

An aerial, black and white photograph of a coastal industrial or urban area. A prominent river or canal winds through the scene from the top left towards the center. The landscape is densely packed with buildings, roads, and infrastructure. The overall tone is industrial and urban. The text is overlaid on this image.

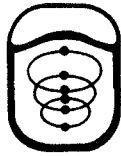
VOLUME I

Coastal Engineering

1976 PROCEEDINGS

RAD

PROCEEDINGS
OF THE
Fifteenth
Coastal Engineering
Conference



July 11-17, 1976 • Honolulu, Hawaii

Sponsored by the
State of Hawaii
University of Hawaii
American Society of Civil Engineers
through its Coastal Engineering Research Council
American Shore and Beach Preservation Association



Published by the American Society of Civil Engineers
345 East 47th Street, New York, N.Y., 10017

Price \$50.00

ACKNOWLEDGMENTS

The following served as the Organizing Committee for the Fifteenth International Conference on Coastal Engineering:

Charles L. Bretschneider
(Chairman)
Department of Ocean Engineering
University of Hawaii

J. Thomas O'Brien
J.K.K. Look Laboratory of
Oceanographic Engineering
University of Hawaii

Harold P. Brown
Conference Center
University of Hawaii

David S. D. Chung
U. S. Naval Facilities
Engineering Command
Pearl Harbor, Hawaii

Ada Marie B. O'Brien
Honolulu, Hawaii

S. Joseph Amaki
Department of Transportation
State of Hawaii

Howard A. Schirmer
Dames and Moore, Engineers
Honolulu, Hawaii

Karl V. Keller
Pacific Division, Corps of
Engineers, U. S. Army
Honolulu, Hawaii

Frederick A. Zobrist
Neighbor Island Consultants

Appreciation is expressed to the Department of Planning and Economic Development of the State of Hawaii and the Hawaii Visitors Bureau for providing the many photographs appearing on the title pages for the various parts of the proceedings.

CONTENTS

PART I

THEORETICAL AND OBSERVED WAVE CHARACTERISTICS

Chapter 1		
REVISIONS IN WAVE DATA PRESENTATION		
Laurence Draper	3
Chapter 2		
WAVE CLIMATE ANALYSIS FOR ENGINEERING PURPOSES		
Hans H. Dette and Alfred Führböter	10
Chapter 3		
WAVES USED FOR INTER-TIDAL DESIGN AND CONSTRUCTION		
D. C. Keiller and T. D. Ruxton	23
Chapter 4		
DATA COLLECTION AND ANALYSIS FOR COASTAL PROJECTS		
E. Loewy, K. G. Witthaus, L. Summers, and R. J. Maddrell	43
Chapter 5		
REGIONAL NETWORK FOR COASTAL ENGINEERING DATA		
Richard J. Seymour and Meredith H. Sessions	60
Chapter 6		
WAVE MEASUREMENTS IN OPEN OCEAN		
Davidson T. Chen, Benjamin S. Yaplee, Donald L. Hammond, and Paul Bey	72
Chapter 7		
GREAT LAKES WAVE INFORMATION		
D. T. Resio and L. W. Hiipakka	92
Chapter 8		
APPLICATIONS OF EMPIRICAL FETCH-LIMITED SPECTRAL FORMULAS TO GREAT LAKES WAVES		
Paul C. Liu	113

CONTENTS

Chapter 9	
WAVES OFF TAICHUNG COAST OF TAIWAN	
Charles C. C. Chang, M. H. Wang, and J. T. Juang	129
Chapter 10	
EXTREME WAVE PARAMETERS BASED ON CONTINENTAL SHELF STORM WAVE RECORDS	
R. E. Haring, A. R. Osborne, and L. P. Spencer	151
Chapter 11	
CONSECUTIVE HIGH WAVES IN COASTAL WATERS	
Winfried Siefert	171
Chapter 12	
PARAMETRIC REPRESENTATION OF A WIND-WAVE FIELD	
Henrik Rye and Roald Svee	183
Chapter 13	
HURRICANE WIND AND WAVE FORECASTING TECHNIQUES	
Charles L. Bretschneider and Elaine E. Tamaye	202
Chapter 14	
OCEAN WAVE STATISTICS FROM FNWC SPECTRAL ANALYSIS	
Warren C. Thompson and F. Michael Reynolds	238
Chapter 15	
APPLICATION OF FETCH AREA METHOD IN MONSOON WAVE HINDCASTING	
Nai-Kuang Liang, Shih-Tsan Tang, and Ben-Juen Lee	258
Chapter 16	
CHARACTERISTIC WAVE PERIOD	
M. Manohar, I. E. Mobarek, and N. A. El Sharaky	273
Chapter 17	
OCEAN WAVE RECORD ANALYSIS BY TUCKER'S METHOD— AN EVALUATION	
J. Dattatri and I. V. Nayak	289
Chapter 18	
SIX-PARAMETER WAVE SPECTRA	
Michel K. Ochi and E. Nadine Hubble	301

CONTENTS

Chapter 19	
DIRECTIONAL SPECTRA ON OCEAN SURFACE WAVES	
H. Mitsuyasu and S. Mizuno	329
Chapter 20	
WAVE DIRECTION COMPUTATIONS WITH THREE GAGE ARRAYS	
D. Esteva	349
Chapter 21	
RANDOM WAVE SIMULATION IN A LABORATORY WAVE TANK	
Akira Kimura and Yuichi Iwagaki	368
Chapter 22	
WAVE HEIGHT DISTRIBUTION OF WIND WAVES OVER LONG WAVES	
Shan-Hwei Ou and Frederick L. W. Tang	388
Chapter 23	
INTERACTION OF WAVES AND A TURBULENT CURRENT	
J. D. A. van Hoften and S. Karaki	404
Chapter 24	
TRANSFORMATION OF NONLINEAR LONG WAVES	
Nobuo Shuto	423
Chapter 25	
RECENT DEVELOPMENTS IN THE STUDY OF BREAKING WAVES	
Michael S. Longuet-Higgins	441
Chapter 26	
KINEMATICS OF BREAKING WAVES	
Edward B. Thornton, James J. Galvin, Frank L. Bub, and David P. Richardson	461
Chapter 27	
DEFORMATION UP TO BREAKING OF PERIODIC WAVES ON A BEACH	
Ib A. Svendsen and J. Buhr Hansen	477
Chapter 28	
WAVE SHOALING OF FINITE AMPLITUDE WAVES	
Masataka Yamaguchi and Yoshito Tsuchiya	497
Chapter 29	
REFRACTION OF FINITE-HEIGHT AND BREAKING WAVES	
James R. Walker	507

CONTENTS

Chapter 30	
THREE-DIMENSIONAL CONDITIONS OF SURF	
William L. Wood	525
Chapter 31	
ENERGY SPECTRA OF IRREGULAR SURF WAVES	
Fritz Busching	539
Chapter 32	
RESONANT INTERACTIONS FOR WAVES BREAKING ON A BEACH	
Robert T. Guza and Anthony J. Bowen	560
Chapter 33	
WAVE SPECTRUM OF BREAKING WAVES	
Toru Sawaragi and Koichiro Iwata	580
Chapter 34	
CONSIDERATION ON FRICTION COEFFICIENT FOR SEA BOTTOM	
Toru Sawaragi, Koichiro Iwata, and Masayoshi Kubo	595
Chapter 35	
PHYSICAL ASPECTS OF WAVE-INDUCED NEARSHORE CURRENT SYSTEM	
Masaru Mizuguchi and Kiyoshi Horikawa	607
Chapter 36	
NEARSHORE CURRENT ON A GENTLY SLOPING BEACH	
Tamio Sasaki, Kiyoshi Horikawa, and Shintaro Hoffa	626
Chapter 37	
LATERAL AND BOTTOM FORCES ON LONGSHORE CURRENTS	
David A. Huntley	645
Chapter 38	
TIME DEPENDENT FLUCTUATIONS IN LONGSHORE CURRENTS	
Guy A. Meadows	660
Chapter 39	
TERRESTRIAL PHOTOGRAMMETRIC MEASUREMENTS OF BREAKING WAVES AND LONGSHORE CURRENTS IN THE NEARSHORE ZONE	
Joseph W. Maresca, Jr. and Erwin Seibel	681

CONTENTS

Chapter 40		
NON-UNIFORM ALONGSHORE CURRENTS		
Michael R. Gourlay		701
Chapter 41		
CURRENT DEPTH REFRACTION USING FINITE ELEMENTS		
Ove Skorgaard and Ivar G. Jonsson		721
Chapter 42		
SET-UP AND RUN-UP IN SHOALING BREAKERS		
William G. Van Dorn		738
Chapter 43		
WAVE RUN-UP ON A SIMULATED BEACH		
A. J. Sutherland, J. N. Sharma, and O. H. Shemdin		752
Chapter 44		
WAVE RUN-UP IN FIELD MEASUREMENTS WITH NEWLY DEVELOPED INSTRUMENT		
Heie F. Erchinger		767
Chapter 45		
CHARACTERISTICS OF FLOW IN RUN-UP OF PERIODIC WAVES		
Ary Roos and Jurjen A. Battjes		781
Chapter 46		
MACH-REFLECTION AS A DIFFRACTION PROBLEM		
Udo Berger and Sören Kohlhasse		796
Chapter 47		
ACTION OF NON-LINEAR WAVES AT A SOLID WALL		
Mohamed S. Nasser and John A. McCorquodale		815
Chapter 48		
ESTIMATION OF INCIDENT AND REFLECTED WAVES IN RANDOM WAVE EXPERIMENTS		
Yoshimi Goda and Yasumasa Suzuki		828
Chapter 49		
DECOMPOSITION OF CO-EXISTING RANDOM WAVE ENERGY		
Dennis B. Morden, Eugene P. Richey, Derald R. Christensen		846

CONTENTS

Chapter 50	
RESONANT REFRACTION BY ROUND ISLANDS	
Richard E. Meyer	866
Chapter 51	
PHYSICS AND MATHEMATICS OF WAVES IN COASTAL ZONES	
H. Lundgren	880
Chapter 52	
HURRICANE TIDE FREQUENCIES ON THE ATLANTIC COAST	
Francis P. Ho	886
Chapter 53	
AUTOMATED FORECASTING OF EXTRATROPICAL STORM SURGES	
N. Arthur Pore	906
Chapter 54	
GENERALIZED MODEL FOR STORM SURGES	
Gour-Tsyh Yeh and Fei-Fan Yeh	921
Chapter 55	
SIMULATION MODEL FOR STORM SURGE PROBABILITIES	
M. H. Fallah, J. N. Sharma and C. Y. Yang	934
Chapter 56	
SPLASH—A MODEL FOR FORECASTING TROPICAL STORM SURGES	
Celso S. Barrientos and Chester P. Jelesnianski	941
Chapter 57	
CURRENTS IN TIDAL FLATS DURING STORM SURGES	
Harald Göhren	959
Chapter 58	
TSUNAMI PROPAGATION IN THE PACIFIC OCEAN	
Manfred Engel and Wilfried Zahel	971
Chapter 59	
TRANSFORMATION OF TSUNAMIS IN A COASTAL ZONE	
Shiegehisa Nakamura, Haruo Higuchi, and Yoshito Tsuchiya	988
Chapter 60	
TSUNAMI INUNDATION PREDICTION	
Charles L. Bretschneider and Pieter G. Wybro	1006

CONTENTS

Chapter 61

NUMERICAL SIMULATION OF TSUNAMIS ORIGINATING IN THE PERU-CHILE TRENCH

A. W. Garcia and H. L. Butler 1025

Chapter 62

NUMERICAL MODELS OF HUGE TSUNAMIS OFF THE SANRIKU COAST

Toshio Iwasaki 1044

Chapter 63

3-D HYDRAULIC MODEL OF WAVES GENERATED BY DISPLACEMENTS

Shin-Lin Liu and R. L. Wiegel 1060

Chapter 64

CALCULATIONS OF WAVES FORMED FROM SURFACE CAVITIES

Charles L. Mader 1079



Hanauma Bay, Island of Oahu

PART I

THEORETICAL AND OBSERVED WAVE CHARACTERISTICS

Wailea Point, Island of Maui



CHAPTER 1

REVISIONS IN WAVE DATA PRESENTATION

LAURENCE DRAPER

Institute of Oceanographic Sciences
Wormley, Godalming, U.K.

In 1966 the author proposed, at the Tenth Conference on Coastal Engineering, methods (Reference 1) of presentation of wave data which were thought likely to be useful to the engineering user. Data obtained from many recording stations have been processed and presented in the formats proposed, and appear to have been able to provide answers to many of the wave questions posed by engineers. However, from time to time additional questions arise, and improvements in technology enable answers to more sophisticated questions to be given. The purpose of this paper is to describe the additions thought necessary to cope with these changes; there are no alterations to the 1966 presentation methods, only additions.

Extreme waves

In the last decade the ability to estimate the likely height of the highest individual wave in some long period of time, say 50 or 100 years, has assumed a new importance. The methods employed all rely on the extrapolation of measured sets of data, but as no one method has an impeccable theoretical parentage several methods have to be resorted to. Considerable effort has been put into such work by this Institute and at present the log-normal, Gumbel and Weibull distributions are used on each set of data.

Persistence

In the original paper the only recommendation made concerning persistence dealt with the persistence of wave conditions with heights at and above given thresholds; this is used mainly in connexion with the estimation of downtime, and is now known as the Persistence of Storms. However, in rougher sea areas it becomes necessary to quantify the number and duration of quiet spells, so that working time on operations such as pipelaying, which can only proceed in prolonged calm conditions, can be estimated. This is known as the Persistence of Calms. It is not possible to derive the Persistence of Calms from the Persistence of Storms, or vice versa.

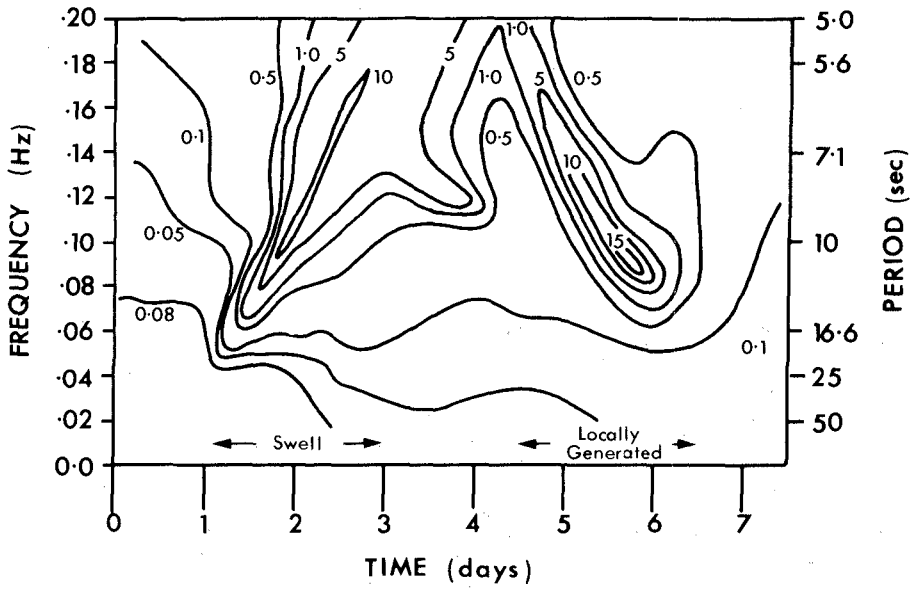


Figure 1. Presentation of hypothetical wave spectra illustrating the characteristics of swell and locally-generated waves

One-dimensional spectra

The most important improvement stems from the arrival of data-logging equipment and the ability to produce spectra on a routine basis at an acceptable cost. A publication listing spectral data for 3000 wave records, the number commonly obtained in a year, would not be easy to comprehend unless the spectra could be extremely condensed. It now seems likely that spectra for a month can be presented on one page in a form which can be assimilated by visual inspection and yet which can give quantitative results. This is an extension suggested by M.J. Tucker to the method used by Snodgrass et al. (Reference 2) in the Pacific swell attenuation study. Each spectrum is presented as a column of numbers giving the energy density in $\text{metres}^2/\text{Hz}$ each plotted at its appropriate frequency level. Subsequent spectra are displayed in the same way one after another and then contours of wave energy are drawn. A hypothetical result is given in figure 1. Apart from giving the actual data, the method identifies immediately where the waves are under generation and where swell is arriving from a distant storm. The arrival of swell is characterized by the appearance of low-energy long-period waves whose energy gradually increases as the frequency increases (period decreases) so that the contours are aligned upwards to the right; in contrast, with locally generated waves the energy and wave period increase together and the contours align downwards to the right. This presentation is a powerful method for the identification of the wave regime at any given time. Once a potentially dangerous time (for the engineer) is defined, the full details of the spectra can be obtained from the original data. Returning to the figure, which is a hypothetical demonstration of this type of presentation, it shows the appearance of swell between days 1 and 3; the slope of a line drawn along the ridge can enable the distance of the source (storm) to be calculated. About noon on day 4 a local storm is beginning to generate waves of increasing period; this continues to day 6, after which calm conditions return.

Actual examples are given in Figures 2 and 3. These present data from a Waverider Buoy situated 6 miles to the west of the island of South Uist in the Outer Hebrides, north west Scotland. Figure 2 illustrates fairly rough conditions with significant heights up to 5.72 m. The highest energy concentrations lie between about 9 and 16 seconds period. The figure covers the time between 10.59 hours on day 100 (9 April) and 0759 hours on day 105 (14 April). The second illustration, figure 3, covers the time between 10.56 hours on day 115 (24 April) and 0459 on day 120 (29 April). It is a time of lower waves, significant heights up to 1.24 m, with a swell of about 9 seconds dying away and another swell of 15 or 16 seconds arriving, reducing in period and dying away. There is a

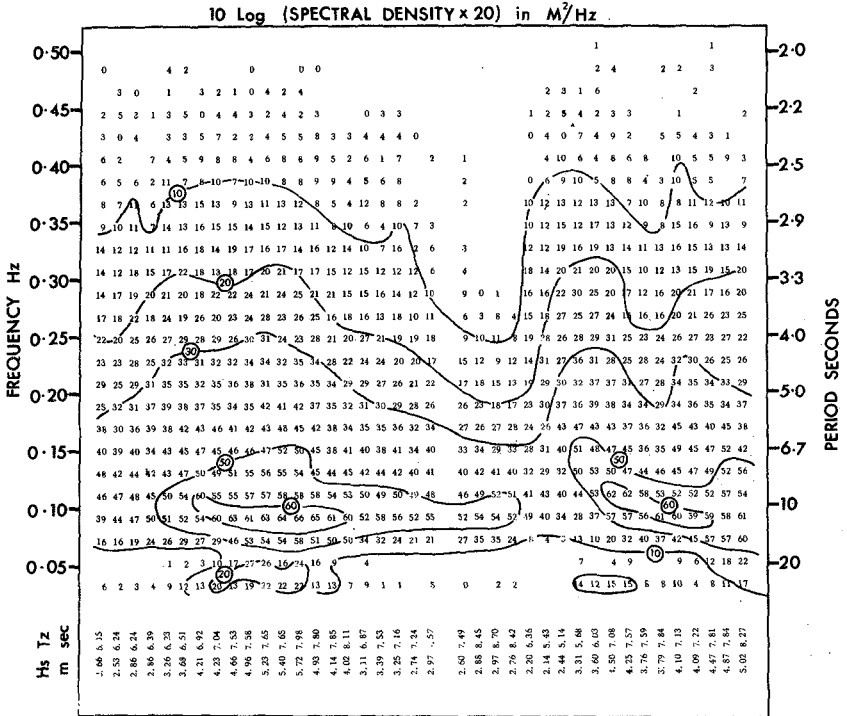
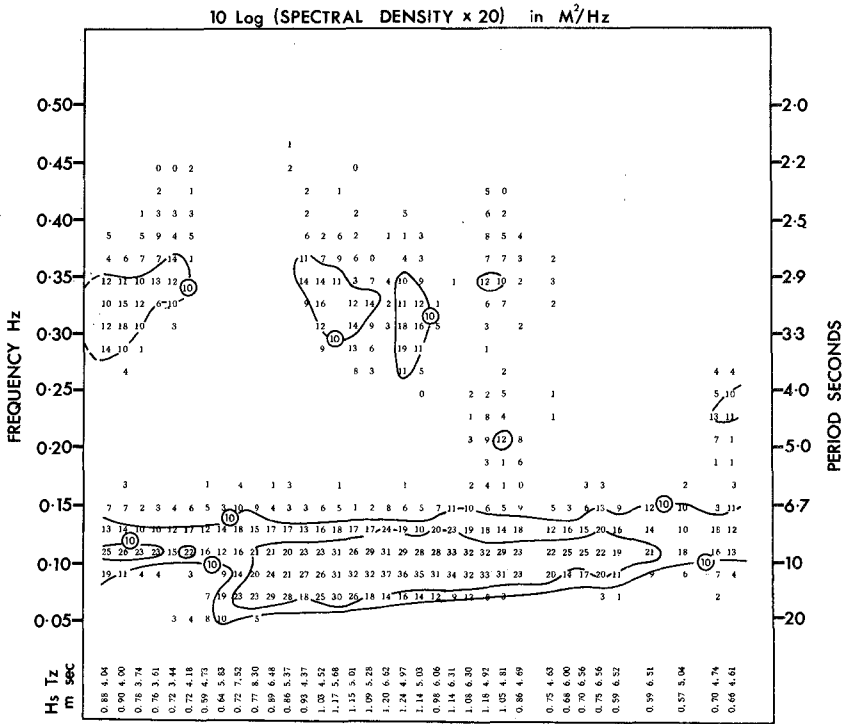


Fig 2

Actual spectra for five days with significant wave height and zero-crossing period calculated from each spectrum



WEST OF SOUTH UIST, OUTER HEBRIDES
 10-56 hr, DAY 115 1976 to 04-59 hr, DAY 120 of 3hr intervals

Fig 3

Actual spectra for five days with significant wave height and zero-crossing period calculated from each spectrum

small amount of local wave generation at about 3 seconds, probably due to winds of around 10 knots. In these cases, to make the presentation more complete, the significant wave height in metres and the zero crossing period in seconds are given below each column. In these two figures the data are not as condensed as in the hypothetical case, figure 1, and because there were several sources of wave energy in the North Atlantic at the time the picture is not as simple as in the idealized figure 1.

Sea-bed waves

With the improvement in techniques there is the possibility of presenting on a routine basis information on the magnitude of the wave motion at the sea bed. This can be done either as spectra in an analogous way to the presentation of surface data, or in a more condensed way as was done for some wave data around the U.K. This is by means of an exceedance diagram for wave-induced particle speeds at the sea bed (Reference 3).

Titles of graphs at present proposed for data presentation:

- | | |
|---|-----|
| (1) Wave Height Exceedance - one for each season. | |
| (2) Zero-crossing Period Histogram - one for each season. | |
| (3) Spectral Width Parameter - annual. | |
| (4) Scatter Diagram - annual. | |
| (5) Persistence of Storms - annual. | |
| (6) Persistence of Calms - annual. | New |
| (7) Extreme Waves - several methods - annual.
1 method at present. | New |
| (8) Spectra if available. | New |
| (9) Sea Bed Spectra if available and desirable. | New |
| (10) Sea Bed particle speed exceedance if surface
spectra available. | New |

ACKNOWLEDGEMENTS

The author gratefully acknowledges the willing assistance of several consultant and university engineers who discussed the proposals in detail and made valuable suggestions. The cooperation of his colleagues, especially Mr E.G. Pitt in the provision of the examples of the spectral presentation, is very much appreciated.

REFERENCES

- (1) Draper, L. 1966 The Analysis and Presentation of Wave Data - a Plea for Uniformity. Proc. 10th Conference Coastal Engineering, Tokyo, Vol. 1, pp. 1-11.
- (2) Snodgrass, F.E., Groves, G.W., Hasselmann, K.F., Miller, G.R., Munk, W.H. and Powers, W.H. 1966 Propagation of ocean swell across the Pacific. Phil. Trans. roy. Soc. (Lond.) A (1103) 259, 431-497.
- (3) Draper, L. 1967 Wave Activity at the Sea Bed around Northwestern Europe. Marine Geol. 5, 133-140.

CHAPTER 2

WAVE CLIMATE ANALYSIS FOR ENGINEERING PURPOSE

by Hans H. DETTE ¹⁾ and Alfred FÖHRBÖTER ²⁾

ABSTRACT

The North Sea (Fig. 1) is known as a random sea with depths in the southern part between 40 m and 100 m so that in contrary to the Atlantic and Pacific coastlines deep sea wave conditions do not exist. After four years of comprehensive wave measurements in the offshore area of the Island of Sylt near the Danish border a general analysis of the wave climate in that region was possible. In this paper results and suggestions will be presented under the aspect of replacing qualitative judgements by quantitative statements which are derived from the knowledge of the adjacent wave climate. Because the wave action varies from year to year a general time unit is not advisable for the evaluation of shore processes; therefore the time scale should be substituted by the integral of incoming wave energy occurring after a certain time. The investigated method of expressing the total energy of one season or one year in the electrical unit Kilowatthour (kWh) per meter (m) width of shoreline could prove in future as a feasible way of classifying the irregular seasonal and yearly wave intensities.

It is further shown that wave measurements over a period of several years can be sufficient for the investigation of correlations between the wind velocities occurring from all directions and the resulting wave heights. In case of satisfying correlation factors it will then be possible to carry out feedback operations for periods from which only records of wind velocities and directions are available and even to hindcast the wave heights for certain not yet measured wind velocities.

¹⁾ Oberingenieur Dr.-Ing., ²⁾ Prof. Dr.-Ing. and Director of Leichtweiss-Institut für Wasserbau of the Techn. Univ. Braunschweig, Germany, Div. of Hydrodyn. and Coastal Eng.

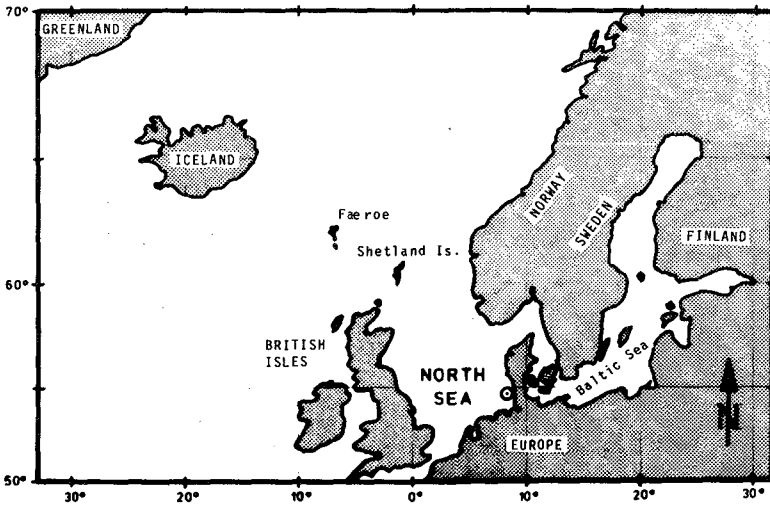


Fig. 1: Location of the North Sea with the region of wave climate analysis

INTRODUCTION

The analysis of the wave climate at a certain location by means of longterm measurements is usually aimed at the investigation of extreme wave parameters and the exceedance frequencies of the maximum or significant wave heights. These informations are needed for the design of offshore structures and coastal protection works. Besides it is often desirable to get some further information about the wave pattern which will normally have to be expected or taken into consideration during certain months or seasons within the year. This is of interest for the determination of the execution time.

Another point of interest is the knowledge of the wave intensity during a certain period or after the completion of an activity. Such informations are especially needed with regard to the feasibility of mobile coastal protection works - e. g. beach nourishments in which sand is used in large amounts as material of construction. As such measures do not grant a protection for ever they will have to be repeated from time to time depending upon the intensity of waves in that region. For this purpose it is necessary to find quantita-

tive statements as it has been for example suggested by the definition of a "half decay time" of a nourishment (FOHRBÖTER 1974) as that point when a nourishment should be renewed.

WAVE RECORDS AND ANALYSIS

With regard to the above mentioned necessities and in order to evaluate an artificial beach nourishment with more than $1.000.000 \text{ m}^3$ of sand dumped in 1972 at Sylt through an extensive surf zone a comprehensive wave measuring program was carried out from 1971 to 1974. Four ultrasonic wave recorders were laid out up to a distance of 1.3 km from the shoreline; from which three stations were located seaward of a longshore bar extending at a distance of 300 m from the shoreline, whereas the fourth was placed in the trough between longshore bar and the beach (Fig. 2).

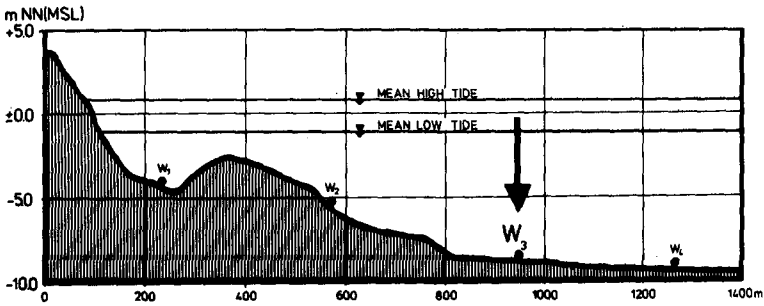


Fig. 2: Wave measuring profile

At least twice a day, about high and low water the waves were recorded simultaneously for a period of 15 minutes. According to a special program, depending upon the actual prevailing wave heights, records were carried out at shorter intervals up to continuous records during heavy storm surges.

For the determination of the statistical wave height parameters (H_{max} , H_s , and H_m) and the wave periods a sequence of 100 waves within the 15 minute record was selected and the zero-up crossing method was applied as suggested by DRAPER, 1966.

Within the four years of measurements a maximum wave height $H_{max} = 7.2$ m was measured at a distance of 1.3 km from the shoreline at position W_4 (Fig. 2).

From a series of several hundred single records the following statistical relationships were obtained (position W_3):

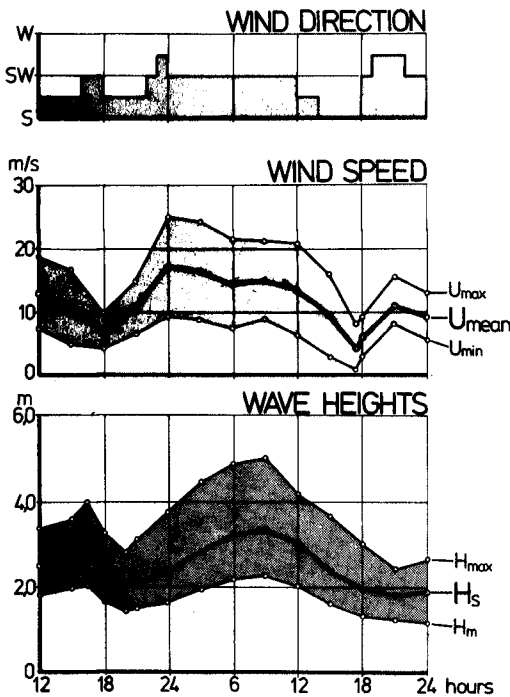
$$H_{max} / H_m = 2.07$$

$$H_{max} / H_s = 1.44$$

$$H_s / H_m = 1.44$$

WIND-WAVE CORRELATIONS

Based on the high number of single records relations between the mean



local wind velocities and the wave heights measured seaward of the longshore bar at position W_3 (Fig. 2) could be carried out by means of electronic computations. For this purpose the hourly records of wind direction and velocity were available from a meteorological station near the wave measuring profile for the period from 1965 to April 1976. General relationships between wind and waves are shown on Figure 3 for a storm period in February 1973. Besides a phase shifting of several hours can be seen between the maxima and minima of wind and wave height records.

Fig. 3: Wind and Wave height conditions during a storm in February 1973

Figure 4 demonstrates the frequency and directional distribution of the hourly wind records in the years from 1965 to 1976. During nearly 20 per cent of the considered time wind velocities higher than $U_{\text{mean}} = 10 \text{ m/s}$ with significant wave heights $H_s \approx 2 \text{ m}$ were predominant. The storm causing wind directions are ranging from South of Southwest (SSW) up to West of Northwest (WNW) with a resultant direction lying in between WSW and W.

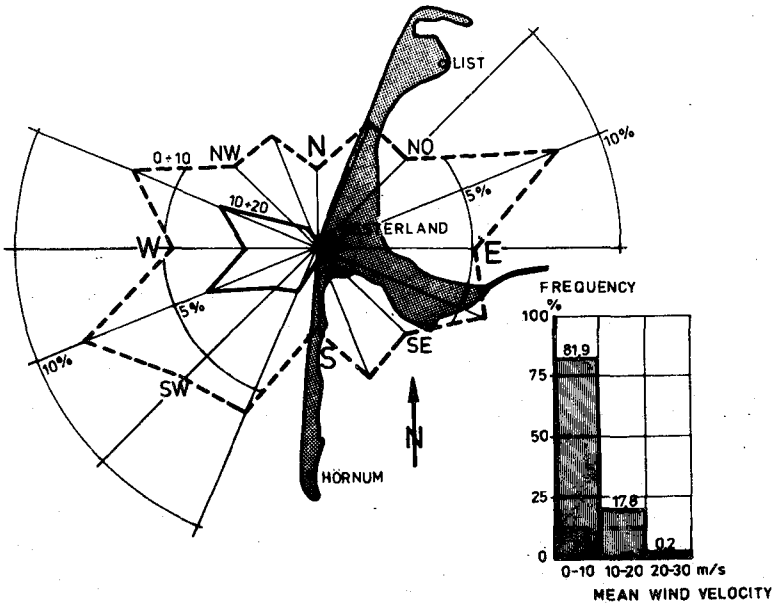


Fig. 4: Frequency and directional distribution of wind records (1965 to 1976)

For wind sectors of 22.5° correlations between the wave generating wind directions ranging from South to Northwest (Fig. 4) and the significant wave heights measured at position W_3 (Fig. 2) were carried out for time differences from one hour up to six hours and besides for the mean wind velocity and direction prevailing during the first to third, the second to fourth and the third to fifth hour before the wave measurement.

The best correlations for all sectors were found for the mean wind direction and velocity prevailing during the second to fourth hour,

The following correlation coefficients were obtained:

Wind Direction	Correlation Coefficient R
S	0.55
SSW	0.80
SW	0.79
WSW	0.91
W	0.96
WNW	0.88
NW	0.49

For the different wave generating wind sectors the measured significant wave heights H_s are plotted as function of the mean wind velocities U_{mean} on Figure 5. Within the wave measuring period from 1971 to 1974 the following highest mean wind velocities lasting for three hours and associated wave heights occurred:

Wind Direction	Mean Wind Velocity for 3 Hours	Significant Wave Height
-	m/s	m
S	12.0	2.7
SSW	14.5	3.2
SW	15.0	3.8
WSW	23.5	5.2
W	22.0	5.2
WNW	20.5	4.9

Additionally the regression lines are drawn for the single wind directions in Figure 5, so that for higher not yet recorded wind velocities the significant wave heights may be extrapolated. The maximum wave heights can be determined by using the already mentioned relationship

$$H_{\text{max}} = 1.44 H_s$$

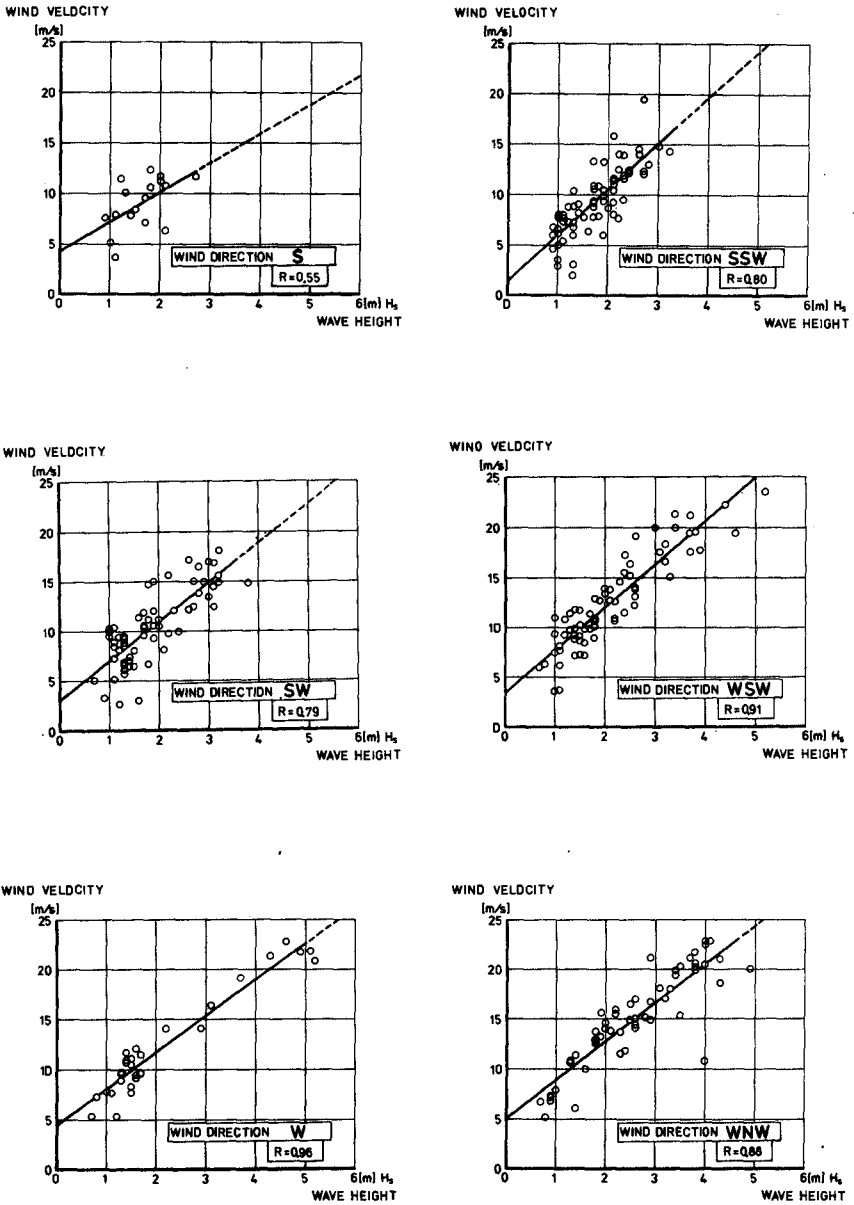


Fig. 5: Correlations between local wind velocities and significant wave heights

Based on the above investigated relationships which yielded satisfying correlations it could be proved that a wave measuring period of a few years can be sufficient in order to find reliable statistical parameters between the wave generating factors and the existing wave heights. The wave measuring period can be regarded as the calibration phase within the effort to evaluate the longterm wave climate in the years before (= feedback operation) and after the wave measurements when only wind data are available which can be obtained with a minimum of efforts and expenses.

In the following a further application of the suggested concept will be presented with regard to the aim of finding objective statements for the evaluation of processes caused by wave action.

WAVE ENERGY LOAD

Because the wave action varies from year to year a general time unit is not advisable for the evaluation of the durability of an offshore structure or a coastal protection work. The time scale should be substituted by a distorted time scale by means of computing the integral of the incoming wave energy load per unit width of wave front. The method of expressing the total wave energy load of one season or one year in the electrical unit Kilowatthour (kWh) per meter width of shoreline is regarded as a feasible way of classifying in future the irregular seasonal wave intensities.

By application of the linear wave theory and inserting the significant wave height $H_{s(j,i)}$ computed from the hourly wind records by the above mentioned correlation the single hourly wave loads \bar{N} were determined for the period from 1965 to 1976 and classified according to different criteria.

The incoming wave load \bar{N} , expressed in the electrical unit kWh per meter width of shoreline was determined in the following way:

$$\bar{N} = 1.225 \cdot c \cdot \Delta t \sum_{j=1}^{24} \sum_{i=1}^{365} H_s^2$$

with $H_s = H_{s(j,i)}$ = wave height at the hour j in the year i

$c = \sqrt{g \cdot d}$ = wave velocity at position W_3 (Fig. 2)

$d = 10$ m = constant = mean water depth at position W_3

$\Delta t = 1$ = one hour

It is no doubt that the above assumptions incorporate uncertainties and rough assumptions with regard to a quantitative reliability. Therefore the calculated wave energy loads are not considered from the quantitative point of view, the method is mainly regarded as a reliable basis for the demonstration of the irregular seasonal wave intensities as it is shown on Figure 6 for the period from 1965 (starting with the month of April) up to the end of March 1976

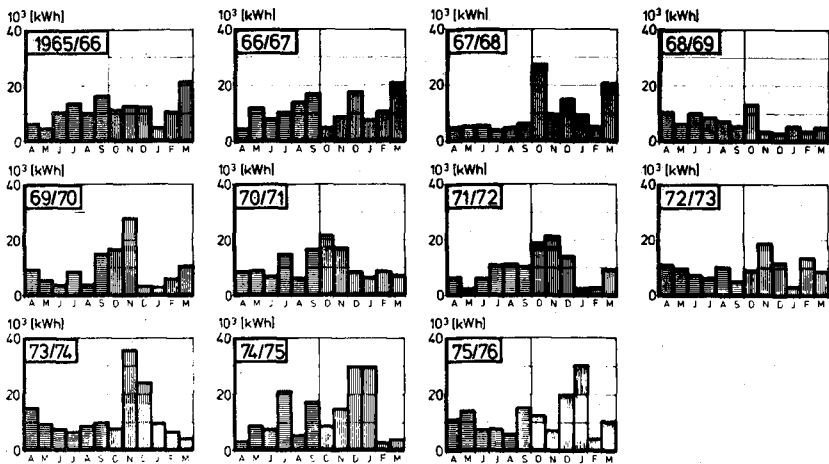


Fig. 6: Monthly wave energy load at position W_3 within the period from 1965 up to 1976

With regard to the classification of the yearly wave energy load as it is demonstrated on Figure 7 the total wave energy load per year (left axis on Figure 7) should be neglected as already mentioned; instead the mean of the

considered period (= 100 per cent) should be determined and deviations from the mean should be expressed in percentage (right axis).

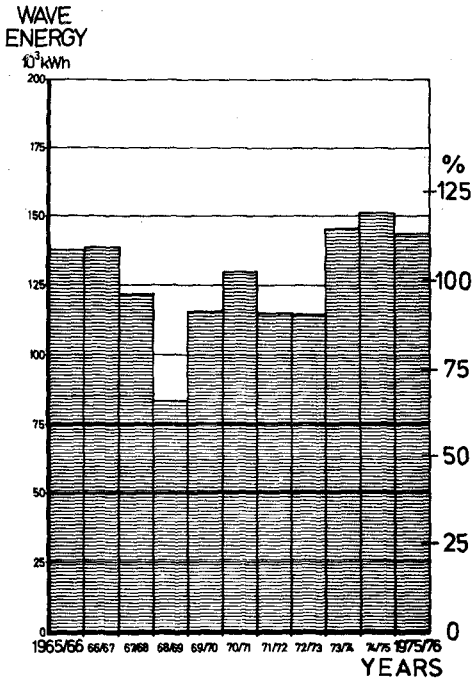


Fig. 7: Yearly wave energy loads in the years from 1965 to 1976

So for example the wave intensity could be classified by means of deviations from the mean wave load as follows:

- > 110 % = high
- 90-110 % = normal
- < 90 % = low

The next figures may help to estimate depending upon the long-term wave climate the risks when a work has to be carried out for example during a certain month or season within the year. Figure 8 shows the classification of the single monthly wave energy loads according to the months and seasons of the year for the period from 1965 to 1976. On Figure 9 the sum of the monthly wave energy loads over the same period has been summarized and the deviations from the mean can be seen.

Finally the consideration of incoming wave energy load can be useful with regard to the resultant direction of wave attack which will give an idea into which longshore direction there will have to be expected a net transport of sediments. From Figure 10 it is obvious that there will be surplus of movements in northern direction for the period from 1965 to 1976.

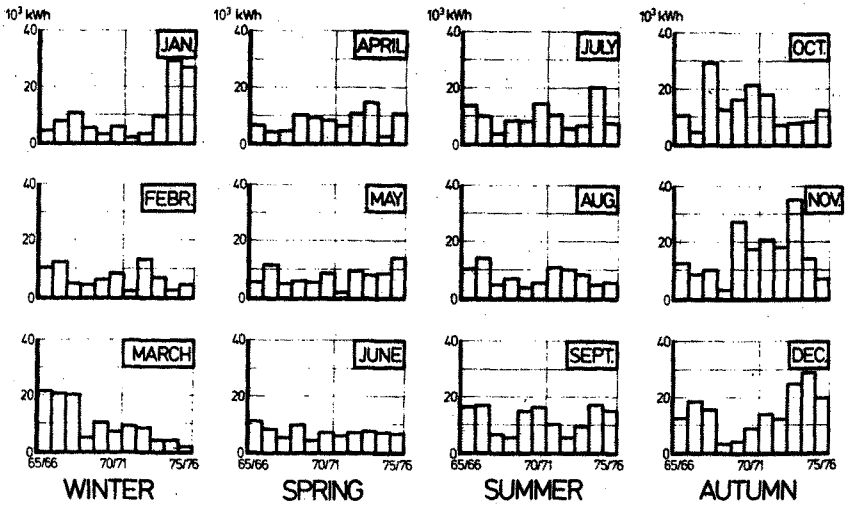


Fig. 8: Classification of the wave energy load according to the months of the year within the period from 1965 to 1976

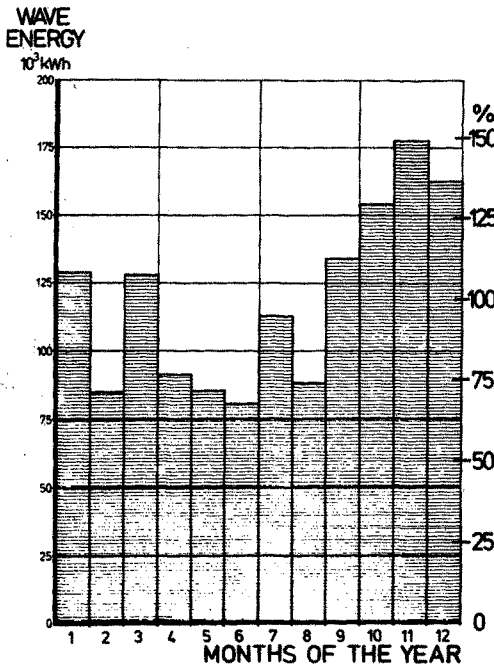


Fig. 9: Total wave energy loads for the months of the year for 1965 to 1976

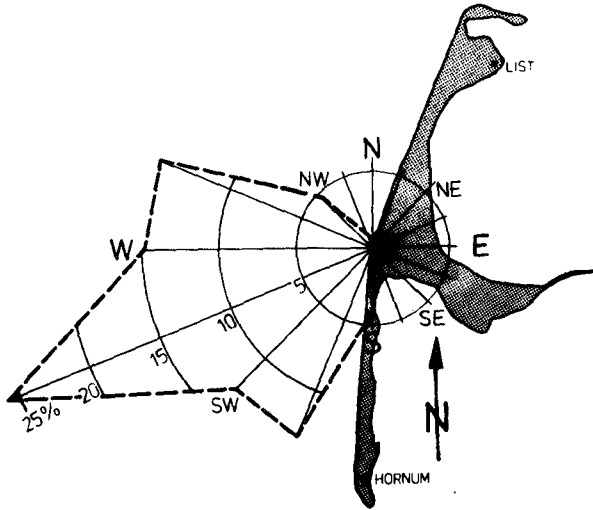


Fig. 10: Frequency and directional distribution of wave energy load for the period from 1965 to 1976

CONCLUSIONS

The attempt to point out relationships between wind velocities occurring from different directions and the wave heights was possible by means of extensive electronic computations. In case it is possible to prove also satisfying correlations for other places of interest the suggested method could be applied in order to receive an objective knowledge of the long-term wave climate and to facilitate the evaluation of processes caused by wave action for an engineer.

ACKNOWLEDGEMENTS

The collection of wave data in the years from 1971 to 1974 was kindly supported by the AMT FÜR LAND- UND WASSERWIRTSCHAFT HUSUM"

CHAPTER 3

WAVES USED FOR INTER-TIDAL DESIGN AND CONSTRUCTION

BY

D. C. KEILLER and T. D. RUXTON,

BINNIE & PARTNERS, LONDON

Introduction

1. The selection of suitable design criteria and methods of construction for works on inter-tidal sand flats has played an important part in a recently completed study (1) which examines the feasibility of storing fresh water in bunded reservoirs built on the foreshore of the Wash bay in the east coast of England (figure 1). Wave, wind and tide conditions have been monitored in the bay for 3 years to provide the information needed for design and construction. Experience gained during the construction of a 15m high trial embankment (figure 2) located 1m below mean sea level and 5 km from the sea defence bank has enabled us to examine the economy of construction methods. Short and long term observations on the bank will provide data on the performance of rip rap surface protection in field conditions.

2. The Wash is an approximately square bay extending over an area of 600km^2 with an entrance 20km wide. Mean spring tides in the bay have a range of 6.4m and tides with ranges above 8.0m are predicted to occur once or twice a year. The large tidal range is associated with extensive foreshores. At low water of a spring tide approximately half the area of the bay is exposed revealing sand and mud flats which in places extend 8km from the sea defence banks. The problems associated with the accurate measurement of water levels in this area with its extensive sand flats have been described by Pugh and Waller (7).

Wave measurement programmes

3. At the commencement of the study there was very little information available on wave conditions in the Wash. To remedy this situation we initiated two separate programmes of wave observation. Three wave recorders were mounted on the foreshore in an area exposed at low water to record wave conditions over the inter-tidal sand flats. These records were obtained for a 15 minute period each tide close to high water. Anemometers installed on the edge of the bay provided a continuous record of wind conditions. The installation and early results from these instruments have been described by Driver and Pitt (3). The second programme of wave observation was the visual estimation of wave height by the skippers of the pilot cutter serving the port of King's Lynn. These seamen observed wave conditions almost every tide at 3 buoys marking the shipping channel which

cuts through the inter-tidal sand flats. Data were obtained from both instrumental and visual programmes for a period of 3 years (1972 - 1975)

4. The aims of the two wave observation programmes were complementary. The storm wave data obtained by the wave recorders were to be used in conjunction with the locally measured wind data and also wind data from long established recording stations to define the wave conditions that should be used for the design of rip rap surface protection for permanent reservoir embankments founded on the foreshores of the southern Wash. The visual estimates of wave height were to show the distribution of typical wave heights experienced in the Wash and the significance of seasonal variations. These results combined with the experience of contractors working in the Wash would enable us to estimate the likely proportion of time wave conditions would limit construction work on the inter-tidal sand flats.

Storm wave conditions on the SE foreshore of the Wash

Wind conditions associated with storm waves

5. An analysis of the operation of the wave recorders during the 3 year study period showed that waves with a significant height of at least 0.5m were recorded on 48 separate tides. The largest waves were as expected associated with NW, N and NE winds since the longest overwater fetches are from these directions. In general, larger waves were associated with stronger winds, though this effect was masked by the influence of tide level on wave height. The largest waves were recorded during storms which coincided with the high waters of spring tides.

6. On every recorded occasion except one a 10m/s wind from the NW, N or NE at high water resulted in 0.5m waves at one or more recorders. The exception occurred at a time when only one recorder (site 1) was operational. There are however many occasions when similar wind speeds and directions occurring at low water failed to generate 0.5m waves at any of the recorders the following high water. This highlighted the fact that waves are generated over the inter-tidal foreshore only when a storm coincides with high water. On such occasions the maximum waves associated with the wind are quickly generated because of the short fetches which exist in almost all directions. For example a NW wind of 20m/s at high water would generate fetch-limited waves at the recorder sites after about $1\frac{1}{2}$ hours.

Analysis of storm wave records

7. The wave recorder output was analysed using the method proposed by Tucker (9) as modified by Draper (2). The data are summarised in figure 3 which shows the significant wave heights and zero crossing periods

recorded at each site. Results have only been included for those occasions (tides) at each site when the recorded significant wave height was at least 0.5m. There were 33 such tides at site 1, 20 at site 2 and 35 at site 3 between September 1972 and May 1975.

8. The wave heights and periods recorded at each site are broadly similar with the highest waves generally being recorded at site 3. The two largest individual values of significant wave height were, however obtained from the recorder at site 1 where significant heights of 2.4m and 1.6m were recorded. The wave heights at site 2 were latterly generally lower than elsewhere. This is thought to result from a 1m increase in bed level during the winter 1973/74.

9. There is only a very weak correlation between the height and period of recorded waves.

10. The wave height distributions (figure 3) cannot be compared in detail because the waves recorded at each site did not all occur on the same occasions. Comparisons may better be made by comparing the differences between the observed waves and those predicted for each occasion by a standard wave-forecasting routine. Although deep-water wave prediction routines cannot be expected to give accurate answers in shallow water, they do provide a standard for comparison taking account of wind speed, duration, direction and fetch length. The differences between the observed and predicted wave conditions will indicate the influence of the shallow and varying water depth on wave generation, refraction, shoaling and friction.

11. Wave hindcasts have been made using the Sverdrup-Munk-Bretschneider (S-M-B) deep water wave forecasting charts (6) for each site on every tide that the significant wave height was at least 0.5m. The waves were hindcast using the average wind speed over a period long enough to generate fetch limited waves. On each occasion the fetch was calculated for high water of a spring tide assuming all wave generation to occur within the confines of the bay. No allowance was made for the effects of refraction in the calculation of fetch.

12. The ratio of observed significant wave height (H_s) to hindcast significant wave height (H_o) has been plotted against water depth for site 1 alone and sites 2 and 3 together on figure 4. The best fit straight lines to each set of wave height data are shown. The results show a rapid increase in wave height ratio with water depth at site 1 but much smaller changes in wave height ratio with water depth at sites 2 and 3. Bounding lines spaced two standard deviations from the mean are also included. Consideration was given to plotting the H_s/H_o ratio against water level relative to Ordnance Datum and using this relationship for the subsequent analysis and design instead of one incorporating water depth. The observed reduction in wave heights at site 2 (paragraph 8) following the rise in sea bed level suggested the use of water depth rather than water level. Furthermore in considering

wave heights at different foreshore levels the use of water depth proved to be more convenient than water level. The bed configuration seaward of the reservoir sites does not include banks or bars that would invalidate the use of water depth and the increase in fetch with increasing depth (due to higher water levels) was shown to have no marked effect on the results at site 2.

13. The magnitude of the random errors that have been introduced into the calculation of wave height by the method of analysis of the wave records (paragraph 7) are fairly significant. These random errors alone are estimated to cause a standard deviation in the wave height ratio of around 13%. The measured standard deviation for the observations from sites 2 and 3 is about 20%. The standard deviation of the observations for site 1 is greater at about 27%, due largely to the two occasions when the wave height ratio exceeded 1.4.

14. These two occasions are interesting as these were also the occasions of the largest waves recorded during the study. The operation and calibration of the wave recorder appeared normal on both occasions. The most likely explanation for these exceptional wave heights is that the recorder was situated close to a point where wave energy was concentrated by wave refraction during both storms. The greater sensitivity of wave height ratio to water depth at site 1 when compared to sites 2 and 3 may also be indicative of a concentration of wave energy resulting from wave refraction as such concentrations depend on water depth as well as wave period.

Extreme storm conditions

Extreme wind conditions

15. The installation of anemometers on the shore of the Wash in 1972 provided the first continuous records of winds in the bay. In the past wind records have been collected at Spurn Head (figure 1) which is 50km north of Gibraltar Point. Wind records are also available at several nearby inland sites including a long record at Cranwell (figure 1) 55km west of Gibraltar Point. As the Wash anemometers have only operated for three years there are insufficient data available for them to be used to give reliable estimates of wind speeds occurring less frequently than once in 5 years.

16. The British Meteorological Office was commissioned to examine the relationship between wind speeds at Gibraltar Point and Cranwell with a view to using the long record available at Cranwell to estimate extreme winds at Gibraltar Point. Cranwell was chosen for this comparison as it was the site nearest the Wash with broadly similar wind characteristics and a long record. Initial comparisons indicated that wind direction and strengths at the two sites were usually similar.

17. The results of the comparison of hourly mean wind speeds confirmed that on average the differences in wind speed between Gibraltar Point and Cranwell were fairly small. Despite this apparent similarity the main significance of the regression equations linking the two stations was that the estimates of wind speed at Gibraltar Point using Cranwell data were poor. If corrections were made to the regression equations based on the wind direction, the difference between the observed and estimated wind speed at Gibraltar Point was reduced. Even with this improvement the standard error of estimate was between $1\frac{1}{2}$ and 2m/s . The use of Cranwell data to estimate wind speeds at Gibraltar Point on particular occasions is thus ruled out.

18. The regression equations linking wind speeds at Gibraltar Point with those at Cranwell are considered adequate to estimate the broad characteristics of winds at Gibraltar Point. The evidence from Cranwell suggests for example that gale force winds (speeds 17m/s) from the NE are rare at Gibraltar Point. The examination showed that large errors would result from the use of the regression equations during individual storms. This prevents us estimating extreme wind conditions at one site on the basis of extreme conditions at the other and is due to many complex effects which influence the relationship on particular occasions. These effects may be expected to be especially pronounced during extreme storms.

19. The meteorological office considered that more reliable estimates would be provided from wind maps prepared by Hardman, Helliwell and Hopkins (4). These wind maps have been updated to take account of extreme winds in East Anglia up to June 1975 and the estimates for the Wash (figure 5) taken off these maps show a wind speed of 29.2m/s (57kt) to have a return period of 50 years. The wind speed frequencies apply to a point in the centre of the entrance to the Wash.

20. The wind directions associated with very high wind speeds cannot be estimated in the same way as the extreme wind speed. Some indication of the most likely directions of extreme winds is provided by the records from Spurn Head from 1922 to 1958. An examination of the directions associated with hourly mean wind speeds of at least 21m/s showed (Table 1 below) that although the most common direction for high winds was W, almost half the occurrences were associated with N or NW winds which are able to generate some of the largest waves in the Wash. There were no recorded occasions of similar NE or S winds at Spurn Head. The large proportion of high winds associated with W, NW and N winds is a feature of observations made along the NE coast of England. Although there may be some differences between the winds at Spurn Head and the Wash, the Spurn Head data are used in the subsequent analysis.

Wind direction	S	SW	W	NW	N	NE	E	SE
Percentage of occasions	0	7	33	30	19	0	7	4

Table 1: Directions associated with mean wind speeds \geq 21 m/s at Spurn Head.

Extreme wind speeds at high water

21. The probability that extreme wind conditions will occur during a high water period is lower than the probability of these winds occurring at any state of the tide. There is only a 1 in 4 chance that the maximum hourly mean wind speed during a storm will coincide with a three hour period at high water. From an analysis of storms recorded at Lerwick, Shellard (8) has estimated the ratio of maximum wind speeds averaged over varying numbers of hours to the maximum speeds over one hour. Shellard considered that these ratios could be used to estimate the wind speeds which, when averaged over different numbers of hours, had the same frequency of occurrence each year as the maximum mean hourly wind speed.

22. The wind ratios derived by Shellard (8) for Lerwick have been applied to the Wash data to estimate the frequency of occurrence of combinations of wind speed and duration (figure 5). In our calculation of duration, the wind speed was assumed to be above the average for half the averaging period. The lower wind speeds which occur more frequently for long periods of time have a greater chance of occurring during a high water period. The frequency of occurrence of particular wind speeds at high water may be obtained by combining the frequency of occurrence of the wind speed for a particular number of hours with the probability that this will coincide with high water and summing the frequencies derived for periods up to 9 hours. All periods of 9 hours or more are considered together as they will all coincide with at least one high water period. No account has been taken of periods which overlap two or more high water periods as these rare occasions are unlikely to increase the derived frequency of particular wind speeds by more than 1%. The estimated frequency of occurrence of various wind speeds at high water is also shown on figure 5. The figure shows that for the same frequency of occurrence each year the maximum hourly mean wind speed at high water is about 2m/s lower than the maximum hourly mean speed recorded at any state of the tide.

23. The frequency of occurrence of a given wind speed from a particular wind direction at high water is estimated by combining the results contained in figure 5 with those in table 1 (paragraph 20).

Extreme wave heights

24. The frequency of occurrence of a particular large wave height at high water in deep water in the southern Wash is estimated by summing the frequency of occurrence at high water of the winds from W, NW, N and E that are capable of generating the desired wave height. The available fetch is taken as the site 3 fetch within the confines of the bay at high water of a spring tide and the relationship between wind speed and wave height in deep water is taken from the S-M-B wave forecasting charts (6). The deep water wave height frequencies were used with the empirical relationship (figure 4) between wave height and water depth for sites 2 and 3 to obtain shallow water wave frequencies for a range of water depths.

25. The calculations we undertook indicated that N winds would probably cause the largest waves in the SE Wash. The greater frequency of occurrence of strong NW winds compared to N winds (Table 1) does not outweigh the effect of the longer N fetch. The longer fetch allows less strong and therefore more frequent N winds to generate large waves more often than NW winds.

26. Up to this point the calculations of wave height frequencies referred to particular water depths. These depths will occur at different foreshore levels as the tides change from springs to neaps. To provide estimates of the frequency of occurrence of large waves at particular foreshore levels, we have combined the probability that high water will reach a particular level with the frequency of occurrence of the required wave height in the appropriate water depth. The results are then summed for all tide levels. The probability that the predicted tide will reach a given level was derived from the annual distribution of predicted tide levels; the assumption has been made that there would be an average tidal residual of +0.5m at high water whenever large waves occurred. This is because strong NW and N winds generally raise water levels in the southern Wash and are quite often associated with North Sea storm surges. The calculations indicated that at foreshore levels above -1m OD large waves are most likely to occur during high spring tides when predicted high water levels are at least +3.3m OD. This is because the frequency of occurrence of wind needed to generate large waves in this depth of water is much higher than that of the wind needed to generate the same size of wave in the shallower water that is more often present.

27. Wave heights which are estimated to have particular frequencies of occurrence at various foreshore levels are shown in figure 6. This figure indicates that at all depths the wave height with a frequency of occurrence of 0.001 each year is only about 2.3 times larger than the wave height that occurs on average once a year. The wave height expected at a foreshore level of -4m OD is about 2.4 times the wave height expected at +2m OD with the same frequency of occurrence.

28. In some areas of the foreshore, wave energy will be concentrated or dispersed by the effects of wave refraction. These local variations in wave energy concentration will change the height of the waves. In areas of severe concentration the wave height may be up to twice that experienced generally. The occurrence of severe concentration of wave energy will be critically dependent on the wave period and water depth on each occasion as well as the offshore bed topography.

Rip rap design for sea-facing reservoir banks

29. The extreme wave heights derived for the southern Wash (figure 6) have been used as the basis for design of rip rap surface protection for the Westmark and Hull Sand reservoir shapes (figure 1). The method of relating wave height to surface protection is based on recent model studies by the British Hydraulics Research Station (HRS) (5). The studies indicate that for a given embankment slope, the amount of damage sustained by a randomly placed quarry stone rip rap layer of given stone size depends principally on the significant height and number of waves attacking the embankment. In the model studies the rip rap was placed over suitable filter material in a layer whose thickness was twice the median size of the rip rap. Failure of the modelled slope protection was deemed to occur when a hemispherical foot with a diameter equal to the median size of rip rap under test could just touch the underlying filter layer.

30. The rip rap design for the proposed sea facing reservoir embankments in the Wash was based on the requirement that the surface protection should not require maintenance even after a design storm containing 2000 waves with a significant height estimated to have a probability of occurrence each year of 0.001 at the level of the foreshore upon which the bank was sited. The number of waves in the design storm was calculated as the maximum number likely to attack the bank during the three hour period around high water when water depth would be greatest. The wave heights experienced on the preceding and following high water are likely to be significantly smaller during such an extreme storm because of the improbability of a sufficiently strong wind being maintained for upwards of 12 hours (figure 5). A further reason for confidence in the restriction of the design storm to 2000 waves is that model tests with up to 5000 waves generally showed little additional damage to that caused by 2000 waves (5). The requirement that no maintenance be needed was interpreted as meaning that during the design storm the damage should be less than 15% of that

causing failure, as defined above, of the rip rap protection. The assumption has been made in this definition that the results of the model studies may be directly applied to the proposed Wash reservoirs. From figure 6 the design wave height for an embankment founded close to 0m OD on the SE foreshore of the Wash is 2.3m. Rip rap with a median size exceeding 950mm placed on a 1:4 slope will satisfy the no-maintenance requirement defined above for this wave height.

31. A second requirement for the rip rap design was that in areas subjected to concentrations of wave energy, the protection should not fail, though greater damage requiring maintenance would be permissible. In such areas the significant wave height will increase and greater damage will be experienced during storm with a given frequency of occurrence.

32. For the Westmark reservoir which is founded at and above 0m OD a median stone size of 950mm satisfying the first requirement is considered adequate. This size of stone should withstand, without failure, waves 1.75 times the height experienced generally during the design storm. Such a measure of concentration of wave energy is unlikely to be exceeded on the flat gently shelving foreshore seaward of the reservoir. This area of foreshore has been stable for 100 years and is accreting in a fairly uniform manner.

33. On the line of the Hull Sand reservoir embankment which crosses a series of channels and areas of complex topography, wave heights up to twice the height experienced generally are considered possible. This implies that in some areas during the design storm waves with a significant height of 4.6m could attack an embankment founded at 0m OD. To resist such waves without failure, rip rap laid on a 1:4 slope should have a median size of at least 1050 mm. As a result of the dependence of the wave height on the foreshore level for a storm with a particular frequency of occurrence (figure 6) the size of rip rap used for surface protection should vary with foreshore level. The size of rip rap required for both Westmark and Hull Sand reservoirs at various foreshore levels is shown in Table 2.

Foreshore level (mOD)	Median size of rip rap (mm)		Top level of protection (mOD)	
	Hull Sand Reservoir	Westmark Reservoir	Heavy	Light
+2	750	650	+8.5	+10.0
0	1050	950	+9.75	+12.0
-2	1450	-	+10.75	+14.0
-4	1700	-	+11.5	+15.75

Table 2: Rip rap design for proposed Wash reservoirs
(Note: design maximum still water level +5.8mOD)

34. The vertical height to which surface protection should be taken depends on the expected extreme still water level and the height above this which may be damaged during a storm which almost causes failure of the protection. The HRS model studies (5) indicated that at failure of a 1:4 slope damage extended for a vertical distance of 3 median stone diameters above and below the still water level. This finding is applied to the full scale embankment design with an added 0.5m allowance for free board. The recommended top level of rip rap protection (table 2) assumes an extreme water level of +5.8mOD which is estimated to have a frequency of occurrence each year of 0.001 at Roaring Middle.

35. Above the main surface protection, lighter protection is required against wave run up. The HRS model studies (5) indicated that wave run up would occasionally reach a level 1.25 times the significant wave height above still water level. Using this information for reservoir design in the Wash, with a similar allowance for free board and an extreme water level of +5.8mOD gives the top levels of lighter protection (table 2).

The trial bank as a test for the rip rap design

36. The trial bank constructed in the Wash (figure 2) is circular in plan with a diameter of 284m enclosing a small area of foreshore. The bank consists of 412,000m³ of sandfill won with a cutter-suction dredger from a nearby foreshore borrow pit. The sand fill is protected against wave attack and erosion by quarry stone rip rap and two filter layers of coarse sand and crushed furnace slag from a phosphate process. The rip rap on the seaward side of the bank consists of hard durable limestone with a median size of 660mm laid in a layer 1300mm thick. On the landward side similar though smaller rip rap is used. The protection on the seaward side is taken from sea bed level (-1m OD) to +7.5m OD. Above this level the bank is protected to +9m OD by slag. The top 5m of the bank is grassed.

37. The surface protection used for the trial bank is less heavy than that recommended for the permanent banks of the Westmark reservoir although the trial bank and the proposed Westmark reservoir are founded at similar levels. If the design assumptions used for the proposed reservoir prove to be accurate the rip rap on the trial bank will suffer damage requiring maintenance during storms with a significant wave height exceeding 1.7m. The frequency of occurrence of such waves at the bank site is thought to be about 0.1 each year if wave energy is not concentrated onto the bank.

38. The surface protection of the trial bank should not fail even if attacked by waves with a significant height of 2.7m which are thought to have a frequency of occurrence of about 0.001 each year. If wave energy was heavily concentrated onto the trial bank by wave refraction, failure may occur during storms with a frequency of occurrence of 0.1. Such concentrations of wave energy are thought unlikely as the bed topography seaward of the bank is flat and gently shelving.

39. The long term performance of rip rap on the trial bank will indicate the validity of the design methods we propose for the main reservoir embankment. To this end a continuing programme of wave, wind and tide measurement has been recommended with associated studies on the performance of the surface protection. The performance of the rip rap will be judged on the basis of stone movement.

Visual wave observations to estimate inclement weather

40. Three of the buoys marking the King's Lynn shipping channel were chosen as sites for visual wave observations (figure 1); No 13 indicative of conditions on the upper foreshore, No. 7 indicative of lower foreshore conditions and No. 1 in deep water at the mouth of the channel. Estimates of wave period were not made, although the skippers reported the presence of swell.

41. The wave height frequency distribution is shown in figure 7 which compared the wave height distribution at buoys 13, 7 and 1 for the year June 1974 to May 1975. Large waves are encountered much more frequently at buoy 1 than at the more landward buoys. For example in 1974/5 waves exceeding 0.6m (2ft) were reported on almost 20% of observations at buoy 1, almost 10% of observations at buoy 7 and less than 3% of the observations at buoy 13. At each buoy there were also a large number of occasions when wave heights less than 0.075m (3ins) were recorded. The proportion varied from 10% at buoy 1 to over 20% at buoy 13.

42. The information provided by the skippers of the pilot cutter was of great value to us in assessing typical wave conditions in the Wash, principally because of the regularity of the observations. Over a period of 3 years December 1973 - November 1975 the skippers recorded their wave height estimates at buoy 7 on 92.5% of the 2116 high waters. The wind conditions on the high waters when no observations were made at buoy 7 were compared with conditions on other high waters and found to be very similar suggesting that severe wave and wind conditions did not usually prevent the pilot cutter putting to sea. On the majority of occasions when the pilot cutter remained in port the reason was the absence of shipping requiring pilotage.

43. There were only four recorded occasions in the 3 years when stress of weather was given as the reason for remaining in port or turning back before reaching buoy 7. On 7 of the 9 occasions when waves above 1.5m were noted at buoy 7, however, no readings were made at buoy 1 suggesting that wave height was a contributory factor in causing the pilot cutter to turn back or meet ships before reaching buoy 1. On one of these occasions the cutter reached buoy 1, but the conditions were so severe that the skipper felt unable to estimate the wave height accurately.

44. The seasonal variations in wave height estimates over the 3 year period at buoy 7 are shown in figure 8. This figure shows that the wave height distribution is fairly similar at all seasons of the year with the exception of the 3 summer months of June, July and August when wave heights are noticeably lower, making these months the prime building period.

45. The seasonal estimates of wave height distribution (figure 8) do not indicate for how long the waves remained above a height which could hinder or damage work nor the length of time between periods of inclement weather when building may proceed. This information is conveyed on figure 9 which shows that the number of separate periods each season when waves exceed 0.22 and 0.30m remained between 20 and 25 with no significant reduction in the summer. The average persistence of small waves was however about $1\frac{1}{2}$ days longer in the summer than during the remainder of the year. There are also likely to be much longer periods with no waves above 0.45 and 0.6m in summer than at other times of the year. Although the other months generally have longer periods of inclement weather, even these months contain occasional long calm spells.

46. Data from the anemometer at Cranwell indicate that the period of the study was fairly windy. In the two years June 1973 to May 1975 there were 45 percent more hours when the wind speed exceeded 10m/s (UK Beaufort force 6) than the average over the nine years July 1966 to June 1975. During a typical construction period, the amount of time that will be lost due to inclement weather would normally be somewhat lower than the proportion of time indicated by the wave height frequency distribution (figure 7).

47. The effects of variations in wind conditions from year to year may be illustrated by considering the wave and wind data from the spring months of March, April and May during the 3 years 1973 to 1975 (figure 10). During these spring months the weather is often dominated by moderate northerly winds which can generate fairly large waves in the Wash. The proportion of time the wind exceeded 8m/s (UK Beaufort force 5) from the NW, N or NE ranged from 3 to 5% in 1973 and 1974 to 15% in 1975. At the same time wave heights exceeding 0.45m (18ins) were reported on 7 to 8% of tides in 1973 and 1974, but 20% of tides in 1975.

48. Experience gained by contractors using using small craft for survey and building purposes suggested that operations were hindered when wave heights exceeded 0.23m (9 ins).

49. The contractor for the trial bank (HAM Dredging Ltd) imported large quantities of rip rap stone and filter material through an offshore transshipment site in which the materials were moved from coasters to barges by floating cranes. The operation of this site was occasionally affected by the inclement weather experienced in the spring of 1975 (figure 10) which delayed the programme 5 days in 7 weeks. The periods

when weather conditions halted the transshipment operation coincided with reports from the pilot skippers of 0.5m waves at buoy 7.

Conclusions

50. For the design of the surface protection for the reservoir embankments proposed in the recent feasibility study for water storage in the Wash we have attempted to estimate the frequency of occurrence and extent of storm damage. To this end we have measured wave and wind and tide conditions at the site for three years to derive empirical relationships between water depth, wave height and wind speed, direction and fetch.

51. We were advised not to use a direct correlation between local recorded wind conditions and the conditions recorded 55km away at a long term anemometer station as the basis for derivation of extreme winds. Instead extreme wind maps based on all available regional wind data have been used as these are considered more reliable than a direct correlation between two individual stations.

52. To assess the frequency of occurrence of various wave heights on the inter-tidal foreshore we have taken into account the duration and direction of extreme wind speeds and the probable incidence of these winds with high water. Our estimates of wave height, based on the empirical relationship between wind, wave and tide conditions, take account of the variation in high water levels between spring and neap tides. We have been able to estimate wave heights with a given frequency of occurrence at foreshore levels ranging from mean high water springs to mean low water springs in an area with a spring tide range of 6.4m.

53. Our estimates of the frequency of occurrence of wave heights at various foreshore levels have been combined with the results of recent model studies at HRS to produce a rip rap design. The frequency of damage and probability of failure of this surface protection has been estimated.

54. Long term tests on the trial bank rip rap combined with continuing wave wind and tide measurements will indicate the validity of the design methods proposed.

55. Estimates of the amount of time that will be lost during construction of the reservoir bank due to wave activity may be made as a result of regular visual observations of wave height over a three year period. These observations enable the frequency and probable duration of waves likely to hinder building operations to be estimated on a seasonal basis.

ACKNOWLEDGEMENTS

This work has formed part of the feasibility study of the Wash Water Storage Scheme undertaken for the Central Water Planning Unit, Reading, England, by Binnie & Partners, London. Thanks are due to O. Gibb, Director of the Planning Unit and Binnie & Partners for permission to publish the paper.

REFERENCES

- (1) Binnie & Partners (1976) Wash Water Storage Scheme, Feasibility Study Report, Central Water Planning Unit, Reading, England.
- (2) Draper L. (1966) 'The analysis and presentation of wave data - a plea for uniformity'. Chap. 1. Proc. 10th Coastal Engineering Conf.
- (3) Driver, J.S. and Pitt, J. D. (1974) 'Wind and wave relationships in a shallow water area'. Chap. 6, Proc. 14th Coastal Engineering Conf.
- (4) Hardman, Carol E., Helliwell, N.C. and Hopkins, J. D. (1973) 'Extreme winds over the United Kingdom for periods ending 1971'. Climatological memorandum No. 50A, Meteorological Office, Bracknell, England.
- (5) Hydraulics Research Station (1975) Rip rap design for wind-wave attack - 'A laboratory study in random waves' EX707, Hydraulics Research Station, Wallingford, England.
- (6) Ippen, A. T. (1966) 'Estuary and coastline hydrodynamics'. Eng. Soc. Mon. McGraw Hill.
- (7) Pugh, D. T. and Waller, W. R. (1974) 'Sea level measurement in the Wash bay'. Chap 149, Proc. 14th Coastal Engineering Conf.
- (8) Shellard, H. C. (1975) 'Lerwick anemograph records 1957-70 and the offshore industry'. The Meteorological Magazine, Vol. 104, No. 1236, July 1975.
- (9) Tucker M. J. (1963) 'Analysis of records of sea waves' Proc. Inst. Civ. Engrs. 26, pp 305 - 316

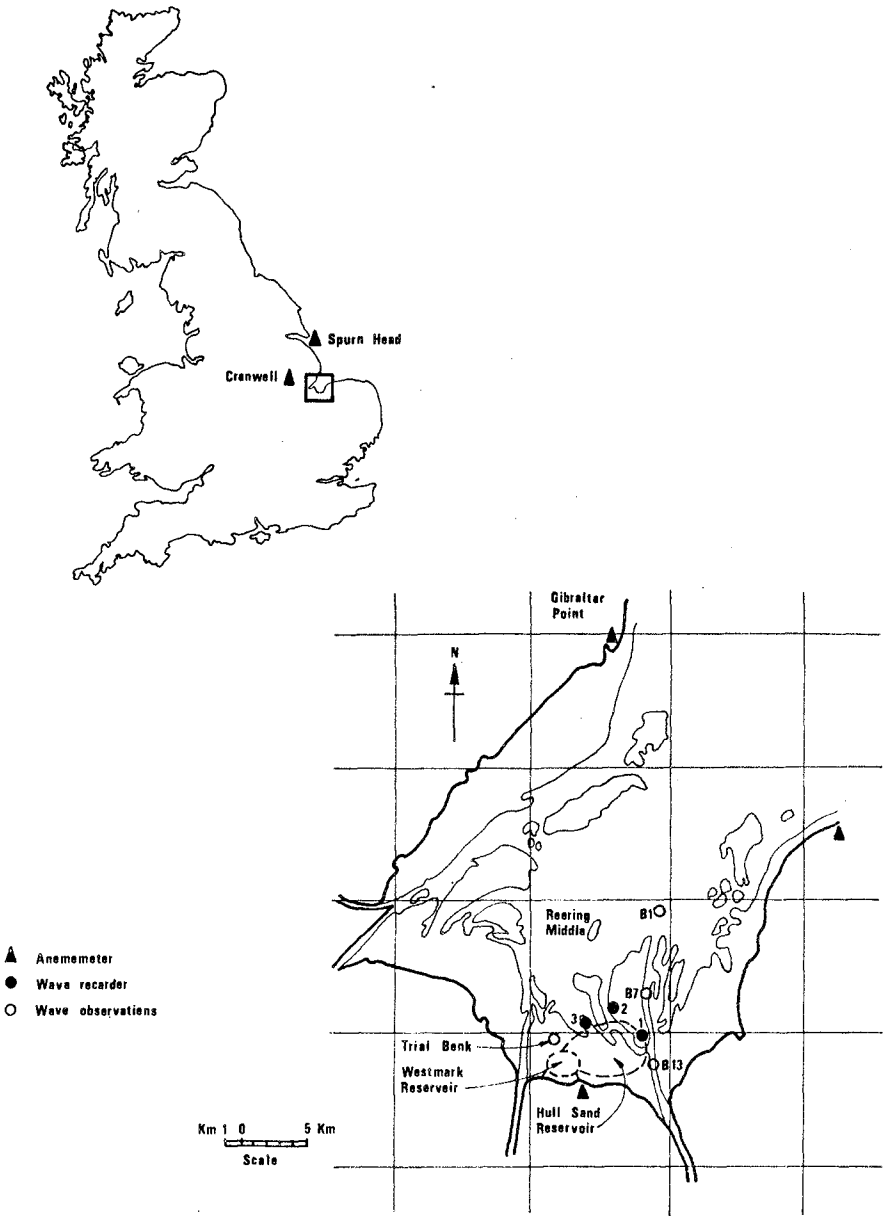


Figure 1. The Wash: General Plan

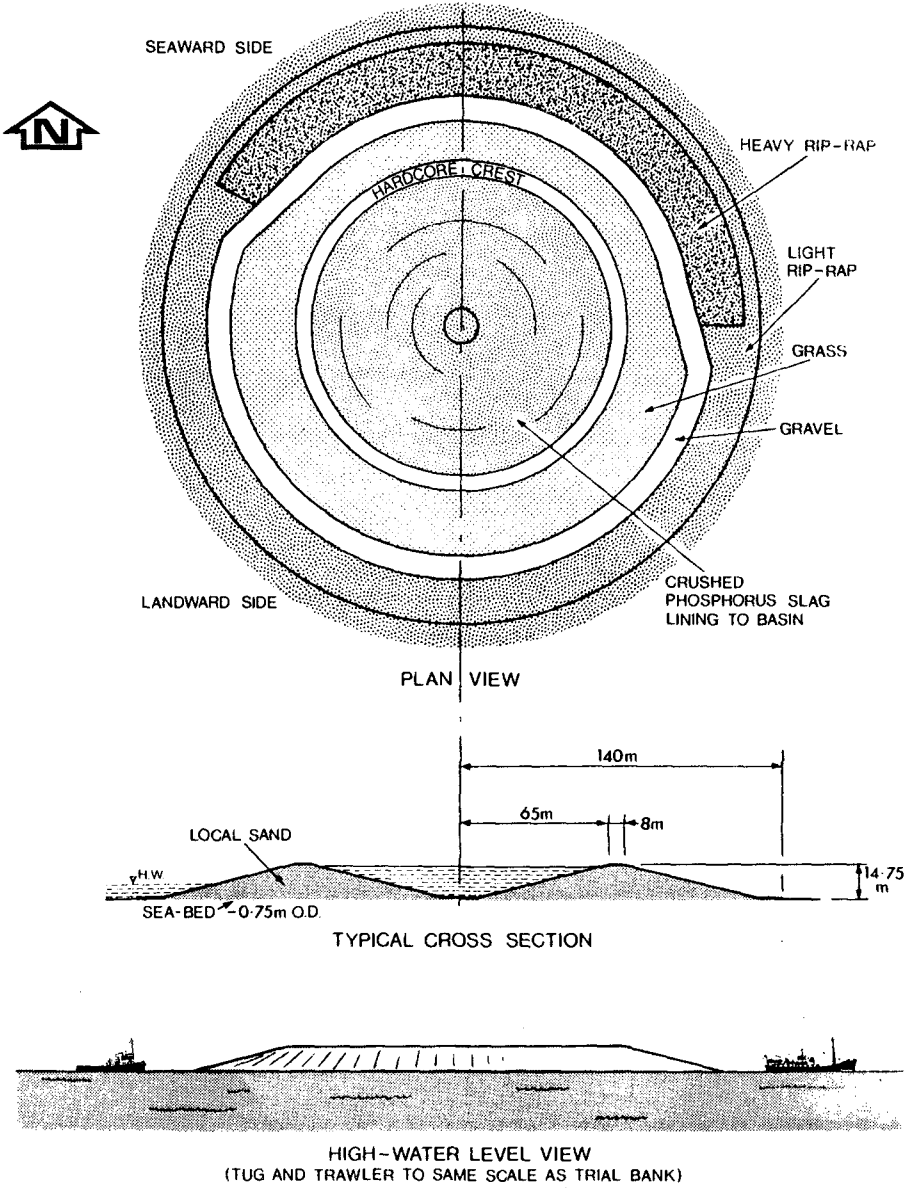


Figure 2. Details of Offshore Trial Bank

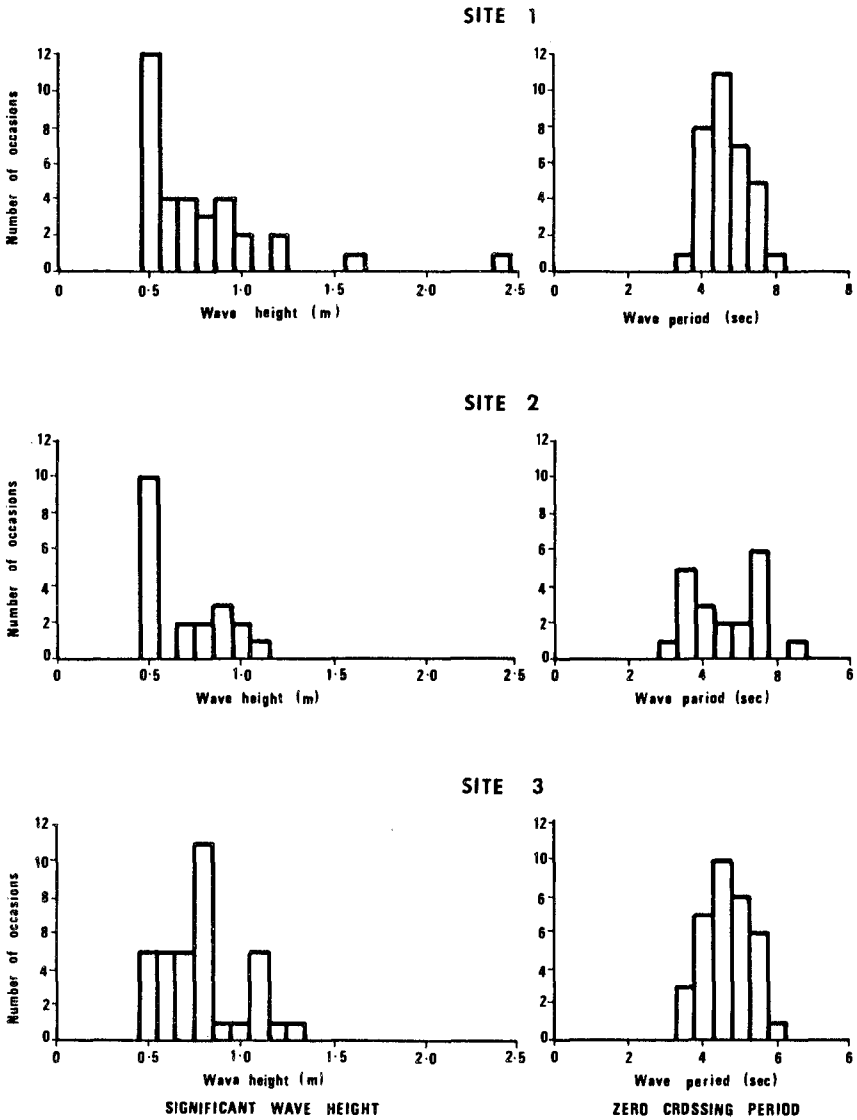


Figure 3. Wave recorder analysis for occasions with wave height 0.5 m or greater

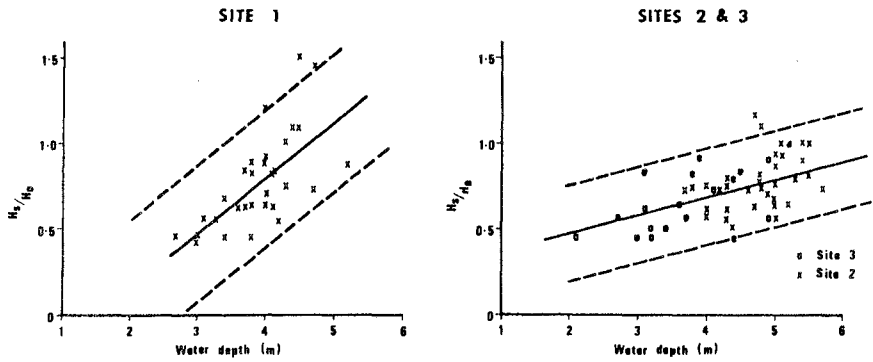


Figure 4. Variation of wave height with water depth

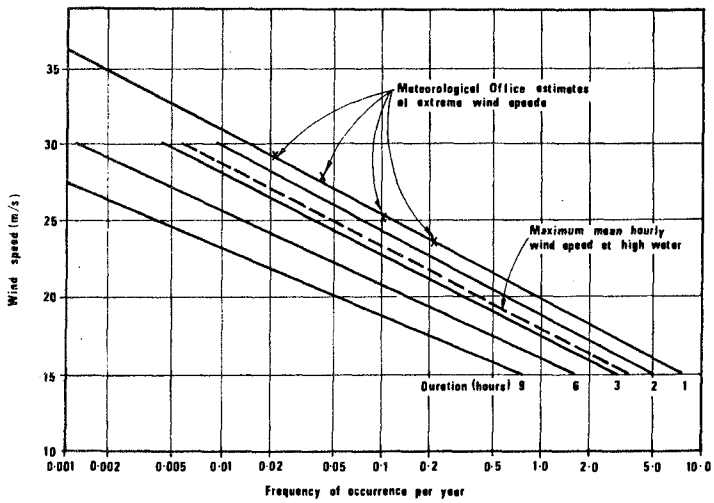


Figure 5. Extreme wind speeds in the Wash

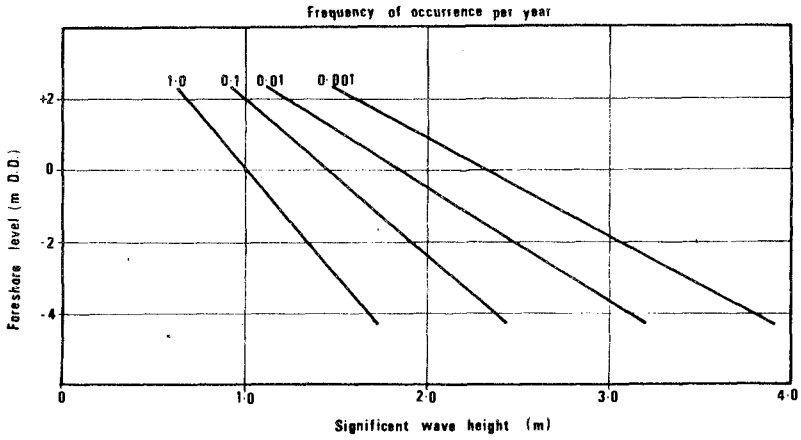


Figure 6. Frequency of occurrence of large waves at various foreshore levels

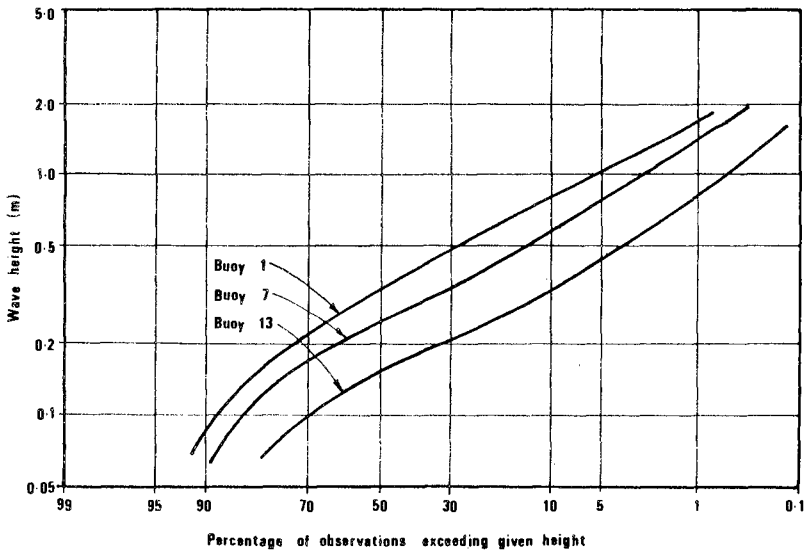


Figure 7. Comparisons of wave heights at Buoys 13, 7 & 1
June 1974 — May 1975

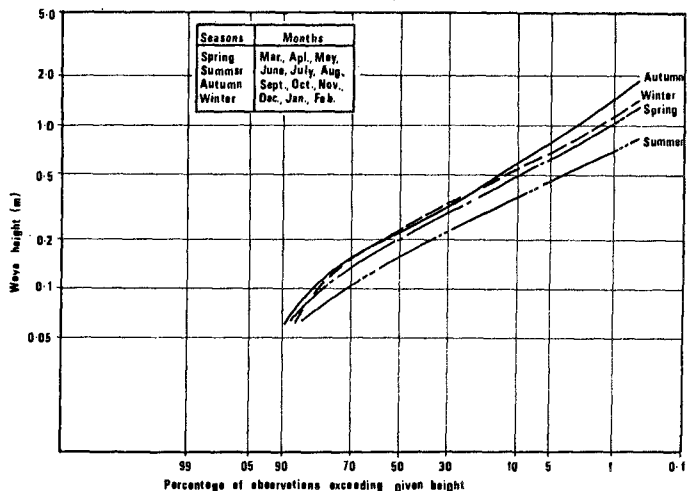


Figure 8. Seasonal variation in wave height distribution at Buoy 7 Dec 1973 - Nov 1975

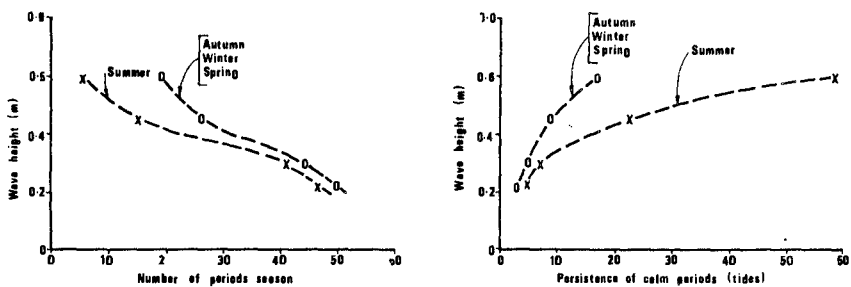


Figure 9. Number and persistence of calm periods at Buoy 7

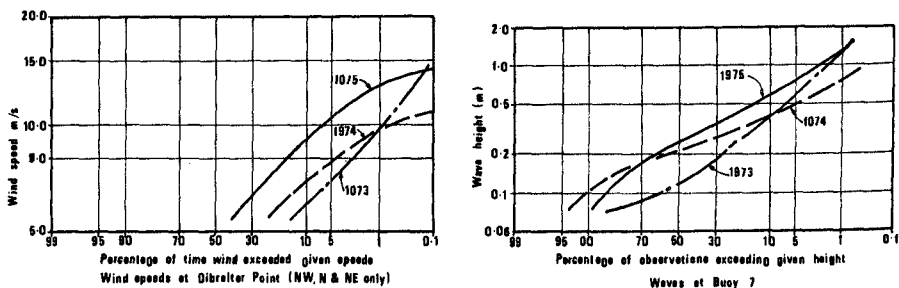


Figure 10. Comparison of wave and wind conditions during spring

CHAPTER 4

DATA COLLECTION AND ANALYSIS

FOR

COASTAL PROJECTS

E. Loewy	Sir William Halcrow & Partners
K. G. Witthaus	Watermeyer, Legge, Piesold & Uhlmann
L. Summers	Sir William Halcrow & Partners
R. J. Maddrell	Sir William Halcrow & Partners

INTRODUCTION

Modern design concepts for coastal engineering works make increasingly heavy demands in respect of the number of variables to be investigated, of the accuracy of the field measurements and of subsequent methods of analysis. In general the larger the projects the greater the demand for accurate site data but frequently, whatever the field data requirement might be, environmental conditions impose severe limitations upon the quality and quantity of the obtainable information.

Before field measurements commenced on the two projects reported in this paper (see Figures 1 and 2) careful consideration was given to the relation between the probable status of the data, the level of statistical analysis to be applied and the constraints the results might impose upon research objectives or upon projected works. Such appraisal was specially relevant since the projects drew upon results from both physical and mathematical models and, in one case, involved assessments of extreme sea conditions related to nuclear safety. This approach provided sufficient flexibility to adjust the method or extent of data collection to take advantage of optimum conditions in the field and changing requirements for input to models and designs.

The time and energy expended in obtaining data of the correct order of confidence was justified by its direct applicability to alternative designs in the face of rapidly inflating construction costs. It was considered essential that the planning and control of data collection be co-ordinated by the design engineer for relating individual items to the project as a whole. It was found equally important that the hydrographic surveyors and oceanographers, familiar with the physical aspects involved, understood how their results were to be applied and hence appreciated the necessity of achieving appropriate tolerances for different parts of the work.

OUTLINE OF CASE STUDIES

The paper describes two data collection programmes which had significant analogies despite being devised for sites remote from each other and for quite different purposes. Both sites had gently shelving sandy shores and seabed and in each case the severity of the wave climate and degree of exposure determined the choice and operating methods of field equipment. These were

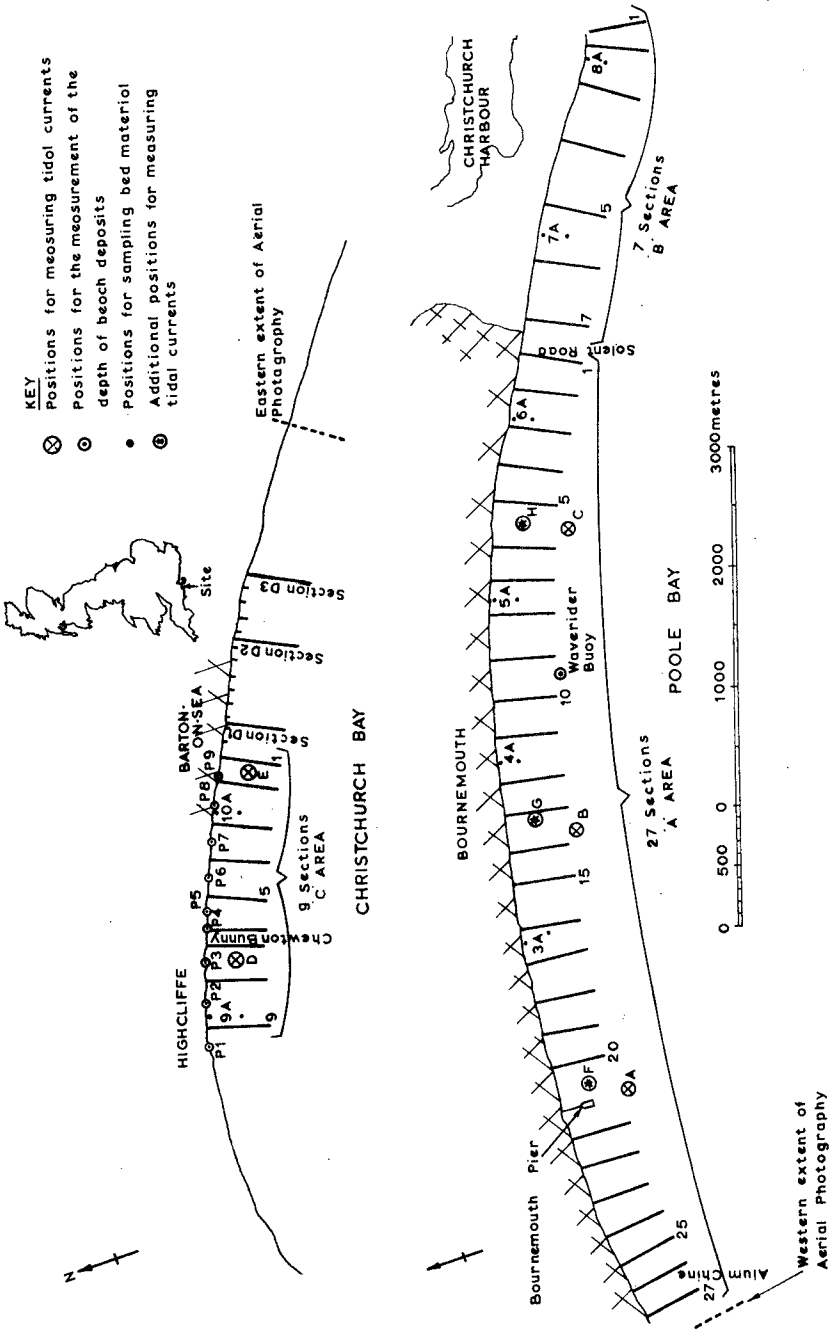


FIGURE 1. POOLE AND CHRISTCHURCH BAYS RESEARCH STUDY. POSITIONS FOR DATA RECORDING.

constraints that greatly affected the value of the data collected and established the tolerance standards for the data requirements.

Poole and Christchurch Bays Research Study

In the first project programme the primary study site was Poole Bay on the south coast of England, fronting the flourishing holiday resort of Bournemouth, where the beach was not only an amenity but provided protection to the promenade and cliffs. A secondary study site covered a short length of an adjoining bay where the beach was very small and had been insufficient to prevent rapid erosion of clay cliffs. As can be seen from Figure 1 both bays faced south, both had limited protection from the prevailing south-westerly storms, and both had fairly shallow shelving seabeds and beaches, the levels of which had been lowered during recent years.

Many of the problems at Poole Bay were analogous to those in other British coastal areas. Therefore the United Kingdom Department of the Environment agreed to sponsor a research project aimed at analysing the beach feeding parameters. The Authors were involved as Project Co-ordinators, being responsible for preparing Contract Documents and ensuring that the data was collected at the required time and was of an adequate standard for subsequent analysis by the Hydraulics Research Station, Wallingford. Collection of data from the two bays extends over a period of three years in association with the following schemes for coast protection:

- a) In Poole Bay, renourishment of the beaches was undertaken by dredging about one million cubic metres of sand from an offshore bank and pumping this onto the beaches.
- b) At the west end of the bay information on beach response was sought to the construction of two long semi-permeable groynes.
- c) The headland between the two bays at the eastern end of 'B' area (see Figure 1) contained bands of ironstone which gave it a greater resistance to erosion than the surrounding material. Information was required on movement trends of mobile material past such a headland and its associated inshore shelf.
- d) In Christchurch Bay, cliffs composed of overconsolidated clay were receding through a pattern of slumps, mud slides and mud flows. More information was required on the rate of recession related to the degree of beach protection at the toe and on the most suitable methods for beach development in this context.

(i) Hydrographic and Topographic Surveys

The surveys extended along 14 km of coastline (see Figure 1) and consisted of 43 survey sections at approximately 400 m intervals. Each section profile began at the toe of the sea wall or cliff and terminated some 500m offshore or at the 9 m contour (5 fathom mark), whichever was the greater. These surveys were carried out immediately before and after the beach feeding and subsequently three times within the first year following completion of the sand replenishment. Further surveys were made at the end of the first year and then at six monthly intervals thereafter.

Each survey section was in fact a combination of topographic and hydrographic surveying carried out during a spring tide, the topographic survey at low water (LWST) and the hydrographic survey at high water (HWST). It was specified in the Contract that the topographic surveys were to be carried out within $1\frac{1}{2}$ hours of LWST, and that the hydrographic survey was to be an extension of the topographic survey line carried out within $1\frac{1}{2}$ hours of HWST. This method of operation ensured that there was a length of profile over which levels were repeated, this overlap serving as a useful check on accuracy achieved, in particular that of the hydrographic work. It was also specified that the surveys had to be carried out within 24 hours of each other to ensure that recorded changes of beach levels were kept to a minimum between the hydrographic and topographic surveys. In the hydrographic work horizontal and vertical tolerance limits were specified not to exceed ± 1 m and ± 80 mm respectively. For the topographic work it was obviously possible to obtain closer limits and the Specification required the points on a section to be within 1 in 5000 horizontally and ± 20 mm vertically.

A recording tide gauge was installed at Bournemouth. This single installation was found to be insufficient to establish a datum for all the hydrographic surveying. The research area was under the influence of two amphidromic points and experienced flood peaks of varying height along its length. Consequently other temporary gauges had to be established along the frontage.

Current velocity measurements were taken every half hour at five stations and at four depths throughout a complete spring tide.

Some 200 bed samples were also taken, both onshore and offshore at regular intervals and their grain size distributions established. The depths of the deposits above the clay bed were also recorded at regular intervals at the various sampling stations. These were repeated at the same time as the surveys.

(ii) Wave Analyses

A waverider buoy was positioned in Poole Bay (see Figure 1). The buoy recorded for 20 minutes every 3 hours, producing information on parameters such as H_1 , H_2 , H_S , T_C , T_2 and E . The buoy had to be inspected once a month, taken out of the water, checked and cleaned, It was recalibrated every six months. The receiver was serviced every two weeks.

Wind data was also analysed from two recorders in the area and the wave data plotted in relation to the wind. Wave directions were observed visually from the cliff top once a day.

(iii) Aerial Survey

This provided stereographic coverage of some 20 km of coastline at a scale of 1 to 2500, the photographic coverage starting and finishing 1 km either side of the boundaries specified on Figure 1. The photography was to be carried out at LWST at six monthly intervals for a period of three years, with a cloud cover less than 10 per cent. Limiting tolerances with regard to crab and tilt were specified.

The aerial survey was later extended to cover the entrance to Poole Harbour to the west of the project area to assist in determining any tendency for the beach feed sand to drift in a westerly direction.

(iv) Film

A film lasting some 20 minutes was commissioned in order to have a record of the research project. The various subjects to be recorded and the minimum duration of viewing time to be allocated to each item were specified. An allowance was made for additional footage of film.

Koeberg Nuclear Power Station

The site area, which lies some 27 km north of Cape Town on the west coast of South Africa (see Figure 2), consists of a zone of active dunes behind a gently sloping beach and sea bed. It is intended that a multi-stage development of nuclear power stations will be constructed at the site which together will generate some 6000 MW for the Electricity Supply Commission (ESCOM). The cooling water for the reactors is to be taken from a dredged basin, protected from wave activity by rubble mound breakwaters, and discharged as a low velocity jet south of the southern breakwater arm (see Figure 2). The site is exposed to the full force of the south Atlantic Ocean, the sea is rarely calm, and throughout most of the year there is a wide surf zone. During the

summer, the site is affected by waves generated from the south and occasionally by storms travelling from this direction. In the winter, storm generation and waves from the north-west appear to predominate. Although the beach and offshore sea bed undergo seasonal changes there is no apparent net change from year to year (1).

On the west coast of South Africa the sea water temperatures are some 10°C below that of the ambient temperatures of freshwater lakes. According to Shannon (2) the main reason for this is that as the cold Benguela current, originating in the Antarctic, passes northward along the Continental shelf, upwelling is generated by the predominant southerly winds. However, this effect could be temporarily modified by north-westerly winds and therefore merited a detailed study as the upwelling of cold water has a direct bearing on the efficiency of the stations.

Mathematical models were used to predict siltation patterns in and around the intake basin (1), the susceptibility of the basin layout to seiche, resonance and recirculation patterns and temperatures for various discharge conditions. Physical models were used to establish the criteria for breakwater design and wave conditions within the intake basin.

Initially studies involving oceanographic measurements were carried out by the Institute of Oceanography of the University of Cape Town as early as 1968, as experience was gained using the data collected and, the project requirements were defined, it became apparent that a more intensive site investigation was required. A definitive data collection and processing programme was evolved by the Authors' firms with relation to the cooling water intake basin and discharge works. Data-gathering procedures were agreed and jointly developed with the National Research Institute for Oceanology (NRIO), together with the University of Cape Town who undertook this work.

(i) Hydrographic and Topographic Surveys

These surveys were undertaken on a quarterly basis for a period of 2 years using the survey markers shown on Figure 2. However, allowances were made for additional ad-hoc surveys after periods of extended calms or severe storms. It was intended that there should be an overlap between the beach and hydrographic surveys but, because of the almost continual occurrence of surf, this overlap was rarely achieved. In fact difficulties of surveying in the surf zone imposed severe restrictions on the data collection and on the accuracy of the survey. This problem was resolved during the course of the studies by the use of a ski boat fitted with a recording echo-sounder and a calibrated vertical pole fixed on it as a mast. When the ski boat indicated that it was making a fix on its echo-sounding trace a shore-based surveyor

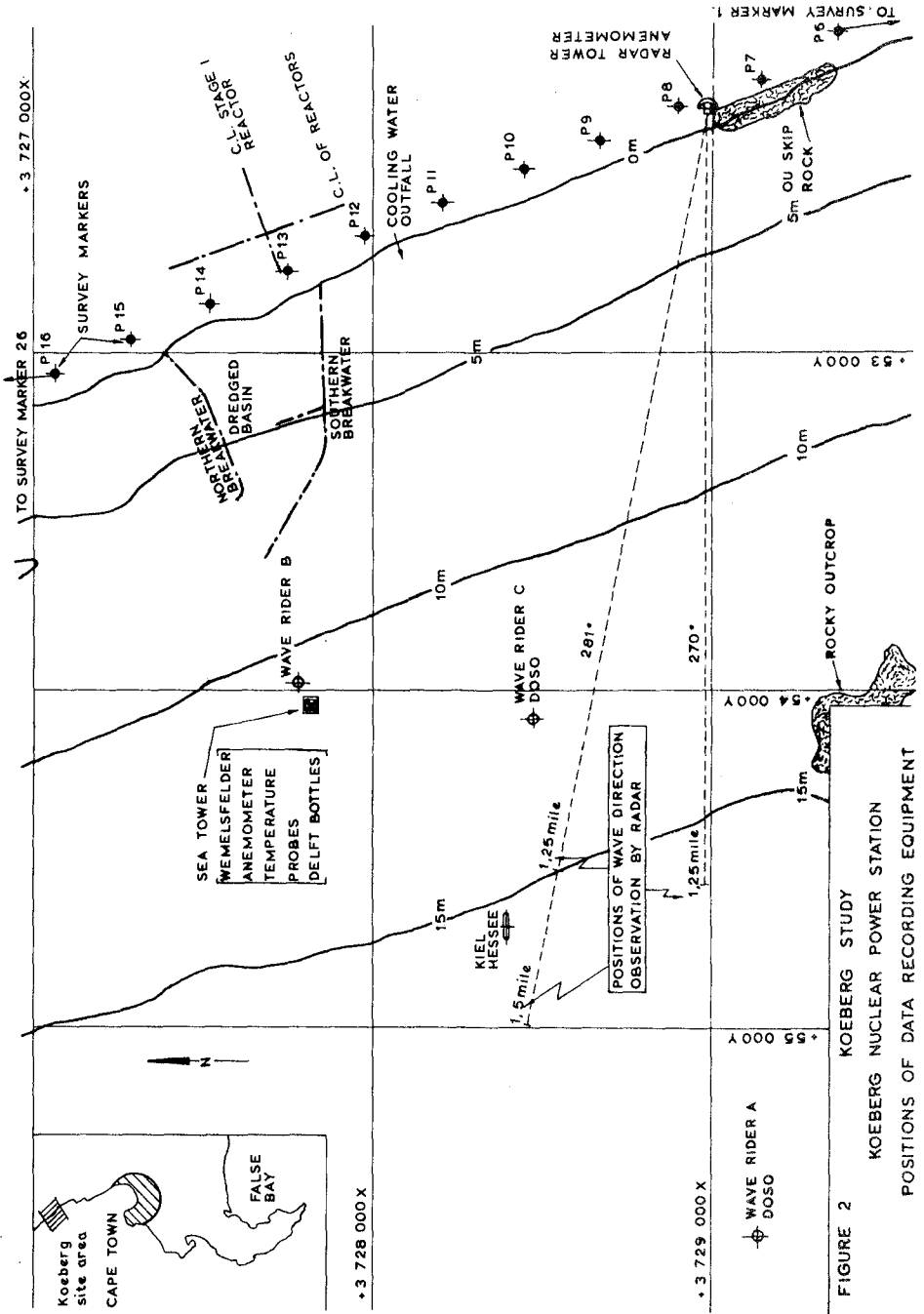


FIGURE 2
 KOEBERG STUDY
 KOEBERG NUCLEAR POWER STATION
 POSITIONS OF DATA RECORDING EQUIPMENT

with a theodolite and camera attachment established the boat's position and elevation. This innovation ensured that the tolerances for the vertical accuracy of the echo survey were kept to an acceptable level.

In addition to the survey markers a series of beach poles was installed opposite the Sea Tower between low water and the dune area. Measurements of beach levels relative to the top of the poles were taken at weekly intervals and enabled a detailed picture of beach erosion and accretion to be established.

(ii) Wave Height and Period Data

Early in the data collection programme it was decided to install a Sea Tower in about 10 m of water (see Figure 2) and to operate it as a data collection centre. A Wemelsfelder float-operated wave height recorder, type W.R.67, which was installed on the Sea Tower in March 1972, provided basic wave data such as H_s , H_{max} , H_{10} , H_{rms} and E .

Wave measurements were also taken using an NIO ship-borne recorder on board the research vessel "Thomas B. Davie" during survey voyages, together with visual observations of wave direction. In general these records of the deep water wave spectra were discontinued once wave recorders were established at the site.

The main information on the wave spectra was provided by Waverider buoys A and B, installed early in 1974, and Waverider buoy C which later replaced buoy B. The buoys recorded for 20 minutes every 6 hours and produced an almost continuous record of wave conditions on the site. The buoys were calibrated and maintained regularly and the records were analysed to give wave parameters, in the same way as on the Poole Bay Project.

(iii) Wave Direction

In 1974 a Decca radar system type RM 919, which is the smallest of the commercial shipping range, was established in a recording hut on Ou Skip rocks at the south end of the study area. This system was based on that developed by the Institute of Oceanographic Sciences (3), with the scanning dish on top of a tower some 33 m (100 feet) above mean sea level. The radar was operated for 10 minutes every 5 hours and recorded the wave patterns photographically, with an exposure time equal to the time of a complete sweep of the radar scanner. This unique method of recording enabled the whole wave front pattern to be recorded as far as 2 km ($1\frac{1}{2}$ miles) seaward of the site. In addition, by recording the photographs on successive frames of a cine film the resulting time-lapse photographs presented a two-dimensional picture of the wave fronts as they were refracted and diffracted. By timing the radar photographs to coincide with wave buoy

recordings, wave direction was added to the other parameters obtained.

The radar system could not be arranged, economically, to record wave directions as far out as Waverider buoy A. Consequently, a Doso meter (4) was introduced in 1975 as an additional tool for measuring these directions in deep water beyond the range of the radar. This recorder, which is a simple bottom-mounted flow direction indicator, was positioned initially next to Waverider buoy C for two months and calibrated against the radar records. Once calibrated it was stationed next to Waverider buoy A.

Observations of wave height, period and direction were also taken from data recorded under the international system operated by Voluntary Observation Ships (VOS) (5). Records for a limited sea area of Marsden Square No.45 were obtained and analysed for use in conjunction with the data obtained on the site in order to improve confidence in the deep water wave spectra. Predictions regarding wave directions were also made by correlating the spectral energy plots obtained for the waves with the low pressure areas in the south Atlantic which generated the waves.

(iv) Wind

Measurements of wind speed, direction and duration were taken both at the Sea Tower and on the observation tower on Ou Skip rocks using Lambrecht recorders. These wind readings were compared with longer term records at nearby airports and at a refinery, as an independent check on the results and as a method of extending the 3 years of site measurements.

(v) Currents

The spring tidal range was 1.5 m (4.9 feet) on this stretch of the South African coast, but the co-tidal lines were almost parallel to the coast. Consequently the tidal currents were small, and not normally measurable on conventional current meters. A Bendix current meter was installed at the Sea Tower and a Keil Hassee current meter was installed on the sea bed near Waverider buoy A, but each meter only recorded current velocities outside instrumental error range during full flood of a spring tide or at times of strong onshore winds.

Most of the data on currents was collected by using free and fixed drogue systems. Measurements using the free drogue system were taken either on an ad-hoc basis or to examine in greater detail the pattern of currents resulting from a specific wind condition. Current data from fixed drogues was obtained by measuring the distances and angles between three drogues connected in series. This was done each morning and evening, and from the

observations the current speeds and directions could be calculated. The results were analysed together with wind records and a relationship between winds and currents was established.

(iv) Bed Samples

A number of samples were taken and analysed during the programme. The bed material throughout the area was in general fine sand with a D₅₀ of about 0.1 mm, but occasionally the bed material was coarser in areas where rip currents predominated.

(vii) Suspended Sediment

Samples were taken initially using Delft bottles, attached to the legs of the Sea Tower, at a number of levels. This sampling method was too crude for prediction of sediment in suspension, needed as essential input data to the sediment transport model that was being developed. However, Professor Kilner was developing a vacuum-operated sediment sampler at the University of Cape Town (6) and it was decided to use this, though at the time it was untried. Initially samples were collected instantaneously in a vacuum bottle, but as this was unsatisfactory as a record for long period storm waves, a later development of the equipment enabled a continuous sample to be taken during the passage of several waves. To operate in the breaker zone the sampler was suspended from a helicopter which, although an expensive method, enabled samples to be collected at a number of depths within the water column and for a variety of wave conditions, without too much difficulty. A more complete description of the method can be found in Professor Kilner's paper to this Conference.

(viii) Sea Water Temperatures

Initially measurements using thermometers were taken at monthly intervals on research vessels within the area. However, this was found not to provide a representative sample and later conductivity type temperature probes were installed at three depths at the Sea Tower. Also, additional measurements were taken regularly over a period of two years at a number of positions by wading into the surf zone. These measurements proved to be most interesting and a clear relationship was established between the sea water temperatures and the wind driving the upwelling current.

PROBLEMS ENCOUNTERED

For major coastal engineering projects which merit extensive data collection programmes the problems encountered are numerous. The cost is high and, as Wright (7) has pointed out, the tender prices for the surveys can vary considerably depending on the engineer's specification and the contractor's assessment of the

actual requirements. Any specification must not only allow for the logistics of collecting each set of data under a variety of sea and weather conditions, but also define the tolerances which can be applied in practice. In addition, it is generally necessary for the different types of data to be collected simultaneously. One set of data alone may be interesting, but to be of use it needs to be time-related to other different sets of measurements, e.g. hydrographic and topographic surveys require the continuous measurement of the wave climate and current patterns if the former are to be successfully analysed. For this it is essential not only to have back up equipment but also to adopt different methods of approach, so that any missing data may be filled in with some degree of confidence from alternative sources, or so that it can be used to correlate with other longer term records.

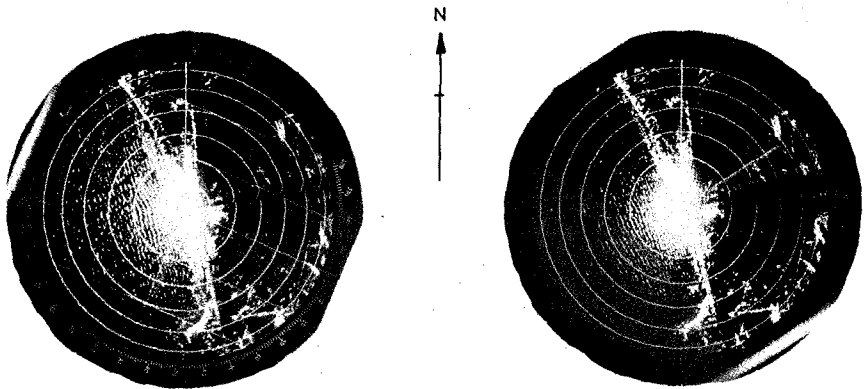
The limits of achievement of data collection from the two survey programmes of the projects described were dependent upon measurement of the wave-dominated environmental climate, the status of the project and the purpose intended for the use of individual observations.

At Koeberg, predictions of extreme events were required in relation to the safety of the nuclear plant. An intensive programme of investigations was called for in order to provide reliable input data for the complex physical and mathematical models. Even so the results obtained were limited by the severe marine environment.

At Bournemouth, the wave climate was far less severe and it was possible to use a much less intensive programme of investigations. However, on occasions important records could still not be obtained during the winter months.

Considering the problems that arise from the wave climate, some of the basic wave parameters can be relatively easy to collect. Waverider buoys were successfully employed on both projects and achieved a very high rate of useful collection. A buoy broke loose during the worst storm on both projects, resulting in a gap in the wave record while the buoy was reinstated. This also meant that the peak wave energy condition went unrecorded and consequently affected the predictions of wave and surge conditions which were dependent upon them. The Wemelsfelder recorder on the Koeberg Sea Tower also failed to provide a continuous record because, during major storms, waves broke over the tower and tended to force the instrument's float into the top of the well chamber.

The VOS observations were useful in that they provided relatively long-term records and gave an indication of the deep water climate.



DATE 27.MAY.74 TIME 09.00

Hmax = 3.8 m

Hs = 2.5 m

Tc = 7.5 secs

DATE 5.JUN.74 TIME 12.01

Hmax = 2.0 m

Hs = 1.3 m

Tc = 9.4 secs

FIGURE 3. WAVE FRONT PATTERNS RECORDED PHOTOGRAPHICALLY USING RADAR.

Establishing the direction of waves has always been a problem. Visual observation from cliff tops, such as at Bournemouth, proved satisfactory but only represented the near-shore, refracted, waves at one point along the 14 km coastal study area. Although this information could be used to back-track the wave rays in order to derive the deep water spectra, which could then be refracted in elsewhere along the coast, this process can pose many problems principally arising from the nature of the model grid. At Koeberg good results were obtained by combining radar records (see Figure 3), which also required a high vantage point, with Doso records. On their own the radar records were not entirely satisfactory as, even in the severe wave climate at Koeberg, only about 35% of the waves were recorded during a year, i.e. those waves which were sufficiently high and steep with, in general, 'fluffy' crests. However the radar faithfully recorded sufficient wave fronts over a fairly wide sea area and, by use of time-lapse photography, the refraction pattern of a wave as it shoaled could

be checked against calculated values. Radar equipment had the further advantage that it was entirely land-based and could be easily serviced. This was not the case with the Doso meter, for which a diver was required to retrieve the records and to service the instrument. If subsequent analysis showed a fault in operation to have occurred, a section of the readings might have been omitted and lost. However, in general the Doso meter gave an excellent point recording of wave direction and proved to be a powerful tool when used in conjunction with radar recordings.

At the time of the project study an alternative concept for determining wave direction was fortunately being developed by Dr Harris of the University of Cape Town and this was expanded in private correspondence.

In brief the deep water wave directions were established by comparing synoptic weather bulletins with contoured plots of spectral wave energy arrivals against wave frequency and the time of recording.

These contoured plots, normally covering a period of about one month, showed a series of high and low areas, representing times of peak energy arrival or of relatively quiescent periods respectively. The scales of the plot were calibrated so that a line drawn through the major axis of the peak area intersected the time abscissa at the date on which the generated storm waves had originated, and the included angles gave the distance to the storm centre in degrees of latitude. Examination of the weather bulletins showing the location of the isobars of the low and high pressure areas for the period preceding the arrival of the peak energy condition provided an essential check on the calibration.

This method was proved by comparing the results against those of the other methods of measuring wave direction and, once proved, was used to fill in missing data.

It was found that the hydrographic and topographic surveys were greatly influenced by wave activity. This was because wave energy not only alters the onshore and offshore topography and bathymetry but, as has been mentioned earlier, also affects the practical aspects of the survey itself. Cross (8) who discusses the many sources of error that can occur in inshore surveying also acknowledges the important influence of the wave climate. At Bournemouth the surveys were timed to coincide with spring tidal conditions to ensure that there was an adequate area of overlap between the topographic and hydrographic surveys.

On at least two occasions, rough seas led to a postponement of the surveys and only three out of eleven surveys were fully completed in the time specified. At Koeberg one of the surveys

was abandoned altogether due to sea conditions. It was found that the zone of overlap on each line could be extended and thus the accuracy of the survey improved by using a survey pole with disc base for topographic surveying which could be taken into the water by a man in a wet suit. This technique was successfully employed at Poole Bay to extend the topographic survey by some 20 m, but at Koeberg the surf conditions rapidly halted progress outwards and overlap was rarely achieved. Even under ideal conditions, as can be seen from Figure 4, the overlap does not always give a good solution.

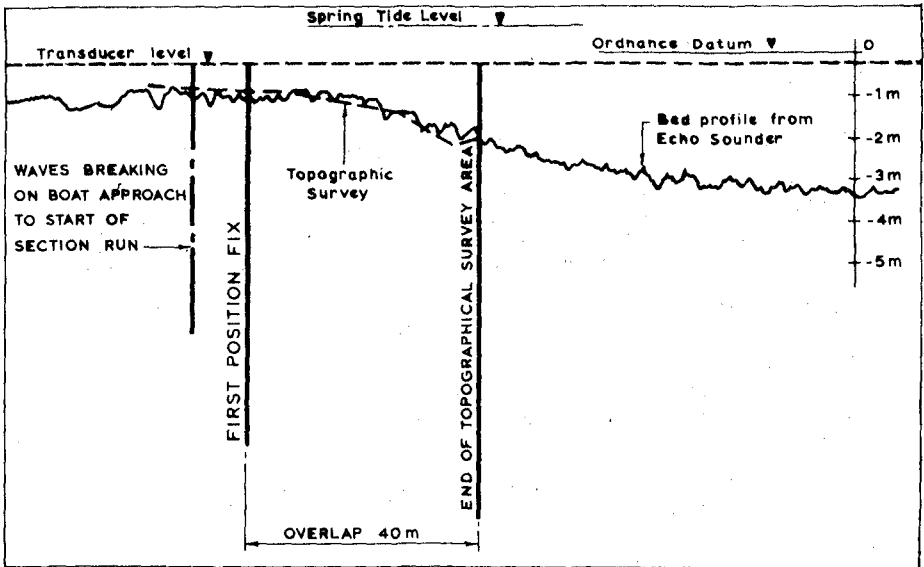


FIGURE 4. POOLE AND CHRISTCHURCH BAYS RESEARCH STUDY. OVERLAP OF HYDROGRAPHIC AND TOPOGRAPHIC SURVEYS.

The overlap between the two surveys cannot be relied upon to provide a datum line for the hydrographic survey. The reference level must be related to datum using the tidal level at the time of the survey, especially at the seaward end of the section. This presented few problems at Koeberg which has a small and reasonably regular tide. The Bournemouth coast, however, under the influence of two amphidromic points (see Figure 5), caused tidal differences in the two bays which were not only notable from tide to tide but also varied during a tide. A careful check had to be made of the tidal level variation along the coast by the installation of additional tide boards.

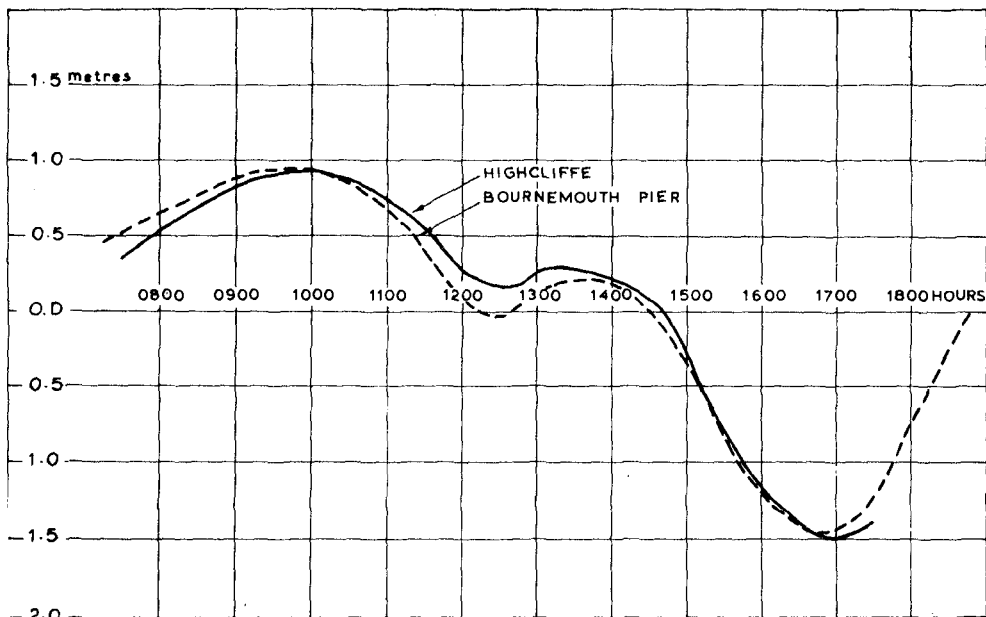


FIGURE 5. POOLE AND CHRISTCHURCH BAYS RESEARCH STUDY.
SPRING TIDAL OBSERVATIONS FOR 17 FEBRUARY 1976

It was realised that the mathematical model for sediment transport, developed specially for the Koeberg project, would rely heavily upon site data records, especially on suspended sediments in relation to wave height. When the studies commenced, no reliable method was known for obtaining suspended sediment samples in the surf zone. Fortunately the 'Kilner' sampler was developed, providing suspended samples in waves up to 6 m high which showed good correlation with those developed from theory (1).

In areas where tidal current predominated conventional current meters were adequate and, if used during spring and neap tidal cycles, the tidal current pattern could be easily established. Where the tidal currents were low or non-existent the current pattern had to be established using drogues. This required at least one year's data, preferably taken on a daily basis, which was possible using a fixed drogue system. A relationship had then to be established between the currents and the wind driving them. This proved possible at Koeberg and the relationship was used together with the continuous records of wind to predict flow patterns.

CONCLUSION

It can be said with confidence that a data collection programme can be accurately planned only when the parameters to be measured are known. Clearly this is an unrealistic situation and consequently latitude must be allowed in the collection programme for lack of knowledge by, if possible, providing for more than one method of measuring the data. This requires thought, planning, finance and an assessment of what the answers will be. A complete set of data taken at the same time is essential to any project, especially if models are employed. No matter how sophisticated the theory or advanced the modelling technique that is adopted, the quality of the answer will directly reflect the quality of the data fed in.

It is also essential that, when planning data collection, the engineer understands the technique to be used and the practical difficulties involved. He must not demand a level of accuracy that is impossible or, unless he makes provision for it, extremely expensive to achieve. On the other hand the hydrographer or University Department must realise how the data which they collect is to be used and what influence it has on the project as a whole. The engineer must not be afraid to experiment but should not rely entirely on new untried equipment which tends to produce results later than expected.

In general the cost of taking measurements of the coastal environment are high but their true value is not always apparent at the beginning. The Authors have found that because of this high cost many institutions are willing to undertake analyses of

data on a shared use basis. Co-operation of this kind between research personnel and practising engineers can be very beneficial to a project as a whole.

ACKNOWLEDGEMENTS

The authors would like to thank both ESCOM and the U.K. Department of the Environment for providing the necessary funds for the projects, for their understanding that data collection is in part an evolutionary process, and for their permission to publish this paper.

They would like to thank personnel from the following South African Institutions; University of Cape Town, the National Research Institute for Oceanology, the Department of Fisheries (VISKOR) and the Atomic Energy Board, and personnel from the following U.K. Institutions; The Hydraulics Research Station, University of Southampton, Longdon and Brownings Surveys Ltd and Huntings Surveys Ltd.

REFERENCES

1. Fleming, C A and Hunt, J N : "Application of a Sediment Transport Model" Proc. 15th Coastal Engineering Conference 1976.
2. Shannon, I V : "Hydrology of the South and West Coasts of South Africa" Investl Rep. Div. Sea Fish. S. Afr. 58, 1966.
3. Gleason, R, Blackley, M W L and Carr, A P : "Beach Stability and Particle Size Distribution, Start Bay, Devon" J. Geol. Soc. Vol 131 Part 1 Jan. 1975 pages 83 - 100.
4. Retief, G de F and Vonk, A P M : "A Low Cost Wave Direction Indicator" Proc. 14th Coastal Engineering Conference, 1974, Vol. 1, pages 212 to 224.
5. Hogben, N and Lumb, F E : "Ocean Wave Statistics" Her Majesty's Stationery Office, 1967.
6. Kilner, F A : "Measurement of Suspended Sediment in the Surf Zone" Proc. 15th Coastal Engineering Conference, 1976.
7. Wright, M : "Surveying by Contract in the United Kingdom. A Critical Review" Proc. XIV International Congress of Surveyors, 1974, Paper 401.3.
8. Cross, R H : "Hydrographic Surveying - Error Sources". Proc. A.S.C.E. J. of Surveying and Mapping Div., 1974, Part SU2, pages 83 to 95.

CHAPTER 5

REGIONAL NETWORK FOR COASTAL ENGINEERING DATA

Richard J. Seymour*
Meredith H. Sessions**

A. Introduction

The California Department of Navigation and Ocean Development (DNOD), responsible for shoreline protection within the state, was particularly aware of the lack of coastal wave statistics to support their beach erosion program. As a direct result of the 1974 ASCE-sponsored New Orleans Conference on Ocean Wave Measurement and Analysis, discussion was initiated within DNOD and then with the Scripps Institution of Oceanography (SIO) at La Jolla, on the feasibility of establishing a regional wave monitoring network for California. The initial specification presented by DNOD was for a 200-station network reporting directional wave spectra twice daily for a period of ten years. SIO ocean engineering personnel responded with a system concept employing low-cost pressure transducers hardwired to shore with a dialup telephone data gathering link to a central station. The initial cost estimates appeared attractive when compared with Corps of Engineers experience as reported in Peacock (1974).

As a result, a small program was funded in February 1975 at Scripps to demonstrate critical hardware items through the breadboard stage. With the successful completion of this work, additional funds were allocated by DNOD as matching funds for a California Sea Grant Project.

The first station in the network began operation on 3 December 1975 at Imperial Beach, California. A second station was added at Ocean Beach (San Diego) on 27 March 1976, a third at SIO (La Jolla) on 18 May 1976 and the fourth at Oceanside, California on 2 June 1976. The locations of these initial stations are shown in Figure 1.

Considerable effort has been directed during the past 10 years toward the development of numerical models to predict deep-water wave conditions from meteorological data. Reasonable results have been obtained and sufficient accuracy achieved to allow routing of both commercial and military ship traffic. There has been some hope by users

* California Department of Navigation and Ocean Development

** Scripps Institution of Oceanography

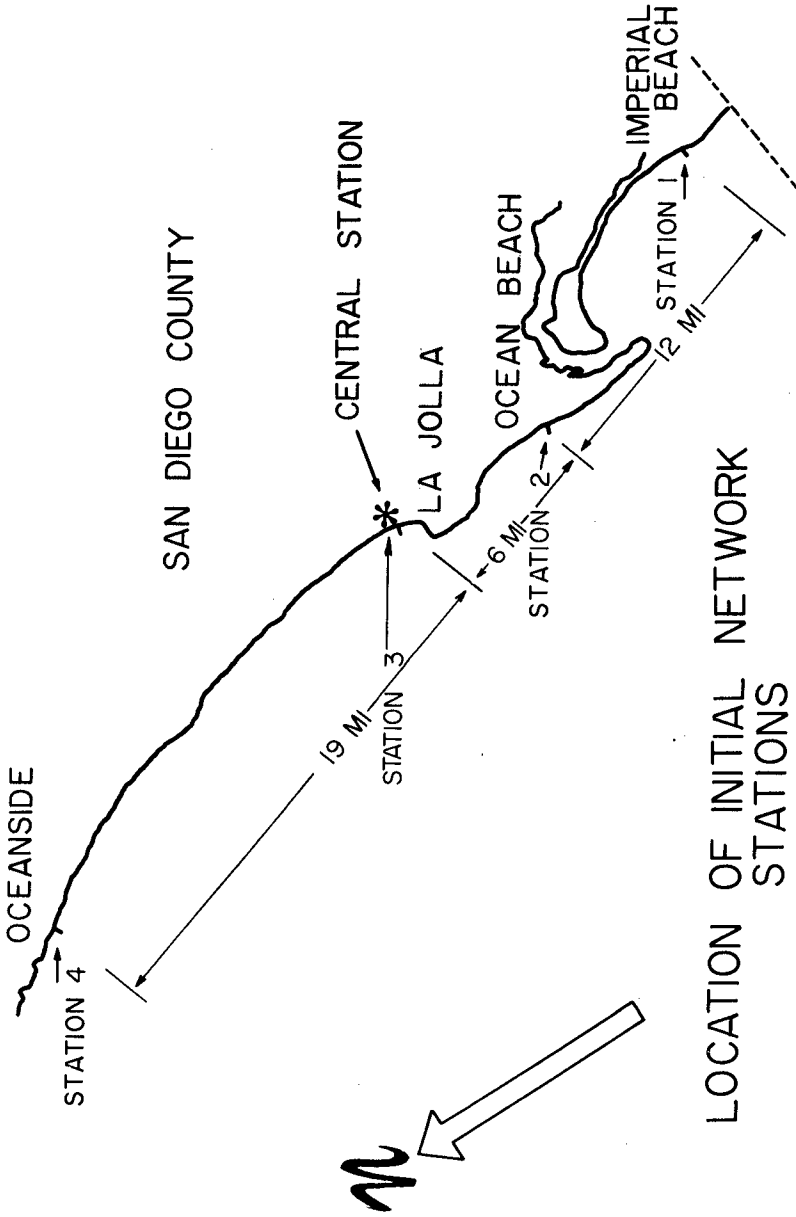


FIGURE 1

of nearshore wave data that hindcasting of meteorological records would allow a relatively low-cost method of accumulating long-term coastal wave statistics. However, the realities of the situation indicate that this may never be possible. Because of the irregularities in the continental shelf topography, a very marked difference in the refracted wave intensity at a particular location results from a small change in the deep-water wave approach angle. Accuracies on the order of one-half degree are needed in predicting offshore directional spectra in order to achieve reasonable estimates of local nearshore wave climates. The best obtainable accuracy that may eventually be expected is still at least an order of magnitude poorer than this.

The situation existing in Southern California is even more difficult than in most coastal regimes. The deep-water waves are not only refracted by the very irregular bathymetry of the shelf but are reflected, scattered and diffracted by a chain of large offshore islands.

Since the observed local wave climate is the sum of the deep-water swell that diffracts around the islands, and the locally generated wind waves, these factors combine, in the case of Southern California, to make wave prediction for coastal areas an extremely difficult task. Therefore, in this region of the coastline, it is even more imperative to find an affordable method for acquiring wave statistics through local nearshore measurements at closely spaced sites.

Any effort by man to alter the coastline shape, to prevent the erosion of valuable shoreline property, to manage the sediment budget within a coastal province -- all require the ability to predict the local capacity of the waves to transport sediment onshore, offshore, and longshore. Since man is most often concerned with the long-term cumulative effect of such sediment transport, only long-term statistics on the wave climate will allow meaningful predictions to be made.

Nearshore currents -- tidal, wind-driven or caused by fresh water flows -- can be significant factors in sediment transport and the dispersion of pollutants. Temperature variations with depth and time can provide data on such stable phenomena as thermoclines and such transient events as internal waves and bores. Both features are important in the engineering of the mixing patterns of outfalls. The wind field over the water can be of value in verifying wave generation models and for atmospheric pollution studies. Thus, a variety of additional sensors might be utilized at certain locations in addition to the basic wave gaging.

B. Objectives of the System

1. Coastal Wave Climate Statistics:

The primary objective of the system is to provide an affordable means of gathering directional wave statistics, at least twice each day, from closely placed stations along the coast of California. These stations are to be selected to allow both a characterization of the wave climate along the entire coastline and to highlight areas of specific interest -- such as a coastal reach undergoing critical erosion. These statistics are to be available in a timely manner to the users (reports containing monthly data are mailed no later than the third working day of the following month). Further, the data are to be archived so that raw data tapes and spectra tapes can be used at a future time by investigators.

The data can also be available in nearly realtime for surf reports and boaters' advisories if desired.

It is an objective of the program to collect these data for a minimum of ten years to establish seasonal trends.

2. Sediment Transport Estimates:

The second priority objective is to make estimates of the longshore sediment transport from the wave data in all locations where this would be appropriate. This prediction will utilize the best available model relating the measured wave characteristics and the sediment transport. Since the original wave data are preserved, these estimates can be updated later with improvements in the transport model.

3. Support of Scientific Experiments:

The ability of the network to provide nearly simultaneous observations over a very broad reach of coastline provides a unique data gathering tool to many coastal experiments. It is an objective of the program to support such work whenever possible, either as the primary data source or as an adjunct to the basic data retrieval system.

C. General Description of the System

1. Station Locations:

As of 30 June 1976, four stations have been installed in the network as shown in Figure 1. All are in San Diego County and have been added in a northerly progression. The Imperial Beach location was chosen as the southernmost site

in California because a critical beach erosion problem has been experienced here. In addition, a beach renourishment project is now underway and the wave data obtained may be of value in monitoring the effectiveness of the sand placement. The Ocean Beach site is just north of the Sunset Cliffs area, which has suffered damaging erosion. The gaging station is also very close to the entrance to Mission Bay, which will be studied by the Corps of Engineers for possible solution to the dangerous entrance conditions due to breaking waves which are encountered several times each year. The site at SIO is close to the Scripps Submarine Canyon, the terminus for a major littoral cell. The Oceanside location is in an area with chronic problems caused by interrupted littoral drift and localized erosion.

2. Central Station Configuration:

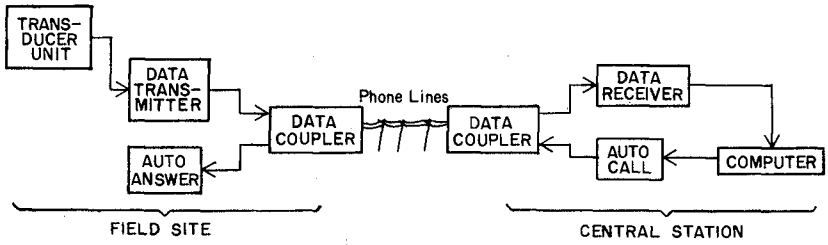
When the multiplexed signal is received at the central station, channel separation is achieved by tuned filters at the carrier frequency. The signal is then demodulated and digitized. The multiplexed data from as many as seven instruments are transmitted over an ordinary voice-grade, dial-up commercial telephone line. The data quality is at least as high as experienced with more costly leased lines over comparable distances.

At the central station, a dedicated minicomputer is interfaced to a receiver and autocall system. Under real-time computer control, a preprogrammed telephone number corresponding to the desired field station is dialed. Each station is called in sequence once every ten hours. This provides a minimum of two reports per day and eliminates the bias possible with fixed polling times. Upon connection to the field site, the digitized words are written to the computer buffer and then to magnetic tape for permanent storage.

The system block diagram is shown in Figure 2.

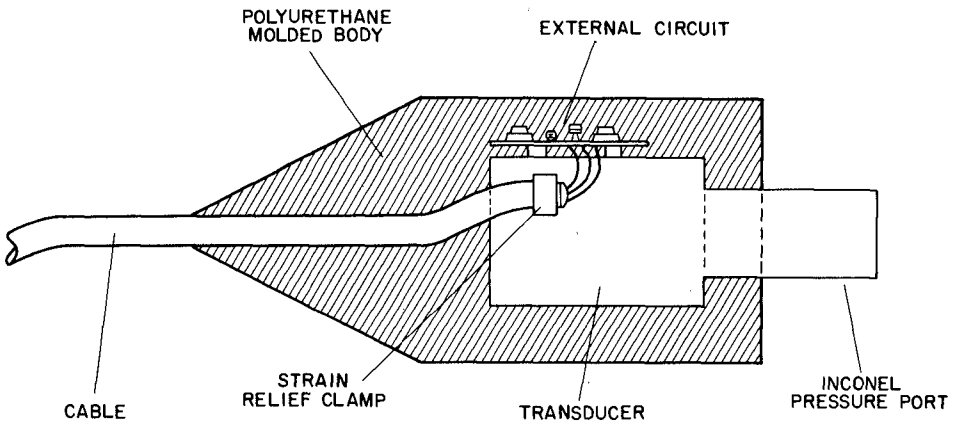
3. Field Station Configuration:

The initial stations utilize existing piers to bridge the surf zone. In the updated configuration, wave measurements are obtained with very stable LVDT (linear variable displacement transformer) pressure transducers which are molded directly on the end of a specially designed high performance armored cable as shown in Figure 3. This construction eliminates the cost and reliability hazards associated with connectors and housings. A single transducer providing one-dimensional wave spectra is the basic station. Three transducers in an array are now being



**BLOCK DIAGRAM,
DATA TRANSMISSION SYSTEM**

FIGURE 2



GULTON WAVE SENSOR ASSEMBLY

FIGURE 3

installed at each station to provide a directional estimate. The underwater cables are terminated in a data control box on the end of the pier. This unit performs the functions of signal conditioning, multiplexing signals from the various sensors, and responding to telephone requests for data from the central computer. The installed cost of the complete field station with an array of three pressure transducers, the underwater cabling and the data control box is projected to be less than \$3,000. Current meters, temperature probes, anemometers and other continuously reporting instruments can be accommodated in addition to the wave measuring devices. The output of each instrument is amplified at the point of measurement and converted to a frequency in the kHz range. At the shore station, this is divided down and used to modulate a carrier tone in the voice range.

4. Reports and Data Analysis:

These data are available for immediate analysis, if required. Normally Fourier transforms of wave data are made once a month and stored on a permanent transform archive tape. From these, a monthly wave climate statistical report is made, including one-dimensional spectra and significant wave height estimates for each data sampling.

D. Data Archiving

It is anticipated that the appropriate federal agency will, at some later time, take over the function of archiving the wave data obtained with this network. Initial discussions with NOAA personnel indicate that they plan a national wave statistics program beginning before the end of this decade. This would meet the needs for a central repository, capable of specifying the format for standard inputs and of meeting the requests of investigators for duplicate tapes or tabulations of data. Until this arrangement is available, the present project organization will attempt to meet the needs of interested investigators for raw data, transforms or tabulations.

Following is a tabulation of data outages which have occurred since the system went into operation in December 1975:

<u>Date</u>	<u>Data Lost</u>	<u>Cause</u>
December 1975	2 runs from 1 site	Power supply failure in central station
April 1976	2 runs from 1 site	Vandalism

<u>Date</u>	<u>Data Lost</u>	<u>Cause</u>
June 1976	2 runs from 1 site	Phone line damaged by construction work
June 1976	1 run from 1 site	Pier power outage

During this time over 1,000 runs have been made, so the data outage rate is 0.7%. Considering only equipment failures, the rate becomes 0.2%.

E. Plans For Expanding Capabilities

1. Additional Stations

As funds become available, other stations will be added to the network. As in the selection of the existing stations, the advice of the Corps of Engineers, the California Department of Navigation and Ocean Development, and other interested agencies will be solicited to aid in selecting future sites.

2. Wave Direction Measurement Capability

During the second half of 1976, the existing stations (and additional stations as they are installed) will have multiple channel capability. This will allow the installation of a minimum of three sensors in an array to estimate wave directional properties.

Two alternate approaches are being evaluated at this time. The first is to calculate a conventional directional spectrum estimate. With the limited array size, this will necessarily result in a poor estimate of actual wave direction. The second approach involves an approximation of the longshore momentum flux, defined by Longuet-Higgins (1970) as the sum over frequency of the products of the energy, the ratio of the phase and group velocities and the sine and cosine of the approach angle. This is expressed symbolically as

$$S_{xy} = \sum E_n \sin \theta \cos \theta$$

This parameter, which can be related to the longshore current induced by waves along straight coastlines, may be a more valuable and concise means for describing the overall directionality of the wave field.

Regardless of which method is employed in monthly reporting, the raw data will be preserved for use in other types of analyses.

3. Wind Measurements

Wind will be measured at pier sites utilizing an aerovane-type sensor which has had wide application on ships and oceanographic buoys. Data will be sampled periodically and a number of samples stored in a temporary memory until called by the central station. Upon receipt of a command from the central computer, data will be converted to a frequency proportional to the values stored in the memory and sent as a sequential series. The entire contents of the temporary memory will be sent upon command but the contents will be retained until overflow occurs with the most recent value pushing the oldest data out of the stack. Sample intervals and durations are programmable and can be varied to suit the experiment requirements.

F. Results and Preliminary Conclusions

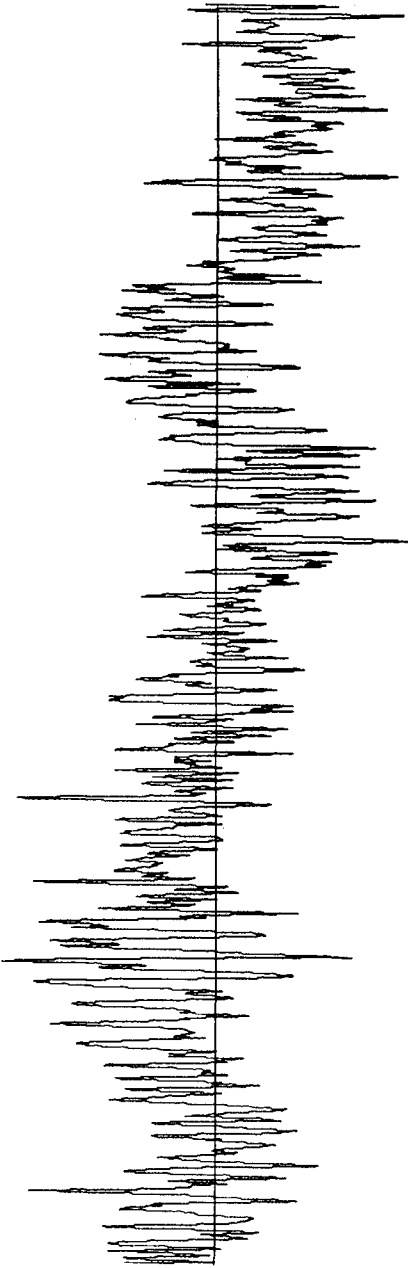
The first seven months of operation of the network have shown gratifying progress. The hardware cost goals have been met or exceeded. The data retrieval reliability has been greater than 99%, including causes beyond the control of the project. Every monthly report has been mailed to users within the first three working days of the following month.

A sufficient data bank has already been acquired to allow some tentative conclusions on the eventual usefulness of these measurements:

.....The ability to discriminate low amplitude, long-period oscillations has been dramatically illustrated by the record of a tsunami reverberation made on 4 December 1975, four days after the earthquake on Hawaii. The uncorrected bottom pressure time history is shown in Figure 4. Although the original tsunami arrival had been detected by the tide gaging station at Scripps Institution of Oceanography, this reverberation was not detectable.

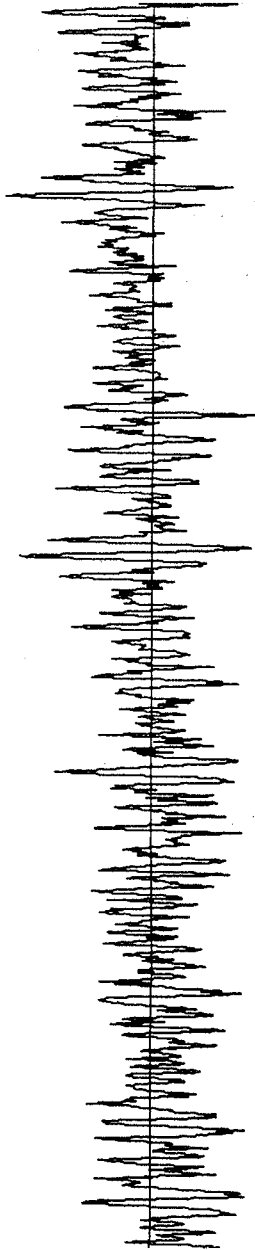
.....The influence of tides on spectral shape is significant when wind waves are small. Figure 5 shows a pressure record in which the mean sea level shift caused by the tide can be easily distinguished.

.....It has long been reasoned that point-to-point variations in nearshore wave climate are large. The present record of the network indicates that these variations may be even larger than anticipated. Figure 6 shows qualitatively the intense spatial variability within an 18-mile stretch of coastline during a single month. The "vertical" dimension suggested by



Pressure-time Record, Imperial Beach Station, 0600 4 December 1975, Showing Reverberations of 29-30 November Tsunami From Earthquake in Hawaii (Period: Approximately 10 Min., Height: Approximately 1 Foot).

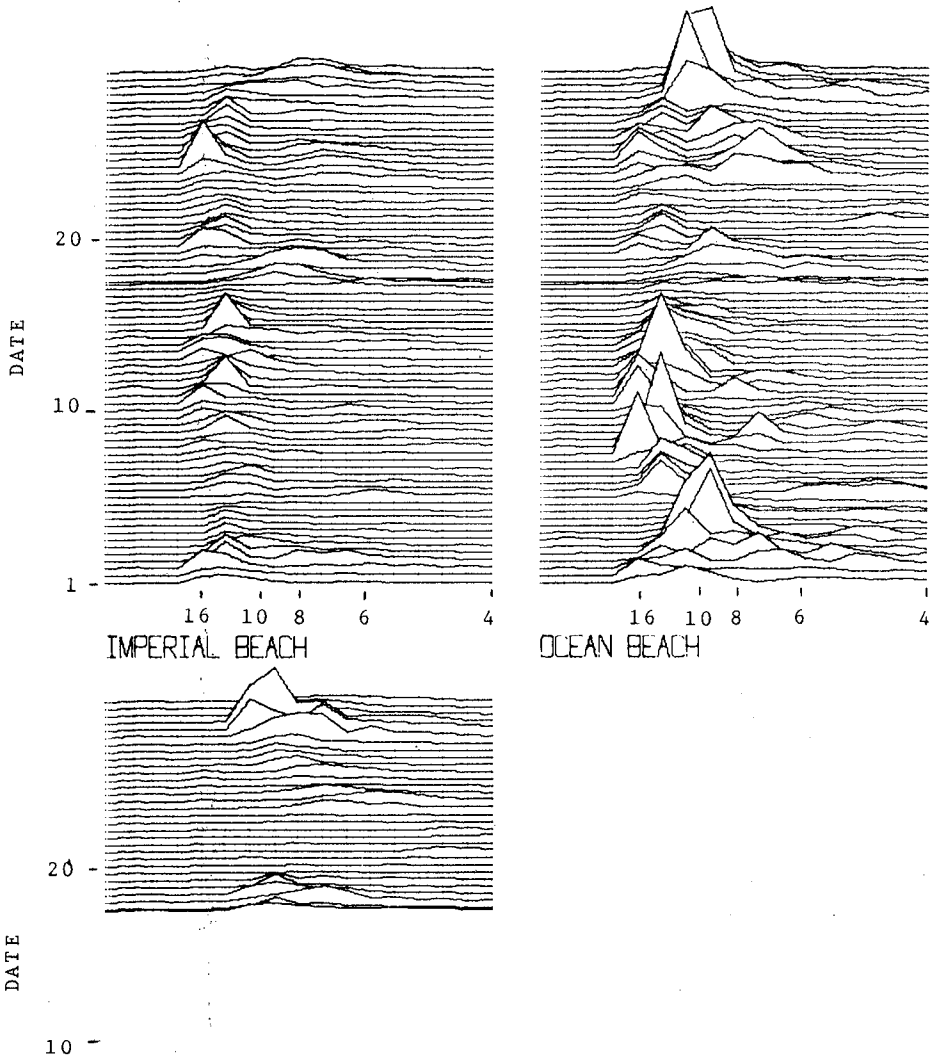
FIGURE 4



Pressure-Time Record Showing Mean Water Level Change Caused By Tide.

FIGURE 5

WAVE ENERGY CONTOURS - MAY 1976



SCRIPPS PIER

FIGURE 6

this plot is absolute energy plotted at the same scale for all stations.

This variability, both temporal and spatial, reinforces the need for closely spaced nearshore wave measuring stations reporting more than once per day in order to characterize the impact of the wave climate on the shoreline.

REFERENCES

1. Peacock, H. G. "CERC Field Wave Gaging Program," Proc. Int'l. Symposium on Wave Measurement and Analysis, New Orleans, September 1974, Vol. II, pp. 1-22, Waves 74.
2. Longuet-Higgins, M. S. "Longshore Currents Generated by Obliquely Incident Sea Waves," Journal of Geophysical Research, November 20, 1970, Vol. 75, No. 33, pp. 6778-6801.

CHAPTER 6

WAVE MEASUREMENTS IN OPEN OCEAN

Davidson T. Chen, Benjamin S. Yapple, Donald L. Hammond
and Paul Bey

Space Science Division
Naval Research Laboratory
Washington, D. C. 20375

I. INTRODUCTION

The ability to measure the wave spectra in the open ocean from a moving vessel has met with varying degrees of success. Each sensor to date has suffered in its performance due to environmental conditions or due to its physical placement aboard the vessel for measuring the unperturbed sea. This paper will discuss the utilization of a microwave sensor on a moving vessel for measuring the open ocean wave spectra. Employing microwaves, some of the limitations of other sensors are not experienced.

Tucker [1] developed the Tuckermeter for measuring the wave spectra from a moving ship by sensing changes in water pressure due to surface wave conditions. The Tuckermeter is placed below the water line and thus requires calibration for each wave frequency, ship speed, and depth. Since the sensor operates on pressure, it performs as a low pass filter and will not sense the higher frequencies.

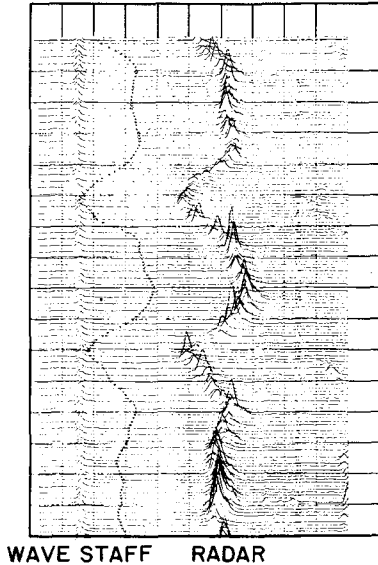
A microwave shipboard wave height radar sensor for measuring the ocean wave spectra was developed by the Naval Research Laboratory (NRL) and was installed on the S.S. McLean in February 1975 and its performance, design, and analysis of data for one data run will be discussed.

II. RADAR SYSTEM

A profile of the ocean waves by measuring their height variations can be used to calculate the ocean wave spectral components. A radar with high angular and range resolution is an ideal sensor for profiling the waves because the narrow antenna beam illuminates a small spot on the ocean surface and the narrow transmitted pulse resolves the vertical height of the waves.

A radar system employing these features was operated from a Coast Guard navigation tower to demonstrate its capability to measure ocean wave spectra as indicated by

Yaplee, et al. [2]. The radar system illuminated a one meter spot with a one-nanosecond pulse permitting a height resolution of 15 centimeters. The radar range measurements were compared with a wave staff mounted around the spot illuminated by the radar. A sample of the radar and the wave staff wave profiles are shown in Figure 1.



PULSE DATA FROM THE
CHESAPEAKE LIGHT TOWER
WAVE HEIGHTS 1.524 meters
HOR. SCALE 0.762 m/division
VERT. SCALE 1 sec/division
DATE June 19, 1970

Figure 1 Measurements from Chesapeake
Light Tower

The encouraging results of the tower measurements led to a radar system designed to be operated from a ship to profile ocean waves. It was desirable to point the antenna beam out at a slight angle to avoid the ship's bow wake to measure the unperturbed sea. However, since the radar in this look angle is not viewing the nadir, the question arises as to what effect the phenomenon of wave foreshortening will be on the wave spectrum. Therefore, a set of tower radar

measurements were made to profile the sea at different look angles between nadir and forty-five degrees. The wave spectra of the tilted radar and wave staff data were obtained and these spectra were almost identical at all look angles from nadir to forty-five degrees [3]. Therefore it was concluded that the results of the shipboard radar would not be compromised as the result of changing look angles.

The principal parameters for the shipboard radar are listed in Table 1. The functional block diagram of the radar system is shown in Figure 2.

TABLE 1

Parameters for Shipboard Radar

Wavelength	3 centimeters
Pulse Width	2 nanoseconds
Peak Transmitted Power	100 watts
Pulse Repetition Rate	10,000 per second
Antenna Diameter	61-centimeter parabola
Receiver Noise Figure	7 db
Equivalent Pulse Processing Rate	100 per second

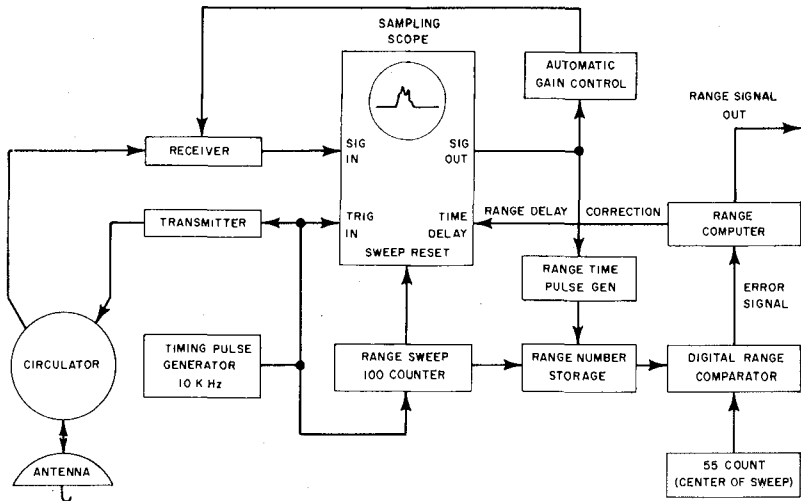


Figure 2 Radar System

The radio frequency components for the transmitter and receiver are mounted in a watertight enclosure on an antenna pedestal located about 23 meters above the ship's water line. The antenna is pointed abeam and tilted down and out about 15 degrees with respect to nadir. Figure 3 is a photograph of the antenna mounted on the starboard side of the ship's bridge and the figure to the right shows a sample of the measured data before processing.

SHIPBOARD WAVEHEIGHT RADAR ON-BOARD SS - McCLEAN

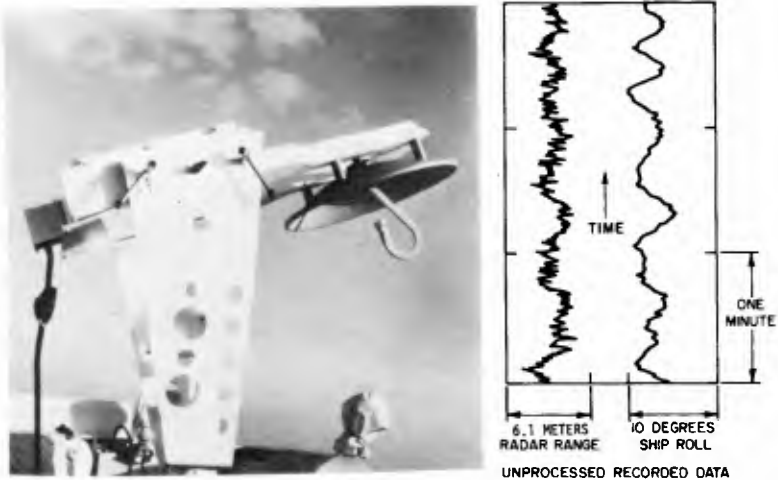


Figure 3

The 10 Kilohertz (KHz) timing generator, shown in Figure 2, triggers the transmitter and synchronizes the receiver signal processing. The radio frequency transmissions consist of 2-nanosecond wide pulses at the 10 Gigahertz (GHz) carrier frequency with a peak power of 100 watts and with a pulse repetition rate of 10,000 per second. The radar pulses reflected by the ocean surface are amplified in the receiver to a usable level. An envelope detector following the amplifier results in a 2-nanosecond wide video pulse.

Processing the 2-nanosecond wide pulses requires circuitry in the system with bandwidths of 500 Megahertz (MHz). It is desirable to operate at a lower bandwidth where components are more easily used and obtained. By using a sampling scope for display and signal processing, it is possible to make this bandwidth transformation to an equivalent video pulse that is 200 microseconds wide or a bandwidth of 5 KHz. Thus the use of standard low speed

logic circuits can be used for signal processing resulting in a simpler and more reliable system. The principle of operation of a sampling scope is well known and will not be discussed. See references [4, 5, 6] for the particular scope used in this radar.

III. EXPERIMENTAL TESTS

The nanosecond radar is located starboard on the bridge of S.S. McLean and adjusted to view the ocean at a look angle of 15 degrees from nadir and away from the bow wake. On February 6, 1975, while the ship was underway from Elizabeth, New Jersey to Portsmouth, Virginia, simultaneous ocean surface data were taken by the shipboard radar while an airborne laser profilometer and airborne nanosecond radar were measuring the same seas. The object of this effort is to establish the validity of the shipboard measured data.

The shipboard radar data were recorded at 30 minute intervals starting at 8:20 A.M. EST on February 6, 1975 and ended at approximately 2:00 P.M. of the same day. Each file of data started with about a minute of zero level setting and followed by a minute of calibrations. The ship was travelling at 14.9 meters per second at 214 degrees heading. Approximately 9:26 A.M. the aircraft intercepted the ship's track at $38^{\circ}3' N$ in latitude and $74^{\circ}41' W$ in longitude. Airborne data were recorded at 152.4 meters and at 304.8 meters altitude in the immediate vicinity of the ship's path. At 152.4 meters altitude, a laser profilometer [7] and an airborne nanosecond radar were used to profile the ocean surface. At 304.8 meters altitude, NRL's airborne nanosecond radar was operated in the wave spectrometer mode. Aircraft data were recorded continuously at intervals of about 90 seconds as the aircraft was flying at 75.2 meters per second ground speed. Exact coincidence of data taking was not possible and comparison of the data is based on approximate times from the ship and aircraft logs.

IV. ANALYSIS

The dynamics of the two platforms (aircraft and ship) while recording ocean surface data was significantly different. In addition to their peculiar motion characteristics, the data were recorded in different manners. One, is continuously in analog and the other, is intermittently and digitally. To effect a better comparison of the data, it was necessary that the data be reduced to some common base.

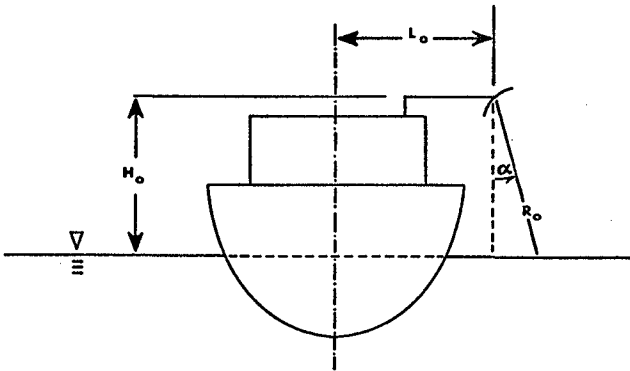
The analog shipboard data were recorded in real time, and then sampled and digitized at 8 Hertz (Hz) off-line. This digitizing rate was a compromise, taking into account the longest ocean wavelengths expected to be experienced by

the ship and the storage capacity of in-house computers to process the data. The aircraft data were digitized at 90 Hz rate in real time but was utilized at 15 Hz rate off-line. Again a compromise was made with the high frequencies which were not overly significant being truncated and at the same time trying to maintain equal spatial resolution with the shipboard data.

The largest amount of dynamic motion or movement other than forward velocity of a ship is its roll. In Figure 3 was shown a sample of the shipboard radar output and the output of the roll sensor. The magnitude and the period of the roll which affect the determination of the true ocean wave spectra must be removed before any real analysis can be conducted. However other motions also need to be corrected for unless they become second order in magnitude and can be ignored.

By assuming rigid body motion the geometry of the radar aboard ship is shown in Figure 4. The upper figure

(A) VERTICAL UPRIGHT POSITION



(B) ROLL POSITION

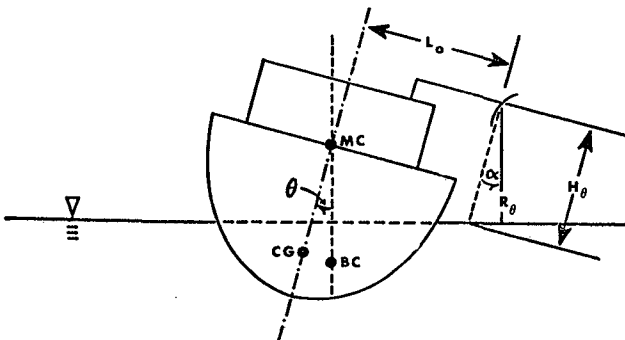


Figure 4 Rigid Body Motion due to Roll

shows the direction of the ship moving into the paper and in still water thus remaining in the upright position. The radar measures $R(t)$, the distance from the radar to the surface of the water at an angle α with respect to the vertical. It is the magnitude and frequency of these radar distance variations that yields information for determining the ocean spectra. As mentioned earlier, ship motions, particularly roll, affects the magnitude of these variations yielding an erroneous wave height change. In the lower illustration of Figure 4 is shown an instantaneous roll position that the ship can assume. In this situation, the change in radar distance $R(t)$ is not due to waves but is due to the ship's motion and the radar then measures the distance R_θ instead of R_0 . The magnitude of the change in R_0 to R_θ needs to be determined. Symbols used in Figure 4 for determining this change are defined as

- H_0 - distance from radar antenna to water surface, in the direction of ship's symmetric axis, and 0 degrees roll angle; 23.2 m for H_0 in these calculations;
- H_θ - distance from radar antenna to water surface in the direction of ship's symmetric axis, caused by θ degrees roll angle;
- L_0 - horizontal distance of radar antenna from center of gravity of the ship at 0 degrees roll angle; 12.2 m for L_0 in these calculations;
- θ - angle of roll; positive in clockwise direction, from vertical upright position, by looking into the direction of ship's heading;
- R_0 - radar distance of 0 degrees roll angle;
- R_θ - radar distance at θ degrees roll angle;
- α - look angle of radar antenna, 15 degrees;
- CG - center of gravity of the ship;
- MC - metacenter of the ship;
- BC - buoyant center of the ship.

From the Law of Sine's, it can be shown that

$$R_\theta = (H_0 - L_0 \tan\theta) \frac{\cos\theta}{\cos(\theta - \alpha)} \quad (1)$$

Using Equation (1) the values for $R_\theta(t)$ can be determined from H_0 , L_0 , α , and θ which can be obtained from the ship's roll sensor.

Using $R_{\theta}(t)$ in the radar distance measurements, the following relationship can be established:

$$R_R(t) = R_{\theta}(t) - \zeta(t) \sec(\alpha - \theta) + \Delta R(t) \quad (2)$$

where

$R_R(t)$ - the radar distance measurement to the water surface;

$\zeta(t)$ - the instantaneous apparent wave height, positive in upward direction from the mean sea surface;

$\Delta R(t)$ - the radar distance changes due to ship motion other than roll.

It is worth noting that, as it has been shown by Hammond, et al. [3], for $|\alpha - \theta| \leq 45^\circ$ the term $[\zeta(t) \sec(\alpha - \theta)]$ will indeed give the correct ocean wave spectrum as calculated from $\zeta(t)$. Thus, for simplicity in data processing, Equation (2) can be approximated as

$$R_R(t) = R_{\theta}(t) - \zeta(t) + \Delta R(t) \quad (3)$$

This relationship shows the effect of ship motion in conjunction with wave motion and their effect on the radar range measurements, but assumes that any flexural and torsional motions which change the distance between the radar antenna and the center of gravity are negligible. All other motion changes such as yaw, pitch and heave, etc. are combined into $\Delta R(t)$. The term of interest, $\zeta(t)$, in describing the sea surface, is small in magnitude and it modulates the distance $R_R(t)$ which is large. The shipboard equipment was designed only to record this modulation and as a result a large distance bias, D , remains.

Let

$$R_A(t) = R_R(t) - D \quad (4)$$

where $R_A(t)$ is called the relative radar range measurement and D is a constant. Substituting Equation (3) into Equation (4),

$$R_A(t) = R_{\theta}(t) - \zeta(t) + \Delta R(t) - D \quad (5)$$

Rearranging the terms

$$R_{\theta}(t) - R_A(t) = \zeta(t) - \Delta R(t) + D. \quad (6)$$

Define

$$R_1(t) = R_{\theta}(t) - R_A(t) \quad (7)$$

where $R_1(t)$ is the relative radar range without the effect of ship's roll. Rearranging the terms

$$\zeta(t) = R_1(t) + [\Delta R(t) - D]. \quad (8)$$

This results in $\zeta(t)$ describing the sea surface variations. There still exist $[\Delta R(t) - D]$ which has not been accounted for because D is basically a DC term. This however can be removed by filtering the data. The term $\Delta R(t)$, as defined, consist of all the other ship motions affecting the radar range measurements. The high frequency components of $\Delta R(t)$ are of such low magnitude that their effects on the wave measurements are negligible, whereas the low frequency components can be effectively removed with a high pass filter. In the reference by Linnette [8] the filtering process employed to remove the $[\Delta R(t) - D]$ term is discussed. After the process $\zeta(t)$ still contains a Doppler term and it must be taken care of before it is possible to study the ocean surface characteristics.

The term $\zeta(t)$ describing the amplitude variations of the waves as the radar profiles the surface while the ship is underway includes a Doppler term. Due to the velocity of the ship and the Doppler effect, the waves encountered are foreshortened. Thus the wavelengths measured are not the true ocean wavelength but an apparent wavelength. If the radar's instrumentation had incorporated a coherent radio frequency signal, the effect of the ship's velocity can, by appropriate instrumentation, be subtracted directly. Since this is not the case, it is necessary to correct the apparent spectra to a true spectra. In order to accomplish this, it is no longer possible to operate in the time domain but one must resort to working in the wave number or frequency domain.

It is straight forward to evaluate the apparent wave number spectrum, $\psi_A(k_A)$, from the foreshortened wave height, $\zeta(t)$, where k_A is the apparent wave number because of the Doppler effect. Neglecting the effect of the direction of propagation of the wave component under consideration, it can be shown, in Appendix, that $\psi_A(k_A)$ can be transformed to $\phi(\sigma_T)$ where $\phi(\sigma_T)$ is the true wave frequency spectrum

and σ_T is the true wave frequency. The spectra shown in the results were calculated by using Equation (10) in Appendix.

Significant wave heights were determined by employing equation (9), [ref. 9],

$$H_{1/3} = 4\sqrt{E} \quad (9)$$

where $H_{1/3}$ is the significant height and E is the total energy of the waves.

V. SPECTRAL BANDWIDTH WITH SPECTRAL RESOLUTION

The 0.61-meter parabolic antenna illuminates a footprint [10] about 0.95 meters in diameter at a radar range of 24.4 meters. This footprint size can only resolve wavelengths longer than 1.83 meters which is equivalent to an apparent cutoff frequency of 0.908 Hz. The true cutoff frequency is 0.358 Hz after removing the Doppler effect. Translating this true cutoff frequency into a true wave period results in wave period of not less than 2.8 seconds. The high pass filter, discussed earlier, removes waves with periods longer than 7 seconds in the data. The wave spectra shown in the results are calculated for the wave period window of 2.8 to 7 seconds.

If different spectral bandwidths are desired, the upper frequency bound can be raised by increasing the antenna size. The lower frequency bound can also be extended but this requires removing the ship's motions without the use of high pass filter. The analysis requires ship motion sensors at the site of the antenna to record the actual excursions of the antenna. In this manner it is possible to resolve the longer wavelengths of the spectra.

VI. RESULTS

Wave spectra from the shipboard measurements are presented in Figures 5 to 12. The significant wave heights for files 1 to 8 of the data, respectively, are 2.10, 2.22, 2.23, 2.17, 2.16, 1.99, 1.99, and 1.94 meters. Since the sea was not in steady state conditions, it is not possible to make comparison with the Pierson-Moskovitz spectrum [11]. Figure 13b shows the analyzed results from the airborne measurements made by laser profilometer and the nanosecond radar. Laser profilometer registered 1.84 meters and the nanosecond radar registered 1.43 meters as the significant wave height based on data taken at the altitude of 152.4 meters. At the altitude of 304.8 meters, operating the nanosecond radar in wave spectrometer mode

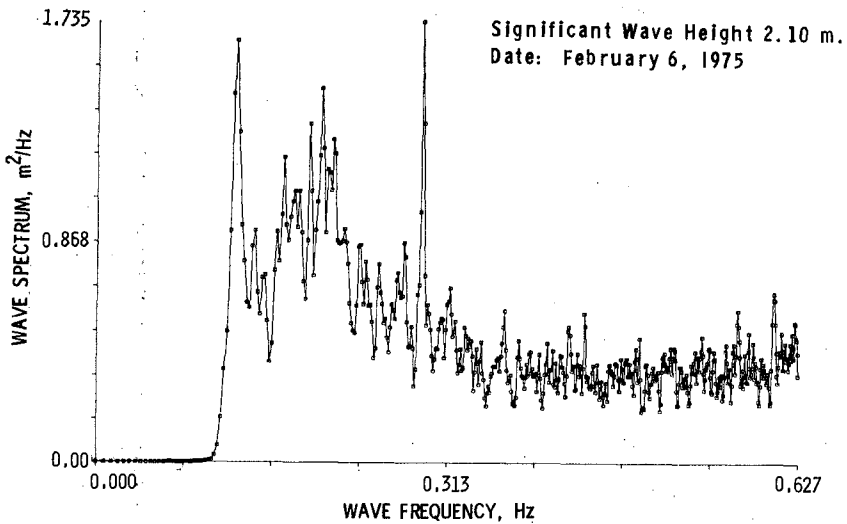


Figure 5 Wave Spectrum from File 1 of the Shipboard Radar Measurements

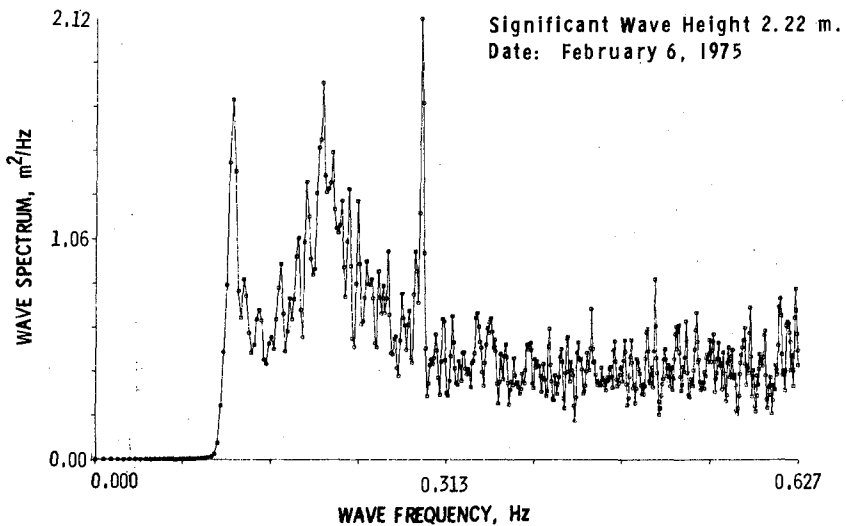


Figure 6 Wave Spectrum from File 2 of the Shipboard Radar Measurements

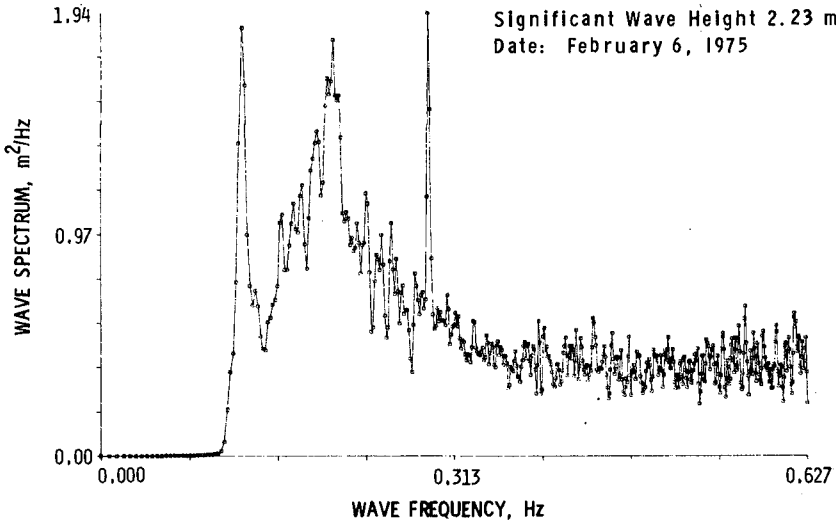


Figure 7 Wave Spectrum from File 3 of the Shipboard Radar Measurements

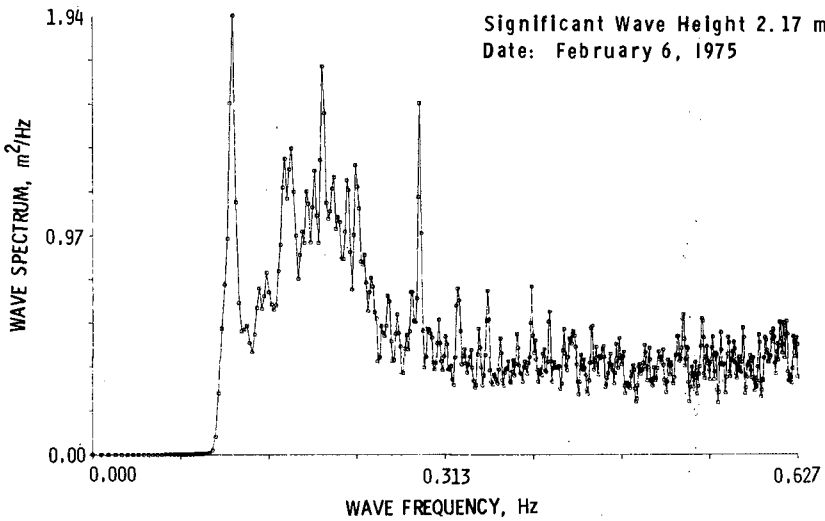


Figure 8 Wave Spectrum from File 4 of the Shipboard Radar Measurements

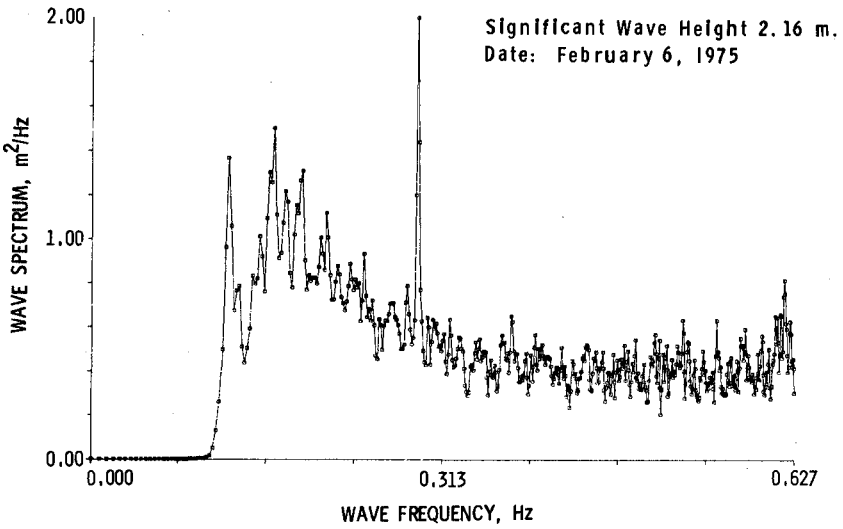


Figure 9 Wave Spectrum from File 5 of the Shipboard Radar Measurements

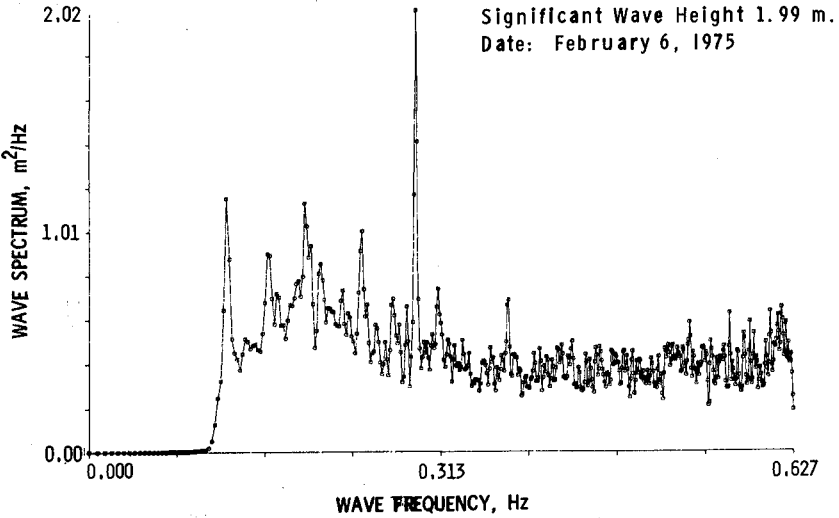


Figure 10 Wave Spectrum from File 6 of the Shipboard Radar Measurements

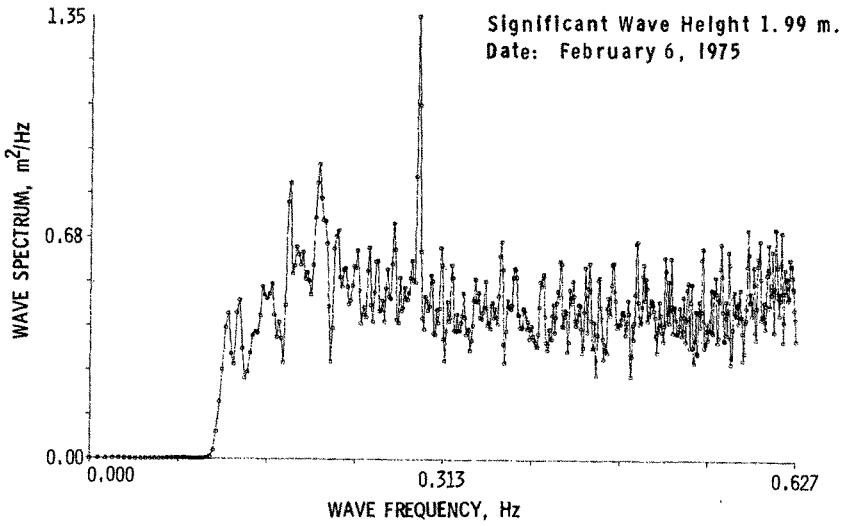


Figure 11 Wave Spectrum from File 7 of the Shipboard Radar Measurements

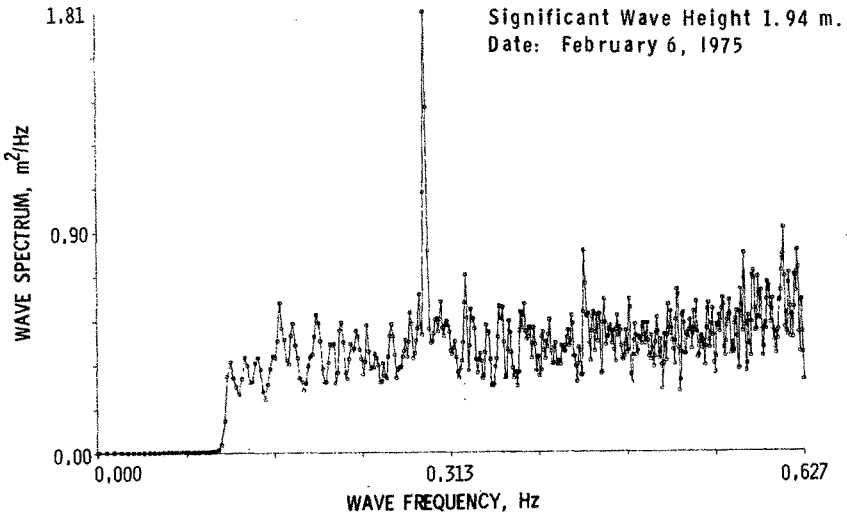


Figure 12 Wave Spectrum from File 8 of the Shipboard Radar Measurements

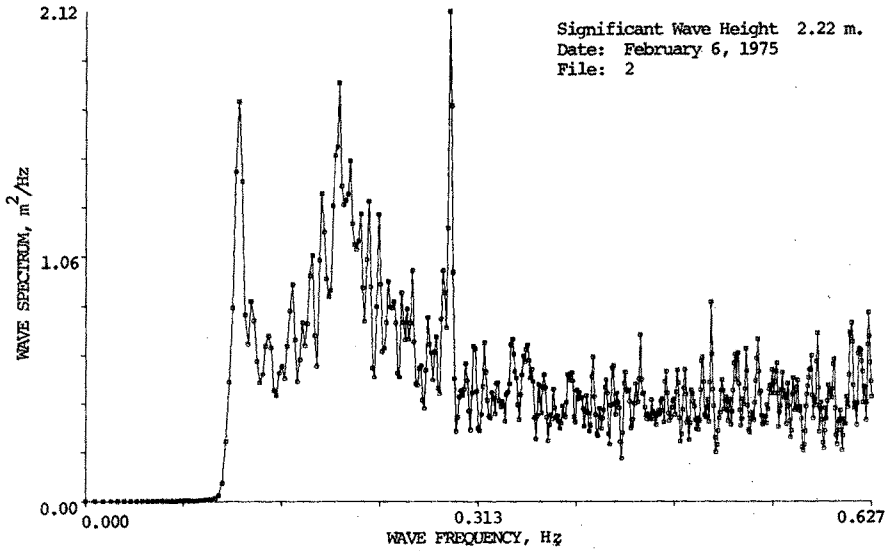


Figure 13a Shipboard Radar Measurements

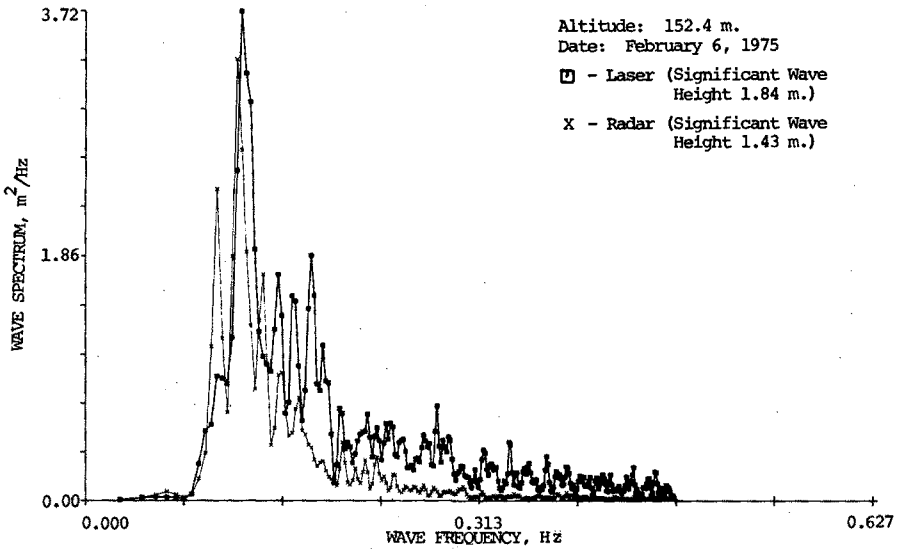


Figure 13b Airborne Measurements

yielded significant wave height of 2.01 meters. All airborne measurements were made in the vicinity of the ship during part of the time the shipboard radar was recording data for file 2. Accordingly Figure 13b, of the airborne measurements and Figure 6 of the shipboard measurements are combined in Figure 13 for comparison. The shapes are very similar. The significant wave heights of all the measurements are shown in Figure 14. The data are in reasonable agreement, especially when time coincidence of the data is not possible and the aircraft covers such large area about the ship.

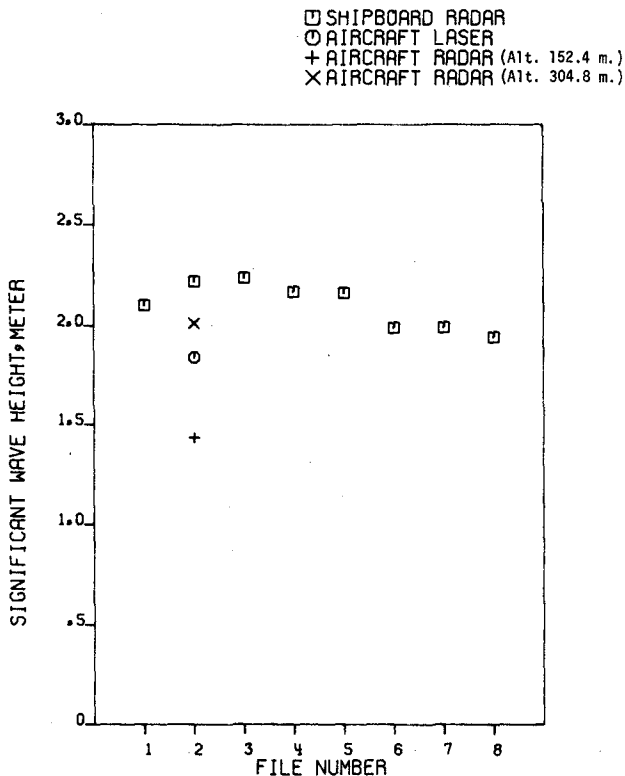


Figure 14 Significant Wave Height Measurements, Feb. 6, 1975

VII. DISCUSSIONS

In any system, one can always find areas for improvement, and this radar is no different. After conducting the analysis of the data, several points should be noted.

1. Future radars for this purpose should record the total range as well as the range modulation by the waves. The advantage is to enable one to make absolute corrections for the ship motions; otherwise, only relative corrections can approximately be made for ship motions, and still leave the DC offset as an unknown quantity.

2. A shipboard radar measurement of wave spectra permit viewing the undisturbed area of the sea. With better time and spatial resolution and by employing accelerometers on the antenna, the ship motion effects can be removed directly. Three accelerometers and three angular sensors at the site of the radar are recommended for future measurements.

3. Shipboard radars can operate in all types of weather, twenty-four hours a day.

ACKNOWLEDGMENTS

The authors of this paper wish to thank Kalen J. Craig for his indomitable spirit in developing the radar system and also the testing and evaluating it at sea. The assistance of James Kenney in preparing the equipment for use in the 1974-1975 season is greatly appreciated. Mr. Charles Buhler's skill in the assembly of the antenna package was an excellent example of assistance from the support services at NRL. Mr. E. A. Uliana's programming assistance made the data analysis possible. The cooperation from the personnel from the Teledyne Materials Research and the crew of the S.S. McLean made our task much easier. The authors also wish to make special thanks to Mr. J. T. McGoogan, of NASA Wallops Flight Center, for his encouragement of the study and for permitting NRL to use the C-54 aircraft for measuring the waves independently and simultaneously with the shipboard measurements.

The research reported herein was supported by Naval Sea Systems Command under Contract N00024-75-WR-51625 and U. S. Coast Guard under Contrast MIPR Z-70099-43693.

APPENDIX

The changing pitch of the sound from, say, a fire-engine siren as it moves by at high speed is familiar to all; this effect, the Doppler effect, is one of the most obvious influences of relative motion between the source and the medium. Similarly, if a wave train of ocean waves propagating at the surface of the ocean is observed by a radar in motion, a Doppler change of frequency also will result. The Doppler effect is purely a kinematic phenomenon and can be evaluated without resorting to dynamical equations of wave motion. By kinematic argument [12], it can be shown that

$$\sigma_T = \sigma_A + \frac{\sigma_T^2}{g} v \cos \xi \quad (10)$$

where

σ_T - true wave frequency, $2\pi/T$ or ck_T ;

k_T - true wave number, $2\pi/\lambda_T$;

λ_T - true wavelength;

σ_A - apparent wave frequency;

k_A - apparent wave number, $2\pi/\lambda_A = (\sigma_T^2/g) + (\sigma_T/v \cos \xi)$;

T - wave period;

λ_A - apparent wavelength;

ξ - angle between the ship's heading and the direction of the wave propagation;

v - speed of the ship;

c - phase speed of wave component;

g - gravitational acceleration.

By employing Equation (10) and Jacobian transformation from the apparent wave number domain to true wave frequency domain in Euclidian space yields

$$\phi(\sigma_T) = \frac{2\sigma_T}{g} \left(1 + \frac{1}{2} \frac{g}{\sigma_T v \cos \xi} \right) \psi_A(k_A) \quad (11)$$

where $\phi(\sigma_T)$ is the wave frequency spectrum and $\psi_A(k_A)$ is the apparent wave number spectrum.

Since data is already digitized, the equations are modified to take into account that the information is sampled at some rate and not continuous. Thus following changes are incorporated to perform the calculations:

by defining

M - total number of lags;

J - lag number;

Δx - distance between observations; $v \cos \xi \Delta t$;

Δt - time between observations, then

$$k_A(J) = \frac{J}{M \Delta x} = \frac{\sigma_T^2(J)}{g} + \frac{\sigma_T(J)}{v \cos \xi}$$

and also

$$\sigma_T(J) = - \frac{g}{2v \cos \xi} + \left[\frac{g^2}{4(v \cos \xi)^2} + \frac{g \pi J}{M \Delta x} \right]^{1/2}$$

from Equation (10).

REFERENCES

1. M. J. Tucker, "A Shipborne Wave Recorder," Transactions, Institute of Naval Architects, XCVIII, 236-250, London, 1956.
2. B. S. Yaplee, A. Shapiro, D. L. Hammond, B. D. Au, and E. A. Uliana, "Nanosecond Radar Observations of the Ocean Surface from a Stable Platform," Institute of Electrical and Electronics Engineers, GE-9(3), 170-174, 1971.
3. D. L. Hammond, E. A. Uliana, K. J. Craig, and B. S. Yaplee, "Ocean Wave Height Measurements with a Shipboard Radar System," Proposal submitted to U. S. Coast Guard (FSP-13/72), Naval Research Laboratory, 1971.
4. "Dual Trace Sampling Unit, Type 3S-1," Instruction Manual, Textronix, Inc.
5. "Oscilloscope, Type 568/R568," Instruction Manual, Textronix, Inc.
6. "Programable Sampling Sweep Type 3T5," Instruction Manual, Tektronix, Inc.
7. Spectra-Physics Geodolite 3A Laser Profilometer.
8. H. M. Linnette, "Statistical Filters for Smoothing and Filtering Equally Spaced Data," Defense Documentation Center, NEL Report 1049, 1961.
9. G. Neumann and W. J. Pierson, Jr., Principles of Physical Oceanography, Prentice-Hall, Inc., Englewood Cliff, N.J., 1966.
10. M. L. Skolnik, Introduction to Radar Systems, McGraw-Hill, Inc., 1962.
11. W. J. Pierson, Jr., and L. Moskowitz, "A Proposed Spectral Form for Fully Developed Wind Seas Based on the Similarity Theory of S. A. Kitaigorodskii," J. Geophysical Research, 69 (24), 5181-5190, 1964.
12. O. M. Phillips, The Dynamics of the Upper Ocean, Cambridge University Press, 1966.

CHAPTER 7

GREAT LAKES WAVE INFORMATION

By

D. T. Resio¹ and L. W. Hiipakka²

I. Introduction.

The lack of reliable Great Lakes wave information has long been a problem for the Corps of Engineers and others involved in planning and design along Great Lakes coasts. In recent years this need has been accentuated by increased water levels and increased demand for coastal land use. The Corps need for wave information became critical with the passage of the River and Harbor Act of 1970 (Public Law 91-611) Section 123 of this legislation authorized design and construction of contained spoil disposal facilities having a ten-year capacity to hold polluted dredged material.

The North Central Division of the Corps of Engineers (NCD) is responsible for dredging 117 navigation projects and connecting channels in the Great Lakes. Of these, 59 are considered polluted, necessitating construction of 41 diked disposal sites at an estimated cost of over \$300,000,000. With a program of this magnitude, it was apparent that unnecessary conservatism in design had to be minimized through development of the best wave information base that the state-of-the-art could provide.

A project was initiated at the Corps of Engineers Waterways Experiment Station (WES) under the sponsorship of NCD to supply design wave information. After a review of all possible sources of available wave information and the potential for obtaining additional gage data, it was determined that a wave hindcast program might best meet the immediate needs of NCD. The actual study has been divided into four phases:

- a. The estimation of over-lake winds,
- b. The establishment of a wave hindcast technique,
- c. The analysis of waves from model outputs, and
- d. The evaluation of errors in Phases a, b, and c.

11. Winds Over A Lake.

Cole (1967) evaluated three methods for estimating winds over Lake Michigan. He compared estimates from these three methods to winds observed at a tower located about a mile offshore from Muskegon, Michigan. Table 1 gives the results of these comparisons to the three techniques in terms of correlation coefficients. The method based on the reduction of geostrophic wind speeds to surface wind speeds produced the highest

¹Research Physical Scientist, USAE Waterways Experiment Station, Vicksburg, Miss.

²Chief, Coastal Engineering and Hydraulic Design Branch, U. S. Army Engineering Division, North Central.

TABLE 1
WIND SPEED COMPARISONS BY COLE (1967)

TYPE OF COMPARISON	NUMBER OF DATA PAIRS	CORRELATION COEFFICIENT
BRETSCHNEIDER WINDS VS 10-M WINDS	36	0.63
JACOBS' 7.5-M WINDS VS 7.5-M WINDS	43	0.55
JACOBS' 19.5-M WINDS VS 16-M WINDS	49	0.37
RICHARDS' WINDS VS 16-M WINDS	44	0.36
RICHARDS' WINDS VS 10-M WINDS	36	0.24

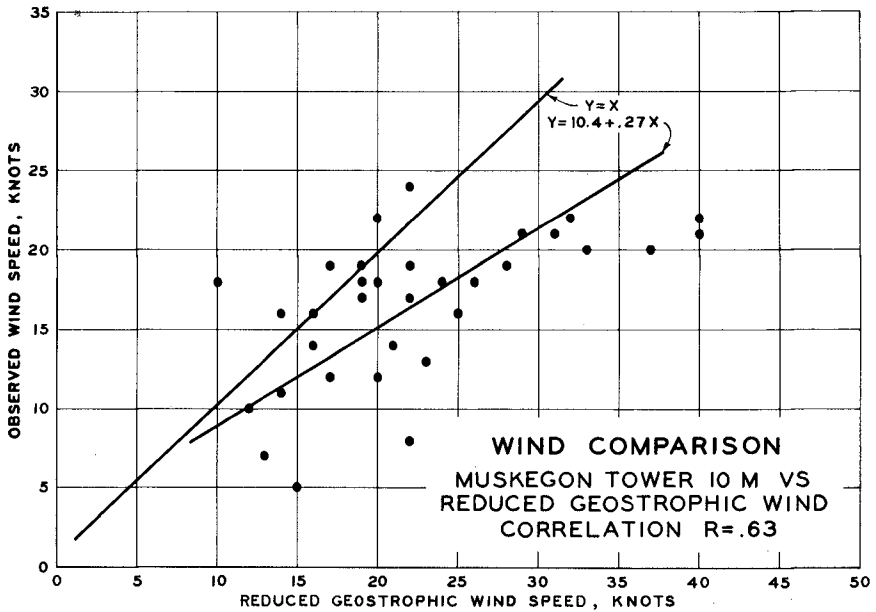


Figure 1 Comparison of wind speeds from Muskegon tower to wind speeds estimated by reduced geostrophic wind speed

correlation coefficient, 0.63. Methods based on the reduction of gradient winds to surface winds (Jacobs, 1965) and on the transformation of over-land wind speeds to over-water wind speeds produced substantially lower correlation coefficients. However, as shown in Figure 1, although the correlation coefficient is high for the geostrophic method there is a pronounced bias toward overestimation of wind speeds, particularly at high velocities. A detailed study of the relationship between geostrophic wind speeds and anemometer-level wind speeds over large lakes (Resio and Vincent, 1976) indicated that this bias is due to the lack of velocity-dependence in the constant used to reduce geostrophic velocities to surface velocities in this method.

During this study two methods were found to produce unbiased estimates of wind speeds over the Great Lakes--a method based on the transformation of geostrophic winds to surface winds using numerical techniques similar to those of Cardone (1969) and a method based on the transformation of wind speeds measured at land sites to over-water wind speeds. The latter of these methods was chosen for application to hindcasting due to its simplicity and the lack of long-term meteorological records at a time and space scale suitable for obtaining accurate geostrophic level winds.

The derivation of the transformation coefficients is discussed in detail in an earlier paper (Resio and Vincent, 1976a). In this paper, the wind speed over water was related to the wind speed over land by

$$U_w = U_L \psi \phi_n \bar{F} \quad (1)$$

where U_w is the over-water wind speed, U_L is the over-land wind speed, and ψ , ϕ_n , and \bar{F} are dimensionless conversion factors accounting for the effects of the velocity-dependence of lake surface roughness, air-sea temperature difference and over-water fetch, respectively. Figures 2 and 3 give the determined forms of ψ and ϕ_n along with corroboratory evidence from other studies for Lake Erie and Lake Ontario. The fetch factor was found to be approximated by

$$\bar{F} = \begin{array}{ll} 0.411 F^{0.297} & \text{for } F < 20 \text{ miles} \\ 1.0 & \text{for } F > 20 \text{ miles} \end{array} \quad (2)$$

where F is the over-water fetch in miles. Whereas the relationships for ψ and ϕ_n were based on more than 52,000 ships observations, the relationship for \bar{F} is based on a limited number of observations tabulated by Richards et al. (1966) and should probably be regarded only as a first estimate.

Using Equation 1 to estimate winds over Lake Erie and Lake Ontario the rms error was found to be a function of velocity (Figure 4). As seen here, the error for wind speeds of importance to design and planning is beneath 5 knots.

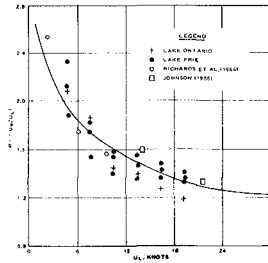


Figure 2. Variation in Ψ with observed land velocity

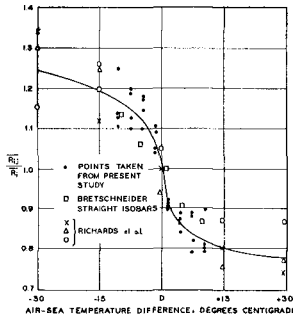


Figure 3. Variation in Φ_n with air-sea temperature difference

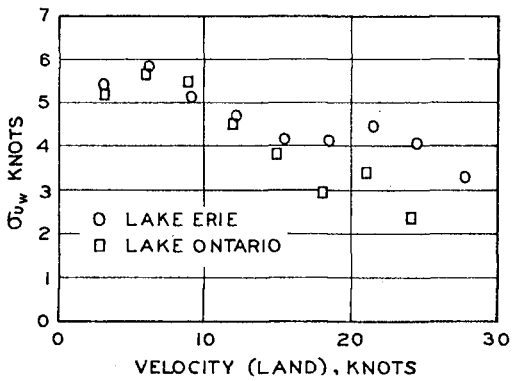


Figure 4. RMS error in wind speed estimate as a function of observed land wind speed

It can be shown (Resio, 1976) that the bias introduced by a random error in wind velocity is represented by

$$\frac{\hat{H}}{H} = \frac{(U^2 + \sigma_e^2)}{U^2} \quad (3)$$

where \hat{H} is the estimated mean wave height for conditions with wind speed U , H is the actual mean wave height for conditions with wind speed U and σ_e^2 is the variance of wind estimates around U . Figure 5 shows the value for \hat{H}/H as a function of wind speed for an rms error of 5 knots. For wind speeds above 25 knots over the water, there is less than 5 percent bias due to the random error in wind estimates.

Further evidence that the wind transformation is reliable even during high wind conditions can be seen in Figures 6a, 6b, and 6c. These figures show comparisons of winds estimated from data obtained at Cleveland and Toledo airports during storms on Lake Erie and simultaneous observations of winds by ships in the lake.

III. The Wave Model.

Three hindcast techniques were evaluated for application to the Great Lakes. These are as follows:

- a. The significant wave method contained in the Shore Protection Manual.
- b. A numerical model of the growth and decay of wave spectra as formulated by Inoue (1966, 1967), Cardone (1969), and Pierson et al. (1966).
- c. A numerical model of the growth and decay of wave spectra as formulated by Barnett (1966).

The first technique has been evaluated in previous studies by Cole (1967) and Brebner and Kennedy (1962) on Lake Michigan and Lake Ontario, respectively. Figure 7 shows the results of their comparisons along with some additional comparisons performed during this study for waves in Lake Ontario and Lake Erie. This figure indicates a pronounced tendency to over estimate wave heights in high wind conditions. Regression coefficients suggest that there is about a 35 percent bias in this method. However, since the winds used for hindcasting in this method appear to be too high (Figure 1), the bias might be more a function of errors in wind speed rather than a discrepancy in the wave hindcast curves. The standard deviation of the scatter about the regression line was 2.5 ft.

As indicated in the previous discussion, the lack of precise measure of wind speed over a fetch complicates the comparison of hindcast wave heights to observed wave heights. Therefore, instead of basing a decision regarding the optimal model for hindcasting in restricted fetches on such comparisons, the results of field efforts (Hasselmann et al., 1973;

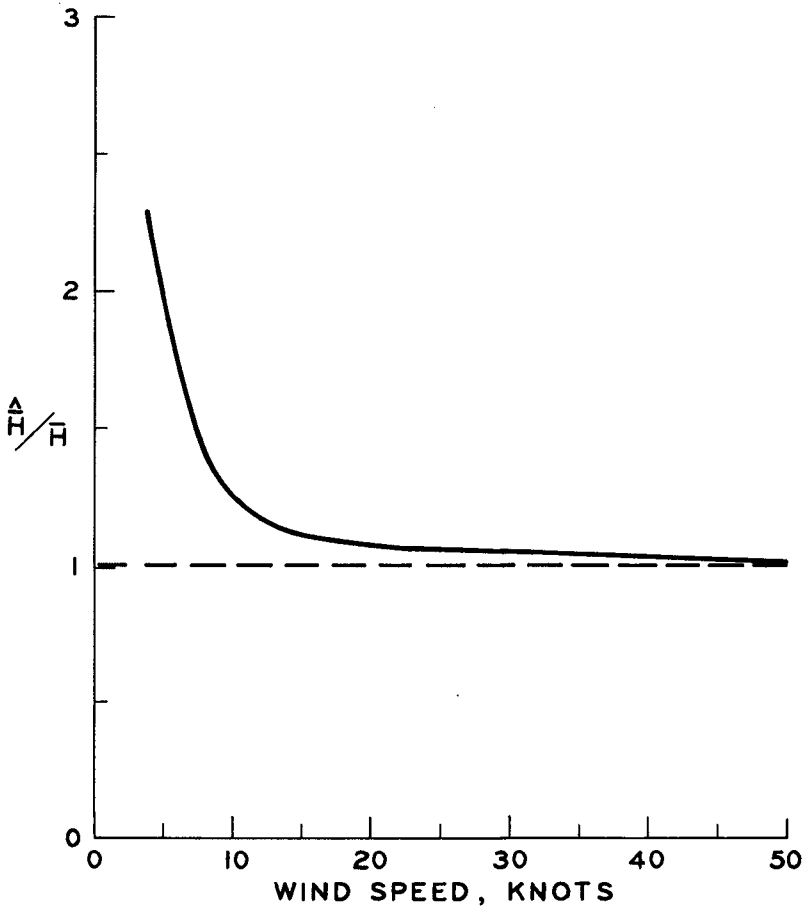
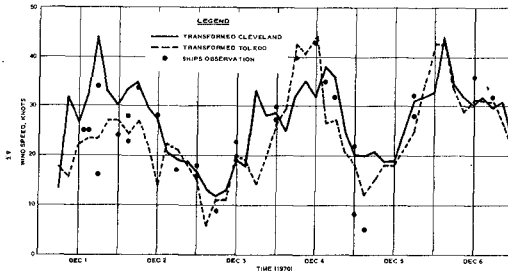
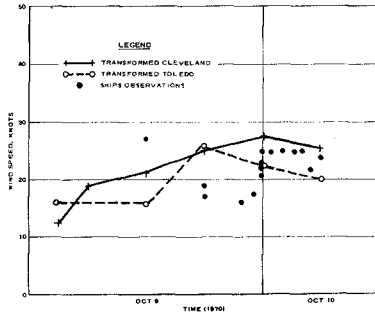


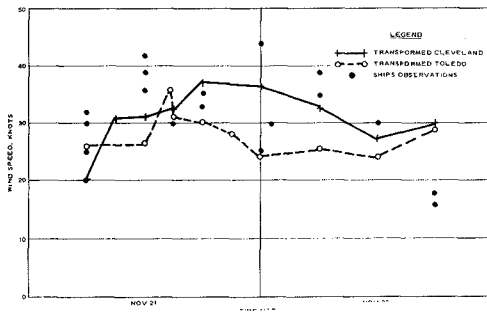
Figure 5. Estimate of bias due to random wind error



a.



b.



c.

Figure 6. Comparison of wind speeds by ships to wind speeds estimated by equation (1)

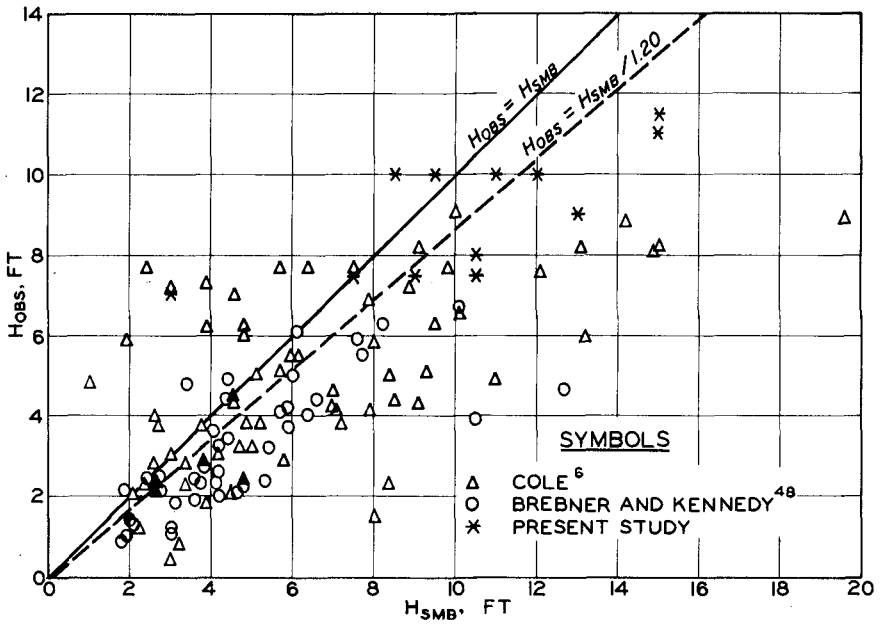


Figure 7. Composite chart showing results of comparison of observed wave heights and wave heights hindcast by SMB methods on the Great Lakes

Mitsuyasu, 1968), which formulated functional relationships between non-dimensional fetch and wave height parameters were used for comparisons. These studies have supported Kitaigorodskii's (1962) similarity theory for the development of wave spectra along a fetch. Figure 8 shows a plot of non-dimensional wave height, defined as

$$\tilde{H} = \frac{g\sqrt{E}}{U_*^2} \quad (4)$$

where U_* is the friction velocity of the wind, E is the total energy in the wave spectrum, and g is the acceleration due to gravity, versus nondimensional fetch defined as

$$\tilde{F} = \frac{gF}{U_*^2} \quad (5)$$

where F is the fetch measured in the same units as g and U_* . This figure indicates that none of the available models produce results in accord with recent observational evidence for limited fetches.

Of the three models, the Barnett model came closest to reproducing the desired relationship between non-dimensional fetch and non-dimensional wave height. Consequently, this model was chosen for modification in an effort to achieve a better fit between predicted and expected values. A review of the field studies by Mitsuyasu (1968) and Hasselmann *et al.* (1973) indicated that a major factor not considered in the Barnett model was the variation in the Phillips equilibrium constant with non-dimensional fetch. This constant was originally proposed by Phillips (1958) as a "universal constant" in the relationship between wave frequency and energy density in that portion of the surface waves dominated by wave breaking. On dimensional grounds, he hypothesized that such a relationship should be of the form

$$S(f) = Bg^2 f^{-5} \quad (6)$$

where S is the energy density of waves with frequency f and B is a constant. Later work by Mitsuyasu (1966, 1968), Hasselmann *et al.* (1973), and DeLeonibus *et al.* (1974) have demonstrated that although the f^{-5} proportionality is almost always preserved in the equilibrium range, B varies systematically with non-dimensional fetch and non-dimensional wave height. Figure 9 shows that this variation can be quite important in the Great Lakes regions where non-dimensional fetches can range over several orders of magnitude. Consequently, an implicit formulation of B was programmed into the wave model to compensate for this effect. Figure 10 indicates that this brings the theoretical growth rates into much better agreement with observation.

In several tests of the modified Barnett model against deepwater gage observations in the Great Lakes, the model performed well. Figure 11

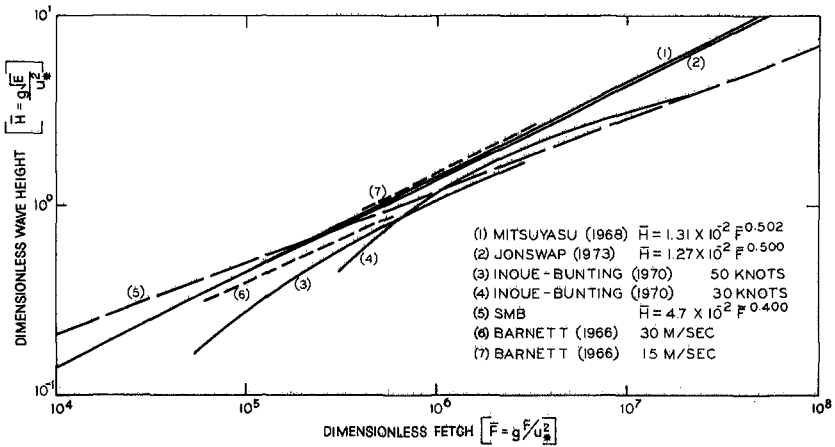


Figure 8. Comparison of wave height growths with fetch from various sources and field results of Mitsuyasu (1968) and Hasselmann et al. (1973)

*SMB too large
short fetch
too small large
fetch*

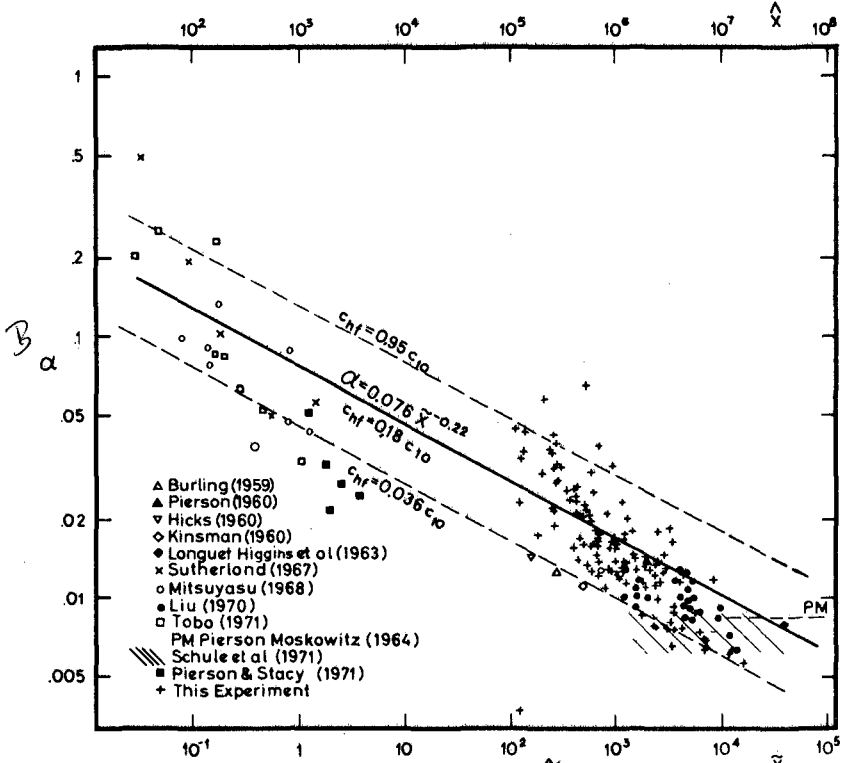


Figure 9. Variation in Phillips constant α with nondimensional fetch \bar{X}

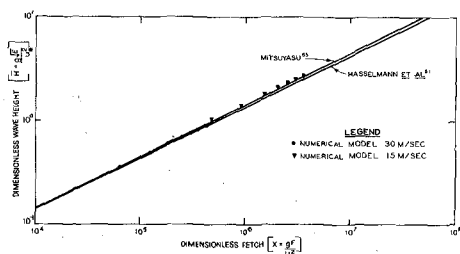


Figure 10. Comparison of rate of change of nondimensional wave height with nondimensional fetch with rates of change observed by Mitsuyasu (1968) and Hasselmann et al. (1973)

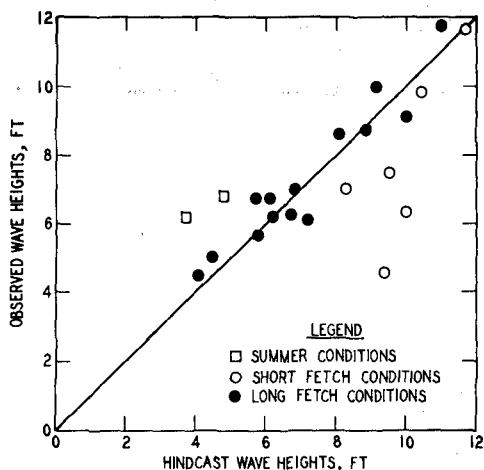


Figure 11. Comparison of maximum significant wave heights for individual storms as recorded by gages (Point Pelee, Lake Erie; and Toronto, Cobourg, and Main Duck, Lake Ontario), and significant wave heights hindcast by the numerical model using Barnett's parameterizations

is a compilation of the comparisons between observed peak significant wave heights and hindcast peak significant wave heights for storms on Lake Erie and Lake Ontario. The input to this model was taken from land winds transformed as described in the previous section. There was only a small positive bias in this sample (4 percent), and the standard deviation of hindcasts around the best fit regression line was about 1.5 ft.

It should be noted that the wave heights calculated in the model are considered to be deepwater wave heights and must be transformed by refraction, shoaling, diffraction and bottom friction before a nearshore wave estimate can be made.

IV. Analyses Of Model Outputs.

Lake Erie, Lake Ontario, and Lake Michigan have now been completed under the present program at WES. Between 200-500 storms, covering a period of 69 years, have been hindcast for each lake. For each storm hindcast, a time series of two-dimensional spectra at 1-hour intervals was retained on magnetic tape for grid points located at about 10-mile intervals along the shoreline. These data permit an extensive set of analyses into the organization of the wave climate on these lakes. A typical set of data analyses is presented here for Cleveland, Ohio, which is on Lake Erie.

a. Analysis of extreme significant wave heights by season and direction of approach:

Since many harbors and design sites in the Great Lakes are protected by ice during the winter, the analysis of extremes was stratified into seasons defined as January-March (winter), April-June (spring), July-September (summer), and October-December (fall). Similarly, since the design of structures requires information on approach direction, the analysis separated the wave heights into direction classes as shown in Figure 12.

The largest significant wave height within each season-direction category was determined for each storm. It is assumed that the maximum significant wave height in one storm is uncorrelated with a maximum significant wave height in another storm. A preliminary study of the return periods of these wave heights indicated that they were adequately described by a Fisher-Tippett Type I distribution; and hence, the logarithm of the return period could be expected to be a linear function of wave height

$$\ln T \sim a + bH \quad (7)$$

where T is the return period of the significant wave height H and a and b are two constants. Figure 13 shows that this is a reasonable assumption for deepwater wave heights in the Cleveland area. In this figure, the return periods were estimated by the USGS method (Dalrymple, 1960)

$$T = \frac{m+1}{n} \quad (8)$$

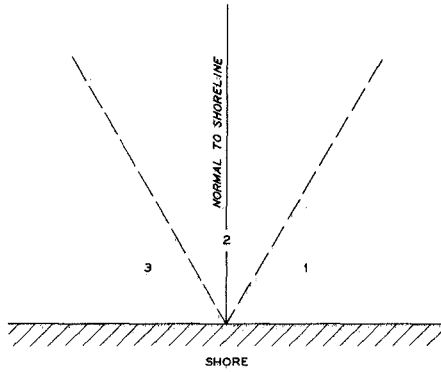


Figure 12. Definition of shoreline angles used in study

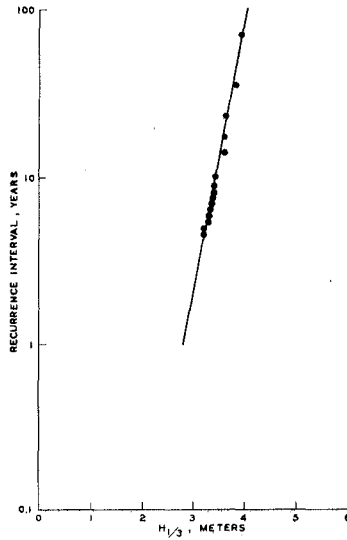


Figure 13. Linear variation of log T with wave height

where m is the total number of years in the sample and n is the rank of the magnitude (i.e., for the largest wave height $n=1$, for the second largest $n=2$, etc.).

Table 2 gives the return periods for deepwater significant wave heights in the Cleveland area for the four seasons and three angle classes previously defined. The return periods for all directions combined within each season are also given in this table along with the confidence bands for each of these estimates calculated from the relationship (Gringorten, 1961)

$$S_x = S\sqrt{\frac{1.1000y^2 + 1.1396y + 1}{N}} \quad (9)$$

where S is the standard deviation of the annual maxima of significant wave heights, S_x is the confidence band estimate (one standard deviation wide) and y is the reduced variate in the Fisher Tippett Type I distribution.

b. Recurrence intervals for wave heights within an arbitrary time interval during a year.*

Although the stratification by seasons is adequate for some purposes, many planning and design criteria at sites around the Great Lakes require other intervals during the year for consideration. To obtain estimates of recurrence within arbitrary time intervals, all extremes were first categorized by 5-day increments within the year. Thirty-day overlapping periods were used to filter some of the irregularities from the distributions, and then the largest 10 significant wave heights in each time interval and direction class were plotted against recurrence intervals using the USGS method. Least squared error regression lines were calculated for each of these sets of data. Table 3 gives a matrix with the recurrence intervals for each 5-day period within the year calculated in this manner. The recurrence interval, T_k , for k 5-day periods can be calculated from the relationship

$$T_k = \frac{1}{1 - \prod_{i=1}^k (1 - 1/T_i)} \quad (10)$$

where T_i is the recurrence interval for a five-day period. As an example of the application of this table, the mean recurrence interval for a 10-ft wave in the angle class 2 in the month of July is 122 years.

*The only constraint on this is that the time interval must be some multiple of 5 days.

TABLE 2

TABLE OF EXTREMES ESTIMATES		PULTNEYVILLE NY		
GRID LOCATION	8,15	LAT=43,37	LN=77,25	
SHORELINE GRID POINT 10				
WINTER				
ANGLE CLASSES				
	1	2	3	ALL
5	6,9(1,3)	10,8(1,6)	13,8(0,6)	13,8(0,6)
10	9,2(1,7)	12,5(2,1)	14,4(0,7)	15,0(0,8)
20	9,8(2,1)	14,4(2,6)	15,1(0,9)	16,2(1,0)
50	10,8(2,6)	17,4(3,2)	16,1(1,1)	18,0(3,4)
100	12,5(3,0)	18,7(3,7)	17,4(1,3)	19,5(3,9)
SPRING				
ANGLE CLASSES				
	1	2	3	ALL
5	4,6(1,2)	5,6(1,3)	8,2(0,7)	8,2(0,7)
10	5,6(1,5)	7,5(1,7)	8,9(1,0)	9,4(1,0)
20	7,2(1,9)	8,5(2,1)	9,8(1,2)	10,6(1,3)
50	8,2(2,4)	9,5(2,7)	12,1(1,5)	12,2(1,5)
100	8,9(2,7)	10,8(3,1)	13,1(1,7)	13,5(1,8)
SUMMER				
ANGLE CLASSES				
	1	2	3	ALL
5	4,3(1,7)	4,6(1,2)	7,5(0,4)	7,9(0,5)
10	5,6(2,3)	5,6(1,5)	8,2(0,6)	8,7(0,6)
20	8,2(2,8)	7,2(1,9)	8,5(0,7)	9,6(0,8)
50	9,8(3,5)	8,2(2,4)	9,2(0,9)	11,1(4,0)
100	12,5(4,1)	8,9(2,7)	9,8(1,0)	12,7(4,1)
FALL				
ANGLE CLASSES				
	1	2	3	ALL
5	5,6(0,9)	12,1(0,9)	13,1(0,4)	13,2(0,4)
10	6,6(1,1)	13,1(1,1)	13,8(0,6)	14,2(0,6)
20	7,5(1,4)	14,1(1,4)	14,1(0,7)	15,2(1,5)
50	8,2(1,8)	17,1(1,8)	15,4(0,9)	16,9(1,7)
100	8,5(2,0)	18,0(2,0)	15,7(1,0)	18,3(2,1)

c. Significant period as a function of significant wave height and approach direction.

Two factors--significant wave height and over-water fetch--were found to explain the majority of the variations in significant periods. At each site, the over-water fetch is related directly to an angle of wave approach; consequently, mean significant period is well represented as a function of significant wave height within each previously defined angle class (Figure 14).

d. The expected duration of significant wave heights.

The amount of water transported over a dike during a storm is related not only to the peak significant wave height but also to the durations of significant wave heights above particular levels. A simple measure of this latter parameter is taken to be the mean duration of wave heights above any level H for all storms in which that wave height or higher occurs. Figure 15 shows the results of this calculation for the Cleveland data for the months of October through December.

e. Probabilities of higher order wave heights.

Estimates of the average wave heights for the highest 10 percent ($H_{1/10}$) or highest 5 percent of the waves in a spectrum are related directly to estimates of $H_{1/3}$ by a simple constant of proportionality. Consequently, recurrence intervals for these wave heights can be obtained by a transposition of the line for the recurrence intervals for $H_{1/3}$ (Figure 16). However, the statistics for the largest single wave in a spectrum also involve the duration of wave heights. As shown by Longuet-Higgins and Cartwright (1956), the probability of a particular wave height occurring is directly related to the wave height, the rms deviations of the surface elevation, and the duration of the sample. Since many storms have been hindcast in this study, there is no need to assume an average duration, but rather the probabilities can be calculated from the time histories.

V. Discussions and Conclusions.

An important question regarding the usefulness of hindcast wave data is the accuracy of the wave height distributions produced by the hindcasts. The answer to this question must be determined on an individual basis for each different type of probability estimate based on the hindcast data set. For example, as shown in Figure 5, the bias created by an error in wind estimates can create a significant bias at low wave heights. The importance of the type of relative bias demonstrated in Figure 5 is dependent on the magnitude of the bias created in the wave height estimates. Consequently, the extreme bias at winds under 10 knots is not significant in most cases, since the estimated wave heights for these winds are still less than a ft. On the other hand, if more accuracy is needed in this very low wave height range, an analysis similar to Figure 5 could provide a simple means of filtering the distribution of hindcast wave heights to obtain a better estimate of actual wave conditions.

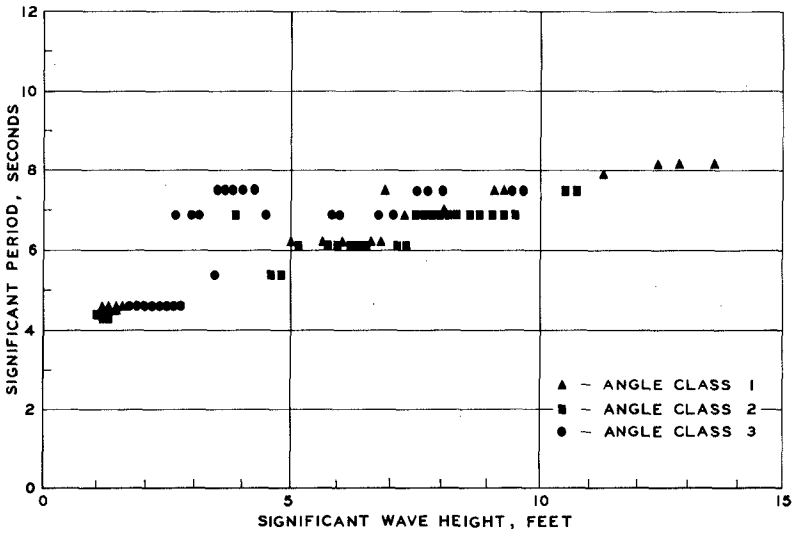


Figure 14. Significant wave period as a function of angle class and wave height

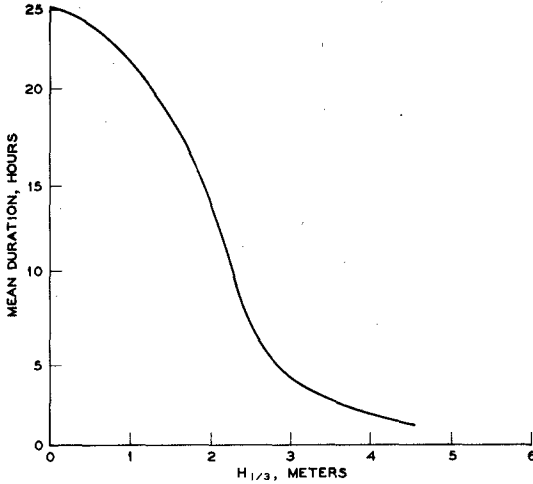


Figure 15. Mean duration of wave heights equal to or above H as a function of H

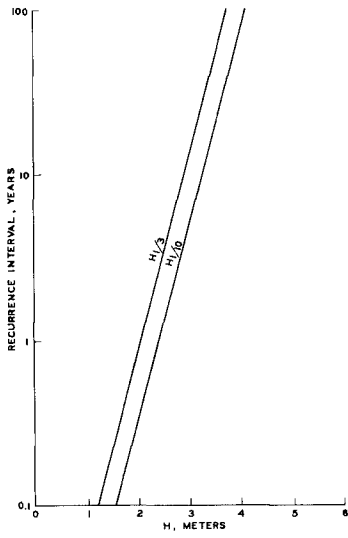


Figure 16. Linear shift in log T between $H_{1/3}$ and $H_{1/10}$

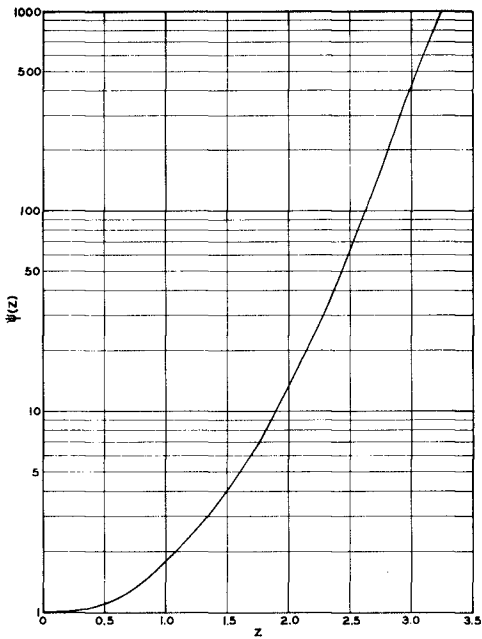


Figure 17. Relationship between $\Psi(Z)$ and Z

At the other end of the distribution, the extremes, the results shown in Figure 5 indicate very little bias; however, as shown in Resio and Vincent (1976b), an additional source of error encountered in this range comes from the effects of the convolution of the extremal distribution and a Gaussian error distribution. This bias can be considered in terms of the ratio of mean recurrence interval estimated from the extremal distribution with the error term \hat{T} , to the mean recurrence interval for the extremal distribution alone, T . In Resio and Vincent (1976b) this was shown for a Fisher-Tippet Type 1 distribution to be given by

$$\frac{\hat{T}}{T} = \frac{1 - F(H)}{1 - F(H)\psi(z)} \quad (10)$$

where the form of $\psi(z)$ is shown in Figure 17 with z defined as

$$z = \frac{\sigma}{B} ,$$

where σ is the rms error in the wave estimates and B is a coefficient of variation in the extremal distribution.

The importance of the above relationships is that it indicates that the possible bias can be quantified. For design wave calculations on Lake Ontario, this bias was shown (Resio and Vincent, 1976b) to be less than 10 percent. Additionally, the implication is that the confidence bands are not seriously affected by the random errors in individual hindcasts for these data. Thus, Equation 9 still provides a good estimate of the confidence bands when using hindcast wave heights, and the width of the confidence band still decreases as the square root of the record length.

This paper has demonstrated the utility of a numerical hindcast model in providing a set of data which can subsequently be analyzed to obtain a wide range of information on the organization of the wave climate at a site. Although there are errors in specific hindcasts, these errors do not appear to create significant bias in many of these statistical estimates. Furthermore, the ability to obtain a long-term, synthetic record of two-dimensional spectra permit an extensive analysis into even complex phenomena with higher confidence than could be obtained from an exact record obtained from exact measurements over a shorter period of time.

REFERENCES

1. Barnett, T. P., 1966, "On the Generation, Dissipation and Prediction of Ocean Wind Waves," Ph. D. Thesis, Univ. of California, San Diego, pp. 194.
2. Brebner, A. and R. J. Kennedy, 1962, "Correlation of Waves and Shore Winds, Lake Ontario," Pub. No. 9, Inst. of Sci. and Tech., Univ. of Michigan, pp. 116-122.
3. Cardone, V. J., 1969, "Specification of the Wind Distribution in the Marine Boundary Layer for Wave Forecasting," Tech. Rep. 69-1, Geophysical Sciences Lab., NYU, p. 137.
4. Cole, A. L., 1967, "An Evaluation of Wind Analysis and Wave Hind-casting Methods as Applied to the Great Lakes," Proc. Tenth Conference on Great Lakes Research, pp. 186-196.
5. Dalrymple, T., 1960, "Flood Frequency Analyses," Manual of Hydrology: Part 3 - Flood Flow Techniques, Water Supply Paper 1543, Chapter A, pp. 1-79.
6. DeLeonibus, P. S., Simpson, L. S. and M. G. Mattie, 1974, "Equilibrium Range in Wave Spectra Observed at an Open-Ocean Tower," JFR, V. 79, No. 21, pp. 3041-3053.
7. Gringorten, I. I., 1963, "Extreme-Value Statistics in Meteorology--A Method of Application," Air Force Surveys in Geophysics No. 125, Air Force Cambridge Research Center, Bedford, Mass., 71 p.
8. Hasselmann, K. et al., 1973, "Measurements of Wind-Wave Growth and Swell Decay During the Joint North Sea Wave Project (JONSWAP)," Deutsches Hydrographisches Institut, Hamburg, Germany.
9. Inoue, T., 1967, "On the Growth of the Spectrum of a Wind-Generated Sea According to a Modified Miles-Phillips Mechanism and Its Application to Wave Forecasting," Tech. Rep. 67-5, Geophysical Sciences Lab., NYU.
10. Jacobs, S. J., 1965, "Wave Hindcasts vs. Recorded Waves," Final Report 06768, University of Michigan.
11. Kitaigorodskii, S. A., 1970, "The Physics of Air-Sea Interaction, Israel Program for Scientific Translations, Ltd. (available from NTIS, U. S. Dept. of Commerce, Springfield, VA).
12. Cartwright, D. E. and M. S. Longuet-Higgins, 1956, "The Statistical Distribution of the Maxima of a Random Function," Proc. Roy. Soc. V. A. 237, pp. 212-232.
13. Mitsuyasu, H., 1966, "Interactions between Water Waves and Wind (I)," Rep. of Res. Inst. for Appl. Mech., Kyushu Univ., Fukuoka, Japan, V. 14, No. 48, pp. 67-89.

14. Mitsuyasu, H., 1968, "On the Growth of the Spectrum of Wind Generated Waves (1)," Rep. of Res. Inst. for Appl. Mech., Kynshu Univ., Fukuoka, Japan, V. 16, No. 55, pp. 459-482.
15. Phillips, O. M., 1958, "The Equilibrium Range in the Spectrum of Wind Generated Waves," J. Fluid Mech., V. 4, pp. 426-434.
16. Pierson, W. J., L. J. Tick, and L. Baer, "Computer Based Procedures for Preparing Global Wave Forecasts and Wind-field Analyses Capable of Using Wave Data Obtained by Spacecraft," Proc. of the Sixth Naval Hydrodynamics Conference.
17. Resio, D. T., 1976, "Extreme Wave Heights for Cleveland Harbor," Proc. ASCE Specialty Conference, June 9-13, Newark, Delaware.
18. Resio, D. T. and C. L. Vincent, 1976, "The Estimation of Winds over the Great Lakes," Misc. Paper H-76-12, U. S. Army Waterways Experiment Station, Vicksburg, MS 72 pp.
19. Resio, D. T. and C. L. Vincent, 1976b, "Design Wave Information for the Great Lakes: Lake Ontario," Tech Rep. H-76-1, U. S. Army Engineer Waterways Experiment Station, Vicksburg, MS, 148 pp.

CHAPTER 8

APPLICATIONS OF EMPIRICAL FETCH-LIMITED SPECTRAL FORMULAS TO GREAT LAKES WAVES¹

Paul C. Liu, M. ASCE²

ABSTRACT

Two episodes of Great Lakes waves for which both wind and wave data are simultaneously available are used to examine the applicability of the empirical fetch-limited spectral wave formulas developed by JONSWAP, Mitsuyasu, Liu, and Sverdrup-Munk-Bretschneider. Comparing the results hindcast from the formulas with those recorded shows that, for hindcasting significant wave heights, Liu's formula gives better results for less than fully developed waves, while formulas by JONSWAP, Mitsuyasu, and Sverdrup-Munk-Bretschneider give better results for fully developed waves. In hindcasting average wave periods and peak-energy frequencies, all the formulas result in a deviation of up to 2 s and 0.5 rad s⁻¹, respectively. These results can be used as a reference in evaluating and interpreting wave predictions made by these formulas as applied to the Great Lakes.

1. INTRODUCTION

Various surface wave studies in recent years have results in the development of several sets of empirical fetch-limited spectral formulas of practical interest in wave predictions. These formulas are all characterized by the dimensionless fetch parameter $X_0 = gX/U_*^2$, where g is the acceleration of gravity, X the fetch distance, and U_* the frictional wind velocity. In terms of X_0 , the significant wave height $H_{1/3}$, peak-energy radian frequency ω_p , and spectral energy density $S(\omega)$ as a function of frequency ω can be expressed by

$$H_{1/3} = A \frac{U_*^2}{g} X_0^a \quad (1)$$

$$\omega_p = B \frac{g}{U_*} X_0^{-b} \quad (2)$$

$$S(\omega) = C g^2 \omega^{-5} X_0^{-c} \exp[-DX_0^{-d} (\frac{U_* \omega}{g})^{-4}] F \quad (3)$$

in which A , B , C , and D = the empirical coefficients; a , b , c , and d = the empirical exponentials; and F = an empirical spectral shape function. Several authors have developed various sets of numbers for these empirical constants. Table 1 represents a summary of the results obtained from these studies. Data

¹GLERL Contribution No. 93.

²Physical Scientist, Great Lakes Environmental Research Laboratory, National Oceanic and Atmospheric Administration, Ann Arbor, Michigan 48104.

TABLE 1.--Empirical Constants Used by Various Authors in Eqs. (1), (2), and (3)

Author	A x 10 ²	B	C	D	a	b	c	d	F
Garratt (1973)	1.264	4.10			0.600	0.300			
Hasselmann et al. (JONSWAP, 1973)	5.060	6.80	0.348	2,665	0.500	0.330	0.220	1.320	$\gamma \frac{\exp \frac{-(\omega-\omega_p)^2}{2\sigma^2\omega_p^2}}{2\sigma^2\omega_p^2}$ *
Kononkova et al. (1970)		14.80				0.360			
Liu (1971)	1.740	8.57	0.400	5,500	0.542	0.333	0.250	1.333	I
Mitsuyasu (1971)	4.520	6.28	1.337	1,948	0.504	0.330	0.312	1.320	I

* γ = ratio of maximum spectral energy to maximum of fully developed Pierson-Moskowitz spectrum ~ 3.3 .

σ = spectral width factor, $\sigma = 0.07$, $\omega < \omega_p$; $\sigma = 0.09$, $\omega > \omega_p$.

collected from many oceans and lakes, as well as laboratory wave tanks, were used. Table 1 reveals that some of the constants derived by these authors are quite close; some of the constants, however, differ significantly. It is of interest to note that, although the authors used their own wave measurements in developing their empirical formulas, they all made an effort to incorporate the results of well-known wave studies published during the past 20 years. Obviously, some of the differences in the coefficients can be attributed to the authors' subjectivity in adjusting the regression line to fit their own data. Because of these differences and because of the simple nature of the formulas, case studies have been made to examine the applicability of the formulas by using available wave data from the Great Lakes. This paper presents two episodes of wave conditions for which recorded data are compared with those hindcast by the formulas of JONSWAP, Mitsuyasu, and Liu. In addition, conventional hindcasts from the Sverdrup-Munk-Bretschneider formulas (Shore Protection Manual, Vol I, 1973) are also included for further comparisons.

2. CHARACTERISTICS OF THE FORMULAS

Before proceeding to the case studies, it is of interest to examine some of the basic characteristics of the formulas that use hypothetical wind conditions. Because frictional wind velocity was not available for this study, logarithmic wind profile and a drag coefficient, C_{10} of 10^{-3} have been used in this paper for converting wind speed at different levels to U_* . Fig. 1 presents a set of examples of wave spectra calculated by empirical formulas (3) for 10-m level wind speeds of 5 and 40 m s^{-1} and fetch distances of 10 and 100 km. As the four cases shown in the figure combine long and short fetches with high and low wind speeds, respectively, the magnitude of spectral energy and peak-energy frequency varies significantly from case to case. However, the relative differences among the three empirical spectra are similar for all cases. In general, JONSWAP and Mitsuyasu spectra are fairly close, especially at high wind speeds, while Liu spectra yield much lower energy content. The energy at the spectral peaks for JONSWAP and Mitsuyasu are approximately an order of magnitude larger than those of Liu. An explanation for this great difference lies in the fact that the wave data used in developing the JONSWAP and Mitsuyasu formulas are from fully developed seas, whereas the wave data from Lake Michigan used in Liu's formula are not.

With energy spectra calculated from the empirical formulas, the spectral moments can be readily obtained. The basic parameters, such as significant wave heights and average wave periods, can then be derived from the moments, based on the theoretical results of Longuet-Higgins (1952) and Rice (1945), as:

$$H_{m_0} = 4m_0^{1/2} \quad (4)$$

and

$$T_{m_{0,2}} = 2\pi(m_0/m_2)^{1/2} \quad (5)$$

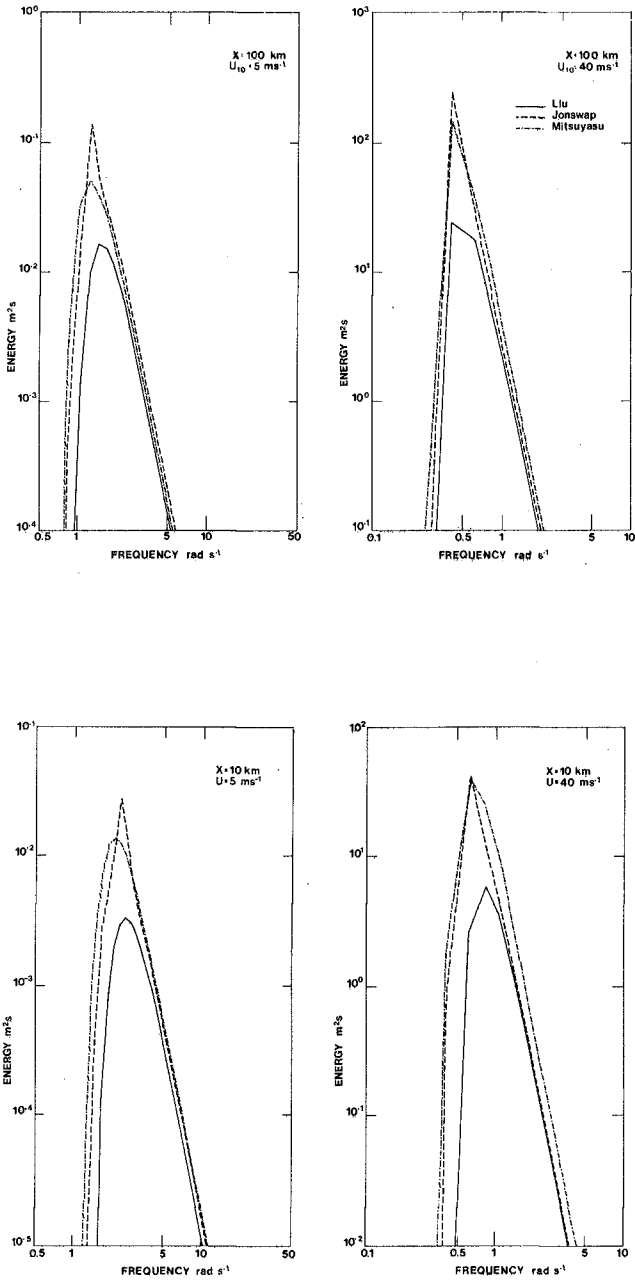


Fig. 1 Examples of wave spectra calculated by empirical formulas.

in which the n th moment of a wave spectrum is given by

$$m_n = \int_0^{\infty} \omega^n S(\omega) d\omega. \quad (6)$$

Here the average wave period $T_{m0,2}$ is presumably equivalent to the wave period given by the Sverdrup-Munk-Bretschneider method. The significant wave height H_{m0} calculated by Eq. (4) should approximate $H_{1/3}$, calculated by (Eq. 1). A correlation of calculated H_{m0} and $H_{1/3}$ is given in Fig. 2. In the case of the JONSWAP method, H_{m0} tends to be larger than $H_{1/3}$. A slightly greater trend is also shown in Mitsuyasu's case. Since Liu's empirical equation for $H_{1/3}$ was a direct derivation from the spectral moments, the close correlation shown is not surprising. In the following discussions, $H_{1/3}$, ω_p , and $T_{m0,2}$ will be calculated from the various empirical formulas and compared with actual data.

3. APPLICATIONS OF THE FORMULAS

Two episodes of Great Lakes waves, with both wind and wave data available, are used to examine the applicability of the various empirical formulas. The first episode occurred in Lake Michigan. Wave data were recorded by a staff gage installed on a research tower located 2 km offshore from Muskegon, Michigan, in 16 m of water (Fig. 3). The wind anemometer was located at 10 m above the lake surface on the same tower. The episode covered approximately 4 days during October 25th through 28th of 1971. The wind conditions, which are typical of the Great Lakes, are shown in Fig. 4. The wind speeds during this episode were quite unsteady with the predominant direction from the south and south-southeast providing moderate fetch distances of the order of 50 km.

Fig. 5 represents the significant wave heights $H_{1/3}$ recorded during this episode as compared with those hindcast by empirical formulas. Here and in the following figures in this paper, the heavy solid lines indicate recorded data; the dotted lines, the long-short dashed lines, the dashed lines, and the light solid lines indicate the hindcast data by Sverdrup-Munk-Bretschneider, Mitsuyasu, JONSWAP, and Liu, respectively. The results of Sverdrup-Munk-Bretschneider, Mitsuyasu, and JONSWAP, shown in Fig. 5, are strikingly close. In this episode, they all overestimated the recorded data by a factor of 2. Liu's results are relatively lower than the others since the energy contents given by Liu's formula are generally less than the others. In this case, Liu's results are closer to the recorded results than the others.

Fig. 6 shows the comparisons for the average wave period $T_{m0,2}$. The relative differences between the results of different authors seem quite similar and distinctive. Sverdrup-Munk-Bretschneider, for the most part, furnished the highest estimate, followed in order by Mitsuyasu and JONSWAP. Liu hindcast relatively lower average wave periods for the same wind condition.

The results for the peak-energy frequency ω_p are shown in Fig. 7. The Sverdrup-Munk-Bretschneider formula does not give estimations for ω_p ; hence,

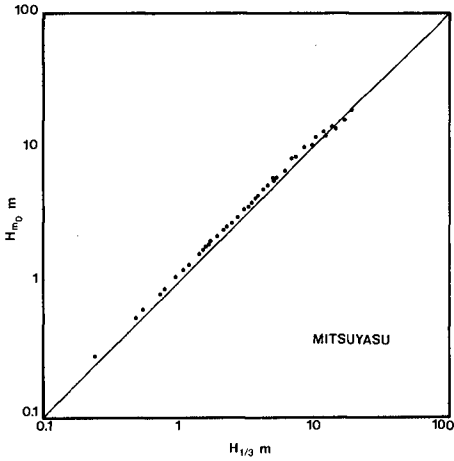
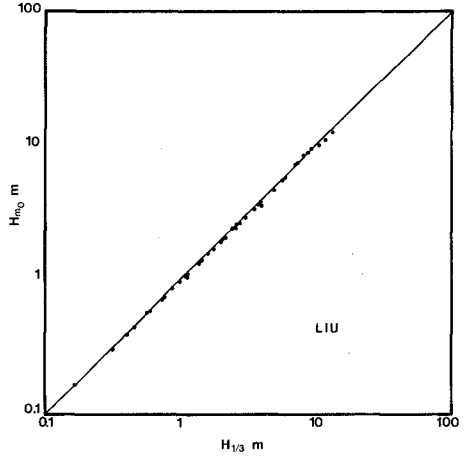
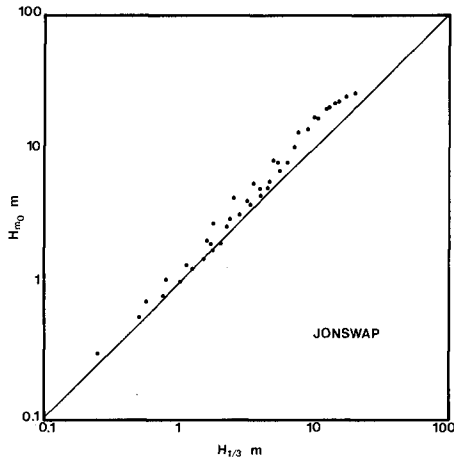
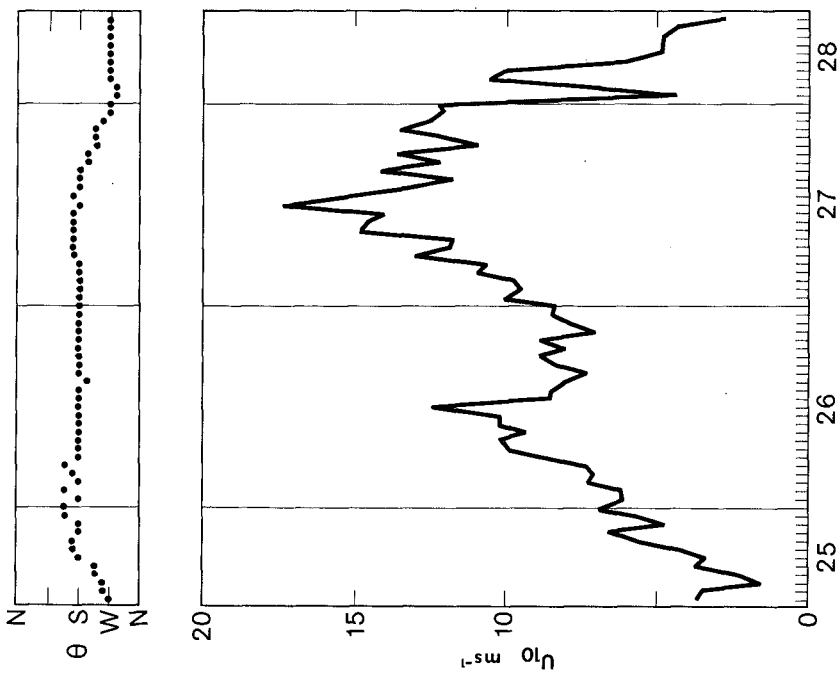


Fig. 2 Correlations of H_{m0} and $H_{1/3}$ calculated by empirical formulas.



OCTOBER, 1971

Fig. 4 Wind conditions during Lake Michigan episode.

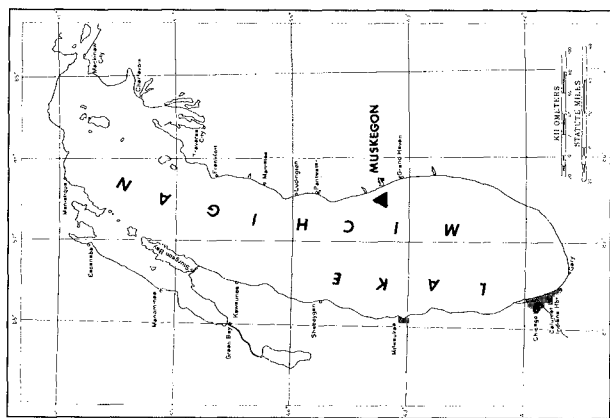


Fig. 3 Location of wave gage in Lake Michigan.

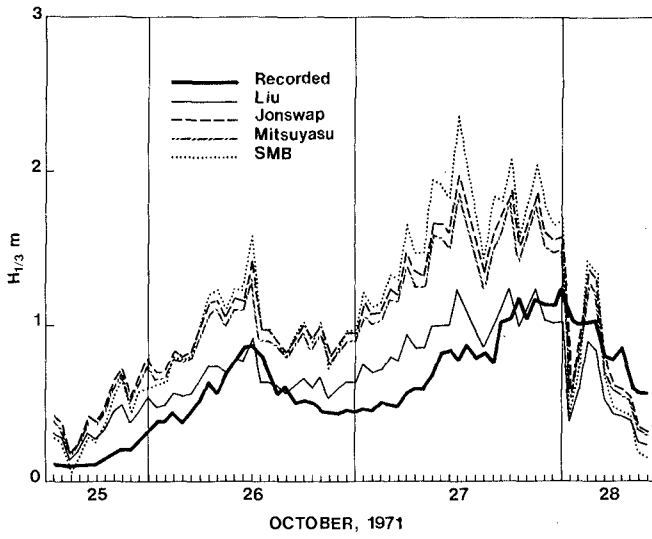


Fig. 5 Comparison of hindcast and recorded $H_{1/3}$ during Lake Michigan episode.

*SMB
overpredicts*

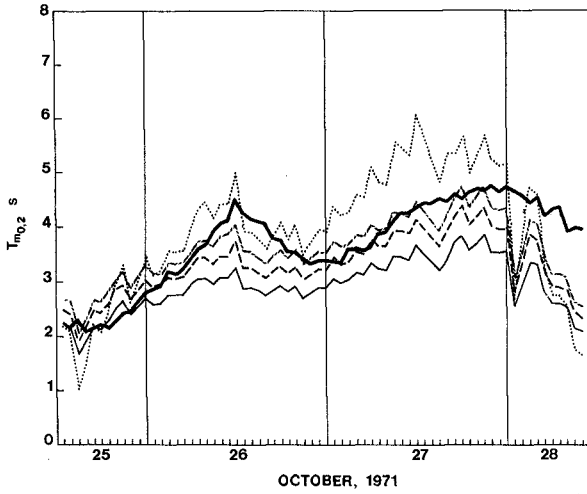


Fig. 6 Comparison of hindcast and recorded $T_{m0,2}$ during Lake Michigan episode.

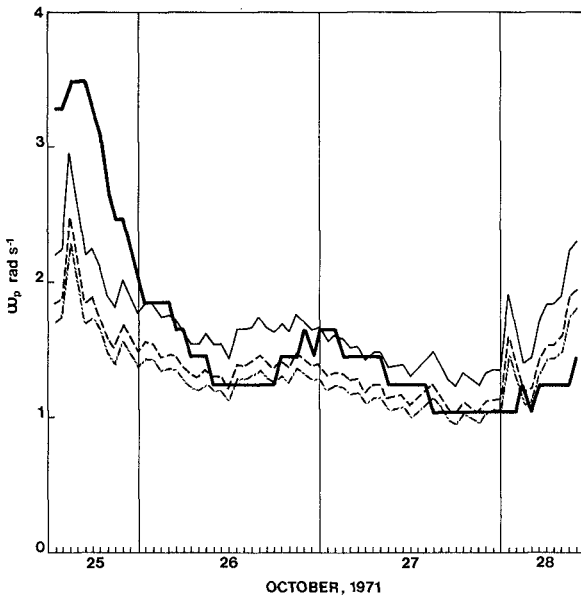


Fig. 7 Comparison of hindcast and recorded ω_p during Lake Michigan episode.

only JONSWAP, Mitsuyasu, and Liu are compared. The relative differences are again quite similar and distinctive. Liu hindcast a higher ω_p , followed by JONSWAP and then Mitsuyasu.

The second episode is from Lake Ontario. The wave gage, a waverider buoy manufactured by Datawell of Holland, was located 30 km northeast of Oswego, New York, in 150 m of water. The solid circle labeled Oswego-2 on the map, Fig. 8, indicates the waverider location. The open circle on the map shows the location of an instrumented buoy where the wind data used in this analysis were recorded. The wind anemometer on the buoy was 4 m above the lake surface.

Fig. 9 gives the wind conditions during this 4-day episode of October 7-11, 1972. The wind speeds were typically unsteady, with directions starting from the north, with a moderate fetch of 40 km, changing to west with a long fetch of 200 km or more when the storm intensified, and gradually switching back to north after the storm subsided.

The comparisons for the hindcast and recorded significant wave heights for this episode are shown in Fig. 10. The relative differences between the empirical results remain the same. The results of this episode are different from the first episode, however, in the sense that Liu's hindcasts, which were closer to the recorded results than the others in Fig. 5, are clearly underestimated in Fig. 10. The hindcasts of Sverdrup-Munk-Bretschneider, Mitsuyasu, and JONSWAP are again close to each other in this episode and also close to the recorded data during the growth part of the storm. All the empirical formulas significantly underestimated $H_{1/3}$ when the wind field decayed and directions switched from long fetches to short fetches.

Figs. 11 and 12 show the comparisons for $T_{m0,2}$ and ω_p , respectively, for this episode. The results are generally similar to those discussed in Figs. 6 and 7. It seems that, at any given time, one of the formulas tends give a better hindcast than the others, but none of the formulas is able to maintain the close hindcast throughout the episode. The inconsistency, therefore, casts doubt over the applicability of all the formulas.

Two examples of comparing computed spectra with the recorded spectra are shown in Fig. 13. The accuracy of the spectrum hindcast by the formulas depends mainly on the accuracy of corresponding formulas in hindcasting significant wave height and peak-energy frequency. If the hindcast significant wave height and peak-energy frequency values are close to those recorded, then the hindcast spectrum will certainly be close to that recorded and vice versa. The comparisons of spectra shown in the figure represent the typical results that can be expected from these empirical formulas.

4. SUMMARY AND CONCLUDING REMARKS

It has been the intent of this paper to present an assessment of the usefulness and applicability of the various empirical formulas in connection with surface waves in the Great Lakes. The assessment has been performed by comparing waves that were hindcast by the formulas with those actually recorded during two storm episodes in Lakes Michigan and Ontario. Based on the detailed

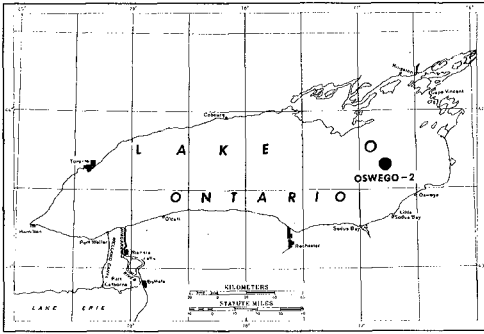


Fig. 8 Location of wave gage in Lake Ontario.

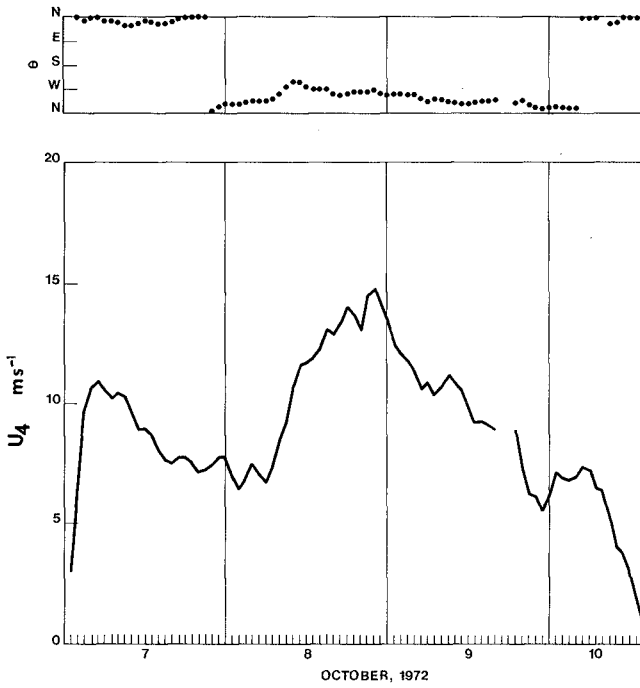


Fig. 9 Wind conditions during Lake Ontario episode.

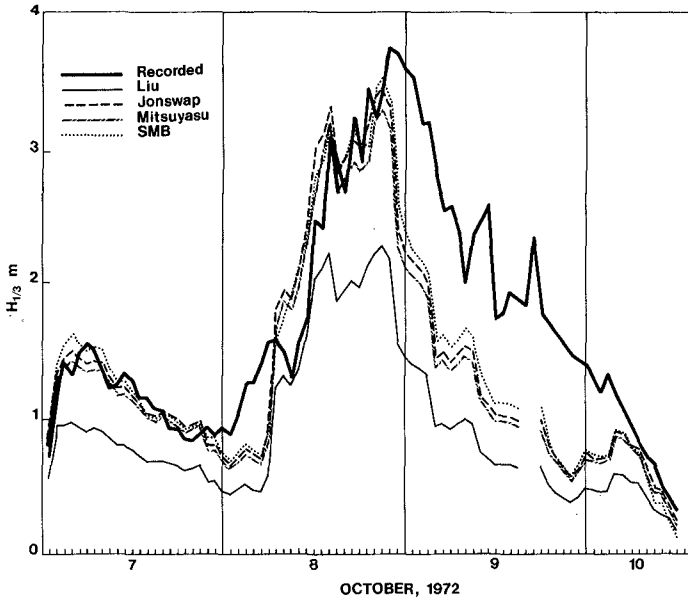


Fig. 10 Comparison of hindcast and recorded $H_{1/3}$ during Lake Ontario episode.

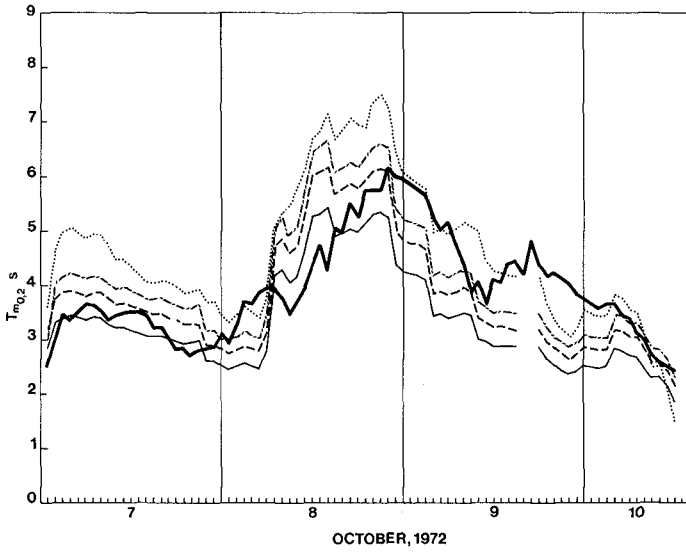


Fig. 11 Comparison of hindcast and recorded $T_{m0,2}$ during Lake Ontario episode.

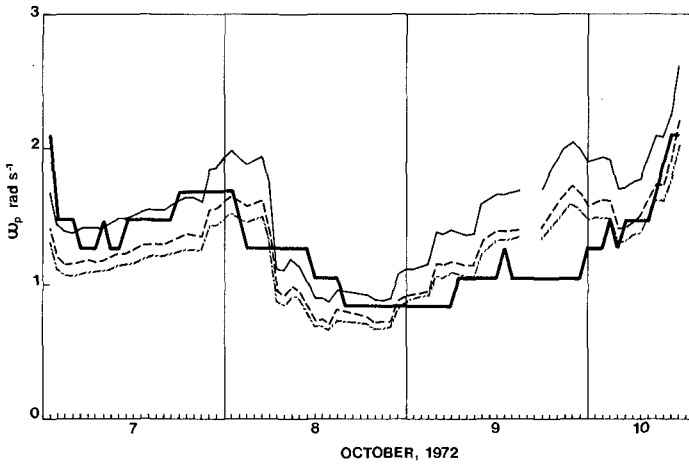


Fig. 12 Comparison of hindcast and recorded ω_p during Lake Ontario episode.

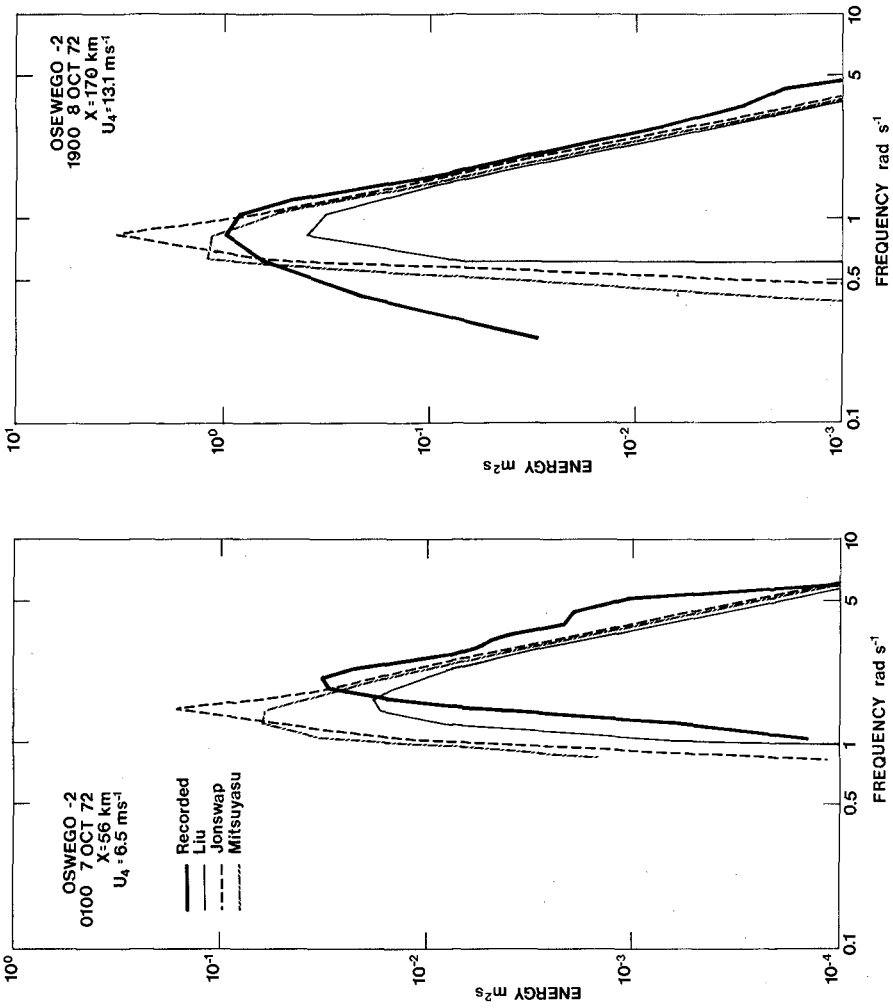


Fig. 13 Examples of hindcast and recorded wave spectra.

comparisons for the three parameters $H_{1/3}$, $T_{m0,2}$, and ω_p , results can be summarized as follows:

a. Significant Wave Height, $H_{1/3}$. The hindcasts by the JONSWAP, Mitsuyasu, and Sverdrup-Munk-Bretschneider methods are generally close to each other and greater than Liu's hindcast by about 50 percent. During the Lake Michigan episode, Liu's results were closer to the recorded results than the others; thus, the other formulas yielded overestimations. During the Lake Ontario episode, JONSWAP, Mitsuyasu, and Sverdrup-Munk-Bretschneider's results were closer to the recorded results than Liu's during the growth part of the storm; hence Liu's results appear to be underestimations.

At first glance, the results rendered by the two episodes seem to be inconsistent. The inconsistency, however, can be clarified by further examination of the two respective wind fields. During the Lake Michigan episode, the 10-m wind speeds started at 2 m s^{-1} and gradually increased to 10 m s^{-1} and higher; thus, the wave spectra were mostly under development. During the Lake Ontario episode, on the other hand, the wind speeds at the 4-m level had reached over 10 m s^{-1} at a very early stage of the storm. The wave spectra under this wind field tended to be fully developed. From these facts, it appears that Liu's formula is applicable for the less than fully developed waves, whereas JONSWAP, Mitsuyasu, and Sverdrup-Munk-Bretschneider formulas are applicable for the fully developed waves. This is consistent with the characteristics of the data from which the corresponding formulas were derived.

The above discussions apply only to the growth part of the storms. All the formulas underestimated the significant wave height when the wind field decayed, especially when the decay involved changes in wind direction as well as reductions in fetch distances. As the formulas were neither derived from, nor intended for, decaying processes, the results are by no means unexpected.

b. Average Wave Period, $T_{m0,2}$. The difference between high and low estimates as hindcast by the formulas for a given time is about 2 s. The recorded data generally lie within this range. Therefore, the error in hindcasting average wave periods by any formula is about 2 s or less. None of the empirical results can be considered substantially close to the recorded results throughout either of the two episodes.

c. Peak-Energy Frequency, ω_p . The difference between high and low ω_p hindcast for a given time is about 0.5 rad s^{-1} . With the exception of the low wind portion of the Lake Michigan episode and the decaying portion of the Lake Ontario episode, the recorded ω_p lies within the range of the empirical hindcasts. An accurate hindcast of ω_p will lead to accurate hindcasting of wave spectra if the hindcast of significant wave height is also accurate. None of the formulas seems to be able to provide an accurate ω_p . During both episodes, Liu's hindcasts were relatively close to the recorded results through a major portion of the storm. JONSWAP and Mitsuyasu's hindcasts came closer to the recorded results at the peak of the storm.

These results, while generally fulfilling most of the objectives of this paper, are by and large both disappointing and encouraging. These results are disappointing because they demonstrate that simple fetch-limited spectral formulas have not provided substantial applicability to the prediction of Great

Lakes waves. Undoubtedly, parameters neglected by the formulas, such as duration and atmospheric stability, play important roles not known at the present time and need to be further explored. On the other hand, these results are encouraging because they provide information on the limitations and error ranges that can be expected in the application of these formulas to predicting Great Lakes waves. Until further developments and additional studies are made, the results presented in this paper will continue to be useful.

5. REFERENCES

- Garratt, J.R., "Studies of Turbulence in the Surface Layer Over Water (Lough Neagh). III. Wave and Drag Properties of the Sea-Surface in Conditions of Limited Fetch," *Quart. J. R. Met. Soc.*, Vol. 99, 1973, pp. 35-47.
- Hasselmann, K., T. P. Barnett, E. Bouws, H. Carlson, D. E. Cartwright, K. Enke, J. A. Ewing, H. Gienapp, D. E. Hasselmann, P. Kruseman, A. Meerburg, P. Müller, D. J. Olbers, K. Richter, W. Sell, and H. Walden, 1973. "Measurements of Wind-Wave Growth and Swell Decay During the Joint North Sea Wave Project (JONSWAP)," *Deutsche Hydrog. Z. Suppl. A(8)*, No. 12, 1973, 95 p.
- Kononkova, G. E., E. A. Nikitina, L. V. Peborchaya, and A. A. Speranskaya, 1970, "On the Spectra of Wind Driven Waves at Small Fetches," *Izvestiya, Atmospheric and Oceanic Physics*, Vol. 6, 1970, pp. 747-751.
- Liu, P. C., "Normalized and Equilibrium Spectra of Wind Waves in Lake Michigan," *J. Phys. Oceanography*, Vol. 1, 1971, pp. 249-257.
- Longuet-Higgins, M. S., "On the Statistical Distribution of the Heights of Sea Waves," *J. Marine Res.*, Vol. II, 1952, pp. 245-266.
- Mitsuyasu, H., "On the Form of Fetch-Limited Wave Spectrum," *Coastal Eng. in Japan*, Vol. 14, 1971, pp. 7-14.
- Rice, S. O., "The Mathematical Analysis of Random Noise," *Bell System Tech. J.*, Vol. 24, 1945, pp. 46-156.
- U.S. Army Coastal Engineering Research Center, "Shore Protection Manual," Vol. I, U.S. Government Printing Office, Washington, D.C., 1973.

CHAPTER 9

WAVES OFF TAICHUNG COAST OF TAIWAN

by

Charles C.C. Chang¹, M.H. Wang² and J.T. Juang³

SYNOPSIS

Many coastal engineers have made studies on the characteristics of waves, but most of them concentrated on waves of the open ocean. Due to the environmental difference, the result drawn for open ocean waves may not be applied to straits or the continental shelf. Based on the observed data, the authors intend to obtain some characteristics or tendency of wave condition in the Taiwan strait. Correlation among wave parameters and meteorological factors is also examined. Comparisons to the result for open ocean waves are made to supply information for planning, design and construction of coastal structures on the coast of the strait. These studies are also useful for wave prediction in the strait area.

GEOGRAPHICAL AND METEOROLOGICAL CONDITIONS

The Taichung coast, on the central-west part of the island of Taiwan, faces the Taiwan strait as shown in Fig. 1. The climate in this area may be classified as winter monsoon, summer and the transitional seasons. The speeds of NNE-NE winds prevailing during the monsoon season beginning in October to the next March are generally higher than those of S-SW winds in summer season from May to August. Due to frequent change of

-
1. Deputy Chief Engineer, Taichung Harbor Bureau, Taiwan, Rep. of China.
 2. Former Assistant Engineer, Taichung Harbor Bureau, Taiwan, Rep. of China.
 3. Assistant Engineer, Hydraulics Laboratory, Taichung Harbor Bureau, Taiwan, Rep. of China.

wind directions, the months of April and September are regarded as the transitional season. However, during the period of July to September, this island is frequently hit by typhoons. Paths of seven typhoons from 1971 to 1975 were plotted in Fig. 2.

DATA COLLECTION

An ultrasonic wave gauge was set at a water depth of 19 meters below low water level in the Taichung harbor construction area off the coast. The gauge was installed in July 1971 to record waves of 20 minute intervals for two hours. Among the wave series, 150 waves were chosen to represent to wave record of this time interval. Parameters of the average wave, the one-third highest wave or the significant wave, the one-tenth highest wave and the maximum wave were calculated. The reference wind speed was compiled from the anemometer records established on this coast. Location of the wave gauge and the anemometer are shown in Fig. 3.

ANALYSIS

The relative occurrence frequency of the significant wave height and that of the significant wave period were calculated by month, by season and finally by 4 years, the duration of all records. In order to investigate the central value and the scatter of probability distribution, both mean and variance of wave characteristics were computed. Since the waves change with the meteorological factors, thus, the difference of wave height statistics for each month and each season is examined. The same procedure is followed for studying the probability distribution of the significant wave period. Moreover, the correlation coefficient between the significant wave height and its reference wind speed for each month was calculated. The coefficient is useful to wave prediction. Because wave steepness plays an important role on the development of coast, the deepwater wave steepness H_0/L_0 has been studied.

For comparisons of the wave condition of this

strait area with the open ocean. Two sources of open ocean wave data are selected. One was obtained by Hogben and Lumb (1966) in the ocean area off the north and east coasts of Taiwan and also analyzed by Bretschneider (1973). The other was collected by Jade Dattatri (1973) off the Mangalore harbor located on the west coast of India as shown in Fig. 4.

Because typhoon waves control the design condition of coastal structures, seven typhoon wave sequences as shown in Fig. 2 have been studied. Correlation coefficient between typhoon wave height and wind speed was calculated and discussed. The relationship between the significant wave height $H_{1/3}$ and period $T_{1/3}$ is also examined with the equation suggested by Bretschneider (1973).

$$T_{1/3} = 3.86 \sqrt{H_{1/3}} \quad (1)$$

The above equation is derived from wave data of open ocean. The unit of $H_{1/3}$ is meter and $T_{1/3}$ is second.

In order to check whether the theoretical Rayleigh's law will apply to strait waves, ratios among wave heights of the significant wave, the one-tenth highest wave, the average wave and the maximum wave are studied. The results are compared with the equations presented by Longuet-Higgins (1952)

$$H_{1/3} = 1.6 H_{ave} \quad (2)$$

$$H_{1/10} = 1.27 H_{1/3} \quad (3)$$

$$H_{max} = 1.583 H_{1/3} \quad (4)$$

RESULTS AND DISCUSSIONS

1. Periodicity of Wave Condition

The distributions of the significant wave height for each season are shown in Fig. 5 and Fig. 6. The accumulated probability of wave height is also shown in Fig. 7. All deviate slightly from the Rayleigh's curves.

The significant wave period for each season was

shown in Fig. 8. The accumulated probability is also shown in Fig. 9. The distribution of $T_{1/2}$ for each season nearly follows the normal law. It seems that the variation of meteorological condition in each season doesn't change the type of wave period distribution as illustrated in these diagrams.

Mean values of monthly significant wave heights and periods with their 90% confidence interval are shown in Fig. 10 and 11 respectively. The periodicity of monthly occurrence of $H_{1/2}$ and $T_{1/2}$ is also shown in Fig. 12. Oceanic condition in summer is quite calm. From May to August, monthly mean of wave height is less than 0.8 meter and wave period less than 5.5 second. Concerning the transitional season, both mean values of monthly wave height and period in September are larger than those in April. As to the monsoon season, mean values of wave heights in October has the largest confidence interval while that in March has the smallest. Comparison of the variance coefficients of wave heights and periods for each month is made in Fig. 13. It is clear that the variation coefficient of $H_{1/2}$ is always larger than that of wave period. Since the typhoon hits this island occasionally, the variation coefficient of wave height in summer is quite high. However, the yearly recurrence of the significant wave period is quite obvious. Typhoons also affect the monthly mean value of wave height, but it has little effect on that of wave period. Meanwhile, the monthly correlation coefficients between wave height and wind speed are also calculated as shown in Table 1 which shows no distinct difference for winter and summer seasons.

2. Monthly Variation of Wave Steepness

The monthly mean of deepwater wave steepness with 90% confidence interval is shown in Fig. 14. During the winter monsoon season from October to March, the wave steepness is rather high, beach erosion might occur. However, due to large tidal range, only a few sand bars appear in this coast.

3. Typhoon Waves and Winds

Wind direction generally changes from NNE through N, NNW, W, WSW and SSW to S during a typhoon assault. The wind is rather steady and duration is long during the former stage. The NNE and N winds are dominant at

this stage. The longest duration of N wind ever recorded is 24 hours and that of NNE wind is 20 hours. Relationships between the significant wave height and the reference wind speed for NNE and N are plotted in Fig. 15 and Fig. 16 respectively. The short vertical line, drawn in Figures, indicates the standard deviation of wave heights from their mean. The wave height increases linearly with wind speed when the peak of typhoon wave sequence is over, unsteady wind is usually observed except from SSW direction. At a later stage, the wind direction changes rapidly from time to time, as a result the duration becomes very short, no definite relationship between wave height and wind speed can be formed except the SSW direction.

Using 90% confidence interval, the ratios of the significant wave height $H_{1/3}$ to the reference wind speed $U_{Ref.}$ for NNE, N and SSW wind are obtained as follows.

$$\begin{aligned} \frac{H_{1/3}}{U_{Ref.}} &= 0.110 - 0.130 && \text{for NNE wind} \\ &= 0.133 - 0.147 && \text{for N wind} \\ &= 0.112 - 0.128 && \text{for SSW wind} \quad (5) \end{aligned}$$

where $H_{1/3}$ is in meter and $U_{Ref.}$ is in meter per second.

The relationship of the wave height and SSW wind speed is shown in Fig. 17. The null hypothesis may be accepted in 1% significance level as follows.

$$H_{1/3} = 0.130 U_{Ref.} \quad (6)$$

The correlation coefficient between wind speed and wave height for each typhoon is listed in Table 2. Typhoon Nina whose center passed by the harbor has the largest correlation coefficient, while Typhoon Gloria passed the Bashi strait, southward of the island, has the least. It may be assumed that a stronger relationship between winds and waves would result if the typhoon path is closer to the location of the wave recorder.

4. Typhoon Wave Height Distribution

The ratios among $H_{1/3}$, H_{ave} , $H_{1/10}$ and H_{max} of typhoon waves have been studied in order to ascertain the conformity to the Rayleigh distribution of wave

height. In accordance with Fig. 18, 19 and 20, the relationship may be expressed as follows:

$$H_{1/2} = 1.41 H_{ave} \quad (7)$$

$$H_{1/10} = 1.20 H_{1/2} \quad (8)$$

$$\begin{aligned} H_{max} &= 3.04 H_{1/2} && \text{for } H_{max} \leq 5.8^m \\ &= 1.16 H_{1/2} && \text{for } H_{max} \leq 4.5^m \end{aligned} \quad (9)$$

The first relationship in Eq. (9) is regarded as the upper limit and the second one, the lower limit. These equations (7, 8 and 9) indicate that the strait wave height distributions may not follow exactly Rayleigh's law. The small wave in the strait has higher probability of occurrence than that in the ocean. The mean value of H_{max} to $H_{1/2}$ ratio for each typhoon wave sequence and its standard deviation are shown in Table 3.

5. Typhoon Wave Height and Period

The correlation curve between typhoon wave height and period of 90% confidence interval is shown in Fig. 21. The scatter diagram of wave height and period is shown in Fig. 22. The most probable relationship may be represented by Eq. (10)

$$T_{1/2} = 4.56 \sqrt{H_{1/2}} \quad (10)$$

It indicates that for the same wave height, the wave period in the strait is longer than that in the ocean. Such a phenomenon is worth further study.

6. Recurrence Period of Wave Height

Based on the wave height distribution compiled from 4-year records, the recurrence period of the specified significant wave height has been calculated. Comparison of the recurrence period of wave height in the strait with that in the ocean (Bretschneider, 1973) has also been made. Bretschneider's result was drawn from ship observation of waves on the north and east coasts of Taiwan (Hogben and Lumb, 1966) as shown in Table 4 and Fig. 23. The wave height in the strait is approximately one half of that in the ocean. However, the curves shown in Fig. 23 may be modified by further observation and analysis, this study may still be used as the

criteria for waves in the strait sheltered area.

7. Comparison of Monsoon Wave Distribution

The wave height and period distribution of the Taichung coast is compared with that of the Mangalore harbor on the west coast of India. It is noted from Fig. 24 and Fig. 25 that the monsoon wind on the west coast of India generates waves heavier than those generated on the Taichung coast. Nevertheless, the wind speed recorded at the Mangalore harbor was lower than that at the Taichung harbor.

CONCLUSIONS

The meteorological factors have little effect on the monthly distribution of wave period, which has a clear recurrence month by month. The significant wave period may be estimated from the significant wave height by Eq. (10). The wind acts as a dominant factor to the wave height. Therefore, the wave height distribution of winter monsoon differs from that of summer season. It is found that the wave height on this coast is approximately one half of that on the north and east coasts of Taiwan based on a comparison with Bretschneider's (1973) results. This phenomenon is also verified by comparing the waves off west coast of India. Though the wind speeds in the India coast area are lower, heavier seas are also observed. However, waves in the straits would have rather a longer period for a given magnitude of wave height. The distribution of strait wave height may not follow the Rayleigh's law. So that the strait wave will be overestimated by means of the result drawn by Longuet-Higgins (1952). The recurrence interval of various significant wave height shown in Table 4 and Fig. 23 may be used as the wave criteria for the structure design on the coast of the strait. Of course, the result is needed to be modified by further study.

ACKNOWLEDGMENT

The authors express their appreciation to Admiral M.C. Chen, director of the Taichung Harbor Bureau, for

kind permission to use the wave and wind records. Acknowledgment is also made to Mr. C.L. Wang, chief engineer of the Taichung Harbor Bureau, and Dr. L.W. Tang, Professor of National Cheng-kung University, for their constant instruction in the presentation of this study. Besides, much of the calculation work herein was done by Mr. Y. C. Huang. The authors are very grateful for all the help which was given and has made this study possible.-

REFERENCES

1. Bretschneider C.L., A Tentative Analysis of Wave Data for Design Wave Criteria Around Taiwan, Science Reports of the National Taiwan University, No. 3. pp. 1-24, December, 1973.
2. Dattatri Jade and Renukardhya, Wave Forecasting for West Coast of India, Journal of Waterways, Harbor and Coastal Engineering Div., ASCE, Aug., 1971.
3. Dattatri Jade, Waves off Mangalore Harbor - West Coast of India, Journal of Waterways, Harbor and Coastal Engineering Div., ASCE, Feb. 1973.
4. Hogben, N. and F.E. Lumb (1966), Ocean Wave Statistics, National Physical Laboratory, Teddington, Middlesex, England.
5. Longuet-Higgins, M.S., On the Statistical Distribution of the Height of Sea Waves, Journal of Marine Research, Vol. XI, No. 3, 1952.

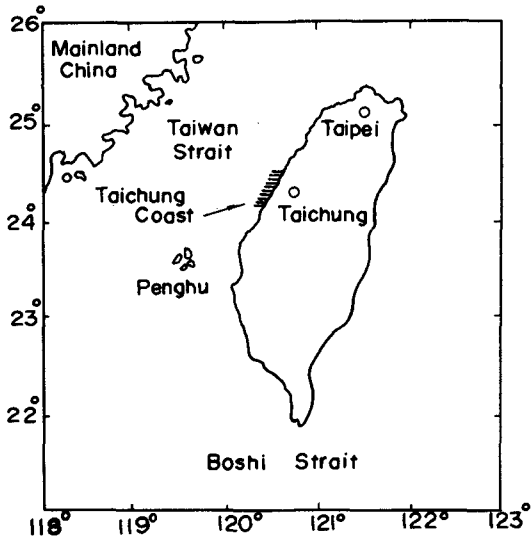


Fig.1 Location of Taichung Coast.

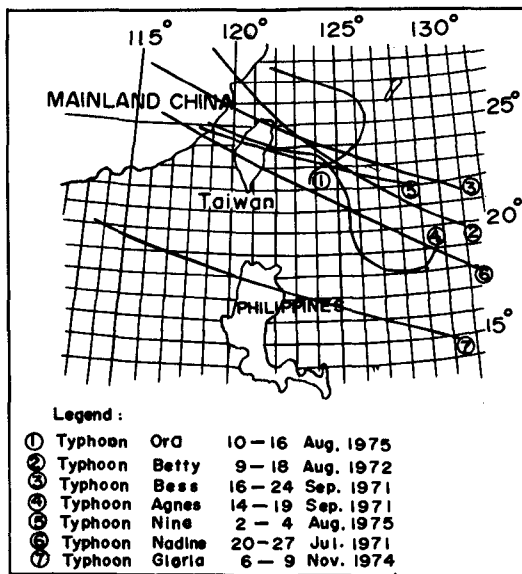


Fig.2 Location map and Tracks of seven Typhoons.

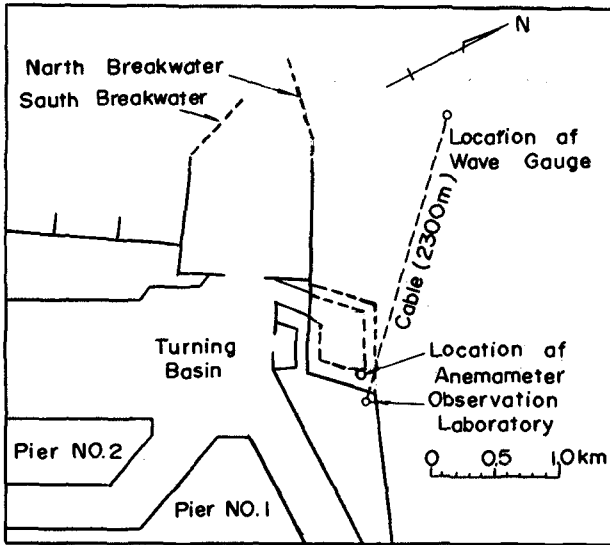


Fig. 3 Locations of Wave Gauge and Anemometer.

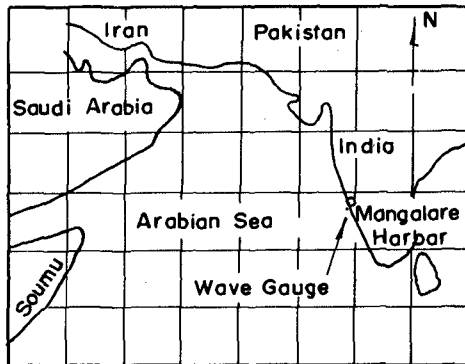


Fig. 4 Location of Mangalore Harbor.

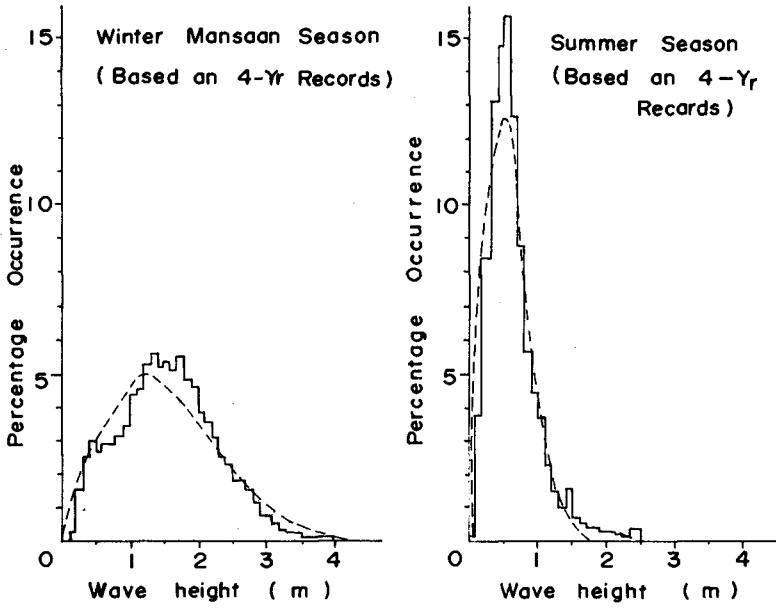


Fig. 5 Distribution of Significant Wave Height.

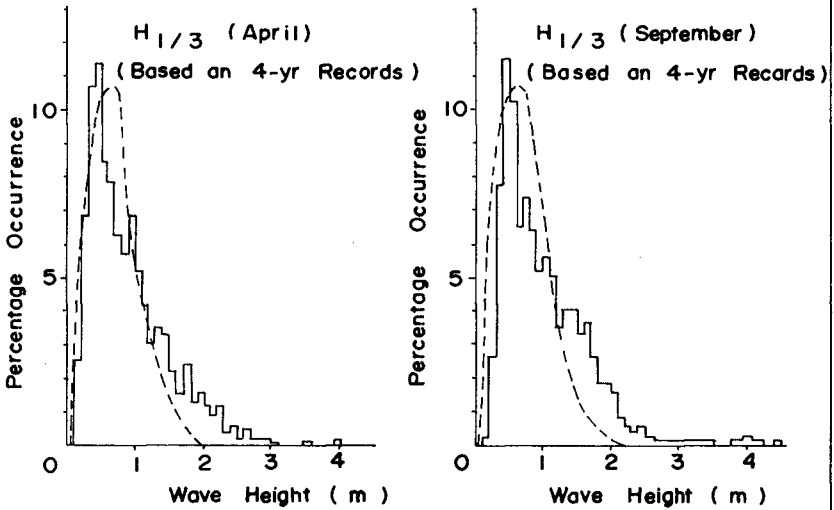


Fig. 6 Distribution of Significant Wave Height, Transition Season.

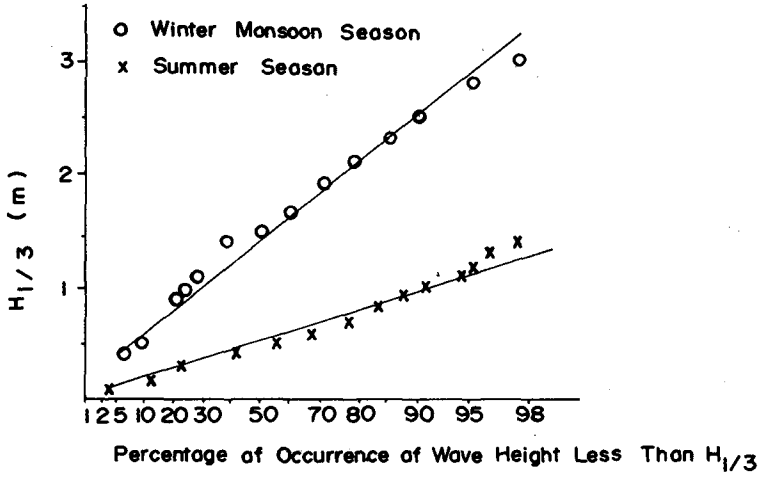


Fig 7 Accumulated Distribution of Significant Wave Height.

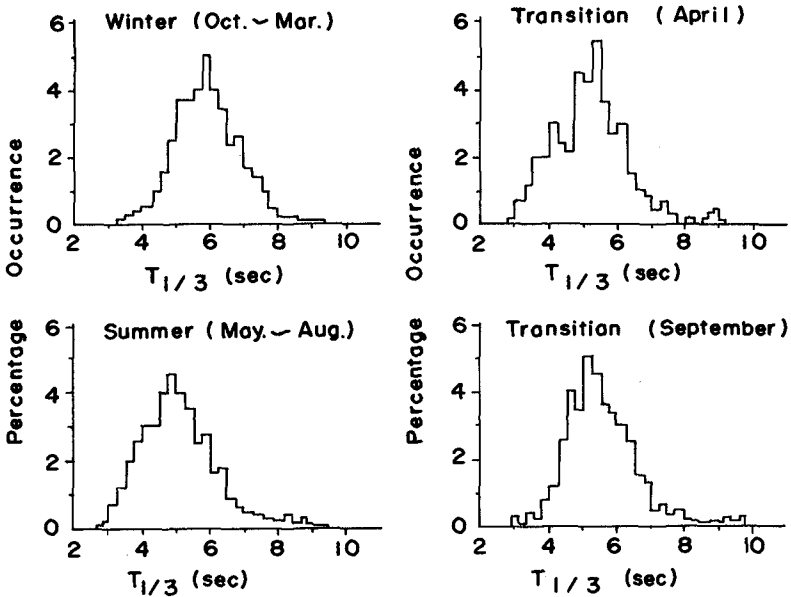


Fig. 8 Distribution of Significant Wave Period (4-Yr Records)

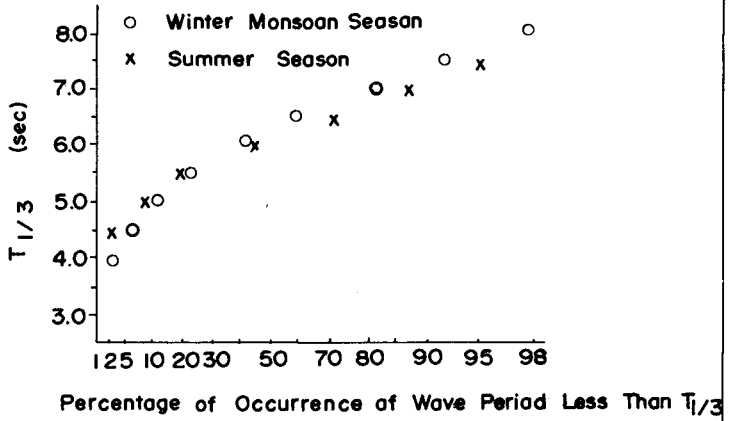


Fig. 9 Accumulated Distribution of Significant Wave Period.

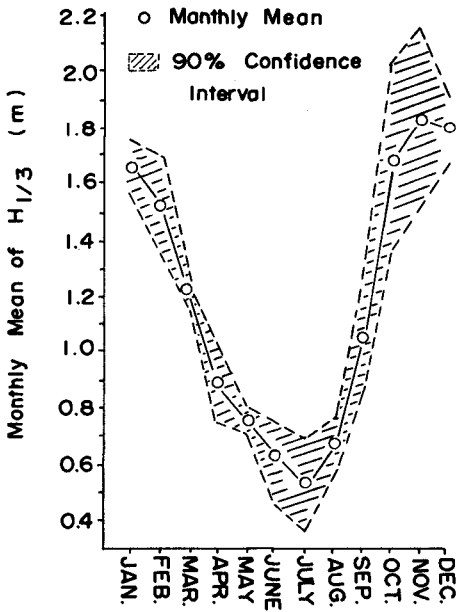


Fig. 10 Monthly Mean of Significant Wave Height.

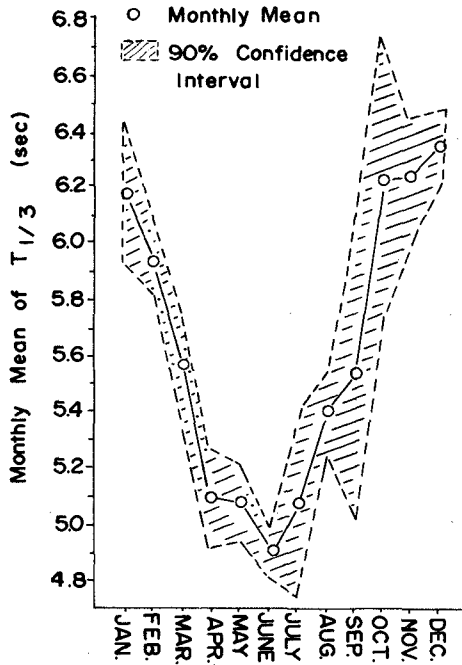


Fig.11 Monthly Mean of Significant Wave Period.

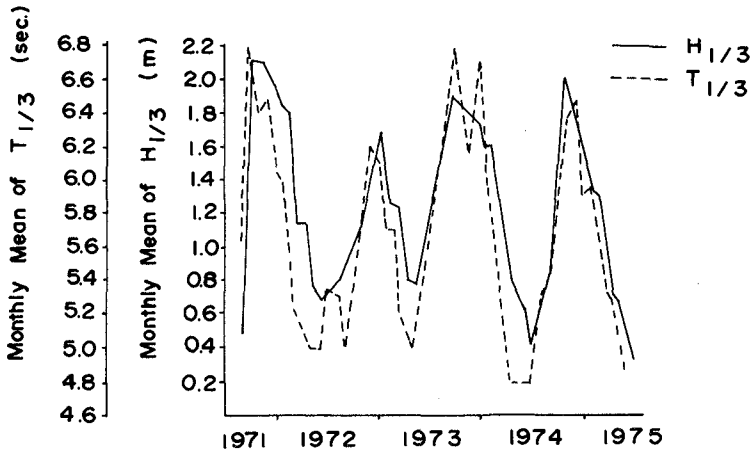


Fig.12 Tendency Comparison of Significant Wave Height and Period.

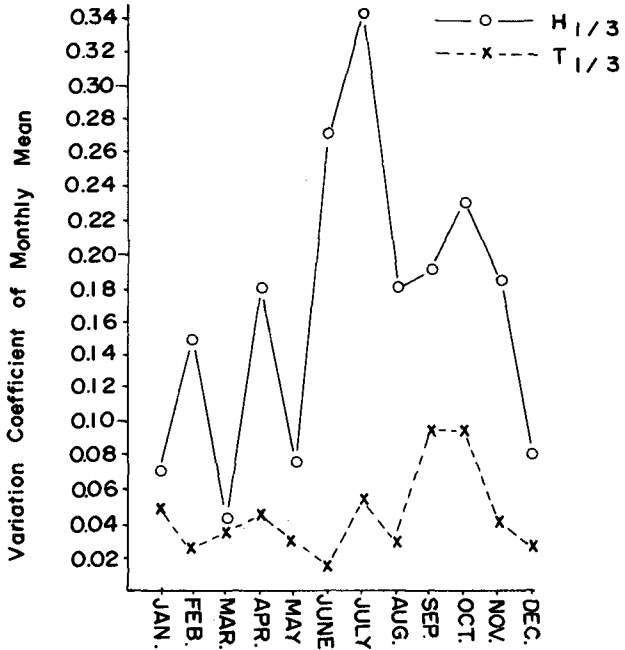


Fig.13 Variation Coefficient Comparison Between Monthly Mean of $H_{1/3}$ and $T_{1/3}$.

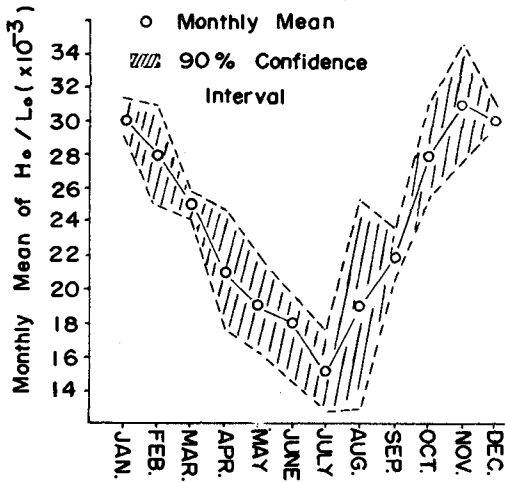


Fig.14 Monthly Mean of Wave Steepness.

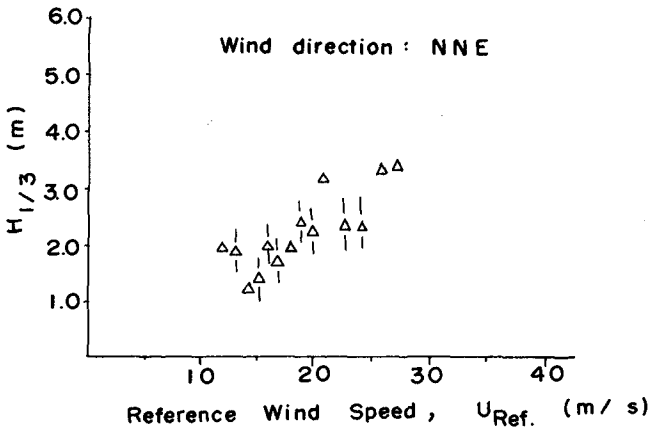


Fig.15 Relationship between Significant Wave Height and Reference Wind Speed.

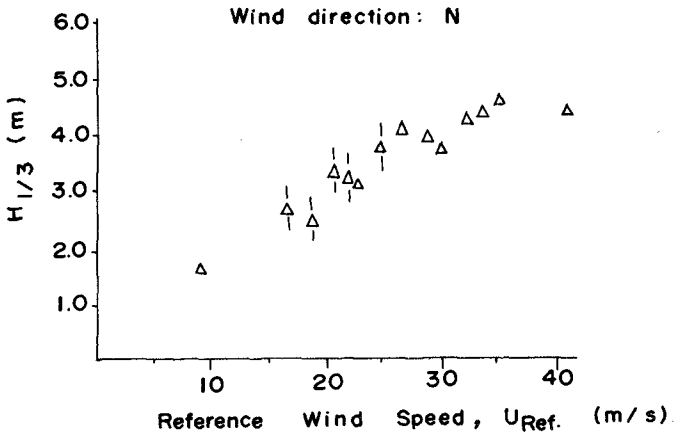


Fig.16 Relationship between Significant Wave Height and Reference Wind Speed.

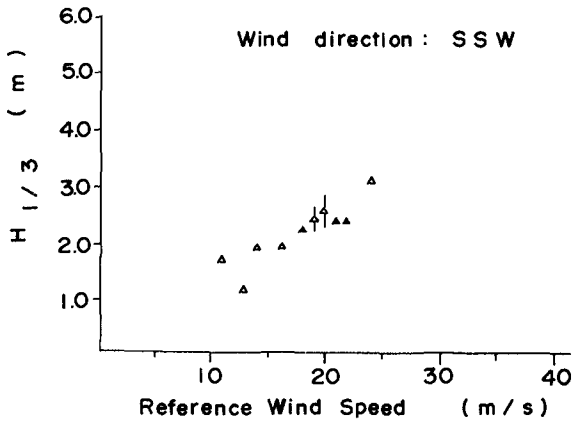


Fig.17 Relationship between Significant Wave Height and Reference Wind Speed.

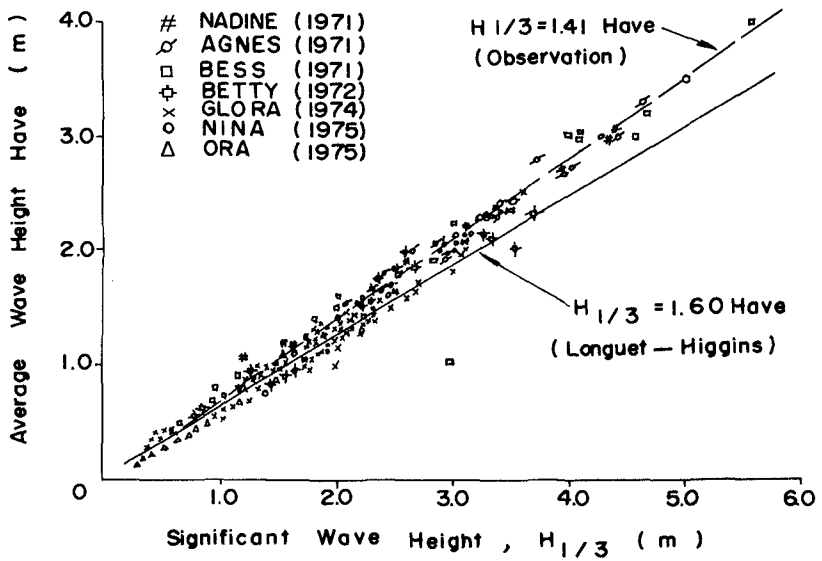


Fig.18 Average Wave Height versus Significant Wave Height .

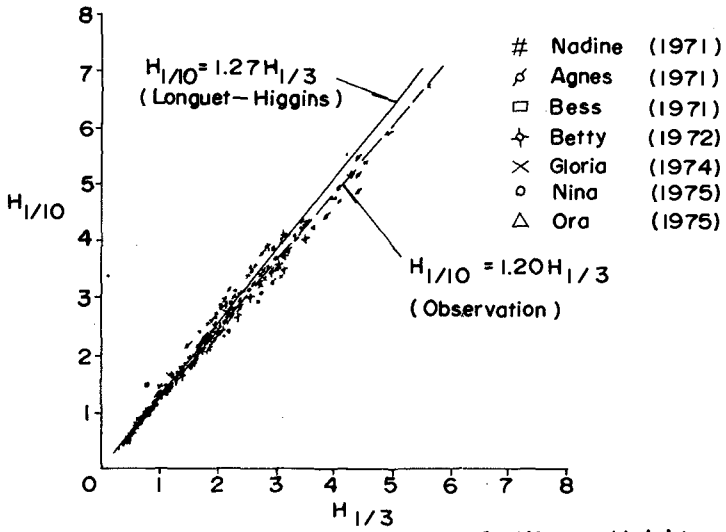


Fig.19 Mean of Highest one tenth of Wave Height versus Significant Wave Height.

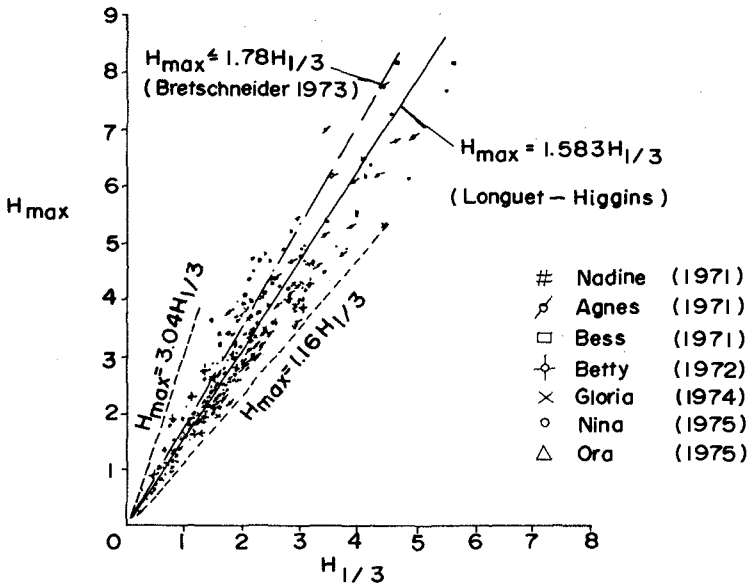


Fig.20 Maximum Wave Height versus Significant Wave Height.

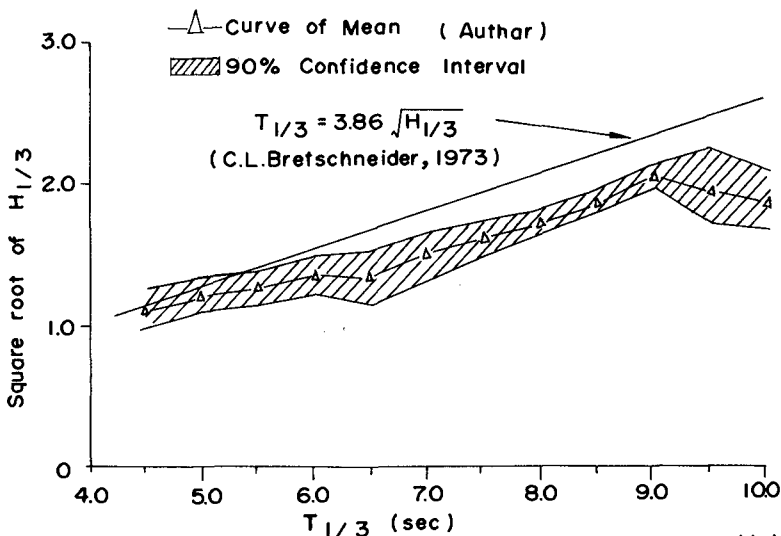


Fig.21 Relationship between Significant Wave Height and Period.

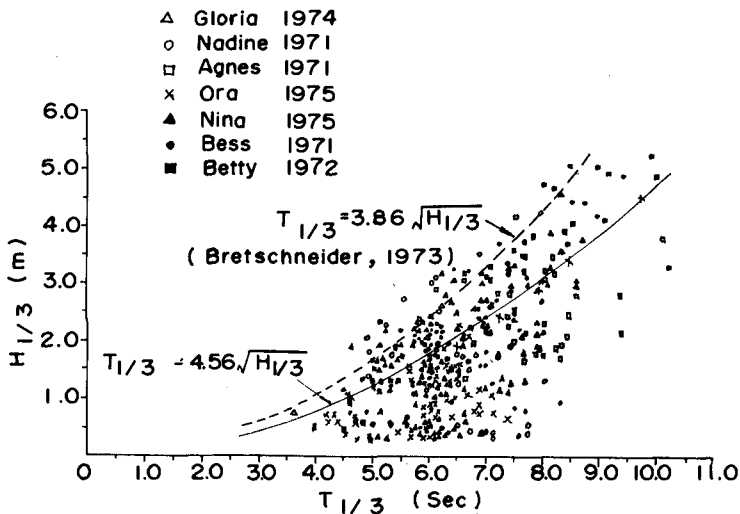


Fig.22 Scatter Diagram Relating Significant Wave Height and Period.

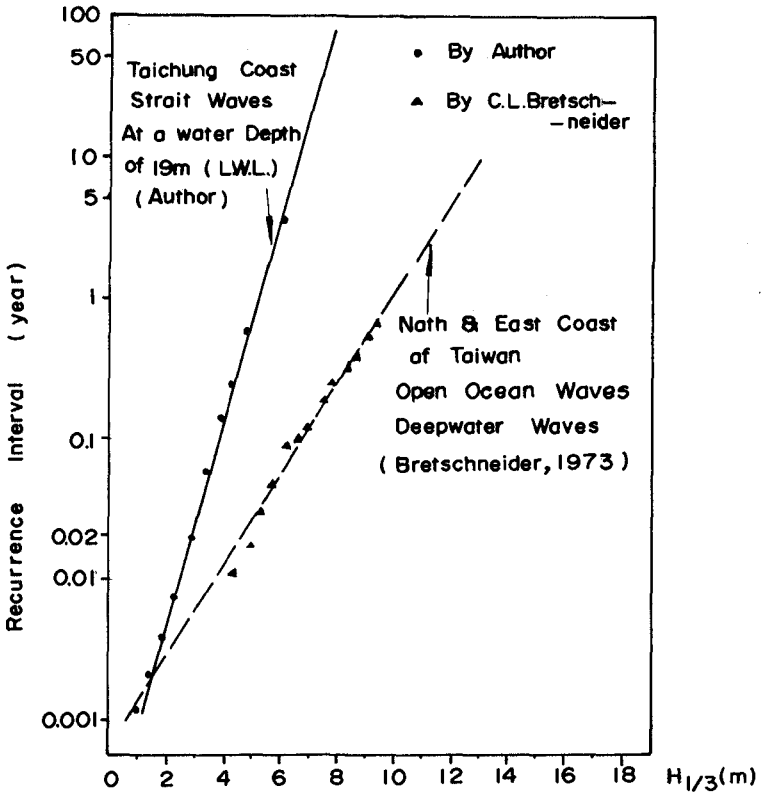


Fig. 23 Significant Wave Height versus Recurrence Interval in years.

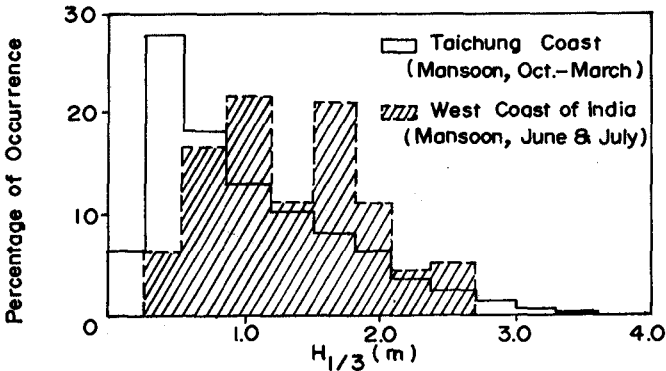


Fig. 24 Comparison of Wave Height Distribution.

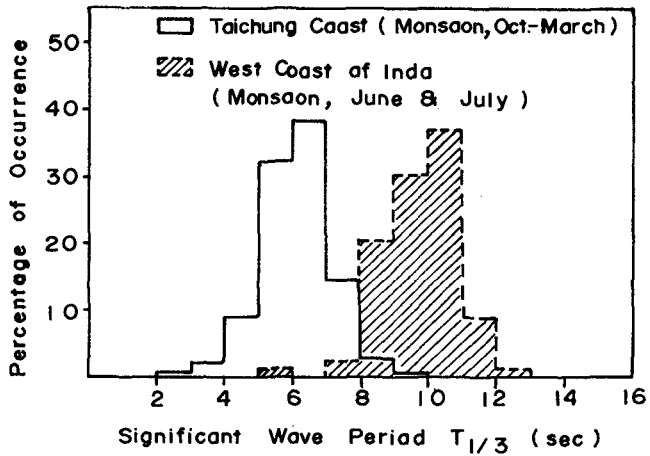


Fig. 25 Comparison of Wave Period Distribution.

Table I. Monthly Correlation Coefficient between Wave Height and Wind Speed

Month year	Jan.	Feb.	March	April	May.	June
1973	—	—	0.61	0.70	—	—
1974	0.60	0.83	0.84	0.68	—	0.56
1975	0.78	0.84	0.88	0.87	0.59	0.80

Month year	July	Aug.	Sep.	Oct.	Nov.	Dec.
1973	—	—	0.66	0.91	—	0.83
1974	0.77	0.52	0.74	0.84	0.63	0.75
1975	0.96	0.76	0.39	0.95	—	—

Table 2. Correlation Coefficient between typhoon
Wind and Wave Height.

Typhoon Name	Ora.	Betty	Bess	Agnes	Nina	Nadine	Gloria
Correlation Coefficient	0.46	0.32	0.68	0.48	0.85	0.36	0.34

Table 3. Ratio of H_{max} to $H_{1/3}$ for Typhoon Waves.

Typhoon Name	Ora.	Betty	Bess	Agnes	Nina	Nadine	Gloria
Mean	1.562	1.497	1.507	1.517	1.654	1.630	1.707
Standard Deviation	0.131	0.177	0.155	0.208	0.223	0.283	0.240

Table 4. Significant Wave Height in Meter for
Various Return Interval (yr.)

Return Interval	1	5	10	25	50	100	Remark
Taichung Coast West Coast of Taiwan	5.0	6.0	6.4	7.1	7.4	7.8	Strait Wave
North & East Coast of Taiwan	9.8	11.9	12.8	14.2	15.0	16.0	Open Ocean Wave

CHAPTER 10

EXTREME WAVE PARAMETERS BASED ON CONTINENTAL SHELF STORM WAVE RECORDS

by

R. E. Haring*, A. R. Osborne* and L. P. Spencer*

SUMMARY

Measured storm wave records from several Continental Shelf areas were used to test the adequacy of estimating formulae for individual wave parameters. In all, 376 hours of storm wave records were analyzed, and their properties nondimensionalized by fundamental spectral parameters. Results are presented for surface deviation statistics, individual wave height statistics and individual wave period statistics. The results can be used by ocean engineers to eliminate unintended bias from wave parameters selected for the design of offshore facilities. The most significant result is that measured rare wave heights in the storm wave records are on the order of 10 percent less than predicted by the Rayleigh distribution at the 1 in 1000 probability level.

INTRODUCTION

Severe storms on the Continental Shelf produce a complex series of waves in time and space. The condition of the ocean's surface which exists over a short time interval is assumed to be a stationary process called a sea state. The spectral definition, a distribution of the amplitude energy density in the frequency domain, contains the necessary information to define the sea state. Fundamental properties derived from the spectral definition are the total energy content (or variance of the sea surface) and the dominant frequency (or frequency of maximum energy density). The shape of the spectral density function is also important because it characterizes the wave amplitude record. Modern wave prediction methods estimate the energy content of the sea surface as a function of both frequency and direction [1]. Instrumental measurements of the stationary, time-varying sea surface can be analyzed mathematically to produce the spectral density as a function of frequency. Such instrumental measurements are often used to verify or calibrate numerical wave prediction models. Figure 1 illustrates the typical sea state spectrum and the derived properties which will be used in this paper.

Conventional engineering design practice for fixed offshore structures requires the specification of an individual wave in terms of trough-to-crest height and zero-crossing period [2]. This design wave should be a realistic estimate of the extreme, rare wave in a severe storm sea state whose return period is appropriate for the design

* Exxon Production Research Company, Houston, Texas.

problem at hand and whose properties are consistent with real sea surface behavior. Selection of design wave parameters is often based on the assumption that the distribution of wave heights in a storm sea state is described by the theoretical Rayleigh distribution. Practical formulae for the selection of wave parameters have been proposed based on this assumption. These formulae can be expressed in terms of the fundamental derived properties from the amplitude energy density spectrum. However, an idealized sea surface is assumed; that is, the distribution of surface deviations about the mean is Gaussian and the energy is narrow-banded in the frequency domain. Neither of these assumptions is satisfied for storm wave records on the Continental Shelf. Jahns and Wheeler [4] have shown that substantial deviations from the Gaussian assumption occur in water depths up to 100 ft. Furthermore, reported storm wave spectra and spectral hindcasts made by modern wave prediction methods may not be sufficiently narrow-banded to justify that assumption. A study was undertaken using measured storm wave records from several Continental Shelf areas to test the adequacy of estimating formulae for individual wave parameters. The results reported in this paper will allow the designer to avoid any unintended bias in selecting design wave parameters. The results also provide a basis for the development of empirical compensation factors for practical use.

DATA SOURCES AND ANALYSES

The offshore petroleum industry has undertaken several measurement programs in areas of present and future interest. Valuable wave records have been obtained in the Gulf of Mexico through the Ocean Data Gathering Program [5], in the North Sea through a measurement program sponsored by the United Kingdom Offshore Operators Association and through the Gulf of Alaska Wave and Wind Measurement Program [6]. Exxon has also obtained storm wave data in conjunction with offshore operations. Analysis of these data is restricted to digitized storm wave records. The arisen sea states provide the opportunity to examine greater deviations from the idealized sea surface than would be expected under ambient wave conditions. Compensation factors developed from the measured storm data should be applicable to design problems because the underlying physical phenomena are similar to those that occur under design level conditions.

Table 1 summarizes the data sources utilized in this study. Widely different geographic areas, water depths, and measurement systems are combined in the results presented in this paper. Altogether, approximately 376 hours of storm wave records were analyzed.

TABLE 1 Summary of Data Sources Utilized

	<u>Gulf of Mexico</u>	<u>Offshore Australia</u>	<u>Northern North Sea</u>	<u>Gulf of Alaska</u>
Locations	Various	38°59'S, 142°33'E	60°20'N, 0°E	Various
Dates	Various	May, 1968	Nov, 1973- Jan, 1974	Nov, 1974- Feb, 1975
No. of Stormy Intervals	7	1	8	6
Water Depth	34-340 ft	327 ft	522 ft	366-600 ft
Minimum H _s	8 ft	15 ft	15 ft	15 ft
Measurement System	Wavestaff (fixed platform)	Heave-Compensated Wavestaff (semi-submersible)	Waverider Buoy	Waverider Buoy

Many investigators have presented characteristic spectra based on wave measurements. The principal ones applied to continental shelf storms are due to Pierson and Moskowitz [7], Robinson, Brannon and Kattawar [8] and Hasselmann et al [9, 10, 11]. These spectra are compared in a nondimensionalized form in Fig. 2. The dimensionless groups used here place the dominant spectral frequency at unity and require that the area under the spectrum be unity. Thus, the spectral density shapes in the frequency domain can be compared directly. The storm wave data analyzed in this study exhibit a broad range of spectral shapes which include all three of the model shapes illustrated in Fig. 2. This is not unexpected because of the variety of meteorological conditions represented by the data. The storm waves in the Gulf of Mexico are produced by tropical storms with their attendant high winds and rapidly changing wind fields. North Sea and Gulf of Alaska storms are produced by large extratropical disturbances which have lower wind speeds but greater fetch lengths and durations. In some cases there is swell propagating into the wind fetch area which alters the character of the storm spectra.

Statistical analyses of the storm wave records were conducted in a hierarchy outlined below:

Data Blocks - Continuous water surface deviation records were digitized, and approximately 20-minute segments were analyzed as a block. A 20-minute wave record is considered long enough to obtain statistically meaningful results, but short enough to warrant the assumption of a stationary, ergodic process. The data were screened to insure that no noise spikes, DC drifts or original analog signal lapses would be inadvertently incorporated into the statistical analysis. An amplitude energy density spectrum was computed for each block of storm wave data. This defined the dominant spectral frequency and the spectral moments for the block. The spectral calculations were conducted by the methods of Blackman and Tukey

[12] with the number of lag products used for the autocorrelation function calculation equal to approximately $100/\Delta t$. Statistics on individual wave crest elevations, heights and zero-crossing periods were accumulated from the wave record. Other special parameters which will be discussed later were also computed for each block of data. Quantities derived from the wave record analysis were nondimensionalized by fundamental spectral parameters. Wave crest and height parameters were nondimensionalized by $\sigma = \sqrt{m_0}$ and wave period parameters were nondimensionalized by T_1 .

Stormy Interval - The stormy intervals analyzed had reasonably constant spectral shape characteristics over the interval of significant wave heights used (cf. Table 1). Statistics for the nondimensional parameters were compiled based on the values accumulated for each block of data within each stormy interval.

Composite Statistics - The results from each stormy interval were combined by area, spectral characteristic (such as bandwidth parameter), water depth or other combinations of data. These are the results that are presented in this paper. In all, approximately 148,000 zero-crossing waves were processed digitally and their statistics accumulated. The results presented below are broadly divided into three categories: surface deviation statistics, individual wave height statistics, and individual wave period statistics.

SURFACE DEVIATION STATISTICS

The non-Gaussian behavior of surface deviations are water depth dependent. Jahns and Wheeler [4] demonstrated that fact with shallow water storm wave records obtained in the Gulf of Mexico. For the data available there is no important non-Gaussian behavior discernible in water depths greater than about 350 ft. However, imperfections in the wave measurement systems utilized could easily mask the small deviations that are expected in these water depths. The non-Gaussian behavior of the sea surface manifests itself as a surplus of rare wave crests and a deficit of rare wave troughs relative to those predicted by the theoretical developments of Cartwright and Longuet-Higgins [3]. For the case of zero-crossing waves only, the rare crests (large η^*/σ) are predicted to follow the Rayleigh distribution.

Jahns and Wheeler [4] suggested a correction to the Rayleigh distribution in the following form.

$$P [\text{wave crest } \eta_c \leq \eta^* | \sigma] = 1 - \exp \left\{ -\frac{1}{2} \left(\frac{\eta^*}{\sigma} \right)^2 \left[1 - B_1 \frac{\eta^*}{d} \left(B_2 - \frac{\eta^*}{d} \right) \right] \right\} \quad (1)$$

This correlation is shown in Fig. 3 along with the composite shallow water data presented by Jahns and Wheeler [4] and Gulf of Mexico data from hurricane Camille in 340-ft water depth [13]. The form of this correlation suggests that the probability of rarely occurring crest heights relative to the storm wave record σ will increase gradually with increasing crest height-to-water depth ratio (η^*/d) and reach maximum

near 0.3. The parabolic form of the correlation reflects the fact that crest heights of breaking waves will be about 0.55-0.60 of the water depth. Thus, the water depth effect cannot continue indefinitely with increasing η^*/d .

Another aspect of surface deviation analysis relates to commonly used methods for estimating the fundamental wave record property σ from an instrumentally-recorded analog wave record. It is often not convenient to digitize and process a large volume of analog wave surface deviation recordings from wave measuring instruments. Two methods are evaluated as part of this study. The mean-rectified deviation is easy to record electronically [14]. This recording procedure was simulated using the digitized storm wave data available. Tucker [15] proposes a method that utilizes the highest crest and lowest trough (or second highest crest and second lowest trough) in an analog wave record. These parameters can often be determined quickly by inspection of a paper chart record of 100 or so waves. This procedure was also simulated digitally.

The equations that apply are found in the paper by Tucker [15]. His equations can be rearranged to provide the following estimates of the RMS surface deviation σ of the wave record, σ_r , σ_1 , and σ_2 , based on the mean-rectified deviation and Tucker's definition of H_1 and H_2 , respectively.

$$\sigma_r = \bar{H}_r \sqrt{\pi/2} \quad (2)$$

$$\sigma_1 = H_1/[2\sqrt{2\theta} (1 + 0.289 \theta^{-1} - 0.247 \theta^{-2})] \quad (3)$$

$$\sigma_2 = H_2/[2\sqrt{2\theta} (1 - 0.211 \theta^{-1} - 0.103 \theta^{-2})] \quad (4)$$

For each block of wave data, the three estimates of σ were calculated and used to normalize the true σ of the wave record. The mean and coefficient of variation of the accumulated ratios were determined. These results are presented in Table 2.

Table 2. Estimates of RMS Surface Deviation

	σ/σ_r	σ/σ_1	σ/σ_2
Range for 4 Areas (Table 1)			
Mean	0.997-1.018	0.996-1.028	0.997-1.026
Coefficient of Variation	1.0-1.4%	8.5-10.1%	5.6-6.6%
Composite Data			
Mean	1.001	1.011	1.013
Coefficient of Variation	1.3%	8.7%	6.1%

It is evident from the results that all three methods on the average give an essentially unbiased estimate of the true RMS surface deviation. However, the method based on mean-rectified wave height produces a much smaller coefficient of variation. The relatively large coefficients of variation obtained for the H_1 and H_2 methods could cause significant error in the estimate of σ (and hence of the spectral estimate of significant wave height $H_s = 4 \sigma$) by infrequent sampling of analog wave records. These errors would compensate over a long time period such as is the case when processing ambient wave statistics. Isolated, severe storm wave records could have true values of H_s substantially different than those assigned by infrequent sampling of the wave record by the H_1 or H_2 method.

INDIVIDUAL WAVE HEIGHT STATISTICS

Proper assessment of individual wave height statistics requires that a consistent definition be adopted for wave height determination. As indicated in Fig. 4, wave height can be defined as the difference between the trough and crest elevation between two successive zero crossings in either the upward direction or in the downward direction. One can also assign a wave height based on the average trough depths about a given crest. Of course, the idealized waves assumed in design practice are symmetric about the crest unlike most large rare waves in a storm sea state. The rare wave heights for all possible wave height definitions were normalized to σ and compared with the commonly accepted Rayleigh distribution. These results are presented in Fig. 5. This analysis is concentrated on the highest 1/10th waves which are in excess of the nominal significant wave height $H_s = 4 \sigma$ for the sea state. The probability of exceeding rare waves on the order of twice the significant wave height was consistently much less for the instrumental storm wave records analyzed than predicted by the Rayleigh distribution. This finding contradicts many publications which assume wave heights are approximately Rayleigh distributed. However, those assumptions are not based on detailed examination of the extreme right-hand tail of data.

A commonly accepted practice for estimating the maximum wave height in a storm sea state is to derive the wave which would be exceeded on the average once in N_z zero-crossing waves. This is given by the following well-known expression:

$$H_{\max} = H_s \sqrt{\frac{1}{2} \ln N_z} \quad (5)$$

which can be derived from Equation 3 for large N_z . Table 3 shows the height actually exceeded based on all the normalized storm wave records (Figure 5) relative to the height that is predicted to be exceeded by the Rayleigh distribution (Equation 5) for the probability level of 1 in 1000 waves.

TABLE 3 Compensation of Rayleigh Height Statistics

	$\frac{H \text{ Actual}}{H \text{ Rayleigh}}$, for $P[H^* \sigma] = 0.999$		
	<u>Downcrossing</u>	<u>Upcrossing</u>	<u>Average</u>
Range for 4 Areas (Table 1)	0.87-0.92	0.89-0.94	0.86-0.92
Composite Data	0.892	0.920	0.867

The results are consistent for all areas from which data are available and show on the average the true rare wave height is about 10 percent less than predicted at the 1 in 1000 probability level. The form of the composite statistics shown in Fig. 5 suggests a linear compensation to the Rayleigh distribution as follows.

$$P[\text{wave height } H \leq H^*|\sigma] = 1 - \exp \left\{ -\frac{1}{8} \left(\frac{H^*}{\sigma} \right)^2 \left[C_1 + C_2 \left(\frac{H^*}{\sigma} \right) \right] \right\} \quad (6)$$

Thus, the exceedance probability for increasingly rare nondimensional wave heights H^*/σ will increasingly depart from the Rayleigh distribution. The extreme wave heights could be renormalized to the true significant wave height ($H_{1/3}$) as measured by the highest one-third waves in the wave records. Of course, the data would then agree with the Rayleigh distribution at a height equal to the significant wave height. However, there would still be a downward compensation of the true wave height distribution relative to Rayleigh statistics required for increasingly rarer waves as a consequence of Equation 6. Furthermore, the true significant wave height $H_{1/3}$ is not necessarily equal to the fundamental property of the wave record, $H_s = 4\sigma$. Only $\sigma = \sqrt{m_0}$ is predicted by spectral wave models, and is related to the energy content of the sea surface. Therefore, the most useful scaling parameter for individual wave height statistics would be based on the wave record RMS surface deviation σ as shown in Fig. 5.

INDIVIDUAL WAVE PERIOD STATISTICS

The design engineer must also estimate the zero-crossing period associated with a design wave height. The kinetics of water particle motion in space and time calculated for design waves can vary significantly with wave period. It is also necessary to estimate the zero-crossing period of all waves so that the number of waves per hour for the duration of a nominal storm sea state can be estimated. If the storm wave spectra were extremely narrow-banded ($\epsilon = 0$), then all wave periods should be essentially equal to the dominant spectral period. Therefore, it is intuitive that the deviations from this ideal situation should be dependent on the bandwidth parameter ϵ . The definition of ϵ which we use is based on the ratio of the number of zero-crossing waves to the total number of double-amplitude waves in the block of wave data N_z/N_w .

$$\epsilon = \sqrt{1 - (N_z/N_w)^2} \quad (7)$$

This is a more stable estimate of ϵ because it does not depend on the higher spectral moments, which depend strongly on the higher frequency energy and which are subject to some uncertainty due to wave recording and digitization procedures. This subject has been treated in detail by Goda [16].

Figure 6 illustrates the average zero-crossing period normalized to the dominant spectral period over each stormy interval versus the average bandwidth parameter ϵ for that interval. The results, while empirical, provide a useful correlation to relate the average number of zero-crossing waves in a storm wave record to the bandwidth. Figure 6 shows that even for relatively narrow-banded storm spectra the zero-crossing periods will average about 0.8 of the dominant spectral period. The standard deviation of the ratio T_z/T_d between individual blocks of wave data within a stormy interval is 0.071.

A similar correlation is shown in Fig. 7 for rare wave zero-crossing periods. Here the rare wave period definitions are the average of the downcrossing periods of the highest one-third waves, of the highest one-tenth waves, and of the maximum wave in the particular block of wave data. The same trend is exhibited for all of the large well formed waves in a storm sea state. This confirms results reported by Goda [16]. Consequently, we can conclude that the average period of the significant waves and larger exhibit an essentially constant ratio to the dominant spectral period of the sea state in which they occur. The ratio is less than unity and is bandwidth dependent. This result implies that the extreme wave heights in a sea state are associated with steeper waves of essentially the same zero-crossing periods on the average as the less rare waves in that sea state. Comparison of Fig. 6 with Fig. 7 shows that the average period of the large waves is always greater than the average zero-crossing period of all the waves in the record. As indicated by the dashed lines in Fig. 7, these correlations are not exact. The standard deviation of the wave periods normalized to the dominant spectral period between individual blocks of data increases as the wave rarity increases.

The empirical results presented in Figs. 6 and 7 also can be presented in terms of wave periods derived from properties of each storm sea state spectrum. Formulae have been suggested [1,3,16] for estimating average wave record properties as follows:

$$\bar{T} = 2\pi m_0/m_1 \quad (8)$$

$$T_0 = 2\pi \sqrt{m_0/m_2} \quad (9)$$

$$\epsilon_s = \sqrt{1 - m_2^2/m_0 m_4} \quad (10)$$

These formulae should account for finite spectral width ($\epsilon \neq 0$) by incorporating the higher spectral moments. These spectral estimates

were normalized by their corresponding true values for each block of data and compiled over each stormy interval analyzed. These results are presented in Figs. 8 and 9 versus the bandwidth parameter. The spectral estimates consistently underpredict the true values of wave period as derived from the wave records, particularly for the wider-banded wave spectra. Note that the standard deviation of the normalized ratios is substantially less than for the results shown in Figs. 6 and 7. There is no consistent correlation between the spectral estimate ϵ_S with that derived from the wave counts. On the average the spectral estimate of bandwidth parameter ϵ_S is about 5 to 15 percent greater than the value defined by Equation 7 for the storm wave records analyzed.

CONCLUSIONS

1. The properties of storm waves that are rare in their sea state show uniform, correlatable behavior when nondimensionalized by the fundamental spectral properties derived from the wave records. This result covers a wide range of geographic locations, water depths, and storm characteristics.
2. Surface deviation statistics are non-Gaussian and exhibit a surplus of rare crests relative to the Rayleigh distribution out to at least 340-foot water depth as determined by hurricane Camille wave records from the Gulf of Mexico.
3. Simplified methods to estimate the true RMS surface deviation σ of a storm wave record are unbiased on the average, but some methods can lead to substantial error when applied to a small sample of wave record.
4. The statistics of extreme wave height, as measured by elevation difference between trough and crest, deviate substantially from the Rayleigh distribution at the 1 in 1000 wave probability level. The true observed wave heights are on the order of 10 percent less than predicted.
5. The zero-crossing wave periods for the entire record and for the rare waves in a sea state can be nondimensionalized by the dominant spectral period and correlated with bandwidth parameter ϵ . The wave periods relative to the dominant spectral period decrease as bandwidth increases.
6. The approximate formulae for individual wave periods and bandwidth parameter based on higher spectral moments do not agree well with results obtained directly from the wave records.

ACKNOWLEDGMENTS

The authors wish to thank the Oceanographic Committee of the United Kingdom Offshore Operators Association and the participants in the Gulf of Alaska Wave and Wind Measurement Program for permission to utilize their proprietary storm wave records in this study. We also acknowledge the efforts of M. A. Williams of Rice University who assisted with the digital wave record processing.

NOMENCLATURE

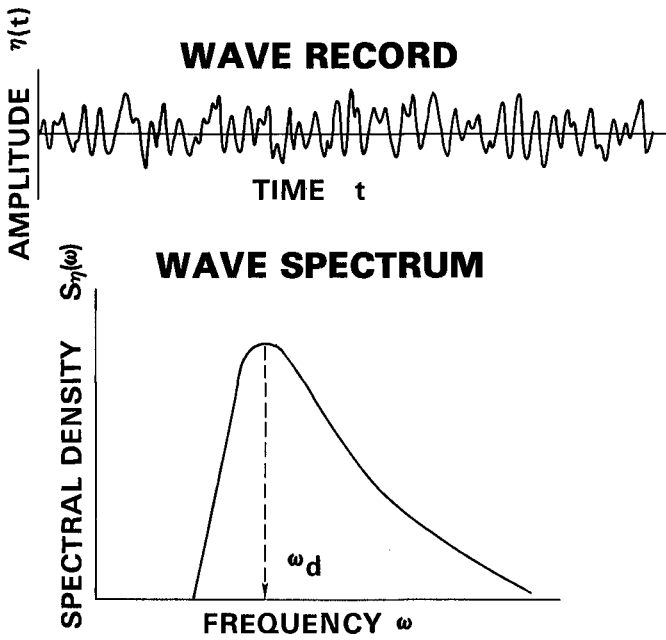
B_1, B_2	= arbitrary constants (Equation 1)
C_1, C_2	= arbitrary constants (Equation 6)
d	= water depth
f	= frequency, Hertz
\hat{h}	= dimensionless wave height, H/σ
H^*	= arbitrary wave height
H_{\max}	= estimate of maximum wave height (Equation 5)
$H_{1/N}$	= average height of highest 1/Nth waves
\bar{H}_r	= mean-rectified wave height
H_s	= $4\sigma = 4\sqrt{m_0}$ = spectral estimate of significant wave height
H_1	= Wave height based on highest crest and lowest trough in wave record
H_2	= wave height based on second highest crest and second lowest trough in wave record
m_k	= kth moment of amplitude energy density spectrum (Figure 1)
N_z	= number of zero-crossing waves in wave record
N_w	= number of double-amplitude waves in wave record (number of crests)
$P[]$	= probability that statement in brackets is true
T_d	= $1/f_d$ = dominant spectral period
$T_{1/N}$	= average zero-crossing period of highest 1/Nth waves
T_{\max}	= period of highest wave in wave record

T_o	= spectral estimate of average wave period (Equation 9)
T_z	= average zero-crossing period in wave record
\tilde{T}	= spectral estimate of significant wave period (Equation 8)
γ	= dimensionless crest height, η_c/σ
Δt	= time interval between digitized wave record points
ϵ	= bandwidth parameter (Equation 7)
ϵ_s	= spectral estimate of ϵ (Equation 10)
η_c	= crest height of zero-crossing wave
η^*	= arbitrary crest height above mean water level
ω	= circular frequency
σ	= RMS surface deviation of wave record
$\sigma_{r,1,2}$	= estimates of σ (Equations 2, 3, 4)
θ	= $\lambda n N_z$

REFERENCES

1. Cardone, V. J., Pierson, W. J., and Ward, E. G., "Hindcasting the Directional Spectra of Hurricane Generated Waves", OTC 2332, Seventh Annual Offshore Technology Conference, Houston, May 5-8, 1975.
2. "API Recommended Practice for Planning, Designing, and Constructing Fixed Offshore Platforms," API RP2A, 7th Edition, January 1976.
3. Cartwright, D. E. and Longuet-Higgins, M. S., "The Statistical Distribution of the Maxima of a Random Function", Proceedings Royal Society, 1956, A237, pp. 212-232.
4. Jahns, H. O. and Wheeler, J. D.: "Long-Term Wave Probabilities Based on Hindcasting of Severe Storms," JPT, April, 1973, p. 473-486.
5. Ward, E. G.: "Ocean Data Gathering Program - An Overview," OTC 2108-B, 6th Offshore Technology Conference, May 6-8, 1974, Houston, Texas.
6. McLeod, W. R.: "A Unique Strategy for Obtaining Wind and Wave Data in the Gulf of Alaska" OTC 2297, 7th Offshore Technology Conference, May 5-8, 1975, Houston, Texas.

7. Pierson, W. J. and Moskowitz, L.: "A Proposed Spectral Form for Fully Developed Wind Seas Based on the Similarity Theory of S. A. Kitaigorodskii," JGR, vol. 69, no. 24, 1964, p. 5181-5190.
8. Robinson, R. J., Brannon, H. R. and Kattawar, G. W.: "Storm Wave Characteristics," SPEJ, March, 1967, p. 87-98.
9. Hasselmann, K. et al.: "Measurements of Wind-Wave Growth and Swell Decay During the Joint North Sea Wave Project (JONSWAP)", Deutsches Hydrographisches Institut, Hamburg, 1973.
10. Rye, H., Byrd, R. C. and Torum, A.: "Sharply Peaked Wave Energy Spectra in the North Sea," OTC 2107, 6th Offshore Technology Conference, May 6-8, 1974, Houston, Texas.
11. Saetre, H. J.: "On High Wave Conditions in the Northern North Sea," Report No. 3, Institute of Oceanographic Sciences, Wormley, England, 1974.
12. Blackman, R. B. and Tukey, J. W.: The Measurement of Power Spectra, Dover Publications, Inc., New York (1958).
13. Patterson, M. M.: "Oceanographic Data from Hurricane Camille," OTC 2109, 6th Offshore Technology Conference, May 6-8, 1974, Houston, Texas.
14. Blair, P.M.: "Buoy for Recording Wave Height and Period," Proceedings of the International Symposium on Ocean Wave Measurement and Analysis, September 9-11, 1974, New Orleans, Louisiana, p. 254-271.
15. Tucker, M. J., "Analysis of Records of Sea Waves", Paper No. 6691, N. I. O. Conference, 1963.
16. Goda, Y.: "Estimation of Wave Statistics from Spectral Information," Proceedings of the International Symposium on Ocean Wave Measurement and Analysis, September 9-11, 1974, New Orleans, Louisiana, p. 320-337.



DERIVED PROPERTIES

$m_K = \int_0^{\infty} \omega^K S_{\eta}(\omega) d\omega$, THE Kth SPECTRAL MOMENT

$T_d = 2\pi/\omega_d$, THE DOMINANT SPECTRAL PERIOD

$\sigma^2 = m_0$, THE VARIANCE OF WAVE RECORD $\eta(t)$

Figure 1. Typical sea state spectrum

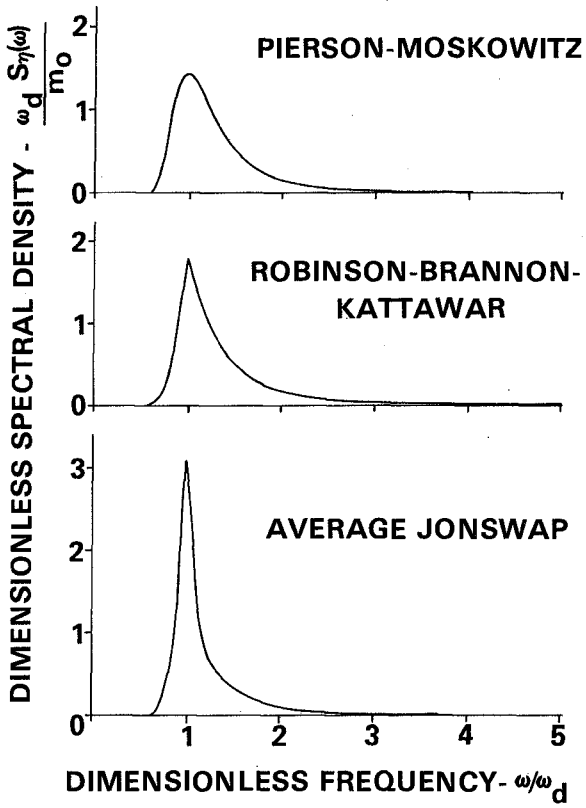


Figure 2. Model spectral shapes

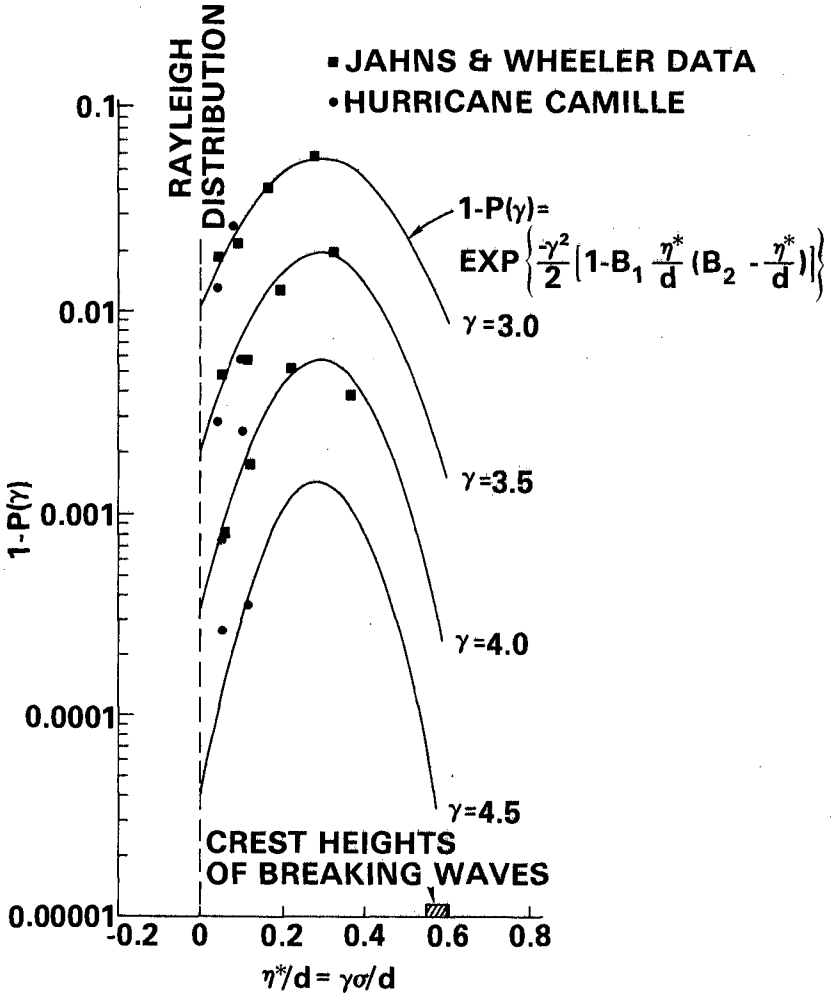


Figure 3. Rare wave crest statistics

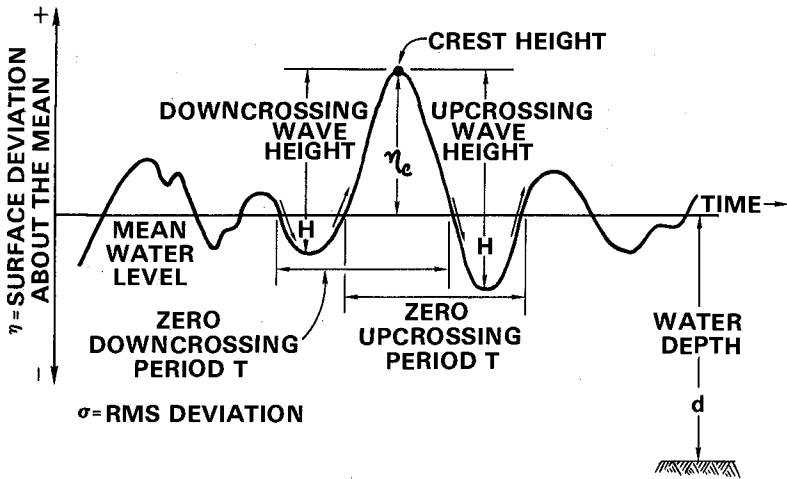


Figure 4. Wave height definitions

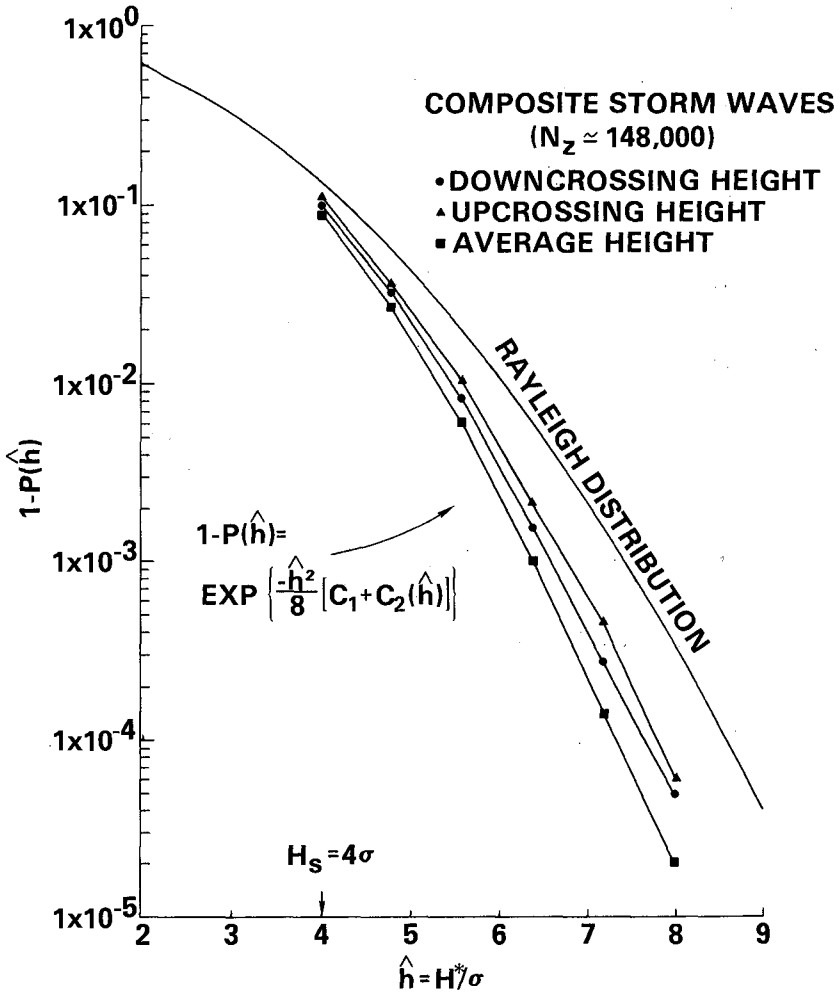


Figure 5. Rare wave height statistics

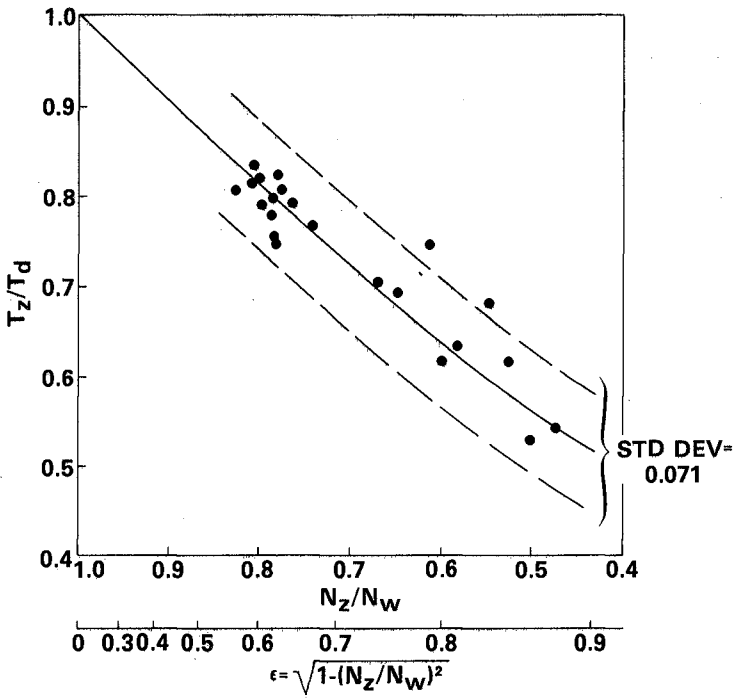


Figure 6. Average zero-crossing period

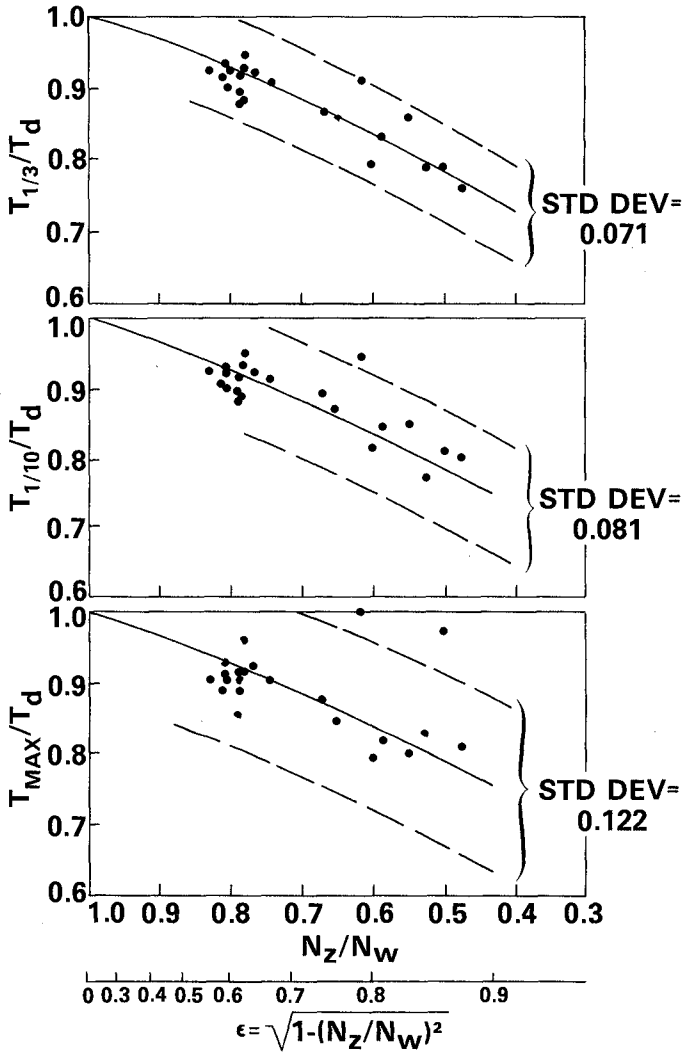


Figure 7. Rare wave periods

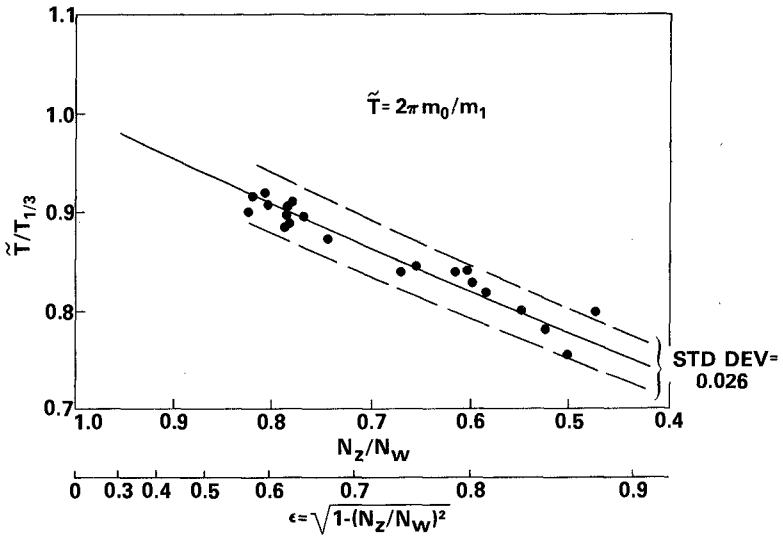


Figure 8. Spectral estimates of wave period

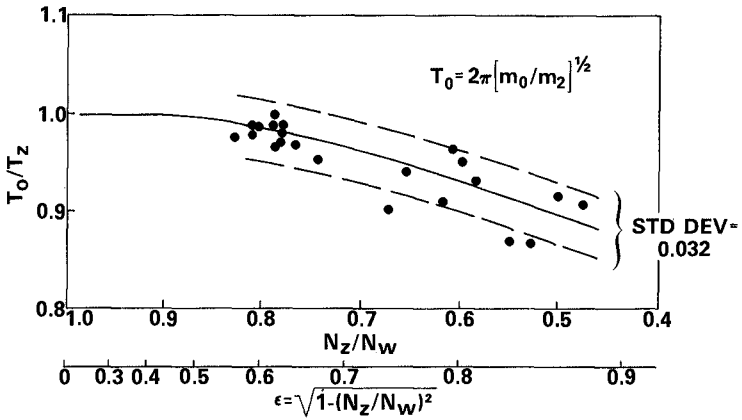


Figure 9. Spectral estimates of wave period

CHAPTER 11

CONSECUTIVE HIGH WAVES IN COASTAL WATERS

by Winfried Siefert^{*)}

Abstract

The problem of statistics of numbers of consecutive high waves has not yet been treated in detail. Some numerical results (Goda, 1970) and evaluations of prototype data in water depths of 100 m (Rye, 1975) and 40 m (Wilson and Baird, 1973) respectively were published. Data from measurements in nearshore coastal waters, with unbroken, breaking and broken waves, obtained in the Elbe estuary, are treated in this paper.

Introduction

For the design of coastal structures as well as for the understanding of coastal processes a lot of prototype wave data is necessary. During the last decade research has been intensified all over the world. Usually the wave climate at a certain position is characterized by representative heights and periods (\bar{H} , $H_{1/3}$, \bar{T} , $T_{H_{1/3}}$) and energy spectra. By correlation with wind data, functions of wave height, period, and spectra occurrence and exceedance can be given. In addition to that distribution functions of wave heights and periods for any wave stage can be derived, as has been done by evaluation of about 15.000 wave records in the Elbe estuary at the German North Sea coast (Siefert, 1974) (Fig. 1).

Concerning stability problems of structures extended to wave attack there is another criterion: the number of waves in a run that exceed a predetermined value. There are

^{*)} Dr.-Ing., Strom- und Hafengebäude Hamburg, Coastal Eng. Res. Group "Neuwerk", 2190 Cuxhaven, West Germany

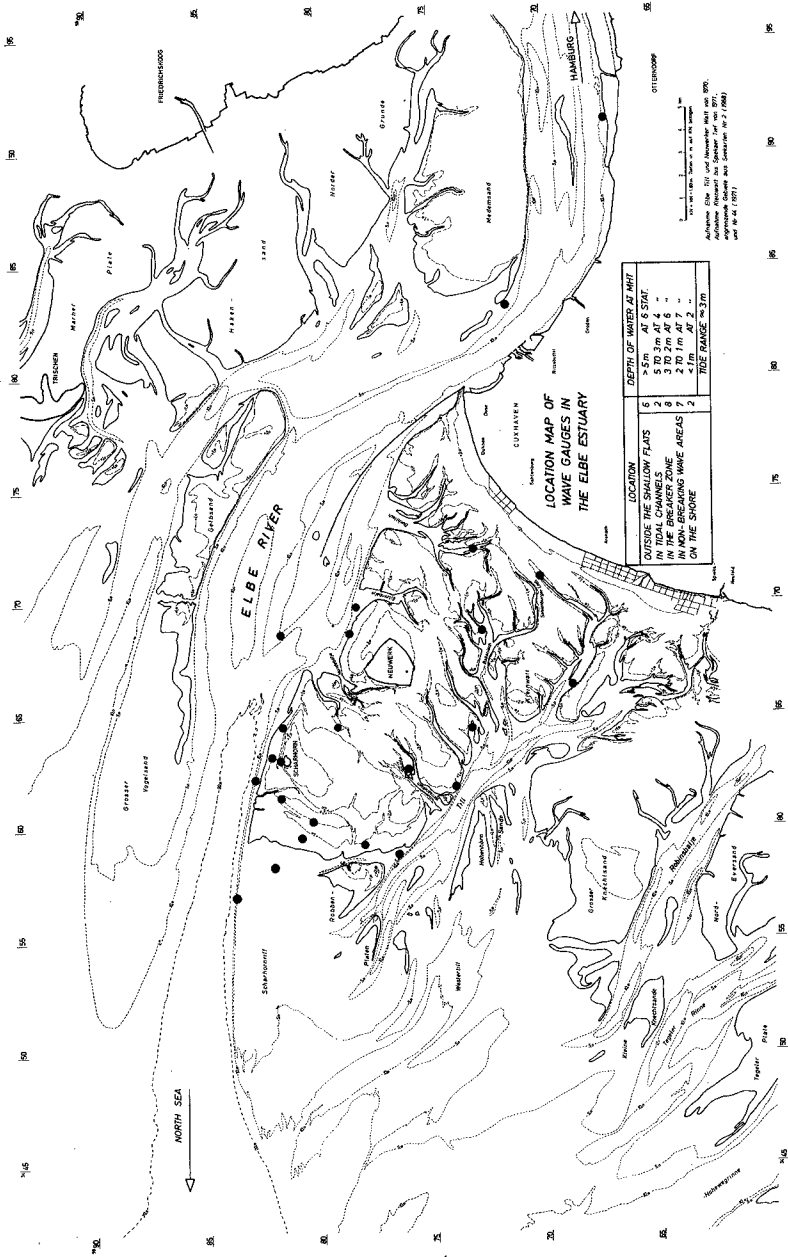


Fig. 1
Wave Investigations in the Elbe Estuary

not yet transfer functions between distributions of heights and periods or energy spectra and the numbers of consecutive high waves. So this problem has to be analyzed separately as an additional information.

The static wave force on a structure is usually characterized by the design water level plus highest wave height. The dynamic force - evaluated by one or the other good or bad formula - is usually derived from the significant wave height or $H_{1/10}$ or something similar. The realistic force, caused by a run of waves of a certain height and generating vibrations and perhaps resonance, is not yet subject to wave design.

Analysis

Numerical treatments of the problem of statistics of consecutive high waves were done by Goda (1970), for wide spectra, with additional derivations for narrow band spectra by Ewing (1973); evaluations of prototype data in water depths of 100 m by Rye (1975) and 40 m by Wilson and Baird (1973). These results are shown together with some results from the Elbe estuary in linear scale on Fig. 2.

The presented values for waves in a run higher than $H_{1/3}$ show large agreement, though there seem to be some specific differences.

Most of the "runs" with waves $>H_{1/3}$ occur in runs of only one wave, i.e. preceded and followed by smaller waves (70 to 85%). About 10 to 20% of the runs consist of 2 waves, up to 7% of 3 waves, up to 2.5% of 4 waves. More than 5 waves $> H_{1/3}$ in a run are not yet identified.

For further analysis this graph will be presented in semi-logarithmic scale. Before that it seems to be useful to do some remarks on the evaluation and the definition of a group or "run". Table 1 gives the height numbers of consecutive waves in a record with the notification of waves $>H_{1/3}$ and numbers of wave groups. In general, one "event" is

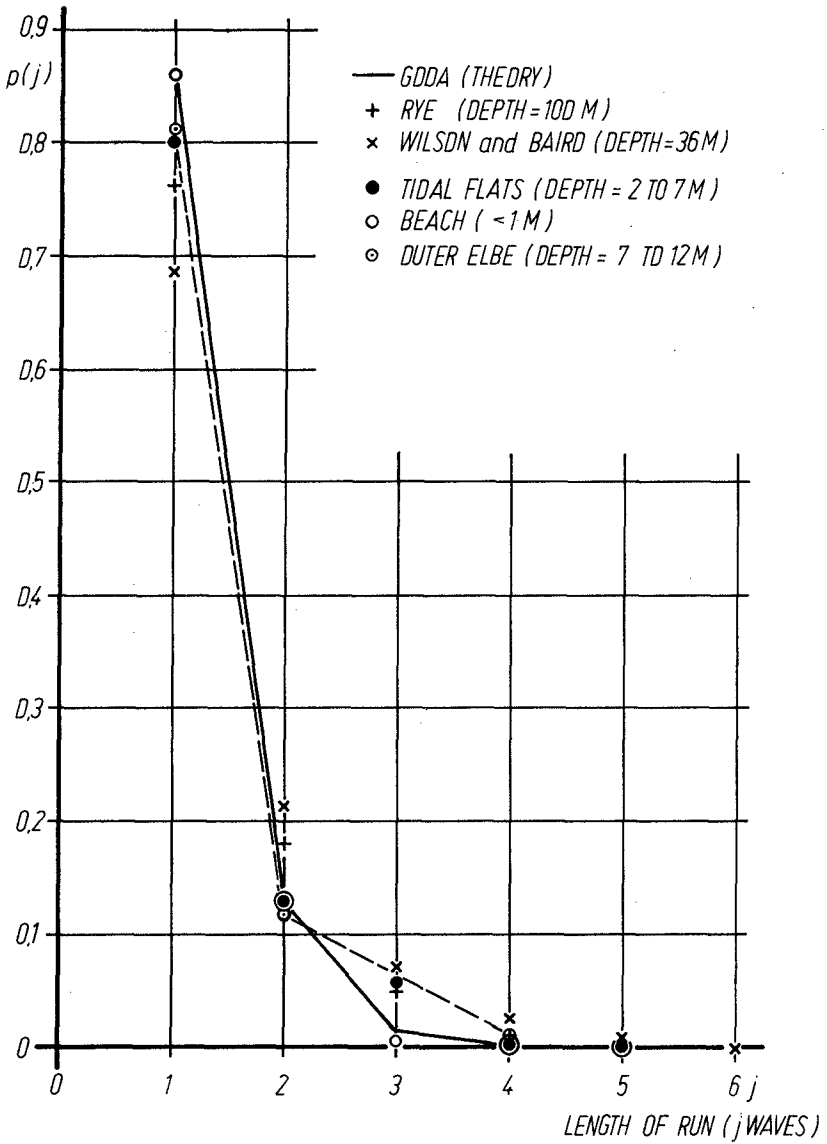


Fig. 2
 Probability of Wave Group Formation,
 Waves Greater than $H_{1/3}$

Table 1

Example for Evaluation of Wave Groups

Wave Heights in cm	Waves greater than $H_{1/3}$	Wave Group No.
23		
<u>73</u>	x	1
12		
40		
<u>66</u>	x	
<u>66</u>	x	2
<u>84</u>	x	
30		
30		
47		
50		
50		
18		
19		
14		
<u>68</u>	x	
<u>65</u>	x	3
45		
50		
36		

Mean values of the complete
record: $\bar{H} = 40$ cm
 $H_{1/3} = 61$ cm
 $\bar{T} = 3.3$ sec

understood as a "group" of consecutive waves above a chosen limit, a "group" consisting of one or more waves in a row.

On the left side of Fig. 3 we see the before mentioned results. Theory seems to give too small probabilities for the occurrence of 3 and more waves $>H_{1/3}$ in a run. The results from the outer Elbe and in greater depths are more or less identical.

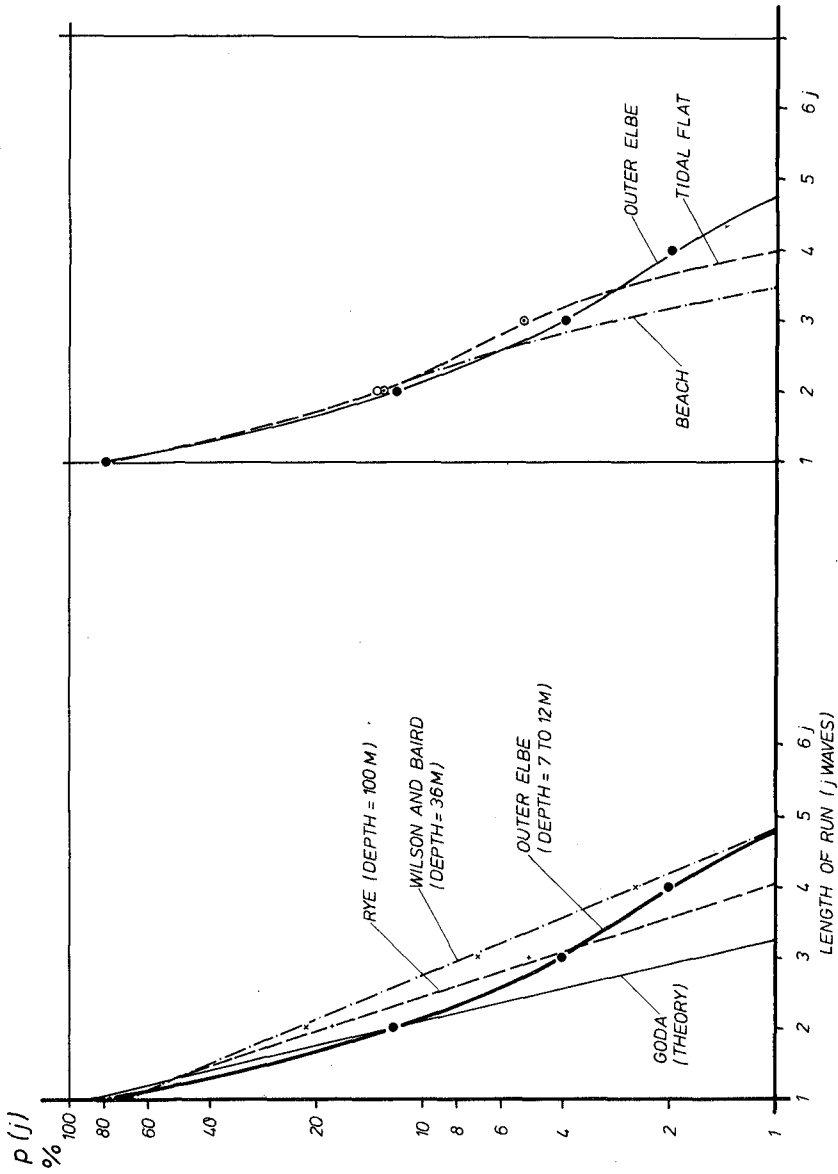


Fig. 3

Probability of Wave Group Formation with Waves Greater than $H_{1/3}$

The comparison on the right side of Fig. 3 shows that in very shallow water the probability of long runs is diminished and nearly the same as Goda's theory.

Some hints of changes of wave group behaviour with mean wave height can be given on Fig. 4. In three different topographic areas with different water depths it turns out that the probability of longer runs with $H > H_{1/3}$ raises with mean wave height. As possible mean wave height raises with water depth, the tendency is the same as on Fig. 3: increase of probability of long runs with high waves with increasing water depth.

The analysis of wave groups $> 1.8 \bar{H}$ shows on the left side of Fig. 5 the same tendency as was seen with groups $> H_{1/3}$: In shallow water the probability of long runs of high waves becomes smaller.

On the right side we see that the probability of long runs diminishes with increasing predetermined height. But this result has to be considered in detail, as is shown on Fig. 6.

These graphs show the probability of wave group formation versus the relation of predetermined and mean wave height.

A certain number of records was evaluated as follows: All waves higher than H^* are 100%. Now each run contains a certain amount of these 100%.

The dots indicate the percentage of waves with $H > H^*$ that occurred in the longest run of a record.

In connection with this the increase of wave periods with wave heights has to be taken into account, i.e. on Table 2 from the right to the left:

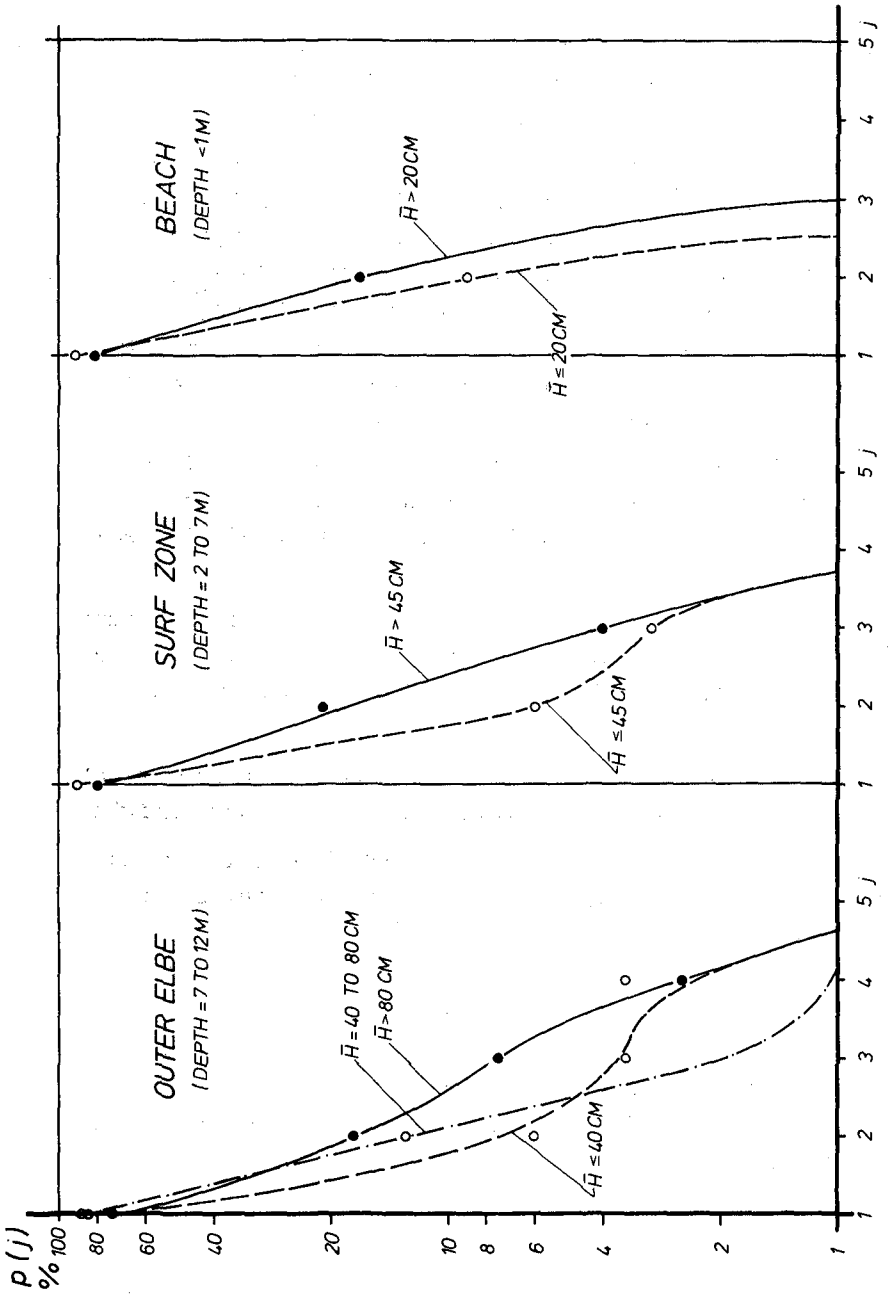


Fig. 4

Probability of Wave Group Formation with Waves Greater than $H_1/3$ for Different Topographic Areas and Mean Wave Heights

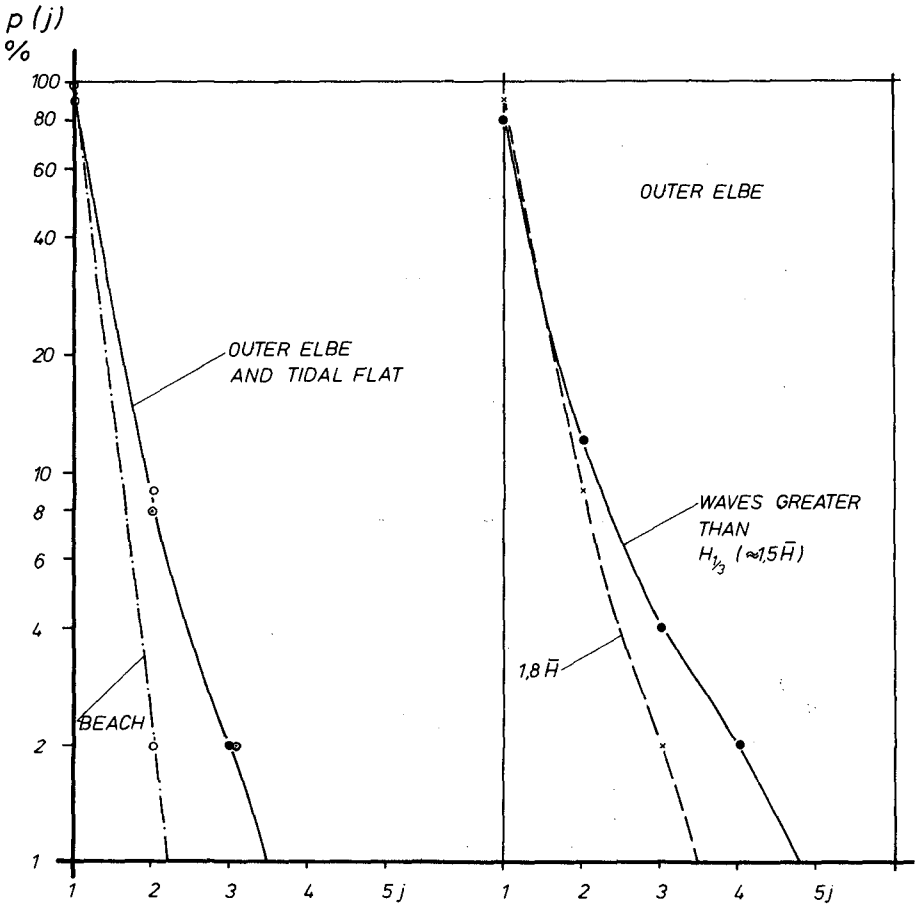


Fig. 5
 Probability of Wave Group Formation
 Waves Greater than $1.8 \bar{H}$

OUTER ELBE

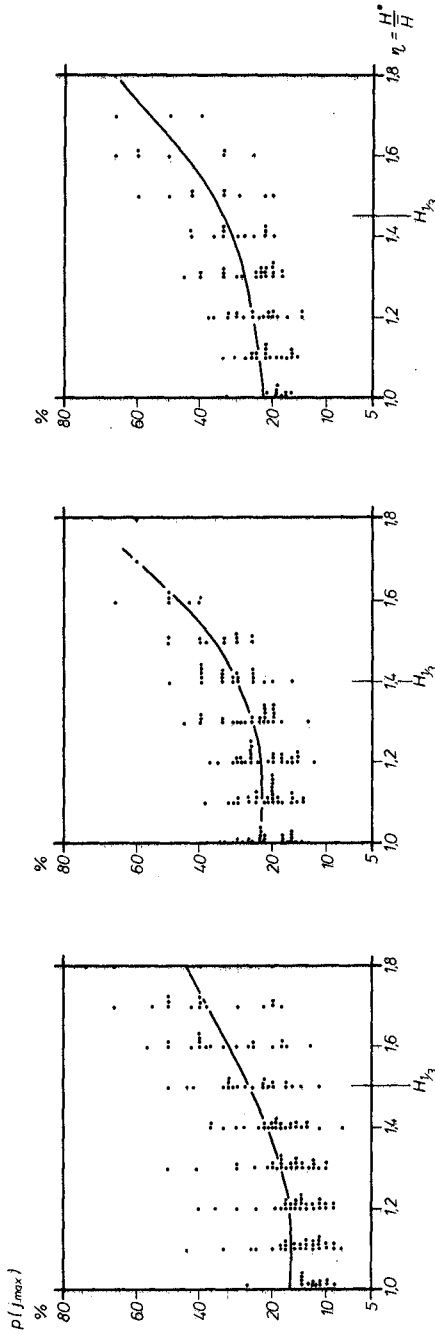
29 RECORDS
 $d = 5.8$ TO 9.9 M
 $\bar{H} = 1.8$ TO 1.52 CM
 $\bar{T} = 2.1$ TO 5.9 SEC

SURF ZONE

29 RECORDS
 $d = 1.5$ TO 6.7 M
 $\bar{H} = 2.3$ TO 7.1 CM
 $\bar{T} = 2.6$ TO 5.3 SEC

TIDAL FLAT

20 RECORDS
 $d = 1.6$ TO 4.4 M
 $\bar{H} = 1.9$ TO 7.1 CM
 $\bar{T} = 1.5$ TO 4.1 SEC



WAVE GROUPS WITH WAVES $H > H^*$

Fig. 6
 Probability of Wave Group Formation
 (Longest Run of Each Record with j_{max} Consecutive Waves $H > H^*$)

Table 2
Connections Between Wave Periods Of
Different Wave Height Groups

<u>SOUTHERN NORTH SEA</u>	<u>SURF ZONE</u>	<u>TIDAL FLATS</u>
$T_{H_{1/3}} = 1.25 \bar{T}$	$T_{H_{1/3}} = 1.19 \bar{T}$	$T_{H_{1/3}} = 1.15 \bar{T}$
$T_{H_{1/10}} = 1.33 \bar{T}$	$T_{H_{1/10}} = 1.30 \bar{T}$	$T_{H_{1/10}} = 1.22 \bar{T}$
$T_{H_{\max}} = 1.46 \bar{T}$	$T_{H_{\max}} = 1.30 \bar{T}$	$T_{H_{\max}} = 1.28 \bar{T}$

Moreover, the formation of wave groups influences oscillations of wave set-up, and this way of wave analysis will also give some hints about the reliability of laboratory test results with monochromatic waves.

Not treated in this paper is the mean number of small waves between runs of high waves. Some informations on this problem are given by Ewing (1973).

Summary

The result of Figs. 3 to 6 is:

1. The greater H^* - the lower limit of the heights in the run - is, the lower is the number of waves above H^* ;
2. The greater H^* is, the greater is the probability that a lot of the waves $>H^*$ occur in one run: Waves greater than $1.6 \bar{H}$ appear in a run of 2 or 3 as often as in a "run" of 1 wave. Groups of 2 and 3 waves of a height greater than 1.7 or $1.8 \bar{H}$ have been recorded.
3. The greater the relation of design wave height and mean wave height is, the more important becomes the dynamic force by consecutive design wave heights.

References

- EWING, J.A.: Mean Length of Runs of High Waves. Jour. of Geoph. Res., Vol. 78, No. 12, 1973
- GODA, Y.: Numerical Experiments on Wave Statistics with Spectral Simulation. Report of the Port and Harbour Research Institute, Vol. 9, Nr. 3, Japan 1970
- RYE, H.: Wave Group Formation Among Storm Waves. Proc. CEC 1974, Copenhagen, ASCE, New York 1975
- SIEFERT, W.: Über den Seegang in Flachwassergebieten. Mitt. des Leichtweiß-Inst. der Techn. Univ. Braunschweig, H. 40, 1974
- SIEFERT, W.,
KALDENHOFF, H.: Analysis of Random Waves in Shallow Water and Laboratory Reproduction. Proc. 16th Congress of the JAHR, Vol. 1, Sao Paulo 1975
- WILSON, J.R.,
BAIRD, W.F.: A Discussion of Some Measured Wave Data. Proc. CEC 1972, Vancouver, ASCE, New York 1973

CHAPTER 12

PARAMETRIC REPRESENTATION OF A WIND-WAVE FIELD

by Henrik RYE^x and Roald SVEE, Dr. techn.^{xx}

The River and Harbour Laboratory (VHL) at
the Norwegian Institute of Technology,
7034 - Trondheim - NTH, Norway

SUMMARY

The applicability of various spectral shape parameters is discussed. The wave height distribution from 60 actual wave recordings is computed and compared to the Rayleigh distribution. The behaviour of various wave period parameters is discussed. Based on results from field data as well as numerical computations, it is concluded that some of the spectral wave parameters frequently used today may not be suitable for characterizing the wave field.

INTRODUCTION

Offshore activity in the North Sea has increased the need for wave data for the design of offshore structures. To overcome the increasing amount of wave data collected in the field, a parametric representation of the data is highly preferable.

This paper considers the usefulness of certain currently used wave parameters and distributions such as wave spectra, spectral width parameters, wave period parameters, and wave height distribution. It should be noted that the International PIANC Commission in their recent wave study /1/ recommended and stressed the need for such studies wherever possible.

The literature on this topic is relatively extensive and the results do not appear to be consistent. Some of the discrepancies from the past may be explained from the fact that reliable wave data from the field may be difficult to collect, especially during severe weather conditions, and that the wave recording equipment applied may not have been reliable. A recent test of the shipborne Tucker wave recorder /2/ concludes that "the pressure signal contains a relatively high level of noise of any kind, in particular in cases of

^x Senior scientist

^{xx} Head, section of harbour and coastal engineering

high wave conditions" /3/.

However, the accelerometer buoy produced by Datawell, Netherlands (the "Waverider" buoy), appears to be reliable /4/.

THE WAVE ENERGY SPECTRUM

It is generally believed today that the wave energy spectrum is able to express all the linear statistical properties of a wind-wave surface. However, the shape of the wave energy spectrum appears to be controversial. Based on the wave data available in 1964, Pierson and Moskowitz /5/ proposed a spectrum of the type

$$S_{PM}(f) = \alpha g^2 2\pi^{-4} f^{-5} \exp \left[-\frac{5}{4} \left(\frac{f}{f_p} \right)^{-4} \right] \quad (1)$$

where $S_{PM}(f)$ is the spectral density, f is the frequency (inverse of the wave period), f_p is the peak frequency (the frequency at which the spectral density reaches its maximum value) and α is Phillips' constant. This spectrum is widely used today for engineering applications /6, 7, 8, 9/.

More recently, K. Hasselmann et.al. /10/ arrived at another spectral formulation for fetch-limited, wave-growth conditions during the first Joint North Sea Wave Project (JONSWAP). This spectrum was shown to be much more sharply peaked than the corresponding Pierson Moskowitz type of spectrum. K. Hasselmann et. al. were able to fit the spectral shape of their observations to the following analytical expression:

$$S(f) = \alpha g^2 (2\pi)^{-4} f^{-5} \exp \left[-\frac{5}{4} \left(\frac{f}{f_p} \right)^{-4} \right] \gamma \exp \left[\frac{-(f-f_p)^2}{2\sigma^2 f_p^2} \right] \quad (2)$$

where $\sigma = \begin{cases} \sigma_a & \text{for } f < f_p \\ \sigma_b & \text{for } f > f_p \end{cases}$

where $S(f)$ is the spectral density of the spectrum (denoted the JONSWAP spectrum), α is the Phillips' /11/ constant (which was shown to vary considerably with the fetch and the wind speed), g is the acceleration of gravity, γ is the ratio of the maximal spectral energy to the maximum of the corresponding Pierson-Moskowitz spectrum (1) with the same values of α and f_p ; σ_a and σ_b define the left and right side widths, respectively, of the spectral peak. Fig. 1 illustrates the physical interpretation of the parameters α , f_p , γ , σ_a and σ_b . It is noted that for $\gamma = 1$, the JONSWAP spectrum reduces to a Pierson-Moskowitz type spectrum.

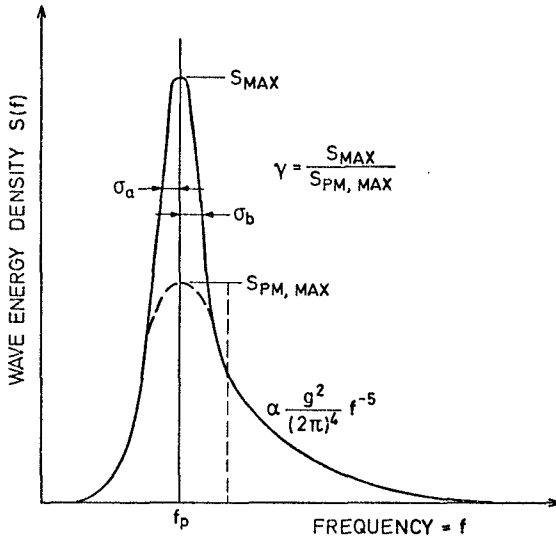


Fig. 1. Illustration of the definition of the five parameters α , f_p , γ , σ_a and σ_b in the JONSWAP spectrum (2). From ^p/10/.

The shape factor γ was found to have values up to 7 with an average value of 3.3. Therefore the wave energy spectrum appears to be much more peaked during wave growth conditions than in the PM-spectrum. Fig. 2 illustrates the JONSWAP spectrum with a γ factor equal to 7 and the corresponding Pierson-Moskowitz spectrum. For a brief review of the JONSWAP results see /12/.

The JONSWAP results were obtained during short-fetched, light wind conditions. However, recently obtained storm wave energy spectra indicate that the spectral shape compares reasonably well to the JONSWAP spectrum during more severe wave conditions also /13, 14, 15, 16/.

The spectral shape of the wave energy field is important to consider for a number of engineering applications. When transfer functions for linear systems are applied, a too low spectral peak in the wave-spectral input may underestimate the forces on an oscillating structure tuned to the peak frequency. D. Hoffmann /9/ stresses the importance of varying the spectral shape when wave loads on ship structures are considered. Wave group formation (i.e. that large waves tend to succeed each other in one single run) tends to be more pronounced for a narrow (or sharply peaked) spectrum /17, 18, 19, 20/. P. Bruun /21/ stresses the importance of wave-group occurrences in the wave field for the breakdown of breakwaters exposed to extreme sea states. Also, for the slow-drift oscillations of moored structures (i.e. oscillations with periods much larger than the periods present in the wave spectrum) the shape of the wave spectrum appears to be an important factor /16, 22/. These oscillations tend to respond to the wave height envelope period /23, 24, 25/ rather than to the individual wave period.

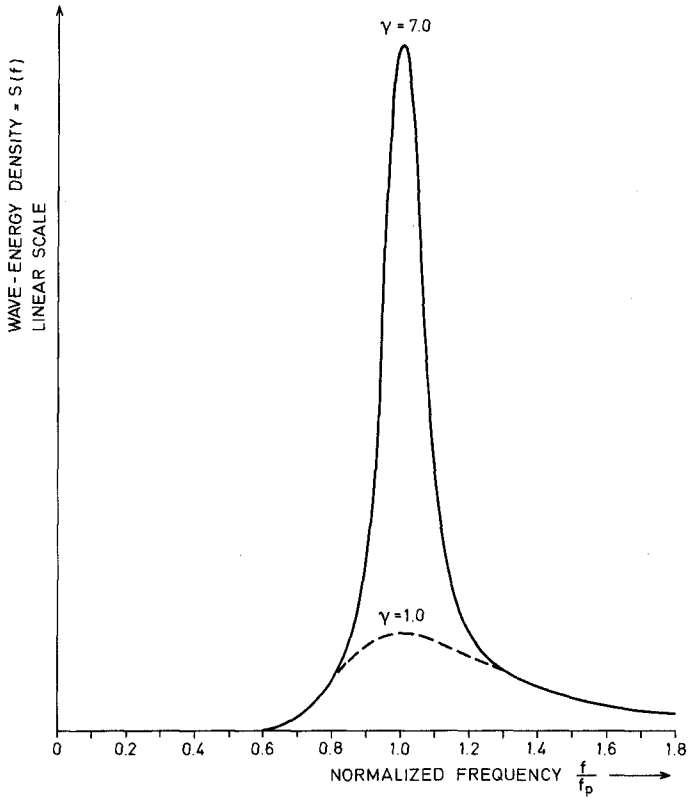


Fig. 2. Illustration of the sharply peakedness of the JONSWAP spectrum. α = arbitrary. The frequency scale is normalized to the peak frequency f_p . Two values of γ are shown, $\gamma = 7$ (full line) and $\gamma = 1$ (broken line). $\sigma_a = 0.07$ and $\sigma_b = 0.09$ which correspond to the average values found during the JONSWAP experiment /10/.

SPECTRAL SHAPE PARAMETERS

The large variations in the spectral shape found for field data /8, 9, 10, 26/ indicate the need of spectral shape parameters. One parameter which has been applied extensively is the spectral width parameter ϵ defined by

$$\epsilon^2 = 1 - \frac{m_2^2}{m_0 m_4} \quad (3)$$

where the moment m of the wave-energy spectrum is defined by

$$m_n = \int_0^{\infty} S(f) f^n df \quad (4)$$

The spectral width parameter was introduced by Cartwright and Longuet-Higgins /27/ in order to describe whether the wave energy was concentrated within a narrow frequency band ($\epsilon \rightarrow 0$) or not ($\epsilon \rightarrow 1$).

Another parameter ν , applied by Longuet-Higgins /17/ to describe the narrowness of the spectrum, is defined

$$\nu^2 = \frac{m_2 m_0}{m_1^2} - 1 \quad (5)$$

A similar parameter ν_1 , also suggested by Longuet-Higgins /29/, is defined

$$\nu_1^2 = 1 - \frac{m_1^2}{m_2 m_0} \quad (6)$$

A parameter Q_p to describe the peakedness of a wave spectrum, was introduced by Goda /18/ and is defined by

$$Q_p = \frac{2}{m_0^2} \int_0^{\infty} f [S(f)]^2 df \quad (7)$$

All these parameters are supposed to characterize the distribution of the wave energy on the frequency scale. However, it appears that some of these parameters depend on the choice of the high-frequency cut-off when the moments (4) are computed. Figs. 3-6 show the dependency of these parameters on the choice of the high-frequency cut-off frequency. The JONSWAP spectrum (2) was applied for $S(f)$, and the integrations were carried out numerically.

It turns out that the parameter Q_p is the only one which is not dependent on the high-frequency cut-off choice. In addition, the parameter seems to distinguish very well between a very sharply peaked JONSWAP spectrum ($\gamma=7$) and a Pierson-Moskowitz type spectrum ($\gamma=1$). It is therefore recommended that this parameter be applied rather than the parameters ϵ , ν or ν_1 .

From Fig. 6, it may even be considered to establish a relationship between γ and Q_p . This relationship is shown graphically in Fig. 7 for a specific choice of σ_a and σ_b .

The reason why ϵ varies with the choice of the high-frequency cut-off in the numerical integrations, is that the wave energy spectra are found to have a high-frequency tail proportional to f^{-5} . When the fourth moment of such a

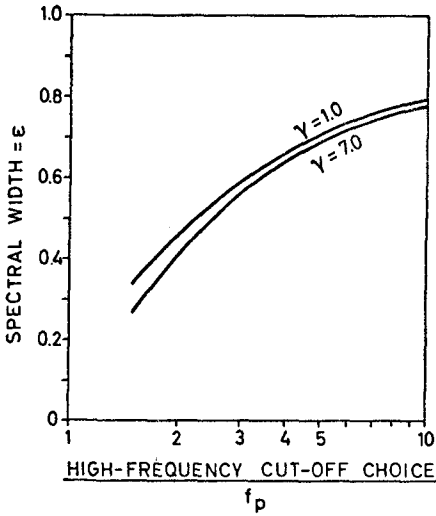


Fig. 3. The spectral width parameter ϵ as a function of the high-frequency cut-off choice. ϵ is computed from (3). α = arbitrary. The frequency scale is normalized to the peak frequency f_p . Two values of γ are shown. $\sigma_a = 0.07$. $\sigma_b = 0.09$.

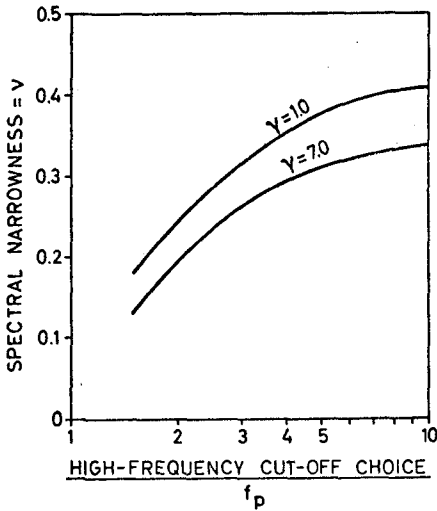


Fig. 4. The parameter ν as a function of the high-frequency cut-off choice. ν is computed from (5). α = arbitrary. The frequency scale is normalized to the peak frequency f_p . Two values of γ are shown. $\sigma_a = 0.07$. $\sigma_b = 0.09$.

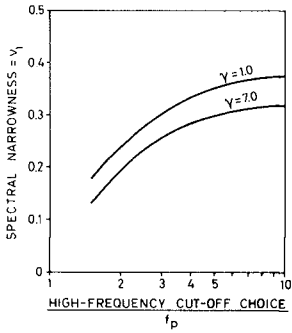


Fig. 5. The parameter ν_1 as a function of the high-frequency cut-off choice. ν_1 is computed from (6). α = arbitrary. The frequency scale is normalized to the peak frequency f_p . Two values of γ are shown. $\sigma_a = 0.07$. $\sigma_b = 0.09$.

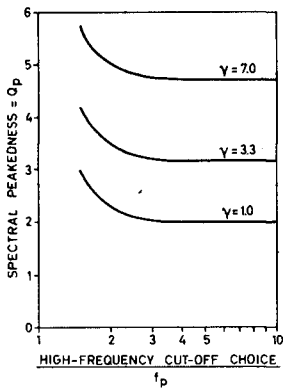


Fig. 6. The peakedness parameter Q_p as a function of the high-frequency cut-off choice. Q_p is computed from (7). α = arbitrary. The frequency scale is normalized to the peak frequency f_p . Three values of γ are shown. $\sigma_a = 0.07$. $\sigma_b = 0.09$.

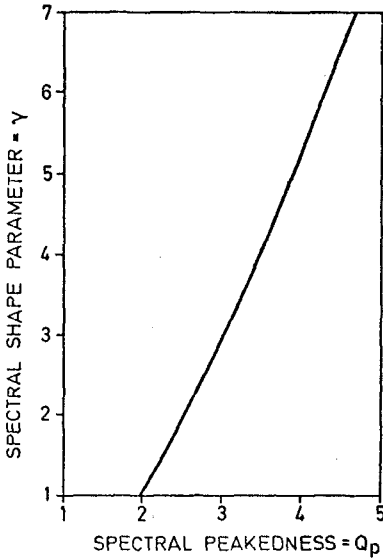


Fig. 7. The relationship between the spectral peakedness parameter Q_p and the spectral shape parameter γ in the JONSWAP spectrum. The other parameters in the JONSWAP spectrum are: α = arbitrary, f_p = arbitrary, $\sigma_a = 0.07$, $\sigma_b = 0.09$.

spectrum is computed, the result will be proportional to the natural logarithm of the high-frequency cut-off. In fig. 3, ϵ is shown to vary between 0.4 and 0.8 for a Pierson-Moskowitz type spectrum, dependent on the cut-off frequency. In addition, ϵ appears to distinguish poorly between a very sharply peaked ($\gamma=7$) wave energy spectrum and a Pierson-Moskowitz type spectrum ($\gamma=1$). These facts may explain some of the conflicting results reported in the literature /14, 30, 31/.

It is possible to obtain a rough estimate of ϵ directly from a wave record /18/ by applying the formula

$$\epsilon^2 = 1 - \left(\frac{N_0}{N_1} \right) \quad (8)$$

where N_1 is the number of maxima and N_0 is the number of zero-up-crossings in the wave record. However, the number N_1 will depend on the resolution of the wave recorder; a recorder with a large resolution will record more maxima than a recorder with a small resolution and thus enlarge the value of ϵ . This effect will be similar to the effect of choosing a larger high-frequency cut-off when ϵ is computed from the moments of the spectrum.

THE WAVE HEIGHT DISTRIBUTION

When the spectrum is narrow, it can be shown that the wave height distribution is approximately a Rayleigh distribution /32/. This distribution has been compared to the actual distribution of the wave heights recorded, and the agreement appears to be good /18, 28, 30, 32, 33/.

In order to compare wave height distribution from actual wave recordings to the Rayleigh distribution, 60 recordings of wind-generated waves were examined. The data were collected with a "Waverider" accelerometer buoy located outside Utsira, Norway. The location is shown in Fig. 8. The water depth was about 100 m. The duration of each recording was between 8 and 20 minutes.

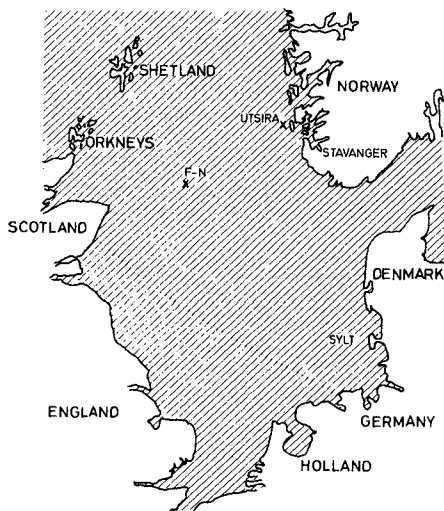


Fig. 8. Location of the "Waverider" wave recorder. From /16/.

The data applied for the analysis were collected from three storms, occurring in October, November and December 1970. All of the recordings were selected so that some waves larger than 4 m were present in each recording.

Wave heights lower than 0.5 m were excluded because these waves were expected to be affected by the resolution of the recording instrument. By excluding these waves, the results were expected to improve /33/.

Fig. 9 shows that the wave heights follow the Rayleigh distribution comparatively well. In order to include all of the 60 recordings on the same diagram, the average wave height \bar{H} was used as unity for each of the recordings.

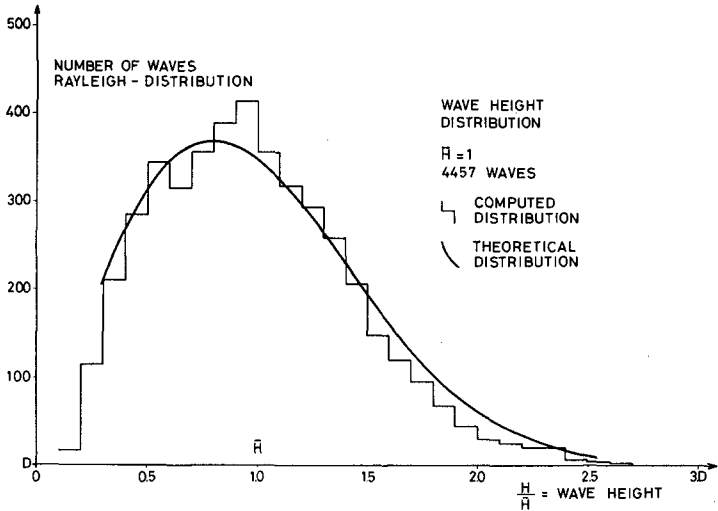


Fig. 9. The distribution of the wave heights from 60 wave recordings. The wave heights are determined from the zero-up-cross method. The heights are normalized to the average wave height of each recording.

THE WAVE PERIOD PARAMETERS

The distribution of the wave periods appears to be more controversial than the distribution of the wave heights. Bretschneider /34/, using semi-empirical relationships, proposed a Rayleigh distribution of the zero-up-crossing wave period squared (T_z^2) which has been applied with variable success /18, 33/. Recently, however, Longuet-Higgins /28/ has arrived at a theoretical wave

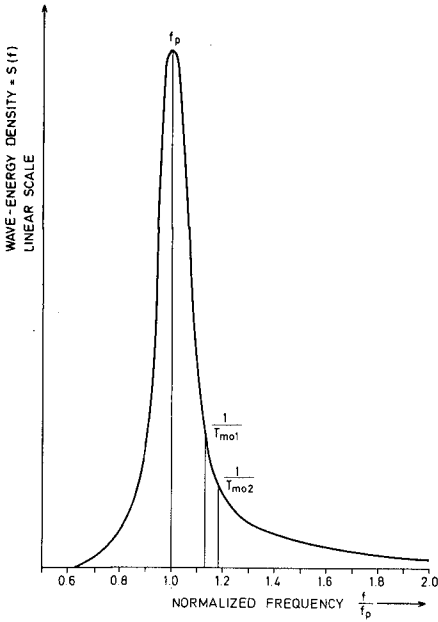


Fig. 10. Illustration of the average periods T_{m01} and T_{m02} for a very sharply peaked JONSWAP spectrum. $\alpha = \text{arbitrary}$. The frequency scale is normalized to the peak frequency f_p . $\gamma = 7$. $\sigma_a = 0.07$. $\sigma_b = 0.09$. T_p is determined according to (11). T_{m01}^a is determined from $P(9)$. T_{m02} is determined from (10).

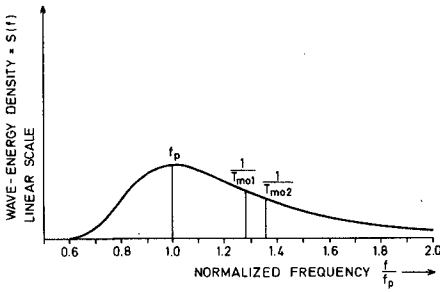


Fig. 11. Illustration of the average periods T_{m01} and T_{m02} for a Pierson-Moskowitz type spectrum. $\alpha = \text{arbitrary}$. The frequency scale is normalized to the peak frequency f_p . $\gamma = 1$. $\sigma = 0.07$. $\sigma_b = 0.09$. T_p is determined according to (11). T_{m01}^a is determined from (9). T_{m02} is determined from (10).

period distribution which seems to compare well with observations.

A number of wave period parameters have been proposed for practical applications. Based on the moments of the spectrum, an average wave period T_{m01} may be defined /9, 28/.

$$T_{m01} = \frac{m_0}{m_1} \quad (9)$$

Sometimes the average periode T_{m02} is also defined /9, 30, 35, 36/.

$$T_{m02} = \left(\frac{m_0}{m_2}\right)^{\frac{1}{2}} \quad (10)$$

In /9/, T_{m02} is denoted "the average apparent period".

The peak period T_p (inverse of the peak frequency f_p) is obtained by derivating the wave spectrum equation:

$$\frac{d}{df} [S(f)] = 0 \quad (11)$$

This period corresponds to the frequency of maximum energy density in the wave spectrum /9, 10/.

The period parameters T_{m01} and T_{m02} were computed by numerically integrating the JONSWAP spectrum. Figs. 10 and 11 show the results from the computation. For a very sharply peaked JONSWAP spectrum ($\gamma=7$), T_{m01}/T_p was found to be ~ 0.885 while T_{m02}/T_p was found to be ~ 0.850 . For a Pierson-Moskowitz type spectrum ($\gamma=1$), $T_{m01}/T_p \sim 0.785$ while $T_{m02}/T_p \sim 0.735$.

The results were also found to depend on the high-frequency cut-off choice as shown in Fig. 12. The numbers above are given for a high frequency cut-off choice approximately equal to $4 f_p$.

For the JONSWAP spectrum, the main part of the energy will be concentrated within a narrow frequency band about the peak frequency. The largest waves (the most important for engineering purposes) will have their periods very close to the peak period because these waves are expected to contribute most to the wave spectrum. However, the computations in this paper show that for a relatively narrow, single-peaked wave energy spectrum with a peak period of, say, 10 seconds, the "average period" (T_{m01} or T_{m02}) is expected to fall within the range 7.1 - 8.9 seconds, dependent of the high-frequency cut-off choice and the peakedness of the spectrum. This computation therefore suggests that the average wave periods computed by means of the moments of the spectra will tend to underestimate the period of the largest waves by about 10 - 25%. This conclusion is consistent with Goda /30/ which states that T_{m02} "requires a correction of +20% on the average when applied for sea waves".

Another wave period parameter frequently applied is the average "zero-up-cross" wave period T_z . This parameter is defined as the ratio between the number of zero-up-crossing of the wave trace and the total duration of the wave record. This parameter depends on the resolution of the recorder. A larger number of zero-up-crossing will be recorded if the resolution is improved. By means of numerical simulation, it has also been shown by Goda /18/ that T_z varies with the spectral shape.

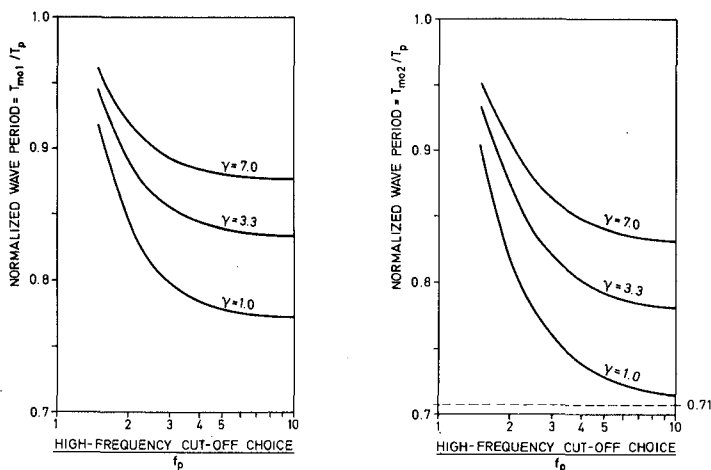


Fig. 12. The "average" wave periods T_{m01} and T_{m02} as a function of the spectral shape parameter γ and the high-frequency cut-off choice. T_{m01} is normalized to the peak period T_p and the high-frequency cut-off choice is normalized to the peak frequency f_p . The following parameters in the JONSWAP spectrum were applied: α = arbitrary, f_p = arbitrary, $\sigma_a = 0.07$, $\sigma_b = 0.09$.

Based on field data, a low correlation has been found /37, 38, 39/ between T_z and the period of the maximum energy density. It is therefore concluded that the period T_z does not appear to be a convenient parameter to characterize the periods of the sea waves.

However, recent findings indicate that the periods of the highest waves in a wave record might be applicable. Thompson /37/ suggests that the average period in trains of large waves in the wave record might be a useful period parameter to apply, and he shows that this period will be very close to the spectral peak period T_p . Goda /30/ concludes that the significant wave period is statistically stable. This parameter appears to be only about 5% smaller than the spectral peak period.

The number 5% is in good agreement with the relation between the peak period T_p and the significant wave period given by Bretschneider /40/.

$$T_p = \sqrt[5]{5/4} T_S \tag{12}$$

$$\approx 1.06 T_S$$

Also, Earle /41/ considered the relationship between the period of the max. wave height T_{HMAX} , T_S and \bar{T} . He also finds that \bar{T} needs a correlation of about + 20%; $\bar{T}_S \approx 0.8 T_{HMAX}$. For T_{HMAX} , he finds it approximately equal to T_S , but T_{HMAX} is less statistically stable than T_S .

A small check on these results was applied on wave data from the North Sea. A quarter of the 60 recordings previously mentioned were selected for spectral analysis. Wave recordings from a growing wind-wave field were digitized and the spectrum computed by means of an FFT algorithm. The peak period T_p was determined from the spectrum and the period of the maximum wave height T_D was found directly from the wave record. Fig. 13 shows the results. Also shown, is the significant wave height determined from $4\sqrt{m_0}$. Fig. 13 indicates that the period of the maximum wave tends to slightly underestimate the period of the spectral peak. The finding is consistent with the results from Goda's investigation /30/, where the period of the maximum wave was found, on the average, to be only about 5% lower than the period of the spectral peak.

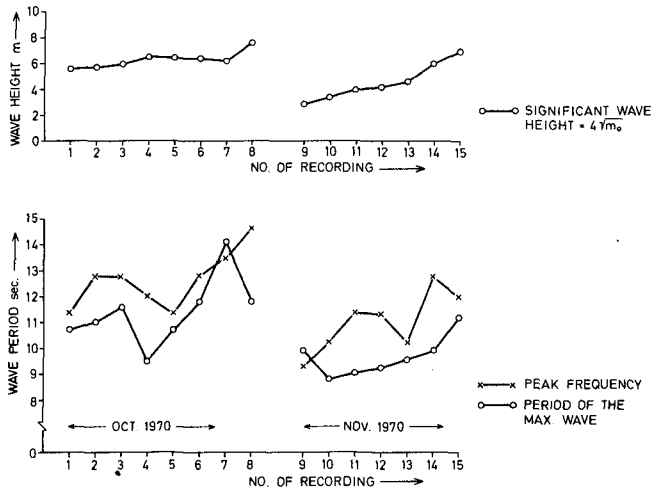


Fig. 13. Comparison of the spectral peak period T_p and the period of the maximum wave height for 15 actual wave recordings from Utsira. The recordings are selected from a growing wind-wave field.

It is concluded that the peak period T_p and the significant wave period T_S characterize the periods of the largest waves in the recording better than the various average wave periods \bar{T} , T_{m01} or T_{m02} do. It is therefore recommended that T_p or T_S are applied rather than the various "average" periods.

CONCLUSIONS

The results derived in this paper may be summarized as follows:

1. The spectral width parameter is shown to vary considerably with the high-frequency cut-off choice. The spectral peakedness parameter Q_p , introduced by Goda /18/, appears to be a more convenient parameter with which to characterize the spectral distribution.
2. The wave height distribution from a wind-wave field compares very well to a Rayleigh distribution.
3. The period of the spectral peak or the significant wave period will correspond relatively close to each other and will characterize the period of the largest waves present in the recording better than the "average" wave periods do.

ACKNOWLEDGEMENTS

The authors would like to thank the Royal Norwegian Council for Scientific and Industrial Research (NTNFK) for permission to use their data in this analysis.

REFERENCES

- [1] LARRAS, J.: Commission Chairman, Final report of the International Commission for the study of waves, Permanent International Assoc. of Navigation Congress (PIANC), Bulletin No. 15, 1973.
- [2] TUCKER, M.J.: "A shipborne wave recorder". Trans. Inst. Nav. Architect. London, 98, pp 236-246, 1956.
- [3] VAN AKEN, H.M. and BOUWS, E.: "Frequency Response of a Shipborne Wave Recorder", Proceedings on the International Symposium on Ocean Wave Measurement and Analysis. Sept. 9-11, 1974, New Orleans.
- [4] DRAPER, L., HUMPHRY, J.D., PITT, E.G.: "The Large Amplitude Response of Two Wave Recorders". Proceedings, 14th Coastal Engineering Conf., Copenhagen, June 1974.
- [5] PIERSON, W.J. and MOSKOWITZ, L.: "A proposed spectral form for fully developed wind seas based on the similarity theory of S.A. Kitaigorodskii". Journ. of Geophys. Res. 69, 1964.
- [6] WARNSINK, W.H. et. al.: Report of Committee 1 on Environmental conditions. Proceedings 2nd International Ship Structures Congress (ISSC). Delft, July 1964.
- [7] ABKOWITZ, M.A.: The interim standard sea spectral formulation of the 11th ITTC - A review and evaluation of its use. Proceedings, 12th International Towing Tank Conference (ITTC). Roma, Sept. 1969.
- [8] HOFFMAN, D.: Discussion to the report on Committee 1 on Environmental conditions. Proceedings, Fifth International Ship Structures Congress (ISSC), Hamburg, Sept. 1973.
- [9] HOFFMAN, D.: "Analysis of measured and calculated spectra". Proceedings, International symposium on The dynamics of marine vehicles and structures in waves. London, April 1974.
- [10] HASSELMANN, K. et al.: "Measurements of wind-wave growth and swell decay during the Joint North Sea Wave Project (JONSWAP)". Deutschen Hydrographischen Zeitschrift, Ergänzungsheft. Reihe A (80), No. 12, 1973.
- [11] PHILLIPS, O.M.: The dynamics of the upper ocean. Cambridge University Press, 1969.
- [12] EWING, J.A.: "Some results from the Joint North Sea Wave Project of interest to Engineers". Proceedings. International symposium on The dynamics of marine vehicles and structures in waves, London, April 1974.
- [13] HOUMB, O.G. and RYE, H.: "Analysis of wave data from the Norwegian Continental Shelf". Proceedings, Second International Conference on Port and Ocean Engineering under Arctic Conditions (POAC). Reykjavik, August 1973.
- [14] SAETRE, H.J.: "On high wave conditions in the Northern North Sea". Proceedings, "Oceanology International 1975". Brighton, March 1975.

- [15] Private communication with Dr. Duncan Ross, Atlantic Oceanogr. & Meteorological Labs (NOAA). Miami, USA.
- [16] RYE, H. et. al.: "Sharply peaked wave energy spectra in the North Sea". Offshore Technology Conference 1974. OTC paper No. 2107.
- [17] LONGUET-HIGGINS, M.S.: "The statistical analysis of a random, moving surface". Phil.Trans. Roy. Soc. London, Vol. 249, A.966. 1957, pp 321-287.
- [18] GODA, Y.: "Numerical experiments on wave statistics with spectral simulation". Report of the Port and Harbour Research Institute. Vol. 9, No. 3, 1970, Japan.
- [19] EWING, J.A.: "Mean length of runs of high waves". Journ. of Geophysical Res. Vol. 78, No. 12, 1973, pp 1933-1936.
- [20] RYE, H.: "Wave group formation among storm waves". Proceedings, 14th International Conference on Coastal Engineering, Copenhagen, June 1974.
- [21] BRUUN, P. and JOHANNESSEN, P.: "A critical review of the hydraulics of rubble mound structures". Institute Rep. R3-74. Div. of Port and Ocean Engineering, Univ. of Trondheim, Norway.
- [22] PINKSTER, J.A.: "Low frequency phenomena associated with vessels moored at sea". Society of Petroleum Engineers of AIME, 1974, SPE Paper No. 4837.
- [23] REMERY, G.F.M. and HERMANS, A.J.: "The slow drift oscillations of a moored object in random seas". Offshore Technology Conference, 1971. OTC Paper No. 1500.
- [24] HSU, F.H. and BLENKARN, K.A.: "Analysis of peak mooring forces caused by slow vessel drift oscillations in random seas". Offshore Technology Conference 1970. OTC Paper No. 1159.
- [25] RYE, H. et. al.: "On the slow drift oscillations of moored structures". Offshore Technology Conference 1975. OTC Paper No. 2366.
- [26] HOFFMAN, D. and MARKS, W.: "Application of wave inputs to sea-keeping". Proceedings, Sea-keeping Symposium, 18-19 Oct. 1973. Webb Inst. of Naval Architecture, Glen Cove, N.Y., USA.
- [27] CARTWRIGHT, D.E. and LONGUET-HIGGINS, M.S.: "The statistical distribution of the maxima of a random function". Proc. Royal Soc., A., Vol. 237, 1956, pp 212-232.
- [28] LONGUET-HIGGINS, M.S.: "On the joint distribution of the periods and amplitudes of sea waves". Journ. of Geophys. Res., Vol. 80, No. 18, June 1975.
- [29] Private communication with Prof. Longuet-Higgins, Dept. of Applied Mathematics and Theoretical Physics, Univ. of Cambridge.
- [30] GODA, Y.: "Estimation of wave statistics from spectral simulation". Proceedings, International symposium on Ocean Wave Measurement and Analysis, Sept. 9-11, 1974, New Orleans.

- [31] CHAKRABARTI, S.K. and SNIDER, R.H.: "Wave statistics for March 1968 North Atlantic storm". To appear in the Journ. of Geophys. Res.
- [32] LONGUET-HIGGINS, M.S.: "On the statistical distribution of the heights of sea waves". Journal of Marine Research Vol. 2, No. 3, 1952, pp. 245-266.
- [33] HARRIS, D.L.: "Characteristics of wave records in the coastal zone". From "Waves on Beaches and Resulted Sediment Transport". Academic Press, Inc., 1972.
- [34] BRETSCHNEIDER, C.L.: "Wave variability and wave spectra for wind-generated gravity waves". U.S. Army Corps of Engineers, Beach Erosion Board, Techn. Memo, No. 113, 192 pp. 1959.
- [35] LONGUET-HIGGINS, M.S.: "On wave breaking and the equilibrium spectrum of wind-generated waves". Proc. Roy. Soc. A. 310, pp. 151-159, 1969.
- [36] RICE, S.O.: "Mathematical analysis of random noise". Reprinted from "Selected Papers on Noise and Stochastic Processes", Dover Pub., Inc., 1954. pp. 133-294.
- [37] THOMPSON, W.C.: "Period by the wave-group method". Proceedings, Coastal Engineering Conference, Vancouver 1972.
- [38] HARRIS, D.L.: "The analysis of wave records". Amer. Soc. of Civil Engrs., Proc. of the 12th Coastal Engineering Conference, 1970.
- [39] WILSON, J.R. et. al.: "A discussion of some measured wave data". Proceedings, 13th International Coastal Engineering Conference, Vancouver 1972.
- [40] BRETSCHNEIDER, C.L.: "On the determination of the design ocean wave spectrum". Proc., Interocean 1976.
- [41] EARLE, M.D.: "Extreme waveconditions during hurricane Camille". Journ. Geophys. Res. Vol. 80, No. 3, January 1975.

APPENDIX - NOTATION

- f = frequency or the inverse of the wave period
 f_p = frequency of the spectral peak
 g = acceleration of gravity
 \bar{H} = average wave height
 m_n = n'th moment of the spectrum
 N = number of zero-up-crossings in a wave record
 N = number of maxima in a wave record
 Q_p = spectral peakedness parameter
 S = spectral energy density distribution
 T_{m01} } "average" wave periods
 T_{m02} }
 T_p = period corresponding to the spectral peak frequency f_p
 T_s = significant wave period
 T_z = zero-up-crossing wave period
 \bar{T}_z = average zero-up-crossing wave period
 α = Phillips' constant in the wave energy spectrum
 γ = spectral shape factor in the JONSWAP spectrum
 ϵ }
 ν } = spectral width parameters
 ν_1 }
 σ }
 σ_a } = parameters to describe the broadness of the spectral
 σ_b } peak in the JONSWAP spectrum

CHAPTER 13

HURRICANE WIND AND WAVE FORECASTING TECHNIQUES

BY CHARLES L. BRETSCHNEIDER¹ AND ELAINE E. TAMAYE²

ABSTRACT

Measurements needed to calibrate both significant wave and wave spectrum methods. These concern extreme waves hence related more to design than operations.

Ratio of one-dimensional wave spectrum $S(f)$ as function of wave frequency (f) to that as function of frequency (f_0) of maximum energy density with slope, $m + 1$ is:

$$\frac{S(f)}{S(f_0)} = e^{-\frac{m+1}{m} \left(\frac{f}{f_0}\right)^{-(m+1)}} - \frac{m+1}{m} \left(\frac{f}{f_0}\right)^{-m}$$

Ratio of period of maximum density (f_0^{-1}) to wind speed (U) in knots with significant wave height (H_s) in feet as a parameter is:

$$\frac{f_0^{-1}}{U} = 0.4 \tanh \left\{ \ln \left[\frac{1 + \frac{40 H_s}{U^2}}{1 - \frac{40 H_s}{U^2}} \right]^{1/2} \right\}^{0.6}$$

and ratio of wind speeds at radial distances r and R in nautical miles from center of stationary hurricane is:

$$\frac{U_r}{U_R} = -\frac{1}{2} \frac{fR}{U_R} \frac{r}{R} + \sqrt{\left[1 + \frac{fR}{U_R} \right] \frac{R}{r} e^{(1-R/r)} + \left[\frac{1}{2} \frac{fR}{U_R} \frac{r}{R} \right]^2}$$

Significant wave heights [H_{Rv} and H_{rv}] in hurricane moving at forward speed [V_F] for significant wave heights [H_R and H_r] for stationary hurricane are:

$$H_{Rv} = H_R \left[1 + \frac{1}{2} \frac{V_F \cos \theta}{U_{Rs}} \right]^2 \quad \text{and} \quad H_{rv} = H_r \left[1 + \frac{1}{2} \frac{V_F \cos \theta}{U_{rs}} \right]^2$$

θ is angle between wind and hurricane forward speed; $H_R = K' \sqrt{R \Delta P}$ and H_r/H_R and K' are functions of fR/U_R where f = coriolis parameter = $2 \times$ Earth's angular velocity \times Sine (average latitude); ΔP = central pressure reduction from normal in inches of mercury; and subscript "s" denotes surface wind speeds.

This technique predicts at one station (N29W89) during Hurricane Camille (11 Aug 69) maximum wave of 42.4 ft compared to 43.1 ft measured and an envelope-of-spectra similar to one from measurements in North Sea (JONSWOP, 15 Sept 68).

Hurricanes in Hawaiian waters have recurrence interval of about 1 in 50 years. One in 1959 [DOT] caused considerable damage especially on island of Kauai.

This paper supported in part by the Univ. of Hawaii Sea Grant College Program of the National Oceanic and Atmospheric Administration (NOAA), Office of Sea Grant, Department of Commerce of the U.S.A. Government under its "Wave Statistics for Extreme Wave Conditions".

¹ Professor and Chairman and ² Graduate Student;
both in Department of Ocean Engineering; University of Hawaii.

FORWARD

The various methods of wave forecasting are summarized briefly including wave spectra and its application to hurricane waves. The latest relationships are presented. Knowledge of the art of forecasting extreme wave conditions is important since tropical cyclones occur in most of the tropical areas of the world, including the Gulf of Mexico and Atlantic Coast of the U.S.A.

WAVE FORECASTING PHILOSOPHIES

Of the various methods of wave forecasting, there are primarily only two concepts: the Significant Wave (Bretschneider, 1970, 72a, 72b) and the Wave Spectrum (Pierson and Moskowitz, 1964; Cordone, Pierson, Ward, 1975).

1. The Significant Wave Concept is a very simple method which forecasts the principle parameters, i.e. the significant wave height, H_S and the significant wave period, T_S , or else the modal period of the frequency spectrum

$$f_o^{-1} = \sqrt[4]{5/4} T_S .$$

The normal unit form of the theoretical spectrum can be used to estimate the wave spectrum; and the normal form of the directional spectrum, frequency dependent, can be used to estimate the complete directional spectrum.

2. The Wave Spectrum concept is on reverse to the significant wave method, i.e., the wave spectrum method predicts the directional spectrum, from which the one-dimensional spectrum and the significant wave are determined.

3. In both methods the Rayleigh distribution is used to determine the most probable maximum wave height.

4. Both methods are based upon use of measured wave data for calibration. If the same or similar wave data are used for calibration, then both methods should give essentially the same results in regard to directional spectrum, the one-dimensional spectrum, the significant wave height and period, and the period (f_o^{-1}) of maximum energy density.

5. The significant wave method is easier to use and certainly less costly, whereas the wave spectrum method requires a highly sophisticated and expensive computer program.

6. Both methods are needed to compliment each other, and also serve as calibration techniques for each other.

7. The methods concern only the extreme wave conditions associated with design criteria, and not associated necessarily with the day by day or operational wind and wave criteria.

Presently, there are about seven methods used in wave forecasting and some methods are not better necessarily than others. Wave

forecasting, or wave hindcasting as the case may be, is an art as well as a science. The accuracy of any method depends upon practice, experience, verification, and correlation. Both the Significant Wave Method and the Wave Spectrum methods are taught at the University of Hawaii, and it is up to the student to make a choice. These methods are presented in Bretschneider, 1967, 68, 72, 73 and Pierson, Moskowitz, 1964, and Silvester, 1974.

OCEAN WAVE SPECTRUM

ONE-DIMENSIONAL WAVE SPECTRUM,--There is very little that can be added to the state-of-the-art on ocean wave spectrum analytical expressions. Opinions have been generated on what is the best form of the wave spectrum. Only minor details exist between the various semi-empirical methods; none are of any significance to ocean engineering. The problem is to select the design wave spectrum for a particular situation, area of operation, and the recurrence interval. The only thing lacking is data for obtaining statistical extremes in some places.

The generally accepted form of the unit wave spectrum is as follows:

$$S(f) = Af^{-(m+1)}e^{-Bf^{-m}} \quad (1)$$

where $S(f)$ = energy density, and f = wave frequency in hertz (sec^{-1}). The form of equation (1) is similar to that of the Weibull distribution function (Weibull, 1951) as used in Bretschneider (1959).

There are three parameters involved in equation (1), namely: the coefficients A and B , and the slope $(m+1)$ of the high frequency end of the spectrum. They can be obtained, either by theory, wave forecasting relationships, or by use of measured wave spectrum data.

Based on past experience, enough information is available to postulate the form of equation (1). For example the value of maximum energy $S(f_0)$ and the wave frequency f_0 at which it occurs can be determined by performing the following simple operation on equation (1):

$$\frac{d[S(f)]}{df} = 0 \quad (2)$$

whence

$$B = \frac{m+1}{m} f_0^m$$

$$A = S(f_0) e^{\frac{m+1}{m}} f_0^{m+1}$$

thus

$$\frac{S(f)}{S(f_0)} = e^{\frac{m+1}{m}} \left(\frac{f}{f_0}\right)^{-(m+1)} e^{-\frac{m+1}{m} \left(\frac{f}{f_0}\right)^{-m}} \quad (3)$$

Note that when $(m+1) = 5$, equation (3) becomes:

$$\frac{S(f)}{S(f_0)} = e^{5/4} (f/f_0)^{-5} e^{-5/4} (f/f_0)^{-4} \tag{4}$$

Equation (4), whose solution is shown in Fig. 1, is a special form of the wave spectrum given in Bretschneider (1959) as is the Pierson-Moskowitz (1964) spectrum. Sometimes engineers prefer the so-called period (T) spectrum, which can be obtained as follows:

$$S(T) dT = -S(f) df$$

where $T = f^{-1}$

and $dT = -f^{-2} df$

This is a simple operation and leads to:

$$\frac{S(T)}{S(T_0)} = e^{\frac{m-1}{m}} \left(\frac{T}{T_0} \right)^{m-1} e^{-\frac{m-1}{m}} \left(\frac{T}{T_0} \right)^m \tag{5}$$

where $S(T_0)$ is maximum with dimension $\ell^2 t^{-1}$ at wave period T_0 , and $(m-1)$ is the slope for very low periods of the period spectrum.

Note that the dimension of $S(T)$ is $\ell^2 t^{-1}$ and $S(f)$ is $\ell^2 t$. When $(m-1) = 3$, equation (5) becomes:

$$\frac{S(T)}{S(T_0)} = e^{3/4} \left(\frac{T}{T_0} \right)^3 e^{-3/4} (T/T_0)^4 \tag{6}$$

Equation (6) is a special form of the period spectrum given in Bretschneider (1959); see Fig. 2.

All of the above equations are special forms of the Weibull Distribution function (Weibull, 1951).

Equations (4) and (6) [figures 1 and 2] are related as follows:

$$f_0^{-1} = \sqrt[4]{5/4} T_s$$

and $T_0 = \sqrt[4]{3/4} T_s$

or $f_0^{-1} = \sqrt[4]{5/3} T_0$

$$T_s = \sqrt[4]{4/3} T_0 = \sqrt[4]{4/5} f_0^{-1} \tag{7}$$

where T_s is a definite definition of the significant wave period, not necessarily as the characteristic period used in the past.

From actual data on frequency spectrum, the corresponding period spectrum can be obtained by use of two operations:

$$\begin{aligned} S(T) &= S(f) \cdot f^2 && \text{(for the ordinate)} \\ T &= f \cdot f^{-2} && \text{(for the abscissa)} \end{aligned} \quad (8)$$

The area under the spectrum in either case remains the same.

The design wave spectrum can be obtained by Froude scaling of measured wave spectrum, but with caution. For example:

$$\left. \begin{aligned} S_p(f) &= \lambda^{5/2} S_m(f) \\ f_p &= \lambda^{-1/2} f_m \end{aligned} \right\} \quad (9)$$

where λ is the linear scale parameter, and p stands for predicted and m stands for measured. This assumes that g^2 and t are the same from one section of gF/U^2 to the next section, which is not necessarily always true; $g = 32.16 \text{ ft/sec}^2$, $F = \text{fetch (feet)}$, and $U = \text{wind speed (ft/sec)}$.

DIRECTIONAL SPECTRUM.—The earliest directional spreading function was the one published by Cote, et al., (1960) as obtained from the Stereo Wave Observation Project (SWOP). Since then, other forms of the directional spectrum have evolved including those by Ou, et al., (1974), Silvester (1974) and Longuet-Higgins, et al., (1963). The choice of the directional spectrum depends upon the engineering solution required. Certainly, more experimental data on the directional spectrum is required especially for engineering problems such as the reaction to wave excitation of ships and of flexible fixed and floating offshore structures. For all practical engineering purposes, it does not seem to make very much difference which of the proposed directional spectrum methods are used. (See Silvester, 1974, Fig. 3.34.)

THE ENVELOPE OF SPECTRA.—The "overshoot" of the high frequency energy during early wave generation has been observed in measurements made in both laboratory and field. The classical field observations were made during JONSWOP, that is the Joint North Sea Wave Project (Barnett, 1972 and Fig. 3), while the classical laboratory observations were made by Mitsuyasu (1968 and Fig. 4). These as well as measurements made on Lake Michigan (Liu, 1971) and on North Atlantic (Miles, 1972) are notable.

The Envelope of Spectra is of the same form as Equation (3) and for demonstration purposes the same as Equation (4), except now the value of maximum energy and the corresponding wave frequency are respectively $S(f_o^*)$ and f_o^* .

The Envelope Spectrum, as discussed by Bretschneider (1975) in fact should be termed "the Envelope of Spectra"; it takes the high frequencies into account and thus includes these "overshoots"

All the spectra under the Envelope of Spectra is preferable to the fully-developed sea spectrum for design purposes because the Envelope of Spectra yields more energy at the high frequencies.

Both the Envelope of Spectra and the fully-developed sea spectrum should be cut off at the particular low frequency defined by the fetch length and wind duration, which limit the length of the wave which can be generated.

As an example, the Envelope of Spectra is superimposed in Fig. 3 on the JONSWOP spectra obtained from measurements at 11 stations situated in the North Sea offshore the Island of Sylt, Germany. The spectra at all stations would be similar if the fetch length at all stations were replaced with the time growth which actually occurred at the station farthest offshore (#11). Thus, the design spectrum should be based on all spectra under the Envelope of Spectra and not on the spectrum at final time of maximum peak. This same effect is apparent in the North Atlantic spectra (Miles, 1972, Figs. 5 and 6). Perhaps a better selection of m would give a better fit, but this demonstration, given of the Envelope of Spectra, seems adequate.

The area under the Envelope of Spectra is considerably more than the area under the fully-developed spectrum $(1/4 H_s)^2$. This is very important for engineering design purposes. In fact, it is for this reason that small boats are swamped and sunk in small lakes, such as those 2 miles in diameter under 40-knot winds, rather than in the open ocean in the roaring forties. A number of challengers have rowed across the Atlantic and the Pacific Ocean, surviving seas 40-foot high, 12-second period. Many so-called pioneers have drowned trying to get ashore during a gale on a small inland lake with waves 2- to 3-foot high, and 1- to 3-second periods. The Envelope of Spectra supports these conclusions.

DEEP WATER WAVE FORECASTING

EQUATIONS FOR PREDICTION OF DEEP WATER WAVES.--The latest Significant Wave forecasting relationships for constant wind speed and direction are as follows (Bretschneider, 1973):

$$\frac{gH_s}{U^2} = A_1 \tanh \left[B_1 \left(\frac{gF}{U^2} \right)^{m_1} \right] \dots\dots\dots (10)$$

$$\frac{C_o}{U} = \frac{gT_s}{2\pi U} = A_2 \tanh \left[B_2 \left(\frac{gF}{U^2} \right)^{m_2} \right] \dots\dots\dots (11)$$

$$t_{min} = 2 \int_0^{F_{min}} \frac{1}{C_o} dx \dots\dots\dots (12)$$

where:

$$\begin{aligned} A_1 &= 0.283 & A_2 &= 1.2 \\ B_1 &= 0.0125 & B_2 &= 0.077 \\ m_1 &= 0.42 & m_2 &= 0.25 \end{aligned}$$

H_s = significant wave height, feet

T_s = significant wave period, sec

F = fetch length, feet

U = U_s (10-min average surface wind speed), ft/sec at 10-meter water level

t = wind duration, sec

C_o = wave crest speed, ft/sec

The form of these equations was given originally by Wilson (1954); only the coefficients have been changed. Graphical solutions of them are given in Bretschneider (1970) and Shore Protection Manual (1973).

The expression gF/U^2 in equations (10) and (11) can be eliminated, and using the above coefficients and expressing U in knots and g as 32.2 ft/sec^2 the following is obtained:

$$\frac{T_s}{U} = 0.4 \tanh \left[1.07 \left(\operatorname{arctanh} \frac{40 H_s}{U^2} \right) 0.6 \right] \quad (13)$$

REVISIONS OF SIGNIFICANT WAVE PERIOD.--Equation (13) seems to give significant wave periods for high wind speeds about 10% too high. Based on wave spectra measured in the North Atlantic, for example, Fig. 5, from Miles (1972), equation (13) has been changed to read:

$$\frac{f_o^{-1}}{U} = 0.4 \tanh \left\{ \ln \left[\frac{1 + \frac{40 H_s}{U^2}}{1 - \frac{40 H_s}{U^2}} \right]^{1/2} \right\} 0.6 \quad (14)$$

where f_o^{-1} = sec. = period of maximum energy density, U = knots and H_s = feet and the significant wave period T_s , from equation (7) is $T_s = \sqrt[4]{4/5} f_o^{-1}$. Hence, equation (13) is needed no longer. The solution to equation (14) is given in Table I.

Incidentally, the Envelope of Spectra given by equation (4) was applied to the wave spectra measured in the North Atlantic (Miles,

1942) and the results plotted in Figs. 5 and 6. It is interesting to note that the Envelope of Spectra is almost in exact agreement with the +90% confidence limit of the mean International Ship Structures Committee (ISSC) spectrum (Fig. 6).

FORECASTING HURRICANE WIND FIELDS

INTRODUCTION.--A method is presented for determining hurricane wind fields and resulting deep water wave field, as proposed by Bretschneider. A detailed development of the hurricane model is given in Bretschneider, 1972 a and b. The wind field itself is based in part on work by the National Weather Service; see Meyers (1954) and Graham and Nunn (1959).

Graphs, formulae and procedures are presented by Bretschneider (1972-b) which make it possible to calculate the entire deep water wave field from model hurricane wind fields. They have been applied successfully to historical hurricanes along the U.S. East and Gulf of Mexico coasts and to U.S. National Weather Service standard project and probable maximum hurricanes for deep water conditions.

BASIC RELATIONSHIPS FOR STATIONARY HURRICANE WIND FIELD.--The balance of the pressure gradient, Coriolis, and centrifugal forces of the equation of motion leads to the non-dimensional stationary hurricane wind field, which is given as:

$$\frac{U_r}{U_R} = -\frac{1}{2} \frac{fR}{U_R} \frac{r}{R} + \sqrt{\left(1 + \frac{fR}{U_R}\right) \frac{R}{r} e^{(1-R/r)} + \left(\frac{1}{2} \frac{fR}{U_R} \frac{r}{R}\right)^2} \quad (15a)$$

where U_r and U_R are the wind speeds at radial distance r and R (radius of maximum winds) from the hurricane center, $f = 2\omega \sin\phi$ (Coriolis parameter) $\omega = 7.29 \times 10^{-5}$ rad/sec (angular velocity of earth), and ϕ is the latitude.

$$P = P_O + (P_N - P_O) e^{-R/r} \quad (15b)$$

where P = atmospheric pressure at radial distance r , P_O = central pressure, P_N = normal pressure = 29.92 inches of mercury, and R = radius to maximum wind.

Figure 7 gives the non-dimensional solution for equation (15a) for values of $r/R \geq 1.0$ vs fR/U_R . Note that r/R did not necessarily occur where U_r/U_R is a maximum. Graham and Nunn (1959) recognized this shortcoming and made modifications based in part on experience and data. The significant change is their recommendation of a single relationship as shown in Figure 7 for $r/R \leq 1.0$. The example which follows utilizes The Graham and Nunn model for $r/R \leq 1.0$ and

the National Weather Service model given by equation (15a) for $r/R \geq 1.0$ (Fig. 7).

The maximum sustained wind speed will occur at R, radius of maximum wind, and refers to a value, averaged over a time of 10-20 minutes, and reduced to the 10-meter elevation above mean sea level. The geostrophic wind speed U_R is given by:

$$U_R = K\sqrt{\Delta P} - 0.5 fR \quad (16)$$

where U_R is in knots, $\Delta P = P_N - P_O$ is the central pressure reduction from normal in inches of mercury, and the constant K varies with latitude from 67 at 20-25°, to about 63 at 45° latitude (see Table II).

The 10-minute average wind speed, U_{RS} , at the 10-meter reference level is given by:

$$U_{RS} = k^* U_R \quad (17)$$

where $k^* = .865$ for all U.S. East Coast and Gulf Coast Zones A and C, and $k^* = .886$ for Gulf Coast Zone B [see Graham and Numm (1959) for zone designations].

CORRECTION DUE TO FORWARD MOTION OF HURRICANE.--The stationary model hurricane wind field is coupled directly to the corresponding model hurricane wind field. Thus, any change in the wind field will result in a directly related change in the wave field. For a moving hurricane, the change in the wind speed component is:

$$\Delta U = \frac{1}{2} V_F \cos \theta \quad (18)$$

thus

$$U_{RS}^* = U_{RS} + \Delta U \quad (19)$$

where θ is the angle of wind deflected from the direction of the incurvature angle of the wind speed and V_F is average forward speed of the hurricane.

Hurricanes moving faster than the critical forward speed are not considered herein. This condition needs further study.

EXAMPLE CALCULATIONS FOR 1969 HURRICANE CAMILLE.--The following are some simple sample calculations for Camille according to parameters obtained from Cordone, Pierson & Ward (1975).

- R = radius of maximum wind = 10 nautical miles
- ΔP = atmospheric pressure reduction at hurricane center from normal = 105 milli-bar = 3.1" mercury
- V_F = average forward speed of hurricane = 10 knots (this increased as Camille moved inland)
- ϕ = approximate average latitude for maximum wave generation = 29°
- f = $.525 \sin \phi$ = coriolis parameter = .255 radians/hour
- β = 25° incurvature angle for stationary hurricane

Determinations of maximum sustained wind speed at R

$$K = 66 \text{ (from Table II)}$$

$$U_R = K\sqrt{\Delta P} - 0.5 fR = 114.9 \text{ knots}$$

$$U_{RS} = .886 U_R = .886(114.9) = 102 \text{ knots}$$

This is for the stationary hurricane and U_{RS} is the 10-minute average wind speed at the 10-meter anemometer level above mean sea level.

WIND FIELD FOR CAMILLE MOVING AT 10 KNOTS.—1. The change in wind components, ΔU , due to the moving hurricane for radii at 20° incremental angles is:

$$\Delta U = 5 \cos \theta$$

2. Thus, the 10-minute average wind speed at 10-meter level (U_{RS}^*) for a moving hurricane is:

$$U_{RS}^* = U_{RS} + \Delta U = .886 U_R + \Delta U = 102 + 5 \cos \theta$$

3. Various values for the isotachs were chosen ($U_{RS} = 20, 40, 50, 60, 70, 80, 90, 100$ knots), and the parameter U_{rs}/U_{RS}^* calculated for each U_{RS}^* .

4. From Fig. 7 the corresponding values of r/R were determined for the calculated parameter $fR/U_R = 0.022$.

5. The wind field was then constructed for the values of U_{rs} and their corresponding radius (Fig. 8).

FORECASTING HURRICANE DEEP WATER WAVES

STATIONARY MODEL HURRICANE WAVE FIELD.—Relationships have been developed in Bretschneider (1972) for obtaining the model hurricane wave field:

$$H_R = K' \sqrt{R\Delta P} \quad (20)$$

where R and ΔP have been defined and K' , a function of fR/U_R , can be obtained from Table III.

The general relationships for the entire stationary hurricane wave field, where $H_r/H_R =$ function of fR/U_R , is shown in Fig. 9.

FORWARD MOTION OF A HURRICANE.—

$$H_{RV} = H_R \left[1 + \frac{1}{2} \frac{V_F \cos \theta}{U_{RS}} \right]^2 \quad (21)$$

$$H_{rv} = H_r \left[1 + \frac{1}{2} \frac{V_F \cos \theta}{U_{rs}} \right]^2 \quad (21A)$$

where H_R is obtained by use of equation (20), H_T is obtained by use of Figure 9, H_{RV} and H_{TV} are a result of the forward speed, V_F , and the direction of wind in relation to direction of forward speed as given by the angle θ . The limitation of equation (21) is that $V_F \leq V_C$, where V_C is the critical forward speed.

CAMILLE DEEP WATER WAVES

FOR SIGNIFICANT WAVES.--Calculate $fR/U_R = .255 (10)/114.9 = 0.0222$. From Table III, $K' = 6.64$, $R =$ radius at maximum wind.

FOR THE STATIONARY HURRICANE.-- $H_R = k' \sqrt{R \Delta P} = 6.64 \sqrt{31} = 37.0$ feet. Calculate

$$\frac{40 H_R}{U_{RS}^2} = \frac{40 (37.0)}{(102)^2} = 0.142$$

From Table I [or equation (14)], $f_0^{-1}/U = 0.121$. Therefore, $f_0^{-1} =$ period of maximum energy = 12.34 sec. And, $T_S =$ significant period = $\sqrt[4]{4/5} f_0^{-1} = 11.67$ sec.

HURRICANE MOVING AT FORWARD SPEED, $V_a \leq V_C$ WHERE $V_C =$ CRITICAL FORWARD SPEED.--The modified significant wave height for actual forward speed is:

$$H_a = H_R \left[1 + \frac{1/2 V_F}{U_{RS}} \right]^2 = 37.0 \left[1 + \frac{5}{102} \right]^2 = 40.7 \text{ feet}$$

The wave period f_0^{-1} may be found by first calculating:

$$\frac{40 H_a}{(U_{RS} + 1/2 V_F)^2} = \frac{40(40.7)}{(107)^2} = 0.142$$

From Table I (or equation 14), $f_0^{-1}/U_i = 0.121$. Therefore, $f_0^{-1} = .121 \times (107) = 12.95$ sec. And, $T_S = \sqrt[4]{4/5} f_0^{-1} = 12.25$ sec.

Similarly the critical forward speed, V_C in knots can be calculated from $V_F = V_C = 1.515 T_C$.

Table IV summarizes the results of the above calculations.

SIGNIFICANT WAVES AT $r/R = 1.8$ TO 2.0 .--Refer to figures 7 and 9. The maximum value of the significant wave does not occur at $R =$ radius of maximum wind, but at 1.8 to $2.0 R$, where $H_{2R} = 1.04 H_R = 37 \times 1.04 = 38.5$ feet and $U_{2RS} = 0.9 U_{RS} = 0.9 (102) = 91.8$ knots.

$$\frac{40 H}{U^2} = \frac{40 (38.5)}{(91.8)^2} = 0.182$$

$$\frac{f_o^{-1}}{U} = 0.139$$

$$f_o^{-1} = 0.139 (91.8) = 12.76 \text{ sec}$$

$$T_S = 12.76 \sqrt[4]{4/5} = 12.07 \text{ sec}$$

For a hurricane moving at 10 knots:

$$U_{2RS} = 91.8 + 5 = 96.8 \text{ knots}$$

$$H_{2RS} = 38.5 \left[1 + \frac{5}{91.8} \right]^2 = 42.8 \text{ feet}$$

$$\frac{f_o^{-1}}{U} = 0.139$$

$$f_o^{-1} (2R) = 0.139 (96.8) = 13.46 \text{ sec}$$

$$T_S = 13.46 \sqrt[4]{4/5} = 12.73 \text{ sec}$$

A summary of the above calculations for $r = 2R$ is given in Table V.

CAMILLE DEEP WATER WAVES AT "2R"

The path of Hurricane Camille and the location of the six wind and wave measuring stations are shown in Fig. 10 taken from Cordone, et al. (1975) as part of the Ocean Data Gathering Program (ODGP) of the Shell Development Co.

The height of the maximum significant wave corrected for a moving hurricane was determined for each ΔU corresponding to radii at 20° incremental angles according to:

$$H_{Rv} = H_R \left[1 + \frac{1}{2} \frac{V_F \cos \theta}{U_{RS}} \right]^2 = 36.97 \left[1 + \frac{\Delta U \cos \theta}{101.8} \right]^2$$

Values of H_T/H_{RV} were determined for the parameter $fR/U_R = 0.022$ and set values of r/R using Fig. 9.

The values of H_T corresponding to the given radius r were then calculated for each H_{RV} and the results plotted in Fig. 11.

The wave field was then constructed for chosen values of H_T (in this example, $H_T = 10, 15, 20, 30, 35, 40$ feet) using Fig. 11.

The results of the above wave predictions are shown in Figure 8, superimposed on the wind field. A comparison is made in Figure 12 between these predictions and measurements made at six stations off the Louisiana coast as part of the ODGP.

In order to make the comparison between the predicted and the measured significant wave heights at the ODGP stations, the predicted wind and wave field was placed along the storm track with forward direction 10° W of N and centered at time 1800 CDT. The predicted significant wave heights are for an instantaneous wave field. The comparison made here is not absolute since the wave heights will change as a function of time with the moving hurricane. The maximum measured significant wave height was 43.13 feet compared to 42.4 feet predicted in the field generally and not necessarily at one of the stations.

A comparison between the measured spectrum (Cordone, et al., 1975) and two predicted spectrum (Cordone, et al., 1975 and Bretschneider, 1970) at ODGP Station 1 at 1600 hours CDT, August 11, 1969, is presented in Fig. 13. Both predictions are well within the measured $\pm 90\%$ confidence limit (Fig. 10 of Cordone, et al., 1970). Fig. 13 includes the Envelope of Spectra (equation 4) based on the measured values (at the maxima where $f_0^{-1} = 14.3$ seconds, $S(f_0) = 4,030 \text{ ft}^2 \text{ sec} = 374.4 \text{ m}^2 \text{ sec}$) in contrast to the predicted spectra which are based upon predicted values of the wave height. This Envelope of Spectra is very similar to that from the JONSWOP measurements (Fig. 3). For example, if Camille were a design hurricane, the design spectrum would be all the spectra under the Envelope of Spectra as shown in Fig. 13 rather than the actual measured spectrum, in order to account for the "overshoot" of early wave generation in time, fetch, and wind speed. Some other value of m might be more appropriate in equations (3) and (4) and thus might fit better the measured spectra.

The purpose was not to determine the proper value of m for the Envelope of Spectra, but was to illustrate the importance of the "overshoot". There is need for more research in this area.

HAWAIIAN DEEP WATER WAVES

The tracks of the major hurricanes near Hawaii for the period 1950-1974 are shown in Figure 14. They include DOT (1959), NINA (1957) and HIKI (1950).

Note that most hurricanes approach the Islands from either the east or south. Although most have done little or no damage, a few

have been devastating such as Hurricane DOT (1959) which did over 5.5 million dollars worth of damage to crops and buildings on the island of Kauai with gusts over 100 mph recorded at Kilauea Point Lighthouse and \$150,000 in damage on the Islands of Oahu and Hawaii. In 1972 Hurricane DIANA generated waves estimated to be 30 feet high along the SE (Puna) coast of the Island of Hawaii.

Using the technique described in "Wind Field for Camille" a graphical presentation was prepared (Fig. 15) which when applied to Figure 14 provides predictions of the wind and wave field that may be expected to occur in the open ocean during a hurricane off the Hawaiian Islands. Its recurrence interval is estimated to be once in fifty years.

As a hurricane approaches the land, the winds are reduced by 1% per mile within 10 miles of the coast and correspondingly the waves are decreased in height, except very close to shore where the waves begin to break. However, the effect of the Islands is fairly negligible since their extent is small compared to that of the hurricane. Therefore, it is reasonable to expect significant waves of up to 30 feet and greater in height with 60 knot (69 mph) winds. In addition, instantaneous gusts of 84 knots (97 mph) may occur, and individual maximum waves could exceed 50 feet in height. Winds in the usually windy Pali (cliff) on the Island of Oahu can be expected to exceed 87 knots (100 mph).

DISCUSSION AND SUMMARY

There is an abundance of information available for calculating in deep water (1) the standard project and probable maximum hurricane wind and wave fields as verified adequately by use of the Ocean Data Gathering Project measurements (2) the maximum sustained wind speed, U_R , and maximum significant wave height, H_R , at radius of maximum wind, R , as applied successfully to historical hurricanes along the U.S. East and Gulf of Mexico coasts and to the standard project and probable maximum hurricanes of the U.S. National Weather Service (Bretschneider, 1972-b). The method is limited to a hurricane moving at speed equal to or less than its critical forward speed. Those faster need further study.

Winds and waves due to a hurricane moving over the Continental Shelf and the Coastline are modified by bottom friction percolation, refraction, shoaling, breaking, and water depth change caused by storm surge and/or tide. These must be taken into account.

ACKNOWLEDGEMENT

This paper was supported in part by the task "Wave Statistics for Extreme Wave Conditions" which is sponsored by the University of Hawaii Sea Grant College Program, National Oceanic and Atmospheric Administration (NOAA), Office of Sea Grant, Department of Commerce of the U.S.A. Government.

NOTE CONCERNING FIG. 4: "D" is wind damper opening in percent and "F" is the fetch in meters. Thus, the index 15-8 denotes a fetch of 8 meters subject to a wind generated when damper is 15% open.

APPENDIX I.--REFERENCES

1. _____ (1973), "Shore Protection Manual", Vols. I, II, and III, U.S. Army Coastal Engineering Center.
2. Barnett, Tim P. (1972), "Observations of Wind Wave Generation and Dissipation on the North Sea; Implications for the Off-shore Industry", OTC Paper No. 1518, Preprints of 1972 Off-shore Technology Conference, Houston, Texas.
3. Bretschneider, C.L. (1959), "Wave Variability and Wave Spectra for Wind Generated Gravity Waves", Beach Erosion Board, T.M. 118, U.S. Army Corps of Engineers, p. 192.
4. Bretschneider, C.L. (1967), "Fundamentals of Ocean Engineering, Part 4-B, Wave Forecasting", Ocean Industry, November 1967, pp. 38-45.
5. Bretschneider, C.L. (1968), "Fundamentals of Ocean Engineering, Parts 8-A, B, C, and D, Decay of Wind Generated Waves to Ocean Swell by Significant Wave Method", Ocean Industry, March, April, May, and June issues.
6. Bretschneider, C.L. (1970), "Forecasting Relation for Wave Generation", Look Lab/Hawaii, Vol. 1, No. 3, July; published by JKK Look Laboratory of the University of Hawaii.
7. Bretschneider, C.L. (1972a), "A Non-Dimensional Stationary Hurricane Wave Model", Proceedings of 1972 Offshore Technology Conference, Houston, Texas, Paper No. OTC 1517, May 1972.
8. Bretschneider, C.L. (1972b), "Revisions to Hurricane Design Wave Practices", Proceedings of the 13th Coastal Engineering Conference, ASCE, July, Vancouver, Canada.
9. Bretschneider, C.L. (1973), "Prediction of Waves and Currents", Look Lab/Hawaii, Vol. 3, No. 1, pp. 1-17; published by JKK Look Laboratory of the University of Hawaii.
10. Bretschneider, C.L. (1975), "The Envelope Wave Spectrum", Third Int'l Conf. on Port and Ocean Engineering Under Arctic Conditions (POAC), Alaska.
11. Cote, L.J., J.O. Davis, W. Marks, R.J. McGough, E. Mehr, W.J. Pierson, J.F. Ropek, G. Stephenson, and R.C. Vetter (1960), "The Directional Spectrum of Wind Generated Sea as Determined from Data Obtained by the Stereo Wave Observation Project (SWOP)", Met. Rep. New York Univ., Vol. 2, No. 6.
12. Cordone, V.J., W. J. Pierson, and E. G. Ward (1975), "Hind-casting the Directional Spectra of Hurricane Generated Waves", Proceedings of Offshore Technology Conference, Dallas, Texas, Paper No. OTC 2332.

13. Gilman, Charles S. and Vance A. Meyers (1957), "Winds and Pressures in Hurricanes", Proceedings, 6th Conf. on Coastal Engineering, Chap. I, pp. 1-13.
14. Graham, H.E. and D.E. Nunn (1959), "Meteorological Conditions Pertinent to Standard Project Hurricane, Atlantic and Gulf Coasts of United States", National Hurricane Research Project, Report No. 33, U.S. Weather Service.
15. Liu, P.C. (1971), "Normalized and Equilibrium Spectra of Wind Waves in Lake Michigan", J. of Physical Oceanography, Vol. 1, No. 4, October.
16. Longuet-Higgins, M.S., D.E. Cartwright, and N.D. Smith (1963), "Observations of Directional Spectrum of Sea Waves Using the Motions of a Floating Buoy", in Ocean Wave Spectra, Prentice-Hall, Englewood Cliffs, N.J.
17. Miles, M. (1972), "Wave Spectra Estimated from a Stratified Sample of 323 North Atlantic Wave Records", Preliminary Report #LTR-SH-118A of Marine Dynamics & Ship Lab of Dept. of Mechanical Engineering of Canada, dated May 1972; 8½ x 11", 10 pages text, 19 pages Tables, 325 pages of Figures in "Sampling of Ocean Wave Spectra at N. Atlantic Station INDIA". Order #516 of Soc. of Naval Arch. & Marine Engrs.; 74 Trinity Place, NY, NY 10006; dated June 1972; along with two reports by D. Hoffman of Webb Inst. of Naval Arch., "The Process of Sampling Ocean Wave Records", December 1971 (6 pages) and "Further Analysis of Ocean Wave Spectra at Station INDIA"; Pages: 5 text, 55 figures, 40 tables.
18. Mitsuyasu, H. (1968), "On the Growth of the Spectrum of Wind Generated Waves (I)", Reports of Res. Inst. for Applied Mechanics, Vol. XVI, No. 55.
19. Myers, Vance A. (1954), "Characteristics of United States Hurricanes Pertinent to Levee Design for Lake Okeechobee, Florida", Hydrometeorological, Report No. 32, U.S. Weather Service.
20. Ou, S.H., C.L. Bretschneider, and F.L.W. Tang (1974), "Relationship Between the Significant Waves and the Directional Wave Spectrum", Int'l Symposium on Ocean Wave Measurement and Analysis, New Orleans, Louisiana, September.
21. Pierson, W.J., Jr. and Y. Moskowitz (1964), "A Proposed Spectral Form for Fully Developed Wind Seas Based on the Similarity Theory of S.A. Kitaigorodski", J. Geophys. Res., Vol. 69, pp. 5181-5190.
22. Silvester, R. (1974) Coastal Engineering, I. Elsevier Scientific Publishing Co.
23. Weibull, W.A. (1951), "A Statistical Distribution Function of Wide Applicability", J. of Applied Mechanics, Vol. 18, pp. 293-297.
24. Wilson, Basil W. (1954), "Graphical Approach to the Forecasting of Waves in Moving Fetches", Tech. Memo. No. 73, Beach Erosion Board, U.S. Army Corps of Engineers, 31 pp.

LIST OF SYMBOLS

ΔH	Change in significant wave height due to a change in wind speed and fetch length, moving hurricane	U_{RS}	Surface wind speed at distance R from hurricane center, stationary hurricane
H_r	Significant wave height at r, stationary hurricane	U_{RS}^*	Surface wind speed at distance R from hurricane center due to change in wind speed, moving hurricane
H_R	Significant wave height at R, stationary hurricane	V_F	Forward speed of hurricane
H_{Rv}	Significant wave height at R due to change in wind speed, moving hurricane	β	Incurvature angle of wind vector
H_x	Component of H along x-axis	θ	Angle of the radius measured counterclockwise from the x-axis
H_y	Component of H along y-axis	ϕ	Latitude
K	Coefficient used in expression for U_R	ω	Angular velocity of earth
K'	Coefficient used in expression for H_R	P	Atmospheric pressure at radial distance r
k^*	Coefficient used in expression for U_{RS}	P_0	Central pressure
ΔP	Central pressure reduction from normal, inches mercury	P_N	Normal pressure = 29.92 inches H_g
r	Radial distance from center of hurricane	ℓ	Length
R	Radius of maximum wind	t	Time
s	A subscript to denote surface wind speed	T	Wave period in general
ΔU	Change in wind speed due to moving hurricane	T_s	Significant wave period
U_r	Geostrophic wind speed at distance r from hurricane center, stationary hurricane	T_c	Critical period
U_s	10-minute average surface wind speed at 10 meters above water surface	f_0^{-1}	Period of maximum energy density
U_R	Geostrophic wind speed at distance r from hurricane center, stationary hurricane	f	Wave frequency; also Coriolis parameter
U_{rs}	Surface wind speed at distance r from hurricane center, stationary hurricane	f_0	Frequency of maximum energy density
		f_0^*	Frequency of maximum energy density for the Envelope Spectrum

TABLE I

$$\frac{f_o^{-1}}{U} \text{ vs } \frac{40 H}{U^2}$$

 $f_o^{-1} = \text{sec}$
 $U = \text{knots}$
 $H = \text{feet}$

$\frac{40 H}{U^2}$	f_o^{-1}/U	$\frac{40 H}{U^2}$	f_o^{-1}/U
0.0	0.0	0.510	0.24383
0.010	0.02521	0.520	0.24638
0.020	0.03814	0.530	0.24892
0.030	0.04856	0.540	0.25143
0.040	0.05760	0.550	0.25393
0.050	0.06572	0.560	0.25641
0.060	0.07317	0.570	0.25888
0.070	0.08010	0.580	0.26133
0.080	0.08661	0.590	0.26377
0.090	0.09276	0.600	0.26619
0.100	0.09860	0.610	0.26861
0.110	0.10419	0.620	0.27101
0.120	0.10955	0.630	0.27340
0.130	0.11470	0.640	0.27579
0.140	0.11966	0.650	0.27817
0.150	0.12446	0.660	0.28054
0.160	0.12911	0.670	0.28291
0.170	0.13362	0.680	0.28528
0.180	0.13800	0.690	0.28764
0.190	0.14226	0.700	0.29000
0.200	0.14642	0.710	0.29237
0.210	0.15047	0.720	0.29473
0.220	0.15442	0.730	0.29710
0.230	0.15828	0.740	0.29948
0.240	0.16206	0.750	0.30186
0.250	0.16576	0.760	0.30426
0.260	0.16938	0.770	0.30666
0.270	0.17293	0.780	0.30908
0.280	0.17642	0.790	0.31151
0.290	0.17984	0.800	0.31397
0.300	0.18320	0.810	0.31644
0.310	0.18650	0.820	0.31895
0.320	0.18975	0.830	0.32148
0.330	0.19295	0.840	0.32405
0.340	0.19610	0.850	0.32665
0.350	0.19920	0.860	0.32931
0.360	0.20225	0.870	0.33202
0.370	0.20526	0.880	0.33479
0.380	0.20823	0.890	0.33763
0.390	0.21116	0.900	0.34056
0.400	0.21405	0.910	0.34359
0.410	0.21691	0.920	0.34675
0.420	0.21973	0.930	0.35005
0.430	0.22252	0.940	0.35356
0.440	0.22528	0.950	0.35731
0.450	0.22801	0.960	0.36140
0.460	0.23071	0.970	0.36599
0.470	0.23338	0.980	0.37139
0.480	0.23603	0.990	0.37844
0.490	0.23865	0.999	0.39082
0.500	0.24125	1.000	0.

TABLE III

K' vs fR/U_R

[Reproduced from Bretschneider(1972-a)]

fR/U_R	K'	fR/U_R	K'
0	7.50	0.15	4.50
.005	7.25	0.16	4.42
.010	7.05	0.17	4.34
.015	6.85	0.18	4.28
.020	6.70	0.19	4.18
.025	6.55	0.20	4.10
.030	6.40	0.21	4.03
.035	6.25	0.22	3.97
.040	6.10	0.23	3.91
.045	5.95	0.24	3.85
.050	5.80	0.25	3.80
.055	5.70	0.26	3.75
.060	5.60	0.27	3.70
.065	5.49	0.28	3.65
.070	5.42	0.29	3.60
.075	5.34	0.30	3.55
.080	5.27	0.31	3.50
.085	5.20	0.32	3.45
.090	5.13	0.33	3.40
.095	5.06	0.34	3.35
.100	5.00	0.35	3.30
.110	4.88	0.36	3.26
.120	4.76	0.37	3.23
.130	4.66	0.38	3.20
.140	4.57	0.39	3.17
.150	4.50	0.40	3.15

TABLE II					
K and f vs ϕ					
(Reproduced from Bretschneider, 1972a)					
ϕ Deg. Lat.	20	22.5	25.0	27.5	30.0
K	67	67	67	66	66
$f(\text{hours})^{-1}$	0.18	0.20	0.22	0.24	0.26
ϕ Deg. Lat.	32.5	35.0	37.5	40.0	42.5
K	66	66	65	64	63
$f(\text{hours})^{-1}$	0.28	0.30	0.32	0.34	0.36

TABLE IV			
SUMMARY OF HINDCAST OF SIGNIFICANT WAVES AT R FOR CAMILLE			
	Stationary Hurricane	Actual Forward Speed	Critical Forward Speed
V_F (knots)	0	10	20.6
H_S (feet)	37.0	40.7	44.8
f_0^{-1} (sec)	12.34	12.95	13.58
T_S (sec)	11.67	12.25	12.84
U_{RS} (knots)	102	107	112.3

TABLE V			
SUMMARY OF HINDCAST OF SIGNIFICANT WAVES AT $r = 2R$ FOR CAMILLE			
	Stationary Hurricane	Actual Forward Speed	Critical Forward Speed
V_F (knots)	0	10	21.7
H_S (feet)	38.5	42.8	48.14
f_0^{-1} (sec)	12.76	13.46	14.26
T_S (sec)	12.07	12.73	13.49
U_{RS} (knots)	91.8	96.8	102.7

Note: For Tables IV and V, U_{RS} is the 10-minute average at 10 meter elevation.

- Fig. 1 Non-Dimensional Wave Frequency Spectrum
- Fig. 2 Non-Dimensional Wave Period Spectrum
- Fig. 3 Spectra of Waves Generated in North Sea by Winds offshore Island of Sylt, Germany on 15 Sept. 1968 during Joint North Sea Wave Observation Project (Barnett, 1972) with the Envelope of Spectra added
- Fig. 4 Spectra of Waves Generated in Kyushu University Laboratory by Wind (Mitsuyasu, 1968) with Envelope of Spectra added. See "note concerning Fig. 4" preceding "References" .
- Fig. 5 Spectra of Waves Measured in 1954-67 in North Atlantic Ocean (station India at about N59 W20) with significant height [H_s] of 25-35 ft compared to spectrum of Intern. Ship Structures Comm [ISSC] for H_s of 29.42 ft and 9.14 sec. period (Miles, 1972). The Envelope of Spectra is added.
- Fig. 6 Spectrum of Waves with Significant Height of 35-45 ft and its standard deviation as measured in 1954-67 in North Atlantic Ocean at about N59 W20 and as predicted by ISSC (Miles, 1972). The Envelope of Spectra is added.
- Fig. 7 Ratio of Wind Speed, U_r , at Radial Distance, r , to Speed, U_R , at Radial Distance, R , of Maximum Wind versus r/R with the Coriolis (f) Function, fR/U_R , as a Parameter. For $r/R \geq 1$ use equation (15) and for $r/R \leq 1$ use Graham and Nunn (1972).
- Fig. 8 Wind and Wave Field Predicted for Hurricane Camille (1969)
- Fig. 9 Ratio of Significant Wave Height, H_r , at Radial Distance, r , from center of a stationary hurricane to that, H_R , at Radial Distance, R , of Maximum Wind Speed with Coriolis (f) Function, fR/U_R , as a Parameter
- Fig. 10 Path of Hurricane Camille (1969) thru Six Measuring Stations of Shell's Ocean Data Gathering Program in the Gulf of Mexico
- Fig. 11 Predicted Height of the Significant Wave Generated by Hurricane Camille (1969) at Various Distances from its Center. Angles are measured clockwise from true North to the particular station.
- Fig. 12 Predicted and Measured Height of the Significant Wave Generated in the Gulf of Mexico at Six Different Measuring Stations of Shell's Ocean Data Gathering Program by Hurricane Camille, 1969. Values estimated from Fig. 11.
- Fig. 13 Spectrum of Waves Generated by Hurricane Camille at ODGP-Station 1 (N29-05 W88-44) on 17 August 1969 at 1600 h CDT and those hindcast by the Significant Wave and Wave Spectrum methods with the Envelope of Spectra added.
- Fig. 14 Tracks of Hurricanes and Tropical Storms in the Vicinity of the Hawaiian Islands for the period 1950-1974 [from National Weather Service of NOAA]
- Fig. 15 Hurricane Wind and Wave Field Model for use with Fig. 14 hence it should be to same scale as Fig. 14. Place on Fig. 14 to obtain wind-wave field in area selected.

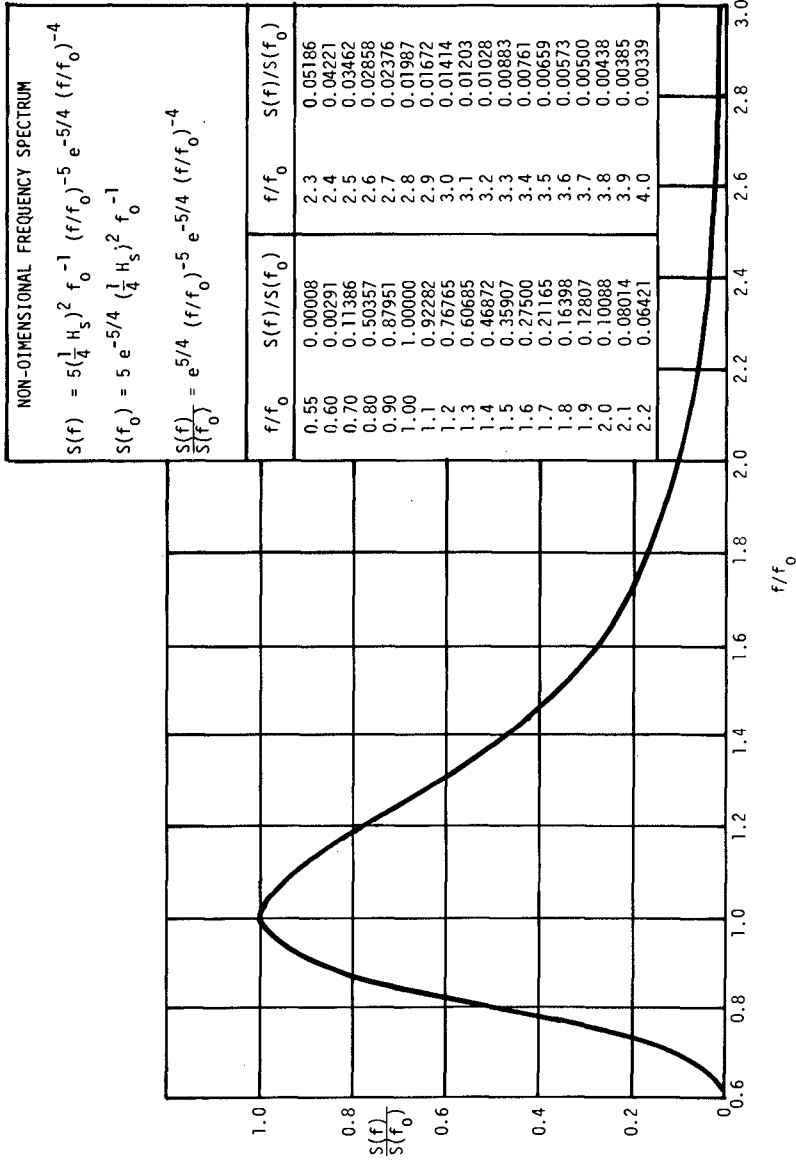


Fig. 1 Non-Dimensional Wave Frequency Spectrum

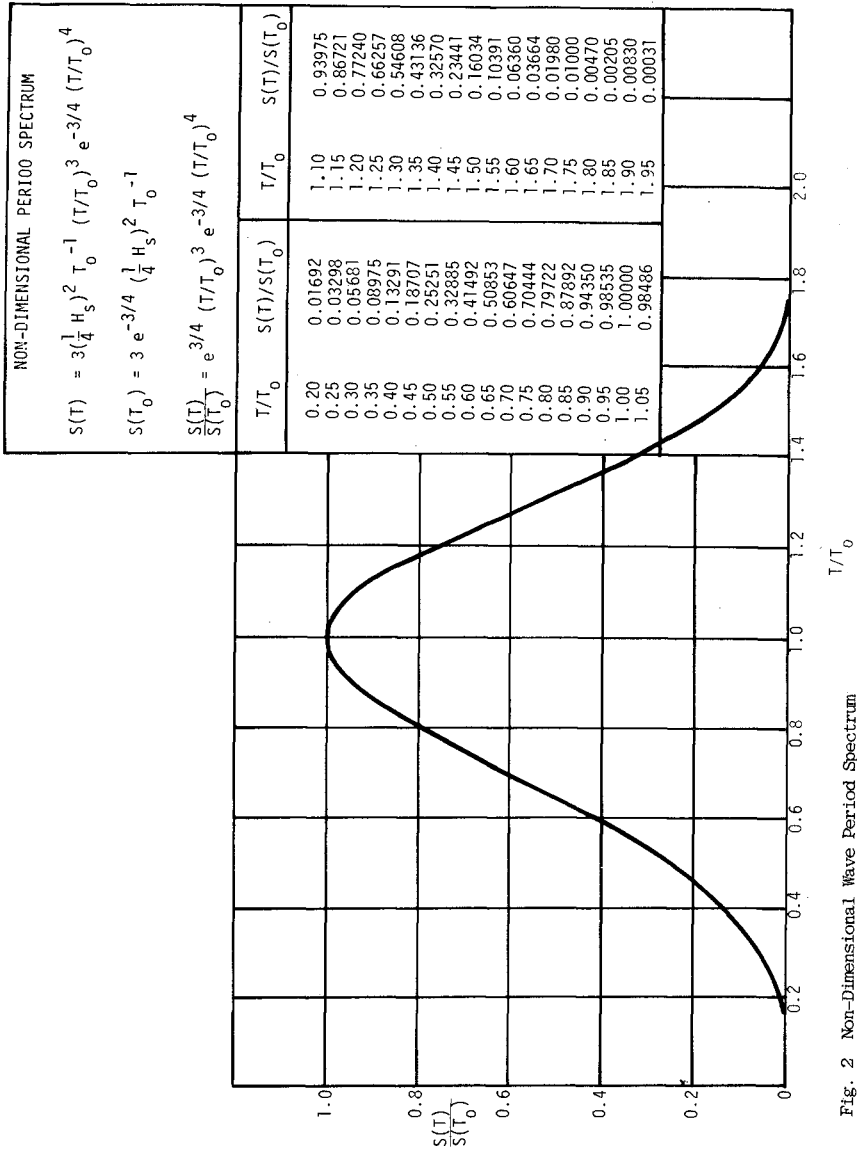


Fig. 2 Non-Dimensional Wave Period Spectrum

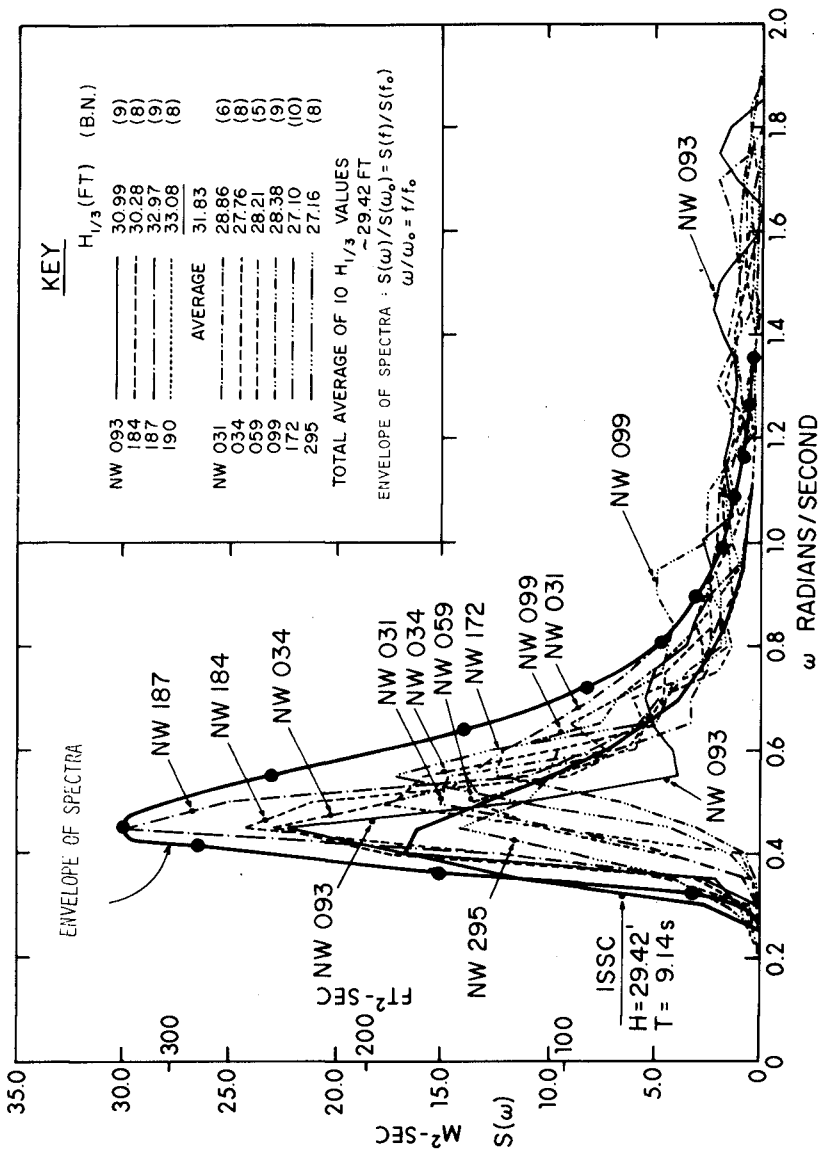


Fig. 5 Spectra of Waves Measured in 1954-67 in North Atlantic Ocean (station India at about N59 W20) with significant height $[H_s]$ of 25-35 ft compared to spectrum of Intern. Ship Structures Comm [ISSC] for H_s of 29.42 ft and 9.14 sec. period (Miles, 1972). The Envelope of Spectra is added.

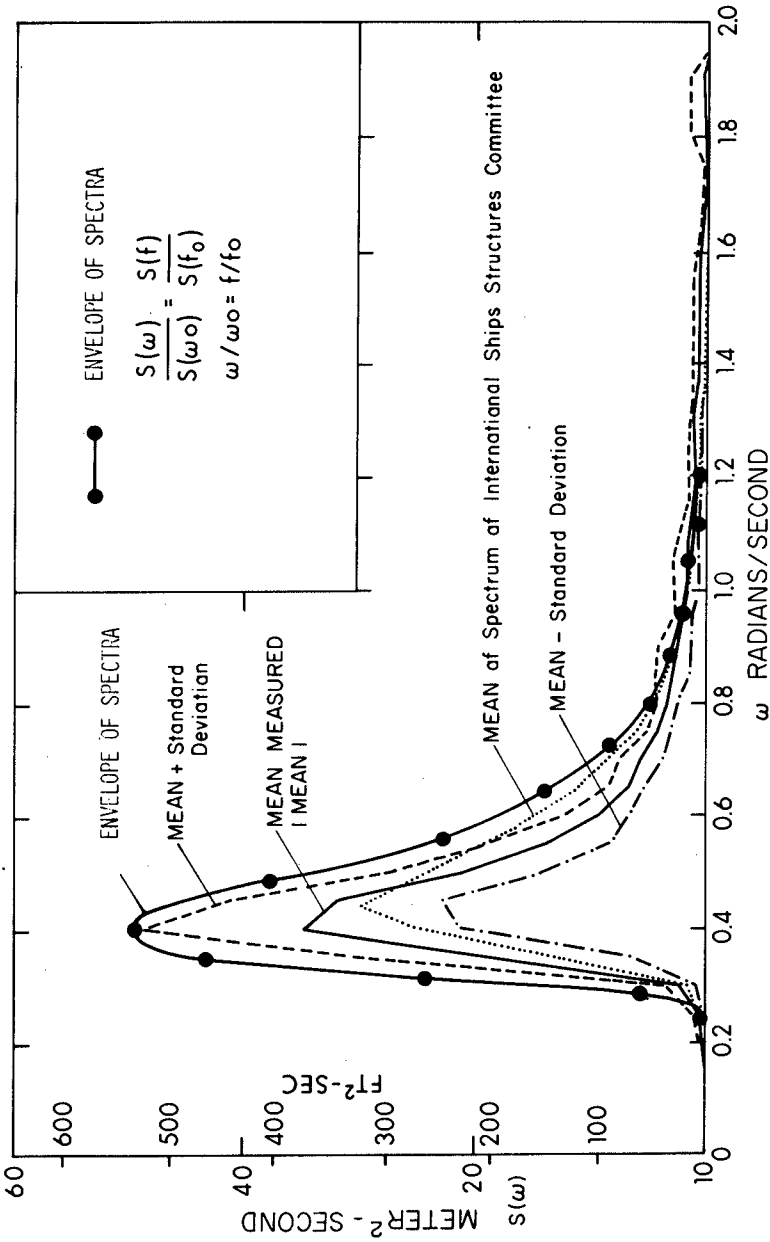


Fig. 6 Spectrum of Waves with Significant Height of 35-45 ft and its standard deviation as measured in 1964-67 in North Atlantic Ocean at about N59 W20 and as predicted by ISSC (Miles, 1972). The Envelope of Spectra is added.

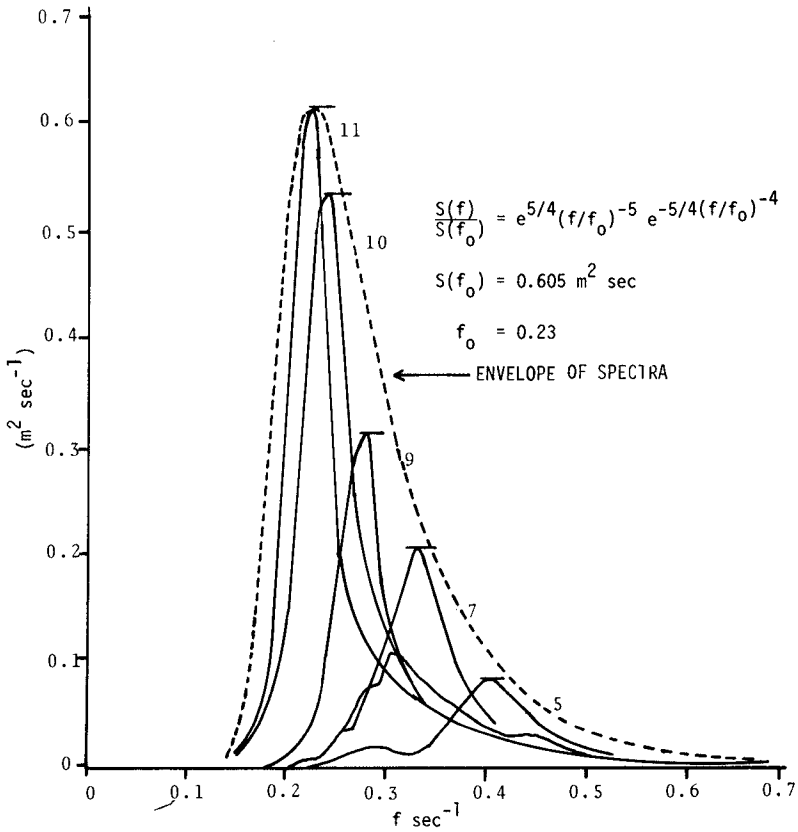


Fig. 3 Spectra of Waves Generated in North Sea by Winds offshore Island of Sylt, Germany on 15 Sept. 1968 during Joint North Sea Wave Observation Project (Barnett, 1972) with the Envelope of Spectra added

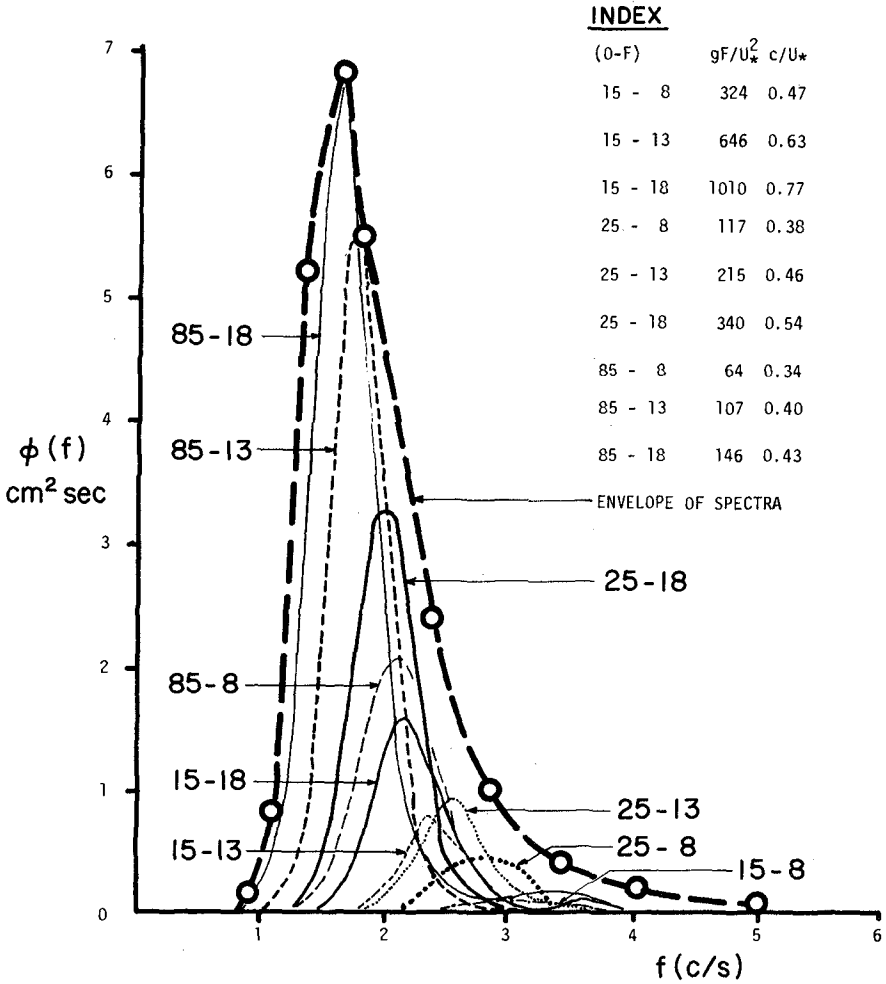


Fig. 4 Spectra of Waves Generated in Kyushu University Laboratory by Wind (Mitsuyasu, 1968) with Envelope of Spectra added. See "note concerning Fig. 4" preceding "References".

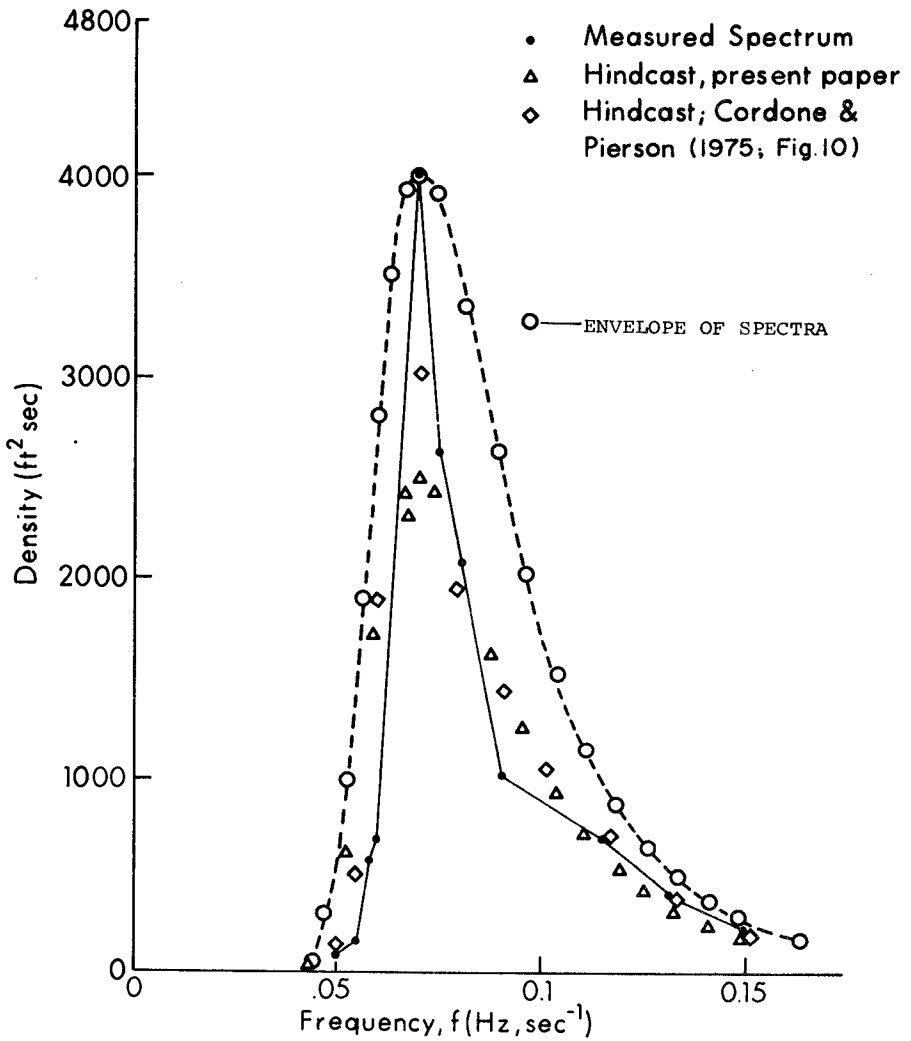


Fig. 13 Spectrum of Waves Generated by Hurricane Camille at ODGP-Station 1 (N29-05 W88-44) on 17 August 1969 at 1600 h CDT and those hindcast by the Significant Wave and Wave Spectrum methods with the Envelope of Spectra added.

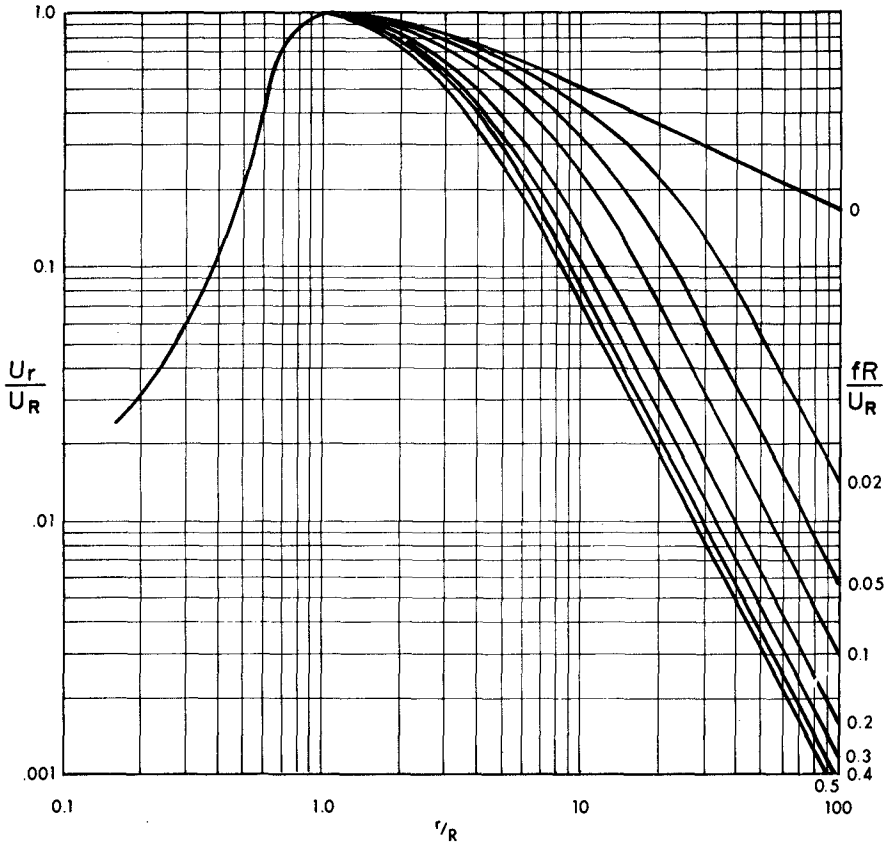


Fig. 7 Ratio of Wind Speed, U_r , at Radial Distance, r , to Speed, U_R , at Radial Distance, R , of Maximum Wind versus r/R with the Coriolis (f) Function, fR/U_R , as a Parameter. For $r/R \geq 1$ use equation (15) and for $r/R \leq 1$ use Graham and Nunn (1972).

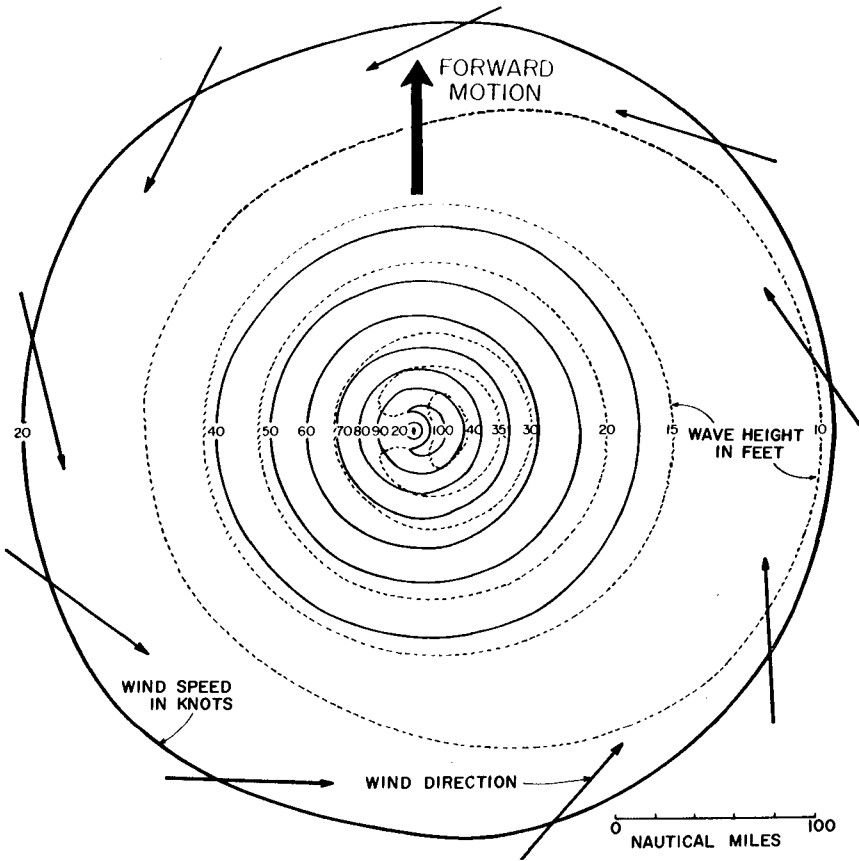


Fig. 8 Wind and Wave Field Predicted for Hurricane Camille (1969)

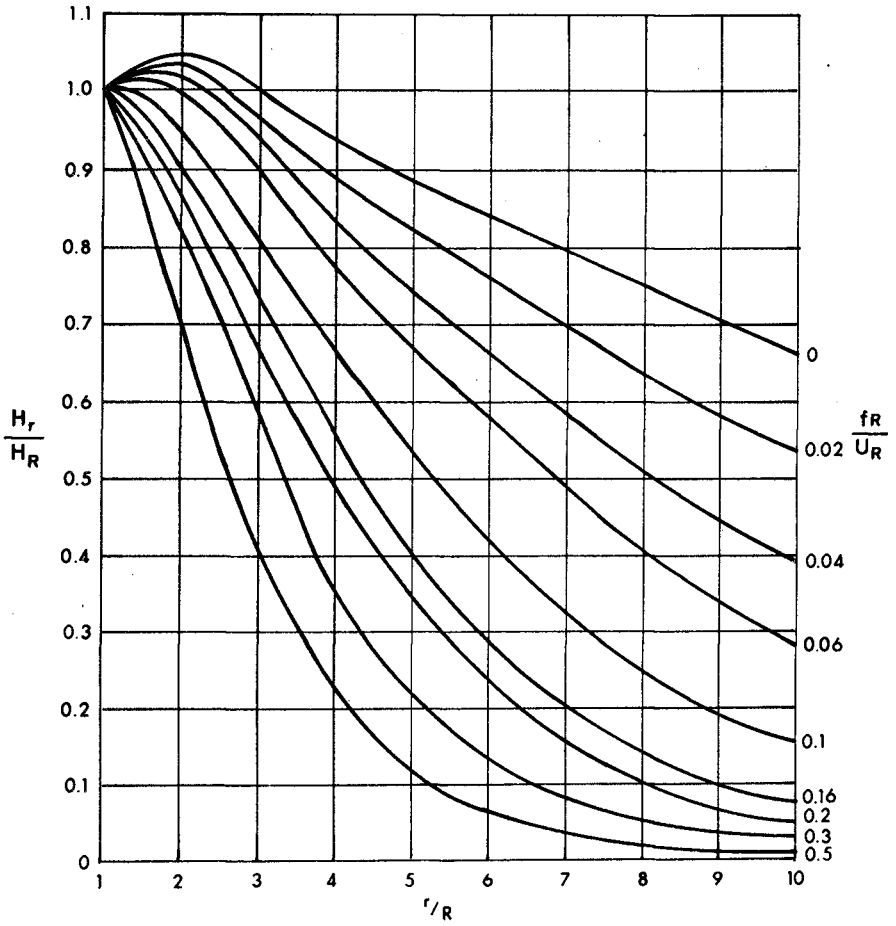


Fig. 9 Ratio of Significant Wave Height, H_r , at Radial Distance, r , from center of a stationary hurricane to that, H_R , at Radial Distance, R , of Maximum Wind Speed with Coriolis (f) Function, fR/U_R , as a Parameter

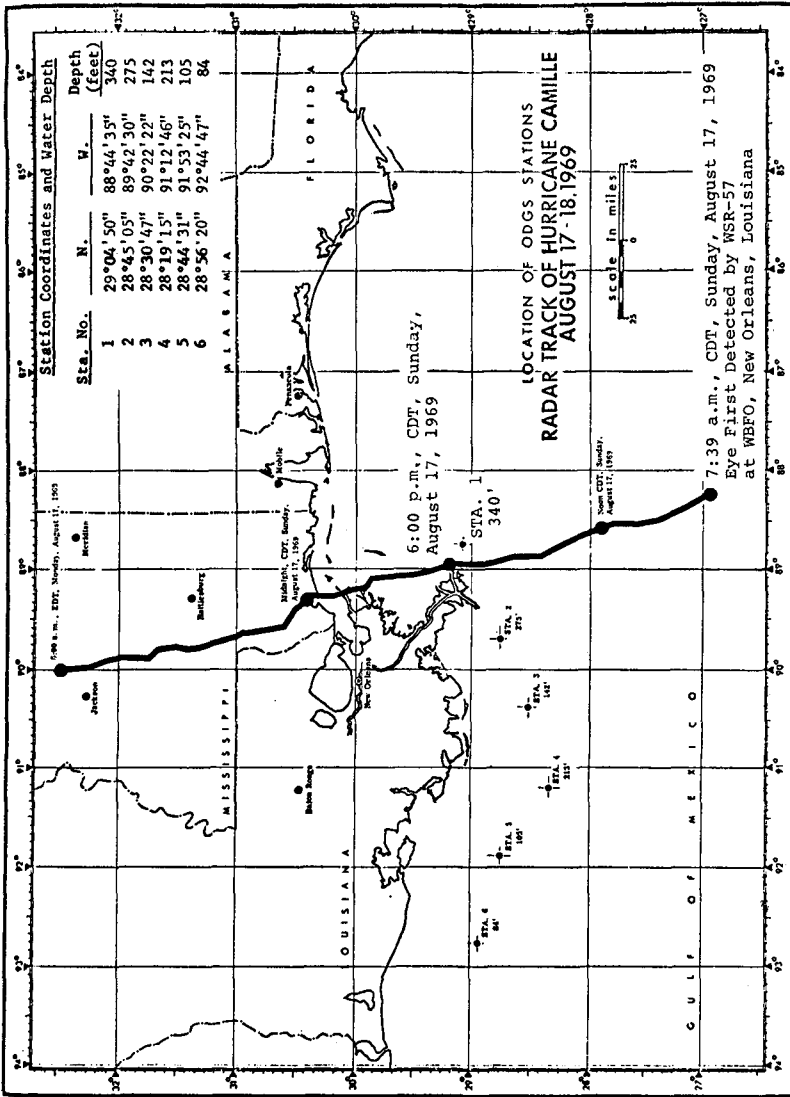


Fig. 10 Path of Hurricane Camille (1969) thru Six Measuring Stations of Shell's Ocean Data Gathering Program in the Gulf of Mexico

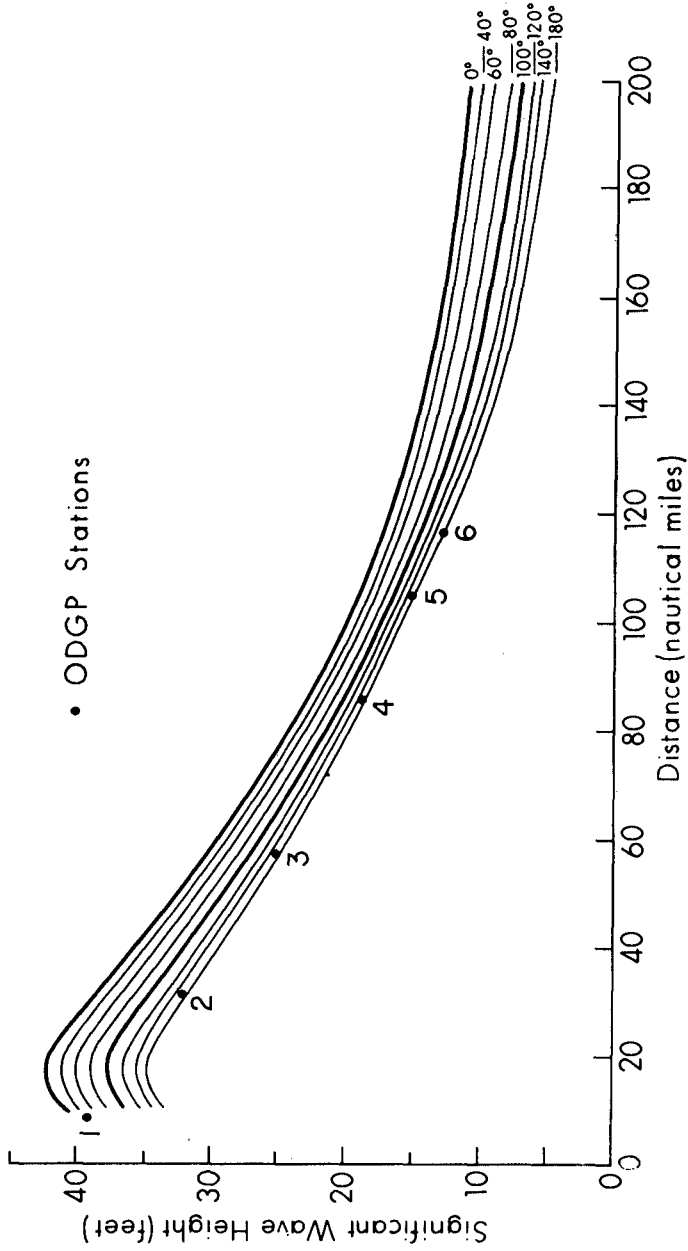


Fig. 11 Predicted Height of the Significant Wave Generated by Hurricane Camille (1969) at Various Distances from its Center. Angles are measured clockwise from true North to the particular station.

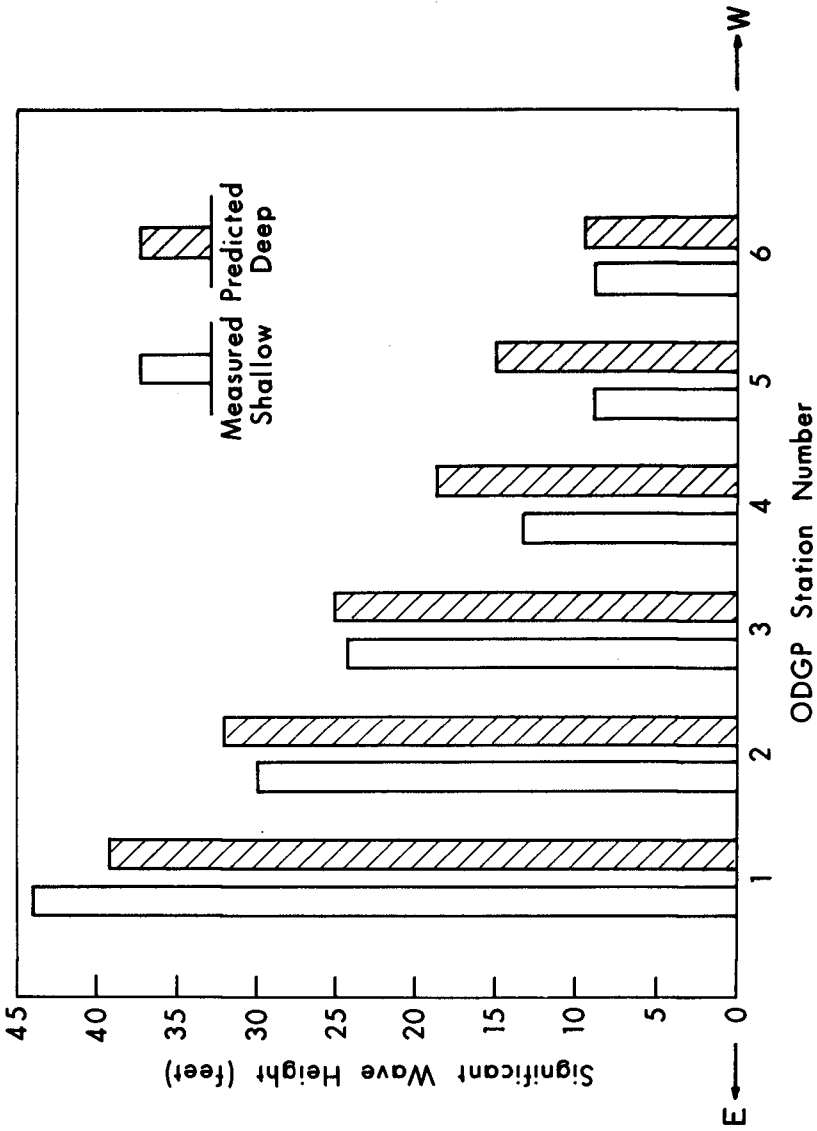


Fig. 12 Predicted and Measured Height of the Significant Wave Generated in the Gulf of Mexico at Six Different Measuring Stations of Shell's Ocean Data Gathering Program by Hurricane Camille, 1969. Values estimated from Fig. 11.

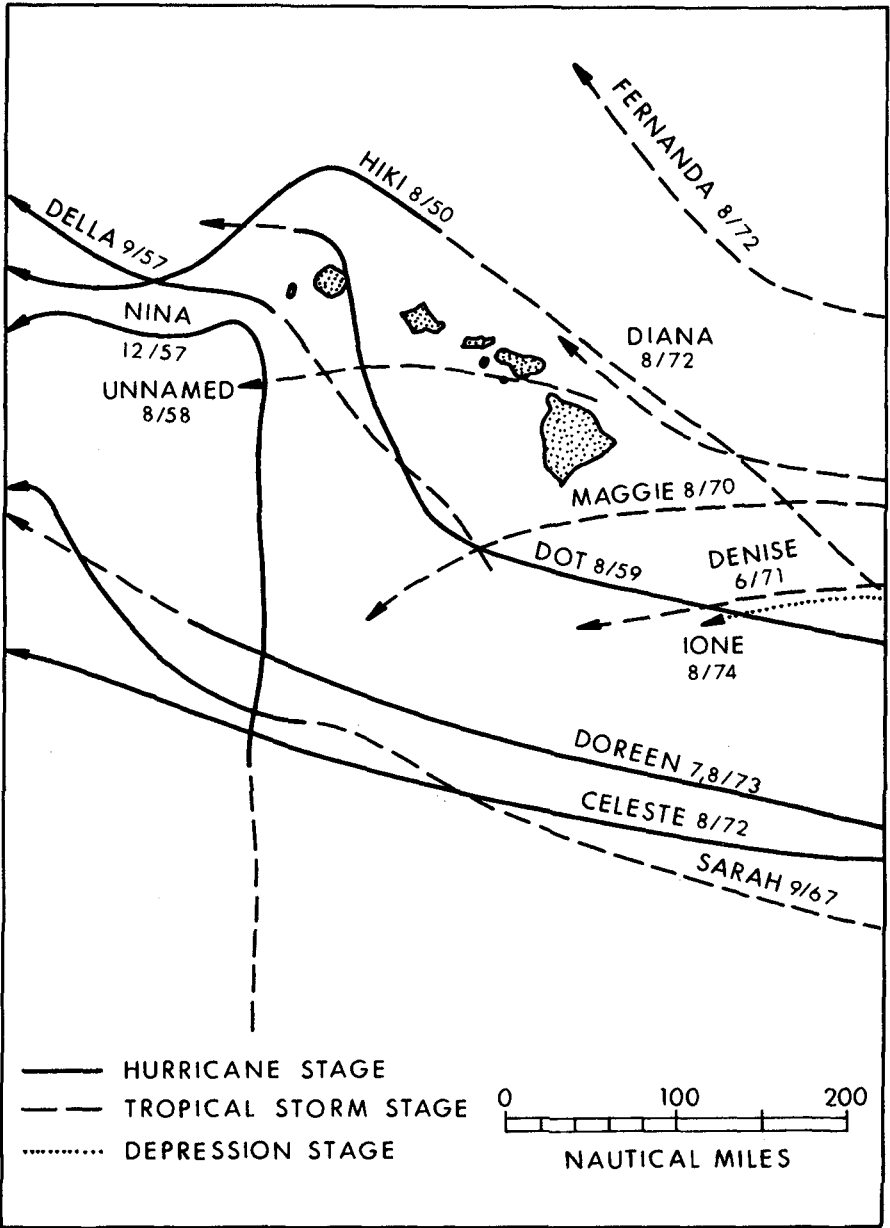


Fig. 14 Tracks of Hurricanes and Tropical Storms in the Vicinity of the Hawaiian Islands for the period 1950-1974 [from National Weather Service of NOAA]

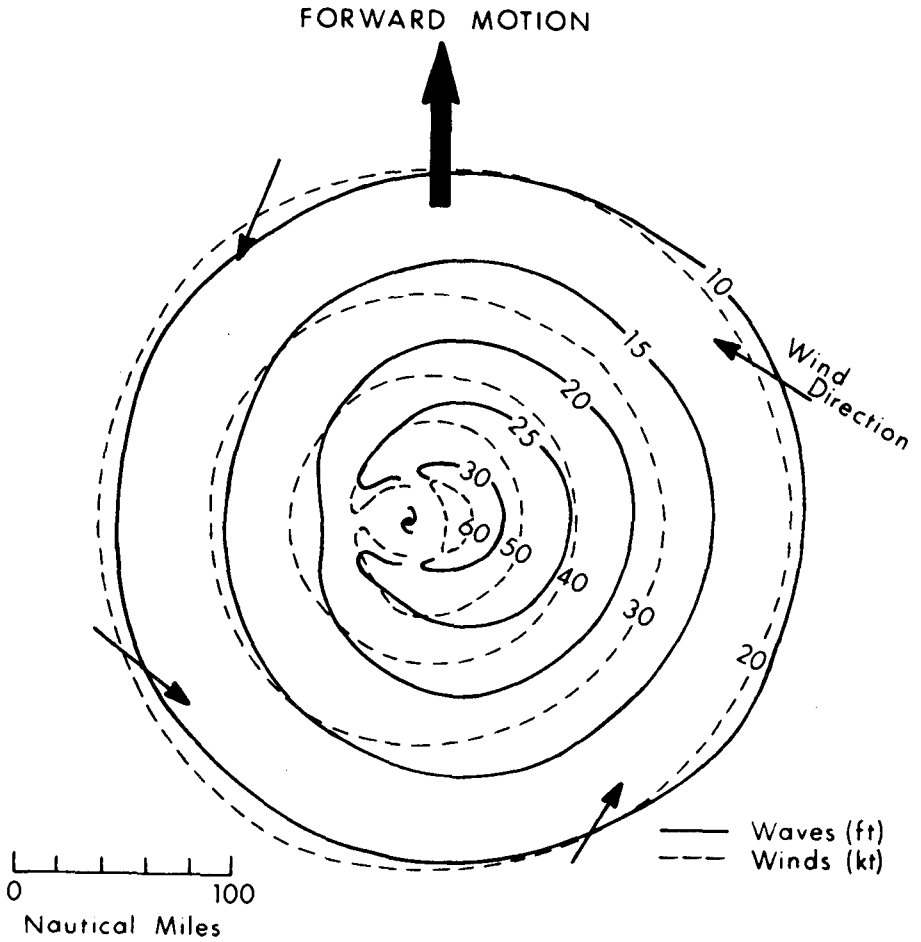


Fig. 15 Hurricane Wind and Wave Field Model for use with Fig. 14 hence it should be to same scale as Fig. 14. Place on Fig. 14 to obtain wind-wave field in area selected.

CHAPTER 14

OCEAN WAVE STATISTICS FROM FNWC SPECTRAL ANALYSES

Warren C. Thompson, Professor of Oceanography
F. Michael Reynolds, Lieutenant, U. S. Navy
Department of Oceanography, Naval Postgraduate School
Monterey, California 93940

ABSTRACT

Climatological wave data that may be shoaled and refracted from a deep-water wave station can be compiled in two forms from spectral ocean wave analyses produced by the Fleet Numerical Weather Central at Monterey, California: (1) significant wave statistics, which are similar to statistical tables currently in use, and (2) spectral element statistics, which give the frequency of occurrence of energy densities contained in a matrix of 15 frequency bands and 12 direction bands. Experimental formats of both types of statistical compilations are presented, their properties are examined, and the coastal engineering applications of these statistics are discussed.

BACKGROUND

For certain purposes coastal engineers require frequency-of-occurrence statistics on ocean waves compiled for a selected deep-water wave station located offshore from the coastal sector of interest. These wave climatology tables characteristically give the statistical frequency with which height-period-direction ($H-T-\psi$) data elements occur per average month or average year. They are of particular value in beach erosion studies because of the fact that the $H-T-\psi$ elements can be shoaled and refracted from deep water to any location in intermediate or shallow depths up to the breaker point. The gradient of the statistical wave field in deep water is generally sufficiently small along the coast that wave statistics prepared for a given deep-water wave station may be carried into shoal water depths for many miles in either direction from the station.

Frequency-of-occurrence statistics are derived from synoptic weather maps by the wave-hindcast method. Heretofore, the analysis of weather maps for wave generation parameters (wind velocity, fetch, and wind duration) has been performed manually. Because of the large amount of labor involved, climatological data of this type are not available for most coasts of the open oceans. Statistical tables have been compiled by the hindcast method for the Atlantic, Gulf, and Pacific coasts of the United States, however, and these have had wide use (tables currently in use were prepared by Saville, 1954; Newmann and James, 1955; Bretschneider and Gaul, 1956; Marine Advisers, 1961, and National Marine Consultants, 1960, 1961). The effort involved in making manual hindcasts has also limited these compilations to three years of weather maps. The yearly variability of the statistical wave field at a given open ocean wave station in middle and higher latitudes is known to be

appreciable; accordingly, a three-year data base for long-term average statistics must be considered minimal.

In December 1974 the Fleet Numerical Weather Central (FNWC) of the United States Navy at Monterey, California put into routine operation a spectral ocean wave computer model that produces "real-time" computations, termed analyses, of the deep-water wave field in spectral form 12-hourly for a grid-point field covering the major oceans of the Northern Hemisphere (waves are not computed for the Southern Hemisphere). The wave field is computed in 3-hour time steps from the surface wind field, which in turn is derived from the observed sea-level pressure field. The grid-point spacing is approximately 150 nautical miles. Details concerning the FNWC Spectral Ocean Wave Model, including comparisons between FNWC wave computations and open-ocean observations, are given by Lazanoff and Stevenson (1975).

In addition to issuing daily wave analyses and forecasts, FNWC has begun running historical weather maps through their spectral wave program and is in the process of storing the 6-hourly wave field for the Northern Hemisphere oceans on magnetic tapes. Present plans call for the production of 20 years of 6-hourly analyses for the period 1955-1974. When the project is completed, which will require many months, the archived wave data will provide the potential to extend the present wave statistics coverage geographically to most coasts and islands of the open North Pacific, North Atlantic, and North Indian Oceans, and to increase the time base nearly an order of magnitude as well.

Wave statistics for coastal engineering use have not previously been produced from FNWC spectral wave computations. In this paper, formats for presenting frequency-of-occurrence statistics are illustrated and applications of the statistics are discussed. Additional information is given by Reynolds (1976).

DEVELOPMENT OF THE TABLES

The approach taken by the authors to develop wave-occurrence statistics from FNWC spectral analyses was to mock up suitable formats manually from a short series of FNWC computer printouts for a given wave station. This permitted experimentation with the format design, including the selection of suitable scales. The wave station chosen is a FNWC grid point located at latitude 50.9°N and longitude 145.6°W near Ocean Weather Station Papa in the open Gulf of Alaska (a deep-water site along an open ocean coast could have been chosen). A summer month and a winter month, August 1974 and February 1975, were selected for extremes in seasonal wave activity and with the expectation of a dominance of swell during one month and sea in the other. The statistical tables for February only are presented here. The equivalent tables for August can be found in Reynolds (1976). It may be noted that the August wave statistics reveal much lower wave activity, shorter wave periods,

and a higher incidence of swell versus sea than occurred in February. Because of missing synoptic analyses, the data for February that are shown in the tables were drawn from 45 12-hourly computer printouts totalling 22½ days of time.

SYNOPTIC SOURCE DATA

Familiarity with the FNWC wave analysis printout is required for a full understanding of the design and characteristics of the tables presented herein. A sample printout for the selected wave station for 00Z on 31 August 1974 is shown in Table 1.

The 15 wave-frequency values shown across the top of the printout (Item 1) each represent the central frequency of a given FNWC frequency band. The central frequencies are seen to cover a period range from 6.1 seconds (0.164 Hz) to 25.7 seconds (0.039 Hz). The limits and width of each frequency band are given in Table 2. The 12 wave-direction values shown in the right-hand column in degrees (Item 2) and in the left-hand column in coded form (Item 3) each represent the central direction of a 30° directional band. The geographical directions are seen to be irregular. They vary from grid point to grid point because of the global map projection used by FNWC (Lazanoff and Stevenson, 1975).

The block of 180 numbers forming the body of the table (Item 4) constitutes the frequency-direction ($f-\psi$) spectrum of the wave field. Each number represents the wave energy density, expressed as variance (ft^2), contained in the frequency and direction bands indicated. The sums of the columns (Item 5) represent the wave energy contained in the 15 frequency bands irrespective of wave direction and constitute the familiar f -spectrum. The sums of the rows (Item 6) give the wave energy contained in the 12 direction bands irrespective of wave frequency, and collectively represent the less familiar ψ -spectrum.

The sums of the component variance values contained in the $f-\psi$ spectrum, the f -spectrum, and the ψ -spectrum (Items 4, 5, and 6) are identical, and for the waves being considered are seen to total 3.145 ft^2 (Item 7). It is of interest to note that two well-defined wave trains from different sources are revealed in the printout. The larger set is a swell train with a dominant period of about 15.0 seconds (0.067 Hz band) and a dominant direction from the West (259° band); the other set is sea of about 9.7 second period (0.103 Hz) from the South (199°).

At this point, some comment is needed regarding the wave frequency bands (Item 1) represented in the printout. The 15 bands have been carefully selected by FNWC to minimize computing time and yet cover the full frequency range for ordinary gravity waves with suitable bandwidths. It may be noted in Table 2 that the bands below a frequency of 0.080 Hz are of constant width (0.0055 Hz), but that at higher frequencies the bandwidth has been widened by multiples of 2, 3, 4, and 18. A consequence of this design is

that in order to properly compare the magnitude of two energy density values, the values must be adjusted to a common frequency bandwidth. Choosing the common or standard bandwidth to be $\Delta f = 0.0055$ Hz, this can be done by multiplying the energy density values in the printout by the appropriate energy density factors listed in Column 4 of the table. By way of example, the secondary peak of the f-spectrum (Item 5 of Table 1) appears to lie at a frequency of about 0.133 Hz, whereas this maximum actually lies at about 0.103 Hz (the primary peak of the f-spectrum lies at about 0.067 Hz). The energy content of these two frequency bands are seen from the printout to have values of 0.41 ft^2 per $\Delta f = 0.0165$ Hz (from Table 2) and 0.33 ft^2 per $\Delta f = 0.0110$ Hz, or about 0.14 ft^2 and 0.16 ft^2 respectively, when adjusted to the common bandwidth of $\Delta f = 0.0055$ Hz. The component variance values of the f- ψ spectrum (Item 4) must be similarly adjusted for direct comparison of their energy contents.

It should be further noted that if the variance values composing the f-spectrum shown in the printout (Item 5) were plotted on a linear frequency scale, the resulting graph would be exaggerated at the high-frequency end of the spectrum because of the choice of variable frequency bandwidths. Nevertheless, the sum of these variance values, 3.145 ft^2 , correctly represents the total energy content computed for the waves present. For a correct graphical representation of the frequency spectrum (to the accuracy permitted by the widths of the frequency bands), the variance values must first be adjusted to a common frequency bandwidth through use of the energy density factors. No such difficulty arises with the ψ -spectrum because of the use of equal directional bandwidths.

The FNWC decision to represent the frequency spectrum by unequal bandwidths affects the way in which statistical tables may be formatted and the statistics compiled, and requires care by the user in order to assure correct interpretation of the data. This is commented upon further in the discussion of the individual tables.

Returning to the spectral printout in Table 1, the waves computed to be present at the station at the designated time are seen to be described in considerable detail by 180 ΔV - Δf - $\Delta \psi$ elements, each being a component, ΔV , of the total variance of the wave field (V) contained in a specific frequency band, Δf , and direction band, $\Delta \psi$. These wave data are referred to herein as spectral element data. The wave information in the printout may also be summarized by designating the significant height, $H_{1/3}$, the period of maximum energy density, T_{\max} , and the direction of maximum energy density, ψ_{\max} . For the wave field shown in the printout, $H_{1/3} = 6.8$ feet ($H_{1/3}^2 = 4V^2$ where $V = 3.145 \text{ ft}^2$), T_{\max} lies in the frequency band centered at 15.0 seconds (or 0.67 Hz), and ψ_{\max} lies in the direction band centered at 259 degrees. Thus, the ψ_{\max} wave field can be described in a gross way by a single $H_{1/3}$ - T_{\max} - ψ_{\max} data unit. Wave data in this form will be significant wave data.

It is evident that wave statistics derived from a time series of FNWC spectral analyses may be compiled as (1) significant wave statistics, consisting of one $H_{1/3} - T_{max} - \psi_{max}$ data unit per FNWC analysis, and as (2) spectral element statistics, composed of $180 \Delta V - \Delta f - \Delta \psi$ data units per FNWC analysis (or fewer than 180 units when variance values of 0.00 ft^2 are excluded from the statistical tabulation). Example formats of each are given in the following sections.

In the statistical tables and the discussion herein, wave frequency and wave period are used interchangeably, in a reciprocal sense, according to convention; frequency is used when reference is made to the FNWC spectral model and period when operational wave products are of interest.

SIGNIFICANT WAVE TABLE

The significant wave statistics compiled for the selected station for February 1975 from FNWC spectral wave analyses are presented in Table 4. Because of the sparsity of the data in the individual direction bands, the entries for all 12 directions have been combined into a single table for illustration purposes in this paper; tables intended for practical use would display each direction component separately. The values in the table represent the number of 12-hourly synoptic analyses occurring during the $22\frac{1}{2}$ day data period. The height scale, coded for brevity (code given in Table 3), is linear with an increment of 2 feet. Regarding the period scale, wave occurrences were compiled from the printouts by the FNWC frequency bands shown in Table 2, but for purposes of convention each column of Table 4 is labelled for the period equivalent to the central frequency of each FNWC frequency band. The equivalent period bandwidths are seen from Table 2 to be variable and to lie mostly in the range of 1 to 2 seconds.

The design of Table 4, except for the use of frequency as a base instead of period, is essentially identical to existing frequency-of-occurrence tables, but with one important exception. In compiling wave statistics derived from the manual analysis of weather maps, wherein wave trains generated in individual wind areas are computed and propagated separately, it has been the general practice to record each set of waves as an independent occurrence whenever two or more trains are present simultaneously at the wave station. This results in tables containing more hours of wave occurrence in a month than actually occurs, particularly when separate tables for sea and swell are compiled. This presents the user with the problem of how to adjust the data to 100% occurrence. In addition, higher wave heights must occur in nature than these tables generally indicate because multiple wave trains are a common occurrence at open ocean wave stations. In the FNWC Spectral Ocean Wave Model, the growth of sea and the propagation of swell are complexly inter-related and individual wave trains are not differentiated in the $f-\psi$ spectrum. Accordingly, the statistics compiled from the

FNWC spectral analyses reflect wave heights associated with the statistical occurrence of multiple wave trains, and the super-occurrence problem does not exist.

In using significant wave tables compiled from FNWC spectral analyses, it may be desirable for some purposes to distinguish swell from sea and to estimate the relative age of the swell, i.e., whether it has travelled over a short, moderate, or long decay distance. Because swell steepness diminishes with increasing travel distance from the generating area, some measure of the steepness of the wave field, γ_s , can be used for this purpose. In this study, γ_s is defined in terms of $H_{1/3}$ and T_{max} by analogy to monochromatic waves as shown in Table 5. The relationship selected between wave age and γ_s is given in the lower part of the table. Thus, young swell has a statistical steepness in the range of about 1/40 and 1/100, has travelled 0 to 250 nautical miles from the location where it was generated, and has been reduced in significant height by a factor of 1.0 to 0.5. It may be observed that because significant wave tables are a matrix of values of $H_{1/3}$ and T_{max} , they are also tables of γ_s and accordingly of wave age. This permits wave-age boundaries to be superimposed, as in Table 4.

It may be recalled that the term "wave age" was introduced by Sverdrup and Munk (1947) to describe the growth stages of sea during wave generation. They defined it as the ratio of wave speed to surface wind speed, C/U , and related it to wave steepness. In extending use of the term to swell, which has considerable practical merit, wave age is defined differently than for sea but remains related to the steepness of the wave field.

The zone labelled "sea" in Table 4 contains all synoptic occurrences where sea is the dominant component of the wave field present, regardless of the wind speed generating the sea or of its stage of growth. The zone is seen to have a cutoff such that wave heights greater than a certain value do not occur for a given period. Young seas, because they are of maximum steepness, should lie along this data envelope, whereas fully arisen seas should fall near the inner margin adjacent to the zone labelled "young swell". A well-defined data cutoff should be expected whenever a significant number of synoptic entries represent seas, but may not be evident in statistics where swell is dominant.

SPECTRAL ELEMENT TABLES

Spectral element statistics compiled for the selected station for February 1975 from FNWC synoptic wave analyses are shown in Table 6. The entries in the table were read directly from the 180 component variance values contained in each of the 45 12-hourly printouts available for the month (eg., Item 4 of Table 1). The entries for all 12 direction bands have been combined into a single table for purposes of comparison with Table 4.

Table 6 is identical to Table 4 with respect to the period scale and the manner of representing frequency of occurrence (i.e., by the number of 12-hourly analyses); however, the significant-height scale is replaced by a variance scale chosen to give a reasonable spread to the data. The variance scale is coded (Table 3) to simplify the table. It should be noted that the units of variance in Table 6 are ft^2/FNWC frequency bandwidth.

Tables 6 and 4 were derived from the same FNWC printouts and the total energy content represented by their entries is identical. Nevertheless, there are no values common to both distributions, and consequently, there are no means by which the data in the two tables can be equated numerically. Neither can one table be derived from the other. These circumstances arise from the fact that although the energy in the waves at a given place and time can be separated analytically into spectral components and can subsequently be reconstituted to yield a significant wave height representing that sea surface, the same spectral components when distributed in a statistical table with components from other synoptic analyses can no longer be identified and re-assembled to produce the significant height.

A comparison of these two tables offers some interesting contrasts, however, and gives some feeling for the coarseness of significant wave data as a descriptor of ocean wave climatology. The spectral element table contains some fifty times more data than the significant height table; specifically, 2126 variance entries ($> 0 \text{ ft}^2$) versus 45 height entries. The variance entries are distributed in a wider range of period bands, from 6.1 to 25.7 seconds versus 9.7 to 18.0 seconds, and extend into what are ordinarily considered very long periods. Further, the entry of maximum energy is centered in the 20.0 second band for the spectral element statistics versus the 16.4 second band for the significant wave statistics. It should additionally be noted that the wave activity in February 1975 was appreciable; this is indicated in Table 4 by the small number of occurrences of waves under 10 feet (Code 05 and under), but is not apparent in Table 6 where most of the entries are in the lowest energy categories.

A peculiarity of Table 6 is that a given energy category or code number does not represent the same energy density for all frequency bands. This is due to the variable widths of the FNWC frequency bands. For example, Code 03 represents an energy level of $0.50\text{-}0.74 \text{ ft}^2/0.0055 \text{ Hz}$ bandwidth in the 12.0 second band but $0.50\text{-}0.74 \text{ ft}^2/0.0110 \text{ Hz}$ bandwidth in the adjacent 10.9 second band, giving the 10.9 second band about half the energy density of the 12.0 second band. Accordingly, energy density values cannot readily be compared across the table. This circumstance would complicate the use of this type of table and would likely result in incorrect interpretation of the statistics.

This difficulty may be avoided by reducing the component variance values to the standard frequency bandwidth, $\Delta f = 0.0055$

Hz, through multiplication by the energy density factors given in Table 2. This operation may be applied either to the 180 variance values in each FNWC printout, or with a slight reduction in statistical accuracy to the statistics compiled directly from these values. Table 7 was derived from Table 6 by the latter method. The variance scale of Table 7 thus has the units of $\text{ft}^2 / 0.0055 \text{ Hz}$ standard bandwidth for all periods in the table.

Table 7 has the desirable quality that a given energy code number represents the same energy level for all frequency bands. On the other hand, the table contains less total energy than Table 6. This is due to the fact that in adjusting the energy of the FNWC frequency bands to the standard bandwidth in the periods from 6.1 to 10.9 seconds, segments of the frequency spectrum lying outside the 0.0055 Hz bandwidth centered about each period are in effect excluded.

A feature of the spectral element tables of particular interest that is best seen in Table 7 is the well-defined energy cutoff extending diagonally across the table. The cutoff represents the energy-saturated frequencies of sea spectra associated with the strongest winds occurring during the month. The cause and nature of the cutoff can be more readily visualized from consideration of Table 8 which shows the spectral entries such as might be extracted from a single FNWC printout for a fully arisen sea of 50 knots (in the absence of swell). The entries in this table show the energy density per 0.0055 Hz and 30° bandwidths (as in Table 7) for the condition in which the mean wind direction coincides with the center of the direction band (this condition gives the maximum variance values possible for the 50-knot sea). The reader may recognize this distribution as a frequency spectrum graph in tabular form that has been rotated 180° about both the energy density and frequency axes. If one now imagines a graph of nested frequency spectra for fully arisen seas generated over a range of wind speeds, the spectra are seen in the higher frequencies to occupy a relatively narrow band on the graph, with the outermost spectrum being associated with the strongest wind and representing the energy cutoff in the equivalent statistical tables. If non-fully developed spectra for the same wind speeds are added to the imagined graph, the unsaturated portions of each will lie inside this band, as will also the saturated low-frequency tails of fully arisen spectra associated with weaker winds.

It is evident from these considerations that the entries in Table 7 lying inside the cutoff zone may represent (1) saturated frequency components associated with fully arisen seas produced by weaker winds, (2) unsaturated components of seas produced by strong or weak winds, or (3) swell. There is no way to associate these entries with sea or swell however, whether or not this might be desired for practical purposes. All that can be said in this vein is that the entries lying in a band along the data envelope clearly represent dominantly sea. It should be

mentioned here that the energy cutoff in Table 7 is not fully analogous to the height cutoff in Table 4; occurrence entries representing sea may be found anywhere inside the data envelope of Table 7 but lie only in the zone labelled "sea" in Table 4.

The wave statistics for February are presented in still another form in Figure 1. This figure was constructed by cumulating the occurrences in Table 7 from high to low energy density within each period band (cumulative table not shown), and plotting the cumulated values against the period. The curves in the graph are isopleths of energy density coded according to Table 3. Figure 1 combines the advantage of Table 6 in that the total energy represented is correct, and Table 7 in which the energy densities are referenced to the standard 0.0055 Hz bandwidth. This graphical presentation gives the user a distinctly better visual impression of the statistical distribution than do the two tables; however tables directly provide the numerical values a user needs.

Figure 1 is of particular interest not so much as a format in which spectral element statistics may be presented but because of the possibility which it suggests for describing climatological wave data by a mathematical function, at least for some ocean regions and seasons. The energy-occurrence curves in the figure are seen to resemble nested wave frequency spectra for fully arisen seas associated with a range of wind speeds, with the dashed curve being the counterpart of the T_{\max} curve for the spectra. The fact that the pattern of this T_{\max} small-sample distribution is so well defined suggests that the long-term average pattern for February is similar at this station. It may be expected, on the basis of continuity, that similar wave climatology patterns occur in adjacent months and over adjacent regions of the North Pacific Ocean; accordingly, it seems possible that all of these distributions might be described by a function having variable coefficients that provide for seasonal and geographical gradients. From a practical standpoint, the availability of wave climatology models for ocean regions would greatly improve data packaging, allow greater versatility in data manipulation, and improve the prediction of infrequently occurring wave conditions.

Consideration of the spectral characteristics of sea and swell further suggests that in ocean regions and seasons where swell is dominant, the wave climatology may not be amenable to mathematical description. A graph similar to Figure 1 prepared for August (not shown) when the swell-to-sea ratio is substantially higher at the selected station is inconclusive on this point because of the low frequency of wave occurrence in that month. It should be recalled that Figure 1 is a data composite of all 12 direction bands. If long-term average statistics for February were displayed for each direction band, it is reasonable to expect that a pattern similar to that in the figure would appear for all or some of the component directions.

USES OF THE STATISTICS

Significant wave statistics tables derived from FNWC spectral analyses are similar in construction to climatology tables currently in use, except for tabulation of the wave data by variable period increments. This design feature may appear untidy but should not restrict the uses of the statistics.

The coastal engineering applications which would be made of these tables appear to be identical to those of existing wave climatology tables. Reasons for favoring use of the FNWC-derived significant wave statistics, however, are that they are free of the familiar super-occurrence problem in which tables contain more total hours of wave occurrence than actually occurs, and that they take into account simultaneous occurrence of wave trains arriving at a wave station and therefore contain higher wave heights.

With regard to spectral element statistics, there are considerable uncertainties concerning their uses and apparently no experience available to provide guidance. The following comments are therefore limited to the more obvious things that can and cannot be done with these statistics.

The $\Delta V - \Delta f - \Delta \psi$ values composing spectral element tables compiled for a deep-water wave station can be shoaled and refracted in the same manner as the spectrum of a given set of waves (described by Pierson, Neumann, and James, 1955); thus, the spectral element climatology can be determined for a selected shoal-water site (except near the surf zone since the breaker height cannot be identified in the spectral statistics). These statistics cannot be converted into wave height statistics, however, and so cannot be used to compute design wave heights, wave forces, breaker-height statistics, or littoral-drift rates by current methodology; these quantities must still be calculated using the more gross significant wave statistics.

The principal uses for wave statistics in spectral element form, both in coastal waters and the open ocean, appear to lie in the realm of resonant reaction of structures to waves. Practical applications can readily be visualized involving piling platforms, spar platforms, tethered breakwaters, floating causeways, surface vessels, and surface-effects craft. The nature of the transform from spectral wave information to structures response and how the transform can be applied quantitatively appear to be little understood, however.

Although specific uses for spectral element climatology are not now developed, the marked differences which these statistics display from the significant wave statistics derived from the same synoptic source data, along with the possibility of modelling these spectral distributions mathematically, compels further attention to these data.

REFERENCES

- Bretschneider, C. L., 1958. Revisions in wave forecasting: deep and shallow water. Proc. of Sixth Conf. on Coast Engr., Chap. 3, pp. 30-67.
- Bretschneider, C. L., and R. D. Gaul, 1956. Wave statistics for the Gulf of Mexico (for 5 wave stations). Army Corps of Engrs., Beach Erosion Board, Tech. Memo. 85-89 (5 reports).
- Lazanoff, S. M., and N. M. Stevenson, 1975. An evaluation of a hemispheric operational wave spectral model. Fleet Numerical Weather Central, Tech. Note 75-3, 103 pp.
- Marine Advisers, Inc., 1961. A statistical survey of ocean wave characteristics in Southern California waters. Prepared for Army Corps of Engrs., Los Angeles Dist., 30 pp. + tables.
- National Marine Consultants, Inc., 1960. Wave statistics for seven deep water stations along the California coast. Prepared for Army Corps of Engrs., Los Angeles and San Francisco Dist., 20 pp. + tables.
- National Marine Consultants, Inc., 1961. Wave statistics for three deep water stations along the Oregon-Washington coast. Prepared for Army Corps of Engrs., Portland and Seattle Dist., 17 pp + tables.
- Neumann, G., and R. W. James, 1955. North Atlantic Coast wave statistics hindcast by the wave spectrum method. Army Corps of Engrs., Beach Erosion Board, Tech. Memo. 57, 23 pp. + tables.
- Pierson, W. J., Jr., G. Neumann, and R. W. James, 1955. Practical methods for observing and forecasting ocean waves. Navy Hydro. Off., H.O. Pub. 603, 284 pp.
- Reynolds, F. M., 1976. Climatological wave statistics derived from FNWC synoptic spectral wave analyses. Naval Postgrad. Sch., Monterey, Calif., M. S. Thesis, 141 pp.
- Saville, T., Jr., 1954. North Atlantic Coast wave statistics hindcast by Bretschneider-revised Sverdrup-Munk method. Army Corps of Engrs., Tech. Memo. 55, 18 pp. + tables.
- Sverdrup, H. U., and W. H. Munk, 1947. Wind, sea, and swell: theory of relations for forecasting. Navy Hydro. Off., H.O. Pub. 601, 44 pp.

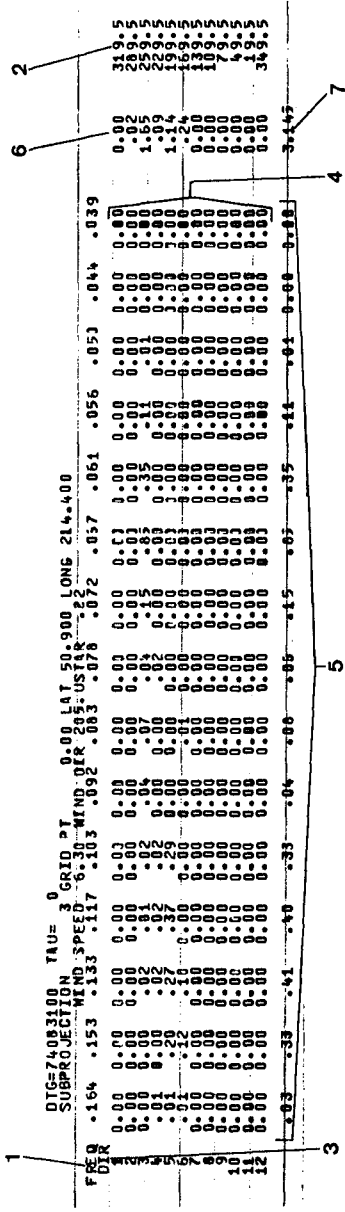


TABLE 1: FNNWC SPECTRAL PRINTOUT OF WAVE FIELD
FOR GRID POINT 164 OF SUBPROJECTION 3 FOR 00Z ON 31 AUGUST 1974

Table 2: FNCW FREQUENCY/PERIOD PARAMETERS
(Modified from Lazanoff and Stevenson, 1975)

Central frequency (Hz)	Frequency band (Hz)	Frequency bandwidth (Hz)	Energy density factor	Central period (sec)	Period band (sec)	Period bandwidth (sec)
0.164*			1/18	6.1		
0.153	0.142-0.164	0.0220	1/4	6.5	7.2- 6.1	1.1
0.133	0.125-0.142	0.0165	1/3	7.5	8.0- 7.2	0.8
0.117	0.108-0.125	0.0165	1/3	8.6	9.3- 8.0	1.3
0.103	0.097-0.108	0.0110	1/2	9.7	10.3- 9.3	1.0
0.092	0.086-0.097	0.0110	1/2	10.9	11.7-10.3	1.4
0.083	0.080-0.086	0.0055	1	12.0	12.5-11.7	0.8
0.078	0.075-0.080	0.0055	1	12.9	13.4-12.5	0.9
0.072	0.069-0.075	0.0055	1	13.8	14.4-13.4	1.0
0.067	0.064-0.069	0.0055	1	15.0	15.7-14.4	1.3
0.061	0.058-0.064	0.0055	1	16.4	17.2-15.7	1.5
0.056	0.053-0.058	0.0055	1	18.0	19.0-17.2	1.8
0.050	0.047-0.053	0.0055	1	20.0	21.2-19.0	2.2
0.044	0.042-0.047	0.0055	1	22.5	24.0-21.2	2.8
0.039	0.036-0.042	0.0055	1	25.7	27.6-24.0	3.6

*Lower limit of frequency band

Note: Periods are derived from the FNCW frequencies.

Table 3: CODE FOR EXPRESSING SIGNIFICANT WAVE HEIGHT AND SPECTRAL ENERGY DENSITY IN THE CLIMATOLOGY TABLES

<u>Significant wave table</u>		<u>Spectral element tables</u>	
<u>Code</u>	<u>$H_{1/3}$ (ft)</u>	<u>Code</u>	<u>ΔV (ft²)</u>
01	0.0 - 1.9	01	0.01 - 0.24
02	2.0 - 3.9	02	0.25 - 0.49
03	4.0 - 5.9	03	0.50 - 0.74
04	6.0 - 7.9	04	0.75 - 0.99
05	8.0 - 9.9	05	1.00 - 1.24
06	10.0 - 11.9	06	1.25 - 1.49
07	12.0 - 13.9	07	1.50 - 1.74
08	14.0 - 15.9	08	1.75 - 1.99
09	16.0 - 17.9	09	2.00 - 2.49
10	18.0 - 19.9	10	2.50 - 2.99
11	20.0 - 21.9	11	3.00 - 3.49
12	22.0 - 23.9	12	3.50 - 3.99
13	24.0 - 25.9	13	4.00 - 4.49
14	26.0 - 27.9	14	4.50 - 4.99
15	28.0 - 29.9	15	5.00 - 5.49
16	30.0 - 31.9	16	5.50 - 5.99
17	32.0 - 33.9	17	6.00 - 6.49
18	34.0 - 35.9	18	6.50 - 6.99
19	36.0 - 37.9	19	7.00 - 7.49
20	38.0 - 39.9	20	7.50 - 7.99
21	40.0 - 41.9	21	8.00 - 8.49
22	42.0 - 43.9	22	8.50 - 8.99

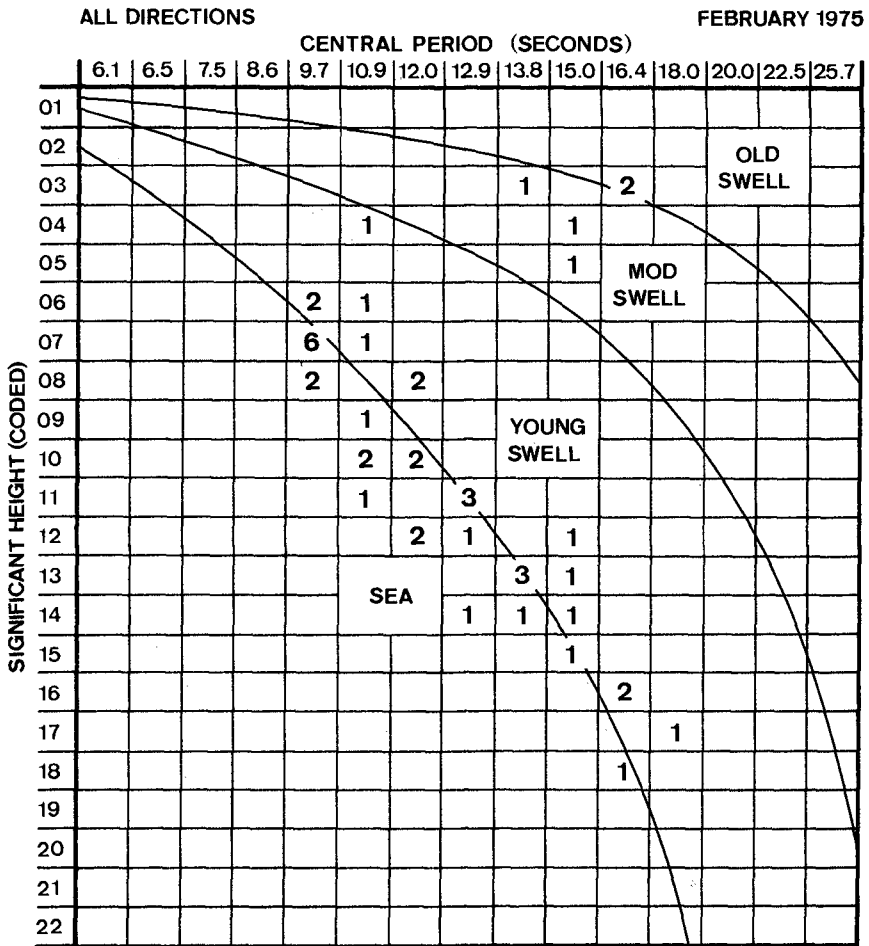


TABLE 4: SIGNIFICANT WAVE STATISTICS

Table 5: DEFINITIONS OF WAVE STEEPNESS AND WAVE AGE
(Applicable to deep water only)

WAVE STEEPNESS, γ

Monochromatic waves

$$\gamma_m = \frac{H}{L} = \frac{H}{\frac{g}{2\pi} T^2} = \frac{H}{5.12 T^2}$$

H = wave height

L = wave length

T = wave period

Spectrum waves

$$\gamma_s = \frac{H_{1/3}}{\frac{g}{2\pi} T_{max}^2} = \frac{H_{1/3}}{5.12 T_{max}^2}$$

$H_{1/3}$ = significant wave height

T_{max} = period of max energy density

WAVE AGE (in terms of γ_s)

<u>Wave age</u>	<u>γ_s</u>	<u>Significant height reduction* (H_D/H_F)</u>	<u>Decay distance* (naut mi)</u>
Sea	1/40	1.00	0
Young swell	1/100	0.50	250
Moderate swell	1/250	0.25	1600
Old swell			

H_F = sea height in the generating area

H_D = swell height at decay distance D

*Approximate values for swell generated in an average extratropical cyclonic storm from the SMB wave forecasting graphs (Bretschneider, 1958).

ALL DIRECTIONS		CENTRAL PERIOD (SECONDS)														FEBRUARY 1975		
		6.1	6.5	7.5	8.6	9.7	10.9	12.0	12.9	13.8	15.0	16.4	18.0	20.0	22.5	25.7		
ENERGY DENSITY / FNWC FREQ. BANDWIDTH (CODED)	01	142	135	122	123	123	153	143	158	129	108	76	60	37	11	13		
	02	141	115	137	40	41	33	39	37	29	27	17	12	2	1			
	03			1	65	49	33	30	17	17	16	9	9	8	1	1		
	04				65	51	18	19	16	7	7	6	3		1	1		
	05				2	29	19	20	13	13	9	6		1	1			
	06						20	9	8	7	4	4						
	07						18	4	8	4	2	1						
	08						16		3	6	3	2						
	09						1		3	3	4	1	1	3				
	10									5			2					
	11										6		3					
	12											5	1		1			
	13										1	2		1				
	14																	
	15											1	1					
	16												1					
	17																	
	18																	
	19												1					
	20																	
	21													1				
	22																	

TABLE 6: SPECTRAL ELEMENT STATISTICS
 ENERGY DENSITY (CODED) PER FNWC FREQUENCY BANDWIDTH
 AND 30° DIRECTION BANDWIDTH

ALL DIRECTIONS

FEBRUARY 1975

	CENTRAL PERIOD (SECONDS)														
	6.1	6.5	7.5	8.6	9.7	10.9	12.0	12.9	13.8	15.0	16.4	18.0	20.0	22.5	25.7
01	283	250	260	228	164	186	143	158	129	108	76	60	37	11	13
02				67	100	51	39	37	29	27	17	12	2	1	
03					29	39	30	17	17	16	9	9	8	1	1
04						34	19	16	7	7	6	3		1	1
05							20	13	13	9	6		1	1	
06							9	8	7	4	4				
07							4	8	4	2	1				
08								3	6	3	2				
09								3	3	4	1	1	3		
10									5			2			
11										6		3			
12											5	1			
13										1	2		1		
14															
15											1	1			
16												1			
17															
18															
19												1			
20															
21													1		
22															

TABLE 7: SPECTRAL ELEMENT STATISTICS

ENERGY DENSITY (CODED) PER 0.0055 Hz STANDARD FREQUENCY BANDWIDTH AND 30° DIRECTION BANDWIDTH

	ALL DIRECTIONS													FEBRUARY 1975		
	CENTRAL PERIOD (SECONDS)															
	6.1	6.5	7.5	8.6	9.7	10.9	12.0	12.9	13.8	15.0	16.4	18.0	20.0	22.5	25.7	
01	1	1														
02			1													
03				1												
04					1											
05																
06																
07						1									1	
08																
09							1									
10																
11								1								
12									1							
13																
14														1		
15										1						
16																
17											1					
18																
19												1	1			
20																
21																
22																

TABLE 8: SPECTRAL ENTRIES FOR A 50-KNOT FULLY ARISEN SEA
 FOR A GIVEN LOCATION AND SYNOPTIC TIME
 0.0055 Hz AND 30° BANDWIDTHS

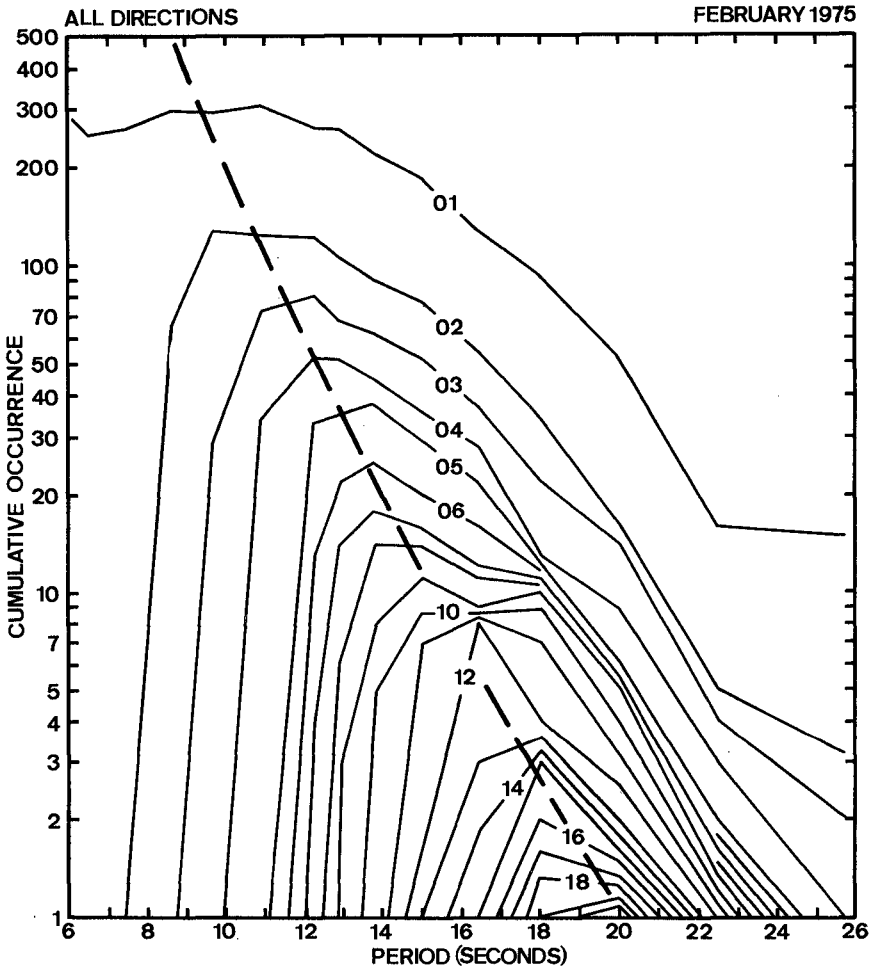


FIGURE 1: CUMULATIVE SPECTRAL ELEMENT STATISTICS
 CURVES ARE ENERGY DENSITY (CODED) PER 0.0055 HZ BANDWIDTH
 AND 30° DIRECTION BANDWIDTH

CHAPTER 15

Application of Fetch Area Method in Monsoon Wave Hindcasting

Nai-Kuang Liang¹, Shih-Tsan Tang²
and Ben-Juen Lee³

ABSTRACT

The Fetch Area Method (FAM) derived from Elementary Wave Model is used to analyze the winter monsoon wave of Taichung Harbour. The empirical wind-wave energy transfer coefficient $\bar{\xi}$ determined by FAM for this area is 7.25×10^{-4} . A relationship between $g T_{1/3} / 2\pi\bar{U}$ and $g t_d' / \bar{U}$ is also found, where \bar{U} is the average wind speed and t_d' the duration. A comparison of the wave hindcasting of FAM has shown that the latter is better than the former, and the former is valid only as the wind velocity increases, once the wind decreases the SMB Method is no more valid.

INTRODUCTION

The Fetch Area Method based on Elementary Wave Model (Liang 1973a, 1973b) is applicable to the wave forecasting or hindcasting, in which the influence of the whole wind field is considered.

The limited water field and the continental shelf of Taiwan Straits make us believe that the wave generated in this area should be different from that of the open sea like Pacific Ocean (Fig. 1). There are some coastal stations in Taiwan where both wind and wave data are available. Among them, we are most satisfied with the completeness and perfectness of the data in the vicinity of Taichung Harbour. The hindcast work of this paper has been made on the basis of the data on the point observation of Taichung Harbour and the weather maps analyzed by Central Weather Bureau. In this paper we analyzed the wave and wind data according to the Elementary Wave Model to determine the empirical coefficient $\bar{\xi}$ and the relationship of $T_{1/3}$, the average wind speed of influencing area \bar{U} and the duration t_d' adapted for Taichung Harbour. Using this coefficient and the relationship, one can hindcast or forecast the monsoon waves of this area.

-
1. Associate professor, Institute of Oceanography, National Taiwan University, Taipei, Taiwan, Rep. of China.
 2. Former research assistant, Institute of Oceanography, National Taiwan University, Taipei, Taiwan, Rep. of China.
 3. Meteorologist, Central Weather Bureau, Taipei, Taiwan, Rep. of China.

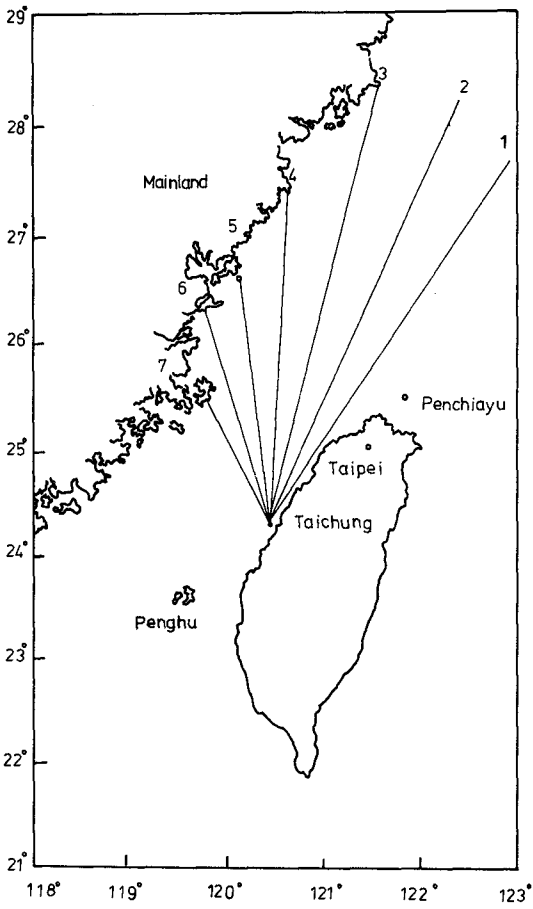


Fig.1 Taiwan Straits

BASIC THEORY

According to the Elementary Wave Model (Liang 1973b, 1975) and some modifications, the wave energy at the observation point 0 (Fig. 2) is as follows:

$$E = \frac{2}{\pi G} \int_r \int_\theta \bar{\Phi}(r, \theta) U^2(r, \theta) \cos^2[\beta(r, \theta)] \exp\left(-\frac{0.08}{U^2} r\right) dr d\theta \quad (1)$$

where G is the equivalent group velocity and defined as

$$G = \frac{g}{2} \frac{\int_0^\infty \bar{\Phi}(\sigma) \sigma^{-1} d\sigma}{\int_0^\infty \bar{\Phi}(\sigma) d\sigma} \quad (2)$$

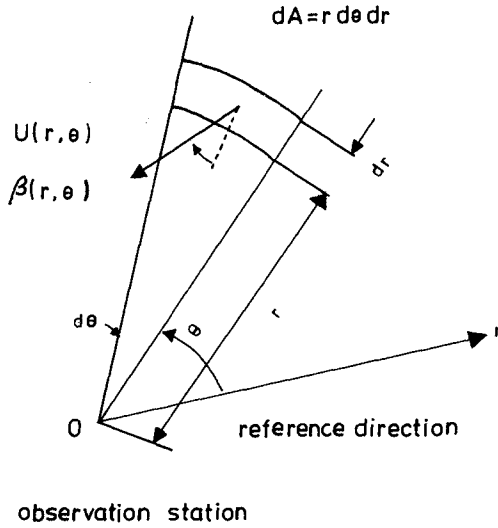


Fig.2 The coordinate system of the wind field.

in which $\bar{E}(\sigma)$ is the wave spectrum. $\bar{\xi}$ is a parameter which characterizes the energy transfer from wind to wave. U (m/s) is the wind velocity at 10m above sea level. $\cos^2 \beta$ is the angular spreading function which is verified by an experiment (Liang 1973a,b). $\exp (- \frac{0.08}{U^2} r)$ is an e-exponential decay term, which is determined by the 100% developed seas after C. L. Bretschneider, i. e.,

$$\frac{gr}{U^2} = 600,000. \tag{3}$$

or
$$r = \frac{600,000}{g} U^2 = \frac{600}{g} U^2 \text{ (km)} \tag{4}$$

It is then supposed that the elementary wave energy at the end of the fetch of this 100% developed seas is decayed to 1/100 of the original amount, as it propagates to the observation point 0,

$$e^{-\alpha r} = \frac{1}{100} \tag{5}$$

$$\alpha r = 4.605 \tag{6}$$

From eq.(4) $\alpha \approx \frac{0.08}{U^2}$ (7)

For simplicity, we take

$$G_{1/3} = \frac{gT_{1/3}^2}{4\pi}, E_{1/3} = H_{1/3}^2 \tag{8}$$

Instead of G and E and assume $\bar{\xi}$ is a constant, then we have

$$H_{1/3}^2 = \frac{2}{\pi G_{1/3}} \bar{\xi} \int_r \int_\theta U^2 (r, \theta) \cos^2 [\beta (r, \theta)] \exp (\frac{-0.08}{U^2} r) dr d\theta \tag{8}$$

$$\text{or, } \bar{\xi} = \frac{H_{1/3}^2}{2 / (\pi G_{1/3}) \int_r \int_\theta U^2 (r, \theta) \cos^2 [\beta (r, \theta)] \exp (\frac{-0.08}{U^2} r) dr d\theta} \tag{9}$$

ESTIMATION OF WIND FIELD AND DETERMINATION OF INFLUENCING WIND FIELD

The preliminary data for wave forecasting or hindcasting is the information of

wind field over sea areas. Unfortunately, there are few wind data available in these areas and it is believed that there are still some difficulties to determine the wind field over the ocean (Bunting, 1970). Hence, we have made some objective judgement of the wind field over these sea areas. Estimates of wind field over sea areas are made on the basis of the isobaric pattern of synoptic weather charts and the wind data of nearby meteorological stations. The sea areas can be roughly divided into two regions, i.e., the region to the north of Pengchiayu and the region in the Taiwan Straits. Since the region to the north of Pengchiayu belongs to an open sea where the isobaric pattern is less influenced than that in the Taiwan Straits, the wind field in this area is estimated from the calculated wind speed and the wind data of the nearby stations.

The calculated wind speed is obtained from the geostrophic balance equation

$$U_g = \frac{1}{f a f} \frac{\Delta p}{\Delta n} \quad (10)$$

and some corrections with geostrophic surface-wind relationship given by

$$U = aU_g + b \quad (11)$$

where $a = 0.54$ and $b = 2.5$ (Hasse and Wagner, 1970)

In the region of Taiwan Straits the isobaric lines are greatly curved and the pressure gradient is too great to be determined precisely from the weather chart. However the wind was observed offshore of Taichung Harbour at 2 hour interval. Hence, the observed wind data at this area will be used to represent the wind field over the Straits.

The 6-hr weather map is always changing, we should assume that the wind is steady during the six hour interval. Since the winter monsoon blows steadily from the north or northeast, it's appropriate to say that the wave in the generating area is quasi-fully-developed. It is then assumed that the elementary wave energy propagates at the speed of the fully-arisen equivalent group velocity determined by the local wind, i.e, $0.5 U$ after Neumann. The authors use a series of surface synoptic charts to determine the influencing wind field. For example, if we try to hindcast the wave at 1400Z, Feb. 26, 1974, the weather chart at 1500Z should be checked at first. The weather charts are available at 0300Z, 0900Z, 1500Z and 2100Z. Since the weather system is assumed unchanged during the 6-hr interval, the wind field is stationary from 1200Z to 1800Z. The wind speed of Taichung Harbour at 1500Z Feb. 26, 1974 is $U_1 = 17.4$ m/s, the first influencing sector has a radius (Fig.3)

$$\begin{aligned} r_1 &= 0.5 \times 17.4 \times \Delta t_1 \\ &= 0.5 \times 17.4 \times 2^1 \times 3600 \text{ (m)} \\ &= 0.6 \text{ (lat.)} \end{aligned}$$

Then we check the former chart (Fig.4) of 0900Z on which the wind speed near r_1 is $U_2 = 11$ m/s, Hence,

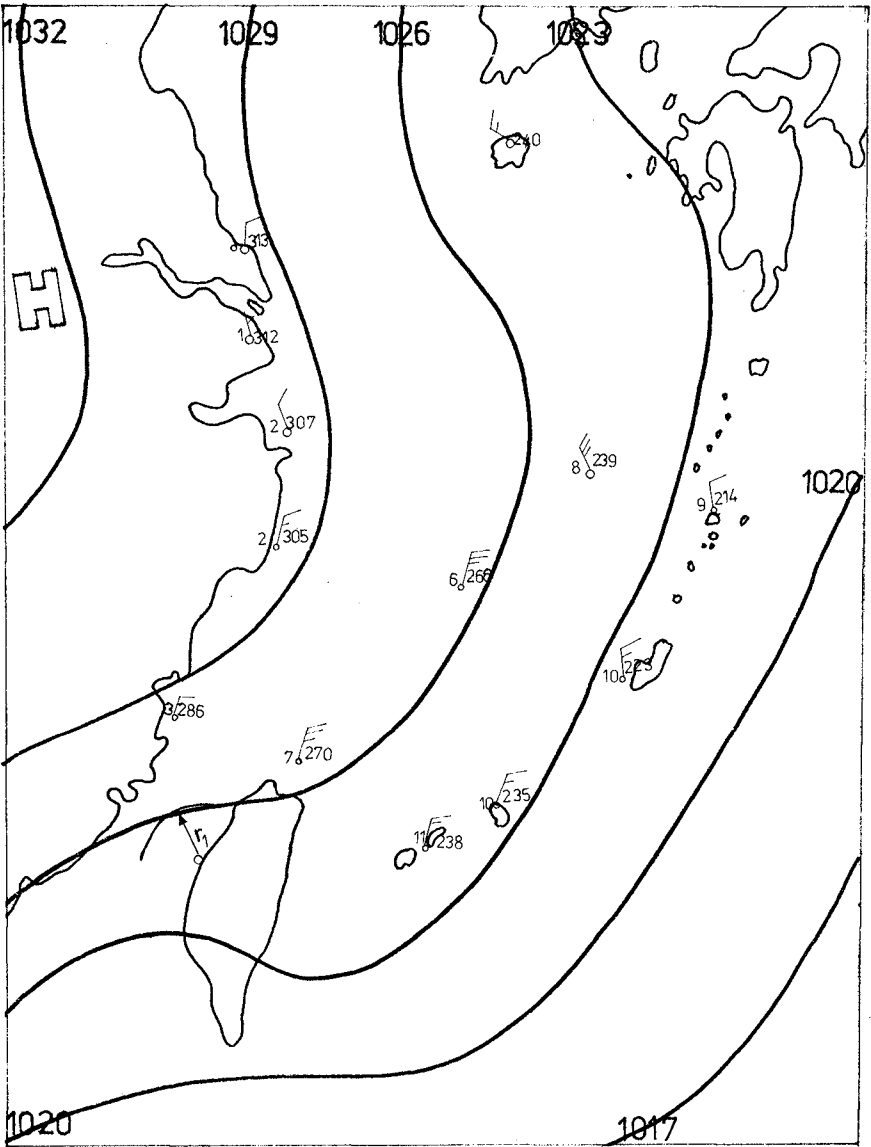


Fig.3 Surface synoptic chart for 1500Z, Feb. 26, 1974

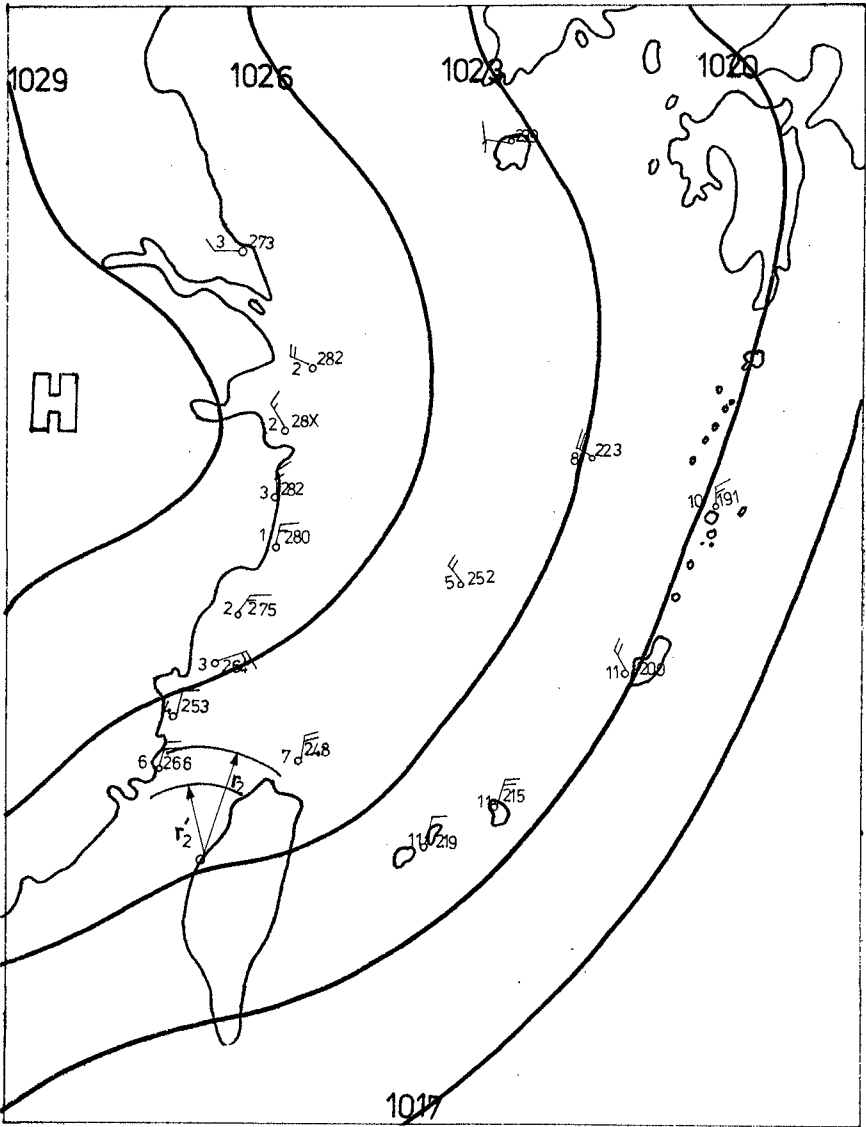


Fig.4 Surface synoptic chart for 0900Z, Feb. 26, 1974

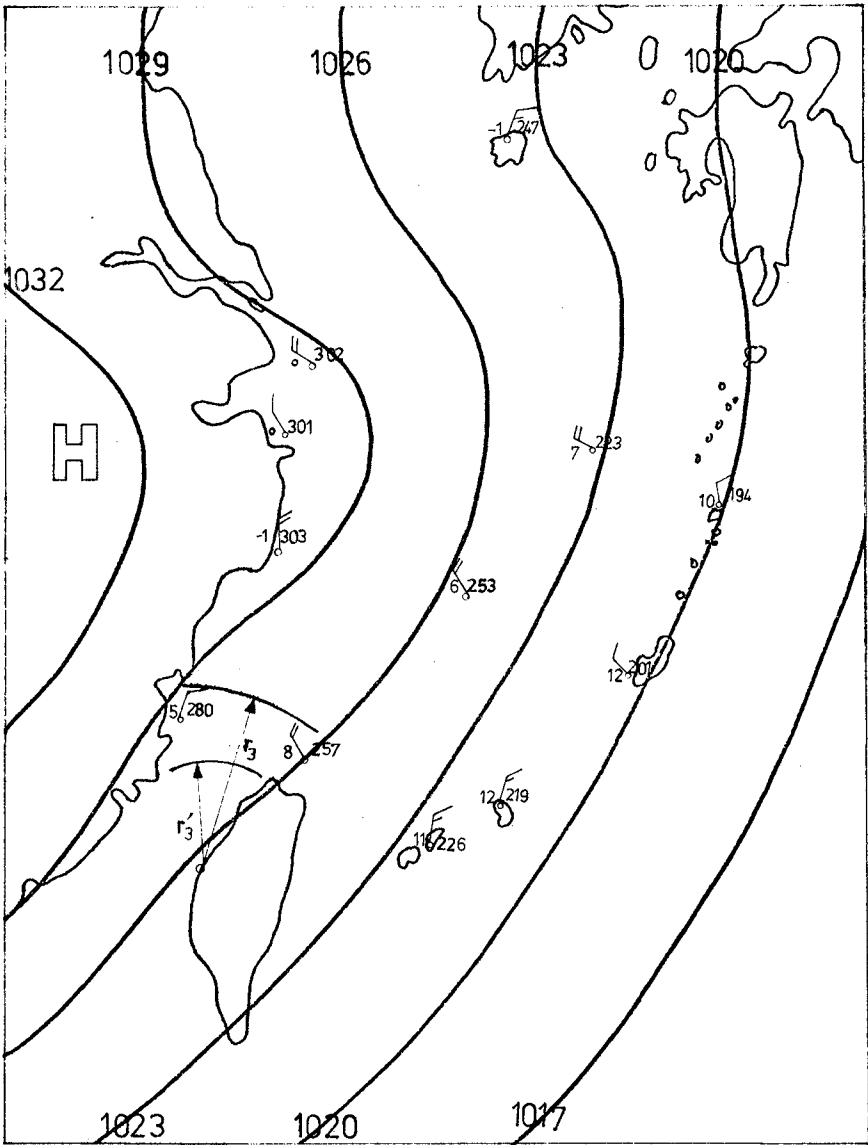


Fig.5 Surface synoptic chart for 0300Z Feb. 26, 1974

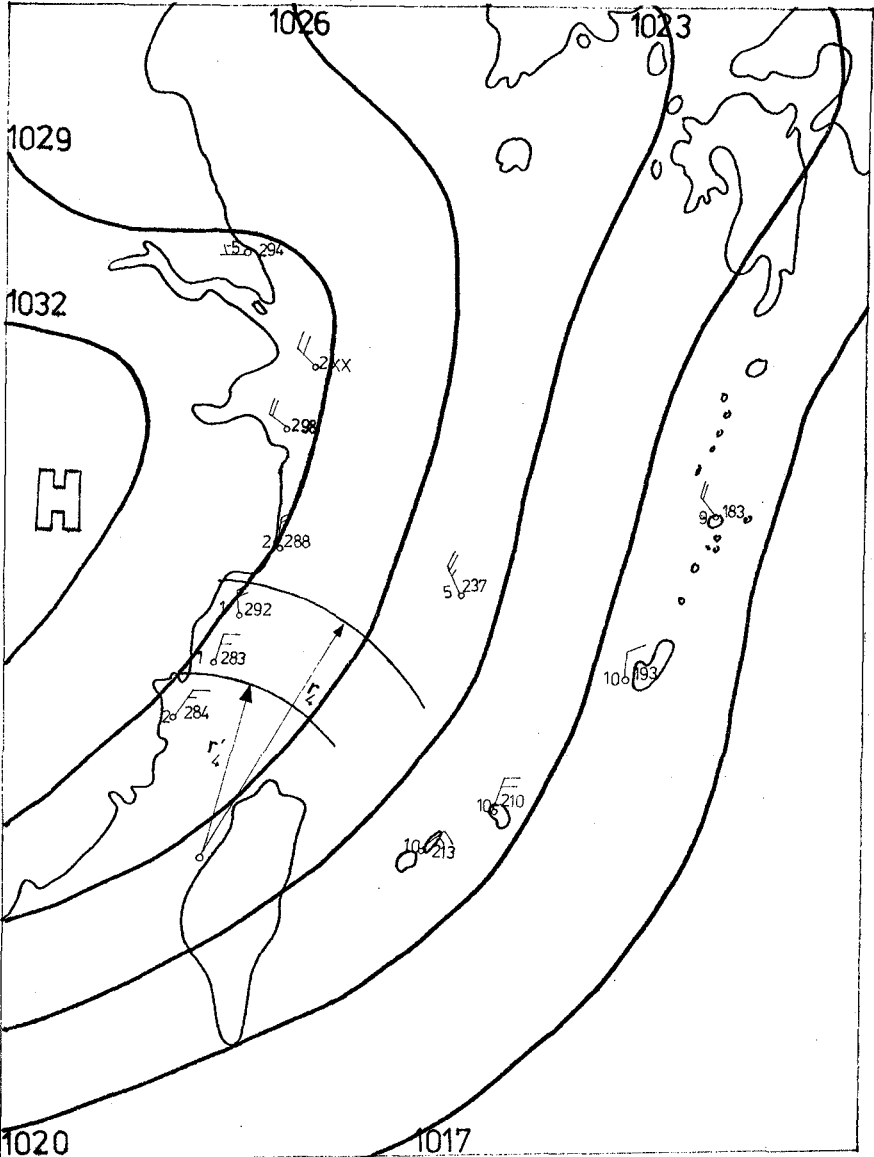


Fig.6 Surface synoptic chart for 2100Z Feb. 25, 1974

$$\begin{aligned} r_2 &= 0.5 \times 11 \times (\Delta t_1 + \Delta t) \\ &= 0.5 \times 11 \times (2 \frac{1}{2} \times 6) \times 3600 \text{ (m)} \\ &= 1.4 \text{ (lat.)} \end{aligned}$$

$$\begin{aligned} r_2' &= 0.5 \times 11 \times \Delta t_1 \\ &= 0.5 \times 11 \times 2 \frac{1}{2} \times 3600 \text{ (m)} \\ &= 0.4 \text{ (lat.)} \end{aligned}$$

Since the wind data to the north of Pengchiayu is not valid for Taiwan Straits of which the radius is about 1.0 lat., we should take $r_2' = 1.0$ lat.

In Fig. 5, the weather chart of 0300Z shows the wind speed near r_2 is $U_2 = 10$ m/s. Then

$$\begin{aligned} r_3 &= 0.5 \times 10 \times (\Delta t_1 + 2\Delta t) \\ &= 0.5 \times 10 \times (2 \frac{1}{2} \times 2 \times 6) \times 3600 \text{ (m)} \\ &= 2.3 \text{ (lat.)} \end{aligned}$$

$$\begin{aligned} r_3' &= 0.5 \times 10 \times (\Delta t_1 + \Delta t) \\ &= 0.5 \times 10 \times (2 \frac{1}{2} \times 6) \times 3600 \text{ (m)} \\ &= 1.3 \text{ (lat.)} \end{aligned}$$

In the weather chart of 2100Z, Feb. 25, 1974 (Fig. 6) the wind speed near r_3 is $U_4 = 11$ m/s, therefore

$$\begin{aligned} r_4 &= 0.5 \times 11 \times (\Delta t_1 + 3\Delta t) \\ &= 0.5 \times 11 \times (2 \frac{1}{2} \times 3 \times 6) \times 3600 \text{ (m)} \\ &= 3.7 \text{ (lat.)} \end{aligned}$$

$$\begin{aligned} r_4' &= 0.5 \times 11 \times (\Delta t_1 + 2\Delta t) \\ &= 0.5 \times 11 \times (2 \frac{1}{2} \times 2 \times 6) \times 3600 \text{ (m)} \\ &= 2.5 \text{ (lat.)} \end{aligned}$$

EVALUATION OF \bar{F} and $T_{1/3} - \bar{U} - t_d'$ - RELATIONSHIP.

The detail to calculate eq. (9) is illustrated in Fig. 1. It consists of 7 radials from the wave station at intervals of 10° and extending these radials until they intersect the shoreline.

With the influencing wind field determined we can calculate the integral along each radial. All the work is finished by a computer program. 233 data during the time from Feb. 7, 1974 till March 15, 1974 are selected to evaluate the $\bar{\xi}$ -value. It seems to have no correlation between $\bar{\xi}$ and wind speed.

The average value of $\bar{\xi}$ of these 233 cases is 7.24990×10^{-4} , its standard deviation is 2.19916×10^{-4} .

Two definitions have been made: \bar{U} is the area average wind speed from the observation point to the sea area where the e-exponential decay term $\exp(-\frac{0.08}{U^2} r) = 0.6$ and the duration t'_d is defined as the time interval between the first and the last weather chart we used to evaluate the average wind speed \bar{U} . A relationship of $T_{1/3}$, \bar{U} and t'_d is expressed as a dimensionless phase velocity $gt'_{1/3} / 2\pi\bar{U}$ and dimensionless duration gt'_d / \bar{U} on log-log plot (Fig. 7). A linear relationship in log-log plot is suggested:

$$\frac{gt'_{1/3}}{2\pi\bar{U}} = 0.00488 \left(\frac{gt'_d}{\bar{U}} \right)^{0.4472} \tag{12}$$

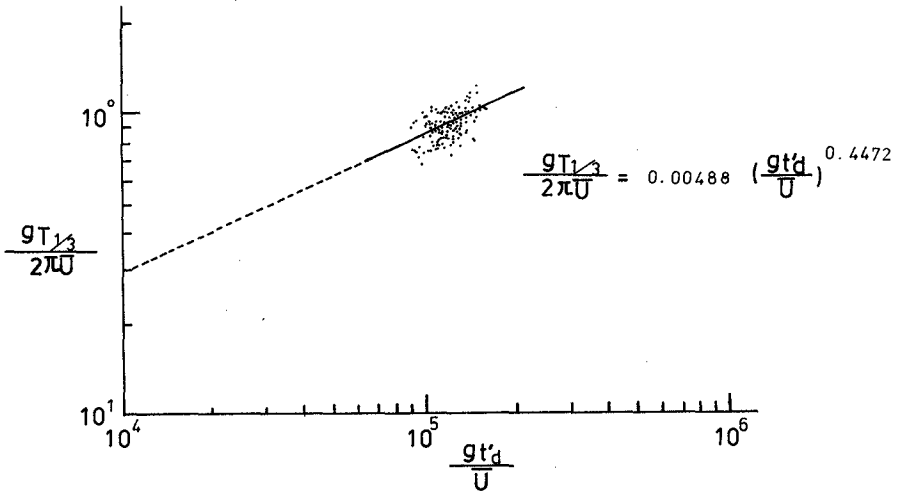


Fig. 7 Dependence of dimensionless phase velocity on dimensionless duration

COMPARISON OF SMB AND FAM

49 wave data during the time from Oct. 28, 1975 to Nov. 1, 1975 are selected to illustrate the comparison of SMB (U.S. Army, Corps of Engineering) and FAM hindcasting. The FAM hindcasting is finished by a computer. We need only give the wind velocities in specified areas at 6-hr interval. The result is shown in Fig. 8. and Fig. 9. It can be seen clearly that SMB has a little better result as the wind velocity increases. Once the wind velocity decreases, SMB is no more valid. In general, FAM has a much better hindcasting. The percentage of $H_{1/3}$ and $T_{1/3}$ within specified percent error by both methods is shown in Table I.

Table I Accuracy of hindcasting

Percent Error	Percentage of $H_{1/3}$ within Percent error		Percentage of $T_{1/3}$ within Percent error	
	SMB	FAM	SMB	FAM
5	8	39	22	16
10	22	61	33	43
15	27	71	53	63
20	35	88	73	84
25	47	92	82	88
30	51	94	90	96
35	57	98	96	100
40	63	100	100	100

CONCLUSION

1. SMB is a good method to predict or hindcast waves when the wind is increasing. Once the wind decreases, SMB is no more valid, at least for limited water field such as Taiwan Straits.
2. In general, FAM is much better than SMB, because the former has considered the influence of the whole wind field.
3. FAM can be used for routine work, such as Fishery Weather Forecasting of the Central Weather Bureau, Taiwan, Rep. of China, if one can precisely predict the wind in the Taiwan Straits.

ACKNOWLEDGEMENT

The authors wish to acknowledge the invaluable assistance rendered by Mr. C. H. Shu in the preparation of data analysis. Thanks also extended to Miss P.L. Chien for drawing the figures and typing the text.

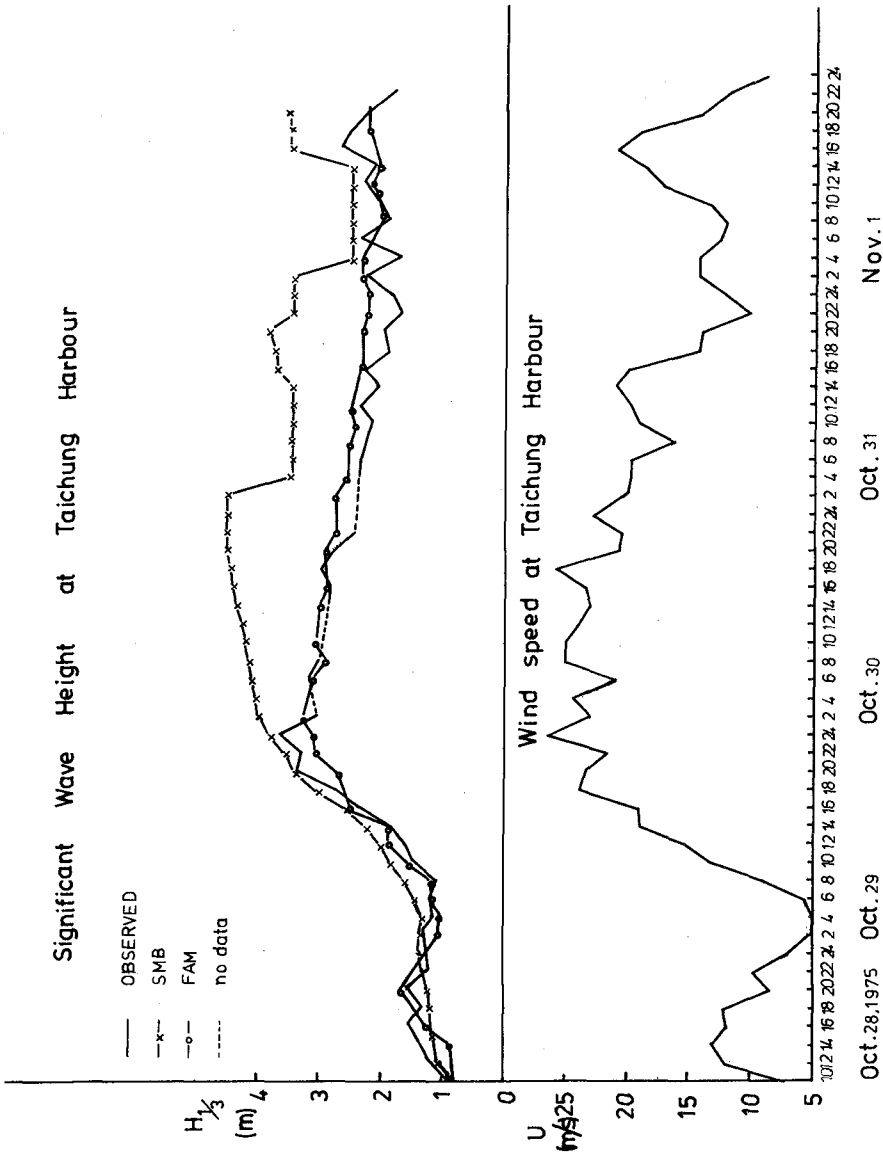


Fig. 8 Comparison of significant wave heights

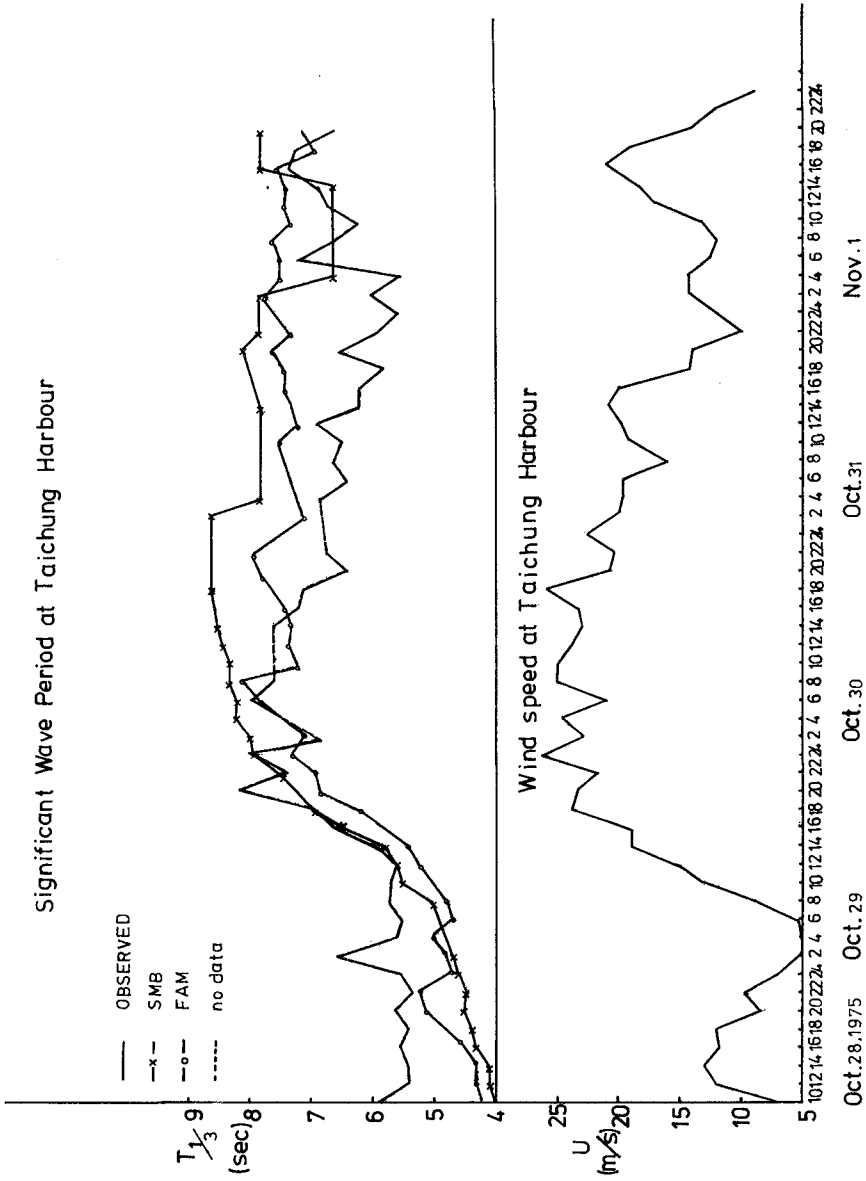


Fig.9 Comparison of significant wave periods

The majority of the work is supported by the National Science Council. The original wave and wind data are provided by Taichung Harbour Bureau.

REFERENCE

- BUNTING, D.C. (1970) Evaluating Forecasts of Ocean-Wave Spectra, Journal of Geophysical Research 75(21): 4131-4143.
- HASSE, L. and V. WAGNER (1970) on the Relationship between Geostrophic and Surface Wind at Sea, Monthly Weather Review 99(4): 255-260.
- LIANG, N.K. (1973a) Ueber den Einfluss des Windfeldes bei der Wellenvorhersage, Mitteilungen des Franzius-Instituts fuer Wasserbau und Kuesteningenieurwesen der Technischen Universitaet Hannover: Heft 39: 218-323.
- LIANG, N.K. (1973b) Elementary Wave Model and the Definition of " Fetch Area " in Wave Prediction, Acta Oceanographica Taiwanica 3: 87-96.
- LIANG, N.K. (1975) The Estimation of Wave Spreading Factor and Significant Wave Direction, Proc. of Ocean Engineering III, Delaware.
- U.S. ARMY, CORPS OF ENGINEERING, Shore Protection Manual, Vol. I, pp. 3.1-3.40, Coastal Engineering Research Center.

CHAPTER 16

CHARACTERISTIC WAVE PERIOD

By

M. Manohar (1), I.E. Mobarek (2) & N.A. El Sharaky (3)

ABSTRACT : The wave period estimates obtained from different procedures are not consistent unlike statistical distribution analysis of wave heights. Thus not one definition of wave period is satisfactory for engineering analysis of coastal processes.

There are at least 10 different measures of wave periods including the zero up-crossing period, the average wave period, significant height period and peak of the energy density spectrum period.

For the analysis of periods, 20 min. records were obtained from offshore pressure recorders. Summer and winter records were analysed separately.

In the analysis, zero up-crossing period and average period were taken as reference periods. There were significant differences between the wave periods and they were found to depend also on the spectral width parameter.

Finally comparison was made between the energy flux obtained under the spectral diagrams and energy flux obtained using various wave periods and heights.

Study shows that if the total energy flux is desired, then the most appropriate values to be used are the root mean square wave height and period corresponding to that wave height. Use of significant wave height, along with zero up-crossing period gives higher values.

INTRODUCTION : Ocean waves are extremely complex in character. The period, celerity, wave length and wave height are irregular. Though individual wave heights vary considerably, they are easier to define statistically and the expected wave heights can be predicted reasonably. Such consistency does not, however, occur with wave periods and therefore, not one definition of wave period is sufficient in wave analysis.

-
- (1) Hydrodynamics Engineer, UNESCO, Coastal Protection Studies, EGY/73/063, P.O.Box 946, Alexandria - Egypt.
 - (2) Assoc. Professor, Civil Engineering Dept., Cairo University - Cairo, Egypt.
 - (3) Head, Abuquir Research Station, Academy of Scientific Research & Technology, Abuquir - Egypt.

There are, at least, 10 measures of wave periods, at present, in use namely (i) average period of all waves called period of wave crests, (ii) zero up-crossing period, (iii) average period of one-third the highest waves, (iv) average period of one-tenth the highest waves, (v) period of root mean square wave height, (vi) average period contained in a single wave group, (vii) period of the highest wave, (viii) period most prominent in the record, (ix) period corresponding to the peak of the energy density spectrum and (x) period of the maximum energy density.

THEORY : At a given point on the ocean surface, the water surface elevation y is a function of time and can be assumed as the sum of an infinite number of sinusoidal waves, each with a frequency

$\omega_i = \frac{2\pi}{T_i}$ and phase angle ϕ_i where ω_i = angular frequency of the i th component of the wave spectrum. Thus

$$y(t) = \sum_i^N a_i \cos(\omega_i t + \phi_i) \quad (1)$$

where $y(t)$ is a stationary random function. The probability density of $y(t)$ is a Gaussian distribution

$$p(y) = \frac{1}{\sqrt{2} m_0} e^{-\frac{y^2}{2 m_0}} \quad (2)$$

where $\sqrt{m_0}$ = square root of the zero moment or area of the energy density spectrum and

$$H_{\text{rms}} = 2 \sqrt{2 m_0} \quad (3)$$

where H_{rms} = root mean square wave height.

Not going into mathematical details of the Raleigh Distribution, it can be stated that consideration of the energy of the component waves leads to the energy density spectrum. The energy of each component

$$e_i = \frac{1}{2} \rho g a_i^2$$

where e_i varies with angular frequency ω depending upon wave characteristics. The energy density of the spectrum $E(\omega)$ is the energy contained in the frequency limits ω , and $(\omega + d\omega)$. Thus :

$$E(\omega) d\omega = \frac{1}{2} \sum_{\omega}^{\omega + d\omega} a_i^2$$

and the total energy in the whole spectrum is

$$m_0 = \int_0^{\infty} \epsilon(\omega) d\omega = \sum_1^N \frac{1}{2} a_i^2 \tag{3}$$

Statistical analysis (3, 4) also shows that average zero up-crossing period T_z of the sea surface and the average crest period T_c can be determined from the wave spectrum. Thus :

$$T_z = 2\pi \sqrt{\frac{m_0}{m_2}} \tag{4}$$

$$T_c = 2\pi \sqrt{\frac{m_2}{m_4}} \tag{5}$$

The spectral width parameter ϵ is given by :

$$\epsilon = \sqrt{1 - \frac{m_2^2}{m_0 m_4}} \tag{6}$$

where m_2 and m_4 are spectral moments of 2nd and 4th order respectively.

If the spectrum has a constant shape, then it may be characterised by a single wave height directly related to the wave energy described by m_0 and a single wave period. The characteristic period (T_0) adopted is often corresponding to the frequency ω_0 of the spectral peak and can be obtained from the energy spectrum (with $\epsilon(\omega)$ on the y axis and $\omega = \frac{2\pi}{T}$ on the x axis). The above period of the maximum energy density obtained from spectral analysis is also useful in finding the average period of the waves composing the dominant wave groups in a swell (7, 8).

ANALYSIS : In the study, waves were recorded by offshore pressure operated recorders (OSPOS) anchored at the bottom in 6 m to 7 m depths at three stations off the Nile Delta Coast.

Draper/Tucker (3,9) method of manual analysis was made of the pressure charts, each record of which was of 20 min. duration recorded at intervals of 4 hours. Analysis was made separately for summer and winter seasons

since the former usually experienced swells from wind waves more or less continuously and the latter generated storms separated by lull periods.

To obtain a more objective analysis and since it represents an integration of waves present in the 20 min. record, the period of zero up-crossing was taken as the characteristic period and other periods were compared to that period. However, since zero up-crossing method depends on a practical method for determining the zero line, the wave crest period was also used as reference period in some cases.

There were significant differences between the various wave periods. Further the differences depended on the type of waves namely swells or storm waves or whether the waves occurred with one or more peaked spectra. Comparing the zero up crossing period with significant period, the former was found to be normally more than the latter, the ratio for summer and winter waves being 1.2 and 1.13 respectively (Fig. 1). The reason for this is probably because a large wave results when several of the spectral components are in phase at a given point and time. The period of the resulting wave will be influenced most by the higher frequencies present and therefore will be less than the zero up-crossing period T_z . Also larger values of ϵ occur for storm waves since wide range of z frequencies are present. Comparison of period of maximum wave height with zero up-crossing period (fig.2) shows similar trend (for the same reasons) but to a lesser extent. Their ratios (T_{Hmax} to T_z) are also dependent upon on the spectral width parameters which vary from 0.4 to 0.8 with summer swells (ϵ small) having smaller values than storm waves (ϵ large). Analysis of the period of the peak of the energy spectrum with zero up-crossing period gave a relationship $T_o = 1.12 T_z$ (fig.3) which corresponds to Bretschneider spectrum (1) for wind generated z waves such as those of Pierson and Moskowitz (6). The above relation was found to be mostly true for swells and for fully risen storm waves. This relationship will, however, differ if a spectrum of different form or of more than one peak occur. Comparison of significant wave height periods with those of maximum wave heights showed periods to be more or less equal though slightly less for swells. Considering spectral peak period in relation to the significant wave period, the former was higher than the latter varying from 1.22 to 1.32 (fig.4), the higher value representing summer waves.

Using wave crest period as reference, the significant wave height period, the spectral peak period, maximum wave height period, period corresponding to the root mean square wave height period were then analysed (figs.5 to 8). The spectral peak period showed the largest variation with the root mean square wave height period showing the least variation and the period of the maximum wave height equalling the period of the wave crests for swells (ϵ small). The fact that the spectral peak period showed the largest variation is not surprising since it represents a single peaked spectra of higher frequencies.

Studies were also made between the period of maximum energy density and the period corresponding to the peak of energy density spectrum. There seemed to be no correlation between them and therefore, no further study was made of the former.

Groups of waves (not swell trains) present in wind waves during storms were then examined and their periods determined. Similarly periods of prominent waves during storms were also analysed. Fig. 9 shows that they are related to T_z in some way or other. The analysis of these is not complete since swell trains have yet to be studied. However, the present indications are that for wind waves, zero up crossing period is fair representation of wave group period.

Unlike the earlier study of Harris⁽⁵⁾ which showed very little correlation of different wave period definitions, this study seems to indicate the existence of relations between some of them and that fact has been made use of to evaluate the total energy flux correctly using various wave height and period definitions.

Fig.10 shows the comparison between the energy flux obtained under the spectral diagrams and energy flux obtained using the various wave periods and heights. It shows that if the correct total energy flux is desired, then the most appropriate values to be used are the root mean square wave height and the period corresponding to that wave height. Use of significant wave height along with the zero up crossing period or spectral peak period results in considerably higher values representing higher energies present in the wave train. Though they may be useful in the study of wave dynamics, they will certainly give higher sediment transport rates than the actual. Lines representing the various energy fluxes using different wave periods have been drawn for the purpose of comparison.

CONCLUSIONS : An extensive study of the various definitions (ten) of wave periods was made. It showed that for wind waves and for swells associated with such wind waves, certain relations exist between some wave period definitions. It also showed that use of zero up-crossing period to represent the period of a wave recording is not to be recommended in all cases. Comparison of the actual energy flux from wave spectrum with the various wave periods and wave heights showed that the most appropriate combinations are those involving root mean square wave height and period corresponding to that height and that combinations involving significant wave height and zero up crossing period gave considerably higher values.

References

- 1) Bretschneider, C.L.- 1970 : Forecasting Relations for Wave Generation
vol.I, No.3, Look Laboratory, Univ. of Hawaii
- 2) Cartwright, D.E. & Longuet Higgins, M.S. - 1956 : Statistical
Distribution of the Maxima of a Random Function.
Ser.A, Vol.237, Proc. Roy. Society, London, p.212-232
- 3) Draper, L. - 1966 : Analysis and Presentation of Wave Data -
A plea for uniformity.
Vol.I, Proc. 10th Conference of Coastal Engineering,
Council of Wave Research, p.1 to 11.
- 4) Gourlay, M.R. - 1973 : Wave Climate at Moffat Beach
Bull. No.16 Dept. of Civil Engineering, Univ. of
Queensland, St.Lucia, Australia, p.74.
- 5) Harris, D.L. - 1970 : Analysis of Wave Records
Vol.I ASCE Proc. 12th Conference of Coastal Engineering
p. 85-100.
- 6) Pierson, W.J.; and Moskowitz - 1964 : A Proposed Spectral Form for
Fully Developed Wind Seas Based on the Similarity
Theory of S.A.Kitaigorodskii
Vol.69, No.24, Journ. of Geophy.Research, p. 5181-5190.
- 7) Thompson, W.C. - 1972 : Period by Wave Group Method
ASCE, Proc. 13th Conf. of Coastal Engineering, p.197-214.
- 8) Thompson, W.C. & Smith, R.C. - 1974 : Wave Groups in Ocean Swell
ASCE, Proc. 14th Conference of Coastal Engineering,
p.338 to 367.
- 9) Tucker, M.J. - 1963 : Analysis of Records of Sea Waves
vol.26, Proc. Inst. of Civil Engineers, p.305-316.

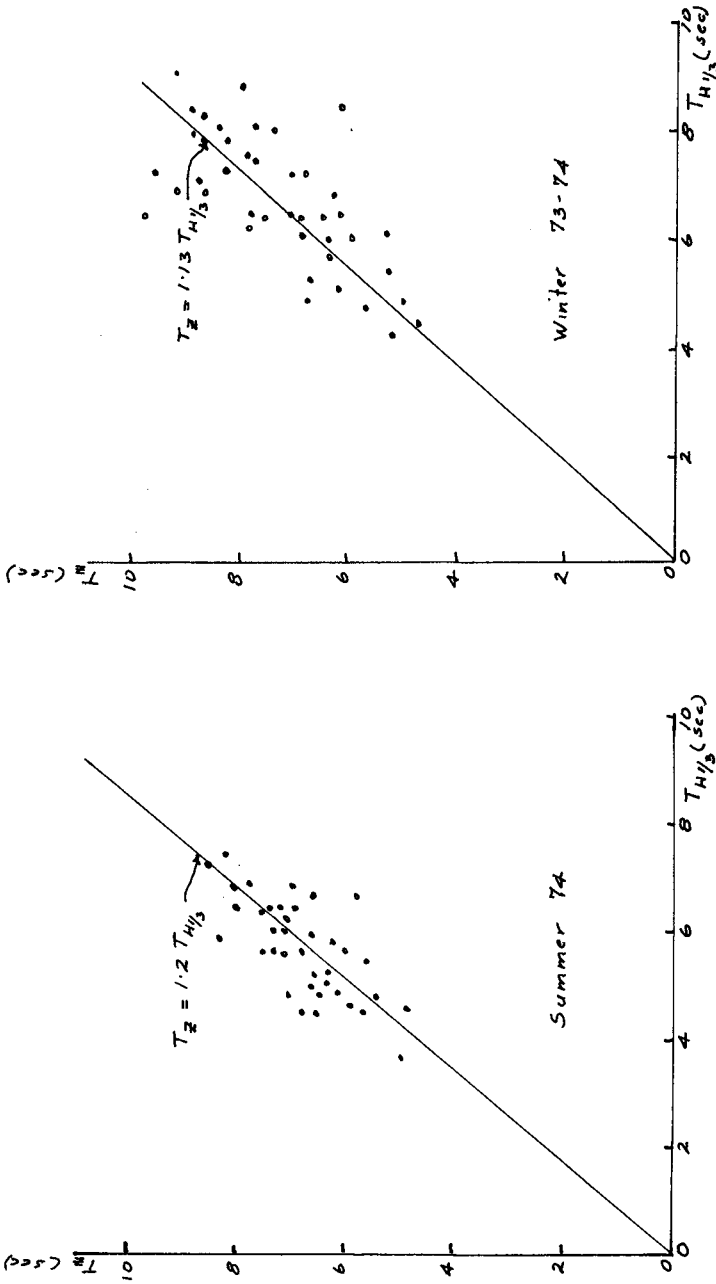


FIG. 1: NILE DELTA COAST : T_z VS $T_{H/3}$

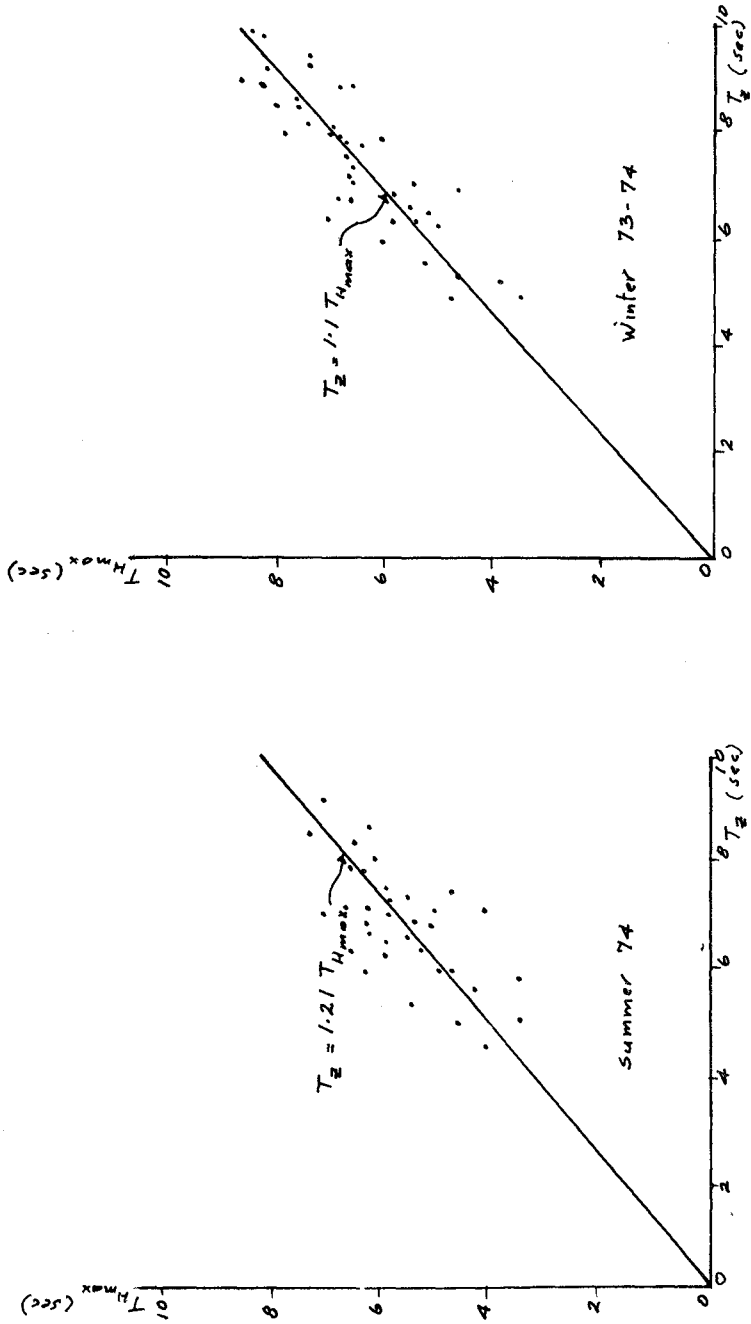


FIG. 2: NILE DELTA COAST : T_z VS T_{Hmax}

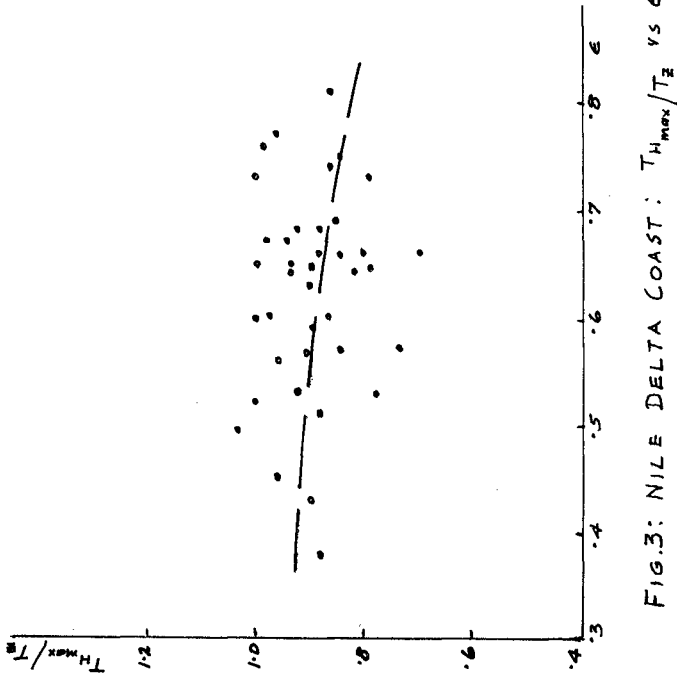
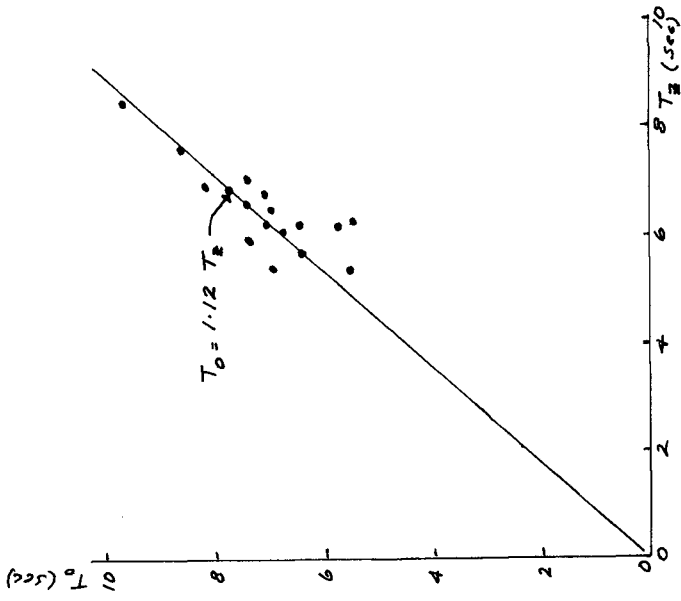


FIG.3: NILE DELTA COAST: T_{Hmax}/T_z VS ϵ AND T_0 VS T_z - WINTER 73-74

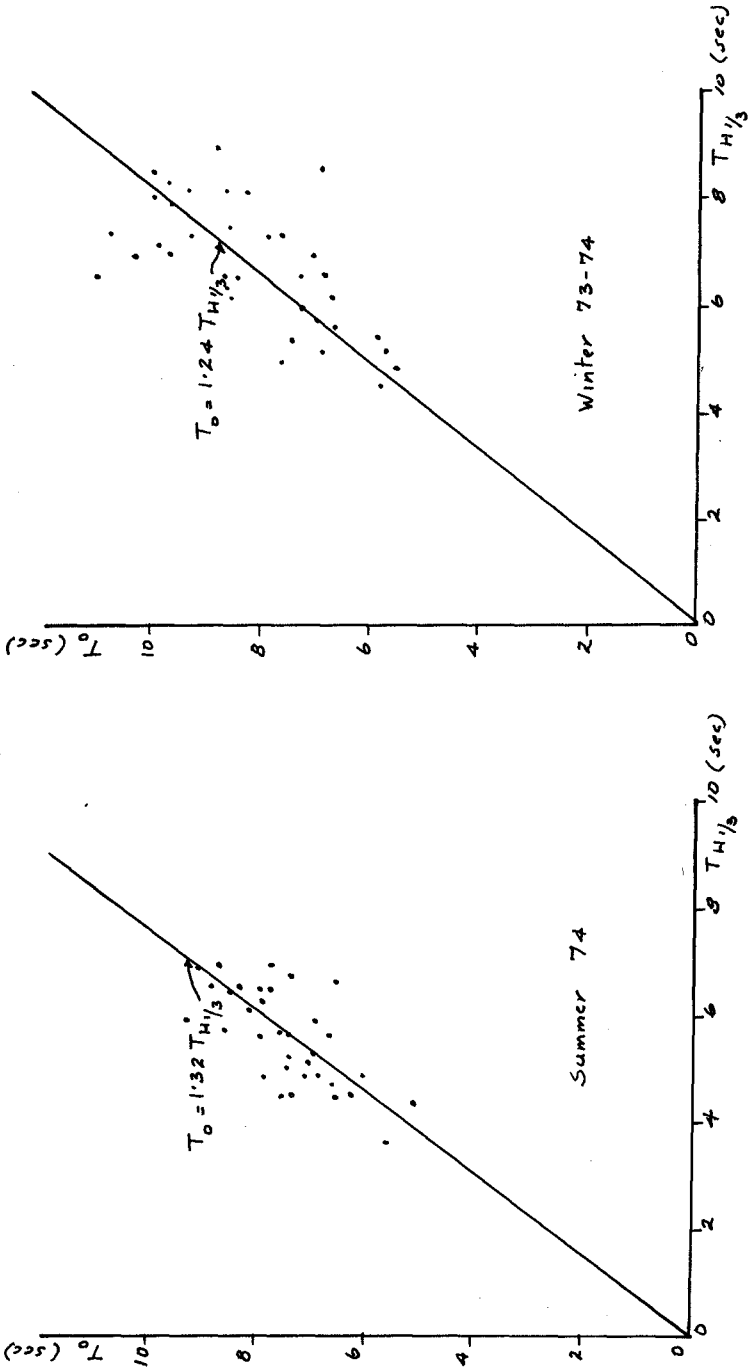


FIG. 4: NILE DELTA COAST : T_0 vs $TH_{1/3}$

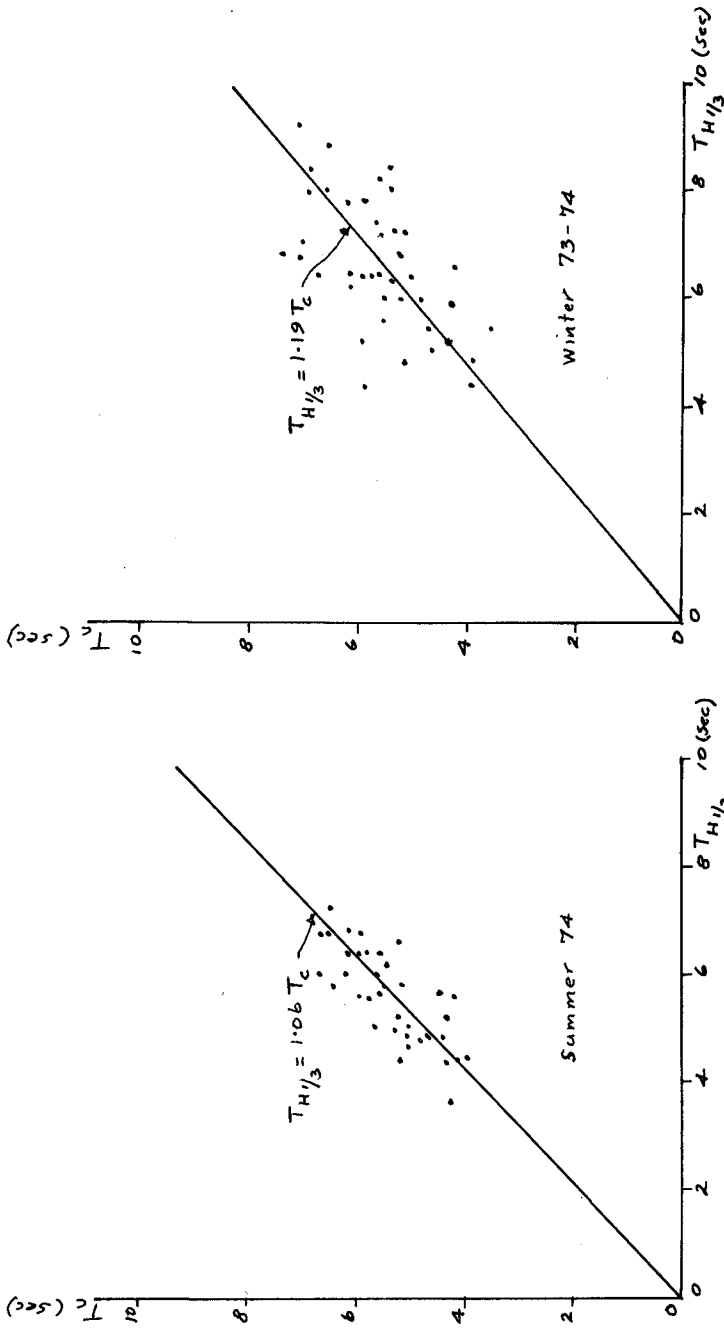


FIG. 5: NILE DELTA COAST: $T_{H/3}$ vs T_c

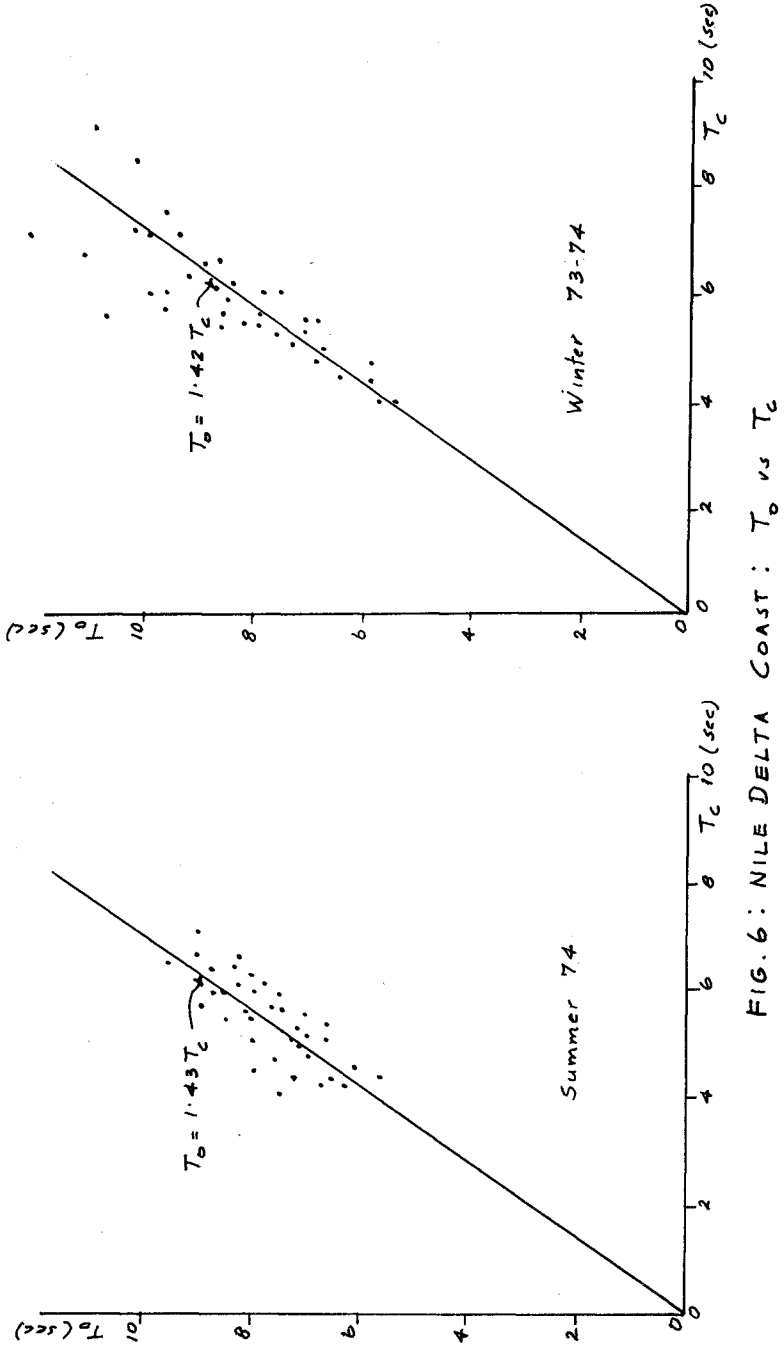


FIG. 6: NILE DELTA COAST: T_0 vs T_c

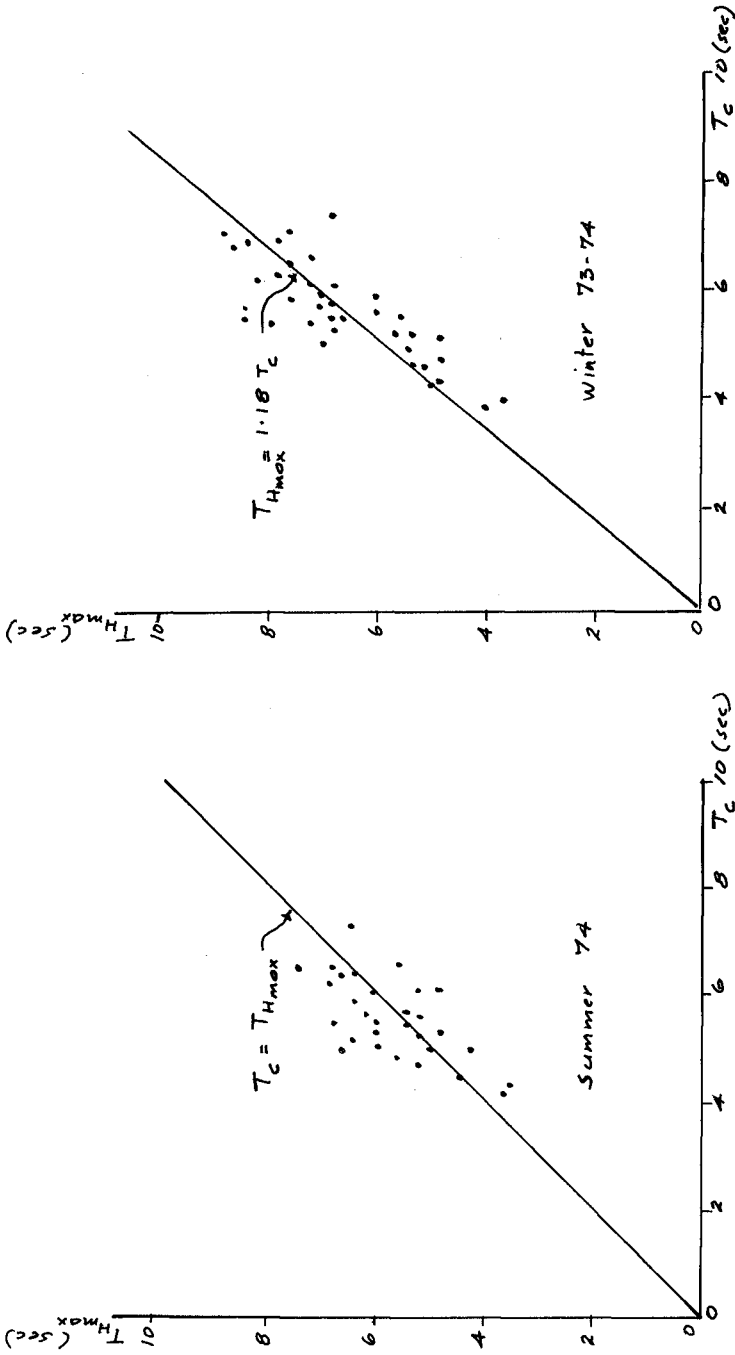


FIG. 7 : NILE DELTA COAST : T_{Hmax} vs T_c

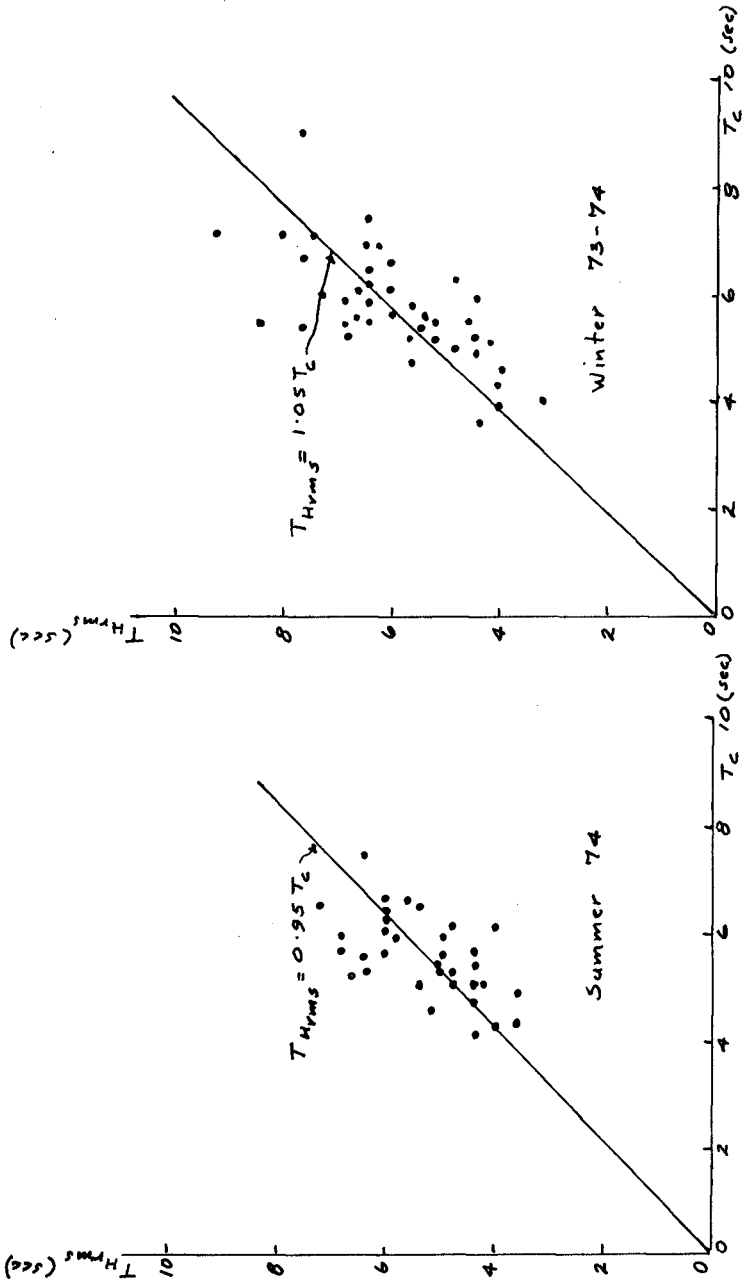


FIG 8: NILE DELTA COAST : T_{Hrms} vs T_c

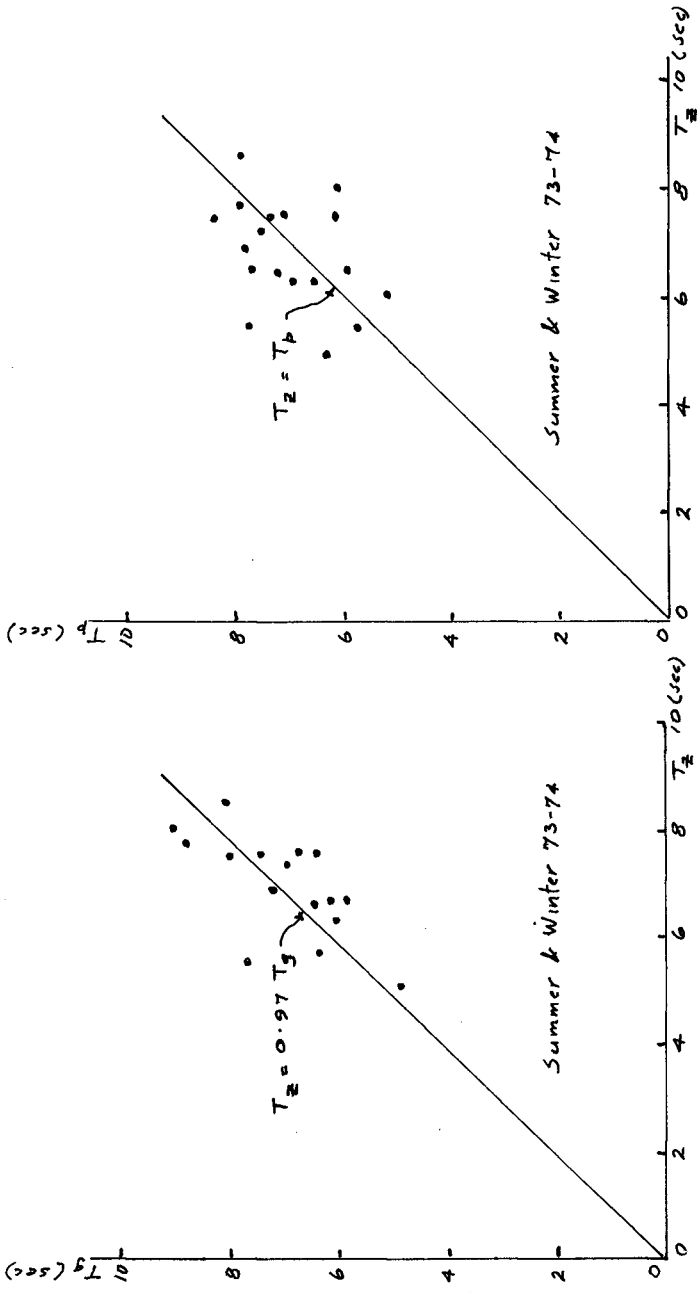


FIG. 9: NILE DELTA COAST: T_z vs T_g & T_p

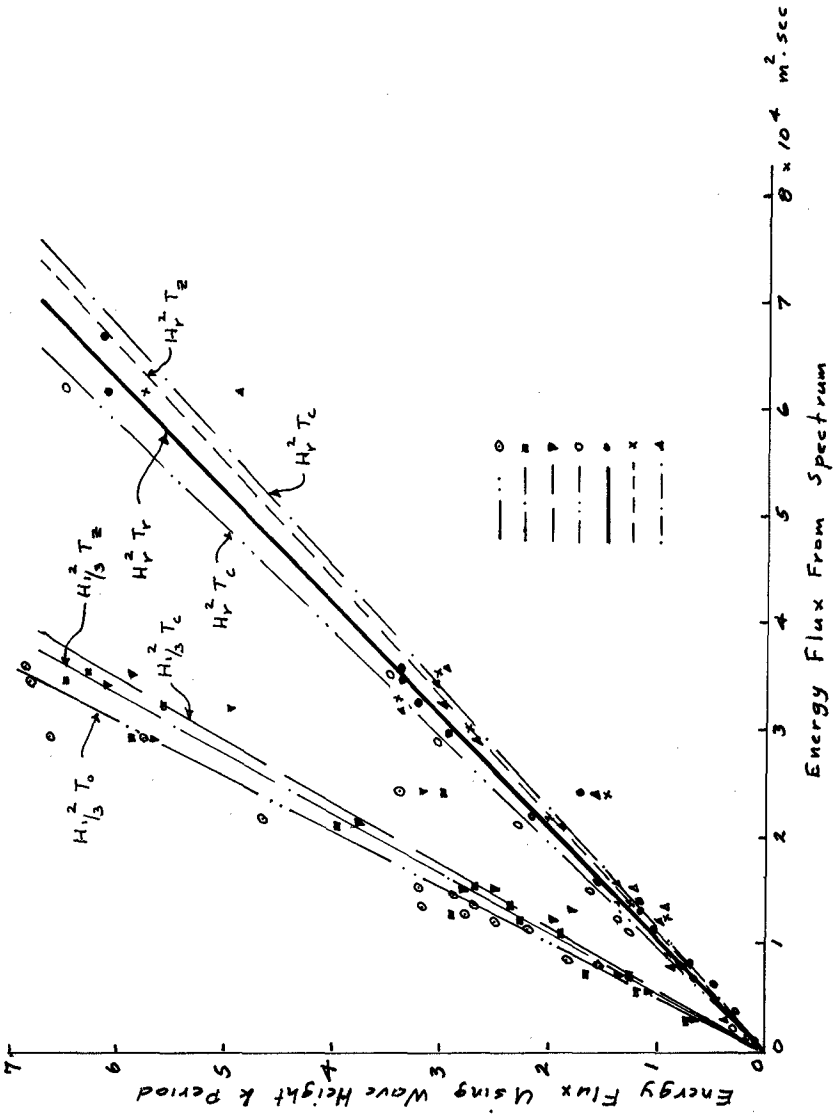


FIG.10: NILE DELTA COAST: ENERGY FLUX

CHAPTER 17

OCEAN WAVE RECORD ANALYSIS BY TUCKER'S METHOD - AN EVALUATION

J. Dattatri¹ and I. V. Nayak²

INTRODUCTION

The planning and design of any Coastal Engineering structure requires adequate knowledge of the wave characteristics. It is desirable that this knowledge of waves is based on instrumentally recorded data over a number of years, so that reliable values could be used for the computation of the design wave. Analysis of instrumentally recorded data to yield the relevant wave characteristics like the significant wave height, though not complicated is too time consuming. A simple method of analysis has been proposed by Tucker (9, 10), wherein the relevant information is obtained with only a few measurements of the larger waves. This method is also recommended by Draper (6) in his plea for uniformity of the analysis and presentation of wave data. This paper deals with the application of the Tucker's method to analysis of waves recorded off the Mangalore Harbour on the West Coast of India.

ANALYSIS OF WAVE RECORDS - TUCKER'S METHOD

Tucker (9, 10) has provided a simple method for obtaining the pertinent information of waves in any wave record, by only a few measurements of the larger waves, the theoretical basis of which is given by Cartwright and Longuet-Higgins (1), and by Cartwright (2). The measurements required

¹Asst. Prof., Dept. of App. Mech. and Hydraulics, Karnataka Regional Engineering College, SURATHKAL (S.K.)-574157, India.

²Prof. and Head, Dept. of App. Mech. and Hydraulics, Karnataka Regional Engineering College, SURATHKAL (S.K.)-574157, India.

for the Tucker's method of analysis are: A, the height of the highest crest; B, the height of the second highest crest measured from the mean water level line; C, the depth of the lowest trough; and D, the depth of the second lowest trough from the mean line as shown in Fig. 1. In addition the number of zero-crossings N_z , that is, the number of times the record trace crosses the mean line in an upward direction in the duration considered (Fig. 1) is also required. From these measurements, Tucker defines $H_1 = A + C$, and $H_2 = B + D$.

Using these measured values, the other wave height parameters can be estimated from H_1 and H_2 . D_{RMS} , defined as the root-mean-square value of the instantaneous distance of the water surface from the mean line, is estimated as follows:

$$D_{RMS} = \frac{1}{2} H_1 (2\theta)^{-\frac{1}{2}} [1 + 0.289 \theta^{-1} - 0.247 \theta^{-2}]^{-1} \dots (1)$$

$$D_{RMS} = \frac{1}{2} H_2 (2\theta)^{-\frac{1}{2}} [1 - 0.211 \theta^{-1} - 0.103 \theta^{-2}]^{-1} \dots (2)$$

$$\text{in which } \theta = \text{Log}_e N_z \dots (3)$$

It should be noted that in the original papers (9, 10), Tucker had used H_{RMS} instead of D_{RMS} , to indicate the root-mean-square value of the displacements of the water surface from the mean line. This results in some confusion as H_{RMS} is also used to indicate the root-mean-square value of the crest to trough heights of waves. To overcome this confusion, Tucker in the closure (5) of one of his paper (10) had suggested the use of D_{RMS} and H_{RMS} to indicate the r.m.s. value of wave displacements and wave heights respectively. For a wave system containing only a narrow band of frequencies, $H_{RMS} = 2\sqrt{2} D_{RMS}$ (5). Introducing this, Eqs. 1 and 2 can now be modified to:

$$H_{RMS} = \sqrt{2} H_1 (2\theta)^{-\frac{1}{2}} [1 + 0.289 \theta^{-1} - 0.247 \theta^{-2}]^{-1} \dots (4)$$

$$= K_1 H_1 \dots \dots \dots (4(a))$$

$$\text{in which } K_1 = \sqrt{2} (2\theta)^{-\frac{1}{2}} [1 + 0.289 \theta^{-1} - 0.247 \theta^{-2}]^{-1} \dots (4(b))$$

$$H_{RMS} = \sqrt{2} H_2 (2\theta)^{-\frac{1}{2}} [1 - 0.211 \theta^{-1} - 0.103 \theta^{-2}]^{-1} \dots (5)$$

$$= K_2 H_2 \dots \dots \dots (5(a))$$

in which $K_2 = \sqrt{2} (2\theta)^{-\frac{1}{2}} [1 - 0.211 e^{-1} - 0.103 e^{-2}]^{-1} \dots (5(b))$

It can be seen from Eqs. 4(b) and 5(b) that K_1 and K_2 are functions of θ only, which in turn is a function of N_z from Eq. 3. Hence K_1 and K_2 can be evaluated as functions of N_z and this is shown in Fig. 2.

The analysis of wave records is now reduced to a simple process of determining H_1 , H_2 and N_z from the wave record and then determining K_1 and K_2 from Fig. 2 using the measured value of N_z . From these values, H_{RMS} can be evaluated using Eq. 4(a) or Eq. 5(a). Once H_{RMS} has been evaluated, the other wave height parameters like the significant wave height can be determined using the relations given by Longuet-Higgins (8). Analysis of ocean wave records in India (3) and abroad (7) have shown that the relations between the various wave height parameters as given by Longuet-Higgins, to be substantially the same for the records analysed.

Tucker (10) recommends that the zero-crossing period T_z , (= duration of record, in seconds/ N_z) could be the relevant period to be used with the above wave heights.

APPLICATION OF TUCKER'S METHOD

The primary objective of the present investigations was to study the applicability of the Tucker's method to waves recorded along the Indian Coasts. For this purpose, the wave records obtained by the Mangalore Harbour Project authorities on the West Coast of India were utilized. About 12 months' records were available for analysis and the results of the analysis regarding the wave height and wave period distributions etc., has been reported in an earlier paper (3). For the present investigations about 50 samples of the wave records of 15 minutes duration, picked at random were utilized for analysis by the Tucker's method.

For each sample, the heights A, B, C and D were directly read from the records. From these values $H_1 = A+C$

and $H_2 = B+D$ were evaluated. For each sample the number of zero-crossings, N_z was also noted. From the known value of N_z , the values of the constants K_1 and K_2 , H_{RMS} was evaluated from Eqs. 4(a) and 5(a), and this H_{RMS} will hereafter be referred to as the H_{RMS} estimated from H_1 or H_2 .

For each wave record sample, the crest to trough heights of the individual waves were also read and the root-mean-square wave height, H_{RMS} , was also directly computed from these individual heights.

As the wave recorder used, was of the sub-surface pressure type, all the wave heights read from the wave records were corrected to account for the attenuation of wave pressure with depth and the frequency response of the instrument as per standard procedures (3).

PRESENTATION AND INTERPRETATION OF DATA

Eqs. 4 and 5 can only give the estimate of the value of H_{RMS} , since a statistical average value like H_{RMS} is being evaluated based on a single reading of H_1 or H_2 . As stated by Tucker (9), the statistical errors in these estimates are less than what might be expected and are not much worse than that of the mean of the highest one third waves in the records. Tucker (9) mentions that the proportional standard error in the estimate of H_{RMS} from H_1 could be approximately 13 percent and from H_2 about 10 percent, under certain conditions. The direct computation of any statistical average like H_{RMS} , from the individual wave heights itself is subject to error depending on the length of the record (4). In view of these considerations, perfect agreement cannot be expected between the H_{RMS} , estimated from H_1 or H_2 , and the H_{RMS} directly computed from all the individual wave heights in the record.

In Fig. 3 the H_{RMS} estimated from H_1 and H_2 is compared with the H_{RMS} directly computed. As discussed

earlier, perfect agreement is absent. But, it can be seen that the H_{RMS} estimated from H_1 or H_2 is within ± 15 percent of the directly computed value. There is a strong tendency for the H_{RMS} estimated from H_2 , to be more than the directly computed value. The spectral width parameter ϵ , for the samples analysed ranged from 0.2 to 0.8. The possibility of the variation in the spectral width parameter being a reason for the deviations of the data was also considered, but no systematic variation was noticed. A possible reason for the scatter could be that crest to trough heights are used in the computation instead of water surface heights from the mean line, and the theoretical relationships are derived using the latter.

Assuming the H_{RMS} directly computed to be the correct value, analysis was made of the percentage error in the estimation of the wave height from the single measurement of H_1 or H_2 , and these results are presented in Fig. 4. It can be seen in Fig. 4, that in nearly 90 percent of the cases, the estimated H_{RMS} differed from the directly computed value by less than 15 percent. These studies show that the H_{RMS} estimated from H_1 or H_2 is close enough to the H_{RMS} directly evaluated, for practical purposes. This supports the usefulness of the Tucker's method as a rapid means of obtaining the pertinent wave characteristics without a detailed and time consuming analysis of the wave records.

Another aspect studied was the relation between H_{Max} (the maximum crest to trough wave height in the sample under investigation) and, H_1 and H_2 . Actually Tucker recommends that for many civil engineering purposes, the relevant wave height could be H_1 and the period T_z .

In Fig. 5 is plotted H_{Max} versus H_1 and H_{Max} versus H_2 . For the data analysed, it can be seen that H_1 is generally greater than H_{max} and $H_2 = H_{Max}$. In general, for records containing only a narrow band of frequencies, H_{Max} should be

nearly equal to H_1 . This is because the narrow band assumption implies that the highest crest is associated with the deepest trough and in that case, it follows that H_{Max} should be equal to H_1 . But the present set of wave records, with the spectral width parameter ranging from 0.2 to 0.8, cannot be regarded as belonging to the narrow band process. For the wide band process, the highest crest is not associated with the deepest trough and it is to be expected that H_1 will be greater than H_{Max} and the results in the present analysis confirm it.

CONCLUSIONS

Tucker's simple method of obtaining the pertinent information of waves in any wave record by only a few measurements of the larger waves is found to be applicable to waves recorded on the West Coast of India. The error involved in such computations in comparison with more refined calculations is found to be generally below 15 percent.

ACKNOWLEDGEMENTS

The data analysed was made available to the authors by the Mangalore Harbour Project authorities and authors express their thanks of gratitude to them. To Prof. Evald Nielsen, formerly UNESCO Professor in Coastal Engineering at the college, who initiated these coastal engineering studies, the authors owe their debt of gratitude. The paper is published with the permission of the college authorities.

REFERENCES

1. Cartwright, D.E., and Longuet-Higgins, M.S., 'The Statistical Distribution of the Maxima of a Random Function', Proc. Roy. Soc. A, Vol. 237, 1956, pp 212-232.
2. Cartwright, D.E., 'On Estimating the Mean Energy of the Sea Waves from the Highest Waves in a Record', Proc. Roy. Soc. A, Vol. 247, 1958, pp 22-48.

3. Dattatri, J., 'Waves off Mangalore Harbour - West Coast of India', Journal of the Waterways, Harbors, and Coastal Engineering Division, ASCE, Vol. 99, No. 1, Proc. Paper 9532, Feb. 1973, pp 39-58.
4. Draper, L., 'Derivation of a 'Design Wave' from Instrumental Records of Sea Waves', Proceedings, The Institution of Civil Engineers, London, England, Vol. 26, Oct. 1963, pp 291-303.
5. Draper, L., and Tucker, M.J., Joint closure to 'Derivation of a 'Design Wave' from Instrumental Records of Sea Waves', and 'Analysis of Records of Sea Waves', Proceedings, The Institution of Civil Engineers, London, England, Vol. 29, Sept. 1964, pp 206-208.
6. Draper, L., 'The Analysis and Presentation of Wave Data - A Plea for Uniformity', Proceedings, Tenth Conference on Coastal Engineering, ASCE, Sept. 1966, Tokyo, Japan, Vol. I, pp 1-11.
7. Goodknight, R.G., and Russel, T.L., 'Investigations of Statistics of Wave Heights', Journal of Waterways and Harbours Division, ASCE, Vol. 89, No. WW2, Proc. Paper 3524, May 1963, pp 29-54.
8. Longuet-Higgins, M.S., 'On the Statistical Distribution of the Heights of the Sea Waves', Journal of Marine Research, Vol. 11, 1952, pp 245-266.
9. Tucker, M.J., 'Simple Measurements of Wave Records', Proceedings, Conference on Wave Recording for Civil Engineers, National Institute of Oceanography, England, Jan. 1961, pp 22-23, Also printed in the Dock and Harbour Authority, No. 493, Vol. 42, 1961, pp 231-232.
10. Tucker, M.J., 'Analysis of Records of Sea Waves', Proc. The Institution of Civil Engineers, London, England, Vol.26, Oct. 1963, pp 305-316.

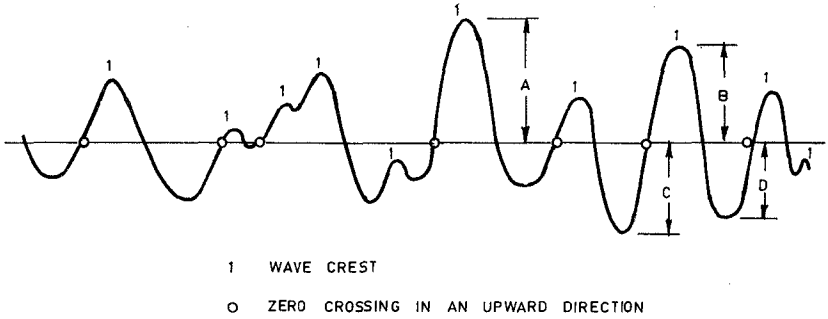


FIG.1 AN ILLUSTRATION OF THE SIMPLE MEASUREMENT
OF A WAVE RECORD (ONLY SHORT LENGTH OF
RECORD SHOWN)

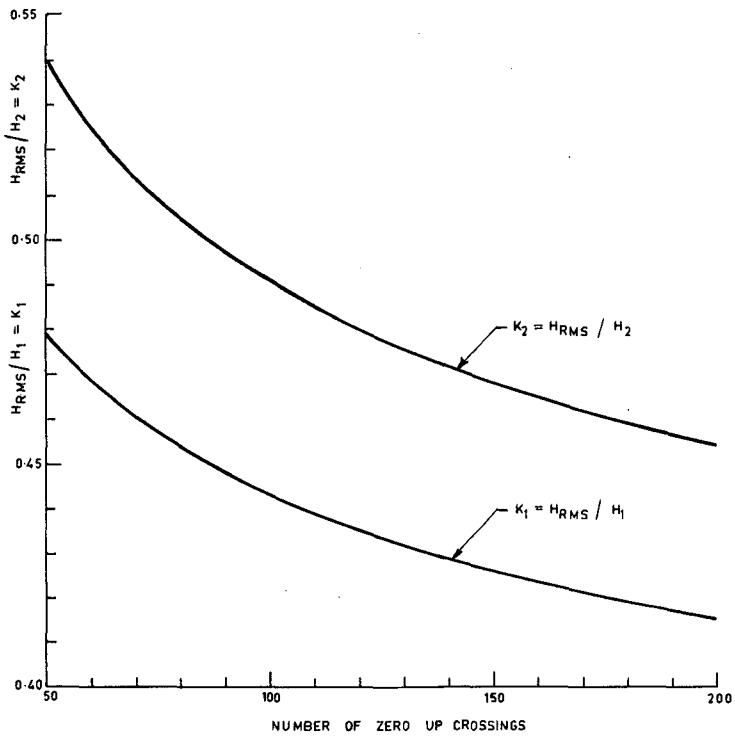


FIG. 2 : K_1 AND K_2 PLOTTED AGAINST THE NUMBER
OF ZERO UP CROSSINGS.

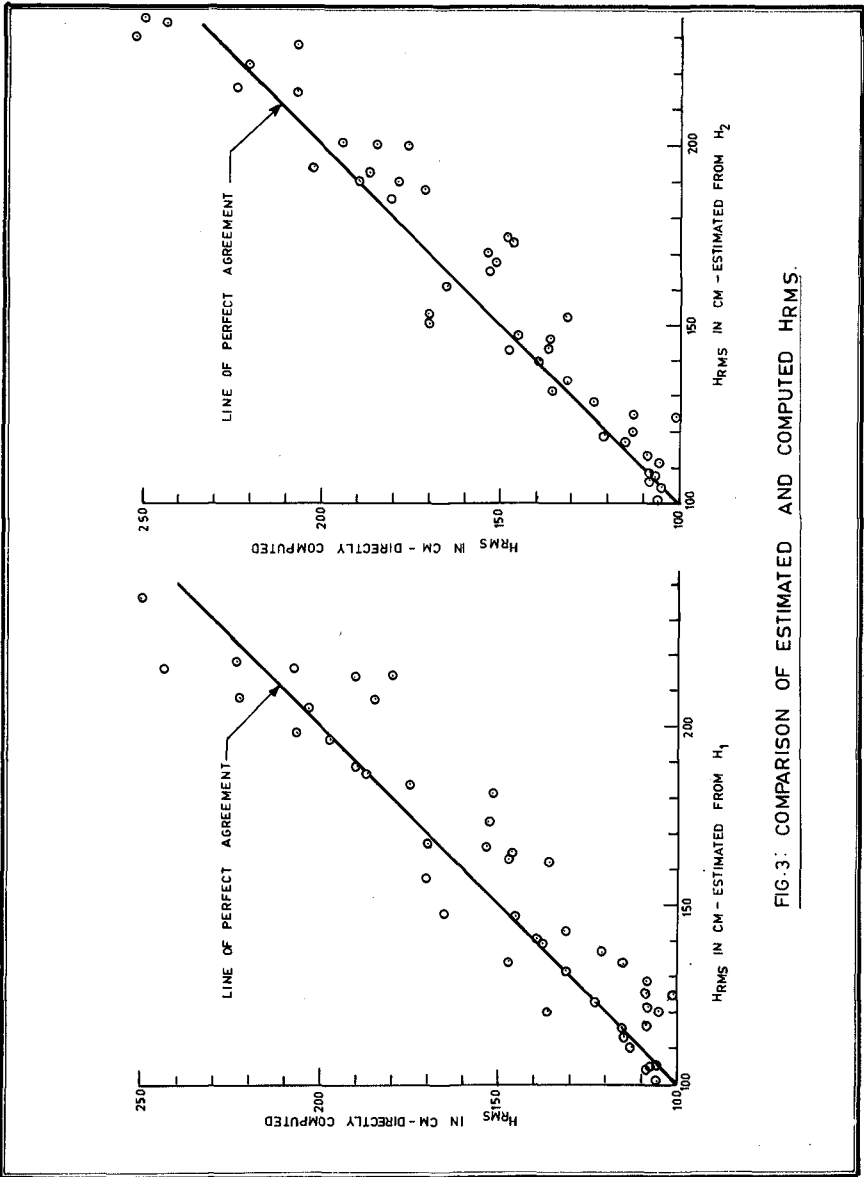
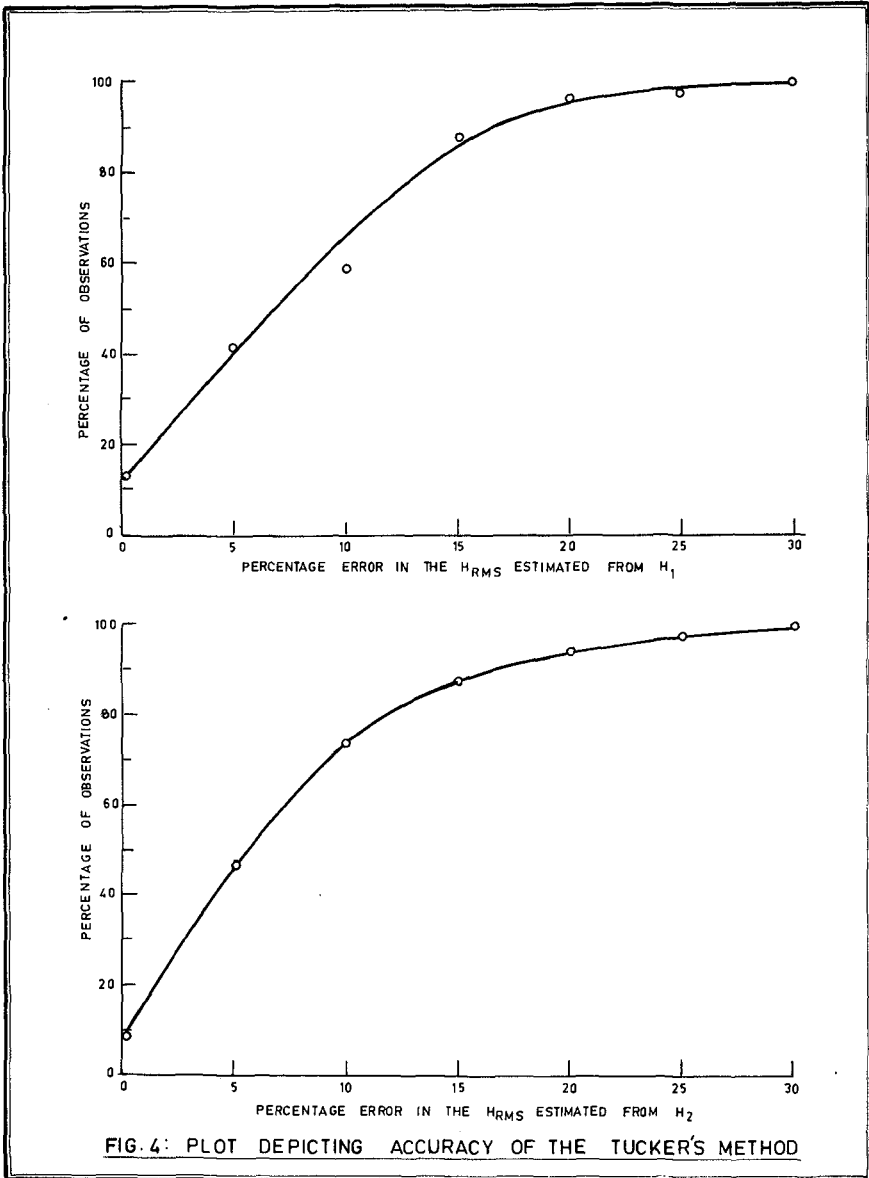


FIG. 3: COMPARISON OF ESTIMATED AND COMPUTED HRMS.



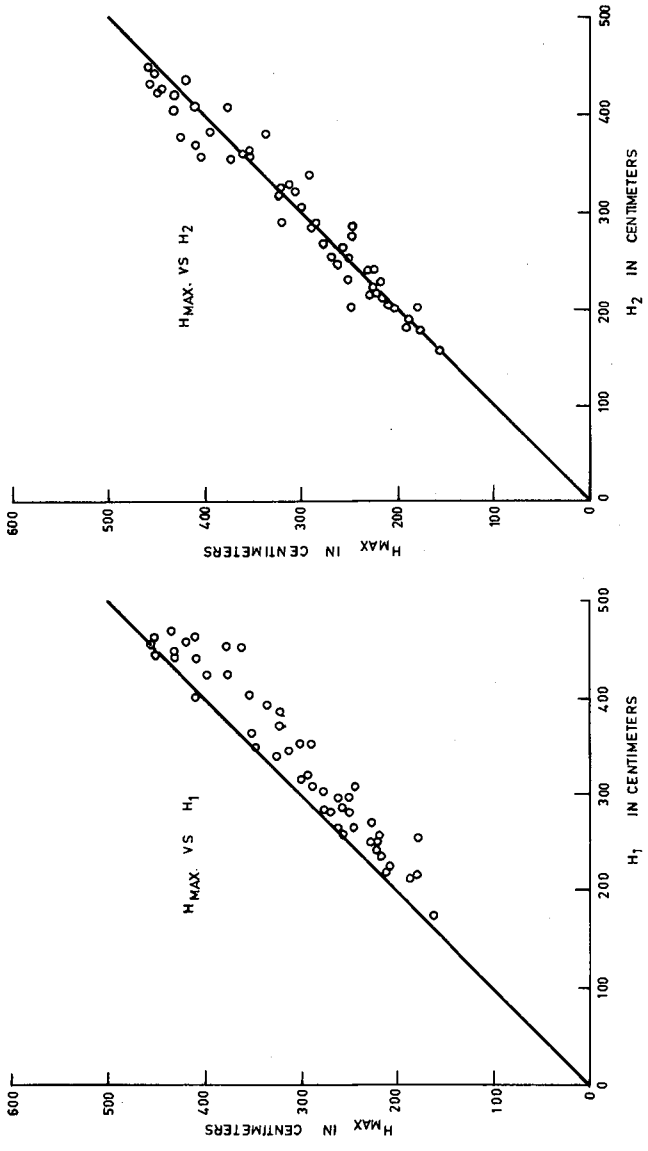


FIG. 5: COMPARISON OF H_{MAX} WITH H₁ AND H₂

CHAPTER 18

SIX-PARAMETER WAVE SPECTRA

by

Michel K. Ochi* and E. Nadine Hubble*

ABSTRACT

In an attempt to develop a systematic series of wave spectra covering a variety of spectral shapes observed in the ocean, this paper presents a newly developed series of wave spectra which involves six parameters. In the development of the six-parameter wave spectra, the spectra are decomposed into two parts. Each part is expressed by a mathematical formula with three parameters, and the total spectrum is expressed by the combination of two sets of three-parameter spectra. Results of analysis have shown that the six-parameter wave spectra thus derived appear to represent almost all stages of development of a sea during a storm. Then, from the statistical analysis of 800 spectra observed at the North Atlantic Ocean, the values of the six-parameters are expressed in terms of significant wave height so that a family of spectra for a desired sea severity can be generated.

INTRODUCTION

Recent progress in application of statistics to ocean and coastal engineering enables us to evaluate responses of ocean structures in a seaway at an early design stage by carrying out spectral analysis. In applying the linear superposition principle for prediction, however, wave spectra in desired seas have to be prepared in advance, and the magnitude of responses of ocean structure is significantly influenced by the shape of wave spectra for a given sea severity.

The shape of wave spectra observed in the ocean varies considerably (even though the significant wave heights are same) depending on the duration and fetch of wind, stage of growth and decay of a storm, and existence of swell. For example, Figure 1 shows a variety of shapes

*David W. Taylor Naval Ship Research and Development Center,
Washington, D.C., U.S.A.

of wave spectra all of which have the same significant wave height of 3.5 m (11.48 ft) (+1%), and wind speeds are between 20 to 25 knots.

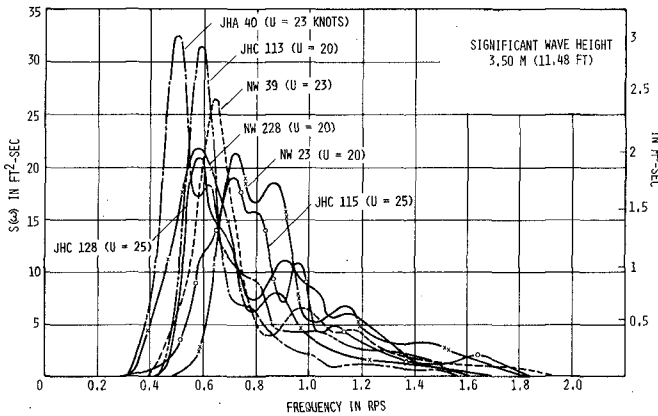


Figure 1 Variety of wave spectra for significant wave height of 3.5 m (11.48 ft)

As can be seen in the figure, the spectrum JHA 40 has a very sharp single peak at the lower frequencies, while some spectra (JHC 128, NW 23, NW 39) have double peaks. Furthermore, three spectra (JHC 113, NW 228, and JHC 128) have the same modal frequency of 0.58. Thus, even though two parameters (significant wave height and modal frequency) are the same, the shape of the spectra are significantly different, and this may result in a significant difference in the evaluated magnitude of responses of ocean structures. This indicates that additional parameters are required for more accurate representation of wave spectra to provide useful information for more rational design of ocean structures.

In an attempt to develop a systematic series of wave spectra covering a variety of spectral shapes, this paper presents a newly developed series of wave spectra which involves six parameters.

In the development of the six-parameter wave spectra, the wave spectra are decomposed into two parts--one which includes primarily the lower frequency components of the wave energy and the second which covers primarily the higher frequency components of the energy. Then, each wave spectrum is expressed in a mathematical formula with three parameters; i.e., significant wave height, modal period, and shape parameter, and the entire spectrum is expressed by a combination of two sets of three-parameter spectra. The parameters are determined numerically such that the difference between the theoretical six-parameter and observed spectra is minimal.

The six-parameter representation of ocean waves is made on a total of 800 observed spectra, and the results are classified into 10 groups depending on the severity. Then, for each group a statistical analysis is carried out on the parameters taking into account the correlation between them. Finally, the results are presented in a family of spectra including the most probable spectrum expected to occur for a specified sea state as well as the limiting spectral shapes which may occur with a confidence coefficient of 0.95. The values of the six-parameters for this set of mathematical spectra are expressed in terms of significant wave height so that a family of spectra for a desired sea severity can be generated.

DERIVATION OF SIX-PARAMETER WAVE SPECTRA

In the development of the six-parameter wave spectra, the spectra are decomposed into two parts as illustrated in Figure 2; one which includes primarily the lower frequency components of the wave energy and the second which covers primarily the higher frequency components of the energy. This concept of decomposing the wave spectrum into two parts was also proposed by Strekalov et. al. in 1972 in their analysis of measured wave spectra [1]. In the present analysis, the spectrum of each part is expressed by a mathematical formula with three parameters so that the total spectrum is expressed by the combination of two sets of three-parameter spectra.

It may be of interest to note here the shape of wave spectra which have been most frequently observed to date. Although numerous shapes of wave spectra have been observed, the results of analysis made on available data indicate that spectral shapes similar to those shown in Figure 3 through 5 have been most frequently observed. In a broad sense, the shape of these spectra have a peak at the lower frequencies which decreases exponentially to a plateau at the higher frequencies. Thus, it is very difficult to express the entire spectral shape in a simple mathematical formula. The lower frequency part of the spectra

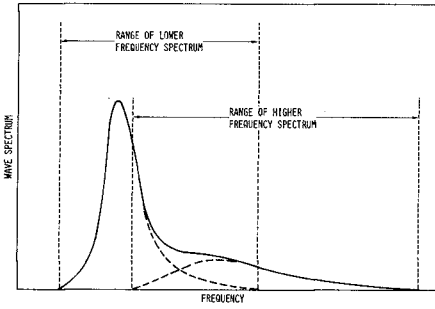


Figure 2 Decomposition of wave spectra

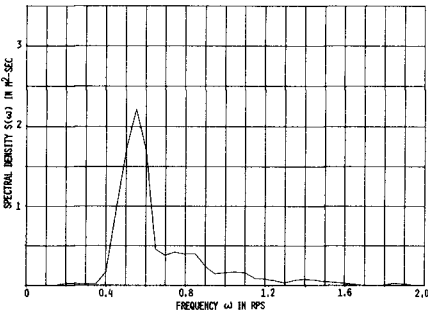


Figure 3 Example of wave spectrum (sig. height 2.89 m, 9.47 ft)

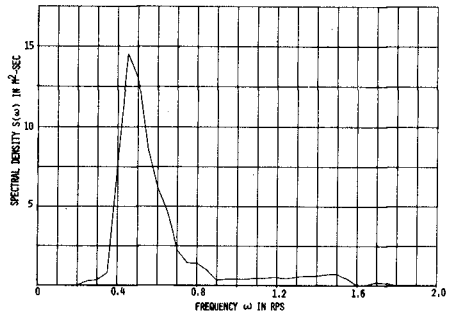


Figure 4 Example of wave spectrum (sig. height 7.47 m, 24.5 ft)

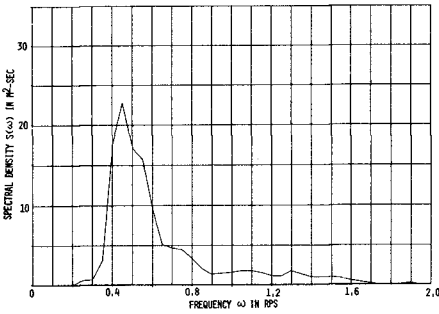


Figure 5 Example of wave spectrum (sig. height 10.09 m, 33.1 ft)

shown in these figures may be well expressed by some currently available spectral formulations; however, in the presently existing formula, the wave energy at the higher frequencies decreases exponentially with increase in frequency and hence the energy at the plateau is not represented. Although the wave energy at the higher frequencies is usually much less than that at the lower frequencies, its contribution to responses of marine vehicles and structures may be significant depending on their size and vehicle speed. Thus, it is highly desirable to represent the shape of the entire spectrum as closely as possible, and this may be achieved by separating the spectra into two parts.

First, we may derive the three-parameter representation for both the low and high frequency part of the spectrum as follows:

From results of dimensional analysis of ocean waves, Phillips has derived the following form of the spectrum of ocean waves over a range of frequencies between the modal frequency and that at which capillary waves become significant [2]:

$$S(\omega) = \alpha g^2 \omega^{-5} \quad (1)$$

where, α = equilibrium range constant
 g = gravity acceleration

The validity of this spectral presentation for wind-generated waves has been shown by Kitaigorodskii [3] from an analysis of Burling's observed data, and many formulae currently available for spectral representation of ocean waves are expressed in the following form [4] [5] [6]:

$$S(\omega) = \frac{A}{\omega^5} e^{-B/\omega^4} \quad (2)$$

Since it is commonly assumed that ocean waves comprise a Gaussian process with a narrow-band spectrum, it can be shown that the significant wave height, ζ , defined as the average of the highest one-third waves becomes,

$$\zeta = 4\sqrt{m_0} = \sqrt{\frac{4A}{B}} \quad (3)$$

where, $m_0 = \int_0^{\infty} S(\omega) d\omega = \frac{A}{4B}$

Next, let the spectrum, $S(\omega)$, be divided by the area, m_0 , so that the spectrum has a unit area. That is,

$$S'(\omega) = \frac{4B}{\omega^5} e^{-B/\omega^4} \quad (4)$$

The unit area spectrum, denoted by $S'(\omega)$, can be considered as if it were a probability density function, since $S'(\omega)$ is a positive, continuous, and integrable function with unit area, and thereby satisfies all conditions required for the probability function. $S'(\omega)$, in fact, yields the exponential probability density function by letting $\omega^4 = 1/x$. Hence, it can be generalized in the form of a new probability density function with an additional parameter, λ , which yields the gamma probability function. That is,

$$S'(\omega) = \frac{4}{\Gamma(\lambda)} \frac{B^\lambda}{\omega^{4\lambda+1}} e^{-B/\omega^4} \quad (5)$$

Under the assumption that the spectrum is narrow-banded, $S'(\omega)$ may be converted to the dimensional wave spectrum $S(\omega)$ which satisfies the condition that the area under the spectrum is equal to $(\zeta/4)^2$ given in Equation (3). Then, we have,

$$S(\omega) = \frac{1}{4} \frac{B^\lambda}{\Gamma(\lambda)} \frac{\zeta^2}{\omega^{4\lambda+1}} e^{-B/\omega^4} \quad (6)$$

The constant, B , in Equation (6) can be expressed in terms of the modal value, ω_m , by setting the differentiation of $S(\omega)$ with respect to ω to be zero. That is,

$$B = \left(\frac{4\lambda+1}{4} \right) \omega_m^4 \quad (7)$$

Thus, from Equations (6) and (7), the following spectral formulation can be made:

$$S(\omega) = \frac{1}{4} \frac{\left(\frac{4\lambda+1}{4} \omega_m^4 \right)^\lambda}{\Gamma(\lambda)} \frac{\zeta^2}{\omega^{4\lambda+1}} e^{-\left(\frac{4\lambda+1}{4} \right) \left(\frac{\omega}{\omega_m} \right)^4} \quad (8)$$

The spectrum given in Equation (8) has three parameters; namely, significant wave height, ζ , modal frequency, ω_m , and a parameter λ .

The parameter, λ , controls the shape (sharpness) of the spectrum when the other two parameters are held constant, and hence it may be called a spectral shape parameter. For example, Figure 6 shows computer printout of a family of wave spectra for various λ while the other two parameters, ζ and ω_m , are held constant at 3.0 m (9.8 ft.) and 0.6 rps, respectively. As can be seen in the figure, the spectral shape becomes sharper with increasing λ .

Let $\lambda = 1$ in Equation (8). Then, we have,

$$S(\omega) = \frac{1.25}{4} \zeta^2 \frac{\omega_m^4}{\omega} e^{-1.25 \left(\frac{\omega_m}{\omega}\right)^4} \quad (9)$$

The spectrum given in Equation (9) is the Bretschneider two-parameter wave spectrum expressed in terms of significant wave height and modal frequency. Thus, the three-parameter spectrum given in Equation (8) includes the Bretschneider two-parameter spectrum as a special case ($\lambda = 1$), and this in turn also includes the Pierson-Moskowitz one-parameter spectrum ($\lambda = 1$ and $\omega_m = 0.4 \sqrt{g/\zeta}$).

By combining two sets of three-parameter spectra, one representing the low frequency components and the other the high frequency components of the wave energy, the following six-parameter spectral representation can be derived:

$$S(\omega) = \frac{1}{4} \sum_j \frac{\left(\frac{4\lambda_j+1}{4} \omega_{mj}\right)^{\lambda_j}}{\Gamma(\lambda_j)} \frac{\zeta_j^2}{\omega^{4\lambda_j+1}} e^{-\left(\frac{4\lambda_j+1}{4}\right) \left(\frac{\omega_{mj}}{\omega}\right)^4} \quad (10)$$

where, $j = 1, 2$ stands for the lower and higher frequency components, respectively.

The six parameters, $\zeta_1, \zeta_2, \omega_{m1}, \omega_{m2}, \lambda_1,$ and λ_2 , involved in Equation (10) are determined numerically such that the difference between theoretical and observed spectra is minimal. For this, appropriate initial values are chosen for each parameter, and then the computation is carried out for various combinations of the parameters in order to determine the final values for which the difference between theoretical and observed spectra is minimal. An example of the computer output is shown in Figure 7. The heavy line in the figure is the measured spectrum and the line with the circles is the six-parameter spectral representation. The values of the parameters for this example are $\zeta_1 = 4.14$ m (13.59 ft.), $\zeta_2 = 3.27$ m (10.73 ft.), $\omega_{m1} = 0.58$, $\omega_{m2} = 1.00$, $\lambda_1 = 2.67$, and $\lambda_2 = 1.37$.

Recently, a computer program has been developed by applying a nonlinear least square fit technique by which the six parameters can be evaluated directly from the information on wave spectra stored on tape. This eliminates the need to generate individual spectra in visual form from the tape to which mathematical formula is fitted.

Examples of comparisons between observed spectra and mathematical six-parameter spectra are shown in Figures 8 through 11. For example, Figure 8 shows a comparison for the case when swell coexists with wind-generated waves and hence the spectrum has double peaks. Figure 9 shows an example of the case when the wind-generated waves are growing and are nearly fully-developed, and spectral shapes similar to this are

frequently observed as mentioned earlier. On the other hand, Figure 10 shows an example for seas of mild severity with a relatively broad-band spectrum while Figure 11 shows a comparison for a very severe sea of significant wave height 14.5 m (47.7 ft) in which the sea is partially developed by strong wind, and has a very sharp peak at the lower frequencies in the spectrum. As can be seen in these examples, the six-parameter spectra derived in Equation (10) appear to represent almost all stages of development of a sea during a storm.

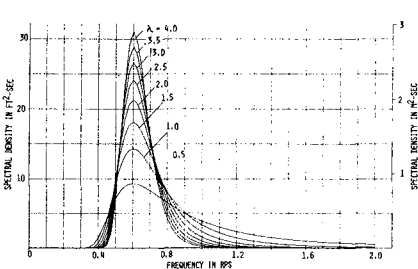


Figure 6 Three-parameter spectra for various λ -values (sig. height 3.0 m, 9.8 ft, modal frequency 0.6 rps)

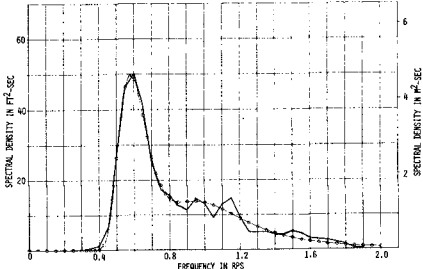


Figure 7 Comparison of measured and six-parameter spectrum (sig. height 5.28 m, 17.3 ft)

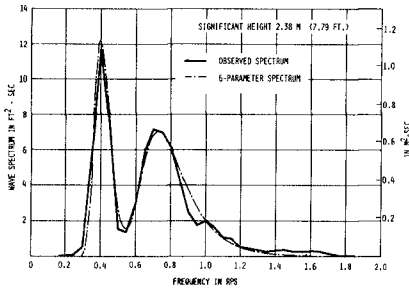


Figure 8 Comparison of measured and six-parameter spectrum (sig. height 2.38 m, 7.79 ft)

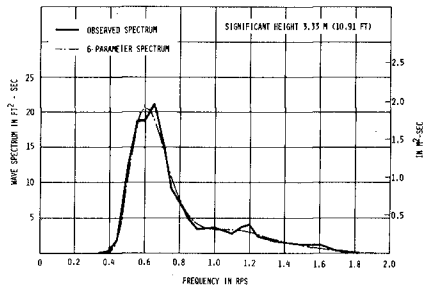


Figure 9 Comparison of measured and six-parameter spectrum (sig. height 3.33 m, 10.91 ft)

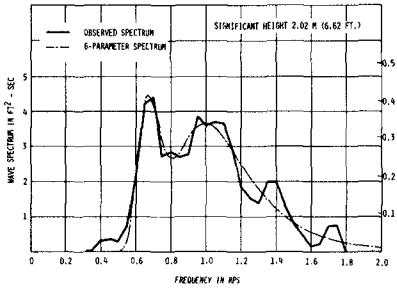


Figure 10 Comparison of measured and six-parameter spectrum (sig. height 2.02 m, 6.62 ft)

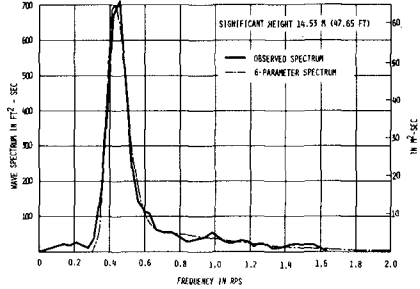


Figure 11 Comparison of measured and six-parameter spectrum (sig. height 14.54 m, 47.65 ft)

STATISTICAL ANALYSIS OF PARAMETERS

It was shown in the preceding section that the six-parameter spectra represent fairly well a variety of spectral shapes observed in the ocean. Perhaps one of the most useful applications of the spectra is to carry out a statistical analysis on each parameter so that a family of spectra for a given sea severity will be generated with a preassigned probability of assurance. For this purpose, a total of 800 available spectra observed in the North Atlantic Ocean [7] [8] [9] are classified into ten groups depending on severity as given in Table 1. Then, for each group a statistical analysis is carried out on the parameters, except for the last two groups IX and X where the number of samples is small.

First, consider the statistical properties of significant wave heights ζ_1 and ζ_2 , for the low and high frequency components, respectively, for a given severity. Consider the i -th group in Table 1 in which the wave spectra with significant heights ranging from $(\zeta_i)_{\min}$ to $(\zeta_i)_{\max}$ are included in the sample. Then, the significant heights for the low and high frequency components (ζ_1 and ζ_2 , respectively) cannot exceed $(\zeta_i)_{\max}$. In other words, the probability density function of ζ_1 and ζ_2 have to be truncated at $(\zeta_i)_{\max}$. The results of the analysis have shown that the significant heights ζ_1 and ζ_2 both obey the normal probability law, and that the concept of truncation is necessary only for ζ_1 , the significant height for the low frequency component.

Figure 12 shows a comparison between the histogram obtained from the data and the truncated normal probability distribution curve of ζ_1 , for Group IV (a nominal significant height $\zeta = 4.57$ m, 15 ft.). Figure 13 shows an example of the comparison for ζ_2 for the same Group IV. Still other examples, Figures 14 and 15 show similar comparisons

made for more severe seas, Group VII ($\zeta = 9.15$ m, 30 ft.). As can be seen in these figures, the significant wave heights ζ_1 and ζ_2 obey the normal probability law from which the confidence band of each parameter can be established. However, for a given sea severity, it is not necessary to consider the confidence band for ζ_1 and ζ_2 individually. This is because the two significant wave heights ζ_1 and ζ_2 , and the significant wave height of the entire spectrum, ζ , are functionally related as discussed in the following:

If it is assumed that the low and high frequency component spectra are both narrow-banded and that their sum (namely, the entire spectrum) is also narrow-banded, then the following simple relationship holds:

$$\zeta^2 = \zeta_1^2 + \zeta_2^2 \quad (11)$$

If one of the component spectra (perhaps, the high frequency component spectrum) is not narrow-banded, then the significant wave height of the entire spectrum is analytically derived as outlined in Appendix A. In order to compare the difference between the two approaches, Figure 16 is prepared.

Table 1 Group of significant wave heights used for analysis

GROUP	SIGNIFICANT WAVE HEIGHT	
	NOMINAL	RANGE
I	4.0 ft (1.22 m)	Less than 5.5 ft (1.68 m)
II	6.5 (1.98)	5.5 ft (1.68 m) ---- 7.5 ft (2.29 m)
III	10.0 (3.05)	7.5 (2.29) ---- 12.5 (3.81)
IV	15.0 (4.57)	12.5 (3.81) ---- 17.5 (5.34)
V	20.0 (6.10)	17.5 (5.34) ---- 22.5 (6.86)
VI	25.0 (7.62)	22.5 (6.86) ---- 27.5 (8.38)
VII	30.0 (9.15)	27.5 (8.38) ---- 32.5 (9.91)
VIII	35.0 (10.67)	32.5 (9.91) ---- 37.5 (11.43)
IX	40.0 (12.20)	37.5 (11.43) ---- 42.5 (12.96)
X	45.0 (13.72)	Higher than 42.5 ft (12.96 m)

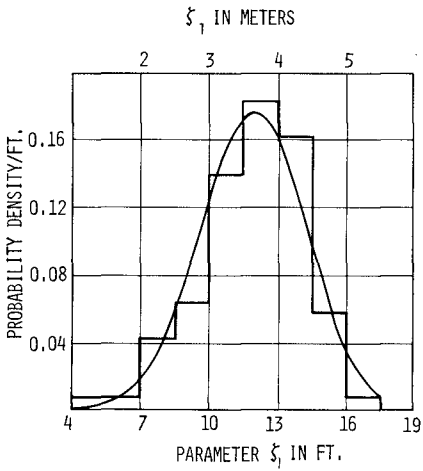


Figure 12 Histogram and probability density function of parameter ζ_1 for Group IV

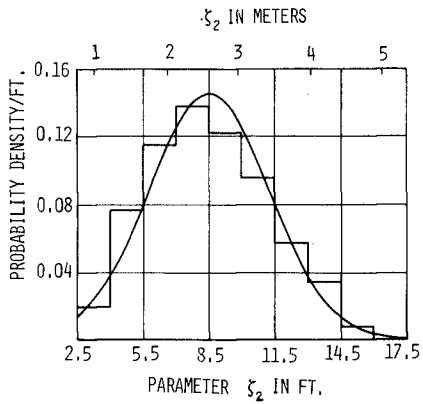


Figure 13 Histogram and probability density function of parameter ζ_2 for Group IV

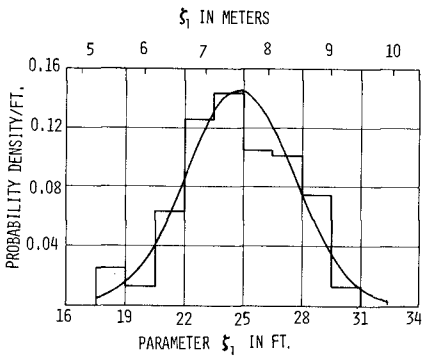


Figure 14 Histogram and probability density function of parameter ζ_1 for Group VII

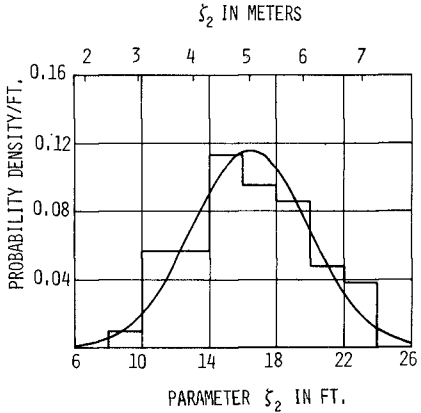


Figure 15 Histogram and probability density function of parameter ζ_2 for Group VII

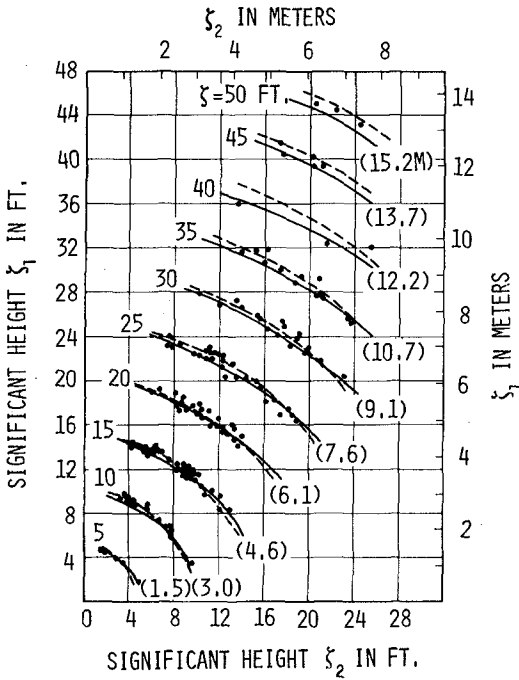


Figure 16 Relationship between significant wave heights ζ_1 , ζ_2 , and ζ

The solid lines in Figure 16 show the relationship between significant wave heights, ζ_1 , ζ_2 , and ζ , as obtained from Equation (A-10) in Appendix A, while the dashed lines show the relationships obtained from Equation (11). Included also in the figure are the results of the analysis of measured wave spectra whose significant wave heights are within ± 2.5 percent of the specified height. For example, for significant wave height, $\zeta = 9.1$ m (30 ft.), the results of the analysis of wave spectra with significant heights from 8.9 m (29.3 ft.) to 9.4 m (30.8 ft.) are plotted in the figure. As can be seen in the figure, the two lines obtained from Equations (A-10) and (11) do not differ appreciably, and that the results of analysis of the measured spectra fall on these lines. Hence, the simple formula given in Equation (11) may be used for the functional relationship between ζ_1 and ζ_2 . Thus, for a given sea severity of significant wave height ζ , the six parameters involved in Equation (10) can be reduced to five parameters by taking the ratio of the two significant wave heights, ζ_1/ζ_2 . For convenience, let $\zeta_1/\zeta_2 = \tan \theta$, and the statistical property of θ will be discussed hereafter.

$\theta = \tan^{-1}(\zeta_1/\zeta_2)$ (where, $0 < \theta < 90$) is outlined in Appendix B, and comparisons between histogram and the probability density function given in Equation (B-3) are shown in Figures 17 and 18 which pertain to Groups IV and VII, respectively. As can be seen in these examples, the derived probability density function agrees well with the histograms and hence the statistical analysis will be made using this probability function.

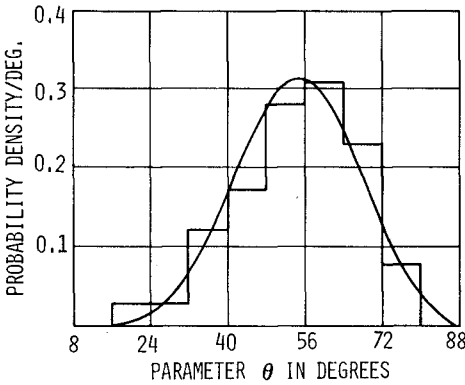


Figure 17 Histogram and probability density function of parameter θ for Group IV

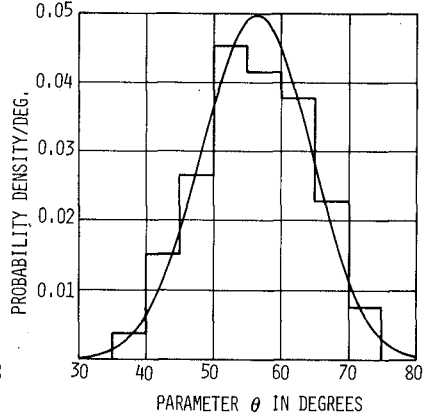


Figure 18 Histogram and probability density function of parameter θ for Group VII

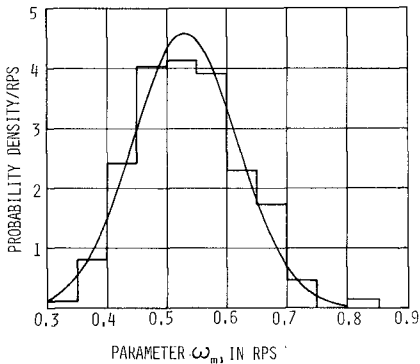


Figure 19 Histogram and probability density function of parameter ω_{m1} for Group IV

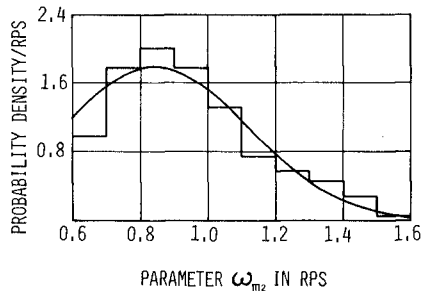


Figure 20 Histogram and probability density function of parameter ω_{m2} for Group IV

Next, the probability density function of the modal frequencies, ω_{m1} and ω_{m2} , will be obtained. In the determination of the modal frequencies for a given wave spectrum, no limitation is set for the value of ω_{m1} , namely, $0 < \omega_{m1} < \infty$. However, the modal frequency, ω_{m2} , has to be greater than ω_{m1} , and furthermore, the restriction is made such that ω_{m2} should not be less than 0.6 in order to avoid the possibility of an unrealistic representation of the spectral shape. For example, suppose a spectrum has triple peaks, two of which are in the frequency range below 0.6, then the computer program may take these two peaks (even though the energy is not appreciable) and discard the third peak in the higher frequency range which is associated with the wind-generated seas. In this case, it may be more appropriate to represent the two peaks in the frequency range less than 0.6 by one peak, and consider the energy in the higher frequency range.

The results of analysis of the available data have indicated that ω_{m1} and ω_{m2} both obey the normal distribution law, although ω_{m2} is truncated at 0.6. As an example, comparisons between histogram and the probability density function for Group IV are shown in Figures 19 and 20.

The value of the shape parameter, λ_1 , is much higher than that of λ_2 , in general; however, it appears that both follow the gamma probability law. Comparisons between the histogram and the gamma probability density function for λ_1 and λ_2 for Group IV are shown in Figure 21 and 22, respectively. Other examples of the comparisons for Group V ($\zeta = 6.10$ m, 20 ft.) are shown in Figures 23 and 24.

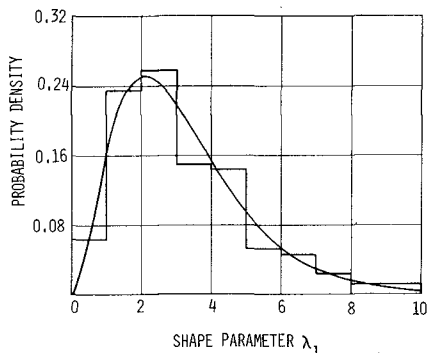


Figure 21 Histogram and probability density function of parameter λ_1 for Group IV

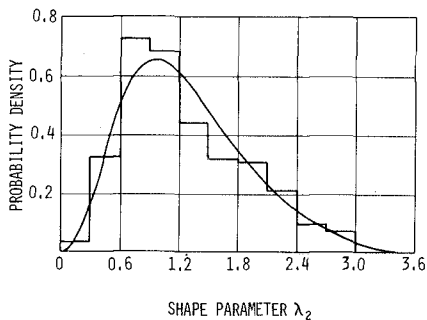


Figure 22 Histogram and probability density function of parameter λ_2 for Group IV

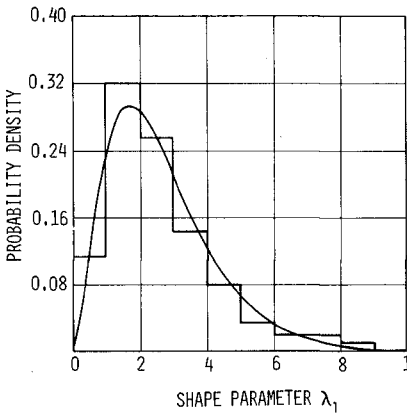


Figure 23 Histogram and probability density function of parameter λ_1 for Group V

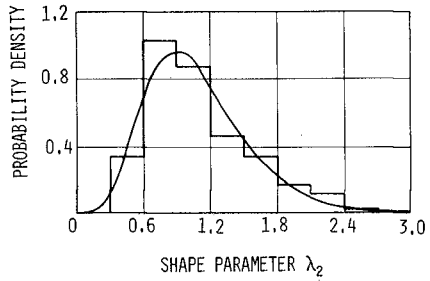
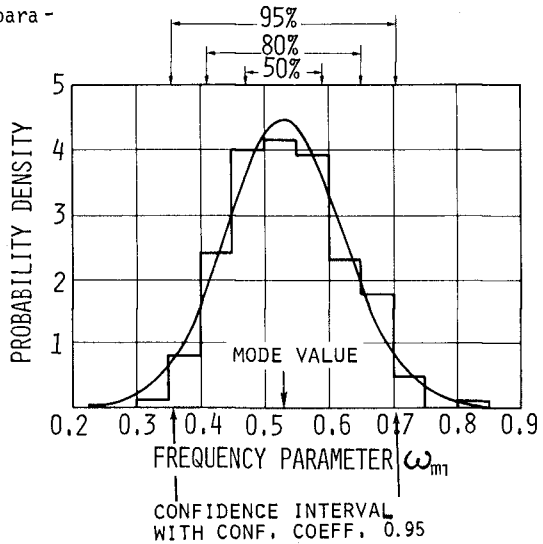


Figure 24 Histogram and probability density function of parameter λ_2 for Group V

Figure 25 Mode value and upper and lower-ground values of ω_{m1} for a confidence coefficient 0.95 (Group IV)



FAMILY OF WAVE SPECTRA

In this section, a family of wave spectra will be developed for a desired sea severity using the probability function applicable for each parameter in an attempt to represent various shapes of spectra associated with a storm.

In the development of the family of spectra, an attempt was made first to divide each probability density function into seven divisions as shown at the top of Figure 25. The figure is an example for the modal frequency, ω_{m_1} for Group IV (nominal significant height 4.75 m, 15 ft.). Then six values were determined by which 50%, 80%, and 95% of the probability density function was covered as shown at the top of the figure. For each value of ω_{m_1} , the value of each of the other parameters was determined from the original data by taking their respective averages in the region of $\pm 5\%$ of ω_{m_1} . For example, the θ -value for $\omega_{m_1} = 0.65$ (the upper value for 80% coverage) was determined by taking the average value of θ from a sample which belonged to $\pm 5\%$ of $\omega_{m_1} = 0.65$ ($0.62 < \omega_{m_1} < 0.68$) in Group IV. Since there are five parameters, θ , ω_{m_1} , ω_{m_2} , λ_1 , and λ_2 , this procedure resulted in a family consisting of a total of 25 spectra for a given sea severity. Judging from the results of this procedure, however, it appears that 25 wave spectra are too many to be considered since many of the shapes look alike.

To reduce the number of spectra involved, another approach is to choose three values for each parameter; namely, the modal value, the upper and the lower values determined from a confidence band for a confidence coefficient of 0.95. For example, the most probable ω_{m_1} is obtained as 0.53 for Group IV as shown in Figure 25, and the upper and lower bound values are 0.71 and 0.36, respectively. Similarly, three ω_{m_1} -values are evaluated for all other groups (except Groups IX and X) listed in Table 1, and the results are plotted in Figure 26 as a function of significant wave height, ζ . Included also in this figure are the formulae representing the data points so that the ω_{m_1} values for a desired sea severity can be evaluated.

Next, the values of the other parameters for each ω_{m_1} are determined for all groups in the same fashion as mentioned earlier, the results of which are plotted in Figures 27 through 30 as a function of ζ . It is noted that the parameter values shown in these figures are all associated with the parameter ω_{m_1} . The formulae representing the data points are also included in these figures. Although the formulae are derived without consideration of data points for severe seas ($\zeta = 12.2$ m, 40 ft. or above), the formulae may still be applicable for severe seas; since the data does not show serious scatter in relatively severe seas. Thus, a set of three spectra associated with the parameter ω_{m_1} can be drawn for an arbitrarily specified sea severity. As an example, Figure 31 shows a set for a significant wave height of 4.0 m (13.1 ft.). As can be seen in the figure, the dominant peaks of the spectra range from $\omega_{m_1} = 0.38$ to 0.74, and the spectral shape becomes more broad as the modal frequency ω_{m_1} increases.

The above discussion along with Figures 25 through 31 pertain to the parameter ω_{m_1} . The same procedure as that to derive a set of three spectra associated with ω_{m_1} , is carried out for the other four parameters, and thus a total of fifteen mathematical spectra can be established for a given sea severity. Of these fifteen spectra, five are associated with the mode value of the five parameters. The results of the analysis have

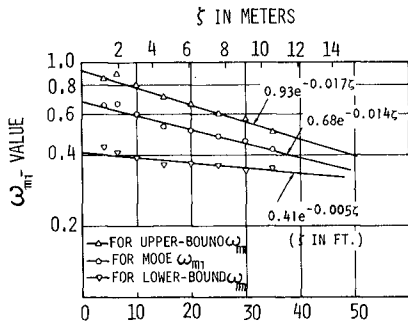


Figure 26 ω_{m1} -values as a function of significant height

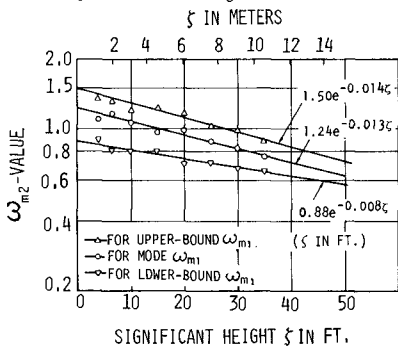


Figure 28 ω_{m2} -values for probable, upper and lower-bound values of ω_{m1} as a function of significant height

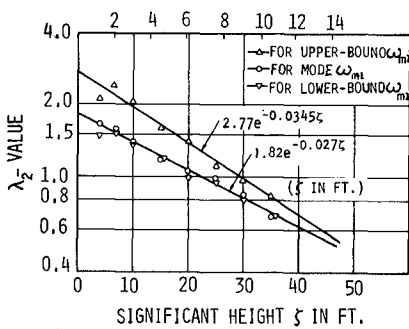


Figure 30 λ_2 -values for probable, upper and lower-bound values of ω_{m1} of significant height

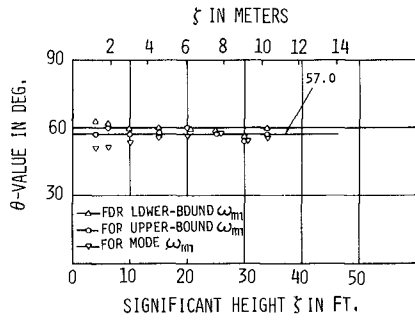


Figure 27 θ -values for probable, upper and lower-bound values of ω_{m1} as a function of significant height

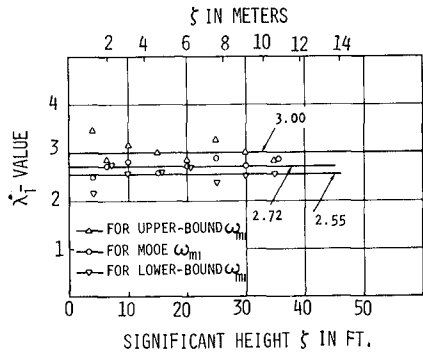


Figure 29 λ_1 -values for probable, upper and lower-bound values of ω_{m1} as a function of significant height

indicated, however, that the shapes of these five spectra are nearly the same as shown in Figure 32. Hence, the spectrum associated with the mode value of the parameter θ may be chosen as representative of the five spectra determined from the mode values of the parameters.

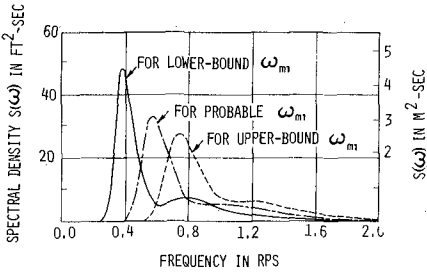


Figure 31 Spectral density function for probable, lower and upper-bound values of ω_{m1} (Sig. height 4.0 m, 12.1 ft)

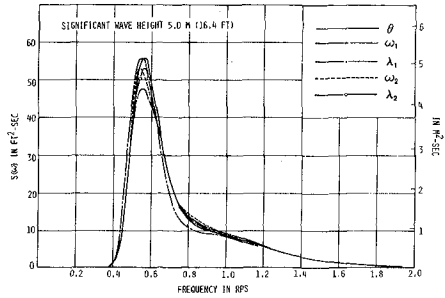


Figure 32 Comparison of five spectra associated with the mode value of five parameters (Sig. height 5.0 m, 16.4 ft)

Table 2a Values of six-parameters (ft-units)

	ζ_1	ζ_2	ω_{m1}	ω_{m2}	λ_1	λ_2
Most Probable Spectrum	0.84 ζ	0.54 ζ	0.70 $e^{-0.014 \zeta}$	1.15 $e^{-0.012 \zeta}$	3.00	1.54 $e^{-0.019 \zeta}$
95% Confidence Spectra	0.95 ζ	0.31 ζ	0.70 $e^{-0.014 \zeta}$	1.50 $e^{-0.014 \zeta}$	1.35	2.48 $e^{-0.031 \zeta}$
	0.65 ζ	0.76 ζ	0.61 $e^{-0.012 \zeta}$	0.94 $e^{-0.011 \zeta}$	4.95	2.48 $e^{-0.031 \zeta}$
	0.84 ζ	0.54 ζ	0.93 $e^{-0.017 \zeta}$	1.50 $e^{-0.014 \zeta}$	3.00	2.77 $e^{-0.034 \zeta}$
	0.84 ζ	0.54 ζ	0.41 $e^{-0.005 \zeta}$	0.88 $e^{-0.008 \zeta}$	2.55	1.82 $e^{-0.027 \zeta}$
	0.90 ζ	0.44 ζ	0.81 $e^{-0.016 \zeta}$	1.60 $e^{-0.010 \zeta}$	1.80	2.95 $e^{-0.032 \zeta}$
	0.77 ζ	0.64 ζ	0.54 $e^{-0.012 \zeta}$	0.61	4.50	1.95 $e^{-0.025 \zeta}$
	0.73 ζ	0.68 ζ	0.70 $e^{-0.014 \zeta}$	0.99 $e^{-0.012 \zeta}$	6.40	1.78 $e^{-0.021 \zeta}$
	0.92 ζ	0.39 ζ	0.70 $e^{-0.014 \zeta}$	1.37 $e^{-0.012 \zeta}$	0.70	1.78 $e^{-0.021 \zeta}$
	0.84 ζ	0.54 ζ	0.74 $e^{-0.016 \zeta}$	1.30 $e^{-0.012 \zeta}$	2.65	3.90 $e^{-0.026 \zeta}$
0.84 ζ	0.54 ζ	0.62 $e^{-0.012 \zeta}$	1.03 $e^{-0.009 \zeta}$	2.60	0.53 $e^{-0.021 \zeta}$	

ζ = significant wave height in feet

Table 2b Values of six-parameters (m-units)

	ζ_1	ζ_2	ω_{m1}	ω_{m2}	λ_1	λ_2
Most Probable Spectrum	0.84 ζ	0.54 ζ	0.70 $e^{-0.046 \zeta}$	1.15 $e^{-0.039 \zeta}$	3.00	1.54 $e^{-0.062 \zeta}$
95% Confidence Spectra	0.95 ζ	0.31 ζ	0.70 $e^{-0.046 \zeta}$	1.50 $e^{-0.046 \zeta}$	1.35	2.48 $e^{-0.102 \zeta}$
	0.65 ζ	0.76 ζ	0.61 $e^{-0.039 \zeta}$	0.94 $e^{-0.036 \zeta}$	4.95	2.48 $e^{-0.102 \zeta}$
	0.84 ζ	0.54 ζ	0.93 $e^{-0.056 \zeta}$	1.50 $e^{-0.046 \zeta}$	3.00	2.77 $e^{-0.112 \zeta}$
	0.84 ζ	0.54 ζ	0.41 $e^{-0.016 \zeta}$	0.88 $e^{-0.026 \zeta}$	2.55	1.82 $e^{-0.089 \zeta}$
	0.90 ζ	0.44 ζ	0.81 $e^{-0.052 \zeta}$	1.60 $e^{-0.033 \zeta}$	1.80	2.95 $e^{-0.105 \zeta}$
	0.77 ζ	0.64 ζ	0.54 $e^{-0.039 \zeta}$	0.61	4.50	1.95 $e^{-0.082 \zeta}$
	0.73 ζ	0.68 ζ	0.70 $e^{-0.046 \zeta}$	0.99 $e^{-0.039 \zeta}$	6.40	1.78 $e^{-0.069 \zeta}$
	0.92 ζ	0.39 ζ	0.70 $e^{-0.046 \zeta}$	1.37 $e^{-0.039 \zeta}$	0.70	1.78 $e^{-0.069 \zeta}$
	0.84 ζ	0.54 ζ	0.74 $e^{-0.052 \zeta}$	1.30 $e^{-0.039 \zeta}$	2.65	3.90 $e^{-0.085 \zeta}$
	0.84 ζ	0.54 ζ	0.62 $e^{-0.039 \zeta}$	1.03 $e^{-0.030 \zeta}$	2.60	0.53 $e^{-0.069 \zeta}$

ζ = significant wave height in meters

Thus, a total of eleven spectra derived in the above are considered as a family of wave spectra for a specified sea severity. The values of six parameters for these eleven spectra are expressed in terms of significant-wave height, ζ , and are tabulated in Table 2 so that a family of spectra for a desired sea can be generated from Equation (10). In these eleven spectra, one is considered as the "most probable spectrum" representing a specified sea, and the remaining ten spectra are those expected to occur with 95 percent confidence.

Examples of the family of spectra thus derived are shown in Figures 33 through 36. Figures 33 and 34 are for significant wave heights of 1.25 m (4.1 ft.) and 3.0 m (9.8 ft.), respectively, and the shapes of wave spectra vary considerably in these seas of relatively mild severity. The frequency domain where the predominant wave energy exists varies to a great extent (from 0.4 to 1.2) depending on the shape of spectra. On the other hand, Figure 35 is for a significant wave height of 9.0 m (29.5 ft.), and the frequency domain where the predominant wave energy exists varies to a much less extent (from 0.3 to 0.7) in this severe sea although a variety of spectral shapes may still be observed.

Figure 36 is for a significant wave height of 13.0 m (42.6 ft.), an example of very severe seas. A family of spectra shown in this figure is of particular interest since the values of all parameters for this fam-

ily of spectra are determined by extending the lines of the analysis of data, examples of which are shown earlier in Figures 26 through 30. In order to examine whether or not the family of spectra thus generated represents the measured spectra, Figure 37 is prepared. The figure shows an observed spectrum which has the same significant wave height as that of the family shown in Figure 36, 13.0 m (42.6 ft.). Included also in the figure is the computer-generated six-parameter spectrum. From the comparison of these two figures, it can be seen that the example given in Figure 37 agrees well with one of the members of the family (the most probable spectrum) given in Figure 36. Thus, it appears that the families of spectra generated using the parameter values obtained from the extension of the lines in the analysis of the data can be considered to represent realistic sea spectra.

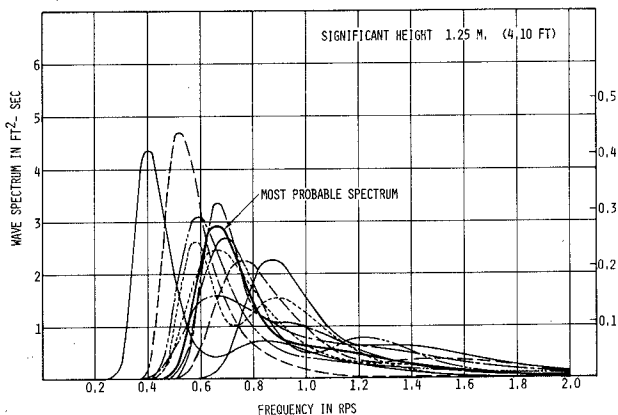


Figure 33 Family of spectra for significant wave height of 1.25 m (4.1 ft.)

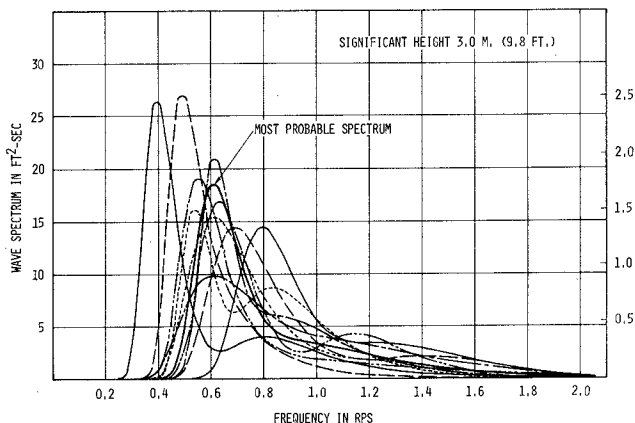


Figure 34 Family of spectra for significant wave height of 3.0 m (9.8 ft.)

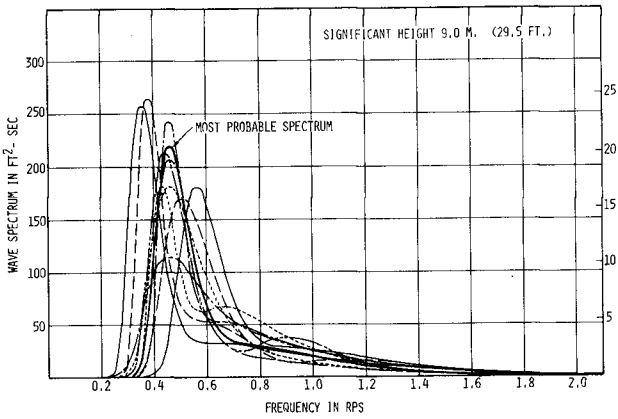


Figure 35 Family of spectra for significant wave height of 9.0 m (29.5 ft.)

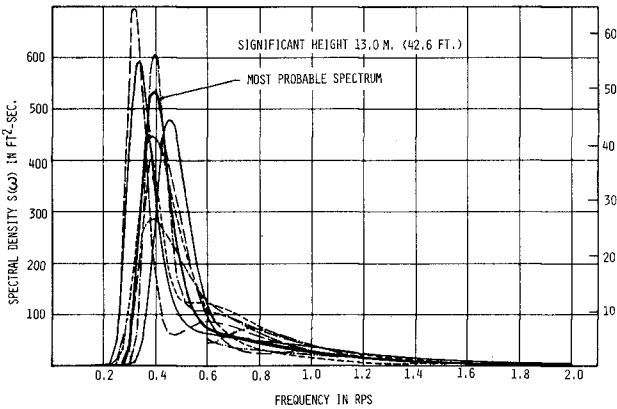


Figure 36 Family of spectra for significant wave height of 13.0 m (42.6 ft.)

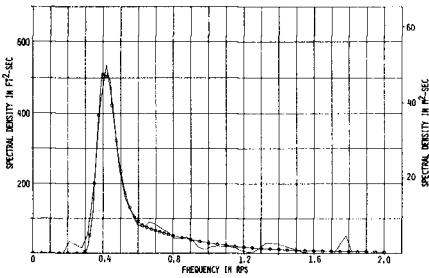


Figure 37 Comparison of measured and six-parameter spectrum (significant height 13.0 m, 42.6 ft.)

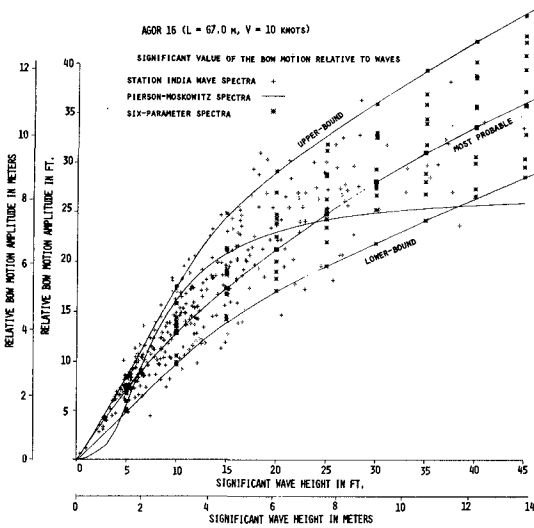


Figure 38 Significant amplitudes of the vertical bow motion of a catamaran in various seas (10-knot speed)

APPLICATION OF SIX-PARAMETER SPECTRA

The six-parameter wave spectra can be applied to evaluate responses such as motions and wave-induced forces, etc., of marine vehicles and structures in a seaway for design consideration. Figure 38 shows, as an example of the application, the significant values of the vertical bow motion relative to waves of a catamaran (length 67 m, 220 ft.) for 10-knot speed in various sea severities. Included also in the figure are the responses evaluated by using the Pierson-Moskowitz fully-developed sea spectra, and those due to individual wave spectra (about 300) observed at Station India in the North Atlantic Ocean [9].

As can be seen in the figure, for a specified sea severity, there are 11 responses (one for each member of the family of the six-parameter spectra), and one of the family members yields the largest response, and another yields the smallest response. The most probable spectrum given in Table 2 yields the most probable response. By connecting the points obtained in each sea severity, we may establish the most probable response, the upper-bound and the lower-bound responses which will provide useful information for design. The upper and lower-bounds cover the majority of the responses obtained from using the measured wave spectra, and it may safely be said for this case that the values of the six parameters obtained from a statistical analysis of the data yield a family of spectra representing realistic seas reasonably well with 95 percent confidence.

The results of a similar application made for predicting extreme wave-induced loads on an ocean structure may be found in Reference [10].

The six-parameter wave representation may be used for the analysis of wave spectra associated with particular situations such as breaking waves, wave run-up, etc. The measured spectra may be expressed in terms of six parameters and a statistical analysis may be carried out on the parameters to find significant factors which influence the spectra.

Another application of the six-parameter representation is to store or file a massive amount of measured data for statistical analysis. In the case where consecutive measurements are made within a certain time interval, the data may be stored in the form of six variables, the values of which change gradually with time, and hence the sea condition associated with the growth and decay of a storm may be discussed from a statistical analysis of the parameters.

CONCLUSIONS

Consideration of various shapes of wave spectra for a given sea severity is of particular significance for evaluation of response of ocean and coastal structures to waves, since the magnitude of responses is greatly influenced by the relative location of the modal frequencies of waves and response of individual structures. In an attempt to develop a systematic series of wave spectra covering a variety of spectral shapes, a series of wave spectra which involves six parameters are newly developed.

In the development of the six-parameter wave spectra, the spectra are decomposed into two parts, and each part is expressed by a mathematical formula with three parameters; i.e., significant wave height, modal frequency, and shape parameter, and the entire spectrum is expressed by the combination of two sets of three-parameter spectra. The parameters are determined numerically such that the difference between theoretical and observed spectra is minimal. The six-parameter spectra thus obtained appear to represent almost all stages of the sea condition associated with a storm.

Then, a total of 800 spectra observed in the North Atlantic Ocean are classified into 10 groups depending on severity, and for each group a statistical analysis is carried out on the parameters taking into account the correlation between them. From the results of analysis, a family consisting of eleven sets of mathematical spectra is established for a given sea severity. In these eleven spectra, one is considered as the "most probable spectrum" representing a specified sea, and the remaining ten spectra are those expected to occur with 95 percent confidence. The values of six parameters for these eleven spectra are expressed in terms of significant wave height, and are tabulated in Table 2 of the paper so that a family of spectra for a desired sea severity can be generated from the formula (Equation 10) given in the paper.

REFERENCES

1. Strekalov, S.S., Tsyploukhin, V.P., and Massel, S.T., "Structure of Sea Wave Frequency Spectrum", Proc. 13th Coastal Eng. Conference, Volume 1, 1972
2. Phillips, O.M., "The Equilibrium Range in the Spectrum of Wind-Generated Waves", Journal of Fluid Mech., Volume 4, 1958
3. Kitaigorodskii, S.A., "Application of the Theory of Similarity to the Analysis of Wind-Generated Wave Motion as A Stochastic Process", Izv. Akad. Nauk. SSSR, Ser. Geophys., Volume 1, 1961
4. Pierson, W.J. and Moskowitz, L., "A Proposed Spectral Form for Fully Developed Wind Seas Based on the Similarity Theory of S.A. Kitaigorodskii", Journal of Geophysical Res., Volume 69, No. 24, 1964
5. Bretschneider, C.L., "Wave Variability and Wave Spectra for Wind-Generated Gravity Waves", Beach Erosion Board, Corps of Eng. Tech. Memo. No. 11B, 1959
6. Hasselmann, et. al., "Measurements of Wind-Wave Growth and Swell Decay During the Joint North Sea Wave Project (JONSWAP)", Deutsches Hydrograph. Inst., 1973
7. Moskowitz, L., Pierson, W.J., and Mehr, E., "Wave Spectra Estimated from Wave Records Obtained by the OWS WEATHER EXPLORER and the OWS WEATHER REPORTER", New York Univ. College of Eng. Res. Div. (Part I) 1962, (Part II) 1963, and (Part III) 1965
- B. Bretschneider, C.L., et. al., "Data for High Wave Conditions Observed by the OWS WEATHER REPORTER in December 1959", Deutsche Hydrographische Zeitschrift, Jahrgang 15, Heft 6, 1962
9. Miles, M., "Wave Spectra Estimated from A Stratified Sample of 323 North Atlantic Wave Records", National Res. Council, Div. of Mech. Eng. Report LTR-SH-11B, 1971
10. Ochi, M.K. and Wang, S., "Prediction of Extreme Wave-Induced Loads on Ocean Structures", Int. Conference on Behaviour of Offshore Structures, The Norwegian Inst. of Tech., 1976

APPENDIX A: SIGNIFICANT WAVE HEIGHT FOR A SPECTRUM CONSISTING OF HIGH AND LOW FREQUENCY COMPONENTS

Let $x(t)$ be the wave profile of an irregular sea which is a normal random process with zero mean and a narrow-band spectrum, and let $x(t)$ be comprised of two components; $x_1(t)$ and $x_2(t)$, which correspond to the wave profile of the low frequency and the high frequency components, respectively. Here, $x_1(t)$ and $x_2(t)$ are both normal random processes; however, in the following it is assumed that $x_1(t)$ is a narrow-banded but $x_2(t)$ is not necessarily narrow-banded. The amplitude, frequency, and variance are denoted by A , ω , and σ^2 , respectively, and the subscripts 1 and 2 refer to the low and high frequency components, respectively.

Then, from the assumption described above, the wave profile $x(t)$ may be written in the following form:

$$x(t) = A(t) \cos(\omega_2 t - \theta(t)) \quad (A-1)$$

The low-frequency component wave profile becomes,

$$x_1(t) = A_1(t) \cos(\omega_1 t - \theta_1(t)) \quad (A-2)$$

On the other hand, the high frequency component wave may be expressed in the following form:

$$x_2(t) = x_{2c}(t) \cos(\omega_2 t) + x_{2s}(t) \sin(\omega_2 t) \quad (A-3)$$

where,

$$x_{2c}(t) = \sum \left[a_n \cos(n\omega - \omega_2)t + b_n \sin(n\omega - \omega_2)t \right]$$

$$x_{2s}(t) = \sum \left[a_n \sin(n\omega - \omega_2)t - b_n \cos(n\omega - \omega_2)t \right]$$

and

$$a_n = \frac{2}{T} \int_0^T x_2(t) \cos(n\omega t) dt$$

$$b_n = \frac{2}{T} \int_0^T x_2(t) \sin(n\omega t) dt$$

Here, $x_{2c}(t)$ and $x_{2s}(t)$ are independent normal processes, and their joint probability density function can be written as,

$$f(x_{2c}, x_{2s}) = \frac{1}{2\pi\sigma_2^2} e^{-\frac{x_{2c}^2 + x_{2s}^2}{2\sigma_2^2}} \quad (A-4)$$

From the condition that $x(t) = x_1(t) + x_2(t)$, Equations (A-1),

(A-2), and (A-3) yield:

$$x(t) = [x_{2c}(t) + A_1(t) \cos \psi] \cos \omega_2 t + [x_{2s}(t) - A_1(t) \sin \psi] \sin \omega_2 t \quad (\text{A-5})$$

where,

$$\psi = (\omega_1 - \omega_2)t - \theta_1$$

Thus, from Equations (A-1) and (A-5), we can derive the following relationship:

$$\begin{aligned} x_{2c} &= A \cos \theta - A_1 \cos \psi \\ x_{2s} &= A \sin \theta + A_1 \sin \psi \end{aligned} \quad (\text{A-6})$$

Since the joint probability density function of x_{2c} and x_{2s} is given in Equation (A-4), the joint probability density function of A and θ can be obtained from Equations (A-4) and (A-6) by transformation of two random variables (x_{2c}, x_{2s}) to (A, θ) , and therefrom the marginal probability density function of A can be obtained. This part of the work was done by Middleton [A-1], and he derived the following formula:

$$f(A) = \int_0^{2\pi} f(A, \theta) d\theta = \frac{A}{\sigma_2^2} e^{-\frac{A^2 + A_1^2}{2\sigma_2^2}} I_0\left(\frac{AA_1}{\sigma_2^2}\right), \quad 0 \leq A < \infty \quad (\text{A-7})$$

The probability density function of the amplitude, A , given in the above, however, is expressed in terms of the amplitude of the low frequency component waves, A_1 . Hence, Equation (A-7) can be considered as a conditional probability density function $f(A|A_1)$. In order to express the probability density function of A in terms of the variance of the two component waves σ_1^2 and σ_2^2 , the condition is used that the low frequency wave component has a narrow-band spectrum and hence its amplitude follows the Rayleigh probability law. Thus, the probability density function of A can be written as follows:

$$\begin{aligned} f(A) &= \int_0^\infty f(A|A_1) f(A_1) dA_1 \\ &= \frac{A}{\sigma_2^2} e^{-\frac{A^2}{2\sigma_2^2}} \int_0^\infty I_0\left(\frac{AA_1}{\sigma_2^2}\right) \frac{A_1}{\sigma_1^2} e^{-\frac{1}{2}\left(\frac{1}{\sigma_1^2} + \frac{1}{\sigma_2^2}\right)A_1^2} dA_1 \end{aligned} \quad (\text{A-8})$$

By carrying through the integration involved in the above equation, the following formula can be derived:

$$f(A) = \left(\frac{1}{1+\mu} \right) \frac{A}{\sigma_2^2} e^{-\frac{A^2}{2\sigma_2^2}} \times \left(1 + \sqrt{\frac{\pi}{2}} \sqrt{\frac{\mu}{1+\mu}} \frac{A}{\sigma_2} e^{\left(\frac{\mu}{1+\mu} \right) \left(\frac{A}{2\sigma_2} \right)^2} I_{\frac{1}{2}} \left(\frac{\mu}{1+\mu} \left(\frac{A}{2\sigma_2} \right)^2 \right) \right) \quad (A-9)$$

where,

$$\mu = \left(\frac{\sigma_1}{\sigma_2} \right)^2, \quad I_{\frac{1}{2}}(Z) = \sqrt{\frac{2}{\pi Z}} \sinh Z$$

Equation (A-9) is the probability density function of the amplitude, A , in terms of two variances, σ_1^2 and σ_2^2 , which are equal to the area under the low and high frequency components, respectively, of the wave spectrum. The significant wave height of the spectrum, ζ , is then obtained numerically from Equation (A-9) as follows:

$$\zeta = 3 \int_{A_*}^{\infty} A f(A) dA \quad (A-10)$$

where, A_* can be found from

$$\int_0^{A_*} f(A) dA = 2/3$$

REFERENCE:

- A-1. Middleton, D., "An Introduction to Statistical Communication Theory", McGraw Hill Book Company, New York, 1960

APPENDIX B: DERIVATION OF PROBABILITY DENSITY FUNCTION OF $\theta = \tan^{-1}(\zeta_1/\zeta_2)$

In the text it is discussed that the significant wave heights ζ_1 and ζ_2 both obey the normal probability law, and that the concept of truncation is necessary for the significant height for the low frequency component, ζ_1 .

Let μ_1 and σ_1^2 be the mean and variance, respectively, of the significant height ζ_1 belonging to the i -th group in Table 1 given in the text, and let μ_2, σ_2^2 be the mean and variance of the significant height ζ_2 . Since ζ_1 and ζ_2 may not necessarily be statistically independent, let ρ be the correlation coefficient which can be evaluated from the sample

belonging to the i -th group. Then, by taking into account the truncation of ζ_1 at $(\zeta_1)_{\max}$, the joint probability density function of ζ_1 and ζ_2 belonging to the i -th group can be written as.

$$f(\zeta_1, \zeta_2) = \frac{1}{1 - \int_{(\zeta_1)_{\max}}^{\infty} f(\zeta_1) d\zeta_1} \frac{1}{2\pi\sigma_1\sigma_2\sqrt{1-\rho^2}} - \frac{1}{2(1-\rho^2)} \left\{ \left(\frac{\zeta_1 - \mu_1}{\sigma_1} \right)^2 - 2\rho \left(\frac{\zeta_1 - \mu_1}{\sigma_1} \right) \left(\frac{\zeta_2 - \mu_2}{\sigma_2} \right) + \left(\frac{\zeta_2 - \mu_2}{\sigma_2} \right)^2 \right\} \quad (\text{B-1})$$

x e

$$0 < \zeta_1 < (\zeta_1)_{\max}, \quad 0 < \zeta_2 < \infty$$

where, $f(\zeta_1)$ is the probability density function of the significant height ζ_1 which is a normal distribution with mean μ_1 and variance σ_1 .

Let $\eta = \zeta_1/\zeta_2$. Then, from Equation (B-1), the probability density function of η becomes,

$$f(\eta) = \frac{1}{1 - \int_{(\zeta_1)_{\max}}^{\infty} f(\zeta_1) d\zeta_1} \frac{1}{2\pi\sigma_1\sigma_2\sqrt{1-\rho^2}} \int_0^{\infty} \zeta_2 - \frac{1}{2(1-\rho^2)} \left\{ \left(\frac{\zeta_2\eta - \mu_1}{\sigma_1} \right)^2 - 2\rho \left(\frac{\zeta_2\eta - \mu_1}{\sigma_1} \right) \left(\frac{\zeta_2 - \mu_2}{\sigma_2} \right) + \left(\frac{\zeta_2 - \mu_2}{\sigma_2} \right)^2 \right\} d\zeta_2 \quad (\text{B-2})$$

x e

$$0 < \eta < \infty$$

Next, let $\theta = \tan^{-1}\eta = \tan^{-1}(\zeta_1/\zeta_2)$. Then, the probability density function of θ can be obtained numerically using Equation (B-2) as follows:

$$f(\theta) = \left[f(\eta) \right] \sec^2 \theta, \quad 0 < \theta < 90 \quad (\text{B-3})$$

$\eta = \tan \theta$

CHAPTER 19

DIRECTIONAL SPECTRA OF OCEAN SURFACE WAVES

by

H. Mitsuyasu and S. Mizuno

Research Institute for Applied Mechanics

Kyushu University, Fukuoka, Japan

ABSTRACT

From 1971-74 seven cruises were made to measure the directional spectrum of ocean waves by using a cloverleaf buoy. Typical sets of wave data measured both in open seas and in a bay under relatively simple conditions have been analyzed to clarify the fundamental properties of the directional spectrum of ocean waves in deep water.

It is shown that the directional wave spectrum can be approximated by the product of the frequency spectrum and a unimodal angular distribution with mean direction approximately equal to that of the wind. The normalized forms of the frequency spectrum show various forms lying between the Pierson-Moskowitz spectrum and the spectrum of laboratory wind wave which has a very sharp energy concentration near the spectral peak frequency. The form of the JONSWAP spectrum is very close to that of laboratory wind waves. The concentration of the spectral energy near the spectral peak frequency seems to decrease with increasing the dimensionless fetch and the spectral form finally approaches to the Pierson-Moskowitz spectrum which can be considered as the spectrum with the least concentration of the normalized spectral energy. However, the definite relation between the shape of the normalized spectrum and the dimensionless fetch has not been obtained.

Concerning the angular distribution, it is shown that the shape of angular distribution of the single-peaked wave spectrum in a generating area can be approximated by the function $G(\theta, f) = G'(s) \left| \cos(\theta - \bar{\theta})/2 \right|^{2s}$ proposed originally by Longuet-Higgins et al. (1963). Here $G'(s)$ is a normalizing function, $\bar{\theta}$ is the mean direction of the spectral component, and s is a parameter which controls the concentration of the angular distribution function.

The significant results of this study are that $\bar{\theta}$ is very close to the wind direction irrespective of the wave frequency, and that the parameter s can be uniquely determined from the dimensionless frequency. The angular distribution is very narrow for the frequencies near the dominant peak of the frequency spectrum, whereas it widens rapidly towards high and low frequencies. Thus, the major energy-containing frequency components of the ocean waves propagate in almost the same direction as the wind with the least angular spreading.

An idealized form of the angular distribution function of the ocean wave spectra is proposed for practical purposes. Qualitatively, the idealized form proposed here has a property which is similar to that of the SWOP spectrum, although they are different quantitatively.

INTRODUCTION

To a first approximation, ocean surface wave can be regarded as a linear superposition of statistically independent free waves and is consequently described by two-dimensional wave spectrum (directional spectrum). During the last twenty years great many studies have been made to clarify the properties of ocean wave spectra. However, in contrast with numerous studies of the one-dimensional (frequency) spectrum, only a few studies have been made of the two-dimensional (directional) spectrum of ocean waves. Particularly, reliable data for estimating the directional spectra of ocean waves are remarkably lacking except for the data reported by Côté et al. (1960), Longuet-Higgins et al. (1963), Ewing (1969) and recently by Tyler et al. (1974). These situations may be partly attributed to the technical difficulties for the measurement of the directional wave spectrum as compared to that of the one-dimensional spectrum. Therefore, many studies on the directional wave spectrum have been concentrated on the measuring techniques and their accuracies rather than the measurements and analysis of the directional wave spectra in various conditions.

In order to save these situations, in 1971 we have developed the cloverleaf buoy which is almost the same as that of the National Institute of Oceanography (Cartwright and Smith 1964). From 1971 to 1974 seven cruises were made to measure the directional spectrum of ocean waves by using the cloverleaf buoy. Typical wave data measured both in open seas and in a bay have been analyzed to clarify the fundamental

properties of the directional spectrum of ocean waves in fairly simple generating conditions. A new standard form of directional wave spectrum is proposed on the basis of typical sets of measured data. The proposed form of the directional spectrum is further verified by the additional data obtained in the East China Sea during the period of AMTEX'75.*

WAVE DATA AND ANALYSIS

Waves were measured by using a cloverleaf buoy which is almost the same as that of the National Institute of Oceanography (Cartwright and Smith, 1964). It can measure the

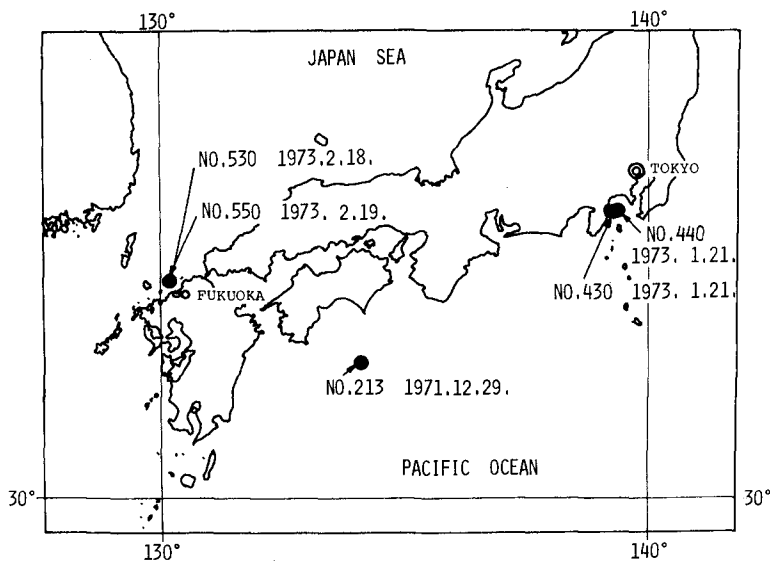


Fig. 1. Locations and dates of the wave observations.

* AMTEX'75 (Air-Mass Transformation Experiment in 1975) is one of the international sub-program of GARP (Global Atmospheric Research Programme).

vertical acceleration η_{tt} , slope η_x , η_y , and curvature η_{xx} , η_{yy} , η_{xy} of the wave surface $\eta(t, x, y)$. The detailed description of the instrumentation including the buoy and of the observational procedures has been given elsewhere (Mitsuyasu et al., 1973a,), and will not be repeated here.

From approximately 50 cases, only five typical data sets (identified as Nos.213, 430, 440, 530 and 550) have been analyzed; each is a continuous record of about 1 h. These data were obtained under the fairly simple generating conditions. That is, the wind speeds and directions are fairly constant within the duration time. Fig.1 shows the locations and dates of the wave observations.

Data sets 213, 530 and 550 correspond to wave data in open seas and data sets 430 and 440, to those for a bay.

Table 1 gives the wind direction θ_w , speed U , and approximate duration t_d , which have been measured from the tending ship near each observation station; H and T are the significant wave height and period, respectively, measured by the cloverleaf buoy.

Data set	θ_w	parameter				
		U ($m s^{-1}$)	t_d (h)	H (m)	T (s)	H/L
213	E-NE	10	26	1.49	6.20	0.025
430	ENE-NE	7	2	0.80	4.45	0.026
440	ENE-NE	7	4	0.74	4.11	0.028
530	NNE	9	4	0.84	4.50	0.027
550	N-NE	10	24	2.34	8.30	0.022

Table 1. Wave parameters from the five data sets.

The wind speeds measured at the observation stations have been determined by taking the mean of the measured wind speeds during the duration. Table 2 gives similar kind of data which have been measured in the East China Sea ($28^{\circ}19'N \sim 28^{\circ}36'N$, $125^{\circ}17'E \sim 125^{\circ}42'E$) and are used for verifying the conclusions derived from the first series of data shown in Table 1.

Original wave data recorded on magnetic tapes in analogue form were digitized by using a high-speed A-D converter. The cross spectral analysis of the data was done on the

computer system FACOM 270-20 using a standard program based on fast Fourier transform procedures. Fundamentals of the mathematical procedure of the data analysis are almost the same as those used by Longuet-Higgins et al. (1963) and by Cartwright and Smith (1964). Condensed descriptions of the data analysis have been given also in our previous papers (Mitsuyasu et al. 1973a, and 1975).

Data set	θ_w	parameter				
		U (m s^{-1})	t_d (h)	H (m)	T (s)	H/L
801	0°	10	55	2.33	7.80	0.025
804	340°	13	18	2.79	8.00	0.028
805	350°	14	23	2.67	7.80	0.028

Table 2. Wave parameters from the additional three data sets

Cross spectra $C_{em}(f) - Q_{em}(f)$ were computed using the measured six signals from the ocean waves. The directional spectrum $E(f, \theta)$ is conveniently expressed in the form

$$E(f, \theta) = \phi_1(f)G(f, \theta), \quad (1)$$

where $\phi_1(f)$ is the one-dimensional wave spectrum and $G(f, \theta)$ an angular distribution function. The one-dimensional spectrum $\phi_1(f)$ is determined from the acceleration spectrum $C_{11}(f)$, i.e.,

$$\phi_1(f) = (2\pi f)^{-4} C_{11}(f). \quad (2)$$

The coefficients A_n and B_n in the Fourier expansion of an angular distribution function $h(f, \theta) [= \pi G(f, \theta)]$ can be determined up to $n = 4$, from the measured cross-spectral elements C_{ym} and Q_{em} . From these Fourier coefficients the angular distribution function $h(f, \theta)$ can be expressed approximately as

$$h_4(f, \theta) = \frac{1}{2} + \sum_{n=1}^4 w_n (A_n \cos n\theta + B_n \sin n\theta), \quad (3)$$

for $w_1 = 8/9$, $w_2 = 28/45$, $w_3 = 56/165$, $w_4 = 14/99$

where the weights w_n are introduced to make $h_4(f, \theta)$ non-negative. The partial Fourier sum with the weights w_n corresponds to the smoothed average of $h(f, \theta)$ by the weighting function $W_4(\theta)$ which is very approximately proportional to $\cos^4 \theta/2$ and has an rms width $\pm 29^\circ$.

RESULTS

a. One-dimensional spectra of ocean waves

In a previous study one of the present authors studied the similarity of the one-dimensional spectra of wind-generated waves by using accurately measured wave data for three different groups A, B and C (Mitsuyasu et al., 1973c). Wave data for groups A and B were obtained in two quite different wind-wave facilities under various conditions. The wave data of group C were obtained in Hakata Bay, where the water depth is approximately 5 m and the fetch is approximately 5 km to the north.

It was found that wave spectra normalized in the form

$$\frac{\phi_1(f) f_m}{E} = \phi\left(\frac{f}{f_m}\right) \quad (4)$$

were quite similar and stable within each the groups; here f_m the spectral peak frequency and E the total energy of the wave spectrum defined by

$$E = \int_0^{\infty} \phi_1(f) df = \int_0^{\infty} \int_0^{2\pi} E(f, \theta) d\theta df \quad (5)$$

Moreover, there were no differences in the normalized spectra between groups A and B. However, the normalized spectra of group C were slightly different from those of groups A and B. These results can be clearly seen in Fig.2 which is reproduced from the previous paper (Mitsuyasu et al., 1973c), and shows the mean form of the normalized spectra of each group together with the normalized spectrum of Pierson and Moskowitz (1964). As can be seen from Fig. 2, the concentration of the normalized spectral energy near the spectral peak is lower in the data of Group C than

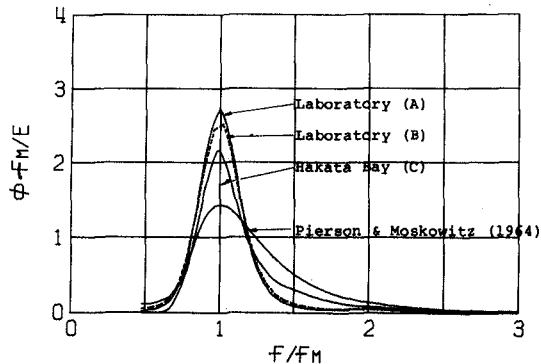


Fig.2 Similarity of the one-dimensional wave spectrum.

in those of groups A and B. The concentration of the normalized spectral energy of the Pierson-Moskowitz spectrum is much smaller than that of group C. The dimensionless fetch gF/u_*^2 is approximately 10^2-10^3 for the wave data of groups A and B, 10^5-10^6 for those of group C, and approximately 10^7 for the Pierson-Moskowitz spectrum. Therefore, within the range of our previous data, it was concluded that the concentration of the normalized spectral energy of wind waves seems to decrease with increasing dimensionless fetch gF/u_*^2 .

The normalized spectra shown in Fig.2 are used as a kind of reference for discussing the present data of one-dimensional spectra measured under various conditions. All of the measured spectra were normalized in the form (4) and compared with the previous results. Some typical examples of the normalized forms of the measured wave spectra are shown in Figs. 3-5.

The dashed line in each figure shows the spectral form which is selected from the typical spectra shown in Fig.2 and which has the closest resemblance to each measured spectrum. It can be seen from these figures that the wave spectrum of No. 430/1 is quite similar to the spectrum of laboratory wind waves, the wave spectrum of No. 550/1 is quite similar to the spectrum observed in Hakata Bay, and the wave spectrum of No. 213/1 is quite similar to the Pierson-Moskowitz spectrum. All of the other spectra were scattered between the spectral form for laboratory wind waves and that of Pierson-Moskowitz (1964), though they are not shown in the figures. Furthermore,

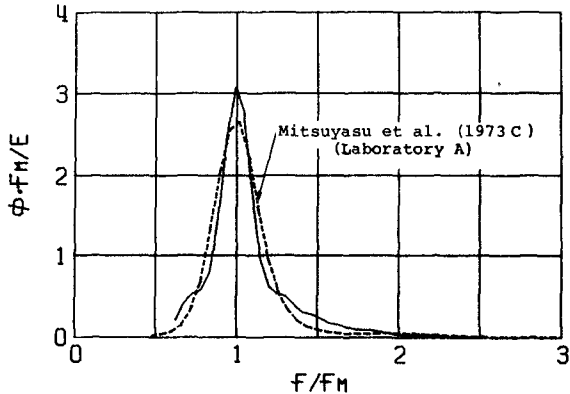


Fig.3. Normalized form of the one-dimensional wave spectrum: Continuous curve, ocean wave data set No. 430/1; dashed curve, laboratory wave data (group A).

within the range of our observed spectra, it was shown that the Pierson-Moskowitz spectrum is the spectrum with the smallest energy concentration, in other words, the spectrum with the largest spectral width. Within the range of the present data, however, a definite relation between the normalized spectral form and the dimensionless fetch has not been obtained.

Recently, a new spectral form, the JONSWAP spectrum, has been reported (Hasselmann et al. 1973). The JONSWAP spectrum has very high concentration of normalized spectral energy, which is comparable to that for laboratory wind waves. Fig.6 shows the comparison of the JONSWAP spectrum, the Pierson-Moskowitz spectrum and the idealized form of laboratory wind wave spectra (Mitsuyasu 1973b). As shown in Fig.6, the JONSWAP spectrum is quite similar to the spectra of laboratory wind waves in the normalized form (4). Therefore, we

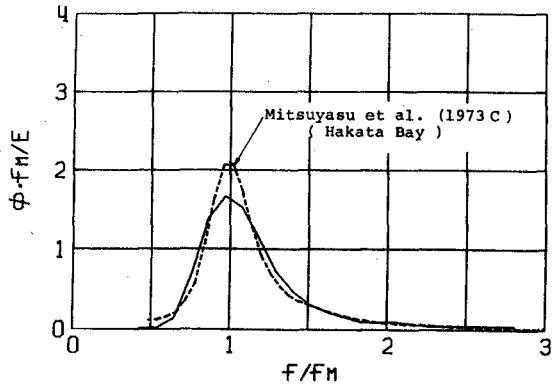


Fig.4. As in Fig.3 except for ocean wave data set No. 550/1, and the wave data of Hakata Bay (group C).

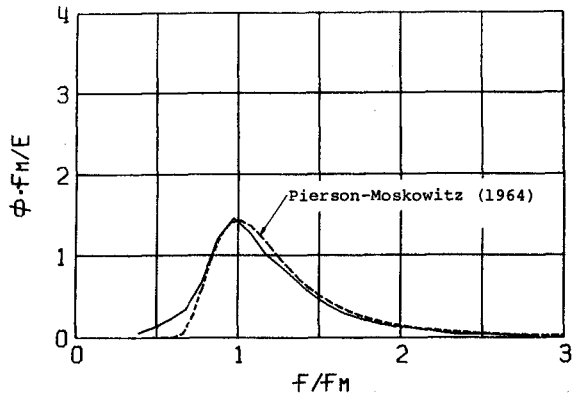


Fig.5. As in Fig.3 except for ocean wave data set No. 213/1, and the Pierson-Moskowitz spectrum.

can say that many of the ocean wave spectra scatter between the JONSWAP spectrum and the Pierson-Moskowitz spectrum. In fact, almost every wave spectra of our additional data sets 801, 804, 805 were just between these two extem forms of the wave spectra. As an example, normalized spectra of wave data No. 805 is shown in Fig.7.

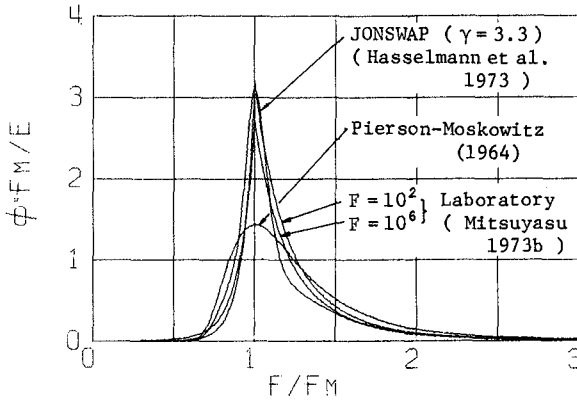


Fig.6. Similarity of the one-dimensional wave spectrum

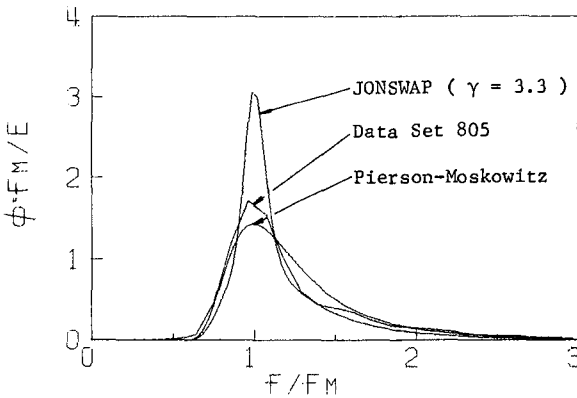


Fig.7. Normalized form of one-dimensional wave spectrum: dats set No. 805, the Pierson-Moskowitz spectrum and the JONSWAP spectrum.

b. The angular distribution function

Fig.8 shows an example of the measured angular distribution $h_4(f, \theta)$ together with $h_2(f, \theta)$ which is given by

$$h_2(f, \theta) = \frac{1}{2} + \sum_{n=1}^2 w_n' (A_n \cos n\theta + B_n \sin n\theta) \quad (6)$$

for $w_1' = \frac{2}{3}$, $w_2' = \frac{1}{6}$.

Here, $h_2(f, \theta)$ is an angular distribution which can be determined only from the signals of η_{tt} , η_x and η_y , and corresponds

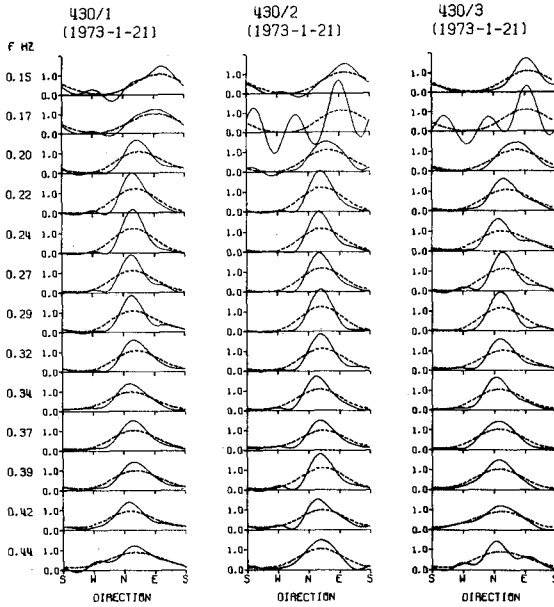


Fig.8. Angular distribution functions of the directional spectrum (wave data case 430/1, 2, 3): continuous curve, $h_4(f, \theta)$; dashed curves, $h_2(f, \theta)$.

to the data measured by a "pitch-roll buoy". Eq. 6, the partial Fourier sum with weights w_n , corresponds to the smoothed average of $h(f, \theta)$ by the weighting function $W_2(\theta)$ which is proportional to $\cos^4 \theta/2$. Since the width of $W_2(\theta)$ is approximately twice as large as that of $W_4(\theta)$, $h_2(f, \theta)$ is smoother than $h_4(f, \theta)$ as shown in Fig.8. In the figure $h(\theta)$ for each frequency component is shown separately. It can be seen from Fig.8 that $h(f, \theta)$ can be well approximated by an unimodal distribution function except for some exceptional cases which are considered to be affected by some errors.

In order to investigate $h(f, \theta)$ more quantitatively, the following function, originally proposed by Longuet-Higgins et al. (1963), is fitted to the measured angular distributions;

$$h(\theta) = G'(s) \left| \cos \frac{1}{2} (\theta - \bar{\theta}) \right|^{2s}, \quad (7)$$

where $G'(s)$ is a normalizing function to make

$$\int_0^{2\pi} h(\theta) d\theta = \pi,$$

i.e.,

$$G'(s) = 2^{2s-1} \chi \frac{\Gamma^2(s+1)}{\Gamma(2s+1)}. \quad (8)$$

The parameter s is, in a general case, a function of the wave frequency f , and $\bar{\theta}$ is the mean direction defined by

$$\bar{\theta} = \tan^{-1} B_1/A_1. \quad (9)$$

In Eq. (8) Γ is the gamma function.

The form of $h(\theta)$ given by the above equation is shown in Fig.9 for different values of s . As can be seen, $h(\theta)$ tends to a narrower distribution with an increase of the parameter s . That is, s can be

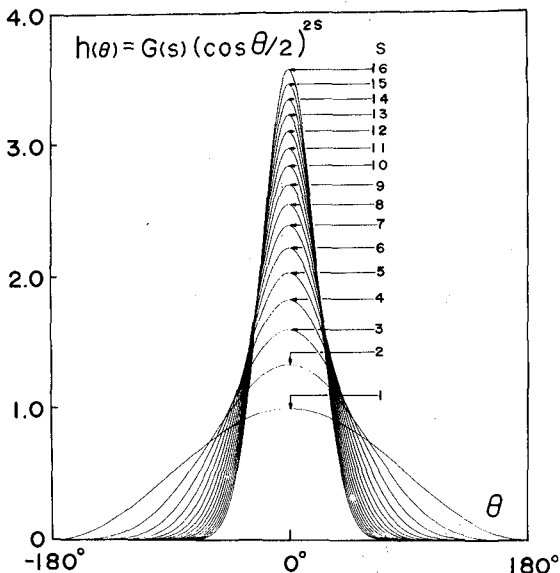


Fig.9. An idealized angular distribution function.

considered as a parameter which controls the concentration of the directional distribution of the wave energy.

If Eq. (7) were a perfect fit to the measured angular distribution, the parameter s would have to satisfy all of the expressions

$$C_n = \frac{s(s-1)\dots(s-n+1)}{(s+1)(s+2)\dots(s+n)},$$

$$n = 1, 2, 3, 4 \quad (10)$$

where

$$C_n = (A_n^2 + B_n^2)^{\frac{1}{2}} \quad (11)$$

By using Eqs. (10) and (11) the parameter s_n can be determined from the corresponding Fourier coefficients A_n and B_n , respectively, for $n = 1, 2, 3, 4$. Furthermore, if Eq. (7) were a perfect fit to the measured angular distributions, all s_n ($n = 1, 2, 3, 4$) should be equal. In fact, s_2 was found to be approximately equal to s_1 , but s_3 and s_4 were somewhat different from s_1 and s_2 . These might be attributed to the fact that the higher terms of the Fourier coefficients of angular distribution function contain non-negligible errors, due to the poor accuracy in the measurement of wave curvature. Therefore, the parameter s_1 and s_2

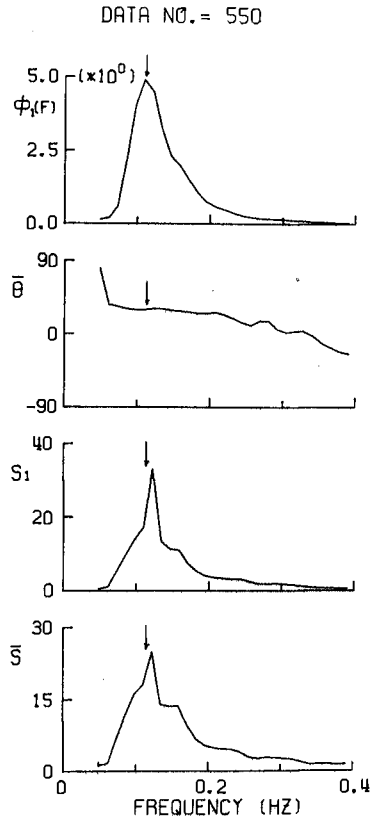


Fig.10. The one-dimensional wave spectrum $\phi_1(f)$, mean direction $\bar{\theta}$, and the spreading parameters s_1 and s for wave data set 550.

will be used for the following discussions.

Fig.10 shows typical set of values of $\phi_1(f)$, $\bar{\theta}$, s_1 and s , where s is the mean of the values of s_1 and s_2 . The location of the arrow shows the frequency of the maximum spectral density. It can be seen from this figure that the value of s_1 or s is very large near the maximum spectral density frequency. However, it decreases rapidly toward higher and lower frequencies. In other words, the angular distribution is very narrow for the frequency components near the spectral peak frequency, whereas it widens rapidly toward higher and lower frequencies. It can also be seen that the mean direction of the dominant spectral component is almost the same as that of the wind (cf. Table 1). Similar results have been obtained from the other sets of data.

Therefore, it can be said that in a generating area, frequency components near the dominant peak of the frequency spectrum, i.e., the most energy-containing frequency components, propagate in almost the same direction as the wind direction and their angular spread is very narrow. However, the angular spreading increases toward higher and lower frequencies as the spectral energy decreases.

AN IDEALIZED FORM OF THE ANGULAR DISTRIBUTION FUNCTION

In order to find the relation between the parameter s and the dimensionless frequency \tilde{f} [$= 2\pi fU/g = U/C$], s [$= (s_1+s_2)/2$] and \tilde{f} are plotted in Fig.11 on a log-log scale. It can be seen that values of the parameter s are almost uniquely determined from the dimensionless frequency \tilde{f} on the high-frequency side of the spectrum, although the data are somewhat scattered due to the insufficient accuracy of the measurements. In Fig.11 the arrow marks the location of the dimensionless frequency \tilde{f}_m that corresponds to the spectral peak frequency f_m . It can also be seen from Fig.11 that in each spectrum the parameter s shows its maximum value near \tilde{f}_m as already shown in Fig.10, and s decreases rapidly with decreasing \tilde{f} at $\tilde{f} < \tilde{f}_m$. Similar results can also be obtained from the data on s_1 .

These facts suggest that for the high-frequency side of the spectrum the parameter s shows an equilibrium form which is given approximately by

$$s = 11.5 \tilde{f}^{-2.5} . \quad (12)$$

In the frequency range below the spectral peak, $\tilde{f} < \tilde{f}_m$, an approximate expression for s can be given by

$$s = k \tilde{f}^m, \quad (13)$$

where k and m are dimensionless constants. The power m in the above expression seems to depend somewhat on \tilde{f}_m . That is, as shown in Fig.11, m is slightly larger in the cases of smaller \tilde{f}_m than in those of larger \tilde{f}_m . At this time, however, since the scatter of the data are considerable, these differences in m are neglected and m is assumed to be

$$m = 5.$$

The constant k can be determined from the condition that s has its maximum value s_m at \tilde{f}_m where Eq. (13) coincides with Eq. (12).

Approximate expressions for s for $\tilde{f} < \tilde{f}_m$ and for s_m are

$$s = 11.5 \tilde{f}_m^{-7.5} \tilde{f}^5, \quad (14)$$

$$s_m = 11.5 \tilde{f}_m^{-2.5}. \quad (15)$$

On the other hand, the dimensionless frequency \tilde{f}_m of the spectral peak can be determined from the dimensionless fetch $F [= gF/U^2]$ by using the so-called fetch relation. For example, the fetch relation (Mitsuyasu 1968)

$$\tilde{f}_m = 1.00 \hat{F}^{-0.330}, \quad (16)$$

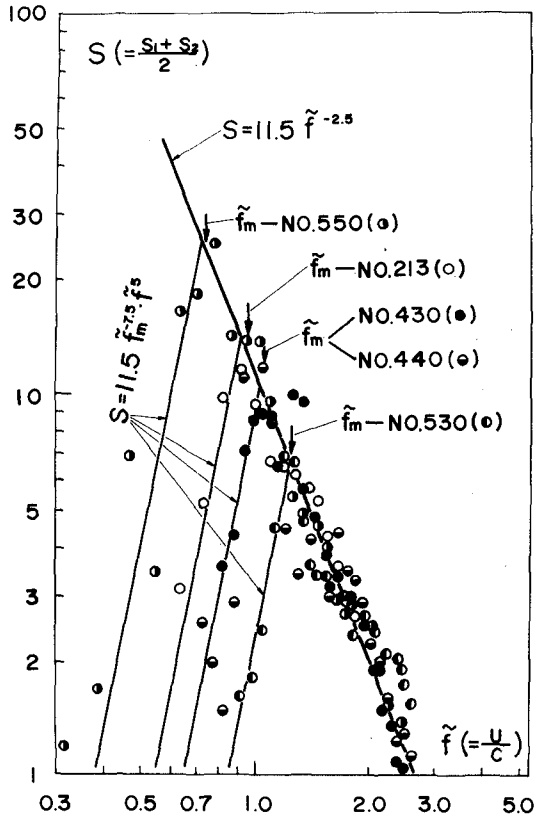


Fig.11. The parameter s as a function of the dimensionless frequency \tilde{f} . \tilde{f}_m is the dimensionless frequency of the maximum density of the one-dimensional wave spectrum.

where

$$\hat{f}_m = u_* f_m / g, \quad \hat{F} = gF / u_*^2 \quad (17)$$

where u_* is the friction velocity of the wind, can be transformed into

$$\hat{f}_m = 18.8 \hat{F}^{-0.330} \quad (18)$$

by using the approximate relation

$$25 u_* = U_{10} = U. \quad (19)$$

From Eqs. (7), (12), (14) and (18) we can derive an idealized form of the angular distribution function that can be used for practical purposes. That is, the angular distribution is given by

$$G_1(f, \theta) = G_1(s) |\cos \theta / 2|^{2s} \quad (20)$$

where

$$G_1(s) = \frac{1}{\pi} 2^{2s-1} \frac{\Gamma^2(s+1)}{\Gamma(2s+1)}. \quad (21)$$

The parameter s is given by Eq. (12) for $\hat{f} > \hat{f}_m$ and by Eq. (14) for $\hat{f} < \hat{f}_m$, and \hat{f}_m can be determined from Eq. (18). Fig.12 shows further check of the proposed relations (12) and (14) by the data sets 801, 804 and 805. Coincidence between the prediction and observation is generally satisfactory.

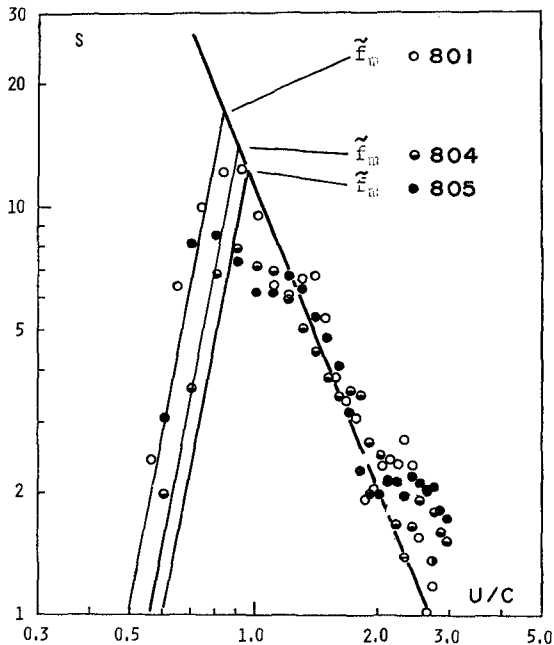


Fig.12. As in Fig.11 except for wave data sets No.801, 804 and 805.

From Eqs. (12), (14) and (15) the other expressions for s are as follows:

$$s/s_m = (\tilde{f}/\tilde{f}_m)^{-2.5}, \quad \text{for } \tilde{f} \geq \tilde{f}_m, \quad (22)$$

$$s/s_m = (\tilde{f}/\tilde{f}_m)^5, \quad \text{for } \tilde{f} \leq \tilde{f}_m. \quad (23)$$

It should be mentioned here that the parameter s at the spectral peak frequency f_m increases with an increase in the dimensionless fetch \tilde{F} . In other words, the angular distribution becomes narrower as the dimensionless fetch increases. This is a rather unexpected result, because it would appear that the angular distribution should broaden with increasing fetch due to the fluctuation of the wind direction in a generating area.

COMPARISON OF VARIOUS ANGULAR DISTRIBUTION FUNCTIONS

Finally, the proposed form of the angular distribution

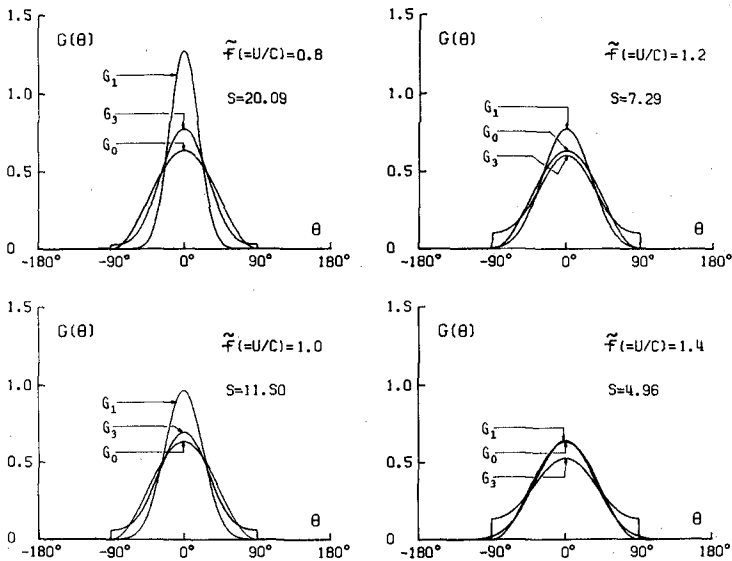


Fig.13. The angular distribution functions $G_0 = (2/\pi)\cos^2\theta$; G_1 , proposed spectrum and G_3 , SWOP spectrum, as a function of the dimensionless frequency \tilde{f} .

function, $G_1(f, \theta)$, is compared with the other forms which have been used frequently for practical purposes. Typical forms of the angular distribution are

1. PNJ type (Pierson et al., 1955)

$$G_0(\theta) = \frac{2}{\pi} \cos^2 \theta \quad (24)$$

2. SWOP spectrum (Coté et al., 1960)

$$G_3(f, \theta) = \begin{cases} \frac{1}{\pi} (1 + a \cos 2\theta + b \cos 4\theta), & \text{for } |\theta| \leq \pi/2 \\ 0, & \text{for } |\theta| > \pi/2 \end{cases} \quad (25)$$

where

$$a = 0.50 + 0.82 \exp \left(-\frac{1}{2} \tilde{f}^4 \right) \quad (26)$$

$$b = 0.32 \exp \left(-\frac{1}{2} \tilde{f}^4 \right). \quad (27)$$

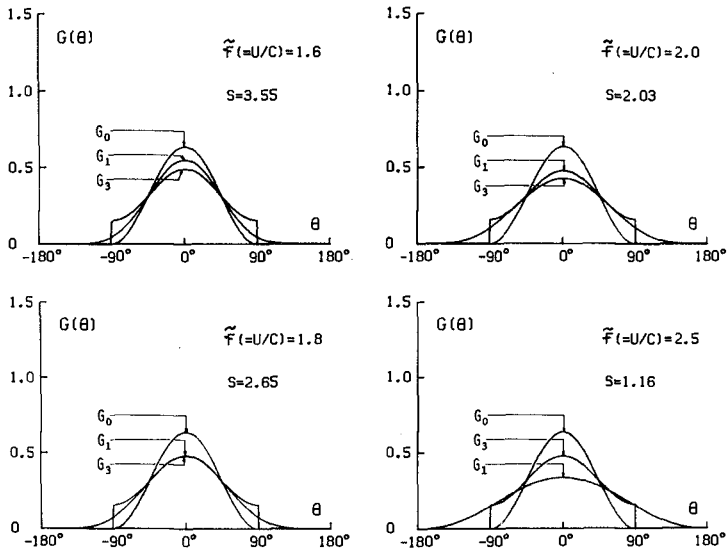


Fig.14. As in Fig.13 for other values of \tilde{f} .

Figs. 13 and 14 show the comparisons of the various forms for the angular distribution functions, $G_0(\theta)$, $G_1(f, \theta)$ and $G_3(f, \theta)$, by taking $\tilde{f} [= U/C]$ as a parameter. Here, $G_1(f, \theta)$ shown in the figures corresponds to angular distributions of the spectral components in a frequency range $\tilde{f} > \tilde{f}_m$. It can be seen from Figs. 13 and 14 that $G_0(\theta)$ is an appropriate form for the spectral components near the frequency $\tilde{f} [= U/C] \doteq 1.5$, but it has a wider angular distribution for the frequency components $\tilde{f} < 1.5$ and narrower angular distribution for the frequency components $\tilde{f} > 1.5$, as compared $G_1(f, \theta)$; $G_3(f, \theta)$ is very close to $G_1(f, \theta)$ for the frequency components $\tilde{f} \doteq 1.8-2.0$, although there exist some discontinuities of the distributions at $|\theta| = \pi/2$. Furthermore, $G_3(f, \theta)$ shows a wider angular distribution for the frequency components $\tilde{f} < 1.8$ and a narrower angular distribution for $\tilde{f} > 2.0$.

In some cases the following form of the angular distribution function has been used for practical purposes:

$$G_2(f, \theta) = G_2'(n) \cos^n \theta, \quad (28)$$

where

$$G_2'(n) = \frac{1}{\pi^{\frac{1}{2}}} \frac{\Gamma(1 + \frac{n}{2})}{\Gamma(\frac{1}{2} + \frac{n}{2})}. \quad (29)$$

It can be shown by comparing $G_2(f, \theta)$ with $G_1(f, \theta)$ that $G_2(f, \theta)$ becomes very close to $G_1(f, \theta)$ if we assume

$$n = 0.46 s, \quad (30)$$

and use Eqs. 12 and 14 for the values of s . The relation (30) is only an approximate relation which gives consistent results for the frequency components $\tilde{f} < 1.6$ or $s > 4$.

CONCLUSIONS

Using typical wave data measured by the cloverleaf buoy we have determined the directional spectrum of ocean waves, in particular, the form of the one-dimensional frequency spectrum and that of the angular distribution function. While final conclusions have not been obtained for the frequency spectrum, an idealized form of the angular distribution function has been determined, which can be used for practical purposes.

The most important findings of the present study are the following properties of the angular distribution of wave energy. The angular distribution is very narrow for the frequency components near the spectral peak, whereas it widens

toward high and low frequencies. Furthermore, the angular distributions of the frequency components near the spectral peak become narrower with increasing dimensionless fetch and, thus, with the growth of the wind waves. These properties are included in the proposed form of the idealized angular distribution function. Finally, it should be mentioned that, in many cases, the variabilities in the angular distribution functions are fairly large. Particularly, the scatter of the parameter s is considerable for the low frequency components ($f < f_m$) of the spectrum. This may be attributed to the effects of background swell and nonlinear wave-wave interactions. It should be also mentioned that the idealized form of the angular distribution function is based only on the ocean wave data and not on the laboratory wave data. Therefore, the extension of the formula to the laboratory wind wave is uncommendable.

ACKNOWLEDGEMENTS

Basic data used in the present study were obtained in a project entitled "Studies on techniques for ocean wave measurements". We are grateful to many members of this project, particularly, to Prof. F. Tasai and Prof. T. Suhara. We also wish to acknowledge to Mr. K. Eto and Mr. M. Tanaka for their constant supports in the study, and Miss N. Uraguchi for typing the manuscript.

REFERENCES

- Cartwright, D. E. and N. D. Smith, 1964: Buoy techniques for obtaining directional wave spectra. *Buoy Technology*, Washington, D.C., Marine Tech. Soc., 112-121.
- Coté, L. J., J. O. Davis, W. Marks, R. J. McGough, E. Mehr, W. J. Pierson, Jr., J. F. Ropek, G. Stephenson and R. C. Vetter, 1960: The directional spectrum of a wind-generated sea as determined from data obtained by the Stereo Wave Observation Project. *Meteor. Papers*, 2, No.6, New York University, 88pp.
- Ewing, J. A., 1969: Some measurements of the directional wave spectrum. *J. Marine Res.*, 27, 163-171.
- Hasselmann, K. et al., 1973: Measurements of wind-wave growth and swell decay during the Joint North Sea Wave Project (JONSWAP). *Deut. Hydrogr. Z.*, 12, 1-95.
- Longuet-Higgins, M. S., D. E. Cartwright and N. D. Smith, 1963: Observations of the directional spectrum of sea waves using the motions of a floating buoy. *Proc. Conf. Ocean Wave Spectra*, Prentice-Hall, 111-132.

- Mitsuyasu, H., 1968: On the growth of the spectrum of wind-generated waves (1). Rep. Res. Inst. Appl. Mech. Kyushu Univ., 16, No.55, 459-482.
- Mitsuyasu, H., F. Tasai, T. Suhara, S. Mizuno, M. Ohkusu, T. Honda, K. Rikiishi, M. Takagi and H. Hiyama, 1973a: Studies on techniques for ocean wave measurements (1). Bull. Res. Inst. Appl. Mech., Kyushu Univ., No.39, 105-181.
- Mitsuyasu, H., 1973b: The one-dimensional wave spectra at limited fetch, Rep. Res. Inst. Appl. Mech. Kyushu Univ., Vol. XX, No.66, 37-53.
- Mitsuyasu, H., F. Tasai, J. Okabe, T. Suhara, S. Taneda and T. Honda, 1973c: Laboratory simulation of ocean waves. Bull. Res. Inst. Appl. Mech., Kyushu Univ., No.39, 183-210.
- Mitsuyasu, H., F. Tasai, T. Suhara, S. Mizuno, M. Ohkusu, T. Honda and K. Rikiishi, 1975: Observations of the directional spectrum of ocean waves using a cloverleaf buoy., J. Phys. Oceanogr., Vol.5, No.4, 750-760.
- Pierson, W. J. and L. Moskowitz, 1964: A proposed spectral form for fully developed wind seas based on the similarity theory of S. A. Kitaigorodskii., J. Geophys. Res., 69, 5191-5203.
- Pierson, W. J., G. Neumann and R. W. James, 1955: Practical methods for observing and forecasting ocean waves by means of wave spectra and statistics. H. O. Publ. 603, U. S. Navy Hydrographic Office.
- Tyler, G. L. et al., 1974: Wave directional spectra from synthetic aperture observations of radio scatter. Deep Sea Res., 22, 987-1016.

CHAPTER 20

WAVE DIRECTION COMPUTATIONS WITH THREE GAGE ARRAYS

by

D. Esteva¹

INTRODUCTION. Wave direction is an important parameter in the solution of many coastal engineering problems such as the estimation of sediment transport and the response of coastal structures. Wave-gage arrays are among the most widely proposed systems for measuring wave direction. In late March 1970, the U.S. Army Coastal Engineering Research Center (CERC) installed an array of five pressure sensors off the California coast.

Figure 1 gives the location of the array, its geometry and dimensions. The water depth at the site was approximately 9.14 meters (30 feet) and the gages were positioned .76 meters (2.5 feet) from the bottom.

One use for the array data would be to compare redundant values of wave direction and estimate the level of accuracy of the computations. Redundant values of direction were obtained from the ten three-gage arrays possible with five gages. Three-gage arrays offer some advantages over arrays involving a larger number of gages and have been proposed by many investigators. An obvious advantage involves economics. Non-linear arrays offer the advantage over linear arrays that straight forward mathematical expressions can be derived for the unambiguous computation of direction. These expressions involve the phase differences between gage pairs for the waves present, no recourse to two-dimensional spectral analysis is necessary. However, it is necessary to assume long and relatively straight crested waves, traveling in well determined directions, and geometrically stationary over the array. The first two assumptions are supported by high altitude aerial photographs, Figure 2 and, by radar scans of the wave field, Figure 3. Fujinawa (1975) conjectures that narrow directional spread is responsible for the incomplete recovery of the true directional spectrum from field records in his computations using high directional resolution.

Direction estimates for all bands .01 hz wide between approximately 30 and 3 seconds were obtained from the ten arrays using cross spectra between gage pairs. The lower limit on period is estimated from the water column over the pressure sensors. The resulting directions at bands of maximum energy disagreed by 20° to 160° . It had been expected that the array would yield directions to better than 20° .

¹Mathematician/Oceanographer, U.S. Army Coastal Engineering Research Center, Ft. Belvoir, VA

The computational model was applied to computer simulated narrow-banded wave trains propagating across the array. Because of the narrow-bandedness of the simulated trains, the frequency resolution used in these computations was increased to approximately .001 hz. It was found that the directional results depend highly on the spectral width, both, in frequency and direction, of the wave train involved and on the relationship between wavelength at the site and gage separations.

The same higher frequency resolution was used to analyze field wave pressure records having standard deviations above 2 feet. Average discrepancies of 20 degrees among computed directions were obtained for narrow-banded trains with periods longer than 10 seconds. Larger discrepancies resulted for shorter periods. Thus, accuracies no better than 20 degrees can be expected for wave directions resulting from three-gage arrays.

ARRAY OPERATION AND DATA SUMMARY. The gages in the array were developed mostly at CERC. The heart of the system is a Fairchild pressure transducer which is potted inside a two-inch plexiglass tube, (Williams 69, Peacock 74). A plastic tube filled with silicone oil transmits the sea water pressure to the transducer. A rubber diaphragm separates the silicone oil from the sea water. A teflon scouring pad dipped in anti-fouling paint separates this rubber diaphragm from the end of the package which admits the sea water pressure. The instrument is mounted vertically on a tripod. The signals from the pressure transducers are brought by cables to a recording and transmitting station on shore.

The water pressure at each of the five gages was registered continuously at four samples per second on digital magnetic tape. The recording proceeded with few interruptions during most of 1970. It can be shown (Kinsman, 1965), that the potential energy in the wave field is proportional to the variance of the time history of sea surface elevation at a fixed location. This energy is also proportional to the square of the wave height. Thus, the standard deviation of sea surface elevations (or of the pressure at a certain depth) is a good measure of wave height. Four times the standard deviation approximately equals the significant wave height.

The standard deviation of the wave pressure in each gage was computed for observations consisting of simultaneous 20-minute recordings. The mean standard deviation was found for each observation. Table 1 gives a breakdown of the largest difference of individual standard deviations in an observation from their mean for 871 observations processed in 1970 regardless of magnitude. This breakdown indicates the system operated in a consistent way. The field wave records used for computing wave direction were chosen from those observations in this Table for which the standard deviations in the five gages differed by 3% or less from their mean and for which the uncompensated significant wave height was above 2 feet.

TABLE 1. PERCENT OF OBSERVATIONS FOR WHICH THE LARGEST DEVIATION OF INDIVIDUAL STANDARD DEVIATION IN THE OBSERVATION FROM THEIR MEAN WAS AS INDICATED. EIGHT-HUNDRED AND 71 OBSERVATIONS IN 1970.

Deviation from mean	Percent of Observations
$\leq 2\%$	41
(3 - 10%)	52
(11 - 20%)	1
$\geq 20\%$	6

COMPUTATION OF WAVE DIRECTION

For a long crested sinusoidal wave with frequency σ_i , propagating in direction α_i , the phase difference between locations 1 and 2 with coordinates (x_1, y_1) and (x_2, y_2) respectively, is given by:

$$\phi_{12} = K_i [(x_1 - x_2) \cos \alpha_i + (y_1 - y_2) \sin \alpha_i] \quad (1)$$

where $K_i = 2\pi/L_i$, is the wave number associated with frequency σ_i , and L_i is the wave length.

Expressions for the phase differences between two pairs of gages in a three-gage array allow solving for the sine and cosine of the direction of wave travel α_i . Thus the angle is determined uniquely. Estimates of a representative phase difference between gage pairs for bands of constant frequency width are easily computed from cross-spectra of the wave (pressure) records. These spectra give average values of the covariance of the wave records along two perpendicular directions for each band. The expediency in these computations is appealing provided the resulting directions are of engineering value.

The co-spectrum (Co) and quad spectrum (Quad) may be defined as, (Jensen and Watts, 1968):

$$C_{o\Delta} = \sum_{\Delta} X_1 X_2 \cos \phi_{12}$$

$$Quad_{\Delta} = \sum_{\Delta} X_1 X_2 \sin \phi_{12} \quad (2)$$

where X_1 and X_2 are the frequency spectral estimates from wave records 1 and 2 and the \sum_{Δ} indicates summation over the adjacent spectral periods combined

to make up a band. The representative phase difference for the band is given by expression 3 below, where the sign of numerator and denominator must be taken into account.

$$\phi_{12\Delta} = \tan^{-1} \left[\frac{\text{Quad}_{\Delta}}{\text{Co}_{\Delta}} \right] \quad (3)$$

Cross spectra between gage pairs were computed for bands approximately .01 hz wide for a few observations. A representative wave direction was computed for each band between 30 and 3 seconds for the 10, arrays. The agreement among these redundant values is an indication of the degree of confidence that can be placed on the resulting directions.

Disagreements on the order of 20° were obtained for bands of maximum energy with central periods above 10 seconds. For bands with maximum energy at shorter central periods disagreements on the order of 160° were obtained.

It had been expected that the array would yield directions to better than 20 degrees and for periods between 25 and 7 seconds.

SIMULATED OBSERVATIONS

To gain understanding of the problems involved, wave records arising from narrow-banded wave trains propagating through the array in a specified direction were simulated in the computer. Each simulated observation consisted of values of the wave profile at the five locations computed at 1/4 second intervals for slightly over 17 minutes (1024 seconds) to simulate the sampling rate and record duration customarily used at CERC for the field data.

Fast Fourier Transform (Cooley and Tukey 1967) computations yield the contribution to the variance at each of a set of frequencies ω_m 's, which are harmonics of a fundamental given by the inverse of the record duration, T. The frequencies of these harmonics will be referred to as *spectral frequencies* and the corresponding periods, given by their inverse the *spectral periods*. The resulting spectrum will be termed the *high resolution spectrum*. For records 1024 seconds in duration, this high resolution approximately equals .001 hz.

Assume a sinusoid with frequency given by

$$\sigma = \frac{2\pi(m + \delta)}{N\Delta t} \quad (4)$$

where Δt is the interval of time between samples and δ is less than or equal to 1/2. This expression provides for assigning frequencies which

differ from the spectral frequencies. The contribution to the variance at the spectral frequencies, of the sampled record is given by:

$$S_m^2 = a_m^2 + b_m^2 \quad m = 1, \dots, N/2 \quad (5)$$

where a_m and b_m are the Fourier coefficients. Harris shows (Harris 1974) that for values of m near \hat{m} ; i.e., for ω_m near the frequency of the sinusoid, and for \hat{m} far removed from one and $N/2$, the expressions below are good approximations to the coefficients.

$$a_m \approx \frac{A \sin \pi \delta \cos (\phi - \pi \delta)}{\pi (\hat{m} - m + \delta)} \quad (6)$$

$$b_m \approx \frac{A \sin \pi \delta \sin (\phi - \pi \delta)}{\pi (\hat{m} - m + \delta)}$$

It is clear that slow convergence of the energy toward the spectral period closest to the assigned period is indicated. Thus the energy is spread over adjacent spectral periods. This spreading, due to the finiteness of the record is usually referred to as spillover.

The technique routinely used at CERC to decrease spillover is to apply the cosine bell data window as indicated below:

$$\hat{Y}_i = \frac{1}{2} \left(1 - \cos \frac{2\pi t_i}{T} \right) Y_i \quad i = 1, \dots, N \quad (7)$$

where Y_i are the values in the original record. The Fourier coefficient for the resulting \hat{Y}_i are given by:

$$\hat{a}_m \approx \frac{A \sin \pi \delta \cos (\phi - \pi \delta)}{2\pi (\hat{m} - m + \delta) [(m - m + \delta)^2 - 1]} \quad (8)$$

$$\hat{b}_m \approx \frac{A \sin \pi \delta \sin (\phi - \pi \delta)}{2\pi (\hat{m} - m + \delta) [(m - m + \delta)^2 - 1]}$$

Thus convergence is greatly increased and spillover is effectively reduced to three adjacent spectral periods.

The cosine bell data window was applied to all records discussed here. Thus, in simulating records it was sufficient to consider wave trains consisting of three sinusoids with nearby periods spread over at most six adjacent spectral periods. Central periods near 16 and eight seconds were chosen to simulate a relatively long period swell and a shorter period swell. Swells with these periods are common in the West Coast.

Figures 4 and 5 are plots of the high resolution spectra for two of the simulated observations. Energy density at each spectral frequency is plotted versus a linear frequency scale in Hz. The corresponding period values are given along the top axis. All of the spectral plots shown here have been plotted in the same way and to the same scale. The spectra in these two figures resulted from combining only three sinusoids; yet, energy contributions appear at from five to nine adjacent periods. In Figure 4 three relative maxima separated by two minima can be identified. The energy shown at these two minima may be interpreted as due to spillover since no sinusoids were combined with the appropriate periods.

Energy minima can easily be identified in the high resolution spectra of field wave observations. The energy at these minima may be used as a measure of spillover and noise in these spectra.

Table 2 gives the characteristics of the first eight simulated observations and Table 3 the computational results at spectral periods closest to the assigned periods.

The last column in Table 3 gives the average resulting directions from the ten arrays. For wave trains 1 thru 3 the computed directions agree for the ten arrays and with the input directions to within 1 degree. Directional results for wave train No. 4 are correct only for spectral period number 62. The main difference between this train and No. 2 is the narrower spectral width. Wave train No. 2 gave the correct direction for all spectral periods while No. 4 did not.

Directional results seem meaningless for simulated wave trains 5 through 8. To determine whether these poor results were due to some programming deficiency another eight sets of simulated records were generated interchanging periods and directions.

The directional results for the sinusoids with periods clustered around 16 seconds were of the same quality regardless of the assigned direction. The directional results for the 8 second sinusoids, however, indicate that the capability to sense the correct direction for these shorter waves depends on the orientation of the three-gage array relative to the direction of propagation of the incoming wave. This is not surprising when it is realized that the effective gage separation for the different gage pairs varies with this relative orientation.

Additional simulated records were generated using the same periods as for observation No. 5 but assigning the additional directions listed in

Table 4. At the top of each column the orientation and shape of the corresponding array is given. Computed directions omitted differed by 87° and more from the assigned directions listed on the left hand column. It is apparent from Table 4 that the more nearly equilateral arrays give correct directions for a wider range of periods.

TABLE 2. CHARACTERISTICS OF SIMULATED WAVE TRAINS

Wave Train	Period (sec)	Amp. (cm)	Direction (degrees)
1	16.75..	11.43	21 S
	15.97...	15.24	21 S
	15.25...	11.43	21 S
2	16.75..	11.43	21 S
	15.97...	15.24	15 S
	15.25...	11.43	21 N
3	16.48..	11.43	21 S
	15.97..	15.24	21 S
	15.72..	11.43	21 S
4	16.48..	11.43	21 S
	15.97..	15.24	21 N
	15.72..	11.43	21 N
5	8.18..	11.43	60 N
	7.99..	15.24	60 N
	7.80..	11.43	60 N
6	8.18..	11.43	60 N
	7.99..	15.24	40 N
	7.80..	11.43	60 S
7	8.11..	11.43	60 N
	7.99..	15.24	60 N
	7.93..	11.43	60 N
8	8.11..	11.43	60 N
	7.99..	15.24	40 N
	7.93..	11.43	60-S

The effect of angular spread in the 16 second wave train was investigated by introducing angular spreads among assigned directions and keeping frequency separations among sinusoids constant (three spectral frequencies). Input angular spreads of 5° , 10° , and 20° gave rise to angular spreads of 0° , 16° , and 32° respectively.

FIELD WAVE OBSERVATIONS

To better evaluate directional results from field observations, spectral periods at or near which wave trains may be present in the field were isolated in the high resolution spectra of 44 field observations. The

average uncompensated significant wave height in each observation was over two feet and discrepancies of individual standard deviations from their mean was 3% or less.

TABLE 3. COMPUTATIONAL RESULTS AT CLOSEST SPECTRAL FREQUENCIES FOR SIMULATED WAVE TRAINS

Wave Train	Closest Spectral Frequency (1/024 hz)	Spectral Period (sec)	Amp. (cm)	Direction (degrees)
1	61	16.79	5.62	20 S
	64	16.00	7.55	20 S
	67	15.28	5.70	20 S
2	61	16.79	5.62	21 S
	64	16.00	7.55	15 S
	67	15.28	5.70	20 N
3	62	16.52	5.52	20 S
	64	16.00	5.35	20 S
	65	15.75	1.19	20 S
4	62	16.52	5.52	21 S
	64	16.00	5.35	25 S
	65	15.75	1.19	36 N
5	125	8.19	5.62	142 N
	128	8.00	7.55	142 N
	131	7.82	5.70	142 N
6	125	8.19	5.62	142 N
	128	8.00	7.55	78 N
	131	7.82	5.70	162 S
7	126	8.13	5.52	142 N
	128	8.00	5.35	142 N
	129	7.94	1.19	142 N
8	126	8.13	5.52	142 N
	128	8.00	7.14	76 N
	129	7.94	5.83	172 S

Plots of the high resolution spectra for these observations will be published in a CERC Technical Report. Figures 6 and 7 are shown here to illustrate the two typical spectral shapes obtained. The spectra on Figure 6 show most of the energy between approximately 13 and 18 seconds. The

Assigned Direction Degrees	Three-Gage Arrays									
	1-2-3	1-2-4	1-2-5	1-3-4	1-3-5	1-4-5	2-3-4	2-3-5	2-4-5	3-4-5
60 N				59 N	60 N	59 N		60 N		60 N
40 N	40 N	40 N	40 N	40 N	40 N	40 N		40 N		39 N
21 N	21 N	20 N	21 N	21 N	20 N	20 N		21 N		20 N
15 N	14 N	14 N	14 N	14 N	14 N	14 N		14 N		15 N
15 S	14 S	14 S		14 S			14 S	14 S	14 S	15 S
21 S	21 S	20 S		20 S			20 S	20 S	20 S	20 S
40 S	40 S	39 S		39 S			39 S	40 S	39 S	39 S
60 S				60 S			60 S	59 S	59 S	60 S

Table 4 Directional results of high resolution spectral computations for 2 second wave.

Results differing by 87° or more from the assigned directions on the left hand column have been omitted.

structure suggests more than one wave train present in that period range. The spectra in Figure 7 display bimodality - a large portion of the energy appearing at shorter periods. A "background" energy was estimated for each observation by systematically averaging the energy at minima between 25 and seven seconds in the spectrum. Adjacent spectral periods in this range showing energy content twice the background or above were identified and considered arising from the same wave train. The number of adjacent periods in each train was used as a measure of the *spectral width* of the train. The energy had to be above the chosen level at all five gages for the spectral period to be included in the group. The spectral period among these showing maximum energy was taken as the "period" of the wave train.

Directions were computed at all the spectral periods in each train for the ten arrays. The total spread among these directions was found; and, an average total spread was computed for trains having the same spectral width. The same was done for the spread in computed directions at the "period" of the train.

Twenty-five percent (25%) of the identified wave trains had total directional (computed) spreads above 100° and were not considered any further. For 89% of the discarded trains, the "period" of the train was under 9.4 seconds. Thus trains with "period" under this value were also discarded.

Table 5 shows the results for the different spectral widths for the 280 trains retained.

TABLE 5. AVERAGE SPREAD IN COMPUTED DIRECTIONS FOR 280 WAVE TRAINS IDENTIFIED IN THE HIGH RESOLUTION SPECTRUM OF 44 FIELD WAVE OBSERVATIONS

Spectral Width (hz)	Average Total Spread in Direction (for all Periods) (Degrees)	Average Spread in Direction for "Period" of Train (Degree)	No. of Cases
.001		21.8	96
.002	30.9	22.9	58
.003	33.6	20.2	41
.004	41.5	20.4	22
.005	38.7	19.8	21
.006	43.8	19.8	16
.007	48.2	17.0	5
.008	84.5	17.6	8
.009	53.0	15.3	6
.010	49.3	13.7	3
.011	38.0	18.0	1
.012	81.0	15.0	1
.013	48.5	15.2	2

These results indicate that narrow peaks consisting of from one to three spectral periods are most frequent. The total spread in direction increases with frequency width. The spread in the direction at the "period" of the train remains relatively constant. Since the average spread at this "period" for narrow-banded trains ($< .003$ hz) is 21.8 degrees; it is to be expected that three-gage arrays cannot yield directional results to any better accuracy.

There are various possible explanations for the large spreads observed in the directions computed from field records. For the long crested wave model to be applicable, it is important that:

- o The phase differences be known accurately or that the probable error in their computed values be known; from expressions 6 and 8 it is clear that the analysis yields accurate phase differences for strictly monochromatic conditions. For each component with nearby period in a wave train the value of δ in expressions 6 (or 8) will be different; thus, no accurate value of the phase difference for the train nor of the error involved can be estimated;
- o the wave crests over the array site be long and straight; waves with periods between 20 and eight seconds had and are undergoing refraction at the site of the array; thus, their crests are not exactly straight; for the longer waves, with wave lengths at the array site several times the gage separations, the curvature will not introduce much error; this is not the case for the shorter waves, and orientation of the array becomes important;
- o the sea surface be stationary in time for the duration of the record, and in space over the span of the array. Stationarity of the wave field is assumed in most wave directional models. The extent and frequency of its applicability either in the open ocean or in coastal waters has not been established.

These three factors are sufficient to account for the discrepancies found in computed directions.

CONCLUSIONS

The results of directional computations both for simulated and field wave data records indicate three-gage arrays have some capability to determine wave direction under certain conditions. This capability depends on:

- o the dimension of the array and the water depth at the site which

place a lower limit on the wave period for which possibly accurate directions may be computed;

- o the orientation of the array for the shorter periods;
- o the nature of the wave field; directional results for wave trains with a narrow frequency distribution and/or for which the computed directions differ little at adjacent spectral periods might be meaningful.

For wave trains with narrow frequency and directional spreads; and, period above 10 seconds, the Pt. Mugu arrays yield directions to an estimated accuracy of 20° .

Bibliography

- Borgman, L. E. and Panicker, N. N., "Design Study for A Suggested Wave Gage Array off Point Mugu, California," Technical Report HEL 1-14 University of California, Hydraulic Engineering Laboratory, Berkeley, California, January 1970.
- Cooley, J. W. and Tukey, J. W., "The Fast Fourier Transform," IEEE Spectrum, Vol. 4, pp 63-70, 1967.
- Fujinawa, Yukio, "Measurement of Directional Spectrum of Wind Waves Using An Array of Wave Detectors" - Journal of the Oceanographical Society of Japan, Vol. 30, pp 10-22, 1974.
- Fujinawa, Yukio, "Measurement of Directional Spectrum of Wind Waves Using An Array of Wave Detectors Part II - Field Observations" - Journal of the Oceanographical Society of Japan, Vol. 31, pp 25-42, 1975.
- Harris, D. Lee, "Finite Spectrum Analyses of Wave Records," International Symposium on Ocean Wave Measurement and Analysis, September 9-11, 1974, New Orleans, Louisiana.
- Jenkins and Watts, "Spectral Analysis and Its Applications," Holden-Day, 1968.
- Kinsman, B., "Wind Waves," Prentice-Hall, Inc., Englewood Cliffs, New Jersey, 1965.
- Peacock, Harold C., "CERC Field Wave Gaging Program," Proceedings of the International Symposium on Ocean Wave Measurement and Analysis, September 1974, New Orleans, Louisiana, USA.
- Williams, Leo C., Technical Memorandum No. 30, U.S. Army Corps of Engineers, Coastal Engineering Research Center, December 1969.

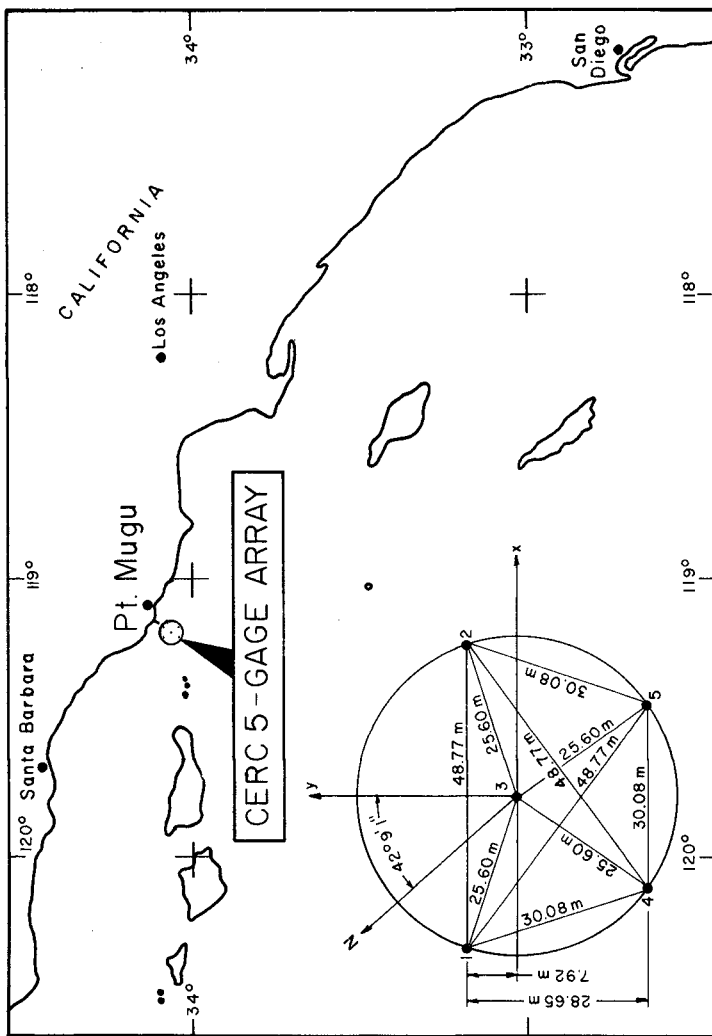


FIGURE 1. LOCATION, GEOMETRY, AND DIMENSIONS OF FIVE-GAGE ARRAY.



FIGURE 2. AERIAL PHOTO OF WAVE FIELD. PT. SAINT GEORGE,
CALIFORNIA.



FIGURE 3. RADAR SCAN OF WAVE FIELD AT NAUSET, MASSACHUSETTS.

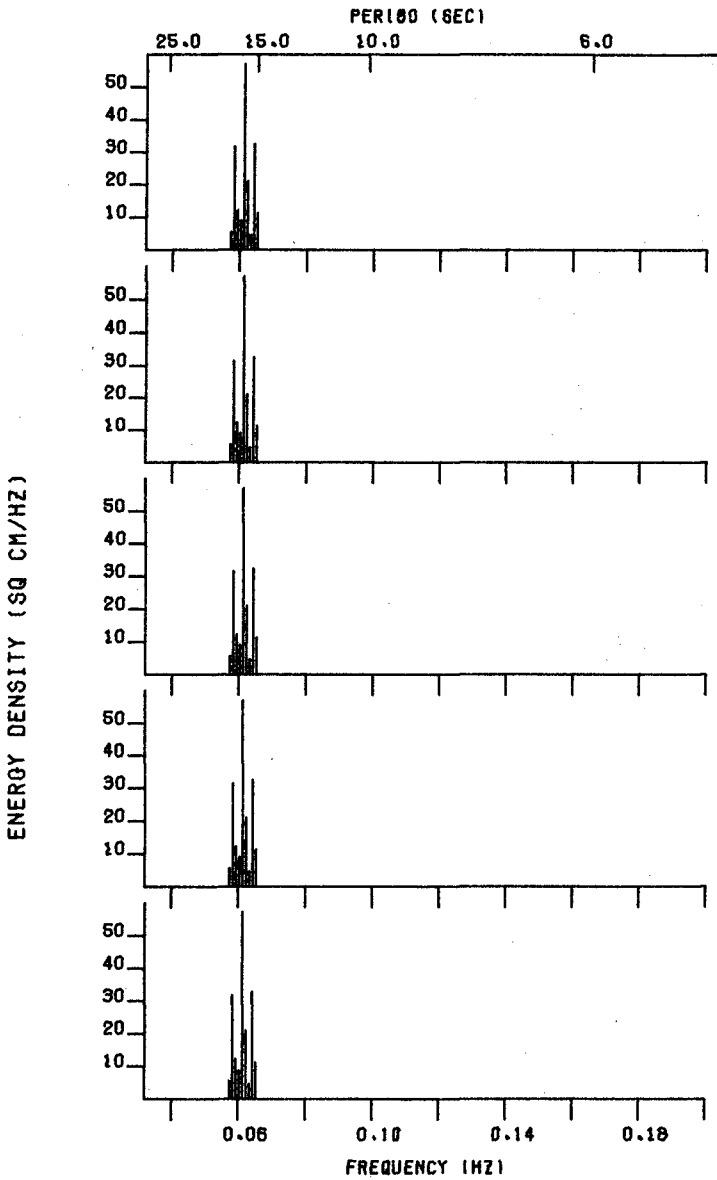


FIGURE 4. HIGH RESOLUTION SPECTRA PRESSURE GAGES ONE THRU FIVE POINT MUGU, CALIFORNIA, SIMULATED OBSERVATION NO. 1.

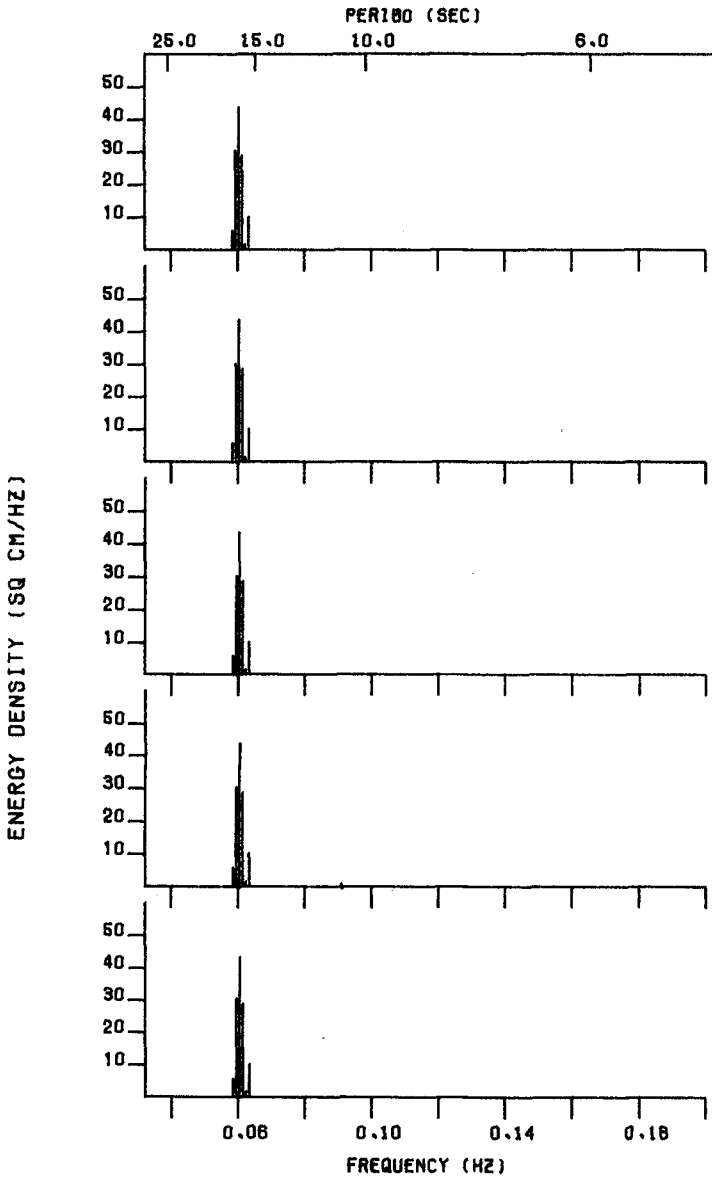


FIGURE 5. HIGH RESOLUTION SPECTRA PRESSURE GAGES ONE THRU FIVE POINT MUGU, CALIFORNIA, SIMULATED OBSERVATION NO. 3.

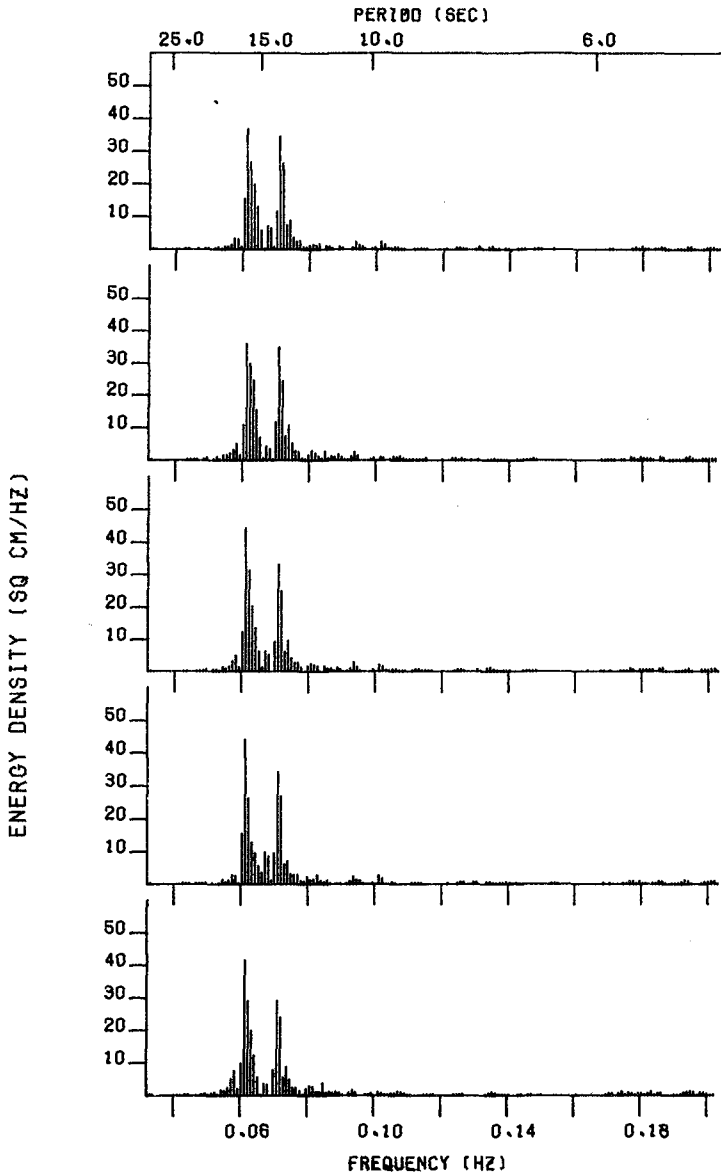


FIGURE 6. HIGH RESOLUTION SPECTRA PRESSURE GAGES ONE THRU FIVE
 POINT MUGU, CALIFORNIA, 307 HRS. JUNE 25, 1970.
 SIGNIFICANT WAVE HEIGHT 76.9 CM (2.5 FT)

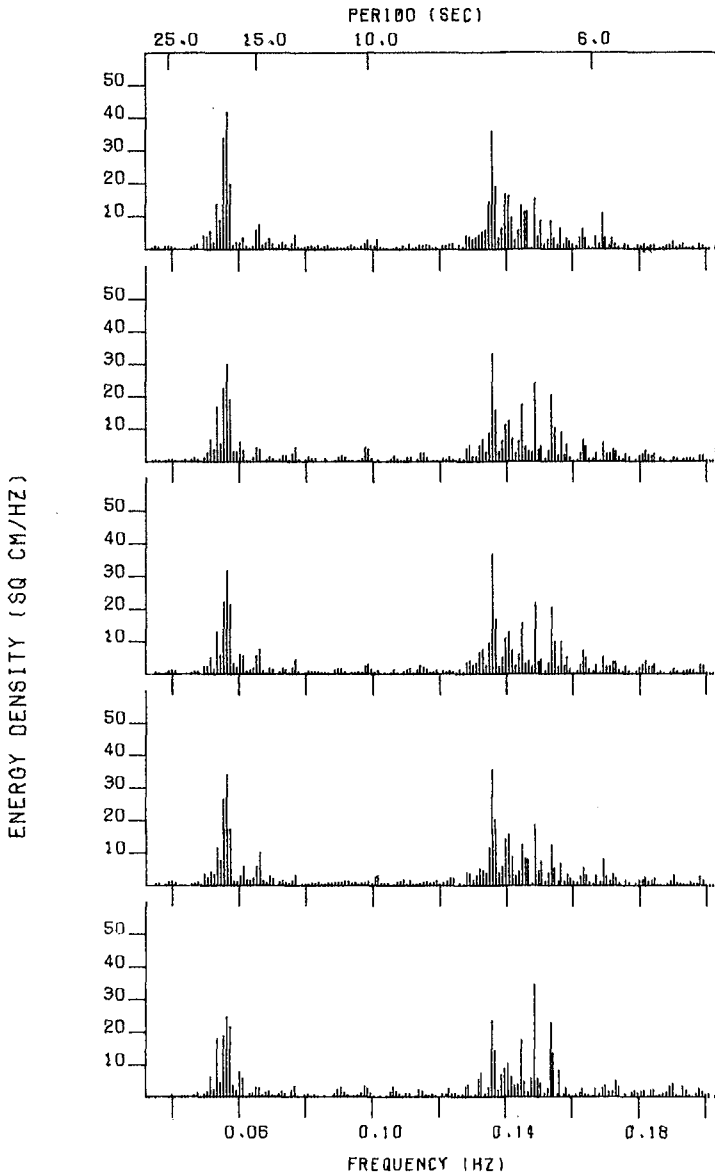


FIGURE 7. HIGH RESOLUTION SPECTRA PRESSURE GAGES ONE THRU FIVE
 POINT MUGU, CALIFORNIA, 1421 HRS. JUNE 10, 1970.
 SIGNIFICANT WAVE HEIGHT 109.3 CM (3.6 FT)

CHAPTER 21

RANDOM WAVE SIMULATION IN A LABORATORY WAVE TANK

Akira Kimura

Research Assistant

and

Yuichi Iwagaki

Professor

Department of Civil Engineering
Kyoto University
Kyoto, Japan

ABSTRACT

Most of coastal engineering problems have been studied with monochromatic waves. However, sea waves which arrive at the coast are random. It is very difficult to estimate exactly the influence of these random waves to coastal structures. Then the model tests in a laboratory wave tank using random wave simulation techniques seem to be most desirable way to estimate the influence of randomness of sea waves. For this purpose, the accomplishment of random wave simulation system, which make possible generating random waves having statistically same properties as those of sea waves, has long been desired. The authors achieved to establish such a new wave simulation system. In this paper, the characteristics of this system are demonstrated experimentally through several cases of random wave simulations.

INTRODUCTION

Random wave simulations are usually performed with a random wave generator in a laboratory wave tank. Then the important problem is how to drive the random wave generator to simulate random sea waves. In other words, how to generate random signals by which the random wave generator is driven becomes important. There are two ways of generating random signals, classifying random wave simulation techniques roughly. One is an analog method and the other is a digital method. In both methods, we must define at first what kind of properties of random waves should be simulated. Power spectrum shapes, Gaussian distribution of the water surface elevation and Rayleigh distribution of the wave height are well known representative properties for random sea waves. Simulated random signals must have the above properties at least. Especially the power spectrum shape of the simulated random signal must be same as that of sea waves.

It is known experimentally that other properties besides the power spectrum shape are almost same as those of sea waves if the power spectrum shape of simulated random waves is similar to that of sea waves. So the main purpose of random wave simulation is how to simulate the power spectrum shape of sea waves.

The analog method is the electrical simulation technique using band-pass filters. Random noise generated electrically is transmitted into a band-pass filter unit which consists of many band-pass filters with slightly different central frequencies. Gains of each filter are controlled so as to make equal the power of the output signal from each filter to the initially specified function in each frequency band. This initially specified function will be called as a target spectrum. Output signals from each filter are superimposed each other. Then the power spectrum of the output signal becomes equal to the target spectrum consequently. Finally this signal is transmitted into the random wave generator (1),(2).

The digital method is usually carried out by means of a digital computer. Random numbers generated by the computer are averaged using a numerical filter with a weighted moving average method. Averaged values are converted into analog record by a D-A converter and transmitted into the random wave generator. In this method, the procedure for designing the numerical filter mathematically, which transforms random numbers to random signals of specified properties, becomes important. Usually this problem can be deduced to solving Wiener-Hopf's integral equation, which is necessary and sufficient conditions that input and output signals must satisfy. But this procedure is very complicated and laborious and there is no assurance of the existence of an analytical solution in any case (3),(4).

From the fundamental knowledge about the Fourier transformation theorem, the numerical filter can be calculated easily by the reverse Fourier transformation of a linear spectrum. This numerical filter does not satisfy Wiener-Hopf's equation. In spite of mathematical discrepancy this method has been used frequently for convenience (5),(6),(7).

Beside these numerical filter methods, the wave superposition method has been treated by Borgman (5) and Goda (8). This is the most simple method to simulate random waves. But the simulated random waves by this method repeat themselves periodically every certain time interval. In order to avoid this periodicity several methods have been examined. Goda (8) recommended that the number of component waves is more than fifty. However, it can be said that when the number of component waves becomes so large it takes more time to calculate random signals than by the numerical filter method.

The authors propose herein a new method to calculate numerical filters. The procedure of this method is very simple and the numerical filter obtained satisfies Wiener-Hopf's equation.

NUMERICAL FILTER

The problem to obtain a numerical filter can be deduced to design mathematically an optimum circuit system which transforms a white noise $x(t)$ to a random wave profile $y(t)$ of desired statistical properties. In Fig.1 showing a linear circuit system, $h(\tau)$ and $g(\tau)$ mean unit impulse response functions in the normal and reverse directions of the circuit respectively. The relations between $x(t)$ and $y(t)$ are expressed as

$$y(t) = \int_0^{\infty} h(\tau) x(t-\tau) d\tau \dots\dots\dots(1)$$

$$x(t) = \int_0^{\infty} g(\tau) y(t-\tau) d\tau \dots\dots\dots(2)$$

Eqs.(1) and (2) can be written as follows in digital form expressions:

$$y_t = \sum_{\tau=0}^{\infty} h_{\tau} x_{t-\tau} \dots\dots\dots(3)$$

$$x_t = \sum_{\tau=0}^{\infty} g_{\tau} y_{t-\tau} \dots\dots\dots(4)$$

where $x_t, y_t, h_{\tau}, g_{\tau}, x_{t-\tau}$ and $y_{t-\tau}$ are digitized values of $x(t), y(t), h(\tau), g(\tau), x(t-\tau)$ and $y(t-\tau)$ with a time interval dt . Substituting Eq.(4) into Eq.(3) gives

$$\begin{aligned} y_t &= \sum_{\tau=0}^{\infty} h_{\tau} \sum_{n=0}^{\infty} g_n y_{t-n-\tau} = \sum_{\tau=0}^{\infty} h_{\tau} \sum_{n=-\infty}^{t-\tau} g_{t-\tau-n} y_n \\ &= \sum_{n=-\infty}^t y_n \sum_{\tau=0}^{t-n} g_{t-n-\tau} h_{\tau} \dots\dots\dots(5) \end{aligned}$$

Then from the condition that y_t appearing in both sides of Eq.(5) are always equal, the following relation is derived:

$$\sum_{\tau=0}^t g_{t-\tau} h_{\tau} = \delta_t \quad (t=0, 1, 2, \dots, \infty) \dots\dots\dots(6)$$

where δ_t is Dirac delta function

$$\delta_t = 1 \quad (t=0), \quad \delta_t = 0 \quad (t \neq 0) \dots\dots\dots(7)$$

In Eq.(6), if either h_{τ} ($\tau = 0, 1, 2, \dots, \infty$) or g_{τ} are known, the other can be determined easily. But h_{τ} and g_{τ} are not yet defined independently. Then other conditions are introduced to define h_{τ} and g_{τ} separately. In Eqs.(3), (4) and (6), it is impossible to sum up τ infinitely in real computation, then the upper boundary of summation is replaced by a sufficiently large number N . Now the white noise having the following characteristics is introduced newly as a random input:

$$E[x_t] = 0, \quad E[x_t x_{t-\tau}] = \delta_{\tau} \dots\dots\dots(8)$$

where $E[]$ means time averaging procedure.

If it is assumed that h_{τ} ($\tau = 0, 1, 2, \dots, N$) are given, g_{τ} are known from Eq.(6). y_t ($t = 0, 1, 2, \dots, \infty$) can be determined by substituting the white noise x_t into Eq.(3). Newly defined white noise x'_t obtained by substituting these y_t into Eq.(4) must be equal to x_t , but there are little differences between them, because the upper value of the

summation is replaced by a sufficiently large but finite number N in Eqs.(3),(4) and (6). Then let us try to obtain h_t and g_t which will minimize the mean squares of the difference between x_t and x_t^1 .

$$D^2 = E[(x_t - x_t^1)^2] = E[x_t^2] - 2E[x_t x_t^1] + E[x_t^1^2] \dots\dots\dots(9)$$

From Eqs.(3), (4) and (8) and the condition $h_i = 0$ when $i < 0$, Eq.(9) can be written as

$$D^2 = 1 - 2 \sum_{\tau=0}^N g_\tau E[x_t y_{t-\tau}] + \sum_{\tau=0}^N \sum_{n=0}^N g_\tau g_n r_{\tau-n} = 1 - 2h_0 g_0 + \sum_{\tau=0}^N \sum_{n=0}^N g_\tau g_n r_{\tau-n} \dots\dots\dots(10)$$

where r_i ($i = 0, 1, 2, \dots, N$) are digital values of the autocorrelation function of the output y_t . In order to obtain g_i ($i = 0, 1, 2, \dots, N$) which minimize D^2 , differentiating Eq.(10) with respect to g_i and putting each equation to be equal to zero, the following equation can be derived:

$$\sum_{\tau=0}^N g_\tau r_{\tau-n} = h_0 \delta_n \quad (n=0, 1, 2, \dots, N) \dots\dots(11)$$

This equation can also be expressed in matrix representation as

$$\begin{pmatrix} r_0 & r_1 & r_2 & \dots & r_N \\ r_1 & r_0 & r_1 & \dots & r_{N-1} \\ r_2 & r_1 & r_0 & \dots & r_{N-2} \\ \dots & \dots & \dots & \dots & \dots \\ r_N & r_{N-1} & r_{N-2} & \dots & r_0 \end{pmatrix} \begin{pmatrix} g_0 \\ g_1 \\ g_2 \\ \vdots \\ g_N \end{pmatrix} = \begin{pmatrix} h_0 \\ 0 \\ 0 \\ \vdots \\ 0 \end{pmatrix} \dots\dots(12)$$

As h_0 appearing in the right hand side of Eq.(12) is still unknown, then an attempt to solve the equations except the top ones including h_0 is made. This means to solve the matrix of rank $N-1$.

$$\begin{pmatrix} r_0 & r_1 & r_2 & \dots & r_{N-1} \\ r_1 & r_0 & r_1 & \dots & r_{N-2} \\ r_2 & r_1 & r_0 & \dots & r_{N-3} \\ \dots & \dots & \dots & \dots & \dots \\ r_{N-1} & r_{N-2} & r_{N-3} & \dots & r_0 \end{pmatrix} \begin{pmatrix} g_1/g_0 \\ g_2/g_0 \\ g_3/g_0 \\ \vdots \\ g_N/g_0 \end{pmatrix} = - \begin{pmatrix} r_1 \\ r_2 \\ r_3 \\ \vdots \\ r_N \end{pmatrix} \dots\dots(13)$$

Now denote the solution of this matrix by g_i^1 ($i = 1, 2, \dots, N$), which are the ratios of g_i to g_0 as seen in Eq.(13).

Putting $n = 0$ in Eq.(11) gives

$$g_0 r_0 + g_1 r_1 + g_2 r_2 + \dots + g_N r_N = h_0 \dots\dots\dots(14)$$

If both sides of Eq.(14) are divided by g_0 , Eq.(14) is written as

$$r_0 + g_1' r_1 + g_2' r_2 + \dots + g_N' r_N = h_0 / g_0 \quad \dots (15)$$

The left hand side of Eq.(15) can be determined by solving Eq.(13). Denoting the total summation of Eq.(15) by q , g_n can be expressed as follows:

$$g_n = \frac{h_0}{q} g_n' \quad \dots (16)$$

Substituting these relations into Eq.(10), the following equation can be obtained:

$$D^2 = 1 - \frac{h_0^2}{q} \quad \dots (17)$$

If q is positive, D^2 has a minimum value zero when $h_0^2 = q$. From Eq.(16), g_n can be finally determined as

$$g_0 = \frac{1}{\sqrt{q}}, \quad g_n = \frac{g_n'}{\sqrt{q}} (n=1, 2, \dots, N) \quad \dots (18)$$

Substituting these g_n into Eq.(6), then h_n ($n = 0, 1, 2, \dots, N$) can be determined. h_n are the numerical filters which transforms the white noise into random signals of a target spectrum.

NUMERICAL SIMULATION

In this section numerical simulations using the method explained previously are treated, and the results are compared with target spectra.

In addition random wave simulations by the Fourier transformation method are compared with those by this method. Two types of numerical filters can be defined by the Fourier transformation method. One is a numerical filter and the other is an asymmetrical one. From the results of numerical simulations in the preceding study, it was found that the asymmetrical filter gives better results than the symmetrical one. Then the results of random wave simulations by the newly proposed method herein will be compared with those by the asymmetrical filter.

Random signals by the Fourier transformation method are calculated by the relation

$$y_t = \sum_{i=-N/2}^{N/2} a_i \cdot x_{t-i} \quad \dots (19)$$

where a_i ($i = -N/2, \dots, 0, \dots, N/2$) are the numerical filters defined by the sine transformation of a linearized target spectrum. Eq.(19) has a similar form to Eq.(3) except lower limit of the summation.

The spectrum for random sea waves is frequently expressed as

$$S(f) = c_1 f^{-m} \exp(c_2 f^{-n}) \quad \dots (20)$$

where c_1, c_2, m and n are constants determined by wave conditions. This equation can be normalized using the peak frequency f_p and the spectral value $S(f_p)$ as follows:

$$S(f) = S(f_p) (f/f_p)^{-m} \cdot \exp\left\{\frac{m}{n} [1 - (f/f_p)^{-n}]\right\} \dots\dots\dots (21)$$

Values of f_p and $S(f_p)$ used in this numerical simulation are tabulated in Table-1. Target spectra are determined by substituting these values into Eq.(21). Autocorrelation functions are calculated by Wiener-Khintchine's theorem.

By substituting the digitized autocorrelation function into Eqs.(6), (13), (15) and (18), numerical filters can be determined. Fig-2 shows the examples of the numerical filters tabulated in Table-1. These numerical filters transform the random numbers, which have flat characteristics of power spectrum density, into the random signals of a target spectrum.

Fig-3 shows a part of uniform random numbers used in these numerical simulations. These random numbers are generated by the mixed congruence method using the computer subroutine. Fig-4 shows a part of numerically simulated random waves in Case-I-b.

Fig-5(a)~(d) and Fig-6(a)~(f) show the plots of the power spectra of simulated random waves by the proposed method and the Fourier transformation method (dotted lines) with the target spectra (solid lines). It is known from these figures that the proposed method gives better results than the Fourier transformation method.

These numerical simulations were performed in same conditions. N in Eq.(3) and Eq.(19) is 128 and the time interval dt is 0.05 sec. So the same degree of accuracy can be obtained by this new method with a smaller value of N than by the Fourier transformation method.

Goda (8) concluded, based on his experimental study that the time interval dt is preferable to satisfy the following relation:

$$dt \leq \frac{0.05}{f_p} \dots\dots\dots (22)$$

This relation is satisfied in all cases. However, dt must be selected not so as to be too little because when the time interval becomes small, N in Eq.(3) must be large. It is known from the accuracy of the simulated random waves that the moderate size of N is 100 or so and dt is desirable to be equal to $0.05/f_p$ which is the largest value that satisfies Goda's criterion.

The numerical filters as shown in Fig-2 must satisfy the following Wiener-Hopf's integral equation which is necessary and sufficient conditions:

$$\psi_{xy}(\tau) = \int_0^\infty h(\sigma) \cdot \psi_x(\tau-\sigma) d\sigma \quad (23)$$

where ψ_{xy} is the crosscorrelation function between the input $x(t)$ and the output $y(t)$, ψ_x is the autocorrelation function of the input $x(t)$ and $h(\sigma)$ is the filter or weighting function.

This equation can be expressed in digital form as

$$E[x_{t-\tau} \cdot y_t] = \sum_{\sigma=0}^N h_{\sigma} \cdot E[x_{t-\tau} \cdot x_{t-\sigma}] \quad \dots \quad (24)$$

The left hand side of Eq.(24) can be written using Eq.(3) as follows:

$$E[x_{t-\tau} \cdot \sum_{s=0}^N h_s \cdot x_{t-s}] = \sum_{s=0}^N h_s \cdot E[x_{t-\tau} \cdot x_{t-s}] \quad (25)$$

This is equal to the right hand side of Eq.(24). Therefore, h_{τ} ($\tau = 0, 1, 2, \dots, N$) satisfy Wiener-Hopf's integral equation.

RANDOM WAVE SIMULATION SYSTEM

Fig-7 shows the flow chart of the random wave simulation system. Two types of information can be available as an input of this system. One is a theoretical expression of the power spectrum or autocorrelation function. The other is the power spectrum or autocorrelation of observed sea waves or records of water surface itself. This system only needs basically the digitized autocorrelation function to simulate random waves. Either power spectra or autocorrelation functions can be available, because both are related each other by Wiener-Khintchine's theorem.

If the observed sea surface elevations are selected as input of this system, the right hand side of this flow chart will be used. This part of the flow chart is mainly aimed to generate random numbers. Because it is a very difficult problem to determine the randomness of sea waves, this part is attached to introduce the randomness in the simulation procedure from the observed sea waves. Reverse numerical filter g_{τ} in Eqs.(4)

and (6) are used to generate random numbers. Other procedures are the same as those at the left hand side of the flow chart.

Random waves in prototype must be reduced to a moderate size in order to generate in a laboratory wave tank. Usually the Froude similitude law is used to reduce the power spectra to a moderate scale. Then this reduced power spectrum will be called as a target spectrum. In the next step, the target spectrum must be modified because the random wave generator does not have flat response characteristics of frequency. Therefore, the wave making characteristics must be considered. In this system, Biesel-Suquet's theoretical relation between the movement of a wave making paddle and generated waves in a wave tank is adopted. Although this relation is for periodic small amplitude waves, it will be valid for random waves as the paddle movement is small. Fig-8 shows the experimental results for the ratio of the component amplitude of random waves to that of paddle movement. Plotted data agree well with the theoretical relations. Biesel-Suquet's theoretical relations shown in Fig-8 are expressed as

for piston type,

$$\frac{H}{2R} = \frac{2 \sinh^2 kh}{\sinh kh \cosh kh + kh} \quad \dots \dots \dots (26)$$

for flatter type $\frac{II}{2K} = \frac{2 \sinh kh}{kh} \frac{1 - \cosh kh + kh \sinh kh}{\sinh kh \cosh kh + kh}$ (27)

The modified target spectrum $S^*(f)$ will be defined by

$S^*(f) = S(f) \cdot [F(f)]^2$ (28)

where $S(f)$ is a target spectrum and $F(f)$ the inverse expression of Eq.(26) or Eq.(27).

Pierson-Moskowitz and Neuman spectra are selected to demonstrate the feasibility of this system. Target spectra are determined by Eq.(21). f_p and $S(f_p)$ of each spectrum are shown in Table-2. Fig-9 shows an example of the target spectrum and modified target spectrum.

Numerical filters were calculated in the same manner as used in the former section. Random numbers were averaged with the numerical filter, and these averaged values were transmitted into a D-A converter. The output signal from the D-A converter should be arranged to the smooth signal with the low pass filter. Then finally the random signals were transmitted into the wave generator.

Magnetic tapes and data recorders included in Fig-7 are attached to store digital and analog signals for future experiments.

Fig-10 shows the wave tank used in this system. This wave tank is 27 m long, 50 cm wide and 75 cm deep with glass side walls. At one end of this tank a random wave generator is furnished. At the other side of the wave tank, a wave absorber is installed and a wave gauge is set at the position of 10 m apart from the wave making paddle. Photo-1 and Photo-2 show the wave tank and random wave generator respectively.

The random wave generator is of servo-controlled electro-hydraulic system. Some typical properties of this wave generator are listed in Table-3. The wave generator has two actuators, which are connected with a piston type wave making paddle and a flatter type one respectively. Each actuator can be controlled independently. When the peak frequency of the target spectrum is higher than 1.0 Hz, random wave simulations will be performed with the flatter type wave making paddle, and if the peak frequency is lower than 1.0 Hz, the piston type wave making paddle is used. Furthermore, each paddle can be controlled simultaneously with different random signals.

A band pass filter unit not included in this system with fifteen band pass filters of 1/3 oct. frequency band from 0.2 to 5.0 Hz is attached as an optional faculty to this random wave generator. Therfor, the random wave simulations by an analog method can be made (2).

Fig-11 (a) ~ (d) and Fig-12 (a) ~ (d) show the experimental results of Pierson-Moskowitz and Neuman spectral simulations. The plotted data in each figure denote the results of power spectral analysis of water surface elevation measured by the wave gauge, and the solid lines show target spectra. From these figures, it is known that the power spectra of simulated waves are very close to the target spectra except in the region of low frequency.

The difference between the data and the target spectra at low frequency may be mainly caused by the surf beat which is usually observed in random waves near the coast.

This random wave simulation system aims to simulate a random wave spectrum. At the same time, other properties such as probability distributions of surface elevation and wave height must resemble those of sea waves.

Fig-13 shows some examples of the probability distributions of water surface elevation of simulated waves for Case-1-b and Case-2-a shown in Table-2. Plotted values are slightly skew to the minus side compared with the Gaussian distribution shown in a solid line, but this tendency is always observed in sea wave data. This is owing to the non-linear characteristics of wave motion.

Fig-14 shows wave height distributions defined by the zero-up-cross method for Case-1-b and Case-2-a. Agreement of data with the Rayleigh distribution is very well. These results means that the simulated waves in a wave tank have the same characteristics as those of sea waves.

CONCLUSION

The random wave simulation system has been discussed with several cases of random wave simulations in a wave tank. New, simple and accurate method to determine the numerical filter in this system has been proposed. The numerical simulation of random waves and experiments in a laboratory wave tank have shown that this system is very satisfactory.

There are some restrictions of wave making in extremely low and high frequency regions not only for this system but also for a regular wave generator, even though the random wave generator adopted in this system is much improved so as to equipt two types of wave making paddles. It is, therefore very difficult to estimate random waves in wide frequency range, for example, random waves of widely separated multiple peaked spectrum by a usual random wave generator only.

The ideal random wave simulation system will be consist of an extremely low frequency random wave generator like a tsunami generator and an ordinary random wave generator and a wind tunnel.

This random wave simulation system was completed in 1973. Since then, more than 40 cases of random wave simulation have been performed, and the statistical characteristics of random waves, such as distributions of the wave period, wave height and wave period and also combined distributions, have been studied using these simulated random waves (9), (10)

REFERENCES

- (1) Mohus, I. : Generation and measurement of simulated ocean waves, Automatic Control Laboratory, Norwegian Institute of Technology, Trondheim, pp. 1-32, 1960.
- (2) Iwagaki, Y. and A. Kimura : A study on simulation of ocean waves by a random wave generator, Proc. 19th Conf. Coastal Eng. in Japan, pp.131-136, 1972. (in Japanese)
- (3) Shvetsov, K.Y. and Shorin, A.N. : The modeling of sea waves by digital computer, Oceanology, Vol.9, pp.578-584, 1969.
- (4) Hino, M. : A predictor filter and transformation filter for ocean waves (1), Proc. 14th Conf. Coastal Eng. in Japan, pp.21-28, 1967. (in Japanese)
- (5) Borgman, L.E. : Ocean wave simulation for engineering design, Proc. ASCE, WW4, pp.557-583, 1969.
- (6) Webber, N.B. and C.D. Christian : A programmable irregular wave generator, Proc. 14th Conf. Coastal Eng., pp.340-351, 1974.
- (7) Funke, R. : Random wave signal generation by minicomputer, Proc. 14th Conf. Coastal Eng., pp.352-371, 1974
- (8) Goda, Y. : Numerical experiments on wave statistics with spectral simulation, Rpt. Port and Harbour Res. Inst. of Japan, Vol.9, pp.7-57, 1970.
- (9) Iwagaki, Y. and A. Kimura : A study on a characteristics of the period distributions of random sea waves, Proc. 22th Conf. Coastal Eng. in Japan, pp.295-300, 1975. (in Japanese)
- (10) Iwagaki, Y. and A. Kimura : A study on a characteristics of zero-up-cross wave length and celerity, Proc. 23th Conf. Coastal Eng. in Japan, 1976. (in Japanese)

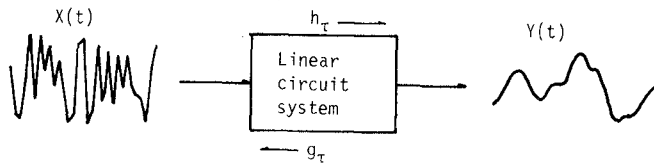


Fig-1 Diagram of linear circuit system

Table-1 Characteristics of target spectra

Case No.	f_p (Hz)	$S(f_p)$	m	n	N
I -a	0.6	1.0	4	4	128
I -b	0.6	1.0	5	4	128
I -c	0.6	1.0	6	4	128
I -d	0.6	1.0	7	4	128
II -a	0.4	1.0	5	4	128
II -b	0.6	1.0	5	4	128
II -c	0.8	1.0	5	4	128
II -d	1.0	1.0	5	4	128
III -a	0.8	1.0	5	4	64
III -b	1.0	1.0	5	4	64

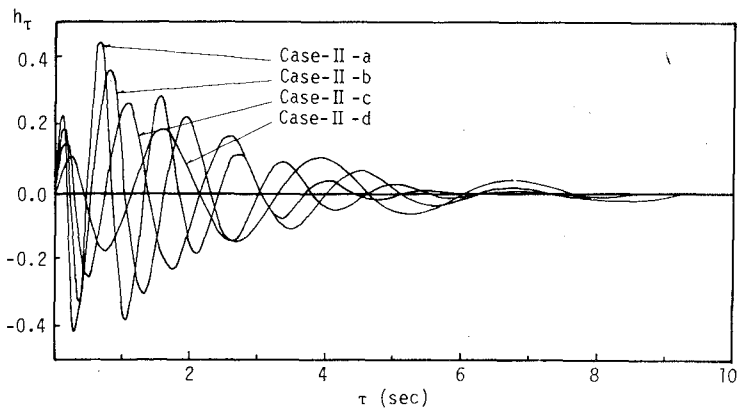


Fig-2 Examples of numerical filters

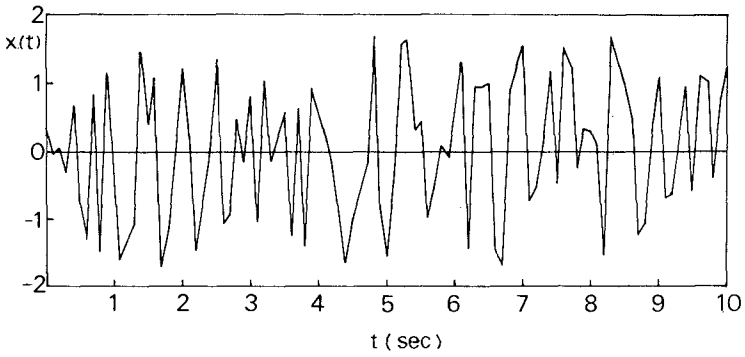


Fig-3 Uniform random numbers

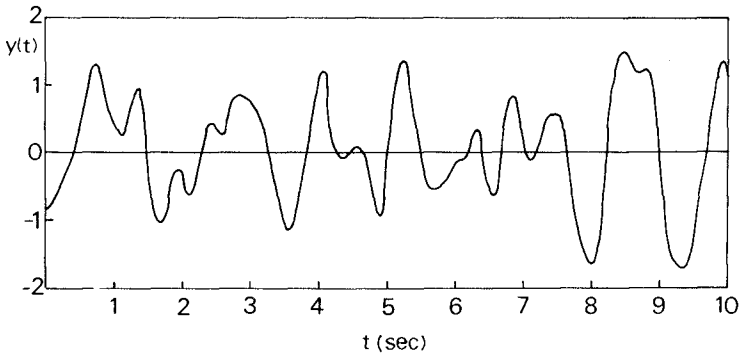
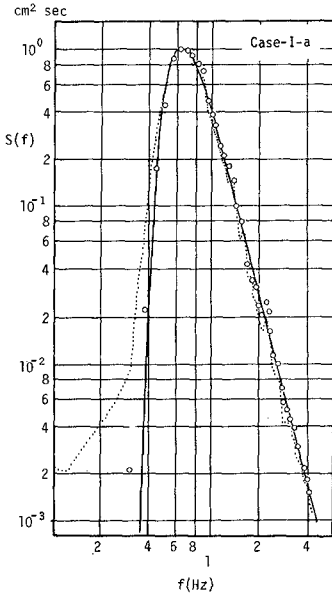
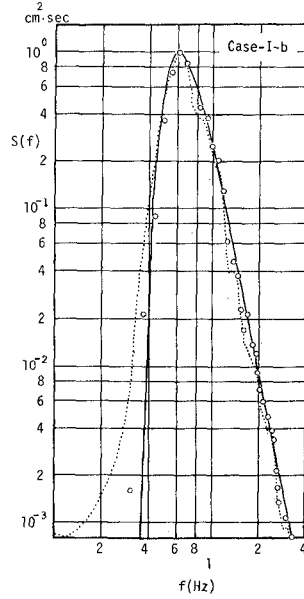


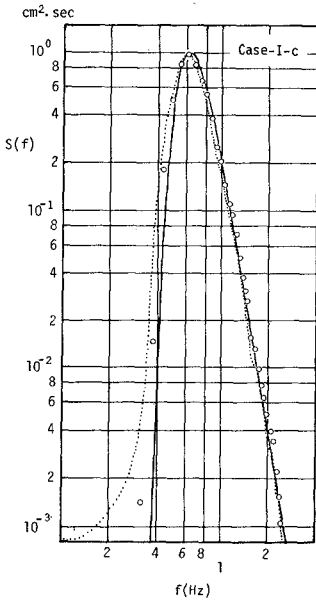
Fig-4 Signals of simulated waves (Case-I-b)



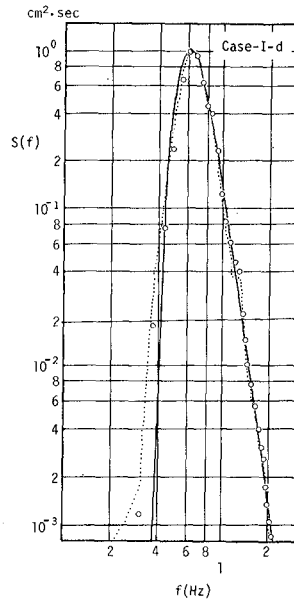
(a)



(b)



(c)



(d)

Fig-5 Power spectra of simulated waves (Case-I)

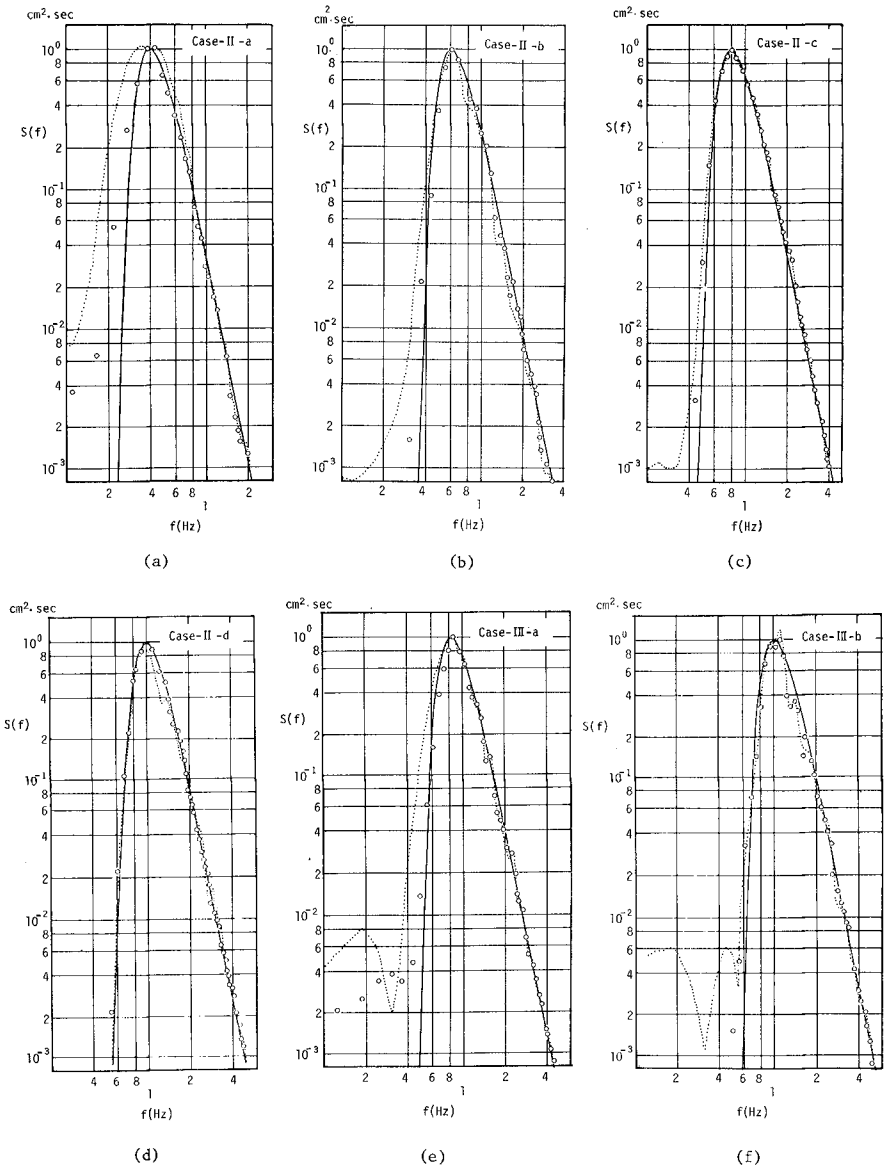


Fig-6 Power spectra of simulated waves (Case-II and Case-III)

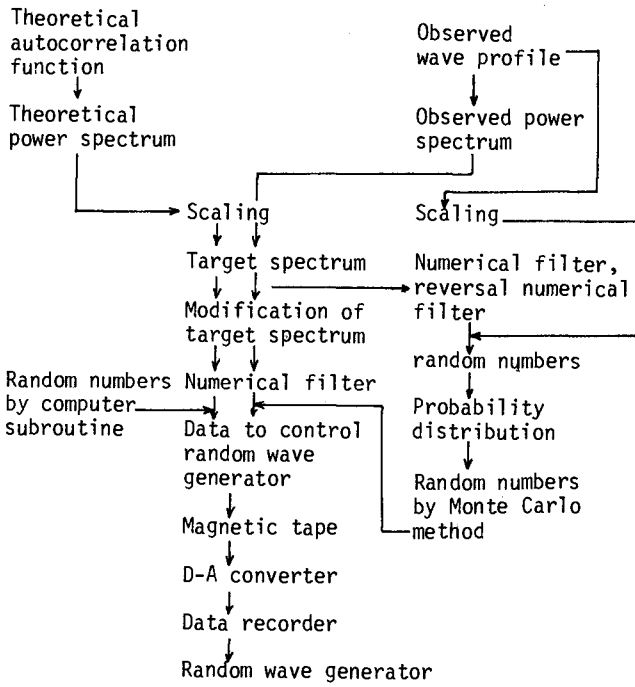


Fig-7 Flow chart of random wave simulation system

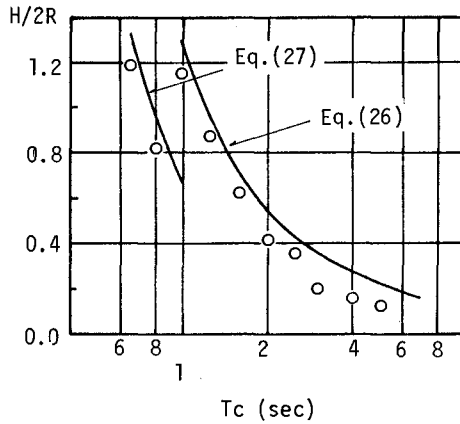


Fig-8 Period characteristics of wave generation by two types of wave paddles ($h=40$ cm)

Table-2 Characteristics of target spectra used in experiments

Case No.	f_p (Hz)	$S(f_p)$ (cm^2sec)	m	n
1-a	0.4	5.0	5	4
1-b	0.5	5.0	5	4
1-c	0.6	7.0	5	4
1-d	0.7	10.0	5	4
2-a	0.5	2.0	6	2
2-b	0.6	2.0	6	2
2-c	0.7	4.0	6	2
2-d	0.8	5.0	6	2

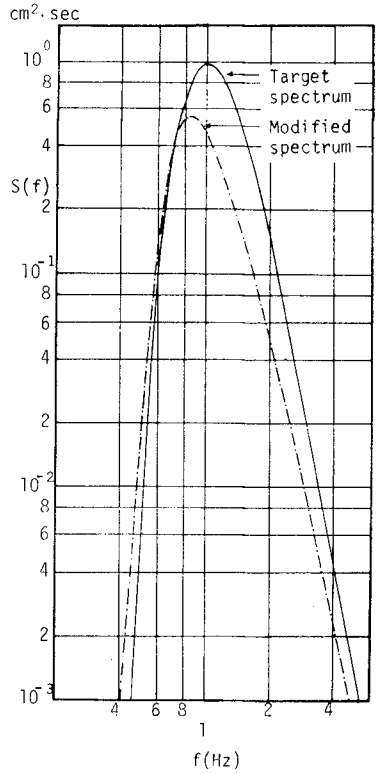


Fig-9 Target spectrum and Modified spectrum

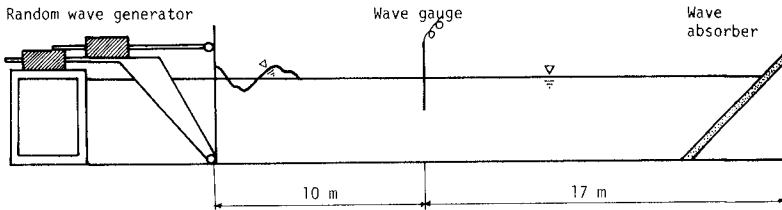


Fig-10 Wave tank



Photo-1 Wave tank

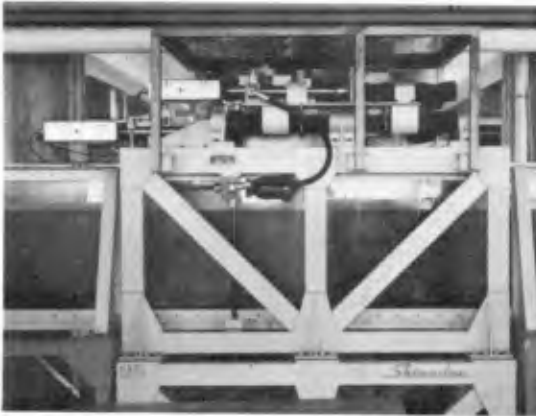


Photo-2 Random wave generator

Table-3 Typical properties of random wave generator

	Maximum power	Maximum stroke	Frequency characteristics
Actuator (A) (Piston)	1.0 ton	± 10.0 cm	0.01 ~ 10.0 Hz
Actuator (B) (Flatter)	0.5 ton	± 10.0 cm	0.01 ~ 10.0 Hz

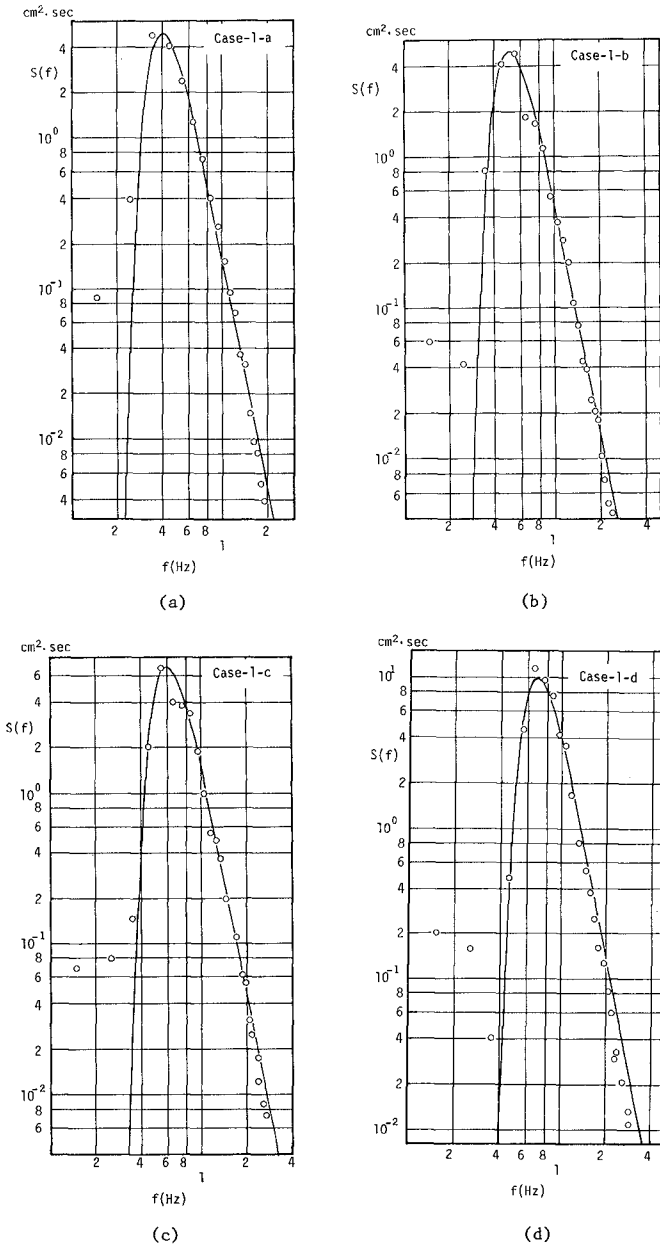
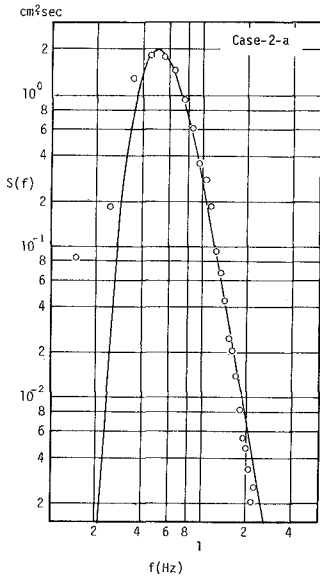
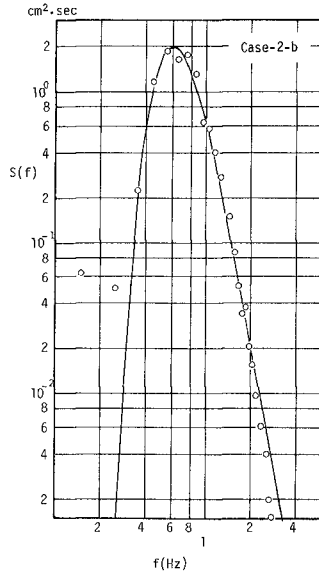


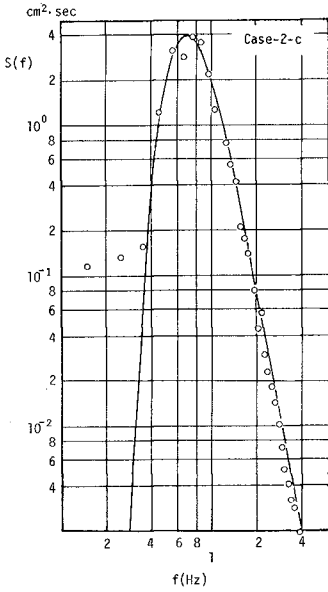
Fig-11 Power spectra of simulated waves in wave tank
(Pierson-Moskowitz spectra)



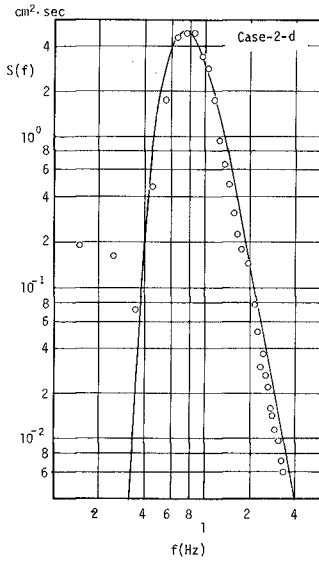
(a)



(b)



(c)



(d)

Fig-12 Power spectra of simulated waves in wave tank
(Neumann spectra)

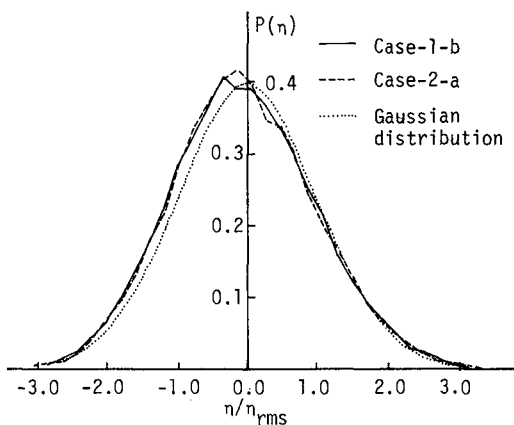


Fig-13 Probability distributions of water surface elevation of simulated waves

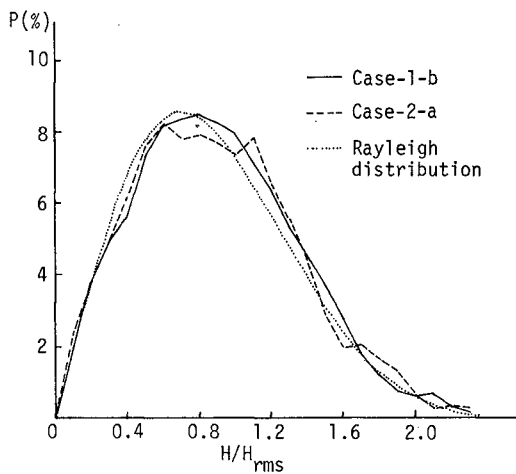


Fig-14 Wave height distributions defined by zero-up-cross method

CHAPTER 22

WAVE HEIGHT DISTRIBUTION OF WIND WAVES OVER LONG WAVES

Shan-Hwei Ou¹ and Frederick L.W. Tang²

ABSTRACT

Influence of long wave on the wave height distribution of wind waves was studied through the laboratory experiment. Experiments were conducted in a wind-wave tank where the wind waves were generated by a wind blower and the long waves were developed by an oscillating pendulum type wave generator.

The wave height distribution of the wind waves over long wave is slightly different from the Rayleigh distribution in the small steepness of long wave. The ratios between the average of highest 1/n-th waves vary with the steepness of long waves. The magnitude and the location of the spectral peak of wind waves are altered. The amount of the attenuation of wind wave energy is larger than the results of Mitsuyasu (1966).

1. INTRODUCTION

The design of marine structures have often been done with the concept of representative wave. Offshore structures are mostly designed against the maximum probable wave at the structure site. Coastal structures are usually designed against the significant wave at the locality. However, marine structures are subjected to the action of irregular waves. The analysis of irregular wave action on marine structures requires the information of statistical distribution of wave heights. Ito, et.al.(1966) employed the wave height distribution function to estimate the possible sliding distance of the breakwater. This method has been adopted in the practical breaker design (The Japan port and Harbour Association, 1970). Goda(1970) calculated the rate of wave overtopping of sea walls from the wave height distribution.

In this kind of analysis, the detailed distribution function of wave heights is needed. Theoretical distribution of wave heights, defined by the crest-to-trough method, was developed by Longuet-Higgins(1952) as the Rayleigh distribution, under the assumptions of narrow spectrum and random phases. There are lots of investigators confirm this wave height distribution. However, it is uncertain in case where the wind waves are propagated over the surface of long waves such as ocean swell or tidal currents.

The interaction of short wave and long wave has been studied by Longuet-Higgins and Stewart(1960) for the case of same wave type and by Mitsuyasu(1966) for the case of different wave type. In this paper, the influence of long wave on the wave height statistics of wind waves is presented.

-
1. Lecturer, Dept. of Hydraulic Engineering, National Cheng Kung University, Tainan, Taiwan 700, R.O.C.
 2. Professor, Graduate School of Ocean and Hydraulic Engineering, National Cheng Kung University, Tainan, Taiwan 700, R.O.C.

2. EXPERIMENTAL EQUIPMENT AND PROCEDURE

The experiment was conducted in a wind - wave tank of 75 m long, 1m wide and 1.2 m deep as shown in Fig.1. The long waves were generated by an oscillating pendulum type wave generator at one end of the tank. Wind waves are generated in the same direction by a 10 Hp motor, located at 10 m down the pendulum wave generator. The cross section of the outlet of wind blower is 1m in width and 0.5 m in height. The bottom of the duct is 0.2 m above the still water level such that the regular waves may pass through the gap. The wind velocity at the center of the wind passage was measured by a pitot - static tube in conjunction with a micromanometer. The micromanometer was allocated in a slope of $\sin \theta = 1/4$, and filled with two insoluble liquids of ink solution and colorless benzene, each has the specific gravity of 0.998 and 0.875 at the temperature of 20°C respectively. The pressure difference bearing at the pitot - static tube can be read out easily and hence the wind velocity was obtained. Waves were measured by the resistance type wave gauge and recorded on the visigraph.

Wind waves were generated by three free stream wind velocities, i.e. 8.10m/s, 10.73m/s and 12.45m/s. The regular long waves were produced by three periods and five wave heights. The properties of regular long waves used in the present experiment were listed in the table 1. The steepnesses of the long waves are all below 0.01. Each experimental condition includes the case of three wind velocities, that makes altogether 45 experimental runs.

Table 1. Regular long waves used in the experiment

Mean period (sec)	Mean wave height (cm)	Steepness
3.06	1.49	0.0010
3.06	2.14	0.0015
3.13	3.62	0.0024
3.07	6.34	0.0043
3.09	7.44	0.0050
2.82	6.94	0.0056
2.81	5.01	0.0041
2.83	4.78	0.0038
2.84	3.48	0.0028
2.80	1.98	0.0016
2.51	2.47	0.0025
2.51	3.64	0.0037
2.48	4.99	0.0052
2.48	5.91	0.0062
2.48	8.10	0.0084

In the experiments the regular long wave was generated first, and then wind was sent over the surface of long wave. Each run lasts for five minutes, and the co - existent system was recorded for last two minutes. The wave data at fetch 16.4 m were presented here.

3. EXPERIMENTAL RESULTS

3.1 General features of the combined wave field

Figure 2 shows the examples of the wave record. In the figure, (a) is the record of wind wave unaffected by the long wave; (b) is the record of mechanically generated long wave; (c) is the record of co- existent system in almost steady state. Figure 3 shows the examples of co - existing system under different wave steepness of long waves. The wave heights are taken as crest-to-trough wave height through out this analysis. The wave statistics of wind waves and long waves are calculated separately, and the combined wave field of wind waves and long wave was also computed as given in Table 2, where the values in bracket denoted the wave statistics for wind waves only.

3.2 Wave height statistics

The theoretical wave height distribution derived by Longuet - Higgins for a narrow band spectrum is given as

$$P(H)dH = \frac{1}{4} \frac{H}{\sigma^2} \exp \left(-\frac{H^2}{8\sigma^2} \right) dH \dots \dots \dots (1)$$

where σ^2 is the variance of surface elevation. The ratios of average heights of the highest 1/n-th waves have been calculated as

$$\frac{H_{1/3}}{H_a} = 1.598, \quad \frac{H_{1/10}}{H_{1/3}} = 1.270 \quad \text{and} \quad \frac{H_{max}}{H_{1/3}} = 1.601 \quad (\text{for } N=160) \dots \dots (2)$$

Although several reasons could affect the wave height distribution, such as the nonlinear wave - wave interaction, the breaking effect, the instrument of wave recorder, and the use of a finite number of component wave heights, etc., the wave height distribution observed in the field (Grodnight, 1963; Collins, 1967; Koele, 1960; Goda, 1974; etc.) has been shown generally in good agreement with the Rayleigh distubution.

In the present analysis, the distributions of crest - to - trough wave heights of wind waves over the long wave are computed. Figure 4 is the wave height distribution of wind waves over the long wave as given in Figure 3. It is seem that the wave height distributions do not deviate too much from the Rayleigh distribution, except for the wind waves only and the low wave steepness. All the experimental data of wave beight distribution are summarized into four groups According to the steepness of long wave, i.e., $H/L = 0, 0.001-0.003, 0.003-0.006, 0.006-0.009$. The data in the same group are averaged and formed the representative wave height distribution as given in Figure 5. Seeing that the wave height distributions vary with the steepness of the long

Table 2. Properties of co-existent system

Run	Wind waves		Long waves		Wind waves plus long waves						
	Velocity (m/s)	(E) ₀ (cm ²)	T (sec)	H (cm)	H/L	E (cm ²)	Hmax (cm)	H _{1/0} (cm)	H _{1/3} (cm)	H _a (cm)	H _r (cm)
1	8.10	0.73	3.06	1.49	0.0010		(3.10)	(2.17)	(1.67)	(1.95)	(2.24)
2			3.06	2.14	0.0015	2.07	5.46	4.16	3.30	2.76	3.06
3			3.13	3.62	0.0024	3.32	6.38	4.23	3.35	2.90	3.23
4			3.09	7.44	0.0050	13.56	3.77	2.77	2.04	1.85	2.28
5			3.07	6.34	0.0043	10.91	7.55	5.30	3.64	2.72	3.45
6			2.82	6.94	0.0056	4.84	6.72	5.19	4.21	3.30	4.36
7			2.83	4.78	0.0038	20.37	13.85	10.23	5.81	4.61	6.54
8			2.81	5.01	0.0041	13.10	8.81	5.87	3.99	3.07	3.86
9			2.84	3.48	0.0028	5.16	5.88	4.67	3.45	2.69	3.70
10			2.80	1.98	0.0016	1.96	5.88	4.40	3.40	2.62	2.94
11			2.51	2.47	0.0025	2.62	6.72	4.01	3.02	2.51	2.83
12			2.51	3.64	0.0037	1.79	6.30	4.19	3.13	2.55	2.87
13			2.48	4.99	0.0052	2.91	6.30	4.38	3.15	2.50	2.85
14			2.48	5.91	0.0062	4.71	6.72	4.51	3.28	2.57	3.05
15			2.48	8.10	0.0084	7.11	7.97	5.59	3.96	2.76	3.42
16	10.73	3.26					(9.65)	(6.95)	(5.95)	(4.93)	(5.22)
17			2.48	8.10	0.0084	10.3	10.53	7.61	5.73	4.45	5.32
18			2.48	5.91	0.0062	7.36	10.50	7.08	5.39	4.00	4.66
19			2.48	4.99	0.0052	5.78	10.50	7.11	5.94	4.76	5.23
20			2.51	3.64	0.0037	5.04	9.65	7.61	6.37	4.95	5.46
21			2.51	2.47	0.0025	4.09	10.92	7.29	6.07	5.27	5.69
22			2.80	1.98	0.0016	4.01	9.54	7.54	6.77	5.31	5.66

Table 2. Properties of co-existent system(continued)

Run	wind waves		Long waves			Wind waves plus long waves					
	Velocity (m/s)	(E) ₀ (cm ²)	T (sec)	H (cm)	H/L	E (cm ²)	H _{max} (cm)	H _{1/10} (cm)	H _{1/3} (cm)	H _a (cm)	H _r (cm)
22			2.84	3.48	0.0028	4.74	8.71	6.14	5.24	4.16	4.73
23			2.81	5.01	0.0041	8.41	12.45	7.70	5.96	4.81	5.59
24			2.83	4.78	0.0038	11.30	9.13	5.39	4.43	4.00	5.16
25			2.82	6.94	0.0056	17.4	10.37	8.54	5.88	4.63	5.72
26			3.07	6.34	0.0043	11.35	10.79	7.52	5.37	4.01	4.78
27			3.09	7.44	0.0050	8.94	9.13	6.84	5.44	4.59	5.24
28			3.13	3.62	0.0024	5.91	9.13	6.66	5.52	4.32	4.87
29			3.06	2.14	0.0015	4.3	8.30	7.08	6.21	5.03	5.38
30			3.06	1.49	0.0010	4.5	8.71	6.99	5.67	5.12	5.60
31	12.45	7.52	3.06	1.49	0.0010	6.95	(18.26)	(10.25)	(8.63)	(7.41)	(7.79)
32			3.06	2.14	0.0015	7.33	12.45	10.01	8.77	7.00	7.39
33			3.13	3.62	0.0024	7.00	10.37	9.67	8.25	6.89	7.23
34			3.09	7.44	0.0050	10.56	14.94	8.37	6.89	5.94	6.35
35			3.07	6.34	0.0043	9.01	15.35	10.37	7.96	6.62	7.27
36			2.82	6.94	0.0056	17.36	15.35	12.27	7.81	5.75	7.00
37			2.83	4.78	0.0038	13.69	14.11	9.77	6.92	5.39	6.51
38			2.81	5.01	0.0041	8.64	12.45	9.10	7.29	5.66	6.22
39			2.84	3.48	0.0028	7.56	10.79	8.90	7.27	6.10	6.59
40			2.80	1.98	0.0016	6.78	14.94	10.01	8.22	6.87	7.28
41			2.51	2.47	0.0025	6.94	12.86	9.70	8.08	6.80	7.18
42			2.51	3.64	0.0037	6.05	10.79	8.76	7.14	5.94	6.43
43			2.48	4.99	0.0052	6.60	11.62	8.29	6.79	5.82	6.50
44			2.48	5.91	0.0062	9.50	14.52	9.82	7.58	5.80	6.55
45			2.48	8.10	0.0084	10.22	13.28	10.07	7.06	5.60	6.44

wave. The wave height distribution of wind waves in absence of long wave does not follow the Rayleigh distribution. As the steepness of long wave increases, the densities in the lower part of the distribution function begin to grow, and the wave height distribution of the co-existent system of wind waves and long wave show slightly close to Rayleigh than before, as in the case of $H/L = 0.001-0.003$ and $H/L = 0.003-0.006$. However, when the steepness of long wave continue to increase as in the case of $H/L = 0.006-0.009$, the distribution shows deviate from Rayleigh again.

Figure 6 shows the values of ratios among various wave height in relation to the steepness of long waves. It is noted that the values of $H_{1/3}^1 / H_a$ and $H_{1/10} / H_{1/3}$ are smaller than the theoretical values given by Equation (2), but the ratio of $H_{\max} / H_{1/3}$ is larger, comparing the theoretical values. The ratios of $H_{1/3} / H_a$, $H_{1/10} / H_{1/3}$, $H_{\max} / H_{1/3}$ are increased in proportion to the steepness of long wave.

Figure 7 shows the relations between $H_{1/10} / H_a - U/C_0$ and $H_{1/10} / H_{1/3} - \epsilon^2$, where U is the free stream velocity, C_0 is the phase velocity of long wave, ϵ is the bandwidth of the co-existent system computed from power spectrum. It is seen that $H_{1/10} / H_{1/3}$ increases with ϵ^2 , and $H_{1/3} / H_a$ seems has nothing to do with U/C_0 .

3.3 The spectrum and the attenuation of wind wave energy

Spectra of wind waves alone and the co-existent system of wind waves and long waves are analysed in order for the better understanding of the detailed properties of wind waves on long waves. Each record of two minutes in length is digitized with 0.1 sec interval. The computation of wave spectrum was done by the IBM 1130 digital computer. Each run consumes 7 minutes of computer time. The adopted program was based on Blackman and Tukey method with sample size $N=1024$, maximum lag $M=102$, Nyquist frequency $f_N = 5.0$ c/s, resolution $f=0.049$ c/s.

In Fig. 8, the solid line shows the power spectrum of wind waves for wind velocity equals to 12.45 m/s. As long waves appear, the spectrum of co-existent system shows a double peaks, which can clearly separated each other. The high frequency peak represents the wind wave spectrum, and the low frequency peak represents the long wave spectrum. Fig. 8 shows that the wind wave spectrum is attenuated gradually with increasing the steepness of long waves. The scale of ordinate in the figure is changed in the high frequency range so as to see more clearly the changes of wind wave spectrum.

The total energy in each run as listed in Table 2 is computed through the spectrum calculation. In Table 2, $(E)_0$ indicates the total energy of wind waves in the absence of long waves; E represents the total energy of the co-existent system of wind waves and long waves. The total energy of the co-existing system is increased in most cases due to the appearance of long waves. But that part of wind waves energy in the co-existent system is decreased, as has shown in Fig. 8. Let E' be the energy contained

in the wind waves of the co-existent system. E' can be obtained by the numerical integration of each spectrum. Fig.9 shows the attenuation of wind wave energy as relation to steepness of the long waves. The attenuation rate according to long wave steepness is larger than the result of Mitsuyasu (1966). The attenuation of wind waves energy might due to the breaking of wind waves near the crest of the long wave, as has pointed out by Longuet-Higgins and Stewart (1960). The other reason of attenuation is due to the change of wind field induced by the passing long waves. The peak of wind wave spectrum is also altered. Fig.9 shows the results.

4. CONCLUSION

The interaction between short wind-generated waves and the long mechanically-generated waves involves complicated energy transfer in the wind field and wave field. The experimental results show the influence of long wave on the wave statistics of wind waves. The wave height distributions of wind waves over small steepness of long waves show not much deviate from the Rayleigh distribution, but the ratios of various wave heights are varied both with the steepness of long waves and the band width of the co-existent spectrum. The attenuation of wind wave energy is directly proportion to the steepness of long wave. The peak of wave wave spectrum is shifted.

Acknowledgment

Discussion with Dr. C.T. Kuo on Rice's theory is acknowledged.

REFERENCES

- Bretschneider, C.L. (1959): Wave variability and wave spectra for wind-generated gravity waves, U.S. Army corps of Engineers, Beach Erosion Board, Tech. Memo. No. 118, 192P.
- Cartwright, D.E. and Longuet-Higgins, M.S. (1956): The statistical distribution of the maxima of a random function, Proc. Royal Soc., A, vol. 237, P. 212-232.
- Collins, J.I. (1967): Wave statistics from Hurricane Doris, J. Waterways and Harbor Div., ASCE, vol. 93, No. WW2, P. 59-77
- Goda, Y. and K. Nagai (1968): Wave observation at the port of Nagoya, Tech. Note of P.J.R.I., Japan, No. 61, 64P.
- Goda, Y. (1970): Numerical experiments on wave statistics with spectral simulation, Rept. of Port and Harbor Res. Inst., vol. 9, No. 3, P. 3-57.
- Goda, Y. (1974): Estimation of wave statistics from spectral information, Proc. of the International Symposium on Ocean Wave Measurement and Analysis, vol. 1, P. 320-337.
- Goodnight, R.C. and T.L. Russel (1963): Investigation of the statistics of wave heights, Jour. of Waterways and Harbor Div., ASCE, vol. 89, No. WW2, 1963, P. 29-55
- Koele, L.A. and P.A. de Bruyn (1964): Statistical distribution of wave heights in correlation with energy spectrum and water depth, Proc. of 9th Conf. on Coastal Eng., P. 123-139.
- Longuet-Higgins, M.S. and R.W. Stewart (1960): Changes in the form of short gravity waves on long waves and tidal currents, J. Fluid Mech., 8. P. 565-583.
- Longuet-Higgins, M.S. (1952): On the statistical distribution of the height of sea waves, J. Marine Res., vol. 11, No. 3, P. 245-266.
- Mitsuyasu, H. (1966): Interactions between water waves and winds (I)- co-existent system of wind wave and regular oscillatory wave, Rept. of Res. Inst. for Applied Mech., Kyushu Univ., Vol. XIV, No. 48, P. 67-89.
- Rice, S.O. (1944, 1945): Mathematical analysis of random noise, Bell System Tech. Jour., vol. 23, P. 282-332, 1944, and vol. 24, P. 46-156, 1945.
- Rice, S.O. (1948): Statistical properties of a sine wave plus random noise, B.S.T.J., Jan. 1948, P. 109-157.
- Siefert, W. (1972): Wave investigation in shallow water, Proc. of 13th Conf. on Coastal Eng., P. 329-346.
- The Japan port and Harbour Association: Design stand ard for port and harbour structures, 1970.

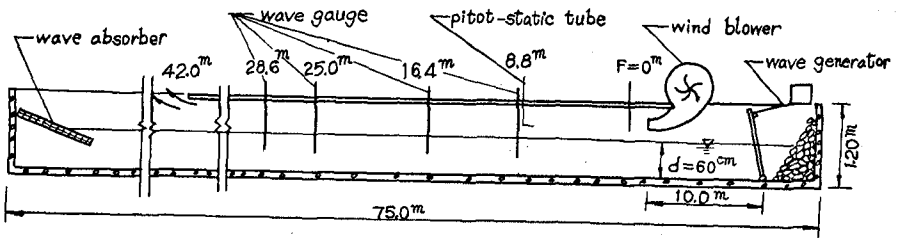


Fig.1 EXPERIMENTAL WIND WAVE TANK.

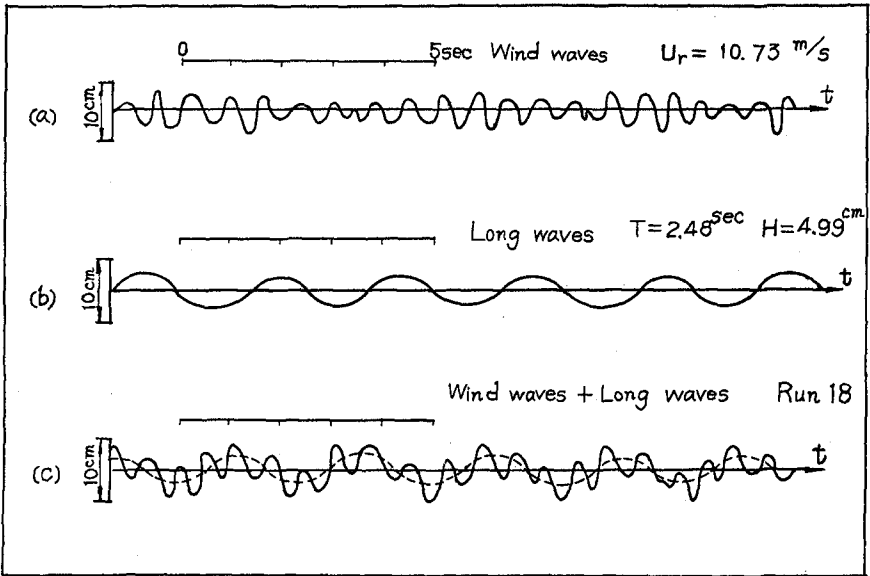


Fig.2 SAMPLES OF WAVE RECORDS (AT 16.40M)

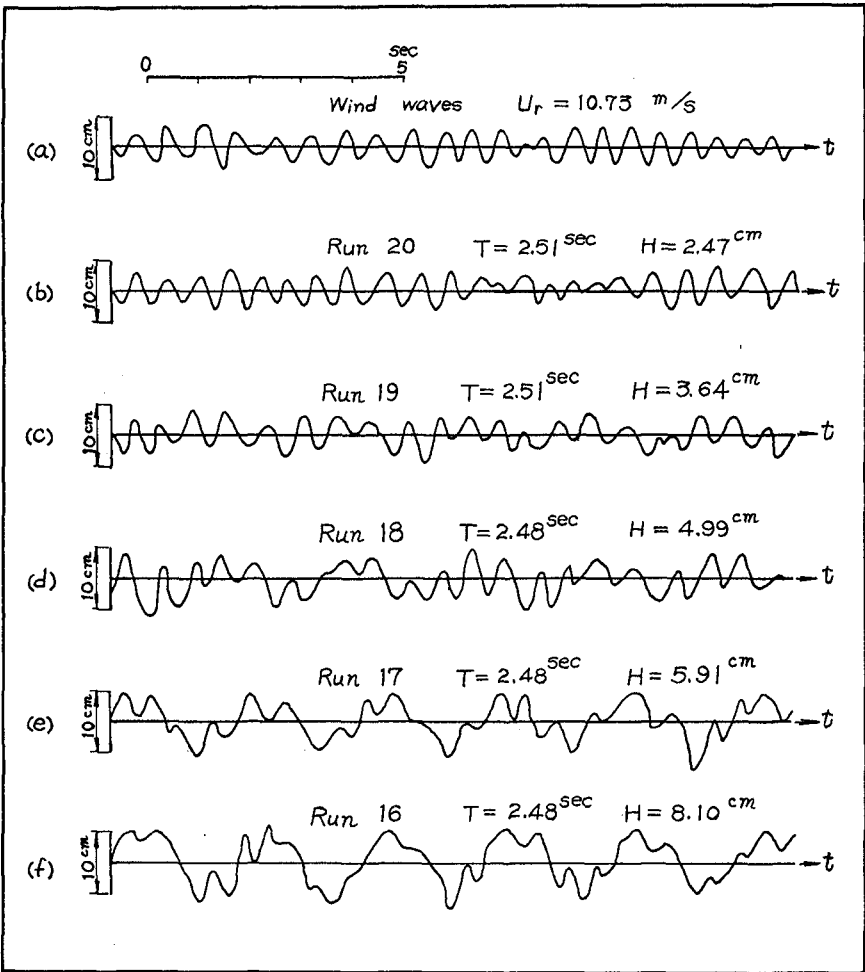


Fig. 3 SAMPLES OF CO-EXISTENT SYSTEM OF WIND WAVES AND LONG WAVES (AT 16.4 M).

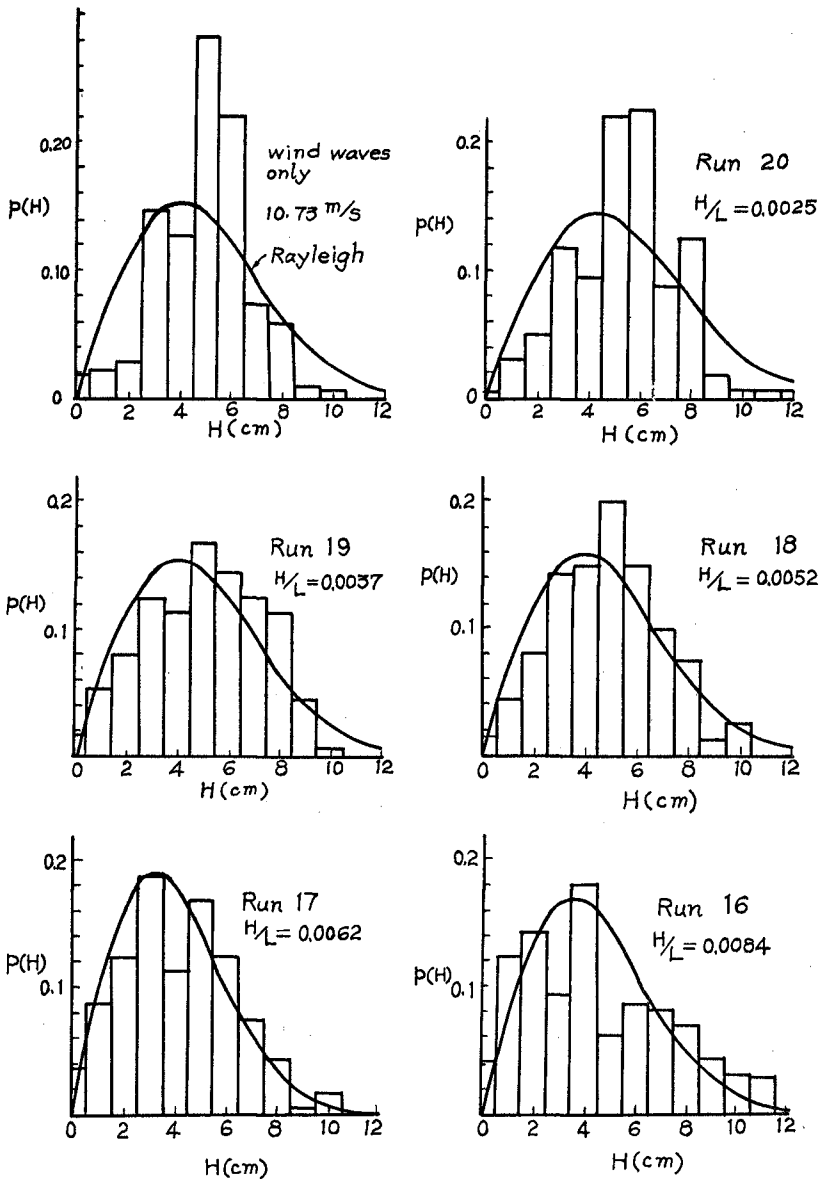


Fig. 4 COMPARISON OF WAVE HEIGHT DISTRIBUTION TO RAYLEIGH DISTRIBUTION (AT 16.4 M).

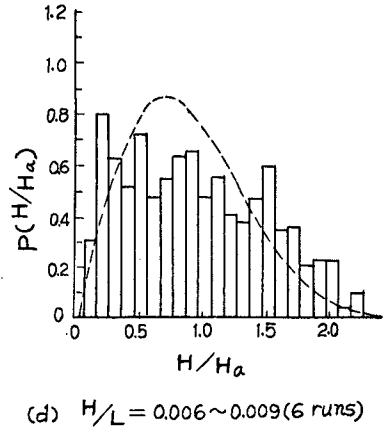
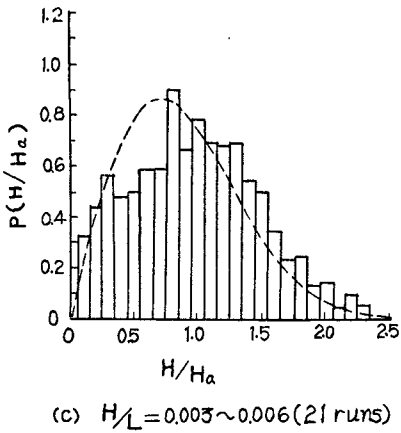
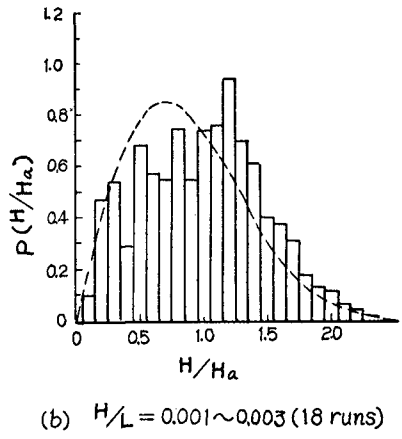
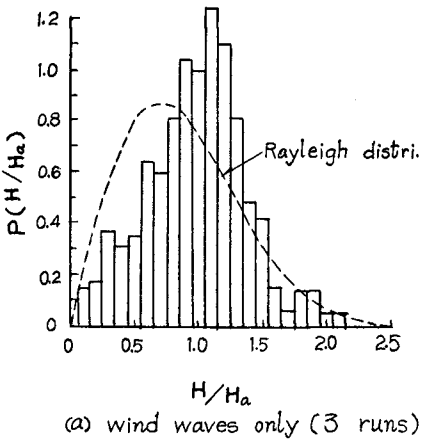


Fig.5 COMPARISON OF OVERALL WAVE HEIGHT DISTRIBUTION TO RAYLEIGH DISTRIBUTION

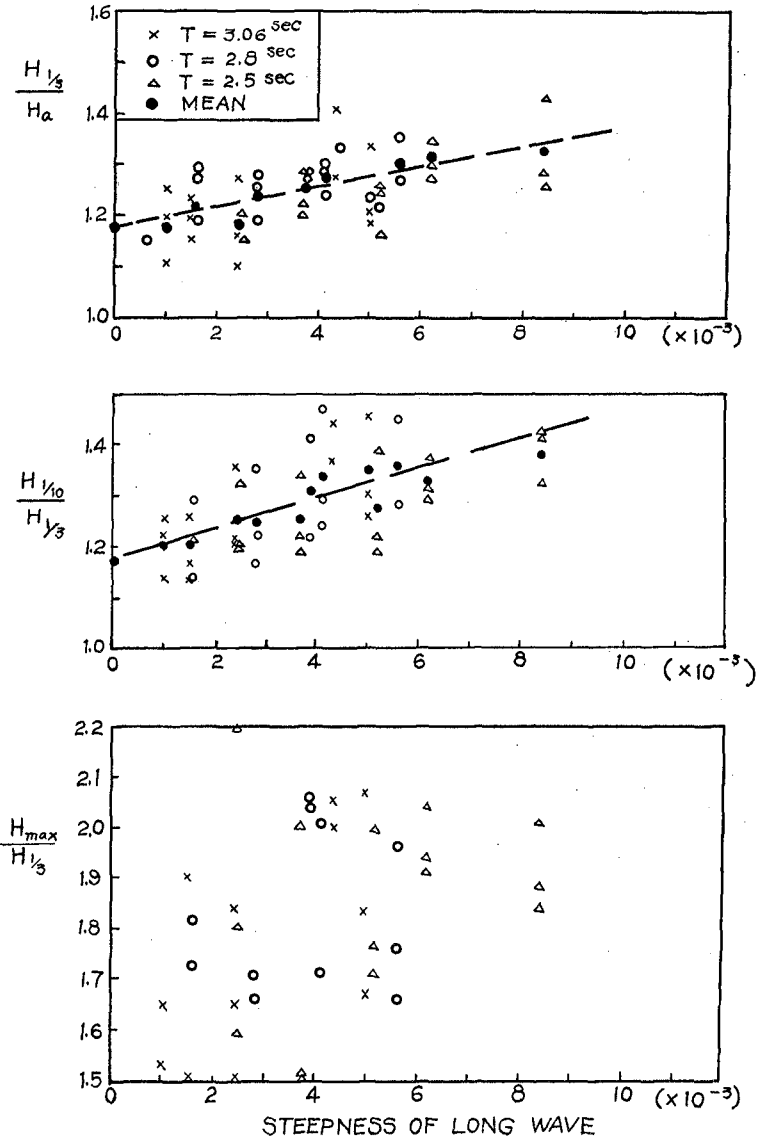
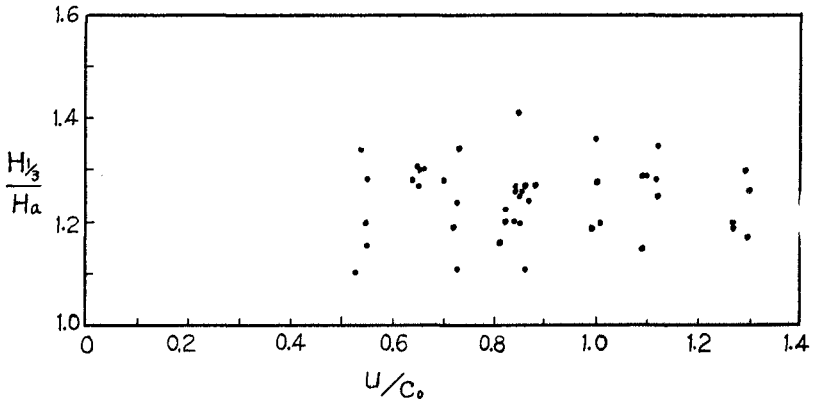
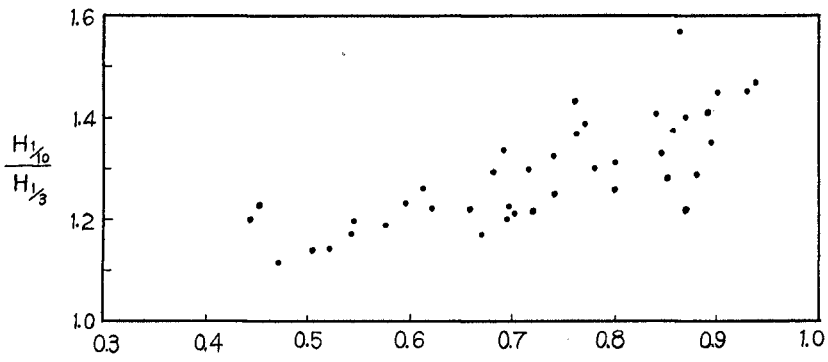


Fig.6 STATISTICAL RATIOS OF WIND WAVE HEIGHTS AND STEEPNESS OF LONG WAVE



(a) $H_{1/3}/H_a \sim U/C_0$



(b) $H_{1/10}/H_{1/3} \sim \epsilon^2$

Fig. 7 CHANGES OF RATIOS OF WAVE HEIGHTS WITH ϵ^2 AND U/C_0

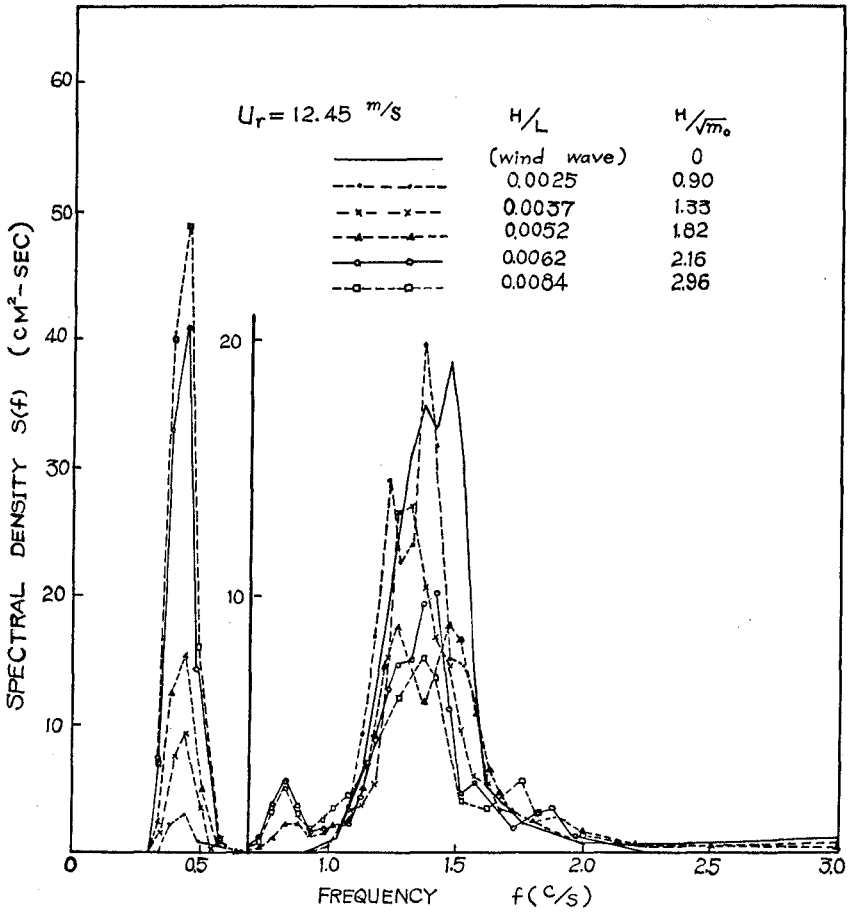


Fig 8 SPECTRA OF CO-EXISTING SYSTEMS OF WIND WAVE AND LONG WAVE.

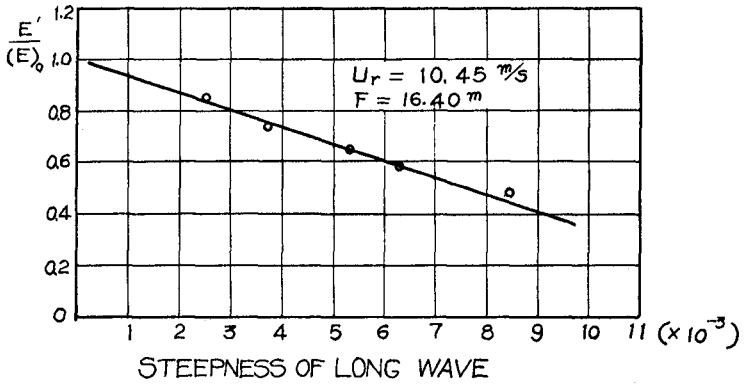


Fig.9. ATTENUATION OF WIND WAVE ENERGY

CHAPTER 23

INTERACTION OF WAVES AND A TURBULENT CURRENT

by

J. D. A. van Hoften¹ and S. Karaki²

ABSTRACT

An experimental investigation was made to study wave-current interaction. Wave amplitude attenuation was measured along a laboratory wave channel to compare wave dissipation with and without flow. Mean, wave, and turbulent velocities were also measured to determine the modifications of the flow imposed by the gravity waves propagating with the current. The process of energy transfer in the wave-current system was studied. Energy was found to be extracted from the waves, diffused downward and dissipated by an increase in bottom shear stress.

INTRODUCTION

The development of a model to accurately describe the generation and decay of ocean surface waves has been a primary objective of oceanographers for decades. In present wave forecasting formulas there is far more agreement on empirical wave growth than on wave dissipation. Numerous studies have dealt with the aspect of laminar wave energy dissipation such as the early theoretical work of Lamb (1932) and Hunt (1952). Experimentally, a large variety of studies have been made relating wave dissipation to near-surface viscous effects or to the oscillatory boundary layers. In real situations, waves seldom travel across non-turbulent waters. Thus an account must be made of the interaction which results as orbital wave velocities work against the shear current and turbulence which likely exist.

This paper describes a laboratory study of the interaction of waves and current as mechanically generated, monochromatic, intermediate-depth gravity waves propagate on a turbulent open channel flow. The two areas of primary concern are:

1. Wave modification - the change in wave form, mainly wave amplitude, resulting in increased wave energy dissipation.
2. Current modification - the alteration of mean and turbulent flow parameters due to the wave interactions, as well as changes in the resistance to flow and energy transport properties.

¹Assistant Professor of Civil Engineering, University of Houston, Houston, Texas (Formerly Research Assistant, Colorado State University)

²Professor of Civil Engineering, Colorado State University, Fort Collins, Colorado

THEORETICAL ANALYSIS

In order to create a set of baseline data for wave attenuation analysis, it is first necessary to examine wave energy dissipation without the effect of channel flow. Hunt (1952) utilized the basic laminar wave dissipation equations and integrated the effects of the oscillatory boundary losses for the side and bottom and derived an expression for a wave attenuation modulus,

$$\alpha = \frac{2k}{b} \sqrt{\frac{\nu}{2\sigma}} \left(\frac{kb + \sinh 2kh}{2kh + \sinh 2kh} \right) \quad (1)$$

where b is channel width, h is flow depth, k is wave number ($2\pi/\text{wave length}$), ν is kinematic viscosity and σ is wave frequency ($2\pi/\text{period}$) derived from $\sigma^2 = gk \tanh kh$. Wave amplitude attenuation is then defined by the exponential form

$$a = a_0 e^{-\alpha x} \quad (2)$$

where a_0 is the initial wave amplitude and a is the attenuated amplitude at distance x .

The analysis of the wave-current amplitude attenuation utilizes a control volume of unit width bounded by upstream and downstream vertical sections, the channel bottom and the free water surface. Whitham (1962) applied the concept of the radiation stress (introduced by Longuet-Higgins and Stewart (1960)) to the momentum and energy flux in water waves. Application of Whitham's concepts to the case of attenuating monochromatic waves propagating on a uniform open channel flow begins with the integral momentum equation,

$$\frac{d}{dx} (\rho h U_m^2) + \rho g h \sin \theta + \frac{dS_{xx}}{dx} = - \bar{\tau}_b \quad (3)$$

$$\text{where } S_{xx} = E \left(\frac{2kh}{\sinh 2kh} + \frac{1}{2} \right) \quad (4)$$

is the longitudinal component of radiation stress, $\sin \theta$ is channel slope, $\bar{\tau}_b$ is the mean bottom shear stress, a is wave amplitude, E is wave energy density ($1/2 \rho g a^2$), and U_m is the mass transport velocity defined by

$$U_m = \bar{u} + \frac{E}{\rho h c} \quad (5)$$

where \bar{u} is mean uniform flow velocity, and c is phase speed. By substituting equations (4) and (5) into (3), differentiating and retaining terms to the order of a^2 and assuming an exponential wave attenuation of the form of equation (2), the resulting equation for bottom shear stress is

$$\bar{\tau}_b = \rho gh \sin \theta + \rho g \alpha a^2 \left[\frac{2}{c} (\bar{u} + c_g) - \frac{1}{2} \right] \quad (6)$$

where c_g is the group velocity defined by

$$c_g = \frac{C}{2} \left[1 + \frac{2kh}{\sinh 2kh} \right] \quad (7)$$

Note that for $\theta = 0$, and $\bar{u} = 0$, equation (6) reduces to the form

$$\bar{\tau}_b = \rho g \alpha a^2 \left[\frac{2c_g}{C} - \frac{1}{2} \right] \quad (8)$$

which is just dS_{xx}/dx . In other words for the case of waves on still water the shear stress on the bottom is balanced by the rate of change of the radiation stress. Also note that if $\theta \neq 0$, $\bar{u} \neq 0$, and $\alpha = 0$, or the case of waves propagating on a current without attenuation,

$$\bar{\tau}_b = \rho gh \sin \theta \quad (9)$$

which is the bottom shear stress without waves.

In the same manner, the equation for the energy flux through the control volume is

$$\frac{d}{dx} \left[\frac{\rho h U_m^3}{2} + \rho gh^2 U_m + S_{xx} U_m + E U_m + E c_g \right] = -D \quad (10)$$

where D is the energy dissipation defined as dE/dt . Again substituting and retaining terms of the order a^2 gives the total dissipation as

$$D = \rho gh \sin \theta \bar{u} + E \left[\frac{g \sin \theta}{c} + \alpha \bar{u} \left(1 + \frac{3\bar{u}}{c} \right) + 2\alpha c_g \left(1 + \frac{2\bar{u}}{c} \right) \right] \quad (11)$$

The first term on the right is the energy dissipation due to channel flow alone as the product of shear stress and mean velocity. The remaining terms represent the additional dissipation due to wave-current interaction and will be denoted D_w . For the case of no flow, $\bar{u} = 0$, $\theta = 0$, and noting that $da/dx = -\alpha a$, equation (11) reduces to

$$D = c_g \rho g \alpha a^2 \quad (12)$$

$$\text{or } D = -c_g \frac{dE}{dx} \quad (13)$$

Thus the energy dissipation in still water is a product of the group velocity and the longitudinal wave energy density gradient.

The above analysis provides a basis for the experimental measurements. Terms of equation (11) may be directly measured and an estimate may be computed for the total dissipation between successive sections of the channel. Limitations are imposed by the

assumption of a uniform velocity profile and the neglect of side-wall losses. Also neglected is the integral effect of the turbulent interaction. A possible improvement may be made to the analysis by the use of the energy equation derived by Brink-Kjaer and Jonsson (1975) which assumes a linear shear profile.

EXPERIMENTAL APPARATUS AND PROCEDURES

Figure 1 shows a schematic of the wind-wave facility at Colorado State University. The flume is 15.8 m long, 60 cm wide and 70 cm deep. Flow was recirculated at a constant depth of 15.2 cm and waves were generated by a vertical plunger of the upstream end. Mean flow velocities ranged from 15.0 to 60.0 cm/sec and wave frequencies varied from 1.3 to 2.5 Hz.

An initial study of wave attenuation in still water was made to compare the experimental results to the theoretical laminar dissipation of equation (1). Water surface elevations were measured with a capacitance probe mounted on a moving carriage. Average or rms wave heights were measured at 15 cm intervals along the centerline of the 10 m test section. Wave lengths were measured directly by longitudinally separating two capacitance probes and observing the corresponding Lissajous figure on an X-Y oscilloscope plot. Integral wave locations were recorded when the figure repeated itself.

Waves were next generated on a series of steady currents and wave profiles were measured. Artificial bottom roughness elements assured a fully developed turbulent flow. Velocity measurements were made with a split hot-film anemometer at various depths in the flow field both with and without waves. Simultaneous wave and velocity data were digitized and stored on magnetic tape.

Iterative computer techniques were used to analyze the split-film data due to the large intensities of the velocity fluctuations. Phase averaging techniques were next used to compute flow quantities relative to the average wave profile. Quantities computed at each depth included mean velocity, wave velocity, longitudinal and vertical turbulence intensities, and turbulent and wave induced Reynolds stress.

To separate the velocity components the instantaneous velocity, u_i , is written as a sum of a time mean, \bar{u}_i , a wave induced component, \tilde{u}_i , and a random component, u_i' . Thus

$$u_i(x, z, t) = \bar{u}_i(x, z) + \tilde{u}_i(x, z, t) + u_i'(x, z, t) \quad i = 1, 2 \quad (14)$$

By first time averaging, the mean signal is removed. The process of phase averaging then identifies wave induced and turbulent velocities as a function of wave phase. Phase averaging is symbolized by brackets ($\langle \bullet \rangle$).

WAVE MODIFICATION

Figure 2 shows three typical mean wave amplitude variation curves for waves in still water. Figure 3 illustrates similar measurements for waves on a flowing channel. The rms amplitudes are normalized by the amplitude at the beginning of the test section. Reflected wave energy creates the regular variation in rms wave amplitude throughout the channel. In most still water cases the pattern obeyed the one-half wave length theory presented by Ursell et.al. (1959). For waves on a current the pattern was distorted due to the modification of wave parameters by the flow, but a regular sinusoidal pattern still existed in the channel.

Attenuation, or wave energy dissipation is demonstrated by the gradual decay of wave amplitude along the channel. The measured exponential decay modulus, α_m , was calculated by a least squares fit of equation (2) to the measured profiles. It is readily apparent that neglecting wave reflection would seriously affect attenuation measurements. Figure 4 is a plot of representative measured attenuation coefficients on still water against the viscous theory of Hunt (1952). In nearly all cases the theory slightly underestimates the measured attenuation modulus, a fact that many investigators have previously noted (Eagleson (1962), and Grosch et.al. (1960)).

In order to compare wave attenuation on still and moving water it is necessary to analyze the wave-current results from a reference system convected with the mean velocity. The results then show a reduced relative frequency and decreased fetch. Figure 5 shows wave dissipation as a function of wave amplitude on still water. Note again that the dissipation is slightly underestimated by viscous theory but increases nearly as the square of the amplitude. Figure 6 is a similar plot of waves on a current, where D_w is the wave dissipation from the convected reference system, calculated from equation (11). Note in this case the large increase in wave dissipation due to the wave-current interaction and the divergence from the A^2 variation as amplitude increases. Figure 7 shows the dissipation as a function of wave steepness, ak , with mean velocity, \bar{u} , as a third variable. Steeper waves on the same flow are shown to dissipate energy faster, probably due to the added-stretching of vortex lines as described by Phillips (1959).

FLOW MODIFICATION

Figure 8 illustrates the effect on the velocity profile of increasing frequency and amplitude of waves superposed on a constant mean velocity. Mean velocities at each relative depth, z/h , are normalized by the bulk mean velocity. As the frequency and amplitude increase, the mean velocity profile flattens near the surface and steepens near the bottom. Equation (16) predicts that $\bar{\tau}_b$ will increase as the wave amplitude and attenuation modulus increase. The increase in velocity gradient near the bottom indicates the relative increase in average boundary shear.

The modification of mean velocity and turbulence quantities for a typical run is shown in Figure 9. Dotted profiles are those measured without waves. Quantities for the wave-current profiles are an average over a wavelength of the phase averaged results. The mean velocity profiles indicate a strong interaction with a large increase in gradient near the bottom. The local longitudinal and vertical turbulence intensities show an increase near the surface and relative reduction in the middle regions. The Reynolds stress becomes positive near the surface due to the reversal of the mean velocity gradient, and its magnitude is lower throughout the depth. It is apparent that the interaction of the waves and shear flow produce turbulence near the surface and that it diffuses downward, likely through the action of wave induced pressure terms. A further analysis of the energy transfer mechanism is given in van Hoften (1976).

Local flow characteristics give insight into the magnitude of the interaction. Figure 10 shows the longitudinal wave induced velocity at various relative depths. Velocity variations are typical of intermediate-depth waves with finite velocities near the bottom. Figure 11 is a plot of the phase averaged longitudinal turbulence intensity and Figure 12 is the turbulent Reynolds stress. Note that both exhibit double frequency behavior and both become less phase dependent as depth increases.

One-dimensional energy spectra of the longitudinal velocity fluctuation, with and without waves, were computed. Figure 13 shows spectra computed at four relative depths without waves. The inertial subrange where the slope obeys the $-5/3$ law appears as a narrow band due to the relatively low flow Reynolds number ($R_e = 36,900$). The high frequency portions of the spectra conform closely to the -7 slope where viscous effects determine energy transfer. A -1 slope at $z/h = 0.07$ is mildly indicated in the region where Tchen (1953) predicts large turbulence production, near solid boundaries. Figure 14 shows spectra of the total longitudinal velocity ($u + u'$) with waves. The large peaks in the plots correspond to the wave induced velocity component at 1.88 Hz. Note that relative peaks decrease with depth, as the velocity plots from Figure 10 indicate. The spectrum at $z/h = 0.95$ appears to have a range of low frequencies where the -1 slope applies, representing a production range. Chang and Cheng (1972) studied turbulent airflow over water waves and predicted that the -1 power law should apply from the dominant wave frequency to the lower bound of the inertial subrange. The low Reynolds number of the present flows, however, prevents an accurate assessment of this concept.

CONCLUSIONS

Waves propagating on an open channel flow are shown to be altered by a combination of the interaction of the waves with the shear gradient and the existing turbulence. The effect is to extract energy from the waves resulting in an increased wave attenuation.

The flow itself is altered by the superposed waves. The induced orbital wave velocities distort the mean velocity profile increasing the gradient near the bed. Turbulence energy is produced near the surface by the interaction of the wave induced Reynolds stresses and the fluctuating velocity gradients. The energy diffuses downward where it is dissipated on the bottom by an increase in apparent boundary shear stress.

REFERENCES

- Brink-Kjaer, O. and I.G. Jonsson (1975), Radiation Stress and Energy Flux in Water Waves on a Shear Current. Progress Report 36, Inst. Hydrodyn. and Hydraulic Engineering, Tech. University of Denmark, p 27.
- Chang, P.C., and I.M. Cheng (1972), Interaction Subrange Spectrum of Turbulent Wind Over the Air Water Interface. J. Physical Oceanography, 2, p 273.
- Eagleson, P.S. (1962), Laminar Damping of Oscillatory Waves. J. Hydraulics Div., ASCE, HY3, May, p 155.
- Grosch, C.E., L.W. Wood, and S.J. Lukesik (1960), Viscous Dissipation of Shallow Water Waves. Physics of Fluids, 3, No. 3, p 477.
- Hunt, J.N. (1952), Viscous Damping of Waves Over an Inclined Bed in a Channel of Finite Width. LaHouille Blanche, December, p 836.
- Lamb, H. (1932). Hydrodynamics, Dover Pub. Inc., New York.
- Longuet-Higgins, M.S., and R.W. Stewart (1960), Changes in the Form of Short Gravity Waves on Long Waves and Tidal Currents. J. Fluid Mechanics, 8, p 565.
- Tchen, C.M. (1953), The Spectrum of Energy in Turbulent Shear Flows. J. Research, National Bureau of Standards, Vol. 50, p 51.
- Ursell, F., R.G. Dean, and Y.S. Yu (1960), Forced Small Amplitude Water Waves: A Comparison of Theory and Experiment. J. Fluid Mechanics, 7, p 33.
- van Hoften, J.D.A. (1976), The Interaction of Gravity Waves and Turbulent Channel Flow, Ph.D. Dissertation, No. CED75-76JDAVH36, Colorado State U., Ft. Collins.
- Whitham, G.B. (1962), Mass, Momentum and Energy Flux in Water Waves. J. Fluid Mechanics, 12, p 135.

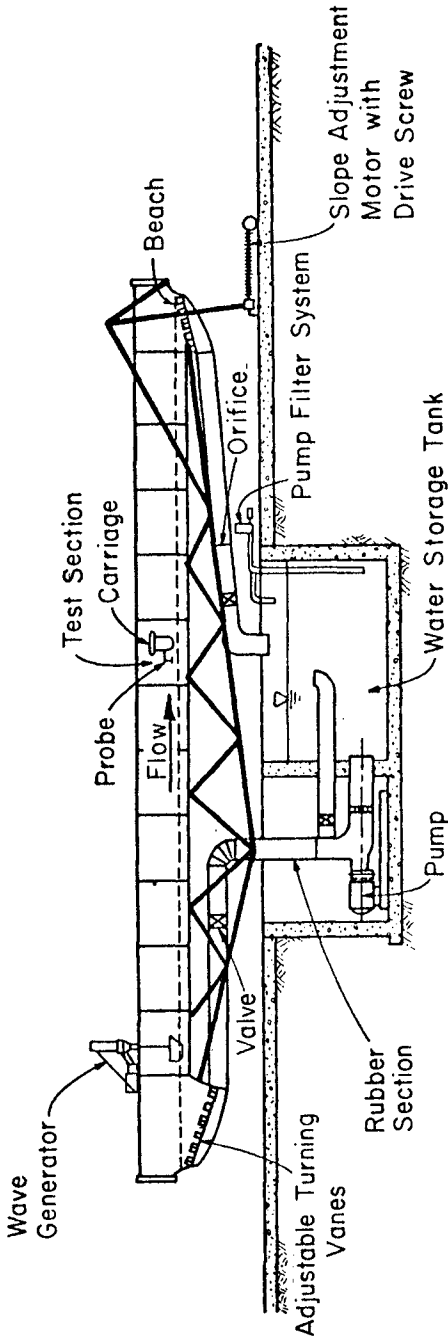


Figure 1. Wind-wave facility of Colorado State University.

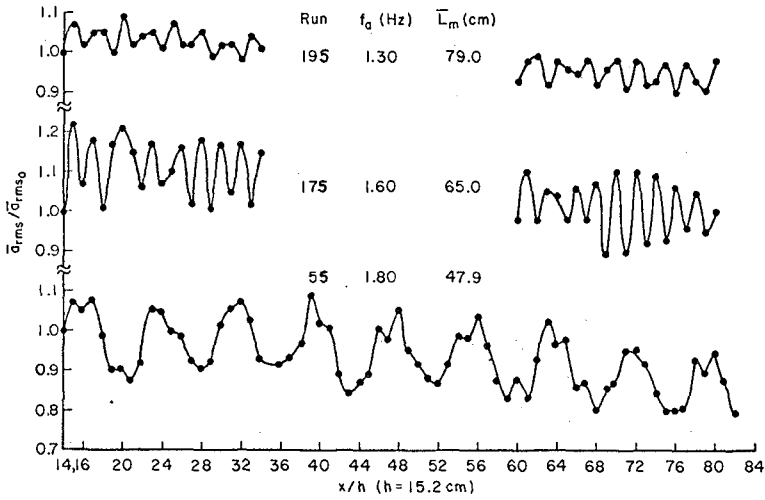


Figure 2. Still water reflection and attenuation profiles

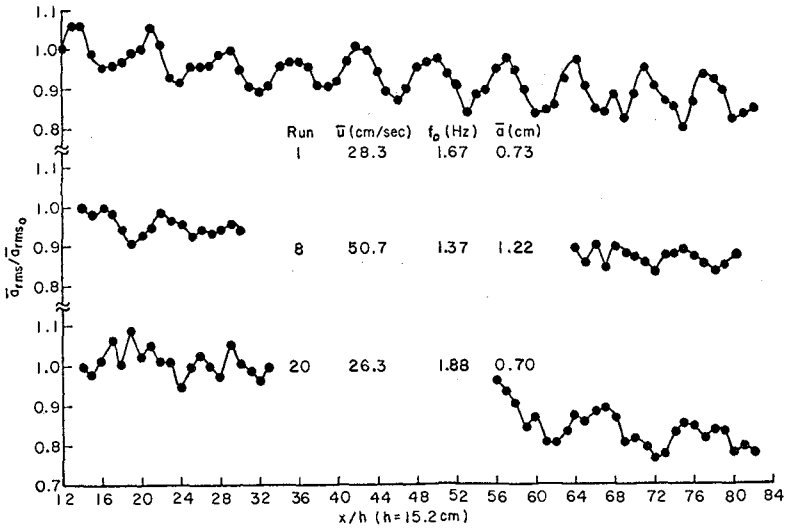


Figure 3. Reflection and attenuation profiles for waves on a turbulent current.

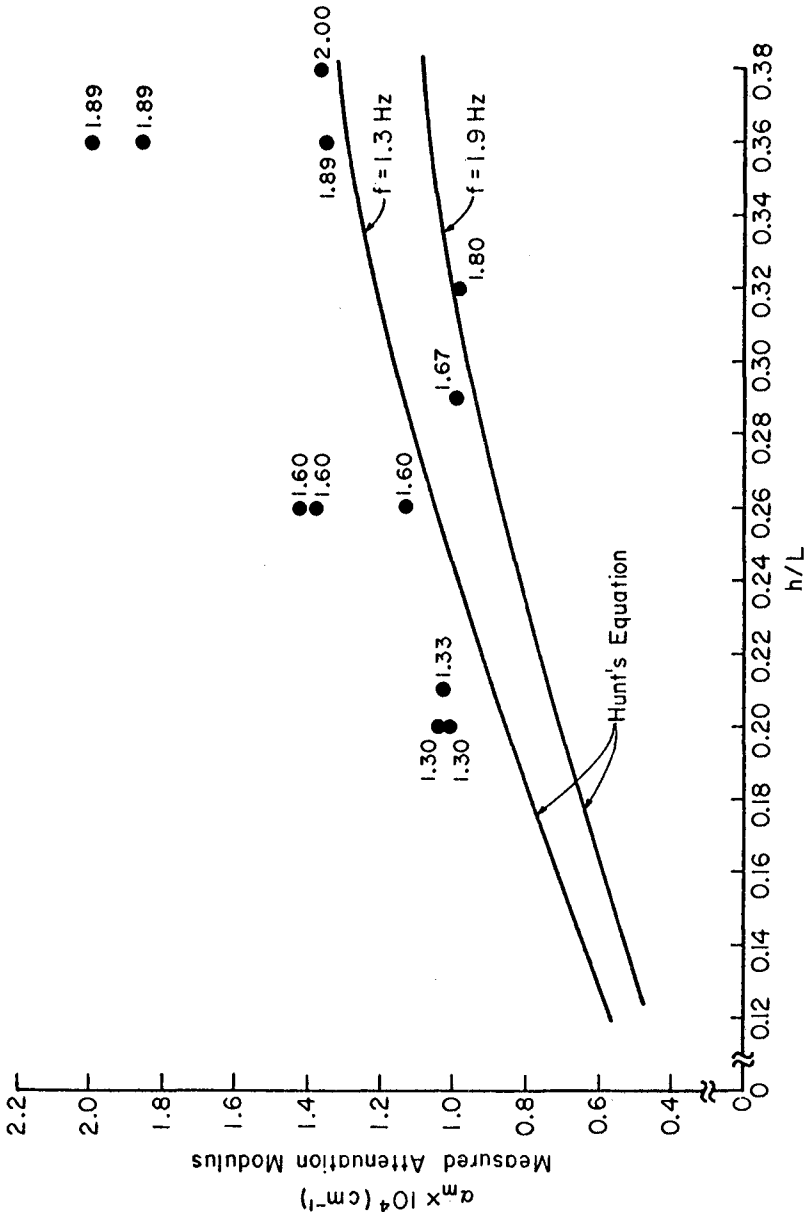


Figure 4. Measured attenuation modulus.

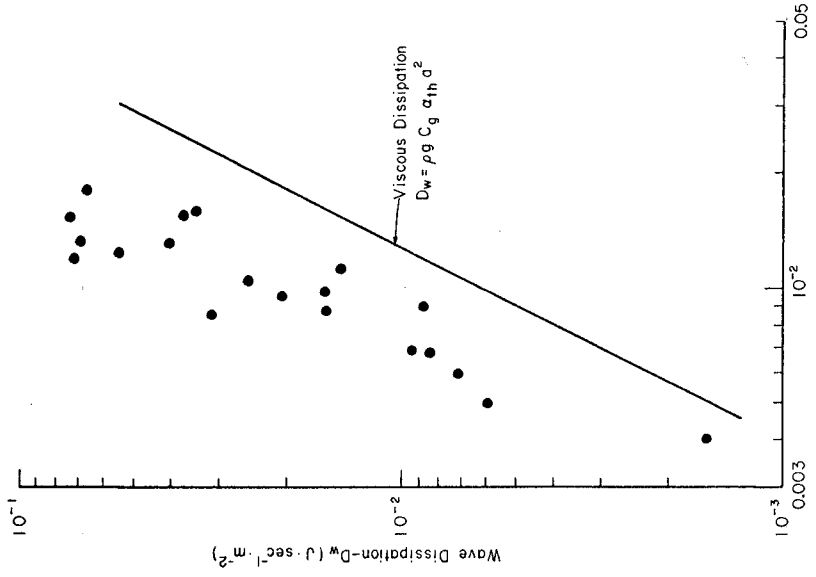


Figure 6. Wave dissipation on a turbulent flow.

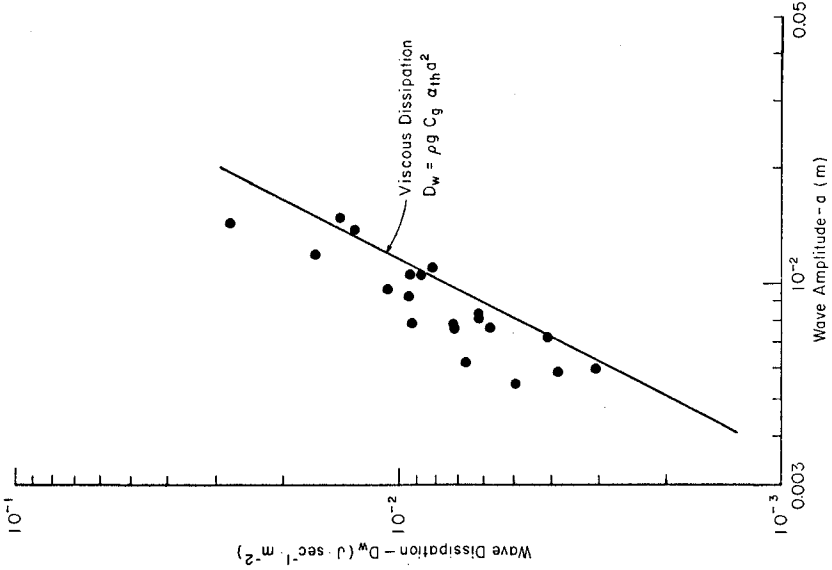


Figure 5. Still water wave dissipation

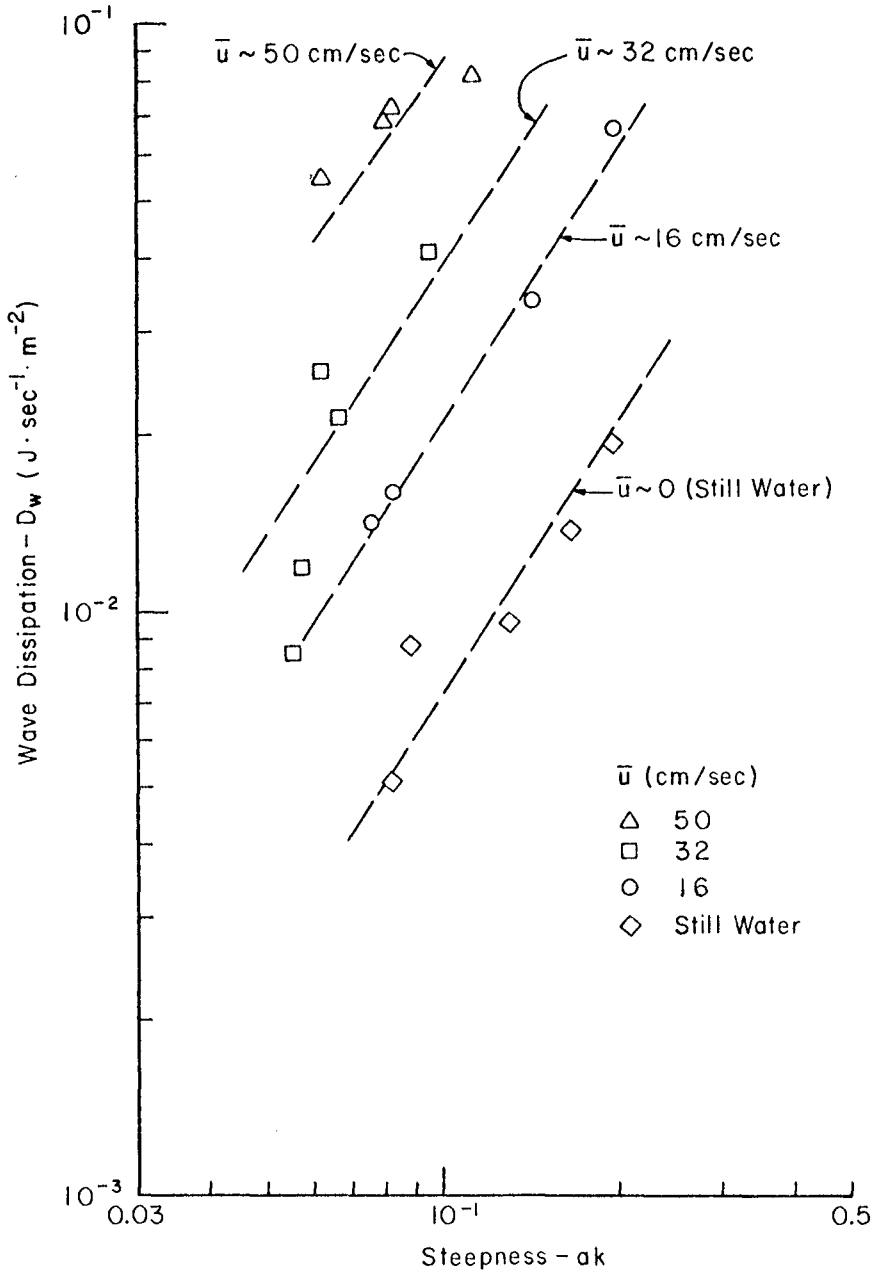


Figure 7. Wave dissipation as a function of wave steepness with constant flow velocity.

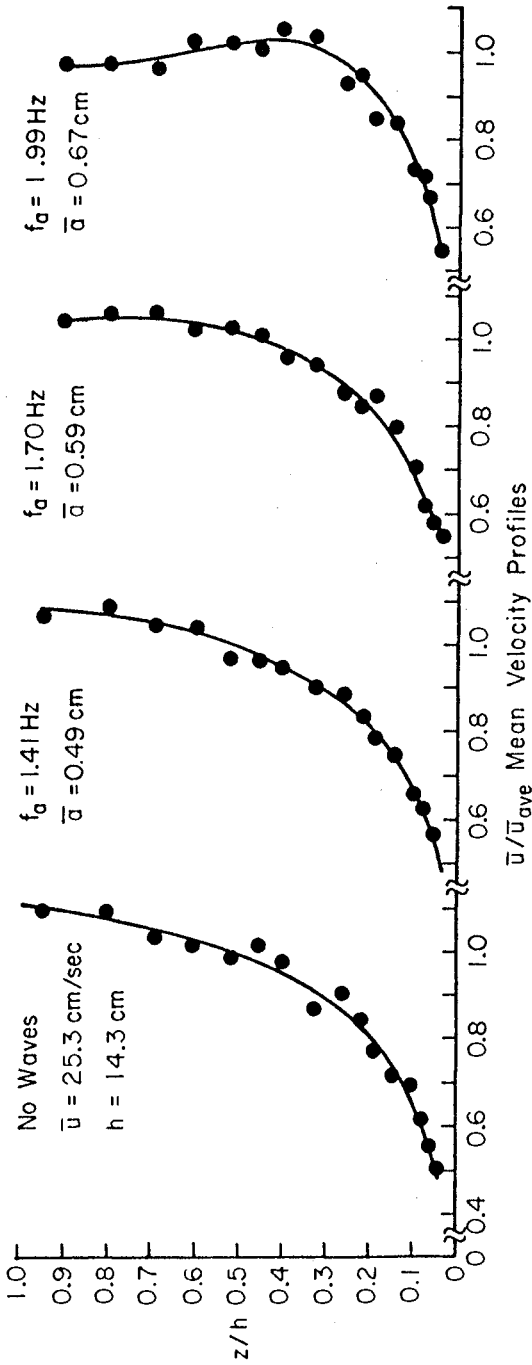


Figure 8. Mean velocity profiles with increasing wave frequency and amplitude.

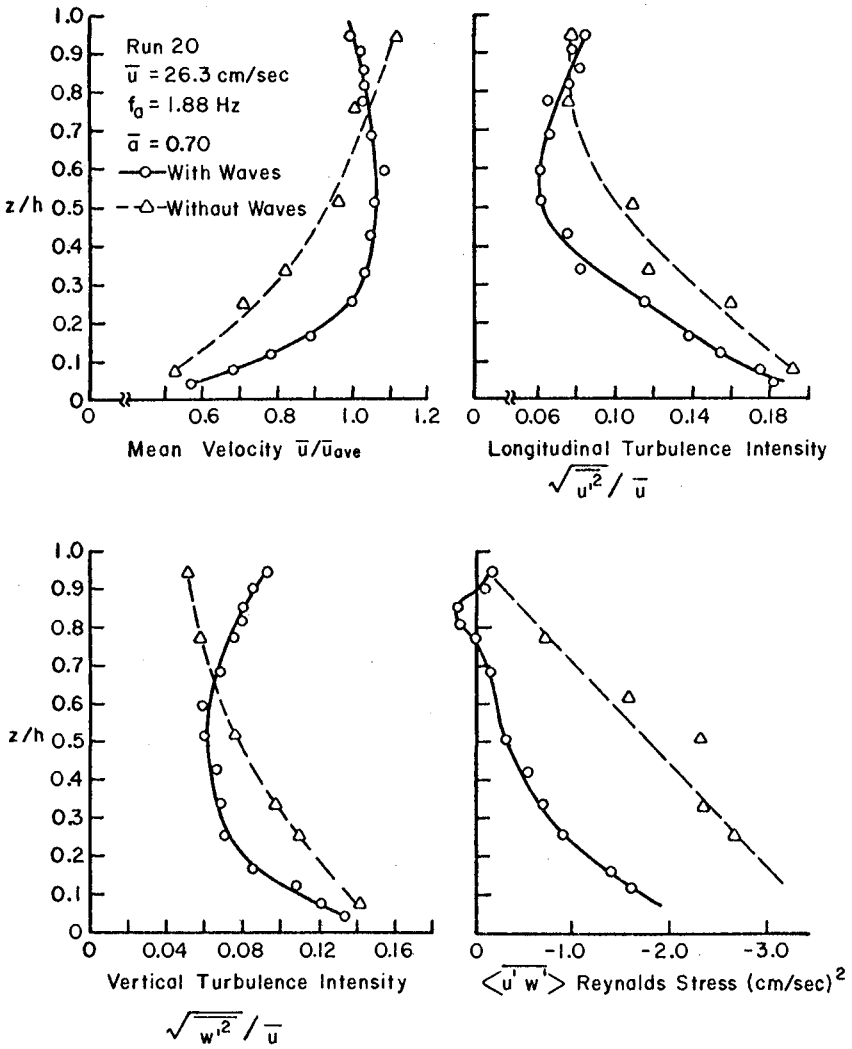


Figure 9. Mean velocity and turbulence profiles with and without waves.

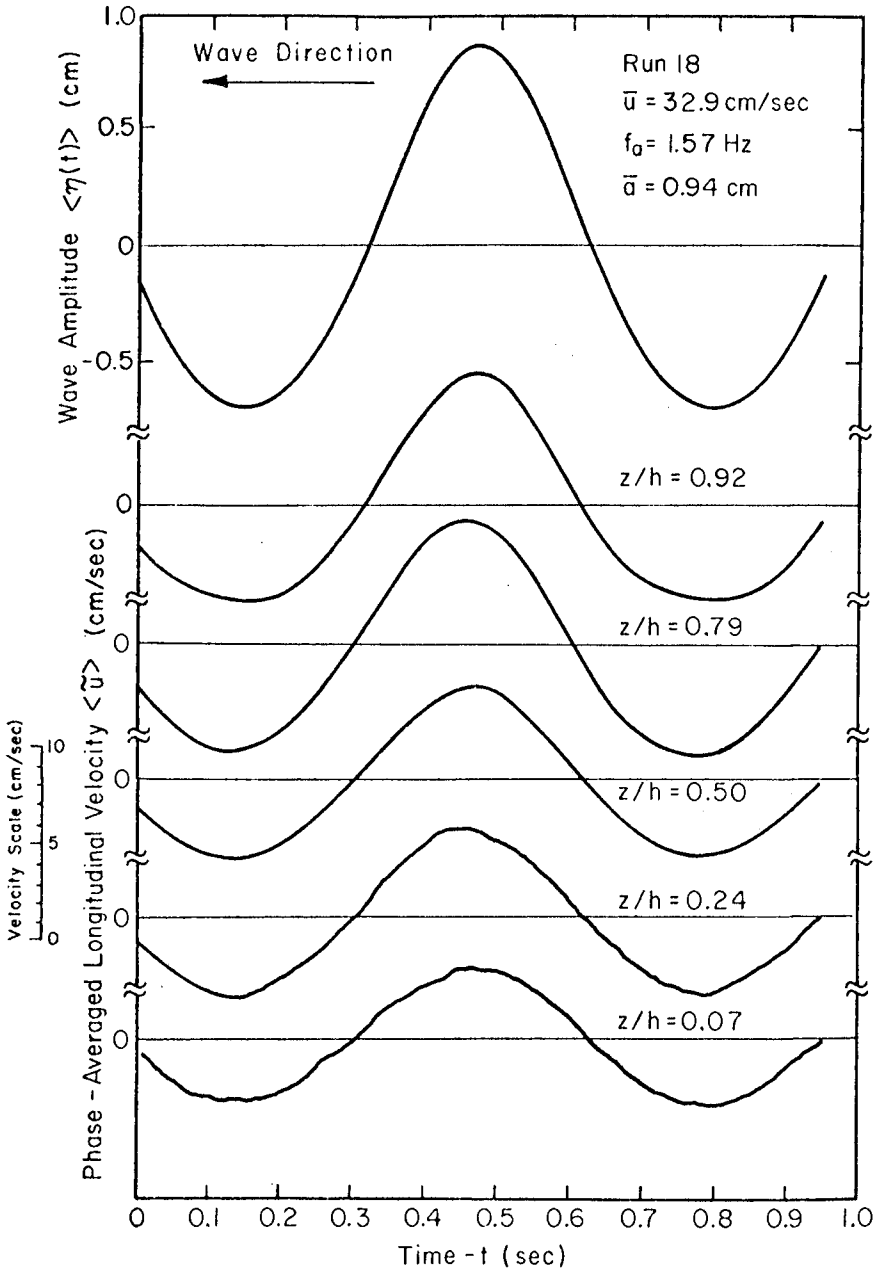


Figure 10. Phase averaged wave induced velocity $\langle \hat{u} \rangle$.

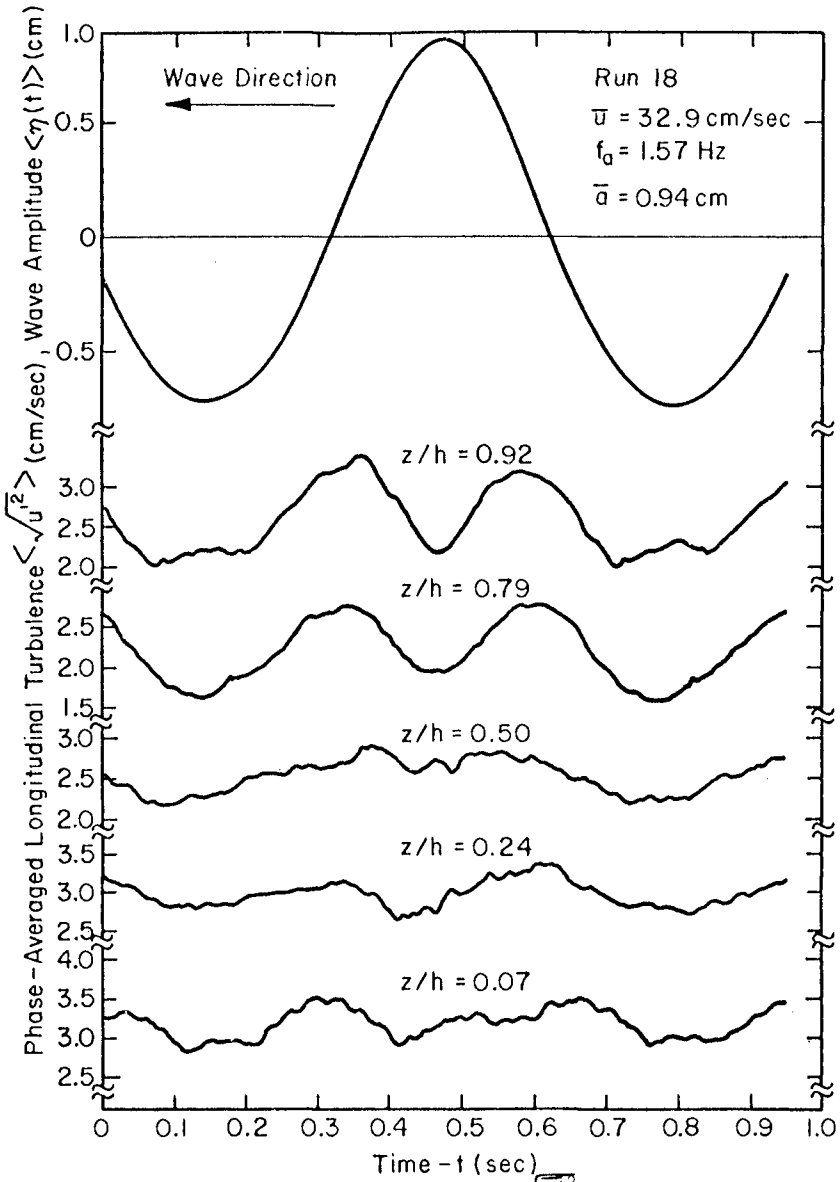


Figure 11. Phase averaged turbulence rms $\langle \sqrt{u^2} \rangle$.

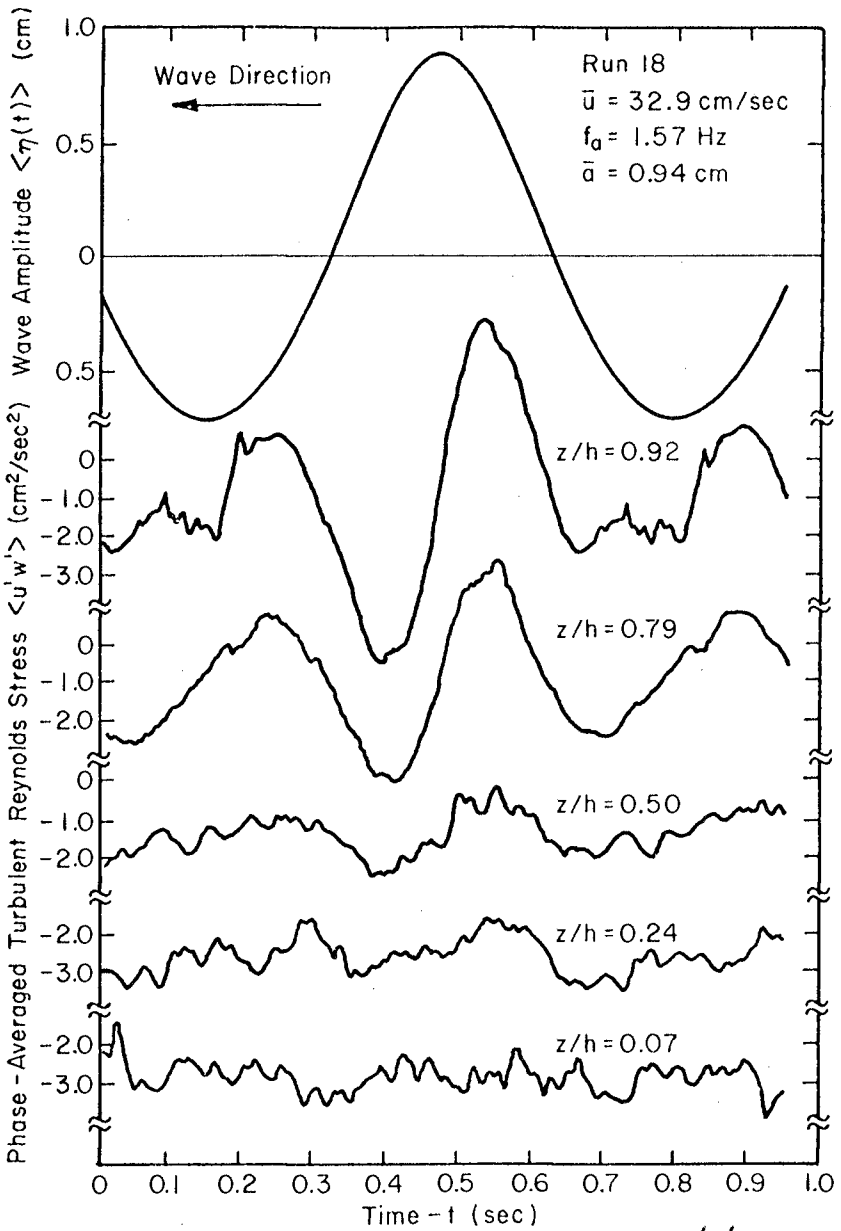


Figure 12. Phase averaged turbulent Reynolds stress $\langle u'w' \rangle$.

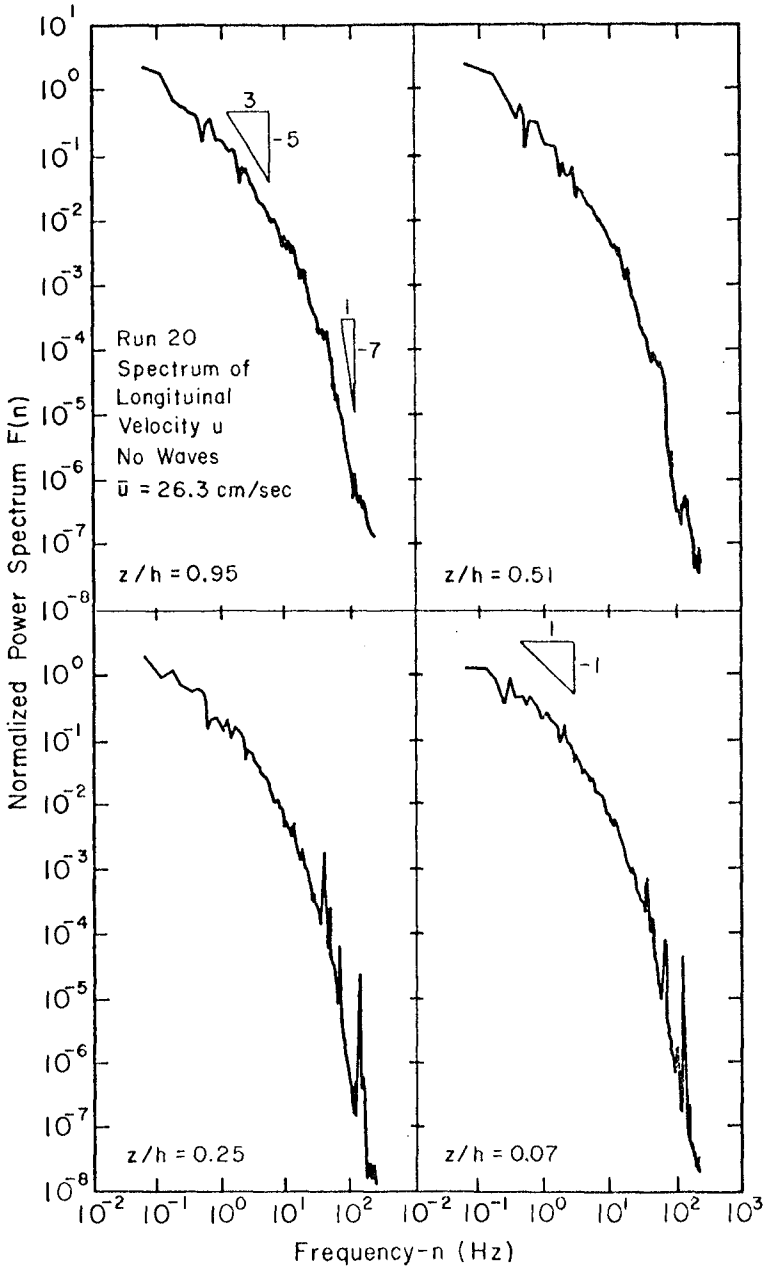


Figure 13. Spectra of longitudinal velocity, u , without waves.

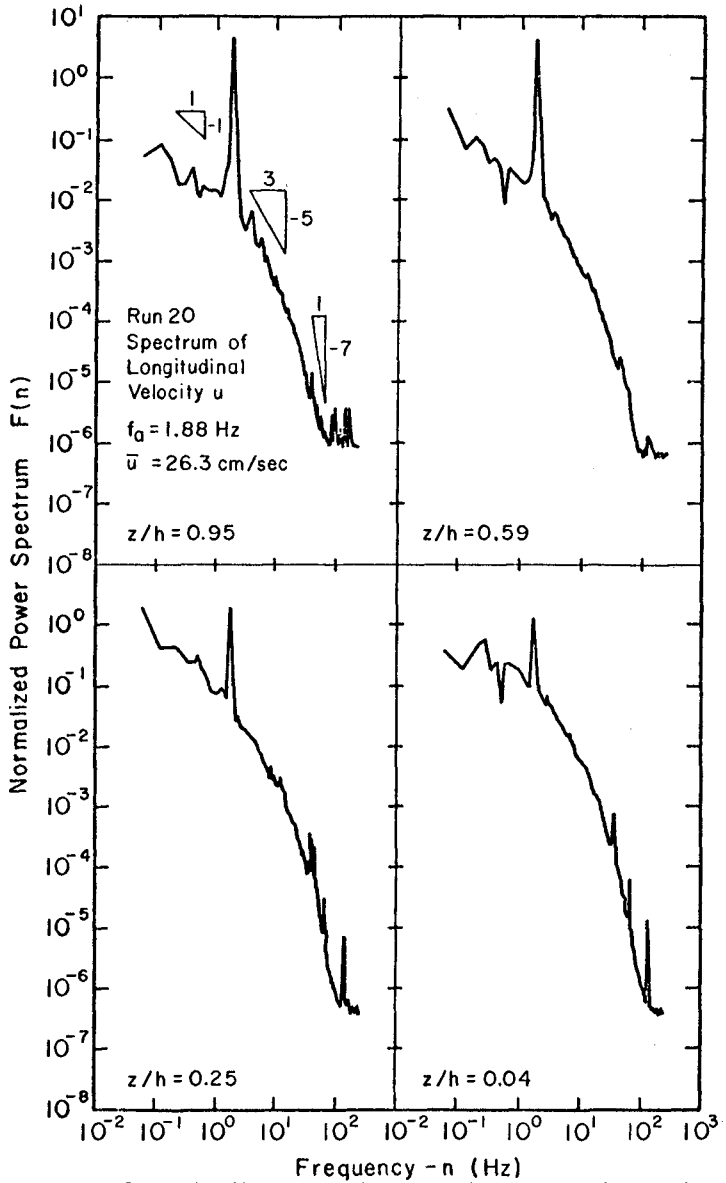


Figure 14. Spectra of longitudinal velocity, u , with waves, $f_a = 1.88$ Hz.

CHAPTER 24

TRANSFORMATION OF NONLINEAR LONG WAVES

by

Nobuo Shuto

Chuo University, Tokyo, Japan.

SYNOPSIS

Kakutani's equation is extended to include the effects of variable width of the channel and the bottom friction. Based on the equation, several solutions are derived and compared with experimental results. For example, Green's law is obtained if the nonlinearity, dispersion and bottom friction are neglected. With the nonlinearity included, it is shown that the wave amplitude follows Green's law and at the same time the wave profile deforms due to the nonlinear effect.

Discussion of the present paper is mainly focused on the effect of the bottom friction. From the experimental results of cnoidal waves in a channel of constant depth and width, on the bottom of which artificial roughnesses are planted, it is shown that the friction coefficient estimated from Kajiura's theories gives good agreements, thus confirming the validity of the method of conversion, proposed in the present paper, between sinusoidal and cnoidal wave motions.

Change in height of cnoidal waves on a slope is also solved. The friction coefficient determined from wave characteristics and bottom conditions, by means of Kajiura's theories and the method of conversion stated above, is used in the comparison with experimental results. Theoretical prediction agrees very well with experimental results.

INTRODUCTION

In shallow water, long waves transform under several effects such as nonlinearity, dispersion, topography and bottom friction. As for the first three effects, the present author has derived an equation and solved in one of his previous papers [1].

In the present paper, an equation which includes all four effects is derived and, therefore, is considered a fundamental equation for water waves in shallow water. In other words, the equation is an extension of Kakutani's equation [2], because if the bottom friction and the effect of the variable width are neglected, it is reduced to Kakutani's one.

The bottom friction here is assumed to be proportional to the square of the horizontal velocity of water particle. This is normally done if the flow is turbulent near the bottom. We encounter two questions as for the expression of the bottom friction. The one is how we select the representative horizontal velocity, and the second problem is how we can estimate the magnitude of the friction coefficient.

In the following derivations, the horizontal velocity of the first order approximation, that is, the horizontal velocity of the linear long waves is used as the representative velocity. Since it has a uniform vertical distribution, it is easy to connect it with the water surface elevation η , for which the equation is derived. At the same time, there is neither ambiguity nor complexity in the definition of the bottom friction.

For the friction coefficient in an oscillatory flow, Jonnson's empirical formula [3] and Kajiura's theories [4], [5] are available. In the present paper, an attempt is made to connect cnoidal waves with Kajiura's theories which assumed sinusoidal waves. It is assumed here that the mean energy dissipation is the same for sinusoidal and cnoidal waves, thus providing the method of conversion of the friction coefficients.

Kajiura derived his first theory, on assuming that the boundary layer thickness is very big and covers the whole water depth. This corresponds to tsunamis or storm surges in natural conditions.

Kajiura's second theory is for wind waves or swells in shallow water. It is assumed that the boundary layer thickness is very thin compared to the water depth.

In the experiments, artificial rectangular roughnesses are planted on the bottom of the channel and on the slope. For a given size and spacing of the roughnesses, Adachi's empirical formula [6] is used to calculate the coefficient of the bottom friction and the roughness length z_0 in steady flow. The friction coefficient thus obtained is always smaller than that required for unsteady flow. Therefore, the roughness length is used to estimate the friction coefficient for unsteady flow, combined with the horizontal velocity of linear long waves, by Kajiura's theories.

Decay of cnoidal waves in a channel of constant depth and width are at first tested in order to examine the validity of the expression of the bottom friction. Dimensions of the roughnesses used in the experiments are big for the water depth, compared with the natural condition. The friction coefficients computed from experimental results are quite big compared with that estimated for steady flow and fall between two Kajiura's theories. Therefore, it is concluded that the present theory combined with Kajiura's theories provides reasonable basis for transformation of nonlinear long waves in shallow water.

Experiments are also carried out on a slope of 1 on 20, on which the same artificial roughnesses are planted. Mean value of the friction coefficient is used to predict the change in wave height and the results agree very well with experimental results.

FORMULATION

The equations to be solved are;

$$\left. \begin{aligned}
 u_x + v_y + w_z &= 0 \\
 u_t + uu_x + vu_y + wu_z &= -\frac{1}{\rho} p_x + \frac{1}{\rho} \tau_z \\
 v_t + uv_x + vv_y + wv_z &= -\frac{1}{\rho} p_y \\
 w_t + uw_x + vw_y + ww_z &= -\frac{1}{\rho} p_z - g
 \end{aligned} \right\} \text{----- (1)}$$

in which the x-axis is taken horizontally and parallel to the direction of wave propagation, the y-axis horizontally and normal to the x-axis, and the z-axis vertically and positive upwards. It is assumed that the bottom friction mainly contributes in the x-direction only.

Boundary conditions are as follows.

On the free surface $z = h_0 + \eta$,

$$\left. \begin{aligned}
 p &= 0 \\
 \eta_t + u\eta_x + v\eta_y &= w \\
 \tau &= 0
 \end{aligned} \right\} \text{----- (2)}$$

On the sea bottom $z = h(x)$

$$\left. \begin{aligned}
 uh_x &= w \\
 \tau &= \tau_b
 \end{aligned} \right\} \text{----- (3)}$$

At the side wall of the channel $y = \pm b(x)$,

$$ub_x = \pm v \quad \text{----- (4)}$$

In these expressions, it is assumed that the centerline of the channel coincides with the x-axis and the water depth does not vary in the y-direction.

Equations and conditions are expressed in dimensionless form by using Johnson's method [7] and are expanded into series by Kakutani's method of perturbation [2]. The details are not stated here because they are almost the same as are given in one of the author's previous papers, except that the bottom friction is developed as $\tau = \epsilon^{1/2} \tau_0 + \epsilon^{3/2} \tau_1 + \text{----}$. With this expression, the effect of the bottom friction does not appear in the first order approximation but in the second approximation.

Solutions of the first order approximation are given as follows.

$$u_0 = \frac{1}{V_0} \eta_0, v_0 = 0, w_0 = \frac{1}{d} \eta_0 \xi (1 - d - z), p_0 = \eta_0$$

----- (5)

where every quantities are expressed in terms of the elevation of free surface η_0 . Up to this point, no restriction is given to the wave profile.

Second order approximation is solved and every terms are expressed again in terms of η_0 and are integrated once with respect to the y-direction in order to include the side wall condition in the equation, and vertically once thus taking into consideration the bottom and free surface conditions. Finally we have the following equation for the first order surface elevation in dimensional expression.

$$\eta_x + \frac{3}{2} g^{-1/2} d^{-3/2} \eta \eta_\xi + \frac{1}{6} g^{-3/2} d^{1/2} \eta_{\xi\xi\xi} + \frac{1}{4} d^{-1} d_x \eta$$

$$+ \frac{1}{2} b^{-1} b_x \eta + \frac{1}{2} C_1 d^{-2} \eta |\eta| = 0$$

----- (6)

in which the subscript 0 is omitted for simplicity. Letter subscripts in the equation denote differentiation with respect to them.

The first term in the equation denotes the spatial rate of change in wave profile and others are the causes. The second term is the effect of finite amplitude, referred hereafter, as the effect of nonlinearity. The third is the effect of dispersion. The fourth is the effect of the variable water depth. With these four terms only, the equation is reduced to Kakutani's equation.

The fifth term gives the effect of the variable width of the channel. With this term included, the equation is extended to two dimensional cases which are important in practical problems such as refraction problem. The bottom friction is given by the last term in which the bottom friction is expressed as $\tau = \rho C_1 u |u|$.

Notations used are as follows. The term x denotes the horizontal distance, ξ a modified time defined by $\xi = \int (1/\sqrt{gd}) dx - t$, t the actual time, g the acceleration of gravity, d the undisturbed water depth, b the width of the channel and C_1 the friction coefficient.

EXAMPLES OF SOLUTION

Decay of linear long waves

Equation (6), with the second and third terms neglected, is reduced to

$$\frac{\eta_x}{\eta} + \frac{1}{2} \frac{b_x}{b} + \frac{1}{4} \frac{d_x}{d} + \frac{C_1}{2} \frac{|\eta|}{d^2} = 0$$

----- (7)

and the solution is

$$\eta b^{1/2} d^{1/4} = \eta_0 b_0^{1/2} d_0^{1/4} \exp\left[-\int_{x_0}^x \frac{C_1}{2} \frac{|\eta|}{d^2} dx\right] \quad \text{----- (8)}$$

If the friction term is neglected, the equation is reduced to Green's law of shoaling.

For a sinusoidal wave in a channel of constant depth and width, when the effect of bottom friction is assumed small enough to be replaced by an equivalent linear friction, then for a small travel distance x , the wave profile is given by

$$\eta = \eta_0 \exp\left[-\frac{4a_0}{3} \frac{x}{d^2}\right] \quad \text{-----(9)}$$

where a_0 is the initial wave amplitude.

Decay of shallow water waves due to bottom friction

It is assumed here that the depth and width of the channel are constant. Equation (6) is reduced to the following expression.

$$\eta_x + \frac{3}{2} g^{-1/2} d^{-3/2} \eta \eta_\xi + \frac{C_1}{2} d^{-2} \eta |\eta| = 0 \quad \text{----- (10)}$$

For the positive η , the equation is simply expressed by

$$\eta_x + A\eta \eta_\xi + B\eta^2 = 0 \quad \text{----- (11)}$$

and its solution which satisfies the boundary condition $\eta = f(-t)$ at $x = x_0$ is given by

$$\eta = \frac{f\left[\xi + \frac{A}{B} \ln\{1 - B\eta(x - x_0)\}\right]}{1 + B(x - x_0) f\left[\xi + \frac{A}{B} \ln\{1 - B\eta(x - x_0)\}\right]} \quad \text{----- (12)}$$

For the negative η , B in the equation is replaced by $-B$. In these expression $A = 3/2 \cdot g^{-1/2} d^{-3/2}$, and $B = C_1 d^{-2}/2$.

CHANGE IN WAVE HEIGHT OF CNOIDAL WAVESEquation

For simplicity, equation (6) is written as

$$\eta_x + \alpha_1 \eta \eta_{\xi} + \alpha_2 \eta_{\xi} \eta_{\xi} + \alpha_3 \eta |\eta| + \alpha_4 \eta = 0 \quad \text{----- (13)}$$

The wave profile is divided into two parts; the one is the principal part η_0 which is cnoidal waves and the other minor part a modification.

$$\eta_0 = H \operatorname{cn}^2 \beta + \delta, \quad \beta = A[\xi - Bx], \quad A = \frac{1}{k} \left[\frac{3gH}{4d^2} \right]^{1/2} \quad \text{----- (14)}$$

It is assumed that the principal part of the wave profile always keeps the cnoidal shape. Main change can occur in its wave height, phase and the position of wave trough. And even if the higher order term is included, the latter should not increase secularly with respect to x . Otherwise, at some time later, the magnitude of the higher order term exceeds that of the basic cnoidal waves and, then, the perturbation applied here is no longer valid. As for the details of the manipulation, one can refer References [1], [8] and [9].

Under this assumption, the following equation is derived and gives the change in wave height.

$$\frac{1}{H} \frac{dH}{dx} - \frac{1}{2U} \frac{dU}{dx} + \alpha_4 + \frac{\delta}{H} \frac{I_2}{I_1} \left[\frac{1}{H} \frac{dH}{dx} - \frac{1}{U} \frac{dU}{dx} + \alpha_4 \right] + \alpha_3 H \frac{I_0}{I_1} = 0 \quad \text{----- (15)}$$

where U^2 is a kind of Ursell's parameter defined by gHT^2/d^2 , and others are as follows.

$$\left. \begin{aligned} \alpha_3 &= \frac{C_1}{2} d^{-2} \\ \alpha_4 &= \frac{1}{2} b^{-1} b_x + \frac{1}{4} d^{-1} d_x \\ \delta &= -\frac{H}{k^2} \left[\frac{E}{K} - k'^2 \right] \\ I_0 &= \int_{-k}^k \left(\operatorname{cn}^2 \beta + \frac{\delta}{H} \right)^2 \left| \operatorname{cn}^2 \beta + \frac{\delta}{H} \right| d\beta \\ I_1 &= \int_{-k}^k \operatorname{cn}^4 \beta d\beta \\ I_2 &= \int_{-k}^k \operatorname{cn}^2 \beta d\beta \end{aligned} \right\} \quad \text{----- (16)}$$

There are difficulties in the above equation if one want to solve it analytically. They are due to two terms, $\delta I_2/HI_1$ and I_0/I_1 .

Approximations of $\delta I_2/HI_1$ and I_0/I_1 for large Ursell's parameter

For Ursell's parameter larger than 50, the following approximation was obtained in Ref. [1],

$$\frac{\delta I_2}{HI_1} = - \frac{2\sqrt{3}}{U} \quad \text{----- (17)}$$

and if we allow errors of 3.5 % at most, this approximation is extended down to $U^2 = 40$.

As for another coefficient I_0/I_1 , we have to approximate it in a form convenient for integration. At first the integral I_0 is rewritten as follows for convenience of numerical computation.

$$\begin{aligned} I_0 &= \int_{-k}^k (cn^2\beta + \frac{\delta}{H})^2 |cn^2\beta + \frac{\delta}{H}| d\beta \\ &= 2 \int_0^k (cn^2\beta + \frac{\delta}{H})^2 |cn^2\beta + \frac{\delta}{H}| d\beta \\ &= 2 \int_0^{\beta_1} (cn^2\beta + \frac{\delta}{H})^3 d\beta - 2 \int_{\beta_1}^k (cn^2\beta + \frac{\delta}{H})^3 d\beta \\ &= 4 \int_0^{\beta_1} (cn^2\beta + \frac{\delta}{H})^3 d\beta - 2 \int_0^k (cn^2\beta + \frac{\delta}{H})^3 d\beta \end{aligned} \quad \text{----- (18)}$$

where β_1 is the value which satisfies

$$cn^2\beta_1 + \frac{\delta}{H} = 0 \quad \text{----- (19)}$$

The above equation is approximated for large Ursell's parameter, that is, for large K, by

$$I_0 = \frac{16}{15} - \frac{16}{\sqrt{3}} U^{-1} + 32 U^{-2} \quad \text{----- (20)}$$

Figure 1 shows the comparison between numerical value of I_0 and its approximation, Eq.(20). Taking into consideration the fact that Eq.(20) is no longer applicable down to $U^2 = 100$ and is still inconvenient for integration, a set of I_0/I_1 shown in Table 1 is proposed as the approximation for integration.

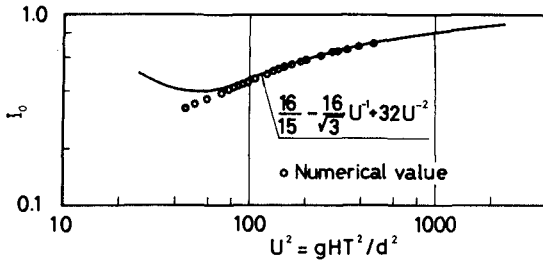


Fig.1. I_0 as a function of Ursell's parameter

U^2	I_0 / I_1
40 - 200	$0.05254 U^{4/5}$
200 - 1 000	$0.1516 U^{2/5}$
1 000 - 2 500	$0.3025 U^{1/5}$
2 500 -	$\frac{4}{5} (1 - \frac{5\sqrt{3}}{U})$

Table 1. Approximate values of I_0/I_1

Case 1. Constant depth and constant width

To examine the validity of the expression of the bottom friction and to correlate the friction coefficient for cnoidal waves to Kajiura's theories, solutions without the topographical effect are derived and are to be compared with experimental results. Since d is constant in this case, Ursell's parameter varies with wave height H . Then, we have

$$U^2 = \frac{gT^2}{d^2} H = \frac{H}{D}, \quad \frac{H}{x} = 2 \frac{U}{x} \quad \text{----- (21)}$$

where D is d^2/gT^2 and takes a constant value, because the wave period T is also considered constant.

For Ursell's parameter between 40 and 2500, the coefficient I_0/I_1 is expressed by

$$\frac{I_0}{I_1} = F U^m / 5 \quad \text{----- (22)}$$

where F and m are constant for given ranges of Ursell's parameter and are given in Table 1.

Equation (15) is now reduced to

$$\frac{3}{2} [U^{-1} - \frac{4}{\sqrt{3}} U^{-2}] \frac{dU}{dx} + \alpha_3 DFU^{(10+m)/5} = 0 \quad \text{----- (23)}$$

or further to

$$[U^{-1-(10+m)/5} - \frac{4}{\sqrt{3}} U^{-1-(15+m)/5}] dU + \frac{2}{3} \alpha_3 DF dx = 0 \quad \text{----- (24)}$$

and the solution is given by

$$\begin{aligned} & \left(\frac{U_0}{U} \right)^{(10+m)/5} \left[1 - \frac{4}{\sqrt{3}} \frac{10+m}{15+m} \frac{1}{U} \right] - \left[1 - \frac{4}{\sqrt{3}} \frac{10+m}{15+m} \frac{1}{U_0} \right] \\ & = \frac{10+m}{15} \frac{C_1}{gT^2} F x U_0^{(10+m)/5} \quad \text{----- (25)} \end{aligned}$$

where the subscript $_0$ denotes the value at a reference point $x = 0$.

Although the wave height is given by Eq.(25), the equation is still a little complicated. More simple relationship, if obtained, is convenient for practical purpose. Therefore, the Ursell's parameter in the first square bracket is replaced by U_0 . A numerical examination shows that if the wave height H remains larger than $0.8H_0$, this replacement yields 3 % errors at most. The wave height H_0 is the wave height at the beginning of an interval where the bottom friction is not negligible and H is the wave height at its end. With the distance x of the interval well chosen so as to satisfy this restriction, wave height can be predicted by simple formulae as shown in Table 2.

For Ursell's parameter larger than 2500, Eq.(15) becomes of the following form.

$$\left(\frac{3}{2} \frac{1}{U} - \frac{2\sqrt{3}}{U^2} \right) \frac{dU}{dx} + \frac{4}{5} \left(1 - \frac{5\sqrt{3}}{U} \right) \alpha_3 DU^2 = 0 \quad \text{----- (26)}$$

For this range of Ursell's parameter, $5\sqrt{3} U^{-1}$ is not larger than 0.17 and the following approximation is used in the integration.

$$\left(1 - \frac{4}{\sqrt{3}} \frac{1}{U} \right) / \left(1 - 5\sqrt{3} \frac{1}{U} \right) \approx 1 + \frac{11}{\sqrt{3}} \frac{1}{U}$$

The solution is given as follows.

$$\left(\frac{U_0}{U}\right)^2 \left[1 + \frac{22}{3\sqrt{3}} \frac{1}{U}\right] - \left[1 + \frac{22}{3\sqrt{3}} \frac{1}{U_0}\right] = \frac{16}{15} \alpha_3 D U_0^2 x \quad \text{----- (27)}$$

Again the fact that $22/3\sqrt{3} \cdot U^{-1}$ is smaller than 0.15 is taken into consideration and U in the first square bracket is replaced by U_0 . The result is also listed in Table 2.

For a solitary wave as a limit when Ursell's parameter tends to infinity, we have

$$H = H_0 / \left(1 + \frac{8}{15} \frac{C_1 H_0 x}{d^2}\right) \quad \text{----- (28)}$$

If one prefer Manning's n in place of C_1 used in the present paper, he can replace C_1 by $gn^2 d^{-1/3}$ although there is an unsolved problem, that is, how to determine the value of n for unsteady flow.

$$40 < gHT^2/d^2 < 200$$

$$\left(\frac{H_0}{H}\right)^{7/5} - 1 = 0.0490 \frac{C_1 x}{gT^2} \left(\frac{gH_0 T^2}{d^2}\right)^{7/5} / \left[1 - 1.70 \left(\frac{gH_0 T^2}{d^2}\right)^{-1/2}\right]$$

$$200 < gHT^2/d^2 < 1000$$

$$\left(\frac{H_0}{H}\right)^{6/5} - 1 = 0.121 \frac{C_1 x}{gT^2} \left(\frac{gH_0 T^2}{d^2}\right)^{6/5} / \left[1 - 1.63 \left(\frac{gH_0 T^2}{d^2}\right)^{-1/2}\right]$$

$$1000 < gHT^2/d^2 < 2500$$

$$\left(\frac{H_0}{H}\right)^{11/10} - 1 = 0.222 \frac{C_1 x}{gT^2} \left(\frac{gH_0 T^2}{d^2}\right)^{11/10} / \left[1 - 1.59 \left(\frac{gH_0 T^2}{d^2}\right)^{-1/2}\right]$$

$$2500 < gHT^2/d^2$$

$$\frac{H_0}{H} - 1 = \frac{8}{15} \frac{C_1 H_0 x}{d^2} / \left[1 + 4.23 \left(\frac{gH_0 T^2}{d^2}\right)^{-1/2}\right]$$

Table 2. Decay of wave height in case of $\alpha_4 = 0$

Case 2. Cnoidal waves in general case

Almost similar calculation is possible for this case except that the water depth in Ursell's parameter is also variable. The following relationship should be substituted in place of Eq.(21).

$$\frac{2}{U} \frac{dU}{dx} = \frac{1}{H} \frac{dH}{dx} - \frac{2}{d} \frac{dd}{dx} \quad \text{----- (29)}$$

The equation to be solved is

$$\begin{aligned} & \frac{1}{U} \frac{dU}{dx} + \frac{1}{3} \frac{1}{b} \frac{db}{dx} + \frac{3}{2} \frac{1}{d} \frac{dd}{dx} + \frac{2}{3} \frac{\delta}{H} \frac{I_2}{I_1} \left[\frac{1}{U} \frac{dU}{dx} + \frac{1}{2} \frac{1}{b} \frac{db}{dx} + \frac{9}{4} \frac{1}{d} \frac{dd}{dx} \right] \\ & + \frac{2}{3} \alpha_3 H \frac{I_0}{I_1} = 0 \quad \text{----- (30)} \end{aligned}$$

For Ursell's parameter between 40 and 2500, the equation is further reduced to the following with the aid of Eqs.(17) and (22).

$$\begin{aligned} & \frac{1}{U} \frac{dU}{dx} \left[1 - \frac{4}{\sqrt{3}} \frac{1}{U} \right] + \frac{1}{2} \left[\frac{1}{b} \frac{db}{dx} + \frac{9}{2} \frac{1}{d} \frac{dd}{dx} \right] \left[\frac{2}{3} - \frac{4}{\sqrt{3}} \frac{1}{U} \right] \\ & + \frac{2}{3} \frac{C_1}{2gT^2} F U^{(10+m)/5} = 0 \quad \text{----- (31)} \end{aligned}$$

The solution is given by

$$U^2 (U - 2\sqrt{3}) b d^{9/2} \exp \left[\int \frac{C_1 F}{gT^2} \frac{U^{(15+m)/5}}{U - 2\sqrt{3}} dx \right] = \text{const.} \quad \text{----- (32)}$$

The value of U in the exponential function of the equation can be replaced by U₀ under the same consideration as in case of constant depth and width of the channel. In terms of wave height H, the relationships are shown in Table 3.

For Ursell's parameter larger than 2500, the equation is given by

$$\frac{2}{U} \frac{dU}{dx} + \frac{1}{U - 2\sqrt{3}} \frac{dU}{dx} + \frac{1}{b} \frac{db}{dx} + \frac{9}{2} \frac{1}{d} \frac{dd}{dx} + \frac{4}{5} \frac{C_1}{gT^2} U^2 \frac{U - 5\sqrt{3}}{U - 2\sqrt{3}} = 0 \quad \text{----- (33)}$$

and the solution is

$$\frac{U^2(U - 2\sqrt{3}) b d^{9/2}}{U_0^2(U_0 - 2\sqrt{3}) b_0 d_0^{9/2}} = \exp\left[-\frac{4}{5} \frac{C_1}{gT^2} U^2 \frac{U - 5\sqrt{3}}{U - 2\sqrt{3}} dx\right]$$

----- (34)

In terms of H, the result is also shown in Table 3.

With C_1 set equal to zero, that is, with no friction, the right-hand sides of the results in Table 3 are reduced to unity and they coincide with the result of the author's previous paper which discussed the shoaling of cnoidal waves.

$$\frac{Hb d^{5/2} (\sqrt{gHT^2/d^2} - 2\sqrt{3})}{H_0 b_0 d_0^{5/2} (\sqrt{gH_0 T^2/d_0^2} - 2\sqrt{3})}$$

$$40 < gHT^2/d^2 < 200$$

$$= \exp\left[-\frac{0.05254 C_1 x}{gT^2} \left(\frac{gH_0 T^2}{d_0^2}\right)^{9/5} / \{\sqrt{gH_0 T^2/d_0^2} - 2\sqrt{3}\}\right]$$

$$200 < gHT^2/d^2 < 1000$$

$$= \exp\left[-\frac{0.1516 C_1 x}{gT^2} \left(\frac{gH_0 T^2}{d_0^2}\right)^{17/10} / \{\sqrt{gH_0 T^2/d_0^2} - 2\sqrt{3}\}\right]$$

$$1000 < gHT^2/d^2 < 2500$$

$$= \exp\left[-\frac{0.3025 C_1 x}{gT^2} \left(\frac{gH_0 T^2}{d_0^2}\right)^{8/5} / \{\sqrt{gH_0 T^2/d_0^2} - 2\sqrt{3}\}\right]$$

$$2500 < gHT^2/d^2$$

$$= \exp\left[-\frac{4C_1 H_0 x}{5 d_0^2} \{\sqrt{gH_0 T^2/d_0^2} - 5\sqrt{3}\} / \{\sqrt{gH_0 T^2/d_0^2} - 2\sqrt{3}\}\right]$$

Table 3. Change in wave height of cnoidal waves under the effects of variable water depth, variable channel width and bottom friction

EXPERIMENTAL PROCEDURE

Experiments were carried out in a wave flume 50 m long, 1 m wide and 1 m high. First series of the experiments was carried out in a channel of constant depth. Water depths during the experiments were kept 10 cm, 20 cm and 30 cm. Wave period was kept constant as 2 sec. Wave heights were varied between 2 cm at minimum and 12 cm at maximum. At the end of the channel, a permeable slope of 1 on 25 was installed, packed with waste films. Even with this wave absorber, we had normally 7-8 % reflection from this end of the channel. The maximum reflection observed during experiments was about 10 %.

Artificial rectangular roughnesses were planted on the bottom in the middle part of the channel. Height and width of a roughness are the same and 8 mm. Its length is 1 m and can cover the whole width of the channel. Spacing of the roughnesses is 8 cm. The roughnesses were arranged at right angles to the direction of wave propagation. Total length of roughened bed measured along the direction of wave propagation is 10 m. From the beginning of this area, wave heights are measured at every 1 m intervals. Since the reflection is not completely negligible, we draw, by using the experimental results, average curves of the change in wave height, from which the friction coefficient C_f is estimated.

In the second series of the experiments, a slope of 1 on 20 was installed. Total horizontal length of the slope was 6 m. Water depths at the toe of the slope were 40 cm, 45 cm and 50 cm. From the upper end of the slope, continues another horizontal bed, on which water depths during the experiments were 10 cm, 15 cm and 20 cm. The same roughnesses as in the first series of experiments were planted on the surface of the slope. Wave height was measured at every 50 cm intervals on the slope. Wave periods were varied between 2 sec and 10 sec. Wave heights at the toe of the slope were varied from 1.5 cm to 10 cm.

COMPARISON BETWEEN THEORY AND EXPERIMENTCharacteristics of roughness in steady flow

According to Adachi's empirical formula [6], the effect of the rectangular ribs arranged at right angles to the stream is expressed in terms of Nikuradse's equivalent sand roughness k'_s by the following relationship.

$$k'_s = 30 k m (R_1 / k)^{-\theta} \quad \text{----- (35)}$$

where R_1 is the hydraulic radius of the channel, k is the height of a roughness, s is the spacing of the roughnesses, m and θ are functions of s and k which were experimentally determined by Adachi.

$$m = 0.79 (s/k)^{-0.26} \quad \text{-----} \quad (36)$$

$$\theta = 0.02 (s/k)^{0.8}$$

The roughness length z_0 is defined by $k'_s/30$. For example, $z_0 = 0.23$ cm for $d = 30$ cm, $k = 8$ mm and $s = 8$ cm.

The friction coefficient C_1 for steady flow is computed by

$$C_1 = [6.0 + 5.75 \log_{10} (d/k'_s)]^{-2} \quad \text{-----} \quad (37)$$

and is 0.0227, 0.0137 and 0.0108 for water depth 10 cm, 20 cm and 30 cm, respectively, in the first series of the experiments.

Estimation of the friction coefficient by Kajiura's theories

Field data and experimental results obtained by many researchers show that the friction coefficient under wave action is different from that in steady flow. Kajiura established two theories, on considering the average state of turbulence over one wave period and adopting the assumption of the eddy viscosity analogous to that for the steady turbulent flow. According to his theories, the frictional coefficient is given as a function of certain dimensionless parameters constructed from known quantities of wave and bottom conditions.

Kajiura's theories are based on the assumption that the oscillatory motion is sinusoidal and the present theory used the cnoidal waves. Direct substitution of the results of Kajiura's theory is not recommended. In order to connect two different definitions of the friction coefficients, mean energy dissipation of sinusoidal motion is equated with that of cnoidal waves.

For the case of long period waves [4], in which the flow is fully turbulent, the mean energy dissipation is

$$\langle E \rangle = \frac{\rho}{2} \frac{8}{3\pi} \hat{C}_{k1} \cos \theta \hat{U} \hat{u}^2 \quad \text{-----} \quad (38)$$

where \hat{u} is the amplitude of the mean velocity vertically averaged over the water depth. The angle θ denotes the phase lead of the bottom stress relative to the vertically averaged velocity and \hat{U} is the amplitude of a formally defined velocity corresponding to the pressure gradient.

For the case of short period waves [5], in which the thickness of the bottom frictional layer is very thin compared with the total depth of water, the mean energy dissipation is given by

$$\langle E \rangle = \frac{\rho}{2} \hat{C}_{k2} \cos\theta \hat{U}^3 \quad \text{-----} \quad (39)$$

where \hat{U} is the amplitude of the horizontal velocity at the top of the bottom frictional layer. The angle θ denotes the phase lead of the bottom stress relative to the velocity at the top of the frictional layer.

For cnoidal waves in the present paper, the mean energy dissipation is given by

$$\langle E \rangle = \frac{\rho}{2} 16 I C_1 \hat{u}^3 \quad , \quad I = I_0 / 2K \quad \text{-----} \quad (40)$$

where \hat{u} is the amplitude of the horizontal velocity which is vertically uniform and I is given in Table 4 in simple expressions convenient for practical application.

Equating these three formulas, the coefficient used in the present paper can be estimated from Kajiura's theories.

$$\hat{C}_{k2} \cos\theta = \frac{\rho}{3\pi} \hat{C}_{k1} \cos\theta \left(\frac{\hat{u}}{\hat{U}} \right)^2 = 16 I C_1 \left(\frac{\hat{u}}{\hat{U}} \right)^3 \quad \text{----} \quad (41)$$

$gHT^2/d^2 = U^2$	I
40 - 200	$0.08089 U^{-1/5}$
200 - 1000	$0.2334 U^{-3/5}$
1000 - 2500	$0.4657 U^{-4/5}$
2500 -	$\frac{32}{15\sqrt{3}} \left(1 - \frac{5\sqrt{3}}{U} \right) \frac{1}{U}$

Table 4. Values of I

Experimental results in case of horizontal bottom

The friction coefficients are determined from the experimental results, converted, by means of Eq.(41), to Kajiura's definition of the friction coefficient, and plotted in Fig.2. In the same figure, Kajiura's theories are given by two oblique lines, and three short horizontal lines correspond to the friction coefficients in steady flow.

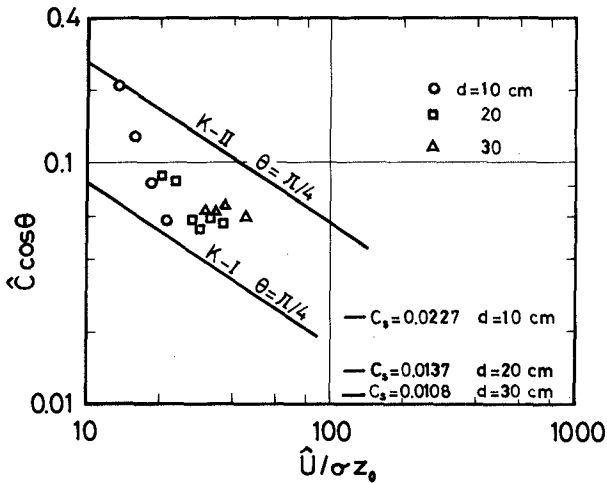


Fig. 2. Friction coefficients compared with Kajiura's theories and Adachi's formula

The friction coefficients in steady flow show very small values and are unable to be used for practical estimation of decay of water waves in shallow sea. The experimental results fall between Kajiura's theories. This suggests that the conversion formula given above is practically valid.

Taking into account the fact that the size of the roughness in the experiments is very big compared to the water depth and this condition does not frequently occur under natural conditions, it is concluded that the present theory with the friction coefficient converted from Kajiura's first theory can be used to predict the change in height of tsunamis and storm surges, while if combined with Kajiura's second theory it can be used to compute the case of wind waves and swells in shallow water.

Change in wave height on a slope

Since the method of evaluating the friction coefficient from given wave and bottom conditions is established, the present theory is compared with the second series of experiments. Figure 3 shows an example. Although values of friction coefficient varies with water depth on the slope, average value, 0.1 for this case, is used in calculation. Broken line in the figure shows the shoaling of cnoidal waves when no friction is taken into account. Solid line is with friction and agrees fairly well with experimental results. Scattering of the experimental data is considered due mainly to the reflection from the slope and the wave absorber installed at the end of the flume.

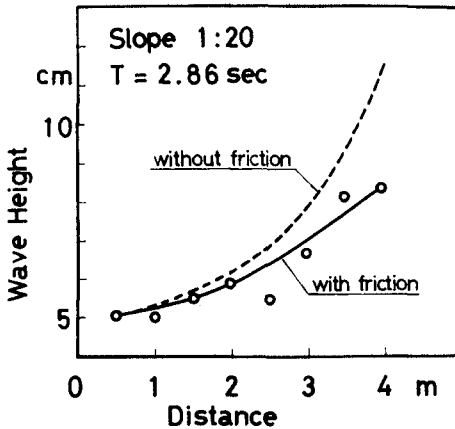


Fig.3. Change in wave height on a slope.

CONCLUSIONS

A fundamental equation for long waves is derived by using Kakutani's and Johnson's methods. The equation includes the effects of nonlinearity, dispersion, water depth, width of the channel and bottom friction.

In addition to several solutions obtained in analytical form, the change in wave height of cnoidal waves is given and listed in Tables 2 and 3. In order to obtain as simple and convenient formulas as possible, imposed, during the derivation, were restrictions which should be remembered at application. The length of an interval, x , should be well chosen so as that the wave height H at the end of the interval remains larger than 0.8 times H_0 , the wave height at the beginning of the interval. If this restriction is not welcome, Eqs.(25) and (27) should be used in place of formulas in Table 2, or H_0 in the right-hand sides of the equations in Table 3 should be replaced by H .

The friction coefficient C_1 is estimated from known quantities of wave and bottom conditions. In the present experiments, artificial rectangular ribs are used, the roughness length, z_0 , of which is evaluated from Adachi's empirical formula. This roughness length and wave characteristics gives the friction coefficient for sinusoidal waves, if one follows Kajiuura's theories. Kajiuura assumed sinusoidal waves and the present theory cnoidal waves. Conversion of the friction coefficient between the two different motions is possible through Eq.(41), provided that the mean energy dissipation is the same for the two motions.

From the first series of experiments, the method of estimation of the friction coefficient is confirmed. Results of the second series of the experiments show that the theoretical prediction of the change in wave height on a slope agrees very well with experiments.

It is concluded that the present theory combined with Kajiura's first theory which assumes that the flow is fully turbulent gives good estimation of the change in wave height of tsunamis and storm surges, and that with Kajiura's second theory which assumes a thin bottom frictional layer the theory predicts the change in height of swells and wind waves in shallow water.

ACKNOWLEDGEMENTS

A part of the present study was supported by a grant from the Ministry of Education.

REFERENCES

- 1) Shuto, N.: Nonlinear long waves in a channel of variable section, Coastal Engg. in Japan, Vol.17, pp.1-12, 1974.
- 2) Kakutani, T.: Effect of an uneven bottom on gravity waves, J. Phy. Soc. Japan, Vol. 30, No.1, pp.272-276, 1971.
- 3) Jonnson, I.G.: Wave boundary layers and friction factors, Proc. 10th Conf. Coastal Engg, pp.127-148, 1967.
- 4) Kajiura, K.: On the bottom friction in an oscillatory current, Bull. Earthq. Res. Inst., Vol.42, pp.147-174, 1964.
- 5) Kajiura, K.: A model of the bottom boundary layer in water waves, Bull. Earthq. Res. Inst., Vol.46, pp.75-123, 1968.
- 6) Adachi, S.: Experimental study on artificial roughness, Trans. JSCE, No.104, pp.33-44, 1964, (in Japanese).
- 7) Johnson, R.S.: On the development of a solitary wave moving over an uneven bottom, Proc. Camb. phil. Soc., Vol.73, pp.183-203, 1973.
- 8) Otto, E. and Sudan, R.N.: Non-linear theory of ion acoustic waves with Landau damping, Phy. Fluids, Vol.12, No.11, pp.2388-2394, 1969.
- 9) Shuto, N.: Shoaling and deformation of non-linear long waves, Coastal Engg. in Japan, Vol.16, pp.1-12, 1973.

CHAPTER 25

RECENT DEVELOPMENTS IN THE STUDY OF BREAKING WAVES

by

Michael S. Longuet-Higgins
Royal Society Research Professor
Department of Applied Mathematics and Theoretical
Physics, Cambridge, England and Institute of
Oceanographic Sciences, Wormley, Godalming, Surrey

1. INTRODUCTION

The sight and sound of breaking waves and surf is so familiar and enjoyable that we tend to forget how little we really understand about them. Why is it, that compared to other branches of wave studies our knowledge of breaking waves is so empirical and inexact?

The reason must lie partly in the difficulty of finding a precise mathematical description of a fluid flow that is in general nonlinear and time-dependent. The fluid accelerations can no longer be assumed to be small compared to gravity, as in Stokes's theory for periodic waves and the theory of cnoidal waves in shallow water, nor is the particle velocity any longer small compared to the phase velocity.

The aim of this paper is to bring together some recent contributions to the calculation both of steep symmetric waves and of time-dependent surface waves. These have a bearing on the behaviour of whitecaps in deep water and of surf in the breaker zone.

Since spilling breakers in gently shoaling water closely resemble solitary waves, we begin with the description of solitary waves of limiting amplitude, then discuss steep waves of arbitrary height. The observed intermittency of whitecaps is discussed in terms of the energy maximum, as a function of wave steepness. In Sections 6 and 7 a simpler description of steady symmetric waves is proposed, using an asymptotic expression for the flow near the wave crest. Finally we describe a new numerical technique (MEL, or mixed Eulerian-Lagrangian) with which it has been found possible to follow the development of periodic waves past the point when overturning takes place.

2. THE LIMITING SOLITARY WAVE

A simple and very accurate approximation to the limiting solitary wave has recently been given by Longuet-Higgins (1974). If x and y are horizontal and vertical coordinates and h the undisturbed depth of water, then the surface profile on one side ($x > 0$) is approximated by

$$y/h = Ae^{-\lambda x/h} + Be^{-\mu x/h} \quad (2.1)$$

The constants A , B and λ , μ are determined by the conditions, first, that the particle at the crest moves with the phase-speed $c = F\sqrt{gh}$. So from Bernoulli's equation,

$$y/h = \frac{1}{2}F^2 \quad (x = 0), \quad (2.2)$$

Secondly, the angle of inclination at the surface is -30° , so

$$dy/dx = -1/\sqrt{3} \quad (x = 0). \quad (2.3)$$

We know thirdly (see Lamb, 1932 § 252), that in the outer fringes of the wave ($x \rightarrow \infty$) the profile behaves asymptotically like $e^{-\lambda x}$, where

$$\frac{\tan \lambda}{\lambda} = F^2 \quad (2.4)$$

exactly. This is satisfied by (2.0) if $0 < \lambda < \mu$. Fourthly we have Starr's exact relation

$$3V/g = (F^2 - 1) M \quad (2.5)$$

where V is the potential energy and M the mass:

$$V/g = \int_{-\infty}^{\infty} \frac{1}{2} y^2 dx, \quad M = \int_{-\infty}^{\infty} y dx;$$

and lastly an exact relation

$$\int_{-\infty}^{\infty} \left[(1 + y/h)(1 - 2F^{-2}y/h)^{\frac{1}{2}}(1 + dy/dx^2)^{\frac{1}{2}} - 1 \right] dx = 0 \quad (2.6)$$

proved by Longuet-Higgins (1974). Equations (2.2) to (2.6) are five relations to determine the constants A , B , λ , μ and F , giving

$$\left. \begin{aligned} A &= 1.5389, & \lambda &= 1.0495 \\ B &= -0.7093, & \mu &= 1.4630 \\ F^2 &= 1.6592. \end{aligned} \right\} \quad (2.7)$$

The resulting profile, plotted in Figure 1, agrees numerically with that given by Yamada (1957) to within 1% everywhere, and generally to within 0.2%.

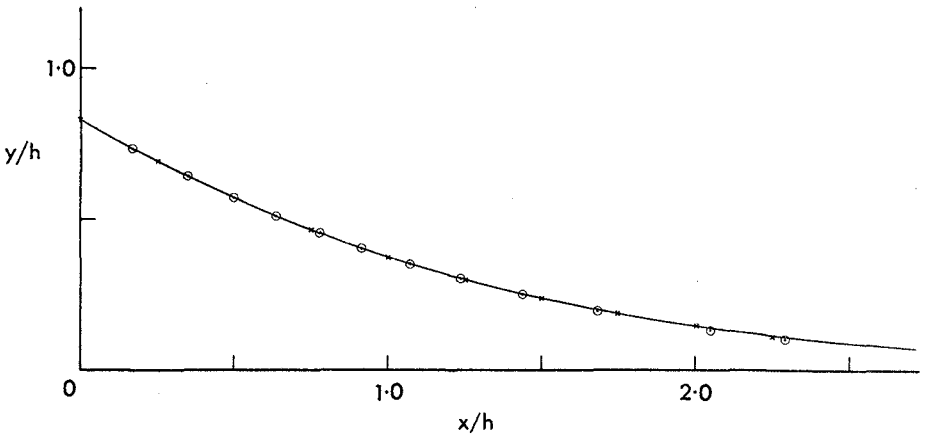


Figure 1. (from Longuet-Higgins, 1974). The profile of the highest solitary wave as given by equation (2.1) (solid line) compared with the numerical calculations of Yamada (1957) (circles) and Lenau (1966) (crosses).

3. SOLITARY WAVES OF ARBITRARY HEIGHT

The properties of solitary waves of arbitrary amplitude a in water of undisturbed depth h have been studied in two recent papers by Longuet-Higgins and Fenton (1974) and by Byatt-Smith and Longuet-Higgins (1976) using quite different methods.

It is convenient to define a parameter ω for the family of solitary waves by the equation

$$\omega = 1 - q^2/gh$$

where q is the particle-speed at the wave crest, in a frame of reference moving along with the phase-speed. For waves of small amplitude, $q \approx \sqrt{gh}$ so ω is small, whereas for limiting waves q vanishes, so $\omega = 1$. In general

$$0 < \omega \leq 1 \tag{3.1}$$

and the complete range of ω is precisely known.

Figure 2 shows a succession of wave profiles, computed precisely for moderate values of ω . The height of the waves increases monotonically with ω . This is in qualitative agreement with the approximate Rayleigh-Boussinesq theory, in which

$$\left. \begin{aligned} y/h &\approx \frac{1}{3} \alpha^2 \operatorname{sech}^2(\frac{1}{2} \alpha x) \\ F^2 &= 1 + \frac{1}{3} \alpha^2 \end{aligned} \right\}$$

and so

$$\omega = 1 - (F^2 - 2a/h) \frac{1}{3} \alpha^2 \approx a/h \tag{3.2}$$

and ω increases almost linearly with a/h . As the wave height increases, so the horizontal width of the profile decreases, like $1/\alpha$ or $(a/h)^{-1/2}$. This implies that successive profiles must intersect each other, and from Figure 2 it is clear that as the amplitude increases, so the point of intersection gradually moves in towards the wave crest.

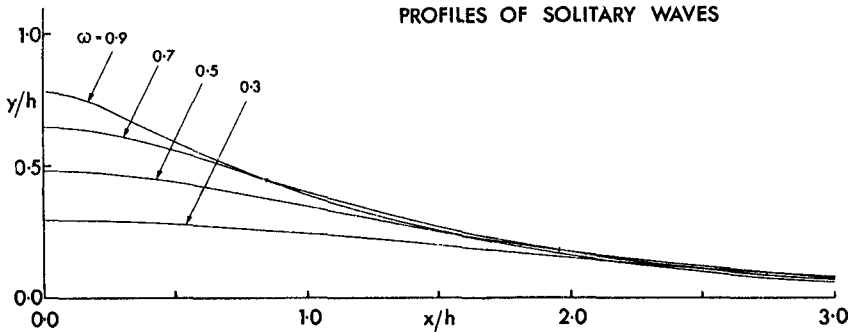


Figure 2. (from Byatt-Smith and Longuet-Higgins, 1976). Profiles of solitary waves at moderate values of the parameter ω .

At finite values of the wave steepness the acceleration near the crest becomes comparable with g and the approximate Rayleigh-Boussinesq theory is no longer valid. An exact theory was however calculated by two methods. In Longuet-Higgins and Fenton (1974) the Rayleigh-Boussinesq theory was treated as the first term in an infinite series in powers of ω , which was carried to high order and then summed by rational approximants (Padé sums). All integral properties converged, up to and including $\omega = 1$, and from these it was possible to calculate also the dimensionless phase-speed F .

Figure 3 shows the dimensionless phase-speed calculated by means of Padé sums, and plotted as a function of the wave steepness a/h . After increasing steadily with a/h , F reaches a maximum and then actually decreases at higher values of a/h . The maximum speed $F = 1.294$ occurs when $a/h = 0.790$, whereas the speed of the highest wave is only $F = 1.286$.

The presence of a maximum in the phase-speed is at first sight surprising, since it implies that over a certain range of steepnesses there can exist two distinct solitary waves in the same depth of water, having the same phase-speed. The reason becomes

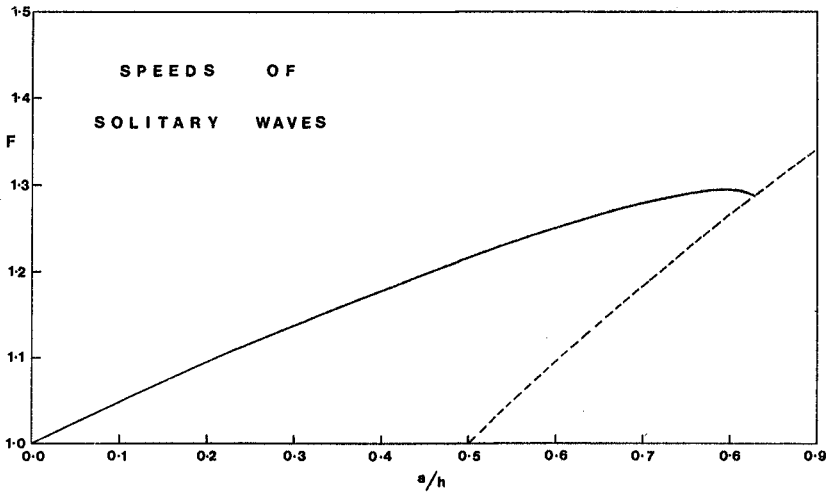


Figure 3. The dimensionless phase-speed $F = c/\sqrt{gh}$ for solitary waves, as a function of the relative crest height a/h .

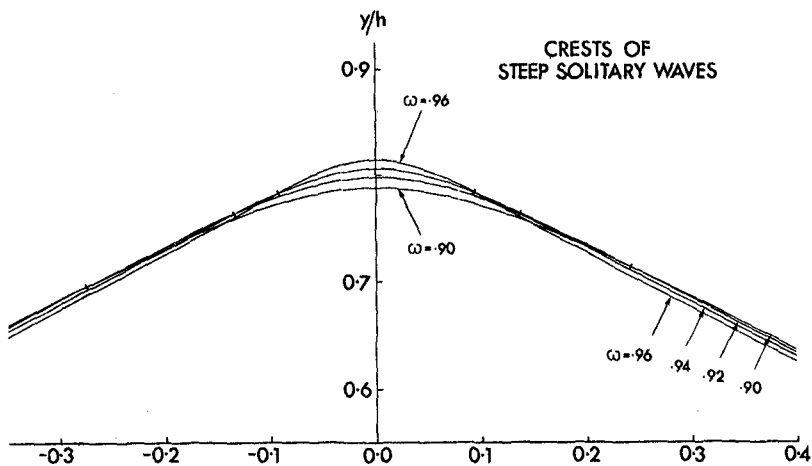


Figure 4. (from Byatt-Smith and Longuet-Higgins, 1976). The form of steep solitary waves close to the wave crest.

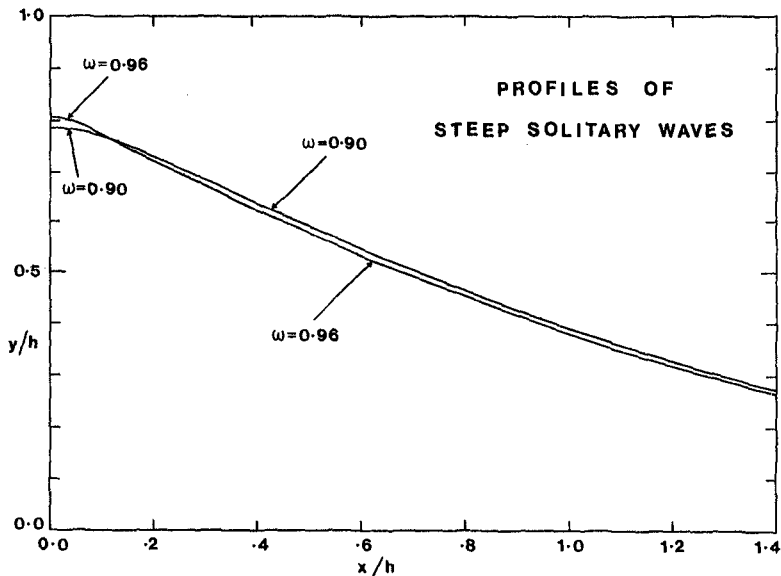


Figure 5. Comparison of the profiles of two steep solitary waves ($\omega = 0.90$ and 0.96).

apparent from Figure 4. This shows some accurately calculated profiles near the wave crest, from $\omega = 0.90$ to $\omega = 0.96$. Evidently the trend begun at the lower wave amplitudes in Figure 2 continues, and as ω increases the point of intersection moves up close to the wave crest. The situation is shown more clearly in Figure 5, from which it will be seen that the higher of the two waves, corresponding to $\omega = 0.96$ actually lies below the lower wave ($\omega = 0.90$) over most of the wave profile. This implies that the average elevation of the higher wave is actually less than that of the lower wave.

Now Starr's exact relation (2.5) can be written in the form

$$(F^2 - 1) = \frac{3}{2} \bar{y}/h \quad (3.3)$$

where \bar{y} is the average surface elevation, defined by

$$\bar{y} = \frac{\int_{-\infty}^{\infty} y^2 dx}{\int_{-\infty}^{\infty} y dx} \quad (3.4)$$

So if \bar{y} decreases as ω increases, so also must F decrease, by equation (3.2).

Although the completeness of the Rayleigh series was questioned by Witting (1975), nevertheless the existence of the maximum speed has been confirmed by a quite different method of calculation based on the integral equation of Byatt-Smith (1970) for solitary waves. In his first paper, Byatt-Smith took the phase-speed F as an independent parameter in the integral equation, and from it calculated the wave height and profile. He was unable to obtain solutions with F greater than about 1.294, and in this neighbourhood convergence was slow. The explanation is apparently that in this neighbourhood a small change in F corresponds to a large change in the profile. But in a second paper (Byatt-Smith and Longuet-Higgins, 1976) ω was taken as independent parameter, and the wave speed F as dependent variable. The solutions converged rapidly and the maximum in F was verified (see Figure 6).

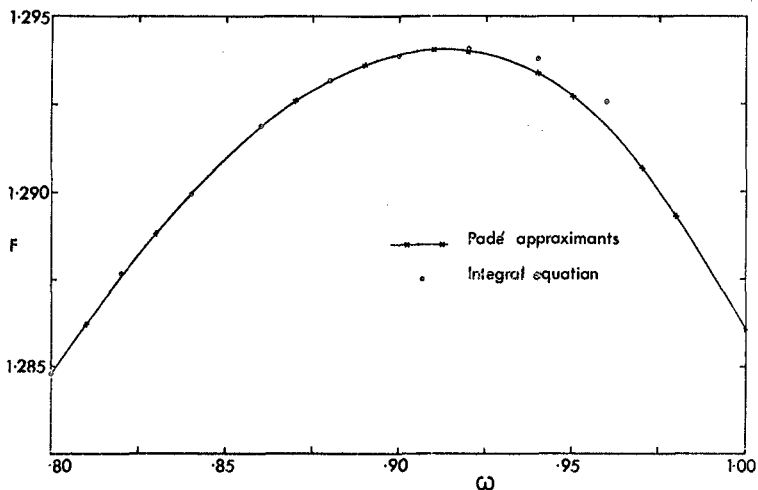


Figure 6. (from Byatt-Smith and Longuet-Higgins, 1976). The dimensionless phase-speed F at high values of ω , calculated by two different methods.

4. WAVES ENTERING SHALLOW WATER

In addition to the maximum in the phase-speed, Longuet-Higgins and Fenton (1974) also found maxima in the mass, momentum and energy of solitary waves, as a function of a/h or of ω (see Figure 7). This has implications for waves entering gradually shoaling water. For, in the absence of appreciable dissipation, the energy E_1 of a solitary wave might be expected to remain a constant. As the mean depth h diminished, the dimensionless energy $E = E_1/\rho gh^3$ would be expected to increase, at first. So, provided the wave remained symmetrical it would be represented by a point travelling up the curve in Figure 7, with both E and a/h increasing.

Before the maximum value of E is reached, however, the wave must leave the energy curve, which it generally does by becoming unsymmetrical and then spilling or plunging forwards (see Section 8). If it plunges heavily, it becomes radically altered. But if it spills gently, it may thereby dissipate enough energy to travel on down the curve more or less as a symmetric wave damped by a whitecap on the forward face. This

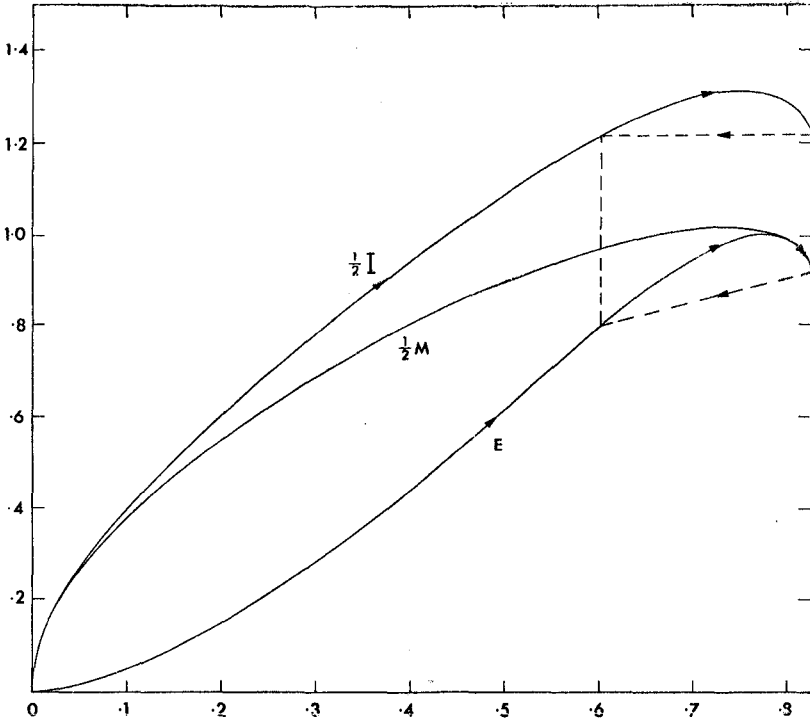


Figure 7. (from Longuet-Higgins and Fenton, 1974). The normalised mass M , momentum I and energy E of a solitary wave, as a function of the relative height a/h .

presumably is a spilling breaker, for which a theory has recently been given by Longuet-Higgins and Turner (1974). In their model, the whitecap was represented as a gravity-current, of density ρ' less than unity, riding down the forward face of an irrotational wave and exchanging mass and momentum by entrainment across the interface. Calculations showed that the flow could exist provided that ρ'/ρ was of order 0.7 (similar to the ratio observed in hydraulic jumps) and that the surface slope exceeded an angle of about 20° .

In this model, however, and also according to observation, the length of the whitecap tends to increase continually*, so producing a disproportionate damping of the wave. What happens when the point in Figure 7 reaches the right-hand edge of the graph, representing the steepest symmetric wave? Longuet-Higgins and Fenton (1974) suggested that it may jump back to a point lower down the curve, representing a wave with almost the same mass and momentum, but with a slightly lower energy. This wave would have a rounded crest and a lower value of a/h . The process might then be repeated.

Some support for this suggestion comes from an analysis of the film of shoaling solitary waves made by Kjeldsen and Olsen (1974). Measurements of the length ℓ of the whitecap as a function of the time t (see Figure 8) show that it increases not continuously but in a series of jumps. At each jump, the crest becomes rounded and a part of the whitecap is lost by being left behind the travelling crest. The remnant appears on the near face of the wave as a patch of aerated water, which quickly subsides.

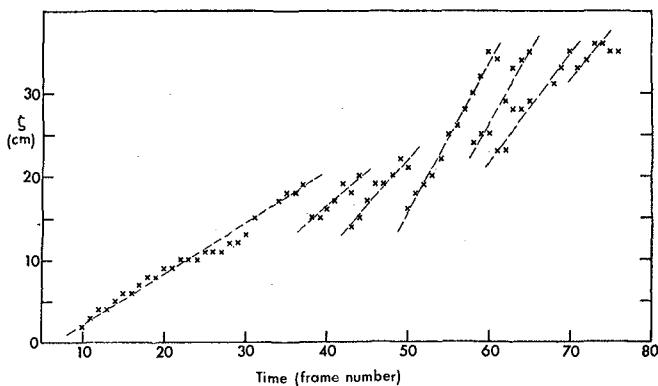


Figure 8. (from Longuet-Higgins and Turner, 1974). Measurements of the length ℓ of the whitecap on shoaling solitary waves as a function of the time, showing intermittency.

*No allowance was made in this model for loss of buoyancy by air bubbles rising through the upper surface.

5. PERIODIC WAVES

For progressive waves in deep water, it has been shown by Schwartz (1974) that the well-known Stokes expansion in powers of the first harmonic a_1 , which is satisfactory at low wave amplitudes, fails to converge at larger wave amplitudes, short of the highest. This is because the waves become markedly non-sinusoidal, developing narrow crests and broad troughs, and the amplitude a_1 of the first harmonic in fact reaches a maximum and then diminishes before the highest wave is reached. So for steepnesses greater than about 0.1 even the higher-order Stokes expansions are divergent and misleading.

Schwartz (1974) overcame this difficulty by using as expansion parameter the wave steepness H/L itself, which increases monotonically throughout the range of possible waves. However, the limiting value of H/L is not accurately known a priori. As an alternative Longuet-Higgins (1975) used the parameter

$$\omega = 1 - \frac{q^2 q'^2}{c^2 c_0^2} \tag{5.1}$$

where q and q' denote the particle speeds at the crest and trough, in a frame moving with the wave, and where c and c_0 are the wave speed and the speed of infinitesimal waves respectively. This parameter is similar to (3.1) and indeed reduces to (3.1) when the depth is finite and the wavelength infinite. The range of ω is from 0 to 1, the value 1 corresponding precisely to the highest wave.

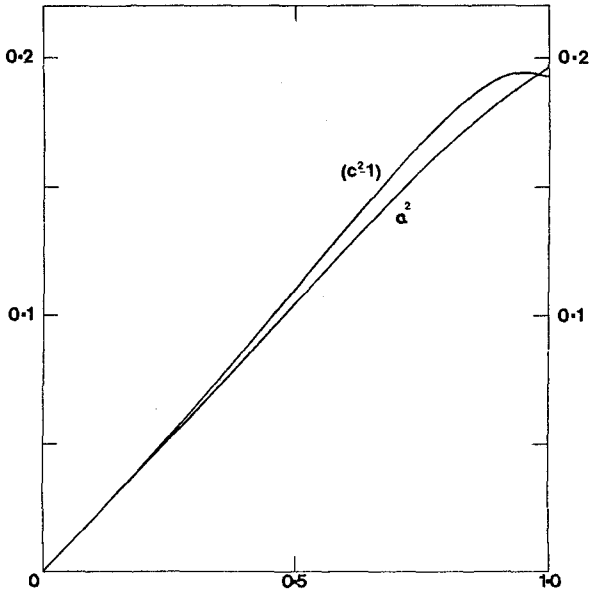


Figure 9. (from Longuet-Higgins, 1975). The square of the wave amplitude a and wave speed c for progressive waves in deep water, as a function of the parameter ω (equation 5.1). The units are chosen so that $g = 1$ and the wavelength $L = 2\pi$. The wave steepness H/L equals a/π .

By using Padé sums, Longuet-Higgins (1975) obtained convergence up to and including the highest wave ($\omega = 1$). Precisely similar effects as for solitary waves, namely maxima in the speed, energy, momentum, momentum flux, etc., as functions of the wave steepness, made their appearance (see Figure 9).

This result is particularly significant since the Stokes series (with ω as parameter) is formally quite different from the Rayleigh-Boussinesq series for the solitary wave. Yet for Stokes's series no question of completeness arises, since Levi-Civita proved actual convergence, for waves of sufficiently small amplitude.

More recently, Cokelet (1976) has calculated and tabulated the speeds, momenta and other integral properties of symmetric gravity waves of arbitrary amplitude and in waves of arbitrary depth h . His method is to use the general Stokes series for waves in finite depth, with an expansion parameter similar to (5.1). For all ratios of the wavelength to depth, he finds maxima in the phase speeds as a function of the wave steepness. There are maxima also in the momentum, momentum flux, energy and energy flux. These accurate calculations may be of considerable use for practical purposes.

6. ASYMPTOTIC SHAPE OF WAVE CREST

The wave crests in Figure 5 suggest that as $\omega \rightarrow 1$ the profile approaches the 120° corner-flow predicted by Stokes. But when $\omega < 1$, and while the crests are still rounded, is there any smooth asymptotic form which the free surface assumes in some neighbourhood of the crest? A natural length-scale for such an asymptotic form

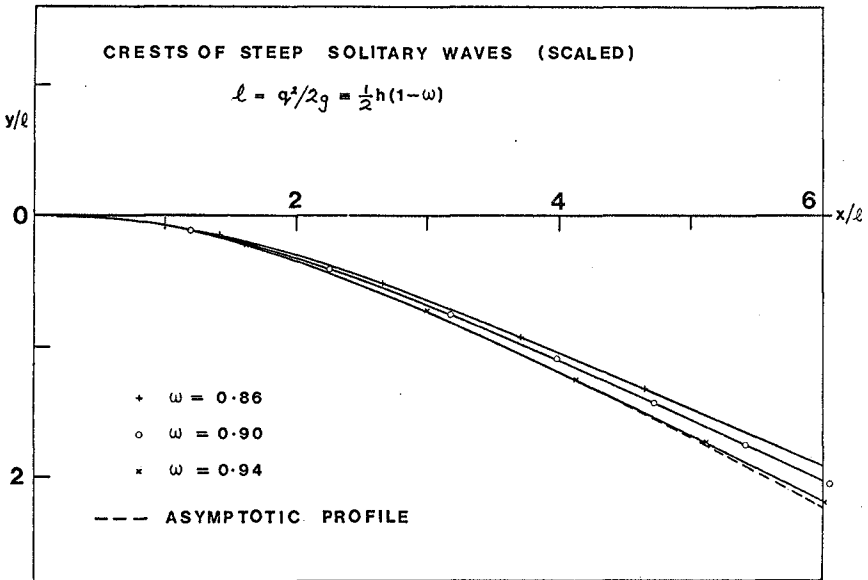


Figure 10. The crests of steep solitary waves (from Figure 5) after rescaling by $l = q^2/2g$, where q is the particle speed at the crest.

is the length

$$\ell = q^2/2g \tag{6.1}$$

where q denotes the particle speed at the crest in the frame moving with the wave. Comparison with equation (3.1) shows that ℓ is directly related to ω by

$$\ell = \frac{1}{2}h(1 - \omega). \tag{6.2}$$

As a test of the conjecture, Figure 10 shows the same wave profiles as in Figure 5 ($\omega = 0.90$ to 0.94) now drawn on the new scale ℓ . When ω approaches 1 they do indeed tend to fall along the same curve.

To define our limiting flow we may take radial coordinates (r, θ) with the origin O at a distance $\ell = q^2/2g$ above the wave crest, and with the line $\theta = 0$ vertically downwards. The Bernoulli condition at the free surface is then

$$\left| \frac{dX}{dz} \right|^2 = 2gr \cos \theta \tag{6.3}$$

where $X = \phi + i\psi$ is the complex velocity potential and $z = re^{i\theta}$. We require a solution which, as $r/\ell \rightarrow \infty$, tends to the Stokes corner-flow:

$$X \rightarrow \frac{2}{3} g^{1/2} z^{3/2} \quad \text{as } r \rightarrow \infty, \quad |\theta| \leq \frac{\pi}{3}. \tag{6.4}$$

This problem has been solved numerically in a recent paper by Longuet-Higgins and Fox (1976). The resulting profile is shown in Figure 11 (and also by the broken line in Figure 10). Not unreasonably, the free surface crosses its asymptote at about $r/\ell = 3.32$ and then approaches it very gradually from the outside. It can be shown analytically that for large values of r/ℓ the normal displacement n of the surface from the straight-line asymptote must have the form

$$n/\ell \sim K(\ell/r)^{1/2} \cos [(3\mu/2) \ln r - \epsilon] \tag{6.5}$$

where K and ϵ are amplitude and phase constants and μ is the positive root of the equation

$$\frac{\mu\pi}{2} \tanh \frac{\mu\pi}{2} = \frac{\pi}{24\sqrt{3}} \tag{6.6}$$

In fact $K = 0.60$, $\epsilon = 0.47$ and $\mu = 0.714$. This means that the free surface approaches its asymptote in a very slowly damped oscillation. There is a second crossing of the asymptote at $r/\ell = 68.5$, a third at $r/\ell = 1286$, and so on.

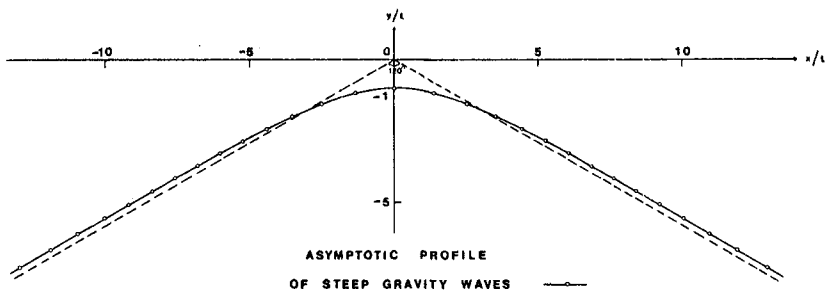


Figure 11. (from Longuet-Higgins and Fox, 1976a). The asymptotic profile of the crests of a steep gravity wave, on a scale $\ell = q^2/2g$.

The results can be checked not only by a direct comparison with the profiles of wave crests calculated independently (such as in Figure 10) but also by a consideration of the maximum surface slope. From Figure 11 it will be seen that between the two crossings of the asymptote at $r/l = 3.32$ and $r/l = 68.5$ the maximum angle of slope must slightly exceed 30° . The actual value is 30.37° . This should correspond to the maximum slope of almost-limiting gravity waves.

Now independent calculations of the complete profiles of steep solitary waves have been made both by Sasaki and Murakami (1973) and by Byatt-Smith and Longuet-Higgins (1976). Their values for the maximum surface slope are plotted against ω in Figure 12. It can be seen that a linear extrapolation of the plotted points passes very close to the asymptotic value that we have obtained independently.

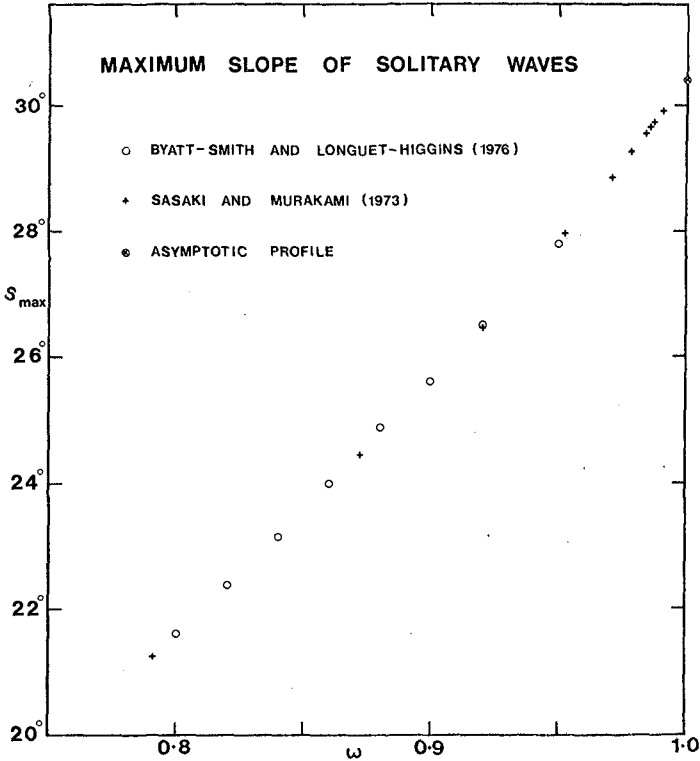


Figure 12. (from Longuet-Higgins and Fox, 1976). The maximum surface slope of steep solitary waves, as a function of the parameter ω . The limiting value at $\omega = 1$ corresponds to the profile of Figure 11.

Figure 13 shows a similar comparison for periodic waves in deep water. The agreement is again very close.

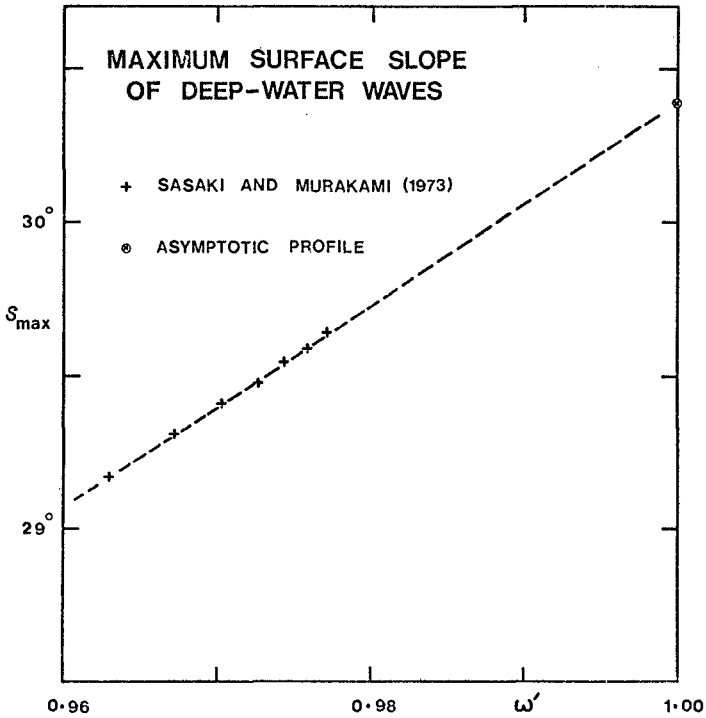


Figure 13. (from Longuet-Higgins and Fox, 1976). The maximum surface slope of progressive waves in deep water, as a function of the parameter ω' .

The acceleration of a fluid particle at the wave crest is given by

$$\ddot{y} = -q^2/R$$

where R is the radius of curvature. From the present profile this is found to be $0.39 g$. In the far-field, as $r/l \rightarrow \infty$, the acceleration tends to the value $\frac{1}{2} g$ directed radially outwards, as in the Stokes corner-flow.

7. IMPROVEMENT IN THE CALCULATION OF STEEP GRAVITY WAVES

The maximum slope will in theory exceed 30° only for very steep, symmetric waves and in a limited region near the crest, which may be affected by instabilities, wind pressures and surface tension. Nevertheless the asymptotic solution found in Section 6 may have practical uses. At present the only accurate calculations of steep, symmetric gravity waves have been obtained by mathematical tour-de-force, either by carrying small-amplitude expansions to very high order or by numerical techniques, such as Fourier series or integral equations, which involve lengthy and complicated numerical schemes. The main value of the asymptotic solution just described is that it may be used as an inner solution, valid near the wave crest, and matched asymptotically to an outer solution representing the flow in the remainder of the wave.

The appropriate matching has already been carried out for periodic waves in deep water by the present author and M.J.H. Fox (1976). As a sample of their results, Figure 14 shows a comparison of the square of the wave speed c^2 plotted against the wave steepness. The peculiar shape of the top of the velocity curve is accurately checked, showing that it is certainly not due to some quirk of the Padé approximants.

Such an approach thus promises to simplify our calculations of steep, symmetric waves, and to improve our understanding of them.

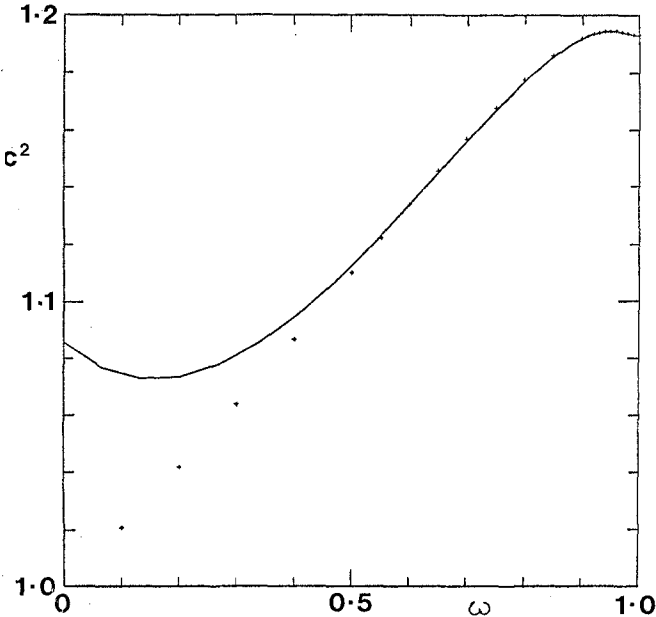


Figure 14. Square of the velocity c for progressive waves in deep water, as a function of ω . The plotted points correspond to the values obtained from Padé sums (Longuet-Higgins, 1975; see also Figure 9). The curve is found independently by matching the asymptotic solution in Section 6.

8. A METHOD FOR CALCULATING UNSTEADY SURFACE WAVES

In natural conditions the occurrence of a steady, steep wave is somewhat exceptional. Even symmetric waves tend to become unsteady and asymmetric long before their energy reaches the theoretical maximum. However, a new and general method for calculating the development of an unsteady wave has recently been given by Longuet-Higgins and Cokelet (1976). So far it has been applied only to waves in deep water but it could readily be extended to waves in water of finite depth.

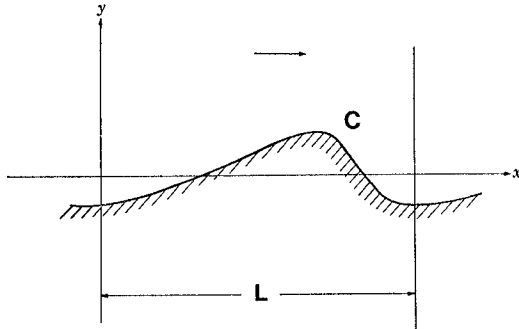


Figure 15. Axes and notation for space-periodic waves in deep water.

The motion is assumed to be irrotational and periodic in space (see Figure 15) though not generally periodic in time. All calculations are carried out with the surface values of the space coordinates (x, y) and of the velocity potential ϕ . For the rates of change of these quantities one has

$$\begin{aligned} \frac{Dx}{Dt} &= \frac{\partial \phi}{\partial x} \\ \frac{Dy}{Dt} &= \frac{\partial \phi}{\partial y} \end{aligned} \tag{8.1}$$

$$\frac{D\phi}{Dt} = -p - gy + \frac{1}{2}(\nabla\phi)^2$$

where D/Dt denotes differentiation following the motion. The last equation follows from the time-dependent Bernoulli equation and the fact that $D\phi/Dt = \partial\phi/\partial t + (\nabla\phi)^2$. Hence, given the surface values of x, y, ϕ and $\nabla\phi$ at some instant t on the surface $C(t)$ one can calculate x, y and ϕ at time $(t + dt)$ on the displaced surface $C(t + dt)$.

To proceed to the next time-step we need to know both components of the velocity on $C(t + dt)$. We can obtain the tangential component $\partial\phi/\partial s$ immediately, by differentiating $\phi(t + dt)$ along the new surface. However we still lack the normal component of velocity $\partial\phi/\partial n$ on $C(t + dt)$.

Now because of the space-periodicity we can transform C into a closed contour C' (Figure 16) simply by writing

$$e^{ik(x + iy)} = \zeta, \quad (k = 2\pi/L). \tag{8.2}$$

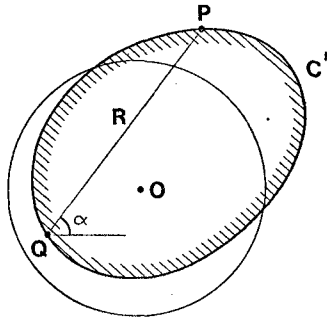


Figure 16. One wavelength in the (x, y) plane transformed to a closed domain in the z -plane.

The domain of the fluid goes into the interior of C' and the points at infinite depth go into the origin $z = 0$. We then have to solve, in effect, the well-known Dirichlet problem, namely to find $\partial\phi/\partial n$ on a contour C' , given ϕ on C' and

$$\nabla^2\phi = 0 \quad (8.3)$$

everywhere inside C' .

This problem can be solved as follows (see Figure 16). Let (R, α) denote the polar coordinates of a running point P on the boundary, relative to a fixed point Q , also on C' . Then it follows from Green's theorem that

$$\int_{C'} \frac{\partial\phi}{\partial n} \ln R \, ds = \pi\phi_Q + \int_{C'} \phi_P \, d\alpha \quad (8.4)$$

where in the right-hand integral we take the principle value. Since ϕ is known everywhere on C' , the right-hand side is given, and equation (8.4) is then a linear integral equation for $\partial\phi/\partial n$, with given kernel $\ln R$. Solution of this equation gives us $\partial\phi/\partial n$ on $C(t + dt)$, and the time-stepping can proceed.

Numerical solution of equation (8.4) has been carried out by Longuet-Higgins and Cokelet (1976) replacing the boundary by a finite number N of integration points. Typically $N = 60$ for one wavelength. Details of the method, which are vital for its accuracy and success, are given in their paper. The method was first tested for accuracy on a free symmetric wave of finite amplitude for which the form and phase-velocity were calculated independently by the method of Section 5, and good agreement was obtained. Then the following experiment was performed. As initial state was chosen a progressive wave of fairly large amplitude, whose energy was 0.80 times the maximum E_{\max} for a steady symmetric wave of that wavelength. The energy was then raised by applying to the surface (numerically) a pressure of the form

$$p = \left\{ \begin{array}{l} p_0 \sin(kx - \sigma t) \sin \sigma t, \quad (0 < \sigma t < \pi) \\ 0 \quad (\sigma t < 0 \text{ and } \sigma t > \pi) \end{array} \right\} \quad (8.5)$$

through the boundary-conditions (8.1). This represented a sinusoidal distribution of pressure, in quadrature with the fundamental harmonic of the surface elevation, increasing and dying away smoothly over half a wave period (π/σ). After the surface pressure had fallen to zero, the wave was supersaturated, that is its level exceeded E_{\max} . It was then allowed to run free. Its subsequent development can be followed in Figure 17.

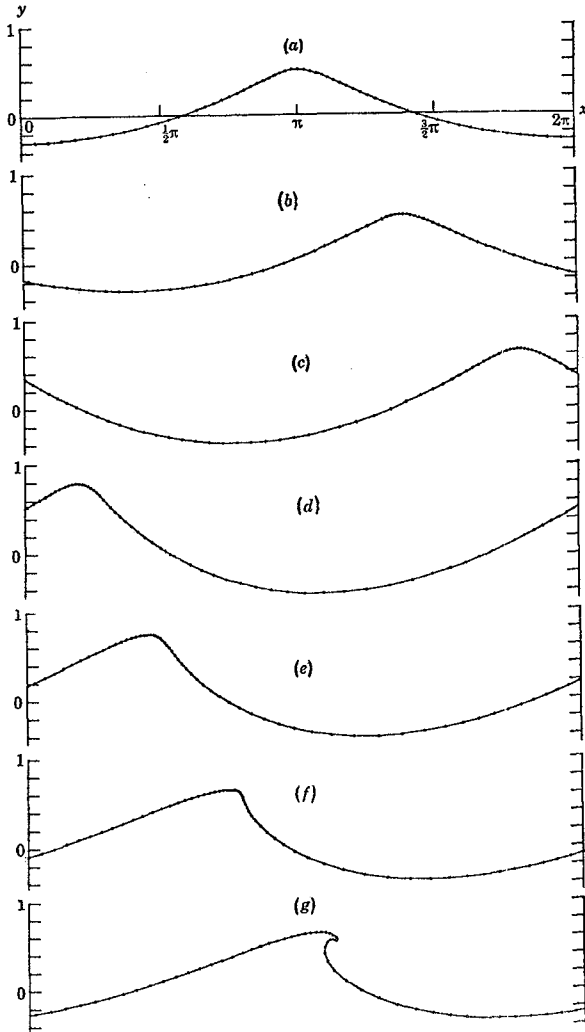


Figure 17. (from Longuet-Higgins and Cokelet, 1976). Development of a progressive wave in deep water. From (a) to (c) a surface pressure (8.5) is applied to the rear face of the wave. From (d) to (e) the wave is free.

Figure 18 gives a close-up view of the free surface near the instant of overturning. The figure shows successive positions of the free surface (actually every 3 time-steps) in a frame moving with the speed c_0 of infinitesimal waves. The plotted points refer always to the same marked particles, so that a line through a succession of points defines a particle trajectory, in this reference frame.

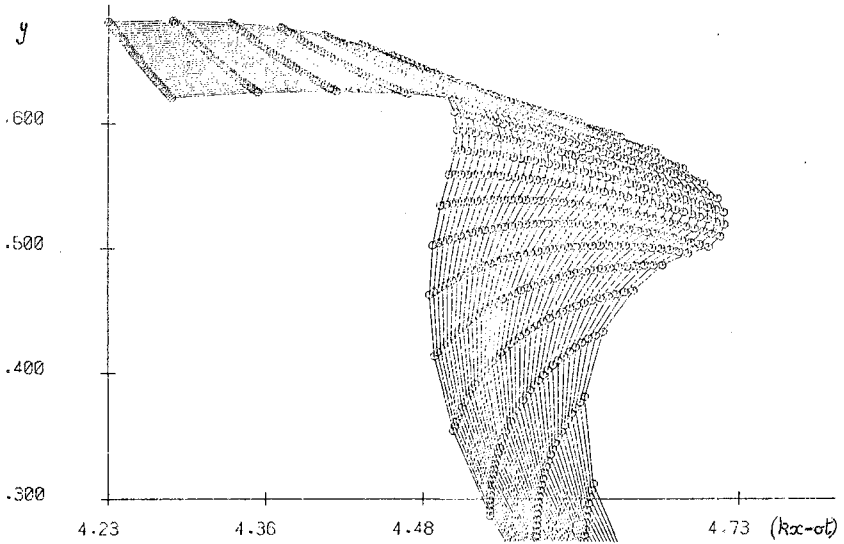


Figure 18. (from Longuet-Higgins and Cokelet, 1976). Successive profiles of the free surface near the instant of overturning, seen in a reference frame moving with speed c_0 .

The particles have a welcome tendency to congregate near points of high surface curvature, which is precisely where they are needed for computational accuracy.

It will be seen that the crest remains rounded until well past the instant when the surface becomes vertical. Thereafter the curvature near the tip of the breaker increases rapidly. The free surface can be followed by this method only so long as the separation between adjacent particles does not exceed a fraction of the local radius of curvature. The question whether the curvature becomes infinite in finite time cannot be decided by this method.

In practice the tip of the jet will be much influenced both by surface tension, which we have neglected, and by air currents. Both these may cause it to break up into spray. Both effects could possibly be included in the calculation. The present calculations were intended to apply only to waves on a sufficiently large scale.

Though the computation involves only the surface values of x , y and ϕ , the pressure and velocity components in the interior may also be found from the surface values, by the use of Cauchy's theorem. The pressure gradients in the tip are small, but there is no evidence of a reversed normal gradient of the pressure.

Because it uses the velocity potential ϕ yet follows marked particles, the above technique may be called MEL (mixed Eulerian and Lagrangian). The example just discussed illustrates only one possible application of the general method. Various other initial conditions might be chosen so as to correspond, for example, to a standing wave, or to a partially reflected wave, or to a mixture of progressive wave trains having rationally related wavelengths. These would constitute a wave group with slowly varying wave envelope. It will be of interest to see how the resulting energy and momentum lost in the jet of the breaking wave are related to the different initial conditions.

9. EXPERIMENTAL CONFIRMATION

Although the above computations were for deep water, nevertheless one would expect the local behaviour of the wave crest to be asymptotically similar whether in deep or shallow water. To test whether the surface could remain smooth and continuous after the tangent became vertical, the author and N.D. Smith, with the collaboration of Dr. N. Hogben, made a high-speed film of waves breaking on a 1:6 beach slope, in the No. 2 Towing Tank of the National Physical Laboratory at Teddington. Figure 19 shows one frame from a film taken at 500 frames/sec. The grid-spacing is 5.0 cm. The film confirms that the free surface can indeed remain smooth and rounded until after overturning takes place.

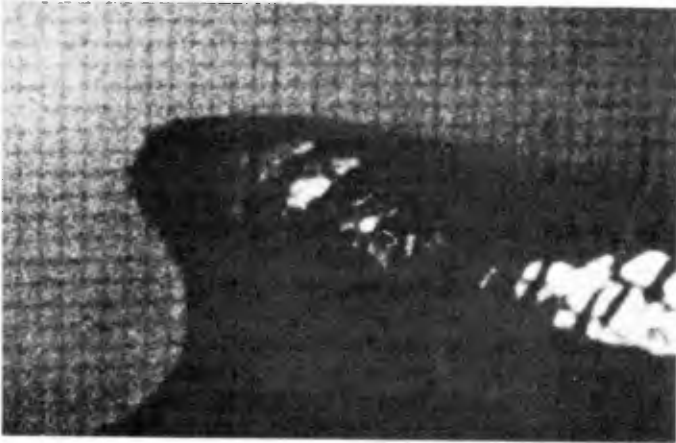


Figure 19. Wave breaking on plane beach, slope 1:6.

REFERENCES

- Byatt-Smith, J.G.B. 1970 An exact integral equation for steady surface waves.
Proc. Roy. Soc. Lond. A. 315, 405-418.
- Byatt-Smith, J.G.B. and Longuet-Higgins, M.S. 1976 On the speed and profile of steep solitary waves.
Proc. Roy. Soc. Lond. A. 350, 175-189.
- Cokelet, E.D. 1976 Steep gravity waves in water of arbitrary uniform depth.
(in preparation).
- Fenton, J. 1974 A ninth-order solution for the solitary wave.
J. Fluid Mech. 53, 257-271.
- Kjeldsen, S.P. and Olsen, G.B. 1971 Breaking waves (16mm film).
Tech. Univ. of Denmark, Copenhagen.
- Lamb, H. 1932 Hydrodynamics, 6th ed.
Cambridge Univ. Press.
- Lenau, C.W. 1966 The solitary wave of maximum amplitude.
J. Fluid Mech. 26, 309-320.
- Longuet-Higgins, M.S. 1963 The generation of capillary waves by steep gravity waves.
J. Fluid Mech. 16, 138-159.
- Longuet-Higgins, M.S. 1973 On the form of the highest progressive and standing waves in deep water.
Proc. Roy. Soc. Lond. A. 331, 445-466.
- Longuet-Higgins, M.S. 1974 On the mass, momentum, energy and circulation of a solitary wave.
Proc. Roy. Soc. Lond. A. 337, 1-13.
- Longuet-Higgins, M.S. 1975 Integral properties of periodic gravity waves of finite amplitude.
Proc. Roy. Soc. Lond. A. 342, 157-174.
- Longuet-Higgins, M.S. and Cokelet, E.D. 1976 The deformation of steep surface waves on water. I. A numerical method of computation.
Proc. Roy. Soc. Lond. A. 350, 1-26.
- Longuet-Higgins, M.S. and Fenton, J.D. 1974 On the mass, momentum, energy and circulation of a solitary wave. II.
Proc. Roy. Soc. Lond. A. 340, 471-493.
- Longuet-Higgins, M.S. and Fox, M.J.H. 1976 Theory of the almost highest wave.
(in preparation).
- Longuet-Higgins, M.S. and Turner, J.S. 1974 An "entraining plume" model of a spilling breaker.
J. Fluid Mech. 63, 1-20.
- Sasaki, K. and Murakami, T. 1973 Irrotational, progressive surface gravity waves near the limiting height.
J. Oceanogr. Soc. Japan 29, 94-105.
- Schwartz, L.W. 1974 Computer extension and analytic continuation of Stoke's expansion for gravity waves.
J. Fluid Mech. 62, 553-578.
- Stokes, G.G. 1880 On the theory of oscillatory waves. Appendix B: Considerations relative to the greatest height of oscillatory irrotational waves which can be propagated without change of form.
Math. and Phys. Pap. 1, 225-228.
- Witting, J. 1974 On the highest and other solitary waves.
SIAM J. Appl. Math. 28, 700-719.
- Yamada, H. 1957a Highest waves of permanent type on the surface of deep water.
Rep. Res. Inst. Appl. Mech. Kyushu Univ. 5, 37-52.
- Yamada, H. 1957b On the highest solitary wave.
Rep. Res. Inst. Appl. Mech. Kyushu Univ. 5, 53-67.

CHAPTER 26

KINEMATICS OF BREAKING WAVES

Edward B. Thornton,
James J. Galvin,
Frank L. Bub and
David P. Richardson

Department of Oceanography
Naval Postgraduate School
Monterey, California 93940

ABSTRACT

Measurement of waves, and vertical and horizontal water particle velocities were made of spilling, plunging and surging breakers at sandy beaches in the vicinity of Monterey, California. The measured breaking waves, derived characteristically from swell-type waves, can be described as highly nonlinear. Spectra and cross spectra were calculated between waves and velocities. Secondary waves were noted visually and by the strong harmonics in the spectra. The strength of the harmonics is related to the beach steepness, wave height and period. The phase difference between waves and horizontal velocities indicates the unstable crest of the wave leads the velocities on the average by 5-20 degrees. Phase measurements between wave gauges in a line perpendicular to the shore show breaking waves to be frequency nondispersive indicating phase-coupling of the various wave components. The coherence squared values between the sea surface elevation and the horizontal water particle velocity were high in all runs, ranging above 0.8 at the peak of the spectra. The high coherence suggests that most of the motion in the body of breaking waves is wave-induced and not turbulent.

INTRODUCTION

Wave theories can be applied outside the surf zone with some degree of certainty, and can be tested in laboratory and field situations. The various theories can be used to carry the waves from deep water through the shoaling process up to the point of near breaking. At the breaker point, however, there is a transition from ordered to apparent turbulent motion and the theoretical description of wave kinematics becomes difficult. One of the greatest deficiencies in our understanding of the surf zone is an appropriate description of breaking waves. The experimental study of the kinematics of breaking waves in the surf zone has progressed slowly due to the problems encountered in making direct field measurements and the difficulty in modeling the surf zone in the laboratory.

The most direct approach to the problem of describing the kinematics of surf zone breaking waves is by field measurements. Advances in instrument design have led to simple, sturdy, devices for measuring waves and velocities with rapid response time. Miller and Ziegler (1964) used both acoustic and electromagnetic flow meters to determine the particle motion

in the surf zone. Walker (1969) made studies using propeller-type flow meters. Wood (1973) measured waves and currents in the surf zone using movies of dye movement and capacitance wave gauges. Fhürbötter Büsching (1974) utilized a two-component electromagnetic current meter and pressure-type wave meters to measure simultaneous orbital velocities and water levels. Thornton (1968) used an electromagnetic flow meter and pressure transducers to measure waves inside the surf zone. Steer (1972), Thornton and Richardson (1973), Bub (1974) and Galvin (1975) used pressure meters, capacitance wave gauges and electromagnetic current meters to measure surface profiles and particle velocities within the surf zone; the work presented here is a synthesis of these latter studies.

EXPERIMENT

The experiments were designed to measure kinematics of various types of breaking waves including spilling, plunging and surging breakers. The manner in which waves break depends very much on the characteristics of the beach and near-shore bottom slope. The experimental sites were in the vicinity of Monterey, California. The beaches here were some of the first intensively studied to gain an understanding of amphibious warfare techniques and were described and popularized by Bascom (1964).

The Del Monte Beach, within Monterey Bay, was chosen to measure plunging and spilling breakers. The waves at this location are generally topographically sheltered and severely directionally filtered due to refraction by the geometry of the bay often resulting in swell type waves impinging perpendicular to the shore. Hence, a simplification to a two-dimensional narrowbanded wave description is allowed. A second experimental site was Carmel River Beach, five miles to the south, where the beach is very steep and often has surging type breakers. Again here, the beach is within an embayment, Carmel Bay, and the generally narrow-banded waves impinge almost perpendicular to the shore.

The median grain size at Del Monte Beach is approximately 0.2 mm (taken at the water line), and the beach slope varies between 1:14 to 1:40. The median grain size at the Carmel River Beach is approximately 0.6 mm and the beach slope varies between 1:6 to 1:12. A typical beach profile and instrument location for Del Monte Beach is shown in Figure 1.

Instrumentation. The surf zone is a formidable environment in which to make measurements. The instruments must be rugged and reliable but at the same time be accurate and have a good time response. The instrumentation set-up described below evolved over a number of experiments.

Measurements at Del Monte Beach were made using two electromagnetic flow meters and three capacitance wave gauges. One flow meter and two wave gauges were used at Carmel River Beach. The instruments were mounted on the towers within the surf zone. All equipment was calibrated in the laboratory prior to the experiments.

The electronics package for each of the 2.5 m capacitance wave gauges was constructed using the design of McGoldrick (1969). The electronics package was housed in a water-tight brass case which was mounted on the tower. This enabled the connecting leads to be less than 30 cm, thereby minimizing wire-to-wire capacitance. Accuracy is estimated to be ± 0.005 m.

The flow meters were Marsh-McBirney Model 721 and 722 Electromagnetic Current meters. The flow meter operation is based on Faraday's principle of electromagnetic induction. Each probe measures water velocity in two orthogonal directions. The flow meters were calibrated with an oscillating platform attached to an eccentric arm driven by a variable speed motor. Measurement accuracy was determined to be ± 0.005 m/sec during calibration.

The instrument towers are 6.3 cm outside diameter steel pipes which were 3.6 m high with a 1.0 m baseplate and 0.6 m steel pipe bottom extension. A typical tower and sensor arrangement is shown in Figure 2. The towers were placed on a line perpendicular to the shore and were erected during low tide when the beach was easily accessible. The measurements were then conducted at high tide. The tidal range in the Monterey area is typically two meters. The towers were supported by steel guy wires fastened to the one meter long blade type anchors. Several types of anchors were tried; the blade anchor was chosen because it works quite satisfactorily in the relatively coarse sand and is easily installed. The flow meters were positioned directly under the wave gauges with the axes aligned horizontally and vertically. A carpenter's level was used to establish axis alignment with an estimated error of ± 2 degrees.

A number of problems arose in the course of the experiments. The greatest difficulties in the field are encountered during periods of storms and large waves, a time when the measurements are often of most interest. Flotsam and, in particular, the giant kelp, *Macrocystis*, torn loose from its hold-fasts are thrust ashore during storms. The kelp at times becomes entangled in the instrument towers, greatly increasing the drag, and making the towers susceptible to being knocked down.

The beaches are composed of fine to coarse sand. During wave conditions when the beaches are being eroded and cut back, considerable scour can occur around the anchors and instrument towers causing towers to topple on several occasions.

The first capacitance wave gauge wires were manufactured from one cm diameter stripped RG-11 coaxial cable, (Bub, 1974); these wave wires were susceptible to strumming and broke soon after installation. The construction of the wave wire was modified to a three-eighths inch outside diameter stainless steel rod as the center conductor covered with a jacket of polyurethane plastic tubing as the dielectric; these wave gauges can withstand the severe forces in the surf.

Wave gauges penetrating the surface were used to obtain a true measure of the surface elevation. Pressure transducers, although easier to install and maintain, do not represent the water surface in breaking waves. Breaking waves are highly nonlinear and the conventional technique of converting the pressure measurements to water surface elevation using the spectral transfer function derived from linear theory results in substantial error. As will be shown, the velocities, and hence dynamic pressures beneath breaking waves, are much greater than calculated using linear theory. Further, pressure does not support sharp discontinuities beneath the sharp crests of breaking waves, hence, the pressure records are much smoother and rounded off compared with the capacitance wave gauge measurements.

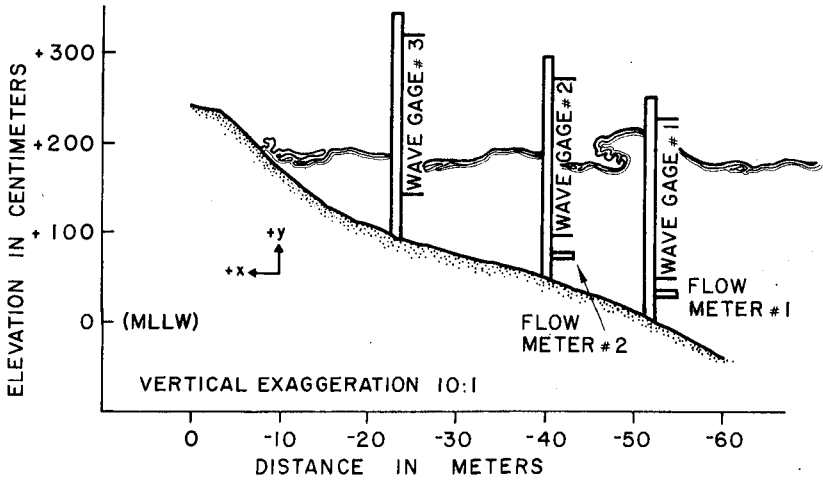


FIGURE 1. LOCATION OF INSTRUMENTS.

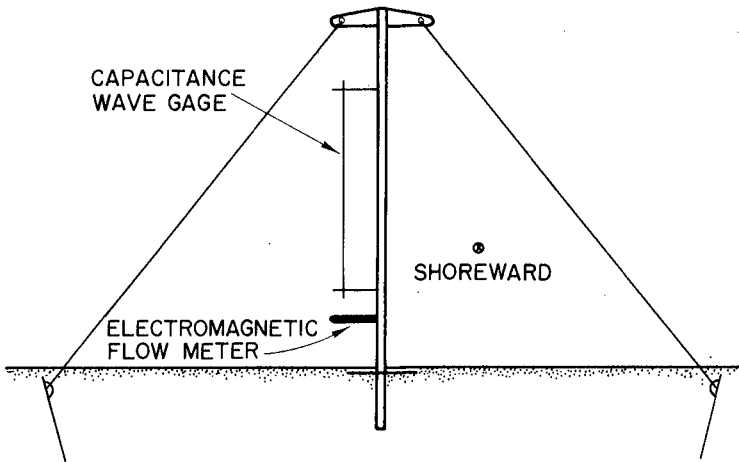


FIGURE 2. INSTRUMENTATION TOWER.

All signals were cabled ashore and recorded on a Vidar Corporation 32-channel digital data acquisition system. A Sangamo Model 3500 14-channel FM tape recorder was utilized as a secondary recording system. A Brush 8-channel strip chart recorder was used to monitor the instrumentation performance during recording and as a means to select the appropriate data sections to be analyzed.

Analysis. A mean value was calculated for all data sets and the data were linearly detrended to exclude the rise and fall of the tide. The variance, standard deviation and average period were calculated. The average period was determined by calculating the time between zero up-crossings.

Correlation functions were calculated for signals and smoothed with a Parzen window. The smoothed correlation functions were Fourier transformed to obtain the power and cross spectra. The coherence and phase were calculated from the cross spectral estimates.

The maximum lag time in calculating the correlation functions was taken as five percent of the record giving a spectral bandwidth resolution of 0.0055 Hz and resulting in 40 degrees of freedom for each spectral estimate. The 90 percent confidence limits for 40 degrees of freedom using a chi-square distribution are found to be between 0.72 and 1.51 of the measured power spectral estimates.

Measurements in the surf zone are not only hampered by the difficulties of a physically hostile environment, but can present conceptual analysis difficulties. The wave heights and spectral characteristics continually change as the waves shoal, break and dissipate across the surf zone. Changes in the wave profile occur over short distances compared to the wave length within the surf zone which does not allow spatial averaging within the surf zone. Point measurements are also troublesome because the breaker position is continually changing. Thus, the waves in the surf zone are spatially nonhomogeneous and tend to be temporally nonstationary.

As the wave height stochastically varies, the wave set-up changes resulting in a change in the mean water level at a particular location in the surf zone. The breaker position is approximately related to the wave height and local depth. Hence, the breaker position tends to wander, depending on the wave conditions. The breaker position tends to wander more on flatter beaches as was evident at Del Monte Beach experiment site. The shoaling processes on steeper beaches occur much more rapidly and over shorter distances, resulting in the breaker position being relatively fixed. The waves broke at nearly the same position for a particular tidal stage at the steeper Carmel River Beach site.

The spatial nonhomogeneity and temporal nonstationarity results in a smearing of spectral information of the breaking processes. This difficulty must be kept in mind when interpreting the results, but does not appear to be a severe limitation.

Handwritten note:
/Cont. surf
mean for
crossing
contours

WAVES AND HORIZONTAL VELOCITY MEASUREMENTS

Qualitative Description. A number of universal similarities of wave form can be observed for various types of breakers occurring on different beaches. Figure 3 is a typical analog record of plunging-spilling breaking waves and horizontal velocities beneath the waves obtained from Del Monte Beach. In general, there is a quick drawdown of water just before the breaker arrives, followed by a steep, vertical leading edge, and a sloping profile toward the trailing edge, giving a generally sawtoothed shape. On the trailing edge, one or more secondary waves are often noted. The secondary waves are harmonics of the primary wave frequency and are indicative of strongly nonlinear waves. The authors have had the opportunity to see in the field the secondary waves develop by standing on an instrument tower as the waves break past the tower. As the wave shoals, the secondary waves start to grow and, as the waves steepen rapidly just before breaking, the secondary waves likewise rapidly develop on the back of the primary wave. The rapid transfer of energy from the primary wave frequency to the secondary wave is "mother nature's" means of maintaining the potential energy across the surf zone rather than converting to kinetic energy in the breaking process. The broken primary wave often reforms and continues toward shore closely followed by the secondary wave; this often results in two waves breaking close behind each other as the beach face is approached.

Surging breakers generally occur on steeper beaches in which the shoaling wave becomes unstable and forms a bore-like profile as the water progresses up the beach face. The breaking process on steep beaches occurs rapidly and secondary waves generally do not have time to develop.

On steep beaches, the swash zone is much more important in the surf zone processes, and on very steep beaches can constitute a major extent of the surf zone. A strong interaction of the backwash of the proceeding breaker and the new breaker can occur which complicates the wave processes. Wave reflection from steep beaches is greater which further complicates the processes.

The water particle velocity trace shown in Figure 3 reflects the general characteristics of the sea surface. The water cannot support sharp discontinuities which results in the velocities being considerably more smoothed. It should be emphasized that the smoothing in the velocity records is real and not a result of the frequency response of the flow meters.

In a spilling breaker, the crest becomes unstable and slides down the face of the wave; the turbulent region is generally confined to the area above the trough and does not penetrate into the body of the flow. The crest of the plunging breaker curls over and penetrates deeper into the water column, although the velocities still have an appearance similar to the wave surface. Surging breakers, which are bore-like, are apparently turbulent on the small scale throughout the water column, but the body of the fluid translates with the wave profile. Hence, the primary motion even under the surging breakers can be associated with the surface and is wave-induced. The important point is that the velocities under breaking waves and in the surf zone appear to be primarily associated with the wave surface and not turbulent, disorganized motion.

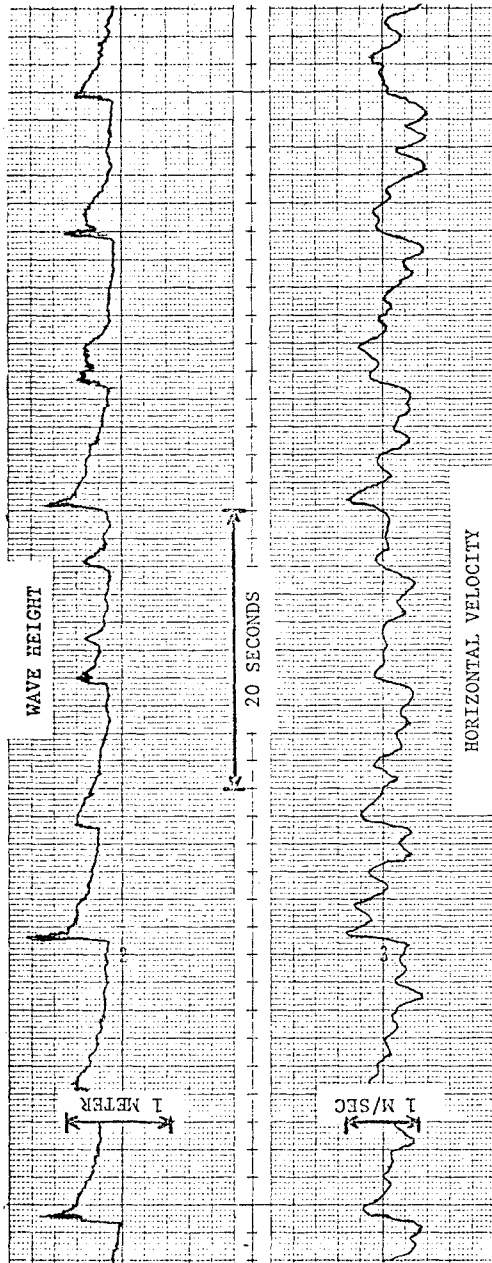


FIGURE 3. TYPICAL ANALOG RECORD OF WAVES AND HORIZONTAL VELOCITIES BENEATH THE WAVES FROM DEL MONTE BEACH.

Comparing Measured and Calculated Velocity Spectra Using Linear Wave Theory. A velocity spectrum was calculated from the wave spectrum using the transfer function derived from linear wave theory. Previous work in deeper water by Simpson (1969), Bowden and White (1966), and Thornton and Krapohl (1974) has shown that using linear wave theory to derive the spectral transfer function gave very good results in calculating the water particle velocity spectra under waves. It was not expected that as good results would be obtained in the surf zone, but would serve as a basis for comparison with other theories. Further, spectral analysis assumes superposition of the spectral component which only allows using a constant parameter linear theory for the transfer function.

The elevation of the surface $\eta(t)$ can be described as the superposition of an infinite number of sinusoids of the form:

$$\eta(t) = \sum_{n=1}^{\infty} a_n \cos(\vec{k} \cdot \vec{x} - \sigma_n t + \epsilon_n) = \sum_{n=1}^{\infty} \eta_n \quad (1)$$

where a_n is the amplitude, x is the horizontal Cartesian coordinate, t is the time, ϵ_n is an arbitrary angle, \vec{k} is a horizontal vector wave number, and σ is the frequency related in linear theory to k by

$$\sigma_n^2 = gk_n \tanh k_n h \quad (2)$$

where g is the acceleration of gravity. The $\eta(t)$ represents the sum total of all component wavelets. Summing in the manner of (1) implies a linear system and restricts the analysis to the use of linear wave theory to describe the wave-induced motion.

Linear wave theory can be used to calculate the wave-induced water particle velocities. The equation for the horizontal velocity is

$$\begin{aligned} u(t) &= \sum_{n=1}^{\infty} a_n \sigma_n \frac{\cosh k_n (h+z)}{\sinh k_n h} \cos(\vec{k}_n \cdot \vec{x} - \sigma_n t + \epsilon_n) \\ &= \sum_{n=1}^{\infty} \frac{\sigma_n \cosh k_n (h+z)}{\sinh k_n h} \eta_n = \sum_{n=1}^{\infty} H_n(\sigma, z) \eta_n \end{aligned} \quad (3)$$

where h is the total depth and z is the vertical coordinate measured positively upward from the still water level. The solution says that the amplitude of the velocities is a function of wave amplitude, frequency and depth, and that the water surface and horizontal water particle velocities are in-phase. The term in (3) in braces represents the complex spectral transfer function, $H_n(\sigma, z)$, and is used to calculate the wave-induced horizontal velocity spectrum, $S_u(\sigma)$, from the wave spectrum $S_\eta(\sigma)$:

$$S_u(\sigma) = |H(\sigma, z)|^2 S_\eta(\sigma). \quad (4)$$

In the formulation of linear wave theory, the boundary conditions are linearized in order to obtain an analytical solution. In the linearization, it is assumed that the amplitude is small in comparison with the wavelength, that is, $ak \ll 1$. Higher-order solutions to the boundary value problem, generally obtained by perturbation analysis, give a better representation of a constant profile wave. However, the nonlinearities introduced in the solution preclude their use where the principle of superposition is invoked.

Figure 4 shows typical spectra of the measured and calculated water particle velocities using Eq. 4 for the case of plunging-spilling breakers in the surf zone taken at Del Monte Beach. The waves are narrow-banded with a primary frequency of 0.06 hz (16.6 second period).

Strong harmonics of decreasing energy density are evident. The measured horizontal velocities were always greater than the calculated by 20-100 percent. That is to say, linear theory underpredicts the horizontal velocities. This is not surprising because of the steepness of the waves, but the amount of underestimation is surprising. The amount of deviation from linear theory demonstrates the strength of the nonlinearities of shallow water waves and some contribution by turbulence.

The strong harmonics are both real and artifices. The secondary waves are real harmonics of the primary wave and show up as energy at harmonic frequencies. Due to the very peaked wave form of the primary wave, spectral analysis will also show energy-density at harmonic frequencies as a result of viewing the breaking waves as an infinite sum of sinusoidal wave components.

Also shown in Figure 4 are the coherence squared (here-after referred to simply as coherence) and the phase difference between waves and horizontal velocity. The coherence between waves and horizontal water particle velocities was high, ranging above 0.75 at the peak of the spectrum and decreasing at higher and lower frequencies. The generally high coherence indicates the water particle motion is primarily wave-induced.

The decrease in coherence can be attributed primarily to the velocities being converted to turbulence during breaking and the nonlinearities associated with finite amplitude wave motion. The decrease in coherence due to turbulence can be demonstrated by considering the horizontal velocity, u , as being decomposed into wave-induced, U , turbulent, u' , and mean, \bar{u} , contributions, such that the velocity is given by

$$u = U + u' + \bar{u}. \quad (5)$$

Assuming the wave-induced and turbulent velocity spectral component are statistically independent, the horizontal velocity spectrum is given by

$$S_u(\sigma) = S_U(\sigma) + S_{u'}(\sigma). \quad (6)$$

The wave-induced velocity spectrum is calculated from the wave spectrum using equation (4). For a constant parameter linear system the coherence is identically equal to unity,

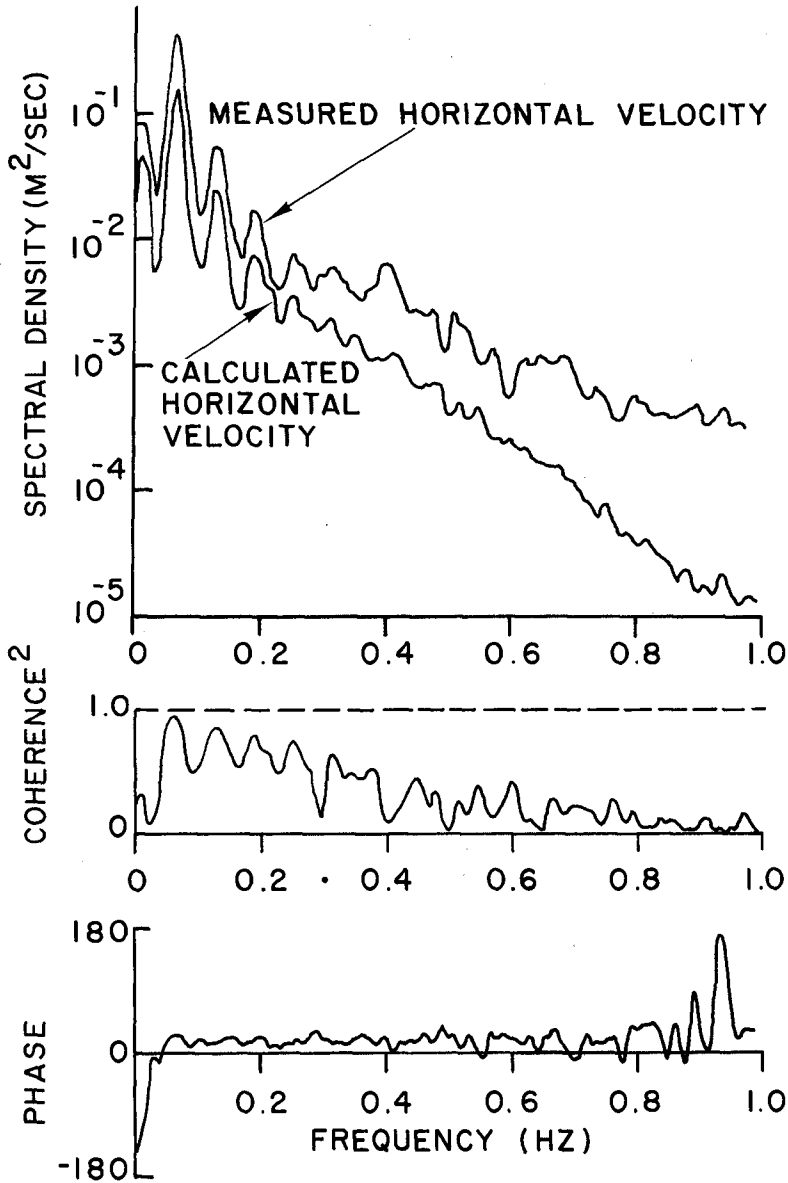


FIGURE 4. MEASURED AND CALCULATED HORIZONTAL VELOCITY SPECTRA UNDER SPILLING-PLUNGING BREAKERS, 4 MARCH 1975.

$$\gamma_{U\eta}^2(\sigma) = \frac{|S_{U\eta}(\sigma)|^2}{S_U(\sigma) S_\eta(\sigma)} \equiv 1 . \quad (7)$$

Since the turbulent and wave-induced velocities are assumed to be statistically independent, then

$$S_{U\eta}(\sigma) = S_{U\eta}(\sigma) . \quad (8)$$

The substitution of (6), (7) and (8) into the definition of coherence between the total horizontal velocity and waves results in

$$\gamma_{U\eta}^2(\sigma) = \left[1 - \frac{S_U(\sigma)}{S_U(\sigma)} \right]^{-1} = \frac{S_U(\sigma)}{S_U(\sigma)} \leq 1 . \quad (9)$$

Increasing lack of coherence is due to an increasingly high ratio of turbulence (noise) to coherent wave-induced velocity fluctuations (signal). Using this interpretation for the coherence, the results of Figure 4 suggest that 94% of the spectral energy at the primary wave frequencies (peak of the spectrum) is wave-induced.

The phase difference between waves and horizontal velocities for all runs varied between 5-30 degrees at the primary frequency. Theory states that the waves and horizontal velocity are in phase, or have a zero phase difference. The measured phase difference is interpreted as showing the breaking wave crest leading the wave-induced velocities beneath.

Wave and velocity spectra characteristic of collapsing breakers taken at Carmel River Beach are shown in Figure 5. Wave No. 1 and horizontal velocity spectra were measured at the breaker line. Wave No. 2 spectrum was measured 3.5 meters shoreward. The spectra do not exhibit the strong harmonics on this steeper beach because the secondary waves do not have time to develop during rapid shoaling. The energy density is greatly attenuated in the breaking process from Wave No. 1 to Wave No. 2. The coherence and phase difference shown are between Wave No. 1 and horizontal velocity. The phase difference shows the waves leading the velocities at the primary frequency by 15 degrees. The coherence is high, again indicating the motion to be primarily wave-induced.

Wave Celerity. The wave speed, or celerity, was measured using two wave gauges separated in a line perpendicular to the propagating wave crests. Consider a spectral wave component propagating perpendicular to the beach in the x direction measured at point, $x_1 = 0$, and a point shoreward by an amount, $x_2 = \Delta x$, given by

$$\begin{aligned} \eta_1(\sigma) &= a_1(\sigma) \cos \sigma t , \\ \eta_2(\sigma) &= a_2(\sigma) \cos(k\Delta x - \sigma t) . \end{aligned} \quad (10)$$

The phase difference of the waves between the two measurement points is given by

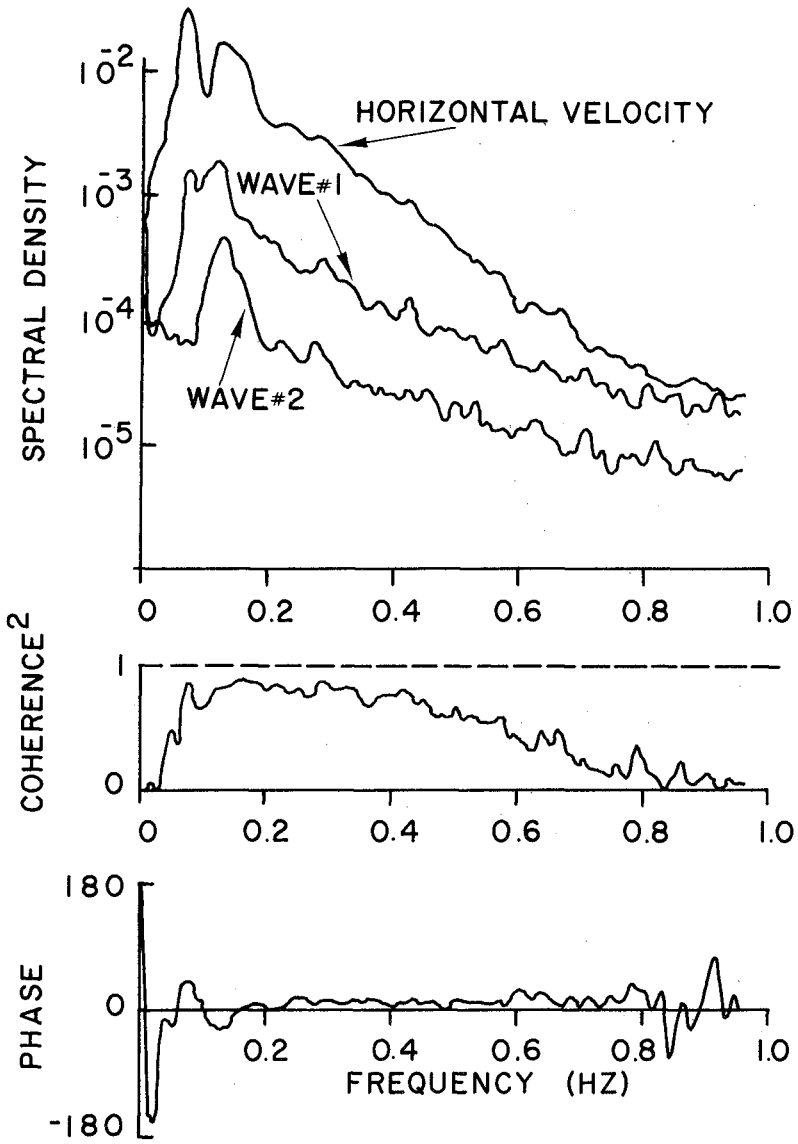


FIGURE 5. WAVE AND VELOCITY SPECTRA CHARACTERISTICS OF COLLAPSING BREAKERS, 29 MAY 1975.

$$\phi(\sigma) = k\Delta x = \frac{\sigma\Delta x}{c} \quad (11)$$

where the celerity, $c = \sigma/k$.

Figure 6 shows two wave spectra measured at Del Monte Beach within the surf zone. Wave gauge one was at the approximate breaker line and wave gauge two was 11 meters shoreward. The wave spectra exhibit strong harmonics. The energy density is shown to decrease as the waves break and progress shoreward. The coherence is high at the primary frequency and decays from the peak. The phase difference between the wave gauges continuously increases with frequency.

Expected phase differences were calculated using both the linear wave theory relationship

$$c = \left(\frac{g}{k} \tanh kh\right)^{1/2} \quad (12)$$

and the shallow water relation assuming nondispersive waves

$$c = \sqrt{g(h + \alpha H)} \quad (13)$$

where h is the total depth of water, H is the wave height and α a constant. It should be noted that even though the water is shallow, the higher frequency wave components can be considered intermediate or even deep water waves.

The phase differences calculated using equation (11) are shown on Figure 6. The dashed line is the phase difference calculated using the nondispersive wave speed, equation (13), for α equal to 0.5. The comparison of all measured and calculated phase differences shows that linear theory wave speed is not valid, but that the waves are nondispersive. The nondispersiveness of the waves across the frequency band of significant wave energy is because the wave components are phase-coupled to the primary frequency wave, i.e., the higher frequency wave components travel at the phase speed of the primary frequency wave. The phase-coupling of the wave components is another indication of the strong nonlinearities of breaking waves.

CONCLUSIONS

The measured breaking waves, derived characteristically from swell-type waves, can be described as highly nonlinear, although the kinematics are more orderly than intuitively presupposed. The measured wave and velocity spectra show strong harmonics of the peak frequency of the waves. The harmonics are secondary waves of the primary wave frequency and are indicative of strongly nonlinear waves. As the wave shoals, the secondary waves start to grow and, as the waves steepen rapidly just before breaking, the secondary waves likewise rapidly develop on the back of the primary wave. The development of secondary waves indicates a transfer of energy to higher frequencies.

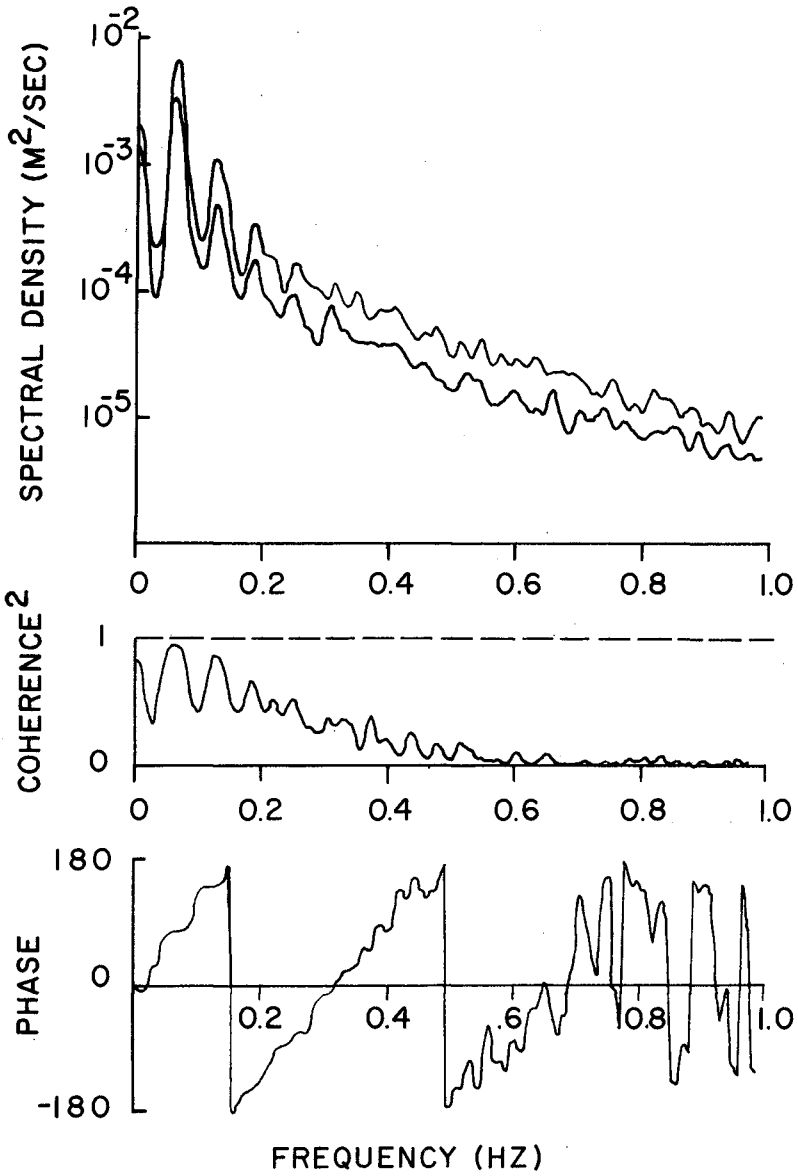


FIGURE 6. WAVE SPECTRA SEPARATED BY 11 METERS IN THE SURF ZONE, 4 MARCH 1976.

Spectra and cross spectra were calculated between waves and velocities measured directly beneath the waves. The wave energy-density spectral components were converted to velocity spectral components using linear wave theory. The measured horizontal velocities were always greater than the calculated by 20-100 percent. The amount of deviation from linear theory demonstrates the strength of the nonlinearities of shallow water waves.

The measured phase difference between waves and horizontal velocities indicates the waves generally led the velocities on the average by 5-20 degrees, implying that the "curling" crest of the wave arrives prior to maximum water particle velocity. The coherence values between the sea surface elevation and the horizontal water particle velocity were high in all runs, ranging above 0.8 at the peak of the spectra and decreasing at higher and lower frequencies. The decrease in coherence can be attributed primarily to the velocities being converted to turbulence during breaking and the nonlinearities associated with finite amplitude wave motion. The high coherence suggests that most of the motion in the body of the breaking waves was wave-induced. Hence, breaking waves may be more amenable to theoretical treatment than previously thought, although still very nonlinear.

The wave speed was measured using two wave gauges separated in a line perpendicular to the propagating wave crests. The measured phase difference was compared with theoretical values calculated using celerity relations from linear wave theory and the shallow water relation assuming nondispersive waves. The measurements show that the breaking waves are frequency nondispersive; this is further evidence of the strength of the nonlinearities of the waves in the surf zone.

ACKNOWLEDGEMENTS

This work was supported by the Office of Naval Research, Geography Branch, under contract NR 388-114.

REFERENCES

- Bascom, W., Waves and Beaches, Doubleday and Co., Inc., 1964.
- Bowden, K. F., and R. A. White, Measurements of the Orbital Velocities of Sea Waves and Their Use in Determining the Directional Spectrum," Geophys. J. Roy Astron. Soc., 12, 33-54, 1966.
- Bub, F. L., Surf Zone Wave Kinematics, M. S. Thesis, Naval Postgraduate School, Monterey, California, 1974.
- Führbötter, A., and Büsching, F., "Wave Measuring Instrumentation for Field Investigations on Breakers," Proceedings of the International Symposium on Ocean Wave Measurement and Analysis, ASCE, 1974.
- Galvin, J. J., Kinematics of Surf Zone Breaking Waves: Measurement and Analysis, M.S. Thesis, Naval Postgraduate School, Monterey, CA, September 1975.

- McGoldrick, L. F., A System for the Generation and Measurement of Capillary-Gravity Waves, Technical Report No. 3, University of Chicago, Department of the Geophysical Sciences, August 1969.
- Miller, R. L., and Ziegler, J. M., "The Internal Velocity Field in Breaking Waves," Proceedings of the Ninth Conference on Coastal Engineering, pp. 103-122, ASCE, 1964.
- Simpson, J. H., "Observation of the Directional Characteristics of Waves," Geophys. J. Roy. Astron. Soc., 17, 93-120, 1969.
- Steer, R., Kinematics of Water Particle Motion Within the Surf Zone, M.S. Thesis, Naval Postgraduate School, Monterey, CA, 1972.
- Thornton, E. B., "A Field Investigation of Sand Transport in the Surf Zone," Proceedings of the Eleventh Conference on Coastal Engineering, pp. 335-351, ASCE, 1968.
- Thornton, E. B., and Krapohl, R. F., "Water Particle Velocities Measured under Ocean Waves," Journal of Geophysical Research, V. 79, pp. 847-852, 20 February 1974.
- Thornton, E. B., and Richardson, D. P., The Kinematics of Water Particle Velocities of Breaking Waves Within the Surf Zone, Technical Report NPS-58TM74011A, Naval Postgraduate School, Monterey, CA, January 1974.
- Walker, J. R., Estimation of Ocean Wave-Induced Particle Velocities from the Time History of a Bottom Mounted Pressure Transducer, M. S. Thesis, University of Hawaii, 1969.
- Wood, W. L., A Wave and Current Investigation in the Nearshore Zone, Department of Natural Science, Michigan State University, E. Lansing, Michigan, 1973.

CHAPTER 27

DEFORMATION UP TO BREAKING OF PERIODIC WAVES ON A BEACH

Ib A. Svendsen* and J. Buhr Hansen*

ABSTRACT

An experimental description is presented for the transformation of periodic waves which approach breaking on a gently sloping beach. The data include the variation of wave height, phase velocity, wave surface profiles, and the maximum value of the wave height to water depth ratio $(H/h)_{\max}$ around the breaking point.

The results are compared with the theories of sinusoidal and cnoidal wave shoaling, and the latter is shown in most cases to agree remarkably well when the laminar energy loss along the walls and bottom of the wave tank is included.

An empirical relation is established between wave length to water depth ratio L/h at the breaking point and the deep water wave steepness H_0/L_0 . Also the maximum wave height to water depth ratio at breaking shows considerably less scattering than found previously, when plotted versus $S = h_x L/h$, h_x being bottom slope.

1. INTRODUCTION

The literature shows a considerable number of experimental investigations of the slow transformation of waves on a sloping bottom, which is denoted shoaling. In particular, data for the variation of the wave height have been reported.

Most of these results, however, do not confirm each other. Thus no definitive conclusion has been obtained so far neither about the real variation of the wave height nor as to which theory will predict the variation sufficiently accurately.

Iversen (1952)[†] presented experimental data which showed that the height of periodic waves on a sloping bottom grows much faster than predicted by the sinusoidal wave theory, and Brink-Kjær and Jonsson (1973) showed that actually the variation resemble a cnoidal wave shoaling.

Similar experiments were made by Ippen and Eagleson (1955), and Eagleson (1956) arrived at the same conclusion though the pattern was

*Assoc. Prof., Institute of Hydrodynamics and Hydraulic Engineering (ISVA), Technical University of Denmark.

[†]The paper by Iversen (1953), 'Waves and breakers in shoaling water,' Third Conf. Coastal Engrg., Cambridge, Mass. 1952, is almost identical with Iversen (1952).

less pronounced, partly due to considerable scattering. Also the experiments by Vera-Cruz (1965) should be mentioned.

Iwagaki (1968) compared his experiments with the theory of hyperbolic waves, in which the wave profiles are approximated by parts of solitary wave profiles. As far as it has been possible to ascertain from the graphical presentation in the paper, the agreement is good for waves with small deep water steepness ($H_0/L_0 < 0.005$), (though the theoretical curves have not been extended to the full region of water depths for which measurements are presented). Actually it may be shown (Svendsen, 1974) that to the first order the hyperbolic wave height varies as h^{-1} , i.e. as a shoaling solitary wave. Further, in particular waves of small deep water wave steepness (swell-type) will more and more resemble a solitary wave in shape as the water depth decreases. Hence the best agreement with hyperbolic waves should be expected for swell-type waves. For steeper waves the comparison seems inconclusive as should also be expected, as the theory does not apply to such waves.

Against this stand the solitary wave experiments by Ippen and Kulin (1954) and by Camfield and Street (1969) indicating that although a solitary wave is as far from a sinusoidal wave as well possible, the variation of its height is much better predicted by the $h^{-1/4}$ rule valid for long sinusoidal waves. This is further confirmed by the numerical calculations by Madssen and Mel (1969), which agree quite well with the results of Camfield and Street.

Finally, Wiegel (1950) claims that in general his experimental results for periodic waves on slopes 1:10.8 and 1:20 follow the linear theory.

One possible reason for these discrepancies is that all the experiments for pure solitary waves, and Wiegel's with periodic waves, have been performed on slopes which are actually too steep to allow the shoaling assumption to be valid. Another important factor is the friction losses, which can be shown to have a considerable effect on the shoaling process, in particular in a relatively narrow laboratory wave flume.

Also part of the surprisingly large scattering which appears in many experimental results for wave quantities is most likely due to the free second harmonic waves generated by the sinusoidal motion of a piston-wave-generator.

The aim of the present investigation has been to try to clear up some of these uncertainties, using the facilities for generation of waves of extremely regular and permanent form, described by Buhr Hansen, Schiolden and Svendsen (1975).

In addition to the wave height, the phase velocity and the mean water level ('set-down') have been measured, and records have been obtained for the wave surface profiles. The results are compared with theory, and since it is rather evident from previous investigations that the linear theory is doomed to fail, the major emphasis is placed on a comparison with cnoidal wave theory. Perhaps it should be added for completeness that a second or higher order Stokes theory will be out of question, too, when the Ursell parameter U (defined as HL^2/h^3)

(as in most cases) grows far beyond 30 or 40, which is about the limit for which a higher order Stokes theory is applicable.*

In each case will be discussed outcome of the comparison, and an analysis will be attempted of the possible reason for discrepancies.

2. DESCRIPTION OF EXPERIMENTAL FACILITIES AND PROCEDURE

The waves are generated by a flap-type wave generator in a flume 33 m long, 60 cm wide, with a plane beach sloping 1:35 (see Fig. 1). The motion of the wave generator is controlled by a PDP 8 mini-computer, which generates a command signal of the form

$$\xi = e_1 \sin \omega t + e_2 \sin(2\omega t + \beta_2) \quad (1)$$

(Buhr Hansen and Svendsen, 1974). Fig. 2 shows a comparison between a resulting measured wave profile (with almost no free second harmonic components) and a second order Stokes wave. The parameter $U = HL^2/h^3$ is about 2. It appears that even for U as large as 40-50 (which is far up in the cnoidal region), the waves generated by (1) remain of clean and constant form.

This is important because the waves in the constant depth part of the wave flume represent the initial conditions for the shoaling process. (It may be noticed that it has no meaning to consider whether the wave produced by (1) is a 'Stokes' or a 'cnoidal' wave, as long as it is of constant form.)

The water surface variation is recorded by a resistance wave height transducer (two silver wires, 0.17 mm diameter, 5 mm apart), the signal of which is scanned by the computer 400 times per second. The transducer is mounted on a carriage which is moving slowly along the flume. Vertical irregularities of the rails for the carriage are eliminated by storing in the computer a zero level correction, which is obtained from the wave transducer during a carriage-run without waves.

In the experiments, the computer determines on line the height H of each wave, the mean water level $\bar{\eta}$, and by means of an additional wave height transducer, the phase velocity c . At the same time selected wave profiles are stored. After each experiment the results may be plotted out on an ordinary pen-recorder.

In all experiments reported, the still water depth was 36.0 cm and the plane slope was 1:35. The wave frequency varied between 0.3 Hz and 1.2 Hz, the wave height in the constant depth part of the flume between 3.5 cm and 10 cm.

The calibration factor for the wave transducers was determined by linear regression on 10-12 data points corresponding to 1 cm increments in the submergence of the transducer. In all experiments the minimum submergence was more than 1.5 cm, corresponding to a regression coefficient larger than 0.999.

*The limit referred to corresponds to the largest value of H for which there is no secondary wave crest in the trough. In the second order this means that $U < (L/h)^3 \pi^{-1} (3 \coth^3 kh - \coth kh)^{-1}$, the maximum of which is 26.3 for $kh \rightarrow 0$ (see Svendsen and Jonsson, 1976). For higher order theories U may be slightly larger.

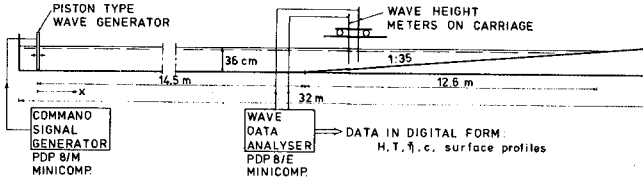


Fig. 1 Experimental facility

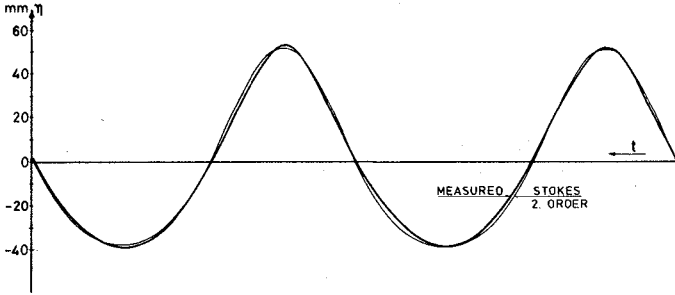


Fig. 2 Comparison between profile measured in front of the wave generator and Stokes second order approximation with the same wave height and period

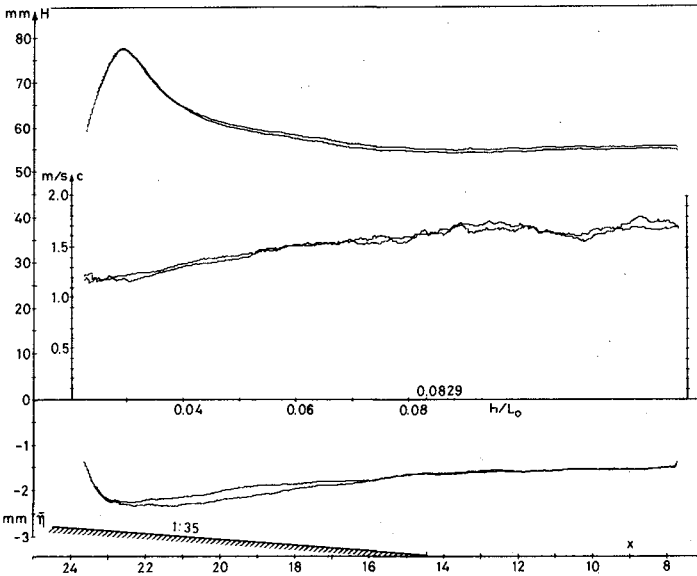


Fig. 3 Illustration of reproducibility of experiments

The reproducibility of the experiments is illustrated in Fig. 3 showing two records of the same experiment. The figure also shows that even most of the small and apparently inexplicable irregularities in the records are obviously repeated exactly the same way. Some may be due to irregularities in the wave flume (though the accuracy of alignment of sides and bottom is well below 1 mm) but most of them seemed to be generated by either capillary waves, secondary waves generated by the breaking process, and perhaps the rest of the free second harmonics.

3. THE SHOALING ASSUMPTION

The notion of wave shoaling or wave transformation on a beach was introduced on an intuitive basis by Rayleigh (1911). In his approach there are three more or less independent assumptions involved:

- (a) The wave will — to the first approximation in bottom slope — continuously adjust its form so that surface profile, phase and particle velocities, pressure variation, etc. can be determined from the horizontal bottom theory, applying the local values of water depth and wave height.
- (b) The wave energy flux through a vertical section is constant, which implies that the reflection is negligible.
- (c) The number of waves remain constant during the shoaling process so that the wave period T is conserved.

Essentially each of these assumptions requires a 'sufficiently gently varying water depth', but how gently will actually depend on the wave theory considered. This question can be analysed theoretically by rigorous perturbation expansions including the effect of the bottom slope h_x .

Rayleigh, of course, presented the ideas in terms of the linear wave theory, and for that case it may be shown that the shoaling assumptions will be satisfied provided the relative change in water depth over a wave length is of the same order of magnitude as the wave steepness (or smaller), i.e.

$$S \equiv h_x L/h = O(H/L) \quad (2)$$

For higher order Stokes waves only smaller values of h_x are allowed (depending on the order considered), and for (first order) cnoidal waves, Svendsen (1974) showed that a consistent shoaling theory requires $S = O(h/L)^3$.

In conclusion we notice that in all cases the parameter S occurs and that shoaling conditions imply that S is too small to be of importance. This will be discussed further later on.

4. THE WAVE HEIGHT VARIATION

Experimental Results

Since the wave period is assumed to be constant, one of the principal problems in wave shoaling is to determine the wave height H as a function of the water depth h .

Figs. 4 and 5 show the recorded variation of the wave height for deep water wave steepnesses ranging from 0.0039 to 0.064. Both dimensionless wave period $T\sqrt{g/h}$, wave height to water depth ratio H/h in the constant depth part of the flume, and the theoretically determined deep water wave steepness H_0/L_0 are given in each figure.

There are two experimental curves in each figure. One represent each individually measured wave height, the other a moving average over the length of the reflection pattern.

Though the curves for the individual wave heights seem to show a continuous variation they are actually step-curves. This is because the carriage with the wave transducer moves 2 - 4 cm (depending on the wave period) along the wave flume during one wave period, i.e. between each new result for the wave height.

In the following the origin of the theoretical curves is described and discussed, but first we consider the effect of energy loss due to friction.

Energy Loss due to Friction

This effect was taken into account in the theoretical curves by reducing the energy flux at each station with the energy lost since the previous station in the calculation, due to friction along the bottom and along the side walls.

In these calculations laminar boundary layers were assumed in all cases although the longest and highest waves according to Jonsson (1966) should have turbulent boundary layers, at least close to the breaking point. The effect, however, of introducing the turbulent value of the wave energy loss on the last part of the slope appears to be insignificant.

In the calculation of friction losses were used wave particle velocities determined by the linear theory. This also applies to the region where the wave height variation was calculated from the cnoidal theory. In fact it is a reasonable simplification since the friction only 'eats' a minor part of the energy flux anyway.

Linear Wave Shoaling

It is not surprising that the present results confirm the conclusion quoted in the introduction from other investigations, namely that shoreward of the point of minimum wave height, i.e. roughly $h/L_0 = 0.10$, the linear theory predicts divergingly smaller wave heights than measured. This is evident from Fig. 4b where the linear curve is shown through to breaking.

On the other hand we notice that as long as the deep water steepness is less than 3-4% (Figs. 4a and 5a), the linear wave theory seems to work quite well in deeper water. This is of particular interest because the cnoidal theory cannot be applied for $h/L_0 \gtrsim 0.10$.

In fact, for the small wave steepnesses the agreement is better than in the interpretation of Iversen's measurements given by Brink-Kjær and Jonsson (1973). They found that even for smaller wave steepnesses an appreciable discrepancy seemed to develop between the linear theory and

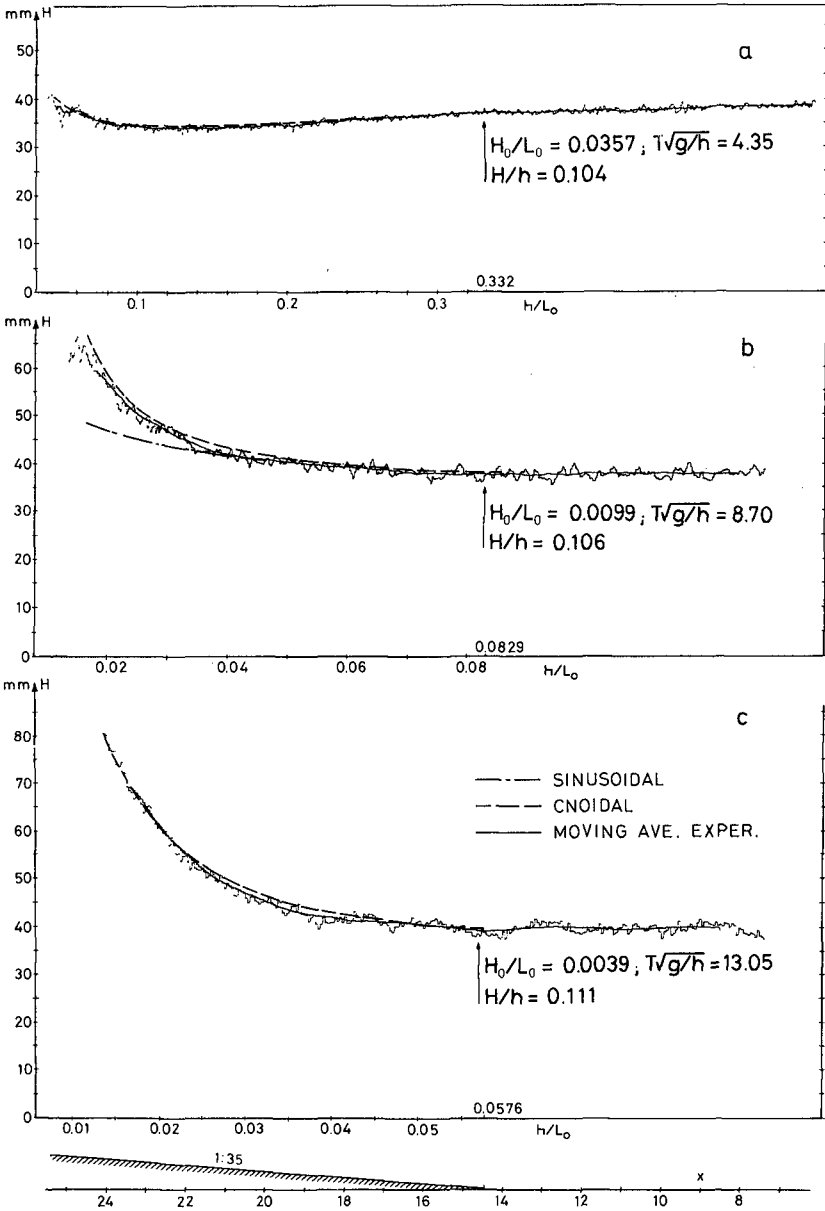


Fig. 4 Variation of wave height for three different wave steepnesses

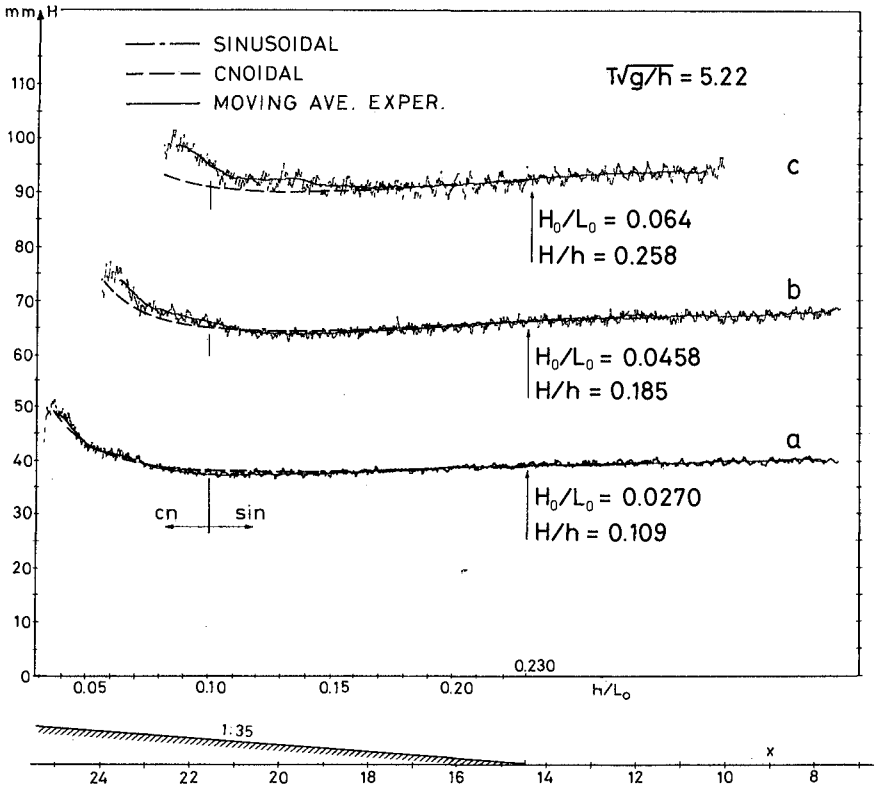


Fig. 5 Variation of wave height, rather steep waves

the measurement as h/L_0 decreased towards the value 0.10. Fig. 6 shows an example of this where H_0/L_0 is 3.58%, and the linear theory yields results up to 8% higher than the measurements (i.e. a minimum value of $H/H_0 = 0.913$ against 0.85 measured).

It has turned out that the major reason for this discrepancy is that friction has been neglected in Brink-Kjær and Jonsson's calculation of the theoretical curves. In particular in Iversen's case, with a wave flume only 30 cm wide and a horizontal bottom depth of 77.8 cm in the case considered, the friction along the side walls has a considerable effect. Taking this into account brings the theoretical minimum value of H/H_0 down to 0.869 in the case shown in Fig. 6, and this must be considered in fair agreement with the measured value. The theoretical variation with friction included is shown in the figure. It may also be noticed that the wave heights measured by Iversen are most likely influenced by the fact that the first 4.6' (= 1.40 m) of Iversen's slope are steeper (1:5.75 = 0.174) than the value 1:13.8 = 0.072 referred to as the slope for the experiment.

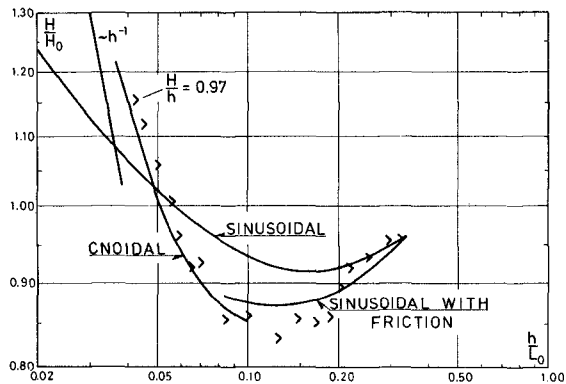


Fig. 6
The effect of friction losses on Iversen's results

For the experiment shown in Fig. 4 a, H_0/L_0 is almost the same (3.57%) and here the measured minimum value of H/H_0 is 0.875 against the calculated value (including friction) of 0.889.

From Fig. 5 a-c, however, we see that if the deep water steepness increases, the wave height to water depth ratio will grow to large values already outside the cnoidal region. In the case of $H_0/L_0 = 6.4\%$ (Fig. 5 c) the wave actually breaks at $h/L_0 \approx 0.10$, so that the entire shoaling process has been determined by the linear theory. And quite obviously, linear theory cannot handle the large values of H/h .

Since we here at the breaking point have $U_{\max} \sim 45$ ($H/h \sim 0.71$ and $L/h \sim 8$) it seems likely that the problem could be overcome by using a second or third order Stokes shoaling theory.

Cnoidal Wave Shoaling

The theory of cnoidal wave shoaling used here was developed by Svendsen and Brink-Kjær (1972) who on the same intuitive basis as Rayleigh

solved and tabulated the variation of the wave height. A more direct presentation of the results can be found in Skovgaard et al. (1974).

Perhaps it should be mentioned that this theory is based on (8) (see Sect. 6). A slightly different version will appear if (10) (in which $\sqrt{1+AH/h}$ is substituted by $1+\frac{1}{2}AH/h$) is used, and other differences of similar nature are possible too. Formally all these versions (as e.g. Shuto (1974) and Ostrovskiy and Pelinovskiy (1970) are equal in that they only differ in the way the small terms are handled. For practical applications, however, where H/h is not really as small as envisaged in the theory they result in considerable differences in the numerical results for e.g. the wave height variation, in particular as we approach the breaking point. In our numerical calculations we have found that the best fit to the measurements is obtained by using the version developed by Svendsen and Brink-Kjær.

As appears from Fig. 4 b and c, the combined linear-cnoidal shoaling model fits the experimental data surprisingly well in those cases where the H/h -ratio remains small for $h/L_0 > 0.10$. The predictions even follow the development all the way to the breaking point, although the theory should not be applicable there.

It should be emphasized, however, that essentially this only indicates that the relationship between cnoidal energy flux and wave height shows a realistic variation with water depth. The absolute value of the energy flux is determined from the wave height in the constant depth part of flume and may not be correct (and other cnoidal wave properties as e.g. the position of the mean water level may be even rather inaccurately predicted by the same theory). This must be recalled in those experiments where $h/L_0 \gtrsim 0.10$ in the constant depth part of the flume. Then linear wave theory is applied for $h/L_0 > 0.10$, and at $h/L_0 = 0.10$ the theoretical result must be matched with the cnoidal shoaling, which is used shoreward of that point.* Svendsen and Brink-Kjær (1972) matched the two theories by assuming continuity in energy flux. However logical this approach seems it results in a discontinuity in wave height at the matching point.

Since, however, neither of the two theories yields the exact energy flux for a given wave height it may be argued that it is equally correct to match the wave heights, which we know are continuous, and accept a discontinuity in the theoretically determined energy flux (which is approximate anyway) at the matching point. This is actually the method chosen here. Finally it is mentioned that in the numerical evaluations the still water depth has been corrected for wave set-down.

Discussion

As mentioned the figures show a reasonable agreement, though discrepancies up to 6-8% in wave height develop close to the breaking point. This cannot surprise, however, since the energy flux used for the calculations was based on the assumptions that $H \ll h$, that the horizontal velocity u is constant over the water depth, and that the excess pressure p^+ due to the wave is constant too, and proportional to the local

*In principle any point shoreward of $h/L_0 \sim 0.10$ could be chosen as the matching point between the two theories.

value of the surface elevation. As is evident from e.g. velocity measurements in waves near breaking (see e.g. Iwagaki and Sakai, 1976), the velocity is far from constant over the water depth, and the constancy of p^+ actually represents neglect of the vertical accelerations in this context.

A few comments will also be appropriate about the matching procedure between linear and cnoidal wave theory.

The wave tables prepared by Skovgaard et al. (1974) are based on continuity in energy flux. The tables may also be used, however, for calculations with continuity in wave height at the matching point, if it is noticed that the corresponding shift in energy flux is represented by a formal shift in the deep water wave steepness. The procedure is illustrated in the appendix.

As mentioned in Sect. 3, a proper measure of the steepness of the sloping bottom is the parameter $S = h_x L/h$.

Since L is approximately proportional to \sqrt{gh} , a plane slope will correspond to $S \sim h_x h^{-1/2}$ so that for fixed h_x the value of S grows with decreasing water depth, indicating that the slope appears steeper and steeper to the waves as they propagate shoreward. Hence the shoaling condition (which requires S small) will sooner or later be invalidated. With reference to the assumptions in Sect. 3 this would cause appreciable reflection and disintegration of the wave form (T not constant). No such phenomena were observed in the experiments recorded here, which suggests that S in all cases have been small enough.

5. WAVE SURFACE PROFILES

Let us assume that a rigorous perturbation expansion is carried out for waves on a sufficiently gently sloping bottom. Then the shoaling of the wave will represent the first approximation, but even though the slope of the bottom does not directly influence this first order solution, a second order solution exists which will represent the first approximation to the effect of the bottom slope, which has the effect of making the wave skew.

Svendsen (1974) carried out the calculations for this second order solution in the case of cnoidal waves, and the result for the skew wave profiles can be written

$$\eta = \eta^{(0)} + \eta^{(1)} \quad (3)$$

where $\eta^{(0)}$ is the constant depth cnoidal wave profile

$$\eta^{(0)} = H \left(\beta(m) + cn^2(2K\theta, m) \right), \quad \theta = \frac{t}{T} - \frac{x}{L} \quad (4)$$

K being the complete elliptic integral of the first kind, m its parameter, and β a function of m . $\eta^{(1)}$ is the above mentioned first approximation to the effect of the sloping bottom. $\eta^{(1)}$ is given by

$$\frac{\eta^{(1)}}{h} = 3 S \frac{L}{h} T \sqrt{g/h} f\left(\theta; U, \frac{H}{h}\right) \quad (5)$$

where

$$f\left(\theta; U, \frac{H}{h}\right) = \frac{\eta_{\theta}^{(0)}}{\sqrt{gh}} \int \eta_{\theta}^{(0)-2} \int \eta_{\theta}^{(0)} \int \left[2(cn^{(0)})_h - c_h \eta^{(0)} \right] d\xi d\zeta d\theta \quad (6)$$

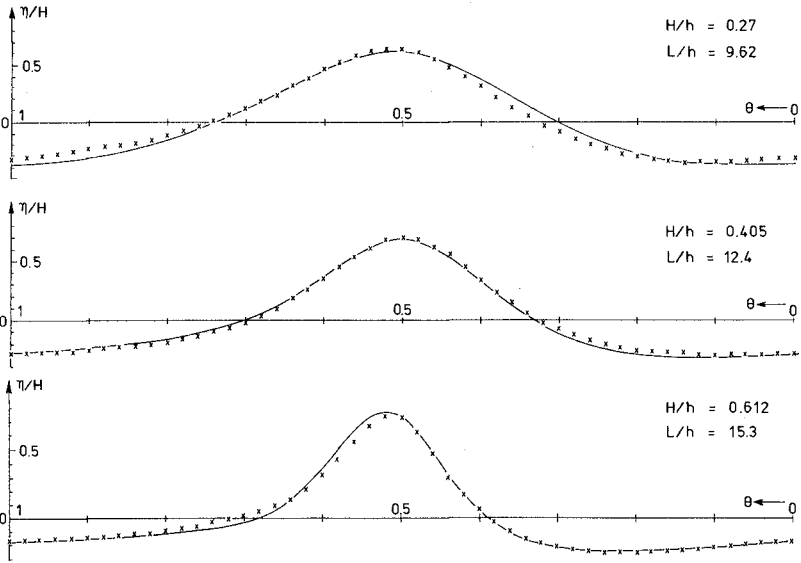


Fig. 7 Wave profiles for wave with $H_0/L_0 = 0.0165$ on slope $h_x = 1:35$

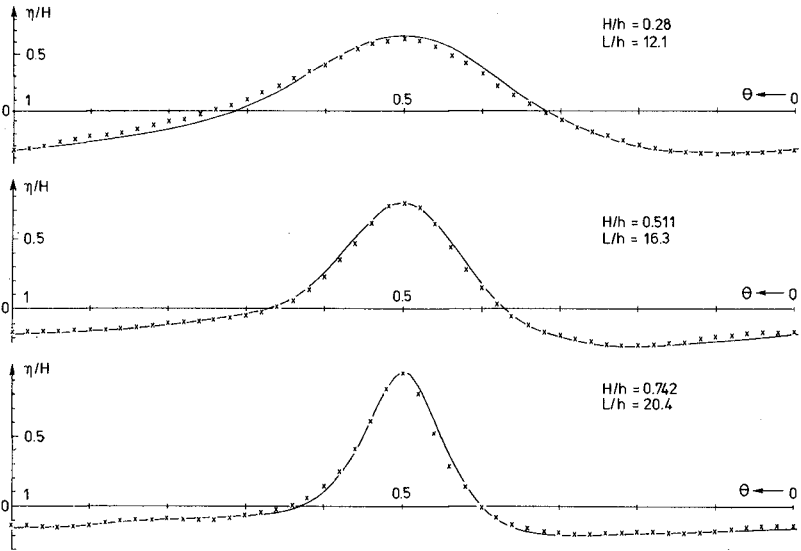


Fig. 8 Wave profiles for wave with $H_0/L_0 = 0.0114$ on slope $h_x = 1:35$

with indexes θ and h denoting partial differentiation with respect to θ and h , respectively, under the restriction that the energy flux E_f is constant. This solution has been evaluated for a number of cases corresponding to wave profiles measured in the experiments. As input for the evaluation of the theoretical profiles has been used the wave period, the local measured wave height, the water depth (including set-down), and the bottom slope.

Figs. 7 and 8 show a comparison between measured and calculated profiles, in each case for three different phases of the deformation of a wave towards the breaking point.

It is immediately evident from the figures that the agreement is good even for wave height to water depth ratios as large as 0.75. It should, however, also be noticed that all the cases in the figures correspond to situations where the deviation from the symmetrical (ordinary) cnoidal wave profile is small. In other words, situations where the shoaling assumption about a local equilibrium is still valid. This is required also in the theory for $\eta^{(1)}$ because $\eta^{(1)}$ has to be a small perturbation on $\eta^{(0)}$. Consequently the large deformations which rapidly develop just before breaking cannot be predicted by this theory.

An interesting feature is that the skewness of the surface slopes is not so pronounced in the wave crest. The major effect of sloping bottom is concentrated in the wave trough, which has its deepest point right in front of the next wave crest.

6. PHASE VELOCITY

The measurements of the phase velocity c were obtained by measuring the time (in milliseconds) it took the wave crest (identified digitally by the computer) to travel the distance between two wave gauges placed 20.0 cm apart in the direction of wave travel.

The results obtained in this way are rather sensitive to small changes in the shape of the wave crest between the two wave gauges. As a consequence, the individual measurements show a considerable scattering ($\pm 10 - 25\%$). This is particularly pronounced for the very small wave steepnesses. Consequently the scattering is much reduced when the waves steepen on the slope.

The results for c presented in Fig. 9 a - d represent a moving average over a number of waves. The results have further been confirmed by a different method based on measuring electrically the time it takes the wave to travel between two pointed metal-rods placed 20 cm apart. The mean value of the measurements obtained in this way confirmed that the results obtained from the computer when the pointed ends of the metal-rods were placed at a level close to the wave crest.

It can be mentioned that one of the reasons for the large scattering in the experimental results is that small free second harmonic waves still exist in the flume. Such disturbances result in phase velocities which are constant in time, but vary from point to point. Hence the tendency mentioned in Sect. 2, that even the irregularities are reproduced when an experiment is repeated.

The measurements are compared with linear and cnoidal results for the phase velocity. From linear theory we have

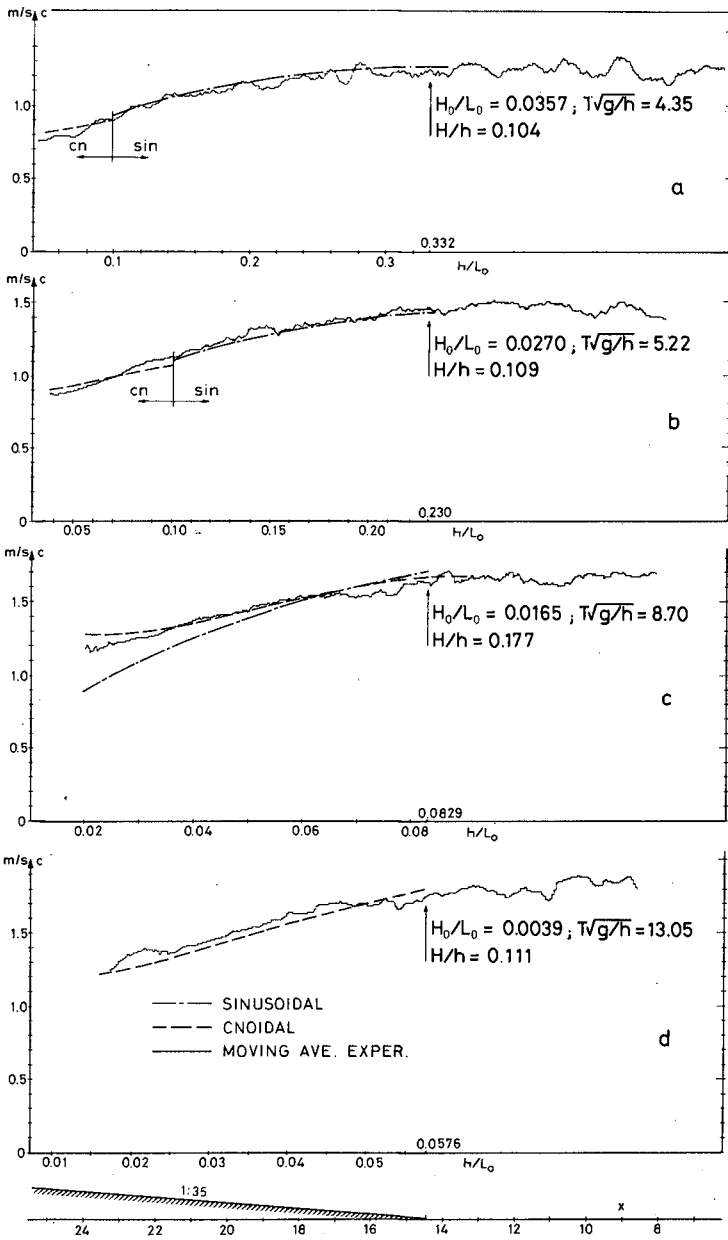


Fig. 9 Variation of phase velocity

$$c = \frac{g}{\omega} \tanh kh \quad (7)$$

which is used for all values of $h/L_0 > 0.10$. As the cnoidal result for c is used (for $h/L_0 < 0.10$)

$$c = \left(g h \left(1 + A \frac{H}{h} \right) \right)^{1/2} \quad (8)$$

$$A = \frac{2}{m} - 1 - \frac{3E}{mK} \quad (9)$$

where E is the complete elliptic integral of the second kind.

Since cnoidal theory assumes $H/h < 1$, (8) may also be written

$$c = \sqrt{g h} \left(1 + \frac{1}{2} A \frac{H}{h} \right) + O\left(\frac{H}{h}\right)^2 \quad (10)$$

which is equally valid. In the analogy with the wave height variation we realize that for waves near breaking the numerical results obtained for (8) and (10) differ appreciably. It turns out that the results obtained from (8) fit the measurements better. In (8) the theoretically determined wave height (i.e. from the shoaling process) has been used.

In general the conclusion is positive. The two theories predict the phase velocity to within a few per cent, the linear theory for $h/L_0 > 0.10$, the cnoidal shoreward of that point. The only exception is close to breaking, where the cnoidal theory overestimates the finite amplitude effect and yields results somewhat above the measurements. In Fig. 9 c is for comparison given the linear curve even though $h/L_0 < 0.10$ everywhere.

7. WAVE BREAKING

The last topic to be discussed in this paper is the characteristics of the waves at the breaking point, including the prediction of the position of this point, e.g. in terms of the water depth where breaking is initiated.

Even though cnoidal theory seems to predict the wave height variation reasonably well, no information can be deduced from that theory (or any other known theory) about where the breaking occurs. In that question we must rely entirely upon empirical data.

One of the problems is to define exactly where the breaking has started. Often breaking is defined to start 'where the front of the wave becomes vertical', though in the case of a spilling breaker there is no such point. Also the initiation of foam may be a very uncertain definition in small scale experiments where the surface tension will cause scale effects for the foam production.

In consequence of these arguments we have chosen to define the breaking point as the point where H/h is maximum. Since the wave height has a maximum close to the point where the energy dissipation starts and h is decreasing, H/h appears to have a rather sharp maximum. In the evaluation of h the set-down is incorporated. The choice of H/h to identify the breaking point has the advantage that from an engineering point of view the maximum of H/h is one of the primary information about the wave breaking.

Part of the large scatter in breaking data for earlier experiments is believed to be due to free second harmonics in the waves (Battjes, 1974). And even when this irrelevant effect is removed, as in our experiments, each breaking wave will generate wavelets which influence the breaking of the next wave etc. This is particularly pronounced for plunging breakers and represents an effect which must be expected also in the nature.

In the attempt to find coherence in the data obtained, many different plots and relationships among the parameters have been tried. One of the most promising is shown in Fig. 10.

It shows the value of the wave length to water depth ratio $(L/h)_B$ at the point where H/h is maximum. Since all the experiments were performed with a slope 1:35, Iversen's (1952) data for slopes, 1:10, 1:20, 1:30 and 1:50, and those reported by Iwagaki and Sakai (1976) for slopes, 1:10, 1:20 and 1:30 have been included, too. For all the points, L has been determined from the cnoidal wave theory using the wave period, and the wave height and water depth at the breaking point.

The abscissa in Fig. 10 is the theoretically determined deep water wave steepness H_0/L_0 . It appears from the figure that within the accuracy expected by the experiments (and the more advanced ISVA-experiments show a smaller variation, as they should) the data can be described by the relationship

$$(L/h)_B = 2.30 (H_0/L_0)^{-1/2} \quad (11)$$

From this relationship several deductions follow. Since L/h is increasing monotonously shorewards, this relation means that breaking starts when the wave length to water depth ratio grows to a value which depends only on the deep water wave steepness.

It is of particular interest to note that $(L/h)_B$ does not depend on the bottom slope h_x , and that the scattering is considerably smaller than for any other correlation between breaking parameters. The first suggests that shoaling conditions are satisfied in most of the experiments (Iversen's 1:10-data showing a weak tendency to larger values of $(L/h)_B$). Since L/h varies rapidly with the position in the breaking zone, the small scattering indicates that the initiation of breaking depends strongly on the value of L/h .

Once the relation (11) has been established, the wave height at the breaking point H_B is actually *theoretically* fixed too for a wave with a given deep water steepness H_0/L_0 . From (11) we get $(L/h)_B$, and since L/h is a monotonous function of h/L_0 for given H_0/L_0 (Svendsen and Brink-Kjær, 1972) this means that $(L/h)_B$ corresponds to one particular value of h_B/L_0 . This value can in principle be determined, though none of the tables published so far are suited for this purpose.* Finally, from h_B/L_0 and H_0/L_0 the value of $(H/h)_B$ can be determined (using e.g. Table 3 in Skovgaard et al., 1974).

Notice that if only H_0/L_0 is given we cannot determine the absolute value of h_B and H_B , only the ratios described above. Often, however, the wave period will be given too, and then $L_0 = g/(2\pi) T^2$ yields the

*The table required should have the entries L/h and H_0/L_0 and yield values of h/L_0 .

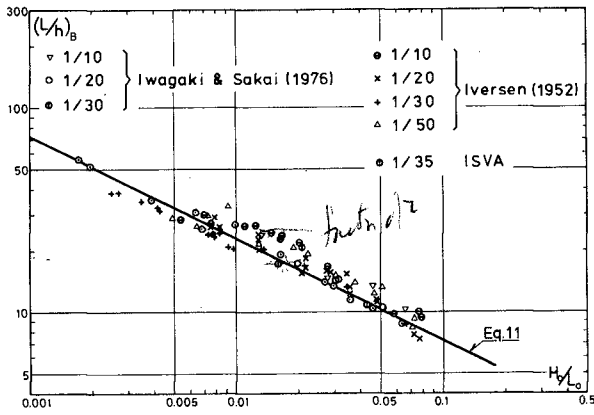


Fig. 10 Wave length to water depth ratio $(L/h)_B$ at the breaking point versus deep water wave steepness H_0/L_0

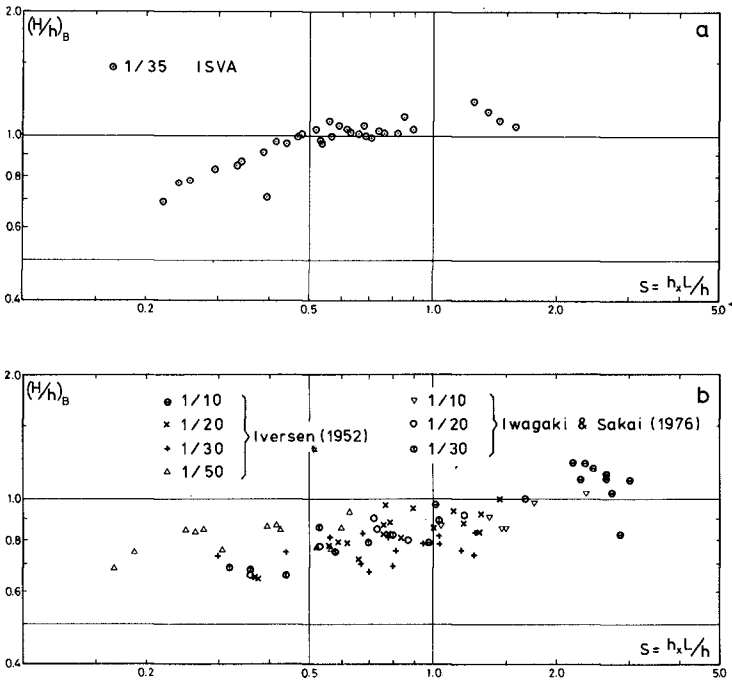


Fig. 11 Maximum value of wave height to water depth ratio $(H/h)_B$ versus slope parameter $S = h_x(L/h)_B$

length required to specify the absolute values from the dimensionless ratios.

In Fig. 11 a the values of $(H/h)_B$ are plotted versus $S = h_x(L/h)_B$. A comparison between theoretical and experimental results here would yield no information, which could not be drawn from Figs. 4 and 5.

The measurements of Iversen, and Iwagaki and Sakai (Fig. 11 b) do not quite fit into the pattern of the present investigation but the tendency is the same. Their results all correspond to smaller values of $(H/h)_B$ and the scattering is considerable. As mentioned before, this is probably to a large extent due to the free second harmonics generated by their wave generator. The scattering, however, is considerably decreased by using S instead of $(L/h)_B$. Thus the value of H/h at the breaking point is actually a function of the bottom slope h_x .

It will be seen that the values of the $(H/h)_B$ are in general somewhat larger than the height $0.827 h$ considered the largest possible for a solitary wave on a horizontal bottom (Longuet-Higgins and Fenton, 1974), and other results usually quoted for the maximum possible height of periodic waves. Also, the largest values of $(H/h)_B$ correspond to the largest values of S .

In both these respects, the results seem to fit into the pattern found by Camfield and Street (1969) who for solitary waves (i.e. theoretically infinitely long waves) found $(H/h)_B$ -values up to 2.

8. CONCLUSION

Linear ('sinusoidal') and cnoidal wave theories are compared with experimental results obtained with waves without free second harmonic disturbance on a plane slope $h_x = 1:35$. It is shown that:

- (a) Linear theory can predict the shoaling as long as the wave height to water depth ratio H/h is small (Fig. 4 a).
- (b) Cnoidal theory, which can only be used for $h/L_0 < 0.10$ (L_0 being deep water wave length), predicts the variation of the wave height quite well even close to breaking (Fig. 4 b and c).
- (c) Linear theory is used for $h/L_0 > 0.10$, and wave height is matched with cnoidal theory at that point. For waves with large deep water steepness H_0/L_0 ($> 3-4\%$) the value of H/h is not small for $h/L_0 > 0.10$. Hence linear theory fails (Fig. 5 b and c). Second or higher order Stokes theory is recommended in this case for $h/L_0 > 0.10$.
- (d) The skew shape of the wave profiles is well predicted by a theory taking into account the effect of the bottom slope (Figs. 7 and 8). The theory cannot predict breaking.
- (e) Both the linear and the cnoidal formulae for phase velocity c fit remarkably well to the data for $h/L_0 > 0.10$ and < 0.10 , respectively (Fig. 9).
- (f) At the breaking point the wave length to water depth ratio $(L/h)_B$ appears to be independent of bottom slope, for bottom slopes less than 1:10, i.e. $(L/h)_B = f(H_0/L_0)$, Fig. 10, whereas $(H/h)_B$ is primarily a function of the slope parameter $S = h_x(L/h)_B$ (Fig. 11).

ACKNOWLEDGMENT

The authors wish to acknowledge help and guidance from Jørgen Christensen and Paul Prescott in the experimental work, and from Ivar G. Jonsson in the calculations of friction losses.

APPENDIX

Given a wave with period $T = 12$ s, and $H_0/L_0 = 0.01$.

Find the wave height H at $h = 7$ m.

Since $L_0 = gT^2/2\pi = 225$ m, we have $h/L_0 = 0.031 > 0.10$ so that cnoidal wave theory is appropriate to use for this wave at $h = 7$ m.

Continuity in energy flux at the matching point, Table 3 in Skovgaard et al., yields directly (using h/L_0 and H_0/L_0 as entry) that $H/H_0 = 1.133$, or $H = 2.55$ m, since $H_0 = 2.25$ m.

Continuity in wave height at the matching point requires that we stage the calculation through that point. Linear theory yields (h_m denoting the depth at the matching point)

$$h_m/L_0 = 0.10 \Rightarrow H/H_0 = 0.933 \quad H = 0.933 \cdot 0.01 \cdot 225 = 2.10 \text{ m}$$

$$h_m = 0.10 \cdot 225 = 22.5 \text{ m}$$

At this point the table for linear (i.e. sinusoidal) waves yields $H_{\sin}/H_0 = 0.933$, whereas the cnoidal result for $H_0/L_0 = 0.01$ is $H_{\text{cn}}/H_0 = 0.867$. If we now require that at the matching point $H_{\text{cn}} = H_{\sin}$, we find that in the cnoidal calculation we must formally use a deep water wave height $H_{0,\text{cn}} = H_0 \cdot 0.933/0.867 = 2.43$ m, i.e. in the cnoidal computation the deep water steepness must be $H_{0,\text{cn}}/L_0 = 0.01076 \sim 0.0108$. The wave height at $h = 7$ m can then be found from Table 3 (Skovgaard et al.) using $h/L_0 = 0.031$ and $H_0/L_0 = 0.0108$ as entry. We get

$$H/H_0 = 1.140 \quad H = 1.140 \cdot 2.43 = 2.78 \text{ m}$$

against 2.55 m obtained by the other matching procedure.

REFERENCES

- Battjes, J.A. (1974) Computation of set-up, longshore currents, run-up and overtopping due to wind-generated waves.
- Brink-Kjær, O., and I.G. Jonsson (1973) Verification of cnoidal shoaling: Putnam and Chinn's experiments. Progr. Rep. 28, pp. 19-23, Inst. Hydrodyn. and Hydraulic Engrg., Tech. Univ. Denmark.
- Buhr Hansen, J., and I.A. Svendsen (1974) Laboratory generation of waves of constant form. Proc. 14th Coastal Engrg. Conf., Copenhagen, Chap. 17, pp. 321-339. (Identical with Part I in Buhr Hansen et al. (1975)).
- Buhr Hansen, J., P. Schioltzen, and I.A. Svendsen (1975) Laboratory generation of waves of constant form. Series Paper 9, Inst. Hydrodyn. and Hydraulic Engrg., Tech. Univ. Denmark.
- Camfield, F.E., and R.L. Street (1969) Shoaling of solitary waves on small slopes. Proc. ASCE, J. Waterways and Harbors Div., 95, WW1, pp. 1-22.

- Eagleson, P.S. (1956) Properties of shoaling waves by theory and experiment. *Trans. Am. Geophys. Union*, 37, 5, pp. 565-572. (Disc. 38, 5, pp. 760-763).
- Ippen, A.T., and G. Kulin (1954) The shoaling and breaking of the solitary wave. *Proc. 5th Conf. Coastal Engrg.*, Grenoble, Chap. 4, pp. 27-47.
- Ippen, A.T., and P. Eagleson (1955) A study of sediment sorting by waves shoaling on a plane beach. Beach Erosion Board, Tech. Memo 63.
- Iwagaki, Y. (1968) Hyperbolic waves and their shoaling. *Proc. 11th Conf. Coastal Engrg.*, London, Chap. 9, pp. 124-144.
- Iwagaki, Y., and T. Sakai (1976) Representation of particle velocity of breaking waves on beaches by Dean's stream function. *Memoirs, Faculty Engrg.*, Kyoto Univ., 38, 1.
- Iversen, H. W. (1952) Laboratory study of breakers. *Gravity Waves*, Nat. Bur. Standards, Circ. 521, pp. 9-32, U.S. Gov. Printing Off., Wash., D.C.
- Jonsson, I.G. (1966) Wave boundary layers and friction factors. *Proc. 10th Conf. Coastal Engrg.*, Tokyo, Chap. 10, pp. 127-148.
- Longuet-Higgins, M.S., and J.D. Fenton (1974) On the mass, momentum, energy and circulation of a solitary wave. II. *Proc. Roy. Soc.*, London, A, 340, pp. 471-493.
- Madsen, O.S., and C.C. Mei (1969) Dispersive long waves of finite amplitude over an uneven bottom. MIT, Hydrodyn. Lab., Rep. 117.
- Ostrovskiy, L.A., and E.N. Pelinovskiy (1970) Wave transformation on the surface of a fluid of variable depth. *Atmospheric and Oceanic Phys.*, 6, 9, pp. 552-555.
- Rayleigh, Lord (1911) Hydrodynamical notes. *Phil. Mag.*, Ser. 6, 21, pp. 177-187.
- Shuto, N. (1974) Non-linear long waves in a channel of variable section. *Coastal Engrg. Japan*, 17, pp. 1-12.
- Skovgaard, O., I.A. Svendsen, I.G. Jonsson, and O. Brink-Kjær (1974) Sinusoidal and cnoidal gravity waves. *Formulae and tables*. 8 pp. *Inst. Hydrodyn. and Hydraulic Engrg.*, Tech. Univ. Denmark.
- Svendsen, I.A., and O. Brink-Kjær (1972) Shoaling of cnoidal waves. *Proc. 13th Coastal Engrg. Conf.*, Vancouver, Chap. 18, pp. 365-384.
- Svendsen, I.A. (1974) Cnoidal waves over a gently sloping bottom. *Series Paper 6*, *Inst. Hydrodyn. and Hydraulic Engrg.*, Tech. Univ. Denmark.
- Svendsen, I.A., and I.G. Jonsson (1976) Hydrodynamics of coastal regions. *Den private Ingeniørfond*, Tech. Univ. Denmark.
- Vera-Cruz, D. (1965) Experimental correlation of gravity wave heights. *Mem. 250, Laboratório Nacional de Engenharia Civil*, Lisboa.
- Wiegel, R.L. (1950) Experimental study of surface waves in shoaling water. *Trans. Am. Geophys. Union*, 31, pp. 377-385.

CHAPTER 28

WAVE SHOALING OF FINITE AMPLITUDE WAVES

Masataka Yamaguchi
Assistant Professor, Department of Ocean Engineering,
Ehime University, Matsuyama, Japan

and

Yoshito Tsuchiya
Professor, Disaster Prevention Research Institute,
Kyoto University, Kyoto, Japan

ABSTRACT

Wave shoaling is calculated, based on finite amplitude wave theories on a uniform depth which were extended by the authors using the Stokes second definition for wave celerity. Change of wave characteristics with decrease in water depth is discussed from numerical computation, and difference in shoaling characteristics is considered in comparison with results obtained from usual wave theories by the first definition. Theoretical results are compared with preliminary experimental ones on the wave transformation in shoaling water conducted by the experimental facilities satisfying the physical conditions corresponding to the definition for wave celerity as well as possible, and the validity of each theory for practical purposes is investigated.

INTRODUCTION

There appears to be some problems in calculating wave shoaling by finite amplitude wave theories on a uniform depth under the assumption that energy flux of waves and wave period are invariable with change in water depth. One of them is the fact that as already pointed out by Stokes (1880), the physical definition is necessary to determine the wave celerity in the extension to the higher order approximate solution of finite amplitude wave theory. The one is the Stokes first definition for wave celerity, which means that the average horizontal water particle velocity over a wave length vanishes, and the other is the Stokes second definition for wave celerity, which means that the average momentum over a wave length vanishes by addition of a uniform motion.

The authors (1972) already calculated finite amplitude wave theories such as Stokes waves and cnoidal waves using the Stokes second definition for wave celerity and investigated the applicability by comparison with experimental results for wave celerity and water particle velocities.

In the calculation of wave shoaling, Le Méhauté and others (1964 and 1966) used usual Stokes wave theories of the third and the fifth orders by the first definition. Iwagaki and Sakai (1967) also used the hyperbolic wave theory of the second approximation. The hyperbolic wave theory was derived by Iwagaki (1968) from Laitone's cnoidal wave theory (1961), in which the wave celerity is calcu-

lated by the second definition.

In this paper, change of wave height and wave length with decrease in water depth is calculated using the above-mentioned theories by the second definition, and difference in shoaling characteristics is considered in comparison with results obtained from the usual wave theories by the first definition. Nextly, the applicability of each theoretical result is briefly discussed by the comparison with a preliminary experimental one.

ENERGY FLUX OF FINITE AMPLITUDE WAVES

According to Whitham (1961), mean energy flux of waves over a wave period \bar{W} is defined as

$$\bar{W} = \frac{1}{T} \int_{-T/2}^{T/2} \int_{-h}^{\zeta} \left(\frac{1}{2} \rho (u^2 + w^2) + p + \rho g z \right) u dz dt \dots \dots \dots (1)$$

in which T is the wave period, h the depth of water, ζ the surface displacement from the still water level, p the wave pressure, ρ the density of fluid, g the acceleration of gravity and u and w are the horizontal and vertical water particle velocities respectively. Eq. (1) is transformed into Eq. (2) from Bernoulli's theorem, in which ϕ is the velocity potential.

$$\bar{W} = -\frac{1}{T} \int_{-T/2}^{T/2} \int_{-h}^{\zeta} \rho \frac{\partial \phi}{\partial t} u dz dt \dots \dots \dots (2)$$

Mean energy flux of waves calculated from the Stokes wave theory of the fourth order by the second definition \bar{W}_{S2} is given as

$$\begin{aligned} \bar{W}_{S2} = & \frac{\rho c^2 \lambda^2}{8k} \left[A_{11}^2 (2kh + \sinh 2kh) + 8\lambda^2 \left\{ kh \left(A_{32}^2 + \frac{1}{2} A_{11} A_{13} + A_{11}^3 \right) + \frac{A_{11}^2 B_{22}}{8} + A_{22} A_{11} \cosh kh + \frac{A_{11} A_{22}}{2} \right. \right. \\ & \cosh kh + \frac{A_{11} A_{13}}{4} \sinh 2kh + \frac{3}{16} A_{11}^3 \sinh 2kh + \frac{A_{11}^2 B_{22}}{8} \cosh 2kh + \frac{A_{11} A_{22}}{2} \cosh 3kh \\ & \left. \left. + \frac{A_{11}^2}{4} \sinh 4kh \right\} \right] + O(\lambda^6) \end{aligned} \dots (3)$$

in which c is the wave celerity, λ the small expansion parameter corresponding to the wave steepness, k the wave number and A_{ij} and B_{ij} are the function of kh respectively. In the calculation, the contribution of the higher order terms than the fourth order term to the result is neglected. Eq. (3) agrees exactly with Le Méhauté's result by the usual Stokes wave theory if $A_{22} = 0$.

On the other hand, mean energy flux of Chappelard's cnoidal wave theory (1962) by the second definition \bar{W}_{C2} is expressed by Eq. (4), based on the second order approximation.

$$\begin{aligned} \bar{W}_{C2} = & \rho g h^2 \sqrt{g h} \left[\frac{L_1^2}{3} \left\{ \kappa^2 - 1 + 2(2 - \kappa^2) \left(\frac{E}{K} \right) - 3 \left(\frac{E}{K} \right)^2 \right\} + \frac{13}{3} L_1^2 L_3 \left\{ \kappa^2 - 1 + 4 \left(\frac{E}{K} \right) - 2 \kappa^2 \left(\frac{E}{K} \right) - 3 \left(\frac{E}{K} \right)^2 \right\} \right. \\ & \left. + \frac{L_1^3}{15} \left\{ 18\kappa^4 + 11\kappa^2 - 29 + (-36\kappa^4 + 6\kappa^2 + 124) \left(\frac{E}{K} \right) - 5(7\kappa^2 + 25) \left(\frac{E}{K} \right)^2 + 30 \left(\frac{E}{K} \right)^3 \right\} \right] + O(L_1^4 L_2^2) \dots (4) \end{aligned}$$

In Eq. (4), γ is the modulus of elliptic function, K and E are the complete elliptic integrals of the first and second kinds respectively and L_1 and L_3 the small expansion parameters given in Eq. (15).

Mean energy flux of waves obtained from cnoidal wave theory by the first definition \bar{W}_{c1} is calculated as the following equation.

$$\bar{W}_{c1} = \rho g h^2 \sqrt{g h} \left[\frac{L_1^2}{3} \left\{ \kappa^2 - 1 + 2(2 - \kappa^2) \left(\frac{E}{K} \right) - 3 \left(\frac{E}{K} \right)^2 \right\} + 5L_1^2 L_3 \left\{ \kappa^2 - 1 + 4 \left(\frac{E}{K} \right) - 2\kappa^2 \left(\frac{E}{K} \right) - 3 \left(\frac{E}{K} \right)^2 \right\} \right. \dots (5)$$

$$\left. + \frac{L_1^3}{15} \left\{ 23\kappa^4 + 6\kappa^2 - 29 + (-46\kappa^4 + 31\kappa^2 + 119) \left(\frac{E}{K} \right) - 15(4\kappa^2 + 7) \left(\frac{E}{K} \right)^2 + 15 \left(\frac{E}{K} \right)^3 \right\} + 0(L_1^m L_3^n) \right]$$

Substituting the relation between expansion parameters in Chappellear's first order approximate theory L_1 and L_3 given as

$$2L_3 + L_1 \left(\kappa^2 + \frac{E}{K} \right) = 0 \dots \dots \dots (6)$$

it is found that Eq. (5) coincides with Eq. (4) within the order of this approximation.

Based on Laitone's cnoidal wave theory expressed by the mean water depth, energy flux \bar{W}_{L2} is given as

$$\bar{W}_{L2} = \rho g h^2 \sqrt{g h} \left[\frac{1}{3\kappa^4} \left\{ \kappa^2 - 1 - 2(\kappa^2 - 2) \left(\frac{E}{K} \right) - 3 \left(\frac{E}{K} \right)^2 \right\} \left(\frac{H}{h} \right)^2 + \frac{1}{30\kappa^4} \left\{ 4(-\kappa^4 + 3\kappa^2 - 2) + (8\kappa^4 - 53\kappa^2 + 53) \left(\frac{E}{K} \right) \right\} \right. \dots (7)$$

$$\left. + 60(\kappa^2 - 2) \left(\frac{E}{K} \right) + 75 \left(\frac{E}{K} \right)^2 \right] \left(\frac{H}{h} \right)^3 + 0 \left(\left(\frac{H}{h} \right)^4 \right)$$

Eq. (7) agrees exactly with that obtained from the second order approximate solution by the first definition within this approximation, and moreover if the parameters L_1 and L_3 are expanded into power series of the ratio of water depth to wave height H/h , energy flux by Chappellear's theory, Eqs. (4) and (5) yields Eq. (7). This is a self-evident truth, because expanding the parameters L_1 and L_3 in Chappellear's theory into the power series of H/h , Laitone's theory coincides with Chappellear's theory to the second order of H/h , as the authors (1974) already proved.

WAVE SHOALING OF FINITE AMPLITUDE WAVES

In general, the calculation of wave shoaling using energy flux from a theory on a uniform depth is based on the two assumption that energy flux and wave period are invariable with change of water depth. Then, under the assumption that energy flux of waves in deep water may be given by the results from the Stokes wave theory of the fourth order, in case which wave theories by both the definitions coincide each other, equations to calculate wave shoaling by Stokes wave theory are formulated by the following ones.

$$\left(\frac{h}{L}\right)^4 \lambda_0^8 \left(1 + \frac{3}{4} \lambda_0^2\right) = \left(\frac{h}{L_0}\right)^4 \lambda^2 \left[\frac{A_{11}^2}{2} (2kh + \sinh 2kh) + \lambda^2 \left\{ 4kh \left(A_{02} + \frac{A_{11}A_{13}}{2} + A_{12} \right) + \frac{A_{11}^2 B_{22}}{2} \right. \right. \\ \left. \left. + 4A_{02}A_{11} \cosh kh + 2A_{11}A_{22} \cosh kh + A_{11}A_{13} \sinh 2kh + \frac{3}{4} A_{11}^2 \sinh 2kh + \frac{A_{11}^2 B_{22}}{2} \cosh 2kh \right. \right. \\ \left. \left. + 2A_{11}A_{22} \cosh 3kh + A_{12}^2 \sinh 4kh \right\} \right] \dots \dots (8)$$

$$2\pi(1 + \lambda_0^2) \left(\frac{h}{L_0}\right) = kh(1 + C_1 \lambda^2) \tanh kh \dots \dots \dots (9)$$

in which C_1 is the function of kh . The parameters λ and λ_0 are given in Eqs. (10) and (11) respectively.

$$\frac{\pi H_0}{L_0} = \frac{3}{8} \lambda_0^3 + \lambda_0 \dots \dots \dots (10)$$

$$\frac{\pi H}{L} = B_{33} \lambda^3 + \lambda \dots \dots \dots (11)$$

Under the similar assumption as the case of Stokes waves, equations to determine shoaling characteristics by the cnoidal wave theory are expressed as

$$\lambda_0^2 \left(1 + \frac{3}{4} \lambda_0^2\right) \left\{ \frac{1}{2\pi} (1 + \lambda_0^2) \left(\frac{h}{L_0}\right) \right\}^{3/2} = 8\pi \left(\frac{h}{L_0}\right)^4 \left(\frac{\bar{W}_0}{\rho g h^2 \sqrt{g h}}\right) \dots \dots \dots (12)$$

$$\frac{1}{2\pi} (1 + \lambda_0^2) \left(\frac{h}{L_0}\right) \left(\frac{L}{h}\right)^2 = \left(\frac{c}{\sqrt{g h}}\right)^2 \dots \dots \dots (13)$$

in which \bar{W} is the energy flux by each cnoidal wave theory mentioned above. Eqs. (14) and (15) are further added to calculate wave shoaling by Chappellear's theory.

$$\frac{H}{h} = \kappa^2 L_1 \left\{ 1 + \frac{1}{4} L_1 (7\kappa^2 + 10) + 6L_3 \right\} \dots \dots \dots (14)$$

$$2L_4 + L_1 \left(\kappa^2 + \frac{E}{K} \right) + L_2 \left\{ -\frac{1}{5} (-9\kappa^4 - 6\kappa^2 + 1) + 2(\kappa^2 + 1) \left(\frac{E}{K} \right) \right\} + 6L_1 L_3 \left(\kappa^2 + \frac{E}{K} \right) + L_5^2 = 0 \dots \dots (15)$$

Numerical computation was done by use of iterative technique composed of the combination with the Regula-Falsi method and the Newton method.

NUMERICAL RESULTS AND CONSIDERATIONS

Fig. 1 shows change of wave height calculated from Stokes wave theories by both the definitions, in which the breaking inception is obtained from the Stokes criterion that the wave celerity equals to the horizontal water particle velocity at the water surface. In addition to the well-known fact that change of wave height calculated from Stokes wave theory is more evident than that by Airy wave theory with increase in deep water wave steepness H/L , the wave height calculated from Stokes wave theory by the second definition⁰ is larger than that by the first definition by about 7 % at most. It is also noted that the ratio H/H_0 is greater than unity in the range of relatively large value of the ratio h/L_0 , in

case when the Stokes wave theory by the second definition is used.

Fig. 2 is the results based on Chappellear's cnoidal wave theory as well as the Stokes wave theories mentioned above. Wave height increases rapidly with decrease in h/L compared with the results by the Airy wave theory, as extended by Iwagaki and Sakai, using the hyperbolic wave theory. Results from cnoidal wave theories by both definitions do not differ from each other in relatively small ratio of h/L . This is expected from the fact that the cnoidal wave theories by both the definitions coincide each other in the case of a solitary wave.

The comparison between change of wave height computed from Chappellear's cnoidal wave theory by the second definition and that from Laitone's theory is given in Fig. 3, in which the ratio from Chappellear's theory becomes greater than that

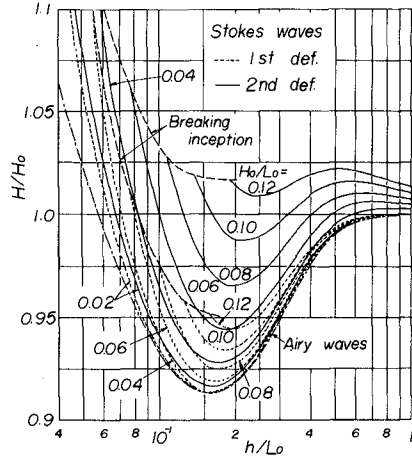


Fig. 1 Change of wave height calculated from Stokes wave theories by both definitions

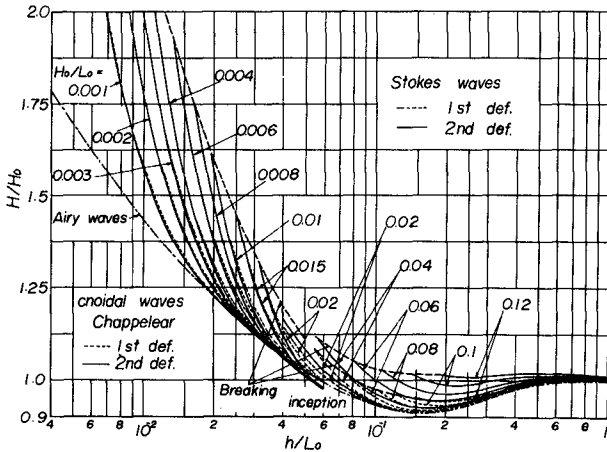


Fig. 2 Change of wave height calculated from Stokes and cnoidal wave theories by both definitions

from Laitone's theory with increase in deep water wave height H_0/L_0 . Since, moreover, the horizontal water particle velocity at phase of wave crest at the water surface by Laitone's theory greatly increases compared to that by other finite amplitude wave theories in the vicinity of breaking point, the ratio H/H_0 at breaking point calculated from the Stokes criterion by Laitone's theory becomes considerably smaller than that by Chappellear's theory.

Fig. 4 shows change of wave length computed from the Stokes wave and cnoidal wave theories by Chappellear. As shown in the figure, the wave length calculated from Stokes wave theory by the first definition as well as the cnoidal wave theories by both definitions increases with H/H_0 for the same ratio of h/L_0 , whereas the result from the Stokes wave theory by the second definition decreases with H/H_0 within a range of the ratio of h/L_0 .

The comparison between result for change of wave length L/L_0 computed from Chappellear's cnoidal wave theory by the second definition and that from Laitone's theory is shown in Fig. 5. There is little difference between them as well as the result for wave height shown previously except for a region near the breaking point and a range of relatively large values of h/L_0 and H_0/L_0 , where the applicability of cnoidal wave theory is questionable.

COMPARISON WITH EXPERIMENTAL RESULTS AND CONSIDERATIONS

A preliminary experiment of wave shoaling was conducted at Ujigawa Hydraulic Laboratory, Disaster Prevention Research Institute. The wave tank used in the experiment is 25 m long, 0.5 m wide and 0.65 m deep. Various devices were made by Tsuchiya and Yasuda in order to keep the uniformity of mass transport induced by waves. That is to say, the wave tank of which both the ends are opened was installed in the wide semi-circular basin of which diameter is 35 m. Next, attaching a big float to the usual piston-type wave generator, the generation of waves with opposing direction was suppressed, and a special wave absorber was set adjacent to the end of wave tank and at the sidewall of wave basin. These are owing to prevent the return flow in relation with the hydrostatic pressure gradient caused by mass transport of waves.

The experiment was carried out in the two cases. In the first case, a sloping model beach which gradient is 1/50 was installed in the wave tank so as

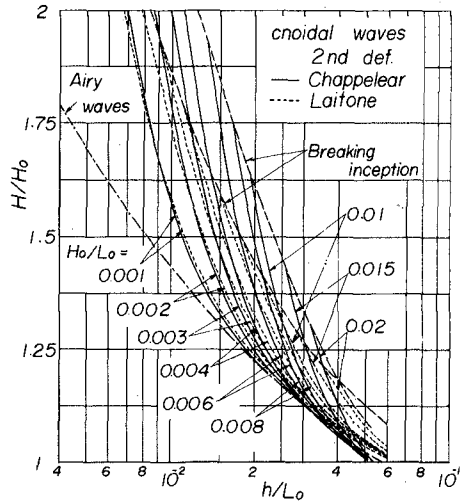


Fig. 3 Change of wave height calculated from Chappellear's theory and Laitone's one

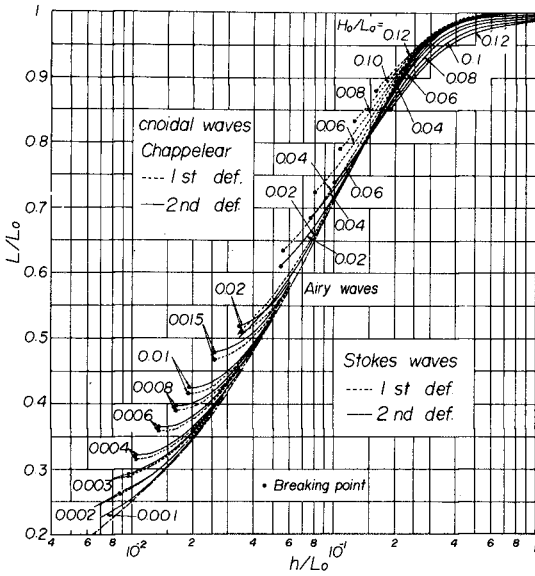


Fig. 4 Change of wave length calculated from Stokes and cnoidal wave theories by both definitions

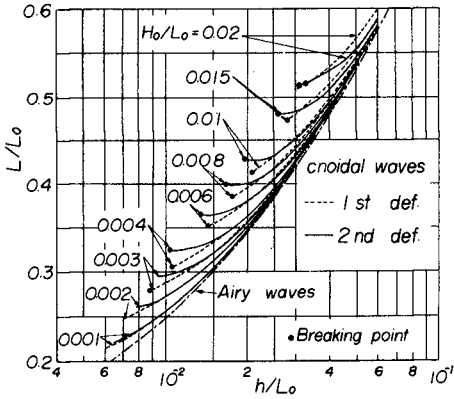


Fig. 5 Change of wave length calculated from Chappellear's theory and Laitone's one

to keep the water depth at the end of wave tank finite. This is corresponding to the experiment to realize the physical condition for the Stokes first definition to some extent. In the experiment, the care not to make the waves break on the sloping beach was taken, because wave breaking at the end of wave tank induces excess mass transport.

In the second case, the sloping beach model was installed under a situation that the outflow and inflow of water through the end of wave tank do not exist. Consequently, the dry bed on which waves are run up was ensured. This is corresponding to the experiment to realize the physical condition for the second definition.

Surface displacement was measured by six resistance-type wave gauges and wave celerity was estimated from propagation time between each gauge.

Since wave height and wave length in deep water are not uniquely determined from the given wave height and wave period at an arbitrary water depth when the wave theories by both the definitions are used, change of wave height and wave length starting from those at the most offshore wave gauge were treated for comparison.

The effect of wave damping due to bottom and sidewall friction on change of wave height with decrease in water depth was estimated by applying the following formula of wave damping step by step. The formula by Iwagaki et al. (1967) is expressed as

$$\left. \begin{aligned} \frac{H_x}{H_l} &= \exp\left(-\frac{\alpha \epsilon_{\beta+\omega} x}{L}\right), \\ \epsilon_{\beta+\omega} &= \left(\frac{4\pi^2}{\beta L}\right) \left(1 + \frac{1}{\psi}\right) \frac{1}{\sinh 2kh + 2kh}, \quad \psi = \frac{kB}{\sinh 2kh}, \\ \beta &= \left(\frac{\pi}{vT}\right)^{\frac{1}{2}} \end{aligned} \right\} \dots \dots \dots (16)$$

which was derived from laminar wave boundary layer theory on a uniform depth, in which x is the distance of wave propagation, B the width of wave tank and ν the kinematic viscosity. The value of α was adopted as 1.4 from comparison with their experiment on wave damping in order to take into account the effect of wave non-linearity and water surface contamination on wave damping. Consequently, it was found that the effect of wave damping on change of wave height is very important to be about 15% for 1/50 slope.

Fig. 6 is one of examples for change of wave height with decrease in water depth, in which h_1 and H_1 are the water depth and wave height measured at the most offshore site respectively. In spite of wide scatter of experimental results, it appears that the qualitative tendencies of experimental results may be explained by each theory.

Fig. 7 shows change of wave length estimated from the experimental results for wave celerity. Wave celerity measured was regarded as the one at the middle point of two wave gauges. The experimental results agree relatively well with the theoretical ones for each experiment.

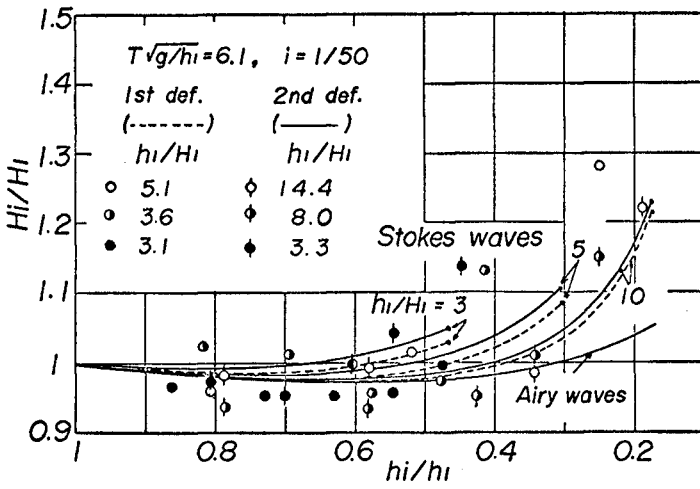


Fig. 6 Comparison between theoretical results and experimental ones for change of wave height

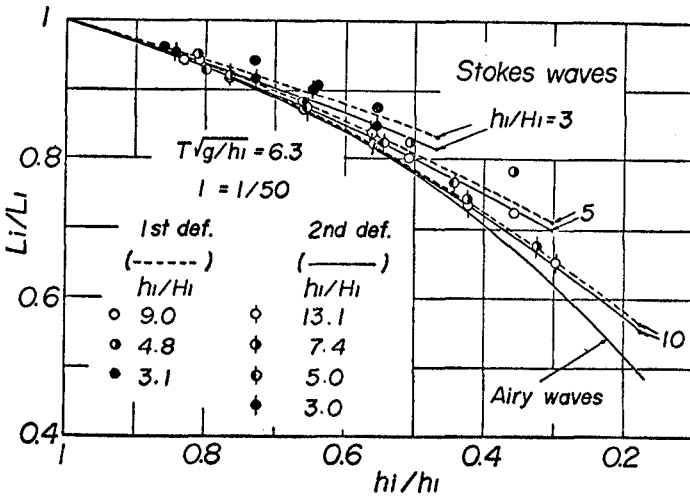


Fig. 7 Comparison between theoretical results and experimental results for change of wave length

CONCLUSIONS

Wave shoaling was calculated, based on finite amplitude wave theories on a uniform depth which were extended by the authors using the Stokes second definition for wave celerity and difference in shoaling characteristics was considered in comparison with results obtained from the usual wave theories by the first definition. It was found that the difference is considerably significant for a region of applicability to Stokes waves.

From comparison with the experimental results made under the considerations to satisfy the physical condition corresponding to each definition for wave celerity as much as possible, the tendency of shoaling characteristics obtained from each wave theory was qualitatively confirmed.

ACKNOWLEDGEMENTS

Part of this investigation was accomplished with the support of the Science Research Fund of the Ministry of Education, for which the authors express their appreciation.

REFERENCES

- Chappelear, J. E. (1962). Shallow-Water Waves, Jour. Geophys. Res., Vol. 67, No. 12, pp. 4693 - 4704.
- Iwagaki, Y., Tsuchiya, Y. and Chen, H. (1967). On the Mechanism of Laminar Damping of Oscillatory Waves Due to Bottom Friction, Bull. DPRI, Kyoto Univ., Vol. 16, Part 3, pp. 49 - 75.
- Iwagaki, Y. and Sakai, T. (1967). Wave Shoaling of Finite Amplitude Waves, Proc. 14th Conf. on Coastal Engg., JSCE, pp. 1 - 7 (in Japanese).
- Iwagaki, Y. (1968). Hyperbolic Waves and Their Shoaling, Proc. 11th Conf. on Coastal Engg., pp. 124 - 144.
- Koh, R. C. and Le Méhauté, B. (1966). Wave Shoaling, Jour. Geophys. Res., Vol. 71, No. 8, pp. 2005 - 2012.
- Laitone, E. V. (1961). The Second Approximation to Cnoidal and Solitary Waves, Jour. Fluid Mech., Vol. 9, pp. 430 - 444.
- Laitone, E. V. (1965). Series Solutions for Shallow Water Waves, Jour. Geophys. Res., Vol. 70, No. 4, pp. 995 - 998.
- Le Méhauté and Webb, L. M. (1964). Periodic Gravity Waves over a Gentle Slope at a Third Order of Approximation, Proc. 9th Conf. on Coastal Engg., pp. 23 - 40.
- Stokes, G. G. (1880). On the Theory of Oscillatory Waves, Math. Phys. Paper, Vol. 8, pp. 197 - 229.
- Tsuchiya, Y. and Yamaguchi, M. (1972). Some Considerations on Water Particle Velocities of Finite Amplitude Wave Theories, Coastal Engg. in Japan, Vol. 15, pp. 43 - 57.
- Whitham, G. B. (1961). Mass, Momentum and Energy Flux in Water Waves, Jour. Fluid Mech., Vol. 12, pp. 43 - 57.
- Yamaguchi, M. and Tsuchiya, Y. (1974). Relation between Wave Characteristics of Cnoidal Wave Theory Derived by Laitone and by Chappelear, Bull. DPRI, Kyoto Univ., Vol. 24, Part 3, pp. 217 - 231.

CHAPTER 29

Refraction of Finite-Height and Breaking Waves

by James R. Walker, Ph.D., P.E.*

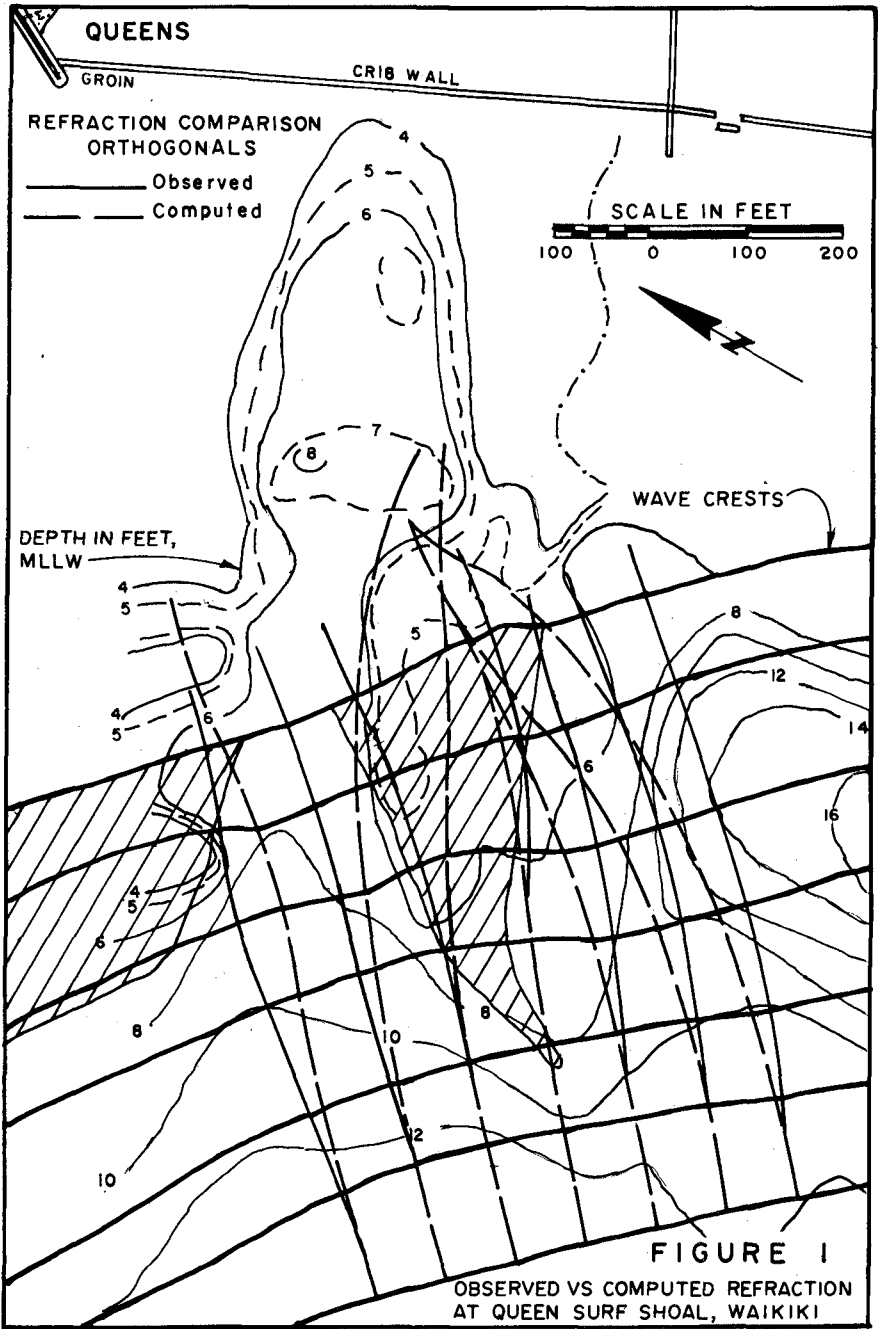
ABSTRACT

The primary objective of this study was to ascertain the influence of wave height and breaking on wave refraction over a three-dimensional shoal. The subject wave transformations were studied in an hydraulic model. Wave shoaling, decay in the breaker zone, and phase velocities were analyzed in a base test series over a bottom slope of 1:30. A second test series was conducted over a three-dimensional shoal. Wave patterns were photographed and wave heights and celerities were measured. The measurements were compared with wave refraction patterns and coefficients computed by analytical methods. Wave shoaling observed over the constant 1:30 slope was 25 percent greater than predicted by Airy theory at the breaking point for wave steepness $H_0/L_0 = .030$ and 50 percent greater than predicted for $H_0/L_0 = .002$. Shoaling measurements were compared with other empirical data sets, confirming the inadequacy of commonly used practice using linear wave theory near the breaker zone. The celerity measurements indicated that the non-breaking celerity was given by $C = (1 + .25 H/d)C_a$, where C_a is the Airy celerity. The discussion and results give a basic understanding of wave refraction near the breaker zone, supplementing analytical papers on refraction procedures using finite amplitude wave theories.

INTRODUCTION

The topic for this study evolved from field investigations of wave transformations over recreational surfing shoals in Hawaii. Walker, Palmer, and Kukea (1972) noted through observation of aerial photographs that, in some cases, breaking waves had a diverging pattern over the centerline of the shoal where linear refraction theory predicted a strong convergence. Figure 1 shows an observed wave at 5-second intervals propagating over Queens surf shoal in Waikiki. Orthogonals drawn from the wave crests are compared with those computed by linear refraction theory. The observed orthogonals tended to be considerably less affected by the bathymetry than were the theoretical orthogonals. This observation raised several questions concerning the applicability of extending refraction analysis into the breaker zone, especially over an irregular shoal. Whalin (1971) observed effects of finite height altering wave refraction patterns, but focused his attention on diffraction. Weigel and Arnold (1957) state that refraction theory is valid within two to three wave lengths seaward of the breaking position. Unfortunately, the coastal engineer often extends the limits of theory

*Moffatt & Nichol, Engineers, Long Beach, California.



into the surf to acquire the required design wave or frequency of occurrence of a given wave height.

The purpose of this study is to determine the influence of finite height and breaking on wave refraction over a three-dimensional shoal for application to surf shoal design and prediction of the influence of the shoal on adjacent beaches. The effects of diffraction, wave-induced currents, reflection, and energy dissipation other than breaker decay are assumed negligible in this study. This study was conducted in an hydraulic model of a shoal of specific shape; however, the results also have general application in understanding the nature of error and order-of-magnitude of error when conventional refraction techniques are employed near the breaking region.

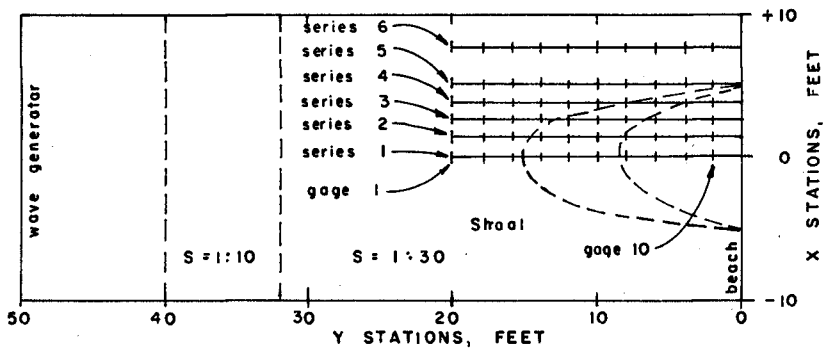
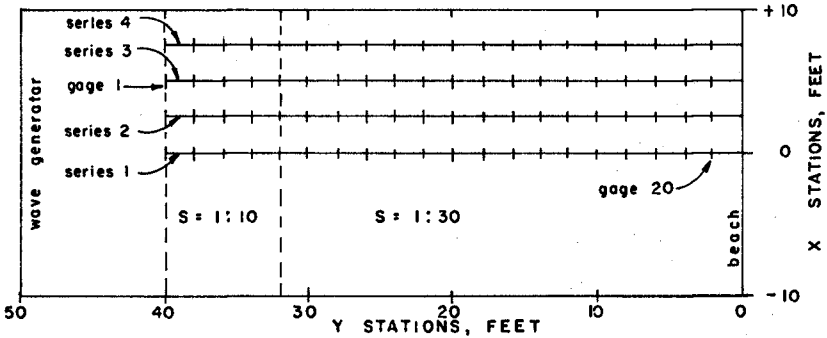
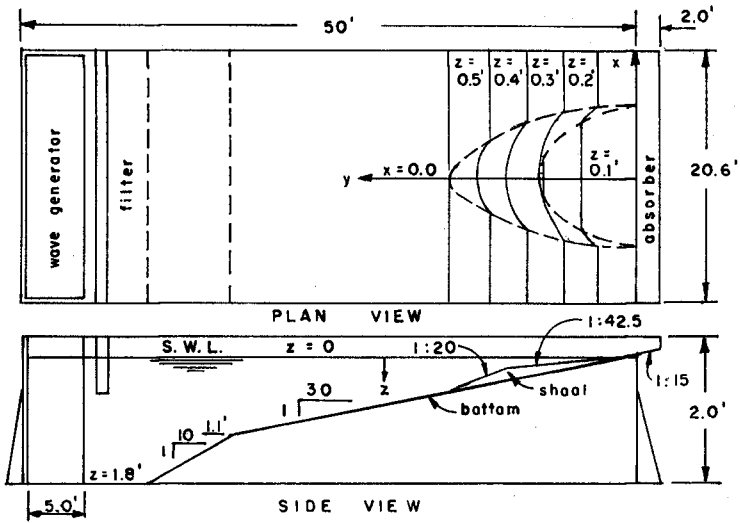
THE MODEL

The primary objective of the model was to study the transformation of waves propagating from deep water into the surf zone over a three-dimensional shoal. Several compromises were made in design of the model basin and test shoal. Since wave propagation was to be followed through the surf zone, the scale should be as large as possible to reduce scale effects due to viscous dissipation and air entrainment. The bottom slope should be constant for a distance of at least a wave length seaward of the test shoal according to criteria developed by Camfield and Street (1966). The bottom slope should be representative of conditions typically found in nature. The wave generator should be located in water depth to wave length ratio $d/L > .1$ such that wave shoaling could be measured from relatively deep water and to ensure that secondary wave crests described by Galvin (1968) would not be generated.

Space limitations restricted the basin length to 50 feet and the wave generator established the basin width at 20.6 feet. Figure 2 shows the model basin dimensions. The basin side walls were 2 feet and the water depth was 1.8 feet. The test shoal was modeled after a general concept of a surf site discussed by Walker and Palmer (1971).

The bathymetry of the test shoal was required to:

- a. induce a theoretical wave orthogonal convergence by application of linear refraction theory;
- b. induce a wave to break in a form similar to that at a recreational surfing shoal;
- c. produce a spilling to plunging breaker-type;
- d. have minimum reflection effects and minimum effects from side walls or beach;
- e. have sufficient water depth to minimize scale effects induced by dissipation at the bottom boundary and in the turbulent breaking region; and,
- f. have the parameters under study be of a scale sufficient to deduce significant conclusions.



The selected shoal shape was a truncated cylinder inclined on a 1:20 slope relative to the horizontal. The cylinder was truncated on the bottom by the 1:30 basin slope and on the top by a 1:42.5 slope. The plan view of a truncated cylinder transcribes an ellipse. The semi-major axis of the 1:30 slope was 15 feet and was oriented parallel to the direction of wave approach. The semi-minor axis was 6.71 feet on a horizontal projection. The shoal and coordinate system are shown in Figure 2. The toe of the shoal starts at station $x=0$ feet, $y=15$ feet and intersects the shoreline at station $y=0$ feet, $x=\pm 5$ feet. The 1:42.5 slope starts at the shoreline to form a plane which also transcribes an ellipse. The 1:42.5 slope intersects the 1:20 slope at $z=0.222$ feet at station $y=9.44$ feet, $x=0$ feet. The bathymetry of the model and shoal for y less than 33 feet is give by three equations:

1. $z_1 = y/30$, for $y < 33$, $|x| \geq 5.0(1. - y^2/15^2)^{1/2}$
2. $z_2 = (y/20) - (15/20)(1. - x^2/45)^{1/2} + 0.5$, for $y < 15$, $|x| \leq 5.0(1. - y^2/15^2)^{1/2}$
3. $z_3 = y/42.5$, for $y \leq 9.44$, $|x| \leq 5.0(1. - y^2/9.44^2)^{1/2}$

The depth, z , is everywhere less than or equal to the z_1 plane and greater than or equal to the z_3 plane. The curved portion of the shoal is described by z_2 .

The model basin and shoal were constructed of reinforced, finished concrete. Measurements of the bathymetry after construction indicated that the 1:30 bottom slope was accurate to within ± 0.005 feet and that the test shoal was accurate to within ± 0.010 feet.

Waves were generated by a 20.5-foot-long plunger-type wave generator. The wave period was adjusted on a variable speed crank and the amplitude of the waves was changed by adjusting the stroke of the plunger. A wave filter was placed in front of the generator to reduce high frequency noise produced by the generator. A wave-absorbing beach was placed at the shoreline along $x=0$ to reduce the entry of reflections into the measurement area. The absorber comprised a 1:15 beach slope covered by two layers of 1/4-inch stone. The stones extended on the 1:30 slope to $y=1.8$ feet.

Wave heights were measured with double-wire resistance-type wave rods. Signals were displayed on a light beam oscillograph recorder. Wave crest patterns were photographed from a platform located 20 feet above the model.

Two series of tests were conducted using 15 test waves in each series. The base test series was conducted over the constant sloping bottom to calibrate the model and waves. The shoal test series was conducted using the same generator settings as the base tests to monitor the changes in wave response induced by the bathymetry.

The 15 test waves selected for study had periods of 1.16, 1.67, 2.00, and 2.33 seconds. Four wave generator settings were used with each wave period with the exception that the four-inch half-stroke was not used with the 1.16-second period. This latter wave overtopped the

basin walls. The tests covered a range of waves which broke approximately between station $y=2$ feet, depth $z=0.067$ feet, and station $y=12.5$ feet, $z=0.42$ feet on the constant slope. The breaker heights ranged from 0.08 feet to 0.38 feet.

Eighty-one gage locations were used for the base tests. Eighty gages were located on I-beams along $x=0, 2.5, 5.0,$ and 7.5 feet and at $y=2, 4, 6, \dots, 40$ feet. Figure 3 shows the locations of the gages during the base tests. In addition to the evenly spaced gages, a portable gage was used during a separate run of the group of test waves to measure breaker heights and locations.

Sixty-one gage locations were monitored in the shoal tests. The gages were located at stations $x=0, 1.25, 2.5, 3.75, 5.0$ feet, and $7.5,$ and at $y=2, 4, 6, \dots, 20$ feet. Figure 4 shows the location of the gages for the shoal series of tests. An additional group of test waves was run with a portable gage to measure the initial breaker height on the centerline of the shoal at $x=0$ feet.

Wave rod calibrations were taken prior to and after each group of test waves had been run. The gage calibrations were slightly non-linear over a large range of submergence. A second order polynomial was fit to seven calibration points by the method of least squares to describe the calibration curve. Calibration on gage 13, located at station $y=16$ feet on the wave test, was unstable and the results were assumed to be unreliable.

Test procedures consisted of running the wave generator for approximately one minute while the recording was made. The recording chart speed was $1/4$ inch per second for the series of gages from stations $y=22$ feet to $y=40$ feet, and one inch per second for the gages located from stations $y=2$ feet to $y=20$ feet.

Small variations in the generated wave height and tolerances in basin depths caused the wave to break non-uniformly across the basin. The variations in wave breaker position induced a current system which influenced the refraction and the breaking patterns. Even on the straight beach, the breaking pattern varied considerably when the generator was allowed to run for an extended period of time. For this reason, measurements were confined to the first five to ten waves, which were relatively unaffected by the induced currents. In most cases, little temporal variation in the wave height was evident. The greatest temporal wave height variations occurred when a gage was located close to the breaking point. The average wave celerity between successive gages was determined by measuring the time differential of crest passage between gages separated by 2-foot intervals.

The results of this investigation may be viewed in terms of dimensionless parameters. However, lengths and times may be scaled for application to coastal design. Scaling of the model was done through use of the Froude modeling relation. Viewed in terms of a model experiment of a prototype surf shoal, the length scale selected in the design of the model was 1:36 and the velocity and time scales were 1:6.

The laminar dissipation was calculated by the method of Keulegan (1950) to obtain an estimate of the dissipation in the model prior to wave breaking. Approximately five percent of the energy from non-breaking waves was dissipated by laminar dissipation by the time the wave reached station $y=2$ feet. Horikawa and Kou (1962) indicated that wave height decay in the breaking region was greater in the model than in the prototype. When applying these data to a prototype situation, these factors must be taken into account. Wave energy reflecting from the beach was computed by the Miche (1951) formula. The maximum calculated reflected wave height, H_r , was less than 14 percent of the incident wave.

The accuracy of the model procedures was estimated from a preliminary test series. The wave rods were spaced 2 inches apart and strung across the basin at $y=26$ and 27. Eight test waves were run to determine the variation in wave height. The measured wave heights were within a ± 10 percent deviation at two standard deviations. Wave height variation across the basin introduced an additional ± 5 percent error. Wave celerity was estimated to be within 10 percent error due to tolerance in positioning the wave gage and in reading the zero phase position on the wave.

RESULTS AND ANALYSIS

Wave Shoaling

The base test series was conducted to study transformations of waves propagating from intermediate water depths over a sloping bottom into the breaking region in shallow water. The primary topics investigated were wave height growth due to shoaling water depths and the influence of wave height and wave breaking on wave celerity. Measurements were compared with values predicted by application of linear wave theory commonly used in refraction analysis.

The characteristics of incident test waves and their breaking properties measured in the model are summarized in table 1. Figure 5 shows a typical wave height profile as a function of distance offshore. The figure indicates the typical scatter and accuracy of the data. The breaking position was measured by a single gage. An equivalent deep-water wave height was determined by application of the Airy shoaling coefficient to the wave measurements at gages located at Stations 26, 28, 30 and 32. Utilizing the calculated deep-water wave height and the Airy shoaling coefficient, the predicted wave height is shown by the dashed line in Figure 5. The wave shoaling measured in the model increases much more rapidly than the predicted wave shoaling. This increase is most noticeable just prior to the wave breaking position. The slope of the measured wave height profile appears to increase significantly when $H/d \geq .25$.

Wave shoaling from each of the tests was plotted in dimensionless form as a function of d/L_0 . The data were smoothed and shoaling curves are shown in Figure 6 as a function of H_0/L_0 . The data are compared with Airy shoaling theory. The rate of shoaling increases rapidly just prior to breaking. The low steepness waves, $H_0/L_0 = .002$, break at a

TABLE 1
SUMMARY OF TEST WAVES

Test No.	Wave Generator Setting		Deep-Water Wave Height & Steepness			Breaking Wave Properties, $X=0.0$			Breaking Wave Parameters, Base Test			
	Generator 1/2 Stroke in.	T sec.	H_o' ft.	L_o ft.	H_o'/L_o	Base Tests		Shoal Tests		H_b/H_o' measured	H_b/H_o' predicted*	
						H_b ft.	Y station ft.	H_b ft.	Y station ft.			
1	1	1.17	0.092	6.9	0.01334	.141	4.5	.163	8.0	1.52	1.38	.942
2	1	1.67	0.062	14.2	0.00437	.119	4.0	.139	7.3	1.92	1.81	.893
3	1	2.00	0.045	20.4	0.00224	.105	3.5	.111	6.0	2.29	2.16	.904
4	1	2.33	0.034	27.8	0.00123	.083	3.0	.097	5.0	2.42	2.51	.832
5	2	2.33	0.074	27.8	0.00267	.168	6.0	.156	7.5	2.25	2.05	1.009
6	2	2.00	0.097	20.4	0.00476	.195	5.5	.198	8.3	2.00	1.78	1.066
7	2	1.67	0.125	14.2	0.00885	.236	6.3	.216	9.0	1.88	1.52	1.126
8	2	1.17	0.180	6.9	0.02595	.250	7.5	.230	10.0	1.38	1.16	1.240
9	3	1.17	0.261	6.9	0.03759	.320	9.8	.269	11.0	1.23	1.06	.980
10	3	1.67	0.185	14.2	0.01301	.312	9.0	.279	10.5	1.67	1.38	1.041
11	3	2.00	0.145	20.4	0.00713	.304	7.2	.271	9.4	2.08	1.61	1.267
12	3	2.33	0.112	27.8	0.00403	.245	6.5	.215	9.1	2.19	1.86	1.131
13	4	2.33	0.152	27.8	0.00546	.285	8.5	.264	10.1	1.89	1.72	1.005
14	4	2.00	0.200	20.4	0.00981	.343	9.0	.266	10.0	1.72	1.49	1.144
15	4	1.67	0.247	14.2	0.01738	.379	12.2	.306	12.5	1.53	1.29	.931

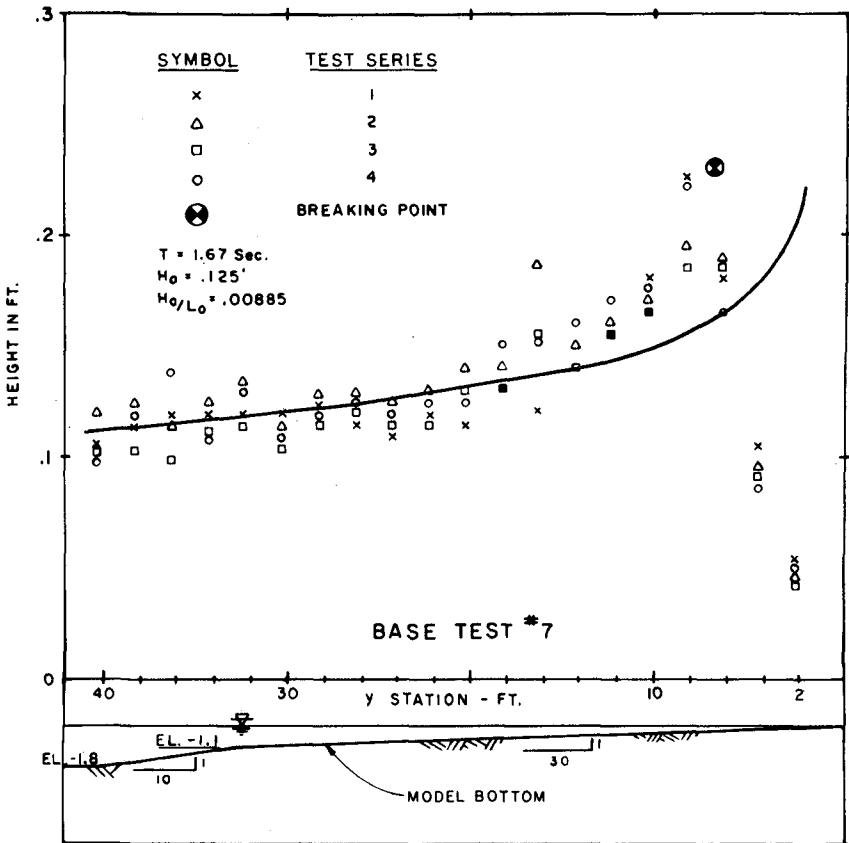


FIGURE 5 - WAVE SHOALING, TEST 7

height 50 percent greater than the Airy shoaling coefficient predicts. The higher initial steepness waves, $H_0/L_0 = .03$, break at a height 25 percent greater than Airy theory predicts.

Figure 6 represents an empirical set of wave shoaling curves for waves propagating over a 1:30 slope. The significance of these results is that the waves in shallow water shoal at a much greater rate than Airy theory predicts. Consequently, application of Airy theory in shallow water predicts a significantly lower wave height than observed in this model. These results are similar to those obtained by Iwagaki and Sakai (1972). The wave shoaling curves given in Figure 7 are compared with the shoaling curves based on cnoidal wave theory developed by Svendsen and Kjaer (1972) and stream function theory by Dean (1974). The comparison shows similar trends, height of shoaling as a function of H_0/L_0 . Cnoidal theory predicts a shoaling height less than unity for d/L_0 greater than .05. This is not confirmed by observation. Cnoidal theory also appears to predict a slightly greater rate of wave shoaling than measured for H_0/L_0 less than 0.01. However, the comparison is not strictly valid since H_0' rather than H_0 was measured. Stream function theory compares well with the expected set for $H_0/L_0 \geq .01$ with the exception that the published data uses the breaker index $H_b/d_b = .78$ compared to the observed index = 0.95. This may be attributable to the effect of bottom slope not accounted for in the theory. For $H_0/L_0 < .01$, the stream function shoaling is significantly greater than the observed. This is attributed in part to the estimate of H_0 made in the model at the low d/L_0 region. The wave had undergone more transformation than predicted by Airy theory. Consequently, the indicated $H_0/L_0 = .002$ curve may in fact be representative of some lower H_0/L_0 . Conversely, the shoaling curves are theoretical over a constant sloping bottom. The breaker index is equal to 1 for the measured data as drawn in Figure 6. Shoaling from deeper water $d/L_0 > .1$ through breaking for $H_0/L_0 < .01$ over different bottom slopes requires further research; however, the results of the studies indicate the magnitude of error when Airy theory is invoked. Figures 6 and 7 could be used in design, model, and field studies and in evaluating wave data.

Comparison of measured breaking height to deep-water height with values predicted by empirical data developed by Koh and Le Méhauté (1966) indicate that predicted values are 10 percent to 15 percent lower than measured. The difference between the observed and predicted values is attributed in part to the method of estimating the deep-water wave height. Rarely in the field or model is the deep-water wave measured and directly related to a shallow water breaking wave. Application of a linear shoaling coefficient to a measured wave height introduces a potential error which increases in magnitude with decreasing d/L_0 . The relative breaker height to breaker depth index, B , is also listed in Table 1. The average value of $B = .95$ for this data set. Application of methods developed by Galvin (1968) predicted an average value of $B = .85$.

Wave Celerity

The average phase velocity, \bar{c} , between two wave gages was determined by dividing the elapsed time for passage of the wave crest between gages by the distance between the gages. Figure 8 shows typical average

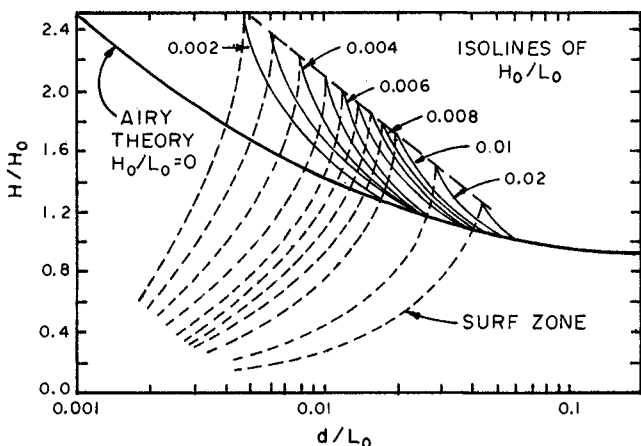


FIGURE 6 - WAVE SHOALING

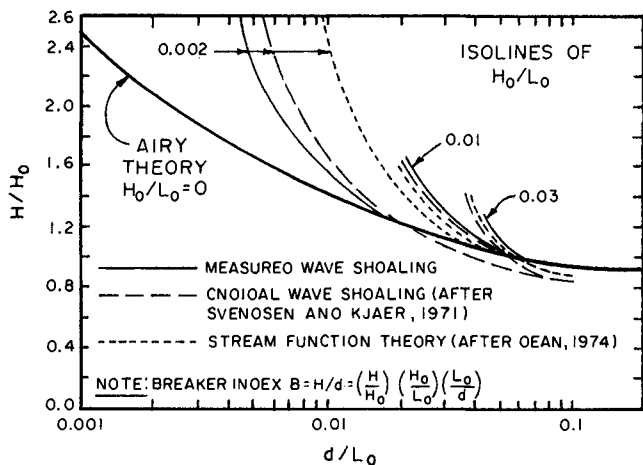


FIGURE 7

COMPARISON BETWEEN MEASURED AND THEORETICAL WAVE SHOALING

celerities measured in the model in the base tests. The celerities increase as a function of wave height.

The measured celerities were compared with celerities commonly used in refraction analysis by defining a Froude number, $F_r = \bar{c}/\bar{c}_a$,

$$\text{where } \bar{c}_a = \frac{1}{y_1 - y_2} \int_{y_2}^{y_1} c \, dy = \frac{1}{y_1 - y_2} \int_{y_2}^{y_1} \frac{gT}{2\pi} \tanh(dk) \, dy,$$

where $k = \frac{2\pi}{L}$, and y_1 is gage 1 coordinate.

The Froude numbers are plotted in Figure 8 as a function of H/d . The results indicated a significant departure from Airy theory which would have had a $F_r = 1$ in all regions. Several theoretical expressions were plotted against the data; however, the simple expression below fits the data through the non-breaking region well:

$$F_r = 1 + 0.25 \frac{H}{d}$$

This expression gives a maximum Froude number of 1.25 at breaking where $H/d = 1$. The curve is applicable to the region prior to breaking. Airy theory predicts celerity approximately 6 percent too low at $H/d = .25$. This is also the region where the shoaling curve deviated noticeably from the Airy theory.

The Froude number increases with H/d until it exceeds 1.25 at breaking. The breaking and broken waves are shown in Figure 8 above $F_r = 1.25$. The maximum value was $F_r = 1.4$. The higher values appear to occur when the wave breaks. A discontinuity in wave phase appears to occur during the plunge of the breaker as the crest curls over the face of the wave. This is a short-duration occurrence, but accounts for observed apparent divergences in wave form in aerial photos and high Froude numbers in Figure 8. Data were insufficient to ascertain a reliable expression for wave celerity in the surf zone. Considering wave decay, scale effects, and the change of phase during breaking, $c = \sqrt{g(d+H)}$ when $H = .78d$ or $F_r = 1.33$ gives a reasonable approximation in the surf zone. An analysis was made using wave setup, η , in the surf zone. Setup was included in the velocity term where $c_b = \sqrt{g(d+\eta)}$; however, the analysis did not reduce the scatter of data significantly. After the wave breaks, however, the application of refraction loses some meaning. The wave crest patterns become the only meaningful relation unless wave decay can be modeled more accurately in the surf zone in regions of converging and diverging orthogonals.

Shoal Tests - Refraction

The shoal test series was conducted to study the influence of finite wave height and breaking on wave refraction. Comparison of wave crest patterns measured in the model and computed by linear refraction theory are shown in Figure 9. The comparison shows the wave pattern of a wave as it propagates over the shoal. The wave crests and initial surf line are traced over the shoal for test waves 3 and 14. Comparison of the theoretical with the measured refraction patterns shows that the low-height wave represented by test 3 tends to follow the conver-

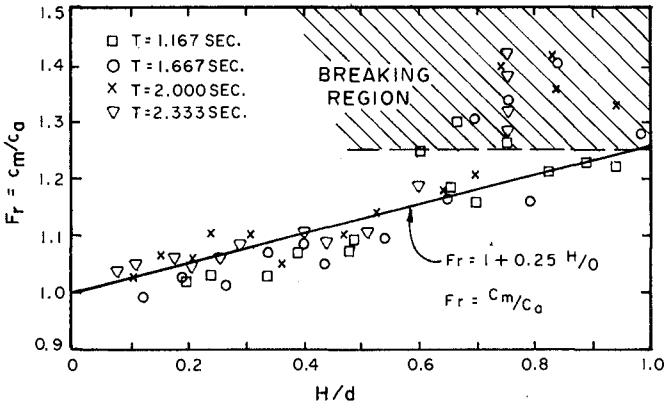


FIGURE 8 - Fr . VS H/d

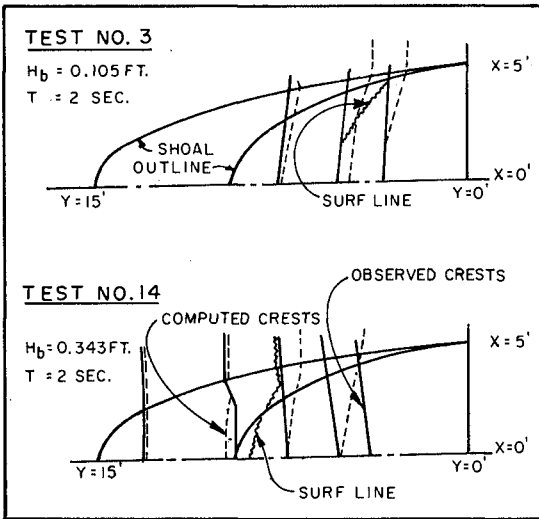


FIGURE 9 - OBSERVED VS COMPUTED WAVE CREST PATTERNS

gent patterns predicted by the theoretical analysis. With increase in wave height represented by test 14, the pattern tends to become divergent over the center of the shoal.

Computed refraction coefficients, K_r , range from 0.75 to 2.0. The waves approaching the shoal converge toward the centerline over the curved portion of the shoal. The conventional refraction analysis predicts wave concentration over the shoal centerline. The high refraction coefficients are located over the center of the shoal and the low coefficients along the side of the shoal. The observed wave patterns vary considerably as a function of wave height. The most noticeable feature of the observed patterns is the marked divergence in the vicinity of breaking as shown in the large wave in test 14.

The conclusion drawn from these observations is that finite height and wave breaking have a very significant influence on wave refraction over a shoal. The waves with small heights in Tests 1 through 5 converged toward the center of the shoal and conformed in general with linear refraction patterns up to a short distance seaward of breaking. The larger waves, however, tended to diverge. The combination of orthogonal divergence and diffraction, current, and reflection effects reduced the breaker height to less than that over the planar 1:30 slope for the larger waves. The application to design indicates that refraction over the shoal may not necessarily increase the wave height as would intuitively be expected.

MODIFIED REFRACTION TECHNIQUE

The influences of wave height and wave breaking were shown to affect wave refraction patterns in the hydraulic model. Linear refraction procedures were modified to account for the effects of wave height and wave breaking. The basic algorithm utilized the results of the base tests on celerity and shoaling to construct wave fronts at successive time intervals. Chu (1974) and Skovard and Petersen (1976) have developed computer programs utilizing the finite height theories to predict refraction of finite height, but not breaking waves.

The modified refraction theory is briefly described below using test 7 as an example. The incident wave parameters were $H_0 = 0.126$ feet and $L_0 = 14.22$ feet, resulting in $H_0/L_0 = 0.00885$. The wave height was determined as a function of depth from Figure 6, neglecting refraction effects by the equation

$$\frac{H}{d} = \left(\frac{H}{H_0}\right) \left(\frac{H_0}{L_0}\right) \left(\frac{L_0}{d}\right)$$

The wave celerity in the region prior to breaking was determined by the equation

$$c = c_a(1 + 0.25 H/d)$$

The wave in the breaking region was determined by $c = 1.33\sqrt{gd}$. Breaking was assumed to occur at $H/d = 1$. Refracted wave crests were drawn by the wave crest method and refraction coefficients were determined from or-

thogonals drawn through the crests. The method is tedious and not recommended for design practice. The wave front method was also employed using conventional refraction procedures for direct comparison of wave crest patterns and refraction coefficients shown in Figure 10.

The modified technique, which incorporates wave height and wave breaking, predicts a smaller degree of orthogonal convergence in the center of the shoal and a smaller degree of orthogonal divergence along the sides of the shoal. The refraction coefficients determined by using the conventional analysis predicts coefficients as high as 2, whereas the modified procedure yielded a maximum refraction coefficient of 1.25. Both procedures had coefficients = .75; however, a smaller area had values less than .75 in using the modified procedure.

The observed refraction patterns have an orthogonal divergence in the vicinity of the initial breaking region over the center of the shoal. During breaking, the wave crest slides down the front of the wave. This is manifested as a greater local wave celerity. This phenomenon was not modeled in the modified refraction procedure.

FINDINGS

The findings of this investigation illustrate the importance of considering the effects of finite height and wave breaking on wave transformation near and in the surf zone. The base test series studying the transformation of waves over a 1:30 slope indicated that the observed increase in wave height at the breaker point relative to the deep-water height was 25 percent greater than that predicted by application of Airy theory for $H_0/L_0 = 0.03$ and 50 percent greater at $H_0/L_0 = 0.002$. This result has a significant application when transforming a shallow-water wave to either a deep-water wave from a gage reading or transforming the wave to a breaker position. The result also suggests that model experiments should generate the waves in as deep water as possible, at least as deep as $H/d < .25$. Simple corrections to Airy theory have been deduced from the data to include the effects of finite height and breaking on wave celerity. In addition, during the breaking process, the lip transforms into a bore resulting in a considerably greater local celerity than the aforementioned correction. The conclusions above are more applicable to long-period wind-generated swell of regular form, as found in the Hawaiian Islands, as opposed to sea or locally generated waves found in the North Sea. Shorter period waves of greater steepness conform better to conventional analysis.

The model tests on the refraction of waves over a three-dimensional shoal illustrated the influence of finite height on wave refraction. The wave orthogonals tend to converge less over a shoal for increasing wave height due to the effects of finite height on wave celerity. This factor becomes important near the surf zone. The waves tend to diverge less over a trough. The influence of finite height and breaking are, therefore, to reduce the effects of refraction. Most existing computer programs using linear theory tend to strive for accuracy of bathymetry interpolation in refracting by the ray equation. Care should be exercised in the application and interpretation of such programs where H/d exceeds about .25 or when c is increased 6 percent over the Airy celerity.

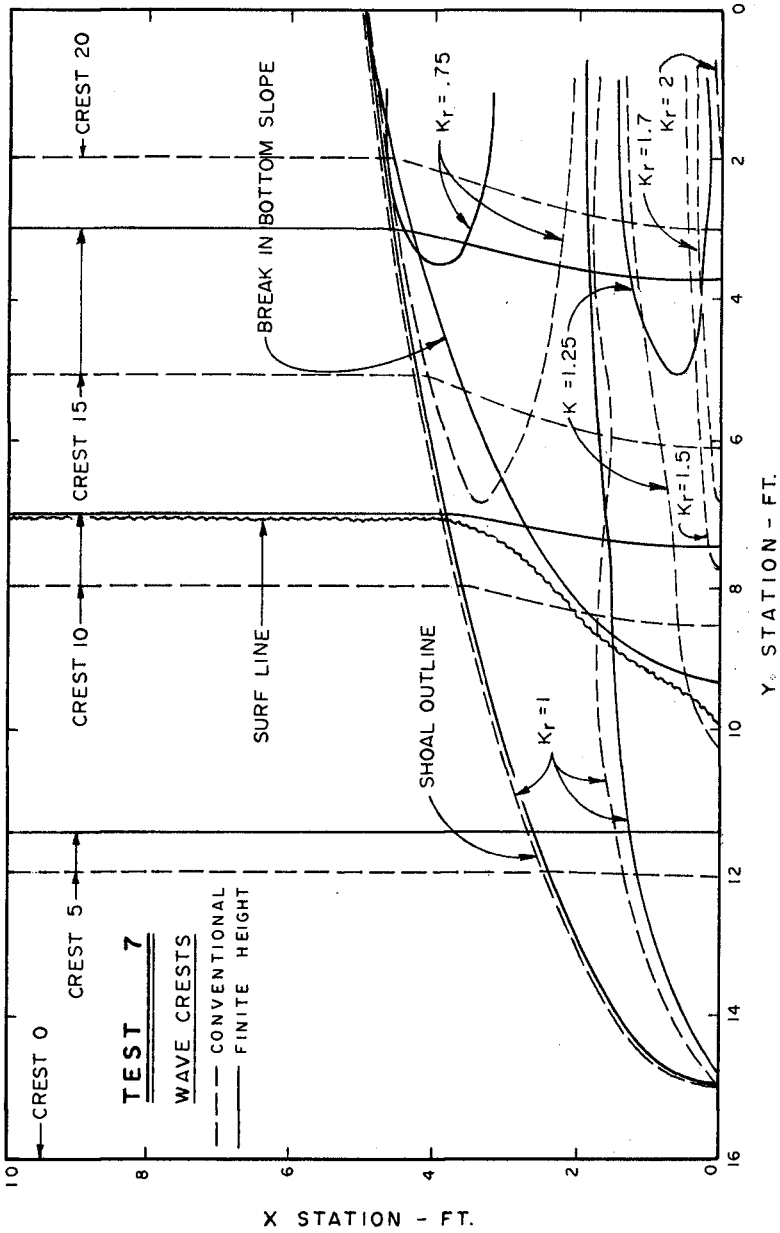


FIGURE 10 - COMPARISON OF CONVENTIONAL U.S. FINITE HEIGHT REFRACTION PATTERNS

ty. The application of cnoidal theory presented by Skovgaard and Petersen, use of stream function shoaling curves, or a finite height scheme such as presented by Chu appears to be a step in the right direction. However, these schemes are for regular bathymetry. A wave front type method should be developed to more accurately predict finite height along a wave crest.

APPLICATION TO DESIGN PRACTICE

Application of a detailed refraction analysis using finite height procedures or corrections to linear analysis can be a time-consuming chore. Linear refraction and shoaling techniques appear valid for $H/d < .25$. The recommended procedure is to generally employ conventional refraction analysis using Airy theory and select a few critical cases to study in more detail starting at $H/d = .25$. The study results indicate that in design of a surf shoal similar to the one tested, wave refraction is of secondary importance relative to wave shoaling. The influence of finite height decreases the wave refraction effects considerably over a shoal. This is not a diffraction effect since the wave front pattern which is prescribed by refraction can be accounted for to a large extent by finite height considerations. Effects of wave-induced currents and diffraction are also of importance, but were not studied in this paper.

ACKNOWLEDGEMENT

Portions of this paper were extracted from a dissertation submitted to the University of Hawaii, Department of Ocean Engineering, in partial fulfillment of the requirement for the degree of Doctor of Philosophy in Ocean Engineering. The project was funded by the Surf Parameters project, a State of Hawaii funded research project. The author wishes to acknowledge Professors C. L. Bretschneider and F. Gerritsen for their guidance; Mr. J. F. O'Brien, Director of Look Lab; Mr. R. Q. Palmer who inspired the study; and Mr. H. Ho, technician who built the basin and associated appurtenances.

REFERENCES

- Battjes, J. A., "Refraction of Water Waves", J. of Waterways and Harbors Division, ASCE, Vol. 94, WW 4, 1968.
- Beitinjani, K. I., and E. F. Brater, "A Study of Refraction of Waves in Prismatic Channels", J. of Waterways and Harbors Division, ASCE, Vol. 91, WW 3, 1965.
- Camfield, F. E., and R. L. Street, "The Effects of Bottom Configuration on the Deformation, Breaking, and Run-up of Solitary Waves", Proc. 10th Conf. on Coastal Engineering, ASCE, London, 1968.
- Chu, H. L., "Numerical Model for Wave Refraction by Finite Amplitude Wave Theories", Symposium on Modeling Techniques, San Francisco, California, September 1975.
- Dean, R. G., "Evaluation and Development of Water Wave Theories for Engineering Application", SR-1, U.S. Army Corps of Engineers, CERC, Ft. Belvoir, Virginia, November 1974.
- Galvin, C. J., "Breaker-Type Classification on Three Laboratory Beaches", J. of Geophysical Research, Vol. 73, No. 12, June 1968.
- Iwagaki, Y., and T. Sakai, "Shoaling of Finite Amplitude Long Waves on a Beach of Constant Slope", Proc. ASCE Conf. on Coastal Engineering, Vancouver, B.C., 1972.
- Keulegan, G. H., "Gradual Damping of Solitary Waves", J. Res. National Bureau of Standards, Vol. 40, page 487, 1950.
- Koh, R. C. Y., and B. Le Méhauté, "Wave Shoaling", JGR, Vol. 71, No. 8, 1966.
- Miche, R., "Le Pouvoir Reflechissant des Ouvrages Maritimes Exposés à l'Action de la Houle", Annales des Points et Chaussées, Vol. 121, pages 285-319, 1951.
- Skovgaard, O., and M. H. Petersen, "Refraction of Cnoidal Waves", Proc. 15th Conf. on Coastal Engineering, Honolulu, Hawaii (Draft), July 1976.
- Svendsen, I. A., and O. Brink-Kjaer, "Shoaling of Cnoidal Waves", Proc. 13th Conf. on Coastal Engineering, Vancouver, B.C., 1972.
- Walker, J. R., and R. Q. Palmer, "A General Surf Site Concept", Look Lab TR-18, University of Hawaii, Honolulu, Hawaii, September 1971.
- Walker, J. R., R. Q. Palmer, and J. K. Kukea, "Recreational Surfing on Hawaiian Reefs", Proc. 13th Conf. on Coastal Engineering, Vancouver, B.C., 1972.
- Walker, J. R., "Wave Transformations Over a Sloping Bottom and Over a Three Dimensional Reef", Dissertation, University of Hawaii, Look Lab Miscellaneous Report-75-11, May 1974.
- Whalin, R. W., "The Limit of Applicability of Linear Wave Refraction Theory in a Convergent Zone", USA Corps of Engineering Waterways Experiment Station, H-71-3, 1971.
- Wiegel, R. L., and A. L. Arnold, "Model Study of Wave Refraction", Beach Erosion Board, TM 103, 1957.

CHAPTER 30

THREE-DIMENSIONAL CONDITIONS OF SURF

William L. Wood
Associate Professor of Marine Science
Director, Great Lakes Coastal Research Laboratory
Department of Geosciences
Purdue University
West Lafayette, Indiana

ABSTRACT

Wave height variability along the crest of breaking waves is shown to be a significant factor in the assessment of surf zone dynamics. Variations in excess of 50 percent of the maximum wave height can occur along a single crest without significant variations in bathymetry. The horizontal scale of this longshore variability in crest height corresponds to the wave length of incident breaking waves. Four possible mechanisms for this variability are postulated and then evaluated individually on the basis of field observations. A major result of these evaluations is that two-dimensional shallow-water wave equations appear to be inappropriate for expressing natural surf zone wave transformations and water motions even under the condition of waves encroaching on a plane sloping bottom. Consequently, three-dimensional equations of surf should be used for describing most natural surf zone dynamics.

INTRODUCTION

Conventional techniques for estimating dynamic conditions in the surf utilize linear or weakly non-linear transformations of a set of deep water wave parameters to predict a set of shallow water wave parameters assumed to be incident at the outer limits of the surf zone. Once this set of shallow water wave parameters has been determined it is then used to establish initial and seaward boundary conditions for calculating two-dimensional wave transformations and water motions within the surf zone. To a first approximation two-dimensional irrotational motion of inviscid fluid on a shoaling beach satisfies nonlinear shallow-water equations (Meyer and Taylor, 1963; Ho, et al., 1963). However, most natural surf conditions are not two-dimensional thus, it is necessary to determine if longshore variations in the initial and seaward boundary conditions are of significant magnitude to invalidate the use of two-dimensional theory.

The three-dimensional time dependent shallow water equations of motion show that longshore variations in surf are caused primarily by longshore variations in the wave field approaching the coast and by longshore variations in bottom geometry within the surf zone (Stoker, 1957). Meyer and Turner (1967) have shown, for initial and seaward boundary

conditions independent of distance parallel to shore, that when the longshore bottom profile slope is gentler than the normal bottom profile slope "weakly three dimensional" surf can still be analyzed directly by two-dimensional theory. However the effect of longshore variations in the incident wave field at the outer surf zone has not yet been investigated.

Therefore, the primary purpose of this study was to measure three-dimensional variations in surf zone wave conditions and to relate them to incident wave conditions at the outer surf zone. An analysis of longshore variations in wave height at the outer surf zone was carried out in order to evaluate uniformity of the incident wave field. Wave height probability distributions were calculated from the observed data in order to show the distributional changes related to wave breaking and transformation through the surf.

THREE-DIMENSIONAL EQUATIONS OF SURF

Derivation of a shallow water wave theory from exact hydrodynamic equations utilizing a formal perturbation procedure, where all quantities are expanded in powers of $\sigma = kh$, (h is the depth and k is the maximum initial curvature of the free surface) has been carried out by Friedrichs (1948) and Stoker (1957). Defining the x, z plane as the undisturbed water surface with the y -axis positive upward, the free surface and bottom position are specified by $y = \eta(x, z, t)$ and $y = -h(x, z)$ respectively. The general three-dimensional problem is then formulated in terms of the equations of motion

$$\frac{\partial u}{\partial t} + u \frac{\partial u}{\partial x} + v \frac{\partial u}{\partial y} + w \frac{\partial u}{\partial z} = -\frac{1}{\rho} \frac{\partial p}{\partial x} \quad (1)$$

$$\frac{\partial v}{\partial t} + u \frac{\partial v}{\partial x} + v \frac{\partial v}{\partial y} + w \frac{\partial v}{\partial z} = -\frac{1}{\rho} \frac{\partial p}{\partial y} - g \quad (2)$$

$$\frac{\partial w}{\partial t} + u \frac{\partial w}{\partial x} + v \frac{\partial w}{\partial y} + w \frac{\partial w}{\partial z} = -\frac{1}{\rho} \frac{\partial p}{\partial z} \quad (3)$$

and continuity

$$\frac{\partial u}{\partial x} + \frac{\partial v}{\partial y} + \frac{\partial w}{\partial z} = 0. \quad (4)$$

It is assumed that the flow is irrotational with kinematic boundary conditions at the bottom and free surface given by

$$u \frac{\partial h}{\partial x} + v + w \frac{\partial h}{\partial z} = 0 \quad \text{at } y = -h \quad (5)$$

$$\frac{\partial \eta}{\partial t} + u \frac{\partial \eta}{\partial x} + w \frac{\partial \eta}{\partial z} = v \quad \text{at } y = \eta \quad (6)$$

respectively and a dynamic boundary condition at the free surface given by

$$p = 0 \quad \text{at } y = \eta. \quad (7)$$

Introduction of dimensionless variables through the use of a typical depth h and a typical horizontal length k into equations (1) through (7) and expanding u , v , w , η , and p in a power series of σ provides the opportunity to equate coefficients of like powers of σ . The first order approximation to u , w , and η are then given by the "three-dimensional shallow-water equations" (Stoker, 1957).

$$\frac{\partial u}{\partial t} + u \frac{\partial u}{\partial x} + w \frac{\partial u}{\partial z} + \frac{\partial \eta}{\partial x} = 0 \quad (8)$$

$$\frac{\partial w}{\partial t} + u \frac{\partial w}{\partial x} + w \frac{\partial w}{\partial z} + \frac{\partial \eta}{\partial z} = 0 \quad (9)$$

$$\frac{\partial \eta}{\partial t} + \frac{\partial [u(\eta + h)]}{\partial x} + \frac{\partial [w(\eta + h)]}{\partial z} = 0. \quad (10)$$

TWO-DIMENSIONAL EQUATIONS OF SURF

It is easily seen that if w is assumed to be zero and all other quantities are assumed to be independent of z that equations (8) through (10) become the "two-dimensional shallow-water equations" [Stoker, 1947; Friedrichs, 1948; Stoker, 1957; Meyer and Taylor, 1963; and Meyer and Turner, 1967]

$$\frac{\partial u}{\partial t} + u \frac{\partial u}{\partial x} + \frac{\partial \eta}{\partial x} = 0 \quad (11)$$

$$\frac{\partial \eta}{\partial t} + \frac{\partial [u(\eta + h)]}{\partial x} = 0. \quad (12)$$

Meyer and Turner (1967) also show these equations to be applicable to "weakly three-dimensional surf". Equations (11) and (12) are further simplified by assuming that u and η and their derivatives are small quantities whose squares and products are negligibly small compared to the linear terms. The resulting equations are the "linear shallow-water equations"

$$\frac{\partial u}{\partial t} + \frac{\partial \eta}{\partial x} = 0 \quad (13)$$

$$\frac{\partial \eta}{\partial t} + \frac{\partial (uh)}{\partial x} = 0 \quad (14)$$

The preceding derivation depends upon three important simplifying assumptions with respect to longshore water motions and bottom variability: that the longshore velocity component is zero; that the incident wave field at the seaward boundary of the surf zone is uniform in the longshore direction; and that the bottom slope in the longshore direction is zero. Meyer and Turner (1967) showed analytically that unless $\beta/\epsilon \rightarrow 1$, where ϵ is the beach slope normal to shore and β is the beach slope parallel to shore, the first and third assumptions above are valid approximations. However, they accepted the second assumption implicitly, asserting it was, in fact, valid whenever initial and seaward boundary conditions were primarily dependent upon beach slope ϵ . This assumption that uniform wave crests are a reasonable expectation for an incident wave field at the outer surf zone is one of the most important assumptions in formulating the two-dimensional equations of surf. A field evaluation of this assumption forms the primary context for this paper.

FIELD EXPERIMENT

In order to evaluate three-dimensional conditions of surf a three by three wave gauge array was positioned in the surf zone with its longshore axis parallel to the crests of incident breaking waves, Figure 1. Separation distance between individual wave monitoring positions was approximately one half the incident wave length. The three outer most stations were located seaward of the zone of active breaking. The six inner stations were located within the breaker zone and bracketed the region of most active breaking. Approximately eighty percent of initial breaking occurred within the monitoring array.

The bottom in the study area was characteristic of a sandy barred coastline with isobaths parallel or slowly varying in the longshore direction. Positioning of the monitoring array was such that ϵ was large (normal beach slope 1:20) and $\beta/\epsilon \rightarrow 0$ (to correspond to the conditions suggested by Meyer and Turner, 1967).

Wave monitoring was carried out continuously for fifteen minute periods separated by fifteen minute intervals. Wave breaking and transformation in the surf zone was monitored using a super 8 mm motion picture camera. The motion picture film records were taken in order to analyze the individual crests behavior as they passed through the monitoring grid. The only conditions monitored were those when waves broke within the monitoring grid. Conditions resulting in breaking or breaking and reforming seaward of the grid were not measured. Conditions during which waves appeared to be arriving from more than one direction, at the outer surf zone, were also excluded from the monitoring periods.

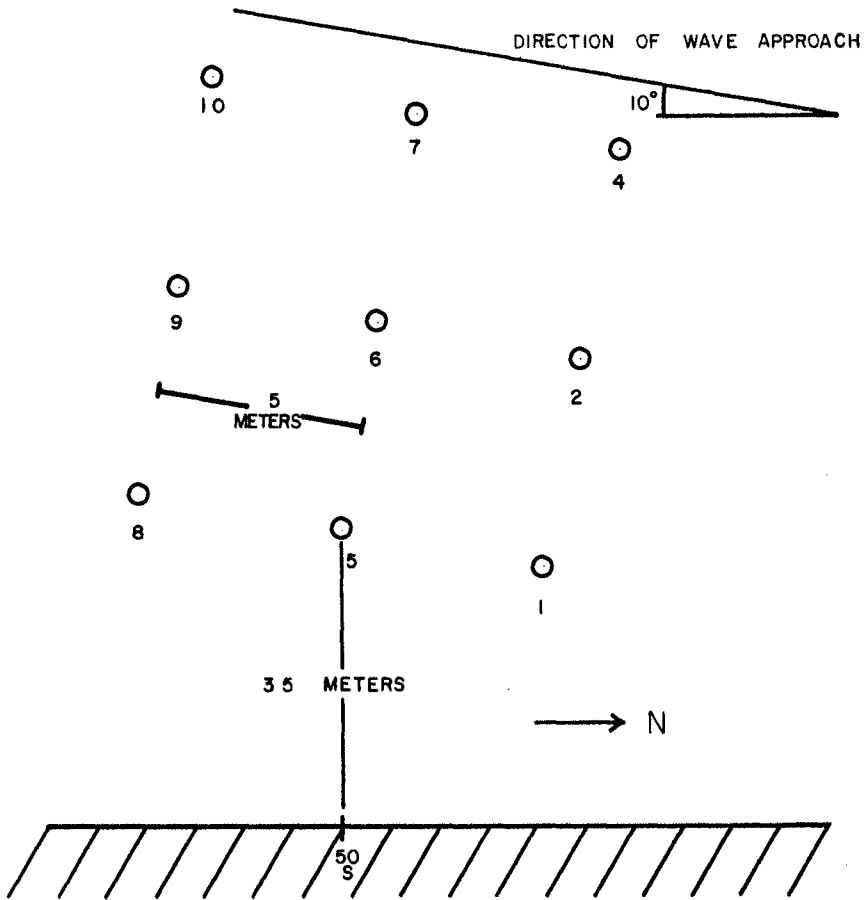


FIGURE 1. STATION CONFIGURATION FOR EXPERIMENT

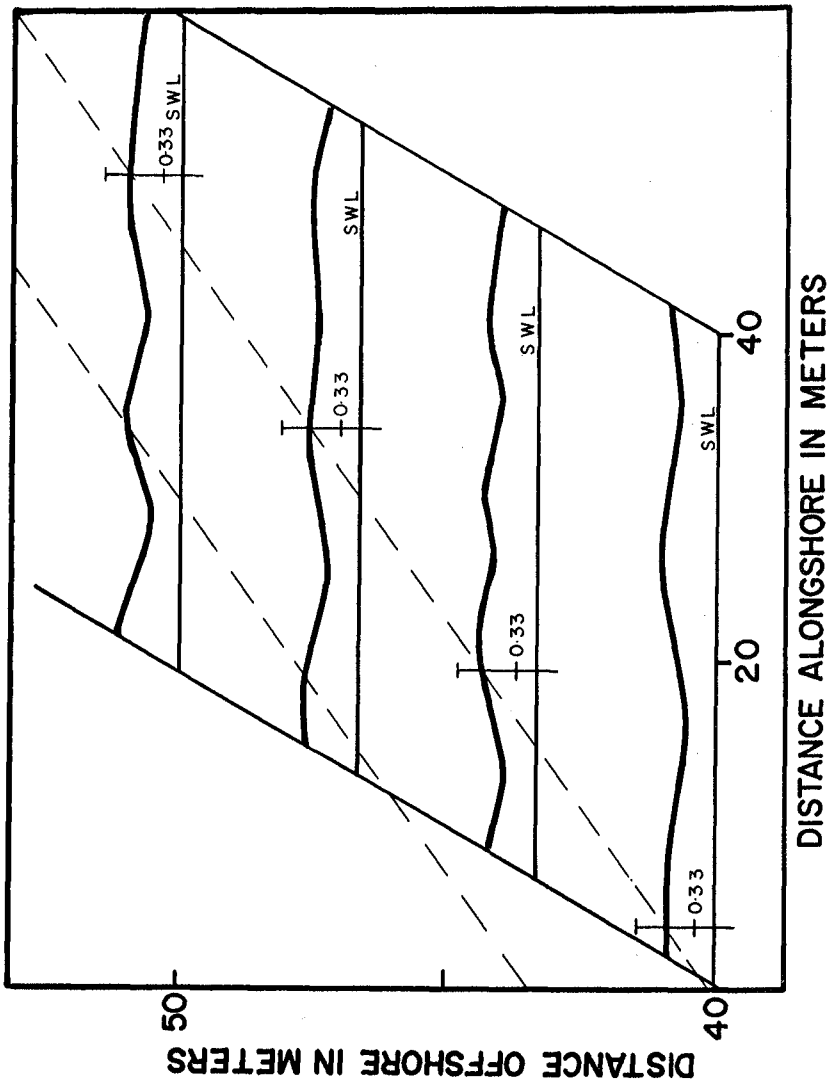
EXPERIMENTAL RESULTS

Initially the movie film records were analyzed using the in situ grid, provided by the wave monitoring stations, as a reference base. Wave height along a single crest was observed to vary noticeably over short horizontal distances. Figure 2 shows successive wave crest height profiles for a single wave from approximately five meters seaward of the breaker zone to a position where fully developed breaking is occurring along the entire crest. The primary result from these film records is that significant variation in wave crest height is observed seaward of the breaker zone and prior to the development of major instability in the wave crest.

Nine free surface time histories from each monitoring period were evaluated directly and analyzed in two separate statistical contexts. First, wave height probability distributions were generated for each of the monitoring positions from the time history data and second, wave spectra were computed from each of the time series. The use of probability distributions was extremely convenient for understanding individual crest transformations in the surf zone.

Figures 3, 4 and 5 show five successive waves, measured at three positions along the crest, at the outer, middle and inner lines of the array (see Figure 1 for station locations). This series of waves is representative of the longer time histories and clearly shows the characteristic variation in wave height along the crest. Seaward of the surf zone, variations in excess of 50 percent of the maximum wave height occur along an individual wave crest, Figure 3. The regions of high crest height, stations 10 and 4, tend to maintain the same relative relationship to the region of low crest height, station 7, for successive wave passages. Many of the wave profiles at stations 10 and 4, appear to be near breaking waves. Film records verify, however, that no local breaking has occurred at or prior to reaching these stations. As this same group of waves pass into the breaker zone the crest height variability appears to be less clearly related, Figure 4. The low wave crests seaward of the breaker zone, station 7, have amplified and are steepening towards breaking limits, station 6. High wave crests seaward of the breaker zone, stations 10 and 4, have generally decreased in height due to breaking, stations 2 and 9. The result of these two inverse processes is to create a relatively uniform crest-wise wave height distribution. Near the shoreward limit of the breaker zone, these same waves again exhibit variations in excess of 50 percent of the maximum wave height along an individual wave crest, Figure 5. In contrast to the outer stations, Figure 3, the region of high crest height, station 5, is flanked by two regions of low crest height, stations 8 and 1. This result is, however, what would be anticipated due to wave height decay through breaking, at stations 8 and 1, and continued steepening or initial breaking at station 5. Thus differential breaking seems to be a reasonable explanation for the systematic changes along the crest as an individual wave passes through the surf zone. It is not, however, a satisfactory explanation for the initial conditions observed at the seaward boundary of the surf zone.

FIGURE 2. WAVE SURFACES FROM FILM RECORDS



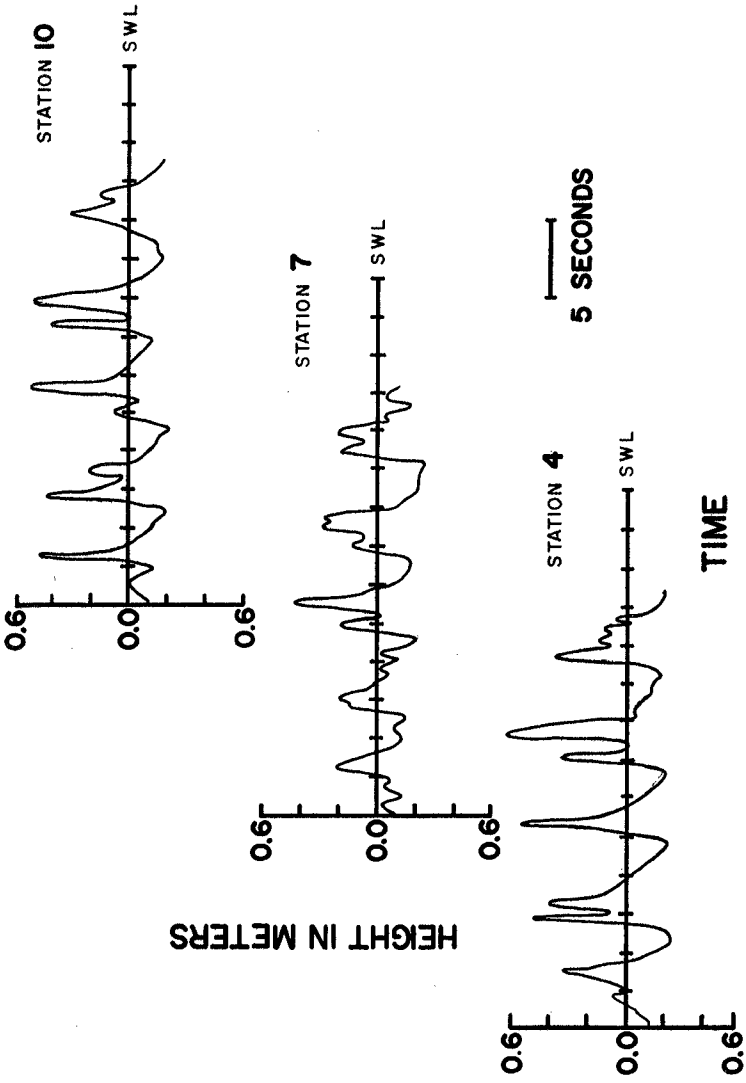


FIGURE 3. FREE SURFACE TIME HISTORIES
AT OUTER LINE OF ARRAY

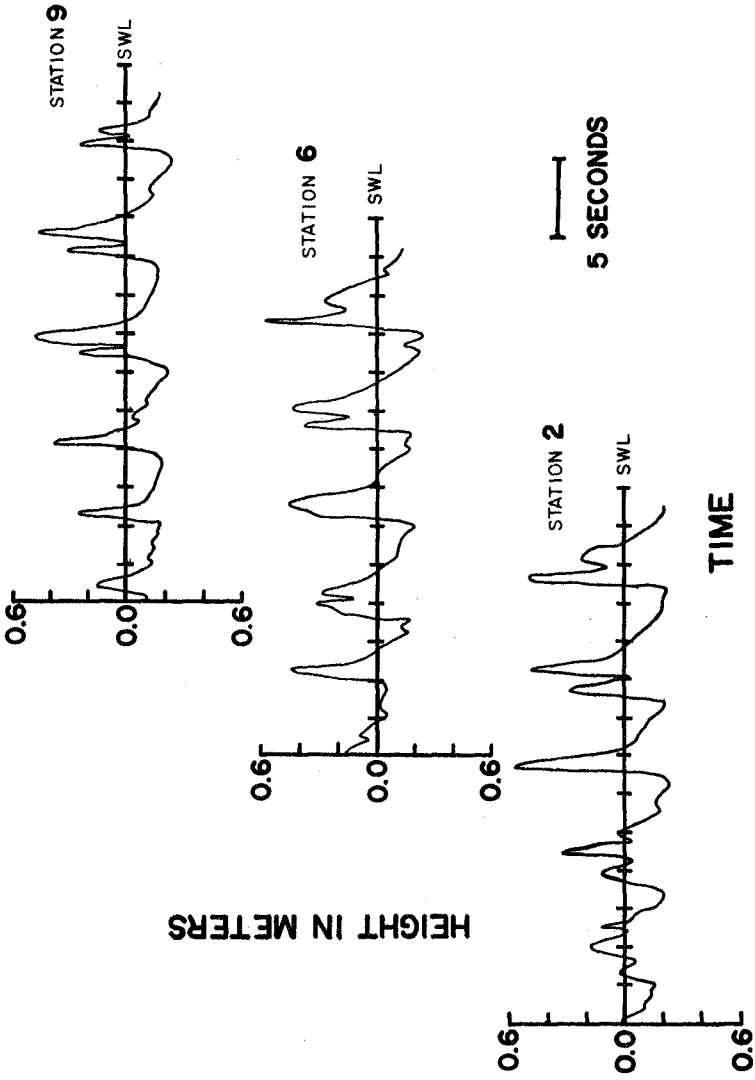


FIGURE 4. FREE SURFACE TIME HISTORIES
AT MIDDLE LINE OF ARRAY

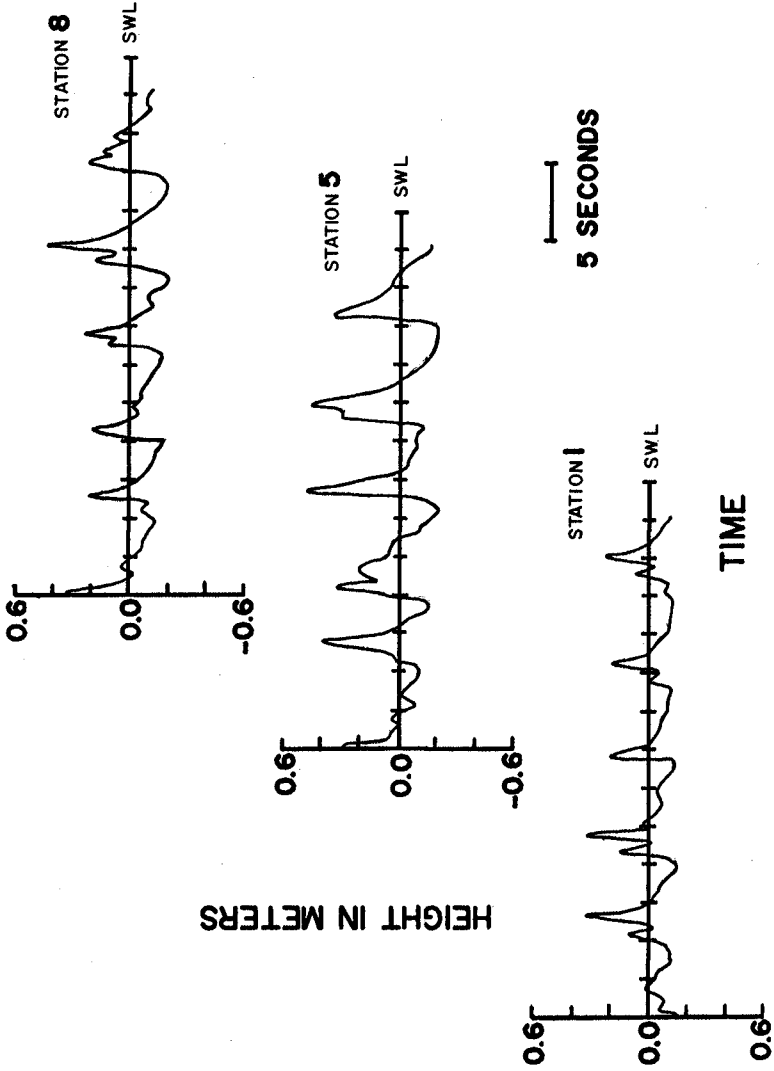


FIGURE 5. FREE SURFACE TIME HISTORIES AT INNER LINE OF ARRAY

In order to verify that the wave crest height relationships, suggested by a limited sample of individual waves, Figures 3, 4 and 5, were characteristic of the entire time series, probability distributions were computed for the entire 15 minute monitoring period (approximately 200 waves). Comparisons of the probability distributions from the outer and inner lines of the array support the relative wave height variability suggested in the analysis of individual waves. Comparison of the probability distributions at the middle line of the array are inconclusive. Although the trend of the individual distributions is consistent with the inverse process argument posed earlier.

Analysis of variance was carried out for each of the three lines of the array. The results of this analysis supported the hypothesis that significant differences exist between individual probability distributions at the outer and inner lines of the array, $F(2,600) = 5.27$, $p < 0.01$ and $F(2,600) = 10.54$, $p < 0.01$ respectively. The results of the analysis failed to support the hypothesis that significant differences exist between individual probability distributions at the middle line of the array, $F(2,600) = 4.09$ rejected at $p < 0.01$.

Spectrum analysis of the nine stations individual time series indicated two major spectral peaks common to all of the series. A 6.0 second peak corresponded to the incident swell period and a 3.3 second peak corresponded to the breaker period. A long period component ($T > 50$ seconds) was present in all of the time series from the monitoring stations seaward of the breaker zone. This component also appears in all but one of the six breaker zone time series.

DISCUSSION

Longshore variation in wave crest height is neither an unexpected nor unrecognized physical occurrence in the surf zone. Bowen (1969) showed that periodic longshore variation in wave height caused by either bottom geometry or mean water level fluctuations was responsible for the generation and spacing of rip cells. Bowen and Inman (1969) suggested that edge waves could account for longshore variations in wave height on a planer beach. Inman, Tait, and Nordstorm (1971) assert that "the interaction of edge waves with incoming waves of the same frequency produces systematic fluctuations in breaker height along the beach." Guza and Davis (1974) showed that waves incident on a planer beach can in fact generate these edge waves, but of a mode different from that of Bowen and Inman (1969). Finally, Dalrymple (1975) has shown that longshore variation in wave height can be anticipated for conditions where two wave trains of the same frequency arrive at the outer surf zone from two distinct directions.

Subsequently there are four mechanisms which can be postulated for the causation of longshore variation in wave crest height: significant longshore variation in bottom geometry $\beta/\epsilon \rightarrow 1$; interaction of edge waves with the incident wave field; interaction of long-crested swell arriving from two distinct directions; and arrival of a "short-crested" wave field generated by local storm winds. Experimental conditions during the observations from this study tend to control for the first and third postulated causations. There were, of course, two distinct frequencies present in the wave spectrum at 6.0 and 3.3 seconds which clearly indicates the presence of two wave groups. However, the direction of arrival of these wave groups appeared to be coincident and their frequency separation was quite large for significant interaction to occur.

The possibility of edge wave interaction with the incident wave field is likely. Fluctuations in the total longshore velocity field with a periodicity close to that of the zero mode edge wave have been observed under similar field conditions (Wood and Meadows, 1975, Meadows, 1976). The wave length of the longshore wave height fluctuations, from this experiment, are equivalent to the incident wave length of the breaking waves. Thus the periodicity of these fluctuations would seem to be much shorter than those calculated from edge wave theory for the observed conditions. Likewise the observed wave height fluctuations are in excess of those anticipated by edge wave theory.

The final postulated mechanism, of an incident wave field arriving with a "short-crested" structure independent of the first three mechanisms, is theoretically possible but, within the limitations of this experiment difficult to substantiate. It has long been recognized that turbulence in a wind field can result in the generation of a short-crested wave field (Jefferies, 1924). Likewise McClenan and Harris (1975) analyzed 40,000 aerial photographs of waves in shallow-water and concluded that the dominant pattern is one of short-crested waves and randomness. Notably missing between these studies is the concurrent observation of wind and wave field structure in shallow-water. The crest height wave length correspondence to incident breaking wave length and the large fluctuations in wave height along the crest do, however, present intriguing possibilities for short-crested wave structure. Clearly, the question left to be answered is whether energy is being transmitted along the crests of these waves.

CONCLUSIONS

Significant variations in wave height occur along the crest of waves incident at the outer surf zone. These variations are independent of bathymetric control and persist through the surf zone due to differential effects of shoaling and breaking. The wave length of these variations is the same as that of the incident breaking waves.

Of the four postulated mechanisms which might cause these variations only bathymetric variability seems an unlikely mechanism under these

experimental conditions. Therefore, the assumption, accepted implicitly by Meyer and Turner (1967), that longshore variability in the incident wave field is negligible whenever $\beta/\epsilon \rightarrow 0$ and the normal beach slope is moderate to steep, is incorrect. Consequently, treatment of surf zone dynamics utilizing two-dimensional shallow-water equations seems to be generally inappropriate. In fact, the full three-dimensional equations of surf (8, 9, and 10) appear to be necessary to properly represent natural surf zone dynamics.

ACKNOWLEDGMENTS

This study was supported by the Geography Programs, Office of Naval Research, through the Great Lakes Coastal Research Laboratory, Purdue University.

REFERENCES

- Bowen, A.J., Rip Currents, 1, Theoretical Investigations, Jour. Geophys. Res., 74, 5467-5478, 1969.
- Bowen, A.J. and D.L. Inman, Rip Currents, 2, Laboratory and Field Observations, Jour. Geophys. Res., 74, 5479-5490, 1969.
- Dalrymple, R.A., A Mechanism for Rip Current Generation on an Open Coast, Jour. Geophys. Res., 80, 3485-3487, 1975.
- Friedrichs, K.O., On the Derivation of the Shallow Water Theory, Commun. Pure Appl. Math., 1, 81-85, 1948.
- Guza, R.T. and R.E. Davis, Excitation of Edge Waves by Waves Incident on a Beach, Jour. Geophys. Res., 79, 1285-1291, 1974.
- Ho, D.V., R.E. Meyer, and M.C. Shen, Long Surf, Jour. Marine Res., 21, 219-232, 1963.
- Inman, D.L., R.J. Tait, and C.E. Nordstrom, Mixing in the Surf Zone, Jour. Geophys. Res., 76, 3493-3514, 1971.
- Jefferies, H., On Water Waves Near the Shore, Phil. Mag., Series 6, 48, 44-48, 1924.
- McClenan, C.M. and D.L. Harris, The use of Aerial Photography in the Study of Wave Characteristics in the Coastal Zone, Technical Memorandum, No. 48, CERC, U.S. Corps of Engineers, 72 pp., 1975.
- Meadows, G.A., Time Dependent Fluctuations in Longshore Currents, Proc. 18th Conf. Coast. Eng. (in press) 1976.
- Meyer, R.E. and A.D. Taylor, On the Equations of Surf, Jour. Geophys. Res., 68, 6443-6445, 1963.
- Meyer, R.E. and R.B. Turner, Some Three-Dimensional Effects in Surf, Jour. Geophys. Res., 72, 2513-2518, 1967.
- Stoker, J.J., Surface Waves in Water of Variable Depth, Quart. Appl. Math., 5, 1-54, 1947.
- Stoker, J.J., Water Waves, Interscience Publishers, New York, 1957.
- Wood, W.L. and G.A. Meadows, Unsteadiness in Longshore Currents, Geophys. Res. Lett., 2, 503-505, 1975.

CHAPTER 31

ENERGY SPECTRA OF IRREGULAR SURF WAVES

by

Fritz BUSCHING¹⁾

ABSTRACT

The investigations under consideration are based on synchronous measurements of waterlevel deflections $\eta(t)$ at some positions in a beach profile with a slope of approximately 1:40.

Surf conditions are studied during a severe storm surge as well as during periods of attenuating wave action.

By the use of a FOURIER ANALYZER 40 energy spectra are calculated which are also presented in integrated form (co-cumulative spectra). Because of different site arrangements it is possible to analyze the deformation of the spectra due to tide dependent changes of the water depth as well as due to coastward decreasing water depth.

It happens that there are some phenomena associated with certain frequency bands.

With the water depth decreasing the energy densities in surf spectra are distributed over a wider frequency band.

In the present case unbroken waves are characterized by energy spectra in which at least 90 % of the energy is represented by FOURIER components in the frequency range $0 \lesssim f \lesssim 0.5$ Hz. Increasing distribution of the energy densities over a wider frequency band represents at first breaking and finally broken waves. Sometimes the amount of energy coastward of the surf zone is higher than seaward of the breakers. This phenomenon can be explained by refraction effects caused by local nearshore bathymetry. All of these investigations were sponsored by the DEUTSCHE FORSCHUNGSGEMEINSCHAFT (German Research Foundation).

1) Dr.-Ing., Div. of Hydrodyn. and Coastal Engineering
Techn. Univ. Braunschweig, Federal Republic Germany

1. INTRODUCTION

As it is well known that the energy dissipation processes taking place in the surf zone cannot completely be simulated in a model (FOHRBÖTER 1970 and 1971), since 1971 comprehensive field investigations have been performed on the west coast of the isle of SYLT/North Sea, see Fig. 1. FOHRBÖTER (1974) investigated the behaviour of waves in the nearshore zone and inside the surf, presented first results on the influence of a longshore bar and on the energy decay perpendicular to the coast. Additionally he proposed a β -number for a quantitative breaker classification.

DETTE (1974) reported on longshore currents in the range of high REYNOLDS-numbers and BÜSCHING (1974) investigated the orbital velocities of irregular surf waves. Subject of the investigations under consideration are the changes in surf energy spectra due to tidal dependent and coastward decreasing water depth.

The intended structural analysis is based for the one thing on synchronous measurements of the waterlevel deflections $\eta(t)$, which were carried out during a heavy storm surge and for another on two measurements during attenuating weather conditions.

2. MEASURING EQUIPMENT AND DATA ANALYSIS

For the purpose of wave height measurements (water level deflections $\eta(t)$) pressure type wave meters working on inductive principle were attached to steel supports driven into the seabed at positions 85 m, 100 m, 120 m and 128 m distant from the shoreline. Thus the deformation of the waves in a beach profile with a slope inclined 1:40 could be analyzed.

During the storm surge of December 13th to 14th 1973, only the devices at measuring positions 85 m and 100 m functioned satisfactorily, whereas during the later measurements also records from the two more offshore situated pressure devices at 120 m and 128 m could be received.

In order to analyze the data on a FOURIER ANALYZER all the measuring signals were fed to an analog magnetic tape recorder.

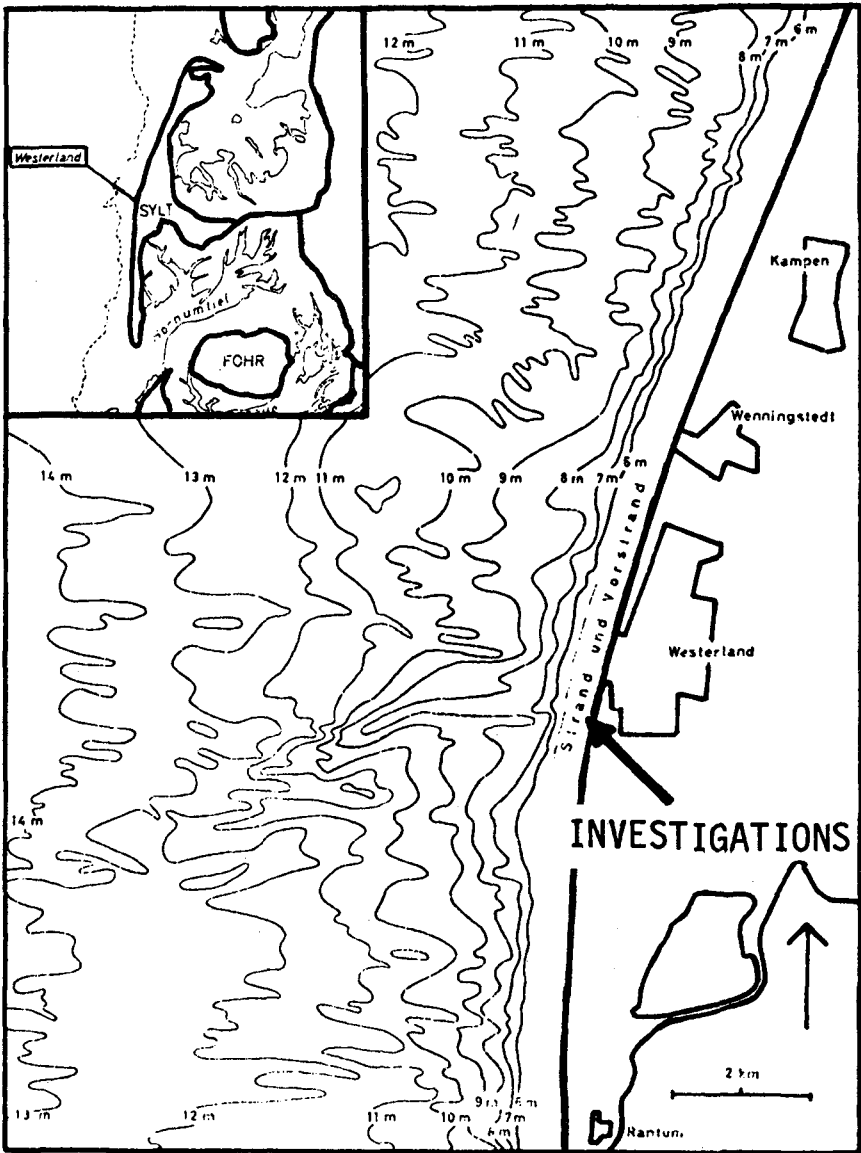


Fig. 1: Investigation area and underwater bathymetry west of the middle part of the isle of SYLT. Measured by surveying ships of DHI and WSA Kiel. After KÖSTER (1974)

The details of the measuring system are commented on by BOSCHING (1974) and FÜHRBÖTER and BOSCHING (1974).

Because of lack of space only a few things will be pointed out here:

1. For a wave analysis the maximum frequency

$$F_{\max} = F_N = \frac{1}{2 \Delta t} = 3.125 \text{ Hz}$$

is relatively high.

2. The frequency resolution is characterized by

$$\Delta f = \frac{F_{\max}}{N/2} = \frac{3.125}{256} = 0.012207 \text{ Hz and}$$

3. By averaging 10 successively calculated energy spectra, each representing $T'_R = 81.92 \text{ s}$ measuring time, the resulting time of measurement was:

$$T_R = 10 \times 81.92 = 819.2 \text{ s.}$$

Comparing spectra calculated in the same manner one can expect to recognize the fundamental changes involved. This is why it seemed not to be necessary to deal with the method of calculation itself.

3. ANALYZED MEASURING SERIES

3.1. Storm Surge of December 13th to 14th, 1973

The present storm surge data (water level deflections $\eta(t)$) had been previously analyzed by the author together with simultaneously recorded orbital velocity data.

Among others in that work an attachment of NORMALIZED ENERGY SPECTRA and surf phenomena could be established.

Contrary to that the present evaluations deal with ABSOLUTE SPECTRA taken simultaneously at measuring positions 100 m and 85 m.

During the storm surge period of about 30 hours at 16 measuring intervals samples were analyzed, see Fig. 2 and 3.

Each measuring interval is represented by 4 diagrams consisting of the energy spectra at positions 100 m and 85 m with the respective co-cumulative spectra beneath them.

In correspondence with wind and tidal dependant water level fluctuations peak energy densities (E_{fp}) occurred in the range of

$$0.87 \text{ m}^2/\text{Hz} \leq E_{fp} \leq 4.38 \text{ m}^2/\text{Hz}$$

3.2 Simultaneous measurements of January 20th and 23rd, 1974 respectively

During the period of attenuating wave activity another two measurements have been carried out, each, however, consisting of 4 spectra, as to be seen from Fig. 4 and 5.

At the farther offshore positions (at 128 m and 120 m) on January 20th a much wider peak due to higher wave activity at Bft. 6 can be seen than on January 23rd at Bft. 3 only.

On the other hand both measurements show similar values of maximum energy density:

$$E_{fp} \approx 1.1 \text{ m}^2/\text{Hz}$$

In order to attach also these spectra to the respective wave deformation the synchronously recorded wave traces of two neighbouring devices have been shifted in such a way that there exists nearly no phase difference between them and thus changes could be recognized very well, see Fig. 6 and 7.

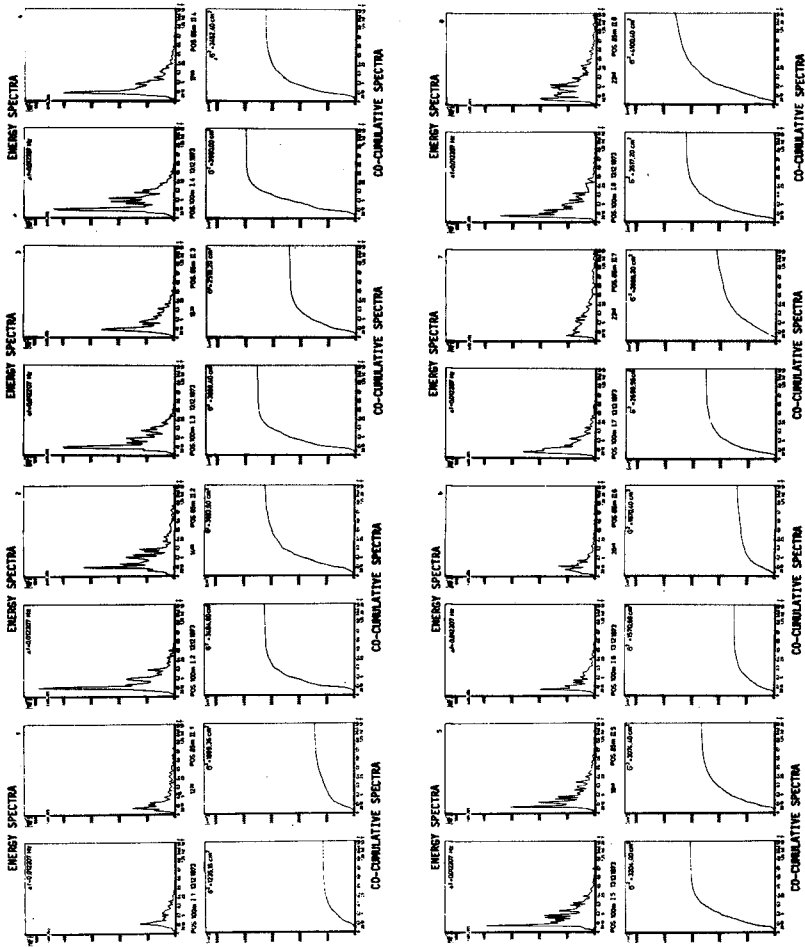


Fig. 2: Energy spectra and co-cumulative spectra at measuring positions

100 m and 85 m during the storm surge period on December 13th, 1973

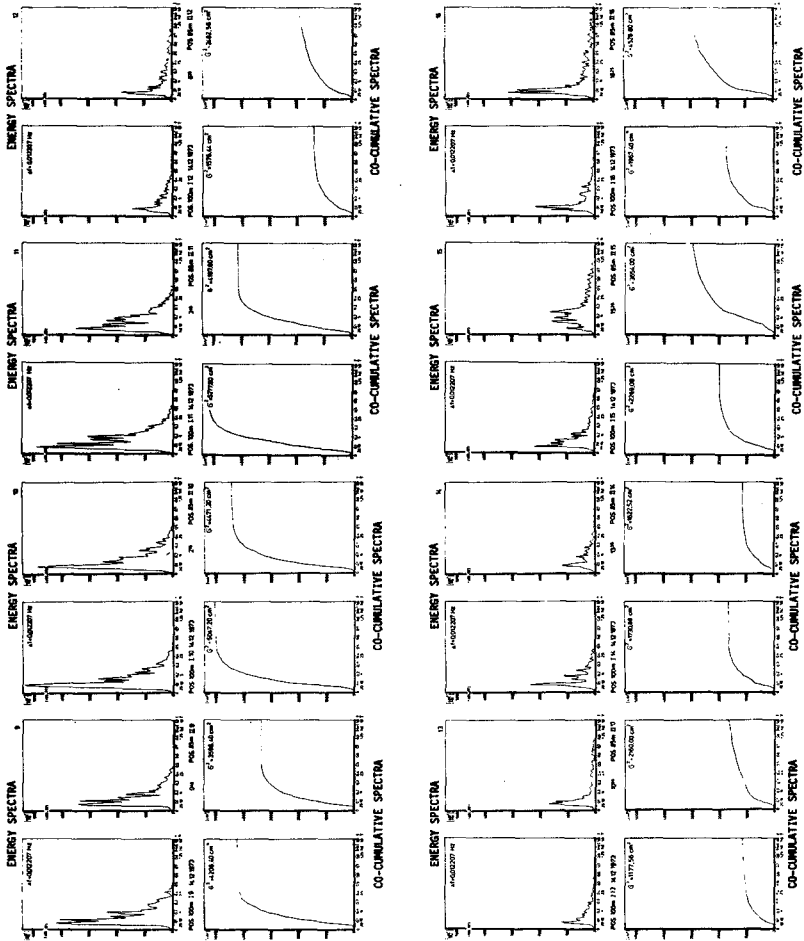


Fig. 3: Energy spectra and co-cumulative spectra at measuring positions 100 m and 85 m during the storm surge on December 14th, 1973

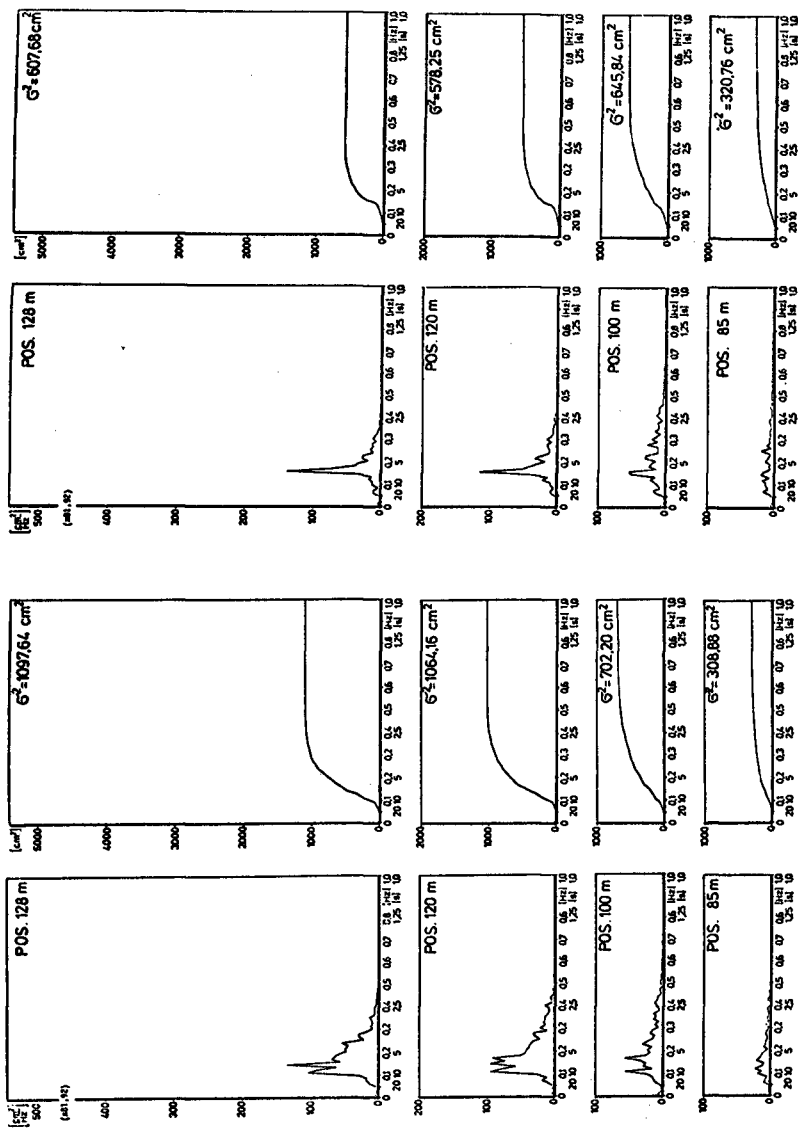


Fig. 4: Energy spectra and co-cumulative spectra on January 20th, 1974

Fig. 5: Energy spectra and co-cumulative spectra on January 23rd, 1974

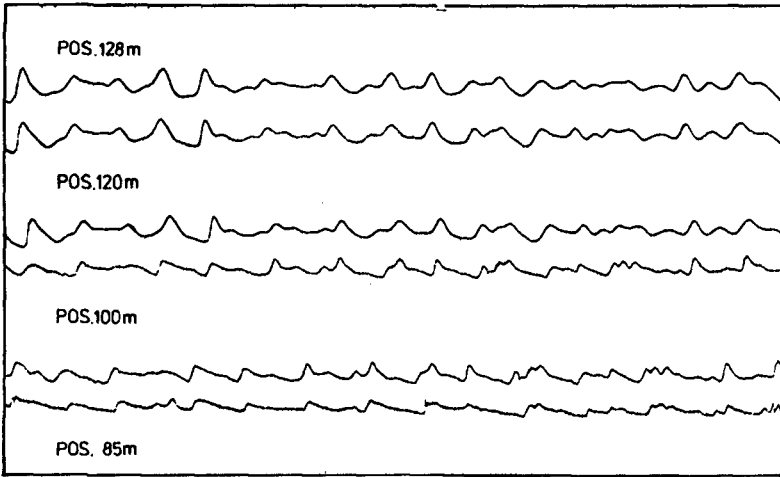


Fig. 6: Synchronous water level deflections $\eta(t)$
on January 20th, 1974, 11.44 a. m.

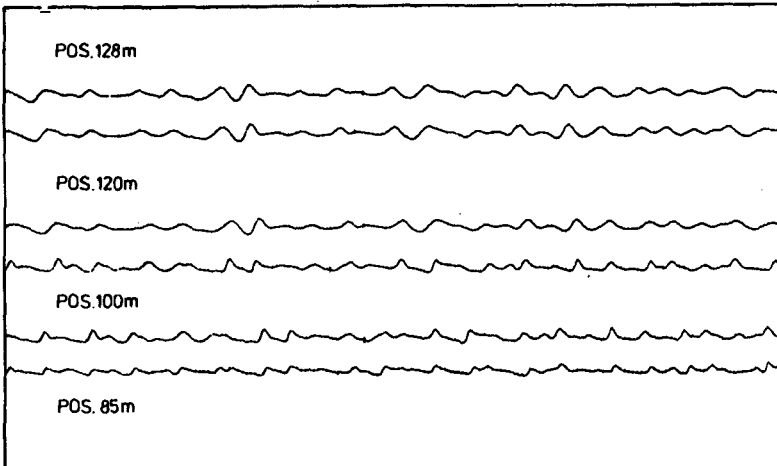


Fig. 7: Synchronous water level deflections $\eta(t)$
on January 23rd. 1974, 00.55 a. m.

Comparing those two sets of strip charts the overall impression is that on January 20th

the magnitude of water level deflections is somewhat higher,
the waves at position 128 m are steeper and
the periods at position 85 m are much larger

As regards, however, the deformation and the stability of the waves in the measuring profile, a similar behaviour can be seen for both measurements:

particularly the traces at positions 128 m and 120 m are similar to a high degree; at Pos. 120 m they are only little steeper. At Position 100 m on an average nearly breaking waves are much steeper and at position 85 m less steepness indicates broken waves.

4. THE STRUCTURE OF SURF SPECTRA

The problem of energy dissipation in limited water depth (in the ELBE estuary) was studied by SIEFERT (1974) using energy spectra. With regard to the structure of the spectra he agrees with the results of WALDEN and RUBACH (1967) and HASSELMANN and COLLINS (1968):

With the energy dissipation increasing the energy density decreases and the peak of energy density shifts to shorter periods (higher frequencies). For the swash zone SONU, PETTIGREW and FREDERICKS (1974) found the contrary to be true:

Energy spectrum variation in the upbeach direction reveals a low-pass filter effect of the beach along with an enhancement of energy density in an infragravity frequency band.

Regarding the appearances in normalised energy spectra of breakers, breaking and broken waves, from the author's previous investigations the breaker zone turned out to be a transitional area:

With the water depth decreasing on the one hand the peaks of energy densities shift to lower frequency FOURIER components and at the same time some energy densities of a certain amount appear at higher frequencies.

In order to have a closer look into the processes taking place in the surf zone in the following the absolute spectra and co-cumulative spectra are analyzed, see Figures 2, 3, 4 and 5.

In the present study evaluations are carried out only to get a better interpretation of surf spectra; conclusions regarding the amount of energy dissipation are not drawn. In order to characterize the differences between the storm surge measurements and the remaining two measurements at attenuating wave action it shall only be mentioned here that the maximum peak energy density $\max E f_p$ as well as the maximum variance $\max \sigma^2$

$$\begin{aligned} \max E f_p &= 4.3817 \text{ m}^2/\text{Hz} \text{ and} \\ \max \sigma^2 &= 0.5278 \text{ m}^2 \end{aligned}$$

both are a multiple of the respective measurements on January 20th and 23rd, 1974.

Already from the graphs of the co-cumulative spectra (see Fig. 2 and 3) one can see that there is only a percentage of the total variance present in the frequency range in between 0 and 1 Hz.

In this connexion total variances are denoted as the numerical values σ^2 calculated for the total analyzed frequency band and plotted into the upper part of the graphs.

The following 4 figures are prepared for further illustration:

In Fig. 8. the development of the variances $\sigma^2 = \int_0^{f_1} G_{nn}(f) df$ at the measuring positions 100 m and 85 m respectively are shown along with the tide curve of the investigation area. The characterizing changes shall be discussed describing the curves ①, ③ and ⑥.

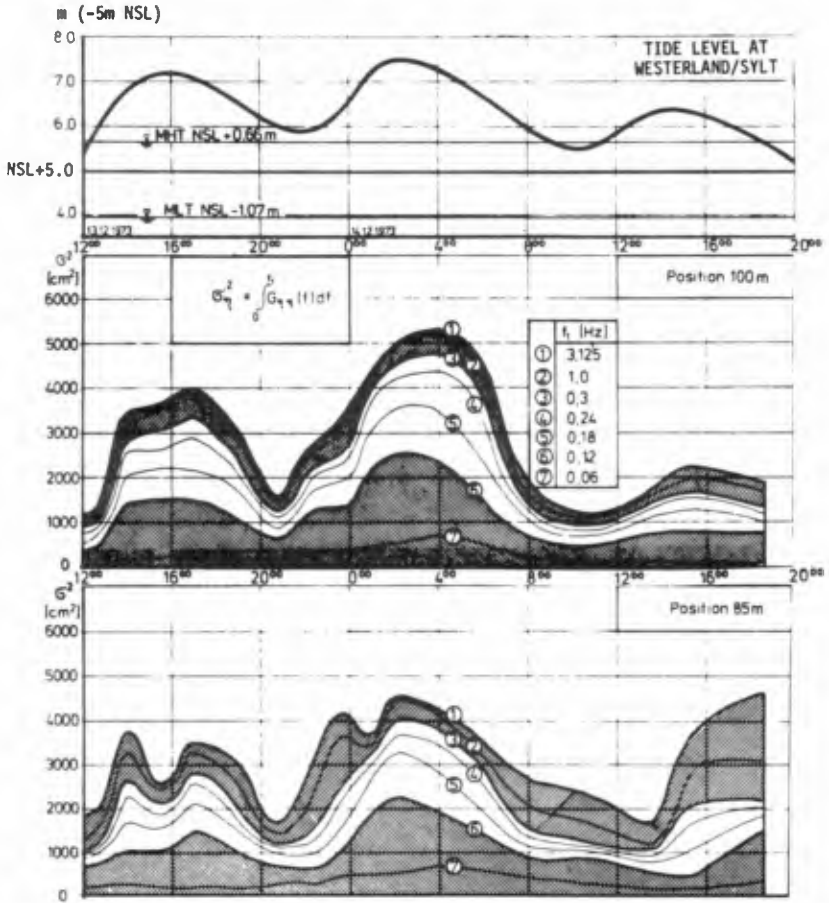


Fig. 8: Changes of the variance σ^2 during the storm surge measuring period of December 13th to 14th, 1973

- A. Frequency range $0 \leq f \leq 3.125$ Hz (Curve ①)
 Apparently the coherence between wave energy and tide level at position 85 m is less than at position 100 m:
 At 100 m distant from the shoreline high tide levels are in agreement with high wave energies whereas this is not true for the development of the variance at position 85 m where 5 maxima are to be recognized and the absolute maximum occurs at an extremely low water level at the end of the measuring period.
 Comparing curves ① at position 100 m and 85 m it is also obvious that sometimes the amount of energy nearer to the shore (i.e. at pos. 85 m) is higher.
- B. Curve ③ describes the variances of FOURIER components in between 0 and 0.3 Hz
 At position 100 m there is not a great difference to curve ① - but at position 85 m it is:
 From the areas between curves ① and ③ it can be stated that the increase of energy is predominantly due to high frequency FOURIER components at low water depth.
- C. Also the amount of energy belonging to the longperiodic Fourier components ($T > 8$ s, curve ⑥) shows good correlation to the water levels at position 100 m. This is also true for the position 85 m until 8.00 a.m. on December 14th 1973, but later on there are some changes to be recognized:
- C.1 There is a minimum of energy coincident with the third high tide level and
- C.2 just before and after this high tide level in this frequency range there are higher energies at position 85 m than at position 100 m.

In Fig. 9 some percentages of the total variances (calculated for the frequency band $0 \leq f \leq 3.125$ Hz) are shown up to 1.0 Hz. In order to illustrate the fundamental changes involved there are 3 areas limited by the 50- and 90 percentage variance isoline respectively.

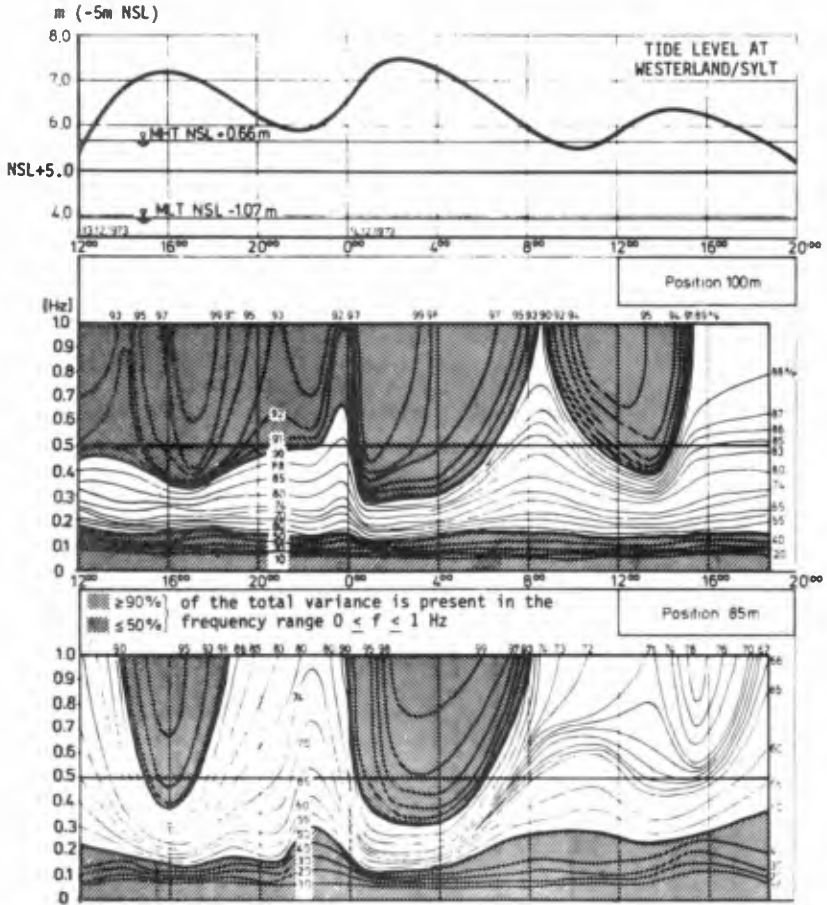


Fig. 9: Percentage variance isolines of the storm surge measuring period of December 13th to 14th, 1973

At the measuring position 100 m from the coastline the relationship between tide level and certain percentage isolines is not quite clear:

The amount of 50 % of the total energy seems to be constantly present at frequencies lower than 0.2 Hz whereas there is a fluctuation in the 90 % isoline.

At position 85 m, however, those two isolines show significant correlations to the tide levels: Exclusively at very high tide levels at least 90 % of the total energy are present at frequencies between 0 and 0.5 Hz, and in correspondence with low tide levels 50 % of the total energy require a wider frequency band, i.e. frequencies up to 0.36 Hz maximum.

The evaluations of the synchronous measurements of 4 pressure devices on January 20th and 23rd have been carried out in a similar manner. Contrary, however, to the plots of the storm surge data in Figures 10 and 11 the changes are shown as functions of the shoreline distance.

During the measurements on January 20th at position 128 m nearly the total energy (more than 99 % of $\sigma^2 = 1097.64 \text{ cm}^2$) is present in the frequency range $0 \lesssim f \lesssim 0.5 \text{ Hz}$. With the waves approaching the shore the energy continuously decreases.

On January 23rd the energy at the farthest offshore position is only about half as much but similar to the above mentioned appearances there is an increase of energy nearer to the shore (at pos. 100 m).

5. CONCLUSIONS:

In consideration of the surf phenomena detected from strip chart records of the storm surge measurements (see BOSCHING 1974) in generell it can be stated that at low tide levels the energy present in surf spectra is distributed over a wider frequency band. This statement is in accordance with

- a) the results of a theoretical investigation on the deformation of sinusoidal waves increasingly deformed (steepened) by

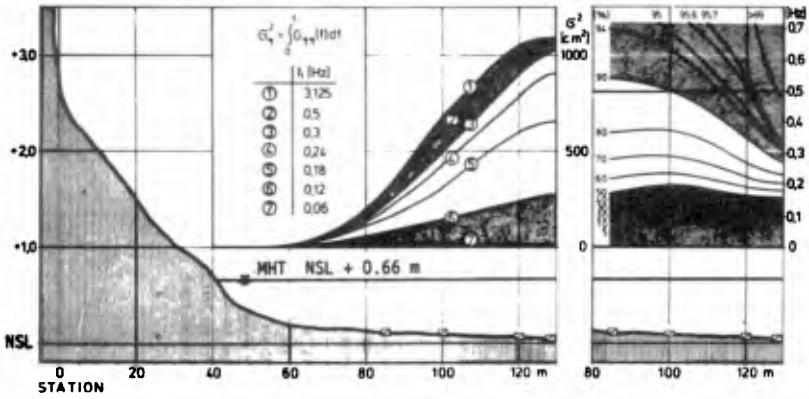


Fig. 10: Coast normal wave energy decrease on January 20th, 1974, 11.44 a.m.

Percentages of the energy present in the frequency range $0 \leq f \leq 0.78$ Hz

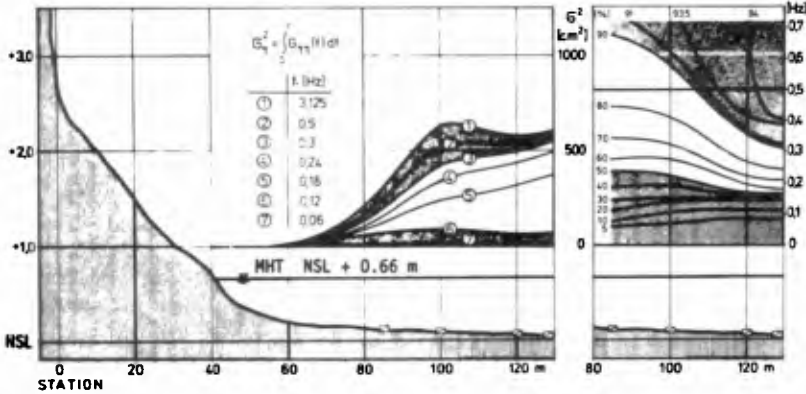


Fig. 11: Coast normal wave energy decrease on January 23rd, 1974, 00.55 a.m.

Percentages of the energy present in the frequency range $0 \leq f \leq 0.78$ Hz

decreasing water depth. SCHULEJKIN (1956) found out that the energy associated with higher harmonics increases at the expense of the fundamental oscillation.

- b) The decomposition of original waves into two or more waves (solitons) reported from wave tank investigations by GALVIN (1972).

Comparing surf energy spectra and respective strip chart records of the storm surge measurements for the present case it can be stated that unbroken waves are characterized by spectra in which at least 90 % of the energy is represented by FOURIER components in between 0 and 0.5 Hz. Increasing distribution of energy densities over a wider frequency band at first stands for breaking and finally signifies broken waves.

The statement is in accordance with the measurement on January 20th, 1974 (see Fig. 10) but for the measurement on January 23rd it demands for the instability of the waves to have occurred seaward of position 100 m (see Fig. 11). Thus it can be concluded that the interpretation of the wave deformation (see Fig. 7) has to be changed in such a way that the wave trace at position 100 m already represents breaking waves - probably spilling breakers.

As far as the energy increase in upbeach direction is concerned, it is obvious that this increase is due to Fourier components of frequencies higher than 0.3 Hz emerging at relatively low water levels. On the other hand at minimum water depth (before and after the last high tide of the storm surge measurement) there is another energy increase in the frequency range $0 \leq f \leq 0.12$ Hz (curve ⑥, Fig. 8).

Apparently this is in accordance with the shifting of peak energy densities to lower frequencies in line with coastward or tidal dependent water level decrease (see SONU et al 1974 and BÜSCHING 1974).

In the following an explanation of the temporary energy increase in the upbeach direction is presented. Fig. 1 shows the investigation area on the isle of Sylt with a bar located offshore perpendicular to the coast. Although this bar is relatively far away from the beach it can not be excluded that some phenomena result from it even on the beach:

The higher energies may be explained by refraction effects (interference) in such a manner that breaking waves are focussed on a special point in the measuring profile. The position of this point, i.e. the distance from the shoreline depends on the water depth present. This explanation is in agreement with visual observations. Frequently wave systems of little differing directions of propagation could be watched thus producing cross surf. Accordingly on January 23rd a focal point must have been near position 100 m whereas on January 20th at a higher tide level broken waves collided coastward of position 85 m and therefore could not be registered by the pressure devices.

As concerns the intensity of the interfering waves another conclusion can be drawn from the above mentioned previous study:

In Fig. 12 the resulting wave directions calculated from orbital velocity components (via transfer functions) are shown for the storm surge measurements on December 13th and 14th at position 85 m together with a levelling curve also describing the changes of the wind directions. In the study under consideration (BÜSCHING 1974) an explanation of the deviations from the mean line could not yet be given.

If, however, those deviations are compared with the fluctuation of wave energy present at position 85 m (see Fig. 8) a rather good correlation turns out until December 14th, 8.00 a.m.

As this agreement also would be significant after 8.00 a.m, if the amount of energy due to long periodic wave run up (just before and after the last high tide level) would not be considered, it might be concluded that the indicated variations of velocity directions result from the differing intensities of the contributing wave systems caused by refraction.

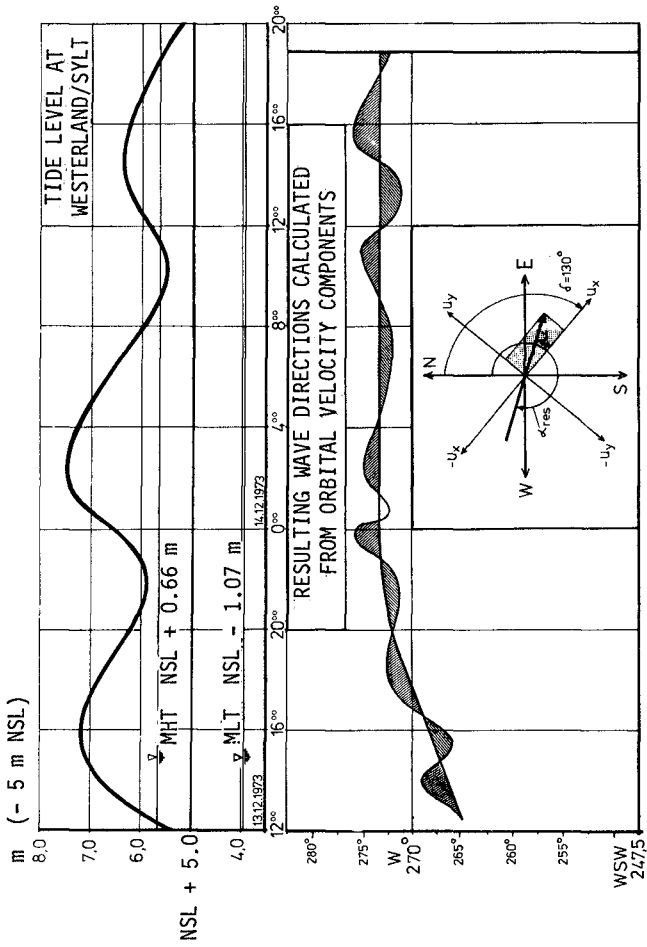


Fig. 12: Variations of horizontal orbital velocity directions during the storm surge of December 13th to 14th, 1973

6. REFERENCES

- BÜSCHING, F.
1974
Über Orbitalgeschwindigkeiten irregulärer Brandungswellen
Mitt. LEICHTWEISS-INSTITUT der Technischen Universität Braunschweig, Heft 42, 1974
- BÜSCHING, F.
1975
Über die Änderungen von Wellenperioden im Brandungsbereich
Mitt. LEICHTWEISS-INSTITUT der Technischen Universität Braunschweig, Heft 47, 1975
- DETTE, H. H.
1974
Über Brandungsströmungen im Bereich hoher REYNOLDS-Zahlen
Mitt. LEICHTWEISS-INSTITUT der Technischen Universität Braunschweig, Heft 41, 1974
- FÖHRBÖTER, A.
1970
Air Entrainment and Energy Dissipation in Breakers
Proc. XIIth Coastal Engineering Conference Washington, 1970
- FÖHRBÖTER, A.
1971
Über die Bedeutung des Lufteneinschlages für die Energieumwandlung in Brecherzonen
a) Mitt. Franzius-Institut
Technische Universität Hannover, Heft 36, 1971
b) Die Küste, Heft 21, 1971
- FÖHRBÖTER, A.
1974
Einige Ergebnisse aus Naturuntersuchungen in Brandungszonen
Mitt. LEICHTWEISS-INSTITUT der Technischen Universität Braunschweig, Heft 40, 1974
- FÖHRBÖTER, A.
BÜSCHING, F.
1974
Wave Measuring Instrumentation for Field Investigations on Breakers
OCEAN WAVE MEASURING AND ANALYSIS, Volume 1, New Orleans; USA 1974, Published by ASCE New York

- GALVIN, C.J.Jr.
1972
Wave Breaking in Shallow Water in "Waves on Beaches", edited by R. E. Meyer, Academic Press, Inc. New York and London, 1972
- HASSELMANN, K.
COLLINS, J.I.
1968
Spectral Dissipation of Finitedepth Gravity Waves Due to Turbulent Bottom Friction
Journal of Mar., Res. Vol. 26, No. 1, 1968
- KÖSTER, R.
1974
Geologie des Seegrundes vor den Nordfriesischen Inseln Sylt und Amrum
MEYNIANA 24, S. 27 - 41, Kiel, 1974
- SCHULEJKIN, W. W.
1960
Theorie der Meereswellen
Akademie-Verlag Berlin 1960
- SIEFERT, W.
1974
Über den Seegang in Flachwassergebieten
Mitt. LEICHTWEISS-INSTITUT der Technischen Universität Braunschweig, Heft 40, 1974
- SONU, C. J.
PETTIGREW, N. und
FREDERICKS, R. G.
1974
Measurement of Swash Profile and Orbital Motion on the Beach
Proc. International Symp. OCEAN WAVE MEASUREMENT AND ANALYSIS
Sept. 9 - 11, 1974, New Orleans, Louisiana, USA, 1974
- WALDEN, H.
RUBACH, H.J.
1967
Gleichzeitige Messungen mit nichtstabilisierten Beschleunigungsschreibern an Orten mit unterschiedlicher Wassertiefe in der Deutschen Bucht
Dt. Hydrogr. Zeitschrift, Bd. 20, Heft 4, 1967

CHAPTER 32

RESONANT INTERACTIONS FOR WAVES BREAKING ON A BEACH

Robert T. Guza
Assistant Professor
Scripps Institution of Oceanography, University of California
La Jolla, California 92093

Anthony J. Bowen
Professor
Dalhousie University
Halifax, Nova Scotia, Canada

ABSTRACT

A laboratory and theoretical study of the transition from strongly reflected surging to dissipative plunging breakers on a relatively steep plane beach (1:8) has revealed the following: (1) The run-up and offshore variation of sea surface elevation of surging waves are well predicted by linear theory. (2) The fluctuating part of the run-up (related to the amplitude of the reflected incident wave) reaches a maximum value; a further increase in incident progressive wave energy results in increased dissipation. (3) Subharmonic edge waves (the growing instabilities of surging waves) are driven primarily by the swash motion, which does not increase with increasing incident breaking wave height. However, the turbulence accompanying incident wave breaking, and the effective eddy viscosity, rapidly increases with increasing breaker height. As a result, subharmonic resonances do not occur with spilling or steep plunging waves; very strong viscous effects suppress the nonlinear instabilities. (4) Edge waves generated by a surging incident wave can be suppressed by superimposing an additional breaking wave of different frequency on the incident wave field. Thus, any excited edge waves are likely to have length scales at least the order of a surf zone width.

INTRODUCTION

The shoaling and breaking of a regular train of surface waves has been the subject of many extensive experimental investigations. However, the primary interest has been in waves which break by spilling or plunging and surprisingly little attention has been given to surging, or collapsing, waves. Surging occurs when the reflection from the beach is strong, and the interference between the incoming and reflected waves results in complex patterns of elevation and velocity markedly different from the essentially monotonic changes in wave height associated with spilling waves.

Surging waves, and the transition from surging to plunging, are of interest for several reasons. One is the suggestion that steady, wave-induced, bottom currents having convergences associated with either nodes or antinodes of a standing wave component, are responsible for the formation of offshore bars. However, except for the field work of Suhayda (1974) involving a complicated

spectrum of waves, there is little data to support the theoretical location of nodes and antinodes. A second motivation for a more detailed study of wave surging involves the resonant generation of edge waves. It has been shown theoretically that completely reflected, monochromatic, incident waves are unstable to edge wave perturbations (Guza and Davis, 1974; Guza and Bowen, 1975). Qualitative laboratory studies (Galvin, 1967; Guza and Inman, 1975) show that the edge waves excited by nonlinear interaction may have amplitudes at the shoreline more than twice as large as surging incident waves. However, as the incident wave amplitude is increased and the waves break by plunging, the resonance ceases and the edge waves disappear. In order to understand why the resonance ceases, it is clearly necessary to have a detailed understanding of the incident wave behavior.

Before considering the complexities which arise in three-dimensions due to edge waves, it is useful to first consider the two-dimensional case. In section II, a linear model is formulated for normally incident waves, partially reflected from a plane beach. This theoretical model is found to be in close agreement with laboratory measurements of sea surface elevation, seaward of the break point, when the coefficient of reflection, r , is greater than about 0.3. For lower reflections, that is steeper incident waves, nonlinear effects become significant.

In the experiments described in section III, the width of the wave basin is adjusted so that edge waves generation becomes possible. The two-dimensional, monochromatic, incident waves can now force edge waves at the subharmonic $\sigma/2$ of the incident wave frequency σ . Measurements show that these edge waves also have an offshore variation very close to that predicted by linear theory. The equilibrium amplitude of the edge waves was determined for various incident wave conditions, and the disappearance of the resonance with increasing incident wave amplitude was investigated in detail. Additional experiments superimposed a second wave train on a resonant situation so that the effects of a surf zone, not associated directly with the primary incident wave of the resonance, could be examined.

II. TWO-DIMENSIONAL WAVES

Linear Theory

When waves approaching the shore are reflected by a beach they propagate from water which is effectively infinitely deep, to zero depth and then back out into deep water. Although exact linear solutions for this problem are known, they are extremely cumbersome, especially for small beach slopes (Stoker, 1947). Simpler linear theories exist, but none provide a satisfactory description of the total motion even if frictional effects are neglected; different approximations apply for deep and shallow water.

Clearly, at the shoreline and for some distance offshore the appropriate approximation is provided by linear, shallow water theory. The solution for a wave, frequency σ , partially reflected from a plane beach of slope $\tan \beta$ is (Lamb, 1932; Suhayda, 1974)

$$\phi^S = \frac{a_S g}{\sigma} \left\{ J_0(x) \sin \sigma t + Y_0(x) \cos \sigma t + r \{ J_0(x) \sin(\sigma t - \theta) - Y_0(x) \cos(\sigma t - \theta) \} \right\} \quad (1)$$

where $\chi^2 = \frac{4\sigma^2 x}{g \tan^2 \beta}$, a_S is the amplitude of the incoming wave, r the reflection coefficient and θ a phase shift in the reflected wave, x is positive in the offshore direction with the shoreline at $x = 0$.

Offshore, in deeper water, the slowly varying Stokes solutions are valid, where in water depth h

$$\phi^d = \frac{a_d g \cosh k(z+h)}{\sigma \cosh kh} \left[\cos \left(\int_0^x k dx + \psi + \sigma t \right) + r \cos \left(\int_0^x k dx + \psi - \sigma t + \theta \right) \right] \quad (2)$$

provided $\sigma^2 = gk \tanh kh$, and $a_d = a_\infty (\tanh kh + kh \operatorname{sech}^2 kh)^{-1/2}$; where a_∞ is the amplitude of the incoming wave far offshore ($kh \rightarrow \infty$) and ψ is a constant.

Friedrichs (1948) showed that the shallow water limit of the Stokes solution and the offshore limit of the shallow water solution smoothly match together at intermediate depths if appropriate values of a_S and ψ are chosen. Then

$$\phi^{\lim} = \lim_{\chi \rightarrow \infty} \phi^S = \lim_{h_*^{-1} \rightarrow \infty} \phi^d = \frac{a_\infty g h_*^{-1/4}}{\sigma \sqrt{2}} \left(\cos \left(\chi - \frac{\pi}{4} + \sigma t \right) + r \cos \left(\chi - \frac{\pi}{4} - \sigma t + \theta \right) \right)$$

$$\text{where } h_* = \frac{\sigma^2 h}{g} = \frac{\sigma^2 x \tan \beta}{g} \quad (3)$$

if $a_S = a_\infty (\pi/2 \tan \beta)^{1/2}$ and $\psi = -\pi/4$. In the matching regions $\chi \gg 1$, $h_* \ll 1$, so that

$$\tan^2 \beta \ll h_* \ll 1 \quad (4)$$

For a wave totally reflected at the shore, a purely standing wave, the ratio of the wave amplitude at the shoreline to that in deep water, given by equation 3, is equivalent to the amplification factor known from the exact solution (Stoker, 1947) if the beach slope is small ($\beta \approx \tan \beta \approx \sin \beta$).

A general solution on a sloping beach, valid everywhere is given by

$$\phi = \phi^S + \phi^d - \phi^{\lim} \quad (5)$$

where if ϕ^S or ϕ^d are outside their range of validity they are cancelled by ϕ^{\lim} leaving the other as the only contribution in the relevant region. We note that the linear Stokes progressive wave solution (equation 2, $r = 0$) may be improved upon by adding a linear correction term of $O(\tan \beta)$ (Chu and Mei, 1970). This correction term smoothly matches to a higher order expansion of the shallow water Bessel function solutions (eq. 1), and it appears possible to produce a matched asymptotic solution which is an arbitrarily good approximation to the

exact linear solution. However, a comparison of the sea surface elevation given by the exact linear (Stoker, 1947) and smoothly matched solutions on a 6° slope shows insignificant differences between the two, and suggests that little is to be gained by linear improvements on equation 5. The marked profile asymmetry attributed to linear $O(\tan\beta)$ corrections by Biesel (1952) and Gaughan and Komar (1975) do not appear in the exact solution. The applicability of eq. 5 is limited because nonlinearities are neglected, and it is not likely to be a particularly good representation of the wave field right in to the break point unless r is large. The larger wave steepnesses which lead to smaller values of r produce plunging or spilling breakers whose size is generally underestimated by linear theory (Komar and Gaughan, 1972). However, the present experiments show that eqs. 1-5, are satisfactory up to breaking if $r > 0.3$, which does include part of the regime in which waves break by plunging. Figure 1 shows the normalized local sea surface displacement for a fully reflected wave ($r = 1, \theta = 0$) calculated from both the shallow water and Stokes solutions for three different beach slopes. Offshore the shallow water solution diverges from the correct solution, errors in amplitude $> 5\%$ occurring for $h_* > 0.25$. The phase of this solution diverges at even smaller values of h_* (phase errors tend to be cumulative) and on small slopes may become large where the amplitude is still well predicted. The parameter which limits the offshore validity of the shallow water solutions is $h_* = \sigma^2 h/g$, not the scale depth which actually appears in the solution $h_* \tan^2 \beta$. Consequently the shallow water solutions are valid much further seawards on beaches of gentle slope. As a rough rule, the shallow water solutions are valid for $h_* < 0.1$.

It is evident in Figure 1 that, regardless of beach slope, the linear Stokes solution will correspond very closely to the matched solution except in the immediate vicinity of the shoreline. Here, however, the discrepancy is serious; the solution has a singularity of order $h_*^{-1/2}$ and cannot provide a reasonable value for the amplitude at the shoreline in terms of deep water conditions. Higher order solutions (both linear and nonlinear) for the Stokes wave have even stronger singularities at the shoreline.

It is perhaps worth noting that although the linear shallow water and Stokes' solutions match smoothly together, their higher order, nonlinear terms do not. To provide a uniformly valid non-linear solution an additional intermediate zone governed by nonlinear equations of the Kortweg-De Vries type on a sloping beach is probably needed. Fortunately, waves which are strongly reflected are of low steepness and nonlinearities are negligible everywhere except on the beach face. Figure 2(a), discussed more fully later, shows the measured values of sea surface elevation for totally reflected waves of three different periods, which are in very good agreement with the theoretical estimation derived from the linear theory (eq. 5).

Partial Reflection

Carrier and Greenspan (1958) used the fully nonlinear, inviscid, shallow water equations to study the maximum possible size a standing wave can attain on an impermeable sloping beach. A review of their work, and of the general problem of waves on a sloping beach is given by Meyer and Taylor (1972). Carrier and Greenspan found that a standing wave solution is possible if

$$\epsilon = \frac{a_0 \sigma^2}{g \tan^2 \beta} \leq 1 \tag{6}$$

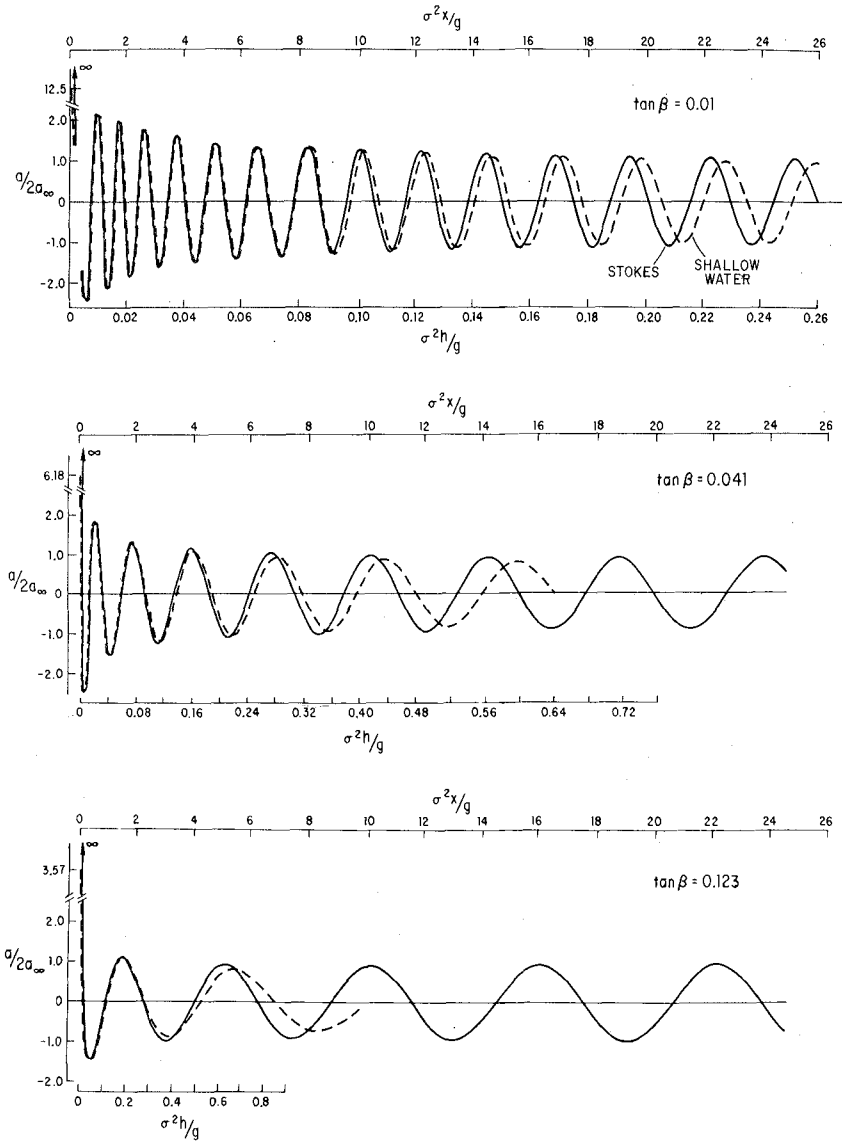


Figure 1. Theoretical local standing wave displacement (a) normalized by offshore amplitude ($2a_\infty$). Stokes solutions are valid offshore, while shallow water solutions properly describe the run-up.

where $2a_0/\tan\beta$ is the total horizontal excursion of the swash, and $a_0 = 2a_s$ (eq. 1; $r = 1.0$, $\theta = 0$) is the standing wave amplitude away from the immediate vicinity of the shoreline. Munk and Wimbush (1969), coincidentally, obtain the same limit condition (eq. 6) using linear theory. If $\epsilon = 1$, the standing wave is of maximum possible size, the nonlinearities producing considerable distortion of the wave profile; in the run-up the Fourier amplitude at frequency 2σ is theoretically about a quarter of the amplitude of the motion at σ . However, for nonbreaking waves the maximum horizontal displacement of the shoreline, $2a_0/\tan\beta$, is exactly the same as presented by the linear standing wave solution with amplitude a_0 . Thus, if the waves are nonbreaking and the effects of viscosity and percolation on the beach face are small, a measurement of the horizontal displacement of the shoreline provides an appropriate value of a_0 to compare to offshore measurements where the wave is essentially linear. Away from the immediate vicinity of the shoreline, the nonlinear shallow water standing wave does not differ appreciably from the linear solution and (3) provides the appropriate patching. The deep water condition for a standing wave which will not break at the shoreline is therefore that

$$\frac{2a_\infty \sigma^2}{g} \left(\frac{\pi}{2}\right)^{\frac{1}{2}} \tan^{-5/2} \beta \leq 1 \tag{7}$$

that is, incoming progressive waves amplitude a_∞ in deep water will be totally reflected provided (Meyer and Taylor, 1972).

$$\epsilon_i = \frac{a_\infty \sigma^2}{g} (2\pi)^{\frac{1}{2}} \tan^{-5/2} \beta \leq 1 \tag{8}$$

This result differs by a constant factor of about two from the formula of Miche (1951) which has been commonly used (Moraes, 1970; Suhayda, 1974; and others) to estimate the maximum amplitude of an incoming wave which will be totally reflected

$$\frac{a_\infty \sigma^2}{g} (2\pi)^{\frac{1}{2}} \beta^{-\frac{1}{2}} \sin^{-2} \beta \leq 2 \tag{9}$$

For small β , Miche's formula therefore implies that complete reflection may occur provided $\epsilon_i < 2$. For $\epsilon_i > 2$ Miche assumes the wave is partially reflected and that the reflection coefficient r decreases with increasing ϵ_i

$$r = \frac{2}{\epsilon_i}, \quad \epsilon_i > 2$$

Now the offshore amplitude of the wave reflected from the beach is ra_∞ so

$$\epsilon_r = \frac{2ra_\infty}{g} \left(\frac{\pi}{2}\right)^{\frac{1}{2}} \tan^{-5/2} \beta = r\epsilon_i \tag{10}$$

and the Miche hypothesis is

$$\epsilon_r = \frac{\epsilon_i}{2/\epsilon_i}; \quad \epsilon_i < 2. \tag{11}$$

Battjes (1974) has suggested a similar expression based on a shallow water parameter similar to ϵ (eq. 6). There is, however, no allowance for the $\tan^{-\frac{1}{2}}\beta$ (theoretical) amplification in shallow water (3), so Battjes deep water reflection parameter differs from (10, 11) by $\tan^{-\frac{1}{2}}\beta$

$$\epsilon_r = \frac{\epsilon_i}{0.787 \tan^{-\frac{1}{2}}\beta} ; \epsilon_i < 0.787 \tan^{-\frac{1}{2}}\beta \quad (12)$$

The formulas (11, 12) are numerically identical when $\beta = 8.8^\circ$, and both follow from the assumption that when wave breaking occurs, the wave field outside the breakpoint (or surge line) consists of an incoming progressive component plus a standing wave of the maximum possible amplitude which can occur without breaking.

Field Observations

The idea that the surf zone can be represented as the sum of a standing wave of some maximum amplitude, and an incoming progressive component which decays shoreward of the break point, suggests that the motion at the shoreline is determined primarily by the standing component and should be given by

$$\epsilon = \frac{a_0 \sigma^2}{g \tan^2 \beta} = \text{constant} = \epsilon_c$$

Therefore, if an incident wave field consists of several narrow banded components, the energy spectrum of the wave run-up (vertical)

$$E(\sigma) \approx a_0^2 = g^2 \tan^4 \beta \sigma^{-4} \epsilon_c^2 \quad (13)$$

provided the wave components behave, at lowest order, as independent (linear) waves. Although the assumption of independence seems a gross approximation with the breaking bores observed in real surf zones, field observations do seem to show a region in the run-up spectrum where the energy varies as σ^{-4} (Huntley, Guza, and Bowen, in press).

An immediate question is whether this agreement provides real support for the conceptual model of the surf zone and run-up as a simple sum of standing and progressive waves which is implicit in the formula for reflection coefficients. If so, then measurements of shoreline displacement should give the size of the standing wave component and hence the amplitude of the wave components reflected from the beach. The critical relation is then between the wave amplitude at the shoreline and the wave amplitude seen in the reflected wave outside the breakers. Clearly, a first look at this relationship will be most easily obtained in the laboratory.

Laboratory Experiments

To investigate the relevance of the various theoretical suggestions, detailed laboratory measurements were made to: (i) check the limits of applicability of the matched linear solutions (eq. 5) for fully and partially reflected waves; (ii) determine the criteria for the onset of breaking in terms of the parameters ϵ and ϵ_i ; and, (iii) to compare the behavior at the shoreline with the reflection coefficients determined from the observations offshore.

Experiments were conducted in the 15.2 m x 18.2 m wave basin at the Hydraulics Laboratory at SIO. The beach was a concrete sloping section ($\beta = 7^\circ$) extending from the shoreline end of the basin for 8.7 m, the depth being constant (65 cm) for the 5.1 m between the toe of the beach and the plunger type wavemaker. The width of the working area was adjusted so that no subharmonic edge waves could be excited by the incident waves. Incident periods of 2.39, 2.76 and 3.39 sec. were studied in detail.

Measurements of sea surface elevation were made with a sensitive resistance gauge from the beach toe to as shallow water (~ 10 cm) as the gauge design allowed. The records were either filtered to remove higher harmonics before the wave amplitude was measured or, equivalently, Fourier analyzed to obtain spectral coefficients. The offshore measurements, therefore, relate linear theory to that part of the wave field at the primary frequency. Ideally, it is possible to measure only the total wave height, and to allow for the harmonics with higher order Stokes theory (Goda and Abe, 1968; Moraes, 1970). However, in real laboratory experiments, a wavemaker producing the primary wave at σ , will in general, generate free waves at harmonics $2\sigma, 3\sigma, \dots$, even if the wavemaker motion is perfectly simple harmonic (Madsen, 1971). As the free harmonic waves and Stokes corrections are dynamically distinct, having different wavenumbers, they are affected differently by reflection and viscosity, and the total motion a 2σ may therefore be a complicated combination of standing and progressive waves of two different wavenumbers. Fortunately, the total Fourier amplitude of 2σ was generally small compared to σ , and the harmonic free waves probably had little effect on the overall wave dynamics. They may, however, provide some errors in the run-up and run-down measurements (done with a meter stick).

To eliminate as far as possible the effects of general boundary dissipation not associated with wave breaking, estimates of reflection are based on measurements of sea surface elevation made in shallow water on a rather steep beach ($\tan\beta = 0.123$). On very gentle beach slopes viscous effects will invalidate the amplification factors predicted by inviscid theory, and measurements in relatively deep water will always indicate less than complete reflection. Moraes (1970) clearly shows lower coefficients of reflection at small β for similar values of ϵ_j . We did some qualitative experiments with 1.5 sec waves on a 15 m long 2.3° beach and found (based on offshore measurements) relatively low coefficients of reflection no matter what the value of ϵ_j . This is to be expected since gentle beach slopes result in a large zone of shallow water waves with high shearing (short wavelengths, Figure 1) and dissipation.

Figure 2a shows some typical measured amplitudes of the primary frequency wave normalized by the amplitude at the shoreline, a_0 , where

$$2a_0 = R \tan\beta \tag{14}$$

and R is the horizontal displacement on the beach face. These very closely fit the theoretical profile for a completely reflected wave, as expected since $\epsilon \leq 1$. The values of a and hence ϵ_j , were computed by fitting the offshore points to eq. 5 (here $r = 1, \theta = 0$). The close correspondence between ϵ and ϵ_j shows that for completely reflected waves, the amplification at the shoreline relative to deep water, is correctly given by

$$a_0 = 2a_s = 2a_\infty \left(\frac{\pi}{2 + \tan\beta} \right)^{\frac{1}{2}} = 7.14 a_\infty \tag{15}$$

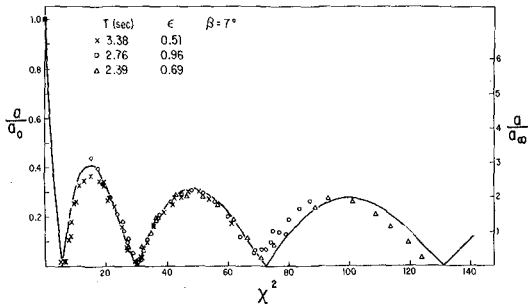


Figure 2a. Measured standing wave displacements (a) compared to linear theory (eqs. 1-5, $r = 1$, $\theta = 0$). Complete reflection occurs because $\epsilon < 1$. $\epsilon_i = 0.49, 0.99, 0.66$ for $T = 3.38, 2.76, 2.39$ sec.

This remains true and the waves are essentially completely reflected provided $\epsilon_i < 1$ as predicted by Carrier and Greenspan (1958). When $\epsilon_i > 1$ the incoming waves are partially reflected. Figure 2b shows data from several experiments where $r \approx 0.4$, the agreement between observations and linear theory is emphasized by the superposition which occurs when experiments of different wave heights and periods are properly scaled. There is some variation of ϵ_i with T for the same value of r . Figure 3 shows a series of experiments for wave period 2.39 sec. where the deep water wave amplitude is the only variable which is changing and provides the corresponding increase in ϵ_i . Generally, the results are well predicted by linear theory for $\epsilon_i < 6$. At larger values the amplitude variation with distance from the shore departs markedly from the theory both in the position and in the relative size of the antinodes outside the surf zone. It is clear that finite amplitude effects must eventually become important both directly in the solutions to the wave equations and indirectly through second order effects such as wave set-up. However, there is a suggestion in Figure 3 that the phase shift of the nodes and antinodes increases roughly as the width of the surf zone. Interactions between incident and reflected bores may also contribute to the discrepancy.

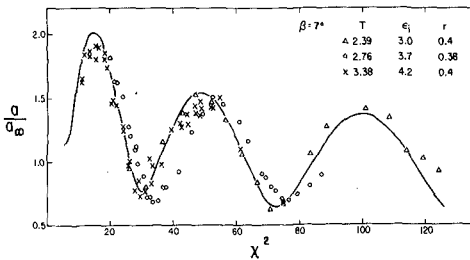


Figure 2b. Measured sea surface displacements (a) of partially reflected waves compared to theory (eqs. 1-5, $r = 0.4$, $\theta = 0$). The agreement is good right up to the break point, $X_B^2 = 10$.

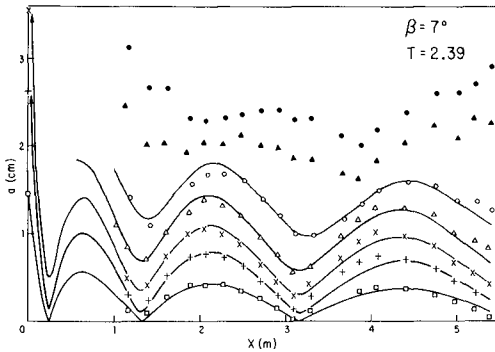


Figure 3. Measured wave displacements (a) for $T = 2.39$ sec, and various a_0, ϵ_i .

	□	+	×	△	○	▲	●
ϵ_i	0.66	1.3	2.1	3.0	4.24	6.9	8.2
r	1.0	0.8	0.55	0.4	0.26	-	-
θ	0	0	0	0	0.25	-	-

The reflected wave amplitudes are shown in Figure 4 in terms of ϵ_r , see eqs. 11-12, with $r = \epsilon_r/\epsilon_i$. The Miche reflection prediction (11) is frequently reduced by an "intrinsic" reflection factor which varies according to roughness of the reflecting surface, ~ 0.8 for smooth surfaces, the maximum ϵ_r is then 1.6. It is emphasized that although Carrier and Greenspan (1958) provides sound theoretical insight into the maximum possible amplitude completely reflected wave, there is no basic theory which predicts the variation in the reflection coefficient with increasing ϵ_i (eqs. 11-12 are essentially empirical). The experimental data (Figure 4) suggests that the offshore standing wave amplitude continues to increase with increasing ϵ_i past the range of total reflection, $\epsilon_i \approx 1$, reaching a slight maximum when $\epsilon_i \approx 2.5$. It is clear from Figure 4 that Miche's concept of a standing wave of constant amplitude provides a reasonable approximation to the data in this range of ϵ_i . However, although the wave begins to break at $\epsilon_i \approx 1$, this does not impose an immediate upper limit on the amplitude of the reflected wave and the standing wave of constant amplitude with $2 < \epsilon_i < 6$ is not the amplitude of the maximum size standing wave which can occur without breaking, $\epsilon_r \sim 1$.

The horizontal displacement at the shoreline R gives a measure of a_0 (eq. 14) and ϵ (eq. 6) as a function of ϵ_i (Figure 5). For $\epsilon_i < 1$, $\epsilon = \epsilon_i = \epsilon_r$ (Figure 2a) and the motion at the shoreline is completely explained by the excursion of the standing wave at the shoreline; for $1 < \epsilon_i < 2.5$ the swash motion continues to be appropriate for the offshore standing wave associated with the partially reflected wave. However, for $\epsilon_i > 2.5$ the motion at the shoreline (ϵ) continues to slowly increase although the reflected wave (ϵ_r) estimated from wave conditions outside the surf zone tends to decrease slightly in amplitude (Figure 4). For very large values of ϵ_i , ϵ appears to reach a maximum value of about 4 (Fig. 5). The odd ϵ_i axis on Fig. 5 (linear when $\epsilon_i \leq 10$) emphasizes the detailed studies for $\epsilon_i \leq 10$ and is intended to show qualitative behavior for larger ϵ_i . Although the measurement of run-up and particularly run-down is somewhat

subjective, these results are substantially different from those reported by Battjes (1974) where $\epsilon \approx 1.26$ is suggested as a reasonable fit to data obtained on steep beaches. However, at the same time Battjes has proposed that reflection takes place as a standing wave where

$$\epsilon_r = 0.787 \tan^{-\frac{1}{2}} \beta$$

For very steep beaches this may be small but even when $\tan \beta = 0.123$ (1:8) this requires $\epsilon_r \approx 2.3$ (Figure 4). For gentler slopes, Battjes requires ϵ_r to become large, reaching 4.0 for the 2.3° slope used for some of the data in Figure 5.

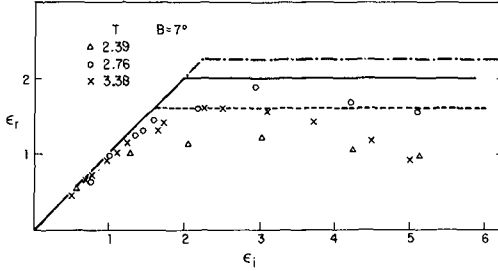


Figure 4. Nondimensional reflected wave amplitude (ϵ_r) as a function of incident wave (ϵ_i), based on data seaward of breakpoint as in Figures 2a, b.

- - - - Battjes (eq. 12)
- — — Miche (eq. 11)

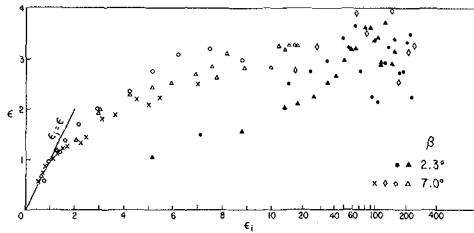


Figure 5. Swash parameter $\epsilon = a_0 \omega^2 / g \beta^2$ versus offshore incident wave parameter ϵ_i (eq. 8). Note the ϵ_i axis is linear for $\epsilon_i \leq 10$, and log for $\epsilon_i > 10$.

	▲	●	X	0	Δ	◇
T (sec)	3.06	2.48	3.38	2.76	2.39	1.00
tan β	0.04	0.04	0.123	0.123	0.123	0.123

In the present experiments ϵ and ϵ_r are very much the same size for $\epsilon_i < 3$, the run-up and down being primarily determined by a standing wave at the incoming wave frequency. For $\epsilon_i > 3$, ϵ tends to increase while ϵ_r remains steady, or slightly decreases. The ratio of the wave amplitude at the shoreline to the amplitude offshore will be effected by set-up, but other non-linear effects are probably more significant and ϵ may reflect the contributions of the various free and forced harmonic frequencies 2σ , 3σ , etc. to the swash on the beach.

III. EDGE WAVE EXCITATION

Normally incident waves strongly reflected at the shoreline are known to be unstable to perturbation by edge waves; edge waves can grow by extracting energy from the primary incident wave via a nonlinear interaction (Guza and Davis, 1974). The edge wave with the most rapid theoretical growth rate, and the experimentally observed wave, is a zero mode subharmonic having velocity potential

$$\phi^e = \frac{a_e g}{\sigma_e} e^{-k_e x} \cos k_e y \sin(\sigma_e t + \theta) \tag{16}$$

where $\sigma_e = \frac{\sigma}{2}$, and $\sigma_e^2 = g k_e \tan \beta$

Various experimenters (Galvin, 1965, 1967; Birchfield and Galvin, 1975; Guza and Inman, 1975) have qualitatively determined the final steady state edge wave amplitude as a function of incident wave parameters and beach slope. In all these experiments, the edge wave amplitude was determined through measurements of the swash. At an edge wave antinode, the run-up of the incident wave is alternately in and out of phase with the edge wave, so the difference between successive uprushes gives an approximation of the edge wave amplitude at the shoreline, a_e .

$$a_e = \frac{(R_2 - R_1) \tan \beta}{2}$$

where R_1, R_2 , are the maximum (horizontal) shoreward intrusions of successive incident wave uprushes. Thus, the existing edge wave amplitude estimates are based on measurements at the shoreline where nonlinear distortion and viscous effects may be significant. In the present experiments the edge wave amplitude is measured as a function of offshore distance and the exponential ($e^{-k_e x}$) decay verified. The offshore amplitude measurements qualitatively agree with the swash observations, especially at low amplitudes. However, when the incident waves break by plunging the swash measurements tend to give too low a value for the edge wave amplitude.

The incident wave amplitudes were also not well determined in the previous experiment; Guza and Inman (1975) measured the fluctuating part of the run-up, R , (with no edge waves present) and determined a_e as a function of ϵ . However, ϵ is not linearly related to ϵ_i , the incident wave parameter in deep water (Figure 5), so there is some ambiguity as to the amplitude of their incident waves. Galvin (1967) measured only "wave height at the toe of the beach". If reflection is significant, it matters whether the measurement is near a standing wave node or antinode. Birchfield and Galvin (1975) present

incident wave data as the "amplitude of the primary wave at the shore" but obtain values of $\epsilon \approx 9$, which is much larger than observed elsewhere; perhaps they refer to the incident wave amplitude at the break (surge) line. Here, we have taken the incident waves studied in detail in II, altered the basin width to allow edge wave excitation, regenerated the same incident waves, and measured the wave field with edge waves present.

The incident waves, periods 2.39, 2.76, and 3.39 sec. studied in II now generate subharmonic edge waves, periods 4.78, 5.52, and 6.78 sec. whose wave-numbers k_e satisfy the boundary conditions of no flow through the side walls separated by distance b ,

$$k_e = \frac{m\pi}{b}, \quad m \text{ integer} \quad (17)$$

for $m = 2, 3$, and 4 if $b = 8.8$ m. Measurements were made at various distances offshore at a longshore position corresponding to an elevation antinode of the edge wave. The wavemaker conditions were identically of those of II, so the form of the incident wave prior to edge wave growth, is known; theoretically, the incident wave may be substantially modified by the interaction with the edge wave.

The measurements of edge wave amplitude show the $e^{-k_e x}$ decay expected from (16), and hence provide a measurement of a_e , the edge wave amplitude at the shoreline. It is useful to also express a_e in a dimensionless form ϵ_e where

$$\epsilon_e = \frac{a_e \sigma_e^2}{g \tan^2 \beta} \quad (18)$$

Figure 6a shows the observed variation of ϵ_e as a function of the incident wave conditions defined by ϵ_i . The edge wave resonance disappears when $\epsilon_i > 8$ for wave period 2.39 secs. The paddle was not powerful enough to make incident waves of the longer periods large enough to suppress the resonance. The $T_i = 1.0$ sec point from Galvin (1967) is based on the amplitude at the beach tow, acceptable in this case of large ϵ_i , and minimal reflection.

Galvin's (1968) classification of breaker type is (Battjes, 1974, gives similar criterion)

$$\begin{aligned} \frac{H_o}{L_o \beta^2} < 0.09 & \quad \text{surging-collapsing} \\ 0.09 < \frac{H_o}{L_o \beta^2} < 4.8 & \quad \text{plunging} \\ 4.8 < \frac{H_o}{L_o \beta^2} & \quad \text{spilling} \end{aligned} \quad (19)$$

and when $\epsilon_i \approx 10$; $H_o/L_o \beta^2 \approx 0.44$ and the resonance ceases near the low steepness end of the plunging wave regime.

Figure 6b shows ϵ_e versus ϵ (the incident wave run-up parameter) and indicates that resonance ceased ($T_i = 2.39$) when $\epsilon \approx 3.2$. Guza and Inman (1975) present similar results for a range of periods and beach slopes, their edge wave

amplitudes are qualitative, being based on a swash measurement rather than detailed measurements offshore. Some maximum values of ϵ for which they observed resonance are shown (—a—, —b—) indicating that ϵ_{max} decreases with decreasing slope and period.

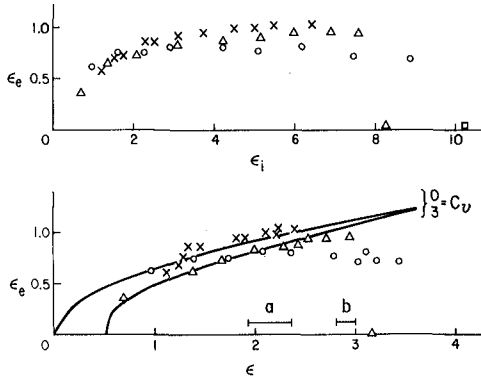


Figure 6a, b. Nondimensional edge wave amplitude ϵ_e (eq. 18) versus nondimensional incident wave offshore (ϵ_i) and swash (ϵ) parameters. Solid line is theory (eq. 21), independent of T_i for $C_v = 0$; $C_v = 3$ corresponds to $T = 2.7$ sec.

	x	0	Δ	\square	a	b
T(sec)	3.39	2.77	2.39	1.0	1.9-2.4	2.7-3.11
tan β	0.123	0.123	0.123	0.149	0.1	0.1

The theory of edge wave excitation by completely reflected incident waves is based on a weak nonlinear interaction formalism using the shallow water approximation for the incident wave (Guza and Davis, 1974; Guza and Bowen, 1976). The forcing of an initially small, zero mode, subharmonic edge wave by the incident wave results in an initial inviscid edge wave amplitude growth

$$a_e = a_e(t = 0) e^{\alpha \epsilon \sigma_i t}, \quad \alpha = \int_0^{\infty} f(x) dx = 0.0169 \quad (20)$$

where $f(x)$ is a complicated function which expresses the spatial coupling between incident and edge waves. Guza and Bowen (1976) have theoretically determined the equilibrium amplitude, based on the assumption that the incident wave is totally reflected ($\epsilon = \epsilon_i$). For a basin width and edge wave frequency satisfying (17)

$$\epsilon_e^2/\epsilon = 7.87 \left[-0.203 d^{1/2} + (2.9 \times 10^{-3} - 3.79 \times 10^{-2} d)^{1/2} \right] \quad (21)$$

where $d = \nu C_v^2 / \sigma_e a_0^2$

and viscous effects have been modeled with laminar boundary layers and an effective viscosity, ν' , where

$$\nu' = C_v^2 \nu \quad (22)$$

For clean water, smooth bottoms, etc., $C_v = 1.0$ and bottom boundary layers account for most of the damping. If ν' is some constant, independent of ϵ_e , viscous effects determine the minimum incident wave amplitude which will excite edge waves but do not limit edge wave growth if it occurs. The edge wave growth is finally curtailed by finite amplitude effects, radiation and finite amplitude detuning (Guza and Bowen, 1976). The condition that nonlinear forcing can overcome viscous damping and initiate resonant growth is

$$\epsilon > \frac{\sigma_i^2}{g\beta^2} \left(\frac{C_v^2 \nu}{\sigma_i} \right)^{\frac{1}{2}} 7.36 \quad (23)$$

Figure 6b shows a comparison between the laboratory measurements and theory (eq. 21) for $C_v = 0$ (inviscid) and $C_v = 3$; using the observed shoreline values for a_0 to calculate ϵ . The agreement is good for $\epsilon \leq 2.4$ (corresponding to $\epsilon_i \leq 5$, $H_0/L_0\beta^2 \leq 0.22$). Above $\epsilon = 2.4$ the edge waves are generally smaller than predicted, the resonance disappearing altogether at large values.

The existing theory is for totally reflected incident waves which do not break and it is not surprising that the observed edge wave amplitudes diverge from theory when the assumption of total reflection is violated. The presence of the progressive incident wave component, and the turbulence which dissipates its energy, have been neglected. We now consider these factors.

The forcing of the edge wave by the incident waves, whether standing or progressive, is expressed as an integral over the entire fluid (eq. 20). It can readily be shown, however, that most of the resonant forcing occurs quite close to shore where the edge wave is large. When only a standing wave is present, $\alpha(20)$ reaches 50% of its total value when $\chi^2 = 8.0$, and 70% when $\chi^2 = 12.8$. Now when $\epsilon_i \approx 3.5$, $r \approx 0.4$, $\epsilon \approx 1.8$, the surge line is about $\chi^2 = 10$ (Figure 2b). Therefore, when ϵ_i is so large that significant dissipation occurs, most of the edge wave forcing by the standing wave occurs inside the breakpoint, and is concentrated in the swash. Hence, ϵ determined by the value of a_0 measured at the shoreline will be assumed to give the edge wave forcing (eq. 20) by the standing component of a partially reflected incident wave. If the progressive incident wave component (whose amplitude after breaking is proportional to the depth) is superimposed on the standing wave the integral in (20) might be recalculated. This simple, surf zone model is clearly related to Miche's concept of reflection, but is probably a gross oversimplification of the actual conditions. However, because the resonant forcing tends to occur very close to the shoreline where the progressive wave vanishes the integral in (20) might be almost unaffected and it seems that the edge wave forcing is not greatly altered by the progressive wave component. The hypothesis that the edge wave forcing is determined primarily by the swash parameter (ϵ) implies that the forcing increases almost linearly with ϵ_i when $\epsilon_i \lesssim 2$, increases more slowly when $\epsilon_i > 2$, and eventually reaches a maximum corresponding to $\epsilon \approx 4$ (Figure 5).

The edge wave damping, however, might be expected to increase dramatically with increasing ϵ_i , when $\epsilon_i > 2$. Significant incident wave breaking is beginning to occur, and the associated turbulence results in an "eddy viscosity" much larger than molecular viscosity. If the edge wave dissipation increases much more rapidly than forcing, then it would be expected that there is some maximum ϵ_i for which resonance can occur; a simplistic model shows that this is indeed the case.

There is no generally accepted form for the eddy viscosity (A) in the surf zone, but the model of Battjes (1976) is certainly plausible;

$$A = Mh(D/\rho)^{1/3}$$

where D is the rate of energy dissipation of incident waves and M is a constant. For completely progressive waves

$$D_p = 0.31 \rho g^{3/2} h^{3/2} \beta \gamma^2 ; x < x_B$$

where the constant ratio between progressive wave height and water depth, $\gamma = H/h \approx 1.0$ on steep beaches. For partially reflected waves, the dissipation rate depends on the progressive component, and we take $D = D_p(1-r)^2$ where $r = 2/\epsilon_i$ (Miche's form, Figure 4). The average (across the surf zone) eddy viscosity is then

$$\bar{A} = 0.4M \left[0.31 \gamma^2 (1-r)^2 \right]^{1/3} \beta^{4/3} x_B^{1/2} (gh_b)^{1/2} \quad (24)$$

Assuming that the eddy viscosity is determined by the breaking incident waves (eq. 24), and that the edge wave damping can be modeled (albeit grossly) by replacing molecular with eddy viscosity, the average edge wave dissipation per unit longshore length is then

$$D_e = \frac{\rho a_e^2 \sigma_e^{5/2}}{2\sqrt{2} \beta^2} A^{-1/2} \int_0^{x_B} e^{-2kx} dx \quad (25)$$

The surf zone width, and hence average eddy viscosity (eq. 24) and edge wave dissipation (eq. 25), depend on ϵ_i . We take as an approximate fit to our data

$$x_B^2 = 0 \quad \epsilon_i < 2$$

$$x_B^2 = 4(\epsilon_i - 2) \quad \epsilon_i > 2$$

which results in

$$D_e = \rho a_e^2 g^2 (8\sigma_i)^{-1} (0.4M)^{1/2} (0.31\gamma^2)^{1/6} \beta^{2/3} \left(1 - \frac{2}{\epsilon_i}\right)^{1/3} (\epsilon_i - 2)^{3/4} \left[1 - e^{-(\epsilon_i - 2)/2}\right] \quad (26)$$

The condition for any subharmonic edge wave excitation is that the rate of energy input from the incident waves (eq. 20) exceed the rate of dissipation. Thus, the maximum ϵ_i which can generate edge wave occurs when (assuming $\gamma = 1$.)

$$\epsilon_i = 3.8\beta^{-1/3} (\epsilon_i - 2)^{3/4} \left[1 - e^{-(\epsilon_i - 2)/2}\right] \left(1 - \frac{2}{\epsilon_i}\right)^{1/3} M^{1/2} \quad (27)$$

Now the present observations (Figure 6) with $\beta = 0.123$ suggest the resonance ceases when $\epsilon_i \approx 3$, and $\epsilon_i \approx 10$, which implies that $M^{1/2} \approx 0.1$. Battjes (1976) has computed values of M from 20 longshore current experiments with fully

developed breakers on steep beaches and finds $0.55 < M^{\frac{1}{2}} < 1.34$. Since the edge wave dissipation rate (26) is proportional to $M^{\frac{1}{2}}$, $M^{\frac{1}{2}} \approx 0.1$ implies a dissipation rate an order of magnitude less than with fully developed surf zones, but an order of magnitude greater than laminar damping. It is possible to use the eddy viscosity model to predict ϵ as a function of ϵ_j (analogous to eq. 2, Fig. 6b) but this seems pointless in view of the unutterable crudeness of the model. The crux of the matter is that if edge wave forcing is approximately constant (or at least the same order) for breaking and non-breaking waves, then the orders of magnitude increase in viscous effects due to wave breaking effectively suppresses the resonance.

To look more closely at the idea that increased damping, rather than the changed form of the incident wave, is responsible for the absence of resonance, experiments were made in which an additional wave was superimposed on a resonant situation. Waves of period 2.76 sec of constant amplitude ($\epsilon_j = 2.16$, $\epsilon = 1.72$), strongly reflected from the beach ($r = 0.77$) generated a subharmonic resonance $\epsilon_e = 0.75$ in the absence of any further waves, in good agreement with theory (Figure 6). Waves of 1.0 sec period were then superimposed, the wave amplitude being measured in deeper water and a value of the breaker index, $H_0/L_0\beta^2$ obtained, the beach slope being 0.123. Table 1 shows the disappearance of the basic resonance, in terms of the edge wave amplitude, as the size of the 1.0 sec wave is increased. Other experiments show this to be a general result, the particular mix of incident wave frequencies and amplitude in Table 1 but one of a multitude of possibilities.

Table 1. Subharmonic edge wave amplitudes in the presence of high frequency waves of 1 sec period

$H_0/L_0\beta^2$ (T = 1 sec)	0	0.74	1.6	2.2	3.0	3.8
ϵ_e ($T_e = 5.56$ sec)	0.75	0.76	0.73	0.62	0.18	0

The question of how much incident wave breaking at other frequencies is needed to suppress a given surging wave resonance is unanswered, and presents great theoretical difficulties. However, it is clearly an important component in the problem of edge wave excitation by an incident wave spectrum. It seems likely that the most important factor will be the ratio between the width of the surf zone (regardless of which breaking waves introduce the turbulence) and the offshore length scale of the edge wave. The instabilities of relatively very long surging waves will be unaffected by very short breakers, where the surf zone, and hence band of increased viscosity associated with the chop is of small extent relative to the incident surging wave and excited edge wave wavelengths. Field situations with offshore breaker bars, and a shoreward zone of reformed potential waves present an even complex problem. Very short edge waves will not "feel" the offshore turbulence!

IV CONCLUSIONS

The model of a surf zone as a simple combination of a standing wave of fixed amplitude plus a progressive wave (decaying shorewards from the breakpoint) seems to provide an accurate representation of the sea surface elevations and run-up for large reflectivities ($r > 0.3$).

The nondimensional amplitude of the standing wave is not, however, determined completely by the condition of the onset of breaking, correctly

predicted by $\epsilon = 1$, but continues to increase to a value of about 1.6 (Figure 4). This agrees quite well with Miche's (1951) empirical suggestion. As the incoming wave height increases, finite amplitude effects seem to complicate the general picture and the relationship between the swash motion ϵ and ϵ_r the reflected wave becomes less clear.

The generation of subharmonic edge waves is known to be dependent on the breaker characteristics, the resonance disappearing when the incoming wave breaks cleanly (Galvin, 1965). Simple calculations suggest that the change is due to an increase in damping and not an alteration in the forcing itself, which seems primarily associated with the standing component of the incoming wave field. Experiments in which a surf zone is generated by a wave unconnected with the resonance, while the forcing remains constant, further supports the idea that the resonance is suppressed by the increase in the effective viscosity of the nearshore region.

This has substantial implications for the existence of any edge waves in surf. To exist at all they must be strongly forced and are most likely to survive if their offshore length scales are large in comparison to the width of the surf zone.

Acknowledgements

The laboratory study would not have been possible without the cooperation of Douglas L. Inman, Reinhard E. Flick and John Powell. Financial support was provided by a National Science Foundation Grant (Robert T. Guza), a Killam Foundation Research Professorship (Anthony J. Bowen), and by the Office of Naval Research under contract N00014-75-C-0300.

References

- Battjes, J. A., 1974, "Surf similarity", Proc. 14th Conf. on Coastal Eng., Amer. Soc. Civil Eng., p 466-88.
- Battjes, J. A., in press, 1976, "A Turbulence model for the surf zone", Proc. 15th Conf. on Coastal Eng., Amer. Soc. Civil Eng.
- Biesel, F., 1952, "Study of wave propagation in water of gradually varying depth", Gravity Waves, Nat. Bur. Stand. U. S. Circ., 521, p 243-53.
- Birchfield, G. E. and C. J. Galvin, 1975, "Generation of edge waves through nonlinear subharmonic resonance", Geol. Soc. Amer. Mem., 142, p 151-61.
- Carrier, G. F. and H. P. Greenspan, 1958, "Water waves of finite amplitude on a sloping beach", Jour. Fluid Mech., vol 4, p 97-109.
- Chu, V. H. and C. C. Mei, 1970, "On slowly varying Stokes Waves", Jour. Fluid Mech. vol 41, no 4, p 873-87.
- Fredrichs, K. O., Commus. Proc. Apl. Maths. vol 1, p 109, 1948.
- Galvin, C. J., 1968, "Breaker type classification on three laboratory beaches", Jour. Geophys. Res., vol 73, p 3651-59.

- Galvin, C. J., 1967, "Subharmonic resonance of edge waves", U. S. Army Corps of Eng., Coastal Eng. Res. Center, unpublished manuscript.
- Galvin, C. J., 1965, "Resonant edge waves on laboratory beaches" (Abstract) EOS Trans. Amer. Geophys. Union, vol 46, p 112.
- Galvin, C. J., 1972, "Waves breaking in shallow water", in Waves on Beaches (Ed) R. E. Meyer, p 413-56, Academic Press, New York.
- Gaughan, M. K. and P. D. Komar, 1975, "The theory of wave propagation in water of gradually varying depth and the prediction of breaker type and height", Jour. Geophys. Res., vol 80, no 21, p 2991-6.
- Goda, Y. and Y. Abe., 1968, "Apparent coefficient of partial reflection of finite amplitude waves", Report Port and Harbor Res. Inst., Amer. Soc. Civil Eng., vol 7, no 3, p 3-58.
- Guza, R. T. and R. E. Davis, 1974, "Excitation of edge waves by waves incident on a beach", Jour. Geophys. Res., vol 79, no 9, p 1285-91.
- Guza, R. T. and D. L. Inman, 1975, "Edge waves and beach cusps", Jour. Geophys. Res., vol 80, p 2997-3012.
- Guza, R. T. and A. J. Bowen, 1975, "The resonant instabilities of long waves obliquely incident on a beach", Jour. Geophys. Res., vol 80, p 4529-34.
- Guza, R. T. and A. J. Bowen, 1976, "Finite amplitude edge waves", Jour. Mar. Res., vol 34, no 1, p 268-93.
- Huntley, D. A., R. T. Guza and A. J. Bowen, in press, "A universal form for shoreline run-up spectra".
- Komar, P. D. and M. K. Gaughan, 1972, "Airy wave theory and breaker height prediction", Proc. 13th Int. Conf. on Coastal Eng., Amer. Soc. Civil Eng., p 405-18.
- Lamb, H., 1932, Hydrodynamics, Sixth Ed., Dover Publications, New York, 738 pp.
- Madsen, O. S., 1971, "On the generation of long waves", Jour. Geophys. Res., vol 76, p 8672-83.
- Meyer, R. E. and A. D. Taylor, 1972, "Run-up on beaches", in Waves on Beaches, (ed) R. E. Meyer, p 357-411, Academic Press, New York.
- Miche, M., 1951, "Le pouvoir reflechissant des ouvrages maritimes exposes a l'action de la houle", Ann. Ponts. Chaussees, vol 121, p 285-319.
- Moraes, Carlos de Campos, 1970, "Experiments of wave reflection on impermeable slopes", Proc. 12th Conf. on Coastal Eng., Amer. Soc. Civil Eng., p 509-21.
- Munk, W. H. and M. Wimbush, 1969, "A rule of thumb for wave breaking over sloping beaches", Oceanology, vol 9, p 56-59.

- Stoker, J. J., 1947, "Surface waves in water of variable depth", Quart. Appl. Math., vol 5, no 1, p 1-54.
- Suhayda, J. N., 1974, "Standing waves on beaches", Jour. Geophys. Res., vol 72, p 3065-71.

CHAPTER 33

Wave Spectrum of Breaking Wave

Toru Sawaragi

Professor of Civil Engineering
Osaka University, Suita, Osaka, Japan

and

Koichiro Iwata

Assistant Professor of Civil Engineering
Osaka University, Suita, Osaka, Japan

ABSTRACT

By wave breaking, an incident monochromatic wave is transformed to a wave composed of its harmonic frequency waves inside a surf zone.

Based on a dimensional consideration, the "-1 power law", the "-2 power law", the "-2/3 power law" and the "-1/2 power law" on the wave height spectrum, $H(f)$, are derived as sorts of equilibrium spectra.

These spectra except "-1/2 power law" are shown to agree with experimental data.

1. INTRODUCTION

The authors¹⁾ already revealed that 25% - 40% of total wave energy was dissipated due to a bottom shear friction and a horizontal roller formed by a plunging breaker in a surf zone.

Therefore, the turbulence with air entrainment will be thought to play an important role in the wave energy dissipation. It is necessary to measure an accurate time-history of water particle velocity in order to clarify the characteristics of turbulence, but, it will be impossible by lack of precise measuring instruments.

Since a wave profile is thought to be an expression of turbulence after breaking, it will be expected that some features of turbulence can be deduced by analysing wave surface profiles.

Inside the surf zone, as the authors already clarified¹⁾, an incident monochromatic wave is transformed to a complicated breaking wave composed of higher frequency component waves due to non-linearity of breaking phenomenon, and dissipates its excess energy which can not be kept for wave motion. Therefore, the wave will be considered to reach some critical state for maintaining the wave motion. In this critical state, there will exist some sorts of critical conditions for wave height distributions of component waves. With this situation, dimensional consideration is an efficient tool for deriving wave height spectral characteristics.

2. DIMENSIONAL ANALYSIS

The physical quantities to be considered in the dimensional analysis of

wave height spectrum, $H(f)$ are gravitational acceleration g , wave frequency f , still water depth h , density of water with air entrainment ρ^* , molecular viscosity of water with air entrainment μ^* , and surface tension K as shown in Eq.(1),

$$H(f) = f (g , f , h , \rho^* , \mu^* , K) . \quad \text{-----(1)}$$

As the significance of these parameters changes according to four kinds of frequency range such as one of shallow water waves, deep water waves, capillary ripple waves and the frequency range in which viscosity is predominant, important physical parameters must be selected to fit the physical situation.

Firstly, attention is paid to the wave frequency range associated with shallow gravity waves which satisfies the relation of $f < f_1$, in which f_1 is given by Eq.(2) deduced from Eq.(3),

$$f_1 = \sqrt{g / 4\pi h} \quad , \quad \text{-----(2)}$$

$$h/L_0 = 0.50 \quad , \quad \text{-----(3)}$$

where, L_0 is a wave length of deep water wave. In this case, the influence of surface tension K is unimportant. Furthermore, the direct effect of ρ^* and μ^* is manifest in wave damping, and under the condition with which we are concerned, these two factors may be the second order terms and may be included in the non-dimensional coefficient of wave height spectrum. Therefore, in this region, three quantities such as g , f , and h are predominant physical factors, and wave height spectrum $H(f)$ has a dimension $[L]$, so that the following wave height spectrum is considered:

$$\begin{aligned} H(f) &= f (g , f , h , \underbrace{\rho^*}_{\text{first order}} , \underbrace{\mu^*}_{\text{second order}}) , \\ &= G_1 (\sqrt{gh^3} / (\mu^* / \rho^*)) \cdot g^{1/2} \cdot h^{1/2} \cdot f^{-1} , \\ &\propto g^{1/2} \cdot h^{1/2} \cdot f^{-1} , \quad \text{-----(4)} \\ &\quad \text{for } f < f_1 (= \sqrt{g/4\pi h}) . \end{aligned}$$

(5)² Next, consider the frequency range of $f_1 < f < f_c$, where f_c is given by Eq.

$$f_c = \frac{1}{2\pi} \sqrt{\frac{\rho^* g}{K}} . \quad \text{-----(5)}$$

This frequency range corresponds to those of deep gravity waves and surface tension K is unimportant as the previous case. ρ^* and μ^* are treated by combining with h as the second order terms, then the predominant physical factors are g and f . Therefore, the following wave height spectrum is considered:

$$\begin{aligned}
 H(f) &= f(g , f , \{ \mu^* , \mathcal{S}^* , h \}) , \\
 &= G_2(\sqrt{gh^3} / (\mu^* / \mathcal{S}^*)) g \cdot f^{-2} \\
 &\propto g \cdot f^{-2} , \quad \text{-----(6)} \\
 &\quad \text{for } f_1 < f < f_c .
 \end{aligned}$$

In deep gravity waves, Michell³⁾ gave the critical wave steepness as a breaking condition as shown in Eq.(7):

$$(H/L)_b = 0.142 . \quad \text{-----(7)}$$

By using the relation of $L=(g/270)f^{-2}$, the critical wave height $H(f)$ is given as follow:

$$H(f) = 0.0226gf^{-2} . \quad \text{-----(8)}$$

Comparing Eq.(6) with Eq.(8), the physical meaning of the dimensional analysis is clear and it may be pointed out that the wave height distribution is limited so as to satisfy a sort of critical wave steepness.

As mentioned above, for a frequency range in which a restoring force is gravitational acceleration, the wave height spectrum $H(f)$ consists of Eq.(4) and Eq.(6). By combining Eq.(4) and Eq.(6), the following expression may be possible:

$$\begin{aligned}
 H(f) &= G^* (\sqrt{gh^3} / (\mu^* / \mathcal{S}^*)) gf^{-2} (\tanh(2\mathcal{X}hf^2/g))^{1/2} , \\
 &\propto gf^{-2} (\tanh(2\mathcal{Z}hf^2/g))^{1/2} , \quad \text{-----(9)} \\
 &\quad \text{for } f < f_c .
 \end{aligned}$$

For a frequency range of $f < f_1$, the relation of $(\tanh(2\mathcal{X}hf^2/g))^{1/2} \approx (2\mathcal{X}hf^2/g)^{1/2}$ is established, and then, $H(f) \propto \sqrt{gh}f^{-1}$ is easily deduced.

Secondly, aiming at the wave frequency ($f_c < f < f_k$) associated with capillary ripples, the influence of gravitational acceleration is ignored, where, f_c is given by Eq.(5), and f_k is the highest frequency for which the surface tension is predominant. In this case, three factors such as f , K , \mathcal{S}^* are very important physical factors and then the following wave height spectrum is considered:

$$\begin{aligned}
 H(f) &= f_3(f , \mathcal{S}^* , K) , \\
 &= G_3 k^{1/3} \mathcal{S}^{*1/3} f^{-2/3} , \\
 &\propto K^{1/3} \mathcal{S}^{*1/3} f^{-2/3} , \quad \text{-----(10)} \\
 &\quad \text{for } f_c < f < f_k ,
 \end{aligned}$$

where, G_3 is a non-dimensional coefficient.

Lastly, treat the very high frequency region ($f > f_k$) in which viscosity of water is only predominant. In this case, we can select only three factors such as f , \mathcal{S}^* and μ^* as predominant physical factors. Therefore, the wave height spectrum given by Eq.(11) is considered,

$$\begin{aligned}
 H(f) &= f_4 (f, \mathcal{S}^*, \mu^*), \\
 &= G_4 \cdot \mu^{*1/2} \mathcal{S}^{*-1/2} f^{-1/2} , \\
 &\propto (\mu^*/\mathcal{S}^*)^{1/2} \cdot f^{-1/2} , \text{----- (11)}
 \end{aligned}$$

for $f > f_k$.

By summarising the above-mentioned wave height spectra given by Eqs.(4), (6),(10) and(11), a wave height spectrum inside the surf zone may be expressed as shown in Fig.-1.

From Fig.-1, it is easily understood that "-1power law", "- 2 power law", "-2/3 power law" and "-1/2 power law" are established in turn as the frequency f increases in the wave height spectrum. The coefficients, G_1, G_2, G_3, G_4 express the levels of wave height spectrum and their features must be examined by various kinds of experiment.

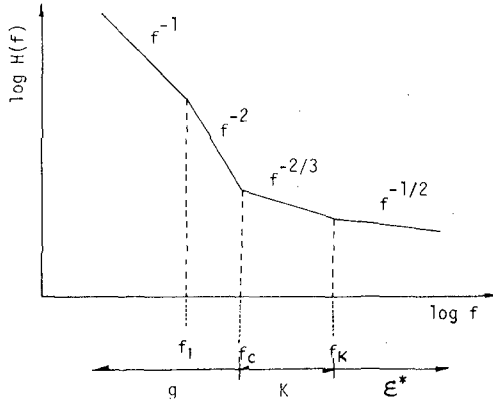


Fig.-1. Schematic view of wave height spectrum.

3 EXPERIMENTAL STUDY

1. Equipment and Procedures

Experiments were conducted to examine the characteristics of wave height spectra predicted by the dimensional analysis. In the experiments, an out-door wave tank in 0.65 m width, 0.95 m height, and 50 m length was used. At one end of the wave tank was installed a plunger-type wave generator and waves were able to be generated in different periods and amplitudes. At the other end of the tank, four kinds of beach slopes such as 1/15, 1/25, 1/40 and a composite slope consisting of an approach ramp with 1/12 slope leading up to a horizontal surface, were installed. Experimental conditions are shown in Table-1.

Wave profiles measured by a resistance-type wave gauge were recorded on magnetic tapes with 60 sec. periods and the data were sampled at each 1/50 sec. interval. Fourier analysis was carried out by FFT method.

For each experimental run, by using a high speed cine-camera (100~200 frames/sec.), a breaking region was filmed through a grid on glass walls at the channel with the camera axis kept at a still water level. From these films, breaking points, breaking depths, domains of existence of horizontal rollers and the regions of air entrainment in breakers were decided.

2. Results and Discussion

Fig.-2 shows a change of wave height spectrum during wave propagation in the horizontal bed. In Fig.-2, the upper figure shows the characteristics of an incident wave, middle two figures are wave height spectra at a breaking point and at $X/L=1.07$ inside the surf zone, and the bottom figure shows the wave height spectrum of a reformed wave after passing through the surf zone. At the breaking point, the wave is composed of high frequency waves against the monocromatic frequency of an incident wave, and harmonic frequency component waves of an incident wave frequency are predominant. Inside the surf zone ($0 < X/L < 1.30$), wave heights of the harmonic frequency waves grow larger than those of the incident wave and the reformed wave after passing through the surf zone. The reformed wave has no higher frequency component wave differing from waves inside the surf zone.

The fact that an incident periodic wave is transformed to a wave composed of its harmonic high frequency waves, shows the remarkable feature of breaking waves. Since wave breaking is non-linear phenomenon, waves in high harmonic frequency will grow due to non-linear terms of the wave motion. But, the effect of non-linear interaction among component waves may be small, because predominant periods of the component waves after breaking are, as mentioned above, harmonic periods of an incident wave period.

Now, consider the relation between a measured height H_{ex} , and its Fourier component wave heights. The equivalent wave heights H_{eq} , calculated by Eq.(11) obtained with the Parceval theorem have good agreement with the measured wave height H_{ex} , as shown in Fig.-3. This shows that the measured wave can be treated as the sum of its Fourier component waves as follows:

$$H_{eq} = \left(\sum_{j=1}^{\infty} H_j^2 \right)^{1/2}, \quad \text{-----(11)}$$

where, $j=1 \sim \infty$ indicates Fourier component waves.

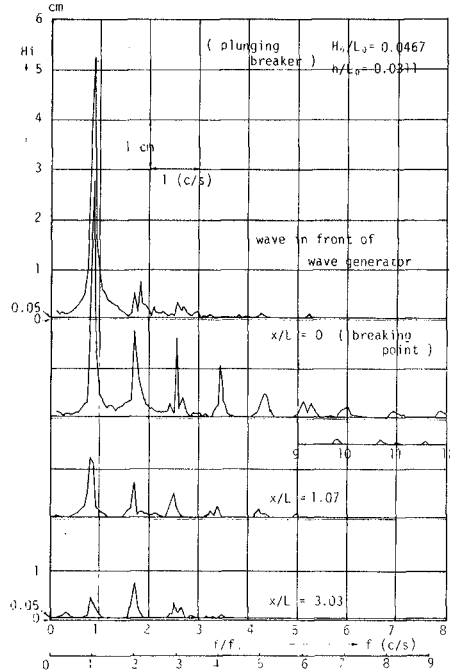


Fig.-2. Variation of wave height spectrum. (S = 0)

Fig.-4 and Fig.-5 show variation of wave height spectra plotted on log - log scale as waves propagate on a horizontal bed. Fig.-5 shows only predominant component waves. $f_1 = 3.3$ (c/s) and $f_c = 13.3$ (c/s) are obtained by Eqs. (2) and (5) for waves shown in Figs.-4 and -5, and the domain of air entrainment X_A/L is given to be $0 \leq X_A/L \leq 1.05$ for the wave shown in Fig.-4 and $0 \leq X_A/L \leq 1.30$ for the wave in Fig.-5 by the experiment.

Fig.-4 and Fig.-5 show that inside the surf zone with air entrainment, the slopes of wave height spectra are approximately proportional to " f^{-1} " for $f < f_1 = 3.3$ (c/s) and " f^{-2} " for $f_1 = 3.3$ (c/s) $< f < f_c = 13.3$ (c/s). In cases of waves before breaking and waves after passing through the surf zone, however, the higher frequency component waves more than 5(c/s) can not be observed, and then, the slopes of wave height spectra are not proportional to " f^{-1} " and " f^{-2} " (see Fig.-4 (a), (g) and (h), and points $X/L = 2.99$ and 3.04 in Fig.-5).

For the case of a spilling breaker, the slope of wave height spectrum at a breaking point is steeper than " f^{-2} " for 3.3 (c/s) $< f < 13.3$ (c/s) in Fig.-4(b) and, at the point $X/L = 0$ in Fig.-5(a). This may be due to the reason that the turbulence of breaking is not saturated⁵⁾ all over the wave as shown in Fig.-6 and that the characteristics before breaking still remain.

In the region such as $X/L = 0.322, 0.523$ and 0.775 in Fig.-4 where the turbulence of breaking is saturated, however, "-1 power law" and "-2 power law" are established as mentioned above.

Figs.-7 and -8 show variation of wave height spectra plotted on the log-log scale on a uniform slope of $1/40$ and $1/25$ respectively. Fig.-9 shows a change of wave height spectrum of predominant component waves piled up on the same graph, where h is a still water depth and h_b is a breaking depth. The characteristics of wave height spectra on uniform slopes are similar to those on the horizontal bed. As shown in Fig.-9, the slopes of wave height spectra are recognized to be nearly proportional to " f^{-2} " for the range of $f_1 < f < f_c$ independent of wave steepness, H_0/L_0 , and beach slope, S . On the other hand, the slopes of wave height spectra for $f < f_1$ is roughly proportional to " f^{-1} ".

In sloping beaches, the values of wave height spectra decrease as waves propagate into shallower water depth as shown in Fig.-10, and inside the surf zone, the pattern of wave height spectrum such that a spectral slope is proportional to " f^{-1} " for $f < f_1$, and " f^{-2} " for $f_1 < f < f_c$, is still maintained. In Fig.-10, the point of $h/h_b = 0.19$ is outside the surf zone.

Summarizing the above-mentioned experimental results, it can be concluded that the wave height spectrum $H(f)$ has the form of which slope is proportional to " f^{-1} " for $f < f_1 (= \sqrt{g/4\pi h})$ and to " f^{-2} " for $f_1 < f < f_c (= 1/2\sqrt{S^*g/K})$ as critical wave height spectrum inside the surf zone where the turbulence of breaking is saturated all over the wave.

On the other hand, since values of wave spectra are very small at the present experiment for $f_c < f < f_k$ in which the surface tension is a restoring force, the characteristics may not be discussed sufficiently. But, in many experimental cases, it is recognized that the slope of wave height spectrum is approximately proportional to " $f^{-2/3}$ " as shown in Fig.-11. Therefore, it may not be said too much that " $f^{-2/3}$ " can be established.

For the frequency range of $f > f_k$ in which water viscosity is predominant, the authors can not discuss about " $f^{-1/2}$ ", because wave profiles were measured by using a low pass filter of which sheltering frequency is more than 25(c/s), and values of spectra are considerably small. In future, the authors will carry out large scale experiments and discuss in detail.

Finally, variation of wave height of component waves will be discussed. The pattern of wave height decay of component waves is different between a spilling breaker and a plunging breaker.

As shown in Fig.-12(a), in case of the spilling breaker, high frequency wave heights grow larger once soon after breaking. On the other hand, in case of the plunging breaker, wave heights of high frequency waves decay uniformly after breaking as shown in Fig.-12(b). This difference may be due to the reason that the spilling breaker is not saturated by the turbulence of breaking at a breaking point, differing from the case of the plunging breaker.

The degree of wave height attenuation of component waves is generally larger as the frequency is higher, as shown in Fig.-12, where f_0 is the monochromatic frequency of an incident wave and f is the frequency of component waves. These mechanism may be due to the internal turbulent shear caused by breaking, and dissipating energy is proportional to νk^2 (k =wave number, ν =kinematic viscosity) as predicted by the classical turbulence theory.

4. CONCLUSION

In this paper, the characteristics of wave height spectrum $H(f)$ inside the surf zone of a monochromatic periodic wave are discussed.

Firstly, due to the dimensional analysis, it is predicted that there exist a critical wave height spectrum $H(f)$ of which slopes are proportional to " f^{-1} ", " f^{-2} ", " $f^{-2/3}$ " and " $f^{-1/2}$ " in turn as the frequency f becomes larger.

Secondly, experiments were carried out to examine the results of the dimensional analysis. It is made clear that inside the surf zone, an incident monochromatic wave is transformed to a wave composed of high frequency component waves and that the subranges of "-1 power law", "-2 power law" and "-2/3 power law" are established in the wave height spectrum as predicted by the dimensional analysis.

REFERENCES

- 1) Sawaragi, T and K. Iwata : On wave deformation after breaking. Proc. of 14th Conf. on Coastal Eng., Copenhagen, Denmark, June 1974, pp.481 - 499.
- 2) Wiegel, R.L. : Oceanographical Engineering, Prentice-Hall, INC., 1964, pp.59 - 60.
- 3) Michell, A.G.M. : The heighest wave in water, Phil. Mag. Vol. 36(5), 1893, pp. 430 - 437.
- 4) Cooley, J.W. and J.W. Tuckey : An algorithm for the machine calculation of complex Fourier series, Math. Compt., 1965, pp.297 - 301.
- 5) Méhauté, B.L. : On non-saturated breakers and the wave run-up, Proc. of 8th Conf. on Coastal Eng., Mexico City, Mexico, 1963, pp.77 - 92 .

Notations	Values
S	0, 1/15, 1/25, 1/40
Ho/Lo	0.0031 - 0.1032

Table - 1. Experimental conditions.

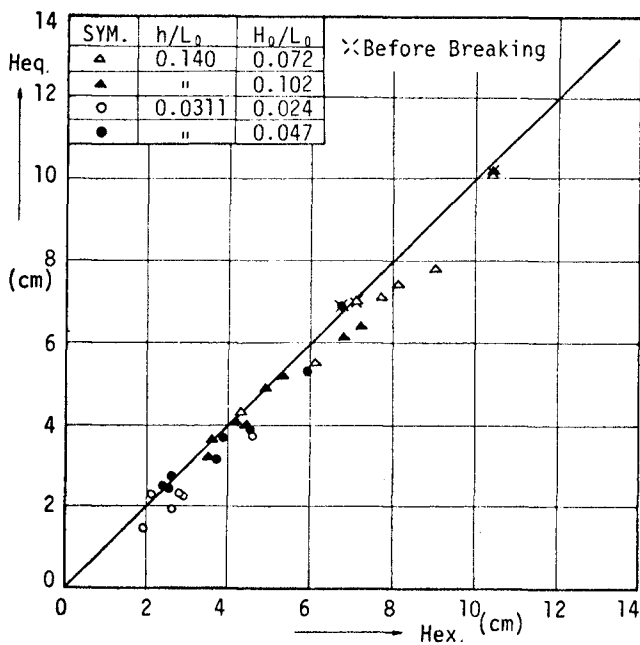


Fig. - 3. Relation between $H_{eq.}$ and $H_{ex.}$.

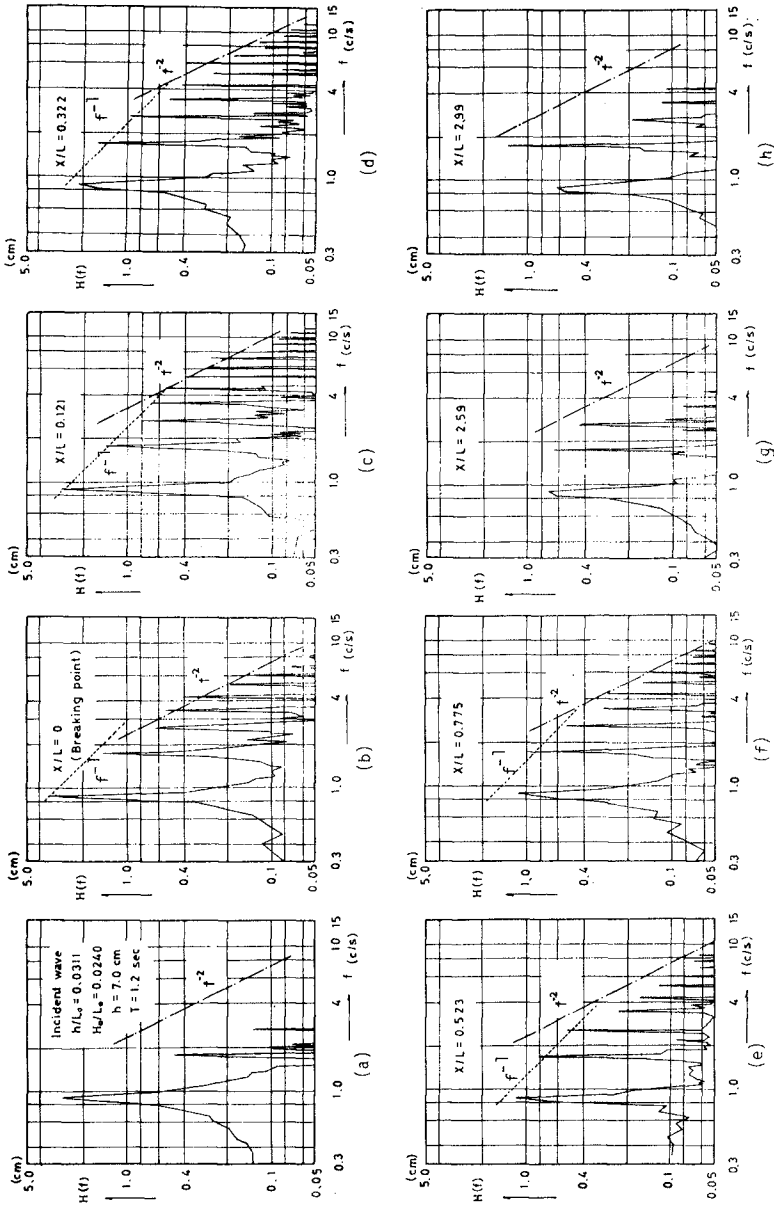


Fig. - 4. Variation of wave height spectrum . ($S = 0$)

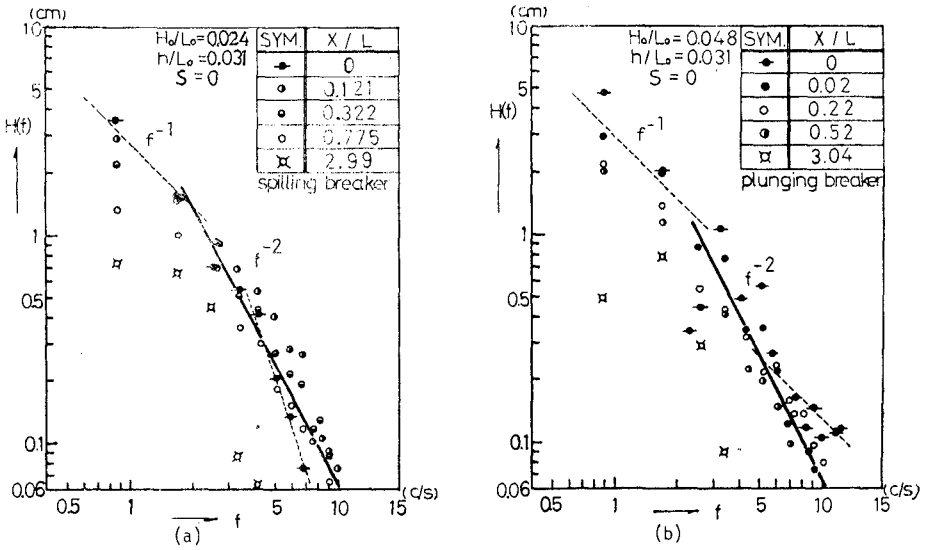


Fig. - 5. Variation of wave height spectrum. ($S=0$)
(Predominant components)

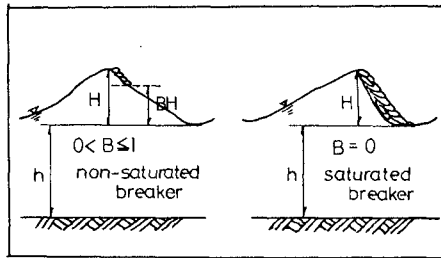


Fig. - 6. Schematic view of non-saturated breaker and saturated breaker.
(from Méhauté 5)

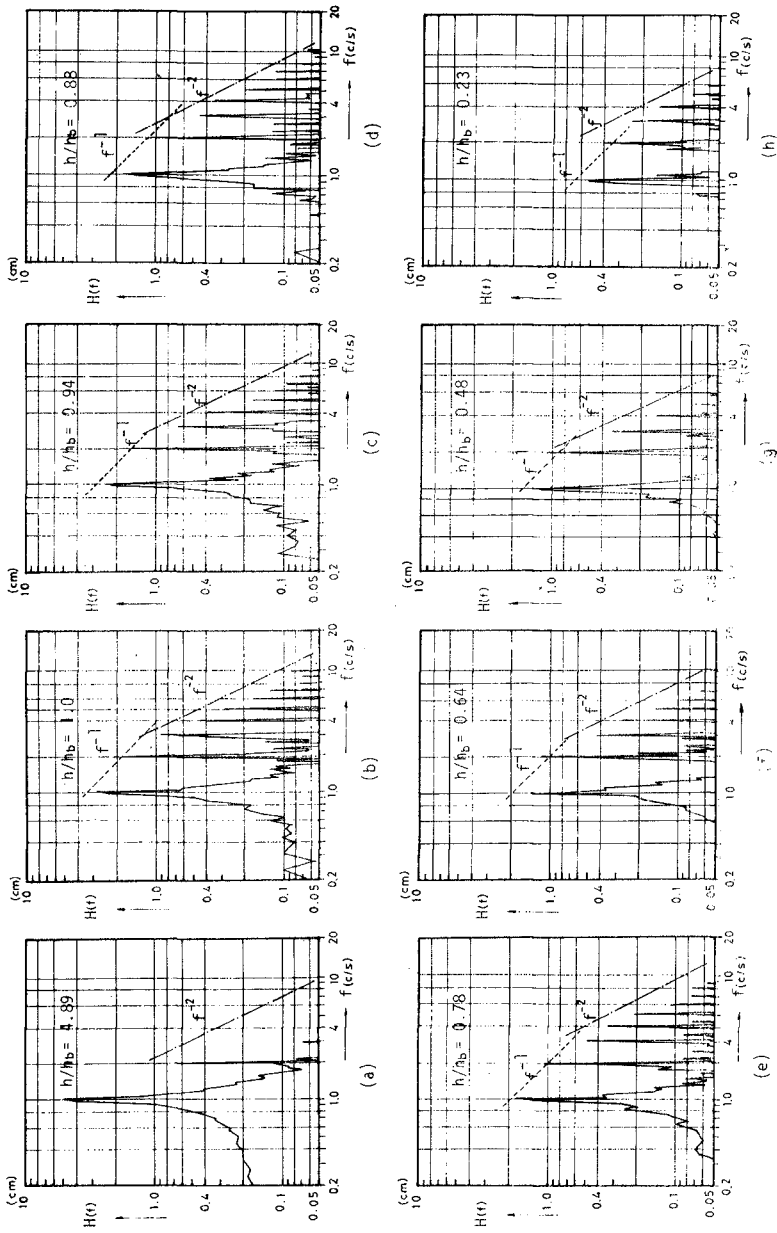


Fig. - 7 . Variation of wave height spectrum. ($H_0/L_0=0.049$, $T=1.0$ sec., $S=1/40$)

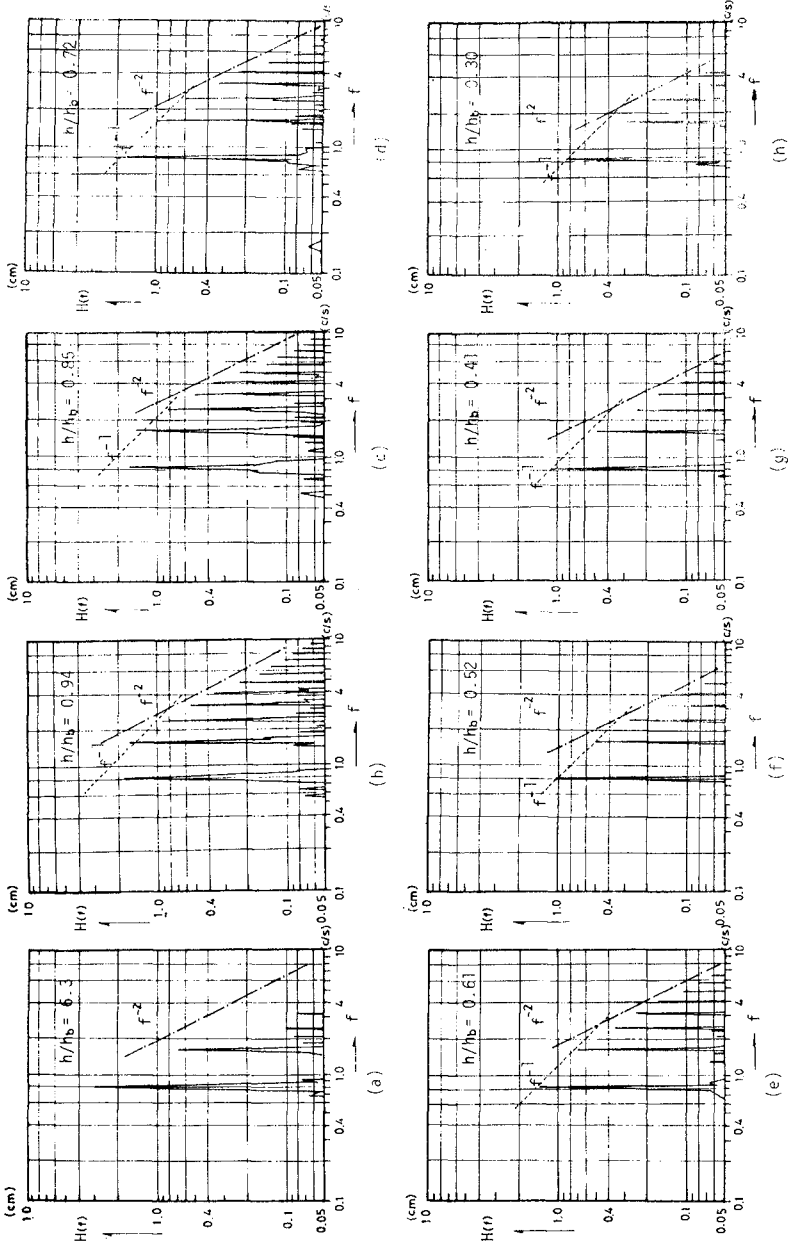


Fig. - 8 . Variation of wave height spectrum. ($H_0/L_0=0.015$, $T=1.22$ sec., $S=1/25$)

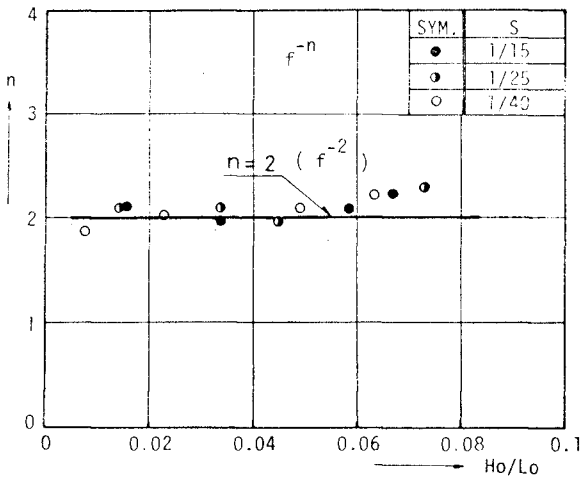


Fig. - 9. " -2 power law " .

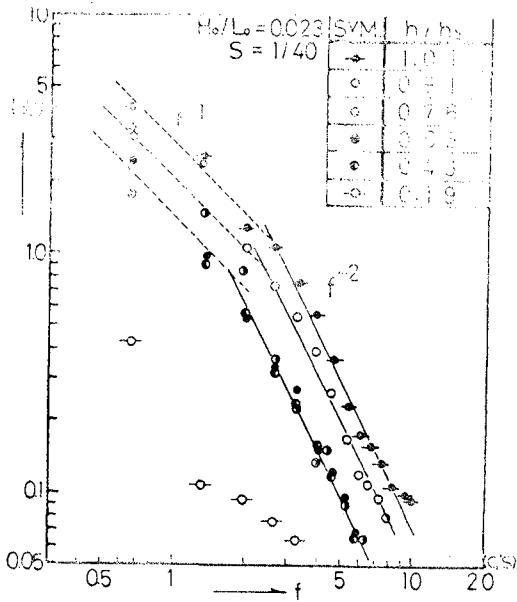


Fig. -10. Variation of wave height spectrum (S=1/40)
(Predominant components)

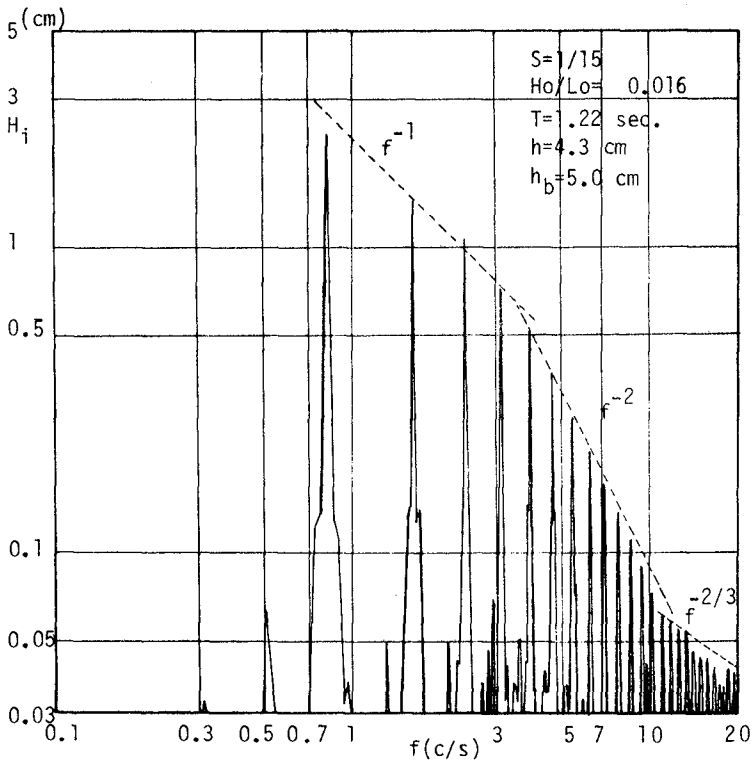


Fig. - 11. Wave height spectrum.

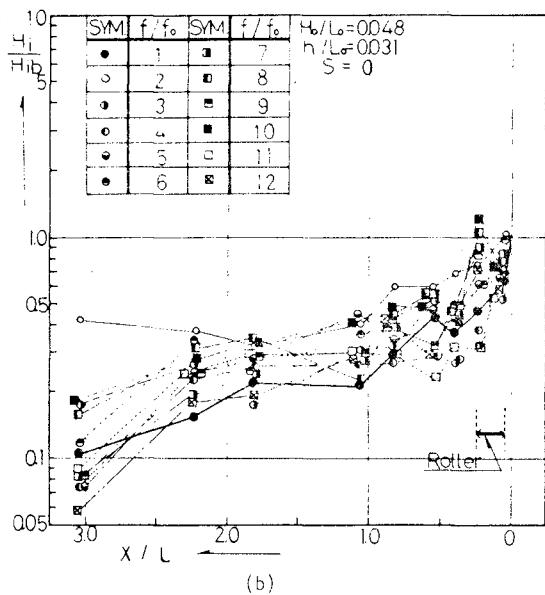
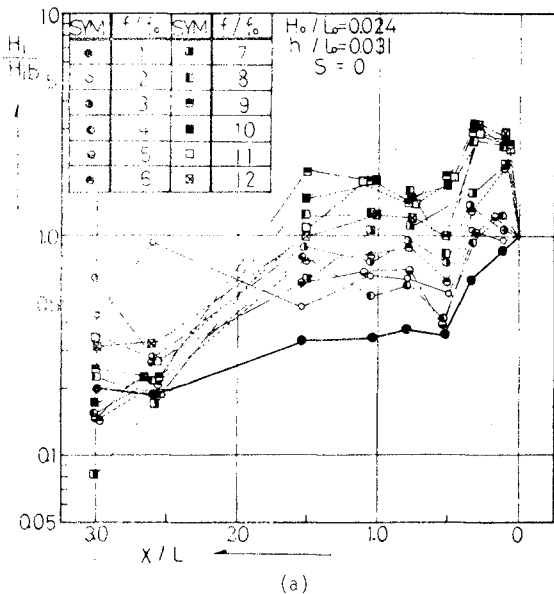


Fig.-12 . Attenuation of predominant component waves. ($S = 0$)
 (H_1 = wave height of component wave,
 H_{1b} = wave height of component wave at breaking point)

CHAPTER 34

Consideration on Friction Coefficient for Sea Bottom

Toru Sawaragi
Professor of Civil Engineering
Osaka University, Osaka, Japan

Koichiro Iwata
Lecture of Civil Engineering
Osaka University, Osaka, Japan

Masayoshi Kubo
Assistant Professor
Kobe University of Mercantile Marine
Kobe, Japan

ABSTRACT

A bottom friction is an effective factor which will prove the deformation of progressive waves in shallow water, and many investigators have obtained the friction coefficients from field observations. However, they have not considered the effect of turbulent loss due to sand ripple at a sea bottom.

The authors, first of all, study on the friction coefficient for artificial fixed ripple by using the boundary layer theory of rough turbulence, and a new formula on the friction coefficient is proposed. The proposed friction coefficients are compared with Zhukovets' experimental results which were performed on a movable bed, and it is found that the theoretical friction coefficients for artificial fixed ripple have to be modified in order to apply for the natural beach. Lastly, the wave deformation due to the bottom friction on the movable bed is calculated by the modified friction coefficient and the effect of bottom friction on the wave deformation is discussed.

1. INTRODUCTION

It is very important to predict a wave height in shallow water for a design of coastal structure. A bottom friction is an effective factor which will prove the deformation of progressive waves in shallow water. Bretschneider¹⁾, Iwagaki and Kakinuma²⁾ and other many investigators have obtained the friction coefficient at the sea bottom from the measuring results of wave height in the field. However, the friction coefficient given by Iwagaki and Kakinuma is larger than 0.01 which was given Bretschneider. We don't know the reason even now. Many investigators have not considered the effect of turbulent loss due to a sand ripple at the sea bottom. But we know that a boundary layer at the sea bottom in shallow water is turbulent in rough state, and that the sand ripple develops at the sea bottom.

As a clue to elucidate the wave deformation due to the bottom friction, the authors, first of all, study on the coefficient for artificial fixed ripple by using the boundary layer theory on rough turbulence which was given by Kajiura³⁾, and a new formula on the friction coefficient is proposed.

Secondarily, the friction coefficient given by the new formula is verified by experimental results at a movable bed, and it is found that the friction coefficient by assuming fixed ripple have to be modified in order to apply for the natural beach.

Lastly, the deformation of shallow water waves on a constant beach slope is calculated by the modified friction coefficient, and the effect of bottom friction on the wave deformation is clarified.

2. FRICTION COEFFICIENT FOR ARTIFICIAL FIXED RIPPLE

The bottom friction under the ripple formation has been investigated by Bagnold⁴⁾, and Putnam and Johnson⁵⁾ have obtained $f = 0.01$ from the field investigation under the consideration of Bagnold's investigation results. This value of friction coefficient was verified by Bretschneider's field observation. However, these studies were not considered the effect of boundary layer.

According to Kajiura theory³⁾ on the boundary layer which expanded Bagnold's experimental results, the ranges of transition are given by the following equations.

$$\left. \begin{aligned} 0.4 \leq \delta^*/D \leq 5.0, \text{ for laminar-turbulent transition} \\ 0.4 \leq D/D_L \leq 5.0, \text{ for smooth-rough transition} \end{aligned} \right\} (1)$$

furthermore,

$$\left. \begin{aligned} D/D_L &= \hat{C}^{1/2} M/N, & \delta^*/D_L &= \hat{C}^{3/2} R^2 N \\ M &= 30 \hat{U}_b Z_0/\nu, & R &= \hat{U}_b / \sqrt{\sigma} \end{aligned} \right\} (2)$$

where, \hat{C} is an amplitude of friction coefficient, ν is a coefficient of kinematic viscosity, σ is an angular frequency of wave, \hat{U}_b is an amplitude of horizontal velocity at the sea bottom, Z_0 is a roughness length, D is Nikuradse's equivalent sand roughness, and $N=12$.

The authors assume the sand ripple to be fixed artificial ripple, and Nikuradse's equivalent sand roughness D equals $30Z_0$. Andmore, it is already revealed that D equals 4η by Motzfeld⁶⁾.

On the other hand, some equations about the sand ripple are given by Homma, Horikawa and Kashima⁷⁾ as follow,

for criterion of ripple formation : $\hat{U}_b / \sigma \lambda > 0.5$ (3)

for height of sand ripple : $\eta = 0.175 (2\hat{U}_b / \sigma)^{-0.915} \lambda^{1.19}$ (4)

for length of sand ripple : $\lambda = \alpha \tau (2\hat{U}_b / \sigma)^{1-2\gamma}$ (4)

where, α and γ are given by the function of sand grain size as shown in Fig. (1) and the authors approximate them by the following equations.

$$\left. \begin{aligned} \alpha &= -389.4 d_{50}^3 + 729.5 d_{50}^2 - 313.0 d_{50} + 40.7 \\ \gamma &= -82.7 d_{50}^3 + 87.2 d_{50}^2 - 28.6 d_{50} + 3.3 \end{aligned} \right\} (5)$$

where, d_{50} is a mean diameter of bed material, in centimeter.

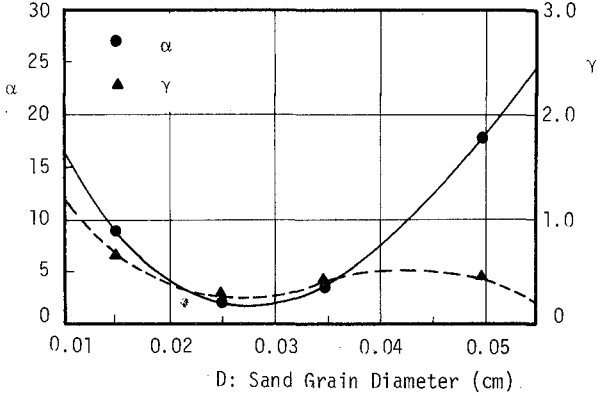


Fig.1 Relation between α , γ and sand grain size.

From the above Eqs.(1) (5), it is known that the state of flow over the ripple due to wave shows almost rough turbulence. Furthermore, the relation between a bottom shear stress and a friction coefficient, C , is given by Eq.(6) due to Kajiura's theory.

$$\tau_b / \rho = C \cdot \hat{U}_b \cdot U_b, \quad C = \hat{C} e^{i\theta} \quad (6)$$

$$\left. \begin{aligned} \hat{C} &= 1.7 (30\lambda / 4\eta)^{-2/3}, \quad \text{for } 0.5 < \hat{U}_b / \sigma \lambda < 1.0 \\ \hat{C} &= A (U_b / \sigma Z_0)^{-B}, \quad \text{for } 1.0 < \hat{U}_b / \sigma \lambda \end{aligned} \right\} (7)$$

where, τ_b is a bottom shear stress, \hat{C} is an amplitude of friction coefficient as shown in Fig.2, θ is a phase of friction coefficient which is given by Kajiura as shown in Fig.3.

Fig.2 and Fig.3 are approximated by the dotted line. From the approximated line, A,B in Eq. (7) and θ in Eq. (6) are given by Table 1.

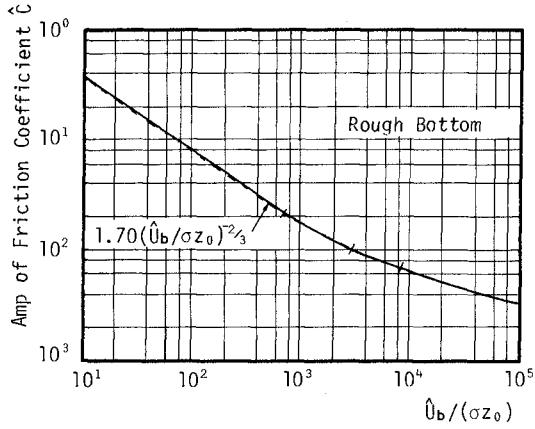


Fig. 2 Change of \hat{C} with $\hat{U}_b / (\sigma z_0)$

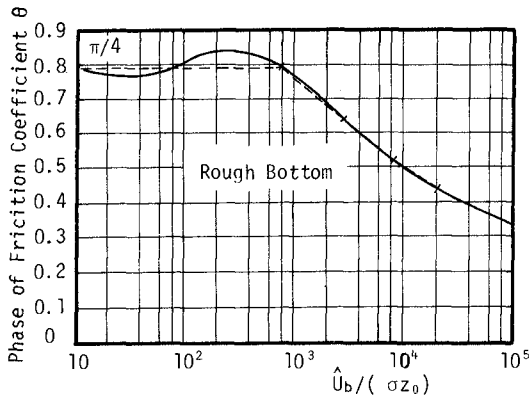


Fig. 3 Change of θ with $\hat{U}_b / (\sigma z_0)$

$\hat{U}/\sigma z_0$	$C=A(\hat{U}_b/\sigma z_0)^{-B}$	θ
~685	$1.7(\hat{U}/\sigma z_0)^{0.667}$	$\approx \frac{\pi}{4}$
$685 \sim 3 \times 10^3$	$0.711(\hat{U}/\sigma z_0)^{0.536}$	$1.558 - 0.266 \log_{10} \left(\frac{\hat{U}}{\sigma z_0} \right)$
$3 \times 10^3 \sim 8 \times 10^3$	$0.240(\hat{U}/\sigma z_0)^{0.4}$	$1.524 - 0.257 \log_{10} \left(\frac{\hat{U}}{\sigma z_0} \right)$
$8 \times 10^3 \sim 2 \times 10^4$	$0.068(\hat{U}/\sigma z_0)^{0.26}$	$1.287 - 0.196 \log_{10} \left(\frac{\hat{U}}{\sigma z_0} \right)$
$2 \times 10^4 \sim 10^5$	$0.068(\hat{U}/\sigma z_0)^{0.26}$	$1.092 - 0.150 \log_{10} \left(\frac{\hat{U}}{\sigma z_0} \right)$

Table 1. Approximated value of A, B and θ

In terms of friction coefficient \hat{C} , a mean energy dissipation $\langle E \rangle$ is given by Eq.(8).

$$\langle E \rangle = \rho/2 \hat{C} \hat{U}_b^3 \cos \theta \quad (8)$$

On the other hand, in the ordinary definition of friction coefficient, f , which is used by many investigators, the energy dissipation, $\langle E \rangle$ is given by Eq.(9).

$$\langle E \rangle = 4/3 \cdot \rho \cdot f \hat{U}_b^3 \quad (9)$$

So, the coefficient, f , is represented by Eq.(10) from the comparison of Eqs.(8) and (9).

$$f = 3/8 \hat{C} \cos \theta \quad (10)$$

Summarizing the above relation, the friction coefficient, f_{fix} , provided that the sand ripple is assumed to be fixed artificial one, is given by Eq.(11).

$$\begin{aligned}
 f_{\text{fix}} &= 0.116 \left(\frac{\nu}{a} \right)^{0.127} Re_T^{-0.127}, \quad \text{for } \left(\frac{1}{a} \right)^{\frac{1}{3}} < Re_T < \pi \left(\frac{2}{a} \right)^{\frac{1}{3}} \\
 f_{\text{fix}} &= 1.18 A \cos \theta \left\{ 0.0467 \left(\frac{\nu}{a} \right)^{1.19} \right\}^B \cdot Re_T^{-1.19B}, \\
 &\quad \text{for } Re_T > \pi \left(\frac{2}{a} \right)^{\frac{1}{3}} \\
 a &= \left(\frac{\nu}{\pi} \right)^{\delta} / \alpha, \quad Re_T = \hat{U}_b^2 T / \nu
 \end{aligned} \quad (11)$$

where, subscript "fix" shows that the sand ripple is assumed to be fixed artificial ripple. α and δ are given by Eq.(5) and A, B and θ are given by Table 1.

Using the above relations, the friction coefficient for an arbitrary

sand grain size is obtained. The relation between f_{fix} and Re_T of Eq.(II) for 4 kinds of sand grain size are shown by the full line in Fig.4.

In Fig.4 the friction coefficients in the field data obtained by many investigators are plotted, and they are scattered and indicate different values according to sand grain sizes. The field data contain the effect of wave directional dispersion, wave breaking, etc., so it is difficult to compare the theoretical coefficient with the field data.

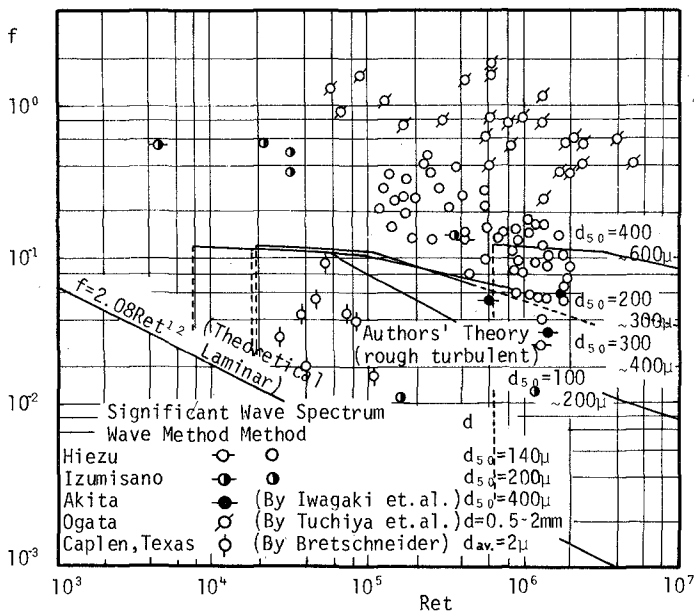


Fig. 4 Relations between f_{fix} and Re_T

3. VERIFICATION OF THE FRICTION COEFFICIENT BY THE EXPERIMENTAL ON THE MOVABLE BED

The friction coefficient of Eq.(II) is compared with the experimental values which were required by Zhukovets⁸⁾ from the wave deformation on horizontal movable bed in a laboratory. In this experiment, the wave height ranged from 3 to 18 cm, and the wave steepness varied from 0.1 to 0.04. As the bed material, the sand which the mean diameter of grain size is 0.25 mm was used.

The comparison of the experimental data within the range of rough turbulence with the theoretical coefficient is shown by Fig.5. In Fig.5, f_{exp} is the experimental friction coefficient and K_{sm} indicates the relative roughness of the bottom and is defined by Eq.(12). Re in this figure shows the Reynolds number which is given by Eq.(13).

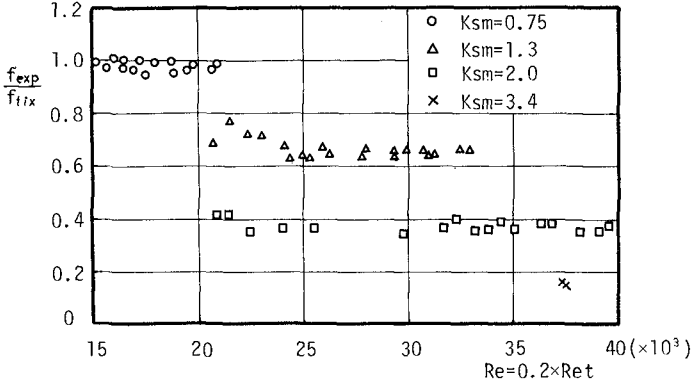


Fig.5 Comparison of f_{fix} and f_{exp} .

$$K_{sm} = V_g^2 / \left\{ 2g d_{50} \sinh^4 \sqrt{1 + \eta / d_{50}} \right\} \quad (12)$$

$$Re = V_g H / \nu \sinh kh \quad (13)$$

where η is the height of sand ripple, and V_g is the velocity of water particle motion at bottom averaged over a quarter period of wave and is given by Eq.(14).

$$V_g = (\sigma H / \pi) \operatorname{cosech} kh + (3k\sigma H^2 / 8) \operatorname{cosech}^4 kh \quad (14)$$

where k is a wave number $k = 2\pi / L$, L is a wave length and H is a wave height.

Then, Re is transformed into Re_T by the following equation.

$$Re = \frac{V_g H}{\nu \sinh kh} \approx \frac{2}{\pi^2} \frac{U_b^2 T}{\nu} = 0.2 Re_T \quad (15)$$

From Fig.5, when K_{sm} is 0.75, f_{fix} has a fairly good agreement with f_{exp} , but when K_{sm} becomes larger, f_{fix} becomes larger than f_{exp} . The reason of this fact is not evident, but it is considered as follow; when K_{sm} becomes larger, V_g becomes large and the bed material seems to have a tendency of suspension. Generally, the friction in suspended state is less than the friction of non-suspended state, so the assumption of the fixed ripple model

for the theoretical friction coefficient is not able to apply for the case of large K_{sm} . Therefore, the theoretical friction coefficient f_{fix} has to be modified with regard to K_{sm} which indicates the characteristics of the movable bed. According to Fig.5, the ratio of f_{exp} to f_{fix} depends only on K_{sm} , and it is independent of the Reynolds number.

Now, the ratio is called a modification factor, F_c . The modification factor varies with K_{sm} as shown in Fig.6. Then, the theoretical friction coefficient for fixed ripple has to be modified into f_m by the modification factor F_c .

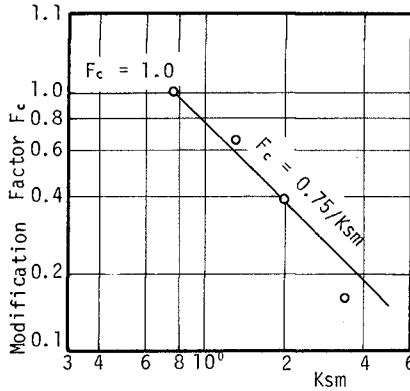


Fig.6 Change of the modification factor with K_{sm} .

The modified coefficient f_m is approximated by Eq.(16).

$$\left. \begin{aligned} K_{sm} &\leq 0.75 & f_m &= f_{fix} \\ K_{sm} &> 0.75 & f_m &= (0.75 / K_{sm}) f_{fix} \end{aligned} \right\} (16)$$

However, when K_{sm} becomes very large, f_m becomes smaller than the friction coefficient in case of laminar boundary layer, f_L , which is represented by Eq.(17).

$$f_L = 2.08 Re_T^{-1/2} \quad \text{for laminar boundary layer}^9) \quad (17)$$

In this case, f_m is assumed to be f_L for convenience.

4. EFFECT OF BOTTOM FRICTION TO WAVE DEFORMATION

The deformation of shallow water wave due to the bottom friction on a constant beach slope is calculated by the modified friction coefficient f_m .

In this calculation, Eq.(18) derived from the law of energy conservation is used.

$$H_{i+1} = \left(\frac{C_{g i}}{C_{g i+1}} H_i^2 - \frac{32 \Delta x}{3 \sqrt{g} C_{g i+1}} f_{mi} \sqrt{U_{bi}} \right) \quad (18)$$

where C_g is a group velocity of wave, the subscript "i" indicates the i-th step, and g is a gravity acceleration.

The calculation is started from the point where a relative water depth l and is stopped at the breaking point which was given by Kishi and Saeki as follows:

$$H_b / h_b = 5.68 S^{0.4} \quad (19)$$

where, S is a beach slope.

The calculation is carried out by the iterative method, that is, the authors evaluate the friction coefficient with the mean value of H_i and the assuming value of H_{i+1} . With the friction coefficient, the calculated value of H_{i+1} will be obtained by Eq.(18). The iteration is continued till the difference between the assuming value of H_{i+1} and the calculated value of H_{i+1} becomes small.

For the wave condition of wave period which equals to 4.0 sec, beach slope of 1/120 and 4 kinds of wave height at deep water, the deformation of wave height is obtained as shown in Fig.7.

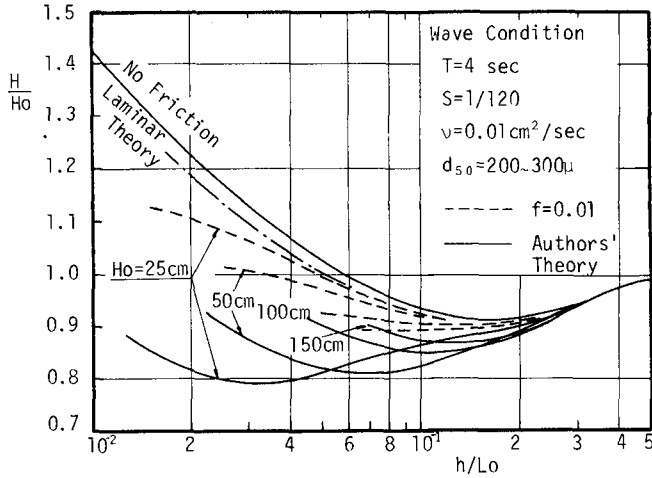


Fig.7 Comparison of wave decay with various friction coefficient

In this figure, the full lines show the change of wave height by the authors' theory, the chain line is the result due to the laminar boundary layer theory and the dotted lines indicate the calculation results in case that the friction coefficient is 0.01. Furthermore, no friction curve, that is, the shoaling curve is drawn in this figure.

From these curves, it is found that the decay of wave height is considerably larger than the laminar case, and the decay curves indicate different tendency of the calculation results for $f=0.01$. According to the authors' theory, when the wave height becomes larger, the effect of bottom friction becomes smaller.

Fig. 8 shows the effect of wave period on the wave deformation due to the bottom friction under the condition that the wave height is 50 cm and the beach slope is $1/120$. From this figure, it is recognized that as the wave period becomes shorter, the wave decay becomes larger.

Fig. 9 shows the effect of beach slope upon the wave decay. From this figure, even if the wave condition at deep water is the same, as the beach slope is gentle, the degree of wave decay becomes larger.

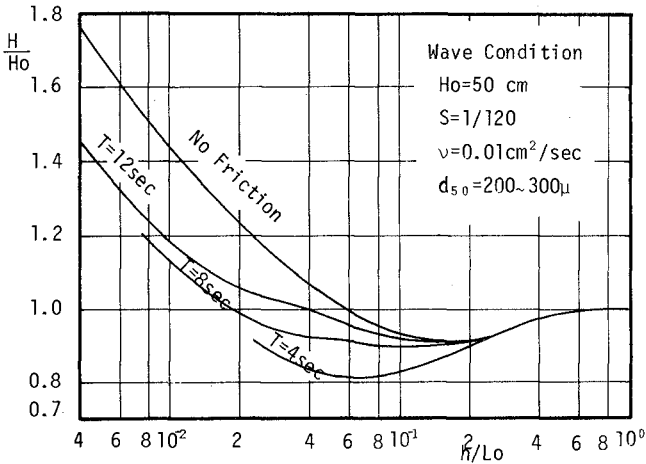


Fig. 8 Effect of wave period for wave decay

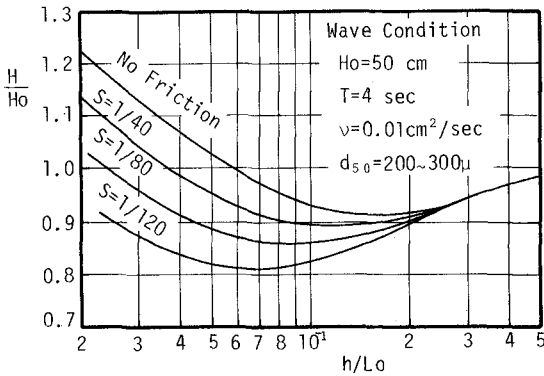


Fig. 9 Effect of beach slope for wave decay

5. CONCLUSION

Considering the effect of sand ripple which is assumed to be fixed artificial ripple, the new formula on friction coefficient is proposed by using the boundary layer theory on turbulence. The proposed friction coefficients are compared with Zhukovets' experimental results which were performed on the movable bed in the laboratory. From the comparison, it is clarified that the proposed friction coefficient for sand ripple has to be modified by the modification factor for a movable bed, and the wave deformation due to the bottom friction on the movable bed is calculated by using the modified coefficient, f_m .

From the calculation, it is pointed out that the wave decay which is considered to be due to the effect of sand ripple under the turbulent condition, is considerably larger than one at laminar case and the wave decay curve indicates the different tendency from that in the friction coefficient $f=0.01$.

REFERENCE

- 1) Bretschneider, C.L. : Field investigation of wave energy loss of shallow ocean waves, B.E.B., Tech. Memo. NO.46, 1954.
- 2) Iwagaki, Y. and T. Kakinuma : On the transformation of ocean wave spectra in shallow water and the estimation of the bottom friction factor, Bull. Disas. Prev. Res. Inst., Kyoto Univ., Vol. 8, 1965.
- 3) Kajiura, K. : A motion of the bottom boundary layer in water waves, Earthquake Research Institute, Vol. 46, 1968.

- 4) Bagnold, R.A. : Motion of waves in shallow water interaction between waves and sand bottoms, F.R.S., 1945.
- 5) Putnam, J.A. and J.W. Johnson : The dissipation of wave energy by bottom friction, Trans. Amer. Geophys. Union, Vol. 30, 1949.
- 6) Motzfeld, H. : Die turbulente strömung an welligen wanden, Angew. Math. U. Mech. Vol.24, 1937.
- 7) Homma, H., K. Horikawa and R. Kashima : Study on a suspension load due to wave action, Proc. of 11th Conf. on Coastal Eng. in Japan, 1964. (in Japanese)
- 8) Zhukovets, A.M. : The determination of the energy losses of swells resulting from eddy and kinematic viscosity, Oceanology, NO. 2, 1963.
- 9) Eagleson, P.S. : Laminar damping of oscillatory waves, Jour. Hydr. Div. A.S.C.E., Vol.88, 1962.
- 10) Kishi, T. and H. Saeki : The shoaling, breaking and run-up of the solitary waves on impermeable rough slopes, Proc. of 10th Conf. on Coastal Eng., 1966.

CHAPTER 35

PHYSICAL ASPECTS OF WAVE-INDUCED NEARSHORE CURRENT SYSTEM

By

Masaru Mizuguchi and Kiyoshi Horikawa

Coastal Engineering Laboratory
 Department of Civil Engineering
 University of Tokyo
 Bunkyo-ku, Tokyo
 JAPAN

INTRODUCTION

Since a theoretical approach on rip currents was made by Bowen (1969), our understandings on that system have progressed steadily.

It will be considered that the dynamics of current system are governed by the following equations which indicate the balance among the gradients of radiation stress and of mean water level, and the friction force induced by the current velocity:

$$\left. \begin{aligned} \frac{\partial S_{xx}}{\partial x} + \frac{\partial S_{xy}}{\partial y} + \rho g(R+\zeta) \frac{\partial \zeta}{\partial x} + fU &= 0 \\ \frac{\partial S_{xy}}{\partial x} + \frac{\partial S_{yy}}{\partial y} + \rho g(R+\zeta) \frac{\partial \zeta}{\partial y} + fV &= 0 \end{aligned} \right\} (1)$$

Here radiation stresses such as S_{xx} are given by the local wave height H and wave ray direction θ . The terms ρ , g , ζ , h , and f denote fluid density, acceleration due to gravity, variation of mean water level above still water level, still water depth, and friction factor, respectively. U and V are components of current velocity which satisfy the following continuity equation:

$$\frac{\partial(Ud)}{\partial x} + \frac{\partial(Vd)}{\partial y} = 0 \quad (2)$$

where $d = h + \zeta$. To solve Eqs.(1) and (2), we need one more relation among the three terms stated above.

Hino (1974) treated this problem by the way of assuming that the wave height in a surf zone is proportional to the water depth as follows:

$$H = \sigma d \quad (3)$$

Iwata (1976) and Mizuguchi (1976) applied the following energy equation in order to close Eqs.(1) and (2):

$$\frac{\partial}{\partial x} \{ E(\bar{U} - c_g) \} + \frac{\partial}{\partial y} (E\bar{V}) + S_{xx} \frac{\partial \bar{U}}{\partial x} + S_{yy} \frac{\partial \bar{V}}{\partial y} = -D \quad (4)$$

where E , c_g , and D denote wave energy, group velocity, and dissipation, respectively. The axis of x is taken offshoreward, and the wave is assumed to come perpendicular to shoreline.

Another approach has been made to clarify the mechanics of rip current system. This is a way to give a wave height distribution or a radiation stress distribution by something came from the outside of the equation system.

Bowen and Inman (1969) and Harris (1967) suggested that generation of edge wave with the same period of incident waves could make a periodic longshore perturbation of wave height distribution. Sonu (1972) found the distinct correlation between the observed current system and bottom topography. While Noda (1974), Horikawa and Sasaki (1974), and others have tried to simulate the current field by using Eqs.(1) and (2) under the conditions of irregular wave height and ray angle field caused by refraction due to irregular bottom topography, and achieved success to calculate it at least in a qualitative sense. Recently Dalrymple (1975) tried to explain the current system from a view point of two intersecting synchronous waves.

These two kinds of approach to the rip current system suggest us the existence of the following two types of current system. The first one which corresponds to the former formulation can be called " the free type rip current system ", because there is no external force to generate the current system. Mathematically it would be formulated as an eigenvalue problem in spite of using either Eq.(3) or Eq.(4). The treatises by Hino, Iwata, and Mizuguchi are included in this category. But the wave height-depth assumption (Eq.(2)) is not verified well enough to go on forward along this assumption. While the energy coupling assumption (Eq.(4)) has also a deficiency of neglecting the first order dissipation term, which might be important on phenomena in a surf zone.

The second one which corresponds to the latter formulation can be called " the forced type rip current system ", because the external factor such as edge wave or irregular bottom topography plays a crucial part of generating the current system. This forced system is of a zero-th order current system caused by irregular radiation stress distribution in a wave breaking area and could be described enough by Eqs.(1) and (2) by using the radiation stress distribution which is externally given. Equation (4) would only contribute to modify the current system as treated by LeBlond and Tang (1974).

There are still some points which must be settled down in order to understand the dynamics of the rip current system. We have done some

laboratory experiments and observed a current system which is similar to that in the field [Sonu (1973)]. Analyzing and discussing the experimental results, we try to make some contribution to clarify the current system.

PRELIMINARY EXPERIMENTS

Experimental set-up and measuring technique are in the following:

- a. A fixed impermeable plane beach made of plywood was installed in a ripple wave tank, the size of which was 1.2m wide, 6m long and 0.15m deep. The selected slopes of beach were $1/20$, $1/10$, and $1/5$.
- b. The direction of incident waves was always perpendicular to the shoreline.
- c. The pattern of current system was observed by a video camera system in tracing the diffusion of dye which was poured into an uprush zone.
- d. Wave height distribution in the nearshore zone was obtained by using wave gages which were travelled parallel to the shoreline. Progressive pattern of wave crests was detected by viewing the video camera records.

We show in the following the experimental results in two cases which are the typical ones.

1. CASE 12 is the one where the wave steepness is not very large and the breaker zone is not very wide. In Fig.1 various curves cover the diffusion area by the current at the indicated time in second. Fine solid lines show a wave crest propagation pattern. Figures 1 and 2 give the following information:
 - 1) The wave crest pattern indicates that the wave propagation is delayed considerably in the region where offshoreward currents (hereafter written offshore currents) exist. We calculated roughly the distortion of the wave crest at the breaker line by using the measured velocity distribution in Fig.5. We get the values of 1.2cm for CASE 12 and 5.2cm for CASE 15 (which will be introduced in the following part) at the breaker line. These results agree well with the observed wave crest pattern.
 - 2) The results of wave height distribution measured in the nearshore area indicate that the wave reduces its height in the region of offshore currents. N

In addition to the above results, we observed that the breaking point in the the region of offshore currents had a tendency to approach the shoreline.

2. CASE 15 is the one where the width of breaker zone is relatively large. In this case the current system is divided into two parts; the first one is the circulation formed in the surf zone which we may call " a closed cell "; and the second one is the two branched feeder currents which join together and finally make an offshore current near the breaker line, thus we may call it " an open cell " (Fig.3). We will name this kind of the current system as a whole a double circulation system.

Another experimental result, which should be mentioned here, is that the beach slope is not important in the qualitative features of the current system except two points stated in the following, at least under the conditions of present experiments:

- 1) As the beach slope is gentler, the width of breaker zone becomes larger for the same condition of offshore waves.
- 2) In some cases for 1/5 beach slope, subharmonic resonant edge waves were clearly observed. The edge waves produced a dye diffusion pattern which is different from the others mentioned above as shown in Fig.4 [Horikawa and Mizuguchi (1975a)].

We calculate the offshore current velocity outside the breaker line by using the data of dye diffusion pattern. The results shown in Fig.5 tell us that the offshore current velocity has its maximum around the breaker line.

We measured the rip current spacing just outside the breaker line. In our experiments the spacings are mainly related to the period of incident waves. The results are plotted in Fig.6 where a solid line indicates the relation of $L_r = L_0$ (L_0 is deepwater wave length).

DISCUSSION: PART 1

As mentioned in Introduction, the senior author has developed a theory to treat the rip current system as an eigenvalue problem, where the wave-current interaction was taken into consideration in the equations of wave and energy conservation. The theory is also confined to the cases of relatively steep slope beach, because the long wave approximation is used all over the concerned area. When we neglect a relevant dissipation term in energy equation (Eq.(4)), an eigenvalue problem is formulated to determine the rip current spacing. This problem can be solved by assuming the bottom friction factor in the surf zone as a power of coordinate taking from the shoreline to offshore.

The theory predicts that the first order perturbation of wave energy has exactly the same alongshore phase as the offshore current perturbation. It means that the wave height in the region of offshore current is greater than that in the remained area. This prediction is completely opposite to our experimental result. From this fact we conclude that the observed current system cannot be explained by the theory in which the wave-current energy interaction is considered to be essential.

On the other hand we (1975) described that one possible explanation for the observed current system stated above is to attribute the origin of such current system to the incident wave itself. If we can assume that free oscillations in a uniform depth area of the wave basin would affect the wave height perturbation at the breaker line, the observed fact will be well explained. Horikawa and Maruyama (1976) found that in a rectangular wave basin resonant synchronous cross waves can occur, and pointed out that the

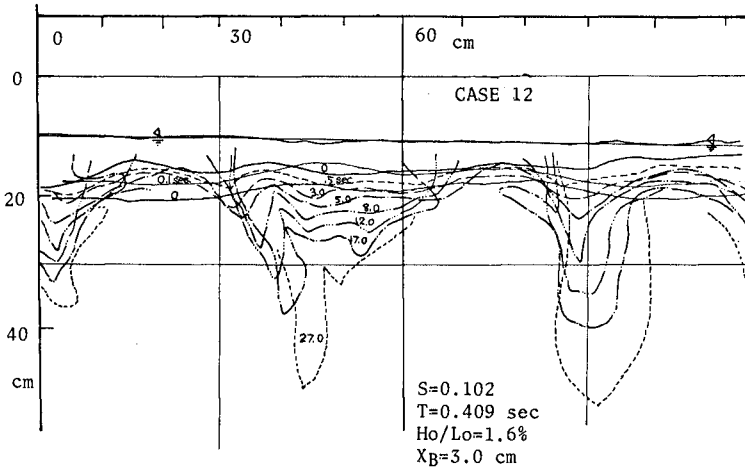


Fig. 1. Wave crest propagation and dye diffusion pattern.

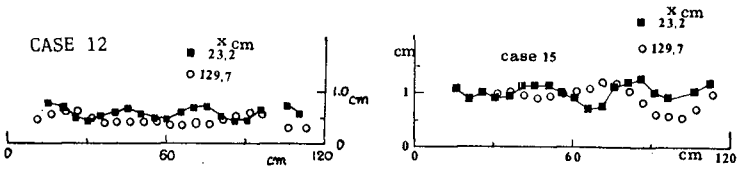


Fig. 2. Alongshore wave height distribution.

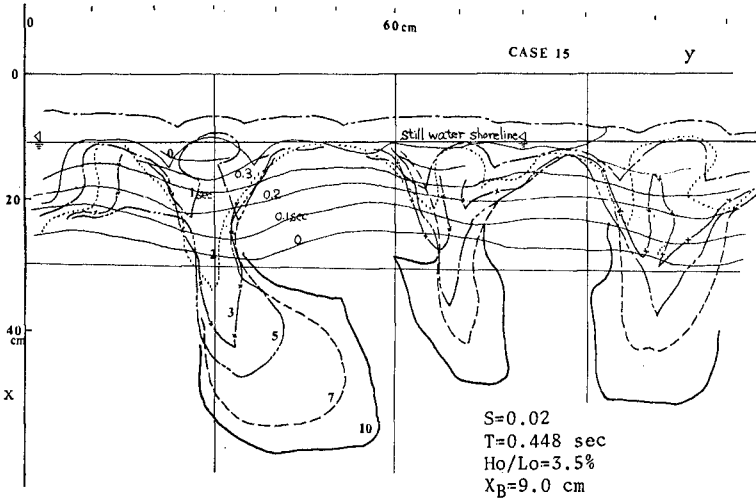


Fig. 3. Wave crest propagation and dye diffusion pattern.

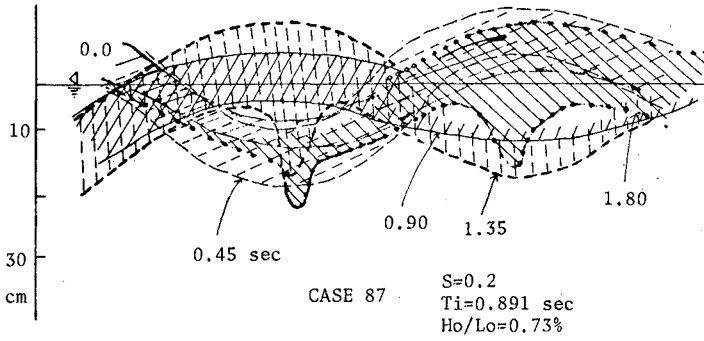


Fig.4. Dye diffusion pattern by subharmonic edge wave.

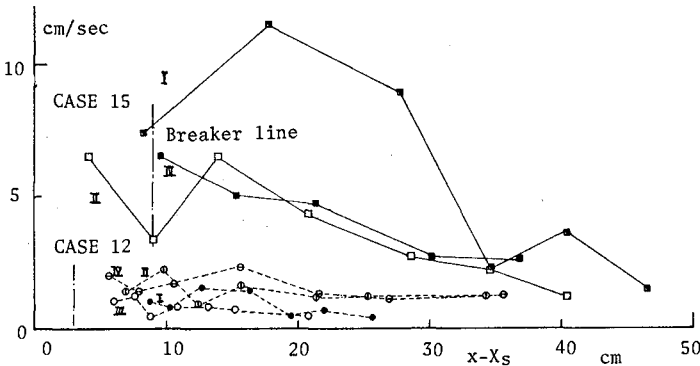


Fig.5. Offshore current velocity profile of rip currents.

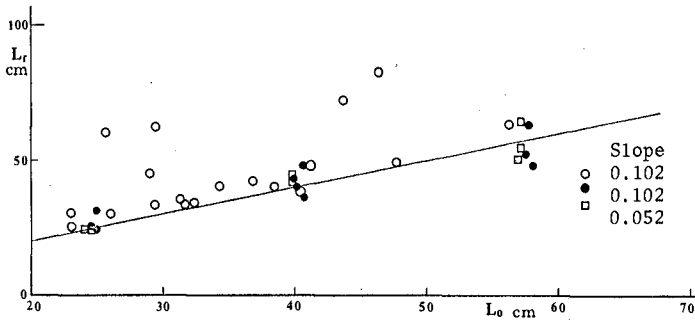


Fig.6. Measured spacings of rip currents.

cross waves generate a wave height perturbation around the breaker line. The wave basin used by them is the same as that we used.

In our experimental set-up with a sloping beach, wave records indicate simple harmonic and steady oscillations at every measuring point. Therefore we interpreted the "cross wave" as follows:

1. The wave maker might generate a little irregular wave component which does travel obliquely to the paddle of wave maker as denoted k_c in Fig.7.
2. Then the side walls select the component wave which satisfies the following boundary condition along the walls:

$$N\pi/R_y = \theta \quad (5)$$

where N is a mode number and not greater than kb/π .

3. The selected component travels across the wave basin, reflects at the side walls and finally makes a wave height distribution in the vicinity of the wave breaking area.

When the cross wave is superposed upon the incident waves, the following wave height distribution appears in the basin:

$$a \sim a_i + 2a_{cN} \cos\left(\frac{N\pi y}{B}\right) \cos\left(\int^x (k_r - k_x) dx'\right) \quad (6)$$

where a_i and a_{cN} are amplitudes of incident wave and of cross wave respectively. A noteworthy characteristic of the cross wave is that the alongshore wave number does not change with refraction.

Considering the fact that the offshore current is always located at the place of lower wave height, we have Fig.8 in which the possible rip current spacings in our experiments are shown. This figure is not in contradiction to the experimental results shown in Fig.6. Reminding the fact that almost every point in Fig.6 is scattering around the relation $L_r = L_0$, we are able to assume that the predominant cross wave is the one that has the largest number of mode in y -direction. Therefore, we can conclude that the phenomena in our experiments show one example of the forced current system, where the cross wave plays an important role to provide an externally given condition.

SECOND SERIES OF EXPERIMENTS (DETAILED OBSERVATIONS)

Based on the above discussions we conducted another series of experiments, paying much attention to the wave height distribution all over the wave basin. Experimental set-up and measuring technique are almost the same as the first series of experiments. We used, this time, static pressure tubes to measure the mean water level in a surf zone, and a wave gage to measure the run-up height distribution.

We selected the following three cases under the condition of the beach slope $1/10$ only as shown in Table 1. There d , T , H_i , H_0 , and X_B denote

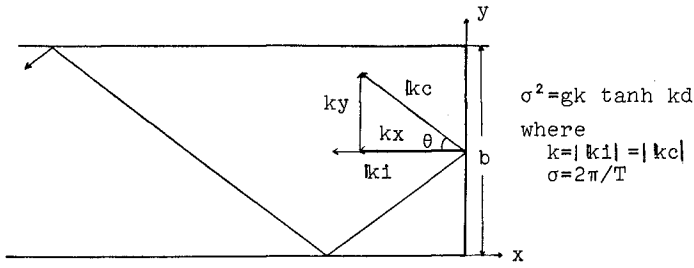


Fig.7. Schematic illustration of " cross wave ".

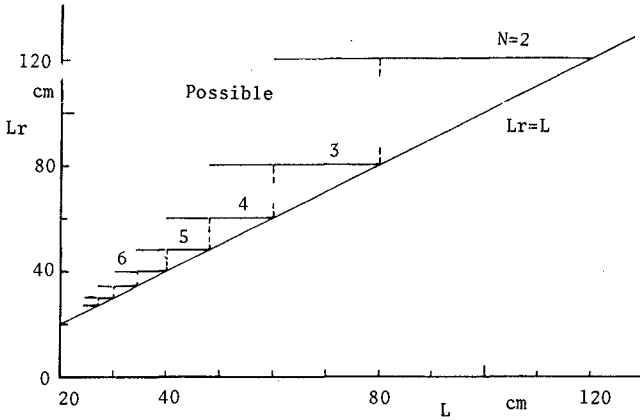


Fig.8. Possible spacings of rip currents by " cross wave ".

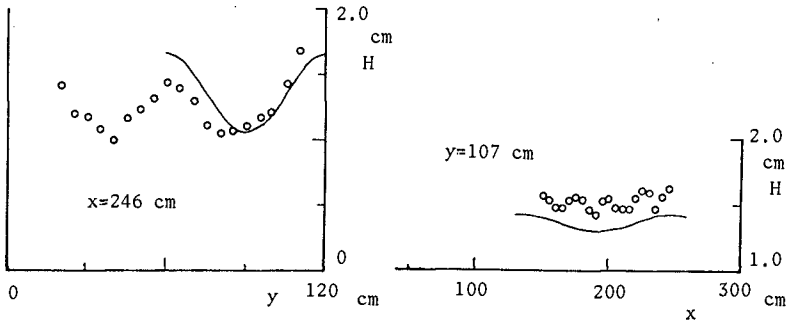


Fig.9. Wave height distribution parallel and perpendicular to the wave maker in uniform depth area (CASE 22B).

water depth in a uniform depth area, period of wave maker, wave height in a uniform depth area, deep water wave height, and width of breaker zone, respectively.

Table 1 Experimental conditions.

CASE	d	T	H_i	H_0/L_0	X_B
22B	11.5cm	0.586sec	1.36cm	2.7%	13cm
26B(=27A)	12.0	0.726	1.70	2.3	12
27B	12.0	0.720	2.60	3.5	21

First we will check the existence of the cross wave in the following:

CASE 22B

Figure 9 shows the wave height distribution at the section of $x = 246\text{cm}$ in the uniform depth area. Resonant oscillations in y -direction exist as shown in Fig.9. Calculating the Fourier components, we get H_i ($i=0-4$) = 1.36, -0.10, 0.28, -0.07, 0.29 cm respectively. Although we can expect the existence of oscillations with mode number $N = 2$ and 4, we consider only $N = 4$. The reason is as follows. Figure 9, also, shows the wave height distribution along the section of $y = 107.0\text{cm}$, and Fig.10 shows that at the section of $y = 0$ for $N = 2$ and 4. These two figures indicate that $N = 2$ is not very important in our experiments.

From the above result shown in Fig.9 we will simulate the wave height distribution by the following equation, where $N = 2$ is neglected and the phase difference in front of wave maker is assumed to be 0 or π .

$$H = 1.36 - 0.30 \cos\left(\frac{4\pi y}{8}\right) \cos\left\{\frac{2\pi}{113}(x-417)\right\} \quad (7)$$

Solid lines in Fig.9 give the curves of the above equation.

CASE 26B AND 27B

Following almost the same procedure as in CASE 22B, we get the next equations to express the wave height distribution in a uniform depth area for CASE 26B and 27B respectively.

$$\left. \begin{aligned} H &= 1.70 + 0.60 \cos\left(\frac{2\pi y}{8}\right) \cos\left\{\frac{2\pi}{395}(x-295)\right\} \\ H &= 2.60 + 0.54 \cos\left(\frac{2\pi y}{8}\right) \cos\left\{\frac{2\pi}{401}(x-270)\right\} \\ &\quad + 0.48 \cos\left(\frac{3\pi y}{8}\right) \cos\left\{\frac{2\pi}{152}(x-270)\right\} \end{aligned} \right\} \quad (8)$$

In these cases a screen was inserted in a uniform depth area in order to diffract the incident waves and to get a stable state of the current system. As a result, phase relations between the incident wave and the cross wave are different from that in CASE 22B. Figures 11 and 12 show that these

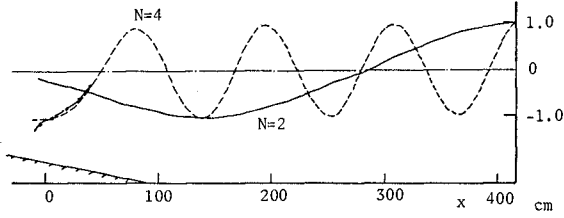


Fig. 10. Calculated wave height undulation along sidewall (CASE 22B);
 with shoaling.

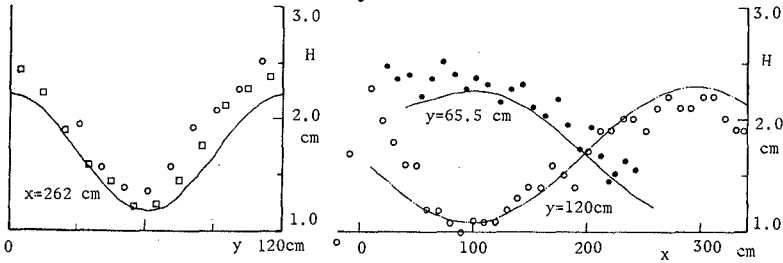


Fig. 11. Wave height distribution in uniform depth area (CASE 26B).

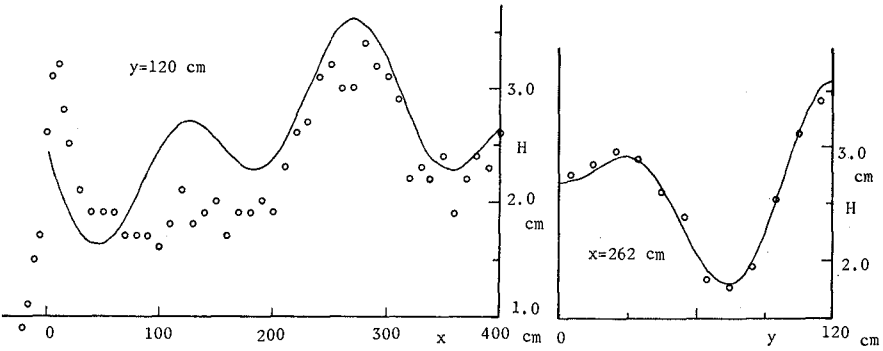


Fig. 12. Wave height distribution in uniform depth area (CASE 27B).

equations can explain well the measured wave height distribution.

From the foregoing figures we can conclude that there exist the cross waves and the assumption on the possible alongshore wave number is supported in CASE 22B and 27B, but not in CASE 26B. It is easy to calculate how the above wave height distribution gives its influences on the phenomena in the wave breaking zone. Snell's law tells us that the wave number of the cross wave in y -direction does not change with refraction. Each wave component makes its refraction process independently so far as the linear wave theory is valid.

One of the purposes of the present experiments is to find out the way how to describe the questioned current system which is now clearly classified into the forced type. We measured in detail the wave height distribution, current and wave crest patterns, and mean water level in a surf zone. In the following, three cases will be taken as representative ones.

CASE 22B

Figure 13 shows the current and wave crest pattern recorded by a video camera system. The area bounded by a hatched line shows the region where the poured dye is remained for a long time. Therefore it indicates the location of a closed cell. This pattern gives the same features as the double-circulation type mentioned previously. While Fig.14 shows the wave height distribution in the surf zone in a three dimensional space. The solid smooth line is the predicted curve of the wave height distribution at the section of $x = -1.5\text{cm}$ based on the offshore wave condition. It agrees well with the experimental result at least in a qualitative sense.

Here we will split the surf zone into two parts; the inner area and the outer area. They are divided by the line where the alongshore wave height perturbation disappears. In this case the line was located at $x = 4.0\text{cm}$. In the outer area offshore currents flow out through the region of lower wave height which is predicted by numerical calculations using the wave conditions in the uniform depth area. In the inner area offshore currents flow out also through the region of lower wave height. But the spacing between them is a half of the spacing in the outer area. Alongshore distribution of run-up measured by the wave gage as well as that given in video records show the same periodicity as the offshore current in the inner area. The region where the run-up height is relatively small corresponds to the place where the offshore current starts. Figure 15 shows the wave height distribution along the section of $y = \text{const.}$ in the surf zone. This result confirms also the above observation on the relationship between current and wave height distribution.

The measured static pressure distribution is shown in Fig.16. It is our regret to say that the data are not so accurate that anything decisive cannot be concluded. This is because the set-down and set-up are very small in our experiments, hence our hand-made apparatus was not very delicate to detect them.

CASE 26B (=27A)

In this case we made longer the period of wave maker, keeping the wave steepness almost the same as the former one (CASE 22B).

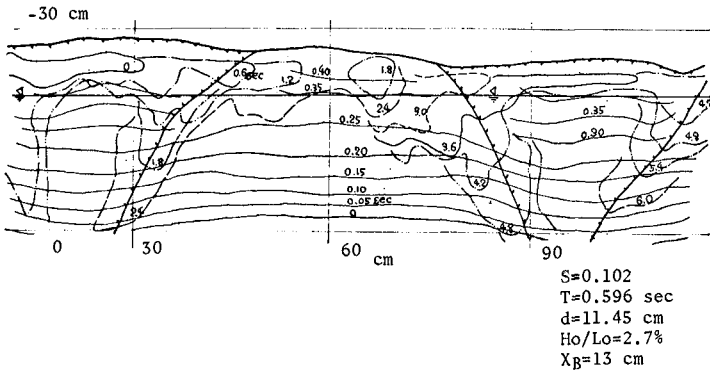


Fig.13. Wave crest propagation and dye diffusion pattern (CASE 22B).

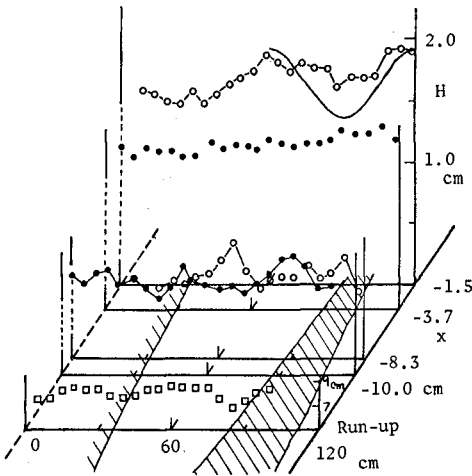


Fig.14. Wave height distribution in surf zone (CASE 22B).

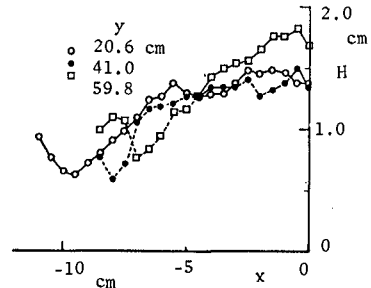


Fig.15. Wave height decreasing in surf zone (CASE 22B).

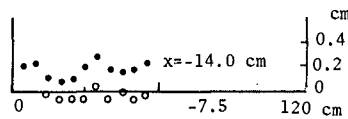


Fig.16. Mean water level variation in surf zone (CASE 22B).

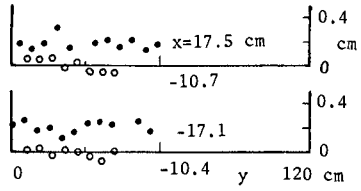
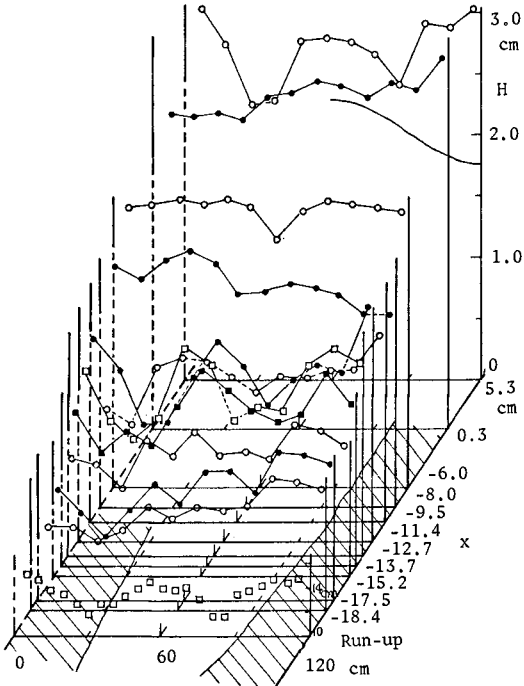


Fig.18. Mean water level variation in surf zone (CASE 26B).

Fig.17. Wave height distribution in surf zone (CASE 26B).

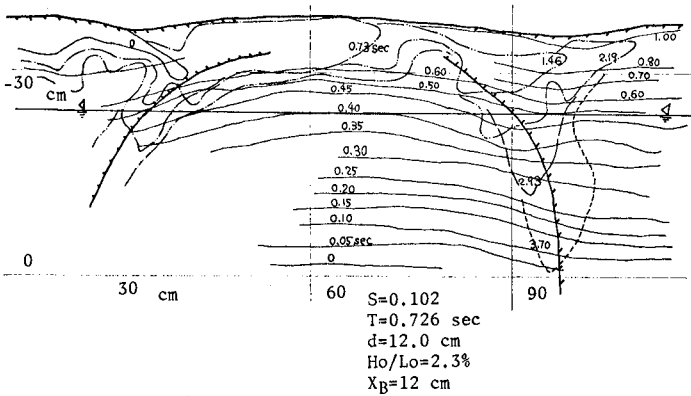


Fig.19. Wave crest propagation and dye diffusion pattern (CASE 26B).

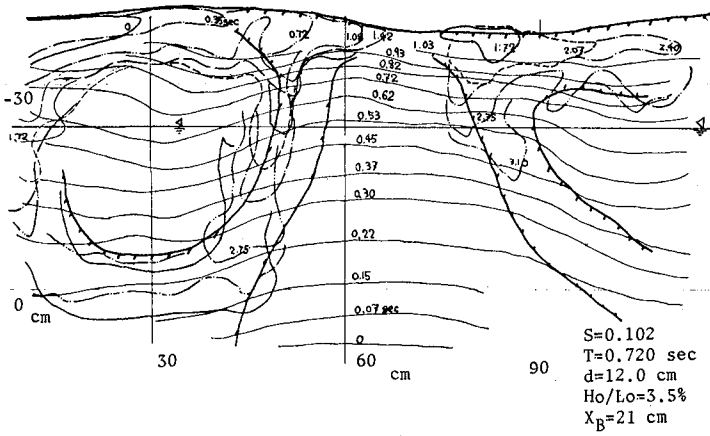


Fig.20. Wave crest propagation and dye diffusion pattern (CASE 27B).

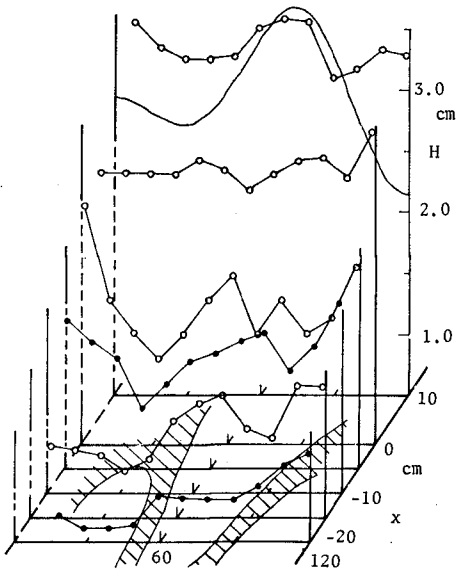


Fig.21. Wave height distribution in surf zone (CASE 27B).

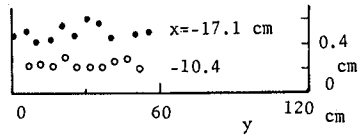


Fig.22. Mean water level variation in surf zone (CASE 27B).

The wave height distribution in this case is shown in Fig.17. Again the smooth solid line in this figure indicates the predicted curve. The measured wave height distribution is different from the predicted one especially near the side walls. The observed current pattern in Fig.19 corresponds well with the measured wave height distribution. The higher wave height region near the wall might be caused partially by the existence of side walls and partially by the wave-current interaction. Another features are the same as that in CASE 22B.

Again in Fig.18 are shown the measured static pressure distributions along the section of $x = \text{const.}$; one is in the inner area and the other in the outer area.

CASE 27B

In this case we made larger the amplitude of wave maker. Experimental results are seen in Figs.20, 21, and 22. New particular feature is that the diffusion pattern induced by the offshore current has a tendency to stay around the breaker line for a while. Therefore the outer area seems to disappear.

Now we have to draw a conclusion about the mean water level. We think that the alongshore variation of mean water level is not so large as that we expect from the measured wave height perturbation based on the wave height-depth assumption.

DISCUSSION: PART 2

Considering the results of the present experiments, we will discuss in the following how the current system can be generated and what kinds of equations can describe its phenomena.

We may say as follows:

- 1) In the surf zone the wave height distribution given externally would produce the radiation stress distribution, where the assumption $S_{xx} = 3/2E$ etc. and $E = 1/2\rho g a^2$ are considered to be still valid. At this stage, Bowen's formulation

$$H = \gamma d (1 + \epsilon \cos \lambda y) \quad (9)$$

would be a proper choice as a first step of approach. This expression is one of the simplest forms which gives an analytical solution and also seems to be a good approximation to the present problem if the wave-current interaction could be neglected as in CASE 12 of the first series of experiments. Outside the breaker line the offshore current velocity decreases monotonically. Therefore it might be reasonable to neglect the radiation stress in the outer area.

- 2) Continuity and momentum equations can be solved. The solution should give both the current field and the mean water level. Momentum equation

(Eq.(1)) may be rewritten as follows:

$$\frac{\partial \xi}{\partial x} \sim - \frac{fU}{fgR} - \frac{1}{fgR} \frac{\partial \delta \xi}{\partial x} \quad (10)$$

so that the currents have a tendency to reduce alongshore variation of mean water level in a surf zone. This fact does not disagree with the above experimental results.

- 3) Then the experimental results show that the wave-current interaction should be taken into consideration, especially in the case that the surf zone is wide enough to generate the double circulation pattern. The wave-current interaction has the following two aspects. One is the wave number interaction which distorts the wave crest line, and the other is the energy coupling which contributes to modify the wave height distribution.

In the outer area, the second one plays an important role to modify the wave height perturbation, as seen in the second series of experiments. The energy coupling contributes finally to weaken the offshore current velocity.

The first one holds a key to generate the double circulation system. The wave crest distortion in the inner area means the alongshore variation of the wave ray direction. As a result the wave in the inner area will refract and make a wave height distribution field as shown in Fig.23, where H and L denote a high and low wave region respectively. Thus the double circulation system could be generated.

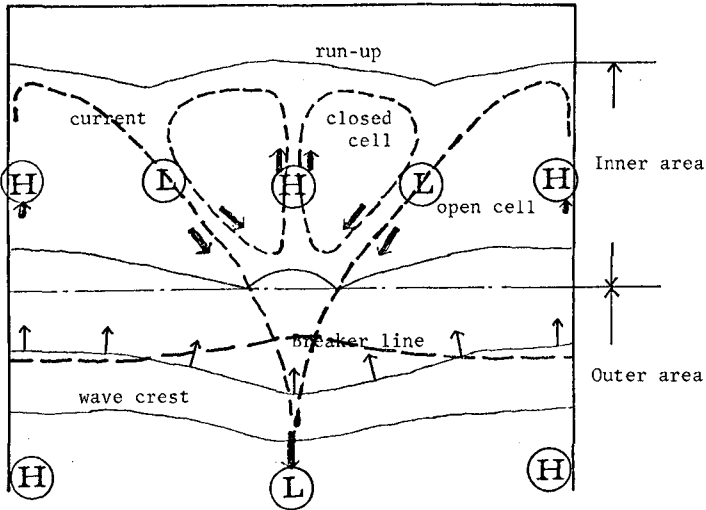


Fig.23. Schematic illustration of a double circulation system.

It is a future problem to formulate the above processes mathematically and to solve and discuss the problem quantitatively

COMMENT ON FIELD OBSERVATIONS

Several papers on the field observations of nearshore current system have been published by Bowen and Inman (1969), Harris (1967), Sonu (1972), Sasaki and Horikawa (1975), Sunamura and Horikawa (1976), Sasaki, Horikawa and Hotta (1976), and others.

The field observations were usually done when the wave condition was not so severe that the change of bottom topography was not rapid even in the surf zone. Moreover wave conditions at the breaker line depend on the bottom topography outside the breaker line, where its change must be very slow and scarce. Therefore we can say that the observed current systems were mainly determined by the bottom topography at least temporarily. Sunamura and Horikawa (1976) reported a case where a distribution of exposed bed rocks near the shoreline determines a current system in that region. The current is very steady in spite of various wave conditions for a long period of time. On the other hand the current system is well simulated by using the refraction method, continuity equation and momentum equation. These facts assure the above idea.

When waves refract both inside and outside of the breaker line, they diverge at depressions and converge at shoals. The high wave region corresponds to the shoals. Applying Bowen's theory, we get outflows at depressions as usually observed.

There are several other explanations. Liu and Mei (1974) calculated radiation stress distribution caused by waves under refraction, and reflection and diffraction at a breakwater. They also calculate a nearshore current pattern as a result. Their idea is essentially the same as the synchronous intersecting wave of Dalrymple (1975). The observed current system in our experiments can be essentially the same kind of them. There is a limitation to apply their idea to the field problem, because monochromatic waves only can make a steady radiation stress distribution.

So far as edge wave is concerned, it creates a very weak current field both in our laboratory experiment (1975a) and that by Bowen and Inman (1969). The current field is completely different from the so-called rip current. Guza and Davis (1974) verified that subharmonic edge wave of Stokes mode is most easily excited under the condition of a standing incident wave. That kinds of edge waves have such a short characteristic length in offshoreward direction that their influence is confined to a region near shoreline.

Hino (1974) energetically approached to this rip current problem by treating it as a time-dependent self generating system on a movable beach. As we stated above, we think that any data obtained so far may not be relevant to compare with his treatment and that the wave height-depth assumption (Eq.(3)) seems to be incorrect.

Sasaki (1974) presented a hypothesis that " infragravity wave " is an essential factor to control the current system on a gently sloping beach through the bottom perturbation. As a result of the present discussion, it will be suggested to consider that the infragravity wave only modifies the current system which is temporarily controlled by bottom topography. For example the infragravity wave may be related to a pulsation of rip current. The bottom perturbation might be caused by the infragravity wave in a long term.

Finally, there must arise a question how an irregular bottom topography could be formed. We consider at present that the answer could be found in the free type rip current system. But it is still an open question what kinds of equations should be applied.

CONCLUSIONS

The wave-induced nearshore current system can be classified into two types; free type and forced type. In our laboratory experiment, we observed a kind of forced current system which is created by a periodic breaking wave height distribution caused by " cross wave ". Offshoreward currents always flow through the lower wave height region both inside and outside of a breaker line. When the surf zone was rather wide, we observed a double circulation pattern, where wave-current interaction might be important.

According to our experimental results, we propose to consider that the observed current system in fields should be interpreted as the forced type current system where irregular bottom topography plays a crucial part.

ACKNOWLEDGEMENT

A part of this research was supported by Science Research Fund of Ministry of Education, Japan.

REFERENCE

- Bowen, A.J. (1969): Rip currents, 1, Theoretical investigations, *J. Geophys. Res.* Vol.74, pp.5467-5478.
- Bowen, A.J. and D.L. Inman (1969): Rip currents, 2, Laboratory and field observations, *J. Geophys. Res.* Vol.74, pp.5479-5490.
- Dalrymple, R.A. (1975): A mechanism for rip current generation on an open coast, *J. Geophys. Res.* Vol.80, pp.3485-3487.
- Guza, R.T. and R.E. Davis (1974): Excitation of edge waves incident on a beach, *J. Geophys. Res.* Vol.79, pp.1285-1291.
- Harris, T.F.W. (1967): Field and model studies of the nearshore circulation, Ph. D. dissertation, Univ. of Natal, South Africa, 188p.
- Hino, M. (1974): Theory on formation of rip current and cuspidal coast, *Proc. 14th Conf. Coastal Eng., Copenhagen*, pp.901-919.
- Horikawa, K and M. Mizuguchi (1975a): Laboratory observation of edge waves, *Abstract 30th Ann. Meeting Japan Soc. Civil Eng.*, pp.37-38. (in Japanese)

- Horikawa, K and M. Mizuguchi (1975b): Laboratory experiments on nearshore current system, Proc. 22nd Conf. Coastal Eng. in Japan, pp.141-147. (in Japanese)
- Horikawa, K. and K. Maruyama (1976): On generation of rip currents in a laboratory basin, Proc. 23rd Conf. Coastal Eng. in Japan. (in print, in Japanese)
- Iwata, N. (1976): Rip current spacing, J. Oceanog. Soc. Japan Vol.32, pp.1-10.
- LeBlond, P.H. and C.L. Tang (1974): On energy coupling between waves and rip currents, J. Geophys. Res. Vol.79, pp.811-816.
- Liu, P.L.F. and C.C. Mei (1974): Effects of a breakwater on nearshore current due to breaking waves. MIT Ralph M. Parsons Lab. Rep. No.192, 256p.
- Mizuguchi, M. (1976): Eigenvalue problems for rip currents spacings, Proc. Japan Soc. Civil Eng. Vol.248, pp.83-88. (in Japanese)
- Noda, E.K. (1974): Wave-induced nearshore circulation, J. Geophys. Res. Vol.79, pp.4096-4106.
- Sasaki, T. (1974): Field studies on the structure of nearshore current systems, Doctoral thesis in Civil Eng., Univ. of Tokyo, Japan, 240p. (in Japanese)
- Sasaki, T. and K. Horikawa (1975): Nearshore current system on a gently sloping bottom, Coastal Eng. Japan Vol.18, pp.123-142.
- Sasaki, T., K. Horikawa, and S. Hotta (1976): Nearshore currents on a gently sloping beach, Proc. 15th Conf. Coastal Eng. (in print)
- Sonu, C.J. (1972): Field observations of nearshore circulation and meandering currents, J. Geophys. Res. Vol.77, pp. 3232-3247.
- Sonu, C.J. (1973): Comment on Paper by C.K.W. Tam, " Dynamics of rip currents ", J. Geophys. Res. Vol.78, pp.8887-8889.
- Sunamura, T. and K. Horikawa (1976): Field investigation of sediment transport pattern in a closed system, Proc.15th Conf. Coastal Eng. (in print)

CHAPTER 36

NEARSHORE CURRENT ON A GENTLY SLOPING BEACH

By

Tamio Sasaki*, Kiyoshi Horikawa** and Shintaro Hotta***

ABSTRACT

The authors developed a new field observation system called STEREO-BACS by which simultaneous measurements of a spacial distribution on waves and currents in the nearshore environment can be obtained. This system was applied on Ajigaura Beach, Japan, and several analyzed results are presented. Also field observations of infragravity low mode edge waves to support the Infragravity Domain Hypothesis on nearshore currents concerning a gently sloping beach [Sasaki(1974,1975), Sasaki and Horikawa (1975)] are introduced.

INTRODUCTION

Extensive studies on nearshore currents have been made over the last several years. As a result, numerous theories on nearshore currents especially on rip current generation have been proposed by Bowen (1967), Bowen and Inman(1969), Sonu(1972), Noda(1972), Hino(1973), Hashimoto and Uda(1974), Noda et al.(1974), Sasaki(1974,1975), Sasaki and Horikawa(1975), Liu and Mei(1974,1976), Birkemeier and Dalrymple(1975), Dalrymple(1975), Iwata (1976), Mizuguchi (1976), Mizuguchi and Horikawa(1976), Horikawa and Maruyama(1976).

However, the validity of these theories have been not clarified in detail due to the lack of precise field data[Sasaki and Horikawa(1975)]. The major difficulties in observing nearshore currents are due to 1) the spatial distribution of their phenomena, 2) multiplicity of affecting factors involved, 3) rough waves and currents in the surf zone, and 4) time dependency. To overcome these difficulties, the authors have been making numerous efforts over the last 6 years.

The best solution conceivable for overcoming these obstacles is to apply the principle of photogrammetry by using a pair of helicopters and/or blimps to secure observation platforms in the air. The authors have once tried utilizing a pair of helicopters called SIHELs [Fig. 1,

* Chief Engineer, Department of Ocean and Coast, INA Civil Engineering Consulting Co., Ltd., Bunkyo-ku, Tokyo, Japan.

** Professor, Department of Civil Engineering, University of Tokyo, Bunkyo-ku, Tokyo, Japan.

*** Research Associate, Department of Civil Engineering, Tokyo Metropolitan University, Setagaya-ku, Tokyo, Japan.

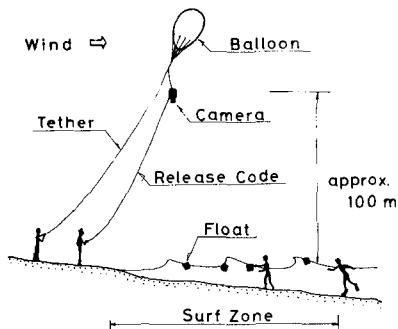
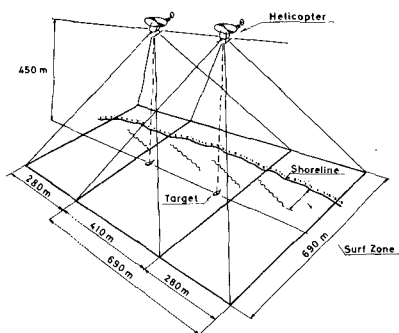


Fig. 1 Schematic diagram of SIHELs. Fig. 2 Schematic diagram of BACS.
(Horikawa and Sasaki, 1972) (Horikawa and Sasaki, 1972)

Simultaneous HELicopter System, Horikawa and Sasaki(1972)], and realized that the obtained accuracy in mapping the wave height distribution was very satisfactory. However the cost was prohibitive, so that this system could only be utilized one time.

In place of the SIHELs, the authors developed a balloon borne camera system called BACS [Fig. 2, Horikawa and Sasaki(1972)]. By this system, the spatial flow field can be easily obtained by tracing floats in successive pictures [Sasaki(1974,1975), Sasaki and Horikawa(1975)]. This system is a very simple and convenient one, however, the wave height field cannot be obtained due to the fact that only a single balloon is used.

Last year, the authors further developed a new system, which consists of a pair of balloons called STEREO-BACS. The aim of this system is to achieve simultaneous measurements of spatial distributions of nearshore waves and currents over a relatively broad area.

In the present paper, the authors first introduce this new system, secondly present an outline of the results obtained from observations made in December, 1976 on Ajigaura Beach, Japan, and lastly show several results to support the Infragravity Domain Hypothesis on a gently sloping beach.

STEREO-BACS

An idea of STEREO-BACS appeared in 1893 by C. B. Adams for terrestrial mapping[Thompson(1966)]. For the application of this idea to unsteady phenomena in the surf zone, the development of a motor-driven camera is required.

Sonu(1969) utilized a Nikon motor-driven camera(35mm) for the study of nearshore current patterns and mixing [Sonu(1972a,1976)]. The Hasselblad 500EL motor-driven camera(70mm) was applied for the first time by Horikawa and Sasaki(1972) to obtain further accuracy in mapping the quantitative flow field in the surf zone.

Figure 3 shows a schematic representation of the STEREO-BACS. Two balloons are lifted about 150 m apart at an altitude of around 300 m. The volume of helium gas necessary to fill a balloon is 33 m³. The effective buoyancy is about 25 kg without tethers or a camera capsule. Two cameras are triggered simultaneously by a radio transmitter. A super-wide angle lens, Zeiss Distagon 40 mm, has been adopted to take wide coverage. About 30 to 50 floats are introduced around the surf zone by divers and from a pier. The floats are made of polyurethane foam coated by red or orange coloured polyvinyl-chloride sheet and equipped with a drogue.

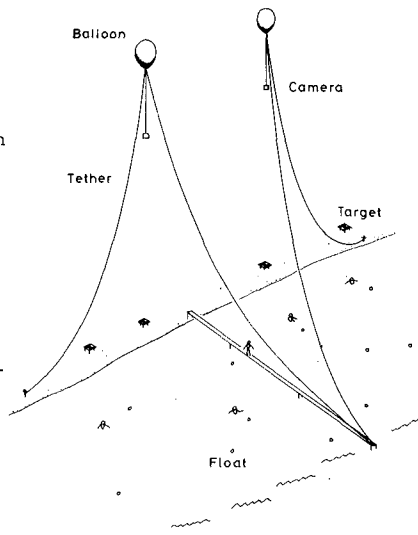


Fig. 3 Schematic diagram of STEREO-BACS.

The pier was 100 m long (presently extended to 200 m), and was constructed by the Public Works Research Institute, Ministry of Construction for research use. Piers play an essential role in operating the STEREO-BACS. Most importantly, they act as a target for absolute orientation of the stereoscopic pairs in onshore-offshore direction. A second role is to secure a foothold for distributing many floats into the surf zone. And a third role is to give a stay for mooring balloons under onshore wind or windless conditions. Two tethers are employed, and the camera is suspended by a single rope from the balloon.

DESCRIPTION OF THE SITE OBSERVED

Field observations by this system were made on Ajigaura Beach. This beach is located 100 km northward from Tokyo and faces the Pacific Ocean (Fig. 4). About 1 km south of the pier, the beach is bounded by a headland. Figure 5 is an overview of the pier. Several rip currents can be seen in this picture.

Fig. 4 Location map of Ajigaura Beach.

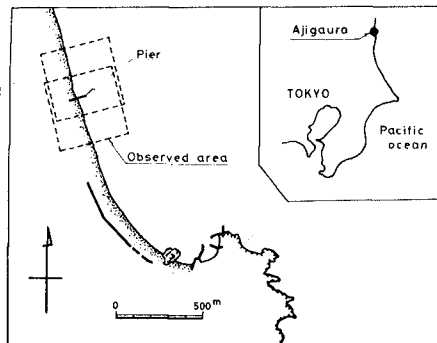




Fig. 5 Overview of Ajigaura Beach.

The beach slope is $1/40$ to $1/70$, and classified as a gentle beach. Strictly speaking, this beach is in Infragravity Domain[Sasaki(1975)] under a relatively rough sea, while under a calm sea it is in Instability Domain.

FIELD OBSERVATION USING THE STEREO-BACS

Wave Climate

Simultaneous measurements of a spatial distribution on waves including infragravity waves, currents, and mean water surface using the STEREO-BACS were carried out in December, 1975.

Figure 6 is a mosaicked picture made from the stereoscopic pairs obtained on December 18, 1975. Because two cameras were used, the long-shore coverage of this picture became very wide compared to that using a single camera (BACS). It is estimated at about 400 m by comparing with the 100 m long pier.

The breaker height and period were around 1.2 m and 13 sec respectively. The wave direction was 2 degrees shifted leftward at the tip of the pier. It was almost windless, and the wave climate was classified as very calm for this coastal region.

Velocity Field

Figure 7 shows the velocity vector field obtained during a quarter



Fig. 6 An example of pictures taken by the STEREO-BACS (December, 1975).

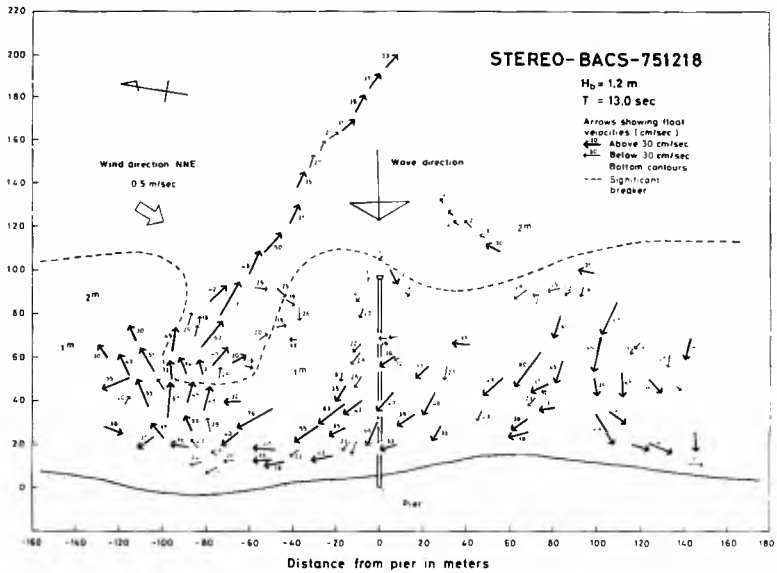


Fig. 7 Velocity vector field (December, 1975).

hour observation. The thick dotted line indicates a significant breaker line, and the thick arrows indicate velocity vectors exceeding 30 cm/sec. The vectors were compiled from interpreting the position of each float in successive pictures taken every 15 sec. Alongshore coverage for the velocity distribution was somewhat limited about 300 m due to the small number of divers in the surf zone available for introducing floats.

On the lefthand side of the pier, a rip current flows out with a maximum velocity exceeding 70 cm/sec. Only one float could overcome the attack of the incoming waves and was able to leave from the surf zone. On the righthand side of the pier, an inflow of offshore water can be seen. This was the first time we were able to catch an entire circulation process of this kind. This is simply due to the combination of the higher altitude of the balloons lifted and the utilization of a pair of balloons. The longshore dimension of the cell was about 200 m.

Figure 8 shows a current speed contour map derived from Fig. 7. By tracing the 40 cm/sec contour line, the shape of the current can be seen vividly. On the shoal located on the righthand side, the inflow is separated into right and left directions. And on the lefthand side, two longshore currents from opposite directions meet to form the rip current at around one half of the surf zone width from the shoreline.

The maximum velocity of the longshore current across the surf zone takes place very close to the shoreline. This fact does not agree with the result based on the theory of Longuet-Higgins (1970) for a plane beach, in which the lateral mixing parameter, P , generally takes a value between 0.1 and 0.4, derived from laboratory data, as pointed out by Sasaki and Horikawa (1975).

Transport Stream Function

Figure 9 is the transport stream function [Arthur (1962)] derived from the longshore component of the observed velocities. The maximum discharge exceeds $20 \text{ m}^3/\text{sec}$.

Figure 10 is a simulated transport stream line using the numerical model originally developed by Noda (1972). However, the treatment of bottom friction was modified with Jonsson's (1966) wave friction factors in the present computation. The roughness length for the bottom was calibrated by the observed velocity field [Sasaki (1975)]. The general current pattern and velocity agree well with observations except near the rip current. The disagreement in the vicinity of the rip current may be the result of the neglect of a lateral mixing and a convective term.

Wave Height Field

Figure 11 shows the maximum wave crest height distribution corresponding to a wave height field. This was made from 5 different instantaneous stereoscopic pairs of water surface configurations. For this, the Hasselblad 500EL motor driven camera, instead of a photogrammetric one, was used, so that the expected accuracy in this mapping might not be so high. However, the characteristic features of the wave height distribution is considered to be significant.

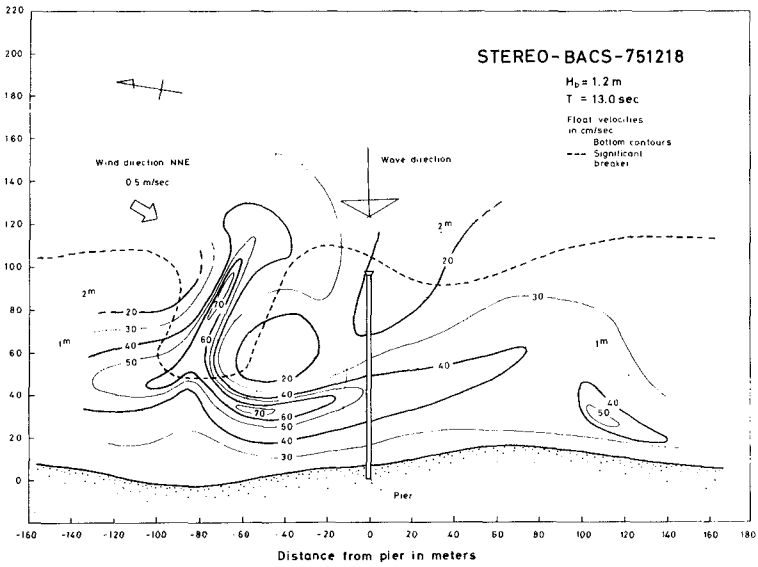


Fig. 8 Current speed contour (December, 1975).

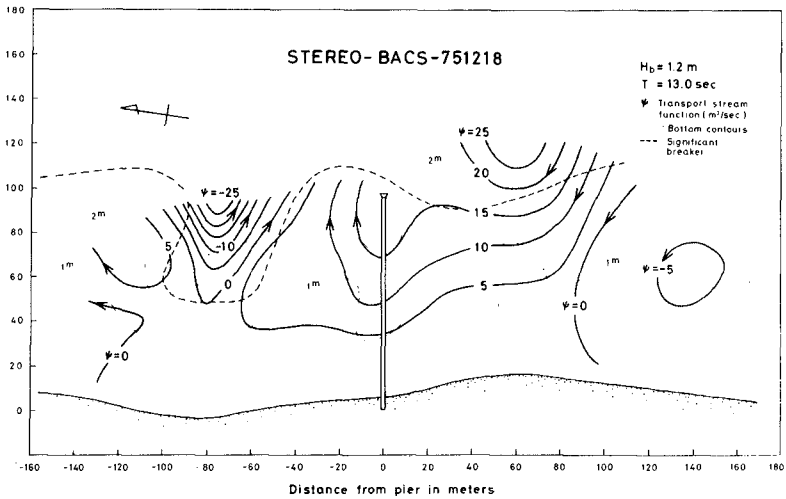


Fig. 9 Observed transport stream function (December, 1975).

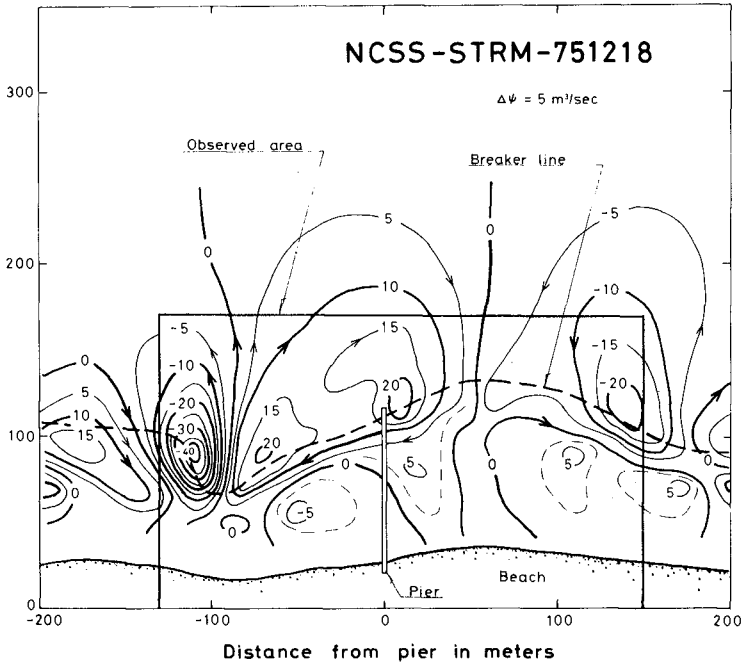


Fig. 10 Simulated transport stream function.

On both sides of the rip current, the maximum wave height appears, and on the lee side of the rip current, wave breaking takes place very close to the shoreline. The main stream of the circulation selects its path where the wave height is lower in the surf zone. A similar phenomena was also observed in the laboratory at the University of Tokyo [Mizuguchi and Horikawa (1976)].

Mean Water Surface

Figure 12 shows a simulated mean water surface elevation of a wave set-up and set-down. The maximum set-up is about 20 cm on a shoal, and the maximum set-down is about 5 cm at the intersection between the breaker line and the rip current. The maximum water surface gradients are seen at a root of the rip current, and are estimated to be approximately $1/200$.

Figure 13 is the mean water surface observed by using the hydraulic filter originally designed by Sonu (1972a). The maximum difference of the water surface elevation is 40 cm, and the maximum water surface arises on a shoal. The longshore current flows from high to low zone like a river. The longshore gradient of the surface is about $1/350$ that is fairly larger than simulated value of $1/200$. Remarkable difference between observed and simulated in water surface distribution is the location where the maximum set-up appears. In the field data, maximum appears somewhat apart from the

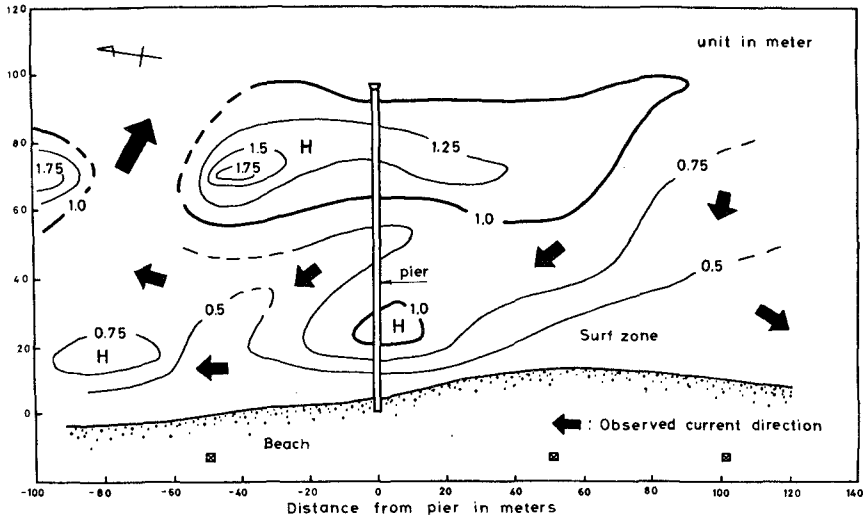


Fig. 11 Observed maximum wave crest height distribution (December, 1975)

shoreline. One of the explanations for this is due to the effect of a percolation in the swash zone.

Estimate of a Convective Term

Noda(1972) and Noda et al.(1974) neglected convective terms in simulating the nearshore current. Based on the above field data, the authors tried to estimate the relative significance of a pressure term with a convective term in the equations of motion. The magnitude of each terms are estimated at every 10 m grid point. Figure 14 shows a comparison of longshore terms(y-axis). Upper diagram is the pressure term, and the lower is the convective term. Near the rip current, convective terms have the magnitudes of 1/3 to 1/5 of the pressure terms. Whereas in the other area, pressure terms have 20 to 30 times larger than convective terms. Therefore, it can be said that near the rip current convective terms may be effective in this case.

FIELD OBSERVATION OF INFRAGRAVITY LOW MODE EDGE WAVES

Infragravity Domain

As for the spacing of rip currents, two theories have been presented [Bowen and Inman(1969) and Hino(1973)]. However, there is some confusion concerning their applicability for the actual phenomena[Sonu(1972b)].

Sasaki(1974,1975) found the existence of three domains on nearshore currents by applying the Iribarren No., I_r , [surf similarity parameter, Battjes (1974)] and the concept of infragravity waves[Suhayda(1974)] and clarified that the previous two theories can only be applied to two of the

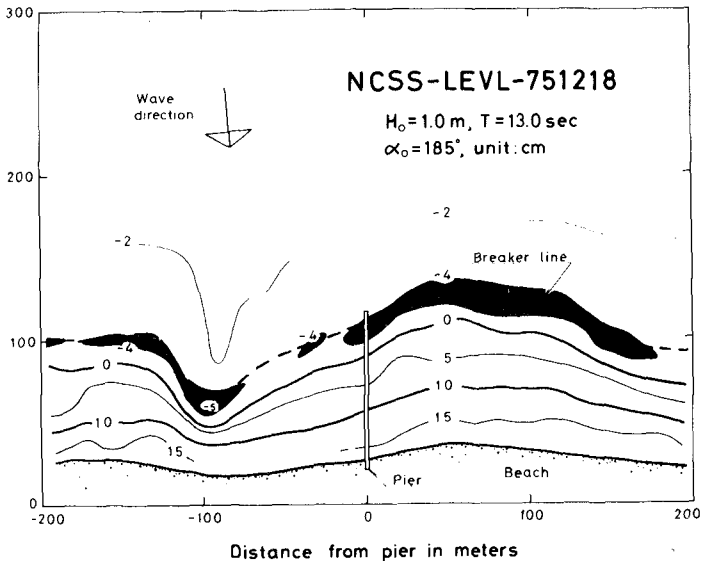


Fig. 12 Simulated mean water surface elevation.

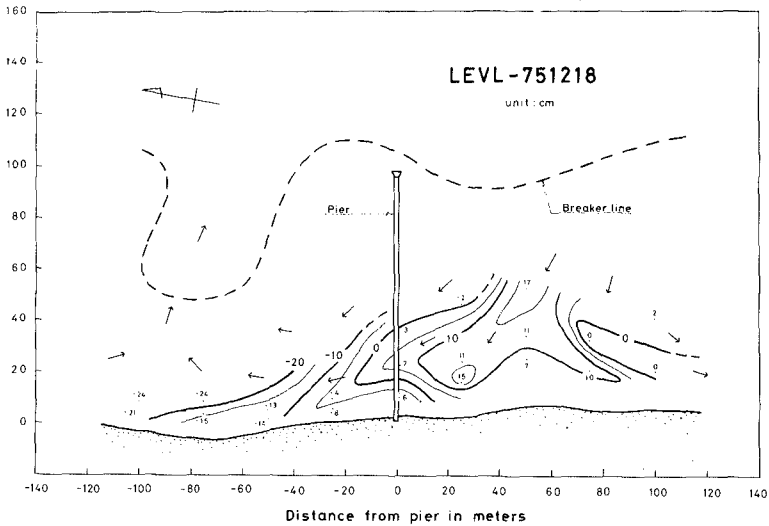


Fig. 13 Observed mean water surface elevation (December, 1975).

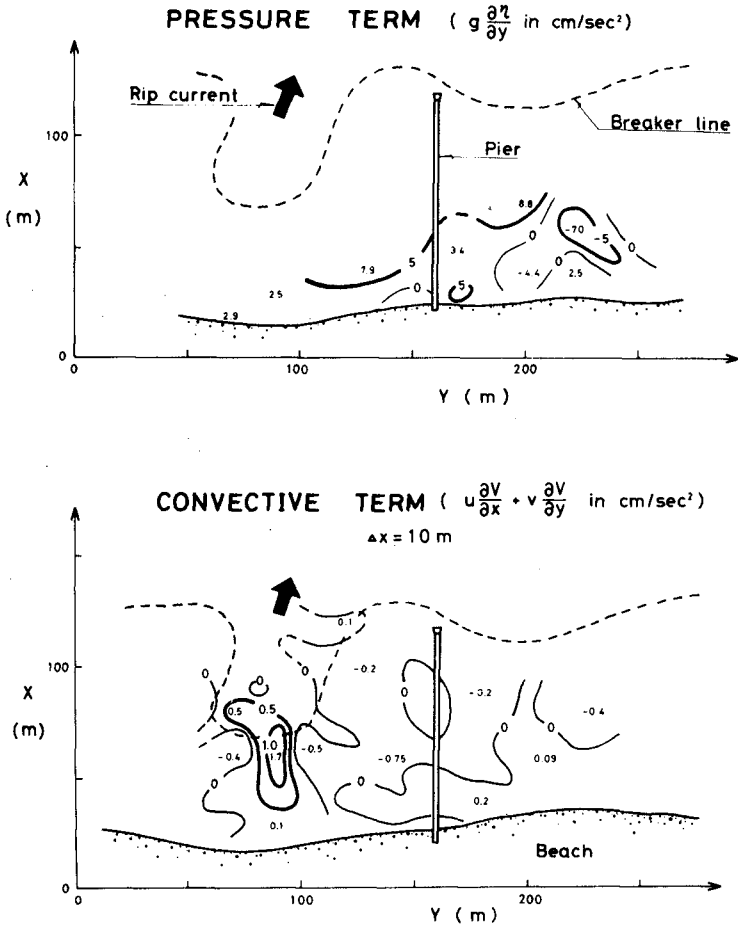


Fig. 14 Pressure term and convective term (December, 1975).

three domains for steep and medium beaches, respectively. For the additional domain, an Infragravity Domain Hypothesis has been proposed for a gently sloping beach [Sasaki(1974, 1975) and, Sasaki and Horikawa(1975)].

Here, the authors review this Hypothesis briefly, and show several observational results to support this. Figure 15 illustrates the concept of the three domains on nearshore currents. The top shows the Infragravity Domain [Sasaki(1974,1975)], the middle is the Instability Domain [Hino (1973)], and the bottom is the Edge Wave Domain [Bowen and Inman(1969)]. These three domains correspond to gentle, medium, and steep beaches, respectively. As shown in Fig. 15, it is easy to understand the concept of

these domains using the number of waves in the surf zone [Battjes(1974)].

The Edge Wave Domain arises when the number of waves in the surf zone is less than 1, and has surging/collapsing or plunging breakers. This domain includes "the reflective system" [Guza and Inman(1975)]. The Instability Domain has 1 to 3 waves in the surf zone, and plunging or spilling breakers. On the contrary, the Infragravity Domain has more than 3 waves in the surf zone, and always has spilling breakers. This domain typically appears when relatively steep waves attack a gently sloping beach. For this domain, Sasaki (1974,1975) presented the next equation for the spacing of rip currents;

$$Y_r^* = 157 I_r^2 \quad (1)$$

where, Y_r^* is a nondimensional spacing of rip currents defined by Eq.(2);

$$Y_r^* = Y_r / X_b \quad (2)$$

I_r is the Iribarren No. [Battjes(1974)] defined by Eq.(3);

$$I_r = \tan\beta / (H/L)_o^{1/2} \quad (3)$$

In Eqs. (2) and (3), Y_r , X_b , $\tan\beta$, H , and L are spacing of rip currents, width of the surf zone, beach slope, wave height, and wave period, respectively. Subscript, o , denotes the value in deep water.

Figure 16 shows the relationship between Y_r^* and I_r for all three domains. The theory of Bowen and Inman corresponds for large values of I_r ($I_r > 1$), and Hino's theory can well be applied for medium values of I_r ($1 > I_r > 0.23$). In the Infragravity Domain ($0.23 > I_r$), Eq.(1) suggests the presence of low mode infragravity edge waves with significant amplitudes. Gravity waves having periods less than 20 sec have negligible reflection from the beach in this domain, while infragravity waves have fairly large reflectivity. So infragravity edge waves can be generated and are able to control nearshore circulation through bottom perturbation. Because the data on infragravity waves are very few, the authors have been trying to detect these waves on numerous occasions.

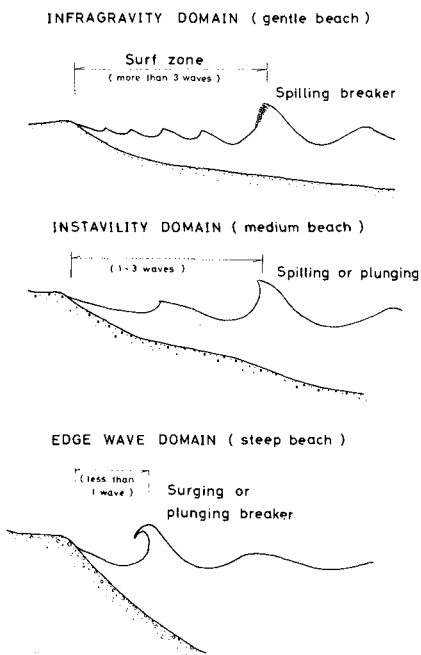


Fig. 15 Concept of three domains. (Sasaki, 1974)

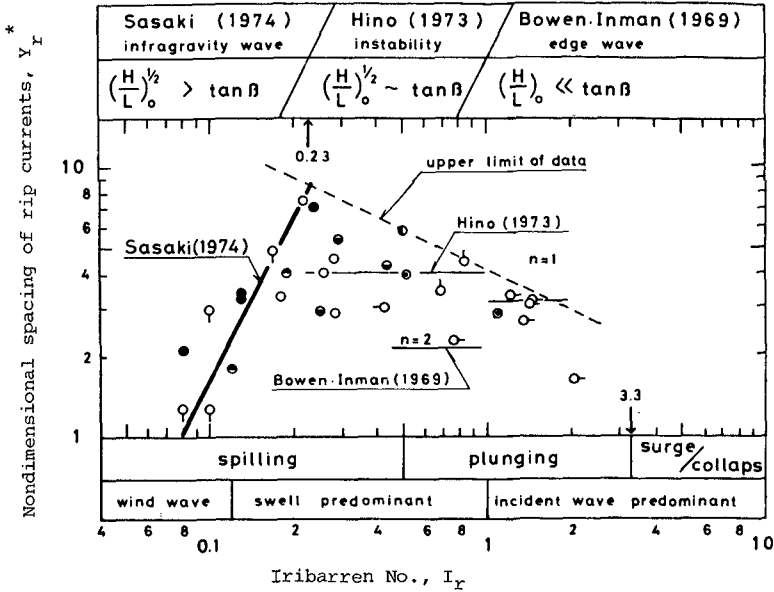


Fig. 16 Y_r^* and I_r (Sasaki, 1974).

Infragravity Low Mode Edge Waves

Figure 17 shows an example of infragravity wave spectrum in the surf zone observed in March, 1976 on Ajigaura Beach. The breaker height at that time was around 3 m. As the width of the surf zone was very wide over 300 m, the 6 wave staffs which were used were all placed in the surf zone. The water surface fluctuations were measured by using 16 mm memomotion cine-cameras.

These three spectra show the results from offshore arrangement of sensors along a pier. There are two dominant peaks. The right peak shows an incident wave peak of 13 sec. The other one is an infragravity wave peak of around 50 sec. In the swash zone(C), the gravity wave peak disappears, and only the infragravity wave peak can be seen. The result of a cross-spectrum analysis by BMD-02T reveals the existence of a nodal line parallel to the shore between B and C sensors.

Figure 18 shows the results from a longshore arrangement of sensors at the same time. In this case, 4 alongshore sensors were located close to the shoreline, so the gravity wave peaks are lower than infragravity wave peaks. The energy levels are somewhat larger than those offshore, and a secondary low frequency peak is found at around 2 min wave period. In each of 6 spectra, the wave height of the infragravity waves is 40 cm to 60 cm.

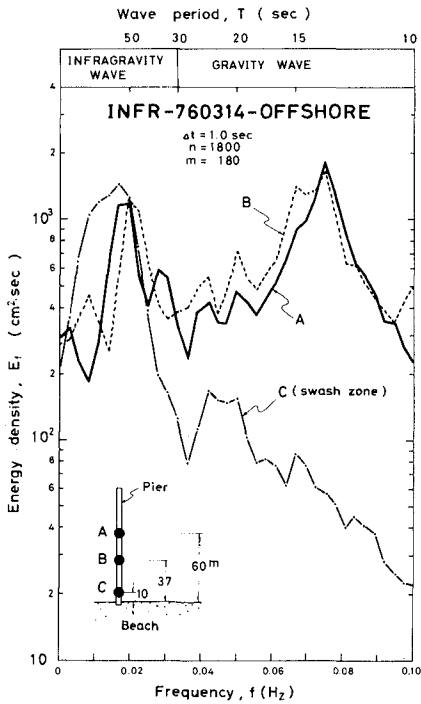


Fig. 17 On-offshore infragravity wave spectrum (March, 1976).

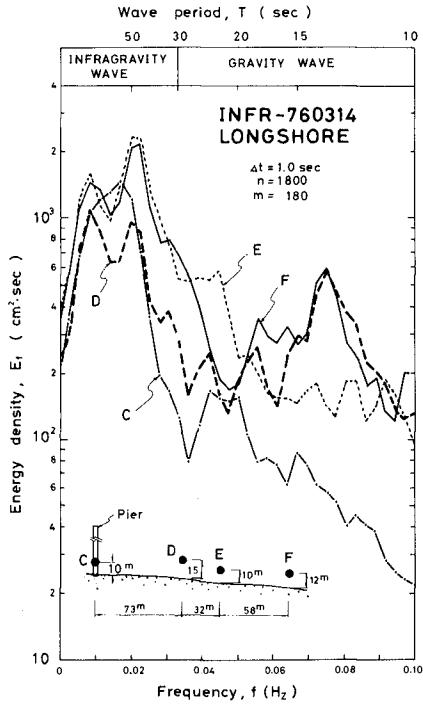


Fig. 18 Longshore infragravity wave spectrum (March, 1976).

An offshore profile of a relative wave height is shown in Fig. 19. The thick solid curve indicates the infragravity low mode edge waves [Eckart (1951)] with an offshore modal number, $n = 1$. Similar result was obtained also on December 18, 1975 (Fig. 20) when the STEREO-BACS was carried out. The short length of the pier prevented us from detecting a perfect envelope of a wave height profile. The case in which a nodal line perpendicular to the shoreline was observed has been reported by Sasaki and Horikawa (1975).

It is very difficult to measure the perfect configuration of edge waves in the field, because numerous wave sensors or flow meters are required to detect it. However, most of our observations carried out on a gently sloping beach show an existence of low mode ($n = 1$ and/or 2) edge waves with infragravity wave frequencies.

Similar results have been shown by Inman and Guza (1976) on the Scripps Beach behind the La Jolla Canyon, and their periods were 70 to 80 sec. Guza and Bowen (1975) and Guza and Inman (1975) introduced Gallagher's (1971) work on surf beat generation; that is incident gravity wave frequency and directional spectra allow infragravity edge wave (30 to 150 sec) excitation through the interaction of different gravity wave components. As for the

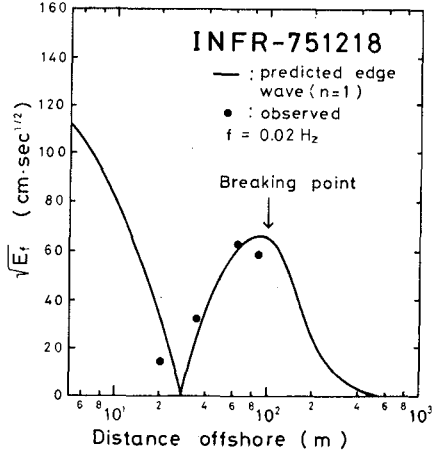
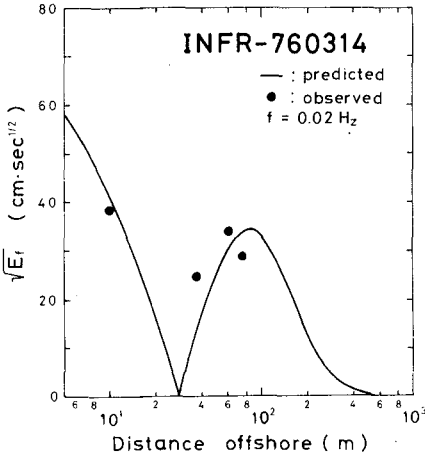


Fig. 19 Infragravity low mode edge wave profile (March,1976).

Fig. 20 Infragravity low mode edge wave profile (Dec.,1975).

cause by nonlinear interactions through different wave frequencies, Yoshida (1950) also derived the generation of 1 to 3 min infragravity waves. As pointed out by Isaacs et al.(1951), surf beats might be, in fact, infragravity low mode edge waves, if some condition [Carrier and Greenspan (1958)] that can be also expressed by Iribarren No. I_r , is satisfied.

Regarding amplitudes of infragravity waves (surf beats), with those periods larger than 20 sec, Goda(1975) has shown several observational results in the surf zone, and revealed that the amplitude of infragravity waves may amount to 40 % of that of offshore waves. This value of 40 % is fairly large compared to that of Tucker(1950) obtained outside the surf zone. This difference may be due to the infragravity edge wave resonances in the surf zone.

The above mentioned several works on infragravity waves, though not fully organized, suggest the validity of the Infragravity Domain Hypothesis, however, further research is needed concerning precise coupling mechanism between nearshore currents, infragravity waves and nearshore topographies on a gently sloping beach.

SUMMARY AND CONCLUSION

1) The authors developed a new field observation system called STEREO-BACS based on a principle of stereophotogrammetry by which simultaneous measurements of a spatial distribution on waves and currents in the near-shore zone can be obtained. Also a broader coverage is achieved compared to the previous system [BACS, Horikawa and Sasaki(1972)].

2) The STEREO-BACS was applied on Ajigaura Beach, Japan, facing the

Pacific Ocean in December, 1975, and observations including infragravity waves and mean water surface elevations were carried out. In this observation, the authors succeeded in catching an entire process of one circulation for the first time.

3) The obtained wave height distribution in the surf zone shows that the rip current flows out at the location where the breaker height is minimum on the breaker line, and the main stream of nearshore currents selects its path where the wave height is lower in the surf zone.

4) Concerning a mean water surface elevation, it is observed that the maximum difference in water surface reached about 40 cm, and longshore currents flow like a river in the surf zone.

5) Based on the above observation, an estimate of a relative significance of a pressure term with a convective term could be made quantitatively, and it was found that the convective term has a magnitude of from 1/3 to 1/5 of the pressure term near the rip current.

6) Our numerous field observations, Goda's(1975) observation, and Gallagher's(1971) work on infragravity waves suggest the existence of infragravity low mode edge waves with significant amplitudes which can cause nearshore circulations through bottom perturbation, and thus support the Infragravity Domain Hypothesis on a gently sloping beach [Sasaki(1974,1975), Sasaki and Horikawa (1975)]. The typical periods of infragravity waves observed are around 1 min.

ACKNOWLEDGEMENTS

The field observations on Ajigaura Beach were financially supported in part by the Public Works Research Institute(PWRI), Ministry of Construction under contract with INA Civil Engineering Consulting Co., Ltd. and partly by the Science Research Fund of the Ministry of Education under the name of second author.

The authors acknowledge the permission given by the PWRI for reproduction of the data and figures concerning the observations on Ajigaura Beach. Without the efforts made by Mr. Hiroshi Hashimoto, Chief of the Coastal Engineering Laboratory at the PWRI to construct and to maintain the Ajigaura Pier, the present research could not have been achieved. The advice in mapping the wave height field kindly given by Dr. Sohtaro Tanaka at the Remote Sensing Technology Center is also acknowledged. The authors are indebted to Dr. Billy L. Edge, Associate Professor, Clemson University, and Dr. Yoshimi Goda, Chief of the Wave Dynamics Laboratory, the Port and Harbor Research Institute, Ministry of Transport, for their kind communications of the literature on edge waves [Edge(1975)] and surf beats [Goda (1975)]. Mr. Hiroshi Sakuramoto and Mr. Susumu Kubota, INA Civil Engineering Consulting Co., Ltd., carried out the essential work in operating the field work, computations and drawings.

REFERENCES

- Arthur, R. S.(1962): A note on the dynamics of rip currents, *J. Geophys. Res.*, 67(7), 2777-2780.
- Battjes, J. A.(1974): Surf similarity, *Proc. 14th Coastal Eng. Conf.*, 466-480, Copenhagen.
- Birkemeier, W. R. and R. A. Dalrymple(1975): Nearshore water circulation induced by wind and waves, *Proc. 2nd Symp. Modeling Techniques for Waterways, Harbors and Coastal Engineering*, San Francisco.
- Bowen, A. J.(1967): Rip currents, Ph. D. dissertation in Oceanography, 115pp., Univ. of Calif., San Diego, La Jolla.
- Bowen, A. J. and D. L. Inman(1969): Rip currents, 2, *Laboratory and Field Observations, J. Geophys. Res.*, 74(23), 5479-5490.
- Carrier, G. F. and H. P. Greenspan(1958): Water waves of finite amplitude on a sloping beach, *J. Fluid Mech.*, 4, 97-109.
- Dalrymple, R. A.(1975): A mechanism for rip current generation on an open coast, *J. Geophys. Res.*, 80(24), 3485-3487.
- Dalrymple, R. A. and G. A. Lanan(1976): Beach cusps formed by intersecting waves, *Geol. Soc. Amer. Bull.*, 87, 57-60.
- Eckart, C.(1951): Surface waves on water of variable depth, *Wave Rep.* 100, Ref. 51-12, 99pp., Univ. of Calif., La Jolla, Calif..
- Edge, B. L.(1975): Present perspective of edge waves and coastal dynamics, *Proc. of the Specialty Conf. on Civil Eng. in the Oceans/III*, 265-293, Newark, Delaware.
- Gallagher, B.(1971): Generation of surf beat by nonlinear wave interaction, *J. Fluid Mech.*, 49(1), 1-20.
- Goda, Y.(1975): Deformation of irregular waves due to depth-controlled wave breaking, *Rep. of the Port and Harbour Res. Inst.*, 14(3), 59-106.
- Guza, R. T. and A. J. Bowen(1975): The resonant instabilities of long waves obliquely incident on a beach *J. Geophys. Res.*, 80(33), 4529-4534.
- Guza, R. T. and D. L. Inman(1975): Edge waves and beach cusps, *J. Geophys. Res.*, 80(21), 2997-3012.
- Hashimoto, H. and T. Uda(1974): A method of a numerical prediction on near-shore currents and its applications, *Proc. 21st Conf. on Coastal Eng. in Japan*, 355-360, (in Japanese).
- Hino, M.(1973): Theory on generation of rip currents, Part III, A simplified theory, *Proc. 20th Conf. on Coastal Eng. in Japan*, 339-344, (in Japanese).

- Horikawa, K. and K. Maruyama(1976): On generation of rip current in a laboratory basin, Proc. 23rd Conf. on Coastal Eng. in Japan, (in press, in Japanese).
- Horikawa, K. and T. Sasaki(1972): Field observations of nearshore current system, Proc. 13th Coastal Eng. Conf., 635-652, Vancouver.
- Inman, D. L. and R. T. Guza(1966): Application of nearshore processes to the design of beaches, Abstracts of 15th Coastal Eng. Conf., 526-529, Honolulu, Hawaii.
- Isaacs, J. D., E. A. Williams, and C. Eckart(1951): Total reflection of surface waves by deep water, Trans. A.G.U., 32(1), 37-40.
- Iwata, N.(1976): Rip current spacing, J. Oceanogr. Soc. Japan, 32(1), 1-10.
- Jonsson, I. G.(1966): Wave boundary layers and friction factors, Proc. 10th Coastal Eng. Conf., 127-148, Tokyo.
- Liu, P. L. F. and C. C. Mei(1974): Effect of a breakwater on nearshore currents due to breaking waves, Tech. Rep. 192, 265pp., R. M. Parsons Lab., M.I.T., Cambridge.
- Liu, P. L. F. and C. C. Mei(1976): Water motion on a beach in the presence of a breakwater, 1. Waves, 2. Mean currents, J. Geophys. Res., 81(18), 3079-3094.
- Longuet-Higgins, M. S.(1970): Longshore currents generated by obliquely incident sea waves, J. Geophys. Res., 75(33), 6778-6789.
- Mizuguchi, M.(1976): Eigenvalue problems for rip current spacings, Proc. Japan Soc. Civil Engineers, 248, 83-88, (in Japanese).
- Mizuguchi M. and K. Horikawa(1976): Physical aspects of wave-induced nearshore current system, Abstracts of 15th Coastal Eng. Conf., 798-800, Honolulu, Hawaii.
- Noda, E. K.(1972): Wave induced circulation and longshore current patterns in the coastal zone, Tech. Rep. 3, 101pp., Office of Nav. Res., Geogr. Br., Washington, D. C..
- Noda, E. K., C. J. Sonu, V. C. Rupert, and C. I. Collins(1974): Nearshore circulation under sea breeze conditions and wave current interaction in the surf zone, REP. TETRAT-P-72-149-4, 216pp., Tetra Tech Inc., Pasadena, Calif..
- Sasaki, T.(1974): Field investigations of nearshore currents on a gently sloping bottom, Doctorial Thesis in Civil Eng., 240pp., Univ. of Tokyo, (in Japanese).
- Sasaki, T.(1975): Simulation on shoreline and nearshore current, Proc. of the Specialty Conf. on Civil Eng. in the Oceans/III, 179-196, Newark, Delaware.

- Sasaki, T. and K. Horikawa(1975): Nearshore current system on a gently sloping bottom, Coastal Eng. in Japan, 18, 123-142.
- Sonu, C. J.(1969): Tethered balloon for study of coastal dynamics, Proc. Symp. on Earth Observations from Balloons, Amer. Soc. Photogrammetry, Tech. Rep., (66), 91-103.
- Sonu, C. J.(1972a): Field observation of nearshore circulation and meandering currents, J. Geophys. Res., 77(18), 3232-3247.
- Sonu, C. J.(1972b): Comment on paper by A. J. Bowen and D. L. Inman, "Edge waves and crescentic bars", J. Geophys. Res., 77(33), 6629-6631.
- Sonu, C. J.(1976): Mixing in the nearshore circulation system, Abstracts of 15th Coastal Eng. Conf., 490-492, Honolulu, Hawaii.
- Suhayda, J. N.(1974): Determining nearshore infragravity wave spectra, Intern. Symp. Ocean Wave Measurement and Analysis, 54-63, A.S.C.E., New Orleans.
- Tompson, M. M.(1966): Manual of Photogrammetry, 1, 536pp., 3rd ed., Amer. Soc. Photogrammetry, George Banta Co., Menasha, Wisconsin.
- Tucker, M. J.(1950): Surf beats; Sea waves of 1 to 5 minute period., Proc. Roy. Soc., London, A, 202, 565-573.
- Yoshida, K.(1950): On the ocean wave spectrum, with special reference to the beat phenomena and the "1-3 minute waves", J. Oceanogr. Soc. Japan, 6(2), 49-56.

CHAPTER 37

LATERAL AND BOTTOM FORCES ON LONGSHORE CURRENTS

David A. Huntley¹

ABSTRACT

A two-component electromagnetic flowmeter has been used on a natural beach of slope 0.01 to measure mean longshore currents and the horizontal fluctuating velocities in the frequency range 0-1 Hz. The measurements extend up to 120 m offshore and span about one third of a wide surf-zone. The cross product of the fluctuating horizontal velocities, assumed to contain the combined effects of radiation and Reynold's stresses, is plotted as a function of distance from the shoreline. The on/offshore gradient of the cross-product is then equated with a bottom friction term either in the form used by Bowen (1969a) or in a form similar to that used by Longuet-Higgins (1970). The apparent values of bottom friction coefficient obtained in this way are at least a factor of two smaller than expected for Reynolds numbers and bottom roughness appropriate to the beach. Attempts to separate the radiation stress and the Reynold's stress contributions to the total stress term using cospectra fail to show distinguishable Reynold's stress contributions. Although this may be construed as being consistent with Battjes' (1975) beach slope dependent form for horizontal eddy viscosity rather than Longuet-Higgins' (1970) form, it is argued that, in fact, the significant horizontal turbulence was not measured at all but was confined to a surface layer above the flowmeter. This leads to the hypothesis that lateral friction, as a surface boundary layer, and the bottom friction act on a less turbulent central layer, and that the small measured friction coefficient in the present experiment is the result of the combined effects of these layers.

INTRODUCTION

Wave-induced longshore currents, confined mainly to the surf-zone, are assumed to be the result of a balance between a gradient of incident wave radiation stress, a gradient of horizontal turbulent Reynold's stress and bottom friction acting on the longshore current (for a recent review see Longuet-Higgins 1972). Recent theories have parametrised these three balancing forces in terms of easily measured macroscopic properties of the flow. Radiation stress is generally calculated from incident wave height and angle of approach; the Reynold's stress acting in the longshore direction is assumed to be the product of the on/offshore gradient of the longshore current and a coefficient of eddy viscosity dependent in some way on distance from the shoreline and beach slope; bottom friction has been parametrised in a number of ways

¹Assistant Professor, Department of Oceanography, Dalhousie University, Halifax, Nova Scotia, Canada

involving a coefficient of friction, the value of the mean longshore current and possibly the wave orbital velocity (calculated in turn from the mean water depth).

Despite the success of these theories in predicting at least the order of magnitude of longshore currents there are a number of uncertainties, particularly in choosing the appropriate parametrization of Reynold's stress and bottom friction. These uncertainties arise primarily because the nature of turbulence within the surf zone is not well understood. Is the appropriate scaling length for the horizontal eddy viscosity coefficient a horizontal distance from the shoreline or a local water depth (Longuet-Higgins 1970; Battjes 1975)? Is a depth mean turbulence picture in fact appropriate or is the wave-breaking turbulence confined to a relatively thin surface layer? What are appropriate values of bottom friction coefficient if much of the turbulence is generated not by bottom roughness but by wave breaking?

The fast response and ruggedness of electromagnetic flowmeters provide an opportunity to begin answering these questions by direct measurement of the fluctuating components of the velocity field, both waves and turbulence, simultaneously with measurement of the mean longshore flow.

This paper discusses an experiment on a shallow beach (beach slope $\beta = 0.01$) in which a two-component flowmeter was used to measure on/offshore and longshore currents in a frequency range 0 - 1 Hz along a line normal to the shoreline. The data provided a direct measurement of the combined local radiation and Reynold's stress forces as well as an on/offshore profile of longshore current. The first part of the paper discusses the friction coefficient obtained from these data, and there follows some discussion of attempts to separate the radiation stress and Reynold's stress components in the data.

THEORY

We assume a co-ordinate system with the x - axis increasing seawards from zero at the shoreline, the y - axis alongshore and the z - axis increasing vertically upwards from the mean still water surface.

The longshore equation of motion for steady currents, assuming hydrostatic pressure and neglecting wave-current interaction, is the shallow water equation

$$\frac{u\partial v}{\partial x} + \frac{v\partial v}{\partial y} = - \frac{g\partial \bar{\eta}}{\partial y} + R_y + \tau_y \quad (1)$$

where u , v are the on/offshore and longshore depth mean currents (including wave-induced mass transport) respectively, $\bar{\eta}$ is the wave induced mean set-up of the water level, R_y is the bottom friction term and τ_y is usually written as the sum of radiation stress and Reynold's stress gradients in the on/offshore directions. If conditions are uniform in the longshore direction then terms in $\partial/\partial y$ disappear and the first term also becomes zero as a consequence of continuity, leaving only

$$R_y + \tau_y = 0 \quad (2)$$

The term τ_y is the on/offshore gradient of the flux towards the shoreline of parallel-to-the-shoreline momentum (Phillips 1969), and can be written

$$\tau_y = \frac{1}{\rho(\bar{\eta}+h)} \frac{\partial}{\partial x} S_{xy} \quad (3)$$

where

$$S_{xy} = \overline{\int_{-h}^{\eta} \rho u'v' dz} \quad (4)$$

Here h is the still water depth and u' , v' are the fluctuating velocity components, including both wave orbital velocities and turbulence. S_{xy} should also contain a term in the cross-product of the horizontal components of mass flux, but this term is proportional to the mean on/offshore flow. Its size can therefore be estimated from the measured mean on/offshore velocities. For the experiment under discussion it was much less than 10% of the term in eqn. 4 and has therefore been ignored.

If the assumption is made that wave and turbulent velocities are uncorrelated it is possible to separate the term on the right of eqn. 4 into a radiation stress part and a Reynold's stress part, and this is the usual way of proceeding. For the data from an electromagnetic flowmeter, however, it is not necessary to make this separation since the components u' and v' are measured directly. Nevertheless it is necessary to make two further simplifications of equation 4 before it relates directly to the measured quantities. These are

$$\begin{aligned} \overline{\int_{-h}^{\eta} \rho u'v' dz} &\approx \int_{-h}^{\bar{\eta}} \overline{\rho u'v' dz} \\ &\approx \overline{\rho u'v'} (\bar{\eta}+h) \end{aligned} \quad (5)$$

The first of these approximations is valid to the same order as

our neglect of the mass flux term in S_{xy} . The second approximation implies that $\overline{u\overline{v}}$ is independent of depth. This assumption must be made a priori since measurements were only made at a single position in the water column. However, the consistency of the results so obtained is later used to assess the validity of the assumption.

Although in principle the vertical and horizontal components of turbulent motion could be measured near the sea bed using the electromagnetic flowmeter, and these could be used to provide a direct measurement of bottom stress, in the present experiment only horizontal velocities were measured and hence the bottom friction must be approximated by empirical expressions involving horizontal components and bottom friction coefficients.

Three different forms of bottom friction have been considered, each involving a bottom friction coefficient. With these bottom friction terms, the equations of motion, eqn. 2, become

$$\begin{aligned} \frac{\partial}{\partial x} [\rho \overline{u\overline{v}} (\bar{\eta}+h)] &= \rho (\bar{\eta}+h) R_Y \\ &= \rho c_b V \quad (\text{Bowen 1969a}) \end{aligned} \quad (6)$$

$$= \rho c_f^1 |U_{\text{orb}}| V \quad (\text{Longuet-Higgins 1970}) \quad (7)$$

$$= \rho c_f^2 |U| V \quad (8)$$

c_b is a linear friction coefficient, with units m/s while c_f^1 and c_f^2 are dimensionless coefficients. In the Longuet-Higgins form U_{orb} is the maximum orbital velocity of the incident waves. In the third formulation $|U|$ is the modulus of the total current vector and differs from $|U_{\text{orb}}|$ mainly in including the steady longshore current V , which Longuet-Higgins assumed was much smaller than U_{orb} .

THE EXPERIMENT

The field experiment was carried out on Saunton Beach, N. Devon, England. This is an essentially straight beach approximately 4 km. long and a survey out to 300 m from the high water mark showed an approximately linear slope of 0.014; this slope is modified to 0.010 relative to the mean water level inside the surf-zone when set-up is taken into account. On the day of the experiments the surf-zone was 300-400 m wide with long-crested spilling breakers.

A single two-component electromagnetic flowmeter was mounted about 20 cms off the sea bed, oriented so as to measure the on/offshore and the longshore components of flow. The effective shoreline distance from this instrument varied as a result of tidal motion and allowed estimates of S_{xy} to be made in the region 0 - 120 m from the shoreline. The experimental technique was discussed in detail at the last Coastal Engineering Conference (Huntley and Bowen 1975a).

FRICTION COEFFICIENTS

Figure 1 shows the measured values of longshore current against distance offshore. The values shown are $8\frac{1}{2}$ minute averages of digital current measurements recorded every $\frac{1}{2}$ second. The measured currents compare well with independent measurements made using drifting floats at different distances offshore and the validity of the tidal excursion technique for measuring on/offshore variation of the velocity field is supported by the similarity of currents at the same offshore distance measured first on the rising and then on the falling tide (Huntley and Bowen 1975a). The current increases almost linearly with distance from the shoreline, as expected since the measurements were made within about $1/3$ of the surf-zone width from the shoreline.

Figure 2 shows the corresponding values of $\overline{u'v'}$ plotted against offshore distance. Here the fluctuating components are taken to be the velocities after removal of the $8\frac{1}{2}$ minute means only. High-pass filtering to remove energy at frequencies below the incident wave band would result in a reduction of about 20% in the values of $\overline{u'v'}$; the cause of this is discussed later. Apart from a single wild point at about 70 m offshore the values are encouragingly stable, the spread of points around 120 m suggesting that the estimates are stable to better than $\pm 40\%$.

Also shown on figure 2 are straight lines corresponding to different values of c_b , the linear friction coefficient. The fit of these straight lines is unconvincing and the values of c_b are lower than might have been expected. Bowen (1969a) estimates values of 0.002m/s for some laboratory data.

The values of c_f^1 and c_f^2 were estimated separately for each $8\frac{1}{2}$ minute section of record. A plot of $(\eta+h) \overline{u'v'}$ vs offshore distance was made and the data approximated by a smooth line increasing monotonically with distance from the shoreline. At the offshore distance corresponding to each $8\frac{1}{2}$ minute record the gradient of this line was measured and equated to the bottom friction terms (eqns. 7 & 8) to obtain values of c_f^1 and c_f^2 . Table 1 shows the results. It is seen that the estimates of c_f^1 and c_f^2 are generally stable, the standard deviations representing approximately $\pm 30\%$, and there is no obvious trend in the values with shoreline distance.

With the exception of the values nearest the shoreline, c_f^1 is consistently larger than c_f^2 . Thus the assumption that U_{orb} is much larger than V is invalid for this data. The ratio of mean values c_f^1/c_f^2 is about 1.4, implying that U_{orb} and V are of the same size. In fact it can be shown using the theory of Longuet-Higgins (1970) that, except for very small angles of approach of the incident waves (of order 1° at the breakpoint), V is generally of the same order as U_{orb} , and the Longuet-Higgins approximation, equation 7, is therefore usually invalid.

The coefficient c_f^1 deduced from longshore current data by various authors (Thornton 1970; Komar 1975) is therefore not a true bottom friction coefficient. The value of c_f^1 will generally be larger than the correct bottom friction coefficient, c_f^2 , but the amount by which it is larger will vary across the surf zone and will be strongly dependent on the angle of approach of the incident waves. This may explain the wide range of values of c_f^1 which have been deduced. [It is worth noting also that estimates of c_f^1 have often been made using the longshore current data of Galvin and Eagleson (1965), but the accuracy of these data is now questioned by Komar (1975) on the grounds of incompatibility with other data. Since the longshore currents of Galvin and Eagleson are larger than expected the estimates of c_f^1 will be low.]

The magnitude of the bottom friction coefficient c_f^2 is less than one half the magnitude expected on the basis of laboratory experiments of flow over rough plates. The experiments of Nikuradse (Prandtl 1952, Longuet-Higgins 1970) suggest that, for the bottom roughness appropriate to the beach and a Reynold's number determined by the incident waves, and friction coefficient should be around 5×10^{-3} (Note that the friction coefficient defined in equation 38 of Longuet-Higgins (1970) and equations 7 and 8 of the present paper is one half the value of c_f given by Prandtl (Longuet-Higgins - private communication)). Other direct estimates of wave friction coefficient have been made by Jonsson (1967) and Teleki and Anderson (1970), and estimates of a combined wave and longshore current friction factor have been made by Jonsson et al (1974), but in each case the values give a bottom friction term at least as large as Prandtl's estimate.

It seems probable that the apparently low value of friction coefficient c_f^2 is the result of the omission of a driving term in the equation of motion, equation 8. The two groups of terms which may have been omitted are the longshore variation terms included in equation 1, or the turbulent Reynold's stress term, which we assumed to be included in equation 5.

If the assumption of uniform conditions in the longshore direction were invalid, then the additional terms in equation 1 would have to be included and could result in a stronger (or weaker) longshore current than would be driven by τ_y alone. If it were nevertheless still assumed that the motion could be described by equations 2, and 6-8, this stronger (weaker) current could only be reconciled with these equations by an apparently smaller (larger) value of friction coefficient. Two mechanisms could be responsible for a longshore variability, edge wave generated circulation cells and refraction of incident waves. Edge wave generated circulation cells (Bowen 1969b, Bowen and Inman 1969) seem very unlikely to be generated on a beach as shallow as 0.01. Theory and experimental evidence suggest that circulation cells have an along-shore wavelength of the same order as the surf-zone width and edge waves of low mode number are most strongly generated; on Saunton beach synchronous edge waves giving circulation cells of the same size as the surf-zone would be of mode number greater than 200. The effect of wave refraction is less easy to dismiss since no

measurements were made alongshore. However offshore topography was relatively smooth and there were no indications of refraction on this long smooth beach. Additional evidence that wave refraction is not responsible for low values of friction coefficient comes from field measurements of longshore currents made by Ramkema (Battjes - private communication). He also found consistently low values of friction coefficient, although his measurements were made for a variety of directions of approach of the waves, and thus for a variety of wave refraction conditions.

The second possible explanation for the low values of bottom friction is that we are just not measuring the Reynold's stress at all. Since the data comes from the 1/3 of the surf-zone closest to the shoreline, a region where the effect of lateral mixing is to increase the longshore current above the unmixed value, we are again ignoring a driving term in the force balance and hence underestimating the friction coefficient.

This hypothesis clearly leads to an attempt to find Reynold's stress contributions to the measured stress term, and this is discussed in the following section.

SEPARATION OF REYNOLD'S AND RADIATION STRESSES

If we could separate the turbulent and wave contributions to the mean u, v product we could examine the hypothesis that turbulence is perhaps not being measured, or possibly test the various parametrisations of horizontal turbulent stresses which have been used in longshore current theories. There are three possible ways in which such a separation might be made. Most obviously we might try to measure elevation at the same time as the horizontal velocities and then remove the calculated elevation-related contributions to the velocities. Alternatively we might measure the variation of the $u\overline{v}$ product across and beyond a surf-zone and attempt to distinguish the two stress components by their different dependences on offshore distance: the Reynold's stress should fall to zero some distance outside the surf-zone and pass through zero at the position within the surf-zone where the longshore current is maximum; these two points and the shoreline limit should allow a reasonable estimate to be made of the radiation stress contribution throughout the nearshore zone. Finally it might be possible to separate the two stresses if they occur predominantly in separate frequency bands.

Unfortunately the data from the present experiment includes neither elevation measurements nor sufficient spread of measurements across the surf-zone to test the first two of these techniques. In fact the first technique would require a rather accurate directional spectrum of elevations, and this would be difficult to measure in the nearshore zone. However frequency separation is in principle possible with the current measurements alone.

The co-spectrum $\overline{u^{\prime}v^{\prime}}(f)$ separates the real part of the $u^{\prime}v^{\prime}$ product into contributions in separate frequency bands. Since the effect of the Reynold's stress gradient is to increase the longshore current within the first one third of the surf-zone we expect the Reynold's stress to contribute to $u^{\prime}v^{\prime}$ with the same sign as the radiation stress, but hopefully within a well defined band at a higher frequency than the incident wave band.

Figure 3 shows a typical example of the co-spectra calculated from the 8½ minute records. The peak just below 0.2 Hz represents the predominant incident wave frequency. The lower frequency contributions may be due to breaker interaction in the wide surf-zone (Huntley and Bowen 1975b) but in any case contribute only about 20% of the total area under the curve. There is no clear frequency band above 0.3 Hz containing a significant peak which may be attributed to Reynold's stress.

It is possible that the level of turbulence was too small to be significant in this co-spectrum. Longuet-Higgins (1970) estimates the total turbulent stress as

$$\overline{u^{\prime}v^{\prime}} = \frac{1}{\rho} N \rho x (gh)^{3/2} \frac{\partial V}{\partial x} \quad (9)$$

where h is local water depth

x is distance offshore

He assumes that the parameter N is a constant with a value ≈ 0.005 ; Bowen and Inman (1972) analyse surf-zone dye diffusion experiments and suggest that N should lie approximately in the range 0.01-0.06. In contrast Battjes (1975) suggests that N should not be constant but beach slope dependent in the form

$$N = \left(\frac{5}{16} \gamma^2 \right)^{1/3} (\tan\beta)^{4/3} M \quad (10)$$

where γ is the ratio of wave height to water depth.

M is a dimensionless parameter deduced by assuming that the N given by equation 10 for $\tan\beta = 0.1$ is similar to the constant N deduced by Bowen and Inman (1972); most experimental determinations of N were made on beaches of slope 0.1. The value of M calculated thus lies in the range 0.3-2.0. The effect of the beach slope dependence of equation 10 is then to give a considerably smaller estimate of turbulent Reynold's stress on a beach of the present slope of 0.01 than would be calculated using a constant N. We have calculated the Reynold's stress, equation 9, using both constant $N \approx 0.01-0.06$, and the beach slope dependent N,

equation 10, which for our slope of 0.01 gives $N \approx (3.5 - 21) \times 10^{-4}$. (we assume also that $\gamma \approx 1.2$ for $\tan\beta = 0.1$ and $\gamma = 0.78$ for $\tan\beta = 0.01$, following Bowen et al (1968), but the choice of γ does not significantly effect the result). Comparison of these predicted Reynold's stresses with the observed contribution to $u\bar{v}$ for frequencies greater than 0.3 Hz shows that the observed values are of a similar magnitude to predictions made using equation 10 but are at least an order of magnitude smaller than predictions made using a constant (independent of beach slope) N . Thus the observed cospectra are not inconsistent with Battjes model for horizontal turbulence but are definitely inconsistent with Longuet-Higgins' model.

It seems more likely however that the flowmeter was not in fact measuring the wave-induced turbulence at all. The mean values of u and v integrated over the complete frequency range can be completely accounted for by the expected values for surface wave breakers propagating in the observed water depths. The coherence between u and v is also around 0.3 in the frequency range 0 - 1Hz as might be expected for short-crested incident waves (Battjes 1975).

DISCUSSION

The conclusion from the present data is therefore that the turbulence is probably not being measured by our single flowmeter and that this omission is likely to be the cause of the low value of friction coefficient obtained.

The probable reason for the absence of turbulence in the flowmeter records is that the flowmeter was too far down in the water column. Laboratory experiments and field experience suggest that the turbulence of breaking is not distributed throughout the water column but is limited to the upper part, especially for spilling breakers. Thus the second approximation of equation 5 is invalid. Turbulence energy would also not be measured if it occurred predominantly at frequencies greater than the approximately 10Hz response frequency of the flowmeter, but this seems unlikely.

Thus the present results suggest a rather different model for longshore currents than has been used before. Rather than a turbulent intensity distributed throughout the water column, wave breaking turbulence is confined to an upper boundary layer which, with the bottom boundary layer, acts on a less turbulent central layer. If indeed the driving force of this upper layer is responsible for the low apparent value of c_f , then an upper limit of about one third the water depth can be put on the thickness of this upper layer, based on the fact that c_f remains small down to as little as 40 m. from the shoreline (table 1).

The hypothesis, then, is that the value of c_f measured here is not a bottom friction coefficient alone but is strongly modified by the

existence of a surface turbulent boundary layer formed by wave breaking. The formulation of the effect of lateral mixing as some kind of boundary layer rather than a depth independent eddy viscosity may explain why Jonsson et al (1974) and Komar (1975) find so little effect on the match of predicted and measured longshore currents when the parameter N (equation 9) is varied over a wide range.

The suggested three layer model may also provide the means to explain Komar's observation (Komar and Inman 1970, Komar 1975, 1976) that for a wide variety of field and laboratory measurements of longshore currents, the ratio of beach slope to the coefficient c_f^1

$$\frac{\tan\beta}{c_f^1} \approx \text{constant} \quad (11)$$

The constant in equation 11 is variously found to be $6.05 + 0.65$ for beach slopes in the range $0.05 - 0.15$ (Komar 1975), ≈ 6.7 (Longuet-Higgins 1972) and ≈ 7 for a beach slope of around 0.05 (Keeley 1975). The beach slope for the present experiment is considerably smaller than for these data, at 0.01 , but, as a consequence of the smaller value of c_f^1 , the ratio is found to be $3.9 +1.1$, in reasonable agreement with the other estimates. In fact, using the correct friction coefficient, c_f^2 , instead of c_f^1 also gives reasonable agreement, with the constant $\approx 5.2 +2.4$.

Komar (1971) assumes that c_f^1 is a friction coefficient and he has attempted to provide a physical explanation for the empirical result of equation 11 by assuming that bottom stress exerted on the beach is proportional to the radiation stress in the incident wave direction at the breakpoint. However, this and other unproven assumptions which he needs to make have been criticized by Longuet-Higgins (1972), also on physical grounds. More recently Komar (1976) has pointed out that, for the field data, a constant ratio $\tan\beta/c_f^1$ suggests an increase in c_f^1 with sand size, as we might expect for flow over a rough bed. However, this argument cannot explain the laboratory results, where most beaches are solid, with a constant, generally small, bottom roughness independent of beach slope.

The three layer model, however, suggests that the measured c_f^1 parameters are strongly influenced by the intensity of breaking turbulence. Increased beach slope will result in a narrower surf-zone over which turbulent breaking occurs, and hence a greater level of turbulence in unit surface area. This increased horizontal mixing will result in a decreased longshore current and hence a greater apparent c_f^1 parameter in our three layer model. This explanation is consistent with Longuet-Higgins' (1972) comments on equation 11.

Clearly what is needed is a new model for longshore currents, involving the correct parametrisation of the bottom friction term in terms of equation 8 rather than equation 7, and involving a new parametrisation of horizontal turbulent mixing as an upper boundary layer. Such a model may provide an explanation for equation 11.

There are several ways that the present three layer hypothesis may be tested experimentally. Direct estimation of bottom friction is possible through use of the electromagnetic flowmeter to measure vertical and horizontal velocities near the bed. Measurements of the distribution of horizontal turbulence in the vertical may also be possible, though measurement in the turbulent surface layer may only be possible by dye diffusion (see Inman et al 1971). Finally the value of c_f^2 deduced from horizontal velocities, as described in this paper, should be measured across and beyond the surf-zone. Since the effect of a surface turbulent layer should be to reduce the longshore current gradient, the maximum longshore current will be less than predicted in the absence of horizontal mixing, the horizontal mixing term will be a retarding force, and the value of c_f^2 should be larger than expected for bottom friction alone. Thus c_f^2 should be smaller near the shoreline increase beyond bottom friction values as the surf-zone is traversed seawards, and then drop again, possibly even becoming negative beyond the surf-zone.

REFERENCES

- Battjes, J. A. A note on modeling of turbulence in the surf-zone. Proceedings, Symposium on modeling techniques, San Francisco, 1050-1061, 1975.
- Bowen, A. J. The generation of longshore currents on a plane beach, J. Mar. Res. 27, 206-215. 1969a.
- Bowen, A. J. Rip currents, 1, Theoretical investigations, J. Geophys. Res. 74, 5467-78, 1969b.
- Bowen, A. J. and D. L. Inman. Rip currents, 2. Laboratory and field observations. J. Geophys. Res. 74, 5479-5490, 1969.
- Bowen, A. J. and D. L. Inman. Nearshore mixing due to waves and wave-induced currents. Rapp. P.-v. Réun. Cons. int. Explor. Mer., 167, 6-12, 1972.
- Bowen, A. J., D. L. Inman and V. P. Simmons. Wave set-down and set-up. J. Geophys. Res. 73, 2569-2577, 1968.
- Galvin, D. J., Jr., and P. S. Eagleson. Experimental study of longshore currents on a plane beach. Coastal Engineering Res. Centre, Tech. Memo. No. 10, 1965.
- Huntley, D. A. and A. J. Bowen. Direct measurement of nearshore and surf-zone velocities. Proceedings, 14th Conference on Coastal Engineering, Copenhagen, June 1974. New York: American Society of Civil Engineers, 1975a.
- Huntley, D. A. and A. J. Bowen. Comparison of the hydrodynamics of steep and shallow beaches. In, Nearshore sediment dynamics and sedimentation, ed. J. Hails and A. Carr. John Wiley and Sons Ltd., London 1975b.
- Inman, D. L., R. J. Tait and C. E. Nordstrom. Mixing in the surf-zone. J. Geophys. Res. 76, 3493-3514, 1971.
- Jonsson, I. G., O. Skovgaard and T. S. Jacobsen. Computation of longshore currents. Proceedings, 14th Conference on Coastal Engineering, Copenhagen, June 1974. New York: American Society of Civil Engineers, 1975.
- Keeley, J. R. Observed and predicted longshore currents on Martinique Beach: A comparison of driving terms. Unpublished M.Sc. thesis, Dalhousie University, Nova Scotia, Canada. 1975.
- Komar, P. D. The mechanics of sand transport on beaches. J. Geophys. Res. 76, 713-721, 1971.
- Komar, P. D. Nearshore currents: Generation by obliquely incident waves and longshore variations in breaker height, in Nearshore sediment dynamics and sedimentation, ed. J. Hails and A. Carr. John Wiley and Sons Ltd., London 1975.
- Komar, P. D. Longshore currents on beaches: A summary, J. Waterways, Harbors and coastal engr. in press, 1976.

- Komar, P. D. and Inman, D. L. Longshore sand transport on beaches. J. Geophys. Res., 75, 5914-5927, 1970.
- Longuet-Higgins, M.S. Longshore currents generated by obliquely incident sea waves. 1 & 2. J. Geophys. Res. 75, 6778-6801, 1970.
- Longuet-Higgins, M.S. Recent progress in the study of longshore currents, in Waves on Beaches, ed. R. E. Meyer. Academic Press, New York, 1972.
- Phillips, O. M. The dynamics of the upper ocean. 261 pp. Cambridge University Press. 1969.
- Prandtl, L. Essentials of fluid dynamics, 452 pp., Haffner, New York 1952.
- Sonu, C. J. Field observations of nearshore circulation and meandering currents, J. Geophys. Res. 77, 3232-47, 1972.
- Teleki, P. G. and M. W. Anderson. Bottom boundary shear stresses on a model beach. Proceedings, 12th Conference on Coastal Engineering Washington, D.C., September 1970. New York: American Society of Civil Engineers, 1970.
- Thornton, E. B. Variation of longshore current across the surf-zone. Proceedings, 12th Conference on Coastal Engineering, Washington, D. C., September 1970. New York: American Society of Civil Engineers, 1970.

TABLE 1

Run I. D.	Distance from shoreline m.	Longshore current m/s	$c_t^{(1)}$ $\times 10^{-3}$	$c_t^{(2)}$ $\times 10^{-3}$
FFC 81	120	0.37	3.25	2.01
FFC 82	117	0.41	2.60	1.46
FFC 83	111	0.38	2.53	1.38
FFC 5	90.5	0.25	3.25	2.03
FF0 1	77	0.26	2.29	1.39
FF0 21	60	0.17	2.27	1.80
FF0 22	50	0.10	3.17	3.13
FF0 23	42	0.10	1.74	2.29

Mean and standard deviation = 2.6 ± 0.6 1.9 ± 0.6

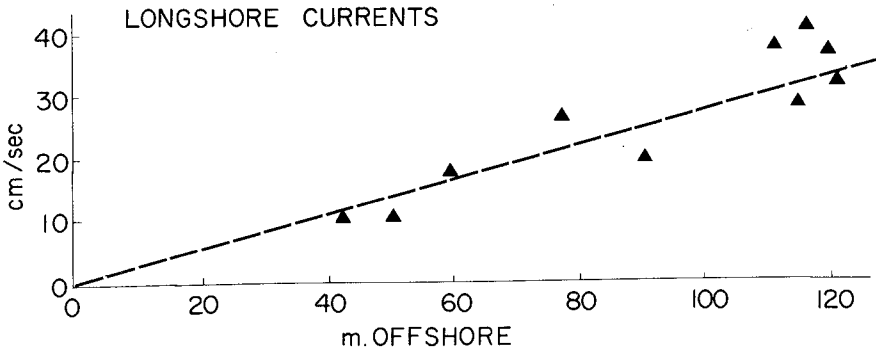


Figure 1.

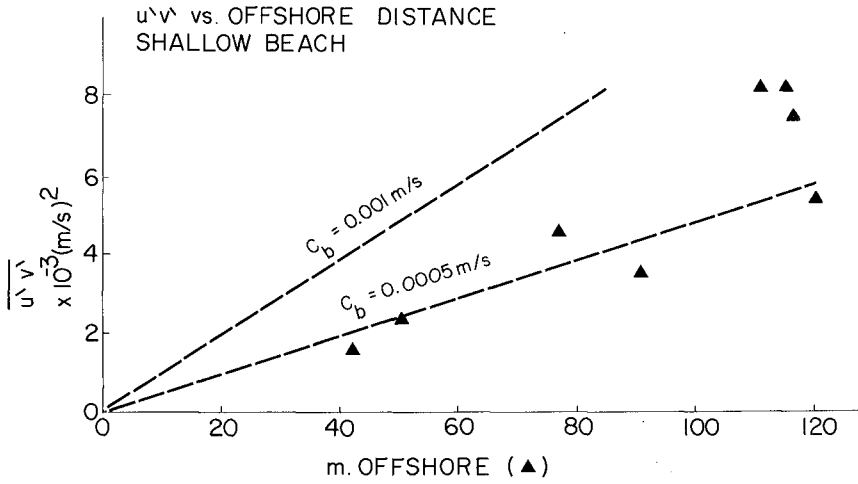


Figure 2.

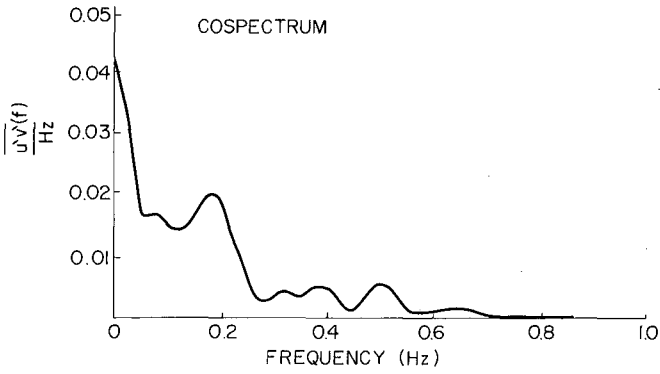


Figure 3.

CHAPTER 38

TIME DEPENDENT FLUCTUATIONS IN LONGSHORE CURRENTS

Guy A. Meadows

Department of Geosciences
Purdue University
West Lafayette, Indiana

ABSTRACT

During constant sea state conditions, longshore current velocities were monitored continuously for fifteen minute periods separated by fifteen minute periods separated by fifteen minute intervals. Three ducted impellor flowmeters were placed at equally spaced vertical positions through the water column. Sequential measurements were made with similar vertical current meter arrays at different locations across the surf zone. Simultaneous measurements of wave height, period and celerity were made at stations placed at equal intervals from the outer surf zone to the beach. The fifteen minute continuous records were subjected to spectral analysis. This analysis showed that the major power associated with fluctuations in the longshore current velocity field occurs in two major frequency bands. A significant spectral peak was coincident with the breaker period of the incident wave field, 4.2 seconds and, another dominant signature occurred at 78.8 seconds. Attenuation with depth of both the steady and fluctuating components of the longshore current flow field was relatively small. The maximum observed velocities for each station and each vertical current meter position varied from 90 to 150 percent above the observed mean longshore current velocity. However, at each station, variation of the means with depth was not appreciable and thus supports the results from time and space averaged theories of vertical uniformity in longshore currents, away from the boundary layer. Results from the field investigation of Wood and Meadows (1975) indicated that the steady state components are dominated by the fluctuating portions of the flow field. Therefore, time averaging of conservation equations in longshore current theory is a physically inappropriate procedure. In order to evaluate the magnitude of the unsteady components, a close examination of surf zone dynamics was made. The most obvious contribution to unsteadiness in longshore currents arises from the longshore component of the maximum horizontal particle velocity. However, the magnitude of observed current fluctuations is too large to be completely accounted for by this component. Spectral peaks at longer periods appear to be related to modes of edge wave phenomena. The long period spectral signature of 78.8 seconds is in direct agreement with the calculated period for a zero mode edge wave in shallow water. This agreement supports the contention that oscillatory components, other than the longshore component of the wave particle velocity,

are contributing to unsteadiness in longshore currents and are manifested throughout a wide range of frequencies.

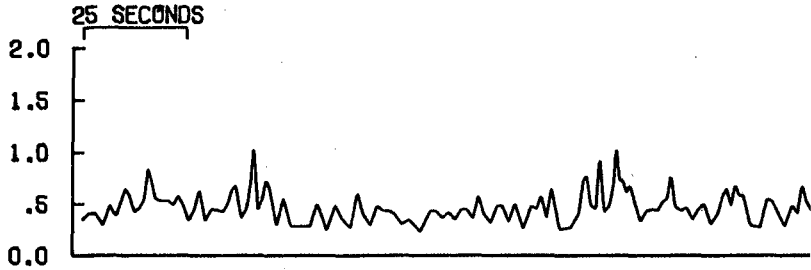
INTRODUCTION

In the presence of an oscillatory wave field incident on a beach it is somewhat unrealistic to expect a steady or slowly varying longshore current. Unsteadiness of longshore currents has been noted for quite some time. However, the magnitude and dominance of the unsteadiness in the flow field has only recently been fully appreciated (Dette, 1974; Wood and Meadows, 1975).

Classically, field and laboratory investigations have relied on averaged results from Lagrangian measurements to establish longshore current velocities. Likewise, conservation equations have been time averaged in the formation of longshore current theories. As a result, design criteria for coastal engineering structures have only considered the periodicity of the incident wave field to be important and local longshore currents have been modeled as steady state and constant with depth. Results from this investigation indicate that these assumptions are inappropriate. Field observations show at a fixed point in the surf zone variations in excess of 150 percent of the mean longshore current velocity occur over time periods from three to eighty seconds (Figure 1). These unsteady motions in longshore currents persist horizontally across the surf zone and vertically from the surface to the bottom. The dominant period of these fluctuations correspond to that of the incident breaker period; however, significant longer period fluctuations are also evident. The magnitude of the time-dependent portions of the flow field as well as their persistence horizontally across the surf zone and vertically with depth suggests that they dominate the steady component. Consequently an analytical formulation for longshore current flow must be carried out in a time dependent framework.

Longshore currents result in a net translation of fluid particles parallel to the shoreline. This fluid flow is bounded by the beach on the nearshore side, by the somewhat arbitrary limit of the surf zone on the seaward side and by the bottom. The flow velocities are hence constrained to vanish at or near these boundaries. There can be no wave generated longshore current flow beyond the maximum wetted extent of the swash zone on the beach. The seaward extent of the longshore current is located where the effects of momentum and energy fluxes, associated with breaking waves, lie beyond the range of lateral mixing in the surf zone. The lower extent of the flow field is characterized by a shear dominated zone terminating in the loosely consolidated sediment comprising the under-water portion of the beach. The flow is constrained to vanish at a sufficient depth into this underlying beach sediment. This depth is not necessarily the top of the mobile sediment layer but a depth at which percolation through the beach material is non-existent. The last remaining boundary is that of the free surface. It is at this

UPPER CURRENT METER



MIDDLE CURRENT METER



BOTTOM CURRENT METER

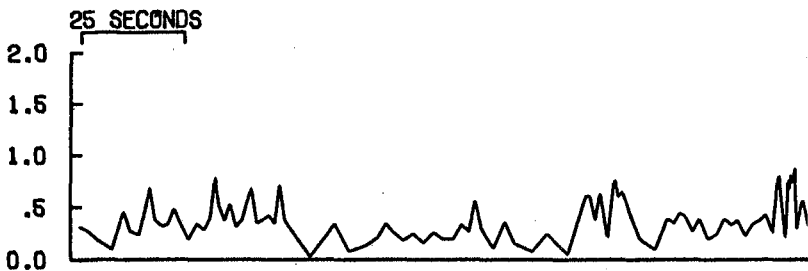


FIGURE 1. THREE REPRESENTATIVE SIMULTANEOUS TIME HISTORIES OF FLUCTUATING LONGSHORE CURRENT VELOCITIES TAKEN AT THREE DEPTH LOCATIONS THROUGH THE SURF ZONE WATER COLUMN.

boundary that the flow velocity is anticipated to be a maximum. Since the shearing stress realized at the bottom must result from a loss of momentum at the bottom boundary, the maximum velocity must be achieved at the greatest possible distance from the bottom. The longshore current flow, outside the viscous boundary layer, appears to be a weak shear flow.

Classically, longshore current velocity has been modeled as a function of wave height, period, celerity and angle of approach at breaking as well as the local water depth (Galvin, 1967). The driving forces necessary to create and sustain the longshore current are most directly related to the breaking wave height, (Putnam, Munk, and Traylor, 1949). This observation led to the development of conservation of momentum and energy approaches to the treatment of the longshore current flow field. It was assumed that in shallow water the wave celerity at breaking can be adequately represented by

$$C_b = \sqrt{g(H_b + Z)}$$

which leads to an ambiguous conclusion. Accepting the premise that energy losses exist that are not accounted for by this approximation, the driving component associated with the horizontal component of the wave particle velocity must be of greater magnitude than the resulting longshore current velocity

$$C_b \sin \theta_b > V.$$

This result is not usually observed in nature, implying that other mechanisms, not accounted for by a simple time averaged momentum balance of the longshore component of the breaking wave horizontal particle velocity, must be associated with the generation of longshore currents.

Early conservation of momentum and energy approaches have led to the investigation of longshore currents based on continuity considerations (Bruun, 1963). The basic assumption in the conservation of mass approach is that a wave breaking at an angle to the beach contributes mass to the surf zone and raises the local mean water level. This creates a slope in the water surface which generates a longshore current. Variation of still water level at different locations along the beach imparts a longshore slope to the free water surface. The differential pressure head associated with this slope initiates flow from areas of high to low pressure. Hence, the velocity of the longshore current is controlled by the frictional pressure head loss within the current itself. The non-uniformity of these conditions implies variation of the longshore current flow field in the longshore direction and forms the basis for theoretical treatments of rip-cell generation (Bruun, 1963; Bowen, 1967). Rip-channels are formed at low areas of wave and slope water set-up and flow perpendicular to the beach. This is a necessary and sufficient condition to satisfy

conservation of mass in the surf zone since the continuity constraint cannot justifiably be met by imposing return flow with depth throughout the surf zone.

Perhaps the most sophisticated and least restrictive approach to longshore currents has been set forth in terms of conservation of energy considerations (Longuet-Higgins, 1970 (1) and (2)).

This approach utilizes the concept of radiation stress to relate the magnitude of the longshore current velocity to the incoming wave energy flux, given by

$$F_x = E c_g \sin \theta \quad (1)$$

outside the surf zone and

$$\frac{\partial F_x}{\partial x} = -D \quad (2)$$

inside the surf zone, where D is the rate of energy dissipation per unit time and horizontal area. The flux of y -momentum across a line $x = \text{constant}$, parallel to the shoreline is given by the radiation stress component

$$S_{xy} = F_x \left(\frac{\sin \theta}{c} \right) \quad (3)$$

and from balance of momentum flux considerations it can be shown that the waves exert a local stress

$$T_y = - \frac{\partial S_{xy}}{\partial x} \quad (4)$$

parallel to the shoreline. Substituting (3) and remembering that $\sin \theta/c$ is independent of x gives

$$T_y = - \frac{\partial F_x}{\partial x} \left(\frac{\sin \theta}{c} \right) \quad (5)$$

or from (2)

$$T_y = D \left(\frac{\sin \theta}{c} \right) \quad (6)$$

A simple momentum balance for steady state conditions on a straight coastline can be expressed as

$$T_y - B = 0 \quad (7)$$

where B is bottom friction and lateral friction is neglected. Applying linear theory of waves in shallow water to (1) under the assumption

that in the breaker zone θ is small enough that $\cos \theta$ can be approximated by unity gives

$$F_x = \frac{1}{2} \rho g a^2 \sqrt{gz} = \frac{1}{2} \alpha^2 \rho g^{3/2} z^{5/2} \quad (8)$$

where ρ is density, g acceleration of gravity, a wave amplitude, z water depth, and $\alpha = a/z$. Longuet-Higgins (1970 1, 2) assumed the Chezy Law

$$B = C\rho |\bar{u}|\bar{u} \quad (9)$$

where \bar{u} is the horizontal velocity, having both a steady and oscillatory component, and C is a constant. Combining equations (5), (8), and the time averaged expression of (9) and substituting into (7) gives a longshore velocity

$$\bar{v} = \frac{5\pi}{8} \frac{\alpha s}{C} gz \frac{\sin \theta}{c} \quad (10)$$

The extension of shallow-water theory out to the breaker line and the inclusion of lateral mixing across the breaker line result in

$$V_o = \frac{5\pi}{8} \frac{\alpha}{C} \sqrt{gz} b (s \sin \theta_b) \quad (11)$$

and

$$V_b = \frac{5\pi}{8} \frac{\alpha \beta}{C} \sqrt{gz} b (s \sin \theta_b) \quad (12)$$

respectively (Longuet-Higgins, 1970 1, 2).

Longshore current velocities predicted from this approach only agree with experimental results under the conditions of a monochromatic sea surface incident at a straight planar beach of constant slope. The assumptions employed in these solutions still remain far too restrictive to produce physically realistic prediction under natural conditions. For an excellent discussion of recent developments in the predictions of steady longshore currents see Longuet-Higgins (1972).

The existence of second order effects across the surf zone with a wide range of incident periods, can add significant contributions to unsteadiness in the longshore current velocity. Wave set-up and set-down (Eagleson, 1965) across the surf zone can add slope water effects to the driving sources. The effect of short crested waves (Fuchs, 1952) and edge waves (Ursell, 1952) can also supply driving forces not accounted for by classic temporal and spatial averaged momentum theory.

Therefore, formulation of longshore current theories based on temporally or spatially averaged quantities appears to be physically inappropriate. It is unrealistic to expect a steady or slowly varying longshore current in the presence of an irregular oscillatory wave

field. Although the oscillatory nature of the longshore current, due to the presence of breaking waves in the surf zone should be expected, the resulting total longshore current velocity field is a far more complex oscillatory field.

FIELD INVESTIGATION

A field investigation was carried out along a section of eastern Lake Michigan shoreline, characterized by a multiple barred configuration and nearly parallel bathymetry. Only conditions of wave breaking on the inner bar were considered for this investigation. This restriction was imposed to avoid the added complication of waves reforming and breaking at multiple locations.

Three ducted impeller flow meters oriented parallel to the shoreline were placed at equally-spaced vertical positions at each monitoring station. The upper meter was placed below the level of the lowest wave trough so that it was continuously submerged. The lower meter was placed adjacent to the bottom and the middle meter half way between the upper and lower meters (Figure 2). Sequential measurements were made with three similar vertical current meter arrays at different locations across the surf zone. The outermost current monitoring station (Station I), was located within the zone of active breaking. The inner stations (Station II and III), were located five and ten meters, respectively, shoreward of Station I. Maximum wave breaking occurred at Station II, hence, the breaker zone was bracketed by the station locations. The total surf zone width was approximately thirty meters.

Simultaneous measurements of wave height, period and celerity were made perpendicular to the shoreline at stations spaced at equal intervals from the outer surf zone to the shore. The spacing of these stations was approximately 5 meters. The incident wave angle at breaking was determined to be 21 ± 5 degrees.

During constant sea state conditions, longshore current velocities and wave characteristics were simultaneously monitored continuously for fifteen minute periods separated by fifteen minute intervals. Constant sea state was determined by requiring that the probability distributions of wave height and period at the outer most wave monitoring station remain stationary. Hydrographic surveys were conducted, at close spatial intervals, offshore to a position outside the surf zone and alongshore to a distance of one surf zone width, which is the theoretical limit of rip cell width. The average nearshore beach slope was found to be 1:40.

ANALYSIS

The most appropriate representation of the longshore current and its associated wave field should be expressed in a statistical context.

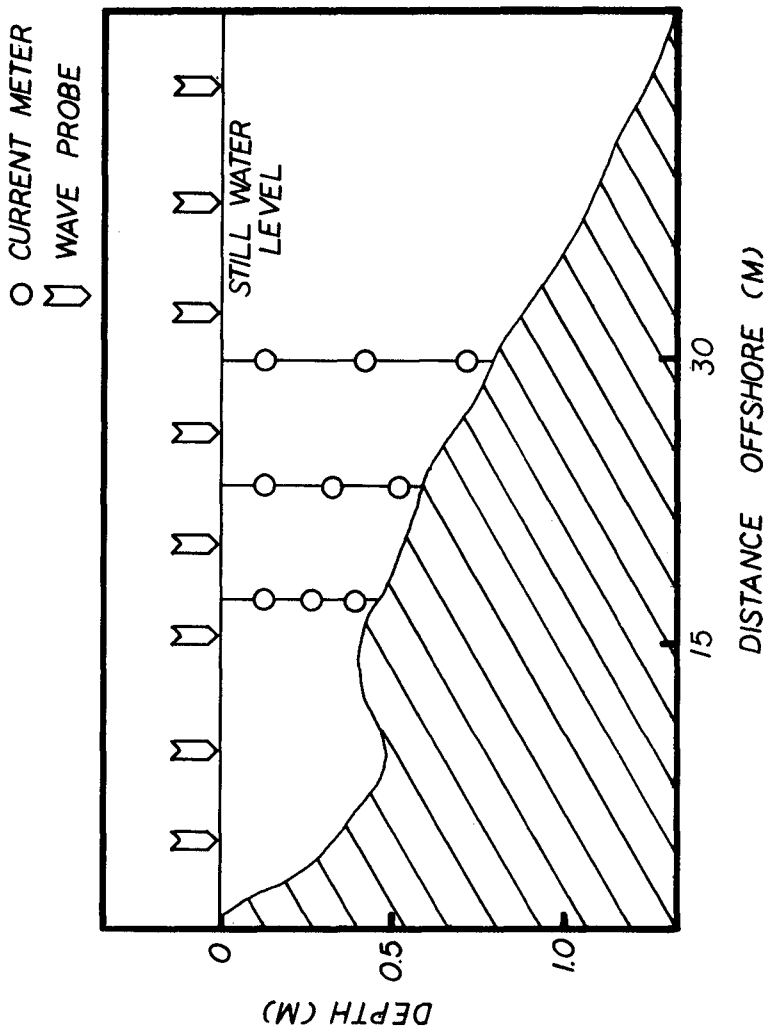


FIGURE 2. BATHYMETRIC PROFILE SHOWING CURRENT METER LOCATIONS AND WAVE MONITORING STATIONS.

Application of this approach to nearshore circulation has been the subject of recent work (Dette, 1974; Earl, 1974; Collins, 1972; and others). Consideration of probability distributions of wave characteristics across the surf zone anticipate a variation in wave height, incidence angle and celerity. Under a monochromatic assumption, all waves are expected to break at the same location in the surf zone. However, with a random distribution of the sea surface, the breaker line becomes a breaker zone and the region over which energy dissipation is active also becomes a broad zone.

Data obtained from the ducted impeller flow meter array were analyzed for their periodic and steady state components. The time intervals between discrete on-off signals of the meter were converted to instantaneous velocities. These velocities were then interpolated on equal time intervals between adjacent points. This data was then subjected to spectral analysis to determine its periodic components. Inherent to the monitoring system are aliasing problems. Data from the flow meter was only available at discrete instants of time, therefore, frequency information was lost from the signal. Frequencies greater than twice the interval between meter signals (averaged approximately 1.0 seconds) can not be resolved. Filtering of the input signal and smoothing of the power spectrum was therefore employed.

The analytical treatment of the longshore current flow field should be developed within the framework of an incompressible, inviscid fluid. The problem also must be formulated in a time dependent context with shallow water wave parameters as inputs. It is therefore necessary to evaluate the initial state of the wave field incident at the outer surf zone (Figure 3).

To evaluate wave induced unsteadiness of the longshore current flow field it is advantageous to remove from the experiment all secondary variations in the velocity field not directly related to the incident breaking waves. For this reason, only wave and current data collected during constant sea state conditions was acceptable for this investigation. The wave field was, therefore, required to be statistically steady in its mean, $\partial\bar{\eta}/\partial t = 0$. This restriction eliminates the existence of significant long period fluctuations in the longshore current velocity field induced by either growth or decay in the wave field incident at the outer surf zone. This restriction, however, does not preclude wave transformations within the surf zone, hence, $\partial\eta/\partial x \neq 0$.

It is not necessary for the incident wave field to be non-uniform in the alongshore direction for periodic unsteadiness in longshore current velocity to exist. Significant unsteadiness in the velocity field should be expected both from direct velocity contributions from breaking waves and from interactive phenomena associated with the entire wave group (Meadows and Wood, 1975).

Incident Wave Field Conditions	
Wave Field Steady in Mean Wave Field Uniform in Y-Direction (Alongshore)	Wave Field Steady in Mean Wave Field Non-Uniform in Y-Direction (Alongshore)
$\frac{\partial \eta}{\partial t} = 0$	$\frac{\partial \eta}{\partial t} = 0$
$\frac{\partial \eta}{\partial x} \neq 0$	$\frac{\partial \eta}{\partial x} \neq 0$
$\frac{\partial \eta}{\partial y} = 0$	$\frac{\partial \eta}{\partial y} \neq 0$
Longshore Current	
Uniform in Y-Direction (Alongshore)	Non-Uniform in Y-Direction (Alongshore)
<u>Steady</u>	<u>Steady</u>
$\frac{\partial u_i}{\partial t} = 0$	$\frac{\partial u_i}{\partial t} = 0$
$\frac{\partial u_i}{\partial x} \neq 0$	$\frac{\partial u_i}{\partial x} \neq 0$
$\frac{\partial u_i}{\partial y} = 0$	$\frac{\partial u_i}{\partial y} = 0$
<u>Unsteady</u>	<u>Unsteady</u>
$\frac{\partial u_i}{\partial t} \neq 0$	$\frac{\partial u_i}{\partial t} \neq 0$
$\frac{\partial u_i}{\partial x} \neq 0$	$\frac{\partial u_i}{\partial x} \neq 0$
$\frac{\partial u_i}{\partial y} \neq 0$	$\frac{\partial u_i}{\partial y} \neq 0$

FIGURE 3. INITIAL CONDITIONS DEFINING POSSIBLE ANALYTICAL CONSIDERATIONS FOR THE DEVELOPMENT OF LONGSHORE CURRENT THEORIES BASED ON THE INCIDENT WAVE FIELD.

The approximation $\partial\eta/\partial y = 0$, requires the incident waves remain long crested and two dimensional as they move through the surf zone. Hence, the initial conditions for a steady, uniform incident wave field have been established.

Another representation of the near shore wave field is that of a non-uniform sea surface in the alongshore direction, $\partial\eta/\partial y \neq 0$. Under this condition, additional driving forces for periodic variations in the longshore current velocity field may be expected. This condition may be a manifestation of either a short-crested sea surface or longer period edge waves. Both of these types of alongshore wave motion result in additional release of energy to the longshore current. However, at a fixed point in the surf zone, the direct cause of these secondary velocity fluctuations can not be established. Their magnitude will at best appear as a residual when all other primary fluctuations are accounted for.

Once the initial conditions describing the incident wave field have been established, the nature of the longshore current flow may be defined. As with the case of the incident wave field, the resulting longshore current flow field may be either uniform or non-uniform in its longshore extent. Classical treatments of longshore current have generally been restricted to a two dimensional long crested incident sea surface encroaching on a bottom with straight and parallel contours. Therefore, with the exception of rip cell formation, the longshore current is treated as uniform in the y -direction.

Figure 3 shows the various analytic assumptions which can be applied to the incident wave field and related longshore current. Existing longshore current theory is formulated on the assumption that only one of the eight possible combinations shown is observed in the surf zone (wave field steady and uniform, longshore current uniform and steady). The major restriction of these classical longshore current theories is that the motion has been confined to steady state, $\partial u_i/\partial t = 0$. The field investigation of Wood and Meadows (1975) has shown that at a fixed point in the surf zone variations in excess of 150 percent of the mean longshore current velocity occur over time periods from three to eighty seconds. These unsteady motions persist horizontally across the surf zone and vertically from the surface to the bottom. The persistence and magnitude of the observed velocity fluctuations imply that time dependent analytical treatments of conservation equations are necessary in order to properly predict longshore current velocity.

It is reasonable to assume that the total longshore current velocity field is composed of a steady and a fluctuating component which result from the incident wave field.

$$v = \bar{v} + v' \quad (13)$$

Recent field measurements (Wood and Meadows, 1975) suggest that the steady flow component and the fluctuating flow component are of comparable magnitude. Similarly, there exists in the surf zone driving components that can be expected to contribute only to the steady portion of the flow field and others that contribute only to the unsteady portions. Therefore, the governing differential equations for longshore current flow (Collins, 1972) should have been retained in their original time dependent form.

Consider the momentum and continuity equations for a two dimensional, incompressible, constant density fluid in the x and y direction (perpendicular and parallel to the beach respectively

$$\frac{\partial u}{\partial t} + u \frac{\partial u}{\partial x} + v \frac{\partial u}{\partial y} = -g \frac{\partial \eta}{\partial x} + T_x - B_x \quad (14)$$

$$\frac{\partial v}{\partial t} + u \frac{\partial v}{\partial x} + v \frac{\partial v}{\partial y} = -g \frac{\partial \eta}{\partial y} + T_y - B_y \quad (15)$$

$$\frac{\partial \eta}{\partial t} + \frac{\partial (uh)}{\partial x} + \frac{\partial (vh)}{\partial y} = 0 \quad (16)$$

where T_x and T_y are the radiation stress components in the x and y direction respectively and B_x and B_y represent corresponding components of bottom friction.

Now let the velocity components u and v be composed of both a steady and a time dependent component of comparable magnitude, in the following form

$$u = \bar{u} + u' \quad v = \bar{v} + v'$$

and the free surface elevation, η , be similarly decomposed into a steady and a fluctuating surface component

$$\eta = \bar{\eta} + \eta'$$

The governing equations now become:

$$\begin{aligned} \frac{\partial u'}{\partial t} + \bar{u} \frac{\partial \bar{u}}{\partial x} + u' \frac{\partial \bar{u}}{\partial x} + \bar{u} \frac{\partial u'}{\partial x} + u' \frac{\partial u'}{\partial x} + \bar{v} \frac{\partial \bar{u}}{\partial y} + \bar{v} \frac{\partial u'}{\partial y} + \\ v' \frac{\partial \bar{u}}{\partial y} + v' \frac{\partial u'}{\partial y} = -g \frac{\partial \bar{\eta}}{\partial x} - g \frac{\partial \eta'}{\partial x} + T_x - B_x \end{aligned} \quad (17)$$

$$\frac{\partial v'}{\partial t} + \bar{u} \frac{\partial \bar{v}}{\partial x} + u' \frac{\partial \bar{v}}{\partial x} + \bar{u} \frac{\partial v'}{\partial x} + u' \frac{\partial v'}{\partial x} + \bar{v} \frac{\partial \bar{v}}{\partial y} + \bar{v} \frac{\partial v'}{\partial y} +$$

$$v' \frac{\partial \bar{v}}{\partial y} + v' \frac{\partial v'}{\partial y} = -g \frac{\partial \bar{\eta}}{\partial y} - g \frac{\partial \eta'}{\partial y} + T_y - B_y \quad (18)$$

$$\frac{\partial \eta'}{\partial t} + \frac{\partial [(\bar{u} + u')h]}{\partial x} + \frac{\partial [(\bar{v} + v')h]}{\partial y} = 0 \quad (19)$$

(Note: previous field observations have shown that $\partial \bar{u}/\partial t$ and $\partial \bar{v}/\partial t$ are non-zero terms due to slight variations in the main flow, however their magnitude is negligibly small).

Spectral analysis of the longshore current velocity series (Figure 4) indicated that significant energy was associated with the incident breaking wave period, 4.2 seconds. However, other dominant signatures occur at longer periods, with the maximum being 78.8 seconds. The observed longshore current velocity fluctuations seem to fall into three period ranges of interest. These periods are: 3 to 10 seconds, order of the incident breaking wave period, 25 to 200 seconds, range of the anticipated long period edge wave modes; and greater than 200 seconds, for the quasi steady state component.

The most obvious contribution to unsteadiness of longshore current velocity arises from the longshore component of the breaking wave horizontal particle velocity. Theory suggests that the longshore current velocity is most directly related to the magnitude of the longshore component of the breaking wave horizontal particle velocity at the surface, $c_b \sin \theta_b$. When time averaged, this oscillatory component was assumed to generate a mean longshore current, $\bar{v} = f(c_b \sin \theta_b)$. In order to evaluate the magnitude and the distribution of this component of the velocity field, only the periodic component of the velocity series is of interest. Hence, the steady state component was removed from the series. The magnitude of the horizontal particle velocity was evaluated throughout the water column. Experimentally derived profiles of maximum horizontal particle velocities and their variation with depth from the tank studies of Morison and Crooke (1953), and Divoky, Le'Mahaute' and Lin (1970), and the field studies of Miller and Zeigler (1964) and Wood (1970) were used for this evaluation. The calculated longshore component of these breaking wave maximum horizontal particle velocity profiles, $U_h' \sin \theta_b$, is plotted for each of the above studies on Figure 5. The velocity range for the three current meter depth locations through the water column of the observed periodic component of the longshore current from this investigation is also plotted on Figure 5.

The observed magnitudes of the fluctuating longshore current velocity compare favorably with the expected magnitudes of the longshore component of the breaking wave horizontal particle velocity. However,

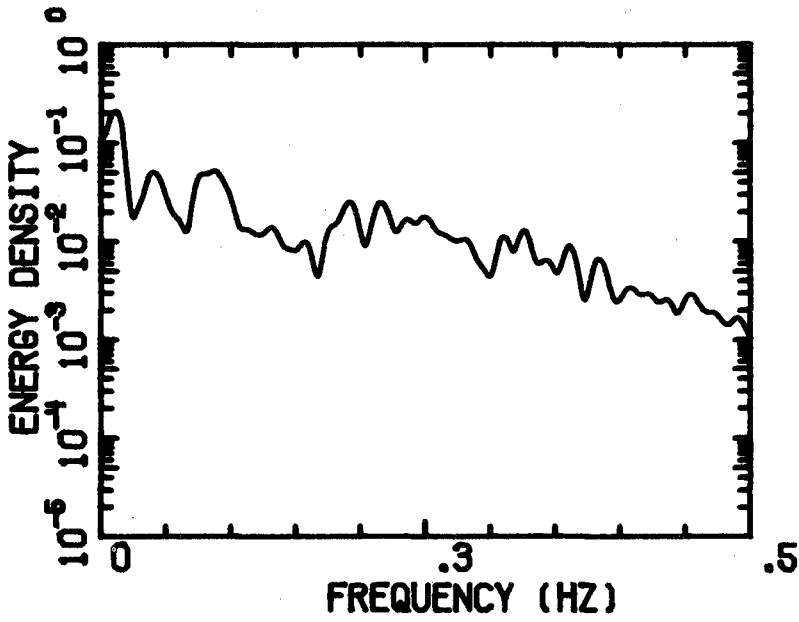


FIGURE 4. POWER SPECTRA FOR UPPER CURRENT METER COMPUTED FROM FIFTEEN MINUTE LONGSHORE CURRENT VELOCITY SERIES.

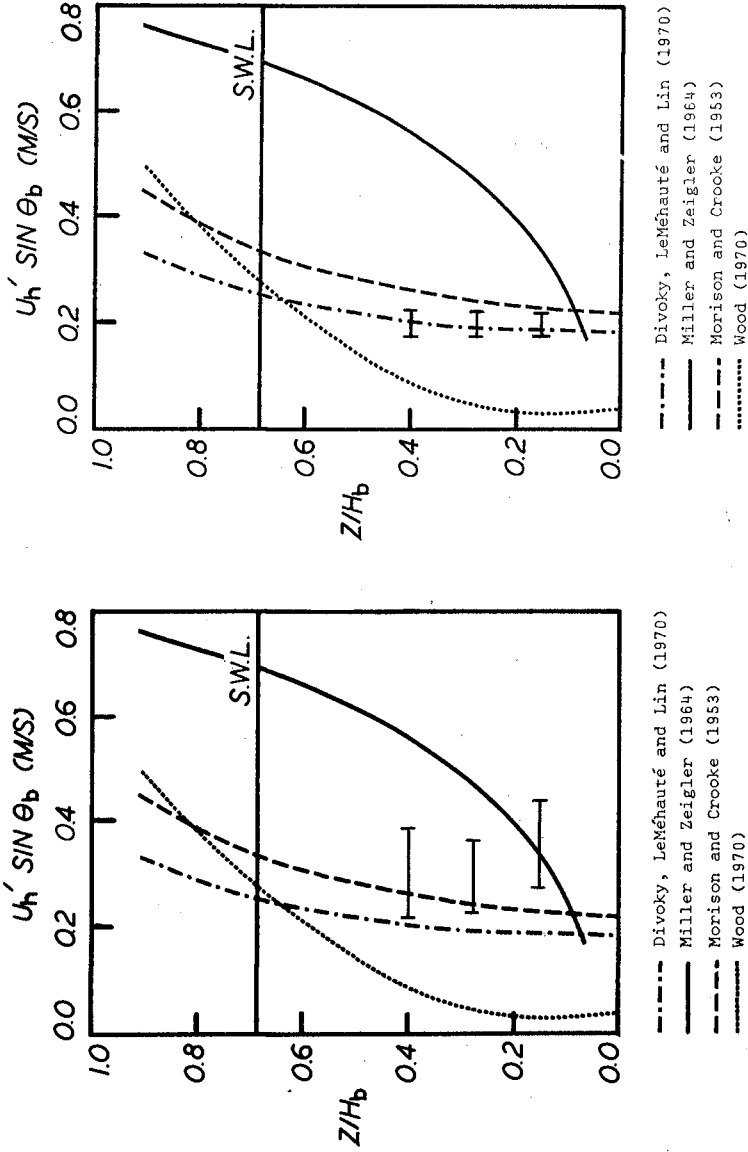


FIGURE 5. COMPUTED LONGSHORE COMPONENT OF BREAKING WAVE MAXIMUM HORIZONTAL PARTICLE VELOCITY COMPARED WITH OBSERVED DE-MEANED LONGSHORE CURRENT VELOCITY FLUCTUATIONS FROM THIS INVESTIGATION.

FIGURE 6. COMPUTED LONGSHORE COMPONENT OF BREAKING WAVE MAXIMUM HORIZONTAL PARTICLE VELOCITY COMPARED WITH OBSERVED DE-MEANED AND FILTERED WAVE PERIOD (3-10 SECONDS) LONGSHORE CURRENT VELOCITY FLUCTUATIONS FROM THIS INVESTIGATION.

the magnitude of the velocity fluctuations from this investigation are generally, with the exception of Miller and Zeigler (1964), 50 to 100 percent larger than would be predicted from these studies. Re-examination of the longshore current velocity series provides an explanation for this discrepancy.

The demeaned longshore current velocity records with which the horizontal particle velocity profiles were compared, contain additional frequencies of longshore current velocity fluctuations. To isolate only that component of unsteadiness associated with the longshore component of the wave horizontal particle velocity, all frequencies other than the breaker zone wave frequencies were removed from the record. Band pass filtering was performed on the fifteen minute longshore velocity records to remove the effect of any long period waves from the observed fluctuations. The filtered series only contained fluctuations whose periods were between 3 and 10 seconds, Figure 6. This filtered series is then the observed longshore current velocity component resulting from the breaking wave horizontal particle velocity, $U_h' \sin \theta_b$. This filtered series of longshore current velocity fluctuations exhibit several characteristics that would be anticipated to be associated with breaking wave induced motions. First, the velocity fluctuations are nearly symmetrical about the abscissas, thus, suggesting that these motions are truly the result of the oscillatory wave particle velocity. Second, the magnitudes of the observed fluctuations are nearly uniform with depth. Near uniformity with depth is suggested by shallow water wave theory as well as by the observed maximum horizontal particle velocity profiles of Morison and Croke (1953) and DiVoky, LeMehaute' and Lin (1970). The observed magnitudes of this filtered series of longshore current velocity fluctuations are in excellent agreement with the results of both previously mentioned tank experiments and are bracketed by the profiles obtained from the field investigations of Wood (1970), on the low side and by Miller and Zeigler (1964), at the upper end. This agreement suggests that the contribution of the breaking wave horizontal particle velocity to fluctuations in longshore current velocity has been isolated from the observed time series.

Results of spectral analysis of the fifteen minute longshore current velocity series has shown significant energy at a period of approximately 80 seconds. Examination of the band pass filtered (3-10 seconds), demeaned longshore current velocity series also shows repeated occurrences of groups of high velocity pulses in the longshore current. The regular occurrence of these pulses at approximately 80 second intervals suggest a correlation with the spectral signature at that same period.

The distinction must be made that the individual high velocity pulses still retain their identity of approximately 5 second period and that groups of these large pulses arrive as a beat phenomenon at

approximately 80 second intervals. However, for the spectral signature at an 80 second period to exist a wave phenomenon at that frequency must be present. Since, periodic amplitude modulation alone of the wave period fluctuating velocity series would not produce a spectral response at that period. It appears that this long period longshore current velocity fluctuation may be driven by the surf beat. Thus the fluctuating portion of the longshore current flow is composed of at least two distinct components. A component of period coincident with the breaking wave period and a long period component of approximately 80 seconds, Figure 7.

The original longshore current velocity series was then low band passed filtered to only allow periods between 200 seconds and 25 seconds to remain. This filtered, demeaned series (Figure 7) shows the existence of the anticipated long period wave phenomena of approximately 80 second period. The maximum magnitude of this velocity component was approximately $\pm .3$ m/sec. The phase of this long period fluctuating component corresponds to the arrival of groups of high velocity pulses of the wave period fluctuation series. If we return to the conservation of mass theory of Bruun (1963) the suggestion was made that the longshore current flow is a response of the surf zone to an influx of mass associated with transitory breaking waves. Since the arrival of the group of high velocity pulses in the longshore current velocity field, is in phase with the long period velocity fluctuation, then perhaps this oscillation is a response of the surf zone to an increased mass flux. As was suggested by Bowen (1967), a corresponding set-up, set-down phenomenon could be expected in the longshore direction. However, since this correlation does appear to exist between the long period and wave period portions of the fluctuating flow, the generation of a low mode edge wave may be a reasonable expectation. The calculated maximum period for a zero mode edge wave for the conditions of this field investigation was 77.8 seconds (Guza and Inman, 1975). The nearshore beach face slope of 5.7° approaches the 6° beach slope for which these calculations were made. This is in agreement with the observed 78.8 second period fluctuation in the longshore current velocity. However, the effect of the well developed barred beach configuration, present during this study, on maximum edge wave periods is not clear, the choice of an "effective" beach slope over this region greatly alters the anticipated edge wave periods. Edge wave period calculations for the area immediately adjacent to the steep beach face suggests a period of 27.7 seconds. Examination of the power spectra for the current meter array at this location in the surf zone does show a weak signal at this frequency.

The major portion of the observed time dependent fluctuations in the longshore current velocity can be accounted for by the two components previously discussed. However, the linear addition of the breaking wave period fluctuating component, V'_w , and the long period component, V'_L does not produce the original longshore current velocity series. The steady state component contributing to the longshore current velocity is absent from the series. The magnitude of the

UPPER CURRENT METER

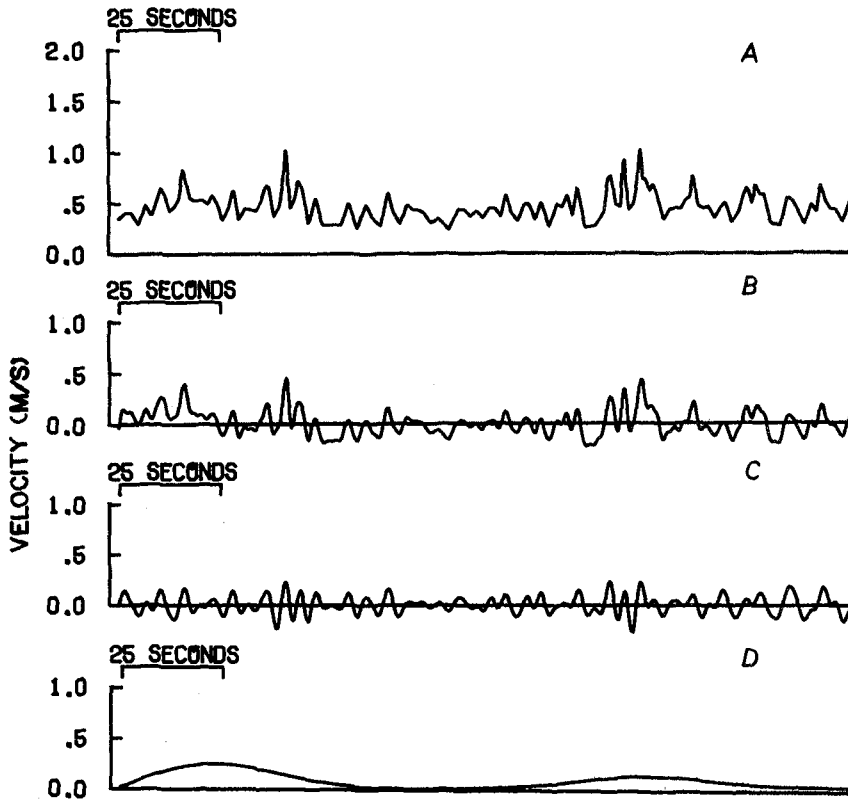


FIGURE 7. REPRESENTATIVE FLUCTUATING LONGSHORE CURRENT VELOCITY SERIES FROM UPPER CURRENT METER: A) TOTAL OBSERVED LONGSHORE CURRENT VELOCITY SERIES; B) Demeaned LONGSHORE CURRENT VELOCITY SERIES; C) Demeaned, BAND PASS FILTERED (3-10 SECONDS) LONGSHORE CURRENT VELOCITY SERIES; AND D) Demeaned, BAND PASS FILTERED (25-200 SECONDS) LONGSHORE CURRENT VELOCITY SERIES.

steady longshore current velocity component \bar{V} , for this set of observations, was approximately 0.65 m/sec. For the purpose of this analysis, the steady state component is defined as the velocity component whose period of variation in magnitude is greater than 200 seconds. Therefore, there must exist a net stress on the fluid within the surf zone of sufficient magnitude to produce the observed steady component of the flow.

The radiation stress concept as applied to the generation of longshore currents by Longuet-Higgins (1970, 1 & 2) states that the presence of waves exerts a net stress on the water of the surf zone. This excess flow of momentum is a result of the flux, toward the shoreline of momentum parallel to the coast

$$S_{xy} = \int_{-h}^{\delta\eta} \rho u V dz. \quad (20)$$

This formulation, employing the radiation stress concept, for the prediction of steady longshore currents has been criticized (S.P.M., 1973) for predicting the magnitude of longshore currents too low. However, for the results of this investigation, the formulation of Longuet-Higgins predicts the magnitude of the steady component, that which it was intended to predict, very well. The calculated value for the steady longshore current component using this formulation was 0.61 m/sec. While the observed steady component ranged from 0.60 to 0.66 m/sec (Wood and Meadows, 1975).

CONCLUSION

Three distinct longshore current velocity components have been isolated which contribute to the total observed longshore current velocity

$$V = \bar{V} + V_w^i + V_L^i \quad (21)$$

where \bar{V} is the steady longshore current velocity component and V_w^i and V_L^i are respectively the wave period and long period fluctuating longshore current velocity components. The mean longshore current velocity component, \bar{V} , was found to be dominated by the combination of the fluctuating components V_w^i , the incident breaking wave period fluctuations, and V_L^i , the long period fluctuations. Variations in the longshore current velocity of 90 to 150 percent of the mean current velocity have been shown to occur over periods from 3 to 80 seconds and these fluctuations have also been shown to persist horizontally across the surf zone as well as vertically from the surface to the bottom. In addition an interactive mechanism appears to be in operation within the surf zone by which short period

velocity fluctuations, order of the incident wave period, appear to interact with long period fluctuations in the longshore current velocity. This interaction seems to be excited by 80 seconds periodic variations in the magnitude of the short period longshore current velocity fluctuations. Decomposition of the longshore current velocity record has shown that a steady state component also contributes to the observed velocity field. The formulation of longshore current theories based on temporally or spatially averaged quantities is a physically inappropriate procedure. In view of the results of the field investigation of Wood and Meadows (1975) it is unrealistic to expect a steady or slowly varying longshore current velocity field in the presence of an irregular oscillatory wave field. Consequently, a reevaluation of the reasonability of the steady state approach to the prediction of longshore current velocity is clearly needed. The success of solutions to problems associated with the coastal environment depends on an appropriate and complete understanding of physical processes active in the environment. The steady state approach to the longshore current velocity field cannot provide this understanding.

ACKNOWLEDGEMENTS

This study was supported by the Geography Programs, Office of Naval Research, through the Great Lakes Coastal Research Laboratory, Purdue University.

I wish to express my sincere appreciation to Dr. William L. Wood, Department of Geosciences, Purdue University, for his helpful comments and discussion during the preparation of this report as well as his untiring assistance in the field. I also wish to extend my appreciation to the staff of the Great Lakes Coastal Research Laboratory for their assistance in the field portion of this investigation.

REFERENCES

- Bowen, A.J., Rip Currents, Ph.D. Thesis, University of California at San Diego, 115 pp. 1967.
- Bruun, P., Longshore currents and longshore troughs, Journal of Geophys. Res., Vol. 68, No. 4, 1963.
- Collins, J.I., Longshore currents and wave statistics in the surf zone, Tetra Tech. Inc., Technical Report, No. TC 149-2, 1972.
- Dette, H.H., Über brandungsströmungen im bereich hoher Reynolds-Zahlen, Heft 41, Leichtweiß-Institut Für Wasserbau der Technischen Universität Braunschweig, 1974.

- Divoky, D., B. L  mehaut  , and A. Lin, Breaking waves on gentle slopes, Journal of Geophys. Res., Vol. 75, No. 9, 1970.
- Eagleson, P.S., Theoretical study of longshore currents on a plane beach, M.I.T. Hydrodynamics Lab., Tech. Rept. 82, 1965.
- Earl, M.D., Longshore currents generated by waves with a Rayleigh wave amplitude distribution, (Abs.), Trans. Amer. Geophys. Union, Vol. 55, No. 4, 1974.
- Fuchs, R.A., On the theory of short-crested oscillatory waves, Gravity Waves - U.S. Dept. of Commerce, N.B.S. Circular 521, 1952.
- Galvin, C.J., Longshore current velocity: A review of theory and data, Rev. Geophys., 5, 287-304, 1967.
- Guza, R.T. and D.L. Inman, Edge Waves and Beach Cusps, Journal of Geophys. Res., Vol. 80, No. 21, 1975.
- Longuet-Higgins, M.S., Longshore currents generated by obliquely incident sea waves 1, J. Geophys. Res., 75, 6778-6789, 1970 1.
- Longuet-Higgins, M.S., Longshore currents generated by obliquely incident sea waves 2, J. Geophys. Res., 75, 6790-6801, 1970 2.
- Longuet-Higgins, M.S., Recent progress in the study of longshore currents, in Waves on Beaches, edited by R.R. Meyer, 203-248, Academic, New York, 1972.
- Meadows, G.A. and W.L. Wood, Unsteady longshore currents in a uniform wave field, (Abs.), Trans. Amer. Geophys. Union, Vol. 56, No. 12, 1975.
- Miller, R.L. and J.M. Zeigler, The internal velocity field in breaking waves, Proc. 9th Conf. Coastal Eng., Lisbon, Portugal, 1964.
- Morison, J.R. and R.C. Crooke, The mechanics of deep water, shallow water, and breaking waves, Beach Erosion Board, Tech. Memo No. 40, Washington, D.C., 1953.
- Putnam, J.A., W.H. Munk and M.A. Taylor, The prediction of longshore currents, Trans. Am. Geophys. Union, 30, 337-345, 1949.
- U.S. Army Coastal Engineering Research Center, Shore Protection Manual, 1, 4-39 - 4-50, U.S. Government Printing.
- Ursell, F., Edge waves on a sloping beach. Proc. Roy. Soc. A214, 1952.
- Wood, W.L., Horizontal particle velocity profiles beneath the crests of waves breaking on a submarine bar, Tech. Rep. 3, Dept. of Natural Science, Michigan State University, 1970.
- Wood, W.L. and G.A. Meadows, Unsteadiness in longshore currents, Geophysical Research Letters, Vol. 2, No. 11, 1975.

CHAPTER 39

TERRESTRIAL PHOTOGRAMMETRIC MEASUREMENTS OF BREAKING WAVES AND LONGSHORE CURRENTS IN THE NEARSHORE ZONE¹

Joseph W. Maresca, Jr.² and Erwin Seibel³

I. INTRODUCTION

We conducted a study to determine the feasibility of shore-based, oblique photographic monitoring of breaking waves, water levels, and currents within the surf zone. The purpose of this paper is to describe a new method of oblique single-image and stereoscopic-image analysis, the potential errors, and the types of measurements that can be made in the surf zone. Examples of application are presented to demonstrate the technique. Sophisticated photographic equipment is not required to collect, analyze, and interpret the data. The analysis and error discussions are directed toward the problems encountered using common equipment.

Vertical images from aircraft, helicopters, and balloons have been used in the past to study shoreline changes,¹ directional ocean-wave spectra,² and longshore currents.³ Oblique images taken from the bridge of a ship have been successfully used to measure whitecap coverage under different wind speeds.⁴ Terrestrial oblique images have been used to study longshore currents,⁵ ice-ridge formation and breakup,^{6,7} and beach changes.⁸

Oblique images, taken with a 35-mm single-lens reflex camera from an elevated point such as a bluff, are particularly suitable for the measurement of breaking waves, water level, beach run-up, and current in the surf zone under storm conditions. In contrast to other techniques of monitoring the surf zone, the photographic technique described in this paper is simple to install, reliable, accurate, and inexpensive. It can be used in all weather conditions, and the analysis of the images is simple. Both stereoscopic and single oblique images can be analyzed, depending on the specific needs and existing environmental conditions. Since the scale of an oblique photograph changes with increasing distance from the camera, the technique is limited in range to about 250 m for a cliff approximately 8 m above the mean water level. Accuracies to within 1% in the horizontal plane and better than 10% in the vertical plane are achievable at this distance.

-
1. Contribution No. 209 of The Great Lakes Research Division, The University of Michigan, Ann Arbor, Michigan 48104.
 2. Stanford Research Institute, Menlo Park, California 94025.
 3. University of Michigan, Ann Arbor, Michigan 48104.

Higher accuracies are obtained as distance from cliff to camera decreases. The unique feature of the oblique image is that it provides a method of delineating changes in space and time without the need for an expensive array of instruments.

II. EXPERIMENTAL METHOD

No special equipment is required for taking the oblique images. If stereoscopic oblique images are required, two 35-mm single-lens reflex cameras can be used. The cameras should be tripod-mounted and separated by a known distance. Polarizing filters are useful to decrease the glare from the water surface. In this study, stereoscopic measurements were taken along the California coast by two cameras placed 8 m apart and 8 m above the mean water level. The focal lengths of the cameras' lenses were 50 mm. The nominal focal length is sufficient for analysis. Although the simultaneous camera exposures could be taken using a long shutter release, we took the exposure by voice command. The two exposures were found to be visually identical, so no more elaborate method was pursued. Kodachrome II color slide film (ASA 25) was used. The color film is necessary for easy identification of points on the image. Slides are necessary, since they can be projected on a screen and enlarged sufficiently until points can be easily identified.

Single and stereoscopic oblique images can be taken along any region, providing the cameras are above the mean water level and the horizon is clearly visible and horizontal in the viewfinder (Figure 1). If the tilt of the horizon is less than 1° , no correction for tilt is required. This is well within the visual judgment of the photographer. The available topography usually dictates the camera elevation. The authors have taken measurements at three camera elevations ranging from 8 to 24 m (depression angles ranging from 2° to 10°) and identified objects at over 600 m from the camera. Generally, for camera elevations of 10 m, measurements offshore are limited to about 250 m. The principal point of the image should be centered on the region of most interest.

For single oblique image analysis, no reference stakes are required if the horizon, the focal length of the camera lens, and the datum elevation are known. However, reference stakes are required for stereoscopic image analysis. The stereoscopic analysis requires that the principal axes of the two cameras are parallel ($\beta = 0^{\circ}$ in Figure 2). The reference stakes should be placed between the cameras. A minimum of three reference stakes are required to mathematically rotate the principal axis of one camera relative to the other camera such that $\beta = 0^{\circ}$. It is not necessary to relate the beach stakes to the camera.

If water level fluctuations are required at known points, it is suggested that plastic buoys supported by polyethylene floating rope be stretched offshore. Theoretically, this is unnecessary, but the floats provide identifiable points. This is unnecessary for the wave measurements.

III. ANALYSIS

The numerous methods of analysis of an oblique image are described in the Manual of Photogrammetry.⁹ The Equivalent Vertical Photographic Method of rectifying points in the oblique image to real ground distances is well suited for surf-zone analysis. Consider an oblique image (color slide) of a plunging breaker taken along the Northern California coastline (Figure 3). The field setup is shown in Figure 1 along with several of the important points of interest such as the plunging breaker, the buoys, and the beach reference stakes. The oblique slide was enlarged using a slide projector (and photographic enlarger), and these points were digitized (Figure 4) with respect to a rectangular coordinate system with the origin at the principal point of the projected image. Fundamental relationships of an oblique image required for the analysis of this digitized image can be derived from the principal-plane diagram (Figure 5) for a slide. The plane of the positive taken by a camera lens of focal length f is defined by the points T, P, I, and N, where T is the intersection of the horizon with the principal plane, P is the principal point of the image, I is the isocenter of the image, and N is the nadir point. The depression angle, θ , is the vertical angle from the horizon plane to the optical axis. The tilt of the photograph is defined as $t = 90 - \theta$. The equivalent vertical photograph is the imaginary photograph that would be obtained if $t = 0$. The equivalent vertical photograph intersects the oblique image at the isocenter. The isoline, the line created by the intersection of the equivalent vertical photograph and the oblique image, is common to both images.

The equations required to calculate real ground distances with the origin at the camera from an oblique slide are given below. The analysis includes the effects of magnification of the slides. The magnification of the slide C is the ratio of the height of a slide, d_1 , to the height of the slide on the screen, d_2 , or

$$C = \frac{d_1}{d_2} . \quad (1)$$

The locations of the points P, T, I, N along the principal plane can be calculated if the positions of any two points are known. Points T and P can be measured directly from the image, and points I and N can be calcu-

lated. Then the coordinates of any point in the equivalent vertical photograph can be determined. The principal point of the enlarged oblique image is the center of the image. The distance from the principal point, P, to the apparent horizon point, T, on the slide, \overline{PT} , can be measured directly. The apparent depression angle, θ' , is

$$\theta' = \arctan (C \overline{PT}/f) \quad (2)$$

The apparent horizon is slightly lower than the true horizon, and a correction angle, $\delta\theta$, can be added to θ' to obtain the true horizon:

$$\delta\theta = 0.98(H)^{\frac{1}{2}} \quad (3)$$

where H is in feet and $\delta\theta$ is in minutes.

Thus,

$$\theta = \theta' + \delta\theta \quad (4)$$

and

$$\overline{PT} = f \tan \theta \quad (5)$$

The following distances in the oblique image are given without derivation:

$$\overline{PI} = f \tan \frac{\theta}{2} \quad (6)$$

$$\overline{PN} = f \tan \theta \quad (7)$$

$$\overline{TI} = \overline{PT} + \overline{PI} \quad (8)$$

$$\overline{TN} = \overline{PT} + \overline{PN} \quad (9)$$

Using Eqs. (1) through (9), we obtain the coordinates of any point in the equivalent vertical photograph (X_{evp} , Y_{evp}), with the origin at the camera (i.e., the principal point of the equivalent vertical photograph, and not the isocenter):

$$X_{\text{evp}} = X_{\text{ob}} C \left(\frac{\overline{TI}}{\overline{TI}-K} \right) \quad (10)$$

$$Y_{evp} = K \left(\frac{\overline{TI}}{\overline{TI}-K} \right) + \overline{NI} \quad (11)$$

where $K = Y_{ob} C + \overline{PI}$, $\overline{NI} = \overline{PI}$, and (X_{ob}, Y_{ob}) are the coordinates of any point on the enlarged oblique image with the origin at the principal point of the oblique image. The real ground coordinates (X_{gr}, Y_{gr}) of any point on the equivalent vertical photograph with respect to the camera are given by

$$X_{gr} = \left(\frac{H X_{evp}}{f} \right) \quad (12)$$

$$Y_{gr} = \left(\frac{H Y_{evp}}{f} \right) \quad (13)$$

where H is the difference in elevation between the camera and the point on the ground. If single images are being analyzed, H is the datum. Usually H is the difference between the elevation of the mean water level and the camera. Thus, horizontal distances can be calculated using Eqs. (12) and (13). The height of an object in a single oblique image can be calculated if the object is vertical. For vertical objects in which the bottom and top points are visible, the height, h , is given by

$$h = \frac{H(K_{top} - K_{bot}) \overline{TN}}{[(TN - TI) + K_{top}] (TI - K_{bot})} \quad (14)$$

where Y_{ob} in K_{top} is the "Y" coordinate of the top point of the vertical object and Y_{ob} in K_{bot} is the "Y" coordinate of the bottom point of the object.

If the datum fluctuates in time and space and the actual elevation of each point is of interest, then stereoscopic images are required. If two cameras with their optical axes approximately parallel are used to simultaneously take overlapping pairs of slides, then the real ground height below the camera of each point in the oblique image can be determined from parallax measurements.

The algebraic difference in the "X" coordinates of the same point in each slide of the stereo-pairs is the parallax, P , and is given by

$$P = X_{\text{evp}} - X'_{\text{evp}} \quad (15)$$

where X_{evp} and X'_{evp} are the left and right "X" coordinates on the equivalent vertical photograph. The difference in elevation between the camera and the point is given by

$$d = \frac{f B}{P} \quad (16)$$

where B is the baseline distance between cameras. Thus the real ground distance of any point in the oblique image is given by Eqs. (12), (13) and (16) if $H = d$.

IV. SINGLE-IMAGE ANALYSIS

Single oblique images can be used to measure horizontal distances such as the location of the breaker zone, nearshore wavelength, run-up on a flat beach, and ice-ridge location, using Eqs. (12) and (13) with the mean water level as the datum. For example, this method was applied to the comparison of the location of the breaker zone to the location of nearshore ice ridges found during the winter on Lake Michigan (Figure 6). These measurements are sometimes difficult to obtain by any other technique. Fluorescein dye and floats are often used to monitor the mean longshore current velocity in the nearshore zone. Consider a sequence of time-interval photographs of a dye patch at times 0, 30, and 60 s [Figures 7(a), (b), and (c), respectively]. Elaborate systems have been used to obtain vertical photographs.³ Single oblique images can be used to make the measurements from shore. The real ground positions of the dye patch are shown in Figure 8. The mean longshore current can be calculated from the displacement of the centroid of the dye patch over time. Plunging-breaker heights can be estimated using Eq. (14). Consider the oblique image of a plunging breaker shown in Figures 3 and 9. The crest of the breaker (point A) and the intersection of the plunging breaker with the mean water level (point C) are points that can be identified on the oblique image. If the crest and the point directly below the crest (point B) could be identified, then Eq. (14) could be used directly to measure the vertical height of the wave. Although the height A-B is not a true measure of breaker height (usually defined as the difference in elevation between the crest and the trough), it does provide a good estimate. In general, point B cannot be precisely identified on images of this type. However, it is possible to estimate point B. Then, using points A and B, Eq. (14) can be applied directly. Since our estimated location of point B may not be directly below point A, an error can be expected. If the oblique image is taken when points B and C are visible along the wavefront, we can estimate the maximum possible error in the selection of point B. This possibility is considered in Figure 9. To

quantify the possible error, assume that the breaker is circular. Therefore, the maximum horizontal displacement is $\frac{1}{2}H_b$. This results in an estimate of the wave height too large by \overline{DE} shown in Figure 9. If a more realistic plunging-breaker shape were chosen, then a better estimate of the true plunging-breaker height would result. The above technique has been used in the field (Figure 10) and gives accurate estimates of the breaker heights.

To determine the accuracy of this simple estimate of the plunging-breaker height, a laboratory study was conducted. Circular waves 4.1, 7.7, 10.8, and 16.8 cm in diameter were constructed out of white paper. Oblique images of the paper waves similar in perspective to those found in nature were taken. The camera was kept at the same elevation but was moved farther away from the paper waves. This also changed the depression angles. The results of the experiment are shown in Figure 11. Errors of less than 5% were found. The greatest fluctuation around the mean occurred at the greatest distance from the camera because the points on the wave, such as the crest, could not be positively identified. We expect that accuracies of better than 10% can be expected routinely in the field. Further tests comparing the photographic method with wave-gauge measurements are planned.

V. STEREOSCOPIC OBLIQUE IMAGE ANALYSIS

More comprehensive measurements can be made if stereo-pairs are taken, since the vertical coordinate can be calculated directly. Thus wave height, water level fluctuations, and beach profiles can be obtained. While the single-oblique-image method can be applied at any location, providing the camera elevation above the datum is known, the stereoscopic oblique-image method requires reference stakes located between the cameras. Using the reference stakes, the angular rotation (Figure 2) of the left camera relative to the right camera can be computed. Any deviation greater than 0.1° , such that the optical axis of the left camera is not parallel to that of the right camera, will induce large errors in the analysis of the vertical coordinate using parallax. From experience, we have found that a minimum of three stakes and preferably five stakes are required. The relative elevation and distances between stakes can be surveyed simply with the stake and horizon method of Emery,¹⁰ using standard surveying instruments. If the cameras are not parallel, the rotation error can be determined and a mathematical correction to the horizontal coordinates (X_{evp}, Y_{evp}) of an equivalent vertical photograph can be made. Assume that the left camera is oriented correctly and rotate the right camera until the absolute values of the "X" coordinates in the left and right oblique image of each reference stake add to the baseline separation difference between cameras - - i.e.,

$$B = |X_{\text{left stake}}| + |X_{\text{right stake}}| \quad (17)$$

Due to measurement error, an average of the rotation error can be determined from three or more reference stakes. The accuracy of the correction can be determined by calculating the relative elevation and separation differences between stakes. Any rotation will result in increasing elevation errors with increasing offshore distance. The corrected equivalent vertical photograph coordinates are given by

$$X_{cevp} = X_{evp} \cos\beta + Y_{evp} \sin\beta \quad (18)$$

$$Y_{cevp} = -X_{evp} \sin\beta + Y_{evp} \cos\beta \quad (19)$$

where X_{evp} and Y_{evp} are given by Eqs. (10) and (11), and β is the rotation angle.

The analysis proceeds as for the single-image analysis except that identical points must be selected in each slide (Figure 12). Identical points can be selected along the wave crest without much difficulty. However, it is not as easy to select points in the wave trough. If repeated measurements are to be made at one site, a string of buoys will provide profile lines to identify the water level at about the same point over time. An example of the water level fluctuation at two buoys separated by 8 m is given in the time series in Figure 13. If identical points are not selected in each photograph, it is usually immediately obvious, because unrealistic fluctuations occur.

VI. ERROR ANALYSIS

There are three primary sources of error in the analysis. These are:

- Measurement error
- Datum error
- Rotation error.

The measurement error is common to both the single and stereoscopic-oblique-image analyses, while the datum error affects only the single-oblique-image analysis and the rotation error affects only the stereoscopic-oblique-image analysis. There are other sources of error - - for example, due to horizontal tilt; uncertainty in the absolute focal length of the camera, uncertainty in the simultaneous exposure of the stereo-pairs, and surveying error. However, these effects are apparently negligible in the analysis.

A. Datum Error

Other than measurement error, the largest error in single-oblique-image analysis is due to the uncertainty in the datum elevation. In single-oblique-image analysis, it is assumed that all points lie on the datum. The datum in our analysis is the mean water level. Since the water surface fluctuates around the mean water level, the horizontal coordinates will have some error (Figure 14). For example, if a dye patch is determined to be 150 m from the camera at an elevation of 8 m, and the water level fluctuates ± 10 cm around the mean, then the error is approximately 1 m in the offshore (Y) direction. The longshore (X) direction error is not reported, since it is not significantly affected by a datum error, and most horizontal measurements in the nearshore zone such as breaker zone, wavelength, and run-up are Y-dependent. The error in the location of a breaking wave is more critically dependent on the datum. If the amplitude of a breaking wave (crest to mean water level) located 150 m offshore is 50 cm, then an error of 7 m in the offshore distance results. However, an estimate of the amplitude of the breaker height can be made and subtracted from H to give a more realistic offshore coordinate. Therefore, a datum error of 10 cm or less can be expected for most measurements.

B. Rotation Error

Rotation primarily affects the calculation of elevation since the parallax is dependent on the "X" coordinates of an object in two oblique images. The angular rotation of one camera relative to the second required to make the line of sight of both cameras parallel is defined as β (Figure 2). If β is greater than zero degrees, an error will result. The effects of rotation error (Figure 15) increase significantly with increasing distance offshore. A relief error of over 5 m is expected at 150 m from shore if the angular rotation is 0.8° . Fortunately, the angle β can be calculated to within $\pm 0.01^\circ$. Therefore, these large errors are not found in the analysis. However, Figure 15 indicates how critically dependent the stereoscopic analysis is on rotation, and emphasizes the need for reference stakes on the beach.

C. Measurement Error

Measurement error is the primary source of error in our oblique-image analysis, because the analysis is done by hand and does not utilize the sophisticated equipment commonly used in aerial surveys. The measurement error includes the effects of outlining the enlarged slide frame, locating the principal point, drawing the (X_{ob} , Y_{ob}) axes through the principal point, drawing and digitizing the horizon, selecting the image point from the slide, and measuring its coordinates with a caliper. All measurements were made with a caliper accurate to ± 0.001 inch. Repeated measurements indicated that an error of ± 0.003 inch can be expected from

any one measurement. The expected measurement error due to all the above sources was found to be about 0.015 inch. The (X_{ob} , Y_{ob}) coordinates of two different reference stakes located about 35 m from the camera were measured from 50 different oblique exposures. The standard deviation of the measurement was 0.016 and 0.015 inch, for the left and right cameras, respectively.

The effects of a possible measurement error in the X direction (ΔX) and in the Y direction (ΔY) of 0.005, 0.010, 0.015, 0.020 and 0.025 inch on the ground coordinates were calculated for three locations. The error analysis was applied at the reference stakes (35 m), the offshore buoys used to calculate mean water (50 m), and the breaking wave (150 m) in Figure 1. Corrected datum levels were used in the calculation. The results are shown in Figures 16 through 20.

The error in estimating a plunging-breaker height by single-oblique-image analysis 150 m from the camera is shown in Figure 16. A total measurement error of 0.015 inch in determining the Y_{ob} coordinate would result in a 15-cm error. This error includes the effects of selecting the points from the image, including the uncertainty of selecting the trough. Since the computation depends on the difference between two " Y_{ob} " coordinates, and the major portion of the 0.015-inch error is a constant bias and not a random error for this calculation, better accuracies are possible.

The possible measurement errors in the longshore (X) and offshore (Y) directions for single oblique images are shown in Figures 17 and 18. Measurement error is linear in the X direction and negligible over the range of offshore distances assumed in the analysis. Although the error in the offshore distance is larger than the error in the longshore direction, it too is small. For example, a measurement error of 0.015 inch in a wave 150 m from shore results in an error of about 3 m. This is about 2%, which is sufficiently accurate for most measurements.

The range of possible relief errors for stereoscopic oblique image analysis due to measurement errors in X_{ob} and Y_{ob} is shown in Figures 19 and 20. Since the calculation of X_{evp} in Eq. (10) is dependent on the calculation of Y_{evp} , the measurement errors in the Y_{ob} direction will effect the parallax. In fact, for increasing offshore distances the effect of ΔY measurement errors increases until it affects the parallax more rapidly than do ΔX measurement errors.

For offshore distances greater than 150 m, the relief errors are more dependent on ΔY measurement errors than on ΔX measurement errors. The family of curves in Figure 19 would be linear if the same datum were assumed for all calculations.

VII. CONCLUSION

Single- and stereoscopic-oblique-image analysis can be used to monitor waves, water level, and longshore currents in the nearshore zone using a 35-mm camera, a tripod, and a slide projector. Accuracies of 10% or better can be attained for these measurements. This technique should find application in coastal monitoring programs.

Acknowledgments. The authors would like to express their appreciation to Messrs. C. Carlson, J. Maresca, Sr., G. Springer, C. Vogelsang, and W. Zavoli for their assistance in the field experiments. We express appreciation for Mr. C. T. Carlson's efforts in assisting in developing and refining this technique for application to nearshore ice studies on Lake Michigan. We would also like to thank Dr. C. Olson for his encouragement and helpful discussions on analysis of oblique images.

REFERENCES

1. D. D. Stafford, R. O. Bruno, and H. M. Goldstein, "An Annotated Bibliography of Aerial Remote Sensing in Coastal Engineering," MP 2-73, Coastal Engineering Research Center, Fort Belvoir, Va. (1973).
2. L. J. Cote, J. O. Davis, W. Marks, R. J. McGough, E. Mehr, W. J. Pierson, Jr., J. F. Ropek, G. Stephenson, and R. C. Vetter, "The Directional Spectrum of a Wind Generated Sea as Determined from Data Obtained by the Stereo Wave Observation Project," Meteorol. Papers, Vol. 2, No. 6, NYU College of Engineering, New York City (1960).
3. C. J. Sonu, "Tethered Balloon for Study of Coastal Dynamics," Proc. Symposium Earth Observation Balloons, pp. 91-102 (1969).
4. E. C. Monahan, "Fresh Water Whitecaps," J. Atmos. Sci., Vol. 26, No. 5, pp. 1026-29 (1969).
5. J. W. Maresca, Jr., "Bluffline Recession, Beach Change and Nearshore Change Related to Storm Passages Along Southeastern Lake Michigan," Ph.D. Dissertation, University of Michigan, Ann Arbor, Michigan (1975).
6. E. Seibel, C. T. Carlson, and J. W. Maresca, Jr., "Lake and Shore Ice Conditions on Southeastern Lake Michigan in the Vicinity of the Donald C. Cook Nuclear Plant: Winter 1973-1974. Part XXI," Special Report No. 55, Great Lakes Research Division, University of Michigan, Ann Arbor, Michigan (1975).
7. E. Seibel, C. T. Carlson, and J. W. Maresca, Jr., "The Interrelationship between Nearshore Ice Ridges, Breaking Waves, and Offshore Bars Along Southeastern Lake Michigan," accepted for publication in Great Lakes Res. (1976).
8. H. J. Pincus, "Some Application of Terrestrial Photogrammetry to the Study of Shorelines," Photogrammetric Eng., Vol. 25, No. 3, pp. 75-82 (March 1959).
9. American Society of Photogrammetry, Manual of Photogrammetry, 3rd Ed., Washington, D.C. (1966).
10. K. O. Emery, "A Simple Method of Measuring Beach Profiles," Limnology and Oceanography, Vol. 6, pp. 90-93 (1961).

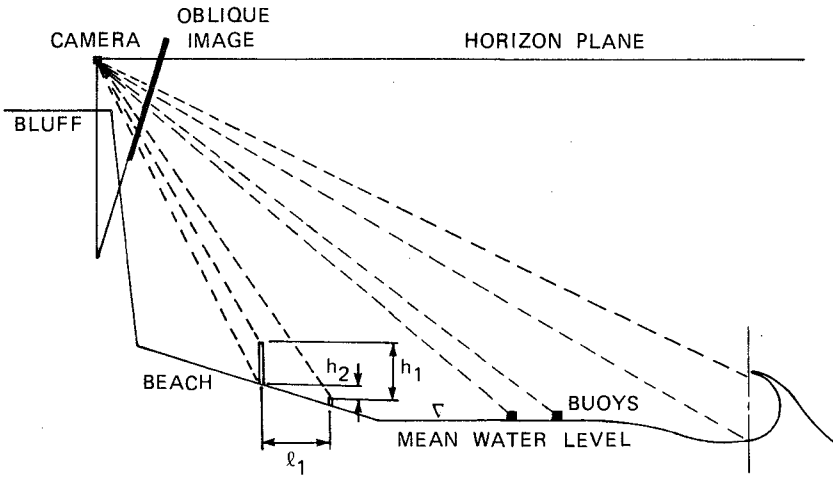


FIGURE 1 OBLIQUE IMAGERY OF THE SURF ZONE

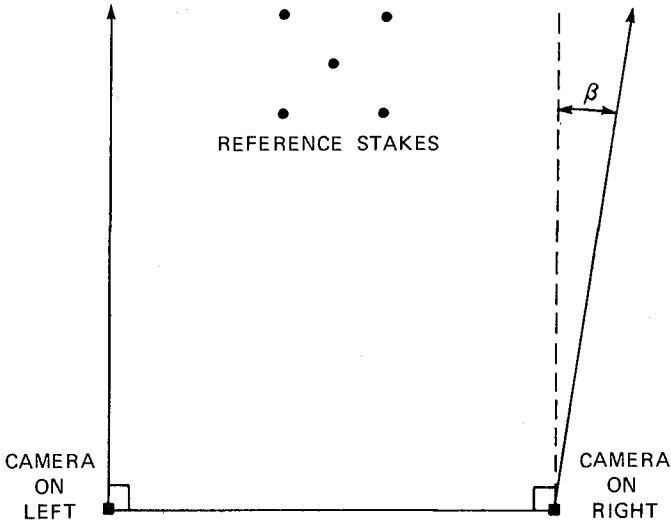


FIGURE 2 EFFECT OF ROTATION ERROR ON STEREOSCOPIC OBLIQUE ANALYSIS. The actual optical axes of the cameras are denoted by the solid line. If $\beta = 0$, the optical axes of the cameras are parallel.



FIGURE 3 SINGLE OBLIQUE IMAGE OF A PLUNGING BREAKER, BUOYS, AND REFERENCE STAKES, AS ILLUSTRATED IN FIGURE 1

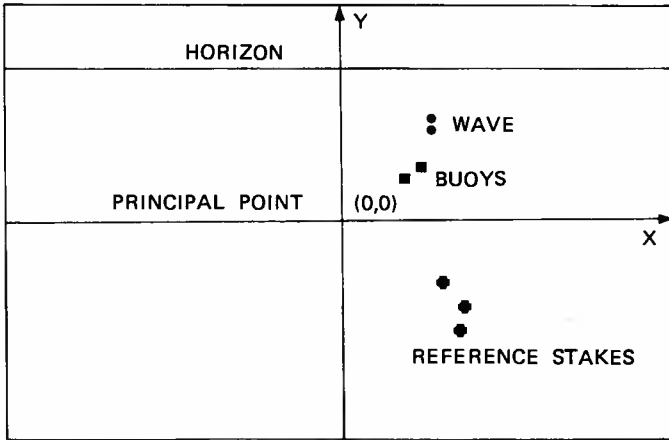


FIGURE 4 DIGITIZED SINGLE OBLIQUE IMAGE

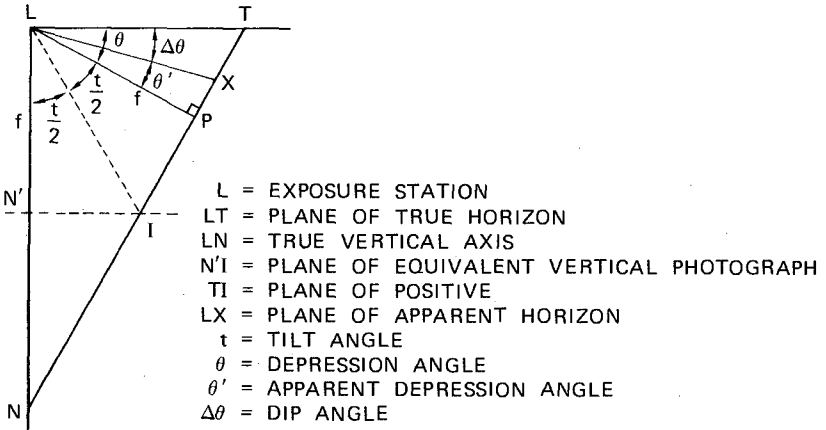


FIGURE 5 PRINCIPAL-PLANE DIAGRAM

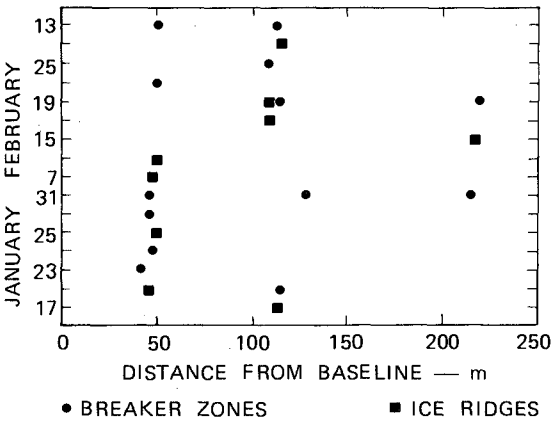


FIGURE 6 LOCATION OF ICE RIDGES AND BREAKER ZONES FOR SINGLE OBLIQUE IMAGES

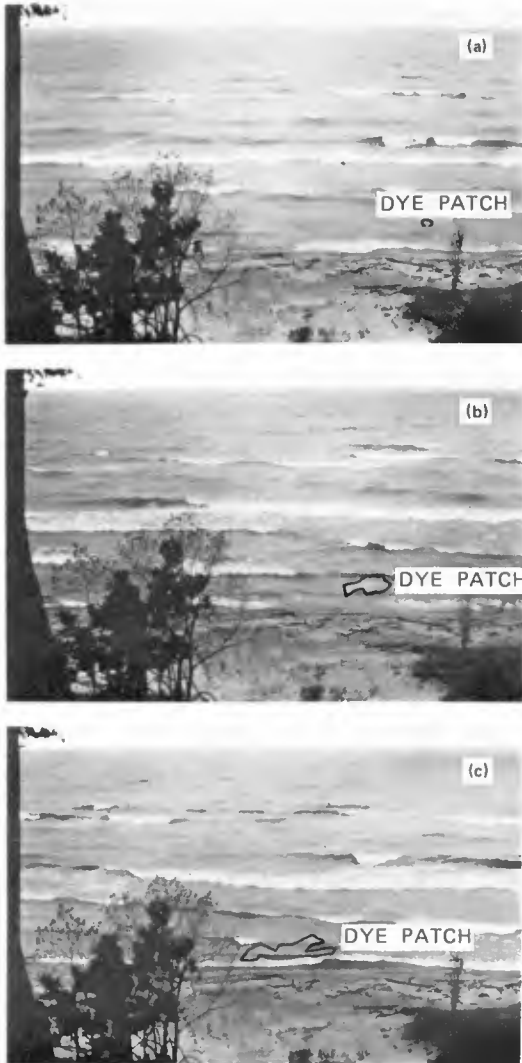


FIGURE 7 SINGLE OBLIQUE IMAGE OF A FLUORESCIN DYE PATCH.
(a) At time of release, (b) 30 s after release, (c) 60 s after release.

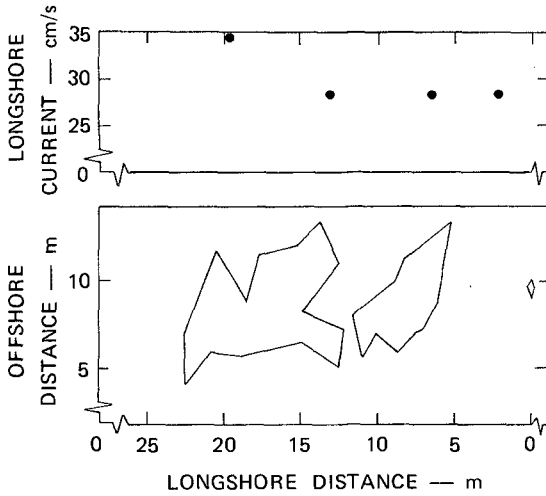


FIGURE 8 SINGLE-OBLIQUE-IMAGE ANALYSIS OF THE LONGSHORE CURRENT

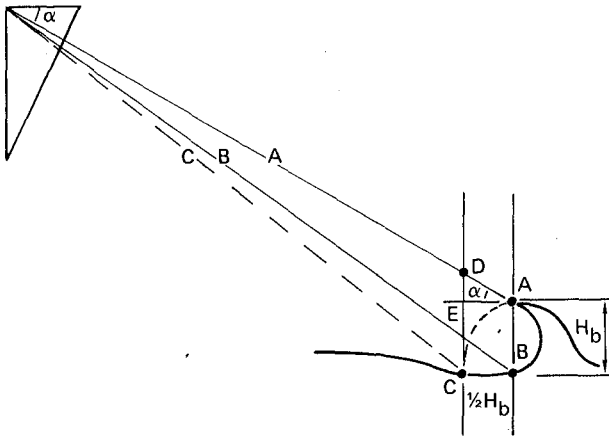


FIGURE 9 DEFINITION OF PLUNGING-BREAKER HEIGHT. Breaker height is defined as \overline{AB} . If points A and C are used to calculate the breaker height, then the breaker height is \overline{DC} . The error is $\overline{DE} = \overline{EA} \tan \alpha = \frac{1}{2} H_b \tan \alpha$.

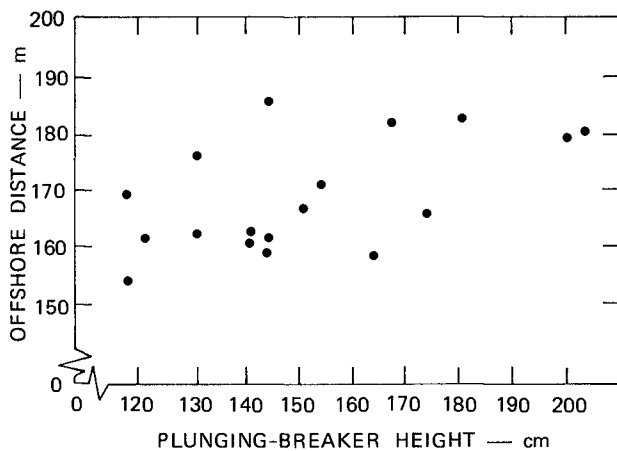


FIGURE 10 SINGLE-OBLIQUE-IMAGE ANALYSIS OF PLUNGING-BREAKER HEIGHTS IN THE FIELD

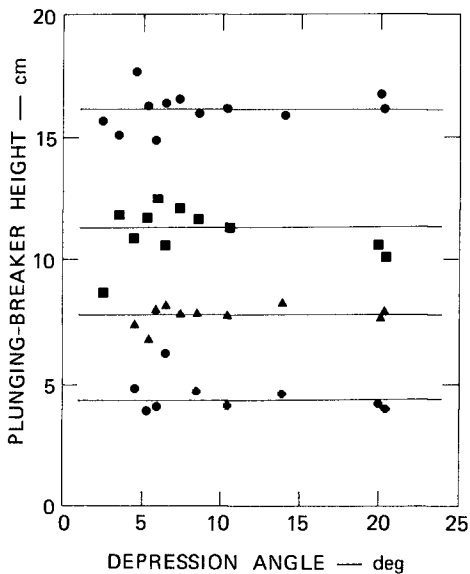


FIGURE 11 SINGLE-OBLIQUE-IMAGE ANALYSIS OF PLUNGING-BREAKER HEIGHTS IN THE LABORATORY

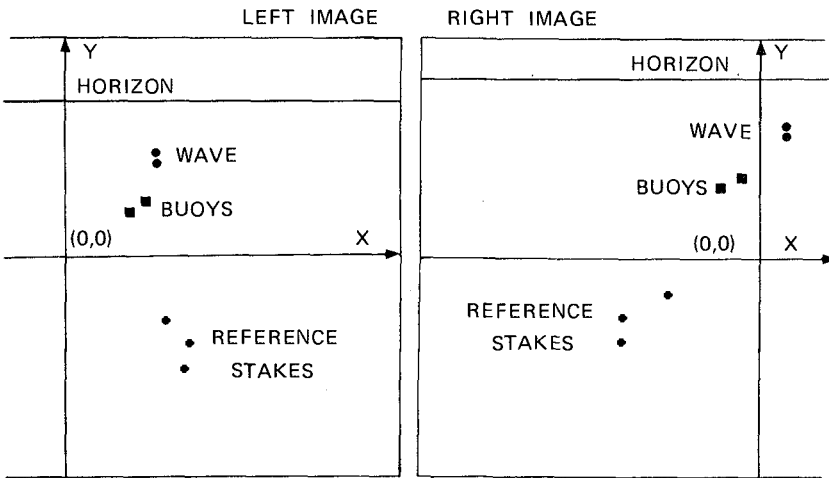


FIGURE 12 DIGITIZED STEREOSCOPIC OBLIQUE IMAGES

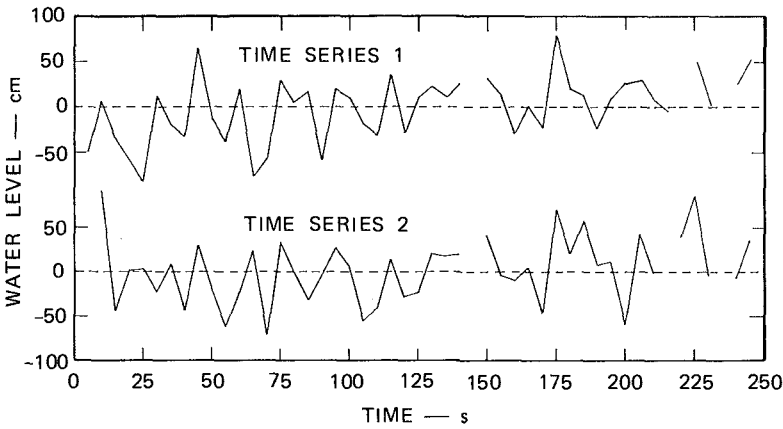


FIGURE 13 WATER LEVEL FLUCTUATION BY STEREOSCOPIC-OBLIQUE-IMAGE ANALYSIS

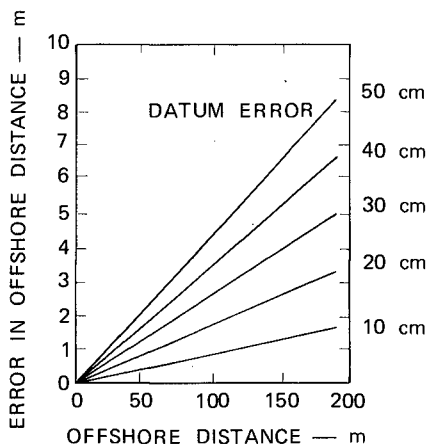


FIGURE 14 ERROR IN OFFSHORE DISTANCE DUE TO DATUM ERROR FOR SINGLE OBLIQUE IMAGE

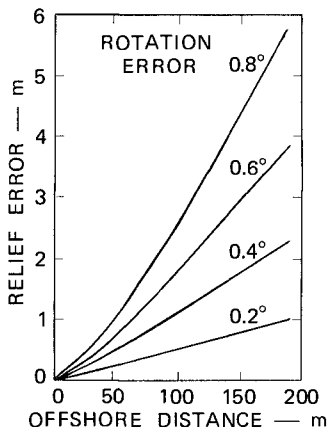


FIGURE 15 RELIEF ERROR DUE TO ROTATION ERROR FOR STEREOSCOPIC OBLIQUE ANALYSIS

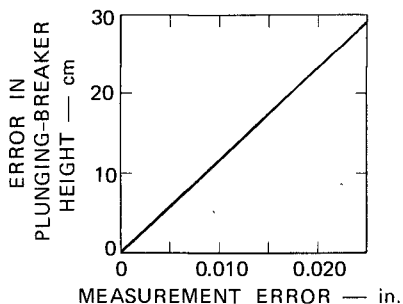


FIGURE 16 ERROR IN PLUNGING-BREAKER HEIGHT FOR SINGLE-OBLIQUE-IMAGE ANALYSIS

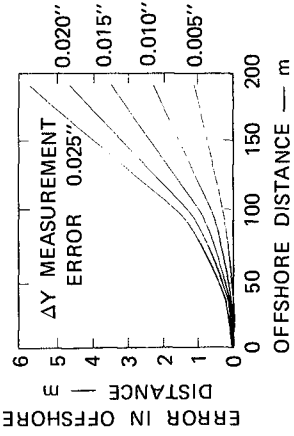


FIGURE 17 ERROR IN X DISTANCE DUE TO ΔX MEASUREMENT ERROR FOR SINGLE OBLIQUE IMAGE

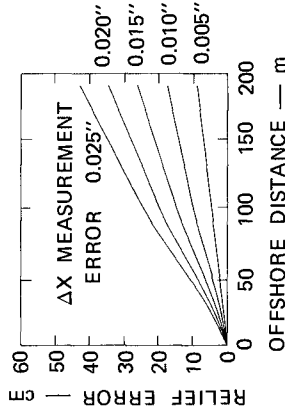


FIGURE 19 RELIEF ERROR DUE TO ΔX MEASUREMENT ERROR FOR STEREOSCOPIC OBLIQUE ANALYSIS

FIGURE 18 ERROR IN OFFSHORE DISTANCE DUE TO ΔY MEASUREMENT ERROR FOR SINGLE OBLIQUE IMAGE

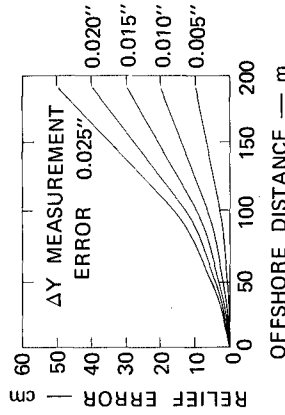


FIGURE 20 RELIEF ERROR DUE TO ΔY MEASUREMENT ERROR FOR STEREOSCOPIC ANALYSIS

CHAPTER 40

NON-UNIFORM ALONGSHORE CURRENTS

Michael R. Gourlay *

Abstract

Alongshore gradients of breaker height have been shown to significantly influence the velocities and circulation patterns of nearshore current systems. Experimental data from an idealized laboratory experiment shows that the form of the nonuniform wave generated current system resulting from diffraction behind an offshore breakwater is essentially determined by the beach-breakwater geometry while its magnitude depends upon the wave height. Furthermore the current may produce significant increases in the magnitude of the wave set-up within the three dimensional system. For the case investigated, where the alongshore gradient of breaker height is comparatively large, the maximum mean alongshore current velocity is not greatly affected by bottom resistance and may be computed for plunging breakers from a relation of the following form;

$$\frac{v}{\sqrt{gH_b^3}} = f\left(\frac{H_b}{d_b}, \frac{x_p}{H_b}, \tan \alpha\right)$$

derived from a simple momentum analysis including "radiation stress" terms. The influence of bottom resistance can be included if necessary.

1. Introduction

The phenomenon of the uniform alongshore current caused by waves breaking at an angle to a straight beach has received a considerable amount of study (1,2). The simple case with waves of uniform height seldom occurs in nature and in practice there is often an alongshore gradient of breaker height which influences the velocity and form of the alongshore current (3). Indeed it is now generally accepted that rip currents are produced by regular alongshore variations in the breaker height (4,5). Moreover it is possible, when the approaching wave crests are parallel to the coast, that the current velocity and circulation pattern are almost completely determined by alongshore breaker height gradients (6).

In the vicinity of coastal structures and coastal features such as reefs and headlands it has been found that wave generated current systems are very much influenced by variations both in the breaker height in the alongshore direction and in the location of the break point relative to those structures and/or features which determine the local coastal geometry (7). In general, any nearshore wave generated current system where breaker height and/or breaker angle varies along the shore may be described as a non-uniform alongshore current.

The author's investigation involved a laboratory study of a non-uniform alongshore current system generated by an alongshore gradient of breaker height with the wave crests parallel to the beach. A previous paper (6) described the experimental arrangements and techniques; presented the general results of a typical test; and treated some aspects involving the calculation of the wave set-up. This paper presents experimental results for various deep water wave heights, H_0 , and two wave periods, T , and describes a simple method for calculating the wave generated current for the situation where the driving force causing the current is created solely by the alongshore gradient of breaker height.

* Department of Civil Engineering, University of Queensland, St. Lucia, Australia

2. Laboratory Experimental Arrangements

The layout of the 12.5 m by 6.6 m outdoor test basin and the measurement methods used were described in a previous paper (6) to which the reader is referred for a more complete description. The experimental arrangement involved the generation of a non-uniform alongshore current by wave diffraction behind an offshore breakwater in a three dimensional fixed bed laboratory model (Figure 1). Waves approached with crests parallel both to the breakwater and the exposed portion of the 1 in 10 concrete beach while the beach in the sheltered area was curved so that it was parallel to the crests of the diffracted waves. Waves thus broke at all times parallel to the beach. The breakwater itself was located at a distance of 3.05 m from the still water line in the exposed area, while the constant offshore water depth at the head of the breakwater was 0.2 m.

Wave heights were recorded using capacitative wave probes and a twin channel pen recorder; wave set-up was measured using piezometer tappings in the beach and a multitube manometer; and current velocities and circulation patterns were obtained from the analysis of movie film records of the paths of small almost neutrally buoyant floats together with some direct measurements with a modified total head tube device (see section 3.1).

3. Results of Laboratory Investigation

3.1 Basic Characteristics of Non-uniform Alongshore Current System

The characteristics of the current system generated in the test basin were described in a previous paper (6). In that description the results of one test only for a specific H_0 and T were considered. To assist in the understanding of the results presented in this paper a brief description of the current system will be given first. Referring to figure 2 it can be seen that as a consequence of the diffraction of the waves by the offshore breakwater, the surf zone is wide in the exposed area where the waves are large while it is narrow within the sheltered area where the waves are of necessity very much smaller. An alongshore gradient of breaker height is thus present and this results in an alongshore gradient of wave set-up since the latter is generally proportional to the breaker height in shallow water.

Now the wave set-up itself is maintained by the onshore thrust created by the change in momentum as the breaking waves are dissipated within the surf zone. However there is no such opposing thrust in the longitudinal direction to balance the alongshore gradient in the mean water level resulting from the alongshore variation in wave set-up. The result is that an alongshore current flows from the surf zone of the exposed area into the sheltered area. Since the geometry of the system is a closed one the alongshore current becomes a circulatory eddy. Referring to figure 2 it is seen that the entire circulation is contained inside the point where the exposed area breaker height is a maximum, i.e. inside of the first interference maximum of the diffraction pattern.* Moreover the seaward limit of the current is initially defined by the location of the plunge point in the exposed area since this represents the point in the onshore-offshore direction where wave set-up commences. Between the point of maximum breaker height and the geometric shadow of the breakwater there is a zone of spatially varied flow where the alongshore current discharge increases as it travels towards the sheltered area since water flows inshore through the breakers from further

* A series of secondary circulation systems is set up in the exposed area where the alternating interference maxima and minima provide the necessary alongshore gradients in energy levels to produce rip currents. The first such rip current occurred within the test basin but as it was affected by the presence of the model sidewall (especially for 1.5 second waves) it was not studied in detail.

offshore. The current discharge itself attains a maximum value at the geometric shadow of the breakwater.

Within the sheltered area the current becomes too large to remain within the rapidly narrowing surf zone and so flows increasingly outside the breaker line until it is eventually completely removed from the surf zone. It is deflected by the stagnation eddy at the corner where the breakwater intersects the curved beach. The return circuit is then completed as the current flows along the shoreward face of the breakwater before turning shoreward at the head of the breakwater to flow back into the surf zone in the inflow region. Inside the primary wave generated current the initially motionless fluid is set in motion by the current and moves as a slow induced eddy within the main current system.

The driving force for the current system appears to be essentially the increase in head created by the breaking waves in the inflow region. Indeed the current system can be visualized as being powered by a "pump" located in the inflow region drawing water in from the offshore zone and discharging it as a high velocity "jet" parallel to the beach. The "jet" is then deflected by the curved beach and breakwater so that it flows back into the "pump" inlet, offshore of the inflow region. Diffusion of momentum offshore creates the induced eddy inside the primary current circulation.

Observations of horizontal velocity profiles of the current, made from photographs of surface floats, indicate that the surface velocity profile is approximately parabolic in shape with a rather well defined offshore boundary between the primary alongshore wave generated current and the induced eddy inside it (figure 3). Measurement of the vertical velocity profile of the alongshore current is much more difficult on account of the very shallow depths in the surf zone and the unsteady nature of the wave orbital motion superimposed at right angles to it. Figure 4 shows one such profile measured along the line of the geometric shadow of the breakwater using a small pitot tube device with two total head tubes, one pointing upstream and the other downstream. Figure 4 includes surface float data from figure 3 which are found to be consistent with the sub-surface measurements resulting in the velocity contours as shown. The maximum velocity occurs within the surf zone, just below the wave trough elevation. Integration of the velocity with respect to depth indicated that the actual current discharge (or mean velocity) is in fact about 50% greater than that calculated from surface float velocities alone. Consideration of the isovel pattern, together with visual observation of the uprush-backwash cycle in the test basin shows that there is spiral secondary flow superimposed upon the primary alongshore current similar to the helicoidal flow observed in the field by Eliot (8) for alongshore currents.

3.2 Influence of Variations in Wave Height and Period upon the Current System

The effect of variations in input wave conditions, upon the wave generated current system was obtained from the results of two series of tests, one made with a wave period of 1.0 seconds, the other with a period of 1.5 seconds. Each test series consisted of four tests with different deepwater wave heights. Two parallel series of tests were also made in which the sheltered area of the test basin was blocked off so as to give two dimensional conditions in the exposed area.

The experimental results indicate that there is a general overall similarity of the current circulation system for all H_0 and T . Variations in detail do occur but the geometrical form of the beach and breakwater determine the overall form of the current system. For instance when breaker height H_b and wave set-up at the still water line $\bar{\eta}_s$ are made nondimensional in terms of H_b^* and $\bar{\eta}_s^*$, their equivalent two dimensional values for the same H_0 and T , general similarity is found for each period (figure 5). Different wave periods which correspond to different

deep water wave lengths, L_0 , cause some differences in the alongshore gradients of breaker height and wave set-up. Specifically, in the region between the maximum wave height in the exposed area and the geometric shadow of the breakwater, the alongshore gradient of dimensionless wave set-up is greater for 1.0 second period waves than for 1.5 second waves. This difference is in agreement with diffraction theory. The alongshore dimensionless breaker height also varies locally in two regions with the deep water wave height. This effect, which occurs in the sheltered area in the vicinity of the stagnation eddy and in the exposed area outside the primary current circulation system, is caused by interaction between the waves and the wave generated currents.

Similarity of the alongshore velocity profiles may be considered from two points of view. The first is to express the velocity profiles in nondimensional parameters based upon the breaking wave conditions which should relate the velocities to those quantities which most directly influence them. Alternatively the alongshore current velocities can be related to the incident or deepwater wave conditions and geometric factors which determine the overall characteristics of the nearshore current system.

Consideration of theoretical investigations for uniform alongshore currents such as that of James (9) suggests that an appropriate set of dimensionless parameters to represent this data would be the following:

$$\frac{v}{\sqrt{gd_b^*}} ; \frac{x}{d_b^*} ; T\sqrt{\frac{g}{d_b^*}}$$

where v is the alongshore velocity at distance x from the still water line;

$$d = \bar{\eta} + h \text{ is the mean water depth;}$$

$$h \text{ is the still water depth.}$$

These parameters are used to plot dimensionless velocity profiles along the geometric shadow for wave periods of 1.0 and 1.5 seconds as shown on figure 6. There is considerable scatter in the data points but it does appear that the dimensionless velocity and distance parameters are satisfactory. However it is evident that the 1.0 second period tests do not show the same consistent variation with the third parameter as shown by the 1.5 second tests. Moreover the magnitudes of this latter parameter are inconsistent for the two wave periods. Analogy between James' theory and theory for non-uniform alongshore currents (e.g. Komar (3)) shows that the velocity profiles could also be affected by the following dimensionless quantities:

$$\frac{dH_b}{dy} ; \gamma = \frac{H_b}{d_b} ; N ; C_f ; \tan \alpha$$

Of these, the bottom slope $\tan \alpha$ was constant in these tests. The bottom friction coefficient C_f is a complex function of the wave orbital velocity and the alongshore velocity. As indicated in section 4.3, bottom friction effects are relatively small in this situation. The factors upon which the lateral mixing coefficient N depends are not yet clear and its exact magnitude remains uncertain. The alongshore gradient in breaker height will only affect the alongshore velocity significantly if bottom friction is important. Otherwise it is the dimensionless difference in alongshore breaker height $\Delta H_b/H_b^*$ which is important and this is the same for both wave periods. This leaves only the breaker index γ as an alternative relevant third parameter. However, while there is some evidence of better agreement between the two series of tests when the equivalent two dimensional breaker index γ^* is considered as the third parameter on figure 6, complete consistency is impossible since γ^* varies in opposite senses for the two wave periods.

Figure 7 shows the dimensionless maximum alongshore velocity as a function of the alongshore distance y for each wave period. This clearly indicates that the magnitude of the velocity is influenced by quantities other than $\sqrt{gd_1^3}$ but as before it is not possible to deduce a simple dependence upon any one of the parameters previously considered which applies to both wave periods.

Considering the alternative of relating the current velocity to the deep water wave conditions it is quite evident that the alongshore current velocity increases with wave height. Consequently the maximum velocity v_m was plotted as a function of H_0 for each location along the shoreline. A simple picture emerged in which $v_m = B(t)H_0$ where $B(t)$ varied consistently along the shoreline. Figure 8a shows the plot of v_m versus H_0 for the profile at the geometric shadow. Similar plots were obtained at the other locations with relatively few discordant points. The magnitude of $B(t)$ has been plotted as a function of the alongshore distance in figure 8b. This figure suggests that, apart from the slight variation with wave period of the location of the point where the current commences, which is a result of the effect of the wave length upon the diffraction process, the wave period does not enter the current velocity similarity parameter. Thus the alongshore current velocity is apparently determined by the deepwater incident wave height H_0 and the geometric characteristics of the system. As the latter were not varied in these tests the relevant variables can only be inferred at this stage. The relevant parameters could be the following:

$$\frac{v_m}{\sqrt{gd_1}} = B\left(\frac{H_0}{X}\right)$$

$$\text{where } B = f\left(\frac{y}{X}, \frac{d_1}{X}, \tan \alpha\right);$$

d_1 is the incident water depth at the breakwater ;

and X is the distance between breakwater and still water line.

3.3 Interaction between Alongshore Current and Wave Set-up

As previously mentioned the alongshore current modifies the breaker heights in certain regions. The wave set-up is also modified by changes in the mean water level created by the current system. In figure 9 the wave set-up at still water level, $\bar{\eta}_s$, is plotted as a function of the corresponding breaker height measured in the three dimensional basin, for each of the four tests with 1.0 second wave period. For comparison the equivalent relation between $\bar{\eta}_s$ and H_b derived from the two dimensional tests is shown on each plot. It can be clearly seen that in the three dimensional case the wave set-up $\bar{\eta}_s$ is relatively greater than its two dimensional value for the corresponding breaker height and that this discrepancy increases with increasing deep water wave height H_0 . Since the current velocity also increases with H_0 (figure 8) it would appear that $\bar{\eta}_s$ increases as the current velocity increases. The tests with 1.5 second period waves indicate a similar result. In figure 10, $\bar{\eta}_s$ is plotted on a very much magnified scale as a function of the distance along the still water line for one of the tests. Also shown on figure 10 is the equivalent two dimensional wave set-up $\bar{\eta}_s^*$ corresponding to the observed alongshore variation in breaker height. $\bar{\eta}_s^*$ is plotted downwards from the corresponding three dimensional value of $\bar{\eta}_s$ and, except at two points, the two dimensional value is generally about 10 to 15% smaller than the three dimensional value.

The following specific characteristics of the alongshore variation of wave set-up may be discerned from figures 9 and 10:

- (i) The wave set-up has its maximum value in the region within the exposed area outside the primary alongshore current system where it is essentially independent of the breaker height (see also figure 5). This represents the effect of the alongshore feeder currents to the rip current, which produce a stagnation condition on the shore at the point where the rip current flows seaward through the breaker zone.
- (ii) The two dimensional wave set-up is greater than the three dimensional set-up at points where there is inflow into the surf zone and alongshore outflow in both directions with a consequent reduction in the magnitude of the backwash.
- (iii) The maximum discrepancy between the three and two dimensional wave set-up generally occurs at or near the geometric shadow line defining the boundary between exposed and sheltered areas. This corresponds to the region where the alongshore velocity attains its maximum value.
- (iv) The minimum value of wave set-up occurs within the sheltered area but not right at the corner on account of refraction of the waves by the current which increases breaker heights within the stagnation eddy but reduces them further upstream.

The explanation for the difference between the three and two dimensional wave set-ups is found in three separate factors. These are breakpoint set-up, $\bar{\eta}_b$; superelevation caused by normal acceleration, $\bar{\eta}_c$; and alongshore translation of the uprush-backwash cycle, $\bar{\eta}_d$. Hence the wave set-up at the still water line at position y within the region influenced by the primary alongshore current is given as follows:

$$\bar{\eta}_s = \bar{\eta}_s^* + \bar{\eta}_b + \bar{\eta}_c + \bar{\eta}_d$$

Breakpoint set-up $\bar{\eta}_b$

In the three dimensional case expansion of the diffracted wave crests behind the breakwater causes a reduction in radiation stress and a consequent increase in mean water level. This results in a breakpoint set-up $\bar{\eta}_b$ in the sheltered area of the order of 1 mm for the particular test shown on figure 10. This factor accounts for about half the observed discrepancy in the stagnation region. In the exposed area there is a breakpoint set-down of similar order of magnitude.

Superelevation caused by normal acceleration $\bar{\eta}_c$

The alongshore current is deflected by the beach and the resulting normal acceleration results in a superelevation of the water surface on the beach. This has been calculated using the relationship

$$\bar{\eta}_c = \sum \frac{v^2}{gr} \Delta r$$

where r is the radius of curvature of the flow streamlines.

The value of $\bar{\eta}_c$ has been plotted on figure 12 upwards from the breakpoint set-up level. It is found that all the three dimensional wave set-up is now accounted for within the stagnation eddy region. With regard to the rip current in the exposed area, calculation of the stagnation velocity of the alongshore feeder currents confirms the previously quoted explanation for the increased wave set-up in this region.

Alongshore translation of uprush-backwash cycle $\bar{\eta}_d$

Visual observation in the test basin suggested that the process referred to earlier in which a helicoidal secondary motion is superimposed upon the primary alongshore current also provides the explanation for the remaining component of the three dimensional wave set-up in the vicinity of the geometric shadow of the breakwater where the alongshore current has its maximum value. Referring to

figure 11 it can be seen that the wave set-up at a point on the beach is in fact determined by waves breaking further upstream along the beach since the alongshore current translates the wave uprush-backwash cycle along the beach. Thus the magnitude of the wave set-up at a point C within the alongshore current depends upon the height of the breaking waves between points A and B upstream of it; and not upon the breaker height at point D on the same profile as point C.

The actual magnitude of the increase in $\bar{\eta}_s$ at point C will depend upon both the velocity of the alongshore current between points A and C and the alongshore gradient of breaker height between points A and B. A simple estimate of this effect was calculated using the observed variation of mean alongshore velocity V and the alongshore variation of the gradient of $\bar{\eta}_s^*$ calculated from the observed breaker heights. Assuming that the mean alongshore displacement distance Δy is equal to the distance travelled by the mean alongshore current during one wave period T , the increase in wave set-up, $\bar{\eta}_d$, at a certain point is given by the following expression:

$$\bar{\eta}_d = VT \frac{d(\bar{\eta}_s^*)}{dy}$$

where the magnitudes of $\frac{d(\bar{\eta}_s^*)}{dy}$ and V are those at a point located a distance equal to $\Delta y = VT$ upstream of the point under consideration.

The results of this calculation are found to give values of $\bar{\eta}_d$ which agree to within 0.3 to 0.5 mm of the observed values. The agreement is particularly good in the inflow zone in the exposed area but not so good in the sheltered area where the current leaves the surf zone. It is however considered adequate for confirmation of this explanation for the influence of the current upon the magnitude of $\bar{\eta}_s$ in the three dimensional case. The remaining small discrepancy may be explicable by the fact that the diffracted wave crests are not exact circular arcs. Consequently the breaker angle may not be exactly zero everywhere along the beach.

4. Computation of Alongshore Current

4.1 General Scheme of Computation

The calculation of the alongshore current from the alongshore gradient of wave set-up has not been found to be easy for a number of reasons. For instance, apart from the nonlinear interaction effects between the current and the wave set-up, there are the problems of defining the seaward extent of the current; the extent of the inflow region where water is being fed into the surf zone from offshore; the point where the current leaves the surf zone and the magnitude of the bottom friction and lateral mixing effects.

The computation process may be considered in four basic stages. These are as follows:

- (i) Determination of the alongshore gradient of breaker height and the location of the break point;
- (ii) Determination of the wave set-up resulting from the alongshore gradient of breaker height;
- (iii) Determination of the wave generated current from the previously determined alongshore gradient of wave set-up;
- (iv) Adjustment of the first estimate of the wave generated current for the effects of interaction between the current and the surf zone conditions.

In a previous paper (6) the author has described how it is possible to determine the location of the breakpoint and the alongshore breaker height gradient

using a graphical combination of 1st order diffraction and shoaling theory together with empirical wave breaking data correlated by Goda (10). The results of this computation were generally promising. However to simplify the treatment of the subsequent stages of the computation process the work described in this paper takes the observed break point and alongshore variation of breaker heights as its starting point.

4.2 Wave Set-up

With regard to the determination of the wave set-up this can be approached from two viewpoints. Firstly a purely empirical approach can be adopted. For instance, the parallel series of two dimensional tests yielded the empirical relationships;

$$\bar{\eta}_s = 0.303 H_b \left[\frac{H_o}{L_o} \right]^{0.12} \quad 1.$$

$$\bar{\eta}_m = 0.288 H_b \quad 2.$$

where $\bar{\eta}_s$ is the wave set-up at the still water line
and $\bar{\eta}_m$ is the maximum wave set-up.

Such empirical relationships derived from this study have the drawback that they allow, neither for the influence of the geometry of the particular two dimensional system in which the measurements were made, nor for scale effects. An alternative approach is to compute the wave set-up using the radiation stress theory of Longuet-Higgins and Stewart as applied by Bowen et al (11), assuming that conditions at the breakpoint and within the surf zone can be represented by the shallow water approximations. On this basis Bowen et al have shown that the mean water level gradient normal to the shore is given by the following expression:

$$\frac{d\bar{\eta}}{dx} = - \frac{1}{1 + 8/3\gamma^2} \cdot \frac{dh}{dx} \quad 3.$$

where $\frac{dh}{dx} = \tan \alpha$ is the bottom slope.

Wave set-down at the breakpoint, assuming the same approximations, is given by:

$$\bar{\eta}_b = - \frac{1}{16} \gamma H_b \quad 4.$$

Simple geometry then permits the derivation of relationships for $\bar{\eta}_s$ and $\bar{\eta}_m$ as functions of γ and H_b in the manner presented by several authors (12, 13 and 14). All these authors assume spilling breakers. Plunging breakers have been treated in a similar manner by Swart (15) and Gourlay (6). In this case an additional parameter is involved, either an energy dissipation factor as in Swart's treatment or the breaker plunge distance x_p in Gourlay's treatment.

For the present study it has been found expedient to adopt slightly modified forms of these empirical relationships in which the wave set-up is referred to the mean water level at the breakpoint rather than the deep water mean water level. This involves neglect of the break point set-down (equation 4) which in the case under consideration varies in the alongshore direction becoming positive in the sheltered area (see section 3.3). In passing it should also be noted that equation 4 generally overestimates the observed wave set-down by a factor of 2 to 3. As the set-down is at least an order of magnitude smaller than the wave set-up, its inclusion at this stage in the calculation of the latter is questionable.

Taking account of the above points the relevant equations for the computation of wave set-up assuming shallow water conditions within the surf zone may be summarized as follows:

$$\bar{\eta}_s^1 = \frac{3}{8} \gamma \frac{(1 - C \gamma \tan \alpha)}{1 + 3\gamma^2/8} H_b \quad 5.$$

$$\bar{\eta}_m^1 = \frac{3}{8} \gamma (1 - C \gamma \tan \alpha) H_b \quad 6.$$

where $C = \frac{x_p}{H_b} = 0$ for spilling breakers
 $= 2$ to 4 for plunging breakers

and $\bar{\eta}_s^1$ and $\bar{\eta}_m^1$ represent wave set-ups measured relative to mean water level at the breakpoint.

The author has previously shown (figure 13 of reference 6) that equation 5. gives reasonable estimates of $\bar{\eta}_s^1$ as measured in the two dimensional tests of this investigation, having regard to the general uncertainty as to what factors determine the magnitude of the dimensionless plunge distance C . Equation 6 has been found to behave similarly with respect to $\bar{\eta}_m^1$.

When plunging breakers are considered it is necessary to be able to determine the depth h_p at the plunge point. Simple geometry gives the following result compatible with equations 5 and 6.

$$h_p = \frac{(1 - C \gamma \tan \alpha)}{\gamma} H_b \quad 7.$$

The analogous directly derived experimental result compatible with equations 1 and 2 is:

$$h_p = 2.55\bar{\eta}_s = 0.773H_b \left[\frac{H_0}{L_0} \right]^{0.12} \quad 8.$$

4.3 Mean Velocity of the Alongshore Current

The following observations of the characteristics of the non-uniform alongshore current have been used in formulating a simple analytical expression for computing the maximum mean velocity of the current.

- (i) Inflow into the alongshore current ceases at the geometric shadow line. Hence discharge Q and mean velocity V are assumed to have attained their maximum values at this point.
- (ii) The seaward limit of the current at this point corresponds to the distance x_{c1} from the still water line to the plunge point of the largest breakers in the exposed area.
- (iii) The landward limit of the current occurs at the point where the onshore-offshore gradient of mean water level intersects the beach, i.e. at the point where the wave set-up equals $\bar{\eta}_m$ located at a distance x_s from the still water line.

The differential equation of motion in the alongshore direction is written as follows:

$$\frac{dS_{yy}}{dy} + \rho g (\bar{\eta} + h) \frac{d\bar{\eta}}{dy} + \rho \frac{d}{dy} [v^2 (\bar{\eta} + h)] + \tau_b + \tau_l = 0 \quad 9.$$

where S_{yy} is the alongshore component of the "radiation stress";

τ_b and τ_l are the shear stresses due to bottom friction and lateral mixing respectively.

For a simple engineering solution we will adopt a control volume type of analysis initially neglecting the effects of bottom friction and lateral mixing,

$$\tau_b \text{ and } \tau_l \rightarrow 0$$

In the alongshore direction (y) the control volume is assumed to be bounded in the upstream direction at the point where the alongshore current velocity V is zero and H_b has its maximum value. The downstream end of the control volume is at the geometric shadow where both velocity and discharge have attained their maximum values. The offshore limit of the control volume in the x direction is assumed to be equal to x_{c1} as noted above. The form of the water surface at either end of the control volume is as indicated in figure 12.

Application of the momentum principle, i.e., the integral form of equation 9, to the flow of the alongshore current into and out of this control volume in the y direction gives the following expression:

$$\rho A_2 V_2^2 = P_1 + S_1 - (P_2 + S_2) \quad 10.$$

where A is the cross sectional area of flow;
 P is the integrated thrust due to hydrostatic pressure
 S is the integrated thrust due to radiation stress;
 V is the mean velocity of flow through a given cross section;
 ρ is the fluid density
 and subscripts 1 and 2 refer to upstream and downstream locations respectively.

Using the shallow water approximation for S_{yy} ,

$$S_{yy} = \frac{1}{16} \rho g \gamma^2 (\bar{\eta} + h)^2 \quad 11.$$

together with equation 3, simple geometry and integration lead to the following relations:

$$P_1 + S_1 = \frac{\rho g}{6 \tan \alpha} \left(1 + \frac{\gamma^2}{8}\right) (h_{p1} + \bar{\eta}_{m1}) h_{p1}^2 \quad 12.$$

$$P_2 + S_2 = \frac{\rho g}{6 \tan \alpha} \left(1 + \frac{\gamma^2}{8}\right) \left(h_{p1}^3 + \frac{64\bar{\eta}_{m1}^3}{9\gamma^4}\right) \quad 13.$$

$$A_2 = \frac{1}{2 \tan \alpha} \left(h_{p1}^2 + \frac{8\bar{\eta}_{m1}^2}{3\gamma^2}\right) \quad 14.$$

In obtaining equation 13 for $P_2 + S_2$ it has been assumed that the ratio between wave height and water depth, γ , is the same outside of the plunge point as inside of it. While this assumption is of course not valid, the simplification of the form of the resulting expression for $P_2 + S_2$ is considered to more than offset the resulting relatively small underestimation of the final value of V.

Substitution into equation 10 yields the result

$$V_2 = \sqrt{\frac{g}{3} \left(1 + \frac{\gamma^2}{8}\right) \frac{h_{p1}^2 \bar{\eta}_{m1} - \frac{64\bar{\eta}_{m1}^3}{9\gamma^4}}{h_{p1}^2 + \frac{8\bar{\eta}_{m1}^2}{3\gamma^2}}} \quad 15.$$

Further simplification is dependent upon the following decisions:

- (i) The choice between equations 8 and 2 or equations 7 and 6 for expressing h_p and $\bar{\eta}_m$ in terms of the incident wave conditions.
- (ii) The specification of the alongshore gradient of $\bar{\eta}_m$ or as a consequence of the substitutions for $\bar{\eta}_m$ referred to in (i) above, the specification of the alongshore gradient of breaker height.

With regard to (i) equations 8 and 2 express h_p and $\bar{\eta}_m$ in terms of H_b and H_0/L_0 with the bottom slope $\tan \alpha$ implicit in the constants while equations 7 and 6 express them in terms of H_b , γ , C and $\tan \alpha$. In the latter case γ is known to be a function of H_0/L_0 and $\tan \alpha$ (10). Since equation 15 already includes the breaker index γ , the substitution of the theoretical equations 7 and 6 will be adopted as most likely to produce a simple consistent result.

As to (ii) this is determined by the system geometry and is of course the result of the combined diffraction - shoaling process behind the breakwater. Consideration of figure 5 suggests that it will be reasonable in the first instance to assume the following relationship for the alongshore change in breaker height.

$$H_{b1} = 2 H_{b2} = H_b^* \quad 16.$$

When the relevant substitutions based upon the above considerations are made in equation 15 the latter becomes

$$\frac{v}{\sqrt{gH_b^*}} = \sqrt{\frac{7}{64} \gamma (1 + \frac{\gamma^2}{8}) \frac{(1 - C \gamma \tan \alpha)}{1 + 3 \gamma^2 / 32}} \quad 17.$$

Equation 17 is compared with experimental values on figure 13.

The general result is similar to that for the two dimensional wave set-up (6) in that most of the experimental values lie within the scatter resulting from the possible variation of the parameter C .

A similar substitution in equation 14 yields

$$\frac{A}{H_b^{*2}} = \frac{(1 + 3\gamma^2/32) (1 - C \gamma \tan \alpha)^2}{2 \gamma^2 \tan \alpha} \quad 18.$$

and combination of equations 17 and 18 leads to an expression for the discharge of the alongshore current of the following form:

$$\frac{Q}{g^{1/2} H_b^{*3/2}} = f(\gamma, C, \tan \alpha) \quad 19.$$

$$\text{where } \gamma = f\left(\frac{H_0}{L_0}, \tan \alpha\right)$$

$$C = f(\tan \alpha, ?)$$

- see Galvin (16).

The comparatively good agreement of equation 17 with experimental observations indicates that the assumption of negligible bottom friction is reasonable. It is however desirable to check this assumption more positively by incorporating the bottom friction force T into the original momentum analysis. Equation 10 now becomes

$$\rho A_2 V_2^2 = P_1 + S_1 - (P_2 + S_2) - T \quad 20.$$

T can be most conveniently evaluated using the non-linear expression for bed shear stress proposed by Jonsson et al (17),

$$\tau_b = f_s \frac{1}{2} \rho V^2$$

where $f_s = f(f_c, f_w \text{ and } \frac{u_{bm}}{V})$

f_c is the current friction factor which is estimated by the usual rough boundary logarithmic formula;

f_w is the wave friction factor which is estimated using the equations of either Jonsson (18) or Kamphuis (19);

u_{bm} is the maximum value of the wave orbital velocity within the surf zone.

Assuming a constant value of f_s determined by average values of f_c , f_w and u_{bm}/V together with a linear variation of mean velocity V with alongshore distance y , within the inflow region, the friction force is given by

$$T = \frac{\rho f_s Y}{6 \tan \alpha} [h_{p1} + \frac{1}{2} (\bar{v}_{m1} + \bar{v}_{m2})] V^2 \quad 21.$$

where Y is the alongshore length of the control volume.

Using the same substitutions as were used to obtain equation 17 from equation 15 the following expression including the effect of bottom friction is obtained:

$$\frac{V}{\sqrt{gH_b^*}} = \sqrt{\frac{7 \gamma (1 + \frac{\gamma^2}{8}) (1 - C\gamma \tan \alpha)}{64 \left(1 + \frac{3\gamma^2}{32} + \frac{f_s \gamma (1 + 9\gamma^2/32)}{3(1 - C\gamma \tan \alpha)} \right) \cdot \frac{Y}{H_b^*}} \quad 22.$$

It is doubtful whether the use of an equation of the complexity of equation 22 is warranted. For instance taking a specific test and substituting actual observed wave conditions and surf zone geometry into equation 20 using equations 12, 13, 14 and 21 enables the effect of bottom friction upon the magnitude of V to be estimated.

For example, for the test with the following conditions

$$\begin{aligned} T &= 1.0 \text{ s} ; & H_o &= 69 \text{ mm} ; & H_b^* &= 77 \text{ mm} ; \\ h_{p1} &= 44 \text{ mm} ; & \bar{v}_{m1} &= 22 \text{ mm} ; & \bar{v}_{m2} &= 11 \text{ mm} ; \\ Y &= 1.2 \text{ m} ; & \gamma &= 1.0 ; & \tan \alpha &= 0.1 ; \\ & & f_s &= 0.025. \end{aligned}$$

the observed value of V was 0.25 m/s.

Neglecting the friction force, V was 0.23 m/s.

and allowing for the friction force, V was 0.21 m/s.

4.4 Further Aspects of Non-uniform Alongshore Current Computations

The planning of the author's experimental work was directed to obtaining a situation where the driving force for the alongshore current resulted solely from an alongshore gradient in breaker height. This represents one limiting case for alongshore currents, the completely non-uniform alongshore current. At the

opposite end of the spectrum lies the uniform alongshore current whose driving force results solely from waves of uniform height breaking at an angle to an infinitely long plane beach. The author's situation represents a current system which is very definitely limited in size and which in fact results in a closed circulation system. The uniform alongshore current on the other hand is ideally of infinite length and open ended in nature.

Once the above contrasts are appreciated it is clear that there may be significant differences in the formulation of theoretical models to allow for the effects of alongshore gradients of breaker height upon the velocity of the alongshore current. In the situation studied by the author the alongshore current is only related to surf zone characteristics within the inflow region where the flow is highly non-uniform and the current discharge is increasing in the alongshore direction. Thus the consideration of the convective acceleration term and variable surf zone width is essential but bottom friction is relatively insignificant. On the other hand if the problem is approached as one where the alongshore gradient of breaker height is modifying the alongshore current produced by waves breaking at an angle to the shoreline, then the bottom friction term is almost certainly more important than the convective acceleration term and the variation in surf zone width with breaker height can be neglected. This latter situation is the one envisaged by Bakker (20) and Komar (3) in their approaches to non-uniform alongshore currents. The differences between the two approaches arise essentially from the assumption of either a large or a small alongshore gradient of breaker height.

The simple methods for computation of non-uniform alongshore currents presented in this paper are subject to the following limitations:

- (i) The breaker angle has been assumed to be negligible.
- (ii) Both the offshore boundary of the current and the alongshore gradient of breaker height have been determined from experimental observations for the particular system considered.
- (iii) The downstream component of the thrust on the control volume due to radiation stress has been overestimated. This results in an underestimation of the alongshore current velocity. However as the magnitude of this error is of the same order but less than the magnitude of the bottom friction force, its overall effect is negligible.
- (iv) The following factors have been ignored or assumed to be negligible:
 - wave set-down or set-up at breakpoint;
 - lateral mixing and the resulting shear stress at the offshore boundary of the control volume as well as the effect of non-uniform velocity distribution upon the momentum thrust;
 - interaction between the alongshore current and the wave surf zone parameters.
- (v) Both the breaker index γ and the dimensionless plunge distance C are based upon laboratory experimental data without any adequate supporting theory to relate them to the offshore wave conditions.

5. Conclusion

For an alongshore current system resulting solely from an alongshore gradient of breaker height produced by diffraction behind an offshore breakwater,

it has been found that the basic current pattern is imposed by the system geometry and that there is a general similarity of alongshore breaker height and wave set-up gradients in terms of their equivalent two dimensional values.

For a given geometry the alongshore current velocity is primarily determined by the deepwater wave height. The wave period appears to have only a secondary effect upon the alongshore current system. The relationship between the current velocity and surf zone parameters has not been clearly established.

The alongshore variation of wave set-up may be considerably influenced by the alongshore current and may be increased above its two dimensional value by the effects of break point set-up, superelevation caused by normal acceleration and alongshore translation of the uprush-backwash cycle.

A simple theoretical analysis has shown that the alongshore current velocity at the point where maximum discharge is attained can be calculated as a function of the equivalent two dimensional breaker height, the breaker constants γ and C and the bottom slope. Bottom friction can be allowed for but has a comparatively small effect in the situation considered.

6. References

1. Galvin, C.J. Longshore current velocity : A review of theory and data. *Reviews of Geophysics* Vol. 5, No.3. Aug. 1967, pp 287-304.
2. Longuet-Higgins, M.S.
Recent progress in the study of longshore currents. *Waves on Beaches and Resulting Sediment Transport* - R.E. Meyer (Editor). Academic Press, New York, 1972, pp 203-248.
3. Komar, P.D. Nearshore currents : Generation by oblique incident waves and longshore variations in breaker height. *Nearshore Sediment Dynamics and Sedimentation* - J. Halls and A. Carr (Editors). Wiley, London, 1975, pp 17-45.
4. Bowen, A.J. Rip currents 1. Theoretical Investigations. *Jour. Geophys. Res.* Vol. 74, No.23, Oct.20, 1969. pp 5467-5478.
5. Bowen, A.J. and Inman, D.L.
Rip currents 2. Laboratory and field observations. *Jour. Geophys. Res.* Vol. 74, No.23, Oct. 20, 1969, pp 5479-5490.
6. Gourlay, M.R. Wave set-up and wave generated currents in the lee of a breakwater or headland. *Procs. 14th Int. Conf. on Coastal Engineering, Copenhagen, 1974, Vol. III, pp 1976-1995.*
7. Gourlay, M.R. Wave generated currents - some observations made in fixed bed hydraulic models. *Univ. of Qld, Dept. of Civil Engineering Bull. No.7, Nov. 1965.*
8. Eliot, J. The persistence of rip current patterns on sandy beaches. *Engineering Dynamics of the Coastal Zone. I.E. Aust., 1st Australian Conference on Coastal Engineering, Sydney, May 1973, pp 29-34.*
9. James, I.D. A non-linear theory of longshore currents *Estuarine and Coastal Marine Science* Vo. 2, 1974, pp 235-249.
10. Goda, Y. A synthesis of breaker indices *Trans. J. S.C.E.* Vol. 2, Part 2, 1970, pp 227-230.

11. Bowen, A.J., Inman, D.L. and Simmons, V.P.
Wave "set-down" and set up.
Jour. Geophys. Res. Vol. 73, No.8, April 15, 1968, pp 2569-2577.
12. Bakker, W.T. Littoral drift in the surf zone.
Rijkswaterstaat, Directorate for Water Management and Hydraulic Research, Dept. of Coastal Research, The Hague, Study Report WWK70-16, 1970.
13. Tait, R.J. Wave set-up on coral reefs.
Jour. Geophys. Res. Vol. 77, 1972, pp 2207-2211.
14. Battjes, J.A. Computation of set-up, longshore currents, run-up and overtopping due to wind-generated waves.
Delft Univ. of Technology, Dept. Civ. Engng. Comm. on Hydraulics. Report No. 74-2, 244 p, 1974.
15. Swart, D.H. Offshore sediment transport and equilibrium beach profiles.
Delft Hydraulics Laboratory. Publication No. 131, 1974.
16. Galvin, C.J. Breaker travel and choice of design wave height.
Procs. ASCE, Vol. 95, No. WW2, May 1969, pp 175-200.
17. Jonsson, I.G., Skovgaard, O. and Jacobsen, T.S.
Computation of longshore currents.
Procs. 14th Int. Conf. on Coastal Engineering, Copenhagen, 1974, Vol II, pp 699-714.
18. Jonsson, I.G. The wave friction factor revisited.
Tech. Univ. Denmark., Inst. Hydrodyn and Hydraulic Engng. Prog. Rep. 37. Dec. 1974, pp 3-8.
19. Kamphuis, J.W. Friction factor under oscillatory waves.
Procs. ASCE, Vol. 101, No. WW2, May 1975, pp 135-144.
20. Bakker, W.T. The influence of longshore variation of the wave height on the littoral drift.
Rijkswaterstaat, Directorate for Water Management and Hydraulic Research, Dept. for Coastal Research, The Hague. Study Report WWK 71-19, 1971.



Figure 1. General View of Test Basin

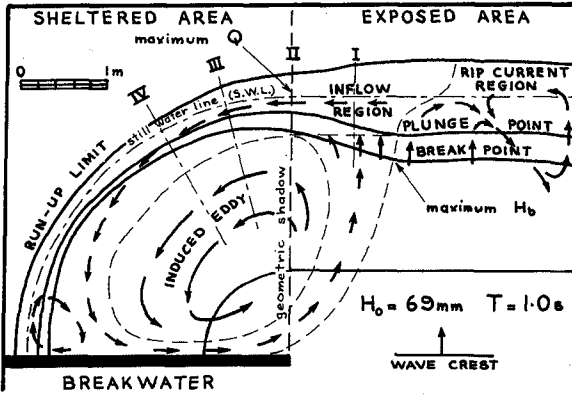


Figure 2 WAVE GENERATED CURRENT SYSTEM

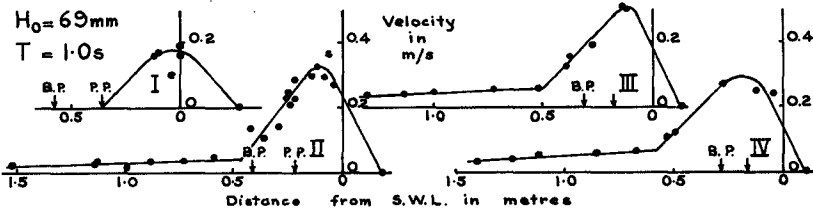


Figure 3 SURFACE VELOCITY PROFILES

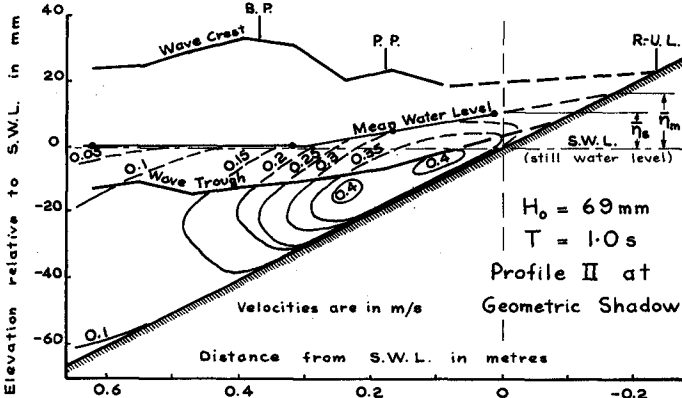
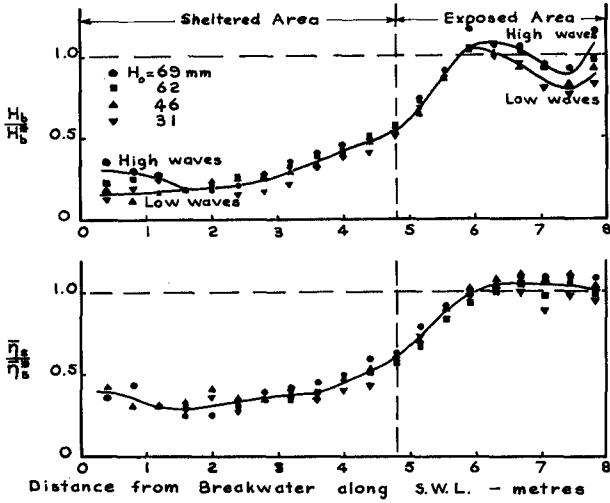
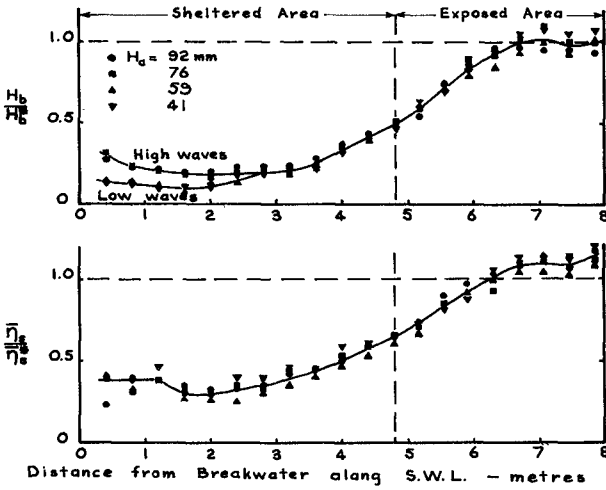


Figure 4 VERTICAL VELOCITY PROFILE



(a) $T = 1.0$ s



(b) $T = 1.5$ s

Figure 5 ALONGSHORE VARIATION OF $\frac{H_b}{H_b^*}$ and $\frac{\bar{\eta}_s}{\bar{\eta}_s^*}$

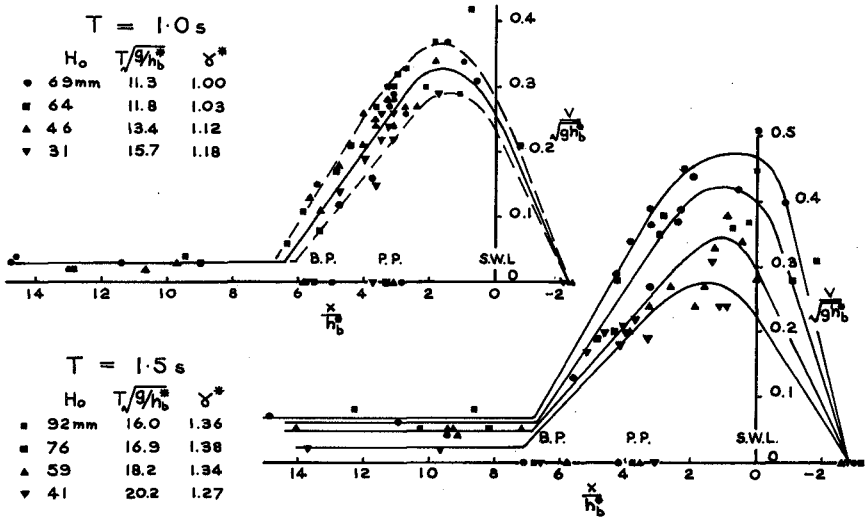


Figure 6 DIMENSIONLESS SURFACE VELOCITY PROFILES AT SECTION II

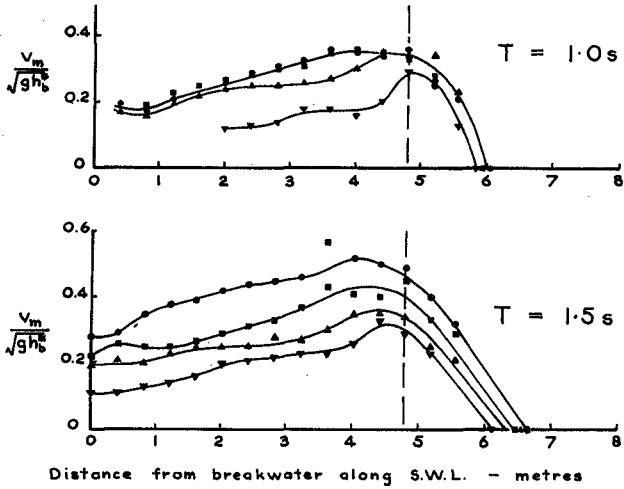


Figure 7 $\frac{V_m}{\sqrt{g h_b}}$ VERSUS ALONGSHORE DISTANCE

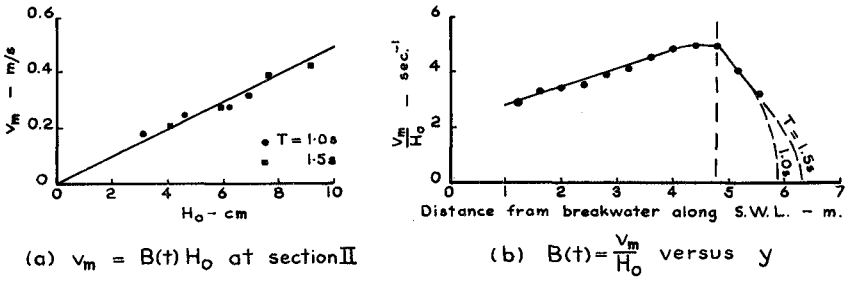


Figure 8 RELATIONSHIP BETWEEN v_m and H_0

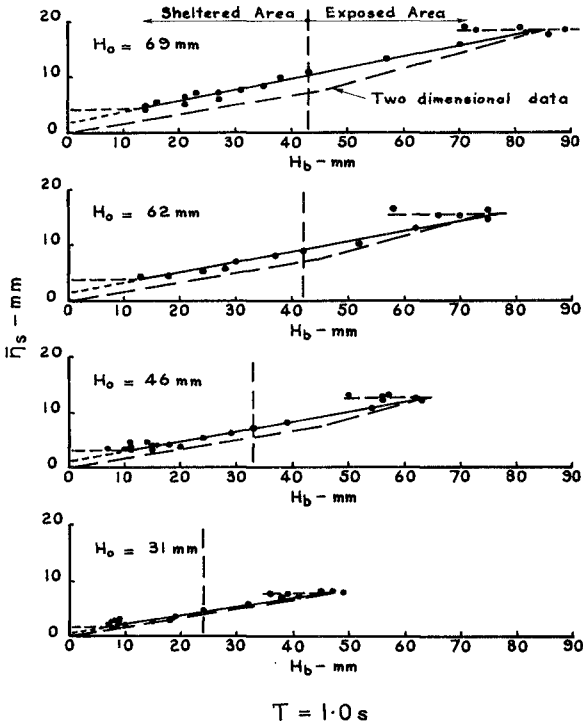


Figure 9 \bar{H}_s VERSUS H_b FOR VARIOUS H_0

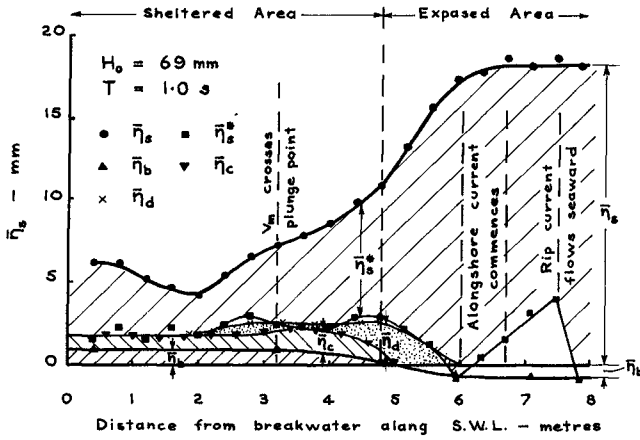


Figure 10 COMPONENTS OF WAVE SET-UP

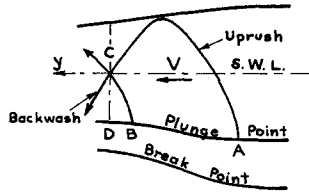
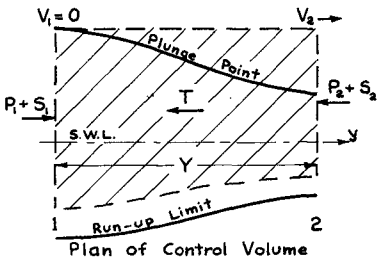


Figure 11

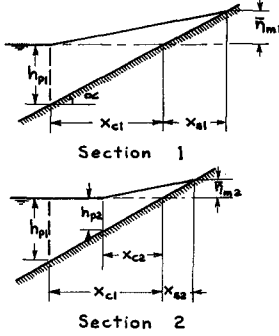


Figure 12

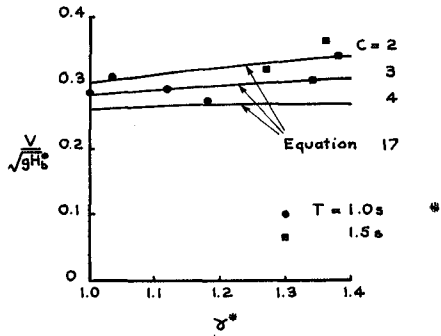


Figure 13

CHAPTER 41

CURRENT DEPTH REFRACTION USING FINITE ELEMENTS

Ove Skovgaard¹ and Ivar G. Jonsson²

ABSTRACT

A computational model is presented for the steady state prediction of currents, waves, and sea surface elevations in a coastal region outside the surf zone. Irrotational flow of surface gravity waves on large-scale steady currents over a gently sloping sea bed is considered. A second order Stokian approach is used, and all dynamic quantities are integrated over depth and averaged over time, in that order. The flow equations and the boundary conditions are presented. A method is developed for the solution of the non-linear steady model by introducing a sequence of two-level calculations, viz. a 'wave level' and a 'current level'. The variables are split on the two levels. The wave field is found, using that the flux of wave action is constant between adjacent wave rays. The current field and the mean sea surface elevation are determined using a Galerkin finite element method. The current field is approximated by triangular elements with linear interpolation functions, and the mean sea surface elevation is approximated by a triangular element with quadratic (parabolic) interpolation functions. A quasi-two-dimensional test solution is tabulated.

1. INTRODUCTION

The purpose of the present computational model is to make a steady state prediction of currents, waves, and elevations of the mean sea surface in a coastal or offshore region outside the surf zone, when the topography of the gently sloping sea bed is given, see Fig. 1.

The computation of depth refraction of regular surface gravity waves presents no fundamental difficulties, see e.g. Skovgaard et al. (1975, 1976) and Skovgaard and Petersen (1976). When the wave height H is small, the combined effect of diffraction and depth refraction can also be calculated in the shallow water region, see Berkhoff (1973, 1975), Chen and Mei (1974, 1976), and Zienkiewicz and Bettess (1975, 1976). On greater water depths, where the intermediate depth wave theory must be applied, combined diffraction and refraction has only been determined for a very simple geometry of the sea bed, see Jonsson et al. (1976b). In the presence of a current the problem becomes much more complex on account of current-wave interaction and anisotropy. Therefore we exclude reflection and diffraction and consider only combined current

¹Senior Research Fellow, Institute of Hydrodynamics and Hydraulic Engineering (ISVA), Technical University of Denmark, DK-2800 Lyngby.

²Associate Professor, ISVA.

depth refraction, i.e. the approach is within the framework of geometrical optics.

Subcritical, irrotational flow of large-scale, horizontally non-uniform and vertically uniform, steady currents over an arbitrary gently sloping sea bed is considered. This means that variations in current velocity and depth are slow, in the sense that changes are appreciable only over many wave lengths. Surface and bottom shear are disregarded, and so is dissipation. The waves are periodic and progressive with the constant absolute wave period T_a ($= 2\pi/\omega_a$), ω_a being the absolute angular frequency. Stokes' second order wave theory is used, and the wave fronts are long-crested. Fluxes of mass, momentum, and energy are integrated over depth and averaged over T_a , in that order. The two-dimensional flow region Ω is simply connected with waves in the whole domain. The fluid is incompressible and homogeneous with density ρ . The Coriolis force and the spherical form of our planet are neglected. The non-linear steady model will be solved by a sequence of two-level calculations, viz. a 'wave level' and a 'current level'.

Another model for current wave interaction in two horizontal dimensions, but with bed shear, is reported by Noda et al. (1974) and Noda (1976). This model is like the present one solved by a sequence of two level iterations; however, the approaches on both calculation levels are completely different from our.

The governing equations for irrotational current depth refraction were introduced by Jonsson (1971b), see also Jonsson and Wang (1976). These equations were solved in one horizontal dimension (no refraction) by Jonsson et al. (1971). Plane flow with vorticity is being reported, see Brink-Kjær (1976), Jonsson et al. (1976a), and Jonsson (1977).

The effect of a combined current wave field is in principle that, when the current has a positive component in the direction of wave propagation, the waves are 'lengthened' and so 'feel bottom' at a greater depth than without the current. So in this case the bending of the wave orthogonal in the combined field is stronger than for pure waves. Conversely, a negative current component will 'shorten' the waves, and the bending of the wave orthogonal is less than for no current (see later).

2. THE GOVERNING EQUATIONS

The arbitrary bottom topography is known (measured from a horizontal datum) in a fixed horizontal Cartesian coordinate system (x,y) . It was

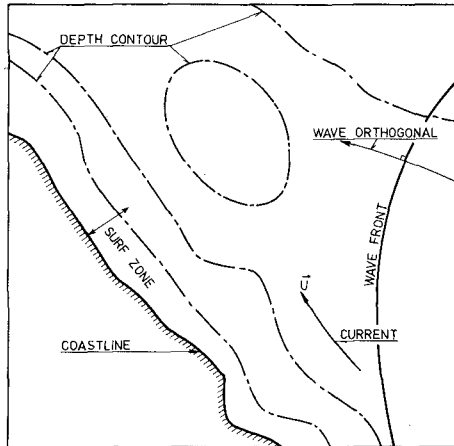


Fig. 1

Horizontal sketch of a coastal region

proved by Jonsson et al. (1971) that for a periodic, irrotational free surface flow a constant horizontal level exists, which is inherently connected with the flow. The level was called the mean energy level (MEL). It is also denoted the mean irrotational stagnation level (MISL), see Jonsson (1977), since it stems from the time mean version of the Bernoulli equation. The distance D between the sea bed and MISL is denoted the geometrical depth. The distance h between the sea bed and the time mean water surface (MWS) is for obvious reasons called the physical depth. The distance η between MWS and MISL is the current wave set-down, see Fig. 2. Notice that our definition of the set-down is opposite in sign to the conventional, see Bowen et al. (1968).

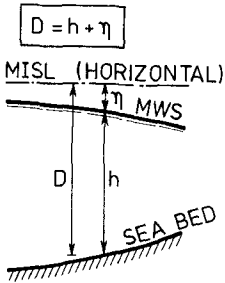


Fig. 2 Vertical definition sketch. Geometrical depth D , physical depth h , and current wave set-down η

The problem has 7 primary dependent variables, which are (see Figs. 2 and 3): (1) and (2) radian wave number vector $\vec{k} = (k \cos A, k \sin A)$, or wave number $k (= |\vec{k}|)$ and wave orthogonal direction characterized by the angle A from the x -axis to the wave orthogonal, (3) wave energy density $E (\equiv 1/8 \rho g H^2)$, where g is the acceleration of gravity, (4) and (5) current vector $\vec{U} = (u, v) = (U \cos \delta, U \sin \delta)$, or current speed $U (= |\vec{U}|)$ and direction characterized by the angle δ from the x -axis to \vec{U} , (6) physical water depth h , and (7) current wave set-down η . Observe that U is an average-over-depth current speed, defined such that the mean volume flux q (per unit width) through a vertical section at right angles to \vec{U} is hU , see Jonsson (1976). The *wave orthogonal* should not be confused with the *wave ray*, see Fig. 3.

The 7 primary governing equations are: (1) conservation of mass, (2) and (3) conservation of momentum, (4) conservation of wave action E/ω_r (ω_r being the intrinsic (i.e. relative) angular frequency, see

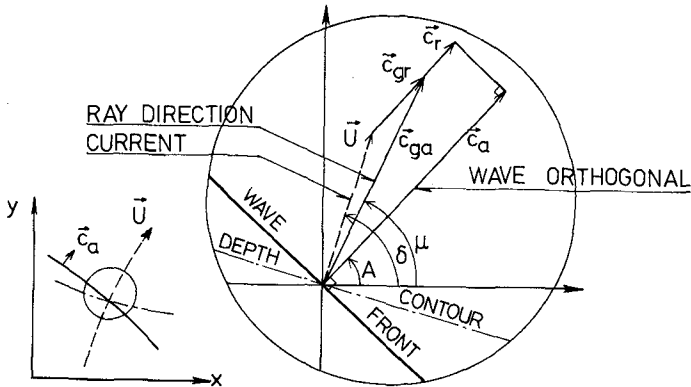


Fig. 3 Horizontal definition sketch for angles and velocities

later), (5) conservation of zero vorticity, (6) conservation of wave crests, and (7) conservation of bottom topography. The conservation equations given by Jonsson (1971b) become in the above mentioned order

$$\frac{\partial}{\partial x}(h u) + \frac{\partial}{\partial y}(h v) = 0 \quad (1)$$

$$\begin{aligned} \frac{\partial}{\partial x} \left[\frac{E}{2} (G + (1+G) \cos^2 A) + \rho h u^2 \right] - \rho g h \frac{\partial \eta}{\partial x} \\ + \frac{\partial}{\partial y} \left[\frac{E}{2} (1+G) \cos A \sin A + \rho h u v \right] = 0 \end{aligned} \quad (2)$$

$$\begin{aligned} \frac{\partial}{\partial x} \left[\frac{E}{2} (1+G) \cos A \sin A + \rho h u v \right] - \rho g h \frac{\partial \eta}{\partial y} \\ + \frac{\partial}{\partial y} \left[\frac{E}{2} (G + (1+G) \sin^2 A) + \rho h v^2 \right] = 0 \end{aligned} \quad (3)$$

$$\frac{\partial}{\partial x} \left[\frac{E}{\omega_r} (u + c_{gr} \cos A) \right] + \frac{\partial}{\partial y} \left[\frac{E}{\omega_r} (v + c_{gr} \sin A) \right] = 0 \quad (4)$$

$$\frac{\partial}{\partial x} \left[v - \frac{E \sin A}{\rho h c_r} \right] - \frac{\partial}{\partial y} \left[u - \frac{E \cos A}{\rho h c_r} \right] = 0 \quad (5)$$

$$c_a = c_r + u \cos A + v \sin A \quad \text{or} \quad \omega_a = \omega_r + k(u \cos A + v \sin A) \quad (6a,b)$$

$$D = h + \eta \quad (7)$$

where we have introduced 5 new (secondary) unknowns: The absolute phase speed (see Fig. 3)

$$c_a = L/T_a \quad (\equiv \omega_a/k) \quad (8)$$

L being the wave length, the relative phase and group speeds

$$c_r = \sqrt{\frac{g}{k} \tanh kh} \quad (9) \quad c_{gr} = \frac{1}{2} c_r (1+G) \quad (10)$$

the relative angular frequency ω_r and the parameter G

$$\omega_r = c_r k \quad (11) \quad G = 2kh / \sinh 2kh \quad (12)$$

In the shallow water limit we have $G = 1$ and $c_r = c_{gr} = \sqrt{gh}$. If we insert these limiting values in eqs. 1-7, we get the shallow water version of the conservation equations, see Skovgaard and Jonsson (1976b).

As shown by Skovgaard and Jonsson (1976a) it is possible to replace any of the conservation equations with the differential equation for the wave orthogonal or with the algebraic equation for the set-down (see later), or to replace any two of the conservation equations with these two equations.

The differential equation for the wave orthogonal reads, see e.g. Skovgaard and Jonsson (1976a)

$$\frac{DA}{Ds} = \frac{1}{c_a} \left(\sin A \frac{\partial c_a}{\partial x} - \cos A \frac{\partial c_a}{\partial y} \right) \quad (13)$$

where s is a coordinate along the wave orthogonal (positive in the direction of the wave propagation). Together with eq. 13 we have the two parametric differential equations

$$Dx/Ds = \cos A \quad (14) \quad Dy/Ds = \sin A \quad (15)$$

The equation for the current wave set-down reads, see Jonsson (1971a, 1976)

$$\eta = \frac{1}{2g}(u^2 + v^2) + \frac{E}{\rho gh} \left(\frac{G}{2} - (u \cos A + v \sin A) / c_r \right) \quad (16)$$

The direction of the wave ray is given by the direction of the absolute group velocity vector $\vec{c}_{ga} (= \vec{U} + \vec{c}_{gr})$, and so is determined by

$$\tan \mu = \frac{v + c_{gr} \sin A}{u + c_{gr} \cos A} \quad (17)$$

where μ is the angle from the x-axis to \vec{c}_{ga} , see Fig. 3. When eq. 17 is differentiated with respect to a coordinate r along the wave ray, the differential equation for the wave ray is obtained

$$\frac{D\mu}{Dr} = \cos^2 \mu \frac{D}{Dr} \left(\frac{v + c_{gr} \sin A}{u + c_{gr} \cos A} \right) \quad (18)$$

Together with the wave ray equation we have two parametric equations

$$Dx/Dr = \cos \mu \quad (19) \quad Dy/Dr = \sin \mu \quad (20)$$

Remark that the wave ray equation presented by Jonsson (1971b), eq. 30, is not correct.

3. BOUNDARY CONDITIONS

The current vector \vec{U} must be given everywhere on the boundary Γ which surrounds Ω , see Fig. 4. The boundary is divided in two parts, Γ_1 and Γ_2 . Γ_1 is that part of Γ where all rays are running in (or out) of Ω , see Fig. 4, and along it the wave field must be known. (Along Γ_2 the wave field is determined by the calculations.)

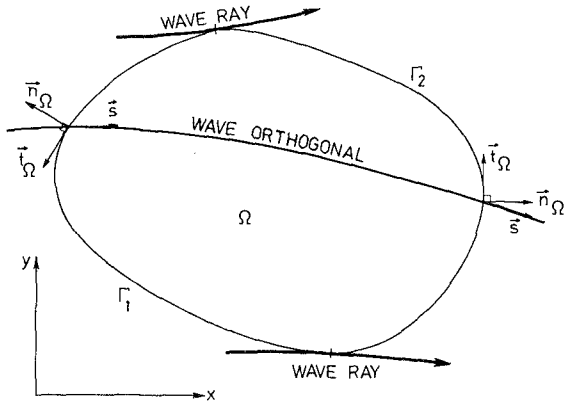


Fig. 4
Definition sketch
of flow domain Ω
with the boundary
 $\Gamma = \Gamma_1 + \Gamma_2$

The wave field is in principle defined by T_a , A , E , L , and h ; however, in an irrotational model it is not necessary to prescribe h in more than one point of Γ_1 for the following reason. For given \vec{U} , T_a , A , E , and h in one point of Γ_1 , we can calculate η in that point by

iteration in eqs. 6, 8, 9, 12, and 16, and then D using eq. 7. Thereby the MISL is determined, which is horizontal in Ω . Combining eqs. 6, 7, 8, 9, 12, and 16 we then can calculate h for all other points of Γ_1 .

We shall later show that it is more convenient if the (incoming) waves are prescribed by the curvature of the ray front κ_e and by A (or μ) in some selected points along Γ_1 rather than by the continuous variation of A along Γ_1 . The angles A and μ are connected by eq. 17 in any point where \vec{U} and h are known, i.e. if A is given we can determine μ , and vice versa. The curvature of the wave action front κ_e is determined by a pure geometrical consideration

$$\kappa_e \equiv D\mu/De = -\sin\mu \partial\mu/\partial x + \cos\mu \partial\mu/\partial y = (D(De)/Dr)/De \quad (21)$$

where De is the infinitesimal distance between two rays, see Fig. 6. Since r is not constant along e-lines, and vice versa, lengths r and e do not form a set of curvilinear coordinates. This is the reason for using the formalism D/Dr instead of $\partial/\partial r$, etc.

In summary we have

$$\vec{U} = \vec{U}_{\Gamma_1} \quad \text{along } \Gamma_1 \quad (22a)$$

$$\kappa_e = \kappa_{e,\Gamma_1} \quad E = E_{\Gamma_1} \quad A = A_{\Gamma_1} \quad \text{or} \quad \mu = \mu_{\Gamma_1} \quad (22b)$$

in some selected points of Γ_1

$$h = h_1 \quad \text{in one point of } \Gamma_1 \quad (22c)$$

$$\vec{U} = \vec{U}_{\Gamma_2} \quad \text{along } \Gamma_2 \quad (22d)$$

For the present irrotational steady state model we can make two integral checks of volume fluxes and velocities. The normal component of \vec{q} ($= h\vec{U}$) along Γ ($= \Gamma_1 + \Gamma_2$) is controlled by mass conservation

$$\int_{\Gamma} \vec{q} \cdot \vec{n}_{\Omega} d\Gamma = 0 \quad (23)$$

where \vec{n}_{Ω} is a unit vector normal to the boundary of and going outward from Ω , and we have assumed that Ω is without sources or sinks. As h is not known along Γ_2 (η is a function also of the unknown wave field) we cannot check in advance that eq. 23 is exactly fulfilled. However, we can calculate h along Γ corresponding to a pure current, and it is expected that for a 'realistic' problem the error introduced in eq. 23 by neglecting the wave contribution to h is small, since it is a second order term. The wave field could also be estimated along Γ_2 before using eq. 23. One could formulate the above as: Eq. 23 must be roughly fulfilled in advance for a realistic problem.

The tangential component of the mean velocity is controlled by the condition of zero vorticity. Introducing the Eulerian mean velocity vector \vec{U}_t ($\equiv \vec{U} - E/(\rho hc_r) \vec{s}$) below wave trough level (\vec{s} being a unit vector in the direction of wave travel), Stokes' theorem gives

$$\int_{\Omega} \text{rot } \vec{U}_t d\Omega = \int_{\Gamma} \vec{U}_t \cdot \vec{t}_{\Omega} d\Gamma \quad (24)$$

where \vec{t}_{Ω} is a unit vector tangential to Γ going counterclockwise around Ω . Using eq. 5 we therefore get

$$\int_{\Gamma} \left(\vec{U} - \frac{E}{\rho hc_r} \vec{s} \right) \cdot \vec{t}_{\Omega} d\Gamma = 0 \quad (25)$$

The wave contribution to the integrand in eq. 25 is a second order term which furthermore has not the same sign along Γ . Thus it can be inferred that the advance neglect of the wave term in eq. 25 will correspond to a realistic problem. Also here we can say: Eq. 25 must be roughly fulfilled in advance for a realistic problem.

4. THE TWO-LEVEL APPROACH

The current depth refraction model is solved by a two-level iterative scheme. In this way we so to speak 'split' the unknowns in two groups, and we do not have to solve all equations simultaneously. The two levels will be named the wave level and the current level.

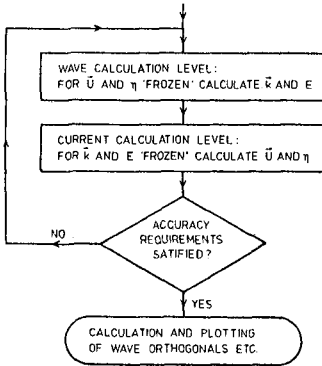


Fig. 5 The two-level splitting of the calculations

two consecutive levels of the same type are lower than a chosen limit for both the wave and the current level, i.e. the number of iterations is determined by accuracy requirements.

After the completion of the two-level iterations the paths of some wave orthogonals are calculated by numerical integration of the three ordinary differential equations 13 - 15, and the wave field is plotted with the wave heights and the current components written at discrete points along these orthogonals. Also the phase field, i.e. the wave fronts is calculated and plotted after the completion of the two-level iterations. Eqs. 13 - 15 cannot be used in the given form to calculate the phase field. Time t must be used as independent variable in this case

$$dA/dt = \sin A \partial c_a / \partial x - \cos A \partial c_a / \partial y \quad (13a)$$

$$dx/dt = c_a \cos A \quad (14a)$$

$$dy/dt = c_a \sin A \quad (15a)$$

5. THE WAVE LEVEL

The approach on this level is a generalization of the method which is used in depth refraction calculations, see e.g. Skovgaard et al. (1975).

In the wave level calculations the 'propagation medium' is held fixed ('frozen'), i.e. \vec{U} , h , and η are known in Ω on this level, and \vec{k} and E are the primary unknowns, see Fig. 5.

In the current level calculations the wave field is frozen, i.e. \vec{k} and E are known in Ω on this level, and \vec{U} , h , and η are the primary unknowns. The governing equations on this level are non-linear, which implies that we have to iterate during the calculations.

The calculations are initiated on a wave level, where we assume $\vec{U} = 0$ and $\eta = 0$ in Ω . The two-level iteration scheme is continued until the differences between

The wave field is determined from one-point conditions (initial conditions) by integration along characteristic lines. By a suitable placing of the boundary points (initial points) along Γ_1 , Ω is covered by a set of characteristic lines. The method is attractive, because we only have to solve a set of four ordinary differential equations along each of the lines.

In depth refraction the characteristic lines are the wave orthogonals, and in current depth refraction the characteristic lines are the wave rays which, of course, for $U = 0$ coincide with the wave orthogonals. The path of the wave ray is determined by eqs. 18 - 20. Bretherton and Garrett (1968) have shown generally that there is no flux of wave action E/ω_r across a wave ray, i.e. between two rays we have a constant flux of wave action, see eq. 4. For water waves, Jonsson (1971a, 1976) found the same result, using quite a different approach. For $U = 0$ the wave action is, of course, proportional with wave energy density, the flux of which is constant between two orthogonals.

$$De_{st} \left(\frac{E}{\omega_r} c_{ga} \right)_{st} = De \frac{E}{\omega_r} c_{ga}$$

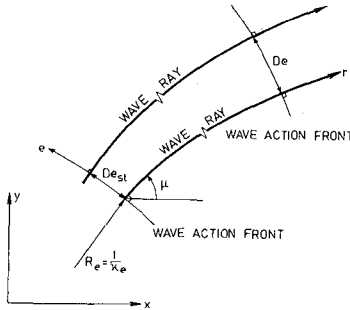


Fig. 6 Two adjacent wave rays and two 'wave action fronts'

Munk and Arthur (1952) derived a differential equation for the wave *orthogonal* separation factor β for $U = 0$. In almost the same manner it is possible to derive a differential equation for the wave *ray* separation factor β_r with distance r along the ray as the independent variable. The factor β_r is defined by

$$\beta_r \equiv De/De_{st} \quad \beta_r > 0 \tag{26}$$

in which suffix 'st' denotes a value at the starting or initial point along Γ_1 , see Fig. 6. The separation factor is found in the following way. Introducing eq. 26 in eq. 21 we get

$$D\mu/De = \beta_r^{-1} D\beta_r/Dr \tag{27}$$

Using the operators

$$\frac{D}{Dr} = \cos \mu \frac{\partial}{\partial x} + \sin \mu \frac{\partial}{\partial y} \tag{28}$$

$$\frac{D}{De} = - \sin \mu \frac{\partial}{\partial x} + \cos \mu \frac{\partial}{\partial y} \tag{29}$$

we have

$$\frac{D}{De} \left(\frac{D\mu}{Dr} \right) - \frac{D}{Dr} \left(\frac{D\mu}{De} \right) = \left(\frac{D\mu}{Dr} \right)^2 + \left(\frac{D\mu}{De} \right)^2 \tag{30}$$

(or $D\kappa_r/Ds - D\kappa_e/Dr = \kappa_r^2 + \kappa_e^2$, κ_r being the curvature of the wave ray). Inserting eq. 27 and using eqs. 28-29 once more, we get an ordinary second-order homogeneous differential equation for β_r

$$\frac{D^2 \beta_r}{Dr^2} + q_s \beta_r = 0 \quad (31)$$

$$q_s = \left(\left(\frac{\partial \mu}{\partial x} \right)^2 - \left(\frac{\partial \mu}{\partial y} \right)^2 - \frac{\partial^2 \mu}{\partial x \partial y} \right) \cos 2\mu + \left(\frac{1}{2} \left(\frac{\partial^2 \mu}{\partial x^2} - \frac{\partial^2 \mu}{\partial y^2} \right) + 2 \frac{\partial \mu}{\partial x} \frac{\partial \mu}{\partial y} \right) \sin 2\mu \quad (32)$$

The coefficient q_s depends on some explicitly known quantities (u , v , h , and η , and their partial derivatives up to the second order) and on some implicitly known quantities (A and E , etc., and their partial derivatives up to second order). The implicit quantities are calculated from some of the conservation equations and the wave orthogonal equation 13.

The condition of constant flux of wave action between two adjacent rays determines in principle E (and so the wave height)

$$E = \frac{E_{st}}{\beta_r} \frac{\omega_r}{\omega_{r,st}} \frac{c_{ga,st}}{c_{ga}} \quad (33)$$

where we have used eq. 26, and c_{ga} ($\equiv |\vec{c}_{ga}|$) is the absolute group speed.

The associated one-point boundary conditions at $r = r_{st}$ for the four ordinary differential equations 18-20 and 31 are

$$\mu = \mu_{st} \quad x = x_{st} \quad y = y_{st} \quad \beta_r = \beta_{r,st} \quad \frac{D\beta_r}{Dr} = \beta_{r,st} \kappa_{e,st} \quad (34)$$

where x_{st} and y_{st} are chosen on Γ_1 , μ_{st} is calculated from eq. 17, $\beta_{r,st}$ is arbitrarily chosen as 1, and $\kappa_{e,st}$ is the curvature of the wave action front in the considered point of Γ_1 . When the differential equation for β_r (eq. 31) is written as a system of two simultaneous first-order equations, eqs. 18-20 and 31 constitute a system of five simultaneous first-order ordinary differential equations, where the five requisite 'initial' conditions at $r = r_{st}$ are given by eq. 34. The system is integrated step-by-step along one ray at a time. A standard variable order code with automatic local control of the error level and corresponding adjustable step length is used.

The calculation along a wave ray stops when one of the following conditions is fulfilled: (1) The boundary of the region of analysis is reached, (2) the orthogonals converge too much, (3) the Stokes parameter is too high (thereby we in practice exclude wave breaking), (4) the bottom slope is too high, (5) the water depth is too small, or (6) the rays converge too much.

The first five conditions equal those for depth refraction, see Skovgaard et al. (1975). Here condition (2) was formulated $D\beta/Ds < -\beta/(1L)$, where l probably is about one. However, since $\beta^{-1} D\beta/Ds = DA/Df = -\sin A \partial A/\partial x + \cos A \partial A/\partial y$, we need not solve the differential equation for β to test condition (2), (Df is the infinitesimal distance between two orthogonals). Nor do we have to determine the wave orthogonal paths. Condition (6) is of the same type as condition (2). Condition (3) reads $HL^2/h^3 > 20$ (say), thus excluding non-Stokian waves.

The solution (i.e. \vec{k} , E etc. and the associate position (x,y) of the ray) is recorded in the computer at a set of prescribed values of distance r along the path of the wave ray. Note that the paths of the rays are new on each level, since the propagation properties of the medium changes on the current level.

6. THE CURRENT LEVEL

On this level the wave field (i.e. \vec{k} and E) is frozen in Ω , and \vec{U} , h and η are the primary unknowns. Using eq. 7, and remembering that D is also known in Ω , we immediately can eliminate h, which implies that we have only three scalar unknowns u, v and η on this level. These three variables are determined by three conservation equations, viz. conservation of mass, eq. 1, and conservation of momentum in the two horizontal directions, eqs. 2-3. We solve the partial differential equations by a direct finite element method, the so-called Galerkin weighted residual process (i.e. a weak formulation). The region Ω is approximated with a domain $\bar{\Omega}$ (with boundary $\bar{\Gamma}$) consisting of a finite number N of triangular subdomains ω . The only difference between Ω and $\bar{\Omega}$ is along the boundary. The triangular subdomains are constructed by connecting the prescribed points along the wave rays with straight lines, see Fig. 7. As the rays are new on each wave level, the triangular subdomains are also new on each current level.

It is well known that we cannot freely select the polynomial order of the shape functions (interpolation functions), see e.g. Hood and Taylor (1974) and Olson and Tuann (1976). We choose to apply the most simple shape functions, which for the present differential equations 1-3 are a linear shape function for u and v, and a quadratic shape function for η . Remark the simple connection in eq. 16 between u, v and η .

It should be explained why we choose to eliminate the physical depth h and not the set-down η . If η was eliminated, and a shape function for h chosen, the indirectly assumed form of the MWS would be influenced by the local form of the sea bed (see eq. 7 and Fig. 2).

We select the most simple placing of the nodal points, i.e. we use for the linear interpolation functions the three vertices as nodal points (see Fig. 8(a)), and for the quadratic interpolation functions the three vertices plus the three mid-side points as nodal points, see Fig. 8(b). Implicit in the preceding discussion is the fact that the same triangular subdomains are used for set-down and velocity fields. Details of these standard elements can be found in e.g. Zienkiewicz (1971), chapter 7. With these two elements the u, v and η solutions become continuous but not differentiable along the sides of the triangular domains. In a typical domain ω we have the following approximations

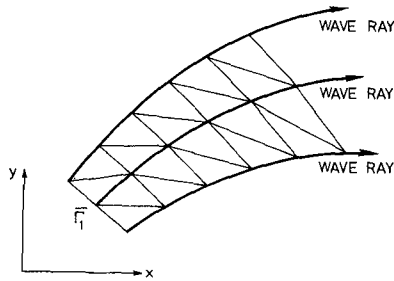
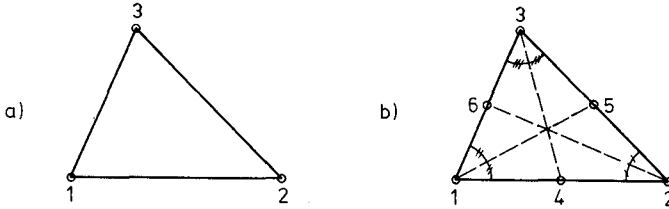


Fig. 7 Placing of triangular elements

$$u = \psi_j(x,y) \bar{u}_j \quad v = \psi_j(x,y) \bar{v}_j \quad n = \phi_1(x,y) \bar{n}_1 \quad (35a,b,c)$$

where the bar indicates a nodal value, and ψ_j , $j = 1,2,3$, and ϕ_1 , $l = 1,2,\dots,6$ are the shape functions. Here and henceforward the repeated nodal indices j , l , etc. are summed over the range of the index.



o NODAL POINT

Fig. 8 Placing of nodal points in isoparametric triangular elements
(a) linear three-node element, (b) quadratic six-node element

For the conservation equation of mass (where h is eliminated) we form the residual $r_e(x,y)$ at point $(x,y) \in \omega$ by inserting eqs. 35 a-c in the left hand side of eq. 1

$$r_e(x,y) = \bar{u}_j \frac{\partial}{\partial x}(D\psi_j) - \bar{n}_1 \bar{u}_j \frac{\partial}{\partial x}(\phi_1 \psi_j) + \bar{v}_j \frac{\partial}{\partial y}(D\psi_j) - \bar{n}_1 \bar{v}_j \frac{\partial}{\partial y}(\phi_1 \psi_j) \quad (36)$$

The residual r_e is multiplied with weight functions which for this residual are the shape functions for the set-down ϕ_m ($m = 1,2,\dots,6$). Support for the appropriate selection of the weight function is given by e.g. Chung and Chion (1976). The functions $(r_e \phi_m)$, $m = 1,2,\dots,6$ are integrated over ω , and each of the results is equated with zero. Oden and Wellford (1972) p. 1592 have given the reason for this approach, 'We can guarantee that the residual vanishes in an average sense over the element by requiring that it be orthogonal with respect to the inner product $\langle f,g \rangle \equiv \int_{\omega} fgd\omega$ to the subspace spanned by the functions $\phi_m(x,y)$, $m = 1,2,\dots,6$. Then $\langle r_e, \phi_m \rangle = \int_{\omega} r_e \phi_m d\omega = 0$, and we obtain the finite element model of the mass conservation equation.'

Using $\int_{\omega} r_e \phi_m d\omega = 0$, we get

$$\bar{u}_j A_{mj} - \bar{n}_1 \bar{u}_j B_{mlj} + \bar{v}_j C_{mj} - \bar{n}_1 \bar{v}_j D_{mlj} = 0 \quad m = 1,2,\dots,6 \quad (37)$$

and A_{mj} , B_{mlj} , C_{mj} , and D_{mlj} denote the four local arrays

$$\left. \begin{aligned} A_{mj} &\equiv \int_{\omega} \phi_m \frac{\partial}{\partial x}(D\psi_j) d\omega & B_{mlj} &\equiv \int_{\omega} \phi_m \frac{\partial}{\partial x}(\phi_1 \psi_j) d\omega \\ C_{mj} &\equiv \int_{\omega} \phi_m \frac{\partial}{\partial y}(D\psi_j) d\omega & D_{mlj} &\equiv \int_{\omega} \phi_m \frac{\partial}{\partial y}(\phi_1 \psi_j) d\omega \end{aligned} \right\} \quad (38)$$

In the same manner we obtain the finite element model of the two momentum conservation equations, the only difference being that the weight functions are ψ_m , $m = 1,2,3$ for both equations. For eq. 2 we get

$$\begin{aligned}
 & \rho \bar{u}_j \bar{u}_p E_{mjpp} - \rho \bar{\eta}_1 \bar{u}_j \bar{u}_p F_{mljpp} - \rho g \bar{\eta}_1 G_{m1} + \rho g \bar{\eta}_1 \bar{\eta}_n H_{m1n} \\
 & + \rho \bar{u}_j \bar{v}_p I_{mjpp} - \rho \bar{\eta}_1 \bar{u}_j \bar{v}_p J_{mljpp} \\
 & = - \int_{\omega} \psi_m \left[\frac{\partial}{\partial x} \left(\frac{E}{2} (G + (1+G) \cos^2 A) \right) + \frac{\partial}{\partial y} \left(\frac{E}{2} (1+G) \cos A \sin A \right) \right] d\omega \quad (39)
 \end{aligned}$$

$m = 1, 2, 3$; where E_{mjpp} , F_{mljpp} , G_{m1} , H_{m1n} , I_{mjpp} , and J_{mljpp} denote 6 local arrays, which are not presented. Nor are the similar equations for eq. 3.

Off-node function values and derivatives of u , v , h , and η , which are used in the wave level calculations, are not formed directly from the finite element method (FEM) solution, using the FEM interpolation functions etc. We follow, however, the guidance given by Carl de Borr (1974), see Roache (1975), p. 235, 'The acknowledged best procedure is to ignore the basis function and evaluate off-node function values and derivatives by standard interpolation formulas.'

Eqs. 37 and 39, and the similar one for eq. 3 represent a set of 12 (= 6 + 3 + 3) non-linear algebraic equations in 12 unknowns, which are $\bar{\eta}_1$, $l = 1, 2, \dots, 6$, \bar{u}_j , $j = 1, 2, 3$, and \bar{v}_j , $j = 1, 2, 3$. Upon assembling the elements, the global stiffness matrix form is sparse, but the system of algebraic equations is non-linear. Along the boundary $\bar{\Gamma}$, the specified current components \bar{u} and \bar{v} are inserted directly in the global matrix form. Using these specified values of \bar{u} and \bar{v} we can calculate $\bar{\eta}$ along $\bar{\Gamma}$ from eq. 16 by iteration, using that E , A , c_r , and G are known from the calculations on the wave level. These values of $\bar{\eta}$ are then inserted directly into the global matrix form.

The global non-linear system of algebraic equations is solved using the Newton Raphson iteration scheme, see e.g. Dahlquist and Björck (1974), p. 250. The iteration is started by interpolation in the current level solution used on the preceding wave level. The number of iterations is determined by accuracy requirements.

Combined diffraction refraction FEM models for short waves are rather expensive in use, as the minimum number of elements is a function of the wave length. The present model for current depth refraction does not have this restriction. The number of elements in our model is a function of the depth variations and the associated variations of the current field. Only the variation of the wave height (amplitude envelope) is modelled. In contrast a diffraction refraction FEM model describes simultaneous amplitudes, i.e. rapid oscillations in horizontal space.

It should be explained why we choose to use both momentum equations, and do not substitute one of them with eq. 16. If we had done this, our model would have been 'tailored' to irrotational flow only, and a later inclusion of bottom friction would be less straightforward. With the present approach we can instead use eq. 16 as a check equation in the nodal points.

7. TEST SOLUTION

For straight and parallel (but arbitrarily spaced) sea bed contours, with the current \bar{u} everywhere parallel with these, a test solution is

calculated numerically (assuming plane incidence in deep water). With these constraints we have a quasi two-dimensional problem in that no phase-independent parameters vary with distance along-shore. Therefore we can calculate the solution (except the ray and orthogonal paths) with D as the only independent variable, without integrating the differential equations for the rays and the orthogonals. In order to simplify the presentation we place the x-axis at right angles to the contours, $\vec{U} = (0, v)$, or $U = v$, and $\delta = \pm 90^\circ$.

For the present problem we can directly integrate the conservation equations (4 and 5) for wave action and zero vorticity

$$\frac{\omega_a}{\omega_r} E c_{gr} \cos A = \text{const}_1 \quad (40)$$

$$v - \frac{E \sin A}{\rho h c_r} = \text{const}_2 \quad (41)$$

When the y-component of the conservation (3) for momentum is integrated and combined with eqs. 8, 10, 11, and 40 we get Snell's law (see Jonsson, 1971a, 1976)

$$c_a / \sin A = \text{const}_3 \quad (42)$$

Further we can easily derive algebraic formulas for the ray and orthogonal separation factors β_r and β ($= Df/Df_{st}$)

$$\beta_r = \cos \mu / \cos \mu_{st} \quad (43)$$

$$\beta = \cos A / \cos A_{st} \quad (44)$$

Note that by combining eqs. 40 and 43 we get eq. 33.

The solution, i.e. the 12 unknowns ($k, A, E, v, h, \eta, c_r, c_a, \omega_r, c_{gr}, G$, and μ) as a function of D, is found by numerical iteration in 12 non-linear algebraic equations (Nos. 6, 7, 8, 9, 10, 11, 12, 16, 17, 40, 41, and 42). After the completion of the iteration, β_r and β are found from eqs. 43 and 44. The ray path is deter-

General information		γ	A_{st}^0	δ^0	T_a	D_{st}	$(D\beta_r/Dr)_{st}$	$v_h \rightarrow \infty$	$\beta_{r, st}$	H_{st}
SI units		9.80665	60	90	8	20	(-4)4.0230	1	1	1
x	y	r	A^0	μ^0	L	D	$\eta = D - h$	v	β_r	H
(+2)2.1117	0	0	(+1)6.0000	(+1)6.3224	(+1)9.8709	(+1)2.0000	(-2)5.2248	1.0046	1.0000	1.0000
(+2)4.0274	(+2)3.7262	(+2)4.2848	(+1)5.3510	(+1)5.7385	(+1)9.1635	(+1)1.5777	(-2)5.2682	1.0050	1.1964	(-1)9.1866
(+2)6.1355	(+2)6.4111	(+2)7.5846	(+1)4.6666	(+1)5.1315	(+1)8.2905	(+1)1.1945	(-2)5.3411	1.0059	1.3874	(-1)8.6927
(+2)7.2377	(+2)8.7224	(+3)1.0715	(+1)3.7557	(+1)4.3540	(+1)6.9477	7.7290	(-2)5.5334	1.0087	1.6091	(-1)8.5039
	(+2)9.6903	(+3)1.2183	(+1)3.1720	(+1)3.8907	(+1)5.9927	5.5245	(-2)5.7931	1.0127	1.7273	(-1)8.6628

TABLE 1 Test solution, plane sloping sea bed, slope 1:50

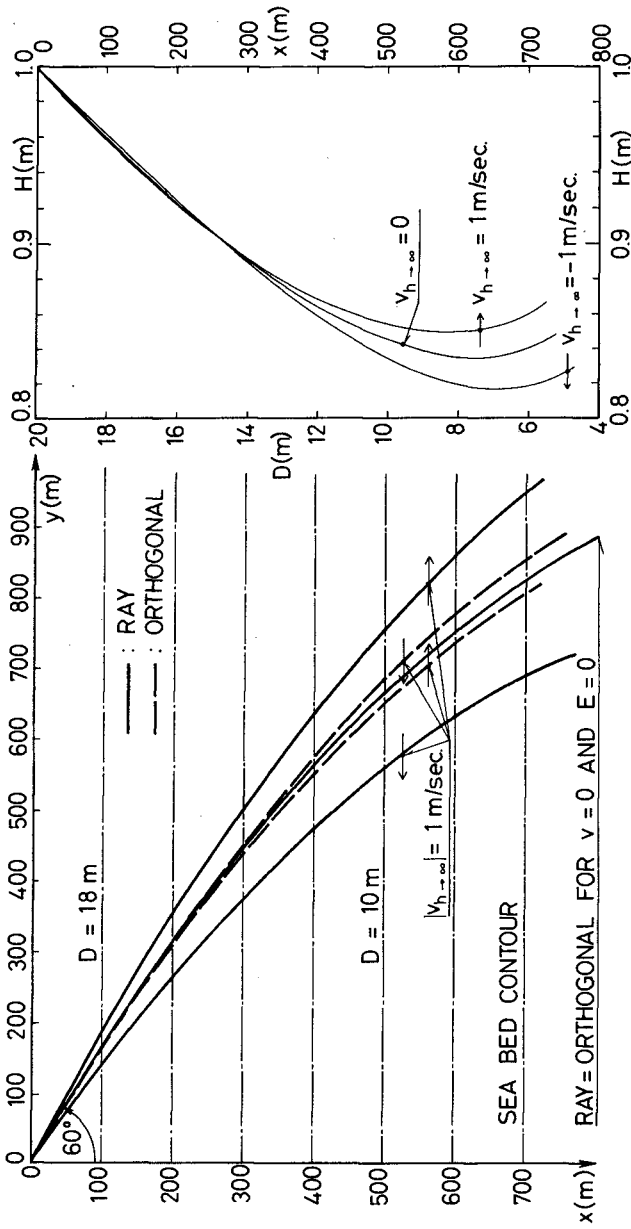


Fig. 9 Paths of wave orthogonals and rays, and variation of wave height. The effect of a 'positive' and a 'negative' current. At $D_{st} = 20 \text{ m}$ the angle A_{st} is 60° . Plane sloping sea bed, slope 1:50

mined by simultaneous integration of the two parametric differential equations for the ray, eqs. 19 and 20 (independent variable r). Similarly the orthogonal path is found by another simultaneous integration of eqs. 14-15 (independent variable s).

The wave level part of the general program can be separately checked using the given test solution.

For a plane sloping sea bed (slope 1:50), $T_a = 8$ sec, $H_{st} = 1$ m, $A_{st} = 60^\circ$, $v_{h \rightarrow \infty} = \pm 1$ m/sec, i.e. $v_{st} = +1.0046$ m/sec, and $v_{st} = -0.99497$ m/sec (both values are rounded with 5 significant digits, 5S), and $D_{st} = 20$ m, the paths of the rays and the orthogonals, and the variation of the wave height are given in Fig. 9. Note that in both cases shown, the rays turn with the current, in contrast to the orthogonals. This phenomenon is explained in the introduction. The figure gives also the path of the orthogonal for $v_{st} = 0$ (and $E_{st} = 0$, i.e. the current $O(H^2)$ is also vanishing, so $v = 0$). It can be shown that if we are in shallow water, the influence of the current on the orthogonal and on the wave height is exceedingly small in this case.

In Table 1 one of the test solutions in Fig. 9 is tabulated for some points along the wave ray. Integers in parentheses indicate powers of 10 by which the following numbers are to be multiplied.

8. CONCLUSION

The irrotational flow equations and the boundary conditions for current depth refraction of surface gravity waves on large-scale steady currents are presented for second-order Stokes waves. An iterative solution algorithm is formulated using a two-level splitting of the calculations, viz. a wave calculation level and a current calculation level. On the wave level, the wave rays are determined in a 'frozen' medium, and wave heights are found using that the flux of wave action is constant between neighbouring rays. On the current level, the waves are 'frozen', and the current field and elevation of the mean surface are determined from the conservation equations for mass and momentum using that the mean irrotational stagnation level (MISL) is horizontal. These conservation equations are solved by a direct finite element method, using triangular linear finite elements for the current and triangular quadratic finite elements for the elevation of the mean sea surface. A test solution is presented, and tabulated for one set of the parameters. The described model is currently being implemented in a general current depth refraction program.

9. ACKNOWLEDGMENT

This study is supported by the Danish Council for Scientific and Technical Research, contract No. 516-5116.B-452.

The authors also wish to thank the Danish Hydraulic Institute, Danish Academy of Technical Sciences, Copenhagen for their financial support to this basic research project.

APPENDIX A: Programming

The numerical methods described are programmed in the IBM OS 360/370 implementation of PL/I. All the floating point calculations are made with 14 hexadecimal digits, i.e. with about 15 decimal digits. The presented results are calculated with about 10S, and the numbers in the test solution in Table 1 are rounded to 5S.

REFERENCES

- Berkhoff, J.C.W., 'Computation of combined refraction-diffraction,' Proc. 13th Coastal Engrg. Conf., Vancouver, July 1972.
- Am. Soc. Civ. Engrs., New York, 1, 24, 471-490, 1973.
- Berkhoff, J.C.W., 'Linear wave problems and the finite element method,' In: Finite Elements in Fluids, Eds. R.H. Gallagher, J.T. Oden, C. Taylor, and O.C. Zienkiewicz, Wiley, London, 1, 251-264, 1975.
- Bowen, A.J., D.L. Inman, and V.P. Simmons, 'Wave "set-down" and set-up,' J. Geoph. Res., 73, 8, 2569-2577, 1968.
- Bretherton, F.P., and C.J.R. Garrett, 'Wave trains in inhomogeneous moving media,' Proc. Roy. Soc. A, 302, 529-554, 1968.
- Brink-Kjær, O., 'Gravity waves on a current: The influence of vorticity, a sloping bed, and dissipation,' Series Paper 12, Inst. Hydrodyn. and Hydraulic Engrg. (ISVA), Tech. Univ. Denmark, 137 pp., 1976.
- Chen, H.S., and C.C. Mei, 'Oscillations and wave forces in an offshore harbor (applications of hybrid finite element method to water-wave scattering),' Rep. 190, Ralph M. Parsons Lab. for Water Resources and Hydrodyn., Dept. Civ. Engrg., MIT, Cambridge, Mass., 215 pp., 1974.
- Chen, H.S., and C.C. Mei, 'Oscillations and wave forces in a man-made harbor in the open sea,' In: Proc. 10th Naval Hydrodyn. Symp., June 1974, Cambridge, Mass., Eds. R.D. Cooper and S.W. Doroff, ACR-204, Office of Naval Res., Dept. of the Navy, Arlington, Va., 573-594, 1976.
- Chung, T.J., and J.N. Chion, 'Analysis of unsteady compressible boundary layer flow via finite elements,' Computers and Fluids, 4, 1, 1-12, 1976.
- Dahlquist, G., and Å. Björck, 'Numerical methods,' Prentice-Hall, Englewood Cliffs, N.J., 573 pp., 1974.
- Hood, P., and C. Taylor, 'Navier-Stokes equations using mixed interpolation,' In: Finite Element Methods in Flow Problems, Eds. J.T. Oden, O.C. Zienkiewicz, R.H. Gallagher, and C. Taylor, Univ. Alabama Press at Huntsville, Huntsville, 121-132, 1974.
- Jonsson, I.G., 'A new proof of an energy equation for surface gravity waves propagating on a current,' Basic Res. - Progr. Rep. 23, Coastal Engrg. Lab. and Hydraulic Lab., Tech. Univ. Denmark, 11-19, 1971a.
- Jonsson, I.G., 'The basic equations for current-depth refraction of surface gravity waves. Irrotational flow,' Progr. Rep. 24, Inst. Hydrodyn. and Hydraulic Engrg. (ISVA), Tech. Univ. Denmark, 39-49, 1971b.
- Jonsson, I.G., 'The energy principle for surface gravity waves propagating on a current,' Submitted for publication, 1976.
- Jonsson, I.G., 'The dynamics of waves on currents over a weakly varying bed,' IUTAM Symp. Surface Gravity Waves on Water of Varying Depth, Canberra, July 1976, Ed. R. Radok, Austral. Acad. Sci., Canberra, 1977.

- Jonsson, I.G., and J.D. Wang, 'Depth-current refraction of water waves,' Submitted for publication, 1976.
- Jonsson, I.G., C. Skougaard, and J.D. Wang, 'Interaction between waves and currents,' Proc. 12th Coastal Engrg. Conf., Wash., D.C., Sep. 1970. Am. Soc. Civ. Engrs., New York, 1, 30, 489-507, 1971.
- Jonsson, I.G., O. Brink-Kjær, and G.P. Thomas, 'Wave action and set-down for waves on a shear current,' Submitted for publication, 1976a.
- Jonsson, I.G., O. Skovgaard, and O. Brink-Kjær, 'Diffraction and refraction calculations for waves incident on an island,' J. Marine Research, 34, 3, 469-496, 1976b.
- Munk, W.H., and R.S. Arthur, 'Wave intensity along a refracted ray,' In: Gravity Waves, Nat. Bur. Stand. Circ. 521, U. S. Gov. Printing Off., Wash., D.C., 95-109, 1952.
- Noda, E.K., 'Wave-current interaction in the nearshore zone,' Abstracts of Papers 15th Coastal Engrg. Conf., Honolulu, Hawaii, July 1976. Am. Soc. Civ. Engrs., New York, 784-786, 1976.
- Noda, E.K., C.J. Sonu, V.C. Rupert, and J.I. Collins, 'Nearshore circulations under sea breeze conditions and wave-current interactions in the surf zone,' Rep. TC-P-72-149-4, Tetra Tech, Pasadena, Cal., AD 776643, 205 pp., 1974.
- Oden, J.T., and L.C. Wellford Jr., 'Analysis of flow of viscous fluids by the finite-element method,' AIAA Journal, 10, 12, 1590-1599, 1972.
- Olson, M.D., and S.Y. Tuann, 'Primitive variables versus stream function finite element solutions of the Navier-Stokes equations,' Preprints, Second Int. Symp on Finite Element Methods in Flow Problems, S. Margherita Ligure, June 1976. Int. Centre for Computer Aided Design (ICCAD), Conf. Series No. 2/76, 55-68, 1976.
- Roache, P.J., 'Recent developments and problem areas in computational fluid dynamics,' In: Computational Mechanics, Int. Conf. on Comput. Methods in Nonlinear Mech., Austin, 1974, Ed. J.T. Oden. Lecture Notes in Mathematics, Springer, Berlin, 461, 195-256, 1975.
- Skovgaard, O., and I.G. Jonsson, 'Connection between the kinematics of current-depth refraction and the conservation equations,' Progr. Rep. 38, Inst. Hydrodyn. and Hydraulic Engrg. (ISVA), Tech. Univ. Denmark, 29-36, 1976a.
- Skovgaard, O., and I.G. Jonsson, 'Current depth refraction using finite elements,' Abstracts of Papers 15th Coastal Engrg. Conf., Honolulu, Hawaii, July 1976. Am. Soc. Civ. Engrs., New York, 787-790, 1976b.
- Skovgaard, O., and M.H. Petersen, 'Refraction of cnoidal waves,' To appear in Coastal Engineering, 1, 1976.
- Skovgaard, O., I.G. Jonsson, and J.A. Bertelsen, 'Computation of wave heights due to refraction and friction,' J. Waterways, Harbors and Coastal Engrg. Div., Am. Soc. Civ. Engrs., New York, 101, WW1, 15-32, 1975.
- Skovgaard, O., I.G. Jonsson, and J.A. Bertelsen, Closure to: 'Computation of wave heights due to refraction and friction,' J. Waterways, Harbors and Coastal Engrg. Div., Am. Soc. Civ. Engrs., New York, 102, WW1, 100-105, 1976.
- Zienkiewicz, O.C., 'The finite element method in engineering science,' McGraw-Hill, London, 521 pp., 1971.
- Zienkiewicz, O.C., and P. Bettess, 'Infinite elements in the study of fluid-structure interaction problems,' Preprint, Second Int. Symp. on Computing Methods in Appl. Sci. and Engrg., Versailles, Dec. 1975, Dept. Civ. Engrg., Univ. Coll. Wales, Swansea, Rep. C/R/255/75, 1975.
- Zienkiewicz, O.C., and P. Bettess, 'Diffraction and refraction of surface waves using finite and infinite elements,' Dept. Civ. Engrg., Univ. Coll. Wales, Swansea, Rep. C/R/274/76, 1976.

CHAPTER 42

SET-UP AND RUN-UP IN SHOALING BREAKERS

William G. Van Dorn
Research Oceanographer
Scripps Institution of Oceanography, University of California
La Jolla, California 92093

ABSTRACT

This paper reports the results of a series of laboratory experiments with periodic waves breaking on uniformly sloping impermeable beaches with the object of distinguishing set-up from dynamic shoreline motions due to partial reflection, the combination of which is normally referred to as 'run-up'. The principal findings are:

1. The mean set-up across the breaker zone was observed to be linear with mean slope proportional to the square of the bottom slope. The mean slope was independent of frequency over slopes of 0.04 or less, and increased with wave period over steeper slopes.
2. The dynamic run-up range was found to be proportional to the square of wave period times beach slope, in agreement with the equation of motion for a nearly frictionless block sliding on corresponding slopes under gravity.
3. The total run-up was poorly correlated with Hunt's empirical formula, nor could any reasonable deterministic justification of this formula be deduced from the present results.
4. Transient run-up was observed to considerably exceed steady-state values in most cases, suggesting that time-dependent momentum flux should be considered in the run-up of variable (natural) waves.

INTRODUCTION

Although commonly lumped together under the ubiquitous headings of run-up and run-down, it is now generally recognized that the shoreline fluctuations in water level observable in the presence of steady, periodic waves breaking on a sloping beach comprise an equilibrium that is the result of at least two different physical effects: (1) periodic oscillations at wave frequency which are the result of partial reflection from the shore slope of that portion of the initial energy of each incident wave not expended through breaking; and, (2) a super-elevation of the mean level against the shore caused by the gradient of momentum flux associated with wave decay in the surf zone.

The transition from a lowering of mean level under the breaker line (set-down) to a positive maximum (set-up) somewhere within the range of periodic shoreline excursions was predicted in principle by Longuet-Higgins and Stewart (1964) as a particular application of their more general theory for momentum flux in non-breaking waves. It was examined in some detail during a series of experiments by Bowen, et al (1968), in which waves of several frequencies and amplitudes were breaking on a uniform beach slope ($S = dD/dx = 0.082$). It was

found that the mean surface gradient $-d\bar{\eta}/dx$ was nearly linear, varied inversely with frequency, and was nearly independent of breaker height. Assuming, as roughly observed, a constant empirical proportionality factor γ between breaker height H and total water depth $(\bar{\eta} + D)$ within the surf zone, they were able to integrate the momentum flux equation of Longuet-Higgins and Stewart to obtain a linear ratio

$$-(d\bar{\eta}/dx)/S = (1 + 8/3\gamma^2)^{-1} \quad (1)$$

The authors note that, although the shoreline set-up $\bar{\eta}_S$ comprised the majority of the observed total run-up R , the latter was still in reasonable agreement with the empirical formula of Hunt (1969)

$$R = HS(H/L_0)^{-\frac{1}{2}} \quad (2)$$

where H is a wave height ordinarily taken as the corresponding deep water wave height H_0 , but, in fact, is most commonly obtained by linear transformation from heights measured in a uniform channel ahead of the slope. Lastly, Bowen, et al suggest that the ratio of beach-to deep water wave-steepness $S/(H_0/L_0)^{\frac{1}{2}}$ may have particular relevance to conditions in the surf zone, since it also appears in the breaking criterion of Iribarren and Nogales (1949). In an attempt to better estimate the quantitative predictions of their slope theory, they present a plot of $\bar{\gamma}$, the average of many determinations of γ across the surf zone, versus $S/(H_0/L_0)^{\frac{1}{2}}$, which includes data for two other beach slopes reported by Putnam (1945), but without drawing any further conclusions.

A more deterministic attempt to predict surf zone set-up is that of Hwang and Divoky (1970), who numerically integrated the momentum flux equation, assuming that (spilling) breakers can be represented by cnoidal waves, whose energy is dissipated at a rate equivalent to a constant fraction of that for a bore of equal local height. Although the many assumptions of this theory are difficult to defend, it provides a means of calculating the set-up and wave height decay simultaneously, and the latter, at least, appears to be in much better agreement with observations than the linear decay assumed by Bowen et al (1968). However, their computed set-up profiles are convex upwards, while the bulk of experimental results suggest that they are linear, or even concave upwards. Even so, the differences are small, and the method deserves further study.

Meanwhile, Battjes (1974a, b) has attempted by dimensional arguments to show that the steepness ratio

$$\xi \equiv S/(H/L_0)^{\frac{1}{2}} \quad (3)$$

is a similarity parameter that, depending upon the interpretation of H , can be used to categorize a wide variety of surf zone phenomena; such as, breaking, breaker type, breaker depth, energy reflectance, and the number of waves simultaneously present between the breaker point and the shoreline. Additionally, Battjes and Roos (1976, in press) present some results of experiments with water velocities and elevations within the swash zone, and try to fit them

into the same mold. But it is difficult to judge the accuracy of these results or conclusions for lack of adequate descriptions of equipment, methodology, or measurement error.

The present paper presents a portion of the results of a two year series of laboratory studies of the dynamics of periodic waves breaking on uniform impermeable beach slopes, in which the time histories of surface elevation, crest velocity, and horizontal fluid velocity, were measured at a plurality of observation stations before and after breaking, as function of slope and wave period. Particular attention was paid to the mean, and periodic, water level excursions across the breaker zone in an attempt to distinguish set-up from the dynamic shoreline excursions caused by reflections. Those experiments dealing with breaking kinematics are described elsewhere (Van Dorn, 1977), and this paper is restricted to shoreline effects, except as regards some pertinent new results from the above paper.

INSTRUMENTATION AND PROCEDURES

All experiments were conducted in a 0.5 m wide by 24 m long glass-sided wave channel with a constant still water depth of 36 cm. Twelve combinations of three plate-glass beach slopes ($S = 0.022, 0.040, \text{ and } 0.083$) and four wave periods ($T = 1.65, 2.37, 3.43, \text{ and } 4.80$ sec) covered the ordinary range of prototype wave conditions for length and time scales of 16:1 and 4:1, respectively. Waves were generated by a planar paddle, hinged 55 cm beneath the channel floor, and driven sinusoidally at the top by a crank shaper. All data runs commenced after at least 5 minutes of generator operation, found by experiment to be about the minimum for low-frequency start-up transients to decay and stable equilibrium to be achieved. Measurements involved the following types of instrumentation.

Surface elevation η versus time, referred to still water, was monitored simultaneously by a plurality of digital (shorting-contact) wave staffs and analog subsurface pressure gages. They were supplemented at specific locations by stroboscopic and flash photography through the channel walls. Comparison of data from these three sources soon established that elevations computed hydrostatically from subsurface pressure were substantially lower than the staff and photo elevations, which generally agreed within 1 cm. The discrepancy was greatest under the wave crests, where it sometimes amounted to 50 percent, diminishing to zero at the shoreline; trough elevations by all three methods agreed within 0.2 cm (Figure 1). This result may substantially affect the assumption of mean hydrostatic equilibrium basic to the theory of time-averaged momentum flux. It may also affect the interpretation of mean elevation given below. Overall elevation accuracy was poorest in vicinity of the plunge and rebound regions of intense breaking, especially on the 0.083 slope, where, in fact, the admixture of air and water made any definition of free surface elevation questionable.

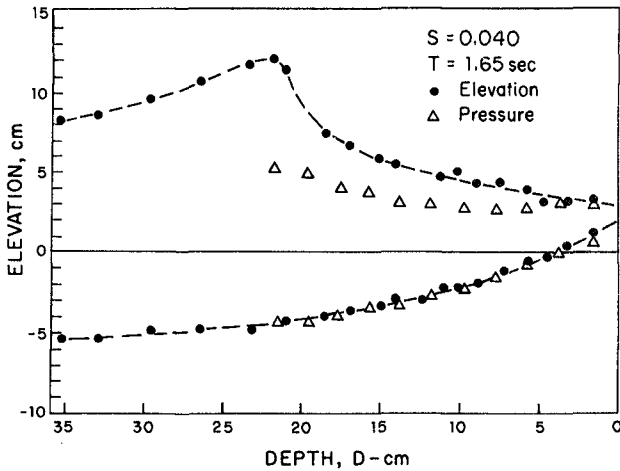


Figure 1. Hodographs of maximum and minimum waves elevations as an individual wave moves toward shore. Pressure and staff elevations agree under troughs, but peak pressure is clearly a poor indication of crest elevation.

Mean elevation $\bar{\eta}$ was observed at fifteen stations evenly distributed between the respective slope toes and the still water shoreline. The sensors comprised 1.0 mm diameter glass tubes taped to channel wall, with their lower ends 1.6 mm above the glass slope. These tubes were connected by plastic tubing via a glass capillary restriction to 2.5 cm diameter, open-ended thistle tubes mounted vertically outside the channel. The time constant of these 'hydraulic hi-pass filters' was adjusted to one minute by varying the capillary lengths. The free surface elevations within the thistle tubes could be rapidly determined by an electric-contact prick probe mounted on a micrometer depth gage. It was found possible to replicate elevations within 0.002 cm after the channel had stabilized, and that annulment of channel seiche fluctuations within these tubes provided the best evidence for stability. While the glass beaches were sealed to the channel walls with rubber gasketing, the slope toes were unsealed, since it was found that sealing them resulted in slow mean elevation drift due to minute seepage between the ground, but unsealed, abutting ends of the glass sections.

Shoreline elevation was monitored versus time by a digital comb-type, shorting contact, wave staff suspended over each beach so that the comb tips cleared the glass surface by about 1 mm, found experimentally to be the minimum elevation required to reduce spurious signals produced by meniscus puddling of water between contacts. Contact spacing was 2 cm on the 0.083 and 0.040 slopes, and 4 cm on the 0.022 slope. The corresponding relative vertical (run-up) resolution of these staffs was always less than 0.2 mm, although the absolute dynamic run-up range may have been slightly larger than reported, owing to elevation of the contacts above the beach. A more-serious problem is the possibility of underestimating the run-up range by virtue of spurious contact shorting in the thin retreating film from a previous wave as a new

bore advanced over the slope. The only ready answer to this question seems to be the nearness of the observations to the limiting possible range, equivalent to the sliding of a frictionless block under gravity only (see Figure 8 and relevant discussion).

Data acquisition of all electric signals was accomplished on a Statos Mark III digital strip chart recorder. This instrument has a 2 khz response, 100 data increments per channel, and prints at a rate of 100 samples per second.

BREAKER CLASSIFICATION

All waves in the present experiments were breaking, and it is appropriate to place them in proper context before discussing results. All relevant breaking point variables are listed in Table 1. Here, phase velocity C_b was obtained from the slope of arrival time curves (accurate to 2%), but later found (Van Dorn, 1977) to be closely approximated by

$$C_b = (2g\eta_b)^{\frac{1}{2}} = (1.54 gH_b)^{\frac{1}{2}} \quad (4)$$

which is substantially slower than the commonly accepted shallow water velocity: $\{g(\eta_b + D_b)\}^{\frac{1}{2}}$. Breaking wavelength is taken as $L_b = C_b T$.

With this preamble, Figure 2 compares breaking steepness H_b/L_b versus beach slope S for the present data on a field of similar data subjectively classified by Galvin (1968) according to breaker type*. The two solid lines $\xi_b = 0.4$ and $\xi_b = 2.0$ represent Battjes (1974a) reinterpretation of Galvin's 'inshore' criteria separating spilling, plunging, and surging or collapsing (non-breaking) waves, where $(\xi_b \equiv S/(H_b/L_b)^{\frac{1}{2}} = 0.32S/(H_b/L_b)^{\frac{1}{2}}$; but the dashed line $\xi_b = 0.6$ appears to be more consistent with the stroboscopic sequences taken during the present study. By either criterion, about half the present waves were spilling and half plunging; but most students of this complicated subject would agree that there is a continuous apparent increase of breaking intensity as either slope or period increases toward the point where no breaking occurs.

* This representation omits Galvin's "plunging altered by reflection", since it has no statistical correlation with any other breaker type.

SLOPE S	PERIOD T, sec	BREAKER HEIGHT H_b , cm	BREAKER DEPTH D_b , cm	PHASE SPEED C_b , cm/s	BREAKER \bar{h}_b , cm OBS.	SET-UP GRAOIENT $m = dD/dx$	BREAKER SET-DOWN \bar{h}_b , cm EQ (5)	MAXIMUM SET-UP \bar{h}_s , cm OBS.	RUN-UP RANGE ΔY , cm	RELATIVE RUN-UP TRANS.	
										R/ H_0 OBS.	EQ (11) Y_t , cm
0.022	1.65	16.6	20.8	160	-0.53	0.0019	-0.71	1.6	0.17	1.5	1.6
	2.37	15.8	18.9	157	-0.44	0.0021	-0.69	1.3	0.26	1.3	1.9
	3.43	13.0	13.8	141	-0.25	0.0018	-0.62	0.8	0.52	1.4	2.0
	4.80	13.0	15.4	141	-0.23	0.0017	-0.65	0.7	0.69	1.3	2.5
0.040	1.65	16.4	21.7	165	-0.69	0.0053	-0.55	2.7	0.48	2.9	3.0
	2.37	14.4	16.9	149	-0.45	0.0055	-0.68	1.7	0.96	2.7	3.5
	3.43	11.8	11.1	131	-0.21	0.0053	-0.56	1.5	1.92	2.9	3.7
	4.80	11.9	11.1	137	-0.21	0.0055	-0.54	1.2	3.24	3.5	4.7
0.083	1.65	15.6	18.3	147	-0.64	0.018	-0.64	2.9	1.84	8.0	6.4
	2.37	12.7	10.8	142	-0.81	0.0260	-0.71	3.4	3.34	5.1	6.8
	3.43	14.8	9.3	145	-0.97	0.047	-1.26	4.0	8.85	11.1	9.3
	4.80	11.2	8.2	169	-1.00	?	-0.85	?	14.4	12.0	10.3

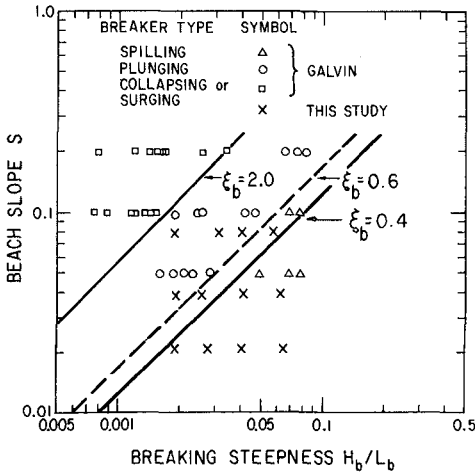


Figure 2. Classification of present breaker types according to Battjes' reinterpretation of Galvin's observations.

RESULTS

As a basic perspective of the results obtained in these experiments, Figures 3, 4, and 5 show, for the three respective beach slopes, comparisons of surf zone variables, ordered downward with increasing wave period. From left to right in each of the twelve period-slope combinations, mean surface elevation (black dots) is increasingly depressed below still water level as the break point (arrows) is approached, reaches a minimum in the vicinity of breaking, and then rises linearly toward the shoreline, although the data do not extend beyond the still water intersection with the beach. The open bars along the beach face give the dynamical range ΔY of steady state water motion, measured vertically from still water level, and whose upper limit represents the engineer's interpretation of run-up. The tic marks on the beach face labeled Y_t give the maximum recorded transient water level excursion associated with the initial surge at the start of each data run. Relevant numerical values of all data are included in Table 1.

Pre-Breaking Set-Down

The depression of mean elevation (set-down) in shoaling water predicted by Longuet-Higgins and Stewart (1964) has been shown by Bowen, et al (1968) to be in good accord with observation where wave growth is governed by linear conservation of energy flux, and to become too small as wave steepness increases beyond the linear range. Near breaking, this trend was reversed: predicted set-down continues to increase, whereas the experimental values were found to reach a flat maximum depression in the vicinity of the break point.

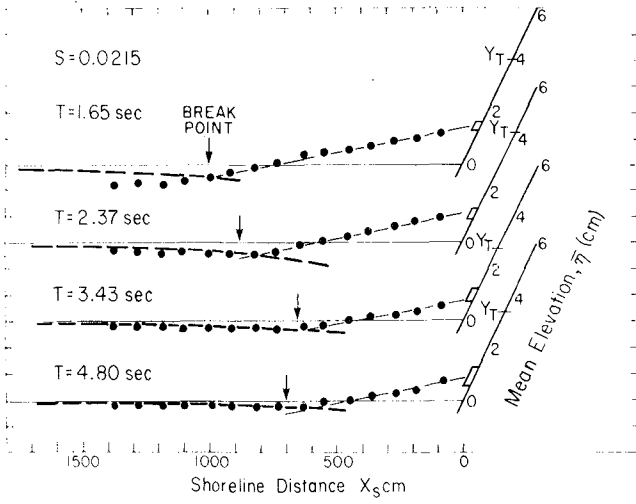


Figure 3. Set-down, set-up, and run-up range for the 0.022 slope.

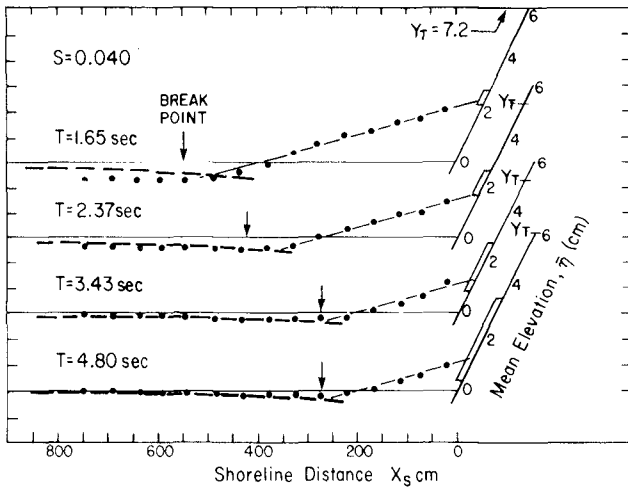


Figure 4. Set-down, set-up, and run-up range for the 0.040 slope.

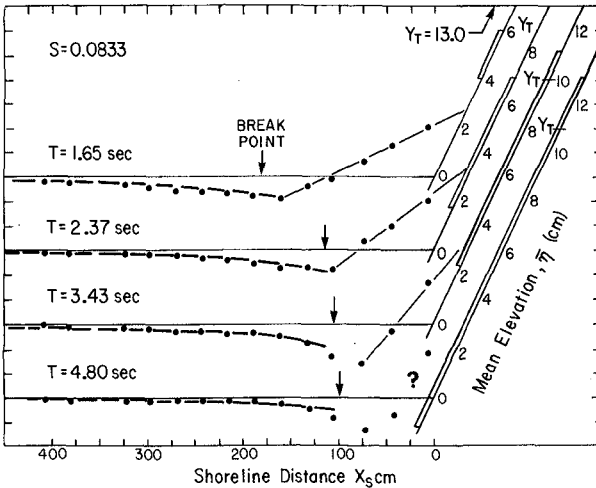


Figure 5. Set-down, set-up, and run-up range for the 0.083 slope.

Much the same results were obtained over the three present slopes, the steepest of which ($S = 0.083$) was the same as that used by Bowen, et al whose experiments were also conducted in the same wave channel. However, in an attempt to find a better approximation to the set-down under steep waves, the dashed curves shown in Figures 3-5 were calculated from the expression

$$\bar{\eta} = -\frac{H^2 k}{8 \sinh 2kD} \quad (5)$$

using observed values of H and D , and taking $k = 2\pi/CT$, where C was observed phase speed. It was hoped that the intersections of these curves with corresponding set-up lines within the surf zone might lead to a means of estimating maximum shoreline set-up, provided that these intersections could somehow be linked to breaker characteristics, and hence to deep water properties (Van Dorn, 1977). As can be seen the computed curves fit the data quite well over most of the growth range, except for those where $T = 1.65$ sec on the 0.022 and 0.040 slopes, where the observed set-down is unexpectedly large in deep water. The reason for this is not known: the experiments were repeated three times with always the same result.

Set-Up

In common with Bowen, et al (1968), set-up within the surf zone was found to be approximately linear, and, on the 0.083 slope, the mean surface slope also appears to increase with wave period, although the definition is doubtful for $T = 3.43$ sec, and completely uncertain for $T = 4.80$ sec, for both of which photographs indicate extremely violent turbulence extending clear to the bottom over most of the very-limited "surf zone". Seemingly, no simple meaning can be attached to 'mean elevation' under such conditions, where there is only one wave or less present simultaneously.

By contrast, the slopes of the set-up lines over the 0.022 and 0.040 slopes appear to be constant and independent of frequency within experimental error. Figure 6 is a plot of set-up slope $m = d\bar{\eta}/dx$ versus beach slope S which includes all present data together with others reported by Bowen, et al and Putnam (1945), where any possible variation due to frequency is represented by error bars. If the line

$$m = 3.4S^2 \quad (6)$$

can be assumed a reasonable fit to the distribution shown, then (1) requires that

$$3\gamma^2/8 = 3.4S/(1 - 3.4S) \quad (7)$$

From the geometry of Figures 3-5, it is evident that, to the extent that the set-down curves and set-up lines intersect at the breaking point (where the wave properties are reasonably predictable), then (1) can be integrated from this intersection ($\bar{\eta} = \bar{\eta}_b$) to obtain the maximum shoreline set-up $\bar{\eta}_s$:

$$\bar{\eta}_s = \bar{\eta}_b + \{3.4S/(1 - 3.4S)\} (\bar{\eta}_b + D_b) \quad (8)$$

Values of $\bar{\eta}_s$ computed from (8) by inserting breaking data into (5) to obtain $\bar{\eta}_b$ are given in Table 1. Comparing these with corresponding values obtained by extrapolating the observed mean slopes to intersection with the beaches shows too great a disparity for (8) to be regarded as a satisfactory prediction method. The principal sources of error are the neglect of the influence of frequency on the 0.083 slope, and the fact that the breaking points do not necessarily coincide with the intersections of the set-down and set-up intersections. Even so, (8) gives set-up values much closer to observations than the shallow water approximation, $\bar{\eta}_s = 0.3H_b$ suggested by Battjes (1974, p 58).

One of the assumptions basic to the set-up theory of Bowen, et al (1968) is the proportionality between breaker height and total water depth across the surf zone. Figure 7 shows plots of observed wave height versus total water depth and horizontal distance, all normalized to their respective breaking values. While the data for the 0.083 slope are scattered, they conceivably could be represented by straight lines, but over both smaller slopes wave height drops rather abruptly from the breaking point, and tends smoothly to some finite value at the still water shoreline. There appears to be relatively little systematic correlation with frequency. This behavior is qualitatively very similar to that predicted by the numerical set-up model of Hwang and Divoky (1970), although their appropriate bottom slopes are numerically too small. This difference might be resolved by a better energy loss coefficient.

Run-Up

Evidence of periodic shoreline oscillations at wave frequency is the most sensitive test that energy is being reflected from a sloping beach. Le Mehaute, et al (1966) and Putnam (1945) observed no perturbation of the mean level over a slope of 1:100, but the run-up range ΔY in these experiments was readily measurable on all three slopes, and increased regularly with slope and wave period, as shown by the open bars along the slopes in Figures 3-5.

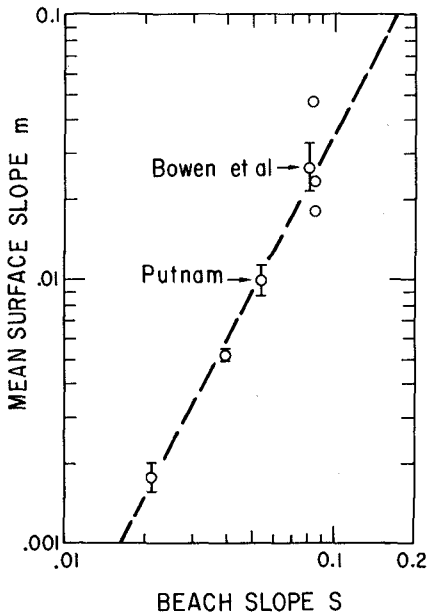


Figure 6. Observed variation of linear mean set-up slope versus beach slope.

In analyzing the motion of bores on slopes, Shen and Meyer (1963) remark that the majority of the motion in $x-t$ space above the still water level should be expected to obey the parabolic law

$$x = u_0 t - \frac{1}{2} gSt^2 \quad (9)$$

where u_0 is the characteristic bore speed at $t = 0$. Equation (9), of course, also describes the motion of a frictionless block projected with velocity u_0 up a slope S . For the periodic shoreline oscillations considered here, the intuitively reasonable picture is that each breaker runs up or the backwash from its predecessor at intervals of a wave period; the whole motion being somehow superimposed on the mean shoreline set-up. Differentiating (9), and noting that $dx/dt = C = 0$ and $x = x_m = \Delta Y/S$ (say) when $t = T/2$, it is easily shown that

$$\Delta Y = gT^2 S^2 / 8 \quad (10)$$

Thus, to the extent that the waves can be considered frictionless bores, and that $S = \tan \alpha = \sin \alpha$, where α is the beach slope angle to the horizontal, (10) should be descriptive of the run-up range. The test of this estimate is: Figure 8, where ΔY is plotted versus $L_0 S^2 = gT^2 S^2 / 2\pi$ for all present data

as well as for that reported by Bowen, et al (1968) and Battjes and Roos (1977, in press)*.

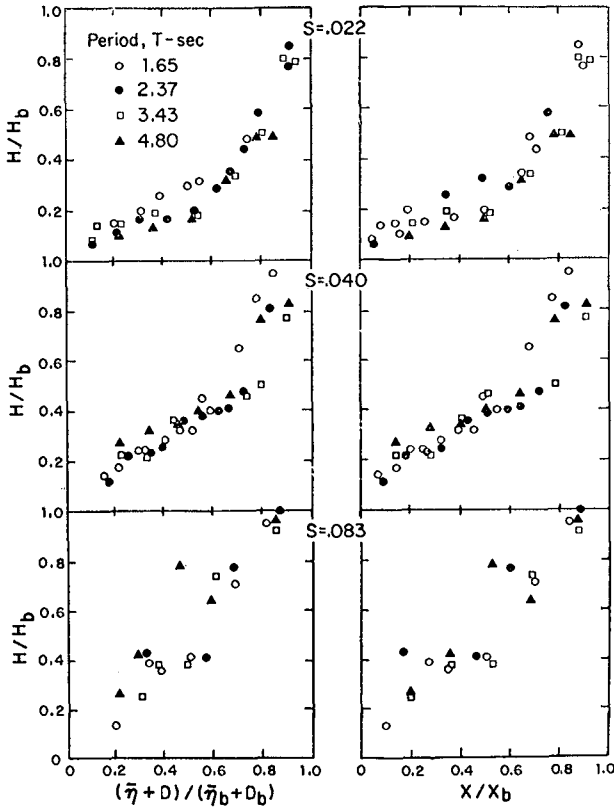


Figure 7. Wave height versus total water depth and surf zone width, all normalized to breaking values.

The straight line labeled frictionless reflection represents (10) in these coordinates, and parallels the data very well. The present experiments, being conducted over plate glass slopes gives results much closer to the frictionless limit than those of Bowen, et al over a plywood slope, and that of Battjes is not described. The conclusion is that run-up range is independent of breaker height, and depends significantly on bottom friction. Indeed, such experiments might provide a sensitive test of frictional losses.

* For Bowen, et al, ΔY was taken as twice run-up, minus mean set-up; for Battjes and Roos, it was taken as ΔX_{cscx} , where ΔX was the observed water excursion along the slope.

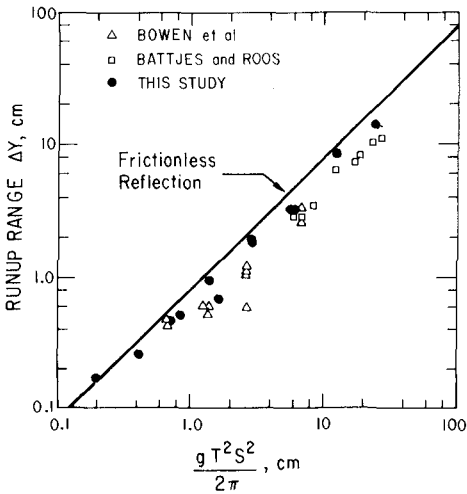


Figure 8. Run-up range versus beach slope and wave period.

Total Run-Up

Nothing said so far provides a clue as to how set-up and run-up range combine to produce the observed maximum run-up, and the above results shed little light on this interesting problem. While no reliable means for predicting set-up has been discovered, Figures 3-5 show clearly that it always amounts to a substantial fraction of the run-up range, since the run-down seldom (if ever) goes below still water level. Second, run-up range, normalized to deep water wave height, is nearly the square of Hunt's (1969) relative run-up:

$$R/H_0 = (L_0/H_0)^{\frac{1}{2}} S \quad (11)$$

which is generally quoted as a reliable run-up index. At least, the comparisons given in Table 1 show that (11) is not a good approximation for small slopes. The values of H_0 used in the calculations were obtained from Van Dorn (1977), and are believed accurate to 10 percent.

Transient Run-Up

Figures 3-5 and the last column in Table 1 give observed values of transient run-up Y_t resulting from the initial surge associated with generator start up. The transient is manifested on the run-up records as a single intumescence, having a duration equal to 3-5 wave periods, that reflect back-and-forth between the wave paddle and beach slope, slowing decaying after several minutes. These transient surges are of interest because their amplitudes substantially exceed the steady-state run-up in many cases, and because they can be expected to occur whenever the momentum flux is varied rapidly, as for example, when waves come in groups. Because their characteristics clearly depend upon the shape of the advancing energy front, no attempt was made here to relate them to other fixed parameters.

ACKNOWLEDGMENTS

This work was supported by the Advanced Research Projects Agency and by the Office of Naval Research and the Department of the Navy, Naval Facilities Engineering Command.

REFERENCES

- Battjes, J. A., 1974a, "Computation of set-up, longshore currents, run-up and overtopping due to wind-generated waves", Delft University of Tech., Report No 74-2, 244 pp.
- Battjes, J. A., 1974b, "Surf similarity", Proc. 14th Coastal Eng. Conf., Amer. Soc. Civil Eng., Vol 1, Chapter 26, p 466-77.
- Battjes, J. A. and A. Roos, 1976 in press, "Characteristics of flow in periodic wave run-up", Jour. Harbors and Waterways, Amer. Soc. Civil Eng.
- Bowen, A. J., D. L. Inman and V. P. Simmons, 1968, "Wave 'Set-Down' and Set-Up", Jour. Geophys. Res., vol 73, no 8, p 2569-77.
- Galvin, C. J. Jr., 1968, "Breaker type classification on three laboratory beaches", Jour. Geophys. Res., vol 73, no 12, p 3651-59.
- Hunt, I. A., 1959, "Design of seawalls and breakwaters", U. S. Corps of Eng., Lake Survey, Detroit, 49 pp.
- Hwang, Li-San, and D. Divoky, 1970, "Breaking wave set-up and decay on gentle slopes", Proc. 12th Conf. on Coastal Eng., Amer. Soc. Civil Eng., Vol 1, Chapter 23, p 377-89.
- Iribarren, C. R. and C. Nogales, 1949, "Protection des ports, Section II", Comm. 4, XVIIth Int. Nav. Congress, Lisbon, p 31-80.
- Longuet-Higgins, M. S. and R. W. Stewart, 1964, "Radiation stress in water waves, a physical discussion with application", Deep-Sea Res., vol 11, p 529.
- Le Mehuate, B. J., G. F. Snow and L. M. Webb, 1966, "Gravity waves on bottom slopes", National Engineering Science Company, Pasadena, California, Final Report, Volume 1, 79 pp.
- Putnam, J. A., 1945, "Preliminary report of model studies on the transition of waves in shallow water", Univ. Calif. Berkeley, Report HE-116-106.
- Shen, M. C. and R. E. Meyer, 1963, "Climb of a bore on a beach, Part 3. Run-Up", Jour. Fluid Mech., vol 16, part 1, p 113-125.
- Van Dorn, W. G., 1977, "Breaking invariants in shoaling waves", Jour. Geophys. Res.

CHAPTER 43

WAVE RUN-UP ON A SIMULATED BEACH

A.J. Sutherland¹, J.N. Sharma², O.H. Shemdin³

ABSTRACT

A set of experiments concerning wave run-up in the presence of an offshore bar is described. Results pertaining to the direct relationship between incident waves and run-up heights are presented. It is clear that in the majority of cases the offshore bar does reduce run-up heights. The experiments showed that under certain conditions very large run-up and run-down heights are produced. This is ascribed to a resonance effect between either the basin, formed between the bar and the beach, or the beach face and the incident waves.

INTRODUCTION

The run-up resulting from the arrival of a train of waves at a beach slope is an important design consideration in many coastal engineering problems. Wave run-up is the maximum vertical height, above the local mean water level, reached by a wave at the end of its travel across the beach.

In reaching the beach, waves pass through the breaking zone and the surf zone in each of which they experience highly non-linear transformations and undergo energy dissipation. Studies of the run-up produced by a bore (Meyer and Taylor, 1972) indicate the importance of frictional dissipation in determining run-up. Other important effects include the interactions between successive waves (by collisions) on the beach slope and the presence of an offshore bar which can cause breaking. The former is important when irregular wave trains are considered while the latter applies to periodic waves as well as to irregular waves. Both effects increase energy dissipation to an unknown extent.

Laboratory measurements of run-up made by van Oorschot and d'Angremond (1968), with mechanically generated waves, and by Webber and Bullock (1968), with wind generated waves, have provided data for conditions in which interactions between waves on the beach slope are an important factor. Battjes (1971) has presented an analytical model of this process but no comparison with data was attempted. Field measurements of run-up by

¹ Reader in Civil Engineering, University of Canterbury, New Zealand.

² Research Fellow, Department of Civil Engineering, University of Delaware, Newark, Delaware.

³ Professor of Coastal and Oceanographic Engineering on leave to Jet Propulsion Laboratory and Scripps Institute of Oceanography, California

Waddell (1973) and Sonu *et al* (1974) must reflect, in addition to the above interactions, the influence of many other factors including the offshore profile, the beach profile, the beach roughness and permeability and the characteristics of the incident waves.

The present study is primarily concerned with the effect of a beach profile which includes a bar. Such profiles are typical of the east coast of Florida. Tests were conducted in the laboratory using a profile modelled on that at Jupiter Island, Florida. Effects of the pronounced offshore bar were determined by measuring wave run-up with a variety of incident wave and water depth conditions.

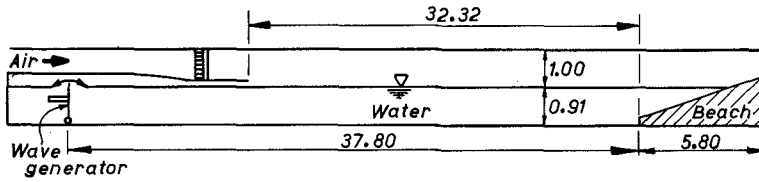
EXPERIMENTAL APPARATUS AND PROCEDURE

The experiments were performed at the University of Florida in the Coastal and Oceanographic Engineering Laboratory air-sea facility, shown in Figure 1, which has been described by Shemdin (1969). Waves are generated by a plate hinged at the bottom and driven by a hydraulic piston. Sinusoidal waves with frequencies in the range 0.2 to 4.0 Hz can be produced with amplitudes up to 10 cm. By using prepared analogue tapes as input the wave generator can be driven so as to produce irregular waves of known spectral shape. There is provision for blowing air over the waves. This was not used in the present experiment.

A model (approximate scale 1:20) of the Jupiter Island beach profile as measured in November-December 1974 was placed at the beach end of the facility. Figures 2 and 3 show the beach profile and the model as constructed. For water depths over the bar of less than 30 cm (68 cm total depth) it was not possible with the wave generator hinged at the base, to generate waves of height comparable to the water depth over the bar. For subsequent tests with reduced water depths at the bar the profile was raised 23 cm and the forward slope of the offshore bar extended at the same slope until it again met the floor of the channel. At the minimum bar depth tested, 5 cm, the water depth in the channel was 66 cm in which waves of sufficient height could be easily generated. For tests with a plane beach slope the horizontal section and the bar were removed from the channel.

Capacitance wave height gauges made from Nyclad insulated wire were placed at the mid-point of the horizontal section 6.10 m "seaward" of the bar at station 2 and 18.29 m "seaward" of the bar at station 4. Most calibration curves were linear with the occasional one consisting of two straight lines meeting near the zero point. Hewlett Packard 7700B recorder bridge circuits conditioned the signals from the gauges. The bridge output, an analogue voltage signal, was taken directly to a Kinematics DDS 1103 (16 channel) Data Acquisition System set to digitize the signal at 10 samples/sec.

A 1.88 cm diameter spiral wound resistance wire wave-staff manufactured by Oceanographic Services was installed parallel to and 6.3 mm from the beach face (see Figure 4). The associated electronics gave an analogue voltage output which was sampled by the data acquisition system at 10 samples/sec, essentially simultaneously with the wave height records. The gauge was calibrated by filling the facility above the level of the



-Dimensions in metres-

Fig.1:- LONGITUDINAL SECTION OF AIR-SEA FACILITY

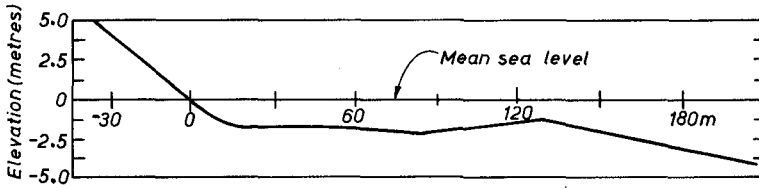
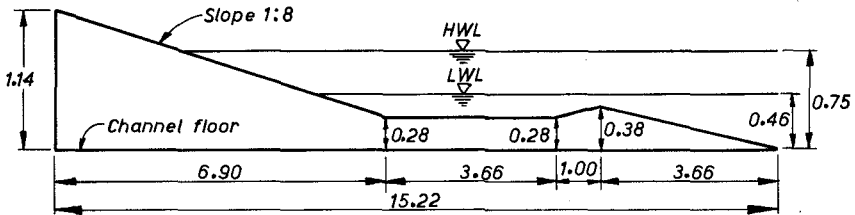


Fig.2:- TYPICAL BEACH PROFILE AT JUPITER ISLAND



-Dimensions in metres-

Fig.3: BEACH PROFILE MODEL

highest expected run-up and then lowering the water level slowly. At selected points the water surface elevation and the resultant output voltage were noted. The calibration curves were closely approximated by two straight lines of similar slope and in a few instances were exactly linear.

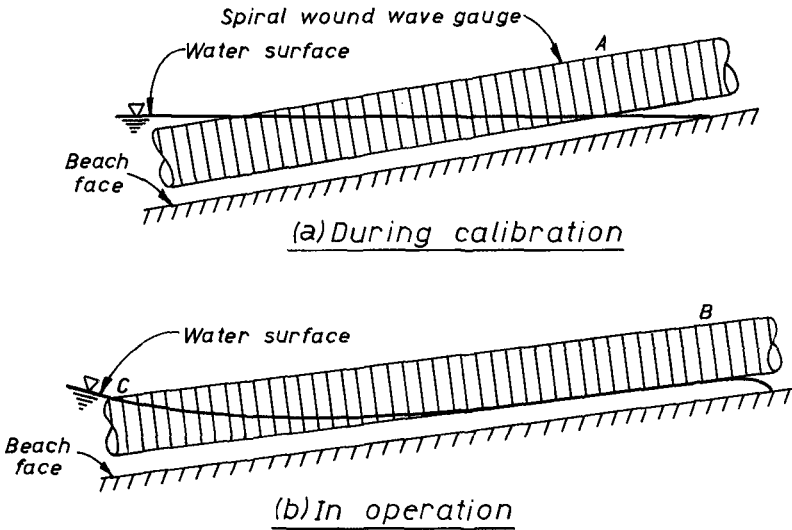


Fig. 4:—SPIRAL WOUND WAVE GAUGE USED FOR MEASURING RUN-UP

A prepared analogue tape was used to provide an input signal for the wave generator. This produced waves having a Bretschneider spectrum and was used for all tests with irregular waves.

At each of eight water depths at the bar a series of tests was performed. Firstly irregular waves having a Bretschneider spectrum were generated and the run-up recorded. Five such runs with different significant wave heights were carried out. Then sinusoidal waves with a frequency of 0.7 Hz, corresponding to the frequency of the peak of the spectrum of the irregular waves, and various wave heights were examined. Sinusoidal waves of 0.3 Hz were also investigated as the peak of the run-up spectrum occurred at 0.3 Hz.

With the bar removed the same series of tests was performed on a plane beach with a water depth of 41 cm in the channel.

The data recorded during each run was the water depth at the bar, the output from the run-up gauge and the three wave height gauges and the RMS voltage supplied to the wave generator. The last being a measure of input wave energy. The digitised records as recorded on tape were processed at the NERDC computing center.

In all, 109 runs were performed. The output from the computer for all these runs is available in the Coastal Engineering Department. The calibrated records have been recorded on a master tape deposited at the NERDC.

RESULTS AND ANALYSIS

Some general observations and impressions are given first. These are followed by the numerical results.

General Observations

Irregular waves cause run-up patterns on a plane slope which differ markedly from those created by regular waves. In these experiments the dominant frequency of run-up (approximately 0.3 Hz) was noticeably less than that of the incident waves (0.7 Hz) and the run-up distribution appeared wider than the wave height distribution. Spectral widths of the run-up ranged from 0.6 to 0.7 compared to 0.42 to 0.49 for the incident waves. Both effects (lower dominant frequency and wider spectrum) result from collision and overtaking on the beach slope. These mechanisms are the significant ones in determining the run-up distribution.

Webber and Bullock (1968) noted that it is often impossible to attribute a particular run-up crest to any individual wave. This was certainly true in the present experiments being most noticeable in the presence of a bar on which a significant number of the incident waves broke.

Most experiments showed a significant rundown which may be defined as the vertical distance below still water level to which the water's edge retreats. There were also negative run-up heights, maxima in the run-up record, which were as much as 2.0 cm below still water level. This would seem to be a result of seiching in the basin lowering the mean water level at the beach as a small wave reached the beach. Such seiching would be excited if the incoming wave has frequency components corresponding to the natural frequency of the basin. With sinusoidal waves of 0.7 Hz both the run-up and the run-down were less than for sinusoidal waves of 0.3 Hz at much smaller incident wave heights. An example is given in Table 1. The high run-up shown for 0.3 Hz could result from the beach having a natural swash frequency of 0.3 Hz, but it is hard to see this producing the observed run-down. Present results do not allow seiching effects to be separated from resonance effects on the beach.

TABLE 1
 RUN-UP AND RUN-DOWN FOR SINUSOIDAL WAVES

Bar Depth (cm)	Wave Frequency (Hz)	Incident Wave Height (cm)	Run-up (cm)	Run-down (cm)
15	0.7	11.0	6.1	-
15	0.3	4.8	11.4	4.9

Having more wave gauges in the basin would possibly allow these effects to be separated. Using the same beach slope with a basin of different geometry may shed light on relative importance of the seiching and the beach resonance.

For a given water depth over the bar the percentage of waves breaking on the bar increased with incident wave height. With sinusoidal waves, spilling from the top occurred when the incident wave height was approximately 60% of the bar water depth. On reaching 70% of the bar water depth all the waves were breaking at the bar crest. For further increase in wave height the break point moved "seaward" down the slope leading to the bar. Observations typical of those made with irregular waves are given in Table 2.

TABLE 2
 BREAKING PERCENTAGE FOR IRREGULAR WAVES

Bar Depth (cm)	Significant Incident Wave Height (cm)	Percentage of Wave Breaking
25	10.4	0
	13.1	5
	16.2	20
	20.4	70
15	7.6	5
	11.5	20
	16.4	70
	20.4	>90

For a water depth at the bar of 5.0 cm the incident wave height seemed almost irrelevant for the run-up. Waves all broke on the seaward slope of the bar and spilled over into the basin. This created waves in the basin which in turn resulted in run-up. The waves were much more regular and much smaller than the incident waves; their properties were probably governed by a combination of the basin geometry and the impulse given to the water in the basin. This represents one end of the spectrum of possible effects caused by the presence of a bar. The other end is when the bar is absent or ineffective.

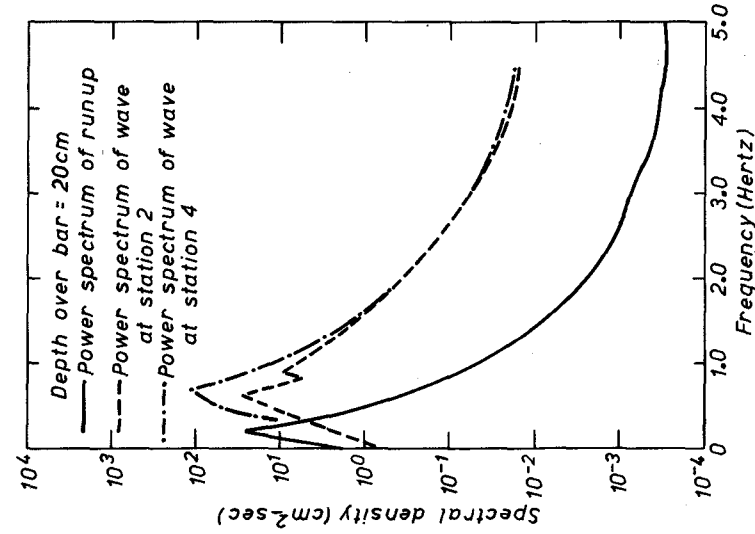


Fig. 6:-- SPECTRA OF RUN-UP, WAVES BETWEEN BAR AND BEACH (St.2) AND INCIDENT WAVES (St.4)

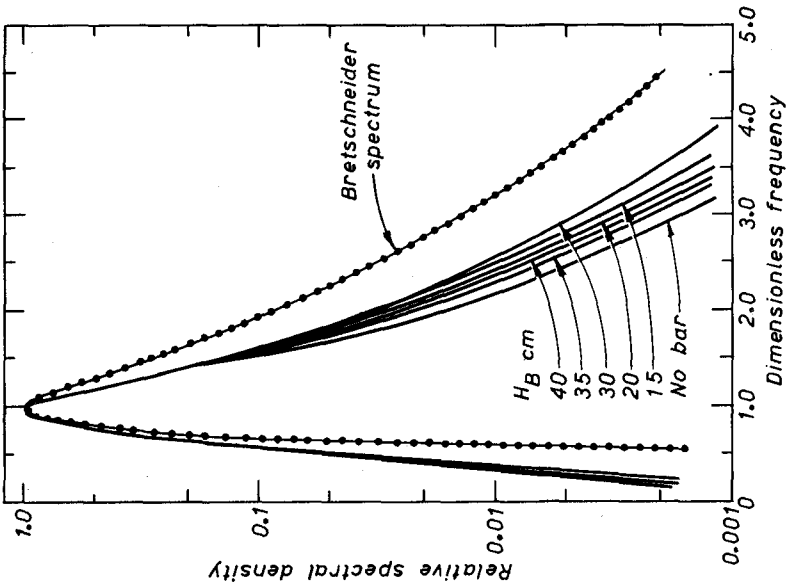


Fig. 5:-- INCIDENT WAVE SPECTRA AND BRETSCHNEIDER SPECTRUM

Numerical Results

Incident Wave Spectra: Smoothed incident wave spectra from all runs at a given bar water depth H_B were plotted in dimensionless form and averaged. Figure 5 shows there is little difference between the spectra at different water depths. However, the generated spectra contain more power at low frequencies and less power at higher frequencies than does the Bretschneider spectrum. The spectral width parameter, ϵ , as defined by Coorschot and d'Angremond (1968) ranged from 0.42 to 0.49 for the generated spectra.

Run-up Measurements: The run-up gauge was designed as a wave staff to be used in a vertical position. When placed on a 1:8 slope and being 1.88 cm in diameter a horizontal water surface intersected the staff over 15.0 cm of its length, see Figure 4a. By calibrating as described above it was assumed that the gauge would be shorted from the last wetted coil down to its lower end, i.e. from coil A in Figure 4a. Then during operating conditions, see Figure 4b, the level recorded would be that of coil B and as such a good measure of the run-up height. However, it appears that simply wetting the coils along the underside of the staff is not sufficient to short them out. The value recorded actually lay somewhere between B and C of Figure 4b where the water surrounds the staff in a way equivalent to that during calibration. The effect is worst when the run-up is highest. Such run-up has a very long thin tongue that extends up the slope and only the underside of the gauge is wet for perhaps 60.0 cm corresponding to a vertical height of 7.5 cm. The error in reading these highest run-ups may thus be 3 or 4 cm in 15 or 20 cm. For the majority of the run-ups, those without very long tongues, the error is of course much less.

This effect was first noticed when values of run-up height on a plane beach divided by incident wave height less than published values were being obtained. A check on the gauge was made in a number of experiments. The run-up height was measured by marking the maximum excursion on the beach face and later measuring its position relative to still water level. These values were later compared with those measured by the run-up gauge. For sinusoidal wave input this is a viable technique because the run-up does not vary significantly between waves. For irregular waves only the maximum could be recorded and an estimate made of the mean.

Such observations confirmed that high run-up values were being under estimated. In some cases this amounted to 25%. One cannot however reliably estimate the error introduced into the results because, particularly for the irregular waves, the shape of the run-up tongue will vary from run-up to run-up. The effect on the run-up spectrum may not be as serious since each run-up event would be recorded and the record would reach a peak at virtually the same time as the run-up peak. The effect is not simply to clip the top off each peak and thus introduce spurious frequency components.

Clearly a different type of gauge must be designed and built for any further tests. It must be such that it responds to point wetting. A step gauge made from a series of electrical contacts each of which records the presence or absence of water is recommended.

In spite of run-up measurement limitations as discussed above, it has been possible to obtain valuable results on run-up dynamics in the

presence of a bar. Spectra of run-up, incident waves (at St. 2) and waves behind the bar (at St. 4) are shown in Figure 6. The spectrum behind the bar is lower than the incident wave spectrum as a result of bottom friction between the two gauges and of dissipation over the bar. The peak frequency of waves remains unchanged before and after the bar. The run-up spectrum, however, shows a distinct shift in the peak frequency to a lower value. Significant dissipation in the higher frequencies and amplification of the lower frequencies in the run-up records is evident. The coherency between the incident waves and run-up height is generally small.

Interesting results on run-up dynamics are also deduced from the equilibrium slope of the spectrum. The incident wave spectrum is shown in Figure 7 and has the (-5) slope expected for gravity waves. The corresponding run-up spectrum exhibits a (-4) slope in the equilibrium range as shown in Figure 8. Dimensional analysis based on the assumption that the dominant spectrum parameters are turbulence intensity, (cm^2/sec^2) and frequency, (Hz) yields a slope of (-4) in the equilibrium range. In contrast gravity and frequency yield a (-5) slope for gravity waves. The result of Figure 8 coupled with the fact that normally significant breaking occurs on the bar suggests that the dynamics of run-up are dominated by turbulence rather than by gravity.

The statistics of the run-up height also differ from those associated with the narrow band gravity wave spectrum. Figure 9 shows the run-up height distribution on probability paper and suggests that run-up can be reasonably described by a Gaussian distribution. This is in accord with the results of Webber and Bullock (1968). It is clear that despite the highly non-linear process affecting run-up, as deduced above, run-up remains a random process but with a different signature. The Gaussian run-up distribution is consistent with the broader band spectrum of Figure 8 compared to that of Figure 7.

Reduction of Run-up Due to Bar:

The direct effect of the bar is to reduce the energy in the wave train. A measure of this energy is the area under the power spectral density curve. The percentage reduction in this value as a function of water depth at the bar H_B is given in Figure 10. The reduction refers to that occurring between a wave gauge 18.29 m from the bar and the gauge in the basin. Some of the reduction is therefore due to viscous action as the waves move along the channel. It appears as though this may be about 25% because at H_B/H_G greater than 3.5, the effect of the bar can be expected to be small.

The effect of this reduction in energy can be seen in Figure 11. Here run-up height has been plotted as a function of incident wave height. The points were derived from the observations made with sinusoidal waves. The number beside each point is the ratio H_B/H_G . As the ratio reduces the points tend to fall further below the standard Beach Erosion Board curve.

Run-up divided by incident wave height as a function of incident wave steepness is shown in Figure 12, in which the points of Figure 11 have been replotted. The number beside each point is again the ratio H_B/H_G . Ignoring those points corresponding to a bar depth H_B of 5 cm (for reasons discussed under General Observations above) there is a tendency for high values of H_B/H_G to be towards the upper left and low

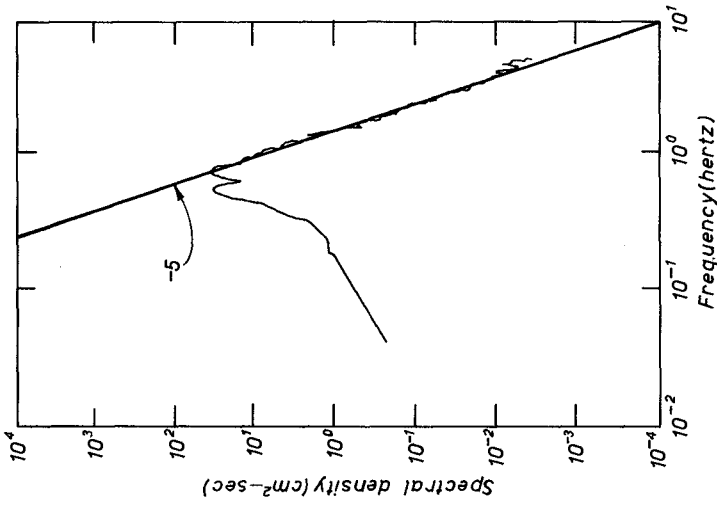


Fig. 8: EQUILIBRIUM RANGE IN
RUN-UP SPECTRUM. WATER
DEPTH OVER BAR 40cm.

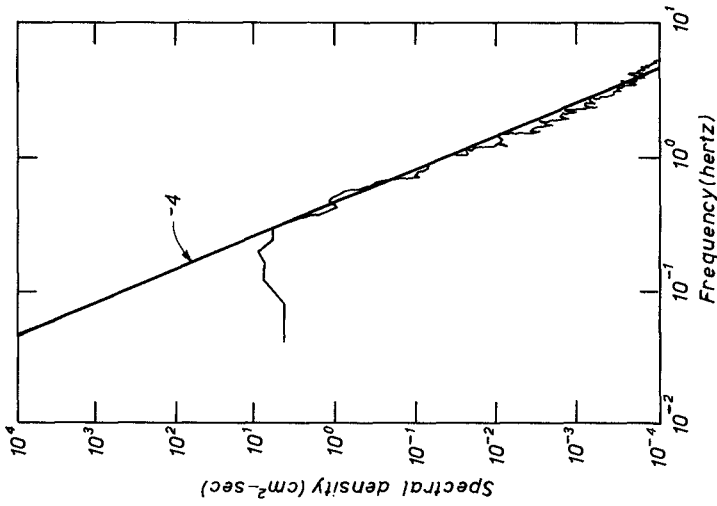


Fig. 7: EQUILIBRIUM RANGE IN
INCIDENT WAVE SPECTRUM
AT ST. 4. WATER DEPTH AT
BAR 40cm.

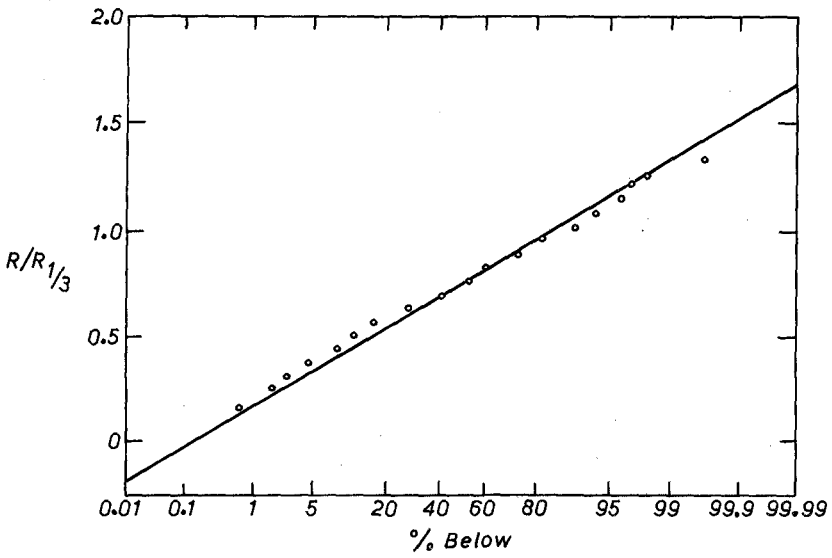


Fig.9:—TYPICAL STATISTICAL DISTRIBUTION OF RUN-UP

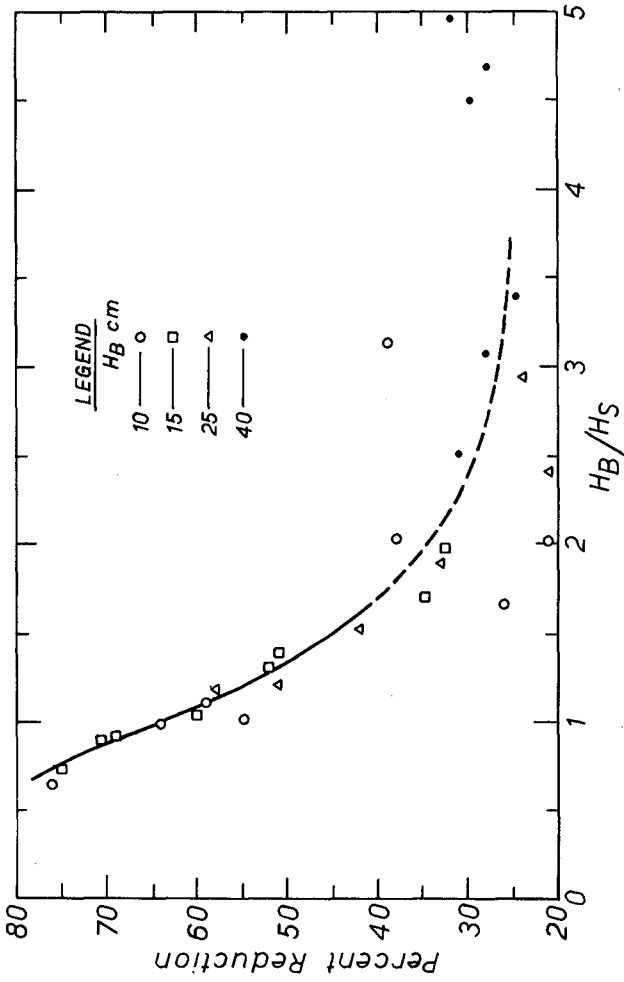


Fig.10:—PERCENTAGE REDUCTION IN ENERGY CAUSED BY THE PRESENCE OF THE BAR AS A FUNCTION OF WATER DEPTH AT THE BAR H_B DIVIDED BY THE SIGNIFICANT INCIDENT WAVE HEIGHT H_s

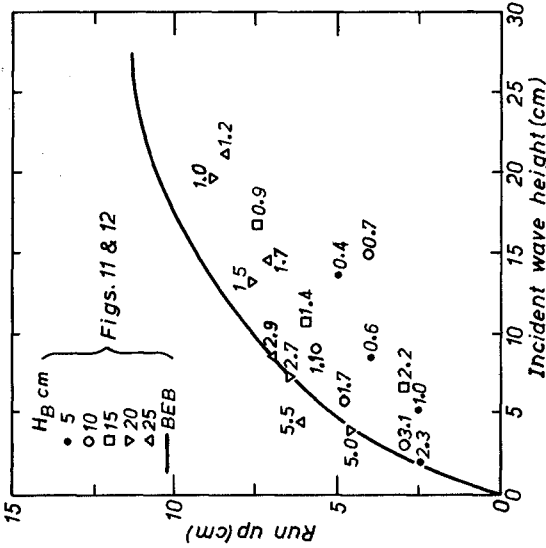


Fig. 11:—RUN-UP AS A FUNCTION OF INCIDENT WAVE HEIGHT (SINUSOIDAL WAVES). NUMBER BESIDE EACH POINT IS THE RATIO H_B/H_S

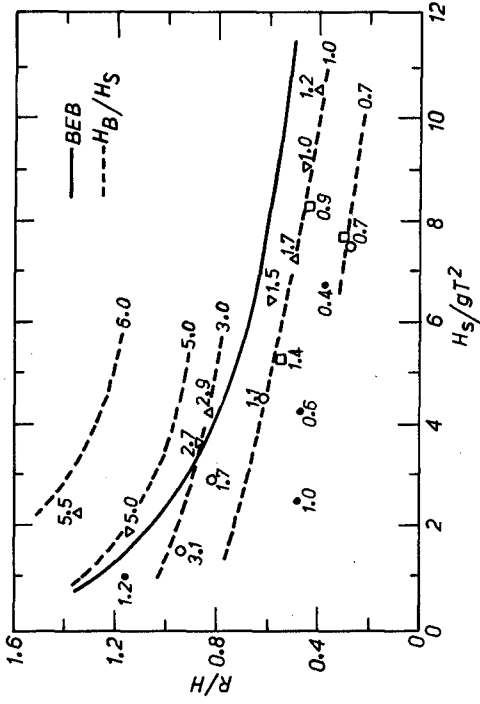


Fig. 12: NORMALISED RUN-UP AS A FUNCTION OF INCIDENT WAVE STEEPNESS

values to be low and to the right. Although these points are barely sufficient to define contours of H_B/H_S , best contour lines are inserted to emphasize trends. The contours suggest that run-up heights can be either smaller or greater than the values predicted by the Beach Erosion Board formula depending on the ratio of water depth over the bar to the incident wave height. An examination of dominant wave height, period and beach conditions during a storm suggests that H_B/H_S is approximately 1.0 and the expected run-up is significantly below the value predicted by the BEB formula.

CONCLUSION

This study has revealed a number of important and interesting aspects of the run-up process occurring in the presence of an offshore bar. The following specific conclusions are derived:

1. The run-up is the product of a highly non-linear process acting on waves approaching a beach. The run-up process is dominated by turbulence generated by breaking waves and friction.
2. The offshore bar has a significant reducing effect on the run-up height. Resonance and seicheing in the region between the bar and the slope can produce significant amplification in run-up and in some cases produce run-down.
3. Continued research is recommended on this problem to investigate the effects induced by movable beds and variable geometry on run-up. Run-up measurements should be made by implanting electronic contact elements in the surface along the beach slope. Field and laboratory studies will be necessary to arrive at adequate modeling relationships for proper prediction of the run-up height.

REFERENCES

- Batjes, J.A. (1971), "Run-up Distributions of Waves Breaking on Slopes", J. Waterways, Harbours and Coastal Engineering Division, Proc. ASCE, Vol. 92, No. WW1, pp. 91-114
- Meyer, R.E. and Taylor, A.D. (1972), "Run-up on Beaches", Waves on Beaches Ed. R.E. Meyer, Academic Press, pp. 357-412
- Shemdin, O.H. (1969), "Air-sea Interaction Laboratory Facility", Tech. Report No. 3, Department of Coastal and Oceanographic Engineering, University of Florida, 44 p.
- Sonu, C.J. Pettigrew, N., Fredericks, R.G. (1974), "Measurement of Swash Profile and Orbital Motion on the Beach", Ocean Wave Measurement and Analysis, Vol. 1, New Orleans, pp. 621-638.
- van Oorschot, J.H., d'Angremond, D. (1968), "The Effect of Wave Energy Spectra on Wave Run-up", Proc. 11th Conference on Coastal Engineering, London, pp. 888-900.

- Waddell, E. (1973), "Dynamics of Swash and Implication to Beach Response", Tech. Report No. 139, Coastal Studies Institute, Louisiana State Univ., 49 p.
- Webber, N.B., Bullock, G.N. (1968), "A Model Study of the Distribution of Run-up of Wind-generated Waves on Sloping Sea Walls", Proc. 11th Conference on Coastal Engineering, London, pp. 870-887.

CHAPTER 44

WAVE RUN-UP IN FIELD MEASUREMENTS WITH NEWLY DEVELOPED INSTRUMENT

Heie F. Erchinger

Coastal Protection Department
D 2980 Norden/Ostfriesland, West-Germany
P.O.-Box 102

ABSTRACT

The height of dikes and other coastal structures can only be calculated after determination of the wave run-up. Several formulas for the calculation of wave run-up are developed after model tests as a rule. But the influences of scale effects and natural wind conditions are practically unknown. To clear these questions further investigations and especially field measurements should be carried out.

By measuring the markerline of floating trash on the slope of the seadikes the maximum wave run-up could be found out after four storm surges in 1967 and 1973. In two graphs it will be shown that on the tidal flats the run-up depends on the waterdepth. The run-up was higher than it could be expected after model tests of 1954.

With a newly developed special echo sounder the run-up could be measured in January 1976. The waves and the run-up could be registered synchronously during two severe storm surges. As shown in Fig. 9 it was found a logarithmic distribution of the wave height, wave period and the higher part of the wave run-up. The found wave run-up is considerably higher than estimated before. The measured 98 % run-up is found about twice the computed value. That is an interesting and important result of the first synchronous recording of wave run-up on sea dikes.

INTRODUCTION

For the design of dikes and other coastal structures and especially for the calculation of their height it is fundamental to determine the wave run-up. The run-up can be calculated with several formulas for different conditions relating to the wave characteristics, the steepness and the roughness of the slope and the position of the structure to the wave propagation direction. As a rule the equations are developed after model tests. But nature and magnitude of scale effects are practically unknown. Also the natural wind conditions are not accurately simulated.

As Professor Führböter has found that model tests with breaking waves do not provide quantitative transferable results, when they are carried out with usual model scales, further investigations are to be done. One way is to carry out field measurements.

THE MARKERLINE OF FLOATING TRASH

Two methods of measuring wave run-up data in the field are usual and carried out at several places:

1. measurement of the markerline of floating trash and
2. visual measuring the run-up of the waves during the storm surge by men on the dike.

Field measurements of the markerline are carried out along the Eastfrisian coast of the German Bight, the south-eastern part of the North Sea. In front of the sea dikes the 5 to 8 km wide tidal flats and the range of sand islands are situated.

After four storm surges in 1967 and 1973 the markerline of the floating trash was measured on the sea dikes in 37 positions. The maximum wave run-up of each position during each storm surge followed from the difference between the storm tide water level and the markerline of floating trash, measured in a

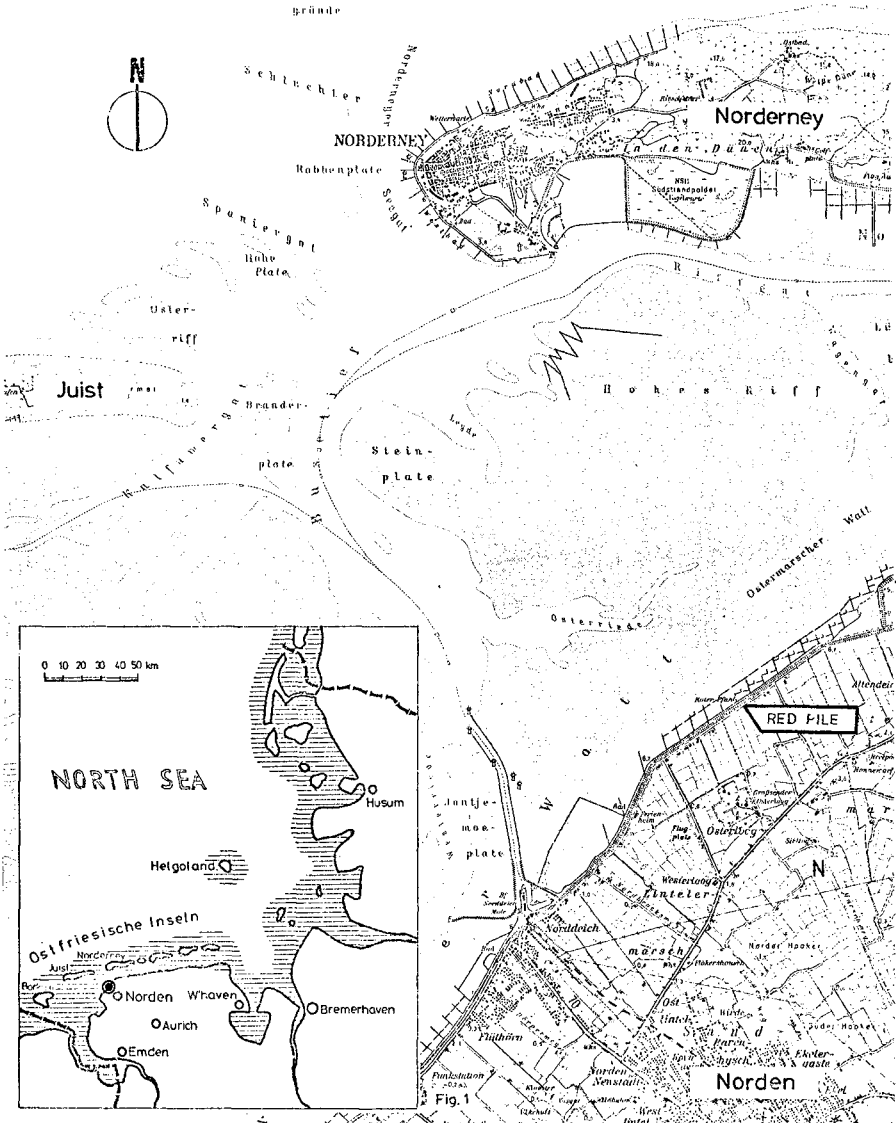
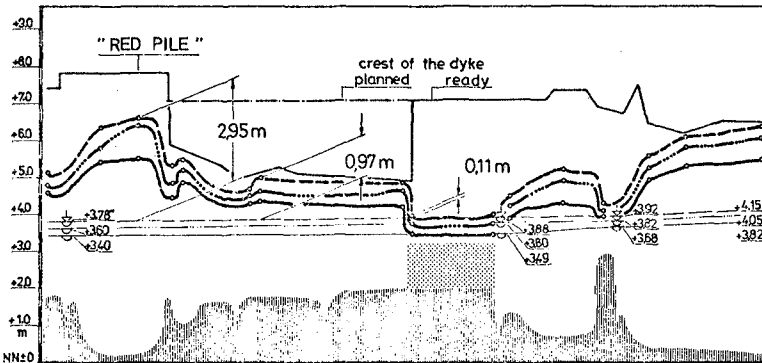


Fig. 1 LAY-OUT PLAN: POSITION "RED FILE" WITH THE TIDAL FLATS AND THE INLET BETWEEN THE ISLES OF JUIST AND NORDERNEY

perpendicular line. Fig. 2 shows the height of the markerline, the highest storm tide level in several locations and the height of the foreland or the tidal flat in front of the dike. It shows further that the markerline is similar to the reflected image of the section through the ground in front of the dike. In three different positions the values of wave run-up during the highest storm tide of this period on Nov. 19th 1973 are specially marked:

	waterdepth near the dike	wave run-up
1. dike without foreland position: "Red Pile"	3.60 m	2.95 m
2. dike with 250 m wide foreland	1.87 m	0.97 m
3. dike with 250 m wide foreland with a summer- dike, 0.57 m waterdepth on its crest	1.87 m	0.11 m



markerline of floating trash	max storm tide water level	storm surges on:
—————	—————	Nov. 13th 1973
—————	—————	Nov. 19th 1973
—————	—————	Dec. 6th 1973

foreland
 summerdyke

Wave Run-up by Measurement of the Markerline of Floating Trash

Fig. 2

These data show the influence of the waterdepth near the dike and mark out the importance of the foreland and the summerdike in reducing the wave run-up and the wave-wash on the dike. The summerdike is a dike on the foreland with a height of approximately 1.5 m, which prevents the inundation of the land behind during lower summer surges.

As wave characteristics on the tidal flats depend on the waterdepth the run-up data were related to the waterdepth in front of the dike. They could not be related to wave data as no wave measurements are carried out on the Eastfrisian tidal flats during these storm surges in 1967 and 1973.

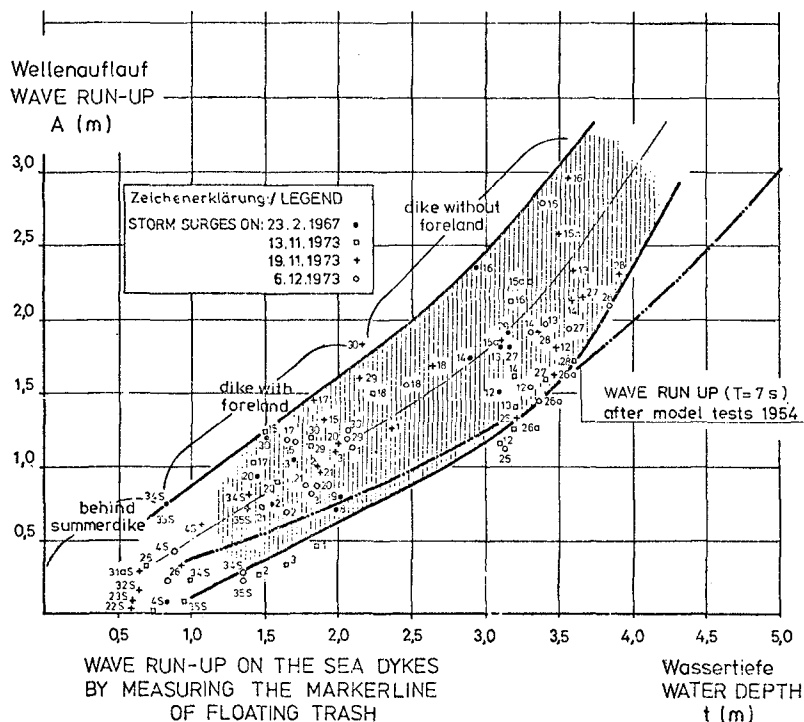


Fig. 3

The graph Fig. 3 shows the "wave run-up" dependent on the "waterdepth". Three groups of data are to be distinguished:

- 1) on dikes without foreland,
- 2) with foreland and
- 3) behind a summerdike on the foreland.

After researching the relation of the values of one place in the four storm-surges the bordering lines with most of the data between them were drawn. We found that wave run-up on the dikes behind a tidal flat with shallow waterdepth and the protection by a range of islands was higher than we could expect after model tests of 1954.

But this measuring of the markerline of floating trash only shows the maximum wave run-up and not the scattering of the values. But the variability is important to know for the determination of the 50 %, 98 % and other values. It is unfavourable, too, that in severe storm surges the trash will be thrown onto the crest or even onto the inside slope of the dike in some places. Sometimes the trash will be scattered by high wind velocities.

Therefore, further study of wave run-up by field measurements was necessary. It would be desirable to get wave and wave run-up data for several positions with different conditions during storm surges and to record synchronously the waves and the wave run-up in these positions.

THE WAVE RUN-UP RECORDER

In December 1975 a special echo sounder record was mounted on the dike near the position "Red Pile". The Red Pile is situated on a dike without foreland, with a low tidal flat in front of it and comparatively high wave action during storm surges as the position lies in a distance of 8 km from the inlet between the isles of Juist and Norderney in south-eastern direction. The normal on the slope of the dike has a direction of approximately North-West, exactly 324 degrees to North.

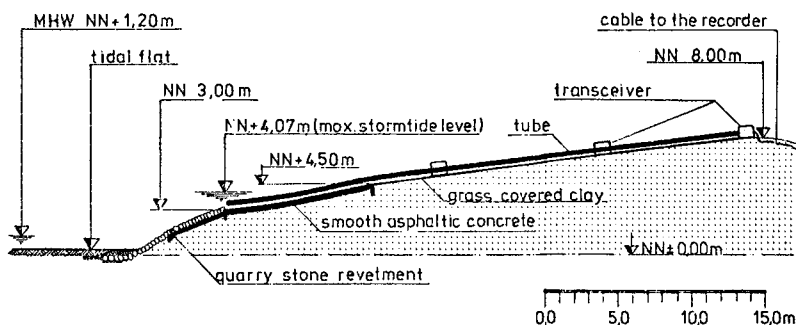


Fig. 4 Slope of a Seadyke with Instruments for Wave Measurement

The dike is covered with a revetment at the outer toe up to NN + 3.0 m that means 1.8 m above MHW, then a slope of smooth asphaltic concrete with an inclination 1 on 6 up to NN + 4.5 m and the upper part with grass covered clay up to NN + 8.0 m also 1 on 6.



Fig. 5 THE STEEL BOX WITH THE TRANSCIEVER
AND THE TUBE WITH THE HOLES

The instrument consists of a waterproof steel box with the transceiver, a small stainless steel tube with a bore of 1 inch and 4 to 8 mm wide holes with a distance of 2 m between each other, and a recorder in a shed at the inside toe of the dike. The tube is fastened on the slope of the dike. Its length is limited at 12 m and, therefore, on the 30 m long slope the system was needed three times. Each second the echo sounder sends 3 pulses into the tube. The pulses are reflected at the non covered holes and each hole is registered in a separate line by the recorder. When the hole is covered by water of the wave uprush the registration is interrupted. The highest interruption shows the maximum run-up of the wave.

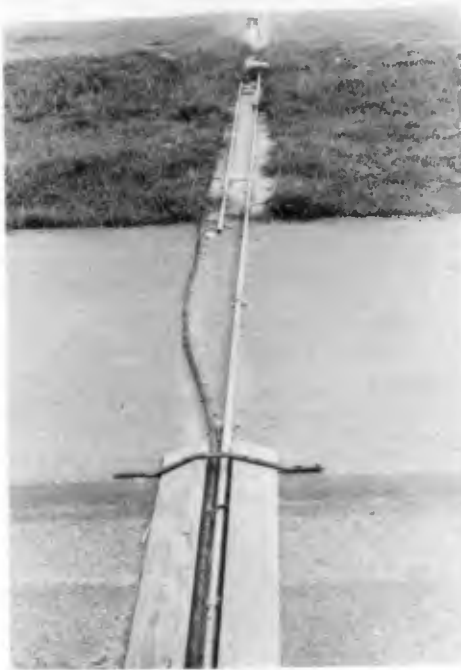


Fig. 6 STEEL BOXES AND TUBES FASTENED
ON THE SLOPE OF THE DIKE

The echo sounder for wave run-up is combined with a supersonic echo sounder for wave measurement. Its receiver is mounted on a frame of steel and placed on the ground of the tidal flat in front of the dike with a distance of 50 m. The time interval between the generation of the sounding signal and the return of its echo after striking the bed is automatically recorded by the instrument and shows the water depth in that moment. The values of both instruments are transmitted by cable to the recorder in the shed inside the dike.



Fig. 7 THE "RED PILE" AND THE SHED FOR THE RECORDER

In the foreground the Red Pile, which formally has signed the border of two sections for the maintainance of the dike.

This wave run-up recorder and the wave recorder are developed by Dr. Fahrentholz in Kiel / West-Germany.

Another type of wave run-up recorder is developed by the Bundesanstalt für Wasserbau in Hamburg. At the lower side of the quadratic steel tube inductive approximity switches are mounted. When they are touched by the wave uprush they give an impulse to

the recorder. As the instrument was mounted this year in springtime no results could be registered by this recorder to date.

REGISTRATION IN JANUARY 1976

Therefore, only the before explained instrument was able to registrate wave run-up in the severe storm surges on January 3rd and 21st 1976. In these storm surges the water level increased 3 m higher than MHW due to wind set up. The following interesting values could be recorded during the hour of the highest water level at station "Red Pile".

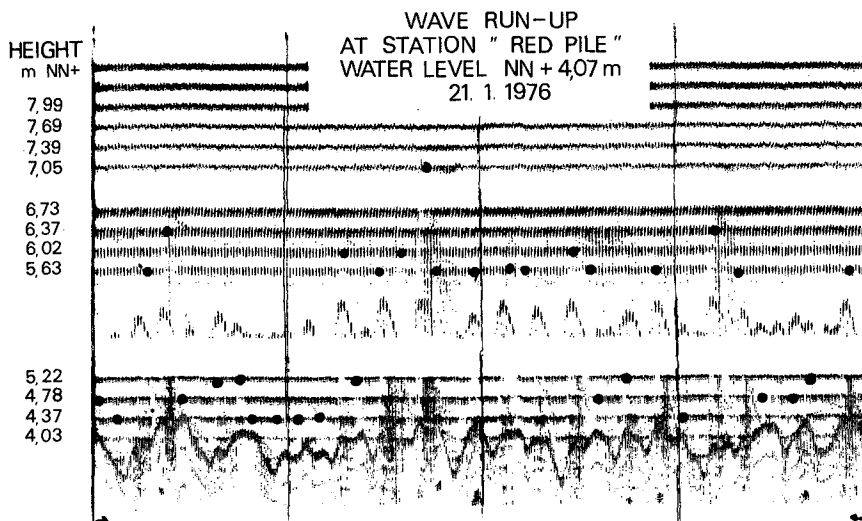


Fig. 8 RECORDING PAPER WITH REGISTERED VALUES

Fig. 8 shows the registration. Three pulses each second are reflected at the holes in the tube. After receiving the pulses they are recorded in a line. Three recording systems with the transceiver and the tubes with holes can be distinguished. As the tubes are open at the low end the water level in the lower tube gives echos, which are recorded too. The single wave uprushes on the slope cover the holes and hence

follows an interruption of the line. The upper interruption gives the highest hole covered by that wave. Hence follows that the run-up reaches the following interval. The plotted black point marks the highest hole covered by water.

During both storm tides the wave run-up data were registered continually but we did not succeed in recording the waves during the high storm tide level without interruption following from two reasons:

1. By the strong movement of the water much silt and fine sand of the ground was kept in suspension and gave an echo which was recorded so that no clear echo of the waves could be distinguished. This trouble will be repaired by varying the transceiver.
2. Near Red Pile the radio station Radio Norddeich for ships broadcast is situated. By a strong radio long-wave transmitter the echos of the wave recorder are influenced and as during stormsthis transmitter is in action very often this second trouble is to be repaired by varying the transceiver.

From these teething troubles follows that only 40 % of the record of waves on January 21st could be analysed and we hope that this part gives a representative section. The wave run-up data have been registered without interruption.

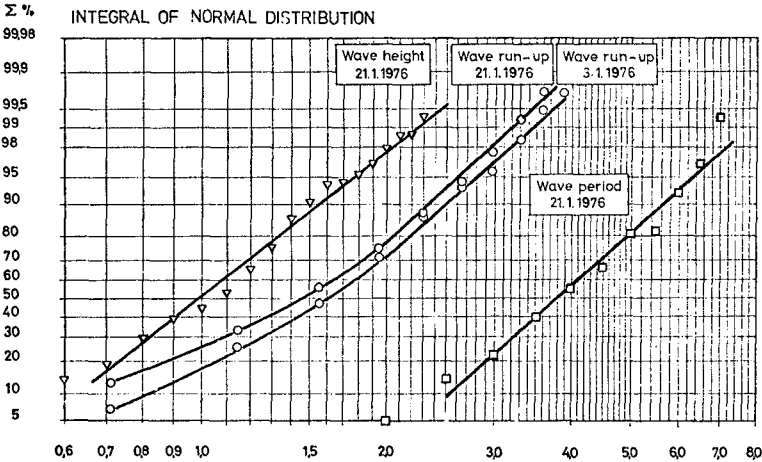


Fig. 9 FIELD MEASUREMENTS OF WAVES AND WAVE RUN-UP AT STATION "RED PILE"

- ▽ Wave height (m)
- Wave run-up (m)
- Wave period (s)

FIRST RESULTS

Fig. 9 shows the analysis of the wave run-up and wave recording during the hour of highest water level. The data of the run-up are prepared after the method of WEIBULL. The curves are plotted with abscissa representing the logarithm of the data of wave height, wave run-up and wave period and with ordinates representing the integral of normal distribution. As the curve of wave height and period approximately follows a straight line we find a logarithmic distribution. The higher part of the run-up data follows a straight line too; only the lower part follows a curve becoming flatter to the low end.

Local conditions at station Red Pile:

Slope of the dike : smooth asphaltic concrete
up to NN + 4.5 m;
the upper part: grass
covered clay;
inclination 1 on 6

	<u>Jan. 3rd</u>	<u>Jan. 21st</u>
Storm tide mean high water level during measurement	: NN + 4.07 m	NN + 4.07 m
Waterdepth in front of the dike	: ~ 4.0 m	~ 4.0 m
Angle of incidence of waves	: ~30 degrees	~30 degrees
Wind conditions (Beaufort force)	: W 10 - 11	W 9 - 10

The main data are:

Wave run-up (m)

	angle of incidence			
	30 degrees		reduced to rightangled (115 %)	
	Jan. 76,	3rd 21st	3rd 21st	
max: wave run-up	3.80	3.50	4.35	4.05
98 % " " "	3.20	2.95	3.70	3.40
<u>sign. wave height</u>	Jan. 21st:	$H_s = 1.44$ m ($H_m = 1.07$ m)		
<u>sign. wave period</u>	Jan. 21st:	$T_{Hs} = 4.9$ s ($T_m = 3.9$ s)		

The found wave run-up is considerably higher than estimated before, even with the probable maximum water level, which is 1.3 m higher than the storm tide level during the measurements.

And at the end an example, controlling some of the numerous formulas for wave run-up:

HUNT VINJE:

$$Z = 1.56 \cdot \sqrt[4]{H_s} \cdot T_{Hs} \cdot \frac{1}{n} = \underline{1.53 \text{ m}}$$

BATTJES:

$$Z_{0.98} = 2.3 \sqrt[4]{H_s} \cdot T_m \cdot \frac{1}{n} = \underline{1.79 \text{ m}}$$

DELFT:

$$Z = 8 H_s \cdot \frac{1}{n} = \underline{1.92 \text{ m}}$$

In fact we measured a 98 % run-up, reduced to rightangled incidence of

$$Z_{0.98} = \underline{3.4 \text{ m}},$$

that is wellrounded about twice the computed value.

That is an interesting and important result of the first synchronous recording of wave run-up on sea dikes. Further investigations will be necessary in several positions with different wave conditions on dikes with foreland and without foreland.

REFERENCES:

- Detta, H.H. Wellenmessungen und Brändungsuntersuchungen vor
Westerland/Sylt
Mitt. d. Leichtweiß-Instituts, Heft 40, Braunschweig 1974
- Erchinger, H.F. Land Reclamation and Groin-Building in the Tidal Flats
Proc. 12th Coastal Engineering Conference,
Washington 1970, Vol. II
- Erchinger, H.F. Küstenschutz durch Vorlandgewinnung, Deichbau und
Geicherhaltung in Ostfriesland,
"Die Küste", Heft 19, 1970
- Erchinger, H.F. Wellenauflauf an Seedeichen - Naturmessungen an der
ostfriesischen Küste.
Mitt. d. Leichtweiß-Instituts, Heft 41, Braunschweig 1974
- Franzius, L. Wirkung und Wirtschaftlichkeit von Rauheckwerken
im Hinblick auf den Wellenauflauf
Mitt. d. Franzius-Instituts, Heft 25, Hannover 1965
- Führbötter, A. Der Druckschlag durch Brecher auf Deichböschungen
Mitt. d. Franzius-Instituts, Heft 28, Hannover 1967
- Führbötter, A. Air Entrainment and Energy Dissipation in Breakers
Proc. 12th Coastal Engineering Conference,
Washington 1970, Vol. I
German draft: "Die Küste", Heft 21, 1971
- Hensen, W. Modellversuche über den Wellenauflauf an Seedeichen
im Wattengebiet
Mitt. d. Franzius-Instituts, Heft 5, Hannover 1954
- Siefert, W. Über den Seegang in Flachwassergebieten
Mitt. d. Leichtweiß-Instituts, Heft 40, Braunschweig 1974
- Technical Advisory
Committee on
Protection against
Inundation Wave Run-up and Overtopping
Government Publishing Office
The Hague, Netherlands 1974

CHAPTER 45

CHARACTERISTICS OF FLOW IN RUN-UP OF PERIODIC WAVES

By Ary Roos¹ and Jurjen A. Battjes²

ABSTRACT

An experimental study is presented of some characteristic parameters of the flow in the up-rush and down-rush of periodic waves breaking on a plane, smooth slope. The water layer thickness has been measured as a function of time at four locations above still water level. Discharges and particle velocities have been calculated. The results have been made non-dimensional on the basis of Hunt's formula for the run-up height. They appear to be either independent of the wave steepness H/L_0 and slope gradient $\tan \alpha$ or to be a function of a single similarity parameter $\xi = \tan \alpha / \sqrt{H/L_0}$ only. An hypothesis is stated concerning a relation between the mean rate of overtopping of a dike by waves, and the run-up which would occur under the same circumstances on an uninterrupted slope. On the basis of this hypothesis the overtopping volume per wave can be normalized so as to make it independent of slope angle and wave steepness. A comparison of the result with measurements from other sources indicates a rough agreement.

1. INTRODUCTION

The run-up of waves is an important factor in the design of shore structures. It has been investigated in many studies, both theoretical and experimental. The experimental studies have mostly been confined to the run-up heights (the greatest heights above still water level, reached by the individual waves on the slope). A simple and reliable formula for the run-up height is given by Hunt (4), based on measurements with periodic waves breaking on smooth plane slopes. However, virtually no data are available regarding the characteristics of the flow in the up-rush and the down-rush on a smooth slope, such as layer thickness, particle velocity, wave front velocity, and so on. Such information can be of use in developing or adjusting schemes for numerical calculation of run-up and overtopping, as well as in problems of stability of cover layer material or of seepage of water into the core material of a dike. The purpose of this paper is to present empirical results concerning the above-mentioned flow parameters, obtained from experiments with periodic waves breaking on smooth plane slopes. In the analysis of the data considerable attention is given to similarities in the run-up process; the existence of such similarities had previously been inferred from Hunt's formula for the run-up height.

2. RUN-UP PARAMETERS

In this study periodic waves of perpendicular incidence are considered, breaking on smooth plane slopes. Only the motion of the relatively thin water layer on the slope above the still water level is dealt with.

The independent parameters considered are (see fig. 1) the height of the incident waves H , the wave period T , the water depth d , the acceleration of gravity g , the slope angle α (a smooth plane slope is considered) and the mass density ρ and the dynamic viscosity μ of the water. A coordinate system is chosen as shown in fig. 1. The origin O is situated at the still water line. The x -axis is directed upwards along the slope. The dependent variables are the layer thickness h , the particle velocity v (averaged over the layer thickness) and the velocity of the run-up wave front c . The variables h and v are functions of the independent variables x and t , in which t is the time; c is a function of x or t .

1. Research Engineer, Directorate for Watermanagement and Hydraulic Research, Rijkswaterstaat, The Hague, The Netherlands.
2. Associate Professor of Fluid Mechanics, Department of Civil Engineering, Delft University of Technology, Delft, The Netherlands.

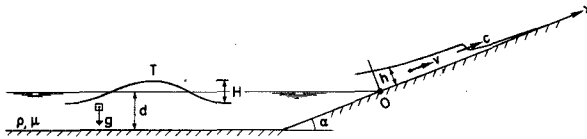


Fig. 1. Definition sketch.

Altogether the following parameter equations are obtained:

$$\begin{aligned}
 h &= F(x, t, H, T, d, g, \rho, \mu, \alpha) \dots\dots\dots (1) \\
 v &= F(x, t, H, T, d, g, \rho, \mu, \alpha) \dots\dots\dots (2) \\
 c &= F(t, H, T, d, g, \rho, \mu, \alpha) \dots\dots\dots (3)
 \end{aligned}$$

Dimensionless combinations can be formed from the variables of Eq. 1 to 3. It may be possible to reduce the number of relevant independent dimensionless parameters by choosing proper scaling quantities. In this way the variables are not merely made dimensionless; they are normalized. Hunt's formula (3), supplemented by an interpretation given by Battjes (1), provides a clue as to the choice of the appropriate scaling quantities.

Hunt's formula is based on measurements of the run-up of periodic waves breaking on smooth plane slopes. It can be written as:

$$R = \sqrt{HL_0} \tan \alpha \dots\dots\dots (4)$$

in which R is the run-up height and L_0 is defined by:

$$L_0 = \frac{gT^2}{2\pi} \dots\dots\dots (5)$$

By substituting Eq. (5) in Eq.(4) this can be written as:

$$R = 0.4 T \sqrt{gH} \tan \alpha \dots\dots\dots (6)$$

From the Eqs. (4) and (6) it appears that the horizontal distance between the still water line and the point of maximum wave run-up is $\sqrt{HL_0}$ or $0.4 T \sqrt{gH}$, independent of the slope angle and the wave steepness. This suggests the use of T , \sqrt{gH} and $\sqrt{HL_0}$ as scaling parameters for the time and the horizontal velocities and lengths of the run-up process. No information is available regarding the scale for the layer thicknesses. Tentatively the same quantity will be chosen as for the horizontal lengths, i.e. $\sqrt{HL_0}$. The following relations are obtained in this way:

$$\frac{h}{\sqrt{HL_0}} = F\left(\frac{x}{\sqrt{HL_0}}, \frac{t}{T}, \frac{d}{L_0}, \frac{\rho H^2}{\mu T}, \frac{H}{L_0}, \alpha\right) \dots\dots\dots (7)$$

$$\frac{v}{\sqrt{gH}} = F\left(\frac{x}{\sqrt{HL_0}}, \frac{t}{T}, \frac{d}{L_0}, \frac{\rho H^2}{\mu T}, \frac{H}{L_0}, \alpha\right) \dots\dots\dots (8)$$

$$\frac{c}{\sqrt{gH}} = F\left(\frac{t}{T}, \frac{d}{L_0}, \frac{\rho H^2}{\mu T}, \frac{H}{L_0}, \alpha\right) \dots\dots\dots (9)$$

The parameter $\rho H^2 / \mu T$ is a Reynolds number for the incident waves. It is assumed that this does not affect the dimensionless dependent variables of Eqs. 7, 8 and 9. The dimensionless variable d/L_0 gives the effect of the water depth. From experiments, such as those reported by Saville (6), it appears that the depth does not affect the run-up heights for periodic waves that break on the slope. Since we are restricting ourselves to breaking waves it is assumed that d/L_0 has no influence on the water movement on the slope. In this way the dependent dimensionless variables appear to be determined only by the location on the slope $x/\sqrt{HL_0}$, the phase t/T , the factor H/L_0 (which for brevity is called the wave steepness) and the slope angle α . Based on the arguments which led to the choice of the

scaling quantities given above, it may be expected that at least some of the dependent normalized variables given in Eqs. 7, 8 and 9 will in fact turn out to be independent of slope angle and wave steepness.

3. RUN-UP EXPERIMENTS

In order to find the effect of the wave steepness and the slope angle on the water movement on the slope, model experiments have been performed.

3.1. Experimental Set-Up

The wave run-up experiments have been performed in a wave flume of the Civil Engineering Department of the Delft University of Technology. This flume is 30 m long, 0.80 m wide and 0.60 m deep. At one end of the flume the waves were generated by a wave board, at the opposite end a plane plywood slope had been installed (see fig. 2).

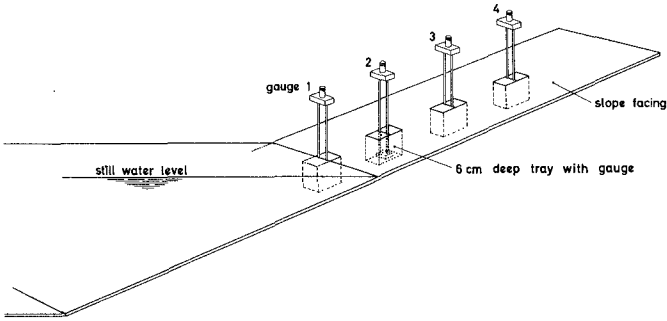


Fig. 2. Slope with gauges for the measurement of layer thicknesses.

On this slope layer thicknesses were measured by means of four wire resistance gauges perpendicular to the slope at equal distances above still water level. They were placed in 6 cm deep trays, which were filled with water and closed by covers flush with the slope facing, in order to maintain the minimum submergence necessary for a linear response. In the constant depth portion of the flume a wire resistance gauge had been placed to measure the incident waves.

3.2. Experimental Procedure

In the experiments the slope angle and the wave characteristics were varied. During each run the incident waves and the layer thicknesses on the slope were registered on recording paper. The measurements on the slope started when the waves reflected from the slope and re-reflected from the wave board arrived at the slope again. The smallest number of waves per run so obtained was thirteen.

The instrumental measurements in each run were supplemented with visual observations of the average run-up length l_u (i.e. the average distance from the still water line to the point of maximum run-up per wave) and the average run-down length l_d (i.e. the average distance from the still water line to the highest point on the slope which appeared to be submerged at all times. During the run-down process the water

tongue becomes relatively thin. For this reason the visually determined values of l_d are not as accurate as those of l_u . However, they turned out to be consistent with the instrumental measurements of the water level variations on the slope.

3.3. Experimental Program

Only waves breaking on the slope are considered. The slope gradients which have been chosen are 1:3, 1:5 and 1:7 (vertical : horizontal); they are typical of dikes. The wave steepness (H/L_0) ranged from 0.02 to 0.07 approximately. Reference is made to table 1. The depth in the constant portion of the flume was 0.45 m in all the runs.

Run number	Slope Gradient	Wave Height H, in meters	Wave period T, in seconds	Wave steepness H/L_0	$\sqrt{HL_0}$, in meters	l_u , in meters	l_d , in meters	$\sqrt{HL_0} \tan \alpha$ in meters	$R = l_u \sin \alpha$, in meters
(1)	(2)	(3)	(4)	(5)	(6)	(7)	(8)	(9)	(10)
1	1:3	0.071	1.26	0.029	0.420	0.45	0.10	0.140	0.142
2	1:3	0.080	1.17	0.037	0.414	0.45	0.13	0.138	0.142
3	1:3	0.106	1.05	0.062	0.426	0.45	0.19	0.142	0.142
4	1:3	0.111	1.01	0.070	0.420	0.45	0.22	0.140	0.142
5	1:5	0.097	1.85	0.018	0.719	0.70	- a)	0.144	0.137
6	1:5	0.116	1.65	0.027	0.702	0.65	-	0.140	0.128
7	1:5	0.131	1.52	0.036	0.687	0.70	-	0.137	0.137
8	1:5	0.156	1.38	0.053	0.680	0.70	-	0.136	0.137
9	1:5	0.169	1.32	0.062	0.678	0.70	-	0.136	0.137
10	1:5	0.183	1.28	0.072	0.685	0.70	-	0.137	0.137
11	1:7	0.116	1.95	0.020	0.828	0.85	0.40	0.118	0.120
12	1:7	0.153	1.63	0.037	0.796	0.80	0.55	0.114	0.113
13	1:7	0.178	1.49	0.052	0.785	0.80	0.60	0.112	0.113
14	1:7	0.213	1.39	0.071	0.801	0.80	0.60	0.115	0.113

a) not recorded

Table 1. Experimental data.

The gauges which measure the layer thickness should cover a constant, fairly large part of the maximum length of the water tongue on the slope in all the runs. Furthermore it was expedient to move the gauges only when the slope angle was changed. For this reason the incident wave characteristics were chosen in such a manner that the run-up length l_u ($\approx \sqrt{HL_0}$ according to Hunt's formula) is about constant per slope angle; see table 1. The value of $\sqrt{HL_0}$ for each slope angle is chosen as large as possible (limited by the flume dimensions) to get the best accuracy of the measurements and the least possible scale effects.

The four gauges on the slope were placed at equal distances, which were constant for each slope angle : 0.125 m for slope 1:3, 0.200 m for slope 1:5 and 0.225 m for slope 1:7. The length covered by the gauges was about $0.9 \sqrt{HL_0}$ for all the runs.

3.4. Experimental Data

A summary of experimental data is given in table 1. For run 7 (which is used as an example throughout the following in this paper) the recorded signals are shown in fig. 3. The index of h in this figure denotes the

gauge number (given in fig. 2).

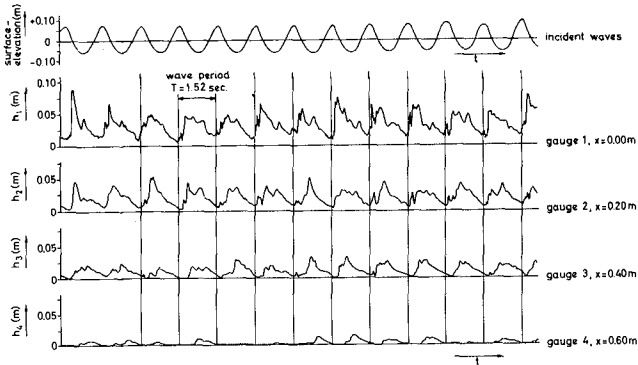


Fig. 3. Recorded waves and layer thicknesses (Run 7).

4. ELABORATION OF THE EXPERIMENTAL DATA

The data available such as those shown in fig. 3 have been elaborated for all the runs presented in table 1. An extensive presentation of the results has been given in ref. (3). In this paper only the results of run 7 are given as an example.

4.1. Phase-Averaging of the Records

From fig. 3 it appears that the records of the layer thicknesses are not quite periodic. To eliminate the irregularities the records have been phase-averaged over ten successive waves at 0.05 sec - intervals. As an example the averaged $h(t)$ -curves of run 7 are presented in fig. 4.

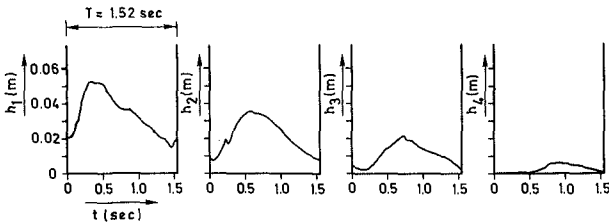


Fig. 4. Phase-averaged $h(t)$ -curves (Run 7).

4.2. Time-History of the Run-Up Front

In the further elaboration the averaged $h(t)$ -curves have been used. The sharp bend in these curves followed by a very quick rise of the water

level (see fig. 4) corresponds with the moment of upward front passage. These passage moments have been used to construct an x-t-diagram of the run-up front (see fig. 5, circled points). Through these points a curve has been drawn, which determines the slope of the curve in S. For the completion of the x-t-curve of the wave front the run-up length (l_u) and the run-down length (l_d) are available. The latter of these determines point Q. These data together determine the shape of the dashed curve in fig. 5 reasonably well.

4.3. Determination of the Particle Velocities

To determine the particle velocities (averaged over the layer thickness) on the slope, the profiles of the water tongues were constructed for successive phases of the wave period with an interval of 0.1 sec. The construction of the profile of the water tongue on the slope for an arbitrary instant $t = t_1$ is illustrated in fig. 6. The layer thicknesses h_1 , h_2 , h_3 and h_4 were read at $t = t_1$ from the $h(t)$ -curves (see fig. 6a, which schematically represents the results given in fig. 4) and were plotted in fig. 6b. This determines the points A, B, C and D.

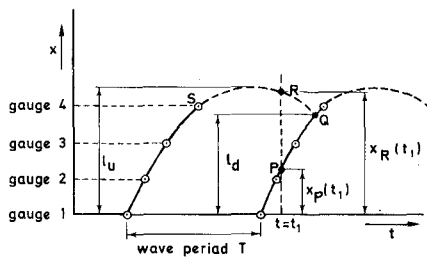


Fig. 5. Construction of the x-t-curve of the wave front on the slope.

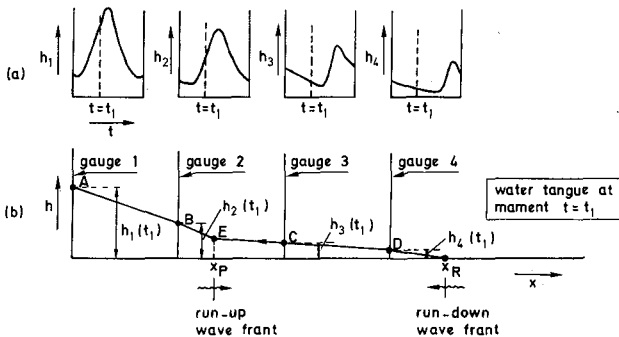


Fig. 6. Construction of the water tongue profile on the slope.

Then the x-coordinates of the run-up wave front (x_p) and the run-down wave front (x_R) were taken at $t = t_1$ from fig. 5 and plotted in fig. 6b. The known points of the profile have been connected by straight lines, except in the area where the run-up wave front is between gauges. In this area the water level of the upper part (between the gauges 3 and 4 in the example of fig. 6) has been extrapolated to x_p ; this gives point E. From this point to point B a straight line has been drawn. An alternative would have been to extrapolate the water level between the gauges 1 and 2 also to x_p , so that a discontinuity in the water level would occur at that location. However, from the $h(t)$ -curves and also from visual observations in the flume it appeared that the run-up front is outlined as a bend in the water tongue profile.

From the constructed water tongue profiles the quantities of water stored above each of the four gauges have been calculated as functions of the time. The curves obtained for these quantities for run 7 are presented in fig. 7a. In this figure B_1 denotes the volume per unit width stored above gauge 1, etc. The particle velocities averaged over the layer thickness have been calculated from these curves according to:

$$v_i(t) = \frac{1}{h_i(t)} \frac{B_i(t + \frac{1}{2}\Delta t) - B_i(t - \frac{1}{2}\Delta t)}{\Delta t} \dots \dots \dots (10)$$

in which i denotes the number of the gauge. The time step Δt is equal to the interval between the successive constructed water tongues, i.e. 0.1 sec. Fig. 7b presents the calculated particle velocities for run 7.

The calculated particle velocities v are less accurate than the water layer thicknesses h because of the procedure used in the elaboration.

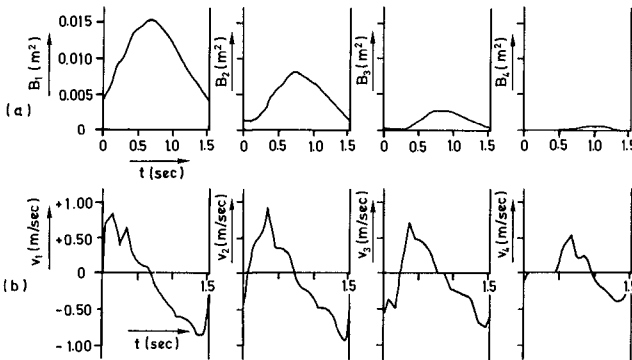


Fig. 7. Calculated volumes of water stored per unit width (a) and particle velocities (b) on the slope (Run 7).

5. EXPERIMENTAL RESULTS

In this section the results of the elaboration as presented in the figs. 4, 5 and 7 are analysed.

5.1. Run-Up Heights

Run-up heights are presented in table 1, column 9 and 10. $\sqrt{HL_0} \tan \alpha$ is the run-up height according to Hunt's formula, while R is the run-up

height calculated from the measured l_u -values and the slope angles. Inspection of the data shows that the measured run-up values are in very good agreement with Hunt's formula.

5.2. Water Layer Thicknesses

Eq. 7 gives the parameter equation for the layer thicknesses. With the elaborated data a relation between $h/\sqrt{HL_0}$ and the independent parameters will be sought. To this end it is useful to characterize the h -values by a single value, for which the maximum layer thickness h_{max} has been chosen. Plots of h/h_{max} versus t/T delivered shape functions (not shown here) which were more or less independent of the wave steepness and the slope angle, for which reason h_{max} can be accepted as the only scale parameter characterizing the h -values. The parameter equation for h_{max} can be obtained as a reduced version of Eq. 7:

$$\frac{h_{max}}{\sqrt{HL_0}} = F\left(\frac{x}{\sqrt{HL_0}}, \frac{H}{L_0}, \alpha\right) \dots \dots \dots (11)$$

In fig. 8a the dimensionless layer thickness $h_{max}/\sqrt{HL_0}$ has been plotted versus the wave steepness H/L_0 . The layer thickness parameter shows virtually no dependence on the wave steepness. Fig. 8b presents a plot of the layer thickness parameter versus the slope gradient. The dependence on the slope gradient is weak. In fig. 8c the dimensionless layer thickness has been plotted versus the location on the slope. In this figure the point $x/\sqrt{HL_0} = 1.0$ is the location of maximum run-up on the slope according to Hunt's formula (apart from a factor $\cos \alpha$).

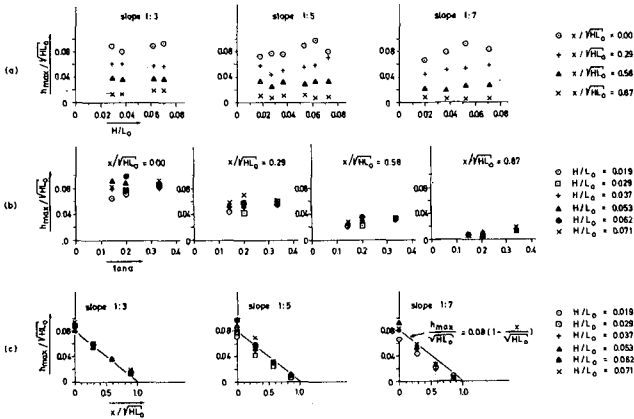


Fig. 8. Normalized layer thickness versus H/L_0 (a), $\tan \alpha$ (b) and $x/\sqrt{HL_0}$ (c).

It is concluded from fig. 8 that $h_{max}/\sqrt{HL_0}$ is roughly independent of H/L_0 and $\tan \alpha$, and that it is related to the location on the slope approximately as follows:

$$\frac{h_{max}}{\sqrt{HL_0}} = 0.08 \left(1 - \frac{x}{\sqrt{HL_0}}\right) \dots \dots \dots (12)$$

This formula is represented in fig. 8c by the straight lines.

5.3. Particle Velocities

Eq. 8 gives the parameter equation for the particle velocities in the water tongue on the slope. The $v(t)$ -curves (see fig 7b) can be characterized by v_{max} (extreme upward velocity) and v_{min} (extreme downward velocity). The shape functions of the $v(t)$ -curves were found to be even more similar than those of the $h(t)$ -curves. In this way the two following parameter equations are obtained from Eq. 8:

$$\frac{v_{max}}{\sqrt{gH}} = F\left(\frac{x}{\sqrt{HL_0}}, \frac{H}{L_0}, \alpha\right) \dots \dots \dots (13)$$

$$\frac{v_{min}}{\sqrt{gH}} = F\left(\frac{x}{\sqrt{HL_0}}, \frac{H}{L_0}, \alpha\right) \dots \dots \dots (14)$$

Various cross-plottings of these parameters were made. In each of the three lowermost gauge locations v_{max}/\sqrt{gH} was found to be approximately inversely proportional to $\sqrt{H/L_0}$ and directly proportional to $\tan \alpha$. This means that in those locations v_{max}/\sqrt{gH} is in fact proportional to the similarity parameter ξ (2) defined by:

$$\xi = \frac{\tan \alpha}{\sqrt{H/L_0}} \dots \dots \dots (15)$$

This is illustrated in fig. 9. The linear dependence of v_{max}/\sqrt{gH} with ξ implies that v_{max} is in fact proportional to $g^T \tan \alpha$, independent of the wave height H . This is a rather surprising result, which obviously can be true in a restricted range of the independent variables only. The coefficient of proportionality of v_{max}/\sqrt{gH} with ξ is the same for the three lowermost gauge locations ($x/\sqrt{HL_0} \approx 0.00, 0.29$ and 0.58). It is only in the upper 1/3 of the run-up length that the particle velocities appear to diminish.

Conclusions such as those stated above for v_{max} also hold for v_{min} (see fig 10).

5.4. Front Velocity

The parameter equation for the dimensionless front velocity is given by Eq. 9. In this equation c is the instantaneous derivative of the x - t -curve of the run-up wave front. A characteristic value for c is its average during run-up, defined by $\bar{c} = l_u/t_u$, in which l_u is the run-up length and t_u is the run-up time (see fig. 11). By dealing with the average front velocity \bar{c} Eq. 9 becomes:

$$\frac{\bar{c}}{\sqrt{gH}} = F\left(\frac{H}{L_0}, \alpha\right) \dots \dots \dots (16)$$

From the analysis of the \bar{c} - data it appeared that \bar{c}/\sqrt{gH} is proportional to $\sqrt{\tan \alpha}$ and inversely proportional to $\sqrt{H/L_0}$. In fig. 12a the parameter \bar{c}/\sqrt{gH} has been plotted versus ξ . From this figure it appears that the following relation holds:

$$\frac{\bar{c}}{\sqrt{gH}} \approx 0.6 \sqrt{\xi} \dots \dots \dots (17)$$

Eq. 17 can also be written as $\bar{c} \approx 0.6 \sqrt{\tan \alpha} \sqrt{g \sqrt{HL_0}}$. The term $\sqrt{g \sqrt{HL_0}}$ in this formula can be interpreted as the velocity of a low shock wave in water with a depth $\sqrt{HL_0}$. It has already been pointed out (see Eq. 12)

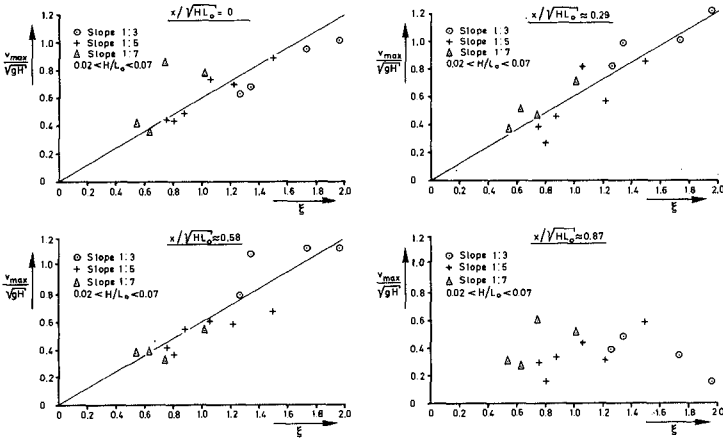


Fig. 9. Normalized upward particle velocity versus ξ .

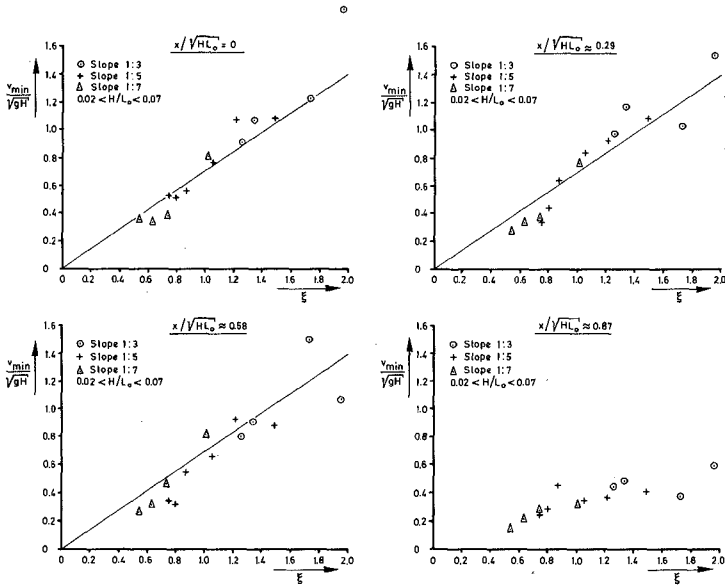


Fig. 10. Normalized downward particle velocity versus ξ .

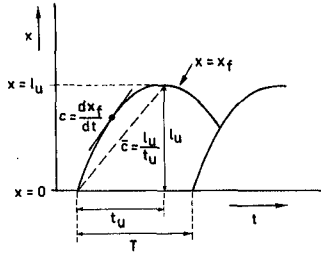


Fig. 11. Definition sketch for the run-up time t_u and the average front velocity \bar{c} .

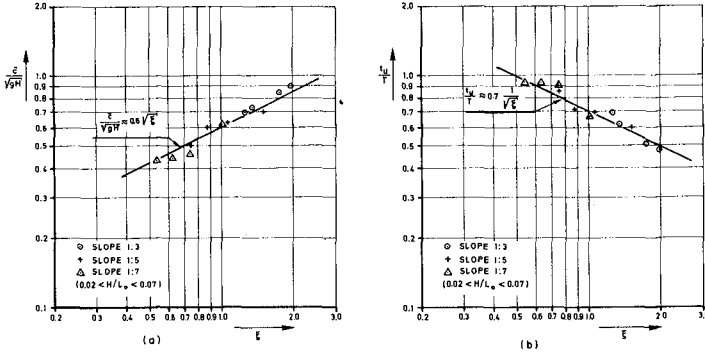


Fig. 12. Normalized average front velocity (a) and run-up time (b) versus ξ .

that the water layer thicknesses on the slope are proportional to $\sqrt{HL_0}$ (although an order of magnitude smaller).

5.5. Run-Up Time

Another characteristic quantity of the x - t -curve of the run-up wave front is the dimensionless run-up time t_u/T . It depends on the wave steepness and the slope angle, expressed by the following parameter equation:

$$\frac{t_u}{T} = F\left(\frac{H}{L_0}, \alpha\right) \dots \dots \dots (18)$$

It appears from the analysis that t_u/T is proportional to $\sqrt[4]{H/L_0}$ and inversely proportional to $\sqrt{\tan \alpha}$. In fig. 12b the dimensionless run-up time t_u/T has been plotted versus ξ . From this figure it can be seen that the following relation is obtained:

$$\frac{t_u}{T} \approx 0.7 \frac{1}{\sqrt{\xi}} \dots \dots \dots (19)$$

5.6. Synthesis to Hunt's Formula

From the expressions for the average front velocity and the run-up time, which have been found independently, Hunt's formula can be reconstructed. From Eqs. 17 and 19 one obtains $\bar{c}t_u/T \sqrt{gH} \approx 0.42$, which can be

written as:

$$l_u \approx 1.05 \sqrt{HL_0} \dots \dots \dots (20)$$

According to Hunt's formula l_u equals $\sqrt{HL_0}/\cos \alpha$, which varies from $1.01\sqrt{HL_0}$ to $1.05\sqrt{HL_0}$ for the three slopes 1:3, 1:5 and 1:7. This agrees well with Eq. 20.

6. WAVE OVERTOPPING

It was deemed worthwhile to investigate to which extent the run-up data obtained could be used in relation to wave overtopping, although no such measurements have been performed in the present study. To this end the following hypothesis is introduced: The maximum quantity of water stored above a certain location on the uninterrupted slope (B_{max}) as measured in the run-up experiments, is equated to the volume of overtopping per wave (V) which would occur if the crest of the dike would be situated at that location (see fig. 13). B_{max} and V are taken per unit width.

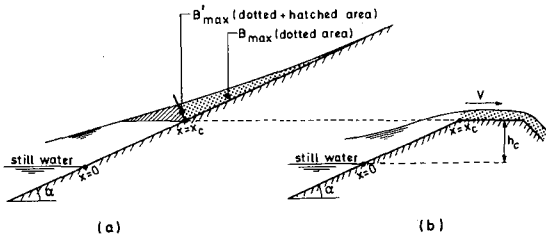


Fig. 13. Definition sketch for the hypothesis on wave overtopping.

It is expected that according to this hypothesis the actual quantity of overtopping is underestimated due to the fact that in the case of overtopping a certain amount of water passes the crest. This implies that the up-rush of the next wave is slowed down less than it would be in the absence of overtopping.

Values for B_{max} are available from the elaboration of the experimental results (see fig. 7a). The variable B_{max} is scaled with HL_0 , because the maximum length of the water tongue is about equal to $\sqrt{HL_0}$ and the layer thicknesses are proportional to $\sqrt{HL_0}$. The dimensionless variable B_{max}/HL_0 depends on the location on the slope, the wave steepness and the slope angle, expressed by the following parameter equation:

$$\frac{B_{max}}{HL_0} = F\left(\frac{x}{\sqrt{HL_0}}, \frac{H}{L_0}, \alpha\right) \dots \dots \dots (21)$$

From the analysis of the B_{max} - data it appeared that B_{max}/HL_0 is independent of H/L_0 and proportional to $\sqrt{\tan \alpha}$. The slope influence is ascribed to phase differences between $h(t)$ at various points along the slope, which increase with decreasing α ; on the 1:3 slope the maximum values of $h(t)$ at the four gauge locations were attained practically simultaneously. So the normalized volume $B_{max} \sqrt{\cot \alpha}/HL_0$ is independent of H/L_0 and $\tan \alpha$ and depends on the location $x/\sqrt{HL_0}$ only. This is shown in fig. 14. A smooth curve has been drawn through the points.

For the case of a dike crest at a finite elevation, a parameter x_c is defined as the x - coordinate of the upper termination of the slope

(see fig. 13b). The ratio $x_c/\sqrt{HL_0}$ is about equal to the ratio of crest height h_c (see fig. 13b) and run-up height according to Hunt's formula $\sqrt{HL_0} \tan \alpha$ (apart from a $\cos \alpha$ -term).

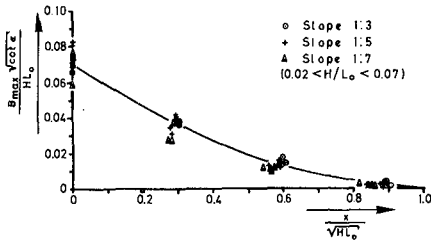


Fig. 14. Normalized maximum volume of water stored on the slope versus $x/\sqrt{HL_0}$

Defining for brevity:

$$R_H \equiv \sqrt{HL_0} \tan \alpha \dots \dots \dots (22)$$

then $x_c/\sqrt{HL_0} \approx h_c/R_H$.

The curve of fig. 14 has been plotted in fig. 15 on double logarithmic paper (drawn line). Along the horizontal axis $(1-h_c/R_H)$ is given, which represents the relative excess of run-up height (R_H) over crest height (h_c).

An alternative definition of a maximum volume stored above a location $x = x_c$ on the slope is given in fig. 13a as B_{max}^I . The behaviour of B_{max}^I is similar to that of B_{max} . The smooth curve through the data points of B_{max}^I has been plotted in fig. 15 as the dashed line.

To check the hypothesis stated above, overtopping data given by Saville (5) have been used. They were obtained with waves breaking on smooth plane slopes of 1:3 and 1:6; the wave steepness H/L_0 varied from 0.026 to 0.066. The data given by Saville have been converted to $V\sqrt{\cot \alpha}/HL_0$ -values and plotted versus $(1-h_c/R_H)$ in fig. 15. The scatter is a known fact in results on wave overtopping and can at least partly be ascribed to the inaccuracy in the measurements, particularly for the relatively small rates of overtopping.

The drawn line in fig. 15, representing $B_{max} \sqrt{\cot \alpha}/HL_0$, is a reasonable lower limit for the overtopping results for the relatively large values of $(1-h_c/R_H)$ (low crest elevations). The dashed line for $B_{max}^I \sqrt{\cot \alpha}/HL_0$ seems to be more nearly a mean value.

Quite apart from the fit of the curves to the data points in fig. 15, it can be seen that the normalization which has been adopted, does serve to bring the data for the 1:3 and 1:6 slopes in a common range for all the wave steepnesses which were used. This means that the rate of overtopping of waves breaking on smooth plane slopes, normalized as $V\sqrt{\cot \alpha}/HL_0$, appears to be a function of the relative crest height h_c/R_H only.

7. DISCUSSION

The variables have been normalized with scaling factors which were chosen on the basis of Hunt's formula. The expectation was that the

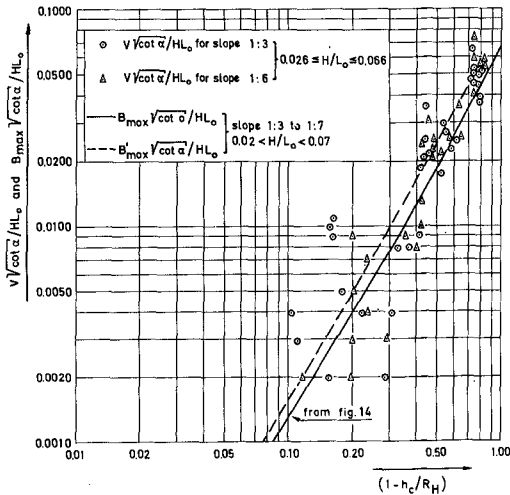


Fig. 15. Normalized maximum volume of water stored on the slope versus $(1-h_c/R_H)$ with plotted data from overtopping measurements.

dimensionless variables so obtained should be independent of the wave steepness H/L_0 and the slope angle α , or nearly so. This turned out to be the case for $h_{max}/\sqrt{HL_0}$, but not for v_{max}/\sqrt{gH} , v_{min}/\sqrt{gH} , \bar{c}/\sqrt{gH} and t_u/T , all of which were found to vary with ξ . It therefore appears that the detailed relationships of the flow in the run-up of breaking waves are somewhat more complex than previously had been inferred from Hunt's formula (1).

The importance of the parameter ξ has been noted before for other characteristics of waves breaking on slopes, such as Iribarren and Nogales' breaking criterion, the breaker type, the reflection coefficient, and the relative importance of (periodic) run-up and (steady) set-up, and to a smaller extent also for the height-depth ratio at breaking. Furthermore, the normalized run-up height itself, if normalized with the incident wave height H , is a function of ξ only, as long as the waves break. This can be seen by writing Hunt's equation in the form $R/H = \xi$. A more detailed discussion of the role of ξ as a similarity parameter for the waves breaking on slopes has been given elsewhere (2).

REFERENCES

1. Battjes, J.A., "Run-up Distributions of Waves Breaking on Slopes", Proc. A.S.C.E., vol. 97, No. WW1, February 1971.
2. Battjes, J.A., "Surf Similarity", Proc. 14th Conf. on Coastal Eng., Copenhagen, 1974.
3. Battjes, J.A., and Roos, A., "Characteristics of Flow in Run-up of Periodic Waves", Report No. 75-3, Communications on Hydraulics, Department of Civil Engineering, Delft University of Technology, 1975.
4. Hunt, I.A., "Design of Seawalls and Breakwaters", Proc. A.S.C.E., vol. 85, No. WW3, September 1959.

5. Saville, T.Jr., "Laboratory Data on Wave Run-Up and Overtopping on Shore Structures", Beach Erosion Board, Techn. Memo 64, 1955.
6. Saville, T.Jr., "Wave Run-Up on Shore Structures", Proc. A.S.C.E., vol. 83, No. WW2, April 1956.

LIST OF SYMBOLS

- B = volume of water stored above a certain location on the slope (per unit width);
- B_{max} = maximum volume of water stored above a certain location on the slope (per unit width);
- B'_{max} = maximum volume of water stored above a certain level on the slope (per unit width);
- \bar{c} = velocity of the run-up wave front;
- \bar{c} = average velocity of the run-up wave front = l_u/t_u ;
- d = constant waterdepth in the flume;
- g = acceleration due to gravity;
- H = height of the incident waves;
- h = layer thickness of the water tongue on the slope;
- h_{max} = maximum layer thickness at a fixed point;
- h^c = crest height of dike above still water level;
- L^c = wave length in deep water = $gT^2/2\pi$;
- l^c_d = run-down length, average distance from the still water line to the highest point on the slope which appeared to be submerged at all times;
- l_u = run-up length, average distance from the still water line to the point of maximum run-up per wave;
- V = volume of overtopping water per wave (per unit width);
- R = run-up height, or greatest height above still water level reached by an individual wave on the slope;
- R_H = run-up height according to Hunt's formula = $\sqrt{HL^c_0} \tan \alpha$;
- T_H = wave period;
- t = time;
- t_u = run-up time, time used by the wave front to run up from $x = 0$ to $x = l_u$;
- v = particle velocity in the water tongue on the slope, averaged over h;
- v_{max} = extreme upward particle velocity at a fixed point;
- v_{min} = extreme downward particle velocity at a fixed point;
- x = coordinate along the slope, positive upwards; origin at still water line;
- x^c = x-coordinate of the crest;
- α^c = slope angle with respect to the horizontal;
- μ = dynamic viscosity of water;
- ξ = similarity parameter = $\tan \alpha / \sqrt{H/L^c_0}$;
- ρ = mass density of water.

CHAPTER 46

MACH-REFLECTION AS A DIFFRACTION PROBLEM

by
Udo BERGER ¹⁾
and
Sören KOHLHASE ²⁾

ABSTRACT

As under oblique wave approach water waves are reflected by a vertical wall, a wave branching effect (stem) develops normal to the reflecting wall. The waves progressing along the wall will steep up. The wave heights increase up to more than twice the incident wave height.

The study has pointed out that this effect, which is usually called MACH-REFLECTION, is not to be taken as an analogy to gasdynamics, but should be interpreted as a diffraction problem.

1. INTRODUCTION

Observations made at vertical walls in prototype as well as in experiments have shown that under certain assumptions gravity waves are apparently not reflected according to the laws of regular reflection. With small angles of wave approach ($\theta_0 < 45^\circ$; angle between wave crest and axis of incidence) the reflected wave will not leave the wall totally; a wave-stem normal to the wall will be developed (Fig. 1a,b). The height of the stem-wave will increase progressively along the length of the wall and will reach a value of more than double the height of the incoming wave (Fig. 1b).

1) Dr.-Ing. Research Assistant Franzius-Institut of the
2) Dr.-Ing. Chief Engineer Technical University,
 Hannover, Germany

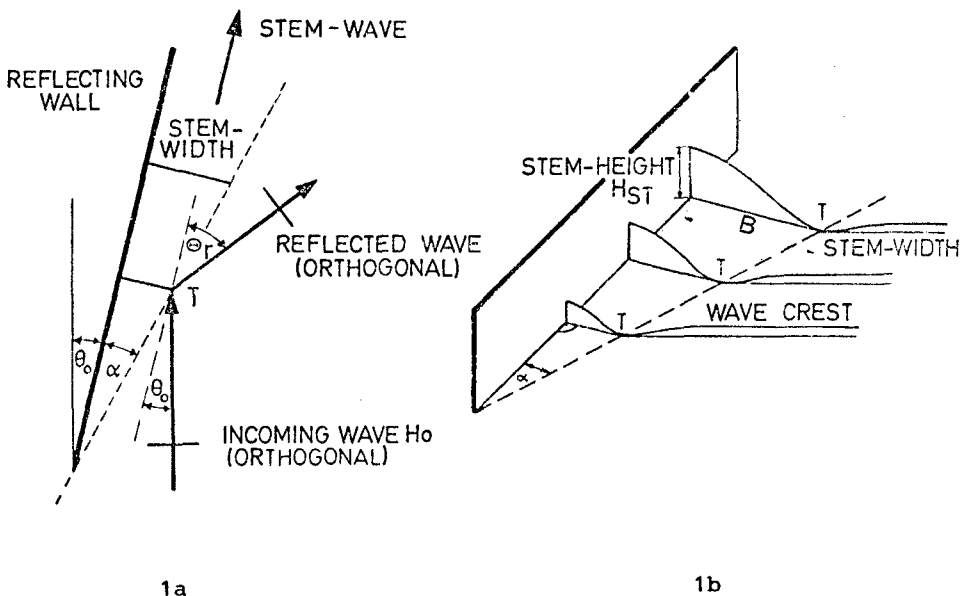


Fig. 1

Explanation of MACH-Reflection

PERROUD (7) and WIEGEL (13) explaining their investigations with solitary waves in analogy to the incoming flow of a compression shock against a re-entrant angle in gasdynamics named this effect MACH-reflection. Fig.1a shows the wave field in front of the wall using wave vectors. The wave strikes the structure with a small angle θ_0 ; a stem-wave and a reflected wave are developed. The point T of intersection between the wave crests of the stem-wave and the incident wave moves on a straight line, cutting the wall with angle α .

Due to the fact that the physical problem is rather unclear and, moreover, the knowledge of the stem-height may be of considerable importance dimensioning structures against wave attack (see SFB 79 (9)) the aim of this investigation was to complete the experiments of NIELSEN and HAGER as follows:

by measurements of both stem-height and stem-width, as a function of the incoming wave-parameters and to give a theoretical explanation of this so-called MACH-effect.

The measurements were carried out at the FRANZIUS-INSTITUTE FOR HYDRAULICS AND COASTAL ENGINEERING, TECHNICAL UNIVERSITY OF HANNOVER using a three-dimensional wave basin from the SONDERFORSCHUNGSBEREICH 79 (Water research in Coastal Regions).

2. REVIEW OF PREVIOUS INVESTIGATIONS

Investigations concerning MACH-reflection of gravity waves have been conducted in the sea and in hydraulic models and with walls of different shape and slopes.

PERROUD (7), CHEN (1) and SIGURDSSON, WIEGEL (8) have studied the MACH-Effect with solitary waves at a vertical as well as at inclined walls. Bended forms also have been investigated. The measurements of NIELSEN (5) and HAGER (4) have been carried out using monochromatic waves and are restricted to straight and vertical walls.

Using a two-dimensional model, NIELSEN established the increase of the stem-height at the reflecting wall, the stem-width as a function of the angle of incidence and of the wave length. However, the number of data is too small to show the results in a functional form. For larger angles of incidence ($> 15^{\circ}$), NIELSEN assumed that the experimental results were influenced by the rather small distance to the boundary of the model at the end of the wall.

In addition to that the reflecting wall is in contact with a lateral boundary at one end which is not in accordance with the conception of a free-standing breakwater. Finally no theoretical explanation of the MACH-reflection is given by NIELSEN.

Contrarily to the investigations of NIELSEN with rather small wave heights and small wave lengths, HAGER's experiments have been carried out under prototype conditions.

HAGER also investigated the increase of the stem-height within an extensive programme at the jetty of the Eckernförde harbour/Germany. However, the limited number of measurements and the scattering of the data only allow qualitative conclusions.

The fundamental results of the investigations of PERROUD,

PREVIOUS EXPERIMENTAL AND THEORETICAL EXAMINATIONS OF THE MACH-REFLECTION AT STRAIGHT VERTICAL WALLS

M A C H - s t e m - p e r a m e t e r						remarks concerning the experiments	remarks on theory																				
author	stem - height	stem-width	stem-width	stem-width	behaviour of the reflecting wave																						
<p>NIELSEN (5)</p> <p>dimensions of the test basin $a = 609,6$ cm $b = 111,7$ cm $h = 12,7$ cm</p> <p>monochromatic wave</p> <table border="1"> <tr> <td>H (cm)</td> <td>$\frac{a}{H}$</td> <td>$\frac{b}{H}$</td> <td>$\frac{h}{H}$</td> </tr> <tr> <td>1.07</td> <td>45,74</td> <td>0.22</td> <td>5</td> </tr> <tr> <td>0.45</td> <td>14,63</td> <td>0.07</td> <td>15</td> </tr> <tr> <td></td> <td></td> <td></td> <td>20</td> </tr> </table>	H (cm)	$\frac{a}{H}$	$\frac{b}{H}$	$\frac{h}{H}$	1.07	45,74	0.22	5	0.45	14,63	0.07	15				20	<p>increase of the stem-height with increasing angle of incidence θ_0</p> <p>the stem width: in independent of the wave length</p> <p>REMARKS: The second MACH-stem is observed in shoaling water.</p> <p>In deep water the 2. MACH-stem increases with increasing wave level</p> <p>Supposition: the stem-width increases linearly with increasing length of the wall</p>	<p>decrease of the stem-width with increasing angle θ_0</p> <p>Increase of the stem-height with increasing wave-height</p> <p>Independent of the wave-height</p> <p>decrease of the stem-width with increasing wave level</p> <p>Supposition: the stem-width increases linearly with increasing length of the wall</p>	<p>the stem-width increases linearly along the length of the wall</p> <p>the stem-width of the reflecting wave is smaller than that of the stem-height wave</p>	<p>the stem-width increases linearly along the length of the wall</p> <p>the stem-width of the reflecting wave is smaller than that of the stem-height wave</p>	<p>WIELSEN shows that there is a reflecting wave with an angle $\theta_0 = 20^\circ$ according to PERROUD</p> <p>the first part of the reflecting wall touches the wall of the test basin</p> <p>the experiments of the 2. MACH-stem have not been done qualitatively</p>	<p>there is a theoretical explanation</p>					
H (cm)	$\frac{a}{H}$	$\frac{b}{H}$	$\frac{h}{H}$																								
1.07	45,74	0.22	5																								
0.45	14,63	0.07	15																								
			20																								
<p>PERROUD (7)</p> <p>the same basin as NIELSEN</p> <p>solitary wave</p> <table border="1"> <tr> <td>H (cm)</td> <td>$\frac{a}{H}$</td> <td>$\frac{b}{H}$</td> <td>$\frac{h}{H}$</td> </tr> <tr> <td>1.52</td> <td>0.38</td> <td>5</td> <td>22.5</td> </tr> <tr> <td></td> <td></td> <td></td> <td>45</td> </tr> </table>	H (cm)	$\frac{a}{H}$	$\frac{b}{H}$	$\frac{h}{H}$	1.52	0.38	5	22.5				45	<p>the stem-height is a function of the angle of incidence and has two minima</p> <p>$\theta_0 = 22,5^\circ$ $\theta_0 = 45,0^\circ$</p>	<p>the stem-width increases linearly along the length of the wall</p> <p>the stem-width of the reflecting wave is smaller than that of the stem-height wave</p>	<p>no reflecting wave for an angle of incidence $\theta_0 > 20^\circ$</p> <p>the wave height of the reflecting wave is smaller than that of the stem-height wave</p>	<p>the stem-width decreases</p>	<p>PERROUD describes the MACH-stem-effect with a solitary-wave connection</p>										
H (cm)	$\frac{a}{H}$	$\frac{b}{H}$	$\frac{h}{H}$																								
1.52	0.38	5	22.5																								
			45																								
<p>HAGER (4)</p> <p>Eckernförde harbour</p> <p>wind wave</p> <table border="1"> <tr> <td>H (cm)</td> <td>$\frac{a}{H}$</td> <td>$\frac{b}{H}$</td> <td>$\frac{h}{H}$</td> </tr> <tr> <td>165</td> <td>3800</td> <td>0.05</td> <td>5</td> </tr> <tr> <td></td> <td></td> <td></td> <td>30</td> </tr> <tr> <td></td> <td></td> <td></td> <td>15</td> </tr> <tr> <td></td> <td></td> <td></td> <td>45</td> </tr> <tr> <td></td> <td></td> <td></td> <td>20</td> </tr> </table>	H (cm)	$\frac{a}{H}$	$\frac{b}{H}$	$\frac{h}{H}$	165	3800	0.05	5				30				15				45				20	<p>the stem-height is a function of the angle of incidence and increases progressively along the length of the wall</p>	<p>the dependence of the stem-height of the incident wave on the angle of incidence, changes</p>	<p>HAGER computes the stem-height along the length of the test basin with the equation system it is easier to PERROUD's</p>
H (cm)	$\frac{a}{H}$	$\frac{b}{H}$	$\frac{h}{H}$																								
165	3800	0.05	5																								
			30																								
			15																								
			45																								
			20																								

Fig. 2.1

NIELSEN and HAGER are summarized in Fig. 2.1. The stem-height increases with the increasing angle of incidence for solitary waves as well as for regular (monochromatic) waves. The stem-height and the stem-width increase in the direction of wave propagation. The stem-width decreases with the increasing angle of incidence. The decrease of the stem-angle is not mentioned very much by NIELSEN, but is readily understood from the decrease of the stem-width with the increasing angle of incidence and is similar to PERROUD's results. The observation of a second MACH-stem for periodical deep-water waves is remarkable.

Theoretical investigations about MACH-reflection of gravity waves have been conducted by PERROUD and HAGER. The analytical solution of PERROUD is connected to the problem of a solitary wave and may not be used in connection with periodical waves. The four unknown parameters - height of the stem-wave, height of the reflected wave, angle of reflection and angle of the stem - are determined by a four-equation-system, which can only be solved implicitly. Two equations of the system are found from geometrical considerations and the other two equations are deduced from the mass and energy-conversion conditions. The theoretical statement of HAGER is similar to PERROUD's and leads to the calculation of the stem-height only. This statement doesn't agree with the experimental results.

3. DIFFRACTION THEORY

From the previous chapter it may be seen that for monochromatic waves there is no theory to calculate the wave pattern, i.e. stem-height and stem-width, with sufficient accuracy. If we suppose that the MACH-reflection has to be interpreted as a diffraction-problem in the area of reflection as opposed to how it was formerly investigated, a new theoretical concept must be examined.

From the linear partial differential equation

$$\Delta \phi = 0$$

and using a polar coordinate system and the well-known boundary conditions of the linear wave theory, we get the scalar wave equation.

$$\Delta F + k^2 \cdot F = 0 \quad ; \quad \Delta \text{ in polar coordinates}$$

$$k = \frac{2 \pi}{L}$$

As shown in (6) after some transformations it can be seen that the modulus of $F(r, \theta)$ is equal to the diffraction coefficient

$$K = \frac{\text{height of diffracted wave}}{\text{incoming wave height}} = |F(r, \theta)|$$

The solutions of the scalar wave equation aren't uniquely determined in infinity through specified sources as opposed to potential equations. The wave equation allows standing waves as a solution, which would physically mean that waves coming from infinity superimpose waves coming from the finiteness. To avoid this, the radiation condition (11) must be determined. This prevents all energy from infinity. Analytically it is enough to say that the solutions of the scalar wave equations have the following condition in infinity

$$F \rightarrow \frac{e^{-ikr}}{\sqrt{r}}$$

SOMMERFELD (12) gives a comprehensive definition of the radiation condition

$$\lim_{r \rightarrow \infty} r \left(\frac{\delta F}{\delta r} - ikF \right) = 0$$

and shows that the solution of the scalar wave-equation is uniquely determined.

For the special case of the half-infinite breakwater, SOMMERFELD has found a solution which allows the computing of the diffraction for all wave-lengths.

SOMMERFELD's solution

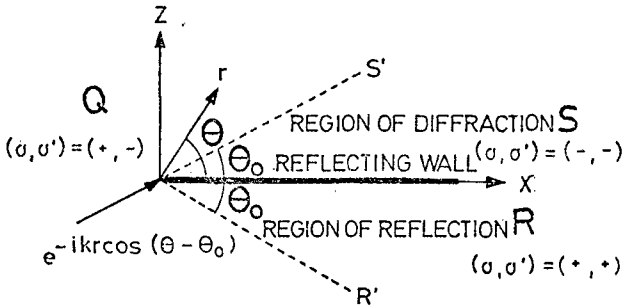


Fig. 3.1

Without mentioning the derivation of the solution function which had been handled in (12), the solution of the searched function is given with the period 4π .

$$F = f(r, \theta - \theta_0) \pm f(r, \theta + \theta_0) \quad (3.1)$$

$$f(r, \theta - \theta_0) = F(r, \theta, \theta_0) \cdot \frac{1+i}{2} \int_{-\infty}^{\sigma} e^{-i \frac{\pi}{2} t^2} dt$$

$$\sigma = 2 \sqrt{\frac{kr}{\pi}} \sin \frac{1}{2} (\theta - \theta_0)$$

Putting the result in equation (3.1) we get the solution of the diffraction problem:

$$F(r, \theta) = e^{-ikr \cos(\theta - \theta_0)} \cdot \underbrace{\left(\frac{1+i}{2} \int_{-\infty}^{\sigma} e^{-i \frac{\pi}{2} t^2} dt \right)}_{\Psi(\sigma)} \pm e^{-ikr \cos(\theta + \theta_0)} \cdot \underbrace{\left(\frac{1+i}{2} \int_{-\infty}^{\sigma'} e^{-i \frac{\pi}{2} t^2} dt \right)}_{\Psi(\sigma')} \quad (3.2)$$

$$\sigma' = -2 \sqrt{\frac{kr}{\pi}} \sin \frac{1}{2} (\theta + \theta_0)$$

In this case the integral $\Psi(\sigma)$ can be written in a similar way

$$\Psi(\sigma) = \frac{1+i}{2} \left(\int_{-\infty}^0 e^{-i \frac{\pi}{2} t^2} dt + \int_0^{\sigma} e^{-i \frac{\pi}{2} t^2} dt \right)$$

Using the LAPLACE-integral after the first integral

$$\int_0^{\infty} -e^{-\alpha \tau^2} d\tau = \frac{1}{2} \sqrt{\frac{\pi}{\alpha}}$$

and splitting up the second integral into a real and an imaginary part, we get:

$$\psi(\sigma) = \frac{1+i}{2} \left(\left(\frac{1-i}{2} \right) + \int_0^{\sigma} \cos \frac{\pi}{2} t^2 dt - i \int_0^{\sigma} \sin \frac{\pi}{2} t^2 dt \right)$$

$$\psi(\sigma) = \frac{1+i}{2} \left(\frac{1-i}{2} + M - i N \right),$$

by which

$$M = \int_0^{\sigma} \cos \frac{\pi}{2} t^2 dt$$

$$N = \int_0^{\sigma} \sin \frac{\pi}{2} t^2 dt$$

M and N are the FRESNEL-integrals.

To discuss the physical problems, in fig.3.1 the lines OS' and OR' are marked as are the shadow borders that are generated through the incoming and reflected wave.

We get three regions S, Q, R. σ and σ' possess a special sign in each of these parts.

That is, for e.g., in the area S:

$$\sigma^{(\pm)} = (-) 2 \sqrt{\frac{k \cdot r}{\pi}} \sin \left(\frac{1}{2} (\theta^{(\pm)} \theta_0) \right)$$

$$\theta - \theta_0 < 0 \Rightarrow \sigma < 0$$

$$\theta + \theta_0 > 0 \Rightarrow \sigma' < 0$$

That is why the regions (fig.3.1) have the following arrangements of signs

$$S - \text{region} \quad (\sigma, \sigma') = (-, -)$$

$$Q - \text{region} \quad (\sigma, \sigma') = (+, -)$$

$$R - \text{region} \quad (\sigma, \sigma') = (+, +)$$

The wave-heights in the three regions finally result in the following solutions:

a) In the region of the geometrical shadow $\sigma < 0, \sigma' < 0$

$$F(r, \theta) = \psi(-\sigma) e^{-ikr \cos(\theta - \theta_0)} + \psi(-\sigma') e^{-ikr \cos(\theta + \theta_0)}$$

b) in the unshadowed region $\sigma > 0, \sigma' < 0$

$$F(r, \theta) = e^{-ikr \cos(\theta - \theta_0)} - \left\{ \begin{array}{l} \psi(\sigma) e^{-ikr \cos(\theta - \theta_0)} + \\ + \psi(-\sigma') e^{-ikr \cos(\theta + \theta_0)} \end{array} \right\}$$

c) in the reflecting region $\sigma > 0, \sigma' > 0$

$$F(r, \theta) = \begin{array}{l} \text{incident wave} \\ e^{-ikr \cos(\theta - \theta_0)} \end{array} + \begin{array}{l} \text{reflected wave} \\ e^{-ikr \cos(\theta + \theta_0)} \end{array} \quad (3.3)$$

$$- \left(\psi(-\sigma) e^{-ikr \cos(\theta - \theta_0)} + \psi(-\sigma') e^{-ikr \cos(\theta + \theta_0)} \right)$$

diffracted wave

This solution in the reflecting region describes the MACH-reflection of gravity waves. Computing the wave-height in front of the wall (stem-height) it is

$$\frac{H_S}{H} = F(r, \theta)$$

The equation (3.3) was computed in Fortran IV.

4. HYDRAULIC MODEL AND TEST CONDITIONS

The wave₂ basin mentioned before has the dimensions 18.3 x 45.0 m², the test area was 11.0 x 45 m². The lateral limitations (guide vanes) in the direction of the wave orthogonals have been installed to control the energy entry of the waves. The length of the reflecting wall has been 7,32 m or 9.80 m respectively. Opposite to the wavemakers, a wave absorber has been installed in the basin consisting of a 7.6°-slope and specially-designed wave absorbing elements which have been tested in some pilot tests (2) before.

The basin is covered by an electrical driven measuring bridge movable with constant speeds of 5 m/min or 20 m/min for measuring the wave field. Resistance-type wave gauges (FÜHR-BÖTER (3)) were used for all tests. The wave heights were registered on a thermosensitive recording instrument.

Mechanical and electrically controlled wavemakers were used for the tests. The movement of the wave paddles was adjustable corresponding to the chosen wave parameters. The combined motion components (translatory + rotary) have been optimized using special tests for these machines at the FRANZIUS-INSTITUT.

Despite this, some model-caused inaccuracies in the experiments should be noted. The reflection-coefficient of the wave-absorber was in the order of 9%, but the error in reproducibility of single tests (measuring time 30 min.) was in the order of 2% only. In addition to the reflection at the wave absorber and re-reflection at the wavemaker-paddle, transverse oscillations in the wave field could be seen leading, to some extent, to disturbances in the wave field. But model-caused reflections have not been investigated in more detail within this programme and the test results reported in this paper show the original (unfiltered) data.

5. RESULTS OF MEASUREMENTS AND COMPARISON WITH DIFFRACTION

THEORY

The stem-height has been measured for different wave heights and wave lengths as a function of the direction of the incident wave as shown in fig. 5.1. The water depth was constant in all tests.

For example, the stem-heights for a wave length of $L = 100$ cm are plotted in fig. 5.1 to 5.4. The full lines show the theoretical development of the stem according to the diffraction theory. The stem-height increases with an increasing angle θ_0 of the incoming wave, as demonstrated by NIELSEN and HAGER (see fig.2.1). Because the theoretical and experimental results were in good agreement, the theoretical development of the stem as a function of the wall-length has been summarized for different angles θ_0 in fig. 5.5.

The oscillating data in fig. 5.1 to 5.4 may be explained by model-caused disturbances (see chapter 4). After about 2/3 of the wall length, the differences between the measured results and the theoretical curve are somewhat greater than at the beginning of the wall. These deviations may be explained by the fact that in addition, a diffraction wave is caused by the end of the wall which is superimposed with the wave field.

For the test conditions given in Tab.1 the stem-widths in front of the wall have also been measured (x/L spaced equidistantly). As an example fig. 5.6 shows the experimental and corresponding theoretical results for an angle of incidence $\theta_0 = 20^\circ$.

The agreement between theory and measurement can be seen rather well. The trough bounding the stem-width becomes steeper and narrower in proportion to the stem-wave's propagation along the wall.

The scattering of the data may be explained by model-caused disturbances (see chapter 4) as mentioned before.

Test conditions

H_I (cm)	L (cm)	θ_0 ($^\circ$)	d (cm)
2,2 3,6	100	10 15	25
4,3	150	20	
	200	25	

Tab. 1

The examples of fig. 5.1 to 5.6 have shown that the diffraction theory describes totally the development of the stem-height at the reflecting wall as well as the wave pattern in front of the wall (stem-width). A comparison with the measurements of NIELSEN and HAGER (see fig. 2.1) although qualitative, confirms both theoretical and experimental results.

The development of a second stem-wave as observed by NIELSEN with larger angles θ_0 of incidence and with a height also greater than double θ_0 the incident-wave height is approved by the diffraction theory, too. Fig.5.7 shows as an example, the water level normal to the wall at a distance of 5 wave lengths from the wall edge for wave-approach angles $\theta_0 = 20^\circ, 25^\circ$ and 30° . A second stem can be seen clearly.

6. CONCLUSION

Investigations with regular waves in connection with the so-called MACH-effect have only been carried out by NIELSEN and HAGER.

From supplementary measurements and by comparing the results with the diffraction theory, it has been proved that the MACH-reflection, i.e. the increase of a wave up to more than double the height of the incoming wave striking a wall with an acute angle, should not to be seen as an analogy to gas-dynamics.

On the contrary, the increase of the wave and the wave pattern before the wall is to be interpreted as a diffraction problem within a region of reflection.

STEM-HEIGHT AT VERTICAL WALL

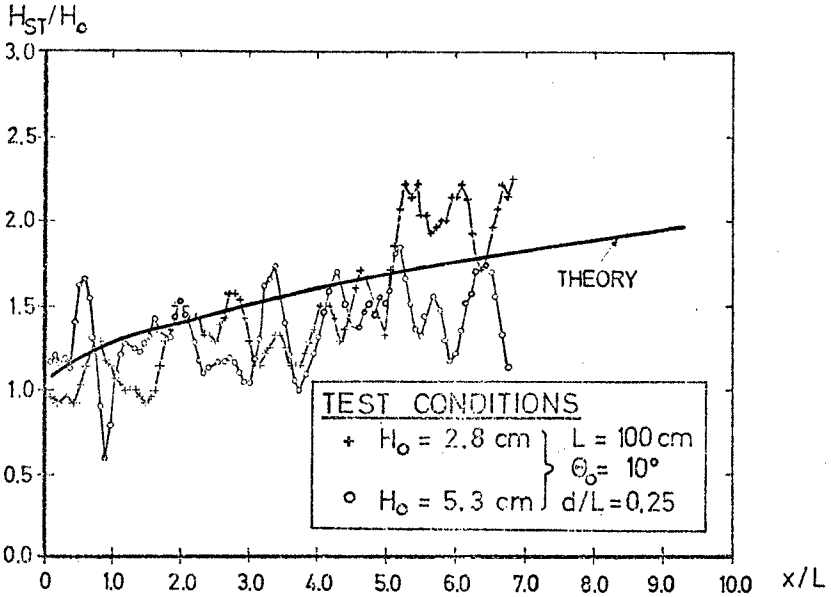


Fig. 5.1

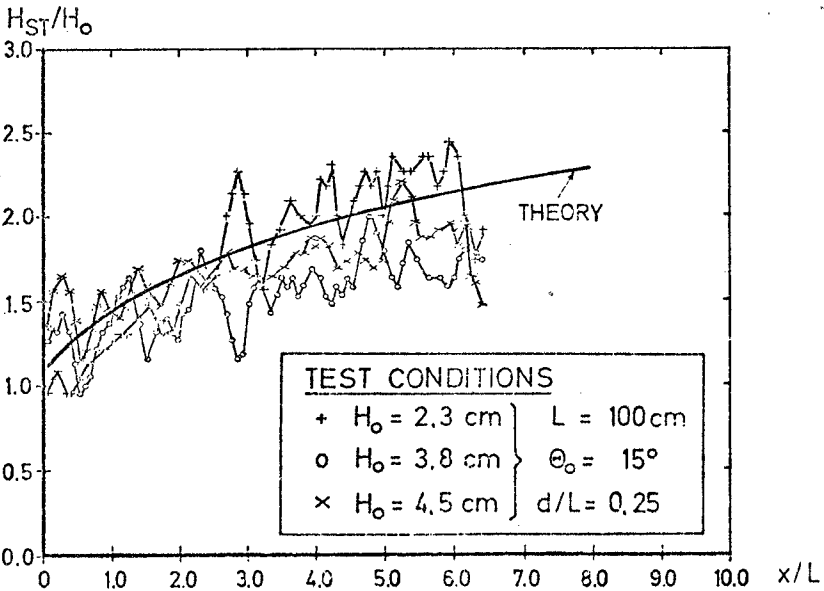


Fig. 5.2

STEM-HEIGHT AT VERTICAL WALL

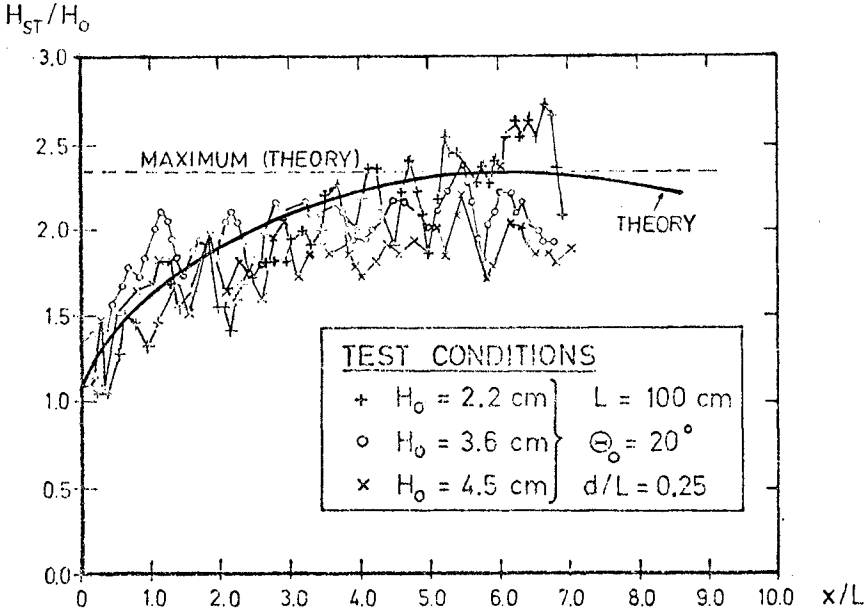


Fig. 5.3

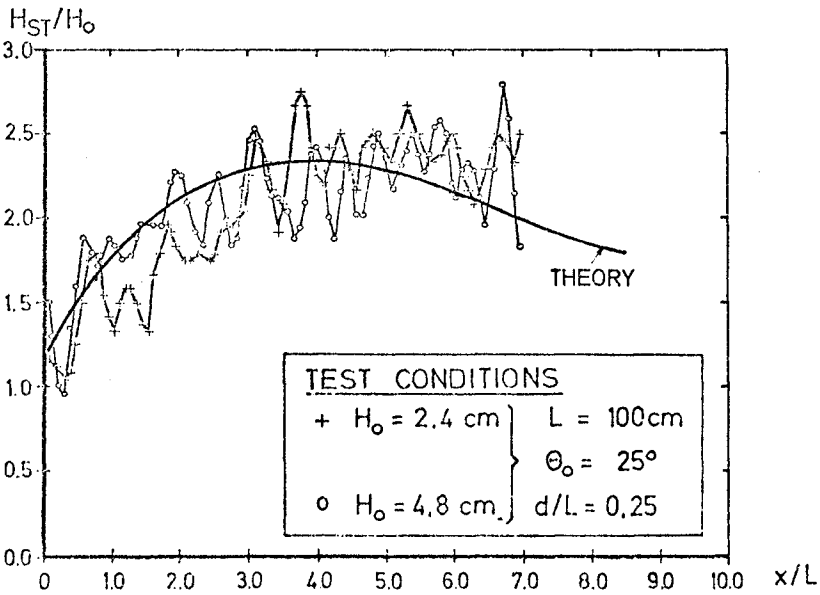


Fig. 5.4

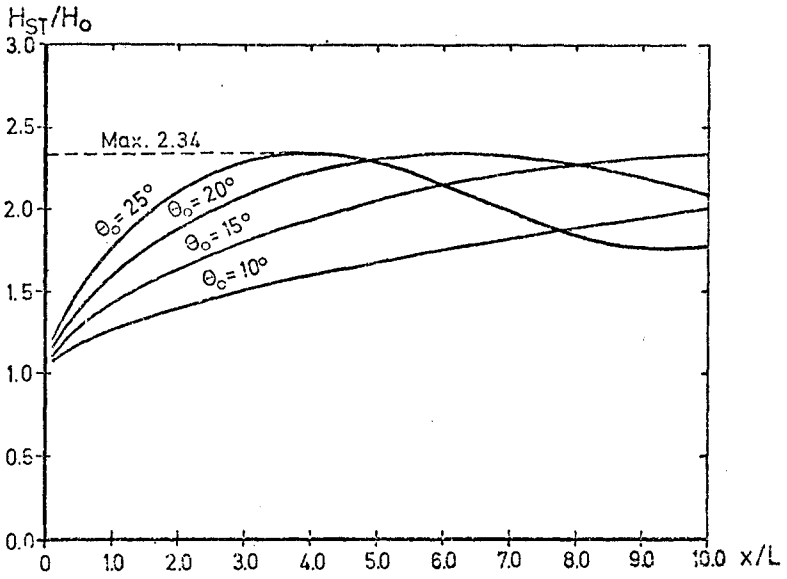


Fig. 5.5

stem-height at vertical wall
diffraction theory

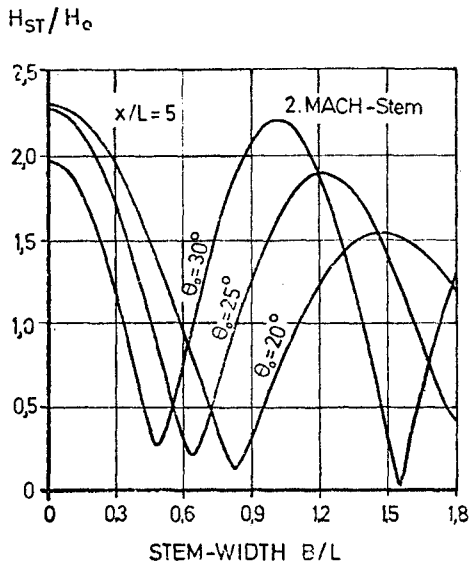


Fig. 5.7

Explanation of a 2.MACH-stem

STEM-HEIGHT IN THE REGION OF REFLECTION
 $\theta_0 = 20^\circ$

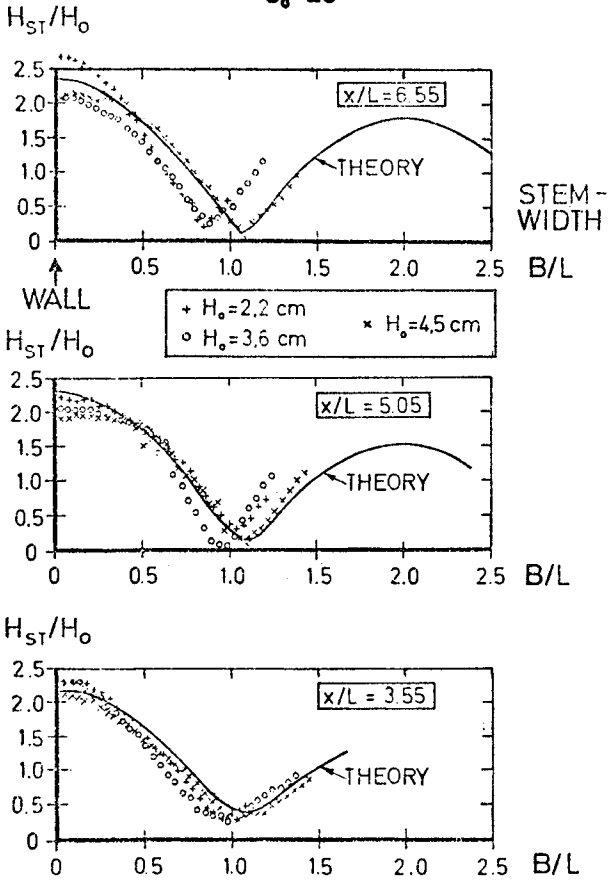


Fig. 5.6



Fig. 5.8

MACH-reflection in the test-basin with monochromatic waves

$\phi_i = 20^\circ$; $H = 5\text{cm}$; $L = 100\text{cm}$

7. REFERENCES

1. CHEN, T.C. Experimental study on the solitary wave reflection along a straight sloped wall at oblique angle of incidence, U.S.Army, Corps of Engineers, Beach Erosion Board, Tech. Memo.No. 124, 24 pp., March 1961
2. FALLDORF, W. Modellversuche zur Reflexion von Wellen an Dämpfungseinbauten, Diplomarbeit am Lehrstuhl für Verkehrswasserbau, TU Hannover, 1971, unveröffentlicht
3. FÜHRBÖTER, A. Einige elektrische Meßverfahren im wasserbaulichen Versuchswesen, Mitteilungen des Franzius-Instituts für Grund- und Wasserbau der Technischen Universität Hannover, Heft 17, 1960
4. HAGER, M. Untersuchungen über MACH-Reflexion an senkrechter Wand, Mitteilungen des Franzius-Instituts für Wasserbau und Küsteningenieurwesen der Technischen Universität Hannover, Heft 42, 1975
5. NIELSEN, A.H. Diffraction of periodic waves along a vertical breakwater for small angles of incidence, Univ.of Calif., Berkeley, IER Rech. Rept. HEL-1-2, 83 pp., Dec. 1962
6. PENNEY, W.G.
and
PRICE, A.T. The diffraction theory of sea waves and the shelter afforded by breakwaters, Philos. Transactions of the Royal Society of London, Series A, No. 882, Vol. 224, pp. 236-253, March 1952
7. PERROUD, P.H. The solitary wave reflection along a straight vertical wall at oblique incidence, Univ. of Calif., Berkeley, IER Tech.Rept.99-3,93 pp.,Sept.1957

8. SIGURDSSON, G.
and
WIEGEL, R.L. Solitary wave behavior at concave
barriers . I.E.R. Series 89, Issue 7,
Hyd. Eng. Lab., Wave Research Pro-
ject. Univ. of Calif.
9. SONDERFORSCHUNGS-
BEREICH 79,
TU HANNOVER Finanzierungsantrag 1975/76 des Teil-
projekts C2, Juni 1974, unveröffent-
licht
10. SOMMERFELD, A. Vorlesungen über theoretische Physik,
Optik, Bd. 4, 1959
11. SOMMERFELD, A. Vorlesungen über theoretische Physik,
partielle Differentialgleichungen
der Physik, Bd. 6, 1959
12. SOMMERFELD, A. Mathematische Theorie der Diffraktion,
Mathematische Annalen, Bd. 47, p. 317,
1896
13. WIEGEL, R.L. Oceanographical Engineering, Prentice-
Hall, 1964

CHAPTER 47

ACTION OF NON-LINEAR WAVES AT A SOLID WALL

by

Mohamed S. Nasser¹, M.ASCE and John A. McCorquodale², AM.ASCE

ABSTRACT

A one-dimensional finite difference model is developed to simulate the action of long non-linear shallow water waves at a solid barrier. A damping parameter is introduced to account for the centrifugal effects in the incident wave. A stability criterion for $\Delta t/\Delta x$ is suggested. The numerical predictions of reflection and run-up compare satisfactorily with experimental results.

INTRODUCTION

The phenomenon of run-up and reflection resulting from water waves impinging on breakwaters is an important problem in coastal engineering. Breakwaters are designed to avoid excessive overtopping. On the other hand, reflection causes local disturbances that persist for some distance outside of the breakwater.

This paper presents a one-dimensional, finite difference model simulating wave motion in front of a vertical, solid breakwater. The discretization of the solution domain is constrained

¹Assistant Professor, Department of Civil Engineering, Concordia University, SGW Campus, Montreal, Quebec, Canada.

²Professor, Department of Civil Engineering, University of Windsor, Windsor, Ontario, Canada.

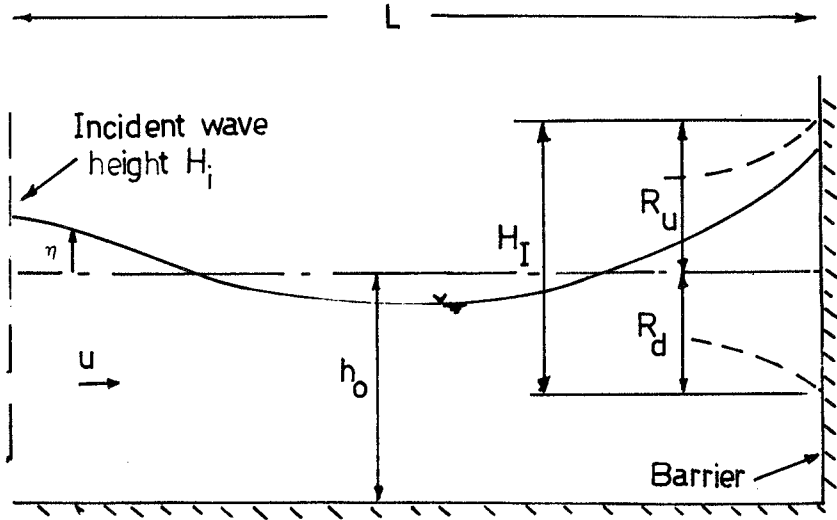


Fig. 1. Definition of Problem

by the characteristic directions to improve numerical convergence and stability. The model predicts wave run-up and rush-down on the breakwater as well as the reflection coefficient. Long, shallow, non-breaking waves are considered in the analysis, and the model is capable of treating both symmetric and asymmetric waves. The model should aid in designing vertical solid breakwaters and is being modified to accommodate sloping sections.

DEVELOPMENT OF MODEL

Figure 1 defines some of the variables of the study. Assuming long, shallow water waves, i.e., approximately hydrostatic pressure distribution, it can be shown that the governing equations of motion and continuity are, respectively (1, 4):

$$\frac{\partial u}{\partial t} + u \frac{\partial u}{\partial x} + g \frac{\partial \eta}{\partial x} = -gS_f \quad (1)$$

$$\frac{\partial \eta}{\partial t} + u \frac{\partial \eta}{\partial x} + (h_o + \eta) \frac{\partial u}{\partial x} = 0 \quad (2)$$

where u = horizontal velocity; η = perturbation height with respect to the still water level, h_o ; g = acceleration of gravity; S_f = friction slope = $\frac{u|u|}{C_f(h_o + \eta)}$; C_f = Chezy friction factor; the bed is assumed horizontal.

Eq. 1 describes fairly accurately the motion of long linear waves. For non-linear, i.e., asymmetric waves, hydrodynamic pressure may become appreciable. However, in this study, Eqs. 1 and 2 are applied to asymmetric waves with an allowance for additional damping due to centrifugal effects. Assuming a sinusoidal wave (Fig. 2), the total head loss, h_t , between sections 1 and 2 may be expressed as

$$h_t = h_f + \epsilon h_c \quad (3)$$

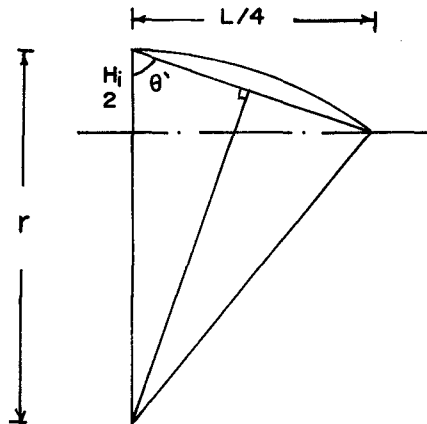
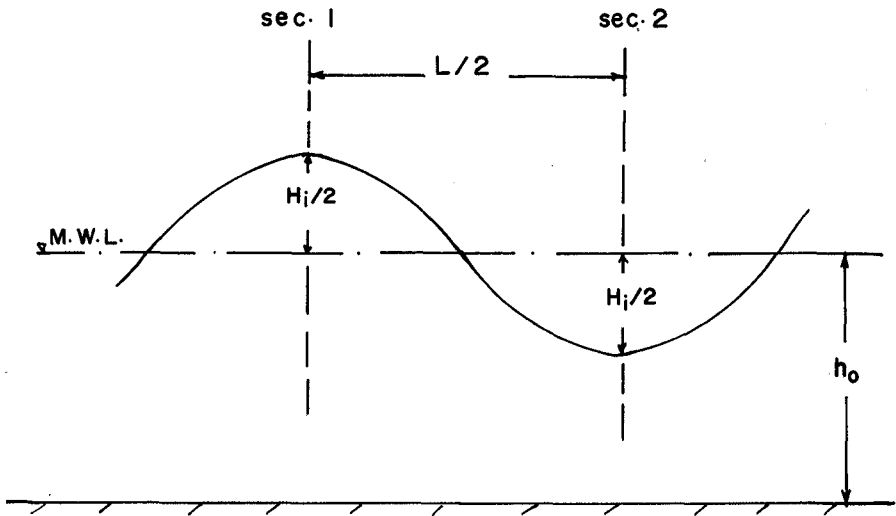


Fig. 2. Approximation of Centrifugal Effect

in which h_f = frictional head loss between sections 1 and 2; h_c = difference in centrifugal pressure head between the two sections; ϵ = empirical constant.

Applying Newton's second law to compute the approximate centrifugal pressure, it can be shown that h_c is given by (3)

$$h_c = \frac{2h_o}{gr} v^2 \quad (4)$$

where r = radius of curvature of water surface;
 v = mean velocity in the vertical.

The frictional head loss, h_f , can be represented by

$$h_f = \frac{v^2 L}{2C_f^2 h_o} \quad (5)$$

in which L is the incident wave length.

Also, the total head loss, h_t , may be assumed as

$$h_t = \frac{v^2 L}{2C_t^2 h_o} \quad (6)$$

where C_t is the equivalent Chezy factor accounting for both frictional and centrifugal effects.

Substituting Eqs. 4 through 6 into 3 and rearranging, gives

$$C_t = \sqrt{\frac{gLrC_f^2}{gLr + 4\epsilon h_o^2 C_f^2}} \quad (7)$$

From Fig. 2, the value of r may be approximated as follows:

$$r \approx [(H_i/2)^2 + (L/4)^2]/H_i \quad (8)$$

Based on a correlation with laboratory experiments, Eq. 7 takes the form

$$c_t = \sqrt{\frac{gLrC_f^2}{gLr+1.2h_o^2C_f^2}} \quad (9)$$

Since r varies inversely with wave steepness, S , Eq. 9 indicates the energy dissipation due to centrifugal action increases with wave steepness.

In order to proceed to the finite difference formulation, η is made dimensionally identical to u through the transformation

$$c = \sqrt{g(h_o + \eta)} \quad (10)$$

which represents a local wave celerity utilized as a measure of η .

The equations of motion and continuity, in terms of c , along with the total differentials of u and c constitute the hyperbolic system of equations governing the phenomenon as given by the matrix form (1):

$$\begin{bmatrix} 1 & u & 0 & 2c \\ 0 & c & 2 & 2u \\ dt & dx & 0 & 0 \\ 0 & 0 & dt & dx \end{bmatrix} \begin{Bmatrix} \frac{\partial u}{\partial t} \\ \frac{\partial u}{\partial x} \\ \frac{\partial c}{\partial t} \\ \frac{\partial c}{\partial x} \end{Bmatrix} = \begin{Bmatrix} -gS_f \\ 0 \\ du \\ dc \end{Bmatrix} \quad (11)$$

The above system yields the following positive and negative characteristic directions:

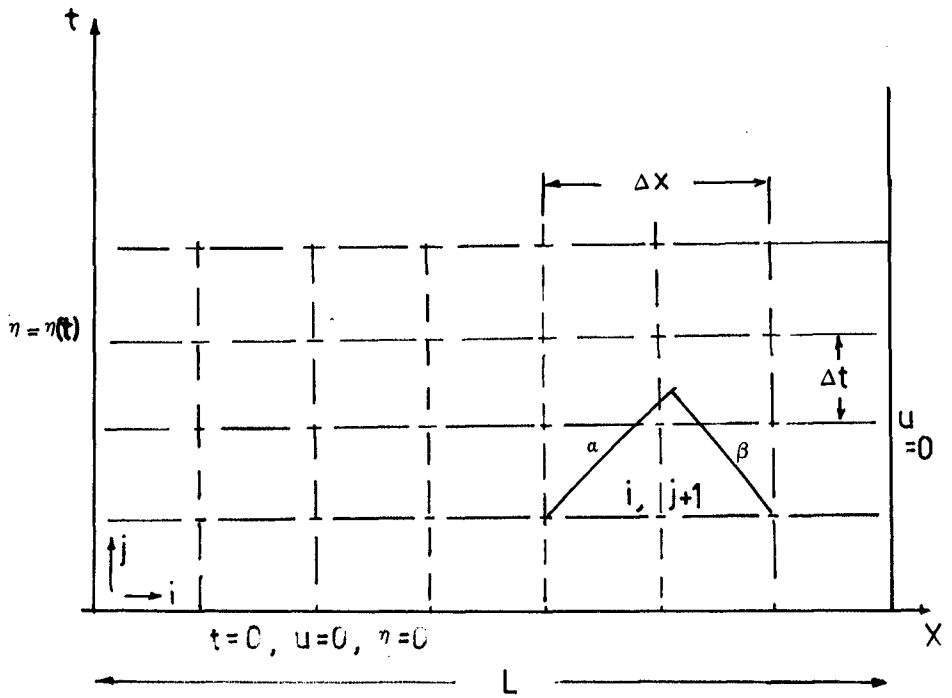


Fig. 3. Boundary Conditions and Discretization of the $x-t$ Plane

$$\alpha = \frac{dx}{dt} \Big|_+ = u + c \quad (12)$$

$$\beta = \frac{dx}{dt} \Big|_- = u - c \quad (13)$$

Based on these directions, the condition,

$$\frac{\Delta t}{\Delta x} \leq \frac{1}{2} (u+c)^{-1} \quad (14)$$

is obtained and used, initially, to control the finite difference, x-t plane (Fig. 3) for stability and convergence (5). The equations of motion and continuity, from Eq. 11, are discretized using central differences in space and forward differences in time, viz.

$$u(i,j+1) = u(i,j) - \frac{\Delta t}{\Delta x} \{u(i,j)[u(i+1,j)-u(i-1,j)] + 2c(i,j)[c(i+1,j)-c(i-1,j)] + g\Delta x S_f(i,j)\} \quad (15)$$

$$c(i,j+1) = c(i,j) - \frac{\Delta t}{\Delta x} \{u(i,j)[c(i+1,j)-c(i-1,j)] + [c(i,j)/2][u(i+1,j)-u(i-1,j)]\} \quad (16)$$

Eqs. 15 and 16 were used to advance the solution from initially still water conditions, i.e., $u = 0$ and $c = \sqrt{gh_0}$.

The boundary condition at the right end of the solution domain, is zero normal velocity at all times. The incident wave is originated in the model at one wave length away from the breakwater; this is the minimum distance required to ensure the generation of at least one loop and one node in the standing wave pattern. The boundary condition simulates the vertical displacement of the incident wave which is represented by a composite as shown in Fig. 4. The amplitudes, A_1 and A_2 , and the periods, T_1 and T_2 , are proportioned so that volume continuity is satisfied which leads to

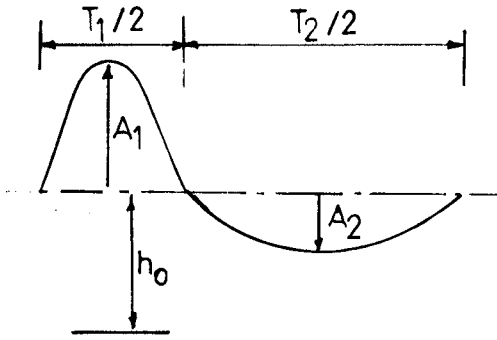


Fig. 4. Composite Input Wave

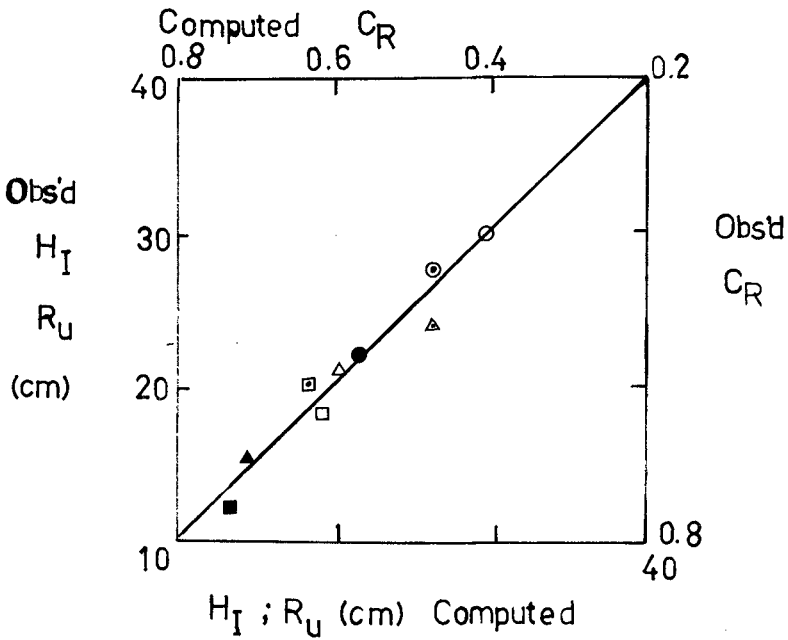


Fig. 5. Comparison of Observed and Predicted Values

$$A_1/A_2 = T_2/T_1 \quad (17)$$

In order to calculate the unknown dependent variable at each boundary, the value of the dependent variable specified by the boundary condition at time (j+1) was included in the calculation. This was achieved by combining the equations of motion and continuity, and discretizing the augmented equation by forward differences in space and time. Assuming that the boundary is located at the ith column, the unknown celerity at the breakwater is calculated by the α -characteristic difference equation,

$$c(i, j+1) = c(i, j) + 2 \frac{\Delta t}{\Delta x} \{c(i, j)u(i-1, j)/2 - c(i, j)[c(i, j)-c(i-1, j)]\} \quad (18)$$

Likewise, a β -characteristic difference equation is used to find the unknown velocity at the left boundary, i.e.,

$$u(i, j+1) = u(i, j) + 2[c(i, j+1)-c(i, j)] + \frac{2\Delta t}{\Delta x} \{2[u(i, j)-c(i, j)][c(i+1, j)-c(i, j)] - [u(i, j)-c(i, j)][u(i+1, j)-u(i, j)] - \Delta x g S_f(i, j)u(i, j)/2\} \quad (19)$$

Throughout the solution, the values of velocity, celerity and the non-linear friction term were improved, within each time increment, by an iterative procedure.

VERIFICATION OF MODEL

A laboratory investigation was conducted to evaluate the proposed mathematical model. The Test flume was 45.8 cm wide and 11 m long with plexiglass walls and aluminum bed. The slider-crank, wave machine used has adjustable stroke and speed that were selected to produce shallow water waves. The breakwater

was simulated by a vertical plexiglass barrier, located at 9.2 m away from the intermediate position of the wave paddle. Wave experiments were performed within the following range of variables:

h_o (cm)	22 - 38
H_i (cm)	4 - 24
Wave Period, T (sec)	2 - 5.8

In the experimental procedure, the stroke and speed were set so as to minimize surface disturbances and secondary waves. The incident wave celerity, c , was determined, prior to the interference of reflection, using a stop watch to time the movement of a wave peak over different distances. The wave period, T , was taken as the average of the rotation time of a point marked on the flywheel of the wave machine. The product of the values of c and T yielded the wave length, L . After a few wave traverses, an asymmetric standing wave pattern was observed to develop and stabilize with nodes and loops forming, alternately, at almost every quarter wave length. The measured loop height, h_p , and node height, h_n , were used to find the "apparent" incident wave height, H_i , and the "apparent" reflected wave height, H_r , according to the linear wave theory, i.e.,

$$H_i = \frac{1}{2} (h_p + h_n) \quad (20)$$

$$H_r = \frac{1}{2} (h_p - h_n) \quad (21)$$

The "apparent" reflection coefficient, C_R , was defined as:

$$C_R = H_r/H_i \quad (22)$$

The maximum limits of run-up, R_u , and rush-down, R_d , bounding the impact wave height, H_T , at the breakwater were recorded. The experimental measurements are estimated to have been within an accuracy of about ± 2 cm.

When the mathematical model was operated, using the equality condition in Eq. 14 with $u \approx c \approx \sqrt{gh_0}$, the procedure was numerically unstable. This instability is thought to originate from the boundary conditions, especially the incident wave boundary condition. The development of Eq. 14 does not consider this type of boundary condition. In order to obtain stability, it was necessary to reduce the time step to between 1/5 and 1/10 of limiting value in Eq. 14.

The stable model was run for the equivalent of 5 wave periods and the third, fourth and fifth periods were used to obtain average values for h_p , h_n , R_u , R_d and H_I . The apparent values of H_I and H_T were calculated from Eqs. 20 and 21, respectively. It is noted that the non-linear values of C_R are much less than for linear waves.

An attempt to make a third order Stokes correction to both experimental and numerical reflection coefficients was unsuccessful because most of the waves had high H_I/h_0 and low h_0/L . Similarly, second or third order Stokes waves were not suitable to describe the observed incident waves. Fifth or higher order Stokes waves or cnoidal waves can be used with the model but more computation time would be required. The crests and troughs of the composite incident waves can be established using information presented by Bretschneider (2).

In Fig. 5 some experimental values of R_u , H_I and C_R are compared with those predicted by the model.

CONCLUSIONS

The simplified numerical model gives representation values for wave reflection and run-up at a solid barrier under attack by long non-linear shallow water waves. Numerical stability was achieved by reducing the method of characteristic time step to about 1/10 of its limiting value. An empirical damping parameter is introduced to account for centrifugal effects in the non-linear waves.

ACKNOWLEDGMENT

This research was supported, in part, by the National Research Council of Canada.

REFERENCES

1. Abbott, M.B., "An Introduction to the Method of Characteristics", American Elsevier Co., New York, 1966.
2. Bretschneider, C.L., "Selection of Design Waves for Offshore Structures", Trans. ASCE, Paper No. 3026, 1960.
3. Chow, V.T., "Open-channel Hydraulics", McGraw-Hill Co., New York, 1959.
4. Henderson, F.M., "Open Channel Flow", The Macmillan Co., New York, 1966.
5. Smith, C.D., "Numerical Solution of Partial Differential Equations", Oxford University Press, London, 1965.

CHAPTER 48

ESTIMATION OF INCIDENT AND REFLECTED WAVES IN RANDOM WAVE EXPERIMENTS

by

Yoshimi Goda and Yasumasa Suzuki

Marine Hydrodynamics Division

Port and Harbour Research Institute, Ministry of Transport

Nagase, Yokosuka, Japan

ABSTRACT

A technique to resolve the incident and reflected waves from the records of composite waves is presented. It is applicable to both regular and irregular trains of waves. Two simultaneous wave records are taken at adjacent locations, and all the amplitudes of Fourier components are analyzed by the FFT technique. The amplitudes of incident and reflected wave components are estimated from the Fourier components, and the incident and reflected wave spectra are constructed by smoothing the estimated periodograms. The wave resolution is effective in the range outside the condition of the gauge spacing being even integer of half wavelength. The ratio of incident and reflected wave energies in the effective resolution range is employed in estimating the overall reflection coefficient. The incident and reflected wave heights are estimated from the composite wave heights by energy consideration.

INTRODUCTION

The importance of wave irregularity concept in coastal engineering study and application is now rightly recognized by many researchers and engineers. A rapid increase in the number of random wave generators in hydraulic laboratories in the world testifies it. With this situation, many researchers are keenly feeling the necessity of developing various experimental techniques inherent to irregular waves. Resolution of incident and reflected waves in a continuous, irregular wave system is one of the most needed techniques. If the resolution becomes feasible, then we can make tests of reflective coastal structures in continuous runs without worrying about the multi-reflection of irregular waves between a wave paddle and a reflective structure. Otherwise, we have to employ a tedious

procedure of repeating a number of short runs of different wave sequences, each of which must be stopped before the return of re-reflected waves by the wave paddle to the structure. Not only the procedure is laborious, but also the test waves are deficient in the spectral component of high frequency band due to the wave dispersion unless a special wave generation technique is employed.

The authors present a resolution technique, which involves a simultaneous recordings of wave profiles at two adjacent stations in a wave flume. The technique is similar to the one employed by Kajima [1] and by Thornton and Calhoun [2], but the use of the Fast Fourier Transform technique in yielding the Fourier components of all the frequency resolutions makes the calculation simple and versatile. For example, the technique is applicable to regular waves too, which has provided a means of calibration of resolution. The paper describes the principle of resolution technique and its accuracy with supporting data. Examples of application in the authors' experiments are also discussed.

PRINCIPLE OF RESOLUTION TECHNIQUE

Suppose we have a multi-wave-reflection system of regular waves in a wave flume. Waves generated by a wave paddle propagate forward in the flume and are reflected by a test structure. The reflected waves propagate back to the wave paddle and are re-reflected. The re-reflected waves propagate forward again and the process is repeated until the multi-reflected waves are fully attenuated. Thus the wave system can be regarded as a superposition of a number of waves propagating in the positive and negative directions of the coordinate, x (see Fig. 1). The waves propagating in each direction form a single train of progressive waves as a whole, because of the constancy of wave frequency (see Appendix). The wave train in the positive direction is called the incident waves and that in the negative direction is called the reflected waves. Let the amplitude of superposed incident waves be a_I and that of reflected waves be a_R . Then these waves are described to have the general form of

$$\left. \begin{aligned} \eta_I &= a_I \cos(kx - \sigma t + \epsilon_I), \\ \eta_R &= a_R \cos(kx + \sigma t + \epsilon_R), \end{aligned} \right\} \quad (1)$$

where η_I and η_R are the surface elevations of incident and reflected waves, k is the wave number of $2\pi/L$ with L being the wavelength, σ is the angular frequency of $2\pi/T$ with T being the wave period, and ϵ_I and ϵ_R are the phase angles of incident and reflected waves.

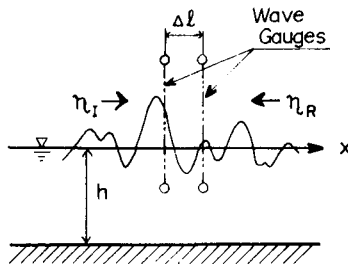


Fig. 1 Definition Sketch

Further, we suppose that the surface elevations are recorded at two adjacent stations of x_1 and $x_2 = x_1 + \Delta l$. The observed profiles of composite waves will be

$$\left. \begin{aligned} \eta_1 &= (\eta_I + \eta_R)_{x=x_1} = A_1 \cos \sigma t + B_1 \sin \sigma t, \\ \eta_2 &= (\eta_I + \eta_R)_{x=x_2} = A_2 \cos \sigma t + B_2 \sin \sigma t, \end{aligned} \right\} \quad (2)$$

where,

$$\left. \begin{aligned} A_1 &= a_I \cos \phi_I + a_R \cos \phi_R, \\ B_1 &= a_I \sin \phi_I - a_R \sin \phi_R, \\ A_2 &= a_I \cos(k\Delta l + \phi_I) + a_R \cos(k\Delta l + \phi_R), \\ B_2 &= a_I \sin(k\Delta l + \phi_I) - a_R \sin(k\Delta l + \phi_R), \end{aligned} \right\} \quad (3)$$

$$\left. \begin{aligned} \phi_I &= kx_1 + \varepsilon_I, \\ \phi_R &= kx_1 + \varepsilon_R. \end{aligned} \right\} \quad (4)$$

Equation 3 can be solved to yield the estimate of

$$\left. \begin{aligned} a_I &= \frac{1}{2|\sin k\Delta l|} \sqrt{(A_2 - A_1 \cos k\Delta l - B_1 \sin k\Delta l)^2 + (B_2 + A_1 \sin k\Delta l - B_1 \cos k\Delta l)^2}, \\ a_R &= \frac{1}{2|\sin k\Delta l|} \sqrt{(A_2 - A_1 \cos k\Delta l + B_1 \sin k\Delta l)^2 + (B_2 - A_1 \sin k\Delta l - B_1 \cos k\Delta l)^2}. \end{aligned} \right\} \quad (5)$$

In the calculation, the dispersion relation of the following is presumed to hold:

$$\sigma^2 = gk \tanh kh. \quad (6)$$

Actual wave profiles usually contain some higher harmonics. Use of the Fourier analysis enables to estimate the amplitudes of A_1 , B_1 , A_2 , and B_2 for the fundamental frequency as well as for higher harmonics. The amplitudes of incident and reflected waves, a_I and a_R , are then estimated by Eq. 5. This is the procedure to be taken for regular wave tests.

The principle of resolution is the same for irregular waves with that for regular waves, because irregular waves can be treated as the superposition of a large number of component waves with the constant amplitudes and frequencies. The number of component waves which can be analyzed in irregular wave records is one half of the number of data sampling. By means of the Fast Fourier Transform technique, the amplitudes of A_1 to B_2 can be calculated for all the component waves and the corresponding amplitudes of a_I and a_R are estimated by Eq. 5. The spectra of incident and reflected waves can be obtained by smoothing the periodograms based on the estimates of a_I and a_R .

ESTIMATE OF INCIDENT AND REFLECTED WAVE HEIGHTS

Calibration of Resolution Technique with Regular Waves

The resolution technique was first applied to regular waves for the purpose of calibration. Trains of waves were generated in a wave flume temporarily built with a partition wall in a wave basin. At the generator side the partition wall was terminated with a gap of about 60 cm and a part of reflected waves could be dispersed into the wave basin. The wave absorber in the flume was built with crushed stone in the slope of 10 to 1. Two wave periods of 1.088 and 1.410 sec were employed. The mean wave heights were 8.98 and 9.23 cm, respectively, at the water depth of 43 cm. The spacing between two wave gauges was varied from $\Delta\ell = 10$ to 250 cm, and continuous wave records of 102.4 sec long were taken at the sampling period of $\Delta t = 1/15$ sec. The records were analyzed for the Fourier components of $f = 0$ to $f = 7.5$ Hz with the frequency resolution of $\Delta f = 0.0084$ Hz. Then, Eq. 5 was applied to estimate a_I and a_R for all the frequencies.

As expected, the resultant estimates showed clear peaks around the frequencies of $f = 0.92$ and 0.70 Hz and their harmonics. The peaks were not confined to one frequency resolution band because of wave fluctuations and signal noises; they were spread in a few neighbouring bands. Thus, the sum of the estimated amplitudes of three to four continuous frequency bands around the peaks was employed as the representative amplitudes of incident and reflected waves. These amplitudes are plotted in Fig. 2 against the ratio of gauge spacing $\Delta\ell$ to the wavelength L . The reference amplitude, a_0 , is the mean of estimated incident wave amplitudes in the range of $\Delta\ell/L < 0.4$ and $0.6 < \Delta\ell/L < 0.9$. The estimated amplitudes of a_I and a_R are seen to diverge around the relative spacing of $\Delta\ell/L = n/2$ with $n = 0, 1, 2, \dots$, at which the divisor of Eq. 5, $\sin k\Delta\ell$, becomes null.

Figure 3 is a similar result of analysis for the case of perfect reflection with the same waves. Divergence of estimated amplitudes around $\Delta\ell/L = n/2$ is observed. The decrease of the reference amplitude a_0 is considered due to the selection of test wave periods which corresponded to the antiresonance condition of the wave flume setup. (The reflective wall was located at the distance of 15 m from the wave paddle.) The divergence of estimated amplitudes is due to the amplification of noises and errors as the divisor of $\sin k\Delta\ell$ approaches 0. For the purpose of application, the zone of inaccuracy (or the effective range of resolution from the other viewpoint) needs to be specified. This will be discussed in the next section.

It is indicated in Fig. 2 that the estimates of a_I and a_R are quite stable except for the diverging zone. The estimates of a_R are several per cent of a_0 , being in agreement with the characteristics of wave absorber. The estimates of a_R for the case of perfect reflection in Fig. 3 are almost equal to a_0 , indicating the reflection coefficient being nearly 1.0. Additional test for a submerged, upright breakwater with the crest submergence of 6 cm yielded the estimate of reflection coefficient of 0.44 to 0.55 (refer to Fig. 6). The conventional method of the measurement of reflection coefficient by means of nodal and antinodal wave heights yielded the reflection coefficient of 0.51 to 0.59 for this case. These estimates of a_R as a whole indicate their consistency with respect to reflecting conditions tested.

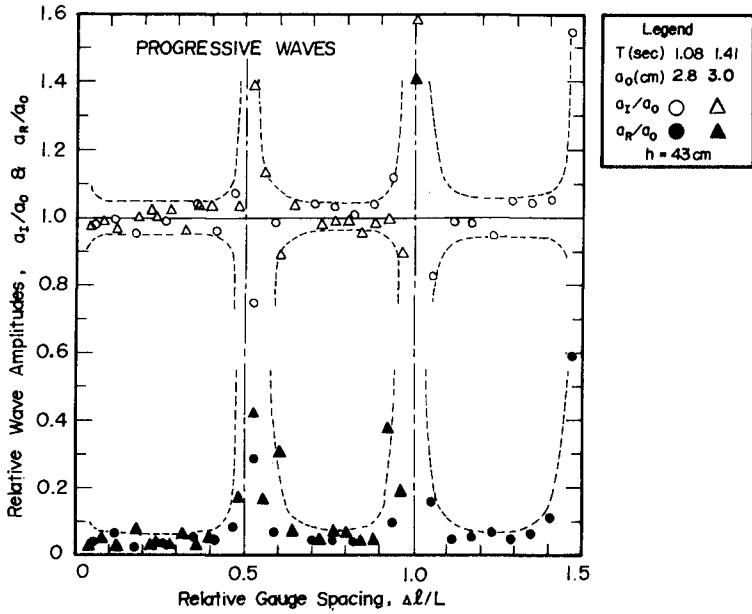


Fig. 2 Variations of Resolved Amplitudes with Wave Gauge Spacing (1)

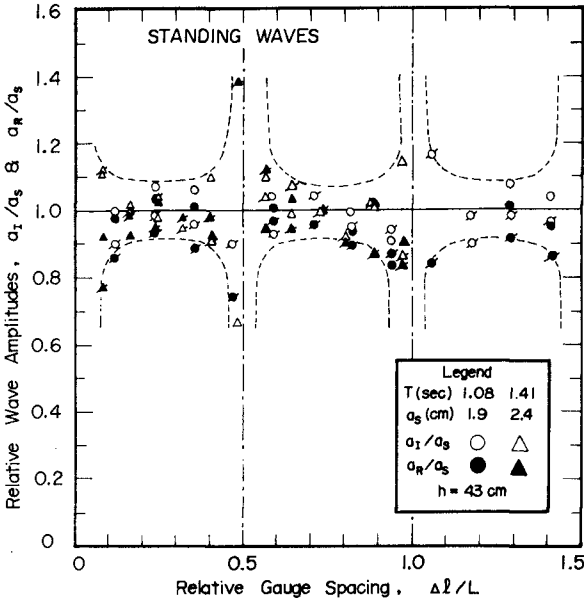


Fig. 3 Variations of Resolved Amplitudes with Wave Gauge Spacing (2)

Application for Irregular Waves

Figure 4 is an example of spectral resolution of irregular waves. A submerged, upright breakwater with its crest at the depth of 6 cm from the mean water level was set at the distance of 15.0 m from the wave paddle. The wave gauges were located at the distance of 4.80 and 5.00 m from the breakwater face. The observed waves at the gauge locations had the significant height of $H_{1/3} = 8.2$ cm and period of $T_{1/3} = 1.44$ sec. The spectra shown in Fig. 4 are the average of three runs with the same source spectrum but with different wave sequences. The duration of a record was 68.3 sec and the data were sampled at the interval of 1/15 sec. The resolved spectra of incident and reflected waves in Fig. 4 indicate the divergence of spectral density near $f = 0$ and $f = 1.97$ Hz; the latter frequency corresponds to the wavelength of $L = 40$ cm or $\Delta\lambda/L = 0.5$. The result is a natural consequence of Figs. 2 and 3. Therefore, the resolution is effective only in some range of wave frequency. The situation is illustrated in Fig. 5.

There may be several methods to estimate the incident and reflected wave heights on the basis of spectral resolution such as shown in Fig. 4. The authors propose the following procedure. First, the effective range of resolution is set for a given gauge spacing; in practise, the latter is to be selected for a given wave condition. The lower and upper limits of frequency, f_{\min} and f_{\max} , are better chosen by a preliminary test for progressive waves. As a reference, the following guideline may be consulted:

$$\left. \begin{aligned} f_{\min} : \Delta\lambda/L_{\max} &= 0.05, \\ f_{\max} : \Delta\lambda/L_{\min} &= 0.45, \end{aligned} \right\} \quad (7)$$

where L_{\max} and L_{\min} are the wavelengths corresponding to f_{\min} and f_{\max} , respectively. Equation 7 is based on the calibration with regular waves such as shown in Figs. 2 and 3 as well as the frequency-wise examination of resolution results of irregular waves. There is a possibility that the effective range may be taken slightly wider than that given by Eq. 7; e.g., f_{\min} may be chosen so that $\Delta\lambda/L_{\max} = 0.03$.

The second step is to evaluate the energies of resolved incident and reflected waves, E_I and E_R , contained between f_{\min} and f_{\max} , i.e.,

$$\left. \begin{aligned} E_I &= \int_{f_{\min}}^{f_{\max}} S_I(f) df, \\ E_R &= \int_{f_{\min}}^{f_{\max}} S_R(f) df. \end{aligned} \right\} \quad (8)$$

The integrations are to be performed on the raw spectra of periodograms without any smoothing to avoid the effect of divergence of resolved amplitudes near $\Delta\lambda/L = n/2$.

The third step is to estimate the overall coefficient of reflection by

$$K_R = \sqrt{E_R/E_I}. \quad (9)$$

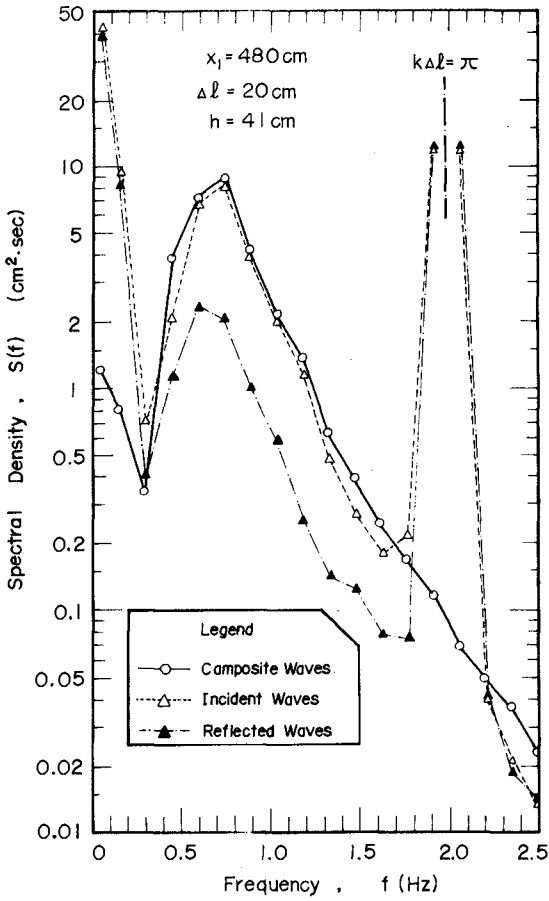


Fig. 4 Example of Spectral Resolution for a Submerged, Upright Breakwater

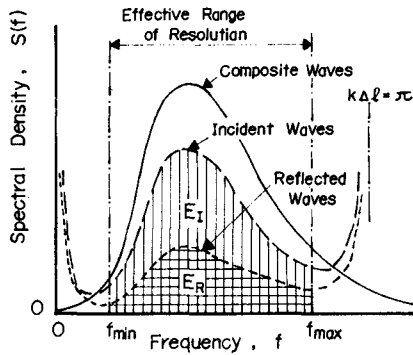


Fig. 5 Illustration of Spectral Resolution

This equation is based on the relation of irregular wave heights being proportional to the square root of wave energy. Then the incident and reflected wave heights, H_I and H_R , are calculated as

$$\left. \begin{aligned} H_I &= \frac{1}{\sqrt{1 + K_R^2}} H_S, \\ H_R &= \frac{K_R}{\sqrt{1 + K_R^2}} H_S, \end{aligned} \right\} \quad (10)$$

where H_S denotes the significant or other representative wave height of composite waves observed by the two wave gauges; the mean of two gauges are employed.

Equation 10 is based on the two presumptions. The first is that the energy of composite waves appearing as the result of superposition of multiple trains of irregular waves is the sum of the energies of individual wave trains. The second is that the proportionality of representative wave heights to the square root of wave energy holds for such composite waves too, regardless of the directions of individual wave trains. The first one may be taken as an axiom for the analysis of irregular waves. The second one can be proved by a numerical simulation of irregular waves. The proof of it by the field data is almost impossible. But the applicability of the Rayleigh distribution of wave heights to ocean waves with multi-peaked spectra or the existence of the relation of $H_{1/3} \approx 4.0 \eta_{rms}$ for such waves [3,4] provides a supporting evidence for the presumption, because a multi-peaked spectrum usually indicates a coexistence of wind waves and swell propagating in the different directions.

Selection of Wave Gauge Stations in a Wave Flume

The present technique of wave resolution can be employed in the vicinity of reflective structure if the magnitude of reflection coefficients only is of concern. Figure 6 shows the variation of resolved, incident and reflected wave amplitudes against the distance of wave gauge from the face of submerged breakwater. The test was done with regular waves at the conditions same with those shown in Figs. 2 and 3. The test result indicates that the wave gauge may be set as near as $0.1 L$ to the reflective face. The dashed line for closed triangles and the dash-dot line for closed circles show the average values of a_R/a_S for the range of $x_1/L > 0.2$. The test was also carried out with irregular waves by shifting the wave gauge position from $x_1 = 1$ to 480 cm, while the wave gauge spacing was fixed at $\Delta x = 20$ cm. The wave spectra shown in Fig.4 were taken from the data of this test. The reflection coefficient defined by Eq. 9 is found to vary little except at $x_1 = 1$ cm, as shown in Fig. 7.

For the estimation of incident and reflected wave heights, on the other hand, wave gauges are required to be away from both the test structure and wave paddle. This is because the composite wave height H_S used in Eq. 10 fluctuates in the neighbourhood of a reflective boundary. The fluctuation of wave heights of irregular standing waves can be calculated with spectral information as demonstrated by Ishida [5]. For a component wave with the angular frequency of σ and wave number of k , the surface elevation of standing waves at the distance of x_1 from the reflective boundary is given as:

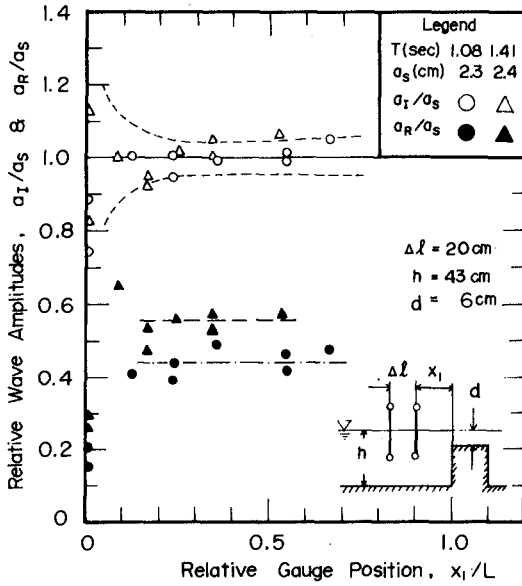


Fig. 6 Variations of Incident and Reflected Wave Amplitudes with Wave Gauge Position

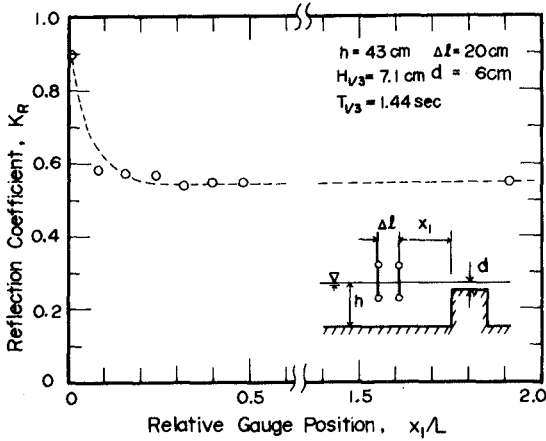


Fig. 7 Variation of Reflection Coefficient of Irregular Waves with Wave Gauge Position

$$\begin{aligned}
 \eta &= a_I \cos(kx_1 - \sigma t) + K_R a_I \cos(kx_1 + \sigma t) \\
 &= (1 + K_R) a_I \cos kx_1 \cos \sigma t + (1 - K_R) a_I \sin kx_1 \sin \sigma t \\
 &= \sqrt{1 + 2K_R \cos 2kx_1 + K_R^2} \cos(\sigma t - \varepsilon_1),
 \end{aligned} \tag{11}$$

where,

$$\varepsilon_1 = \tan^{-1} \frac{(1 - K_R) \sin kx_1}{(1 + K_R) \cos kx_1}. \tag{12}$$

The root-mean-square value of surface elevation of standing waves, $(\eta_S)_{\text{rms}}$, is calculated with the relation of Eq. 11 and the information of incident wave spectrum, $S_I(f)$, as

$$(\eta_S)_{\text{rms}}^2 = \int_0^{\infty} (1 + 2K_R \cos 2kx_1 + K_R^2) S_I(f) df. \tag{13}$$

The significant or any other representative height of irregular standing waves is then obtained as

$$H_S = \frac{(\eta_S)_{\text{rms}}}{(\eta_I)_{\text{rms}}} H_I. \tag{14}$$

Figure 8 is an example of the fluctuation of irregular standing wave heights; the test condition is the same with those of Figs. 4 and 7. The curves represent the result of calculation by Eq. 13 and 14. The incident wave spectrum was obtained from the measurement of progressive waves without a reflective structure. The reflection coefficient of 1.0 and 0.55 were used for the case of a high vertical wall and that of submerged, upright breakwater, respectively. The observed heights of significant waves are represented with the open and closed circles. Though the observed heights are somewhat larger than the calculation possibly because of the multi-reflection and nonlinearity effects, the magnitude of fluctuation is quite in agreement with the calculation. Such the fluctuation of standing wave heights directly affects the estimate of incident and reflected wave heights as the consequence of Eq. 10. The fluctuation becomes negligibly small, however, at the distance of more than one wavelength. A similar phenomenon will take place in front of a wave paddle with the high reflectivity. Therefore, the wave gauges for wave resolution are recommended to be located at the distance of more than one wavelength from both the test structure and wave paddle.

ACCURACY OF THE ESTIMATES OF INCIDENT AND REFLECTED WAVE HEIGHTS

Possible Sources of Inaccuracy

There are several sources of inaccuracy in the present resolution technique. They are:

- 1) Deviation from the dispersion relation of Eq. 6 due to nonlinear effect and others,
- 2) Existence of nonlinear harmonic terms in progressive waves,

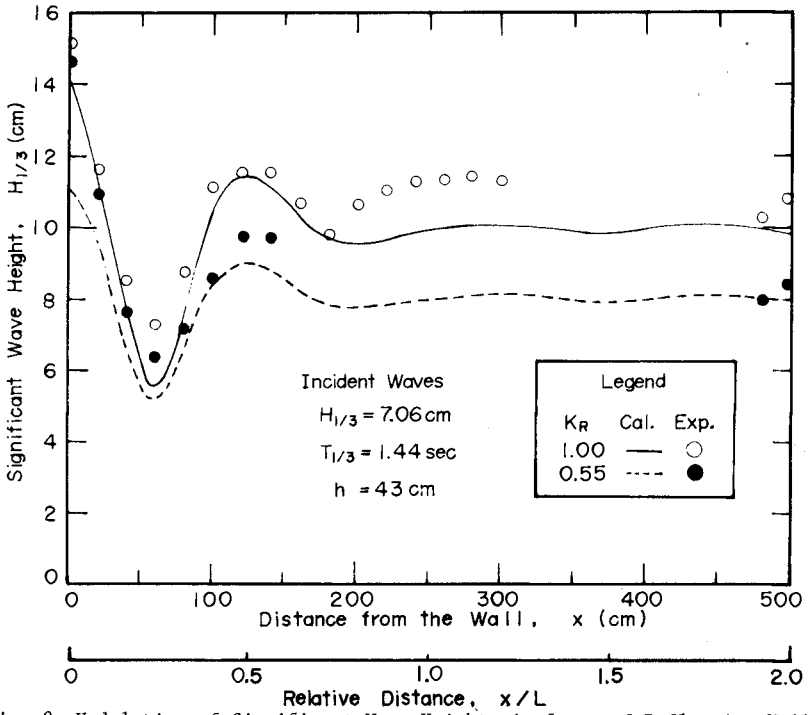


Fig. 8 Undulation of Significant Wave Heights in front of Reflective Wall

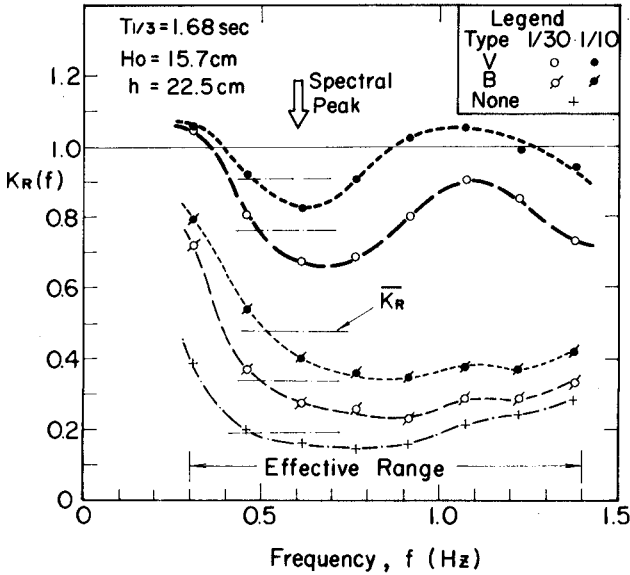


Fig. 9 Frequency-wise Resolution of Reflection Coefficient of Seawalls

- 3) Generation of nonlinear interaction terms in standing waves,
- 4) Appearance of transversal waves and other disturbances in a wave flume,
- 5) Signal noises.

The dispersion relation of Eq. 6 is for the small amplitude waves. The regular waves of finite amplitudes are known to deviate from that relation. The wave number decreases for progressive waves [6,7], while it increases for standing waves in relatively shallow water [8,9]. The existence of the deviation for wind waves has also been reported [10], though not examined yet for mechanically generated irregular waves. Any deviation from Eq. 6 leads to the inaccuracy in the estimates of a_I and a_R in Eq. 5 because the resolution is based on the relative phase difference of $k\Delta\lambda$. The inaccuracy is greatest at the condition of $k\Delta\lambda = n\pi$ where $\sin k\Delta\lambda = 0$ and smallest at $k\Delta\lambda = (n+1/2)\pi$ where $\sin k\Delta\lambda = 1$. The divergence of a_I and a_R in Figs. 2 and 3 or $S_I(f)$ and $S_R(f)$ in Fig. 4 is due to the deviation of wave number from Eq. 6 to a large extent.

The second source of inaccuracy affects not the spectral peak of irregular waves nor the fundamental component of regular waves but the estimates of harmonic components. The regular waves of finite amplitudes are accompanied by the harmonics which propagate with the same celerity with the fundamental one to keep the wave profile permanent despite of their high frequencies. For such harmonic components Eq. 6 does not apply and errors may be evoked. The situation in a wave flume is more complicated, however. There are free waves with the frequencies of harmonics and nonlinear interacting waves, both of which contribute to the generation of travelling, secondary waves in a wave flume [11, 12, 13]. Similar situation exists in case of irregular wave experiments, though the analysis of nonlinear harmonics and their behaviour is difficult. At present, we should content ourselves by taking caution in the interpretation of the resolution results in the range of harmonic components.

When two trains of finite amplitude waves interact such as in the case of wave reflection, there appear nonlinear interaction terms the frequencies of which are the sums and differences of fundamental and harmonic components. Calculation of the third order solution of partial standing waves [9] has shown the generation of the terms of $\cos[(\bar{k} + 2\Delta k)x \pm 3\sigma t]$ and $\cos[(3\bar{k} \pm 2\Delta k)x \mp \sigma t]$ in which \bar{k} and Δk are the mean and difference of the wave numbers of incident and reflected waves in the standing wave system for the angular frequency of σ . The phase velocities of these nonlinear interaction terms are different from those of free waves having the angular frequency of σ or 3σ , and therefore they become a source of inaccuracy in wave resolution. Similar phenomenon occurs in irregular waves having frequency spectra, though detailed analysis will be complicated.

An indication of such nonlinear effects can be seen in Fig. 9, which shows the frequency-wise representation of reflection coefficient of a seawall with vertical face (type V) and a seawall with a mound of artificial concrete blocks (type B) on the bottom slope of 1 in 10 and 1 in 30. Thin dash-dot lines indicate the overall reflection coefficient estimated by Eq. 9 for the effective range of resolution. Humps of $K_R(f)$ around twice the spectral peak frequency for the type V seawall may be due to the nonlinear effects. When the reflection coefficient is low such as for the type B seawall or the case of no seawall, the humps become insignificant. Experiments with waves of longer periods have exhibited another

humps around thrice the spectral peak frequencies. Therefore, the frequency-wise representation of reflection coefficient should be treated with due regard for the nonlinear effects. The employment of the overall reflection coefficient by Eq. 9 is based on this consideration.

Estimation of Accuracy of the Resolution Technique

Indication of the accuracy of the present technique is seen in Figs. 2, 3, and 6 as the dispersions of resolved amplitudes. In case of progressive waves and partial standing waves, the dispersion is of the order of $\pm 5\%$ except for the diverging zone, while it becomes about two times in the case of standing waves. These dispersions are partly due to the variability of waves in a laboratory flume, and the error involved in the resolution technique is considered less than those indicated in these figures.

The effect of nonlinear terms of finite amplitude waves upon the wave resolution is difficult to quantitate. It should be mentioned here that the conventional method of estimating the reflection coefficient with the observed heights of maxima and minima of partial standing wave systems is much susceptible to the nonlinear effects. For example, the conventional method tends to yield an apparent reflection coefficient of low value for a highly reflective structure and a correction is required [9]. The conventional method is essentially for the fundamental frequency component of small amplitude waves. It cannot detect other associated components such as the harmonics, but it is influenced by them instead.

The overall accuracy of wave height estimation is considered rather small for incident waves. Suppose that the significant height of $H_G = 20$ cm was measured for an irregular standing wave system and the reflection coefficient of the structure in test is 0.6. The true incident wave height is $H_I = 17.1$ cm by Eq. 10. If the wave resolution have produced the estimate of $K_R = 0.7$ by some reason, the estimate of H_I would be 16.4 cm, which is smaller than the true value by 4%. When the reflection coefficient is small, the error in the estimate of incident wave height becomes negligible.

EXAMPLES OF APPLICATIONS

The resolution technique has been employed in the authors' laboratory for irregular wave experiments since 1973. A series of wave overtopping tests have been carried out for seawalls with vertical faces and other types of seawalls [14]. Trains of irregular waves of about 200 waves long were generated and exerted upon model seawalls. The total amount of overtopped water was measured for each wave train, which yielded the rate of wave overtopping per second per unit length of seawall. At the same time, wave records of composite waves were taken by the two gauges in the offshore, and the incident and reflected wave heights were estimated from those records by the present technique. Figure 9 for the frequency-wise reflection coefficient is an example of the results of wave overtopping tests. Without the use of the resolution technique, the tests would have been much laborious since a number of short wave trains would have had to be employed to avoid the multi-wave-reflection problem. The tests have produced a set of twelve diagrams for the estimation of wave overtopping rate of seawalls under irregular wave actions, covering the full range of water depth from the offshore to the foreshore.

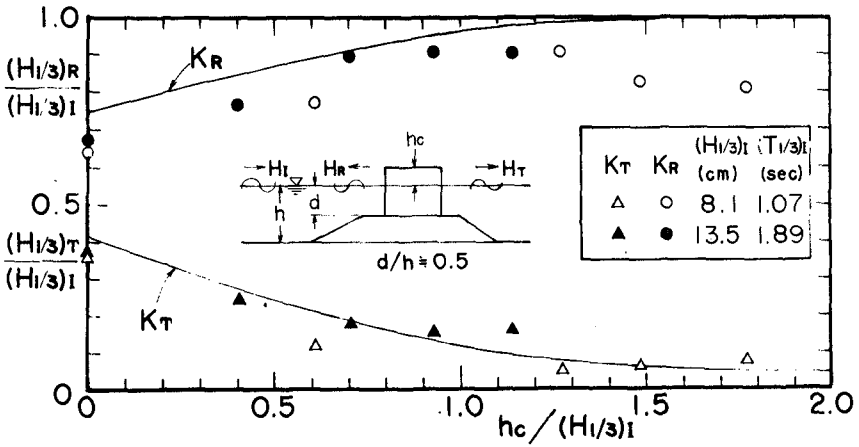


Fig. 10 Transmission and Reflection Coefficients of a Composite Breakwater

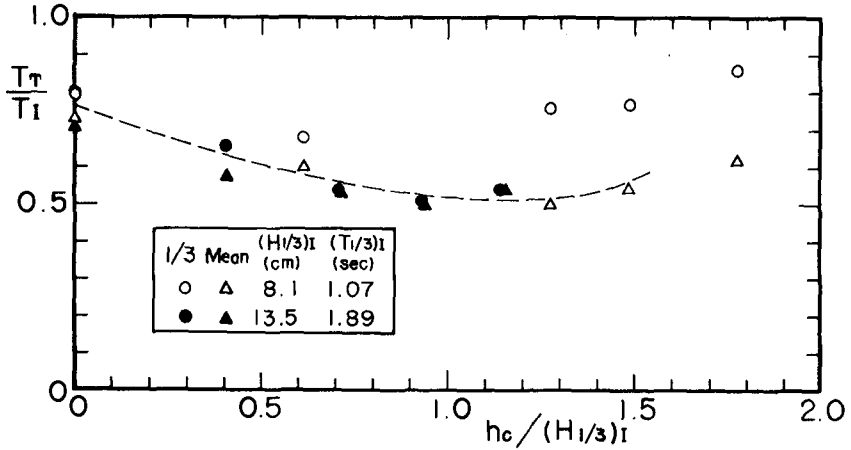


Fig. 11 Change of Wave Periods by Wave Transmission over a Composite Breakwater

Another example of wave tests for continuous wave actions is the wave transmission characteristics of a composite-type breakwater, which consists of a caisson rested upon a rubble mound. When the crest of breakwater is not high enough, some waves overtop it and new waves are generated behind it. The characteristics of transmitted waves by irregular wave actions can be revealed by experiments with continuous runs only. Figure 10 is a result of such experiments [15]. The ratio of significant height of transmitted waves to the incident significant wave height, $(H_{1/3})_T / (H_{1/3})_I$, as well as the reflection coefficient are plotted against the ratio of crest height to incident wave height, $h_c / (H_{1/3})_I$. The curves are those of regular waves previously formulated by the senior author [16]. The transmitted waves have two distinct properties. The one is the distribution of wave heights being broader than the Rayleighian. The second is the wave period being shorter than the incident waves. Figure 11 shows the latter characteristic. Both the mean and significant wave periods decrease to 50 to 80% of the incident wave periods.

The present resolution technique is also effective to detect the enhancement of harmonic components of waves through the interaction with structures. Figure 12 is one of such examples. A slit caisson with the opening ratio of 20% was tested for wave absorbing characteristics. As listed in the figure, the reflected wave height was estimated as 4.9 cm for the incident waves of $(H_{1/3})_I = 10.3$ cm and $T_{1/3} = 2.65$ sec, and the overall reflection coefficient was 48%. An interesting feature of the slit caisson is that it enhances the third harmonic component when it reflects waves. The feature has been predicted by Mei, Liu, and Ippen [17] in general form and is demonstrated in Fig. 12 as a hump of reflected wave spectrum around $3f_0 = 1.05$ Hz, where $f_0 = 0.35$ Hz corresponds to the spectral peak of incident waves. Though a caution should be taken in the interpretation of resolved harmonic components as discussed earlier, the result of Fig. 12 is judged to represent actual generation of the third harmonics because it is not observed in the spectrum of incident waves and the overall reflection coefficient is relatively low.

The enhancement of odd harmonic components by wave reflection was more conspicuous when the slit caisson was tested for regular waves. The undulation of wave heights by formation of partial standing wave system was obscured by the presence of odd harmonics and the conventional method for the measurement of reflection coefficient had difficulty to obtain the correct value of reflection coefficient.

The application of the present technique of wave resolution is not confined to the above examples. It is applicable to any wave test with regular or irregular trains of waves. Though the question of wave nonlinearity effects remains to be clarified, it will provide the most needed means to measure the coefficient of reflection of irregular waves.

CONCLUSIONS

A technique to resolve the incident and reflected waves from the records of composite waves has been proposed. Examination of the technique with wave tests has shown the followings:

- 1) The wave resolution is not possible around the condition of $\Delta\ell/L = n/2$ where $n = 0, 1, 2, \dots$. As a guideline, the wave resolution may be performed in the range of $0.05 < \Delta\ell/L < 0.45$.

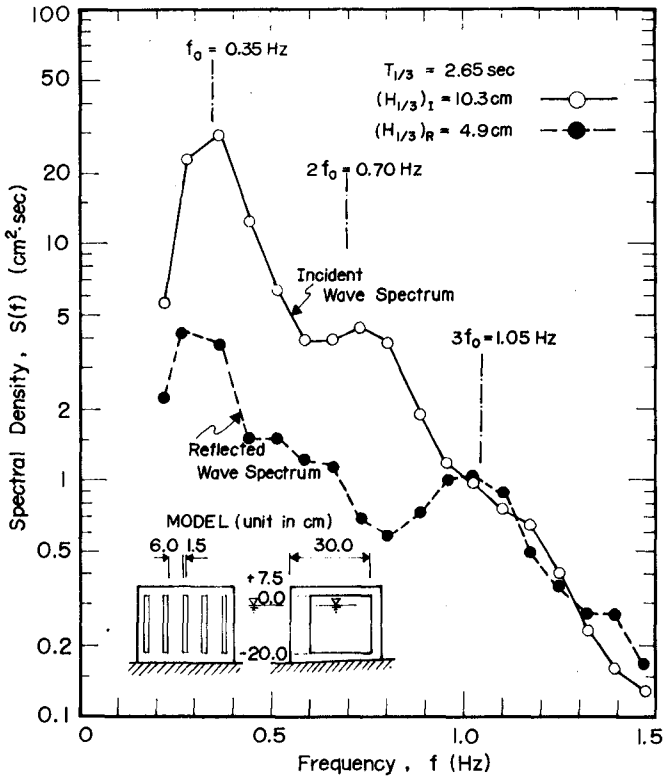


Fig. 12 Example of Spectral Resolution of a Slit Caisson

- 2) The wave gauges are recommended to be located at the distance of more than one wavelength from the test structure and wave paddle in the irregular wave test. In the regular wave test, the wave gauges may be set as near to the structure as at the distance of 0.2 L.
- 3) There remains the problem of nonlinear wave interaction which may affect the accuracy of the wave resolution technique.
- 4) The technique is effective in detecting the enhancement of odd harmonics in the wave reflection by a structure such as a slit caisson.

The authors sincerely express their thanks to Messrs. Yasuharu Kishira and Osamu Kikuchi, members of the authors' laboratory, for their earnest cooperation in carrying out the experimental verification.

REFERENCES

- 1) Kajima, R.: Estimation of incident wave spectrum in the sea area influenced by reflection, Coastal Engineering in Japan, Vol. 12, J.S.C.E., 1969, pp.9-16.
- 2) Thornton, E. B. and R. J. Calhoun: Spectral resolution of breakwater reflected waves, Proc. A.S.C.E., Vol. 98, No. WW4, 1972, pp.443-460.
- 3) Goda, Y. and K. Nagai: Investigation of the statistical properties of sea waves with field and simulation data, Rept. Port and Harbour Res. Inst., Vol. 13, No. 1, 1974, pp.3-37,(in Japanese).
- 4) Coda, Y.: Estimation of wave statistics from spectral information, Proc. Int. Symp. on Ocean Wave Measurement and Analysis, New Orleans, 1974, Vol. 1, pp.320-337.
- 5) Ishida, A.: Transformation of power spectra of wind-generated waves caused by reflection, Coastal Engineering in Japan, Vol. 15, J.S.C.E., 1972, pp.25-33.
- 6) Stokes, G. G.: On the theory of oscillatroy waves, Trans. Camb. Phil. Soc., Vol. 8, 1847.
- 7) Skjelbreia, L.: Stokes' third order approximation, Tables of function, Council on Wave Research, The Engineering Foundation, Berkely, 1958.
- 8) Tadjbaksh, I. and J. B. Keller: Standing surface waves of finite amplitudes, Jour. Fluid Mech., Vol. 8, 1960, pp.442-451.
- 9) Goda, Y. and Y. Abe: Apparent coefficient of partial reflection of finite amplitude waves, Rept. Port and Harbour Res. Inst., Vol. 7, No. 3, 1968, pp.3-58.
- 10) Hidy, G. M. and E. J. Plate: Wind action on water standing in a laboratory channel, Jour. Fluid Mech., Vol. 26, 1966, pp.651-687.
- 11) Hansen, J. B. and I. A. Svendsen: Laboratory generation of waves of constant form, Proc. 14th Coastal Engg. Conf., Copenhagen, 1974, pp.321-339.
- 12) Hulsbergen, C. H.: Origin, effect and suppression of secondary waves, Proc. 14th Coastal Engg. Conf., Copenhagen, 1974, pp.392-411.

- 13) Ishida, A.: On the characteristics of splitting solitons in shallow waters, Proc. 22nd Coastal Engg. Conf. in Japan, J.S.C.E., 1975, pp.41-46, (in Japanese).
- 14) Goda, Y., Y. Kishira, and Y. Kamiyama: Laboratory investigation on the overtopping rate of seawalls by irregular waves, Rept. Port and Harbour Res. Inst., Vol. 14, No. 4, 1975, pp.3-44, (in Japanese).
- 15) Goda, Y., Y. Suzuki, and Y. Kishira: Some experiences in laboratory experiments with irregular waves, Proc. 21th Coastal Engg. Conf. in Japan, J.S.C.E., 1974, pp.237-242, (in Japanese).
- 16) Goda, Y.: Re-analysis of laboratory data on wave transmission over breakwaters, Rept. Port and Harbour Res. Inst., Vol. 8, No. 3, 1969, pp.3-18.
- 17) Mei, C. C., P. L-F. Liu, and A. T. Ippen: Quadratic loss and scattering of long waves, Proc. A.S.C.E., Vol. 100, No. WW3, 1974, pp.217-239.

APPENDIX: MULTI-REFLECTED WAVES IN A LABORATORY FLUME

As described in the text, waves in a closed, laboratory flume may travel many times between a reflective model structure and the wave paddle as the result of wave reflections at the both boundaries. This composes a multi-wave-reflection system. Let the amplitude of initially generated waves be denoted by a_0 , the reflection coefficients of the test structure and wave paddle by r and R , respectively, and the distance between them by ℓ . Then the wave profile of multi-wave-reflection system can be expressed as an infinite series of

$$\begin{aligned} \frac{\eta}{a_0} = & \cos(\sigma t - kx) + R \cos(\sigma t + kx - 2k\ell) \\ & + r R \cos(\sigma t - kx - 2k\ell) + r R^2 \cos(\sigma t + kx - 4k\ell) \\ & + r^2 R^2 \cos(\sigma t - kx - 4k\ell) + r^2 R^3 \cos(\sigma t + kx - 6k\ell) \\ & + \dots \end{aligned} \quad (A.1)$$

where η is the surface elevation of waves, σ is the angular frequency of $2\pi f$, and k is the wave number of $2\pi/L$. The infinite series can be summarized after a few manipulations as a closed form of

$$\eta = \frac{a_0}{\sqrt{1 - 2rR \cos 2k\ell + r^2 R^2}} \{ \cos(\sigma t - kx + \theta) + R \cos(\sigma t + kx - 2k\ell + \theta) \} \quad (A.2)$$

where,

$$\theta = \tan^{-1} \left\{ \frac{r R \sin 2k\ell}{1 - r R \cos 2k\ell} \right\} \quad (A.3)$$

This proves the formation of two trains of waves propagating in the opposite directions as the result of multi-wave-reflections.

CHAPTER 49

DECOMPOSITION OF CO-EXISTING RANDOM WAVE ENERGY

Dennis B. Morden¹, Eugene P. Richey² and Derald R. Christensen³

INTRODUCTION

Of the several transformations that water waves may undergo, the phenomenon of reflection has received relatively little quantitative attention, although the analyst is sensitized to reflection in a qualitative way. Commonly the investigator is interested in progressive or transmitted waves and the characteristics of reflected waves and the energy dissipated during the reflection process are of little consequence. There are, however, certain structures, such as piers, floating bridges, bulkheads, etc., where waves reflecting from the structure can be of concern if they should impinge on a site or shoreline sensitive to a new, or changed, wave climate. Quantitative assessment of the energy dissipated during reflection is essential to the evaluation of devices which are intended to reduce site interaction problems and/or reduce the loading on structures and anchor systems.

This paper examines the analysis of sea states where wind-generated waves and their reflection co-exist. Using the results of a field test the characteristics of co-existing sea states are discussed. The decomposition of these waves to obtain separate incident and reflected wave spectra requires two applications of spectral analysis. First, spectral estimates are computed from co-existing wave data acquired simultaneously at multiple, fixed sensor locations. These spectra are then divided into frequency increments and the amplitude associated with each increment used as an independent input into a technique to decompose the co-existing waves into appropriate incident and reflected wave spectra. Because the incremental amplitudes of the original spectral estimates are used as independent inputs, the shape and accuracy of these original estimates naturally have a profound influence on the final separated wave spectra. Various spectral estimating techniques were used on the field data and the accuracy of the results were compared to three validation criteria.

Because the findings and discussion are validated primarily by the analysis of specific data it seems appropriate to first describe the relevant features of the field test. Though the present study involves deep water waves and zero transmission, the principles apply equally well to any situation where wave reflections are of interest.

TEST DESCRIPTION

Test Site - Sea states composed of wind-generated deep water waves and their reflections were examined in Lake Washington which adjoins Seattle.

-
1. Research Engineer, The Boeing Company, Seattle, Washington, U.S.A.
 2. Professor of Civil Engineering, Department of Civil Engineering, University of Washington, Seattle, Washington, U.S.A.
 3. Research Engineer, Department of Civil Engineering, University of Washington, Seattle, Washington, U.S.A.

Washington, U.S.A. A sixty-foot wide floating bridge with a seven-foot draft traverses the lake in a generally east-west direction and is exposed to waves generated over a 2.8 mile effective fetch by the prevailing southerly winds of the region. Near the center of the span a test site was established to evaluate the waves reflected from the solid vertical walls of the bridge pontoons (which extended 11 feet above SWL) and those reflected from a perforated wall breakwater appended to the pontoon. For the waves occurring at the site the bridge forms an excellent barrier, completely eliminating transmitted waves. The 200-foot depth of the lake is sufficient to classify all waves as deep water waves. During storms reflected wave trains are apparent as far as 4,000 feet south of the bridge.

Figure 1 depicts an aerial close-up of the test site. Co-existing incident and reflected waves were monitored using pressure transducers located five feet below stillwater level (SWL). Analog data were recorded simultaneously at four locations: two in front of a breakwater and two more 150 feet away in front of the solid vertical wall of the bridge. Viatran Model PTB 101 transducers were rigidly mounted 7'9" and 12'9" away from each barrier, as shown in the figure. Morden (1975) shows details of the apparatus and test procedure.

Perforated Wall Breakwater - To produce reflected waves with amplitudes substantially different from those at the solid vertical bridge wall, a perforated vertical wall and solid (but removable) bottom were appended to the bridge, as shown in Figure 2. This "L"-shaped structure and resulting chamber form a perforated wall breakwater of the type originated by Jarlan (1961). The test breakwater section was long enough to avoid diffraction effects on the outer wave sensors, and terminated by solid vertical end plates to maximize the two-dimensional response of the chamber.

Several authors have tested and analyzed the behavior of this type of breakwater; their results have been reviewed by Morden (1975). Richey and Sollitt (1970) successfully model the behavior of the breakwater in monochromatic waves as a linear damped oscillator. As such the amplitude and phase angle of a wave are altered during the reflection process, but its frequency is not changed.

The reflection coefficient for the breakwater in monochromatic waves (Fig.3) is defined as the ratio of reflected to incident wave heights, and has a minimum value at a particular frequency, which depends primarily upon breakwater geometry. This definition must be modified for the random wave case, and becomes the square root of the ratio of the reflected to incident energy over a specified frequency band width, i.e.,

$$R = \sqrt{\frac{\sigma_r^2}{\sigma_i^2}} \quad (1)$$

CHARACTERISTICS OF CO-EXISTING* SEA STATES

Ippen (1966, p. 58) points out that the average potential energy density (i.e., potential energy per unit surface area) is a function of distance from

* Sea states composed of the superposition of wind-generated waves and their reflections. Superposition of unrelated waves are not considered.

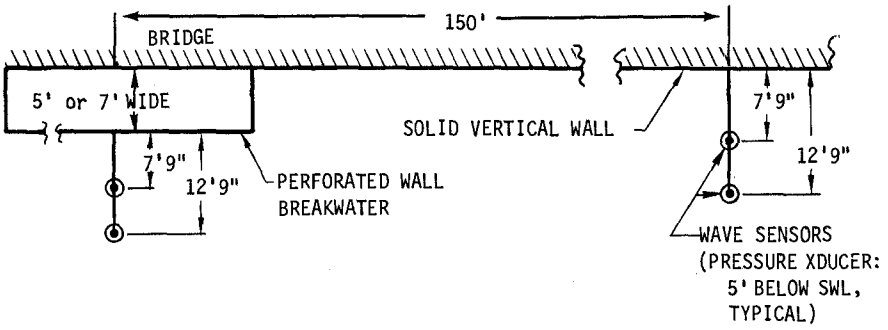


FIGURE 1: AERIAL SCHEMATIC OF TEST SITE SHOWING WAVE SENSOR LOCATIONS

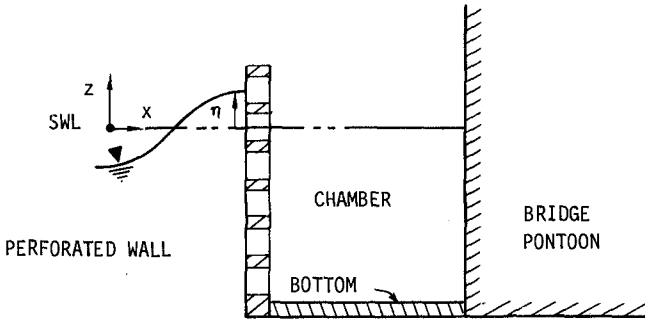


FIGURE 2: CROSS SECTION OF PERFORATED WALL BREAKWATER

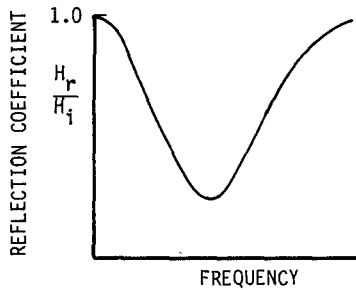


FIGURE 3: TYPICAL PERFORMANCE OF PERFORATED WALL BREAKWATERS

the reflecting barrier. For a single linear wave component the time averaged potential energy at a fixed location, x , obtained from the application of linear wave theory is

$$PE(x) = \frac{\gamma}{4} (a_i^2 + a_r^2 - 2 a_i a_r \cos(\theta_r + \frac{4\pi x}{L})) \quad (2)$$

where a_i , a_r , L , and θ_r are the incident and reflected wave amplitudes, wave length, and relative phase angle, respectively. Since the wave sensors monitor the potential energy, the time averaged energy density at a fixed location in a co-existing sea state is not the same as the sum of the time averaged energy densities (taken independently) of the incident and reflected progressive waves that combine to form the co-existing waves. The measured amplitude is modulated by the last term of Eq. 2.

Inherent in the computation of average energy density for a progressive wave is the assumption that the time average of the wave amplitude at a fixed location is the same as the spatial average of the wave amplitude at a fixed time. For random progressive waves this requirement is met statistically by assuming that the random process is ergodic; i.e., that the ensemble average equals the time average for any location and time. Random waves progressing in a given direction are represented as the superposition of a number of components each with its own characteristic amplitude, frequency, speed, length, and phase angle. The phase angles for random progressive waves are taken to be independent, random, and uniformly distributed between 0 and 2π . When a random progressive wave and its reflection co-exist there is a deterministic relationship between each incident and reflected wave component. The relationship is a function of the speed of the wave component, the distance between the sensor and the location of reflection, and the phase change occurring during the reflection process, if any. The speed associated with each component is linearly related to the frequency such that product of the frequency and speed is a constant.

Any two components of a progressive wave move into and out of phase with each other as time progresses, causing a beat effect. If energy density for progressive waves is averaged over a beat period, the average energy density is not a function of location and the average value equals the sum of the energy densities for each component.

On the other hand, the time series obtained at a fixed location in a co-existing incident-reflected sea state not only contains the beat effect for each wave system but also the amplitude modulation which is a consequence of being, in effect, at different locations on a partial standing wave envelope for each frequency component. For each frequency component the amplitude modulation has a different value (due to the space and frequency dependence of the last term in Eq. 2). The net result is a time series with a beat effect and an amplitude modulation causing the peak measured amplitude values to be strongly dependent on sensor location. The effects are evident in the typical time series shown in Figure 4 for data acquired simultaneously at two fixed locations in front of a solid vertical wall. The effect of position in a standing wave envelope is evidenced by the maximum values recorded. Signals obtained in front of the breakwater are similar in appearance.

Spectra obtained from these time series are shown in Figure 5. The

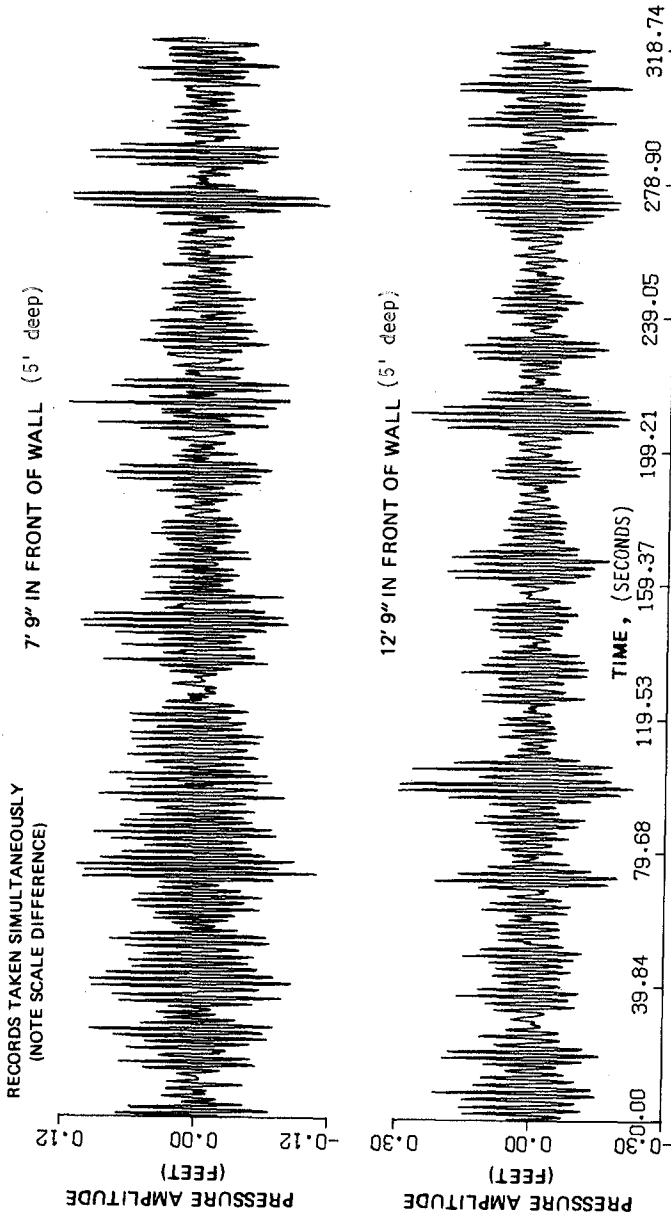


FIGURE 4: TYPICAL TIME SERIES AT TWO LOCATIONS IN FRONT OF A SOLID VERTICAL WALL.

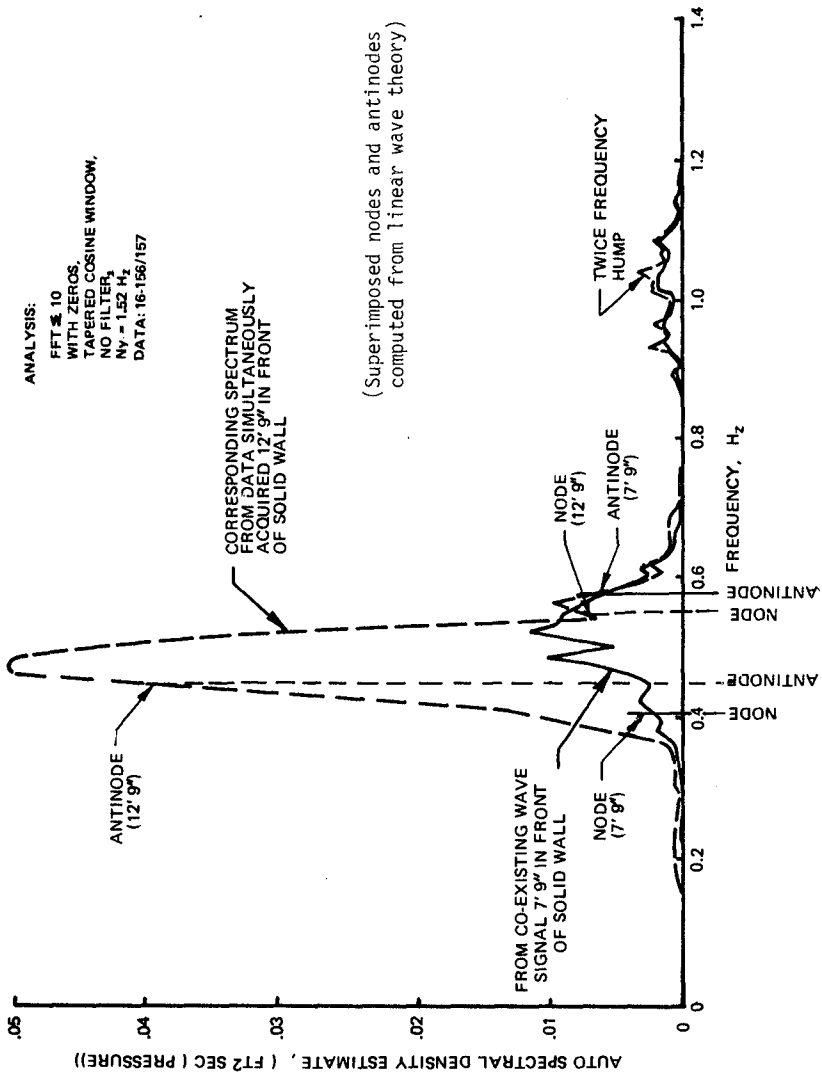


FIGURE 5: CO-EXISTING WAVE SPECTRA FROM PRESSURE DATA IN FRONT OF SOLID VERTICAL WALL.

variances computed at the two distances in front of the solid wall display a strong dependence on sensor location. The twice frequency hump is due to using subsurface pressure sensors. Longuet-Higgins (1950) and Silvester (1974) established that in co-existing sea states a second order pressure variation of the form $\frac{\gamma \pi a_1 a_r}{L} \cos(4\pi ft)$ exists in addition to the usual. The

term is not attenuated with depth and ultimately dominates over the first order term (with its $e^{2\pi z/L}$ pressure response factor) as depth increases. The second order term can be attributed to the movement of the center of gravity in the water column as above the sensors, the fluctuations, occurring at twice the frequency of the surface wave components, are not "real" in the sense of contributing to the surface energy density and therefore must be filtered from spectra obtained using pressure sensors in co-existing sea states.* In the present study the filtering was not a problem, but in co-existing sea states where the spectrum is relatively broad band (the twice-frequency hump might be buried in the spectrum) surface piercing gauges should be used.

The characteristics of the remaining spectra may be better understood by considering a single frequency component of both the incident and reflected wave system. Conceptually, the resulting sea surface at a fixed location due to these two components can be thought of as the sum of a progressive wave and a standing wave. The progressive component eliminates the possibility of true nodes, while the standing wave component produces maxima and minima in the wave envelope which are functions of location. Since these locations are determined by the standing wave component, the phase angle and distance relationships producing the amplitude extremes can be obtained by examining the nodes and antinodes for a perfect reflection. The frequencies associated with node and antinode locations for perfect reflection were computed from linear theory and superimposed on Figure 5. The nodes and antinodes suggest frequencies at which the spectra for each fixed location should contain minimum and maximum (respectively) amounts of information about the wave process. When simultaneously acquired co-existing wave data are examined at two fixed locations, the effects of spatial dependence of the information contained in the spectra can be seen. No location exists where the computed spectrum contains the appropriate ordinate values for the process at all frequencies. Instead, the location where the largest variance (and spectral area) will be calculated is at the position where the frequency for an antinode most nearly matches the peak frequency of the incident wave (assuming that the band width of the process is on the order of, or less than, the frequency difference between nodes). For the wind condition represented by Figure 5, the majority of the incident wave energy occurs at frequencies (.4 - .5 HZ) near a node at the inner (7'9") station and near an antinode for the outer (12'9") station. The opposite occurs in the high frequency tail of the curves where the spectral ordinate value associated with the outer station is less at a frequency corresponding to a node. Since the energy in the incident wave was concentrated

* Alternative one could analyse only the twice frequency spectrum because it is not attenuated with depth, provided the size of the $\frac{\gamma \pi a_1 a_r}{L}$ terms are sufficient to analyse. Due to the considerable reduction in a_r caused by the breakwater the twice frequency hump was exceedingly small for spectra obtained from data taken in front of the breakwater.

in a frequency range near the antinode for the outer station, its calculated variance is much larger than that for the inner one (in this case 4.6 times as large). For all wave conditions tested, the peak incident wave frequency was nearer the antinode frequency for the outer station. Thus, the variance calculated at that station was always larger than the variance at the inner one. The ratio of the variance at the two stations (outer/inner) ranged from 1.4 to 8.1 for the wave conditions of record.

When a linear reflection process occurs at barriers other than solid vertical walls, the location of the node and antinode associated with each frequency increment is altered due to the phase change occurring during the reflection process. As a result of the phase change during reflection altering the frequencies associated with nodes and antinodes, a fixed location in front of the breakwater is not monitoring the same portion of the partial standing wave envelope as that being monitored at the same physical distance in front of a solid vertical wall. Thus, direct comparison of spectral ordinate values obtained from co-existing wave data taken at the same physical distance in front of two types of barriers is a comparison of "apples and oranges."

Having discussed the behavior of co-existing sea states and demonstrated that the variance obtained from any fixed sensor data does not represent the true average energy density, a technique is now discussed to circumvent the problems and decompose multiple co-existing wave spectra into separate incident and reflected spectra.

DECOMPOSITION TECHNIQUE

Thornton and Calhoun (1972) initially presented a theory for separating incident and reflected wave spectra using co-existing wave data acquired simultaneously at two fixed locations in line along the wave ray. The sea state is presumed to result from the superposition of random waves progressing in opposite directions. Each wave is assumed to pass over both sensors. As commonly done in spectral analysis, the random waves progressing in a given direction are represented as the superposition of a number of components each with its own characteristic amplitude, frequency, speed, length, and phase angle. The phase angles for random progressive waves are taken to be independent, random, and uniformly distributed between 0 and 2π . Spectral analysis is used to compute mean square spectra (as well as cross spectra) for the co-existing waves at each sensor location.

The theory was developed by applying linear wave theory to mono-chromatic waves. For a single wave component frequency, the incident and reflected component wave amplitudes are related to the co-existing wave amplitude at two stations. The resulting equations are:

$$\theta_r = \tan^{-1} \left[\frac{A_1 \cos kx_2 - A_2 \cos \theta}{A_1 \sin kx_2 - A_2 \sin \theta} \right] \quad (3)$$

$$\theta_i = \tan^{-1} \left[\frac{a_r \sin \theta_r}{A_1 - a_r \cos \theta_r} \right]$$

$$\theta_i = \tan^{-1} \left[\frac{A_1 \cos kx_2 - A_2 \cos \theta}{A_1 \sin kx_2 + A_2 \sin \theta} \right] \quad (4)$$

$$a_r = \frac{-A_2 \cos \theta + A_1 \cos kx_2}{2 \sin kx_2 \sin \theta_r} \quad (5)$$

$$a_i = \frac{a_r \sin \theta_r}{\sin \theta_i} = \frac{A_1 \cos kx_2 - A_2 \cos \theta}{2 \sin kx_2 \sin \theta_i} \quad (6)$$

The quantities A_1 and A_2 are the amplitudes of the particular frequency component under consideration as calculated from spectral analysis of the signals at 1 and 2. x_2 is the measured distance between gauges; k is calculated from linear wave theory to be $k = 2\pi/L = (4\pi^2/g)f^2$ (in deep water). The phase relationship θ can be obtained directly from the data through cross-spectral analysis of simultaneously acquired records at the two in-line sensor locations. The cross-spectrum is obtained from the Fourier transform of the cross-covariance function in the same manner that the energy spectrum is obtained from the Fourier transform of the auto-covariance function. The inverse tangent of the odd contribution to the cross-spectrum (quadrature spectrum, $Q_{12}(f)$) divided by the even contribution (co-spectrum, $C_{12}(f)$) can be used to calculate the average phase shift, θ , within each frequency band; i.e.,

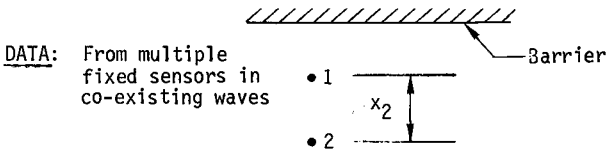
$$\theta(f) = \tan^{-1} \left[\frac{Q_{12}(f)}{C_{12}(f)} \right] \quad (7)$$

These quantities are sufficient to solve for θ_r and θ_i using Equations 3 and 4. The values of a_r and a_i are then available as a function of these phase angles for the given frequency.

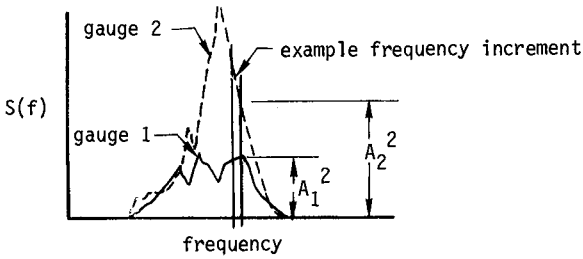
Thus, by evaluating each frequency bandwidth using Equations 3 - 7 the component incident and reflected wave amplitudes can be calculated and the corresponding separate incident and reflected wave spectra computed. In random waves, A_1 and A_2 are obtained by applying spectral analysis to the measured co-existing wave data. The resulting co-existing wave spectra are necessarily only estimates of the distribution of amplitudes (squared) with frequency (i.e., each co-existing wave spectrum is divided into frequency increments and the amplitude representative of that frequency band used as an independent input to equations 3 - 7.). Incident and reflected spectra are then created by plotting the solution to the equations (at each frequency increment) over the range of frequencies. Thus, the accuracy of the resulting spectra is strongly dependent on the shape as well as the variance of the co-existing wave spectra. The process is reviewed schematically in Figure 6. The assumptions inherent in the application of the technique include:

1. Linear wave theory applies. This requirement, which is a reasonable engineering approximation for most non-breaking sea states, is due to the linear wave theory applied to solve the equations.

2. The reflection process does not alter the frequency. Since each



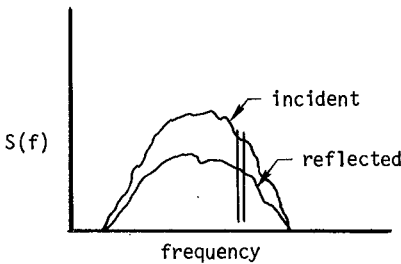
SPECTRAL ESTIMATES OF CO-EXISTING WAVE SIGNALS:



DECOMPOSITION:

- Divide co-existing spectrum into frequency increments
- Apply linear wave theory to each frequency increment independently
- 4 equations $f(A_1, A_2, x_2, \text{relative phase})$
- Solve for incident and reflected wave amplitude and phase

OUTPUT:



- If accurately computed, σ_i^2 and σ_r^2 are independent estimates and can be used directly to evaluate reflection coefficients and energy dissipation

FIGURE 6: OUTLINE OF DECOMPOSITION TECHNIQUE

frequency increment is treated independently there is no analytical mechanism to account for frequency alterations.

3. Wave crests are sufficiently long and parallel to the reflecting barrier that the incident wave passes both sensors, is reflected and passes both sensors again.

4. The surface at each sensor location is the linear superposition of progressive incident and reflected waves.

5. The process is statistically stationary. Typically this requirement is met by comparing calculations based on different portions of an analogue data record.

The distance between sensors must be known, but it is not necessary to know the distance to the reflecting barrier nor the characteristics of the reflection process (except for requirement #2 above).

To evaluate the accuracy of various spectral analysis techniques three performance criteria were specified for the test data. Before the particular techniques are compared, some general characteristics of the spectra resulting from decomposing the co-existing waves are presented.

The required inputs for the decomposition technique are the incremental amplitude and phase information obtained from spectral estimates of two simultaneously acquired co-existing wave signals taken at two different distances in front of a reflecting barrier. The incident waves must have crests nearly parallel to the reflection barrier and the sensors sufficiently in-line with the wave advance that any given incident wave component can be assumed to pass both gages, be reflected, and again pass both gages. Linear wave theory is then used to separate the incident and reflected components from the co-existing wave components at the two fixed locations on the partial standing wave envelope. Because each frequency increment is treated independently, it is necessary to know or assume that the reflection process does not appreciably alter the frequency of the incident wave component. It is not necessary to know anything else about the location or characteristics of the reflection process.

The technique produces the phase and amplitude for both the incident and reflected spectra at each frequency increment. These are presented in Eqs. 2 - 6 and are functions only of the physical distance between sensors and the characteristics of the co-existing wave signals.

Surface or subsurface wave sensors can be used to obtain the co-existing wave information. If subsurface transducers are used the twice frequency components must be filtered from the spectra before they are input to the decomposition technique.

Eqs. 3 - 6 are consistent if the outer gage is designated 1 and inner gage 2. The two signals can be interchanged if the sign on the phase angle, θ , is changed. Usually, an auto spectrum can be calculated without regard to the sign of the amplitude. Due to the use of information from two auto spectra in calculating the incident and/or reflected spectra using this technique, the

signs must be consistent with the physical signal (or both opposite from reality).

Figure 7 shows the reflected wave spectrum in front of a solid vertical wall (from the co-existing wave spectra shown in Figure 5). From Figure 5 it can be seen that the amplitude values at frequencies below .2 Hz are extremely small. Terms involving the difference of these small values are used in the denominator of the equation for amplitude (Eq. 5). Thus, the values of the reflected spectra calculated where the amplitudes of both co-existing spectra are nearly zero ($f < .2$) is erroneous and should be set to zero.

The denominator of Eq. 5 goes to zero when the wave length equals twice the spacing between the sensors. For the distance between the sensors in the present investigation of five feet the amplitude should go to infinity at $f = .716$ Hz. This is clearly evident on Figure 7. For any application of the technique the distance, x_2 , between the sensors should be chosen so that $\sqrt{x_2}/2.56$ is greater than any frequency containing surface wave data of interest.*

The remaining spectral information, which for the figure shown is concentrated between $f = .35$ and $.65$ Hz., is the actual spectral estimate associated with the reflected wave that contributed to the co-existing sea state of Figure 5. Due to the equation similarity, the incident spectrum has identical characteristics.

Eqs. 4 and 6 are written in two forms which are trigonometrically identical. The numerical problems discussed relative to frequencies below .2 Hz produce different spectral calculations for the different identities below $f = .2$ Hz and above $f = .75$ Hz (because the input amplitudes were nearly zero). Over the range of interest, i.e., the range of frequencies when the co-existing wave spectra indicated wave activity, the identities produced identical answers.

For any application of this technique, the range of frequencies containing surface wave information should be established from the co-existing wave spectra and/or knowledge of the specific test conditions. Outside the desired range the extraneous incident and reflected spectral amplitude should be filtered off. The variances of the resulting incident and reflected spectra can then be obtained.

These variances now represent the average energy densities in the incident and reflected wave process and are independent. Since they are separate from each other and independent of spatial location, they can now be used directly to calculate the reflection coefficient of a barrier and/or the dissipation occurring during reflection. The dissipation is easily expressed as the decrease in average incident energy (\sim incident variance, σ_i^2 , and reflected variance, σ_r^2).

$$\text{Percent dissipation during reflection} = \left(1 - \frac{\sigma_r^2}{\sigma_i^2}\right) \cdot 100 \quad (8)$$

* From linear deepwater wave theory, $f = \sqrt{\frac{5.12}{L}}$. The decomposition is valid for wave lengths greater than $2x_2$. decomposition is valid for $f < \sqrt{x_2}/2.56$.

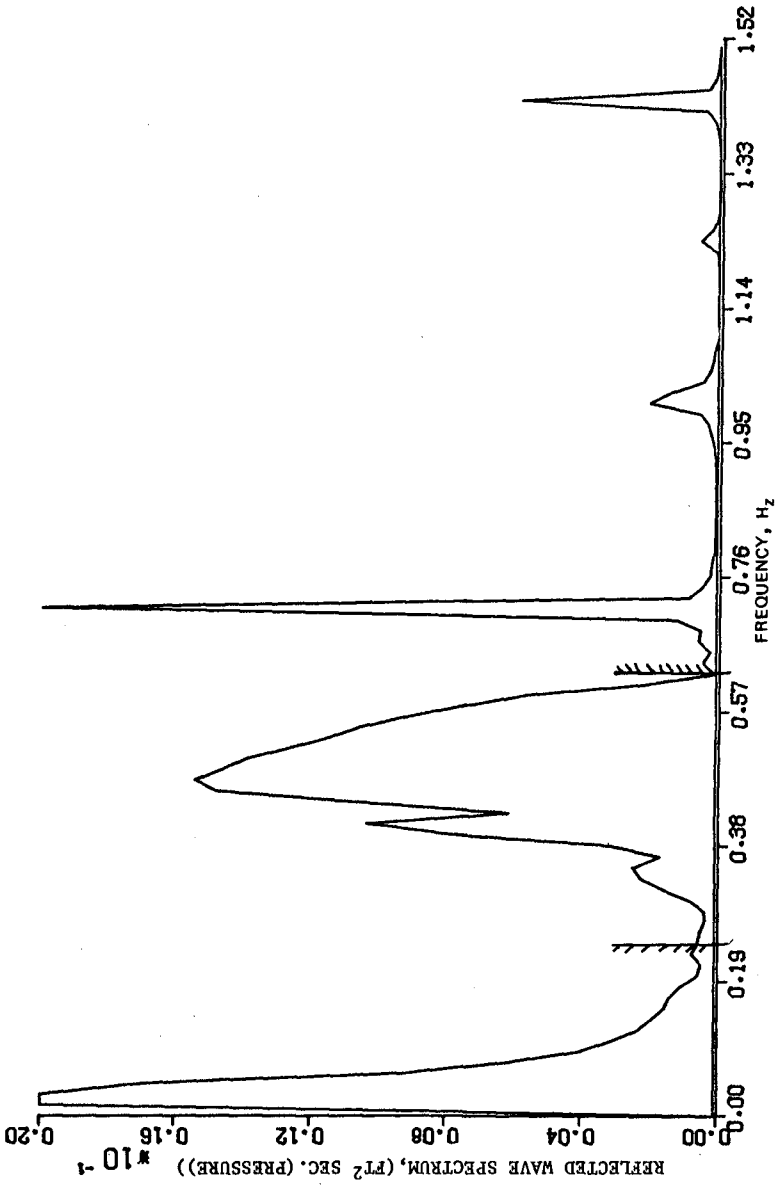


FIGURE 7 : AUTO-SPECTRUM FOR REFLECTED WAVE IN FRONT OF SOLID WALL; COMPUTED BY DECOMPOSITION OF CO-EXISTING WAVES.

Either the reflection coefficients or the dissipation can be calculated equally well from the surface or sub-surface sensor data once the desired frequency range has been defined (and provided the pressure response factor does not reduce the signal strength to an unacceptable level within the range of interest).

A technique has thus been shown to circumvent the problems associated with co-existing random wave data, and produces separate incident and reflected spectra from which the desired reflection characteristics of a barrier can be obtained. The only requirements to using the technique are (1) that the reflection process be known or assumed to occur without altering the wave component frequency, (2) that the distance between two in-line sensors be known, and (3) that the co-existing wave spectra from the two sensors be used as inputs to the decomposition technique where each frequency increment of the spectra is operated on independently. The effect of the last requirement on the numerical computation of incident and reflected spectra is now considered.

COMPARISON OF LAG PRODUCT AND FAST FOURIER TRANSFORM METHODS APPLIED TO THE DECOMPOSITION TECHNIQUE

The decomposition technique requires, as input information, the auto and cross spectra from data acquired simultaneously at two "in-line" locations in a sea state where random incident waves and their reflections co-exist. Increments of the auto spectra become the inputs to Eqs. 3 - 6 and increments of the cross spectra are used to evaluate the phase, Eq. 7. The technique operates on each frequency increment of the spectra independently. Thus the shape and accuracy of the co-existing wave spectral estimates could profoundly influence the computed incident and reflected spectra.

Two methods are commonly used to obtain spectra from random signals; namely, lag product and fast Fourier transform techniques. The lag product method follows the procedure given by Jenkins and Watts (1968). A fast Fourier transform program is described by Paniker (1971). Programmed versions of both methods are widely available. The lag product method involves computing the autocovariance function, which is the correlation of the random signal with itself for the desired number of lags (time increments). The zero lag product of the process is the variance, or mean square value of the signal about the mean. The mean is always zero for the present investigation and the variance is directly proportional to the average energy in the wave signal, and the Fourier transform of the autocovariance function is the spectrum.

Parseval's Theorem (Brigham, 1974) establishes that the spectrum also results from the direct Fourier transform of the continuous time series. For digital computation the Discrete Fourier Transform, DFT, provides a Fourier transform pair made up of the digital time series and a discrete approximation of the continuous spectrum. The fast Fourier transform, FFT, is just an algorithm for efficiently computing the DFT (Bergland, 1969).*

* For 1024 data points used for most of the present analysis the FFT produces a 2DD to 1 reduction in computation relative to the DFT.

The transformations above are defined for infinite time. For the finite length records actually used the transformation can be thought of as an infinite time series multiplied by a window with length equal to the data record. Since multiplication in the time domain is convolution in the frequency domain, the transform of the data (or autocovariance function) is automatically convolved with the transform of the window function. When no window shape is specified it automatically becomes a function which equals zero for all time except the time of the data record and equals one (i.e., has no effect on the time series) during the time of the record (referred to as a rectangular window). The transform of the rectangular window has substantial side loops, which when convolved with the transform of the data produces undesirable positive and negative contributions to the spectral value at each frequency. To minimize this effect several window functions are in common usage which, when transformed, have smaller or better behaved side loops and produce more desirable or less noticeable contributions to the spectral estimate. Though the effect of convolving the data with a window can be reduced through the choice of window functions, the resulting spectrum is always an estimate of the true spectrum for the process.

The spectrum resulting from the transformation of the finite digitized data is referred to as a raw periodogram. Since the periodogram is the direct transform of the finite data from the time to the frequency domain, it is the least squares representation of the raw data (convolved with a window), and it contains the raw coefficients of the Fourier line spectrum. For random signals, the individual component amplitudes do not converge to the true spectrum as the data record length increases. To estimate the true spectrum for the process, adjacent values of the line spectrum are summed together. If too many points are summed together the spectrum becomes oversmoothed (biased). The appropriate number of points to sum to best approximate the true spectrum is more of an art than a science. The window most commonly applied to the data for the FFT technique is the tapered cosine window where the first and last 10 percent of the time series is smoothed using a quarter period segment of the cosine function. The effect of varying the number of line spectral components summed together will be considered further.

The lag product method involves transforming a number of lags of the autocovariance function. The resulting spectral estimate is a function of the number of lags transformed and the window used to multiply the autocovariance function (lag window). When the number of lags transformed is too few the spectrum is oversmoothed (biased). As the number of lags increases, the spectrum approaches the true spectrum of the autocovariance function, then becomes very jagged and unstable. The jagged spectrum produced by the lag product method does not converge to the raw line spectrum produced by the FFT technique. The number of lags necessary to produce the best estimate is unknown and will be considered further. Several window functions are commonly used to smooth the spectral estimate and minimize the effects of side loops (Jenkins and Watts, 1968).

A decision must be made about which combination of windows and transform techniques should be used to produce the best estimate of spectra for co-existing waves which can then be broken into frequency components and used as inputs into the decomposition technique. Experimental data were acquired at four stations simultaneously; two in front of a solid wall (7'9" and 12'9")

and two at the same distances in front of a perforated wall breakwater, 150 feet away (Figure 1). The co-existing waves at the two stations should be different because of the different reflecting processes, but the energy density of the incident waves averaged over the 5.6 minutes of the record should be the same at two stations, only 150 feet apart. Decomposition can be used to compute the incident spectra and average energy density (proportional to the variance) at the two locations. A perfect estimate of the actual incident wave process would require that the incident variance at the two locations be identical. Defining this desired condition as C,

$$C = \sqrt{\frac{\sigma_{I\infty}^2}{\sigma_{I\infty}^2}} \rightarrow 1 \quad (9)$$

where a perfect decomposition requires $C = 1$.

Reflections from a solid vertical wall are nearly perfect below a critical wave camber (Morden, 1975, Section IIC). Over most of the wave conditions encountered in the present investigation, the reflection coefficient in front of the solid wall, R_{∞} , should equal .99-1.0. Co-existing wave data in front of the wall can be decomposed and the resulting variances for the incident and reflected components used to obtain R.

$$R_{\infty} = \sqrt{\frac{\sigma_{R\infty}^2}{\sigma_{I\infty}^2}} \rightarrow .99-1.0 \quad (10)$$

A perfect decomposition requires $R_{\infty} = .99-1.0$.

Perforated walled breakwaters reduce co-existing wave action enough that several observers qualitatively claim that the devices work well. A reduction in co-existing waves substantial enough to be clearly seen in a random sea state would require a considerable dissipation during the reflection process. Therefore, properly decomposed spectra should show a reflection coefficient significantly less than 1. Model-scale predictions (Richey and Sollitt, 1970) suggest overall reflection coefficient (R_{BW}) values in the range of 0.4 to 0.7.

$$R_{BW} = \sqrt{\frac{\sigma_{R_{BW}}^2}{\sigma_{I_{BW}}^2}} \rightarrow .4 \text{ to } .7 \quad (11)$$

These criteria can now be applied to the data for various combinations of lags and windows for the lag product techniques and various sums of spectral line components for the FFT technique. The variations are applied to the co-existing wave data, the resulting spectra can then be incremented and used as inputs into the decomposition technique. The computed incident and reflected variances and spectra can then be judged by the natural criteria.

Stationarity was established for each set of data by analysing the different portions of long analog data records and using only those without changes in computed spectra. Following analysis of many combinations the data was digitized and sampled with a sampling rate of .328 second/sample. (Nyquist frequency 1.52 Hz) 1024 data points represent 5.6 minutes of analog data.

Jenkins' and Watts' (1968) window closing technique was initially used to examine 20, 40, 60, 80 and 95 lags of the co-existing wave data. The lag product method produces very smooth unbiased input spectra when the number of lags equals 50, approximately 5 percent of the record length. Progressive wave spectra often become unstable with lag numbers approaching twice this number. Since the co-existing wave record is expected to be much less smooth because of the effects of partial nodes and antinodes, a high number of lags, say 95, were also tried. The window which produces the least stable spectra is the rectangular window (with its large negative side loops). Tukey and Parzens windows were also applied to smooth the spectra (with the Parzens window presenting the advantage of no negative side loops). The effect of the extremes of these conditions on the shape of the co-existing wave data is shown in Morden (1975). The resulting incident and reflected spectra can be grouped to display the spectral shapes corresponding to the natural criteria. Even transforming 95 lags of the autocovariance of a co-existing sea state produces a spectrum (convolved with appropriate window) which is too smooth to be broken into increments which can be treated independently.

The FFT technique provides the advantage of transforming the data directly. The number of raw periodogram coefficients to be summed together to produce co-existing wave spectra can be varied to show their effect on the computed incident and reflected spectra. Sums of 3, 10, and 15 points (denoted $\sum 3$, $\sum 10$, $\sum 15$) were considered. To increase the number of line spectral components computed, zeroes can be added also to the record. The effect of adding the same number of zeroes as original data points was also considered. The tapered cosine window is an accepted window for use with FFT and is used in all the following comparisons (Bergland 1969). The FFT spectra appear less smooth than those computed from the lag product method, and they do satisfy all three criteria.

Table I summarizes the results of applying the various conditions above to the arbitrarily chosen data set. In all cases the reflection co-efficients are defined over the range of frequencies containing measurable data, .25 to .65 Hz. Application of FFT $\sum 3$ to fourteen sets of field data records produced root mean square error from the criteria for perfect estimation of 4.0 percent for the reflection coefficient (Eq. 10) and 12.7 percent for C (Eq. 9). FFT $\sum 10$ with zeroes added produced r.m.s. values of 3.9 percent for all R_{∞} and 10.7 percent for all C.

It is concluded that the decomposition technique is indeed sensitive to the shape of the input co-existing wave spectra. The lag product method, with its intermediate computation and transformation of the autocovariance function, produces too much smoothing to allow independent treatment of frequency increments. While not perfect, the decomposition technique incorporating the FFT produced input spectra is capable of reducing co-existing wave spectra differing by almost an order of magnitude and produce spectra which satisfy the established criteria within 10 percent.

Based on the examination of the available data, the FFT technique incorporating the summation of 10 spectral line components of co-existing wave data with zeroes added is recommended. Finally, it is suggested that any desired smoothing be done on the output incident and reflected spectra after decomposition. One effective smoothing technique is the moving average.

TABLE I. SUMMARY OF TECHNIQUES APPLIED TO AN ARBITRARY DATA SET
(DATA 16-156/157)

CO-EXISTING WAVE DATA - INPUT										
Technique	Lag or Sum	Window	SOLID WALL				BREAKWATER			
			Sensor Data				Sensor Data			
			σ^2 outer	fq	σ^2 inner	fq	σ^2 outer	fq	σ^2 inner	fq
LP	95	Rect.	.00549	.49	.00104	.53	.00347	.50	.00120	.46
LP	95	Parz.	.00549	.49	.00104	.52	.00347	.49	.00120	.46
LP	95	Tuk.	.00549	.49	.00104	.53	.00347	.50	.00120	.46
LP	50	Parz.	.00549	.49	.00104	.52	.00347	.49	.00120	.47
LP	50	Tuk.	.00549	.49	.00104	.52	.00347	.49	.00120	.46
FFT	$\sum 3$	T.C.	.00568	.50	.00101	.50	.00385	.50	.00130	.50
FFT	$\sum 10$	T.C.	.00568	.49	.00117	.55	.00385	.49	.00130	.46
FFT	$\sum 10$	T.C.	.00568	.48	.00112	.52	.00371	.48	.00128	.45
(w/z)										
FFT	$\sum 15$	T.C.	.00568	.48	.00112	.55	.00370	.52	.00113	.46
(w/z)										

OUTPUT FROM DECOMPOSITION TECHNIQUE													
Technique	Lag or Sum	Window	SOLID WALL				R_∞	BREAKWATER				R_{BW}	C
			Reflected		Incident			Reflected		Incident			
			σ_r^2	fq	σ_i^2	fq		σ_r^2	fq	σ_i^2	fq		
LP	95	Rect.	.00178	.49	.00172	.47	1.01	.00134	.46	.00160	.50	.92	1.04
LP	95	Parz.	.00161	.49	.00173	.47	.96	.00132	.48	.00165	.50	.89	1.03
LP	95	Tuk.	.00166	.49	.00176	.47	.97	.00131	.49	.00163	.50	.90	1.04
LP	50	Parz.	.00160	.49	.00168	.47	.98	.00136	.46	.00168	.50	.90	1.00
LP	50	Tuk.	.00159	.49	.00172	.49	.96	.00133	.46	.00166	.49	.89	1.02
FFT	$\sum 3$	T.C.	.00180	.50	.00179	.50	1.00	.00066	.50	.00183	.49	.60	.99
FFT	$\sum 10$	T.C.	.00183	.50	.00182	.47	1.00	.00060	.49	.00188	.49	.56	.98
FFT	$\sum 10$	T.C.	.00175	.48	.00179	.47	.99	.00062	.50	.00179	.50	.59	1.00
(w/z)													
FFT	$\sum 15$	T.C.	.00175	.48	.00175	.46	1.00	.00057	.50	.00178	.50	.57	.99

LP = Lag Product Method

FFT = Fast Fourier Technique

(w/z) = with zeroes added

σ^2 outer = Variance at outer gage

σ^2 inner = Variance at inner gage

σ_r^2 = Calculated variance for reflected wave system

σ_i^2 = Calculated variance for incident wave system

fq = Frequency of peak spectral ordinate

Since the variance is not affected, the application of smoothing to the final computed incident and reflected spectra would primarily be for visual effect. (This was not done on any spectra shown.) Comparison of smoothed spectra could affect the incremental reflection coefficients, but not the overall reflection coefficient.

CONCLUSIONS AND RECOMMENDATIONS

Sea states where wind-generated waves and their reflections co-exist cannot be analyzed using the techniques commonly applied to progressive random waves. The co-existing sea surface consists of modulated waves contained in a complicated standing wave envelope. As a consequence, the time-averaged energy density varies continuously with position along wave rays. The average energy in a co-existing wave at any fixed location was shown to be a function of a phase relationship as well as the incident and reflected wave amplitudes.

By combining the appropriate spectral analysis with a theory based on linear waves relationships, the stochastic process of wind generated waves and their reflection are amenable to analysis in spite of their deterministic phase relationships. The decomposition technique provides a means of separating incident and reflected wave spectra using spectral estimates computed from data obtained simultaneously at two fixed, in-line sensor locations in wave fields where incident and reflected waves co-exist. Data from either surface or sub-surface sensors can be used, provided the wave energy is sufficiently narrow banded to allow filtering of the "twice frequency hump." The distance, x_2 , between sensors affects the maximum frequency component obtainable in the decomposed spectra. ($f_{\max} = \sqrt{x_2/2.56}$ for deep water waves). Though it is necessary to know or assume that the frequency of a wave component is unaltered during the reflection process, no other knowledge is needed of either the location or fluid dynamics of the reflection.

The accuracy of the technique depends on the spectral analysis method applied to estimate the co-existing wave spectrum. The fast Fourier transform method, which produces a spectrum by directly transforming the digitized data, provides a more accurate assessment of reflection characteristics than the lag product or autocovariance method. Based on the application of validation criteria to field test data obtained in wind generated deep water waves, it is recommended that a number of zeroes equal to the length of the digital data record be added to the co-existing wave data before analysis, that the tapered cosine window be applied, and that ten components of raw periodogram be summed together to produce the best input spectra for the decomposition technique.

As a result of accurate decomposition, the characteristics of waves reflected from, and the dissipation of wave energy occurring at, a barrier can be quantitatively evaluated for any reflected wave process where the wave frequency is not significantly altered during reflection.

REFERENCES

- Morden, Dennis B., "The Decomposition of Co-existing Random Incident and Reflected Wave Energy," Ph. D. Dissertation, University of Washington, 1975.

- Richey, E. P. and C. K. Sollitt, "Wave Attenuation by Porous Walled Breakwater," Journal of Waterways, Harbors and Coastal Engineering Division, ASCE, 69, WW3, New York, New York, August 1970, p. 643-663.
- Ippen, A. T., ed., Estuary and Coastline Hydrodynamics, Engineering Societies Monographs, McGraw-Hill Book Co., 1966.
- Thornton, E. B. and R. J. Calhoun, "Spectral Resolution of Breakwater Reflected Waves," Journal of Waterways, Harbors, and Coastal Engineering Division, ASCE, 98, November, 1972, p. 443-460.
- Brigham, E. L., The Fast Fourier Transform, Prentice Hall, Inc., Englewood Cliffs, New Jersey, 1974.
- Bergland, G. E., "A Guided Tour of the Fast Fourier Transform," IEEE Spectrum, 6, July 1969, p. 41-52.
- Paniker, N. N., "Determination of Directional Spectra of Ocean Waves from Gage Arrays," University of California Hydraulic Engineering Laboratory Research Report HEL 1-18, August, 1971.
- Jenkins, G. M. and D. G. Watts, Spectral Analysis and Its Applications, Holden-Day, Inc., San Francisco, 1968.

CHAPTER 50

Resonant Refraction by Round Islands

Richard E. Meyer
Mathematics Department, University of Wisconsin
Madison, WI 53706

Wave trapping by refraction can give rise to resonance of a kind unfamiliar in oceanography. Trapping over realistic seabed topographies is incomplete, but conversely, possesses a mechanism for direct, harmonic excitation from the open sea that is unknown in classical resonance. These phenomena have been studied for the simplest example of an axisymmetric island of typical shape with small seabed slope. Asymptotic analysis has led to simple formulae for resonant frequencies, energy leakage rates and resonant response coefficients. Resonances of extraordinarily large but narrow response have been found.

I. Introduction

Localized natural surface wave modes in the open sea had long been known to be impossible, because their energy could propagate away freely. Edge waves, however, are just such modes, and their practical significance has come to be appreciated rapidly since their mathematical discovery [Ursell 1952] . Meanwhile, much more unfamiliar resonances have been studied, which are also caused by refraction. The key example of a round island exhibits these novel phenomena in their simplest form, and the following summarizes some recent results.

The mechanism of trapping by refraction is simple. The propagation velocity of surface gravity waves on water increases with depth. Therefore, if parts of a wave crests lie over deeper water, those parts travel faster and in brief, all wave crests over water of uneven depth always turn towards the shallows, during propagation. The possibility thus arises that waves coming from shore might be turned back shoreward, by and by, before they can reach the open sea: such waves are trapped. (The invisible barrier beyond which they do not travel seaward is called a caustic by analogy with optics.) If the phase relationships are just right, moreover, then resonance becomes a plausible possibility.

Such a direct approach, however, proves inadequate because realistic trapping turns out to be much less straightforward. Over an axisymmetric seabed topography, for instance, the depth level lines themselves are circles and to be trapped, the crests must therefore be turned faster than the local level circle. That is impossible [Longuet-Higgins 1967, Shen, et al. 1968] at sufficiently large distances from the

center. The far field is therefore always a field of progressive waves radiating energy from and to the open sea. This stands in striking contrast to edge waves which decay exponentially with distance from shore (a behavior now recognized as rather special and exceptional).

Figure 1 shows the most typical pattern of wave crests for a trapped wave mode around an island. An inner wave ring around the island is separated from the far field of radiation by a quiescent zone, in which the motion is damped exponentially rapidly with distance from the zone edges. All the same, since the damping zone has finite width, the two wave motions separated by it cannot be independent. For instance, if such a wave mode be set up and left to develop freely, without further energy supply, then a non-zero amount of wave energy will pass through the damping zone to the outer wave field, whence it will ultimately be radiated to infinity. Such "leakage" makes complete trapping impossible. There can be no resonance in the clear-cut classical sense. Rather, any resonance must be a matter of degree, depending on the leakage rate.

II. Natural Frequencies

A first question is what trapped wave modes are possible and at what frequencies? Shen, Meyer and Keller [1968] obtained estimates for round islands of quite realistic seabed topography by an approximation based on smallness of the seabed slope ϵ . If horizontal distances are measured in units of the island radius L and vertical distances, in units of ϵL , then the standard equations [e.g. Stoker 1957] of the classical, linear theory of surface waves for the velocity potential $\phi = \phi(x, y, z) \exp(-i\omega t)$ read

$$\frac{\partial^2 \phi}{\partial x^2} + \frac{\partial^2 \phi}{\partial y^2} + \epsilon^{-2} \frac{\partial^2 \phi}{\partial z^2} = 0 \quad \text{for } 0 > z > -h(x, y)$$

$$\partial \phi / \partial z = \epsilon \omega^2 \phi \quad \text{at } z = 0 \quad (1)$$

$$\epsilon^{-2} \frac{\partial \phi}{\partial z} + \frac{\partial \phi}{\partial x} \frac{\partial h}{\partial x} + \frac{\partial \phi}{\partial y} \frac{\partial h}{\partial y} = 0 \quad \text{at } z = -h(x, y)$$

The first is Laplace's equation, the second combines the linearized, kinematical and dynamical surface conditions, the last expresses impermeability of the seabed; viscosity and surface tension are ignored. In the form (1), for $\epsilon \ll 1$, they lead to a refraction approximation for gentle water depth variation, but not to any short- or long-wave approximation in a usual oceanographical sense.

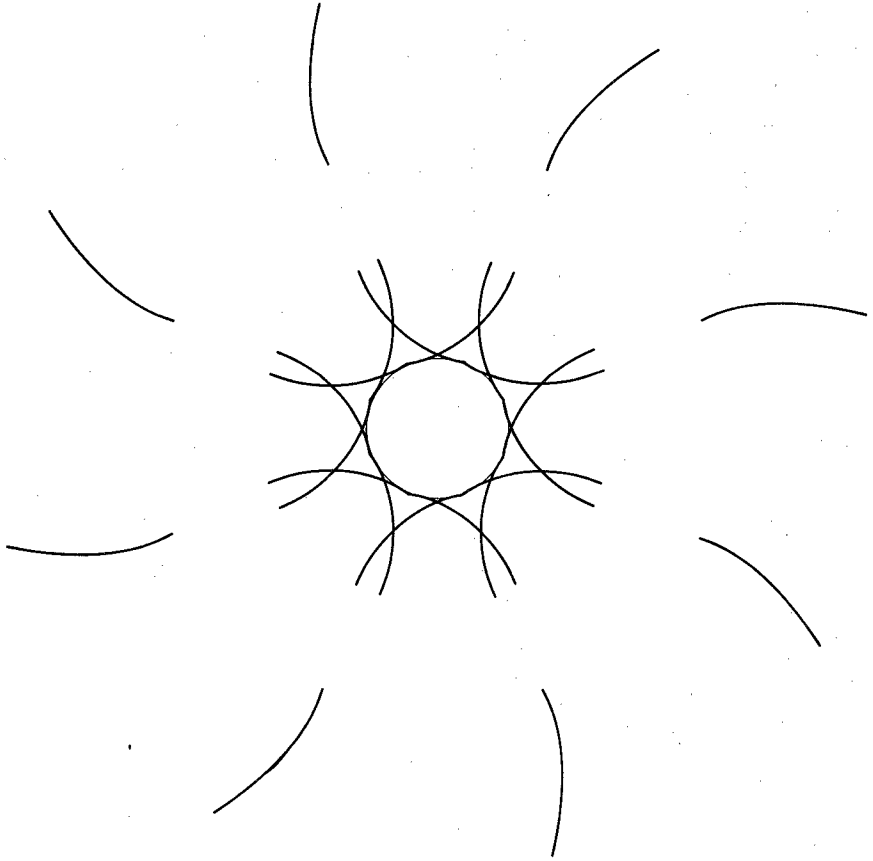


Figure 1

The manner in which ϵ appears in (1) suggests application of Keller's [1958] Geometrical Optics Approximation, a sophisticated and very powerful form of familiar ray methods. The fuss with rays and orthogonals, etc., is cut out by the simple idea that a natural mode must accommodate precisely an integer number of wave lengths both (i) around the island and (ii) between shore and the inner caustic circle bounding the trapped wave ring (Fig. 1. Only patterns with a single trapped wave ring will be considered here; more complicated patterns and spectra are possible, but rare for round islands [Shen et al. 1968]). Condition (i) is easy to apply at a caustic circle because the crests must be perpendicular to this refraction boundary. The wave length along the inner caustic $r = r_1$ is therefore $\lambda_1 = 2\pi/[\omega^2 k(r_1)]$, if $\omega^2 k(r)$ denotes the wave number magnitude (this notation reflects convenience of scaling for $\epsilon \ll 1$), and (i) says simply

$$2\pi r_1 / \lambda_1 = r_1 k(r_1) = n \quad n = 1, 2, 3, \dots \quad (2)$$

For (ii), it will be seen in Section V below that $\omega^2 \xi(r) / 2\pi$ with

$$\xi(r) = \int_1^r |k^2 - n^2 / (\omega^4 r'^2)|^{1/2} dr' \quad (3)$$

counts radial distance in units of local wave length (which varies greatly with the radius r), if the wave number function $k(r)$ is determined from the full dispersion relation [e.g. Stoker 1957].

$$k \tanh(kh) = 1. \quad (4)$$

Condition (ii), actually, is not quite correct as first stated. A full propagation loop goes, say, from shore through refraction at the caustic back to shore (Fig. 1), and the radial distance

$\omega^2 \xi(r_1) / 2\pi$ from shore to inner caustic in wave length units must therefore be a half-integer,

$$\frac{\omega^2}{\pi} \int_1^{r_1} |k^2 - n^2 / (\omega^4 r'^2)|^{1/2} dr = m - \frac{1}{2}, \quad m = 1, 2, \dots \quad (5)$$

The extra $-\frac{1}{2}$ stems from the phase shifts of shore reflection and caustic refraction [Shen and Keller 1975, Shen et al. 1968] and may serve as a reminder that the simplicity of the present account represents, of course, use of hindsight for shameless corner-cutting; for slightly longer, more tenable derivations see [Shen et al. 1968, Meyer 1971].

Given n and m , (2) and (5) are two equations for the frequency ω and caustic radius r_1 , which turn out [Shen et al. 1968] to have at most one solution for realistic topography $h(r)$. Those are the discrete eigenfrequencies and it is clear from (i), (ii) that n counts the number

of crests around the island at fixed radius, while m counts (twice) the number of crests radially outward from shore to caustic and back. Of course, $r_1 < \infty$ for a pattern as in Fig. 1 and a closer look at (2)-(5) [Shen et al. 1968] shows this to set an upper bound to the values of m (and hence, also of ω) for which (2), (5) do have a solution, given n . That bound, moreover, usually rules out the lowest pairs (n, m) , which general experience would have suggested to furnish the most prominent and important modes... For a conical island, for instance, there is no natural mode for any pair (n, m) with $n < 3$ [Shen et al. 1968].

For each n , on the other hand, (2) and (4) can be satisfied with $r_1 = \infty$ (which makes condition (ii) irrelevant) for any frequency ω exceeding a "cut-off" value, and those are the continuous spectra. In sum, there is a countably infinite discrete spectrum embedded in a continuous spectrum of countably infinite multiplicity. That is, as the frequency increases, the continuous spectrum gains more and more progressive wave modes coexisting at the same frequency; but always, further discrete frequencies are encountered at which trapped modes also exist. It is remarkable that so complicated a physical situation can be described by as simple and practical a set of formulae as (2), (4) and (5); Keller's Geometrical Optics Approximation can therefore cope with more complicated circumstances and holds promise of a practical approach to real topographies.

The simple version [Keller 1958, Shen et al. 1968] of this theory actually fails at shore and caustics, but Shen and Keller [1975] have constructed a uniform approximation which now offers a practical approach to the estimation of wave amplitudes at just those places where they are maximal and of most direct interest.

III. Leakage and Response

The theory so far outlined ignores, however, that every natural wave mode must involve leakage of energy from the trapped wave ring through the damping zone to the far field whence that energy is radiated away to the ocean. All eigenvalues are therefore complex. (The real part will continue to be called frequency and the imaginary part will be called "leakage rate.") The flaw in the use of this form of refraction theory for the present purpose is not only that it is logically based on reality of the eigenvalues, which its own results on natural modes show to be impossible. A more weighty objection is that resonance is now a matter of degree, and we need actual estimates of the leakage rate before we can distinguish effectively resonant eigenvalues from harmlessly damped ones.

Indeed, the organic connection between the waves trapped near shore and the associated waves in the far field implies an equal possibility of energy leakage outward and inward across the damping zone. It thereby creates a mechanism for direct excitation of resonant modes by plane waves of the same frequency incident from the ocean. This is a new mechanism, entirely absent in classical water wave resonance.

Classical edge waves [Ursell 1952], for instance, have no far field and, therefore, linear theory has no mechanism by which they could possibly be excited (short of an earthquake, which Ursell [1952] had to use for his experiments). Accordingly, they remained academic until Galvin [1965] showed how to excite them subharmonically, a process dependent on small effects of the second order. That is typical of classical resonance. "Leaky modes," by contrast, possess an inherent, first-order, and therefore potentially highly effective, mechanism of direct harmonic excitation by the natural wave environment, which is new in oceanography although not unfamiliar in some other fields.

This first-order mechanism also implies an opportunity of calculating, from the classical linear theory, the amplitude response of the water surface around an island to a given wave input from the ocean. It turns out to depend greatly on the energy spectrum of the input which, in turn, depends a good deal on the circumstances. The extreme cases are a single, plane wave pulse and a steady monochromatic plane wave input. In the absence of fairly definite specification of the input spectrum, the latter, standing-wave extreme may be the most practical estimate, conservative in that it overestimates the response to be expected in a real situation. For that extreme, the "response coefficient," that is, the standing trapped wave amplitude for unit incident wave amplitude, turns out, plausibly enough, to be just the reciprocal of the leakage rate [Longuet-Higgins 1967, Lozano and Meyer 1976].

This reciprocal relation, on the other hand, creates the paradoxical situation that an estimate of the imaginary part of the eigenvalues is the more important, the smaller this imaginary part. The main engineering interest is precisely in the most negligibly small needles in the haystack, and this imposes a severe demand for precision on any approximate analysis.

These notions of leakage and response were first set out by Longuet-Higgins [1967] and Summerfield [1972] in their long wave approximation for wave trapping by a "hedge," that is, a steep slope terminating a pronounced shelf around an island. (They also offer helpful estimates and comments on the relation between input spectrum and trapping response in their approximation.) That somewhat exceptional topography lends itself, in the long wave limit, to idealization by a topography of piecewise constant depth, for which the natural modes can be represented classically in terms of Hankel functions. Detailed computation of many complex eigenvalues was made possible thereby, and among many others, also quite a number of modes of very large response were found. Their frequency band width of response is so narrow [Longuet-Higgins, 1967], however, that they are virtually inaccessible to a more directly numerical approach. Indeed, some brilliant computational efforts [Lautenbacher 1970] have been defeated by this feature of the response.

IV. Generalized Refraction Theory

The Geometrical Optics Approximation, on the other hand, is defeated by the complex eigenvalues, which are incompatible with its basic formulation [Keller 1958] as an asymptotic expansion in powers of the small parameter ϵ . Leakage introduces factors exponential in ϵ^{-1} , which transcend approximation to any order in powers of ϵ . Such inherent contradictions are, of course, less obvious in more vaguely based ray methods. In short, the better known refraction methods are designed for self-adjoint problems and fail decisively, like many well-known mathematical methods, for non-self-adjoint problems such as trapping.

A more general refraction approximation to (1) is therefore needed. Preferably, it should not be a long wave approximation because we have already seen in Section II that the usual, longest modes are absent, whence the longest actually present are doubtful candidates for strong resonance. For application to the most common topographies, it should be based on the gentleness of seabed variation expressed by the parameter ϵ , that is, on the assumption that the seabed topography varies only on a scale large compared with the local wave length. Such an approximation has been proposed independently by a number of authors who arrived by diverse reasoning at the hypothesis that, over such "gentle" topographies, the vertical velocity profile depends to the first approximation only on the local water depth, but not also on the horizontal derivatives of the water depth.

To express this, write the exact potential

$$\Phi(x, y, z, t) = \phi_s(x, y; \epsilon) F(z; x, y, \epsilon) \exp(-i\omega t)$$

with $F(0; x, y, \epsilon) \equiv 1$ so that ϕ_s is the surface value of the potential. Then F expresses the vertical structure and its dependence on z must, to first approximation, be that predicted by the classical linear theory for waves over water of uniform depth equal to the local value of $h(x, y)$. But that is well known [Stoker, 1957] and implies that $\alpha(h)F$ is to be approximated by

$$F_0 = e^{-kh} \cosh [k(z+h)], \quad k \tanh(kh) = \alpha^2 \quad (6)$$

(The convenience factor $\alpha = \frac{1}{2} [1 + \exp(-2kh)]$ is used to avoid formal degeneracy as $h \rightarrow \infty$.) Vertical averaging of (1) [Lozano and Meyer 1976] then shows $\Psi = \alpha^{-1} \phi_s$ to be governed by the short-scale Helmholtz equation

$$G^{-1} \nabla(G\Psi) + \epsilon^{-2} k^2 \Psi = 0, \quad (7)$$

with

$$G = \int_{-h}^0 F_0^2 dz = [\sinh(2kh) + 2kh] / [4k \exp(2kh)].$$

Equations of the form (7) have been proposed by Battjes [1968] and derived by Berkhoff [1973] from an assumed asymptotic expansion of the potential which, however, is known [Shen and Keller 1975] to be incorrect, especially in the present context. To avoid such pitfalls, Lozano has given a vertical averaging argument [Lozano and Meyer 1976] supporting (6), (7), but a mathematical proof is not claimed. On the other hand, (6), (7) are there shown to include as special cases all known exact solutions of (1), and all the best known approximations (including Geometrical Optics and other ray approximations).

From an oceanographers viewpoint, it is noteworthy that the generalized refraction equations (6), (7) encompass long and short waves impartially: the full, exact dispersion relation $k \tanh(kh) = \varepsilon \omega^2$ is used.

V. Leakage Rates

The Generalized Refraction Equations (6), (7) have been applied to trapping by axisymmetric islands, since those are the simplest topographies exhibiting the new physical effects. Apart from that symmetry, a general, realistic topography is envisaged: the water depth $sh(r)$ increases monotonically and (analytically) smoothly from shore to ocean. To restrict attention to the simplest and most common trapping pattern (Fig. 1), exceptionally pronounced shelves are excluded (which makes the study complementary to Longuet-Higgins' [1967] and Summerfield's [1972], who specialized on the effect of such shelves). Attention has also been restricted to natural modes harmonic in the angular variable because the geometrical optics approach [Shen et al. 1968] has not revealed any others and the new study does not, in any case, aim at an exhaustive calculation of all possible such modes. The surface potential can then be written as

$$\phi_s = e^{in\theta} [\alpha(h)/g(r)] w(r), \quad n = 1, 2, \dots \quad (8)$$

in polar coordinates r, θ based on the island center, with factor

$$g(r) = (rG)^{1/2} = \frac{1}{2} e^{-kh} [2rh + (r/k) \sinh(2kh)]^{1/2}$$

introduced to simplify the differential equation for the unknown function $w(r)$.

Substitution in (7) shows that equation to be

$$\frac{d^2 w}{dr^2} = \left(\frac{f(r)}{\varepsilon^2} + \frac{g''}{g} \right) w, \quad (9)$$

$$f(r) = (n\varepsilon/r)^2 - k^2, \quad (10)$$

$$k \tanh(kh) = \varepsilon \omega^2. \quad (11)$$

It is formidable, not only because of the complexity of the coefficient g''/g , but because even the main coefficient, $f(r)/\varepsilon^2$, can be defined only implicitly through the dispersion relation (11) for $k(r)$. The general form of $f(r)$ is determined by the assumption of a simple trapping pattern (Fig. 1), which implies [Shen et al. 1968] that $f(r)$ has precisely one maximum for $1 < r < \infty$. With $n\varepsilon$ chosen to exceed a certain cut-off value--which implies $n = O(\varepsilon^{-1})$, i.e., a rather large number of wave crests around the island-- $f(r)$ then has precisely two roots, r_1 and $r_2 > r_1$ (Fig. 2). They mark the caustic radii because the basic form of (9) is

$$\varepsilon^2 w'' - f w = 0(\varepsilon^2) \quad (12)$$

so that the solution are oscillatory for $f < 0$, i.e., in the trapped wave ring $1 < r < r_1$ (Fig. 2) and the far field $r > r_2$. For $r_1 < r < r_2$, $f > 0$ and the solutions are non-oscillatory; this is the damping ring.

Since $f(r)$ varies so much (Fig. 2), comparison of (12) with the standard equation $y'' + y = 0$ is assisted by the variable

$$\xi(r) = \int^r | -f(r') |^{1/2} dr'$$

which brings (11) into the form

$$\varepsilon^2 \frac{d^2 w}{d\xi^2} + v(\xi) \frac{dw}{d\xi} + w = 0$$

This shows $\xi/(2\pi\varepsilon)$ to measure radial distance in local wave lengths and explains (3) (with the normalization $\varepsilon\omega^2 = 1$).

Actually, all this holds only for real ω , which has been seen to be impossible for natural modes! With leakage, $k(r)$ is complex for real r , by (11), and so are $f(r)$ and its caustic roots r_1, r_2 , which Fig. 3 shows in the complex plane of the radius r .

That figure also shows the Stokes lines of the differential equation (9) with each of which is associated an abstract pair of exact solutions of (9) of progressive wave character. The pair of L_0 (Fig. 3) represents the fundamental, incoming and outgoing, wave solutions near shore, the pair of L_∞ represents those in the open sea. The main object of the analysis is to calculate the matrix T which relates these pairs of fundamental solutions of (9), or at least, to estimate T adequately. The difficulty is that adequacy, in view of the importance of modes of the very smallest leakage rate, implies a precision unprecedented for differential equations of the generality and inexplicitness of (9) - (11). Adequate precision, however, has now been achieved [Lozano and Meyer 1976] in respect of the leakage rate.

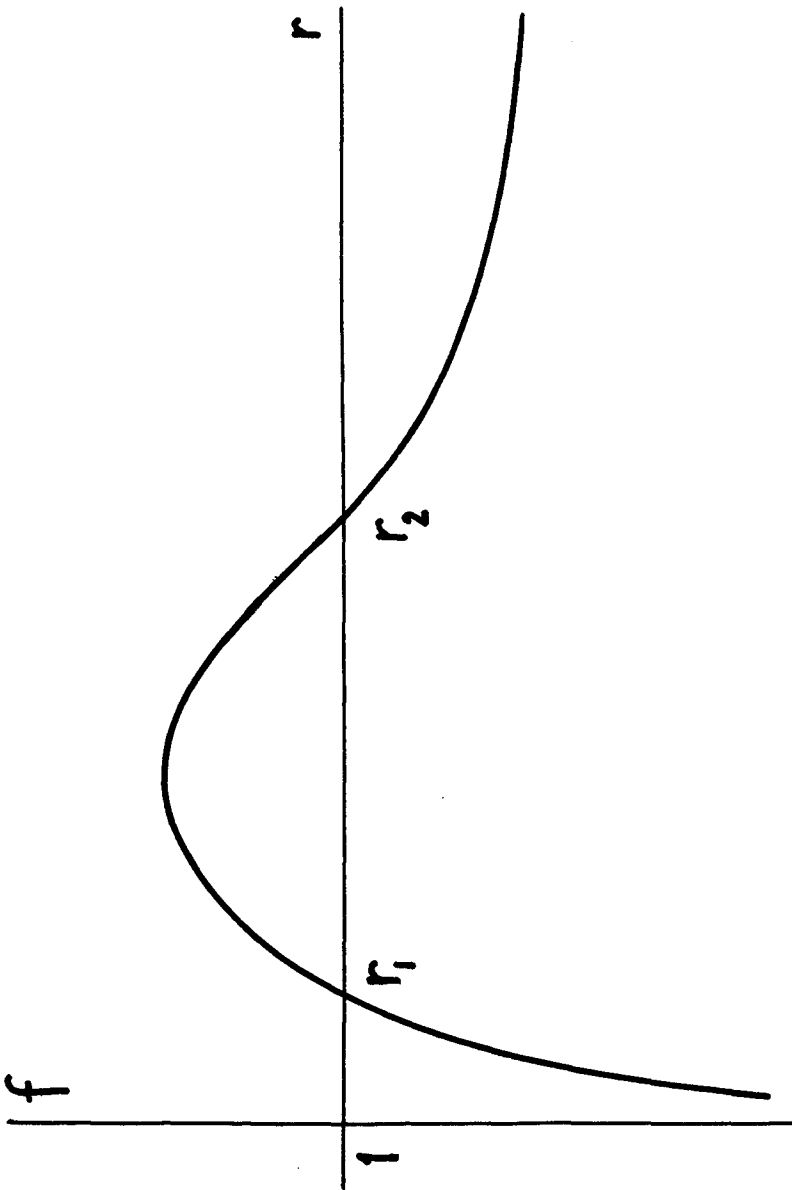


Figure 2

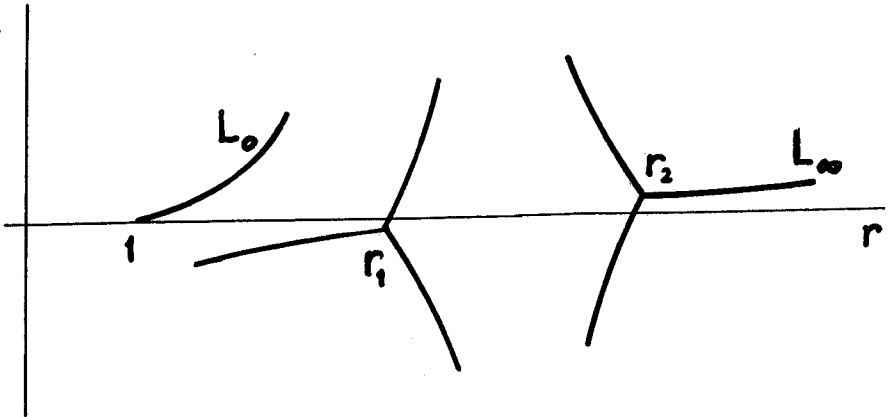


Figure 3

The exact wave solution pairs of the Stokes lines L_0 and L_∞ are of interest because physical boundary conditions are most naturally phrased in their terms. To-date, the radiation condition adopted for natural modes has been that no energy be supplied by radiation from infinity; we envisage a trapped wave mode to be set up, and watch it decay slowly in time by radiation damping. The shore boundary condition adopted to-date has been boundedness of the water velocity at the shore. The reason for it is two-fold, despite its implication of perfect reflection. First, it is successful in edge wave theory [Ursell 1952] and secondly, while a better shore condition could be incorporated into the analysis just as readily, none appears to be known...

The matrix T , which depends on ω , connects these boundary conditions into a characteristic equation [Lozano and Meyer 1976] which can be solved abstractly to deduce rigorous estimates for the eigenvalues. The result is that the frequencies ω_{mn} of Shen, Meyer and Keller [1968] (cf. Section II) are confirmed, with a correction factor of only $1 + O(\omega_{mn}^{-4}) = 1 + O(\epsilon^2)$. In addition, the imaginary part of the eigenvalues is found to be

$$\text{im}(\omega^2) \sim -(2q)^{-1} \exp(-4\pi d) \quad \text{as } \omega_{mn} = \epsilon^{-1/2} \rightarrow \infty \quad (13)$$

where

$$d = (2\pi)^{-1} \omega_{mn}^2 \int_{r_1}^{r_2} |k^2 - n^2 / (\omega_{mn}^4 r^2)|^{1/2} dr \quad (14)$$

would be the width of the damping zone in local "wave lengths," if there were waves in the damping zone... The leakage rate (13) is therefore seen to be exponentially small in ϵ and reciprocally, the response coefficient is exponentially large! In (14), ω_{mn} is found from (2), (5), with $k(r)$ found from the dispersion relation (4). Similarly,

$$q = \int_1^{r_1} |k^2 - n^2 / (\omega_{mn}^4 r^2)|^{-1/2} \frac{k^2 dr}{1 + (k^2 - 1)h}$$

is readily computed by the help of (4).

VI. Quasiresonance

One of the immediate applications of this result is to the standing waves around an island, i.e. monochromatic waves of real frequency ω and surface potential (8). For real frequency, (1) exhibits energy conservation in fixed space-domains [Stoker 1957] and (6), (7) preserve this property. A ratio of respective energy flux levels in the trapped wave ring and in the far field in the open sea is therefore definable [Lozano and Meyer 1976] and its square root represents an amplitude ratio $\rho(\omega)$ characteristic of wave amplification by trapping. This amplification may be computed from the matrix T , given the shore condition of bounded velocity, and is found extremely frequency-dependent. It varies from an exponentially small minimum

$$\min \rho = \frac{1}{2} \exp(-2\pi d) [1 + O(\epsilon)]$$

at a frequency midway between successive eigenfrequencies to an exponentially large maximum

$$\max \rho = \exp(2\pi d) [1 + O(\epsilon)] \quad (15)$$

close to an eigenfrequency [Lozano and Meyer 1976]. The occurrence of such large standing wave amplifications is called quasiresonance in quantum mechanics.

An advantage of the analytical approach is that it promotes an understanding of cause-and-effect relations. The amplification (15) is expressed directly in terms of the intrinsic width (14) of the damping zone that separates the trapped waves from the far field of progressive waves extending to the open sea. This confirms the plausible idea that the wider (in an appropriate sense) the zone of damping, the more it inhibits leakage and promotes amplification. Closer scrutiny permits us to distinguish two effects which promote amplification. First, natural

modes with a large number m of half-wavelengths counted radially across the trapped wave ring have usually a correspondingly wide damping zone. (There are exceptions when n/ω_{mn}^2 is close to the cut-off value so that the maximum of $f(r)$ in Fig. 2 is small and the interval (r_1, r_2) of positive f -values is narrow.)

Secondly, natural modes with $n \gg m$, i.e., with many more crests around the island than radially across the trapped wave ring can occur, and such crests have local character akin to edge waves on a straight coast, which have no leakage. Indeed, as $n \rightarrow \infty$, the analysis can be shown to cover the modes with m not large, even $m = 1$, and the trapped wave ring then becomes narrow by comparison with the island radius. For the spectral conditions (i), (ii) of Section II, however, the relevant scale is the width of the trapped wave ring, and on that scale, the island radius tends to ∞ , the shore appears straight, the waves approach ordinary edge waves, the leakage almost disappears. An indication of this second effect is numerically apparent in Longuet-Higgins' [1967] and Summerfield's [1972] results for long wave trapping by idealized "hedges." Both effects can combine to produce exceptional amplifications due to leakage rates as tiny as [Lozano and Meyer 1976]

$$\text{im } \omega^2 \sim -\pi^{-1} \varepsilon^{2n-1}, \quad n \rightarrow \infty$$

where ε denotes the small beach angle.

The asymptotic estimates for the eigenvalues also permit estimation of the half widths of the resonant peaks of the $\rho(\omega)$ curve of amplification vs. frequency as

$$(4q\omega_{mn}^2 \sqrt{3})^{-1} \exp(-4\pi d)$$

[Lozano and Meyer 1976]. The frequency band width of resonance is therefore seen to be exponentially narrow!

This feature balances the large amplification to some extent, but the resonant modes should still be prominent under many circumstances [Longuet-Higgins 1967] --much in contrast to oceanographical experience and intuition (based on the classical prominence of the lowest modes). Of course, a balanced judgment of such unfamiliar phenomena is not easy at this early stage of their study.

The narrow band width of resonance also suggests experimental and observational difficulties. Scale effects, however, dominated the first experiments [Pite 1973], which indicated the resonant modes to be suppressed by viscous damping in a table-top tank. Laboratory tests on a larger-scale [Barnard and Pritchard 1976] have now detected some of the resonant modes of a sill [Longuet-Higgins 1967].

References

- B. J. S. Barnard and W. G. Pritchard 1976, personal communication.
- J. A. Battjes 1968, Proc. Am. Soc. Civ. Engrs. 94, 437.
- J. C. W. Berkhoff 1973, Proc. 13th Coastal Engrg. Conf., Vancouver, Am. Soc. Civ. Engrs., New York, 1, 471.
- C. J. Galvin 1965, Trans. Amer. Geophys. Union 46, 110.
- J. B. Keller 1958, J. Fluid Mech. 4, 607.
- C. C. Lautenbacher 1970, J. Fluid Mech. 41, 655.
- M. S. Longuet-Higgins 1967, J. Fluid Mech. 29, 781.
- C. Lozano and R. E. Meyer 1976, Leakage and response of waves trapped by round islands, Phys. Fluids 19, 1075.
- R. E. Meyer 1971, Lec. Appl. Math. 13, Amer. Math. Soc., p. 189.
- H. D. Pite 1973, Studies in Frictionally Damped Waves, Ph.D. Thesis, School of Civil Engrg., Univ. New South Wales.
- M. C. Shen, R. E. Meyer and J. B. Keller 1968, Phys. Fluids 11, 2289.
- M. C. Shen and J. B. Keller 1975, SIAM J. Appl. Math. 28, 857.
- J. J. Stoker 1957, Water Waves, Interscience, New York.
- W. Summerfield 1972, Phil. Trans. Roy. Soc. A 272, 361.
- F. Ursell 1952, Proc. Roy. Soc. A 214, 79.

CHAPTER 51

PHYSICS AND MATHEMATICS OF WAVES IN COASTAL ZONES

H. Lundgren*

ABSTRACT

This paper presents a discussion of four methods available for the computation of small amplitude periodic waves in coastal zones of arbitrary topography. With no reflections (or reflection from a single structure) the methods that proceed in space (Refraction and Propagation) or time (Timestep) seem the natural ones from a physical point of view. With repeated reflections, recourse must be taken to the solution of an Elliptic boundary value problem. - It is suggested that a P-method based on (energy) flux lines and energy fronts be developed for cases where the R-methods give crossing orthogonals.

1. WAVE EQUATION

In 1949 Lowell (Ref. 9) derived, for shallow water waves, the wave equation

$$(c^2 \eta_x)_x + (c^2 \eta_y)_y = \eta_{tt} \quad (1)$$

where $c = \sqrt{gh}$ is the local phase velocity, $\eta(x,y;t)$ the surface elevation, and $h(x,y)$ the local depth, while indices x,y,t denote differentiation. For shorter waves c is a function not only of h but also of the period T , and the (reduced) wave equation must be confined to a fixed T , for which $\eta_{tt} = -\omega^2 \eta$, where $\omega = 2\pi/T$. In 1951 Pierson (Ref. 11) asked whether (1) could be derived for an arbitrary period. Indeed, this was easily done from simplified considerations of continuity and equilibrium (Ref. 10).

In 1952 Biéssel (Ref. 4) published the potential theory solution for the two-dimensional case correct to terms of order h_x (slope of bed). On this basis, Svendsen (Ref. 14) in 1967 derived a two-dimensional form of the wave equation that later (Ref. 8) was shown to agree with the three-dimensional form

$$(c c_g \eta_x)_x + (c c_g \eta_y)_y + \frac{c_g}{c} \omega^2 \eta = \nabla \cdot (c c_g \nabla \eta) + \frac{c_g}{c} \omega^2 \eta = 0 \quad (2)$$

where $\nabla = (\partial/\partial x, \partial/\partial y)$. In 1972 Berkhoff (Ref. 2) derived (2) using a surface potential ϕ_0 instead of η (and Schönfeld had obtained it in a different form). c_g is the group velocity.

With the local wave number $k = 2\pi/L = \omega/c$ it is easily seen that the classical shoaling formula for a progressive wave

*Professor of Marine Civil Engineering, Institute of Hydrodynamics and Hydraulic Engineering, Technical University of Denmark, DK-2800 Lyngby. Consultant, Danish Hydraulic Institute.

$$\eta = \frac{1}{2} H_0 \sqrt{c_{g,0}/c_g} \sin \left[\omega t - \int_{x_0}^x k \, dx \right] \quad (3)$$

satisfies the mild-slope equation (2), including terms of the order c_x and $(c_g)_x$, both corresponding to the order h_x , but excluding terms of the order $(h_x)^2$ and h_{xx} . Assuming that (3) holds good also for steeper and curved slopes

$$\nabla \cdot (c c_g \nabla \eta) + \left[\sqrt{c_g} \nabla \cdot (c \nabla \sqrt{c_g}) + \frac{c_g}{c} \omega^2 \right] \eta = 0 \quad (4)$$

(which includes terms $(h_x)^2$ and h_{xx}) should be slightly better than (2). However, Eq. 4 (or the correct formula!) would have to be derived from potential theory and, the improvement is of limited value for most waves, which are not sinusoidal in small depths.

The important *conclusion* of (2) and (3) is that a mild slope does not reflect any energy of the order h_x but, at most, of the order h_x^2 (and hardly of the order h_{xx}). It should be noted that derivatives of η are normally an order of magnitude larger than derivatives of c .

2. R-METHODS (REFRACTION METHODS)

The development of R-methods can be said to have been completed with the establishment of fast, inexpensive computer programs that plot not only the orthogonals but also the wave heights along the orthogonals, taking account of bottom friction (Refs. 12-13). The R-methods will continue to be useful tools in most applications where it is not justified to mobilize better and more expensive methods. In principle, R-methods may be applied to an arbitrary directional spectrum.

The main deficiencies of the R-methods are due to converging and, particularly, crossing orthogonals, in which cases the solutions are unreliable or unusable.

3. E-METHODS (ELLIPTIC METHODS)

An elliptic equation pertains to a problem the solution of which is defined when the boundary conditions along a closed curve are given. (2) is an elliptic equation in (x,y) , corresponding to the fact that wave energy might enter the region bounded by a closed curve from all sides. Particularly, if there are many successive reflections, such as inside harbours, E-methods are the natural tool.

The most common elliptic problem is Laplace equation for which various computational methods are available. The wave equation, however, is distinctly different from Laplace equation because of the last term in (2), giving rise to solutions with wavelengths that are small compared to the region considered. This circumstance eliminates several computational methods.

Finite elements were used by Berkhoff (Ref. 2-3) for the wave motions around an island, over a shoal, and in a harbour basin. Chen and Mei (Ref. 6) also used finite elements, correcting Berkhoff's functional. According to Ref. 3, 5 and 10 elements per wavelength give errors of 10% and 4%, respectively.

In their very nature, E-methods are confined to regions outside the breaker zone.

4. T-METHODS (TIMESTEP METHODS)

By a T-method is understood a method by which the development of the water surface and velocity field is followed over the entire coastal zone, one timestep after the other. Because of the large number of grid points and timesteps, the requirements to storage and machine time are heavy. Despite these difficulties a T-method is, in principle, the only one that - probably in a rather distant future - would be able to handle the general situation of irregular waves in a coastal zone, including breaking, surf and wave-induced currents.

Ito and Tanimoto (Ref. 7) presented examples of T-method calculations, applying an approximate version of the wave equation.

5. P-METHODS (PROPAGATION METHODS)

According to the conclusion in Sec. 1, the reflection from a gently sloping bottom of waves approaching the coast is definitely negligible. (Some swell-exposed beaches are so steep though that they reflect an essential part of the energy.)

In the case of shoals the R-methods give orthogonals that meet at a point (focus) or are tangential to certain curves (caustics), cf. Fig. 1. No reflection can be expected from foci or caustics because, by means of diffraction theory, it has been shown that the rays from a lens pass through the focus without reflection.

It is thus concluded that waves from the sea normally propagate without essential reflection onto the beach where their energy is dissipated. Hence, for periodic waves the elliptic character of the wave equation is rather a mathematical than an important physical property and, therefore, it is highly natural to look for methods where the propagation is followed from deep water into shallower areas, without consideration of the 'future' of the wave motion nearer the beach.

For small waves P-methods should also be applicable if there is a single reflecting structure such as a breakwater. With repeated reflections inside a harbour they are not fit.

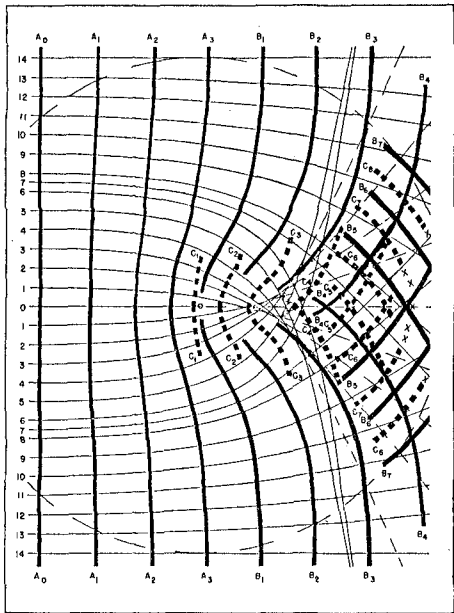


Fig. 1
Refraction orthogonals (thin lines)
and actual fronts (heavy lines)
for waves passing over a clock glass
(from Ref. 11)

The R-methods represent the simplest type of P-methods. A proper P-method should be able to account for the conditions around foci, caustics and crossing orthogonals (Fig. 1).

In principle, the deformation of waves over a gently sloping bottom may also be treated as a P-problem. Hence, in the future computations by P-methods might be continued through breaker and surf zones, though the interaction with wave-induced currents would require iteration.

6. HUYGENS' PRINCIPLE

Historically, Huygens' principle was the first P-method proposed, dealing with the progressive construction of wave fronts. However, because of the smoothing of the wave fronts, it could never produce the crossing orthogonals known to occur in nature (Ref. 11). An attempt at computing refraction with 'moderate diffraction' was made in Ref. 5, with the result that the interference behind the shoal was expressed by wavy orthogonals rather than crossing ones.

Mathematically, any solution to (2) may be written $\eta(x,y;t) = A(x,y) \exp i\omega t$, where A is the complex amplitude satisfying

$$(c c_g A_x)_x + (c c_g A_y)_y + (c_g/c) \omega^2 A = 0 \quad (5)$$

For constant depth (5) simplifies to $A_{xx} + A_{yy} + k^2 A = 0$, valid for all waves in a homogeneous medium. For this special case it has been derived from Green's formula, in 3 dimensions by Helmholtz and in 2 dimensions by Weber (Ref. 1), that A at a point Q_2 inside a closed surface (or curve), S , can be expressed as an integral over S . Weber's formula is

$$A(Q_2) = \frac{1}{4} \iint_S \left[Y_0(kr) \frac{\partial A}{\partial n_1} - A(Q_1) \frac{\partial Y_0}{\partial n_1} \right] ds \quad (6)$$

where Y_0 is the Bessel function of the second kind, $\partial/\partial n_1$ denotes differentiation along the inward normal at the point Q_1 on S , and r is the distance $Q_2 Q_1$, cf. Fig. 2, where line l is only a part of S .

Though (6) has been called the 'mathematical theory of Huygens' Principle' in commemoration of this genius (who advocated the wave nature of light in opposition to Newton), it hardly represents what has been on his mind physically, for the following reason: (6) gives the solution A inside S in the general case where wave energy passes S both inwards and outwards. Since the elliptic wave equation is of the second order, the complete solution A inside S is defined if the values $A(Q_1)$ are given along S . In (6) it seems that $\partial A/\partial n_1$ must also be known on S ; however, in principle, these derivatives can be found by solving a large number of equations established by applying (6) to points inside of and close to S . Thus (6) is the mathematical solution to an elliptic problem with one boundary condition at each point of the closed curve S . In contrast to this, Huygens' physical intuition said that the field of progressive waves would be defined if, along one open curve (a wave front) two boundary conditions were given, viz. elevation + phase (i.e. A) and phase velocity (i.e. $\partial A/\partial n_1$).

7. APPLICATIONS OF HUYGENS' PRINCIPLE

Since the author felt that the physical possibilities of Huygens' principle had not been fully explored, he made - in cooperation with

Dr. Uri Kroszynski - an attempt at calculating the wave motion at Q_2 (Fig. 2) from a knowledge of the wave conditions along line 1.

It was found that the basic formula should be

$$A(Q_2) = \frac{1}{2} \iint \left[Y_0(k_2 r) \frac{\partial A}{\partial n_1} - k_2 A(Q_1) Y_1(k_2 r) \cos q_1 \right] ds_1 \quad (7)$$

where k_2 is the wave number at Q_2 and Y_1 the negative derivative of Y_0 . The factor $1/2$ in (7) indicates that, for constant depth, the integral along the infinite line 1 contributes one half to $A(Q_2)$ in (6), while the other half originates from the integral over an infinitely large semicircle.

It is assumed that the computation of the propagating wave has reached line 1, which is straight or curved. Normally, lines 1 and 2 will not be wave fronts but be chosen in a convenient manner in relation to the topography of the sea bed. According to (7), all points along line 1 have an influence on the wave motion at any point Q_2 on line 2.

The influence coefficients, Y_0 and $k_2 Y_1 = -dY_0/dr$, appearing in (7) correspond to the effects at Q_1 of a wave that spreads from Q_2 uniformly in all directions. These Bessel functions define the diverging wave exactly only when the depth is constant. When r is large, an essential depth variation may be expected between Q_2 and Q_1 , introducing an error by the application of the Bessel functions. The error is reduced, however, partly by the oscillatory character of these functions (corresponding to the varying phase difference from Q_1 to Q_2) partly because the influence from Q_1 diminishes as $1/\sqrt{r}$ when r approaches infinity. Still, the assumption underlying (7) is that the distance between lines 1 and 2 is not too large.

Eq. 7 has been applied to the case of simple shoaling over a plane slope with a depth reduction of 10% in one wavelength. For a distance of $L/8$ from line 1 to line 2, $A(Q_2)$ was found to deviate 0.5% from the correct value, while the error was 2% for a distance of $L/4$.

Thus there is hope that Huygens' principle will eventually materialize in a numerical method applicable to general situations with a reasonably large space propagation step. With the accumulation of errors in a purely explicit method, it is believed that (7) should be somewhat modified. Because of the step size, asymptotic expressions requiring little computation may be used for the Bessel functions Y_0 , Y_1 and Y_2 , of which Y_2 occurs in the expression for the derivative $\partial A/\partial n_2$ (Fig. 2).

It is probable that (7) can also be applied to the combined diffraction and refraction around a breakwater, including reflection from it.

8. FLUX LINE METHOD

In analogy to the R-methods it seems possible to construct diagrams of energy flux lines, transcribing (5) into orthogonal, curvilinear coordinates consisting of flux lines and energy fronts. The computation

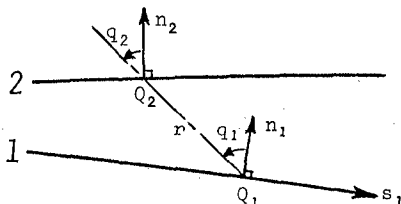


Fig. 2 Influence at Q_2 of wave motion at Q_1

progresses simultaneously along all flux lines. The crucial point of the method is, in analogy to (3), to utilize the energy velocity c_e for direct integration along the flux lines, thus reducing the difficulty of the spatial phase variation, which requires much machine time for E- and T-methods.

The variation of A along the energy fronts influences c_e , as can be seen from the interference of two similar wave trains propagating at right angles to each other. The phase velocity is then $c\sqrt{2}$ with maximum flux along the lines where the 'double crests' propagate.

REFERENCES

1. Baker, B.B. and E.T. Copson: The mathematical theory of Huygens' principle. (Oxford Clarendon Press) 2nd edit. 1953.
2. Berkhoff, J.C.W.: Computation of combined refraction-diffraction. Proc. 13th Coastal Engrg. Conf., Vancouver (1972). Am. Soc. Civ. Engrs., 1, pp. 471-490, 1973.
3. Berkhoff, J.C.W.: Linear wave propagation problems and the finite element method. In: Finite Elements in Fluids, Eds. R.H. Gallagher et al. (Wiley), 1, pp. 251-264, 1975.
4. Biésel, F.: Study of wave propagation in water of gradually varying depth. Gravity Waves. Proc. NBS Semicentennial Symp. on Gravity Waves, Wash., D.C. (1951). Nat. Bur. Stds. Circ. 521, pp. 243-253, (U.S. Gov. Print. Off.) 1952.
5. Biésel, F.: Refraction de la houle avec diffraction modérée. Proc. 13th Coastal Engrg. Conf., Vancouver (1972). Am. Soc. Civ. Engrs., 1, pp. 491-501, 1973.
6. Chen, H.S. and C.C. Mei: Oscillations and wave forces in an offshore harbor. Applications of hybrid finite element method to water-wave scattering. Ralph M. Parsons Lab. for Water Resources and Hydrodyn., Mass. Inst. Tech., Rep. 190, 215 pp., 1974.
7. Ito, Y. and K. Tanimoto: A method of numerical analysis of wave propagation. Application to wave diffraction and refraction. Proc. 13th Coastal Engrg. Conf., Vancouver (1972). Am. Soc. Civ. Engrs., 1, pp. 503-522, 1973.
8. Jonsson, I.G. and O. Brink-Kjær: A comparison between two reduced wave equations for gradually varying depth. Inst. Hydrodyn. and Hydraulic Engrg., Tech. Univ. Denmark, Progr. Rep. 31, pp. 13-18, 1973.
9. Lowell, S.C.: The propagation of waves in shallow water. Comm. Pure and Appl. Math., 2, No. 2/3, pp. 275-291, 1949.
10. Lundgren, H.: The wave equation for gravity waves in water of varying depth. Coastal Engrg. Lab. and Hydraulic Lab., Tech. Univ. Denmark, Basic Res. - Progr. Rep. 7, pp. 2-5, 1964.
11. Pierson, W.J.: The interpretation of crossed orthogonals in wave refraction phenomena. Beach Erosion Board, Tech. Memo. 21, 1951.
12. Skovgaard, O. and J.A. Bertelsen: Refraction computations for practical applications. Proc. Int. Symp. Ocean Wave Meas. and Anal., New Orleans. Am. Soc. Civ. Engrs., 1, pp. 761-773, 1974.
13. Skovgaard, O., I.G. Jonsson, and J.A. Bertelsen: Computation of wave heights due to refraction and friction. Proc. Am. Soc. Civ. Engrs., 101, WW1, pp. 15-32, 1975.
14. Svendsen, I.A.: The wave equation for gravity waves in water of gradually varying depth. Coastal Engrg. Lab. and Hydraulic Lab., Tech. Univ. Denmark, Basic Res. - Progr. Rep. 15, pp. 2-7, 1967.

CHAPTER 52

HURRICANE TIDE FREQUENCIES ON THE ATLANTIC COAST

FRANCIS P. HO¹

I. INTRODUCTION

HISTORICAL BACKGROUND

Hurricane surge is a serious and not uncommon event along the Gulf of Mexico and Atlantic coasts of the United States. The most disastrous display of hurricane forces in recent decades was by Camille, which struck the Mississippi coast in 1969. The storm tide reached 24.6 ft MSL. Reported storm tides on the Atlantic coast have reached elevations of 15 to 20 ft in Florida, Georgia, the Carolinas and New England.

One of the latest coordinated efforts to alleviate losses from hurricanes -- supplementing warning services, community preparedness, and evacuation plans-- is the Flood Insurance Program.

NATIONAL FLOOD INSURANCE PROGRAM

The National Flood Insurance Act of 1968 provides for a cooperative program between the United States Government and private industry for insuring residences and small businesses against floods. The program is administered by the Federal Insurance Administration (FIA). Other federal agencies assist by making technical studies.

Essential to establishing flood insurance rates in any community, whether on the coast or an inland valley, is a flood frequency analysis. Flood frequencies are also used as guides in formulating local zoning and flood plain occupancy ordinances. The 100-yr level (1% chance of being exceeded in any year) is the main criterion for this. The 10-, 50-, and 500-yr levels are also required by FIA regulations.

II. JOINT PROBABILITY METHOD OF THE TIDE FREQUENCY ANALYSIS

Hurricane tide frequency analyses have been made by the National Oceanic and Atmospheric Administration (NOAA) for the open coasts of the states of Florida, Georgia, the Carolinas, Virginia, Maryland, and Delaware, and also Puerto Rico (Fig. 1). The method that NOAA has developed for coastal tide frequency analysis, has come to be known as the joint probability method, and was first applied to Atlantic City, N.J. (13). Refinements of this method have been made over several years and the method extended to other sections of the Atlantic coast (e.g., 1, 14).

¹Meteorologist, Office of Hydrology, National Weather Service, National Oceanic and Atmospheric Administration, Silver Spring, Md.

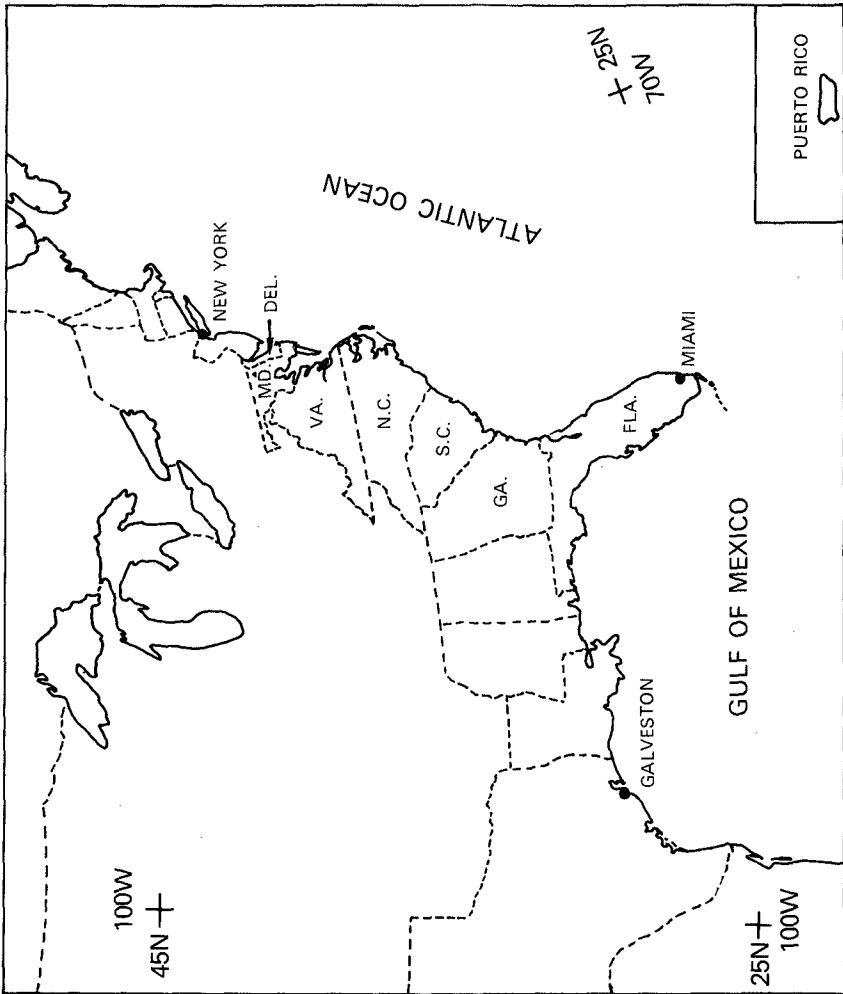


Figure 1.--Location map.

With geophysical data of all kinds, models are used to convert available information to other forms needed but not directly available. The application here is to derive storm tide data from hurricane atmospheric parameters. The first step is to assess from past records the magnitude and frequency distribution of hurricane parameters that are related to surge generation along the coast. The second step is to calculate the coastal surge levels that each of a number of combinations of the hurricane parameters would produce. For this, a dynamic calculation method is used that has been demonstrated to reproduce hurricane surges within an acceptable tolerance. Enough combinations are used to represent the entire range of possibilities. Third, the computed hurricane surges are each combined with the astronomical tide with various time displacements between surge peak and high and low tide. The range of the astronomical tide is also varied.

The frequency of each computed storm tide is worked out from the hurricane parameter and astronomical tide probabilities in a manner briefly described later. Winter coastal storm tide frequencies are estimated at tide gage sites by a statistical analysis. Finally, the hurricane and winter storm tide frequencies are summed to yield the total tide frequencies from all storms.

HURRICANE PARAMETERS

There are four parameters used to compute the surge associated with a hurricane. The first of these is the central pressure, a universally used index of hurricane intensity. The radial profile of sea-level pressure vs. distance from storm center (panel A of Fig. 2) shows a sharp increase within the first few miles with the curve flattening out at greater distances. The distance from the storm center to the area of maximum winds is symbolized by R (schematically shown on B of Fig. 2). R is used as the index of the lateral extent of the storm and referred to as radius of maximum winds. The third and fourth parameters are the forward speed of the storm and the direction of the storm motion. These parameters can be scaled from a hurricane track as illustrated in panel C of figure 2. The lower righthand panel (D) illustrates the dimensions of a hurricane tide. This is a profile of hurricane Hazel's tide observed along the coast. The coastal distance is measured from the point of landfall of the storm center near the North Carolina - South Carolina border.

PROBABILITY DISTRIBUTION OF HURRICANE PARAMETERS

Figure 3 illustrates the climatological analysis of these hurricane parameters. The data sample is collected from all hurricanes exceeding a certain intensity and striking or passing close to the coast within a prescribed span of years. The data are plotted on accumulated probability diagrams as shown in the figure for coastal segments approximately 400 n.mi. in length, for each of the four hurricane parameters. Similar graphs are obtained for the entire coast, for about 60 overlapping zones centered at 50-n.mi. intervals.

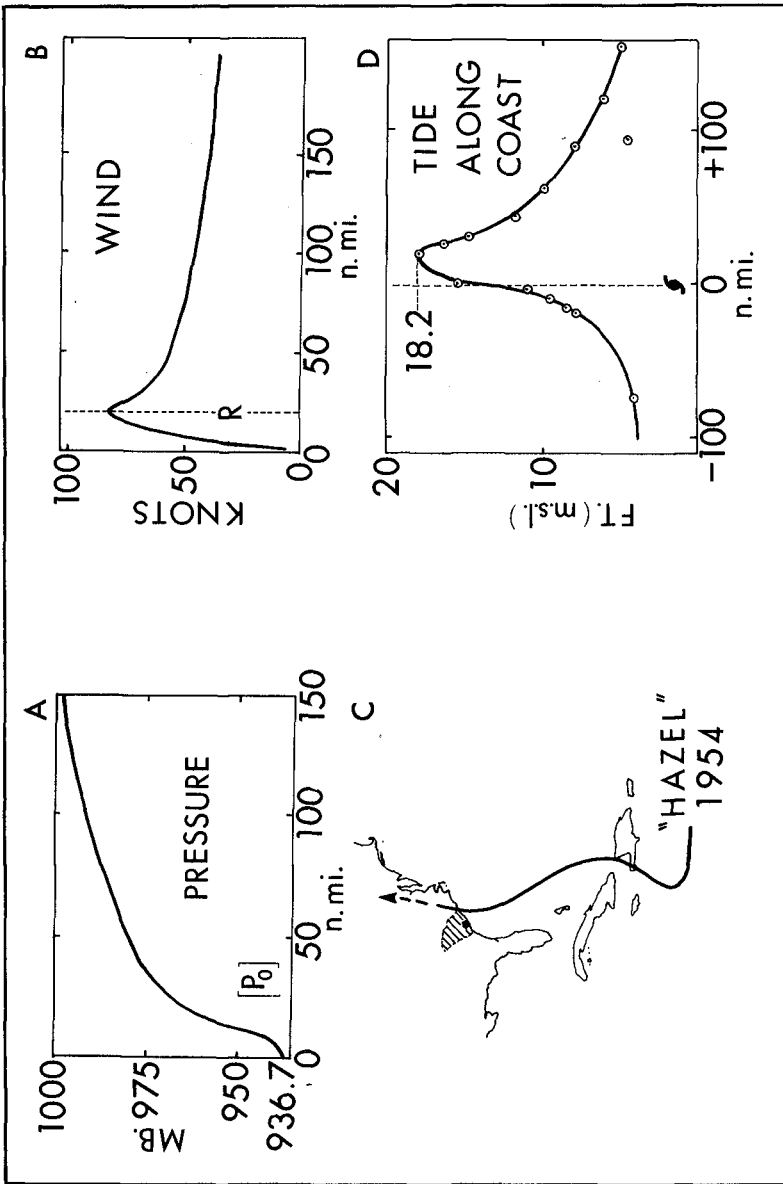


Figure 2.--Examples of basic characteristics of hurricanes from Hurricane Hazel.

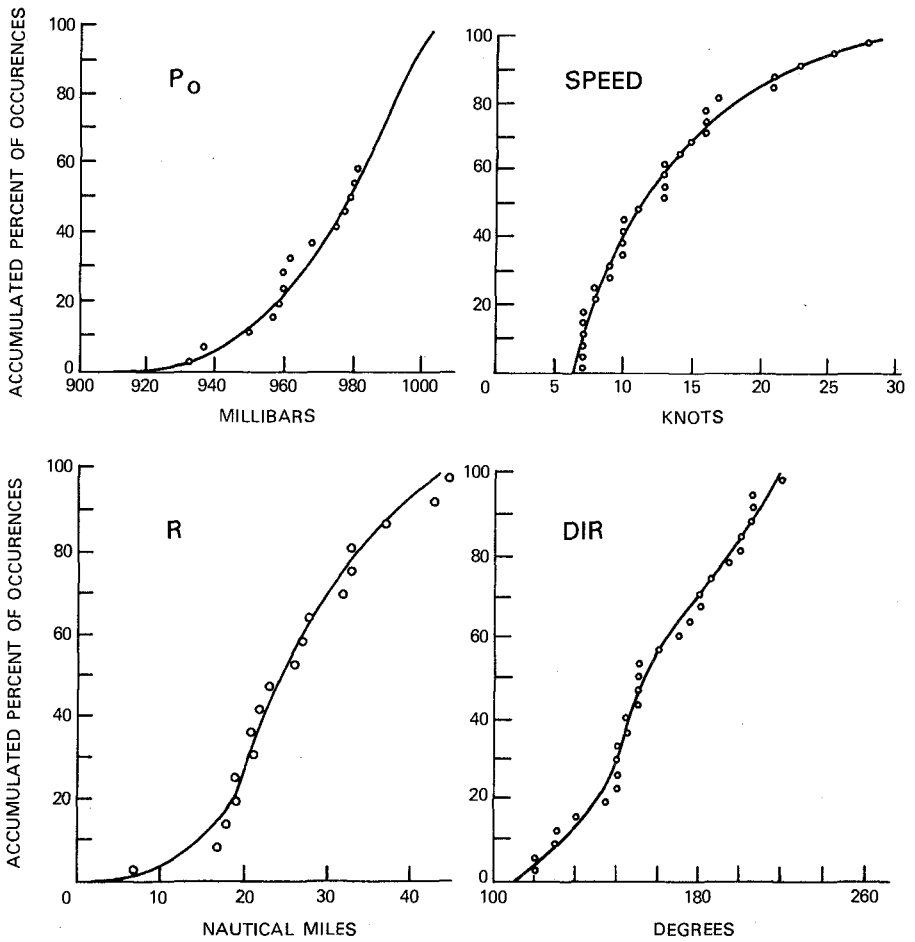


Figure 3.--Hurricane parameters -- data and probability distribution curves for a coastal zone.

Next, values at certain probability levels are read from each of these graphs and smoothed along the coast by applying a weighting function. The resultant coastal profiles for the central pressure are shown in figure 4 (reproduced from Fig. 11 of ref. 4), depicted as lines joining values at the percentiles indicated inside the right margin. The distance scale for the abscissa is measured along a smoothed coastline running from Texas to Maine. The diagram indicates that the minimum central pressures are expected in the Florida Keys, where the most intense hurricane in the western hemisphere, with central pressure of 892 mb, was reported. The trends in the curves reflect the fact that hurricanes tend to become less intense with increasing latitude.

The R in hurricanes affecting the United States coast since 1900 was subjected to a frequency analysis in overlapping zones in the same manner as central pressure. Forward speeds were scaled from track charts and a probability analysis made as with the other parameters, except that hurricanes landfalling on the coast and those bypassing the coast (alongshore hurricanes) were analyzed separately. The direction of forward motion analysis was restricted to landfalling storms. For this, all tracks of tropical cyclones since 1871 were used. For numerical calculations of surges, alongshore hurricanes are treated as if they were moving exactly parallel to the coast.

HURRICANE FREQUENCY

In addition to the distributions of these hurricane characteristics, the overall frequency of hurricane occurrences is basic to calculating hurricane tide frequencies. The frequency of occurrences is assessed by counting tracks (separately for landfalling and alongshore) and smoothing the counts along the coast, similar to the other parameters.

Figure 5 shows the frequency of landfalling hurricanes (from ref. 4). The frequency varies from a minimum of 0.1 storms per 10 n.mi. of smoothed coastline per 100 years near Boston, to maxima of 2.2 in the middle of the Gulf coast and in the Florida Keys.

Similar analyses were made for alongshore hurricanes, and for hurricanes that exited the coast after an earlier entry of the coast elsewhere. Because of hydrodynamic factors, exiting hurricanes give half or less the surge heights as landfalling hurricanes of the same intensity. Exiting hurricanes also tend to have weakened while passing over land and contribute little to the frequency of high storm tides.

WINTER COASTAL STORMS

From time to time, winter coastal storms originating in mid-latitudes also cause millions of dollars of damage along the northern part of the Atlantic coast. At the 100-yr return period storm tide magnitude the activating storms are hurricanes and the additional contribution by winter coastal storms is generally small. The contribution to storm tide frequency of the latter may be evaluated with sufficient precision by direct analysis of long period tide gage records, and interpolation along the coast. These storms are taken into account in coastal storm tide frequency analysis north of Cape Hatteras, but their frequency of occurrence and characteristics are not discussed further in this paper.

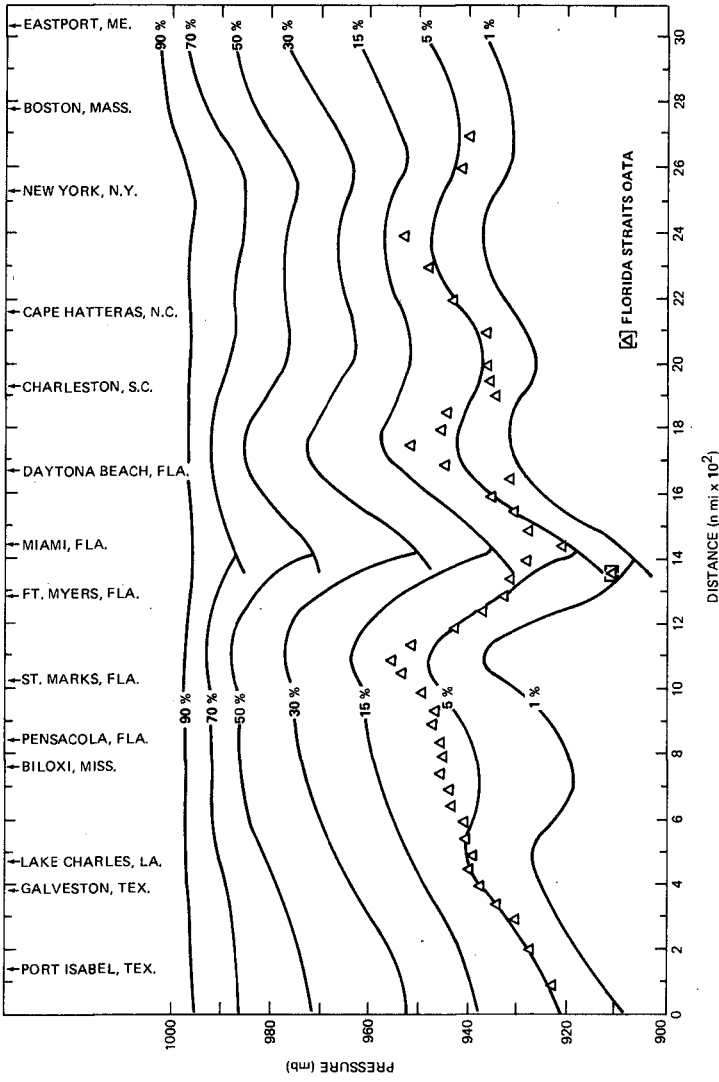


Figure 4.--Hurricane parameter probability profiles along coast -- central pressure. Based on 1900-74. Plotted points (Δ) are taken from frequency analyses at 50-n.mi. intervals for the 5th percentile.

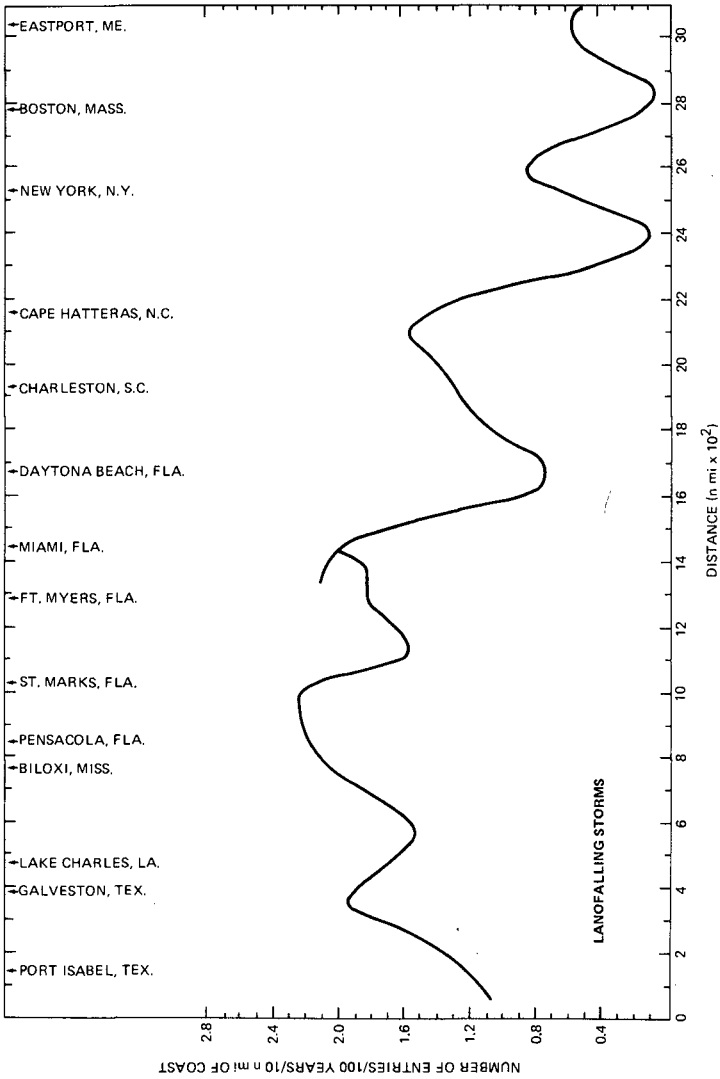


Figure 5.--Frequency of landfalling hurricanes and tropical storms based on 1871-1974.

HYDRODYNAMIC SYNTHESIS

Having defined the hurricane climatology, the next step in the tide frequency analysis is the simulation of hurricane surges. A hydrodynamic-numerical model, called SPLASH, has been developed by Jelesnianski (9, 10) for calculating the surge produced by a hurricane moving over the continental shelf. The model simulates the moving wind and pressure fields over the sea from the basic parameters described above, then computes the surge produced by these fields. This model was developed to predict storm tides when a hurricane approaches, as part of the public warning service of the National Weather Service. The operational application of this model is described in separate reports (11, 12). The same model is used here to compute storm surges from climatological possibilities for frequency analysis.

SHOALING FACTOR

Because of dynamic effects, the surge height that a given hurricane will produce at the coast varies with the shape of the continental shelf. The bathymetry effect on storm surges is handled by the use of a shoaling factor². The shoaling factor is the ratio of the peak surge height that a standard hurricane would produce in a given locale compared to the maximum surge height the same storm would produce over a "standard basin." Figure 6 shows the coastal profiles of the shoaling factor for two different radii of maximum winds. The application of this will be described later.

ASTRONOMICAL TIDE

Another feature of hurricane tides, shown in figure 7, is illustrated by observed tides at Charleston, S.C. in Hurricane Gracie. This diagram includes curves depicting three different water levels. The normal astronomical tide is shown by the solid curve. The dashed curve is the tide level actually observed during the storm. The difference between these is by definition the "surge." That is, the surge is the storm effect, and the graph of this is shown in the lower panel. The surge reached a magnitude of 8.3 ft MSL but, since this was coincident with low astronomical tide, the observed tide peaked at only 5.6 feet. If the same storm had coincided with the normal high astronomical tide, the hurricane tide would have reached 11.2 ft; if the storm were coincident with spring tide, the water level would have been 12 ft. This illustrates the fact that in a synthetic calculation of storm tide frequencies, the relative phasing of storm surge and astronomical tide should be taken into account.

FREQUENCY DISTRIBUTION OF HIGH AND LOW TIDES

Most of the combinations of forces producing the astronomical tides are experienced during a 19-yr cycle. There is also a seasonal variation in the mean water level with the maximum in September-October in most of the study

²The same topic is also discussed by Barrientos and Jelesnianski: "A Numerical Model for Forecasting Hurricane Storm Surges," in the storm surge section of these proceedings.

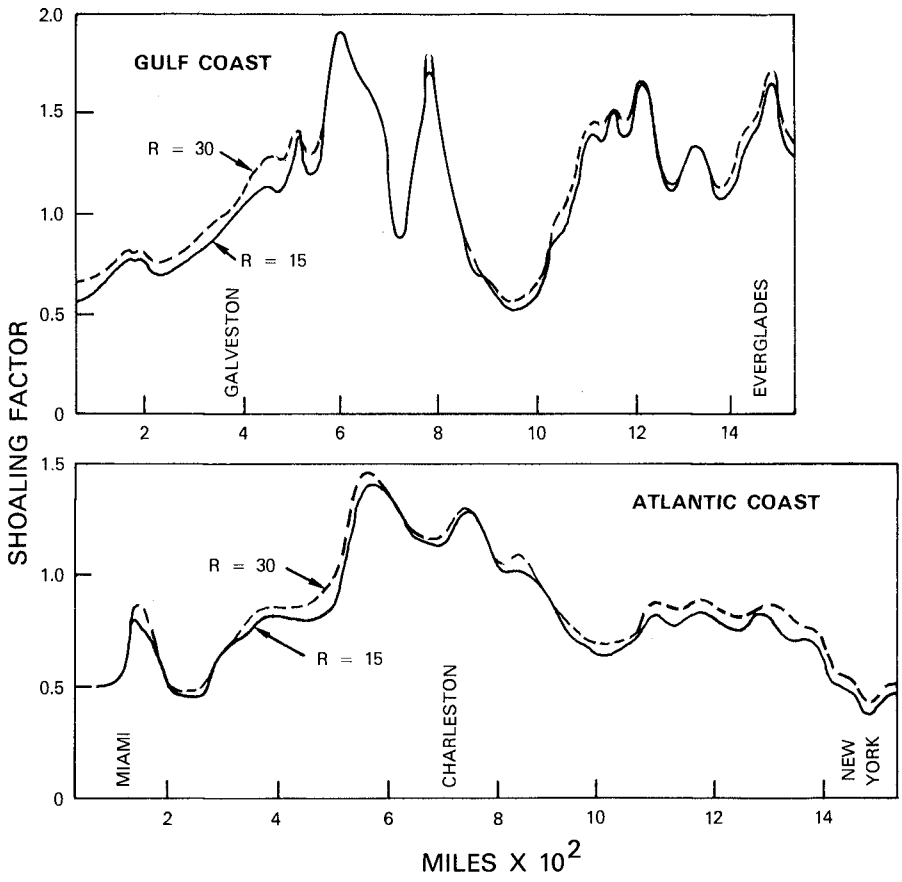
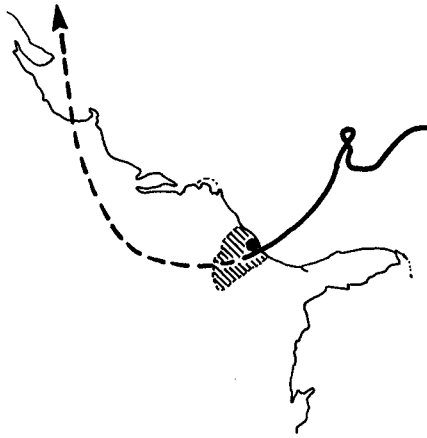
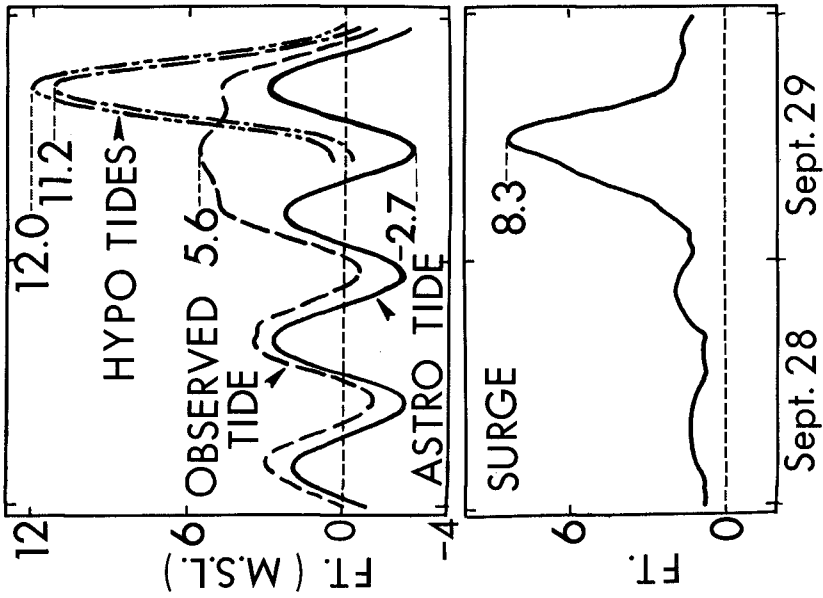


Figure 6.--Shoaling factor curves for Gulf of Mexico and east coasts. R in statute miles.



"GRACIE"
Sept. 1959

Figure 7.--Difference between surge, astronomical tide, and storm tide. Hypothetical combination illustrated by Hurricane Gracie of September 1959 at Charleston, S.C.

area. The months July, August, September, and the first half of October are taken to represent the hurricane season. Astronomical high and low tides for these representative months are recomputed for a 19-yr period with the standard tide computation program written by Pore and Cummings (18). The accumulated frequencies of the high and low tides are calculated separately by months, then weighted in proportion to hurricane occurrences in each month at a particular location. Each distribution is divided into four range class interval values. The representative astronomical tide marigrams needed to combine with each hurricane surge marigram are then approximated as cosine waves with a period of 12.42 hours oscillating between corresponding high tide and low class interval values. This assumes that the highest high tides occur with the lowest low tides, etc. The foregoing calculations are carried out at tide stations and then interpolated along the coast as needed.

COMBINATION OF ASTRONOMICAL TIDE AND HURRICANE SURGE

To combine calculated storm surges with the astronomical tide in search of the maximum height of the combination, the time variation of both is needed. The SPLASH program computes the surge height at grid points every 2.5 minutes. For combining surge profiles and the astronomical tides for the indicated purpose of finding the statistical distribution of maximum total, the asymmetry of the rise and fall of the surge and the non-simultaneity along the coast of the time of maximum surge height in a particular case make no difference. The only requirement is to know how long the surge remains above each height. A saving in computation time is made by precomputing the time variation from a number of representative SPLASH surge computations, then normalizing these by fitting to two parameters. The time variation of the coastal surge is then approximated by a Gaussian curve defined by the maximum surge height, S_x , (in feet) and the time that the surge exceeds 2/3 of S_x , $t_{2/3}$ (in hours). The time variation is then described by:

$$s = S_x e^{-.40547(2t/t_{2/3})^2} \quad (1)$$

where t is the time (in hours) after the occurrence of the maximum surge and $t_{2/3}$ is the time duration indicated above. For the justification for this, the reader is referred to a previously cited report (13).

Each surge is combined with astronomical tide in 84 different ways. These are 21 phasing displacements from low-tide coincidence to high-tide coincidence and four amplitudes of the astronomical tide, ranging from neap tide to spring tide.

III. HURRICANE TIDE FREQUENCY

Hurricanes striking a point of interest are represented by all possible combinations of selected values of the hurricane parameters. This could be, for example, six different central pressures, three R's, three directions of motion, and six speeds, a total of 324 hurricanes. Surges are computed for the 324 storms, with both time and space variation defined. (A SPLASH computation yields surge heights at 8-mi intervals on the coast for specified time increments).

Allowing the same set of hurricanes to strike various points up and down the coast gives a multiple of 324 hurricanes. The surge height produced by each of these hurricanes can be approximated by shifting the surge envelope from a SPLASH computation and applying the shoaling factor adjustment mentioned earlier. Each surge is combined with astronomical tides in the ways described.

The frequency of each of these hurricane tides is the product of the storm parameter probabilities, the landfalling frequency, and the astronomical tide probability. The accumulative frequencies of all these hurricane tide events are plotted as a tide frequency curve for the landfalling hurricanes. Alongshore storms are treated in a similar manner and the two frequency curves summed.

Statistical interdependence of hurricane parameters is handled by assigning conditional probabilities. For example, the speed of storm motion is defined separately for landfalling and alongshore hurricanes. Similarly, a different central pressure distribution is used for small R storms than for medium and large R storms. Details are given in cited reports.

Figure 8 illustrates a typical tide frequency diagram -- a plot of storm tide level against return period, for Rehoboth Beach, Del. The landfalling hurricane tide frequency curve and the alongshore hurricane tide frequency curve are computed separately by the procedure just described. The tide frequency curve from winter coastal storms is obtained by direct statistical analysis of tide gage data.

Summing the frequencies (reciprocal of return periods) of these three classes of storms at each tide level gives the frequency that level of tide is equaled or exceeded, from all storm classes. The figure indicates the contributions made by the different classes of storms. The winter coastal storm is the major factor contributing to the lower end of the frequency curve. The alongshore hurricanes contribute significantly to the recurrence intervals of 100 - 200 years; the landfalling hurricanes contribute most to the more rare return periods. This is typical in the study area north of the entrance of Chesapeake Bay (8). For coastal areas to the south, the tide level produced by landfalling hurricanes is the prime factor in the total storm tide frequencies (e.g., 6, 7).

COMPARISON OF FREQUENCY CURVE WITH HISTORICAL HURRICANE TIDE DATA

Repeating the same process at another point on the coast, we obtain a tide frequency curve, as shown in figure 9 for Savannah Beach, Ga. (1). The 100-yr tide level reaches 14-1/2 ft MSL. It should be noted here that the computed tide frequencies are of still-water levels on the open coast that would be measured in a tide gage house or other enclosure, excluding wave action. The plotted points are the five highest observed high-water marks at Savannah Beach since 1854. This is to verify the correspondence of the computed frequency curve to the local historical record. Other localities with a long period of observed high-water mark records also indicate similar good fit to the computed tide frequency curves, but there are exceptions in some places. The indirect method described, of course, gives hurricane tide frequencies where there are no or few historical storm tide data.

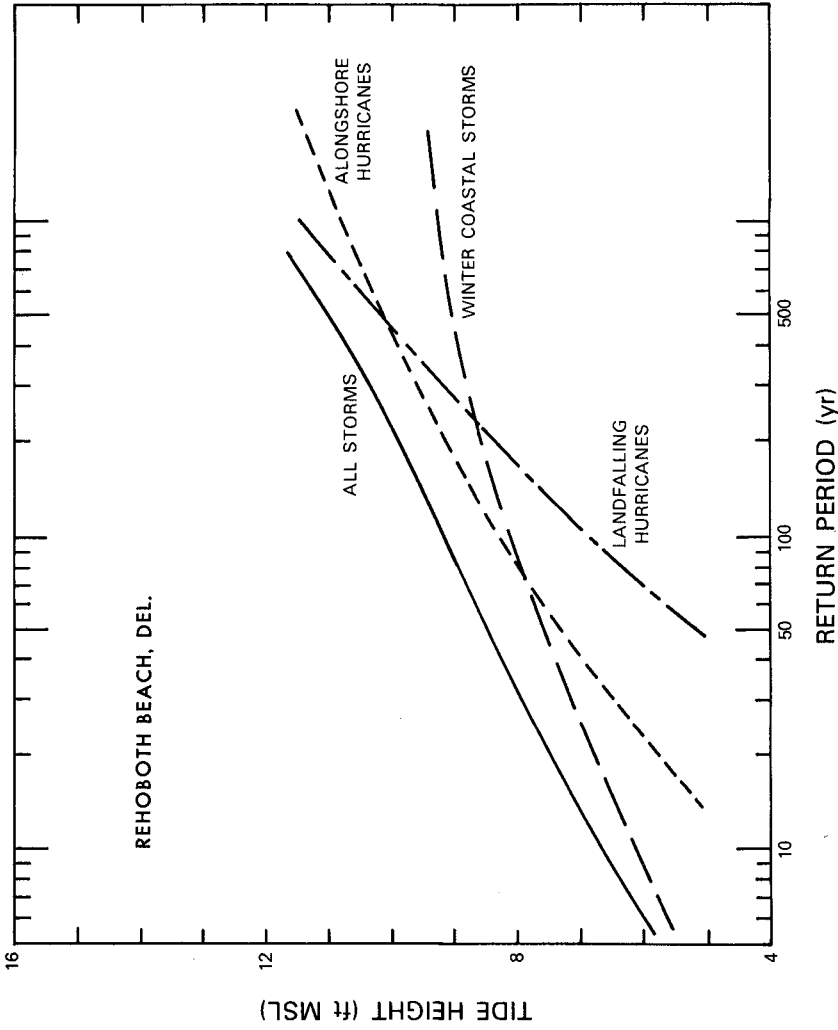


Figure 8.--Tide frequency curves to illustrate significant contribution of alongshore hurricanes, landfalling hurricanes and winter coastal storms.

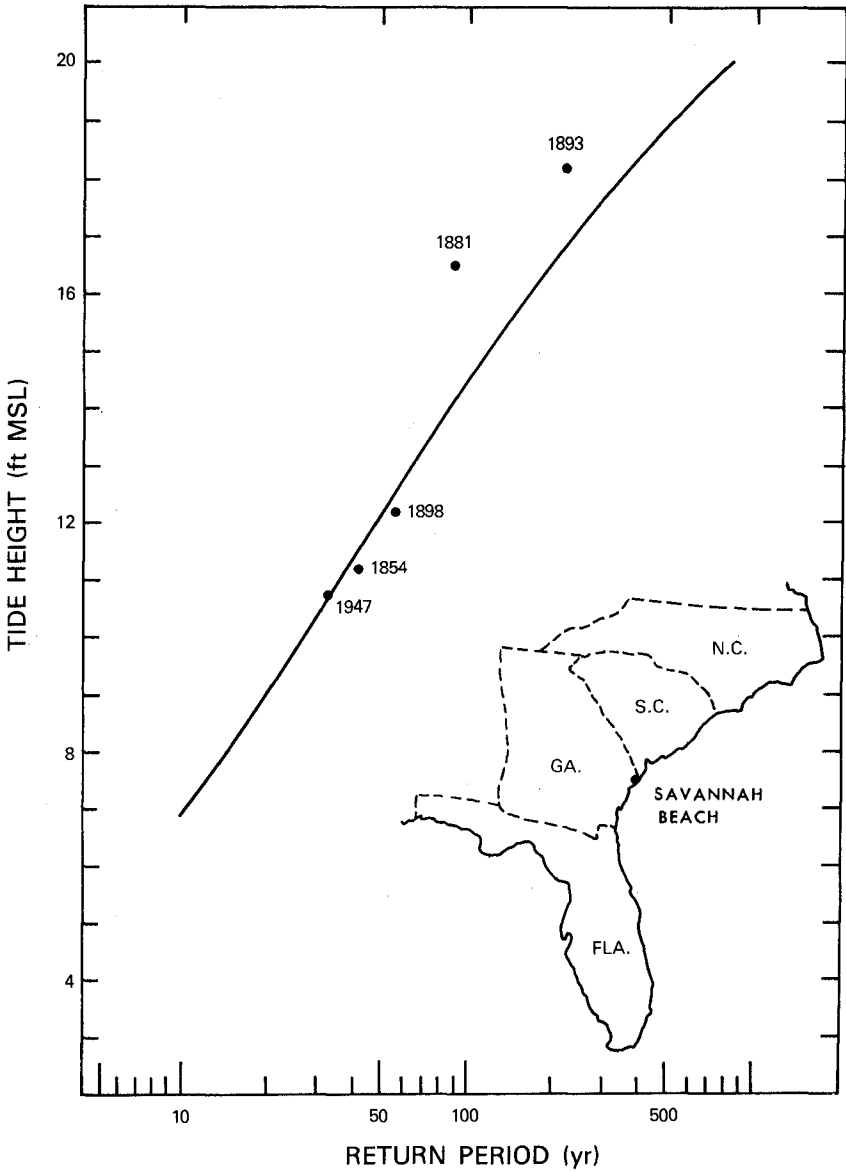


Figure 9.--Comparison of computed tide frequency curve at Savannah Beach, Ga., and high-water marks.

COASTAL PROFILES OF TOTAL TIDE FREQUENCY

Interpolating from results of tide frequency analyses at many points, we have coastal profiles of tide frequencies. Figure 10 shows such profiles for a portion of the Atlantic coast for the 10-yr, 100-yr, and 500-yr recurrence intervals. The 100-yr tide frequencies vary from about 16 ft MSL south of Savannah, Ga., and 14 ft near Miami, Fla., to a low of about 8 ft along the northern portion of the Florida peninsula.

In summary, these coastal variations are associated with the variations of hurricane parameters and the shoaling factor along the coast, illustrated schematically in figure 11. The 100-yr tide frequency profile in the figure is copied from figure 10 (heavy line). Effects of bathymetry are reflected in both the 100-yr tide profile and the shoaling factor curve. The rapid northward decrease of the 100-yr tide level on the Florida coast is related to both the decreasing frequency of hurricane occurrence northward, and weaker hurricane intensities as indicated by the decreasing ΔP curves, ΔP being the depression of the central pressure of a hurricane below its peripheral pressure.

North of Cape Hatteras both the ΔP and the hurricane frequency curve (which pertains to landfalling storms) decrease. The 100-yr flood level remains about the same because of increased frequency (not shown on the diagram) of by-passing hurricanes. Higher storm speeds and larger R 's are also compensating factors which tend to increase the storm tide levels in this region.

IV. OTHER STUDIES

Hurricane tide frequency profiles along the Gulf coast of Florida have been obtained in the same manner as for the southern Atlantic coast (5). Other sections of the Gulf coast are not covered in this series of studies. Hurricane tide frequencies on the coast of Puerto Rico have also been developed from a set of climatologically representative hurricanes, using the NWS numerical dynamic surge model adapted to local conditions (2).

NOAA has also extended the joint probability method of tide frequencies in bays and estuaries as part of the Flood Insurance Program (3, 15). Apalachicola Bay in Florida and the Cape Fear River estuary in North Carolina were selected for pilot projects. Hydrodynamic models had to be developed for routing hurricane tides into the bay and the estuary respectively (16, 17). Again, without going into details, this development leads to hurricane tide frequency estimates in the selected bay and estuary by storm tide simulation.

V. CONCLUSION

The tide frequency analysis technique developed by NOAA has been extended along the Atlantic coast. The simulation method has the advantages of giving results that are consistent from one stretch of coast to another, and for giving a result where there is little local data available. Tide frequencies estimated in this way form the technical basis for flood hazard boundary maps prepared for the Flood Insurance Program for communities subject to inundation from the sea.

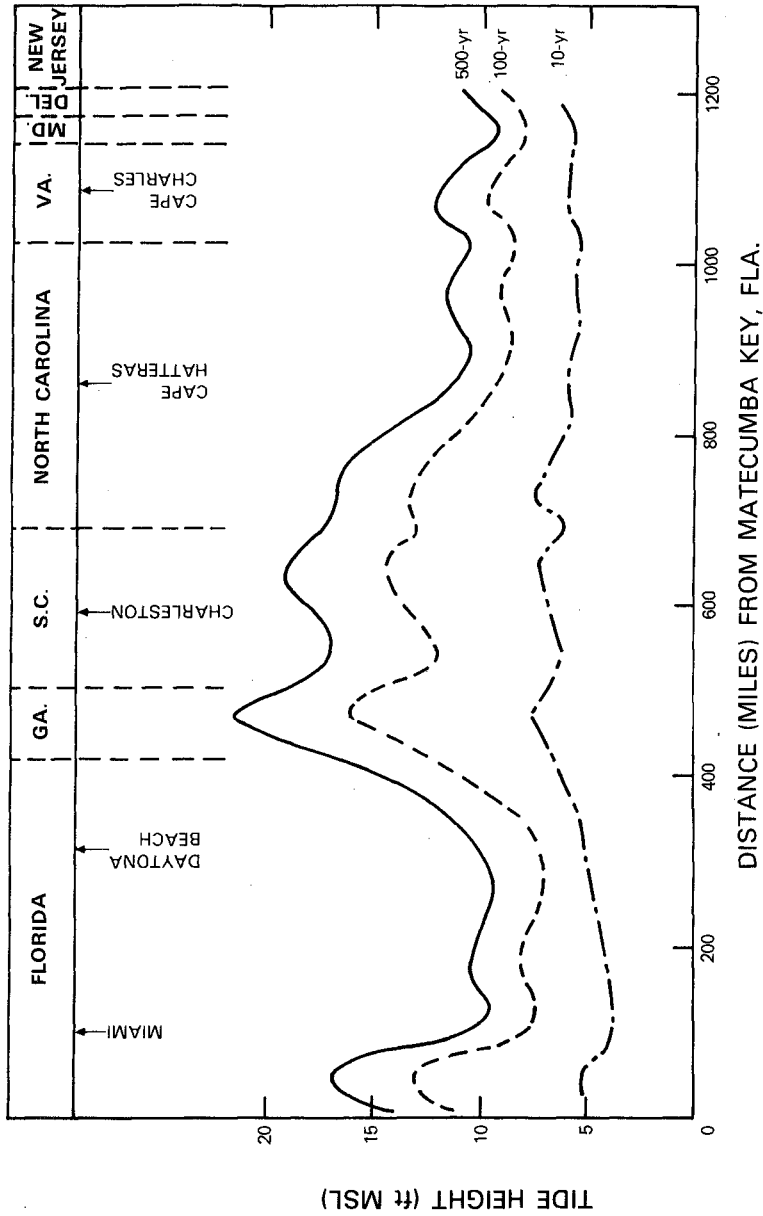


Figure 10.---End product -- tide frequency profiles along open coast.

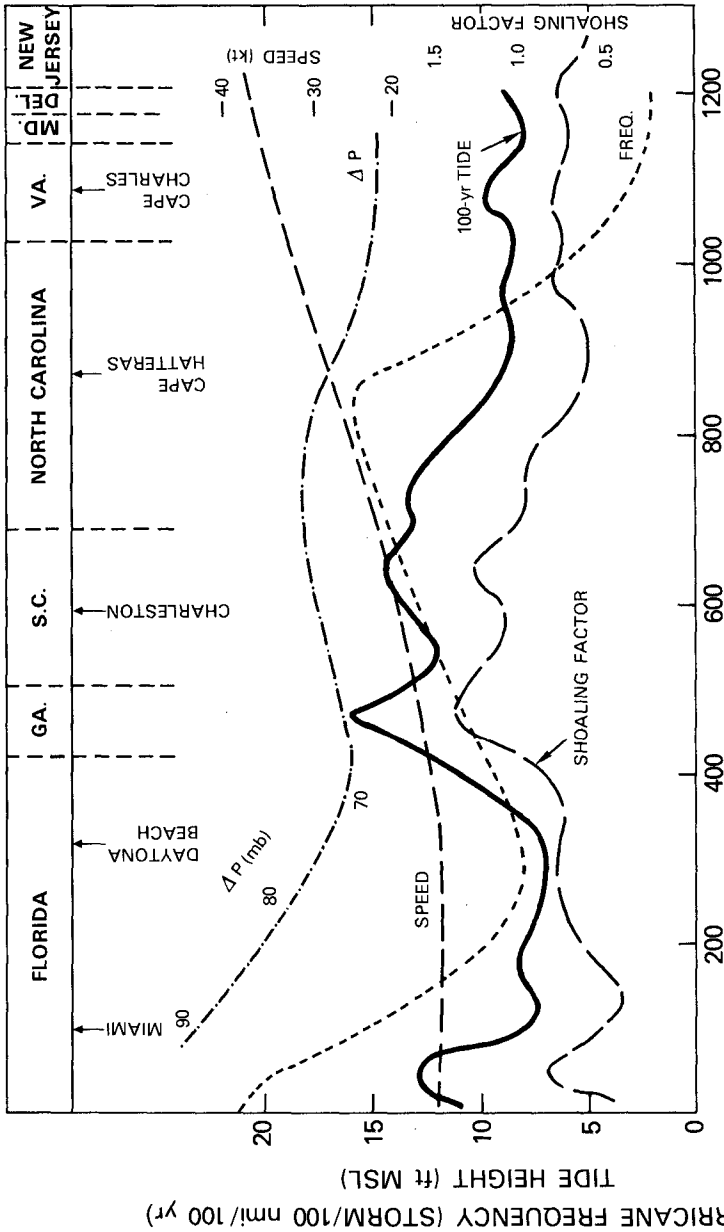


Figure 11.--Schematic illustration of regional relations along the Atlantic coast between storm tide frequency, shoaling factor, and hurricane climatology: landfalling hurricane frequency, pressure deficit (ΔP), and speed of forward motion.

APPENDIX I.--REFERENCES

1. Ho, Francis P., 1974: "Storm Tide Frequency Analysis for the Coast of Georgia," NOAA Technical Memorandum NWS HYDRO-19, National Weather Service, National Oceanic and Atmospheric Administration, U.S. Department of Commerce, Silver Spring, Md.
2. Ho, Francis P., 1975: "Storm Tide Frequency Analysis for the Coast of Puerto Rico," NOAA Technical Memorandum NWS HYDRO-23, National Weather Service, National Oceanic and Atmospheric Administration, U.S. Department of Commerce, Silver Spring, Md.
3. Ho, Francis P., and Myers, Vance A., 1975: "Joint Probability Method of Tide Frequency Analysis Applied to Apalachicola Bay and St. George Sound, Florida," NOAA Technical Report NWS-18, National Weather Service, National Oceanic and Atmospheric Administration, U.S. Department of Commerce, Silver Spring, Md.
4. Ho, Francis P., Schwerdt, Richard W., and Goodyear, Hugo, V., 1975: "Some Climatological Characteristics of Hurricanes and Tropical Storms, Gulf and East Coasts of the United States," NOAA Technical Report NWS-15, National Weather Service, National Oceanic and Atmospheric Administration, U.S. Department of Commerce, Silver Spring, Md.
5. Ho, Francis P., and Tracey, Robert J., 1975: "Storm Tide Frequency Analysis for the Gulf Coast of Florida from Cape San Blas to St. Petersburg Beach," NOAA Technical Memorandum NWS HYDRO-20, National Weather Service, National Oceanic and Atmospheric Administration, U.S. Department of Commerce, Silver Spring, Md.
6. Ho, Francis P., and Tracey, Robert J., 1975: "Storm Tide Frequency Analysis for the Coast of North Carolina, South of Cape Lookout," NOAA Technical Memorandum NWS HYDRO-21, National Weather Service, National Oceanic and Atmospheric Administration, U.S. Department of Commerce, Silver Spring, Md.
7. Ho, Francis P., and Tracey, Robert J., 1975: "Storm Tide Frequency Analysis for the Coast of North Carolina, North of Cape Lookout," NOAA Technical Memorandum NWS HYDRO-27, National Weather Service, National Oceanic and Atmospheric Administration, U.S. Department of Commerce, Silver Spring, Md.
8. Ho, Francis P., Tracey, Robert J., Myers, Vance A., and Foat, Normalee S., 1976: "Storm Tide Frequency Analysis for the Open Coast of Virginia, Maryland, and Delaware," NOAA Technical Memorandum NWS HYDRO-32, National Weather Service, National Oceanic and Atmospheric Administration, U.S. Department of Commerce, Silver Spring, Md.
9. Jelesnianski, Chester P., 1966: "Numerical Computations of Storm Surges Without Bottom Stress," Monthly Weather Review, Vol. 94, pp.379-394.

10. Jelesnianski, Chester P., 1967: "Numerical Computations of Storm Surges With Bottom Stress," Monthly Weather Review, Vol. 95, pp.740-756.
11. Jelesnianski, Chester P., 1972: "SPLASH (Special Program to List Amplitudes of Surges From Hurricanes) I. Landfall Storms," NOAA Technical Memorandum NWS TDL-46, National Weather Service, National Oceanic and Atmospheric Administration, U.S. Department of Commerce, Silver Spring, Md.
12. Jelesnianski, Chester P., 1974: "SPLASH (Special Program to List Amplitudes of Surges From Hurricanes) Part Two. General Track and Variant Storm Conditions," NOAA Technical Memorandum NWS TDL-52, National Weather Service, National Oceanic and Atmospheric Administration, U.S. Department of Commerce, Silver Spring, Md.
13. Myers, Vance A., 1970: "Joint Probability Method of Tide Frequency Analysis Applied to Atlantic City and Long Beach Island, N.J.," Weather Bureau Technical Memorandum HYDRO-11, National Weather Service, U.S. Department of Commerce, Silver Spring, Md.
14. Myers, Vance A., 1975: "Storm Tide Frequencies on the South Carolina Coast," NOAA Technical Report NWS-16, National Weather Service, National Oceanic and Atmospheric Administration, U.S. Department of Commerce, Silver Spring, Md.
15. Myers, Vance A., and Overland, J.E., 1976: "Storm Tide Frequencies for Cape Fear River," unpublished manuscript, National Weather Service, National Oceanic and Atmospheric Administration, U.S. Department of Commerce, Silver Spring, Md.
16. Overland, James E., 1975: "Estimation of Hurricane Storm Surge in Apalachicola Bay, Florida," NOAA Technical Report NWS-17, National Weather Service, National Oceanic and Atmospheric Administration, U.S. Department of Commerce, Silver Spring, Md.
17. Overland, James E., and Myers, Vance A., 1976: "A Model of Hurricane Tide in Cape Fear Estuary," Journal of the Waterways, Harbors, and Coastal Engineering Division, ASCE, (in press).
18. Pore, N.A., and Cummings, R.A., 1967: "A Fortran Program for the Calculation of Hourly Values of Astronomical Tide and Time and Height of High and Low Water," ESSA Technical Memorandum WBTM TDL-6, Environmental Science Services Administration, U.S. Department of Commerce, Silver Spring, Md.

CHAPTER 53

AUTOMATED FORECASTING OF EXTRATROPICAL STORM SURGES

N. Arthur Pore*

ABSTRACT

The Atlantic coast of the United States is affected by extratropical storm surges several times each winter. The most devastating storm of this type on record is that of March 1962. This storm caused damage estimated at over \$200 million. The National Weather Service has developed an automated technique for forecasting such storm surges. Statistical forecast equations have been derived for 11 locations from Portland, Me., to Charleston, S.C. Input data to these equations are values of sea-level pressure as forecast by an atmospheric prediction model of the National Meteorological Center. A sample forecast equation is shown.

The method was put into operation in 1971. Forecasts are transmitted via teletypewriter and extend to 48 hours at 6-hour intervals. A sample teletype message is shown. Forecasts of the devastating storm surge of Feb. 19, 1972, are discussed. These forecasts agreed reasonably well with observations of the storm surge. Experience with the method indicates it to be useful and therefore it will be expanded to include additional forecast locations.

INTRODUCTION

The extratropical storm of March 5-8, 1962, affected much of the east coast of the United States and caused record breaking high tides at locations between Long Island and Cape Hatteras. This storm was the most devastating on record, as it caused damage estimated to be over \$200 million. Figures 1 and 2 show some of the damage at Virginia Beach, Va., and Rehoboth Beach, Del. It is fortunate that storms causing this much damage are rare. However, storms of lesser damage potential occur several times each winter. Accurate and timely forecasts of flooding caused by these storms are important. The crucial times to

*Techniques Development Laboratory, National Weather Service, NOAA, Silver Spring, Md.

forecast these conditions are also the times when forecasters already have burdens brought on by poor weather conditions associated with coastal storms. Therefore, the National Weather Service has developed an objective forecast technique for forecasting extratropical storm surges. This technique has been automated and operates with meteorological input data from an atmospheric prediction model.

SURGE CHARACTERISTICS

Storm surge is defined as the meteorological effect on sea-level and is computed as the algebraic difference between observed tide and the normal astronomical tide. Figure 3 illustrates this definition with a 2-day length of tide record. Here the observed tide is shown by the upper solid curve, the normal (or predicted) astronomical tide by the dashed line, and the storm surge by the lower curve.

The principal factors involved in the generation and modification of the extratropical storm surge are as follows:

1. The rise of water caused by the action of the wind stress on the water surface. It can be thought of as consisting of two components. One component is the set-up of water by the onshore wind in which the slope of the water surface is directly proportional to the wind stress and inversely proportional to the water depth. The other component is the effect of the alongshore wind that generates a current parallel to shore. The effect of the earth's rotation is to have water piled up along the shore if the shore is to the right of the current.

2. The reduction of atmospheric pressure, generally called the inverted barometer effect that causes an increase in sea level in areas of low pressure.

3. The transport of water by waves and swell in the shallow water area near shore.

4. The modifying effects of coastline configuration and the bathymetry, such as convergence or divergence in bays.

The effect of the time of occurrence of the storm surge with respect to the stage of the normal astronomical tide is shown in Figure 4. Here, two identical storm surges are combined with different phases of the normal tide, one occurring at normal high tide and the other at normal low tide, with the one at high tide resulting in a higher actual tide. The time of occurrence of the storm surge with respect to the normal tide can mean the difference between serious and minor flooding.

The recurrence intervals in cases per year for storm surges of 2 ft or greater, 3 ft or greater, and 4 ft or greater for Portland, Boston, Newport, New York, Atlantic City, Breakwater Harbor, Baltimore, and Norfolk are shown in Figure 5. For example, New York City experiences a 2-ft or greater storm surge about six times a year. A 4-ft or greater surge would be expected to occur only once every 2 years.

DEVELOPMENT OF FORECAST EQUATIONS

The forecast technique is a statistical method based on actual storm surge data during the months of November through April from 1956 through 1969. Storm surge values were determined by subtracting hourly values of the astronomic tide from hourly values of observed tide as shown in Figure 3. Data were selected on the basis of storm surge occurrence. Those storms that produced surges of 2 ft or more at four or more of the stations considered were used. Sixty eight storms were selected in this manner.

Earlier studies related surface wind conditions at coastal weather stations to the storm surge Pore (1964, 1965). In the operations of the National Meteorological Center (NMC), meteorological information at computational grid points is more readily available than at weather stations. For that reason, sea-level pressure forecasts at specific grid points were used to represent the generating winds off the east coast in the storm surge generation process. Every 12 hours the NMC runs their numerical atmospheric model (primitive equation model) that produces forecasts for most of the northern hemisphere. Figure 6 shows the grid points where sea-level pressure was considered in this study. Sea-level pressure at these grid points was obtained at 6-hour intervals from analyzed weather charts for the 68 storm cases. These pressure values, with appropriate lag times, were considered as possible predictors of storm surge.

Forecast regression equations were derived by the statistical screening procedure that has been described by Klein (1965) as follows:

"The object of the screening procedure is to select from a large set of possible predictors only those few which contribute significantly and independently to the forecast of a predictand. This is accomplished by a forward method of multiple regression in which significant predictors are picked in a stepwise fashion, one by one. As a result, a small number of predictors can be selected which contain practically all the linear predictive information of the entire set with respect to a specific predictand. The importance

of using a small set of predictors to prevent redundancy and instability of the multiple regression equation and to insure good results when applying it to new data has been emphasized by Lorenz (1956, 1959), Grant (1956), Panofsky and Brier (1958), and others."

A detailed description of the selection of predictors by screening is given by Miller (1958). The manner in which predictors of storm surge are screened is shown below:

$$SS = A_1 + B_1X_1 \dots \dots \dots (1)$$

$$SS = A_2 + B_2X_1 + C_1X_2 \dots \dots \dots (2)$$

$$SS = A_3 + B_3X_1 + C_2X_2 + D_1X_3 \dots \dots \dots (3)$$

·
·

$$SS = A_n + B_nX_1 + C_{n-1}X_2 + \dots + N X_n \dots \dots \dots (n)$$

where SS is storm surge; A_1, A_2, A_3, \dots , are constants; X_1, X_2, X_3, \dots , are predictors; and B_1, B_2, C_2, \dots , are regression coefficients.

The procedure is to first select the best single predictor (X_1) for regression Eq. 1. The second regression equation contains the first predictor (X_1) and the predictor (X_2) that contributes most to reducing the residual after the first predictor is considered. This screening procedure is carried out until the desired number of predictors is included.

A separate forecast equation was derived for each of the locations shown in Figure 7, so that local effects at each location are considered. The locations extend from Portland, Me., on the north to Charleston, S.C. on the south. These locations were chosen because they are in densely populated areas that are frequently threatened by extratropical storm surges. Also, accurate tide observations, necessary for verification of forecasts, are available from the National Ocean Survey and U.S. Army Corps of Engineers for these locations.

Figure 8 shows, as an example, the forecast equation derived for storm surge at New York. Predictors are the sea-level pressure expressed in millibars at the indicated grid points. The subscripts on these terms indicate the time lags in hours. In this case, nearly all the predictors have time lags of 6 hours. Similar equations were derived for the other 10 locations.

APPLICATION TO THE MARCH 1962 STORM

The waves and storm tides generated by the storm of March 5-8, 1962, caused unprecedented damage to coastal areas from southern New England to Florida. The very persistent strong northeast winds blowing over an extremely long fetch were responsible. Another important factor is that the storm occurred at a time of very high astronomical tide. Articles by Stewart (1962) and Cooperman and Rosendal (1962) give details of the storm.

At 7 a.m. EST on March 5th there was an ill-defined low pressure area with a frontal wave northeast of the Bahamas. Low pressure also extended northwestward through the Carolinas and Virginia. By 7 a.m. EST on the 6th, the entire low pressure area had deepened, resulting in a long easterly fetch over the western Atlantic north of Cape Hatteras. The storm continued to intensify and resulted in an elongated low with strong northeast wind over a very long fetch. Four pressure analyses for the storm are shown in Figure 9.

Since the automated method described in this paper did not become operational until Oct. 8, 1971, automated forecasts were not made for the 1962 storm. However, we have made calculations of the storm surge for this storm based upon actual sea-level pressure analyses.

Curves of observed storm surge and calculated storm surge are shown in Figure 10 for the eight locations, for which we have data, for the period March 5-8, 1962. The heavy solid curves show the observed storm surges based on hourly values. The dashed lines connect the computed values of the storm surge made at 6-hour intervals.

We feel there is considerable skill in the calculation of surge for this storm, even though it was a very intense, record-breaking storm.

OPERATIONAL FORECASTING

In operational use, sea-level pressure forecasts at the appropriate grid points are used as input to the storm surge equations. The pressure forecasts are available twice daily from the numerical weather model of the NMC. Pressure forecasts to 48 hours at 6-hour intervals are used.

A sample teletype bulletin of storm surge height forecasts for the 11 locations is shown in Figure 11. The forecasts are expressed in feet at time intervals of 6 hours for the 48-hour forecast period. Such messages are transmitted on a Weather Service teletype circuit to

forecast offices along the east coast where they are used as guidance in preparing the official storm tide bulletins.

AN ACTUAL FORECAST CASE

A very severe coastal storm, to which the automated storm surge method was applied during its first year of operation, was the storm of Feb. 18-20, 1972 (Pore, 1973). The northern portion of the U.S. Atlantic Coast suffered extensive damage and beach erosion. Conditions were very bad as the time of maximum storm surge was near the time of astronomical high tide.

A low pressure system centered over the Great Lakes at 7 a.m. EST on Feb. 18th had a frontal system extending southward over eastern Tennessee, Georgia, Alabama, and into the Gulf of Mexico. Subsequent developments, as depicted on the Northern Hemisphere surface charts of NMC, are shown in Figure 12. By 1 p.m. EST, a closed low had developed over Georgia. Further development occurred and the storm moved rapidly toward the north-northeast, to a position just north of Cape Cod at 1 a.m. EST on the 20th.

Some of the numerical weather model forecasts of storm position and central pressure are shown in Figure 13. The storm center positions and central pressures, taken from the NMC Northern Hemisphere surface charts can be compared to these 12-hour, 24-hour, and 36-hour forecasts. The shorter-range numerical forecasts of the track were very consistent with the longer-range forecasts and are considered to be quite good.

The numerical weather sea-level pressure forecasts, valid about the time of maximum storm surge, can be compared to the NMC pressure analysis in Figure 14. Here it is seen that the longer-range forecasts, such as the +30-hour forecast, did not have the storm intense enough. The shorter-range forecasts, such as the +6-hour forecast, look quite good, both for storm intensity and position.

Calculations of the storm surge based on sea-level pressure analyses and forecasts are shown in Figures 15 through 18. Storm surge calculations, based on sea-level pressure analyses of the NMC Northern Hemisphere surface charts, are shown in Figure 15. Here the observed storm surges, based on hourly values, are shown by the solid curves. Maximum values of observed surge are printed near the peak of each curve. Calculations of storm surge, based on pressure analyses, are shown by dots at 6-hour intervals. It is felt that these storm surge calculations agree fairly well with the observations. Figures 16 through 18 show, in the same manner, actual forecasts of surge based on the sea-level

pressure forecasts. Figure 16 shows 6- and 12-hour forecasts of the surge. Two forecast intervals are combined on one chart so that there is a forecast value every 6 hours rather than every 12.

The actual forecasts of storm surge, of course, are not as accurate as the calculations based on the pressure analyses. The underforecasting of storm intensity of the numerical weather model in the longer-range forecasts was discussed earlier and is reflected in the longer-range forecasts of storm surge, as shown in Figure 18. The 6- and 12-hour surge forecasts were closer to the observed surge than the longer-range 30- and 36-hour forecasts. It is felt that the automated storm surge forecasts provided useful guidance material, especially on the timing of the surge.

CONCLUSION

The statistically derived extratropical storm surge forecast method uses the meteorological forecasts of the NMC as input to provide guidance material for Weather Service coastal forecast offices. The accuracy of the surge forecasts depends greatly upon the accuracy of the meteorological forecasts. Experience, so far, has shown the method to be useful and for that reason it is being expanded to include more locations.

ACKNOWLEDGMENTS

Appreciation is expressed to the National Ocean Survey and the U.S. Army Corps of Engineers for the observed tide data. Appreciation is also expressed to W. S. Richardson and H. P. Perrotti of the Techniques Development Laboratory of the National Weather Service for their assistance and to Mercedes Bakon for the typing of the manuscript.

REFERENCES

- Cooperman, A. I., and H. E. Rosendal, "Great Atlantic Coast Storm, 1962," Climatological Data, National Summary, Vol. 13, No. 3, U.S. Department of Commerce, March 1962, pp. 137-145.
- Grant, A. M., "The Application of Correlation and Regression to Forecasting," Meteorological Study No. 7, Bureau of Meteorology, Commonwealth of Australia, Melbourne, Jan. 1956, 21 pp.
- Klein, W. H., "Application of Synoptic Climatology and Short-Range

Numerical Prediction to Five-Day Forecasting," U.S. Weather Bureau Research Paper 46, 1965, 109 pp.

- Lorenz, E. N., "Empirical Orthogonal Functions and Statistical Weather Prediction," Statistical Forecasting Project Scientific Report No. 1, Contract No. AF19(604)-1566, Department of Meteorology, Massachusetts Institute of Technology, Cambridge, Mass., Dec. 1956, 49 pp.
- Lorenz, E. N., "Prospects for Statistical Weather Forecasting," Statistical Forecasting Project Final Report on Contract No. AF19(604)-1566, Department of Meteorology, Massachusetts Institute of Technology, Cambridge, Mass., 1959, pp. 1-78.
- Miller, R. G., "The Screening Procedure. Studies in Statistical Weather Prediction," Final Report, Contract No. AF19(604)-1590 Hartford, Conn., Travelers Weather Research Center, 1958, pp. 86-95.
- Panofsky, H. A., and G. W. Brier, "Some Applications of Statistics to Meteorology," College of Mineral Industries, Pennsylvania State University, University Park, Pa., 1958, 224 pp.
- Pore, N. A., "The Relation of Wind and Pressure to Extratropical Storm Surges at Atlantic City," Journal of Applied Meteorology, Vol. 3, No. 2, April 1964, pp. 155-163.
- Pore, N. A., "Chesapeake Bay Extratropical Storm Surges," Chesapeake Science, Vol. 6, No. 3, September 1965, pp. 172-182.
- Pore, N. A., "Marine Conditions and Automated Forecasts for the Atlantic Coastal Storm of February 18-20, 1972," Monthly Weather Review, Vol. 101, No. 4, April 1973, pp. 363-370.
- Stewart, J. Q., "The Great Atlantic Coast Tides of 5-8 March 1962," Weatherwise, Vol. 15, No. 3, June 1962, pp. 116-120.



Figure 1.—Damage at Virginia Beach, Va., caused by the Severe March 1962 storm.



Figure 2.—Boardwalk at Rehoboth Beach, Del., destroyed by the March 1962 storm.

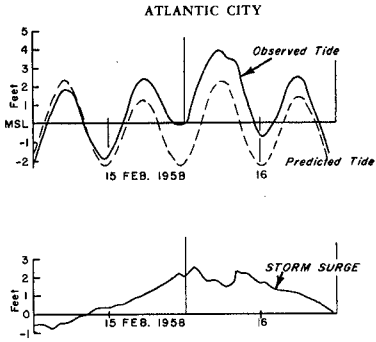


Figure 3.-Tide data showing the observed tide, predicted astronomical tide, and the storm surge.

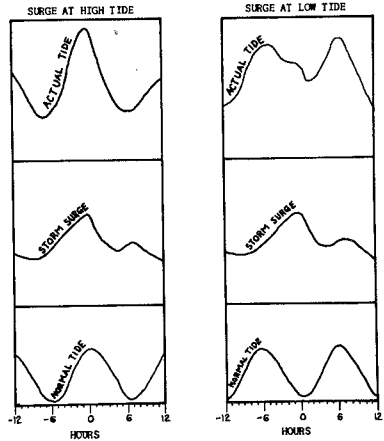


Figure 4.-The actual tide and its components.

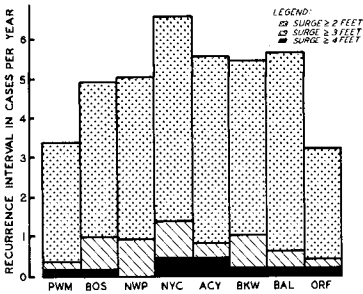


Figure 5.-Frequency of extratropical storm surges of 2, 3, and 4 ft or greater. Stations locations are shown in Figure 7.

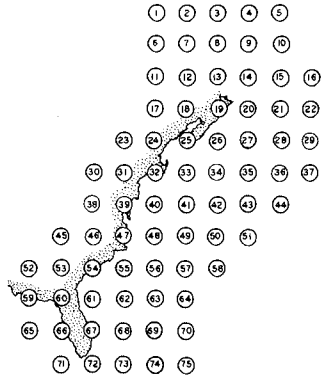


Figure 6.-Grid points where values of sea-level pressure were considered as predictors of storm surge.

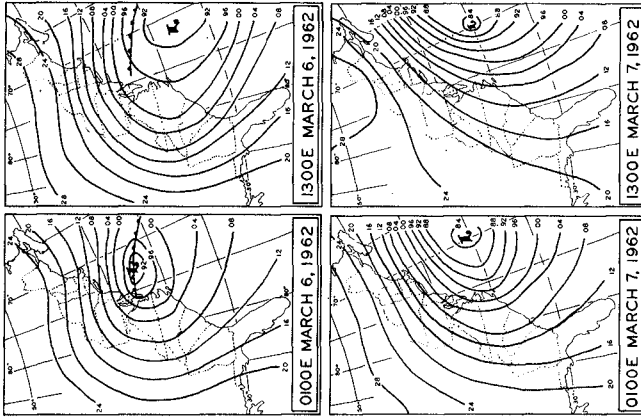
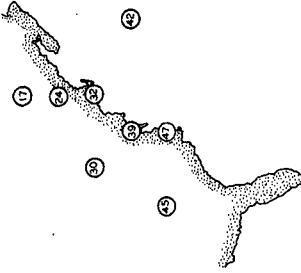


Figure 9.-Sea-level pressure charts for the coastal storm of March 1962.



$$SS(NYC) = A - B(47)_{t-6} + C(17)_{t-6} - D(42)_{t-6} - E(30)_{t-6} + F(24)_{t-6} - G(39)_{t-6} + H(32)_{t-6} + I(45)_{t-6}$$

Figure 8.-Storm surge forecast equation for New York. SS is storm surge, the number in parentheses of each term is the grid point for which sea-level pressure is used as a predictor, and the subscript on each term is the time lag of the predictor in hours.

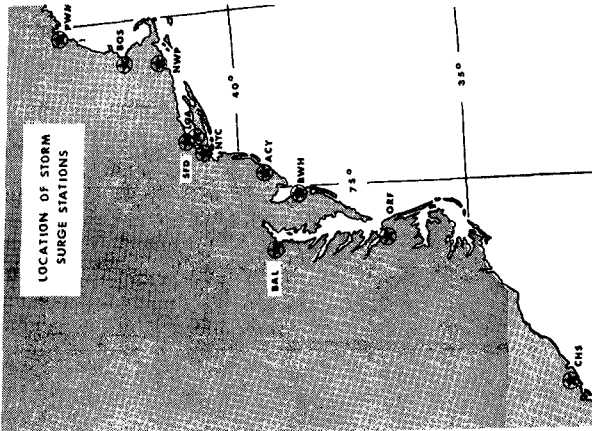


Figure 7.-The 11 forecast locations for which storm surge equations were derived.

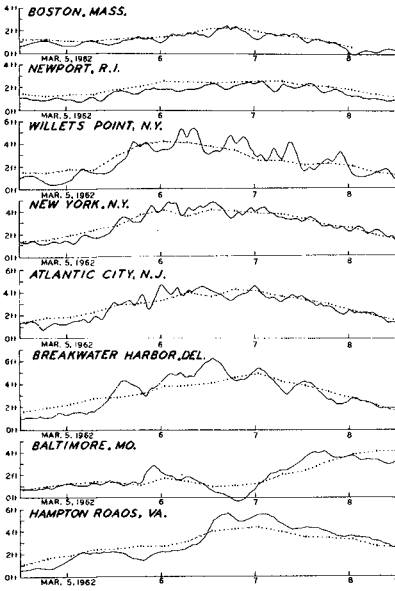


Figure 10.-Observed storm surge and calculated storm surge for seven locations during the March 1962 storm. Solid curves are observed storm surge. The dashed lines connect storm surge calculated at 6-hour intervals, based upon analyses of sea-level pressure.

FZUS3 KWBC 070000
 STORM SURGE FCST FEET INVALID FOR TROPICAL STORMS

	06Z	06Z	12Z	18Z	00Z	06Z	12Z	18Z	00Z
PWM	0.6	0.4	0.6	0.5	0.8	1.1	1.5	1.9	1.7
BOS	0.1	0.1	0.2	0.2	0.5	0.9	1.3	1.7	1.3
NWP	0.7	0.6	0.6	0.5	0.9	1.4	1.7	1.6	1.1
SFD	1.5	1.2	1.2	1.5	2.2	2.7	2.9	1.9	0.4
LGA	0.2	-0.2	0.0	-0.2	0.4	0.8	1.1	0.3	-0.9
NYC	0.3	0.3	0.4	0.5	1.0	1.4	1.5	0.6	-0.4
ACY	0.1	0.1	0.1	0.2	0.7	1.0	0.8	0.5	-0.0
BWH	-0.2	-0.3	-0.1	-0.2	0.4	0.6	0.5	0.1	-0.5
BAL	0.5	0.2	0.5	0.9	0.8	1.4	1.4	0.2	-0.8
ORF	-0.9	-0.5	-0.0	-0.1	-0.1	-0.4	-0.9	-0.5	-0.7
CHS	-0.5	-0.6	0.0	-0.5	-0.5	-1.1	-0.7	-0.5	-0.5

Figure 11.-Storm surge forecast teletype message. Forecast heights are in feet. Valid times are indicated above each column of heights. Forecast point locations are shown in Figure 7.

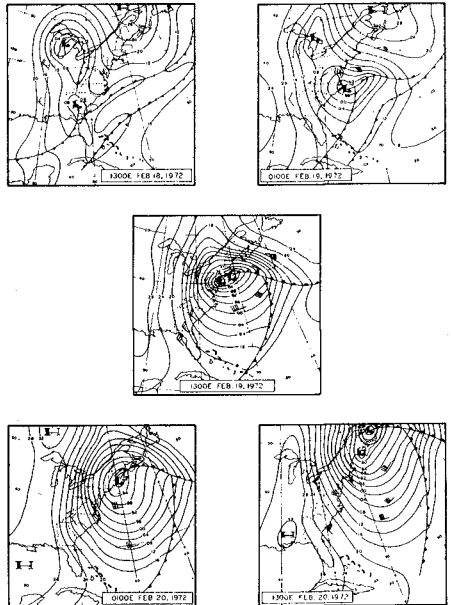


Figure 12.-Sea-level pressure analyses as shown on the Northern Hemisphere surface charts for the National Meteorological Center for Feb. 18-20, 1972.

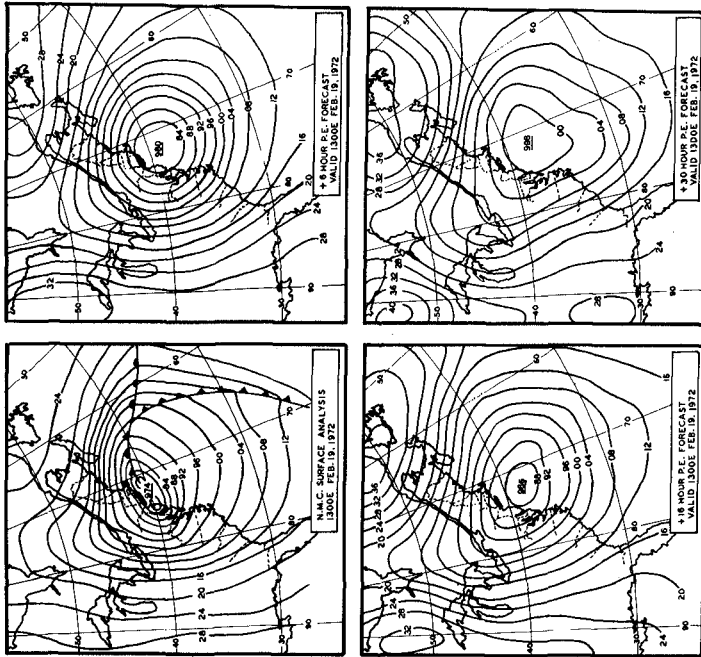


Figure 14.-Sea-level pressure analysis for 1300 EST on Feb. 19, 1972, and the 6-, 18-, and 30-hour forecasts by the numerical weather model of the National Meteorological Center.

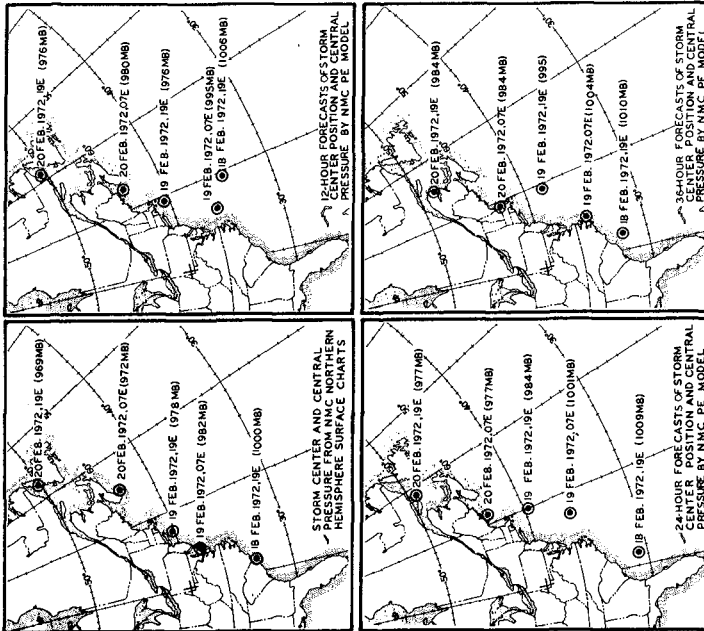


Figure 13.-Analyzed and forecast values of storm center position and central pressure. Data obtained from National Meteorological Center analyzed surface pressure charts and grid point values of sea-level pressure forecasts.

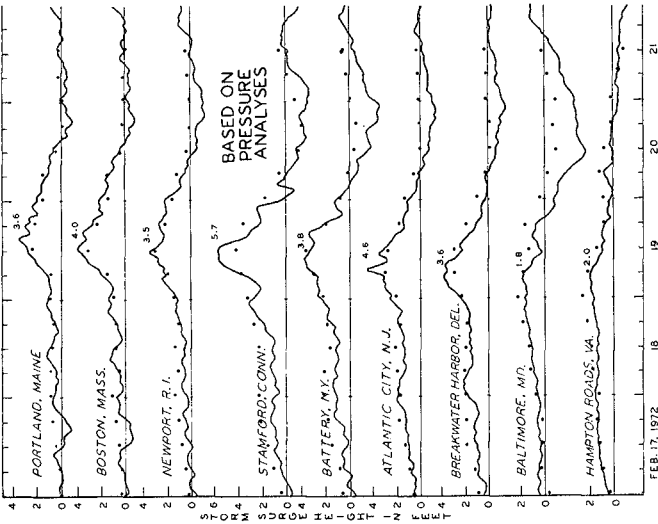


Figure 15.—Observed (solid curves) and calculated (dots) storm surges. Calculated values are based on sea-level pressure analyses. Maximum value (ft) of observed surge is placed near the peak of each curve and the date is placed at the 1200 EST position.

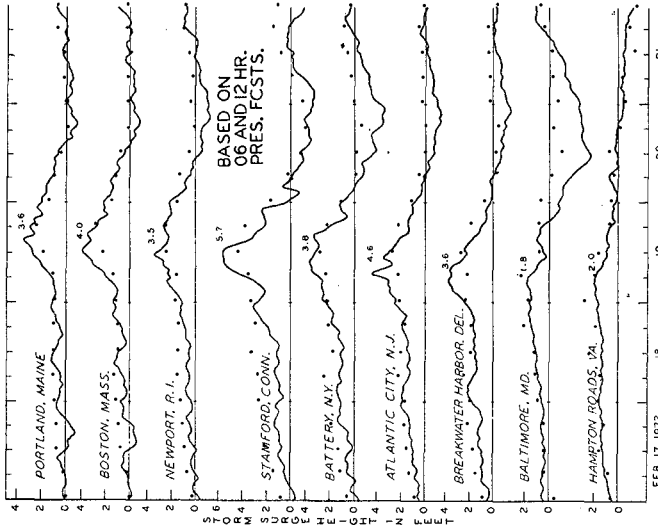


Figure 16.—Same as Figure 15 except dots indicate forecast storm surges. Forecast values are based on 6- and 12-hr sea-level pressure forecasts of the numerical weather model of the National Meteorological Center.

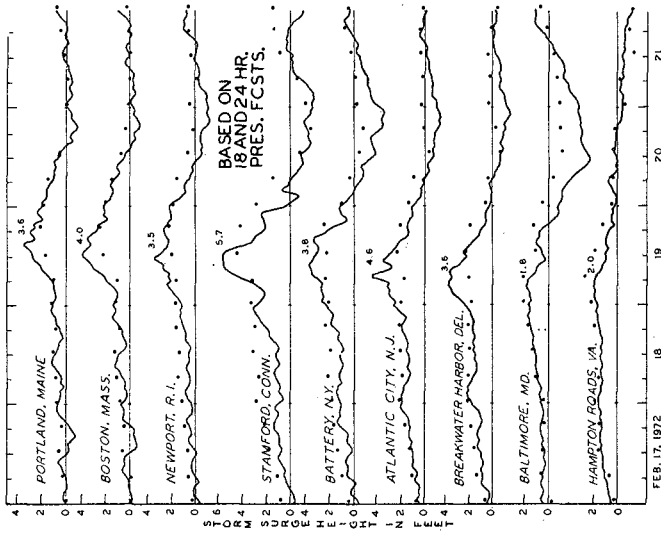


Figure 17.-Same as Figure 16 except forecast values are based on 18- and 24-hr sea-level pressure forecasts.

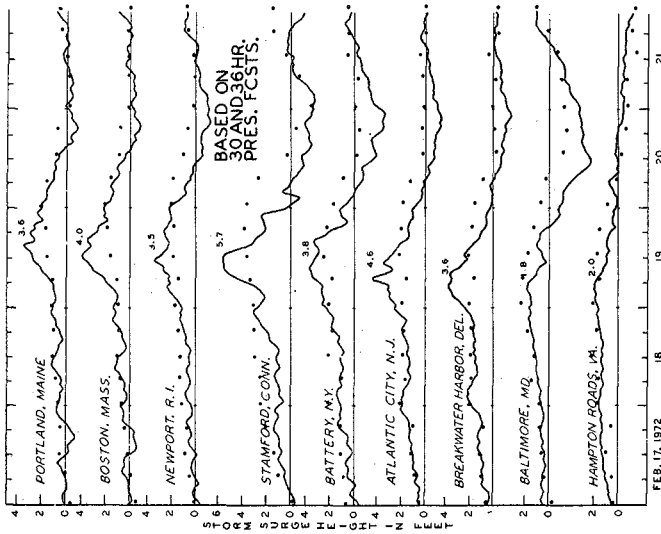


Figure 18.-Same as Figure 16 except forecast values are based on 30- and 36-hr sea-level pressure forecasts.

CHAPTER 54

Generalized Model for Storm Surges

Gour-Tsyh Yeh¹, M. ASCE

and

Fei-Fan Yeh², M. ASCE

Abstract. A two-dimensional numerical simulation model of storm surges based on the vertically integrated hydrodynamic equations of continuity and momentum is adopted. The model embodies the inundation over the low-lying land surface with moving water-land interfaces. Wind stress coefficient is considered not only function of wind speed but also dependent on the temperature differential between air and water. Bottom stress is treated by an evaluation of convolution integrals over the surface slope pressure depression and wind shear. The contribution of momentum by river inflows is taken into account. Particular attention is directed to the treatment of nonlinear terms in the governing equations to insure the improvement of numerical stability and accuracy. The model is applied to the New Jersey Coastal area and reproduces the historical storm surges quite well both at Atlanta City and Sandy Neck.

¹ With Stone & Webster Engineering Corporation, Boston, Massachusetts.

² Formerly with Ebasco Services, Inc., now with Tetra Tech, Inc.

INTRODUCTION

Reliable estimates of water-level changes under storm conditions are essential for the planning and design of coastal engineering works. Determination of design water elevations during storms is a complex problem involving interaction among the bathymetry and geometry of the water body, the forces of the wind field and atmospheric depression, the resistance of the bottom, the momentum generated in the water body, and the effects caused by other mechanisms unrelated to the storms, such as astronomical tides, earth rotation, etc.

The development of numerical models for predicting storm surges has been advanced rapidly during the past decade, from simple one-dimensional bathystropic theory (Bretschneider and Collins, 1963) to more complex two-dimensional simulation of arbitrary water bodies (Reid and Bodine, 1968; Pearce, 1972; Tsai and Chang, 1974; Pearce and Pagenkopf, 1975; Wanstrath, 1975; Damsgaard and Dinsmore, 1975). Most of the models are found to be useful only for specific localities to where one must approximate its underlying assumptions. In view of the various deficiencies in the existing storm surge models, additional considerations to improve the accuracy of the results and the generalization of the applications are listed as follows:

1. Inundation boundary conditions over the low-lying land surface are incorporated automatically with the rationale of both mathematical and physical justification rather than based on the empirical or a weir-type formula.
2. Bottom stress is time varying and may be obtained by an evaluation of convolution integrals over the surface slope, pressure depression, and wind stress. Only with this wind dependent bottom stress, it seems possible to facilitate the computational scheme over the low-lying land surface.
3. Wind stress coefficient is not a unique function of wind speed but also a function of temperature differential between the air and water. This inclusion of temperature effects is highly significant for the estimation of wind stress coefficients in the Northern United States, and should greatly enhance the predictability of storm surges in the Great Lake of Northern America where the temperature has significant change during storms.
4. The surge elevations at the lateral open boundaries perpendicular to the coastline are obtained by assuming zero gradient of total water depth. This would allow the selection of the locations of lateral boundaries with less restriction.

5. The stream inflows in estuarine areas are included in the momentum equations. Conventional assumption by neglecting the stream momentum but adding only the stream mass flux into the continuity equation is not totally true for many estuarine conditions.
6. All nonlinear terms such as advections are not linearized in order to account for the bathymetries involving irregular coastlines and bay complexes.

The numerical techniques used for computing long wave equations generally fall into one of the three schemes: (i) Explicit Finite Difference Method, (Reid and Bodine, 1968; Pearce, 1972; Wanstrath, 1975), (ii) Implicit Finite Difference Method (Leendertse, 1967; Tsai and Chang, 1974), and (iii) Finite Element Method (Pearce and Pagenkopf, 1975; Gallagher, etc., 1973; Gallagher and Chan, 1973). Engineering practice has indicated that the explicit scheme having to satisfy the Courant stability condition is too strenuous. Although the finite element method offers smooth treatment on irregular boundaries, it has serious drawback in the requirements of computing time and computer storages. Furthermore, the lack of provability on the stability of the method often leads to obscure trial and error. The alternate direction (ADI) implicit scheme has gained the popularity. It is unconditionally stable to the long wave equations without nonlinear advection terms (Leendertse, 1967). The authors have been unable to make practical use of this advantage for the cases when the nonlinear terms are included in the long wave equations. It is surmised that this may be due to the way these nonlinear terms are approximated as part implicit and part explicit. A modified ADI scheme, which considers all terms implicit, is therefore adopted.

MODEL FORMULATION

Basic Equations and Assumptions

The mathematical equations describing storm driven surges can be obtained by integrating vertically the Navier-Stokes equations for fluid motions. In this development, it is assumed that density over the depth is constant, pressure variation with the vertical coordinate is hydrostatic, and the variation of momentum transport with vertical coordinate dominates those with horizontal coordinates. The vertically integrated forms of the conservation equations in a Cartesian Coordinate system with x and y on the horizontal plan can be written as

$$\frac{\partial H}{\partial t} + \frac{\partial U}{\partial x} + \frac{\partial V}{\partial y} = qH \quad (1)$$

$$\frac{\partial U}{\partial t} + \frac{\partial}{\partial x} \left(\frac{U^2}{H} \right) + \frac{\partial}{\partial y} \left(\frac{UV}{H} \right) - 2qU - fV = - \frac{g}{2} \frac{\partial H^2}{\partial x} + gH \left(\frac{\partial h}{\partial x} - \frac{1}{\rho g} \frac{\partial p_s}{\partial x} \right) + \frac{\tau_x^w - \tau_x^b}{\rho} \quad (2)$$

$$\frac{\partial V}{\partial t} + \frac{\partial}{\partial x} \left(\frac{UV}{H} \right) + \frac{\partial}{\partial y} \left(\frac{V^2}{H} \right) - 2qV + fU = - \frac{g}{2} \frac{\partial H^2}{\partial y} + gH \left(\frac{\partial h}{\partial y} - \frac{1}{\rho g} \frac{\partial p_s}{\partial y} \right) + \frac{\tau_y^w - \tau_y^b}{\rho} \quad (3)$$

The symbols used in Equations (1), (2), and (3) are defined as follows:

- H = total water depth
- h = undisturbed water depth
- U, V = flux density in x- and y-directions, respectively
- g = gravitational acceleration
- f = coriolis coefficient
- τ_x^w, τ_y^w = wind stress components in x- and y-directions, respectively
- τ_x^b, τ_y^b = bottom stress components in x- and y-directions, respectively
- p_s = atmospheric pressure
- x, y = horizontal orthogonal coordinates
- t = time
- ρ = water density

The terms included in the momentum equations are from the left to the right representing inertia term; nonlinear longitudinal and lateral advection momentum terms; the momentum attributed to the artificial discharges or river inflows and outflows; coriolis acceleration; nonlinear gravity terms; forces due to bottom slope and atmospheric pressure gradient; and wind and bottom stresses. It is interesting to note that the atmospheric depression column and the water depth column are equivalent. Therefore, the accurate reading of the undisturbed water depth is more important than the consideration of atmospheric pressure depression.

Variables in Equations (1), (2), and (3) are H, U, V, h, q, p_s , τ_x^w , τ_y^w , τ_x^b , and τ_y^b . Among these variables, p_s , τ_x^w , and τ_y^w are the forcing functions

depending on the atmospheric pressure and wind field distributions of the storms; h and q are given functions of x and y . Thus, if bottom stress components, τ_x^b and τ_y^b , are related to H , U and V , Equations (1), (2) and (3) will constitute three simultaneous partial differential equations for three unknowns, H , U , and V .

Wind and Bottom and Stresses

The most important and sensitive parameter in storm surge modeling is the wind shear stress since it is the primary driving force. In general, the wind shear stress is related to the wind speed, w , through the following expression

$$\tau^w = \rho_a K w^2 \quad (4)$$

where ρ_a is the density of air and K is the wind stress coefficient. The values of K should be a function of other parameters involving wind speed, surface roughness, and stability and turbulence of the atmosphere. A model treating K as function of wind speed has been presented elsewhere (Van Dorn, 1953; Reid and Bodine, 1968),

$$K = K_1 \quad \text{for} \quad W \leq W_c \quad (5a)$$

$$K = K_1 + K_2 (1 - W_c/W)^2 \quad \text{for} \quad W > W_c \quad (5b)$$

in which the constants, K_1 , K_2 and the critical wind speed have been taken as

	K_1	K_2	W_c
Van Dorn (1953)	$1.2 \cdot 10^{-6}$	$1.8 \cdot 10^{-6}$	6.7 m/sec
Reid & Bodine (1968)	$1.1 \cdot 10^{-6}$	$2.5 \cdot 10^{-6}$	7.2 m/sec

A slightly different formula for describing K has been proposed (Tsai and Chang, 1974) as follows:

$$K = \begin{cases} 1.25 \cdot 10^{-6} & \text{for } W \leq W_1 \\ 1.25 \cdot 10^{-6} + 1.75 \cdot 10^{-6} \sin\left(\frac{\pi}{2} \frac{W-W_1}{W_2-W_1}\right) & \text{for } W_1 < W < W_2 \\ 3.0 \cdot 10^{-6} & \text{for } W \geq W_2 \end{cases} \quad (6)$$

In which $W_1 = 5.1$ m/sec and $W_2 = 15.4$ m/sec. Most of the investigators has not included the atmospheric stability in the formulation of K . However, it has been demonstrated that the temperature differential between the water and air has a significant effect on the value of K (Gillies and Punhani, 1971). It is, therefore, proposed in this paper that K be given by the following equation:

$$K = \begin{cases} K_1 + K_3 \Delta T & \text{for } W \leq W_c \\ K_1 + K_2 (1 - W_c/W)^2 + K_3 \Delta T & \text{for } W > W_c \end{cases} \quad (7)$$

The values of K_1 , K_2 and K_3 will have to be determined from further numerical experiments on storm surges.

The relationships describing the bottom stress have been taken for granted by many authors (Reid and Bodine, 1968; Dansgaard and Dinsmore, 1975) as simply given by the following formula:

$$\tau_x^b = \frac{\rho g \sqrt{U^2 + V^2} U}{C^2 H^2} \quad (8a)$$

and

$$\tau_y^b = \frac{\rho g \sqrt{U^2 + V^2} V}{C^2 H^2} \quad (8b)$$

where C is the Chezy coefficient. Bottom stress formulation based on this line of approach may sometimes yield large error, since there are possible flows in which the transport is small but there still may be a significant bottom shear layer. This problem can be avoided by calculating the drag from the flow profile calculations based on linear theory of long wave equations, as done by Jelesnianski (1970) and Forristall (1974). Accordingly, the bottom stress is given by

$$\vec{\tau}^b = \frac{2u}{H^2} \int_0^t \left(\frac{\vec{t}}{\rho} - \frac{1}{\rho} \vec{v}_p^s \right) K_F(t-\tau) d\tau - \frac{2u}{H^2} \int_0^t g \vec{v}_\eta^s K_Q(t-\tau) d\tau \quad (9)$$

in which ν is the eddy viscosity, $\eta = H - h$, and K_P , K_Q , ∇_p^{\rightarrow} , $\nabla\eta^{\rightarrow}$, $\tau^{\rightarrow w}$, and $\tau^{\rightarrow b}$ denote

$$K_P = \sum_{n=0}^{\infty} (-1)^n (n + 1/2)\pi \text{Exp}\{-\nu(n + 1/2)^2 \pi^2 t/H^2 - (if - 2q)t\} \quad (10a)$$

$$K_Q = \sum_{n=0}^{\infty} \text{Exp}\{-\nu(n + 1/2)^2 \pi^2 t/H^2 - (if - 2q)t\} \quad (10b)$$

$$\nabla_p^{\rightarrow} = \frac{\partial p_s}{\partial x} + i \frac{\partial p_s}{\partial y}; \quad \nabla\eta^{\rightarrow} = \frac{\partial \eta}{\partial z} + i \frac{\partial \eta}{\partial y}; \quad \tau^{\rightarrow b} = \tau_x^b + i \tau_x^b; \quad \tau^{\rightarrow w} = \tau_x^w + i \tau_y^w \quad (10c)$$

respectively. The adoption of Equation (9) is more physically appealing and consistent with the overall method than Equation (8). The derivation of Equation (8) involves more assumptions than that of Equation (9).

Finite Difference Equations

A space-staggered scheme is used to approximate the differential equations with finite difference equations (Leendertse, 1967). The scheme describes the flux density, total water depth, and undisturbed water depth at different grid points as shown in Figure 1.

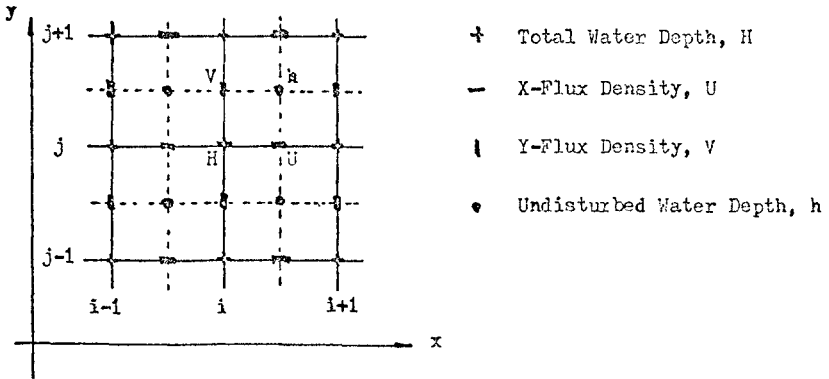


Figure 1

To simplify the discussion on the formulation of finite difference equations, Equations (1), (2), and (3) can be written as

$$\frac{\partial \vec{V}}{\partial t} + \frac{\partial \vec{F}}{\partial x} + \frac{\partial \vec{G}}{\partial y} - I = 0 \tag{11}$$

where

$$\vec{V} = \begin{bmatrix} H \\ U \\ V \end{bmatrix}; \quad \vec{F} = \begin{bmatrix} U \\ \frac{U^2}{H} + \frac{gH^2}{2} \\ \frac{UV}{H} \end{bmatrix}; \quad \vec{G} = \begin{bmatrix} V \\ \frac{UV}{H} \\ \frac{V^2}{H} + \frac{gH^2}{2} \end{bmatrix} \tag{12}$$

and

$$I = \begin{bmatrix} qH \\ gH\left(\frac{\partial h}{\partial x} - \frac{1}{\rho g} \frac{\partial p_s}{\partial x}\right) + fV + 2qU + \frac{\tau_x^w}{\rho} - \frac{\tau_x^b}{\rho} \\ gH\left(\frac{\partial h}{\partial y} - \frac{1}{\rho g} \frac{\partial p_s}{\partial y}\right) - fU + 2qV + \frac{\tau_y^w}{\rho} - \frac{\tau_y^b}{\rho} \end{bmatrix} \tag{13}$$

Let

$$\vec{V}_{i,j}^{(n+1)} = \begin{bmatrix} H(i\Delta x, j\Delta y, (n+1)\Delta t) \\ U(i\Delta x, j\Delta y, p\Delta t) \\ V(i\Delta x, j\Delta y, q\Delta t) \end{bmatrix}$$

where p and q will be replaced by (n+1) or (n) as demanded by the ADI algorithm, then the finite difference approximation of Equation (11) is

$$\frac{\vec{V}_{i,j}^{(n+1)} - \vec{V}_{i,j}^{(n)}}{\Delta t} + \frac{1}{2\Delta x} \left[\vec{F}_{i+1,j} - \vec{F}_{i-1,j} \right] + (1-\theta) \left[\vec{F}_{i+1,j} - \vec{F}_{i-1,j} \right] + \dots = O(\Delta t, \Delta x^2) \tag{14}$$

where θ is a weighting factor ranging from 0 to 1, and $\tilde{F}_{i,j}^n$ is given by

$$\tilde{F}_{i,j}^n = \frac{F_{i+1,j}^+ + F_{i,j}^+ + F_{i-1,j}^+}{4} \tag{15}$$

Expansion of Equation (14) in Taylor series, it becomes,

$$\frac{\partial V}{\partial t} + \frac{\partial F}{\partial x} + \frac{\Delta x^2}{4}(1-\theta) \frac{\partial^3 F}{\partial x^3} + \dots = 0 \tag{16}$$

The third term which has the magnitude of the order of Δx^2 is the numerical filter term to screen the short wave number. For complete implicit scheme, $\theta = 1$, and therefore, no filter term is encountered. This would probably explain the frustration experienced by many model practitioners when Equation (14) with $\theta = 1$ is applied to the solution of circulation problems. Under such circumstances, the noise caused by the short wave would amplify very fast and blow out the computations. Instead of $\tilde{F}^{(n)}$, if $\bar{F}^{(n)}$ is used in Equation (14), similar problems will also arise since no filter term is involved to dampen the short wave noise.

Since \bar{F} , \bar{C} and \bar{I} are nonlinear functions of H , U , and V , Equation (14) is a system of nonlinear algebraic equations. These equations can be solved directly by iterative method. However, iterative solution to a large number of simultaneous equations at each time step is not only time consuming but also causes convergent problems in many areas. Hence, linearization techniques must be used to render these equations to a system of linear algebraic equations that direct solution can be obtained. In general, Taylor series expansion is adopted, i.e.,

$$\bar{F}^{(n+1)} = \bar{F}^{(n)} + \frac{\partial \bar{F}}{\partial H}(H^{(n+1)} - H^{(n)}) + \frac{\partial \bar{F}}{\partial U}(U^{(n+1)} - U^{(n)}) + \dots$$

For example, the term U^2 in the second component of \bar{F} in Equation (12) can be expanded as

$$U^2(n+1) = U^{(n)}(U^{(n+1)} + U^{(n+1)} - U^{(n)}) + \dots \tag{18}$$

Most of the numerical modelers would linearize this term by treating it as part explicit and part implicit (Leendertse, 1967; Tsai and Chang, 1974), i.e.,

$$U^2(n+1) = U^{(n)}U^{(n+1)} \tag{19}$$

It is seen from Equations (18) and (19) that the former will render the latter as its special case if $U^{(n+1)} \rightarrow U^{(n)}$. The implicit scheme, Equation (14), has been proved unconditionally stable when it is applied to linear partial differential equations (Leendertse, 1967). However, frustrations have been experienced more than often when it is applied to nonlinear equations in along with Equation (19), unless the time step is smaller than that given by Courant stability criteria. This fact may be explained by comparing Equations (8) and (19). The comparison indicates that the time step has to be small for the two to agree.

Boundary Conditions

There are two types of boundaries in the numerical simulation of storm surges. One is the water-land interface while the other is the fictitious open boundaries which are artificial termination of the flow field. During a storm, the wind generated surge close to shoreline is most prominent. For locations further seaward, the magnitude of the wind setup (or setdown) becomes progressively insignificant for several reasons. The first effect occurs due to decreased hindrance of the boundary. The increase in water depth accounts for the second reason as the water mass would be more difficult to set in motion at a location of greater depth by the water surface shear forces.

For locations beyond the Continental Shelf, the water elevation due to wind shear would be insignificant. Thus, at seaward boundary the setup (setdown) could be reasonably assumed equal to the barometric and astronomical tides. The treatment of lateral open boundaries is still very controversial. Reid and Bodine (1968) proposed radiative boundary conditions. Pearse and Pagenkopf (1975) assumed zero onshore transport. Zero gradient of water surface slope has been used with the requirements that the lateral boundaries be chosen roughly perpendicular to the bottom contours lines (Stone & Webster, 1976). In this paper, this requirement will be removed by specifying the gradient of total water depth equal to zero at lateral boundaries.

Most of the existing storm surge models does not consider the moving boundaries at the water-land interfaces. General practice is to assume vertical wall interface that the normal flow is zero (Pearse and Pagenkopf, 1975). A few investigators model the inundation of low-lying land with weir type approach (Reid and Bodine, 1968; Dansgaard and Dinsmore, 1975). In the present model, the moving boundaries are accomplished by progressively advancing (retreating) the land-water interface as surges increase (decrease). Both continuity and momentum equations are actually utilized in tallying these moving inundation boundary grids.

MODEL APPLICATION

The storm surge model is applied to the New Jersey coastal area for 1944, hurricane, whose track parallels the east coast and lies well within the confines of the Continental Shelf. The track of the pressure center in the storm is taken from the report by Graham and Hudson (1960). The hurricane characteristics were given both near Hatteras, North Carolina, and Point Judith, Rhode Island (Graham and Hudson) as follows.

	<u>Hatteras, NC</u>	<u>Point Judith, RI</u>
Radiative of maximum winds, R	49 N. Mi	36 N. Mi
Center pressure index, p_o	27.88 in.	28.31 in.
Peripheral pressure, p_n	30.66 in.	29.39 in.
Maximum gradient wind, V_{gx}	113 mph	71 mph

Based on these hurricane parameters and the track, wind and pressure fields are constructed using the method suggested by Graham and Nunn (1959).

The New Jersey coastal area is constructed on a rectangular grid of 22 by 31 with grid size of 33,333 ft. It included the Continental Shelf to a depth of approximately 600 ft and is extended far north and south of the area of interest that the lateral boundary conditions are applicable.

Surge histories for 1944 hurricane are available at both Atlanta and Sandy Hook tidal gage stations in the southern and northern New Jersey coast, respectively (Harris, 1963). Both recorded and computed surges with the model at Atlanta City are shown in Figure 2. Figure 3 shows comparisons between the tidal gage measurements and the simulated results at Sandy Hook. The agreements at both Atlanta City and Sandy Hook are considered favorably. The peak surge as computed at Sandy Hook is higher than the measured.

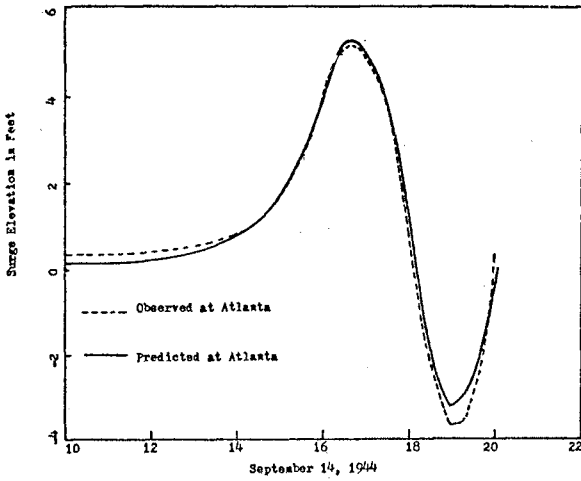


Figure 2

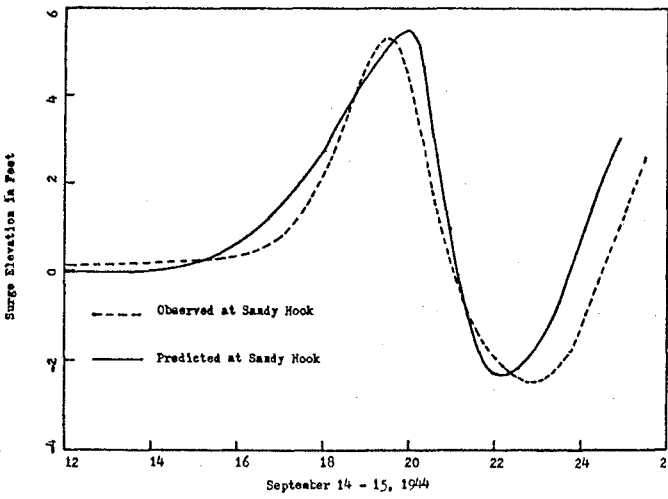


Figure 3

REFERENCES

- Bretschneider, C. L. and J. I. Collins, Prediction of Hurricane Surge: An Investigation for Corpus Christi, Texas and Vicinity, NESCO Technical Report No. SN-120, Prepared by National Engineering Services Company for U.S. Army Engineer District, Galveston, Texas, 1963.
- Damsguard, A. and A. F. Dinsmore, Numerical Simulation of Storm Surges in Bays, Symposium of Modeling Techniques, Vol. II, 1535-1551, Second Annual Symposium of the Waterways, Harbors, and Coastal Engineering San Francisco, California, September 3-5, 1975.
- Forristall, G. Z., Three-Dimensional Structure of Storm-Generated Currents J. Geophys. Research, Vol. 79, No. 18, 2721-2729, 1974.
- Gallagher, R. H., Liggett, J.A. and S. T. K. Chan, Finite Element Shallow Lake Circulation Analysis, J. Hydraulic Division, ASCE, Vol. 99, 1083, 1973.
- Gallagher, R. H. and S. T. K. Chan, Higher-order Finite Element Analysis of Lake Circulation, Computers and Fluids, Vol. 1, 119, 1973.
- Graham, H. E. and E. e. Nunn, Meteorological Considerations Pertinent to Stand Project Hurricane, Atlantic and Gulf Coasts of the U.S., National Hurricane Research Project, Report No. 33, U.S. Weather Bureau, Washington, D.C., 1959.
- Gillies, D.K.A. and A. L. Punhani, Dynamic Forecasting of Lake Erie Water Levels, Ontario Hydro Research Quarterly, Fourth Quarter, 1-6, 1971.
- Harris, D. L., Characteristics of the Hurricane Storm Surge, Technical Paper No. 48, U.S. Weather Bureau, Washington, D.C., 1963.
- Leendertse, J. J., Aspects of a Computational Model for Long Period Water Wave Propagation, RM 5294-PR, The Rand Corporation, 1967.
- Pearce, B. R., Numerical Calculation of the Response of Coastal Waters to Storm Systems, Technical Report No. 12, Coastal and Oceanographic Engr. Laboratory, University of Florida, 1972.
- Pearce, B. R. and J. R. Pagenkopf, Numerical Calculation of Storm Surges: An Evaluation of Techniques, Paper Presented at Seventh Annual Offshore Technology Conference, Houston, Texas, May 5-8, 1975.
- Reid, R. O. and B. R. Bodine, Numerical Model for Storm Surges in Galveston Bay, J. Waterways and Harbor Division, ASCE, Vol. 94, No. WW1, 33-57, 1968.
- Stone & Webster Engineering Corporation, Two-Dimensional Coastal Storm Surge Model, SWECO-17501-P, January, 1975.

CHAPTER 55

SIMULATION MODEL FOR STORM SURGE PROBABILITIES

by

M. H. Fallah¹, J. N. Sharma², C. Y. Yang³

I. INTRODUCTION

Storm surge and its impact on the coastal regions have been of interest to many researchers and engineers for a long time. Deterministic models based on classical hydrodynamics can be used for reliable predictions only for short terms, e.g. up to 24 hours for which the characteristics of the storm can be projected accurately. Long-term predictions, on the other hand, is a statistical problem due to the random nature of the storms. Such long-term prediction is becoming increasingly important as the coastal regions are rapidly developed into residential, recreational and industrial areas.

One of the first statistical studies on coastal storm surge predictions was published in 1961 by Wemelsfelder who used a Poisson probability law to fit the observed high tide data at Hook of Holland. From this fitted law, risk curves for long-term in years can be constructed for design purposes. In 1970 Yang et al applied the extreme value model to fit storm surge data for Atlantic City, New Jersey and Breakwater Harbor, Delaware. This so-called "purely" statistical method is sound in concept and simple to use. It has some serious limitations, however. First, it requires a collection of long term data (say 100 years for reliable design predictions) which is difficult to obtain in general. Secondly, the prediction for one location is not valid in general for other locations even when they are not far apart. To overcome the first limitation on the unavailability of long-term data at least partially, it is recognized that although storm tide data is limited, the general meteorological data is relatively abundant, so that more data on storm tide can be derived from meteorological data (wind field) via a hydrodynamic analysis. The analysis, of course, involves a general coastal area and consequently, the spatial variation of the storm tide can be predicted and the limitation on the location can be removed also. These observations lead to the concept of a combined statistical and hydrodynamic model which takes into account both the randomness of the long-term meteorological data and the physics of the storm surge.

¹ Senior Research Scientist, Mathematica, Inc., Philadelphia, PA

² Research Fellow, Civil Engineering Department, University of Delaware Newark, DE

³ Professor, Civil Engineering and College of Marine Studies, University of Delaware, Newark, DE

The first study known to the authors by this combined statistical and hydrodynamic approach was conducted by Bretschneider (1959) for Delaware Bay and Chesapeake Bay. In this study, the 1944 hurricane which was the most severe storm recorded along the Atlantic Coast at that time was selected as the so-called standard project hurricane. The track of this hurricane was then varied in position and orientation relative to the location in question. For each position and orientation of the hurricane, maximum storm surge height was calculated using a simplified hydrodynamic model. Following Bretschneider's study, a severe winter storm hit the Atlantic City area in 1962 and caused loss of lives and disastrous damage of properties. The following year, through an act of the Congress, the Corps of Engineers did a study for hurricane surge along the Atlantic Coast. A report was published in 1963 in which maximum surge heights were predicted for several locations based on the same standard project hurricane concept as used by Bretschneider (1959). In particular a 500 year return period was estimated for the standard project hurricane, unfortunately with little technical details. Subsequent to the 1963 study, under a contract with the Federal Insurance Administration, the Corps of Engineers in 1972 conducted a study of storm surge for the city of Rehoboth Beach, Delaware. Design surge heights of 500-year and 100-year return periods were predicted based on tide observations at Atlantic City, New Jersey and the 1963 prediction through the standard project hurricane with the estimated 500-year return period. Parallel to the studies by the Corps of Engineers (1963, 1972), Myers (1970) of the National Oceanic and Atmospheric Administration developed a refined method which he called the joint probability method to study the frequency of high tides at Atlantic City, New Jersey. It is refined in two respects. First, a thorough frequency analysis was made for the parameters of all hurricanes so that for a selected set of severe hurricanes, a frequency of occurrence can be calculated under the assumptions of independent hurricane parameters. Secondly, a refined hydrodynamic model due to Jelesnianski (1967) was used in the surge calculations from hurricane wind field. The same method was used to predict storm surge for the South Carolina coast by Myers in 1975 and for the Atlantic Coast by Ho in 1976, using a revised hydrodynamic model from Jelesnianski (1974).

The purpose of this paper is to present a simulation model which includes the generation of random artificial hurricanes and the hydrodynamic model of Jelesnianski (1974) for the long-term prediction of design storm surge. The model is then applied to the Delaware coast. Finally a comparison with other predictions and suggestions for further work are made.

II. SIMULATION MODEL

A Monte Carlo simulation model (see for example, p. 124, Benjamin and Cornell, 1970) is developed to predict storm surge probabilities. This model consists of six essential parts: (1) estimating the statistical distribution of historical hurricanes and hurricane parameters, (2) generating artificial hurricanes associated with the set of random hurricane parameters, (3) computing the surge heights in each artificial hurricane by a suitable hydrodynamic model, (4) combining the hurricane surge with astronomical tide, (5) generating random winter total tide (storm plus astronomical) and (6) constructing extreme value distribution based on yearly maxima.

A flow chart is shown in Figure 1 for the simulation and combination of the hurricane storm surge, astronomical tide and winter tide in a year. This chart is explained in the following steps.

- (1) Generate a uniformly distributed random number, U , between 0 and 1.
- (2) If $U < P$ (the probability of occurrence of a hurricane in the area during one year), a hurricane occurs; otherwise it does not.
- (3) If a hurricane occurs, then generate a set of hurricane parameters, center pressure drop ΔP , radius R , forward speed V and direction θ , consistent with their distributions.
- (4) Generate another uniformly distributed random number, U , to compare with P_L (the probability of a landfalling hurricane) and decide whether it is a landfalling hurricane or one moving parallel to the coast.
- (5) Calculate temporal surge profile due to the artificial hurricane.
- (6) Generate random amplitude and phase for astronomical tide.
- (7) Calculate the combined maximum tide S_H (hurricane surge plus astronomical tide). If a hurricane does not occur, set $S_H = 0$.
- (8) Generate a total winter tide S_W (storm plus astronomical) based on the distribution of observed total winter tide.
- (9) Take the larger of the two values, S_H and S_W , and set it as the extreme event of the year.
- (10) Plot the extreme events on extreme value probability paper.

III. APPLICATION TO DELAWARE

For Delaware coast, data source and input data to the simulation model consists of (1) hurricane occurrence frequency and hurricane parameters for 70 years from Bretschneider (1972), (2) amplitudes of astronomical tide in September from Myers (1970) and (3) total winter tide (1953-1974 storm plus astronomical) from U. S. Geological Survey. These raw data were first analyzed to obtain statistical distributions for use in the model as explained in the previous section. It should be pointed out, however, that due to the inefficiency of the computer available, the cost in running the hydrodynamic model of Jeleznianski (known as SPLASH II) was found to be prohibitive when hundreds of runs are needed in the simulation process. Accordingly, only four runs of the SPLASH II were made to furnish the needed information (the shoaling factor) in the simplified analysis based on Jeleznianski's monographs. This known crudeness and other major assumptions such as the independence of random parameters of a hurricane indicates the approximate nature of the final result.

A total of 792 sample years were used in the final simulation analysis from which key values of the total tide (either hurricane surge plus astronomical tide or winter storm surge plus astronomical tide) together with their frequency of occurrences are sorted out. To facilitate design application, these values are plotted on extreme value probability paper as shown in Figure 2, where the abscissa on the bottom of the figure is the probability distribution function, i.e. the probability that the yearly extreme is equal or less than the indicated tide; and that on the top of the figure is the so-called return period in years. The return period in years means that on the average, the indicated tide level will be exceeded at least once in these many years.

IV. COMPARISON AND DISCUSSION OF RESULTS

In Figure 2, a comparison is presented among the predictions by Yang et al (1970) for Breakwater Harbor, Delaware, by Myers (1970) for Atlantic City, New Jersey, by Corps of Engineers (1972) for Rehoboth Beach, Delaware and by the present simulation model for Breakwater Harbor, Delaware (1976). Although the present analysis is admittedly crude in many aspects, the large discrepancies among these four sources indicate that the prediction by the Corps of Engineers in 1972 based on the concept of a standard project hurricane of 500 year return period and by Myers in 1970 for Atlantic City, New Jersey are probably overly conservative for the Delaware coast. This comment is based on the seemingly lack of technical basis for the assessment of the 500 year return period for the Corps study and the result by Ho (1976) which indicates a higher tide at Atlantic City, New Jersey than at Delaware. To be more specific than this requires further improvement of the simulation analysis on at least the following aspects: (1) a more complete hydrodynamic model taking into account the effect of the Delaware Bay should be used in place of Jelesnianski's (1974) SPLASH model which considers a straight coastline only; (2) the correlation among the hurricane parameters should be taken into account; (3) amplitudes of astronomical tide should be analyzed for all the hurricane season rather than the month of September only; (4) all of the raw data used should be constantly updated and examined for accuracy; (5) a hydrodynamic model for winter storm needs to be developed to improve the prediction reliability particularly for locations like Delaware where winter storms are perhaps more important in the sense of severity than hurricane storms.

V. ACKNOWLEDGMENT

The authors wish to acknowledge their appreciation to Dr. Jelesnianski for providing the SPLASH II computer program and technical advice in its use, and to NOAA and the State of Delaware for financial support of this study.

VI. REFERENCES

Benjamin, J. and Cornell, C. A., Probability, Statistics and Decisions for Civil Engineers, McGraw-Hill, 1970.

Bretschneider, C. L., "Hurricane Surge Predictions for Delaware Bay and River," U. S. Army Corps of Engineers, Miscellaneous Paper No. 4-59, November 1959.

Bretschneider, C. L., Revision to "Hurricane Design Wave Practices," Proceedings of the 13th Coastal Engineering Conference, ASCE, Vol. 1, pp. 167-196, 1972.

Corps of Engineers, Philadelphia District Report, Hurricane Study, Delaware River and Bay, Pennsylvania, New Jersey and Delaware, 1963.

Corps of Engineers, Philadelphia District, Flood Insurance Study, City of Rehoboth Beach, Delaware, June 1972.

Ho, Francis S., "Hurricane Tide Frequencies on the Atlantic Coast," Abstract, Proceedings of the 15th Coastal Engineering Conference, ASCE, 1976.

Myers, V. A., "Joint Probability Method of Tide Frequency Analysis Applied to Atlantic City and Long Beach Island, New Jersey," U. S. Department of Commerce, Weather Bureau, ESSA, Technical Memo WBTM HYDROII, April 1970.

Myers, V. A., "Storm Tide Frequencies on the South Carolina Coast," National Weather Service, NOAA, Technical Report NWS-16, June 1975.

Jelesnianski, C. P., "Numerical Computation of Storm Surge with Bottom Stress," Monthly Weather Review, Vol. 95, No. 11, November 1967.

Jelesnianski, C. P., "SPLASH II (Special Program to List Amplitudes of Surges from Hurricanes)," "General Track and Variant Storm Conditions," NOAA, Technical Memo NWS-TDL-52, 1974.

Wemelsfelder, P. J., "On the Use of Frequency Curves of Storm Floods," Proceedings of the 7th Coastal Engineering Conference, ASCE, 1961.

Yang, C. Y., Parisi, A. M. and Gaither, W. S., "Statistical Prediction of Hurricane Storm Surge," Proceedings, 12th Coastal Engineering Conference, ASCE, pp. 2011-2030, September 1970.

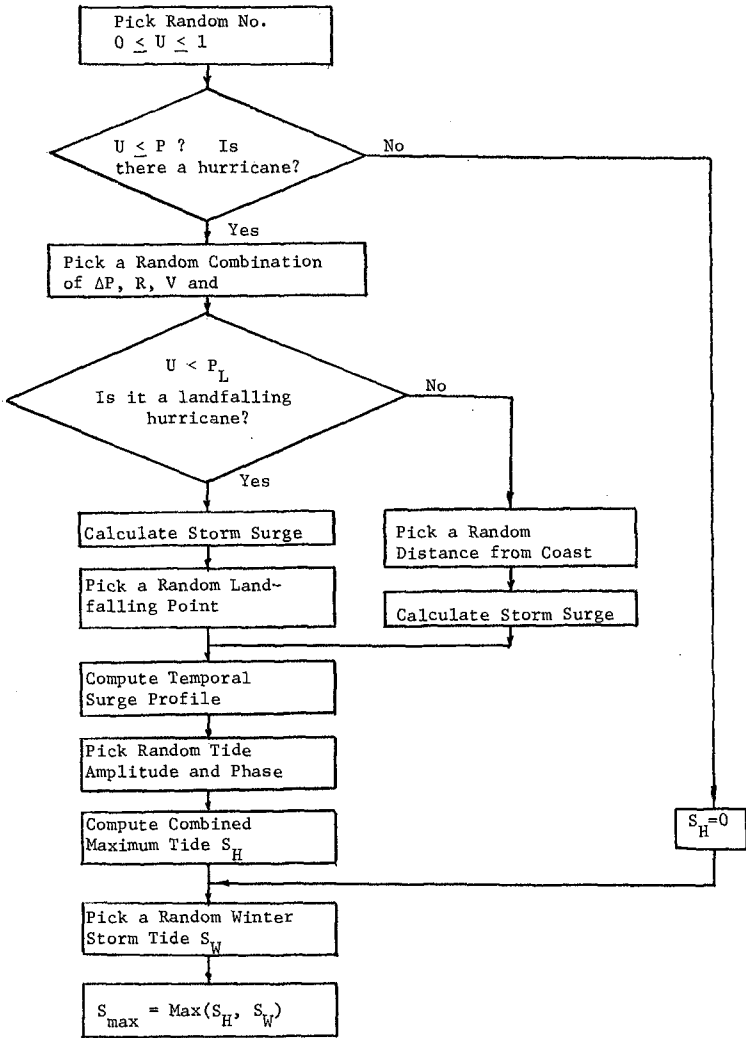


Figure 1 Flow Diagram for Simulation of Maximum Combined Tide in One Year

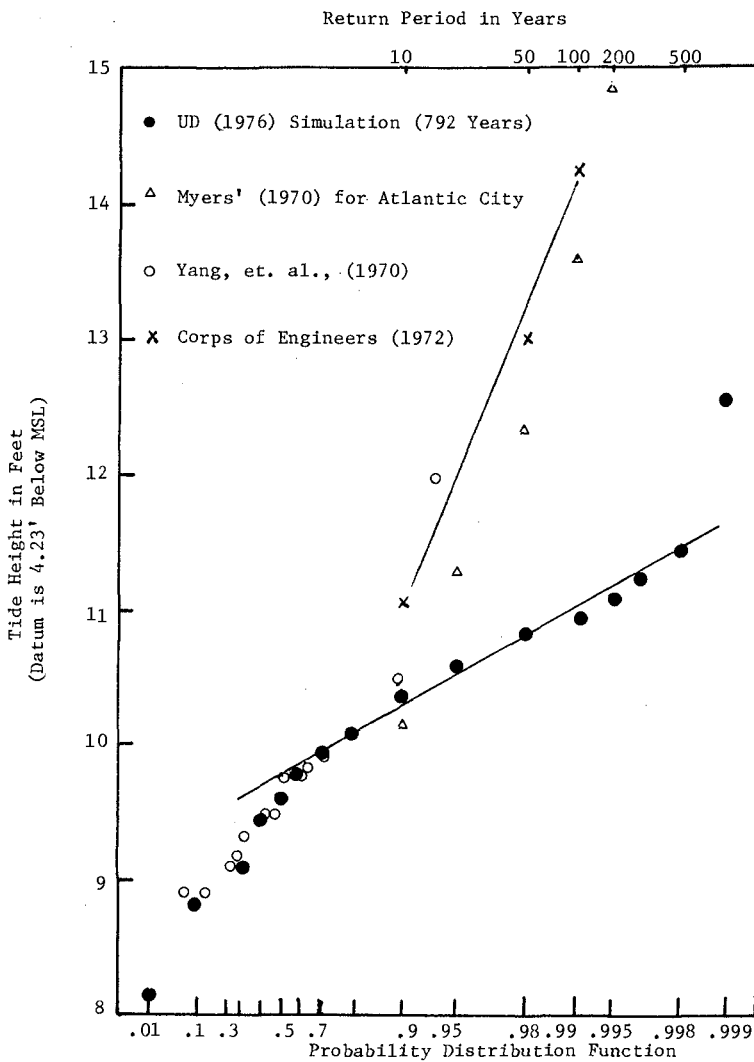


FIGURE 2 Comparison of Extreme Tide Distribution from Simulated Model for Breakwater Harbor with Yang, et al. (1970) Result Based on Historical Tide Record at Breakwater Harbor and with Vance Myers' (1970) Result for Atlantic City Based on His Combined Statistical Model, and with the Corps of Engineers (1972) for Rehoboth Beach, Delaware Based on the Standard Project Hurricane and Tide Data for Atlantic City.

CHAPTER 56

SPLASH - A MODEL FOR FORECASTING TROPICAL STORM SURGES

Celso S. Barrientos
Chester P. Jelesnianski

Techniques Development Laboratory
National Weather Service, NOAA
Silver Spring, Maryland

ABSTRACT

A significant portion of the damage by hurricanes is the storm surges. The National Weather Service has developed a dynamical-numerical model to forecast hurricane storm surges. The model is used operationally for prediction, warning, and planning purposes.

The model requires fixed oceanographic and real time meteorological input data. The oceanographic data were prepared for the Gulf and East coasts of the U.S. and are stored as an essential part of the program. Meteorological data for any tropical storm are supplied by the forecasters or planners using the model.

The model was applied to hurricane Camille 1969. Comparison between the observed and computed surges for Camille was satisfactory for prediction purposes.

INTRODUCTION

Coastal high waters (commonly called surge) generated by tropical storms can cause a significant fraction of the total storm damage. Because the potential for destruction can be enormous, it is useful to have at hand an estimate of the height of the potential surge and the extent of the coastal areas that can be affected by the flooding. Such an estimate can be given by a numerical model such as SPLASH.

What is SPLASH? SPLASH is an acronym for "Special Program to List Amplitudes of Surges from Hurricanes." It is the name of a computer program for a dynamical surge model to predict hurricane storm surges. The program is used operationally at the National Weather Service (NWS).

SPLASH is a numerical-dynamical model to predict storm surges generated by tropical storms (Jelesnianski 1972, 1974, 1976). The model solves the linearized transport equations of motion with storm driving forces on the

surface and bottom stress. The model uses an input basin truncated from the ocean which contains coastal areas of interest. We use a truncated basin of proper size so that numerical computations can be performed at reasonable cost and yet not compromise on the dynamics of the open coast surge.

A very useful adjunct of the SPLASH model is a shoaling curve. (The meaning of shoaling correction will become clear in later parts of the paper.) The shoaling curve indicates the relative increase (or decrease) of the surges if a storm's landfall position changes along the coast. This is important because the surge varies as bathymetry varies along the basin, and bathymetry relative to the storm will vary as landfall is varied. For application purposes, the shoaling curve serves as a powerful tool to determine how surges change if the landfall point is varied. Also, with the aid of the shoaling curve, dangerous and ill-conditioned situations can be anticipated without resorting to extensive computer runs. For planning purposes, a shoaling curve is most effective to obtain added information with a minimum number of computer runs.

SPLASH is used operationally at the National Hurricane Center of NWS in Miami. In this paper, we will discuss the model, the basin, input data, a shoaling correction, and applications of the model. The program is applicable for the Gulf and East coasts of the U.S., from Brownsville, Texas, to Shinnecock Inlet, Long Island, N.Y. This stretch of coast is approximately 300 miles long. Recently, we extended the application of SPLASH to the New England area up to the U.S.-Canadian border.

The SPLASH product is also used to estimate flooding potentials in the coastal areas of the U.S. and Puerto Rico (Jelesnianski and Barrientos 1973). This work is being done by the National Oceanic and Atmospheric Administration (NOAA) as a reimbursable project for the Federal Insurance Administration of the Department of Housing and Urban Development to fix flood insurance rates. A discussion of the NOAA procedure to compute storm tide frequencies is in Myers (1975).

SPLASH MODEL

The SPLASH model has been partially documented in three publications, the mathematical technique in Jelesnianski (1967), and three operational techniques to run and interpret the results for forecasting purposes, Jelesnianski (1972, 1974, 1976). The mathematical techniques are adapted from Platzman (1963). The tropical storm model used to generate surges is discussed in Jelesnianski and Taylor (1973).

SPLASH is a dynamic model which numerically solves the linearized transport equations of motion in a basin bounded by a curvilinear parallel surface;

the curved coastline is a vertical wall and the remaining three boundaries are open to the sea. Initially, the sea in the basin is assumed at rest. Driving forces from the storm are applied on the water's surface; also, a time-history formulation of the bottom stress is utilized.

Initially, the storm is set at zero strength and then allowed to grow to maturity in a continuous but rapid manner. Initial positioning of the storm is unimportant, if on reaching maturity the storm lies in deep water beyond the continental shelf. For storms traveling more or less parallel to the coast and along the continental shelf, initial placement must be at least sufficiently distant from the area of interest so that the surge has time to form; this can be determined by empirical tests through variation of initial storm placement, growth time of storm to maturity, etc.

The grid distance used in our numerical computations must be fine enough to portray not only the storm surge but also the driving forces of the storm. The grid length may be determined by empirical tests.

On the two lateral, open boundaries, the boundary condition used is $\partial V/\partial y=0$; where V is the component of transport along the coastal y -coordinate. This boundary condition is arbitrary and used purely for convenience. In any case, reflections from these boundaries eventually corrupt the interior of the basin. However, if the boundaries are placed sufficiently far from an area of interest along the coast, there will be a time interval before the area is corrupted by reflections from the boundaries. The placement of these side boundaries are determined by empirical tests.

The deep water open boundary is placed somewhat arbitrarily, near the juncture of continental shelf and slope. In deep water away from coastal influences, the dynamic surge is small and corresponds very closely to the inverted barometer effect. The boundary condition used is $h=h_0$; where h_0 is the static height of the surface.

BASIN AND STORM DATA

The dynamic model, SPLASH, computes storm surges via numerical computations for particular storms in particular basins. A basin is described by two-dimensional depth fields, coastal boundaries, local and geographical references, and geographical orientation. To acquire basin data, we used the National Ocean Survey marine charts with scale 1:500,000. The chart delineates coastlines, the continental shelf, depth contours in shallow water, and spot depths in deep water. Detailed descriptions of preparing basin data are presented in our two reports to the Federal Insurance Administration (Barrientos and Jelesnianski, 1973; Barrientos and Chen, 1974).

For orientation purposes regarding the basin, the observer is at sea and facing the coast. The coast to his right will be considered relative north, to his left relative south. Crossing angles of the storm's path to this oriented coast will be described as follows: A storm moving from relative north has a crossing angle of 0° , moving normal to the coast from sea, a crossing angle of 90° , exiting (moving from land to sea), a crossing angle of 270° , etc.

Figure 1 positions pre-selected stations on the East and Gulf coasts of the U.S. used by the SPLASH operational model to indicate approximate positions of basin centers. Some of the location names are abbreviated. The abbreviations are exactly as used in the model for routine operations at NOAA's National Hurricane Center. The stations are 100 miles apart (more or less) and are situated at (or near) the center of the various basins.

To refine the technique for planning and flood insurance study, we find it necessary to add additional basins between the stations (Figure 1); i.e., basins are now overlapped every 50 miles instead of every 100 miles. Geographical locations of the basin centers are included in the basin data. We have not identified the additional basins with any new cities because we want to keep these reference cities to a minimum.

Due to computer core limitations and economics of machine operations, it is impossible to consider an entire ocean as a basin. Open boundaries are therefore used as an artifice in the model. (The basin used is 600×72 statute miles in size and grid length is 4 miles. Thus, total grid points are $1/2(151 \times 20) = 1510$ for each basin.) A more detailed description of basin preparations is in the report of Barrientos and Jelesnianski (1973).

Two versions of the dynamical model are in use. SPLASH I to compute storm surges for landfalling (or exiting) storms only, and SPLASH II for storms moving along the coast. SPLASH requires input meteorological parameters that have to be supplied by weather forecasters. The data for a computer run are shown schematically in Figure 2. In SPLASH I, these are: (a) the pressure drop, $\Delta p = p_\infty - p_0$, where p_∞ is the ambient pressure outside the influence of the storm and p_0 is the central pressure of the hurricane; (b) the radius of maximum wind R ; (c) the vector storm motion, U_s/θ , where U_s is the storm speed of translation θ is the compass (meteorological) storm direction of motion; and (d) landfall point referenced to stations or cities (Figure 1).

The landfall point is important, for it determines which basin will be used in the model. SPLASH I deals with a steady state storm, of constant size and intensity, and constant, linear, vector storm motion. This idealization in SPLASH I has been proved useful in actual operations and climatological studies.

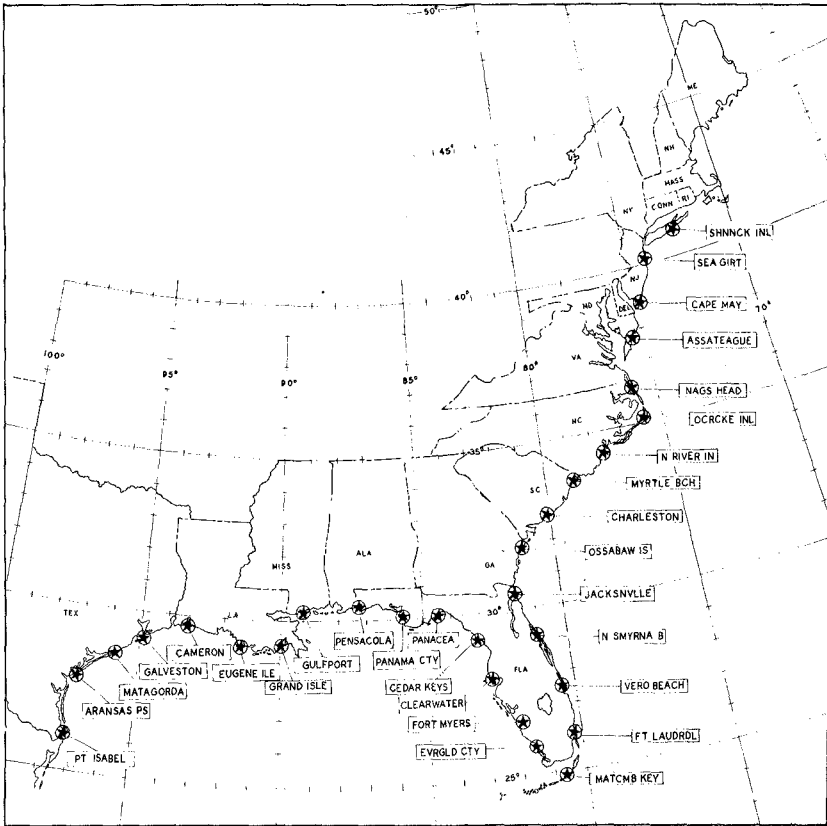


Fig. 1. Selected stations on the East and Gulf coasts of the U.S., used by the SPLASH operational model to indicate positions of basin.

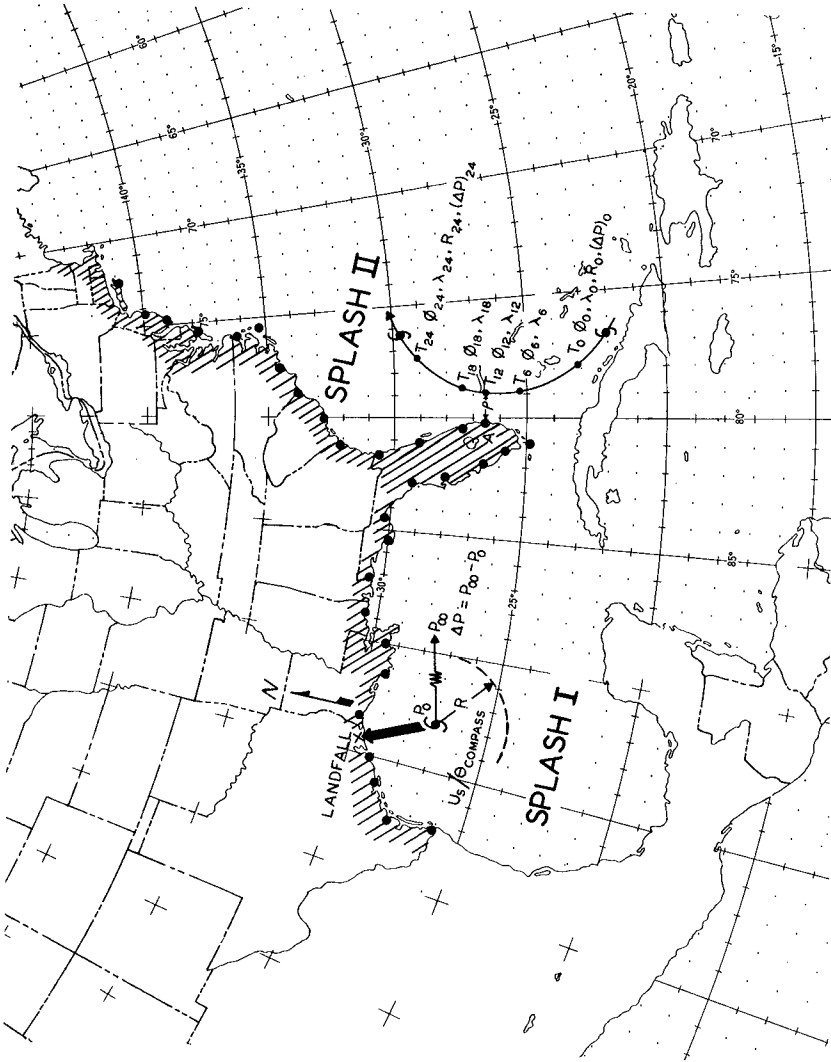


Fig. 2. A schematic representation of the use of the SPLASH programs and input meteorological data.

In contrast, SPLASH II deals with variant conditions of the storm and its track; i.e., a nonsteady state storm. The storm track is quite general; it can landfall (or exit--moving from land to sea) at any angle with the coastline, move parallel to the coast, be bow-shaped, etc. The speed of the storm can be variable along the storm track and even remain stationary. Note that SPLASH I is a special case of SPLASH II. For this program, the weather forecaster supplies a 24-hour track segment (Figure 2). The track is defined by latitude, ϕ , and longitude, λ , for five points on the track staggered six hours apart for a 24-hour period. These input latitudes and longitudes define the track, and the speed of propagation of the storm, i.e., vector storm motion. Other input data are the size of the storm, that is the radius of maximum wind, at initial and final time of the 24-hour period; also, the intensity or pressure drop at initial and final time of the 24-hour period. Both the size and the pressure drop can vary with time. The storm track is very important in the surge computations. A slight shift of the track either toward the coast, or toward the sea, can make a significant difference in coastal surges (Jelesnianski and Barrientos, 1975). Several dynamic phenomena, such as resonance and wave transients, can be generated by storms with generalized motions (Jelesnianski, 1974).

With the basin data and input meteorological parameters, peak surges, profiles, and envelopes of high water along the coast are computed by the SPLASH model.

SHOALING CORRECTIONS

A very important property derived by SPLASH is a normalized shoaling correction. It is a powerful tool to correct surge computations along the coast if the landfall point is shifted.

A shoaling curve for both the East and Gulf coasts is derived from the ratio of the peak surge computed in a local basin to that of the peak surge computed in a standard basin. A shoaling correction curve in a particular basin indicates the change in the coastal surge envelope* as it is displaced by a change in landfall point. The change of the surge envelope is due to changes in the bathymetry of the continental shelf with respect to landfall point. We used a standard storm and standard vector motion in the computations. (A standard storm has a maximum wind speed of 100 mph.) Peak surges computed by the SPLASH model with a standard storm in local basins are normalized with the peak surge computed in a standard basin. A standard basin has a continental shelf sloping linearly at 3 feet per mile, with a depth of 15 feet at the coast; its coast is a straight line, and the depths

*Envelope means the plot of the coastal high water heights during passage of a storm. Highest surges at various points along the coast don't occur simultaneously.

vary in one dimension only. This standard basin may be considered as the mean depth field averaged throughout the continental shelf of the Gulf and East coasts.

We define the standard vector motion to be perpendicular to the coast with a speed of 15 mph from sea to land. Hurricanes, of course, ordinarily do not landfall precisely normal to the coast, but for the purpose of computing shoaling curves our approach is the most convenient. Another alternative is to compute shoaling curves for various track angles to the coast. This kind of approach however would require voluminous amounts of data and staggering computer expense.

Storm surges are related to storm size (radius of maximum wind). For the same maximum wind, the larger storm will give larger surges, up to a critical size. Storm size is even more important for storms moving along the coast (Jelesnianski, 1974; Jelesnianski and Barrientos, 1975).

For convenience in our derivation of shoaling curves, we form the storm's pressure drop so that maximum winds are 100 mph; this wind is maintained for any storm size and also for latitude of real basins on the coast. We can follow this procedure because the storm model accommodates these parametric values (Jelesnianski and Taylor, 1973). In previous work, we found that peak surges along the coast depend only mildly on latitude, but to some extent on radius of maximum wind (storm size). Thus, we computed two reference peak surges in the standard basin with a standard storm for two storm sizes, or radii of maximum winds, of 15 and 30 miles. These two peak surges are used to scale maximum surges computed with the same storms in real basins.

To produce peak surges for standard storms along the Gulf and East coasts, we made SPLASH runs on all 50 basins for two storm sizes: 15 and 30 miles radii of maximum wind. We then plotted the resulting peak surges on the coast. For each basin, we chose a minimum of three landfall points: at the center of the basin baseline, and 16 miles on either side of the center. In complicated locations, e.g., Mississippi Delta, Cape Fear, and Sandy Hook, we made more runs to get better resolution for the shoaling curve. For landfall on either side of the basin center, the track was made normal to the true coastline.

In addition to the location of peak surges for each storm size, we successively plot a portion of the computed envelope on either side of the peak surge. Figure 3 is an example of the process. We plot only a portion of each envelope that is within about one storm radius on both sides of the peaks. We now hand draw an envelope of peak surges, that is, an envelope of surge envelopes. This is done separately for the two storm sizes. The final envelope of peak surges is an unscaled shoaling curve.

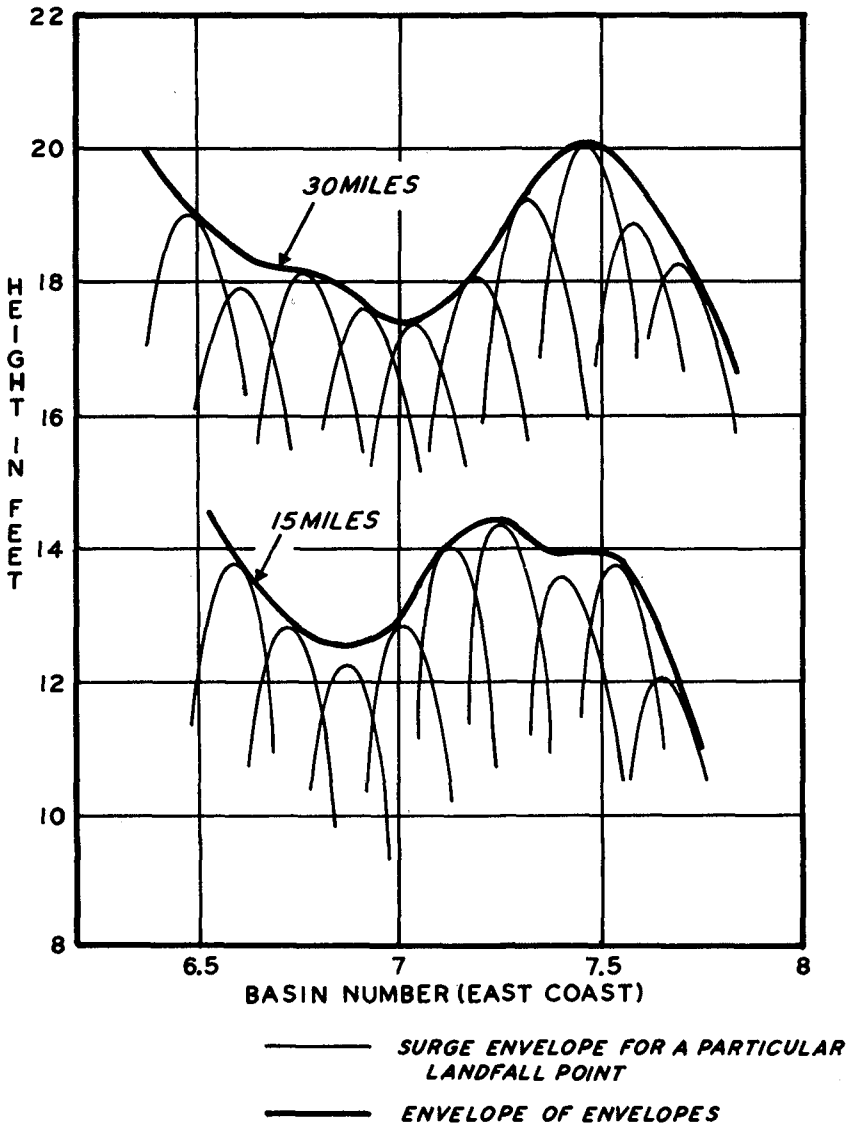


Fig. 3. Analysis of the envelope of surge envelopes to arrive at shoaling curves. The upper envelope is for storm size of 30 miles, the lower for storm size of 15 miles.

In Figure 3, some peak surges are not on the shoaling curve because subjective adjustments of the envelope were made considering the bathymetry of the continental shelf. If more runs of the SPLASH program were made at closer spacings along the coast, then peak surges would have been computed to fit the shoaling curve. The shoaling curve was based on all individual envelopes as shown in Figure 3.

We don't want to be constrained to peak surge values generated by standard storms only. Hence, the shoaling curve must be scaled locally for each basin if it is to be useful in the SPLASH model. The procedure for scaling is now discussed.

The peak surge computed for a standard storm along the coast is a function of the slope of the continental shelf. Hence if we scale the final envelope of Figure 3 according to the peak surge generated by a standard storm in a standard basin, then we reduce the final envelope to a common denominator. We call such a scaled, final envelope a shoaling curve. The shoaling curves for the Gulf and East coasts are shown in Figures 4a and 4b for both 15- and 30-mile storm sizes. The curved coasts are extended linearly for convenient display. The ordinate is the shoaling factor or surge potential (the ratio of peak surge on any point of the coast to that of peak surge on a standard basin).

Also included in Figures 4a and 4b are depth contours on the continental shelf. There is close correlation between the shoaling curve and depth contour, i.e., the shallower the shelf the higher the potential. This is illustrated in Eugene Isle in the Gulf and Ossabaw Island in the East coast. The surge potential is small between Pensacola and Panama City in the Gulf and on the east coast of Florida due to the narrow shelves in these areas.

The shoaling curve varies by a factor of about four on both coasts. The highest surge potential on the Gulf coast is higher than on the East coast for both storm sizes. We can conclude that for the same storm, the Gulf coast has higher storm surge potential than the East coast. However, we point out that storms are not necessarily the same on the Gulf and Atlantic shelves.

To correct a computed surge envelope for alternate landfall points, we have designed an individual shoaling correction curve for each basin. The basin shoaling correction curve is composed as follows: (1) Read from Figure 4a the shoaling value at the center of each basin. (2) Along the shoaling curve of Figure 4a for a given basin, divide the shoaling factors by the shoaling value from (1), for a shoaling correction curve. The value of the correction is unity at basin center. Because the coastal distances

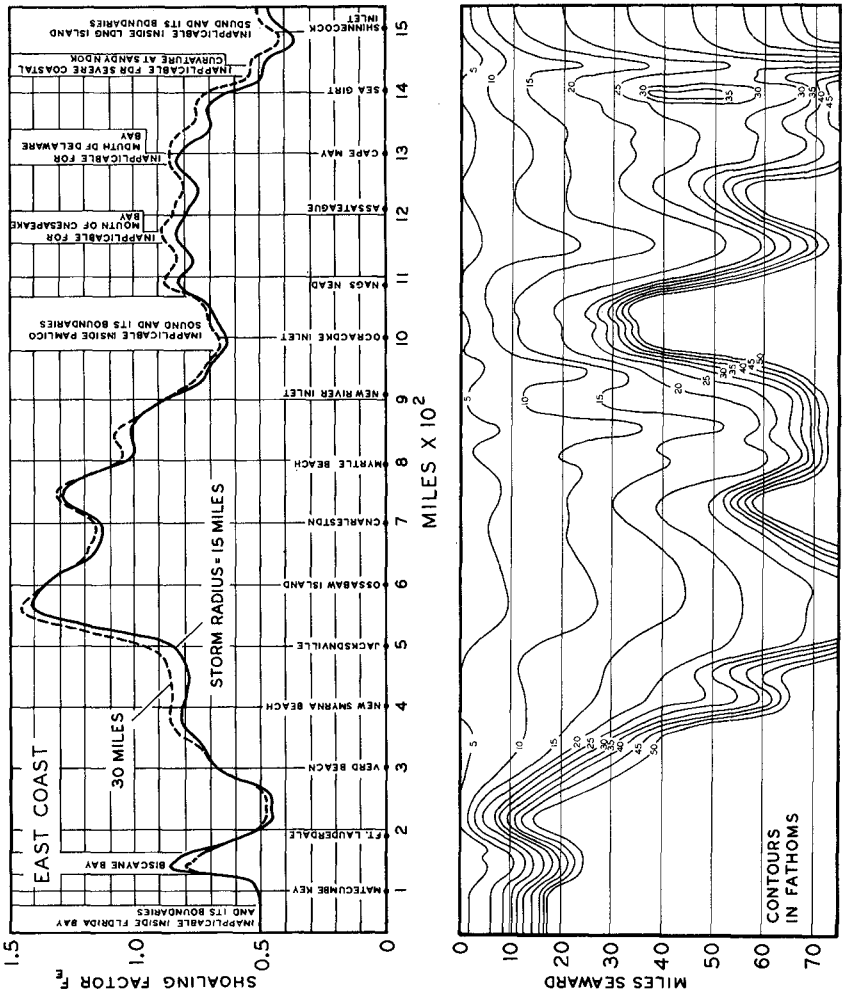


Fig. 4a. Shoaling correction curves along the Gulf coast.

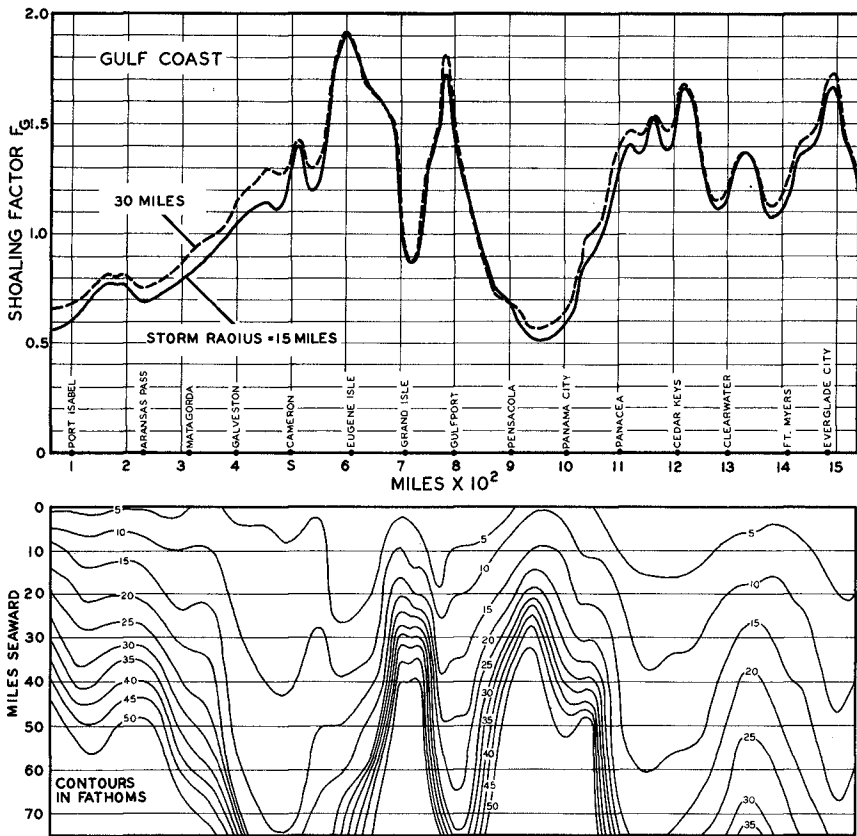


Fig. 4b. Shoaling correction curves along the East coast.

represented by abscissa distances on Figure 4a are curvilinear lengths, whereas the SPLASH model calculations are for equidistant coastal points on a tangent to the coast (a baseline), then the correction curve must be compressed to the linear lengths along the baseline.

After local shoaling corrections are computed, they are stored in the SPLASH program for instant use. The basin shoaling corrections are part of the basin data. The corrections operate on a computed surge envelope; if landfall point is hypothetically shifted on the coast, then the computed envelope is also shifted and operated on by the shoaling curve to correct for changing bathymetry.

The basin shoaling corrections are included in the SPLASH program for each of the 58 basins in the Gulf and East coasts. The program is used operationally at the National Hurricane Center, NWS and by the Office of Hydrology, NWS, NOAA, to compute outer coast surges with climatological input data for flood insurance projects.

APPLICATION TO HURRICANE CAMILLE 1969

To run the SPLASH program in NOAA, users will feed the computer with necessary meteorologic data as shown in Figure 2. For users without access to NOAA computers, we have an earlier version of the program available at the National Technical Information Service. The program includes the file of basin data.

To illustrate the SPLASH program we show a verification run for hurricane Camille 1969. Camille was probably the most devastating hurricane to hit the coast of the U.S. The important result of SPLASH is shown in Figure 5 for Camille.

On the top of Figure 5, the input data that the forecaster supplied are repeated for a visual check. The next group of data are the correction factors for the pressure drop. This is useful to correct the computed surges without rerunning the program. We gave corrections for ± 10 mbs deviation of pressure drop.

We also predict the astronomical tides, above MSL, for various stations near the Landfall point. In operational use, the forecaster's may modify the computed surges accordingly. We don't add the astronomical tide to the storm surges because it is very hard to phase the two waves together.

The main output of the SPLASH program is the surge envelope indicated by asterisks in Figure 5. The symbol \sim^* represents the landfall point of

STORM SURGE HEIGHTS (FEET)
30 25 20 15 10 5 0

UNLESS OTHERWISE SPECIFIED, THE FOLLOWING TIDE PARAMETERS
APPLY TO ALL STATIONS IN THE GULFPORT
AREA. THESE PARAMETERS ARE BASED ON
THE MEAN HIGH WATER (MHW) AND MEAN
LOW WATER (MLW) DATUMS. THE TIDE
GAUGES ARE LOCATED AT THE FOLLOWING
STATIONS: GULFPORT, MISSISSIPPI; STOP
ON BEACH, MISSISSIPPI; STOP
ON BEACH, MISSISSIPPI; STOP

IF YOU WANT TO UPDATE YOUR SET OF PRESSURE CORP. USE THE FOLLOWING CORRECTION FACTORS ON THE COMPUTED SURGE VALUES

CORRECTION FACTOR CORP. .08 .02 .03 .04 .05 .06 .07 .08 .09 .10 .11 .12 .13 .14 .15 .16 .17 .18 .19 .20 .21 .22

CONDITION FACTOR .08 .02 .03 .04 .05 .06 .07 .08 .09 .10 .11 .12 .13 .14 .15 .16 .17 .18 .19 .20 .21 .22

ESTIMATED TIME OF LANDFALL

11:00 AM AUG 17 1969

12:00 PM AUG 17 1969

1:00 PM AUG 17 1969

2:00 PM AUG 17 1969

3:00 PM AUG 17 1969

4:00 PM AUG 17 1969

5:00 PM AUG 17 1969

6:00 PM AUG 17 1969

7:00 PM AUG 17 1969

8:00 PM AUG 17 1969

9:00 PM AUG 17 1969

10:00 PM AUG 17 1969

11:00 PM AUG 17 1969

12:00 AM AUG 18 1969

1:00 AM AUG 18 1969

2:00 AM AUG 18 1969

3:00 AM AUG 18 1969

4:00 AM AUG 18 1969

5:00 AM AUG 18 1969

6:00 AM AUG 18 1969

7:00 AM AUG 18 1969

8:00 AM AUG 18 1969

9:00 AM AUG 18 1969

10:00 AM AUG 18 1969

11:00 AM AUG 18 1969

12:00 PM AUG 18 1969

1:00 PM AUG 18 1969

2:00 PM AUG 18 1969

3:00 PM AUG 18 1969

4:00 PM AUG 18 1969

5:00 PM AUG 18 1969

6:00 PM AUG 18 1969

7:00 PM AUG 18 1969

8:00 PM AUG 18 1969

9:00 PM AUG 18 1969

10:00 PM AUG 18 1969

11:00 PM AUG 18 1969

12:00 AM AUG 19 1969

1:00 AM AUG 19 1969

2:00 AM AUG 19 1969

3:00 AM AUG 19 1969

4:00 AM AUG 19 1969

5:00 AM AUG 19 1969

6:00 AM AUG 19 1969

7:00 AM AUG 19 1969

8:00 AM AUG 19 1969

9:00 AM AUG 19 1969

10:00 AM AUG 19 1969

11:00 AM AUG 19 1969

12:00 PM AUG 19 1969

1:00 PM AUG 19 1969

2:00 PM AUG 19 1969

3:00 PM AUG 19 1969

4:00 PM AUG 19 1969

5:00 PM AUG 19 1969

6:00 PM AUG 19 1969

7:00 PM AUG 19 1969

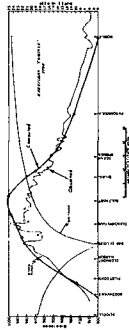
8:00 PM AUG 19 1969

9:00 PM AUG 19 1969

10:00 PM AUG 19 1969

11:00 PM AUG 19 1969

12:00 AM AUG 20 1969



280	1.7	9.0
270	1.1	0.0
260	1.1	0.0
250	1.1	0.0
240	1.1	0.0
230	1.1	0.0
220	1.1	0.0
210	1.1	0.0
200	1.1	0.0
190	1.1	0.0
180	1.1	0.0
170	1.1	0.0
160	1.1	0.0
150	1.1	0.0
140	1.1	0.0
130	1.1	0.0
120	1.1	0.0
110	1.1	0.0
100	1.1	0.0
90	1.1	0.0
80	1.1	0.0
70	1.1	0.0
60	1.1	0.0
50	1.1	0.0
40	1.1	0.0
30	1.1	0.0
20	1.1	0.0
10	1.1	0.0
0	1.1	0.0
-10	1.1	0.0
-20	1.1	0.0
-30	1.1	0.0
-40	1.1	0.0
-50	1.1	0.0
-60	1.1	0.0
-70	1.1	0.0
-80	1.1	0.0
-90	1.1	0.0
-100	1.1	0.0
-110	1.1	0.0
-120	1.1	0.0
-130	1.1	0.0
-140	1.1	0.0
-150	1.1	0.0
-160	1.1	0.0
-170	1.1	0.0
-180	1.1	0.0
-190	1.1	0.0
-200	1.1	0.0
-210	1.1	0.0
-220	1.1	0.0
-230	1.1	0.0
-240	1.1	0.0
-250	1.1	0.0
-260	1.1	0.0
-270	1.1	0.0
-280	1.1	0.0
-290	1.1	0.0
-300	1.1	0.0

Fig. 5. A verification run of the SPLASH program for hurricane Camille 1969.

the hurricane. The peak surge generally occurs at a distance equal to the radius of maximum wind, R to the right of landfall. Below the graph, we print the values of the computed surge envelope. Note these values are the highest surges on the coast but not necessarily occurring at the same time. For Camille, the computed peak surge is 25.0 ft. We also print the stations along the coast for reference and the distances along the coast from landfall point.

The second row of numbers, from the bottom of Figure 5, is the surge envelope if the landfall is shifted 100 miles to the right; the first row is when landfall is shifted 100 miles to the left. It is possible to compute these surge values because of the shoaling correction factors.

The inset in Figure 5 shows a comparison of the observed surges and computed surges by SPLASH for Camille. Considering that the observations are taken at various distances from the coastline, we believe the comparison here is quite good. Also errors in measurements are very difficult to account for.

SUMMARY AND CONCLUSIONS

Rising coastal waters are generated by hurricane driving forces. These forces are low atmospheric pressure (inverted barometer effect) and wind force. Thus a rotating mound of water forms under a storm in deep water. If the variable momentum in the sea (i.e. rotating mound of water or vorticity) is transformed into divergence, then storm surges are further generated. The bathymetry or sloping depths of continental shelf and the coastal boundary are effective mechanisms to transform vorticity to divergence.

NOAA has an existing dynamical-numerical model to compute surges, called SPLASH. To compute surges with this model, basin data are stored for all basins of the Gulf and East coasts of the United States. Basin data consist of depth values at grid points, orientation of the basin with respect to north, local and geographical references, and shoaling corrections.

We have numerically computed surge envelopes at equally spaced landfall intervals of 16 miles, along the 3000-mile stretch of the Gulf and East coasts. At each landfall point, we made computer runs for two storm sizes, 15- and 30-mile storm radius. We then derived envelopes of peak surge to obtain shoaling curves. When the storm size is not 15 or 30 miles, then whichever of the two sizes is nearest to R is used, e.g., $R = 25$ the shoaling curve for $R = 30$ is used.

Finally, shoaling corrections were prepared for each basin in the SPLASH model.

The shoaling curves are used: (a) for comparing the peak surge potential at one location to another, along the Gulf and East coasts, provided the storm characteristics are the same; (b) for pointing out critical coastal areas to planners and developers; (c) for guiding climatologists in collecting and processing hurricane data; and (d) for giving meteorologists information on the isobathic effects on surge along coastal areas.

The shoaling correction curves, localized for each basin, are used even more extensively. In NOAA's work for flood insurance projects, a shoaling correction curve is used to redefine the surge envelope for variable landfall points along the coast, without additional computer runs. Shoaling correction is very convenient for the frequency method of NOAA for estimating flood potentials on the outer coast. In studies for a coastal county, the outer coast tide frequency curve is based on many hypothetical hurricanes determined from hurricane climatology. Because of shoaling corrections, it is not necessary to run the SPLASH program with these storms at successive landfall points on the coast; it is only necessary to run storms for one landfall point.

In operational use of SPLASH, we provide the forecasters with two additional surge envelopes based on landfall point left or right of the forecast landfall. Additionally, the peak surges for the 600-mile long basin are included in the output for any conceivable landfall point in the basin. We are able to provide this extra information because of shoaling correction curves.

We showed the SPLASH run for hurricane Camille 1969. The comparison between the observed and computed surges is quite good; although it is not perfect. Similar runs have been performed for many other historical storms.

Since there are many storm parameters which can be adjusted, as well as coefficients in the equations of motion, a model comparison against a single event does not constitute verification. Our model was verified against 43 actual recorded storms along the Atlantic and Gulf coasts and has been field tested for six hurricane seasons. The calibration for our model is in a global (not local) sense, and no attempt was made to force agreement between computed and observed results for particular storms in local regions. This is one reason why our verification for hurricane Camille is not perfect.

Simple versions of SPLASH are being used in the Philippines, India, and Hong Kong. SPLASH was modified for application to these countries because they don't have similar big computers as the U.S. They told us that satisfactory results were obtained in the SPLASH applications for their areas of the world.

ACKNOWLEDGMENTS

We are grateful to Jye Chen and Mark Flaherty for their help in preparing the basins and shoaling corrections and to Mercedes Bakon for the typing of the manuscript.

REFERENCES

- Barrientos, C. S., and C. P. Jelesnianski, 1973: Storm surge shoaling corrections along the Gulf coast. A report to the Federal Insurance Administration, U. S. Department of Housing and Urban Development, 26 pp.
- _____, and J. Chen, 1974: Storm surge shoaling corrections along the East coast. A report to the Federal Insurance Administration, U. S. Department of Housing and Urban Development, 16 pp.
- Jelesnianski, C. P., 1967: Numerical computations of storm surges with bottom stress. Monthly Weather Review, 95, 740-756.
- _____, 1972: SPLASH (Special Program to List Amplitudes of Surges from Hurricanes) I. Landfall Storms. NOAA Technical Memorandum NWS TDL-46, National Oceanic and Atmospheric Administration, U. S. Department of Commerce, Washington, D. C., 52 pp.
- _____, 1974: SPLASH (Special Program to List Amplitudes of Surges from Hurricanes), Part Two. General Track and Variant Storm Conditions. NOAA Technical Memorandum NWS TDL-52, National Oceanic and Atmospheric Administration, U. S. Department of Commerce, Washington, D. C., 55 pp.
- _____, 1976: A sheared coordinate system for storm surge equations of motion with mildly curved coast. NOAA Technical Memorandum NWS TDL-61, National Oceanic and Atmospheric Administration, U. S. Department of Commerce, Washington, D. C., 52 pp.
- _____, and C. S. Barrientos, 1973: Storm surge model for Puerto Rico. A report to the Federal Insurance Administration, U. S. Department of Housing and Urban Development, 16 pp.
- _____, and C. S. Barrientos, 1975: A preliminary view of storm surges before and after storm modifications for alongshore-moving storms. NOAA Technical Memorandum NWS TDL-58, National Oceanic and Atmospheric Administration, U. S. Department of Commerce, Washington, D. C., 16 pp.

- _____, and A. D. Taylor, 1973: A preliminary view of storm surges before and after modifications. NOAA Technical Memorandum ERL WMPO-3, National Oceanic and Atmospheric Administration, U. S. Department of Commerce, Washington, D. C., 33 pp.
- Myers, V. A., 1975: Storm tide frequencies on the South Carolina Coast. NOAA Technical Report NWS-16, National Oceanic and Atmospheric Administration, U. S. Department of Commerce, Washington, D. C., 79 pp.
- Platzman, G. W., 1963: The dynamical prediction of wind tides on Lake Erie. Meteorological Monographs, 4, American Meteorological Society, Boston, Mass., 44 pp.

CHAPTER 57

CURRENTS IN TIDAL FLATS DURING STORM SURGES

by Harald Göhren *)

Wind action in the viewpoint of coastal engineering is mainly a topic for discussions or investigations of waves, breakers, storm surges, sand transport on beaches and so on. Offshore currents, generated by wind shear stress concern more the scientific field of oceanographers.

But in shallow coastal water windinduced drift currents indeed may be important for coastal engineering problems, as sediment transport, sewage spreading, salinity and so on. For example, along the German North Sea Coast (Fig. 1) we have a rim of extended tidal flats, built up by sand and mud and covered only by a water layer of 1 to 2 m at high tide. At low tide sands and mud flats fall dry. Fig. 2, an aerial view, gives an impression of a typical tidal flat, the "Neuwerker Watt" at the south side of the Elbe Estuary. The distance between main land and the sea side border of the flat is here about 20 km. A lot of investigations have been carried out here - initiated by a harbour planning task - giving some interesting results about currents in the tidal flat area during strong winds and storm surges.

For the current measurements a recording current meter (Fig. 3) has been used, fixed at a tripod aluminum frame in 40 cm above bottom. The propeller meter starts at velocities of 5 cm/s. Tests in a flume proved that orbital currents give no disturbance if unidirectional currents of a certain magnitude are superimposed.

*) Strom- und Hafengebäude Hamburg, W. Germany

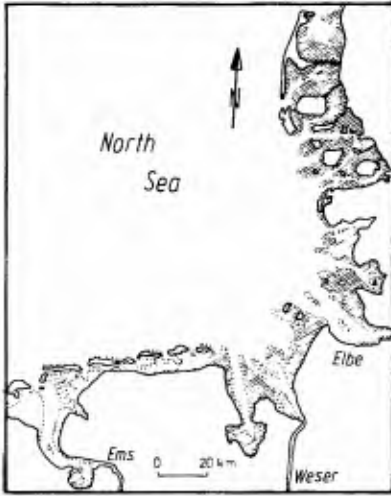


Fig. 1 Tidal Flats in front of the German North Sea Coast

Fig. 2 Aerial View of the "Neuwerk" Tidal Flat



The diagram in Fig. 4 presents a typical example of one measurement of 17 days duration, including a severe storm surge (2.11.1965). Velocities are comparatively small at normal tides, in maximum 30 to 40 cm/s. Directions are adverse in flood and ebb tide. Towards the end of the observation period wind increases to 8 and 9 Bft, blowing from west, that means coastwards. Water level raises and a storm surge occurs on 2. November. The currents increase with wind speed and exceed about 1 m/s in the storm surge. Current directions obviously are influenced - the adverse ebb and flood current is substituted by a more unidirectional movement towards northeast, that means in the direction of the acting wind shear stress.

The wind influence can still better be seen at another graph (Fig. 5) of the same measurement - it is a plot in form of a vectorial track, adding the consecutive data of velocity and direction. The zero point is at tide Nr. 564. The residual flow of the first 15 tides - to Nr. 580 - is comparatively small. The wind induced water motion starts with a significant turning of the vectorial track towards north-east. The residual current velocity increases up to 20 km/tide and more in the storm tides Nr. 590 and 591.

This is a single but typical result. A lot of data of that kind have been collected, suitable for some statistical evaluations. Fig. 6 presents the data of 50 storm surges, stemming from different stations.

In the upper diagram frequency curves of maximum velocities at normal tides and storm tides are compared. At normal tides there is a peak at 30 cm/s, that is the average maximum velocity in tidal flats. The storm surge frequency curve covers the range from 40 to 120 cm/s.

In the lower diagram a frequency curve for the relationship storm tide velocities over normal tide velocities is plot-



Fig. 3
Recording Current Meter

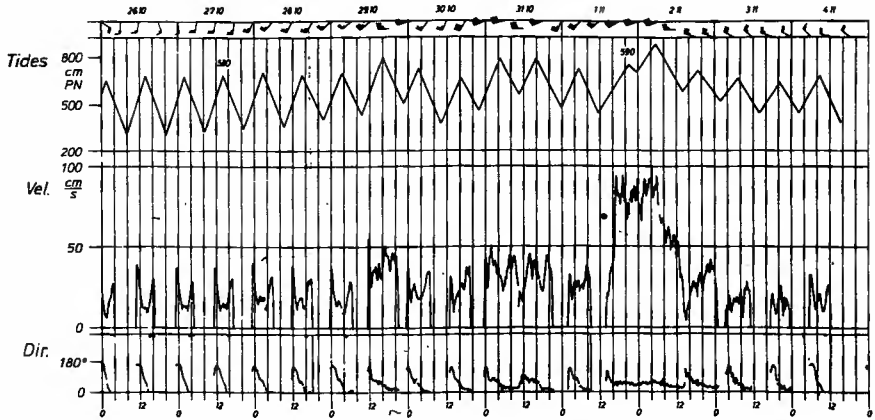


Fig. 4
Record of a Current Meter Station containing
a Storm Surge

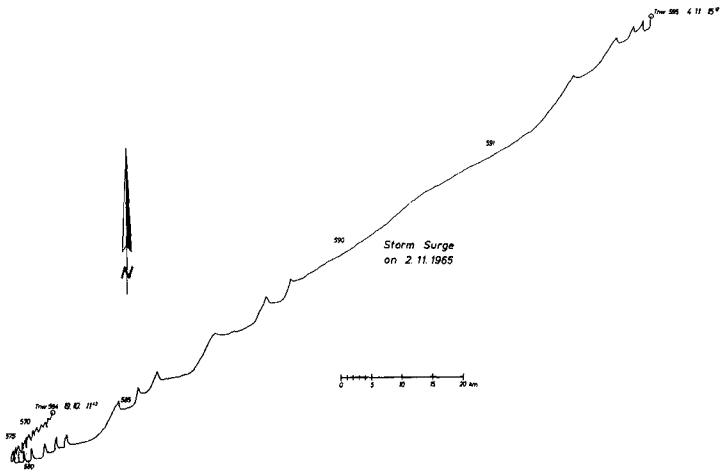


Fig. 5

Currents plotted as Vectorial Track Containing a Storm Surge (s. Fig. 4)

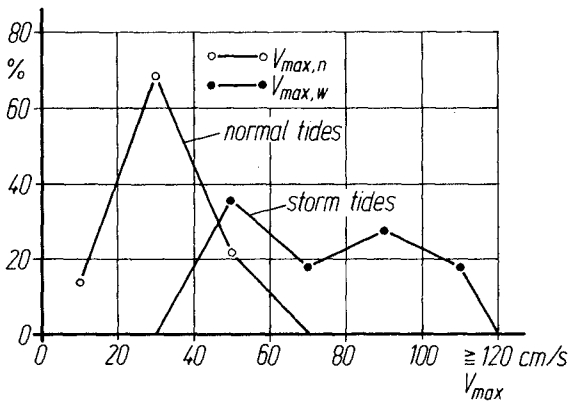


Fig. 6

Frequency of Maximum Velocities in Tidal Flats

ted. Here again a significant peak exists indicating that during storm surges the maximum velocities in tidal flats in average increase about 100%.

Fig. 7 presents curves of residual current velocities over wind speed, again evaluated from some hundred measurements at different stations. The scale in the upper plot is km/tide and the increase of residual current with wind speed - about 1 km at normal tides and about 12 km/tide at storms of 8 Bft and more - is remarkable. But this curve includes the longer duration of water cover in the tidal flat due to the raising water level. This effect is eliminated in the lower diagram with a scale of cm/s for the magnitude of the residual current. In the same range of wind velocities the residual current increases from 5 to 30 cm/s. Especially these statistical results may be helpful for example for estimations of sewage spreading under different wind conditions.

Of special interest is the dependency of current direction. Flume tests and simple mathematical models show that in a rectangular basin we have a flow in the direction of the wind shear stress in the upper layer and an adverse flow beneath that layer, the boundary being $2/3$ over bottom. The current meter used in the field program measures 40 cm above bottom, so that the records present mainly the bottom layer. There is no motion adverse to wind direction in the tidal flats in this layer. This was already shown in Fig. 4 and 5 and is proven by the Fig. 8, presenting residual currents from a simultaneous measurement at 5 different stations over 17 days plotted as vectorial tracks. At the beginning - tides Nr. 600 to 610 - there is no wind stronger than 4 Bft. This part of the track presents normal tidal currents. After that a wind period begins, the wind velocity increasing up to 10 Bft and turning from south-west over west, north-west and north to south-west again. The track of the residuals

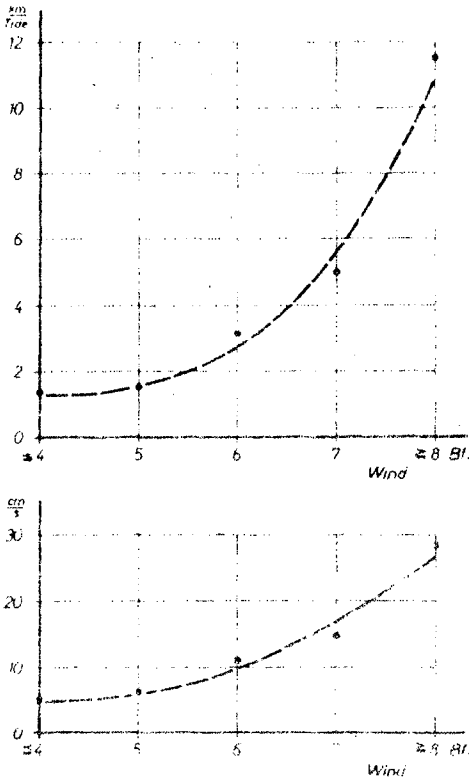


Fig. 7 Residual Current over Wind Speed

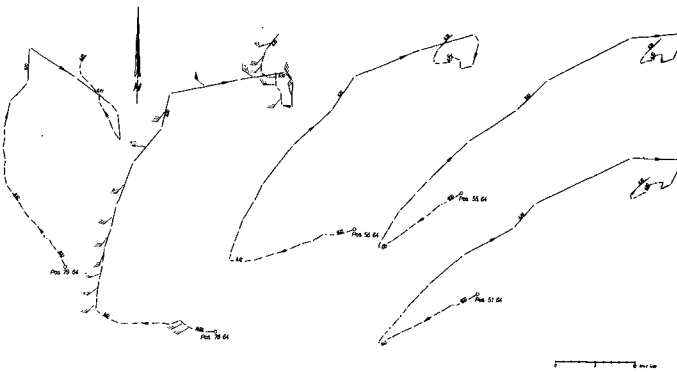


Fig. 8 Residual Currents influenced by Wind

follows that changing of wind direction. Fig. 10 gives another statistical evaluation. At one station inmidst of the Neuwerker tidal flat continuous measurements over two years have been carried out. The collected data of current directions in a 5 minute sequence were classified in groups of wind direction and wind velocity and plotted in the form of direction frequency schemes. With increasing wind velocity the normal tide direction pattern changes and currents in wind direction prevail.

It is to expect that the adverse flow in the bottom layer, which must be present to counterbalance the water transport in the upper layer in wind direction, occurs in the gullies and channels of the shallow water areas. This is proven by Fig. 11. From all measurements with considerable wind influence drift current vectors were computed by a vectorial subtraction of wind induced residual currents and normal tidal residual currents. This vector presents the pure wind influenced current under the assumption that there exist a simple superimposition of tidal and wind induced currents. This is of course a rough approximation. Then the angles between wind direction and drift current directions were computed and plotted as frequency curves. These data include measurements from the bottom layer in the channels and gullies. The left curve presents the frequency of difference angles for the tidal flat, the right curve for the channels. There is a very clear tendency that in the shallow water drift currents prevail in wind direction while in the deeper layer of the channels (superimposed to the much stronger tidal currents) a flow adverse to the wind sheer stress exists.

The question of vertical distribution of the described current pattern is of great interest, but difficult to investigate as waves prevent accurate measurements in the surface layer and tidal currents are superimposed. Flume tests and theoretical considerations show that there is a

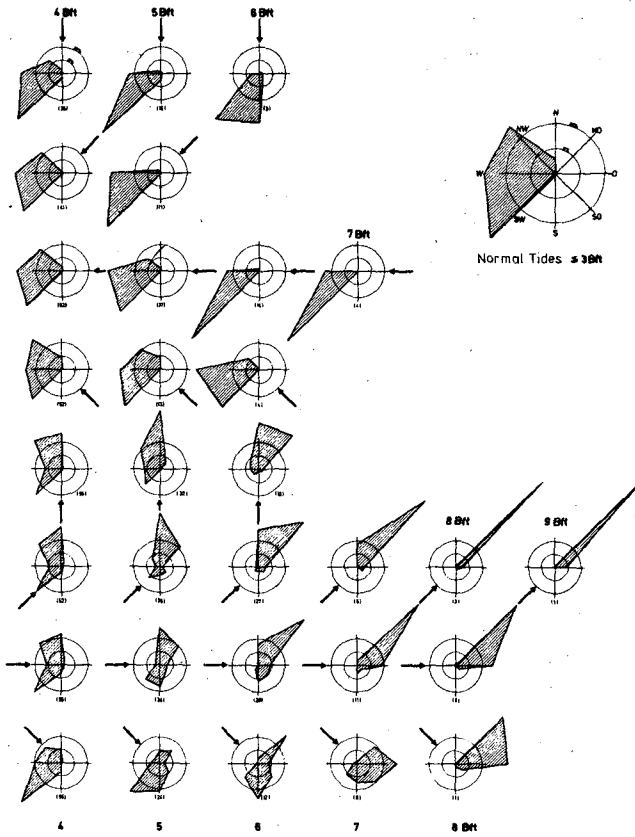


Fig. 10. Frequency Schemes of Currents at one Tidal Flat Station dependent on Wind Velocity and Direction

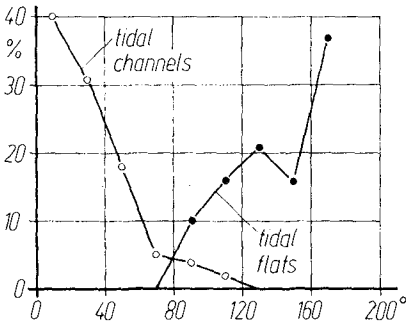


Fig. 11
Difference Angle
between Wind Di-
rection and Re-
sidual Current
Direction

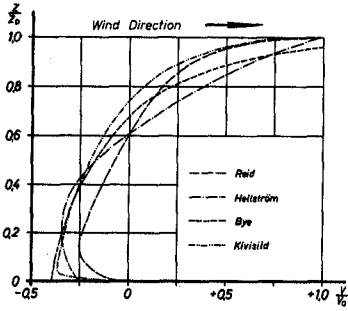


Fig. 12
tical Distribution
Velocity due to
d Shear Stress

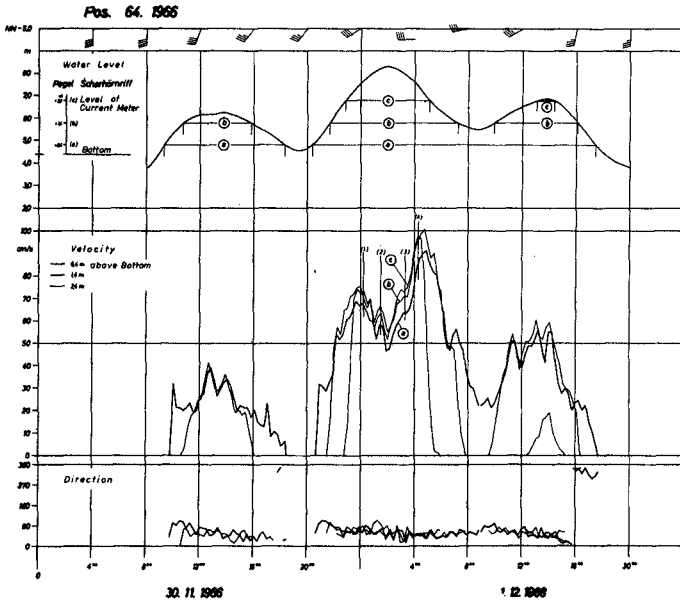


Fig. 13
Currents in 3 Levels during a Storm Surge

strong decrease of velocity in the surface layer (Fig. 12). To get some field data a special station with 3 current meters was set up in levels of 0.4, 1.4 and 2.4 m above bottom. The upper instrument was only to work at higher water levels i.e. at storm surges.

Good observations during a storm surge in December 1966 were obtained. Fig. 13 presents the most interesting part of the record. The three current meter levels a), b) and c) are marked. Neglecting some parts during raising and falling water where the upper meter may be disturbed by waves, a significant but comparatively small decrease of velocities over depth can be seen. There is no indication of a strong velocity gradient as shown in Fig. 12.

Using the data from the two lower instruments it was tried to evaluate a relationship between velocity gradient and wind speed (Fig. 14). Though there is a considerable scattering, the plot indicates that the velocity gradient decreases with increasing wind velocity up to a wind speed of 10 m/s. From this point the gradient increases with further increasing wind velocity. This result can be explained as follows: At calm weather currents at that measuring point are very small - 10 to 20 cm in average. This is a more laminar motion which indeed should have a higher gradient. Increasing wind speed leads to waves and higher turbulence with the effect of a decreasing gradient. But from a certain point - here at a wind velocity of 10 m/s - the gradient increase due to the laws of wind generated flow becomes predominant.

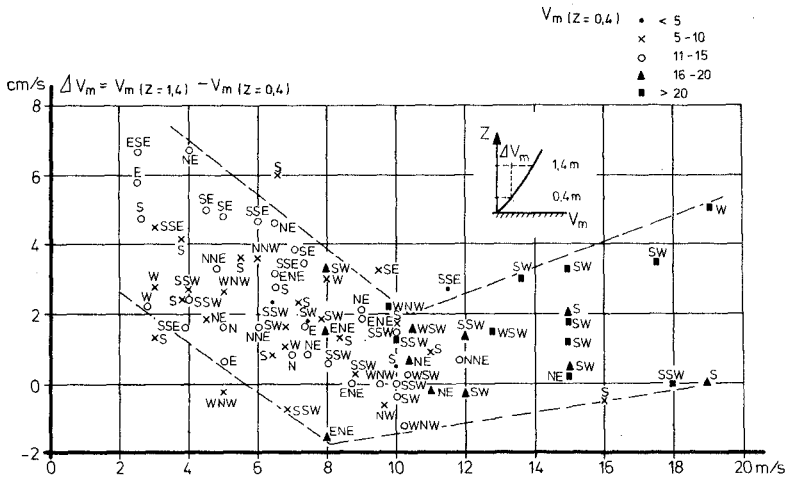


Fig. 14
Velocity Gradient over Wind Velocity

References:

GÖHREN, H.: Triftströmungen im Wattenmeer. Mitt. Franzius-Inst. d. TU Hannover, H. 30, 1968

GÖHREN, H.: Strombeobachtungen an Langzeit-Meßstationen im Watt. Die Küste, H. 25, 1974

HELLSTRÖM, B.: Wind effect on lakes and rivers. Inst. Hydr., Roy. Inst. Techn. Stockholm, Bull. 41, 1941

HUGHES, P.: A determination of the relation between wind and sea surface drift. Quart. Jour. Roy. Met. Soc., Vol. 82, 1956

KIVISILD, H.R.: Wind effect on shallow bodies of water with special reference to Lake Okeechobee. Inst. Hydr., Roy. Inst. Techn. Stockholm, Bull. 43, 1954

CHAPTER 58

TSUNAMI PROPAGATION IN THE PACIFIC OCEAN

by

Manfred Engel⁺ and Wilfried Zahel⁺⁺

ABSTRACT

The Alaska tsunami of March 28, 1964, caused by a tectonic uplift, propagated across the Pacific Ocean and was even recorded at the shores of New Zealand and the Antarctica. The large distance propagation of this tsunami is investigated by a numerical model based on the shallow water equations. The model includes bottom friction, eddy viscosity and Coriolis acceleration and yields the water elevation and the vertically integrated current velocity. The generation mechanism is given by a simplified initial condition, that is derived from the observed average uplift of 1.8 m for an area of 110000 km² on the Continental Shelf. The computed tsunami propagation is presented by means of the first wave travel time and height on Pacific Ocean maps and by giving sea surface time series for selected stations. These computed results are compared with observations, especially considering the limitations of the model due to the coarse grid net having been used.

INTRODUCTION

Research of tsunami hydrodynamics until now seems to be split up into three parts: generation mechanisms, propagation of tsunamis in open ocean, amplification and run up at coasts. A great variety of methods is used for these investigations, such as model building on the basis of analytical or numerical solutions to the hydrodynamic equations and carrying out experiments with hydraulic models of the prototypes.

The present contribution shall be understood as an attempt to simulate the open ocean propagation of an actual tsunami by hydrodynamic-numerical modelling considering as many physical properties as possible. Use was made of a 1°-World-Ocean-model, that yielded realistic results when it was applied to the computation of oceanic tides by ZAHEL, 1975. Because of the far smaller characteristic wave lengths of tsunamis, some preinvestigations had to be performed in order to throw light upon the question, whether the grid net resolution suffices to comprehend the main features of tsunami propagation and initiation. Reference will be made to these considerations in the Chapter PREINVESTIGATIONS.

The 1964 Alaska tsunami was characterized by an extended uplifted area with an average sea surface elevation of 1.8 m and by

⁺ Institut für Meereskunde, Universität Hamburg

⁺⁺ do.

a period of about 1.3 hours of the radiated wave (BERG et al., 1972). Because of these relatively proper conditions for the application of the available model we decided to simulate this actual tsunami. A description of the model is given in the Chapter THE HYDRODYNAMIC MODEL, the grid net arrangement and the numerical treatment of the differential equations are outlined there.

The Chapter COMPUTATIONAL RESULTS contains a discussion of the computational results in view of observations. The distributions of propagation times and heights of the first crest are presented on Pacific Ocean maps, time series of the surface elevation are given for selected positions being as near as possible to gauge positions and originating from all over the Pacific Ocean.

PREINVESTIGATIONS

In order to get an insight into the problems of a large scale numerical tsunami propagation model, we first ran some one-dimensional models. Especially the usefulness of a 110km-grid-resolution with respect to the propagation of the main wave train had to be investigated. As already can be seen from the dispersion relation yielded by the explicit difference equation scheme, the phase velocity for waves with periods longer than 1.3 hours, a value which was observed in connection with the Alaska tsunami, is only insignificantly falsified by the applied numerical treatment in deep ocean areas. Also the decay time due to eddy viscosity remains proportional to the square of the wavelength and to the inverse eddy coefficient for such long period waves in the numerical procedure, so they are insignificantly affected by eddy viscosity while propagating across the Pacific Ocean. Because of the exclusion of small scale processes in the model the convective terms were neglected. A simple shelf radiation model, allowing no reflection to take place at the right hand side open boundary, gave a good impression of the continuous energy radiation from the shelf area for a given initial water elevation distribution (Fig.1). This distribution was well resolved by the used grid net with a spatial grid point distance of 7.4 km. Against that the global model is far from being able to take care of a realistic generation mechanism, only the estimated potential energy of the realistic uplift in the generation region could be considered.

In a $1^{\circ} \times 2^{\circ}$ -testing-model two different schematic distributions of the uplift with the same potential energy content were prescribed, one with different uplifts, the other with a uniform uplift at the eight marked grid points. Fig.2 shows the travel times of the first wave crest for both tsunamis thus having been initiated, that means there is no difference appearing within the accuracy of the plot. Because of this conformity in travel times we finally ran the global model for the Alaska tsunami with the simplest generation mechanism, a uniform initial surface elevation of 2 m at these grid points, the initial potential energy amounting to 2.0×10^{22} erg by this way.

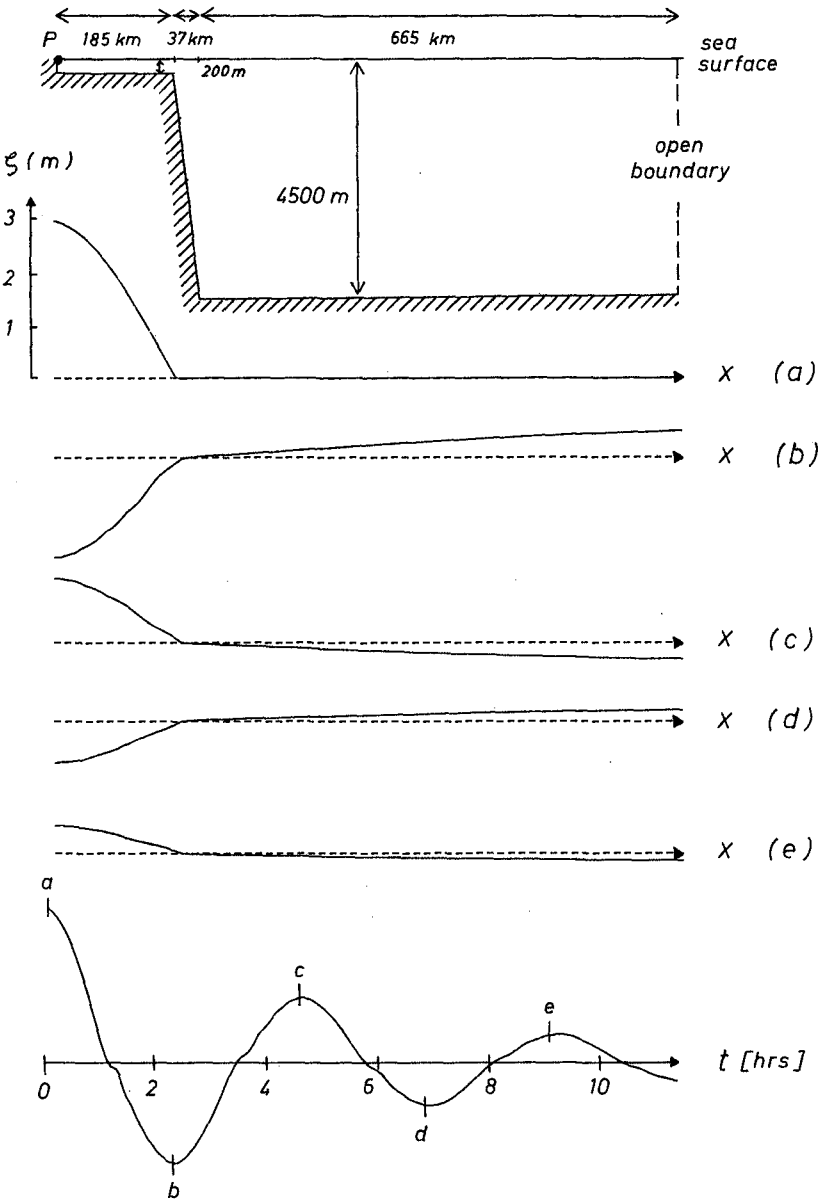


Figure 1. Distribution of sea surface elevations in space and time(at Point P) for computed wave radiation from an idealized shelf.

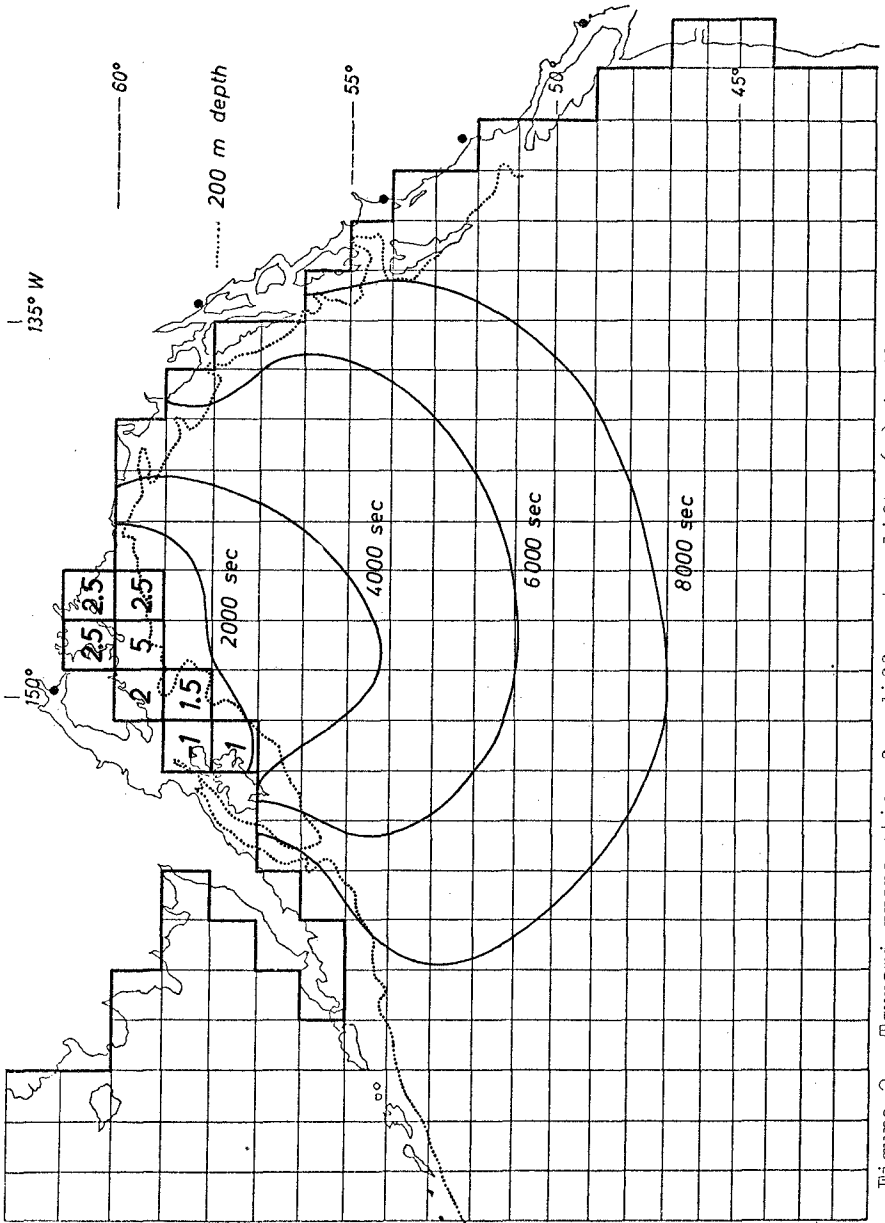


Figure 2. Tsunami propagation for different uplifts (m) in the source area.

THE HYDRODYNAMIC MODEL

The model has already been used for ocean tide investigations by ZAHLE, 1975 and it was developed from that one presented by ZAHLE, 1970 in detail. The equations of motion for long waves and the equation of continuity are taken as a basis for the model. With t =time, λ =geographic longitude, φ =geographic latitude they are given by:

$$\frac{\partial u}{\partial t} - 2\omega \sin\varphi v + \frac{r(u^2+v^2)^{1/2}}{D} u + R\lambda + \frac{g}{R \cos\varphi} \frac{\partial \zeta}{\partial \lambda} = 0$$

$$\frac{\partial v}{\partial t} + 2\omega \sin\varphi u + \frac{r(u^2+v^2)^{1/2}}{D} v + R\varphi + \frac{g}{R} \frac{\partial \zeta}{\partial \varphi} = 0$$

$$\frac{\partial \zeta}{\partial t} + \frac{1}{R \cos\varphi} \left(\frac{\partial (Du)}{\partial \lambda} + \frac{\partial (Dv \cos\varphi)}{\partial \varphi} \right) = 0$$

$u=u(\lambda, \varphi)$, $v=v(\lambda, \varphi)$ denote the vertically integrated current velocity components, eastward and westward respectively, $D = d + \zeta$ the actual depth and $\zeta = \zeta(\lambda, \varphi)$ the surface displacement. The lateral eddy viscosity terms

$$R\lambda = A_h \Delta u + A_h R^{-2} (-u(1 + tg^2\varphi) - 2 \frac{tg\varphi}{\cos\varphi} \frac{\partial v}{\partial \lambda})$$

$$R\varphi = A_h \Delta v + A_h R^{-2} (-v(1 + tg^2\varphi) + 2 \frac{tg\varphi}{\cos\varphi} \frac{\partial u}{\partial \lambda})$$

roughly take account of turbulence effects on the mean flow. A_h is a constant coefficient, $A_h = 10^5 \text{ m}^2/\text{sec}$ is assumed in this case.

As the model is a global one, the domain of integration of the differential equations is only bounded by coasts, which are defined to be impermeable. Therefore the normal component of the current velocity is assumed to be zero at the boundary. Provided that proper initial conditions are prescribed, this condition uniquely determines the solution of the first order equation system. The inclusion of the second order term requires the further homogeneous boundary condition of zero current velocity. The initial conditions defining the tsunami generation mechanism, in strong simplification are given by an uplift distribution of the sea level and zero current velocity at $t = 0$.

Although in the present problem the polar regions are unimportant, the numerical procedure shall for completeness briefly be described as it is applied to the world ocean as a whole. In order to avoid a strong reduction of the grid-point-distance due to the convergence of meridians, poleward doubling of the zonal angular grid-point-distance is performed at five parallels, namely at 55°N, 55°S, 72°N, 72°S, 81°N. Hence the grid net covering the globe is characterized by a mesh size of 1°x1° between 55°N and 55°S, of 1°x2° between 55°N and 72°N as well as between 55°S and 72°S, of 1°x4° southward of 72°S as well as between 72°N and 81°N. Finally, northward of 81°N adjacent grid points are 1° distant on a meridian and 8° distant on a parallel, respectively. The parallels defining the mentioned transitions are marked on Fig.3, which shows the approximated coastlines and the bottom topography that is used in the model.

The numerical scheme has been used in the following form :

$$D_+^t u_{i,j}^n - 2\omega \sin\varphi_i \bar{v}_{i,j}^n + \frac{r\sqrt{(u_{i,j}^n)^2 + (\bar{v}_{i,j}^n)^2}}{D_{i,j}^n} u_{i,j}^n + (R\lambda)_{i,j}^n +$$

$$+ \frac{g}{R \cos\varphi_i} (D_0^\lambda \zeta_{i,j}^n a(\varphi_i) + D_0^\lambda \zeta_{i,j}^{n+1} b(\varphi_i)) = 0$$

$$i=1,3,5,7,\dots ; j=1,3,5,7,\dots$$

$$D_+^t v_{i,j}^n + 2\omega \sin\varphi_i \bar{u}_{i,j}^n + \frac{r\sqrt{(\bar{u}_{i,j}^n)^2 + (v_{i,j}^n)^2}}{D_{i,j}^n} v_{i,j}^n + (R\varphi)_{i,j}^n +$$

$$+ \frac{g}{R} (D_0^\varphi \zeta_{i,j}^n) = 0 \quad i=0,2,4,6,\dots ; j=0,2,4,6,\dots$$

$$D_+^t \zeta_{i,j}^n + \frac{1}{R \cos\varphi_i} (D_0^\lambda (D_{i,j}^n u_{i,j}^{n+1}) + D_0^\varphi (D_{i,j}^n v_{i,j}^{n+1} \cos\varphi_i)) = 0$$

$$i=1,3,5,7,\dots ; j=0,2,4,6,\dots$$

$$D_+^t w := \frac{w(t+\Delta t) - w(t)}{\Delta t} ; \quad D_0^\psi w := \frac{w(\psi+\Delta\psi/2) - w(\psi-\Delta\psi/2)}{\Delta\psi} \quad \psi = \lambda, \varphi;$$

$$w_{i,j}^n := w(i\Delta\varphi/2, j\Delta\lambda/2, n\Delta t) \quad w = \zeta, u, v ; \quad a(\varphi_i) + b(\varphi_i) = 1$$

$0 \leq a \leq 1$, $0 \leq b \leq 1$. Except from a small neighbourhood of the North Pole $a=1$, $b=0$ is taken. Thus the applied time stepping scheme is explicit in the area of tsunami propagation in question. The only transition from one uniform grid net to another in this area takes place at 55°N . Because of technical reasons arrival times and surface elevations of the first maximum were only stored for the $1^\circ \times 1^\circ$ area and for the Gulf of Alaska separately, so that this information was lost for the Bering Sea north of 55°N , as can be seen on Fig.5 and Fig.10.

To give an impression what global results gained by this 1° -model look like, amplitudes and phases of the rather well reproduced M_2 -tide are presented on Fig.4, which is taken from ZAHTEL, 1975. When computing tsunami propagation, calculations are, of course, not performed for areas where the tsunami will not get in the time of interest.

The same hydrodynamic method was applied by ENGEL, 1974 to tsunami simulation in the Black Sea.

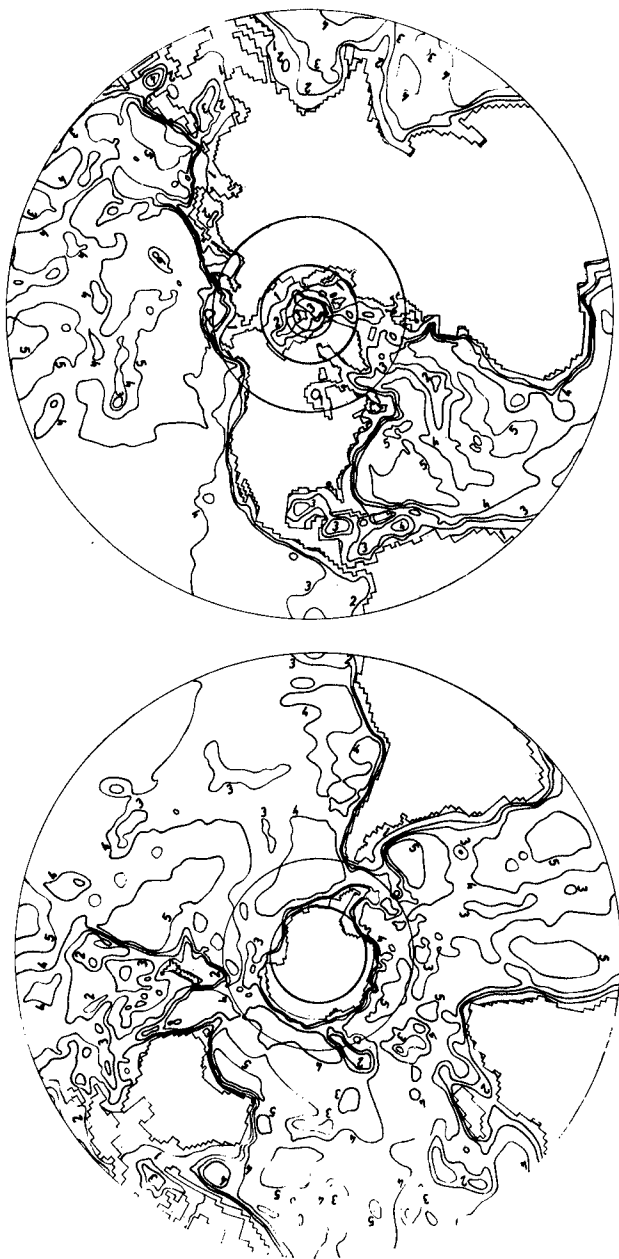


Figure 3. Depth distribution and boundaries as used in the 1° -World-Ocean-model.
Lines of equal depth given for 200m (1), 2000m (2), 3000m (3), 4000m (4) and
5000m (5). Northern and southern hemisphere in stereographic projection.

1° - OCEAN - MODEL
 M_2 - Tide

coidal lines (—) and corange lines (---)
 phases in lunar hours referred to meridian passage at Greenwich
 amplitudes in centimetres (10, 25, 50, 75, 100, 125, 150, 200)

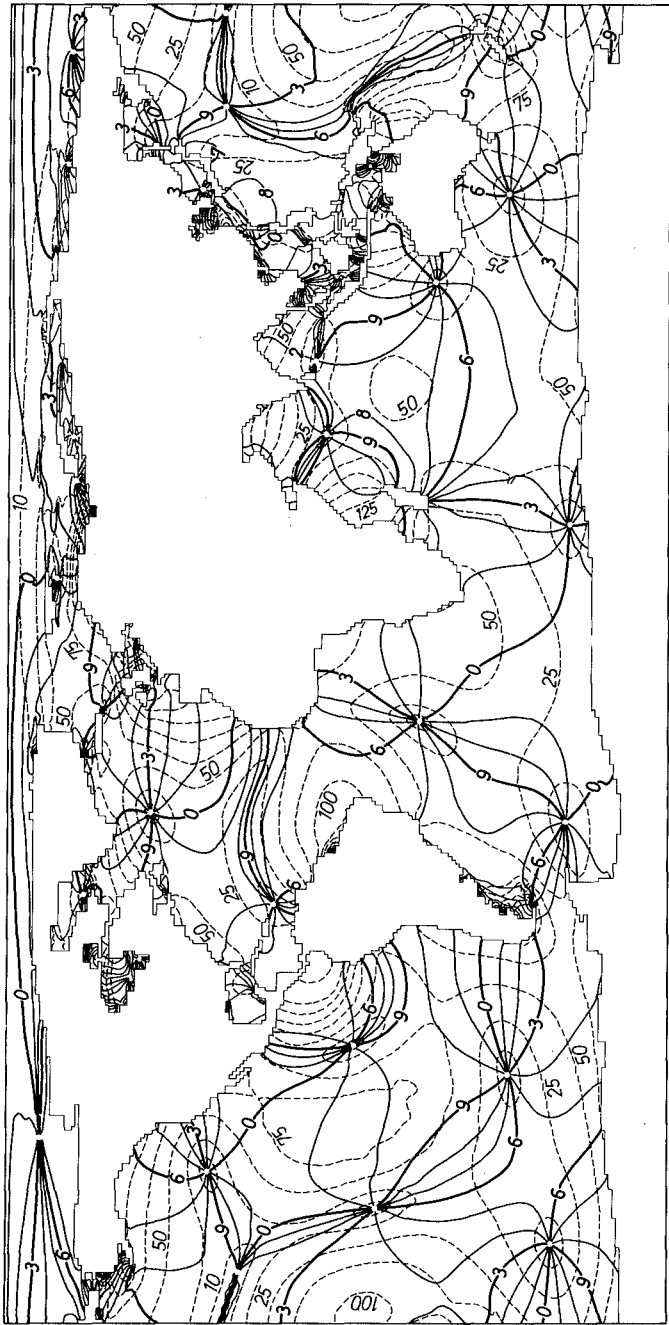


Figure 4.

COMPUTATIONAL RESULTS

To give an idea of computed tsunami propagation properties we at first refer to the propagation time of the first maximum. The isolines of this time, that can better be defined than the arrival time of the first disturbance, are displayed on Fig.5. Due to the applied simple generation mechanism even the tsunami propagating in the open ocean will differ from the real one when being computed by the η^0 -model. This fact gets obvious when considering e.g. the slow ascent of the computed water level compared with the real one at certain oceanic islands. Nevertheless, it is expected from the computations, having been carried out on the basis of a hydrodynamic model, that the characteristic features of the radiated long wave are yielded concerning its propagation in the open ocean. In order to give an impression of the effects of depth distribution on the wave propagation, the lines of equal depth have been entered into the presentation. There are obvious features as to the deformation of travel time isolines due to the bottom topography as e.g. the high speed propagation in the central South Pacific and the comparatively delayed propagation through the shallower parts of the south-eastern Pacific. Refraction effects gathered from Fig.5 at the transition zone from the open ocean to the American coast are evidently not realistic in all cases because of the poor resolution of the narrow shelf there. An improvement of the results, concerning phenomena that arise on small scale areas, could be obtained by including nested grids into the global one. A very distinct effect due to reflection can be recognized at the Japan Trench as well as at the Kuril Trench. While the reflected wave contributes to the formation of the first maximum, superposition with the arriving second wave takes place before the first one has reached its maximum, and in this way the particular propagation pattern comes about. Other effects of reflection cannot be detected from the presentation of the first maximum, although, of course, being fully inherent in this model.

Before comparing computed arrival times with gauge observations, some limitations of the model shall be summarized. As the wave generation was performed rather schematically, the computed wave train only reflects the gross features of the shelf source area and the initial condition in sea level variation and current velocity and therefore it cannot be considered to be directly comparable with the real one. The phase velocity in any numerical model is subject to discretization errors depending on the difference scheme, on the grid resolution and on the wave length governing the physical process being modelled. The described η^0 -model admits long waves with at least thousand kilometers wavelength to propagate in the deep ocean with a phase velocity deviating less than 1 per cent in magnitude from the real phase velocity. A somehow generated wave train containing a broad spectrum of wave lengths will at all events be dispersed numerically. The leading wave of the investigated Alaska tsunami, characterized by a period of 1.3 hours, thus proves to be long enough in deep water to be subject to an appropriate approximation concerning the phase velocity. On extended shelf areas, like that of the Yellow Sea, the computed wave properties are unreliable because of numerical dispersion effects.

Moreover the poor resolution of shelf areas extending in front of coasts leads to insufficient approximation of the wave arriving at the coast, since gauge records coming from such coasts are characterized by the response behaviour to the local topography. As the most available gauge records refer to such positions, computed and observed values can also for this reason not directly be compared.

The positions for which the water elevations have been printed out for every time step are marked on Fig.6, they are close to places where gauge data were gained. Fig.7 and Fig.8 show the computed water elevations at these locations, with the arrival time of a significant disturbance, defined by a water level rise of 2 mm and indicated by the beginning of the curves. The longer vertical lines represent observed arrival times, taken from the gauge records published by SPAETH and BERKMAN, 1967 and others. The above remarks are applicable to the comparison at the mentioned positions, showing itself by the fact that opposite to the observations the computed water elevations yield similar curves for all stations. There is an almost constant time difference between the computed first disturbance and the first wave crest, it amounts to about 65 minutes. Hence, taking this first disturbance instead of the first wave maximum when representing tsunami propagation, a picture of high similarity to that one given on Fig.5 would result. In all cases the observed arrival time is later than the computed one, the difference running up to about 10 minutes except for Galapagos and Lyttelton, where it is nearly 3 times larger. The relatively large time difference at Galapagos may result from the fact that the gauge position at San Cristobal is located farther from the source area than the nearest grid point, which moreover lies on the other side of the island. Because of its backward position in a bight there are similar difficulties in adjoining a grid point to Lyttelton. Finally, it proves to be difficult to recognize a 2 mm disturbance on a gauge record in any case.

Three N-S-surface profiles are plotted on Fig.9, beginning in the source area and extending southward as far as the wave has propagated. As can be seen also from this picture, the form of the leading wave is preserved, although its energy decreases successively. To get an idea of the spatial energy supply, reference to at least the surface elevations shall be made. Fig. 10 shows the computed surface elevation of the first wave maximum in mm. Effects of bottom topography can easily be recognized, e.g. regarding the increased magnitude of elevations at the Hawaiian Ridge, at the north-east coast of Australia and at the American coast. Obviously these surface elevations are not suitable for being compared with the observed ones, they at best can be hoped to be a first approximation for the wave entering coastal areas.

Thus applying the global hydrodynamic model to the 1964 Alaska tsunami is understood as a first step in trying to bridge the gap between investigations concerned with generation mechanisms and those studying run up processes. No model can explicitly include all physical processes governing tsunamis, and therefore besides the application of nesting techniques parameterizations

of significant processes will have to be introduced, in order to achieve an overlapping modelling of generation, propagation and run up of tsunamis that will be of use for practical purposes.

REFERENCES

- BERG, E. et al., Source of the Major Tsunami, Contributions of the Hawaii Institute of Geophysics, University of Hawaii, No. 310, 1972
- ENGEL, M., Hydrodynamisch-numerische Ermittlung von Bewegungsvorgängen im Schwarzen Meer, Mitt. d. Inst. f. Meereskd. der Univ. Hamburg, XXII, 1974
- SPAETH, M.G., and S.C. BERKMAN, The tsunami of March 28, 1964, as recorded at tide stations, Environmental Science Services Administration Technical Report C&GS 33, 1967
- ZAHSEL, W., Die Reproduktion gezeitenbedingter Bewegungsvorgänge im Weltozean mittels des hydrodynamisch-numerischen Verfahrens, Mitt. d. Inst. f. Meereskd. der Univ. Hamburg, XVII, 1970
- ZAHSEL, W., Mathematical and Physical Characteristics and Recent Results of Ocean Tide Models, Proceedings of the IRIA International Colloquium on Numerical Methods of Scientific and Technical Computation, December 1975, Lecture Notes in Mathematics (in press)

ACKNOWLEDGMENTS

This investigation was supported by the Deutsche Forschungsgemeinschaft, SFB 94 Meeresforschung Hamburg. The computations were performed at the Regionales Rechenzentrum Niedersachsen in Hannover.

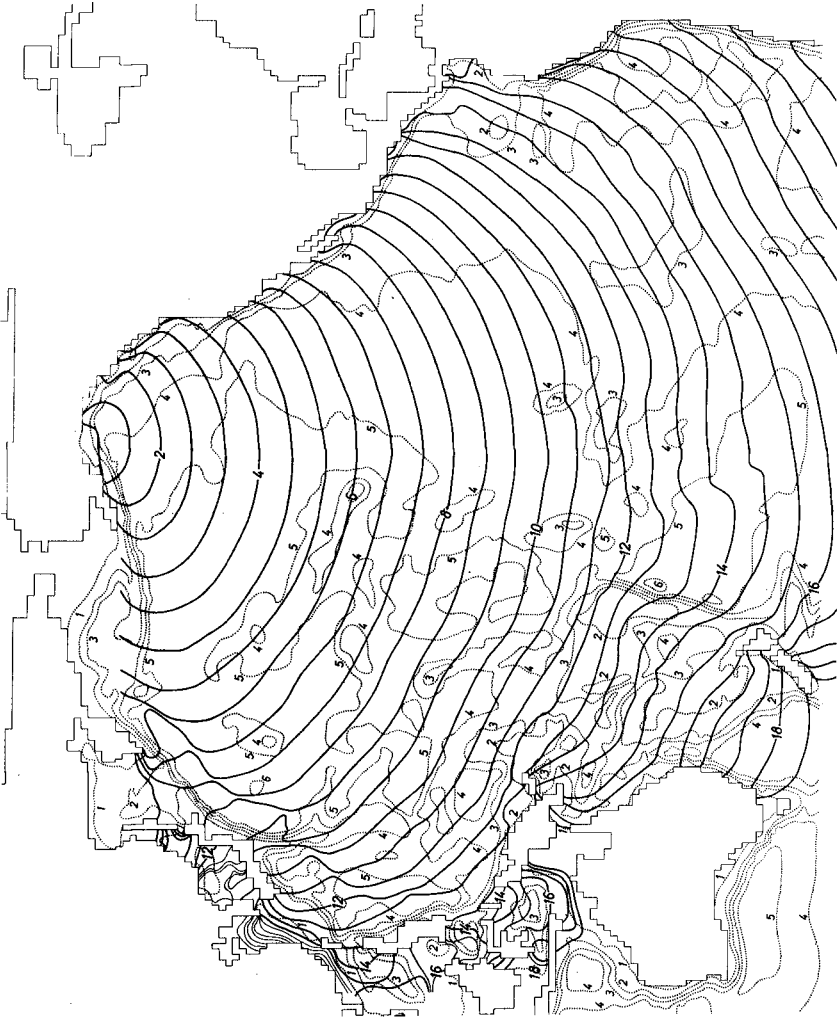


Figure 5. Computed propagation of the 1964 Alaska tsunami.
 Full line —2— propagation time of first wave crest in hours.
 Dotted line depth isoline with 1: 200m ,
 2: 2000m, 3: 3000m, 4: 4000m, 5: 5000m .

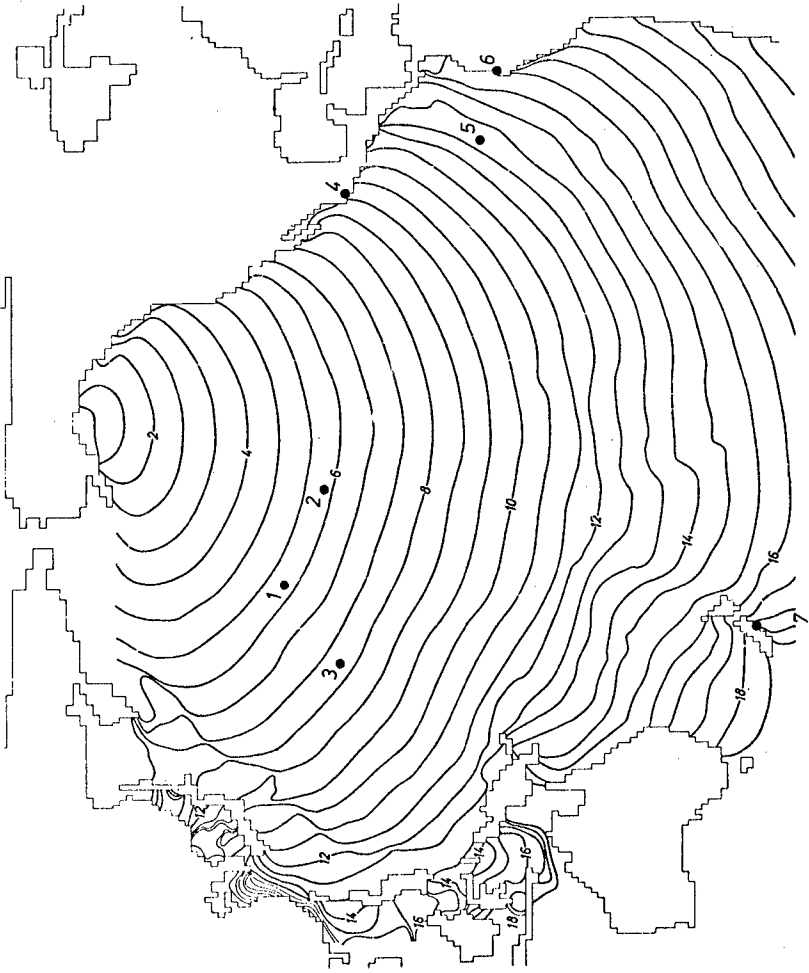


Figure 6. Site of special points for which water elevation time series are given

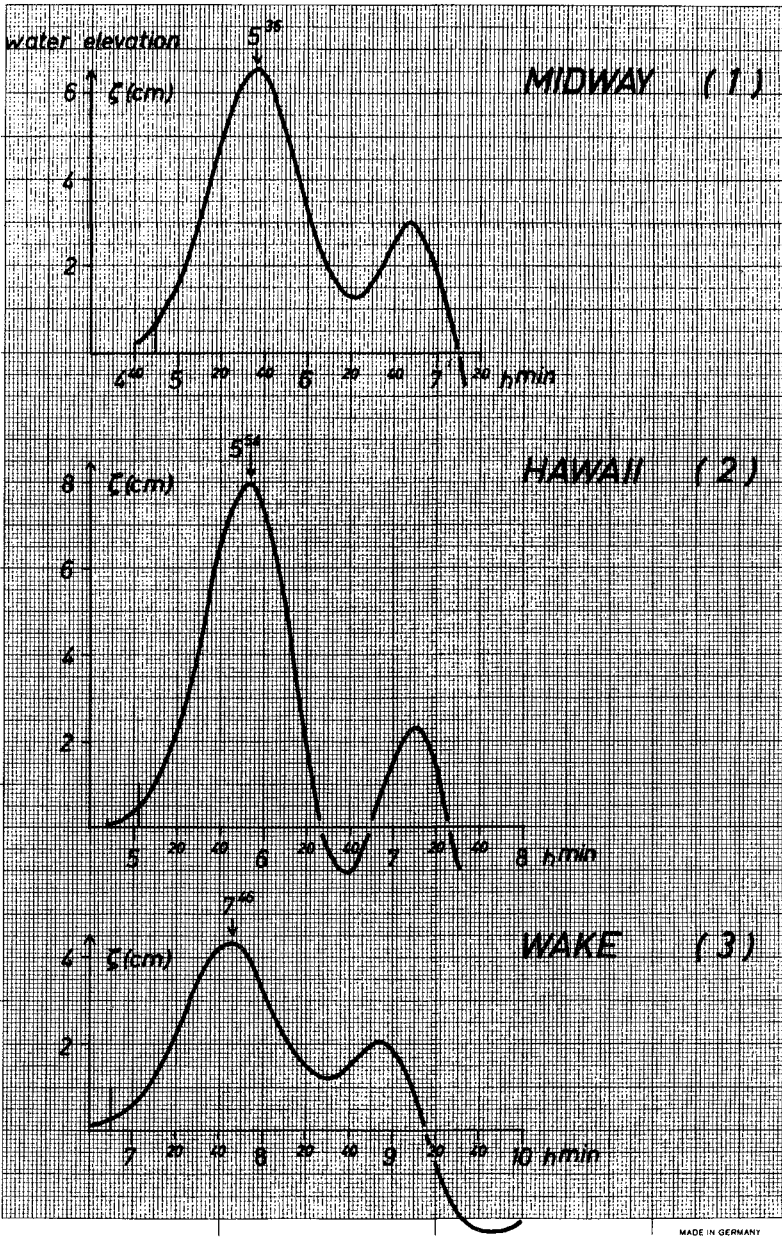


Figure 7. Computed surface elevations ζ

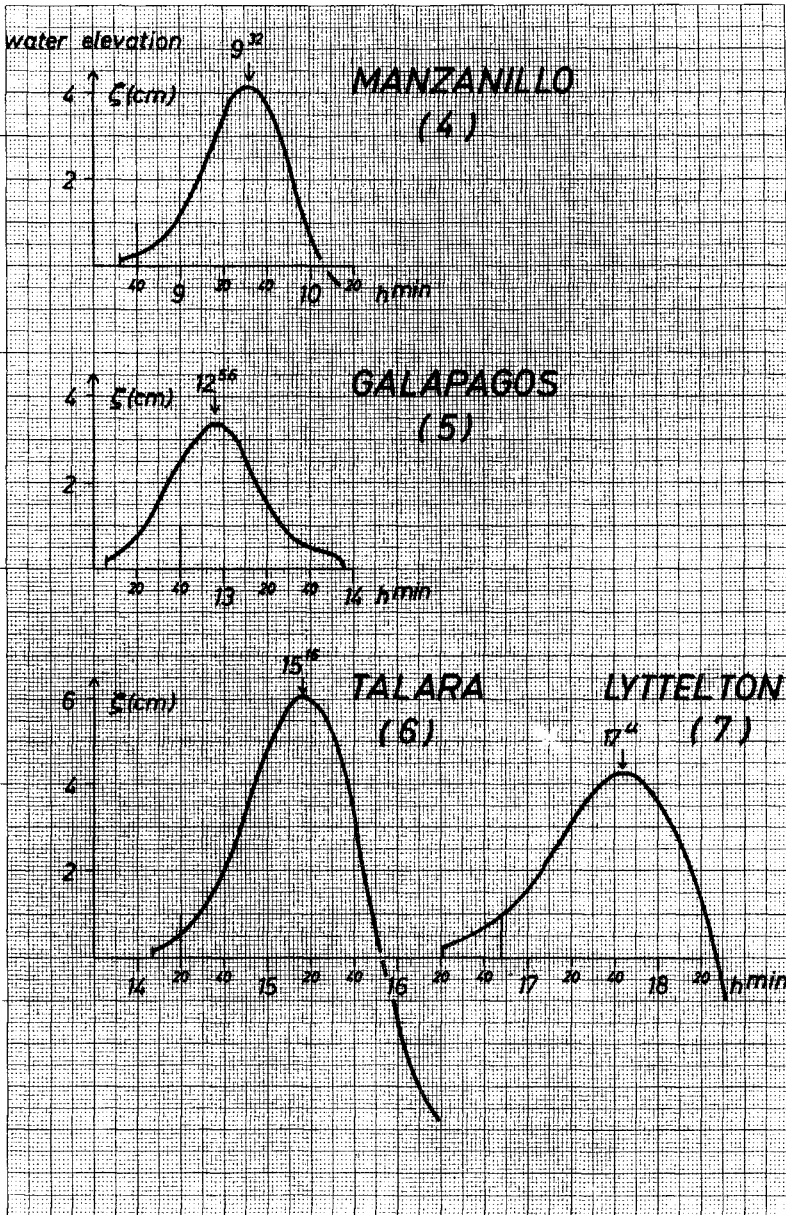


Figure 8. Computed surface elevations ζ

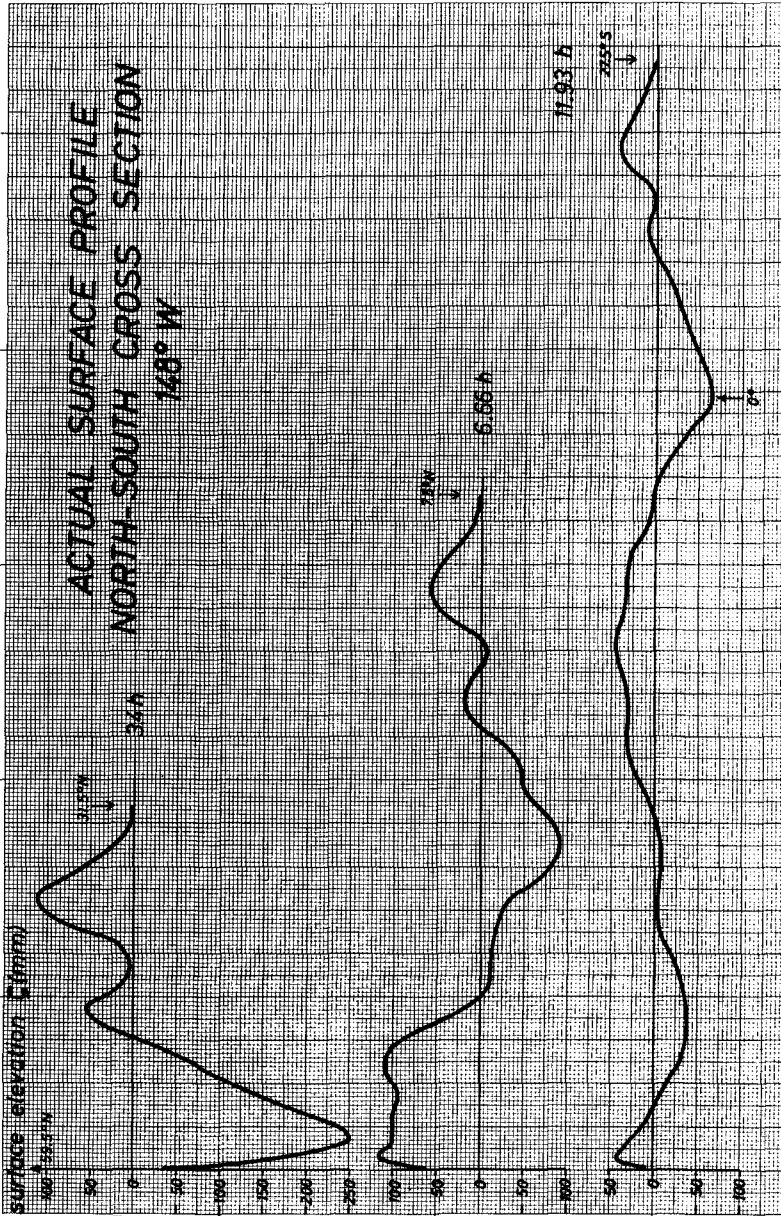


Figure 9.

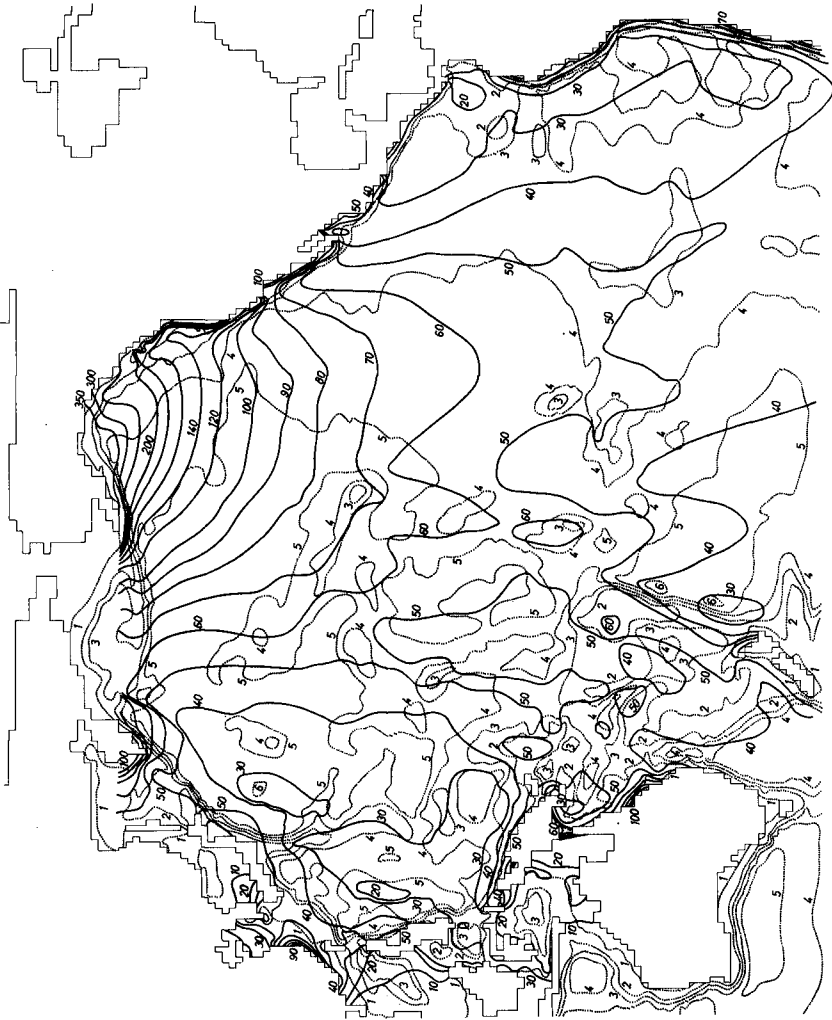


Figure 10. Computed propagation of the 1964 Alaska tsunami.
 Full line --- surface elevation of the first wave maximum in mm.
 Dotted line depth isoline with 1: 200m, 2: 2000m, 3: 3000m, 4: 4000m, 5: 5000m, 6: 6000m .

CHAPTER 59

TRANSFORMATION OF TSUNAMIS IN A COASTAL ZONE

Shigehisa NAKAMURA¹⁾

Haruo HIGUCHI²⁾

and

Yoshito TSUCHIYA³⁾

ABSTRACT

In order to obtain fundamental informations to establish warning practices and effective countermeasures against the tsunamis on the coast, the authors have studied on refraction of the tsunamis propagating into Osaka Bay and on tsunami spectra. The refraction of the tsunami is studied by a numerical computation for a program of refraction and shoaling of small amplitude wave. An example is shown for Chilean Tsunami in 1960 to reveal that the refraction is an important factor to study on the tsunami wave height distribution along the coast of Kii Peninsula and Shikoku Island. The mareograms of the tsunamis are analyzed to obtain power spectra to study on transformation of the tsunamis from the Pacific Ocean to the head of Osaka Bay. The result suggests that it is necessary to be careful to study on transformation of the tsunamis with use of the refraction diagram because the tsunami is not a simple monochromatic and small amplitude plane wave. A brief remark is given for the analysis of the tsunami as non-stationary process.

1. INTRODUCTION

There are various kinds of the external forces acting on the coast. The occurrence of tsunami is one of the remarkable phenomenon in relation to the destructive suffers on the coast. And it is not yet solved the protection of the tsunami at present even though many efforts have been concentrated to the tsunami. On the other hand, in these years, reclamative land use for the industrial zones and the higher utilizations of the coastal zone have become triggers to increase and spread the destructive suffers. Now, it is necessary to study and solve the problems of the tsunami in order to give any effective countermeasure for it. In this paper, at first, a reviewal remark is given. And then, refraction characteristics of tsunami is studied through a numerical computation for Chilean Tsunami in 1960 as a small amplitude wave. And the actual existing tsunamis are not necessarily similar to the exact small amplitude wave but the finite amplitude wave in the coastal zone. Tsunami spectra are studied as a linear transform of the mareogram of the tsunami as a stationary stochastic process, and after that, a remark is given to be studied it as a non-stationary process.

-
- 1) Dr.Eng., Research Assistant, Disaster Prevention Research Institute, Kyoto University, Uji, Kyoto, Japan
 - 2) Dr.Sci., Professor, Department of Ocean Engineering, Ehime University, Matsuyama, Ehime, Japan
 - 3) Dr.Eng., Professor, Disaster Prevention Research Institute, Kyoto University, Uji, Kyoto, Japan

2. REVIEWAL REMARKS

As for Kwanto district and Tokyo Bay, the surveys and researches have been concentrated to solve the problem (for example, since Meiji Era (Omori, 1918)). In the recent years, a countermeasure is introduced as a political practice referring to the results of the researches (for example, Kawasumi, 1969). And as for Ise Bay, a similar countermeasure is offered in a report by Iida (1975). By the way, there have been no researches and surveys for Osaka Bay systematically. It might be a fresh report by Tsuchiya and Nakamura (1974) that is related to a filing of the data and an analysis of the tsunamis propagated into Osaka Bay. They have focused to the mareograms of the recent tsunamis which gave any significant influences to the water level in Osaka Bay from the reports published in the past and the filed mareograms in Osaka District Meteorological Observatory in order to analyze and clarify the mechanisms of the propagation and transformation of the tsunamis. They have traced the historical procedures for the tsunamis, for example, the geographical distributions of the tsunami heights, the travel time of the tsunami fronts, refraction diagrams of the tsunamis etc. The authors have also studied on the tsunami spectra (Nakamura et al., 1976).

The studies on the tsunamis in the past, for example, the geographical distributions of the tsunami wave heights, had been studied with a little consideration on dependency of the refraction of the tsunamis. It might be caused by the difficulty of the surveys of the tsunami refractions in the past. The authors would like to introduce a refraction diagram with use of high speed electronic computer to study the propagation of the wave front, the wave ray, the shoaling effect caused by the water depth, the transformation of the wave caused by refraction etc. They have focused to study on the transformation of the wave by refraction and shoaling.

Adding to that, a method of ocean wave spectrum is introduced into the study on the transitional phenomena of the tsunamis to treat the tsunamis as a stationary Gaussian processes to obtain the tsunami spectra. The transformation of the tsunami spectra is also the authors' interest in this paper. Spacial and time dependent transformation of the waves are considered for the tsunami spectra. And a remark will be given for the tsunami spectral analysis as non-stationary process.

3. REFRACTION DIAGRAM

Judging from the results of the surveys, the researches (for example, by Iida, 1956) and the tabulated catalogues (Imamura, 1942; Iida et al., 1967; Soloviev and Gao, 1974) concerning the tsunamis on the coast of Japan, it might be statistical expect that the one third of the earthquake exceeded Richter's magnitude $M = 6$ those of which had occurred around Japan Islands has the epicenter under the sea, and the one third of the earthquakes which had occurred under the sea accompanied the tsunamis to attack the coastal zone of Japan. In Japan, the records concerning the tsunamis can be found since the seventh century.

The tsunamis which have propagated into Osaka Bay are included not only in the tabulated records introduced above but in the records of the tsunamis occurred off the Aleutian arc, off Alaska and off South America propagated across the Pacific Ocean to attack the coast of Japan Islands. One of the examples is

Chilean Tsunami in 1960 which is surveyed and observed along the coast of Japan Islands exactly and in the detail as far as possible by the organized group in Japan. The refraction diagrams are drawn from the wave source in the neighbour of the coast of Japan by Meteorological Agency of Japan, University of Tokyo and the other related organizations(1961).

In this section, Chilean Tsunami in 1960 is taken as an example in the tsunamis propagated into Osaka Bay, because the details and the accuracy of the data and the records of Chilean Tsunami in 1960 are reliable and abundant in comparison to the other tsunamis.

In order to find the process of the propagation of Chilean Tsunami in 1960, a schedule is arranged to draw a refraction diagram from the Pacific Ocean to Osaka Bay by a numerical computation and a manual drawing. For a convenience of practice, the authors referred to the refraction diagram of Chilean Tsunami in 1960 by Meteorological Agency of Japan, in which the location of the tsunami front just arrived at the south of Shionomisaki is taken as a boundary to start the computation and to draw the refraction diagram of the tsunami propagating into Osaka Bay. A schematical topography from the Pacific Ocean to Osaka Bay is shown in Fig.1. And for a convenience of analysis, the wave heights are assumed to be same along the line which is introduced above as the boundary for the in-put data.

The manual drawing of the refraction diagram is obtained under the assumption of the tsunami as a long wave and with the considerations of the effects of the water depth and of refraction. This manual method has been widely utilized for studying on the propagation of the tsunami fronts and for estimation of the source areas of the tsunamis. As the first step to construct a refraction diagram the wave fronts are drawn time to time successively at a given time step, after that the wave rays are drawn as the orthogonals to the wave fronts. And the wave transformation in height may be estimated to apply Green's formula to the water depth and the width of the neighbouring two wave rays for a linear theory.

On the other hand, a method to use a high speed electronic computer is introduced to obtain the refraction diagram of the tsunami. In this case, the tsunami is assumed to be a small amplitude wave to apply the computer program for refraction of wave, which is developed by Worthington and Herbich(1970) in Texas A and M University.

In order to practice the computation, the areas are taken as shown in Fig.2. Initially the wave front is assumed to be located on the line stretching toward southwest from off Kushimoto. The line forms a part of the large square(about 160 km square). And the wave front is assumed initially to propagate perpendicular to the initial line, which is taken to approximate to a line corresponding to a wave front of Chilean Tsunami in 1960 off Nankaido at a certain time.

For the first step of the computation, the large square is divided to form a mesh with the points of 15×16 , in which the water depth is given by an interpolation from the nautical charts published by Hydrographic Office, Maritime Safety Agency of Japan.

The results of the computations are shown in Figs.3 and 4. In the computa-

tions, the period of the wave is taken to be 30 min. In Fig.3, the wave rays and the wave fronts at every one minute are shown by the solid lines and the dot lines respectively. The refraction coefficient and the shoaling factor are obtained at the same time at the each step of the computations. Relative wave height is also obtained by a product of the refraction coefficient and the shoaling factor. The result is shown by curves in Fig.4, which are characterized by a parameter to indicate the relative wave height referring to the initial wave height.

After the computation in the first area, the twenty two small areas of square (about 15 km square) with the mesh points 25×25 are considered to practice the successive computations from the open ocean to Osaka Bay under the consideration of the availability of the computer at the Data Processing Center of Kyoto University. The wave directions of the last steps in each area are the next initial data of the wave directions as the in-put data. For the practical computation, one of the authors, Tsuchiya, has insisted not to fail the generality of the small amplitude wave in the application of the computing program to the tsunami so that no approximation and no simplification of the equations are considered except the numerical truncations even if the cpu time in the computation is elongated.

As the result of the computation in the first area, it is easily found that the wave front needs more than twelve minutes to travel from off Kushimoto to the entrance of Kii Channel, if the given wave front behaves similar to the tsunami. And, only two or three rays initiated not far from the coast in Fig.3 are passing Kii Channel. The wave rays far from the coast attack the coast of Shikoku Island, on the way to which the wave rays are strongly refracted by the effect of the water depth in the area of the large square. The wave rays in Fig.3 are quite similar to those in the refraction diagram obtained by Nakamura(1974) manually.

In these computations, the wave height and direction are assumed to be uniform along the initial line. Through the successive computations, the wave heights are obtained on the wave rays at each step of one minute. The estimated wave height distribution along the coast of Kii Peninsula from Kushimoto to Osaka is shown by the curve A in Fig.5. The abscissa is a convenient distance from Kushimoto and the wave height referred to that at Kushimoto is the ordinate. The curve B is the estimated wave height distribution obtained by the computations along Awaji Island. And the curve C is the wave height distribution estimated along the axis of Osaka Bay from Tomogashima Passage to Osaka. The dots and circles are the observed heights of the first and the second wave respectively. The simple dots and circles are the data along the coast of Shikoku, Awaji Island and Kobe. The crossed dots and circles are the data along the coast of Kii Peninsula. For the region from the open ocean to Tomogashima Passage ($0 \leq x < 110$ km), the observed wave heights are much smaller than the computed ones and the second wave heights are fairly good correspondence to the computations. In Osaka Bay, the observed wave height is a few but seems to be good agreement to the computed wave height distribution along Awaji Island (curve B). Although, the computed wave height along the axis of Osaka Bay (curve C) cannot be expected as an actual phenomenon. The curve C is anomalous as an actual trend, which might be caused by the given conditions and the matching conditions in the computer program through the successive computations. The authors have been aware of that it is necessary to effort to avoid the unstable results appearing in the computation of the long period waves in the very shallow water. At the cross point of the wave

rays, the computed wave height is anomalously large as far as the computation is referred to the linear theory of wave refraction. In the successive computation, the initiative of the wave direction is essential. And this might be a cause of an undesirable result. Adding to that, it is necessary to remark that no reflection is considered through the computation.

Judging from these refraction diagrams and the analysis, the wave height of Chilean Tsunami might be not so large as the computed results along the axis of Osaka Bay and not so small as the expected results from the hand written refraction diagram. It is necessary to consider not only a simple travel time of the tsunami for a glance but the wave rays or the effect of refraction when the arrival time of the tsunami at the coast is discussed.

There have been obtained and collected the records of the tsunamis caused by the earthquake off Tonankai in 1944, off Nankaido in 1946, off Alaska in 1964, off Aleutian arc in 1965, Hiuganada in 1968 and the others. Even when these records are only reliable ones, the authors may expect that the wave height at the head of Osaka Bay cannot be larger but much smaller than the wave height at Kushimoto.

It is necessary to remark that the initial wave front is different from the exact location of the wave source. And the essential remarks are that the tsunamis are the phenomena of transitional rather than a linear long wave or a small amplitude wave, so that the discrepancy is more or less inevitable between the computed results and the observed wave heights. The tsunamis are not necessarily periodical, so that frequency analysis or spectrum analysis should be also introduced to study on the mechanism and the characteristics of the tsunamis.

4. TSUNAMI SPECTRA

The concept of the tsunami spectrum might be originated and introduced to detect what component of frequency is dominant in the mareogram including a tsunami. When the water level as a time series is assumed to be a stationary Gaussian process, the method of the spectrum analysis might be useful in studying the frequency characteristics of the tsunami.

The introduction of the spectrum analysis in the problem of the tsunamis might be carried out at first by Takahashi(1961a,t). And recently, the records of the tsunamis in the world have been compiled at International Tsunami Information Center(for example, ITIC,1975) to offer the records as well as the informations and contributions of the latest tsunami spectra analyzed with use of Fast Fourier Transform(or FFT). As mentioned by Kajiura, it is essential to study what length of the data is necessary in obtaining the tsunami spectrum. On the other hand, one of the authors, Higuchi had ever analyzed the mareograms of Chilean Tsunami in 1960 by the use of periodogram(Higuchi,1963) and he had been desired to have a chance to cooperate in a study on tsunami spectra.

In this paper, the records are selected so as to study on tsunami spectra for the significant four examples, i.e., the tsunamis caused by the earthquakes off Tonankai in 1944, off Chile in 1960, off Alaska in 1964 and off Aleutian arc in 1965. In this section, the focus is to study on the transformations of the tsunami spectra through the propagations of the tsunamis from the open ocean to Osaka Bay. Before start of analysis, the elevation of the water surface is

read from the mareograms of the tsunamis at a certain constant step or a constant time interval. The discrete values of the elevations in a tsunami are assumed to be a time series of a stationary Gaussian process and treated to analyze by Blackman-Tukey's method which has been widely utilized for the spectrum analysis of ocean waves.

5. TIME DEPENDENCY OF TSUNAMI SPECTRA

When the assumed stationary process is sure, the length of the data for the analysis might not affect the form of the tsunami spectrum. The freedom of the data should be also considered statistically through the analysis. The time dependency of the data length in the analysis might show that the assumption is not suitable. In this section, the two tsunamis in 1944 at Osaka and in 1960 at Kushimoto are taken up for the analysis. The mareograms are read at the step of every three minutes to give a time series of the water level (cf. Table 1). The analysis is followed as that for ocean waves so that the number of the data is taken to be six hundred or much more under the consideration of freedom by the successive folding of the original data (see the sixth column in Table 1).

As for the tsunami caused by the earthquake off Nankaido at Osaka, the spectrum analysis is carried out for the data length of 2.5, 5 and 10 hours of the tsunami record to show the spectra in Fig. 6. In this figure, it is easily found that the principal peak of the spectrum is at the period of near 70 min ($f = 2.2 \times 10^{-4}$ cps) for the initial stage of 2.5 hours, and the other peaks are smaller than one hundredth of the principal peak. For the longer data of 5 hours and 10 hours, the second and the third harmonics of the principal peak become significant which might be caused by shoaling effect or the other effects. And the wave might be transformed into a nonlinear wave in the shallow water. The longest data (10 hours) gives the power spectrum which have the less significant higher harmonics to show that the energy of the wave is decreasing with the time elapse. The principal peaks of the three are quite similar and a little variation to give the similar form of the power spectra except the details of the forms for the significant higher harmonics.

And for Chilean Tsunami in 1960 at Kushimoto, the three kinds of the data lengths are considered, i.e., 3, 6 and 12 hours for the data originated at the time three hours before the arrival of the tsunami. The spectra are shown in Fig. 7. The power of the spectra after the arrival of the tsunami are ten times at least comparing to that before the arrival of the tsunami as a whole of the frequency. The spectra after the arrival of the tsunami have the two peaks at the periods of 40 min and 23 min (that is, $f = 4.4 \times 10^{-4}$ cps and 7.4×10^{-4} cps) respectively. In these two peaks, the one for the period of 23 min is fairly sharp and significant in the three spectra. This peak might be formed by the local resonant oscillation excited by the energy supply from the incident wave. The tsunami might be characterized by the peak at the period of 40 min in Fig. 7. After the arrival of the tsunami, the form of the spectra show the dependency of the analyzed data lengths to give significant higher harmonics. The existence of these higher harmonics suggests that the waves are transformed into the nonlinear waves or affected by the water depth to appear so called shoaling effect.

In the mareogram, the tsunami and tides are recorded in a superposed form.

When the focus is at the problem of the tsunami, the components except the tsunami should be treated as a background noise. In the spectrum, the components except the tsunami are taken to be the background spectrum as is considered by Munk, Snodgrass and Miller(1962). In Fig.7, the power spectrum before the arrival of the tsunami may correspond to the background spectrum mentioned above. When the principal peak and the pattern of the power spectrum are referred to discuss the frequency characteristics, and when the principal peak is sharp with a narrow band width, the assumption might be acceptable that the tsunami is similar to the monochromatic waves as is considered in the refraction diagram. Judging from Figs.6 and 7, the above assumption should be a fairly rough assumption. This assumption might be sufficient for only the initial part of the tsunami as considered in the refraction diagram.

6. TSUNAMI SPECTRA FROM OPEN OCEAN TO OSAKA BAY

In this section, the transformation of the forms of the tsunami spectra is considered from the Pacific Ocean to Osaka Bay for the significant tsunamis listed up in Table 2 except the tsunami caused by Hiuganada Earthquake in 1968. In order to obtain the tsunami spectra of each station, the data are treated and processed in similar manner as done for Figs.6 and 7. For the convenience of a glance to detect the transformation of the tsunami spectra, the distance from Kushimoto is taken as the ordinate and the abscissa is taken as frequency to form a diagram with a parameter of power density for each tsunami respectively. The obtained results are shown in Figs.8, 9, 10 and 11 for each tsunami respectively.

One of the example is Fig.8 which is for Tonankai Earthquake in 1944, the mareograms are obtained only at Shimotsu and Osaka so that the detail cannot be detected. The increase of the power density with the distance is easily found in the lower frequency region in Fig.8. -- And the principal peak(at $f = 9 \times 10^{-4}$ cps) in Kii Channel decreases in Osaka Bay down to less than one tenth and the incidence of the wave induces the local other oscillations.

As for Chilean Tsunami in 1960, as is shown in Fig.9, the frequency at the principal peak of the spectra is almost uniform from Kii Channel to Osaka Bay except Kushimoto. The local effect in the spectra might be characterized by the higher harmonics. The peak of $f = 8 \times 10^{-4}$ cps at Kushimoto may be caused by the effect of the local topography as mentioned for Fig.6. In case of the propagation, the reflection and refraction might cause the significant transformation of the tsunami for the tail part. The peak of $f = 3 \times 10^{-4}$ cps suggests that a oscillation is induced and formed to locate the node at Tomogashima Passage and the loops at the head of Osaka Bay and the mid Kii Channel. This oscillation is easily found by a glance of the diagram as shown in Fig.9. And the trend shows that the power density for the higher frequency region decreases gradually with the distance.

The other examples similar to Chilean Tsunami in 1960 are the tsunamis in 1964 and 1965, which are analyzed and shown in Figs.10 and 11. The wave sources are in each cases far from Japan and the waves come to Japan across the ocean. And the analyses of these tsunamis suggest that the tsunami wave heights and the power density of the tsunami spectra depend on the locations of the wave sources and the paths of the wave rays as well as the magnitude of the waves at the source areas.

The above results are obtained from the tsunami spectra obtained by Blackman-Tukey's method which has been widely utilized in the spectrum analysis of the ocean waves. Exactly speaking, it is necessary to remark that all phenomena of the tsunamis are transitional and to consider to treat the tsunamis as nonstationary processes. The appreciation of the tsunami in the scope of the nonstationary stochastic process might be an important and interesting problem to be solved as remarked by Nakamura(1975).

7. CONCLUSIONS

The authors have analyzed the tsunamis propagating into Osaka Bay in order to study the transformation of the tsunamis through the propagation. (1) At first, Chilean Tsunami in 1960 is taken to study on the wave height distribution along the coast from Kushimoto to Osaka(from the Pacific Ocean to the head of Osaka Bay) in a fairly good correspondency between the refraction diagrams which are obtained by the numerical computations and the manual drawings. The observed wave height along the coast seems to fit well to the computed ones for the initial part of the tsunami, especially for the second wave, except along the axis of Osaka Bay. (2) The tsunamis are analyzed to study the tsunami spectra as a tool to reveal what are the peak frequencies of the tsunamis and what are the induced local oscillations with the consideration of the above refraction diagrams. An oscillation is found by the spectrum analyses of the tsunamis on the frequency-distance diagram with a parameter of the power density to form an oscillation with a node at Tomogashima Passage and two loops at the head of Osaka Bay and at the mid Kii Channel. (3) Adding to the above, it might be necessary to develop a study of tsunami spectrum as a nonstationary stochastic process in relation to the generating processes of the tsunamis.

ACKNOWLEDGEMENT

In this study, the authors have owed to refer to the records and data which are systematically filed by Messers. K.Onishi and H.Sato of Osaka District Meteorological Observatory. And Prof. K.Kajiura and Drs. T.Hatori and I.Aida in University of Tokyo stimulated the authors to construct the refraction diagrams by a numerical computation. The computations are carried out by the computer FACOM 230-75 in the Data Processing Center of Kyoto University and the tsunami spectra are obtained by the use of the computer FACOM 230-25 in Information Processing Center of Disaster Prevention Research Institute, Kyoto University.

REFERENCES

- Higuchi, H. 1963 Geophysical Papers Dedicated to Professor Kenzo Sassa, pp.49-57
 Higuchi, H. 1966 Proc. 11th Pacific Congress, Vol. 2
 Iida, K. 1956 Jour. Earth Sci., Nagoya Univ., Vol. 4, No. 1, pp. 1-43
 Iida, K. 1975 Report for Disaster Prevention Meeting of Nagoya City, pp. 1-30
 Iida, K., D.C. Cox and G. Parraras Carayannis 1967 Data Report No. 5, HIG-67-10, Univ. Hawaii, 131 sheets
 Imamura, A. 1942 Zishin, Ser. 2, Vol. 2, No. 1, pp. 23-28
 ITIC 1975 News Letter, Vol. 8, No. 1, pp. 1-24
 Kawasumi, H. 1969 Reports for Disaster Prevention Meeting of Tokyo, pp. 1-8
 Munk, W.H., F.E. Snodgrass and G.R. Miller 1962 Jour. Mar. Res., Vol. 20, pt. I, pp. 3-30; pt. III, pp. 119-120
 Nakamura, S. 1974 Doctoral thesis in Kyoto University, pp. 1-194
 Nakamura, S. 1975 Abstracts of Autumnal Convention of Oceanographical Society in Japan, Nagasaki, pp. 81-82
 Nakamura, S.H. Higuchi and Y. Tsuchiya 1975 Bull. Disaster Prevention Res. Inst., Kyoto Univ., Vol. 25, Pt. 4, pp. 37-53
 Omori, F. 1918 Report of Committee for Survey of the Drastic Earthquakes, No. 89, pp. 19-48
 Soloviev, S.L. and Ch. Gao 1974 Catalogue of Tsunamis in Western Part of the Pacific Ocean, Sakhalin, pp. 1-308
 Takahashi, R. 1961a Proc. Tsunami Meeting - Honolulu, pp. 19-25
 Takahashi, R. 1961b Proc. Tsunami Meeting - Honolulu, pp. 77-86
 The Committee for Field Investigation of the Chilean Tsunami of 1960 1961 Report on the Chilean Tsunami of May 24, 1960, as observed along the coast of Japan, pp. 1-397
 Tsuchiya, Y. and S. Nakamura 1974 Report for Disaster Prevention Meeting of Osaka City, pp. 1-57
 Wadati, K. 1960 Tsunamis, Storm Surges and Oceanic Disasters, Kyoritsu Pub., Tokyo, pp. 1-208
 Watanabe, H. 1968 Zishin, Ser. 2, Vol. 21, pp. 293-313
 Worthington, H.W. and J.B. Herbitch 1970 Report No. PB-194668, Sea Grant Pub., No. 219, Report No. 127-C.O.E., Texas A and M University, pp. 1-57

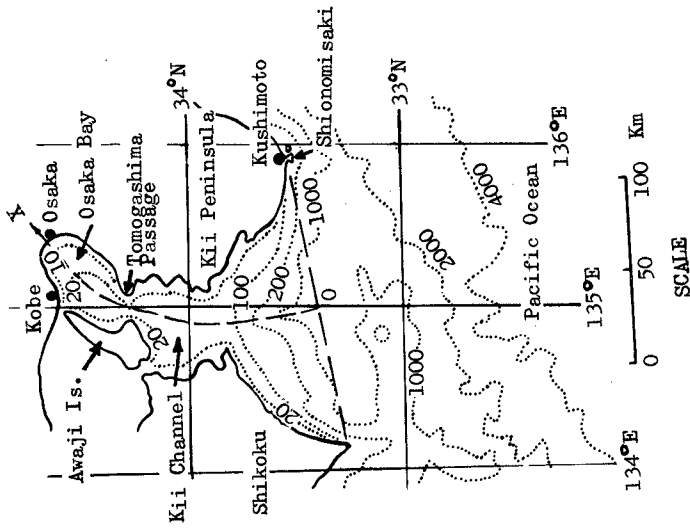


Fig.1 Area of the problem: from the Pacific Ocean to Osaka Bay

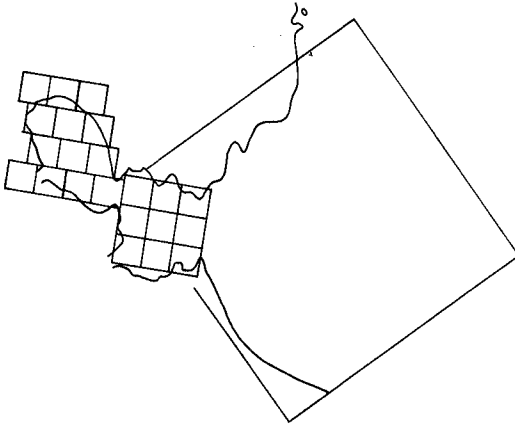


Fig.2 Zoning of the areas for computations of the refraction of the tsunami

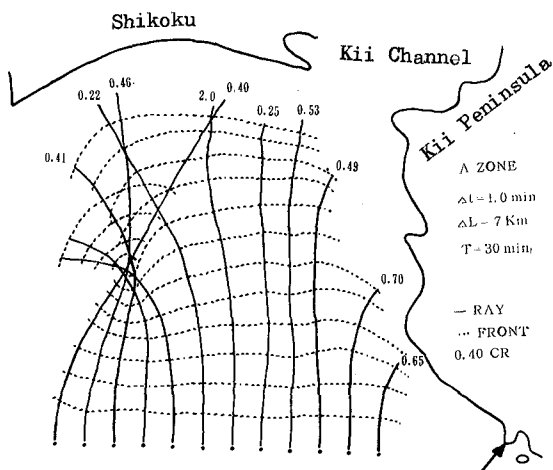


Fig.3 Refraction diagram of simulated Chilean Tsunami in 1960 by a computer

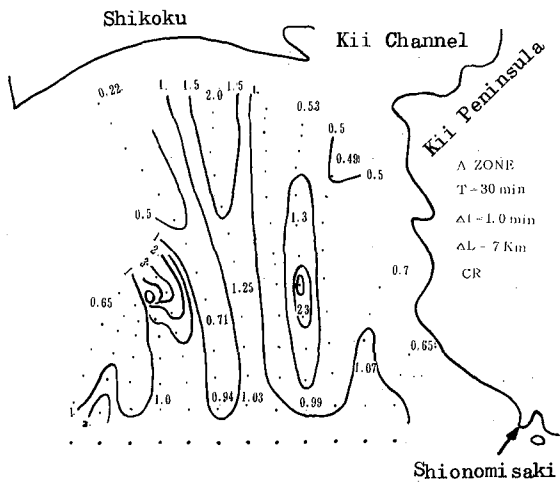


Fig.4 Wave height distribution of simulated Chilean Tsunami in 1960 by a computer

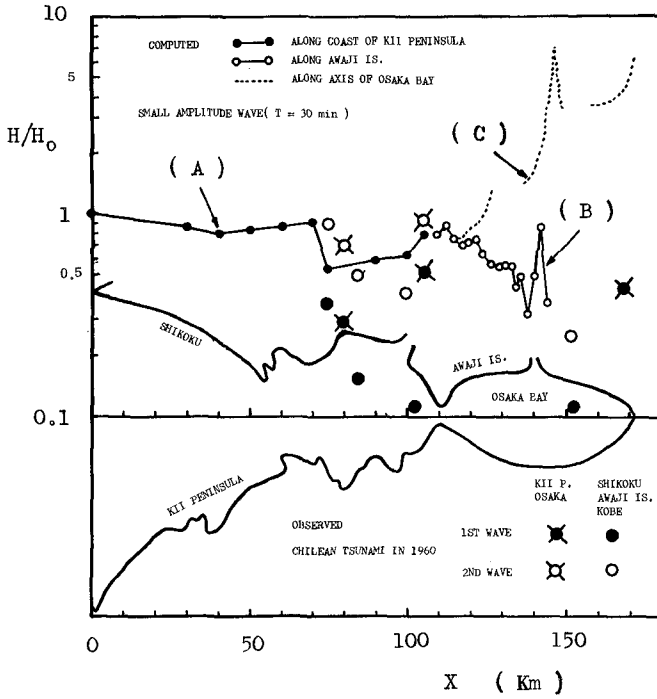


Fig.5 Transformation of simulated tsunami in wave height by a computer along the coast from the Pacific Ocean to Osaka Bay

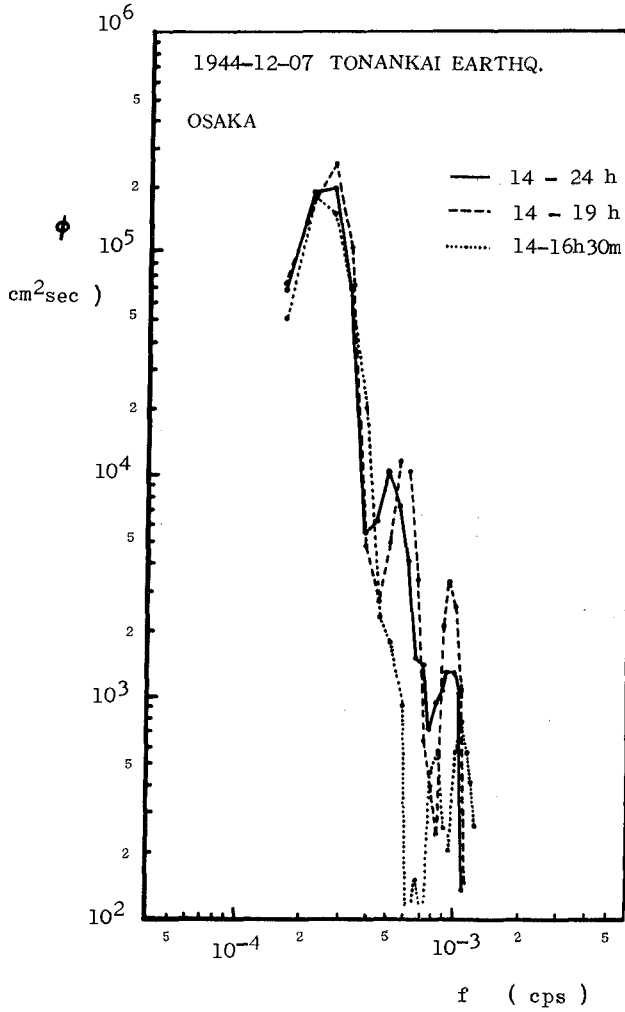


Fig.6 Tsunami spectrum as a function of time elapse at Osaka for the Earthquake off Tonankai in 1944

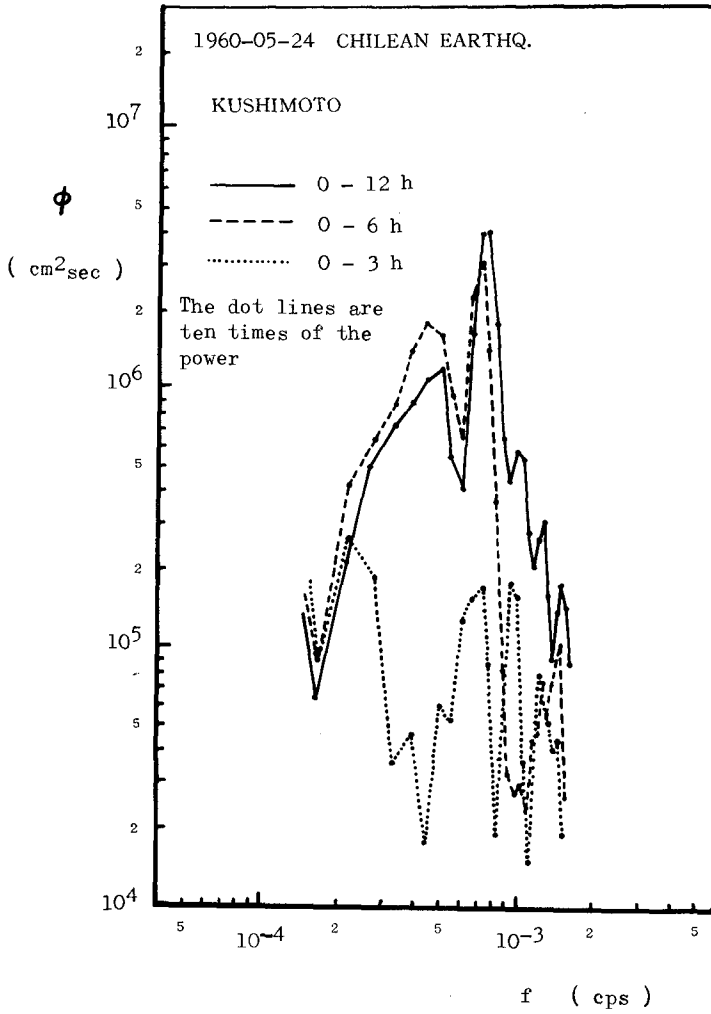


Fig.7 Tsunami spectrum as a function of time elapse at Kushimoto for the Earthquake off Chile in 1960

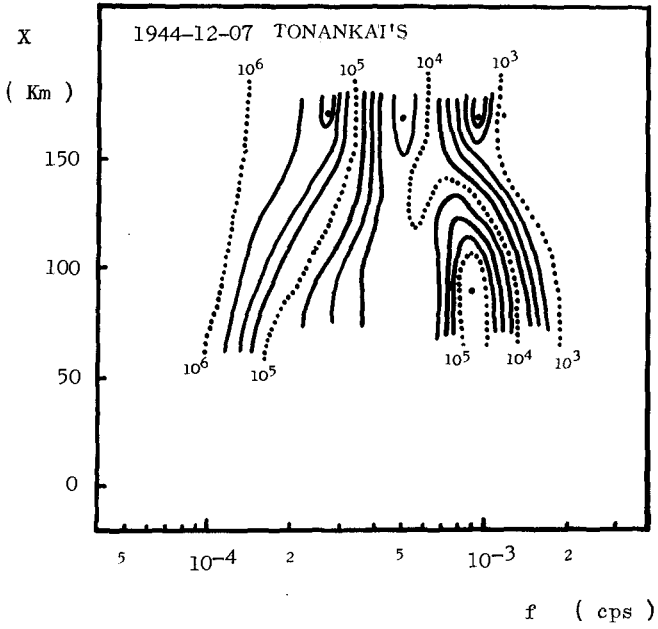


Fig.8 Local transformation of tsunami spectra with distance for the Earthquake off Tonankai in 1944

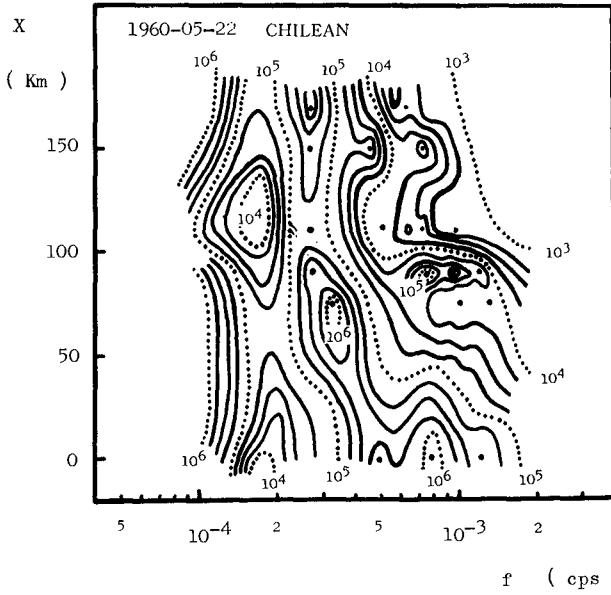


Fig.9 Local transformation of tsunami spectra with distance for the Earthquake off Chile in 1960

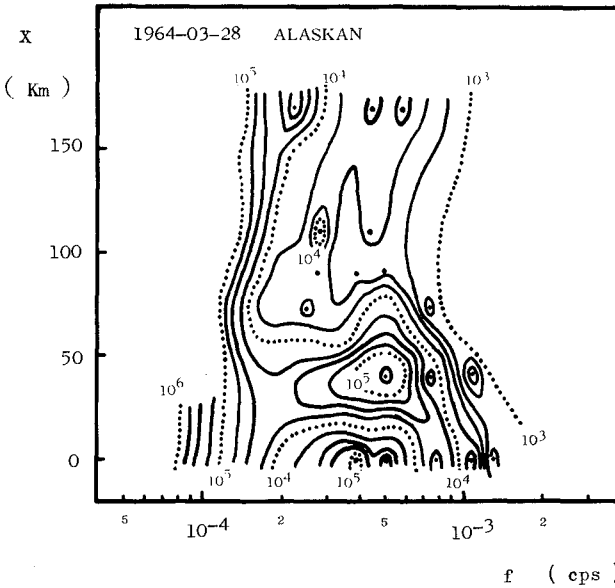


Fig.10 Local transformation of tsunami spectra with distance for the Earthquake off Alaska in 1964

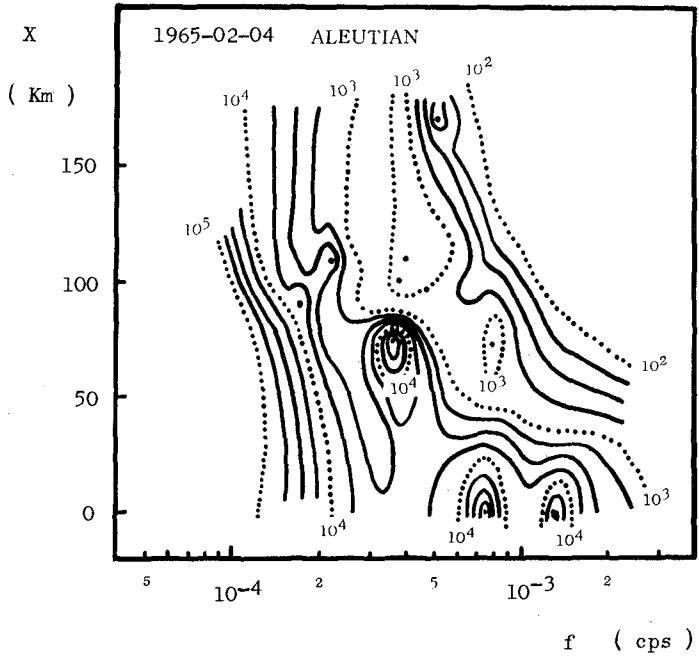


Fig.11 Local transformation of tsunami spectra with distance for the earthquake off Aleutian arc in 1965

Table 1 Number of data used for power spectral analyses of tsunamis

LOCATION	TIME	EARTHQUAKE	TIME STEP	ORIGINAL NUMBER OF THE DATA	NUMBER OF DATA USED FOR ANALYSIS	NUMBER OF FOLD
OSAKA	14-24(10 hs)	TONANKAI	3 min	$N_0 = 200$	$N = 600$	(2)
	14-19(5 hs)			100	600	(5)
	14-16h30m(2.5 hs)			50	600	(11)
KUSHIMOTO	0-12(12 hs)	CHILEAN	3 min	240	720	(2)
	0-6 (6 hs)			120	600	(4)
	0-3 (3 hs)			60	600	(9)

Table 2 Numbers of data used to study on local transformations of tsunami spectra

EARTHQUAKE ACCOMPANIED WITH TSUNAMI	1944-12-07	1960-05-22	1964-03-28	1965-02-04	1968-04-01
	TONANKAI	CHILEAN	ALASKAN	ALEUTIAN	HIUGANADA
LOCATION	NUMBER OF DATA (NUMBER OF FOLD)				
OSAKA (X = 180 km)	400 (1)	340 (1)	720 (0)	680 (0)	-
KIIBE (170)	-	480 (1)	-	-	-
SUMOTO (110)	-	480 (1)	680 (0)	482 (1)	-
NUSHIMA (85)	-	-	670 (0)	-	-
KOMATSUJIMA (75)	-	480 (1)	500 (1)	319 (1)	230 (2)
WAKAYAMA (90)	-	-	480 (1)	480 (1)	-
SHIMOTSU (70)	290 (2)	450 (1)	-	560 (1)	-
MORI (40)	-	-	540 (1)	-	-
KUSHIMOTO (0)	-	480 (1)	480 (1)	681 (0)	230 (2)

CHAPTER 60

TSUNAMI INUNDATION PREDICTION

Charles L. Bretschneider¹ and Pieter G. Wybro²

ABSTRACT

This paper concerns the run-up and inundation characteristics of tsunami surges. The forces and moments produced by the waves are not discussed, however, the proposed technique does provide the necessary information for their determination. The method relies on the knowledge of the wave elevation at the coast (as determined from historical data or other means) and an estimation of the bed roughness. The considerations and calculations involved in determining these parameters are discussed in detail. Twenty-four observed run-ups on the island of Hawaii in the case of the 1946 Aleutian tsunami, and 18 run-ups on the island of Maui for the Chilean 1960 tsunami are used to illustrate the technique. Methods are also presented to predict the shoreline heights and extent of inundation of tsunami surges where historical data is not available.

INTRODUCTION

This paper presents the theory and technique for determining the extent and profile of flooding due to tsunamis as affecting the coastal zone, especially the State of Hawaii. An earlier paper by Bretschneider and Wybro (1973) gave results for tsunami flooding over a flat, dry bed as in Hilo, Hawaii. These results are extended for the case of sloping land profiles and also for composite slopes consisting of a flat foreshore and sloping backshore.

To determine the wave height at the coastline, it is necessary to select an appropriate value of a roughness parameter, namely Manning's n , to account for the frictional effect of the bed on the inland advance of the surge. From this, then, flooding under existing or improved conditions can be determined. For improved conditions, it should be expected that the extent of flooding will be greater than that which occurred during past conditions.

The distribution of coastline elevations obtained from historical data provide an extrapolation base for which coastline elevation at intermediate locations can be determined.

BASIC EQUATIONS

The frictional shear stress opposing the flow of water is given by the Darcy-Weisbach (1858) relationship

$$\tau = \frac{f \rho u^2}{2} \quad (1)$$

¹Chairman and Professor, Dept. of Ocean Engineering, University of Hawaii

²Graduate Student, Dept. of Ocean Engineering, University of Hawaii

where τ is the bottom shear stress, ρ is the fluid density, u is the mean velocity, and f is a non-dimensional friction coefficient. Because the frictional coefficient is dependent not only on the bed roughness, but also on the depth of fluid, various laws have been formulated to attempt to separate these effects.

The most common formulation that attempts to correct this defect is Manning's formula

$$u = \frac{1.486}{n} R^{2/3} S^{1/2} \quad (2)$$

where R is the hydraulic radius (feet), S is the slope of the water surface, and n is Manning's n which is a measure of the roughness of the boundary and has dimensions ($\text{ft}^{-1/3} \text{ sec}$). The hydraulic radius is defined by

$$R = A/P \quad (3)$$

where A is the cross-sectional area of flow and P is the wetted perimeter. R is equal to the depth of water, h , in the case of very wide channels.

The Chezy-Kutter formula is given by

$$u = C_h \sqrt{RS} \quad (4)$$

where C_h is the Chezy coefficient ($\text{ft}^{1/2} \text{ sec}$) and is related to Manning's n by

$$C_h = \frac{1.486}{n} R^{1/6} \quad (5)$$

Manning's n is related to the Darcy-Weisbach f as follows:

$$f = 0.9 g n^2 h^{-1/3} \quad (6)$$

Hence, if Manning's n is only a function of bed roughness, then the friction factor f varies inversely to the 1/3 power of the water height. Bretschneider and Wybro (1973) showed that Manning's n for any particular roughness remains essentially constant with water depth. This is particularly so for values of n less than 0.04 and water heights between 5 and 50 feet.

Values of Manning's n can be found in numerous references such as Creager and Justin (1950) or Parsons (1965) in the case of effects of vegetation.

The classical long wave equations consist of the momentum and continuity equations which are, respectively:

$$\frac{\partial u}{\partial t} + u \frac{\partial u}{\partial x} = -g \frac{\partial h}{\partial x} - gm \frac{-g u |u|}{C_h^2 (d_0 + h)} \quad (7)$$

$$B \frac{\partial h}{\partial t} + \frac{\partial}{\partial x} (Au) = 0 \quad (8)$$

where: A is the cross sectional area of flow
 B is the surface width of flow
 d_0 is the natural water depth
 h is the depth of water above d_0
 m is the bottom slope

and differentiation with respect to x and t denote flow direction and time, respectively.

The last term in equation (7) accounts for frictional dissipation and can be rewritten in terms of Manning's n as

$$\frac{g u |u|}{C_h^2 (d_0+h)} = \frac{n^2 g |u| u (d_0+h)^{-4/3}}{(1.486)^2} \quad (9)$$

SOLUTIONS TO EQUATIONS

We will first consider the special case of a tsunami surge propagating inland over an open coast and a flat dry bed. This case was examined earlier by Bretschneider and Wybro (1973).

The momentum equation becomes (for $m = 0$, and $u = F\sqrt{gh}$ where $F = \text{constant}$ and assuming negligible local accelerations in comparison to the convective terms)

$$\frac{\partial h}{\partial x} = - \frac{n^2 u^2 h^{-4/3}}{(F^2/2+1)(1.486)^2} \quad (10)$$

for which it is found:

$$\frac{h}{h_0} = \left[1 - \left(\frac{x}{x_R} \right) \right]^{3/4} \quad (11)$$

and

$$x_R = \frac{3}{4} \frac{h_0^{4/3}}{F^2 n^2} \cdot \frac{(1.486)^2}{g} \left(\frac{F^2}{2} + 1 \right) \quad (12)$$

where h_0 is the initial surge depth, h is the surge depth after travelling x feet inland, and x_R is the distance to complete dissipation (see Fig. 1). Note that equation (12) differs from that of Bretschneider and Wybro (1973) in the constant term 6.5. However, the earlier report fitted inundation profiles to the observed data, whence Manning's n was determined. To convert the Manning's n so determined to the correct value in equation (12) involves multiplying by the factor $\sqrt{3} = 1.73$. The resultant inundation curves are hence identical, except the Manning's n obtained in the earlier work are to be corrected.

Solutions to equations (11) and (12) are depicted graphically in Figures 2 through 5. Each figure, for a particular roughness value, describes the envelope curve of the surge height as it propagates inland for various initial heights and for Froude numbers $F = 1$ and $F = 2$.

In the theoretical dam break problem, considering frictionless flow, Keulegan (1949) arrives at $F = 2$. Experiments by Fukui, et al., (1963) found that $F = 1.73$ for a bore propagating over a dry bed with $n = 0.013$. More recent experiments by Cross (1966) for tsunami surges finds $F = 1.41$ for a bed roughness of $n = 0.02$.

Miller's (1968) experiments indicated that the characteristic Froude numbers are functions not only of the roughness, n , but also of the ratio of surge depth to depth of water prior to sloping bottom. The relationships $F = f(n, h/d)$ was not determined, however. It appears from Figures 2 through 5 that $F = 2$ causes greater frictional dissipation than $F = 1$ because of higher fluid velocities. It is, hence, conservative to use $F = 2$ to predict shoreline elevations from run-up data and for conservative purposes, until more exact information is known, it appears desirable to use $F = 2$ (as, for instance, if forces are calculated).

In the case of surges advancing over a sloping bottom, equation (7) becomes (neglecting local acceleration and friction)

$$u \frac{\partial n}{\partial x} = -g \tan \alpha - g \frac{\partial h}{\partial x} \quad (13)$$

where α is the bottom slope. For the case of $u = F \sqrt{gh}$ then

$$\frac{\partial h}{\partial x'} = - \frac{\sin \alpha}{(F^2/2+1)} \quad (14)$$

where x' is the coordinate along the flow length. Upon integrating, the expression for the vertical runup, R'' , becomes

$$R'' = h_c + h_t + \frac{u_t^2}{2g} \quad (15)$$

where h_c is the vertical rise of the berm or beach (Fig. 1) and h_t and u_t are the surge height and surge velocity, respectively, at the toe of the slope.

Equation (15) can be compared to the value $u_t^2/2g$ arrived at by Freeman and LeMehaute (1964) where $h_c = 0$ and also $h_t = 0$ as a result of the first-order, non-linear long wave analysis. In this analysis, the surge collapses at the shoreline to a thin sheet of water with a velocity u_t .

Note that for $h_c = 0$ and $F = 2$, $R'' = 3$ or the vertical rise in water will triple.

It appears that for tsunami surges, the inclusion of h_t in equation (12) is justified as it is well known that the surge height does not collapse at the shoreline. This was experimentally justified by Miller (1968).

Cross (1966) found experimentally that the rise of water on a vertical wall is approximately $1.33 u_t^2/2g$ for a dry bed. In equation (15) with $F = 1.41$ and $h_c = 0$ yields $R^u = 1.9 u_t^2/2g$ which is conservative.

In the case of a roughened slope, equation (7) becomes the governing equation, and equation (14) becomes (neglecting the local acceleration)

$$\frac{\partial h}{\partial x'} = -\left\{\sin\alpha + \frac{n^2 g F^2 h^{-1/3}}{(1.486)^2} \cos\alpha\right\} [F^2/2 + 1]^{-1} \quad (16)$$

and the runup, R , is found by numerical integration. This has been done for various slopes (2.5° and 5°), various roughness ($n = 0.025, 0.035, 0.045,$ and 0.055) and a range of surge depths, h_t . The results are depicted in Figures 6 and 7, wherein R is plotted versus h_t for various Manning's n values.

For composite profiles (horizontal foreshore and sloping backshore), Figures 2 through 5 can be used to determine h_t , and this value is entered in Figures 6 or 7 with the corresponding Manning's n value to determine the run-up, R . Note that for the composite slopes, the roughness of the sloping portion need not be the same as the flat portion.

APPLICATION TO HISTORICAL DATA

Bretschneider and Wybro (1973) investigated the results of the tsunamis of 1946 and 1960 for the case of Hilo, Hawaii using the flat bottom equations. It was found that the land profiles were ideally suited due to the very gentle grade and an excellent comparison was obtained between the computed and observed inundation profiles. In this section, the analysis is extended to include composite land profiles whence equations (10) and (11) are used along with Figures 6 and 7. The areas of interest are the north coast of the island of Hawaii as experienced by the 1946 Aleutian tsunami and the southwest coast of the island of Maui for the case of the 1960 Chilean tsunami.

Island of Hawaii

Figure 8 shows the wave advancement of the 1946 tsunami as affecting the north coast of the island of Hawaii. The solid lines represent the wave fronts, the light dashed lines represent orthogonals and the heavy dashed lines represent orthogonal intersections, as was computed by Shepard, et al. (1950). The region of interest extends from Upolu Point in the west to Kumukahi Point in the east, a coastal distance of roughly 100 miles. The reported run-ups, also shown, were obtained from the Tsunami Research Center, University of Hawaii as documented on 1:24,000 scale USCGS quadrangle charts. The land profiles were obtained from these charts and the coastal terrain and roughness conditions were estimated from a field survey coupled with infrared aerial photographs taken from U-2 flights in 1974 and 1975.

It is found that the land profiles for a majority of the locations can be very adequately described by the composite slope method, using backshore slopes of 0.5° up to 10° with an average of about 2° to 3° . The steep,

nearly vertical cliffs that are common to this coastline were not used as these regions are inaccessible, hence, no run-ups were reported.

The reported run-ups are plotted in Figure 9 (solid circles) versus coastal distance measured west to east. These run-ups are projected back to the coast by means of Figures 2 through 7 using the iteration method described in the previous section and where the values of Manning's n are determined from Table I. The coastal elevations are indicated by open circles in Figure 9. Table II lists the run-ups, inundations, coastal elevation and Manning's n determined at each location.

A somewhat smooth curve can be passed through the coastline distribution, and on the basis of this curve, an equivalent, uniform wave of height z_r in open ocean is

$$z_r = \sqrt{\frac{1}{\lambda} \int_0^L z_0^2 ds} \quad (17)$$

where λ = projected distance of coast along the wavefront, ds is the increment of length along the shoreline, and L is the length of the coast. Note that z_r is a fictitious height in that shoaling has already been taken into account. In this case, projecting to the 6:30 a.m. wavefront (Fig. 8) gives $\lambda = 80$ miles, $L = 100$ miles, and $z_r = 46$ feet. On this basis the refraction coefficient is

$$K_R = \frac{z_0}{z_r} \quad (18)$$

The distribution of K_R as obtained by equation (18) is compared to the values obtained from the refraction diagram, Figure 8. The results are shown in Figure 10. The agreement is good, and both curves exhibit the same trends. The discrepancies can be attributed to the basic assumptions involved in arriving at the frictional effect (equation (16)) and the neglect of reflection and diffraction effects.

The determination of the appropriate friction factor involves some subjectivity, especially in the case where the flow length is composed of various roughnesses. The values in Table I were, however, determined not only from a literature review, but also from the fitting of envelope curves to the known inundation profiles (such as Hilo) and hence determining Manning's n . For example, Kolekole Beach Park is situated somewhat midway along the northern coast (see Fig. 11). Field observations made after the 1946 tsunami show that the wave overtopped and destroyed the existing railroad bridge and overtopped the Nanahoa highway bridge by three feet. A fitting of the inundation profile using Figures 2 through 7 determined Manning's n to be 0.04 which is as expected from Table I.

Suppose that the terrain was cleared to an open area with finely cut grass, etc., whence $n = 0.025$. If the same tsunami surge advanced inland under the new conditions, then it would have overtopped the highway bridge by 11 feet and the vertical run-up would be 30 feet instead of 17 feet. This exemplifies the changes in inundation characteristics corresponding to terrain changes as, for instance, when development occurs.

TABLE I
SUGGESTED VALUES OF MANNING'S n FOR VARIOUS COASTAL TERRAIN CONDITIONS

n	Conditions
0.015 - 0.025	Very smooth (mud flats, ice, well maintained concrete paved ways, beaches of fine sand)
0.025 - 0.030	Smooth (dried earth, coarse sand beaches, badly maintained concrete paved ways, very thin lawn grass up to 1 cm high)
0.030 - 0.035	Average for developed areas (lawn grass up to 5 cm high, gravel, presence of some buildings, houses, and other obstructions)
0.035 - 0.045	Open coast, relatively smooth and open area (grass up to 10 cm, sparse population of trees*, sparse bush, even bottom)
0.045 - 0.055	Moderately rough open coastal areas (thick grass, uneven bottom consisting of large rocks, coral, etc., presence of trees with low foliage, brush, lava rock, etc.)
0.055 - 0.070	Unusually rough coastal areas (dense brush, dense tree population with exposed roots, coarse lava rock formations)

* Trees with high foliage such that only trunks are exposed to flow

TABLE II
 HEIGHT, RUN-UP, AND INUNDATION OF 1946 TSUNAMI
 ALONG NORTH COAST OF ISLAND OF HAWAII

Location No. (west to east)	Run-up, R (ft)	Inundation, X_L (ft)	Manning's n (ft ^{1/6})	Elevation at Coast, Z_0 (ft)
1	18	100.	.052	20.
2	40	80.	.035	42.
3	(33)	80.	.045	(34.)
4	50	100.	.045	52.
5	26	4600.	.045	60.
6	40	500.	.045	46.
7	23	5200.	.026	42.
8	40	2300.	.024	50.
9	36	600.	.055	53.
10	28	100.	.035	31.
11	30	200.	.043	33.
12	38	150.	.035	39.
13	(23)	75.	.045	(25.)
14	38	200.	.045	40.
15	37	150.	.050	40.
16	37	50.	.045	39.
17	27	230.	.050	33.
18	34	70.	.043	36.
19	38	100.	.035	39.
20	35	100.	.045	38.
21	20	1800.	.031	30.
22	23	1500.	.029	32.
23	18	360.	.065	32.
24	19	250.	.050	28.

\bar{n} = 0.04236, mean of n

σ_n = 0.01006, standard deviation of n

\bar{n}_r = 0.04354, root mean square of n

Island of Maui

A second coastline is examined in detail, that being the southwest coast of the island of Maui, a coastal distance of roughly 35 miles (see Fig. 12). In this case the 1960 tsunami, which originated from Chile, is examined in much the same manner as the previous case. The reported run-ups were substantially lower due to the sheltering effect of the island of Kahoolawe, however, there is a preponderance of data. This coastline is also ideally suited for the composite slope model.

The results of this analysis are depicted in Figures 13 and 14 and Table III where generally good agreement is obtained between the expected and calculated refraction effects. The discrepancy in the southeast region (right hand side, Fig. 14) can be attributed to diffraction effects due to Kahoolawe.

The method of fitting curves to the distribution of coastline elevations allows for the determination of heights at intermediate locations having no historical data. This is a common occurrence, especially for newly developed areas.

SUMMARY AND CONCLUSIONS

The prediction of the height and extent of flooding due to tsunamis should take into account the initial height, Green's law, convergences or divergences, and friction effects. The equations developed in this report take all of the above into account except convergences and divergences, i.e. they are valid only for the open coastline.

It appears from an analysis of historical run-up data that frictional effects can account for the generally wide data scatter, and on this basis coastline elevations can be determined at locations other than where data is present. When these values have been determined for existing conditions, it is then possible to predict flooding contours under existing conditions and also for extreme conditions. If the existing conditions are changed because of development, then it will be important to select the appropriate value of Manning's n in order to predict the extent of normal and extreme flooding under the improved conditions.

Although the technique has been tested and verified by field conditions, it appears that experimental justification is necessary, especially in regards to the following:

1. The Froude number relationship in regards to bore height and roughnesses.
2. The constancy of the Froude number over the flow length, especially in the case of composite slope.
3. The quantitative criteria for bore formation.

ACKNOWLEDGEMENTS

Appreciation is given to the Sea Grant College Program; the Pacific Urban Studies and Planning Program, University of Hawaii; and the Structural Engineers Association of Hawaii for partial support of this paper.

TABLE III
 HEIGHT, RUN-UP, AND INUNDATION OF 1960 TSUNAMI
 ALONG SOUTHWEST COAST OF MAUI

Location No. (west to east)	Run-up, R (ft)	Inundation, X_L (ft)	Manning's n (ft ^{1/6})	Elevation at Coast, Z_o (ft)
1	7	1600.	.038	11.5
2	9	2200.	.026	11.8
3	9	250.	.052	10.8
4	9	220.	.043	9.8
5	8	1000.	.026	9.1
6	9	300.	.035	9.3
7	8	200.	.043	9.0
8	7	100.	.060	10.5
9	11	150.	.026	11.5
10	7	400.	.035	10.5
11	8	1500.	.021	9.1
12	8	500.	.024	9.0
13	5	650.	.035	8.8
14	4	1000.	.026	9.0
15	5	400.	.047	9.1
16	7	200.	.052	9.2
17	9	100.	.035	10.0
18	9	500.	.031	11.0

\bar{n} = 0.03686, mean of n

σ_n = 0.01101, standard deviation of n

\bar{n}_r = 0.03847, root mean square of n

REFERENCES

1. Bretschneider, Charles L. and Pieter G. Wybro (1973) "On the Determination of Manning's n for Flood Problems Over an Initial Dry Bed", Second Int. Conf. on Port and Ocean Engineering Under Arctic Conditions, University of Iceland.
2. Creager, William P. and Joel D. Justin (1950) HYDROELECTRIC HANDBOOK, Second Edition, John Wiley and Sons, Inc., New York, 1151 pp.
3. Cross, Ralph H. (1966) "Tsunami Surge Forces", University of California, Berkeley, Hydraulic Engineering Laboratory, Report HEL 9-10, 106 pp.
4. Darcy, H. (1858) "Recherches experimentales relatives an mouvement de l'eau dans les tuyaux" (Experimental Research on the Flow of Water in Pipes) Memoires de l'Academic Scientifique, Paris.
5. Freeman, J.C. and B. LeMehaute (1964) "Wave Breakers on a Beach and Surges on a Dry Bed", Journal of the Hydraulics Division, Proceedings of the American Society of Civil Engineers, Vol. 90, No. HY2, March.
6. Fukui, Y., M. Nakamura, H. Shiraishi and Y. Sasaki (1963) "Hydraulic Study of Tsunami", Coastal Engineering in Japan, Vol. 9, pp. 67-82.
7. Keulegan, G.H. (1949) "Wave Motion", Chapter XI, ENGINEERING HYDRAULICS, H. Rowe, Editor, John Wiley and Sons, Inc., New York, pp. 711-768.
8. Miller, Robert L. (1968) "Experimental Determination of Run-up of Undular and Fully Developed Bores", Journal of Geophysical Research, Vol. 73, No. 14.
9. Parsons, D.A. (1965) "Vegetative Control of Streambank Erosion", Proc. Federal Inter-Agency Sedimentation Conf., Jackson, MS, Paper No. 20, pp. 130-136, U.S. Gov. Printing Office, Washington, D.C.
10. Shepard, F.P., G.A. McDonald and D.C. Cox (1950) "The Tsunami of April 1, 1946", Bull. Scripps Inst. Oceanography, University of California, Vol. 5, No. 6, pp. 391-528.

LIST OF SYMBOLS

A	cross sectional area of flow
B	surface width of flow
C_h	Chezy coefficient
F	Froude number
K_R	refraction coefficient
L	length of coastline
P	wetted perimeter
R	hydraulic radius, vertical run-up
R'	vertical run-up not including slope effect
R''	vertical run-up not including frictional effect
S	slope of water surface
d_0	natural water depth
f	Darcy-Weisbach friction factor
h	surge height
h_c	height of flatland above MSL
h_0	depth of surge at coastline
h_t	depth of surge at toe of slope
ℓ	projected distance of coast along wavefront
m	slope of backshore
n	Manning's n
t	time
u	surge velocity
u_t	surge velocity at toe of slope
x	coordinate measured inland from coast
x_R	extent of inundation
z_0	total depth of surge above MSL at coast
z_r	equivalent unrefracted wave height
α	angle of backshore
ρ	density of fluid
τ	bottom shear stress

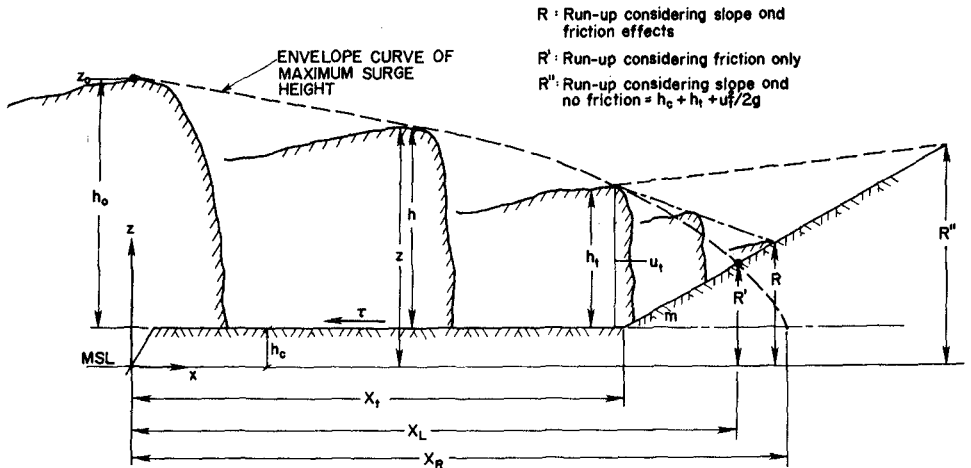


FIGURE 1 SCHEMATIC DIAGRAM OF BORE ADVANCEMENT AND DEFINITION OF SYMBOLS

FIGURE 2 ENVELOPE CURVES OF WATER SURFACE ELEVATION, h , VERSUS INLAND TRAVEL DISTANCE, x , FOR SEVERAL COASTAL ELEVATIONS. MANNING'S $n = 0.025$ FOR $F = 2$ AND MANNING'S $n = 0.017$ FOR $F = 1$.

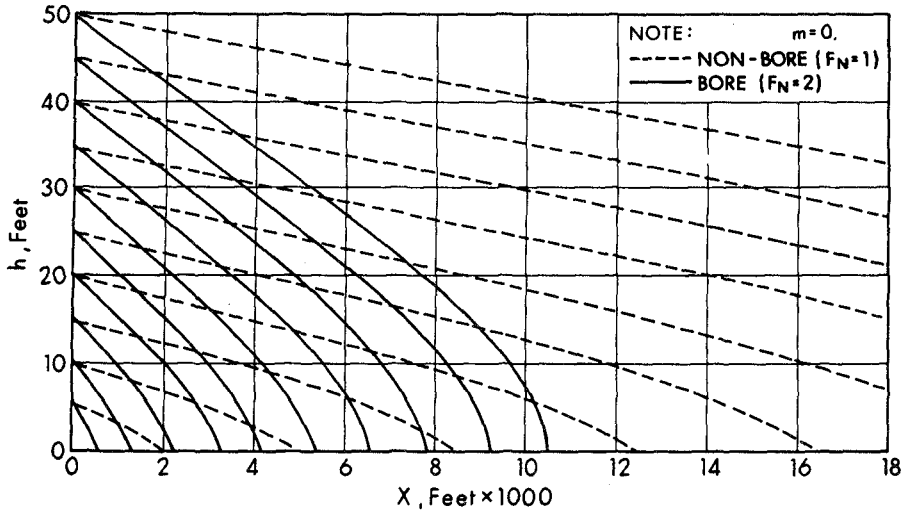


FIGURE 3 ENVELOPE CURVES OF WATER SURFACE ELEVATION, h , VERSUS INLAND TRAVEL DISTANCE, x FOR SEVERAL COASTAL ELEVATIONS. MANNING'S $n = 0.035$ FOR $F = 2$ AND MANNING'S $n = 0.025$ FOR $F = 1$.

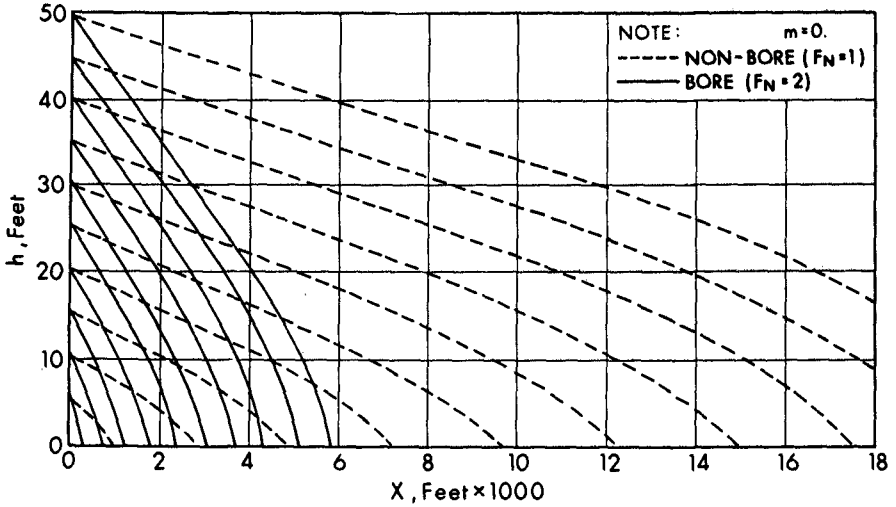


FIGURE 4 ENVELOPE CURVES OF WATER SURFACE ELEVATION, h , VERSUS INLAND TRAVEL DISTANCE, x , FOR SEVERAL COASTAL ELEVATIONS. MANNING'S $n = 0.045$ FOR $F = 2$ AND MANNING'S $n = 0.032$ FOR $F = 1$.

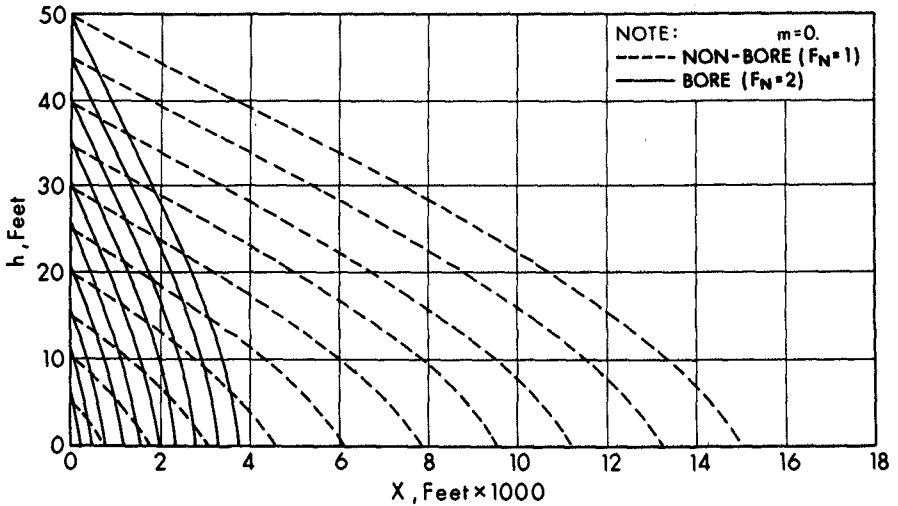


FIGURE 5 ENVELOPE CURVES OF WATER SURFACE ELEVATION, h , VERSUS INLAND TRAVEL DISTANCE, x , FOR SEVERAL COASTAL ELEVATIONS. MANNING'S $n = 0.055$ FOR $F = 2$ AND MANNING'S $n = 0.039$ FOR $F = 1$.

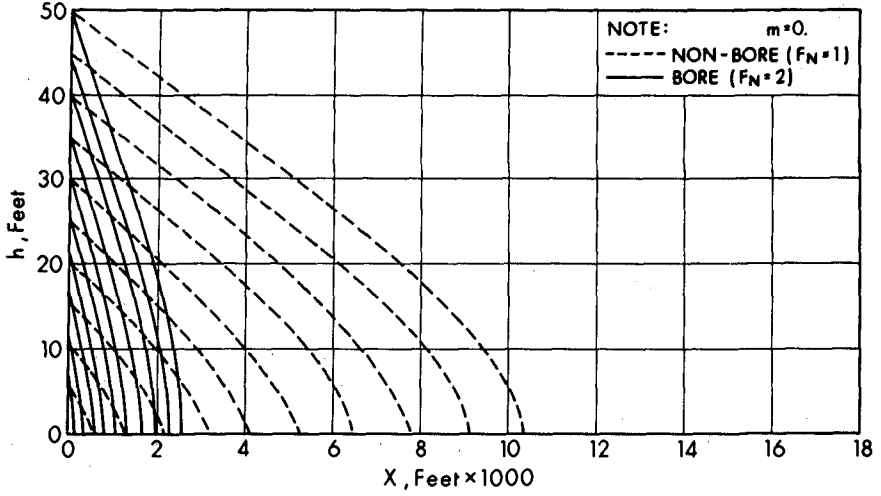


FIGURE 6 RUN-UP, R , VERSUS DEPTH OF SURGE AT TOE, h_t , FOR VARIOUS MANNING'S n . BED SLOPE = 2.5° .

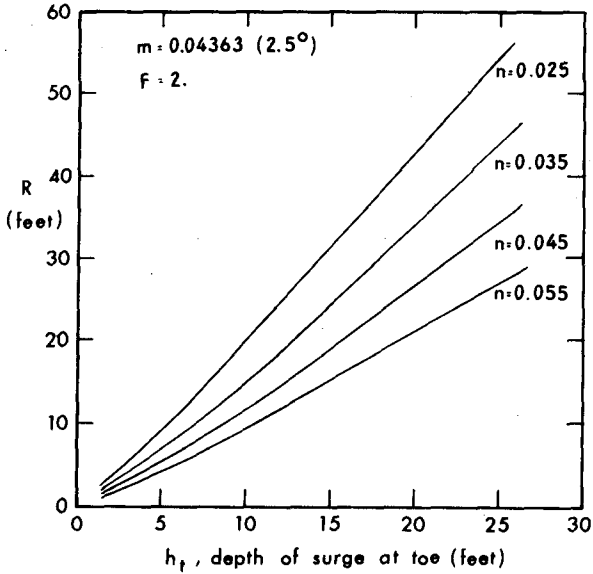


FIGURE 7 RUN-UP, R, VERSUS DEPTH OF SURGE AT TOE, h_t , FOR VARIOUS MANNING'S n. BED SLOPE = 5° .

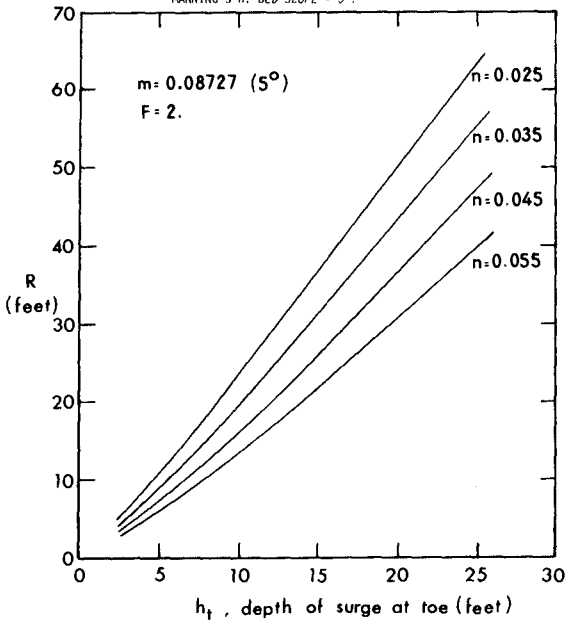


FIGURE 8 NORTH COAST, ISLAND OF HAWAII, SHOWING 1946 WAVE ADVANCE AND OBSERVED RUN-UP HEIGHTS

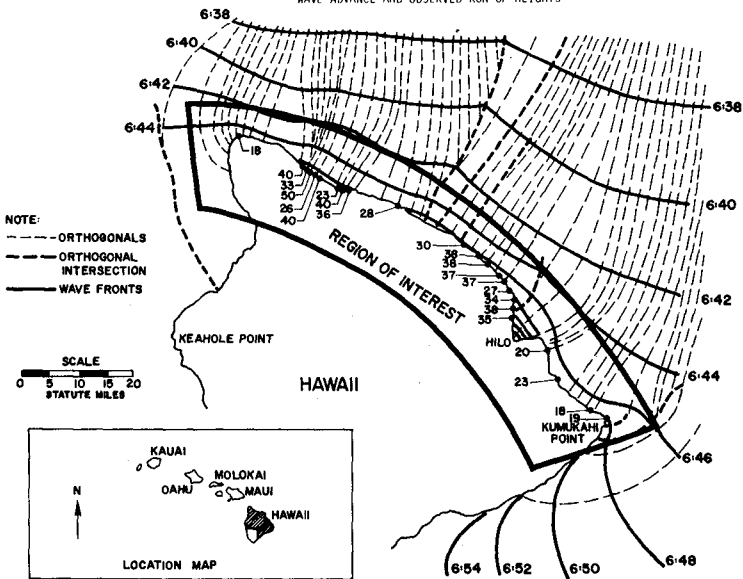


FIGURE 9 OBSERVED RUN-UPS AND PREDICTED ELEVATIONS AT COAST VERSUS COASTAL DISTANCE ALONG NORTH SHORE OF HAWAII FOR 1946 TSUNAMI

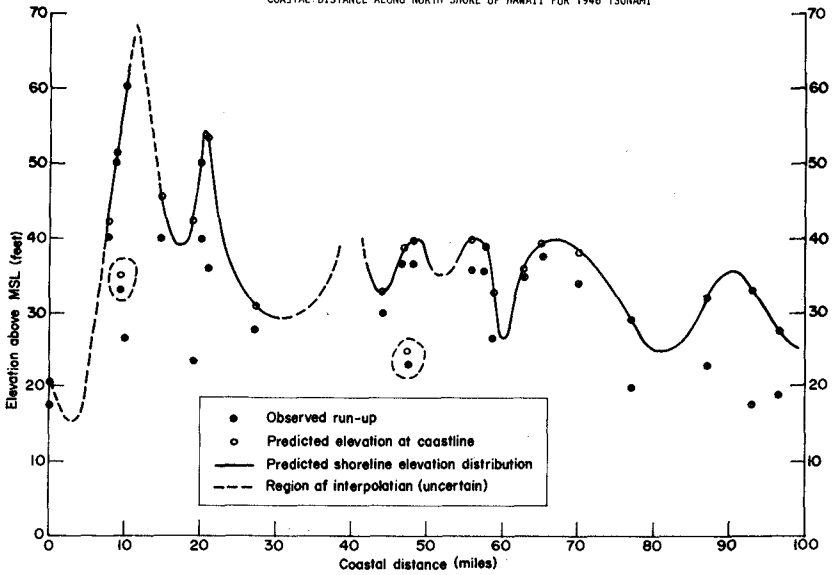


FIGURE 10 COMPARISON BETWEEN REFRACTION COEFFICIENT AS DETERMINED FROM EQUATION (19) AND REFRACTION ANALYSIS FOR THE NORTH COAST, ISLAND OF HAWAII, FOR 1946 TSUNAMI

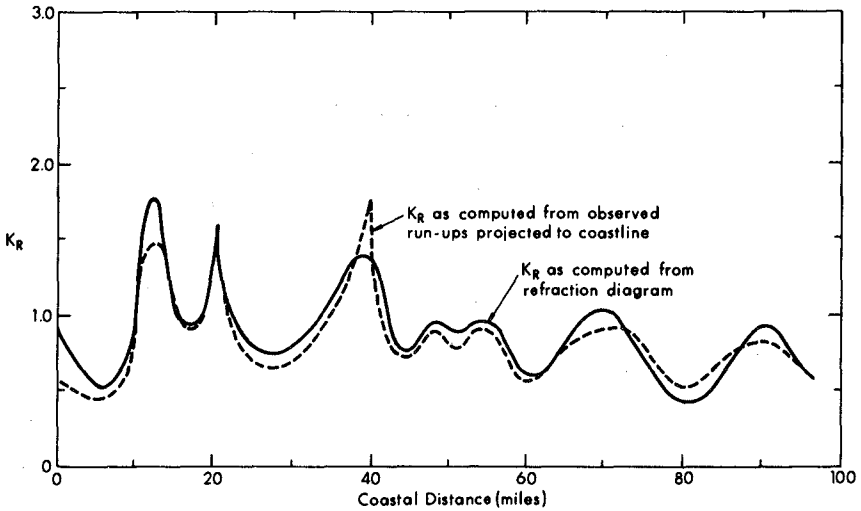


FIGURE 11 THEORETICAL INUNDATION PROFILE OF 1946 TSUNAMI (SOLID CURVE) FOR KOLEKOLE BEACH PARK, ISLAND OF HAWAII, SHOWING OBSERVED ELEVATIONS

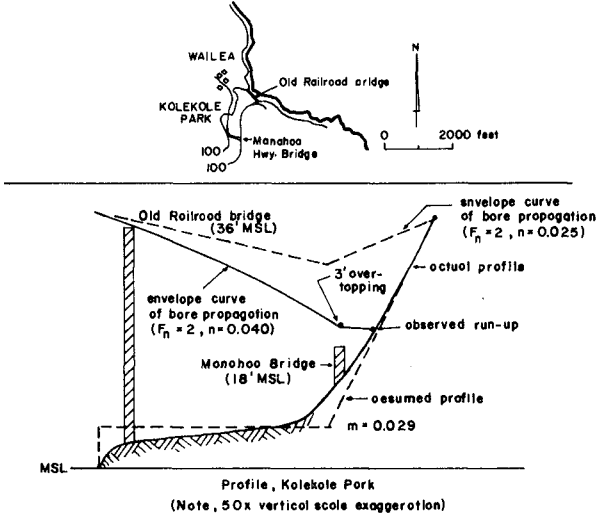


FIGURE 12 SOUTHWEST COAST, ISLAND OF MAUI, SHOWING 1960 WAVE ADVANCE AND OBSERVED RUN-UP HEIGHTS

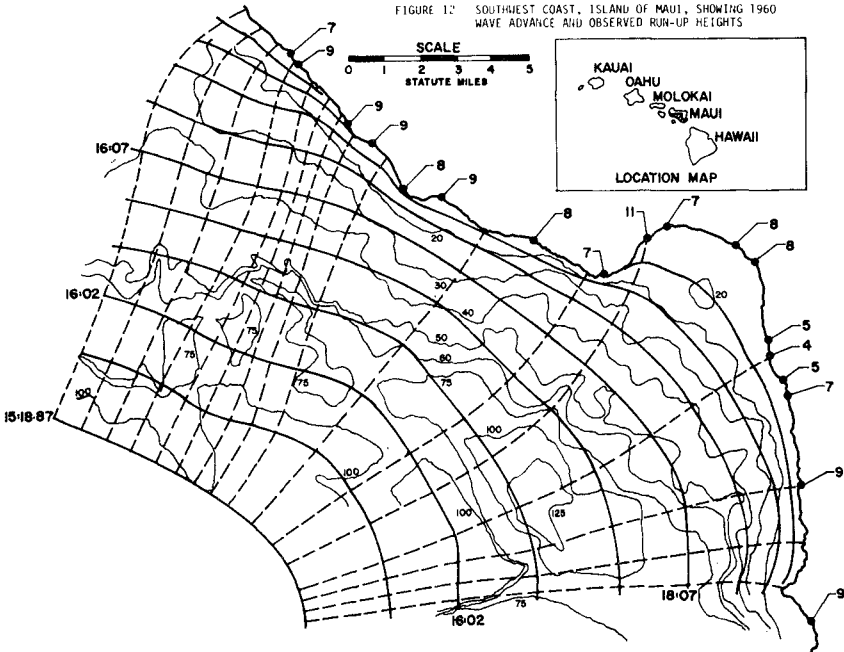


FIGURE 13 OBSERVED RUN-UPS AND PREDICTED ELEVATION AT COAST VERSUS COASTAL DISTANCE ALONG SOUTHWEST COAST OF MAUI FOR 1960 TSUNAMI

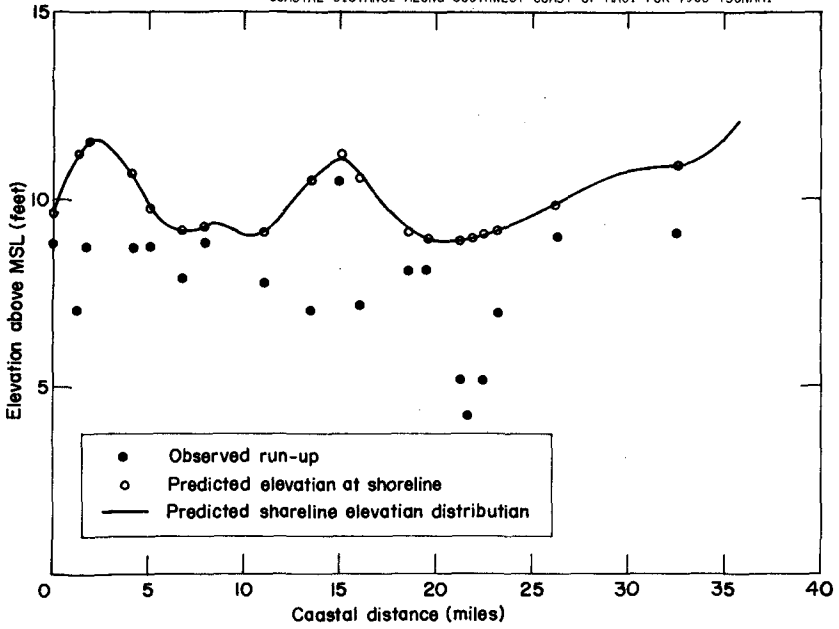
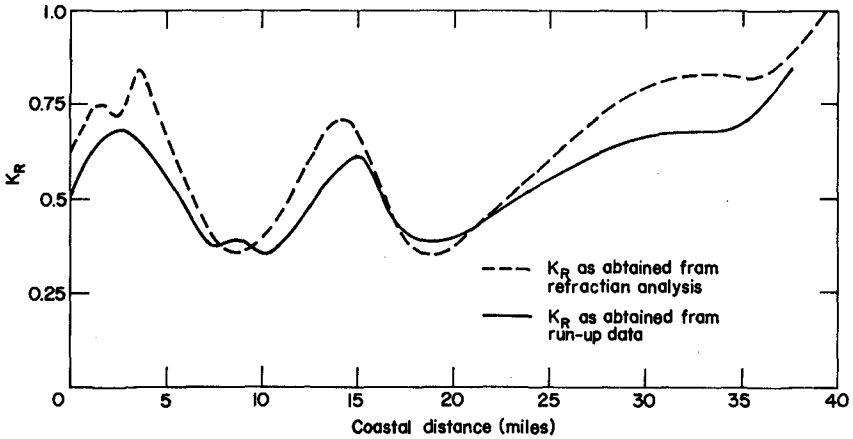


FIGURE 14 COMPARISON BETWEEN REFRACTION COEFFICIENT AS DETERMINED FROM EQUATION (19) AND REFRACTION ANALYSIS FOR SOUTHWEST COAST, ISLAND OF MAUI, FOR 1960 TSUNAMI



CHAPTER 61

NUMERICAL SIMULATION OF TSUNAMIS ORIGINATING IN THE PERU-CHILE TRENCH

BY

A. W. Garcia¹ and H. L. Butler²

I. Introduction

1. The U. S. Army Corps of Engineers has as an objective of its research and development program the determination of better harbor design criteria for tsunami protection. A previous report (Houston, et. al., 1975b) addressed the subject of tsunami vulnerability of the Pacific Coast of the continental United States to tsunamis originating in the Aleutian Trench. That report determined the variation in tsunami amplitude as a function of coastal distance due to a standard uplift source at different locations in the Aleutian Trench. The present report is a continuation of that study and addresses the subject of tsunami vulnerability along the same stretch of coast to tsunamis originating in the Peru-Chile Trench. In addition, modifications to the numerical code used in the previous report allowed the simulation of the Chile tsunami of May 22, 1960.

II. Historical Narrative

2. There have been four well documented major tsunamis to strike the Pacific Coast of the United States in recent times; the Great Aleutian tsunami of 1946, the Alaska tsunami of 1957, the Chile tsunami of 1960 and the Alaska tsunami of 1964. The 1964 Alaska tsunami claimed 107 lives in Alaska, 4 in Oregon and 11 in Crescent City, California. In addition to 330 lives in Chile, the 1960 Chile tsunami claimed 61 in Hawaii and 199 in Japan. Table 1 (Symons, et al., 1960) shows a comparison of maximum wave heights for the tsunamis of 1946, 1952, 1957, and 1960. The comparative intensity of the 1960 tsunami is evident. Indeed, the generating earthquake was of magnitude 8.6, one of the largest ever recorded.

3. The association of large submarine earthquakes with island arcs and deep submarine trenches is well documented (Kelleher, et. al., 1974; Kelleher, 1972; Sykes, 1971). The Japan-Kurile-Kamchatka, the Aleutian and the Peru-Chile Trench regions have long recorded histories of tsunamigenic activity. Of these, however, only tsunamis originating in the Aleutian and Peru-Chile Trenches have a history of causing significant runup along the Pacific Coast of the United States. Because tsunamis originating in the Aleutian Trench is the subject of a previous report, (Houston, et. al., 1975b) it will not be recounted here.

¹Research Oceanographer, USAE Waterways Experiment Station, Vicksburg, MS.
²Research Physicist, USAE Waterways Experiment Station, Vicksburg, MS.

Table 1
Maximum Recorded Rise or Fall

(This table lists only places at which gages were operating during all four tsunamis)

Station	1946	1952	1957	1960
	Feet	Feet	Feet	Feet
Honolulu, Hawaii	4.1	4.4	3.2+*	5.5+*
Sitka, Alaska	2.6	1.5	2.6	3.0
Neah Bay, Wash.	1.2	1.5	1.0	2.4
Crescent City, Calif.	5.9	6.8	4.3	10.9
San Francisco, Calif.	1.7	3.5	1.7	2.9
Port Hueneme, Calif.	5.5	4.7	3.5	8.8
Los Angeles (Berth 60), Calif.	2.5	2.0	2.1	5.0
La Jolla, Calif.	1.4	0.8	2.0	3.3
San Diego, Calif.	1.2	2.3	1.5	4.6

*Measured rise or fall. No extrapolation made for height beyond gage limit.

4. There is some evidence, however, to indicate that Richter scale magnitudes tend to underestimate the source parameters (fault length, width and uplift) and thus the tsunamigenic potential of very large earthquakes. Cumulative frequency vs. surface wave magnitude (M_s) plots show a linear trend for earthquakes with M_s values less than about 7.0 but for higher values of M_s the locus becomes increasingly steep tending toward vertical at M_s approximately equal 8.6. Therefore, it has been commonly assumed earthquakes with M_s greater than about 8.6 do not occur which may indeed be true. This, however, does not necessarily imply there is an upper limit on earthquake source parameters. Conventional analyses of earthquake energy spectra to determine M_s are frequency dependent. Chinnery and North (1975) hypothesize that because very large earthquakes produce spectra that have significant proportions of energy at frequencies below the band where M_s is normally measured and have dislocations which propagate for times significantly greater than 20 seconds that an upper limit to M_s will be observed no matter how large the true earthquake size.

III: Peru-Chile Trench As A Tsunamigenic Region

5. In terms of plate tectonics, the shallow seismic zone of western South America is a continuous boundary along which one plate (the Nazca plate) underthrusts the adjacent plate (the Americas plate). Kelleher (1974) cites numerous studies that indicate this plate motion is accomplished by large magnitude earthquakes, consequently any segment of the boundary that has not ruptured for many decades should be considered a zone of high risk. Moreover, Kelleher (1972) has observed that about once each century the entire fault segment near the Central Valley province

of central and southern Chile (approx. 32° -- 46° S) has fractured in a general north-south direction by a progression of large earthquakes and hypothesizes that a new series of quakes might start about the end of this century near Valparaiso (33° S) and progress southward.

6. Hayes (1966) states that crustal thinning beneath the trench is evidence the major tectonic forces involved are not laterally compressive and the absence of these compressive forces can be produced by a combination of faulting and flexure in the transition region of an ocean-continent margin. He also observes that almost all quake epicenters in the area lie shoreward of the axis of the trench.

7. Plafker and Savage (1970) report that records kept by the Japanese suggest that the subsea tectonic displacement of the 1960 Chile earthquake is probably greater than those associated with any of the earlier earthquakes during a period of nearly 500 years. Indeed, vertical movements of a larger regional scale appear to be characteristic of that portion of the trench extending from Columbia to southern Chile.

IV. Tsunami Source Characteristics

8. Figure 1 shows the contours of elevation of the initial sea surface deformation used as input to the simulation of the Chile tsunami of May 22, 1960. The shape of the deformation is inferred from the works of Plafker and Savage (1970) and Hwang, et. al., (1970). Plafker and Savage show the maximum upward vertical displacement of their preferred interpretation of the fault model to be about 10 m although the maximum observed upward vertical displacement was about 6 m. To avoid distorting the large scale features, the available data were smoothed, that is the maximum vertical uplift of 24 ft was chosen to compromise between the maximum predicted uplift of 10 m and maximum observed uplift of 6 m. Because the data indicate there was little downthrow (less than 2 m) associated with the tectonic deformation this feature was neglected in the model. The length of the deformation was determined from the spatial distribution of the epicenters of the initial quake and aftershocks as shown in Plafker and Savage (1970) and both its meridional and latitudinal extent are consistent with the area of the rupture zone as shown in Figure 2 (from Kelleher et. al., 1974).

9. There is little question that the deformation used for the simulation of the 1960 Chile tsunami is not known with the confidence of that used to simulate the Alaska tsunami of March 28, 1964. Nonetheless, there are enough data available to credibly reconstruct the bottom deformation which generated the tsunami.

10. Figure 3 shows the idealized axis of the Peru-Chile Trench as divided into 12 segments. A hypothetical sea surface deformation which generates a tsunami of approximately four intensity is centered in and aligned with segments one, eight and twelve. In order to facilitate comparison with results of a previous study (Houston, et. al., 1975b), the present hypothetical uplift is identical to that of the previous study.

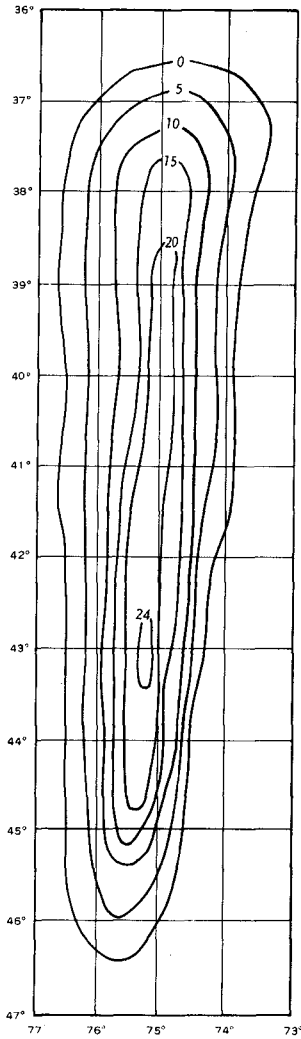


Figure 1. Contours of elevation of uplift used to simulate 1960 Chile earthquake.

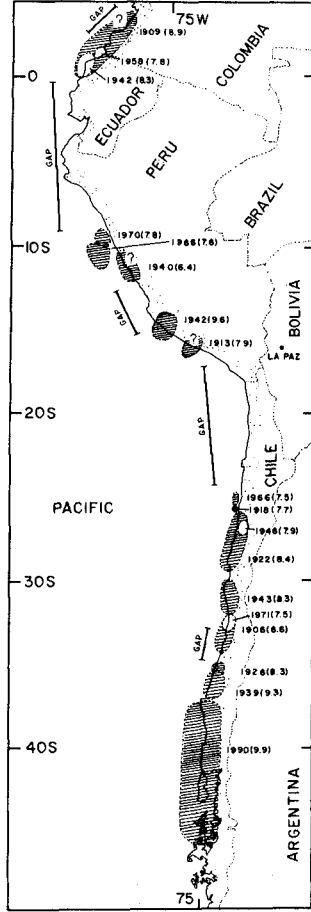
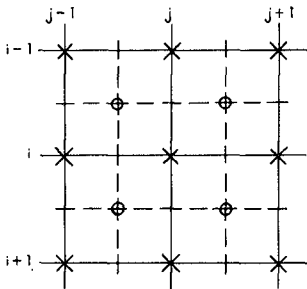


Figure 2. Rupture zones for large shallow earthquakes of this century and existing seismic gaps (after Kelleher, et. al., 1972).

SOUTH
PACIFIC OCEAN



LEGEND

- X - WATER ELEVATION, η
- O - WATER DEPTH, d
- - U VELOCITY IN DIRECTION, θ
- | - V VELOCITY IN DIRECTION, ϕ

Figure 4. Graphic representation of the finite difference grid.

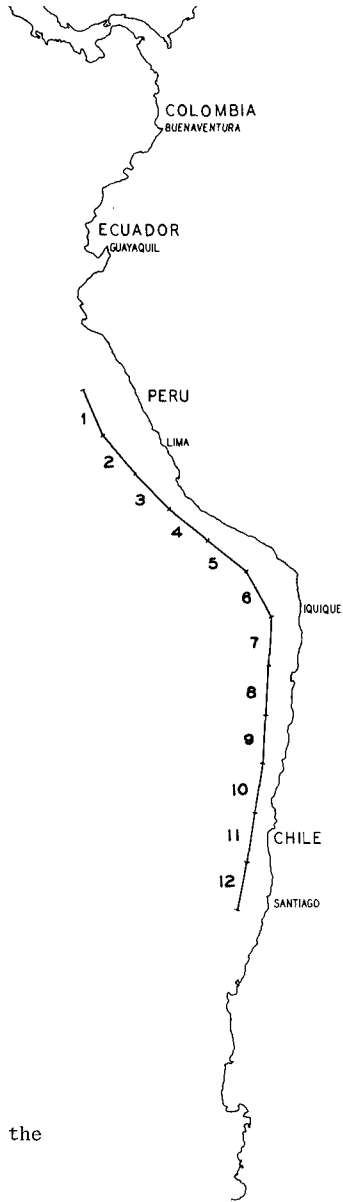


Figure 3. Idealized axis of Peru-Chile Trench showing 12 segments.

V. Computational Model

11. The numerical code used to simulate the 1960 Chile tsunami and the idealized hypothetical disturbances is based upon the linearized longwave equations obtained by vertically integrating the Navier-Stokes equations and equation of continuity. The equations used in the code are formulated in a spherical system as follow:

$$\frac{\partial U}{\partial t} = - \frac{g}{R_e} \frac{\partial \eta}{\partial \theta} \quad (1)$$

$$\frac{\partial V}{\partial t} = - \frac{g}{R_e \sin \phi} \frac{\partial \eta}{\partial \phi} \quad (2)$$

$$\frac{\partial \eta}{\partial t} = - \frac{1}{R_e \sin \phi} \left\{ \frac{\partial}{\partial \theta} (\eta+d) U \sin \theta + \frac{\partial}{\partial \phi} (\eta+d) V \right\} \quad (3)$$

where

U = depth-averaged wave velocity component in the θ direction

V = depth-averaged wave velocity component in the ϕ direction

g = acceleration due to gravity

R_e = radius of earth

η = wave elevation from reference water level

θ = latitude measured positive from north pole

ϕ = longitude measured positive eastward from Greenwich

d = local water depth

The validity of using linearized equations and the conditions under which they hold are discussed in Houston, et. al., (1975b).

12. In order to facilitate simulation of the tsunami of May 22, 1960, modifications were made to the code used for previous reports (Houston and Garcia, 1974; Garcia and Houston, 1975, Houston et. al., 1975b) to permit larger grids and faster execution. In the above mentioned reports the finite difference forms of Equations 1, 2, and 3 were solved by an alternating direction multistep technique whereby during the first half-time step, η and U were computed implicitly along lines of constant longitude and V explicitly along lines of constant latitude; in the second half-time step η and V are computed implicitly along line of constant latitude and U explicitly along lines of constant longitude. In the present report, Equations 4-6 are the finite difference forms of Equations 1-3.

$$U_{i,j}^{n+1/2} = U_{i,j}^{n-1/2} - \frac{g \Delta t}{R_e \Delta \theta} (\eta_{i+1,j} - \eta_{i,j})^n \quad (4)$$

$$V_{i,j}^{n+1/2} = V_{i,j}^{n-1/2} - \frac{g \Delta t}{R_e \Delta \phi \sin \theta} (\eta_{i,j+1} - \eta_{i,j})^n \quad (5)$$

$$\eta_{i,j}^{n+1} = \eta_{i,j}^n - \frac{1}{R_e \sin \theta} \left\{ \frac{\Delta t}{\Delta \theta} \left[(U d \sin \theta)_{i,j} - (U d \sin \theta)_{i-1,j} \right] + \frac{\Delta t}{\Delta \phi} \left[(V d)_{i,j} - (V d)_{i,j-1} \right] \right\}^{n+1/2} \quad (6)$$

(where it is assumed $n \ll d$)

Figure 4 shows the grid scheme used. The depth, d , is considered the averaged depth over the grid square j to $j+1$, i to $i+1$. Equations 4 and 5 are solved explicitly at the same halftime step along lines of constant longitude and latitude respectively. Equation 6 is then solved for η onehalf time step later. The boundary conditions, reflective at land boundaries and transmissive at the open ocean grid boundaries, are treated in the same manner as in the previous report (Houston, et. al., 1975b).

13. The explicit code was verified by comparing the results of hindcasting the Alaska tsunami of March 28, 1964 with results of hindcasting the same tsunami using the earlier implicit-explicit code. There was almost exact agreement of the results.

14. To further reduce the computational time required and to allow a greater area to be covered, a one-third by one-third degree grid was used instead of the onethird by one-fifth degree grid used in the previous report (Houston, et. al., 1975b). The validity of using the coarser grid to propagate tsunamis over the open ocean has been demonstrated by Houston, et. al., (1975a). Use of the latest bathymetric information for the Pacific Coast of the United States allows significant improvement in the detailing of the coastline and continental shelf area.

15. Depths for the open ocean portion of the numerical grid were interpolated from data of ocean depths averaged over areas of one-degree squares of latitude and longitude (Smith, et. al., 1966) available from the National Oceanographic Data Center. Normally, the numerical code interpolates depth data from one point per square degree to nine points per square degree. However, for the continental shelf area, the interpolation process was not used; instead data taken directly from bathymetric charts in a form compatible with the numerical code were inserted.

16. By the modifications made to the finite difference form of the equations used in the numerical code and the use of coarser depth grid, the computational time for similar problems is reduced by a factor of approximately three relative to the previous code.

VI. Procedure

17. To locate the hypothetical uplifts, the Peru-Chile Trench was divided in twelve equal segments as shown in Figure 3. An uplift of the same configuration used in the previous report (Houston, et. al., 1975b) was centered in segments 1, 8 and 12. Segment 1, although closest to the Pacific Coast of the continental United States, is least favorably oriented for producing large waves which propagate in that direction. Segment 8, although more favorably oriented for production of large waves, would be the segment most influenced by the "shadowing" effect of the reach of coast immediately northward of the perimeter of the uplift area. In principle, an uplift centered in segment 7 would experience more shadowing effect, but the uplift placed there would have had a significant proportion on land and therefore produce a smaller tsunami. The orientation of segment 12 is very similar to that of segment 8, that is, more favorably oriented than segment 1 for production of large waves in the direction of the United States, but without the "shadowing" effect experienced by segment 8. One therefore would expect the overall amplitudes of the tsunamis arriving at the Pacific Coast of the United States to be least for those produced by the uplift centered in segment 8 (excluding segment 7) with tsunamis originating in the remaining eight segments producing values between those of segments 1 and 12.

18. To compare the amplitude of the leading wave of the tsunami generated by the three hypothetical ground motions as a function of distance along the Pacific coast of the United States, the amplitudes were normalized to a depth of 600 ft. This is done by analytically solving a one-dimensional standing wave equation (Lamb, 1932). This is done in detail in (Houston et. al., 1975b) but will be recounted briefly here.

19. Combining the one-dimensional long-wave equation of motion and the continuity equation (in rectangular coordinates) yields the wave equation

$$\frac{\partial^2 \eta(x)}{\partial t^2} = g \frac{\partial}{\partial x} d \frac{\partial \eta(x)}{\partial x} \quad (7)$$

Under the assumption of simple harmonic motion,

$$\eta \propto \cos(\omega t + \epsilon) \quad (8)$$

and Equation 7 becomes

$$g \frac{\partial}{\partial x} \frac{\partial \eta(x)}{\partial x} + \omega^2 \eta(x) = 0 \quad (9)$$

If we now substitute $d(x) = d_a x/a$ and $K = \omega^2 a/g d_a$ where d_a is the water depth at the gage location some distance $x = a$ from the shoreline in Equation 9 we get,

$$\frac{\partial}{\partial x} \left[x \frac{\partial \eta(x)}{\partial x} \right] + K \eta(x) = 0 \quad (10)$$

The solution to Equation 10 is

$$\eta(x) = AJ_0(2k^{1/2} x^{1/2}) \quad (11)$$

or with the time dependence restored

$$\eta(x,t) = AJ_0(2k^{1/2} x^{1/2}) \cos(\omega t + \epsilon). \quad (12)$$

Because a tsunami has a very long wave length, we can assume the entire local water surface oscillates in the vicinity of some local depth, d , where $x \geq a$, thus

$$\eta(x) = C \cos(\omega t + \epsilon) \quad (13)$$

for $x \geq a$. Equating equations 12 and 13 yields

$$A = \frac{C}{J_0(2k^{1/2} a^{1/2})} \quad (14)$$

Therefore

$$\eta(x) = C \frac{J_0(2k^{1/2} x^{1/2})}{J_0(2k^{1/2} a^{1/2})} \cos(\omega t + \epsilon) \quad (15)$$

Solving for C at $x = a$

$$C = \frac{\eta(a)}{\cos(\omega t + \epsilon)} \quad (16)$$

From Equation 15,

$$\eta(b) = C \frac{J_0(2k^{1/2} b^{1/2})}{J_0(2k^{1/2} a^{1/2})} \cos(\omega t + \epsilon) \quad (17)$$

and substituting Equation 16

$$\eta(b) = \frac{J_0(2k^{1/2} b^{1/2})}{J_0(2k^{1/2} a^{1/2})} \eta(a) \quad (18)$$

Since $\eta(a)$ is known from the numerical simulation, η at $x = b$ can be determined. The values of a , b and d_a are determined from U. S. Coast and Geodetic Survey charts.

20. Because the method described above is one dimensional, it accounts for the effects of shoaling and reflection but not refraction or diffraction. However, since a tsunami wavelength is so great in waters deeper than 600 ft, few bathymetric features are large enough to significantly refract or diffract the waves over the relatively short distance from the nearest gage location to the 600 ft contour.

VII. Results

21. Table 2 shows a comparison of amplitudes of the leading wave of the 1960 Chili tsunami as recorded by tide gages at selected exposed locations with results of the numerical simulation at locations nearest the tide gages. To avoid the false appearance of exact agreement at locations such as Port Hueneme, the results of the numerical simulation are rounded to the nearest hundredth foot rather than the nearest tenth.

Table 2
Comparison of Elevations of Maximum Rise of Initial Wave
of 1960 Peru-Chile Tsunami to Numerical Simulation

<u>Gage Location</u>	<u>1960 Peru-Chile Tsunami (feet)</u>	<u>Numerical Simulation (feet)</u>
La Jolla, Calif.	1.4	1.05
San Clemente Island, Calif.	0.9	0.89
Port Hueneme, Calif.	1.9	1.86
Presidio (San Francisco), Calif.	1.3	1.46
Crescent City, Calif.	1.3	1.02
Neah Bay, Wash.	0.9	0.73

22. Ideally, the amplitudes resulting from the simulation should be slightly less than those recorded at corresponding tide gages because of shoaling of the wave into shallower gage locations. With the exception of the Presidio gage, this is indeed the case. Two factors which could account for the anomaly at Presidio are frictional dissipation of the actual tsunami over the shallow shelf seaward of Presidio (frictional effects are neglected in the governing equations of motion), and the inadequacy of the averaged depths used in the finite difference code to represent the small detail of the shelf accurately.

23. Figure 5 shows contours of sea surface elevation of the leading tsunami waves 15 hours after generation by simulation of the 1960 Chile quake. The reason for the extensive damage caused by the 1960 Chile tsunami in the Hawaiian Islands and Japan is evident as the highest section of the wave front is directed toward these locations. The preferential radiational patterns of non-circular uplifts are well documented (Takahashi et. al., 1962; Hatori, 1963).

24. Figure 6 shows the locations of the 64 gages used to determine the leading wave amplitude as a function of distance along the Pacific coast of the United States. Figures 7-9 are plots of the amplitude of the leading wave of tsunamis generated by hypothetical uplifts located in segments 1, 8 and 12 respectively. While tsunamis generated in segments 1 and 12 generally produce similar responses along the Pacific coast, the response to the tsunami generated in segment 8 is markedly less. This

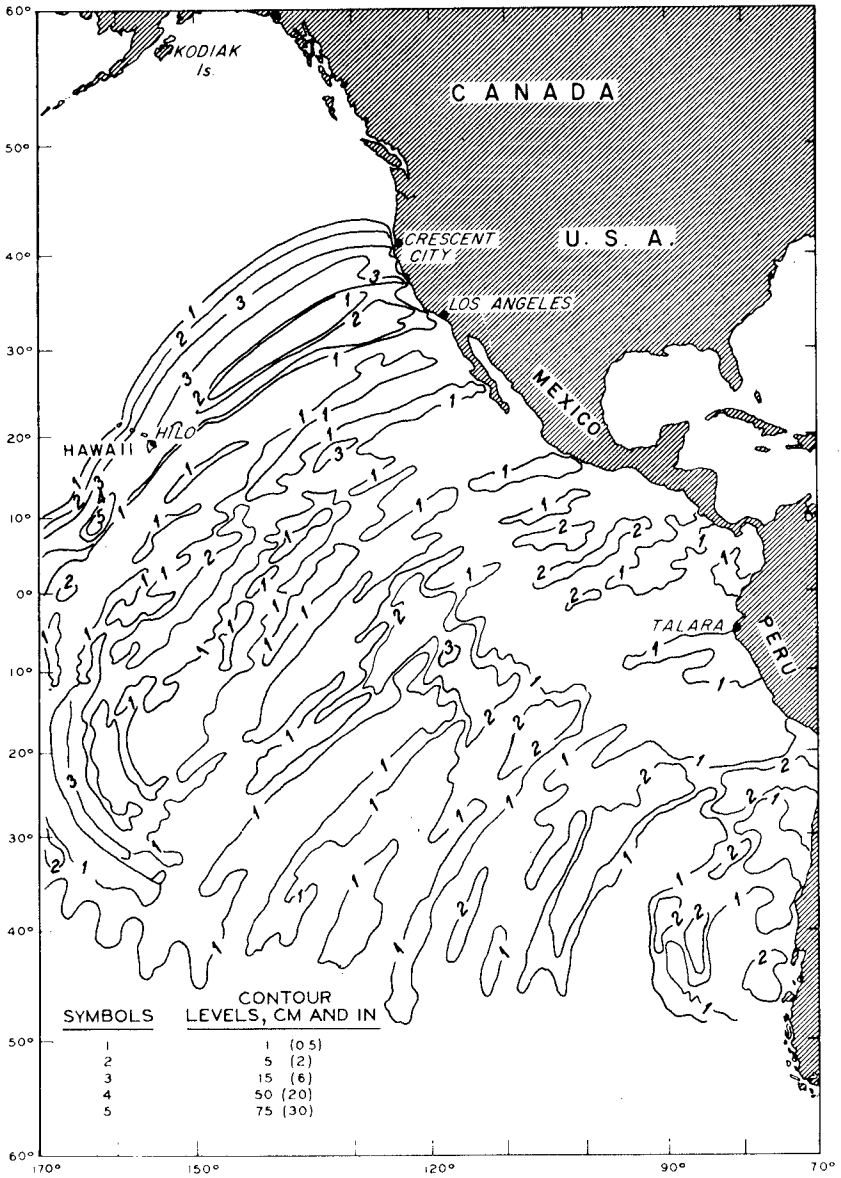


Figure 5. Contours of water-surface elevation for the leading tsunami waves 15 hrs after simulation of the 1960 Chile earthquake.

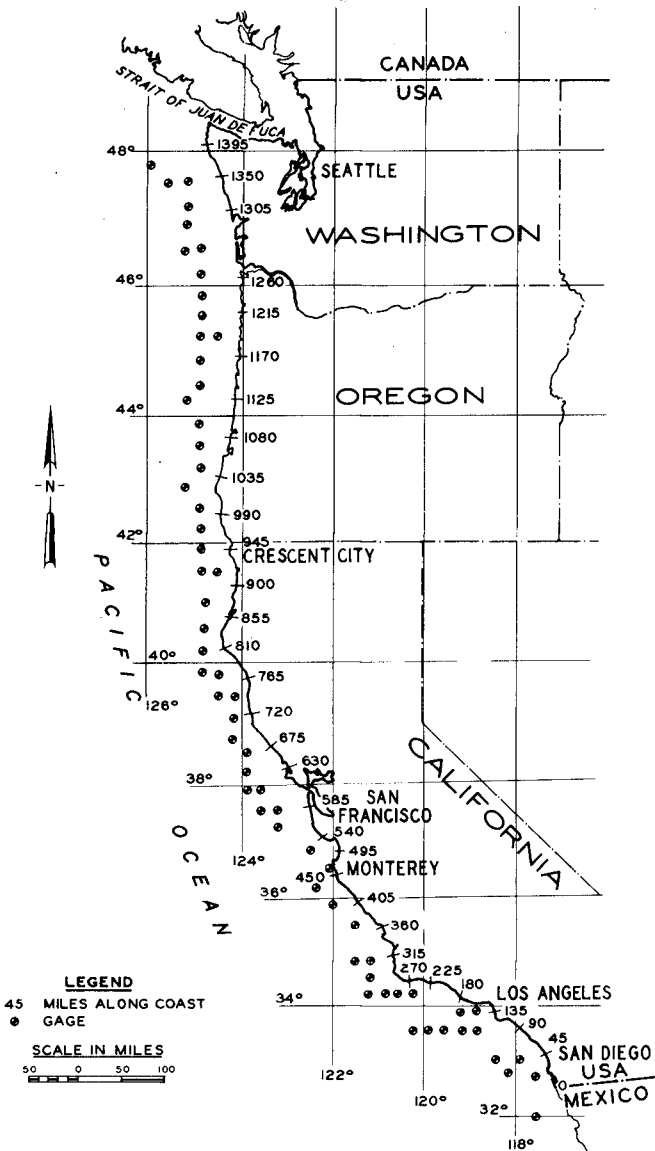


FIGURE 6. GAGE LOCATIONS ALONG THE WEST COAST

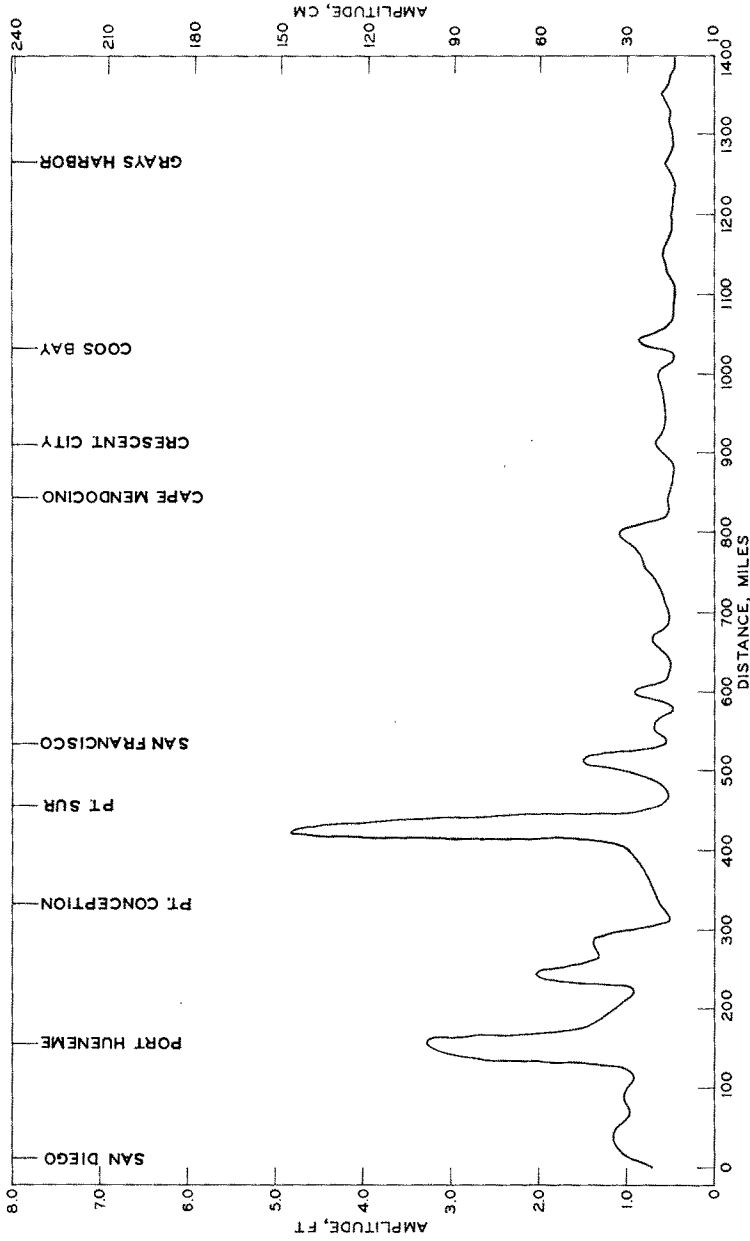


Figure 7. Wave amplitude of leading tsunami wave generated in Segment 1 versus distance of the recording gage from the U. S. - Mexico border.

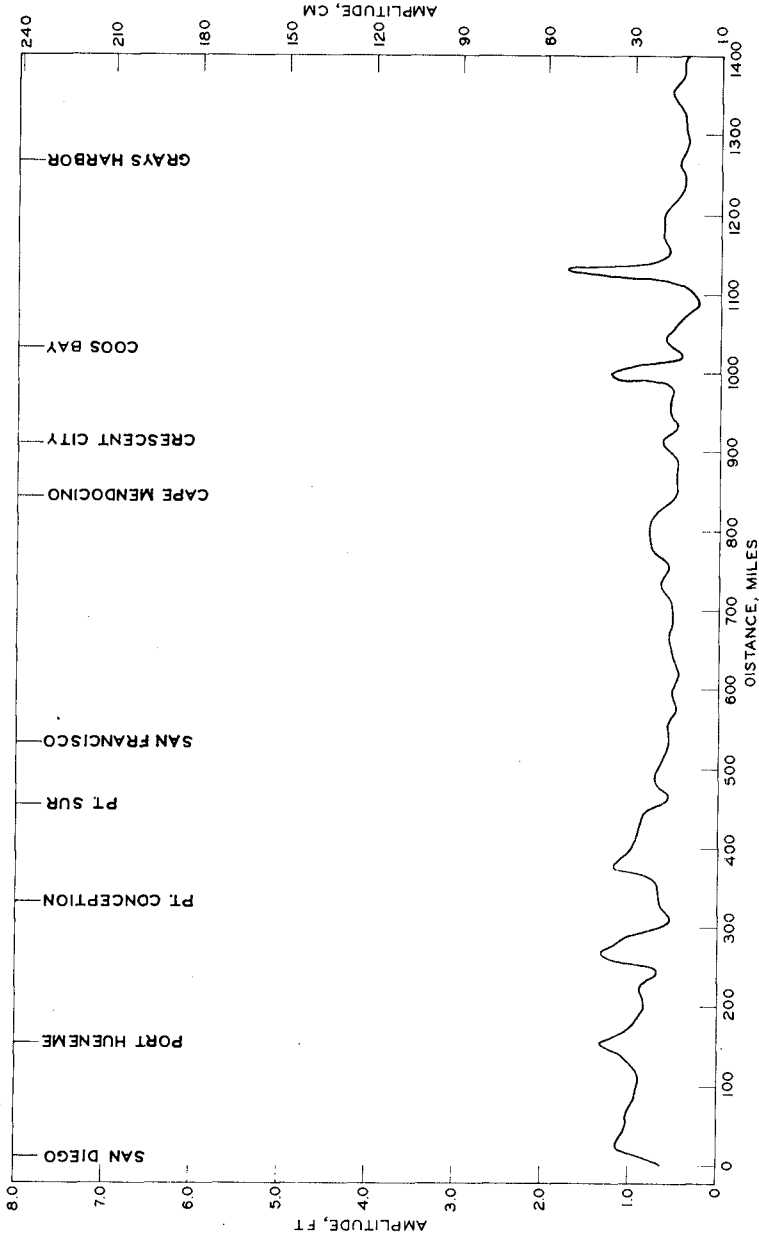


Figure 8. Wave Amplitude of leading tsunami wave generated in Segment 8 versus distance of the recording gage from the U. S. - Mexico border.

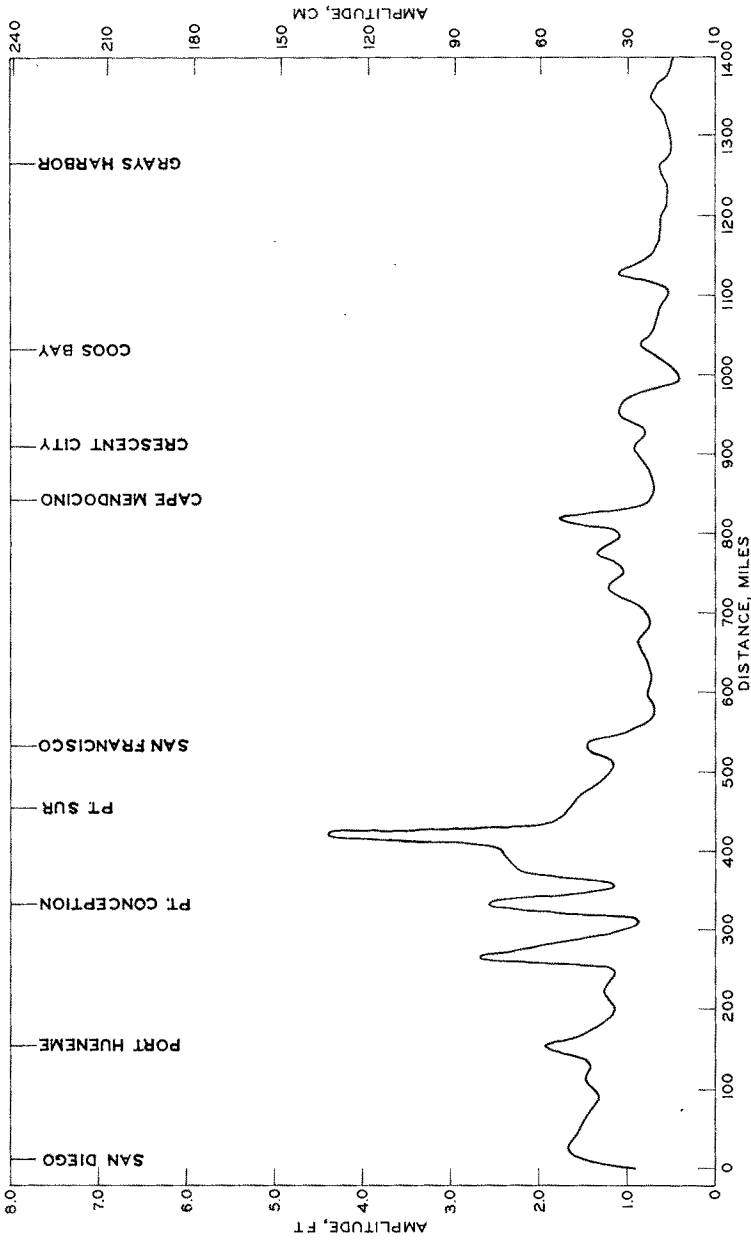


Figure 9. Wave Amplitude of leading tsunami wave generated in Segment I2 versus distance of the recording gage from the U. S. - Mexico border.

is probably due to the "shadowing" by the northwestward to southeastward oriented stretch of South American coast between 15 and 20 degrees south latitude. The generally low response exhibited along the coast from about San Diego to Los Angeles due to tsunamis generated in the three segments is probably the result of sheltering by the Channel Islands. The peaks shown in the vicinity of Port Hueneme (1.4 to 3.3 ft) agree fairly well with heights recorded there during past tsunamis, e.g., 1960 Chile, 2 ft; 1957 Aleutian, <3.5 ft. The validity of the large peaks shown in Figures 7 and 9 just south of Pt. Sur is unknown. There are no gage records existant near that location with which to compare results and it is alsb a relatively uninhabited stretch of coastline. The response of the remainder of coastline is relatively uniform with a maximum amplitude variation of about 1.5 feet. This is not unexpected due to the gradual eastward turning of the coastline as one proceeds northward.

VIII. Summary

25. The Peru-Chile Trench has a long recorded history as an area of generation of tsunamis which cause significant runup along the Pacific coast of the continental United States. An explicit numerical code has been developed and is demonstrated to adequately hindcast the Chile tsunami of 22 May 1960. The code is used to simulate the generation and propagation of tsunamis of approximately four intensity which originate in the Peru-Chile Trench. The amplitudes of the tsunamis are normalized to 600-ft depth and are plotted as a function of distance along the U. S. west coast from the Mexican to the Canadian Borders, thus allowing a relative comparison of the vulnerability of various locations along the U. S. west coast to tsunamis originating in the Peru-Chile Trench.

REFERENCES

1. Chinnery, Michael A. and North, Robert G., "The Frequency of Very Large Earthquakes," Science, Vol. 190, No. 4219, 1975.
2. Garcia, A. W. and Houston, J. R., "Type 16 Flood Insurance Study: Tsunami Predictions for Monterey and San Francisco Bays and Puget Sound," U. S. Army Waterways Experiment Station Report TR-H-75-17, 1975.
3. Hayes, D. E., "Geophysical Investigation of the Peru-Chile Trench," Marine Geology, Vol. 4, pp. 309-351, 1966.
4. Hatori, T., "Directivity of Tsunamis," Bulletin Earthquake Research Institute, Vol. 41, pp. 61-81, 1963.
5. Houston, J. R. and Garcia, A. W., "Type 16 Flood Insurance Study: Tsunami Predictions for Pacific Coastal Communities, U. S. Army Waterways Experiment Station Report TR-H-74-3, 1974.
6. Houston, J. R., Butler, H. L., Whalin, R. W. and Raney, D. C., "Probable Maximum Tsunami Runup for Distant Seismic Events - Islote Site, Puerto Rico," Amendment 23, NORCO-NP-1 PSAR, Puerto Rico Water Resources Authority, Fugro, Inc., May, 1975a.
7. Houston, J. R., Whalin, R. W., Garcia, A. W. and Butler, H. L., "Effect of Source Orientation and Location in the Aleutian Trench on Tsunami Amplitude along the Pacific Coast of the Continental United States," U. S. Army Waterways Experiment Station Report RR-H-75-4, 1975b.
8. Hwang, Li-San, Divoky, D. and Yuen, A., "Amchitka Tsunami Study," Tetra-Tech Report TC-177, 1970.
9. Kelleher, John A., "Rupture Zones of Large South American Earthquakes and some Predictions," J. Geophysical Research, Vol. 77, No. 11, pp. 2087-2103, 1972.
10. Kelleher, John, Sarvins, J., Rowlett, H., and McCann, W., "Why and Where Great Thrust Earthquakes Occur Along Island Arcs," J. Geophysical Research, Vol. 79, No. 32, pp. 4889-4899, 1974.
11. Lamb, Horace, Hydrodynamics, 6th ed., Dover Publications, New York, 1945.

12. Plafker, G., and Savage, J. C., "Mechanism of the Chilean Earthquakes of May 21 and 22, 1960, Geo. Soc. America Bull., Vol. 81, No. 4, pp. 1001-1030, 1970.
13. Smith, S. M., Menard, H. W. and Shorman, G., "World-Wide Ocean Depth and Continental Elevations Averaged for Areas Approximating One Degree Squares of Latitude and Longitude," Scripps Institution of Oceanography, La Jolla, Calif., March 1966.
14. Sykes, Lynn R., "Aftershock Zones of Great Earthquakes, Seismicity Gaps and Earthquake Prediction of Alaska and the Aleutians," J. Geophysical Research, Vol. 76, No. 32, pp. 8021-8041, 1971.
15. Symons, J. M. and Zetler, B. D., "The Tsunami of May 22, 1960 as recorded at Tide Stations," U. S. Department of Commerce, Coast and Geodetic Survey, Preliminary Report.
16. Takahashi, R. and Hatori, T., "A Model Experiment on the Tsunami Generation from a Bottom Deformation Area of Elliptic Shape," Bulletin Earthquake Research Institute, Vol. 40, pp. 873-883, 1962.

APPENDIX A: NOTATION

a	Distance along x-axis, ft
A	Amplitude constant
C	Amplitude constant
d	Depth of Water
d_a	Water depth a distance "a" from shore
e	Base of natural logarithms
g	Acceleration of gravity
J_0	$J_0()$ Zeroth order Bessel function of the first kind
k	Variable, ft^{-1}
L	Characteristics length of the wave in its direction of propagation
n	Refers to a time, $n\Delta t$
R_e	Radius of the earth
t	Time
U	Depth-averaged wave velocity component in the θ direction
V	Depth-averaged wave velocity component in the ϕ direction
x	Distance, ft
Δt	Length of a half-time step
ϵ	Phase factor
η	Wave elevation from reference water level
θ	Latitude measured from the north pole
ϕ	Longitude measured from Greenwich
ω	Wave frequency, sec^{-1}
∂	Partial differential

CHAPTER 62

NUMERICAL MODELS OF HUGE TSUNAMIS OFF THE SANRIKU COAST

Toshio Iwasaki
Professor of Tohoku University

Abstract

Although numerical computations of the generation and propagation of tsunamis are successfully achieved in recent years, modeling of their wave sources is still a big problem. Three kinds of wave source model, that is statistical, oceanographic and fault model, are studied in this paper.

It is found that the first model gives reasonable wave heights as shown in the previous paper, the second one presents roughly one half of those for the first model and the last one produces too small wave heights.

Based on the analysis of computed results, nature of undulations off from the shore boundary, directivity of wave propagation and the spindle-shaped leading part are discussed.

Comparing magnitude of various wave parameters for the leading wave along the minor axis of the wave source, it is shown that the long wave approximation modified by the slope effect illustrates the tsunamis in deep region of the sea and the slope effect is most dominant in shallow region.

INTRODUCTION

For the numerical computation of the generation and propagation of tsunamis, one of the most important problem is the knowledge of the wave sources, such as their location, their dimensions and the motion of the sea beds. A set of empirical equations were proposed by the author in 1974 which gave dimensions of source ellipse assuming the earthquake magnitude M or the tsunami magnitude m^1 (Iwasaki, 1974, hereafter referred to as the previous paper). A wave source derived from these equations is called a statistical model in this paper since these equations are obtained from data collected statistically.

However concerning on the motion of the sea bed, uniform distribution with a rumped function is assumed in this model. This seems to much simple to be realistic.

Dr. I. Aida tried to extract information on the crustal deformation from available data for the Tokachi-oki Tsunami in 1968²). Performing numerical experiments for several models with various distributions of sea bed deformation in the wave source area and comparing amplitudes of water surface oscillations thus calculated with actual tide gauge records, he selected a model. Since bay oscillations were not taken into account in his analysis which should be included in actual records, his method of

selection was somewhat immature. Nevertheless this is one of more developed model. Since it is derived by comparison with actual marigrams, this model is called an oceanographic model.

The Alaskan 1964 Earthquake was an epoch-making which investigation started the study of huge earthquakes along submarine ditches since survey on the bed deformation due to the earthquake was successfully achieved which made possible the interpretation of source mechanism³⁾. Until today there were three other examples for which survey on the bed deformation were accomplished, that is the Kanto 1923 Earthquake, the Nankaido 1946 Earthquake and the Chilean 1960 Earthquake. Owing to these experiences such huge earthquakes are explained as accompanied by the rupture of lithospheres. Thus although huge earthquakes off the Sanriku Coast have their sources in quite deep areas which make bottom survey impossible, estimation of source mechanism was presented by Dr. Kanamori⁴⁾⁵⁾⁶⁾. He urged that the most reliable and quantitative data concerning the deformation of the lithosphere could be obtained by his method. Distributions of sea bed deformations thus derived are called fault models.

It is intended in this paper to obtain the most creditable information of tsunami waves by comparing results of numerical computations for three kinds of source models mentioned above with each other and with observed values. Then a number of special characteristics inherent to tsunami waves are discussed.

SOURCE MODELS FOR THREE TSUNAMIS

The Sanriku Coast is the name of the coast which situates in northern part of the main island of Japan facing the Pacific Ocean stretching from 38° N to 41.5° N. Although a lot of tsunamis have attacked there in the past, there were only three cases for which scientific records were obtained among those which originated off this coast and caused severe damage. They are the Sanriku Tsunami in 1896, the Sanriku Tsunami in 1933 and the Tokachi-Oki Tsunami in 1968.

Fig. 1 shows the region of computation where the Japan Sea Trench lies almost parallel with the Japan Island arcs.

Numerical Computation scheme and the boundary conditions are mostly similar with those in the previous paper in which inertia terms and friction terms are included. Alteration is that Corioli's terms are added and the time and space steps are changed from 10 seconds to 6 seconds and from 20 km to 10 km respectively on account of resolution of networks. Depth at the shore boundary is assumed as 20 meters so that the sea bed is not exposed by negative waves.

Fig 2 shows the wave sources of the statistical models for three tsunamis mentioned above which locations are estimated from inverse-refraction diagrams. Dimensions are computed by the equations proposed by the previous paper such that,

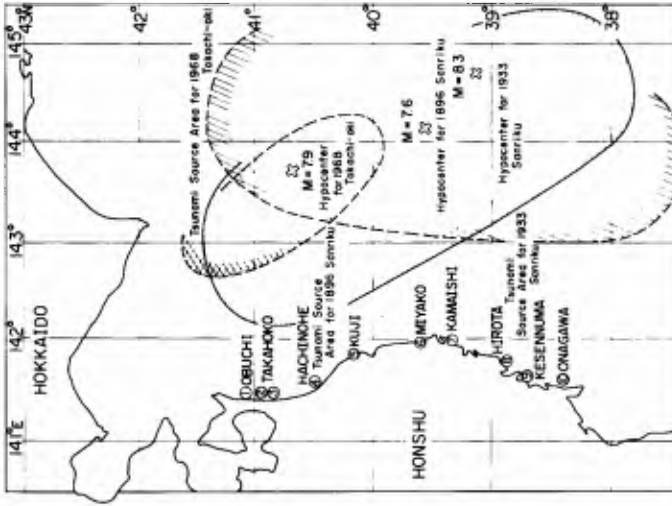


Fig. 2 Wave Sources of the Statistical Models for Three Tsunamis.

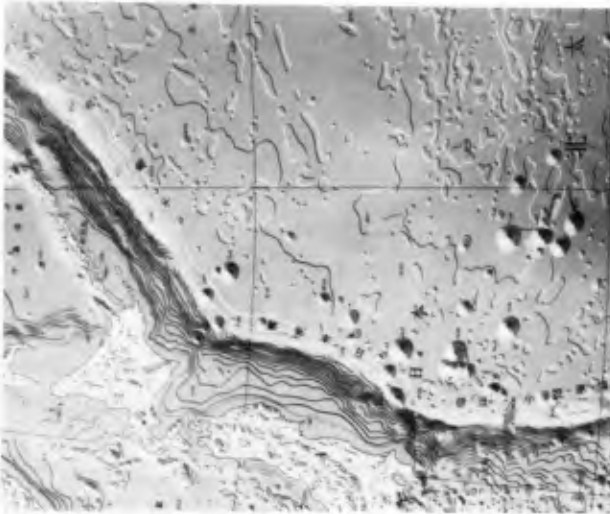


Fig. 1 Japan Islands and the Japan Sea Trench.

$$\ell = 10 \exp [(M - 6.27) / 0.76] \tag{1}$$

$$\epsilon = \tanh [1.5 \tanh ((\frac{\pi}{2012})^{1/2} \cdot \ell^{2/3})] \tag{2}$$

$$2a = \ell / \epsilon \tag{3}$$

$$2b = \ell (1 - \epsilon^2)^{1/2} / \epsilon \tag{4}$$

$$S = \pi ab \tag{5}$$

$$m = 2.61 M - 18.44 \tag{6}$$

$$E_t = 10 \exp [0.6 m + 11.4 - \log_{10} 9.8] \tag{7}$$

$$\eta_{\max} = (2E_t / w_o S)^{1/2} \tag{8}$$

, in which m and M are the magnitudes of tsunami and earthquake respectively. ϵ , ℓ , a, b, S are the eccentricity, the distance between foci in km, the half length of the major axis in km, that of the minor axis in km and the area of the source in square km respectively. And E_t is the tsunami energy in ton-meter units. Table 1 shows the dimensions of wave sources for these three tsunamis.

Table 1. Dimensions of the Wave Sources for Statistical Models

Tsunami		M	2a(km)	2b(km)	η_{\max} (m)	T(sec)
Sanriku	1896	7.6	307	272	8.15	96
Sanriku	1933	8.3	420	190	7.54	60
Tokachi-oki	1968	7.9	168	94	9.18	60

Although the earthquake magnitude of Sanriku 1896 was very small if compared with that of Sanriku 1933, the source area derived from the inverse refraction method was comparable with the latter. Dr. Kanamori illustrated this was due to the abnormal slow deformation with the time constant of about 100 secs of the former which was out of the instrument response at that time⁶). So, from eqs. (1) to (7), M is estimated so as to produce the dimensions of such source areas, which is $M = 8.12$. η_{\max} in table 1. is derived by eq. (8) using this value. T is the duration time of earth movement and is selected to be approximately equal to the time constant proposed by Dr. Kanamori.

For another two tsunamis, source dimensions are derived using values of M in table 1 and T are given as illustrated in the previous paper.

Fig. 3 shows the oceanographic model for the Tokachi-oki 1968 presented by Dr. Aida²). It is noted that there is a region of subsidence in northwest part which is separated by the longitude of 143°E from a region of upheaval where the maximum dislocation is roughly 5 m.

For another two tsunamis, such model is not obtained.

Fig. 4 shows fault parameters defining a faulting plane and its motions, which are a breadth W , a length L , a dislocation D , a dip direction ϕ , a dip angle δ and a slip angle λ with a duration time T and a rupture velocity ν . Displacements of the sea bottom can be computed from such fault parameters. Dr. Maruyama⁷⁾ and also Dr. Mansinha and Smylie⁸⁾ presented theories for them. Fig. 5 shows an example in which abscissa is in unit of breadth of the fault plane. In lower figure, the adverse dip slip planes with the dip angles are shown. In the upper figure, the vertical displacements of the surface of the earth are shown in unit of dip slip component. The length of horizontal bars show the horizontal displacements.

Fig. 6 shows the sea bed displacements for the Sanriku 1933 drawn from fig. 5 taking rupture velocity ν 3.5 km/sec, dip angle δ 45°, dip direction ϕ 90° and the time duration T 10 sec which were presented by Kanamori⁴⁾. As shown in this figure, a zone of upheaval is recognized in the east half and a zone of subsidence in the west half. The motion is the normal faulting without the strike component. There is some ambiguity on the wave source motion. Thus we assume the displacement started at the fault line and propagated to east- and westward.

Fig. 7 shows for the 1969 Tsunami presented by Dr. K. Abe⁹⁾. It was said this earthquake was caused by the low angle thrust faulting with a considerable strike-slip component, in which the ocean side underthrust beneath the continent.

Wave sources thus obtained are summarized in table 2.

Table 2 Wave sources

Tsunamis	Statistical models	Oceanographic models	Fault models
1896	x	-	-
1933	x	-	x
1968	x	x	x

MAXIMUM WAVE ELEVATIONS ABOVE STILL WATER LEVEL

A lot of data on the inundation levels were reported by many sources. Fig. 8, 9 and 10 show such data collected. Northern to Hachinohe, the coastline is monotonous with sloping beach. Since these area was still undeveloped, reliable informations were not available except few places. Remaining area is composed of a large number of bays with various size, shape and topography. Five bays which are Kuji, Miyako, Kamaishi, Hirota and Kesenuma and Onagawa are shown in more detail with dotted contour lines at bay entrances. It is noted that remarkable discrepancy is

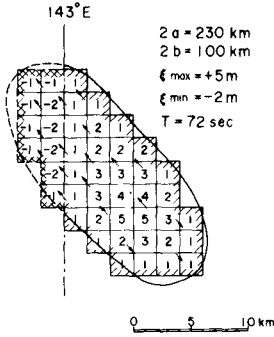


Fig. 3 The Oceanographic Model for the Tokachi-oki Tsunami in 1968 by Aida.

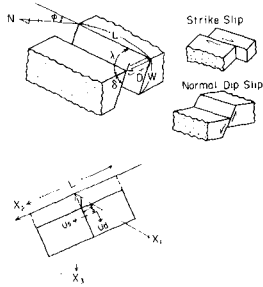


Fig. 4 Fault Parameters which define a Faulting Plane and its Motion.

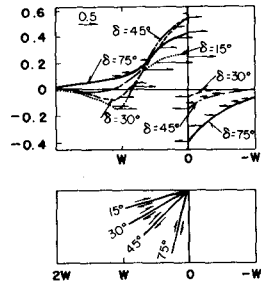


Fig. 5 Vertical and Horizontal Displacements of the Sea Bed due to the Adverse Dip Slip Faulting. (The Vertical Scale is in Unit of Dip Slip Component.)

W = 100 km T = 10 sec
 L = 185 km phi = 90 degrees
 v = 3.5 km/sec delta = 45 degrees

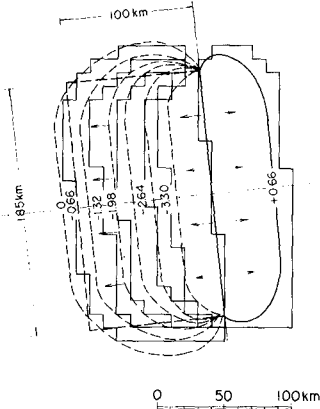


Fig. 6 The Fault Model for the Sanriku Tsunami in 1933.

W = 100 km
 L = 150 km
 dislocation 4 m
 rupture velocity 3.5 km/sec
 T = 48 sec

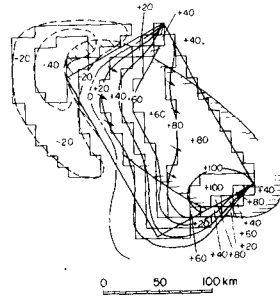


Fig. 7 The Fault Model for the Tokachi-oki Tsunami in 1968 by Abe.

recognized between maximum wave heights even in a same bay. So it is extremely difficult to examine justifiability of source models by comparison of numerical results with observed values.

One procedure tried in this paper is to calculate wave heights at 5m deep for sloping beach areas or those at bay mouths for remaining areas from those at output points which are 20 kms off the shore boundaries by the Green's law. These are shown in frames also in figs 8, 9 and 10.

It is noticed that computed wave heights by the statistical model give reasonable values at Kuji, Miyako, Kamaishi, Hirota and Kesennuma for the Sanriku 1896 Tsunami, but too large at Hachinohe and Onagawa. Also those derived for the Sanriku 1933 by the statistical model which are denoted by S in frames give acceptable values except Onagawa. However the statistical model for the Tokachi-oki 1968 produces too large wave heights.

The computed wave heights by the oceanographic model are probably too small and it seems that they should be doubled.

Results by the fault models are mostly very much small and those for the 1933 tsunami should be multiplied by 18 times in order to give comparable values with results by the statistical model. Similarly those for the 1968 tsunami are to be multiplied by 8 times.

However it should be noted that such estimation is reduced simply by comparison of numerals shown in figures without detailed inspection on hydrodynamic effects due to locality.

SURFACE OSCILLATIONS AT OUTPUT POINTS IN NEAR-COAST OFFSHORE REGION

In spite of the difference of the wave heights with each other, it is possible to examine oscillation pattern at output points in nearcoast offshore region since water depths of these points are deep enough such that effects of non-linear terms in equations of motion can be neglected and surface oscillations thus computed are linearly proportional to the amount of sea bed deformation which make possible relative comparison of wave pattern with each other by adjusting vertical scales.

Fig. 11 shows surface oscillations of the Sanriku 1933 Tsunami, in which full lines are results by the statistical model and dotted lines are plotted of values multiplied by 20 times of results by the fault model. It is noticed that oscillation patterns are not so different except Obuchi and Hachinohe where free oscillations may be invoked in the water body bounded by the Hokkaido and the Honshu which are superposed on the oscillations over the continental shelf. Since the wave source is roughly parallel with the meridian line, the tsunami waves proceed to the coast as if one dimensional waves. So such indifferent pattern of undulations with the distributions of the sea bed movement lead an expectation such that one depressed and one elevated wave may be appeared forcedly at first which are not be effected remarkably by higher order components of the bed movement and following oscillations may be free oscillations over the

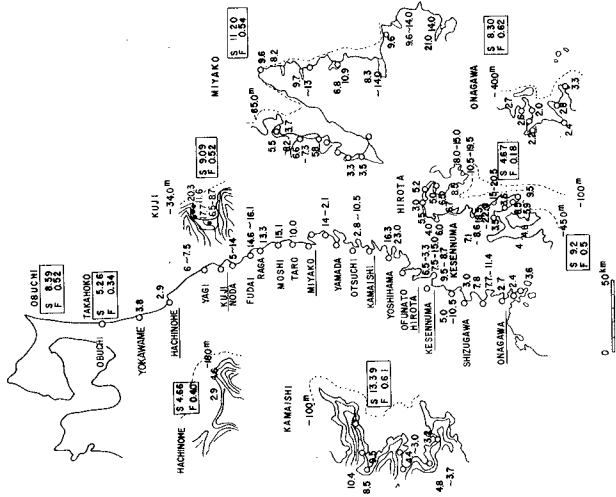


Fig. 9 Maximum Water Levels above MSL in meters for the Sanriku Tsunami in 1933. (Figures in Frames are computed Values. S for the Statistical Model. F for the Fault Model.)

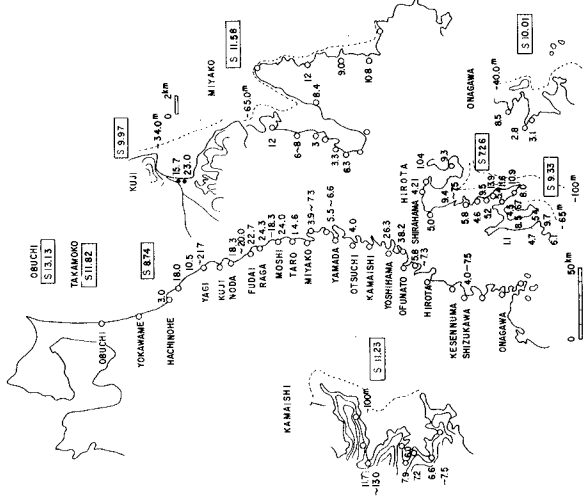


Fig. 8 Maximum Water Levels above MSL in meters for the Sanriku Tsunami in 1896. (Figures in Frames are computed Values. S for the Statistical Model. F for the Fault Model.)

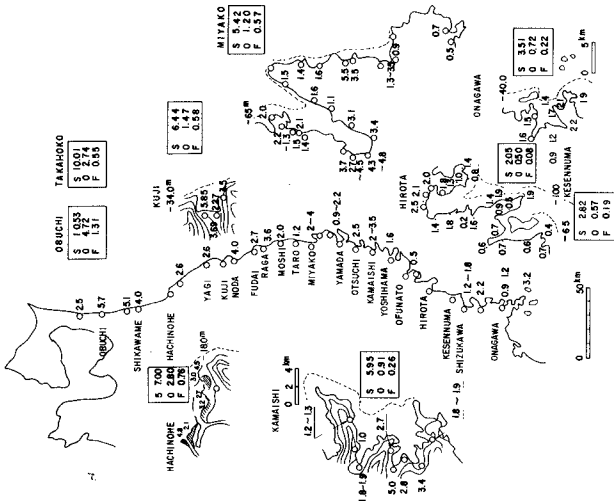


Fig. 10 Maximum Water Levels above T.P. in meters for the Tokachi-oki Tsunami in 1968. (Figures in Frames are computed Values. S for the Statistical Model O for the Oceanographic Model F for the Fault Model.)

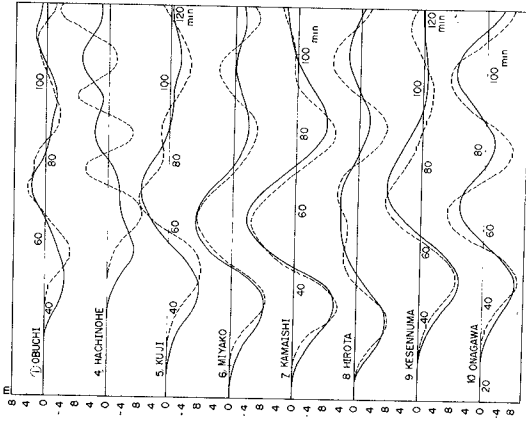


Fig. 11 Surface Oscillations of the Sanriku Tsunami in 1933.

continental shelf.

Oscillations of the 1968 tsunami are somewhat more complicated as shown in fig. 12. Full lines show waves by the statistical model, broken lines are obtained by the oceanographic one which are multiplied twice and dotted lines are those by the fault model multiplied by eight times. It is noticed that the first oscillations reflect the different pattern of the source movement. For the oceanographic and the fault models, the negative waves appear at first at Takahoko and Hachinohe and the positive waves appear at Miyako and Kamaishi which are also reported in field survey. At Kuji the sign of the first waves is opposite with each other. The marigram of this tsunami supports the oceanographic model. Free oscillations of the water body on the continental shelf and those of the water body bounded by the Hokkaido and the Honshu are also noticed.

By the way, readings of actual marigrams are plotted in figures for Hachinohe and Miyako by lines connecting white circles. However they seem to be incorrect informations, since time scale of original recording is too much reduced to make possible one week long recording in a sheet which is attached around a drum rotating once during a week.

SPATIAL WAVE FORMS

Fig. 13 and fig. 14 show spatial wave forms of the 1968 tsunamis by the statistical and the fault models respectively, in which horizontal axis are taken along the 41°N latitude between the most eastward end of the wave source and the coastal boundary at Takahoko. Figures a) are on the progressive stage, figures b) are when the leading fronts have arrived just at the coast and figures c) are when the maximum waves appear there.

The non uniform distributions of the sea bed displacement are reflected on the wave forms in figures a) and b) for progressive stages. The steepness of the leading waves is the order of 10^{-5} , which is very small when compared with those of surface waves.

At the coast, there occurred standing waves and the maximum deviations from the still water are nearly twice of those of the progressive waves.

The spatial wave forms along the major and the minor axis of the source ellipse computed by the fault model for the 1933 tsunami are shown in fig. 15, in which lowest figures show the bottom topography. Along the major axis a depression wave is generated at first, which is disappeared in relatively short period. However along the minor axis, waves are propagated as if one dimensional waves, in which the leading part is composed of one negative and one positive wave. The dispersive nature is recognized and there seems to be so called ripples behind the leading part.

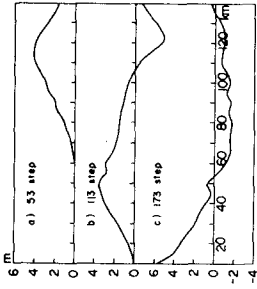


Fig. 13 Spatial Wave Forms of the Tokachi-oki Tsunami in 1968 by the Statistical Model.

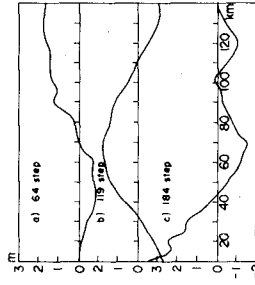


Fig. 14 Spatial Wave Forms of the Tokachi-oki Tsunami in 1968 by the Fault Model.

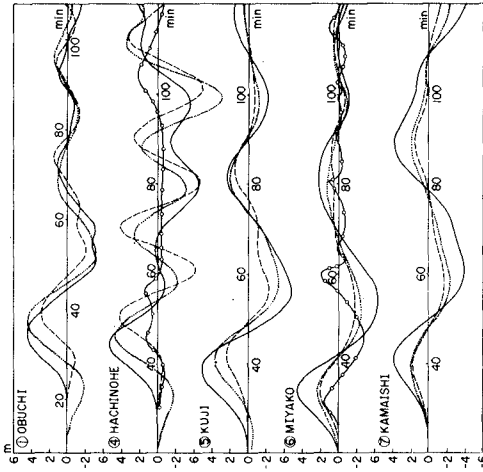


Fig. 12 Surface Oscillations of the Tokachi-oki Tsunami in 1968.

WAVE PARAMETERS ALONG THE MINOR AXIS

Various wave parameters are computed for the leading wave along the minor axis, which are the non-linear parameter a/h , the long wave parameter $(h/l)^2$, the slope parameter $h_x l/h$ and the Ursell's parameter $U = al^2/h^3$, in which a , h and h_x are amplitude, depth and slope respectively and Ursell's parameters are computed by Dr. Raichlen and Dr. Hammack's method for which the inflection point of the leading waves is selected to define the slope and points of intersection of the tangent with the undisturbed and the highest wave elevations define the length l by their horizontal distance.

Fig. 16 shows these no-dimensional parameters with depth as abscissa. Where it is deeper than 3000 meters, the long wave parameter is nearly equal to the slope parameter and is much larger than the non-linear parameter. Shallower than 3000 meters, the slope parameters are dominant to the other two. So in a deep sea tsunami can be approximated by the long wave theory with modification by the slope effect. However in a shallower region theories which take into account the slope effect such as Green's law are most powerful for explaining tsunami waves.

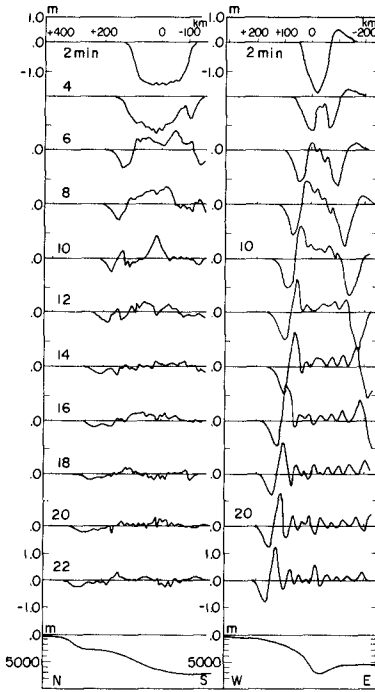
TWO DIMENSIONAL PROPAGATION

Thus far various aspects of tsunami waves are discussed mostly in one dimensional. However computations are made in two dimensional horizontal scheme, so features on two dimensional propagation are studied here.

Fig. 17, 18 and 19 show wave contours at 10, 20 and 30 minutes after the outbreak of the Sanriku earthquake in 1933 in which contours are drawn in every 10 cms by thin full lines and those in every 50 cms by heavy lines from results by the fault model. In fig. 15 it is recognized that the first dropdown proceeds westwards followed by ascension as reaction and the first rising up proceeds eastward with the following falling limb with large size. In fig. 17 these are found in relatively limited area which are spindle-shaped. Behind them, corrugated patches parallel with the major axis are noticed. As shown in fig. 18 and 19, wave fronts are becoming distorted by effects of bottom topography tending to be parallel with bottom contours. However the frontal spindles seem their size and the maximum wave height unchanged remarkably during procession.

The theory of the long wave approximation in shallow water with constant depth derived by Dr. Kajiura gives the following equation for the surface elevations.¹⁰⁾

$$\zeta(x, y, t) = \iint_S H_S \cdot P \, ds \quad (9)$$



a) along the Major Axis. b) along the Minor Axis.

Fig. 15 Spatial Wave Forms of the Sanriku Tsunami in 1933 by the Fault Model.

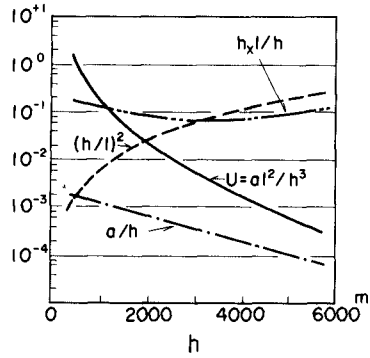


Fig. 16 Wave Parameters of the Leading Wave along the Minor Axis.

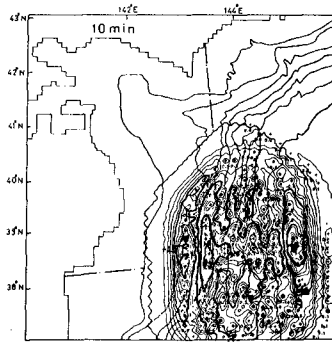


Fig. 17 Wave Contours at 10 min. after the Outbreak of the Sanriku Earthquake in 1933.

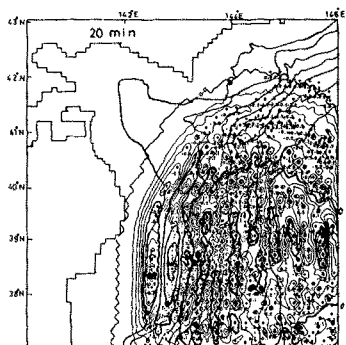


Fig. 18 Wave Contours at 20 min. after the Outbreak of the Sanriku Earthquake in 1933.

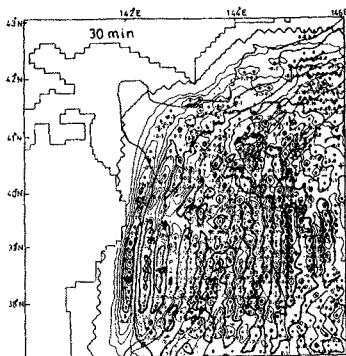


Fig. 19 Wave Contours at 30 min. after the Outbreak of the Sanriku Earthquake in 1933.

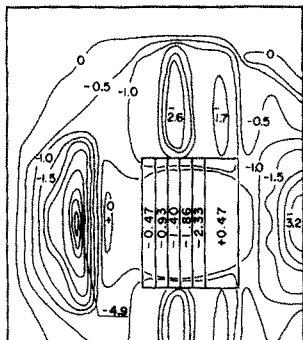


Fig. 20 Wave Contours at 20 min. after the Outbreak of an Earthquake computed by Kajiura's Theory setting the Distributions of the Sea Bed Displacements at the Sanriku Earthquake in 1933. Depth is assumed uniformly 3000 m.

, in which $P = -\frac{1}{2\pi} \operatorname{ct}((ct)^2 - r^2) - \frac{3}{2}$, $c = (gh)^{1/2}$ and $r^2 = (x-x_0)^2 + (y-y_0)^2$. H_s is the water surface elevation above still water level at the wave source (x_0, y_0) , h is the water depth and ds is a surface element of the source area S respectively.

Assuming the same distributions of the surface elevation with those of the bottom displacements of the fault model for the 1933 tsunami and taking the water depth as 3000 m uniformly, wave height distributions 20 minutes after the outbreak of the earthquake are roughly estimated by eq. (9) which are shown in fig. 20. The spindle-shaped hump and depression around both ends of the minor axis and corrugated patches around both ends of the major axis are also noticed, which can be illustrated that contributions from source subelements are inaugurated along the minor axis and are cancelled along the major axis with each other since in the wave source the positive half and the negative half lie almost parallel with the major axis.

CONCLUSIONS

Although slight modifications are still necessary on the method of assuming locations and dimensions of wave sources, it is concluded that statistical models give reasonable wave heights at near-coast offshore points. Oceanographic model is not recommended since trial and error procedure to obtain it is troublesome and method of evaluation for selection of the most suitable model is doubtful.

Perhaps fault models are the most reliable ones as quoted by Dr. Kanamori on relative distributions of sea bed deformations. However the absolute values proposed until now are too much small.

The leading part of tsunami is generated so as to reflect the pattern of the sea bed dislocation, propagates under the effect of dispersion and exits the forced oscillation in near-coast region where free oscillations follow it which periods are governed by oscillation systems there.

For the Sanriku 1933 tsunami, it is found a depression wave generated along the major axis disappeared in relatively short period and one drop down and one ascension form the leading part along the minor axis which proceed to the shallower region without change the wave height remarkably. This leading part forms spindle-shaped two dimensionally. Such directivity of tsunami is illustrated by the bottom movement with opposite sign against the major axis.

ACKNOWLEDGEMENT

The author wishes his acknowledgement to Master of Eng. Akira Mano, a graduate student of Tohoku University for his excellent achievement of

numerical calculations employing NEAC 2230-700 and CDC 6600.

REFERENCES

- 1) T. Iwasaki, " Computer Aid for Optimum Design of Tsunami Waves." Proc. of the 14th Coastal Engineering, vol. 1 (1974)
- 2) I. Aida, " Numerical Experiments for Tsunamis caused by Moving Deformations of the Sea Bottom." Bull. Earthquake Research Institute vol. 47 (1969)
- 3) for example, E. Berg, D.C. Cox, A.S. Furumoto, K. Kajiura, H. Kawasumi and E. Shima, " Field Survey of the Tsunami of 28 March 1964 in Alaska, and Conclusions as to the Origin of the Major Tsunami." Hawaii Inst. of Geophysics, Univ. of Hawaii (1970)
- 4) H. Kanamori, " Seismological Evidence for a Lithospheric Normal Faulting - The Sanriku Earthquake of 1933." Phys. Earth Planet. Interiors, vol. 4 (1971)
- 5) H. Kanamori, " Focal Mechanism of the Tokachi-oki Earthquake of May 16, 1968: Contortion of the Lithosphere at a Junction of two Trenches." Tectonophysics, vol. 12 (1971)
- 6) H. Kanamori, " Mechanism of Tsunami Earthquakes." Phys. Earth Planet. Interiors, vol. 6 (1972)
- 7) T. Maruyama, " Statistical Elastic Dislocations in a Infinite and Semi-Infinite Medium." Bull. Earthquake Research Institute, vol. 42 (1964)
- 8) L. Mansinha and D.E. Smylie, " The Displacement Fields of Inclined Faults." Bull. Seismological Society of America, vol. 61 (1971)
- 9) K. Abe, " Tsunami and Mechanism of Great Earthquakes." Phys. Earth Planet. Interiors, vol. 7 (1973)
- 10) K. Kajiura, " The Leading Wave of a Tsunami." Bull. Earthquake Research Institute, vol. 41 (1963)

CHAPTER 63

3-D HYDRAULIC MODEL OF WAVES GENERATED BY DISPLACEMENTS

by

Shin-Lin Liu* and R. L. Wiegel**

ABSTRACT

Measurements were made of the water waves generated by the horizontal motion of submerged plungers. The results obtained in a three-dimensional hydraulic model experiment, using a plunger 0.5 ft. wide and 0.25 ft. high, were compared with both the experimental results and theory for the two-dimensional case. It was found that at a given location the ratio of the elevation above the still water level (SWL) of the first wave (the largest wave of the group for the range of variables tested) to the displacement of the plunger (H_3/λ) was found to be dependent upon the Froude Number N_{Favg} (based upon the average plunger speed and the water depth) and upon the ratio of the height of the plunger to the water depth (D/d). For a constant value of θ , H_3/λ increased with increasing N_{Favg} and D/d . A few additional tests were made using a plunger 2.0 ft. wide and 0.25 ft. high. The results show that H_3/λ depends also upon the ratio of water depth to the width of the plunger (d/W).

INTRODUCTION

The generation of waves by a tectonic displacement has been solved for the two-dimensional case by Garcia (1972) using a numerical model (ABMAC, Arbitrary Boundary Marker And Cell). Garcia compared the results from his

*Engineer, General Electric Company, San Jose, California

**Professor of Civil Engineering, University of California, Berkeley

numerical model with those obtained from a hydraulic model study of several types of boundary motions for a fairly large range of Froude numbers and found that the numerical model is quite good. It appears, however, that the largest existing digital computer in the U.S. does not have the capability to permit the use of ABMAC to solve three-dimensional problems of this type, except for the case of radial symmetry. The two-dimensional case is useful as an approximation to some prototype cases. For other cases it is not. Owing to this it was decided to test the applicability of the two-dimensional numerical results in three-dimensional cases, making use of a hydraulic model.

LABORATORY ARRANGEMENTS AND PROCEDURES

The experimental arrangements are shown in Fig. 1. The experiments were conducted in a tank which was 5.5 feet wide by 16 feet long by a little less than 3 feet deep. "Steps" were placed along one side wall of the tank. They were 0.50 ft. and 2.00 ft. wide, with both of them being 0.25 ft. high, containing a movable plunger. The design and operation of the mechanism used to cause the plungers in the steps to move horizontally has been described by Garcia (1972) and by Das and Wiegel (1972).

A rotating boom was constructed which pivoted about a pin connection which was located at the centerline of the step, above the front end of the plunger. Parallel wire resistance wave gages (Wiegel, 1953) were mounted on the boom to sense the disturbance of the water surface. A transducer to measure the displacement of the plunger was installed between the tank frame and the moving arm (Fig. 1). The outputs of the wave gages and the plunger displacement transducer were amplified and recorded on an 8-channel strip chart recorder. A number of tests were made to check the reproducibility of results, which was found to be excellent.

Falling weights were used to drive the plunger, with the total plunger displacement (λ) occurring during a time interval τ .

Wave-absorbing material was placed along the three sides of the tank to minimize reflections.

TWO-DIMENSIONAL TESTS

A series of tests were made to be certain that the new arrangements were such that Garcia's (1972) hydraulic model studies could be reproduced. To do this a vertical training wall was placed alongside the $W = 0.50$ ft. wide step, extending the entire length of the tank. Thus, a two-dimensional channel was formed, as in Garcia's tests. A typical example of a water surface profile is shown in Fig. 2. The agreement between

measurements and predictions made using the numerical model of Garcia was found to be very good.

THREE-DIMENSIONAL TESTS

The training wall described in the previous section was removed, and the waves were permitted to radiate in an entire half plane. The ratio of the first wave crest elevation above the SWL (measured along the wall) to the equivalent measurement for the two-dimension case (H_3/H_2), as a function of the normalized distance from the plunger (x/d) is shown in Fig. 3. In this figure, λ is the total displacement of the plunger, W is the width of the plunger, τ is the time required for the displacement to occur, N_{Favg} is the Froude number (V_{avg}/\sqrt{gd}), V_{avg} is the average speed of the plunger movement (λ/τ), g is the acceleration of gravity and d is the water depth in the tank. For the range of conditions tested (three values of Froude number, N_{Favg}), the first wave was the highest wave. It is evident for a source of the type tested, that H_3 is much smaller than H_2 , except near the source. The averages of the data shown in Fig. 4 have been plotted on logarithmic paper in Fig. 4. It can be seen that H_3/H_2 decreases as $(x/d)^{-3/5}$ for values for $x/d > 0.7$. For x/d greater than about 6, H_3/H_2 is less than 0.2.

Some data on the surface spread of the waves are given in Fig. 5. Data for two of these cases were plotted in Fig. 6. The elevations of the first crest above SWL were measured at a radius of 0.50 ft. for $0 \leq \theta \leq 90$ degrees. These values of H_3 were plotted versus $r \sin \theta$, and it was found that there was a nearly linear relationship between the two variables. In these tests $d = 0.50$ ft., and the water depth above the step was 0.25 ft. ($D/d = 0.50$).

A number of additional tests were made, for values of $d = 4, 5, 6, 7, 8$ and 9 inches. The relationship between the Froude number and H_3/λ is shown in Fig. 7. The data shown in Fig. 7 and tabulated in Table 1 were obtained along the centerline in the direction of the plunger motion. These data are for a constant average plunger speed, V_{avg} , with different water depths. The two-dimensional results obtained by Garcia (1972) for a constant water depth, at $x = 5$ ft., are also shown in Fig. 7 for comparison. Although the location at which the measurements were made is different, it is still interesting to note that the relationship between H_3/λ and N_{Favg} has a less steep slope than is the case for the results from the two-dimensional tests. It also can be seen from Fig. 7 that for a constant Froude number the ratio H_3/λ tends to vary only slightly with λ/d within the range of variables tested. Furthermore, the ratio H_3/λ tends to be linearly related to the Froude number for values of Froude number between 0.3 and 0.4.

The variables affecting the ratio of the normalized crest elevation of the first wave for the 0.50 ft. wide plunger are the ratios, x/d , D/d , λ/d , the angle θ as defined in Fig. 5, and the Froude number. In order to study the relationship between H_3/λ and D/d , the other dimensionless variables were kept constant. The Froude number was kept constant by varying the plunger speed for different water depths. The desired plunger speed was obtained by using different weights that were dropped to move the plunger. To hold x/d and λ/d constant, a set of appropriate distances along the x axis and plunger displacements were chosen. The values of these parameters are given in Table 2. The results for different values of θ are shown in Fig. 8 and tabulated in Table 3. The locations at which the measurements were made are shown in Fig. 9.

The work described above (Table 3 and Fig. 8) was extended to include additional values of θ , up to 180 degrees. The results are shown in Tables 4 and 5 and in Fig. 10. A comparison of the results given in the three tables for values of $\theta = 0, 15, 30, 45$ and 60 degrees shows that the results are closely reproducible.

The curves shown in Fig. 10 were cross-plotted in Fig. 11. For large values of D/d , no data for $\theta > 135$ degrees are shown as there was no or very little water over the step and measurements were nearly meaningless. Note that for small values of D/d the curves of H/λ versus θ were approximately symmetrical about $\theta = 90$ degrees, but were very nonsymmetrical for large values of D/d . Examples of the wave records are given in Figs. 12 and 13. It can be seen for large values of D/d that the shape of the wave is different for $\theta = 15$ than for $\theta = 165$ degrees, etc. Thus, the phenomenon is more complicated than one might expect from an observation of Fig. 11.

With the same experimental setup that was used for the 0.50 ft. wide and 0.25 ft. deep plunger, additional tests were made using a step and plunger 2.00 ft. wide and 0.25 ft. high to obtain some information on the effect of the width of the source on the height of the crest of the leading wave. Unexpected difficulties were encountered in constructing and operating the wider step and plunger, so that insufficient data were obtained. However, enough data were obtained to be of some value in understanding the phenomenon.

The locations at which the waves were measured are shown in Fig. 14. The experimental results given in Table 6 were obtained along the centerline of the step. Comparing these data with the results obtained for the 0.50 ft. wide step (Table 2) shows that H_3 for the narrow ($W = 0.50$ ft.) step and plunger was about 35 percent of the value for the wide ($W = 2.00$ ft.) step and plunger for a value of D/d of about 0.40, and a little more than 55 percent of the value for D/d equal to 1.0 (Fig. 15), all other conditions being equal.

Fig. 16 shows that for $D/d < 0.5$ and $d/W > 1$, values of ratio H_3/λ are fairly independent of y for the narrow plunger. The first wave crests in this region, behave as if they came from a point source and are nearly independent of θ . The same tendency is apparent for the wide plunger for the smallest values of D/d for which tests were made. For large values of D/d the values of H_3/λ become quite nonuniform with respect to a constant value of r/d for both the narrow and wide plungers. It also can be seen that the waves behave as if they were generated by a combination of a line source and a point source for the case of $W = 2.00$ ft. for large values of D/d .

The plots of H_3/λ versus y shown in Fig. 16 for the $W = 0.50$ ft. plunger were shifted to the left by a value of 1.50 ft., and replotted in Fig. 17. The values are plotted as if the edge of the $W = 0.50$ and the $W = 2.0$ ft. plunger were along the same line. It is interesting to note the similarity of the two sets of data. It is also evident that the waves for the $W = 2.00$ ft. plunger were always higher than the waves for the $W = 0.50$ ft. plunger.

CONCLUSIONS

1. For the source mechanism tested, the wave crest elevation is considerably less for the three-dimensional case than for the two-dimensional case, with H_3/H_2 decreasing in proportion to $(x/d)^{-3/5}$ for $0.7 < x/d < 10$ and $W/d = 1.0$.
2. For small values of D/d the values of H_3/λ are fairly uniformly distributed with respect to θ for a given value of r/d , but become very nonuniform for large values of D/d .
3. Measurements of H_3 at a given value of r/d for various values of θ from 0 to 90 degrees showed that H_3 decreased in a nearly linear manner with the $r \sin \theta$, that is with the projection of the measurement point on the y axis, at least for the narrow ($W = 0.50$ ft.) source.
4. Values of H_3 along the centerline of the step and plunger were substantially higher for the wide ($W = 2.00$ ft.) source than for the narrow ($W = 0.50$ ft.) source, all other conditions being held constant.
5. Whether the plunger acts like line source or point source depends on the values of W/d and r/d .

ACKNOWLEDGMENTS

The work reported herein was partially supported by Contract DACW-72-67-C-0002 between the Coastal Engineering Research Center, Corps of Engineers, U.S. Army and the University of California.

REFERENCES

1. Das, Madan M., and Robert L. Wiegel, "Waves Generated by Horizontal Motion of a Wall," *Jour. Waterways, Harbors and Coastal Engineering Division, Proc. ASCE*, Vol. 98, No. WW1, February 1972, pp. 49-65.
2. Garcia, William J., Jr., *A Study of Water Waves Generated by Tectonic Displacements*, University of California, Berkeley, Ph.D. Thesis in the Department of Civil Engineering; also Tech. Report No. HEL 16-9, Hydraulic Engineering Laboratory, May 1972, 114 pp.
3. Wiegel, Robert L., "Parallel Wire Resistance Wave Meter," *Coastal Engineering Instruments*, ed. by Robert L. Wiegel, Council on Wave Research, The Engineering Foundation, 1953, pp. 39-43.
4. Wiegel, R. L., Edward K. Noda, Edward M. Kuba, Dennis M. Gee and Gordon F. Tornberg, "Water Waves Generated by Landslides in Reservoirs," *Jour. Waterways and Harbors Division, Proc. ASCE*, Vol. 96, No. WW2, May 1970, pp. 307-33.

NOTATION

d = undisturbed water depth (except over step and plunger), feet (or inches, as specified)

D = height of step (also plunger) above bottom of tank, feet

H₂ = elevation of first wave crest above SWL, 2-dimensional case, ft.

H₃ = elevation of first wave crest above SWL, 3-dimensional case, ft.

N_{Favg} = Froude number, V_{avg}/\sqrt{gd} , dimensionless

r = radius, measured from origin, $r^2 = x^2 + y^2$

SWL = still water level

t = time, seconds

V_{avg} = average velocity of plunger (λ/τ), feet per second

W = width of plunger, feet

x = horizontal distance along the side wall of the tank measured from the front end of the step, feet

y = horizontal distance normal to the side wall of the tank, feet

z = vertical coordinate

λ = total plunger displacement, feet (or inches, as specified)

τ = total time of plunger motion, seconds

θ = horizontal angle, measured counterclockwise from the centerline of the step, degrees

TABLE 1
Elevation of First Wave Crest Above SWL, as a Function of λ/d
and N_{Favg} ($W = 0.50$ ft., $\theta = 0$ degrees, and $x = 1.00$ ft.)

Water Depth d , inches	4			5			6		
Displacement λ , inches	6.82	5.75	4.50	6.82	5.75	4.50	6.82	5.75	4.50
$\frac{\lambda}{d}$	1.70	1.44	1.13	1.36	1.15	0.90	1.14	0.96	0.75
Wave Crest (measured) H_3 , feet	0.066	0.054	0.040	0.046	0.037	0.027	0.038	0.039	0.022
$\frac{H_3}{\lambda}$	0.12	0.112	0.107	0.082	0.076	0.072	0.067	0.065	0.059
Froude Number	0.44	0.44	0.44	0.39	0.39	0.39	0.36	0.36	0.36
Water Depth d , inches	7			8			9		
Displacement λ , inches	6.82	5.75	4.50	6.82	5.75	4.50	6.82	5.75	4.50
$\frac{\lambda}{d}$	0.98	0.82	0.64	0.85	0.72	0.56	0.76	0.64	0.50
Wave Crest (measured) H_3 , feet	0.034	0.027	0.020	0.027	0.023	0.015	0.024	0.020	0.015
$\frac{H_3}{\lambda}$	0.060	0.056	0.053	0.048	0.047	0.040	0.042	0.043	0.039
Froude Number	0.33	0.33	0.33	0.31	0.31	0.31	0.29	0.29	0.29

TABLE 2
 Elevation of First Wave Crest Above SWL, as a Function of D/d
 (W = 0.50 ft., x/d = 3.0, λ/d = 0.75, N_{Favg} = 0.44, θ = 0 degrees and W/d = 2.0)

Water Depth d inches	Distance Along x Axis x, feet	Displacement of Step Motion λ, inches	Displacement Velocity of plunger v _{avg} , ft/sec	Weight Used To Cause Motion lbs	Wave Crest Elevation at x = H ₃ feet	H ₃ / λ	D / d
3	0.75	2.25	1.25	1.8	0.034	0.18	1.00
4	1.00	3.00	1.44	8.2	0.021	0.086	0.75
5	1.25	3.75	1.61	19.5	0.017	0.055	0.60
6	1.50	4.50	1.77	34.0	0.014	0.037	0.50
7	1.75	5.25	1.90	75.0	0.012	0.028	0.43
8	2.00	6.00	2.04	100.0	0.012	0.022	0.38
9	2.25	6.75	2.16	121.0	0.010	0.018	0.33

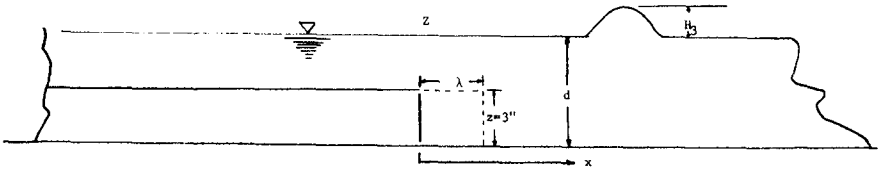


TABLE 3

Elevation of First Wave Crest Above SWL, as a Function of D/d and θ
 (W = 0.5 ft., r/d = 3.0, $\lambda/d = 0.75$, $N_{Favg} = 0.44$ and W/D = 2.0)

Water Depth d inches	Elevation of First Wave Crest at r/d = 3.0, H_3 (feet)					$\frac{H_3}{\lambda}$					$\frac{D}{d}$
	0°	15°	30°	45°	60°	0°	15°	30°	45°	60°	
3	0.034	0.027	0.025	0.019	0.014	0.18	0.14	0.13	0.099	0.075	1.00
4	0.021	0.019	0.016	0.013	0.011	0.086	0.077	0.064	0.054	0.042	0.75
5	0.017	0.015	0.013	0.011	0.009	0.055	0.049	0.042	0.035	0.029	0.60
6	0.014	0.012	0.011	0.009	0.008	0.037	0.033	0.029	0.025	0.021	0.50
7	0.012	0.011	0.010	0.008	0.007	0.027	0.025	0.022	0.018	0.016	0.43
8	0.012	0.010	0.009	0.008	0.006	0.022	0.020	0.017	0.015	0.013	0.38
9	0.010	0.009	0.008	0.006	0.006	0.018	0.016	0.014	0.011	0.011	0.33

TABLE 4

Elevation of First Wave Crest Above SWL, as a Function of θ (0 to 180 degrees), Plunger Displacement and Water Depth (W = 0.5 ft., $r/d = 3.0$, $\lambda/d = 0.75$, $N_{Favg} = 0.44$ and $W/D = 2.0$)

Water Depth d inches	Elevation of First Wave Crest Above SWL, H_3 , feet													Displacement of Plunger λ inches
	0°	15°	30°	45°	60°	75°	90°	105°	120°	135°	150°	165°	180°	
3	0.037	0.031	0.025	0.019	0.013	0.010	0.008	0.006	0.005	0.004				2.25
4	0.021	0.019	0.016	0.013	0.010	0.009	0.007	0.006	0.006	0.007	0.006			3.00
5	0.018	0.016	0.014	0.011	0.010	0.008	0.007	0.006	0.007	0.008	0.007	0.010		3.75
6	0.015	0.014	0.012	0.010	0.008	0.007	0.006	0.006	0.007	0.009	0.009	0.009	0.011	4.50
7	0.013	0.012	0.011	0.009	0.008	0.006	0.005	0.005	0.006	0.009	0.009	0.009	0.014	5.25
8	0.012	0.010	0.009	0.008	0.007	0.006	0.005	0.005	0.007	0.009	0.010	0.011	0.013	6.00
9	0.010	0.009	0.008	0.007	0.006	0.005	0.004	0.004	0.006	0.009	0.010	0.011	0.012	6.75

TABLE 5

Normalized Elevation of First Wave Crest Above SWL, as a Function of θ (0 to 180 degrees) and D/d (W = 0.5 ft., $r/d = 3.0$, $\lambda/d = 0.75$, $N_{Favg} = 0.44$ and $W/D = 2.0$)

Water Depth d inches	H_3/λ													D/d
	0°	15°	30°	45°	60°	75°	90°	105°	120°	135°	150°	165°	180°	
3	0.200	0.168	0.132	0.102	0.069	0.054	0.042	0.030	0.024	0.023				1.00
4	0.086	0.077	0.065	0.054	0.041	0.35	0.028	0.023	0.025	0.027	0.025			0.75
5	0.057	0.050	0.045	0.036	0.031	0.026	0.022	0.020	0.022	0.026	0.022	0.038		0.60
6	0.041	0.037	0.032	0.028	0.022	0.019	0.017	0.016	0.018	0.024	0.024	0.025	0.030	0.50
7	0.031	0.028	0.024	0.021	0.018	0.014	0.012	0.011	0.014	0.020	0.021	0.021	0.032	0.43
8	0.023	0.020	0.018	0.015	0.013	0.011	0.010	0.010	0.013	0.018	0.020	0.022	0.026	0.36
9	0.018	0.016	0.015	0.013	0.011	0.009	0.008	0.008	0.011	0.015	0.017	0.020	0.022	0.33

Table 6

Elevation of First Wave Crest Above SWL, as a Function of D/d
 (W = 2.0 ft., x/d = 3.0, λ/d = 0.75, N_{Favg} = 0.44, θ = 0 degrees, W/D = 8.0)

Water Depth d Inches	Distance Along x Axis, x ft.	Displacement of Plunger λ Inches	Displacement Velocity of Plunger Motion Vavg, ft/sec.	Weight used to cause motion lbs.	Wave Crest Elevation at x, feet	$\frac{H_3}{\lambda}$	$\frac{D}{d}$
3	0.75	2.25	1.25	24.0	0.059	0.318	1.00
4	1.00	3.00	1.44	53.0	0.051	0.205	0.75
5	1.25	3.75	1.61	84.0	0.045	0.145	0.60
6	1.50	4.50	1.77	110.0	0.037	0.010	0.50
7	1.75	5.25	1.90	134.0	0.034	0.078	0.43
8	2.00	6.00	2.04	156.0	0.031	0.062	0.38

Note: No measurements were made for a water depth of 9 inches

TABLE 7

Elevation of First Wave Crest Above SWL, as a Function of (x,y) and Water Depth
 (W = 2.00 ft., x/d = 3.0 for 3" < y < 21" and r/d = 3.0 for y > 21", θ/d = 0.75, N_{Favg} = 0.44 and W/D = 8.0)

Water Depth d Inches	Elevation of First Crest Above SWL, H ₃ , test along y Direction											x Inches	
	y = 3 inches	6	9	12	15	18	21	21+ xSin15°	21+ xSin30°	21+ xSin45°	21+ xSin60°		21+ xSin75°
3	.060	.060	.060	.056	.053	.049	.042	.035	.028	.022	.018	.013	9
4	.056	.056	.056	.051	.047	.043	.037	.029	.023	.018	.014	.010	12
5	.050	.050	.049	.045	.042	.038	.033	.025	.019	.016	.012	.010	15
6	.046	.044	.042	.038	.036	.030	.029	.022	.017	.013	.009	.008	18
8	.040	.038	.037	.034	.031	.027	.024	.021	.018	.014	.010	.009	24

Table 8

Normalized Elevation of First Wave Crest Above SWL, as a Function of θ
 (W = 2.0 ft., x/d = 3.0 for 3" < y < 21" and r/d = 3.0 for y > 21", λ/d = 0.75, N_{Favg} = 0.44 and W = 8.0)

Water Depth d inches	$\frac{H_3}{\lambda}$											$\frac{D}{d}$	
	y = 3 inches	6	9	12	15	18	21	21+ Sin15°	21+ Sin30°	21+ Sin45°	21+ Sin60°		21+ Sin 75°
3	0.322	0.322	0.322	0.300	0.285	0.260	0.223	0.186	0.150	0.118	0.099	0.068	1.00
4	0.223	0.223	0.223	0.206	0.187	0.171	0.149	0.117	0.093	0.071	0.058	0.040	0.75
5	0.160	0.160	0.156	0.146	0.136	0.121	0.107	0.080	0.062	0.052	0.039	0.033	0.60
6	0.123	0.116	0.111	0.103	0.097	0.082	0.077	0.059	0.045	0.035	0.025	0.022	0.50
8	0.080	0.077	0.074	0.069	0.062	0.056	0.048	0.041	0.035	0.029	0.020	0.017	0.36

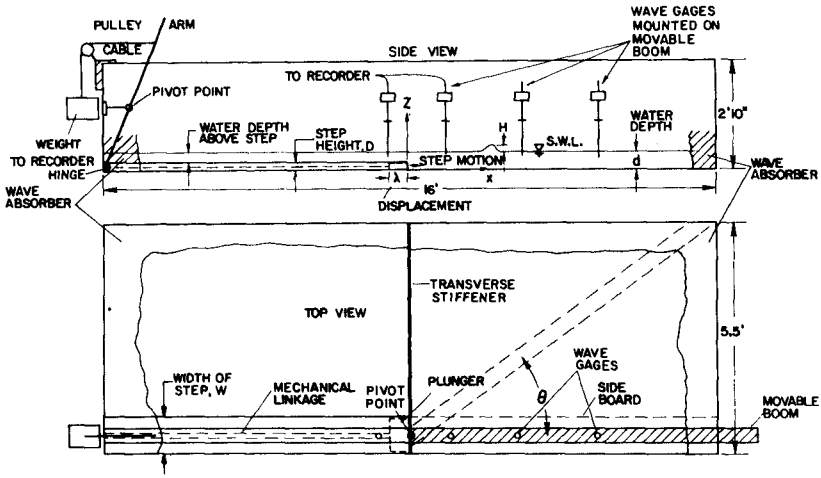


FIG. 1 EXPERIMENTAL ARRANGEMENTS

MEASURED WAVE ELEVATION ABOUT SWL

DISTANCE ALONG FLUME, ft.	-0.5	0.33	1.0	2.0	2.5
ELEVATION ABOUT SWL, ft.	0.025	-0.05	0.016	0.034	0.014

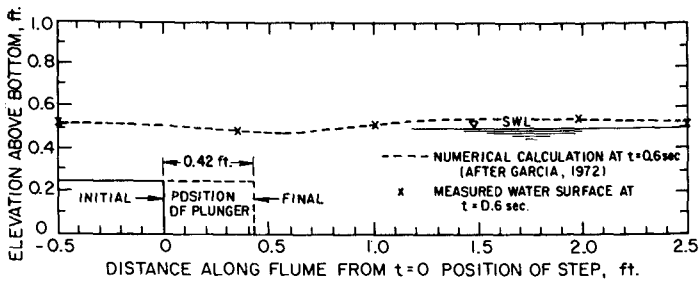


FIG. 2 MEASURED WATER SURFACE PROFILE FOR WAVE GENERATED BY HORIZONTAL MOTION OF SUBMERGED STEP, COMPARED WITH THEORY, TWO-DIMENSIONAL MODEL, PLUNGER DISPLACEMENT = 0.42 ft., FROUDE NUMBER = 0.32, AND $d/W = 1.0$

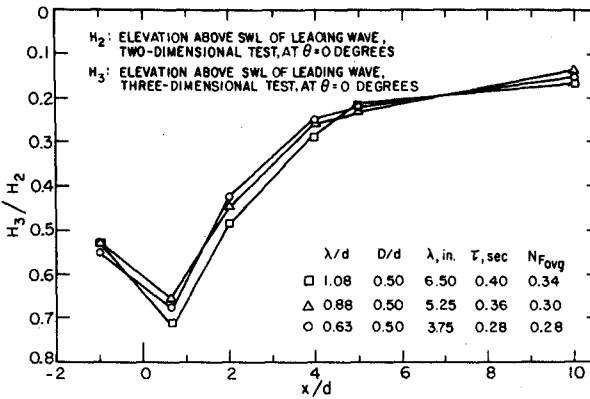


FIG. 3 H_3/H_2 VERSUS x/d , FOR $W=0.50$ FT, $d/W=1.0$
(FROM LIU AND WIEGEL, 1974)

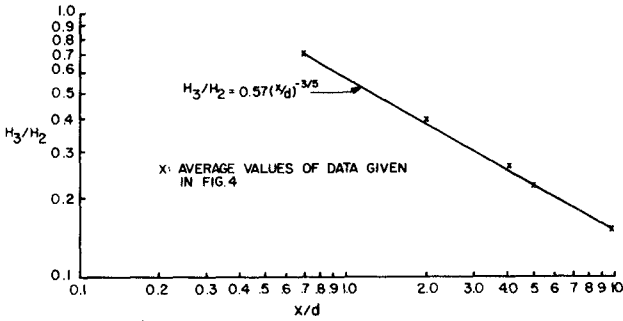


FIG. 4 H_3/H_2 VERSUS x/d FOR $W=0.50$ FT AND $d/w=1.0$

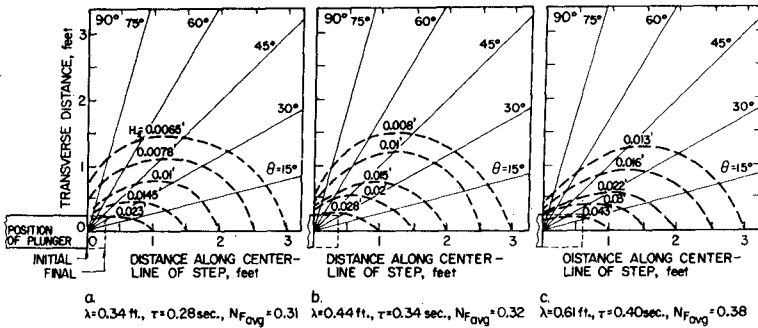


FIG. 5 CONTOURS OF EQUAL CREST ELEVATION ABOVE SWL. ($D/d=0.50$, $d/W=1.0$, $d=0.50$ FT., $W=0.50$ FT.) (FROM LIU AND WIEGEL, 1974)

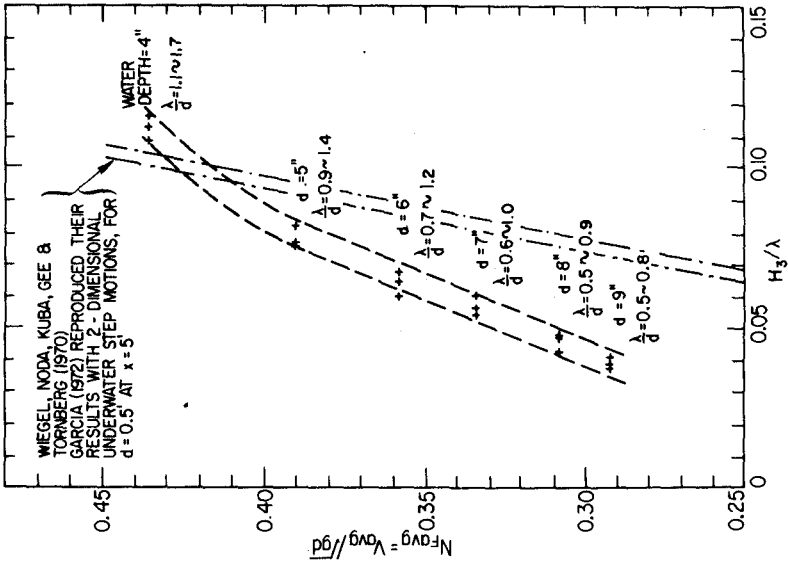


FIG. 7 RELATIONSHIP BETWEEN H_3/λ AND $N_{Favg} (V_{avg}/gd)$ FOR UNDERWATER 3-DIMENSIONAL STEP MOTIONS FOR $W=0.50$ FT., $d=4"$ TO $9"$, 0.025 FT. AND $x=1.0$ FT.

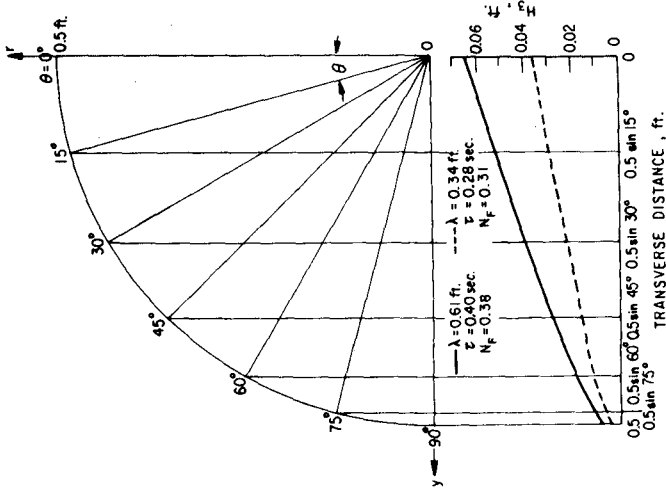


FIG. 6 ELEVATION OF FIRST WAVE CREST ABOVE SWL AT $r=0.50$ FT. RADIUS VS PROJECTION ONTO THE TRANSVERSE AXIS, $W=0.50$ FT. (FROM LIU AND WIEGEL, 1974)

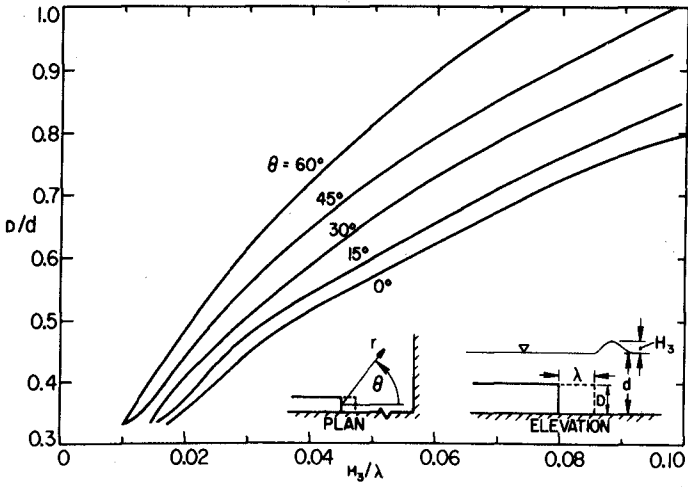


FIG. 8 RELATIONSHIPS AMONG H_3/λ , D/d AND θ , FOR $N_{Favq} = 0.44$, $r/d = 3.0$, $\lambda/d = 0.75$, AND $W = 0.50$ FT.

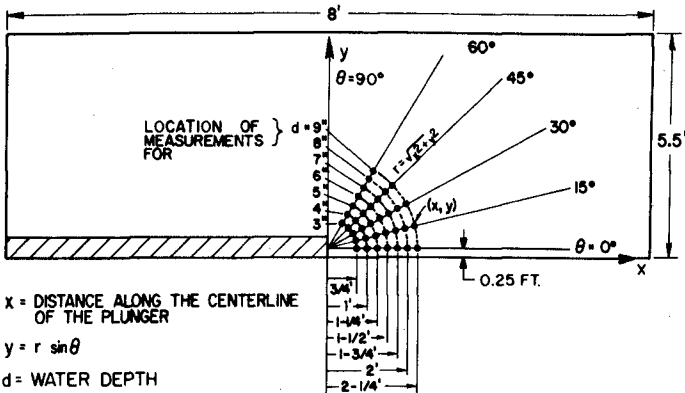


FIG. 9 LOCATIONS AT WHICH MEASUREMENTS WERE MADE OF THE WAVE TIME HISTORIES FOR THE 0.50 FT. WIDE PLUNGER

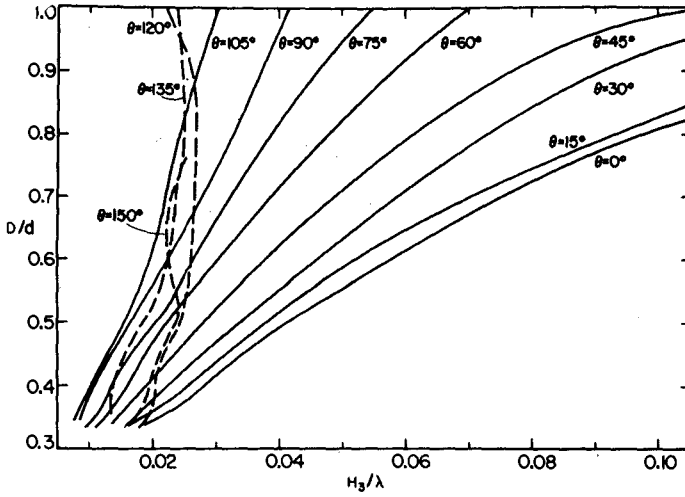


FIG. 10 RELATIONSHIP BETWEEN H_3/λ AND D/d AS A FUNCTION OF θ , FOR $r/d=3.0$, $\lambda/d=0.75$, $N_{Favg}=0.44$, AND $W=0.50$ FT.

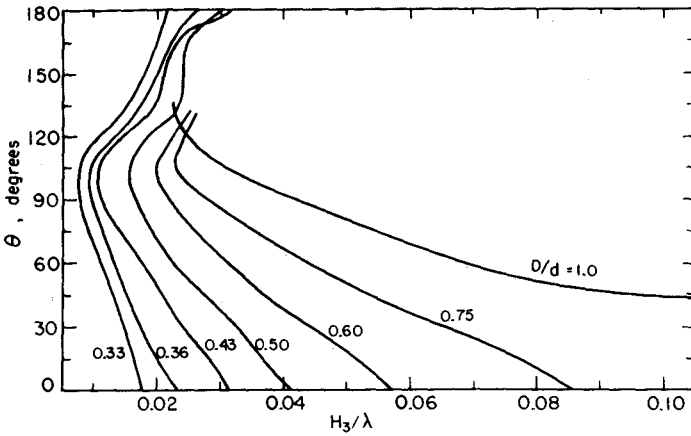


FIG. 11 RELATIONSHIP BETWEEN H_3/λ AND θ AS A FUNCTION OF D/d FOR $r/d=3.0$, $\lambda/d=0.75$, $N_{Favg}=0.44$, AND $W=0.50$ FT.

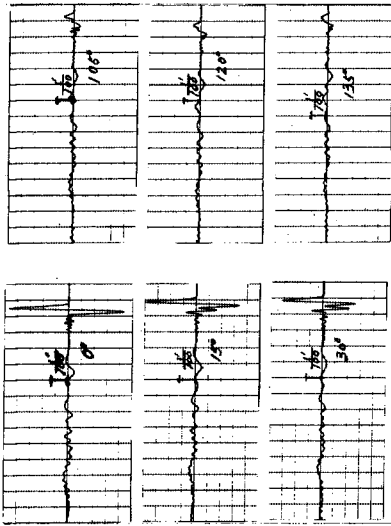


Fig. 12 Water surface time histories as a function of θ for water depth = 1.0 ft. $A = 2.25$ in., $b/d = 1.0$ and $W = 0.50$ ft.

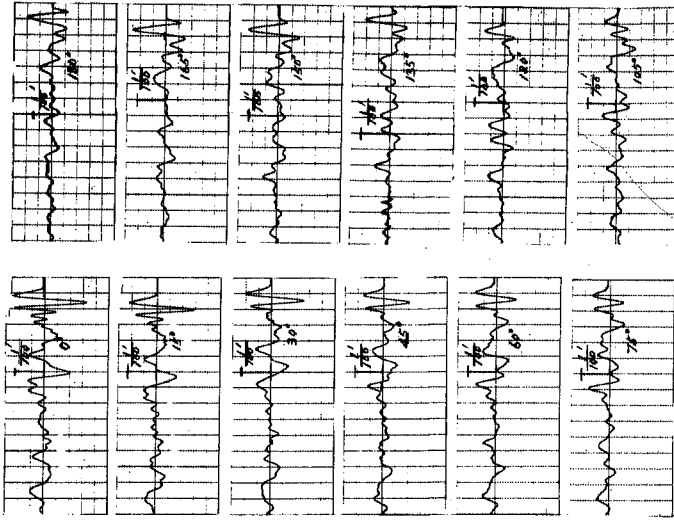


Fig. 13 Water surface time histories as a function of θ for water depth = 9 in., $A = 2.25$ in., $b/d = 0.333$ and $W = 0.50$ ft.

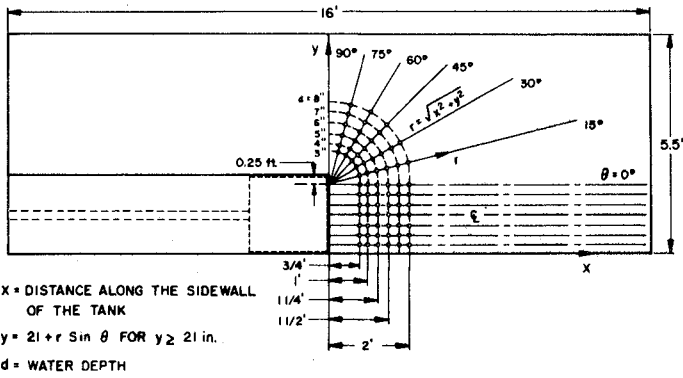


FIG. 14 LOCATIONS AT WHICH MEASUREMENTS WERE MADE OF THE WAVE TIME HISTORIES FOR THE 2.0 FT. WIDE PLUNGER

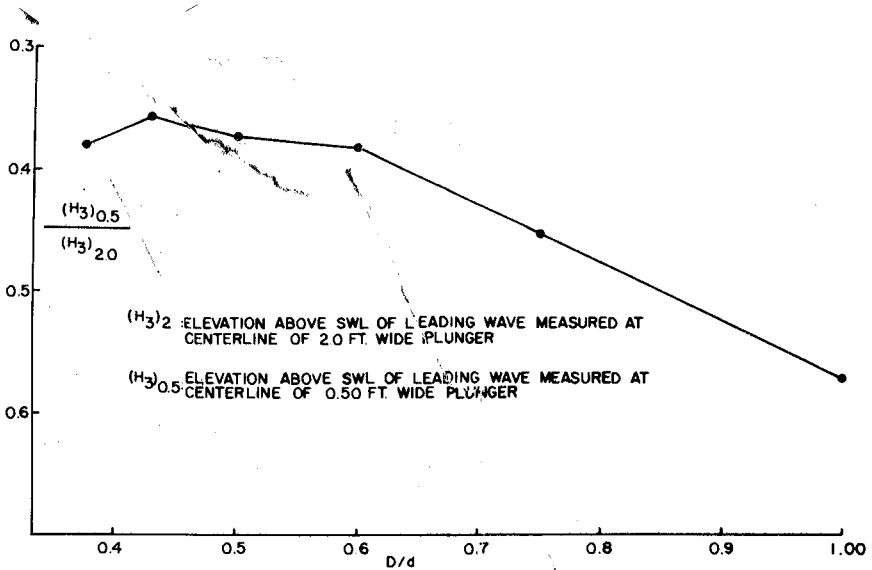


FIG. 15. $(H_3)_{0.5} / (H_3)_{2.0}$ VERSUS D/d FOR: $x/d = 3.0$, $\lambda/d = 0.75$, $N_{Fovg} = 0.44$ AND $\theta = 0^\circ$

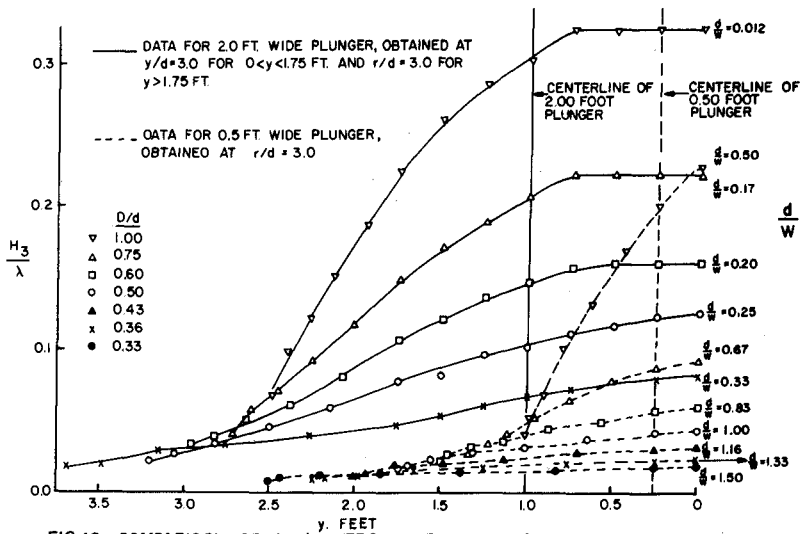


FIG. 16 COMPARISON OF H_3/λ VERSUS y FOR THE NARROW PLUNGERS FOR SEVERAL VALUES OF d/W AND D/d , WITH $N_{Favg} = 0.44$

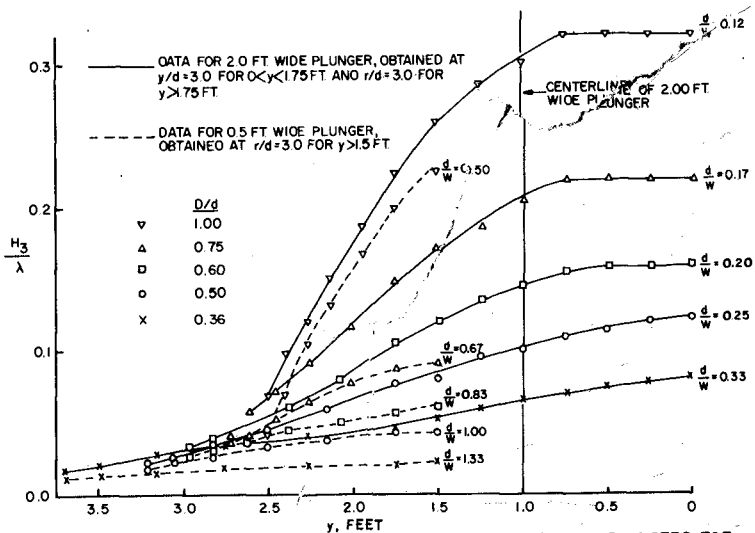


FIG. 17 COMPARISON OF H_3/λ VERSUS y FOR THE WIDE AND NARROW PLUNGERS FOR SEVERAL VALUES OF d/W AND D/d , WITH $N_{Favg} = 0.44$. THE VALUES FOR $W=0.5$ FT. DISPLACED 1.5 FT.

CHAPTER 64

CALCULATIONS OF WAVES FORMED FROM SURFACE CAVITIES Charles L. Mader*

ABSTRACT

The wave motion resulting from cavities in the ocean surface was investigated using both the long wave, shallow water model and the incompressible Navier-Stokes equations. The fluid flow resulting from the calculated collapse of the cavities is significantly different for the two models. The experimentally observed flow resulting from explosively formed cavities is in better agreement with the flow calculated using the incompressible Navier-Stokes model. The resulting wave motions decay rapidly to deep water waves. Large cavities located under the surface of the ocean will be more likely to result in Tsunami waves than cavities on the surface. This is contrary to what has been suggested by the upper critical depth phenomenon.

I. INTRODUCTION

The prediction of water waves generated by large-yield explosions has been based on extrapolation of empirical correlations of small-yield experimental data, usually assuming the waves were shallow water waves. Because the accuracy of such predictions is questionable, the need exists for a detailed description of the mechanism by which waves are generated by explosions. In particular the "upper critical depth" phenomenon needs to be understood. The upper critical depth phenomenon is an experimentally observed wave height maximum that occurs when an explosive charge is approximately two-thirds submerged. The observed height at the upper critical depth is twice that observed for completely submerged explosive charges. If the waves formed are shallow water waves capable of forming Tsunamis, then the upper critical depth phenomenon is important to evaluating the probability of a Tsunami event from other than tectonic events.

Theoretical evaluation of the early interaction of the detonation products of an explosive charge with the water and air interfaces and the resulting wave profile near the detonation has been performed by Mader¹ using the multicomponent reactive compressible hydrodynamic code 2DE.² The pressure and velocity contours for the early interaction of the explosive with the water and air are shown in Fig. 1. The initial formation of the lip or splash wave on the water cavity is also numerically described and it has been suggested that the concentration of momentum near the water surface in the splash wave is a contributing

*Theoretical Division, Los Alamos Scientific Laboratory, University of California, Los Alamos, New Mexico 87545

factor in the upper critical depth phenomenon, resulting in a bubble cavity radius about the same as if the explosive bubble was completely confined by water. The high velocity present in the splash wave is a result of the initial water shock being quickly rarefied and permitting a second shock to be delivered from the explosive products. Subsequent shocks and rarefactions occur while the detonation products have high pressure. Each reverberation increases the particle velocity of the splash wave by an increment that decreases as the pressure of the driving detonation products decreases. The particle velocity of the remainder of the water cannot be increased by reverberations during the early high pressure motion because a free interface is not present. The consequence of this complicated interaction is that the maximum bubble radius achieved by a partially submerged explosive charge is slightly larger than one would expect to observe if the explosive sphere and its bubble was confined by water at one bar.

The bubble is observed to increase to a maximum radius of about 0.5 meter in 0.2 second and then take about 0.3 second to collapse as described in Refs. 1 and 3 for a 1.27-cm radius 9404 explosive sphere initiated at the center and immersed to a depth of 1.59 cm.

In this paper we shall describe an investigation of the flow after the cavity reaches its maximum dimensions. We assume that the flow is essentially incompressible at the times of interest and that the surrounding fluid is approximately at rest at maximum bubble radius.

The waves observed by Craig³ from the collapse of the bubble resulted in a train of waves moving at about 1.25 meters/second with a one-meter wavelength. Mass markers located one meter below the water surface and markers located half a meter below the surface and one meter from the explosive did not show any appreciable movement compared with those located nearer the surface or explosive charge. This result suggests that the fluid flow will not be well described by the usual shallow water-long wave model.

We have calculated the fluid dynamics of a cavity initially 0.5 meter in radius with and without a lip, using a shallow water long wave model and a model based upon the incompressible Navier-Stokes equations.

II. SHALLOW WATER, LONG WAVE MODEL

The long wave theory applies when the depth relative to the wavelength is small, and when the vertical component of the motion does not influence the pressure distribution, which is assumed to be hydrostatic. It is appropriate for Tsunami wave formation, propagation and early shoaling behavior as described in Ref. 4. The SWAN code described in Ref. 4 was modified to solve the long wave equations using an improved numerical difference technique.

The long wave equations solved by the SWAN code are:

$$\frac{\partial U}{\partial t} + U \frac{\partial U}{\partial X} + V \frac{\partial U}{\partial Y} + g \frac{\partial H}{\partial X} = FV + F(x) - g \frac{U(U^2 + V^2)^{1/2}}{C^2(D + H)}$$

$$\frac{\partial V}{\partial t} + U \frac{\partial V}{\partial X} + V \frac{\partial V}{\partial Y} + g \frac{\partial H}{\partial Y} = FU + F(y) - g \frac{U(U^2 + V^2)^{1/2}}{C^2(D + H)}$$

$$\frac{\partial H}{\partial t} + \frac{\partial(D + H - R)U}{\partial X} + \frac{\partial(D + H - R)V}{\partial Y} - \frac{\partial R}{\partial t} = 0$$

- where U = velocity in X direction (i index)
 V = velocity in Y direction (j index)
 g = gravitational acceleration
 t = time (n index)
 H = wave height above mean water level
 R = bottom motion
 F = Coriolis force parameter
 C = coefficient of DeChezy for bottom stress
 F(x), F(y) = forcing functions of wind stress and barometric pressure in X and Y direction
 D = depth .

To obtain stable numerical solutions, the finite difference equations must not have negative diffusion. The following difference equations are stable but require that the time step be kept near the maximum or the numerical results will become smeared. C. W. Hirt⁵ suggested this approach when the difference equations described in Ref. 4 were found to be unstable in certain directions of the flow.

The wave height H and depth D are taken as cell centered and the velocities are centered at cell boundaries. The difference equations at each time step are in order:

$$H_{i,j}^{n+1} = H_{i,j}^n - \Delta t \left[\frac{U_{i+1,j}^n}{\Delta x} (TD1) - \frac{U_{i,j}^n}{\Delta x} (TD2) + \frac{V_{i,j+1}^n}{\Delta y} (TV1) - \frac{V_{i,j}^n}{\Delta y} (TV2) \right]$$

$$+ R_{i,j}^{n+1} - R_{i,j}^n$$

$$TD1 = D_{i+1,j} + H_{i+1,j}^n - R_{i+1,j}^n \quad (U_{i+1,j} < 0)$$

$$TD2 = D_{i,j} + H_{i,j}^n - R_{i,j}^n \quad (U_{i,j} < 0)$$

$$TV1 = D_{i,j+1} + H_{i,j+1}^n - R_{i,j+1}^n \quad (V_{i,j+1} < 0)$$

$$TV2 = D_{i,j} + H_{i,j}^n - R_{i,j}^n \quad (V_{i,j} < 0)$$

$$TD1 = D_{i,j} + H_{i,j}^n - R_{i,j}^n \quad (U_{i+1,j} > 0)$$

$$TD2 = D_{i-1,j} + H_{i-1}^n - R_{i-1,j}^n \quad (U_{i,j} > 0)$$

$$TV1 = D_{i,j} + H_{i,j}^n - R_{i,j}^n \quad (V_{i,j+1} > 0)$$

$$TV2 = D_{i,j-1} + H_{i,j-1}^n - R_{i,j-1}^n \quad (V_{i,j} > 0)$$

$$U_{i,j}^{n+1} = U_{i,j}^n - \Delta t \left[\frac{U_{i,j}}{\Delta x} (TU1) + \frac{TV}{\Delta y} (TU2) \right] - g \frac{\Delta t}{\Delta x} [THU]$$

$$+ \Delta t \left\{ -FV_{i,j}^n - F_{i,j}^{(x)} + S_{i,j}^B \right\}$$

$$TV = 0.25 (V_{i,j} + V_{i,j+1} + V_{i-1,j+1} + V_{i-1,j})$$

$$TU1 = U_{i+1,j} - U_{i,j} \quad (U_{i,j} < 0)$$

$$TU2 = U_{i,j+1} - U_{i,j} \quad (TV < 0)$$

$$TU1 = U_{i,j} - U_{i-1,j} \quad (U_{i,j} > 0)$$

$$TU2 = U_{i,j} - U_{i,j-1} \quad (TV > 0)$$

$$THU = H_{i,j} - H_{i-1,j}$$

$$v_{i,j}^{n+1} = v_{i,j}^n - \Delta t \left[\frac{TU}{\Delta X} (TV1) + \frac{v_{i,j}}{\Delta Y} (TV2) \right] - g \frac{\Delta t}{\Delta Y} [THV] \\ + \Delta t \left\{ F U_{i,j}^n - F_{i,j}^{(y)} + S_{i,j}^B \right\}$$

$$TU = 0.25 (u_{i,j} + u_{i+1,j} + u_{i,j-1} + u_{i+1,j-1})$$

$$TV1 = v_{i+1,j} - v_{i,j} \quad (TU < 0)$$

$$TV2 = v_{i,j+1} - v_{i,j} \quad (v_{i,j} < 0)$$

$$TV1 = v_{i,j} - v_{i-1,j} \quad (TU > 0)$$

$$TV2 = v_{i,j} - v_{i,j-1} \quad (v_{i,j} > 0)$$

$$THV = H_{i,j} - H_{i,j-1}$$

and

$$S_{i,j}^B = g U_{i,j}^n \left(\frac{u_{i,j}^n}{U_{i,j}^n} + \frac{v_{i,j}^n}{V_{i,j}^n} \right)^{1/2} / c^2 (D_{i,j} + H_{i,j}^n)$$

The calculations were performed with 69 cells in the X direction and 130 cells in the Y direction. The cells were .06 meters square and the time step was 0.001 seconds. The gravity constant was -9.8 m sec^{-2} . Although the problem described in this report was symmetrical and required only one direction, the calculations described were performed with the two dimensional SWAN code.

The computed wave profiles using the shallow water equations in the SWAN code for the collapse of a 0.5-meter radius hole are shown in Fig. 2 and for the collapse of a 0.5-meter radius hole with a 0.25-meter high and 0.50-meter wide triangular lip (which approximates the experimentally observed bubble profile) are shown in Figs. 2 and 4. Figure 4 also shows the velocity in the Y direction. The initial water depth was three meters.

III. INCOMPRESSIBLE NAVIER-STOKES MODEL

The Marker and Cell (MAC) method of Harlow and Welch⁶ is a numerical technique for calculation of viscous, incompressible flow with a free surface.

The method uses a finite-difference technique for solving the time-dependent Navier-Stokes equations.

These equations for two-dimensional flows are

$$\frac{\partial U}{\partial X} + \frac{\partial V}{\partial Y} = 0 \quad ,$$

$$\frac{\partial U}{\partial t} + \frac{\partial U^2}{\partial X} + \frac{\partial UV}{\partial Y} = - \frac{\partial \phi}{\partial X} + g_x + \nu \left(\frac{\partial^2 U}{\partial X^2} + \frac{\partial^2 U}{\partial Y^2} \right) \quad ,$$

$$\frac{\partial V}{\partial t} + \frac{\partial UV}{\partial X} + \frac{\partial V^2}{\partial Y} = - \frac{\partial \phi}{\partial Y} + g_y + \nu \left(\frac{\partial^2 V}{\partial X^2} + \frac{\partial^2 V}{\partial Y^2} \right) \quad ,$$

where ϕ is the ratio of pressure to constant density, g_x and g_y are the X and Y components of body acceleration, and ν is the kinematic viscosity coefficient. The MAC method is based on an Eulerian network of rectangular cells, with velocities centered at cell boundaries and the pressure cell-centered. Just as the differential equations of motion are statements of the conservation of mass and momentum, the MAC finite-difference equations express these conservation principles for each cell, or combination of cells, in the computing mesh.

After the introduction of MAC, much attention was given to devising more accurate treatments of the free surface boundary conditions. Chan and Street⁷ developed a technique for more accurate delineation of the free surface. This permitted the free surface pressure to be specified at the surface itself, rather than at the center of the surface cell. Nichols and Hirt⁸ modified the Chan and Street procedure, devising a technique for defining the fluid surface by a set of surface marker particles that move with local fluid velocity. These particles allow surface-cell pressures in MAC to be accurately specified by means of linear interpolation or extrapolation between the known values of pressure in the nearest full cell and the desired fluid surface.

A Simplified MAC (SMAC) has been described by Harlow and Amsden.⁹ The SMAC technique has been modified to include the Nichols and Hirt free surface treatment. The computing program used for the calculations is called ZUNI and is described by Amsden.¹⁰ The calculations were performed with 100 cells in the X direction and 60 cells in the Y direction. The cells were 0.05 meters square and the time step increment was 0.0003 seconds. The convergence criterion is the maximum permitted change in pressure from hydrostatic pressure in any cell between iteration steps divided by the sum of the changes at two iteration steps and was 0.01. Three or more surface particles were used in each cell. The gravity constant was -9.8 m sec^{-2} . The viscosity coefficient was $0.01 \text{ gm sec}^{-1} \text{ m}^{-1}$. Preliminary calculations showed that the results were independent of whether the water depth was 3.0 or 1.5 meters; therefore in the calculations presented in this paper the cavity was in

water initially 1.5 meters deep. The wave amplitude at late times and the details of the bubble collapse after first collapse and jetting were sensitive to the amount of viscosity used in the calculation so the value chosen was the smallest that would also permit numerically stable results. The computed wave profiles using the ZUNI code to solve the incompressible Navier-Stokes equations for the collapse of a 0.5-meter radius hole with a 0.25-meter high and 0.5-meter wide triangular lip are shown in Fig. 5.

IV. COMPARISONS

The experimental and calculated wave parameters are summarized in Table I. The experimental wave parameters are given for the first three waves after four meters of travel from the center of the explosive charge. The calculated wave parameters for the Airy wave were calculated using the WAVE code⁴ for a depth of three meters and using the experimentally observed wave height and wave length. Since the group velocity is almost exactly half the wave velocity, the Airy wave is a deep water wave. The deep water Airy wave is a good approximation to the experimentally observed wave.

The collapse of the cavity is quite different between the SWAN and ZUNI calculation as shown in Figs. 3 and 5. The shallow water cavity calculation collapses from the side in less than 0.1 second while the Navier-Stokes cavity calculation collapses from the bottom in about 0.5 seconds. The experimentally observed bubble collapses approximately symmetrically from the bottom in about 0.3 seconds, so the Navier-Stokes calculation is a more realistic description of the observed flow.

As shown in Table I the Navier-Stokes calculation results in wave parameters more closely approximating those observed experimentally than those calculated using the shallow water theory. The waves calculated using the incompressible Navier-Stokes equations have complicated wave patterns and the waves quickly decay into deep water waves with the particle motion rapidly decreasing with increasing depth below the water surface. This is also in agreement with the experimental observations of mass markers described in the introduction.

TABLE I
CALCULATED AND EXPERIMENTAL WAVE PARAMETERS

	<u>Experimental*</u>	<u>Airy Wave</u>	<u>Shallow Water</u>	<u>Navier-Stokes</u>
Wave Velocity (m/s)	1.25 ± 0.1	1.2489	5.42	1.50 ± 0.50
Amplitude (cm)	1, 1.8, 2.5	2.5 (input)	10.1	< 4.0
Wave Length (m)	1.5, 1.0, 1.0	1.0 (input)	1.0	1.0
Period (s)	1.2, 0.8, 0.8	0.8007	0.18	0.66 ^{+0.3} _{-0.2}
Group Velocity (m/s)		0.6244		

*First three waves observed.

V. CONCLUSIONS

The experimentally observed waves from the cavities formed by explosions near the water surface are better reproduced by models solving the incompressible Navier-Stokes equations than by models solving the shallow water, long wave equations. The experimentally observed waves are deep water waves and the observed upper critical depth phenomenon is apparently a result of a partition of energy near the water surface which results in high amplitude deep water waves (of high potential and low kinetic energy) and not the shallow water waves required for Tsunamis. As the explosive is detonated under the water surface, more of the energy is imparted to the water resulting in waves that have smaller amplitude but more of the energy is present in the water as kinetic energy rather than potential energy. The waves formed will more closely resemble shallow water waves and will not disperse as rapidly as waves formed from surface detonation.

The upper critical depth phenomenon is apparently not important to the formation of Tsunami waves. Large cavities located under the surface of the ocean will be more likely to result in shallow water Tsunami waves than cavities on the surface. A cavity would have to be quite large and reach very deep into the ocean before it could be an effective agent for forming significant Tsunami waves.

To obtain a more realistic solution to the problem of wave formation from explosions one would need to follow the hydrodynamics from the early compressible to late incompressible stages with one of the implicit continuous fluid methods currently under development. Of particular interest would be to determine the source and significance for wave formation of the water jet and root experimentally³ observed before the explosive bubble reaches maximum radius at depths similar to the upper critical depth.

ACKNOWLEDGMENTS

The author gratefully acknowledges the contributions of A. A. Amsden, F. H. Harlow, B. D. Nichols, T. D. Butler, C. W. Hirt, and K. H. Olsen of the Los Alamos Scientific Laboratory, of G. R. Miller, H. G. Loomis, and E. N. Bernard of the Joint Tsunami Research Effort, National Oceanic and Atmospheric Administration, Hawaii Institute of Geophysics, and of George Carrier of Harvard University.

This study was performed for the Energy Research and Development Administration Tamarin Committee.

LITERATURE CITED

1. Charles L. Mader, "Detonations Near the Water Surface," Los Alamos Scientific Laboratory report LA-4958 (1972).
2. James D. Kershner and Charles L. Mader, "2DE: A Two Dimensional Continuous Eulerian Hydrodynamic Code for Computing Multicomponent Reactive Hydrodynamic Problems," Los Alamos Scientific Laboratory report LA-4932 (1972).

3. Bobby G. Craig, "Experimental Observations of Underwater Detonations Near the Water Surface," Los Alamos Scientific Laboratory report LA-5548-MS (1974).
4. Charles L. Mader, "Numerical Simulation of Tsunamis," Hawaii Institute of Geophysics report HIG-73-3 and Joint Tsunami Research Effort report NOAA-JTRE-85 (1973), also J. Physical Oceanography 4, 74-82 (1974).
5. C. W. Hirt, private communication.
6. J. E. Welch, F. H. Harlow, J. P. Shannon and B. J. Daly, "The MAC Method," Los Alamos Scientific Laboratory report LA-3425 (1965).
7. R. K. C. Chan and R. L. Street, J. Comput. Phys. 6, 68-94 (1970).
8. B. D. Nichols and C. W. Hirt, J. Comput. Phys. 8 434-448 (1971).
9. Anthony A. Amsden and Francis H. Harlow, "The SMAC Method: A Numerical Technique for Calculating Incompressible Fluid Flows," Los Alamos Scientific Laboratory report LA-4370 (1970), also J. Comput. Phys. 6 322-325 (1970).
10. Anthony A. Amsden, "Numerical Calculation of Surface Waves: A Modified ZUNI Code with Surface Particles and Partial Cells," Los Alamos Scientific Laboratory report LA-5146 (1973).

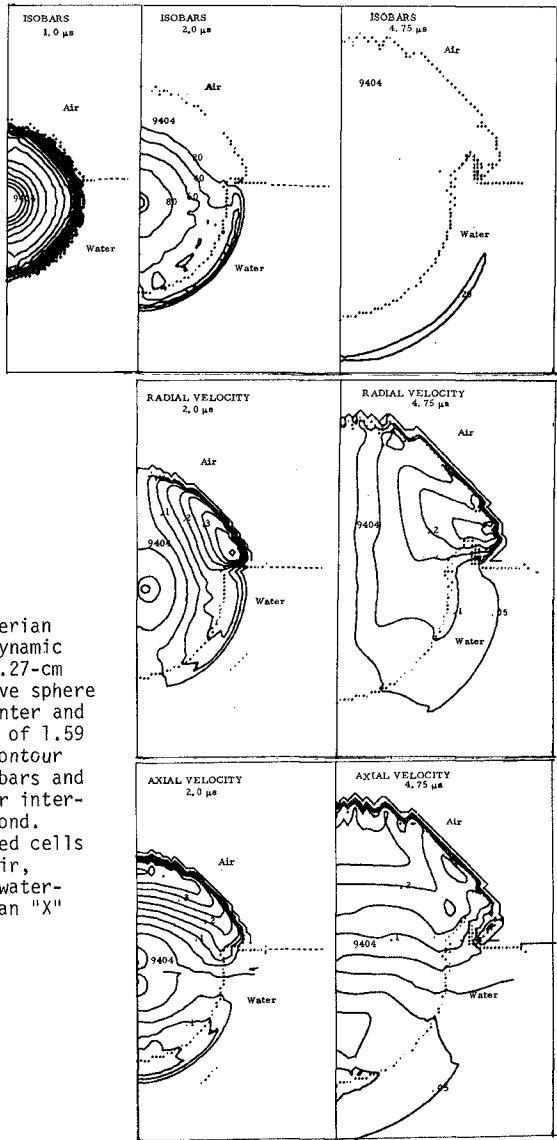


Fig. 1. Two-dimensional Eulerian compressible hydrodynamic calculations of a 1.27-cm radius 9404 explosive sphere initiated at its center and immersed to a depth of 1.59 cm. The pressure contour interval is 20 kilobars and the velocity contour interval is 0.05 cm/μsecond. The position of mixed cells (9404-water, 9404-air, water-air, or 9404-water-air) is shown with an "X" plotting symbol.

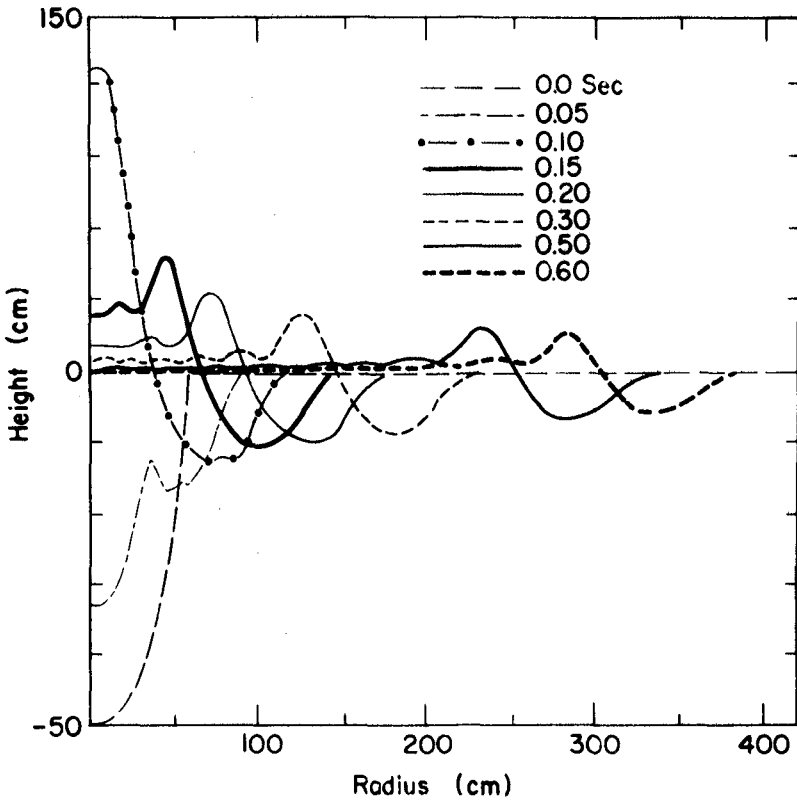


Fig. 2. The computed surface height vs radius at various times of the collapse of a 50-cm radius hole in three meters of water using the shallow water-long wave model and the SWAN code.

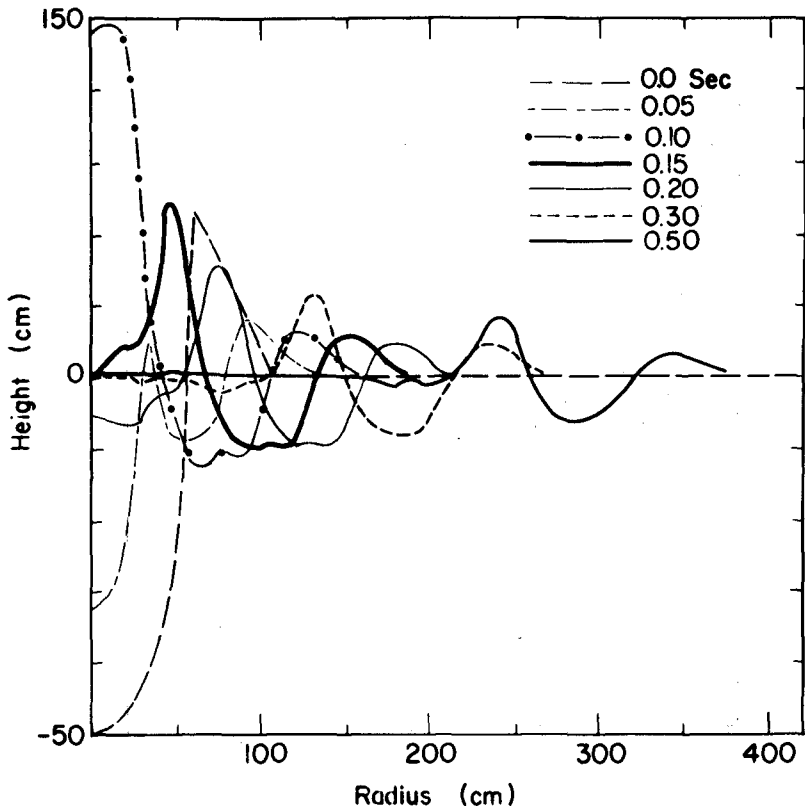


Fig. 3. The calculated surface height vs radius at various times of the collapse of a 50-cm radius hole with a triangular lip using the shallow water-long wave model and the SWAN code.

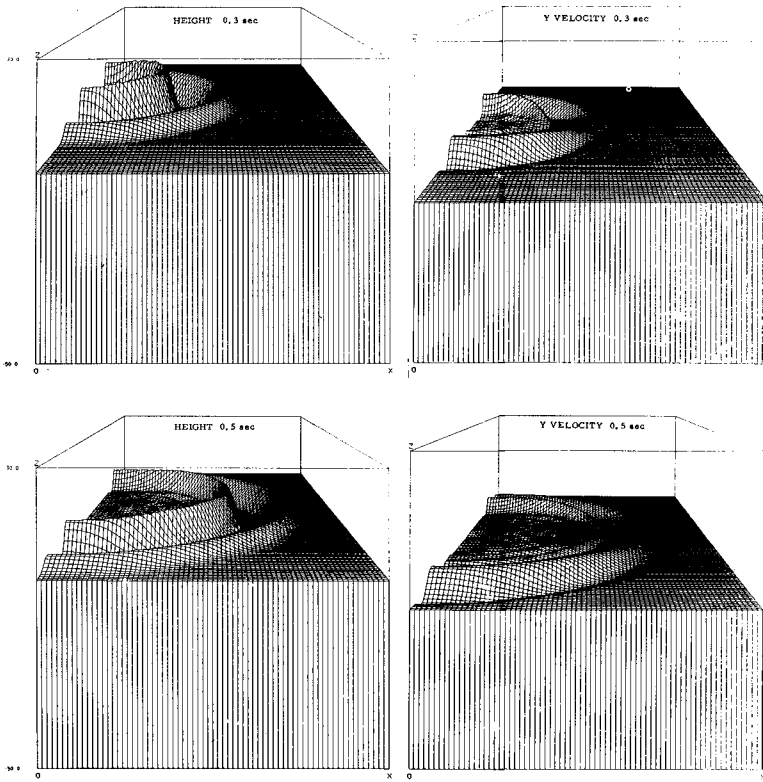


Fig. 4. Picture plots in three dimensions of the surface profiles and the velocity in the Y direction profiles at 0.3 and 0.5 seconds for the calculation described in Fig. 3.

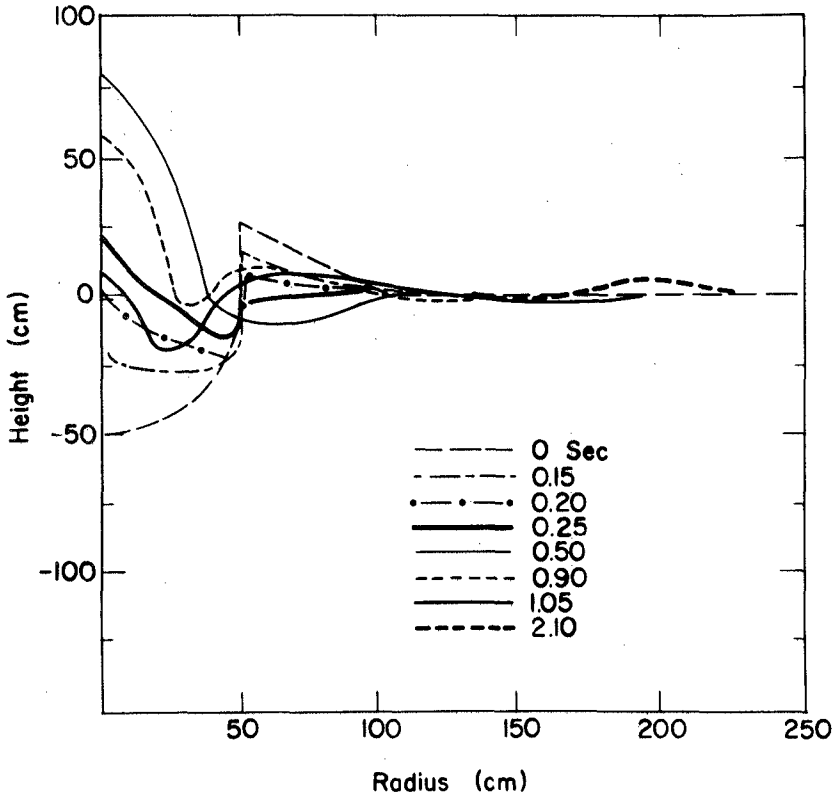


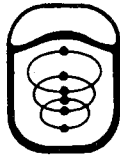
Fig. 5. The calculated surface height vs radius at various times of the collapse of a 50-cm radius hole with a triangular lip using the incompressible Navier-Stokes model and the ZUNI code.

BILLY L. I

DR. BILLY L. EDGE
DEPT. OF CIVIL ENGINEERING
CLEMSON UNIVERSITY
CLEMSON, S. C. 29631

PROCEEDINGS
OF THE

Fifteenth Coastal Engineering Conference



July 11-17, 1976 • Honolulu, Hawaii

Sponsored by the
State of Hawaii
University of Hawaii
American Society of Civil Engineers
through its Coastal Engineering Research Council
American Shore and Beach Preservation Association



Published by the American Society of Civil Engineers
345 East 47th Street, New York, N.Y., 10017

Price \$50.00

ACKNOWLEDGMENTS

The following served as the Organizing Committee for the Fifteenth International Conference on Coastal Engineering:

Charles L. Bretschneider
(Chairman)
Department of Ocean Engineering
University of Hawaii

J. Thomas O'Brien
J.K.K. Look Laboratory of
Oceanographic Engineering
University of Hawaii

Harold P. Brown
Conference Center
University of Hawaii

David S. D. Chung
U. S. Naval Facilities
Engineering Command
Pearl Harbor, Hawaii

Ada Marie B. O'Brien
Honolulu, Hawaii

S. Joseph Amaki
Department of Transportation
State of Hawaii

Howard A. Schirmer
Dames and Moore, Engineers
Honolulu, Hawaii

Karl V. Keller
Pacific Division, Corps of
Engineers, U. S. Army
Honolulu, Hawaii

Frederick A. Zobrist
Neighbor Island Consultants

Appreciation is expressed to the Department of Planning and Economic Development of the State of Hawaii and the Hawaii Visitors Bureau for providing the many photographs appearing on the title pages for the various parts of the proceedings.



CONTENTS

PART II

COASTAL SEDIMENT PROBLEMS

Chapter 65	
QUANTITATIVE DESCRIPTION OF SEDIMENT TRANSPORT BY WAVES	
Ole Secher Madsen and William D. Grant	1093
Chapter 66	
PREDICTIVE EQUATIONS REGARDING COASTAL TRANSPORTS	
D. W. Swart	1113
Chapter 67	
LONGSHORE TRANSPORT PREDICTION—SPM 1973 EQUATION	
Cyril Galvin and Philip Vitale	1133
Chapter 68	
SAND TRANSPORT BY WAVES	
E. W. Bijker, E. van Hijum, and P. Vellinga	1149
Chapter 69	
WAVE ACTION AND BOTTOM MOVEMENTS IN FINE SAND	
Michael W. Tubman and Joseph N. Suhayda	1168
Chapter 70	
APPLICATION OF SEDIMENT TRANSPORT MODEL	
C. A. Fleming and J. N. Hunt	1184
Chapter 71	
LONGSHORE TRANSPORT AT TOTAL LITTORAL BARRIER	
Richard O. Bruno and Christopher G. Gable	1203
Chapter 72	
CONCEPT FOR INFERRING LITTORAL DRIFT TREND	
Masataro Hattori and Takasuke Suzuki	1223

CONTENTS

Chapter 73	
FIELD INVESTIGATION OF SEDIMENT TRANSPORT PATTERN IN CLOSED SYSTEM	
Tsuguo Sunamura and Kiyoshi Horikawa	1240
Chapter 74	
EQUILIBRIUM PROFILES AND LONGSHORE TRANSPORT OF COARSE MATERIAL UNDER OBLIQUE WAVE ATTACK	
E. van Hijum	1258
Chapter 75	
STUDY OF EQUILIBRIUM BEACH PROFILES	
Robert A. Dalrymple and William W. Thompson	1277
Chapter 76	
BEACH PROFILES AT TORREY PINES, CALIFORNIA	
David G. Aubrey, Douglas L. Inman, and Charles E. Nordstrom	1297
Chapter 77	
STABILITY AND IMPULSE RESPONSE OF EMPIRICAL EIGENFUNCTIONS	
Clinton D. Winant and David G. Aubrey	1312
Chapter 78	
RIP-CURRENT AND COASTAL TOPOGRAPHY	
Mikio Hino	1326
Chapter 79	
SAND BYPASSING SYSTEM USING A JET PUMP	
E. C. McNair, Jr.	1342
Chapter 80	
SAND-BYPASS AND SHORE EROSION, BRIDGMAN, MICHIGAN	
C. N. Johnson and L. W. Hiipakka	1361
Chapter 81	
DESIGN AND BEHAVIOR OF SANDTRAPS IN REGIONS OF HIGH LITTORAL DRIFT	
P. C. Saxena, P. P. Vaidyaraman, and R. Srinivasan	1377
Chapter 82	
HEADLAND DEFENSE OF COASTS	
Richard Silvester	1394

CONTENTS

Chapter 83	
COASTAL PROTECTION BY MEANS OF OFFSHORE BREAKWATERS	
I. Fried	1407
Chapter 84	
ENCLOSING SCHEME FOR BATHING-BEACH DEVELOPMENT	
Joseph Tauman	1425
Chapter 85	
EXPERIMENTAL VERIFICATION OF GROUYNE THEORY	
C. H. Hulsbergen, W. T. Bakker, and G. van Bochove	1439
Chapter 86	
GROIN LENGTH AND THE GENERATION OF EDGE WAVES	
Michael K. Gaughan and Paul D. Komar	1459
Chapter 87	
COMPREHENSIVE MONITORING OF A BEACH RESTORATION PROJECT	
O. H. Shemdin, H. K. Brooks, Z. Ceylanli, and S. L. Harrell	1477
Chapter 88	
LABORATORY INVESTIGATION OF SHORE EROSION PROCESSES	
E. F. Brater and David Ponce-Campos	1493
Chapter 89	
CAPE HATTERAS BEACH NOURISHMENT	
John S. Fisher and Wilson N. Felder	1512
Chapter 90	
THREE DIMENSIONAL TESTS ON DYNAMIC EQUILIBRIUM AND ARTIFICIAL NOURISHMENT	
J. W. Kamphuis and R. M. Myers	1532
Chapter 91	
PROPOSED "IMPROVEMENT" OF KAIMU BEACH, HAWAII	
Dook C. Cox, Frans Gerritsen, and Theodore T. Lee	1552
Chapter 92	
CHANGES OF SEA BED DUE TO DETACHED BREAKWATERS	
Osamu Toyoshima	1572

CONTENTS

Chapter 93	
LOCAL SCOUR AND CURRENT AROUND A POROUS BREAKWATER	
Shintaro Hotta and Nobuo Marui	1590
Chapter 94	
PREDICTION OF WAVE-INDUCED SEAFLOOR MOVEMENTS	
Leland Milo Kraft, Jr. and David James Watkins	1605
Chapter 95	
SCOUR AROUND MODEL PIPELINES DUE TO WAVE ACTION	
John B. Herbich	1624
Chapter 96	
HYDRAULICS OF GREAT LAKES INLET-HARBORS SYSTEMS	
Robert M. Sorensen and William N. Seelig	1646
Chapter 97	
CHARACTERISTICS OF TIDAL INLETS ON THE PACIFIC COAST OF JAPAN	
Toshiyuki Shigemura	1666
Chapter 98	
TIDAL INLET FLOW DYNAMICS AND SEDIMENT MOVEMENT	
J. L. Machemehl, N. E. Bird, and A. N. Chambers	1681
Chapter 99	
MEASUREMENT OF BED FRICTION IN TIDAL INLETS	
A. J. Mehta, R. J. Byrne, and J. T. DeAlteris	1701
Chapter 100	
MORPHODYNAMICS OF A WAVE-DOMINATED RIVER MOUTH	
L. D. Wright	1721
Chapter 101	
RESULTS OF RIVER MOUTH TRAINING ON THE CLARENCE BAR, NEW SOUTH WALES, AUSTRALIA	
Cyril D. Floyd and Bruce M. Druery	1738
Chapter 102	
SEDIMENTATION PROBLEMS AT OFFSHORE DREDGED CHANNELS	
A. A. Kadib	1756

CONTENTS

Chapter 103	
STABILITY OF TIDAL CHANNELS DEPENDENT ON RIVER IMPROVEMENT	
Volker Barthel	1775
Chapter 104	
CHANGES DUE TO JETTIES AT TILLAMOOK BAY, OREGON	
Paul D. Komar and Thomas A. Terich	1791
Chapter 105	
CHANGES IN INLET OFFSET DUE TO STABILIZATION	
Dennis K. Hubbard	1812
Chapter 106	
TOPOGRAPHIC CHANGE RESULTING FROM CONSTRUCTION OF A HARBOR ON A SANDY BEACH; KASHIMA PORT	
Norio Tanaka and Shoji Sato	1824
Chapter 107	
IMPACT OF YACHTING MARINAS ON BEACHES	
J. P. Lepetit	1844
Chapter 108	
HARBOR INLETS ON TIDAL ESTUARIES	
Hans Vollmers	1854
Chapter 109	
SAND CIRCULATION PATTERN AT PRICE INLET, SOUTH CAROLINA	
Ducan M. FitzGerald, Dag Nummedal, and Timothy W. Kana	1868
Chapter 110	
BEACH HAVEN AND LITTLE EGG INLETS, A CASE STUDY	
Joseph DeAlteris, Thomas McKinney, and James Roney	1881
Chapter 111	
OFFSHORE SEDIMENTARY PROCESSES AND RESPONSES NEAR BEACH HAVEN—LITTLE EGG INLETS, NEW JERSEY	
Thomas McKinney, Joseph DeAlteris, Yung Y. Chao, Lloyd Stahl, and James Roney	1899
Chapter 112	
CAPACITY OF INLET OUTER BARS TO STORE SAND	
Todd L. Walton, Jr. and William D. Adams	1919

CONTENTS

Chapter 113	
INLET CHANGES OF THE EAST FRISIAN ISLANDS	
Günter Luck	1938
Chapter 114	
BARRIER ISLAND DYNAMICS: OVERWASH PROCESSES AND EOLIAN TRANSPORT	
Stephen P. Leatherman	1958
Chapter 115	
PROCESS AND MORPHOLOGY CHARACTERISTICS OF TWO BARRIER BEACHES IN THE MAGDALEN ISLANDS, GULF OF ST. LAWRENCE, CANADA	
E. H. Owens	1975
Chapter 116	
GEOMORPHOLOGY OF THE SOUTHERN COAST OF ALASKA	
Miles O. Hayes, Christopher H. Ruby, Michael F. Stephen, and Stephen J. Wilson	1992
Chapter 117	
TRACING ESTUARINE SEDIMENTS BY NEUTRON ACTIVATION	
Richard M. Ecker, John F. Sustar, and William T. Harvey	2009
Chapter 118	
SAND MOVEMENT INVESTIGATIONS BY MEANS OF RADIOACTIVE TRACERS IN A HYDRAULIC MODEL AND IN THE FIELD	
Hans Rohde	2027
Chapter 119	
MEASUREMENT OF SUSPENDED SEDIMENT IN THE SURF ZONE	
F. A. Kilner	2045
Chapter 120	
IOWA SEDIMENT CONCENTRATION MEASURING SYSTEM	
Tatsuaki Nakato, Frederick A. Locher, John R. Glover, and John F. Kennedy	2060
Chapter 121	
FACTORS INFLUENCING ESTUARY SEDIMENT DISTRIBUTION	
Mary P. Kendrick and B. V. Derbyshire	2072

CONTENTS

Chapter 122	
SEDIMENT TRANSPORTATION AND DEPOSITION MODELS FOR MOBILE BAY, ALABAMA	
Gary C. April, Samuel Ng, and C. Everett Brett	2092
Chapter 123	
WAVE-FORMED RIPPLES IN NEARSHORE SANDS	
John R. Dinger and Dougals L. Inman	2109
Chapter 124	
ORIGIN OF SUBMARINE DUNES	
N. S. Yalin	2127
Chapter 125	
TRANSPORT MECHANISM IN TIDAL DUNES	
Horst Nasner	2136
Chapter 126	
SEDIMENTATION STUDIES ON THE NIGER RIVER DELTA	
Ramiro Mayor-Mora, Preben Mortensen, and Jorgen Fredsoe	2151
Chapter 127	
GENERATION OF TROUGHS BY DENSITY CURRENTS	
Hans Speekenbrink	2170
Chapter 128	
CONCEPT OF MINIMUM SPECIFIC ENERGY AND ITS RELATION TO NATURAL FORMS	
Gordon Mckay and Ahad K. Kazemipour	2186



Wainae Harbor, Island of Oahu

PART II
COASTAL SEDIMENT PROBLEMS

Lumahai Beach, Island of Kauai



CHAPTER 65

QUANTITATIVE DESCRIPTION OF SEDIMENT TRANSPORT BY WAVES

by

Ole Secher Madsen⁽¹⁾, M.ASCE and William D. Grant⁽²⁾, A.M.ASCE

1. Introduction

With the apparent desire of man to move some of his activities into the offshore region the problems associated with the assessment of the impact of large structures in this environment will be of increasing importance. One of the impacts of a large offshore structure, such as for example the Atlantic Generating Station proposed by Public Service Electric and Gas Company of New Jersey, would be its effect on the wave and current pattern in the vicinity of the structure. These changes in wave and current conditions will induce changes in the sediment transport pattern and may disturb an existing equilibrium thus causing large changes in bottom topography in the vicinity of the structure. These topographical changes may extend all the way to the adjacent shoreline and thus cause deposition in some and erosion in other areas. To assess the severity and extent of topographical changes induced by an offshore structure an ability to quantify not only the effects of the structure on the wave and current pattern but also the mechanics of the interaction of the resulting fluid motion with the bottom sediment is clearly needed. The purpose of this paper is to establish quantitative relationships for the fluid-sediment interaction in this environment.

To avoid misunderstandings it should be pointed out from the outset that the results obtained in the following are limited to non-cohesive sediments and to reasonably well behaved wave conditions. The former of these limitations does not seem severe in view of the fact that the bottom sediments for the major part of the continental shelf may be characterized as cohesionless; the latter limitation excludes the direct application of the results in the immediate vicinity of the structure and in the surf zone where the conditions are complicated by the occurrence of wave breaking. It is, however, hoped that the results of the present research are of a sufficiently general nature to provide at least some insight also into these complicated processes.

With these limitations in mind the first question to ask if concerned with the sediment transport caused by a moving fluid would be: when does the sediment start to move? At the outset of this study a review of the literature on the initiation of sediment movement in oscillatory unsteady flow revealed that there were as many answers as there were publications pertaining to this question. By reanalyzing some of these previously published results

(1) Associate Professor, Ralph M. Parsons Laboratory, Massachusetts Institute of Technology, Cambridge, MA 02139

(2) Research Assistant, Ralph M. Parsons Laboratory, Massachusetts Institute of Technology, Cambridge, MA 02139

and making use of Jonsson's (1966) wave friction factor concept, which enables one to determine the magnitude of the maximum bottom shear stress associated with an oscillatory fluid motion, the differences between various investigations are essentially reconciled. In Section 2 it is shown that the Shields Criterion obtained for unidirectional steady flow is applicable as a general criterion for the onset of sediment movement also in oscillatory unsteady flow.

With a general criterion for the initiation of sediment movement established the next logical question to ask is: at which rate is sediment being transported once the critical bottom shear stress is exceeded? This question, in the context of purely oscillatory flow, has previously been addressed in a search for quantitative relationship by Einstein and co-workers at the University of California at Berkeley in the early sixties (Einstein, 1972), i.e., prior to the availability of the work of Jonsson (1966) on the wave friction factors. In Section 3 the Berkeley data is reanalyzed, using the wave friction factor concept, in terms of more fundamental parameters than those employed by Einstein and co-workers. It is found that their experimental data are well represented by a quasi-steady application of the empirical Einstein-Brown relationship (Brown, 1950) for sediment transport in unidirectional steady flow. Provided the equivalent sand roughness of the bottom is taken as the sediment grain size when evaluating the bottom shear stress for the purpose of predicting the rate of sediment transport it is found that the quasi-steady application of the Einstein-Brown relationship represents the Berkeley data obtained for a plane bed as well as for a bed exhibiting bed forms (ripples).

Some aspects of the application of the general sediment transport relationship, which was established in Section 3 based on experiments performed in purely sinusoidal flow, to predict net sediment transport rates in the coastal environment are discussed in Section 4. The net sediment transport in this wave dominated environment arises from differences in the rate at which sediment is transported back and forth with the wave motion. These differences arise from second order effects such as wave asymmetry, wave induced mass transport and superposed tidal or wind-induced currents. Due to our limited knowledge of the near-bottom turbulent flow conditions associated with unsteady boundary layer type flows the discussion of the factors producing a net sediment transport is rather qualitative, and serves primarily to identify topics in desperate need of further research. It is, however, felt that the quantitative relationships for the sediment transport by waves may serve as the framework for further quantitative studies of sediment transport in the coastal environment. The presentation is rather brief and a general reference is given to Madsen and Grant (1976) for a more detailed discussion.

2. Initiation of Sediment Movement in Oscillatory Flow

For unidirectional steady flow a widely accepted criterion for the initiation of sediment motion on a plane bed is given by Shields Criterion (Shields, 1936). This criterion essentially expresses the critical value of the ratio of entraining to stabilizing forces acting on a sediment grain on the sediment-fluid interface. The entraining force is related to the shear stress exerted on the bottom by the moving fluid, the stabilizing force is related to the submerged weight of a sediment grain and when the ratio of the two forces, re-

ferred to as Shields Parameter, exceeds a critical value sediment movement is initiated. The Shields Criterion is an empirical relationship which is quite general in that it applies for any fluid, flow and sediment characteristics so long as the sediment is cohesionless.

For oscillatory unsteady flows, such as the to and fro motion of the near bottom fluid particles under waves, several empirical criteria for the onset of sediment movement have been advanced. Bagnold (1946) and Vincent (1958) thus relate the amplitude of the near-bed fluid particle motion relative to the bed and the period of oscillation corresponding to the critical condition of initiation of sediment motion. A set of curves, each corresponding to particular sediment characteristics results. Relationships of this kind are usually limited by the range of experimental conditions from which they were derived and are not of the general nature of the Shields Criterion for unidirectional steady flow. The considerable differences between the critical conditions for initiation of sediment movement under waves exhibited by the comparison of some 13 such relationships (Silvester and Mogridge, 1971) clearly demonstrate this.

More general criteria for the initiation of sediment movement under waves have been proposed by Horikawa and Watanabe (1967) and Kajjura (1968). Both of these investigations evaluate the stability of a single grain on the sediment-fluid interface based on the concept of the maximum bottom shear stress associated with the oscillatory flow. Madsen and Grant (1975) presented Bagnold's data on initiation of motion in oscillatory flow in the form of a Shields Diagram in a discussion of a paper by Komar and Miller (1973). Madsen and Grant (1975) utilized the results of the comprehensive study of Jonsson (1966) to evaluate the maximum bottom shear stress associated with an oscillatory flow and this procedure was adopted by Komar and Miller (1975) in their reply. Despite the demonstration of the general validity of the Shields Criterion provided by Komar's and Miller's (1975) analysis their final recommendation for the quantitative description of the initiation of sediment movement under waves is essentially equivalent to their earlier paper.

In an unsteady flow one might expect that an inertia force in addition to a drag force, expressed by the bottom shear stress, contributes to the entraining force acting on a sediment grain on the sediment-fluid interface. An approximate analysis (Madsen and Grant, 1976) as well as a comparison with experimental data, however, shows that the entraining force is adequately represented by the bottom shear stress. Thus, adopting Jonsson's results, it is possible to evaluate the shear stress exerted on the bottom by the oscillatory fluid motion above the bed and present various experimental data for the onset of sediment motion in oscillatory flow in a Shields Diagram based on a Shields Parameter

$$\psi_m = \frac{\tau_{om}}{\rho g (s-1) d} \quad (1)$$

in which ρ is the fluid density, g is the acceleration of gravity, s is the specific gravity of the sediment material, d is the grain diameter and τ_{om} is the maximum bottom shear stress defined by

$$\tau_{om} = \frac{1}{2} f_w \rho u_b^2 \quad (2)$$

in which u_b is the maximum velocity of the fluid relative to the bed and f_w is the wave friction factor as given by Jonsson (1966).

From knowledge of the oscillatory motion, the fluid and sediment characteristics Jonsson's results may be used to evaluate the value of τ_{om} and hence the Shields Parameter given by Eq. (1). Rather than presenting the results in a conventional Shields Diagram the more practical presentation using the parameter

$$S_* = \frac{d}{4\nu} \sqrt{(s-1)gd} \quad (3)$$

in place of the boundary Reynolds number is used. The experimental results analyzed are summarized in Table 1 and presented graphically in Fig. 1.

All experiments on the initiation of sediment movement were performed using an initially flat bed and the equivalent boundary roughness was taken as the sediment diameter. From the sediment and fluid characteristics S_* is obtained from Eq. (3). When no information on the fluid temperature was available the kinematic viscosity of the fluid (in all cases water) was taken as 10^{-5} ft²/sec ($9.3 \cdot 10^{-3}$ cm²/sec). The various sets of experimental data are presented by the heavy vertical lines in Fig. 1 and are identified by a letter in the left hand side of the diagram indicating the investigator (e.g., M for Manohar, 1955) and by the symbol identifying the particular sediment (e.g., S1) whose characteristics may be found in Table 1.

The range of the critical values of the Shields Parameter obtained by a particular investigator for a given sediment indicates a variation of at most some 30% around the mean value. In the context of sediment transport and, in particular, when realizing the subjectiveness involved in determining the point of incipient sediment motion (defined as the condition when one or two grains are dislodged and move a few places) this scatter must be considered reasonable. The possibility, however, remains that the scatter exhibits a systematic variation with period of oscillation as suggested by Komar and Miller (1973). By examining the data it was, however, found that no general trend of the variation of the critical value of the Shields Parameter with period of oscillation was exhibited by the data. In some cases ψ_m increased with decreasing period (e.g., VPU, Vincent, 1958) in others the reverse was true (e.g., MS5, Manohar, 1955) and in some ψ_m varied randomly with period (e.g., Horikawa and Watanabe, 1967).

From the preceding discussing it is concluded that the variation exhibited by individual experiments is due primarily to experimental scatter. When comparing the sets of experimental data by Bagnold (1946) and Manohar (1955) who both used an oscillating plate in their studies, it is, however, seen that the results of Bagnold consistently plot below those of Manohar. This difference, which was also noted by Komar and Miller (1973), could be attributed to imperfect motion of the tray in the case of Bagnold's experiments. The close agreement between Bagnold's results and those of Rance and Warren (1968), who used an oscillating water tunnel, suggests that this reason must be discarded and the differences must be attributed to individual differences in determining just when initial sediment movement occurs.

Type of Exp.	Investigator	Material	Symbol	Spec. Gravity	Diameter (mm)	Range of Periods (sec)	Number of Exp.
Oscillating Plate	Bagnold (1946)	Sand	BS1	2.65	3.30	1.0- 4.8	7
		Sand	BS2	2.65	0.80	1.4- 7.8	6
		Sand	BS3	2.65	0.36	2.2- 7.0	6
		Sand	BS4	2.65	0.16	0.8-10.5	8
		Sand	BS5	2.65	0.09	3.1-15.7	5
		Coal	BC1	1.30	8.00	2.4- 7.0	6
		Coal	BC2	1.30	2.50	2.1-12.5	6
		Coal	BC3	1.30	0.36	2.1-14.3	8
		Steel	BST	7.90	0.60	1.1- 2.7	4
	Manohar (1955)	Sand	MS1	2.63	1.98	2.4- 8.5	18
		Sand	MS2	2.60	1.83	2.7- 8.2	19
		Sand	MS3	2.60	1.01	3.1-10.2	15
		Sand	MS4	2.63	0.79	3.2-10.5	18
		Sand	MS5	2.65	0.28	3.1-11	21
		Glass	MG1	2.54	0.61	3.9-13	19
		Glass	MG2	2.49	0.24	3.7-14.5	21
		Polystyrene	MP	1.052	3.17	9.2-27	13
Polyvinyl	MPC	1.28	3.17	6.5-14	13		
Laboratory Waves	Vincent (1958)	Sand	VS1	2.65	0.63	1.5- 2.1	4
		Sand	VS2	2.65	0.46	1.5- 1.9	3
		Sand	VS3	2.65	0.24	1.0- 2.7	10
		Pumice	VPU	1.38	1.20	0.9- 1.7	5
		Plastic	VP	1.46	0.39	0.8- 1.5	8
	Horikawa and Watanabe (1967)	Sand	HWS	2.65	0.20	0.8- 2.2	17
Water Tunnel	Rance & Warren (1968)	Sand	RWS1	2.65	0.82	5.2-16.1	4
		Sand	RWS2	2.65	0.39	5.0-15.0	4
		Sand	RWS3	2.65	0.24	6.0-13.8	4
		Coal	RWC	1.30*	7.00	3.6-15.7	6
		Limestone	RWL	2.72*	4.10	5.9-13.9	4

* Estimated values.

Table 1: Experiments on Initiation of Motion Presented in Figure 1.

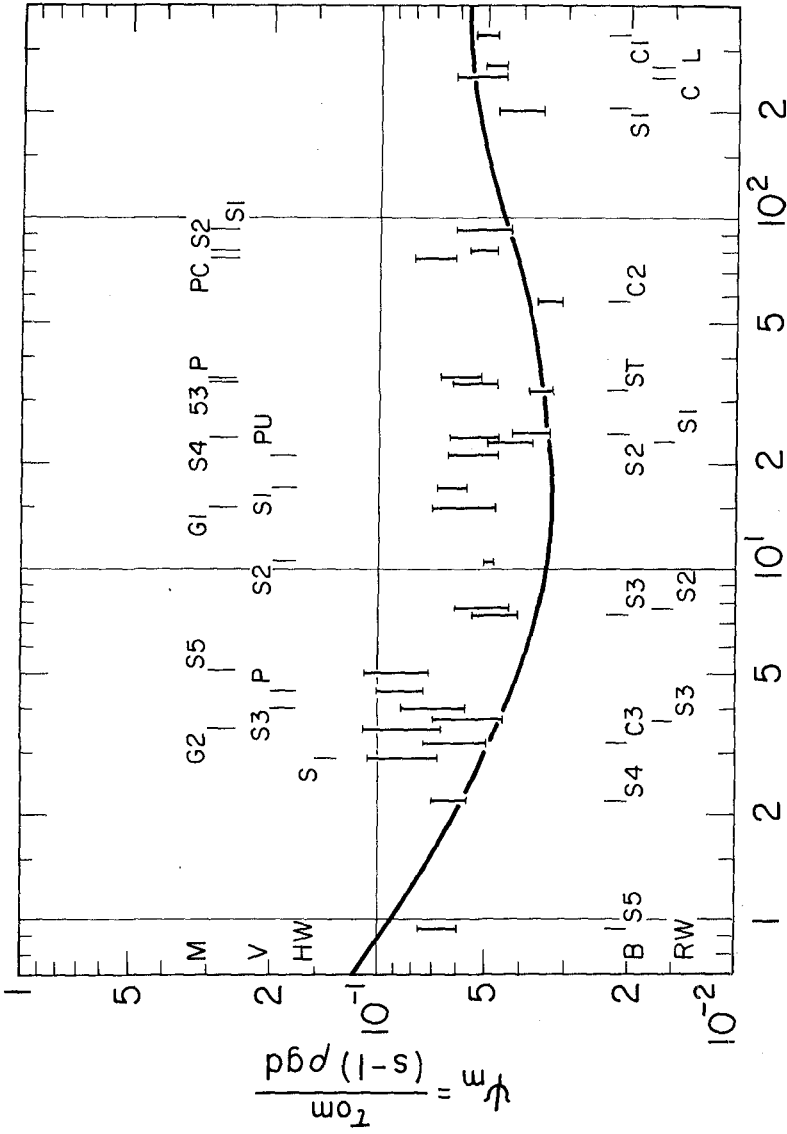


Figure 1: Experimental Observations of the Initiation of Sediment Movement in Oscillatory Flow.

When considering all the experimental data presented in Fig. 1 which were obtained from quite different experimental set-ups and for a wide range of periods (0.8-16 sec) and materials ($s = 1.052 - 7.90$) and keeping in mind the subjectiveness involved in obtaining the experimental results the overall scatter is not alarming. In this respect it should be pointed out that experimental results for unidirectional flow also exhibit some scatter. The general trend of the data indicate a critical value of the Shields Parameter slightly above that associated with the Shields Curve determined from unidirectional steady flow experiments. Despite this minor discrepancy, the conclusion of the results presented in Fig. 1 is that: Shields Criterion for the initiation of sediment movement as derived from steady unidirectional flow conditions serves as a quite accurate and general criterion for the initiation of sediment movement in oscillatory flow, provided the boundary shear stress is properly evaluated.

Since it is to be expected that a bed generally would exhibit bed forms rather than being flat the Shields criterion may seem to be of limited usefulness. The general applicability of Shields Criterion, as demonstrated in Fig. 1 for the purpose of defining the threshold conditions for a flat bed does, however, establish the importance of the Shields Parameter in quantifying the fluid-sediment interaction for unsteady flow conditions. Thus, when the critical value of the Shields Parameter is exceeded, sediment transport is initiated and the rate of sediment transport may be expected to be related to the value of the Shields Parameter.

3. Rate of Sediment Transport in Oscillatory Flow

For a unidirectional steady flow the sediment will, once it is set in motion, be transported in the direction of flow. Hence, in a steady current, the answer to the question of sediment transport rate once the critical shear stress is exceeded would be equivalent to establishing a relationship between fluid and sediment properties as well as flow characteristics and the rate at which sediment is transported. In the oscillatory unsteady flow associated with a wave motion the answer is somewhat more involved.

In an oscillatory flow, the flow above the bed and hence the sediment transport is constantly varying in magnitude as well as direction. To the first approximation the near-bottom fluid velocity associated with a wave motion may be described by linear wave theory as a purely oscillatory motion. Consequently, if the threshold value of the bed shear stress is exceeded during the wave period the amount of sediment transported forward (in the direction of wave propagation) during half of the cycle will equal the amount being transported backwards during the other half of the cycle by virtue of the symmetry of the motion. This means that, to the first approximation, no net sediment transport is associated with a wave motion. Now, water waves do not induce a purely sinusoidal flow near the bed. Nonlinear effects such as wave asymmetry and wave induced mass transport currents are likely to disturb the equilibrium between the amounts of sediment transported forward and backward during a wave period, thus producing a net sediment transport. It is, however, important to realize that such a net sediment transport is brought about by the, possibly small, difference between the, possibly large, quantities of sediment moving forward and backward with the waves.

The preceding qualitative discussion of the mechanics of sediment transport by waves points out the undesirable, but unavoidable, problem of determining a small difference between two large quantities, if one attempts to derive a relationship for the net sediment transport due to wave action. It does, however, pose the fundamental question: What is the rate at which sediment moves forward and backward in a purely oscillatory flow? The answer to this fundamental question is tantamount to the successful solution of the problem of net sediment transport caused by wave action.

As suggested by the analysis of the initiation of sediment motion data presented in the previous section one would expect the Shields Parameter defined by Eq. (1) to be a physically significant parameter in quantifying fluid-sediment interaction. For this reason the experimental data on the average rate of sediment transport in a purely oscillatory flow obtained at the University of California at Berkeley by Einstein and co-workers are reanalyzed in an attempt to establish an empirical relationship

$$\bar{\phi} = \bar{\phi}(\Psi_m) \quad (4)$$

in which

$$\bar{\phi} = \frac{\bar{q}_s}{wd} \quad (5)$$

is the average sediment transport rate, \bar{q}_s , nondimensionalized by the fall velocity w of an equivalent spherical sediment grain of diameter d .

For given sediment and fluid properties the fall velocity, w , may be obtained (Madsen and Grant, 1976, Fig. 6) and from the measured sediment transport rate the value of the dimensionless sediment transport function, Eq. (5) is readily evaluated. Since the experiments analyzed here were performed for an initially flat bed it seems reasonable to take the equivalent sand roughness of the boundary as the sediment grain size. Whether bed forms developed during the experiments is not quite clear; however, a particular set of experiments where bed forms definitely were present (Manohar, 1955) will be analyzed later. At this point we may regard the experiments performed by Kalkanis (1964) and Abou-Seida (1965) to correspond to a plane bed. From knowledge of the oscillatory motion of the plate, and taking the equivalent sand roughness of the boundary to be the sediment grain diameter Jonsson's (1966) results may therefore be used to obtain the value of the maximum boundary shear stress, and the value of Ψ_m may be determined. The results obtained in this manner are plotted in Fig. 2 of $\bar{\phi}$ versus Ψ_m .

From Fig. 2 it is noted that the sediment transport rate drops off for values of the Shields Parameter of the order 0.035. This is not surprising since the threshold of sediment movement in terms of the Shields Parameter as determined in Section 2 corresponds to values of Ψ_m of the order 0.04 to 0.05 for the sediments used by Kalkanis (1964). It is, however, worthwhile to note the fact that sediment transport does occur for these rather low values of the Shields Parameter, whereas Manohar (1955) as mentioned in Section 2 from direct observations of the movement of sediment grains consistently found critical values of the Shields Parameter higher than those indicated by

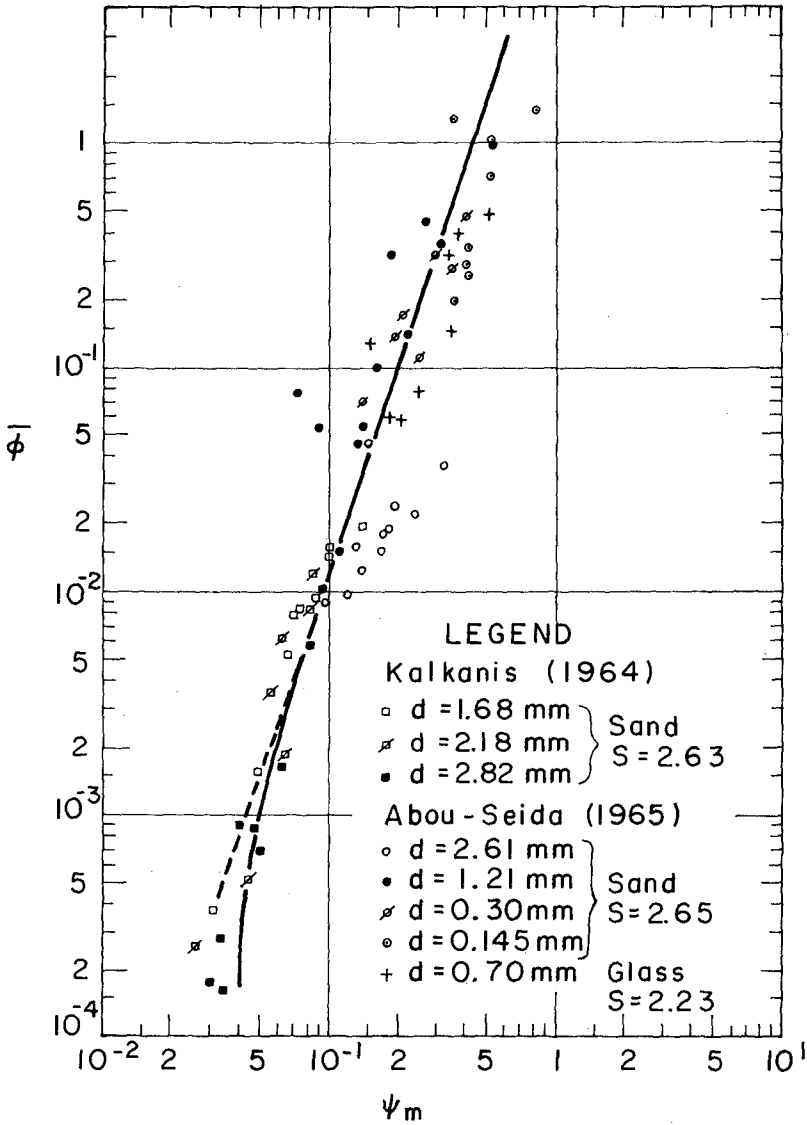


Figure 2: Empirical Relationship for the Average Rate of Sediment Transport in Oscillatory Flow (Plane Bed).

Shields Criterion. The difference between these results, both obtained from oscillating plate experiments, must therefore be attributed to the difference between the methods used to define the condition of incipient sediment movement.

For values of the Shields Parameter somewhat greater than the critical value the results presented in Fig. 2 indicate a rather well defined functional relationship among the two parameters of the type

$$\bar{\phi} \propto \psi_m^3 \quad (6)$$

as evidenced by the dashed straight line drawn onto the diagram.

The experimental data from which this empirical relationship is derived exhibit a scatter similar to the scatter exhibited by the same data when plotted in terms of the parameters used by Einstein and co-workers (Einstein, 1972). It should, however, be noted that the trend of the data in Fig. 2, for large values of the Shields Parameter, is in reasonable agreement with the empirical relationship suggested by the straight line, whereas the Einstein relationship (Einstein, 1972, Figure 16) in this region deviates from the experimental data. Furthermore, it should be noted that, in the present analysis of the Berkeley data, it was not found necessary to introduce any correction factor for the experimental results obtained by Abou-Seida (1965) with fine sediments. This very convenient finding may partially be attributed to the particular choice of the dimensionless sediment transport function, Eq. (5), made in the present analysis.

The rather well defined empirical relationship, Fig. 2, between the average rate of sediment transport in oscillatory flow and the Shields Parameter which was obtained in the preceding section bears a strong resemblance to the Einstein-Brown formula for the sediment transport in unidirectional steady flow. This empirical relationship, suggested by Brown (1950), reads

$$\bar{\phi} = 40\psi^3 \quad (7)$$

where the bar over ϕ and the subscript m have been omitted to indicate that this formula applies in steady flow.

In the context of fluid-sediment interaction a similarity between steady unidirectional and unsteady oscillatory flow was previously noted in Section 2 when establishing a criterion for the initiation of sediment movement. In the present context of rate of sediment transport in an oscillatory flow, the similarity between Eqs. (6) and (7) suggests that a quasi-steady application of the Einstein-Brown relationship may represent the Berkeley data. Hence, one is led to adopt a sediment transport relationship of the form

$$\phi(t) = 40\psi^3(t) \quad (8)$$

in which $\phi(t)$ is the instantaneous value of the sediment transport function

$$\phi(t) = \frac{q_s(t)}{wd} \quad (9)$$

$q_s(t)$ being the instantaneous rate of sediment transport and

$$\Psi(t) = \frac{\tau_o(t)}{(s-1)\rho g d} \quad (10)$$

is the instantaneous value of the Shields Parameter.

The basic assumption inherent in the application of the Einstein-Brown formula in this quasi-steady manner is that the response time of the rate of sediment transport, $q_s(t)$, is short relative to the time it takes the Shields Parameter, $\Psi(t)$, to change appreciably. Limited evidence for the very short response time of the sediment to the time varying forces associated with an oscillatory flow was found in Section 2 where the maximum value of the Shields Parameter was found to govern the initiation of sediment movement. Although this finding by no means constitutes a proof of the applicability of Eq. (8), it is taken to support the adoption of Eq. (8) as the basis for analyzing sediment transport rates in unsteady oscillatory flow.

The problem in applying Eq. (8) in oscillatory unsteady flow becomes that of determining the instantaneous value of the Shields Parameter or, as seen from Eq. (10), the instantaneous value of the boundary shear stress, $\tau_o(t)$, associated with an oscillatory flow. To tackle this problem, the expression for the maximum boundary shear stress given by Jonsson (1966) may be generalized to reflect the temporal variation associated with an oscillatory flow above the bed

$$\tau_o(t) = \frac{1}{2} f_w \rho |u(t)| u(t) \quad (11)$$

in which

$$u(t) = u_b \cos \omega t \quad (12)$$

is the near-bottom velocity relative to the bed, having a maximum value u_b and a radian frequency $\omega = 2\pi/T$ with T being the period of oscillation.

This simple form, Eq. (11) for the time-varying boundary shear stress preserves the varying direction as well as varying magnitude of the shear stress. It neglects a possible phase difference between the velocity and the shear stress, which according to Jonsson (1966) is small for fully turbulent flow in the boundary layer and immaterial in the present context. Furthermore, the assumption of f_w , the wave friction factor, being constant throughout the period of oscillation will be invoked in the following. Both of these assumptions indicate the applicability of Eq. (11) to be limited to conditions when the boundary layer flow is highly turbulent, which incidentally is the case for the Berkeley experiments presented in Fig. 2.

Introducing Eq. (12) in Eq. (11) and making use of Eqs. (1) and (2) lead to an instantaneous value of the Shields Parameter, Eq. (10), given by

$$\Psi(t) = \frac{\tau_{om}}{(s-1)\rho g d} |\cos \omega t| \cos \omega t = \Psi_m |\cos \omega t| \cos \omega t \quad (13)$$

The sediment transport formula, Eq. (8), may therefore be written

$$\phi(t) = 40\psi_m^3 (|\cos\omega t| - \cos\omega t)^3 \quad (14)$$

corresponding to purely oscillatory flow with a turbulent boundary layer.

This formula clearly has a zero mean value when averaged over a full period of oscillation. Thus indicating, as it should, that the amount of sediment transported in the positive direction (when $\cos\omega t > 0$) equals the amount transported in the negative direction (when $\cos\omega t < 0$) when the flow is purely sinusoidal. From the assumption, inherent in the adoption of Eq. (8), of instantaneous response of the sediment transport rate to changes in the transport function, $\Psi(t)$, it follows that sediment will be transported only when the value of the Shields Parameter exceeds the critical value for initiation of movement, ψ_{mc} , whose value is readily determined from Fig. 1. Hence, time-averaging Eq. (14) over the time interval during which $\cos\omega t > 0$ and $\Psi(t) > \psi_{mc}$ leads to a prediction of the time average transport rate, $\bar{\phi}$. The result of this analysis is the full line shown in Fig. 2! For values of ψ_m/ψ_{mc} greater than two the average sediment transport rate is closely described by the equation

$$\bar{\phi} = 12.5 \psi_m^3 \quad (15)$$

This equation is the equation for the straight line drawn in Fig. 2, which represents the experimental data reasonably well. The curved part of the line shown in Fig. 2 reflects the small value of the Shields Parameter relative to the critical value corresponding to initiation of sediment movement and has been drawn corresponding to $\psi_{mc} = 0.04$. Since the Berkeley experiments used in Fig. 2 were regarded as corresponding to conditions of a flat bed the boundary roughness was taken as the sediment grain diameter and the influence of turbulence is limited to a thin boundary layer. In fact, the boundary layer thickness can be estimated from Jonsson (1966) corresponding to the experimental conditions and it can be shown that the boundary layer thickness is of the order 5 times the boundary roughness. Hence, sediment movement is for the experiments analyzed so far restricted to a very thin layer near the bottom. This ensures a rapid response of the sediment transport rate to changes in the transporting forces as was assumed in the quasi-steady application of the Einstein-Brown formula. Furthermore, the limited vertical extent of the region in which sediment is being transported would suggest that if one were to characterize the transport as suspended or bed load, the present experiments would be categorized as bed load. That a bed load formula, here chosen as the Einstein-Brown formula, is successful in representing the experimental data can therefore hardly come as a surprise.

Experimental confirmation backed up by physical reasoning supported the quasi-steady application of the Einstein-Brown formula to describe sediment transport on a plane bed. Experimental evidence, Manohar (1955) and Carstens *et al.* (1969), however, shows that for flow conditions exceeding only slightly those corresponding to initiation of sediment movement the resulting sediment transport leads to the formation of bed forms, ripples. This points out that a sediment transport relationship restricted to plane bed conditions is of limited practical importance.

For a bed exhibiting bed forms, the equivalent sand roughness of the boundary will be related to the scale of the bed forms. The boundary layer thickness and hence the region of turbulent fluid motion may consequently be of considerably larger extent than corresponding to a plane bed. Kennedy and Locher (1972) thus report measurements of the sediment concentration in a layer of considerably thickness above a rippled bed. These observations may cast some doubt on the notion of the sediment transport being characterized as bed load as well as possibly invalidating the assumption of instantaneous response of the sediment transport rate to changes in the transporting forces. Even if these questions are disregarded there still remains the problem of determining the transporting forces, the bottom shear stress, which now may be a function of the scale of the bed forms.

The approach to the similar problems encountered in the context of unidirectional steady flow, Einstein (1950), is to separate the boundary resistance into two components: one, a skin friction component based on the sediment grain size the other being a form drag component which is associated with the bed forms. The former of these components is regarded as expressing the transporting force. In view of the similarities between steady unidirectional and unsteady oscillatory flow already uncovered in this investigation of fluid-sediment interaction it seems natural to pursue an analogous line of approach in the present context of unsteady flow. Hence, one may adopt Eq. (8) as the basic sediment transport relationship with an evaluation of the bottom shear stress, Eq. (11), appearing in the Shields Parameter based on the boundary roughness being taken as the sediment grain size, i.e., essentially disregarding the presence of the bed forms.

The approach outlined in the foregoing may be tested against some experiments performed by Manohar (1955) who undertook a study of bed form geometry and migration using the oscillating plate set-up. In contrast to the Berkeley experiments which were presented in Fig. 2, the oscillations of the sediment carrying plate were in this set of experiments not purely sinusoidal. An asymmetric motion was achieved by changing the radian frequency of the fly-wheel driving the plate when this was at its extreme positions while the excursion amplitude was held constant. The resulting forward and backward motions of the plate were essentially sinusoidal and choosing the subset of Manohar's (1955) experiments in which sediment transport occurred only during the forward motion a test of the procedure suggested above for sediment transport rates in the presence of bed forms is available. Thus, taking

$$\psi'_m = \frac{\tau'_{om}}{(s-1)\rho g d} \quad (16)$$

where the prime indicates that the boundary roughness is taken as the grain diameter, i.e., corresponding to skin friction, we may present Manohar's (1955) experiments whether bed forms were present or not as done in Fig. 3.

It is seen from Fig. 3 that the bed remained flat in some of the experiments. As shown by Manohar (1955) the reason for this is that ripples form only for a certain range of values of the transporting force. For low values of the transporting force, ψ'_m , the sediment transport is insufficient to cause the development of bed forms whereas the sediment transport is so intense for high values of ψ'_m that bed forms are washed away.

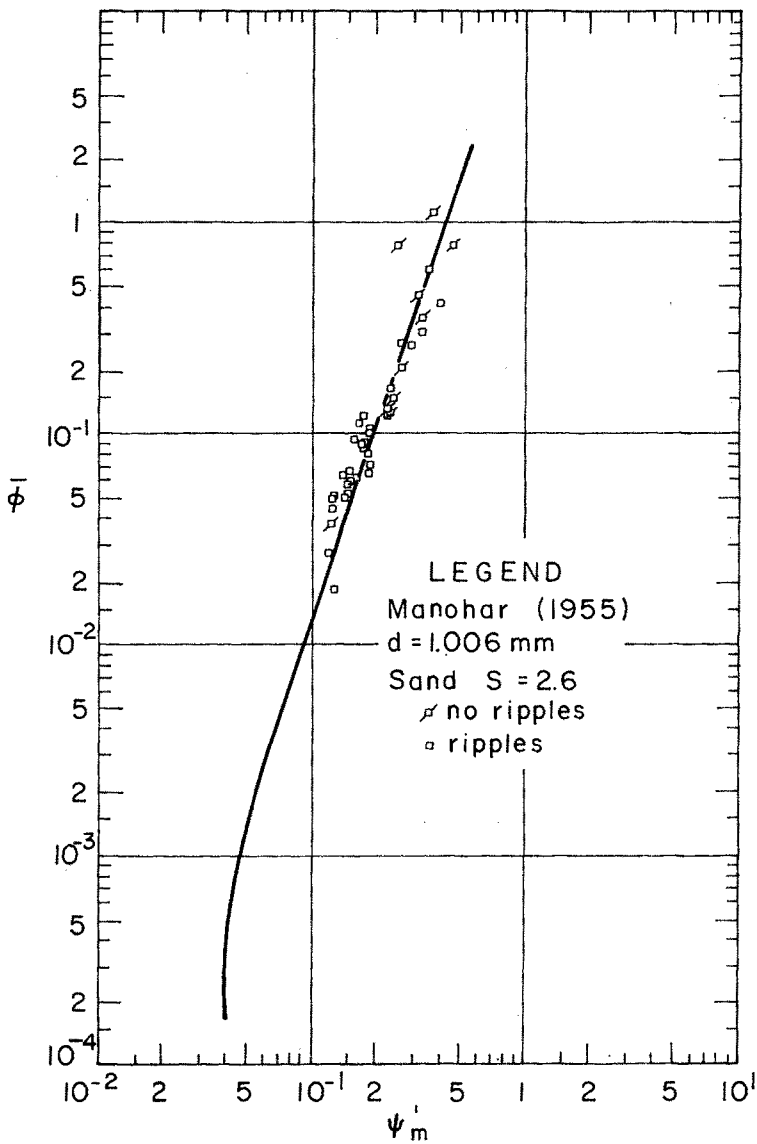


Figure 3: Empirical Relationship for the Average Rate of Sediment Transport in Oscillatory Flow (Plane and Rippled Bed).

The excellent agreement between the experimental data and the quasi-steady application of the Einstein-Brown relationship, the full line in Figs. 2 and 3, suggests that the procedure of disregarding the presence of the bed forms and taking the boundary roughness as the sediment grain size for the purpose of evaluating the transporting forces may be applied with some confidence.

4. Some Aspects of the Prediction of Net Sediment Transport and Resulting Topographical Changes in the Coastal Environment

The sediment transport relationship, Eq. (8), established in the previous section may be used as the basis for a discussion of the problems involved in quantifying the factors which produce a net sediment transport in the coastal environment. It is emphasized that the following discussion, despite the experimental support of Eq. (8) presented in Section 3, must be considered qualitative since it involves considerable generalizations which await experimental confirmation before they may be accepted with confidence. With this in mind the sediment transport relationship, Eq. (8), may be generalized to read

$$\vec{\phi}(t) = 40[\vec{\tau}'(t)]^3 \tag{17}$$

in which $\vec{\phi}(t)$ is the instantaneous dimensionless sediment transport vector given by Eq. (5) with the sediment transport rate, $q_s(t) = (q_{s,x}(t), q_{s,y}(t))$.

The instantaneous value of the bottom shear stress based on the grain roughness is given by

$$\vec{\tau}'(t) = \frac{1}{2} \rho f_s [\vec{u}(t)]^2 \frac{\vec{u}(t)}{|\vec{u}(t)|} \tag{18}$$

in which f_s is a generalized friction factor and $\vec{u}(t) = (u(t), v(t))$, is the instantaneous velocity vector.

Introducing Eq. (18) into (17) the following expressions in terms of the components of the sediment transport vector result

$$q_{s,x}(t) = 40wd \left[\frac{\frac{1}{2} \rho f_s (u^2(t) + v^2(t))}{(s-1) \rho g d} \right]^3 \frac{u(t)}{\sqrt{u^2(t) + v^2(t)}} \tag{19}$$

$$q_{s,y}(t) = 40wd \left[\frac{\frac{1}{2} \rho f_s (u^2(t) + v^2(t))}{(s-1) \rho g d} \right]^3 \frac{v(t)}{\sqrt{u^2(t) + v^2(t)}} \tag{20}$$

Eqs. (19) and (20) express the instantaneous rate of sediment transport in the x and y direction, respectively. In principle it is possible to evaluate these equations if the instantaneous velocity and the appropriate value of the generalized friction factor f_s are known.

In general there is little interest in knowing the instantaneous value of the sediment transport rate. The quantity of importance is the time averaged value of the transport rate, i.e., the net sediment transport rate, since this quantity through the sediment continuity equation determines the rate of topographical changes. For the purpose of predicting the net sediment transport rate one would therefore time average Eqs. (19) and (20)

$$\bar{q}_{s,net} = \frac{1}{T} \int_0^{T'} (q_{s,x}(t), q_{s,y}(t)) dt \quad (21)$$

where the integration is carried out over the time interval, formally identified as 0 to T' , during which the sediment is in motion, i.e., when $|\bar{\psi}'(t)| > \psi_{nc}$. For a periodic motion of period T the average is, of course, taken over the period.

Once the net sediment transport rates have been determined the sediment continuity equation may be used to evaluate the rate of change in bottom elevation, $\partial n / \partial t$,

$$\frac{\partial \bar{q}_{s,net,x}}{\partial x} + \frac{\partial \bar{q}_{s,net,y}}{\partial y} = -(1-\epsilon) \frac{\partial n}{\partial t} \quad (22)$$

in which the factor $1-\epsilon$, where ϵ is the porosity of the sediment, is introduced to account for the fact that the net sediment transport rates are obtained in terms of the actual volume of sediment transported.

The preceding discussion explains the general use of the sediment transport relationship for the prediction of topographical changes. If the water motion is a sinusoidal oscillation, as discussed in Section 3, the net sediment transport is, of course, zero. The second order effects which, when added to a basic sinusoidal wave motion, will produce a net sediment transport are: (1) effect of a sloping bottom; (2) wave asymmetry; (3) wave induced mass transport currents; (4) currents other than mass transport currents.

4.1 The Effect of a Gently Sloping Bottom. The influence of a gently sloping bottom on the rate of sediment transport may qualitatively be examined by considering the entraining forces acting on a sediment grain on the sediment-fluid interface. Even under the influence of a purely sinusoidal wave propagating towards shallower water (up-slope) the gently sloping bottom will give rise to an asymmetry in the forces acting on a sediment grain and hence induce a net sediment transport. Thus, under the wave crest the bottom shear stress acting up the slope will be counteracted by the component of the submerged weight of the particle acting down the slope whereas the two forces will both act in the down-slope direction under a trough. This asymmetry in entraining forces will result in a net sediment transport towards deeper water. No experimental data are available on the influence of bottom slope on the rate of sediment transport in oscillatory flow. Until such data are available this effect cannot be quantified with confidence.

4.2 The Effect of Wave Asymmetry. For a small amplitude wave progressing over a horizontal bed, linear wave theory predicts a purely sinusoidal orbital

velocity above the bed. However, if finite amplitude, i.e., nonlinear, effects are considered the wave profile is no longer symmetric about the mean water level. For nonlinear waves the wave crests become more peaked (higher and steeper) than the wave troughs (shallower and flatter). This lack of symmetry of the surface profile is also reflected in the near-bottom velocity which shows a larger forward velocity of shorter duration under the wave crests and a smaller backward velocity of longer duration under the troughs than predicted by small amplitude wave theory. In principle one might therefore take the friction factor, f_s , in Eq. (19) as Jonsson's wave friction factor f_w and evaluate the net sediment transport from Eq. (21). This procedure is applied to the experiments performed by Manohar (1955), of which a subset was presented in Fig. 3, with reasonably good agreement between predicted and observed net transport rates (Madsen and Grant, 1976, Fig. 9).

4.3 The Effect of Wave Induced Mass Transport Currents. When the analysis of the viscous flow in the bottom boundary layer associated with progressive waves is advanced to include second order effects a steady streaming in the direction of wave propagation is predicted based on the assumption of laminar flow in the boundary layer. This effect, which is referred to as mass transport, has been investigated theoretically by Longuet-Higgins (1953) and by Unluata and Mei (1970) under the assumption of laminar flow. For laminar flow in the bottom boundary layer this steady streaming, which immediately above the bottom is in the direction of wave propagation, will produce a non-zero time average shear stress in the direction of wave propagation acting on the bottom. This, in turn, would indicate that wave induced mass transport currents will result in a net sediment transport in the direction of wave propagation when the asymmetrical shear stress variation is introduced in the sediment transport relationship, Eq. (17).

Recent results reported by Bijker et al. (1974) clearly demonstrate that there are serious reasons to doubt the validity of Longuet-Higgins' solution in the case of a strongly turbulent boundary layer flow. As the roughness of the slope over which the waves propagate is increased from smooth to sand roughness to rippled bed the observed value of the near-bottom mass transport velocity is found to be increasingly smaller than the theoretical results based on a laminar flow assumption. In fact, the experiments with the slope roughness consisting of artificial ripples show a complete reversal of the direction of the near-bottom mass transport velocity. Bijker et al. (1974) conclude that much more data are needed to clarify the nature of mass transport in water waves when the boundary layer flow is turbulent.

In the present context of sediment transport by waves mass transport in addition to wave asymmetry discussed in Section 4.2 is undoubtedly an important factor in producing a net sediment transport. This makes it doubly unfortunate that the state of our knowledge is such that we cannot predict even the direction of this velocity with confidence not to mention its magnitude. For this reason further progress must be awaited before the effects of mass transport can be incorporated in the sediment transport relationship for the purpose of predicting net sediment transport rates associated with progressive waves.

4.4 The Effect of Currents. As a final second order effect which would produce a net sediment transport even if the wave motion were purely sinusoidal, the effects of a weak steady current superposed on the wave motion are considered. The action of these currents, for example, tidal or wind-induced, when combined with a wave motion will produce a net rate of sediment transport. If the current is weak, i.e., essentially a second order effect, the wave motion may be considered a stirring agent which by itself produces no net sediment transport. It does, however, make sediment available for transport by a current, although this current by itself would be incapable of even initiating sediment movement.

Assuming that the instantaneous velocity vector is known, this may be introduced in the general sediment transport relationship and one may numerically integrate Eq. (21) to obtain the time average value of the net sediment transport rates in the x and y direction, respectively. Thus, it is in principle quite simple to apply the general sediment transport relationship to determine the net sediment transport associated with the combined action of waves and currents. The major obstacle in performing this analysis is, however, the determination of the appropriate value of the generalized friction factor $f_s = f_{cw}$ for the combined action of waves and currents. Presently it is possible to estimate with some confidence the bottom shear stress only for a pure wave motion or for a pure current from knowledge of the bottom roughness. As shown by Madsen (1976) the friction factor, f_w , for a pure wave motion may be an order of magnitude larger than the friction factor, f_c , for a pure current of comparable magnitude, thus leaving the value of the friction factor f_{cw} for the combined action of waves and currents rather uncertain. In addition to this problem there is also some indication of a rather peculiar behavior of the sediment transport resulting from a weak current superimposed on a wave motion when the bottom exhibits bed forms. Thus, Inman and Bowen (1963) reported a net sediment transport in the direction opposite of the weak current superimposed on a wave motion. Although Inman's and Bowen's experiments and data analysis have certain deficiencies, as discussed by Madsen and Grant (1976), their observation and the experimental investigation of Natarajan (1969) show that the quantitative description of sediment transport over a rippled bed resulting from the combined action of waves and currents may present problems in addition to the problem of the determination of the wave-current friction factor f_{cw} .

Disregarding the problems mentioned above Grant and Madsen (1976) adopted a formula suggested by Jonsson (1966a) for the wave-current friction factor to investigate the topographical changes in the vicinity of the tip of a semi-infinite breakwater. The waves were assumed to be normally incident on the breakwater and a uniform current parallel to the breakwater produced with the diffracted wave pattern a spatially varying net sediment transport. The details of this investigation may be found in the above paper or in Madsen and Grant (1976). Here, the resulting prediction of erosion and deposition rates a distance of two wave lengths behind the breakwater are presented in Fig. 4. From Fig. 4 it is seen that no change, i.e., no sediment transport, occurs a distance of 3-4 wavelengths into the shadow region behind the breakwater. This is due to the decrease of wave activity in this region and emphasizes the importance of wave motion as being the stirring agent making sediment available for transport by currents which by themselves would be incapable of initiating sediment movement.

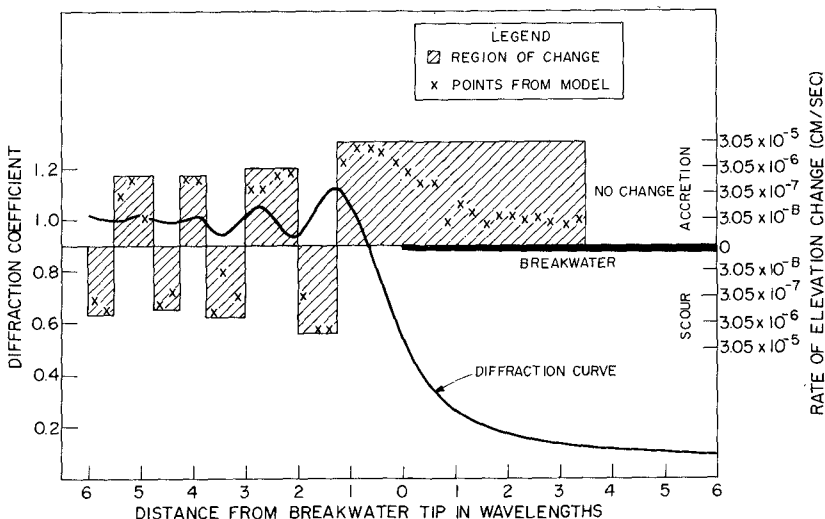


Figure 4: Diffraction Coefficient and Areas of Erosion and Accretion Two Wavelengths Behind Breakwater (From Grant and Madsen, 1976).

5. Concluding Remarks

It is not excluded that further analyses of the experimental data obtained by the Berkeley group may produce different sediment transport relationships for unsteady flow, just as the Einstein-Brown formula is far from being the only relationship for sediment transport in steady flow. Further documentation of the quasi-steady application of the Einstein-Brown sediment transport relation, suggested by the present investigation, is called for before this approach may be accepted with confidence.

The discussion given in Section 4 demonstrates an urgent need for further research and an improved understanding of the nature of the flow in the oscillatory turbulent bottom boundary layer associated with waves and currents in order to treat the problem of sediment transport in the coastal environment in a general manner. The problems of the quantitative description of the fluid flow and its interaction with a solid bottom in the coastal environment must be overcome before one can hope to establish an accurate sediment transport model for this environment. It is hoped, however, that the present study has produced a framework within which sediment transport in the coastal zone may be approached in a rational manner. At the very least the present research serves to point out that it is absurd to attack the problem of sediment transport in the coastal environment without considering the influence of waves.

Acknowledgment: The research reported here was supported by Public Service Electric and Gas Company of New Jersey.

References:

1. Abou-Seida, M.M. (1965), U. Cal., Berkeley, Hydr. Engrng. Lab., Rep. HEL-2-11, 78pp.
2. Bagnold, R.A. (1946), Proc. Roy. Soc. London, A, 187, p. 1-15.
3. Bijker, E.W. et al. (1974), Proc. 14th Conf. Coastal Engrng., ASCE, pp. 447-465.
4. Brown, C.B. (1950), In: Rouse H., Ed., Engineering Hydraulics, John Wiley and Sons, Inc., N.Y., 1039pp.
5. Carstens, M.R. et al. (1969), U.S. Army, CERC, Tech. Memo No. 28, 39pp.
6. Einstein, H.A. (1950), U.S. Dept. Agric. S.C.S., Tech. Bull. No. 1026.
7. Einstein, H.A. (1972), In: Meyer, R.E., Ed., Waves on Beaches and Resulting Sediment Transport, Academic Press, New York, 462pp.
8. Grant, W.D. and O.S. Madsen (1976), Proc. 3rd Inter-Agency Conf. Sed., W. Res. Council, p. 6.28-6.38.
9. Horikawa, K. and A. Watanabe (1967), Coastal Engrng. Japan, 10, p. 39-57.
10. Inman, D.L. and A.J. Bowen (1963), Proc. 8th Conf. Coastal Engrng., ASCE, p. 137-150.
11. Jonsson, I.G. (1966), Proc. 10th Conf. Coastal Engrng., ASCE, 1, p. 127-148.
12. Jonsson, I.G. (1966a), Basic Res. Pro. Rep. No. 11, Tech. U. Denmark, p. 1-12.
13. Kajiwara, K. (1968), Bull. Earthquake Res. Inst., U. Tokyo, 46, p. 75-123.
14. Kalkanis, G. (1964), U.S. Army, CERC, Tech. Memo No. 2, 38pp.
15. Kennedy, J.F. and F.A. Locher (1972), In: Meyer, R.E., Ed., Waves on Beaches and Resulting Sediment Transport, Academic Press, N.Y., 462pp.
16. Komar, P.D. and M.C. Miller (1973), J. Sed. Petrology, 43, 4, p. 1101-1110.
17. Komar, P.D. and M.C. Miller (1975), J. Sed. Petrology, 45, 2, pp. 362-367.
18. Longuet-Higgins, M.S. (1953), Phil. Trans. Roy. Soc. London, A, 903, pp. 535-581.
19. Madsen, O.S. (1976), In: Stanley, D.J. and D.J.P. Swift, Marine Sediment Transport and Environmental Management, J. Wiley and Sons, N.Y., 600pp.
20. Madsen, O.S. and W.D. Grant (1975), J. Sed. Petrology, 45, 2, p. 360-361.
21. Madsen, O.S. and W.D. Grant (1976), R.M. Parsons Lab., MIT, Tech. Rep. No. 209, 105pp.
22. Manohar, M. (1955), U.S. Army, BEB, Tech. Memo, No. 75, 121pp.
23. Natarajan, P. (1969), Ph.D. Thesis, U. of London, Imperial College.
24. Rance, P.J. and N.F. Warren (1968), Proc. 11th Conf. Coastal Engrng., ASCE, p. 487-491.
25. Shields, A. (1936), Mitteil. Preuss. Versuchsanst. Fur Wasserbau and Schiffbau, Berlin, No. 26.
26. Silvester, R. and G.R. Mogridge (1971), Proc. 12th Conf. Coastal Engrng., ASCE, 2, p. 651-667.
27. Unluata, U. and C.C. Mei (1970), J. Geophys. Res., 75, 36, p. 7611-7617.
28. Vincent, G.E. (1958), Proc. 6th Conf. Coastal Engrng., ASCE, p. 326-354.

CHAPTER 66

PREDICTIVE EQUATIONS REGARDING COASTAL TRANSPORTS

by

D. H. SWART*

1. INTRODUCTION

Morphological changes are the result of gradients in longshore and onshore-offshore sediment transport. The coastal engineer is continually faced with engineering problems in which a quantitative knowledge of these morphological changes is required. For this purpose predictive equations have been developed for both longshore and onshore-offshore sediment transport, which are being used in practical applications. In this paper a few of these predictive techniques, as well as one of their typical applications, viz. to a beachfill problem, will be discussed.

2. ONSHORE-OFFSHORE SEDIMENT TRANSPORT

2.1 General

The basics of Swart's *onshore-offshore sediment-transport theory* were described in detail in [14]. A paper about this subject was presented at the 1974 Coastal Engineering Conference in Copenhagen [13]. Subsequently it had become clear that the computational method described in [14] is too complicated for normal use, and that it could be modified to simplify the computations, without affecting the results significantly. In the present paper a summary will be given of the basic principles underlying the theory, as well as of the modified computational approach used at present. In Chapter 4 the method will be applied to a *beachfill problem*, to illustrate one of its typical applications.

2.2 Underlying principles

(1) The development in a normal beach profile is characterized into *three definite zones*, (Figure 1), each with its own transport mechanism, viz.

- (a) the *backshore*, i.e. the area above the wave run-up limit in which "*dry*" transport takes place,
- (b) a *developing profile* (D-profile) where a combination of *bed load- and suspended load-transport* takes place, and
- (c) a *transition area*, seawards of the D-profile, and landwards of the point where sediment motion by wave action is initiated, where normally only *bed load* transport takes place.

(2) The most basic assumption in the schematization of onshore-offshore sediment transport is that the developing profile (D-profile) will eventually reach a *stable situation* under persistent wave attack. This stable situation implies both an *equilibrium form* and an *equilibrium position* of the beach profile. This last concept is illustrated in Figure 2, where the *schematized* volume of sediment in the D-profile is plotted as a function of time. Similar variations are found for the different locations in the D-profile, thus also confirming the equilibrium form concept.

(3) The sediment transport rates into (or out of) the D-profile from (or to) the backshore and the transition area ($S_e(t)$ and $S_t(t)$ respectively) form the boundary conditions for the computation of profile changes in the D-profile. These transport rates were found in [14] to be given by :

* Coastal Engineering and Hydraulics Division
National Research Institute for Oceanology, South Africa

$$S_e(t) = s_e W_e \exp\left(\frac{-s_e t}{\delta_e}\right) \quad \dots (2.1)$$

$$\text{and} \quad S_t(t) = s_t W_t \exp\left(\frac{-s_t t}{\delta_t}\right) \quad \dots (2.2)$$

where s_e and s_t are the backshore- and transition area-coastal constants and

$$W_e = L_e(t=0) - L_e(t=\infty) \quad \dots (2.3)$$

$$W_t = L_t(t=\infty) - L_t(T=0)$$

$$t = \text{time}$$

The other variables are defined in Figure 1.

(4) With the aid of the assumption in step (2) above, the rate of onshore-offshore sediment transport S_{yit} at a specific location i in the profile at any time t can be shown to be a function of the difference between the values of a profile characteristic P at time t ($P(t)$) and time $t = \infty$ ($P(\infty)$).

$$S_{yit} \propto P(\infty) - P(t) \quad \dots (2.4)$$

(see Figure 3)

Experiments showed that the best description of the transport is found if the profile characteristic is taken to be a horizontal length in the profile $(L_2 - L_1)_{it}$.

$$S_{yit} = s_{ym} \left(\frac{s_{yi}}{s_{ym}}\right) (W_i - (L_2 - L_1)_{it}) \quad \dots (2.5)$$

where s_{ym} and s_{yi} are transport coefficients and

$$(L_2 - L_1)_{it} \xrightarrow{t \rightarrow \infty} W_i \quad \dots (2.6)$$

The meaning of $(L_2 - L_1)_{it}$ and the geometry of the beach profile at time t is defined in Figure 1. Relationships are presented in [13], whereby s_{ym} , (s_{yi}/s_{ym}) and W_i , as well as the limits of the D-profile (i.e. the area in which equation (2.5) is valid) can be found in terms of the boundary conditions.

(5) A subsequent study of the given relationships indicated that the computation of time-dependent profile development can be significantly improved and simplified if it can be assumed that at each location i in the developing profile the same fraction f_{it} of the total transport ($\int_0^\infty S_{yit} dt$) of sediment passing that location until time $t = \infty$, will have occurred at any given time t , i.e.

$$f_{it} = \left\{ \frac{\int_0^t S_{yit} dt}{\int_0^\infty S_{yit} dt} \right\} = f_t = \text{constant for all locations } i \text{ in the developing profile at time } t. \quad \dots (2.7)$$

The results of morphological tests with durations in excess of 1 000 hours, given in Figures 4 and 5, show that the above-mentioned assumption (equation (2.7)) is a *good engineering approximation*.

(6) With the principle of continuity of mass, and by using steps (1) - (5) above, it is possible to derive analytical expressions for the time variation of the length $(L_2 - L_1)_{it}$ and the sediment transport, viz. :

$$(L_2 - L_1)_{it} = W_i - (K_{ei} + K_{ti}) \exp(-X_b t) \quad \dots (2.8)$$

$$S_{yit} = s_{yi} (K_{ei} + K_{ti}) \exp(-X_b t) \quad \dots (2.9)$$

$$v_{yit} = \int_0^t S_{yit} dt = s_{yi} (K_{ei} + K_{ti}) X_b^{-1} (1 - \exp(-X_b t)) \quad \dots (2.10)$$

Substitution of equation (2.10) above into equation (2.7) yields an expression for f_t :

$$f_t = 1 - \exp(-X_b t) \quad \dots (2.11)$$

where

$$K_{ei} = \frac{W_e \delta_e}{\delta_{1i} (X_b^{-1} X_i - 1)} \quad \dots (2.12)$$

$$K_{ti} = \frac{W_t \delta_t}{\delta_{2i} (X_b^{-1} X_i - 1)} \quad \dots (2.13)$$

$$X_b = \frac{s_e}{\delta_e} = \frac{s_t}{\delta_t} \quad \dots (2.14)$$

$$X_i = \frac{\delta s_{yi}}{\delta_{1i} \delta_{2i}} \quad \dots (2.15)$$

(7) The theory is valid, not only for perpendicular waves, but also for oblique wave attack. In the latter case the transport coefficients s_{yi} and s_{ym} are increased, to allow for the effect of the increase in shear stress at the bed, due to the presence of nearshore currents, generated by the oblique waves. The data used to derive the relationship for the increase in s_{yi} and s_{ym} , as presented in [14] and [13], was derived from model tests in which a strong rip-current formation was found. A subsequent study into the effect of the rip-currents on the increase in offshore transport, showed that the increase in transport, which is due to the presence of longshore currents alone, can best be written in terms of the increase (due to longshore currents) of the sediment mobility F (refer to [17] and [1]).

$$\frac{(s_{yi})_{wc}}{(s_{yi})_w} = \frac{(F_i)_{wc}}{(F_i)_w} \quad \dots (2.16)$$

(see Figure 6)

where F_i is the sediment mobility at location i and the subscripts wc and w refer to *combined wave and current action* and *wave action only* respectively.

In order to comply with step (5) above, the mean value of equation (2.16) over the whole area of profile development will be applied to all transport coefficients.

$$\frac{(s_{yi})_{wc}}{(s_{yi})_w} = \left\{ \frac{(F_i)_{wc}}{(F_i)_w} \right\} \quad \dots (2.17)$$

Keeping in mind the normal uncertainty factor in the evaluation of sediment transport data, it can be stated that the validity of equations (2.16) and (2.17) is proved by the data in Figure 6.

2.3. Representative wave height

The theory described above was derived and verified for regular wave attack. In order to make it generally applicable to prototype conditions, the effect of irregular waves on the theory must be known. The irregular waves will affect not the underlying principles, but the empirical predictive equations which will be described in section 2.4 below.

Observations showed that the higher waves in the wave spectrum will define the profile limits described in section 2.2, step (1) above. The lower limits of the D-profile and transition area respectively are both found by using the significant wave height in the empirical formulae derived for regular wave attack, whereas the upper limit of the D-profile is found from the regular-wave formula by using a wave with a height twice that of the significant wave height

If it is assumed that the transport-formulae are still applicable in the transport zones defined by these representative wave heights, the single representative wave height which will yield the same resultant transport as the spectrum, can be computed (the wave heights are assumed to be Raleigh-distributed).

The formulae for irregular wave attack, derived in this manner, and those for regular wave attack, will be given in section 2.4.

2.4 Predictive equations

The various equations needed for the application of the theory in section 2.2, will be summarized below for the sake of convenience.

2.4.1 Limits of profile development (refer to Figure 1)

The upper limit of the backshore is chosen at the highest level from which sediment can be eroded indirectly by wave action.

h_e is chosen

upper limit D-profile :

$$h_o = 7650D_{50} \left[1 - \exp \left(-0.000143 \frac{H_{mo}^{0.488} T^{0.93}}{0.786 D_{50}} \right) \right] \quad \dots (2.18)$$

where H_{mo} = maximum wave height in the spectrum = $2(H_o)_{sign}$. ; T is the wave period and D_{50} is the median particle diameter. For regular wave attack, such as in small-scale hydraulic models, $H_{mo} = H_o$.
lower limit D-profile

$$h_m = 0.0063\lambda_o \exp \left(4.347 \frac{(H_o)_{sign}^{0.473}}{T^{0.894} D_{50}^{0.093}} \right) \quad \dots (2.19)$$

where λ_o is the deepwater wave length. For regular wave attack $(H_o)_{sign} = H_o$.

lower limit transition area

The maximum orbital velocity at the bed at the location where initiation of sediment movement takes place (u_{SEGAR}), is found from the following formula, which represents the weighted mean of a number of different initiation of movement-Formulae. [12], [16].

$$u_{SEGAR} = 4.58 D_{50}^{0.38} T^{0.043} \quad \dots (2.20)$$

The depth at which this velocity occurs is h_t . The corresponding wave length is λ_t . The first order wave representation of the orbital velocity can now be used to obtain a value for h_t/λ_t , whereafter it follows that :

$$h_t = \lambda_o \left(\frac{h_t}{\lambda_t} \right) \tanh \left(2\pi \left(\frac{h_t}{\lambda_t} \right) \right) \quad \dots (2.21)$$

In the case of irregular wave attack the significant wave height should be used for the computation of (h_t/λ_t) . Finally, with the aid of equations (2.18), (2.19) and (2.21), it follows that :

$$\delta_e = h_e - h_o \quad \dots (2.22)$$

$$\delta = h_o + h_m \quad \dots (2.23)$$

$$\delta_t = h_t - h_m \quad \dots (2.24)$$

(see Figure 1).

2.4.2 Equilibrium profile characteristics (refer to [14] and [13])

The computation of the equilibrium length w_i is subdivided into two parts, viz. :

- (1) the computation of a reference value $w_r (=w_i$ at the still-water level), and
- (2) the computation at all other locations in the D-profile of the ratio w_i/w_r .

in (1)

$$w_r = \frac{1.51 \times 10^3 D_{50}^{1.06} H_o^{0.39}}{\lambda_o^{0.71}} + 0.11 \times 10^{-3} \left(\frac{\lambda_o}{H_o} \right) \quad \dots (2.25)$$

$$W_r = \frac{\delta}{2m_r} \quad \dots (2.26)$$

In the case of irregular wave attack, equation (2.25) is rewritten as :

$$m_r = \frac{1.21 \times 10^3 D_{50}^{1.06} (H_o)^{0.39} \text{sign}}{\lambda_o^{0.71}} + 0.22 \times 10^{-3} \frac{\lambda_o}{(H_o) \text{sign}} \quad \dots (2.27)$$

re (2)

For any location *i* in the D-profile the ratio W_i/W_r is given by :

$$W_i/W_r = 0.7\Delta_r + 1 + 3.97 \times 10^7 b D_{50}^2 \Delta_r^{1.36} \times 10^4 D_{50} \quad \dots (2.28)$$

where
$$\Delta_r = \frac{\delta_{1i} - h_o}{\delta} = \frac{h_m - \delta_{2i}}{\delta} \quad \dots (2.29)$$

and
$$b = \begin{cases} 0 & ; \Delta_r < 0 \\ 1 & ; \Delta_r > 0 \end{cases} \quad \dots (2.30)$$

With the aid of equations (2.25) - (2.30) above the form of the equilibrium D-profile, measured relative to the position in the profile where $\delta_{1i} = 0$ (see Figure 1), can be written as :

$$Y_{i\infty} = W_r [2.1 z^2 - (1.4 + 2Q) z + P (1 - 2z)(h_r - z)^E EP (z^2 - z) (h_r - z)^{E-1} + (2Q - 0.7)] \quad \dots (2.31)$$

where $h_r = h_m/\delta \quad \dots (2.32)$

$z = \delta_{2i}/\delta \quad \dots (2.33)$

$Q = 0.7 h_r + 1 \quad \dots (2.34)$

$P = 3.97 \times 10^7 b D_{50}^2 \quad \dots (2.35)$

$E = 1.36 \times 10^4 D_{50} \quad \dots (2.36)$

The equilibrium slope $\alpha_{t\infty}$ of the deposited material in the transition area can be found from the equation of Eagleson et al [6] :

$$\alpha_{t\infty} = \frac{\Delta Z_t}{\Delta L_t} \quad \dots (2.37)$$

$$\Delta L_t = 42.73 \frac{J}{K} \lambda_o [\ln (0.01335 - 0.0161 \frac{d}{\lambda_o}) + 0.7271 (\frac{d}{\lambda_o})^2 + 1.206 (\frac{d}{\lambda_o}) - 1.50] \left\{ \begin{array}{l} h_m/\lambda_o \\ (h_m + \Delta Z_t)/\lambda_o \end{array} \right. \quad \dots (2.38)$$

where ΔZ_t is a depth increment and ΔL_t is the horizontal distance in the equilibrium depositional profile between the depths bracketing ΔZ_t .

The values of the schematized recession of the backshore (W_e) and the schematized growth of the transition area (W_t) can be found by drawing up equations for :

- (1) the conservation of mass (re Figure 7a)
- (2) the geometrical form of the equilibrium profile (re (Figure 7b), and
- (3) the distribution of the sediment in the transition area at equilibrium (re Figure 7b). The

reason why three equations are necessary to solve for the two unknowns W_e and W_t , is that δ_{tr} (see Figure 7a) is also an unknown.

2.4.3 Coastal constants (see [17])

At the elevation where $\delta_{li} = 0.5\delta$, the value of s_{yi} approximates s_{ym} very closely. s_{ym} is given by :

$$s_{ym} = \frac{D_{50}}{T} \exp [10.7 - 28.9 \left\{ (H_o)_{50}^{0.78} \lambda_o^{0.9} D_{50}^{-1.29} \left(\frac{(H_o)_{sign}}{h_m} \right)^{2.66} \right\}^{-0.079}] \quad \dots (2.39)$$

where $(H_o)_{50}$ is the median deepwater wave height and $(H_o)_{sign}$ is the significant deepwater wave height. In the case of regular wave attack, both $(H_o)_{50}$ and $(H_o)_{sign}$ are replaced by H_o .

With the aid of section 2.2, step (5), it follows that :

$$X_b = \left(\frac{s_e}{\delta_e} \right) = \left(\frac{s_t}{\delta_t} \right) = \left\{ \frac{(y_2 - y_1)_{io}}{W_{bi} + (y_2 - y_1)_{io}} \right\} X_i \quad \dots (2.40)$$

with as a result

$$\frac{s_{yi}}{s_{ym}} = \frac{4\delta_{li} \delta_{2i}}{\delta^2} \left[\frac{(y_2 - y_1)_{mo}}{W_{bm} + (y_2 - y_1)_{mo}} \right] \left[\frac{W_{bi} + (y_2 - y_1)_{io}}{(y_2 - y_1)_{io}} \right] \quad \dots (2.41)$$

$$\text{where } W_{bi} = \left(\frac{\delta_e}{\delta_{li}} \right) W_e + \left(\frac{\delta_t}{\delta_{2i}} \right) W_t \quad \dots (2.42)$$

$$(y_2 - y_1)_{io} = W_i - (L_2 - L_1)_{io} \quad \dots (2.43)$$

Subscript m refers to middepth ($\delta_{li} = 0.5\delta$) and subscript o refers to time $t = 0$.

The characteristic quantities K_{ei} and K_{ti} can now be found from equations (2.12) and (2.13) respectively.

2.4.4 Mobility number

(for a more detailed description of the mobility number and the following equations, reference should be made to [15] and [17]).

$$(F_i)_{wc} = \left\{ \frac{v_i I_{wc}^n}{C_D^{1-n} C_h^n (\Delta_s D_{35})^{\frac{1}{2}}} \right\}_i \quad \dots (2.44)$$

$$(F_i)_w = \left\{ \frac{2^{-n} f_w^{n/2} u_o}{C_D^{1-n} C_h^n (\Delta_s D_{35})^{\frac{1}{2}}} \right\}_i \quad \dots (2.45)$$

$$\text{where } I_{wc} = \left\{ 1 + \frac{1}{2} \left(\frac{\xi_J u_o}{v} \right)^2 \right\}_i^{\frac{1}{2}} \quad \dots (2.46)$$

$$\xi_{Ji} = \left\{ C_h \left(\frac{f_w}{2g} \right)^{\frac{1}{2}} \right\}_i \quad \dots (2.47)$$

$$C_{hi} = \left\{ 18 \log \left(\frac{12 d_i}{r} \right) \right\}_i \quad \dots (2.48)$$

$$C_{Di} = \left\{ 18 \log \left(\frac{10 d_i}{D_{35}} \right) \right\}_i \quad \dots (2.49)$$

$$f_{wi} = \left\{ \exp \left(-5.977 + 5.213 \left(\frac{a_o}{r} \right)^{-0.194} \right) \right\}_i \quad \dots (2.50)$$

(if $f_{wi} > 0.3$; $f_{wi} = 0.3$)

$$r = \text{hydraulic bed roughness}$$

$$= 25 \Delta_r \left(\frac{\Delta_r}{\lambda_r} \right) \quad \dots (2.51)$$

(See Figure 8)

a_o is the orbital excursion at the bed, Δ_r is the ripple height and λ_r is the ripple length.

$$n = 1 - 0.2432 \ln (D_{gr}) \quad (\text{with } 0 \leq n \leq 1) \quad \dots (2.52)$$

$$D_{gr} = \left(\frac{g \Delta_r}{\sqrt{2}} \right)^{1/3} D_{35} \quad \dots (2.53)$$

D_{35} = particle diameter which is exceeded in size by 65% (in weight) of the total sample.

In the case of irregular wave attack the median wave height (H_o)₅₀ should be used in the equations (2.44) - (2.50).

2.5 Computational Method

The computation of *time-dependent profile changes* (Y_{it}) and *onshore-offshore sediment transport rates* S_{yit} , as well as of *integrated onshore-offshore transport rates* ($\int_0^t S_{yit} dt$) up to any time t , can all be performed by using the following simple procedure :

- 1) compute the *equilibrium condition*,
- 2) compute the value of the *fraction f_t* as a function of time with the aid of section 2.4,
- 3) combine 1) and 2) to *predict time-dependent conditions*.

In the case of *profile-prediction*, the *location of the equilibrium profile* can be predicted, because the *initial profile* is given and the *equilibrium profile form* as well as the values W_e and W_t can be computed from section 2.4. The position Y_{it} of the profile at elevation Z_i and time t is then given by:

$$Y_{it} = Y_{i\infty} + f_t (Y_{i0} - Y_{i\infty}) \quad \dots (2.54)$$

(see Figure 9)

In the case of *transported-volume prediction* the total volume of transported material up to time $t = \infty$ ($V_{yi\infty}$) can be computed from equation (2.10) by putting $t = \infty$, whereafter V_{yit} , the total volume of sediment transported past the location in the profile with elevation Z_i , can be computed from :

$$V_{yit} = f_t V_{yi\infty} \quad \dots (2.55)$$

The *onshore-offshore sediment transport rate* at location i can also be found in terms of $V_{yi\infty}$ and f_t :

$$S_{yit} = V_{yi\infty} X_b (1 - f_t) \quad \dots (2.56)$$

3. LONGSHORE SEDIMENT TRANSPORT

3.1 General

Longshore sediment-transport computations can be used, either to gain an insight into the *overall sediment budget* of an area, or to study *detail problems* (such as deposition of sediment in an entrance channel to a harbour). The *total sediment load at various locations* will be needed in the first case, whereas the *vertical distribution of sediment load* (and specifically the division between bed and total load) will also be needed in the second case.

The available formulae for the prediction of longshore sediment transport rates can be classified into two groups, viz. :

- (1) *overall predictors*, such as the *SPM-formula* and the *Galvin-formula*, and
 (2) *detail predictors*, such as the *Bijker-formula* and the analogous *SWANBY-method*.

When a prediction of longshore sediment transport rates has to be made, it is useful to perform the computations with two or more of the available formulae, and to *base the final prediction* on the outcome of *all the results* obtained. In this chapter a detail-predictor method (SWANBY) will be described in detail, as well as a *modified version* of the SPM-predictor, which is used to back up the detail-predictor results.

3.2 Overall predictors

Although the overall predictors are by definition only applicable in areas with negligible longshore gradients, and cannot be used to obtain reliable estimates of the longshore transport rates in areas with strong longshore tidal flow, they can be useful in assessing the overall longshore sediment budget in an area. As such they can be used in conjunction with the detail predictors.

The SPM-formula, which relates the overall longshore transport rate S_{xtot} to a quantity resembling the longshore component of the wave-energy flux, is the best-known overall predictor available. This SPM-relationship can be rewritten to read :

$$S_{xtot} = K_o (T (H_o)_{rms}^2 k_r^2 \sin \theta_b \cos \theta_b) \quad \text{(see [19])} \quad \dots (3.1)$$

where k_r is the refraction coefficient, θ_b is the angle between the wave crest and the shoreline at wave breaking, and K_o is a coefficient which is assumed to be constant.

However, as lighter material will be transported more readily than heavier materials under the same wave conditions, it is to be expected that K_o will be a function of the grain size of the bed material. A re-evaluation of the data given in [19] and [3] yielded Figure 10, from which a clear tendency can be seen for K_o to vary with grain size. Although a steeper curve is to be expected intuitively, the data suggests K_o to vary as :

$$K_o = 365 \times 10^4 \log \left(\frac{0.00146}{D_{50}} \right) \text{ for } 0.1 \times 10^{-3} < D_{50} < 1.0 \times 10^{-3} \quad \dots (3.2)$$

Equations (3.1) and (3.2) are normally used to back up computations performed with the detail predictor, which will be described in section 3.3.

3.3 Detail predictors

3.3.1 Underlying principles

In 1966 Bijker [2] published a method for the computation of the longshore sediment transport at any specific location in the coastal environment, which constituted a major breakthrough in Coastal Engineering. Bijker assumed that it will be possible to use, in the coastal environment, a sediment transport formula which had been developed for uniform flow conditions, provided that the shear stress terms in the chosen formula are adapted to incorporate the effect of the wave action. He chose as basis for this adaptation the formula of Frijlink, which was at the time a much-used formula in river-flow problems in the Netherlands. Although the resulting Bijker-Frijlink equation sometimes yielded unrealistic results, it has been used since then with a reasonable amount of success in numerous applications in the coastal environment. However, the insight into the fundamentals of sediment transportation under wave action has increased over the past decade. Furthermore, various evaluations of the available predictor methods revealed recently ([5], [7], [18], [20]) that there are more reliable methods for the computation of sediment transport under uniform flow conditions than the Frijlink-equation, which can also be used over a wider range of boundary conditions. Therefore, a new pre-

dicator method was developed by Swart [15] under the auspices of the Coastal Sediment Group of the Dutch Applied Coastal-Research Programme, for application in the coastal environment. The basic differences between the new technique (called the SWANBY-method) and the old Bijker-Frijlink approach will be discussed below.

(1) The Frijlink-formula, used in the original approach, is a bed load formula. The total load was computed from the bed load by adding the suspended load, as computed with the aid of the Rouse/Einstein description of the vertical distribution of suspended sediment. The thickness of the bed layer is in such an approach an important parameter in the determination of the total load. Due to the uncertainty in the definition of the layer in which the bed load takes place, it will be more convenient to choose a total load formula as basis for computations in the coastal environment. If necessary, a definition can then be made of a bed layer thickness, and the amount of sediment transported in that layer can be computed.

(2) Various comparative investigations [5], [7], [18], [20], showed that the two most reliable total load formulae available for uniform flow conditions, are those of *Engelund-Hansen* and *Ackers-White*. Both these formulae give comparable results over a wide range of boundary conditions, the only exception being cases where the sediment transport rate was low (near initiation of motion). In such cases the *Engelund-Hansen method over-predicted* the transport rates, where *Ackers-White* showed a good comparison. *Engelund-Hansen will thus not yield proper scale relationships*, that can be used for the scaling of three-dimensional small-scale models. For the above-mentioned reasons the *Ackers-White approach was chosen* as the basic theory, which was to be adapted for use in the coastal environment.

(3) When evaluating the shear stress at the bed due to combined wave and current action, Bijker assumed the orbital velocity u_z , at the edge of the viscous sublayer to be :

$$u_z = p_B u_o \sin \left(\frac{2\pi t}{T} \right) \quad \dots (3.3)$$

where $p_B = \text{constant} = 0.45$ (see [2])

It is, however, to be expected that the effect of the wave motion on the shear stress will vary with a variation in the flow regime at the bed. Jonsson [9] defined the flow regime at the bed in terms of the ratio a_o/r where r is the hydraulic bed roughness and a_o the maximum wave particle excursion at the bed. Using Jonsson's work, it can be shown that

$$u_z = p_J u_o \sin \left(\frac{2\pi t}{T} \right) \quad \dots (3.4)$$

where $p_J = \left(\frac{f_w}{2k^2} \right)^{1/2}$... (3.5)

C_h is the Chezy-roughness value and f_w is the wave friction factor. In the SWANBY-approach equation (3.4) was used instead of equation (3.3).

(4) In the Bijker-Frijlink approach the hydraulic bed roughness was taken equal to one-half the ripple height. A subsequent study [15] has shown the relative roughness (r/Δ_r) to vary with the ripple steepness Δ_r/λ_r (see Figure 8). This was used in the SWANBY-theory. It was shown in [15] that the thickness of the layer near the bed in which vortices (filled with sediment) are formed and diffused, is of the same order of magnitude as the hydraulic bed roughness r . The thickness of the layer in which bed load takes place was thereafter also assumed to be equal to the hydraulic bed roughness r .

(5) A comparative study of the various methods for the computation of the vertical distribution of suspended sediment (\bar{c}_z/\bar{c}_r) in the coastal environment [15] showed that there is little difference

between the prediction of \bar{c}_z/\bar{c}_r by various theories. The *best correlation* with data covering a wide range of boundary conditions in the coastal environment was, however, obtained with a theory in which the *diffusion coefficient* for solids ϵ was assumed to *vary linearly* over the depth. The corresponding variation in \bar{c}_z/\bar{c}_r is :

$$\frac{\bar{c}_z}{\bar{c}_r} = \left(\frac{z}{r} \right)^{-b_1} \quad \dots (3.6)$$

where b_1 is a constant for each specific suspended sediment distribution over the depth.

With the assumption of a logarithmic variation in velocity over the depth, equation (3.6) yields an expression for the amount of suspended sediment which is transported, which is *easier to apply than any of the other* approaches tested. Due to these reasons it was decided to use equation (3.6) in the SWANBY-method instead of the Rouse/Einstein approach.

In Figure 11 longshore sediment transport rates, measured in a small-scale model, are compared with predicted transport rates, as given by the Bijker-Frijlink and SWANBY (Adapted Ackers-White) formulae. It is obvious that the SWANBY-method shows the better comparison with the data.

3.3.2 Predictive equations

The equations needed for the application of the SWANBY-method for the computation of the longshore sediment transport, will be given below.

total load

The total longshore sediment transport S_{xt} (bed plus suspended load) at any specific location is given by :

$$S_{xt} = \left(\frac{1}{1-p} \right) D_{35} v \left(\frac{C_h}{1} \right)^n I_{wc}^{-n} \frac{C}{A^m} (F_{wc} - A)^m \quad \dots (3.7)$$

where $\left(\frac{1}{1-p} \right)$ = determined by the porosity of the bed, normally taken = 1.45 and v = uniform current velocity in the longshore direction. The values of C_h , I_{wc} , F_{wc} and n are defined in section 2.4.4 (equation (2.44), (2.46) - (2.53)). Furthermore

$$m = \frac{9.66}{D_{gr}} + 1.34 \quad \dots (3.8)$$

$$A = \frac{0.23}{D_{gr}} + 0.14 \quad \dots (3.9)$$

$$C = \exp \{ 2.86 \ln (D_{gr}) - 0.4343 (\ln (D_{gr}))^2 - B.128 \} \quad \dots (3.10)$$

The hydraulic bed roughness r is related to the ripple dimensions as given in equation (2.51). The ripple dimensions can either be known from observations or be computed from one of the available methods (for instance [11] and [15]).

bed load

The bed load can be computed from equation (3.7) and points (4) and (5) in section 3.3.1 above, viz. :

$$S_{xb} = \left(\frac{K_b}{K_b + K_s} \right) S_{xt} \quad \dots (3.11)$$

where $K_b = \ln \left(\frac{er}{\Delta} \right)$ for $b_1 = 1$

and $K_b = \left(\frac{1}{1-b_1} \right) \left(1 - b_1 \left(\frac{\Delta}{r} \right)^{1-b_1} \right)$ for $b_1 \neq 1$... (3.12)

$$K_s = 0.205 \ln \left(\frac{9.12d}{r} \right) \ln \left(\frac{d}{r} \right) \quad \text{for } b_1 = 1$$

and

$$K_s = 0.41 (1-b_1)^{-2} \left[(1-b_1) \left\{ \left(\frac{d}{r} \right)^{1-b_1} \ln \left(\frac{30.2d}{r} \right) - 3.4 \right\} + \left\{ 1 - \left(\frac{d}{r} \right)^{1-b_1} \right\} \right] \quad \text{for } b_1 \neq 1 \quad \dots (3.13)$$

b_1 was found empirically to be [15] :

$$b_1 = 1.05 \left(\frac{w}{\kappa v_* w_c} \right)^{0.96} \left(\frac{r}{d} \right)^{0.013} \left(\frac{w}{\kappa v_* w_c} \right) \quad \dots (3.14)$$

3.4 Representative wave height

The *single representative wave*, which will yield the same resultant longshore sediment transport as the *complete wave spectrum* in the case of irregular wave attack, will again be a function of the boundary conditions. By assuming (1) a Raleigh-distributed wave height spectrum, and (2) the superposition of the transports generated by the individual waves in the spectrum, a *representative wave height* H_r was computed for the SHANBY-detail predictor in the same manner as in Chapter 2. A design curve is presented in Figure 12, whereby it becomes possible to determine the *representative wave height* H_r in terms of the rms - wave conditions. The representative height varies between the median wave height (H_{50}) and the significant wave height (H_{sign}), with a tendency towards H_{sign} at the lower transport rates. Seeing that the lower waves in the spectrum will not transport sediment as readily in cases near the initiation of motion, this tendency is to be expected. The single representative wave height for the SPM-overall predictor is by definition the rms wave height.

4. APPLICATION

4.1 General

Normally the losses from an area which had been replenished by a beachfill, can be estimated by using methods which are based on the *grain size distribution of the borrow and native material* only. The three most-used formulae in this category are those of *Krumbein-James* [10], which is suggested for use in the Shore Protection Manual [19], *Dean* [4] and *James* [8].

The *Krumbein-James* and *Dean* methods predict an *overflow ratio*, i.e. the ratio between the *volume of sediment* that has to be placed in order to retain the design volume and the *required design volume* of sediment in the fill. The *Krumbein-James* method assumes some portion of the borrow material (which has the same grain size distribution as the native material) to be absolutely stable and to stay on the beach indefinitely, whereas the rest of the borrow material will be lost. The *Dean*-method, on the other hand, assumes that the borrow material which is coarser than the native material will *not be lost*.

James assumes that no material is absolutely stable, and that fine material is less stable than coarse material. He then computes a *relative retreat rate*, which is basically the ratio between the *loss rate* of the borrow material in the fill and that of the native material in the original beach profile.

In order to allow the comparison of the losses, as predicted by the techniques described in this paper, and those given by the above-mentioned three beachfill methods [10], [4], [8], the following two definitions were made :

$$\text{Overflow Ratio (SEGAR)} = \frac{(\Delta S_y)_{\text{borrow}} + (\Delta S_x)_{\text{borrow}}}{V_{\text{fill}}} \quad \dots (4.1)$$

and

$$\text{Relative Retreat Rate (SEGAR)} = \frac{(\Delta S_y)_{\text{borrow}} + (\Delta S_x)_{\text{borrow}}}{(\Delta S_y)_{\text{native}} + (\Delta S_x)_{\text{native}}} \quad \dots (4.2)$$

where (ΔS_y) and (ΔS_x) are the losses in the offshore and longshore directions respectively, and V_{fill} is the volume of sediment placed in the beachfill. When computing (ΔS_y) it should be kept in mind that the dimensions of the transport rates S_y in chapter 2 are $\text{m}^3/\text{m}/\text{s}$, while those in chapter 3 (S_x) are m^3/s . In equations (4.1) and (4.2) sediment is considered lost when it moves out of the area in which it was placed, i.e. that volume of sediment which has to be replaced in, for instance, an *annually recurring replenishment*. Due to the fact that the sediment moved in the offshore direction will eventually build a new equilibrium condition, which will conform to the borrow material and the wave climate, the annual losses, i.e. the required recurring replenishment, as characterized by equations (4.1) and (4.2), will gradually diminish with time. The present calculations only show the losses during the first replenishment period. The longshore losses were computed by both the SWANBY-detail predictor method and the SPM-overall predictor, whereafter a representative loss was computed from these two figures.

Due to the fact that both the *overflow ratio (SEGAR)* and the *relative retreat rate (SEGAR)* are time-dependent, a time-duration of 10 days was chosen as basis for the comparison, during which time one wave condition took place. When doing an actual beachfill design, the wave conditions in an average year should be applied *consecutively* to the gradually developing profile.

4.2 Beachfill characteristics

A typical beach profile for Natal (situated on the South African east coast) was taken as the initial profile for the computations. The geometry of the initial profile and the two beachfills, as well as the grain size characteristics, are given in Figure 13. As can be seen, six different cases result, viz. $\alpha_{\text{borrow}} = 1/10$ and $1/5$, each with $D_{50} = 200 \times 10^{-6}$, 500×10^{-6} and 1000×10^{-6} m. It was assumed that the beachfill has a longshore length $l_x = 1000$ m, and is situated in an area with no updrift supply of sediment. No gradients initiated by the placing of the fill itself, will be considered, i.e. edge effects at the longshore extremities of the fill will be neglected.

The wave condition in the area was taken to be :

$$(H_0)_{\text{sign}} = 2 \text{ m} ; T = 10 \text{ s} ; \theta_b = 5^\circ .$$

4.3 Discussion of results

The computed losses, as given by the various methods, are represented graphically in Figure 14. The following general observations regarding the results are relevant :

(1) The beachfill methods of Krumbein-James, Dean and James are all independent of the profile geometry, whereas the Krumbein-James and Dean methods are also independent of the wave climate. In the James-method the wave climate can perhaps be included via the choice of the measure of selectivity of the sorting process Δ (as defined by James [8]). Both the wave climate and the profile geometry do, however, influence the losses. Consequently, the above-mentioned three methods can only be used to obtain comparative results for various possible borrow materials.

(2) If all the consecutive wave conditions in an average year are taken into account, the resultant

losses will be lower than those given by the higher waves only, due to the fact that the lower waves will initiate an *onshore* sediment movement.

(3) Both the relative retreat rate (as given by James) and the overfill ratio (as given by Krumbein-James and Dean) are equal to unity in the case of a borrow material which is *identical* to the native material. The method presented in this paper (called the SEGAR-method) yields higher values of both the relative retreat rate and the overfill ratio (of approximately 2) in the case where the native and borrow materials are identical. This higher loss rate seems logical, seeing that the initial profile with fill is steeper than the initial profile alone (see Figure 13). Offshore losses will thus increase (re chapter 2).

(4) The relative retreat rates predicted by the James-method are appreciably smaller than those predicted by the SEGAR-method, for all values of D_{50} except $D_{50} = 200 \times 10^{-6}$ m. A study of the original paper by James reveals that if $\Delta = 1.0$ as suggested in [8], the relative retreat rate is actually < 1 for 330×10^{-6} m $< (D_{50})_{\text{borrow}} < 1000 \times 10^{-6}$ m, which is unfeasible from a physical viewpoint. For $(D_{50})_{\text{borrow}} < 200 \times 10^{-6}$ m, on the other hand, the relative retreat rate R_b increases drastically to completely unrealistic values (for instance, for $D_{50} = 100 \times 10^{-6}$ m; $M_{\phi_b} = 3.23$, $\sigma_{\phi_b} = 1.08$:- $R_b = 6.8 \times 10^3$ if $\Delta = .6$ and $R_b = 9.2 \times 10^4$ if $\Delta = 1.0$). As was already pointed out by James [8], the relative retreat rate is very dependent on the value of Δ . As Δ is mostly unknown, this represents a serious restriction in the applicability of the theory.

(5) The overfill ratios predicted by Dean and especially by Krumbein-James for values of $D_{50} < 500 \times 10^{-6}$ m (in the present illustration), are exceedingly high. The Dean-method seems to have the soundest physical background of the two methods.

(6) The SEGAR-method described in the present paper can, if necessary, be used to obtain the relative losses in the offshore and longshore directions respectively, as the transports in both these directions are already computed. This is not possible for the Krumbein-James [10], Dean [4] and James [8] methods.

4.4 Concluding remarks

Although the SEGAR-method, which takes into account the local wave climate and the geometry of the beachfill, is more complicated to apply than the other three beachfill methods [10], [4] and [8], it yields results which seem to be more comparable with the known prototype behaviour of a beachfill area, than the results given by [10], [4] and [8]. It is accordingly suggested that the SEGAR-method is used for beachfill design. *Back-up computations, yielding comparative results only*, of both the *relative retreat rate* and the *overfill ratio*, can be made by using the *James-method* (provided that an appropriate choice of Δ can be made) and the *Dean-method* respectively. The Krumbein-James method generally over-predicts the overfill ratio, and is not recommended for use.

5. SUMMARY

Predictor techniques have been presented, whereby it is possible to compute *onshore-offshore* and *longshore sediment transports* respectively. These respective techniques can be used in combination to compute sediment losses in numerous applications. One such application, viz. to a beachfill problem, was described in detail. The results were shown to be realistic.

A *comparison of computed results with actual field measurements* at a beachfill location will be the logical next step in the testing of the techniques.

LIST OF REFERENCES

1. ACKERS, P. and WHITE, W.R. Sediment transport : New approach and analysis; Proc. ASCE Journal of the Hydraulics Division, HY 11, November 1973.
2. BIJKER, E.W. Some considerations about scales for coastal models with movable bed; Delft Hydraulics Laboratory, Publication No. 50 142 pp, November 1967.
3. DAS, M.M. Suspended sediment and longshore sediment transport data review; Proc. 13th Coastal Engineering Conference, Vancouver, Volume II, 1972.
4. DEAN, R.G. Compatibility of borrow material for beach fills, Proc. 14th Coastal Engineering Conference, Copenhagen, Volume II, 1974.
5. DE HAAN, Evaluatie zandtransporten bij eenparige stroming ("Evaluation of sediment transport for uniform flow"); Delft University of Technology, graduation thesis, to be published in 1976.
6. EAGLESON, P.S., GLENNE, B. and DRACUP, J.A. Equilibrium characteristics of sand beaches; Proceedings, ASCE, Journal of the Hydraulics Div., 89, Paper No. 3387, pp 35-57, January 1963.
7. GOLE, C.V., TARAPORE, Z.S. and DIXIT, J.G. Applicability of sediment transport formulae to natural streams; Proc. 15th Congress IAHR Istanbul, September 1973.
8. JAMES, W.R. Beach fill stability and borrow material texture; Proc. 14th Coastal Engineering Conference, Copenhagen, Volume II, 1974.
9. JONSSON, I.G. Wave boundary layers and friction factors; Proc. 10th Conference on Coastal Engineering, Tokyo, Volume I, Chapter 10, pp 127-148, 1966.
10. KRUMBEIN, W.C. and JAMES, W.R. A lognormal size distribution model for estimating stability of beach fill material; T.M.-16, U S Army, Corps of Engineers, Coastal Engineering Research Center, Washington, D.C., November 1965.
11. MOGRIDGE, G.R. and KAMPHUIS, J.W. Experiments on bed form generation by wave action; Proc. 13th Coastal Engineering Conference, Vancouver, Vol. 2, pp 1123-1142, 1972.
12. SILVESTER, R. Coastal Engineering, 2; Developments in Geotechnical Engineering, Vol. 4B; Elsevier Scientific Publishing Company, Amsterdam, 1974.
13. SWART, D.H. A schematization of onshore-offshore transport; Proc. 14th Coastal Engineering Conference, Copenhagen, June 1974.
14. SWART, D.H. Offshore transport and equilibrium beach profiles; Delft Hydraulics Laboratory, Publication No. 131, December 1974.
15. SWART, D.H. and DELFT HYDRAULICS LABORATORY. Coastal sediment transport : computation of longshore transport; Delft Hydraulics Laboratory Report R968, November 1975.
16. SWART, D.H. Weighted value of depth of initiation of movement; Unpublished note, June 1976.
17. SWART, D.H. Sediment transportation in the coastal environment; Lecture notes for post-graduate ECOR-course in Coastal Engineering, Port Elizabeth, South Africa, June 1976.
18. TASK COMMITTEE FOR PREPARATION OF SEDIMENT MANUAL. Sediment transportation mechanics : H. Sediment discharge formulae; Proc. ASCE, Journal of the Hydraulics Division, Vol 97, HY 4, April 1971.
19. U.S. ARMY COASTAL ENGINEERING RESEARCH CENTER. Shore Protection Manual, Vol. 1 - 3; U.S. Government Printing Office, 1973.
20. WHITE, W.R., MILLI, H. and CRABBE, A.D. Sediment transport : an appraisal of available methods, Volumes 1 and 2; Hydraulics Research Station, Wallingford, Report INT 119, November 1973.

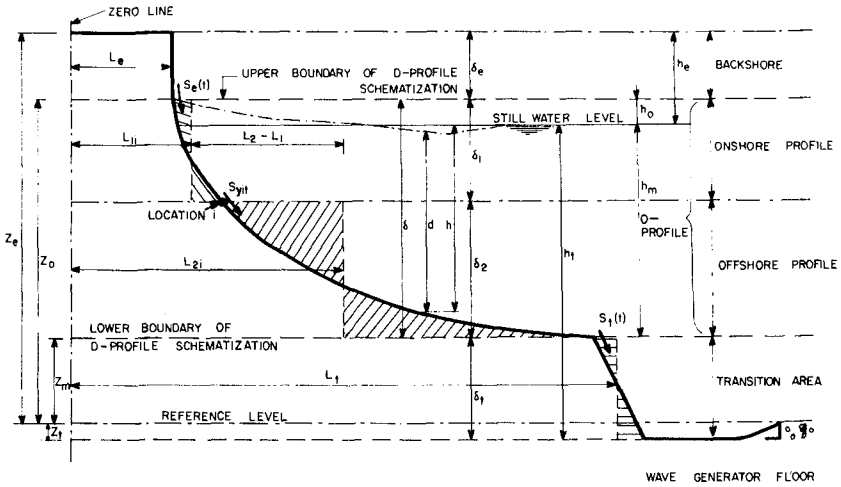


Figure 1 : Schematization of beach profile at time t

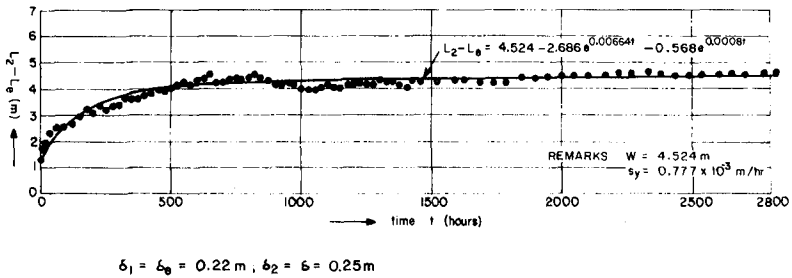


Figure 2 : Schematized time-variation of sediment in D-profile

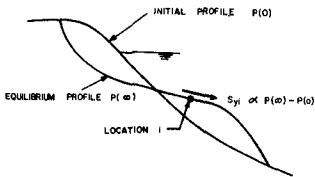


Figure 3 : Relationship between transport S_{yi} and profile form

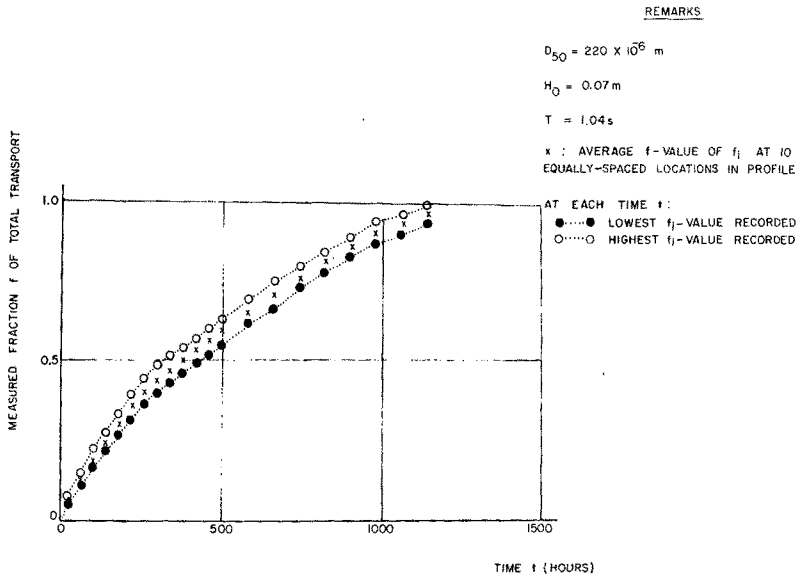


Figure 4 : Time- and depth-variation of measured fractions f_i

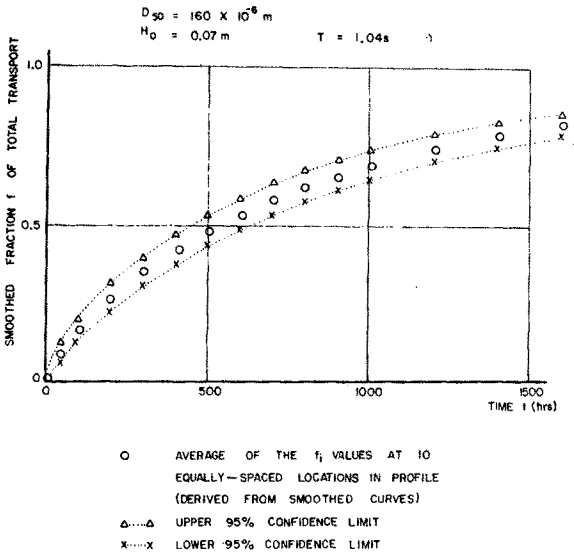
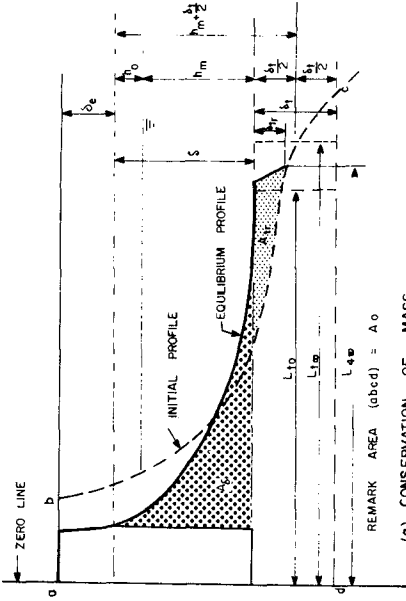
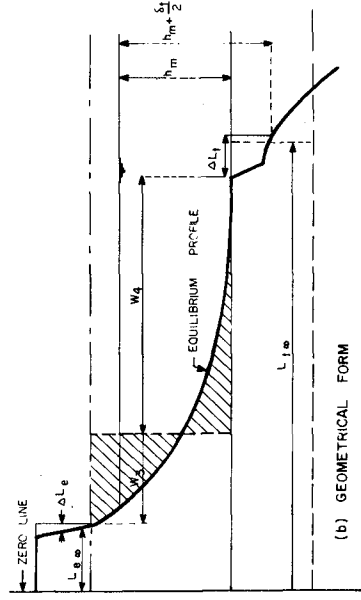


Figure 5 : Time- and depth-variation of smoothed fraction f_i



(a) CONSERVATION OF MASS



(b) GEOMETRICAL FORM

Figure 7 : Definition sketch: computation of W_e , W_t and δ_{tr}

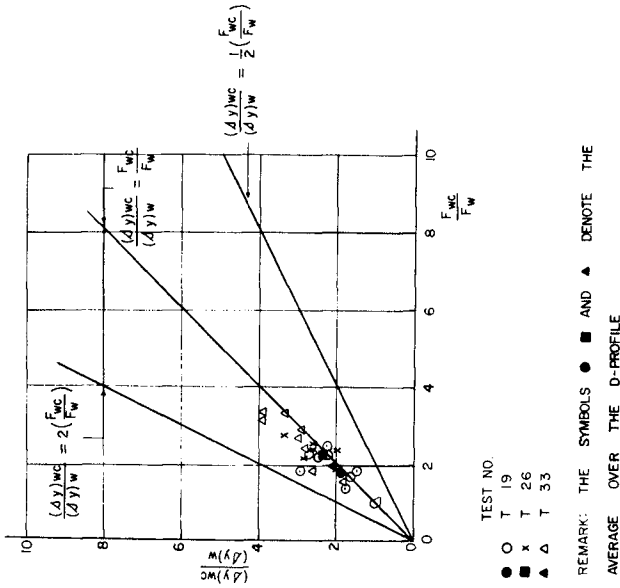


Figure 6 : Increase in coastal constant S_{yi}

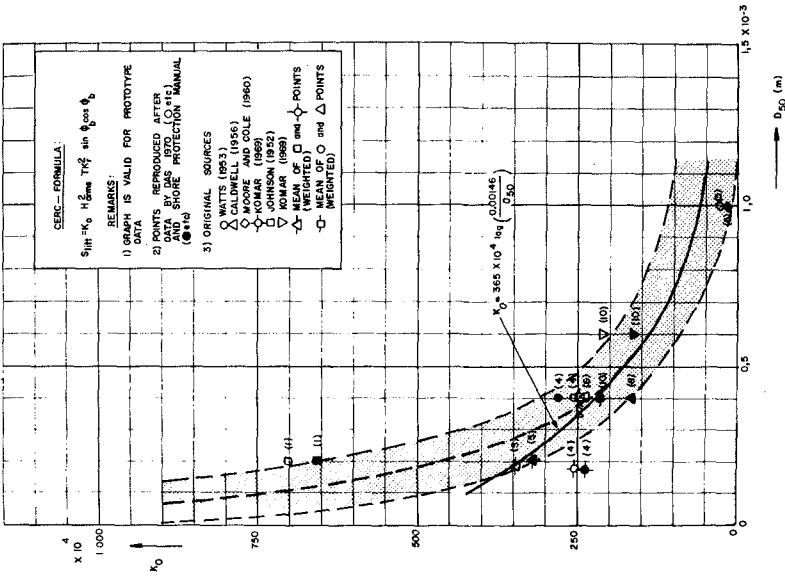


Figure 10 : Grain-size dependence of K_0

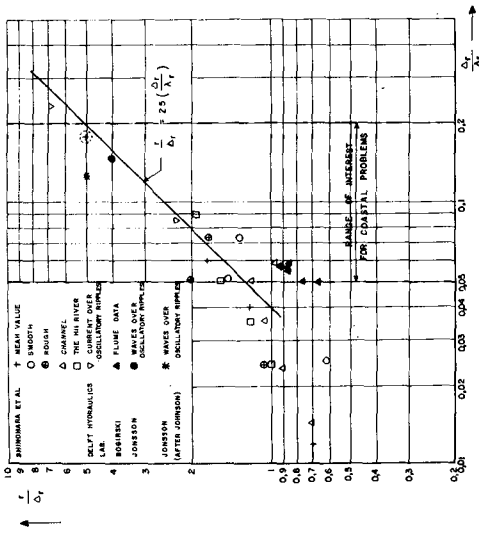


Figure 8 : Computation of relative roughness

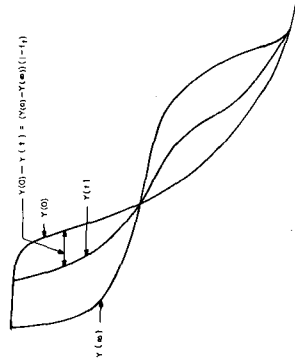


Figure 9 : Computation of time-dependent profiles

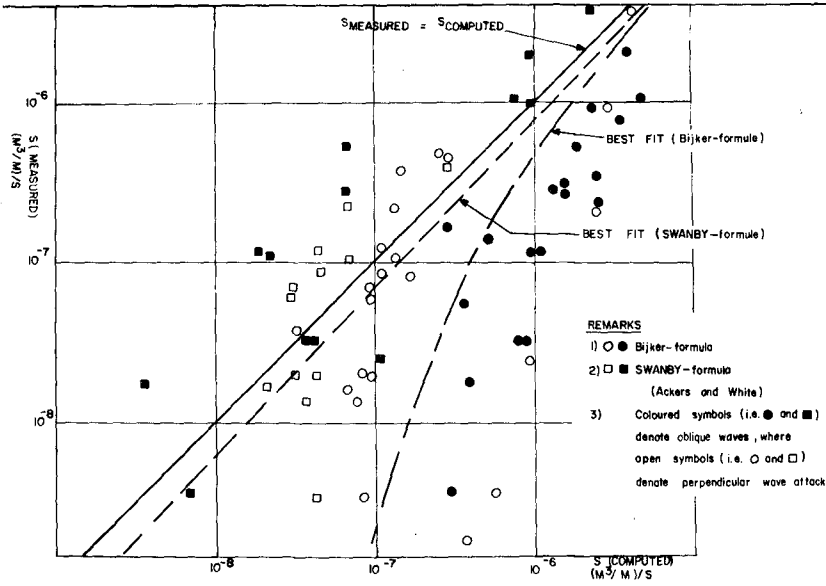


Figure 11 : Comparison between measured and computed longshore transport rates

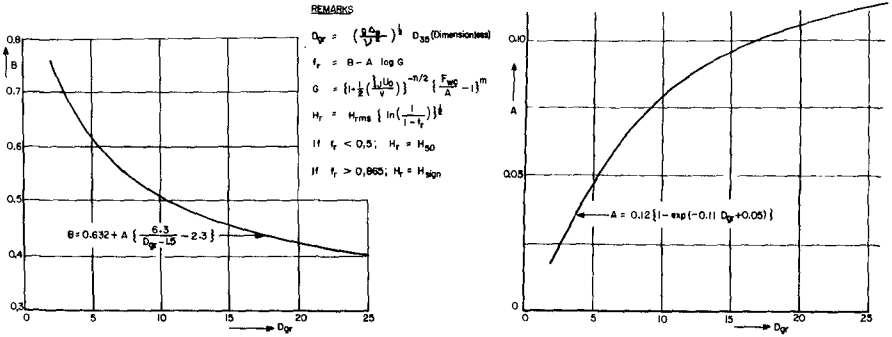
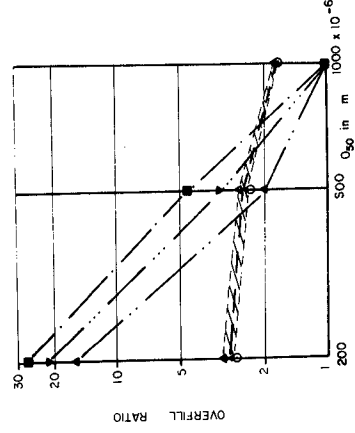
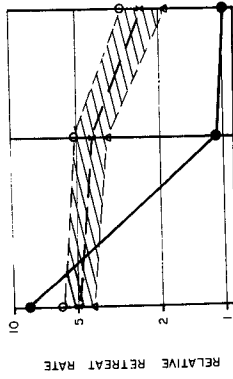


Figure 12 : Computation of representative wave height H_r

REMARKS

- PRESENT PAPER $\phi_{borrow} = \frac{1}{10}$
- △ PRESENT PAPER $\phi_{borrow} = \frac{1}{10}$
- x PRESENT PAPER (AVERAGE OF $\phi_{borrow} = \frac{1}{10}, \frac{1}{10}$)
- JAMES ($\Delta = 0.6$)
- KRUMBEIN - JAMES
- ▲ OGAN
- ▼ AVERAGE OF KRUMBEIN - JAMES AND DEAN (■, ▲)



- FILL I, 1:10 INITIAL SLOPE
- ◻ FILL II, 1:5 INITIAL SLOPE

GRAIN SIZE DISTRIBUTIONS

Grain size in m x 10 ⁶	Native Material			Borrow Material		
	A	B	C	A	B	C
D ₁₅	770	220	90	1000	500	200
D ₅₀	1300	1300	1100	1300	1100	450

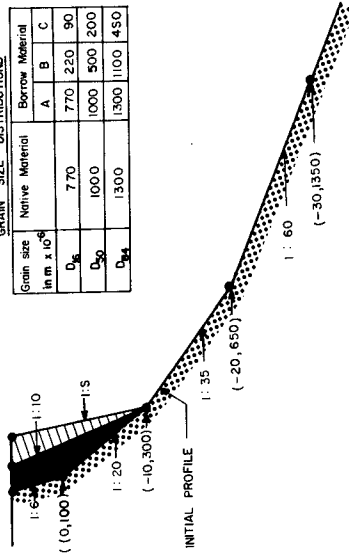


Figure 13 : Characteristics of beachfill

Figure 14 : Beachfill-stability results

CHAPTER 67

LONGSHORE TRANSPORT PREDICTION — SPM 1973 EQUATION

Cyril Galvin¹, M. ASCE and Philip Vitale², A.M. ASCE

ABSTRACT

The 1973 Shore Protection Manual (SPM) predicts longshore transport rates that are 83% higher than its 1966 predecessor, for the same wave conditions. This upward revision is the result of concurrent increases due to (1) deletion of all laboratory data used to establish the 1966 prediction, (2) addition of Komar's (1969) field observations, and (3) limiting energy flux values computed from previously unused data obtained at Santa Barbara (Johnson, 1952). A derivation based on conservation of energy shows that P_{ℓ} is the longshore component of the energy flux confined between two wave orthogonals spaced a unit distance apart in the longshore direction, and that a term previously identified as the onshore component of energy flux is identical with the total energy flux in the direction of wave travel between these orthogonals. Use of submerged weight transport rates has no engineering benefit at the present time because: (1) all available data are in terms of volume rates, (2) conversion to submerged weight requires estimates of the void ratio and sand grain density which have been assumed constant in practice, and (3) the engineering problem needs volume rates which would require reconversion back to volume rates if an immersed weight prediction were established.

INTRODUCTION

Energy flux method. Experience indicates that the best way to predict longshore transport at a given site is to adopt proven values from nearby sites, or to estimate values from surveyed changes in sand volume at suitable places along the shore. However, such data are often not available. In the absence of actual field-based estimates, the recommended procedure is to use the energy flux method.

The energy flux method empirically relates longshore transport rate, Q , to a computed variable called the energy flux factor, $P_{\ell S}$, by an equation of the form:

$$Q = K P_{\ell S} \quad (1)$$

¹P.O. Box 623, Springfield, Virginia 22150

²CERC, Kingman Bldg., Fort Belvoir, Virginia 22060

The energy flux factor depends on some combination of wave direction, height, and period. The coefficient of proportionality, K , is empirically determined.

The relation between Q and $P_{\ell s}$ has been published in many forms, with wide variations in the suggested value of K . This paper compares two published versions of equation (1): the SPM and TR4 versions. (SPM is the "Shore Protection Manual" of the Coastal Engineering Research Center [CERC], U.S. Army Corps of Engineers. SPM replaces the CERC Technical Report Number 4 [TR4], "Shore Protection, Planning and Design". SPM has been issued under two dates [1973, 1975], but both editions are identical for the material referred to in this paper. The third, and final, edition of TR4 [1966] is used for comparison with SPM.)

Units. The units in this paper are those used in SPM. The longshore transport rate, Q , is a volume per unit time, reported as cubic yards per year (yd^3/yr). This rate measures volume of beach sand in place, including voids. This is the volume rate of importance in beach erosion and shoaling studies.

The other side of equation (1) is the energy flux factor, $P_{\ell s}$, a power per unit length of shoreline, reported here as foot - pounds per second per foot of shoreline ($\text{ft} - \text{lbs}/\text{sec}/\text{ft}$). The proportionality constant, K , has units to balance the equation ($\text{yd}^3 - \text{sec}/\text{lb} - \text{yr}$).

It is believed that these units give the most effective engineering formulation at the present time. A later section of this paper discusses the applicability of immersed weight rates of transport instead of volume rates, and the physical meaning of the longshore energy flux factor.

To convert the volume rate and the energy flux factor units of this paper to their metric equivalents, the following conversions are required:

$$Q: 1 \text{ yd}^3/\text{yr} = 0.76 \text{ m}^3/\text{yr} \quad (2)$$

$$P_{\ell s}: 1 \text{ ft} - \text{lb}/\text{sec}/\text{ft} = 4.45 \text{ newton-m}/\text{sec}/\text{m} \quad (3)$$

Purpose. The energy flux prediction in SPM (Figure 4-37 and equation 4-40 on pages 4-100 and 4-101) replaces the energy flux prediction in TR4 (Figure 2-22, page 175). A comparison (Figure 1) between the two versions shows that the SPM prediction yields transport rates that are 83% higher than those in TR4, for the same wave conditions.

The purpose of this paper is to document the reasons for this significant upward revision of the predicted longshore transport rate.

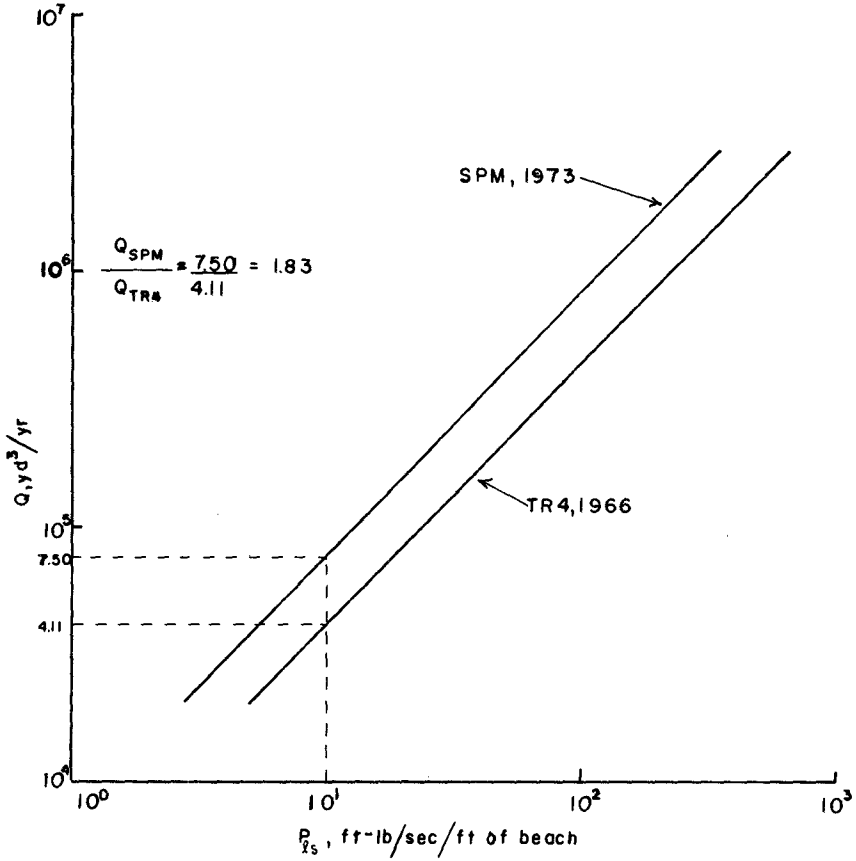


FIGURE 1. UPWARD REVISION OF LONGSHORE TRANSPORT PREDICTION

THEORY

For a field engineer applying a design curve to predict longshore transport rate, the background behind the curve is usually not of immediate interest. However, sooner or later questions arise about the method, or about the relation between the energy flux method and the apparently different methods available from other sources. For this reason, the following sections describe the basic theory behind the energy flux method and how it relates to the immersed weight rate of transport.

Derivation of P_{ls} . The energy flux factor, P_{ls} , is a quantity related to the power, P^* , supplied by the waves to the coast. The equation for P^* , from small amplitude wave theory, is

$$P^* = C_g E \quad (4)$$

where C_g is the group velocity of the wave and E is the energy density. Group velocity is related to wave speed, C , by

$$C_g = nC \quad (5)$$

where n is a factor that has a value of $1/2$ in deepwater and 1 in shallow water. The energy density depends only on wave height, H

$$E = \gamma H^2/8 \quad (6)$$

γ is the weight density of water.

The power, P^* , is in units of energy per second per unit length along the wave crest (ft - lb/sec/ft). In general, the value of P^* will change as the wave travels to shore. A point on a wave crest moving from deepwater to the shore describes a curved path that gradually approaches perpendicular to the bottom contours and the shoreline (Figure 2). This path is a wave orthogonal. Conservation of energy, according to the small amplitude wave theory used to obtain equation (4), requires that no energy can cross through a wave orthogonal, so that between any two orthogonals, the total wave power is constant in the direction of wave travel. Total wave power is the product of P^* and the length, w , along the wave crest between the orthogonals. Thus, from conservation of energy, with symbols from Figure 2,

$$w_0 P_0^* = w_1 P_1^* \quad (7)$$

For the remaining steps of the derivation, it is necessary to assume that the bottom contours are straight and parallel, although not necessarily evenly spaced. If this is the case, then for a given wave condition, any wave orthogonal has exactly

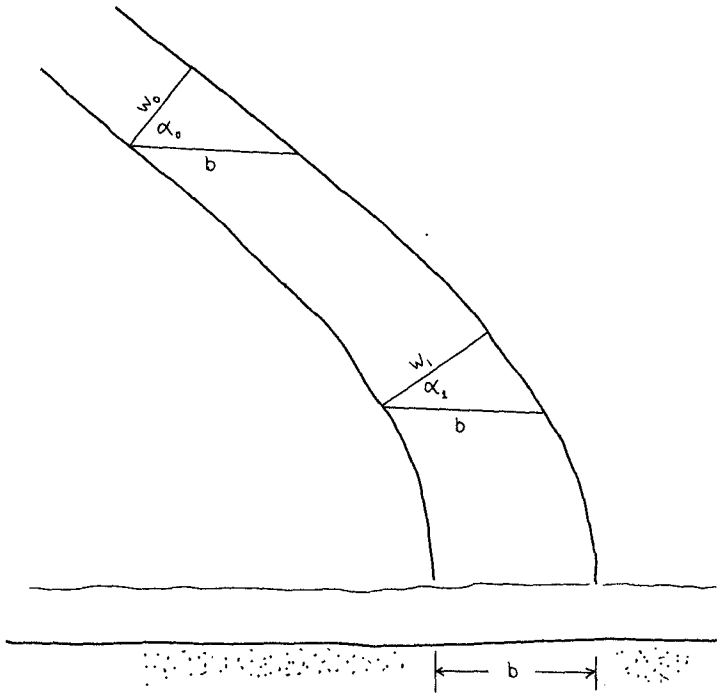


FIGURE 2. WAVE ORTHOGONALS EVENLY SPACED IN LONGSHORE DIRECTION OVER STRAIGHT, PARALLEL, BOTTOM CONTOURS

the same shape as any other. Thus, if the longshore distance between two orthogonals is b at the shoreline, then the longshore distance between those orthogonals remains b at any distance from the shoreline (Figure 2).

This constancy in longshore spacing, b , between orthogonals allows getting rid of the variable distance, w , in equation (7), since

$$w = b \cos \alpha \quad (8)$$

where α is the angle between the wave crest and the shoreline. Thus, the total wave power between wave orthogonals becomes

$$\text{Total Wave Power} = b P^* \cos \alpha \quad (9)$$

Divide both sides of equation (9) by b and set b equal to 1 foot. Equation (9) then becomes total wave power per unit length or shoreline, given as P

$$P = P^* \cos \alpha \quad (10)$$

P and P^* are both power per unit distance, but the unit distance is the longshore spacing between orthogonals in the case of P and a distance along the wave crest in the case of P^* . From energy conservation (equation [7]), the value of P defined by equation (10) is a constant that does not change along the wave path. Equation (10) for P is formally identical with the equation (7.2.5) of Longuet-Higgins (1972) for his F_x which is called the "onshore component of the energy flux" (Longuet-Higgins, 1972, p. 210). However, the derivation just shown indicates that P (or F_x) is constant in the direction of wave travel, rather than in the onshore direction.

At any point along the wave path, the wave power per unit shoreline has a magnitude (P) and a direction (α), and therefore P can be broken into components. The longshore component is

$$P_\ell = P \sin \alpha \quad (11)$$

from Figure 2. Since α will change as the wave refracts while P remains constant, it is evident that P_ℓ varies along the wave path. Equation (11) can be rewritten using equations (10), (4), and (5) and a trig identity to get:

$$P_\ell = \frac{1}{2} C_g E \sin 2 \alpha \quad (12)$$

Longuet-Higgins (1970, p. 210) has stated that P_ℓ has no obvious physical meaning, and that it should be banished from the literature. However, according to the derivation of this paper, P_ℓ has a physical meaning: it is the longshore component

of the energy flux between two wave orthogonals spaced a unit distance apart in the longshore direction.

Since P_{λ} has units of energy per second per foot, it is called a longshore energy flux. The basic assumption behind the energy flux method is that the longshore transport rate, Q , depends on P_{λ} evaluated at the outer edge of the surf zone where the waves break. This evaluation requires approximation, since wave breaking is outside the linear wave theory used to develop the equation for P_{λ} . To indicate the approximation involved, the subscript s (surf zone) is added to P_{λ} , and equation (12) is written

$$P_{\lambda s} = \frac{1}{2} C_b E_b \sin 2\alpha_b \quad (13)$$

The subscript, b , indicates evaluation of the group velocity (equation [5]), energy density (equation [6]), and wave direction (α), all at the breaker point.

The appropriate height to use for H in the energy density equation (6) is the root-mean-square height. However, by custom, most coastal engineers use the significant height which is proportional to the rms height. Because of this and other approximations, the term $P_{\lambda s}$ is described as the "energy flux factor", and in effect, it is calibrated for significant wave height.

Equation (13) has been formulated in explicit terms using wave direction, height, and period (SPM, Table 4-8, p. 4-97). These and other relations are the subject of a separate report in preparation by the authors which has as its aim a complete documentation of the energy flux method.

The derivation presented above benefited from the work by Walton (1972) and Longuet-Higgins (1970).

Immersed Weight. From a scientific viewpoint, a number of investigators (Bagnold, 1963; Komar and Inman, 1970; Longuet-Higgins, 1972) recommend using the immersed weight rate of transport, I_{λ} , rather than Q . The immersed weight rate leads to a dimensionally homogeneous equation with a dimensionless coefficient, instead of the peculiar units that K has in equation (1). The immersed weight is related to the volume rate by

$$I_{\lambda} = a' \Delta \gamma Q \quad (14)$$

where a' = volume solids/volume sand in place and $\Delta \gamma$ is the difference in specific weight between sand grain and water.

In practical application, the immersed weight formulation does not now improve the engineering prediction. The required engineering quantity is a volume rate of sand in place (Q), and all the existing data were originally measured in terms of Q , or in Q equivalents. Therefore, in order to develop the immersed weight formulation from existing data, it is necessary to estimate values of a' and $\Delta \gamma$ and convert Q values to I_{λ} by equation (14). Then, to use the immersed weight formulation to solve a problem, one must reverse the procedure and convert back to the required Q .

Available data have led those investigators who have worked with I_{λ} to assume that both a' and $\Delta \gamma$ are constants. To the extent that this is a fact, I_{λ} is directly proportional to Q , independent of any other variables. If this is the case, nothing is gained toward an engineering solution by using I_{λ} , and something may be lost since the procedure would add two unnecessary calculations.

It appears fairly certain that most sand grains on beaches with longshore transport problems are quartz, so that specific gravity in equation (14) is not expected to vary very much. It is less certain that the porosity of the littoral sands is effectively constant. The I_{λ} formulation will be necessary if future work on the soil mechanics of beaches shows that average a' varies significantly from one locality to another.

EVOLUTION OF ENERGY FLUX PREDICTIONS

The initial application of what has become the energy flux method to predict longshore transport rate appears to have been made by the Los Angeles District, U.S. Army Corps of Engineers in the 1940s (U.S. Army Corps of Engineers, Los Angeles District, 1948; Eaton, 1951).

Since then there have been a number of empirical equations that relate volume longshore transport rate to longshore wave energy flux. They range chronologically from Watts (1953) to the present form, SPM (1973), including the six which are listed in Table 1. Column A of Table 1 lists the published reference, column B gives the equation as presented in the original paper, with the original units described in column C. In column D, the equation is presented with the units used in the SPM (1973). Figure 3 is a graphical comparison of these column D equations.

Watts' (1953) equation (row 1, Table 1) was based on four monthly field data points collected at South Lake Worth Inlet in Florida. The longshore transport rate was measured by surveying the amount of sand pumped into a detention basin at the inlet. $P_{\lambda S}$ (E_T in Watts' paper) was computed using significant wave height and period taken from the analysis of the wave

TABLE 1. SIX ENERGY FLUX PREDICTIONS FOR LONGSHORE TRANSPORT RATE

A	B	C	D	
REFERENCE	EQUATION AS GIVEN IN REFERENCE, Q equals:	UNITS USED IN COLUMN B ←Transport/ Wave Power→	EQUATION IN SPM UNITS* Q equals:	
1.	Watts (1953)	$0.011 (E_T)^{0.9}$	$\frac{yd^3}{day} \frac{ft \cdot lb}{day \ ft}$	11,130 $(P_{\ell s})^{0.9}$
2.	Caldwell (1956)	$210 (E_1)^{0.8}$	$\frac{yd^3}{day} \frac{10^6 \ ft \cdot lb}{day \ ft}$	10,810 $(P_{\ell s})^{0.8}$
3.	Savage (1962)	$1.30 E_a$	$\frac{yd^3}{day} \frac{10^4 \ ft \cdot lb}{day \ ft}$	4110 $P_{\ell s}$
4.	TR4 (1966)	$130 E_a$	$\frac{yd^3}{day} \frac{10^6 \ ft \cdot lb}{day \ ft}$	4110 $P_{\ell s}$
5.	Das (1972)	$0.000193 \times 10^{-4} E_a$	$\frac{yd^3}{day} \frac{ft \cdot lb}{day \ ft}$	6090 $P_{\ell s}$
6.	SPM (1973)		$\frac{yd^3}{yr} \frac{ft \cdot lb}{sec \ ft}$	7500 $P_{\ell s}$

*SPM units given in Row 6, Column C.

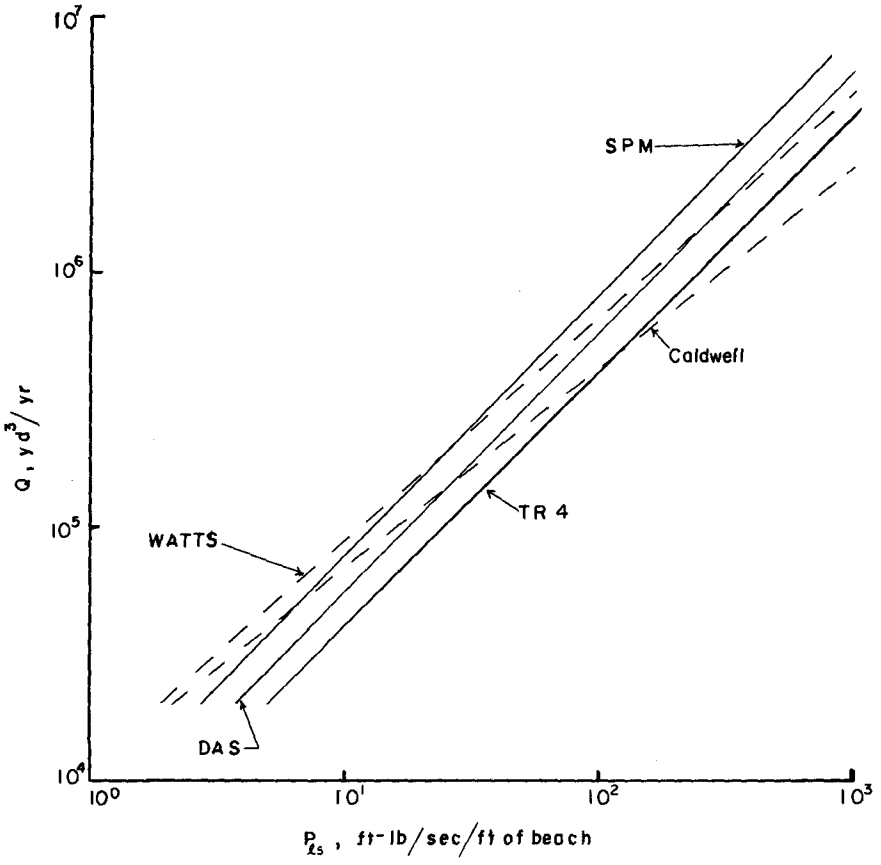


FIGURE 3. FIVE PREDICTIONS OF Q
FROM ENERGY FLUX (1953 - 1973)

records of a pressure gage installed at the seaward end of a pier located eleven miles north of South Lake Worth Inlet. Wave direction was obtained from visual observations.

Caldwell (1956) calculated five more field data points. The longshore transport was measured by comparing successive sets of surveys of the beach along the 11,000 foot study area immediately south of the jetties at Anaheim Bay, California. $P_{\lambda s}$ (E_i in Caldwell's paper) was calculated from wave records of a step resistance wave gage installed on the seaward end of the Huntington Beach Pier, located about six miles south of Anaheim Bay. Wave direction was obtained from wave hind-casting and wave refraction analysis using synoptic weather charts. The equation in row 2 of Table 1 was determined by Caldwell using his five and Watts' four data points.

Savage (1962) added numerous laboratory data points to those of Watts (1953) and Caldwell (1956) to produce a curve described by the equation in row 3 of Table 1. This relation was eventually presented as Figure 2-22, page 175 in TR4 (1966), the only change being in $P_{\lambda s}$ units (E_a in Savage [1962] and TR4 [1966]) as is shown in column C of Table 1.

Das (1972) added field data points from Komar (1969) and Moore and Cole (1960) to those used by Savage (1962) to obtain the equation in row 5 of Table 1. However, in determining this equation, Das deleted those laboratory data based on experiments with lightweight sediment.

As can be seen in Table 1, Watts and Caldwell used $P_{\lambda s}$ raised to a power less than 1 (0.9 and 0.8 respectively). The other references showed linear equations in $P_{\lambda s}$. Das, in unpublished work leading to his 1972 paper, found no statistical advantage to using a power equation if the linear coefficient is chosen correctly.

Figure 3 shows that, in the range of the most commonly occurring values of longshore transport rate (10^5 to 10^6 yd³/year), Watts' (1953) prediction comes closest to the curve now given in SPM (1973). In this range of transport rates, both Watts and SPM predict the highest values of Q for a given $P_{\lambda s}$ of the six equations in Table 1. It is interesting that Watts' (1953) was the earliest equation; SPM (1973) the most recent.

CHANGE FROM TR4 TO SPM

Although the difference between the SPM curve and the early curve of Watts is small, the difference between SPM and its immediate predecessor, the TR4 curve, is large (Figure 3). As shown earlier on Figure 1, the SPM curve gives a transport rate that is 83% higher than the TR4 curve for the

same wave conditions. There are three principal reasons leading to the higher placement of the SPM curve, as illustrated on Figure 4 and described below.

Deletion of Lab Data. The TR4 curve is based on nine field observations and 150 laboratory data points (Table 2). The SPM curve is based on 23 plotted field observations, but no laboratory data. The laboratory data were deleted in SPM because additional field information had become available and because the numerous laboratory data overwhelmed the few field data in locating the curve. The effect of the laboratory points is indicated by the strippled field on Figure 4.

TABLE 2. NUMBER OF DATA POINTS - TR4 AND SPM PREDICTIONS

<u>Lab</u>	<u>TR4</u>	<u>SPM</u>
Krumbein, 1944	15	0
Saville, 1950	9	0
Shay and Johnson, 1951	99	0
Sauvage and Vincent, 1954	17	0
Savage, 1962	<u>10</u>	<u>0</u>
	150	0
 <u>Field</u>		
Watts, 1953	4	4
Caldwell, 1956	5	5
Komar, 1969	<u>0*</u>	<u>14</u>
	9	23

*Komar's data became available after TR4 curve was published.

Komar's Field Data. The field measurements of Komar (1969) added fourteen data points to the curve (Figure 4). In general, these field data plotted above the TR4 trend, which was heavily weighted by the lower laboratory results and the lower field data of Caldwell (1956). Caldwell's data fall in the lower part of the region identified as "Field Data, SPM and TR4" on Figure 4.

Santa Barbara Estimate. Johnson (1952) published values of Q , P_0^* , and wave period for intervals of high longshore transport rates at Santa Barbara. These Santa Barbara data have been identified as exceptional (M. P. O'Brien, personal communication, 1969), but they had not previously been used with longshore transport predictions because the data lack wave direction.

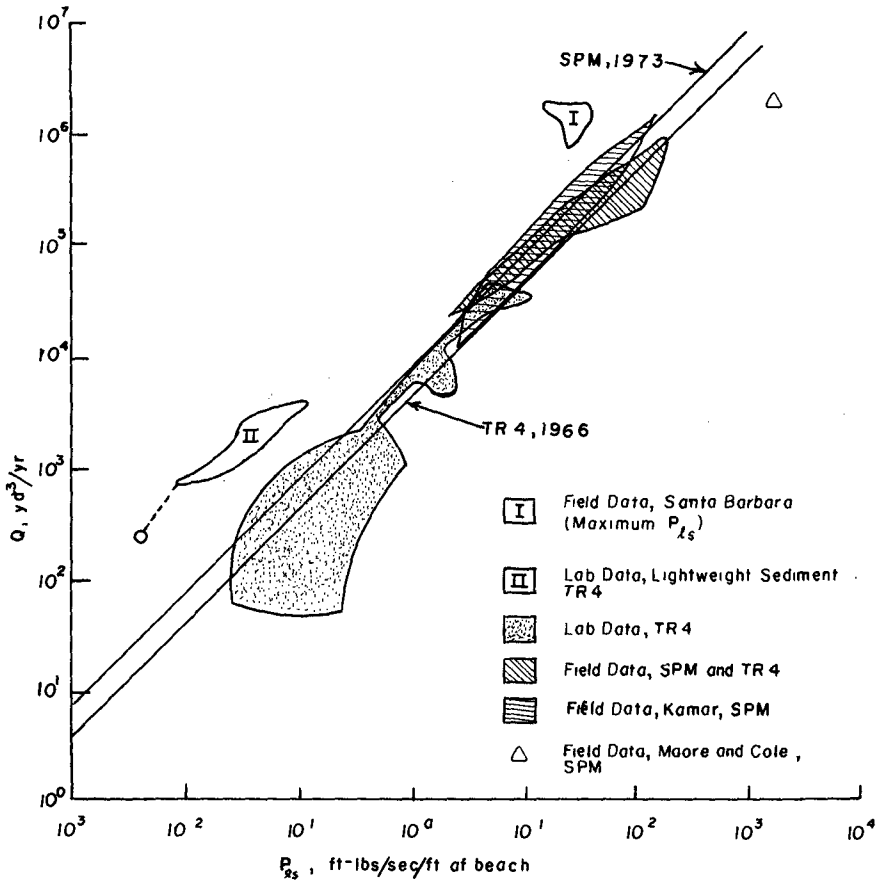


FIGURE 4. DATA USED TO ESTABLISH SPM AND TR4 LONGSHORE TRANSPORT PREDICTIONS

In order to benefit from the Santa Barbara data, the equation for P_{ℓ} , equation (12), was written as the product of two terms, one being P_{\circ}^* and the other dependent only on wave direction.

$$P_{\ell} = M P_{\circ}^* \quad (15)$$

where

$$M = \cos \alpha_{\circ} \sin \alpha_{\text{D}} \quad (16)$$

By using Snell's law, an estimated breaker depth, and trial and error, it is possible to get a maximum value of M (Galvin, 1969). Using this maximum value of M in (15) with Johnson's data for P_{\circ}^* yields equivalent values of $P_{\ell S}$ that are well above the TR4 curve and above even the SPM curve (Region I on Figure 4).

These Santa Barbara data were not plotted on the SPM curve (Figure 4-37 of SPM), but their existence added confidence to the placement of the SPM curve. Since 1972 when the SPM curve was developed, new data have come available from CERC studies at Channel Island Harbor, California, which also support the higher curve.

CONCLUSIONS

1. The SPM prediction for the volume rate of sediment transport, Q , as a function of the longshore energy flux factor, $P_{\ell S}$, is, in the recommended units,

$$Q = 7500 P_{\ell S} \quad (17)$$

This equation gives volume transport rates 83% higher than the rates from the predecessor curve in TR4, for the same wave conditions (Figure 1).

2. The 83% increase from TR4 to SPM is due to deleting the TR4 laboratory data (Table 2), adding Komar's (1969) field data, and determining feasible upper limits for Johnson's (1952) previously unused Santa Barbara data (Figure 4).

3. The recommended units for Q and $P_{\ell S}$ are yd^3/yr and $\text{ft} - \text{lb}/\text{sec}/\text{ft}$, respectively, or their metric equivalents in equations (2) and (3). The volume rate, Q , is preferred over the immersed weight rate, I_{ℓ} , at least until an I_{ℓ} curve can be constructed without assuming values for specific gravity and void ratio of the beach sands. Even if I_{ℓ} can be shown necessary because of significant variability in void ratio, Q is still the variable of engineering interest.

4. P_{ℓ} has a readily understood physical meaning. It is the longshore component of the energy flux conserved between two orthogonals spaced a unit distance apart in the longshore direction (Figure 2). $P_{\ell s}$ is P_{ℓ} evaluated at the seaward edge of the surf zone.

5. A review (Table 1) of six predictions of Q developed over a twenty-year interval indicates that the first prediction (Watts, 1953) is the one closest to the last (SPM, 1973).

REFERENCES

- Bagnold, R. A., 1963, "Mechanics of Marine Sedimentation", The Sea, v. 3, Wiley, New York, pp. 507 - 528.
- Caldwell, J. M., 1956, "Wave Action and Sand Movement Near Anaheim Bay, California", TM-68, U.S. Army Corps of Engineers, Beach Erosion Board.
- Das, M. M., 1972, "Suspended Sediment and Longshore Sediment Transport Data Review", 13th International Conference on Coastal Engineering, Vancouver, B.C., Canada.
- Eaton, R. O., 1951, "Littoral Processes on Sandy Coasts", Proceedings of the First Conference on Coastal Engineering, Council on Wave Research, Engineering Foundation.
- Galvin, C. J., 1969, "Comparison of Johnson's Littoral Drift Data for Santa Barbara with the Empirical Relation of CERC TR4", Memorandum for Record, Coastal Engineering Research Center, 16 Feb 69, 3 pages.
- Johnson, J. W., 1952, "Sand Transport by Littoral Currents", Proceedings of Fifth Hydraulic Conference, State Univ. of Iowa, Studies in Eng. Bull. 34, pp. 89 - 109.
- Komar, P. D., 1969, "The Longshore Transport of Sand on Beaches", Unpublished PhD thesis, University of California, San Diego, Calif. 1969.
- Komar, P. D., and Inman, D. L., 1970, "Longshore Sand Transport on Beaches", Journal of Geophysical Research, v. 75, No. 30, pp. 5914 - 5927.
- Krumbein, W. C., 1944, "Shore Currents and Sand Movement on a Model Beach", TM-7, U.S. Army Corps of Engineers, Beach Erosion Board, Washington.
- Longuet-Higgins, M. S., 1972, "Recent Progress in the Study of Longshore Currents", Waves on Beaches and Resulting Sediment Transport, R. E. Meyer, ed., Academic Press, New York.

- Longuet-Higgins, M. S., 1970, "Longshore Currents Generated by Obliquely Incident Sea Waves, 1", J. of Geophysical Research, v. 75, no. 33, pp. 6788 - 6801.
- Sauvage, M. G., and Vincent, M. G., 1954, "Transport Littoral Formation de Leches et de Tombolos", Fifth Conference on Coastal Engineering, Grenoble, France.
- Savage, R. P., 1962, "Laboratory Determination of Littoral-Transport Rates", J. of Waterways and Harbors Division, Proceedings of American Society of Civil Engineers, v. 88, no. WW2, pp. 69 - 92.
- Saville, Thorndike, Jr., 1950, "Model Study of Sand Transport Along an Infinitely Long Straight Beach", Trans-American Geophysical Union, v. 31.
- Shay, E. A., and Johnson, J. W., 1951, "Model Studies on the Movement of Sand Transported by Wave Action Along a Straight Beach", Issue 7, Ser. 14, Institute of Engineering Research, University of California, Berkeley.
- U.S. Army Corps of Engineers, Coastal Engineering Research Center, 1973 "Shore Protection Manual", 3 volumes, U.S. Govt. Printing Office.
- U.S. Army Corps of Engineers, Coastal Engineering Research Center, 1966, "Shore Protection, Planning and Design", Technical Report No. 4, (3rd ed).
- U.S. Army Corps of Engineers, Los Angeles District, 1948, "Harbor and Shore Protection in the Vicinity of Port Hueneme, California", 1 - 71.
- Walton, T. L., 1972, "Littoral Drift Computations Along the Coast of Florida by use of Ship Wave Observations", Unpublished Masters Thesis, University of Florida, Gainesville.
- Watts, G. M., 1953, "A Study of Sand Movement at South Lake Worth Inlet, Florida", TM-42, U.S. Army Corps of Engineers, Beach Erosion Board, Washington.

CHAPTER 68

SAND TRANSPORT BY WAVES

by

E.W. Bijker^{*}), E. van Hijum^{***)} and P. Vellinga^{****)}

1 Summary

Sand transport parallel to the direction of wave propagation by waves of arbitrary form over a rippled bed has been investigated in a flume, at the Laboratory of Fluid Mechanics of the Dept. of Civ. Eng. of the Delft Univ. of Techn. The transport has been measured by means of a special procedure which does not disturb the process. The measured sand transport is related to the measured wave form parameters. The results indicate that the direction of net sand transport depends upon the form of the waves.

2 Introduction

This study has been carried out with the aim to understand the onshore and offshore movement of sand which determines the development of beach profiles. From movable bed model tests it has become clear that beach profile formation may be severely affected by secondary waves which, together with the primary wave always originate from a sinusoidally moving wave-board. Even a hardly measurable second harmonic free wave can cause bar formation over a horizontal bottom. Since secondary waves are present in nature the study of the effect is of great interest in the understanding of beach profile development.

3 Description of the tests

To obtain insight into the transport phenomenon 27 tests have been conducted in a flume (see Fig. 1) with a horizontal sand bed with a mean particle diameter of 250 μm with different combinations of water depths, wave periods and wave heights as shown in Table 1. The Ursell parameter ($Ur = HL^2/d^3$) ranged from 12 to 57. Since the presence of secondary waves results in a spatially varying wave form, the wave form parameters and the resulting sand transport have been measured at 0.50 m intervals along the flume.

^{*}) Professor of Coastal Engineering, Delft University of Technology, Department of Civil Engineering, The Netherlands.

^{***)} Project Engineer, Maritime Structures Branch, Delft Hydraulics Laboratory, Laboratory de Voorst, The Netherlands.

^{****)} Project Engineer, Harbours and Coasts Branch, Delft Hydraulics Laboratory, Laboratory de Voorst, The Netherlands.

water depth	d	m	0.20	0.25	0.30
wave period	T	sec	1.50	1.70	1.90
relative wave height	Hd^{-1}	-	0.2	0.3	0.4

Table 1

4 Measuring procedure

It is very difficult to measure sand transport under undisturbed conditions. The use of sandtraps usually causes such a discontinuity that the upwave as well as the downwave sandtrap is filled with sediment. An uncovered part in the flume bottom however causes hardly any discontinuity and creates an excellent boundary condition for the balance of sand volume (see Fig. 1).

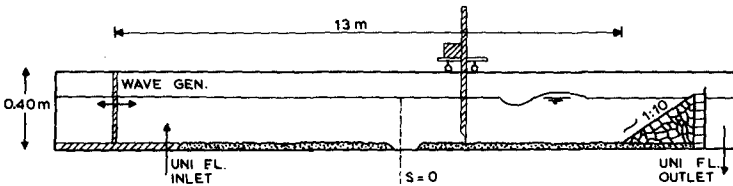


Fig. 1 A schematic illustration of the model

An electronic bottom-profile indicator together with a recorder was used to measure the bottom profile along the flume. By integrating the measured profiles before and after the test, the sediment transport through any cross-section is known. The essence of this procedure is that it is assumed that the transport across the uncovered part is zero. To eliminate the initial effects, the $t=0$ measurements were done only after ripples of the equilibrium form were developed. Also the tests were finished before any secondary interaction processes influenced the results; disturbing processes may originate from the discontinuity at the uncovered part, while also bottom deformation may cause interaction effects on the wave parameters. Taking this into account, it was decided to use test durations between 20 and 60 minutes, depending on the transport intensity. During this period usually bottom elevation variations of the order of 1 mm had occurred. The accuracy of the measuring procedure is of the order of 0.1 mm.

As the bottom profile measurement was done along the length of the flume and as the width of the flume was 0.50 m, the bottom profile was measured along the

center line and the quarter lines and the volume change between two cross-sections was found by taking the average of the three quantities.

The sand transport rate was computed at intervals of 0.50 m. At the same cross-sections the wave parameters were measured: the velocity profile was measured with a micro propellor $1/3 d$ above the bottom, d being the waterdepth, and the wave heights were measured using a resistance type wave gauge.

During the analyses of the test results, only the velocity profile was used when relating the wave parameters to the resulting sand transport, because for sand transport, the velocity profile is of more direct interest than the surface wave form, especially since in latter tests a uniform current was superimposed on the oscillatory motion. Furthermore with waves only the form of the velocity profile is about the same as the form of the wave.

During the analyses no specific attention has been paid to the ripple pattern since the aim of the study is to find a relation between the wave parameters and the resulting transport; the ripple pattern is not an independent variable in this relation and as such not of direct interest in finding this relation. However, the ripple patterns were measured to enable comparisons with other experiments to be carried out on a different scale.

5 Test results

As described by Hulsbergen [1] and Buhr Hansen [2] the wave form varies along the length of the flume. When the velocity variation is analysed in harmonic components it appears that the variation is repetitive in the same form at certain distance intervals. The distance is equal to the distance which is required for the primary wave (period T) to overtake the secondary wave (period $T/2$). The repetition especially appears in the variation of the second harmonic component (see Fig. 2). To see how this overtake length is related to the measured overtake length by Hulsbergen [1] and the theoretical overtake length according to Miche, the distance between two places where the second harmonic component \hat{u}_2 reaches it's maximum (L_{ov-2}) is plotted against the waterdepth (see Fig. 3).

Because of the similarity it may be assumed that the wave form variation in these tests agrees with the theory as described by Hulsbergen [1] and Buhr Hansen [2]. According to Hulsbergen [1] one may separate the \hat{u}_2 component into a contribution from the second order Stokes wave and a contribution from the secondary wave. These contributions can be found by taking the average of \hat{u}_2 over an overtake length as the $\hat{u}_{2-stokes}$ and the amplitude of the variation as the $\hat{u}_{2-fontanet}$ (see Fig. 2).

amplitude of the harmonic components
 derived through fourier analyses (cm/sec)

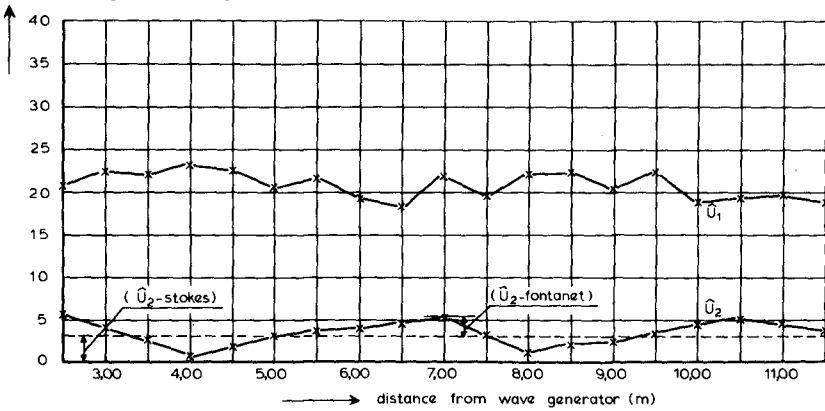


Fig. 2 Variation of the amplitudes of the harmonic components of the orbital velocity with the distance from the wave generator ($T = 1.70$ sec, $d = 0.30$ m, $Hd^{-1} = 0.3$)

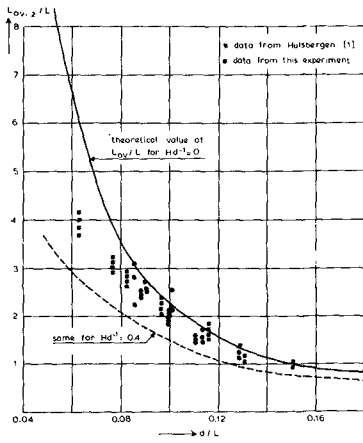


Fig. 3 Dimensionless overtake length

Sand transport variation

From the experiments it is clear that the sand transport varies with the distance from the wave generator. Along the length of the flume sand transport in the direction of wave propagation alternates with sand transport opposite to the direction of wave propagation. For further analyses the sand transport along the flume is divided into the average \bar{S} and the amplitude of the variation \hat{S} (see Fig. 4).

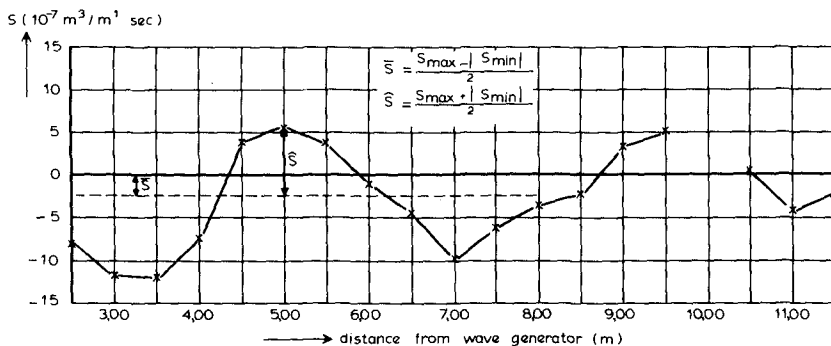


Fig. 4 Variation of the sand transport with the distance from the wave generator

Relation between sand transport variation and wave form variation

To demonstrate that the variation of the sand transport corresponds with the behaviour of secondary waves, the overtake length (L_{ov-2}) is plotted against the distance over which the variation in sand transport is repeated (see Fig. 5). From this figure it is clear that the distances are about equal, hence it may be concluded that the variation in sand transport is caused by the occurrence of secondary waves.

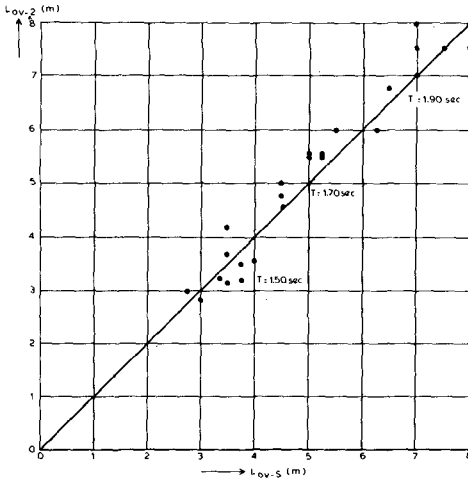


Fig. 5 Overtake length of the secondary wave against the repetition distance of the sand transport variation

6 Analyses of the results

Mechanism of sand transport by waves

The sediment movement under a wave can be described as follows (see Fig. 6): a vortex is generated behind the ripple crest at t_1 . From t_1 to t_2 this vortex is filled with sediment. At t_3 the sediment of this vortex is brought into suspension and is carried backwards by the negative orbital velocity to the preceding ripples. At t_3 at the other side of the ripple crest, a new vortex is formed. At t_5 the sediment of this vortex is brought into suspension and is carried forwards by the positive orbital velocity, etc.

This way a big quantity of sand is in oscillatory motion. A resulting transport can be caused by a small asymmetry in the orbital motion.

In further analyses the following assumptions have been made:

- the quantity of sand moving back and forth under oscillatory motion is proportional to \hat{u}_1^2 .
- the difference between the two quantities is proportional to \hat{u}_2 .
- the resulting sand transport is related to the product of \hat{u}_1^2 and \hat{u}_2 .

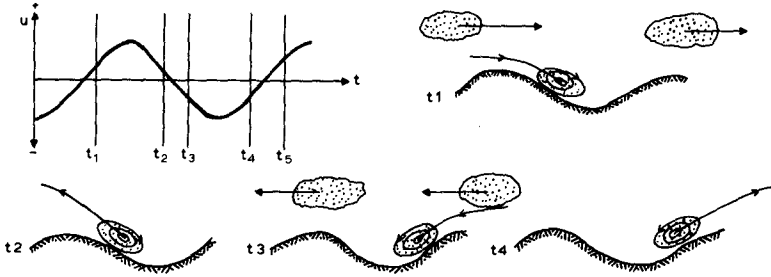


Fig. 6 Sand movement over sand ripples

Relating sand transport to the second harmonic component of the velocity profile
 Fourier analyses of the velocity profile shows that the value of the second harmonic component varies with the distance from the wave board. This variation can be described by the average and the amplitude of the variation. Also the sand transport variation with the distance from the wave board can be described by the average and the amplitude of the variation. Now the averages and the amplitudes can be compared.

In Fig. 7 the average sand transport \bar{S} has been plotted against $\hat{u}_1^2 \cdot \hat{u}_{2-stokes}$. From this figure it is clear that the average sand transport under these test conditions is in all cases opposite to the direction of wave propagation and that there exists a rather consistent relationship with $\hat{u}_1^2 \cdot \hat{u}_{2-stokes}$. From this it may be assumed that a wave which can be described by second order Stokes theory causes a sand transport opposite to the direction of wave propagation and that the size of the transport can be described by an equation of the type

$$S = c_1 \hat{u}_1^2 \cdot \hat{u}_{2-stokes} + c_2$$

In Fig. 8 the variation of the sand transport has been plotted against $\hat{u}_1^2 \cdot \hat{u}_{2-fontanet}$. From this figure it is clear that a straight line with an equation of the type

$$\hat{S} = q_1 \hat{u}_1^2 \cdot \hat{u}_{2-fontanet} + q_2$$

may be fitted reasonably well through the plotted points.

Although in these comparisons the wave period has not been included it is shown that the measured results follow a trend which support the validity of the suggested relations.

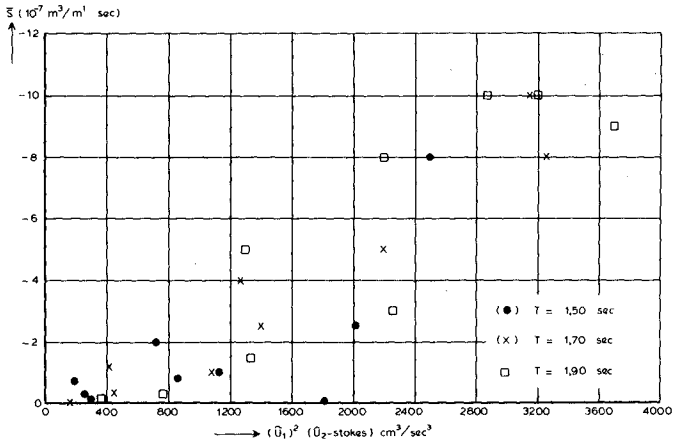


Fig. 7 Average sand transport as a function of wave parameters (negative \bar{S} corresponds with sand transport opposite to the direction of wave propagation)

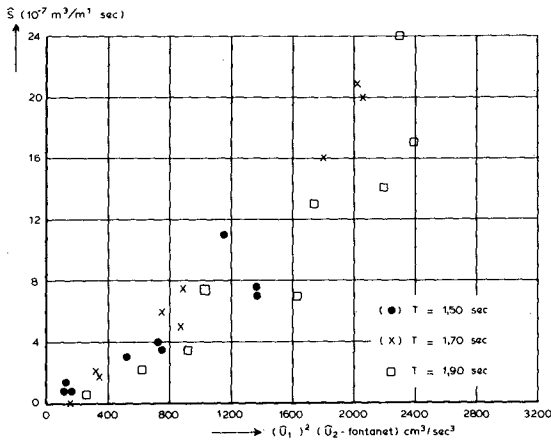


Fig. 8 Variation of sand transport as a function of the variation of wave parameters

A better way of analysing the results, however, is to compare the actual form of the velocity profile with the resulting sand transport. The velocity profile of the two interacting waves is only adequately described by the value of \hat{u}_1 , \hat{u}_2 and the difference in phase between the two. Since this amounts to three variables it makes the physical understanding of the problem more difficult. That is why a small simplification of the velocity profile has been introduced, such that the profile is described by \hat{u}_1 and the difference between the acceleration and the deceleration of the fluid particles as defined in Fig. 9.

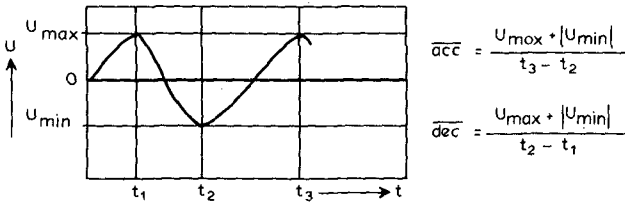


Fig. 9 Definition sketch of acceleration (\overline{acc}) and deceleration (\overline{dec})

This simplification has been carried out for all the measured velocity profiles, and the difference between the acceleration and the deceleration of the fluid particles has been plotted for all tests as a function of the distance from the wave generator (see Fig. 10). In the tests it is apparent that the variation of the value of the $\overline{acc} - \overline{dec}$ is in phase with the variation of the sand transport along the flume (compare Fig. 4 with Fig. 10).

Now another relationship for the amplitude of sand transport can be tried. Like before \hat{u}_1^2 is proportional to the quantities moving back and forth but in this case the resulting transport is caused by the difference between \overline{acc} and \overline{dec} . In Fig. 11 the amplitude of the variation in sand transport has been plotted against the amplitude of the variation in $\hat{u}_1^2 \cdot (\overline{acc} - \overline{dec})$. For each wave period the proportionality constant is different. This is understandable from the fact that the simplification does not really hold for the longer periods. The relation for the shorter period: $T = 1.50$ sec holds very well since the coefficient of linear regression equals 0.995.

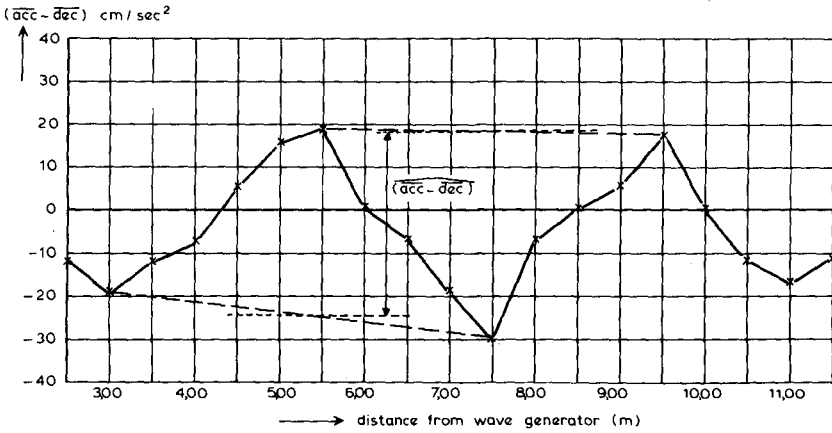


Fig. 10 Variation of the difference between acceleration and deceleration of the fluid particles with the distance from the wave generator ($T = 1.70$ sec, $d = 0.30$, $Hd^{-1} = 0.3$)

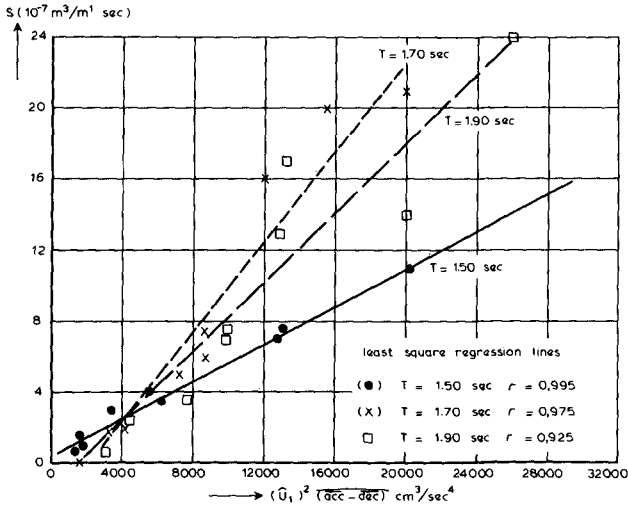


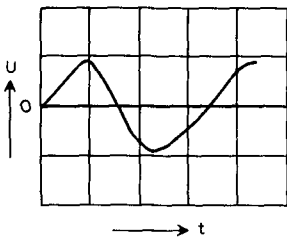
Fig. 11 Amplitude of variation in sand transport against \hat{u}_1^2 times the amplitude of $\overline{acc - dec}$

No attempt has been made to develop a relationship between the pertinent dimensionless parameters as the testing range is limited and the process may be different on another scale.

By the simplification of the velocity profile and comparing the result with the sand transport it has been found that there exists a qualitative relationship which holds for all the tests carried out with sand with a mean particle diameter size of 250 μm :

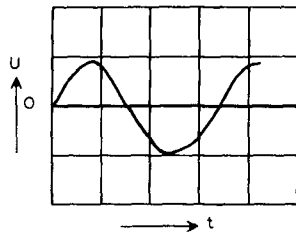
- Sand transport by waves is in the direction of wave propagation when the $\overline{\text{acc}}$ is greater than the $\overline{\text{dec}}$, and opposite to the direction of wave propagation when the $\overline{\text{dec}}$ is greater than the $\overline{\text{acc}}$.
- When the $\overline{\text{acc}}$ equals the $\overline{\text{dec}}$ and there is a second harmonic component present, the sand transport is opposite to the direction of wave propagation.

This phenomenon can be explained as follows: from visual observations it has become clear that the extent of vortex formation is closely related to the acceleration and the deceleration of the fluid particles, so that a small acceleration creates a large vortex whereas by the following large deceleration this sand laden vortex is brought up high in suspension and the sand is carried quite far backwards by the orbital velocity so transport opposite to wave propagation will result (see Fig. 12a). In the same way a small deceleration creates a large vortex on the upwave side of the ripple and the following large acceleration lifts the sand laden vortex high in suspension and the sand is carried quite far forwards by the orbital velocity, so transport in the direction of wave propagation will result (see Fig. 12c).



velocity profile at 3,50 m
from the wave generator

a



velocity profile at 4,50 m
from the wave generator

b

Fig. 12 a,b Velocity profile along the length of the flume ($T = 1.70$ sec,
 $d = 0.30$ m, $Hd^{-1} = 0.3$)

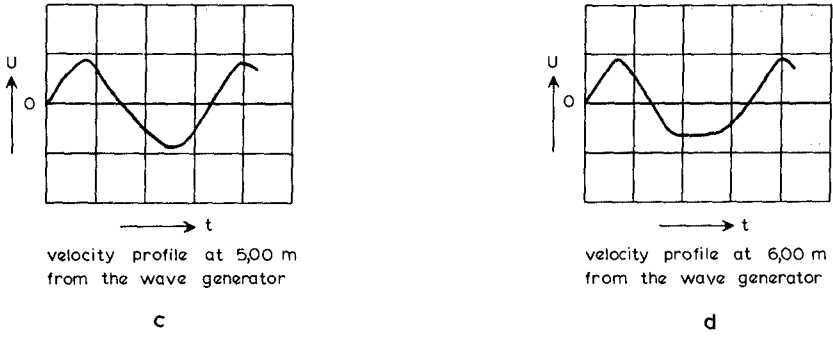


Fig. 12 c,d Velocity profile along the length of the flume ($T = 1.70$ sec, $d = 0.30$ m, $Hd^{-1} = 0.3$)

During tests with standing waves, conducted in the past, it has been possible to observe the vortex formation in photographs. Through this it has been possible to find a certain relationship between the phase of orbital velocity and the development of the vortex (see Fig. 13 and the corresponding photographs). It appears that due to inertial effects vortex formation starts at about $\frac{1}{4} T$ after the zero crossing of the orbital velocity. This means that with a small acceleration the developed vortex reaches its maximum during a high orbital velocity.

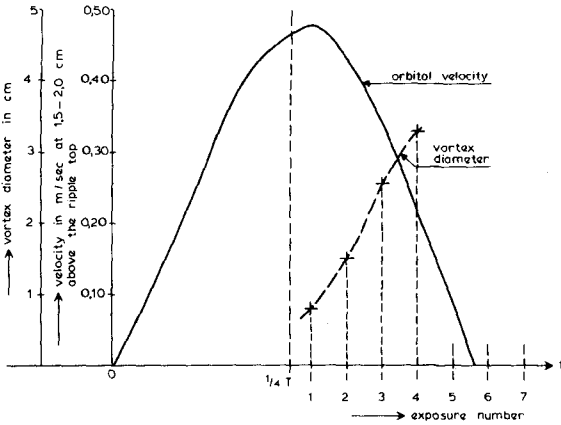


Fig. 13 Vortex development in relationship with orbital velocity (photographs 1-7 are shown at the end of this paper)

7 Sand transport when a small uniform current is superimposed in the direction of wave propagation

Under these circumstances sand transport in the direction of net water transport can be expected. From tests however, it appears that this is not always the case (see Fig. 14). When the uniform flow velocity is zero, the direction of sand transport can be in the direction of wave propagation, as well as opposite to it, depending on the wave form. Under the combined action of waves and current the sand transport can still be opposite to the direction of net water transport.

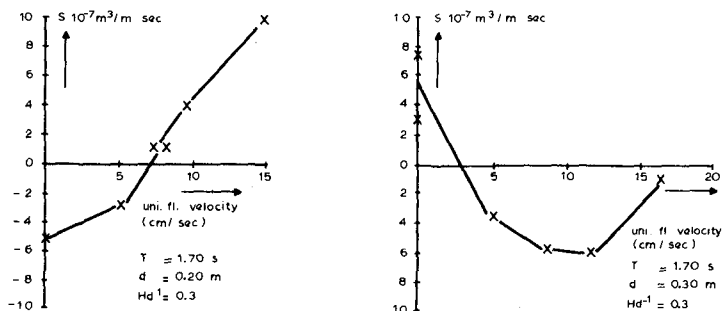


Fig. 14 Sand transport as a function of the velocity of uniform flow superimposed on waves

The explanation for the initial increase of the sediment movement in the direction opposite to wave propagation is the growth of the vortex at the fore-front of the ripple, so that more sand is brought into suspension and is carried backwards by the orbital motion. Only with large uniform flow velocities this effect is overruled. Because of this it can be concluded that insight into the vortex formation as a function of wave and flow parameters is essential for the understanding of sand transport caused by waves and currents.

8 Sand transport under standing waves

Under standing waves also it has been found that the direction of sand transport with sand having a mean particle diameter of 250 μm is in the direction corresponding with the largest temporal gradient of orbital velocity [3]. At first the difference in inertial forces on the grains was considered to be the cause of this. However, further tests showed that the difference in vortex formation was more likely to be the cause.

In the test series with standing waves, finer sand ($D_m = 150 \mu\text{m}$) was also used as bottom material. It was apparent that in this case the direction of sand transport did not agree with the results of the coarser sand. With the finer sand the transport direction was according to the net water transport close to the bottom as described by Longuet Higgins. These results show that two mechanisms of sand transport are present: a first mechanism where sand transport is caused by a small asymmetry in orbital motion and a second mechanism where sand transport is caused by a net water transport. With coarse sands the first mechanism will prevail whereas with finer sands the second mechanism will prevail. When the net water transport is large compared to the orbital velocity, then of course the second mechanism will dominate. The existence of these two mechanisms make it necessary to be very careful in extrapolating data since the domination of a certain mechanism will depend on the scale.

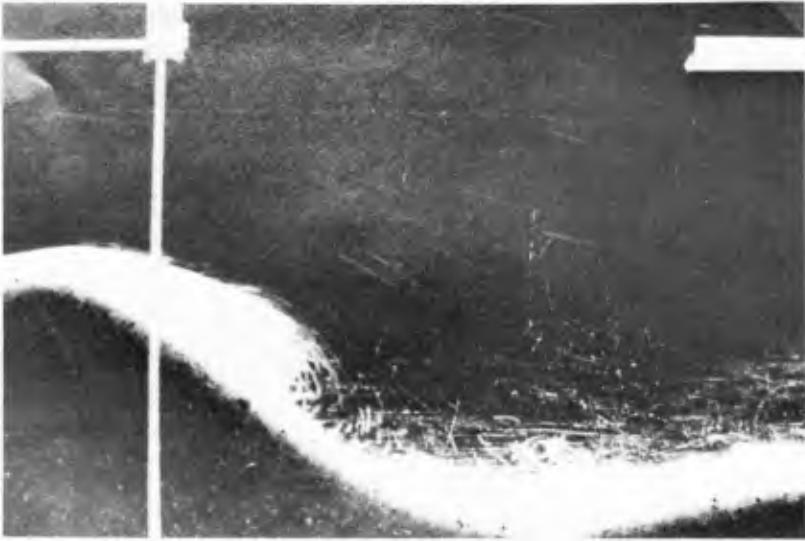
9 Conclusions

- A specially designed procedure for measuring sand transport by waves has given good results. This measuring procedure does not disturb the transport process and very small transports can also be measured.
- Secondary waves which together with the primary wave always originate from a sinusoidally moving wave board cause a spatially varying sand transport resulting in the formation of bars and troughs. The distance between the generated bars is equal to the distance which is required for the primary wave to overtake the secondary wave.
- In all tests with sand of a mean particle diameter of 250 μm , the average of the sand transport along the flume is opposite to the direction of wave propagation and is proportional to $\hat{u}_1^2 \cdot \hat{u}_{2\text{-stokes}}$, whereas the amplitude of the variation in sand transport is proportional to $\hat{u}_1^2 \cdot \hat{u}_{2\text{-fontanet}}$, where \hat{u}_1 is the first harmonic component of the velocity profile, $\hat{u}_{2\text{-stokes}}$ is the spatial average of the second harmonic component and $\hat{u}_{2\text{-fontanet}}$ is the amplitude of the variation of the second harmonic component.

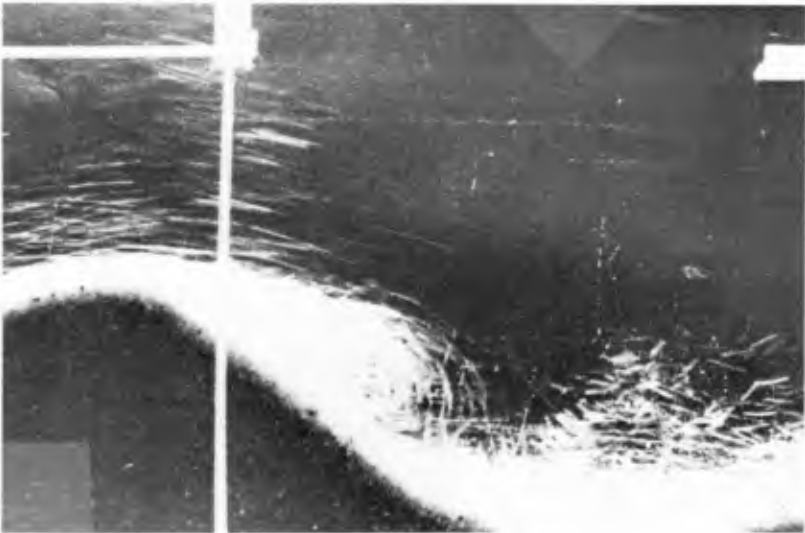
- Throughout these tests it has been found that:
 - 1 sand transport is in the direction of wave propagation when the front of the wave is steeper than the rear face
 - 2 sand transport is opposite to the direction of wave propagation when the rear face of the wave is steeper than the front.
- With sand transport by waves two mechanisms are present; a first mechanism where sand transport is caused by a small asymmetry in orbital motion and a second mechanism where sand transport is caused by a net water transport.
- One should be aware of the different sand transport mechanisms when extrapolating results from movable bed wave-models since the dominating transport mechanism can be different under different scales. Recent tests with finer sands and propagating waves have already shown that the dominating mechanism with sand with a mean particle diameter (D_m) of 150 μm is different from the dominating mechanism with sand with a D_m of 250 μm .
- The test results can be of significant interest in the explanation of the origination of bars in model as well as in nature.

REFERENCES

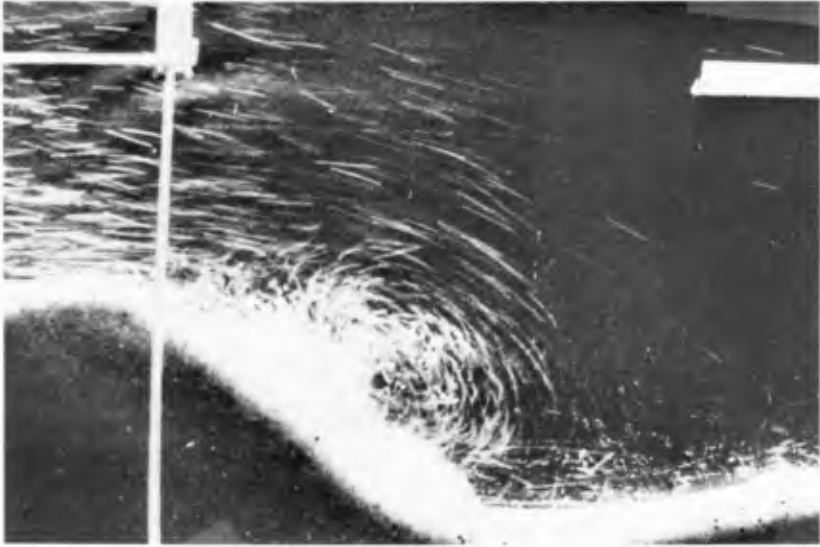
- 1 HULSBERGEN, C.H.,
14th C.E.C., chapter 22, Origin, effect and suppression of secondary waves,
1974
- 2 BUHR HANSEN, J. and SVENDSEN, Ib.A.,
14th C.E.C., chapter 17, Laboratory generation of waves of constant form,
1974
- 3 BIJKER, E.W. de BEST, A. and WICHERS, J.E.W.,
Proc. 1st Conf. on Port and Ocean Engineering under arctic conditions, vol.
2, pp. 1077-1086, Trondheim, 1971
- 4 HIJUM, E. van,
Master thesis, Dept. of Civ. Eng., Delft Univ. of Techn., in Dutch, 1972
- 5 VELLINGA, P.,
Master thesis, Dept. of Civ. Eng., Delft Univ. of Techn., in Dutch, 1975



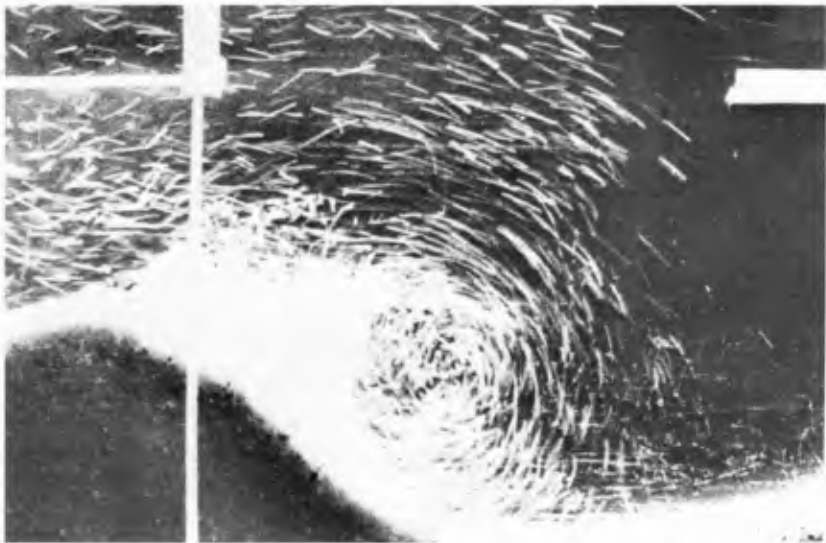
exposure 1



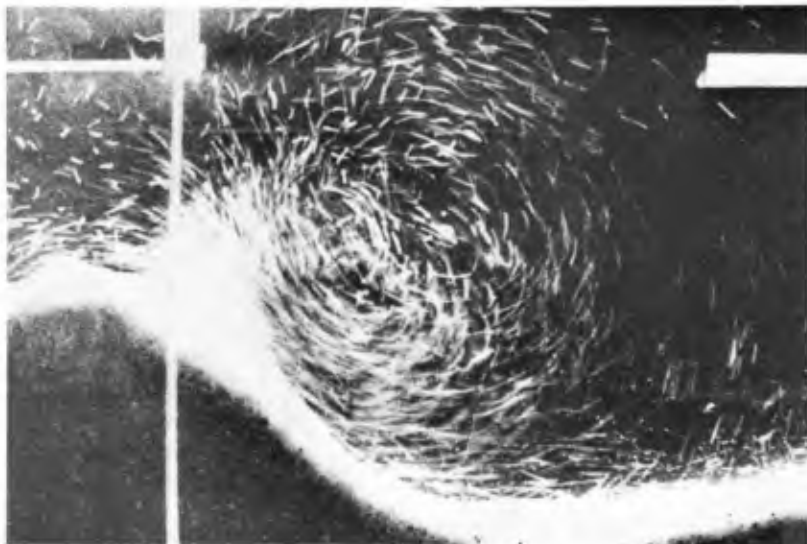
exposure 2



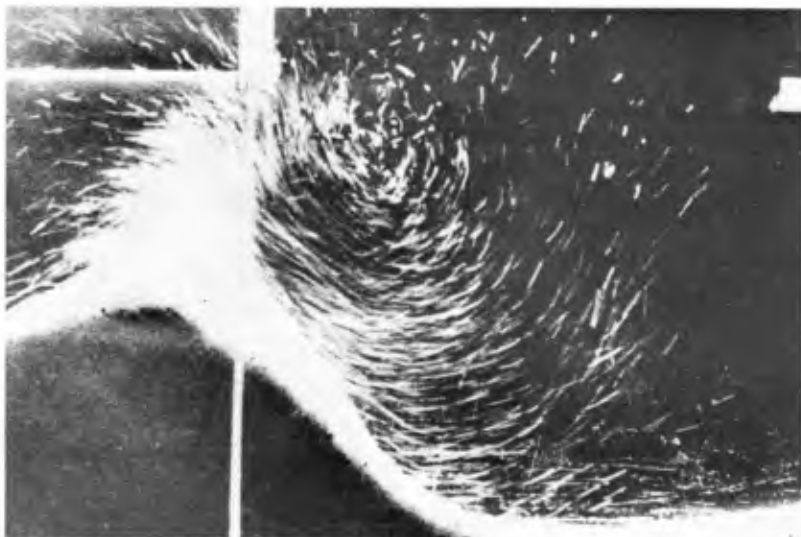
exposure 3



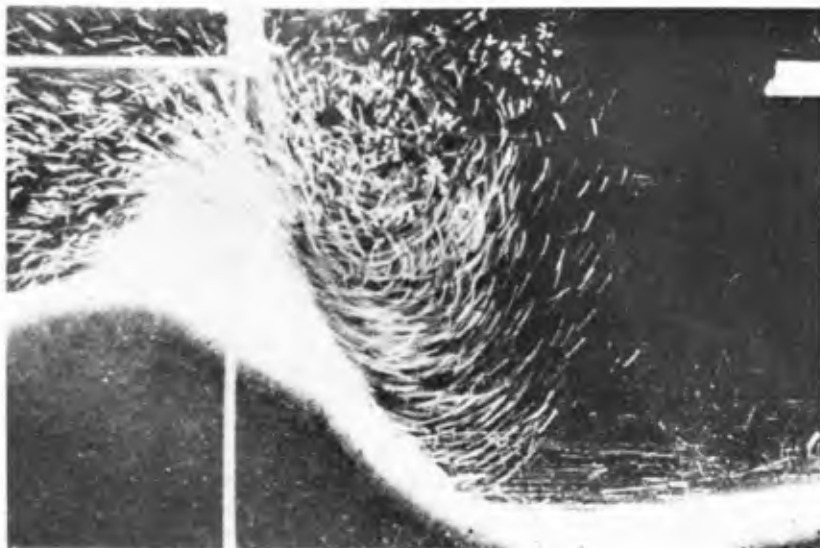
exposure 4



exposure 5



exposure 6



exposure 7

CHAPTER 69

WAVE ACTION AND BOTTOM MOVEMENTS IN FINE SEDIMENTS

Michael W. Tubman and Joseph N. Suhayda
Coastal Studies Institute, Louisiana State University
Baton Rouge, Louisiana 70803

Abstract

Mudbanks have been observed to have an extraordinary calming effect on the sea surface. In certain cases this effect is due primarily to the transfer of energy through the sea/mud interface and its frictional dissipation within the bottom sediments. This paper describes an experiment that measured wave characteristics and the resulting sea floor oscillations in an area where the bottom is composed of fine-grained sediments. The energy lost by the waves at the position of the experimental setup is calculated and compared with a direct measurement of the net energy lost by the waves in going from the point of the experiment to a station 3.35 km inshore. Results show that bottom motions in the range of wave-induced bottom pressures from near zero to 2.39×10^3 Pascal have the appearance of forced waves on an elastic half space. The apparent effect of internal viscosity is seen in a phase shift between the crest of the pressure wave and the trough of the mud wave. Measurements show this angle to be 22° ($\pm 11^\circ$) for the peak spectral component ($T = 7.75$ seconds). The energy lost to the bottom by the waves at the field site was found to be at least an order of magnitude greater than that resulting from the processes of percolation or that caused by normal frictional effects. This newly observed mechanism for the dissipation of wave energy is particularly important for waves in intermediate-depth water and could be a prime factor in determining design wave heights in muddy coastal areas.

Introduction

The extraordinary calming effect that mudbanks exert on surface waves has been recognized for at least two centuries. With the development of the offshore oil industry there also came a recognition that large vertical and horizontal dislocations of the sea floor could occur in areas where the bottom is composed of fine-grained sediments. That these large-scale movements might be linked to wave activity was dramatically suggested in 1969 when two oil platforms were toppled during Hurricane Camille (Sterling and Strohbeck, 1973). The problem of fine-grained sediment mass movements has led to both theoretical and laboratory studies of the interaction of surface-wave-induced bottom pressures and fine-grained sediments. However, direct measurements of wave-induced pressures and resulting bottom movements have not been reported prior to our work.

The results of our work describing the response of bottom sediments to wave pressures were first presented by Suhayda et al. (1976). The analysis

of the field data presented here concentrates on the effect that this interaction has on the loss of wave energy. In the area where our study was conducted (see Fig. 1), the sediment concentration of the water column was not a significant factor contributing to the loss of wave energy. It has been suggested that water column sediment concentration is the key factor in the calming effect of mudbanks (Delft Hydraulics Laboratory, 1962); however, the forcing of a mud wave by wave-induced pressures is also a part of the physical processes wherever fine-grained sediments occur. An understanding of this process is important not only in the Mississippi Delta but also in such coastal areas as the Guianas, the northern coast of China, and southwest India, where extensive areas of fine-grained sediments occur.

Methods

As a cooperative research effort by scientists of the Marine Geology Branch, United States Geological Survey, Corpus Christi, Texas, and the Coastal Studies Institute, Louisiana State University, two field sites were instrumented in East Bay, Louisiana. The primary experimental station and the location of a nearby soil boring are shown in Figure 1.

Results of analysis of the boring (Fig. 2) show the bottom sediments to be very soft, recently deposited material from the Mississippi River. Shear strengths range from 1.57 kilonewtons/meter² (kN/m²) near the water/sediment interface to 2.36 kN/m² 3 meters into the sediment. These low values of shear strength are common in the Mississippi Delta. The boring log shows no evidence of the crust zone that often occurs in these sediments between -3 and -10 meters. In places where the sharp increase in shear strength that defines a crust zone occurs, it is convenient to model the physical system as a light Newtonian fluid overlying a dense, non-Newtonian fluid with a rigid bottom.

The measurement of bottom movement was complicated by two factors. First, the measurements had to be made away from a platform to ensure that the motion of natural muds would be measured. Secondly, bottom motions under typically encountered wave conditions were thought to be small, and therefore high resolution was needed. Both problems were overcome by burying accelerometers in the mud. Though displacements were around 1 cm, accelerations were such that they could be reliably measured and required no fixed reference.

Three Bruel and Kjoer type 8306 accelerometers were mounted so as to measure the accelerations in three dimensions (Fig. 3). They were placed in a water-proof cylindrical PVC housing measuring 0.215 meter in diameter and 0.635 meter in length and having a submerged weight of 5.5 kg. The housing was pushed into the mud by a diver so that the top of the package was 0.15 meter below the mud line. The electronic cable coming from the top of the package was given 4.5 meters of slack, all of which was buried in the mud, and then fixed to a taut galvanized cable that was laid along the bottom between a nearby well jacket and our main instrumented site, Platform V. Platform V, in 19.2 meters of water, is shown in Figure 4. The cable from the accelerometer was brought along the galvanized cable and up the platform leg to the recorders. The location of the accelerometer was

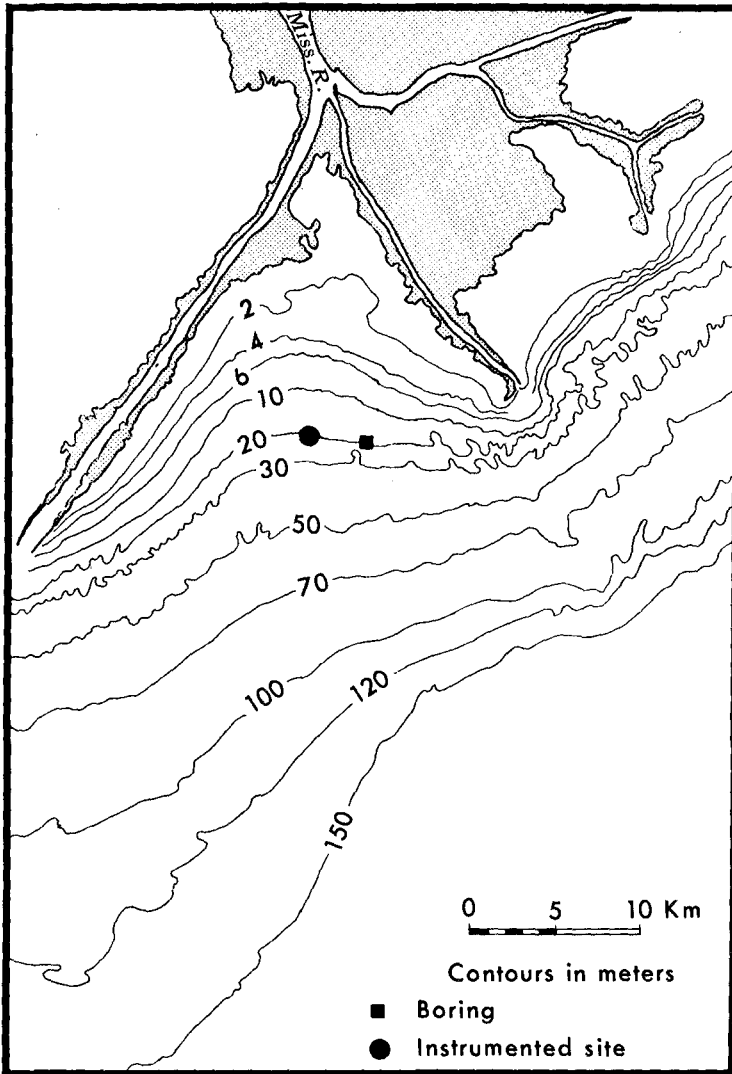


Figure 1. Location of the field site in East Bay, Louisiana.

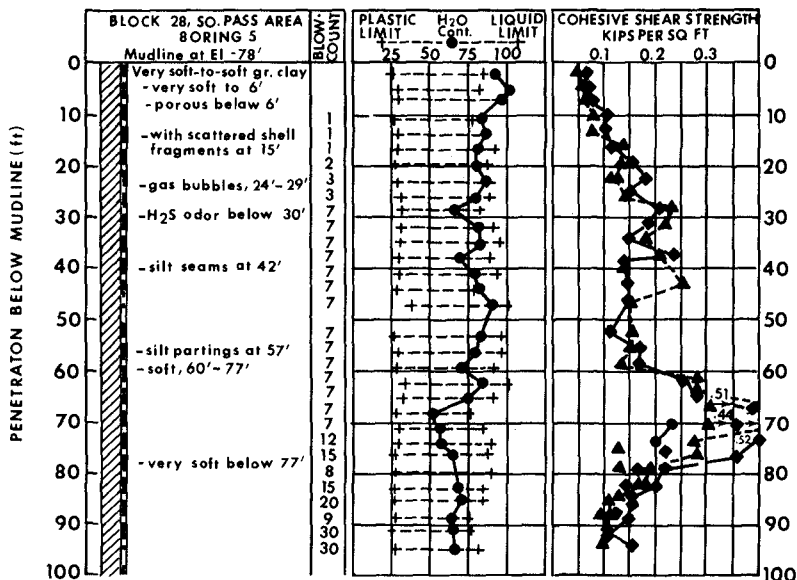


Figure 2. Results of soil boring taken near field site ($1 \text{ kip/ft}^2 = 48 \text{ kilonewtons/m}^2$). For location see Figure 1. (Boring courtesy U.S. Geological Survey, Marine Geology Branch, Corpus Christi.)

directly beneath the catwalk between the two structures so that a pressure cell attached to a weighted cable could be suspended over the package. Figure 5 is a schematic representation of the experiment and the physical system. The location of the pressure sensor was known to be within a radius of 2 meters from the accelerometer. This uncertainty in position could cause an error in the measured phase angle ϕ between the crest of the surface wave and the trough of the mud wave of $\pm 11^\circ$ for a characteristic wave with a period of 7.75 seconds. The importance of such an error will be seen in the calculation of the dissipation of wave energy. Wave properties were measured with a wave staff, a pressure sensor, and a two-axis electromagnetic current meter attached to wire cables that were suspended from the platform and anchored to the bottom through pulleys. A system of winches and pulleys allowed us to adjust the instruments to any depth.

Platform S (see Fig. 10), 3.35 km inshore of Platform V in 5.3 meters of water, was instrumented with an anemometer, a Bendix Q-15 ducted current meter, two pressure sensors, and a wave staff. By running the instruments on Platform S simultaneously with those on Platform V it was possible to compare the net energy lost by the waves while traveling between the two data

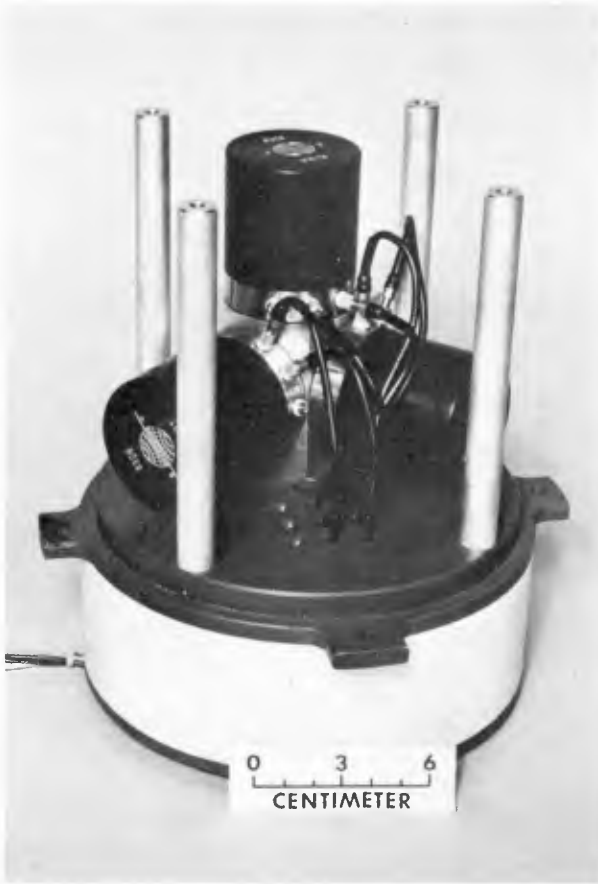


Figure 3. Array of three accelerometers.

stations with a rate of energy loss calculated from the measurements of mud movement at Platform V.

Results

Simultaneous measurements of wave height and wave-induced pressure resulted in the data represented in Figure 6. The term n is a correction



Figure 4. The main instrumented site, Platform V.

factor that matches linear theory with observed pressures and wave heights in the manner shown (where $K_p = \cosh k(h + Z) / \cosh kh$). If the observed data were in perfect agreement with linear theory, the data points would fall along the line n equal to 1.00. Further experimentation using two pressure cells placed at different depths in the water column showed that linear theory accurately predicts the change in wave-induced pressures from near the surface to within 0.5 meter of the bottom. The fact that other researchers have obtained similar results (Homma et al., 1966) supported the use of a corrected linear theory for determining surface wave heights from pressure measurements made in the water column above the accelerometer. The actual values of the correction factor n that were used were those values lying along the two least squares fit lines shown in Figure 6.

A sample of the data taken in the study is shown in Figure 7. The accelerations appear sinusoidal in form and have the same general appearance as the wave record.

The shape of the bottom pressure spectrum is similar to that of the spectrum of the vertical acceleration, and the peaks occur at the same

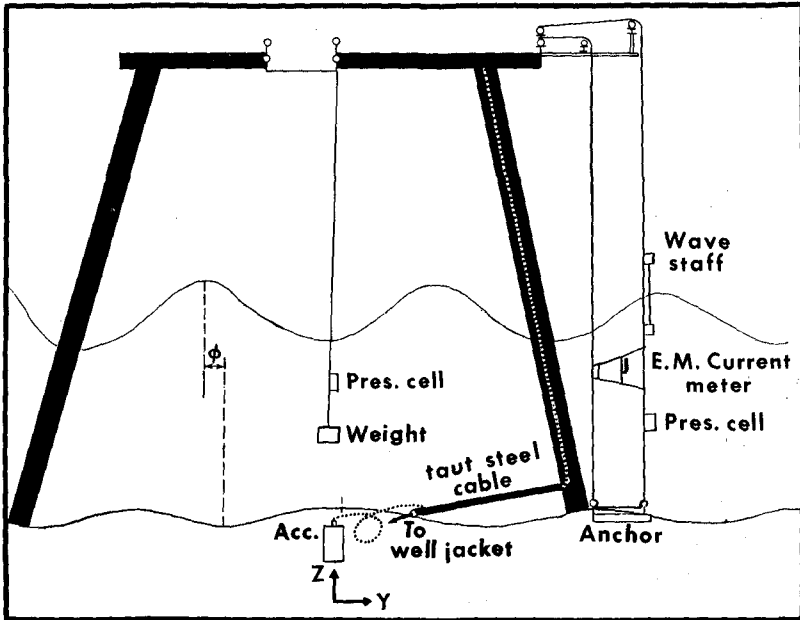


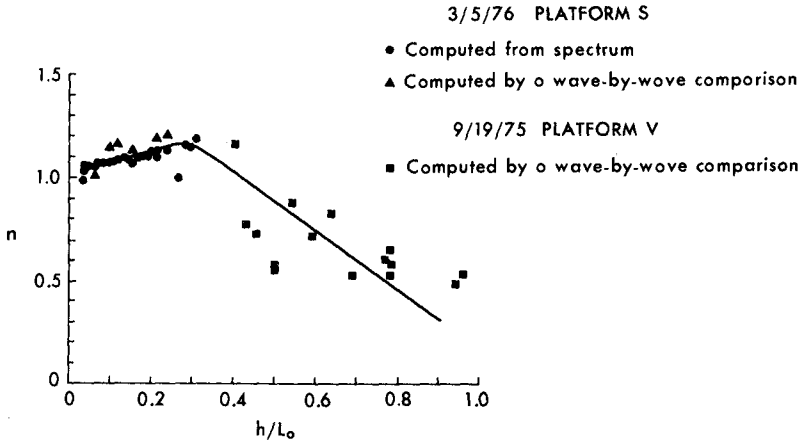
Figure 5. Experimental setup at Platform V.

frequency (Fig. 8). The low-frequency spectral components visible in the acceleration spectrum are believed to be electronic drift. (The phase angle between the crest of the mud wave and the crest of the pressure wave was 202° for the peak spectral component.) Horizontal mud motions are approximately 90° out of phase with the vertical motions, and a backward horizontal movement occurs at the crest of the bottom wave. Similar motion occurs for forced waves on an elastic half space. The ratio of vertical displacement to horizontal displacement over several sets of data averaged about 2.0.

A plot of the amplitude of the pressure wave at the bottom versus the amplitude of the mud wave (Fig. 9) reveals a roughly linear relationship for the range of pressures from near zero to 2.39×10^3 Pascal.

The average energy transmitted through the sea/sediment interface per unit and time over one wave cycle is (Gade, 1958)

$$D_m = -\frac{1}{T} \int_0^T P \frac{dh}{dt} dt \quad (1)$$



h = depth

L_0 = deep water wave length

$$n = \frac{\text{observed wave height}}{\text{observed pressure}} \rho g K p$$

Figure 6. Comparison of observed wave height and observed wave pressure with small-amplitude wave theory.

where T = wave period

P = wave-induced bottom pressure

dh = an infinitesimal increase in the height of the interface

The general characteristics of the data show that the following functions will accurately describe the motions:

$$P = P_a + A \cos (kx - \sigma t)$$

$$h = h_0 + MA \cos (kx - \sigma t + \psi)$$

where P_a = steady-state bottom pressure

A = amplitude of the wave-induced bottom pressure

h_0 = depth of mud over which motion occurs

M = proportionality constant between the amplitudes of the mud wave and the pressure wave

ψ = phase angle between the crest of the bottom pressure wave and the crest of the mud wave

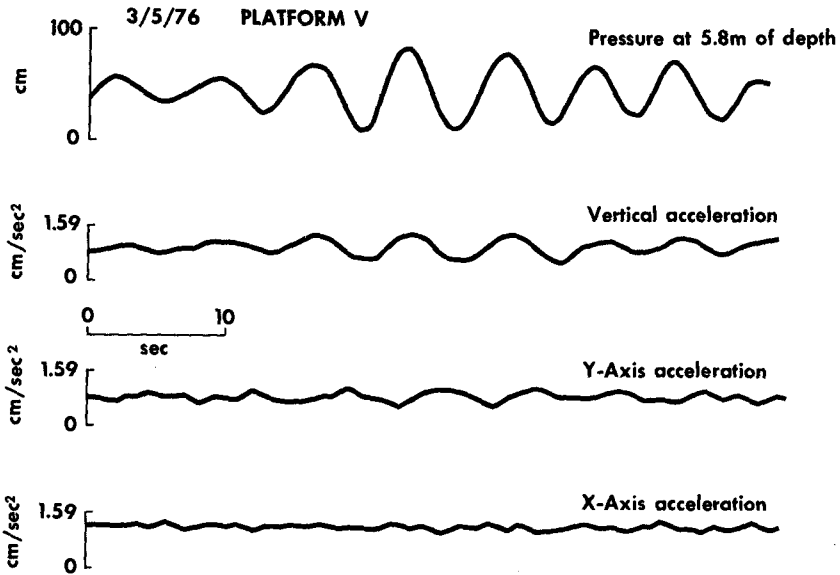


Figure 7. Sample of the data taken during the study.

After substituting equations (2) and (3) into (1) and integrating, and then using linear theory to put bottom pressures in terms of surface wave height, the equation for the rate of energy loss to the bottom is obtained:

$$D_m = \frac{\pi \rho g M H^2 \sin \phi}{4T \cosh^2 kh} \quad (4)$$

where $\phi = 180^\circ - \psi$.

For purposes of comparison with other theories for the dissipation of wave energy, the pressure correction factor for linear theory is not incorporated into the equation. At most this can change the energy loss rate by 20 percent. From equation (4) it can be seen that the dissipation of wave energy by the soft bottom involves only two important factors, determined by the physics of the sediment movement: (1) the relationship between the pressure force on the sediment and the resultant vertical displacement, given by M , and (2) the phase angle between the crest of the pressure wave and the trough of the mud wave, given by ϕ .

The results of the two-station experiment allowed us to estimate the energy lost from the waves. Conditions during the two-station experiment

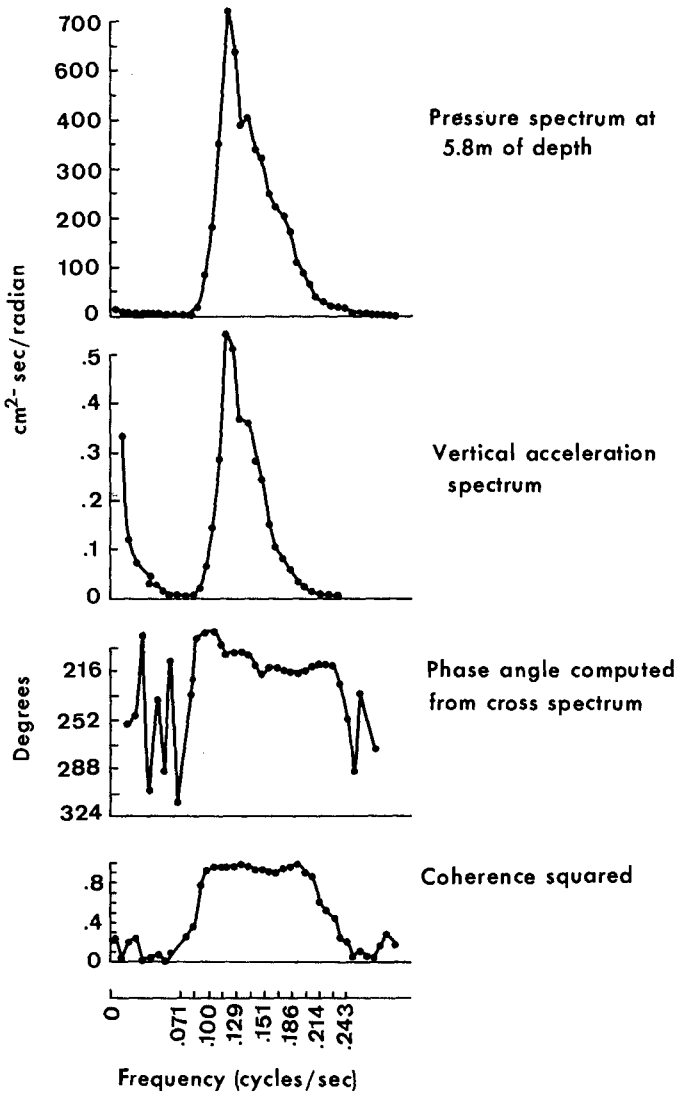


Figure 8. Results of spectral analysis of data.

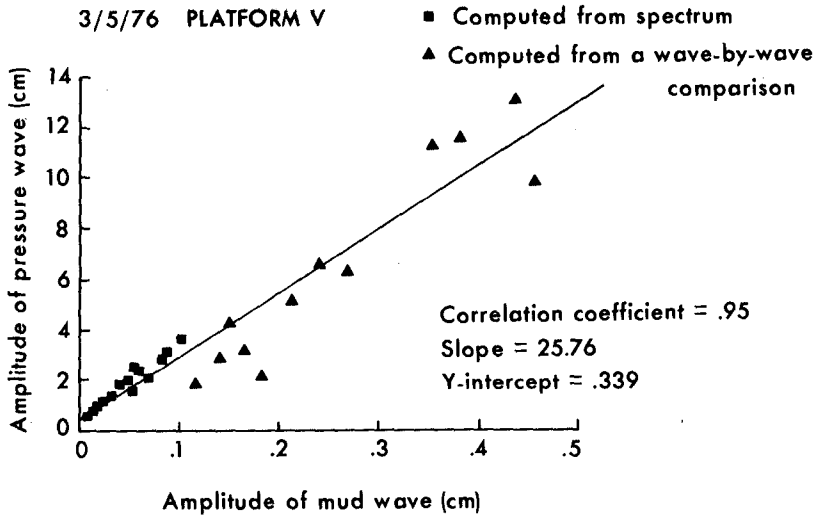


Figure 9. Amplitude of pressure wave plotted as a function of the amplitude of the mud wave.

are illustrated in Figure 10. The instruments on platform V and Platform S were run simultaneously, a procedure that resulted in a surface wave spectrum at V and at S and a bottom movement spectrum at V. For the experiment the effects of the wind, the current, and shoaling and refraction required a small correction to the measured wave height difference. The theoretical wave heights between Platforms V and S were calculated using the energy dissipation equation (4) derived for the forcing of a mud wave and taking into account shoaling and refraction based upon the period of the peak spectral component. The root mean square wave height at Platform V was used for the initial wave height. It was found that to produce agreement with the measured wave height at Platform S and keep M constant the value of the phase angle ϕ would have to be 10° .

Discussion of Results

A comparison of the results of our study with other theories for the dissipation of wave energy is shown in Figure 11. The phase angle ϕ between the crest of the surface wave and the trough of the mud wave is given two values: 22° is the angle that was actually measured at V, and 10° is the angle that results in the correct average dissipation of wave energy between Platforms V and S, assuming that M is constant. Note that the use of the smaller angle does not significantly reduce the magnitude of the dissipation

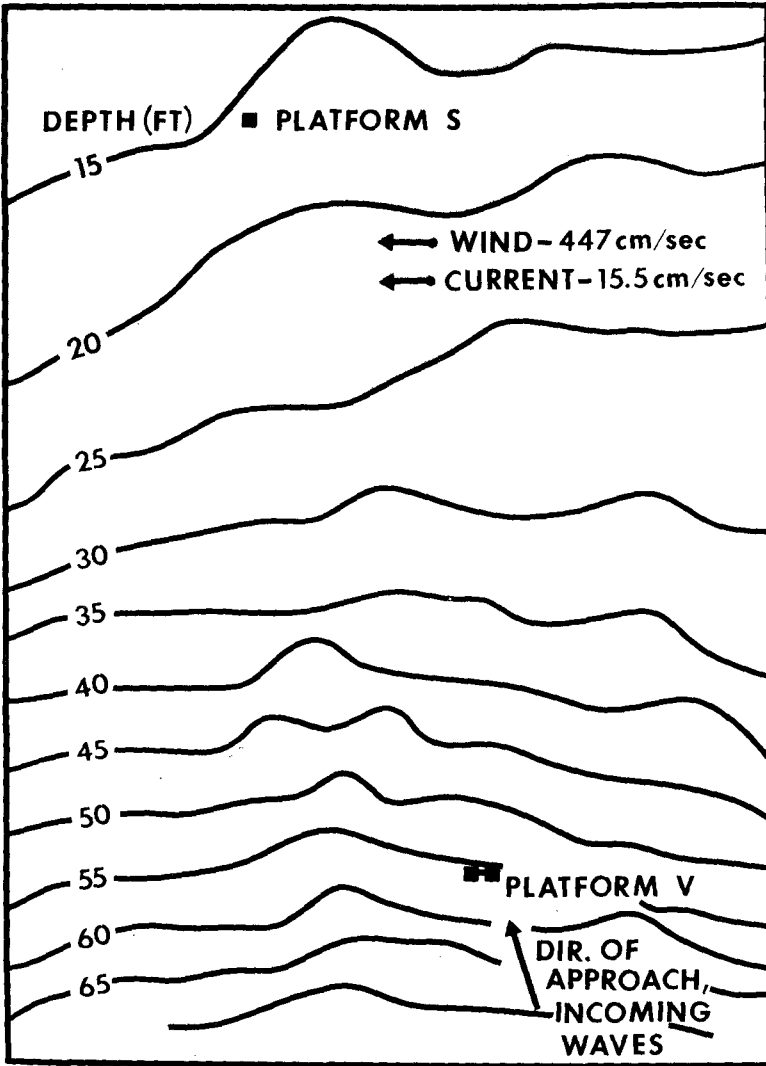


Figure 10. Conditions during two-station experiment.

DISSIPATION OF WAVE ENERGY

J. A. Putnam & J. W. Johnson Impermeable rigid bottom	R. O. Reid & K. Kajjura Permeable rigid bottom	Results of East Bay Study
$D_f = \frac{4}{3} \frac{\pi^2 \rho f H^3}{T^3 \sinh^3 kh}$	$D_p = \frac{\pi \rho g^2 K H^2}{4 L v \cosh^2 kh}$	$D_m = \frac{\pi \rho g M H^2 \sin \phi}{4 T \cosh^2 kh}$
	IN 19.2m OF WATER	
$f = .01$	$T = 7.75 \text{ sec}$	$M = .0388$
$D_f = 3.67 \times 10^{-12} H^3$	$K = 10^{-6} \text{ cm}^2$	$\phi = 22^\circ$
	$D_p = 1.86 \times 10^{-10} H^2$	$D_m = 2.99 \times 10^{-8} H^2$
		$\phi = 10^\circ$
		$D_m = 1.25 \times 10^{-8} H^2$
	IN 4.5m OF WATER	
$D_f = 1.23 \times 10^{-10} H^3$	$D_p = 1.14 \times 10^{-9} H^2$	$D_m = 1.07 \times 10^{-7} H^2$
		$D_m = 4.99 \times 10^{-8} H^2$

Figure 11. Comparison of the rate of dissipation of wave energy for the soft bottom in East Bay with theories for dissipation rates for rigid bottoms (Putnam and Johnson, 1949; Reid and Kajjura, 1957).

rate. The dissipation rates for 19.2 and 4.57 meters of water are in joules/cm²-sec, and H is the wave height in centimeters. The relationship derived by Putnam and Johnson (1949) for dissipation by bottom friction is of particular interest because it is the one most often used even for energy dissipation on coasts. The presence of the mud is often taken into account by making the value of the frictional coefficient (f) larger than 0.01, which is the value commonly used for sandy coasts. It can be seen from this that for reasonable heights the effect of a flexible bottom is to cause an energy dissipation rate that is at least an order of magnitude greater than that for a rigid, impermeable bottom.

The results of the two-station experiment are illustrated in Figure 12. Using 10° in the formula for the dissipation of energy while holding M constant in order to make the total dissipation agree with theory is somewhat an arbitrary choice. It is entirely possible that the properties of the sediments change between V and S and cause changes in M as well as φ, but it should be remembered that because of the uncertainty in the

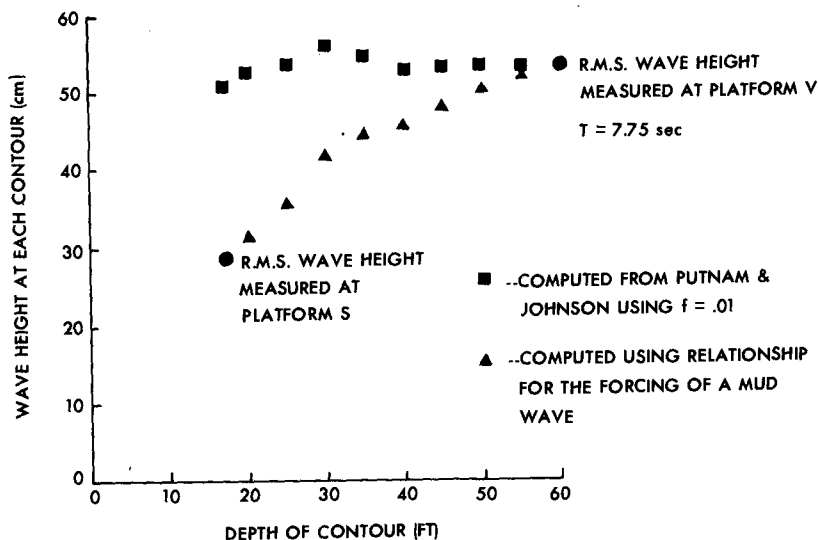


Figure 12. Comparison of the dissipation of wave energy for East Bay and that predicted using the theory of Putnam and Johnson (1949) with the measured wave height change.

position of the pressure sensor relative to the accelerometer it is possible that 10° was the true and constant phase angle.

Figure 12 also illustrates another important point concerning the dissipation of wave energy on muddy coasts. The predicted wave heights between Platforms V and S are shown in the figure as they would be predicted by Putnam and Johnson (1949). Certainly order-of-magnitude higher dissipation rates on sandy coasts can occur when well-formed ripples and the proper velocities are present (Tunstall, 1973), but even in such cases the contrasting trend, made more extreme by using Putnam and Johnson's theory, is present. By comparing the two curves in Figure 12 it can be seen that for bottom friction the dissipation of wave energy occurs mainly in shallow water, whereas for a flexible bottom a relatively greater amount of wave energy is dissipated in intermediate-depth water. Nearshore wave energy for muddy coasts can therefore be expected to be greatly reduced from that present on the outer shelf. Such coasts, in comparison to sandy coasts, tend to protect their shoreline by the dissipation of wave energy in the bottom sediments.

Summary

1. Bottom motions in the pressure range from near zero to 2.39×10^3 Pascal appear to be forced waves on an elastic half space, with the effect of internal viscosity being seen in a phase shift between the crest of the forcing wave and the trough of the mud wave. This results in the transfer of energy to the bottom sediments.
2. The energy loss at the field site was found to be at least an order of magnitude greater than that resulting from percolation over a typical sandy bottom or caused by normal frictional effects.
3. A relatively greater amount of wave energy is dissipated on a muddy coast at intermediate water depths than on a sandy coast.
4. Design criteria for offshore structures and predictions of sediment transport in the nearshore region of a muddy coast based on standard frictional dissipation rates may be significantly inaccurate.

Acknowledgments

Financial support for this project was provided under contracts with the Coastal Studies Institute, Louisiana State University, by the U.S. Geological Survey, Marine Geology Division (Contract 14-08-0001-14963) and the Geography Programs, Office of Naval Research. We thank Shell Oil Company for cooperation during the project.

References

- Delft Hydraulics Laboratory, 1962, Demerara coastal investigation. The Netherlands, 240 pp.
- Gade, H. G., 1958, Effects of a non-rigid, impermeable bottom on plane surface waves in shallow water. *J. Mar. Res.*, 16:61-82.
- Hom-ma, M., K. Horikawa, and S. Komori, 1966, Response characteristics of an underwater wave gauge. *Proc.*, 10th Internat. Conf. on Coastal Engr., Tokyo, Japan,
- Putnam, J. A., and J. W. Johnson, 1949, The dissipation of wave energy by bottom friction. *Trans.*, Am. Geophys. Union, 30(1):67-74.
- Reid, R. O., and K. Kajiura, 1957, On the damping of gravity waves over a permeable sea bed. *Trans. Am. Geophys. Union*, 38(5):662-666.
- Sterling, G. H., and E. E. Strohbeck, 1973, The failure of the South Pass 70 "B" platform in Hurricane Camille. Fifth Offshore Technology Conf., Houston, Texas, Preprint 1898.
- Suhayda, J. N., T. Whelan, III, J. M. Coleman, J. S. Booth, and L. E. Garrison, 1976, Marine sediment instability, interaction of hydrodynamic forces and bottom sediments. Eighth Offshore Technology Conf., Houston, Texas, Preprint 2426.
- Tunstall, E. B., 1973, Experimental study of vortices generated by oscillatory flow over rippled surfaces. Ph.D. dissertation, Univ. of California at San Diego.

CHAPTER 70

APPLICATION OF A SEDIMENT TRANSPORT MODEL

by C.A. Fleming* and J.N. Hunt**

Abstract

A mathematical model for sediment transport under waves has been developed from concepts that have been used successfully for unidirectional flow. This model has been combined interactively with numerical models of wave refraction, wave diffraction, longshore currents and circulation currents in order to predict local topographical changes in the vicinity of a cooling water intake basin for a nuclear power station. The sediment model is calibrated using field data of sediment concentration profiles. Verification and adjustments may be made by analysing deep water wave statistics corresponding to periodic beach and hydrographic surveys.

The model can be used to investigate the effects of any wave climate and consequently different layouts of coastal structures can be examined very rapidly. For the particular problem considered it was necessary to optimise the configuration of the breakwaters forming a cooling water intake basin in order to minimise the sediment concentration at the intake, estimate maintenance dredging quantities and investigate extreme events.

Introduction

A mathematical sediment transport model for unidirectional flow has recently been developed (1). This model assumes that sediment is transported in a bed load region, adjacent to the stationary part of the bed, where the grains are supported by inter-particle collisions, and a suspended load region where gravitational forces are overcome by fluid turbulence. Continuity of sediment concentration and velocity between the two regions was assumed and consequently the exact definition of the transition level is not of critical importance as the sediment flux immediately above and below the transition level will be similar. Whilst not attempting a complete physical description, the model relies on the simplest formulations of bed load and suspended load that are required for predictive use. The unidirectional model was tested against the best existing empirical theories and found to give comparable estimates of sediment transport rates.

* Mathematics Dept., Reading University, England, and Sir William Halcrow and Partners, Consulting Engineers, London, England.

** Professor of Mathematics, Reading University, England.

It is proposed that under certain conditions it is reasonable to assume that there are some basic physical similarities between the movement of sediment in unidirectional flow and in the combination of waves and currents. The latter case can be treated as a quasi-steady condition with respect to the shear stresses acting on the bed and the dispersion of shear stress due to the orbital wave motion. The wave motion is assumed to act principally in stirring up the sediment while the currents act principally in transporting the sediment. Some concepts from the unidirectional model have been extended in order to develop a model to predict sediment transport rates in the presence of waves and currents.

Attempts have been made to apply the theory to the prediction of local sediment movement and hence topographical changes over a coastal region situated on the S.W. coast of South Africa. Such an application requires the evaluation of wave heights, wave directions and near-shore currents over the region. This is achieved by using a wave refraction model combined with a longshore current model. Comparison of predicted and measured topographical changes can be made to verify and adjust the model parameters.

The model has also been used to optimise the layout of breakwaters forming a cooling water intake basin for a nuclear power station with a particular emphasis on minimising maintenance dredging. This requires the use of a wave diffraction model and a potential-flow model to determine the flow in the vicinity of the basin due to wave induced currents and the proposed cooling water recirculation currents. A physical model of the area has also been constructed and detailed comparisons will be made in due course.

Sediment Transport-Bed Load

The shear stress in excess of the critical shear must be dispersed within the bed load layer. Otherwise successive layers of material would be removed from the bed. This type of argument was substantiated experimentally by Bagnold (2,3) who proposed the relationship

$$\tau_d \approx p \tan \alpha \quad (1)$$

where τ_d is the dispersed shear stress, p is the normal pressure and α is a friction angle which may be approximated by static angle of repose. For the oscillatory case

$$\bar{\tau}_d = \bar{\tau}_w - \tau_c \quad (2)$$

where $\bar{\tau}_w$ is the mean wave shear stress, τ_c is the critical shear stress and generally $\bar{\tau}_w \gg \tau_c$.

The relationship proposed by Jansson (4 and recently reviewed 5) was used to evaluate the shear stress due to waves. A friction factor is given by

$$\frac{1}{4\sqrt{f_w}} + \log_{10} \frac{1}{4\sqrt{f_w}} = -0.08 + \log_{10} \frac{a_o}{R_N} \quad (3)$$

where a_o is the water particle orbital amplitude at the bed, R_N is a roughness length. f_w is the friction factor defined by

$$\hat{\tau}_w = \frac{1}{2} \rho f_w \hat{u}_o^2 \quad (4)$$

where $\hat{\tau}_w$ is the maximum shear stress acting on the bed, ρ is the fluid density and \hat{u}_o is the maximum particle velocity at the bed. It has been shown by Madsen and Grant (6) that the Shields criterion for incipient sediment motion in unidirectional flow can also be applied to oscillatory flow when the bottom shear stress is evaluated using equations (3) and (4).

If it is assumed that the bed load layer is supported entirely by grain interaction and that the local change in dispersed shear is proportional to the local concentration, a concentration distribution may be implied such as (1)

$$C = C_m \left(\frac{C_e}{C_m} \right)^{y/e} \quad (5)$$

C_e is the concentration at the upper boundary of the bed load layer and C_m is the maximum concentration at the bed (≈ 0.52 to be consistent with grain movement in all directions).

As the excess shear is to be dispersed within the bed load layer, the bed load thickness, assumed to be the height of the transition level, is

$$e = \frac{\bar{\tau}_d \ln(C_e/C_m)}{g(\rho_s - \rho)(C_e - C_m)(\tan \alpha + \tan \theta) \cos \theta} \quad (6)$$

where ρ_s is the sediment density and θ is the slope of the bed.

Hunter (7) has shown that, in the presence of tides, the current friction factor, for the case of a degenerate tidal ellipse, is twice as large in the direction parallel to the wave orbit plane as in the direction normal to the wave orbit plane. This analysis can also be applied to short period gravity waves so that the corresponding components of shear due to a current are

$$\begin{aligned} \bar{\tau}_{cw} &= 4 \rho f_c \hat{u}_o u_{cw} / \pi \\ \bar{\tau}_{cn} &= 2 \rho f_c \hat{u}_o u_{cn} / \pi \end{aligned} \quad (7)$$

where f_c is the current friction factor, u_{cw} and u_{cn} are the currents parallel and normal to the wave direction respectively. The bed load that should be transported by the combination of the wave and current shears can be determined from the thickness (e') required to disperse the resultant shear. However, for the application considered it is assumed that generally $\hat{u}_0 \gg u_c$ and that $e \approx e'$.

Due to the high concentration of sediment within the bed load layer the fluid and sediment mixture has an effective viscosity much greater than the normal fluid viscosity. This is dependent on and increasing with volumetric concentration. It is therefore assumed that the shape of the velocity distribution may be given by

$$\bar{v}_d = \mu_s \frac{du}{dy} \tag{8}$$

where μ_s is the effective viscosity of the fluid and sediment mixture. This is subject to the boundary condition, $u = u_{ce}$ at $y = e$. The bed load transport rate is therefore

$$T_b = \int_0^e c u dy \tag{9}$$

Sediment Transport-Suspended Load

The simplest one dimensional suspended load distribution may be found from

$$\frac{\partial c}{\partial t} = \frac{\partial}{\partial y} (E \frac{\partial c}{\partial y} + c \omega) \tag{10}$$

where E is a coefficient of eddy viscosity and ω the characteristic fall velocity of the sediment. For the assumed quasi-steady state in oscillatory flow the time dependent term may be omitted. It is also necessary to specify the vertical distribution of eddy viscosity. Johns (8) has developed a turbulent boundary layer model for which a Fourier analysis is carried out for the computation of time means (with respect to turbulent velocity fluctuations) of the distribution of eddy viscosity. He found that according to his model the eddy viscosity distribution is sensibly constant over the whole wave cycle. It is assumed that the distribution takes the form

$$\frac{E}{E_e} = \left(\frac{y}{e}\right)^\xi \tag{11}$$

where subscript e refers to values at $y = e$ and ξ is a positive non dimensional constant. Equation (11) should only be applicable to the lower regions of the depth as it cannot satisfy the necessary boundary conditions at the free surface. However, as the sediment concentration diminishes so rapidly away from the bed this inconsistency can be considered to be admissible. The solution of equation (10)

with $\frac{\partial c}{\partial t} = 0$ and equation (11) is

$$\ln \frac{c}{c_e} = \frac{\omega e}{E_e(1-\xi)} \left\{ 1 - \left(\frac{y}{e} \right)^{1-\xi} \right\} \quad (12)$$

when $\xi \neq 1$.

The current velocity distribution is assumed to be

$$u_c = \hat{u}_c \left(\frac{y}{h} \right)^{1/7} + \text{constant} \quad (13)$$

where \hat{u}_c is the maximum current velocity at the free surface and h is the total depth so that the suspended load transport rate is therefore

$$T_s = \int_e^h c u_c dy \quad (14)$$

By combining the bed load and suspended load models the unknown parameters are c_e , E_e and ξ . Using some results from Johns (8) a value for the exponent ξ was chosen to give the best overall fit to the theoretical distributions in the region adjacent to the bed. A suitable value was found to be approximately 0.25 for a fairly wide range of wave conditions.

The remaining two parameters may be evaluated from suitable experimental or field data.

It should be noted that due to equation (7) the resultant shear acting on the bed and hence bed load movement is not necessarily in the same direction as that of the suspended load which must move in the same direction as the current. However, this difference is generally quite small.

Application

An area of coastline some 6 km long on the S.W. coast of South Africa at Durnfontein has been studied. Site investigations (9) include periodic beach and hydrographic surveys, wave rider recordings, radar and sea bed observations of wave direction, current meter and drogue measurements and suspended sediment profiles (10). The foreshore is gently sloping at approximately 1:100 and has sensibly parallel contours. The wave climate is comparatively severe with a predominant wave period between 10 - 11 secs. and wave heights between 1.5 - 2.0 m but with frequent storms in excess of 4.0 m.

The beach and hydrographic survey data were interpolated onto regular grids so that successive surveys could be compared to give volume changes over the area. Figure 1 shows a typical plot of accumulative volume change that has occurred along the coast, calculated to a distance offshore of 1400 m, for the period February to June 1974 during which there has been general accretion. The broken line and full line show the

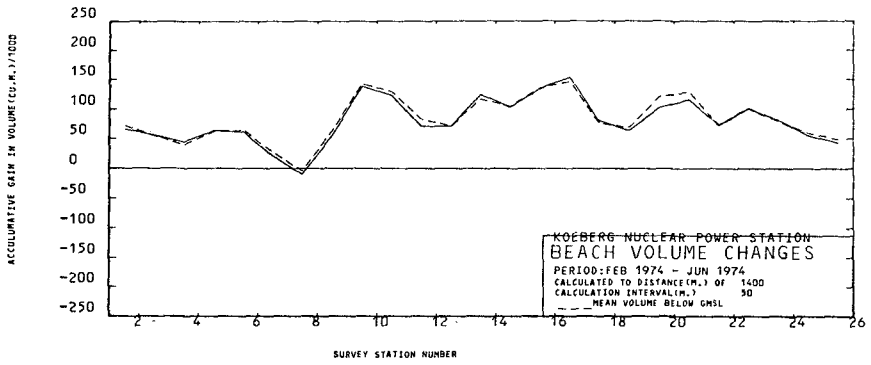


Figure 1. Beach Volume Changes Between Survey Lines , Feb.1974 - Jun. 1974

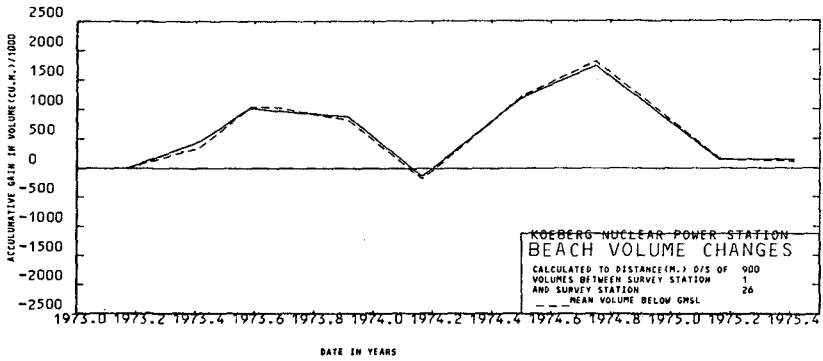


Figure 2. Total Beach Volume Changes

measured volume changes below geodetic mean sea level (GMSL) and below the beach survey station levels respectively, indicating that volume changes above GMSL are generally negligible. The survey stations are shown in Figure 5. Successive volume changes for each survey period could then be plotted to produce a time history of the beach with respect to accumulative volume changes for a common area. Figure 2 shows the results of this analysis of prototype data covering a period of two years and it can be seen that, although there is considerable seasonal variation, the net annual sediment movement is approximately zero.

Due to the wave conditions sediment sampling was extremely difficult. However, concentration profiles both inside and outside the surf zone and for a reasonable range of wave heights and periods were obtained. For each profile it is possible to evaluate a value for the coefficient of eddy viscosity at some arbitrary distance above the bed from equation (11). These values were found to be close enough to take an average for all of the profiles, although some trends with the ratio of wave height to depth can be detected. By combining the bed load and suspended load models and assuming continuity of sediment flux at the transition level it is possible to determine a reference sediment concentration at this level consistent with each set of field data. These values have been plotted against a dimensionless parameter $(\tau_w / g(c_s - c)T\omega$ where T is the wave period) and it can be seen from Figure 3 that a clearly defined relationship exists. Consequently using this relationship the sediment transport model can be used predictively given wave heights, periods, directions, current magnitudes and directions.

A wave refraction model is used to evaluate wave directions and heights over the region. The wave ray tracking method, developed by Abernethy and Gilbert (11), is used. In this method the wave speed is assumed to vary linearly over each triangular element so that the wave ray follows a circular arc across each element. Refraction coefficients are simultaneously calculated using the wave intensity equation of Munk and Arthur (12). The grid spacing is chosen according to the local topography and some initial topographical smoothing is applied as discussed by Coudert and Raichlen (13). The wave heights and directions are interpolated onto a regular sediment transport grid which is a sub-area within the refraction grid and, of necessity, completely covered by wave rays. The relative positions and dimensions of the grids are shown in Figure 4. The offshore topography for the area considered is uniform such that it is possible to assume that the sea bed is plane between the refraction grid boundary and "deep water" and consequently starting conditions for each wave ray can easily be established. A typical wave refraction plot is shown in Figure 5 together with the positions of instrumentation and field measurements.

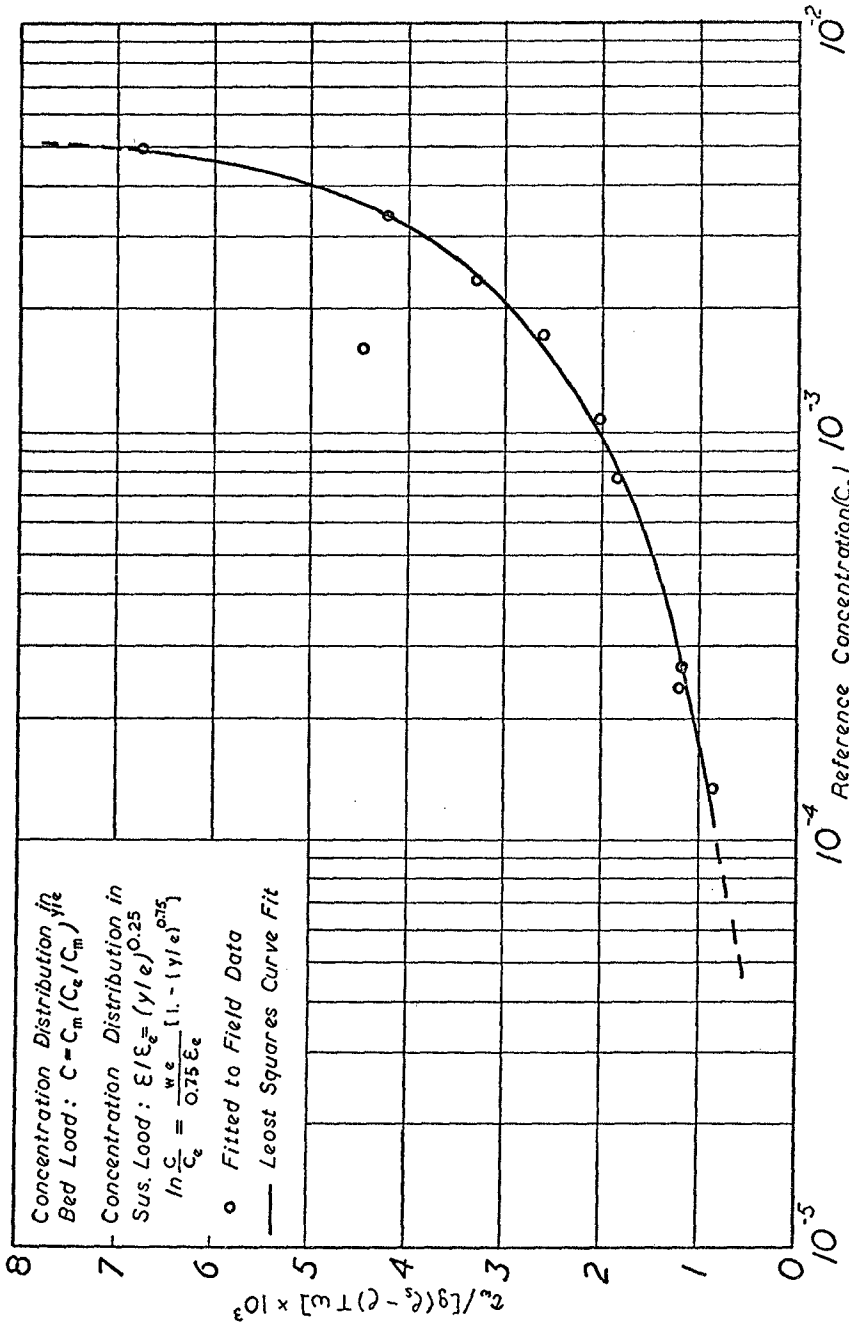


Figure 3. Reference Concentration Fitted to Field Data

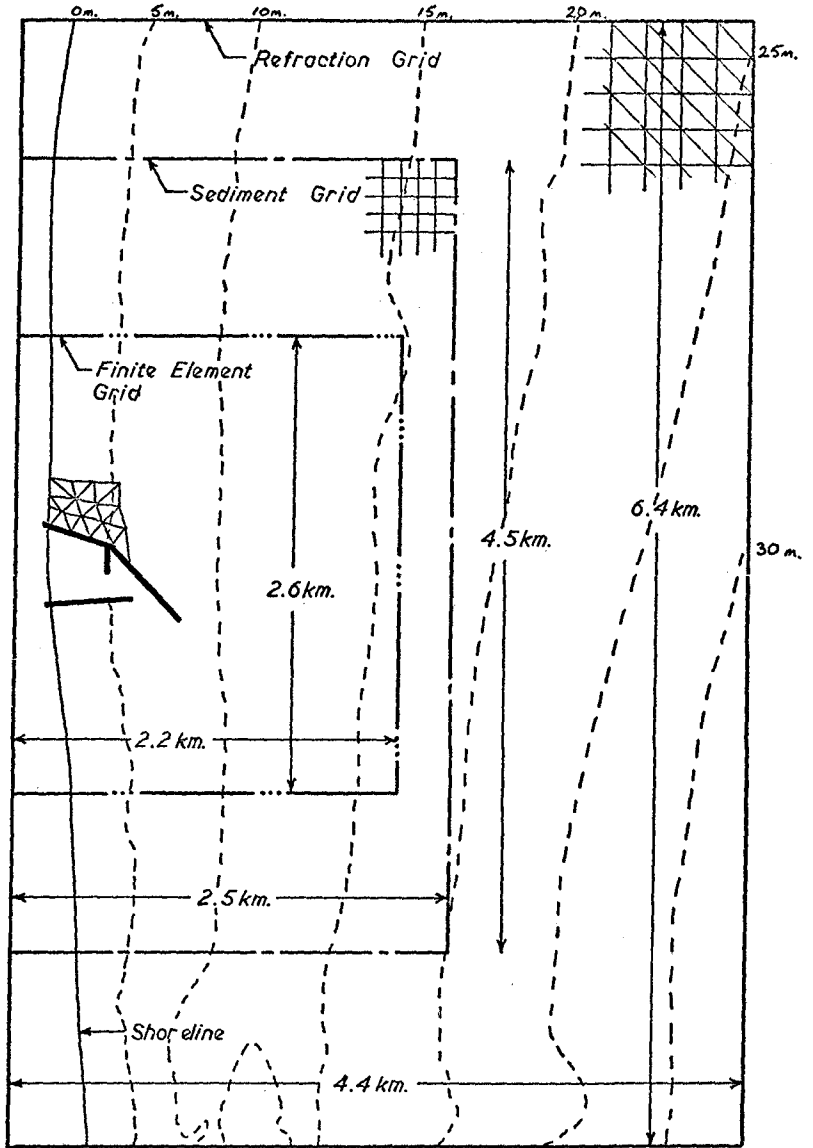


Figure 4. Interrelationship of the Numerical Schemes

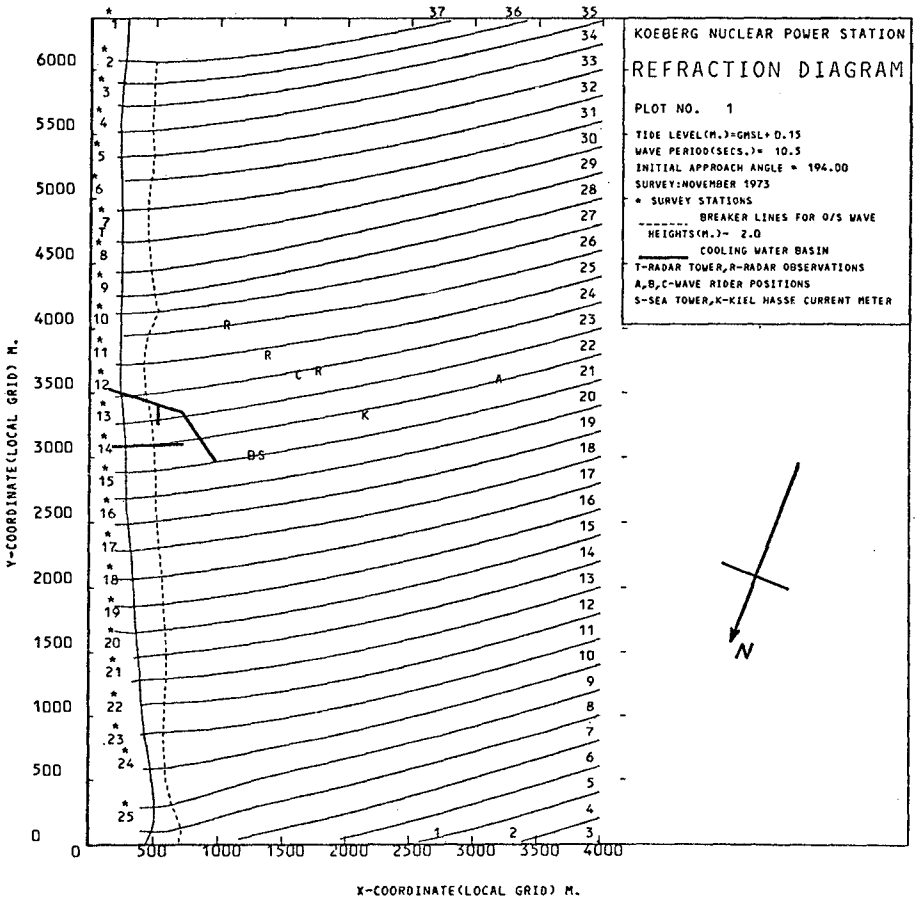


Figure 5. Wave Refraction Diagram

There are very many published wave breaking criteria. However, for this application a relationship of the form

$$d_b = H_b / K_b \quad (15)$$

is used, where H_b is the breaker height, d_b is the breaker depth and K_b a constant coefficient estimated to be 0.7 from physical model tests and field observations.

The longshore current model after Longuet-Higgins (14,15) is then used to calculate wave induced currents inside and outside the surf zone. The foreshore is represented by a series of overlapping planes such that the longshore current profile is calculated at regular sections along the beach. These current vectors are then interpolated onto the discrete points forming the regular sediment transport grid.

Given any combination of offshore wave period, direction and height, the refraction and longshore current models are used to give the required parameters at each point in the mesh and by applying the sediment transport model at these points, predictions of local topographical changes can be made.

The wave data corresponding to each survey period was separately analysed into subsets of wave period, direction and height. These were used as input data and attempts to reproduce historic events, with respect to depth changes and hence volume changes, were made. Initially the model used the wave data for a complete survey period, of approximately three months duration, without intermediate depth adjustments. Consequently the sediment transport for each wave condition was assumed to be accumulative regardless of the order of events. This approach was found to give unrealistically large depth changes. Obviously refinements were necessary and the wave data was reduced to several incremental periods of approximately two weeks duration. Corresponding intermediate depth corrections to the region at the end of each of these periods were made. By comparing the historic and predicted topographical changes for several survey periods it is possible to optimise some of the unknown model parameters. These are

- (i) the current friction factor used in the calculation of longshore currents and reflected by differences in the magnitude of predicted and measured volume changes
and
- (ii) the coefficient of horizontal mixing which determines longshore current velocity profiles.

It is intended that a nuclear power station should be sited at Duynfontein and the breakwater formed intake basin is required to protect the intakes from unacceptable wave attack, alleviate associated cooling water recirculation problems and minimise the intrusion of sediment into the intakes.

The proposed layout of the intake basin as shown in Figure 5 consists of a leading breakwater arm giving shelter from the predominant wave direction. This allowed the use of a wave diffraction numerical model, assuming a semi-infinite breakwater, to define wave heights and directions around the entrance and within the intake basin.

The cooling water outfall is to be situated on the beach between 200 and 500 metres from the root of the southern breakwater with the intake located inside the basin. A finite element potential flow numerical model is used to calculate the currents due to the combination of longshore currents and cooling water recirculation currents in the vicinity of the basin. The finite element mesh, consisting of six noded triangular elements, was chosen to cover a sub-area of the sediment transport grid as shown in Figure 4. The offshore boundary was located at a distance where currents are assumed to be negligible and the boundaries normal to the beach are located at distances where the longshore currents would not be influenced by the presence of the coastal structure. The remaining inshore boundary was located along an idealized line corresponding to mean sea level. The longshore currents outside the finite element mesh are calculated as previously described. The current profile at the edge of the finite element mesh is then used as a boundary condition for the potential flow model together with the cooling water intake and outfall flows. The resulting current velocities and modified wave heights are interpolated onto the regular sediment mesh and estimates of local topographical changes and rates of sediment accumulation inside the basin can be made.

A framework for the sequence of operations for the analysis of field data, the overall mathematical model and the interaction between each activity is shown in Figure 6. The model can deal with many options allowing for numerous sets of wave data to be used successively to reproduce historic events or hypothetical sequences. Figures 7(a) and 7(b) show the current vectors (broken lines) and wave height vectors (full lines) for two examples of typical waves approaching the shoreline from the northern and southern sectors respectively. The generated longshore currents for the examples are in opposite directions and different current patterns around the basin are clearly shown.

The model may also be used to investigate equilibrium sea bed conditions by repeating the same wave data and updating the depth grid at each iteration. An example is shown in Figures 8(a) and 8(b) for a cooling water basin with a shortened outer breakwater arm. Figure 8(a) is a contour plot for November 1973 and Figure 8(b) shows the contours after running a 2.0 m wave of 10.0 seconds period from a direction of S.W. for 20 days in 5 day steps. It should be noted that these contour plots are produced by an automatic computer plotting program and there is some difficulty with the inclusion of discontinuities such as the breakwater arms. Consequently the contours cannot terminate on the breakwaters. However, it can be seen

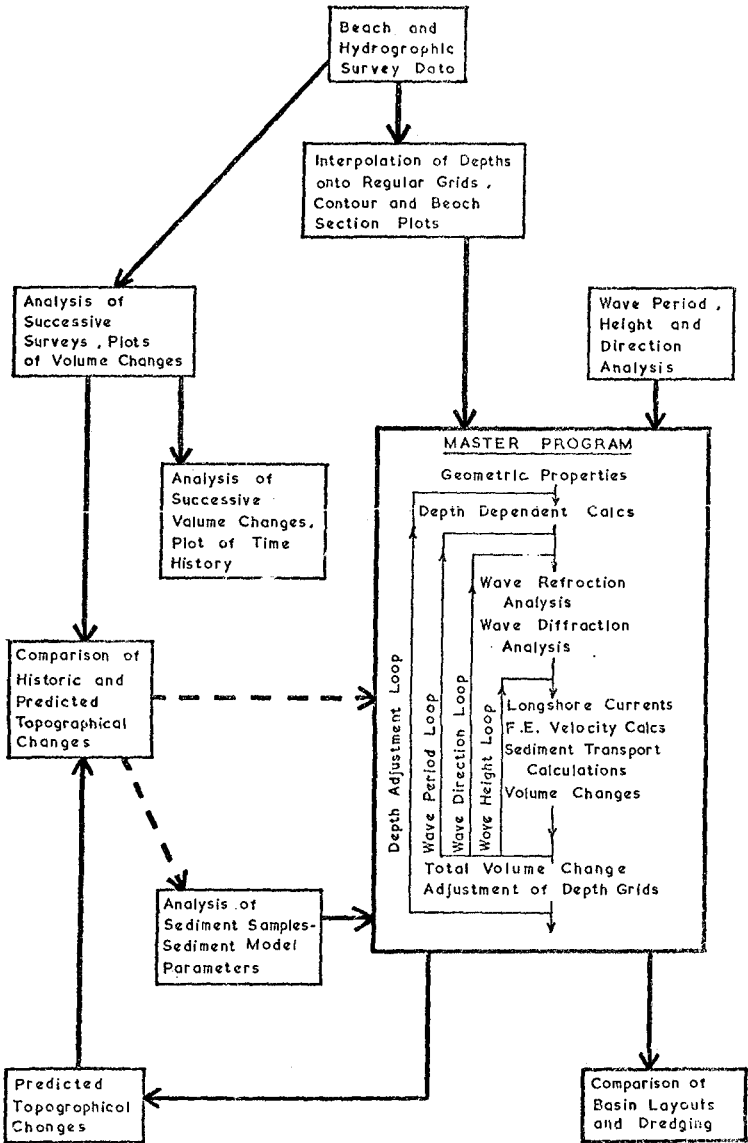
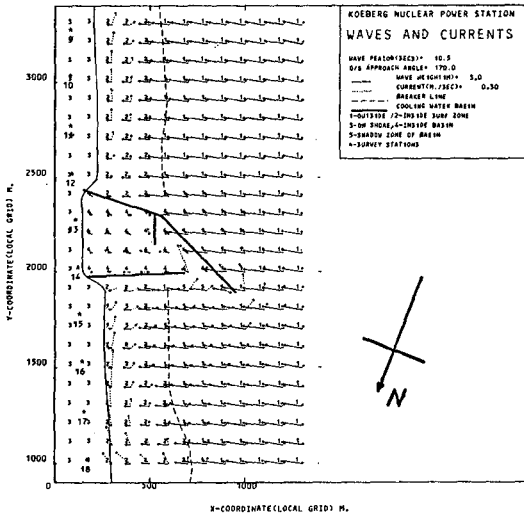
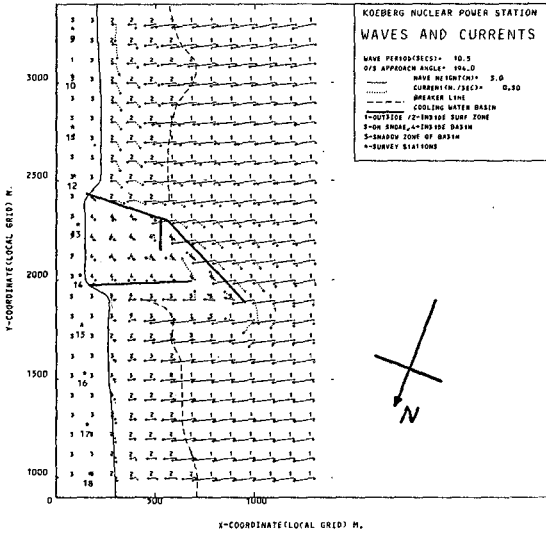


Figure 6. Framework for Sediment Transport Model

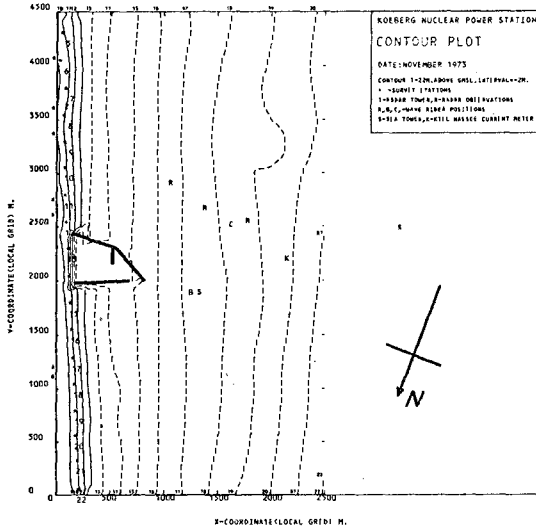


(a) Offshore Wave Direction - WSW

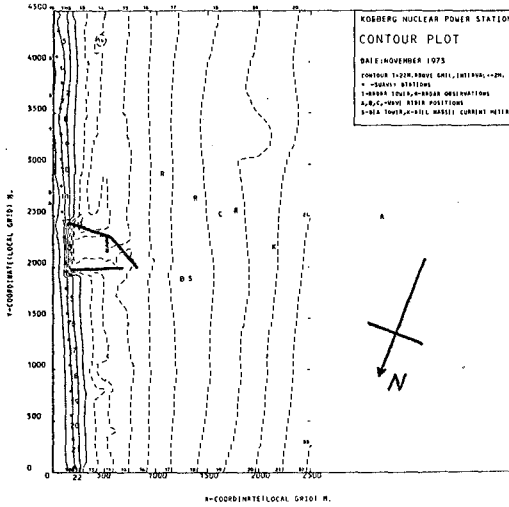


(b) Offshore Wave Direction - SW

Figure 7. Predicted Wave and Current Fields



(a) November 1973 (measured)



(b) November 1973 + 20 days (predicted), wave height=2.0m., period=10.0secs., direction=SW, time step=5 days

Figure 8. Contour Plots

that a bar is shown to be formed in the entrance to the basin, as would be expected. A bar and depression is also shown on the southern side of the southern breakwater indicating the influence of the cooling water outfall as well as some erosion to the north of the intake basin.

Another part of the intake basin investigation was to optimise the distance offshore and hence the depth at which the basin entrance should be situated. The results of this exercise are shown in Figure 9 where the predicted annual maintenance dredging quantities are plotted against entrance depth. The wave data used was based on the one year of complete records available and the range of values indicated by the hatched area represents upper and lower bounds for different assumptions with regard to the wave breaking criteria and wave data analysis. It can be seen that the general trend is for a large increase in predicted dredging quantities as the basin entrance depth decreases below 6 m, a negligible difference of dredging quantity between 6 m and 7 m entrance depth and a decrease in the dredging quantity as the depth is increased beyond 8 m. The shape of this curve is thought to result from the larger waves, possessing the larger sediment transport potential, breaking seaward of the basin entrance and losing much of their energy. The wave height reduces so that a basin entrance located in an intermediate water depth is to a certain extent protected from the larger sediment transporting waves. However, as the depth is further decreased the effect of waves on the bed becomes more pronounced and results in increases to the sediment transport rates. The comparative cost of maintenance dredging and capital cost of construction must be balanced when choosing the optimum depth for the basin entrance. The results of this type of analysis will depend very much on the wave climate for the area considered and in this case the design depth for the entrance was chosen to be 6 m.

Preliminary comparisons between the current patterns and wave heights measured in the physical model show a large measure of agreement. However, more detailed analyses will be carried out.

Conclusions

A mathematical model for sediment transport under waves has been developed from concepts that have been used successfully for unidirectional flow. The model has been applied to the problem of optimising the layout of a cooling water intake basin for a power station in order to minimise both sediment concentrations at the intake and maintenance dredging. This required the simultaneous development of numerical models for wave refraction, longshore currents, wave diffraction and cooling water recirculation as well as the sediment transport model. The longshore current model assumes plane beach sections and does not take account of variations in alongshore wave breaker height and is therefore capable of improvement. The potential

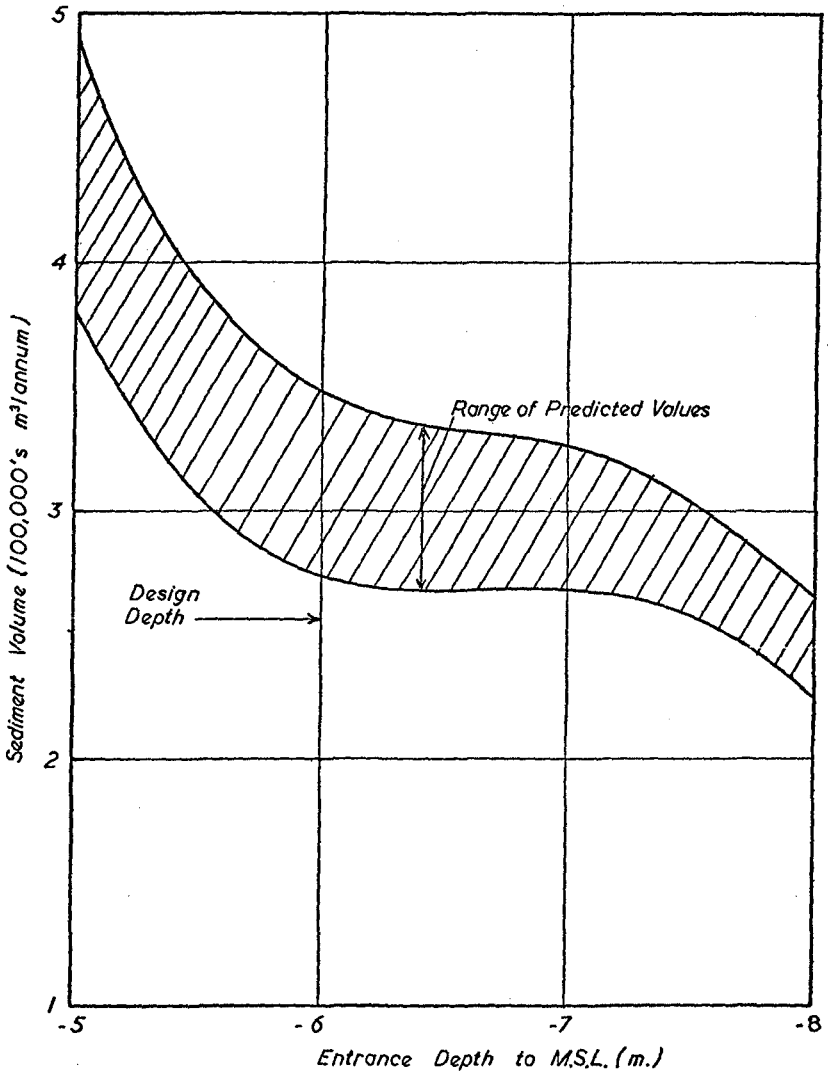


Figure 9. Predicted Annual Dredging Volumes against Entrance Depth

flow model does not account for frictional effects in the vicinity of the basin and the diffraction model should only be used for simple breakwater configurations. However, development work concerning all these aspects will be continued and it is hoped that it will be possible to include such phenomena as the formation of rip currents and mass transport and hence additional forces causing onshore-offshore sediment movement. Nevertheless results from the model are realistic and comparisons to the physical model are reasonable.

An important factor when considering the use of higher order models is the practical limits of computer time. However, there are few detailed field measurements available which do suggest that extra computing effort can be justified. A considerable part of the effort expended in the formulation of the present model was devoted to keeping the execution time to within reasonable bounds and still allow several wave conditions to be processed.

The sediment model is not universal in as far as there are certain parameters that must be calibrated from field data. The consistency of the in-situ sediment concentration profiles collected at Duynfontein and fitted to the model is very good. However, there is a general scarcity of detailed field or experimental data for either concentration profiles or sediment transport rates under waves and it was therefore not possible to generalise the model. Consequently the results from further development of the model to include such non-linear effects as mass transport will be difficult to confirm.

The overall model can be used to examine several different harbour or basin configurations very rapidly and is therefore a very useful engineering tool for the planning of new works or for investigation into modification to existing works.

Acknowledgements

The first author gratefully acknowledges the support given to this work by industrial studentship grants from the Science Research Council, Swindon and Sir William Halcrow and Partners, London. Thanks are also due to the Electricity Supply Commission (ESCOM, South Africa) who financed the site data collection carried out by the University of Cape Town and without which the model could not have been developed.

References

1. Fleming, C.A. and Hunt, J.N., "A Mathematical Sediment Transport Model for Unidirectional Flow", Proc. Instn. Civ. Engrs., London, Part 2, 1976, 61, June. 297-310.
2. Bagnold, R.A., "Experiments on a Gravity Free Dispersion of Large Solid Spheres in a Newtonian Fluid Under Shear", Proc. Roy. Soc., Series A, 1954, 225, 49-63.
3. Bagnold, R.A., "The Flow of Cohesionless Grains in Fluids", Phil. Trans. Roy. Soc., Series A, 1956, 249, No. 964, 235-297.

4. Jonsson, I.G., "Measurements in the Turbulent Wave Boundary Layer", Proc. 10th Conf. I.A.H.R., London, 1963, 1, 85-92.
5. Jonsson, I.G., "The Wave Friction Factor Revisited", Prog. Rep. No. 37, Inst. Hydrodyn. and Hydraulic Engrg, Tech. Univ. Denmark, 1975, 3-8.
6. Madsen, O.S. and Grant, W.D., "Sediment Transport in the Coastal Environment", Ralph M. Parsons Laboratory for Water Resources and Hydrodynamics, Report No. 209, Dept. of Civil Eng. M.I.T., 1975.
7. Hunter, J.R., "A Note on Quadratic Friction in the Presence of Tides", Estuarine and Coastal Marine Science (1975), 3, 473-475.
8. Johns, B., Reading University, Personnel communication.
9. Loewy, E., Witthaus, K.G., Summers, L., and Maddrell, R.J., "Data Collection and Analysis for Coastal Projects", Proc. 15th Coastal Engineering Conference, Hawaii, July 1976.
10. Kilner, F.A., "Measurement of Suspended Sediment in the Surf Zone", Proc. 15th Coastal Engineering Conference, Hawaii, July 1976.
11. Abernethy, C.L. and Gilbert, G., "Refraction of Wave Spectra", Hydraulics Research Station, Report No. INT 117, May 1975.
12. Munk, W.H. and Arthur, R.S., "Wave Intensity Along a Refracted Ray", Gravity Waves, Nat. Bur. St. Circ. 521, U.S. Gov. Printing Office, Wash. D.C., Nov. 1952, 95-109.
13. Coudert, J.F. and Raichlen, F., (Discussion to Jen.Y., Wave Refraction Near San Pedro Bay, California) Proc. A.S.C.E., 96, WW3, 1970, 737-747.
14. Longuet-Higgins, M.S., "Longshore Currents Generated by Obliquely Incident Sea Waves, 1", Journal of Geophys. Res., 75, No. 33, Nov. 1970, 6779-6789.
15. Longuet-Higgins, M.S., "Longshore Currents Generated by Obliquely Incident Sea Waves, 2", Journal of Geophys. Res., 75, No. 33, Nov. 1970, 6791-6801.

CHAPTER 71

LONGSHORE TRANSPORT AT A TOTAL LITTORAL BARRIER

Richard O. Bruno and Christopher G. Gable

ABSTRACT

Analysis of longshore transport at a littoral barrier is presented. Channel Islands Harbor, California was selected as the study site because its offshore breakwater and jetties form a unique complete littoral barrier. Through repetitive surveys an accurate determination of longshore material transport in one direction was made. Measured transport rates ranged from 160,000 to 1,284,000 cubic meters per year. Utilizing visual observations of surf parameters, estimates of longshore wave thrust were computed. The range of wave thrust was 145 to 1,988 Newtons per meter. Comparison of the relation of wave thrust and longshore sediment transport is made. This study indicates that in an environment of high transport, nearly twice as much transport is predicted under corresponding wave thrust as that of the data summarized in the Coastal Engineering Research Center's Shore Protection Manual.

INTRODUCTION

The relation between longshore material transport and nearshore wave thrust (energy) is of vital interest to coastal engineers concerned with design and maintenance of navigation and beach erosion control projects. Past field and laboratory studies have produced an empirical relationship now widely used. However, these studies were conducted in areas where total transport may not have been measured. In this study, Channel Islands Harbor, California was selected because an offshore breakwater and jetties form a unique sand trap (Figure 1). This site is considered a nearly total littoral barrier to longshore transport. A further advantage to this site is its exposure to a high wave energy climate and high transport rates not encountered in previous studies. Dredge records from this harbor show annual transport in excess of one million cubic meters. The objective of this study is to reevaluate the empirical relationship between nearshore wave thrust and longshore material transport.

Coastal Engineering Research Center, Kingman Building, Fort Belvoir, Virginia 22060

Coastal Engineering Research Center, Field Office, Port Hueneme, California 93043

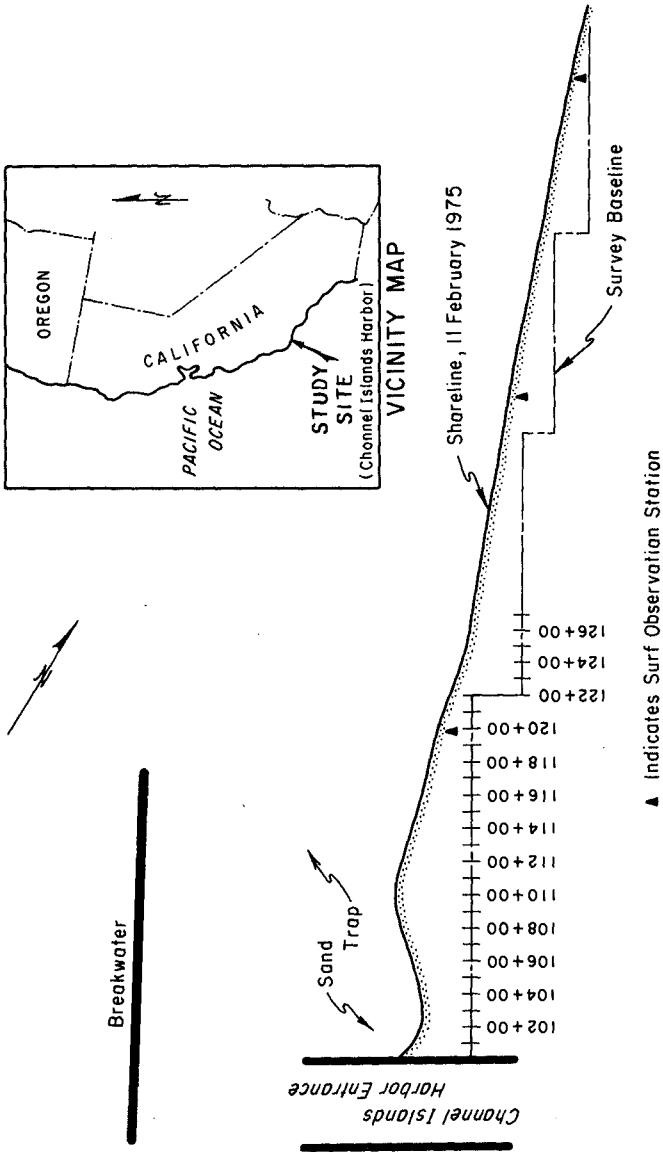


Figure 1. Longshore Transport Study Area .

DATA COLLECTION

The data collection program consists of periodic bathymetric and topographic surveys and routine collection of wave data from which longshore transport and wave thrust can be estimated.

Assistance in making surveys was provided by the Corps of Engineers, Los Angeles District. For these surveys a base line parallel to the shore was established. Profile lines, normal to the baseline, were spaced at about 30.5 meters (100 feet) for a distance of about 823 meters (2700 feet) as shown in Figure 1. At each of these stations elevations were measured from the baseline to the detached breakwater. Surveys were scheduled at intervals of 4 to 6 weeks although this scheduling was frequently modified due to survey crew availability, equipment failures, and unfavorable surf conditions.

Table 1 summarizes survey data, showing survey dates, ranges surveyed, type of fathometer calibration, survey method, and qualitative estimate of overall data quality. The notation "standard" survey indicates an analog fathometer record was made and the survey vessel was located by standard survey techniques of the Los Angeles District. For this method the vessel operator was directed by a man onshore to steer along the profile line. At ten second intervals the analog recording was marked and vessel position was recorded via plane table and alidade.

The notation "hybrid" indicates an analog fathometer record was made and position of survey vessel determined by use of electronic ranging equipment. Under this method the vessel operator was directed by a man onshore to steer profile lines, but the position of the vessel was monitored by telemetering the data to a field office where a minicomputer was used to produce a real time plot of position. By this monitoring of the survey in progress errors in positioning were determined and eliminated. For recording the data an electronic timer was used which simultaneously marked the analog record and recorded the vessel's position on magnetic tape every two seconds.

Both of these methods used an amphibious vehicle, known as LARC V for the bathymetric portion of the survey. The LARC enables measurement of the survey line to be continued through the surf zone by using rod and level methods when the vehicle's wheels contact the bottom. Profile lines were measured over the dry beach areas by standard level and rod transects.

Equally important to the data collection program are the

TABLE 1 - SUMMARY OF SURVEY DATA

DATE	RANGES SURVEYED	FATHOMETER CALIBRATION	METHOD USED	DATA QUALITY
14 APR 74	101 - 122	LEADLINE	STANDARD	5
7 MAY 74	101 - 127	LEADLINE	STANDARD	6
18 JUN 74	101 - 127	LEADLINE	STANDARD	0
30 JUL 74	101 - 127	LEADLINE	STANDARD	7
20 AUG 74	101 - 127	LEADLINE	STANDARD	7
24 SEP 74	101 - 127	LEADLINE	STANDARD	7
6 NOV 74	101 - 127	LEADLINE	STANDARD	4
7 JAN 75	101 - 127	LEADLINE	STANDARD	5
11 FEB 75	101 - 122	LEADLINE	STANDARD	6
4 MAR 75	101 - 127	LEADLINE	STANDARD	7
27 MAR 75	101 - 127	BAR CHECK	HYBRID	0
14 APR 75	101 - 127	BAR CHECK	HYBRID	7
6 MAY 75	101 - 127	BAR CHECK	HYBRID	9
1 AUG 75	101 - 127	BAR CHECK	STANDARD	9
13 AUG 75	101 - 127	BAR CHECK	HYBRID	9
16 SEP 75	101 - 127	BAR CHECK	HYBRID	9

surf data. Figure 1 shows the sites where twice daily surf data were collected using procedures developed under the Coastal Engineering Research Center (CERC), Littoral Environment Observation (LEO) program (Bruno and Hiipakka, 1973; Berg, 1968). These data include observations of surf conditions, local winds and littoral currents. For this study the estimates of breaker height and breaker direction were of primary concern. To aid in estimating the breaker direction the observer is provided with a protractor on the data form. Longshore current data is also considered in this report. Longshore currents were measured using small packets of dye which disperse upon injection in the surf zone. The observer measures the distance the dye travels parallel to the shoreline. Current speed is estimated from the movement of the dye patch centroid over a one-minute period and current direction is noted. Surf zone current velocities are not uniform; therefore, the width of the surf zone is estimated as well as the distance from the shoreline to the point of dye injection. To augment the surf data two wave gages were installed 1300 meters upcoast of the trap at six meters depth. However, gage data have not yet been analyzed and are not used in this report.

ACCURACY

Late in the study it was found the "standard" surveying method was not providing the reliable, accurate data desired. Figure 2 shows profiles plotted from "standard" surveys. These data are on a line sheltered by the breakwater and at a point beyond normal sand deposition. To verify no deposition divers measured underwater reference stakes and determined there was no change in bathymetry at this point. These plots indicate that unacceptable errors were introduced on several surveys. These errors were a result of poor position data, poor fathometer calibrations, and errors in data reduction.

The "standard" surveying method assumes that the LARC is on line for all fixes and that the instrument man has precisely marked its position simultaneously with the fathometer mark. This is not always true and errors which occur can never be recovered. Even with no errors produced in field collection, reduction of working scale plane table data sheets is limited to an accuracy of about 3 meters which is seldom attained.

In the "hybrid" method an electronic timer was employed to simultaneously mark the fathometer at 2 second intervals and to control the recording of the LARC's position. As a result the human errors in determining position are eliminated. Position accuracy, which was limited by the electronic ranging equipment, was found to be about 2 meters and is consistently attained.

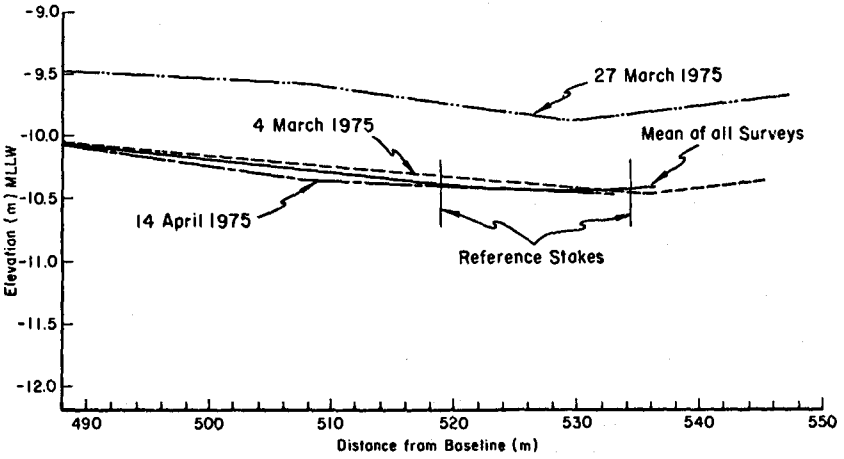
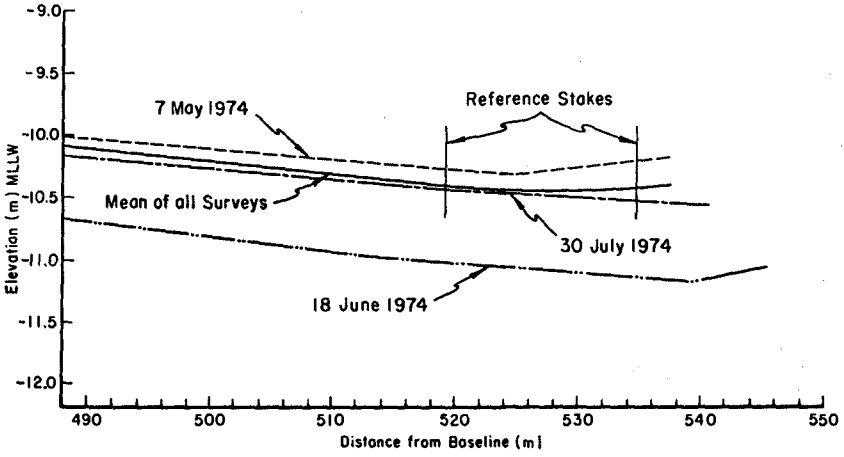


Figure 2. Illustrations of Survey Errors at Reference Station.

In addition to positional errors, fathometer calibrations and data reduction procedures were found to produce errors. Under the "standard" method leadline soundings were used for fathometer calibration. In taking leadline soundings numerous factors determine accuracy including skill and care of the operator, motion of the vessel, and roughness of the water's surface. Later surveys utilized a bar lowered at 5 foot intervals under the fathometer for calibration. This type of calibration removes human factors and is complete in that it shows any non-linearity which may occur in the fathometer readings.

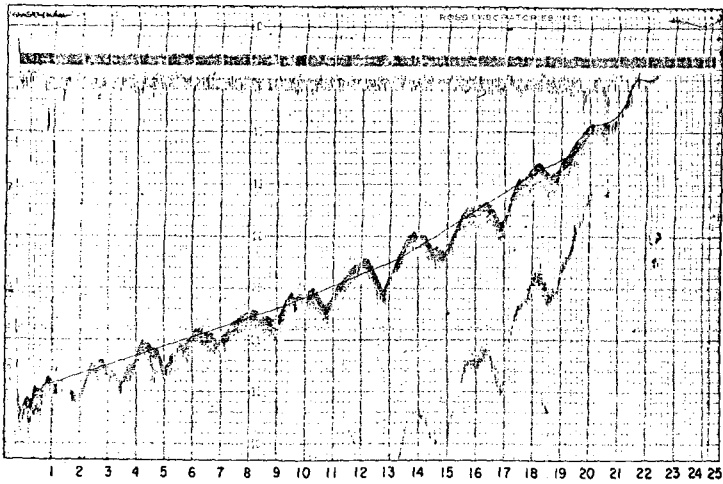
Another source of error which was discovered lies with uncertainty in interpreting the fathometer records. Figure 3 shows two profiles both with similar features which appear to be waves, but in fact on one record these features are the irregular bottom left after dredging. For this reason under the "hybrid" method all data reduction was performed by the authors, who were present at the time of data collection and noted conditions as records were being made.

The last column in Table 1 labeled "survey quality" is a subjective rating from 0 (poor) to 10 (good). These values were determined by the authors after examining the data on hand, field notes, and all profile plots. By using this approach it was determined that data collected 18 June 1974 and 27 March 1975 should be discarded as unreliable.

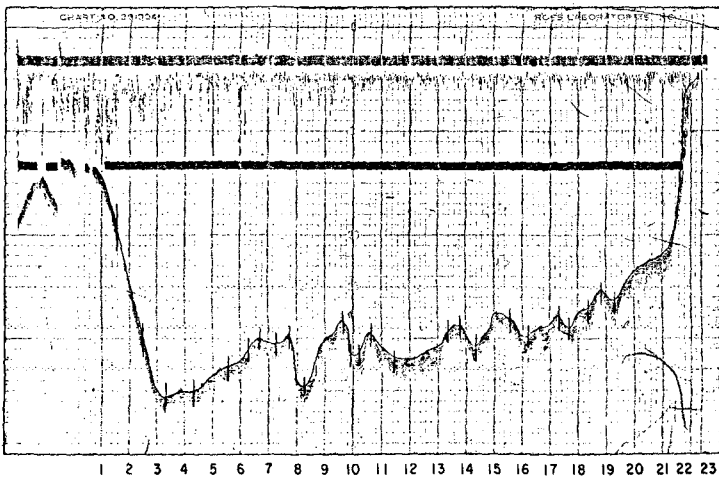
ANALYSIS

Table 2 is a summary of the analysis showing the survey intervals selected for computations, transport rates, longshore thrust, longshore thrust times wave velocity, and longshore currents.

Transport rates were determined by calculating volume changes between surveys. It is assumed that all material deposited into the trap was a result of longshore energy from upcoast; effects of reversal in the wave direction and resulting diffraction around the detached breakwater have been ignored. Diffraction can be illustrated in the case where wave approach is directly onshore. In this case there would be no general longshore component of wave energy. However, due to diffraction, a local zone of longshore wave thrust would develop as shown in Figure 4, (Weigel, 1962). The expected results would be an erosional zone and a depositional area downcoast (to the southeast). If both the local erosion and deposition zones are included in the total area used to calculate volume changes, this shore-parallel wave approach would result in no net volume change. In this study, the area of volume computations was



RANGE 124+00 - FATHOMETER RECORD WITH WAVES



RANGE 104+00 - FATHOMETER RECORD WITHOUT WAVES

Figure 3. Fathometer Record of Regular Bottom with Waves and Irregular Bottom without Waves.

Table 2 - Data Summary

Survey Dates	Transport Rate ($\frac{\text{meters}}{\text{year}}$)	Wave Thrust ($\frac{\text{Newton}}{\text{meter}}$)	Wave Thrust X Wave Velocity ($\frac{\text{Newton-meter}}{\text{meter-second}}$)	Longshore Current ($\frac{\text{centimeters}}{\text{second}}$)
4/17/74	1,194,000	1,988	547	45
5/7/74	689,000	1,276	349	36
7/30/74	537,000	644	159	27
8/20/74	426,000	611	152	22
9/24/74	500,000	689	183	36
11/6/74	1,284,000	665	167	34
1/7/75	1,174,000	877	245	44
2/11/75	716,000	801	208	36
3/4/75	954,000	712	190	66
4/14/75	1,108,000	545	133	35
5/6/75	402,000	366	89	34
8/1/75	160,000	390	84	18
8/13/75	430,000	145	29	21

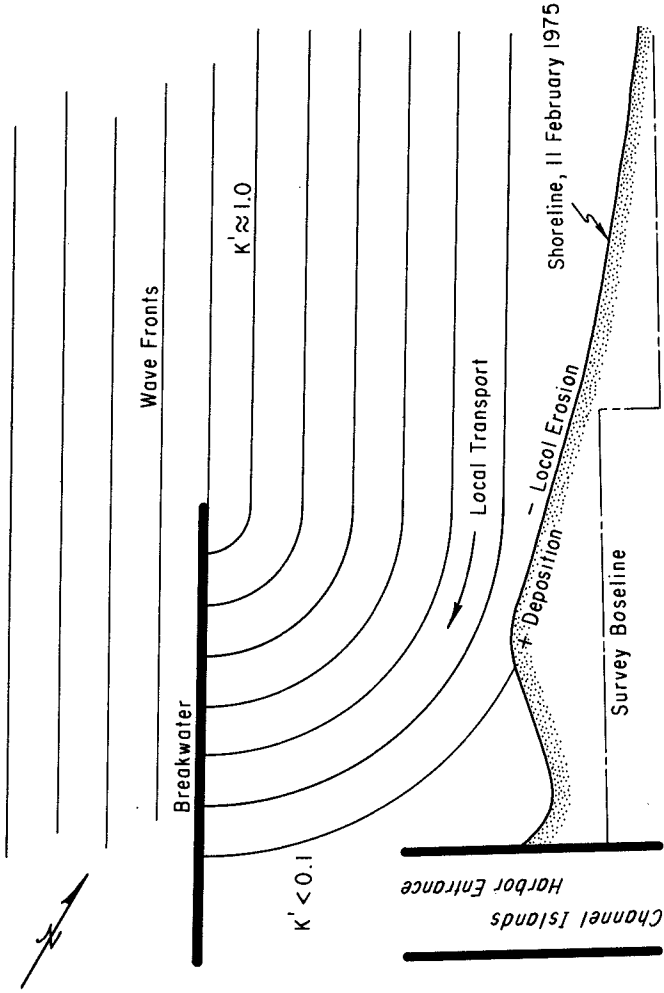


Figure 4. Wave Diffraction Pattern with Incident Waves Normal to the Breakwater (after Wiegel, 1962).

extended 300 meters beyond the north end of the breakwater to include diffraction effects. Diffraction diagrams (Weigel, 1962), indicate that diffraction transport is included for all wave approaches from the West or North which are predominant at the study site. Under periods of wave reversals only small errors are introduced by diffraction since most of the erosion and part of the deposition are included in the area of volume calculation.

Deposition from upcoast (northerly) transport during times of reversals in wave direction can be examined. The area of the trap seaward and upcoast of the jetties will show deposition due to reversals. Figure 5 is a plot of the first profile upcoast of the jetties. Survey dates of spring 1974 and fall 1975 are plotted and show the total change at this profile over the period of the study. This plot shows little deposition at the end of the jetty. Detailed examination of all profile data enabled the authors to define the area of deposition attributable to influx of material from north (upcoast) to the trap. No significant deposition was measured at distances more than 425 meters from the baseline. By using 425 meters from baseline as an outward boundary to calculate volumes, errors due to influx of material from reversals is minimal.

The area used in volume change calculations is between the baseline and 425 meters offshore and the north jetty and 670 meters upcoast. Over this area we expect a volume accuracy of within 15,000 cubic meters.

In 1972 Longuet-Higgins summarized his earlier work and presented an expression for the momentum flux tensor component which he termed lateral thrust. This lateral thrust, or longshore wave thrust, is "the flux towards the shoreline of momentum-parallel-to-the-coast". It is given as:

$$H = E (c_g / c) \cos \theta \sin \theta \quad (1)$$

where E is wave energy density, c_g the local group wave velocity, c the wave velocity, and θ the wave angle. Longuet-Higgins gives an expression for E as:

$$E = 1/8 \rho g h^2 \quad (2)$$

where h denotes wave height, ρ the water density and g the acceleration of gravity. The expression for H , valid outside the breaker zone, implies the waves exert a longshore thrust on water and sediment inside the surf zone. It is therefore

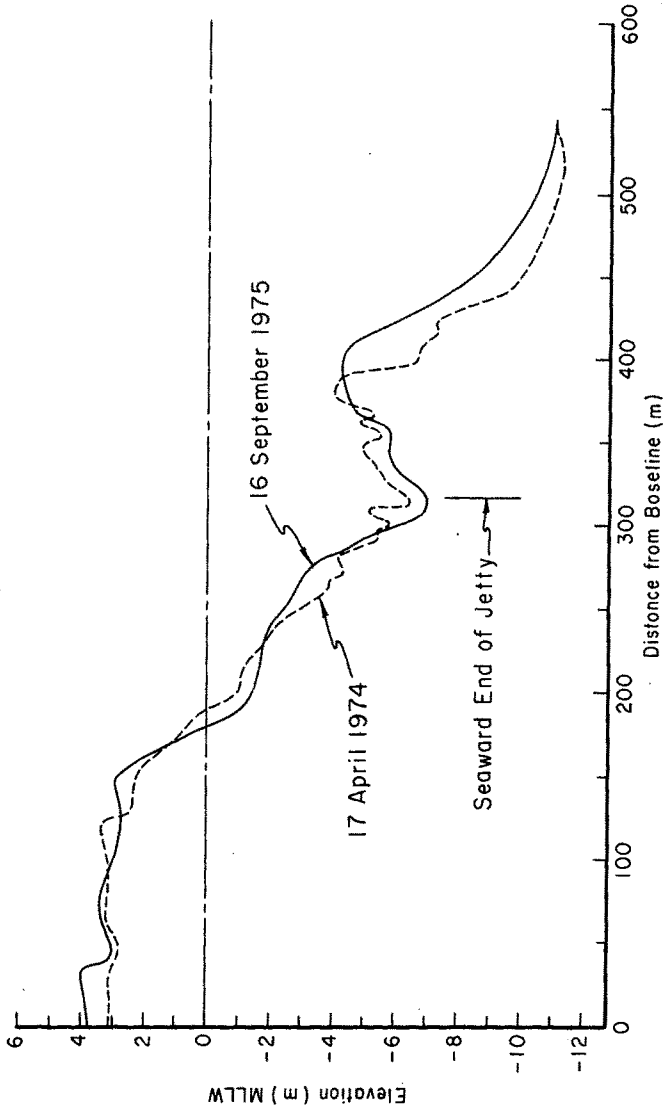


Figure 5. Range 101 + 00 at Beginning and End of Study.

reasonable to expect a direct relation between longshore thrust and longshore transport. At the breaker line $c \cong c_g$, therefore by combining equations (1) and (2) above:

$$H = 1/8 \rho g h_b^2 \cos \theta \sin \theta \quad (3)$$

Unfortunately, previous works of this type have not used H, but rather, have plotted transport rates against an expression which is equivalent to H times the wave velocity c. This expression is given by:

$$Hc = 1/8 \rho g h^2 c_g \cos \theta \sin \theta \quad (4)$$

In shallow water $c_g \cong c \cong \sqrt{gd}$ where d is local depth and g is the acceleration of gravity. At breaking $d = 1.28h$ (Munk 1949); thus, equation (4) can be written as:

$$Hc = \sqrt{1.28}/8 \rho g^{3/2} h_b^{5/2} \cos \theta \sin \theta \quad (5)$$

For comparison with previous work Hc is computed. Values for H and Hc have been calculated using breaker height and angle from the two upcoast observation stations, (Figure 1). Each observation was time weighted to represent a period from mid-time of previous observation to mid-time of next observation. Only those values of "Hc" and "H" toward the trap are considered. These results are tabulated in Table 2.

To complete this analysis the longshore currents are also considered. Longuet-Higgins (1970) derived a theoretical relation for the average longshore current generated by obliquely incident waves which depends only on a horizontal mixing parameter "p" and a reference velocity, " v_0 ", (v_0 would be the longshore current velocity if there were no horizontal mixing). If one assumes a value for P then v_0 and the average current can be determined from the data collected in this study. Longuet-Higgins indicates that a reasonable value for P is 0.4 for the study area. Assuming $P=0.4$, average velocity is equal to $55/196v_0$. But v_0 is given by:

$$v_0 = \frac{v_x}{\left(\frac{10}{49} \frac{x}{x_b}\right) - \left(\frac{5}{7} \frac{x}{x_b} \ln \frac{x}{x_b}\right)} \quad (6)$$

where v_x is velocity at a distance x from the shoreline and x_b is the distance from shore to the breakers. Accordingly average currents toward the trap are given in Table 2.

RESULTS

Figure 6, a plot of transport rate versus time, shows the seasonal nature of the transport in this area. Maximum transport rates were measured during winter and early spring and minimum rates during summer and early fall. These results are consistent with other studies of Southern California. In contrast Figure 7, plot of longshore thrust versus time, does not show high wave thrust expected during winter/spring 1975. Yet this Figure does show the expected high value in spring 1974. However, the expected seasonal trends are evident in Figure 8, a plot of average current versus time. A reasonable explanation for the unexpected low longshore thrust values of winter/spring 1975 is observer error in surf estimates.

Our principal result is the relation between longshore transport and longshore thrust shown in Figure 9. The four outlying points indicated on this Figure represent those data obtained during winter/spring 1975 when high transport was measured but low biasing of observed wave conditions is suspected. Omitting those four points a simple regression line has been plotted. For comparison with CERC Shore Protection Manual (SPM), values of H_c are plotted against transport rate (Figure 10). Note that the regression line of this study predicts nearly twice the transport rate predicted in the SPM.

SUMMARY

In this study repetitive surveys were made at a littoral barrier. These survey data were carefully scrutinized to eliminate errors. Later surveys included the use of electronic positioning equipment for high accuracy. As a result these data represent an accurate determination of longshore material transport through a 16-month period. It is felt that these data are the best estimates of longshore transport measured under field conditions.

Estimates of longshore wave thrust were computed from visual wave observations. Poor agreement with transport rates and longshore currents measured during winter/spring 1975 indicates possible observer bias. These anomalies will be studied in future work.

Comparison of the relation in wave thrust and sediment transport is made. This study indicates that in an environment of high transport, such as the United States Pacific coast, nearly twice as much transport is predicted under corresponding wave thrust as that of the data summarized in the SPM.

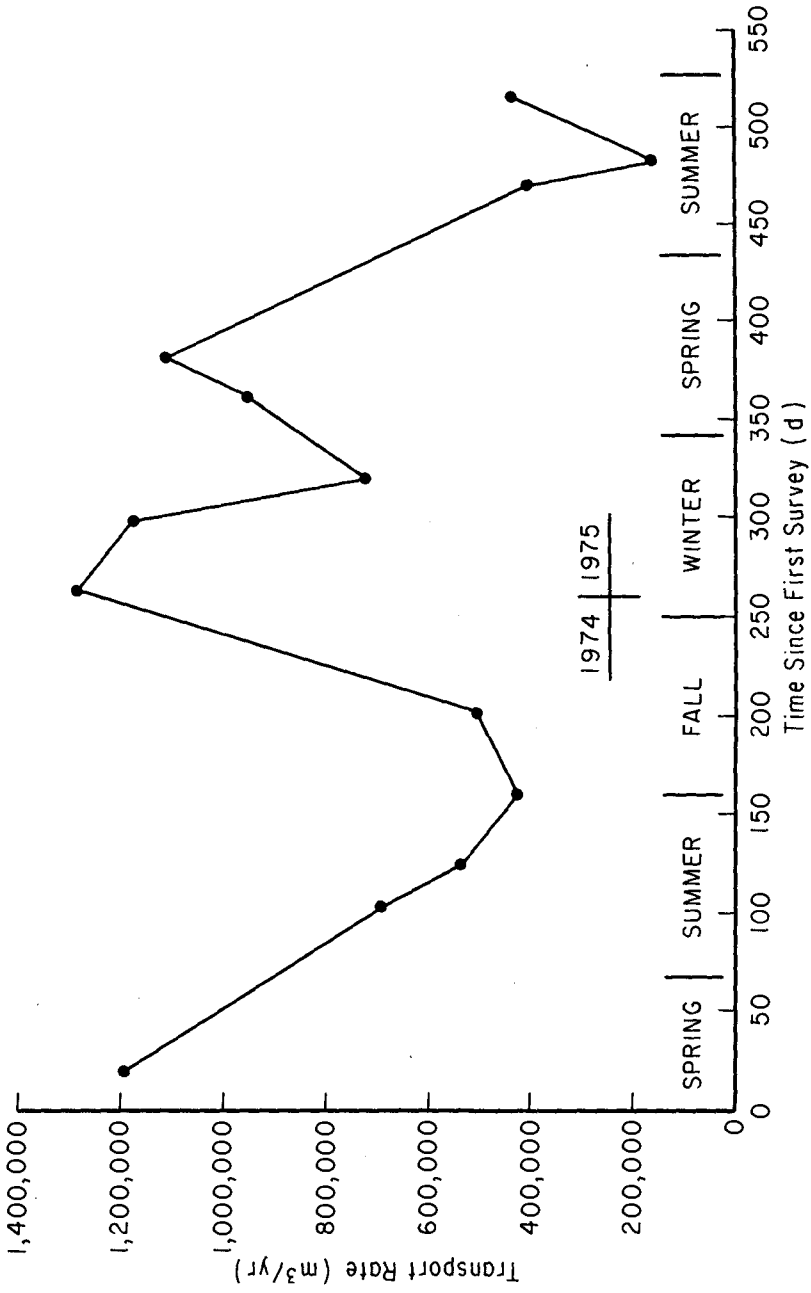


Figure 6. Transport Rate versus Time.

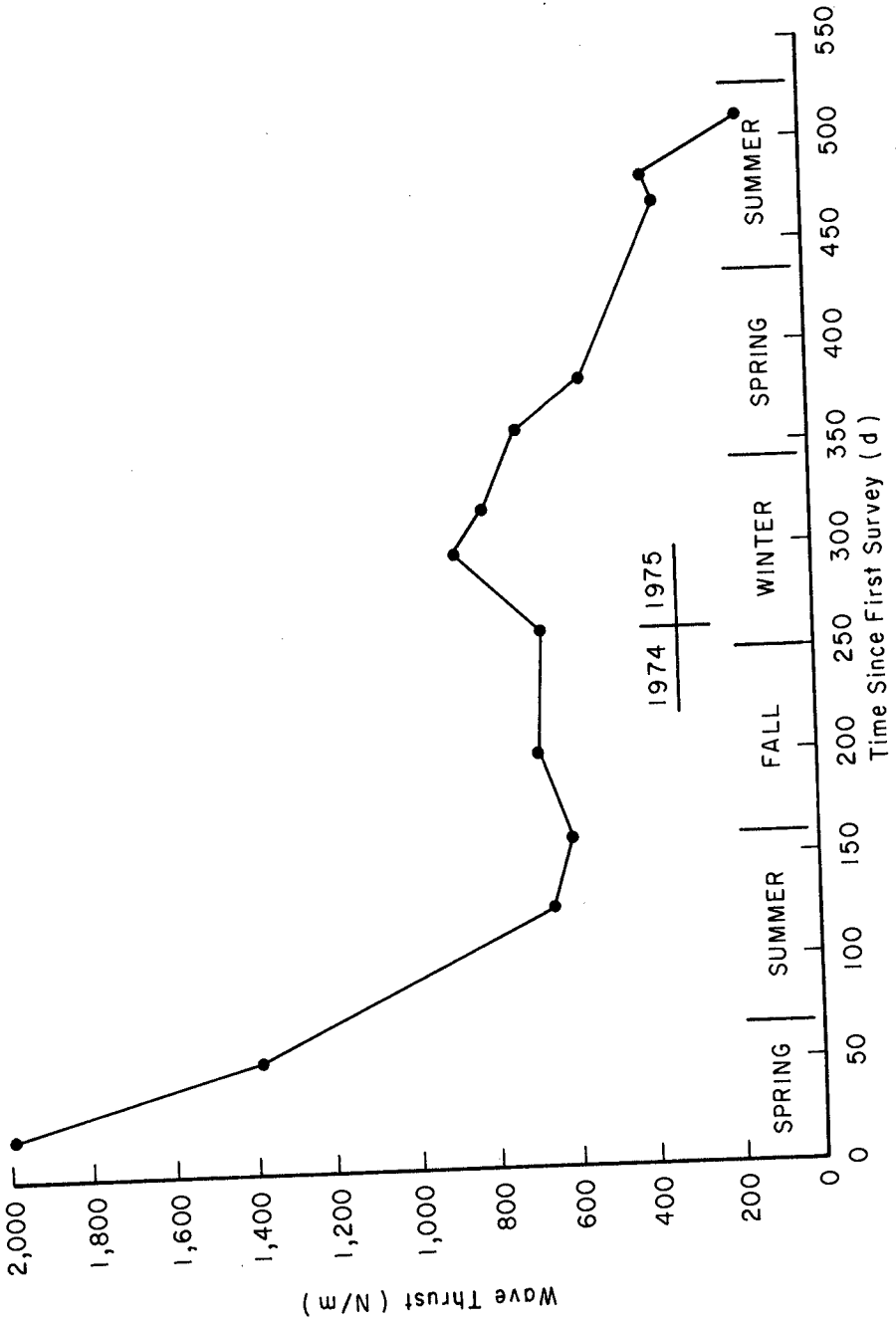


Figure 7. Wave Thrust versus Time.

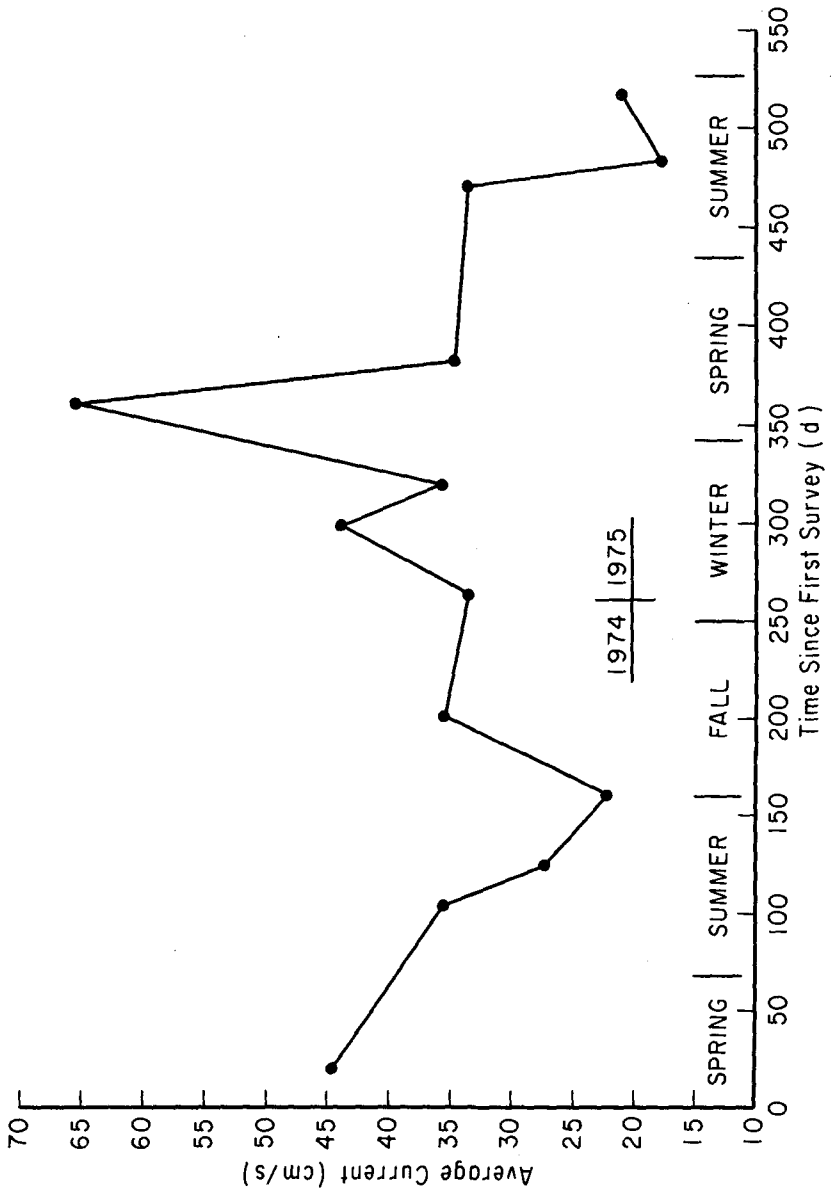


Figure 8. Average Current versus Time.

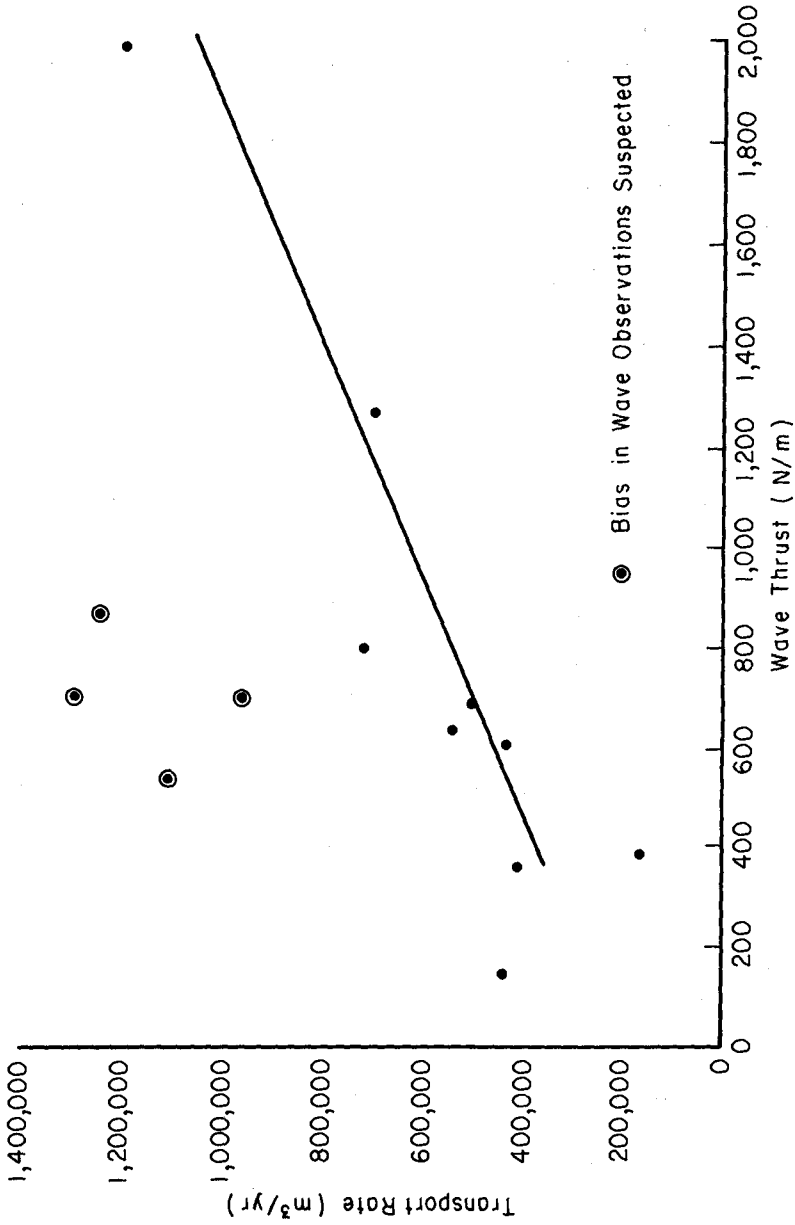


Figure 9. Transport Rate versus Wave Thrust.

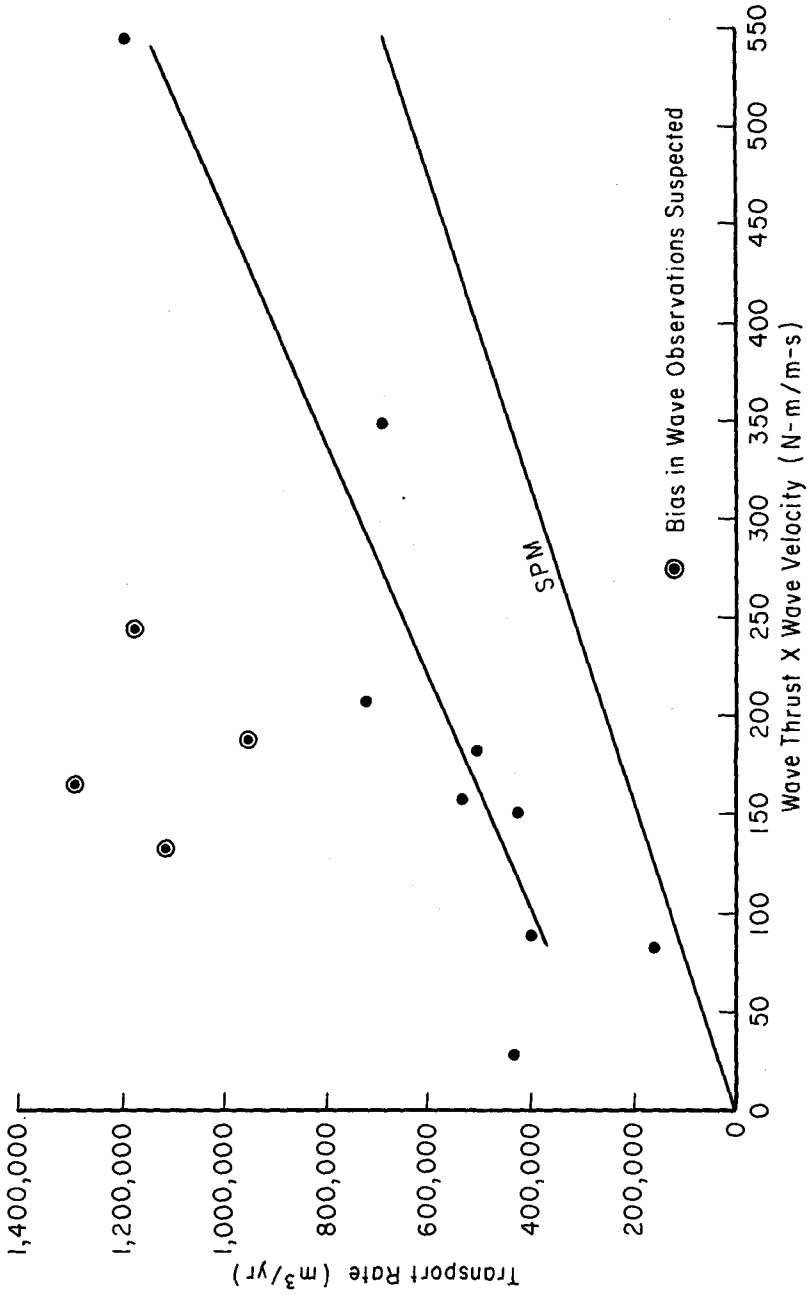


Figure 10. Transport Rate versus Wave Thrust X Wave Velocity .

This work has warranted further study and plans are to continue the data collection program through 1977. Future work will address the questions of accuracy of wave measurements, characteristics of sediment, influence of a dredged deposition basin, wave diffraction influence, and factors in addition wave thrust which contribute to longshore transport of sediment.

ACKNOWLEDGEMENTS

This paper resulted from research conducted by the Coastal Engineering Research Center under the Civil Works research and development program of the United States Army Corps of Engineers. The findings of this paper are not to be construed as official Department of the Army position unless so designated by other authorized documents.

REFERENCES

- BERG, D.W., "Systematic Collection of Beach Data", Eleventh Conference on Coastal Engineering, American Society of Civil Engineers, Chapter 17, pp.273-297.
- BRUNO, R.O., AND HIIPAKKA, L.W., "Littoral Environment Observation Program in the State of Michigan", Proceedings, Sixteenth Conference on Great Lakes Research, International Association on Great Lakes Research, pp. 497-507.
- LONGUET-HIGGINS, M.S., "Longshore Currents Generated by Obliquely Incident Sea Waves, 1 and 2", Journal of Geophysical Research, Vol 75, No 33, Nov. 1970, pp. 6778-6801.
- LONGUET-HIGGINS, M.S., "Recent Progress in the Study of Longshore Currents", Waves on Beaches and Resulting Sediment Transport, 1st ed., Academic Press, New York, 1972, pp. 203-248.
- MUNK, W.H., "The Solidary Wave and Its Application to Surf Problems", Annals of the New York Academy of Science, Vol. 51, 1949, pp. 376-462.
- US ARMY COASTAL ENGINEERING RESEARCH CENTER, Shore Protection Manual, Vol. 1, Chapter 4, 1973.
- WEIGEL, R.L., "Diffraction of Waves by Semi-Infinite Breakwater", Journal of Hydraulics Division, ASCE, Vol 88, No HY1, Jan. 1962, pp. 27-44.

CHAPTER 72

CONCEPT FOR INFERRING THE LITTORAL DRIFT TREND

by

Masataro HATORI* and Takasuke SUZUKI**

* Department of Civil Engineering

** Institute of Geosciences

Chuo University

Bunkyo-ku, Tokyo, Japan

INTRODUCTION

To infer the rate and prevailing direction of littoral transport along a given coast is of prime importance in the functional and rational designing of coastal structures as well as in the environmental consideration of coastal zones. Many efforts have been made to develop the inferring method from field evidences such as 1) coastal landforms and shore configurations in the vicinity of existing structures¹⁾⁻⁶⁾, 2) along-shore variations in beach and bed sediment properties⁷⁾⁻¹²⁾, 3) statistical analysis of incident wave properties¹³⁾⁻¹⁶⁾, 4) movements of natural or artificial tracers¹⁷⁾⁻²⁰⁾, and so on.

Among these evidences, the alongshore variations of indigeneous beach materials have served as a powerful, practical and economical tool in the inference of general trend of littoral transport.

Properties of beach sediment, such as grain size of sand and volume and shape of gravels, indicate some progressive trends with along-shore distance from supply sources²¹⁾. Thus the littoral transport direction along a given coast is inferable from variations in beach sediment properties.

However, inferring criteria of prevailing direction from variations in various beach sediment properties have not yet been fully established. For example, the prevailing direction of littoral transport should be defined to be alongshore component of intergrated vector of littoral transport during several years or decades along a given coast. But this direction is often confused with the alongshore dislocating or traveling direction of beach sediment, which is indicated by the variations.

It has also been concluded simply that the variation series obtained from backshore samples show a long-term trend of littoral transport, whereas those from foreshore indicate a short-term trend such as seasonal changes. In this inferring procedure any considerations have never been paid on differences in grain size of beach materials (sand and gravels) and in wave conditions during the period of field study. Rate or intensity of littoral transport has scarcely been inferred from the variation series of beach sediment properties even quantitatively.

To solve these problems, the present study proposed a new concept on the basis of field evidences obtained on the Enshu Coast, Central Japan.

OUTLINE OF THE STUDIED COAST

The Enshu Coast extends about 115 km between Cape Irigo in the west and Cape Omae in the east and is separated into two arched beaches, at the junction of which the Tenryu River flows into the Pacific Ocean (Fig. 1). The Tenryu, one of the largest rivers in Japan, is 213.7 km in length, 5,093 km² in drainage area and 8,440 m³/sec in the maximum recorded discharge. Since its bed slope in the downstream part is about 1/800, the Tenryu supplies a huge amount of gravels and sand to the Enshu Coast during its flood period. The other rivers flowing into this coast during its flood period. The other rivers flowing into this coast are of very small scales in length, drainage area and discharge, hence they supply only a small amount of sand and silt.

On the western part of this coast, are developed actively receding coastal cliffs, which are composed of the lowest Pleistocene unconsolidated strata named Atsumi formation and are receded by wave actions at a rate of 0.6 to 1.0 m/year. These cliffs supply the weathered gravels of granite, sandstone, slate, rhyolite, etc. to the Enshu Coast. On the coastal plains from the Imakireguchi, an inlet of Lake Hamana, to the eastern end of the coast, some parallel or echelon rows of coastal dunes are developed (Fig. 1).

In the nearshore zone of the coast one or two rows of longshore bars are developed almost continuously²²⁾ (Fig. 2). This suggests that active sediment transports are occurred by breaking waves in this zone. Off the mouth of the Tenryu a submarine canyon exists below a water depth of about 20 m (Fig. 1). Excepting this canyon, offshore topography upto a water depth of 100 m is generally gentle in shape and its slope becomes smaller toward both ends of the Enshu Coast from the canyon.

Beach width is 100 - 170 m in the central part of the Enshu Coast, but becomes narrower toward both ends of the coast²³⁾. The beach consists of sand and gravels. Petrologically the beach gravels are composed of sandstone, slate, granite, and others, and their frequency percentages are 68%, 13%, 11%, and 8%, respectively. This petrological composition agrees fairly with that of the Tenryu River. Yamanouchi²³⁾ demonstrated the variation diagrams of the mean weight of the largest beach gravels along the coast and concluded that most of the beach gravels supplied from the Tenryu are distributed on the central part of the Enshu Coast, between Imakireguchi and the mouth of Bezaiten River. This conclusion is supported by the authors' results described later.

In view of the above-mentioned outline of the Enshu Coast, the authors carried out field surveys for the central part of the Enshu Coast (Fig. 3) and investigated the variations in beach sediment properties.

Only a few data on the wave climate on this coast are available. Figure 4 indicates the occurrences of heights and periods of incident waves observed at Akabane fishery port located at the western part of this coast. According to Fig. 4, the significant wave height and period are about 1.5 m and 10 sec. Swell generated by typhoon often attacks the Enshu Coast and its period observed at Akabane varies in a range from 9 to 15 sec.

Dominant direction of incident waves to the studied coast was in a range of the south-west to the south during the field surveys. To

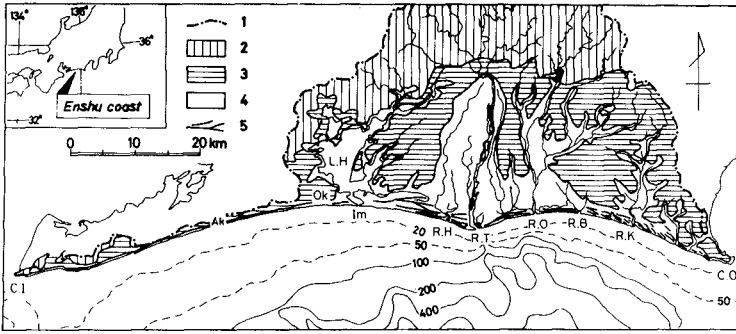


Fig. 1 Generalized topography around the Enshu Coast, Japan.
 1: Main divides, 2: Mountains, 3: Terraces, 4: Lowland, 5: Dunes, C.I.: Cape Irigo, Ak: Akabane fishery port, Ok: Okurato, L.H.: Lake Hamana, Im: Imagire-guchi, R.H.: River Ho, R.T.: River Tenryu, R.O.: River Ota, R.B.: River Bezaiten, R.K.: River Kiku, C.O.: Cape Omae-zaki

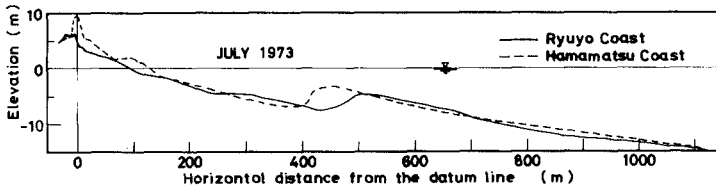


Fig. 2 Typical nearshore profiles of the studied area.

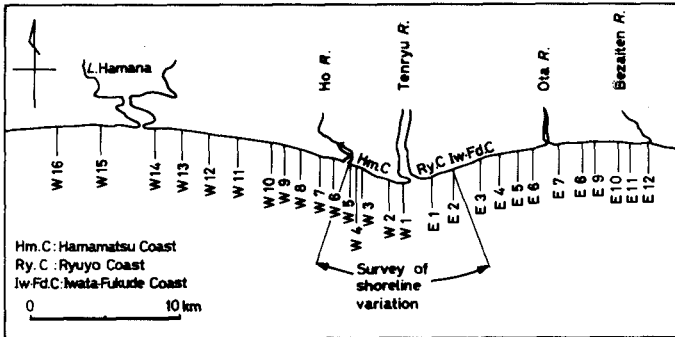
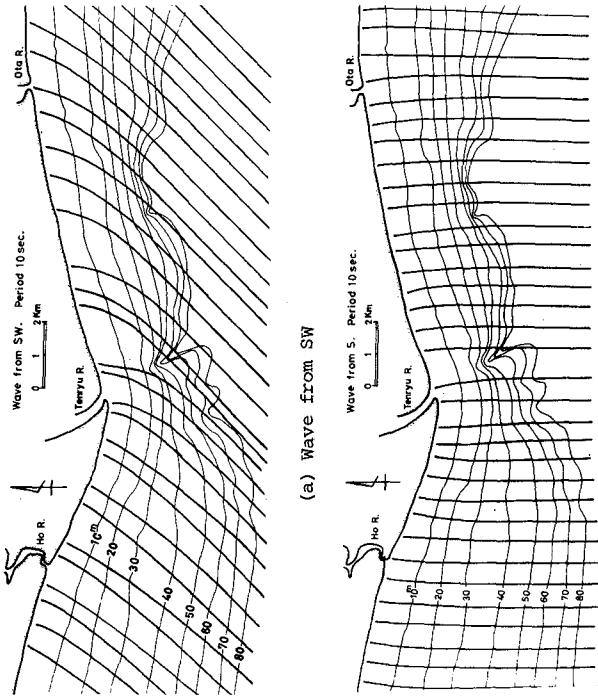


Fig. 3 Location map of the studied coast and sampling stations



(a) Wave from SW
(b) Wave from S

Fig. 5 Refraction diagrams for the studied coast.
(Wave period: 10 sec)

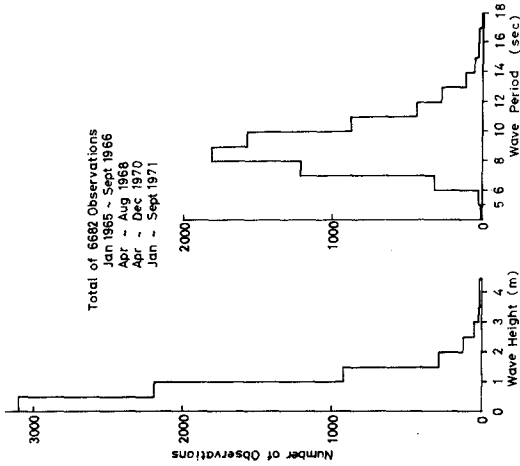


Fig. 4 Distributions of wave heights and periods. Irrespective direction

predict the trend of littoral transport along the coast, refraction diagrams are prepared for a case of wave period of 10 sec (Fig. 5).

It appears from Fig. 5(a) that waves from the south-west are strongly refracted and give rise to the eastward longshore component of energy flux due to incident waves along all over stretch of the studied coast. For waves from the south, negligible refraction occurs (Fig. 5(b)). Along the west coast adjacent to the Tenryu River, the westward longshore component of energy flux is predicted from the refraction diagram.

In addition, construction of many dams along the Tenryu since 1950's results in a remarkable reduce in sediment supply to the coast, and hence in erosion on the west coast adjacent to the river mouth (Hamamatsu Coast, Fig. 6). To prevent the beach recession some coast protection works such as groins and offshore breakwaters have been constructed on this coast.

Littoral transport direction can be inferred from the configuration of river mouth. The changes in migration of river mouths on the Enshu Coast are obtained from the topographic maps surveyed in 1946 and 1970 (Fig. 7).

SAMPLING AND ANALYSIS OF BEACH MATERIALS

Sand and gravel samples were collected from the surface layer of beach both at foreshore and backshore of 28 stations at an interval of about 2 km in June, August and November, 1973 (Fig. 3).

At each station large gravels scattered on the beach surface in an area of about 20 m x 20 m were sampled. Their nominal volumes were calculated from measurements of their long, intermediate and short diameters. The nominal volume is defined as the product of these three diameters. Thus, alongshore variation diagrams of mean nominal volume of the largest ten gravels for three dominant kinds of gravels are obtained (Fig. 8).

Median diameter of beach sand was determined by the sieve analysis of dried samples in the laboratory. By using the Hallimond 5-Pole Magnetic Separator, sand grains ranging from 0.25 to 0.125 mm in diameter were separated into the following three groups: A) ferro-magnetic minerals, most of which are magnetite and hematite, B) feeble-magnetic minerals such as pyroxene, hornblende, sircon and olivine, and C) non-magnetic minerals such as quartz and feldspar. Their specific gravities range from 5 to 4, 4 to 3, and 3 to 2, respectively. Accordingly, variation diagrams of the weight percentage of these three groups can be taken as these of the heavy mineral composition of beach sand.

CRITERIA FOR INFERRING LITTORAL TRANSPORT TREND

Criteria based on the variation diagram of gravel volume

Since the grain size of beach materials generally decreases with increasing distance from the supply source, the littoral transport direction is inferable from the variation diagram showing the size-distance relationship along a given coast.

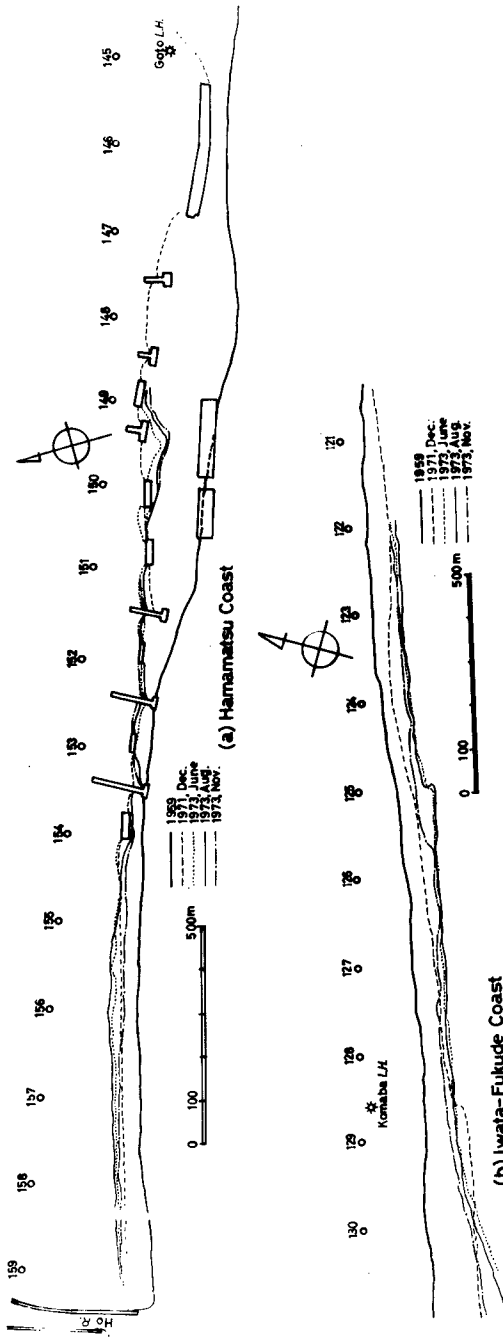


Fig. 6 Shoreline changes of the studied coast (1959-1973)

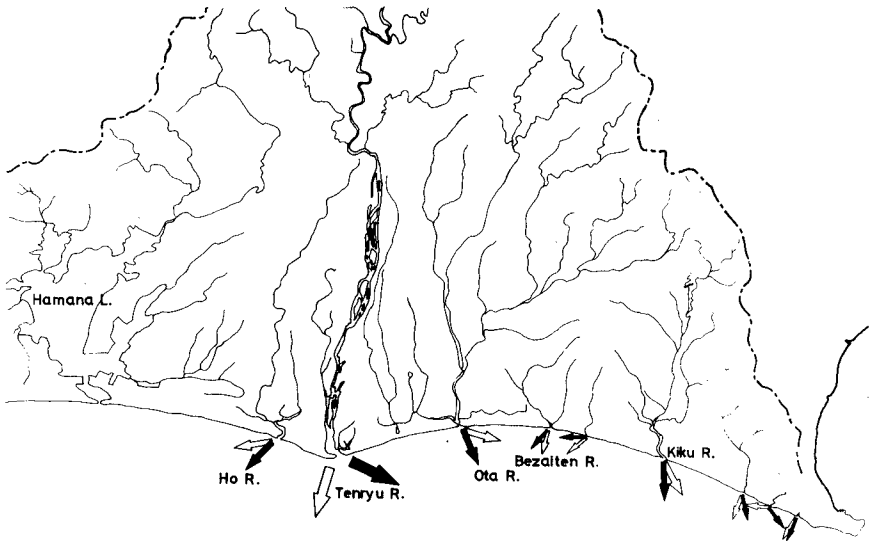
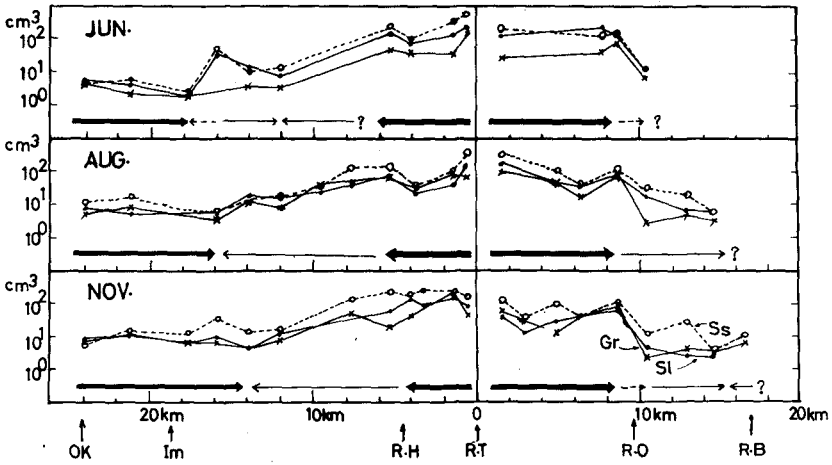
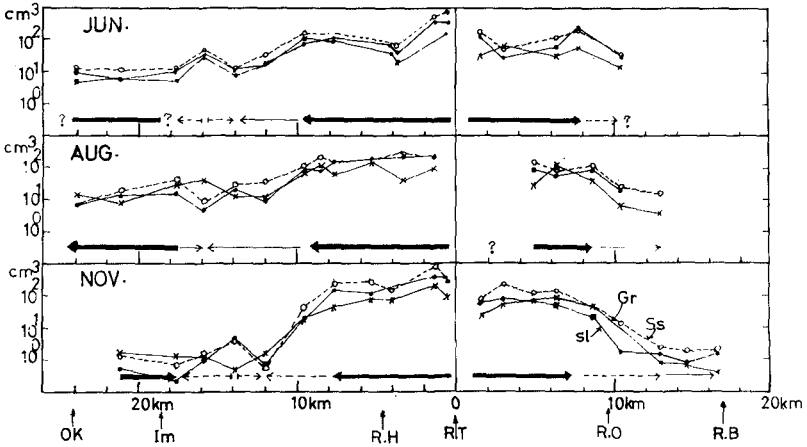


Fig. 7 River mouth deviations. (White arrow: 1946,
Black arrow: 1970)



(a) Foreshore



(b) Backshore

Fig. 8 Variation diagrams of mean volume of the largest ten gravels, and inferred directions and intensities of littoral transport. Ss: Sandstone, Sl: Slate, Gr: Granite.

It is therefore inferred from Fig. 8 that littoral transport directions within extents of about 16 km from the Tenryu River along the coast are eastward and westward, respectively. These inferred directions seem to be independent of the sampling position, kind of gravels and seasonal change.

As seen in Fig. 8, however, the variation diagrams of gravel volume on a semi-logarithmic graph are generally divided into some straight segments with different slope, average over certain stretch of several kilometers long. For example, in case of the backshore gravel in November (Fig. 8(b)), the slope is very gentle within a stretch of about 9 km from the Tenryu River in the westward direction along the coast, but beyond that point the slope becomes steeper abruptly. Such abrupt changes are seen in the other cases of studied coast and also known on the other coasts such as Sagami 24), Niigata 25), and Ishikawa 26) coasts in Japan.

The slope of the variation diagram indicates a ratio of size-decreasing per unit alongshore distance. This ratio must depend both on the intensity of littoral transport parallel to shoreline and on the resistivity of gravels for attrition.

The intensity of littoral transport must imply the net or integrated effects of the following three factors: 1) alongshore velocity component of the swash on the beach, 2) directional frequency distribution of incident waves, and 3) duration of beach sediment dislocation. The factors of 1) and 2) must be affected mostly by the wave climate and the coastal topography.

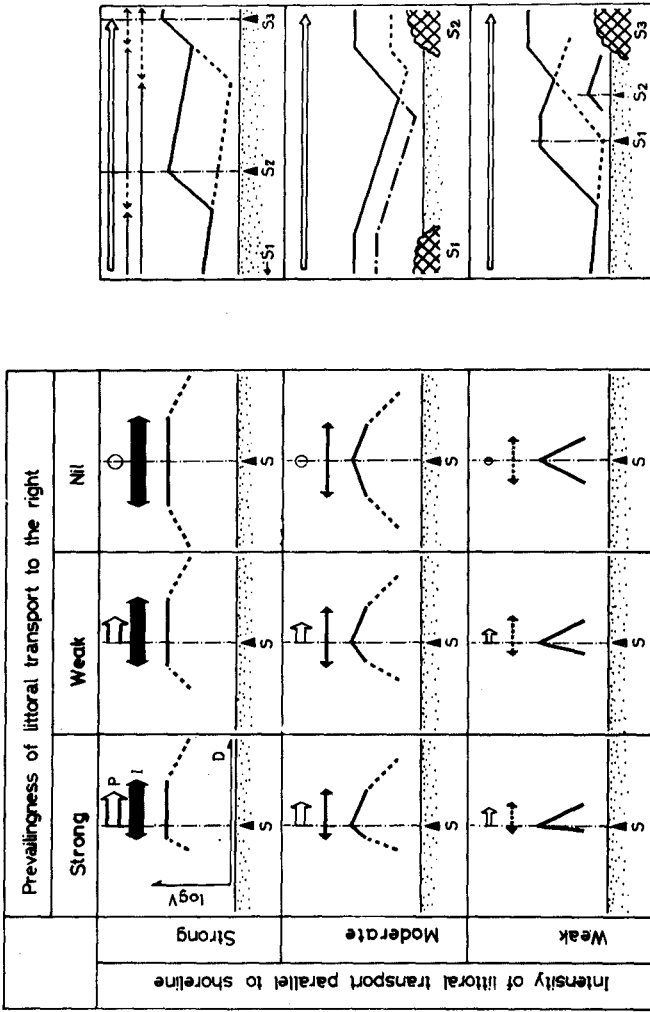
The resistivity of gravels for attrition is related to the mechanical properties of gravels 27), but the effect of the original size of gravel on the rate of attrition has not been clarified. The relationship of the alongshore transport rate of gravels with various sizes to the alongshore energy flux of incident waves has not been known. Thus, interrelationships among these various factors can not be discussed qualitatively from our present knowledge.

For this reason, in the present paper, the term of intensity is used to express the above-mentioned net effects of various factors. It is assumed that the difference in the segment slope of the variation diagram implies that in the intensity of littoral transport, if the size-distance relationship of gravels of the same lithology is concerned.

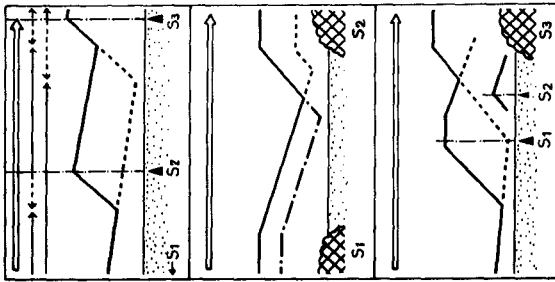
On this assumption, the magnitude of the intensity of littoral transport is divided qualitatively into three degrees: strong, moderate and weak, which are represented by thick, thin and dotted arrows on Fig. 8, respectively. The arrow direction indicates the inferred dislocating direction.

Prevailing direction of littoral transport on a given coast should be inferred from asymmetry of the variation diagram with respect to the supply source of beach gravels; that is, from asymmetry of the intensity and/or from asymmetry of the stretch length with the same intensity. The magnitude of the asymmetry can be called prevailingness of littoral transport.

Based on this consideration, proposed criteria for inferring the prevailing direction and the prevailingness of littoral transport are given by Fig. 9(a). On this figure, ideal variation diagrams of gravel volume for nine cases are shown in semi-logarithmic graph, and the inferred magnitude of intensity is shown by the three kinds of black arrow mentioned



(a)



(b)

Fig. 9 Inferring criteria of the prevailing direction and prevailingness of littoral transport from the variation diagram of gravel volume.

before. The inferred prevailing direction for each case is shown by a white arrow, of which the length and thickness represent the prevailingness qualitatively.

Figure 9(b) shows some inferred examples of prevailing direction in cases where two or more supply-sources exit on a coast. In case of the top of this figure, the prevailing direction is inferred to be toward the right on the figure as shown by a white arrow, based on asymmetry of the intensity with respect to the source of S_2 . If S_2 is lacking in this case, the variation diagram may change into that shown by dotted line. But the inferred prevailing direction is the same, because in this case asymmetry of the intensity with respect to the descending nodal point of dotted line becomes the key for inference. Similarly, prevailing directions of the other cases are inferred to be toward the right.

Criteria based on the variation diagram of sand properties

Generally speaking, the variation diagrams of beach sand properties such as median diameter, sorting coefficient, and heavy mineral composition display a cyclic pattern which has a very shorter pitch as compared with that of beach gravels, as exemplified by Figs. 10 and 11. This seems to be dependent on the following two reasons: (1) Position of the sand-supply source can not be determined easily, because the beach sand is supplied not only from rivers and coastal cliffs, but also from receding beach and sea bottom. (2) Sand properties vary with minor beach topography such as beach cusps owing to sorting effect by wave actions. Therefore, the variation diagrams of beach sand are influenced largely by sampling technique. Beach sand seems to play a less important role than beach gravels as an indicator of littoral transport trend.

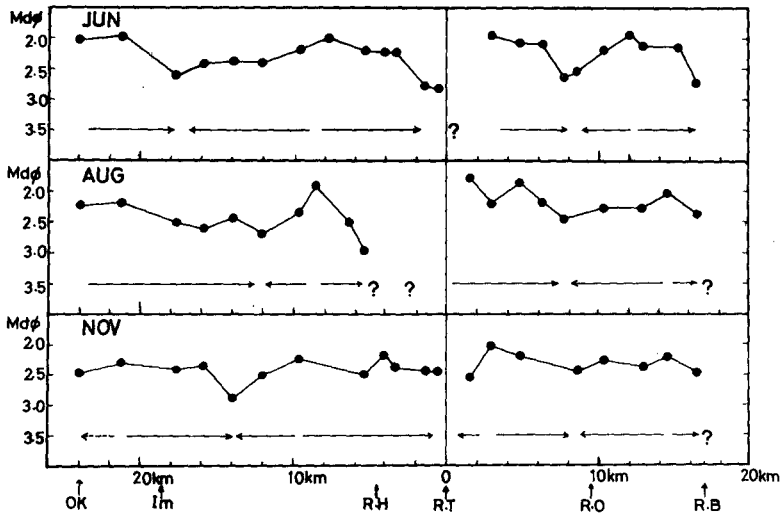
However, the inference of littoral transport direction from the variation diagram of sand properties is made on the basis of the conventional concept, in which the littoral transport direction is considered to coincide with the decreasing direction of grain size and heavy mineral component of beach sand. The prevailing direction is inferred from the same concept as the case of beach gravels discussed in the previous section (Figs. 10 and 11).

SEQUENTIAL MODEL FOR INTERPRETING THE DIFFERENCE AMONG THE INFERRED RESULTS

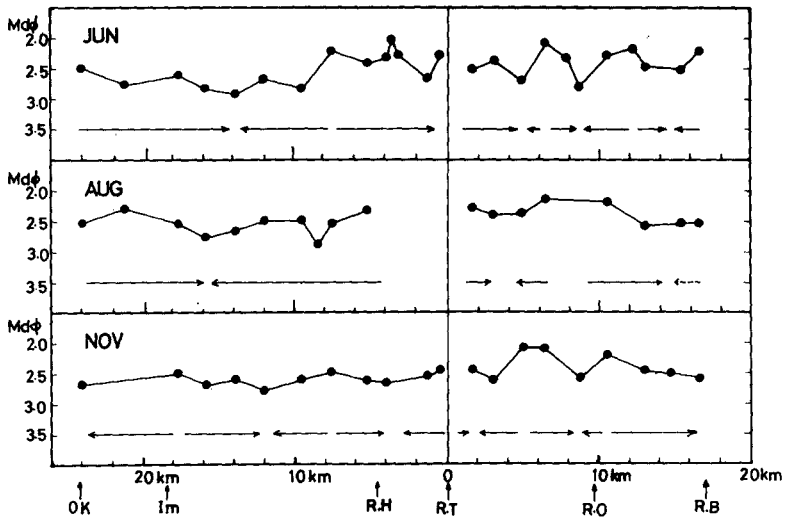
Figure 12 shows the summary of inferred directions and intensities of the littoral transport along the studied coast from the variations in beach sediment properties together with those from the river mouth deviation.

It is noticed from this figure that the inferred results display different tendencies according to the sampling position or elevation (fore-shore and backshore) and to the grain size of beach sediments (sand and gravels). On the other hand, seasonal effect on the inferred results seems to be relatively weak.

The alongshore processes of beach sediment transport are closely related with the size of beach sediment and the position of the zone in which



(a) Foreshore



(b) Backshore

Fig. 10 Variation diagrams of median diameter of beach sand, and inferred directions and intensities of littoral transport.

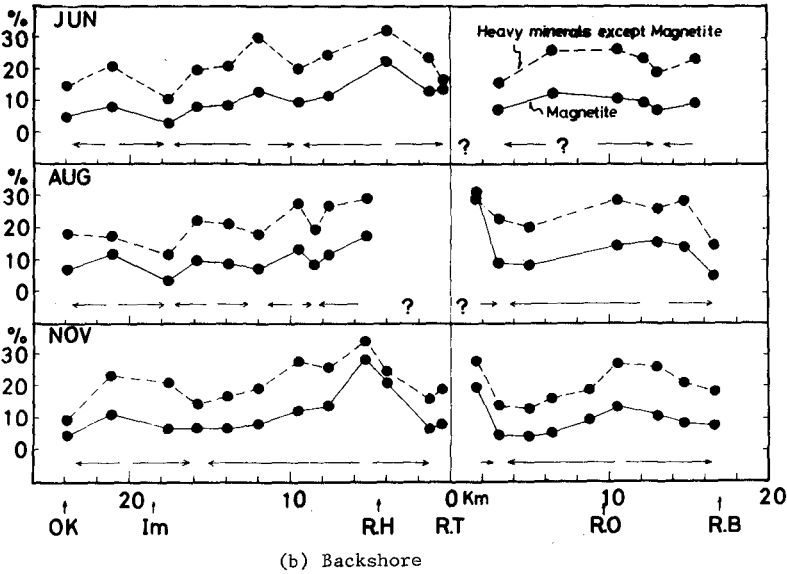
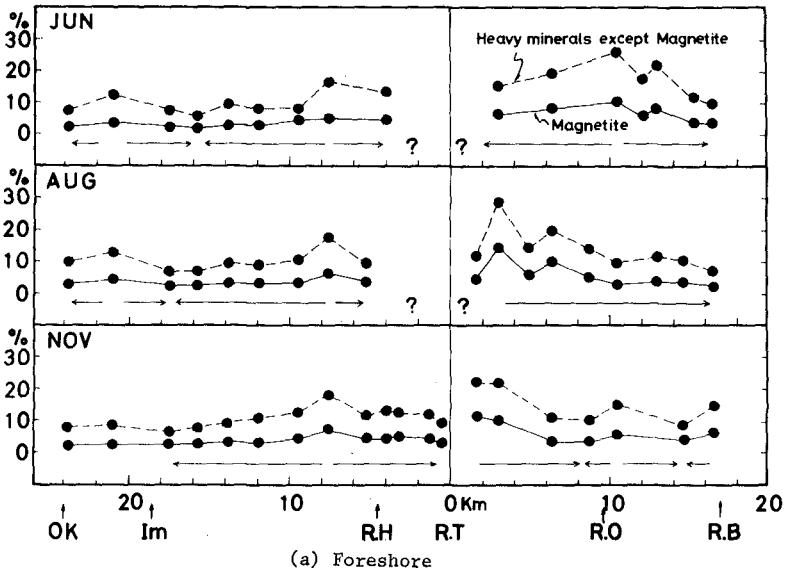


Fig. 11 Variation diagrams of heavy mineral composition of beach sand, and inferred directions and intensities of littoral transport.

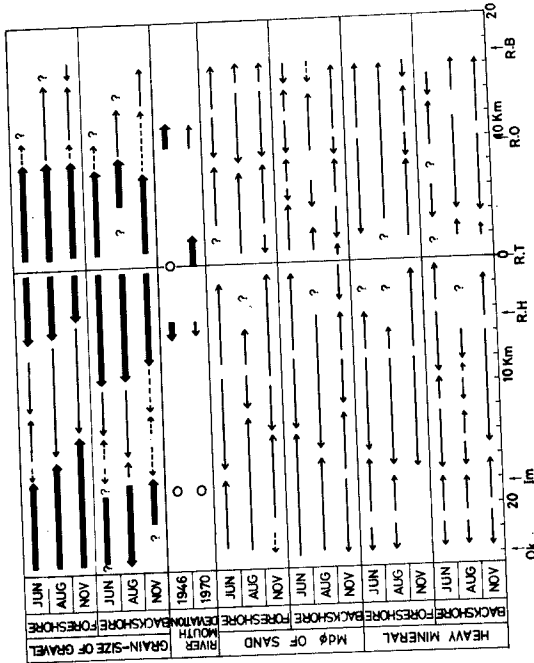


Fig. 12 Summary of the inferred direction and intensity of littoral transport from the variation diagrams of beach sediment on the Enshu Coast, Central Japan.

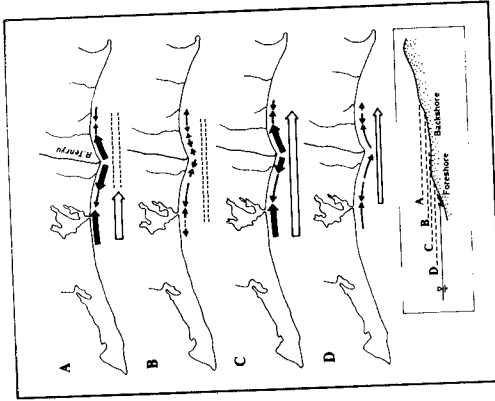


Fig. 13. Littoral transport trends under four sea conditions on the Enshu Coast.

the dislocation occurs²⁸). In addition, the wave runup height on beach and the tractive force acting on beach grains depend on properties of incident waves.

The alongshore variations in beach sediment properties are conceived as the consequences of complex interactions among these factors. The differences in the inferred results, as seen in Fig. 12, can be explained by taking account of differences in sea conditions governing the dislocation of beach sediments.

Based on this concept, a following sequential model is proposed here, as shown in the inset of Fig. 13 schematically: Stage A shows a climax state of rough to high sea condition, in which the littoral transport trend is inferred from the variation diagram of backshore gravels; Stage B is a decay state of the stage A, from backshore sand; Stage C is a slight sea condition, from foreshore gravels; Stage D is a smooth sea condition, from foreshore sand.

According to this model, the directions and intensities of littoral transport along the studied coast under the four sea conditions are concluded to be shown in Fig. 13 by thick and thin arrows.

CONCLUSIONS

Overall prevailing direction and intensity of the littoral transport along a given coast can be inferred from asymmetry both of the slope of variation diagram and of the alongshore distance of the same slope segment on the diagram with respect to the sediment supply source or to the ascending or descending nodal points on the variation diagram.

The prevailing direction along the studied coast is concluded to be eastward clearly under the slight and smooth sea conditions, whereas under the rough to high sea conditions prevailingness is not found, according to the criteria proposed in this paper. This conclusion is supported by the fact that the west coast adjacent to the Tenryu River (Hamamatsu Coast) has been receded severely, whereas the east coast (Iwata-Fukude Coast) has been proceeded (Figs. 6 and 14).

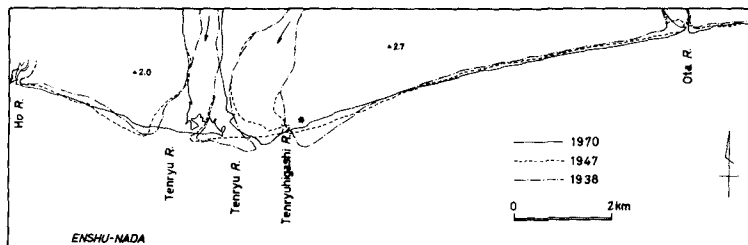


Fig. 14 Long-term shoreline changes on the Enshu Coast.

REFERENCES

- 1) Shepard, F.P.: Beach cycles in Southern California, Tech. Memo. No. 20, B.E.B., 1950.
- 2) Trask, P.D.: Beaches near San Francisco, California 1956-1957, Tech. Memo. No. 110, B.E.B., 1959.
- 3) Bowen, A.J. and D.L. Inman: Budget of littoral sands in the vicinity of Point Arguello, California, Tech. Memo. No. 19, CERC, 1966.
- 4) El-Ashry, M.R. and H.R. Wanless: Shoreline features and their changes- Photogrammetric Engineering, Vol. 33, No. 2, pp. 184-189, 1967.
- 5) Komar, P.D., J.R. Lizarraga-Arciniega, and T.A. Terich: Oregon coast shoreline changes due to jetties, Proc. ASCE, Vol. 102, No. WW1, pp. 13-30, 1976.
- 6) Hom-ma, M., K. Horikawa and C. Sonu: A study on beach erosion at the sheltered beaches of Katase and Kamakura, Japan, Coastal Engineering in Japan, Vol. 3, pp. 101-122, 1960.
- 7) Taney, N.B.: Littoral materials of the south shore of Long Island, New York, Tech. Memo, No. 129, B.E.B. 1961.
- 8) Aramaki, M. and T. Suzuki: The prevailing direction and mechanics of beach drift inferred from variation series of beach sediments along the Sagami Bay Coast, Japan, Geogr. Rev. Japan, Vol. 35, pp. 17-34, 1962. (in Japanese)
- 9) Mino, Y., T. Machida, M. Aramaki and H. Yamanouchi: Physiographical studies on littoral drift along the Niigata Coast, Central Japan, Tokyo Geogr. Papers, No. 7, pp. 1-22, 1963. (in Japanese)
- 10) Cherry, J.: Sand movement along a portion of the Northern California Coast, Tech. Memo. No. 14, CERC, 1965.
- 11) Aramaki, M. and S. Takayama: A petrographic study on littoral drift along the Ishikawa Coast, Japan, Proc. 10th Conf. Coastal Eng., pp. 615-631, 1966.
- 12) Sunamura, T. and K. Horikawa: Predominant direction of littoral transport along Kujyukuri Beach, Japan, Coastal Engineering in Japan, Vol. 14, pp. 107-117, 1971.
- 13) Caldwell, J.M.: Wave action and sand movement near Anaheim Bay, California, Tech. Memo No. 68, B.E.B., 1956.
- 14) Savage, R.P.: Laboratory determination of littoral-transport rates, Proc. ASCE., Vol. 88, No. WW2, pp. 69-92, 1972.

- 15) Fairchild, J.C.: Correlation of littoral transport with wave energy along shores of New York and New Jersey, Tech. Memo. No. 18, CERC, 1966.
- 16) Galvin, Jr., C.J.: A gross longshore transport rate formula, Proc. 13th Conf. Coastal Eng., pp. 953-970, 1972.
- 17) Russell, R.C.H.: The use of fluorescent tracer for the measurement of littoral drift, Proc. 7th Conf. Coastal Eng., pp. 418-444, 1958.
- 18) Kamel, A.M. and J.W. Johnson: Tracing coastal sediment movement by naturally radioactive minerals, Proc. 8th Conf. Coastal Eng., pp. 324-330, 1962.
- 19) Sato, Sh: Sand movement at Fukue Coast in Atsumi Bay, Japan, and its observation by radioactive glass sand, Coastal Engineering in Japan, Vol. 5, pp. 81-92, 1962.
- 20) Sato, Sh., I. Irie and T. Horie: On supply source and dominant direction of littoral drift along the Tyoama Coast, Japan, Proc. 17th Conf. Coastal Eng. in Japan, pp. 297-304, 1970. (in Japanese)
- 21) Russel, R.D.: Effects of Transportation on Sedimentary Particles, Recent Marine Sediments (ed. by P.D. Trask), Am. Assoc. Petrol. Geol., pp. 32-47, 1939.
- 22) Mogi, A: On the shore types of the coasts of Japanese Island, Geogr. Rev. Japan, Vol. 36, pp. 245-266, 1963. (in Japanese)
- 23) Yamanouchi, H.: On the distribution of beach gravels on the eastern part of the Enshu Coast, Jour. Fac. of Education, Gum-ma Univ., Vol. 18, pp. 111-124, 1968. (in Japanese)
- 24) Aramaki, M. and T. Suzuki: loc. cit. 8).
- 25) Mino, Y. et al.: loc cit. 9).
- 26) Aramaki, M. and S. Takayama: loc. cit. 11).
- 27) Suzuki, T. and K. Takahashi: Laboratory experiment on the rock abrasion due to sand impact, Proc. 10th Symp. on Rock Mechanics, JSCE, pp. 66-70 1976. (in Japanese)
- 28) Zenokovich, V.P.: Processes of Coastal Development (ed. by J.A. Steers), Oliver & Boyd, Edinburgh & London, pp. 317-325, 1967.

CHAPTER 73

FIELD INVESTIGATION OF SEDIMENT TRANSPORT PATTERN IN A CLOSED SYSTEM

by
Tsuguo Sunamura and Kiyoshi Horikawa

Coastal Engineering Laboratory
Department of Civil Engineering
University of Tokyo
Bunkyo-ku, Tokyo
Japan

INTRODUCTION

In order to elucidate the transport pattern of sediment in a closed system, a pocket beach was chosen and investigated from various aspects. This investigation included the following studies: (1) bathymetric survey by an echo sounder, (2) survey of submarine geology using an acoustic probe, (3) observation of nearshore current systems using floats, (4) documentation of the transport pattern of suspended sediment by aerial photographs, (5) examination of depositional environments of bottom and beach material by sieve analysis, (6) inference of long-term alongshore sediment transport pattern from the grain size properties of beach sand, and measurement of short-term trends by use of fluorescent sand, and (7) examination of long-term shoreline change using old and recent maps.

STUDY AREA

A study area was located at the bay head of Katsu'ura bay, Chiba prefecture, Japan, facing the Pacific Ocean (Fig. 1). The bay is a semicircular shape (approximately 2 km in diameter) having a south-oriented bay axis, and is bordered by coastal cliffs made of Pliocene sedimentary rocks (Fig. 2). The coastal cliff

in the study area is made of Katsu'ura formation which is the alternation of sandstone and siltstone strata; these strata strike N40-50°E and dip 5-10°N. In front of the cliff a narrow sandy beach stretching 1.3 km develops. Little seasonal change of this beach has been observed. There is no major supply source of beach sand in or near the study area. The direction of wave approach is nearly normal to the beach. Tidal range at spring tide is about 1.5 m, while at neap tide is about 0.7 m.

SUBMARINE TOPOGRAPHY AND GEOLOGY

The topographical and geological surveys revealed that (1) the submarine topography consisted of portions having smooth submarine contours and irregular ones (Fig. 3), (2) the former portion was of sandy sediment, while the latter of exposed bedrock (Fig. 4), (3) from the shoreline up to a water depth of about 5 m, there was little difference between the depths of the bedrock surface and the adjacent sand bottom, while in deeper regions there existed a marked topographic break that the bedrock surface was located 2-3 m higher than the sand bottom (Fig. 5), (4) the submarine bedrock was also made of Katsu'ura formation, and (5) a veneer of sandy sediment developed spottedly on the bare bedrock.

Submarine bedrock configuration shows the existence of a large depression in the western part of the study area (Fig. 6). Figure 7 is an isopach map of sandy sediment, which was plotted on the basis of Figs. 3 and 6; the western portion constitutes a notable sedimentary region.

NEARSHORE WATER CIRCULATION PATTERN

For the measurement of nearshore current pattern, floats with current-crosses were released and traced by transits. The result showed a characteristic pattern: in the areas of exposed bedrock onshore currents developed, while in the adjacent sandy areas offshore currents occurred. This water circulation pattern is shown in Fig. 8, in which H_b = breaker height, T = wave period, U = average wind velocity obtained by the observatory located near the study area, and the letters in brackets show wind direction. Since the nearshore bedrock areas are higher than the adjacent sand areas, it is clear that the underwater topography gives rise to wave convergence in the bedrock regions and to divergence in the sandy areas; longshore currents flowing away from the zones of convergence

turn seaward in the zones of divergence, forming the offshore currents.

Since the surface of exposed bedrock has changed little, submarine topography has determined the nature of wave-induced current fields: in the areas of the bedrock onshore currents dominate, while in the adjacent sandy areas the prevailing offshore currents occur.

SUSPENDED SEDIMENT TRANSPORT PATTERN

The transport pattern of suspended sediment was investigated by air-photo interpretation. Photographs were taken on Nov. 27-29, 1974 by attaching a blue-cut filter to an air-born camera in order to obtain clear underwater information (Lockwood et al., 1974). The photo scale was 1/10000. Figure 9 shows the transport patterns obtained from these photographs.

On the basis of ordinary black and white aerial photographs (scale: approx. 1/10000) taken at several different times, the locations of offshore transport of suspended sediment were depicted (Fig. 10).

Figures 9 and 10 indicate that the prevailing offshore transport occurs in the regions of sand bottom, irrespective of input wave conditions. This result reconfirms the occurrence of offshore currents in the sandy regions, and furthermore suggests the existence of onshore currents in the bedrock regions.

DEPOSITIONAL ENVIRONMENTS OF BOTTOM AND BEACH MATERIAL

On the basis of sieve analysis of submarine and backshore sand samples, the mean diameter in phi scale, $M\phi$, as a grain size parameter and its standard deviation, $\sigma\phi$, as a sorting measure were calculated. Figure 11 shows the areal distribution of $M\phi$ of 63 underwater samples; $M\phi$ in the bedrock regions is generally smaller than that in the sandy area. Namely, sediment in the former is larger than that in the latter. On the other hand, $\sigma\phi$ did not show such a distinctly zonal distribution.

The existence of coarser sediment in the zones of the exposed bedrock suggests that this material would probably be produced by bedrock erosion, although its quantity would be very small due to high resistivity of the bedrock to wave erosion.

Figure 12 illustrates the alongshore variation of $M\phi$ and $\sigma\phi$ of the backshore sand samples which were taken from 24 locations shown in Fig. 3; there is larger and poorly sorted beach sand in the vicinity of location Nos. 5 and 13. Since the areas of bare bedrock in the seaward regions of these localities are larger (Fig. 4), this result suggests that the coarser material on the bedrock could be transported to the beach by the onshore currents dominating in the bedrock regions.

ALONGSHORE SEDIMENT TRANSPORT PATTERN

Considering the beach locations of Nos. 5 and 13 as supply sources of littoral drift to the whole beach, the direction of alongshore sediment transport was inferred from the variation series of $M\phi$ and $\sigma\phi$ (Sunamura and Horikawa, 1972). The result is shown by arrows in Fig. 12: westward transport dominates in the western part of the beach, while transport pattern in the eastern part is complicated.

In addition to this study of long-term trends of transport pattern, short-term phenomena were investigated by tracing different-colored fluorescent sand which was released at three different alongshore locations (Fig. 13). Figure 13 shows that the transport direction at each location varies according to wave conditions.

LONG-TERM SHORELINE CHANGE

The examination of shoreline change during the period of 87 years from 1883 to 1970 indicated that the beach had been suffering erosion at a mean annual rate of 0.1-0.4 m/year (Fig. 14). Since (1) the study area was uplifted 30 cm at the time of Great Kanto Earthquake in 1923 (Omura, 1926) and (2) it was also uplifted about 5 cm during the period from 1923 to 1965 (Fujii, 1968), it is clear that this whole beach has been eroded more severely. This means that all the material once washed away from the beach has not been returned to the beach, i.e. that the pattern of long-term sediment transport has not formed a closed loop.

INFERRED SEDIMENT TRANSPORT PATTERN

Figure 15 is an illustration of the sediment transport pattern inferred from the above various investigation results. Material resting on the exposed bedrock is transported shoreward by the on-shore currents, drifted alongshore on the beach or in the surf zone, and eventually transported offshore by the offshore currents. The characteristics of submarine topography tell that the material transported offshore to the regions shallower than a water depth of 5 m has the possibility of being carried to the bedrock regions again by circulating currents; this transport pattern would probably form closed loops. On the other hand, the material once transported to deeper regions has less possibility of returning due to the existence of the marked topographic break. Therefore, the transport pattern would not be closed.

CONCLUSION

In the present study area, submarine topography greatly influences nearshore current fields and also governs the resultant sediment transport pattern.

ACKNOWLEDGMENT

A part of this study was supported by National Institute of Resources, Science and Technology Agency, Japan.

REFERENCES

- Fujii, Y., 1968, Vertical deformation of the crust in Boso peninsula, Chiba prefecture, Japan (1): Jour. Geodetic Soc. Japan, v.13, pp.136-145 (in Japanese).
- Hatai, K., 1958, Boso peninsula, Chiba prefecture: Jubilee publication in the commemoration of Professor H. Fujimoto sixtieth birthday, pp.183-201.
- Koike, K., 1955, Geo-historical significance of inter-formational disturbances: Jour. Geol. Soc. Japan, v.61, pp.566-582 (in Japanese).
- Lockwood, H. E., Perry, L., Sauer, G. E., and Lamar, N. T., 1974, Water depth penetration film test: Photogrammetric Eng., v.40, pp.1303-1314.

- Omura, H., 1926, The change of elevation of land caused by the great earthquake of September 1st. 1923: Bull. Earthq. Res. Inst., Univ. Tokyo, v.1, pp.65-68 (in Japanese).
- Sunamura, T., and Horikawa, K., 1972, Improved method for inferring the direction of littoral drift from grain size properties of beach sands: Annual Rep. Eng. Res. Inst., Univ. Tokyo, v.31, pp.61-68.

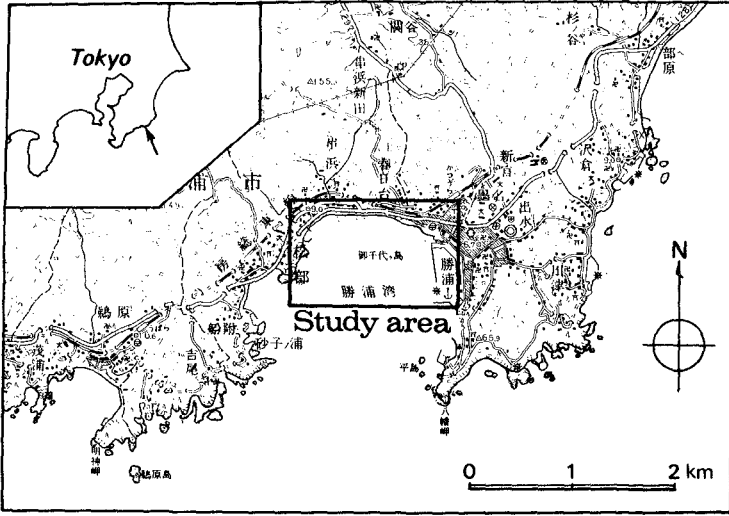


Figure 1 Study area.

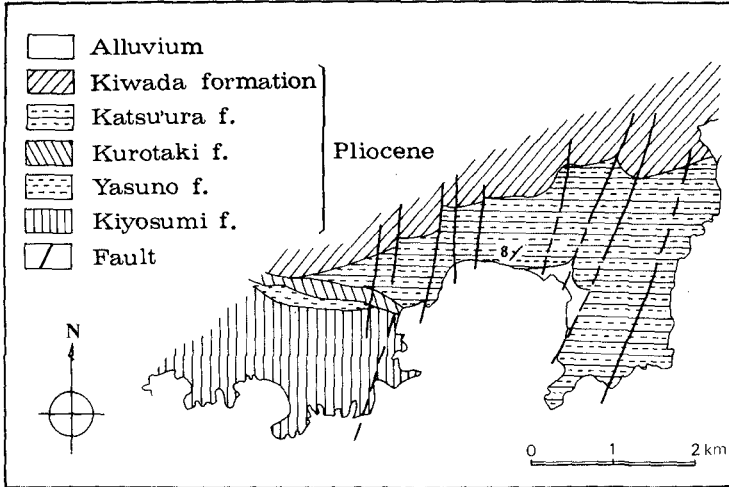


Figure 2 Geology around study area (modified after Koike, 1955; Hatai, 1958).

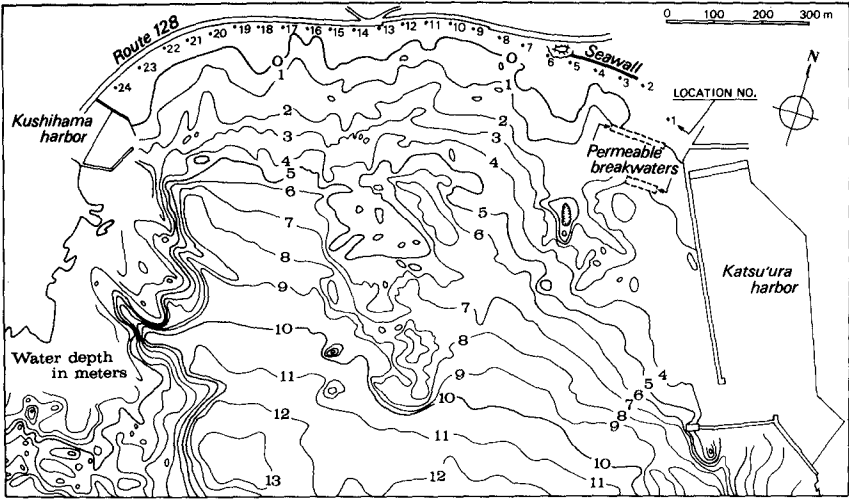


Figure 3 Submarine contour map.

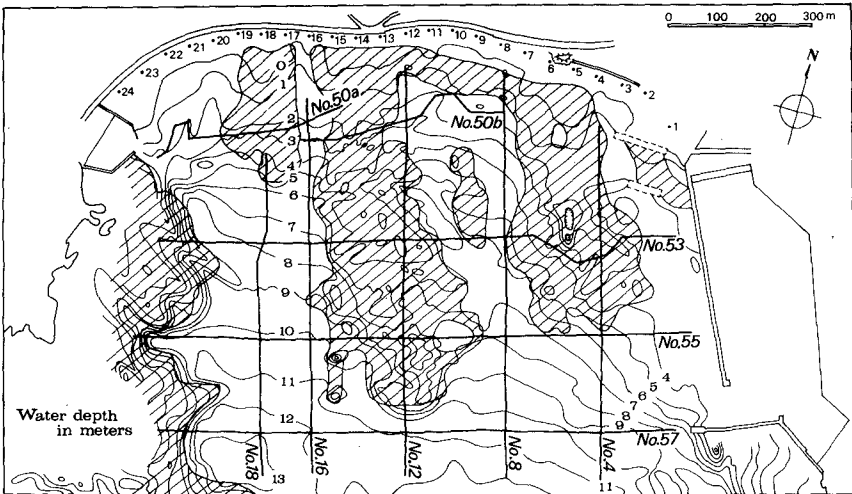


Figure 4 Area of exposed submarine bedrock: hatched portion.

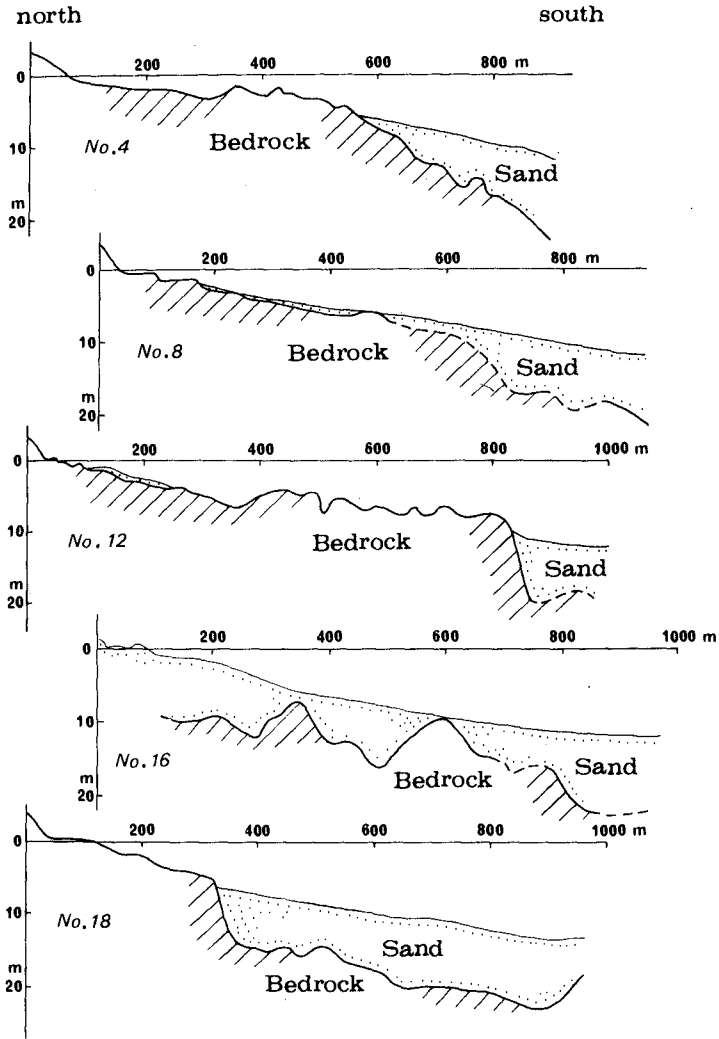


Figure 5a Geological cross sections along survey lines shown in Fig. 4.

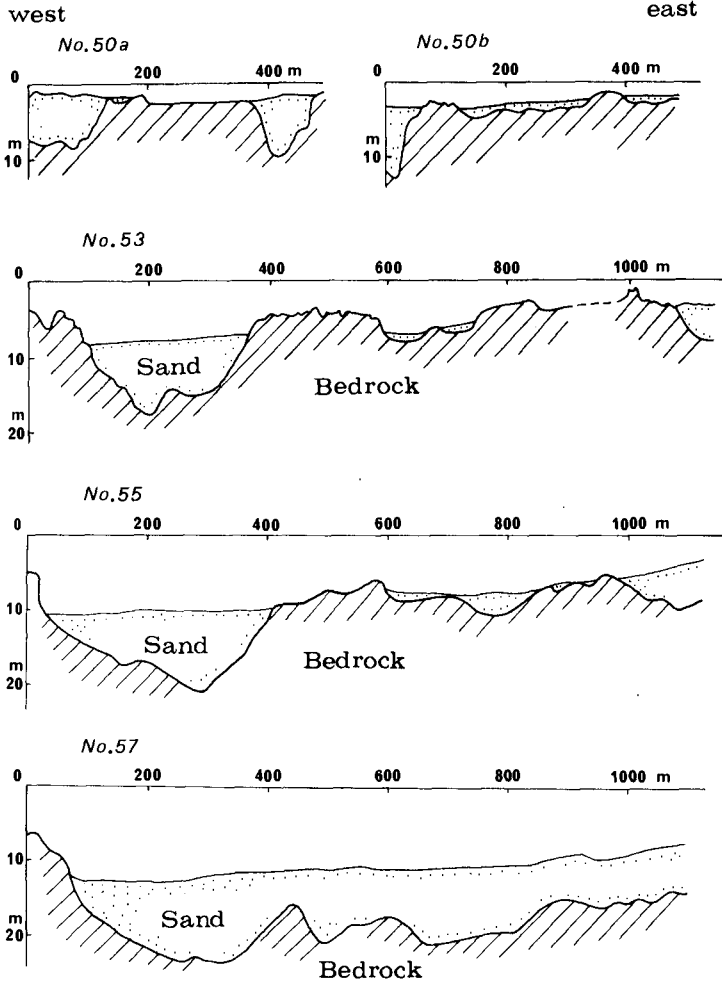


Figure 5b Geological cross sections along survey lines shown in Fig. 4.

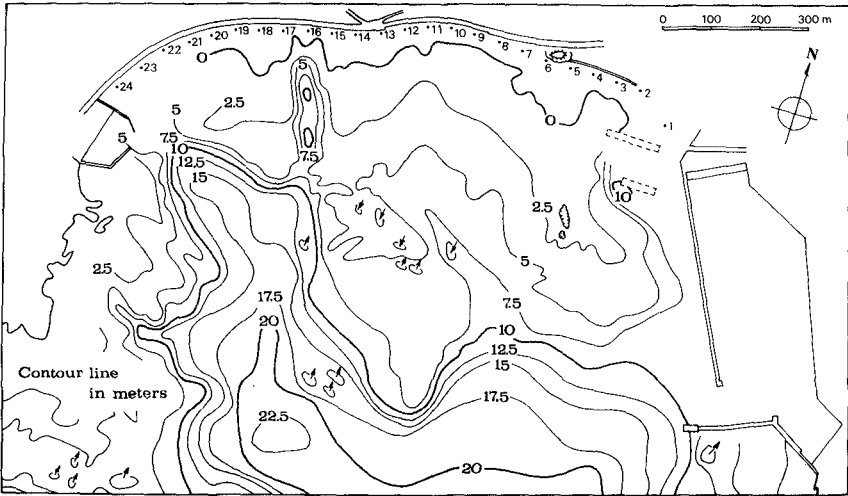


Figure 6 Submarine bedrock configuration.

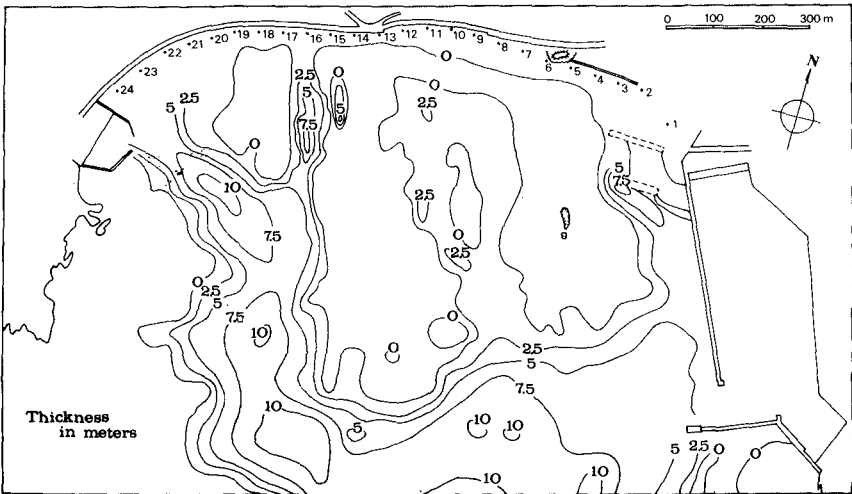


Figure 7 Isopach map of sandy sediment.

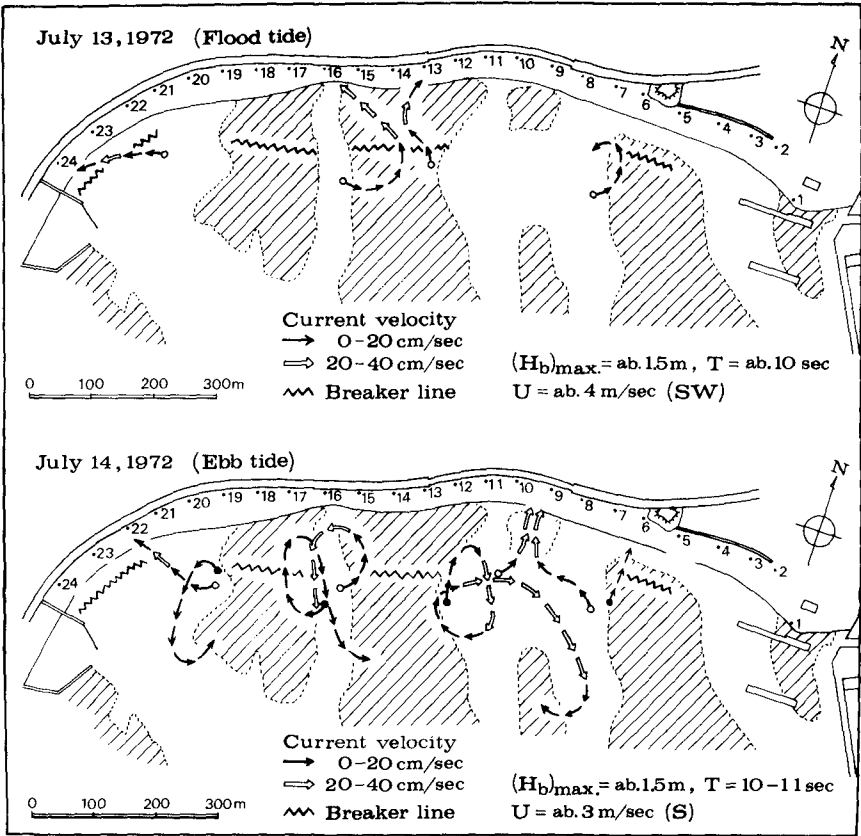


Figure 8 Water circulation pattern.

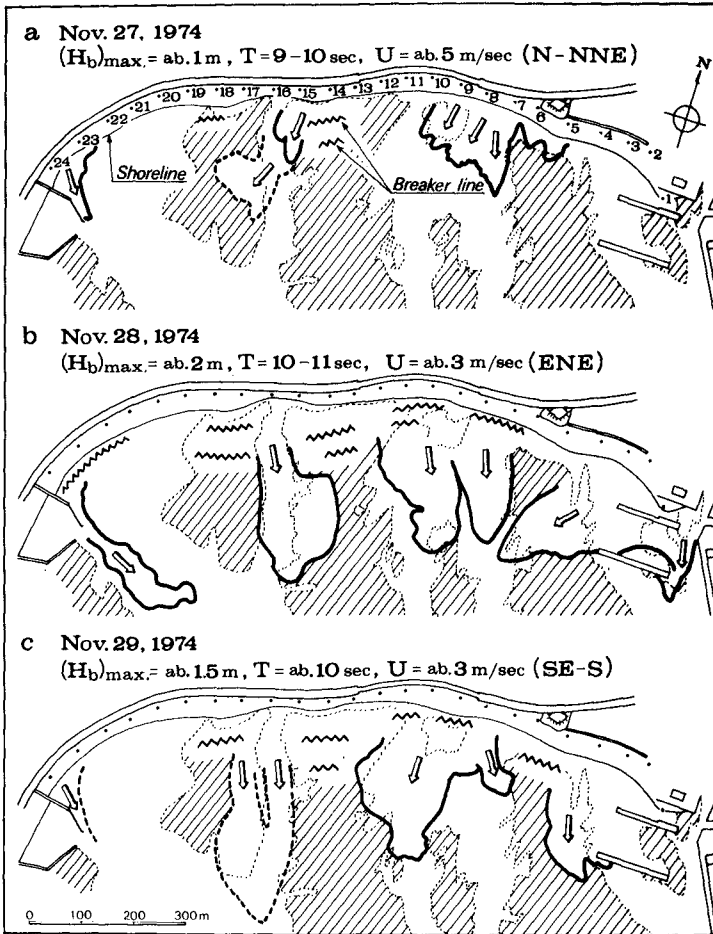


Figure 9 Suspended sediment transport pattern.

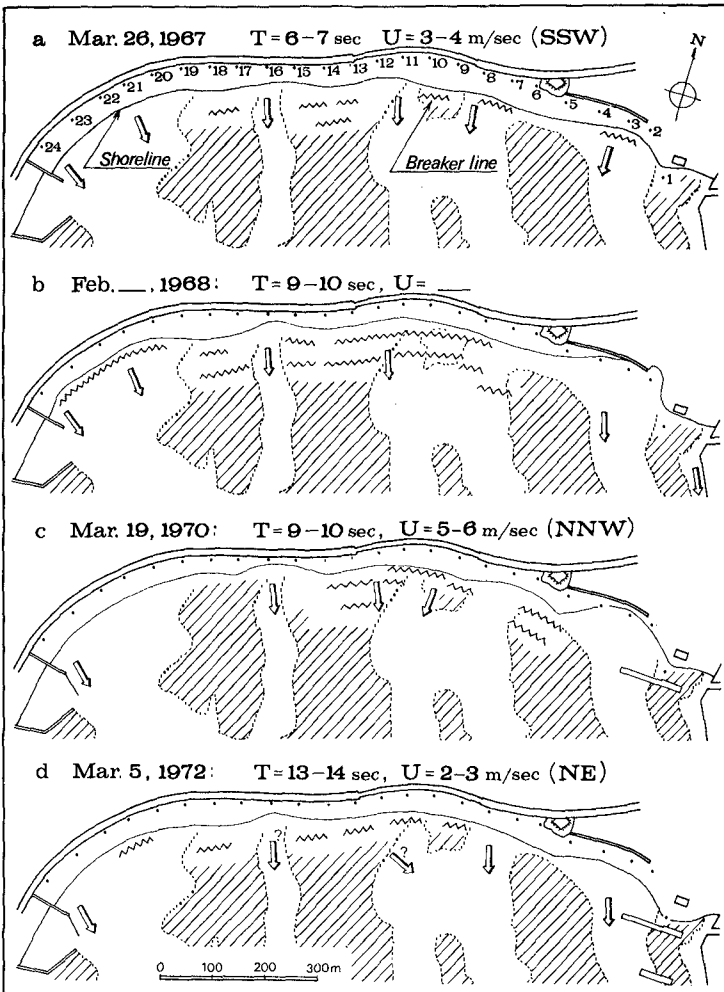


Figure 10a Locations of offshore transport of suspended sediment.

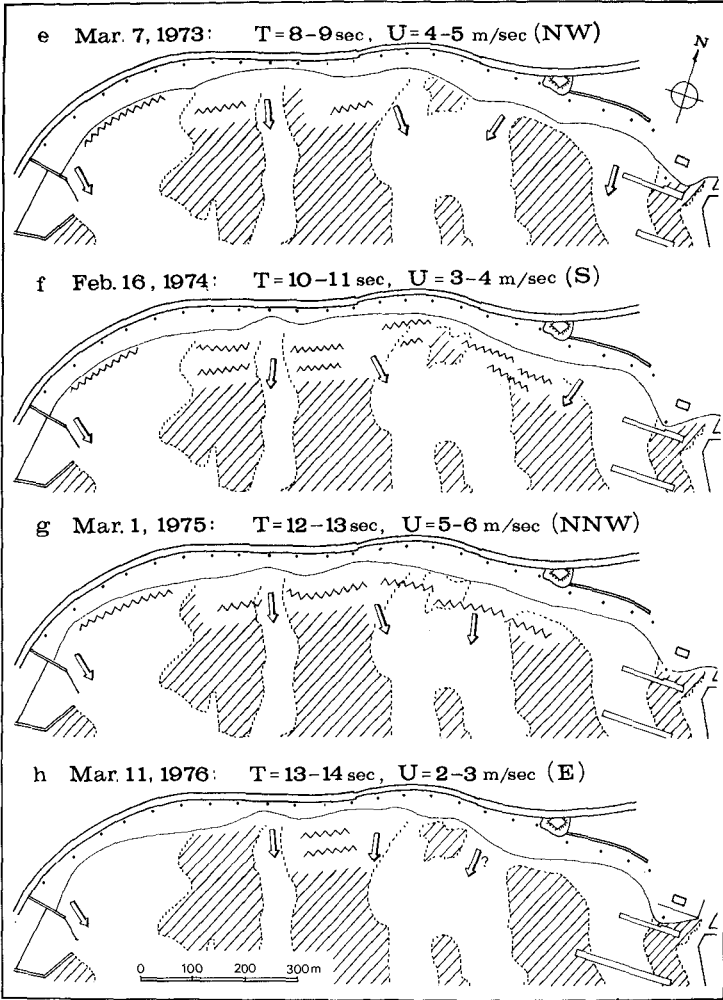


Figure 10b Locations of offshore transport of suspended sediment.

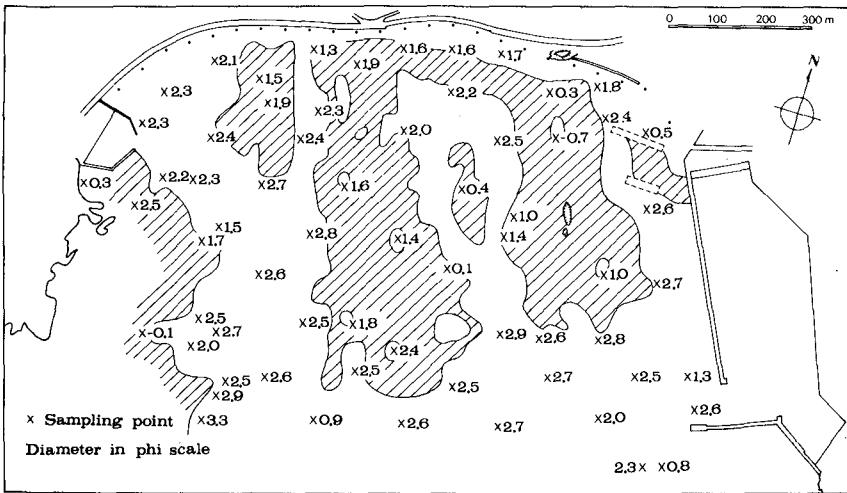


Figure 11 Mean diameter of bottom material.

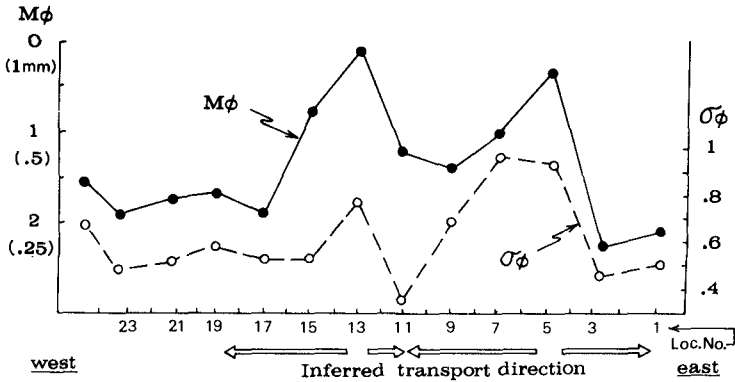


Figure 12 Mean diameter and standard deviation of beach sand, and inferred transport direction.

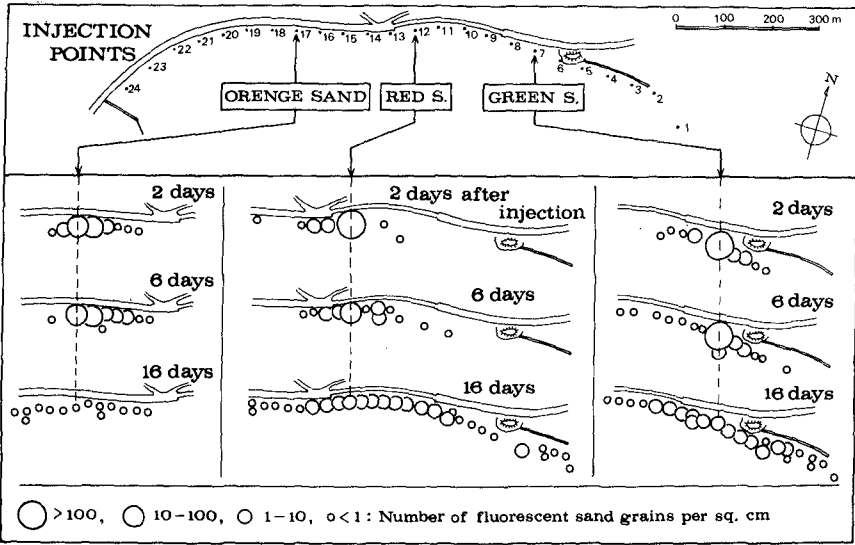


Figure 13 Dispersion of fluorescent sand.

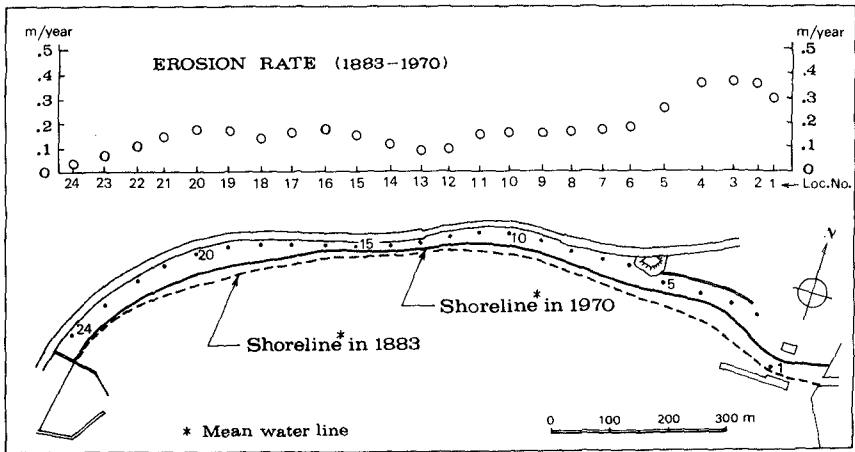


Figure 14 Long-term shoreline change.

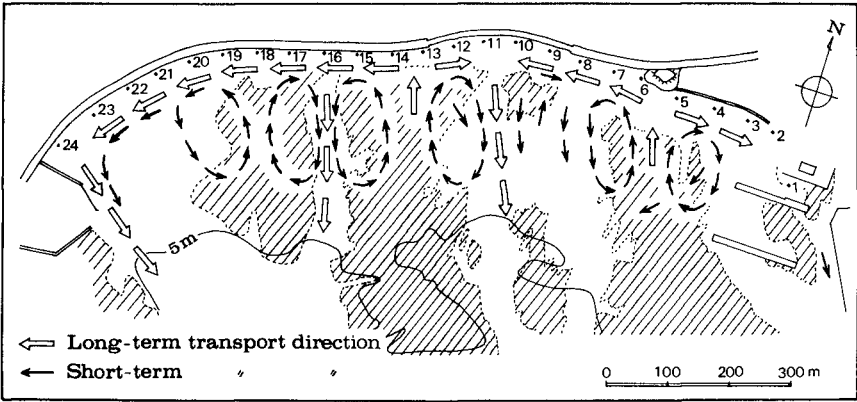


Figure 15 Inferred sediment transport pattern.

CHAPTER 74

EQUILIBRIUM PROFILES AND LONGSHORE TRANSPORT OF COARSE MATERIAL UNDER OBLIQUE WAVE ATTACK

by E. van Hijum *

Abstract. In order to obtain design criteria for artificial gravel beaches, a research programme was drawn up to study the behaviour of gravel beaches under wave attack. The present paper gives the main results of the investigations into beach formation and equilibrium profile characteristics, including the longshore transport rate of beach material under regular wave attack with varying angles of wave approach.

1 Introduction. Coarse material, such as gravel and light rubble, has recently been applied in the Netherlands as a bank protection in areas exposed to wave attack. An example is the gravel beach at the Zuidwal, the southern bank of the harbour entrance to Rotterdam (Figure 1). In order to reduce the waves inside the new harbour mouth and the connected basins, a wave-damping beach is now planned. To achieve the desired energy absorption, such a beach should consist of granular material under a small angle of inclination. For nautical and hydraulic reasons it is not possible to make the beach slope flatter than about 1:10. If loose material is used as slope protection such a slope can only be achieved by using gravel. Contrary to conventional types of bank protection, the profile of such a gravel layer will be deformed when exposed to wave attack. Data on the fluctuation of the profile under design wave conditions are required to ensure an adequate design. For this reason the Public Works Department, Harbour Entrances Division, of the Dutch Government commissioned the Delft Hydraulics Laboratory to investigate the behaviour of gravel beaches under wave attack. The tests were performed in the De Voorst Laboratory of the Delft Hydraulics Laboratory.

2 Beach formation. The process of beach formation has been described extensively by Zenkovich [1] and many others. Changes in coastline are a result of the displacement of beach material along the shore. This process is governed by the size of the material and the position of the zone in which the displacement occurs. Bottom transport, which occurs on the submarine slope under the action of waves that have not yet broken, differs fundamentally from shore transport, which takes place in the surf zone. Silt and fine sand are displaced by both wave and currents; coarser sand and gravel are affected to a lesser extent by currents, whilst larger material is displaced only by wave action. Perhaps due to percolation, gravel

* Project engineer, Maritime Structures Branch, Delft Hydraulics Laboratory, Laboratory de Voorst, The Netherlands.

beaches are rather steep: in general steeper than about 1:8. The mass of water that is formed after a wave breaks on this slope, the swash, is driven by inertia up the beach and then flows back by gravity to meet the following wave (Figure 2). The swash, which has completely lost the nature of wave motion, is exposed to the continuously interchanging forces of inertia and gravity. When the waves approach the shore obliquely, these forces operate differently. As the swash reaches its upper limit it slows down, describes a curve and flows back directly to the sea along the line of steepest gradient. Dependent on the coarseness of the material and the wave conditions, either a thin layer of material or only a few grains are set in motion. The path traversed by particles of material depends on the following factors:

- The wave conditions: wave height, wave period, angle of wave approach;
- the diameter of the particle;
- the shape of the particle and affixtures;
- the initial positions on the beach;
- the time; and
- the initial beach slope.

As an example Figure 3 shows the influence of the initial position of a particle on an equilibrium beach, beyond the breaker-line. The length of the path parallel to the coast traversed by particle 3 is much shorter than that of particle 1. The influence of the time is demonstrated in Figure 4. If the wave conditions alter, the bed will create a new equilibrium. If the waves decrease, path 1 is followed; if the waves increase, path 3 is followed and in the equilibrium phase path 2 is followed.

3 Problem schematization. In the research programme a line was followed as demonstrated in Figure 5. For correct profile development and longshore transport the sediment motion in the model had to fulfil the following conditions:

- The mechanism had to be the same as in nature, and
- in this mechanism scale effects had to be of such an order that they could be neglected.

As the mechanism of sediment transport changes completely once ripples appear, and it is up to this moment impossible to scale down this mechanism, the diameter of the material and the wave conditions were chosen in such a way that no ripples were formed.

Step 1 of the research programme, on deducing scale effects and fluctuation of the profile at perpendicular regular wave attack, has been reported in [2].

The present paper will be restricted to step 2.

4 Problem analysis. In describing profile formation and longshore transport, two groups of parameters may be composed:

a. The external parameters, characterizing the wave attack and the initial beach geometry, viz., wave height and wave length on deep water (H_0 , L_0), wave period (T), depth of foreshore (h), height of beach top (k), initial slope ($\text{tg } \alpha$), grain diameter (D) and angle of wave approach on the foreshore (ϕ). Because of the fact that the larger grains of a grain distribution seem to be determinant for the bed load transport, the D_{90} was chosen to characterize this grain size distribution. D_{90} means that 90% of the weight of a sample has a diameter smaller than D_{90} .

b. The internal parameters, characterizing the resulting equilibrium profile and the sediment transport during the formation of the profile. These parameters are shown in Figure 6:

- h_A = height of wave run-up above the still-water level on the initial (straight) slope
- h_F = height of the beach crest \approx height of wave run-up above the still-water level on the equilibrium profile
- h_B = depth below the still-water level of the point of initial movement on the initial slope
- l_S and l_K = defining the position of the step or bar
- l_E = defining the height of the bar
- $\text{tg } \gamma$ = gradient of the equilibrium profile at the still-water level
- β = angle of repose under water
- $S(y)$ = mean resulting sediment transport in y-direction between two points in time. The time between these points has to be much longer than the wave period
- $S(x)$ = mean resulting sediment transport in x-direction.

For equilibrium of the external parameters in the model the Froude law of similarity was chosen. From [2] it follows that under the conditions tested the Froude law of similarity is also applicable for the internal parameters provided $D_{90} > \sim 6 \times 10^{-3}$ m. The equilibrium profile may show either a bar-type or step-type form, of which the first one has a more pronounced bar, located in the vicinity of the breaker point (see Figure 6). Appearance of a beach crest depends on the initial beach geometry and the erosion rate. If $\phi \neq 0$, then, between two points with $S(x) = 0$, three characteristic sections can be distinguished on a beach (see Figure 7): section A (erosion), section B (equilibrium) and section C (accretion). During a test the section lengths A and C increase and section length B decreases. It is a requirement that the test is finished before section B has

vanished and after the perpendicular cross-section in B has reached an equilibrium condition. These two factors determine the minimum length of the gravel beach section.

5 Description of the model. The model, a straight beach section, was built in a wave basin with the dimensions length * width * depth = 40 * 24,5 * 1,5 m³. The gravel section of the model beach was located between two concrete sections. A carriage with an echo-sounder could be moved over two rails parallel to the beach to make soundings of the profile. In the model two points with $S(x) = 0$ were made (gravel traps). Figure 8 gives a plan view of the model.

6 Tests. A summary of the test program is shown in Table 1. This table includes the two-dimensional tests from step 1. In choosing the external parameters the following four conditions were taken into account:

1. The dimensions of the wave basin.
2. The H-L diagram of Galvin [3], in order to avoid the area of secondary waves.
3. The requirement to remain below the ripple criterion.
4. The condition $D_{90} > \sim 6 * 10^{-3}$ m in order to avoid scale effects in the mechanism of the bottom transport.

Measurements were made of the waves, the wave run-up, the critical velocities at the point of initial movement of the gravel, the changes in time of the beach profile, and of the sorting of the gravel. The waves were measured in 3 rows of about 20 points each. $S(y)$ and $S(x)$ were calculated from frequent profile soundings, being the only way to determine these transports without disturbing the dynamical action of the gravel under wave attack. The procedure used to compute $S(y)$ is shown in Figure 9. In section B, with $\frac{\partial S(x)}{\partial x} \rightarrow 0$, $S(y)$ can be calculated via the continuity equation in y-direction:

$$\frac{\partial S(y)}{\partial y} + \frac{\partial z}{\partial t} = 0, \text{ if } \frac{\partial S(x)}{\partial x} = 0.$$

In x-direction $S(x)$ can be calculated via the continuity equation:

$$\frac{\partial S(x)}{\partial x} + \frac{\partial 0}{\partial t} = 0,$$

where 0 stands for the area of a cross-section in y-direction (see Figure 10).

7 Test results. Only the main results of the tests are given here. In Figure 11 the equilibrium conditions as reached in one of the tests is shown, together with the measured mean incident wave height in the 3 measuring rows. The symbol H_v stands for the wave height on the foreshore. The three characteristic sections A, B and C can clearly be distinguished. $S(x)$ as function of x , in the equilibrium phase, is shown in Figure 12. $S(y)$ as function of y , in section B, is given in Figure 13.

Summarizing all tests, the following conclusions can be drawn:

- It appears to be possible to determine an optimum initial beach profile in y -direction which shows minimum erosion and accretion for a given wave condition. Profile characteristics described in terms of the external parameters are shown in Table 2. The wave run-up on the initial slope (l_A), a vertical profile parameter (h_b), and a horizontal profile parameter (l_s) are shown in their relationships with the external parameters on the Figures 14, 15 and 16 respectively. The transition from step-profile to bar-profile is demonstrated in Figure 17. This criterion only yields for profiles in areas with $\frac{\partial S(x)}{\partial x} \rightarrow 0$. The behaviour of erosion and accretion profiles can deviate considerably, so it will be difficult to check the criterion from Figure 17 with data from beaches in nature.
- The total longshore transport of material in x -direction can be described in terms of grain diameter and design wave conditions (regular waves) by the relationships between internal and external parameters as shown in Table 2 and Figure 18. Both parameter groups in this figure are achieved by simply supposing that a layer of sediment moves along the beach with a velocity proportional to $c_b \sin \phi_b$, where c_b stands for the phase velocity of the breaking wave and ϕ_b for the angle between breaking wave and shoreline. The moving layer is supposed to have a width perpendicular to the coast proportional to l_s and a thickness proportional to D_{90} . The coefficients of proportionality appear to be related to the external parameters too. As shown in Figure 19 there exists a very poor relationship between longshore gravel transport and the so-called "energy flux". In this Figure the model conditions are enlarged with a length scale = 4. As a comparison between longshore sand transport and longshore gravel transport some measurements by Komar are also shown (from [4]).
- Sediment sorting along the equilibrium profile in y -direction seems to be a function of wave height and wave period. At low waves the coarsest material is found on the beach crest and at higher waves in the vicinity of the breaker

point. In x-direction no sorting was found.

- Measurements of critical velocities at the point of incipient motion on the initial slope support the conclusion drawn after the two-dimensional tests, indicating an increase of the critical velocity with increasing water depth.

8 Limitations in use of the results. It is clear that it is only permissible to use the obtained results within the tested range of the parameter groups. An important factor is the translation from a wind-wave field to the regular wave conditions as used in the tests. At the moment at the Delft Hydraulics Laboratory tests are being performed concerning step 4 of the research programme. In the meantime at a project in Italy (see Figure 20) good results were obtained in predicting the longshore transport rate of a natural gravel beach by characterising the wind-wave field by the significant values H_s and T_s .

REFERENCES

1. ZENKOVICH, V.P.,
Processes of coastal development.
Oliver and Boyd, Edinburgh and London, 1967
2. VAN HIJUM, E.
Equilibrium profiles of coarse material under wave attack.
14th Conference on Coastal Engineering, Copenhagen, 1974
3. GALVIN, C.J.,
Finite amplitude shallow water waves of periodically recurring form.
CERC-note, Sept. 1970
4. CERC,
Shore protection manual, 1973

grain diameter ($\rho_s = 2650 \text{ kg m}^{-3}$)	$D_{90} = 1.8; 4.4; 5.9; 7.1; 9.3; 16.5 (10^{-3} \text{ m})$ $D_{50} = 1.3; 3.4; 5.0; 6.1; 8.2; 13.0 (10^{-3} \text{ m})$
wave height	0.04 - 0.47 (m)
wave period	1.20; 1.47; 1.60; 1.83; 2.00; 2.36; 2.44; (s)
angle of wave approach	$0^\circ; 20^\circ; 45^\circ$
initial slope	1:5; 1:8; 1:10
depth of foreshore	0.25; 0.40; 0.50; 0.80; 1.00 (m)
height of beachtop	∞ and still-water level

Table 1 Summary of external parameters

internal parameters	external parameters
$h_B D_{90}^{-1}$	$c_o H_o g^{-1/2} D_{90}^{-3/2} (\cos \phi)^{1/2}$ (if < 700)
$h_B D_{90}^{-1}$	else $H_o D_{90}^{-1} (\cos \phi)^{1/2}$
$l_S D_{90}^{-1}$	$H_o D_{90}^{-1} (\cos \phi)^{1/2}$
$l_K D_{90}^{-1}$	$H_o D_{90}^{-1} (\text{tg } \alpha)^{-1/3} (\cos \phi)^{1/2}$
$h_F D_{90}^{-1}$	$c_o H_o g^{-1/2} D_{90}^{-3/2} (\cos \phi)^{1/2}$
$l_A D_{90}^{-1}$	$c_o H_o g^{-1/2} D_{90}^{-3/2} (\cos \phi)^{1/2}$
γ	$H_o D_{90}^{-1} (\cos \phi)^{1/2}$
β	angle of repose under water ($\sim 30^\circ$)
$l_E D_{90}^{-1}$	$H_o D_{90}^{-1} (\text{tg } \alpha)^{-1/3} (\cos \phi)^{1/2}$
$S(x) g^{-2} D_{90}^{-1} T^{-3}$	$H_o (\cos \phi)^{1/2} D_{90}^{-1}, \{\tanh(kh)\}^{-1} \sin \phi$

$D_{90} > 6 \times 10^{-3} \text{ m}$ only!

Table 2 Relationships between internal and external parameters

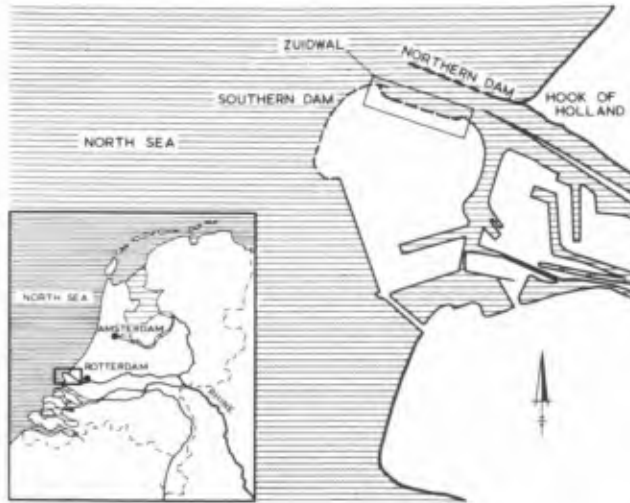


Fig. 1 Location Zuidwal



Fig. 2 Beach formation

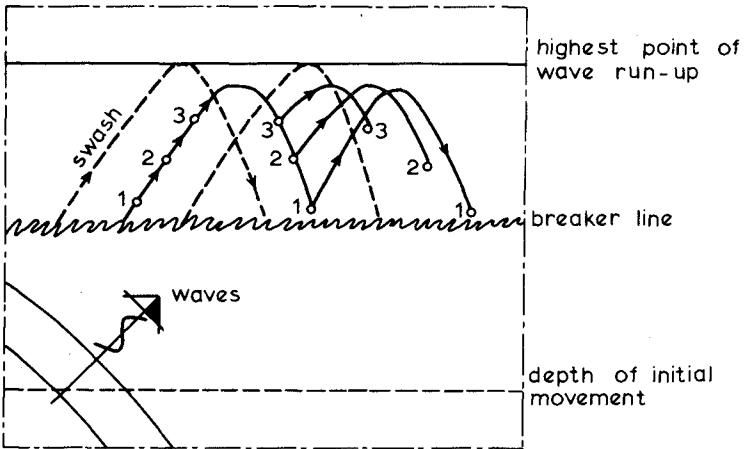


Fig. 3 Influence of the initial location on the beach on particle motion

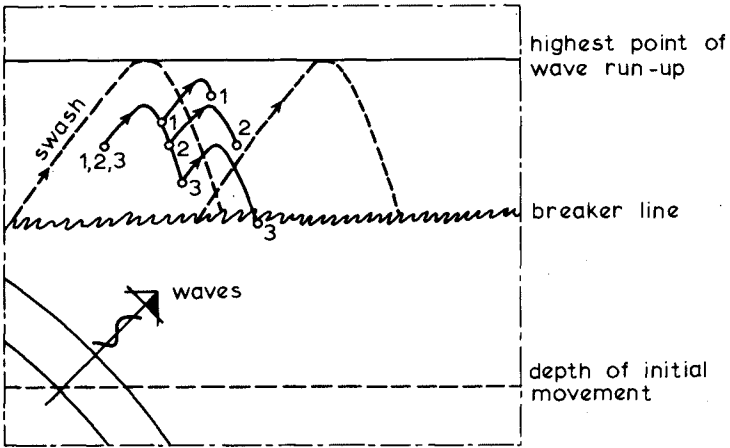


Fig. 4 Influence of the time on particle motion

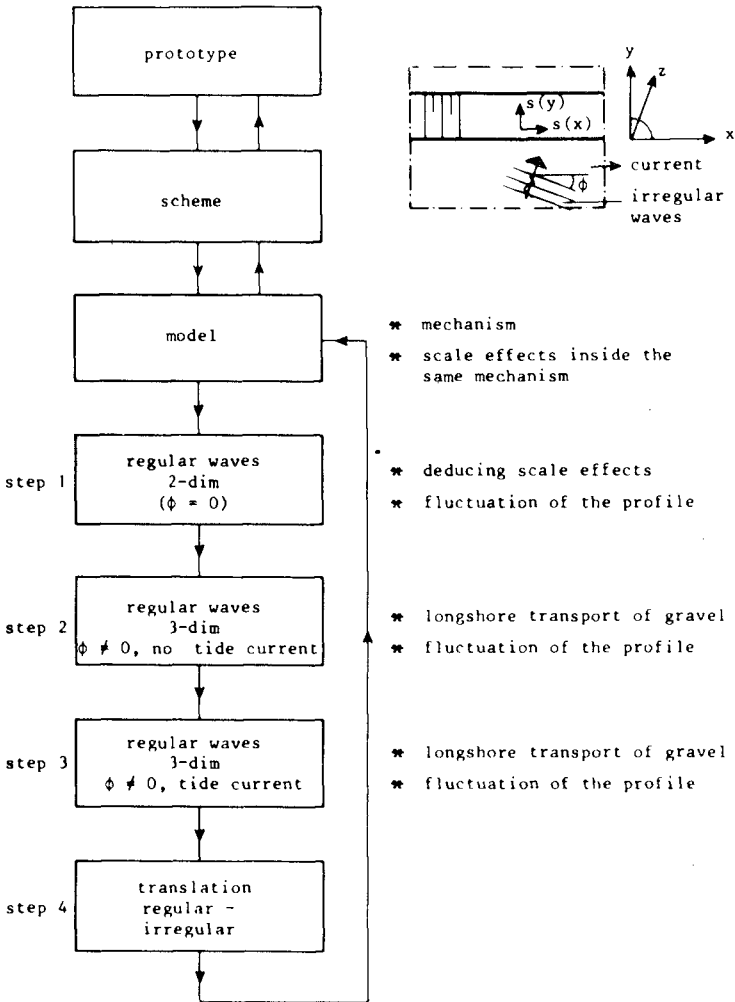


Fig. 5 Problem schematization

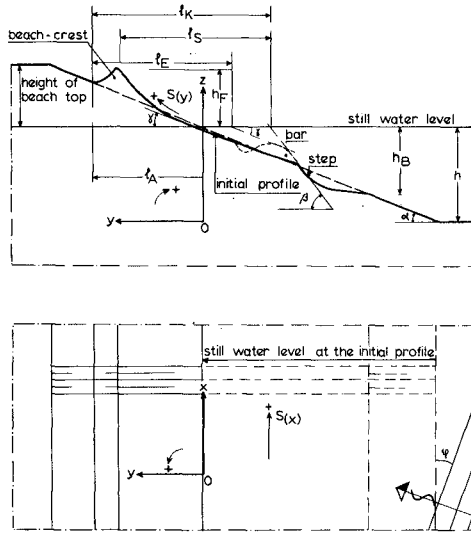


Fig. 6 Definition sketch

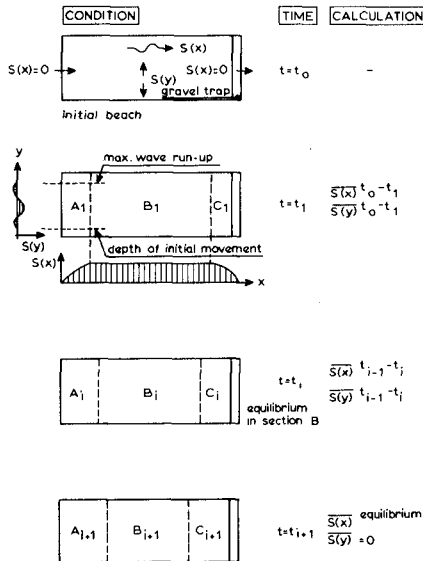


Fig. 7 Beach deformation during a test

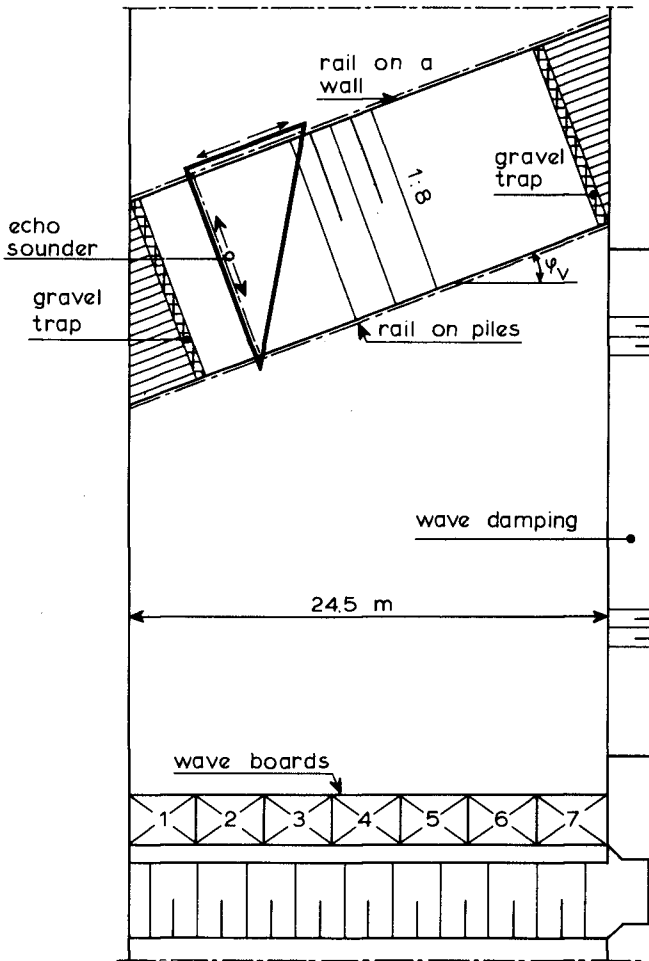


Fig. 8 Plan view of the model

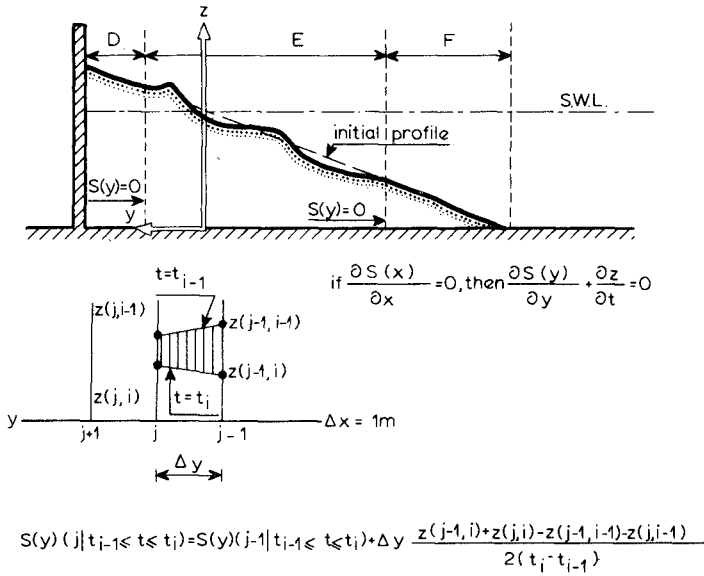


Fig. 9 Computation of onshore-offshore transport S(y)

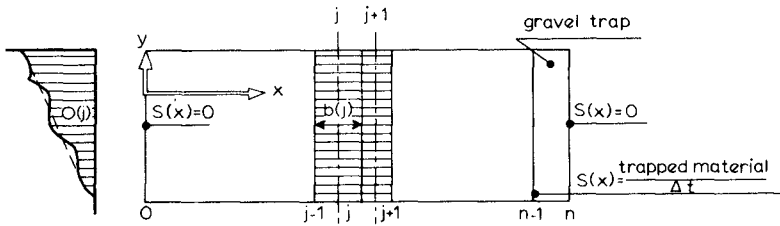


Fig. 10 Computation of longshore transport S(x)

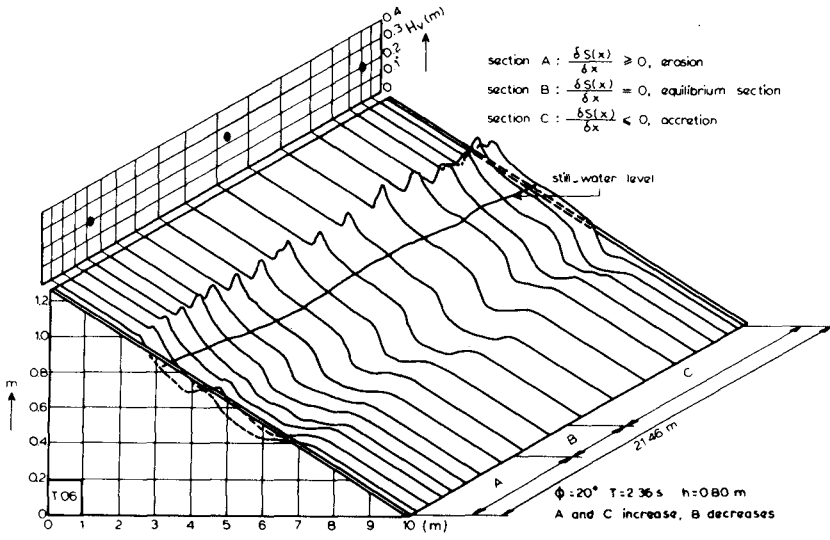


Fig. 11 Equilibrium condition

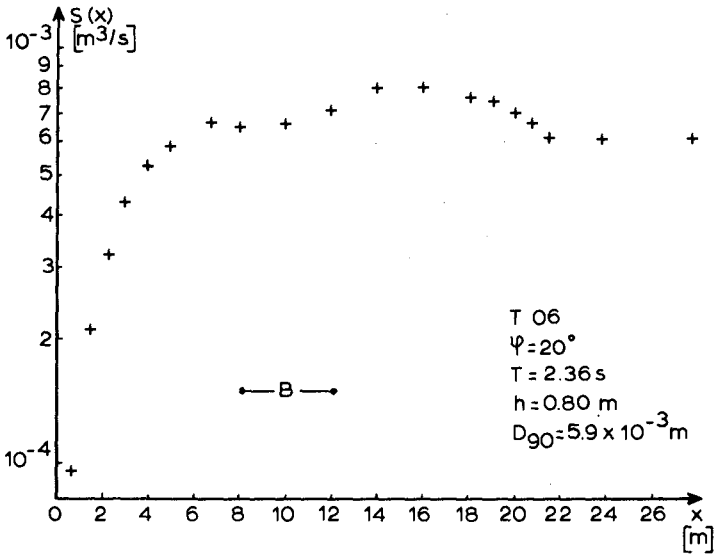


Fig. 12 Longshore sediment transport

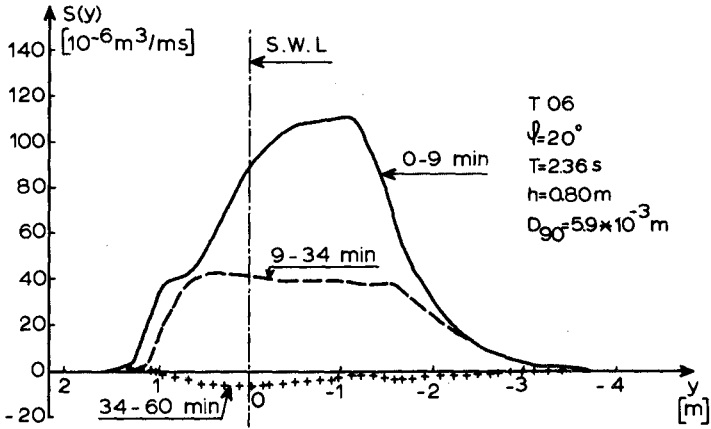


Fig. 13 Onshore-offshore transport in section B

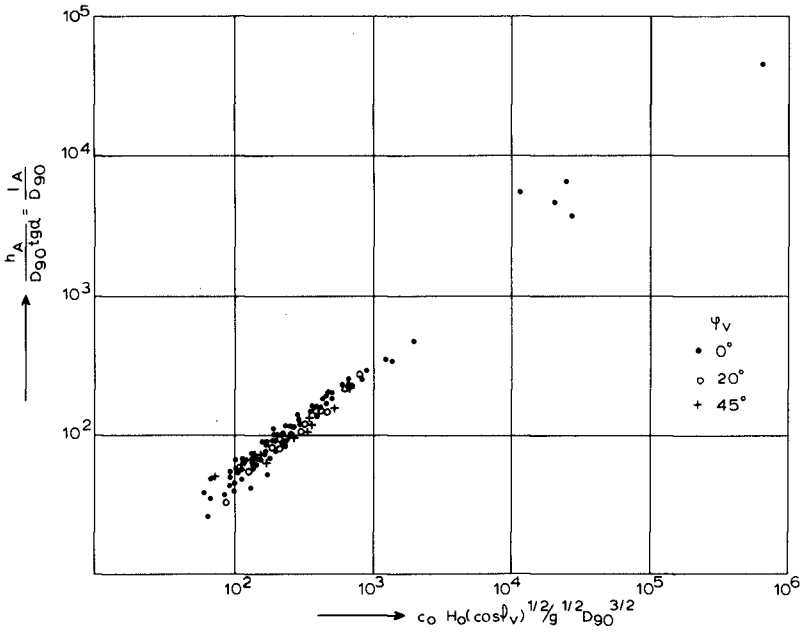


Fig. 14 Wave run-up on the initial slope

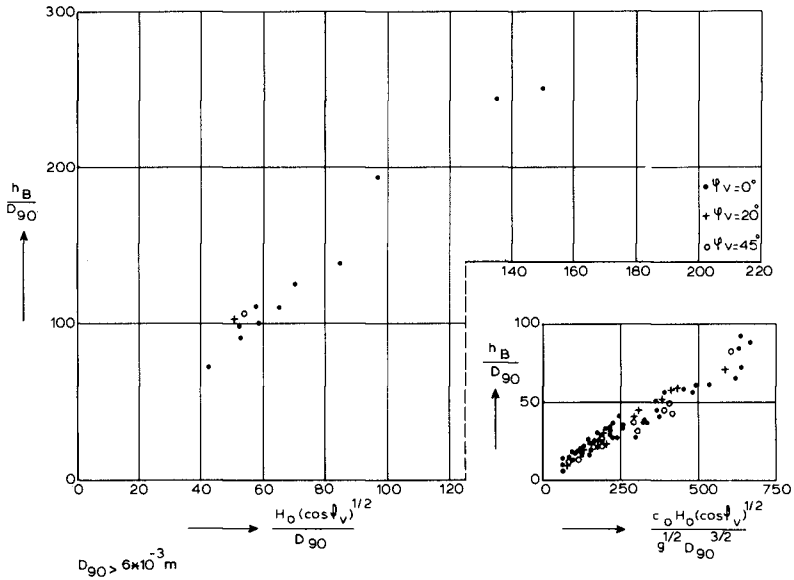


Fig. 15 Depth of incipient motion on the initial slope

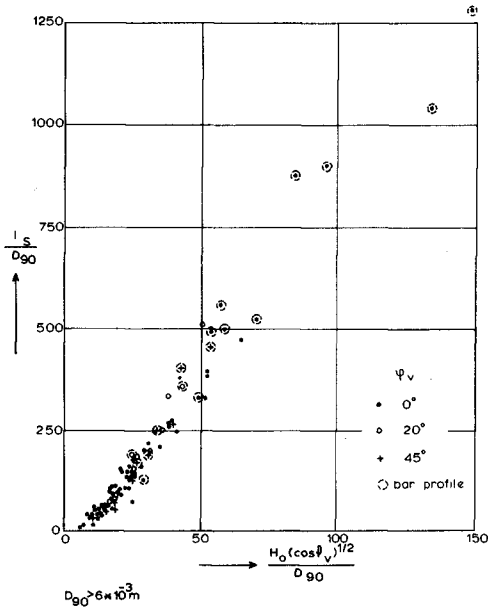


Fig. 16 Location of the step

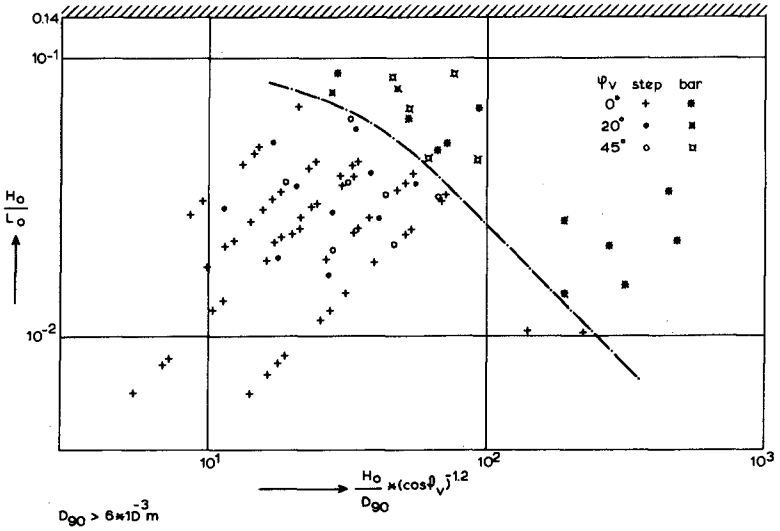


Fig. 17 Bar-step criterion

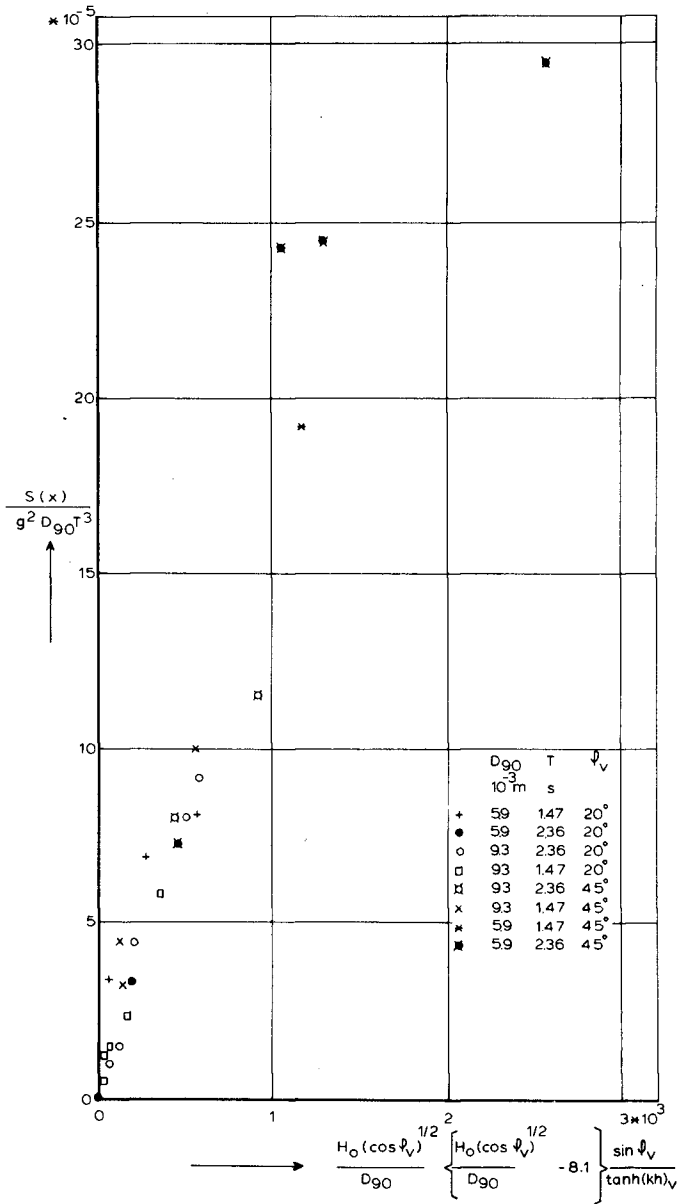


Fig. 18 Longshore transport

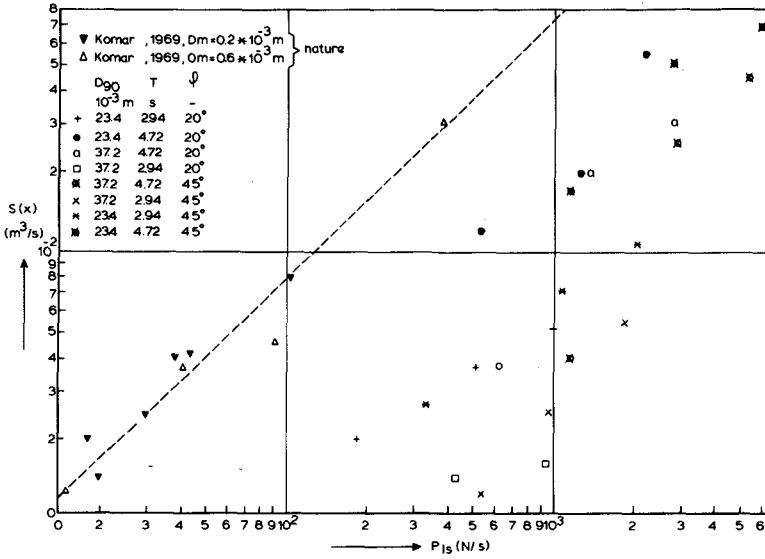


Fig. 19 Longshore transport vs. energy flux

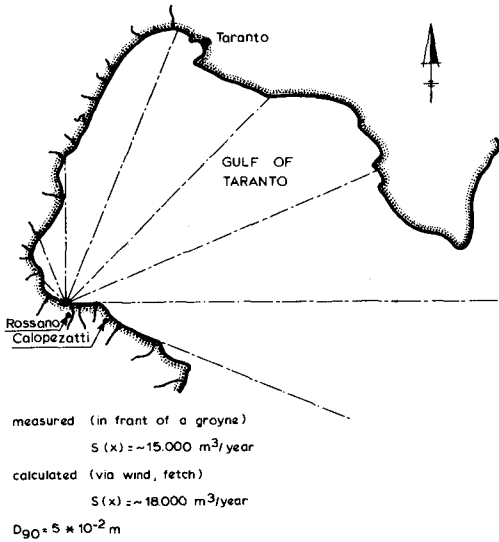


Fig. 20 Predicted and measured longshore gravel transport at Rossano beach

CHAPTER 75

STUDY OF EQUILIBRIUM BEACH PROFILES

by

Robert A. Dalrymple¹ and William W. Thompson²

Abstract

The use of the dimensionless fall velocity for determining equilibrium foreshore slopes, modeling of natural beaches in the laboratory, and for determining shoreline erosion rates is examined. Encouraging results are found for relating foreshore slope uniquely to the dimensionless fall velocity and possible model law is proposed.

Introduction

At the University of Delaware, work has been progressing on the development of computer models for nearshore processes and coastal modification (Wang, Dalrymple and Shiau, 1975; Birkemeier and Dalrymple, 1975). During the course of the work it was necessary to be able to predict equilibrium beach slopes, based not only on the grain size of the material that comprised the beach as was done by Bascom (1951), but also as a function of the incident wave characteristics. Work of this nature has been conducted previously by Kemp (1968), Nayak (1970) and Carter, Mei and Liu (1973). This paper presents the foreshore slope as a function of the dimensionless fall velocity of the sediment, a parameter introduced by Nayak on dimensional grounds and by Dean (1973), based on a physical argument.

Based on the success of the dimensionless fall velocity as a measure of the beach slope and also as an indicator of the reflection from the beach (see Nayak, 1970), numerous model laws were developed for the modeling of beaches in the laboratory, keeping the dimensionless fall velocity ratio constant. Several of these relationships were tested in the laboratory and compared against prototype data in the same manner as Noda (1972) and Paul, Kamphuis and Brebner (1972).

¹Assistant Prof., Dept. of Civil Engineering, Univ. of Delaware, Newark, DE 19711.

²Formerly, Graduate Student, Univ. of Delaware, now with Transworld Drilling Co., Morgan City, La.

A major area of coastal engineering that is still not adequately understood is onshore-offshore sediment transport. From the laboratory tests mentioned above, a speculative empirical relationship is presented for foreshore erosion/deposition based again on the dimensionless fall velocity, which has been shown to be an indication of when erosion or deposition will take place.

Equilibrium Beach Profile and Foreshore Slope

Equilibrium profiles have been studied extensively through the history of coastal engineering, and as early as 1939, Waters postulated that the type of profile (that is, whether a normal profile, with steep foreshore slope and possibly a step at the breaker line, or a bar profile, with a milder foreshore slope and a longshore bar at the breaker line) was determined by the deep water steepness, H_0/L_0 , the ratio of the deep water values of the wave height and wave length. For many years it has been held as a basic tenet that $H_0/L_0 = 0.025$ is the dividing wave steepness between profile types with barred profiles resulting from steeper waves, despite some evidence to the contrary (e.g., Saville, 1957; King, 1972). In 1973, Dean found that the wave steepness separating bar profiles from normal profiles varied with the fall velocity of the sediment, V_f , divided by the deepwater celerity, $C_0 = L_0/T$, where T is the wave period.

$$\frac{H_0}{L_0} = 0.85 \frac{V_f}{C_0}$$

which can be written as $H_0/V_f T = 0.85$. The fall velocity was calculated using the median grain size, d_{50} . Köhler and Galvin (1973) using different data recommended, $H_0/V_f T = 0.70$, while the CERC Shore Protection Manual (1973) recommends 1.0 - 2.0.

The physical significance of the dimensionless fall velocity, $H_0/V_f T$, as presented by Dean is that the parameter is a measure of whether a particle lifted into suspension by the passage of a wave can fall to the bottom during the time when its net displacement due to the horizontal water particle motion is shoreward. If so, the net sediment transport in the surf zone is shoreward, or zero, and we expect a summer profile to develop or to have been developed. Also the parameter can be viewed as the tangent/ π of the angle made by the maximum horizontal velocity in deepwater and the fall velocity.

If the parameter, $H_0/V_f T$, is an important parameter for profile type, it follows (by dimensional analysis) that it is also important for determination of the foreshore slope, θ , measured in degrees at the still water line. Collecting data from different experimenters, including Rector (1954), Fairchild (1959), Raman and Earattupuzha (1972), van Hijum (1974) and Thompson (1976), foreshore slopes were measured and are presented in Fig. 1 versus the dimensionless fall velocity. The figure shows a reasonable trend despite the significant scatter which could be attributed to any number of things including inaccuracy in our

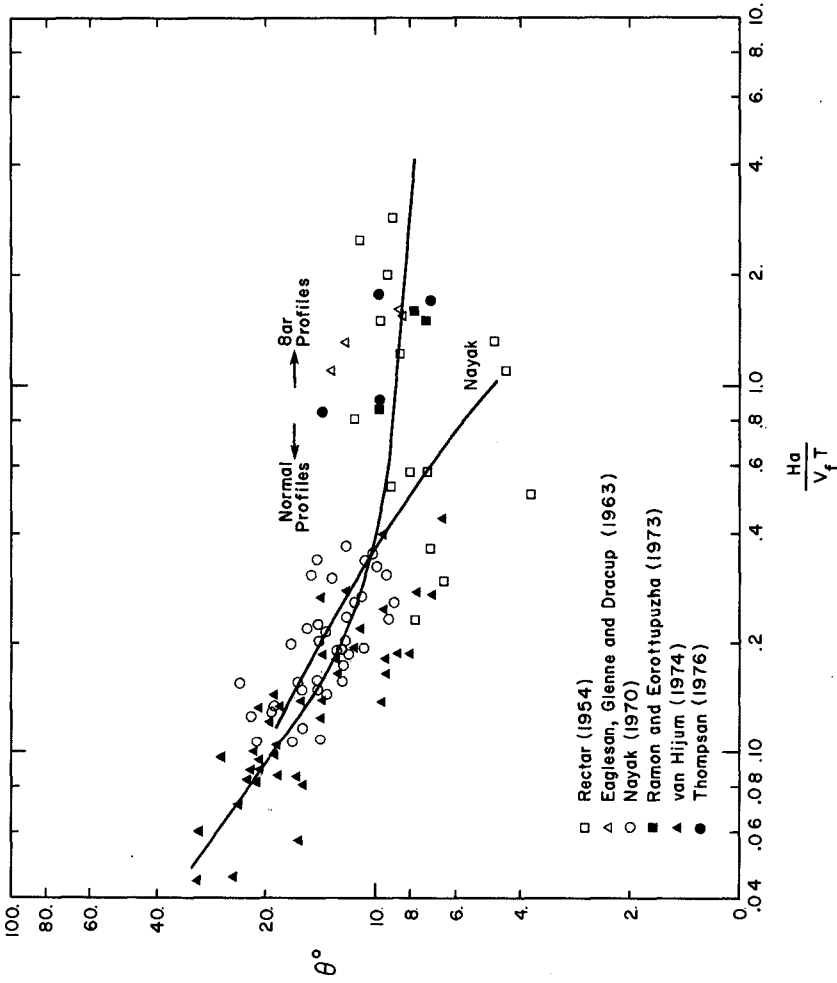


Figure 1 Foreshore Beach Slope Versus Dimensionless Fall Velocity

measurement of θ from the experimenter's figures, profile measurement errors, lack of equilibrium³ and spurious tank reflections. The scatter, however, is less than was obtained by attempting to plot the data versus H_0/L_0 with a third parameter, such as d_{50}/H_0 , d_{50}/L_0 and C_0/V_f .

Nayak's (1970) curve is also shown in the figure, but only over the range for which he used quartz sand. When he used much lighter material, his beach slopes became very mild and, in fact, the whole beach itself was in motion with the waves. Also Kemp (1968) has plotted θ versus a dimensional parameter, $H_b/Td_{50}^{1/2}$, which is similar to the dimensionless fall velocity as V_f is directly proportional to $d_{50}^{1/2}$ for large sand sizes. Ours appears to be significantly different from his, particularly for larger values of $H_0/V_f T$.

Modeling Relationships

From Fig. 1, which indicates a unique foreshore slope for a given value of $H_0/V_f T$, it follows that in order to reproduce in a model the same equilibrium profile that occurs in the prototype (neglecting tidal effects) that the parameter $H_0/V_f T$ should be the same in model and prototype. Based on different modeling requirements seven model laws were developed and are presented in Table 1. The derivations are shown in the Appendix.⁴ Four of the model laws (#3,5,6,7) accommodate the same sand in model and prototype and were tested in the laboratory. However, of these, only #7 maintains geometric similarity (that is, the horizontal length scale, λ , is equal to the vertical length scale, μ), and, therefore, only it should yield a corrected modeled beach slope, while it was hoped that the others might adequately model other features of the profile.

Experiments were conducted in a 21.3 m long x 0.61 m wide wave tank with a piston wavemaker at one end and the sand beach at the other. The experimental program was to run prototype tests for a normal and barred profile and then to model these with tests based on the model laws. The beach material consisted of a quartz sand with a median diameter, d_{50} of 0.40 mm (a Trask sorting coefficient of 1.38 and a skewness of 1.0). Due to tank size restrictions, the maximum practical scaling was only $\mu = 1/2$. Most of the tests were initiated with a plane profile (1:10 for the prototype tests) and allowed to run to equilibrium which was defined as a lack of significant profile change with time in the foreshore region. For the foreshore region,

³ Chesnutt and Galvin (1974) report never achieving equilibrium in their tests despite holding H_0/L_0 constant as the air temperature and hence $H_0/V_f T$ changed.

⁴ The derivation of the model laws utilized the Stokes equation for fall velocity which is valid only for low Reynolds numbers. For larger Reynolds numbers, a different fall velocity relationship is necessary and, in fact, for Model Laws 1 and 2, it is only necessary to scale the fall velocity as $\mu^{1/2}$ and then choose the sand size accordingly.

TABLE 1 SUMMARY OF MODEL LAWS
(See Appendix A for Derivation)

Law	$n\gamma'$	$n_{d_{50}}$	n_T	λ	Note
1	1	$\mu^{1/4}$	$\mu^{1/2}$	μ	Preserves Froude No., H_0/L_0 , geometric similarity, Stokes fall velocity
2	$\mu^{3/2}$	$\mu^{-1/2}$	$\mu^{1/2}$	μ	Preserves bed particle Reynolds number, densimetric Froude number, H_0/L_0 .
3	1	1	μ	$\mu^{3/2}$	Assumes laminar boundary layer. Preserves bed shear stress, Froude No.
4	$\mu^{-0.1875}$	$\mu^{+0.063}$	$\mu^{1.0625}$	$\mu^{1.5625}$	Assumes turbulent boundary layer.
5	1	1	μ	$\mu^{3/2}$	Preserves Froude No.
6	1	1	μ	μ^2	Preserves bed particle Reynolds number, bed shear stress.
7	1	1	μ	μ	Preserves geometric similarity, H_0/L_0 .

$n_{\text{parameter}, a} = \frac{a_{\text{model}}}{a_{\text{prototype}}}$	d_{50} = median grain size diameter
$\gamma' = \frac{\gamma_{\text{sediment}} - \gamma_{\text{fluid}}}{\gamma_{\text{fluid}}}$	T = wave period
	λ = horizontal length scale
	μ = vertical length scale

the foreshore slope and the related profile was achieved quickly, in the matter of several hours; however, the offshore region, dominated by migratory ripples, equilibrium took much longer to achieve, particularly for the barred profile.

A summary of the tests is presented in Table 2, including the initial variables and the time to equilibrium, t_e . The resulting model beach profiles obtained for the different model laws (note that #3 and 5 have the same scaling relationships despite different assumptions) were scaled up to prototype scale and plotted with a common still water line intersection. The results are shown in Figs. 2 and 3 for the normal and barred profiles. As can be seen

TABLE 2 EXPERIMENTAL TEST VALUES

	$\frac{d}{L}$	$\frac{H}{L}$	$\frac{H_o}{L}$	$\frac{H}{V_f T}$	$\frac{H_o}{L_o}$	$\frac{H_o}{V_o T}$	t_e (hrs)			
<u>Prototype</u>										
Summer	1:10	27.0	4.00	4.28	2.1	13.5	2.20	.0158	.928	21
Winter	1:10	27.0	7.50	8.05	2.1	14.0	2.20	.0297	1.745	18.5
<u>Model Law #7</u>										
Summer	1:10	13.5	2.00	2.18	1.05	22.0	2.44	.0323	.850	12
Winter	1:10	13.5	3.75	4.09	1.05	14.5	2.24	.0605	1.740	15
<u>Model Laws</u>										
<u>#3, #5</u>										
Summer	1:7	13.5	2.00	2.18	1.05	25.0	2.52	.0323	.825	8
Winter	1:7	13.5	3.75	4.09	1.05	25.5	2.52	.0605	1.540	11
<u>Model Law #6</u>										
Summer	1:5	13.5	2.00	2.18	1.05	23.0	2.44	.0323	.850	*(24)
Winter	1:5	13.5	3.75	4.09	1.05	14.0	2.20	.0605	1.760	*(18.5)

¹Median water temperature

*Test Time, did not attain equilibrium

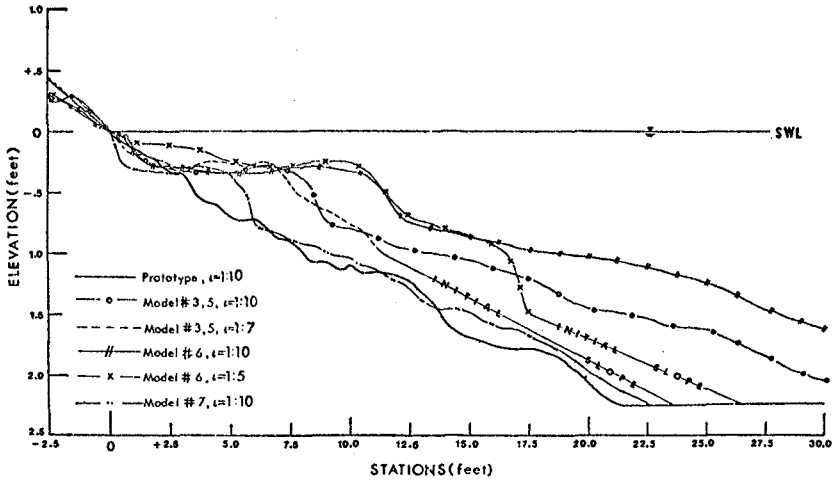


Figure 2 Comparison of Model Laws for Normal Profile. Station 0 = Intersect of SWL and Equilibrium Profile

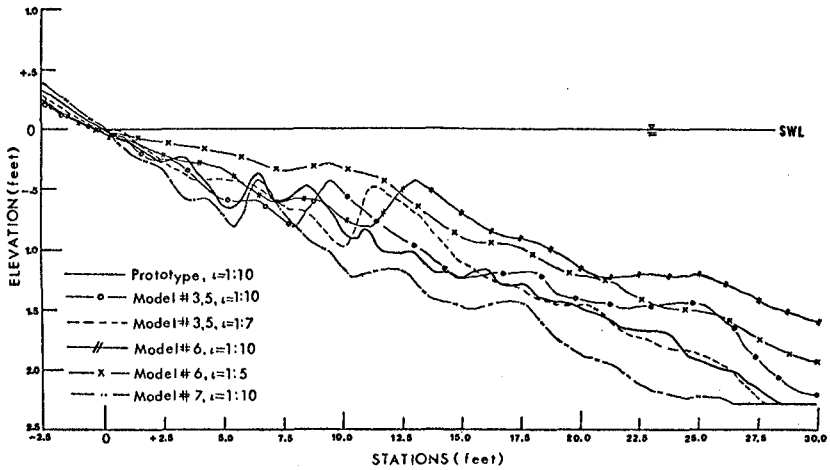


Figure 3 Comparison of Model Laws for Barred Profile. Station 0 = Intersect of SWL and Equilibrium Profile

despite the small scaling ($\mu = 1/2$), there are wide discrepancies in the results, despite the fact that the dimensionless fall velocity was nearly the same (varying due to temperature effects on the fall velocity). The "best" model law of the four tested appears to be #7, as it predicted the location of the primary bar for the steep waves (bar profile) and it follows the normal profile reasonably well for the milder waves. A discrepancy occurs in the model in that it predicts a bar for this case also, however, the problem lies (experimentally) in the fact that $H_o/V_f T$ differs slightly between model and prototype, and both values are near the transition line between profile types as discussed in the first section. The primary reason for the inability of the other models to predict the prototype equilibrium profile appears to be the distortion of these models.

The only difference between the four models is the length scale and, therefore, only the initial slopes were varied to start each test. Comparing the model test results prior to scaling to prototype gives an indication of the effect of initial slope on final profile. Fig. 4 shows the results for the normal profiles. In the onshore region the initial slope makes no difference at all, and, thus, has no effect on the foreshore slope. However, in the offshore region it is important as it is a measure of the amount of sand available to be moved by the waves. For model tests where the depth of water at the toe of the beach is deeper than the depth at which material is moved by the waves then the initial slope will have no effect on the final equilibrium profile.

Three of the proposed models' laws were not tested. Of them, Model Laws 1 and 2 appear to be better ones in that they, like Model Law 7, are undistorted models. As Model Law 1 only requires modeling the sediment size, it appears to be the most practical.

Onshore-Offshore Sediment Transport

The amount of material transported between the foreshore and the offshore region is of importance for beach erosion considerations. Based on dimensional analysis, an erosion parameter, $Q/H_o d_i$, was chosen to represent this volumetric transport. The variable, Q , is the volume of material per unit width of tank eroded or deposited onshore of the breaker line and d_i , the product of the depth of water at the toe of the beach and the initial beach slope is a measure of the amount of material in the tank. The initial slope, i , is also important as the erosion or deposition in the onshore zone depends on whether or not the initial slope is greater than or less than the equilibrium slope. The results which are extremely speculative are shown in Fig. 5. Clearly more data is necessary to verify if the form of the curve is correct.

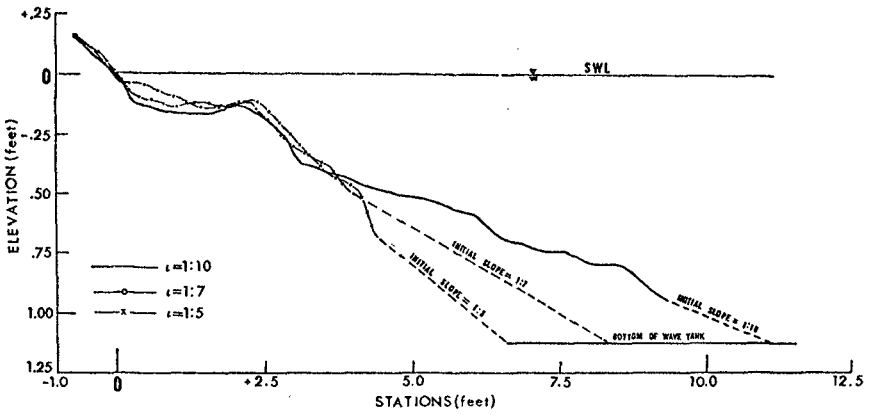


Figure 4 Comparison of Initial Slopes for Normal Profile

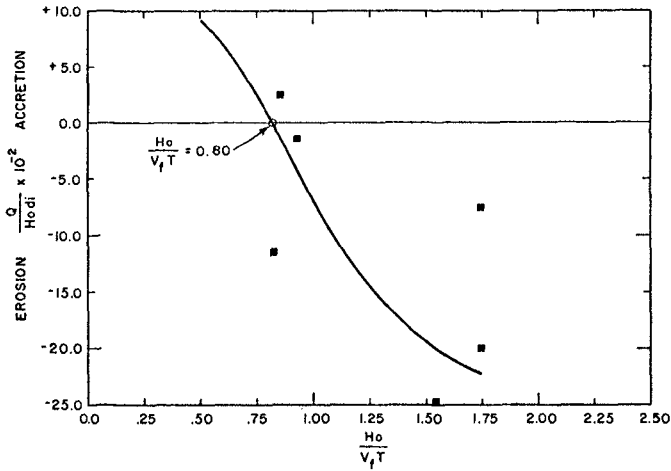


Figure 5 Inshore Erosion Versus Dimensionless Fall Velocity

Conclusions

The foreshore slope angle is uniquely related to the nondimensional parameter $H_o/V_f T$ which accounts for the major wave and material properties. For mild waves, the beach slope will be steeper than for steeper waves. Based on experimental results, the slope is independent of initial conditions and can be repeated for similar laboratory conditions. The slope is also a very important characteristic feature of the application to natural beaches as the region inshore of the Breaker line is the region of most concern to the users of the beach. The slope angle is relatively easy to identify and measure in the field as compared to the identification of an offshore bar.

A model law preserving the parameter, $H_o/V_f T$ has not been proven experimentally although Model Law #1 apparently includes the most important assumptions. Based on the experimental verification of four of the proposed model laws, the model should be geometrically similar to the prototype and should preserve the wave steepness ratio and the parameter, $H_o/V_f T$. To preserve both the wave steepness ratio and $H_o/V_f T$, the material size must also be modeled and the same material used in the model and prototype to eliminate the alien effects of light-weight materials.

References

- Bascom, W.J., "The Relationship Between Sand Size and Beach-Face Slope," Trans., Amer. Geophys. Union, Vol. 32, No. 6, 1951.
- Birkemeier, W.A. and R.A. Dalrymple, "Nearshore Water Circulation Induced by Wind and Waves," Proc. Symp. on Modeling Tech., ASCE, San Francisco, 1975.
- Carter, T.G., Liu, P. L-F. and C. C. Mei, "Mass Transport by Waves and Offshore Bed Forms," J. Waterways, Harbors and Coastal Engrg., ASCE, Vol. 99, No. WW2, May, 1973.
- Chesnut, C.B. and C.J. Galvin, "Lab Profile and Reflection Changes for $H_o/L_o = 0.02$," Proc. 14th Conf. on Coastal Engrg., ASCE, Vancouver, 1974.
- Dean, R.G., "Heuristic Models of Sand Transport in the Surf Zone," Proc. Conf. on Engrg. Dynamics in the Surf Zone, Sydney, May, 1973.
- Eagleson, P.S., Glenne, B. and J.A. Dracup, "Equilibrium Characteristics of Sand Beaches," J. Hyd. Div., ASCE, No. HY1, Jan., 1963.
See also U.S. Army Beach Erosion Board Tech. Memo. 126, July, 1961.
- Fairchild, J.C., "Suspended Sediment Sampling in Laboratory Wave Action," U.S. Army Beach Erosion Board Tech. Memo. 115, June, 1959.
- Henderson, F.M., Open Channel Flow, MacMillan Company, New York, 1966.

References (Continued)

- Jonsson, I.G., "Wave Boundary Layers and Fraction Factors," Proc. of 10th Conf. on Coastal Engrg., ASCE, London, 1966.
- Kamphuis, J.W., "Short Wave Models with Fixed Bed Boundary Layers," J. Waterways, Harbors and Coastal Engrg., ASCE, No. WW4, 1973.
- Kemp, P.H., "Beaches Produced by Waves of Low Phase Difference," J. Hyd. Div., ASCE, No. HY 5, Sept., 1968.
- King, C.A.M., Beaches and Coasts, 2nd Ed., St. Martins Press, New York, 1972.
- Kohler, R.R. and C.J. Galvin, "Berm-Bar Criterion," unpublished Memorandum for the Record, U.S. Army CERC, Washington, Aug.,
- LeMehaute, B., "A Comparison of Fluid and Coastal Similitude," Proc. of the 12th Coastal Engrg. Conf., Washington, 1970.
- Nayak, J.V., "Equilibrium Profile of Model Beaches," Doctoral Dissertation, Univ. of Calif., at Berkeley, June, 1970.
- Noda, E.K., "Equilibrium Beach Profile Scale-Model Relationships," J. Waterways, Harbors and Coastal Engrg., ASCE, No. WW4, Nov., 1972.
- Paul, M.J., Kamphuis, J.W. and A. Brebner, "Similarity of Equilibrium Beach Profiles," Proc. 13th Coastal Engrg. Conf., ASCE, Vancouver, 1972.
- Raman, H. and J.J. Earattupuzha, "Equilibrium Conditions in Beach Wave Interaction," Proc. 13th Coastal Engrg. Conf., ASCE, Vancouver, 1972.
- Rector, R.L., "Laboratory Study of Equilibrium Profile of Beaches," U.S. Army B.E.B.T.M. 41, Aug., 1954.
- Saville, T., "Scale Effects in Two Dimensional Beach Studies," Trans. Int. Assoc. of Hyd. Res., 7th General Meeting, 1957.
- Thompson, W.W., "A Study of Equilibrium Beach Profiles," M.C.E. Thesis, Univ. of Delaware, June, 1976.
- U.S. Army Coastal Engineering Research Center, Shore Protection Manual, Washington, DC, 1973.
- van Hijum, E., "Equilibrium Profiles of Course Material Under Wave Attack," Proc. 14th Coastal Engrg. Conf., ASCE, Copenhagen, 1974, also personal communication, 1976.
- Wang, H., Dalrymple, R.A. and J.C. Shiau, "Computer Simulation of Beach Erosion and Profile Modification Due to Waves," Proc. Symp. on Modeling Tech., ASCE, San Francisco, 1975.

References (Continued)

Waters, C.H., "Equilibrium Studies of Sea Beaches," M.S. Thesis, Univ. of California at Berkeley, 1939.

APPENDIX A

DEVELOPMENT OF EQUILIBRIUM PROFILE MODEL LAWS

To completely define the following model laws, the horizontal scale, the median grain diameter, the submerged specific weight of the beach material and the time scale will be expressed in terms of the vertical scale. As only equilibrium profiles are considered, the time to equilibrium is not modeled. The variable H_0/V_{FT} will be preserved in all model laws. Further, the scale ratio of a parameter $n_{\text{parameter}}$, equals the ratio of the parameter in the model to the same parameter in the prototype. The following notation will be incorporated in the derivations:

$$n_{\text{vertical length}} = \mu$$

$$n_{\text{horizontal length}} = \lambda$$

$$n_{\text{time scale}} = n_T$$

$$n_{\text{median grain diameter}} = n_{d_{50}}$$

$$n_{\text{sediment relative specific weight}} = n_{\gamma'}$$

$$\text{where } \gamma' = \frac{\gamma_{\text{sediment}} - \gamma_{\text{fluid}}}{\gamma_{\text{fluid}}}$$

The resulting model relations are summarized in Table 1.

1. Model Law #1

The deepwater wave steepness, H_0/L_0 , has been shown to be a governing factor in the shaping of beach profiles. Preserving H_0/L_0 and defining $n_{H_0} = \mu$ and $n_{L_0} = \lambda$,

$$\mu = \lambda \quad (1.1)$$

Modeling the deepwater wave length, $L_0 = g/2\pi T^2$, or requiring Froude similitude

$$n_T = \mu^{1/2} \quad (1.2)$$

From Equation 1.2, the modeling of $H_o/V_f T$ yields $\mu = n_{V_f}^{1/2}$ or

$$n_{V_f} = \mu^{1/2} \quad (1.3)$$

This defines a model law in terms of n_{V_f} , n_T , μ , λ . The scale parameter $n_{d_{50}}$, may be obtained from curves of V_f versus d (see, e.g., Shore Protection Manual).

For low Reynolds numbers, the Stokes equation for the sediment fall velocity is

$$V_f = \frac{1}{18} \frac{d_{50}^2 g \gamma'}{\nu} \quad (1.4)$$

Preserving the Stokes equation and using the same fluid in the model and the prototype, $n_\nu = 1$,

$$n_{V_f} = n_{d_{50}}^2 n_{\gamma'} \quad (1.5)$$

For the same material in the model and the prototype, $n_{\gamma'} = 1$, Equation (1.5) reduces to upon substitution of Equation (1.3),

$$n_{d_{50}} = \mu^{1/4} \quad (1.6)$$

2. Model Law #2

Eagleson, Glenne and Dracup (1963) concluded that the equilibrium profile shape is a function of the incipient point for sediment movement. This point is determined by the relative magnitudes of the sediment weight and the bed shear stress. A nondimensional ratio of the gravitational force and the shear stress, the densimetric Froude number is defined as $F_* = \mu_* / (g \gamma' d_{50})^{1/2}$. Modeling F_* ,

$$n_{\mu_*}^2 = n_{\gamma'} n_{d_{50}} \quad (2.1)$$

Preserving the bed particle Reynolds number which is defined as $R_{e_s} = \mu_* d_{50} / \nu$ and using the same fluid in the model and the prototype,

$$n_{\mu_*} = \frac{1}{n_{d_{50}}} \quad (2.2)$$

Simplifying Equation 2.2 by means of Equation 2.1,

$$n_{\gamma'} = \frac{1}{n_{d_{50}}^3} \quad (2.3)$$

Preserving the Froude number, $F = V/(gd)^{1/2}$,

$$n_V = \mu^{1/2} \quad (3.5)$$

Upon the substitution of $n_V = \mu^{1/2}$ in Equation 3.4,

$$n_{u_*} = \mu^{1/4} n_T^{-1/4} \quad (3.6)$$

Modeling the bed particle Reynolds number, $n_{u_*} = 1/n_{d_{50}}$, Equation 2.2,

$$n_{d_{50}} = \mu^{-1/4} n_T^{1/4} \quad (3.7)$$

From the modeling of the densimetric Froude number, $n_{u_*}^2 = n_{\gamma} n_{D_{50}}$, Equation 2.1,

$$n_{\gamma} = \frac{\mu^{3/4}}{n_T^{3/4}} \quad (3.8)$$

upon the substitution of the expressions for n_{u_*} , Equation 3.6 and $n_{d_{50}}$, Equation 3.7. For the same material in the model and the prototype, $n_{\gamma} = 1$, $n_T = \mu$. Preserving $H_o/V_f T$, $n_{V_f} = 1$ and subsequently, $n_{d_{50}} = 1$. A kinematic condition proposed by LeMehaute (1970) stipulates that the ratio of the horizontal, V , and vertical velocity, V_f , be scaled as the ratio of the length scales, λ and μ , $n_V/n_{V_f} = \lambda/\mu$. For $n_V = \mu^{1/2}$, Equation 3.5,

$$\lambda = \mu^{3/2} \quad (3.9)$$

4. Model Law #4

Assuming a turbulent boundary layer, the friction factor is defined by Kamphuis (1973) as

$$f = .47 \left(\frac{k_s}{a_\delta} \right)^{3/4} \quad (4.1)$$

Modeling f ,

$$n_f = n_{k_s}^{3/4} n_{a_\delta}^{-3/4} \quad (4.2)$$

The term a_δ is defined as the wave orbital amplitude at the top of the boundary layer. For shallow water waves, the orbital amplitude equals

$$\delta = \frac{HT}{4\pi} \sqrt{\frac{g}{d}} \quad (4.3)$$

The scale factors λ and n_T are modeled similarly in accordance with Equations 1.1 and 1.2 for the modeling of H_o/L_o . By modeling of $H_o/V_f T$,

$$n_{V_f} = \mu^{1/2} \quad (2.4)$$

Again a model law now exists for the general case with $n_{d_{50}}$ determined

from the V_f-d_{50} curve. In this case the same material could even be used in model and prototype provided a different fluid or possibly different temperature is used. For low Reynolds numbers modeling the Stokes equation for fall velocity, $n_{V_f} = n_{d_{50}}^2 \gamma'$,

$$n_{d_{50}} = \mu^{-1/2} \quad (2.5)$$

$$\text{and} \quad n_{\gamma'} = \mu^{3/2} \quad (2.6)$$

upon substitution of Equations 2.3 and 2.4. For this model law, both the sediment specific weight and the size are modeled.

3. Model Law #3

Assuming a laminar boundary layer, the bed shear stress for incipient motion will be formulated differently from Model Law #2 based on the definition of the bed friction factor. The friction factor for a laminar boundary layer for gravity wave flow is expressed by Jonsson (1966) as

$$f = \sqrt{\frac{\pi}{2}} \frac{v^{1/2}}{V\sqrt{T}} \quad (3.1)$$

Modeling f and assuming the same fluid in the model and the prototype,

$$n_f = n_V^{-1} n_T^{-1/2} \quad (3.2)$$

Henderson (1966) defined the bed shear velocity, u_* , as

$$u_* = \frac{f^{1/2}}{\sqrt{8}} V \quad (3.3)$$

Modeling u_* and simplifying per the Equation 3.2 for n_f ,

$$n_{u_*} = n_V^{1/2} n_T^{-1/4} \quad (3.4)$$

Modeling a_δ ,

$$n_{a_\delta} = \mu^{1/2} n_T \quad (4.4)$$

The term k_s is defined as the bottom sand grain roughness and is assumed proportional to the median grain diameter. Defining the scale ratio as k_s as $n_{k_s} = n_{d_{50}}$ and incorporating the relations for n_{k_s} and n_{a_δ} , the expression for n_f , Equation 4.2, reduces to

$$n_f = \frac{n_{d_{50}}^{3/4}}{\mu^{3/8} n_T^{3/4}} \quad (4.5)$$

Modeling the bed shear velocity, $u_* = (f^{1/2}/\sqrt{8}) V$, as previously defined by Henderson (1966),

$$n_{u_*} = n_f^{1/2} n_V \quad (4.6)$$

Preserving the Froude number, $n_V = \mu^{1/2}$, n_{u_*} simplifies to

$$n_{u_*} = \frac{\mu^{5/16} n_{d_{50}}^{3/8}}{n_T^{3/8}} \quad (4.7)$$

upon the substitution of the equations for n_V and n_f . Preserving the bed particle Reynolds number, $n_{u_*} = 1/n_{d_{50}}$, n_{u_*} reduces to

$$n_{d_{50}} = \frac{n_T^{3/11}}{\mu^{5/22}} \quad (4.8)$$

Using the equations, $n_{u_*} = 1/n_{d_{50}}$ which preserves the bed particle Reynolds number and $n_{u_*}^2 = n_\gamma$, $n_{d_{50}}$ which preserves the densimetric Froude number,

$$n_\gamma = \frac{1}{n_{d_{50}}^3} \quad (4.9)$$

Modeling the Stokes equation for the fall velocity, $n_{V_f} = n_{d_{50}}^2 n_\gamma$,

$$n_{V_f} = \frac{1}{n_{d_{50}}} \quad (4.10)$$

per the substitution of $n_{\gamma'}$, Equation 4.9. Expressing n_{V_f} in terms of $n_{d_{50}}$, Equation 4.8,

$$n_{V_f} = \frac{\mu^{5/22}}{n_T^{3/11}} \quad (4.11)$$

Reexpressing the equation for n_{V_f} based on the modeling of the Stokes fall velocity in terms of $n_{d_{50}}$, Equation 4.8 and n_{V_f} , Equation 4.11,

$$n_{\gamma'} = \frac{\mu^{15/22}}{n_T^{9/11}} \quad (4.12)$$

For the modeling of $H_o/V_f T$,

$$n_T = \mu^{17/16} = \mu^{1.0625} \quad (4.13)$$

for the expressions of $n_{H_o} = \mu$ and n_{V_f} , Equation 4.11. Therefore, Equation 4.12 reduces to

$$n_{\gamma'} = \mu^{-0.1875} \quad (4.14)$$

and Equation 4.8 reduces to

$$n_{d_{50}} = \mu^{+0.063} \quad (4.15)$$

For the modeling of the horizontal velocity, $n_V = \lambda/n_T$. Substituting $n_V = \mu^{1/2}$ which models the Froude number and Equation 4.13 for n_T into the expression for n_V ,

$$\lambda = \mu^{25/16} = \mu^{1.5625} \quad (4.16)$$

This model law scales both the grain size and the particle specific weight. For a small scale model, the model grain size would be smaller than the prototype but the specific weight would be larger.

5. Model Law #5

For the same material in the model and the prototype, $n_{\gamma'} = 1$, and for the same median diameter, $n_{d_{50}} = 1$, $n_{V_f} = 1$. Modeling $H_o/V_f T$,

$$n_T = \mu \quad (5.1)$$

Preserving the Froude number,

$$n_V = \mu^{1/2} \quad (5.2)$$

Modeling the horizontal velocity, V ,

$$n_V = \frac{\lambda}{n_T} \quad (5.3)$$

Introducing the expressions for n_T and n_V ,

$$\lambda = \mu^{3/2} \quad (5.4)$$

6. Model Law #6

Open channel flow can be represented by the Chezy equation as

$$V^2 = C_h^2 RS \quad (6.1)$$

where R , the hydraulic radius, equals the water depth, d , for wide channels and S , the slope of the channel bed, equals the change in vertical elevation per horizontal length. Defining the water depth, d , and the slope, S , in terms of λ and μ , the modeling of the Chezy equation yields

$$n_V^2 = n_{C_h}^2 \frac{\mu^2}{\lambda} \quad (6.2)$$

Modeling the Froude number, $n_V = \mu^{1/2}$, and introducing this expression into Equation 6.2,

$$n_{C_h}^2 = \frac{\mu}{\lambda} \quad (6.3)$$

The Chezy coefficient is defined as $C_h^2 = \frac{8g}{f}$. Modeling the Chezy coefficient, $n_{C_h}^2 = 1/n_f$ and substituting Equation 6.3 for n_{C_h} ,

$$n_f = \frac{\mu}{\lambda} \quad (6.4)$$

Modeling the bed shear velocity, u_* ,

$$n_{u_*} = n_f^{1/2} n_V \quad (6.5)$$

Introducing $n_V = \mu^{1/2}$ per the modeling of the Froude number,

$$n_{u_*} = n_f^{1/2} \mu^{1/2} . \quad (6.6)$$

Substituting Equation 6.4 for n_f in Equation 6.6,

$$n_{u_*} = \frac{\mu}{\lambda^{1/2}} . \quad (6.7)$$

Preserving the bed particle Reynolds number, $n_{u_*} = \frac{1}{n_{d_{50}}}$ and substituting this expression into Equation 6.7 for n_{u_*} ,

$$n_{d_{50}} = \frac{\lambda^{1/2}}{\mu} . \quad (6.8)$$

Per the preserving of the densimetric Froude number,

$$n_{u_*}^2 = n_\gamma n_{d_{50}} . \quad (6.9)$$

Introducing Equations 6.7 and 6.8 into Equation 6.9,

$$n_\gamma = \frac{\mu^3}{\gamma^{3/2}} \quad (6.10)$$

Substituting Equations 6.8 and 6.10 into the model expression for the Stokes fall velocity, $n_{V_f} = n_{d_{50}}^2 n_\gamma$,

$$n_{V_f} = \frac{\mu}{\lambda^{1/2}} \quad (6.11)$$

Preserving $H_o/V_f T$,

$$n_T = \lambda^{1/2} . \quad (6.12)$$

For the same material in the model and the prototype, $n_\gamma = 1$, Equation 6.10 reduces to

$$\lambda = \mu^2 \quad (6.13)$$

Equation 6.8 for $n_{d_{50}}$ reduces to $n_{d_{50}} = 1$ and Equation 6.12 for n_T reduces to

$$n_T = \mu . \quad (6.14)$$

7. Model Law #7

Preserving the wave steepness ratio, H_o/L_o ,

$$\mu = \lambda . \quad (7.1)$$

For the same material in the model and the prototype, $n_p = 1$, and the same grain size, $n_{d_{50}} = 1$, $n_{V_f} = 1$ and the modeling of γ'

$H_o/V_f T$ yields $\mu = n_T$. In this case, however, the Froude number is not modeled.

Acknowledgements

This work was partially sponsored by the Office of Naval Research Geography Program.

CHAPTER 76

BEACH PROFILES AT TORREY PINES, CALIFORNIA

David G. Aubrey, Douglas L. Inman and Charles E. Nordstrom
Scripps Institution of Oceanography, University of California
La Jolla, California 92093

ABSTRACT

Beach profiles have been measured at Torrey Pines Beach, California for four years and correlated with tides and accurate spectral estimates of the incident wave field. Characteristic equilibrium beach profiles persist for time spans of up to at least two weeks in response to periods of uniform incident waves. These changes in the beach profiles are primarily due to on-offshore sediment transport which can be related to variations in wave characteristics and tidal phase. The most rapid readjustment of the beach profile occurs during high wave energy conditions coincident with spring tides. Alternatively, the highest berm building is associated with moderate to low waves that coincide with spring tides.

INTRODUCTION

The movement of sediment in the nearshore zone can be divided into two distinct directional modes: transport along the shore and transport onshore-offshore. It is convenient to think in terms of these two orthogonal modes when evaluating the erosion and accretion of sediment on a coast exposed to waves having seasonal variations in both energy and direction. Prediction of the longshore transport of sediment as a function of incident wave parameters is possible using empirical relations (e.g., Inman, Komar and Bowen, 1968; Galvin, 1976) and quasi-theoretical considerations (Inman and Bagnold, 1963; Komar and Inman, 1970; and Longuet-Higgins, 1970). However, at this time it is not possible to predict the magnitude of onshore-offshore sediment motion given a knowledge of sediment characteristics, tidal variations, and incident wave characteristics. The present study represents an attempt to provide empirical correlations between incident wave and tidal characteristics and onshore-offshore sediment motion.

It is necessary initially to determine whether the concept of an equilibrium beach profile is valid in a natural environment. The equilibrium energy profile is defined by Inman and Bagnold (1963) as the profile (depth as a function of distance offshore) which would eventually be attained when a nearshore area with a particular set of environmental characteristics (e.g., sand size, shelf width, and slope) is acted upon by a given set of driving forces (e.g., waves, currents, and tides). The equilibrium concept implies that the profile has ceased to vary with time and the driving force is constant. The equilibrium profile has been generated in the laboratory, but never fully documented in the field. Winant and Aubrey (1976) and Winant, Inman and Nordstrom (1975) verify the existence of characteristic stable beach forms for summer and winter wave conditions at Torrey Pines Beach, California, by analyzing the profiles using the objective analytical technique of empirical eigenfunctions.

The seasonal onshore-offshore motion of sediment has been previously described by numerous investigators (e.g., Shepard, 1950; Zeigler, et al, 1959; Gorsline, 1966; Sonu and Van Beek, 1971). Shepard (1950) measured seasonal beach changes along the Southern California beaches of the order of two meters vertically. A comprehensive study by Nordstrom and Inman (1975) along a section of coastline north of La Jolla, California, described changes at the location of the summer berm and winter bar of the order of 1 meter. Other researchers have found similar changes in different geographic locations. The beaches cited in the above references respond to the energetic waves characteristic of winter conditions by eroding the berm and moving the sediment offshore. The less energetic waves typical of summer conditions move sediment shoreward, building up the berm. Besides these seasonal large scale motions, the beach responds to smaller time scale events such as storms or long periods of extremely low wave energy. No field studies to date have been able to adequately quantify these wave-related sediment redistributions.

Laboratory studies have been undertaken in an attempt to delineate the erosional and accretionary regimes. These studies emphasize the importance of the wave steepness in determining the form of the profile. The results are given in terms of a critical wave steepness: for wave steepness above this value, a barred (no berm) profile develops, while for a wave steepness below this critical value, a profile with a berm develops (Johnson, 1949; Rector, 1954; Scott, 1954; Watts, 1954; Saville, 1957). The laboratory results are not directly applicable to natural beaches because of an inability to correctly scale both kinematics and dynamics in laboratory experiments. Kemp (1961) suggested that the critical wave steepness is inversely proportional to the wave period, so the critical steepness on natural beaches with a 10 second wave period would be only 10 percent of the critical steepness of a one second wave.

Field experiments have not yet defined the critical wave steepness for natural beaches, primarily because intensive beach profiling projects have not been complemented by good wave measurements. The general observation is that large waves create a barred profile, but the effect of wave period is uncertain. The present study attempts to determine empirically the effect of seasonally varying incident waves on a fine-grained sand beach at Torrey Pines Beach, California. Figure 1 shows the location of the study area. The beach is a long, relatively straight stretch of coastline backed by 100 meter high cliffs. In general, the cliffs contribute little to the sediment budget in the area. The net direction of longshore transport is to the south, where sediment is lost down the La Jolla and Scripps Submarine Canyon systems (Inman, Nordstrom, and Flick, 1976). The direction of littoral drift is seasonally dependent. During the winter, the waves are primarily from the north, while during the summer, there is a high incidence of waves coming from the south. The mean energy density for the area, as defined by the variance, $\langle \eta^2 \rangle$, is approximately 550 cm^2 ; where the variance is related to the energy per unit surface area of the waves $E = \rho g \langle \eta^2 \rangle = 1/8 \rho g H_{\text{rms}}^2$. This is equivalent to a root-mean-square wave height of 66 cm.

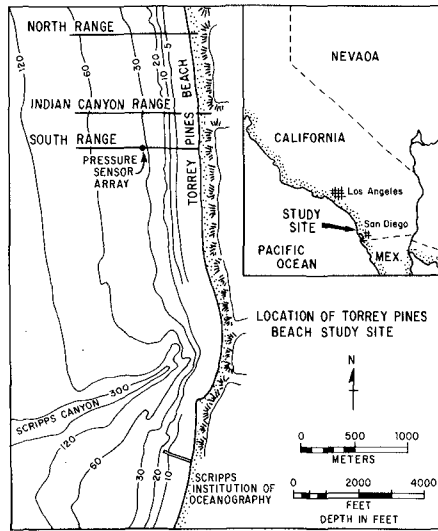


Figure 1. Location map of Torrey Pines Beach, California, showing position of the three rangelines (from Nordstrom and Inman, 1975).

DATA COLLECTION

The profile data was taken over a four year period along the three rangelines shown in Figure 1. For the first two years, the profile data was taken at monthly intervals, while in the succeeding two years, the profile data was taken at daily, weekly, or biweekly intervals. The surveying technique is described in Nordstrom and Inman (1975). Briefly, the surveys consist of an onshore profile extending from the beach backshore at the base of the sea cliffs out to a depth of approximately 1.5 meters. The profile is taken at low tide with a surveyor's rod and transit. Since the survey line is well defined by rangeline marker, this part of the survey is extremely accurate. At least once a month, an offshore survey is also made on the same day as one of the onshore surveys. The method is shown schematically in Figure 2. At high tide, a fathometer survey is made along the rangelines. The boat position is defined by the rangeline and a sextant angle. As soon as practical after the fathometer survey, scuba divers measure a series of arrays of four brass reference rods extending from the bottom at depths of 5, 7, 10, 15, and 20 meters along each rangeline. Since the change in length of the reference rods from survey to survey is an accurate measure of the actual change in sand level, the fathogram can be corrected to minimize the errors that are inherent in fathometer surveys (Inman, 1953). This surveying combination is sufficient to define almost all portions of the profile. During periods of intense wave activity, it is not always possible to measure the profile in the breaker zone, so there is some uncertainty about the profile at this point while the storm waves are present.

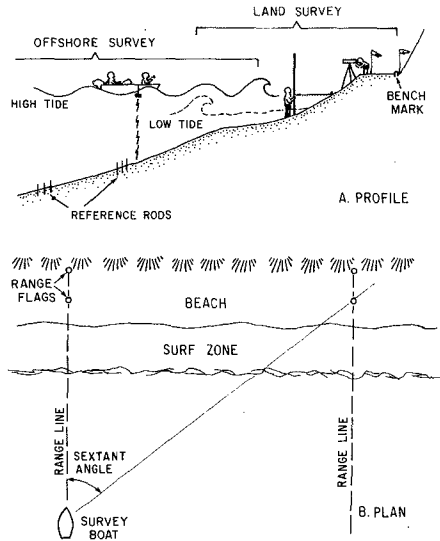


Figure 2. Schematic diagram of the onshore-offshore profiling technique employed in this study (from Nordstrom and Inman, 1975).

The wave data consists of both frequency and directional spectral estimates. The wave measuring system was described by Lowe, Inman and Brush (1972). Data is collected at one of the shelf stations of the Shelf and Shore (SAS) System depicted in Figure 3, and telemetered directly to the laboratory four times a day, each run having an hour duration. The data is automatically stored on digital magnetic tape. The shelf station consists of a surface piercing buoyant spar which is connected by a universal joint to an anchor assembly. The spar contains the transmitting package, which transmits the output of two accelerometers, mounted on the spar, and the output from a linear array of pressure sensors mounted on the bottom. Both frequency and directional spectral estimates are derived from the pressure sensor array (Pawka, Inman, Lowe and Holmes, 1976).

The shelf station is located in 10 meters of water off Torrey Pines Beach. The wave data cited in this study is the energy measured at the 10 meter depth location, corrected to energy density at the water surface. Since directional data were obtained, the resolution into on-offshore and longshore components, and the effect of breaker characteristics will be considered in a later paper. The solid lines in the figures to follow which refer to wave energy represent the energy variance, $\langle \eta^2 \rangle$, as measured by the SAS system. The dashed lines were taken from visual wave observations of breaker height at Torrey Pines Beach, at times when the SAS system was inoperative. The dashed values represent estimates of the energy density at the 10 meter depth calculated from the observed breaker heights.

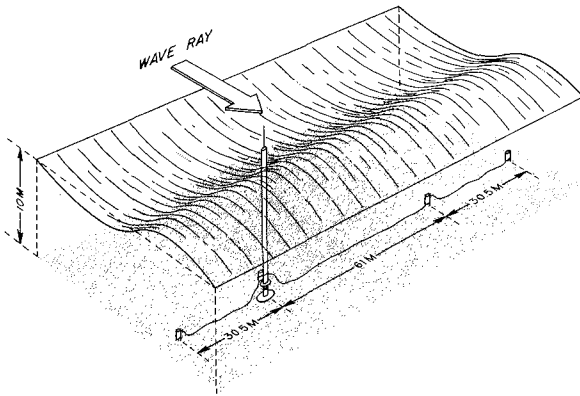


Figure 3. Shelf station portion of the Shelf and Shore (SAS) System used to collect frequency and directional spectral estimates. The pressure sensors are aligned in a linear array parallel to the beach in a water depth of 10 meters (from Pawka, et al, 1976).

The beach profile data is stored on magnetic tapes, and is processed on an Interdata Model 70 minicomputer. The volume calculations plotted on the following figures were evaluated by the computer. Tide data was taken from local tide calendars.

RESULTS

As a further test of the validity of the concept of equilibrium profiles on natural beaches, a series of profiles associated with high and low energy waves are compared. Figures 4 and 5 show equilibrium beach configurations for a high energy wave condition (winter type) and a lower wave energy condition (summer type), respectively. These profiles were taken at Indian Canyon Range. Figure 4 shows a sequence of three profiles taken over a two week time period during the winter of 1975-76. The wave energy was high immediately preceding each of the surveys. On 30 December 1975, there was an intense winter storm with an energy variance of 2100 cm^2 . Prior to the 9 January 1976 survey, wave energies were greater than 600 cm^2 , while before the 15 January 1976 survey, wave energies were about 750 cm^2 . The maximum change in sand volume above mean sea level (MSL) between any of the two profiles during this two week period was 2.5 m^3 per meter length of beach. It has been established that the seasonal summer to winter beach changes for this beach are about $120 \text{ m}^3/\text{m}$ beach length (Nordstrom and Inman, 1975). Thus, this small change implies that after the storm eroded the beach on 30 December 1975, the beach above MSL maintained itself in a constant, or equilibrium, configuration.

Figure 5 shows a sequence of three profiles taken over a two week period in August 1975, showing an equilibrium configuration for summer conditions. The maximum volume change among these profiles was $5 \text{ m}^3/\text{m}$ of beach length. During this time period, the waves were uniform and had an average energy density of about 250 cm^2 . Although a little accretion occurred at depths of approximately -2 meters, the beach face slope was extremely constant.

Both of these examples demonstrate that in natural beach environments, a dynamic equilibrium can be established given the same input wave conditions acting on a stable profile over a period of time. The presence of tidal variations complicates the situation, but does not alter the essential concept of a dynamic beach equilibrium.

INDIAN CANYON RANGE

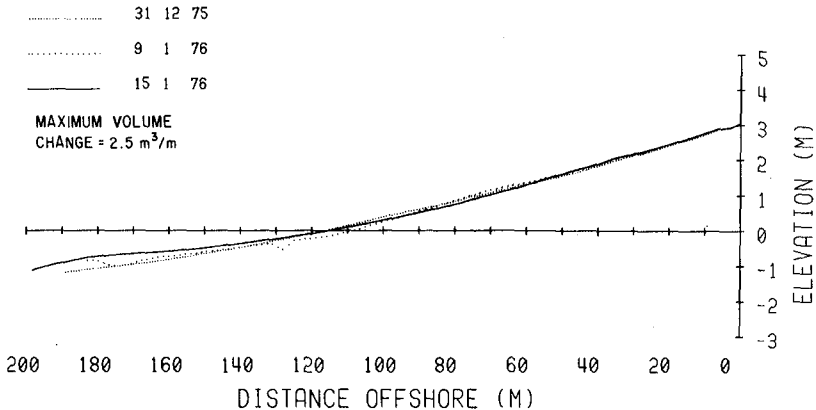


Figure 4. Typical equilibrium beach profiles for Torrey Pines Beach during winter wave conditions.

The second part of this study examines the response of the beach to varying wave and tidal conditions. Figures 6, 7, and 9 show three examples of the response of the beach to these varying forcing conditions. Figure 6 covers the time period from November 1973 through March 1974. The top part of the figure is a plot of the sand volume changes on the beach for the three ranges. The sand volume changes are those above a datum of 1 meter below mean sea level, and are relative to the surveys of 6 June 1972 as reported in Nordstrom and Inman (1975). The sand volume change is calculated from the backshore out to approximately 1 meter depth in these figures. The middle part of the figure plots the maximum daily tidal range (the tide at Torrey Pines is mixed with a pronounced diurnal inequality). The lower part of the figure is a plot of the wave energy variance $\langle \eta^2 \rangle$. The storms during this period were intense, and pronounced beach erosion occurred. After the storms of late December 1973, the beach eroded along all three ranges, and a winter-type profile was established. After that, North and South Ranges remained at a nearly constant level, while Indian Canyon continued to erode due to the action of rainwater flowing down the canyon immediately behind the rangeline. The maximum erosion is normally associated with the coincidence of large waves and high spring tide. The lower energy waves in late March were accompanied by accretion at all three ranges.

INDIAN CANYON RANGE

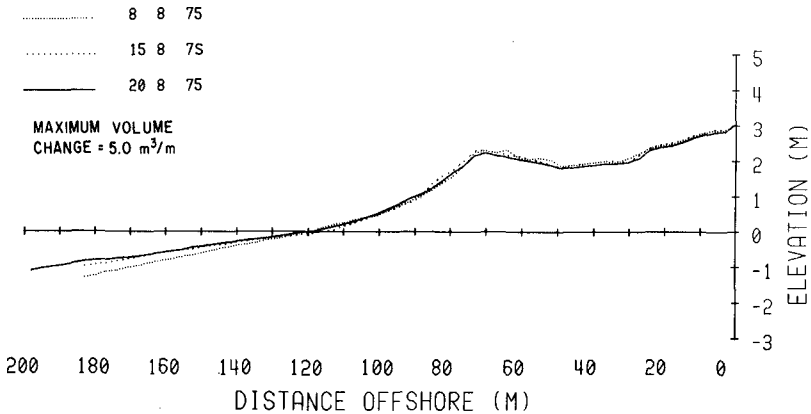


Figure 5. Typical equilibrium beach profiles for Torrey Pines Beach during summer wave conditions.

Figure 7 shows the gradual accretion of a summer beach by the lower energy waves that occurred during the spring and summer of 1975. As before, the bottom portion of the figure shows the wave energy density. The maximum daily tidal range is shown in the middle part of the figure, while the top part shows the sand volume changes for all three ranges. Several large wave events occurred during this time period. Except for these five events, the energy density is low. The volume changes indicate a gradual accretion on the beaches. The slow accretion during the summer is due in part to the periods of erosion of the beach associated with the occasional large waves of summer. Note that the high energy waves of 20-21 July 1975 which coincided with a spring tide caused erosion at all three ranges. The erosion accompanying the large waves of 5 May, 21 May, and 18 June 1975 was minimized in part because the large waves were coincident with neap tides, so that the waves were not as effective in eroding the berm. Had the tidal range been large, more erosion would have taken place.

Figure 8 shows a series of profiles measured from April through July 1975 at South Range. The berm that is evident in the 24 April 1975 (24-4-75) profile is gone in the 7 May profile, following the passage of the storm of 5 May 1975. Between 4 June and 27 June, there is a net progressive accretion of sand on the beach face, and a migration of sand shoreward as shown by the middle portion of Figure 8. The three profiles in July 1975 illustrate the pronounced berm accretion associated with spring tides and moderate wave action (compare profiles 8-7-75 and 15-7-75); and the subsequent rapid erosion associated with a brief period of high waves on 20 July 1975 (see profile 22-7-75).

BEACH FACE SAND VOLUME CHANGES

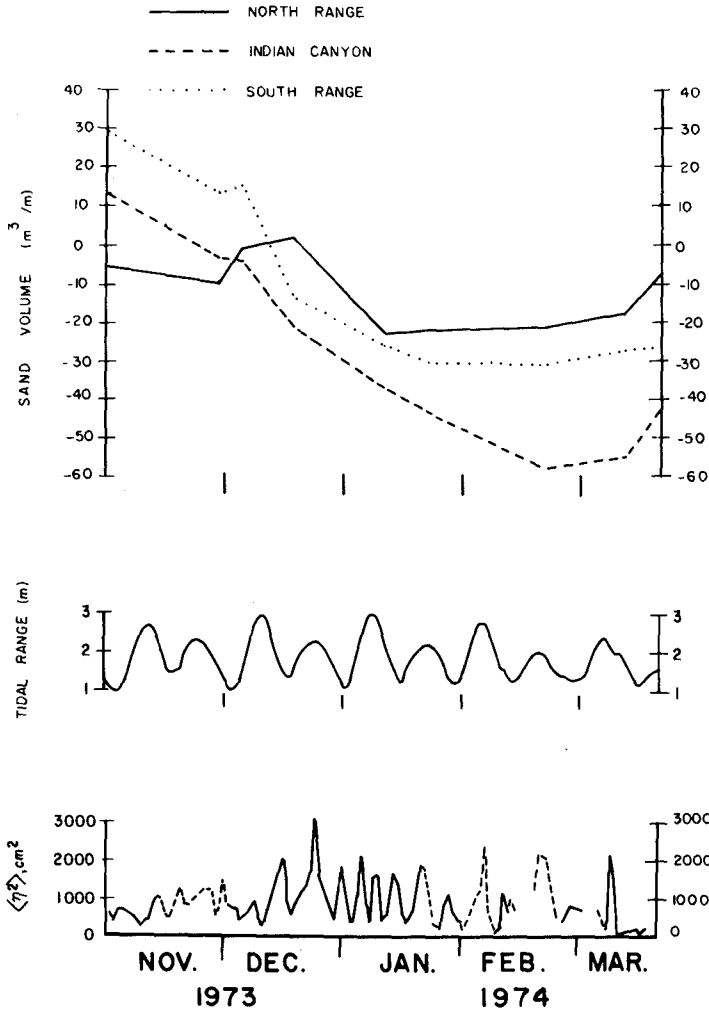


Figure 6. Changes in sand volume above the datum of 1 m below mean sea level relative to the surveys of 6 June 1972, compared with the maximum daily range and total wave energy density for the period of November 1973 through March 1974. The data for this figure was obtained from Nordstrom & Inman (1975).

BEACH FACE SAND VOLUME CHANGES

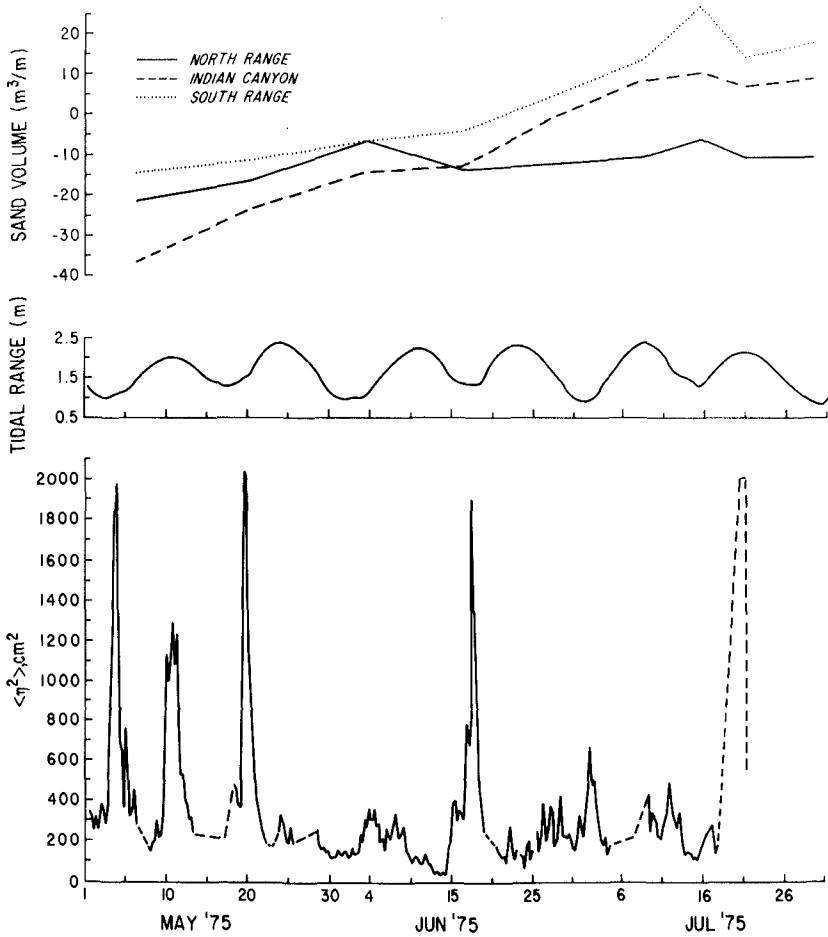


Figure 7. Changes in sand volume above the datum of 1 m below mean sea level relative to the surveys of 6 June 1972, compared with the maximum daily tidal range and total wave energy density for the period of May through July 1975.

SOUTH RANGE

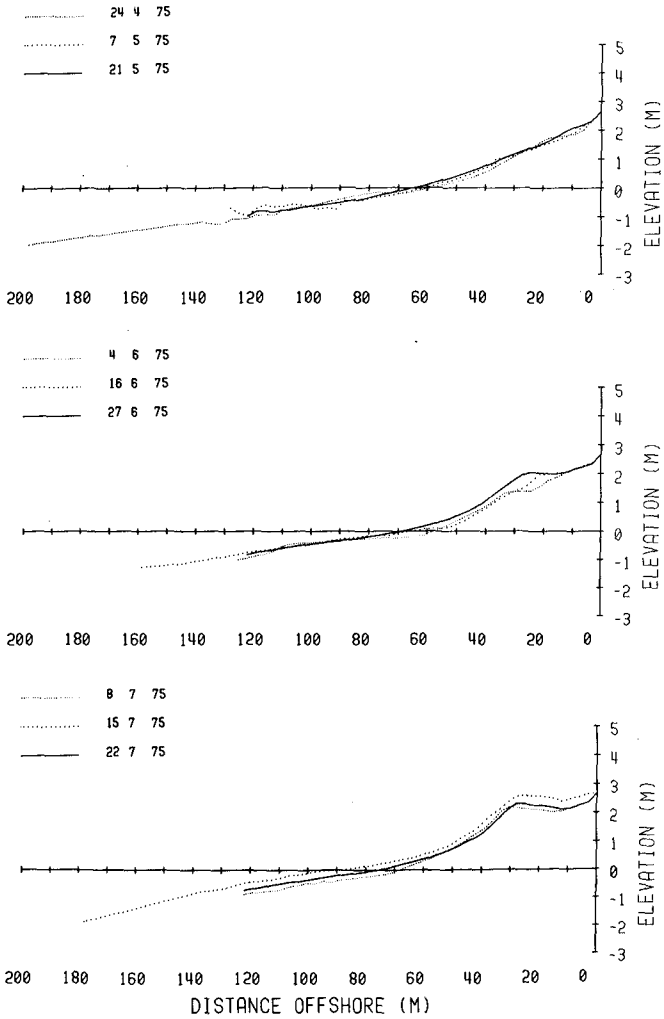


Figure 8. Sequence of beach profiles at South Range for period of May through July 1975.

Figure 9 shows the beach response for the period of December 1975 through February 1976. As before, the lower portion of the figure shows the wave energy density, the middle portion shows the maximum daily tidal range, and the upper portion shows the sand volume changes for the three ranges. Two distinct storms dominate the wave activity, one on 27 December and one on 30 December 1975. The first of these occurred during a period of neap tides and was accompanied by erosion at all three ranges. The second storm occurred during spring tides and was accompanied by more intense erosion at all three ranges. Following these storms, the volume changes at North and South Ranges were similar, and responded to the lower wave energies in the aftermath of the storms. Indian Canyon Range showed some erosion in mid-January, contrary to the trend at the other two ranges. This was due to erosion from rain runoff channeled onto the beach by the canyon behind the rangeline. The rain was accompanied by low energy waves, but the stream discharge was sufficient to erode the beach at Indian Canyon Range. Stream discharge across the beach was also responsible for the erosion in mid-February 1976 at Indian Canyon Range. North and South Ranges both eroded following the coincidence of large waves and spring tides on 14 February 1976. Indian Canyon showed an apparent accretion as the cut in the beach due to rain runoff was beginning to fill in.

Figure 10 shows a sequence of beach profiles at South Range for this same time period. The erosion associated with the storm of 30 December 1975 is apparent in the upper plot of the figure. The berm was totally eroded and the material deposited at a depth greater than -2 meters. The beach face slope decreased during the storm. The slight erosion associated with the 27 December 1975 storm can also be seen. The central plot shows that there was little change in the profile during January 1976, as the wave energy was similar during this time span. The lower plot shows a migration of sediment shoreward between 28 January and 11 February 1976, while there was slight erosion accompanying the larger waves of 14 February 1976. Similar plots for North Range and Indian Canyon Range show the same trends, except for the aforementioned erosion at Indian Canyon due to stream discharge across the beach.

CONCLUSIONS

A condition of approximate dynamic equilibrium is attained on natural sand beaches when the incident wave field remains approximately uniform over sufficiently long periods of time. Once achieved, a condition of approximate equilibrium may exist for periods of two weeks or longer, as evidenced by a minimal redistribution of sediment of 2 to 5 m³ per meter length of beach. Also, the variation in the distribution of sediment along a range perpendicular to the beach can be explained in large part by assuming these variations are due to onshore-offshore movement of sediment, and not a divergence or convergence in the longshore drift. Furthermore, these changes are correlated with the input wave conditions; in this paper they were examined only in terms of the total energy density of the waves, $\langle \eta^2 \rangle$.

The profile associated with large, winter-type waves is most rapidly achieved when large waves are coincident with spring tides. Large waves coincident with neap tides do not maximize the foreshore erosion.

Waves of low energy density build up the beach face and berm, creating a steep beach face slope. The most pronounced berm accretion is associated

BEACH FACE SAND VOLUME CHANGES

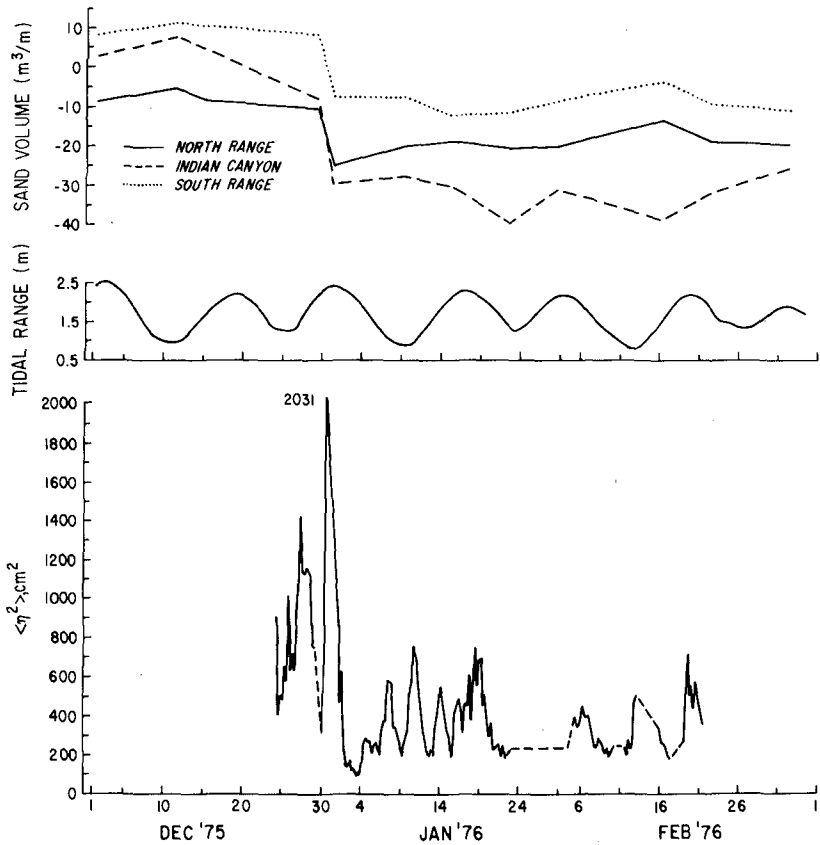


Figure 9. Changes in sand volume above the datum of 1 m below mean sea level relative to the surveys of 6 June 1972, compared with the maximum daily tidal range and total energy density for the period of December 1975 through February 1976.

SOUTH RANGE

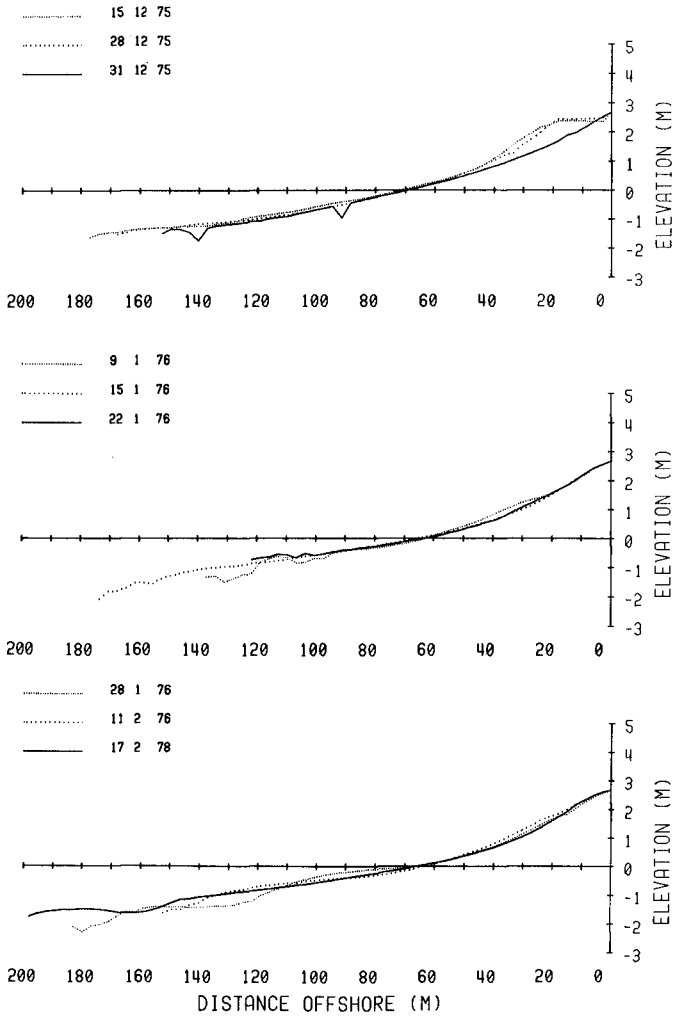


Figure 10. Sequence of beach profiles at South Range for period of December 1975, through February 1976.

with the coincidence of low to moderate wave intensity and spring tides. The profile which is associated with these low waves is rapidly modified by changing wave conditions such as storms.

ACKNOWLEDGMENTS

This study was supported by the Office of Naval Research, Geography Programs, under contract with the University of California.

REFERENCES

- Galvin, C. J. Jr. and P. Vitale, 1976, "Longshore transport prediction -SPM 1973 revision", Abstracts Volume, 15th Int. Conf. on Coastal Eng., Amer. Soc. Civil Eng., p 133-35.
- Gorsline, D. S., 1966, "Dynamic characteristics of west Florida Gulf Coast beaches", Marine Geol., vol 4, p 187-206.
- Inman, D. L., 1953, "Areal and seasonal variations in beach and nearshore sediments at La Jolla, California", U. S. Army Corps of Eng., Beach Erosion Board, Tech Memo 39, 82 pp.
- Inman, D. L. and R. A. Bagnold, 1963, "Littoral Processes", p 529-553 in M. N. Hill (ed) The Sea, vol 3, The Earth Beneath the Sea, Interscience Publ., 963 pp.
- Inman, D. L., P. D. Komar and A. J. Bowen, 1969, "Longshore transport of sand", Proc. 11th Conf. on Coastal Eng., Amer. Soc. Civil Eng., vol 1, p 298-306.
- Inman, D. L., C. E. Nordstrom, and R. E. Flick, 1976, "Currents in submarine canyons: an air-sea-land interaction", p 275-310, Annual Review of Fluid Mech., vol 8, 418 pp.
- Johnson, J. W., 1949, "Scale effects in hydraulic models involving wave motion", Trans. Amer. Geophys. Union, vol 30, p 517-25.
- Kemp, P. H., 1961, "The relationship between wave action and beach profile characteristics", Proc. 7th Conf. on Coastal Eng., Amer. Soc. Civil Eng., p 262-77.
- Komar, P. D. and D. L. Inman, 1970, "Longshore sand transport on beaches", Jour. Geophys. Res., vol 75, no 30, p 5914-27.
- Longuet-Higgins, M. S., 1970, "Longshore currents generated by obliquely incident sea waves, parts 1 and 2", Jour. Geophys. Res., vol 75, no 33, p 6778-6801.
- Lowe, R. L., D. L. Inman, and B. M. Brush, 1972, "Simultaneous data system for instrumenting the shelf", Proc. 13th Conf. on Coastal Eng., Amer. Soc. Civil Eng., p 95-112.

- Nordstrom, C. E. and D. L. Inman, 1975, "Sand level changes on Torrey Pines Beach, California", U. S. Army Corps of Eng., Coastal Eng. Res. Center, Misc. Paper No 11-75, 166 pp.
- Pawka, S. S., D. L. Inman, R. L. Lowe, and L. C. Holmes, 1976, "Wave climate at Torrey Pines Beach, California", U. S. Army Corps of Eng., Coastal Eng. Res. Center, Tech Paper No 76-5, 372 pp.
- Rector, R. L., 1954, "Laboratory study of the equilibrium profile of beaches", U. S. Army Corps of Eng., Beach Erosion Board, Tech Memo No 41, 38 pp.
- Saville, T., 1957, "Scale effects in two-dimensional beach studies", Int. Assoc. Hydraulic. Res., Lisbon, Portugal.
- Scott, T., 1954, "Sand movement by waves", U. S. Army Corps of Eng., Beach Erosion Board, Tech Memo No 48, 37 pp.
- Shepard, F. P., 1950, "Beach cycles in Southern California", U. S. Army Corps of Eng., Beach Erosion Board, Tech Memo No 20, 26 pp.
- Sonu, C. J. and J. L. Van Beek, 1971, "Systematic beach changes on the outer banks, North Carolina", Jour. Geol., vol 79, p 416-425.
- Watts, G. M., 1954, "Laboratory study on the effect of varying wave periods on the beach profiles", U. S. Army Corps of Eng., Beach Erosion Board, Tech Memo No 53, 21 pp.
- Winant, C. D. and D. G. Aubrey, 1976, "Stability and impulse response of empirical eigenfunctions", Proc. 15th Int. Conf. on Coastal Eng., Amer. Soc. Civil Eng.
- Winant, C. D., D. L. Inman, and C. E. Nordstrom, 1975, "Description of seasonal beach changes using empirical eigenfunctions", Jour. Geophys. Res., vol 80, no 15, p 1979-86.
- Ziegler, J. M., C. R. Hayes, and S. D. Tuttle, 1959, "Beach changes during storms on outer Cape Cod, Massachusetts", Jour of Geol., vol 67, no 3, p 318-336.

CHAPTER 77

STABILITY AND IMPULSE RESPONSE OF EMPIRICAL EIGENFUNCTIONS

Clinton D. Winant and David G. Aubrey
Scripps Institution of Oceanography, University of California
La Jolla, California 92093

ABSTRACT

The statistical method of empirical eigenfunctions has been applied to four years of beach profile data. The eigenfunctions associated with the three largest eigenvalues are shown to be stable for data sets of one, two, three, and four years length, and they correctly describe beach changes caused by storm activity. The usefulness of the eigenfunction representation is confirmed as a concise means of representing beach profile variability.

INTRODUCTION

The onshore-offshore movement of nearshore sediments in response to changing incident wave energy makes an important contribution to coastal zone variability. The basic motivation for this paper is to concisely describe the nearshore variability associated with selected beach profiles by means of empirical orthogonal eigenfunctions. In this manner the seasonal onshore-offshore movement of sediment can be distinguished from shorter-term changes in beach profiles. In addition, the method has the advantage of describing all of the variability of the beach profiles by means of just a few simple functions.

The data set consists of four years of beach profile data taken at Torrey Pines Beach, California, at monthly intervals. These profiles were taken by the method described by Nordstrom and Inman (1975), and include measurements from the backshore out to a depth of 20 meters. The study location is a fine-grained sand beach approximately 3 km north of Scripps Institution of Oceanography. The beach is straight with uncomplicated offshore bathymetry exposed to wave energy coming from all offshore quadrants.

Figures 1 and 2 illustrate the magnitude of the seasonal changes in Southern California. Figure 1 shows a portion of the beach in La Jolla at the end of winter, 1975, when the "winter" beach was fully developed. The rocks are exposed approximately one meter. Figure 2 shows the same beach at the end of summer, 1974, when the "summer" beach was fully developed; the rocks are completely covered with sand.

More quantitatively, seasonal changes at North Range, Torrey Pines Beach, are shown in Figure 3 for two successive winter and summer profiles. The summer berm is built up about one meter above the sand level present at the same place during the winter. Similarly, the bar at a depth of 5 meters builds up approximately one meter. These seasonal trends can be obscured by short-term events, such as storms or periods of extremely low wave energy. The method of empirical eigenfunctions can be used to distinguish between variability on these different time scales.



Figure 1. Beach in La Jolla in winter of 1975 with rocks exposed one meter.



Figure 2. Beach in La Jolla in summer of 1974 with rocks fully covered with sand.

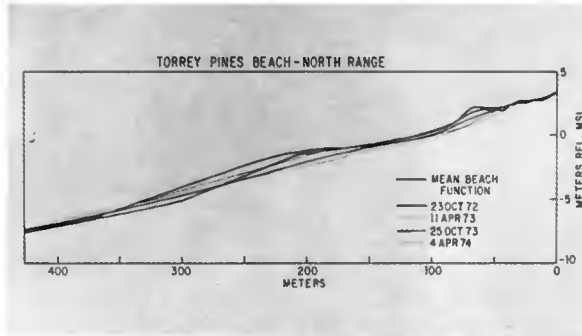


Figure 3. Comparison of winter and summer beach profiles showing seasonal erosion and accretion of sand.

An earlier attempt to depict the seasonal variability of beach profiles using an objective statistical technique was described in Winant, Inman and Nordstrom (1975). The method of empirical eigenfunctions was used to describe the first few modes of variability in two and one-half years of beach profile data taken at monthly intervals. This data set was subsequently expanded to four years (Aubrey, Inman, and Nordstrom, 1976). Over 99.75% of the variability of the data can be accounted for by the three eigenfunctions associated with the three largest eigenvalues. Figure 4 shows the spatial and temporal variation of these eigenfunctions. The first eigenfunction is the mean beach function which reflects the mean beach level. Its time dependence is nearly constant. The second function is the bar-berm function, which shows a large maximum at the location of the summer berm as well as a minimum in the area of the winter bar. The time dependence of this function shows a one year periodicity. The third function is the terrace function, which shows a broad maximum over the low-tide terrace. Its time dependence cannot be simply interpreted.

The present paper addresses two problems not considered in previous work. In order to usefully represent beach variability, the spatial and temporal behavior of the eigenfunctions must be stable with respect to various data sample lengths. Data sets of one, two, three, and four years of beach profiles are examined, and their eigenfunctions are compared. In addition, the first few eigenfunctions should correctly yield the magnitude of beach erosion due to storm waves. This point is investigated by analyzing the first winter storm in October 1974, and its effect on the beach.

STATISTICAL METHOD

One seeks to represent the variability of the beach profile data in terms of a set of orthogonal functions. Obviously any one of a number of such orthogonal series can be generated, one example being a Fourier series. One could then ascribe the variability associated with a one year period to the seasonal variations. Unfortunately, there is no *a priori* reason to suspect that the seasonal dependence of onshore-offshore sand movement is sinusoidal. In fact, there is evidence to the contrary, as when the beach erodes rapidly as the first winter storm waves erode the "summer" beach.

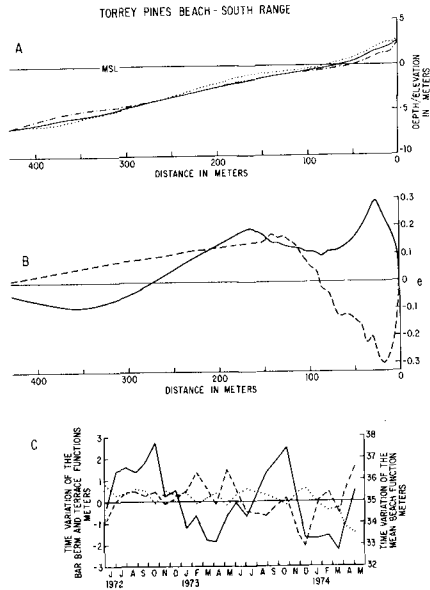


Figure 4. Spatial and temporal dependence of the first three eigenfunctions for a two year period. (a) solid line, mean beach function; dash-dot line, profile of 11 April 1973; and dotted line, profile of 23 October 1972. (b) solid line, bar-berm function; and broken line, terrace function. (c) time variation of bar-berm function (solid line), terrace function (broken line), and mean beach function (dotted line).

A better choice is a set of empirical eigenfunctions which most concisely describe the beach profile variability. The properties of these functions have been summarized by Davis (1976):

(a) They provide the most dense representation of a data set in the sense that the first n terms in the expansion represent more of the data variability than the first n terms of any other orthogonal expansion.

(b) Both the spatial and temporal eigenfunctions are orthonormal sets, so that each corresponding set (λ_n, c_n, e_n) may be regarded as representing a mode of variability which is uncorrelated with any other mode.

The method has been described by Winant, et al (1975). In brief, one seeks an eigenfunction expansion in the form

$$h_{xt} = \sum_n c_{nt} e_{nx} (\lambda_n n_t)^{\frac{1}{2}}$$

where h_{xt} are the beach profile data, c_{nt} represent the temporal eigenfunctions,

e_{n_x} represent the spatial eigenfunctions, n_x represents the number of data points per profile, n_t represents the number of different profiles, and the λ_n are the eigenvalues. In this study, $n_x = 51$ and $n_t = 46$.

The spatial correlation matrix A is formed by the elements

$$a_{ij} = \frac{1}{n_t} \sum_{t=1}^{n_t} h_{it} h_{jt}$$

Similarly, a time correlation matrix B is formed with the elements

$$b_{ij} = \frac{1}{n_t} \sum_{x=1}^{n_x} h_{xi} h_{xj}$$

Both A and B are real symmetric matrices with only positive real eigenvalues. In fact, A and B can be easily shown to have the same non-zero eigenvalues λ_n . The functions e_n then are the eigenvectors of A and the functions c_n are the eigenvectors of B:

$$Ae_n = \lambda_n e_n$$

$$Bc_n = \lambda_n c_n$$

The physical interpretation of the first few of these eigenfunctions has been previously discussed by Winant, et al (1975).

STABILITY OF THE EIGENFUNCTION REPRESENTATION

In order to evaluate the stability of the eigenfunction representation, the spatial eigenvectors were calculated for data sets of one, two, three, and four years length, while the temporal eigenvectors were calculated for data sample lengths of two years and four years. If the eigenfunctions are to accurately represent the beach variability, they should exhibit similar features for the different data sets.

The results of the analysis for the mean beach function are shown in Figure 5. The spatial eigenvectors for the four different data sets are nearly indistinguishable, so this function has no dependence on the length of the data sample. Figures 6 and 7 show the time dependence of the first three eigenfunctions. Figure 6 is for a two year data set; Figure 7 is for a four year data set. The time dependence of the mean beach function is almost constant and is independent of the length of the data set.

Table 1 shows the percentage of the total mean square value of the data associated with each of the first five eigenvalues. The percentage represented by the eigenvalue associated with the mean beach function is essentially independent of the length of the data set. This suggests that the mean

beach function is constant at North Range. No appreciable net erosion or accretion is seen in this function for the four year period.

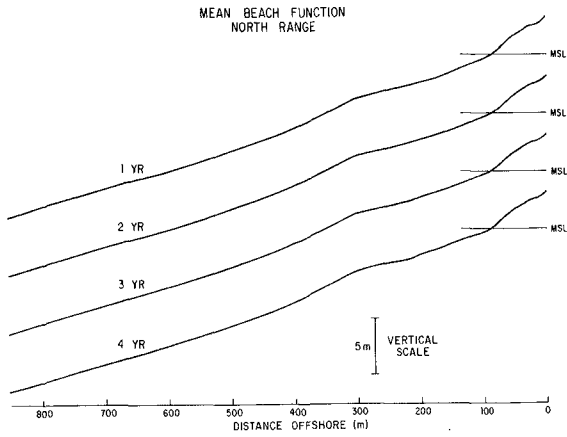


Figure 5. Spatial dependence of mean beach function for data sets at one, two, three, and four years length.

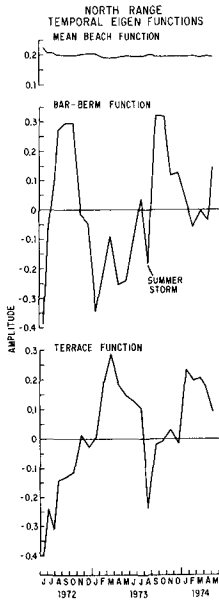


Figure 6. Temporal dependence of first three eigenfunctions for a two year data set.

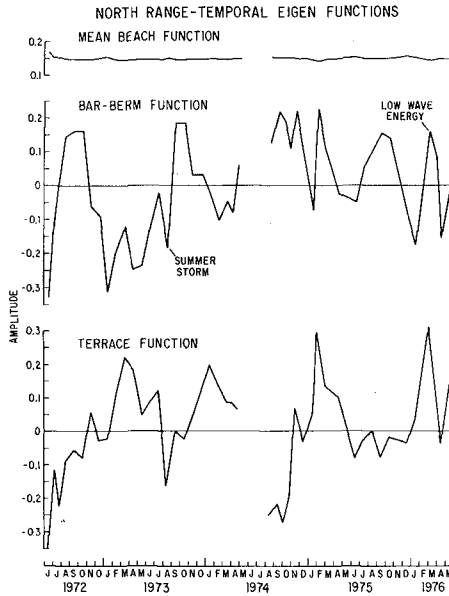


Figure 7. Temporal dependence of first three eigenfunctions for a four year data set.

Table 1. Results of Eigenfunction Analysis. The numbers describe the percentage of the total mean square value of the data associated with each of the five largest eigenvalues.

	One Year	Two Year	Three Year	Four Year
MEAN BEACH FUNCTION	99.33	99.32	99.39	99.43
BAR-BERM FUNCTION	0.30	0.24	0.27	0.24
TERRACE FUNCTION	0.21	0.17	0.18	0.16
EIGENVALUE 4	0.07	0.06	0.07	0.07
EIGENVALUE 5	0.04	0.03	0.03	0.03

The results for the spatial dependence of the bar-berm function are shown in Figure 8 where this function is plotted for each of the four data sets. The shape of the function is the same, except for the tendency of the extrema to broaden. This broadening occurs because the summer berm and winter bar do not form in the identical locations every year. The magnitude of this function also varies somewhat, reflecting the variability in heights of the berms and bars. Figures 6 and 7 show the time dependence of this function for the two data sets. In the two-year overlap in these graphs, the time dependence is nearly identical. The time dependence has a distinct seasonal trend. Table 1 shows that, for the spatial dependence of this function, the same amount of variance is accounted for by the associated eigenvalue in all four data sets.

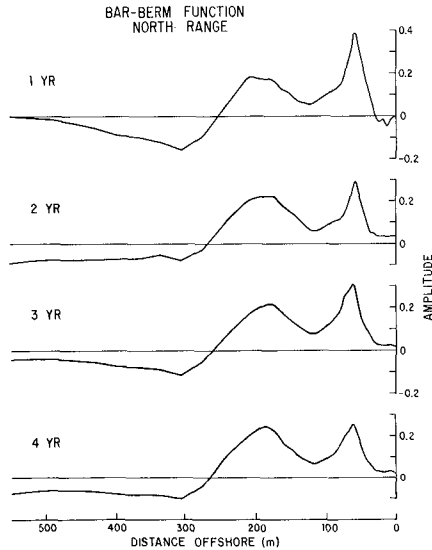


Figure 8. Spatial dependence of bar-berm function for data sets of one, two, three, and four years length.

Figure 9 shows the variation in the spatial dependence of the terrace function for the four data sets. The general shape of the curves is conserved, as are the relative magnitudes of the extrema. The location of the extrema vary slightly in response to the fact that sand erosion and deposition occur in slightly different locations along the profiles in response to different wave conditions. The dominant feature in the spatial dependence is the broad maximum across the low tide terrace. Figures 6 and 7 show the temporal dependence of this eigenvector. Table 1 shows that approximately the same percentage of the total variability is explained by the eigenvalue associated with this eigenvector.

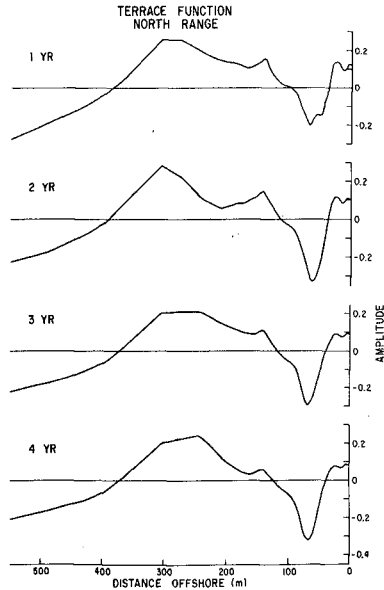


Figure 9. Spatial dependence of terrace function for data sets of one, two, three, and four years length.

IMPULSE RESPONSE OF THE EIGENFUNCTIONS

The response of these empirical eigenfunctions to impulses in the form of storm waves has been examined. Several examples demonstrate that the first few eigenfunctions are sensitive to short-term events. Two qualitative results are shown in Figure 9. On 27 August 1973, the time dependence of the bar-berm function became more negative instead of increasing according to the normal seasonal trend. This reflects the occurrence of a major summer storm on 23 August 1973 which eroded the developing summer profile. Similarly, the large positive values for February and March of 1976 reflect the anomalous occurrence of long, low waves which began to build the beach toward its summer configuration before it was eroded again by the more energetic waves more typical of winter conditions.

In October of 1974 the first large winter storm to hit the Southern California coast was generated off the low pressure center in the Gulf of Alaska. Storm front positions on 27, 28 and 29 October 1974 are shown in Figure 10. Significant environmental parameters measured at or near Scripps Institution of Oceanography during this time period are shown in Figure 11. The barometric pressure dropped from 1017 to 1005 mb and wind speeds reached 15 ms^{-1} . Coincidentally the rms wave amplitude increased to 0.5 m in 10 m of water. Wave energy spectra for the period just preceding and during the

storm are shown in Figure 12. The storm spectra are characterized by an order of magnitude higher spectral peak as well as a broader frequency band.

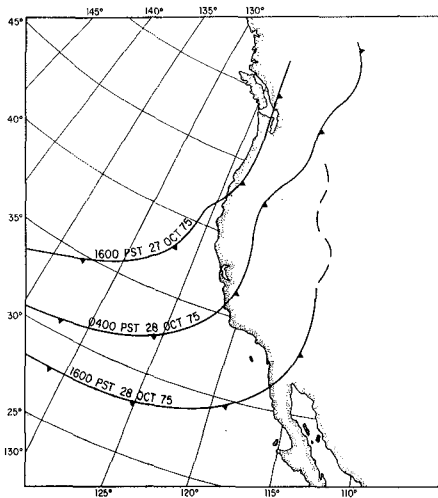


Figure 10. Storm front positions for first winter storm in late 1974.

The increased wave energy was coincident with spring tides of 2 m amplitude. These combined occurrences maximized the erosion on the beach. Figure 13 shows a comparison of a series of beach profiles at North Range taken before, during, and after the storm. The well-developed "summer" profile on 24 October was rapidly eroded as the storm passed through the area. At a distance of 70 m from the profile benchmark where the berm was located, 46 cm of sand was eroded.

This rapid erosion is reflected in the behavior of the temporal dependence of the bar-berm function shown in Figure 14. The 31 October profile shows an erosion in the beach on the order of 15 cm. For this particular storm, the terrace function showed an erosion of 17 cm, while the fourth eigenfunction showed an erosion of 13 cm. The bar-berm function correctly responds to the wave energy impulse, while the magnitude of the beach change can be fully accounted for in the first few eigenfunctions.

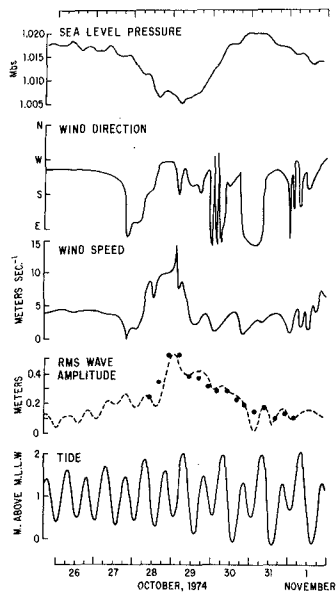


Figure 11. Environmental parameters measured at or near Scripps Institution of Oceanography during first winter storm in late 1974.

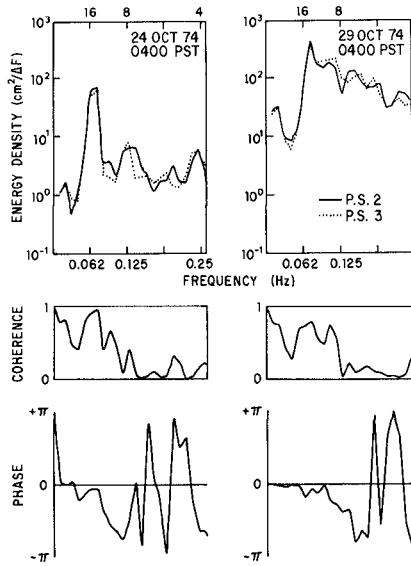


Figure 12. Frequency spectra of ocean surface waves measured before and during the first winter storm of late 1974.

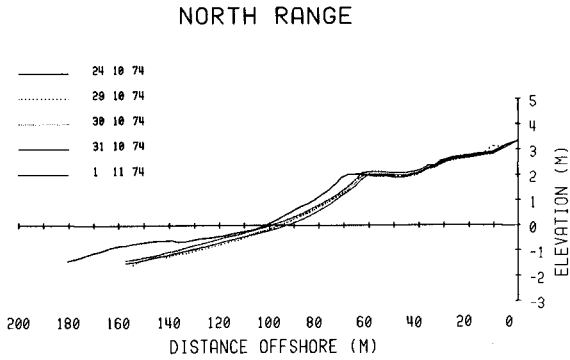


Figure 13. Beach profiles measured at North Range before, during, and after the first winter storm of late 1974.

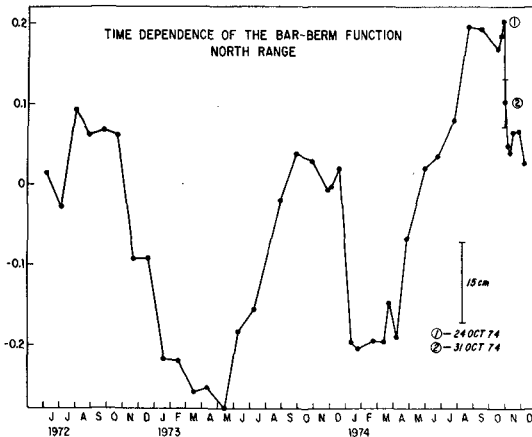


Figure 14. Time dependence of the bar-berm function for a two and one-half year data set at North Range.

CONCLUSIONS

The method of empirical eigenfunctions has been shown to be of great value in analyzing beach profile data. Using no a priori assumptions on the structure of the orthogonal functions, the most concise orthogonal set is generated by the data. The first three eigenfunctions describe over 99.75% of the variability in the data, and can be used instead of the data themselves to quantify the variability. The functions are stable with respect to the length of the data set examined, so an analysis of one year of data will indicate significant trends in the eigenfunctions. Erosion or accretion caused by short term events such as storms can be accurately predicted by the behavior of the temporal dependence of the bar-berm function, while the magnitude of this impulsive change is correctly given by the first four eigenfunctions.

REFERENCES

- Aubrey, D. G., D. L. Inman and C. E. Nordstrom, 1976, "Beach profiles at Torrey Pines, California", Abstracts Volume, 15th Int. Conference on Coastal Engineering, Amer. Soc. Civil Eng., p 711-712.
- Davis, R. E., 1976, "Predictability of sea surface temperature and sea level pressure anomalies over the North Pacific Ocean", Jour. Phys. Ocean. vol 6, p 249-66.
- Nordstrom, C. E. and D. L. Inman, 1975, "Sand level changes on Torrey Pines Beach, California", Miscellaneous Paper No 11-75, U. S. Army Corps of Eng., Coastal Engineering Research Center, 166 pp.

Winant, C. D., D. L. Inman, and C. E. Nordstrom, 1975, "Description of seasonal beach changes using empirical eigenfunctions", Jour. Geophys. Res., vol 80, no 15, p 1979-86.

ACKNOWLEDGMENTS

This research was sponsored by the Geography Programs of the Office of Naval Research under Contract N00014-75-C-0300.

CHAPTER 78

RIP-CURRENT AND COASTAL TOPOGRAPHY

Mikio Hino

Professor, Department of Civil Engineering,
Tokyo Institute of Technology,
O-okayama, Meguro-ku, Tokyo, 152,
JAPAN

SUMMARY

At the 1974 Conference on Coastal Engineering (Copenhagen), the writer proposed a new theory on the mechanism of generation of rip-current and cuspidal coast that the alongshore homogeneous structure of wave field and movable sedimental bottom (that is two-dimensional wave setup and bottom topography) is unstable to a small perturbation, the motive force of instability being the radiation stresses caused by incident wave.

In this paper, based on the response concept and the mathematics already presented at the previous conference some improvements in solving the fundamental equations are attempted, since the direct solution of the full system of basic equations did not necessarily result in the sufficient conclusion.

The response of water-wave system to an infinitesimal perturbation in bottom boundary is quick enough compared with that of sediment system to a change occurring in water-wave system. Consequently, the water system is treated as quasi-stationary. By solving the equation of mass conservation of sediment transport under the prescribed boundary conditions, the preferred wavelength of rip-current as well as the profiles of velocity distribution and the bottom perturbation have been determined as an *eigenvalue* problem.

INTRODUCTION

Recently, various theories have been proposed on the mechanism of rip-current generation. These theories may be grouped into three categories; The forced formation theory, the variational principle of the energy dissipation and the instability or eigenvalue theory.

Bowen and Inman's theory published in 1969 is based on the forced mechanism caused by standing edge waves which induce the spatially periodic distribution of radiation stress.

On the other hand, the writer (Hino 1972) has proposed a hydrodynamic instability mechanism. The writer does not necessarily deny the mechanism proposed by Bowen & Inman. However, there may be a possibility of another mechanism for generation of rip-current system.

In 1971, the writer was staying about a month at the Louisiana State University where the writer and Dr. Sonu who is now at Tetra Tech, frequently discussed on this problem. Dr. Sonu considered that the bottom material would change to sinusoidal forms by the action of alongshore current, as if sandbars on river bed are formed by the unidirectional flow. While, the writer asserted on the instability of uniform wave setup.

ESSENCE OF THE PRESENT THEORY

The basic idea of the writer's theory is as follows;

(a) If waves are incident on a straight coast, and if the water depth is uniform along the shore, the uniform wave setup along it should be formed, caused by the radiation stress of incident waves.

Such a uniformly long wave setup may be unstable to an infinitesimal disturbance, as if a slender elastic cylinder compressed axially becomes buckled when a critical compressive stress is exceeded. This is the *buckling analogy*.

In other words, the wave system itself on a rigid plane bottom may be unstable to form the periodic rip-current. However, in real situations, the rip current is accompanied by the corresponding periodic perturbations in the bottom topography.

As has been indicated in the previous paper, the direct solution of the full system of equations yields the two types of instability; one with the high increase rate and the rapid translation velocity along the shore is called the "*fluid mode*", while the other with the slow rate of increase and the low convection velocity is terminated the "*bottom mode*". Except for the normal wave incidence or the standing wave case caused by positive and negative progressive waves, the fluid mode could not manifest itself because of the too rapid alongshore translation for the perturbation to grow into appreciable intensity.

(b) In solving for bottom mode the basic equations, a physical interpretation of the phenomenon concerned will be introduced. One important way of analysis of the modern fluid dynamics is to attack complicated problems not necessarily purely mathematically but to solve them after the simplification of original equations through the physical interpretation of the basic equations. This attitude has been established by L. Prandtl when he proposed the concept of boundary layer in 1904.

Turning to our problem, the response of water-wave system is quick enough to the deformation of bottom boundary, while the bottom materials respond very much slowly to the change in the water-wave system. Therefore, the state of fluid system may be considered to be quasi-stationary. This is the *concept of response time* (Hino 1974). This idea has already been presented and applied in the writer's first paper (Hino and Hayashi 1972).

(c) Consequently, the flow field for an arbitrary bottom profile is solved from the continuity and momentum equations which include the radiation stress terms introduced by Longuet-Higgins and Stewart (1964). The resulting solutions of velocity components and the water surface elevation still contain the undetermined parameters which describe the bottom profile.

(d) Finally, the above solutions are substituted into the balance equation of bottom material transport. The problem is thus reduced to the *eigenvalue problem*. The rate of increase in the bottom perturbation is determined by the real part of eigenvalues dependent on the alongshore wavenumber of perturbation. On the other hand, the imaginary part of the eigenvalue predicts the propagation velocity of bottom perturbation, that is sand bars.

The components of an eigen-vector determine the unknown coefficients to describe the resulting perturbation in bed profile and thus velocity distribution.

In this way, we can determine not only the predominant spacing of rip-current but also the resulting bottom shape, the velocity field and the water surface elevation.

The idea of the response concept and a simplified mathematical treatment have already been presented at the previous Copenhagen conference.

THEORY

(a) Basic Equations

The basic equations are the same as the previous paper ;

[Equations of motion]

$$\begin{aligned} \frac{\partial [\rho(h+\eta)u]}{\partial t} + \frac{\partial [\rho(h+\eta)u^2]}{\partial x} + \frac{\partial [\rho(h+\eta)uv]}{\partial y} + \frac{\partial S_{xx}}{\partial x} + \frac{\partial S_{xy}}{\partial y} \\ = -\rho g(h+\eta) \frac{\partial \eta}{\partial x} - \rho \zeta u \end{aligned} \quad (1)$$

$$\begin{aligned} \frac{\partial [\rho(h+\eta)v]}{\partial t} + \frac{\partial [\rho(h+\eta)uv]}{\partial x} + \frac{\partial [\rho(h+\eta)v^2]}{\partial y} + \frac{\partial S_{xy}}{\partial x} + \frac{\partial S_{yy}}{\partial y} \\ = -\rho g(h+\eta) \frac{\partial \eta}{\partial y} - \rho \zeta v \end{aligned} \quad (2)$$

[Continuity equation]

$$\frac{\partial (h+\eta)}{\partial t} + \frac{\partial [u(h+\eta)]}{\partial x} + \frac{\partial [v(h+\eta)]}{\partial y} = 0 \quad (3)$$

[Radiation stress relationship]

$$\begin{aligned} S_{xx} &= \frac{3E}{2} - Ec^2 \left(\frac{\sin\theta}{c}\right)^2 \\ S_{yy} &= \frac{E}{2} + Ec^2 \left(\frac{\sin\theta}{c}\right)^2 \\ S_{xy} &= Ec \cos\theta \left(\frac{\sin\theta}{c}\right) \end{aligned} \quad (4)$$

$$E = (\rho g \gamma^2 / 8) (h + \eta)^2 \quad (5)$$

$$c = \{g(h + \eta)\}^{1/2} \quad (6)$$

where $\tilde{\gamma}=1$ inside of breaker zone and zero outside of it.
[Balance equation of bottom material transport]

$$\frac{\partial h}{\partial t} = \frac{\partial(C_s u)}{\partial x} + \frac{\partial(C_s v)}{\partial y} \quad (7)$$

In the above equations, the coordinate system is chosen as shown in Fig. 1 ; u, v mean the velocity components in the x - and y -direction, respectively ; η and h are the mean water-level elevation above still water surface and the depth of bottom, respectively ; S_{xx}, S_{xy} , and S_{yy} represent the radiation stress tensor components ; c is the wave velocity, E the wave energy per unit area, \tilde{C} and C_s are the coefficients of bottom friction and bottom material transport, respectively.

(b) Perturbation Equations

Variables are expressed as sum of equilibrium states ($0, V_0, \eta_0$, and h_0) and small perturbations (u, v, η and h)

$$\begin{aligned} u(x, y, t) &\rightarrow u(x, y, t) \\ v(x, y, t) &\rightarrow V_0(x) + v(x, y, t) \\ \eta(x, y, t) &\rightarrow \eta_0(x) + \eta(x, y, t) \\ h(x, y, t) &\rightarrow h_0(x) + h(x, y, t) \end{aligned} \quad (8)$$

Furthermore, variables are nondimensionalized by L_b (the distance from shore to breaker) and $\sqrt{gL_b}$,

$$\begin{aligned} u/\sqrt{gL_b} &\rightarrow u, \quad v/\sqrt{gL_b} \rightarrow v, \quad V_o/\sqrt{gL_b} \rightarrow V_o \\ x/L_b &\rightarrow x, \quad y/L_b \rightarrow y, \quad h_o/L_b \rightarrow h_o \\ t\sqrt{g/L_b} &\rightarrow t, \quad c/\sqrt{gL_b} \rightarrow c, \quad C_s/L_b \rightarrow C_s \end{aligned} \quad (9)$$

Substituting eq.(8) into eqs.(1) through (7) and linearizing, a set of the linear partial equations are derived,

$$\begin{aligned} \frac{\partial w_i}{\partial t} + A_{i1}(x) \frac{\partial u}{\partial x} + A_{i2}(x) \frac{\partial u}{\partial y} + a_i(x)u \\ + B_{i1}(x) \frac{\partial v}{\partial x} + B_{i2}(x) \frac{\partial v}{\partial y} + b_i(x)v \\ + C_{i1}(x) \frac{\partial \eta}{\partial x} + C_{i2}(x) \frac{\partial \eta}{\partial y} + c_i(x)\eta \\ + D_{i1}(x) \frac{\partial h}{\partial x} + D_{i2}(x) \frac{\partial h}{\partial y} + d_i(x)h = 0 \end{aligned} \quad (10)$$

(i=1,2 and 3)

$$\frac{\partial h}{\partial t} = \frac{\partial C_s u}{\partial x} + \frac{\partial C_s v}{\partial y} \quad (11)$$

where $w_1=u$, $w_2=v$ and $w_3=\eta$, and V_o and $d\eta_o/dx$ which are given as the zero-th order approximation of the perturbation mean the alongshore current velocity and the gradient of wave-setup, respectively ;

$$\begin{aligned} V_o(x) = - \frac{5\gamma^2}{16C_d} (\cos\theta \cdot \sin\theta_b \cdot \sqrt{h_{ob} + \eta_{ob}}) \\ \cdot \frac{h_o + \eta_o}{h_{ob} + \eta_{ob}} \frac{d(h_o + \eta_o)}{dx} \end{aligned} \quad (12)$$

$$\frac{d\eta_o}{dx} = - \left(\frac{3\gamma^2}{8} \right) \frac{\cos^2\theta}{[1+(3\gamma^2/8)\cos^2\theta]} \cdot \frac{dh_o}{dx} \quad (13)$$

Coefficients A_{ij} , B_{ij} etc. are generally functions of x (For details, reference should be made to a paper (Hino 1975).).

(c) Quasi-steady Solution of Water System to Bottom Perturbation

The perturbation in depth profile $h(x,y)$ is expressed by the orthogonal Hermite functions as eq.(14),

$$h(x,y) = \delta \sum_n \mu_n / (\sqrt{(n-1)!}) \cdot H_{n-1}(x) e^{-x^2/4} e^{iky} \tag{14}$$

where δ expresses a parameter of amplitude, H_n is the Hermite function of n -th order and the expansion coefficients μ_n are unknown arbitrary constants to be determined later as a result of the eigenvalue problem.

The solution of fluid system (the velocity components u and v , and the mean surface elevation η) is assumed to be expanded also by the Hermite series as

$$\begin{aligned} u(x,y;t) &= \sum \frac{\alpha_{2n'}}{\sqrt{(2n'-1)!}} H_{2n'-1}(x) e^{-x^2/4} e^{iky} \\ v(x,y;t) &= \sum \frac{\beta_n}{\sqrt{(n-1)!}} H_{n-1}(x) e^{-x^2/4} e^{iky} \\ \eta(x,y;t) &= \sum \frac{\gamma_n}{\sqrt{(n-1)!}} H_{n-1}(x) e^{-x^2/4} e^{iky} \end{aligned} \tag{15}$$

where the boundary condition that u equals zero at $x=0$ is considered by using only the odd-order Hermite functions ; and the boundary conditions that at infinite x variables approach zero by the property of Hermite

functions ($H_n(x)e^{-x^2/4} \rightarrow 0$, when $x \rightarrow \infty$).

Substitution of eqs.(14) and (15) into eqs.(10), and applying the Galerkin method, i.e. integrating them between $(0, \infty)$ after multiplication of both hand side by $H_{m'-1}(x)e^{-x^2/4}/\sqrt{(m'-1)!}$ and putting the residue equal to zero, a set of simultaneous equations for coefficients vector $X = [\alpha_2, \alpha_4, \dots, \beta_1, \beta_2, \dots, \gamma_1, \gamma_2, \dots]^T$ is obtained as a function of $h(x,y)$ or coefficients μ_n ,

$$\begin{aligned} X &= -\delta(A^{-1}B)\mu \\ &= \delta D\mu \end{aligned} \tag{16}$$

$$\begin{aligned} X &= [\alpha_2, \alpha_4, \dots, \alpha_{N'}, \beta_1, \beta_2, \dots, \beta_N, \gamma_1, \gamma_2, \dots, \gamma_N]^T \\ & \quad ((N'+2N)+1 \text{ matrix}) \end{aligned} \tag{17}$$

$$A = \begin{bmatrix} I^{(1)} & J^{(1)} & K^{(1)} \\ I^{(2)} & J^{(2)} & K^{(2)} \\ I^{(3)} & J^{(3)} & K^{(3)} \end{bmatrix} \begin{matrix} ((N'+2N) \\ \times (N'+2N) \text{ matrix}) \end{matrix} \tag{18}$$

$$B = \begin{bmatrix} L^{(1)} \\ L^{(2)} \\ L^{(3)} \end{bmatrix} \quad (19)$$

$$D = \begin{bmatrix} a'_1 \\ \vdots \\ a'_N \\ b_1 \\ \vdots \\ b_N \\ c_1 \\ \vdots \\ c_N \end{bmatrix} \quad (20)$$

$$\begin{aligned} a'_k &= [a_{k1}, a_{k2}, \dots, a_{kN}] \\ b_k &= [b_{k1}, b_{k2}, \dots, b_{kN}] \\ c_k &= [c_{k1}, c_{k2}, \dots, c_{kN}] \end{aligned} \quad (21)$$

$$\mu = [\mu_1, \mu_2, \dots, \mu_N]^T \quad (22)$$

The elements of submatrices $I^{(i)}$, $J^{(i)}$, $K^{(i)}$ and $L^{(i)}$ are given in terms of coefficients A_{ij} , B_{ij} , \dots , a_i , b_1 and so on (Hino 1975).

Matrix D ($(N'+2N) \times N$ matrix) which can be decomposed into row vectors represents the contribution rate of bottom perturbation component $H_{n-1}(x)e^{-x^2/4}$ to velocity and mean surface elevation, u , v and η .

(c) Stability of Bottom Perturbation (Eigenvalue Problem of Bottom Mode Instability)

From the response concept, the amplitude factor δ of eq.(14) is assumed now a slowly varying function of time. Substitution of equations of u , v , η and h where the unknowns are the coefficient vector μ and the amplitude factor δ into eq.(11) yields

$$\begin{aligned} \dot{\delta}(t) & \sum_{n=1}^{\infty} \frac{H_n}{\sqrt{(n-1)!}} H_{n-1}(x) e^{-x^2/4} e^{iky} \\ & = \delta(t) C_s \left[\sum_{n=1}^{\infty} a_n \mu \{ H'_{n-1}(x) - \frac{x}{2} H_{n-1}(x) \} \right. \\ & \left. + (ik) \sum_{n=1}^{\infty} b_n \mu H_{n-1}(x) \right] e^{-x^2/4} e^{iky} \end{aligned} \quad (23)$$

Again applying the Galerkin technique, the following equation is obtained,

$$T\mu = p\mu \quad (24)$$

where p is the exponential growth rate

$$p = (d\delta/dt)/(C_s \delta) \quad (25)$$

and matrix T is composed of coefficients in matrix D (eqs.(43) through (47) in Hino, 1975).

Eq.(24) poses an eigenvalue problem for matrix T , the unknowns p and μ being eigenvalues and eigenvectors, respectively. These are solved numerically by a digital computer HITAC 8700/8400 of Computer Center, Tokyo Institute of Technology.

Two non-dimensional parameters, χ and ψ , are defined from factors affecting the phenomenon,

$$\begin{aligned} \chi & = s(\sin \theta/c)^2 \\ & = (h_b/L_b) \cdot (\sin \theta_b / \sqrt{h_b/L_b})^2 \\ & = \sin^2 \theta_b \end{aligned} \quad (26)$$

$$\begin{aligned} \psi & = s^2(\sin \theta_b/c) \\ & = (h_b/L_b)^{3/2} \sin \theta_b . \end{aligned} \quad (27)$$

RESULTS

(a) Instability diagram:

Fig. 2 shows some examples from the instability diagrams. The exponential growth rates (the maximum values of the real part of eigenvalues), $(Pr)_{\max}$, are plotted against the alongshore wavenumber k of perturbation for a selected combination of bottom slope $h_b = sL_b$ (L_b : distance to breaker zone). In these graphs, the parameter θ expresses the incident angle of waves.

It is shown that the perturbation in bottom configuration and consequently in wave field is most unstable to a certain wave number k_* of alongshore periodicity. Except for the normal incidence, $\theta=0$, the amplification rates become maximum at the nondimensional alongshore wave number of about $k=1.5$ or at the wave length of about 4 times the distance from shore to breaker.

Fig. 3 shows the relation between the most preferred alongshore wavenumber (nondimensional) k_* , the angle of incidence θ and the slope of the initial bottom s . As the bottom slope becomes steep, the preferred nondimensional spacing of rip current ($L_R = 2\pi/k_*$) increases. However, since the distance of breaker from shore also reduces, the real spacing of rip current (L_R)

$$\begin{aligned} L_R &= (2\pi/k_*) L_b \\ &= 2\pi h_b / s k_* \end{aligned} \quad (28)$$

(where h_b is the breaker depth) is estimated generally to become shortened.

(b) Propagation celerity of sandbars:

Moreover, it should be added that the present theory gives the celerity of alongshore translation of bottom perturbation as

$$C_* = p_i C_S / k \quad (29)$$

where p_i represents an imaginary part of the eigenvalue. Fig. 4 is a plot of the propagation velocity of sand bars.

(c) Rip-current and rip-channel:

By substituting the eigenvectors μ which determine the coefficients of perturbed bottom profile in eq. (24), into the series expression (eqs.(14) and (10)) of variables u , v , ζ and h , we are able to obtain the profiles of sand bars and the velocity fields.

Fig. 5 is the cross-sectional profile of a sand bar at various position along the shore. From this graph, a conclusion is derived that sand bars seem to progress onshore when observed at a cross-section perpendicular to the shore, although in reality they are propagated alongshore.

In Fig 6, the upper solid line gives the velocity of offshore current u , that is the rudimentary rip-current. The strength of velocity is the highest at the breaker zone. The lower thin solid curve is the change of bottom profile. This is the so-called rip-channel. The bottom is eroded inside and near the breaker zone, while sand materials are deposited offshore.

These results of theoretical analysis (Figs. 5 and 6) agree well with observed facts.

(d) Effect of initial bottom shape:

The initial bottom profiles are assumed to be represented by

$$h_0(x,y) \propto x^n \quad (30)$$

The upward convex bottom and the upward concave bottom are represented by $n > 1$ and $0 < n < 1$, respectively. Fig. 7 shows the instability diagrams for both cases, indicating that the upward convex shallow bottom is apt to change into rip current system.

(e) Relative importance of wave-setup, alongshore current and bottom friction:

The writer is interested in the relative importance of various intrinsic factors, such as those,

- (i) the wave setup which is caused by the radiation stress,
- (ii) the intensity of alongshore current which is also driven by the radiation stress,
- (iii) the friction factor which influences the intensity of alongshore current.

Since these factors are closely inter-connected each other, it is difficult separated them experimentally. However, in the theoretical analysis, it is possible to change artificially, for instance, the intensity of alongshore current alone, keeping the radiation stress or wave setup unchanged.

Fig. 8 (b) is the instability diagram when the radiation stress parameter γ is varied, keeping the alongshore current (lsc) unchanged. As the intensity of radiation stress is decreased the amplification rate of perturbation decreases. In reality, as the intensity of radiation stress is decreased, the alongshore current is also reduced. The left hand side figure (Fig. 8 (a)) shows the theoretical result for this case ($lsc = \text{real}$).

Fig. 8 (c) gives the instability diagram for a hypothetical case of no alongshore current ($lsc = 0$) even if there is the wave setup, when waves are incident obliquely. In this hypothetical case, the infinitesimal perturbation is also unstable; however there exist no predominant preferred wave number. The tendency is similar to the case of normal wave incidence ($\theta = 0$).

Fig. 9 (a) and (b) summarizes the results on the relationship between the radiation stress intensity and the preferred wavenumber of rip-current spacing ($\gamma \sim k_*$) and the exponential growth rate ($\gamma \sim \rho_*$), respectively.

One the other hand, Fig.10 examines the effects of the bottom friction, keeping the wave setup unchanged ; i.e. $\gamma=1$. Fig.10 (a) is the result for real case, Fig.10 (b) and (c) being the results for hypothetical cases of unchanged and no-alongshore current, respectively.

Fig. 11 (a) and (b) summarizes these results.

From these analytical computation, the following conclusion may be deduced ;

- (i) The main trigger of rip-current generation is the wave-setup caused by the radiation stress, rather than the alongshore current.
- (ii) The spacing of rip-current is dependent on the strength of alongshore current. If there were no alongshore current, there occurs no predominate wavenumber. As the intensity of alongshore current is increased, or the bottom friction is decreased, the preferred wavenumber of rip-current decreases. In other words, the spacing of rip-current becomes longer.
- (iii) When there is no wave-setup, the rip-current would not be formed, even if there were the alongshore current (c.f. especially, Fig. 8 (b) where the intensity of the alongshore current is as strong as for the case of real case caused by the radiation stress).

REFERENCES

- 1) Bowen, A.J. (1969): J. Geophy. Res., Vol.74, No.23, pp.5467-5478.
- 2) Hino, M. and Hayashi, N. (1972): Coastal Engineering in Japan, Vol. 16, pp.55-60, (in English).
- 3) Hino, M. (1974): Proc. 14th International Conference on Coastal Eng., Copenhagen, June.
- 4) Hino, M. (1975): Proc. Japan Soc. Civil Eng., No.237, pp.87-98.
- 5) Longuet-Higgins, M.S. and Stewart, R.W. (1964): Deep-Sea Res., Vol. 11, pp.529-562.
- 6) Sonu, C.J. (1972): J. Geophy. Res., Vol.77, No.18, pp.3232-3247, June.

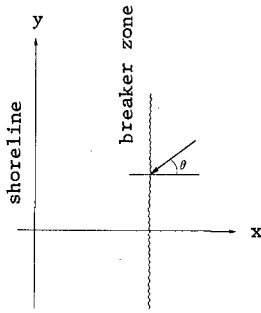


Fig. 1 ; Coordination system, x:offshore direction, y:alongshore direction, θ :incidence angle of wave.

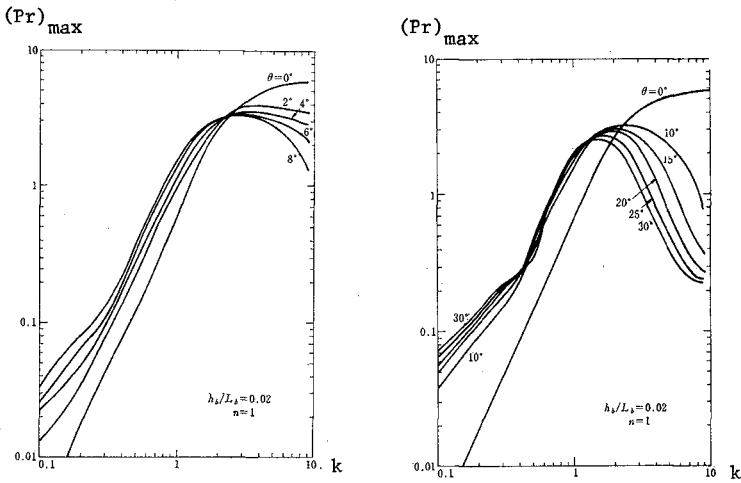


Fig. 2 ; Longshore wave number and the maximum exponential growth rate.

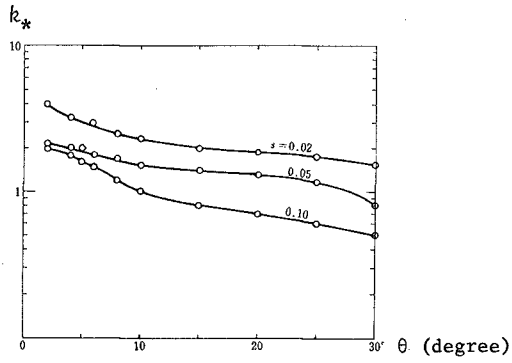


Fig. 3 ; Relationship between the most preferred longshore wave number k_* , the angle of wave incidence θ_b and the bottom slope s .

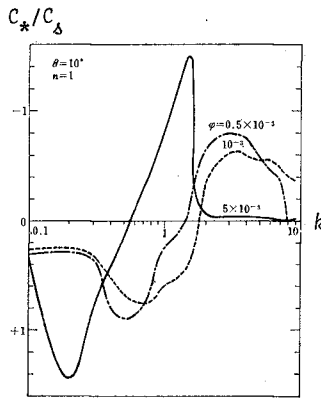


Fig. 4 ; Longshore wave number and translation celerity of sand-bar.

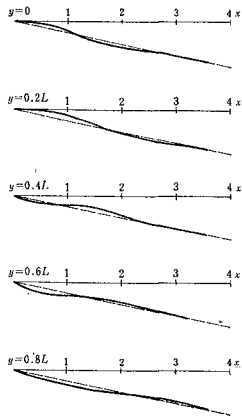


Fig. 5 ; Cross-sectional profiles of sand-bar at various position of y ,

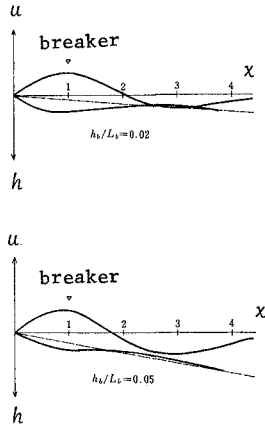


Fig. 6 ; Velocity distribution of offshore current at the rudimentary rip-current $u(x, y_0)$ and the depth variation of bottom (the so-called rip-channel) $h(x, y_0)$.

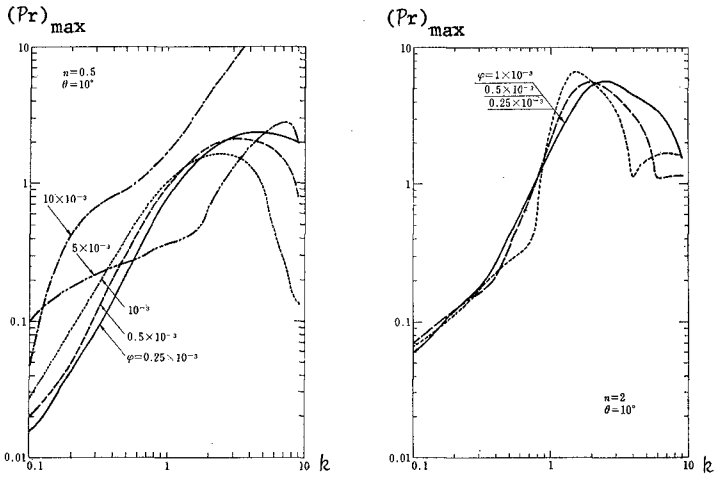


Fig. 7 ; Effects of the initial bottom shape ($h_0(x) \propto x^n$) on the relationship k and $(Pr)_{max}$, (a) for a concave bottom of $n=0.5$ and (b) for a convex bottom of $n=2$.

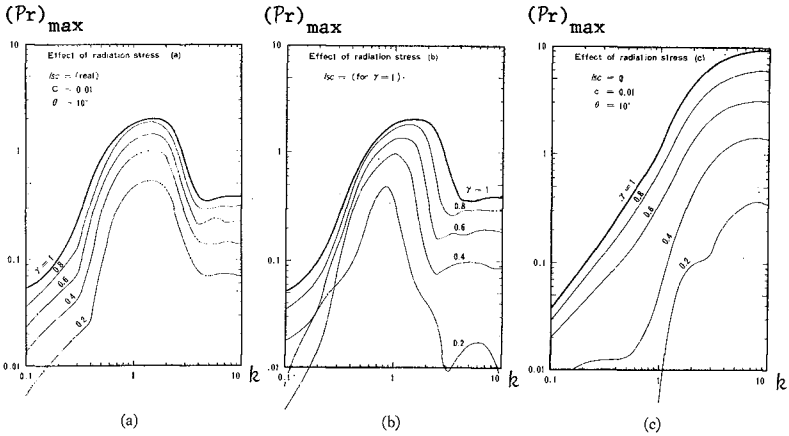


Fig. 8 ; Effect of the radiation stress intensity (γ) on the exponential growth rate $(Pr)_{max}$ and longshore wave-number k .

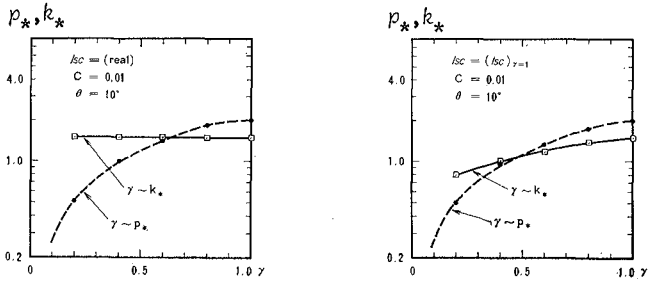


Fig. 9 ; Effect of the intensity of radiation stress γ on the most preferred longshore wave-number k_* and the corresponding exponential growth rate p_* .

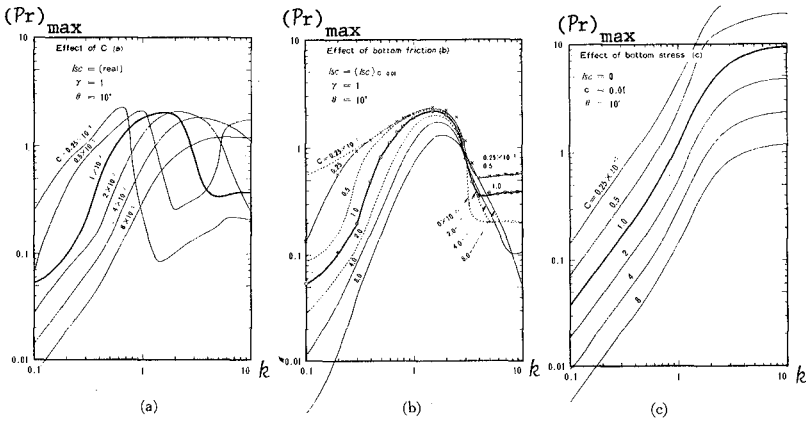


Fig.10 ; Effect of the bottom friction on the instability diagram.

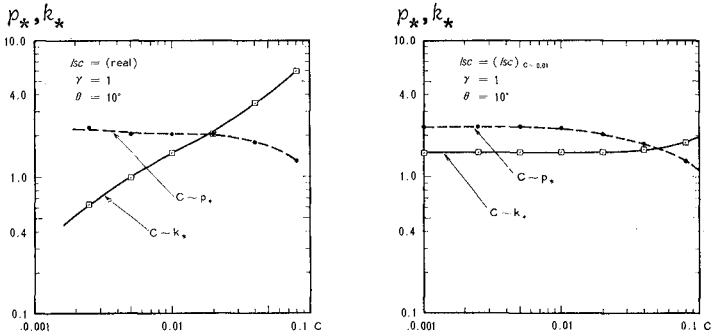


Fig.11 ; Effect of the bottom friction on the most preferred longshore wave number k_* and the exponential growth rate p_* .

CHAPTER 79

A SAND BYPASSING SYSTEM USING A JET PUMP

by

E. C. McNair, Jr.¹

INTRODUCTION

All harbors and tidal inlets that are located in coastal areas have one characteristic in common--the need to bypass littoral materials that collect nearby. If natural harbors and tidal inlets are left unattended, bypassing will often occur naturally, but in the process, the harbor or inlet is usually rendered unfit for commercial or navigation purposes. Quite often, the inattention results in the total closure of the inlet. Therefore, at almost all harbor entrances and controlled tidal inlets, the natural bypassing must be augmented by secondary, usually mechanical, means.

The customary technique for bypassing sand and maintaining harbors and inlets is the use of floating dredge equipment. This equipment is rugged, reliable, has been proved over and over, and appears to be irreplaceable for many applications and locations. However, there are many locations and situations for which this floating equipment is not suitable and may, in fact, be detrimental or prohibitively costly. Waves of even moderate height, moderate-to-high tidal excursion and currents, draft limitations, limited maneuvering area, and interference with normal navigation operations are examples of conditions which decrease the desirability and application of floating dredge equipment. Small volumes of material to be bypassed are an economic liability for the floating plant since mobilization and demobilization costs contribute extraordinarily to the unit cost for bypassing work.

THE PROBLEM

In general, it is at the larger harbors and tidal inlets where the floating dredge equipment can be used effectively, efficiently, and economically.

¹Chief, Research Projects Group, Hydraulics Laboratory, U. S. Army Engineer Waterways Experiment Station, Vicksburg, MS.

Also, it is usually at the smaller harbors and tidal inlets that the use of floating dredge equipment to accomplish the desired bypassing activities becomes questionable.

Until the present time, the coastal engineer with the responsibility for maintaining the smaller coastal harbors and inlets had little choice in the selection of the mechanical means for bypassing sand. Floating dredge equipment was usually scheduled regardless of economy except in isolated cases where land-based pumping plants could be effectively used.

Obviously a need for improved operations and maintenance techniques and equipment for bypassing sand at tidal inlets and other littoral barriers exists. The problem is one to which the methods and procedures of research and development may be profitably applied. Therefore, a research program, sponsored by the Office, Chief of Engineers (OCE), was formulated and implemented for the purpose of improving operations and maintenance techniques specifically to develop effective and economical methods for sand bypassing at tidal inlets and other obstructions to littoral drift.

A review of existing equipment and proposed concepts identified the jet pump as having great potential as a primary component in a sand bypassing system. The survey conclusion was that a jet pump bypassing system requiring limited watercraft and personnel and capable of great portability and reliability can be assembled at a reasonable cost using off-the-shelf equipment. The research program was therefore designed to provide performance criteria, systems design parameters, and deployment and operational techniques for sand bypassing systems using jet pumps.

JET PUMP THEORY

Currently, jet pumps are, in general, used as suction boosters on centrifugal dredge pumps. There are several instances where eductors have been used alone for sand and gravel mining, but all of the equipment in use to date has been designed to meet low head applications. However, there is adequate theory and empirical information to show that the jet pump is capable of producing the higher discharge heads required for a bypassing installation.

The basic principle behind the operation of the jet pumps is the exchange of momentum. High-pressure fluid, normally supplied by a centrifugal pump, is forced through a converging jet nozzle and is converted into a high-velocity, low-pressure jet stream. This jet stream contacts the suction fluid at the nozzle exit and drags it into the pump, thus initiating and sustaining secondary flow of suction fluid from the surrounding water mass. If the surrounding water mass contains solids, or if solid particles are entrained in the secondary flow approaching the jet pump intake, then solids are introduced into the pump mixing chamber. In the mixing chamber, the high-energy jet stream and the suction fluid mix further, exchange momentum, and experience a pressure recovery. The mixed fluids or slurry then pass through a diverging diffuser and into a discharge pipe for delivery to a booster or to a discharge point.

Operational characteristics of the slurry jet pump can be described by three dimensionless ratios^{1,3}:

$$\text{Area ratio } B = \frac{\text{nozzle area}}{\text{mixing chamber area}} = \frac{A_j}{A_{mc}} \quad (1)$$

$$\text{Flow ratio } \phi = \frac{\text{pumping capacity}}{\text{driving capacity}} = \frac{Q_{suc} \gamma_{suc}}{Q_{sup} \gamma_{sup}} \quad (2)$$

$$\text{Head ratio } H = \frac{\text{net jet pump head}}{\text{net driving head}} = \frac{h_{dis} S_{dis} - h_{suc} S_{suc}}{h_{sup} S_{sup} - h_{dis} S_{dis}} \quad (3)$$

where

- A_j = nozzle area
- A_{mc} = mixing chamber area
- Q_{suc} = suction flow rate, gpm
- γ_{suc} = unit weight of suction slurry
- Q_{sup} = supply flow rate, gpm
- γ_{sup} = unit weight of drive fluid
- h_{dis} = total discharge head in feet of slurry
- S_{dis} = specific gravity of discharge slurry

- h_{suc} = total suction head in feet of slurry
- S_{suc} = specific gravity of suction slurry
- h_{sup} = total supply head in feet of drive fluid
- S_{sup} = specific gravity of drive fluid

Using conservation of momentum, mass, and energy, Govatos¹ derived the following equation to give the relationship between H , \emptyset , and B .

$$H = \frac{U - V - W}{W - U + X} \quad (4)$$

where

$$U = 2B + \frac{2(\emptyset B)^2 \gamma_w}{(1 - B) \gamma_{suc}} - \frac{B^2 (1 + \emptyset)^2 \gamma_w (2 + K_{mc})}{\gamma_{dis}} \quad (5)$$

$$V = \frac{\emptyset B}{1 - B} \frac{2(1 + K_s)}{S_{suc}} \quad (6)$$

$$W = B^2 (1 + \emptyset)^2 \frac{K_{dis} - 1}{S_{dis}} \quad (7)$$

$$X = 1 + K_j \quad (8)$$

and

- γ_w = unit weight of water, pcf
- K_{mc} = loss coefficient due to the mixing chamber
- γ_{dis} = unit weight of discharge slurry, pcf
- K_s = loss coefficient due to the suction nozzle
- K_{dis} = loss coefficient due to the diffuser
- K_j = loss coefficient due to the drive jet nozzle

A set of curves similar to those in Figure 1 (from Reference 2) can be plotted by using the above equations and assuming a suction concentration and average loss factors for water.

The efficiency of the jet pump is dependent on several factors, but primarily on pump geometry. The four major geometrical parameters affecting

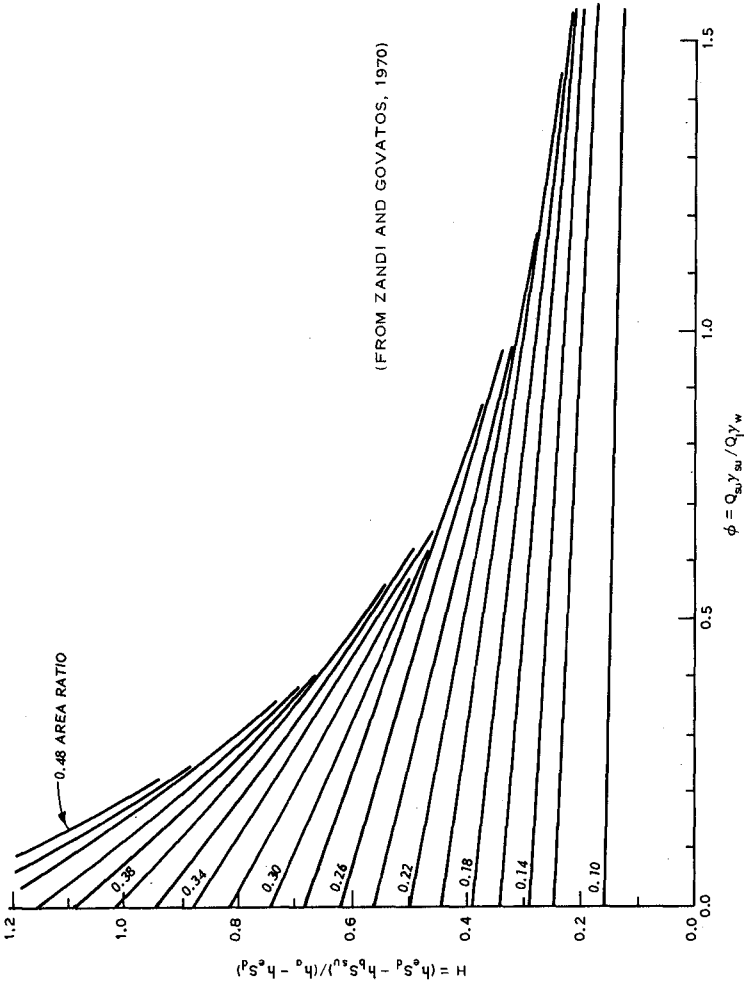


Figure 1. The relationship between dimensionless head ratio H , dimensionless flow ratio ϕ , and dimensionless area ratio for assumed arbitrary loss factors in the jet pump

efficiency are area ratio, the nozzle distance or distance from the tip of the nozzle to the entrance of the mixing chamber, the mixing chamber length, and the diffuser angle. With the exception of the area ratio, which can be varied by changing the nozzle characteristics, the geometry of the jet pumps tested was not altered in the research program.

LABORATORY TESTS

A laboratory test program was begun in 1973 and is continuing at this time. The purpose of these tests is to verify the theoretical and empirical relationships describing jet pump performance, to develop pumping techniques and methods for deployment and application, and to develop auxiliary devices such as hydraulic cutting assists and flow measuring techniques. The laboratory tests are designed to develop practical, reliable components and techniques for field evaluation as well as criteria for system design.

The laboratory facility, shown on Figure 2, consists of an excavation with sloping sides approximately 150 ft square. The facility is lined with plastic membrane to prevent local soil contamination of 2400 cu yd of medium sand (400 μ) used in the test. The size of the facility allows testing of prototype-size (6-in. discharge line) equipment to eliminate problems in scaling and also to provide valid information on deployment techniques.

The pipe network consists of 6-in. schedule 40 steel pipe, 6-in. floating rubber hose, and 6-in. PVC hose. The rubber hose is commonly used in dredging and gives the laboratory system sufficient flexibility to be moved about the basin. Instrumentation of the pumping system consists of magnetic flowmeters on the supply and discharge lines, a nuclear density meter to measure the sand concentration in the discharge line, and pressure transducers which monitor supply pressure, discharge pressure, suction pressure, and ambient pressure.

The flotation system for the jet pump assembly consists of a hollow spherical buoy attached to the jet pump, 6-in. rubber hose, air lines, and an air compressor. Through the use of a simple valving system on the pier, the air compressor can be used to regulate the buoyancy of the sphere. Air can also be pumped into the 6-in. rubber hoses to increase their buoyancy.

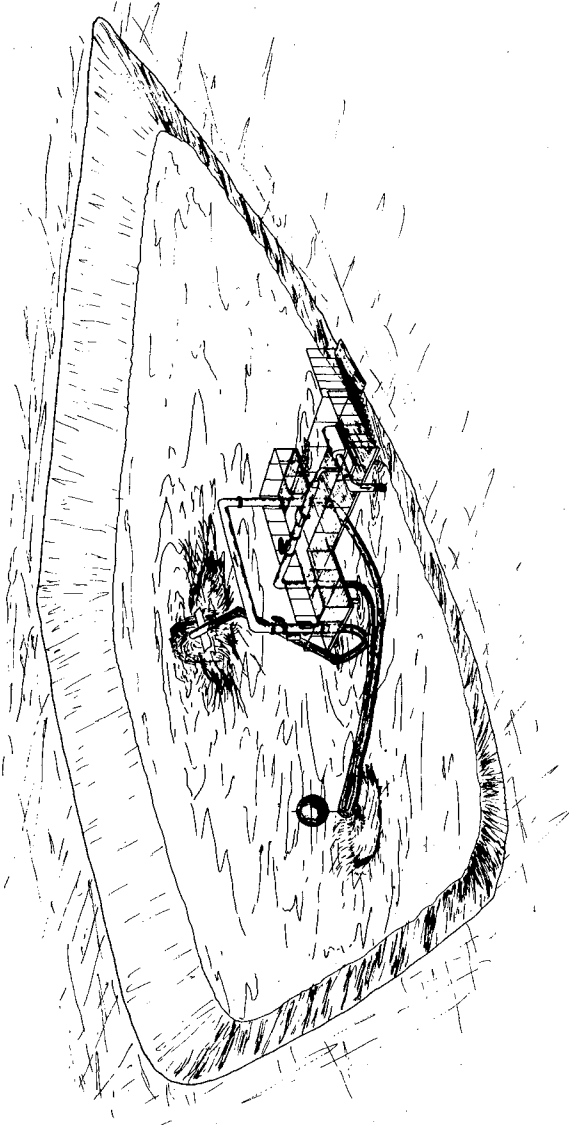


Figure 2. Artist's concept of laboratory facility showing 150-sq ft basin, work platform and piping arrangement

The initial series of laboratory tests were performed to verify the observations and accounts of other investigators as reported in the literature. Tests were first performed by pumping only clear water. In later tests, mixtures of sand and water were pumped and system parameters were observed for those conditions. Examples of the results of some of these tests are shown on Figures 3a and 3b.

A sufficient number of observations were obtained from the initial laboratory experiments to support the design of a prototype system for field testing. It was expected that the ideal conditions of the laboratory facility would be only an approximation of field conditions and that many of the conclusions reached and techniques developed in the laboratory tests would be modified or discarded after field testing of the system.

FIELD TESTS

Several potential field sites were evaluated for their suitability for initial field testing. Among the sites considered were: Santa Cruz and Oceanside, California; Port Mansfield and Colorado River Mouth, Texas; Perdido Pass, Alabama; Michigan City, Indiana; Moriches, New York; Masonboro, North Carolina; and Mexico Beach, Florida. The evaluation procedure determined that Mexico Beach, Florida, was the most suitable site for our initial field testing.

Mexico Beach is located in the Florida Panhandle approximately 30 mi east of Panama City. The test site is adjacent to a small navigation inlet maintained by the township. Local conditions at the inlet (see Figure 4) consist of a sizable sand accretion westward of the two jetties protecting the inlet and eroding beach conditions to the east of the inlet. The littoral drift is estimated to be almost entirely eastward and is in the order of 40,000-50,000 cu yd annually.

A field test unit comprised of a truck-mounted centrifugal pump, instrumentation, discharge and supply lines, and a single four-inch-diameter intake jet pump was put into operation at Mexico Beach in 1973 (see Figure 5). These tests immediately revealed the need for improved deployment techniques, a more manageable buoy system, more efficient operational techniques, and cutting

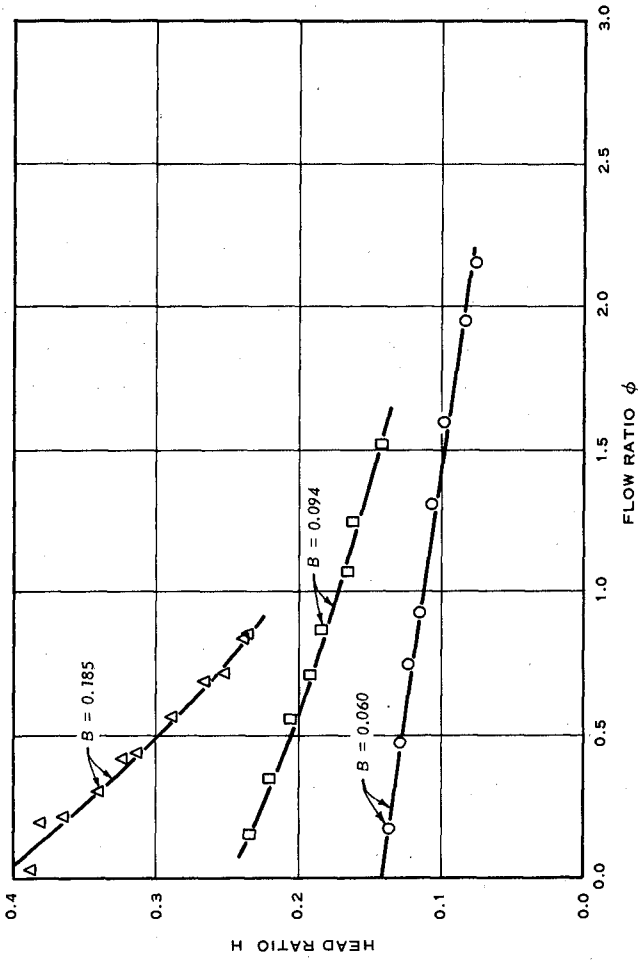


Figure 3a. Head ratio, H, flow ratio, ϕ , relationships for clear water data

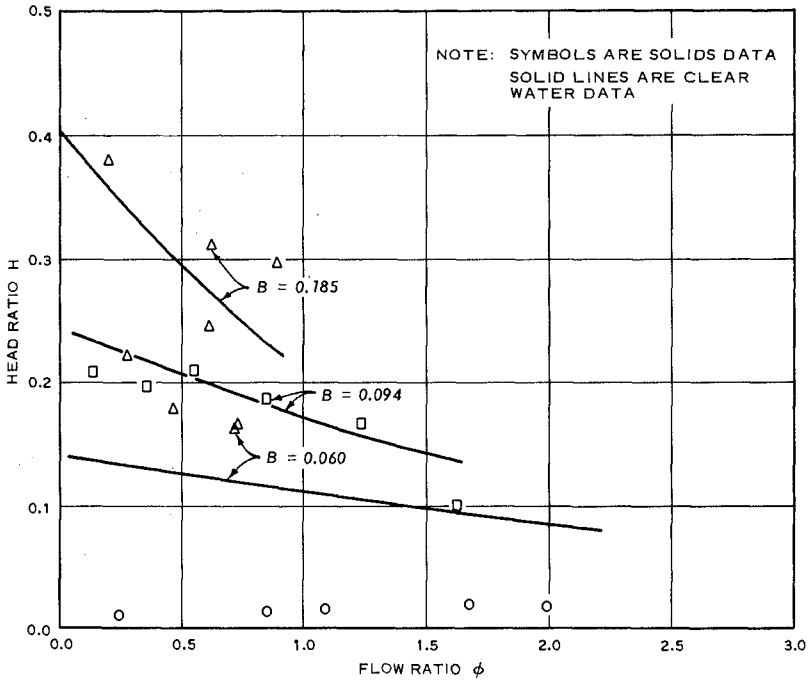


Figure 3b. Head ratio, H , flow ratio, ϕ , relationships for solids flow compared to clear water relationships



Figure 4. Mexico Beach, Florida, field site in 1972

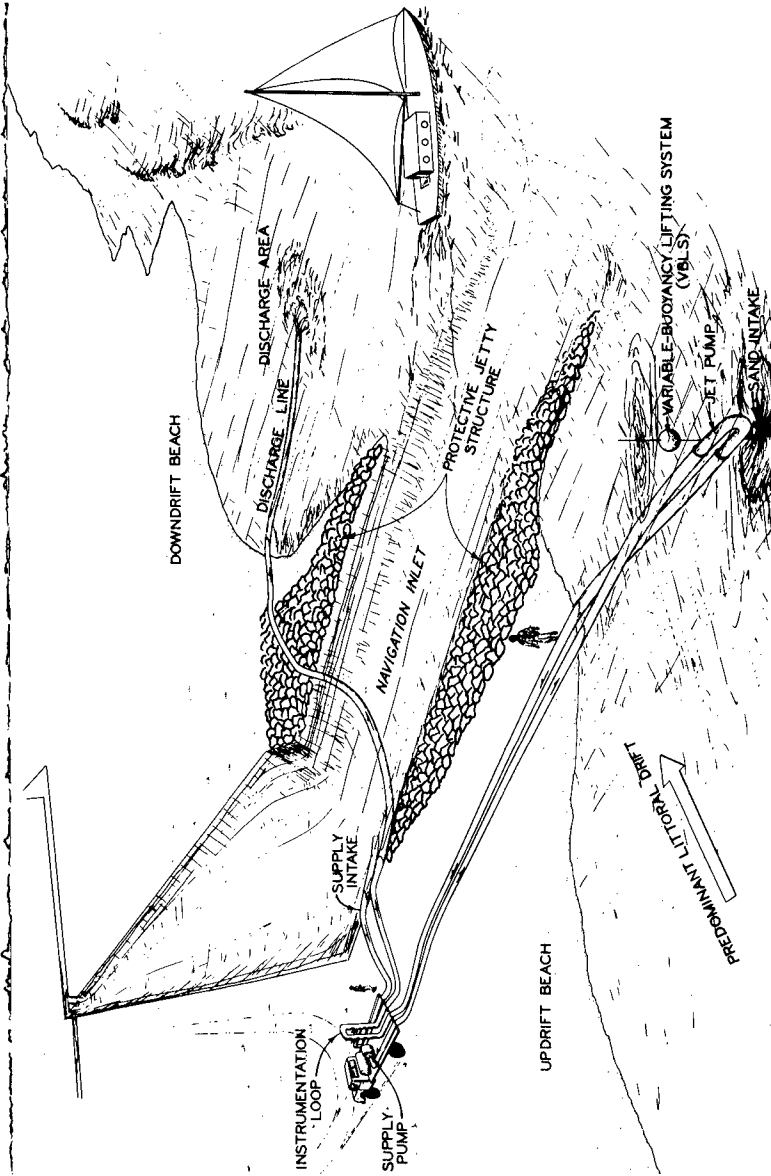


Figure 5. Artist's concept of sand bypassing installation at Mexico Beach, Florida

assists to overcome the cementing agents found in most natural beach sands. Other problems were also identified, including that of plugging of the jet pump intake port by shell fragments or other foreign materials and weaknesses in the various system components.

The jet pump, rigidly attached buoys, and flexible hoses were deployed from the beach using a vehicle winch and two anchors on the offshore bar with a block attached. A system of two or more permanent anchors with blocks can readily be used to reposition the jet pump. A 1/2-in.-diameter pipe was tapped into the supply side of the jet pump and teed into a two-jet cutting assist. The cutting assist was required to initiate a crater when the suction pipe was oriented other than perpendicular to the bottom. The jet pump will self-enplace in its own crater. The pump can also be shut down at any time by balancing the supply flow and discharge flow (zero suction flow) for a sufficient time to flush the sand from the discharge line. The jet pump was left in a crater bottom on several occasions until the crater was completely filled. When the sand was about 8 ft over the suction pipe, several hours of pumping were required before the flotation buoys could free the jet pump. When temporary clogging of the suction pipe was encountered, a valve in the discharge line was closed and the supply water forced out of the suction pipe. This technique is termed backflushing and was required frequently due to significant amounts of large shells blocking the suction pipe. Backflushing is also useful in jetting the suction pipe into the bottom in order to obtain an overburden on the suction pipe.

Most problems were satisfactorily worked out for the Mexico Beach site, and the system was put into a more-or-less operational mode. Over a period of several months, approximately 20,000 cu yd of material were bypassed from the fillet west of the entrance. The production rate of the operational system varied considerably with local conditions, but averaged about 75 cu yd per hour of operation.

The concept of overland portability where the relatively expensive drive-water and booster pumps are used to service several jet-pump locations in a local area was also evaluated during the Gulf of Mexico field tests. A site at Destin, Florida, which is within reasonable driving distance of Mexico

Beach and which has problems with maintenance of a small navigation channel into a harbor area was selected for this evaluation. A jet pump with associated supply and discharge lines was deployed at the Destin site (see Figure 6). The truck-mounted pump was uncoupled at Mexico Beach, driven to the Destin site, and recoupled to the jet-pump piping. The discharge point at the Destin site was such that a booster was added to the system. Otherwise, operational procedures at the Destin site and at the Mexico Beach site were similar.

The overland portability concept was successfully demonstrated at the Gulf of Mexico sites. This technique is to be recommended when several bypassing problems exist in a local area.

The experience, knowledge, and techniques derived from the initial laboratory work and the Gulf of Mexico field work were called upon for design of a system for an Atlantic coast site. Rudee Inlet, Virginia, which has a low-weir sand impoundment basin, was selected as the research site.

The system, as finally configured (see Figure 7), consisted of two electrically driven centrifugal-pump jet-pump units coupled with a single diesel-driven slurry booster pump. The jet pumps and associated piping are suspended from a row of piling near the center of the deposition basin. By maneuvering the jet pumps, the deposition basin can be cleared of most sand deposits. During the field test at Rudee Inlet, approximately 75,000 cu yd of sand were pumped from the impoundment basin to the beach area north of the inlet.

The entrance to Santa Cruz Harbor, California, shown in Figure 8, has been selected as a Pacific coast research site with tests beginning in the summer of 1976. The installation consists of dual-jet-pump, single-booster system with bypassing being accomplished from the shoals which form near the entrance channel. The pumping system will be based on the west jetty of the harbor, and the jet pumps will be maneuvered either by cables from shore or by a small work boat.

DISCUSSION

The jet pump sand bypassing system is simple in design and application and offers the coastal engineer an additional option in his search for solutions

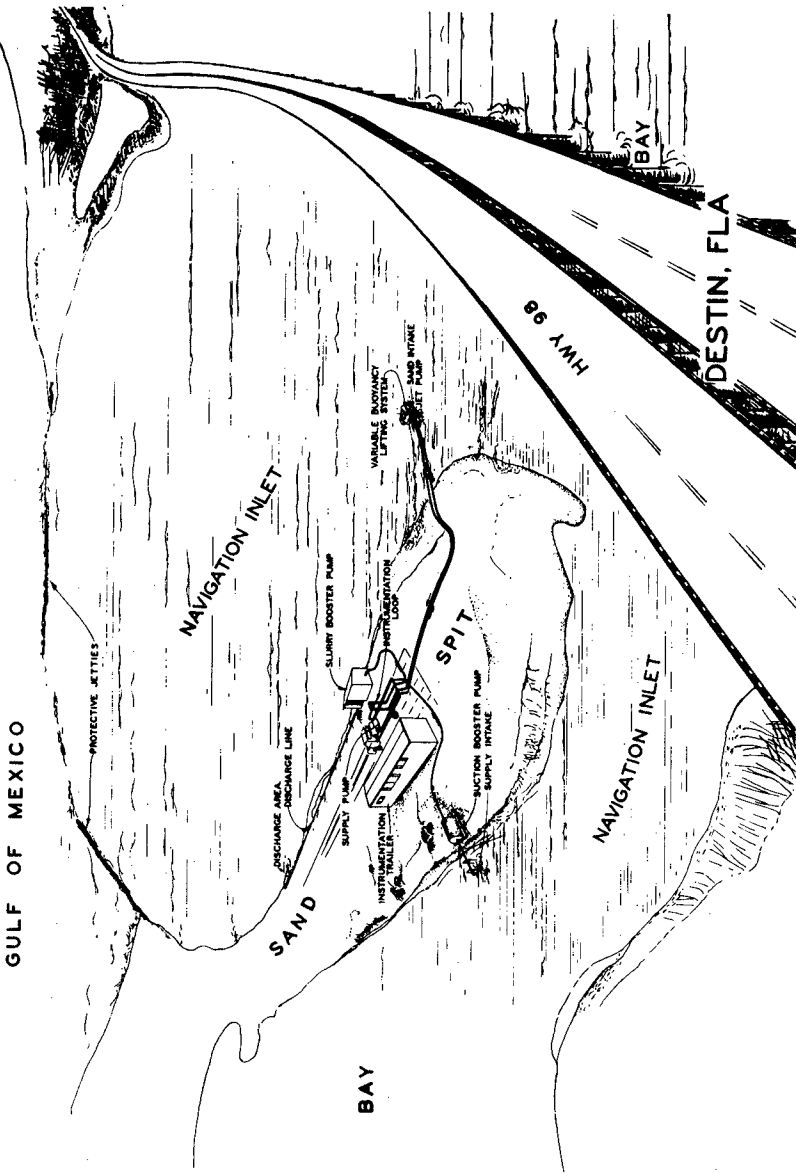


Figure 6. Artist's concept of sand bypassing installation at East Pass (Destin), Florida

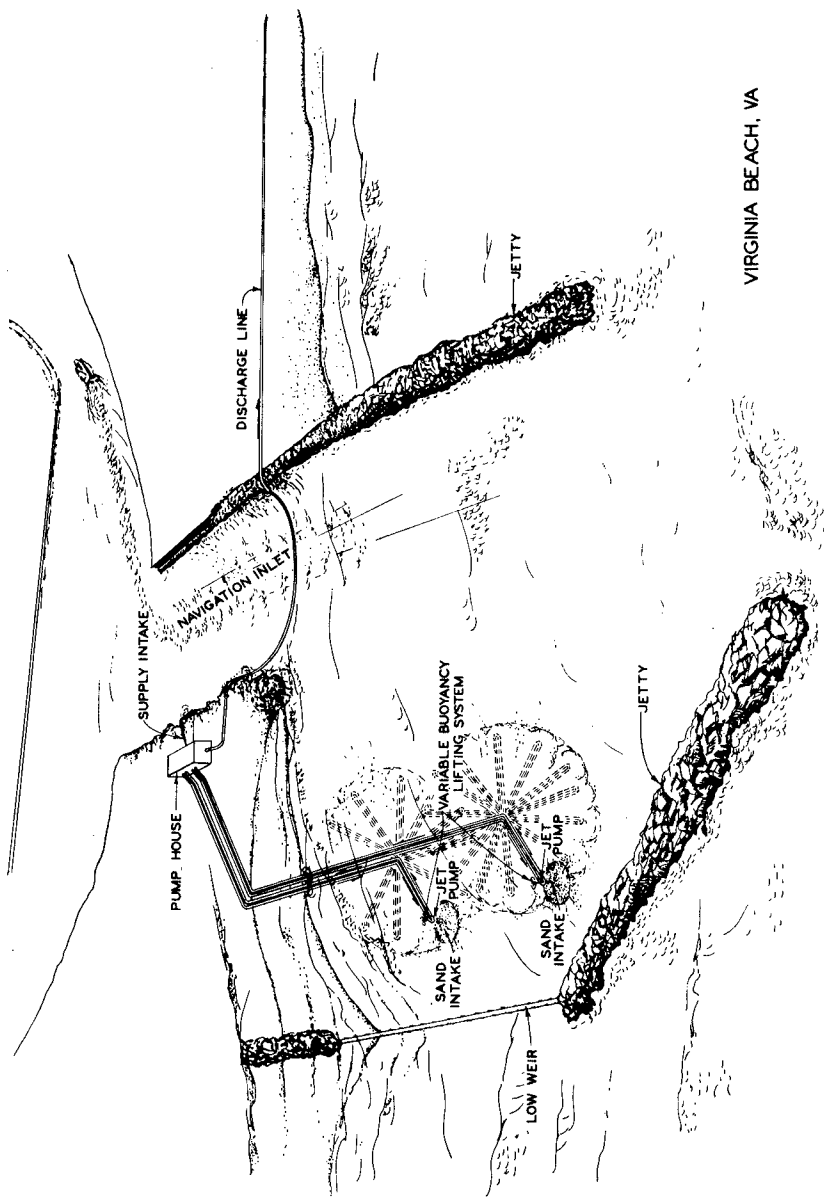


Figure 7. Artist's concept of sand bypassing installation at Rudee Inlet (Virginia Beach), Virginia



Figure 8. Sand bypassing test site at Santa Cruz Harbor, California

to coastal problems. The system has been demonstrated to be rugged, reliable, and effective. During the field tests on the Gulf of Mexico and at Rudee Inlet, Virginia, the system operated successfully in the surf zone, in areas where the currents exceeded 2 knots, and in one instance, through a squall where wind speeds exceeded 50 knots and breaker heights were estimated at 8 ft. Principle advantages of the system are: its relatively low first cost; its tremendous flexibility in location of the jet pump intakes; its relative immunity to wave and current action; its simplicity of operation; and its noninterruption of navigation activities at a bypassing site. Disadvantages are: its proneness to plugging by shell fragments or other debris; and its relatively low production capacity (requiring perhaps continuous operation).

The research program is scheduled for completion in 1978 and publications to be released by that time will include systems design criteria.

ACKNOWLEDGEMENT

The work described herein is a portion of the Improvement of Operations and Maintenance Techniques research program of the U. S. Army Corps of Engineers, sponsored by the Office, Chief of Engineers, and performed at the U. S. Army Engineer Waterways Experiment Station. Permission to publish this description of this work is hereby acknowledged and is appreciated.

APPENDIX - REFERENCES

1. Govatos, George C., "An Experimental and Theoretical Study of a Solids Handling Center Drive Jet Pump and Its Application in Beach Nourishment Operations," Dissertation in Civil Engineering, University of Pennsylvania, 1971.
2. Zandi, I., and Govatos, G., "Jet Pump in Slurry Transport," Proceedings of Hydrotransport 1, British Hydromechanics Research Association, Paper L2, 1970, pp. L2-17 - L2-32.
3. O'brien, M. P., and Goslin, J. E., "The Water Jet Pump," University of California Publications in Engineering, Vol. 3, No. 3, pp. 167-190, 1942.

APPENDIX - NOTATION

- A_j = nozzle area, ft^2
 A_{mc} = mixing chamber area, ft^2
 B = area ratio = A_j/A_{mc}
 h_{dis} = total discharge head in feet of slurry
 h_{suc} = total suction head in feet of slurry
 h_{sup} = total supply head in feet of drive fluid
 H = head ratio = $(h_{dis} S_{dis} - h_{suc} S_{suc}) / (h_{sup} S_{sup} - h_{dis} S_{dis})$
 K_{dis} = loss coefficient due to the diffuser
 K_j = loss coefficient due to the drive jet nozzle
 K_{mc} = loss coefficient due to the mixing chamber
 K_s = loss coefficient due to the suction nozzle
 Q_{suc} = suction flow rate in gallons per minute
 Q_{sup} = supply flow rate in gallons per minute
 S_{dis} = specific gravity of discharge slurry
 S_{suc} = specific gravity of suction slurry
 S_{sup} = specific gravity of drive fluid
 γ_{dis} = unit weight of discharge slurry in pounds per cubic foot
 γ_{suc} = unit weight of suction slurry in pounds per cubic foot
 γ_{sup} = unit weight of drive fluid in pounds per cubic foot
 γ_w = unit weight of water in pounds per cubic foot
 ϕ = flow ratio, $(Q_{suc} \gamma_{suc}) / (Q_{sup} \gamma_{sup})$
 U, V, W, X = dimensionless computational parameters

CHAPTER 80

SAND-BYPASS AND SHORE EROSION, BRIDGMAN, MICHIGAN

BY

C. N. JOHNSON AND L. W. HIIPAKKA¹

The objectives of this paper are two-fold:

- a. Demonstrate by means of a well-documented full-scale case history in the Great Lakes that beach nourishment can mitigate shore damage due to a littoral barrier;
- b. Detail a methodology for analysis of the effectiveness of mitigation measures which lead to conclusions on the needed frequency of nearshore soundings as a tool for monitoring.

In 1970 a temporary harbor was installed by private interests along the southeastern Lake Michigan shoreline near Bridgman, Michigan, (Figure 1). The harbor was necessary to protect floating plant involved in building a large privately-owned electric generating facility. The harbor was constructed of steel sheet pile and extended lakeward about 125 meters from the water's-edge to a depth about 3 meters below low water datum (LWD)². Net littoral transport is about 75,000 cubic meters per year southward. The updrift and downdrift lakebed and bluff materials consist of sand.

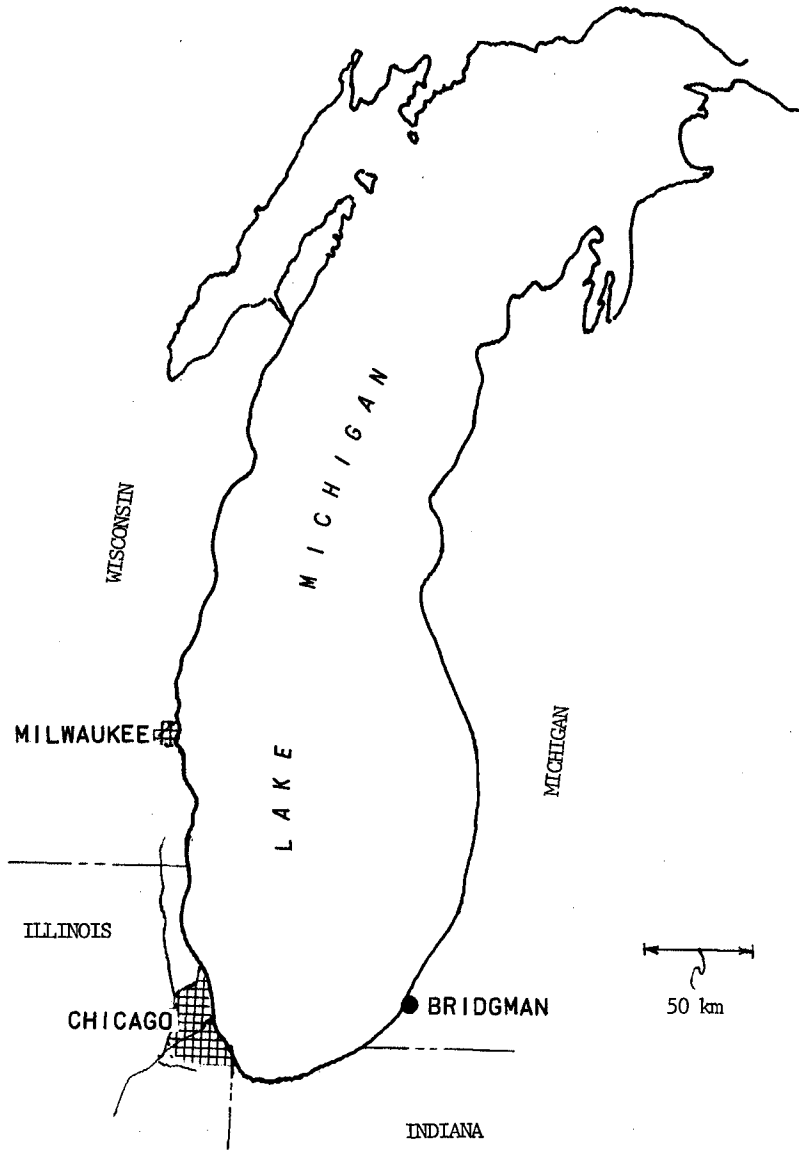
To ensure that this littoral barrier would not have an adverse effect on adjacent properties it was necessary for the Corps of Engineers to impose stringent requirements for issuance of a Federal permit for the installation. Bypass of at least 75,000 cubic meters per year of sand was required to mitigate potential erosion of downdrift beaches due to interruption of littoral transport. The permit also required intensive monitoring of the shoreline to ensure that any adverse effects of the harbor would be promptly detected and remedied. The monitoring consisted of:

- a. Monthly 1:3000 scale aerial photographs of the shoreline sixteen kilometers north (updrift) to sixteen kilometers south (downdrift) of the harbor.
- b. Monumenting and thrice-yearly measurement of backshore-nearshore profiles spaced 150 meters apart, for a distance of 2450 meters north and 2450 meters south of the harbor, extending about 900 meters lakeward to about -8 meters LWD (Figure 2). The nearshore soundings were made by acoustic sounder every 30 meters along each profile. The survey boat was located along the profile by triangulation. Backshore profiles were provided by photogrammetric mapping.

¹The authors are Hydraulic Engineers in the Coastal Engineering and Hydraulic Design Branch, U. S. Army Engineer Division, North Central, Chicago, Illinois, USA.

²Low water datum for Lake Michigan is 175.81 meters (576.8 feet) above mean sea level at Father Point, Quebec.

Figure 1. Location Map



- NOTES:
1. Circles denote end points of nearshore profiles
 2. Crosses denote locations of benchmarks

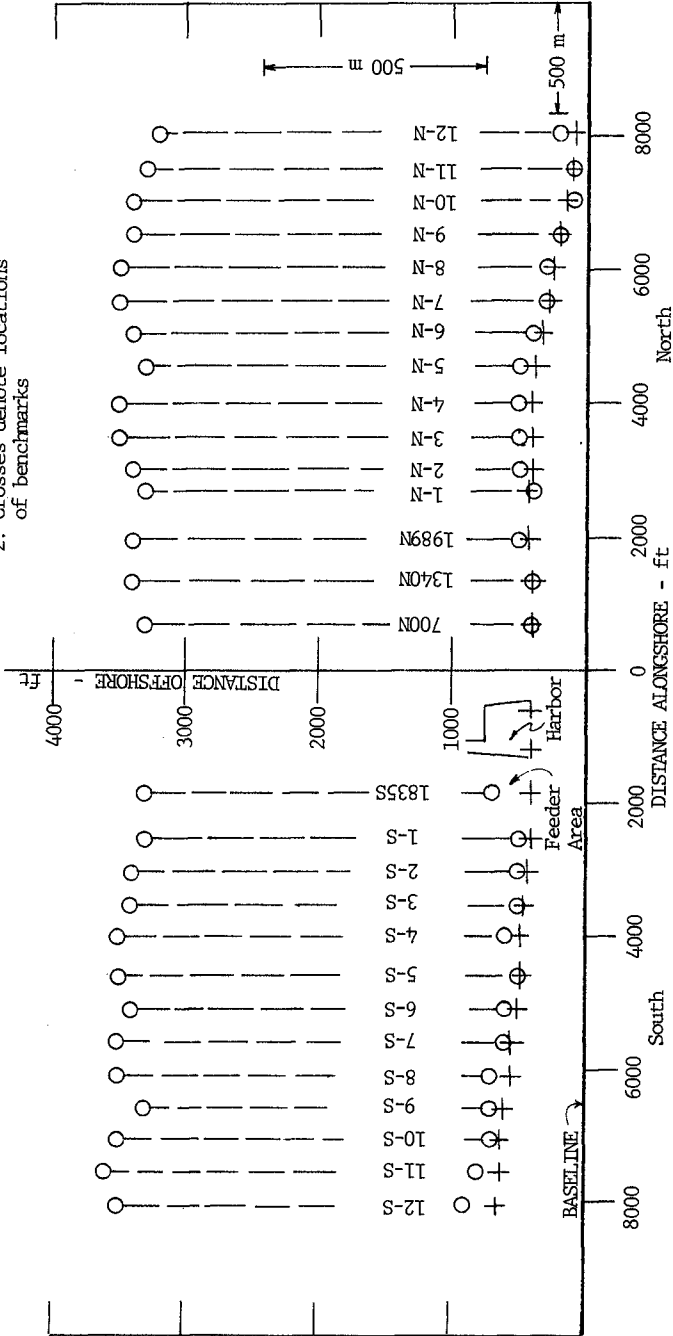


Figure 2. Layout of Harbor and Profiles

- c. Sand samples were taken during May 1973 at the water's edge, on the first and second sandbars for each profile and from the borrow sites. Additional water's-edge samples were taken during October 1973 near the property lines updrift and downdrift from the harbor.
- d. Wind speed and direction were recorded hourly near the water's-edge at an anemometer height of about 10 meters above LWD.

The permit went into effect and the temporary harbor was constructed in late 1970. The harbor was removed in late 1973. The monitoring program continued until December 1974. Tanner (1974) reported on an analysis of some of the resulting data. There is little overlap between his work and that of the authors.

The power company emplaced the following approximate quantities of sand in the feeder beach south of the harbor: 129,000 cubic meters in 1971, 143,000 cubic meters in 1972, and somewhat more than 230,000 cubic meters in 1973. About 40,000 cubic meters of those quantities were obtained by hydraulically bypassing sand from the accretion fillet. The remainder came from mining of the backshore dunes. The dune sand was used to comply with the permit requirements for a total of at least 75,000 cubic meters bypassed per year. The mined sand was much finer and better sorted than that of the beach north of the harbor. About 90% of the mined sand would be lost from the beach, based on overfill-ratio calculations (Shore Protection Manual, 1973) from the May 1973 sampling.

A thorough interim analysis of the data obtained as of October 1972 was done in early 1973 to determine if the sand-bypassing operation was mitigating the effects of the structure.

The results were as follows:

- a. There was no detectable net nearshore erosion or accretion. The nearshore profiles exhibited large volumetric fluctuations with time but little net change. Figures 3, 4, and 5 are examples. The straight lines on the plots are the regression lines of volume with time. Nearly all of the net changes were shown by t-test (Li, 1964) to be statistically insignificant at about the 80 percent level (Figure 6). There was no perceptible seasonal pattern.
- b. Volumetric bluff erosion varied considerable from profile to profile, but the average rate was essentially the same on both sides of the harbor (Figure 7). The symmetry of the average bluff erosion rates about the harbor indicate that the sand-bypassing and dune-mining operation compensated for sand entrapment by the littoral barrier.
- c. The analysis represented in Figure 8 shows that the nearshore profiles which eroded or accreted the most from July 1970 to

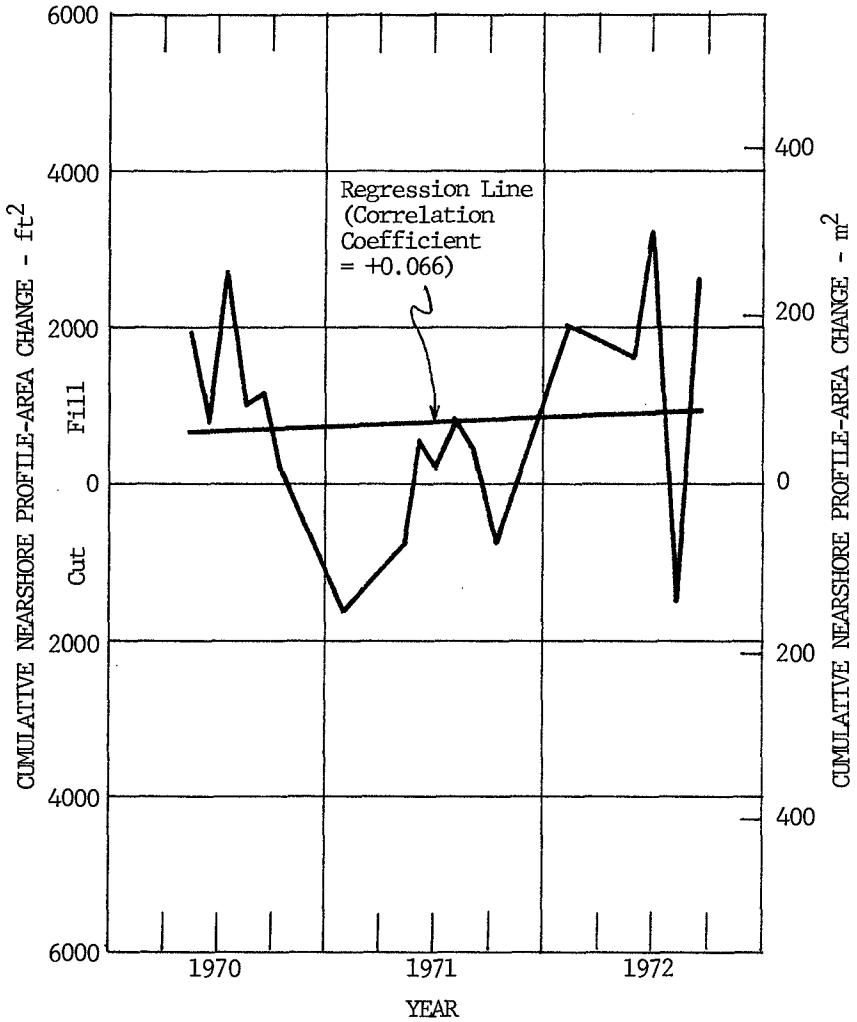


Figure 3. Time History of Cumulative Cut and Fill - Sec 4-S

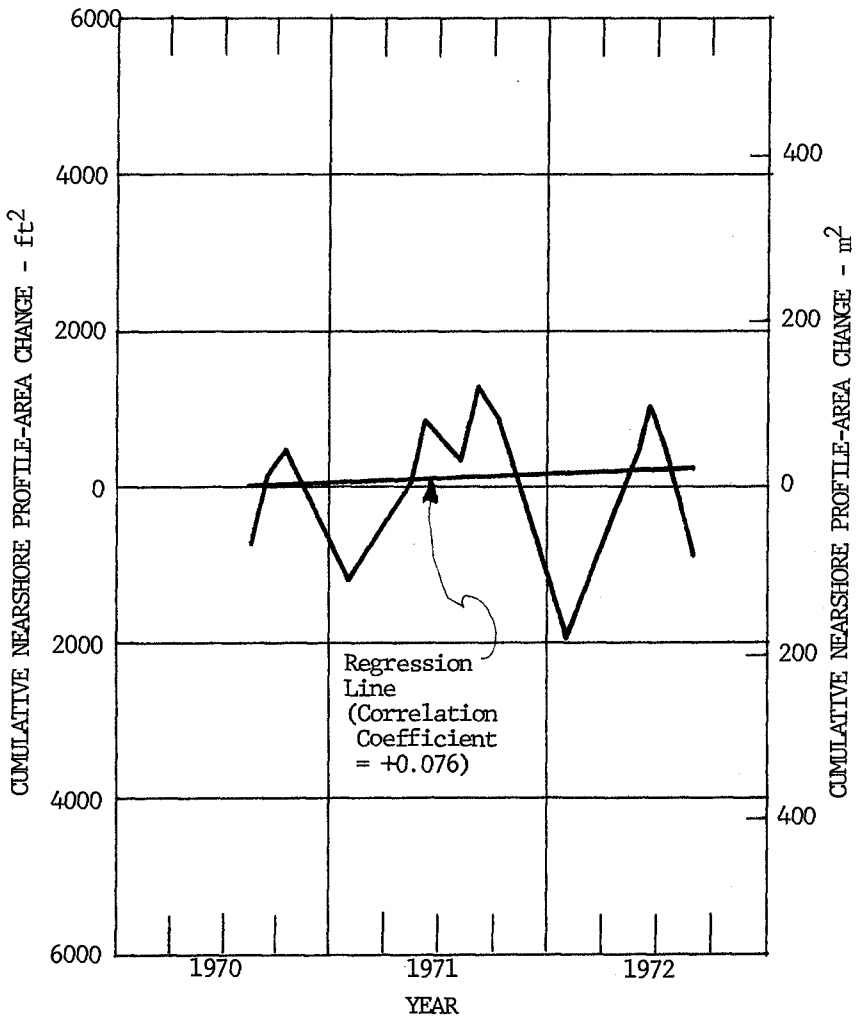


Figure 4. Time History of Cumulative Cut and Fill
Sec 4-N

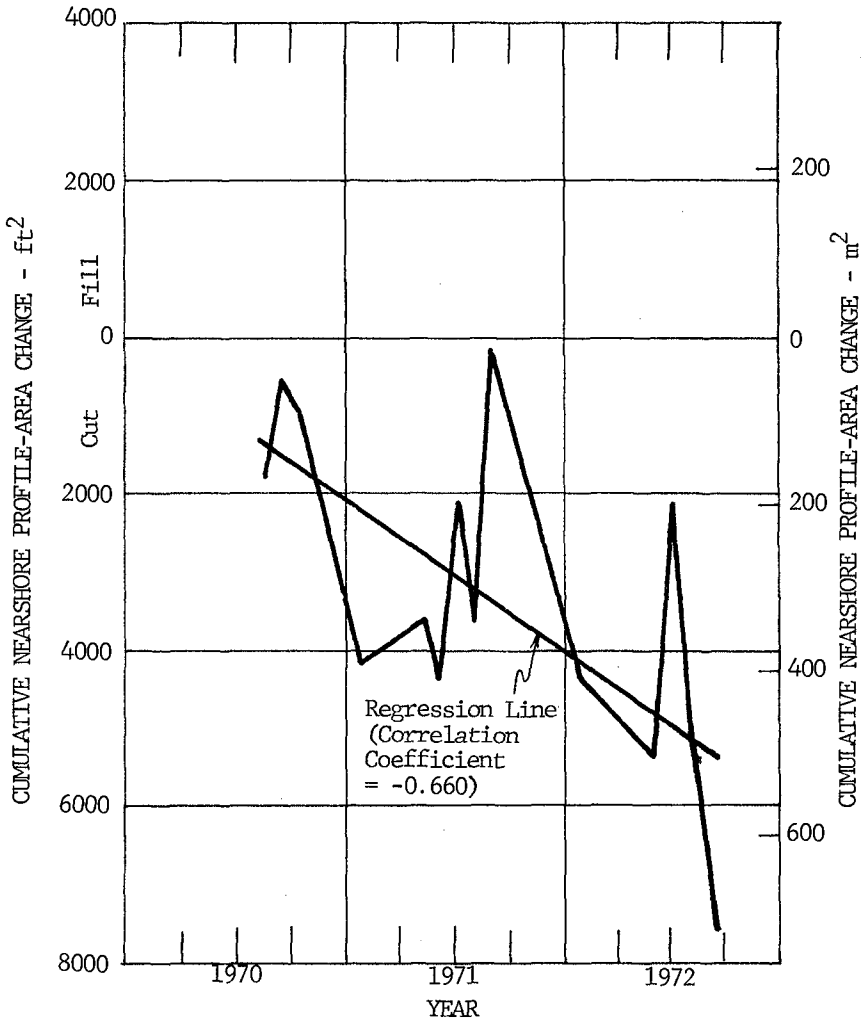
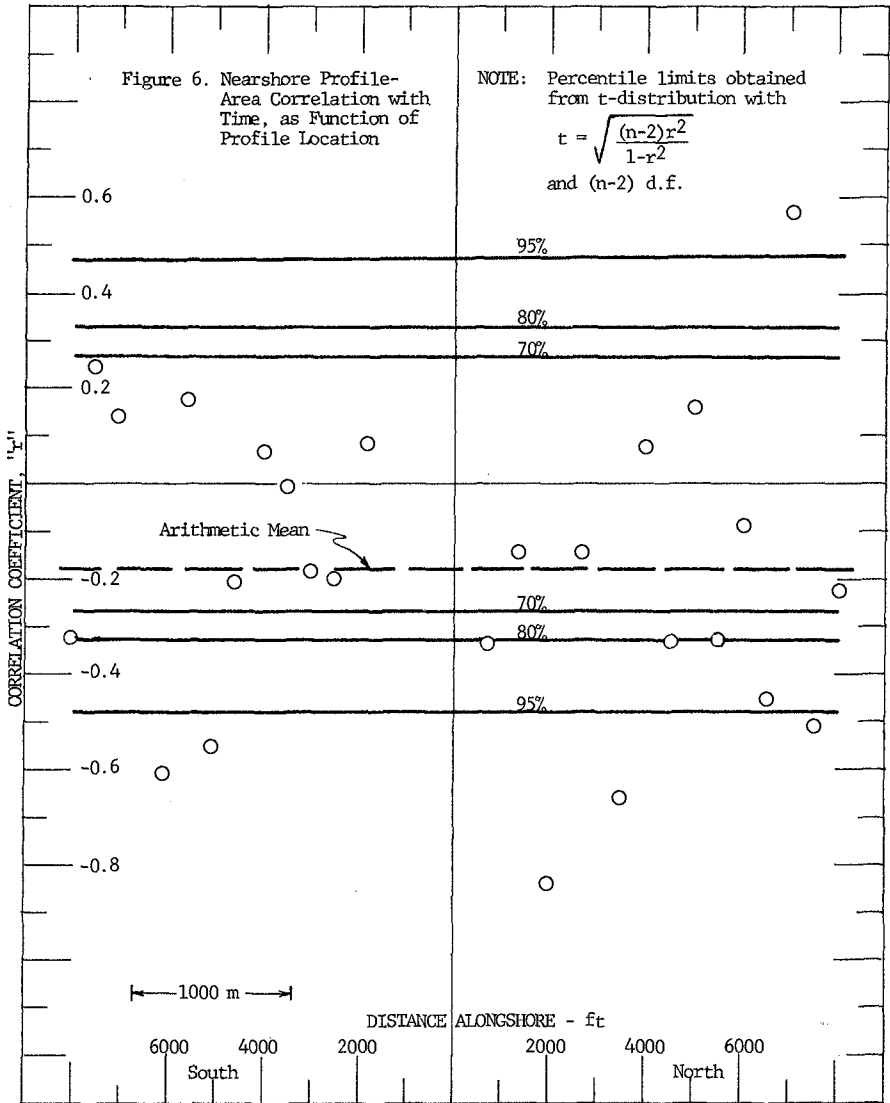


Figure 5. Time History of Cumulative Cut and Fill - Sec 3-N







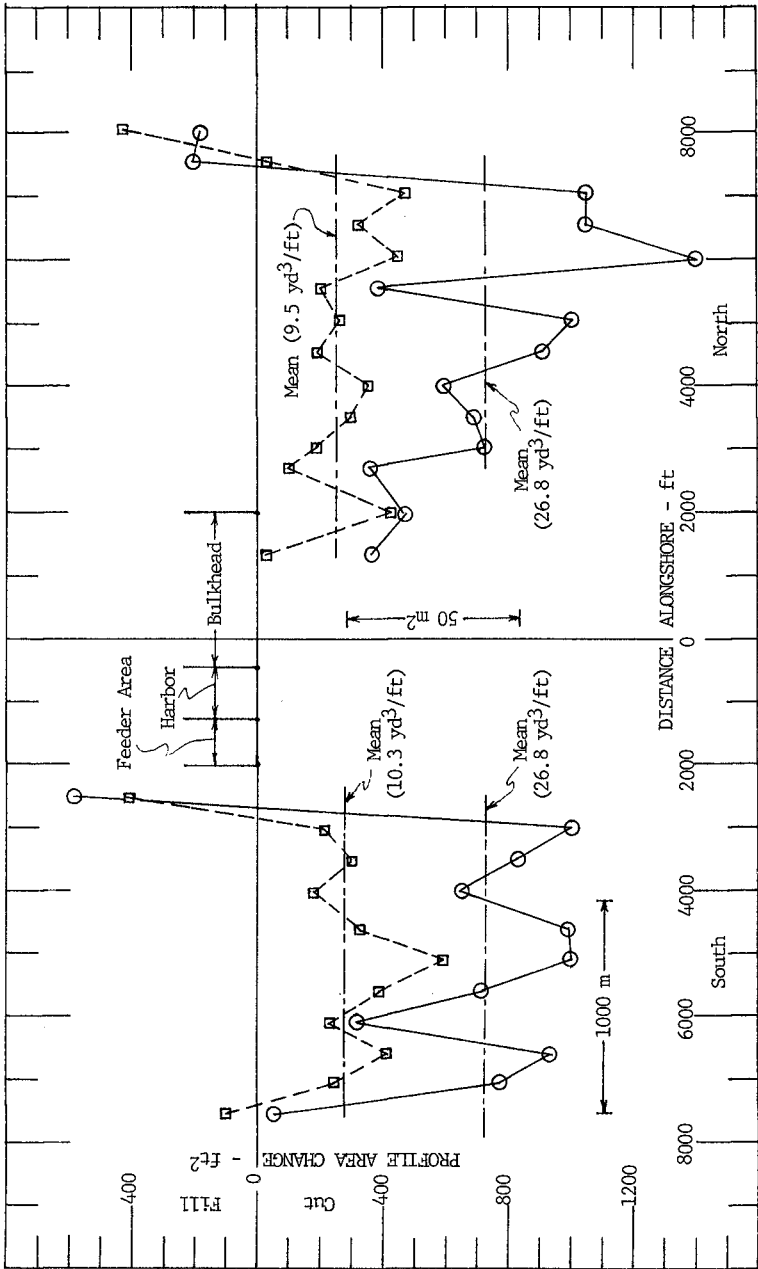
Apr 70 - Oct 72  - - - - - 
Apr 70 - Jul 73  - - - - - 

Figure 7. Beach and Bluff Volumetric Erosion Rates



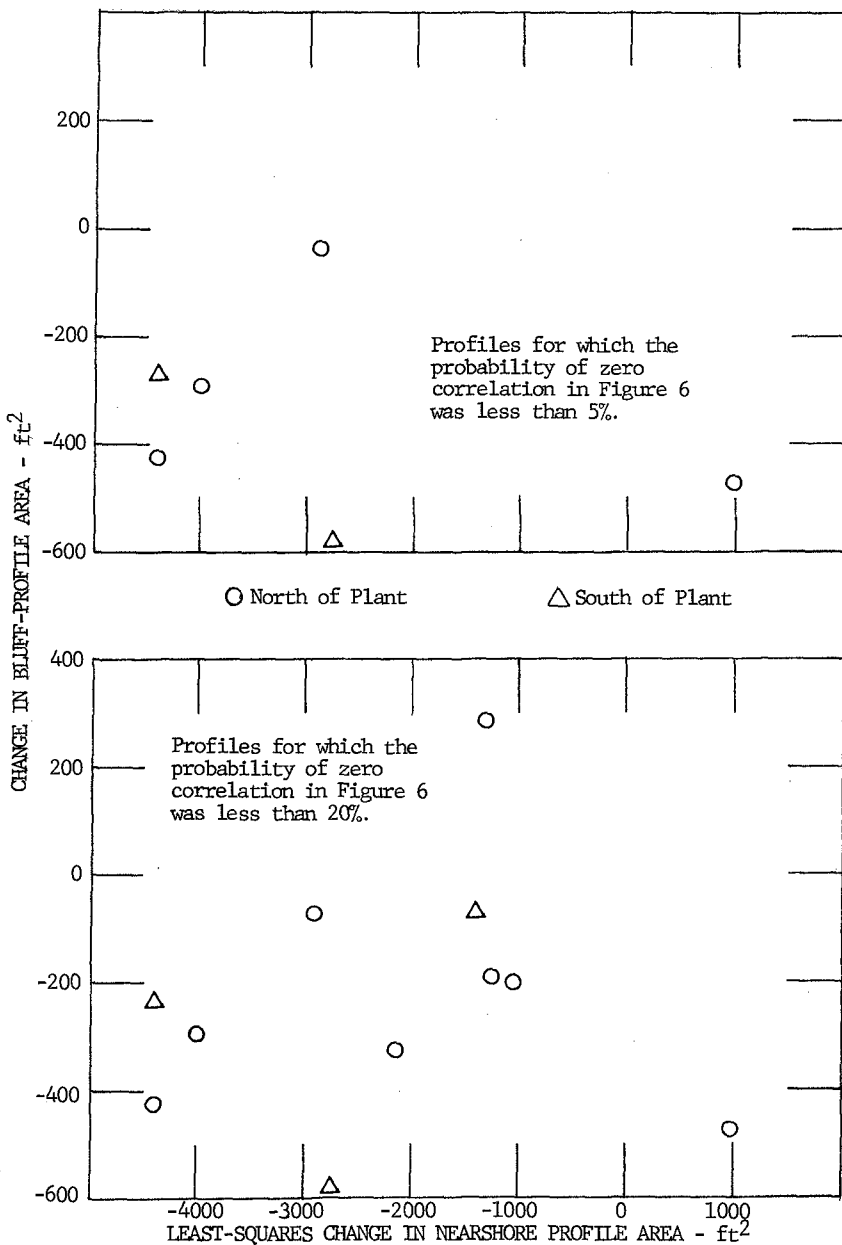


Figure 8. Lack of relation between bluff profile-area changes and nearshore least-squares profile-area changes

October 1972 did not coincide with the bluff profiles which exhibited the greatest changes. The profiles chosen for this figure are those whose correlation coefficients fell outside of 95 percent lines and the 80 percent lines, respectively, in Figure 6.

- d. The lack of any perceptible trends in Figures 6 and 8 indicate that no net deposition of eroded bluff material could be detected in the nearshore zone.

A second analysis was done in late summer 1973, using additional data from April and July 1973. Two unusually severe storms occurred during the 1972-73 storm season. These two storms evidently eroded about 1.5 times as much bluff material as had occurred in the preceding 2.5 years. However, average erosion was the same on both sides of the harbor (Figure 7). This symmetry indicates the continuing success of the sand-bypassing operation since natural updrift bluff erosion equalled bluff erosion downdrift of the harbor.

The third and final analysis, using data from October 1973 through July 1974, was done in late 1974. The harbor was removed early in this period. Storm-season water-levels were about 1.0 meters above LWD, the same as during the 1972-73 storm season. This level was about 0.3 meters higher than during the 1970-71 and 1971-72 storm seasons. There were no storms during the 1973-74 storm season as severe as in the preceding storm season. Bluff erosion took place at roughly the same rate as during the first two years, even though the water level was much higher (Figure 9). Average erosion rates were lower south of the harbor (1.7 m³/m) than north of it (5.3 m³/m). Much of this difference may be due to the large volume of sand emplaced when the harbor was removed.

The sand samples were not taken over a sufficient number of years to justify making firm conclusions from them. However, a few working hypotheses for future research seem to be noteworthy.

- a. Figures 10 and 11 show typical particle-size gradations from the May 1973 samplings. These samples were taken at the end of the severe storm-season discussed above. For all profiles, the median particle sizes were larger at the water's-edge than on the bars. Figure 12 compares the May 1973 water's-edge computed composite and borrow samples with the October 1973 samples (Krumbein, 1957, describes how computed composites are derived). The May water's-edge samples are coarser than the October ones. The May borrow-material gradation was similar to the October water's-edge gradation. If the observed changes in water's-edge material from May to October are typical of seasonal effects, considerable caution should be used in specifying artificial beach-fill gradations based on summertime beach samples.
- b. Trend estimates of nearshore erosion in Lake Michigan and, probably, the other four Great Lakes can be very misleading if

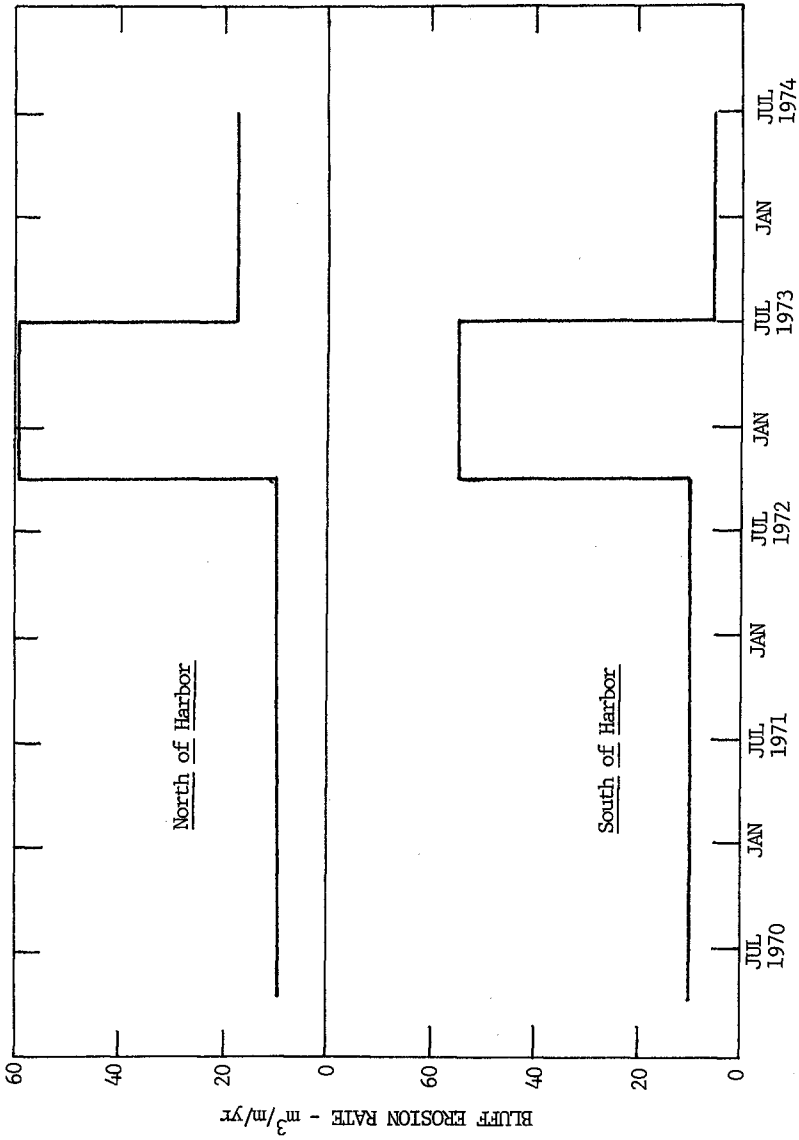


Figure 9. Variation of Bluff Erosion Rate with Time

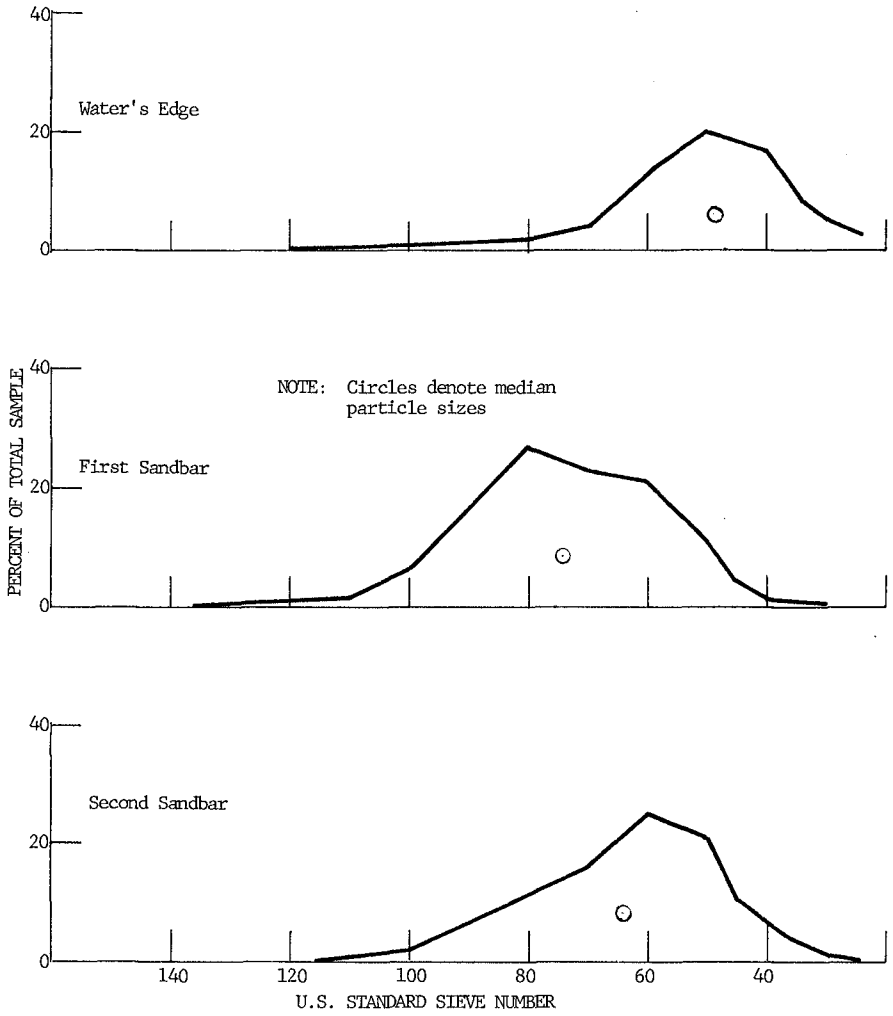


Figure 10. Particle Size Gradations as Function of Location
 - May 1973 Sampling, Profile 10-N

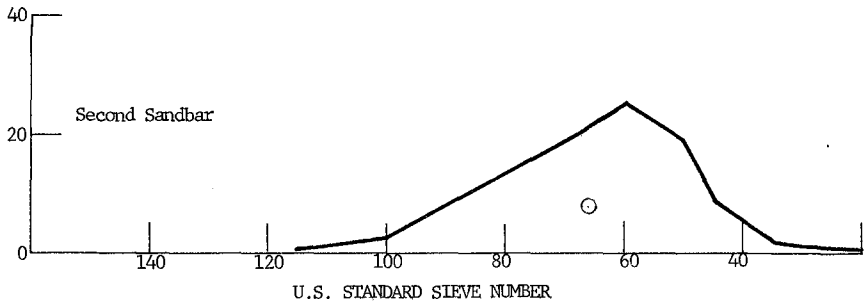
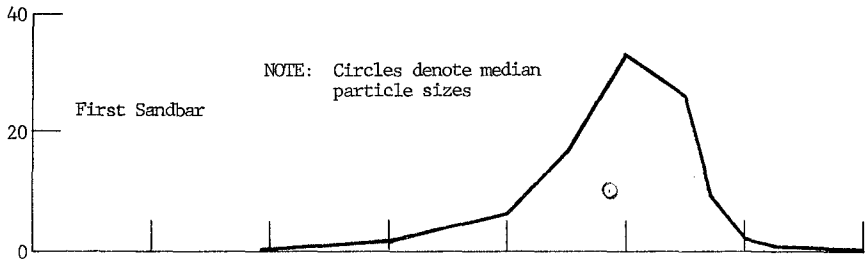
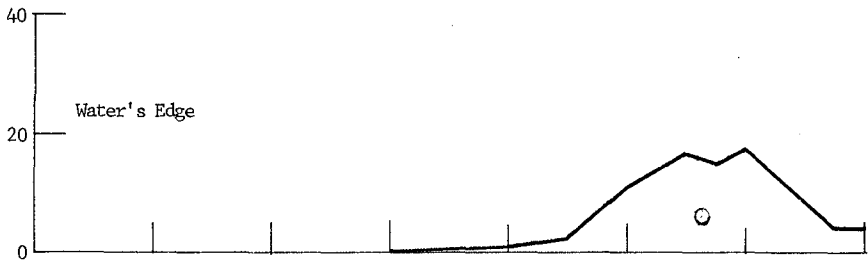
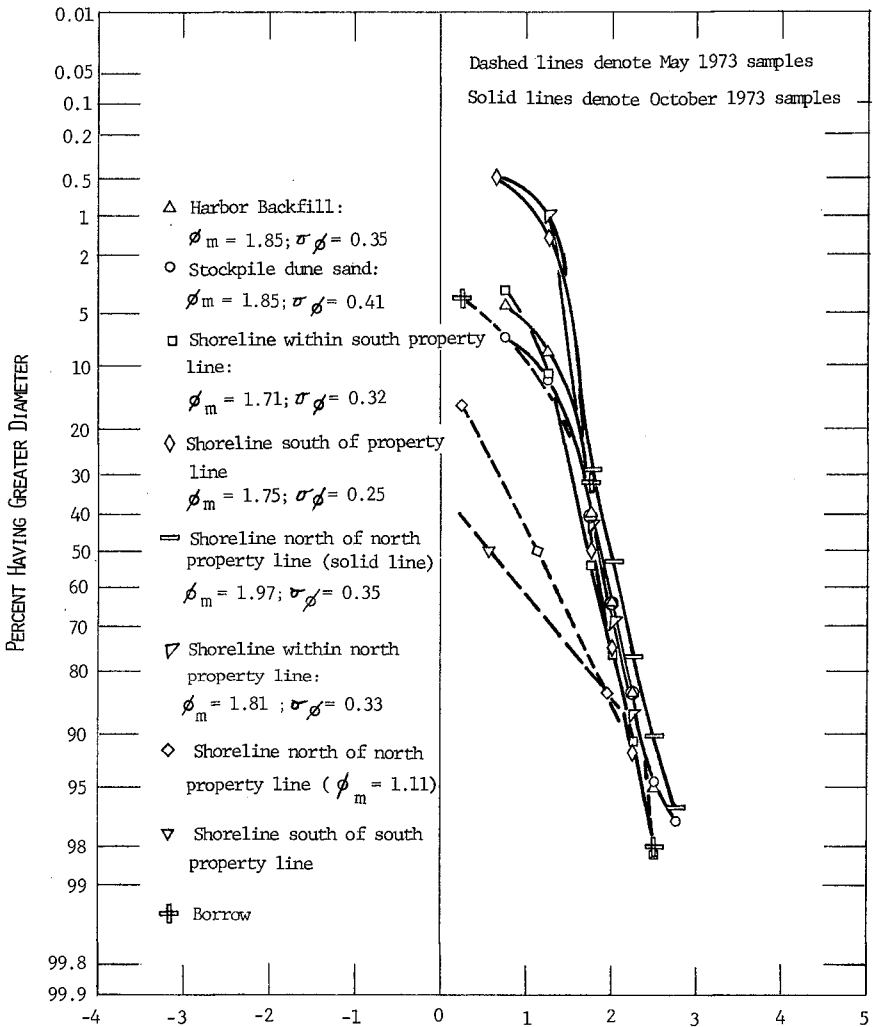


Figure 11. Particle Size Gradations as Function of Location
 - May 1973 Sampling, Profile 10-S

Figure 12. SAND PARTICLE SIZE DISTRIBUTION



based on soundings taken one or more years apart. As a consequence, soundings every three months apart for at least two years may be necessary to estimate the effects of random fluctuations on nearshore profiles.

- c. There was only weak correlation between Lake Michigan water levels and bluff erosion rates. Bluff erosion rates were highly variable from profile to profile. Severe storms seem to be the dominant factor in Lake Michigan shore erosion. Limited beach accretion, not erosion, took place when water levels were seasonally highest (summer). Erosion was severest during the late autumn and early spring when water levels were about 0.2 to 0.3 meters lower than their summer highs.
- d. Large quantities of finer-than-native sand, in excess of the longshore transport rate, were placed on the shore south (downdrift) of the harbor. Downdrift bluff erosion rates were the same as updrift in spite of the excessive quantities. These results imply that beach nourishment with finer-than-native sand may be an inefficient way to control erosion. In spite of the massive quantities of material, erosion still proceeded at the natural rate.

Acknowledgements

Appreciation is expressed to the Chief of Engineers, United States Army, Corps of Engineers for permission to publish this paper. The authors are grateful to the District Engineer, U. S. Army Engineer District, Detroit, and his staff for their assistance in preparation of the paper.

References

Krumbein, W. C., "A Method for Specification of Sand for Beach Fills," TM-102, U. S. Army Corps of Engineers Beach Erosion Board, Washington, D. C., October 1957.

Li, Jerone C. R., Statistical Inference, Ann Arbor: Edwards Brothers, Inc., 1964.

Tanner, W. F., "Beach Processes, Berrien County, Michigan," Seventeenth Conference on Great Lakes Research, 1974.

Shore Protection Manual, U. S. Army Coastal Engineering Research Center, 1973.

CHAPTER 81

DESIGN AND BEHAVIOUR OF SANDTRAPS IN REGIONS OF HIGH LITTORAL DRIFT

By

P.C.Saxena, P.P.Vaidyaraman, and R.Srinivasan

Central Water and Power Research Station, Pune, India.

1. Introduction :

Siltation in harbours and their approach channels is one of the major problems connected with the development of harbours. The economics of harbours are directly related to their annual maintenance dredging, and as such a proper assessment of the quantity of siltation and provision of adequate measures for the maintenance of depths would form an important part of planning the development programmes.

Siltation could occur due to various reasons viz. deposition of littoral drift which is interrupted by the approach channel, deposition of sediments brought into suspension by wave action (including during storm/cyclone) Whenever the alongshore drift is large, wave action obviously is quite substantial which renders the maintenance of depths during this period by dredging difficult. In such cases it would be necessary to make adequate provision to ensure that the depths are not deteriorated to any substantial extent by the movement of the drift. One of the common means for achieving this is the provision of sandtraps on the updrift side of the approach channel which would 'store' the drift material temporarily and from where the material could be dredged at convenience. The design of the sandtrap would be governed by a number of factors such as the extent over which a major part of the drift takes place, quantity of material transported, size distribution of sediments, velocity of currents, mode of dredging etc.

Waves of moderate to high intensity occurs along the eastern coast of India from south and south west direction during south west monsoon period from May to September and from North Easterly direction during North East monsoon beginning from November. In view of this climate the direction of drift along the shore changes with season. The quantities of drift during these periods are also different owing to the magnitude and periods of wave action which differs between the two seasons.

The net drift along this coast varies from 0.60 million m^3 at Madras on the south which increases progressively to 1.00 million m^3 at Paradip further North (Fig. 1).

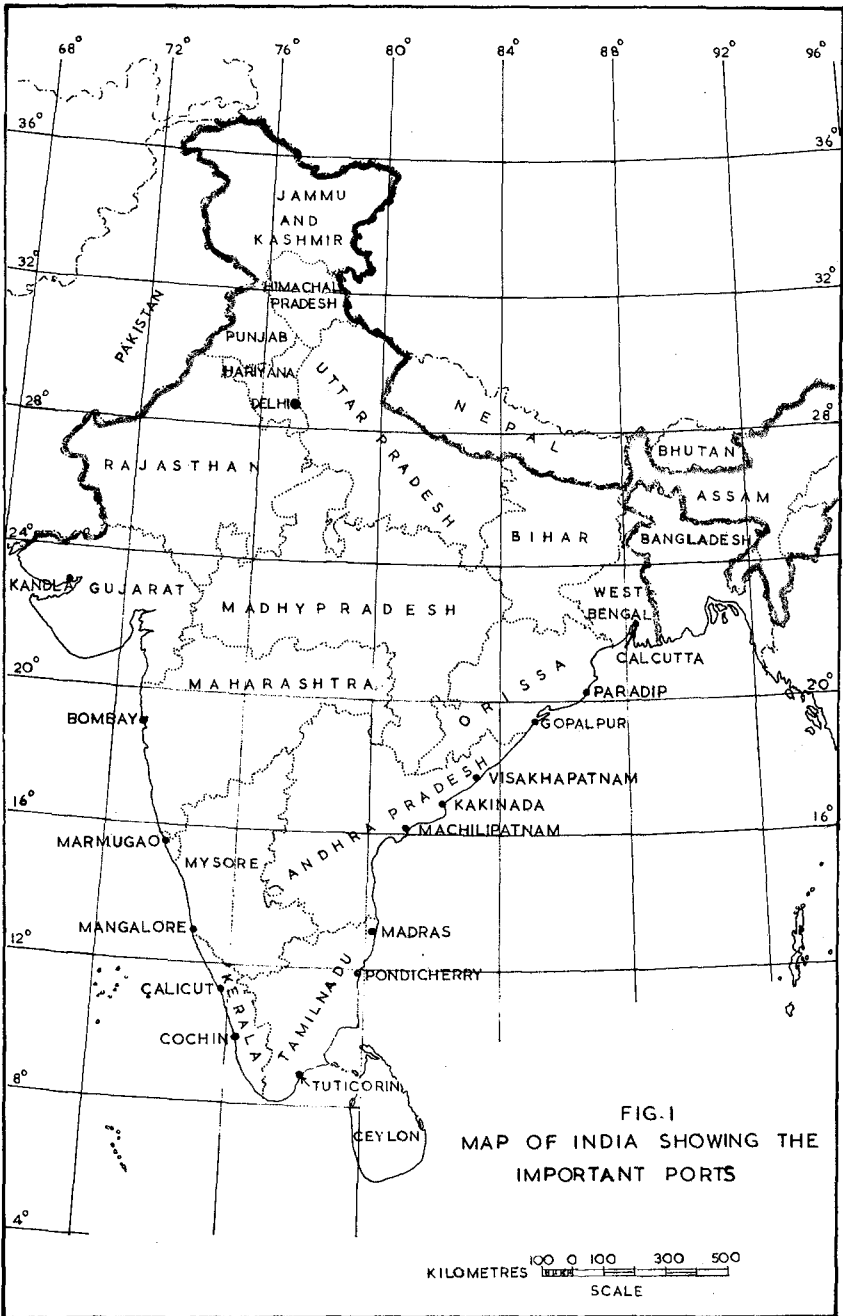


FIG. 1
MAP OF INDIA SHOWING THE
IMPORTANT PORTS

KILOMETRES 100 0 100 300 500
SCALE

Sandtraps are successfully employed for a number of ports along this coast to prevent the drift from deteriorating the channels. In this paper the case histories of some of these ports are discussed together with reference to the model studies carried out at the Central Water and Power Research Station, Pune for the design and layout of these sandtraps.

2. Methods of tackling littoral drift :

The method adopted for the tackling of littoral drift would be governed by the wave climate, the quantum of drift, the nature of operation of the port etc. The configuration of the coastline would also be modified by the drift as shown by Silvester *(1) who has made a comprehensive study of the sediment movement along the various coastlines of the world. Though this information is qualitative, it helps in a broad sense for the identification of the length of coastline which can affect the sediment supply to any specific location.

An idea of the rate of drift is generally obtained by making observations of the rate of accretion updrift of jetties as well as from the records of maintenance dredging. Johnson (2) has used this method of analysis in order to tabulate the rates of drift along the coastlines of the world. It could be seen from his tabulation that the littoral drift along Madras coast obtained by the measurement of rate of accretion south of the breakwater of Madras port is of the order of 0.60 million m³ (0.74 million cubicyards).

It is also well known that a major portion of the littoral transport occurs within the breaker zone. Hence other things remaining the same, the rate of drift per unit width of the coastline would be higher along a steeper coast as compared to a flatter one.

One of the methods adopted to maintain the inlets for navigation in a littoral drift zone has been by use of sand pumps. The material dredged from the entrance to the inlet by the sand pumps are generally pumped on to the down drift side for re-establishing the littoral drift cut off by the inlet. This method has been found to be successful along the Atlantic coast of USA for the maintenance of small inlets. Similar method was also adopted for the maintenance of the approach channel to Durban Harbour South Africa. In India, this type of dredging for a major harbour was considered for the first time in the case Paradip port (in Orissa State) on the east coast.

Though a Sand pump mounted on a trestle forms a fairly simple method for tackling the drift problems, various difficulties connected with the maintenance of the pumps, cavitation and their limited mobility render them unsuitable for universal adoption. Accordingly, provision of sand traps of maintenance by mobile dredger etc. have been found to be more favourable during recent times.

*. References are given at the end of the text.

3. Types and sizes of sandtraps :

Depending upon the site conditions, the orientation, size and location of the sandtraps would vary from place to place. A shallow irregular natural depression at Durban Harbour has been utilised to serve as a sandtrap whereas at Paradip and Visakhapatnam Ports trapezoidal shapes have been adopted. As already mentioned earlier, the inability to dredge during the period of occurrence of littoral drift necessitates storage of the drift material in the trap. The quantum to be stored (and the allowable extent of sand bypassing) would depend upon the individual site conditions. Where the coastline is steep the available space for provision of the trap would also be limited in the seaward direction.

The provision of an island breakwater would considerably help in overcoming this difficulty in that the capacity requirement of the trap could be somewhat reduced since the tranquillity conditions made available by the breakwater would help in continuing the dredging operations over a longer period of time than otherwise possible. Such an example is found in the case of Visakhapatnam Outer Harbour, a major port on the east coast of India, as well as in the case of the Port of Gopalpur also located along the same coast (Fig. 1). The following illustrations are given in order to highlight the aspects mentioned above.

4. Case histories:

4.1 Visakhapatnam Port:

The Port of Visakhapatnam is located on the eastern coast in the State of Andhra Pradesh at a distance from 12.50 km north of the tip of the Indian Peninsula. This port is one of the oldest ports in India and was originally brought into operation in order to cater to vessels drawing upto 10 m for a traffic of 4 million tonnes of general cargo (Fig. 2). The littoral drift being large, a sandtrap existed updrift of the approach channel from where the material was periodically dredged. During 1967, with the advent of iron ore mining industry and the mechanisation of mining at Baladilla, Madhya Pradesh and the expansion of the harbour facilities the development of an Outer Harbour for deep draft ocean carriers was found essential. The total traffic anticipated was then estimated to be of the order of 12 million tonnes of iron ore. The layout of the outer harbour consisting of three breakwaters (southern, northern and eastern) providing thereby a sheltered basin for the development of berths was envisaged to cater for this traffic. The net littoral drift in this region is estimated to be of the order of 0.70 million cubic metres per annum with the predominantly northerly drift of 0.88 million cubic metres during the SW monsoon period

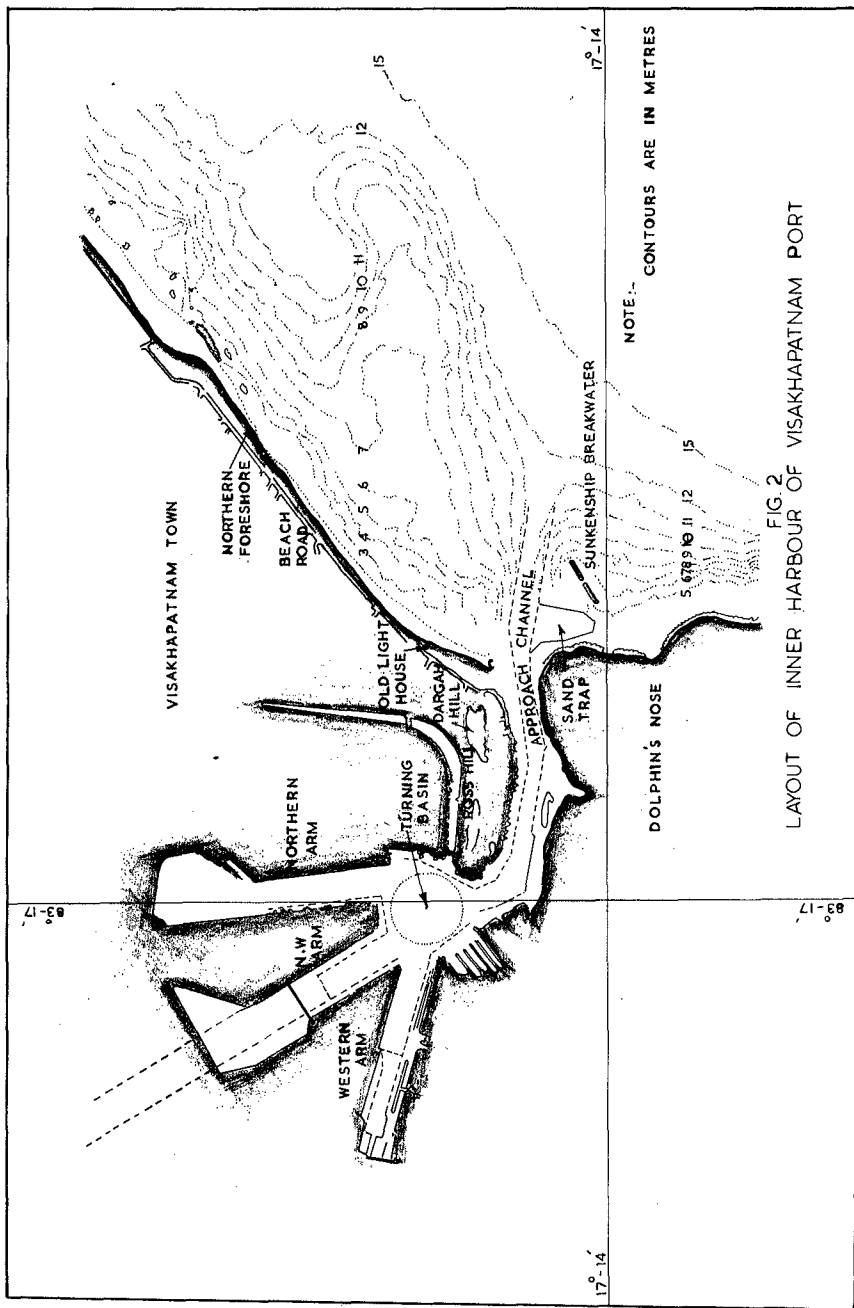


FIG. 2 LAYOUT OF INNER HARBOUR OF VISAKHAPATNAM PORT

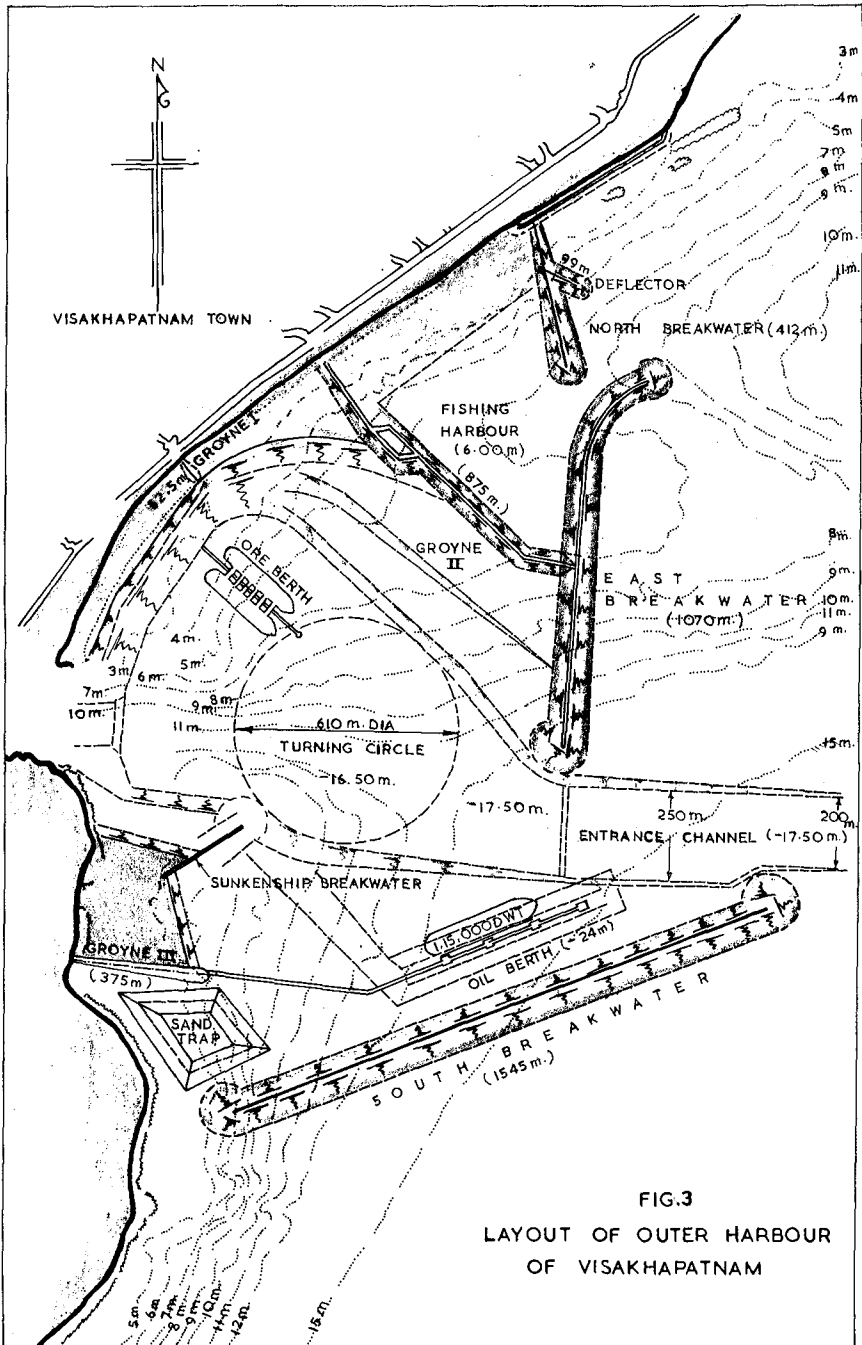


FIG.3
LAYOUT OF OUTER HARBOUR
OF VISAKHAPATNAM

from April to September and weaker return drift of 0.18 million cubic metre during the NE monsoon period from November-January. The coastline in this region is very steep being of the order of 1:10 in the nearshore region, and the 6 m contour is only at a distance of 150 m from the coastline. This obviously would result in the establishment of the breaker zone near the shoreline. As a major part of the drift is confined only to the region between the shoreline and the breaker zone, the conditions for locating the sandtrap are critical and accordingly a sandtrap was located in the gap between the sunken ship breakwaters and the shoreline as shown in Fig. 2. With the development of the outer harbour, this sandtrap originally provided no longer served the needs and its location had to be changed.

Extensive model studies were carried out at the CWPRS in order to determine the best location and the alignment of the sandtrap. The southern breakwater was located in this layout in such a way as to provide the necessary width for the entry of littoral drift into the sandtrap. It was found necessary to ensure that consequent upon the filling of the sandtrap the entrance does not get choked which, if allowed to happen, would have the result of making the trap ineffective during subsequent seasons. A mobile bed wave model built to scales 1:240 H, and 1:80 V was utilised for these studies and the sediment movement was reproduced by using crushed walnut shell having a specific gravity of 1.36 and a median diameter of 0.50mm. Deposition in different areas with the drift reproduced was ascertained from these model studies from which it was ensured that the trap having dimensions of 260m x 180m should provide a capacity of 0.62 million cubic metre which would be quite effective in trapping the material. The final layout is shown in Fig. 3. The sandtrap has been recently dredged at the Port and it is understood that its performance is satisfactory.

4.2 Paradip Port:

Paradip, another major harbour on the eastern coast of India is located 450 km north of Visakhapatnam Port. The main export through this port is iron ore to Japan to an extent of 2 million tonnes. The facilities at present consist of an iron ore jetty capable of accommodating 60,000 DWT ore carriers and a cargo berth for 18,000 tonne cargo vessels. The physical conditions at Paradip are somewhat different from those existing at Visakhapatnam. The slope of the beach at Paradip is much flatter, of the order of 1:80. The frequency and intensity of cyclones at Paradip are also much higher as compared to Visakhapatnam. Flatter beach slopes at this Port result in much longer approach channel for this port and as the littoral drift will be taking place over a much wider region, the size of the sandtrap would also have to be larger to trap a substantial part of the drift. This would necessitate providing a much wider gap between the shoreline and the island breakwater which would increase the transmission of wave energy into the harbour entrance and consequently create more wave disturbance. Accordingly it was necessary to modify the location of the sandtrap and the layout of

the breakwaters to overcome this problem. This layout is shown in Fig. 4. In order to bypass the northerly drift material which would get accumulated south of the southern breakwater, it was proposed to use a sand pump having a capacity of 350 cubic metres per hour moving on a trestle 250 m long for pumping sand and discharging the same to the northern side for nourishment by means of a floating pipeline across the harbour entrance. This would also help in minimising erosion of the coastline north of the harbour.

The harbour construction was completed during 1965 and the port started functioning formally from March 1966. However, due to various problems, the sand pump could not come into operation within the stipulated time. Consequently considerable accretion on the southern side of the breakwater took place besides erosion on the northern side. By 1967 the fillet on the south side was completely saturated with drift material and gradually the material found its way into the approach channel around the tip of the roundhead resulting in the formation of a shoal in the approach channel restricting the entrance width and depth considerably.

Detailed studies were carried out in a hydraulic model and it was considered that a sandtrap having a capacity of 0.8 m cubic metre as shown in Fig. 4 was necessary for this port. This sandtrap could intercept the drift during the south-west monsoon period and could be dredged during the subsequent fair weather season by the port's dredger (cutter suction hopper dredger). Accordingly the sandtrap was dredged during 1969-70 by a contract dredging. The data available subsequently has been analysed in order to examine the behaviour of the trap. Fig. 5 shows the differential depth contours during the monsoons from 1970 to 1974 at the sandtrap. It could be seen from this figure that during the year, 1970 and 1971, the loss of depth outside the sandtrap is practically negligible, whereas considerable loss of depth is found to occur east-wards beyond the confines of sandtrap subsequent to 1971 thereby indicating that the zone of pre-dominant sediment movement is extended east-wards due to the flattening of the beach slope. Fig. 6 shows a comparison of the cross sections of the beach updrift of the trap. It may be mentioned that the design of the sandtrap is evolved assuming that the sand pump could come into the operation so that it could help in maintaining the beach slope updrift of the trap. However, even after the installation of the pump during 1971, the dredging was not very satisfactory resulting in the flattening of the slope mentioned earlier. Fig. 7 shows the loss of mean depths during different monsoons at various sections of the channel. It could be seen from this figure, that during the initial periods after the dredging of the trap, the loss of depth was confined only to a small distance from the approach channel from the tip of the breakwater, the length extending further east-wards during the subsequent periods for reasons already mentioned.

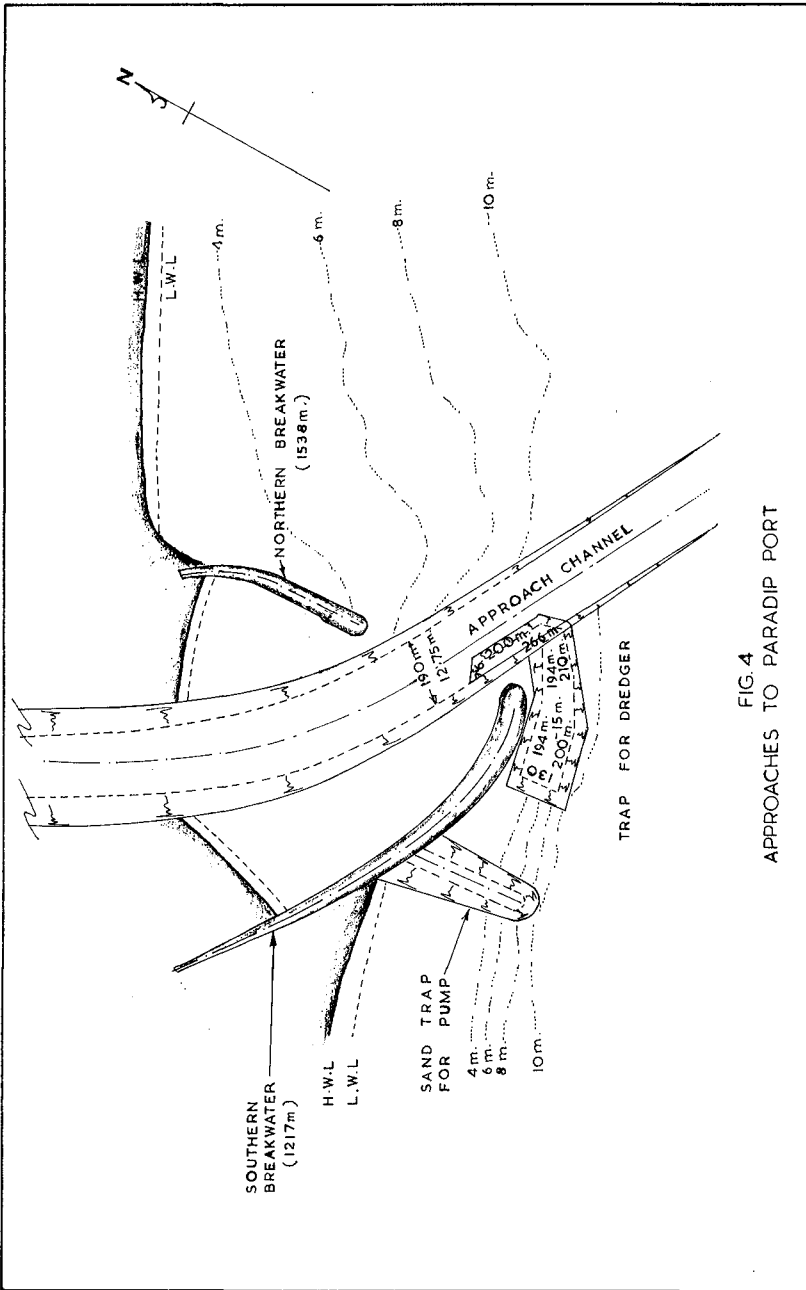
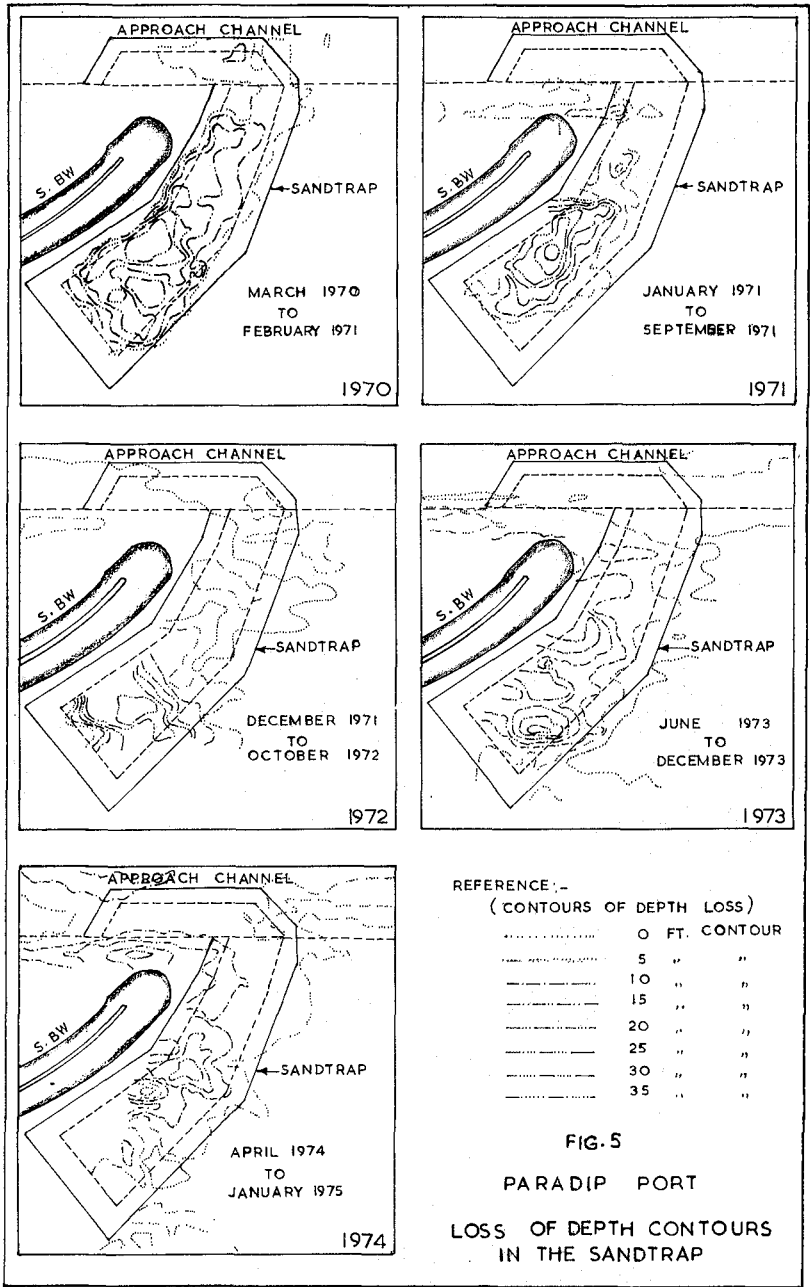


FIG. 4
APPROACHES TO PARADIP PORT



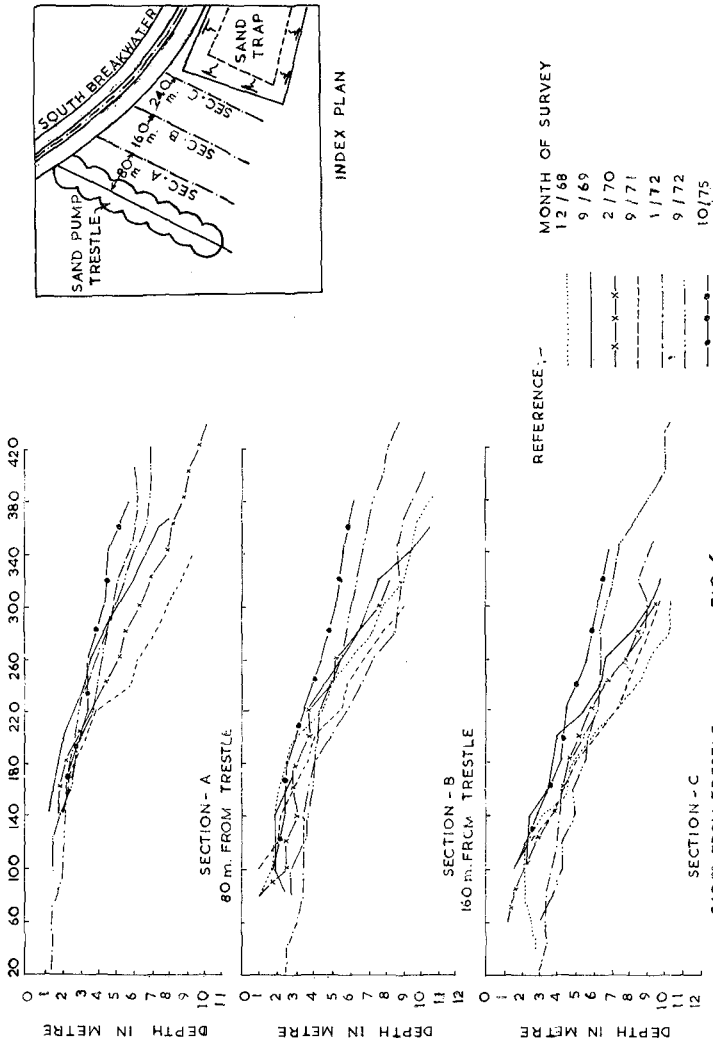
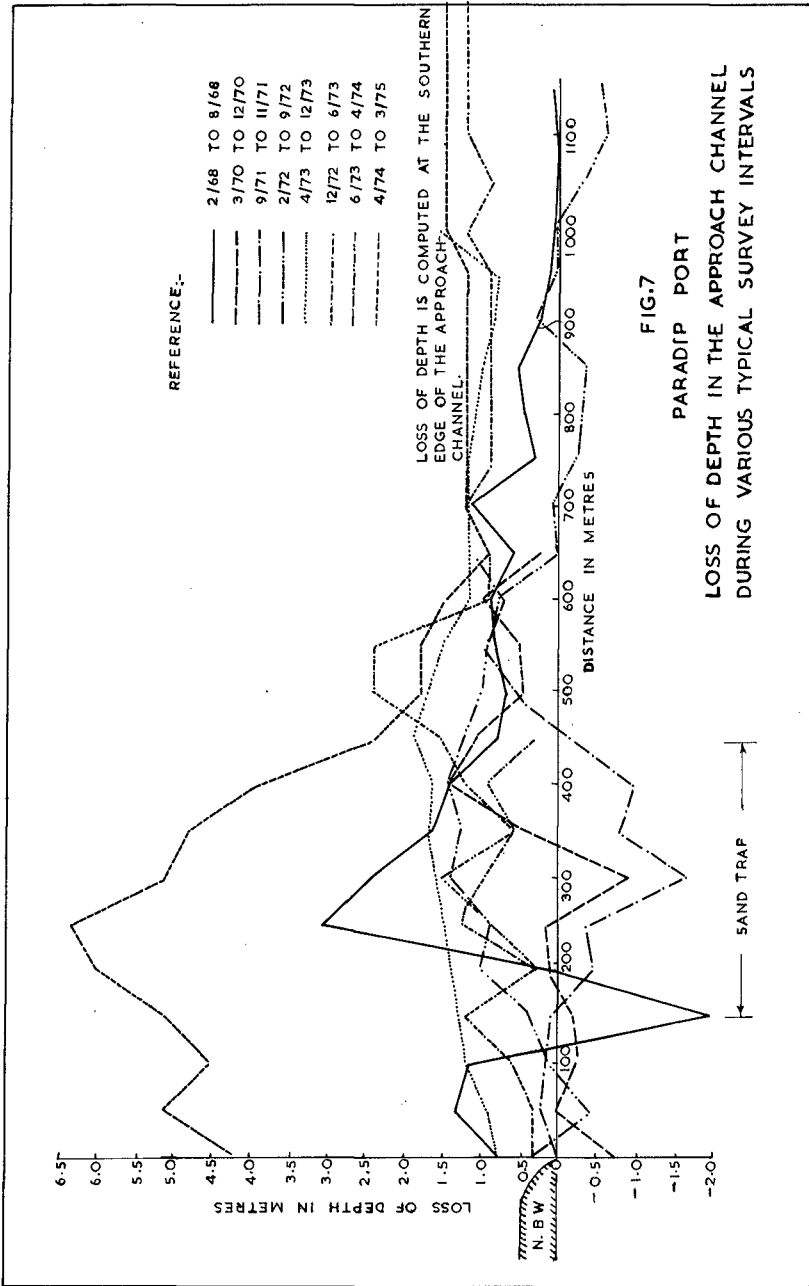


FIG. 6
CHANGE OF CROSS SECTIONS BETWEEN THE TRESTLE AND THE SANDTRAP DURING DIFFERENT PERIODS.



Since this region is situated in an intensely cyclonic zone, the effect of cyclones on the siltation pattern in the approach channel also needs consideration. The currents due to cyclones some times tend to act in a direction opposite to the prevailing littoral currents and affect siltation in the approach channel. This could be seen from the effect of a typical cyclone which occurred during 1-10-1971, during which the siltation was along the northern edge of the channel. An additional sandtrap in continuation with the approach channel along the northern edge of the approach channel was dredged by the port authorities in order to provide for such eventualities.

4.3 Kakinada Port:

The Port of Kakinada is an intermediate port located at Kakinada to a distance of 120 km south of Visakhapatnam. The total traffic through this port is of the order of 0.3 million tonnes consisting mainly of iron ore, rice bran etc. The old port is located 4 km inside a canal into which barges requiring upto 2 m draft navigate. The canal meets the bay called the Kakinada Bay which is formed by a sandspit about 10 km long bordering along the eastern side (Fig. 8).

The history of the sandspit is very interesting from the engineering point of view. Before 1850 the sandspit was completely absent in this region and subsequently due to the changes in the outfall in the River Godavari the formation of the sandspit took place gradually. Fig. 9 shows the formation of the sandspit at different times. With the absence of river flows into the Kakinada bay, the flushing characteristics changed considerably, and siltation of the bay started taking place from the south and SW side. The bay was gradually converted into a tidal bay. The opening at the mouth of the bay would therefore be the function of the relative flushing ability of the bay vis a vis strength of the littoral drift. The cross section area of the mouth of the inlet would therefore follow a law similar to O'Brien (3) who studied the effect of tidal prism in maintaining the inlets in the number of cases.

Recently, expansion of the port has been envisaged by the port authorities for traffic upto 1.5 million tonnes. One of the proposals for this expansion is the provision of mooring facilities west of the sandspit taking advantage of the shelter offered by the spit from wave action. The development and the stabilisation in the sandspit would therefore be of major importance in this programme.

Extensive model studies were conducted in a tidal-cum-wave model built to scales 1:600 Horizontal and 1:40 Vertical and injecting crushed walnut shell for reproducing littoral drift. It

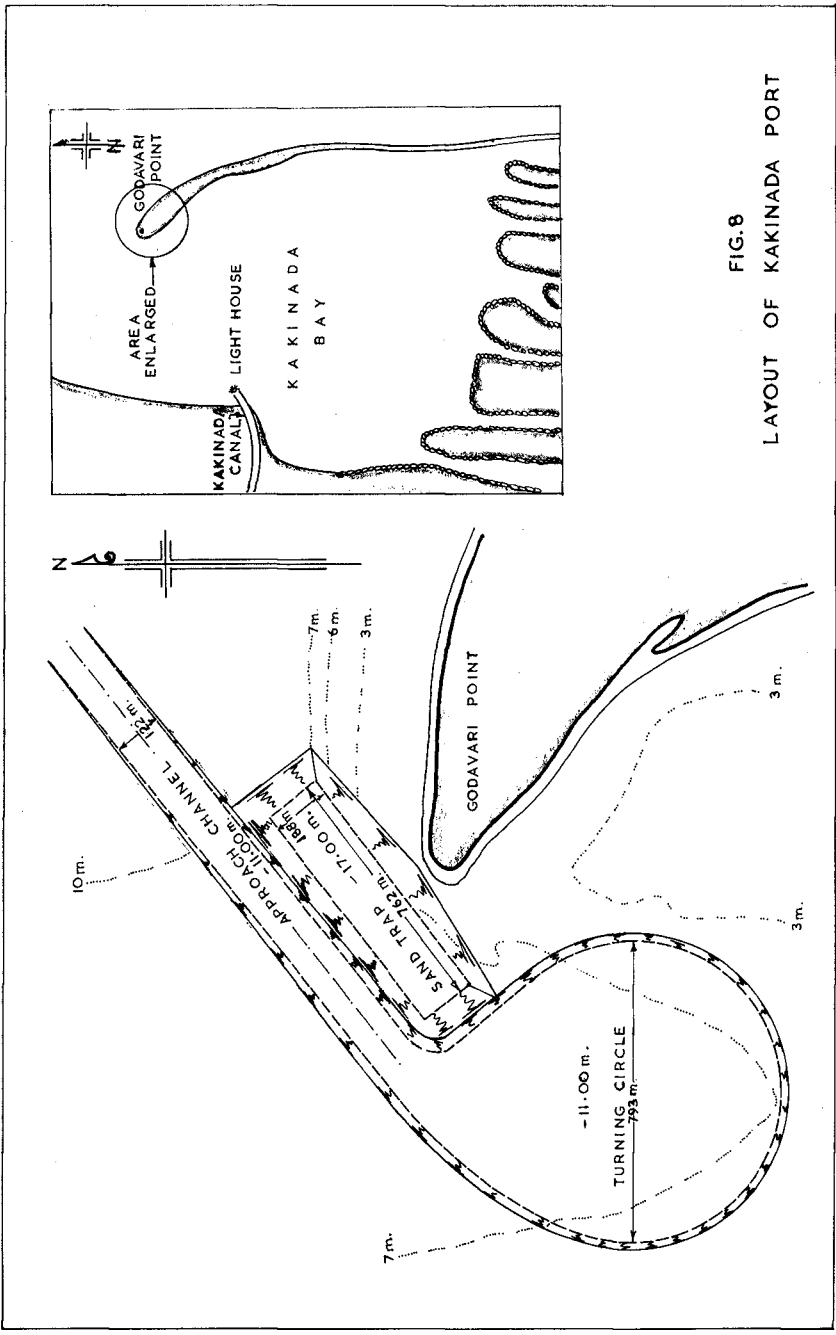
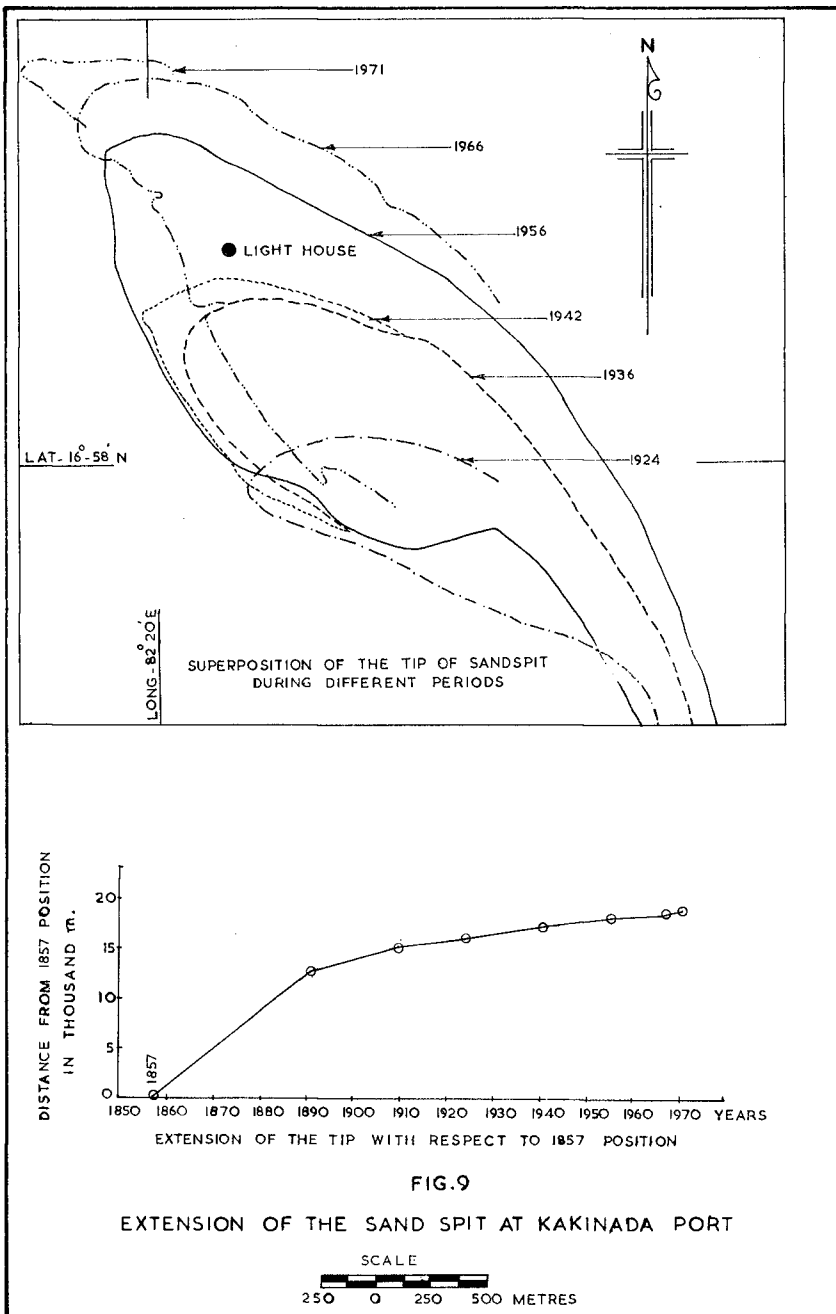


FIG.8
LAYOUT OF KAKINADA PORT



was found that the provision of a sandtrap in the vicinity of the tip of the sandspit would be helpful in preventing the deterioration of the channel due to littoral drift.

These experiments were carried out reproducing in the model a duration equivalent of 25 years in the prototype. The annual maintenance dredging was also reproduced during these tests. It was found that during initial years when the tip of the sandspit is away from the edge of the sandtrap the quantity of siltation in the trap is low and a major part of the drift is utilized only in shallowing of the regions between the edge of the trap and the tip of the sandspit. As this region becomes shallower, the quantum of siltation in the trap increased progressively so that after a period of 10 years, the total quantity of siltation is 60 % of the drift which increases to practically the entire drift after a period of 20 years.

These studies illustrate the long term experiments that would be required as a progressive increase in the quantum of siltation necessitate a corresponding increase in the capacity of the trap.

A proposal to construct a breakwater across the bay from the shore and provide berthing facilities near the entrance where depths are adequate is also under consideration. Studies in the model indicated that this would result in increasing the flushing velocities to a considerable extent because of the constriction of the bay and the area at the mouth. As a consequence it was also found necessary to alter the orientation and location of the sandtrap since a shifting of the direction of extension of the sandspit was seen to take place towards the easterly direction.

5. Conclusions:

The above examples are intended to illustrate the means of effectively maintaining the channel and prevent the drift from affecting depths at the approach channel and the harbour entrance. The variation in the meteorological, geomorphological and physical conditions would require different considerations in their design and where one type would be suited, it may prove to be unsuitable in a different location even along the same coast because of the different physical factors. Further the fact that the slope of the beach on the updrift side should be maintained without too much of a change for an efficient functioning of sandtrap is well brought out in the case of Paradip. The experience in Paradip also indicates that besides the pre-dominant direction of drift due to wave action the effects of currents generated by storms would also need to be carefully considered. The sandspit development in the case of Kakinada is a unique feature which calls for a different type of analysis and studies in the proper location and design of sandtrap. The need for studying the behaviour of the sandtrap over a long term period has also been brought out.

The above studies also indicated the relatively minor role played by sand pumps in the regions where the littoral drift are substantially large. It is necessary to go in for more reliable dredging equipment and methods in order to ensure the infallibility of the proposals.

Acknowledgements:

The data obtained from the respective project authorities have been made use of in the above discussions which is gratefully acknowledged. Extensive use has also been made of the various reports and notes of the Research Station prepared from time to time.

The authors also acknowledge the help received from Mr. V.V.Vaze in the analysis of the data and carrying out the model studies.

References:

1. Silvester R. 'Sediment movement around the coastlines of the World', Conference on Civil Engineering problems overseas, Inst. of Civil Engineers, Paper 14, 1962.
2. Wiegel R.L. 'Oceanographical Engineering', Prentice Hall, 1965.
3. O'Brien M.P. 'Equilibrium flow area of inlets on sandy coasts', Proc. ASCE, Vol. 95, WW1, Feb 1969.

CHAPTER 82

HEADLAND DEFENSE OF COASTS

Richard Silvester, University of Western Australia
Nedlands, 6009, W.A.

ABSTRACT

Crenulate shaped bays are ubiquitous and constitute the largest proportion of coastline length. The characteristics of stable bays (i.e., no littoral drift) are known, so that realistic encroachment limits can be defined. Allowances for long term changes in direction of persistent swell and annual attack from multidirectional storm waves may have to be made. The exposure of a rock outcrop during an erosive sequence will create a new fixed point on the coast and hence a new bayed system. An existing non-stable bay can be prevented from indenting to its equilibrium shape by the construction of one or more fixed points around its periphery. Research should be conducted to minimise the cost of headlands which might start off as offshore breakwaters, even mobile units.

INTRODUCTION

Observance at the shoreline itself, or better still hydrographic charts of same, will immediately highlight the predominance of bays as coastal features. These sandy stretches are strung between headlands, with outlines that are produced by the incoming persistent waves (generally the swell). The presence of such features, together with other obvious indicators, has been used by the author in 1962 to determine net-sediment movement around the coastlines of the world (1) (2).

A worthwhile analogy appears to be clothes hanging loosely on a clothesline. When the wind arrives normal to the wire, the edges of the fabric assume a symmetric cartenary between the pegged points. No matter what the spacing some curvature will occur. The degree of indentation of the cartenary is dictated by the length of fabric caught between the pegs, as illustrated in Figure 1A. In coastal terms the variable is the volume of sand available to construct the beach. Sometimes when there is a surfeit of sand in a batch supply a spit may be formed which encloses a body of water in the form of a lake or lagoon. This is exemplified in Figure 2A, a feature which exists along many sea margins.

There is no equivalent to the sand spit in the cloth hanging analogy but it can be pursued with advantage a little further. When the wind blows obliquely to the peg line the cartenaries are skewed as depicted in Figure 1B. A large section of the cloth edge is pulled normal to the wind vector, causing the remainder to be stressed into a curve. The indentation as before is dependent upon the tautness of the original pegging. Again the analogy can breakdown, by nature constructing spits to form the crenulate shape that has the characteristics of an equilibrium bay. (See Figure 2B)

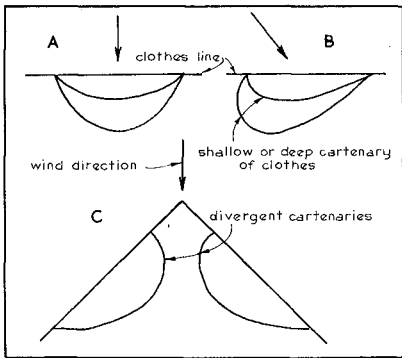


Fig.1. Analogy for crenulate shaped bays of clothes pegged to a line.

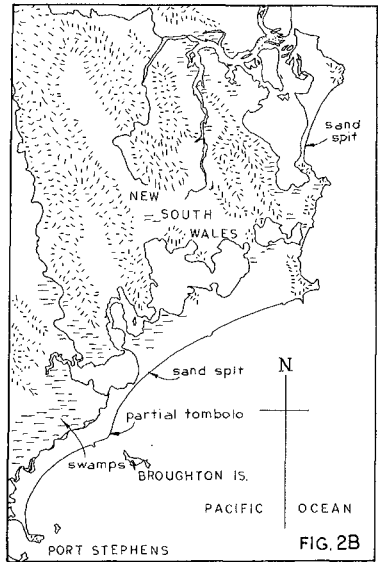
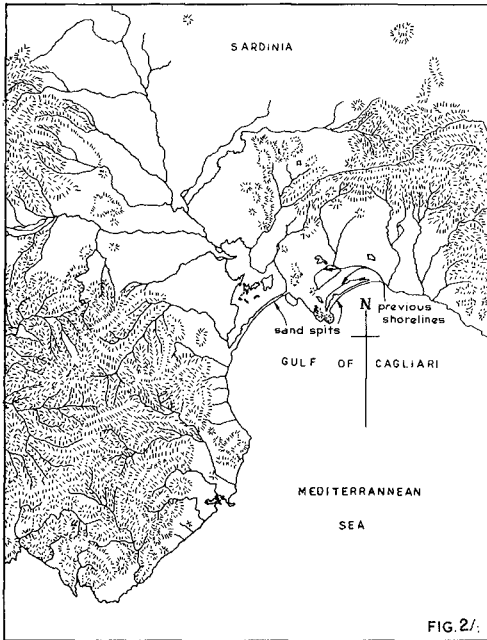


Fig.2 Sand spits formed between headlands enclosing bodies of water. A: with normal wave approach B: with oblique wave approach.



Where a clothesline changes direction, say at right angles as in Figure 1C, the fabrics will be skewed differing amounts and perhaps in differing directions by a given wind. The author has noted this drastic change in two adjacent bays at Point Reyes, California (3) but a further example is illustrated in Figure 3.

The forcing function in the clothesline case is the wind, which produces immediate results on the clothes. The sculpturing strength for shorelines also originates from the wind but is effective per medium of the waves it generates, both locally and far away. As noted by the author elsewhere (4) the generation of waves in the various oceans is reasonably repetitive and hence natural bays exhibit the integrated influence of swell over decades and centuries.

BAY FEATURES

The characteristic of crenulate shaped bays produced by waves arriving obliquely to the alignment of two consecutive headlands has been detailed already (4) (5) but should be recapitulated here. As seen in Figure 4, such a bay comprises a tangential downcoast section and a curved upcoast zone. The resultant shoreline shape is caused by both wave diffraction and refraction (6) in the lee of the upcoast headland. The degree of indentation (termed a in Figure 4) is dictated by a number of variables, namely, the obliquity of the predominant waves (β) to the headland alignment the spacing (b) between the headlands and the supply conditions of sand from upcoast or from river mouths within the bay.

As illustrated in Figure 4 the angle β between the incoming wave crests and the headland alignment is similar to the angle between the tangential coastline and this alignment. This is easier to measure because wave approach from deep water to some representative depth along the seaward extremity of the bay is difficult to determine, even if the predominant 12 second swell is adopted (7) for this purpose. It is the value of β at the fully stable condition that should be used in relationships to be discussed later. However, at the downcoast extremity of the tangent zone this angle is exhibited even in a bay still eroding to its final stable shape. Progressive indentation is achieved by the lengthening of this beach line angled β to the headland alignment.

The spacing (b), within which the bay can form, is related to (a) and (β) by a graph as in Figure 5. This has been derived (6) from model tests and measurements made of natural bays known to be in equilibrium, from their location on a coast and obvious lack of sediment supply. Although the ratio a/b tends to zero as β decreases there will always be a little indentation even with normally approaching swell. This is because a net longshore drift of zero may be made up of an annual drift in each direction of similar magnitude. The other limit of 50° for waves arriving parallel to the headland alignment is not likely ever to be realised because of prior refraction across the continental shelf. It could only result in a lake situation where the predominant waves are locally generated and they are of short period. In this case the curved shoreline will be almost circular in character due to diffraction dictating the crest curvature in this shadow zone.

It has been shown (4) (8) that the curved portion of the coast generally follows a logarithmic spiral, the details of which are illustrated in Figure 6. The ratio of successive radii (R_2/R_1) results from the angle (θ)

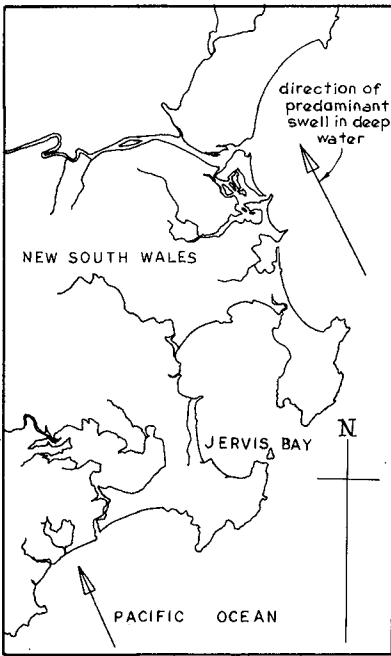


Fig.3. Variable shape and orientation a/b of crenulate shaped bays for a specific approach direction of predominant swells in deep water.

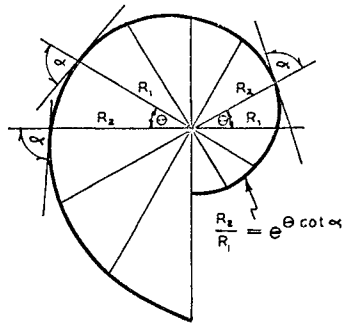


Fig.6. Definition sketch of logarithmic spiral.

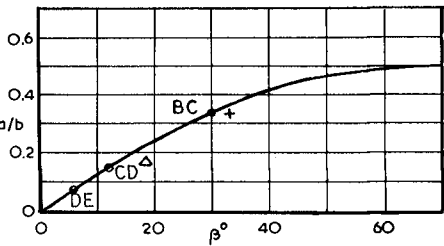
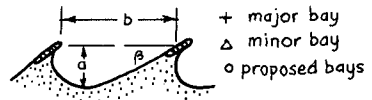


Fig.5. Indentation ratio a/b versus wave approach angle β .

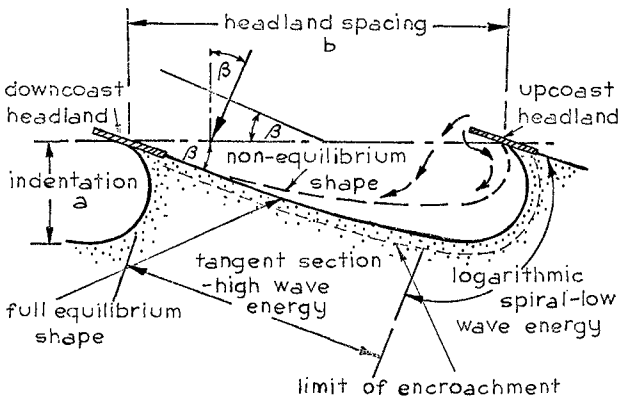


Fig.4 Definition sketch of crenulate shaped bay.

between them and the constant angle (α) between the radius and the tangent. The degree of curvature is given by α whence a logarithmic spiral can be drawn once θ has been chosen. A series of such spirals have been provided by the author (4). It should be noted that the size of the bay or of the plan being examined is of little consequence as the same value of α or R_2/R_1 will result, only a different section of the curve will be utilised. For equilibrium conditions the curve relating β to α is given in Figure 7. Whilst a bay is receding to this stable shape, values of α vary in a consistent manner with angle β as shown elsewhere (3) (4).

When in equilibrium a bay suffers no littoral drift since the predominant waves are arriving normal to the beach at all points around the periphery. This does not preclude the possibility of batches of sediment arriving sporadically from upcoast. This will mainly be transmitted across the bay to the intersection of the tangent curved zones as proven by tracer tests in Australia (9). Because of the almost normal approach of the waves the longshore component of their energy is slight, so requiring the offshore zone to accrete to the stage where the waves can handle the load to be transmitted.

The offshore shoaling lessens the demand for material to construct the bar during storm sequences. This reduces the berm width which is indicative of the active beach which goes to sea and back again in the course of each two or three years. The good protection so afforded makes little or no demand on the sand dunes being constructed by wind blown sand which therefore grow to much greater height along the tangential section of the bay than along the curved zone.

USE OF CHARACTERISTICS

Whilst the evaluation of a/b and α for a measured β may indicate a bay to be in a non-stable condition, this is not the case if the present sand supply to the bay equals the rate of removal by the waves. If an embayment is not fully receded the plotted point will fall below the curve in Figure 5 and above the curve in Figure 7. By using the a/b and α values on the curves an equilibrium shape can be drawn for this bay which indicates the limit of erosion if and when all sediment supply is stopped. It is on this basis that more realistic encroachment lines may be determined than setting back fixed distances along the whole periphery of a bay.

When so determining building lines, due allowance should be made for annual give-and-take by storm waves. These waves can arrive from almost any seaward direction. The erosive effects of arrival from three major obliquities are illustrated in Figure 8, where the width of lost beach varies according to this angle. The presentation does not take into account the likely offshore slope variation around the bay. The tangential stretch should have a milder bed slope than the curved zone, which infers that less material is demanded to construct the protective offshore bar during storm sequences.

A point to note about Figure 8 is that a rip current will form in the vicinity of the greatest indentation. This means that longshore drift brought from both directions towards this zone will quickly construct a shoal and the seaward current will also aid the dissipation of storm waves.

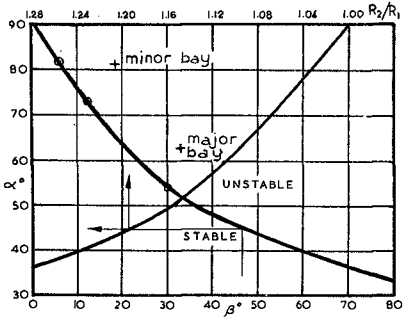


Fig. 7. Logarithmic spiral constants (α and R_2/R_1) versus wave approach angle β .

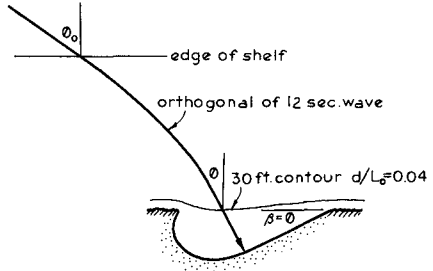


Fig. 9. Typical wave orthogonal across the continental shelf.

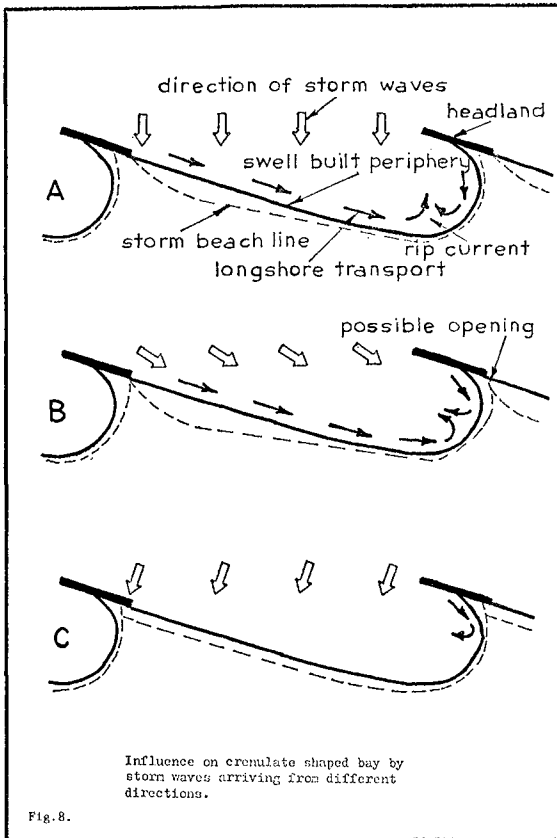


Fig. 8.

This most landward region is therefore better protected than other sections of coast closer to the headlands.

In Figure 4 it is seen that for a non-stable bay the greatest future retreat of the shoreline will take place near the intersection of the curved and tangential zones. But even the whole curved section must erode to accommodate enlargement of the bay. The portion least affected by future progression to an equilibrium shape will be the tangential strip adjacent to the downcoast headland. This reaches its final alignment long before the remainder of the bay. Only a drastic change in the long-term approach angle of the swell or predominant wave system could cause erosion of any significance in this region. With this observation must be considered the added volume of sand offshore due to the milder bed slope, as already discussed.

It is worth working an example on the deep-water changes in direction necessary to effect a given change in approach angle β to the headland alignment. Figure 9 shows a wave orthogonal traversing the continental shelf to arrive at the line joining the headlands at its deepest point. If a wave period of 12 seconds is assumed (7) and the operative depth as 30 ft., the relevant $d/L_0 = 0.04$ as illustrated. Table I shows that for increments of 5° in deepwater obliquity (ϕ_0) the variation in $\phi = \beta$ at $d/L_0 = 0.04$ is around 2° . If a β change of 5° were considered significant, this implies a ϕ_0 variation of 12.5° .

TABLE I - Variations in ϕ at $d/L_0 = 0.04$ for 5° increments in ϕ_0 at $d/L_0 = 0.5$

ϕ_0°	20	25	30	35	40	45	50
ϕ°	9.6	11.7	14.0	16.	18.	19.9	21.7
$\Delta\phi^\circ$		2.1	2.3	2.1	1.9	1.9	1.8

If the storm source for this persistent swell were 1500 nautical miles distant this implies a lateral change in position of 300 NM_s or 6° latitude. Whilst seasonal changes of this order can occur in storm location, it would take a dramatic change in climatic pattern to effect such a shift in the long term. It is difficult to verify such changes by swell observation and any 7 to 10 year cycle of bay erosion due to this source would possibly be overshadowed by more local changes perpetuated by man.

COASTAL DEFENSE

It has been illustrated above that there is a limit to which a bay will erode when all sources of sand are intercepted by whatever means, natural or man-made. If during the course of this recession a rock outcrop is exposed it will become a new fixed point in the coastal system. Such a case is exhibited in Figure 10 which is a bay on the border of South and Western Australia, where a predominant South West swell is known to exist. It is seen that the reef in the curved section of the bay has prevented the removal of material in its vicinity. It has, in fact, created two bays where one would have existed otherwise. Take the reef away and the shoreline would recede to the line indicated in Figure 11 as "major bay profile". This figure is a tracing of Figure 10, in which reefs have been identified by breaking waves.

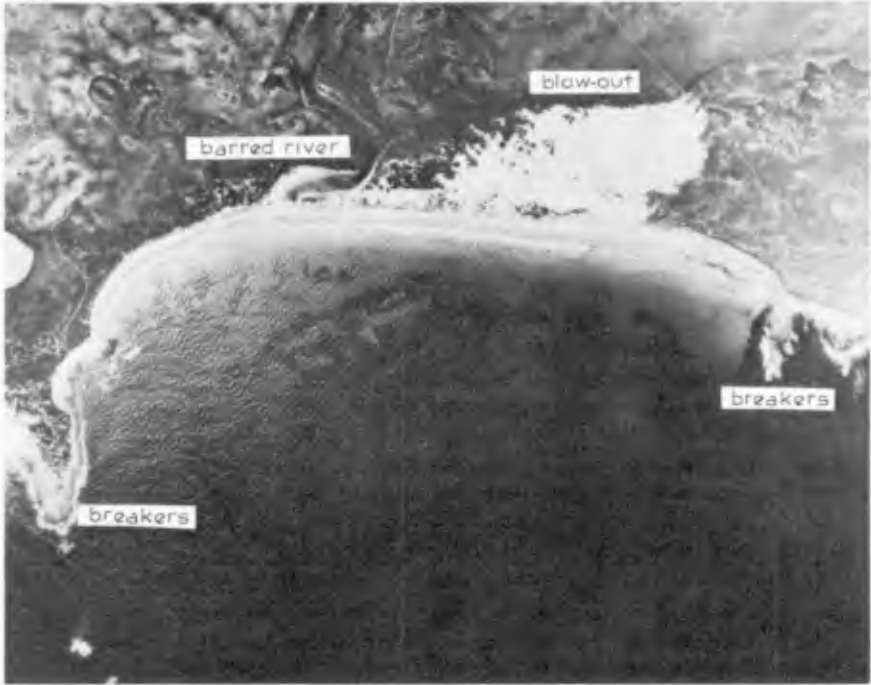


Fig.10. Natural bay showing the influence of intermediate reef serving as a headland.

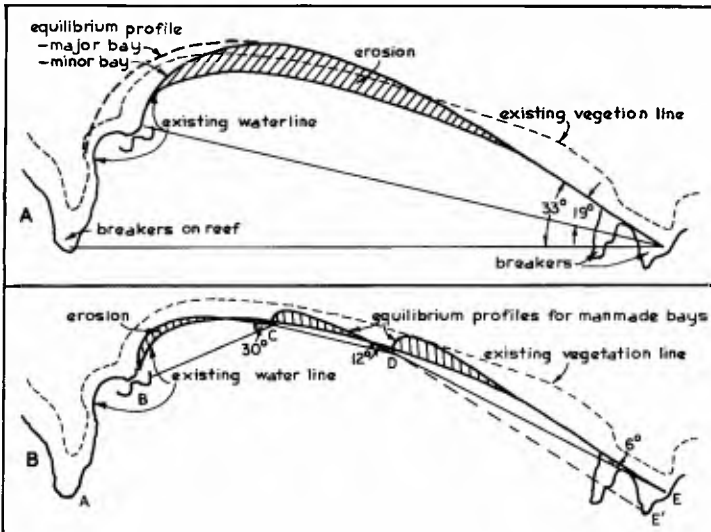


Fig.11. Tracing of features in Fig.10. showing characteristics A: of major and minor bays and B: of proposed bays from headland construction.

It can be gathered from Figures 5 and 7 that this major bay or its larger minor bay have not reached equilibrium due to the deviation of their points from the curves. The relevant values for stability produce the two logarithmic spiral curves shown in Figure 11A. The possible retreat from the present water line indicates an erosion area which is hatched. It is seen that this encompasses even the existing vegetation line which is where the primary dune is located. Whilst the natural reef in the figure is at present retaining quite a modest piece of real estate, it will have saved substantially more as full equilibrium is reached.

There is a lesson to be learnt from this example, namely that reefs or headlands occurring naturally or synthetically within a large eroding bay can prevent its recession to an equilibrium limit. To illustrate this point two further fixed points have been suggested at C and D in Figure 11B. They have been located just seaward of the present waterline. The appropriate headland alignment lines have been drawn and the approach angle β determined from the normal orthogonal to the equilibrium coastline in that region. Hence for bay BC with $\beta = 30^\circ$ a limiting indentation ratio of 0.33 was used (see Figure 5). In bay CD for $\beta = 12^\circ$ the a/b value is 0.15, whilst accepting E as the continued downcoast fixed point the angle $\beta = 6^\circ$ for bay DE results in a/b = 0.08.

It can be observed that with these headlands set close to the present shoreline progressive erosion to an equilibrium state entails some loss of the present beach zone. However it is much less than would occur under natural conditions, as illustrated by the zone of hatching in Figure 11A. If no beach loss between DE were to be permitted the better solution would be to construct a headland at E. The resultant shoreline is shown dotted. This probably implies a reclamation since the volume of material now available from bays BC and CD for natural accretion appears insufficient. Of course a headland or groyne in this case, at E can be constructed to any point between E and E¹ or may be progressively built to catch any sediment that is still passing through the bay system. In so intercepting this drift the influence on the next downcoast bay must be taken into account.

If the suggested erosion within bays BC and CD were deemed undesirable the new headlands at C and D could be located further seaward. This could be carried out to provide equal erosion and accretion areas or even net gain in beach volume (10). This might demand more sand than is available from external sources, in which case supply from the adjoining dunes may be necessary.

This proposal of utilising sand dunes in a stabilization programme is submitted as a squeak from the proverbial mouse who is addressing the environmental lions. When ever such a valuable piece of real estate is wanted for some commercial or even recreational use there is a tumult of opposition from lay persons, and even some engineers, to retain the dunes for safety of the coast. It has already been noted that where the bay is most stable, along the tangential section, the dunes are highest. This is one of nature's anomalies, that she has not engineered the coast efficiently.

The retention of dunes for some future unknown erosion event is equivalent to using factors of safety. The point to be made is that as progress is made in stabilizing coasts by natural and scientific means, such as through adding headlands, there is less need for such factors of ignorance. The necessary reserve of sand for present and future storm activity can be stored in the form of new beach area where in the meantime it is useful. This is equivalent to commercial enterprises keeping their reserve funds in use rather than stacking them in a vault for the rainy day. As long as they are liquid enough to serve the day to day fluctuations in demand their employment in commercial activities is to the benefit of all.

In the process of levelling sand dunes in order to construct wider beach zones the problem of wind blown sand must be overcome. This calls for a big "think tank" involving coastal engineers, geomorphologists, soil scientists and botanists. The costs of vegetating these areas, plus the investment in the associated headlands, must be balanced against the long term gain in land area and the greater protection of facilities through a stable coastline. To this must be added the value of previously dined area which is now put to use for residential, commercial or recreational purposes. Another saving is the continual cost in trying to maintain these mounds of sand in their natural state.

The structures involved in this stabilization programme are necessarily large and may not be undertaken simultaneously. This situation calls for an overall plan which is then implemented in stages. For this purpose it is wise to start construction at the downcoast end of an eroding coast in order quickly to retain sediment within the system to be treated. This is assuming that further downcoast the lack of sand nourishment will have no political or financial repercussions.

The lengths of coast involved in a headland-control system will generally be greater than where groynes or seawalls are attempted. This may call for co-operation between a number of local councils and even between adjacent State Legislatures. Such sharing of costs and profits has been forthcoming for rivers and other waterways and hence its extension to the seacoast should not prove too difficult. In this regard it is to be remembered that littoral drift is a "river of sand" extending hundreds or even thousands of miles, over widths varying from a few hundred yards to many miles. This inter-dependence applies equally to pollution as it does to sediment supply.

If a long enough section of shoreline can be treated at once, or the downcoast zones can be discarded, the ultimate goal should be to stop all littoral drift, at least close to the coast if not further out on the continental shelf. The bulk of coastal engineering problems emanate from longshore sediment transport. It causes erosion in one area, siltation in another, and during transmission from the former to the latter constructs bars across river and harbour mouths or blocks dredged channels. Even with stabilized bays, with no net drift, there will be annual longshore and lateral movement to be controlled, but this will be predictable soon after the major equilibrium shape has evolved.

HEADLANDS

Offshore breakwaters have been advocated by the writer as a starting point for headlands. These can cause accretion on their lee side without becoming attached to the mainland. This occurs frequently in nature as illustrated in Figures 2B and 12, which is a sandy protuberance

known as Quinns Rock on the Western Australian coast near Perth. The offshore reef is a half mile in longshore dimension and a mile from the mainland. The displacement of the apex northwards from the centre line of the reef is due to the persistent swell arriving from the Southwest. The diffraction of such waves is exhibited in the figure. In spite of the lack of local controls at the beach itself such triangular features are exceedingly stable, since they have been produced and are maintained by a wave system that alters very little decade after decade.

Man-made islands or offshore breakwaters are more likely to be closer to shore and smaller in dimension. If a sand spit or tombolo is to be formed, which then acts like a groyne and subsequently as a headland, the further offshore the structure the larger should be its longshore length (11). This seaward location implies deeper water and hence massive mounds of rock. This tendency can cause the whole proposition to become uneconomical, especially when considered in concert with a mammoth reclamation task to prevent downcoast erosion. The prizes of area won from the sea or saved from the sea are gained long after the investment has been made. The larger the outlay the more convincing must be the argument that the rewards are actually obtainable.

Because of the expensive nature of marine structures, especially those for dissipating wave energy, much thought must be given to minimizing their cost. This hydrodynamic requirement only demands reef-type structures which trigger the waves, particularly the persistent swell. The sporadic storm waves will readily break over such a shoal. Any contact with the mainland through a tombolo may quickly be broken in these circumstances, but will just as quickly be remade when subsequent swell arrives. This low profile structure not only saves in volume of material but is also more aesthetic in that a synthetic mound is not imposed on the sea panorama.

But even a mound rising to a foot or two below low water can become expensive if set initially in a deeper zone, where its length is around one wave length in order for a tombolo to form. One solution to this problem is to create a horizontal platform which will break the predominant waves. If such a submerged platform breakwater were buoyant it could be relatively mobile. After accreting sand at a point on the coast, and perhaps upcoast from it, the structure could be towed seawards to continue the action (10). When a suitably indented bay were formed a rubble mound headland could be constructed on the beach. This need not be of a high profile, only sufficient to be at mean sea level after subsidence has occurred. The mobile platform could then be hauled to a new site.

Research has been carried out for some years at the University of Western Australia on submerged platform breakwaters (12). This concept is more economical than the surface floating structure because to attenuate the same swell wave it need be only a fraction of the width. An example will illustrate this: To reduce the energy of a 10 second wave in 15 ft., depth of water a floating breakwater must be at least one wave length or 105 ft., in width. A similar platform, either impervious or perforated, moored at a level 5 ft., below the water surface will require a width of only 30ft., since it need be only half the length of this 10 second wave in 5 ft., of water. The submerged platform can be slung from floats or if buoyant held down with weights. Research is being aimed at minimizing the mooring forces and coping with stresses imposed by maximum waves at the site.

In respect to the final wave tripper to be built on the accreted beach apex, it would appear that the cheapest material to use is sand at the site. The cartage of rubble stone is costly at any time, but especially when roads must be provided in remote locations to the breakwater site. To provide vehicular access the structure must be constructed to a meter or two above high water mark and be of such a width to carry such large trucks. The seaward and landward forces as well as the top must be protected by armour units of such a weight as to withstand the fiercest storm waves. A degree of interlocking, plus dissipation of wave energy within large voids, are desirable characteristics sought when designing concrete units for this purpose.

A more economical approach has been reported in the literature for groyne and seawall construction of sand confined in a flexible sheath. Plain sand or cemented material has been employed in this large scale "sand-bag" approach. Perforated polyethylene tubes are available up to about 7 ft., in diameter. Sand is flushed in whilst the water percolates through the skin. Use of these sausages singly or in heaps as headlands or reefs provides a new outlook for coastal engineers.

When cement additives are used the sausages become a solid rock mass immediately. This obviates the problem of splitting or cutting of the polymer during construction, or later through human vandalism. Research is needed into the most effective mixtures to achieve the minimum strength required in such massifs. Lime may be found a better proposition than cement in this saline situation. Means of pumping beach sand into tubes whilst adding chemicals at a fixed rate needs investigation.

There is little question that coastal defense structures need a new outlook since conservatism has proved very costly in the decades gone by.

REFERENCES

1. Silvester R. "Sediment movement around the coastlines of the world" Proc. Conf. Inst. Civil Engrs. (London) 1962, 289-315.
2. Silvester R. "Sediment movement - long term net movement" Encyclopaedia of Earth Sciences, Reinhold Publ. Corp. (Ed. R.W. Fairbridge) 1968, 985-988.
3. Silvester R. "Development of crenulate shaped bays to equilibrium" Proc. ASCE 96 (WW2), 1970, 275-287.
4. Silvester R. Coastal Engineering Vol II Elsevier Publ. Co. 1974.
5. Silvester R. and S.K. Ho "Use of Crenulate shaped bays to stabilize coasts" Proc. 13th Conf. Coastal Eng. 2, 1972, 1347-1365.
6. Ho. S.K. "Crenulate shaped bays" M. Eng. Thesis No. 346. Asian Inst. Tech., Bangkok, 1971
7. Silvester R. "Design waves for littoral drift models" Proc. ASCE 89(WW3), 1963, 37-47.
8. Yasso W.E. "Plan geometry of headland - bay beaches" J. Geol. 73, 1965, 702-714.

9. Hughs E.P.C. "The investigation and design for Portland Harbour, Victoria" J. Instn. Engrs. Aust. 29, 1957,55-68.
10. Silvester R. "Stabilization of sedimentary coastlines" Nature (London) 188, 1960 467-469.
11. Silvester R. "Offshore breakwaters" Trans. ASCE 124, 1959, 356-365.
12. Silvester R. "Submerged platform breakwaters" Proc. 1st Aust. Conf. Coastal Eng., 1973, 182-189.



Fig.12. Coastal protuberance crested by an offshore reef at Quinns Rock, Western Australia.

CHAPTER 83

PROTECTION BY MEANS OF OFFSHORE BREAKWATERS

by I. Fried, C.E., Director
Civil & Marine Engineering Co. Ltd., Haifa - Israel.

INTRODUCTION

The coast of Tel-Aviv is characterised by a narrow sandy beach, and the seabed in the nearshore shallow waters is strewn with rocky ledges and outcrops. These rocks are of a marine conglomerate type and are covered with layers of fine to medium grained sand of various thickness. At depths greater than 5 m the seabed is predominantly sandy. During the summer season, when waves and swells seldom exceed 2 m in amplitude, the sandy strip of the beach maintains its minimum width of about 20 m. However, winter storms reduce the width of the beach in some places to zero, and there is a marked tendency to erosion and scour of the beach in front of the retaining walls of the alongshore promenade or in front of the coastal bluff.

In order to prevent this erosion and at the same time to enlarge the sandy beach area, we have proposed to erect in front of the beach a series of offshore breakwaters, either detached or groyne-connected. (Fig. 1)

The first of the series was erected off the Tel-Baruch beach just north of Tel-Aviv. There beach sand was practically non-existent, and in order to enable bathers to enter the water, a breach in the shallow rocky belt had to be blasted.

The Tel-Baruch breakwater is of a rubble-mound type, 200 m long and connected with the shore by a 100 m long groyne. It is founded on a rocky seabed at -3.0 m below M.S.L. and consists of a quarry-run core (0.5 to 250 kg units), protected on its seaward slope by a rock armour (2-6 tons units) laid on a 1:3 grade, and on its landward slope by a secondary armour (1-2 tons units) laid on a 1:1.5 grade. Its crown is topped by R.C. 0.25 thick slabs to a level of +1.0 m above M.S.L.

Shortly after its erection in 1965, a sandy tombolo has formed at both sides of the groyne, increasing in area until a permanent equilibrium has been achieved. Erosion of the beach on both sides of the breakwater was avoided, owing to a belt of beach rock which protects the foreshore to the south and to the north of the breakwater.

The second system was erected in front of the Tel-Aviv Sheraton and Hilton hotels. (Fig. 2)

It consists of twin breakwaters here connected by groins. Each of the rubble-mound type breakwaters is about 250 m long and 200 m distant from the shore. They are based on a practically rocky seabed at a -4.0 m level and constructed of quarry-run (0.5 - 500 kg units) core and blanket, a seaward armour slope 1:2.5, consisting of 4-8 tons rock units and a landward slope 1:1.5 of 3-4 tons rocks. The crown of the breakwaters is capped by R.C. slabs, 0.25 m thick, and reach a level of +1.25 m. The gap between the breakwaters' heads is 135 m wide.

Soon after the completion of these breakwaters in 1968 the barren rocky foreshore behind them was transformed into a wide sandy beach protected from summer swells and safe to bathers. The sandy tombolos expanded steadily, reaching an equilibrium in about 3 years time, thus permitting the erection of beach amenities (wardrobes, services, showers, refreshment stands) on the vast sandy areas. Behind both these breakwaters the apices of the tombolos from a permanent contact with their inner edge, thus obstructing free passage of water, even during the winter season.

For this and other reasons it was decided to create protected beaches at the central coast of Tel-Aviv south of the newly built "Gordon" boating marina in such a way that all the year round ample gaps should be left between the breakwaters and the sandy tombolos behind them. Moreover, it was deemed desirable from the aesthetic and beach utilisation points of view to form the new shoreline behind the row of detached breakwaters in a sinusoidal shape. The crests of such sinusoids should lie behind the breakwaters at a distance of about 60 m from the actual shoreline, whilst their troughs, situated opposite the gaps between the breakwaters, should be about 20 m distant from the original shoreline. (Fig. 5)

This new concept put before the designers a dilemma how to proportionate the row of detached breakwaters (their length, distance from the shore and between each other) in order to fulfil the basic requirements of the new beach. In order to help the designers to find the right answers to these questions it was decided to resort to movable bed tri-dimensioned hydraulic model tests.

MAIN CHARACTERISTICS OF THE LOCAL CONDITIONS

In order to build a suitable movable bed model in a hydraulic laboratory wave basin and to submit it to a series of tests, it is necessary to collect as many data as possible concerning the physical conditions ruling in the coastal zone under investigation.

For this purpose a series of preliminary surveys and studies of the central Tel-Aviv coastal zone has been undertaken, consisting of:

- a. Topographic and hydrographic mapping;
- b. Wave observations and recordings;
- c. Longshore currents measurements at various depths; littoral transport evaluation;
- d. Sampling of sand from the beach and from the seabed at various depths;
- e. Pricking into the seabed in order to ascertain the depth of hardpan underneath the sandy layers.
- f. Assembly of meteorological and geomorphological data.

The results of the above-mentioned surveys and studies have made it possible to characterise and to analyse the coastal conditions as follows:

The tidal range seldom exceeds 50 cm; however, strong easterly winds may lower the water level to -50 cm below M.S.L., whilst persisting westerly storms may cause a temporary piling up of coastal waters, bringing their level to 70 cm above M.S.L.; but these are extreme events.

The shore of Tel-Aviv is basically sandy with an underlying rocky bottom, which is partly based in shallow water, and in some places near the coastline rocky ledges protrude above M.S.L. The sand cover above the rocky bottom increases in thickness from 1-2 m at the coastline to about 7 m at the -12 m contourline. The seaward slope ranges from an average of 1 to 40 nearshore, to 1 to 75 beyond the -7 m contour. Between the two zones there is a sand bar with a levigation ditch at about -4 m to -5 m depth. The orientation of the shoreline is about 19° East of North. The grain-size distribution of sand samples taken at the foreshore and at certain depths indicates uniformity and sediment sorting, the foreshore samples being much coarser than the offshore samples. The mean diameter changes with the depth as follows:

Depth (m)	foreshore	-5	-7	-13
d (mm)	0.26	0.17	0.16	0.14

The maximum 90% diameter of foreshore samples reaches 0.40 mm.

The winds blow mainly from the NW to SW sector, i.e. from the open sea. Winds above 5 Beaufort (16 knots) strength blow only 5% of the time.

The distribution of significant waves amplitudes and periods shows that most of the storms and all waves higher than 5 m occur between November and April. Their direction is from the WSW and WNW sector, and they account

only for 1% of all waves. The average number of moderate storms (3-4 m high waves) during the summer period is 2 or 3 (1.5% of all waves).

The frequency of amplitudes and periods were found as follows:

Amplitudes									
(m)	6-8	5-6	4-5	3-4	2-3	1.5-2	1-1.5	0.5-1	0-0.5
%	0.37	0.45	1.1	1.58	4.1	9.9	28.0	11.9	42.6

Periods									
(sec)	10-12	9-10	8-9	7-8	6-7	5-6	4-5	3-4	Calm
%	2.0	2.8	7.9	16.5	19.6	23.3	14.4	3.1	10.4

The pattern of wave distribution around the year had to be simulated in the model in order to find the movements of the bottom observed in nature. The currents were measured, both at the surface and at various depths. The results of these measurements have shown that their pattern is irregular and their maximum velocities seldom exceed 25 cm/sec. These low velocities point to the fact that the currents themselves play only an auxiliary role in the movement of sediments put into suspension by shoaling waves.

The estimates concerning the littoral drift at the coast of Tel-Aviv were as follows:

The northward transport - about 400,000 cu.m. a year, the southward transport - much less, about 80,000 cu.m. a year. This leaves a net northward littoral transport of at least 320,000 cu.m. a year.

HYDRAULIC MODEL TESTS

The movable bed hydraulic model was built in the wave basin of the hydraulic Engineering Laboratory of the Haifa Technion (Israel Institute of Technology). The basin's dimensions were 40 m x 25 m x 0.9 m, and it was equipped with a 30 m long movable wave generator, capable of turning in various directions; an overflow level regulator and a movable measuring bridge spanning the area occupied by the model. Frequency and amplitude modulations were effected according to a prescribed program.

The model study began at the end of May 1971 and was completed 16 months later, i.e. October 1972.

The choice of the model scales was influenced by many factors, the most important being the relation between the length of the coastal strip to be tested and the actual dimensions of the wave basin. It was decided to reproduce the model beach with a distortion 1:2, using ground ebonite

as model sand. Thus the adopted horizontal scale was 1:150 and the vertical scale 1:75, while the model sand, the average specific gravity of which being about 1.8, was prepared with a grain size distribution found in the prototype, using a 1:1 scale. The scale of the sand is based in principle on the similitude of fall-velocities, assuming that the major part of the sand transport is usually carried in suspension, and the setting in the protected area is basically governed by the fall velocity - carrying capacity relation, too.

Calibration of the model was effected relative to the sedimentological processes observed in the vicinity of the existing structures (Tel-Aviv lighter basin, Sheraton and Hilton breakwaters). (Fig. 3) There were some indications in the calibration tests that the velocities reproduced on the Froudian scale with the adopted distortion were insufficient for the establishment of a reasonably small sedimentological time scale. Therefore it was decided to increase the model scale for waves, using a scale of 1:50 for wave heights, which were calculated on an energy basis. However, breaking of waves and overtopping of low breakwaters by them are governed by Froudian similitude. Therefore, the breakwaters had to be heightened in the model in such a way that the height of their crest above mean water level corresponds to a 1:50 scale, too. The most difficult problem was to establish a sedimentological time scale. It could not be made before the reproduction of sedimentological changes around the existing structures. Therefore, at the beginning of the calibration a tentative wave program was adopted, which corresponded to the statistical distribution of wave energy and wave direction, but the corresponding wave cycle did not necessarily represent a model year. Then theoretical calculations were made as to the possible sedimentological time scale, and the overall time of the wave cycle was modified accordingly.

Practically the time-scale was found by comparing the time-rate of the tombolo formation at the two existing breakwaters with their development rate in the model. Comparing model to prototype has led to the unavoidable conclusion that two different time scales have to be applied relative to the tombolo formation - one for the initial stage, when the changes are due to shifting of the local sand stock and to longshore transport, and the other when the development of the tombolos is due to the trapping of sand which arrives mainly from the unprotected offshore area. This is because an offshore transport was observed in the model, which was believed to be in excess of the corresponding offshore transport in the prototype and which could not easily be eliminated. However, the final equilibrium state of the tombolos was correctly reproduced, and this indicates that the similitude of the sedimentological process to be studied in the model was basically correct. The basic sedimentological time scale adopted in the beginning was $1:2190 = 1:2200$, i.e. 4 model hours equivalent to one prototype year.

Inasmuch as the development of the tombolos in the first year was correctly reproduced on the adopted time scale, however, the additional growth caused by accretion of sand supplied by onshore transport was slowed down by about 1:3, as proved by the Hilton-Sheraton breakwaters test. At a later stage the sedimentological time scale was re-checked, and as average of 12 hrs. equivalent to one prototype year adopted. Altogether 14 different alternatives were tested in the model study.

TEST RESULTS

The original concept of the outlay of a complete system was a row of offshore breakwaters parallel to the shore with evenly distributed gaps between them, except two wider gaps: one 225 m and the other 310 m long. Also the existence of the first northernmost breakwater, which was erected at the same time as the "Gordon" marina breakwaters, had to be accounted for. The breakwater is situated about 250 m from the original shoreline. Therefore, alternatives 1 to 9 have shown breakwaters situated all at this distance from the shore.

Testing the first alternatives with two wide gaps between the breakwaters indicated serious erosion opposite these gaps. Therefore, other solutions were sought that would provide sufficient widening of the beach. It was made clear by the results of the tests that the proportion between breakwater lengths, gaps and distances from the original shoreline must have definite values, to be found by testing procedure, in order to meet the prescribed requirements concerning controlled tombolo formation. The fact that the hydrographic conditions are quite uniform along the shore section in question, and architectural considerations as well, lead to a symmetrical outlay of similar breakwater units equally spaced.

Alternative 9 was tested with six uniform breakwaters, 130 m and 120 m long gaps, all aligned with the existing northernmost breakwater (Fig. 4).

The result of the tests with this alternative seemed to be quite satisfactory, except that the tombolos showed an undesirable tendency to reach the northern units of the system, contrary to requirements.

Another alternative, No. 10, was then composed, similar to alternative No. 9, of six 130 m long breakwaters; however, the five intermediary breakwaters were displaced offshore by 45 m. Thus a wider lagoon was created, which made the connection of the tombolos with the breakwaters unlikely, except with the existing one, the position of which could not be changed anymore.

In addition, two oblique gaps were formed, which made the penetration of longshore currents, and thus circulation and exchange of water, easier. It was then decided to choose alternative No. 10 as the most suitable outlay of the system.

The choice of the best outlay was based on comparative tests using artificial fill; however, the final version had to be re-tested with a natural process, when the building schedule of the system is correctly reproduced in the model. Owing to the considerable differences in the sedimentological time-scales at the beginning and at the end of the construction period, a mixed average of 12 hours, equivalent to one prototype year for the building period of the whole breakwater system, was finally adopted.

The testing of the natural sedimentological process in the chosen outlay was repeated with three different versions, called alternatives Nos. 12, 13 and 14, differing between them in the time sequence of the construction and other details. Alternative 12 was tested for a construction period of one year for the whole system. In alternative 13 two other time schedules were tested, building of 3 breakwaters per year and building 3 breakwaters in 2 years. This would mean extension of the building period to two and a half and five years, respectively, considering additional five offshore breakwaters and the southern end unit.

The purpose of alternative No. 14 was to improve the distribution of sand accumulating along the protected beach by partition of the protected water area, leaving the groin of the central unit in place, or dismantling, if only partially. The nearshore part of it would very soon be covered, while the gap left between the groin and the breakwater would facilitate the exchange of water between the northern and the southern parts of the lagoon.

In the final version the central breakwater was moved back by 45 m to its position in alternative No. 9, i.e. in line with the end units. (Fig. 5) Thus two inter-connected symmetrical lagoons were formed with considerably improved sedimentological and hydraulic behaviour. The results of the test have shown that the accumulation of sand in the protected area is caused partly by the longshore transport. With an open ended system more sand is attracted from the longshore current, and consequently sedimentation is quicker than in a closed one. If the system is closed, this sand will probably by-pass the breakwaters, apart from the small part trapped behind them. This means that the influence of the construction of the system on the coastline is spread over a longer period, which is certainly beneficial to the coast. Consequently, the building schedule has a direct influence on the rate of sand accretion, though not on the final state of equilibrium. Construction of the whole scheme can be sped up by using artificial feeding. However, if the rate of construction is not exceeding one breakwater a year

(as it actually is), sufficient widening of the beach will be achieved by a natural process. After completion of the model study it was decided to extend the breakwater scheme to the south in order to connect it with the "Clöre" park reclamation. It was suggested on the basis of the model study that this can be done by adding one more breakwater to the system, maintaining however the dimensions of the breakwater units and of the gaps, which were found to be optimal. Thus the finally recommended outlay is composed of seven offshore breakwaters and an end unit shore connected to the seawall of the "Clöre" park reclamation. The head of the southern end breakwater No. 8 and the central breakwater No. 4 are aligned with the existing breakwater No. 1, nearest to the Gordon marina. The remaining five breakwaters are displaced by 50 m in the offshore direction. The length of each offshore breakwater is 130 m, and the gaps between their heads are 120 m long.

The central groin No. 4 will be dismantled only partially, leaving a distance between its head and the central offshore unit. The crests of the offshore breakwater are at +1.75 m above M.S.L.

With an outlay of the system described above, the shore development of the protected beach was expected to satisfy the basic requirements when its new equilibrium is established. (Fig. 6)

The model indicated a 100 to 200 m wide lagoon for swimming purposes, protected from waves mostly in the leeward (the "shadow") of the breakwaters where the beach widens, and to a lesser extent opposite the gaps where the beach narrows. At any rate, the average wave energy along the beach should actually be less than 50% of the energy in the open sea. As long as the waves do not overtop the breakwaters - and this will not happen if the wave heights are less than 2.0 m, as they actually are during the summer season - the water in the lagoon will be calm in general. If overtopping occurs during stormy periods, the reduction of wave heights by the breakwaters is less effective.

FIELD CONSTRUCTION WORKS

Breakwater No. 1 was completed in 1971, and a tombolo has formed that was very similar to the one predicted by the model for the same period of existence. In 1972 No. 2 breakwater was completed and its groin dismantled, using the rock to build the groin of No. 3 system. However, due to war and the policy of the authority concerned, No. 3 breakwater was completed only in 1975. It was decided to proceed with the construction, and this year No. 4 breakwater is in the process of being completed. (Fig. 6)

The method of constructing the offshore breakwaters is as follows:(Fig. 7)

First, rubble-mound type groins are constructed from the shore outwards by dumping on the seabed a core material to a +0.75 m level. This core material consists of a well graded quarry-run (0.5 to 500 kg units), protected on both sides by 3-5 ton rocks placed at a 1:1.5 stope. The width of the groin crest is about 5 m (a minimum necessary to enable the passage of crawler cranes, which place rock armour on the breakwaters). Then the construction of the breakwaters proceeds from their mid-section outwards by laying first on the seabed a 1.0 m thick quarry-run blanket, which is to protrude 3 m outside the outer toe and 2 m outside the inner toe of the breakwater mound. This blanket constitutes an anti-scour device, protecting the toes of the breakwaters and preventing excessive penetration of the armour rock into the sandy seabed.

The quarry-run core of the breakwaters is then dumped on the blanket and protected on its outer (offshore) slope by rock armour (5-8 ton units), placed on a 1:3 grade on its inner (inshore) slope by a somewhat lighter armour (3-5 ton units) laid on a 1:1.5 grade. The breakwater crests are capped to a +1.75 m level by the heavier armour rocks. Also the heads of the breakwaters are protected all around by 5-8 ton rock units placed on a 1:3 grade. The width of the breakwaters at their crest level is 5.25 m.

After completion of each breakwater, the connecting groin is dismantled and the rocks transferred to the next groin. These rubble-mound type structures have proved to be very stable, and even after heavy storms no significant damage have been observed until now.

Periodical hydrographic surveys executed in the area, as well as air photos, indicate that the sedimentation process is generally well in accordance with the prediction of the model study. Now one can see a substantial widening of the protected beach and the appearance of a convenient new bathing area. There has, however, been less sand accumulation at the two northernmost tombolos just behind breakwaters No. 1 and No. 2 than anticipated in the model study. This indicates that sand distribution along the protected shore is more balanced than predicted. No permanent erosion was observed on the adjacent shore due to the above development. This fact corroborates the preliminary assumption that the newly developed beach will not be widened on account of the neighbouring shore sectors, but on account of the differential alongshore sand transport, reducing only the quantity of sand that would otherwise be carried offshore due to the local hydrographical and sedimentological circumstances. (Fig. 8)

The implementation of the offshore breakwaters scheme, together with a substantial widening of the sandy beach behind them, will enable the establishment of a new ample alongshore promenade seawards of the existing one without jeopardising the newly created beach.

CONCLUSIONS

Many factors are involved in the reproduction of natural sedimentological processes in a wave basin with movable bed, and a misinterpretation of some of them may lead to erroneous conclusions. In the long run, the exact definition of the sedimentological time-scale is less important than the reproduction of seabed configuration, representation of sand grain particles and of wave spectra.

The exact full-scale sedimentation processes in the prototype are hardly known in detail. However, we can assume that the formation of sandy tombolos in the lee of offshore breakwaters results mainly from the interception of the littoral drift. Some of the sand enters directly downdrift the onshore zone behind a breakwater, whilst other sand particles by-pass the breakwater on the outside and are then directed by waves diffraction around its opposite head into the calm foreshore zone as a result of onshore movement caused by waves agitation. The accelerated sedimentological process in the model enables however to reproduce quite exactly the natural development of tombolos formation in the prototype, which, in order to reach a state of equilibrium requires a considerable period of time. Nowadays, even a well experienced designer of coastal structures requires a corroboration of his ideas by model studies, which by themselves are not substitutes for a careful and sound design, but serve as practical indicators of their behaviour in the prototype.

REFERENCES

1. Shore Protection Manual - U.S. Army Coastal Engineering Research Center - 1973.
2. Dr. M.L. Vajda - Final Report on Tel-Aviv Shore Development Model Study - Technion, Israel Institute of Technology, January 1975.
3. I. Fried - "New Coastal Works at Nahariya, Beach Protection and Development". The Dock and Harbour Authority, Vol. XVI No. 532, February 1965.
4. I. Fried - "Foreshore and Beach Development of Tel-Aviv and Nathanya" - Symposium on Foreshore and Beach Development from the Coastal Engineering Aspect - Tel-Aviv, January 1975 (in Hebrew).
5. Giorgio Berriolo & Giorgio Siritto "Spiagge e Porti Tusistici", Edizione Hoepli, Milano 1972.

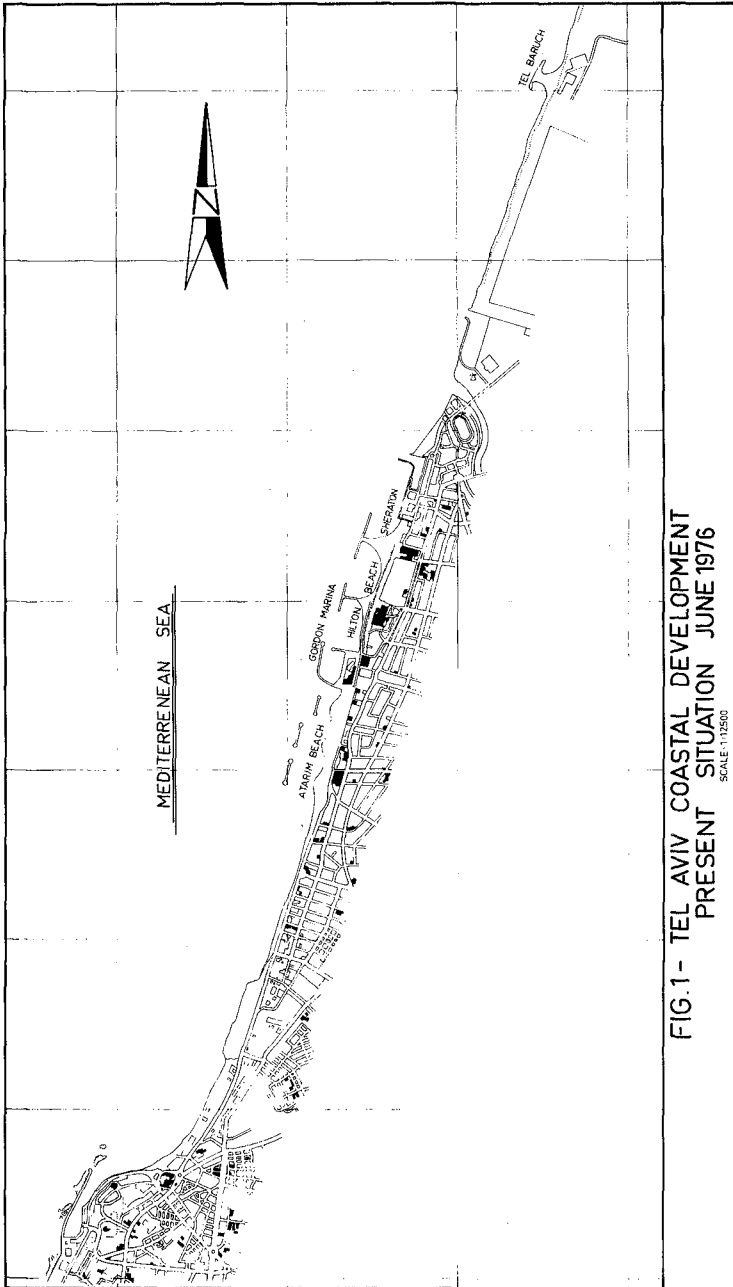
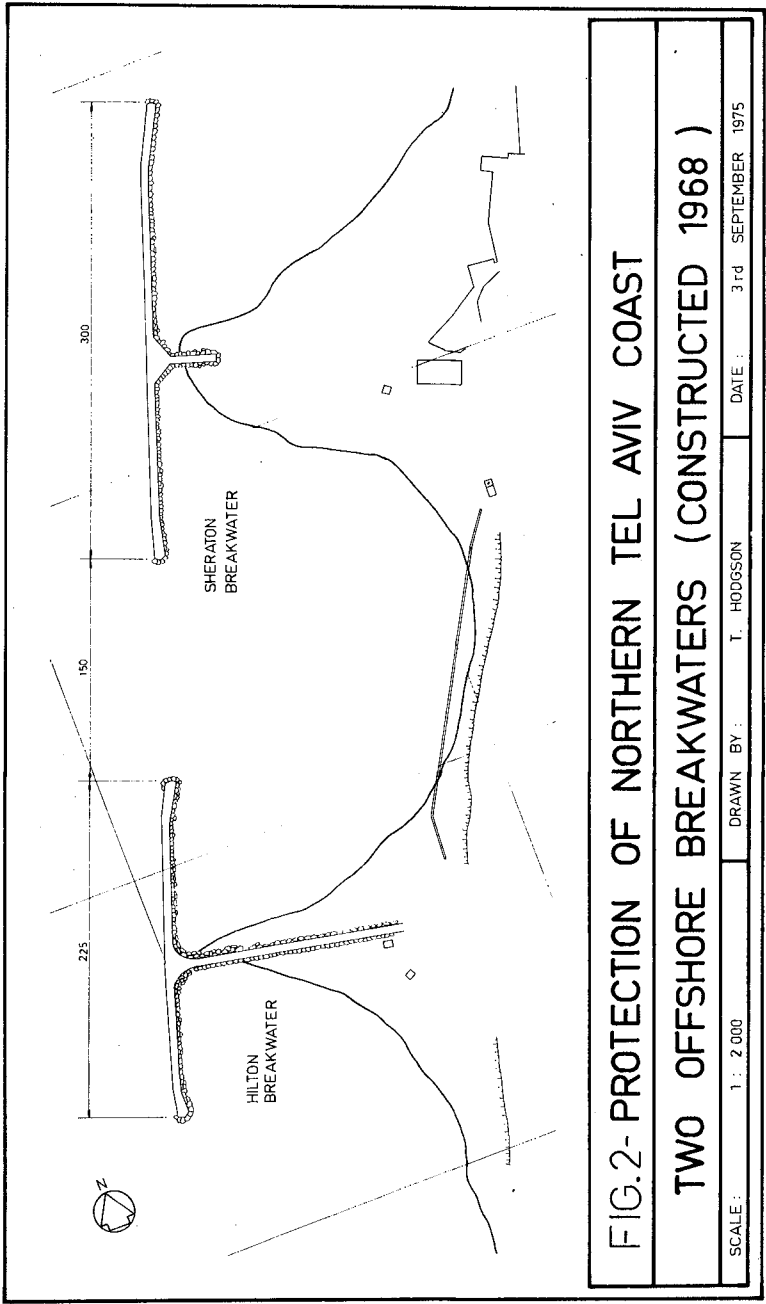


FIG.1- TEL AVIV COASTAL DEVELOPMENT
PRESENT SITUATION JUNE 1976
SCALE 1:10,000



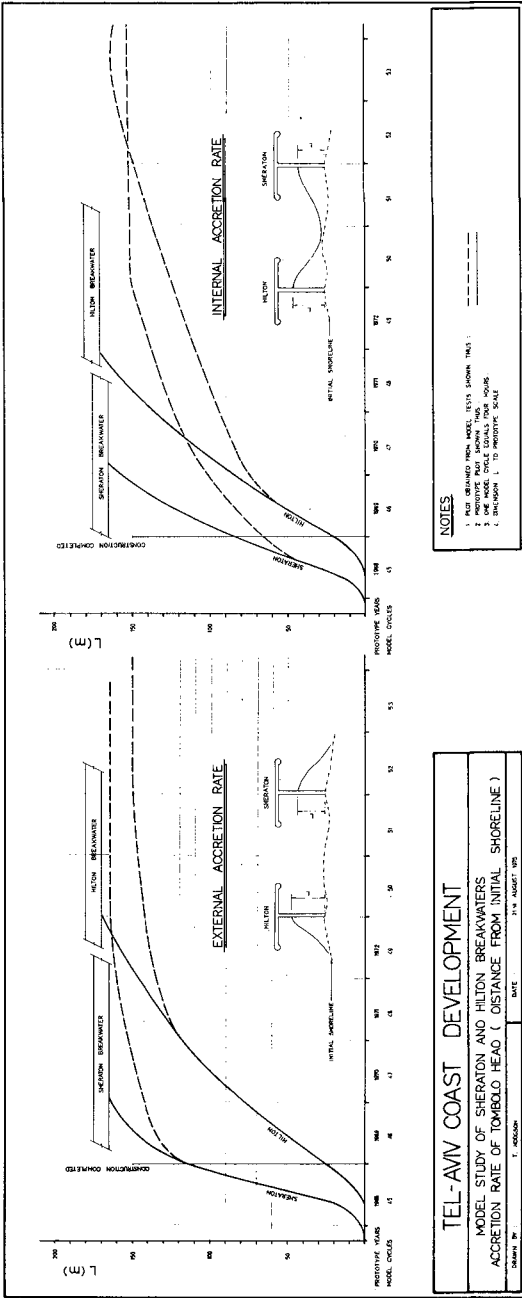
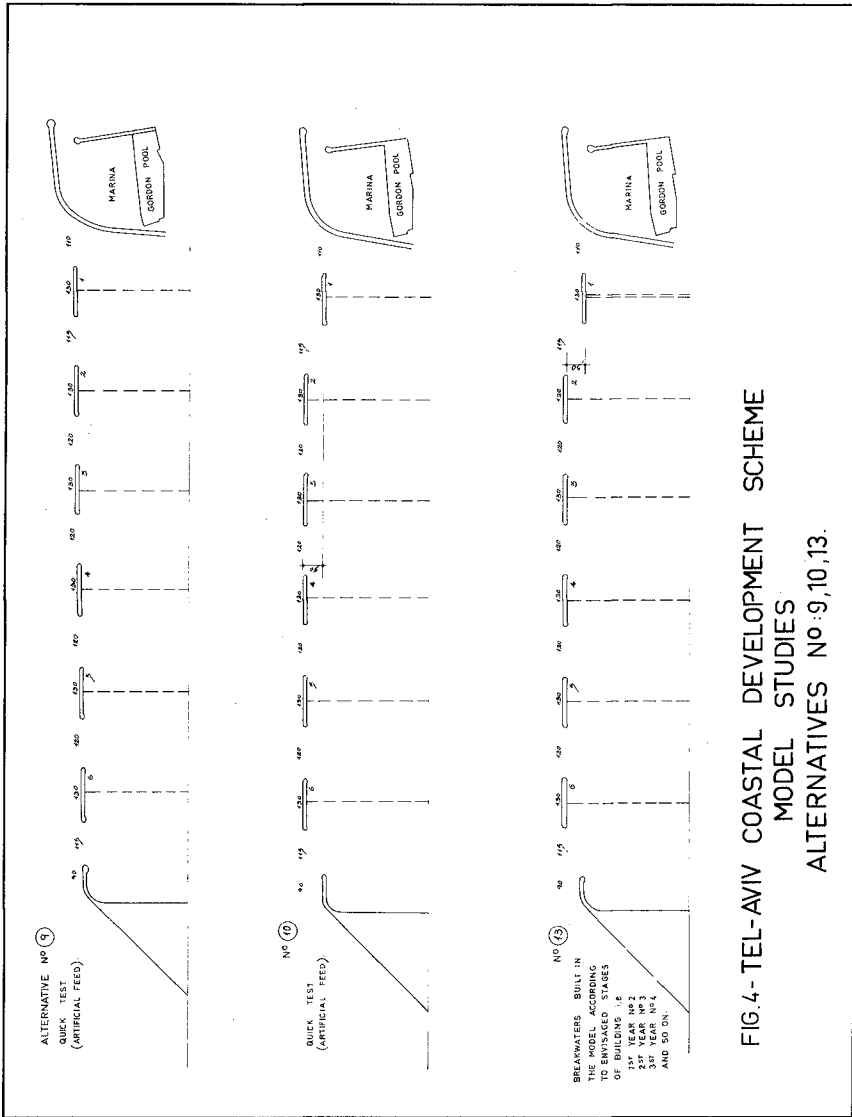


FIG.3 - SHERATON AND HILTON BREAKWATERS ACCRETION RATE OF TOMBOLOS



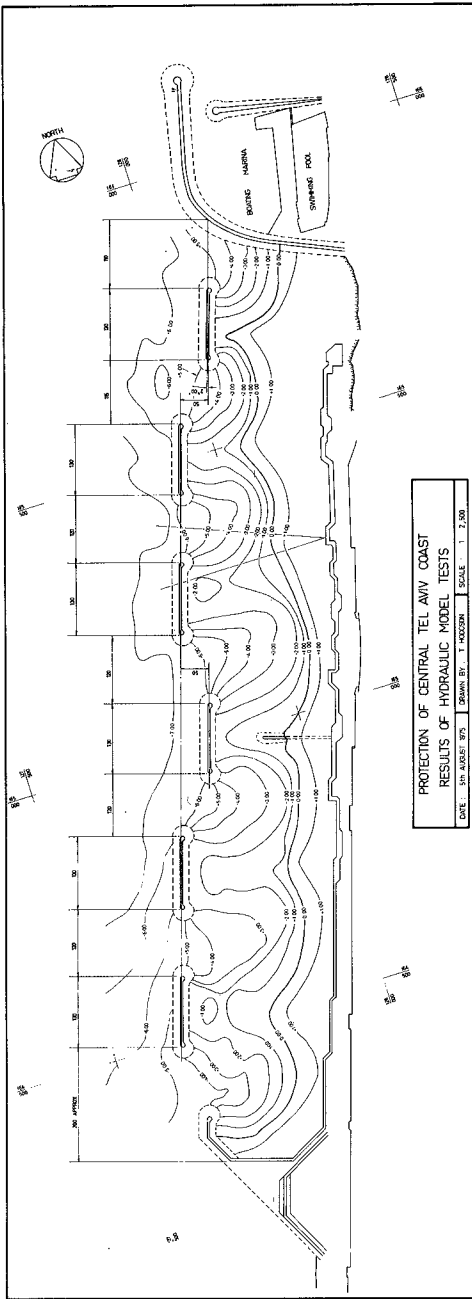
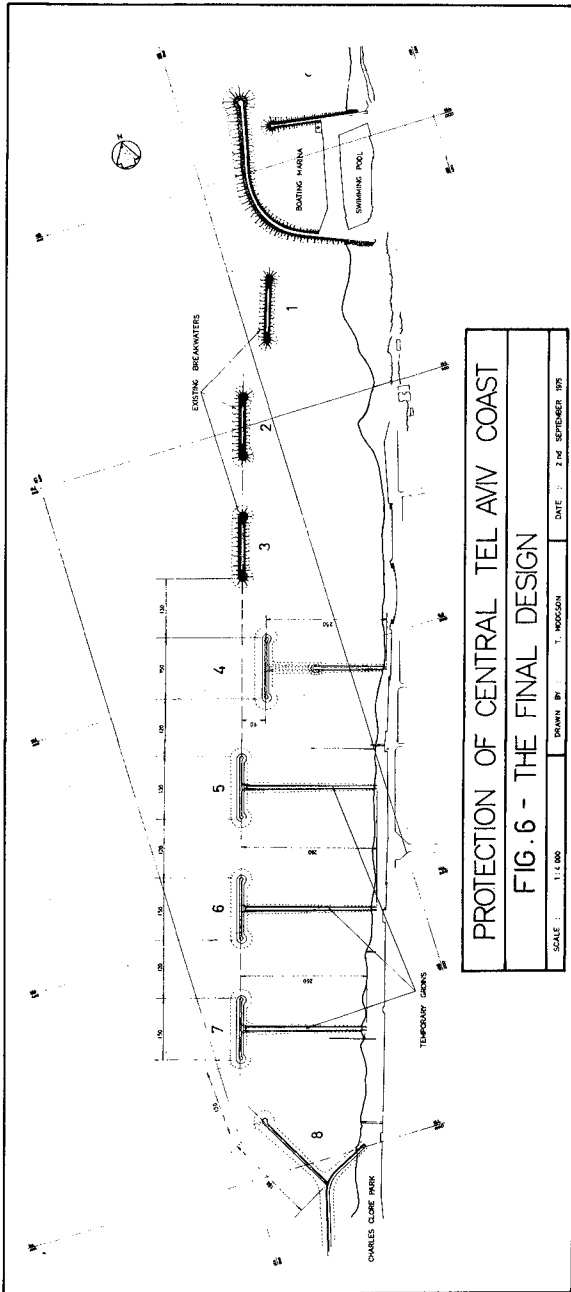


FIG.5 - FINAL RESULTS OF HYDRAULIC MODEL TESTS



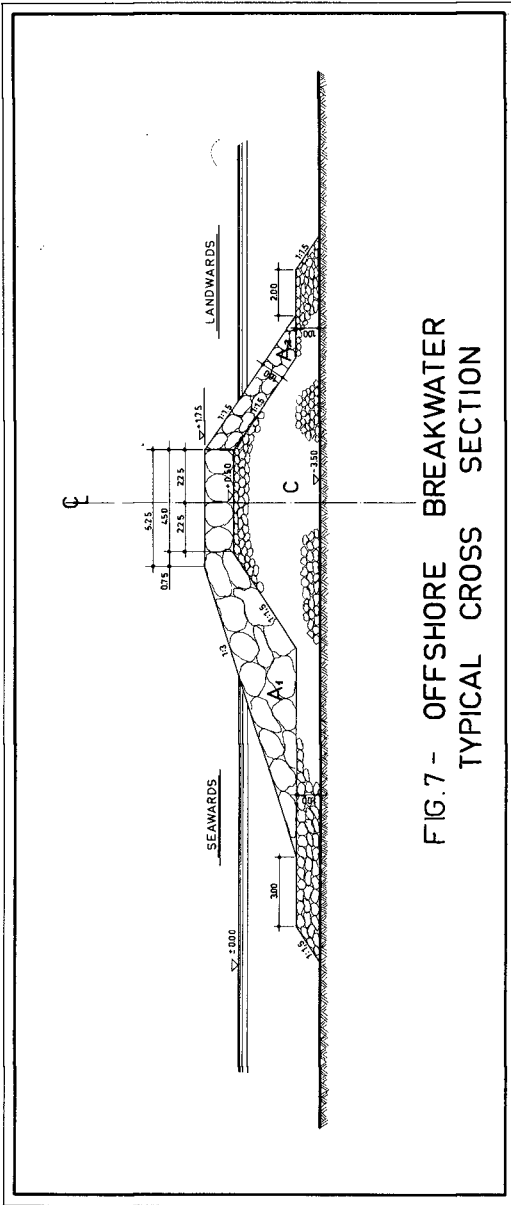


FIG.7 - OFFSHORE BREAKWATER
TYPICAL CROSS SECTION



FIG. 8 - CENTRAL COAST OF TEL AVIV - JUNE 1976

CHAPTER 84

ENCLOSING SCHEME FOR BATHING-BEACH DEVELOPMENT

by

Joseph Tauman
J. Tauman, Coastal and Harbour Eng. Ltd.
Consulting Engineers, Ramat Hasharon, Israel

ABSTRACT

This paper refers to bathing beaches. It presents a method for beach design which provides both coastal protection and protection for the bathing public. Reasons are pointed out as to why the open sea foreshores are, in many cases, not suitable for recreation.

The method uses an enclosing submerged breakwater coupled with short groins to provide a bathing beach with a safe swimming area and a controlled sand plaza. Economical in execution and maintenance, the method can be used for sandy or rocky coasts.



Fig. 1. Enclosed Sela Beach at Bat-Yam. General View. 400 m. long by 175 m. wide.

INTRODUCTION

The use of beaches for recreation has assumed tremendous proportions (Ref. 1) and, with growing frequencies of heat waves, it may be expected that sea bathing will continue to rise in demand.

Various coastal protection measures (Ref. 2) used in coastal engineering emphasize mainly the protection and creation of sandy plazas. The problems of sea bathing were left open. This paper is devoted foremost to the human aspect of coastal protection rather than to sedimentation or to structural problems.

Bathing in the open sea foreshore (where most bathing takes place) is in many cases a safety hazard, and swimming or other recreational activities are hardly possible. Besides the good swimmers, the surfers and those who enjoy jumping to the rhythm of breakers, there is a vast public of ordinary people, including families with children, the handicapped and the elderly, which require controlled sea conditions for bathing, swimming, rubber boating and just playing around in the water. This last group of people is often deterred from bathing in the sea by conditions and warnings of waves, currents, changing depths and rocky sea bottoms, pollution, reappearing sludges dumped in deep sea, sharks, jellyfish, fear of drifting out into the sea, strict lifeguard discipline, etc.

The Enclosing Scheme is aimed at developing a method by which bathing beaches will provide side by side enclosed and open sea coastal protected sections for the benefit of almost all groups of bathers. The following paragraphs describe the results of two built, enclosed beaches. They also describe general open sea conditions, emphasizing the need for beaches, public and private, to be properly utilized.

DESCRIPTIVE SUMMARY OF RESULTS

In general, the Scheme was meant to provide beaches with safe bathing areas, sand plazas and hinterlands protected against winter storms. In the Scheme, the submerged breakwater encloses a water area of reduced wave heights, cut off from open sea dangers. The short groins maintain the plaza sands and the seawall protects the hinterland at the back of the plaza. For rocky beaches, sand has to be brought in.

The Scheme was introduced at two locations of differing coastal characteristics along the Mediterranean shores of Israel. In 1969, an area about 400 m. long by 175 m. wide was enclosed at the sandy Sela Beach of Bat-Yam, at the central west coast of the country (Fig. 1). A rocky pocket beach about 75 m. long by 50 m. wide was enclosed, in 1974, at Achziv in the north of the country (Fig. 2). This enclosure is the first part of a planned future development and, being limited in size and water depth, it mainly serves families and children visiting the adjacent park.



Fig. 2. Enclosed Achziv Beach. General View. 75 m. long by 50 m. wide.

Sela is a very popular beach and from the time of its enclosure, seven years ago, soundings, field observations and water quality tests have been performed. The following summary of results and respective layout of the Scheme refer to Sela Beach, with occasional reference to Achziv Beach.

1. Layout. Fig. 3 presents the general layout of the Scheme and of the structural elements. The overall enclosed area is some 65,000 sq. m. (Achziv 4,000 sq. m.). The water area is about 40,000 sq. m., at present. The enclosure follows the lines of existing submerged beach rock. The reason for this was mainly economical. (In Achziv, too, advantage was taken of existing beach rock.) The submerged breakwater was based partially on sandy seabottom and partially on rocky bottom. The outer groins, on top of the beach rock, were designed to top the sides of the submerged breakwater. The location of the inner groins was influenced by the existence of the refreshment kiosk. The inner groins are not yet at their proposed full length. The sea wall follows the front line of the refreshment kiosk, leaving a limited hinterland up to the cliff. The plaza is some 25 m. wide at its narrowest, between the mean sea water line and the sea wall. The plaza is expected to be widened an additional 15 m. by lengthening the inner groins and by adding a groin at the southern sector.

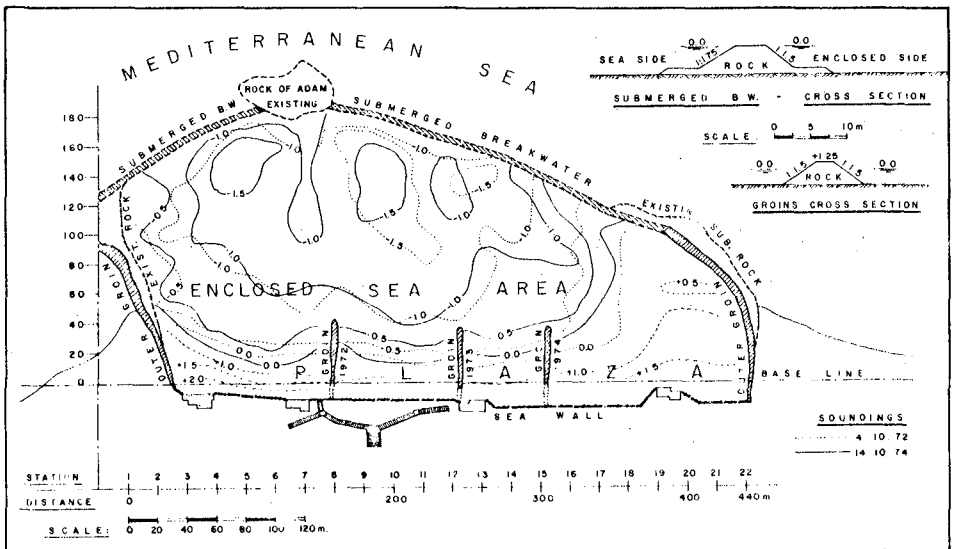


Fig. 3. Sela Beach. Layout of Enclosure, Structural Elements, Cross Sections and Soundings. Dated October 1972 and October 1974.

Long beaches can be developed step by step as was proposed for the whole beach length of Bat-Yam (Fig. 4).

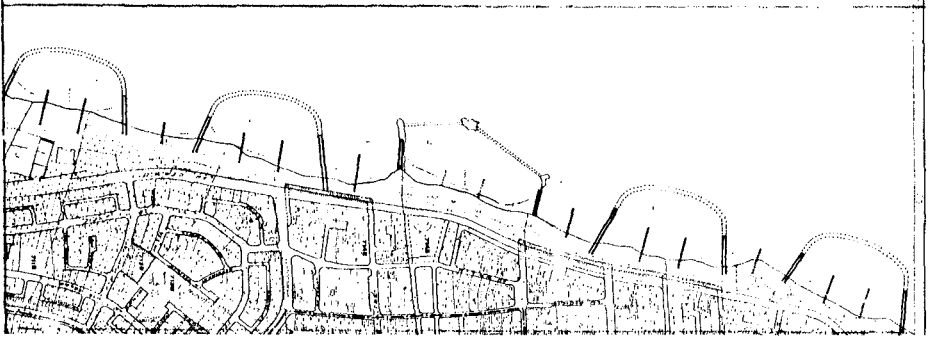


Fig. 4. Proposed Development for Bat-Yam Coast.

2. Waves and Currents. Wave heights in the enclosed area are considerably reduced, compared to outside wave heights. Those measured in the enclosed area were a maximum of 0.5 m., while estimated heights outside were around 1.5 m.

During most of the bathing season, bathing, swimming and rubber boating were safe inside, whereas they were hardly possible outside.

Waves sliding over the breakwater re-form in the area, some distance from the breakwater. The re-formed waves are of an oscillatory nature and swimming is pleasant. There are almost no currents. In certain wind conditions, relatively weak currents were occasionally reported between the breakwater and re-forming line.

During winter storms, wave heights in the area may reach up to 1 - 1.5 m. and currents of significant strength were reported by good swimmers.

The difference between wave and current conditions inside and outside are significant (Fig. 5). Bathing in the enclosed area is possible throughout the year, except during winter storms.



Fig. 5. Sela Beach. Difference in Agitation Between Inside and Outside the Enclosed Area. Limited Bathing Outside.

3. Water Depth and Sediment Movement. In most of the enclosed area, water depth is no more than 1.0 m. from mean sea level, i.e., about 1.5 m. from inside, still, high water level. In some areas, the water is deeper, up to 2.5 m. The shallow areas are usually preferred by the majority of the visitors. Figures 3 and 6 show soundings related to mean sea level, taken at beginnings and ends of bathing seasons. The depth lines seem to be relatively stable and the slopes gentle.

During and after construction of the breakwater and groins, sand movement took different forms. During the construction period,

sand drifted into the area and a tombolo was formed in the lee of the Rock of Adam. During the first two years after construction, the sand of the tombolo moved to the northern corner creating there a wide plaza. During the same period - prior to building the inner groins and prior to securing the southern outer groin against outflanking - the whole center and southern plaza areas were washed out, leaving beach rock exposed above and below sea level. Since the construction of the inner groins and the placing of sand between them, the plaza width became relatively stable, the beach rock became covered with sand, and seasonal sand movement takes place in the enclosed area. During the summer months, sand drifts from the plaza towards the breakwater creating shallow water areas near the breakwater, opposite the southern and central groins (Fig. 6).

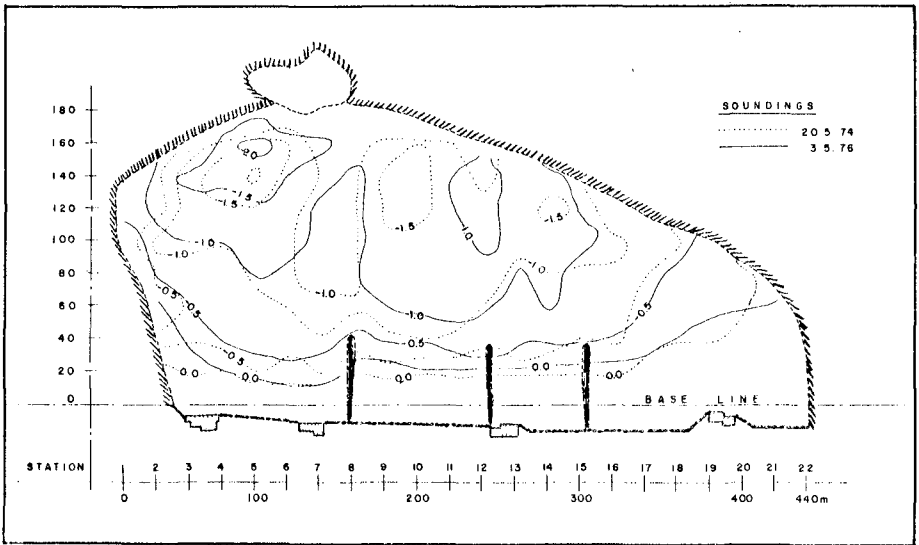


Fig. 6. Sela Beach. Soundings May 1974 and May 1976, (also see Fig. 3), Related to MSWL.

These shallow water areas may reach a height of -0.5 m. below mean sea level. The winter storms push the sand back, but it appears that not all of the sand goes back and not to its original plaza sections. During the last two years, some 2,500 cu. m. of sand remained in the water area. So far, no maintenance has been done in the water area, but it is expected that in years to come sand will have to be shifted from the water area back to the plaza. Shifting of sand in the plaza area takes place at the beginning of each bathing season for shaping up the area after winter storms. So far, since the building of the inner groins, there have been no noticeable changes in the overall balance of the sand in the enclosed area.

Outside the area, at the sides of the outer groins, accretion took place. This accretion undergoes seasonal changes within the general on- and off-shore movement of the sediments. The littoral drift appears to bypass the area around the breakwater.

4. Water Quality. Water quality inside is the same as outside and the enclosed area cleanses itself. The still water level is higher inside than outside, resulting in a constant out-flow of water.

A water temperature difference of 2°C, higher inside than outside, was measured during the bathing season.

During construction, contamination from the open sea penetrated into the enclosed area resulting in an odour in the northern part of the enclosure. This odour faded during the first bathing season after construction.

Afterwards, the following facts were reported: a) A pipeline, located some 150 m. to the south of the area, discharges fluid spoil of brown color. Even under southwesterly winds, a small part of this fluid was seen penetrating the area. The bulk of it was seen bypassing outside the breakwater; b) Before the beginning of the 1975 bathing season, the Bat-Yam beaches were accidentally flooded by untreated sewage. In July, the waters were retested and all the beaches, including the Sela, were found clean - fit for bathing; c) This 1976 season, the Sela Beach was declared open for bathing whereas the other two beaches to the south were closed due to contamination.

5. Recreation. The enclosed area provides sea bathing recreation also to a public which, in open sea conditions, could not bathe. It has been noticed at many locations that wide, sandy, open sea plazas are used to capacity by visitors, while actual sea bathing is very limited.

In the enclosed area, a considerable part of the visiting time is spent in the water and a wide range of recreational activities are available. Bathing, swimming and swimming lessons, rubber boating and shallow water diving are exercised inside; amateur fishing takes place from the breakwater to the outside.

Enterprise could still broaden the recreational activities of the water and hinterland areas. It should be emphasized that the enclosed area gives the impression and feeling of open sea bathing and not of a swimming pool. The sand plaza, sea water, sandy bottom, space, low waves, open horizon, onshore breeze, security and lenient attitude of the lifeguards provide sea bathing and recreation in a relaxed atmosphere. For the good swimmers, entrance to the open sea can be either through the open sections of the beach at both sides of the outer groins or, in order to avoid bypassing the dangerous foreshore, from specified places along the breakwater.

Most bathers prefer shallow water. In the enclosed beach, bathing is spread over wide areas, whereas outside it is limited to narrow strips and only as directed by the lifeguards (Fig. 7).



Fig. 7. Sela Beach. Bathing Mostly in Shallow Areas. Outside Bathing Limited to Narrow Strips. Inside Bathing Spread Over Wider Areas.

6. Design and Construction. Design of the enclosed Sela Beach started in 1968, and continued through the construction period and until the inner groins were built. At that time, wave data and personnel experience with submerged breakwaters and enclosed sea areas were available from the building of Ashdod Port, about 30 km. to the south of Bat-Yam. Partial soundings of the Sela area were taken at the beginning of the design, and field observations in the area and along other bathing beaches were made through the whole design period. No laboratory tests were made because of lack of local data, time and the high cost in foreign currency in comparison to the overall cost of the structure.

The beach rocks at both ends of the area were thought to serve as parts of the enclosing structure, but a closer survey during construction indicated the necessity of full enclosure by means of dumped rock and the necessity of elevated outer groins at both ends.

The necessity of the inner groins became evident during the first winter of construction. The inner groins were built only after serious damage occurred to the inner plaza. Close observations were made as to sand movement prior to and after the building of the groins.

The submerged breakwater was built at a water depth of approx. 2.5 - 3 m. The nominal crest elevation was designed to be at mean sea level. In reality, some rocks are lower and some are up to +0.6 m. and more (Fig. 3). The armour rock, of 5 - 8 ton class, was designed for wave heights of 3.5 m. The placing of the rocks was carried out from both ends, simultaneously. The equipment operated from an overbuilt elevation of 1.5 - 2.0 m. above mean water. After enclosure was achieved, the overbuilt rock was removed and used as berms at both sides of the breakwater. The quantities of rock were about 100 tons per lineal meter of breakwater. The work was done during one summer season.

OPEN SEA CONDITIONS

Open sea bathing is in many cases a safety hazard and of limited recreational value. Along our Mediterranean coast, the foreshore is particularly dangerous and there most drownings occur.

1. The Foreshore. The foreshore is the area between the

*The author served as supervising engineer for design and construction of breakwaters at the Port of Ashdod

water line and the outer limit of the nearshore bar. The assumed conditions in the foreshore, as described, are based on observations during a bathing season prior to the construction at the Sela Beach.

During most days of the summer months, the eastern coast of the Mediterranean Sea is exposed to onshore winds resulting in waves 0.6 - 1.2 m. high and sometimes up to 2.0 m. high (Fig. 8).

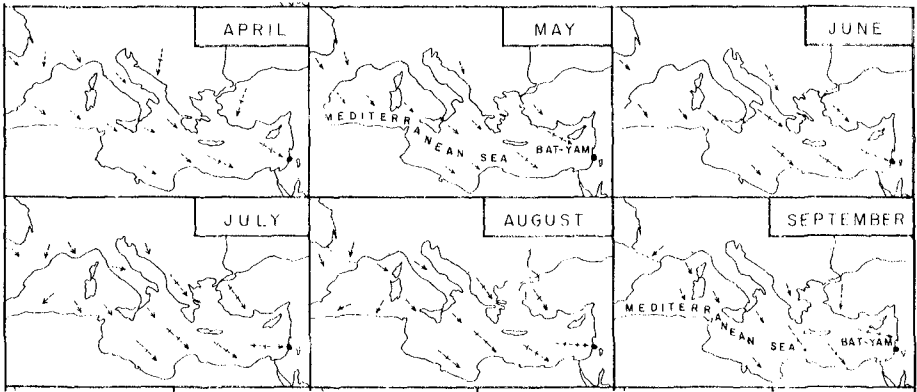


Fig. 8. Monthly Wind Conditions at Mediterranean Sea.

At the same time, a nearshore bar with a crest elevation of about 1.0 m. below sea level exists parallel to the coast.

The nearshore bar was sounded (Ref. 3)(Fig. 8a) and appears to be in fair agreement with the assumptions based on previous observations.

The waves break to the seaside or on top of the bar and almost the entire width of the foreshore is covered by surf. It appears that the area between the water line and the inner limit of the bar acts as a current velocity field in which flow takes place in all directions (Fig. 8b). Studies made in the past provide a wider range of information (Ref. 5 & 6).

Along the bar, there are breaks or rip-passes through which rip-currents are forced out into the sea. On top of the bar the water seemed to be air entrained, absorbing currents from both sides (Fig. 8c). The bar configuration, the rip-passes, current velocities and current directions seemed to be changing under changing wave conditions. In the area, drownings occurred as near as 5 m. from the water line and difficulties in returning

to shore were experienced by ordinary bathers, while rip-currents endangered even fairly good swimmers. Because of frequent drownings during bathing seasons, a law was enforced banning entrance into the sea except under supervision and as directed by lifeguards.

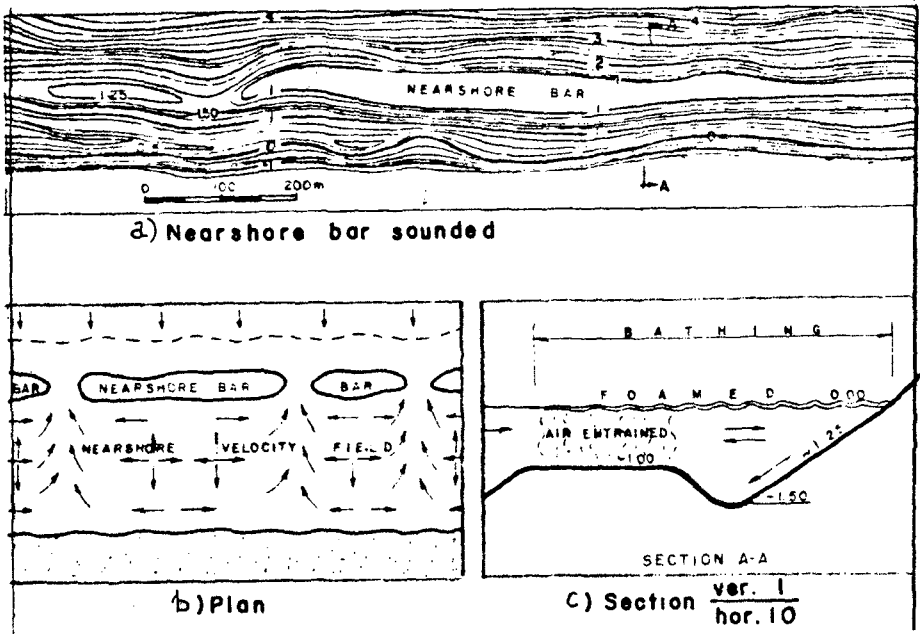


Fig. 8. Schematic Diagram of Nearshore Bar and of Nearshore Current Velocity Field.

2. Open Sea Bathing. Open sea bathing is in many cases confined to jumping to the rhythm of the breakers. The ordinary bathers' time in the water is short and at a very limited distance from the water line. The great responsibility resting with the lifeguards results in their enforcing stringent restrictions on the movements of the bathers, and bathing takes place in narrow areas perpendicular to the shore.

Swimming, rubber boating or other recreational activities are hardly possible during most days of the bathing season (Fig. 9). Visitors often spend their time on the plazas without going into the water, or they wade for short periods. In many cases, even wide beaches with lifeguards cannot be rated as bathing beaches.



Fig. 9. Open Sea Beach Near Achziv. August 1976.

SUMMARY

With the increasing demand for recreational beaches, beach design should include the problems of sea bathing and related recreational activities.

During its seven years of existence, the Enclosing Scheme proved that safe sea bathing and recreation for private and public beaches can be achieved and long sections of shore can be developed step by step with relative economy.

ACKNOWLEDGEMENTS

Sincere thanks to the Municipality of Bat-Yam, to the National Parks Authorities and to Sulam-Zur Council for their permission to use material prepared for them.

REFERENCES

1. Ippen, Arthur T., "Environmental Problems and Monitoring in Coastal Waters." Proc. Thirteenth Coastal Eng. Conf., 1972, Vancouver, B. C., Canada, ACCE, Vol. 1, pp. 15, 16.
2. Bruun, Per., "The History and Philosophy of Coastal Protection." Proc. Thirteenth Coastal Eng. Conf., 1972, Vancouver, B. C., Canada, ACCE, Vol. 1, pp. 43-50.
3. Eitam, Y., "Changes Along the Coast of Maagan Michale." 1974 Study for M.Sc. at the Hebrew University, Jerusalem, and Israel Oceanographic & Limnological Research, Haifa (Text in Hebrew).
4. Shepard, F. P., and Inman, D. L., "Nearshore Circulation." Proc. First Conf. on Coastal Eng., 1950, Long Beach Calif., Council on Wave Research, Chapter 5.
5. U. S. Army Coastal Eng. Research Center., Shore Protection Manual, 1973, Vol. 1, pp. 4-44. *
6. Tauman, J., "Bathing Beach Development by Means of Enclosing Scheme." Journal of the Assoc. of Eng. & Arch. in Israel, July-August, 1975 (in Hebrew), and Symposium on Foreshore and Beach Development from the Coastal Engineering Aspect, January 1975, Tel-Aviv.

CHAPTER 85

EXPERIMENTAL VERIFICATION OF GROUYNE THEORY

by

C.H. Hulsbergen¹, W.T. Bakker² and G. van Bochove³

1 Abstract. In order to check the results of Bakker's theory [1], [2] concerning the influence of groynes on a sandy beach, a comparison is made with experimental results obtained in model tests performed in the Delft Hydraulics Laboratory [3], and in the Laboratorio Nacional de Engenharia Civil, Portugal [4]. The theory gives the bathymetric development in terms of a set of two schematized contour lines, representing the onshore and offshore parts of the model where longshore sand transport occurs. As input in the theory the characteristics of the undisturbed sand transport should be known, i.e. without groynes. This is achieved by computing the longshore sand transport according to Bijker's method [5] and the transverse sand transport according to Swart's method [6], starting from the hydraulic conditions as measured in the model without groynes. In order to make a comparison with the theoretical lines, the bathymetric development as measured in the model with groynes is also schematized to a set of two contour lines. In some cases the result is quite good, whereas in other conditions the theory does not even show the right trend; see [7] for details. Possible causes are discussed, and shortcomings of the model as well as of the theory are mentioned.

2 Theory. For details of the theory reference is made to [1] and [2]. Only a few basic assumptions and limitations are mentioned here. The theoretical approach may be summarized as follows:

- a) The coastal profile is schematized according to Fig. 1. The active zone of the profile, i.e. from an upper dune erosion level down to a depth where relevant changes are no longer significant, is split into two layers with a thickness D1 and D2. Each layer extends seaward from a common base line over a certain distance, L1 and L2, respectively. The area of the schematized step-type cross-section is equal to the area of the actual profile. The elevation of the horizontal interface is defined by the point where the seaward toe of the groyne intersects the actual beach profile. In top view, the two layers appear as a set of two lines, referred to as beach-line and foreshore-line respectively (Fig. 2).
- b) The rates of littoral drift S1 and S2 along beach and foreshore each have a linear relationship with the local angle of wave incidence:

$$S1 = \underline{So1} - \underline{s1} \frac{\partial y1}{\partial x} \quad \text{and} \quad S2 = \underline{So2} - \underline{s2} \frac{\partial y2}{\partial x} \quad (1)$$

where So1 (So2) = undisturbed longshore transport along beach-line (foreshore-line); s1 (s2) = factor of proportionality; $\partial y1/\partial x$ ($\partial y2/\partial x$) = local angle between beach-line (foreshore-line) and base line.

- c) The transport Sy perpendicular to the coast, taking place between the beach and the foreshore, depends on the steepness of the (schematized) profile. Whenever the distance L2 - L1 is smaller than a certain equilibrium distance W, the profile is too steep, causing a seaward transport. In the opposite case there is a landward transport (Fig. 2):

1 Delft Hydraulics Laboratory, Project Engineer.
2 Rijkswaterstaat, Head Study Department Flushing.
3 Rijkswaterstaat, Coastal Research Engineer.

$$S_y = \underline{s_y} \left[\underline{W} - (L_2 - L_1) \right] \quad (2)$$

where s_y is a factor of proportionality.

In (1) and (2) the underlined terms are "coastal constants", which control both the time scale and the geometric scale of the coastal development, and which have to be determined in order to achieve quantitative results. Here, the "coastal constants" are quantified from:

- experiments without groynes
- Bijker's theory [5] for longshore transport
- Swart's theory [6] for perpendicular transport.

d) Continuity of the sand volume is specified by

$$- \frac{dS_1}{dx} - S_y = D_1 \frac{\partial y_1}{\partial t} \quad \text{and} \quad - \frac{dS_2}{dx} - S_y = D_2 \frac{\partial y_2}{\partial t} \quad (3)$$

e) The main boundary condition is formed by the complete obstruction of that fraction of the littoral drift which moves along the beach-line. Moreover, there is continuity in the location and in the orientation of the foreshore-lines on both sides of every groyne.

A visualization of a typical theoretical result is given in Fig. 3. It gives rise to a few comments. The theory, in its basic form as outlined above, gives only one type of coastal evolution, i.e. a certain amount of accretion upstream and an equal amount of erosion downstream, in a pattern which is basically fixed. That is so, because the hypotheses concerning the sand transport tacitly assume a quite neat and "nicely" behaving breaking wave and longshore current. In fact, the theory is not dealing with any detail of the coastal current system or the sand transport phenomenon. In order to make the theory more realistic, the possibility has been added to include such influences as rip-currents, stream refraction, and diffraction. However, except for a single case (Chapter 4), these options have not been used here, because their application presumes detailed a priori knowledge about the current pattern, which was not available. For this reason Chapter 3 gives the experimental results against the background of the theory in its basic form, as represented by Fig. 3. The procedure for this comparison is outlined in Fig. 4.

3 Experiments in Delft Hydraulics Laboratory

3.1 Model facility and test procedure

The lay-out of the model basin is given in Fig. 5. A large amount of various conditions were installed, details of which are extensively discussed in [3]. As bed material dune sand was used with $\rho = 2650 \text{ kg m}^{-3}$ and $D_m = 0.220 \text{ mm}$. Either 0, 1 or 3 impermeable groynes were present, with their crests well above the water level, with rough 1:1 slopes and aligned perpendicularly to the coast. The spacing was 6 m and their length so that they obstructed the longshore current partly or completely. The regular waves had a period of 1.55 s or 1.15 s, and a height between 0.07 m and 0.14 m. Depending on the wave steepness and the local beach slope, either spilling or plunging breakers occurred, under an angle of appr. 5° with the shore line. Water and sand were fed upstream and caught downstream in order to represent an infinitely long, straight beach.

In short, the procedure was to try and establish a dynamic equilibrium along a straight beach without groynes, and to assess meanwhile the development of the wave heights, the current velocity, the morphology and the trapped sand distribution. Then, after adding a groyne system, the new hydraulic and bathymetric development were recorded and subsequently compared with the theory. Here only a limited, though typical, selection of the numerous test results is presented, while in Chapter 5 a discussion is given, making use of some more selected measuring

data which are deemed useful for a good interpretation of the results.

3.2 Tests with a single groyne.

Representative as a "good" tests is T22, where the main conditions were: wave height 0.075 m, wave period 1.55 s, water depth 0.38 m in front of the wave generators. The average rate of sand nourishment was $71 \text{ dm}^3\text{hr}^{-1}$, while $55 \text{ dm}^3\text{hr}^{-1}$ was caught in the traps. The rate of water supply was constant at $30 \text{ dm}^3 \text{ s}^{-1}$ in order to feed the longshore current. The groyne extended seaward to 4.2 m, whereas the waves broke at appr. 3.5 m. Fig. 6 and 7 depict the beach, looking upstream, after 0.5 hr and 50 hrs. They show a quite regular accretion upstream, and erosion downstream of the groyne. This is also represented by Fig. 8, a difference chart displaying the extent and the locations of erosion and accretion during the 50 hrs of the test. In an attempt to monitor the actual longshore sand transport by local measurements, the wave height and the longshore current distribution were frequently measured in sections perpendicular to the shore. These data, together with the local depth and the bed material characteristics, are enough to compute the longshore sand transport according to Bijker. Examples are given in Figs. 9 and 10 for a section 8 m upstream of the groyne, and at the groyne itself, respectively. The obvious decrease of the longshore sand transport capacity is in good accordance with the observed accretion of the beach. Fig. 11 shows both rates of longshore sand transport in the course of time. Typical accreting and eroding coastal profiles are given in Figs. 12 and 13, respectively, the latter together with the distribution of the longshore sand transport as caught in the sand traps.

From Bijker's and Swart's theories, together with the appropriate data from the experiment, the following quantities were derived for application of the theory:

upper level of beach	: 0.51 m	}	with respect to the level of the wave generator floor.
elevation of interface	: 0.24 m		
lower level of foreshore	: 0.18 m		

$S_{01} = 87 \text{ dm}^3\text{hr}^{-1}$, $s_1 = 994 \text{ dm}^3\text{hr}^{-1}$, $S_{02} = 29 \text{ dm}^3\text{hr}^{-1}$, $s_2 = 332 \text{ dm}^3\text{hr}^{-1}$, $W = 7.62 \text{ m sy} = 0.0338 \text{ dm hr}^{-1}$.

The resulting schematized beach- and foreshore-lines for 0.10 and 50 hrs are given in Fig. 14, together with the comparable theoretical lines. The fit is quite good, especially for the beach-lines. It is thought that this favourable result was reached under the influence of an extraordinarily regular breaker type (plunging), which was accompanied by a very regular longshore current. Moreover, the groyne interrupted the longshore current almost entirely, thus obstructing the longshore transport of sand to a great extent.

Another test with a single groyne, T18, contrasted sharply with the above result. Its main conditions were: wave height 0.10 m, wave period 1.55 s, water depth 0.38 m in front of the wave generators, average rate of sand nourishment $88 \text{ dm}^3\text{hr}^{-1}$, while $106 \text{ dm}^3\text{hr}^{-1}$ was caught in the traps. The water discharge was constant at $55 \text{ dm}^3 \text{ s}^{-1}$. In Fig. 15 the contours after 60 hrs are shown, where the attention is drawn to the clear accretion, but this time downstream of the groyne. Locally even a new beach line appeared seaward of the original one. The development can be followed on Figs. 16 and 17, where difference charts of 0-20 hrs and 20-60 hrs are showing how the bulk of the longshore sand transport moved around the groyne in two stages. In the intermediate stage the maximum accretion amounted to 20 cm at some distance downstream and seaward of the head of the groyne. After 20 hrs the bulk of this sand deposit was removed and shifted in shoreward direction, and somewhat more downstream. Fig. 18 shows that neither the upstream nor the downstream overall profile was subject to large changes. It also points towards a possible reason for the remarkable developments encountered here: the trapped sand distribution, averaged over 60 hrs, indicates that the groyne could hardly be expected to stop the longshore transport. However, the average trapped sand distribution in the preceding test T17 (without groyne), was used

to design this groyne length such that it would stop approximately 50% of the existing longshore sand transport.

After the above explanation it is not surprising that the experimental results are not well covered by the theoretical beach- and foreshore-lines (Fig. 19), which are based on the following data:

upper level of beach	: 0.46 m	} with respect to the level of the wave generator floor.
elevation of interface	: 0.235 m	
lower level of foreshore:	0.06 m	

So1 = 73.5 dm³hr⁻¹, s1 = 840 dm³hr⁻¹, So2 = 65 dm³hr⁻¹, s2 = 743 dm³hr⁻¹, W = 10.08 m, sy = 0.029 dm hr⁻¹.

The impression exists from various observations (see also Chapter 5) that secondary wave formation, caused by the bar at a distance of 11 m (Fig. 18), may have played an important part in re-establishing the original coastal profile after 20 hrs. It is felt that this type of secondary waves has an important influence on coastal profile dynamics.

3.3 Tests with a row of three groynes.

In Fig. 20 the contours after 50 hrs of test T23 with three groynes are presented. The conditions were: wave height 0.075 m, wave period 1.55 s, water depth 0.38 m in front of the wave generators. The average rate of sand nourishment was 44 dm³hr⁻¹, while 27 dm³hr⁻¹ was caught in the traps. The average rate of water supply was 25 dm³s⁻¹. The groynes extended to 3.7 m. Until 20 hrs a plunging breaker occurred at appr. 3.7 m, whereas later on the spilling type dominated, with variations in breaker location. In Fig. 21 a clear rhythmic behaviour is revealed by the difference chart, both in longshore direction (as caused by the groynes) and in perpendicular direction (as caused by an overall coastal profile development). The various quantities with respect to the theoretical computations are:

upper level of beach	: 0.51 m	} with respect to the level of the wave generator floor.
elevation of interface	: 0.255 m	
lower level of foreshore:	0.160 m	

So1 = 87 dm³hr⁻¹, s1 = 995 dm³hr⁻¹, So2 = 29 dm³hr⁻¹, s2 = 331 dm³hr⁻¹, W = 8.10 m sy = 0.032 dm hr⁻¹.

Fig. 22, displaying the experimental and theoretical lines representing the beach and the foreshore, reveals a reasonable equality as far as the beach is concerned. However, large deviations occur in the foreshore, where the typical rhythmic variations are not found back in the theory.

Test T34 had unusual conditions in so far that the water level fluctuated in a one-hour cycle 0.025 m plus and minus the average of 0.38 m above the wave generator floor. This was done in order to shift also the type and the location of the breaking waves, in an attempt to avoid rip-current formation at fixed locations. The other conditions were: wave height 0.115 m, wave period 1.15 s, average rate of caught sand 74 dm³hr⁻¹. The rate of sand nourishment was constant at 70 dm³hr⁻¹, and the rate of flow was constant at 50 dm³s⁻¹. The groynes extended to 3.27 m, whereas the breaker location varied widely during the test.

The quantities for the theoretical analysis were:

upper level of beach	: 0.49 m	} with respect to the level of the wave generator floor.
elevation of interface	: 0.27 m	
lower level of foreshore:	-0.01 m	

So1 = 32.4 dm³hr⁻¹, s1 = 370 dm³hr⁻¹, So2 = 35.6 dm³hr⁻¹, s2 = 407 dm³hr⁻¹, W = 8.11 m, sy = 0.108 dm hr⁻¹.

The result was not much better than that of test T23, as can be seen on Figs. 23, 24 and 25. Fig. 24 is a special chart, displaying the difference between test T34 and test T33 (without groynes but further with exactly the same conditions as T34) after 30 hrs. The pattern of alternating erosion and accretion between the groynes is opposite to what should be expected from the theory. This is most probably caused by an intricate and unstable pattern of currents, stagnation areas, rip currents and regions of lower and higher waves.

4 Experiments in Laboratorio Nacional de Engenharia Civil.

4.1 Model facility and test conditions.

Reference is made to [4] for details. Fig. 26 shows the lay-out of the model. A convex beach profile of pumice-stone ($\rho = 1670 \text{ kg m}^{-3}$, $D_m = 1.25 \text{ mm}$) was molded between two rockfill groynes E1 and E3. These groynes had 2:1 absorbent slopes and acted as training walls for the beach. A smaller groyne E2 in between with steep 1:5 slopes completely obstructed the littoral drift. The waves were 0.02 m high, had a period of 1 s and were generated under an angle of 20° in a water depth of 0.40 m.

4.2 Test results and theoretical beach lines.

Various beach line positions were recorded during the 35 hr test, as presented in Fig. 27. These are compared to theoretical lines, which were determined as follows [8]. The active profile was schematized to a single beach line, because perpendicular transport across the 0.063 m depth contour was assumed negligible. This depth is twice the breaker depth as calculated for straight, parallel depth contours. Diffraction calculations were performed in the deeper, horizontal part of the basin, whereafter refraction was calculated up to the 0.063 m contour line, again assuming straight and parallel depth contour lines, remaining so during the whole test. The resulting values for the wave height H_1 and the angle of wave attack ϕ_1 at the 0.063 m depth contour are given in Fig. 28.

The final position of the beach is now assumed to be defined by ϕ_1 and H_1 in a first approximation. By ϕ_1 alone, the final beach line is determined by being parallel to the local wave crest as defined by ϕ_1 , because only then the net transport along any part of the beach is equal to zero. By H_1 alone on the other hand, differences in wave set-up will develop, causing a varying longshore current velocity V_l along the beach, where V_l is a function of various parameters among which the beach line orientation [9]. By putting V_l equal to zero, the final beach alignment is found. After adding the partial solutions for H_1 and ϕ_1 , the final coastline is found as Y_0 in Fig. 29. By comparing this line to the experimental 35 hrs-line in Fig. 27, some differences can be found:

- In the experiment a certain amount of material does disappear into deeper water. Because Barcelo reports a rip-current near groyne E2, the theoretical line is adapted by taking a sand transporting rip-current into account near E2 with an adequate transport capacity. This will at the same time increase the theoretical beach line angle near groyne E2, bringing it closer to the measured position.
- Differences near groyne E1 are likely to be caused by a very low transport capacity in the model, whereas in the calculation no critical velocity for beginning of movement is used.

For the calculation of the coastline after 1, 4, 7, 15 and 35 hrs the dynamic equation is used (with $s_y = 0$), together with equation (1). Relevant quantitative parameters are: $S_{\text{ripcurrent}} = 3.4 \text{ dm}^3\text{hr}^{-1}$, $S_{01} = 27.8 \text{ dm}^3\text{hr}^{-1}$ acc. to Barcelo, $s_1 = 150 \text{ dm}^3\text{hr}^{-1}$. The resulting theoretical lines are given in Fig. 29; they fit quite well with the experimental lines of Fig. 27.

5 Discussion of the results. The above examples are typical in so far that they indicate the rather large variation in the ability of the theory to fit with the experimental results. One should not be too surprised, in view of the wide deviations which were often present in the actual experimental conditions, as compared to the ideal conditions which were (tacitly) assumed in the theory. The main causes of deviation are discussed below.

- Variations in wave height as measured in cross-sections very close to each other, were frequently noted and were judged to have a strong negative effect on the homogeneous conditions sought. Fig. 30 shows a rather dramatic example, in which the wave height variations are at least partly due to the varying bed profiles. Of course there exists a strong mutual interaction between wave behaviour and coastal profile development.
- An example of the progressively deteriorating homogeneity in longshore direction of the coastal profiles is given in Fig. 31. It shows the envelopes of all cross-sections after 10, 30 and 50 hrs in test T19 (without groyne).
- An effect, and simultaneously a cause, of the above mentioned non-homogeneity is present in the chaotic current pattern in the same test, as presented in Fig. 32. This test, too, began with a nice homogeneous and steady longshore current.
- Apart from being non-homogeneous, the current pattern was unsteady, as is shown in Fig. 33. It gives values of the longshore current in test T25, measured in two points 1 m apart perpendicular to the coast. The measurements were performed by timing floats over a distance of 1 m.
- Secondary waves were present under certain conditions. Apart from those, generated by the sinusoidally moving wave board [10], also secondary waves were generated while the regular waves passed over a large bar without breaking. In this respect it is interesting to not that Byrne [11] reports the same wave behaviour (long regular swell conditions) in the prototype (Fig. 34). Fig. 35 presents a coastal profile of test T19, with a bar and with the wave height over it; the wave breaks only at a distance of appr. 5 m. The respective wave forms as shown in Fig. 36 clearly show the presence of secondary waves (with period $T/2$) which are overtaken gradually by the faster main waves. Their presence has undoubtedly a large influence on the perpendicular sand transport [10], and further on the type of breaking and the kinematic results thereof. It is felt that the presence of those secondary waves can have a dominating effect on the formation and the stability of coastal profiles.
- The pair of Fig. 37 and 38 illustrates the strong relationship between secondary waves, bar formation, type of breaker, and subsequently the rate and distribution of the longshore transport. The conversion of the breaker type from spilling to plunging was in very good agreement with Galvin's results as far as the influence of the seaward slope of the breaker bar is concerned [12]. After this conversion the rate of longshore transport was appr. three times as large as before, and much more concentrated.
- The most obvious visible result of the increasingly non-homogeneous conditions in many tests was the formations of beach cusps. Both small (Fig. 39) and large (Fig. 40) examples have been recorded. It goes without saying that this is most unwelcome in tests which are meant to verify the effect of groynes on a sandy beach. Fortunately, the presence of a groyne appeared to induce a more stable condition, in which the cusp formation was partly suppressed.

6 Conclusions. The conclusions which follow from these tests and their comparison with the theory can be summarized as follows.

- The theory is good in cases with a stable, neat, and well defined longshore current system, and if the groyne(s) intercept a substantial part of the longshore sand transport.
- In other, more complex systems, the theory in its present form is not adequate on a forecast basis. However, if the current pattern is well enough defined and specified, the theoretical result may be improved by taking into consideration the effects of stream refraction, diffraction, and rip-currents.
- The coastal current system should be studied in more detail in order to improve the theory of Bakker.

REFERENCES

- 1 BAKKER, W.T., The dynamics of a coast with a groyne system. 11th Conf. on Coastal Engineering, Ch. 31, London 1968
- 2 BAKKER, W.T., KLEIN BRETELER, E.H.J. and ROOS, A., The dynamics of a coast with a groyne system. 12th Conf. on Coastal Engineering, Ch. 64, Washington 1970
- 3 DELFT HYDRAULICS LABORATORY, The influence of groynes on the coast, Report M 918 part I (experiments) March 1976 (in Dutch)
- 4 BARCELO, J.P., Experimental study of the hydraulic behaviour of groyne systems. 11th Conf. on Coastal Engineering, Ch. 13, London 1968
- 5 BIJKER, E.W., Longshore transport computations. Proc. A.S.C.E., vol. 97, WW 4, pp. 687-701, November 1971
- 6 SWART, D.H., A schematization of onshore-offshore transport. 14th Conf. on Coastal Engineering, Chapter 51, Copenhagen 1974
- 7 DELFT HYDRAULICS LABORATORY, Comparison of theoretical and experimental coast lines, Report M 918 part III, 1976 (in Dutch)
- 8 BOCHOVE, G. van, Elaborations of a model test conducted by Barcelo. Memo 72-21 of Rijkswaterstaat, Dir. Water Management and Water Movements, Section Coastal Research, The Hague 1972
- 9 BAKKER, W.T., The influence of longshore variation of the wave height on the littoral current. Study-Report WWK 71-19 of Rijkswaterstaat, Dir. Water Management and Water Movements, Section Coastal Research, The Hague 1971
- 10 HULSBERGEN, C.H., Origin, effect and suppression of secondary waves. 14th Conf. on Coastal Engineering, Chapter 22, Copenhagen 1974
- 11 BYRNE, R.J., Field occurrences of induced multiple gravity waves. Journ. of Geoph. Res., vol. 74, 1969, no. 10, May 15, pp. 2590-2596
- 12 GALVIN, C.J., Classification of breaking waves on three laboratory beaches. C.E.R.C. Res. Divn, 1967.

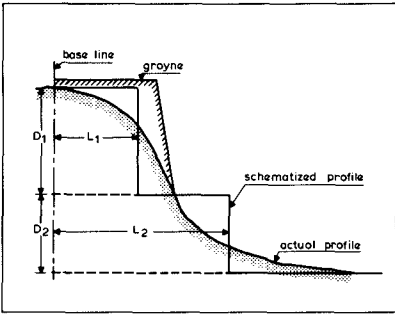


Fig. 1 Schematization of coastal profile

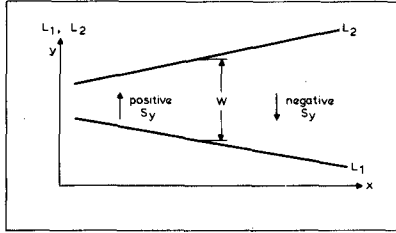


Fig. 2 Top view of schematized coast lines

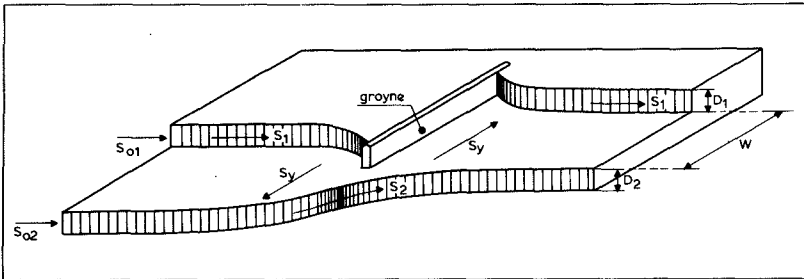


Fig. 3 Visualization of theoretical coast

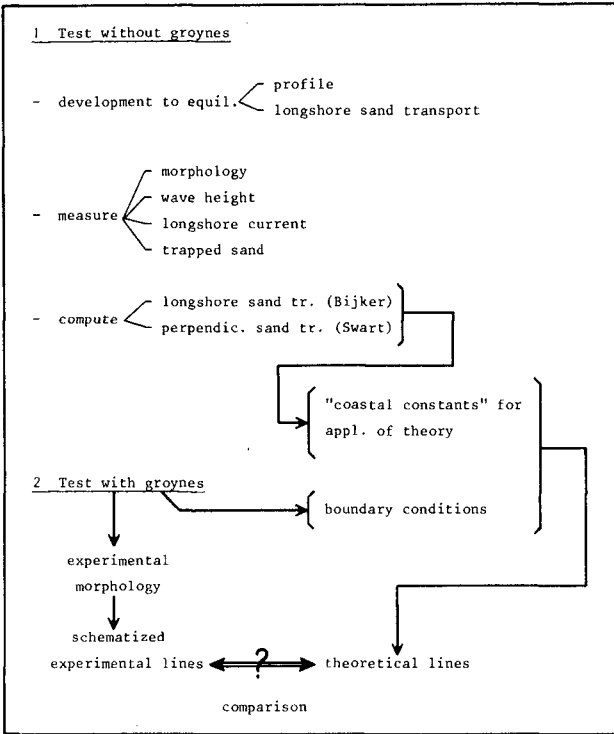


Fig. 4 Procedure of verification

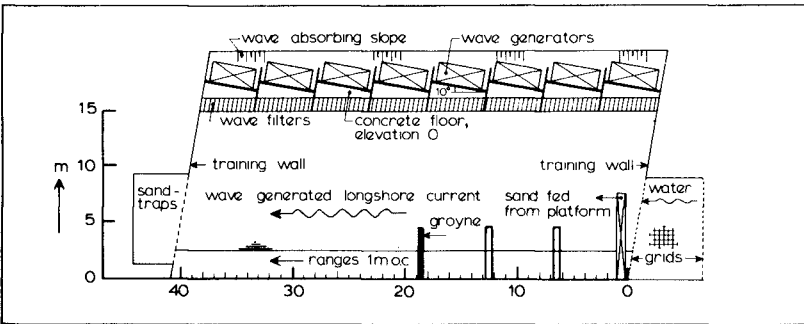


Fig. 5 Lay-out of model facility



Fig. 6 Test T22 after 0.30 hrs.



Fig. 7 Test T22 after 50 hrs.

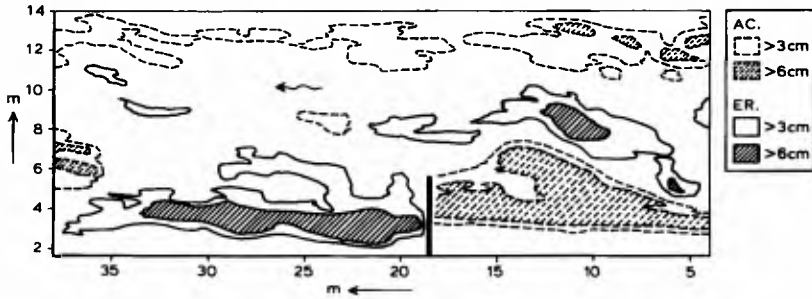


Fig. 8 Test T22, difference chart 0-50 hrs.

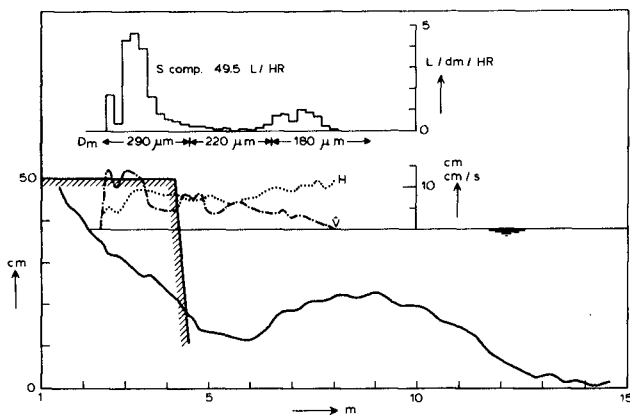


Fig. 9 Test T22, 8 m upstream of groyne after 3 hrs.

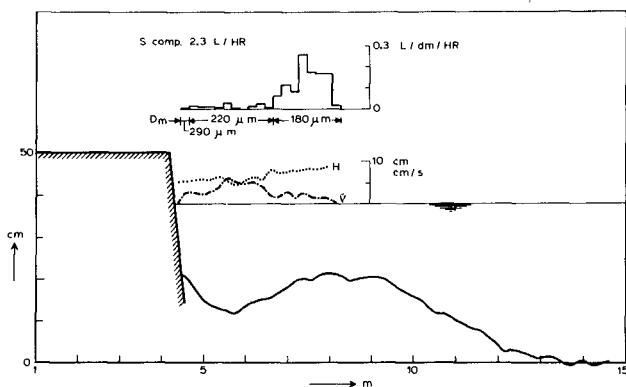


Fig. 10 Test T22, at groyne after 4 hrs.

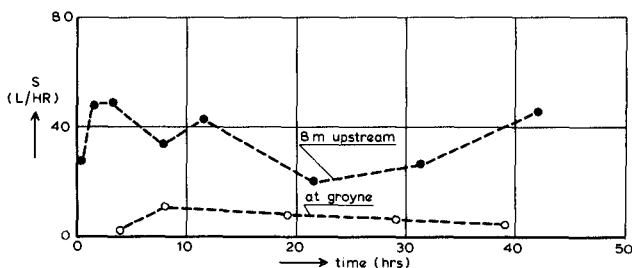


Fig. 11 Test T22, longshore transport according to Bijker

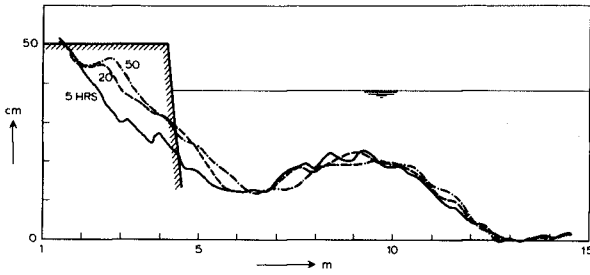


Fig. 12 Test T22, 3.5 m upstream of groyne

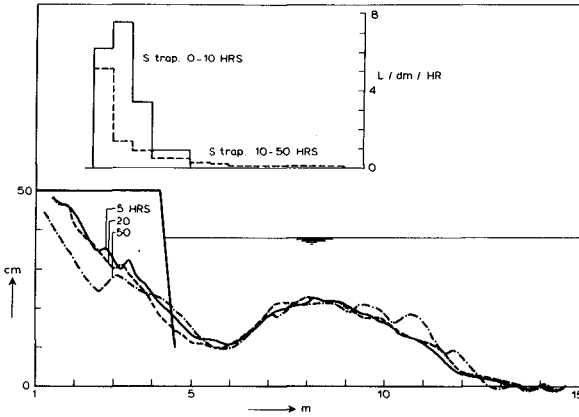


Fig. 13 Test T22, 3.5 m downstream of groyne

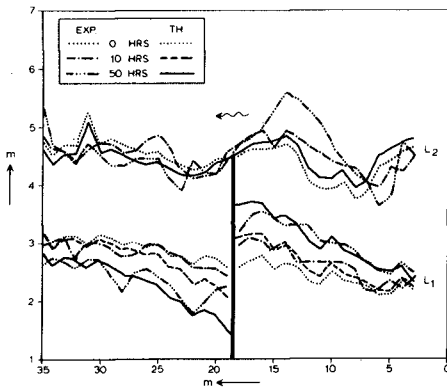


Fig. 14 Test T22, comparison of beach- and foreshore-lines

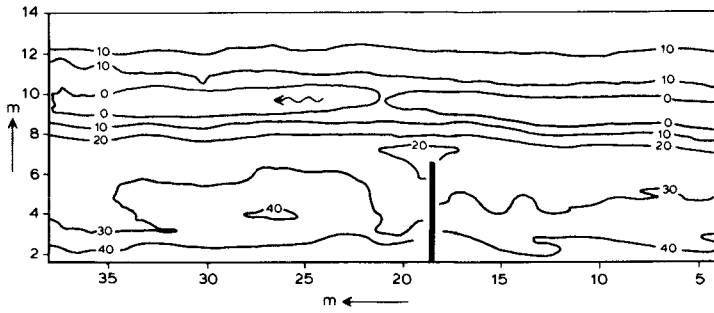


Fig. 15 Test T18, 60 hrs, contours in cm above model datum

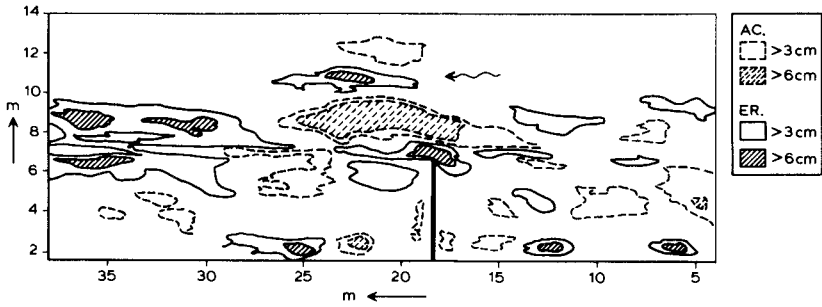


Fig. 16 Test T18, difference chart 0-20 hrs.

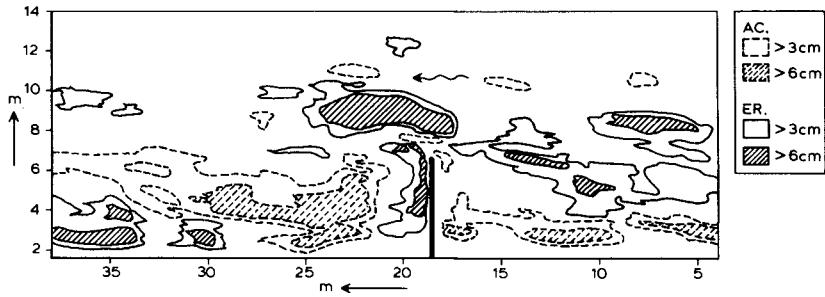


Fig. 17 Test T18, difference chart 20-60 hrs.

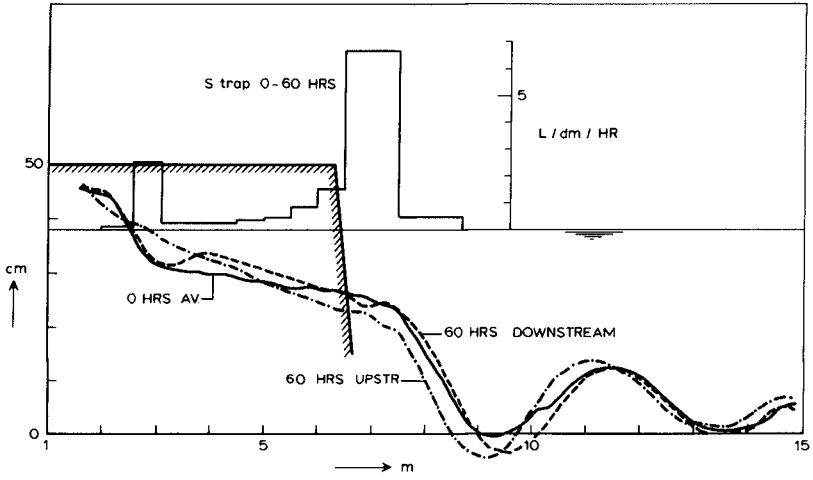


Fig. 18 Test T18, average upstream and downstream profiles

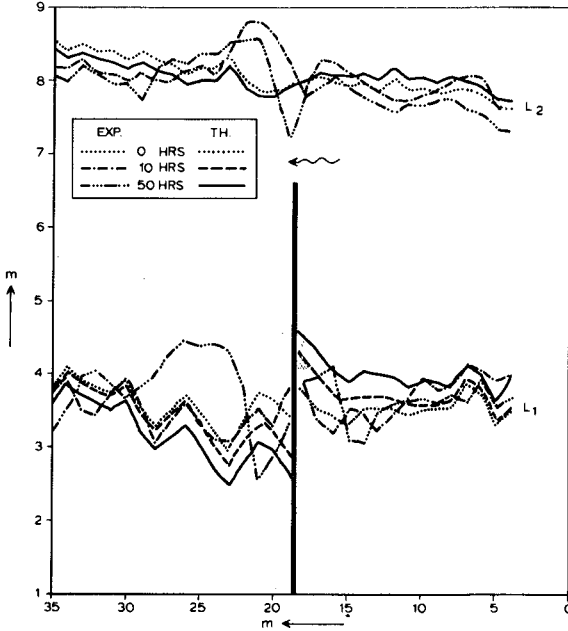


Fig. 19 Test T18, comparison of beach- and foreshore-lines

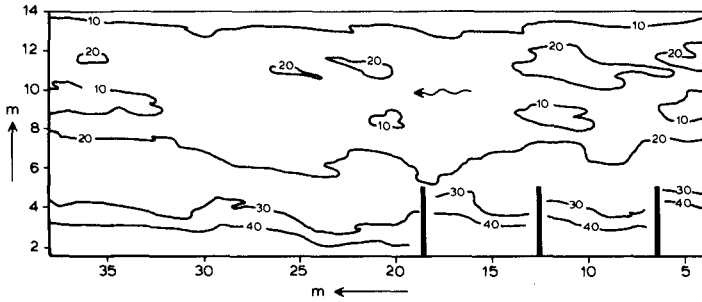


Fig. 20 Test T23, 50 hrs, contours in cm above model datum

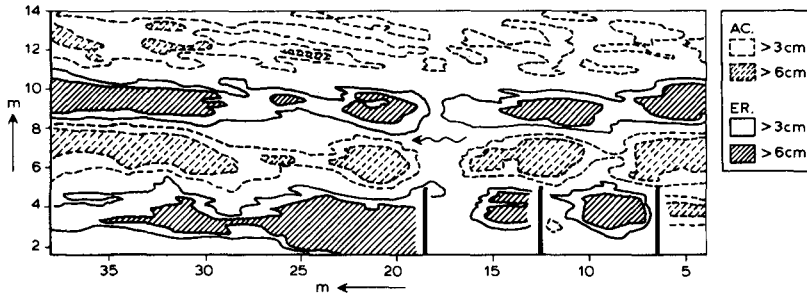


Fig. 21 Test T23, difference chart 0-50 hrs.

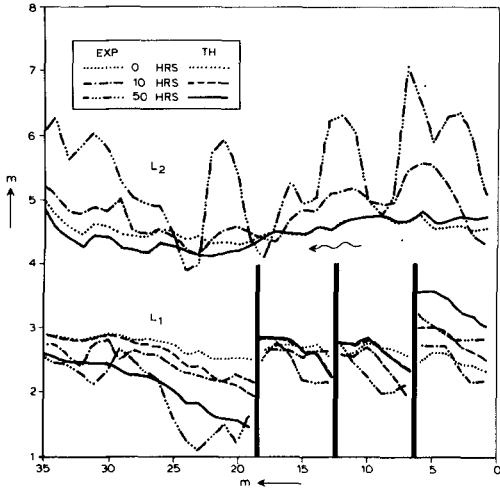


Fig. 22 Test T23, comparison of beach- and foreshore-lines

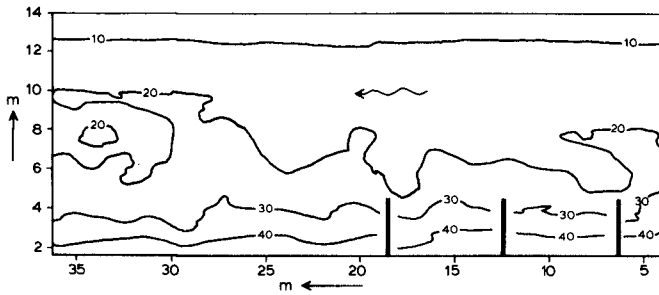


Fig. 23 Test T34, 45 hrs, contours in cm above model datum

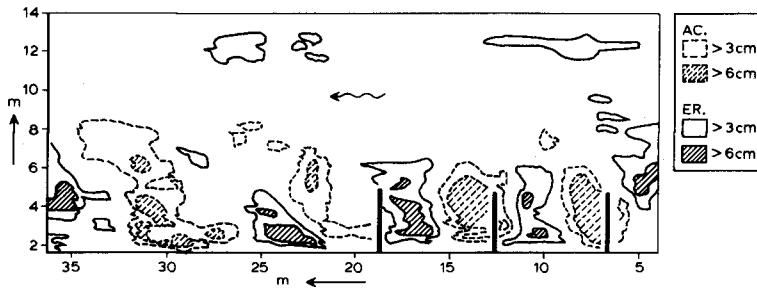


Fig. 24 Test T33/34, groyne effect 30 hrs.

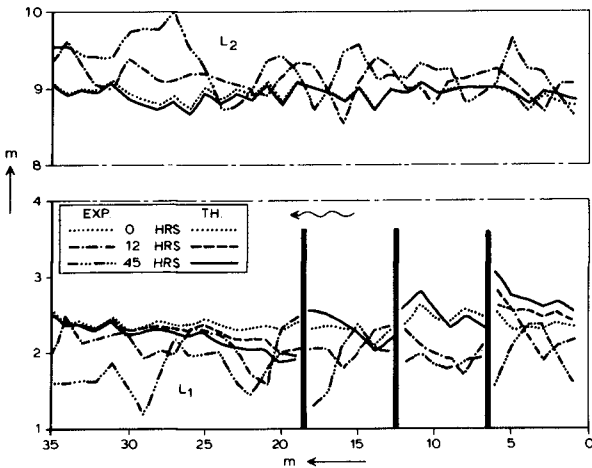


Fig. 25 T34, comparison of beach- and foreshore-lines

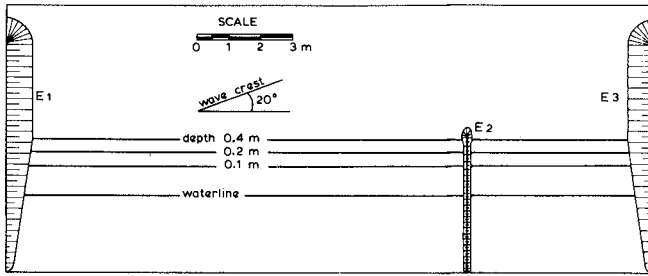


Fig. 26 LNEC test, lay-out of model basin

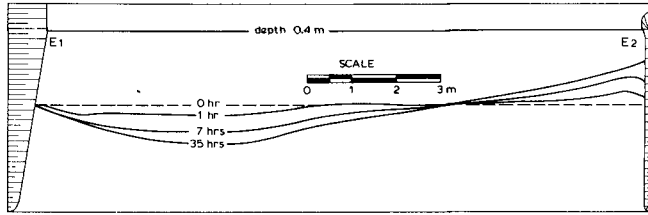


Fig. 27 LNEC test, experimental beach-lines

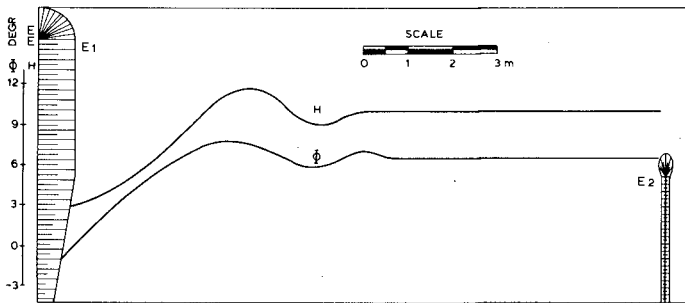


Fig. 28 LNEC test, wave height and angle of wave incidence

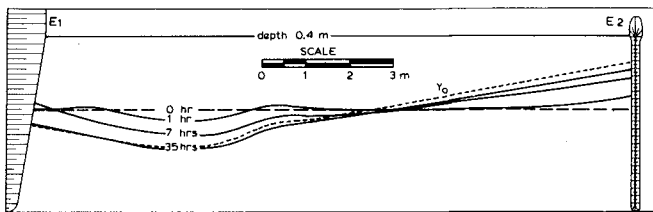


Fig. 29 LNEC test, theoretical beach-lines

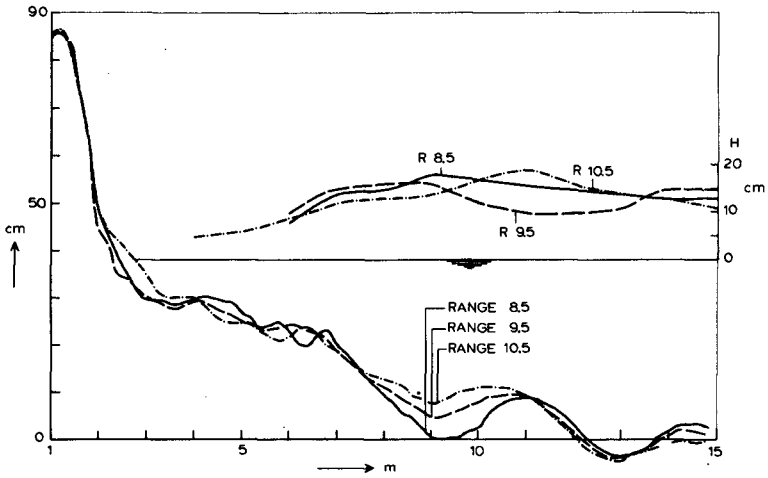


Fig. 30 Test T2, variety in beach profiles and wave heights

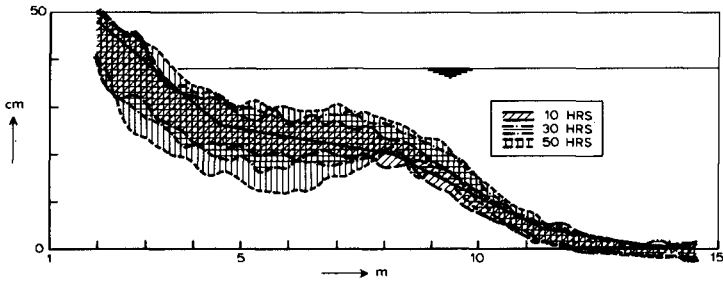


Fig. 31 Test T19, envelopes of beach profiles

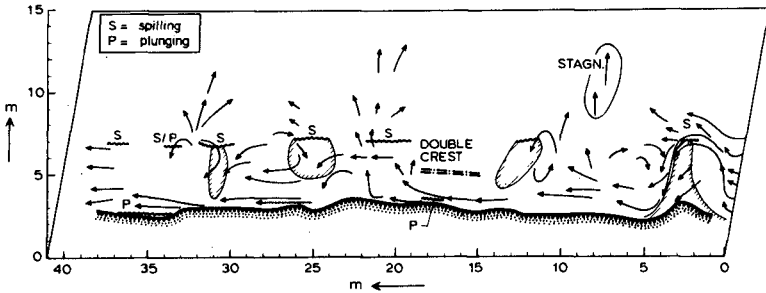


Fig. 32 Test T19, current pattern 77 hrs.

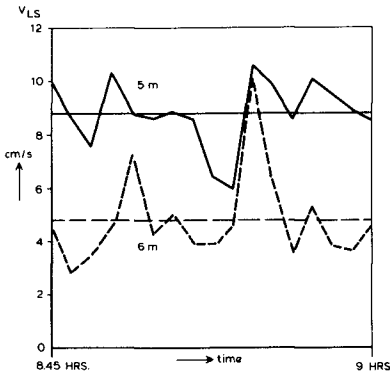


Fig. 33 Test T25, unsteadiness in longshore current velocity

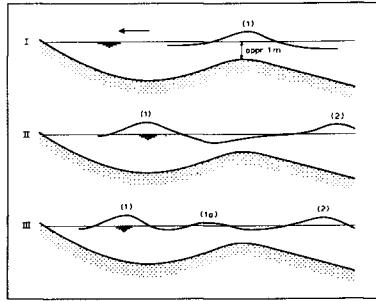


Fig. 34 Prototype observation of induced multiple gravity waves (after Byrne)

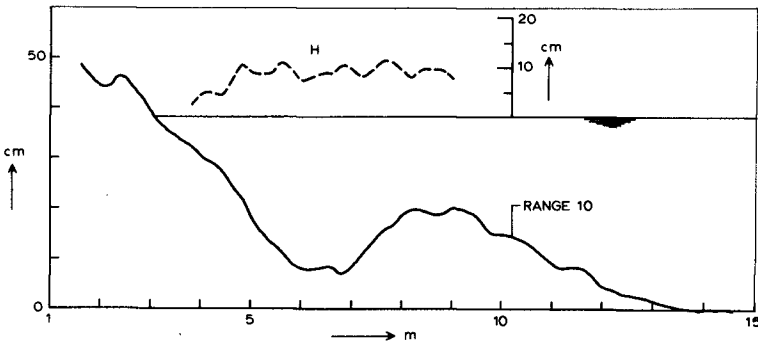


Fig. 35 Test T19, 105 hrs, bar profile and wave height

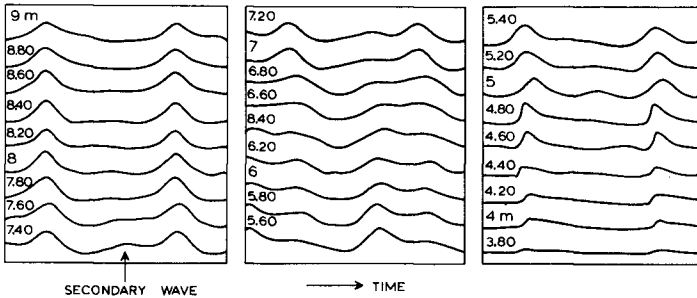


Fig. 36 Test T19, wave forms over bar profile from Fig. 35

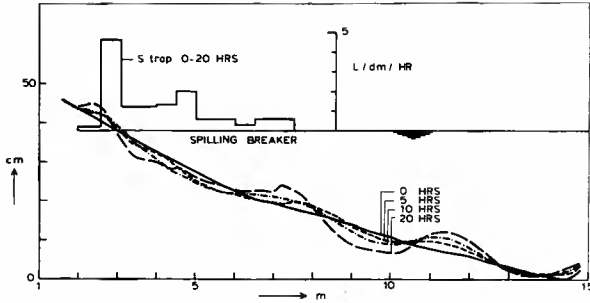


Fig. 37 Test T17, spilling breaker conditions 0-20 hrs.

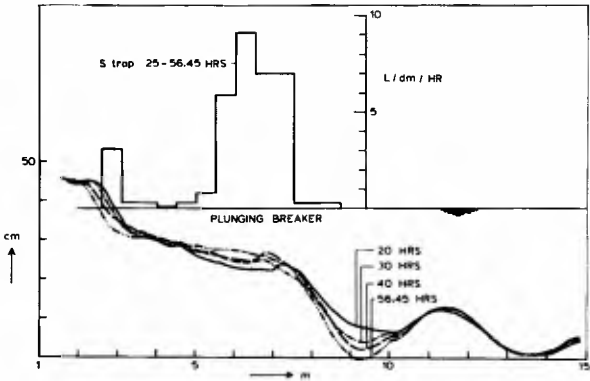


Fig. 38 Test T17, plunging breaker conditions 20-56.45 hrs.



Fig. 39 Test T19, small scale beach cusps



Fig. 40 Test T27, large scale beach cusps

CHAPTER 86

GROIN LENGTH AND THE GENERATION OF EDGE WAVES

Michael K. Gaughan¹ and Paul D. Komar²

ABSTRACT

A series of wave basin experiments were undertaken to better understand the selection of groin spacings and lengths. Rather than obtaining edge waves with the same period as the normal incident waves, subharmonic edge waves were produced with a period twice that of the incoming waves and a wave length equal to the groin spacing. Rip currents were therefore not formed by the interactions of the synchronous edge waves and normal waves as proposed by Bowen and Inman (1969). Rips were present in the wave basin but their origin is uncertain and they were never strong enough to cause beach erosion.

The generation of strong subharmonic edge waves conforms with the work of Guza and Davis (1974) and Guza and Inman (1975). The subharmonic edge waves interacted with the incoming waves to give an alternating sequence of surging and collapsing breakers along the beach. Their effects on the swash were sufficient to erode the beach in some places and cause deposition in other places. Thus major rearrangements of the sand were produced between the groins, but significant erosion did not occur as had been anticipated when the study began.

By progressively decreasing the length of the submerged portions of the groins, it was found that the strength (amplitude) of the edge waves decreases. A critical submerged groin length was determined whereby the normally incident wave field could not generate resonant subharmonic edge waves of mode zero with a wavelength equal to the groin spacing. The ratio of this critical length to the spacing of the groins was found in the experiments to be approximately 0.15 to 0.20, and did not vary with the steepness of the normal incident waves.

¹CICESE, Av. Gastelum No. 898, Ensenada, Baja California, Mexico.

²School of Oceanography, Oregon State University, Corvallis, Oregon

INTRODUCTION

Rational criteria for selecting groin lengths, spacings, heights, and angles to the shoreline for a given beach and wave conditions are not well developed. Some general criteria, founded on past experience, are mentioned in the literature. For example, Coastal Engineering Research Center (1973) recommends that groins be spaced two to three times the offshore groin length. A general review of beach protective structures, including groins, can be found in Bruun (1972).

In this study a series of wave basin experiments were undertaken for the purpose of better understanding the selection of groin spacings and lengths. It was initially supposed that a certain groin spacing would cause resonant conditions with the incoming waves such that strong edge waves would be generated with the same period as the normal waves. As shown by Bowen (1969) and Bowen and Inman (1969), such edge waves can interact with the incident waves to generate steady rip currents. Our working hypothesis was that such resonant conditions should be avoided as the resulting rip currents would be a hazard to swimmers and the rips would wash the sand offshore, defeating the purpose of the groins. We felt that some groin failures might have been an inadvertent selection of a groin spacing that resonated with the existing beach and wave conditions.

Our experiments quickly demonstrated that our initial hypothesis was incorrect, at least for the wave-basin scale and groin geometry tested. Rather than obtaining edge waves with the same period as the normal waves in the basin, subharmonic edge waves were produced with periods twice those of the incoming waves so that rip currents were not formed by the interactions of the edge waves and normal waves as proposed by Bowen (1969) and Bowen and Inman (1969). Rip currents were present in the wave basin but their origin is uncertain and they were not strong enough to cause beach erosion. They commonly originated at the node position of the subharmonic edge waves, but then migrated alongshore to the antinode positions, obtaining their best development when adjacent to a groin.

Guza and Davis (1974), Guza and Inman (1975) and Guza and Bowen (1975) had previously demonstrated theoretically and experimentally that the subharmonic edge wave with a period twice that of the incident waves is most

easily generated and the one most often occurring. The second most likely edge wave to be generated is that with a period equal to the incoming wave (termed the synchronous edge wave) of low modal number. Our wave basin experiments, therefore, agree with their conclusions. In all our experiments, subharmonic edge waves were easily generated in the wave basin, while synchronous edge waves were not detected even when the appropriate boundary conditions were employed. Guza and Inman (1975, p. 3005) found that when the incident wave period was chosen so that the groin and beach geometry excluded subharmonic resonances, synchronous edge waves were sometimes clearly visible in the run-up. This was not the case in our study. The reason is unknown; perhaps it is due to the smaller scale of our wave tank.

Our finding strong subharmonic edge waves in the wave tank tests also agrees with the field studies of Huntley and Bowen (1973, 1975a). Through measurements of the horizontal water particle velocities across the near-shore on a steeply sloping beach, they obtained clear evidence for the existence of subharmonic edge waves; synchronous edge waves were not detected.

Because we obtained only subharmonic edge waves, our study shifted to an investigation of their effects on the beach between the groins, and to the strength of the edge waves as a function of the groin geometry and wave conditions. The strength of the edge waves was taken as indicated by its swash distance up the beach face and its amplitude computed from this swash distance. As will be seen, the strength was found to be a function of the groin length and spacing.

A series of experiments were conducted with a thin layer of sand covering the otherwise evenly sloping solid beach for the purpose of determining what effects the presence of the sand might have on the edge wave strength and how the sand is redistributed on the beach by the combination of edge waves and incoming waves. The interest was whether general erosion or accretion of the beach would result from the presence of the subharmonic edge waves, and therefore whether they are to be avoided in the design of groin fields.

COMBINED FLOW OF EDGE WAVES AND NORMALLY INCIDENT WAVES

Recent research by Bowen (1969), Bowen and Inman (1969, 1971), Guza and Davies (1974), Guza and Inman (1975), Guza and Bowen (1976), and Huntley

and Bowen (1973, 1975a) have shown that waves incident on a beach can generate standing edge waves. Standing edge waves have their crests normal to the shoreline and their wave lengths from crest to crest parallel to the shoreline. Thus they are rotated ninety degrees in orientation to the incident swell waves. As shown in Figure 1, there are alternate positions

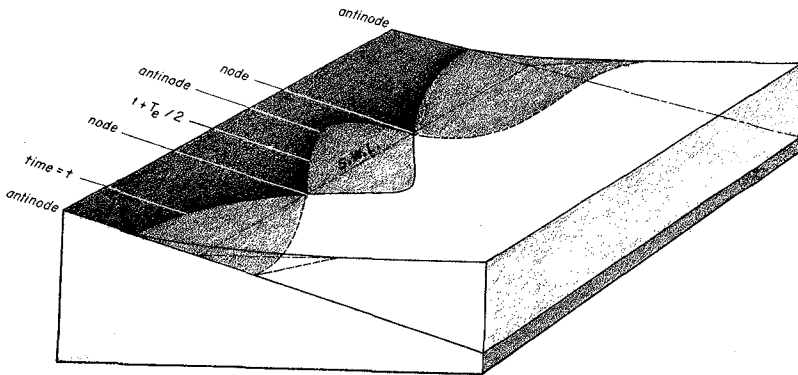


Figure 1: One possible type of standing edge wave (zero mode) with nodes and antinodes along the beach length, and decreasing in amplitude offshore. Higher-mode edge waves have a more complicated offshore variation in amplitude.

of nodes and antinodes along the beach. At the nodes there is no up and down motion of the water surface due to the edge waves, and at the antinodes the full edge wave height can be observed. The edge wave oscillations are best detected as run-up on the sloping beach. The edge wave height is maximum at the shoreline and decays offshore in a manner depending on the offshore modal number (Ursell, 1952).

Since in our experiments we obtained only subharmonic edge waves, our discussions will be limited to their interactions with the incoming waves and the resulting effects on the beach. The combined motion of the incident waves and the generated subharmonic edge waves is shown in Figure 2. The groins are located along the right and left hand boundaries, defining a

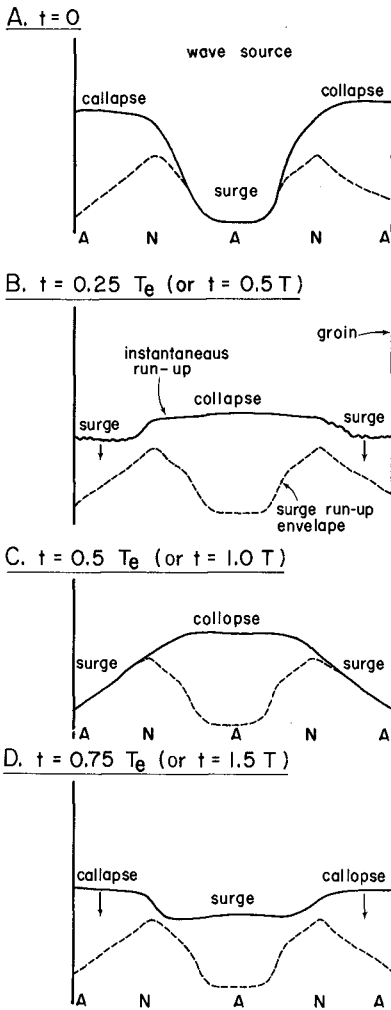


Figure 2: The interactions of the subharmonic edge waves with the normal waves to give a varying pattern of run-up and breaker type. Note that the edge wave period T_e is twice the period T of the paddle-produced waves.

limited length of beach. Figure 2 is based on actual photographs of the wave basin tests. The continuous line indicates the instantaneous position of the leading edge of the combined wave run-up, while the dashed line depicts the maximum wave run-up envelope. The groin spacing is 3.0 meters, and antinodes (A) are located at each groin and midway between them. The two nodes (N) are midway between the antinodes. The wave run-up at the edge wave nodes is approximately equal to the run-up due to the paddle-driven waves alone.

In Figure 2A the run-up is maximum at the central antinode where the breaker surged up the beach face. Figure 2B shows the next wave collapsing at the central antinode due to its interaction with the backwash from the previous surging breaker. In addition, in Figure 2B the breakers at the bounding antinodes can be seen beginning to surge up the beach slope. In Figure 2C the run-up is maximum at the bounding antinodes and minimum at the central antinode; this run-up pattern occurs one half of an edge wave period (equal to one period of the incident waves) after the run-up pattern in Figure 2A. Figure 2D displays the run-up approximately one-fourth edge wave period later. The incident wave at the central antinode is beginning to surge up the beach face while the breakers at the bounding antinodes are of a collapsing type.

As the wave height of the incident paddle-driven waves was increased, the breaker types become more plunging, and the edge wave amplitude decreases until it is no longer observable in the run-up pattern. Guza and Inman (1975) obtained the same results. The indication is then that under larger waves on beaches the edge waves will be relatively less important and may disappear altogether. However, the measurements by Huntley and Bowen (1973, 1975a) of standing subharmonic edge waves even under plunging wave conditions suggest that they do not disappear entirely, although they may not be observable in the swash run-up.

Reflection of the incident waves from the beach face is important in the generation of edge waves according to the theoretical considerations of Guza and Davis (1974) and Guza and Bowen (1975). This again appears to be borne out by the field measurements of Huntley and Bowen (1973, 1975b) who did not find incident-wave related edge waves on a low sloping beach (slope

tangent 0.014) but did on a steep beach (slope tangent 0.13). Our laboratory tests are limited to a steep beach (slope 0.125) where wave reflection and edge wave development can be expected to be important.

Longshore periodicities observed on laboratory beaches may be due to cross waves produced at the wave paddle and extending down the entire wave basin length (Garrett, 1970). Cross waves can be ruled out as producing the run-up patterns observed in the present study. In most tests, wave periods were selected so as to give resonant conditions for the generation of sub-harmonic edge waves. In addition, the run-up patterns already described closely conform to those recounted by Guza and Inman (1975) for edge waves.

GROIN LENGTH ON NONERODABLE BEACHES

A series of experiments were conducted to determine the effect of the groin length and spacing on the run-up and amplitude of the generated edge waves. As in the other tests, the wave basin in the hydraulics laboratory of the School of Engineering, Oregon State University, was employed. This wave basin is 6.1 m wide and 9.1 m in length along the direction of wave propagation. Wave guides were placed parallel to the side walls and adjacent to the paddle edges to eliminate wave reflection and diffraction as the waves travel toward the sloping beach. Because of the relatively short length of the basin, a steep beach slope $s = 0.125$ had to be used. Wooden impermeable groins were placed perpendicular to the shoreline a distance b apart.

To satisfy the boundary conditions of no flow through the groins,

$$b = m L_e / 2 \quad (1)$$

for the groin spacing b , where m is an integer equal to the number of half edge wave lengths in the longshore direction, L_e denoting the full edge wave length in the longshore direction. Using this equation and the dispersion relationship for standing edge waves (Guaz and Inman, 1975), the relationship

$$b = g T_e^2 m (1 - 2p) s / 4\pi \quad (2)$$

is obtained where g is the gravitational acceleration, T_e is the edge wave

period, m the modal number of equation (1), p is the slope truncation effect, and s is the beach slope. For the conditions of these experiments, $m = 2$ and $p = 0$, yielding the simplified equation

$$b = \frac{g T_e^2 s}{2\pi} \quad (3)$$

To generate the resonant edge waves associated with a groin spacing b , the normally incident paddle-driven waves must have a period equal to one half the edge wave period T_e in equation (3). For the groin spacings used, $b = 2$ m, 2.5 m, 3 m, and 3.5 m, the corresponding edge wave periods are $T_e = 3.20, 3.60, 3.92,$ and 4.24 sec respectively.

In order to observe the maximum possible run-up at the antinodes due to the edge waves alone, very long groins were initially used. The run-up due solely to the edge wave was determined at the central antinode by measuring the total maximum run-up at time intervals equal to the incident wave period. Subtracting two successive run-up measurements eliminated the run-up due to the incident waves and yielded the edge wave run-up portion. These measurements were repeated for ten waves and averaged. Once a run-up value for the long groins was obtained, both groins were shortened and the measurements repeated. The groins were thus progressively decreased in length until edge waves were no longer observed in the run-up.

Figure 3 and Table 1 summarize the results of these experiments for the series of groin spacings $b = 2.0, 2.5, 3.0$ and 3.5 m. The beach slope tangent was held at $s = 0.125$, and the deep-water wave steepness remained nearly constant at $H_{\infty}/L_{\infty} = 0.005$ to 0.0064 . The ordinate in Figure 3 is the run-up R_e due to the edge waves, divided by the maximum edge wave run-up R_{e-max} which occurred for the longest groin length. The abscissa is the ratio of the groin length L_g to the groin spacing b . The submerged groin length is used for L_g , and is defined as the offshore length measured from the intersection of the still-water line with the beach face.

From Figure 3 it is seen that for all four groin spacings, as the submerged groin length L_g is decreased, the run-up due to the edge waves is decreased. When the submerged groin length is decreased to about $0.15b$,

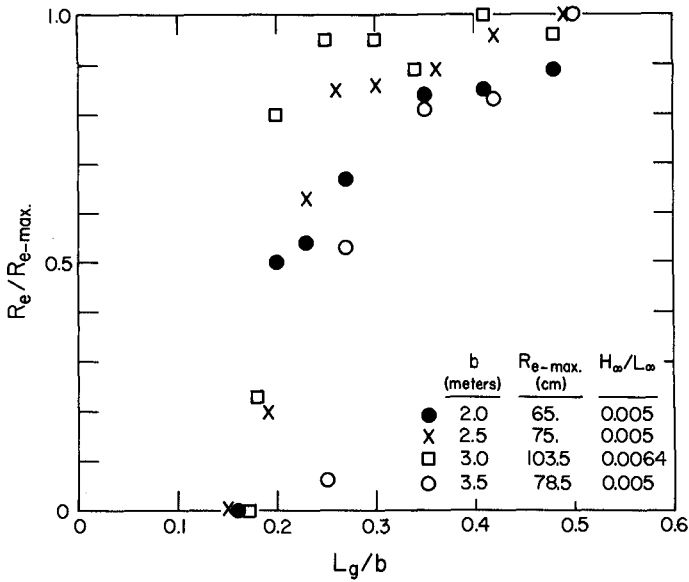


Figure 3: The strength of the subharmonic edge waves as indicated by their run-up R_e , the strength decreasing as the length of the grains L_g are decreased relative to the grain spacing b .

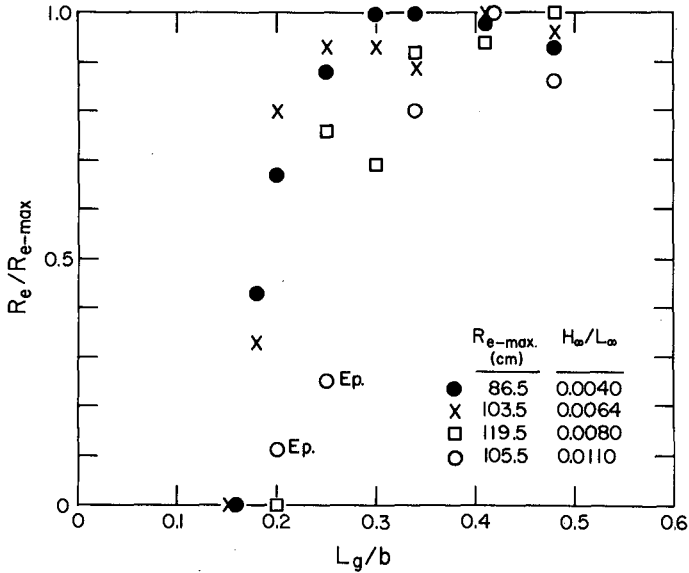


Figure 4: Experiments similar to those of Fig. 3 but where the grain spacing is held constant at 3 meters and the wave steepness varied.

TABLE 1: Edge Wave Run-up Versus Groin Length

A. Experiments on nonerrodable smooth slope

1. $b = 2.0$ m; $T_i = 1.58$ sec; $H_i = 2.2$ cm; $h_i = 37.0$ cm; $R_{e-max} = 65.0$ cm; $H_\infty/L_\infty = 0.005$;

L_g/b 0.77 0.48 0.41 0.35 0.27 0.23 0.20 0.16

R_e/R_{e-max} 1.0 0.89 0.85 0.84 0.67 0.54 0.48 0.0

2. $b = 2.5$ m; $T_i = 1.80$ sec; $H_i = 2.5$ cm; $h_i = 36.0$ cm; $R_{e-max} = 75.1$ cm; $H_\infty/L_\infty = 0.005$;

L_g/b 0.49 0.42 0.36 0.30 0.26 0.23 0.19 0.16

R_e/R_{e-max} 1.00 0.96 0.89 0.86 0.85 0.63 0.20 0.0

3. $b = 3.0$ m; $T_i = 1.88$ sec; $H_i = 3.5$ cm; $h_i = 35.6$ cm; $R_{e-max} = 103.5$ cm; $H_\infty/L_\infty = 0.0064$;

L_g/b 0.48 0.41 0.34 0.30 0.25 0.20 0.18 0.16

R_e/R_{e-max} 0.96 1.00 0.89 0.93 0.93 0.80 0.33 0.0

4. $b = 3.5$ m; $T_i = 2.21$ sec; $H_i = 3.5$ cm; $h_i = 36.0$ cm; $R_{e-max} = 78.5$ cm; $H_\infty/L_\infty = 0.005$;

L_g/b 0.50 0.42 0.35 0.27 0.25 0.23

R_e/R_{e-max} 1.00 0.83 0.81 0.53 0.06 0.0

5. $b = 3.0$ m; $T_i = 1.88$ sec; $H_i = 2.2$ cm; $h_i = 35.6$ cm; $R_{e-max} = 86.5$ cm; $H_\infty/L_\infty = 0.0040$;

L_g/b 0.48 0.41 0.34 0.30 0.25 0.20 0.18 0.16

R_e/R_{e-max} 0.93 0.98 1.00 1.00 0.88 0.67 0.43 0.0

6. $b = 3.0$ m; $T_i = 1.88$ sec; $H_i = 4.6$ cm; $h_i = 35.6$ cm; $R_{e-max} = 119.5$ cm; $H_\infty/L_\infty = 0.0080$;

L_g/b 0.48 0.41 0.34 0.30 0.25 0.20 0.18 0.16

R_e/R_{e-max} 1.00 0.94 0.92 0.69 0.76 0.0 0.0 0.0

7. $b = 3.0$ m; $T_i = 1.88$ sec; $H_i = 6.0$ cm; $h_i = 35.6$ cm; $R_{e-max} = 105.5$ cm; $H_\infty/L_\infty = 0.0110$;

L_g/b 0.48 0.41 0.34 0.30 0.25 0.20 0.18 0.16

R_e/R_{e-max} 0.86 1.00 0.80 0.00 0.23 0.11 0.00 0.00

8. Experiments on sand-covered slope

1. $b = 3.0$ m; $T_i = 1.88$ sec; $H_i = 2.2$ cm; $h_i = 37.0$ cm; $R_{e-max} = 36.4$ cm; $H_\infty/L_\infty = 0.0022$;

L_g/b 0.52 0.43 0.37 0.32 0.27 0.21

R_e/R_{e-max} 0.79 1.00 0.39 0.53 decay decay

Definitions: L_g = submerged groin length; R_e = edge wave run-up; b = groin spacing; T_i and H_i are incident wave period and height; h_i = water depth in constant-depth portion of basin.

the characteristic combined flow pattern of subharmonic edge waves and normal paddle waves is no longer observed. There is some variation in this critical groin length, the value of L_g/b being 0.15 for three of the experimental groin spacings, and about 0.25 for $b = 3.5$ m. The decrease in the edge wave run-up is sharp, indicating an abrupt termination in the edge wave's presence. For groins shorter than the indicated critical value of L_g/b , the side-wall boundary conditions imposed by the groins are no longer effective in the generation of edge waves with a wavelength equal to the groin spacing.

Figure 4 and Table 1 contain a similar series of experiments, but where the groin spacing was held at $b = 3$ m and the wave steepness H_∞/L_∞ varied. Although the scatter is large, the experiments yield the same range of critical L_g/b values for the termination of edge wave run-up as found in Figure 3. The indication in Figure 4 is that if there is any dependence of the critical L_g/b ratio on the wave steepness, it must be small. In the case of $H_\infty/L_\infty = 0.011$, Figure 4, as L_g/b approached the critical value, the edge waves were observed to be episodic, appearing for a time and then disappearing. These are labeled Ep. in the diagram.

Our results then indicate that there is a critical groin length to spacing ratio, L_g/b , below which subharmonic edge waves apparently are not generated, or are at least not observed in the run-up. This critical condition is not appreciably affected by the steepness of the normal incident waves. The basin utilized in our experiments is not sufficiently long to install low beach slopes, so we were not able to test for a beach slope dependence of the critical L_g/b value.

The reduction in the edge wave amplitude at the shoreline as the groin length is decreased can be related to the edge wave's amplitude dependence on the offshore distance. When the long groins are installed the edge wave is fully developed with its amplitude maximum at the shoreline and, according to theory (Guza and Inman, 1975), decaying exponentially offshore as shown by the dash-dot curve in Figure 5. The nondimensional offshore distance is zero at the intersection of the beach slope and the still-water level. Also graphed in Figure 5 is the measured edge wave amplitude at the shoreline for two of the groin spacings as functions of the nondimensional submerged groin length. The

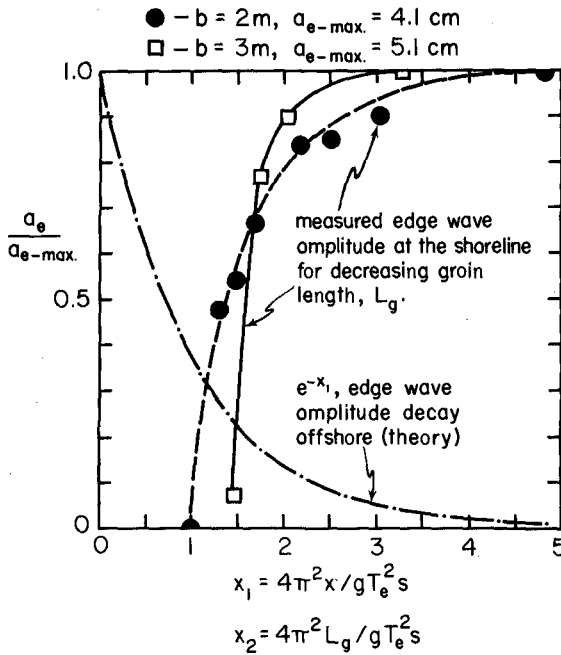


Figure 5: The edge wave amplitude a_e , obtained from the measured run-up, as functions of the submerged groin length and distance x offshore from the still-water line, both expressed in nondimensional form.

edge wave amplitude, a_e , is obtained from the measured run-up R_e by the equation (Guza and Inman, 1975)

$$a_e = R_e s / 2 \tag{4}$$

where s is the beach slope.

The measured edge wave amplitude at the shoreline ($x_1 = 0$) decreases to zero for nondimensional groin lengths between 1.0 and 1.5 (Figure 5). These lengths correspond to an offshore distance where the edge wave amplitude is equal to e^{-1} and $e^{-1.5}$ of its value at the shoreline for the fully developed state (which in these experiments occurred with the longest groin lengths). In other words, subharmonic edge waves were not generated when the groin

lengths did not extend seaward of the offshore distance where the maximum edge wave has an amplitude equal to approximately e^{-1} of its value at the shoreline. For groins shorter than the defined critical length the boundary condition of no flow through the groin wall is not a factor in enhancing the generation of the subharmonic edge wave corresponding to the groin spacing b .

EXPERIMENTS ON NONERODABLE BEACHES COVERED WITH SAND

A series of experiments were undertaken with a thin veneer of sand initially uniformly covering the solid evenly sloping beach. These were performed to determine if the presence of the sand appreciably changes the edge wave run-up values. The results also allow insight into the possible effects of the edge wave's existence on erosion or accretion between the groins.

For each groin length the sand was initially smoothed out 1 to 2 cm thick, covering the beach slope between the groins from the still-water level to depths beyond the influence of the waves. After 1.5 to 2 minutes of normally incident, paddle-driven waves arriving at the beach, edge waves would appear, beginning the redistribution of the sand alongshore as well as in the on-offshore direction. After about 15 minutes the sand would reach an approximately unchanging configuration, although the sand diameter was not in equilibrium with the beach slope.

The general tendency of the combined edge wave and incident waves is to reform the sand into the characteristic pattern shown in Figure 6. The sand extends much further up the beach slope from the still-water level at the antinodes (located near both groins and midway between them) than at the nodes (located midway between the antinodes). This sand has been removed from the now barren slope section (Figure 6) at and just shoreward of the breaker zone. Most of the total volume of sand accumulated on the upper beach is at the edge wave antinode positions not only because it extends further up the beach there, but also because the sand is at least three times as thick. For the groin length in Figure 6, the maximum sand depth at the antinodes is 2.0 cm whereas at the nodes it is only about 0.5 cm. Note

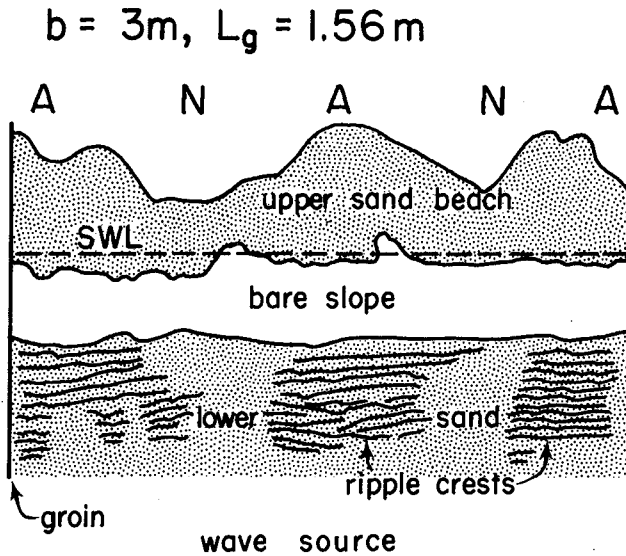


Figure 6: Redistribution of sand on beach face by subharmonic edge waves. Sand initially covered the solid beach in a thin even layer below the still-water level. A and N denote respectively the edge wave antinode and node positions.

that the barren section of the beach slope (the sand source to the upper beach) is very nearly uniform in the longshore direction, indicating that some of the sand seaward of the nodes is transported to the sand accumulations at the adjacent antinodes. The much larger flow velocities occurring at the antinodes are indicated by the sand ripple formations seaward of the barren slope; definite ripple patterns exist offshore of the antinodes while only very weak ripples or none at all exist seaward of the nodes.

When the beach slope is initially entirely covered with a thin layer of sand, rather than covered just below the still-water line as before, the subharmonic edge waves together with the incident waves reform the sand into a series of beach cusps. The intense swash at the antinode positions hollows out the beach sand, producing the embayments; the cusp horns were located at the nodes of the edge waves. This has already been demonstrated by Guza and

Inman (1975), also in a wave basin (see their Figure 8, page 3007). Beach accretion occurs at each cusp while erosion occurs in the embayments at the antinode positions of the subharmonic edge waves; this is just opposite to our previous test with sand initially only below the still-water line. Either way, the presence of the strong subharmonic edge waves caused local rearrangements of the sand on the beach face and local areas of erosion and beach accretion. However, there was no significant offshore losses of sand from the beach face as might have been the case had strong rip currents been produced as originally envisioned.

Experiments similar to those conducted on the nonerodable beach were executed to determine the effect of groin length on edge wave generation in the presence of the sand. For each groin length the maximum combined wave run-up at the central antinode was measured for successive waves and used to compute the edge wave run-up portion R_e as before. Because the sand is not in complete equilibrium with the beach slope, some difficulties were encountered in obtaining realistic edge wave run-up values for all groin lengths.

The general result of these measurements (Table 1) is that the critical groin length determined for the nonerodable solid beach (Figures 3 and 4) is still adequate in the presence of the sand. Although the $R_e/R_{e-\max}$ values tend to decrease with decreasing groin length, a larger amount of variability about this trend is exhibited as compared to the experiments using no sand cover. Part of this variability is due to the uneven distribution of the sand cover alongshore; run-up just to the sides of the antinode positions is not opposed by as thick a sand cover. This run-up, in many cases, flows as high or higher up the beach face than the run-up at the antinode position. This pattern of run-up occurred for the steady sand cover condition described above.

The greatest effect of the sand on the run-up can be seen by comparing the maximum edge wave run-ups with and without the sand present. The $R_{e-\max}$ value with the sand was 36.4 cm, and without the sand it was 86.5 cm.

The decrease in the edge wave run-up as a function of decreasing groin length is demonstrated in Figure 7, obtained from overhead photographs, where

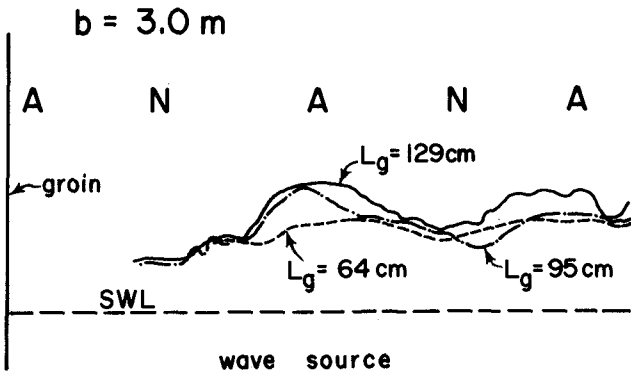


Figure 7: The decrease in the edge wave run-up as a function of the groin length L_g . Run-up lines determined from overhead photographs of sand cover, the sand initially being a uniform thin layer below the still-water level. Lines terminate on left due to inadequacy of photographic coverage.

the beach was again initially covered with sand only below the still-water line. Contours of the maximum distance up the slope of the sand covered beach are plotted for three groin lengths. The general trend of lower maximum contour with decreasing groin length is apparent. For $L_g = 64$ cm, the edge waves developed after two minutes and decayed after six minutes.

SUMMARY AND DISCUSSION

In all our wave basin experiments, we obtained subharmonic edge waves of period twice that of the incident paddle-produced waves. This lends additional support to the theoretical and experimental work of Guza and Davis (1974), Guza and Inman (1975), and Guza and Bowen (1975, 1976), who found that the subharmonic edge wave is most easily generated and the one most often occurring.

We were unable to generate synchronous edge waves with the same period as the paddle-driven waves. This precluded the formation of rip currents as outlined by Bowen (1969) and Bowen and Inman (1969), where the synchronous edge waves interact with the incident waves to produce longshore variations

in breaker heights and therefore a cell circulation. Rip currents were present in our tests, but at all times they were very weak, too weak to cause any erosion of beach sands between the groins. Initially, we set out to study the resonant conditions leading to strong rip currents, producing beach erosion and thereby defeating the purpose of the groins. Under prototype conditions rip currents do appear to be particularly strong between groins, causing offshore losses of sand. For example, Per Bruun (pers. communication, July 1976) indicated that rip currents were important in sand losses in the groin field at Miami Beach, Florida. Thus our initial working hypothesis seems to have been correct, but our inability to generate strong rip currents in the laboratory wave basin precluded its study. Why we were unable to generate synchronous edge waves and strong rip currents is uncertain; perhaps our wave basin (6.1 m by 9.1 m) is too small.

Subharmonic edge waves were readily produced so our study shifted to an examination of how the groin spacings and lengths control their strength, as manifested in the run-up on the beach face, and how they rearrange sand between the groins. We found that as the submerged lengths of the groins are decreased relative to the spacing, the edge wave strength and run-up decreased. When the ratio of groin length to spacing reached about 0.15 to 0.20, the effects of the subharmonic edge waves on the run-up were no longer observable. Thus subharmonic edge waves can be avoided in groin fields by making the groin lengths sufficiently short relative to their spacings.

A series of tests were undertaken with a thin covering of sand on the otherwise solid beach face to determine how much redistribution of the beach sand would be produced by the subharmonic edge waves. In all tests the edge waves produced a cusped shoreline so there were local areas of erosion and deposition. However, there were no offshore losses of sand from between the groins so the presence of the subharmonic edge waves posed no threat to the groins nor defeated their purpose. When the beach was initially entirely covered with a thin layer of sand the beach cusps formed had their embayments at the antinode positions of the subharmonic edge waves and the cusp horns at the node positions. This agrees with the results of Guza and Inman (1975) and supports their contentions concerning the origin of beach cusps by subharmonic edge waves.

ACKNOWLEDGEMENTS

This work is a result of research sponsored (in part) by the Oregon State University Sea Grant Program, supported by NOAA Office of Sea Grant, Department of Commerce, under Grant #04-6-158-44004.

REFERENCES

- Bowen, A. J. (1969) Rip currents, 1, Theoretical investigations: Jour. Geophysical Research, v. 74, n. 23, p. 5467-5478.
- Bowen, A. J., and D. L. Inman (1969) Rip currents, 2, Laboratory and field observations: Jour. Geophysical Research, v. 74, n. 23, p. 5479-5490.
- Bruun, Per (1972) The history and philosophy of coastal protection: Thirteenth Coastal Engineering Conf., p. 33-74.
- Coastal Engineering Research Center (1973) Shore Protection Manual: U. S. Army, Corps of Engineers, Washington, D. C., 3 volumes.
- Garrett, C. J. R. (1970) On cross waves: Jour. Fluid Mechanics, v. 41, p. 837-849.
- Guza, R. T., and A. J. Bowen (1975) The resonant instabilities of long waves obliquely incident on a beach: Jour. Geophysical Research, v. 80, n. 33, p. 4529-4534.
- Guza, R. T., and A. J. Bowen (1976) Finite amplitude edge waves: Jour. Marine Research, v. 34, n. 1, p. 269-293.
- Guza, R. T., and R. E. Davis (1974) Excitation of edge waves by waves incident on a beach: Jour. Geophysical Research, v. 79, n. 9, p. 1285-1291.
- Guza, R. T., and D. L. Inman (1975) Edge waves and beach cusps: Jour. Geophysical Research, v. 80, n. 21, p. 2997-3012.
- Huntley, D. A., and A. J. Bowen (1973) Field observations of edge waves: Nature, v. 243, n. 5403, p. 160-162.
- Huntley, D. A., and A. J. Bowen (1975a) Field observations of edge waves and their effect on beach material: Jour. Geological Society, v. 131, p. 69-81.
- Huntley, D. A., and A. J. Bowen (1975b) Comparison of the hydrodynamics of steep and shallow beaches: in *Nearshore Sediment Dynamics and Sedimentation*, edited by J. Hails and A. Carr, John Wiley and Sons, London, p. 69-109.
- UrSELL, F. (1952) Edge waves on a sloping beach: Proc. Royal Society of London, Series A, v. 214, p. 79-97.

CHAPTER 87

COMPREHENSIVE MONITORING OF A BEACH RESTORATION PROJECT

by

O. H. Shemdin (1), H. K. Brooks (2),

Z. Ceylanli (3), S. L. Harrell (4)

ABSTRACT

This paper outlines the results obtained from monitoring the Beach Nourishment Project at Jupiter Island, Florida. Jupiter Island is a 16 mile long barrier island on the east coast of Florida. Five miles of the beach were nourished in two stages in 1973 and 1974. A total of 3.4 million cubic yards of sand were dredged from an offshore borrow area and placed on the beach. The monitoring program included: seasonal hydrographic surveys of beach and offshore profile to 3000 feet offshore; climatological monitoring of wind, waves, tides and currents over a one-year period; tracer and dye studies; and sand sampling and coring at selected beach and offshore locations. The results indicate that beach restoration has a groin effect in the sense of producing favorable changes in littoral drift due to shore alignment changes. A net accretion updrift of the restored area occurs. The results demonstrate the importance of the offshore profile in accounting for the total sedimentary balance. Shoreline recession coupled by a build up in the offshore profile may reflect accretion rather than erosion. Finally, the results show that the littoral drift formula using the wave climate as input provides inadequate prediction estimates for erosion or deposition following construction of a beach restoration project.

-
- (1) Professor of Coastal and Oceanographic Engineering, University of Florida, Gainesville, Florida; on leave to Jet Propulsion Laboratory and Scripps Institution of Oceanography.
 - (2) Professor of Geology, University of Florida, Gainesville, Florida.
 - (3) Graduate Research Assistant, Coastal and Oceanographic Engineering, University of Florida, Gainesville, Florida.
 - (4) Assistant in Engineering, Coastal and Oceanographic Engineering, University of Florida, Gainesville, Florida.

I. INTRODUCTION

Jupiter Island is a barrier island about 16 miles long on the east coast of Florida. The island lies between St. Lucie inlet, on the north, and Jupiter inlet, on the south, Figure 1. The island has had a long history of erosion problems and has been a subject of extensive studies (see references 1, 2, 3, 4, and 5). In the past several years the residents of Jupiter Island, Florida have financed the construction of seawalls, revetments and groins in an effort to prevent loss of beach-front property. In addition to structural protection, several beach fill techniques have been tested including scrapers and draglines recovering material from the surf zone. These efforts were not successful - [6]. It was proposed that a long term solution to the problem was artificial nourishment of the beach from offshore borrow.

In 1973 the town of Jupiter Island agreed to restore a 5 mile portion of the beach with about 2.4 million cubic yards of sand to be obtained from an offshore borrow area about 3000 feet from the shore [5]. Due to construction difficulties the restoration project was completed in two stages, 68% of restoration completed in the summer 1973 (Stage I), and 32% completed in the summer of 1974 (Stage II) and a total of 3.4 million cubic yards of sand was placed on the beach. About 1000 feet of beach, public beach in Figure 1, was left unrestored because of an alleged biologically important reef in the surf-zone immediately offshore.

Artificial beach nourishment from offshore borrow as a method to combat beach erosion and provide recreational areas is now utilized over most other engineering practices. The costs of placing large volumes of suitable beach fill are high. It is therefore important that criteria be developed for evaluating and predicting the effectiveness of borrow material from offshore sources. At the present time no completely satisfactory test for evaluating the feasibility of utilizing available offshore borrow has been developed. Though much more work must be done, it has become evident that more emphasis must be given to total onshore and offshore volumetric transport and the range in size gradation of the borrow material.

II. MONITORING OF THE RESTORED BEACH

A monitoring program was undertaken to evaluate the fill performance. The specific objectives were to observe the changes in the sand balance, shoreline shape, sand characteristics, and to explain these changes in terms of causative factors. The monitoring study was initiated in March, 1974 and included the following:

- (1) Seasonal hydrographic surveys of the beach and the offshore profile to 3000 feet offshore along six miles of the restored beach and adjacent areas.
- (2) Continuous monitoring of wind, waves, tides and currents over a one year period.
- (3) Tracer and dye studies.
- (4) Sand sampling and corings at selected beach and offshore locations.

(1) The Hydrographic Surveys

Hydrographic surveys including the offshore profile were conducted along six miles of beach before construction, after first construction

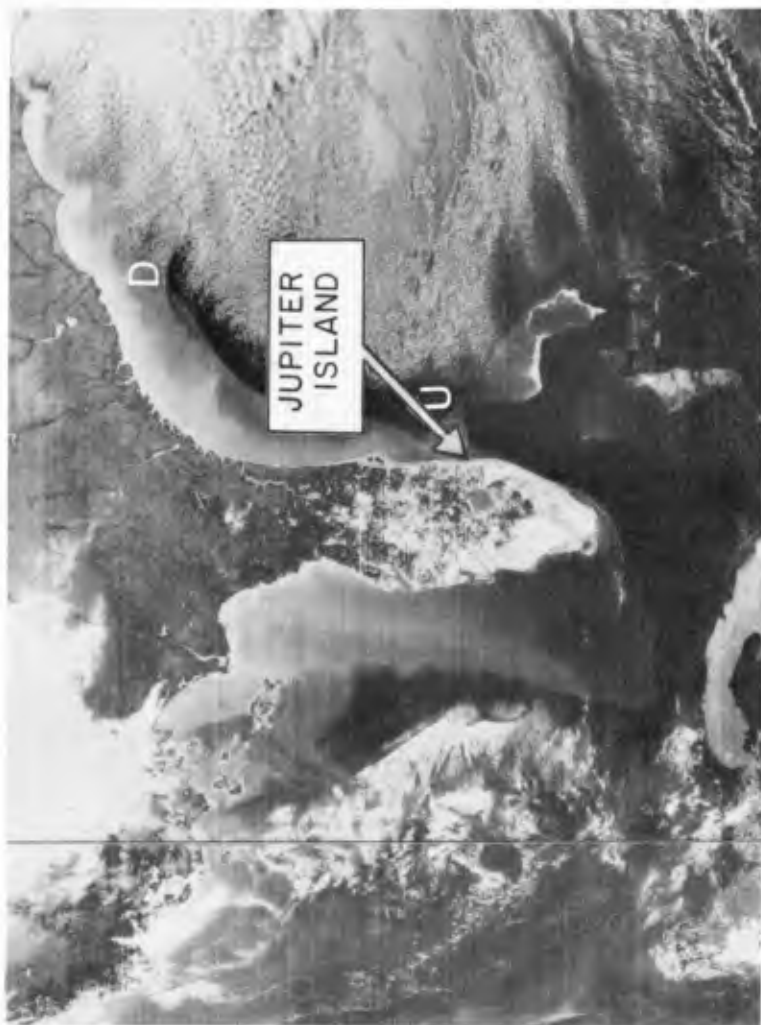


Figure 1. Location Map .

and at different intervals afterwards. Pre-construction and post-construction surveys of stages I and II were conducted by Arthur V. Strock & Associates, Inc. of Deerfield Beach, Florida. Their surveys were limited to 1200 feet from shore. More frequent and detailed surveys were conducted by the Coastal and Oceanographic Engineering Laboratory (COEL), covering the offshore profile to 3000 feet. Table I shows the summary of hydrographic surveys conducted.

Table I. Summary of Hydrographic Surveys.

Date	Description	Surveyed By	Reference Date
June-Sept., 73	Pre-Construction stage I	Strock&Assoc. Inc.	June, 1973
July-Nov., 73	Post-Construction stage I	Strock&Assoc. Inc.	Nov., 1973
May-June, 74	Follow-up (This also serves as pre-constr. for stage II)	COEL, Strock & Assoc., Inc.	May, 1974
June-July, 74	Post-Construction stage II (This is a partial survey covering only stage II fill area)	Strock&Assoc. Inc.	June, 1974
Aug., 74	Summer survey	COEL	Aug., 1974
Nov., 74	Fall survey (after Oct.	COEL	Nov., 1974

(2) Monitoring of Wind, Waves, Tide, and Currents

- a) Continuous recordings of wind speed and direction were obtained from March 1974 to May 1975. Use was made of a MRI Anemometer Model 1071. The anemometer was installed on a tower 30 feet above ground level inside the study area, shown as square number 1, in Figure 2.
- b) Continuous recordings of the tide were obtained from March 1974 to May 1975. A Leopold Stevens tide gauge, type F, was placed at the end of a pier 10 miles south of the south end of the study area.
- c) The monitoring of waves presented a more troublesome task than anticipated. No piers or other convenient structures could be found near the study area. It was decided to use a self recording pressure type wave gauge, Bass Engineering model WG/100M, which was installed in 20 feet depth within the study area (square number 2 in Figure 2). This gauge did not perform satisfactorily and no significant data was collected during the period of use. An Ocean Applied Research (OAR) Telemetry Wave Gauge was subsequently installed at a depth of 30 feet in October 1974 (square number 3 in Figure 2). It operated satisfactorily until January 1975. In April 1975 a Hydroproducts Wave and Tide gauge, Model 621, was installed. The shore based monitor was connected to an offshore pressure transducer by a 3000 foot armored cable. The location of this installation is shown as square number 4 in Figure 2. The latter gauge operated satisfactorily

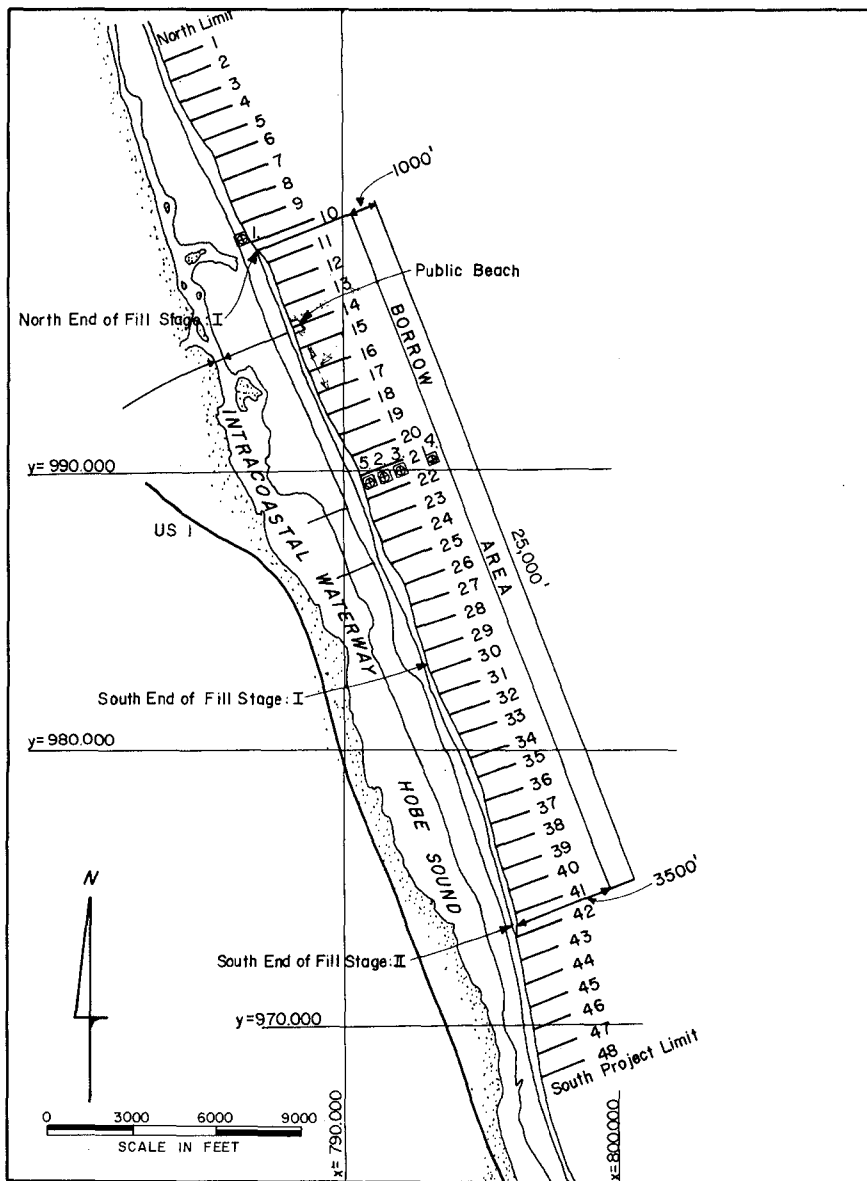


Figure 2. Profile lines and instrument location map.

until the end of the study period (May 1975). Wave directions were obtained by measuring the angle between the shoreline and the breaker line. These measurements were obtained at two locations two to five times a day during the periods of wave recording. One observation post was immediately shoreward of the wave gauge and the other was at the pier near the tide gauge installation.

- d) Current measurements were obtained using a Bendix Model Q-16 self-recording current meter. This meter was installed in 11 feet water depth. The impeller duct was placed 3 feet above the bottom (square number 5 in Figure 2). Current magnitudes and directions were continuously recorded from October 1974 to May 1975 with only intermittent failures.

(3) Tracer and Dye Studies

The littoral drift pattern and longshore velocities in the study area were periodically measured. Fresh water filled balloons with attached fluorescent dye bags were placed at different distances from shore. Each balloon was followed along its travel path and its speed recorded. At the same time wave characteristics, beach profiles and wind speeds were recorded.

In August 1974 a tracer study was conducted in the study area. Four tons of original borrow material were treated in the Laboratory. The sand was sieved into three different diameter size categories and each size dyed with different fluorescent dye colors. The quantities dyed and their respective diameters were: 4000 lbs. with a median diameter of 0.13mm, 1350 lbs. with a median diameter of 0.21 mm and 1350 lbs. with a median diameter of 0.50 mm. The various color sands were then mixed and point injected at the beach face during low tide. The position of the tracer particles in the dynamic zone were monitored after 1/2, 2, 10 and 40 tidal cycles by taking sand samples at established grid points. Profile locations were sampled at high water mark, low water mark, and at depths 3 feet, 5 feet, 10 feet, 15 feet, and 20 feet.

(4) Sand Sampling and Coring

A limited coring program was completed in May 1974 in which continuous cores, four to ten feet in length were obtained from the beach face, the breaker bar and at distances of 500 and 1000 feet offshore. Relatively undisturbed subsurface samples were obtained by utilization of a double walled piston coring device which employed circulating drillers mud to overcome external friction on the core barrel. It was anticipated that sampling lines at the north, center and southern end of the beach fill would best represent the adjusted areal and stratigraphic distribution of the artificially placed sediment. However, bedrock was encountered at a shallow depth in the first two cores attempted at the north end of the project and the line of sampling was not completed. Thus, multiple cores were obtained only from lines 31 and 37, Figure 2.

Grain size frequency, bulk density, grain density and percent shell were determined in subsequent laboratory analysis. The cores were zoned and analyzed based upon evident changes in the physical parameters of the sediment with depth in the core.

One set of surface sediment samples obtained in the August 1974 tracer study was analyzed for size frequency only. Certainly, more intervals of sampling would have been desirable. The core samples do, however, represent depositional changes through time. From the cores obtained in May 1974 from the "adjusted" 1973 beach fill and the August 1974 surface samples, consistent results were obtained. Thus, we believe the sampling program provided data upon which evaluation of the behavior of the artificial beach fill at Jupiter Island could be made.

III. DATA ANALYSIS AND RESULTS

(1) The Hydrographic Surveys

The hydrographic surveys were analyzed to yield information on the total sand volume in the nourished area and its gradual depletion with time. Figure 3 shows a summary of the total sand volumes in the study area during the different stages of construction and post construction periods. It is surprising to see no net loss of sand after one year following completion of the first stage. This was not expected since it is believed that a net littoral transport towards the south prevailed in this area of the shoreline, see reference [7].

Although unexpected at the outset the above result is easily explained by the fact that both the shoreline and the offshore profile advanced following restoration. The latter produced a groin effect at the northern extremity of the fill. The shoreline alignment with respect to breaking waves is altered and induces a net decrease in the longshore current at the north end of the restored section. The nourished area therefore received sand from the then prevailing littoral system at its north end. The gain is evidently equal to the loss from the central and southern segments of the fill during the first year. The analysis of the hydrographic surveys indicated a small net gain during this first year.

The distribution of volumetric changes along the study area is shown in Figure 4(a). As indicated before, the shore area at the public beach was left unrestored to satisfy biological concerns for a reef offshore. Both sides of the public beach were restored, however. It is evident from Figure 4(a), that large quantities of sand were transported by littoral drift from the nourished area north of the public beach to the void in front of the public beach. This is shown in Figure 4(a) as erosion north of the public beach and accretion at the public beach. The groin effect discussed previously is also evident by the accretion pattern at the north end of the fill. The central region of the fill (south of the public beach) shows minor erosion as expected because of prevailing southerly longshore drift. Near the south end of the fill a net accretion occurred. This is probably due to the wave refraction pattern generated in the vicinity of a recessed shoreline.

Figure 4(a) shows that erosion patterns can not be determined by observing changes in the shoreline profile alone. Two shoreline contours obtained from the November 1973 and May 1974 surveys are drawn with respect to the reference prefill shoreline of June 1973. Near the north end of the fill the shoreline is receding while a net volumetric gain is computed due to the groin effect discussed before. A similar pattern is observed near the southern end of the fill. In the central

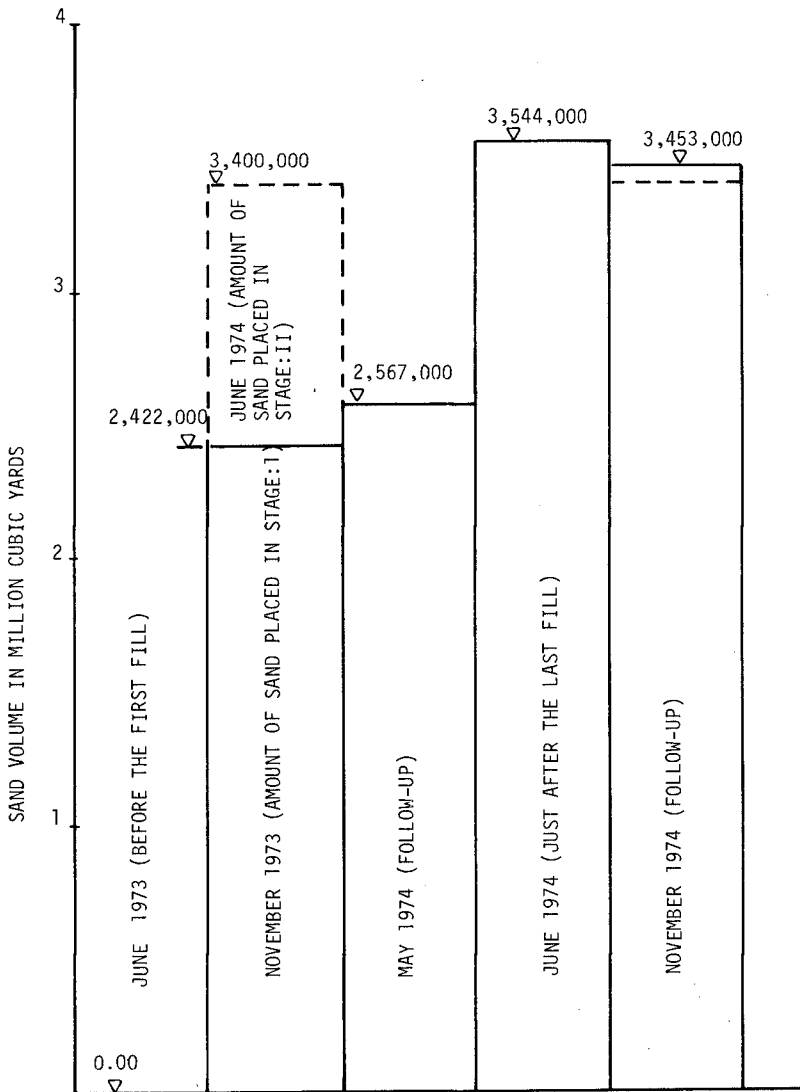
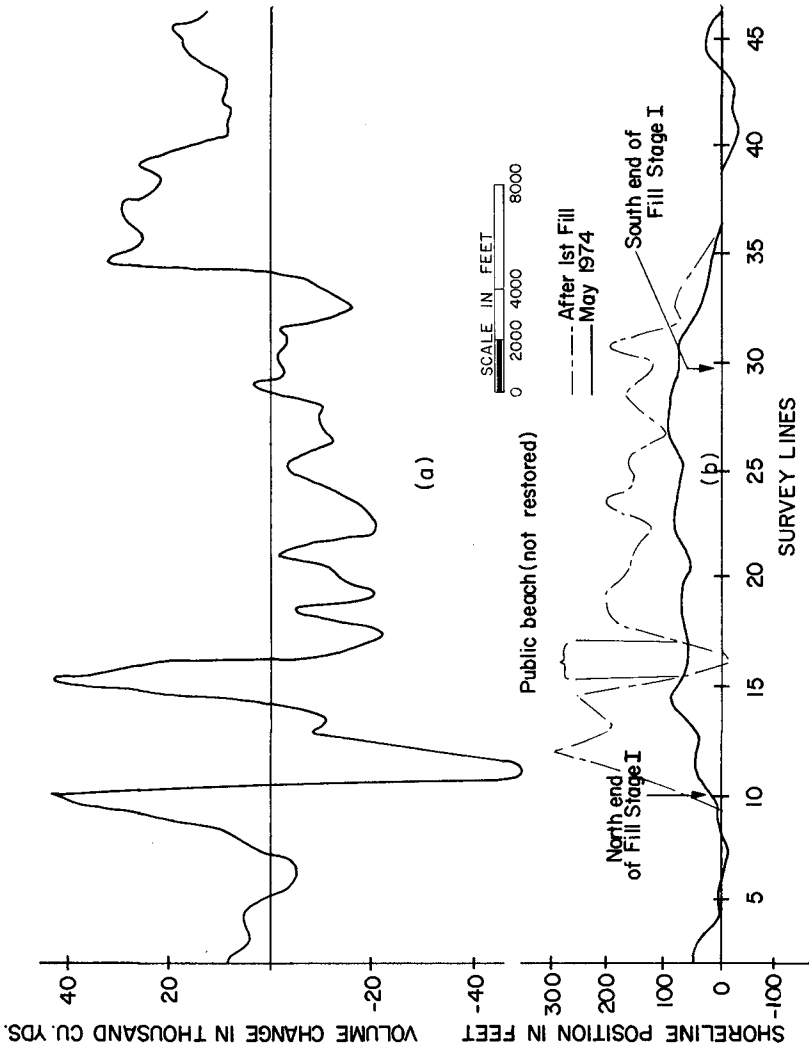


Figure 3: Summary of volume calculations obtained from hydrographic surveys.



(a) OBSERVED VOLUME CHANGES ALONG THE SHORELINE FROM NOVEMBER 1973 TO MAY 1974. (+ ACCRETION; - EROSION); (b) SHORELINE POSITIONS AS REFERENCED TO 1973 PREFILL SHORELINE

Figure 4

region (south of the public beach) on the other hand, the shoreline contour is advancing towards offshore while the volumetric curve shows a net erosion. This can only be explained by the shoreward retreat of the offshore profile.

Further insight on the advance of the offshore profile and the simultaneous retreat of the shoreline contour is presented in Figure 5. In the top portion 11 foot depth contours are depicted to show the advance of the offshore profile. During the same period a general recession in the shoreline contour occurs and is shown in Figure 5(b). Figures 4 and 5 clearly demonstrate the role of the offshore profile; the central conclusion being that shoreline advances and recessions are poor indicators of accretion or erosion in a nourished area.

The borrow area and the locations of borrow holes also produce substantial variations in the offshore profile. These are shown in Figure 6. Five foot contours are drawn to show variation of the offshore bar during the period of the study. This depth is typical of the near shore bar. The May 1974 contour shows the beginning of a cyclic variation which has correspondence to the offshore borrow holes. The variation is accentuated in the November 1974 contour following the October 6-7, 1974 storm. The borrow holes induce nearshore concentration of energy by uneven refraction of wave rays in the vicinity of borrow holes. The refraction calculations were not carried out due to lack of hydrographic data in the vicinity of borrow holes.

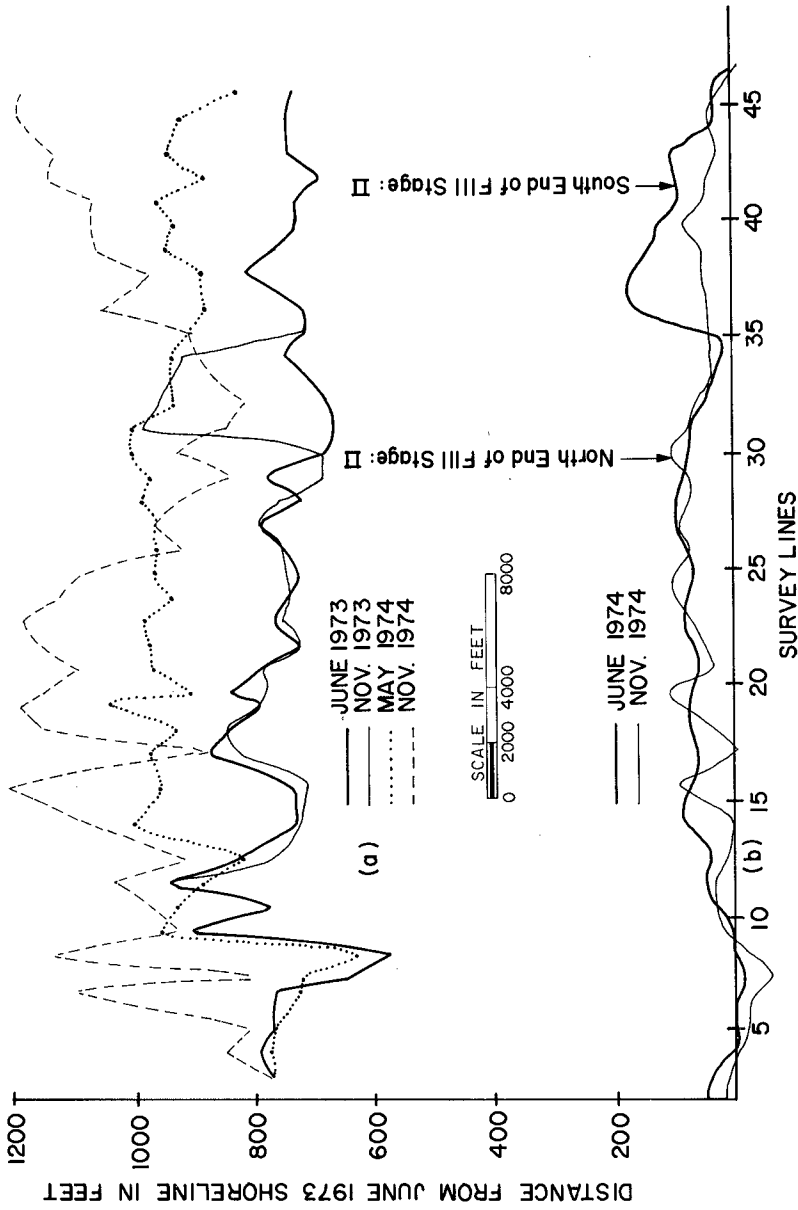
(2) The Wave Climate and Longshore Transport

The analysis of the wave data was aimed at determining the monthly averages of the long shore current (and sand transport) at different stations along the restored beach. The in situ measurements were supplemented by available wave statistics corresponding to the period of study from NOAA, Surface Marine Observations, National Climatic Center. This data was found to be especially useful in filling in situ measurement gaps. The measured wind speeds and directions were found helpful in producing correlations between different wave data sets. Hydrographic information was obtained from monitoring surveys and USGS boat charts.

The analysis procedure consisted of generating equivalent deep water wave heights and directions from nearshore point measurements of wave height, period and breaking angle. A modified Dobson [8], refraction program was utilized with a nested grid system. A nearshore fine grid network was used to relate the measured breaker angle to a mean wave direction at the wave measuring station. Then using a large grid the measured wave heights and the derived wave directions were used to yield deep water wave heights, and directions.

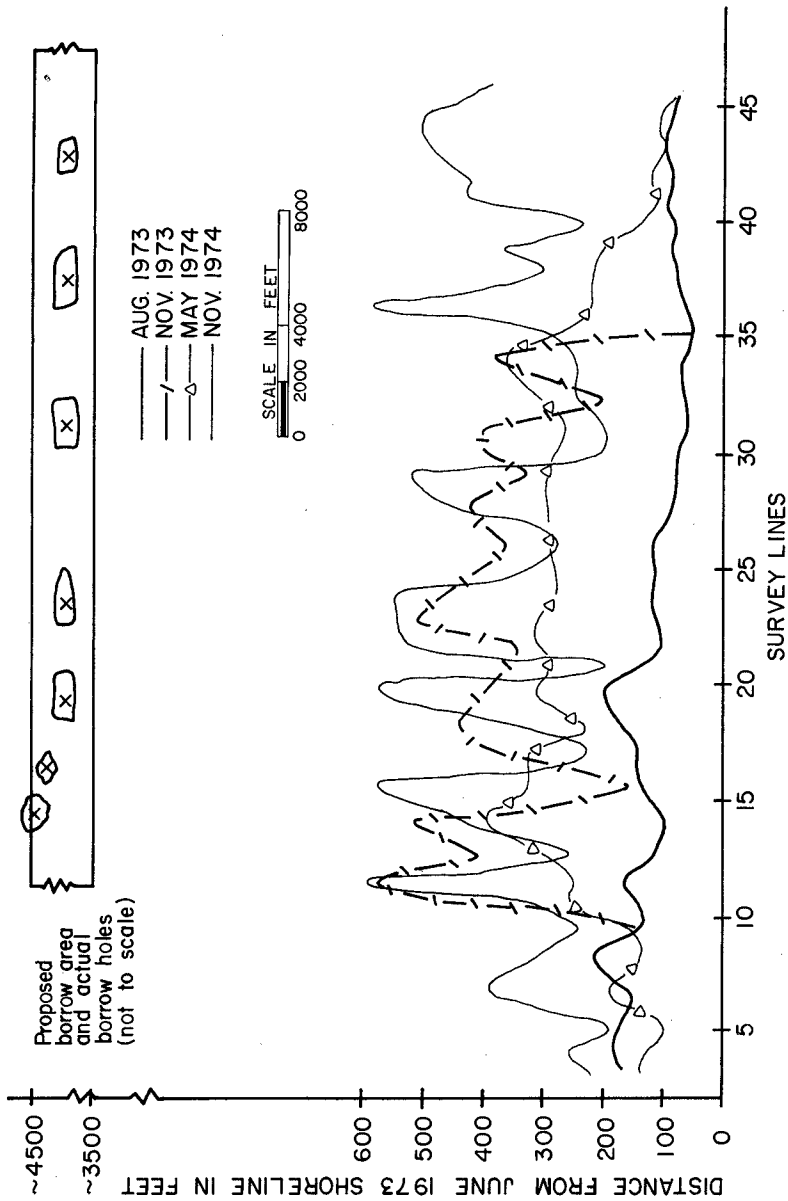
The surface Marine Observations of NOAA were calibrated by correlating the derived deep water wave heights and directions during the periods when both data sets were available. Calibration constants were derived to make the ship observations compatible with in situ measurements.

The monthly averages of equivalent deep water wave parameters were computed and are shown in Table 2. The period covered is bounded by two hydrographic surveys. The intent was to predict the net erosion or deposition during this period by using the wave climate and the littoral drift formula and to compare with corresponding erosion or deposition patterns calculated directly from the hydrographic surveys.



(a) CHANGES IN 11 feet CONTOUR; (b) CHANGES IN SHORELINE, BOTH AS REFERENCED TO 1973 PREFILL SHORELINE

Figure 5



CHANGES IN 5 FEET CONTOUR POSITION IN RELATION TO JUNE 1973 SHORELINE

Figure 6

Table 2. Deep Water Wave Climate.

Date	T (sec.)	H _o (ft.)	θ (deg.)
March	8	1.0	109
April	8.5	1.48	110
May	7.4	1.04	119
June	7.7	0.84	120
July	8.2	0.96	98
August	9.1	0.99	110
September	7.9	0.99	106
October	8.9	2.6	69

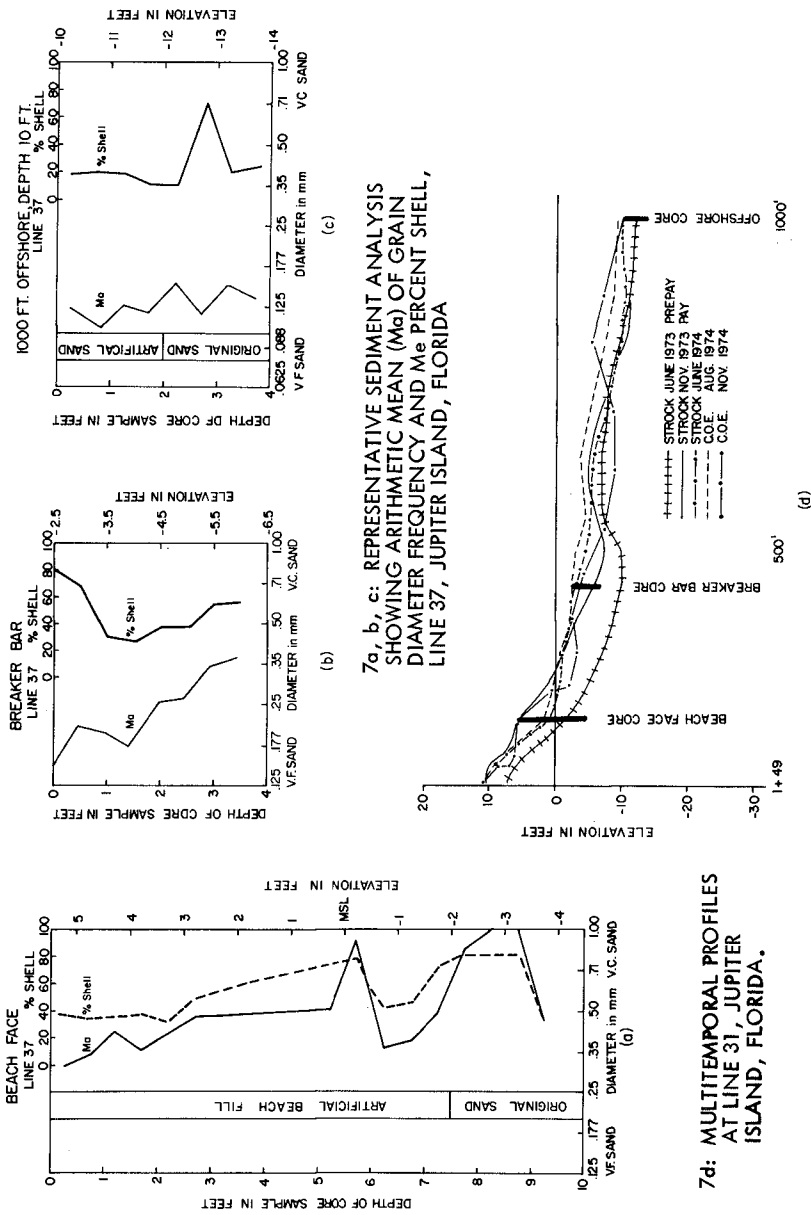
The predicted volumetric changes using the littoral drift formula were found to be one order of magnitude larger than calculated values from hydrographic surveys. The discrepancy raises a number of questions regarding present technical capability to predict erosion and deposition patterns following a beach restoration construction. Two primary areas of concern are suggested:

- a) The littoral drift formula in present form is empirically derived from gross volumetric sand accumulation near littoral drift barriers. The formula is very useful for gross calculations but evidently less useful for more detailed changes along a shoreline with varying longshore wave activity. Research is needed to develop more detailed relationships for sand transport due to waves, current, wind, and grain size distribution.
- b) The wave climate as determined from deep water wave measurements is only part of the total climate affecting littoral drift. The local wind, for example, plays an important role in a manner not completely understood yet. Definition of the total climatological factors in impacting sand movement and the consequent collection of pertinent data remains prerequisite to adequate prediction of sand movement following a restoration project.

(3) Sedimentological Results

At present, relatively little is known about the nature of onshore-offshore movement of sand in the surf zone. An indication of the onshore-offshore movement is found in the analysis of the sediment cores. As indicated these cores were taken at the beach face, the breaker bar and at distances 500 and 1000 feet offshore.

The mean diameter and shell content of the beach face core is shown in Figure 7 (a). Underlying the beach face there are layers representing different



7a, b, c: REPRESENTATIVE SEDIMENT ANALYSIS SHOWING ARITHMETIC MEAN (Mg) OF GRAIN DIAMETER FREQUENCY AND Me PERCENT SHELL, LINE 37, JUPITER ISLAND, FLORIDA

Figure 7

energy conditions. There are even differences in the layers deposited during high and low tides. The beach face consists of medium to coarse sand with layers of shell.

The near-shore bar is composed of fine sand as shown in Figure 7(b); and very fine sand is found 100 feet offshore as shown in Figure 7(c). The shell content was found useful in distinguishing between the native sand and the new sand that moved towards offshore.

It is clear from these sedimentological results that the fine and very fine sand is moved offshore and is the main constituent for building the offshore profile. This sand is not totally lost to the system as volumetric computations such as those of Krumbein and James [9] would suggest. The beach face has been protected by coarser particles and the winnowed fine sand has contributed to energy dissipation through the buildup of the profile in the dynamic zone, especially the breaker bar.

The project engineer [8] stated the mean grain diameter in the proposed borrow area was 0.23 mm. whereas the native receding beach material had a mean grain size of 1.20 mm. When the size gradation, i.e. standard deviation, of these sand bodies are taken into consideration by utilization of the "critical ratio" formula of Krumbein and James [9], it is determined that 7.8 cubic yards of fill material would be required to yield one cubic yard of sand comparable to the original sand on the unstable beach. Fortunately, the project has developed better than preliminary statistics predicted. This is because a material with favorable parameters was placed on the beach.

IV. CONCLUSIONS

The conclusions derived from this monitoring study are the following:

- (1) Beach Fills Have a Groin Effect - The placement of sand on a beach has the effect of extending the shoreline seaward and therefore inducing shoreline alignment changes at both extremities of the restored area. The restored beach consequently interferes with the previously prevailing littoral drift balance and induces a net deposition near the updrift end. The groin effect increases the half life of the restored beach.
- (2) The Offshore Profile Serves an Important Role - Shoreline recessions do not reflect the true state of erosion or accretion following a beach restoration. The total sand volume contained in a restored area is critically dependent on the offshore profile. Shoreline recessions are normally accompanied by a buildup of the offshore profile.
- (3) Borrow Holes Cause Energy Focusing on Shore - Local concentrations of wave energy at the shoreline are induced by wave refraction in the vicinity of borrow holes when they are located close to shore. Lateral variations in the shoreline contour and the offshore profile are induced by close to shore borrow holes.

- (4) Prediction of Erosion or Accretion along a Restored Beach Is Not Possible by the Littoral Drift Formula - The presently used littoral transport formula does not give a reasonable prediction of erosion or deposition along a restored beach. The formula is derived empirically from gross transport rates and cannot be expected to provide accurate predictions for relatively detailed shoreline erosion following a restoration construction.
- (5) The Need for Research in Nearshore Dynamics - This study points out the need for continued research on dynamical aspects of offshore-onshore and along-shore transport of sand. Relevant contributions were reported at the Hawaii conference; it will be instructive to apply the techniques proposed.

V. REFERENCES

1. House Document No. 765, 80th Congress, 2nd Session, "Jupiter Island," 1947.
2. Coastal and Oceanographic Engineering Laboratory, Tech. Prog. Rep. No. 5, "Coastal Engineering Investigation at Jupiter Island," University of Florida, Gainesville, 1957.
3. Dept. of the Army, Jacksonville District, Corps of Engineers Serial No. 54, "Beach Erosion Control Study on Martin County, Florida," 1968.
4. Coastal and Oceanographic Engineering Laboratory, "Cooperative Study at Jupiter Island, Florida," University of Florida, Gainesville, 1969.
5. Arthur V. Strock and Associates, Inc., "Town of Jupiter Island Beach Restoration Project," Deerfield Beach, 1973.
6. A. V. Strock, and A. D. Noble, "Artificial Nourishment Projects in Southeast Florida," M.T.S. Journal, Vol. 9, No. 3, 1975.
7. U. S. Army, Civil Engineering Research Center, "Shore Protection Manual, Vol. 1," Washington, D. C., 1973.
8. R. S. Dobson, "Some Applications of a Digital Computer to Hydraulic Engineering Problems," Tech. Rep. No. 80, Dept. of Civil Eng., Stanford, 1967.
9. W. C. Krumbein and W. R. James, "A Lognormal Size Distribution Model for Estimating Stability of Beach Fill Material," Tech. Mem. No. 16, U. S. Army Coastal Engineering Research Center, 1965.
10. W. N. Bascom, "The Relationship between Sand Size and Beach-Face Slope," Trans. Am. Geophys. Union, Vol. 32, 1951.

CHAPTER 88

LABORATORY INVESTIGATION OF SHORE EROSION PROCESSES

by

E. F. Brater¹ and David Ponce-Campos²

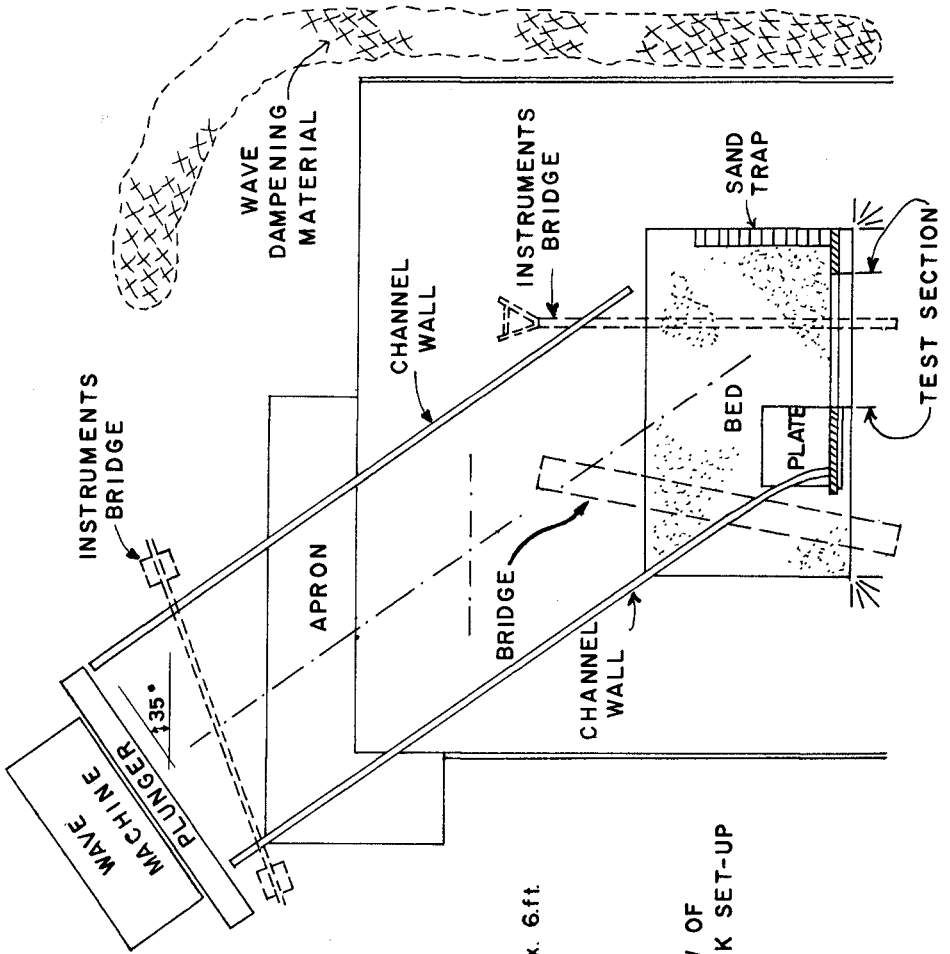
The laboratory investigation was undertaken as part of a shore protection demonstration program sponsored by the Michigan Department of Natural Resources. Subsequently funding was also provided by the Sea Grant Program. The laboratory work is being done in the Lake Hydraulics Laboratory, a facility of the Department of Civil Engineering of the University of Michigan. The field demonstration program consists of 19 field installations at locations on Lakes Michigan, Huron and Superior. The laboratory program was planned to supplement information from the field installations by testing over a wider range of variables and to test procedures not included in the field program. This program has also proven to be useful in the demonstration of shore erosion processes to groups concerned with shore problems. Although erosion rates determined in a model cannot be converted quantitatively to nature it was reasoned that if natural shore erosion processes could be simulated and if repeatable erosion rates could be produced in the model the results could help to evaluate the relative effectiveness of many protective methods. The advantages of using a model are the much lower cost compared with field installations, the control over such variables as wave height and water level and the speed with which results can be obtained.

The Testing Arrangement

The tests were conducted in a wave tank located in the University of Michigan Lake Hydraulics Laboratory. The tank is about 40 feet (12 m) square. The testing arrangement is shown in Fig. 1. The movable bed area indicated as "sand" in Fig. 1 was about 11 feet (3.3 m) by 16 feet (5 m). The test section consisted of six feet (1.8 m) of bluff. The area of the model outside of the movable bed portion was surfaced with concrete. At the beginning of each test the sand bottom was formed to a slope of 1 to 20 which conformed with the surrounding concrete

¹Professor of Hydraulic Engineering, Dept. of Civil Engineering, University of Michigan, Ann Arbor, Michigan.

²Research Assistant, Dept. of Civil Engineering, University of Michigan, Ann Arbor, Michigan.



SCALE
1 in. approx. 6 ft.

FIG. 1
PLAN VIEW OF
WAVE TANK SET-UP

bottom. The sand bluff test section was formed with a smooth surface having a slope of 60° with the horizontal. The waves were created by a plunger type wave machine and projected at an angle of 35° with the shoreline in order to produce a natural littoral current. In order to prevent lateral dispersion of the wave energy the portion of the waves which attacked the test section were confined in a channel until near the testing zone. Waves outside of the test section were destroyed by dampening material placed along the walls of the tank.

The Testing Procedure

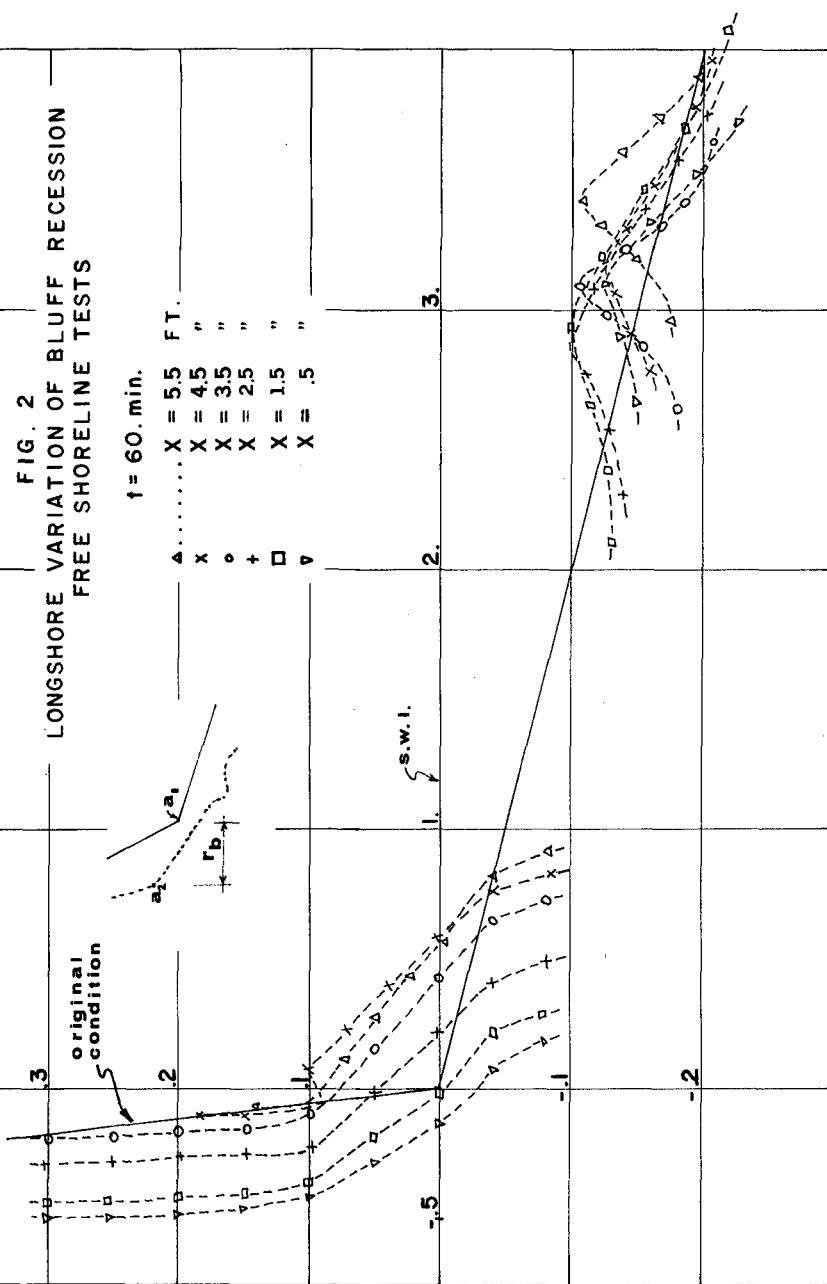
The wave selected as a standard for most of the tests had a deepwater height of 0.20 feet (6.1 cm) and a period of 1.0 seconds. At a scale ratio of 1:50, which was the basis for constructing the model protective devices, this model wave would correspond to a prototype wave having a height of 10 feet (3 m) and a period of 7 seconds. The standard water surface elevation which was used in most of the tests was the elevation of the junction between the bluff face and the bottom which is designated as a_1 in Fig. 2. The standard test durations were 30 and 60 minutes. At a scale ratio of 1:50 these durations correspond to storms lasting 3.5 and 7 hours, respectively. The preliminary tests showed that 60 minute tests provided sufficient data to meet the objectives of the program. At the end of 30 minutes of testing and again at 60 minutes the bluff and bottom profiles were determined and the littoral drift was measured. The distance along the test section starting at the updrift end was designated as x (See Fig. 1) and six profiles were taken at one foot (0.3 m) intervals with the first one at $x = 0.5$ feet (0.15 m). The rate of littoral drift was measured in 12 sand traps extending 6 feet (1.8 m) from the shore line at the down-drift end of the test section as shown in Fig. 1.

The first tests were made with a well graded sand which was too coarse to produce a typical continuous erosion pattern. The bluff erosion started in a typical manner but the coarser eroded material could not be readily moved by the littoral currents and therefore created a protective revetment which prevented further erosion. This problem was overcome by using a finer sand. This sand was quite uniform in size with about 80 percent less than 0.4 mm and about 20 percent less than 0.3 mm. No noticeable portion of this sand went into suspension during the tests. Thereafter, the most difficult modelling problem was the development of a procedure for re-forming the bluff and bottom which was not too time consuming and would produce repeatable results of a given set of conditions. The procedure which gave satisfactory results consisted of forming a rectangular volume of sand after which the front form was removed and the face of the bluff was cut at the desired angle. Uniform compaction of the sand was achieved by simultaneous vibration and saturation.

FIG. 2
 LONGSHORE VARIATION OF BLUFF RECESSION
 FREE SHORELINE TESTS

t = 60. min.

- Δ X = 5.5 FT.
- x X = 4.5 "
- o X = 3.5 "
- + X = 2.5 "
- X = 1.5 "
- ∇ X = .5 "



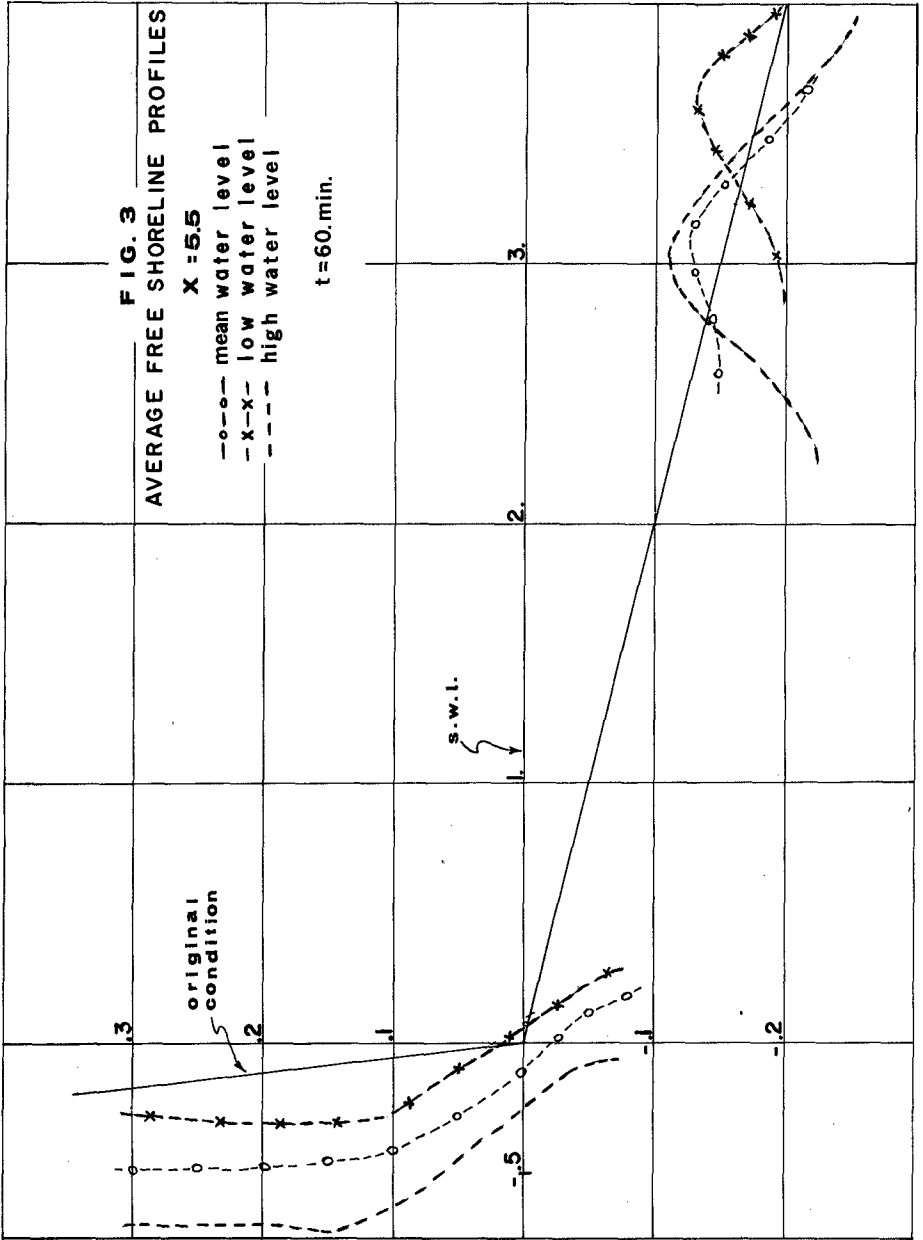
Creating a Typical Repeatable Natural Shore Process

As previously stated, the experimental arrangement produced typical bluff erosion. Similarity between the model processes and natural processes is illustrated in Fig. 2 by six profiles which show the decreasing bluff recession as one proceeds down-drift along the bluff. This is due to the protection provided by the increasing amount of littoral drift in the down-drift direction. As shown in Fig. 1 a section of the bottom just up-drift from the test section was a plate rather than a sand bed. Therefore the only source of littoral drift along the bluff test section was the erosion and slumping of the bluff itself. Consequently at the first test section ($x = 0.5$) there was virtually no littoral drift and at each successive section the amount of littoral drift was greater thus providing increasing natural protection by the presence of this increasing amount of beach material. It may be seen in Fig. 2 that the recession was a maximum at $x = 0.5$ and decreased at successive sections to nearly zero at $x = 5.5$ feet. Checks on wave height along the breaker zone indicated no significant orderly change in wave height along the test section. Other indications that the model was creating typical natural shore processes were the creation of typical sand bars in the breaking area, as shown in Figs. 2 and 3 and the increase in recession rates with an increase in water surface elevation as illustrated in Fig. 3. The profiles in Fig. 3 show bluff recession at the same section ($x = 1.5$) for the normal water level, and for levels 0.02 feet (0.6 cm) above and below normal respectively. This change in level in the model corresponds to an increase in level in nature of 1.0 feet (0.3 m). In studying the profiles shown in Figs. 2 and 3 it should be noted that the vertical and horizontal scales differ in a ratio of 1 to 5.

The investigation of the repeatability of the tests required that consideration be given to the fact that it was impossible to reproduce identical test conditions. This was because there was no control over the water temperature in the wave tank and because the actual average wave height was not known until the end of the test when it was determined from the oscillograph charts. In order to take into account these variables an application of dimensional analysis was made to develop a parameter which would include the effect of small variations in wave height and viscosity as well as the duration of the tests. The following parameter was found to serve the purpose of coordinating the test results.

$$N = k \left(\frac{gTH}{\nu} \right)^2 \quad (1)$$

In this parameter g is the gravitational acceleration, T is the wave period, H is the wave height, ν is the kinematic viscosity and k includes various constants and the duration of the tests. Since the only variable in k was the duration of the tests k was taken as unity for 30 minute tests and as two for 60 minute tests. The presence of H in the numerator is a measure of the original wave energy and ν in the denominator is related to the energy dissipation. The usefulness of this parameter will be demonstrated



but it should be noted that additional work is in progress which indicates that a more rational parameter can be developed which will also include the distance from the breaker zone to the bluff.

In order to relate bluff recession to the parameter N , the recessions at any section was represented by r_b , the recession of the toe of the bluff. As illustrated in Fig. 2, r_b is the recession of a_1 to the new position a_2 . The parameter r_b was considered to be the best single measure of the recession of the bluff. The use of this procedure is illustrated in Figs. 4 and 5 where values of r_b are plotted against N for three test conditions. In Fig. 4 the results are for section $x = 1.5$ and Fig. 5 shows the results at section $x = 2.5$. Consider first the center group of nine points in each figure. These show the results of tests made with a standard wave height on the free shoreline. The five points with the smaller values of N show the recessions produced in 30 minutes and the four with the greater values of N give recessions produced by 60 minute tests. The lines drawn through the values plotted in Figs. 4 and 5 were determined by a least squares analysis. The correlation coefficients shown are much higher than the values required for a one percent confidence level, thus indicating that these lines represent a logical relation between recession and important variables. Considering the random nature of the sand slumping process it was concluded that these correlations provided satisfactory evidence that repeatable recession rates were being obtained. The upper and lower graphs in Figs. 4 and 5 give two additional examples of groups of test points, the upper sets being for a smaller wave height with a free shoreline and the lower sets show the effect of a groin system using the standard wave height. Again, the high correlation coefficients indicate that the linear relationship is a reasonable interpretation of the trends and that a good repeatability was being obtained.

It is of interest to note in Figs. 4 and 5 that the smaller wave height of 0.12 feet (3.7 cm) produced greater bluff recession than the normal wave height which was 0.20 feet (6.1 cm). This is believed to be because the larger waves broke nearly twice as far from the bluff as the smaller waves and therefore had nearly twice as much energy dissipation. This research did not include sufficient tests on variable locations of the breaker zone to permit drawing conclusions. However, as previously mentioned, it is expected that future work may provide more information on this important variable.

The relations between bluff recession, r_b , and the parameter N provide a better way of presenting test results than the comparison of beach profiles because the effect of small variations in wave height and viscosity do not obscure the trends and because the two different test durations can be included in one graph. For example, the difference in bluff recession between the up-drift and downdrift portion of the model which was demonstrated

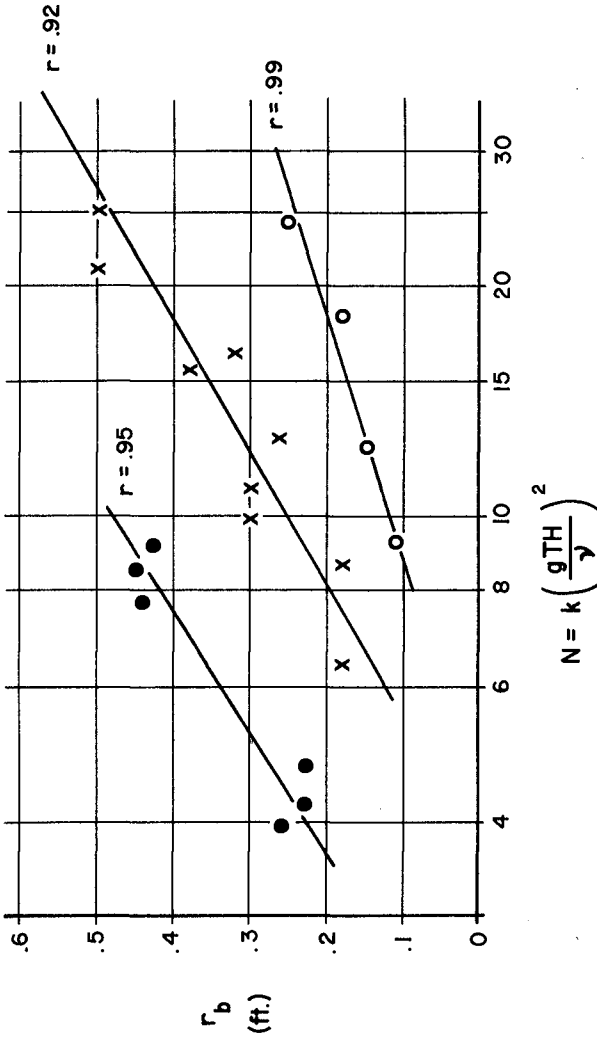


FIG. 4
PROFILE AT $X = 1.5$

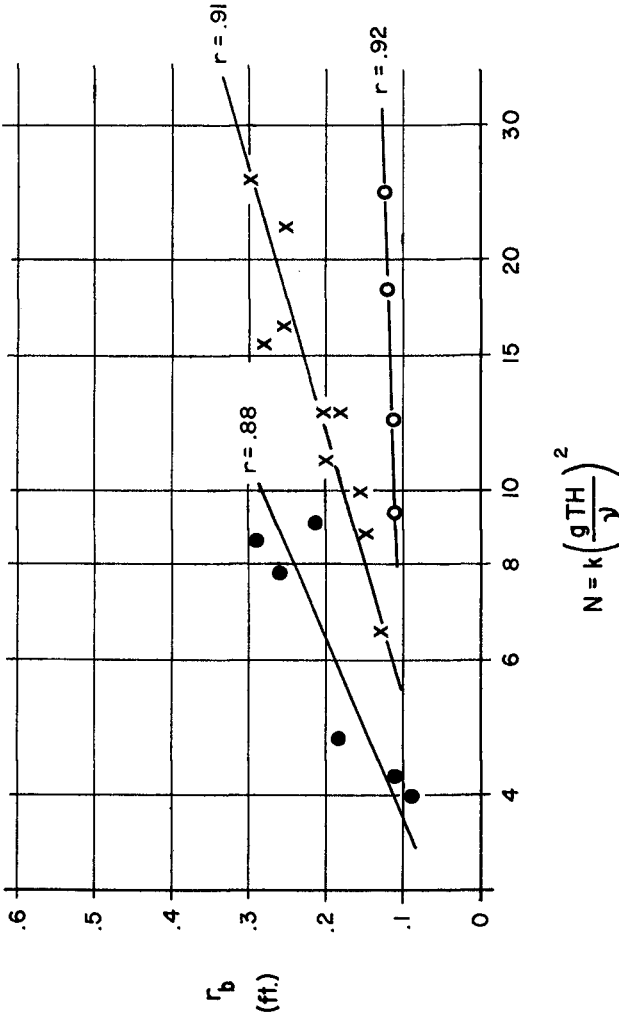


FIG. 5
PROFILE AT X = 2.5

x : FREE SHORELINE ; H/L = .039
 o : F. S. ; H/L = .023
 o : GROINS ; H/L = .039 ; g/s = 1.0

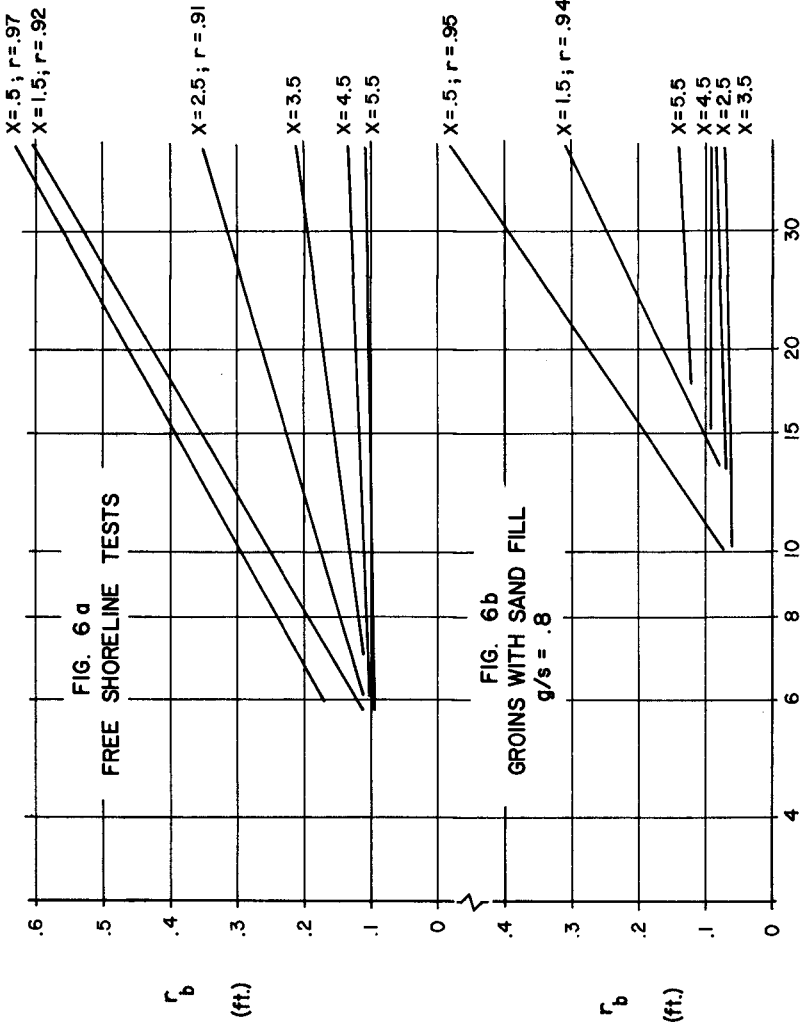
with individual profiles from a single test in Fig. 2 is shown in Fig. 6 by lines relating r_b to N . Each of these lines is the best fit line for all the values of r_b determined at a given section from a series of test runs. The individual test points are not shown in order to simplify the presentation. The information in Fig. 6a is for a free shoreline. The lines are for successive test sections from $x = 0.5$ to $x = 5.5$. Again, the protection provided by increasing littoral drift is demonstrated. Figure 6b shows a similar set of curves for the same wave conditions but with a groin system which was initially nourished. Again, the maximum erosion occurred at the updrift sections, $x = 0.5$ and $x = 1.5$. However, section 5.5 experienced slightly more erosion than sections $x = 2.5, 3.5,$ and 4.5 . The reason for this is believed to be that the groin system delayed some of the littoral drift near the center of the groin system and there was slightly less sand present at $x = 5.5$.

Another indication of the reproduceability of the tests is obtained by plotting total sand transport against the parameter N as shown in Fig. 7. Here again, there is some random scatter as one would expect in a process so susceptible to variations in behavior but points fell well within the one percent confidence level based on the statistical test provided by the linear correlation coefficient. It should be reiterated that except for the difference in the test duration (30 to 60 minutes) the variations in N within each group of points are due to variations in the viscosity of the water and to minor variations in wave height.

The Effect of Shore Protection Procedures

Various procedures were tested and compared with recession rates for free shoreline conditions. Some of the procedures were selected to supplement data from the demonstration projects, others because of ideas advocated by public groups and some to check procedures observed in the field.

Some results of tests on groin systems are shown in Fig. 8. The curves of recession versus N are shown for two locations $x = 1.5$ (Fig. 8a) and $x = 2.5$ (Fig. 8b). The results are shown for three groin systems having different lengths and spacing and for one of these systems combined with a permeable wall. In all cases the freeboard of the groins was 0.02 feet (0.6 cm) in the model which corresponds to one foot (0.3 m) in nature. For each set of tests the length of the groins (g) as well as the ratio of length to spacing (g/s) is shown. Comparison with the free shoreline results which are also shown in Fig. 8 shows that the erosion rate was reduced by means of all the groin systems. The two sets of tests for the same length to spacing ratio ($g/s = 0.8$) give approximately the same results and when g/s was increased to 1.0 the protection was much greater. While this is as would be expected the range of variables used in the tests may be too limited to warrant reaching any general conclusion regarding groin spacing. It should be noted that the two groins



$$N = k \left(\frac{q_{TH}}{y} \right)^2$$

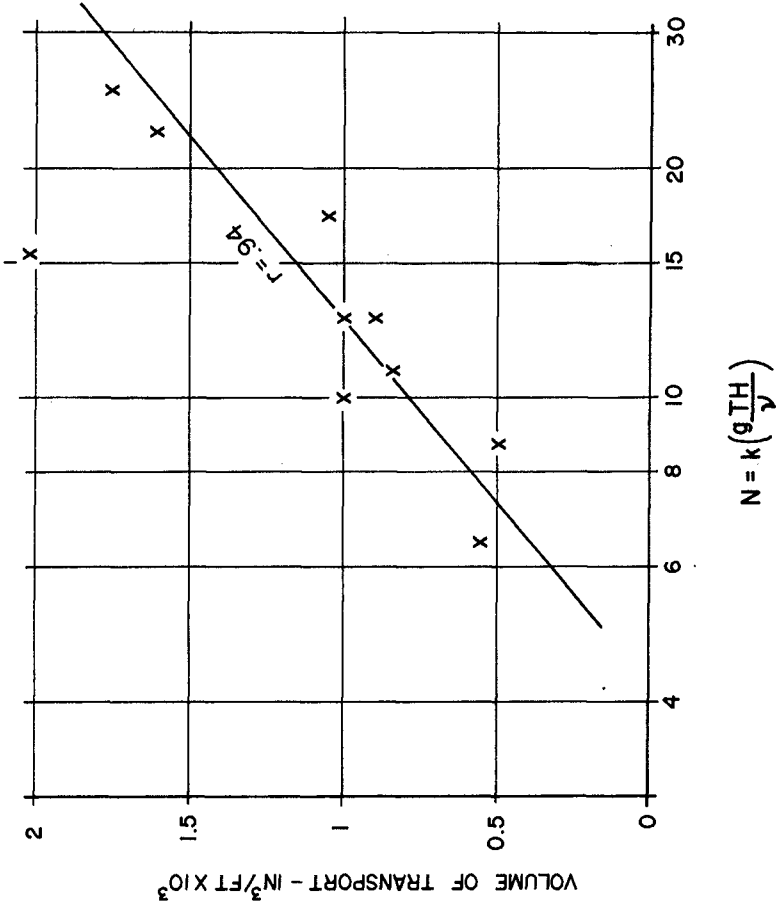


FIG. 7

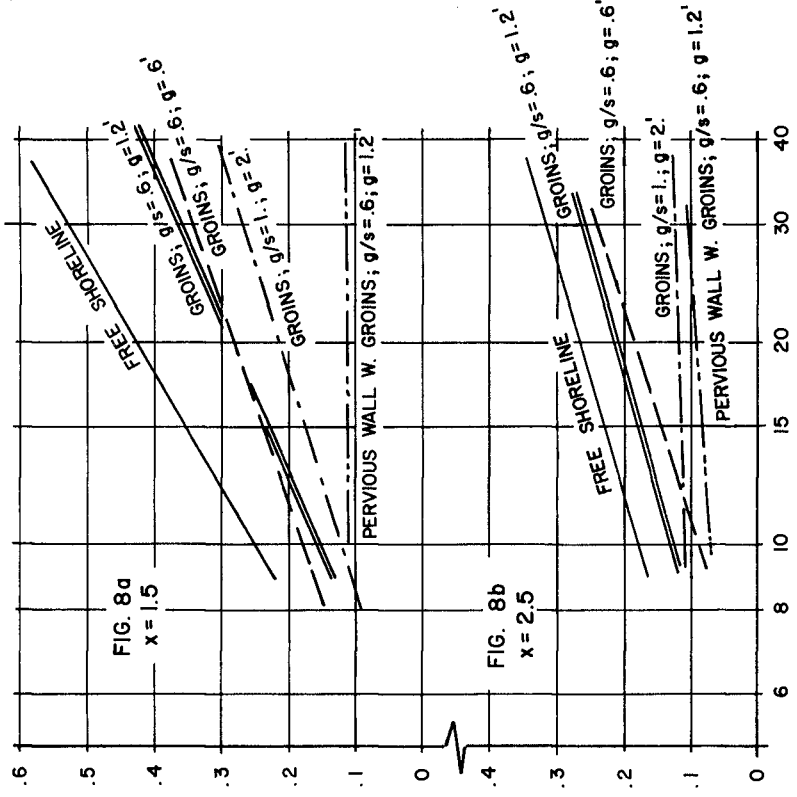
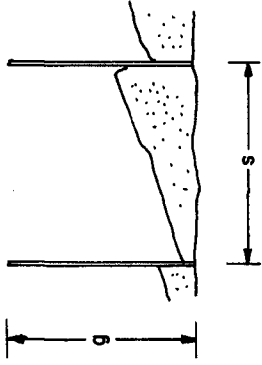


FIG. 8a
x = 1.5

FIG. 8b
x = 2.5

r_b
(ft.)



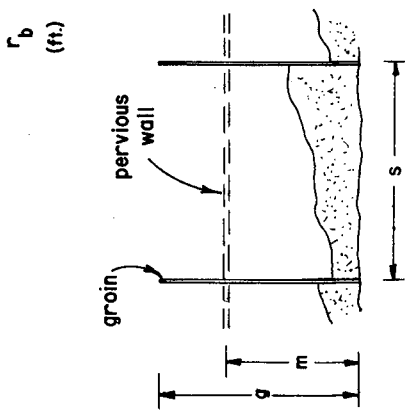
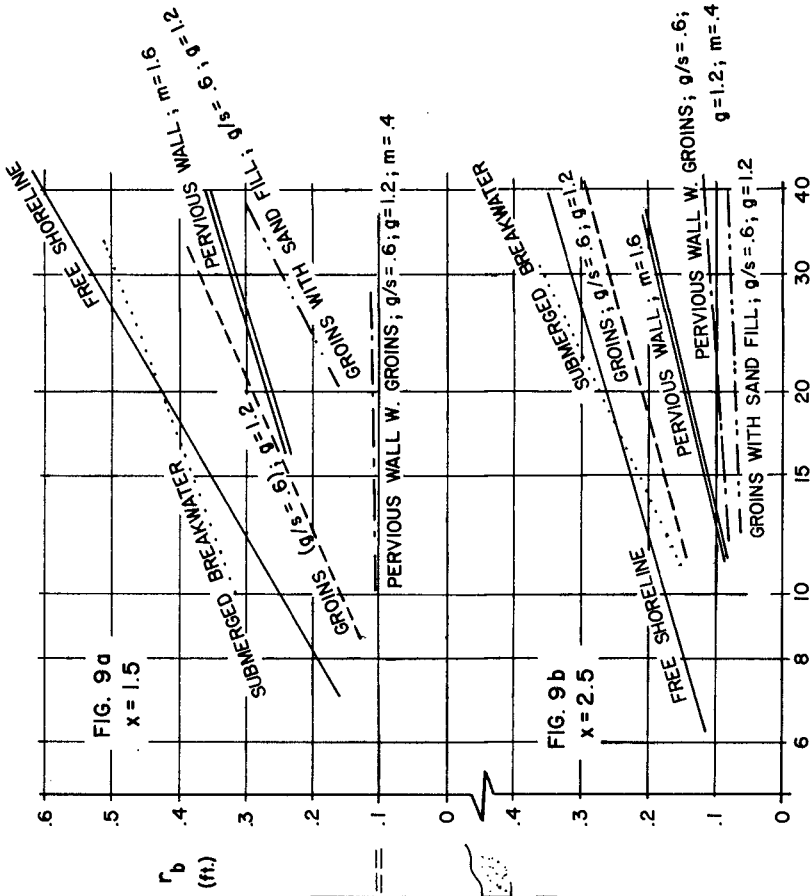
$$N = k \left(\frac{g \cdot T_H}{v} \right)^2$$

lengths used in the tests correspond to lengths of 40, 80, and 100 feet (12, 24 and 30 m) in nature. The greatest reduction in erosion occurred when a permeable wall was combined with the groins. The system was tested because it has been extensively used with considerable success on the Michigan coast. The location of the pervious wall is shown in Fig. 8c. The wall had a porosity of 30 percent which simulated a wall made with 2 inch x 8 inch (5 cm x 20 cm) lumber placed vertically with 3 inch (7.5 cm) gaps. The addition of the pervious wall to the groin system brings the cost up to the upper range of "low cost" shore protection.

Some of the graphs from Fig. 8 are repeated in Fig. 9 where results are also shown for groins with sand fill, pervious walls without groins and for a submerged breakwater. The sand fill consisted of the same sand used in constructing the model bluff and bottom. It was placed in the space between the groins, with the top of the sand at the elevation as the tops of the groins. At the outer ends of the groins the sand was allowed to assume its natural slope. It will be seen in Fig. 9 that this provided very effective protection through the full 60 minutes of testing. Note that at $x = 1.5$ the pervious wall with groins is more effective than the nourished groins, whereas at $x = 2.5$ the reverse is true. The pervious wall for which results are shown in Fig. 9 had a porosity of 40 percent and was located a distance from the shore line which corresponds to 20 feet (6.1 m) in nature. It may be seen in Fig. 9 that this wall provided considerable protection.

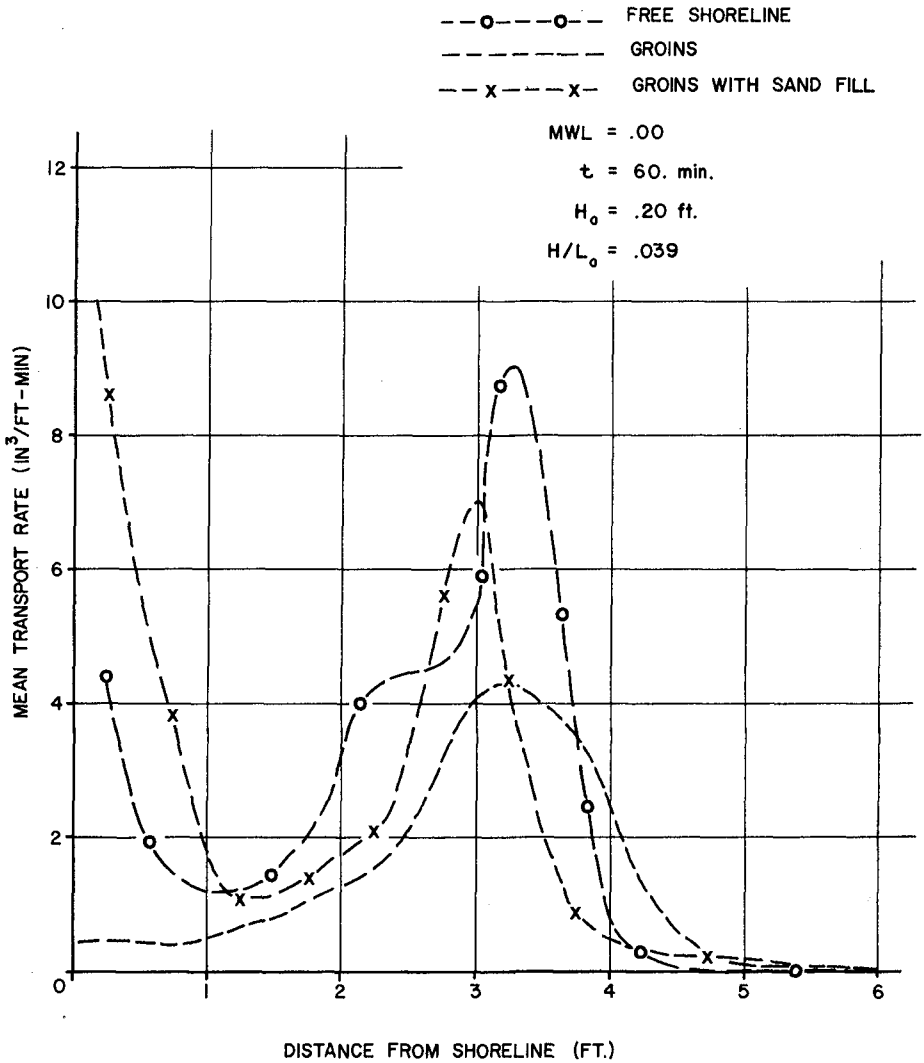
The submerged breakwater was tested because of considerable public interest in this type of protection. It was installed in the breaker zone. When originally installed the ratio of its height above the bottom to the depth was 1:3.4. After the model was in operation for a few minutes this ratio became about 1:2.5. The use of such a low barrier produced no noticeable reduction in bluff recession.

The effect of groin systems on littoral drift is shown in Fig. 10. The ordinates of the graphs are rate of transport and the abscissas are distance from the shore line, zero being point a_1 in Fig. 2. The twelve plotted points give the rate at which sand was collected in the twelve individual pans and each point is plotted at the center of the pan. The values of total transport plotted in Fig. 7 were obtained by integrating the area under one of the curves. Each of the curves in Fig. 10 represents an average of the curves for that series of repeated tests. The free shoreline curve shows that the littoral drift is large in the uprush zone near shore and in the breaker zone. The curve for a groin system shows that the groins stopped most of the littoral drift in the near shore area and reduced the drift in the breaking zone. However, the curve for groins with sand fill shows that when nourishment was supplied to the groin system the littoral drift is even greater than with the free shoreline. It should be recognized that the transport during tests with the



$$N = k \left(\frac{qTH}{y} \right)^2 \times 10^{12}$$

FIG. 10
SAND TRANSPORT



groins, without and with nourishment, would probably change if the tests were continued longer. The un-nourished groins would be expected to fill with sand naturally and then littoral drift could be expected to resume in the near shore area. On the other hand, the nourished groins would eventually lose enough of the fill material so that the littoral drift could be expected to drop back to a more normal rate. Some tests were made with higher groins. These created wave reflections which directed the wave energy toward shore on the updrift sides of the groins. This is illustrated by the shorelines plotted for high and low groins in Fig. 11.

Tests were also made to gain more information on one of the field demonstration projects. This project consisted of an off-shore breakwater constructed of zig-zag concrete walls. The structure provided considerable protection for a number of years but during a large storm severe erosion occurred behind the structure. The model studies also showed that some protection was being provided by this structure when compared with a free shoreline. However, when the water level in the model was raised one foot (0.3 m) to the top of the structure the bluff erosion was more than doubled. This information showed that the wind tide which occurred during the destructive storm was an important factor in reducing the effectiveness of the structure.

Summary

A laboratory investigation of shore erosion processes was undertaken to supplement a shore protection demonstration project in Michigan. The purpose of both the field project and the laboratory studies was to familiarize individuals and public agencies with shore protection methods and to provide information on the selection and construction of protective procedures. Although it was recognized that erosion rates could not be converted quantitatively from the model to nature it was hoped that the relative effectiveness of various protective procedures could be evaluated. If this could be done, the advantage of the model over field projects would be lower cost, the control over variables such as wave height and water surface elevation and the shorter time required. One of the chief difficulties with field demonstration projects is the random nature of the occurrences of on-shore storms of a size sufficient to test but not destroy the structures.

The preliminary tests showed that natural processes were simulated in the model and after considerable experimentation in constructing the model it was found that repeatable results could be obtained. Because, even in the model, it was impossible to control wave height exactly and because there was no control over the water temperature it was necessary to test for repeatability by plotting bluff recession against a parameter which was related to the ratio of original energy and energy dissipation.

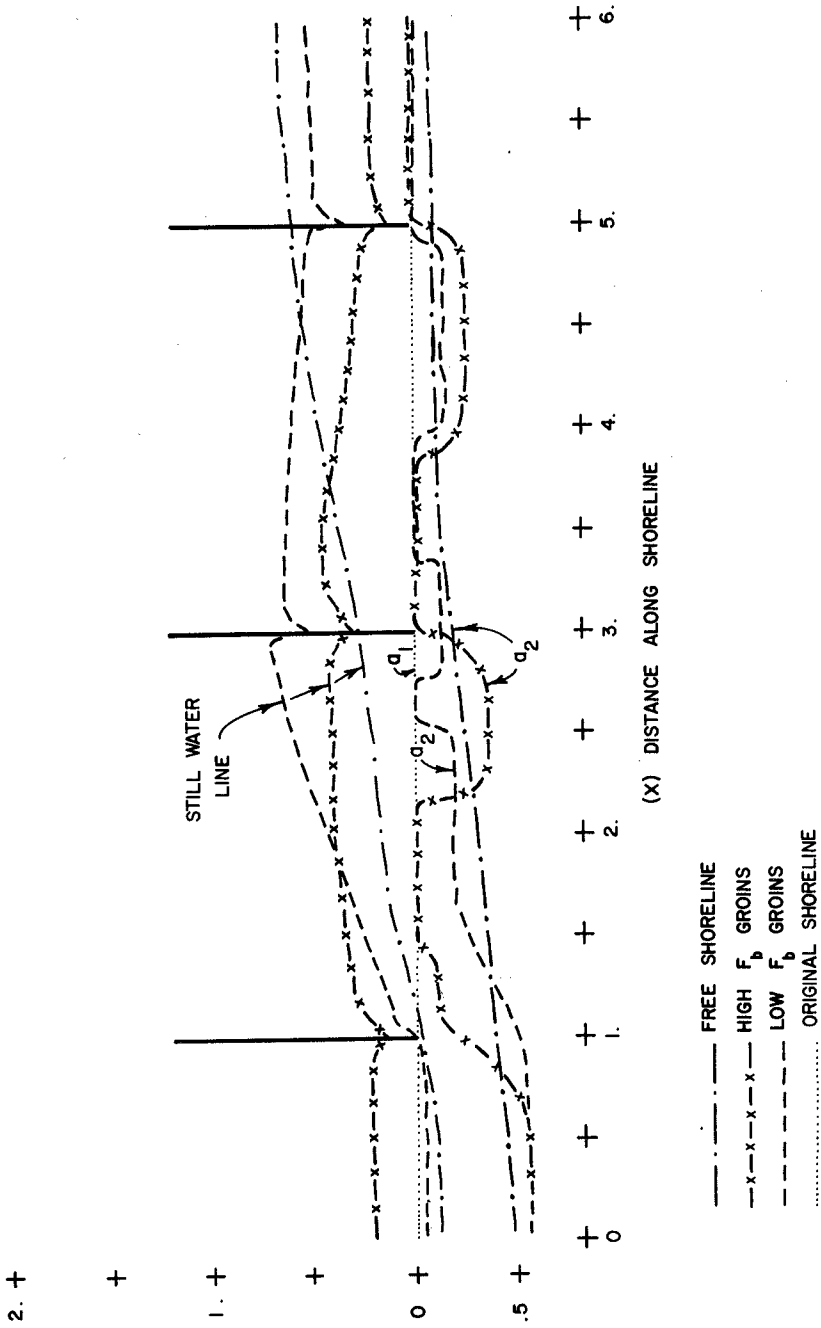


FIG. 11: PLAN VIEW OF EROSION PATTERNS

This parameter also included the duration of the model storms. It was found that comparison of results of tests on various methods of shore protection with the erosion of a free shoreline could also be made by means of plotting bluff recession against this parameter. This parameter also served to coordinate rates of littoral drift. The model was used to evaluate some well established procedures such as groin systems and beach nourishment. Tests were also made to provide additional information on one of the demonstration projects and to determine the effectiveness of some procedures which had considerable public interest but were not included among the field projects.

CHAPTER 89

Cape Hatteras Beach Nourishment

John S. Fisher¹

Wilson N. Felder²

Abstract

The 1973 beach nourishment at Cape Hatteras placed approximately 465,000 m³ on the subaerial beach. Eighteen months later, about 51 percent of this material remained on the beach. During this period there were relatively few major storms, and this mild wave climate is largely responsible for this high retention. At the end of this monitoring period the beach was stable and fully capable of providing shoreline protection and recreation.

A correlation is presented relating storm erosion with the complete storm wave climate, including a post-storm period. A new parameter is defined which includes a measure of wave steepness and longshore current velocity.

¹Assistant Professor, Department of Environmental Sciences, University of Virginia, Charlottesville, Virginia

²Research Assistant, Department of Environmental Sciences, University of Virginia, Charlottesville, Virginia

Introduction

The placement of sand as beach nourishment is one of coastal engineering's most successful techniques for the short-term arresting of coastal erosion. This practice is particularly popular when the endangered beach is primarily valued for recreation, including motel sites, piers, etc.. In these situations the use of groins, seawalls, and other alternatives is often undesirable and to be avoided when possible. Of course, the suitability of a beach nourishment plan depends upon the availability of nearby sand, as well as several legal and economic considerations.

This paper describes a recently completed beach nourishment project at Cape Hatteras, North Carolina. During an eighteen month period ending in the fall of 1973, approximately 1.25 million cu yds ($956,000 \text{ m}^3$) were placed along a 1.5 mile (2400 m) stretch of shoreline at Buxton, North Carolina, Figure 1. This particular beach at Cape Hatteras has experienced a relatively high erosion rate in recent years. As a consequence, several different coastal engineering schemes have been tried, including groins, sand bags, and two previous nourishment projects. Although some of these projects have had limited success, the beach has continued to erode, necessitating this latest project. This paper describes the scope of the project, and the condition of the beach eighteen months after its completion. We have included the beach volume changes, the observed wave climate and the frequency and dimensions of the severe storms during this period. Finally, we present some preliminary thoughts on how these data can be used in developing a rationale for the prediction of nourishment retention.

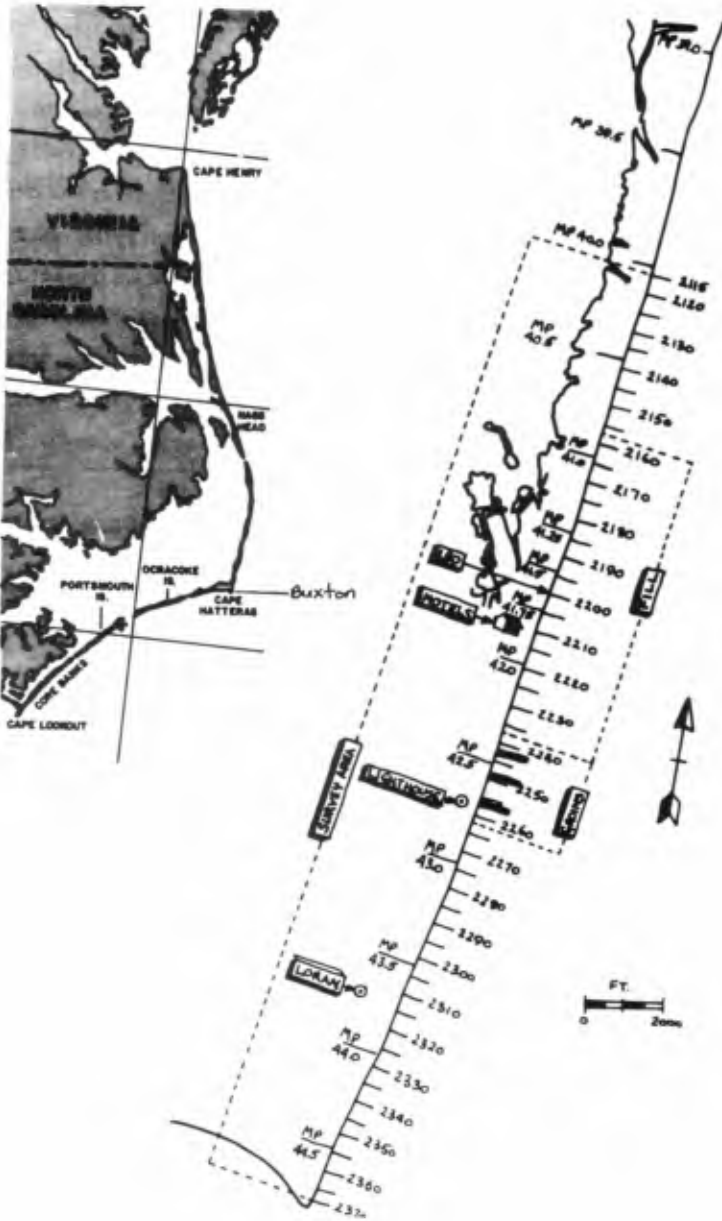


Figure 1 Location map and project dimensions

Project Description

Cape Hatteras is well known for its dramatic series of barrier islands and their beaches, as well as the large waves and severe storms which frequent them. Most of this shoreline is included in the Cape Hatteras National Seashore, as is the beach nourishment site at Buxton, on Cape Point. The fill area is located on the northern side of Cape Point, where Hatteras Island makes an abrupt change in orientation, turning to the west, Figure 1. The predominant longshore drift on the northern side of the point is to the south, in part forming this classic spit feature. This spit provided an excellent source of fill material, being both nearby and similar in texture to the beach sand. The nourishment sand had a mean diameter of .37 mm, and the area to be filled a diameter of .38 mm.

A borrow pit was excavated at the spit and the material was pumped 4 miles (6400 m) to the north. At the completion of the dredging and pumping, the borrow pit was approximately 2500 ft (762 m) by 1000 ft (304 m) with an average depth of 15 ft (4.6 m). There was no connection with the ocean initially, but an inlet cut into the southwest side at a later date and has remained open.

The fill material was placed along a 1.5 mile (2400 m) segment of shoreline. The dredge pipe was located so that the discharge was immediately above the mean high water line, with no effort made to shape or bulldoze the sand into a designed profile. In general, the nourishment resulted in an increase in subaerial beach width of roughly 250 feet (76 m) along the 1.5 mile (2400 m) beach, Figure 1. This material was intended to provide some immediate shoreline protection to the lighthouse, Naval Station, and public and private property. To a limited extent, this goal was accomplished, and the previously eroded and narrowed beach at Buxton

was restored to a width providing more shoreline protection and increased recreation.

In order to assess the impact and performance of the nourishment project, a program of field studies was initiated by the National Park Service. This monitoring program included frequent surveys of the beach, portions of the nearshore bathymetry, the borrow pit, as well as daily wave climate observations. Dolan, et al. (1) summarize this data for the period from the project beginning to completion of pumping. Fisher, et al. (2) report on the survey results for the succeeding 18 month period. In addition to the measurement of volume changes, an analysis of the ecological impact of the fill material on the native beach was undertaken, Hayden and Dolan (3). Their study suggests that there is no significant damage to the beach ecology as a result of the fill activities.

As with many coastal engineering projects, the measurement of the wave environment proved to be one of the most difficult problems in the monitoring program. The nearest wave gage is 60 miles (97 km) north of the fill area at Nags Head. The wave conditions at the site were estimated according to the LEO, Littoral Environment Observation Program, as developed by the Coastal Engineering Research Center, CERC, Bruno and Hipakka (4). The LEO program includes the daily observation of wave period, angle and height of breaking, as well as a simple estimate of the longshore current velocity. These wave observations suffer from the usual symptoms of non-instrumentated data collection, nonetheless, they did provide an important reference in documenting significant changes in the wave climate. In particular, they enabled us to observe the change in wave conditions associated with storm systems.

The survey program included the borrow pit, the beach and the offshore. The latter two areas included the immediate fill area as well as adjacent areas to the north and south, for a total of 4.5 miles (7200 m). The entire borrow pit was surveyed once during the study period, and the southern end was surveyed five additional times, when possible change was suggested. The offshore was profiled with a Raytheon Fathometer a total of five times during the 12-month period discussed here. Unfortunately, the survey vessel was unable to cross the inner bar, and therefore the beach profile could not be extended out to the Fathometer profiles. The data for both the borrow pit and offshore are not presented here.

The subaerial beach was surveyed bi-weekly as well as immediately after a storm. Fifty-three survey stations were established on 500 ft (152 m) intervals from Mile Post 40.0 to Cape Point, Figure 1. Nine of these stations were north of the fill area, 16 in the fill area, and 28 to the south. The profiles were made with level and rod, and extended from a project baseline on the backshore into the swash to the mean low water level.

Figure 2 illustrates the changes at three of these stations, one in the fill area, and one both north and south of the fill. Station 2200 is located approximately in the middle of the nourishment area, it also is the site of the LEO wave observations. The post pumping profile, September 1973, clearly shows the increase in beach width with the additional material, at this site, over 300 ft (91 m). The depression landward of the beach crest is a result of the decision not to shape the fill material or otherwise attempt to develop a predetermined beach profile. At this particular site, this depression was within the National Seashore boundaries. Further to the south, the resulting depression was within private property, and

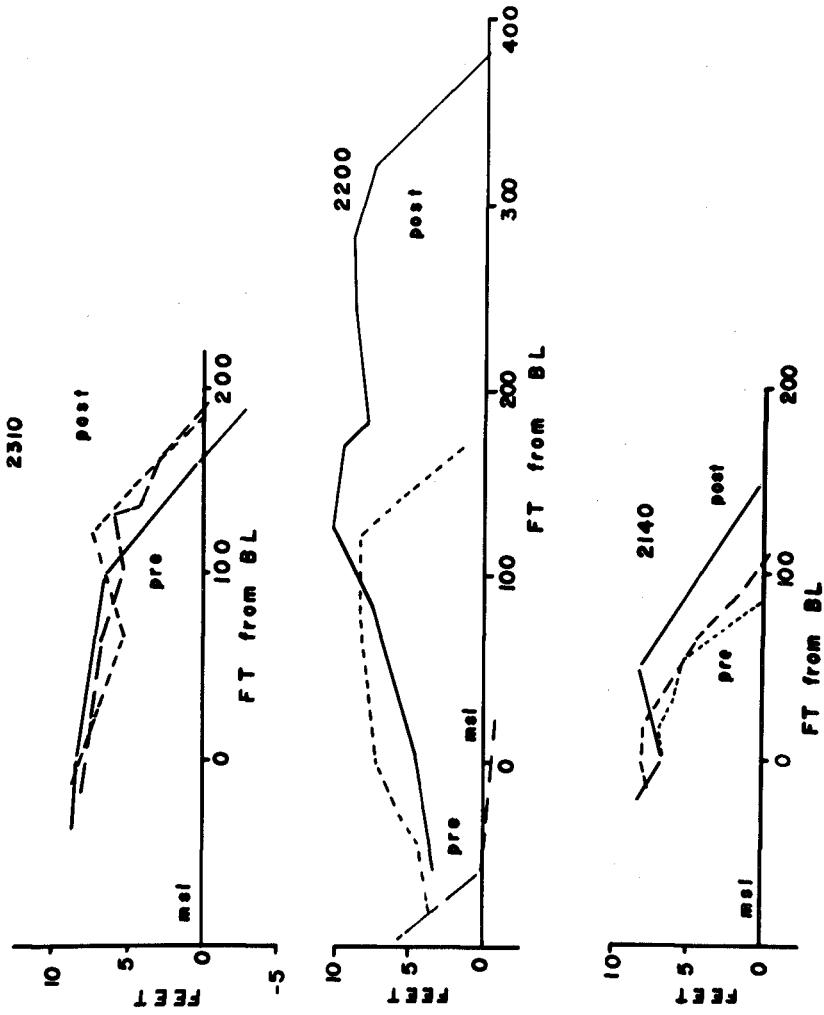


Figure 2 Subaerial beach profiles

thus there was no intentional placement of fill outside of the National Seashore. The profile for February 1975 at this same station illustrates the extent of subaerial beach erosion during this period. The 50 per cent decrease in beach width is typical of the fill area, with the bulk of the material transported offshore, as evidenced by the relatively small change in the dimensions of the landward depression.

Station 2140 is one mile (1600 m) north of station 2200, and is about .5 mile (800 m) north of the limits of the nourishment area. There was a relatively small increase in beach width just after the completion of nourishment, and a more recent erosion, with only a modest net increase in width by February 1975. The beach to the south of the fill area, is illustrated by station 2310, about one mile (1600 m) south of the fill area. Again, there is only a small net change in beach dimensions outside of the fill area.

Wave and Storm Climate

According to the record from the CERC wave gage, the annual mean wave height along Cape Hatteras is the largest for the mid-Atlantic coast. The gage at Nags Head, 60 miles (97 km) north of Buxton has a mean value of 3.0 ft (.9 m), CERC (4). Our LEO observations covered the period from April 1974 to February 1975, and were made at station 2200, 3.4 miles (5.4 km) north of Cape Point, Figure 1. The mean wave height from this data is 2.2 ft (.67 m), the mean period is 7.9 sec, and the mean longshore current is approximately zero. This latter parameter does not accurately reflect the net longshore drift, which is clearly from the north, towards the point. This low net current magnitude does suggest that large wave conditions, i.e., during storm periods transport the bulk of the littoral

material. This observation is consistent with the literature, including the discussion presented in the Shore Protection Manual, CERC (5).

Figure 3 illustrates a portion of the LEO data, including the wave period, longshore current velocity squared, and the square of the wave height. Of particular interest in this data are the episodes of high waves and large currents, both from the north and the south. These dates are associated with storms, although the correlations are not as high as one might expect for this coastline. It is difficult to assemble a reasonable model for wave observations and storm intensity when the available data is this limited. However, by simply using a hindcast deep water wave height, one can gain a limited feeling for this system.

The bottom graph on Figure 3 is the SMB hindcast deep water wave height H_0 for all storms with H_0 greater than 5 feet (1.5 m). This technique, Bretschneider (6), depends upon the available meteorological observations for the estimation of the storm fetch and duration, as determined from the synoptic weather charts. Figure 3 shows the storms to be generating the larger waves and currents, although there is some noise in the data. A notable exception occurs during the period from October 19th to the 21st. In fact, a small low pressure did move rapidly up the coast during this period, but its deep water waves were only hindcast to be 4 ft (1.2 m). This event helps to dramatize the weakness of this simple model. Although the storm's deep water waves were relatively small, its LEO waves were the same magnitude as some of the larger events.

As stated above, the mean net longshore current is almost zero, although the shoreline geometry indicates significant longshore sediment transport to the south. Of the larger storms, all but one had a longshore current towards the south, the exception being the early December storm.

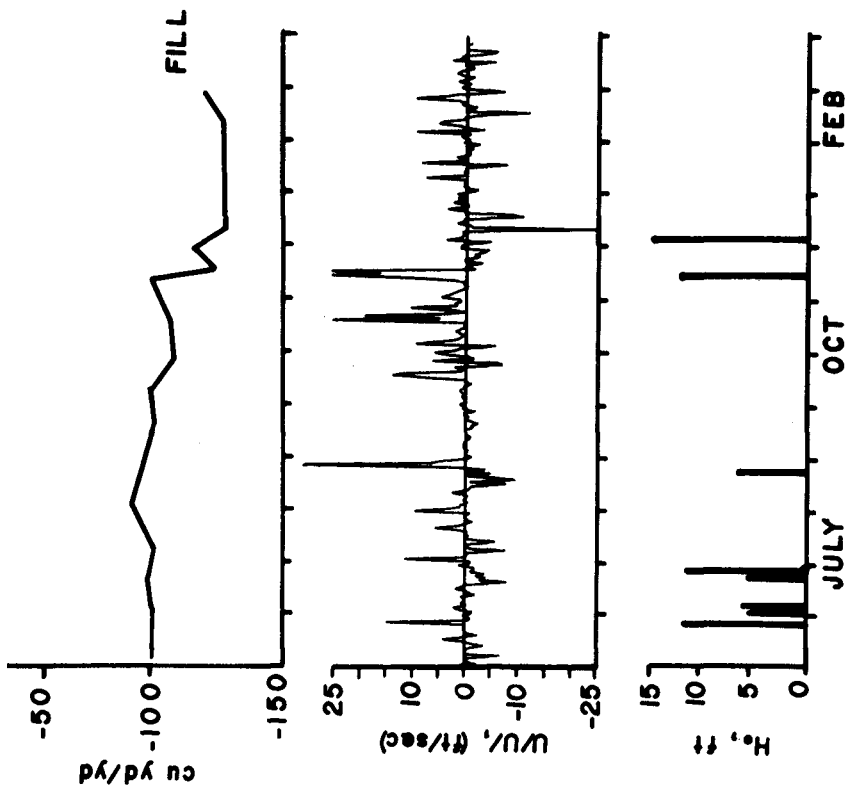


Figure 3 Wave and storm climate.

This storm developed off of the South Carolina coast and maintained its strongest winds while still south of Cape Hatteras, hence the south to north current direction. This direction, although followed for approximately one half of the LEO observations, is unusual during periods of high wave energy. It is probable that this strong northerly flow was in part responsible for the overall impact this storm had on the subaerial beach volume change.

For the observation period from April 1974 to February 1975, there were ten storms with deep water waves hindcast greater than 5 ft (1.5 m). As will be discussed in the following section, only a few of these storms had any significant impact on the nourished beach. In terms of storm frequency, 1974 was a relatively mild year for Cape Hatteras. According to Dolan and Hayden (1) this section of the mid-Atlantic coast averages about 34 storms per year, whereas 1974 had a total of only twenty.

Nourishment Retention

From June to September 1973, approximately 1.25 million cu yd (956,000 m³) of fill were pumped. Using surveys made immediately preceding and following the completion of pumping, the volume of fill which contributed to the accretion of the subaerial beach has been calculated. This data fails to account for the material which was washed into the inshore zone, which must have been a large percentage of the original fill volume. The lack of data in this zone because of the difficulty of surveying in the breakers, is an obvious handicap to our computations of fill retention and overall project performance. The following discussion and analysis, limited to the beach above the mean low water level, must be recognized as only a portion of the complete sand budget.

Table 1 presents the net volume of sand accumulated at each of the 16 stations within the fill area. The total for this area was 646,667 cu yd (494,442 m³), an average gain of 243 cu yd/yd (203 m³/m). During this same period, stations to the north and south of the fill area accreted an average of 14 cu yd/yd (12 m³/m). Using this mean value outside the fill area as an estimate of natural deposition throughout the study area, we have assumed the mean gain due to fill was 229 cu yd/yd (191 m³/m) between stations 2165 and 2240, and the total deposition above MSL of 608,480 cu yd (465,243 m³), or 49 percent of the material pumped. The remaining material was deposited below sea level at each station.

In terms of beach restoration and protection, the volume accumulated below MSL is an important component of the overall nourishment project. This material, the bulk of which was presumably retained within the nearshore zone, provides a source of material to the beach, and helps maintain the inner bar system and hence wave energy dissipation. Because of the inability to accurately survey the nearshore, no data is available to analyse the volume changes in this zone.

The remainder of this retention discussion deals with the volume of nourishment sand on the beach itself, above MSL. Figure 4 shows the volume changes along the entire project, both for before and after pumping, and from completion of pumping to 18 months later. The significant area of change is within the fill area itself. Eighteen months after the completion of the pumping, 51 percent of the nourishment sand remained in place in this area, or 307,343 cu yd (235,000 m³).

Outside of the fill area the changes have been relatively small. To the north, there has been no significant erosion or accretion. South of the nourishment area there has been a small amount of accretion.

TABLE 1

VOLUME OF MATERIAL REMAINING ON THE
SUBAERIAL BEACH UPON COMPLETION OF PUMPING

Station	Cu Yds/Yd
2165	63
2170	160
2175	270
2180	250
2185	250
2190	210
2195	330
2200	350
2205	230
2210	280
2215	270
2220	300
2225	240
2230	290
2235	260
2240	27

Mean accretion in fill area:	243 cu yds/yd
Mean accretion outside fill area:	14 cu yds/yd
Net accretion of fill:	229 cu yds/yd
Total accretion:	608,480 cubic yards
Total pumped:	1,250,000 cubic yards
Net percent of fill material retained on subaerial beach:	49 percent

Inasmuch as the longshore drift during high wave conditions is towards the south, we can reasonably assume that this accretion is derived in part from the nourishment area. There are three short groins just south of the fill area. The volume change within the groin field both during and after nourishment has been rather small. The impression one gets from Figure 4 is that this groin field is behaving like a filter in that it appears to have dampened the volume changes immediately downdrift from the fill area.

Figure 5 shows the post-fill volume changes over the 18 month period of our surveying. The shoreline is divided into four increments, north, fill, groins, and south, and the combined changes are also shown in this figure. Again, it is clear that the only section undergoing significant change during this period is the fill area itself. And in fact, even the fill area appears relatively stable with the exception of the loss in early November. This large loss of sand occurred at all four of the project areas, although it was most severe within the nourished beach. From Figure 3 we can relate this large volume of erosion to a single November storm, with H_o of about 10 ft (3 m). This figure presents the volume change for the combined project area as well as the hindcast wave height and longshore current. It is apparent that this relatively large November storm, with its strong north to south current is responsible for the erosion. However, there are two other events illustrated on this figure which tend to confuse the correlation. During mid-October, a smaller storm generated longshore currents just as strong as the November event, but the beach accreted. And in early December, an even larger storm, $H_o > 15$ ft (4.6m) caused considerably less erosion than the November storm. Thus, from this series of events, we are presented with a rather

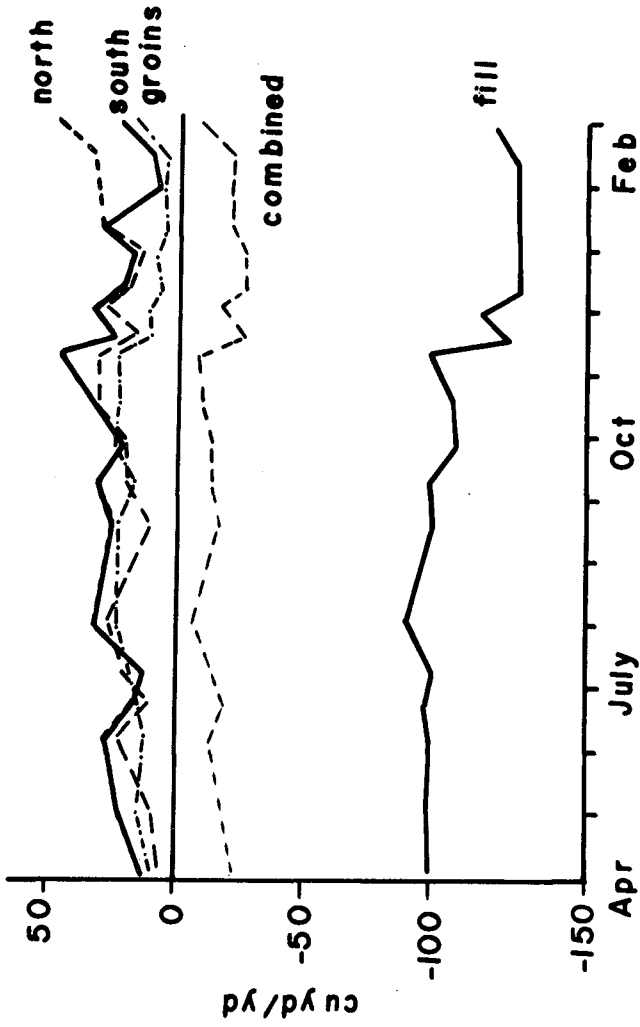


Figure 4 Volume changes for project period

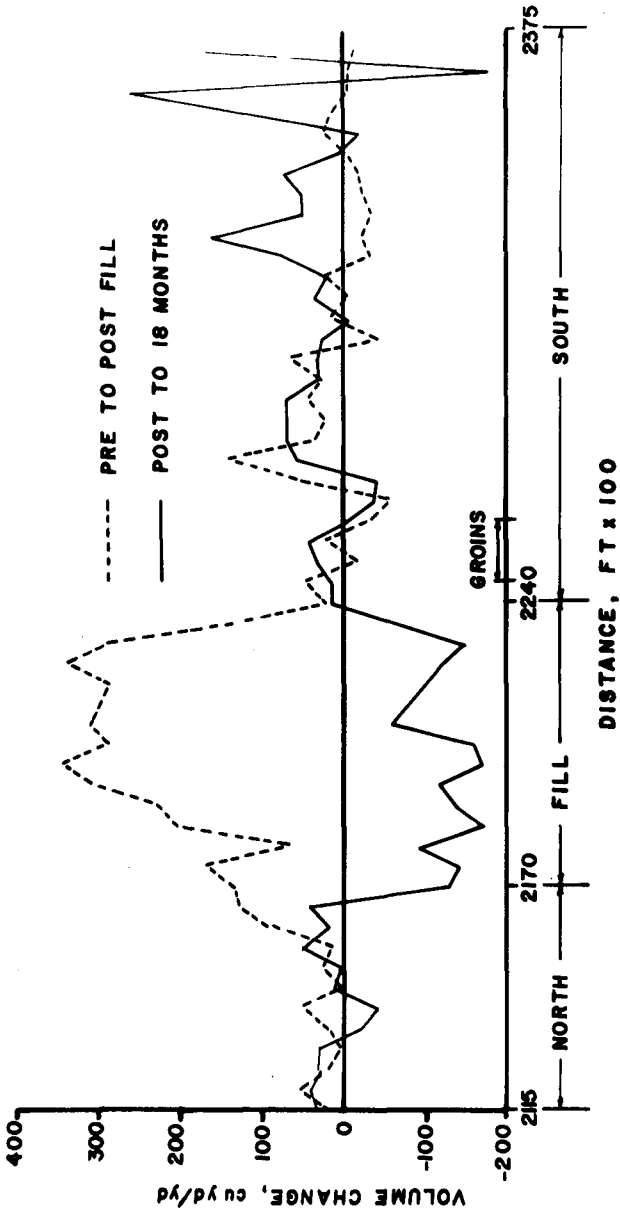


Figure 5 Pre and post fill volume changes

complex set of relationships regarding the impact of individual storms on the beach.

There is one interesting difference between these three storms and their associated beach changes which we feel is notable. The longshore drift immediately after the November storm was from the south whereas the post-October drift was from the north. If we consider the principle source of sand for this beach to be from the north, as suggested by its morphology, then it follows that a post-storm wave climate generating a drift to the south will be an ideal condition for beach recovery. Conversely, a post-storm drift from the south will not provide the beach with an equivalent quantity of sand. In addition the characteristics of the post-storm waves, i.e., their period, steepness, etc., should also play a role in this recovery process.

As a preliminary analysis of this hypothesis, we have made a simple correlation of the post-storm waves and drift. A dimensionless parameter, S, has been defined which includes the fall-time parameter $\frac{H}{V_f T}$ with the square of the longshore current normalized by the fall velocity,

$$S = \left(\frac{H}{V_f T} \right) \left(\frac{U}{V_f} \right)^2$$

As stated above, our assumption is that the impact of an individual storm is a function of the post-storm drift direction, i.e., from a source or sink of sand. To evaluate this assumption we have correlated the surveyed beach volume changes with this parameter S, assigning the sign of the post-storm drift.

$$\hat{S} = \bar{S} \operatorname{sgn} (U_{ps}),$$

where \bar{S} is the mean of S over the survey period. Figure 6 shows the correlation of \hat{S} with the mean volume change ΔV for the study period. The solid dots are for surveys which bracketed storms. There appears to be a high correlation, suggesting that we should take a serious look at this assumption and its implications for evaluating storm impact. We are presently analysing this data in this context, and will present our results in a forthcoming paper.

Conclusions

The success of a beach nourishment project cannot reasonably be measured in terms of the percent retention of material at a specified period after placement. There are too many political and social questions which must be included in the final appraisal. We have not looked at these problems, and will not comment on them. However, if we restrict our view to the impact of the fill on the subaerial beach, we can comment on the measured changes.

Eighteen months after pumping, about 50 percent of the subaerial nourishment was still in place. In as much as this period included a relatively mild storm climate, we consider this volume of sand to be greater than what might have been predicted. The remaining sand is providing a wide beach for recreation as well as some additional protection to the various public and private structures. The immediate threat of storm damage present prior to the nourishment has been, and continues to be alleviated.

The problem of designing future fill projects, and predicting their project life has been addressed in this paper in the context of identifying the impact of individual storms on the beach. We are presently able

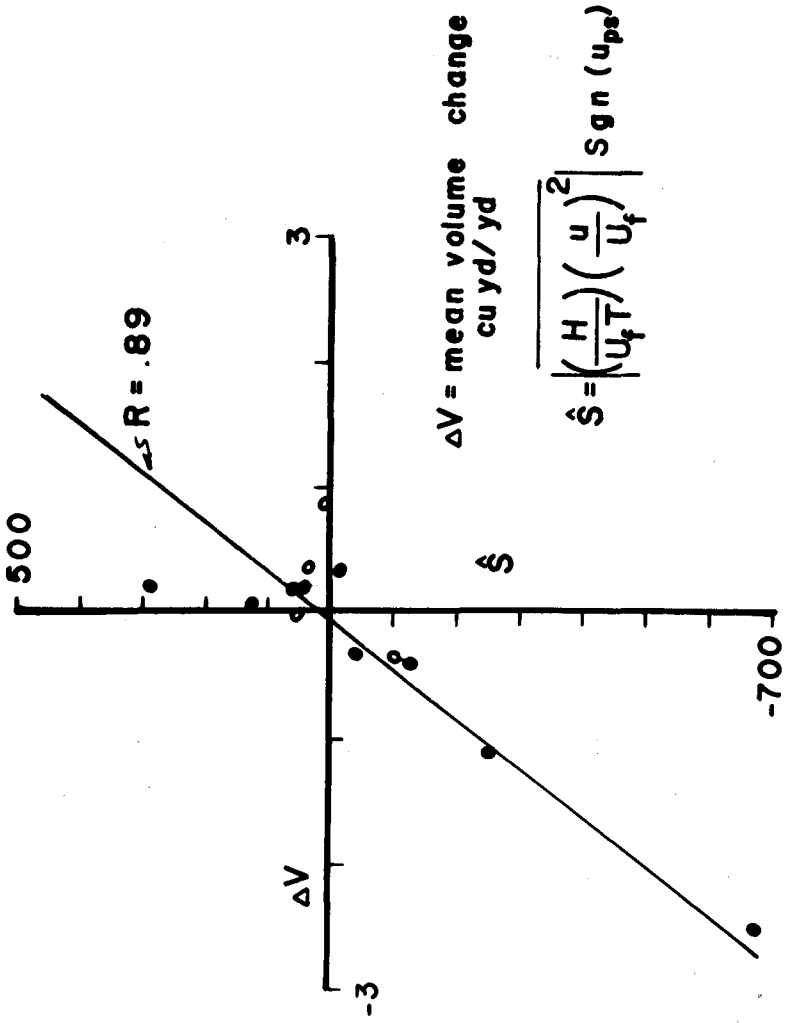


Figure 6 Correlation of volume change and wave conditions

to make crude predictions of storm and wave climates for a given stretch of shoreline. The problem is in estimating the erosion or accretion resulting from this simulated climate. Our analysis at Cape Hatteras suggests that in attempting to develop a relationship between storms and volume changes, that the post-storm wave conditions may be important. The preliminary results presented here indicate a strong correlation between volume change and direction of post-storm littoral drift.

Finally, we note that the analysis of aerial photography presented at the conference is being prepared for separate publication, as space limitations precluded its inclusion in this paper.

Acknowledgements

This project has been supported by the Southeast Regional Office, National Park Service, Grant No. CX500040462. The authors wish to thank Mr. John Ponton and Mr. Leif Gulbrandsen for their assistance in this analysis.

References

- (1) Dolan, Robert. 1973. Beach Nourishment Project, Cape Hatteras, North Carolina, Post-Pumping Summary. Coastal Research Associates, Charlottesville, Virginia.
- (2) Fisher, J.S., Felder, W., Gulbrandsen, L., Ponton, J. 1975. "Cape Hatteras Beach Nourishment Study, Post-Pumping Report, March 1974 - February 1975," Department of Environmental Sciences, U. Va.
- (3) Hayden, B.P. and R. Dolan. 1974. "Impact of beach nourishment on distribution of Emerita talpoida, the common mole crab," Journal of Waterways, Harbors, and Coastal Engineering Division, ASCE, WW2, pp. 123-132.
- (4) Bruno, Richard and Hiipakka. 1973. "Littoral Environment Observations Program in the State of Michigan, " Proc. 16th Conf. Great Lakes Res.
- (5) U.S. Army Coastal Engineering Research Center. 1973. Shore Protection Manual, Vol. 1 and 2.

CHAPTER 90

THREE DIMENSIONAL TESTS ON DYNAMIC EQUILIBRIUM AND ARTIFICIAL NOURISHMENT

by

J.W. Kamphuis
Professor of Civil Engineering
Queen's University, Kingston, Canada

and R.M. Myers
Engineer, MacLaren Atlantic Ltd.
Halifax, Canada

ABSTRACT

A three dimensional facility for testing dynamic equilibrium and artificial nourishment of beaches was developed. Specific conclusions are drawn with respect to trap location and re-reflection of waves. It was found that dynamic equilibrium is achieved faster in three dimensional tests than in previous two dimensional work and that the profiles are eroding profiles rather than potential (limit) profiles. It was seen that profiles develop around the offshore bar which is shaped early in the experiments. Also the depth of the summer step was found predictable from critical shear stress considerations. Finally, onshore nourishment of eroding beaches was found to be successful.

SYMBOLS

- D = particle diameter; D_{90} - 90% of the particles are smaller;
 d_G = depth of water at the wave generator;
g = gravitational acceleration;
H = wave height;
 n_{t_s} = sediment transport scale for wave action only (Ref. 8);
 n_{t_m} = sediment transport scale for bed morphology and littoral transport;
R = runup distance; distance from SWL to maximum limit of uprush;
SWL = still water line; distance from an arbitrary measuring base line to the intersection of the still water level and the beach;
 S_{SWL} = beach slope at SWL ;
T = wave period;
 v_* = shear velocity;
 α = angle of approach of the waves; α_G - at the wave generator;
 α_0 - in deep water;
 β = distance from the still water level to the crest of the offshore bar;
 γ_s = sediment unit weight under water ($= (\rho_s - \rho)g$);
 θ = distance from the still water level to the trough behind the offshore bar;

- λ_b = bar distance; distance from SWL for a winter profile to the point where the bar rises suddenly out of the offshore beach slope;
 λ_s = step length measured between the intersections of the summer step with the offshore beach slope and the onshore beach slope;
 ν = kinematic viscosity of water;
 ρ = density of water;
 ρ_s = density of sediment;
 Σ = distance from the still water level to the summer step;
 τ_o = bottom shear stress; $(\tau_o)_c$ - critical value; $\hat{\tau}_o$ - maximum value;

INTRODUCTION

In an earlier paper (7) the first of a series of two dimensional tests on artificial beach nourishment were presented. The tests were performed on a model beach made up of the relatively coarse sand shown in Fig. 1.

($D_{50} = 0.61$ mm). This material was subjected to a simulated Great Lakes wave climate (neglecting tidal fluctuations and seasonal water level changes).

Since an equilibrium profile in the usual sense of the word is never achieved in the prototype, the term "dynamic equilibrium profile" was coined. Dynamic equilibrium is said to occur when a beach is acted upon long enough by a simulated, annually recurring cycle of waves so that each year, the profile returns to the same shape at the same time of year. For the simulated Great Lakes wave climate it was assumed that the total annual wave climate could be subdivided and grouped into three wave categories:

- a. approximately 250 days of "background wave action", where the wave height is equal to or less than 0.3 m and the wave period of the order of 4 seconds,
- b. approximately 15 days of "small storm waves" with a wave height of about 1.2 m and a wave period of 6 seconds,
- c. about one and one half days of "large storm waves" with a wave height of about 3 m and a wave period 7.5 seconds.

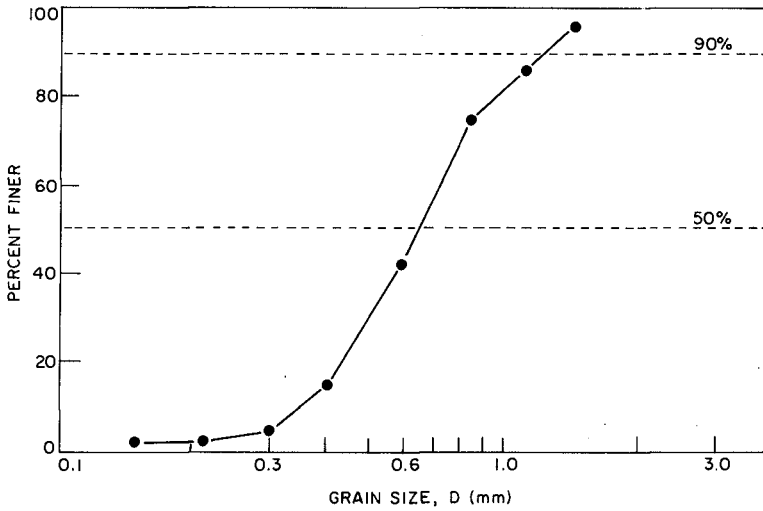


Figure 1: Grain size distribution of beach material used.

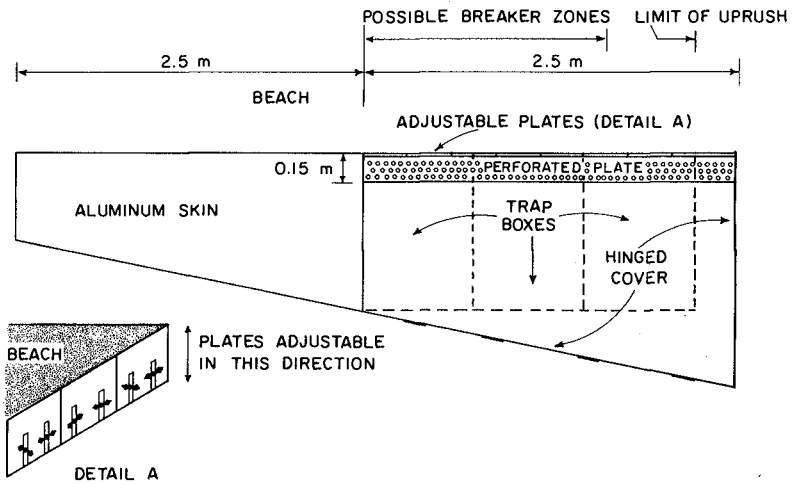


Figure 2: Sediment trap.

Although the background and small storm wave action may occur any time, the large storm waves are strictly confined to late autumn and winter. For modelling purposes, however, it was necessary to group the classes of waves together and run them in a cyclical pattern. Thus dynamic equilibrium in these studies occurs when the above wave action simulated in neat cyclical form has taken place long enough so that the profiles at the same time during each cycle are the identical. From preliminary tests it was found that the background waves moved very little or no material and thus the model wave cycle was reduced to alternate small storm waves and large storm waves. The model scale chosen was 25, i.e., the wave time scale was equal to 5. The ideal wave sediment transport time scale for two dimensional sand models (8) was found to be 210, for an assumed field particle size of 1 mm: not an unreasonable size for Great Lakes beaches under relatively heavy wave attack. Therefore the annual wave climate was simulated by a cycle of 110 minutes of 4.6 cm waves at 1.2 seconds followed by 11 minutes of 12.2 cm waves of 1.5 second period. The beaches were essentially shaped in the first five minutes of the large storm wave cycle and in the first fifteen minutes of the smaller storm wave cycle. Therefore the beach movement was correctly modelled with each of the above portions of the cycles coming to a pseudo equilibrium and errors in the estimate of sediment transport time scale resulting from the above assumptions did not result in errors in the beach profile development.

Because of the simplification of the wave climate as a two phase cycle it is difficult to define real time accurately. It may be postulated that spring or early summer occurs when the large storm wave portion of the cycle is completed. The profile resulting after the 11 minutes of large storm waves was therefore called the "winter profile". This would mean that late summer and autumn occur just before the start of the large wave portion of the cycle and thus the profile after the 110 minutes of small storm waves was called the "summer profile".

It was concluded from these earlier tests (7) that the dynamic equilibrium (even with only two phases) was much to be preferred over the normal long term equilibrium as an aid to understanding the prototype. With respect to beach nourishment, it was found that offshore nourishment (material placed seaward of the offshore bar) could be instrumental in accreting the beach as long as the material was placed in early summer and above the normal summer step level.

Nourishment placed offshore in late summer (before the large storm waves) remained trapped in the breaking zone and would not move onshore; it would only lengthen the profile. Onshore nourishment was only successful on long profiles which are normally associated with erosion. When the profile became shorter than a limiting value, called the "potential profile", onshore nourishment was totally unsuccessful. The combination of offshore nourishment to lengthen the profile and onshore nourishment yielded excellent results.

The initial impressions gained from these early tests are obviously highly incomplete without considering the presence of transport in the longshore direction as well as grain size sorting which takes place as the profile forms. Therefore, the next series of tests were performed in a three-dimensional basin. This paper is a description of the gradual development of a workable three-dimensional test basin to perform these tests and of the dynamic equilibrium achieved. Also the results of some preliminary applications of beach nourishment are described.

TEST BASIN DEVELOPMENT

Three-dimensional testing basins have been used in many studies (including Refs. 4,13,14,15,17) and each of these layouts had its own peculiarities and shortcomings as described by the various authors. At Queen's the major limitation was space, thus requiring a highly efficient sediment trapping-feeding system to give a workable beach length.

Sediment Trap

The sediment trap, as shown in Fig. 2, consisted of three boxes covered with a hinged lid, leaving a 15 cm wide slot. This slot was covered with perforated plates to allow the sediment to pass into the trap while causing as little interference as possible with the wave pattern. The leading edge of the trap (end of the beach) consisted of 30 cm long, vertically adjustable plates which were moved up and down to match the existing beach profile.

Originally the trap was placed outside of the downdrift wave guide to yield as much usable beach as possible but it was soon noted that the littoral drift was forced seaward as it approached the trap. This left a buildup of material

offshore at the downdrift end of the model causing the beach to rotate in the direction of wave approach. This phenomenon could be explained using the concept of wave set-up and set-down (2), which takes place in the basin but not over the trap (Fig. 3). The set-up, landward of the breaking zone, causes a current toward the trap while within and seaward of the breaker zone, the set-down causes a current away from the trap. By continuity, the water level at point A will be high, forcing the longshore transport to seaward. This problem was rectified by placing the trap inside the downdrift wave guide, as shown in Fig. 4, so that the trapping zone was subjected to the same set-up and set-down conditions as the remainder of the beach.

Sediment Feeder

For a short laboratory beach to behave like an infinitely long beach, the trapped material must be re-introduced with complete similarity at the upper end of the beach. This similarity must pay particular attention to variations in sediment volumes and grain size distributions with respect to distance offshore. The feeder system used in this study is shown in Fig. 5 and consisted of a conveyor belt which sheared sand from the bottom of a hopper onto a vibrating plate which in turn distributed the sand on the beach so that the waves could sort the material before it actually reached the test section.

Wave Re-reflection

Some earlier studies (4,11,14) noted that wave heights were not constant across the basin but had a tendency to increase in the downdrift direction. This was found also to be the case in this study. Most of this wave variability may be explained by re-reflection of waves within the model basin.

The incident wave in the model, as well as in the prototype, is partially reflected by the beach, resulting in a reflected wave which is approximately one order smaller than the incident wave. In the model, however, this reflected wave is re-reflected off the wave generator and the wave guides. The magnitude of this re-reflected wave depends on the quality of the wave filters used, but will be of the same order as the reflected wave. Considering only the first re-reflected wave (since subsequent reflections at the beach again reduce the wave by approximately one order) it may be seen that the simple model beach in

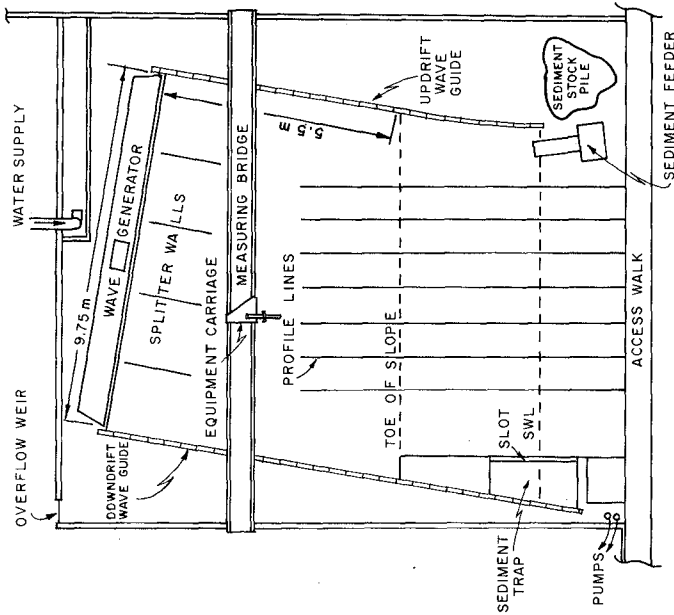


Figure 4: Basin layout.

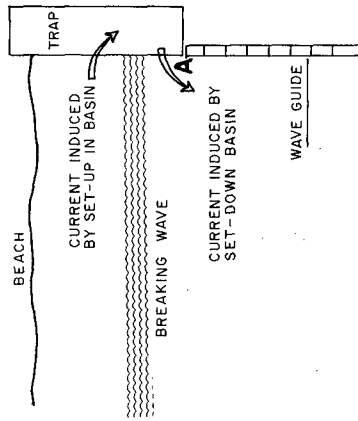


Figure 3: Induced current at trap.

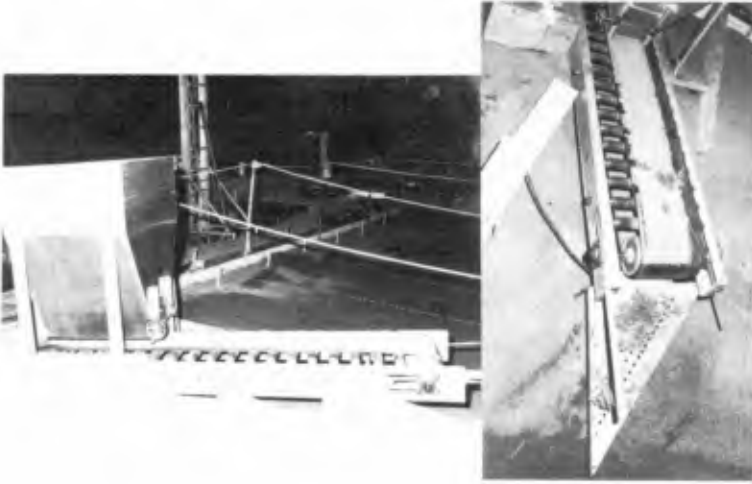


FIGURE 5: SEDIMENT FEEDER.

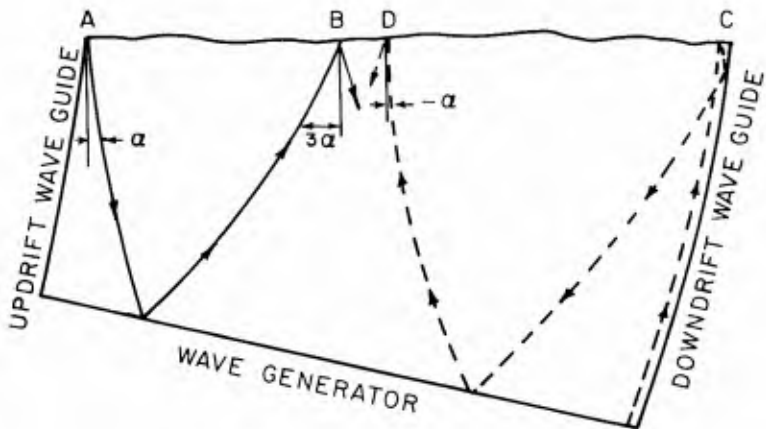


FIGURE 6: LIMITS OF RE-REFLECTED ORTHOGONALS.

Fig. 6 consists of a section AB where only the incident wave at angle α occurs (like in the prototype), a section BC where the reflected wave, re-reflected by the generator only is superimposed at an angle 3α and a further section CD where the reflected wave after suffering a double re-reflection from the wave guide and wave generator is superimposed at an angle $-\alpha$. Thus it may be expected that wave heights (and wave steepnesses) increase in the downdrift direction. This has important implications with respect to erosional patterns and the formation of the offshore bar, as shown in Fig. 7. An increase in wave height in the downdrift direction tends to rotate the model beach parallel to the wave generator. This phenomenon is completely independent from set-up problems near the trap as outlined above. Further, since littoral drift is a function of twice the angle of incidence, the littoral transport will increase considerably in the downdrift direction as a result of the large angle of incidence of the wave which is re-reflected off the generator only. In order to eliminate most of this model effect the basin was reconstructed for the last few tests to triple the shortest distance between the toe of the beach and the wave generator from 5.5 m as shown in Fig. 4 to 16.5 m. This resulted in elimination of the wave from direction 3α while the wave at $-\alpha$ came completely across the whole beach, yielding more uniform conditions. The wave splitter walls shown in Fig. 4 are also conducive to spreading the re-reflected waves more successfully across the whole basin.

THE DYNAMIC EQUILIBRIUM PROFILE

Most of the tests were carried out in the basin shown in Fig. 4. A beach consisting of 12 cm of sand (Fig. 1) laid over a concrete beach sloping at 1:10 was subjected to a simulated wave climate shown in Table 1.

TABLE 1 Simulated Great Lakes Wave Climate Used

	Duration min	H cm	T sec	d_G cm	α_G degs	α_0 degs
Large Storm Waves	11	14.0	1.5	48.5	9.4	11.8
Small Storm Waves	110	4.6	1.2	48.5	9.4	10.4

where d_G is the depth of water at the wave generator
 α_G is the angle between the generator and the beach
 α_0 is the extrapolated deep water angle of incidence

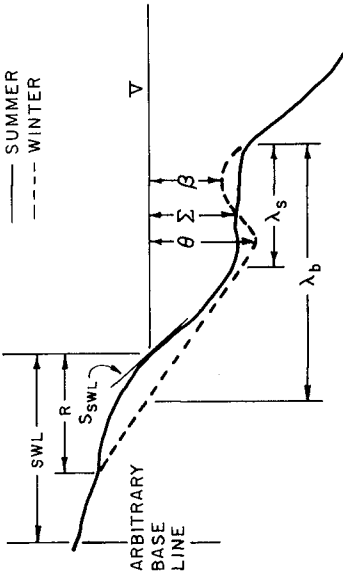


Figure 8: Profile definition.

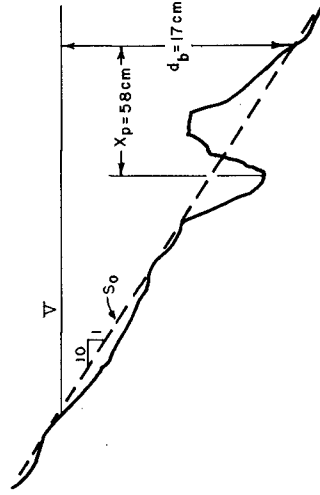


Figure 9: Beach profile after the initial half cycle of large storm waves.

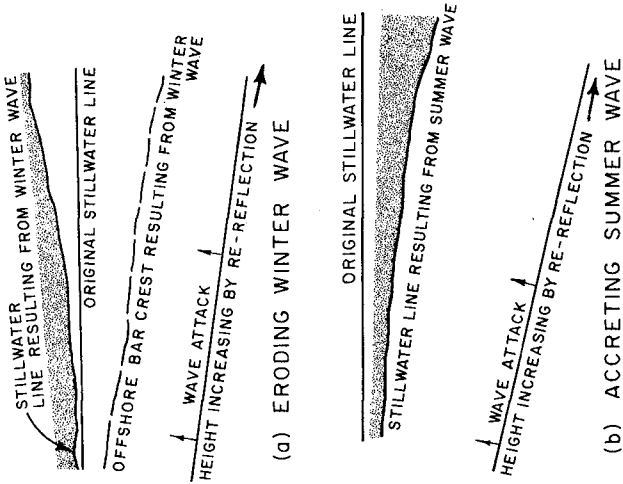


Figure 7: Effect of increasing wave height.

Soundings were made every 5 cm and to the nearest millimeter along the profile lines in Fig. 4 after each portion of the wave cycle was completed and these profiles were plotted to determine when dynamic equilibrium was reached. An "average profile" was also plotted. This can only be done meaningfully if model is so well controlled that the beach is relatively straight and does not rotate. The profiles may be summarized by a number of key parameters shown in Fig. 8.

The first waves (large storm waves) shaped the beach so that the longshore bar was formed exactly where the breaking process takes place and Fig. 9 shows the relationship between the bar location and d_b , the depth of breaking, and X_p , the breaker travel distance, as derived using the methods of the Shore Protection Manual (16, Ch 7).

After one completed wave cycle very little change took place in the profiles and the equilibrium profiles were set up much more rapidly than in the two dimensional tests. This is a direct result of modelling the littoral processes in these tests. In the two-dimensional tests supply and removal of material could only take place in the onshore-offshore directions and a great deal of moving back and forth and balancing from cycle to cycle accomplished a final equilibrium. In the three-dimensional tests excess material was removed promptly by littoral drift and conversely, material was brought in rapidly to the areas needing supplies. The only parameter with a definite trend after one complete cycle was λ_b which slowly decreased until the seventh wave cycle. The final equilibrium parameters are listed in Table 2.

TABLE 2 Dynamic Equilibrium Parameters

Parameters Units	λ_b cm	λ_s cm	θ cm	β cm	Σ cm	SWL cm	R cm	S_{SWL}
Winter Profile	147		15.7	9.5		96	56	.21
Summer Profile		76			12.3	106	36	.20

Comparison with the two-dimensional dynamic equilibrium profiles (7) yields some interesting results. The two-dimensional λ_b was found consistently to be in the range 112 ± 10 cm. This was achieved by redistributing the 1:10

initial slope in the onshore-offshore direction using as an anchor the offshore bar which was no doubt established by the initial breakers, as in this study. The two-dimensional profile represented a "potential profile" - a limiting condition. In the three-dimensional case, however, this lengthy redistribution process was not allowed to take place since littoral transport removed all excess material quickly leaving an eroded profile with a dynamic equilibrium considerably short of the potential profile developed in the two-dimensional work. It will be seen later that upon nourishment, the potential profile is achieved. The longer λ_b also resulted in a longer λ_s in three-dimensional work. The slope at still water is somewhat greater than in the two dimensional case, again because material is removed by littoral drift. The uprush R is somewhat smaller in three dimensions because of the steeper SWL slope as well as the angle of approach of the waves. The other parameters are quite comparable.

The littoral transport during the period of larger storm waves at the time of equilibrium was $.05 \text{ m}^3$ while for the longer period of smaller storm waves it was $.13 \text{ m}^3$. Scaling up to prototype these figures represent a littoral drift rate of $2800 \text{ m}^3/\text{yr}$ which is quite low for coarse beaches subjected to Great Lakes wave climates. This needs further investigation. Two factors will contribute to this low and distorted value of littoral transport. The simulation of a wave climate by grouping similar waves together as portions of cycles causes considerable scale effect in the littoral drift rate. Littoral drift is greatest at the beginning of each individual storm and decreases with time. As a result of the grouping of storms, these individual time histories are modelled by one time history, causing considerable distortion. Further, Ref. 8 gives two time scales, n_{t_s} the time scale for sediment transport by wave action only and n_{t_m} the scale for coastal morphology, and for sediment transport in the littoral direction. For this study using the assumptions mentioned earlier, the ideal time scales are

$$n_{t_s} = 210 \quad \text{and} \quad n_{t_m} = 38.4$$

The first time scale was used in the three-dimensional study for two reasons. First, it would allow comparison with the two-dimensional study. Second, although it is more likely that the second scale is the correct scale to use in the three-dimensional work, the wave durations would be increased by a factor of about 5.5.

During the experiments it was noticed that all the beach shaping took place in the first three minutes of the larger storm waves and the first 10 minutes of the smaller storm waves. Again this can be ascribed to the littoral transport effectively removing excess material and supplying depleted material rapidly. Thus it was felt that using the scale of 210 gave sufficiently long durations to model the process properly even though the term "year" might not be directly applicable. Using the second time scale, the annual littoral drift would be $15000 \text{ m}^3/\text{yr}$ which is very close to the value observed in the field for the assumed conditions.

CRITICAL SHEAR STRESS AND THE SUMMER STEP

Since the summer step is flat in the two-dimensional as well as three-dimensional tests it was decided to use the work of Refs. 6 and 8 to determine the shear stress on the summer step to find out if a critical shear stress existed. The shear stress used is $\hat{\tau}_o$, the maximum value of the shear stress on the bottom during the wave cycle. A number of tests varying H and T were specifically run for this purpose and for 19 two-dimensional tests with wave periods in the range $0.95 \leq T \leq 2.96$ sec and wave heights $3.6 \leq H'_o \leq 6.6$ cm the mean value of the critical maximum shear stress $(\hat{\tau}_o)_c$ was 1.26 N/m^2 with a standard deviation of 0.12 N/m^2 . A further six tests in the three-dimensional basin, keeping T constant at 1.2 seconds but varying H'_o from 3.3 to 5.5 cm indicated a mean value of $(\hat{\tau}_o)_c$ of 1.39 N/m^2 with a standard deviation of 0.13 N/m^2 . The critical shear stress appeared to be constant. Dimensional analysis indicates for unidirectional flow that

$$\frac{(\tau_o)_c}{\gamma_s D} = f_1 \left(\frac{v_* D}{v} \right) \quad (1)$$

which is represented by the Shields diagram. It is not unreasonable to assume that for wave motion

$$\frac{(\hat{\tau}_o)_c}{\gamma_s D} = f_2 \left(\frac{\hat{v}_* D}{v}, \text{ wave-inertia interaction} \right) \quad (2)$$

Since only one particle size was used in these tests, other profile tests from the literature (5,10,12) and at Queen's (9,11) were used in conjunction with the methods of Refs. 6 and 8 to determine the effect of particle size. Because of armouring of the beach surface D_{90} was used in the analysis and Fig. 10 shows that

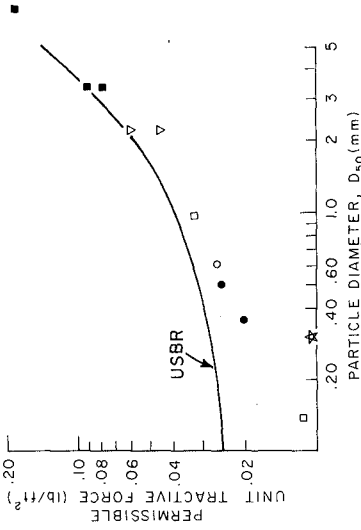


Figure 12: Comparison with permissible tractive force.

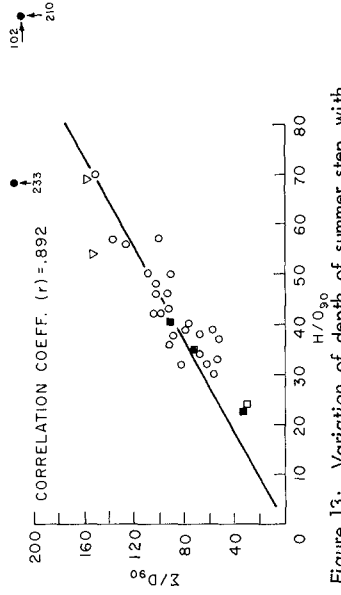


Figure 13: Variation of depth of summer step with increasing wave height.

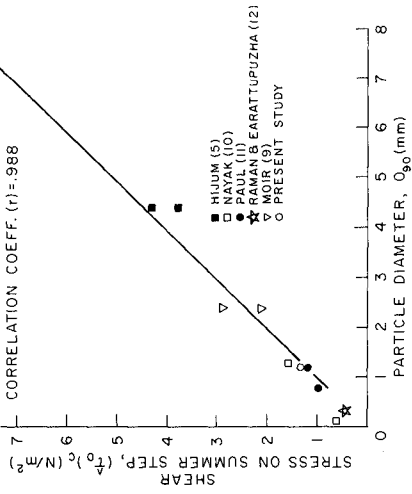


Figure 10: Critical shear stress on summer step as a function of particle size.

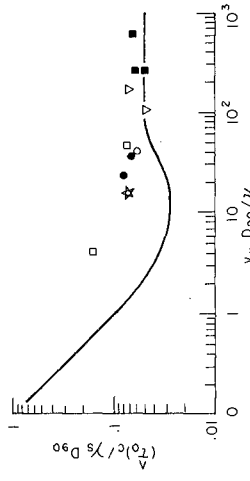


Figure 11: Comparison with shields curve.

$$(\hat{\tau}_o)_c = 1000 D_{90} \quad (3)$$

in S.I. units, or

$$\frac{(\hat{\tau}_o)_c}{\gamma_s D_{90}} = 0.061 \quad (4)$$

Since $(\hat{\tau}_o)_c$ is a maximum value and considering that a number of assumptions were made about the tests performed by the other authors, this is quite close to the normal Shields condition for incipient motion at higher Reynolds numbers:

$$\frac{(\tau_o)_c}{\gamma_s D} = .05 \quad (5)$$

In order to assess the validity of the Shields criterion in this work, the points were replotted as in Fig. 11 which shows all points above the Shields line reflecting the use of the maximum value of τ_o as well as some wave-inertia effect. The points were also plotted in Fig. 12 to compare them with "critical tractive force" work (3, p 173). The USBR line implies some sediment motion and all points are below this line.

Further attempts were made to relate the summer step depth, Σ directly to wave parameters as was done by Bagnold (1) and Hijum (5). Figure 13 shows the results considering wave heights only. The scatter in this figure is mostly due to ignoring the wave period effect.

ARTIFICIAL BEACH NOURISHMENT

After dynamic equilibrium was reached and much time was expended in developing a basin, there was only time for a few nourishment tests. Although only few tests were performed, the test results will be given and these should be considered tentative until further work has been completed. In order to maximize the usefulness of the results, the winter profile was nourished in the onshore region. This had been found to be the most efficient method of nourishment under two-dimensional conditions (7). The nourishment material had the same grain size characteristics as the parent beach material (Fig. 1) but because the waves had sorted the original beach material, many of the fines had been removed from the onshore zone of the parent beach and transported offshore. Thus the nourishment material contained more fines than the native beach in the nourishment area.

The original average dynamic equilibrium, the average profile of the nourishment and the average equilibrium profiles subsequent to another 10 test cycles, are shown in Fig. 14. The test cycles were kept the same as before (including the sediment feed rate). During the first cycle after nourishment, the small storm waves eroded the new foreshore and planed off the offshore bar. This resulted in an excess of material in the summer step region, which in turn resulted in a more violent summer breaker, which yielded a summer bar corresponding to X_p and d_b of the summer wave. The new SWL slope returned to 20% immediately although the nourishment material had been placed at 29%. Figure 14 shows that no nourishment material ended up seaward of the bar and that 72% of the original nourishment remained, while the rest was removed from the test section by increased littoral drift.

The parameters for the new dynamic equilibrium are given in Table 3

TABLE 3 Dynamic Equilibrium Parameters after Nourishment

Parameters Units	λ_b cm	λ_s cm	θ cm	β cm	Σ cm	SWL cm	R cm	S_{SWL}
Winter Profile	116		11.4	8.8		119	50	.19
Summer Profile		32			12.9	128	36	.21

and comparison with Table 2 shows that λ_b has now decreased to 116 cm, close to the potential value for the two-dimensional tests. This has resulted in an attendant decrease in λ_s . Further, θ and β have both decreased indicating much more material present behind the offshore bar, SWL has moved out an average of 22.5 cm showing a net benefit at the shoreline. The other parameters remained the same.

The littoral drift during the period of larger storm waves was 0.067 m^3 while during the smaller waves it was 0.128 m^3 which makes for a total prototype drift of $3050 \text{ m}^3/\text{cycle}$, up slightly from the value for the initial dynamic equilibrium.

A further nourishment was subsequently applied to the dynamic equilibrium winter profile described in Fig. 14 and Table 3. During the first summer, the

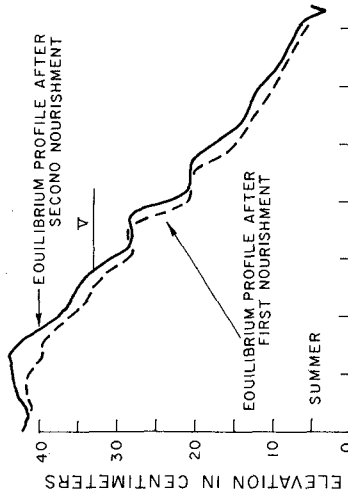
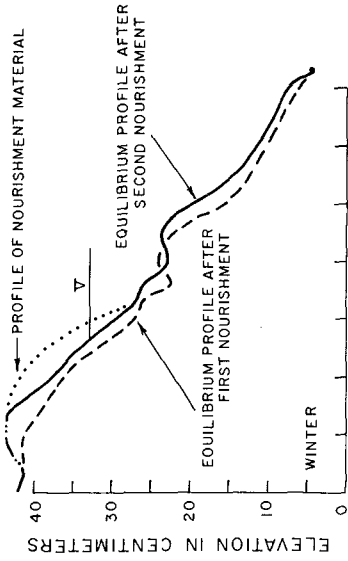


Figure 15 Summary plot of second nourishment

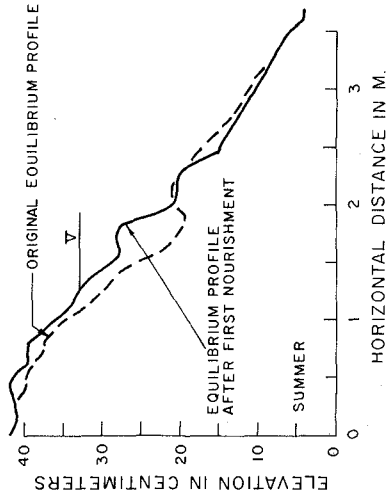
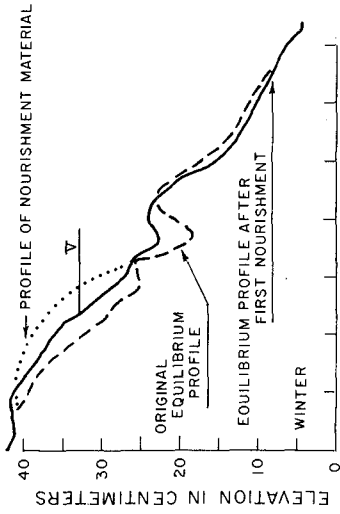


Figure 14: Summary plot of first nourishment

original nourished slope at SWL of 37% was reduced to about 20% again. The much shorter profile could not support the material eroded from the vicinity of SWL as had been the case in the previous nourishment and material was moved offshore of the existing bar. Here it was shaped by the first winter waves into a new bar 18 cm seaward of the previous bar. Equilibrium profiles occurring after a further nine cycles are given in Fig. 15 and the parameters are given in Table 4.

TABLE 4 Dynamic Equilibrium Parameters after a Second Nourishment

Parameters Units	λ_b cm	λ_s cm	θ cm	β cm	Σ cm	SWL cm	R cm	S_{SWL}
Winter Profile	113		10.9	8.5		131	51	.21
Summer Profile		31			12.6	137	34	.20

It may be seen that SWL has moved out an average distance of 10.5 cm and all other parameters are very much the same. This would indicate that the previous equilibrium profile was close to a potential profile which was shifted bodily to seaward by the nourishment. In this case only 8% of the material was removed by increased littoral drift and thus the profile behaved very much like the two-dimensional tests of Ref. 7. The littoral drift during the period of larger waves was $.091 \text{ m}^3$ (up from the previous time) while for the period of smaller waves it was $.104 \text{ m}^3$ (down from the previous time). The total drift still represents $3050 \text{ m}^3/\text{cycle}$ as before.

CONCLUSIONS

With respect to development of a three-dimensional testing facility it was learned that

1. The sediment trap must be within the area subjected to wave action.
2. Wave re-reflection from the generator alone causes superimposed waves at an angle of incidence of (3α) , while re-reflection from both the generator and the wave guides results in waves at angle $(-\alpha)$. The waves at $-\alpha$ cannot be avoided but the waves at 3α should be avoided in order to
 - a. bring about uniform wave heights across the basin
 - b. cause uniform littoral drift across the basin

- c. prevent rotation of the beach in the direction of the wave generator.

With respect to dynamic equilibrium profiles it was found that

3. Dynamic equilibrium is achieved faster in three-dimensional tests.
4. The profiles resemble eroding profiles rather than potential profiles in three-dimensional tests. Potential profiles are defined as those profiles which are as short as possible.
5. The profiles develop around the offshore bar which is shaped early in the experiments at the breaking position of the large storm waves.
6. The depth to the summer step is a function of critical shear stress resulting from wave action on the beach material.

With respect to artificial beach nourishment,

7. Onshore nourishment on eroding beaches is successful.
8. Onshore nourishment on potential profiles results in a seaward shift of the whole profile.

Further study of many of these aspects is continuing at Queen's.

ACKNOWLEDGEMENTS

The funding by the National Research Council of Canada is gratefully acknowledged. Comments and suggestions by colleagues of both authors were also very helpful.

REFERENCES

1. Bagnold, R.A., "Beach Formation by Waves; Some Model Experiments in a Wave Tank", *Jour. Inst. Civil Eng.*, Vol 15, 1940, pp 27-52.
2. Bowen, A.J., Inman, D.L., Simmons, V.P., "Wave Set-Down and Set-Up", *Journal of Geophysical Research*, Vol 31, 1968, pp 2569-2577.
3. Chow, V.T., *Open Channel Hydraulics*, McGraw-Hill, (1957), p 173.
4. Fairchild, J.C., "Laboratory Test of Longshore Transport", *Proceedings 12th Conference on Coastal Engineering*, Washington, 1970, pp 867-889.
5. Hijum, E.V., "Equilibrium Profiles of Coarse Material Under Wave Attack", *Proceedings 14th Conference on Coastal Engineering*, Copenhagen, 1974, pp 939-957.

6. Kamphuis, J.W., "Friction Factor Under Oscillatory Waves", *Waterways, Harbours and Coastal Engineering Journal*, ASCE, WW2, May, 1975, pp 135-144.
7. Kamphuis, J.W., Bridgeman, S.G., "Placing Artificial Beach Nourishment", *Proceedings Oceans III Conference*, Delaware, 1975, pp 197-216.
8. Kamphuis, J.W., "The Coastal Mobile Bed Model", *Queen's University, C.E. Report No. 75*, Kingston, 1975.
9. Moir, J., Ph.D. Thesis in Progress, Queen's University, Kingston, 1976.
10. Nayak, I.V., "Equilibrium Profiles of Model Beaches", *Tech. Report HBL-2-25*, University of California, 1970.
11. Paul, M.S., "*Similarity of Bed Evolution and Sediment Transport in Mobile Bed Coastal Models*", Ph.D. Thesis, Queen's University, Kingston, 1972.
12. Raman, H., Earattupuzha, J.J., "Equilibrium Conditions in Beach Wave Interaction", *Proceedings 13th Conference on Coastal Engineering*, Vancouver, 1972, pp 1237-1256.
13. Savage, R.P., "Laboratory Study of the Effect of Groins on the Rate of Littoral Transport", *Beach Erosion Board TM 114*, 1959.
14. Saville, T. Jr., "Model Study of Sand Transport Along an Infinitely Long, Straight Beach", *Transactions, American Geophysical Union, Vol 31*, 1950, pp 555-565.
15. Shay, E.A., Johnson, J.W., "Model Studies on the Movement of Sand Transported by Wave Action", *Inst. of Engrg. Research, Univ. of California, Berkeley, Issue 7, Series 14*, 1951.
16. *Shore Protection Manual*, Coastal Engineering Research Centre, 1974.
17. Swart, D.H., "Offshore Sediment Transport and Equilibrium Beach Profiles", *Publication 131, Delft Hydraulics Laboratory*, 1974.

CHAPTER 91

PROPOSED "IMPROVEMENT" OF KAIMU BEACH, HAWAII

By Doak C. Cox, Frans Gerritsen, and Theodore T. Lee*

Abstract

Proposals to "improve" a pocket beach at Kaimu, Hawaii have been under active consideration for a decade. The beach, which is famous for its jet black color has been receding for at least a century. The plans proposed have called for its enlargement, and most of them for its protection by an offshore breakwater. Advantages of a larger beach area, and of the improvement of swimming conditions if the breakwater were constructed, are undeniable. Loss of surfing sites would, however, have resulted from the adoption of any of the plans involving breakwater. Other disadvantages associated with some of the plans proposed would have included alteration of beach color, other visual impacts, and threats to archaeological sites from the quarrying of breakwater stone. Sand-loss estimates and breakwater construction criteria dependent on them were based on probably erroneous interpretations of historical evidence. Possible alternative sites for the provision of the swimming opportunity were not investigated.

Serious question was raised whether the project would result in overall improvement. However, recent coastal subsidence has rendered all of the plans obsolete and the question is probably moot.



Fig. 1 Photograph of Kaimu Beach in 1968 (Corps of Engineers)

*Respectively Environmental Center, Department of Ocean Engineering, and Look Laboratory of Ocean Engineering; University of Hawaii, Honolulu, Hawaii, USA

Introduction

Kaimu beach (fig. 1) is a pocket beach in the Puna District on the southeast coast of the island of Hawaii (fig. 2). Although no more than about a quarter mile in length (fig. 3), the beach would be considered important simply because of the scarcity of beaches on that island and especially in that district. It is in fact famous, but primarily because of the jet black color of its sand. It has been a visitor attraction longer than there has been a recognized tourist industry in Hawaii. However, the beach has long been retreating--indeed measures to control the erosion of its sand were considered as early as the 1910's or 1920's. This paper relates primarily to proposals for its "improvement" dating from 1966 when the Mayor of the County of Hawaii requested the Corps of Engineers to investigate possibilities for its restoration and preservation.

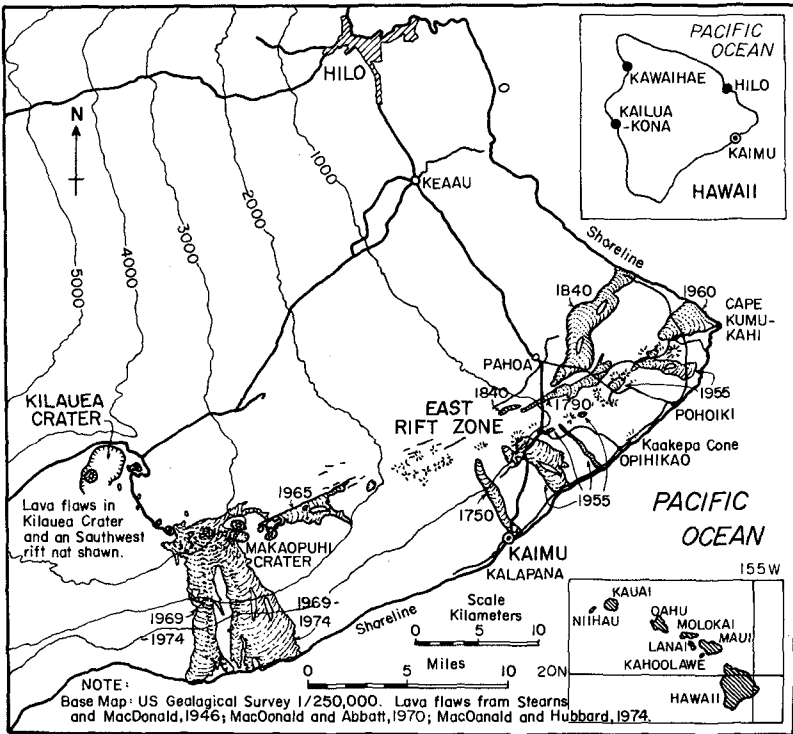


Fig. 2 Topographic and geologic map of Puna District, showing location of Kaimu Beach

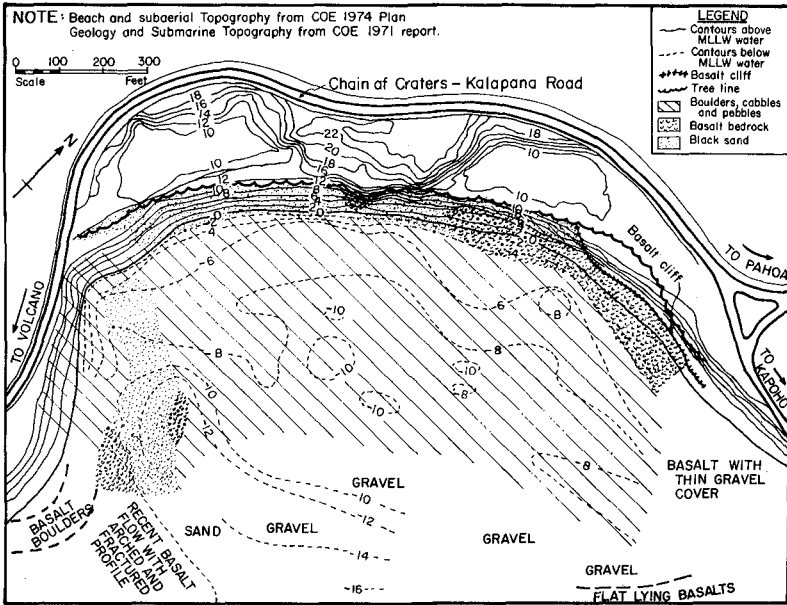


Fig. 3 Topography and geology of Kaimu Beach

In the subsequent decade, plans for enlarging and protecting the beach have been made and revised several times by the Corps. At one time or another, in spite of considerable controversy, all approvals for a construction project were secured, and federal, state, and county funds were released, but the necessary simultaneous correspondence of plans, approvals, and funding was never secured. All of the plans were rendered obsolete by coastal subsidence associated with an earthquake in late 1975 and the future of what is left of the beach may now be left primarily to nature to determine.

The likelihood of an event such as has thus intervened was foreseen, but this likelihood was but one of several environmental aspects that led us, before the event, to propose a Kaimu discussion as a case history of a project whose characterization as an "improvement" was highly questionable. It seems best, even though it appears that the project will not be undertaken, to use a historic outline for this discussion.

Origin and natural fate of the beach

The Island of Hawaii consists essentially of the peaks of five predominantly basaltic volcanoes rising from the ocean floor. Kilauea volcano, whose east rift is the source of lava flows forming most of the Puna district (fig. 2), is one of three that have been active in historic times.

Significant geologic events that have affected this district in historic times are listed in table 1 (Stearns and Macdonald, 1946; Macdonald and Abbott, 1970; Macdonald and Hubbard, 1974). As will be noted, several of the historic lava flows reached the coast.

Table 1. Significant historical geologic events in Puna district

<u>Year</u>	<u>Event</u>	<u>Effects</u>
1750	Eruption	Lava flow from rift to S. coast
1790	"	Lava flow on rift
1840	"	Lava flow N. from rift
1868	Earthquake	Subsidence of S. coast
1884	Eruption	Brief shallow submarine eruption
1923	"	Small lava flows on rift
1955	"	Cones and lava flows covering 6 sq. mi., 3 reaching S. coast
1960	"	Cones and lava flow covering 4 sq. mi. and extending to N. and S. coasts near Cape Kumakahi
1961	"	Small lava flows on rift
1962	"	Small lava flows on rift
1963	2 eruptions	Mostly lava fills in pit craters on rift
1965	2 eruptions	Lava flows covering 3 sq. mi. on rift
1968	Eruption	Small lava flows on rift
1969	2 eruptions	Lava flow from first eruption covering 2 sq. mi. near rift. Lava flows from second eruption, which continued into 1971, covering 22 sq. mi., 3 of them reaching the S. coast
1972	Eruption	Lava flows covering 14 sq. mi., one extending to S. coast
1973	3 eruptions	Lava flows covering 4 sq. mi. near rift
1974	Eruption	Lava flows covering 1 sq. mi. on rift
1975	Earthquake	Subsidence of S. coast

Kaimu beach resulted from the entrance of a lava flow into the sea. Upon such entrance, lava often explodes forming deposits of volcanic ash. To the extent these deposits are within wave reach, the ash fragments are subject to reworking and transport. The resulting sand may be deposited, at least temporarily, in a beach at some relatively protected part of the coast. Such a beach is, however, an evanescent feature. The sand is subject to further comminution and transport by waves and wind, and the beach is certain to recede if not covered by a later lava flow.

It is uncertain what lava flow was responsible for the ash from which the black glass sand of Kaimu was derived. The flow may have been a pre-historic one (Stearns and Macdonald, 1946). If so, the ash deposits that were the source of its sand may have been covered by the lava flow of approximately 1750, which entered the sea just northeast of Kaimu beach (fig. 4). In this case the beach has probably been somewhat protected by the coastal extension resulting from the lava flow. Alternatively, the 1750 flow itself may have both been responsible for both the bay in which it was



Fig. 4 Aerial photograph of Kaimu in 1959 (U.S. Navy)

deposited and the source of the sand (COE, 1971). In this case the ash deposits have subsequently been eroded away.

In either case, the beach has been subject to erosion since the sand source was exhausted or covered. Some of the sand has been blown inland at Kaimu, some of it has undoubtedly moved into deep water offshore, and much of it has been transported northwestward to Kalapana (fig. 2) where it has been blown inland to form dunes.

Evidence of the subsidence of Kaimu beach, possibly combined with retreat, was reported as early as the 1870's by Nordhoff (1874) in the form of coconut tree stumps sticking up out of the surf. Photographic evidence of coconut trees being toppled into the water in the 1880's was published by Agassiz (1889) (Fig. 5). Similar photographs have been taken at numerous times since (figs. 6-8); and rough or precise estimates of the rates of retreat may be made by comparisons of shoreline maps dating from 1892 to 1968 and from beach profile surveys made in 1968 and subsequently (fig. 10). By the mid-1960's a rock ledge was exposed near the middle of the beach, and by the mid-1970's this ledge formed a conspicuous promontory (fig. 7).

Table 1 does not include the several tsunamis that may have accelerated the beach retreat temporarily. Tsunamis accompanying the earthquakes of 1868



Fig. 5 Photograph of Kaimu Beach in 1880's (Alexander Agassiz)



Fig. 6 Coconut tree roots exposed by beach erosion, 1972 (Corps of Engineers)



Fig. 7 Underlying lava exposed
by beach erosion (1972)
(Corps of Engineers)



Fig. 8 Kaimu beach in 1973
(Rick Scudder)

and 1975 had runup heights of several tens of feet on the coast farther northwest, but the latter tsunami, at least, was of slight importance at Kaimu. Recent beach erosion was evident after the 1946 tsunami, but it is not clear that any significant addition to rate of retreat resulted.

Project as proposed in 1971

Proposal

In response to the 1966 request of the Mayor of Hawaii for investigation of means to restore and protect Kaimu Beach, the Corps of Engineers issued a favorable reconnaissance report in 1967. Detailed project plans were then prepared which were described in a report issued in September 1971 (COE, 1971).

From shorelines supposedly mapped in 1910 and 1938 and a 1968 shoreline survey, average beach retreat was estimated at about 4 ft. per year, and average sand loss at 2000 cu. yds. per year. The Corps proposed enlargement of the beach, its protection by an offshore breakwater, and periodic replenishment of sand to replace subsequent losses that would occur in spite of the protection.

The enlargement proposed would have required 40,000 cu. yds. of sand, which was to be produced by crushing and screening cinders from a nearby cinder cone, Kaakepa. With this volume, a dry-beach area of 100,000 sq. ft. would have been created. The breakwater proposed would have been about 1350 feet long, extending across the entire bay and would have had a crest height of 2.5 ft. above mean lower low water. Use of stone of at least 6 tons was proposed. The beach enlargement would have been similar and the breakwater alignment identical to those shown in figure 11. Sand losses after breakwater construction, necessitating periodic sand replenishment, were estimated at 600 cu. yds. per year.

The Corps pointed out that this plan would produce, not only an enlarged and protected beach, but a protected swimming area where swimming has been hazardous because of the waves and a rip current. They recognized that the breakwater would have a visual impact, and that its construction would interfere with two surfing sites.

Alternatives to the proposed plan included enlargement of the beach without a breakwater, with a submerged breakwater on the same alignment and with the same length as the proposed exposed breakwater, and a submerged breakwater on the same alignment but extending only 450 feet from the southwest shoreline.

Objections

Although the swimming opportunity that would have been created by the proposed project would clearly have been advantageous, there were expectable objections to the visual impact of the breakwater, the loss of surfing sites, and other alleged detriments. The University of Hawaii Environmental Center, in reviewing the proposal, pointed out the scarcity of surfing sites on the island of Hawaii, and also the traditional importance of surfing at Kaimu as a spectator as well as participant sport (Fig. 9) (Bretschneider et al, 1972).



Fig. 9 Surfing at Kaimu
(Rick Scudder)

In addition, the Center called attention to the effects of using the crushed cinders for the beach enlargement. Spread on the beach, this material would have been harsh underfoot, and because it was brown, the jet black appearance on which the fame of the beach depended, would have been lost. The Center also questioned the Corps estimates of historic rates of beach retreat and sand loss.

The source of the stone for the breakwater was described in the Corps report merely as within 10 miles of Kaimu. It later appeared that the principal source in mind was a lava ledge at Kalapana. The Center pointed out the existence of archaeological sites in the vicinity and questioned whether the quarrying operation could be carried out there without disturbance to these sites or esthetic detriments.

The Center also commented that, although beach enlargement without a breakwater and use of lower or shorter breakwaters on the proposed alignment had been considered as alternatives, there was no evidence of consideration of

alternative modes of beach protection or of alternative sites at which the swimming opportunity could be created. The Center called attention to the opinion of the Look Laboratory of Oceanographic Engineering that the choice among alternative breakwater designs should be based on hydraulic modeling (Bretschneider et al, 1971).

Project as proposed in 1972

Proposal

In response to some of the objections and questions mentioned above, and others, the Corps of Engineers revised its estimates and its proposed plan (COE 1972a) and prepared and issued an environmental impact statement on the project (COE 1972b, 1973). Estimates of beach retreat and sand loss, were revised on the basis of shoreline positions mapped in 1892, 1915, and 1940, and beach surveys in 1968 and 1972. From the description of the 1892 shoreline, it is assumed to have been that dated 1900 in the earlier Corps report (COE 1971). This shoreline and those plotted in the 1972 Project Report (COE 1972a) are shown in figure 10. The histories of the position of the beach front and of the sand volume in the beach as estimated by the Corps are shown in figure 12.

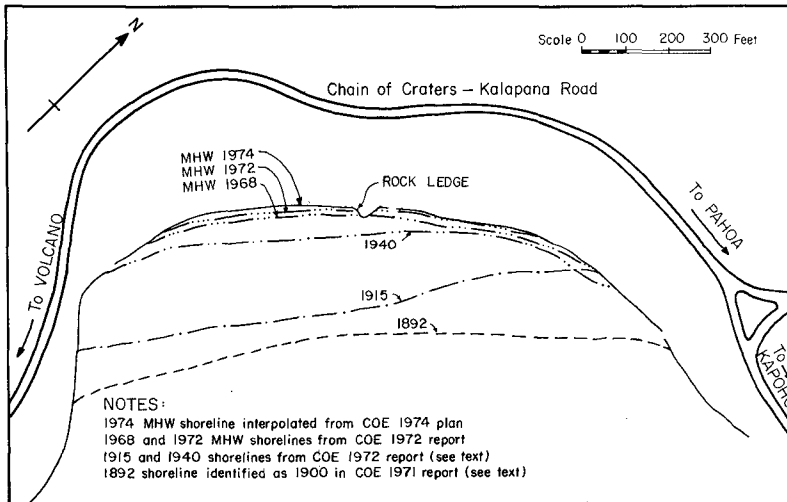


Fig. 10 Shoreline history of Kaimu Beach

The revised plan called, in sequence, for:

- 1) Removal and stockpiling of 5,800 cu. yds. of sand from the beach.
- 2) Adding 38,000 cu. yds. of new sand to the beach.

3) Monitoring for about two years, during which sand loss at a rate of 3000 cu. yds. per year was expected.

4) Construction of the breakwater to the same length and on the same alignment as in the original plan, but with its crest at mean lower low water (fig. 11).

5) Adding an additional 5,000 cu. yds. of new sand to the beach and topping off with the 5,800 cu. yds. of original stockpiled sand.

6) Periodic replenishment of sand, averaging 1,200 cu. yds. per year, to compensate for continuing sand losses.

The dry beach area on completion was estimated at 133,000 sq. ft., an increase of 101,000 sq. ft. over the existing area. It was recognized that the breakwater would still interfere with surfing. It was also recognized that the water inshore of the submerged breakwater (crest at mllw) would not be as quiet as in the case of the exposed breakwater originally proposed (crest at 2.5 ft. mllw), but considered that this would not seriously detract from the swimming opportunity.

Recognizing the importance of the color of the sand, the Corps proposed, as a possible alternative to the use of crushed cinders, the use of greenish-black sand-sized ash derived from shoreline explosions of the 1960 lava flow at Kumukahi (fig. 2).

Objections

In reviewing the 1972 proposal, the Environmental Center called attention to the fact that the original sand removed from the beach, stockpiled, and later replaced on top of new sand, would be most immediately affected by subsequent erosion (Johnson, 1973). The estimation of sand loss rates was again questioned. The Center pointed out that the Corps had assumed that the 1915 and 1940 shorelines were mean high water lines, whereas in Hawaiian usage they were more likely to be wave wash lines, and that the rates of retreat and sand loss had probably slowed as the beach retreated.

The matter of alternatives was again brought to attention. An alternative of gradual sand replenishment without a breakwater, either at a rate just sufficient to balance the erosion or at a larger rate to induce increase in beach width, was pointed out as having seeming economic advantage (Cox, 1973). In addition, the importance of geologic hazards to the beach and the proposed project was discussed, with special reference to the hazards of lava flows and coastal submergence or emergence.

Project as proposed in 1974

Initiation

Weighing the benefits, detriments, and uncertainties, the Environmental Council, advisory to the Governor of the State of Hawaii, recommended initially against the undertaking of the proposed project. However, on the request of the Hawaii County Council, the Environmental Council reconsidered

the matter, and in June 1973 recommended the planning of a project similar to that proposed in 1972, but with the breakwater construction to be contingent on the results of monitoring:

- 1) Construction phase I: Beach enlargement
- 2) Monitoring phase of two or, preferably, three years
- 3) Contingent construction phase II: Breakwater construction
- 4) Periodic replenishment of sand to compensate for continuing losses.

The Corps of Engineers was requested to "apply, whenever possible, the recommendations of geologists, ocean scientists, and other experts from the University of Hawaii" to the design of the first phase, and to consult with University experts on the monitoring program and the design of the breakwater.

First proposal

An initial proposal was presented to the Environmental Council by the Corps in November 1974. Enlargement of the beach (fig. 11) was to be accomplished using 30,000 cu. yds. of sand from the Kalapana ash deposits, which approached the Kaimu sand in color and size distribution. Stability of the enlarged beach was an important consideration in the design configuration (fig. 11). A monitoring period was called for with monthly surveys for three months after completion of sand emplacement, bimonthly for the rest of a two-year period, and annually thereafter for 10 years, unless it were decided earlier to construct the breakwater.

It was proposed that the breakwater would not be constructed if all of the following sand-loss criteria were met:

- a) Initial rate: less than 10,000 cu. yds. per yr.
- b) Rate during each subsequent monitoring interval: less than 3,000 cu. yds. per yr.
- c) Average rate from completion of enlargement to any survey date in the first two years: less than 1,300 cu. yds. per yr.
- d) Rate during any subsequent year: less than 3,000 cu. yds. per yr.
- e) Average rate to any subsequent survey: less than 1,300 cu. yds. per year.

A decision to construct was to be made at the end of two years if any of the first three criteria were not met, and at any time thereafter if either of the last two criteria were not met. The breakwater, if constructed, was to be a submerged one as in the 1972 plan (fig. 11).

Beach-retreat and sand-loss estimation

The Environmental Center considered that, in the light of the Council's recommendation to defer the breakwater construction pending actual observation of the rate of sand loss after beach erosion, the criteria for

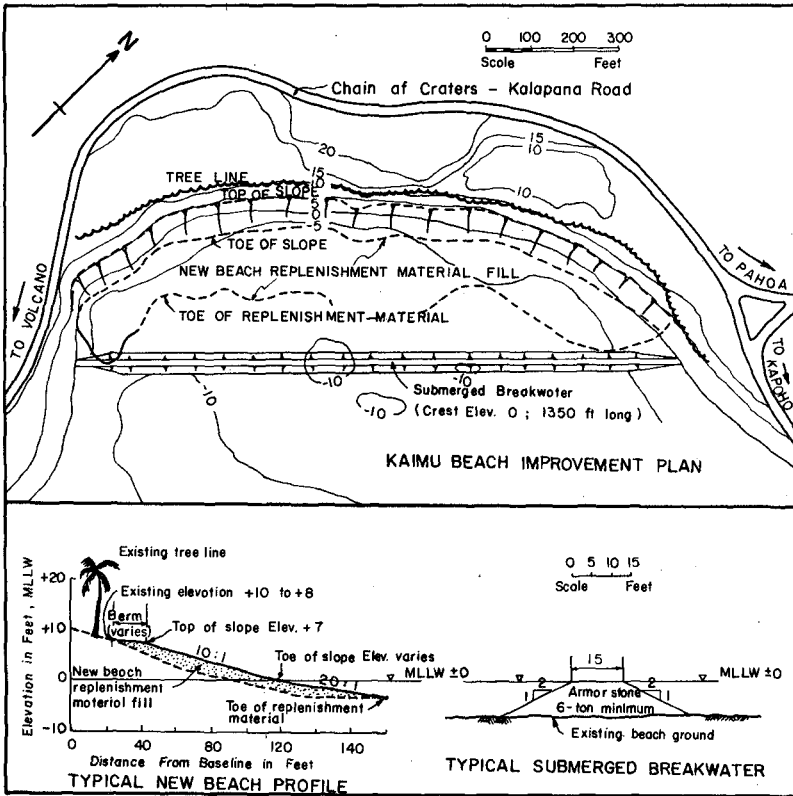


Fig. 11 Kaimu breakwater as proposed in 1972 and beach enlargement as proposed in 1974

determining whether or not the breakwater should be built were critical, and that for this reason the estimates of beach retreat and sand loss should be reexamined. In the Center's opinion, the criteria should exceed, but not exceed greatly, the loss rates expectable considering average natural loss rates at beach front positions equivalent to post-enlargement positions, expectable short-term departures from average loss rates, and some increase over natural loss rates due to non-equilibrium configuration of the beach, especially immediately after construction.

The Center developed estimates of long-term beach retreat and sand loss rates, that were based on Corps of Engineers data, including the approximate position of the shoreline in 1892 and the results of a 1974 survey that had

just been completed (Cox, 1974b). Like the Corps, the Center was forced to assume that, in profile, the shape of the beach at the times when only shorelines had been mapped was similar to the shape when the entire beach front was surveyed in 1968, 1972, and 1974. Beach retreat and sand loss rates were related through use of a smoothed curve of loss-retreat ratios, obtained from Corps data, plotted against shoreline position. However, the Center assumed that the shorelines mapped in 1892, 1915 and 1938 were not the high water line, as assumed by the Corps, but the "kahakai" or mark of the sea, the uppermost reach of waves as indicated by the vegetation line, as was conventional in Hawaiian cadastral surveying.

The histories of beach retreat and sand loss in accordance with the Center assumption are compared with those in accordance with the Corps assumption in figure 12. In this figure the beach-front positions and beach-sand volumes at the times of successive shoreline and beach-front surveys are plotted relative, respectively, to the 1972 position and volume. Beach-retreat and sand-loss rates as estimated by the Center are compared with those estimated by the Corps in figures 13 and 14. In these figures, retreat rates and loss rates are plotted over the respective ranges in beach-front position between successive mapping or survey dates. It will be seen from the latter figures that much more regular relationships between retreat and sand loss rates and beachfront position resulted from the Center estimation than the Corps estimation.

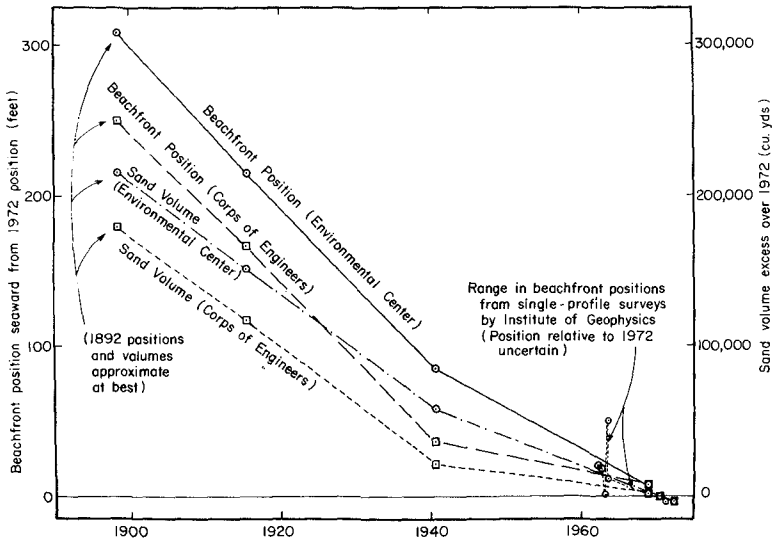


Fig. 12 Historic beach front-positions and sand volumes in accordance with Corps of Engineers and Environmental Center assumptions

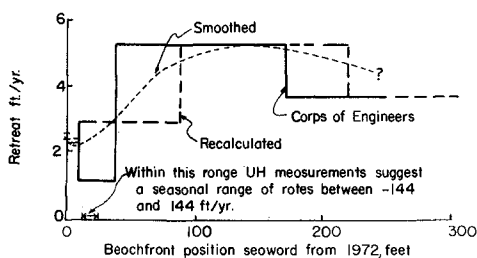


Fig. 13 Beach retreat rates as estimated by Corps of Engineers and Environmental Center assumptions

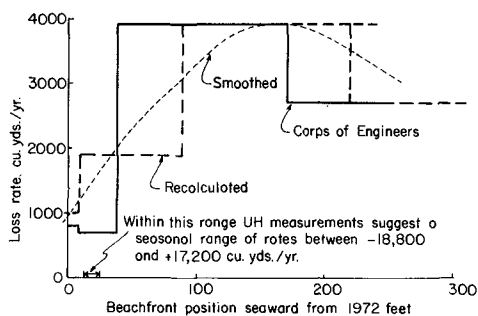


Fig. 14 Sand-loss rates as estimated by Corps of Engineers and Environmental Center in relation to beachfront positions

The Center also made use of profiles of the beach surveyed by the Hawaii Institute of Geophysics in June and September 1962; January, April, and July 1963; and July 1971 (Moberly and Chamberlain, 1964). Because the Institute of Geophysics surveys were made on a single range, it was necessary to assume that, in plan, the shape of the beach was essentially the same on the various survey dates.

Unfortunately, the position of the Institute range was never related to the positions of the ranges used by the Corps. Hence the relation in figure 12 between the beach-front history based on Institute data and the longer term history is somewhat uncertain, and the implications of the Institute data are shown in figures 13 and 14 merely as ranges of uncertainty.

The Institute data were, however, of use, together with the Corps beach surveys of December 1968, May 1972, and February 1974, in estimating short-term departures from long-term beach-retreat and sand-loss rates. From the rates of sand loss indicated by various pairs of surveys, the normal (long-term) rates indicated by figure 14 were subtracted, and the resulting departures were compared, without regard to sign, in a log-log plot against the time intervals between the respective surveys. Retreat rates were treated similarly. The results indicated that departures from normal sand-loss rates

could well be as large as 25,000 cu. yds./yr. over a period of 2 months, 5,000 cu. yds./yr. over a period of 6 months, 1,800 cu. yds. per year over a period of a year, and 600 cu. yds. per year over even a period as long as two years.

The combination of normal rates of sand loss for various beach-front positions as plotted in figure 14, expectable departures from normal rates for periods of various durations, and sand-loss/retreat-rate ratios for various beach front positions, provided a basis for estimating the expectable rates of sand loss after the beach was enlarged and as it subsequently retreated (fig. 15), if it were assumed that the effects of any failure to attain an equilibrium configuration in construction would be small or of short duration. Expectable cumulative sand losses after beach enlargement, estimated as indicated, are shown in figure 15. This figure also shows the losses implied by the criteria for breakwater construction originally proposed by the Corps, and the losses that the representatives of the Corps and Environmental Center agreed jointly should be reflected in revised criteria.

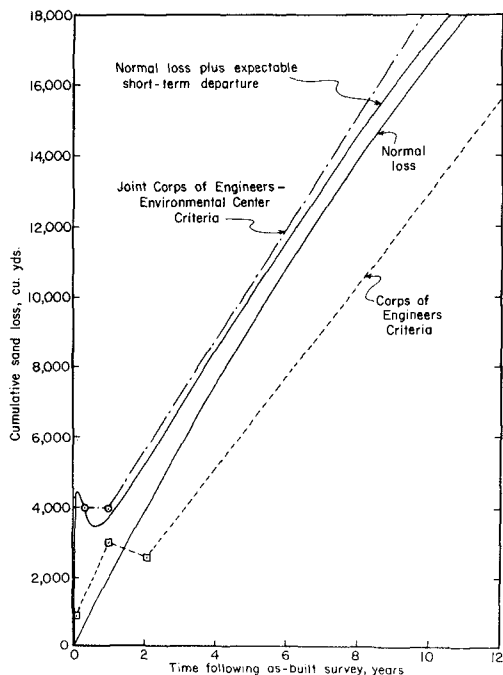


Fig. 15 Expectable cumulative sand loss after beach enlargement and proposed breakwater construction criteria

Revised proposal

The Corps-Center conferees reported back to the Environmental Council in December 1974 (Beishe et al, 1974). In brief their joint recommendations, if the project were to proceed, were as follows:

1. The 30,000 cu. yds. of sand to be placed on the beach should be drawn in accordance with the earlier plan (fig. 11) from the Kalapana ash deposits.
2. A first monitoring survey should be made before beach enlargement, a second as soon as possible after completion of the enlargement, and subsequent surveys at two-month intervals during the first year thereafter, four-month intervals during the second year, and annually thereafter for 10 years.
3. The breakwater would be built if, and only if, the cumulative loss of sand after the as-built-survey exceeded 4,000 cu. yds. at any time during the first year or 2,400 cu. yds. plus the product of 1,600 cu. yds. per year and the time in years elapsing from the as-built-survey (fig. 15).
4. The breakwater, if built, was to be constructed in accord with the submerged breakwater plans (fig. 11) using stone quarried from sites of no archaeological significance where scenic detriments and nuisance would be minimized.

No estimate was reported of the rate of continuing sand loss after the breakwater was constructed, if it were constructed. Assuming the validity of the Corps estimate of the ratio of loss rates with and without the breakwater, the periodic replenishment of sand needed to compensate for sand losses continuing after breakwater construction would have averaged about 1,100 cu. yds. per year.

Independently, the Center suggested that the Council should reconsider its decision to approve any modification of Kaimu Beach, calling attention to some of the objections that had been raised previously but seemingly not adequately considered. However, the joint Corps-Center recommendations were approved by the Council and transmitted to the Governor of the State of Hawaii and the Mayor of the County of Hawaii.

Project as proposed in 1975

Although the County Council of the County of Hawaii had approved the staged project, as proposed by the Corps in 1972, and had not objected to the proposal of the Environmental Council to make the breakwater construction contingent on monitoring results, and in spite of the subsequent planning efforts of the Corps and Environmental Center and endorsement of their recommendations by the Environmental Council, the County Council rejected the recommendations, in favor of a plan in which the breakwater would be constructed first and the beach enlargement accomplished second. In spite of the State Environmental Council's position, the State Department of Land and Natural Resources, which controlled the necessary state funds, concurred with the County Council.

The breakwater was presumably to be a submerged one, and the sand used for beach enlargement was presumably to come from Kumukahi, but it is not clear what volume of sand would have been placed on the beach nor where the breakwater stone would be obtained because, during the long delay, the federal funds originally allocated to the project had been committed elsewhere, and the preparation of revised plans and undertaking of construction had to await a further allocation.

Natural intervention

Nature then intervened. On 29 November 1975 there was an earthquake with a magnitude and effects similar to those of 1868. A tsunami was generated that was responsible for two deaths on the coast southwest of Kaimu. The coast again subsided to a maximum of about 10 feet to the southwest and about 3 feet at Kaimu. Some subsidence seems to have continued since the quake, although the results of surveys have not as yet been published.

As had been reported after the 1868 subsidence, the erosion of Kaimu beach accelerated after the 1975 subsidence (figs. 16 and 17). However, the height of the beach above sea level was reduced by about 3 feet and the depths along the proposed breakwater alignment as well as elsewhere were increased by the same amount. Hence neither the plans for beach enlargement nor those for breakwater protection could be considered at all appropriate. In addition County plans for other aspects of coastal development at Kaimu, private and public, were rendered questionable by the subsidence and the obvious exposure to the effects of earthquakes and tsunamis. Hence the economic justification for the project appeared to need reexamination.

No final decision has yet been made that the construction project affecting Kaimu Beach should not be undertaken. The Corps of Engineers has indicated its possible availability for further planning. However, the County has decided that no further planning effort should be made for a while, at least until the question of continuing coastal subsidence has been settled.



Figs. 16 and 17 Kaimu beach in December 1975 (Joseph Halbig)

Analysis and conclusions

As in the case of most projects intended to modify natural conditions or processes, the Kaimu Beach project, in any of the plans proposed, would have resulted in a combination of benefits and detriments, some of both accruing as side effects, incidental to the benefits for which the project was proposed. The weighing of such benefits and detriments is supposed to be facilitated by the combined availability of project reports and environmental impact statements, after public review and resulting response, to decision makers. The process seldom approaches perfection, and this review of the Kaimu case was undertaken to call attention to some sources of imperfection to which special attention might usefully be paid in reviewing the process or applying it to similar cases.

The benefit originally sought by the County of Hawaii was the restoration and protection of Kaimu Beach. All of the plans called for enlargement of the beach, but in a strict sense none of them could have restored the beach to its natural condition at some time in the past. It is quite doubtful that, without public review, the color change which would have resulted from the implementation of the 1971 plan would have come to general attention until the change had been effected, although there is little doubt that preserving the natural color of the beach was considered important. When the color change detriment was called to attention, the plans were revised to call for the use of sand more nearly matching the natural sand in color.

More or less protection of the beach would have been afforded by any of the plans that incorporated a breakwater, and all of the plans called for sand replenishment after the project was complete to compensate for the lack of complete protection. The loss of surfing sites that would result from breakwater construction was recognized from the outset by the Corps, but the importance of these sites, on account of their traditional and continuing use, was highlighted in the public review process and more or less well recognized in the final environmental statement.

The potential detriments associated with quarrying for breakwater rock, which came to light in the public review process, were circumvented by changes in the plans for quarry sites in response to the review comments.

The swimming opportunity that the breakwater would have provided was identified by the Corps from the outset as a major benefit. Retention of the breakwater in the plans probably resulted from considerable public agreement with the importance of this benefit. However, in spite of the requirement in federal environmental law for the consideration of alternatives, possible alternatives for the provision of this benefit were never investigated because the Corps is not authorized to investigate the creation of beaches or swimming sites, but only their restoration and protection, and the state and county could not have counted on federal support for the investigation or construction where there was not an existing beach.

Some of the detriments of the project that were alleged in the public review process were examined and shown to be of little consequence--an alleged loss of fishing opportunities, for example. Some alternatives suggested in review were, however, brushed aside as being impractical without evidence of adequate investigation, for example, alternative types and alignments of breakwaters. Trial dumping of sand cinders (or of cinders from which sand might be generated) east of the beach to nourish the beach indirectly (Johnson, 1973) was dismissed simply because "this alternative is not a positive approach to the problem and there is a possibility that the introduced sand would bypass the eroded areas completely" (COE, 1973).

The questions initially raised in the first public review about the retreat and sand loss estimates, on which the benefit and cost appraisals of the project depended, were not satisfactorily addressed until the Environmental Council intervened.

Of three geologic hazards, only the least consequential, that of tsunamis, was initially recognized. The lava-flow hazard, to which attention was called in the review process, was never analyzed, although historical statistics on which a reasonable analysis could be based became increasingly available during the planning period. Attention was called in the review process to the hazard of subsidence, but this hazard could not have been analyzed because there had been but one prior incidence of this hazard at Kaimu. Oddly, it was a second incidence of this hazard, that brought the project planning to a halt, at least temporarily.

It seems quite questionable that, if all of the detriments, hazards, and alternatives had been recognized at the outset, any of the plans formally proposed would have been considered as representing, overall, an improvement. During the long planning period, however, increasing public and private commitments were made for land uses in the vicinity under the assumption that the Kaimu beach would be enlarged and a swimming opportunity created there. The decisions in early 1975 were almost certainly biased by developments that were stimulated by the initial proposal of 1971, although this would be difficult to document. Unfortunately the event that led to the halt also hastened the end of Kaimu beach, of which there are left only remnants.

Acknowledgements

Many members of the University of Hawaii community contributed to the Environmental Center reviews on which this paper is based, and several members of the staff of the Corps of Engineers were helpful in supplementing and clarifying the information in official reports in the review process. Information and photographs provided by Joseph Halbig and G. A. Macdonald of the University of Hawaii, Rick Scudder of the Office of Environmental Quality Control, and Clarence Fujii and Karl Keller of the Corps of Engineers were used in the preparation of this paper. The assistance of all, whether here named or not, is gratefully acknowledged.

References

- Agassiz, Alexander. 1889.
The coral reefs of the Hawaiian Islands. Bull. Mus. Comparative Zool. Harvard Coll., vol. 17, no. 3, pp. 121-170.
- Belshe, J., C. Fujii, K. Keller, O. Swenson, O. C. Cox, F. Gerritsen, and T. T. Lee. 1974.
Recommendations concerning Kaimu Beach. Joint recommendations from U.S. Army Corps of Engineers and Univ. Hawaii Environmental Center. 5 December 1974.
- Bretschneider, C. L., T. T. Lee, and J. T. O'Brien. 1971.
Kaimu Beach on island of Hawaii; site inspection of. Univ. of Hawaii Look Lab. of Oceanographic Eng. Misc. Rept. 2., March 1971.
- Bretschneider, C. L., D. C. Cox, and J. R. Healy. 1972.
[Review of] Kaimu beach plan. Univ. Hawaii Environ. Center RG-0006, 9 March 1972.
- Corps of Engineers. 1971.
Detailed project report, shore protection, Kaimu Beach, Island of Hawaii. U.S. Army Engineer Division, Pacific Ocean, September 1971.
- Corps of Engineers. 1972(a).
Preliminary detailed project report, shore protection, Kaimu Beach, Island of Hawaii. U.S. Army Engineer Division, Pacific Ocean, June 1972.
- Corps of Engineers. 1972(b).
Draft environmental statement. Kaimu Beach, Hawaii, proposed shore protection. U.S. Army Engineer Division, Pacific Ocean, 17 November 1972.
- Corps of Engineers. 1973.
Final environmental statement, Kaimu Beach, Hawaii, proposed shore protection. U.S. Army Engineer Division, Pacific Ocean, August 1973.
- Cox, D. C. 1973.
Critique of draft environmental impact statement, Kaimu Beach; and Natural hazards on the southeast coast of Puna. Univ. Hawaii Environ. Center suppl. to RE-0082, 1 February 1973.
- Cox, D. C. 1974(a).
Suggested reconsideration of Kaimu Beach decision. Univ. Hawaii Environmental Center RG:0017, 5 December 1974.
- Cox, D. C. 1974(b).
Kaimu beach retreat and sand loss, Univ. Hawaii Environmental Center RG:0015, 29 November 1974.
- Johnson, J. M. 1973.
[Review of] Draft environmental impact statement, Kaimu Beach. Univ. Hawaii Environmental Center RE-0082, 19 January 1973.
- Macdonald, G. A. and A. T. Abbott. 1970.
Volcanoes in the Sea. Univ. Hawaii Press.

- Macdonald, G. A. and D. H. Hubbard. 1974.
Volcanoes of the National Parks in Hawaii. Hawaii Natural History Assn. 7th ed.
- Moberly, Ralph Jr., and T. Chamberlain. 1974.
Hawaiian beach systems. Hawaii Inst. Geophysics Rept. 64-2, May 1964.
- Nordhoff, Charles. 1874.
Northern California, Oregon, and the Sandwich Islands. Low, Marston, Low & Searle, 1874. Reprinted by Ten Speed Press, 1974.
- Stearns, H. T. and G. A. Macdonald. 1946.
Geology and Ground-water Resources of the Island of Hawaii. Hawaii Div. Hydrography Bull. 9.

CHAPTER 92

CHANGES OF SEA BED DUE TO DETACHED BREAKWATERS

Osamu Toyoshima

Director, Public Works Research Institute, Akabane Branch
Ministry of Construction

Ex-Director, Sea Coast Division, River Bureau
Ministry of Construction, Japan

INTRODUCTION

Since most of the coast lines of Japanese Islands are faced on the open sea and are always attacked by severe waves, beach erosion is one of serious problems in the coastal engineering field. Although Japan has all types of coastal land-forms except the glacial shoreline, remarkable recessions of coast line have been observed at sea cliffs and sandy beaches. The recession of sea cliffs has been found at several districts in Japan since old times. But, beach erosion has become increasingly severe since the early 1950's. The main causes of beach erosion are the reduction in sediment supply from rivers and the interception of the longshore paths of sediment. The former is caused by the river improvement works and by the construction of dams and debris barriers or Sabô works. The later is caused by the coastal structures, such as jetties, groins, breakwaters, and flood-control outlets. In addition a new type of beach erosion has been observed at the coast where coast protection works such as seawalls and bulkheads exist.

The beach erosion defence works are being executed at more than 300 sites in Japan. Considerable number of the works were commenced in the 1960's.

The author proposed ten years ago a detached breakwater system to develop the sand deposition behind the breakwater. Up till now, about fifty or more works of the detached breakwater system have been constructed under the guidance of the author, and most of them have brought about successful results. The details of the design method about a detached breakwater system were presented by the author at the fourteenth International Conference on Coastal Engineering, titled "Design of a detached breakwater system".

The paper takes an example in Kaike coast, and describes the changes of coastal protection works against beach erosion and the changes of sea bed after the construction of the detached breakwaters.

OUTLINE OF THE KAIKE COAST

Kaike, one of the most famous hot spring resorts, located on the root of the Yumiga-hama Peninsula which has been believed to be a sand spit formed by sand deposition discharged from the Hino River that fed sand to this coast.

Rough waves from the east-northeast is refracted in Miho Bay as a result of the offshore topography and configuration of the coast as shown in Figure 2. These refracted waves give rise to the longshore current in the western direction along the Yumiga-hama Peninsula.

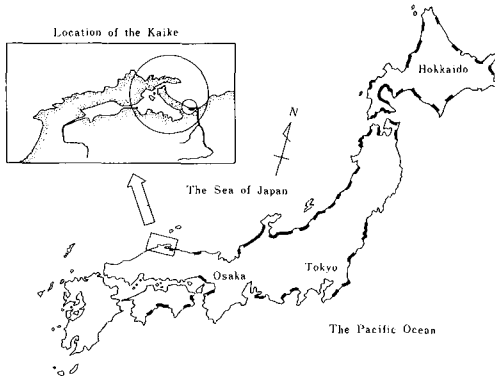


Fig.1 Location map showing the Kaike coast and sites where beach erosion has been comparatively severe.

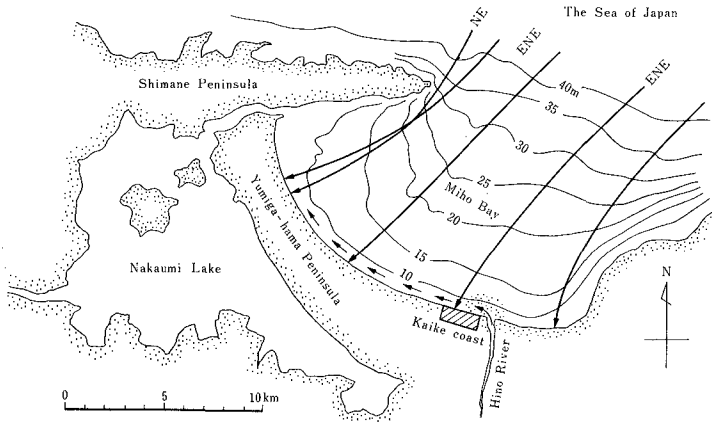


Fig.2 The longshore current formed the Yumiga-hama Peninsula in ancient times, and now-a-days it erodes the Kaike coast on account of reduction of sand supply from the Hino River.

In the early 1870's, a fountainhead of hot spring was discovered by fishermen in shore of the Kaike coast by chance. In those days, the shoreline of the Kaike coast had been advancing offshorewards year by year. In the 1910's, the former sea bed where the fountainhead of hot spring was discovered, changed into backshore, and the first spa was built on the beach. At that time, Kaike had sandy beach of width of more than 200 meters.

About 1920, iron sand collecting for Japanese traditional steel making was abandoned in the upper reaches of the Hino River. In addition to this, a number of Sabô dams and agricultural weirs were constructed along the Hino River. These facts brought a remarkable reduction in sediment supply from the Hino River and the advancing tendency of the Kaike coast turned into the receding one. The shoreline at Kaike has receded more than 200 meters during the last half century.

CHANGES IN COASTAL PROTECTION WORKS AT THE KAIKE COAST

In the face of acute construction material shortage during the World War II, an attempt was made to weaken the rate of beach recession by means of primitive crib works using pine logs which had commonly

used in the river bank protection works in Japan.

Unfortunately almost of the works were destroyed soon after their completion by very strong actions of stormy waves.



Fig.3 In 1942, people in the seabord tried to weaken the longshore current by means of primitive crib works using pine logs, but these works were destroyed soon.

In 1947, after the War, Tottori Prefecture organized a research committee on the littoral drift control with experts and engineers representing the universities and central and local governments. There have never been any attempts to organize the technical and research committee concerning with the problems in the coastal engineering until the establishment of this committee.

Before the establishment of this committee, Tottori Prefecture had constructed an experimental groin composed of rubble stones on the Kaike coast. But this groin subsided under the sea water level soon after its completion.

In paralleling with the committee's research work, between 1949 and 1950, the local government constructed more five experimental groins which composed of large scale concrete blocks.

Figure 4 indicates the change in the shoreline configuration during that period together with locations of constructed groins. It is noticed from this figure that groins resulted in accretion on the up-drift side and in erosion on the downdrift. However the shoreline in front of Kaike Spa advanced seawards in comparison with that before the scheme commenced. The fountainhead of hot spring, indicated in the figure, was the No. 3. Nos. 1 and 2 fountainhead, located more off-

shore side than the No.3, had been destroyed by the heavy beach erosion, and vanished under the sea bed before 1940.

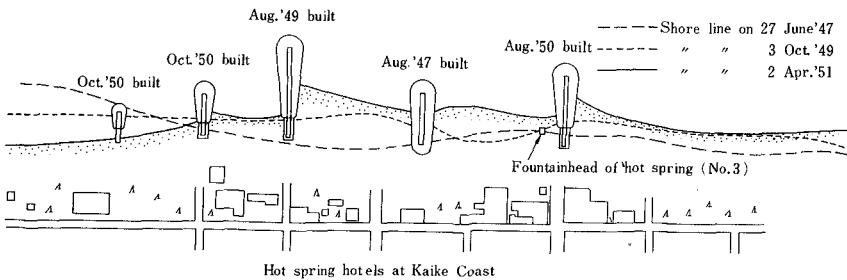


Fig.4 Five groins were constructed between 1947 and 1950 in front of the Kaike Spa. Their performances in the initial stage were very effective and shoreline advanced seaward compared with that before the construction.

Based on the proposal of the research committee and the success in the construction of groin system, Tottori Prefecture decided to construct eight groins in addition to that previously constructed. As seen in Figure 5, the function of groin system gave the satisfactory effect in 1954.

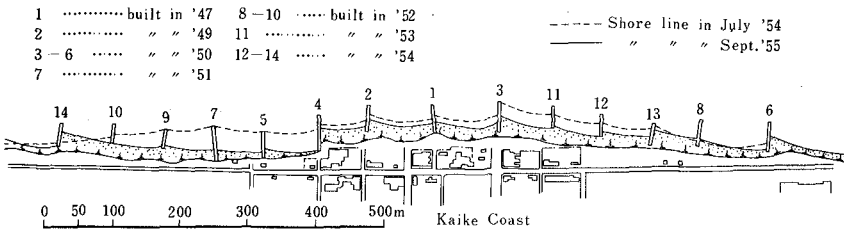


Fig.5 In the next summer after the completion of the construction of the groin system, August 1955, the Kaike coast was eroded again.

In August 1955, the Kaike coast was heavily eroded by rough waves caused by Typhoon and the shoreline was in full retreat.

Immediately after the heavy erosion due to Typhoon, Tottori Prefecture constructed seawalls along the shoreline to withstand severe wave actions. Based on the technical consideration in those days,

concrete stepped face seawalls illustrated in Figure 7 have been adopted as a suitable prevention structures against beach erosion in Japan. The construction of the seawalls had been made between 1955 and 1961.

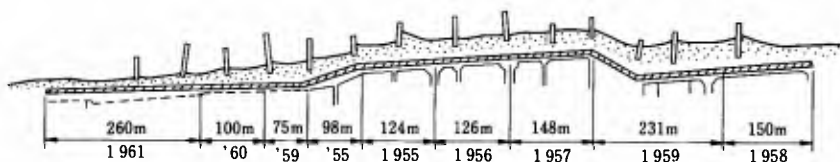


Fig.6 The seawalls have been constructed between 1955 and 1961, and most of the Kaike Spa have been protected from the severe waves by the seawalls in length of about 1300 meters.

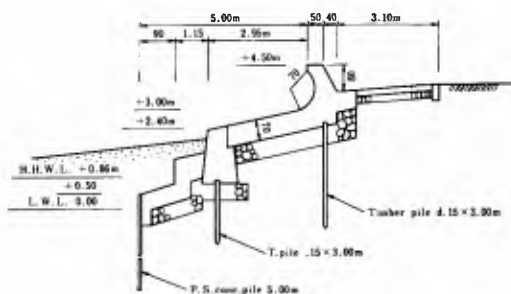


Fig.7 Concrete stepped face seawall was adopted in 1955.

For several years after the completion of the seawalls, the Kaike coast had been seen like a stable beach, where very wide sandy beach extended in front of the seawall.

Fig.8 In 1957, the Kaike beach had been seen a stable wide sandy beach. The berm height of sandy beach in front of the seawall was nearly equal to that of the crest of the seawall.



Even when the Kaike coast was seemed to be stable, a large amount of beach sediment carried offshoreward with every attack of severe wind waves in winter. As the result of wave attacks groins and seawalls on the Kaike coast were damaged locally in January 1961.

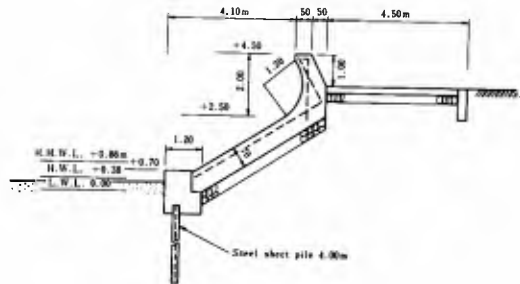
Fig.9 In December 1960, most of the sandy beach were vanished. The arrow mark on the center of the picture shows the fountainhead No.3 shown in Figure 4.



Fig.10 In January 1961, the stepped face seawall had been partly destroyed by the winter strong wave force. Waves had scoured beach at the foot of the seawall, and the body of the seawall had been scattered. The seawall had been reconstructed at once.



Fig.11 Reinforced inclined-face type seawall was adopted as the restored seawall.



The profile of seawall restored by the local government was an inclined-face type seawall with sandtight cutoff wall by steel sheet pile as shown in Figure 11.

After a lull in beach retrogression Kaike coast begun to retreat again in the early 1960's. Incident waves directly struck seawalls and overtopped. In order to reduce wave overtopping, wave defence works composed of artificial concrete blocks were constructed in front of the seawalls.



Fig.12 As the wave defence works, armour concrete blocks, named Hexa-leg block, were piled up in front of the seawall. But a number of these blocks have sank under the sea bed (photo in 1970).

As severe waves have repeatedly hit the Kaike coast, the combination system of groins and seawalls with wave defence works has shown its inadequacy in the protection function against beach erosion. When incident waves approach normally to the shoreline, some portions of incident wave energy are reflected from the seawall.

This wave reflection results in considerable scour in front of seawalls and receding waves take away beach sediment seawards. Due to these unfavourable effects by the seawall, groins and wave defence works settled and scattered. Therefore the local government often faced to restore and reinforce the protection works on the Kaike coast. In the early 1970's, the Kaike coast severely eroded again.

Then, the author proposed to construct detached breakwaters as a countermeasure against beach erosion.

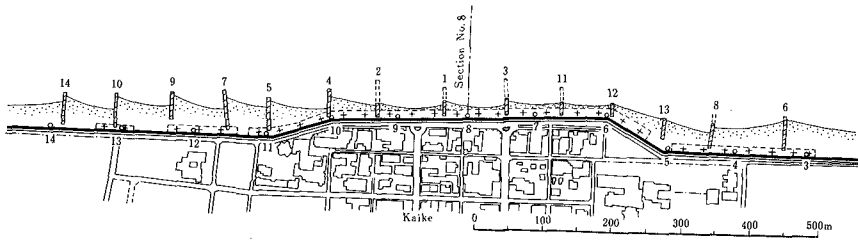


Fig.13 The shoreline of the Kaike coast in 1970.

PROPOSAL OF A DETACHED BREAKWATER SYSTEM

For more than twenty years, in Japan, as a countermeasure against beach erosion, many preventive constructions, such as seawalls and groins, have been built. However, it turned out that the seawalls and groins are not necessarily effective measures to prevent beach erosion, and that they have even accelerated beach erosion in some cases. Then the author proposed a detached breakwater system ten years ago.

This system has two major functions. One is the dissipation of incident wave energy, by which beach erosion due to wave actions can be stopped. The other is generation of diffraction waves, by which development of a tombolo, sand deposition behind a breakwater, is encouraged. A detached breakwater system consists of a group of breakwaters, parallel with the shoreline, and is usually located in the surf zone.

The first experimental work of this system was carried out at Ishizaki coast Hokkaido Prefecture under the direction of the author in 1966. Soon after the completion of the work, the tombolo was formed behind the breakwater, and the system were effective in the restoration of shoreline. Further twenty or more experimental works had been carried out on another coasts, and most of them have been successful.

Although a considerable experimental works were carried out, this system is comparatively new and there are fewer examples compared with groins. Generally, of cause, construction work of the detached breakwaters is not easy and maintenance cost is also high, when they

are constructed on steep and deep sea bed.

CONSTRUCTION OF THE DETACHED BREAKWATERS AT KAIKE

The detached breakwaters at Kaike were positioned in water considerably deeper than that where the previous experimental breakwaters constructed. Therefore, the adoption and its positioning were determined after long series of field surveys and researches.

In June 1971, the construction of the first breakwater at Kaike was commenced under the direct administration of the Ministry of Construction, and was completed in September the same year. The breakwater with the length of 150 meters was constructed at the water depth of about 5 meters where was 110 meters offshoreward from the seawall. The breakwater as seen in Figure 14 was comprised of rubble stones and armoured by tetrapods.

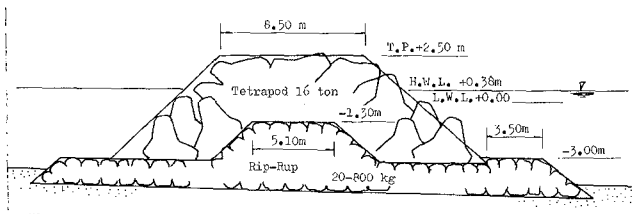


Fig.14 Cross-section of the detached breakwater at Kaike.

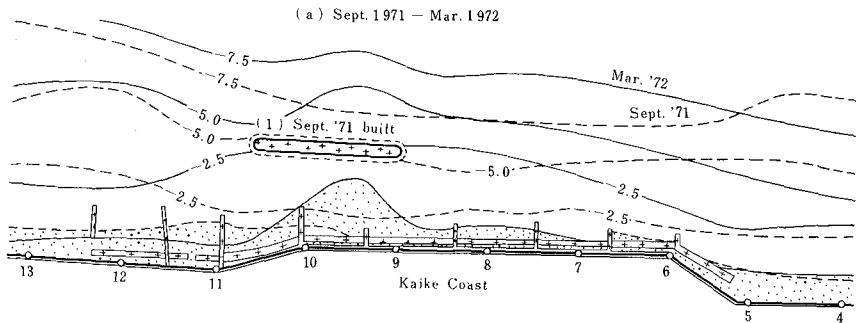


Fig.15 Changes of shoreline and equi-depth line before and after the construction of the No.1 detached breakwater at Kaike.

After the construction of the first breakwater, the tombolo was formed in front of the seawall, and every equi-depth line around the breakwater greatly advanced offshoreward in comparison with that before the construction. The thickness of deposit sand was about 4 meters at the apex of the tombolo, and about 2 meters in front of the seawall.

According to the changes of sea bed before and after the construction of the breakwater, it was estimated that most of the deposit sand was carried from the offshore sea bed at a depth of more than 12 meters.

Encouraged by the successful result of the first experimental detached breakwater, the No.2 breakwater was constructed in the following year, on the updrift side of the No.1 breakwater. The No.2 breakwater was also effective in bringing back sand transported from offshore zone and in forming a large scale tombolo behind it.

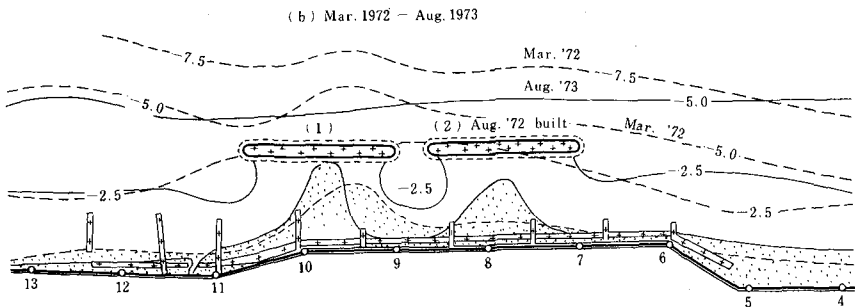


Fig.16 Changes of sea bed after the construction of the No.2 breakwater.

In progress of No.2 breakwater construction it was observed beach retrogression in the downdrift zone of No.1 breakwater. To eliminate the undesirable effect by Nos. 1 and 2 breakwater, No.3 breakwater was sited on the downdrift side of No.1 breakwater. The No.4 breakwater was in the updrift side of the No.2 breakwater in order to increase the covering area.

These two breakwaters were constructed in the following two years, and were positioned at equal spaces of 50 meters.

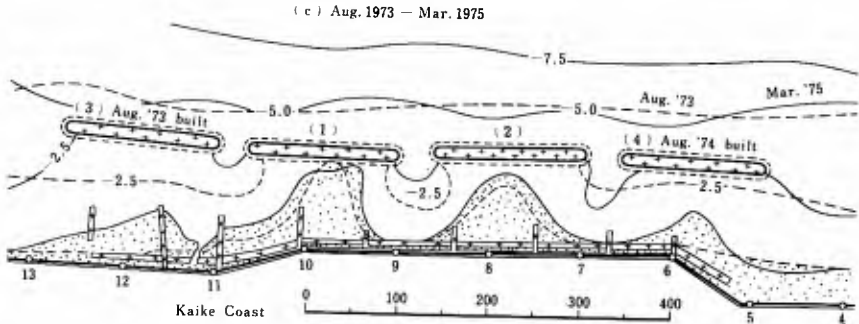


Fig.17 Changes of sea bed after the construction of the Nos. 3 and 4 breakwater.

Before the construction of the breakwaters, the shoreline has usually been retreated by attacks of strong waves in winter. But after the construction, the sand depositing action of the breakwaters has continued and tombolos have become larger in their sizes even under the severe wave condition.

At the Kaike coast, the progress of the construction of the breakwaters and changes in shoreline features have frequently been recorded by means of the radio controlled model plane. From the sequential aerial photographs, we can see the development of the tombolos and the refracting wave patterns due to the breakwaters.

Fig.18 Aerial view of the Nos. 1 and 2 breakwater and tombolos by means of a radio controlled model plane.



1) July 27 '72
No.2 breakwater is under the construction.

- 2) Aug. 24 '72
Just after the construction.



- 3) Sept. 11 '72
Small tombolo appears.



- 4) Sept. 29 '72
The tombolo grows larger
gradually.



- 5) March 9 '73
Strong waves attack the
breakwaters and tombolos.



6) April 25 '73
The tombolos are stable.



CHANGES OF SEA BED DUE TO DETACHED BREAKWATERS

In order to investigate the changes of sea bed, the survey of beach profile on each section have been made since 1958. Before the construction of the breakwaters, there were considerable changes in the sea bed configuration. However, since the construction, the changes of the sea bed have become very little.

Figure 19 are a typical example of survey results for the section No.8 which is located at the center of the Kaike Spa. There had been severe erosion on the sea bed between March 1963 and August 1963, and it had continued. After the construction of the detached breakwater (No.2), large amount of sand deposition have accumulated on the shore.

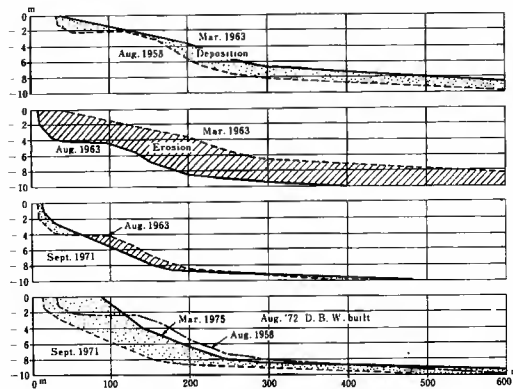


Fig.19 Changes of sea bed on the section No.8.

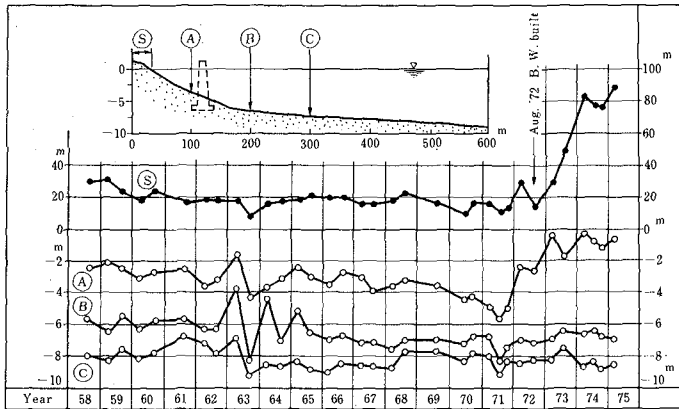


Fig.20 Annual changes of shoreline and sea bed on the section No.8.

Figure 20 shows the annual changes of the sea bed on the same profile line No.8. In this figure, (S) represents the horizontal distance of shoreline from the seawall, and (A), (B) and (C) the water depth from the still sea water level at the points of 100, 200 and 300 meters distant from the seawall. The No.2 breakwater was constructed on the profile line No.8 in August 1972, and it was very effective for depositing sand. After its construction, the sea bed at the point (A) indicated a remarkable shoaling, and the shoreline (S) greatly advanced.

Above-mentioned severe erosion are also expressed in this figure, and the point (B) indicates remarkable change of sea bed three times during the period from 1962 to 1965.

Similar changes of sea bed occurred at the same time within the nearby area. Figure 21 also shows the annual changes of sea bed at the points of 200 meters distant from the seawall (like point (B)) on each profile line. We can see remarkable erosion of sea bed in 1963 on the profile lines No.6 to No.12. On the other hand, there were violent rise of sea bed on the profile lines No.2 and 4 in 1966, and we cannot find out significant changes of sea bed in 1963 on these profile lines such as the profile line No.8.

There are furthermore noticeable facts in this figure that, every sea bed have been going to rise since 1971, after the first detached breakwater was built, in spite of those offshoreward situation.

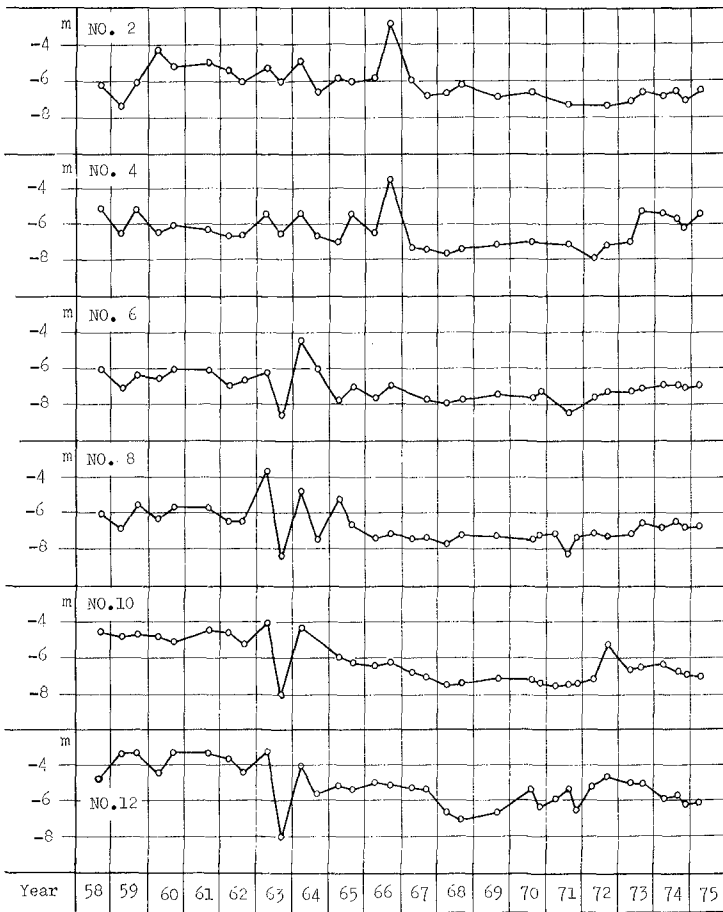


Fig.21 Annual changes of sea bed at the points of 200 meters distant from the seawall on each profile line.

The survey of sea bed, that is sounding, have been made within the limits of about 600 meters offshoreward from the seawall. After the construction of the detached breakwaters, a lot of sand were transported from offshore zone to the nearby area of the detached breakwaters not only onshore side but also offshore side of the breakwaters. However, we cannot find out the eroded zone as the source of the sand supplied to the onshore zone.

Table 1 Volumetric changes in the sea bed after the construction of the detached breakwaters at the Kaike Coast.

Unit : cubic meters			
Number of breakwater	Onshore side of breakwater	Offshore side of breakwater	Total volume
No.4 break-water zone	+ 41,260	+ 61,845	+ 103,105
No.2 break-water zone	+ 39,790	+ 99,770	+ 139,560
No.1 break-water zone	+ 35,835	+ 101,575	+ 137,410
No.3 break-water zone	+ 1,200	+ 45,265	+ 46,465
Total	+ 118,085	+ 308,455	+ 426,540

Table 1 shows volumetric changes in the beach profiles calculated from the survey results during the period from September 1971, before the construction, to March 1975, after the construction of the fourth breakwater. It is noticed from this table that a considerable volume of sand has been deposited on the sea bed in the onshore and offshore zones of the breakwaters since the construction scheme of detached breakwaters commenced. And now, the Kaike coast has gained a stable sea bed by virtue of this detached breakwater system.

CONCLUSION

The detached breakwater system at the Kaike coast is one of the symbolical work in the countermeasure against the beach erosion in Japan. It is very effective in the shoreline protection, however, some problems involved this system still remain to be solved. The most important problem is subsidence of the breakwaters. Up to now, the subsidence of the breakwaters on the Kaike coast is considered to be moderate, but it is urgently needed to develop methods by which the speed of subsidence can be minimized.

Hereupon, our efforts must be continued without a break, so that the re-created beach may not be lost again.



Fig.22 The latest aerial view of the Kaike coast (in 1975).

Reference:

Osamu Toyoshima, Design of a detached breakwater system,
Proceedings of the Fourteenth International Conference on
Coastal Engineering, Vol.II pp. 1419 - 1431, 1975.

CHAPTER 93

LOCAL SCOUR AND CURRENT AROUND A POROUS BREAKWATER

By

Shintaro Hotta* and Nobuo Marui**

ABSTRACT

Scour at the foot of vertical homogeneous crib style walls which were used as models for detached breakwaters, and the rise of mean water level in the shoreside region of the breakwaters were experimentally investigated, and the experimental results were compared to some field data.

Introduction

Scour around coastal structures has been studied by many researchers. For examples, the scour at the foot of or in front of solid sea walls have been of special interest to many coastal engineers and researchers, and a quite good number of papers concerning it have already been presented. [Sawaragi and Kawasaki(1960), Sato, Tanaka and Irie(1969), Herbick, Murphy and Van Weels(1965), Herbick and Ko(1968) and many others] The scour around breakwaters due to construction of harbors at sandy coasts were investigated by Sato(1972), Sato, Tanaka and Irie(1969) and Wada, Nishimura and Nirei(1970). The scour around the pier structures in the surf zone was observed by Hotta, Uda and Sasaki(1976).

Recently, the construction of permeable detached breakwater systems of concrete blocks has become widely practiced as a counter-measure against beach erosion. Most of these breakwaters function effectively. It is, however, reported that some of them exhibit unexpected defect in their construction. Many factors are related to the construction of the breakwaters and interact with one another in complicated ways. Of these, the local scour and wave-induced currents around the breakwaters are especially considered to be very important in successful construction of the breakwaters. In relation to these problems, the scour at openings of detached breakwaters systems was studied by Toyoshima(1972) and Kawaguch and Sugie(1972), and a series of excellent

* Research Associate, Dept. of Civil Engineering,
Tokyo Metropolitan University, Tokyo Japan

** Associate Professor, Dept. of Civil Engineering,
Tokyo Metropolitan University, Tokyo Japan

field works on the scour at foot of the breakwaters have been carried out by the First Port Construction Bureau, The Ministry of Transport, at Nigata Coast where continuous detached breakwaters of concrete blocks about 5 km in length are situated 150m offshore. [Katayama, Irie and Kawakami(1973)] However, the problems of these breakwaters are still not fully understood, and thus, the problems still remain unsolved.

The purpose of this study is an attempt to clarify the characteristics of the local scour and wave-induced currents, and the interactions between them around permeable detached breakwaters by laboratory experiments. A difficulty in experimental study is the similarity problems between the laboratory and the field. As a means of solving this problem, some researchers have used light specific gravity bed materials in their experiments. Horikawa and Sasaki(1970) reported in their experiments concerning a study of artificial nourishment of beaches that the Mesalite, which is a kind of light-weight concrete aggregate with a specific gravity of 1.65, was a good movable bed material. Due to Horikawa and Sasaki(1970)'s results, fine Mesalite was used in these experiments as a bed material.

Detached breakwaters usually have a trapezoid cross section. To simplify the scouring phenomenon, however, vertical homogeneous crib style walls were used as the model of the breakwaters in these experiments. Details about the model breakwaters will be described in succeeding section.

Experimental Facilities and Procedure

Experimental Facilities

Experiments were carried out in a rectangular glass walled wave tank 0.8 m deep, 0.5 m wide and 27 m long. At one end, the tank is equipped with a piston type wave generator. The wave height can be changed by varying the stroke of the piston arm, and the wave period can be changed by adjusting the rotation of a rotary disk. At the other end of the tank model beaches were moulded with a compound slope, 1/10 and 1/40.

Measurements and Observations

Wave heights were measured by hook point gauges, electric platinum wire resistance wave meter and 16 mm memo-motion cameras. The former two of these were used in the offshore zone. To take the mean water level and the envelopes of wave crest and trough, beach and wave profiles were photographed by a 35 mm camera and 16 mm memo-motion cameras each measurement time. The scouring depths and beach profiles were measured by a point gauge which ran along fixed rails on the wave tank and which was able to measure the water depth by moving up and down a rod with constant speed automatically. Manometers were used as another way to measure the mean water levels, and their results were compared with the results gained from the 16 mm cameras.

Bed Materials and Model Beaches

Two bed materials were used in these experiments. One was the Mesalite mentioned above and the other was a fine natural sand, specific gravity, 2.65. These were used to discover how the scouring patterns and beach changes differ with different bed materials. Grain size distribution curves of the two bed materials are shown Figure 1. As an initial beach slope, a compound slope with 1/10 and 1/40 was used. This initial slope was chosen to produce a wide surf zone similar to these of natural beaches in rough sea conditions within the limited wave tank length.

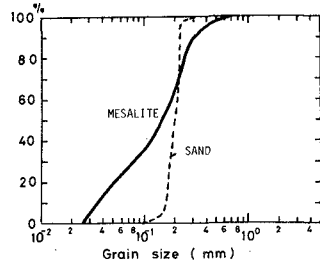


Figure 1 Grain size distribution curves.

Model Breakwaters

It would seem that scouring patterns and beach changes would be affected by the hydraulic properties of the breakwaters. From this reason, four kinds of vertical homogeneous crib style walls were experimentally investigated. Two thicknesses of model breakwaters and three kinds of filler were used. The characteristics of the model breakwaters are shown in Table 1.

Table 1

symbol of the walls	thickness of the walls	filler materials
W_1	2 cm	gravel 5-8 mm
W_2	2 cm	gravel 10-13 mm
W_3	2 cm	glass ball 18 mm
W_4	5 cm	glass ball 18 mm

Experimental Conditions

Only one type of wave was used in this experiment. The wave characteristics were as follows;

wave period, T , = 1.1 second
deep water wave height, H_o , = 10.8 cm
wave steepness, H_o/L_o , = 0.057

The deep water wave height was calculated from the shallow water wave height which was decided by means of Hely's method from wave data taken at constant water depth of the tank, 0.45 meters.

Experimental Procedure

After moulding the model beaches carefully, the walls were installed. First at 50, 100, 130 and the at 250 cm from the shoreline. After a wall was installed, the waves were started. At the time of each measurement, the waves were first observed, then the wave generator was stopped, and the scouring depths and beach profiles were measured by using the point gauge. A first series of experiments was finished, the Mesalite bed was removed, and it was replaced by the fine natural sand for the next set of experiments. Each test was run until wave number t/T , was over 70,000, where t was experimental duration. This number was decided on the basis of the following consideration; that is, we assumed that if storm wave periods would be within from 6 to 8 seconds, and storms would not continue over three day, the number of waves which would attack the breakwaters during a single storm would be roughly about 70,000.

Experimental Results and Discussion

Relationship between local scour and beach change (sea bottom topography change)

One difficulty in the study of local scours is that both beach change and local scour exist together. That is, the local scour is superimposed on the bottom topography, and their changes are complicatedly interacted. Figure 2 shows an example of the local scour around a pier structure surveyed by the Authors, and P shows positions of piers. In this case, we can easily recognize that local scour is superimposed on the natural beach profile, and that the pier will not influence major changes in the beach profile because it is understood that the disturbance of wave motion around pier is small. It is, however, not hard to imagine that the existence of a system of detached breakwaters on beaches will greatly influence wave motion, and it is difficult to predict the beach changes accompanying the change of the wave motions at the present time. In fact, this prediction is an important problem with which we are confronted right now and which must be solved. As of right now, the correlationship between local scour and beach change from this study has not become clear.

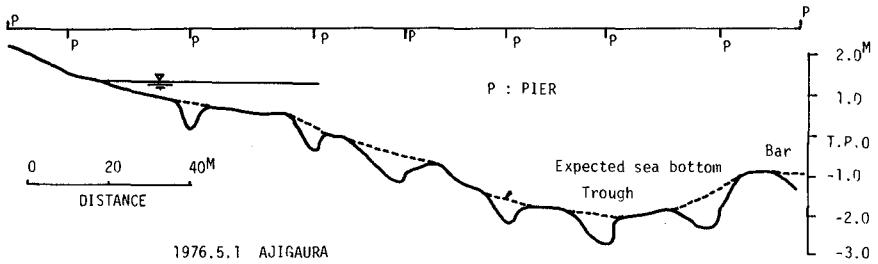


Figure 2 An example of local scour around pier structure.

Scouring Process

The authors defined the scouring depth at the foot of the walls as the vertical distance from the sand surface of the initial slope to the scoured bottom. Figure 3 shows the processes of scouring depth. According to Sawaragi and Kawasaki(1960) the scouring process at the foot of vertical solid walls could be classified as 4 types depending on the position in which wall was situated. Sato, Tanaka and Irie (1969) classified it as 5 types. However, in the case of permeable vertical walls, it is hard to find a tendency by which the scouring process can be classified according to the differences in the positions of the walls, bed materials or hydraulic properties of the walls.

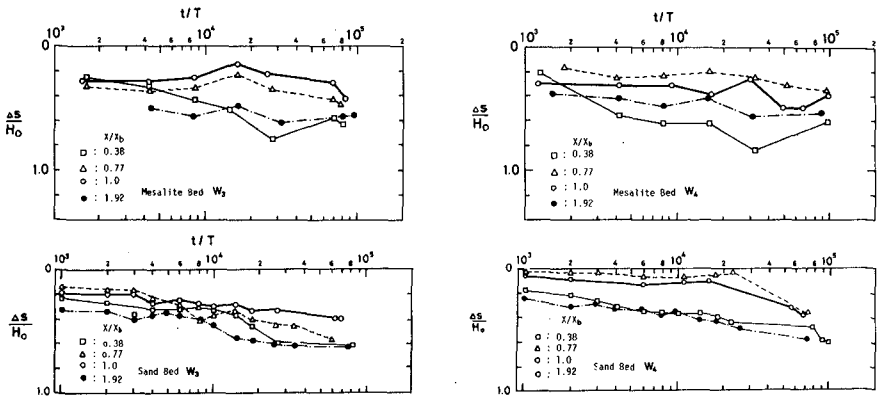


Figure 3 Scouring process.

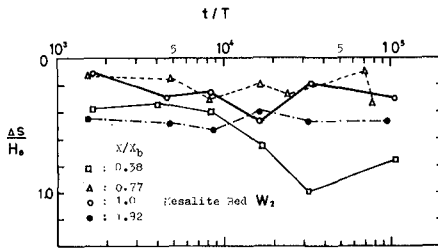
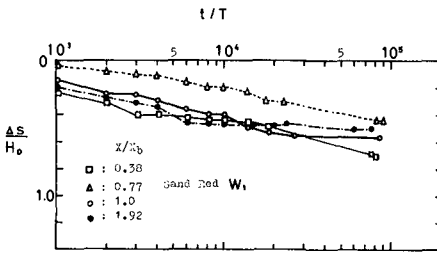
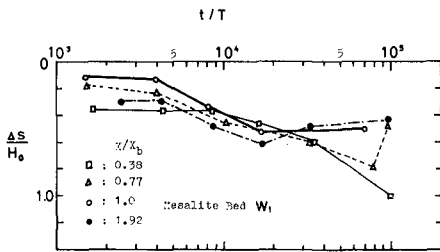


Figure 3 Scouring process.

Change of Beach Profile

Figure 4 shows examples of final beach profiles and the ratios between wave heights with walls to wave heights with no wall at each point, X . From this figure, the following are pointed out;

(1) Influence of bed material appears on the final beach profile when no wall are used, that is, the retreat of shoreline of a Mesalite bed is much larger than that of the sand bed. When a wall is used the retreat of the shoreline is small. However this retreat does not necessarily mean that the beach in the shoreside of wall is being eroded. The retreat makes the swash zone steeper, and a swash bar is formed. After that the shoreline retains its stability. Walls exhibit a sufficiently effective function.

(2) On the offshore side of walls, waves become much larger than when no wall was used and become partial standing waves, and the loops and nodes of

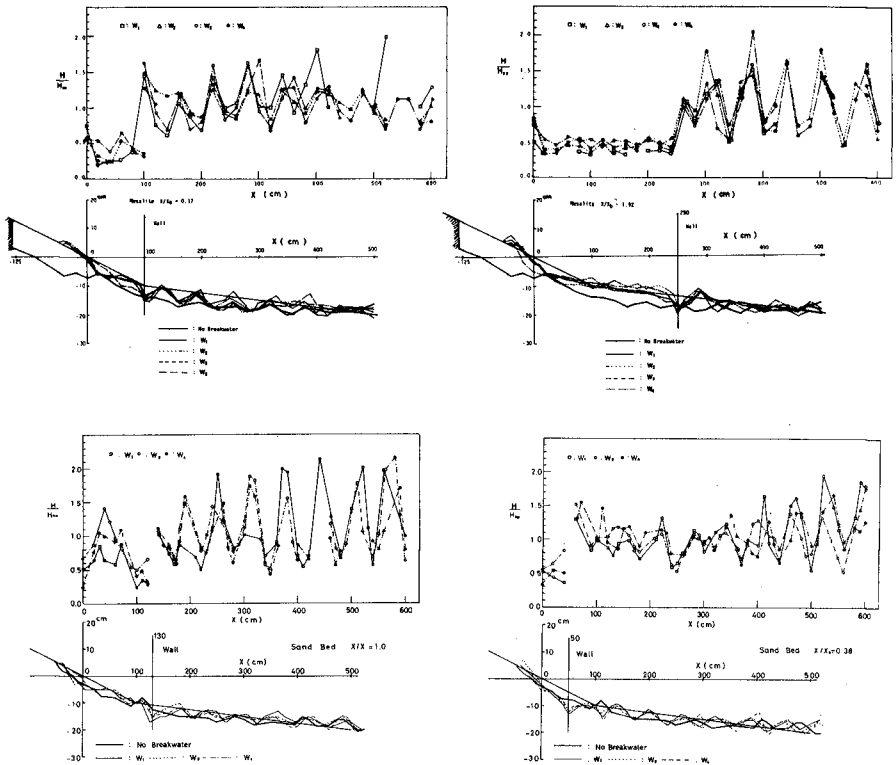


Figure 4 Beach profiles and ratios between wave height with walls to wave height no wall.

the standing waves closely correspond to the troughs and crests on the beach profile. This result agrees with that on scour in front of solid seawalls obtained by Herbich and Ko(1968).

The configuration of beach profiles in front of walls suggests that large sea bottom changes on natural beaches will occur in front of detached breakwaters.

The Maximum Scouring Depth

In Figure 5, the ratios of scouring depths to deep water wave height, $\Delta S/H_o$, are plotted against the relative positions of the walls, X/X_b , where X is the distance from the shoreline to the positions at which the walls are situated, and X_b is the distance from the shoreline to break-point. As seen from Figure 5, the scouring depths are largest at $X/X_b = 0.38$ and are small in the neighborhood of the break-point regardless of the bed materials and hydraulic properties of walls. It is not clear why the scouring depths are the largest at $X/X_b = 0.38$. However, it may depend on beach change. As seen in Figure 6 and Figure 4, the initial beach slope of this position, $X/X_b = 0.38$, was steeper, and the bed material moved largely offshore. That is, one may say that the local scour overlapped on the lowering of initial slope due to beach change. Might the local scour be $\Delta S'$ in Figure 6? In any cases, the scouring depth is not greater than the order of the deep water wave height.

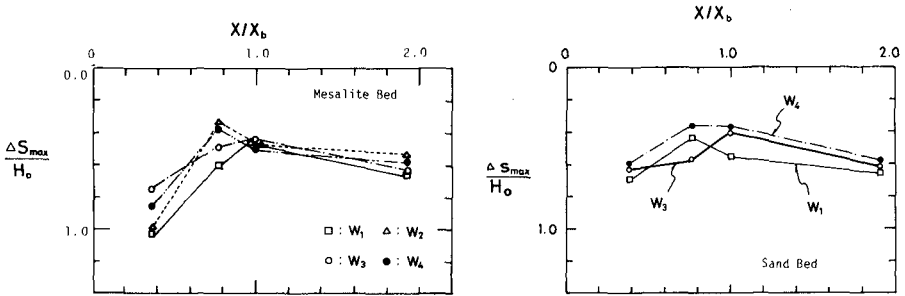


Figure 5 The maximum scouring depth.

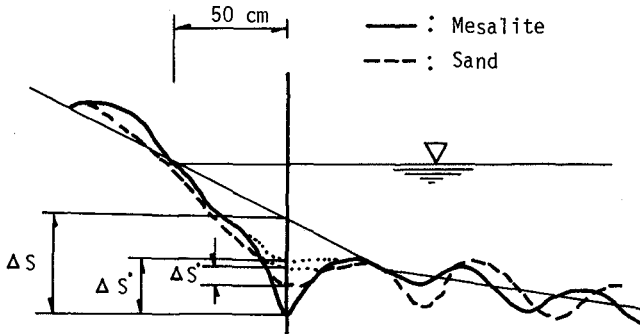


Figure 6 Examples of beach profile at $X/X_b = 0.38$

Figure 7 shows the relationship between $\Delta S/H_0$ and X/X_b in the case of solid walls. In this case, the maximum scouring occurs when the walls are situated at the break-point or a little inside the break-point. On this point, there is a remarkable difference between solid and porous walls. Conversely, the fact that maximum scouring depth is not greater than the deep water wave height under stormy conditions is the same for each.

Figure 8 shows scouring depths with $\Delta S/h$ instead of $\Delta S/H_0$. An advantage of this expression is that one can see the percent of scouring depths for the water depth in relation to the positions of the walls. From this Figure 8, $\Delta S/h$ is not greater than 0.6 without $X/X_b = 0.38$. A maximum of about 2 m scouring depths was observed at Nigata Coast where detached breakwaters were situated in water depth of 3 m about 150 m offshore. [Katayama, Irie and Kawakami (1973)] In this case, the ratio of $\Delta S/h$ was about 0.66. This figure almost agrees with the results gained in our experiments.

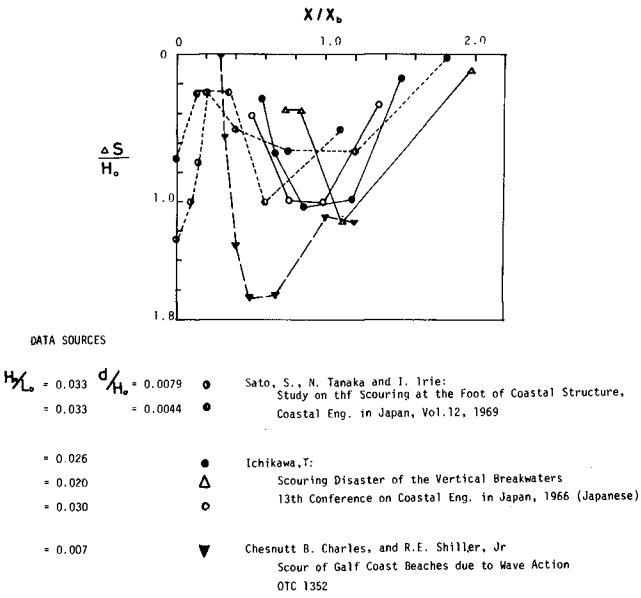


Figure 7 The maximum scouring depth of solid seawalls.

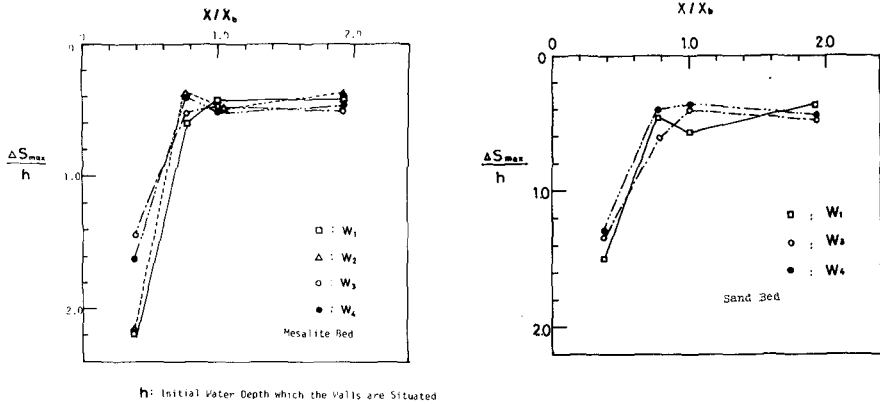


Figure 8 The ratios between the maximum scouring depth to the water depth.

Transmitted Wave heights

Figure 9 shows the ratio between the wave height transmitted to the inside region of walls and the deep water wave height. As seen in the Figure 9, the ratio depends on the size and shape of the filler materials and the width of the wall. The larger the size of the filler, the larger H_t/H_0 becomes. The greater the width of the wall, the smaller H_t/H_0 becomes. H_t/H_0 is smallest at $X/X_b = 0.77$ regardless of the hydraulic properties of the model breakwaters. In the same Figure, the field data observed by The First Port Construction Bureau at Nigata Coast are also plotted. In this plot, X/X_b is decided as follows: That is, because the position of the breakwaters is fixed X is constant ($X = 150$ m). The wave heights observed offshore at 10 m water depth were taken as the deep water wave height, H_0 . Using Goda's Breaking Index [Shore Protection Manual, U.S. Army, Coastal Engineering Research Center, pp 2-121] and assuming $K_f = K_r = K_d = 1$, the water depths of the break-point were read from the Figure. Then X_b were read from the sounding map.

Field data show similar tendencies to those of the experiments.

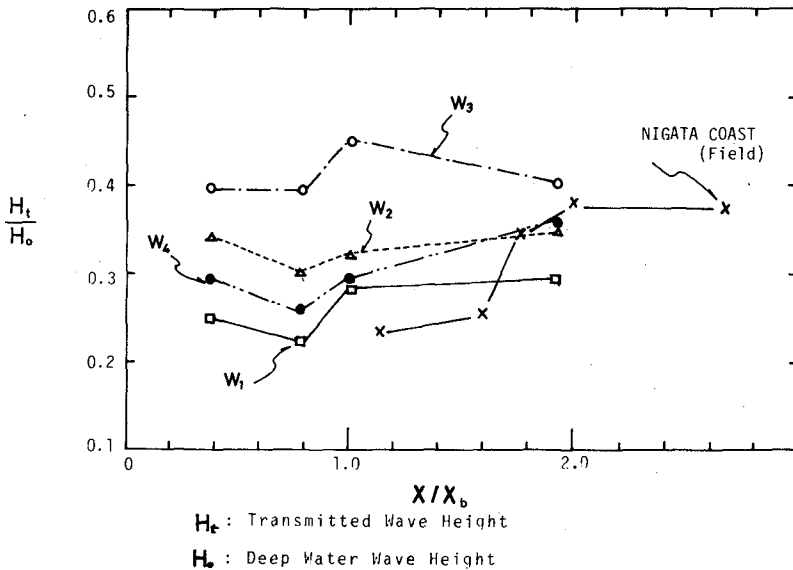


Figure 9 Transmission coefficient.

Rise of the Mean Water Level inside the Wall

A rising of the mean water level was observed in the shoreside region of the breakwaters. On the contrary, a lowering of the mean water level was observed in the offshore region of the breakwater. This rising and lowering has a great influence on the current around the breakwaters. Figure 10 shows a dimensionless plot of η/H_o and X/X_b . It seems that the rising of the mean water level depends on the position and hydraulic properties of the model breakwaters, but these influence are not clear within this experimental works. The magnitude of the rising of the mean water level is about 5 - 10 % of the deep water wave height. Field data [Katayama, Irie and Kawakame(1973)] are also plotted in the Figure 10. X/X_b in Figure 10 is decided in the same way as that described the previous section. The results of the field data are a little larger than those of the experiments. From Figure 10, it seems that the rise of mean water level in the shoreside of the wall is not beyond 10 % of the deep water wave height. The lowering of the mean water level in the offshore region from the wall fluctuated according to nodes and loops of the partial standing waves.

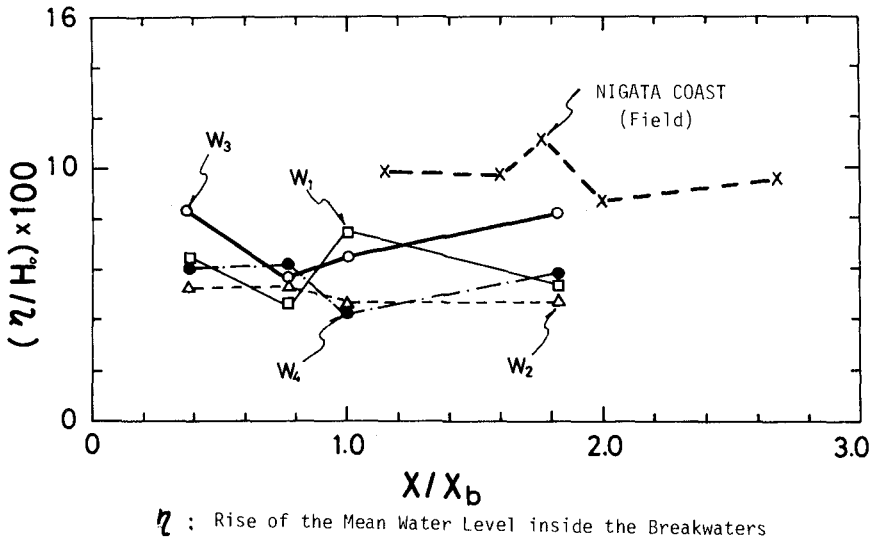
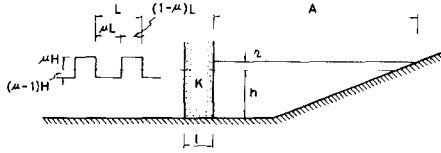


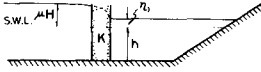
Figure 10 Rise of mean water level inside of walls.

The rising of the mean water level was analyzed. Authors assumed the wave to be shown in Figure 11. In equilibrium condition, if the Forchheimer's formula is assumed, the four equations in Figure 11 are given. From these equations, finally, the rise of mean water level, η , is approximatedly given by a equation 1. In this equation, a problem is to give μ and K (coefficient of permeability). It seems that the equation 1 will predict the rise mean water level in shoreside of the breakwaters, but it remains in discussion.

*** DEFINITION ***



(1) WHEN THE CREST OF WAVE COME IN TOUCH WITH THE WALL



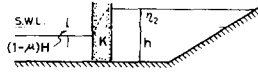
$$q_1 = \frac{K}{2l} \{ (h + \mu H)^2 - (h + \eta_1)^2 \} \dots\dots (1)$$

$$\frac{dq_1}{dt} = \frac{q_1}{A}$$

$$= \frac{K}{2lA} (2h + \mu H + \eta_1)(\mu H - \eta_1) \dots\dots (2)$$

$$\therefore \frac{d\eta_1}{(2h + \mu H + \eta_1)(\mu H - \eta_1)} = \frac{K}{2lA} dt$$

(2) WHEN THE TROUGH COME IN TOUCH WITH THE WALL



$$q_2 = \frac{K}{2l} \{ (h + \eta_2)^2 - \{ h - (1-\mu)H \}^2 \} \dots\dots (1)$$

$$- \frac{dq_2}{dt} = \frac{q_2}{A}$$

$$= \frac{K}{2lA} \{ 2h - (1-\mu)H + \eta_2 \} \{ \eta_2 + (1-\mu)H \} \dots\dots (2)$$

$$\therefore \frac{d\eta_2}{\{ 2h - (1-\mu)H + \eta_2 \} \{ \eta_2 + (1-\mu)H \}} = - \frac{K}{2lA} dt$$

$$\boxed{ \eta = \frac{H^2}{h} \mu(1-\mu) - \frac{Kl\mu H}{lA} \mu(1-\mu)^2 \left(1 + \mu \frac{H}{h} \right) \dots\dots\dots }]$$

Figure 11 Analysis of rise of mean water level.

Conclusion

In respect to transmitted wave heights and local scour, detached breakwaters function best when situated at the break-point or a little inside the break-point.

Acknowledgements

The authors gratefully acknowledge the help and advise by Mr. Kouichi Oobori, Head of the Planning Section, and Mr. Michio Yajima, Senior Engineer, the Planning Section, The First Port Construction Bureau, The Ministry of Transport. The authors also thank Mr. Kenji Moriyama and Mr. Tadao Yoshimura, student of Tokai University, for their assistance in these experiments.

A part of this study was supported by The Grant in Aid for Co-operative Research A, 035016,(1975) "Study of dynamic systems on coastal process" represented by Dr. Kiyoshi Horikawa, Professor, Dept. of Civil Engineering, University of Tokyo. The Grant is offered by The Ministry of Education, Science and Culture.

References

- Sawaragi, T. and Y. Kawasaki(1960): Scour at foot of seawalls, Disaster Prevention Research Institute Annuals, Kyoto University, Vol. 4, pp. 198-203, (in Japanese).
- Sato, S., N. Tanaka and I. Irie(1969): Study on scouring at the foot of coastal structures, Coastal Eng. in Japan, Vol. 12, pp. 83-98, JSCE.
- Herbick J. B., H. D. Murphy and B. Van Weels(1965): Scour of flat sand beaches due to wave action in front of seawalls, Proc. Coastal Eng. Santa Barbara Specialty Conference, pp. 703-726, ASCE.
- Herbick, J. B., S. Ko(1968): Scour of sand beaches in front of seawalls, Proc. 11th Conf. on Coastal Eng., pp. 622-643, ASCE.
- Sato, S and Y. Goda(1972): Coastal and Harbour Eng., pp. 339, Shokokushya Publishing Co. Ltd., Tokyo, Japan, (in Japanese).
- Wada, Y., K. Nishimura and Y. Nirei(1970): Scour around breakwaters and erosion on adjacent beaches, Proc. 17th Conf. on Coastal Eng. in Japan, pp. 311-316, JSCE, (in Japanese).
- Hotta, S., T. Uda and T. Sasaki(1976): Local scour around pier structures on surf zone, Proc. 23rd Conf. on Coastal Eng. in Japan, pp. 244-248, JSCE, (in Japanese).
- Toyoshima, O.(1972): Coastal Engineering for practical Engineer, Erosion Section, Scour at opening on detached breakwater system, pp. 314, Morikita Publishing Co. Ltd., Tokyo, Japan, (in Japanese).
- Kawaguchi, T. and M. Sugie(1972): Study of arrangement of detached breakwaters, Proc. 19th Conf. on Coastal Eng. in Japan, pp. 77, JSCE, (in Japanese).
- Katayama, T., I. Irie and T. Kawasaki(1973): Field observation of effectiveness of detached breakwaters on Niigata Coast, Proc. of 20th Conf. on Coastal Eng. in Japan, pp. 519-524, JSCE, (in Japanese).
- Horikawa, K. and T. Sasaki(1970): An experimental study of artificial nourishment of beaches, Proc.17th Conf. on Coastal Eng. in Japan pp. 324, JSCE, (in Japanese).

CHAPTER 94

PREDICTION OF WAVE-INDUCED SEAFLOOR MOVEMENTS

by

Leland Milo Kraft, Jr.¹, M. ASCE and David James Watkins², A.M. ASCE

ABSTRACT

Foundation design for offshore structures in areas where wave-induced bottom pressures cause submarine mud slides requires a knowledge of the potential depth of slide and of the magnitude and distribution of soil movements below the slide. Several methods have been developed to evaluate the stability of the seafloor due to wave-induced bottom pressures. These methods are reviewed and an improved procedure is presented. This procedure makes use of finite element analysis and combines in a rational manner oceanographic information on wave statistics with stress-strain behavior of soils under cyclic load conditions in order to evaluate the effects of a given storm history on the behavior of submarine sediments.

INTRODUCTION

Storm-generated surface waves can cause cyclic variations of pressure on the seafloor that trigger large scale soil movements manifested by massive soil failures to penetrations as deep as about 100 ft (30 m) below seafloors with slopes of one degree or less. Seafloor sediments most susceptible to these bottom pressure induced movements are the very soft to soft, underconsolidated clays found at the mouths of many major river systems, such as the Mississippi, Amazon, Niger, Ganges-Brahmaputra and Mekong, where active deltaic development results in a rate of sediment accumulation that exceeds the rate of pore pressure dissipation by consolidation. Fig. 1 illustrates that many of these deltaic regions are the site of major activity related to the installation and operation of offshore oil and gas production platforms and pipelines.

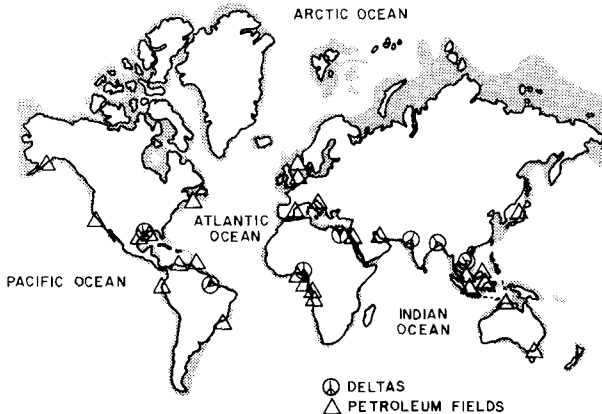


FIG. 1-MAJOR PETROLEUM ACTIVITY ON THE CONTINENTAL SHELVES

1 Manager, Special Projects Group, McClelland Engineers, Inc., Houston, Texas

2 Project Engineer, McClelland Engineers, Inc., Houston, Texas

When the seafloor is unstable the moving soil mass exerts lateral forces on offshore structures that can exceed the combined wind, wave and current force. Fig. 2 illustrates the soil loading mechanism. This paper outlines procedures currently used to assess the depth of the failure zone and the magnitude and distribution of accumulated soil movements produced by a given storm history. The application of these results to analyses of soil-structure interaction, which is required for reliable and economic structural design of foundations in these sediments, is beyond the scope of this paper.

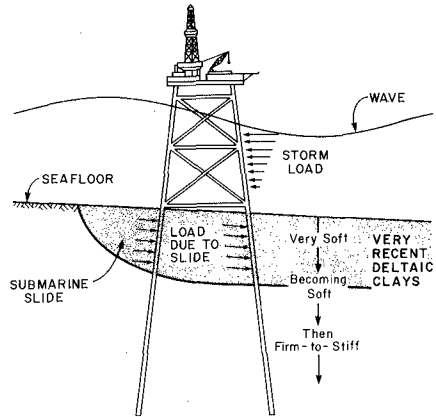


FIG. 2—LOADS DUE TO STORM WAVE AND SUBMARINE SLIDE

HISTORICAL DEVELOPMENT

Fig. 3 shows the failure of a 30-in. (76 cm) diameter flare pile that occurred during Hurricane Carla in 1961. This failure was an early demonstration of the potential depths of soil failure and the magnitude of lateral soil movement that may occur in very soft deltaic sediments. In August 1969, Hurricane Camille demonstrated convincingly the devastating impact of a submarine slide on offshore platforms. In about 300 ft (90 m) of water in South Pass Block 70 one platform was overturned and displaced about 100 ft downslope, and significant lateral soil movements occurred to at least 80 ft (24 m) below the seafloor (20). A second platform was displaced about 3 ft (1 m) downslope without overturning, and a third platform was destroyed in nearby South Pass 61.

These failures stimulated extensive and continuing programs to study submarine slides caused by storm-induced bottom pressure perturbations. The current state-of-the-art has evolved through many studies with contributions from and support by governmental agencies, academia, the petroleum industry and geotechnical consultants. To set the stage for the current state-of-the-art, the significant developments and results of earlier studies are highlighted.

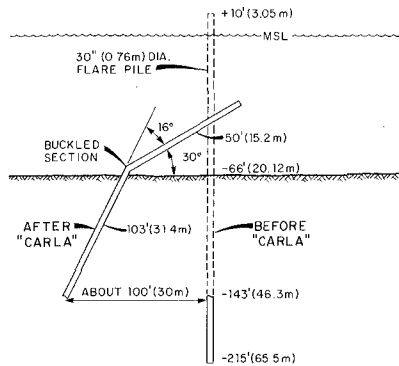


FIG. 3—FLARE PILE FAILURE CAUSED BY SEAFLOOR SLIDE (After McClelland and Cox, 1976)

Limit Equilibrium Analysis

One of the earliest published contributions that demonstrated the significance of storm-induced bottom pressures on submarine slope stability was presented by Henkel(7), who used a limit equilibrium method with an assumed circular failure surface. This concept, which is illustrated in Fig. 4, has been extended in practice to other shapes of potential failure surfaces and is used to estimate the depth of submarine slides, defined by the location of the deepest potential failure surface having a safety factor of one. Fig. 5, which shows the results of a limit equilibrium stability analysis for a location in the Mississippi Delta, illustrates that the potential failure surface with the minimum safety factor may underestimate the depth of the potential slide.

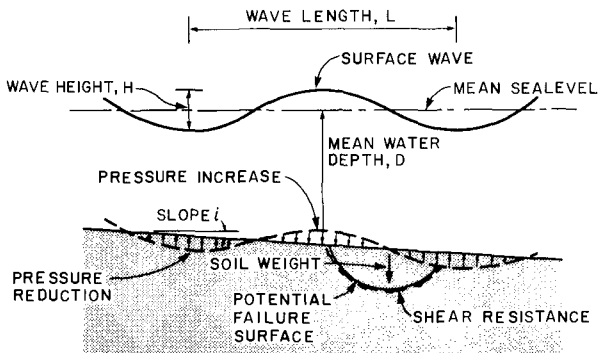


FIG. 4-LIMIT EQUILIBRIUM ANALYSIS FOR WAVE INDUCED SUBMARINE SLIDES

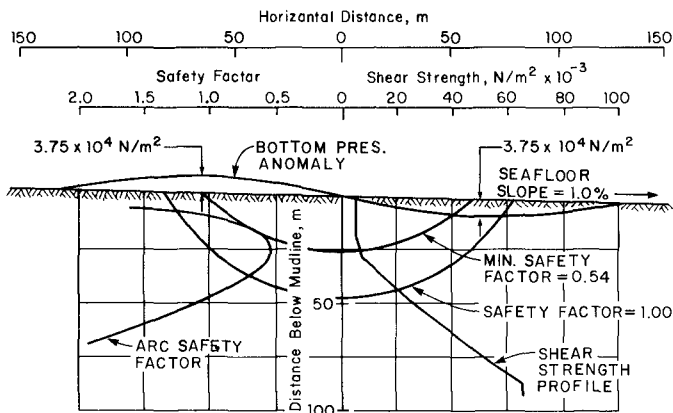


FIG. 5-RESULTS OF TYPICAL LIMIT EQUILIBRIUM ANALYSIS

The depth of slide zone is affected by the shear strength and unit weight profiles of the soil, and the amplitude and wave length of the bottom pressures. The interdependence between the influence of the amplitude and wave length of the bottom pressure anomaly on the stability of seafloor slopes for a very underconsolidated soil mass is illustrated in Fig. 6. Greater bottom pressures associated with longer wave lengths tend to cause deeper slides. If the design wave spectrum is known, analysis using combinations of wave lengths and amplitudes are made to determine the combination of wave data yielding the maximum depth of slide.

Limit equilibrium analyses, however, do impose certain approximations that challenge the accuracy of the depth of slide predicted with this procedure. Limit equilibrium analyses treat the soil as a rigid-plastic material and do not account for either soil softening and strength loss produced by a large number of successive waves or for dynamic effects. Nevertheless, limit equilibrium analyses are useful during preliminary studies to assess the likelihood of submarine slides for a given oceanographic and geotechnical environmental setting. Results of limit equilibrium analyses, however, do not provide estimates of the magnitude and distribution of soil movements.

Shear stresses computed using the theory of elasticity with a sinusoidal loading have also been used to evaluate stability. In this case the computed profile of maximum shear stress is compared to the shear strength profile.

Model Studies

To gain further insight into the stability and deformational patterns of seafloor soils subject to wave-induced bottom pressures and to evaluate the applicability of limit equilibrium approaches, model studies have been performed using wave tanks(4,7,15,19,22). Results of these model tests have demonstrated the validity of the failure mechanism and have shown that the vertical component of the movement decays more rapidly with depth than the horizontal component, but there is a net lateral translation downslope. Below the failure zone the net downslope movement decreases to about zero where the soil experiences nearly elastic behavior.

Results of these model studies demonstrated also that the yielding and movements of the seafloor soils can influence the development of bottom pressure amplitudes, which are usually computed from oceanographic data using linear wave theory that assumes a rigid seafloor. Doyle(4) found the bottom pressures on the soils in the wave tank were about 0.27 of those

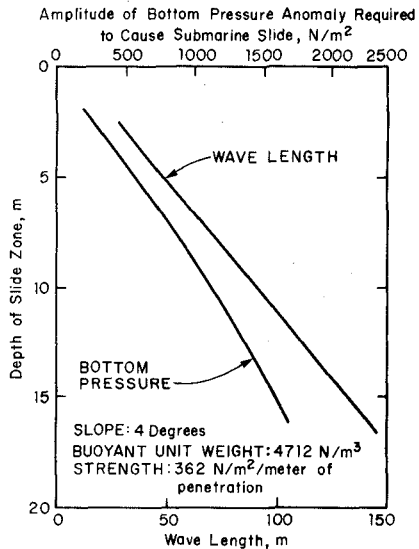


FIG. 6-DEPTH OF FAILURE ZONE FOR ANOMALIES OF VARYING AMPLITUDE AND LENGTH

computed for a rigid bottom. Gade(6) discusses the importance of soil yielding on the interaction between the water and soil. Due to the complex interaction between wave length, water depth and soil properties, the bottom pressure amplitude computed for a rigid bottom may not always exceed the value experienced on a yielding bottom. Since the magnitude and distribution of soil movements are strongly influenced by the amplitude and wave length of the bottom pressure, more attention is required, as will be discussed subsequently, on the interaction between the water and soil.

The qualitative results obtained from the wave-tank studies provided insight into a complex phenomenon and served to confirm general findings from analytic techniques in view of the limited field data available.

Finite Element Analysis: First Generation

At the time some of the wave-tank studies were being made the finite element analysis was being applied to the problem, and laboratory studies were initiated to develop stress-strain data for soft soils subjected to cyclic loads having periods coincident with storm loads. Wright and Dunham (25) first applied a finite element method with a nonlinear stress-strain response for the soils to evaluate seafloor response to wave-induced pressures. Since this model does not include the effects produced by gravity loads, the lateral boundaries are located one-quarter wave length apart for reasons of symmetry and antisymmetry, as shown in Fig. 7. In this case, displacements are allowed parallel to but not normal to the boundary under the crest, and below the null point displacements are allowed normal to but not parallel to the boundary. The lower boundary of the mesh is located at a penetration where soil movements are negligible so that restricting soil movements at this penetration in the model provides a reasonable approximation to in situ conditions. The distribution and size of the elements are selected to be compatible with soil property variations and the wave length and to provide reasonable numerical accuracy.

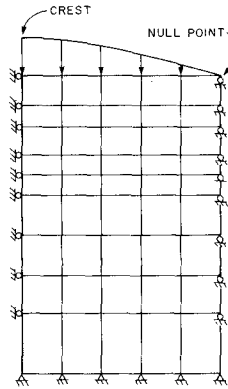


FIG. 7-QUARTER WAVE LENGTH FINITE ELEMENT MESH

The nonlinear and inelastic behavior typified by the undrained behavior of cohesive soils were incorporated into the finite element model using an interactive-incremental procedure(5,25) and a hyperbolic approximation(8) of the soil stress-strain response for loading conditions:

$$\sigma_1 - \sigma_3 = \frac{\epsilon}{\frac{1}{E_i} + \frac{R_f \epsilon}{2 S_u}} \quad , \quad \epsilon \leq \epsilon_f$$

$$\sigma_1 - \sigma_3 = 2 S_u \quad , \quad \epsilon \geq \epsilon_f \quad \dots \dots \dots (1)$$

where $\sigma_1 - \sigma_3$ = deviator stress; ϵ = axial strain; E_i = "elastic" tangent modulus at $\epsilon = 0$; S_u = undrained shear strength; and R_f = failure ratio, influence of the failure strain ϵ_f . The comparison in Fig. 8 between

Eq. 1 and laboratory measured stress-strain response of a Gulf of Mexico clay shows remarkable agreement. For unloading conditions, a decrease in maximum shear stress, the soil modulus value, E_{ur} , is approximately constant with a value that generally equals or exceeds E_i . The parameters associated with Eq. 1 were based on stress-strain data obtained from isotropically consolidated data.

Even though in situ gravity stresses were unaccounted for in these early finite element analyses, it was recognized that with vertical displacement of the seafloor mass under the action of a bottom pressure anomaly the gravity forces would tend to retard the tendency for instability, especially in very soft sediments where larger vertical displacements may occur. The counter pressure due to the buoyant weight of the elevated soil is illustrated in Fig. 9. Wright and Dunham(25) describe an approximate procedure for adjusting displacements to account for the counter buoyant effect. Arnold(1) and Bea and Arnold(2) used the finite element method to evaluate soil movements at a site in South Pass Block 70. Fig. 10 shows some results of their analyses to give perspective to the magnitude and distribution of computed movements due to wave-induced bottom pressures.

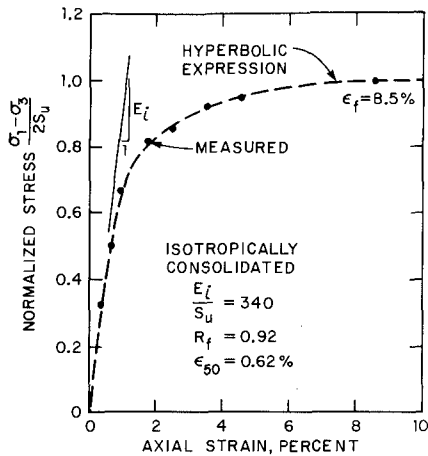


FIG. 8—COMPARISON BETWEEN MEASURED AND THEORETICAL STRESS-STRAIN RESPONSE

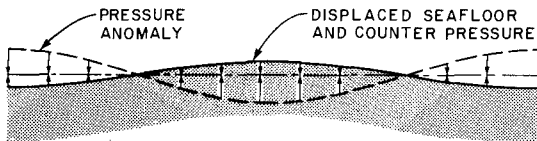


FIG. 9—COUNTER BUOYANT EFFECT DUE TO LARGE SEAFLOOR MOVEMENTS

Finite Element Analysis: Second Generation

Although results from the first generation finite element studies provided reasonable assessments of the distribution of stresses and displacements in a soil mass subjected to bottom pressure anomalies, the previously reported finite element analyses did not accurately account for either alterations in the soil properties due to the storm history or for gravity

stresses on the predicted soil movements. These factors were addressed, but only accounted for in a very approximate way. In addition, the interaction between the soil and water on the development of bottom pressures was neglected. Recently, Wright(24) described a procedure, based on a finite element analysis that includes initial gravity and geologic stresses, for predicting stress distribution and soil movements.

In situ shear stresses due to gravity and geologic stresses influence the seafloor response to wave-induced bottom pressures in three ways. The magnitude of soil stiffness is influenced by the shear stress in the soil due to its non-linear stress-strain behavior, and the increment of additional shear stress that the soil can sustain due to wave-induced loading may be reduced as the initial in situ shear stresses increase. Furthermore, when the gravity and geologic stresses are included, the stiffness moduli in the slope are usually not symmetrical about any parallel lines oblique to the slope. This lack of symmetry exists also when the wave-induced stresses are superposed. For an infinite train of uniform waves and negligible changes in soil properties with each wave cycle, the displacement patterns on lateral boundaries oriented perpendicular to the slope and separated by one wave length should be identical. Therefore, results of finite element analyses are based on equal displacements at corresponding penetrations on the two boundaries. An example finite element mesh for one wave length is shown in Fig. 11 together with the boundary conditions normally used.

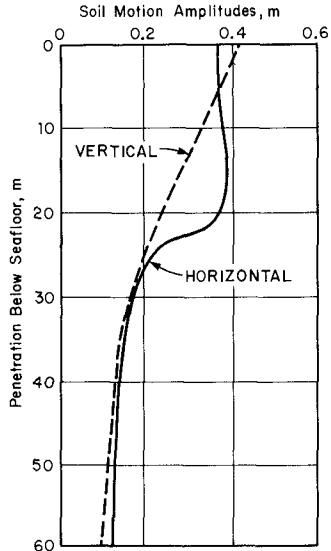
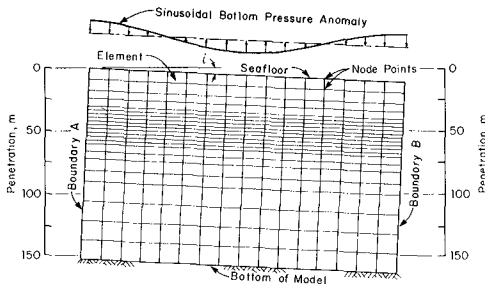


FIG. 10-TYPICAL MAXIMUM SOIL MOVEMENT INDUCED BY A SINGLE WAVE (After Bea and Arnold, 1973)



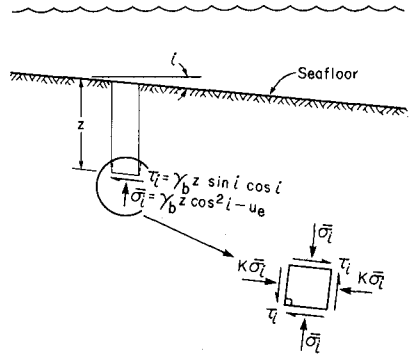
BOUNDARY CONDITIONS
 1. Points on Boundary B move identically to Points on Boundary A
 2. Bottom Fixed
 351 Elements; 391 Nodes

FIG. 11-FINITE ELEMENT MESH - ONE WAVE LENGTH

The seafloor may often be approximated as an infinite slope inclined at an angle i , as illustrated in Fig. 12. In an underconsolidated soil mass, excess hydrostatic pore pressure, u_e , results in a hydraulic force; the resultant hydraulic force being perpendicular to the surface. As shown in Fig. 12, the excess pore pressure, which is required to determine the effective stress state, may be related to the ratio of undrained shear strength of a normally consolidated soil to effective consolidation pressure (referred to as the c/p ratio), the buoyant overburden pressure, and the in situ undrained shear strength of the underconsolidated soil, S_u .

An additional assumption, which is used to compute the complete state of stress in the soil mass, is that the effective normal stresses on some two planes are proportional. For slopes less than a few degrees and for either the principal planes or planes parallel and perpendicular to the slope, the constant of proportionality between normal stresses on these planes may be about equal to the effective coefficient of earth pressure "at rest". These stress conditions are summarized in Fig. 12.

Early finite element results suggested that the magnitude of initial stress can have a significant influence on the computed soil movements. These previous analyses, however, have used stress-strain response measured on isotropically consolidated specimens. The soil in situ experiences anisotropic consolidation, and the stress-strain response of an anisotropically consolidated specimen may differ appreciably from the response of an isotropically consolidated specimen, as illustrated in Fig. 13. The comparison of secant moduli at equal levels of mobilized shear stress, shown in Fig. 13, indicates that larger soil movements may be computed with the smaller secant moduli associated with the isotropically consolidated specimen. Wright(24) attempts to include the effects of both anisotropic consolidation and cyclic loading on the soil



- γ_b : Soil Buoyant Unit Weight
- u_e : Excess Hydrostatic Pore Pressure
 $= \gamma_b z - S_u / (c/p)$
- S_u : In situ Undrained Shear Strength of Underconsolidated Soil
- c/p : Ratio of Undrained Shear Strength of Normally Consolidated Soil to the Effective Consolidation Stress, p

FIG. 12-EFFECTIVE STRESSES IN AN INFINITE SUBMERGED SLOPE

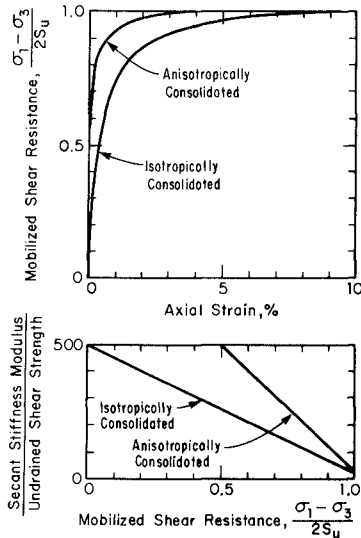


FIG. 13-COMPARISON OF STRESS-STRAIN CURVES

stress-strain response by combining the shear stresses computed from finite element analysis on a plane parallel to the slope with strains obtained from cyclic simple shear tests that simulate the computed stress history.

The second generation finite element procedure for computing wave-induced seafloor movements does not account for:

- (1) the soil stress-strain behavior for an anisotropic-consolidated condition, which is more representative of in situ conditions than the isotropic-consolidated condition;
- (2) the degradation in soil strength and stiffness that occurs due to cyclic stress reversals induced during the passage of a storm; and
- (3) the interaction between the water and soil on the development of the amplitude of wave-induced bottom pressure.

A procedure for overcoming the first two limitations is presented in subsequent paragraphs. A procedure to overcome the third limitation has been developed, but will not be reported here.

CURRENT PROCEDURE

Stress-Strain Model

The finite element model currently used is basically the same as the second generation model with the exception that the stress-strain behavior is described by a hyperbolic expression that accounts for anisotropic consolidation. Results of a recent study by Donaghe and Townsend⁽³⁾ showed that the undrained response of cohesive soils consolidated under a deviatoric stress σ_{dc} could be mathematically described by the modified hyperbolic expression:

$$\sigma_1 - \sigma_3 - \sigma_{dc} = \frac{\epsilon}{\frac{1}{E_i} + \frac{R_f \epsilon}{2S_u - \sigma_{dc}}} \dots \dots \dots (2)$$

Eq. 2 represents soil stress-strain response for a single application of a static load. With the passage of a number of waves the soils may soften and lose strength. This degradation in soil resistance is influenced by the spectrum of bottom pressure anomalies and in general decreases with penetration. The cumulative soil displacements, however, can be estimated using Eq. 2 with appropriately modified parameters, which are determined from the spectrum of bottom pressures, estimates of induced stresses from finite element analysis using unmodified stress-strain parameters, and results from laboratory cyclic testing.

Spectrum of Bottom Pressures

A spectrum of bottom pressure anomalies is developed from deep-water wave statistics and characteristics of the seafloor in the vicinity of the site. A deep-water storm wave record, such as the one in Fig. 14, can be defined by a spectrum, the number of storm waves with various combinations of periods and heights. Depending on the water depth and soils at the site, the shorter period waves

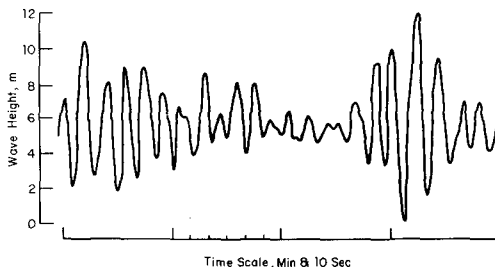


FIG. 14—FOUR MINUTE PORTION OF A TYPICAL STORM WAVE RECORD (After Tricker, 1964)

of smaller heights that do not cause significant bottom pressure amplitudes are not considered in the analysis.

The wave length L at a site with water depth D is computed for each wave period T from linear wave theory(23).

$$\left(\frac{2\pi}{T}\right)^2 = \frac{2\pi g}{L} \tanh\left(\frac{2\pi D}{L}\right) \dots \dots \dots (3)$$

where g is the acceleration of gravity. Analyses, which include the effects of refraction, reflection, shoaling and bottom friction, are then made to determine the changes in heights of storm waves as they prograde from deep water across the continental shelf and over the site. After determining the heights and lengths of waves at the site for each wave period, the bottom pressure amplitude, Δp, produced by this storm-wave spectrum is computed from

$$\Delta p = \gamma_w H/[2 \cosh(2\pi D/L)] \dots \dots \dots (4)$$

As previously mentioned, the yielding of the seafloor with the passage of waves affects the development of wave heights and bottom pressures. Although analyses are not available to fully account for this effect, through a cooperative and interactive effort between the oceanographer and geotechnical consultant, approximate methods are available to evaluate the relative influence of a yielding seafloor on the development of bottom pressure amplitude for a given wave height. These methods are based on a dynamic visco-elastic model(14). The term "yielding" refers to a failure of the soil mass and not simply "elastic" deformations for which analytic methods are available.

A 100-year storm wave spectrum along with its spectrum of wave-induced bottom pressure at a site located in about 200 ft (60 m) of water in the Gulf of Mexico is shown in Table 1. This data demonstrates that the maximum deep-water wave height does not always induce the maximum amplitude of bottom pressure.

Initial Finite Element Analyses

To obtain data for planning a laboratory test program of cyclic loading and to evaluate and interrelate cyclic tests data with finite element analyses for predicting the cumulative soil displacements during a storm, finite element analyses are first performed for a range in amplitudes and wave lengths typical of the expected spectrum on bottom pressure anomalies. Usually results are obtained for 3 to 5 wave length conditions and for 5 to 15 amplitudes. The stress-strain-strength properties of the soils used in these initial analyses are usually based on Remote Vane data(9) and on laboratory data obtained from the SHANSEP concept(10) for a single load cycle preferably applied at a rate representative of the mean period of wave loads. For a given spectrum of bottom pressures, a spectrum of stresses at any location

Wave Period, sec	7-7.9	8-8.9	9-9.9	10-10.9	11-11.9	12-12.9	13-13.9	14+
Mean Wave Length, m	87.8	112.5	139.3	167.7	196.0	224.9	254.2	282.6
Amplitude of Surface Wave in Deep Water, m	Number of Cycles/Pressure Amplitude for Average Wave, kN/m ²							
3.1 - 4.6	112	149	144	125	85	56	24	11
	1.25	2.92	5.22	8.24	10.78	13.22	13.22	16.96
4.6 - 6.1	54	66	65	56	33	28	12	7
	1.77	4.12	7.33	11.60	15.09	18.39	21.27	23.76
6.1 - 7.6	19	24	23	21	15	10	5	3
	2.30	5.27	9.44	14.80	19.40	23.85	27.00	30.56
7.6 - 9.1	4	4	7	7	6	5	2	
	2.78	6.47	11.54	18.11	23.71	29.12	33.48	
9.1 - 10.6	2	2	3	5	5	4	2	
	3.31	7.62	13.65	21.41	28.07	34.44	39.61	
10.6 - 12.1			2	3	2			
			15.76	24.72	32.38			

Note
 (1) Wave Statistics are of waves having an amplitude greater than 3.0m and a period greater than 7.0 seconds
 (2) Mean Period 9.9 seconds
 (3) Mean Amplitude 5.6 m
 (4) Water Depth at Site 57.9 m

**TABLE 1
 100 YEAR HURRICANE WAVE STATISTICS
 AND TYPICAL BOTTOM PRESSURE
 SPECTRUM**

below the seafloor can be determined from the stress distribution computed with the finite element method.

Fig. 15 illustrates a profile of computed lateral movements and the cyclic variation of shear stress on planes parallel to the slope for one wave length, but different amplitudes of bottom pressure. Fig. 15 also includes the soil properties and initial in situ stress conditions. The variation in stresses experienced by an element of soil during one wave cycle is shown in Fig. 16.

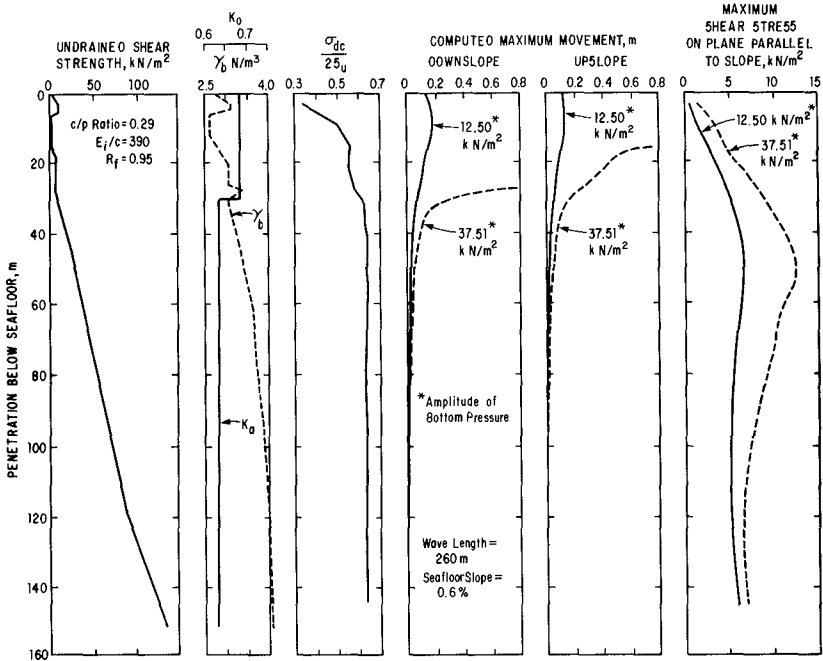


FIG. 15—SOIL PROPERTIES, LATERAL MOVEMENTS AND STRESSES

The depth of soil failure determined from the finite element results for the conditions described in Fig. 15 was approximately 45 ft less than the depth determined from a limit equilibrium analysis. Deviations between the predicted depth of slide from limit equilibrium and finite element results depend on several factors including the strength profile. The predicted depths obtained from the two procedures tend to better agree when the failure occurs in a relatively weaker soil layer at some depth⁽²⁾.

To illustrate the importance of using a stress-strain model representative of anisotropically consolidated conditions, a finite element analysis was made for the conditions shown in Fig. 15, but using stress-strain data representative of isotropically consolidated conditions. The results of this comparison, shown in Fig. 17, demonstrate that stress-strain response in terms of isotropically compared to anisotropically consolidated conditions may result in much larger predicted displacements, but

the differences in stresses computed with both data sets deviated by less than about 30 percent.

Stresses and displacements below the seafloor due to wave-induced bottom pressures can be computed for the other wave lengths in the spectrum, and combining these with the results in Fig. 15, an initial estimate of the soil stress spectrum can be developed. During the progress of a storm the seafloor response to a bottom pressure perturbation depends on the history of cyclic stresses due to previous wave action. The degree of progressive softening and loss of strength affects the stress distribution and the development of soil displacement that may accumulate during the storm. Knowing the spectrum of induced stress, a laboratory testing program is designed to provide modified stress-strain data for incorporation into the finite element analysis to predict cumulative soil displacements with the passage of a storm over a site.

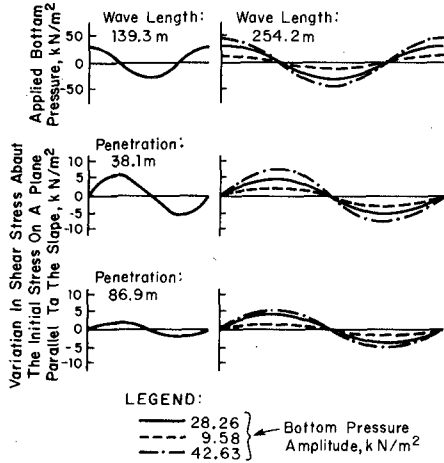


FIG. 16-STRESS VARIATIONS

Modified Stress-Strain Response

A series of cyclic stress pulses can be superposed on the initial consolidation stress in the laboratory to determine the accumulation of strain with each additional stress pulse. Laboratory tests are generally performed by either cycling with a constant stress or by applying a spectrum of stress pulses. Fig. 18 shows data obtained from cyclic tests on a Gulf of Mexico clay.

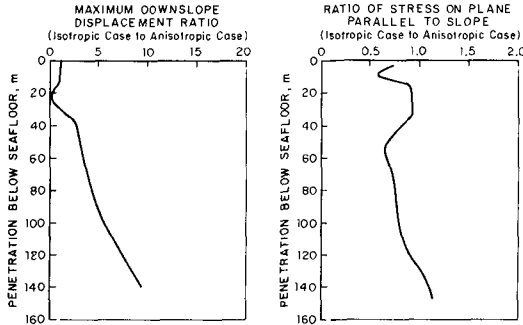


FIG. 17-COMPARISON OF RESULTS FOR ISOTROPICALLY AND ANISOTROPICALLY CONSOLIDATED STRESS-STRAIN DATA

The amount of cumulative strain and reduction in shear strength due to cyclic loading with a constant stress is shown in Fig. 19. If an element of soil experiences an equivalent of 10 stress cycles, the

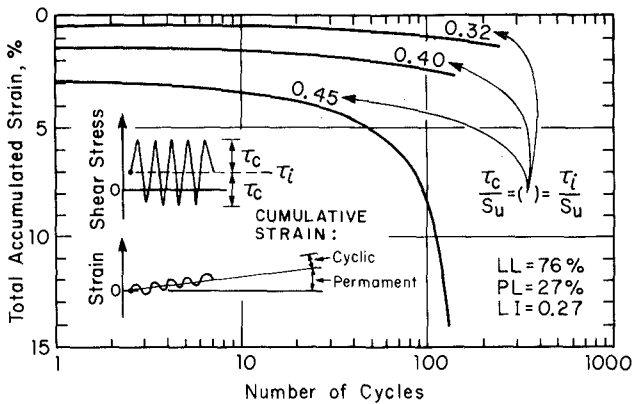


FIG. 18-CYCLIC LOADING TEST RESULTS

stress-strain curve marked $N = 10$ provides a realistic estimate of the expected cumulative displacement. Studies by Lee and Focht⁽¹²⁾ and Norwegian Geotechnical Institute^(17,18) summarize the current experience of cyclic load test data for cohesive soils. The stress-strain response of soil subjected to cyclic loading is a function of the initial stress condition about which the cyclic stress oscillates. Preliminary research results⁽¹⁸⁾ demonstrate that cyclic test data obtained for equal magnitudes of cyclic stress about different initial stresses can be equated if the results are interpreted with a normalized stress R ,

$$R = \frac{\tau_c}{S_u} \left[\frac{1}{1 - (\tau_i/S_u)^4} \right] \dots (5)$$

where τ_c = cyclic maximum shear stress; τ_i = mean maximum shear stress; and S_u = static undrained shear strength.

The degradation to soil stress-strain-strength properties induced by a series of N cycles of variable stresses can usually be equated to an equivalent number of cycles, N_{eq} , of some reference stress τ_{ref} . Combining this premise with laboratory cyclic test data and the profile of stress spectra, modified stress-strain-strength data can be generated for use with the finite element analysis to determine the accumulation of soil movements due to a spectrum of bottom pressures. The procedure used

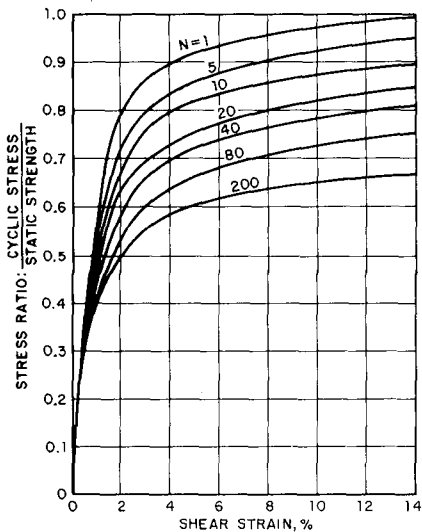


FIG. 19-STRESS-STRAIN RELATIONSHIPS AFTER CYCLIC LOADING

to determine the appropriate modified stress-strain responses to predict these cumulative displacements, representative of the complete storm or some fraction of its history, is explained for a given penetration. The process is repeated to determine the degree of degradation for other penetrations.

For the purpose of analysis, it is necessary to find a cyclic stress of uniform amplitude that has the same effects as the random stress history due to the storm loading. Lee and Focht(11) have presented a method for determining this equivalency, which is based on Miner's damage potential concept(16) developed for the study of metal fatigue. The essential elements of the method are presented in Fig. 20. As shown schematically in Fig. 20(a), the cyclic stress history, which was estimated from initial finite element analysis, contains

N_i cycles of amplitude S_i . The number of cycles of stress of this amplitude, N_{if} , required to produce some predetermined strain, ϵ_p , is determined from the results of laboratory cyclic loading tests as shown in Fig. 20(c). If superposition is assumed then the same strain, ϵ_p , is produced by N_e cycles of stress with amplitude S_e . Thus, N_{if} cycles of stress of amplitude S_i are equivalent to N_e cycles of amplitude S_e . Therefore, N_i cycles of amplitude S_i are equivalent to $(N_i \cdot N_e) / N_{if}$ cycles of amplitude S_e . This procedure is repeated for every cycle in the irregular stress history to yield the number of uniform cycles of stress, N_{eq} , of amplitude S_e that produce the same accumulated strain as the irregular stress history. The equivalency is expressed by:

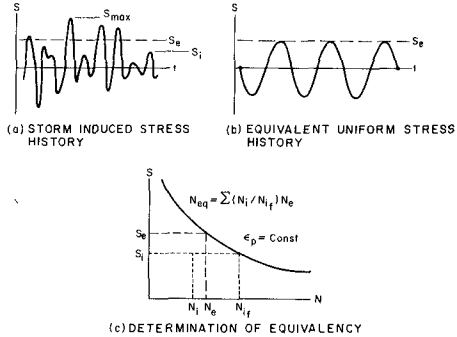


FIG. 20-CONVERSION OF IRREGULAR STRESS HISTORY TO EQUIVALENT UNIFORM STRESS HISTORY

$$N_{eq} = \sum (N_i / N_{if}) N_e \dots \dots \dots (6)$$

Theoretically the amplitude S_e of the uniform stress history equivalent to the random stress history may be selected arbitrarily. Changing S_e leads to a change in N_{eq} in Eq. 6, but any combination of N_{eq} and S_e is equivalent to any other. Each defines the number of uniform cycles required to produce a specified accumulation of strain. However, a program of laboratory tests to confirm the validity of the procedure for a given soil is recommended.

Reference Anomaly

When computing the equivalency, it is convenient to convert the irregular stress history into an equivalent number of cycles of stress corresponding to the stress induced by the "most severe" anomaly present in the spectrum being analyzed because analysis of the effects of this anomaly are used for the basic studies of seafloor response. The term "most severe" refers to the anomaly that induces the largest stresses and displacements in the seafloor. The anomaly of greatest amplitude is not necessarily the "most severe", nor does the anomaly of maximum amplitude

necessarily coincide with the surface wave of maximum height. The "most severe" anomalies are usually those of long wave length and large amplitude. The anomaly used to compute the equivalency is called the "reference" anomaly. Because the anomaly-induced stresses are a function of penetration below the seafloor, the equivalency number, N_{eq} , also varies with penetration.

Fig. 21 shows the profile of N_{eq} values representative of the conditions shown in Fig. 15 for the wave spectrum in Table 1. Fig. 21 also shows a comparison of profiles of downslope movement computed with the appropriate stress-strain curves shown in Fig. 19 for the N_{eq} profile and with the unmodified stress-strain curves. Above approximately 135-ft penetration the downslope movements accumulating with the passage of the storm exceeds the movement due to one application of a larger wave with unmodified soil properties. Below about 135-ft penetration the reverse is true. As the storm develops, the reduction in strength and softening in the upper material prevents transmission of the greater stresses due to larger waves, which generally occur near the middle of the storm.

If sufficient degradation of the soil occurs the material in the failure zone acts essentially as a fluid-like mass. Once this occurs additional accumulation of displacements below the failure zone are very small. When displacement analyses are conducted to assess the forces that must be sustained by structures founded in the seafloor, it is necessary to determine at what stage of the storm the combined effects of progressive softening and changes in the magnitude and distribution of soil movements result in maximum structural loading.

CONCLUDING COMMENT

The depth of submarine slides and profiles of soil movements, such as those illustrated in Fig. 15 and 21, are important input for analyses of soil-structure interaction and for the design of foundations at sites susceptible to submarine slides. Evaluation of the soil movement problem and the effect of soil movements on offshore platform design requires an interaction between the oceanographer, marine geologist, geotechnical engineer, and structural engineer. The scope of this paper has been limited to only oceanography and geotechnical considerations required to estimate soil movements.

The state-of-the-art for prediction of soil movements due to wave-induced bottom pressures has improved significantly during the past eight years. The procedures presented here were based on a static analysis, even though the wave-induced bottom pressures are dynamic loads. Although static analyses are often appropriate for the 10 to 15-second period loads, prediction of soil response in the failure zone and the transfer of stresses into the unfailed soils would be better modelled with a dynamic analysis. More work, however, is required to better define the behavior of soils in post-failure conditions before further improvements in the state-of-the-art can be expected.

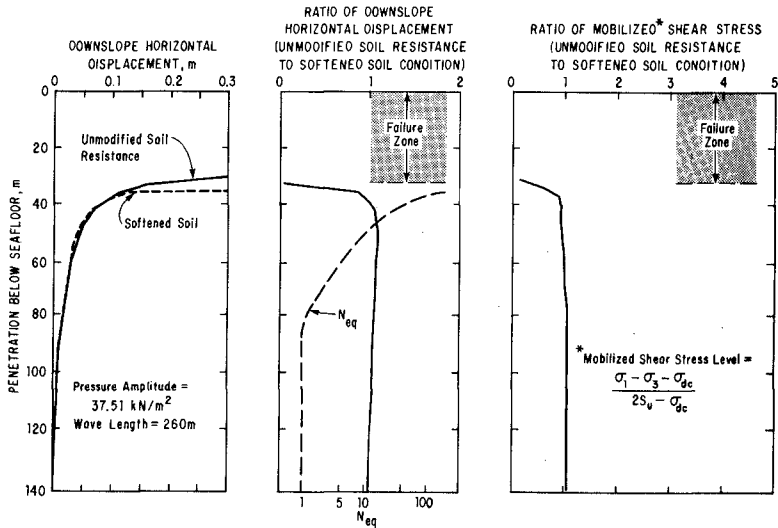


FIG 21-COMPARISON OF LATERAL MOVEMENTS AND STRESSES FOR UNMODIFIED AND SOFTENED SOIL

APPENDIX I - REFERENCES

- (1) Arnold, P., "Finite Element Analysis - A Basis for Sea-Floor Soil Movement Design Criteria," Proceedings, Fifth Annual Offshore Technology Conference, Houston, Vol. 2, May 1973, pp. 743-752.
- (2) Bea, R. C. and Arnold, P. "Movements and Forces Developed by Wave-Induced Slides in Soft Clays," Proceedings, Fifth Annual Offshore Technology Conference, Houston, Vol. 2, May 1973, pp. 731-742.
- (3) Donaghe, R.T. and Townsend, F.C., "Effects of Anisotropic Versus Isotropic Consolidation in Consolidated-Undrained Triaxial Compression Tests of Cohesive Soils," Technical Report No. S-75-13, U.S. Army Engineer Waterways Experiment Station, Vicksburg, Mississippi, October 1975.
- (4) Doyle, E. H., "Soil-Wave Tank Studies of Marine Soil Instability," Proceedings, Fifth Annual Offshore Technology Conference, Houston, Vol. 2, May 1973, pp. 753-766.
- (5) Duncan, J.M. and Chang, C-Y, "Nonlinear Analysis of Stress and Strain in Soils," Journal of the Soil Mechanics and Foundations Division, ASCE, Vol. 96, No. SM5, 1970, pp. 1629-1653.
- (6) Cade, H. G., "Effects of Nonrigid, Impermeable Bottom on Plane Surface Waves in Shallow Water," Journal of Marine Research, Vol. 16, No. 2, 1958, pp. 61-82.
- (7) Henkel, D. J., "The Role of Waves in Causing Submarine Landslides," Ceotechnique, Vol. 20, No. 1, March 1970, pp. 75-80.

- (8) Kondner, R.L., "Hyperbolic Stress-Strain Response: Cohesive Soils," Journal of the Soil Mechanics and Foundations Division, ASCE, Vol. 89, No. SM1, February 1963, pp. 115-143.
- (9) Kraft, L.M., Jr., Ahmad, N., and Focht, J.A., Jr., "Application of Remote Vane Results to Offshore Geotechnical Problems," Proceedings, Eighth Annual Offshore Technology Conference, Houston, May 1976, Vol. 3, pp. 75-96.
- (10) Ladd, C.C. and Foott, R., "New Design Procedure for Stability of Soft Clays," Journal of the Geotechnical Engineering Division, ASCE, Vol. 100, No. GT7, 1974, pp. 763-786.
- (11) Lee, K.L. and Focht, J.A., Jr., "Cyclic Testing of Soil for Ocean Wave Loading Problems," Proceedings, Seventh Annual Offshore Technology Conference, Houston, Vol. 1, May 1975, pp. 343-354.
- (12) Lee, K.L. and Focht, J.A., Jr., "Strength of Clay Subjected to Cyclic Loading," Marine Geotechnolgy, Vol. 1, No. 3, 1976, pp. 165-185.
- (13) McClelland, B. and Cox, W.R., "Performance of Pile Foundations for Fixed Offshore Structures," International Conference on Behaviour of Offshore Structures, Norwegian Institute of Technology, Norway, August 1976.
- (14) McClelland Engineers, Inc., Unpublished Proprietary Research, 1976.
- (15) Mignoit, C., "A Study of the Physical Properties of Various Forms of Very Fine Sediment and Their Behavior Under Hydrodynamic Action," La Houille Blanche, No. 7, 1968.
- (16) Miner, M.A., "Cumulative Damage in Fatigue," Transactions, ASME, Vol. 67, September 1945, pp. A159-164.
- (17) Norwegian Geotechnical Institute, Research Project, Repeated Loading on Clay, Literature Review, Report No. 74037-5, Norwegian Geotechnical Institute, Oslo, September 1975.
- (18) Norwegian Geotechnical Institute, Research Project, Repeated Loading on Clay, Summary and Interpretation of Test Results, Report No. 74037-9, Norwegian Geotechnical Institute, Oslo, October 1975.
- (19) Singh, H., "The Behavior of Normally Consolidated and Heavily Over-consolidated Clays at Low Effective Stress," Thesis presented to Cornell University, Ithaca, New York, January 1971, in partial fulfillment of the requirements of the degree of Doctor of Philosophy.
- (20) Sterling, G.H. and Strohbeck, E.E., "The Failure of the South Pass 70 "B" Platform in Hurricane Camille," Proceedings, Fifth Annual Offshore Technology Conference, Houston, Vol. 2, May 1973, pp. 719-730.
- (21) Tricker, R.A.R., Bores, Breakers, Waves and Wakes, Mills and Boom, Ltd., London, 1964.
- (22) Tsui, K.K., "Stability of Submarine Slopes," Thesis presented to Queen's University, Ontario, Canada, in January 1972, in partial fulfillment of the requirements of the degree of Doctor of Philosophy.

- (23) Wiegel, R.L., Oceanographical Engineering, Prentice-Hall, Inc., Englewood Cliffs, New Jersey, 1964.
- (24) Wright, S.G., "Analysis for Wave Induced Sea-Floor Movements," Proceedings, Eighth Annual Offshore Technology Conference, Houston, Vol. 1, May 1976, pp. 41-52.
- (25) Wright, S.G., and Dunham, R.S., "Bottom Stability Under Wave Induced Loading," Proceedings, Fourth Annual Offshore Technology Conference, Houston, Vol. 1, May 1972, pp. 853-862.

APPENDIX II - NOTATION

γ_b	= soil buoyant unit weight
γ_w	= unit weight of water
Δp	= bottom pressure amplitude
ϵ	= axial strain
ϵ_f	= failure strain
ϵ_p	= predetermined amount of strain
ϵ_{50}	= axial strain at a shear stress equal to $1/2 S_u$
σ_{dc}	= deviatoric consolidation pressure
$\bar{\sigma}_i$	= effective normal stress on plane parallel to slope
$\sigma_1 - \sigma_3$	= deviatoric stress
τ_c	= cyclic maximum shear stress
τ_i	= mean maximum shear stress or stress on a plane parallel to infinite slope
τ_{ref}	= reference shear stress
c/p	= strength ratio
D	= water depth
E_i	= "elastic" tangent modulus at $\epsilon = 0$
E_{ur}	= "elastic" unloading modulus
g	= gravitational constant
H	= wave height
i	= slope angle
K	= earth pressure coefficient
L	= wave length
N	= number of cycles
N_e	= number of cycles of amplitude S_e
N_{eq}	= equivalent number of cycles
N_i	= number of cycles of amplitude S_i
N_{if}	= number of cycles of amplitude S_i required to cause a strain of ϵ_p
R	= normalized stress

R_f	=	failure ratio, influence of the failure strain ϵ_f
S_e	=	stress amplitude
S_i	=	stress amplitude
S_{max}	=	maximum stress amplitude
S_u	=	undrained shear strength
t	=	time
T	=	wave period
u_e	=	excess hydrostatic pore pressure
z	=	penetration below seafloor

CHAPTER 95

SCOUR AROUND MODEL PIPELINES DUE TO WAVE ACTION

by

John B. Herbich, Ph.D., P.E.
Professor of Ocean and Civil Engineering
Ocean Engineering Program
Texas A&M University
College Station, Texas

ABSTRACT

The size, number and application of offshore pipelines are steadily increasing. At the same time, the incidence of reported pipeline failures is also increasing. There appear to be several reasons for these failures, and they can be placed in two basic categories:

1. inadequate cover, and
2. low "specific gravity" of the pipeline.

Under the first category the depth of burial may be insufficient, the type of burial material may be inferior to the material alongside the trench, or the compaction of cover material may be inadequate. Under the second category the pipe may actually float up to the surface from the ocean bottom as material around the buried pipe liquifies.

An extensive literature search revealed that many studies were conducted by Meyers (1936), Waters (1939), Johnson (1940), W.E.S. (1940), Rector (1954), Wiegel, et al (1954), Saville (1957), Iwagaki and Noda (1962), Nayak (1972), Noda (1972), and Earattupuzha (1974). In general, two types of "equilibrium profiles" were developed in the laboratory flumes, the "ordinary" and the "storm" (sometimes referred to as summer and winter profiles). Despite numerous previous investigations, knowledge of the "scale effects" involved in equilibrium beach profiles is inadequate. Many authors have analyzed model data without stating the relation between model and prototype dimensions. In addition, many have claimed certain phenomena observed in the model to be independent of initial slope.

An extensive laboratory study was conducted to evaluate the development of underwater bars and scour patterns with the pipeline buried at various depths below the ocean bottom. Pictures of the beach profile were taken at specific time intervals through the glass wall of the wave tank.

Attempts were made to correlate equilibrium profile geometric quantities, such as depth of offshore bar, scour depth and berm height with the wave characteristics. Qualitative agreement between laboratory and natural beach profiles were demonstrated by trial and error fitting of one to the other.

INTRODUCTION

In more recent times, the energy crisis has caused acceleration of exploitation and exploration of the oil and gas reserves under the continental shelf. The most economical way of transporting oil and gas is through pipelines from offshore platforms or underwater completions to shore.

In another widespread application of pipelines, environmental considerations and regulations call for the disposal of municipal and industrial waste in deeper water, both in lakes and oceans, than previously. Here, as in all engineering design work, a better understanding of soil-pipe interaction and magnitudes of various forces acting on an unburied pipe is required before good design criteria and engineering practices can be well defined.

Experimental studies, mainly in the laboratory, but some in the field, have been conducted in many countries, notably in the U.S.A., the Netherlands and Japan.

While the petrochemical industry is evaluating pipeline failures and design practices, such technical information is generally restricted and not available. Since design engineers have been made more conscious of failures in more recent years, pipelines are sometimes over-designed and excessively expensive to construct. Over the past 10 or so years, the incidence of reported submarine pipeline failures, particularly of large diameter pipelines, has increased markedly.

The American Society of Civil Engineers appointed a Task Committee on Pipelines in the Ocean in 1969 to define the problems of pipelines in the oceans and to determine the state-of-the-art in the design and construction of pipelines in the oceans.

This effort, which has not been sponsored financially, has attempted to define the problem and review the current state-of-the-art in the areas of environmental factors, design factors and construction factors. The deficiencies were uncovered in the state-of-the-art¹, in

- (a) structural and external pressure effects,
- (b) depth of burial,
- (c) economics of submarine pipelines, and
- (d) documentation.

The current project deals with the aspects described in (a), (b), and (d).

The American Gas Association has been sponsoring a study on offshore pipelines², particularly those in water depths greater than 200 ft. The conclusions of the study to date indicate that

- (a) considerable additional data are required to more fully evaluate pipeline-soil interaction, and

- (b) field measurements of storm-driven bottom particle velocities and accelerations should be obtained.

Recent pipeline failures include the following:

- (a) One gas line, one telephone line and two water lines have moved upward through silty sand at the bottom of a ship channel from an elevation -51 ft to elevation -41 ft. These lines were subsequently cut by maintenance dredging operations.
- (b) One 10-ft diameter steel bitumen-coated pipeline failed three times during construction. The failure, which occurred during one major and two minor storms, was probably due to liquifaction of the silty sand sediment around the pipe. One section of the pipe, weighing about 80 tons was found some 150 ft away from the trench in which it was placed and partially backfilled.
- (c) One 48-inch sewer outfall pipe failed during its first year of operation. Higher than design wave forces are thought to be responsible for failure. The pipeline was unburied.
- (d) One 48-inch water intake pipe was damaged and three sections of it displaced. The pipe was buried and an analysis is being made as to the possible causes of failure.
- (e) One 60-inch intake pipe at a nuclear power plant failed before the plant was placed in operation. Scour of sediment around the pipe exposed the buried pipe which was then subjected to forces for which the pipe was not designed.

The information on pipe failures is difficult to obtain as construction companies or owners are reluctant to discuss or even admit failure occurred. The problem is complicated by the fact that disputes arise as to who is responsible for failure -- the designer or the contractor. It is not unusual for some cases to be taken to court. It is hoped that permission will be obtained to eventually summarize and document recent pipeline failures.

LITERATURE REVIEW

The relationship between many variables which govern beach deformation are quite complex as was pointed out by many researchers studying beach formation, beach erosion, scour around piers and piles, and in front of seawalls, etc. A large number of variables and their mutual interaction further complicate analysis of experiment data.

Assuming a two-dimensional approach, a review of the literature revealed numerous studies of model beach profiles conducted by Meyer³ (1936), Waters⁴ (1939), Johnson⁵ (1940), Rector⁶ (1954), Wiegel, et al⁷ (1964), Saville⁸ (1957), Iwagaki and Noda⁹ (1962), Nayak¹⁰ (1972), Noda¹¹ (1972),

and Earattupuzha¹² (1974). Figure 1 shows a classification scheme developed by Sunamura and Horikawa¹³ (1974) for model beach profiles. Type II profile was generally observed in this study. Despite numerous previous investigations, knowledge of scale effects is inadequate.

A literature survey relating to scour and stability of submarine pipelines was conducted and reported by Ralston and Herbich¹⁴ (1968). The present study is partially an outgrowth of previous work which was supported in part by the U.S. Corps of Engineers. An additional survey dealing with the design of offshore pipelines was conducted in 1971-73 and reported by Manley and Herbich¹⁵ (1976).

Coastal deformations can be divided into two general groups: long-term and short-term. Long-term changes are those changes in a coastline which occur over hundreds of years and result in a general prograding or recession of the shoreline. Of more interest to the coastal engineer is the short-term change which is associated with the variable wave climate and resulting sediment motion. Wave induced sediment motion can be divided into two components: alongshore motion and motion normal to the coast. This paper is concerned with the onshore-offshore motion.

As waves progress onto a beach sediment motion occurs. The magnitude of the sediment transport depends on the wave characteristics. The resulting changes in the beach have a feedback control on the incident waves. For example, changes in depths caused by breaking waves require changes in location of the breaking waves. Intuitively, it would seem that when a given beach is subject to waves of constant characteristics for a sufficient length of time, an equilibrium state will develop. In nature, the variable meteorological conditions and resulting variable wave conditions probably seldom allow an equilibrium to be attained. In the hydraulic model, where one has control over wave parameters, such as wave height and wave period, and beach parameters, such as grain size and size distribution, the concept of the equilibrium profile can be more readily studied. Thus, in nature the equilibrium profile needs to be defined in terms of statistical averages. However, in the laboratory the equilibrium profile is defined as a stable configuration in which the oscillatory motion of a given sediment particle is about a mean position, the sorting action of waves presumably having reached an equilibrium. The net transport across any section parallel to the beach is zero.

The objective of this part of the study was to determine, through physical modeling, the effect of storm waves on buried pipelines approaching the shoreline. Scour depth and scour patterns have been evaluated in a two-dimensional wave tank. Three-dimensional effects have also been studied in a larger wave basin. The number of variables included wave characteristics such as height, period, wave crest direction, water depth, pipe burial depth, and beach slope. Preliminary results on three-dimensional effects indicate that local scour may be quite significant when pipes are placed at an angle to the approaching waves.

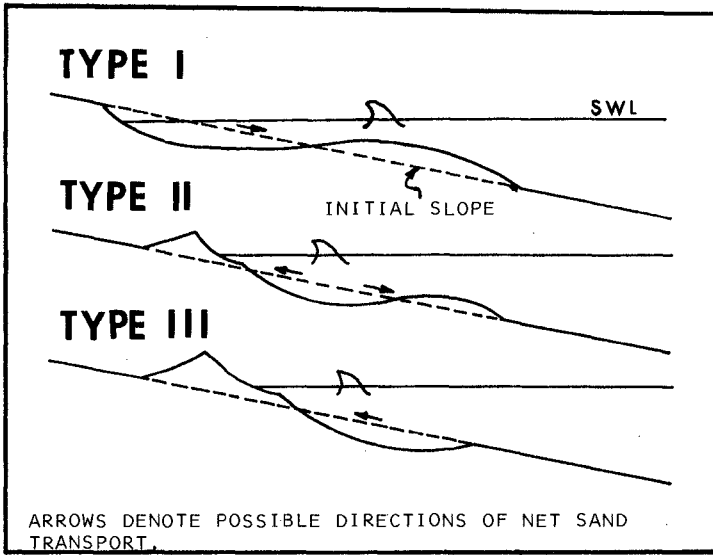


FIGURE 1. NEW BEACH PROFILE CLASSIFICATION. AFTER SUNAMURA AND HORIKAWA (1974).

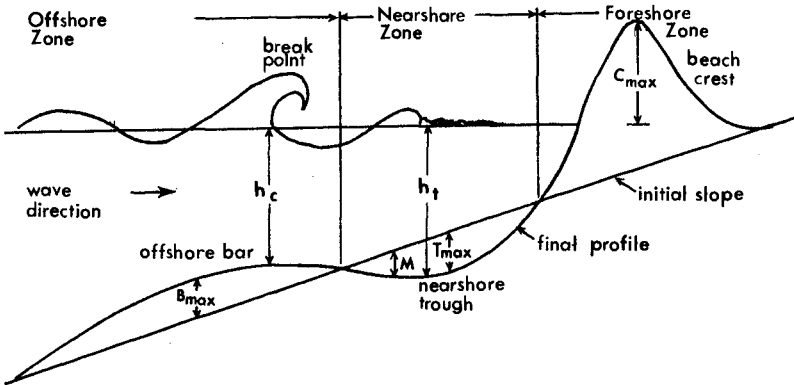


FIGURE 2. NOTATION USED IN THE STUDY.
(FROM REFERENCE 16)

EXPERIMENTAL STUDY

Experimental studies were conducted to assess the required depth of burial for a pipeline through the surf zone. The problem was approached by using a two-dimensional beach profile. Beach profiles were allowed to come to equilibrium in a 2-ft wide wave tank. Two-dimensional profiles were recorded for a number of wave conditions and initial slopes of 1:10, 1:20, 1:30 and 1:60. The 1:60 slope study was limited because of instability of profiles associated with minor water level variations as observed by Smith¹⁶ (1975).

A sample dimensionless plot of beach profiles for the slope of 1:20 is shown in the Appendix (Fig. A-1).

Attempts were made to correlate equilibrium profile geometric quantities, such as the maximum depth of the nearshore trough (T_{max}) and maximum height of the beach crest (C_{max}) with the wave characteristics. Figure 2 indicates the notation used in this study. It was found that wave height varies spacially and temporally in the tank making it an unsuitable independent variable for determining linear regressions. Deep water wave length (a function of wave period), however, was found to exhibit constant characteristics throughout a given test. Thus, the deep water wave length was used as the independent variable in the linear regression analysis.

Of the four attempted regressions, three were determined significant at the 5% significance level. Table I shows the correlation coefficients and regression results¹⁶.

Table I

L_o vs. C_{max}	r	r ²	v	r(.05, v)	significant
1:20	.94	.88	8	.632	yes
1:30	.86	.75	14	.497	yes
L_o vs. T_{max}					
1:20	.708	.502	8	.632	yes
1:30	.002	.048	10	.576	no

Where r = correlation coefficients; v = degrees of freedom = no. of obs. - 2; r(.05, v) = tabulated values of r at 5% significance level; r² = % variance explained by the linear relationship of C_{max} and L_o ; C_{max} = maximum height of the beach crest above the still water level; T_{max} = maximum height of the nearshore trough below the still water level, and L_o = deep water wave length.

Confidence intervals were determined for the C_{max} regression slopes and intercepts. The 95% confidence intervals for the slope and intercept of the 1:20 data are: $b_1 = .014 \pm .003$, $a_1 = .085 \pm .028$. Similarly for

1:30 data, $b_2 = .025 \pm .006$, $a_2 = .030 \pm .061$. Based on a 2-tailed t-test it was determined that at the 95% confidence level the populations represented by the 1:20 and 1:30 data are significantly different. Thus, for the range of tested variables, the dependence of C_{max} on L_0 is not independent on initial slope of the model beach. The failure of the T_{max} regression for the 1:30 data indicates that possibly some of the 1:30 T_{max} values had not reached equilibrium. This is in agreement with earlier observations indicating that steeper beaches reached equilibrium in a shorter time.

Hence the following relationships were obtained for a 1:20 initial slope: $C_{max} = .085 + .014 L_0$, for a 1:30 initial slope; $C_{max} = .030 + .025 L_0$, for a 1:20 initial slope: $T_{max} = .001 + .075 L_0$.

Qualitative agreement between laboratory and natural beaches was demonstrated by trial and error fitting. Figure 3 shows such a fit. The required distortion of scales results in an unnatural repose angle at the foreshore. In addition, the wave parameters responsible for the natural profile are unavailable. However, the trial and error method is useful in determining a general scale factor. For example, a comparison between laboratory-obtained profiles and field profiles near Sabine Pass, Texas, indicate a horizontal scale of 1 to 25 and vertical scale of 1 to 8, or a distortion of about 3 to 1.

PIPELINE STABILITY

An offshore pipeline must have sufficient horizontal and vertical stability against all environmental and imposed forces. Although environmental and gravitational forces are of primary importance, constructional and operational loadings should also be taken into account.

The gravitational forces include the weight of the pipe (either steel or concrete), weight of the corrosion protection coating, weight of the concrete coating (in case of steel pipe), and weight of the fluid in the pipeline.

The environmental forces depend on the storm severity, location of the pipeline and water depth. They are quite complex and variable. The forces acting on the pipeline include those due to storm or hurricane waves, vortex shedding and foundation strength.

Since forces due to waves may be considerable, particularly in shallow water, the most obvious solution is to place the pipeline in an excavated trench and cover it with suitable material up to the original underwater beach profile. There is no easy answer to this question as the depth of cover required will depend on a great many variables, including the wave climate, sediment size, littoral current, liquefaction potential, etc.

Buried pipelines approaching and passing through the surf zone must be placed below the storm beach profiles, or below the "winter" profiles. Such profiles must be determined prior to the design of the pipeline's profile and selection of burial depth. It has been found that in many cases

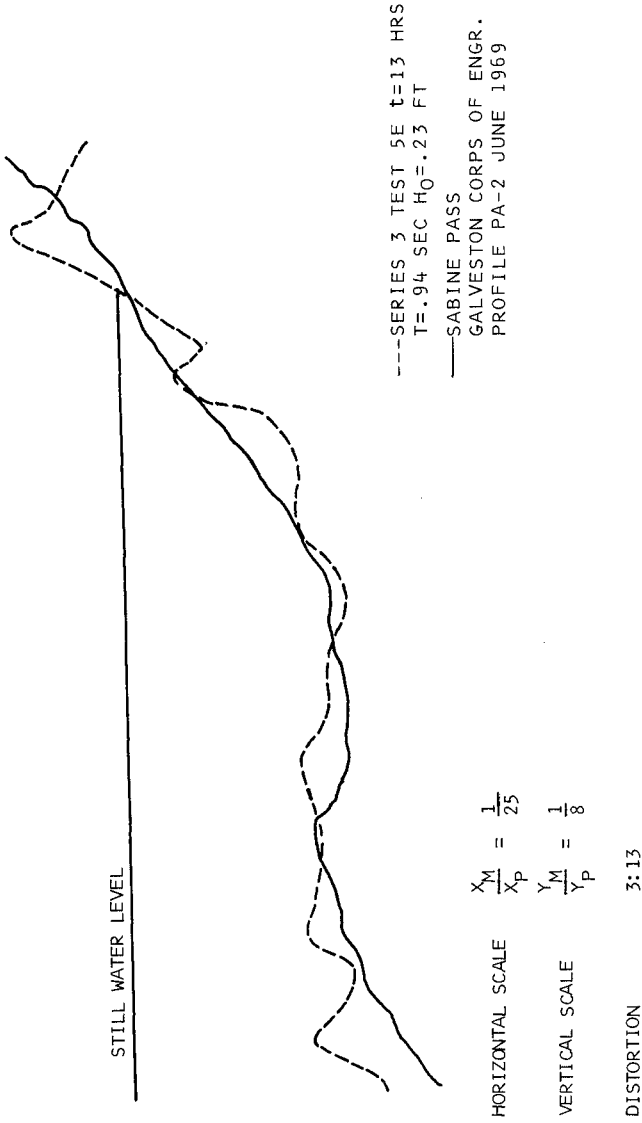


FIGURE 3. COMPARISON OF EXPERIMENTAL AND NATURAL PROFILE.

offshore pipelines failed due to inadequate cover or due to the fact that the pipeline profile generally followed the underwater beach profile observed at one time of the year, sometimes only during the summer period (or having a "summer" profile).

DEPTH OF COVER OVER PIPELINES







For safe design the pipeline should be buried under the storm beach profiles. The actual depth of burial would depend on the storm frequency selected, the importance of the project, and on possible environmental impact should the pipe fail, etc. The forces induced by waves on the buried pipe are generally not large, particularly as compared with unburied or partially buried pipe. Figure 4 indicates the coefficient of drag (C_D), coefficient of inertia (C_M) and coefficient of lift (C_L) on pipes located above the bottom, touching bottom and partially buried (2). For example, the forces due to drag on a pipe suspended 20 inches above the bottom are five times as large as on the pipe partially buried (protruding 0.25 of its diameter above the bottom). The effects of drag causing scour are shown schematically in Figure 5.

In order to develop safe design criteria for pipe cover two types of profile characteristic dimensions were considered:

1. (a) Maximum depth of trough below initial slope - T_{max} ,
 (b) Maximum height of offshore bar above initial slope - B_{max} ,
2. (a) Depth of trough below mean low tide - h_T ,
 (b) Depth of bar below mean low tide - h_C .

Ideally, all measurements should be taken either during the storm or as soon as practical after the storm. If no measurements are available, laboratory developed "equilibrium" profiles may be used provided a distorted scale is determined on the basis of laboratory-field comparisons.

Plots of h_T as a function of h_C have been determined from both field and laboratory data (Figure 6). The experimental laboratory data for beach profiles of 1 on 10, 1 on 20, and 1 on 30 are shown in Table II. A summary of recent laboratory results indicates that beach slope affects the ratio of h_T to h_C (Tables III and Figure 7). For example, the h_T/h_C value for 1 on 10 slope is 1.80 with a 95% confidence interval of ± 0.21 while the value for 1 on 30 slope is 1.35. Previously analyzed profiles are shown in Figure 6.

Pipe Position with respect to Mudline		C_D	C_M	C_L
	$L^* = 20^*$	1.0	1.5	0.5
	$L = 3^* - 20^*$.95	1.5	0.5
	Pipe Touching Bottom	.75	1.5	1.0
	$L = 0.25$ Diameter	.50	1.5	.85
	$L = 0.50$ Diameter	.25	1.5	.75
	$L = 0.75$ Diameter	.20	1.5	.20

* L = Distance from bottom of pipe to mudline.

Figure 4. Recommended Drag (C_D), Inertial (C_M) and Lift (C_L) Coefficients for Different Pipe Positions with Respect to the Mudline (Reynolds Numbers $> 200,000$)

(from Reference 2)

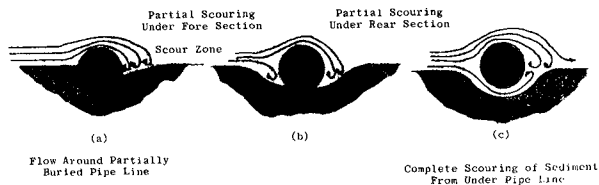


Figure 5. Drag Effects on Partially Buried Pipelines

(from Reference 2)

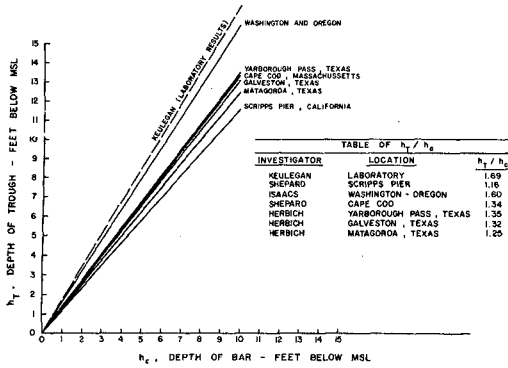


FIGURE 6. RELATIONSHIP BETWEEN DEPTH OF TROUGH AND DEPTH OF BAR

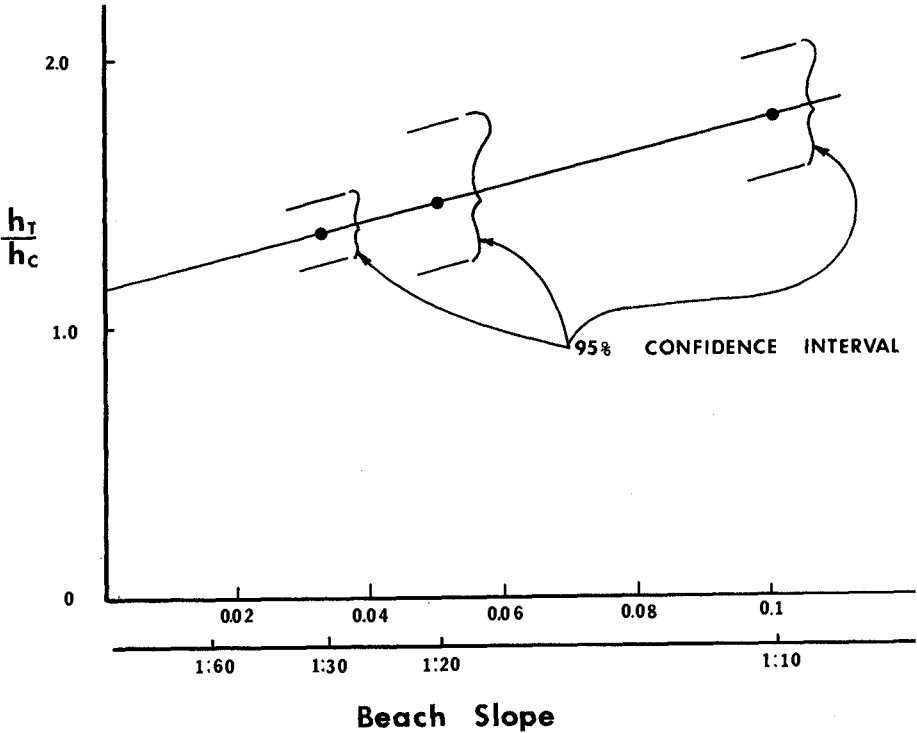


FIGURE 7. RATIO OF $\frac{h_T}{h_c}$ AS A FUNCTION OF BEACH SLOPE

TABLE II
EXPERIMENTAL TEST DATA

Series No. 1 Beach Slope 1:10

Test No	Depth of Trough h_T (in)	Depth of Bar h_C (in)	$\frac{h_T}{h_C}$	Time (hrs)
2B	3.7	1.7	2.18	13
2C	2.9	1.4	2.07	15
3C	2.2	0.9	2.44	11
4A1	3.2	1.9	1.68	5
4B1	3.3	1.8	1.83	15
4C1	3.8	1.6	2.38	13
4D1	3.2	1.8	1.88	13
4E1	2.6	1.6	1.63	13
5A1	3.6	2.4	1.50	13
5B1	3.1	2.9	1.07	13
5C1	3.8	2.0	1.90	13
5D1	3.2	2.0	1.60	13
5E1	4.2	3.1	1.35	13
6C2	8.4	3.5	2.4	7
6E2	2.4	1.2	2.00	7
7C2	3.7	2.5	1.48	7
7E2	3.3	2.8	1.18	7

Series No. 2 Beach Slope 1:20

1C	2.5	1.7	1.47	13
2C	1.5	0.7	2.14	13
3C	2.1	1.4	1.5	13
4C	4.3	4.1	1.05	13
5C	4.1	3.6	1.14	13
1E	3.7	1.9	1.95	13
2E	3.3	2.2	1.50	13
3E	3.4	1.9	1.79	13
4E	3.4	2.7	1.26	13
5E	3.5	3.1	1.13	13

Series No. 3 Beach Slope 1:30

4C	2.7	2.3	1.17	13
5C	4.5	3.4	1.32	13
4E	4.7	3.1	1.52	13
5E	4.8	3.6	1.33	13
6E	4.8	3.4	1.41	74
7E	5.9	4.4	1.34	48
8E	4.6	3.3	1.39	30

TABLE II (continued)
EXPERIMENTAL TEST DATA

Series No. 3 Beach Slope 1:30

Test No.	Depth of Trough h_T (in)	Depth of Bar h_C (in)	$\frac{h_T}{h_C}$	Time (hrs)
9E	4.7	3.9	1.21	65
10E	3.5	2.3	1.52	45
11E	3.6	2.2	1.64	13
12E	4.6	3.0	1.53	45
13E	4.8	4.2	1.14	30
14E	6.4	5.5	1.16	30
15E	7.2	5.8	1.24	45

Series No. 6 Beach Slope 1:6D

1X	6.4	4.8	1.33	77
1Y	6.1	5.6	1.09	77
4A	6.4	4.4	1.45	45
5A	8.2	6.6	1.24	96
6A	4.1	1.9	2.16	45
7A	5.0	3.8	1.32	30
1D	4.9	4.0	1.23	45
2D	5.5	4.8	1.15	145

TABLE III
SUMMARY OF RESULTS

Beach Slope	$\frac{h_T}{h_C}$	95% Confidence Interval
1:10	1.80	± 0.21
1:20	1.49	± 0.26
1:30	1.35	± 0.09

REFERENCES

1. Task Committee on Pipelines in the Ocean, "Pipelines in the Ocean", Final Report, ASCE Pipeline Division, 1973.
2. Pipeline Research Committee, "Forces Acting on Unburied Offshore Pipelines", Project PR-91-68, AGA Report, September 1974.
3. Meyer, R.D., "A Model Study of Wave Action on Beaches", M.S. Thesis, Dept. of Engr., University of California, unpublished, 1936.
4. Waters, C.H., "Equilibrium Slopes of Sea Beaches", M.S. Thesis, Dept. of Engr., University of California, unpublished, 1939.
5. Johnson, J.W., "Scale Effects in Hydraulic Models Involving Wave Motion", Trans. Amer. Geophys. Union, 30, 517-525, 1949.
6. Rector, R.L., "Laboratory Study of Equilibrium Profiles of Beaches", Beach Erosion Board, Tech. Memo. 41, 1954.
7. Wiegel, R.L., Patrick, D.A., and Kimberley, H.L., Wave, Longshore Current, and Beach Profile Records for Santa Margarita River Beach, Oceanside, California, Trans. Amer. Geophys. Union, 35, 887-896, 1949.
8. Saville, T., Jr., "Scale Effects in Two-Dimensional Beach Studies", Trans. IAHR 7th General Meeting, A3-1 to A3-10, 1957.
9. Iwagaki, Y., and Noda, E., "Laboratory Study of Scale Effects in Two-Dimensional Beach Processes", Chapter 14, 8th Conference on Coastal Engr., 194-210, 1962.
10. Nayak, I.V., "Equilibrium Profiles of Model Beaches", Hyd. Engr. Lab Reports, HEL2-25, University of California, Berkeley, 1970.
11. Noda, E.K., "Equilibrium Beach Profiles Scale-Model Relationships", Journal of W.W. Div. of ASCE, Paper 9367, 511-527, 1972.

12. Earattupuzha, J.J., "Equilibrium Conditions in Beach Wave Interaction", Ph.D. Thesis, Dept. of Civil Engineering, Indian Institute of Technology, Madras, India, 1974.
13. Sunamara, T. and Horikawa, K., "Two-Dimensional Beach Transformation Due to Waves", Proc. 14th Conf. Coast. Engr., 920-937.
14. Ralston, D.O. and Herbich, J.B., "The Effects of Waves and Currents on Submerged Pipelines", Project Report No. COE-101, Texas A&M University, 1968.
15. Manley, R. and Herbich, J.B., "Foundation Stability of Buried Offshore Pipelines. A Survey of Published Literature", Report No. COE-174, Texas A&M University, 1974.
16. Smith, D.C., IV, "Factors Influencing Equilibrium of a 1:60 Model Sand Beach", unpublished M.S. thesis, Texas A&M University, December 1975.

Table A-116
1:20 Test Data

Parameter	Test									
	1E	1C	2E	2C	3E	3C	4E	4C	5E	5C
T(sec.)	1.55	1.55	1.45	1.46	1.26	1.27	1.11	1.11	.96	.96
L_0 (ft.)	12.30	12.30	10.79	10.85	8.18	8.22	6.33	6.33	4.73	4.73
H_0 (ft.)	.36	.35	.33	.35	.26	.27	.21	.21	.21	.21
d(ft.)	1.75	1.75	1.75	1.75	1.75	1.75	1.75	1.75	1.75	1.75
t_{max} (hrs.)	13.00	13.00	13.00	13.00	13.00	13.00	13.00	13.00	13.00	13.00
C_{max} (ft.)	.25	.25	.22	.25	.21	.21	.19	.18	.12	.15
T_{max} (ft.)	.17	.13	.13	.14	.12	.11	.13	.08	.11	.11

Table A-2¹⁶
1:30 Test Data

Parameter	1C	2C	2E	3C	3E	4C	4E	5C	6E	7E
T(sec.)	1.55	1.45	1.44	1.26	1.26	1.10	1.10	.95	1.42	1.69
L ₀ (ft.)	12.30	10.76	10.58	8.13	8.13	6.20	6.20	4.61	10.32	14.54
H ₀ (ft.)	.38	.35	.35	.27	.27	.21	.24	.22	.22	.35
d(ft.)	1.75	1.75	1.75	1.75	1.75	1.75	1.75	1.75	1.75	1.75
t _{max} (hrs.)	13.00	13.00	13.00	13.00	13.00	13.00	13.00	13.00	13.00	13.00
C _{max} (ft.)	*	*	.25	.17	.21	.15	.17	.14	.29	.38
T _{max} (ft.)	+	+	+	+	+	.10	.17	+	.05	.16

Parameter	8E	9E	10E	11E	12E	13E	14E	15E
T(sec.)	1.04	1.15	1.39	1.07	1.36	1.37	1.43	1.32
L ₀ (ft.)	5.54	6.77	9.82	5.81	9.40	9.61	10.47	5.99
H ₀ (ft.)	.20	.23	.26	.15	.34	.23	.32	.32
d(ft.)	1.75	1.75	1.75	1.75	1.75	1.75	1.75	1.75
t _{max} (hrs.)	30.00	65.00	45.00	13.00	45.00	30.00	30.00	45.00
C _{max} (ft.)	.15	.23	.31	.25	.33	.27	.29	.15
T _{max} (ft.)	.19	.20	.18	.15	.23	.20	.25	.24

* Beach crest equilibrium not indicated by profile sequences.

+ Nearshore trough equilibrium not indicated by profile sequences.

Test Series No. 2
Length of Test = 13 hrs.

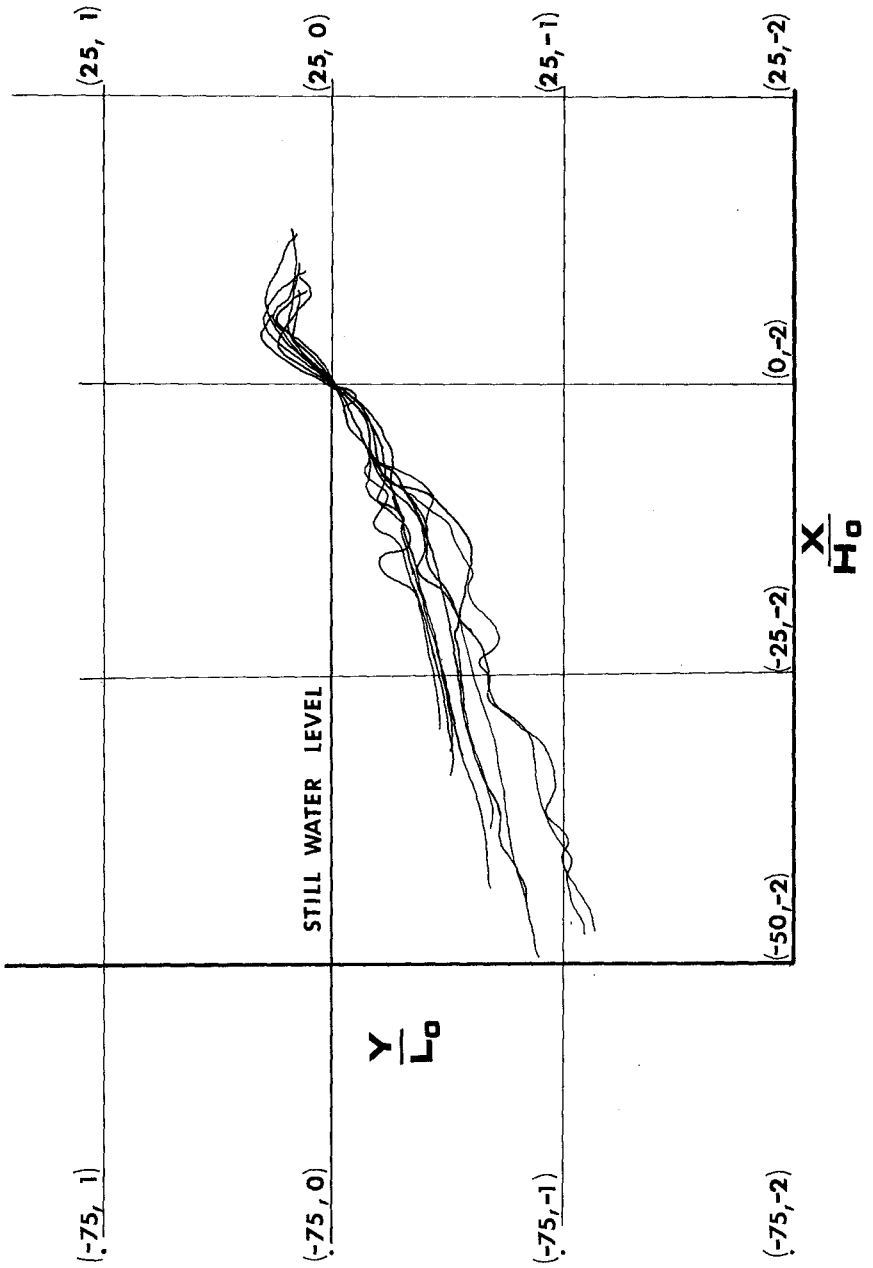


FIGURE A-1

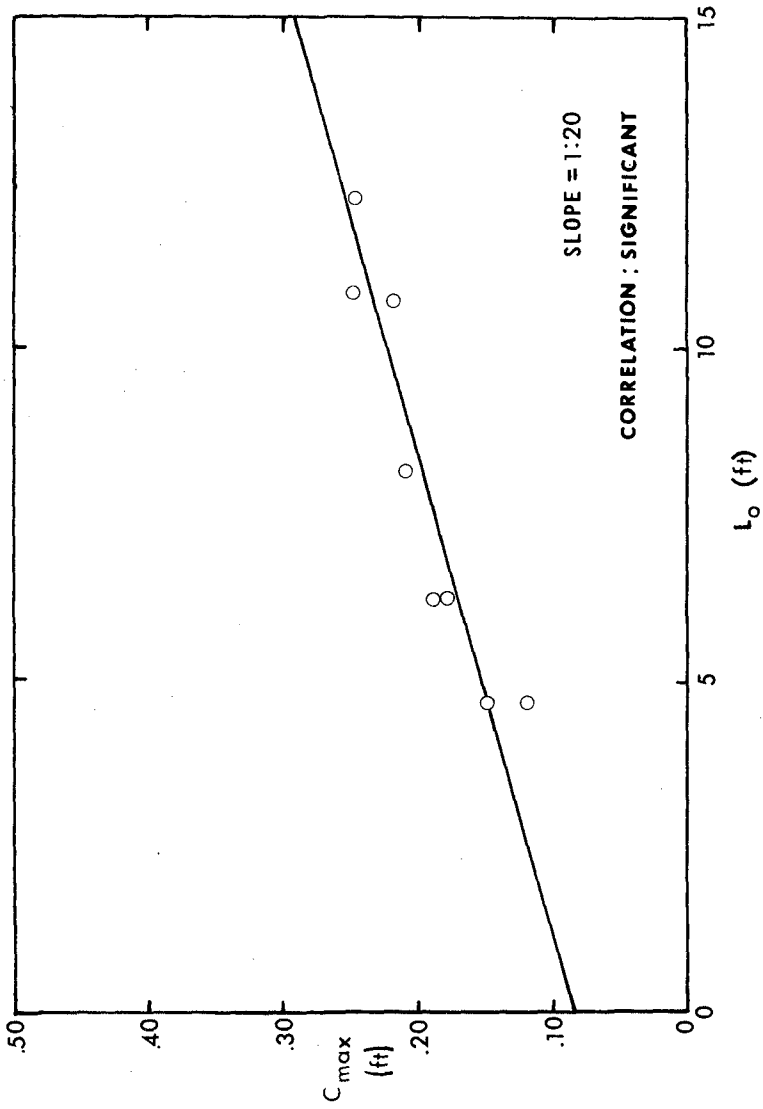


FIGURE A-2. LINEAR REGRESSION OF MAXIMUM HEIGHT OF BEACH CREST ON DEEP WATER WAVE LENGTH FOR ALL 1:20 TESTS. (FROM REFERENCE 16)

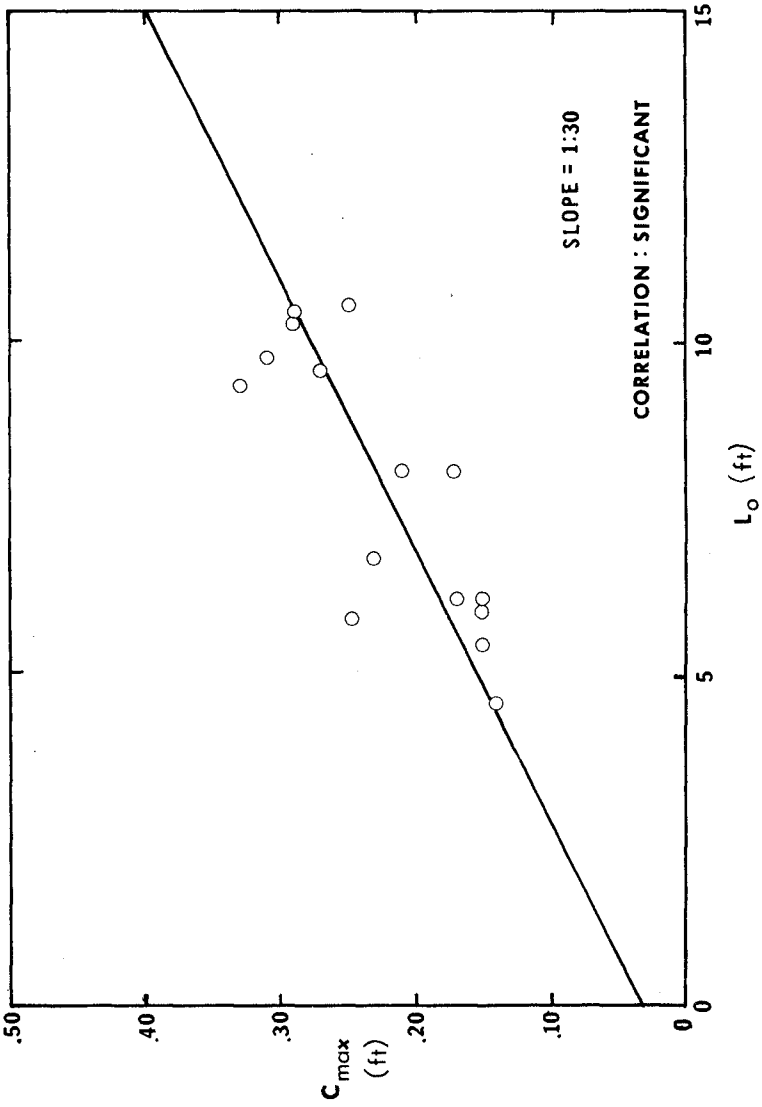


FIGURE A-3. LINEAR REGRESSION OF MAXIMUM HEIGHT OF BEACH CREST ON DEEP WATER WAVE LENGTH FOR ALL 1:30 TESTS. (FROM REFERENCE 16)

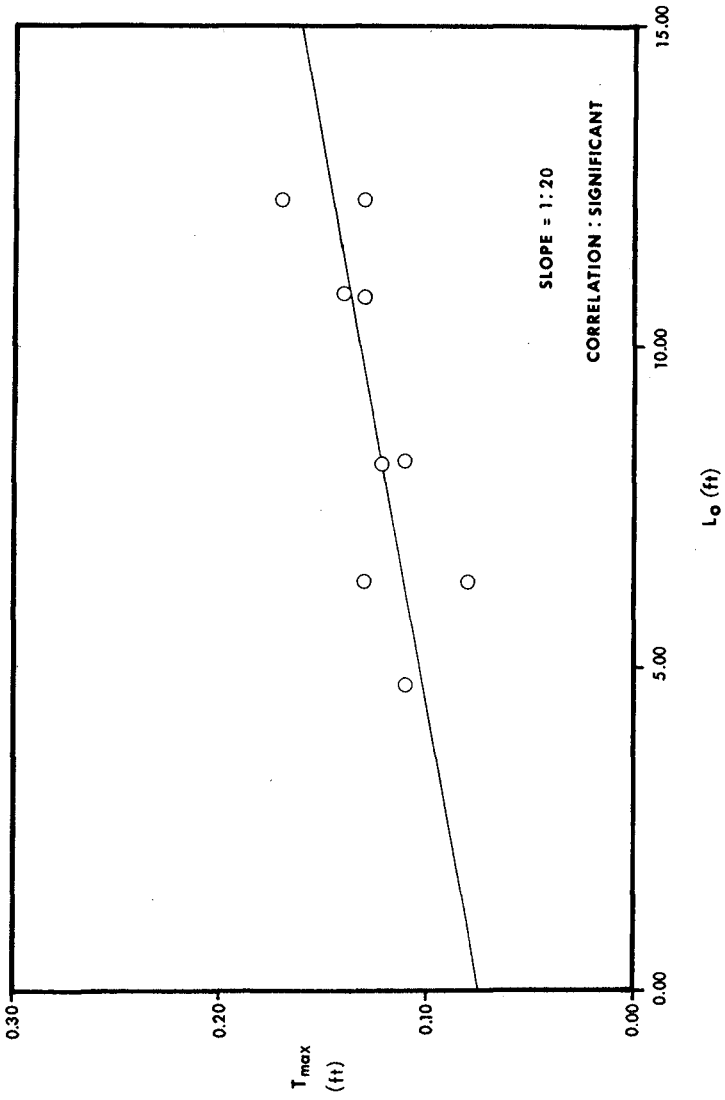


FIGURE A-4. LINEAR REGRESSION OF MAXIMUM DEPTH OF BEACH TROUGH ON DEEP WATER WAVE LENGTH FOR ALL 1:20 TESTS.

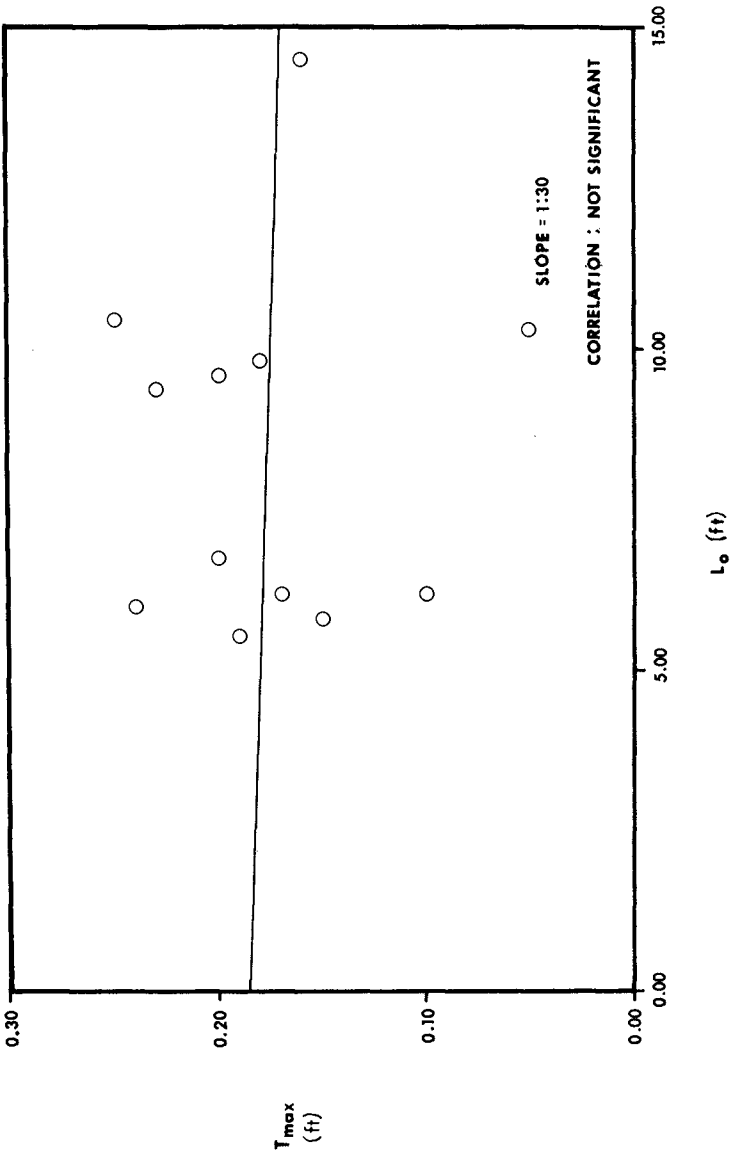


FIGURE A-5. LINEAR REGRESSION OF MAXIMUM DEPTH OF BEACH TROUGH ON DEEP WATER WAVE LENGTH FOR ALL 1:30 TESTS.

CHAPTER 96

HYDRAULICS OF GREAT LAKES INLET - HARBORS SYSTEMS

Robert M. Sorensen¹

and

William N. Seelig²

Abstract

Reversing currents in inlets on the Great Lakes are generated primarily by long wave seiching modes of the lakes rather than by the tide. In order to investigate the nature of long wave excitation and the generating mechanism for significant inlet velocities, to establish techniques for predicting inlet-harbor system response, and to develop base data for future planning and design studies, field measurements were conducted in 1974-75 at several harbors on the Great Lakes. Data collected includes continuous harbor water level measurements at all sites, inlet velocity measurements at the primary site (Pentwater, Michigan), and channel hydrographic surveys at the sites where more recent data were needed. Historic water level and velocity data for some of the harbor sites was also available.

Amplification of harbor oscillations and generation of the highest inlet velocities are caused by the Helmholtz resonance mode which has a period of 1 to 3 hours for the inlet-harbor systems studied. A recently developed simple lumped-parameter numerical model is shown to be quite effective in predicting inlet-harbor response over the range of excitation periods encountered. Selected data from Pentwater are presented to demonstrate the hydraulic response of the inlet harbor system and the applicability of the lumped-parameter numerical model.

Introduction

Situated along the coastlines of the U.S. - Canadian Great Lakes are several inlet-harbor systems that consist of lakes or other embayments which are connected to the adjacent Great Lake by one or more artificial jettied inlets. There are also a few inlet-harbor systems that have natural uncontrolled inlets, but most inlets are jettied and periodically dredged to maintain adequate navigation channels.

Higher velocity reversing currents at these inlets are generated in response to storm-generated seiching of the individual Great Lakes. Of particular importance to the generation of higher velocities is the resonant amplification of Great Lakes seiches by the inlet-harbor systems. Although high

¹Chief, Coastal Structures Branch, US Army Coastal Engineering Research Center, Ft. Belvoir, Virginia 22060

²Research Hydraulic Engineer, Coastal Structures Branch, US Army Coastal Engineering Research Center, Ft. Belvoir, Virginia 22060

velocities can be generated by excitation of resonant conditions, a cumulative frequency distribution of channel velocities at most Great Lakes inlets will show that velocities in excess of 1 ft/sec typically occur less than 5 percent of the time.

A field data collection program was conducted at nine inlets on the U.S. coast of the Great Lakes. Also, historic field data were available for some of these nine inlets as well as for three additional inlet sites. Historic and project field data includes continuous measurements of Great Lake and harbor water levels and inlet velocities over periods of a few weeks to nearly a whole ice free season, and hydrographic surveys at inlet channels where insufficient hydrographic data were available. The primary site for field data collection was at Pentwater, Michigan.

The three objectives of this project were: (1) to define the hydraulic mechanisms that generate the dominant inlet currents and related harbor oscillations, (2) to establish analytical techniques for prediction of inlet-harbor response to Great Lakes oscillations, and (3) to develop background data that will demonstrate the hydraulic behavior of these inlet-harbor systems as well as the validity of analytical prediction techniques, and that will provide base data for guidance in future project design studies.

This paper will summarize the hydraulic behavior of Great Lakes inlet-harbor systems and the techniques used herein to predict the hydraulics of these systems; it will outline the field data collection program; and it will present results from the data collection program at the primary study site in order to demonstrate details of the hydraulic response of these inlet-harbor systems as well as the ability of analytical techniques to predict this response.

Inlet-Harbor System Hydraulics

Figure 1 schematically depicts a prismatic inlet channel that connects a large body of water such as a sea or one of the Great Lakes to a much smaller bay, lake or harbor (herein referred to as the harbor). The inlet channel has a length, L , width, B , average depth, d , cross-sectional area, A_c , and time dependent instantaneous horizontal velocity, V . A_h is the surface area while η_s and η_h are the time dependent instantaneous sea and harbor surface elevations. The harbor surface is assumed to remain horizontal as it rises and falls in response to excitation from the sea. This assumption requires that the harbor surface response period be long compared to the time required for a shallow water wave to propagate from the inlet to the farthest point in the harbor.

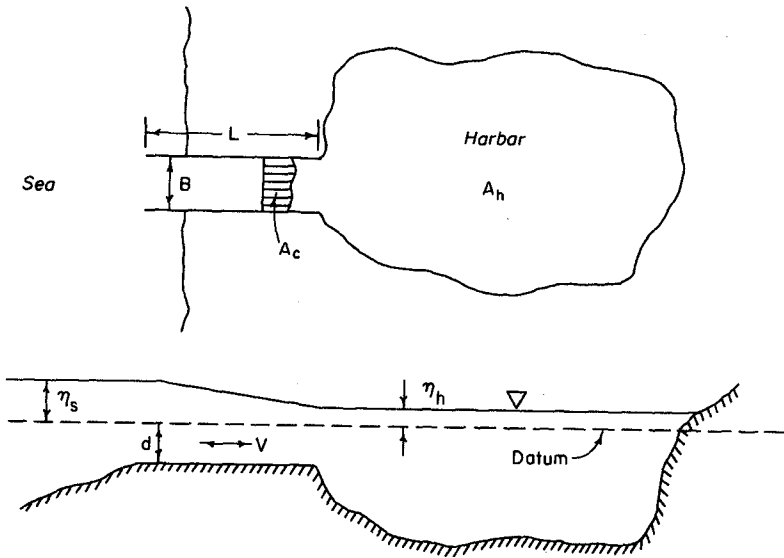


Fig. 1 Inlet - harbor system

For purposes of discussion it is helpful to write a simple inlet-harbor continuity equation and the one-dimensional equation of motion for flow in the inlet channel. The continuity equation

$$Q = VA_c = A_h \frac{\partial \eta_h}{\partial t}, \quad (1)$$

where Q is the instantaneous channel discharge, equates the volumetric flow through the inlet to the harbor water surface rise or fall needed to balance that flow. An accurate record of the harbor surface elevation time-history can thus be used to calculate the instantaneous channel discharge and velocity using Eq. 1 (provided that the harbor surface remains horizontal as it oscillates).

The one-dimensional equation of motion along the inlet channel axis can be written

$$-g \frac{\partial \eta}{\partial x} = \frac{f V |V|}{8R} + V \frac{\partial V}{\partial x} + \frac{\partial V}{\partial t} \quad (2)$$

where R is the channel hydraulic radius, x the distance along the channel axis from some reference point, f the channel friction factor, and g the acceleration of gravity. Eq. 2 equates the horizontal driving force due to the water surface slope with the three terms on the right which are the channel frictional resistance, the convective acceleration owing to velocity variation along the channel axis, and the temporal acceleration (or inertia) owing to velocity variation at a point with time. In nearly prismatic channels the convective acceleration is often negligible.

At U.S. tidal inlets, because of the magnitude of common tidal periods and amplitudes, friction strongly dominates the effects of inertia. The result is that at most tidal inlets inertia can be neglected in hydraulic calculations, the harbor tidal range is less than the range at sea, and the phase lag between the sea and harbor tides is much less than 90° .

On the Great Lakes, the components of the long wave energy spectrum that excite the dominant inlet-harbor system response modes typically have amplitudes in the order of 0.1 to 0.2 ft and periods of less than 3 hours. This causes the inertia term to be larger than the friction term throughout most of the cycle of oscillation. (Friction will dominate only around times of peak ebb and flood velocity, which are also the times of minimum temporal acceleration.) As a result, the harbor response is amplified and its phase lag can exceed 90° .

The inlet-harbor system response is analagous to the response of a slightly damped spring-mass system or its acoustic counterpart, the Helmholtz resonator (see Kinsler and Frey, 1950). The motion of the mass of water in the inlet channel corresponds to the motion of the mass of the spring-mass system, and the action of gravity on the rising and falling harbor water surface corresponds to the restraining force of the spring. Details of the response characteristics of this mode of oscillation (usually called the Helmholtz mode) are demonstrated by Figure 2 which depicts the classical behavior of a single-degree of freedom oscillating system.

In Figure 2, the phase lag between the sea and harbor surface elevations as well as the amplification of the harbor surface response are plotted as a function of excitation period divided into the frictionless resonance period, T_H . The series of curves represents different degrees of frictional damping of the system. Note that increased friction tends to shift the resonant or Helmholtz period to slightly higher values. For excitation at periods much longer than the Helmholtz period (A) the harbor amplitude

equals the sea amplitude and the phase lag is small (pumping condition). With decreasing excitation periods and significant friction (B) the ratio of

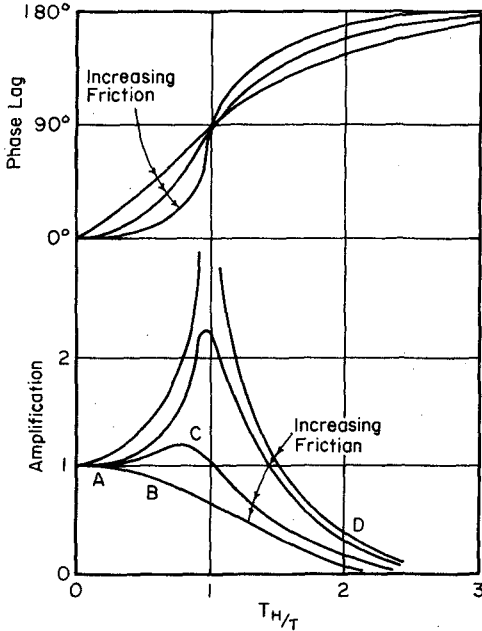


Fig. 2 Amplification, phase lag for inlet - harbor system

harbor to sea amplitude is less than unity and the phase lag less than 90° . This is the typical response of most tidal inlets. As the Helmholtz period is approached, particularly with lesser frictional damping (C), the harbor response is amplified and the lag increases toward (or above) 90° . A significant decrease in the harbor response occurs for all levels of frictional dissipation when the excitation period is much less than the Helmholtz period (D). At a harbor on the Great Lakes, excitation will occur at a number of periods in the long wave energy spectrum (typically $\frac{1}{2} T_H$) and cause a range of responses for these different periods as indicated in Figure 2.

The Helmholtz period is longer than the fundamental free seiching period of the harbor. A simple equation for the Helmholtz period can be derived (Carrier, Shaw and Miyata, 1971) by neglecting the friction and convective acceleration terms in Eq. 2 and solving this equation and continuity for the conditions depicted by Figure 1. This yields

$$T_H = 2\pi \sqrt{\frac{L A_h}{g A_c}} \quad (3)$$

Eq. 3 ignores the water mass that is just outside each end of the inlet channel but is part of the mass of water set in motion at resonance. Miles (1948), using an acoustic analogy, developed an equation for the added channel length, L' , necessary to account for this additional water mass where

$$L' = \frac{-B}{\pi} \ln \left[\frac{\pi B}{\sqrt{gd} T_H} \right] \quad (4)$$

Thus, an improved form of Eq. 3 can be written as

$$T_H = 2\pi \sqrt{\frac{(L + L') A_h}{g A_c}} \quad (5)$$

The inclusion of end effects is particularly important for short channels (i.e. $L < L'$). For the inlet-harbor systems encountered in this study Eq. 5 proved to be reasonably effective for determining the Helmholtz period. A numerical method for determining the Helmholtz period for a harbor with more than one entrance channel is given by Freeman, Hamblin and Murty (1974).

Note from Eq. 5 that the Helmholtz period increases as the channel length or the bay surface area increases and as the channel cross-sectional area decreases. The Helmholtz mode of oscillation is independent of the harbor depth which is not the case for the free seiching modes of harbor resonance.

A recently developed simple lumped-parameter numerical model for inlet hydraulic calculations has been used at CERC to predict inlet-harbor response to Great Lakes long wave motion. Details of the development and application of this model are given by Seelig et al. (1977).

In the lumped-parameter model the oscillating harbor water surface is assumed to remain horizontal and continuity of flow is defined by Eq. 1

written in finite difference form. The equation of motion is integrated along the channel axis to yield

$$\frac{\partial Q}{\partial t} = \frac{FQ^2}{2} \left(\frac{1}{A_{cs}^2} - \frac{1}{A_{ch}^2} \right) + gF(\eta_s - \eta_h) - \frac{Fg}{2} \sum_{i=1}^S \frac{1}{\sum_{j=1}^C A_{ij}} \sum_{j=1}^C \frac{n_{ij} |W_{ij} Q| W_{ij} Q B_{ij} L_{ij}}{(d_{ij})^{1/3} A_{ij}^2} \quad (6)$$

The inlet channel is divided into C subchannels and S sections along its length by construction of a flow net to yield SXC grid sections. Each grid section is assigned a Manning's n (n_{ij}), depth, d_{ij} , width, B_{ij} , length, L_{ij} , area normal to flow, A_{ij} , and flow weighting factor, W_{ij} . The flow weighting factor determines what fraction of the total flow, Q, passes through each grid. It may be selected (1) to distribute flow equally in all subchannels (2) to distribute flow across subchannels so friction is minimized at each section or (3) to distribute flow in each subchannel (no cross over between subchannels) so friction is minimized in each subchannel. F is a channel geometry factor that develops from integration of the equation of motion and A_{cs} and A_{ch} are the inlet channel cross-sectional areas at the sea and harbor ends respectively.

Given the harbor surface areas, inlet hydrography, and $\eta_s = f(t)$, the channel flow net is drawn, n_{ij} and W_{ij} distributions are established and the model is solved in time steps by a fourth order Runge-Kutta-Gill technique to yield η_h at $t, t+1, \dots$ and Q (or V distribution) at $t + 1/2, t + 3/2, \dots$. If (η_s, η_h and V) = $f(t)$ data are available for an inlet-harbor system the model can be calibrated by adjusting n_{ij} .

The lumped parameter model is particularly appropriate for Great Lakes inlet-harbor system hydraulic calculations because of the nature of the harbor water level response during Helmholtz resonance and because the model allows input of irregular sea level time-histories common to Great Lakes long wave spectra. Also, because it has the capacity to handle harbors with more than one inlet channel as are found at some locations on the Great Lakes.

Field Data Sites and Collection Program

A field data collection program was conducted during October and November 1974 and July through November 1975. The harbor sites where data were collected are shown in Figure 3 along with the sites where usable historic data are available.

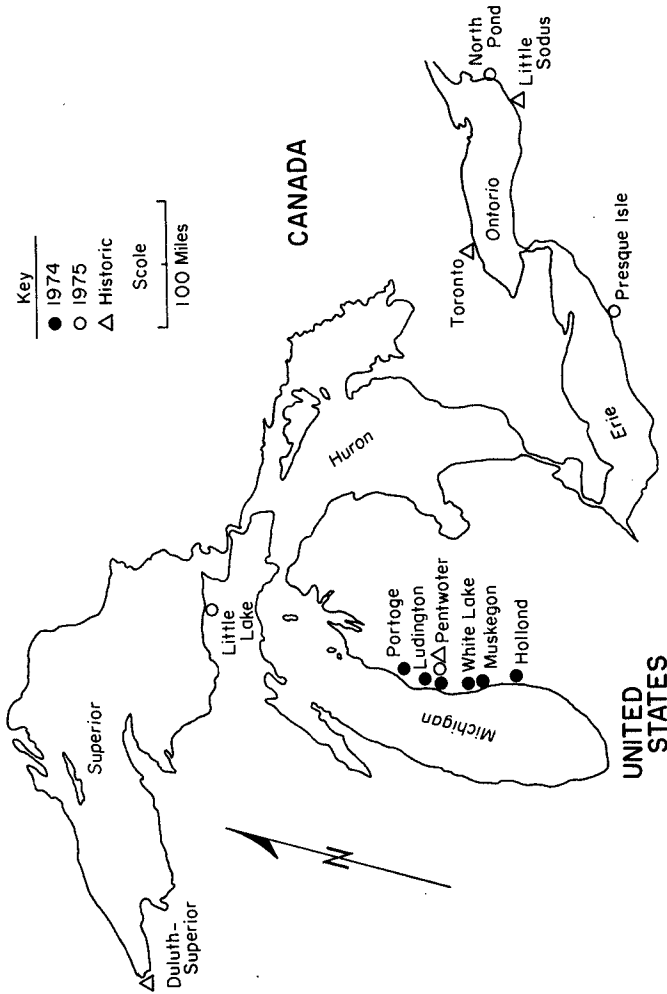


Fig. 3 Field data collection sites

The field program included harbor water level and inlet channel velocity measurements as well as inlet channel hydrographic surveys. The water level measurements were taken at 2 or 5 minute intervals on a continuous basis at the harbors indicated in Figure 3. Continuous current velocity measurements were made in the Pentwater inlet channel at a point middepth, midlength and 7 ft from the north jetty.

Historic lake and harbor water level and channel velocity data at Pentwater are available (Duane and Saylor, 1967) for July and August 1967. Figure 4, a map of Pentwater Lake, shows the locations where water level and

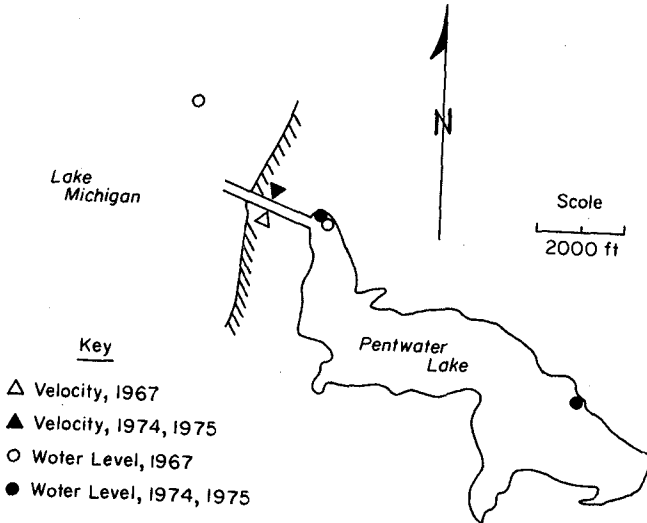


Fig. 4 Pentwater Lake, Michigan

current data were measured. Pentwater was chosen as the primary site for this study (and paper) because of its uncomplicated inlet channel geometry, the availability of the 1967 data, and the existence of concurrent field studies at Pentwater by other CERC personnel.

Pentwater Lake has a surface area of 1.81×10^7 ft² and is connected to Lake Michigan by a jettied inlet channel 2000 ft long and 145 feet wide. The average inlet channel depth at the time of the field data collection was 12.8 ft while Pentwater Lake has an average depth of 30 ft. A report by Seelig and Sorensen (1977) gives additional information on the field data collection sites, measurements made, instrumentation used, and results obtained.

Table 1 lists the Helmholtz period for each of the six field study sites located on the eastern shore of Lake Michigan. The Helmholtz period was calculated by Eq. 5 so the true period will be somewhat higher than listed owing to frictional resistance in the channel. Also listed in Table 1 are the fundamental seiching periods, T_1 , in each harbor calculated by the classical Merian equation.

Table 1 - Helmholtz and fundamental seiching periods

<u>Location</u>	<u>Helmholtz period (hrs)</u>	<u>Fundamental seiching period (hrs)</u>
Portage	2.17	0.16
Ludington	1.22	0.32
Pentwater	1.39	0.13
White Lake	2.55	0.37
Muskegon	3.80	0.27
Holland	2.23	0.63

At most locations on the Great Lakes the amplitude of the astronomical tide is less than 0.3 ft. The amplitudes of the various components of the longwave spectrum on the Great Lakes are of the same order of magnitude but their periods (particularly for higher harmonics) are significantly lower and closer to the resonant period than are the tidal periods. Thus, Great Lakes seiching is more likely to generate noticeable inlet velocities.

Table 2 lists the periods of the longitudinal free seiching modes in Lake Michigan (information is from a variety of field data and numerical model analyses). Owing to the geometry of Lake Michigan, the transverse seiching modes are hard to generate. Note that the 6th through 9th longitudinal modes have periods around the Helmholtz period for Pentwater. It appears (see Mortimer, 1965) that the 7th and 9th modes have nodes near Pentwater while the 6th and 8th modes have antinodes and thus should cause greater hydraulic activity at Pentwater.

Table 2 - Longitudinal free seiching periods, Lake Michigan

Mode:	1	2	3	4	5	6	7	8	9
Period (hrs):	9.0	5.2	3.7	3.1	2.5	1.85	1.58	1.44	1.25

Field Data Measurement and Analysis

Water level data were measured by stilling well-float type gages and recorded digitally (at 5-minute intervals) on punch tape with a Fisher-Porter Model 15-42 level recorder. Vertical resolution of the water level records was to the nearest 0.01 ft. Extreme care must be taken in the design of a stilling well-recorder combination when digital water level measurements are made because the signal of interest is of much lower amplitude than that of the higher frequency "noise" owing to wind waves. Special linear damping stilling wells (Seelig, 1976) with a design based on the work of Noye (1974) were used in this study. The punch tape water level records were machine converted to standard computer punch cards for spectral and other analyses.

Inlet current speed and direction data at Pentwater were measured with a Bendix Q-9 current meter and recorded on strip chart. The velocity records were digitized for analysis at 5-minute intervals timed to coincide with the nearby water level data. Owing to the uniform geometry of the Pentwater inlet channel, measured current velocities should give a good indication of the average channel velocities.

Spectral analyses of water level and velocity data were conducted using the Cooley and Tukey Fast Fourier Transform algorithm with a cosine bell window (Harris, 1974). As a compromise, a record length of 1.78 days (512 data points) was used to maintain the assumption of a weakly stationary system and still give good resolution for the range of periods of interest.

Field Data Results

Selected data from Pentwater are presented in this section to demonstrate the response of the inlet-harbor system to Lake Michigan water level oscillations. Figure 5 shows records of storm generated water levels in Lake Michigan at Pentwater along with the resulting Pentwater Lake levels and channel velocities. These data are typical of storm conditions at Pentwater. High wind waves at Pentwater will often occur when the wind is from the west but during this time inlet velocities will remain low. When the wind shifts to parallel the axis of Lake Michigan and generate seiching action in the Lake, harbor oscillations and inlet velocities increase.

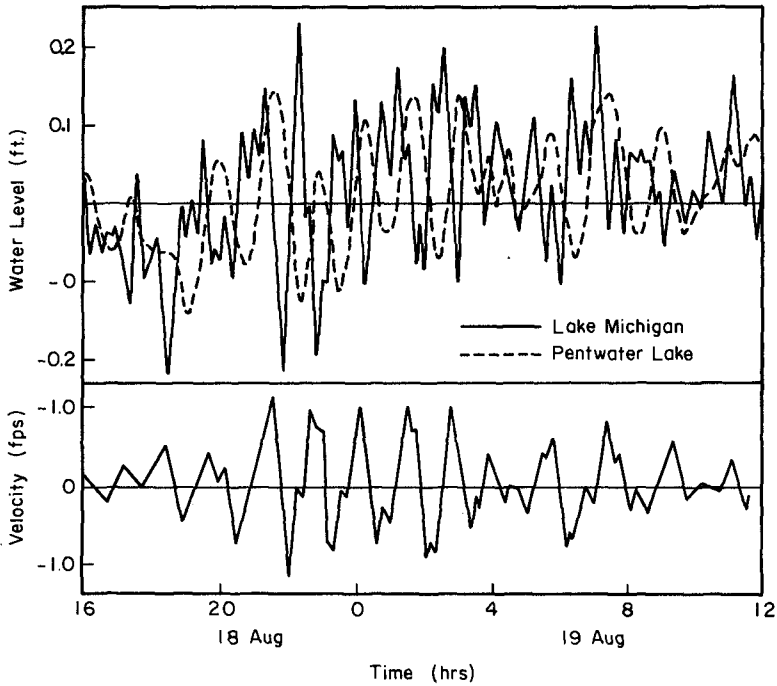


Fig. 5 Lake Michigan water level and resulting Pentwater channel velocity and harbor water level

As demonstrated by Figure 2, higher frequency oscillations are strictly damped by the inlet-harbor system so the harbor water level record is smoother than the Lake Michigan record. The harbor water level oscillation in Figure 5 has a predominant period of 1.5 to 2 hours and is approximately 180° out of phase with the oscillation of Lake Michigan. Harbor response like that shown in Figure 5 typically lasts for a period of 2 to 3 days.

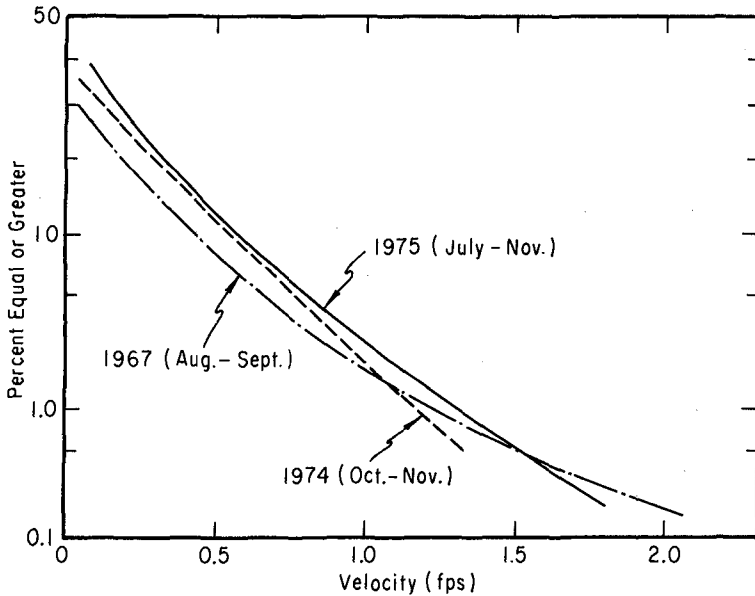


Fig. 6 Velocity cumulative frequency distributions at Pentwater inlet

The cumulative frequency distributions of velocities measured at Pentwater in 1967, 1974 and 1975 are plotted in Figure 6. Although the data were collected during the summer and fall they should be somewhat representative of a typical year at Pentwater. Because of the low frequency of occurrence of significant velocities, inlet currents should only rarely cause concern for navigation. Also, velocities high enough to flush sediment from the inlet (say $V > 1$ fps) occur only about 1 percent of the time so continuous inlet maintenance would likely be required.

Inlet velocity cumulative frequency distributions at all of the other inlets studied (except Duluth-Superior) were approximately the same or lower than the distribution at Pentwater. These distributions were constructed from velocity measurements, when available, or from velocities calculated (by Eq. 1) from harbor water level records. A comparison of measured and

calculated velocity cumulative frequency distribution from Pentwater showed the distributions to be quite compatible.

The Duluth-Superior harbor is located at the end of Lake Superior (see Figure 3) where the shorelines converge and seiche antinodes occur. Oscillation with amplitudes greater than 0.5 ft and periods close to the resonant period have been measured at Duluth-Superior. Inlet velocities up to 7 fps were generated.

Lake Michigan and Pentwater Lake water level spectra for a period bracketing that in Figure 5 are shown in Figure 7. Spectral peaks in the Lake Michigan record occur at 5.3, 1.8, 1.44, 1.0 and 0.85 hours - the second, sixth and eight longitudinal seiching modes plus two undetermined higher frequency modes. As expected, the 5.3 hour mode is only very slightly amplified, the 1.8 and 1.44 hour modes which are near the Helmholtz period are strongly amplified, and the 1.0 and 0.85 hour modes are strongly damped.

Water level spectra for several of the storms that occurred during the periods of record at Pentwater showed responses similar to Figure 7. Quite often the 1.44 hour period was dominant although occasionally other periods such as the 5.3 hour mode would dominate. Of course, the 5.3 hour mode would not be significantly amplified and lower velocities could be expected because of the lower amplitude of harbor oscillation and the longer oscillation period.

Application of Lumped Parameter Numerical Model

The lumped parameter model was calibrated for Pentwater (with $C = 1$, $S = 5$, $n_{ij} = n$, $W_{ij} = 1$) by adjusting the friction term (Manning's n) until there was agreement with the field data. This was accomplished by comparing the amplification predicted by the model for incident sinusoidal waves

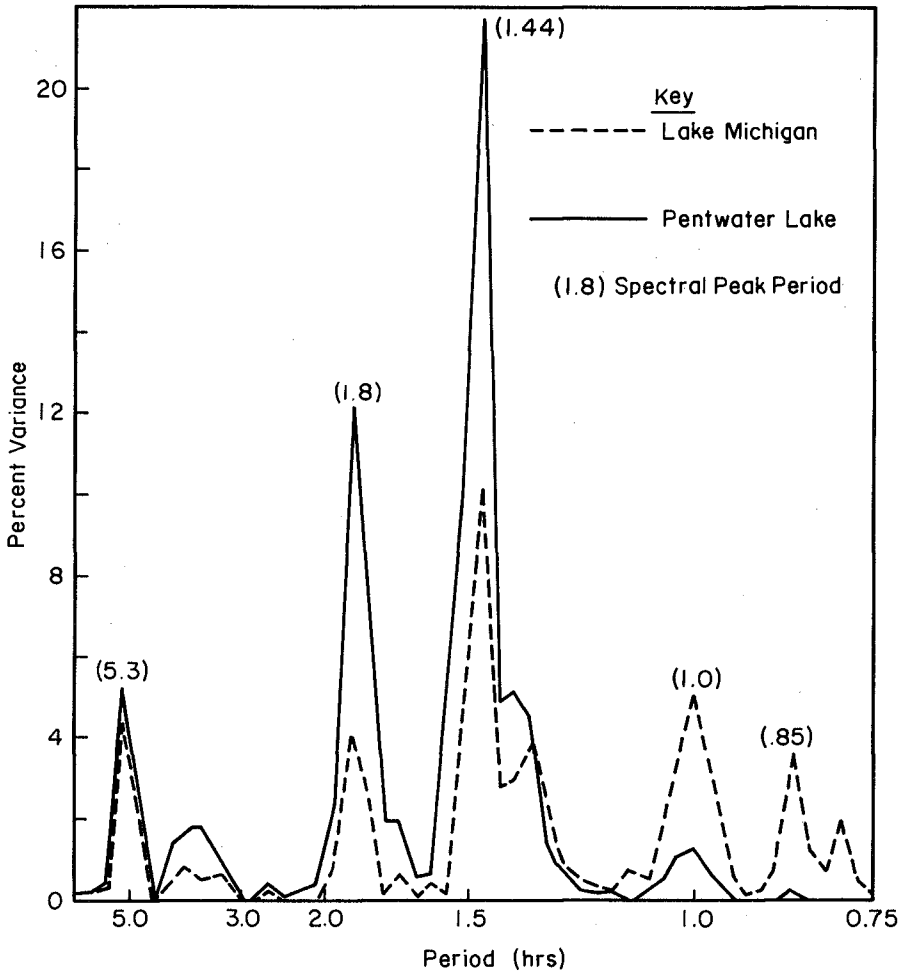


Fig. 7 Lake Michigan and Pentwater Lake spectra,
18 - 20 August 1967

having a 0.1 ft amplitude and a range of periods, to the amplification observed in the field. The calculated amplification for the calibrated condition (solid line) and the amplification determined from the field data (circles) are plotted in Figure 8. The numerical model usually had to be run for two or three cycles for the harbor response to build to equilibrium. In the prototype harbor it is likely that equilibrium (full amplification) is never fully achieved. Thus, the calibration curve in Figure 8 forms the upper envelope of the field data.

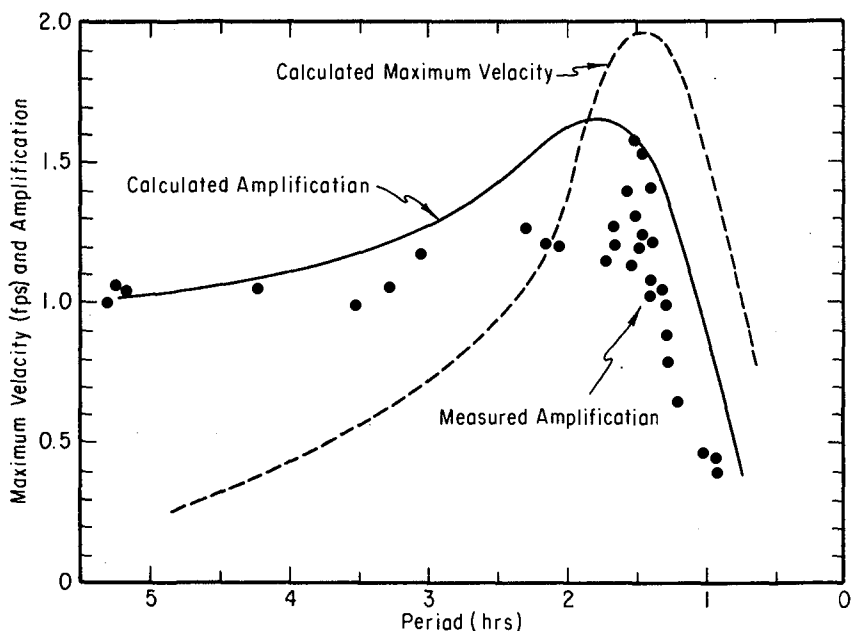


Fig. 8 Response to long wave excitation
at Pentwater (wave amplitude = 0.1 ft)

A Manning's n (see Eq. 6) of 0.036 was required to calibrate the model. This value is probably somewhat higher than the true prototype value because Eq. 6 is applied from the sea to the harbor and inlet channel entrance and exit losses thus become incorporated in the friction term.

The peak resonant period in Figure 8 is 1.8 hours as compared to a period of 1.39 hours predicted by Eq. 5; the difference being due to the effects of friction. Also plotted on Figure 8 are the calculated maximum channel velocities for the range of excitation periods and a Lake Michigan excitation amplitude of 0.1 ft. Because inlet velocity is dependent on both the period and amplitude of the harbor oscillations, the peak velocity occurs at the lower period of 1.4 hrs (which is coincidentally close to the resonant period predicted by Eq. 5).

The harbor level and inlet velocity time-histories computed for an incident sinusoidal wave of 0.1 ft amplitude and 1.5 hour period are plotted in Figure 9. As indicated by Eq. 1 and shown in Figure 9 the inlet velocity is maximum when the gradient of the harbor water level time-history curve is maximum and the velocity is zero at the instant of high and low slack water in the harbor. The phase lag between the sea and harbor water levels is about 0.35 hours or 84° which conforms to Figure 2.

Also plotted in Figure 9 are the magnitudes of the channel friction, head differential and temporal acceleration terms of the equation of motion, normalized by dividing by the highest instantaneous value among the three. Note that the temporal acceleration or inertia term exceeds the friction term over more than half of the cycle.

Figure 10 shows a selected water level record from Lake Michigan along with the measured and calculated ($n = 0.036$) water level response in Pentwater Lake. After three to four hours of record the numerical model stabilized and quite accurately predicted the remaining portion of the measured harbor water level record. This further confirms the model calibration based on Figure 8. The high frequency oscillations in the measured harbor water level record were not predicted by the numerical model. Perhaps these oscillations are due to harbor seiching ($T_1 = 0.13$ hrs) which is not accounted for in the model.

Conclusions

Field and historic hydraulic data for several Great Lakes inlet-harbor systems were collected and analyzed. The primary conclusions from this effort are:

Reversing inlet currents are generated in response to various modes of low amplitude (<0.4 ft) seiching of the Great Lakes. The strongest currents develop when Great Lake seiching excites the Helmholtz resonance mode of the inlet-harbor system and when the seiching mode has an antinode in the vicinity of the system.

Other than a few percent of the time, at most inlets on the Great Lakes current velocities are less than 0.5 fps.

The simple lumped-parameter numerical model used in this study is effective in predicting the hydraulic response of most inlet-harbor systems of the type found on the Great Lakes.

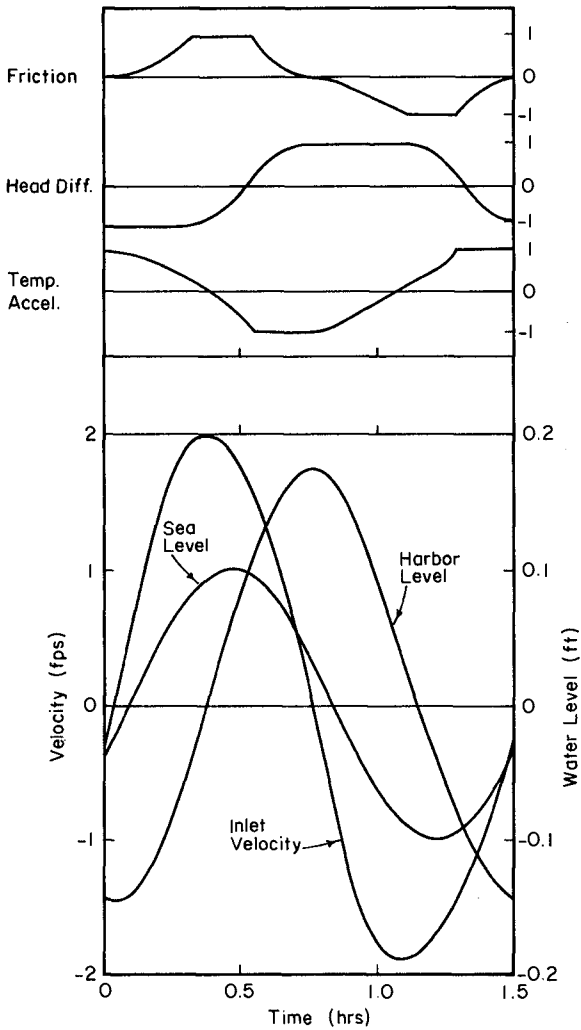


Fig. 9 Pentwater response to sinusoidal wave
(period = 1.5 hrs, amplitude = 0.1 ft)

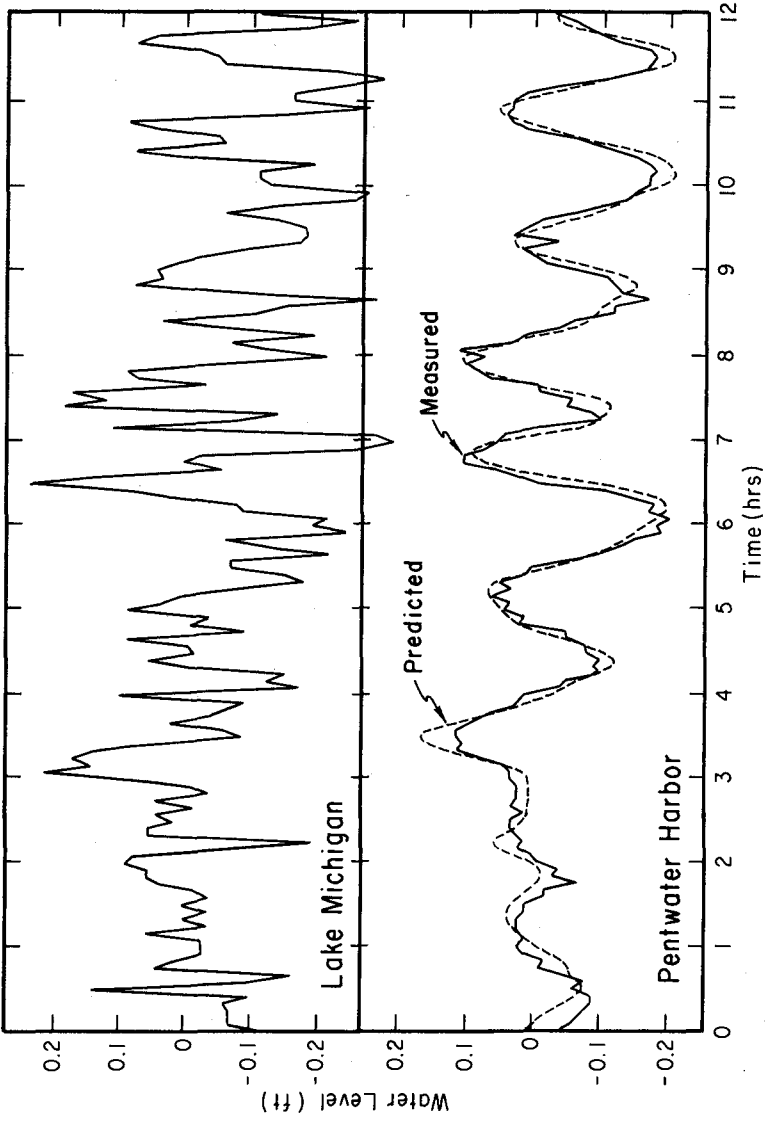


Fig. 10 Numerical model water level predictions at Pentwater

Acknowledgements

The NOAA Lake Survey Center and the U.S. Army Engineer District, Detroit conducted a large portion of the field data collection. This research, conducted by the U.S. Army Coastal Engineering Research Center, is part of the Civil Works research program of the Corps of Engineers. Permission from the Chief of Engineers to publish this research is appreciated. No statements in this paper are to be construed as official Department of the Army policy unless so stated in other authorizing documents.

References

- Kinsler, L. E. and A. R. Frey (1950), Fundamentals of Acoustics, John Wiley and Sons, Inc., New York, pp. 198-208.
- Carrier, G. F., R. P. Shaw, and M. Miyata (1971), "Channel Effects in Harbor Resonance" Journal, Engineering Mechanics Division, ASCE, December, pp. 1703-1715.
- Freeman, N.G., P. F. Hamblin, and T. S. Murty (1974), "Helmholtz Resonance in Harbours of the Great Lakes" Seventeenth Conf. on Great Lakes Research, TAGLR, August, 28 p.
- Miles, J. W. (1948), "Coupling of a Cylindrical Tube to a Half Space" Journal, Acoustical Society of America, pp. 652-664.
- Seelig, W. N., D. L. Harris, and B. E. Herchenroder (1977), "A Generalized Lumped-Parameter Numerical Model of Inlet Hydraulics" U. S. Army Coastal Engineering Research Center and Waterways Experiment Station Joint General Investigation of Tidal Inlets Report (in publication).
- Duane, D. B. and J. H. Saylor (1967), unpublished data taken by NOAA Lake Survey Center, Detroit, Michigan.
- Seelig, W. N. and R. M. Sorensen (1977), "Hydraulics of Great Lakes Inlets" U.S. Army Coastal Engineering Research Center, Technical Memorandum (in publication).
- Mortimer, C. H. (1965), "Spectra of Long Surface Waves and Tides in Lake Michigan and at Green Bay, Wisconsin" Publication 13, Great Lakes Research Division, University of Michigan, pp. 304-325.
- Seelig, W. N. (1977), "Stilling Well Design for Accurate Water Level Measurement" U.S. Army Coastal Engineering Research Center, Technical Paper (in publication).
- Noye, B. J. (1974), "Tide-well Systems II: The Frequency Response of Linear Tide-well System" Journal of Marine Research Vol. 32, May, pp. 155-181.
- Harris, D.L. (1974), "Finite Spectrum Analyses of Wave Records" International Symposium on Ocean Wave Measurement and Analysis, ASCE, New Orleans, September, pp. 107-124.

CHAPTER 97

CHARACTERISTICS OF TIDAL INLETS ON THE PACIFIC COAST OF JAPAN

By Toshiyuki Shigemura¹, M. ASCE

ABSTRACT

Tidal inlets on the Pacific coast of Japan were studied with respect to three characteristic variables of the throat section: (1) Throat area, A; (2) Throat width, B; and (3) Direction of throat section, θ_{ts} . For each of these three variables, multiple regression analysis was performed stepwise by introducing external variables such as tidal prism, mean flow rate of tidal flow, wind energy, wave energy and so on into a linear regression model. Exposure condition of throat section to open sea was also introduced into the analysis.

First step analysis derived quite reliable result on the direction of throat section; $\theta_{ts}(\text{degree}) = -60.0 + 0.88 \theta_{pwv}(\text{degree}), r=0.964$

where θ_{pwv} is the direction of wave energy which penetrates into a backed bay through tidal inlet and r the correlation coefficient between θ_{ts} and θ_{pwv} . However, results on both throat area and throat width were not satisfactory enough even after the performance of more than eighth step analysis on them.

Similar analysis was further performed on both throat area and throat width of the classified data due to the magnitude of geometrical parameters r_{as} and r_{hxb} respectively, where r_{as} is the ratio of throat area to mean surface area of backed bay and r_{hxb} the ratio of the maximum depth at the throat section to throat width. As a result, the former regressions on both throat area and throat width were improved remarkably. Multiple correlation of the regressions were all greater than 0.930.

INTRODUCTION

Tidal inlet problems have been a big concern for coastal engineers who are engaged in maintaining or developing water basins such as bays, lagoons, and estuaries. Especially, characteristics of the minimum flow section or throat section of tidal inlet have been the most important subjects to be investigated since they govern the functional operation of various facilities built inside the basins above.

Many distinguished works have been done on the characteristics of throat section. In 1931, M.P.O'BRIEN(4) made a survey on the tidal inlets located on sandy beaches on the Pacific coast of the United States, and found the following well known relationship between the cross sectional area of throat section and the corresponding tidal prism;

$$A(\text{km}^2) = 4.063 \times 10^{-2} P(\text{km}^3)^{0.85} \dots\dots\dots(1)$$

where A is the cross sectional area of throat section measured below mean sea level and P the corresponding tidal prism for spring tidal range. In 1969,

¹ Dr-Engrg., Asst. Prof. of Ocean Engrg., National Defense Academy of Japan.

O'BRIEN(5) further found that the same relationship held for a large number of additional jettied inlets located on sandy beaches of the Pacific, Atlantic and Gulf coasts of the United States although a slightly different relationship did for a limited number of unjettied inlets;

$$A(\text{km}^2) = 6.65 \times 10^{-2} P(\text{km}^3) \dots\dots\dots(2)$$

In 1973, J.W.JOHNSON(3) made similar analysis on the tidal inlets located on sandy beaches on the Pacific coast of the United States and found the following relationship between their throat areas and corresponding tidal prisms;

$$P(\text{km}^3)/A(\text{km}^2) = 1.729 \times 10^1 P(\text{km}^3)^{0.1} \dots\dots\dots(3)$$

He also showed that different relationship held for a limited number of unjettied inlets on the above coast;

$$P(\text{km}^3)/A(\text{km}^2) = 1.676 \times 10^1 \dots\dots\dots(4)$$

Here, it should be noted that JOHNSON used mean tidal range for the evaluation of tidal prism instead of spring tidal range. These are similar results obtained by O'RRIEN since Eq.(3) and (4) would be transformed into the following equations respectively;

$$A(\text{km}^2) = 5.784 \times 10^{-2} P(\text{km}^3)^{0.9} \dots\dots\dots(5)$$

$$\text{and } A(\text{km}^2) = 5.965 \times 10^{-2} P(\text{km}^3) \dots\dots\dots(6)$$

On the other hand, P.BRUUN and F.GERRITSEN(1) analysed the throat areas of tidal inlets on sandy coasts of the United States, Holland, Denmark and Portugal by introducing the idea of so called "Stable shear stress". As a result, they pointed out that stable throat area could be better described by the maximum flow rate of tidal flow than by tidal prism.

Through the brief review of the previous works, the following facts can be noticed;

- 1). Tidal inlets on sandy beaches were mainly investigated.
- 2). Throat area was the major concern among the characteristics of tidal inlet.
- 3). Effects of a single external variable such as tidal prism or the maximum flow rate was introduced into the analysis of throat area although investigators pointed out the necessity of evaluationg the effects of (1) Other external variables;(2) Geometrical features of both inlets and backed bays; and (3) Geological features of tidal inlets and backed bays in the analysis of throat area.

Similar statistical analysis on tidal inlets are quite few in Japan. So, the author will perform a statistical analysis on the characteristics of tidal inlets located on the Pacific coast of Japan. Here, it should be noted that most tidal inlets on the Pacific coast of Japan are not on sandy beaches but on the rugged rocky coasts. In this study, characteristics of throat section will be investigated as well. Figure 1 shows a model of throat section. Investigation will be made on the following three variables;

- 1). Throat area, A, measured below mean lower low water, in square kilometers.
- 2). Throat width, B, measured below MLLW, in kilometers.
- 3). Direction of throat section, θ_{ts} , measured in azimuth, in degree.

Among these variables, the last two are those added specially in this study since often usage of tidal inlets by super-tankers or big container

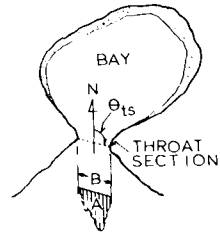


Fig.-1. Model of throat section.

ships has necessitated to obtain full information on both throat width and direction of throat section for both functional operation of ports and safety navigation.

On the other hand, the following ten external variables will be provided for the analysis of the characteristic variables;

- 1). Wind energy off the tidal inlet :E_{owd}
- 2). Direction of wind energy off the tidal inlet : θ_{owd}
- 3). Wind energy penetrating into throat section :E_{pwd}
- 4). Direction of wind energy penetrating into throat section : θ_{pwd}
- 5). Wave energy off the tidal inlet :E_{owv}
- 6). Direction of wave energy penetrating into throat section : θ_{owv}
- 7). Wave energy penetrating into throat section :E_{pwv}
- 8). Direction of wave energy penetrating into throat section : θ_{pwv}
- 9). Volume of tidal prism for mean tidal range :P
- 10). Mean rate of tidal flow at the throat section :V_n

Multiple regression analysis will be performed stepwise on each of the characteristic variables by introducing external variables one by one into a linear regression model preset. The details of the analysis will be presented in the following Chapters.

SURVEY OF THE BASIC DATA

Figure 2 shows the map of Japan. Along the Pacific coast of Japan, ninety five tidal inlets were chosen for analysis.

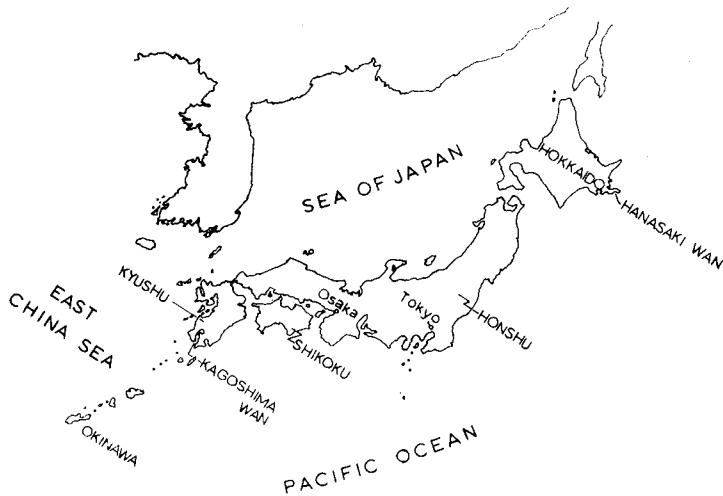


Fig. 2. Map of Japan and her adjacent areas.

Those inlets are distributed almost evenly along the Pacific coast of Japan from Hokkaido to Kagoshima. The inlets whose throat sections are stabilized either by jetties or other artificial works were not considered in the sampling stage. For each inlet selected, the following data were collected through

the various sources;

- A). Geometrical features of inlets and their backed bays.
- B). Geological features around inlets and their backed bays.
- C). Wind data around the inlets.
- D). Wave and tidal data around the inlets.

Details of the data survey will be described in the following sections.

A. Geometrical features of inlets and their backed bays.

Basing on the most recent nautical charts, published by the Japan Maritime Safety Agency, the following data were measured;

- 1). Surface area of bay measured below mean higher high water: $S_h(\text{km}^2)$
- 2). Surface area of bay measured below mean lower low water : $S_l(\text{km}^2)$
- 3). Shore length of the bay measured below MLLW : $l_s(\text{km})$
- 4). Principal axial length of bay measured below MHHW : $l_p(\text{km})$
- 5). Width of the throat section measured below MLLW : $B(\text{km})$
- 6). Direction of the throat section : $\theta_{ts}(\text{degree})$
- 7). Opening angle of tidal inlet against open sea : $\theta_{op}(\text{degree})$
- 8). Throat area of tidal inlet measured below MLLW : $A(\text{km}^2)$
- 9). Maximum depth of the throat section measured below MLLW : $h_x(\text{m})$
- 10). Mean tidal range at the bay : $2a_n(\text{m})$

B. Geological features around the inlets and their backed bays.

Geological information along beaches were surveyed through the "Geological Maps of Japan"(6) published by the Economical Planning Agency of Japan. Information on bottom materials were checked through the "Bottom Sediment Chart of the Adjacent Seas of Japan"(10) published by the Japan Maritime Safety Agency. Those information were also referred to those shown in the corresponding nautical charts.

C. Wind data around the inlets.

Thirty four meteorological stations were chosen along the Pacific coast of Japan. These stations are all located near the selected inlets. At each station, the monthly maximum winds recorded during the period of 1967 to 1971 were picked up through the "Annual Report of the Japan Meteorological Agency". At the inlets where stations were not located nearby, wind data were estimated by the interpolation method basing on the monthly maximum winds obtained at the close stations.

D. Wave and tidal data around the inlets.

Wave data available were all collected through various sources(2,7,8,9, 11,12). However, reliable data were obtained only at a few spots where waves were recorded continuously during the period of 1967 to 1971. Among these data, the monthly maximum waves were picked up for the analysis. At the inlets where reliable wave data were not obtained, waves were estimated by the method of SVERDRUP-MUNK-BRETSCHNEIDER basing on the data of monthly maximum winds at the corresponding inlets. The monthly maximum waves recorded continuously during the other period than the above were also referred to the waves estimated by S-M-B method, and the larger ones were adopted as the monthly maximum waves.

Data of tidal range at each inlet were collected through the correspond-

ing nautical charts.

EVALUATION OF THE EXTERNAL VARIABLES

As shown in INTRODUCTION, ten external variables were provided. These are the variables related to wind energy, wave energy, tidal prism, and mean rate of tidal flow at the throat section of tidal inlet. In the following sections, derivation of the equations on these variables will be described briefly.

A. Equations of wind energy and the related terms.

Basing on the monthly maximum winds, wind diagram at the offshore of each selected inlet was produced. Figure 3 shows a wind which blows from the i th direction.

Suppose the velocity of this wind to be $V(i)$ and its frequency of occurrence over five years to be $f(i)$. Then, the horizontal component of wind energy off the inlet, $E_{owdh}(i)$, is evaluated by

$$E_{owdh}(i) = \frac{1}{2} \rho_a V(i)^2 (f(i)/60) \sin(22.5(i-1)) \dots (7)$$

where ρ_a is the air density. Similarly, the vertical component of this energy, $E_{owdv}(i)$, is evaluated by

$$E_{owdv}(i) = \frac{1}{2} \rho_a V(i)^2 (f(i)/60) \cos(22.5(i-1)) \dots (8)$$

then, the probable wind energy off the inlet, E_{owd} is evaluated by

$$E_{owd} = \sqrt{\left(\sum_{i=1}^{16} E_{owdh}(i)\right)^2 + \left(\sum_{i=1}^{16} E_{owdv}(i)\right)^2} \dots (9)$$

The direction of this energy, θ_{owd} , can be obtained by

$$\theta_{owd} = \sin^{-1}\left(\frac{\sum_{i=1}^{16} E_{owdh}(i)}{E_{owd}}\right) \dots (10)$$

Figure 4 shows a wind which penetrates into the throat section from the i th direction. The penetrating energy, E_{pwd} , and its direction, θ_{pwd} , are then obtained through Eqs. (9) and (10) respectively by summarizing the corresponding terms over the opening angle of the tidal inlet instead of full range.

B. Equations of wave energy and the related terms.

Basing on the monthly maximum waves, wave diagram was produced at the offshore of each inlet. Now, suppose the height of wave coming from the i th direction to be $H(i)$, wave length to be $L(i)$, wave period to be $T(i)$, and the frequency of occurrence over five years to be $f(i)$. Then, the horizontal component of wave energy off the tidal inlet, $E_{owvh}(i)$, is given by

$$E_{owvh}(i) = \frac{1}{2} \rho_w g H(i)^2 L(i) (f(i)/60) \sin(22.5(i-1)) \dots (11)$$

Similarly, the vertical component of this energy, $E_{owvv}(i)$, is given by

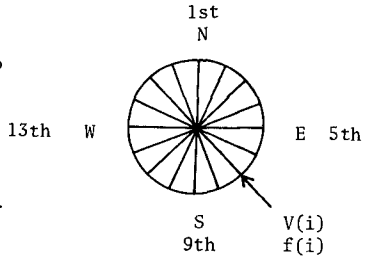


Fig.-3. Wind data which blow from i th direction.

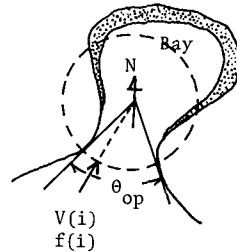


Fig.-4. Wind data which penetrates into throat section from i th direction.

$$E_{OwVv}(i) = \frac{1}{8} \rho_w g H(i)^2 L(i) (f(i)/60) \cos(22.5(i-1)) \dots\dots\dots(12)$$

where ρ_w is the density of sea water. The probable wave energy off the inlet is then given by

$$E_{OwV} = \sqrt{\left(\sum_{i=1}^{16} E_{OwVh}(i)\right)^2 + \left(\sum_{i=1}^{16} E_{OwVv}(i)\right)^2} \dots\dots\dots(13)$$

The direction of this wave energy, θ_{OwV} , is given by

$$\theta_{OwV} = \sin^{-1} \left(\frac{\sum_{i=1}^{16} E_{OwVh}(i)/E_{OwV}}{\dots\dots\dots} \right) \dots\dots\dots(14)$$

Penetrating wave energy, E_{pWV} , and its direction, θ_{pWV} , can be obtained through Eq.(13) and (14) respectively by summarizing the corresponding terms over the opening angle of the tidal inlet instead of full range.

C. Equations of tidal prism and mean rate of tidal flow.

Tidal prism, P, was evaluated by the following equation;

$$P(\text{km}^3) = S_n(\text{km}^2) \times 2a_n(\text{m})/1000 \dots\dots\dots(15)$$

where S_n is the mean surface area of the backed bay which was obtained by averaging the surface area measured at MHHW and that measured below MLLW, and $2a_n$ the mean tidal range in the backed bay.

The mean rate of tidal flow at the throat section, V_n , was evaluated by the following equation;

$$V_n(\text{m/sec}) = \frac{P(\text{km}^3)}{A(\text{km}^2) \times T/2(\text{sec})} \times 1000 \dots\dots\dots(16)$$

where T is the duration of tidal cycle.

STEPWISE MULTIPLE REGRESSION ANALYSIS ON THE CHARACTERISTIC VARIABLES

The following equation shows a linear regression model assumed between each of the characteristic variables and external variables;

$$Y = C_0 + \sum_{i=1}^m A_i X_i \dots\dots\dots(17)$$

where Y indicates one of the characteristic variables, C_0 the regression constant, X_i the *i*th external variable introduced into the regression model, A_i the partial regression coefficient of X_i , and m the number of the external variables introduced into the analysis. Thus, Eq.(17) actually shows the linear regression model assumed for the *m*th step analysis on Y.

Analysis is performed stepwise by introducing external variables one by one at each step of analysis into the regression model above. A variable is introduced into the regression model at each step of analysis in such an order that the maximum multiple correlation may be obtained by its introduction. F test is performed at each step of analysis by setting the significance level of 5 %, and the analysis will be proceeded until the introduction of new variable becomes insignificant.

The actual analysis was initiated by checking the correlation coefficients between the characteristic variables and external ones. Correlation coefficients between each of the characteristic variables and external ones were investigated on the following cases;

1). When the values of both characteristic variables and external ones are

original ones.

2). When the values of characteristic variables are original although the values external variables are converted into logarithmic values.

3). When the values of both characteristic variables and external ones are all converted into the logarithmic values.

Exposure condition of throat section was also introduced into the analysis. Table 1 summarizes the results of correlation analysis. In this table, exposed inlets mean the inlets whose throat sections are exposed to open sea, and protected inlets indicate the ones whose throat sections are protected against the intrusion of winds and waves by either islands or peninslas.

Table 1. Correlation coefficients between each of three characteristic variables and ten external variables.

External variable	Exposed inlets(N=66)						Protected inlets(N=29)					
	A B θ_{ts} (orig. values)			A B θ_{ts} (log values)			A B θ_{ts} (orig. values)			A B θ_{ts} (log values)		
P	.643	.718	-.133	.844	.873	.062	.928	.777	.187	.824	.772	.276
V _n	.268	.413	-.124	.286	.443	-.075	.560	.439	-.058	.051	.162	-.182
E _{owd}	.095	.077	.002	.030	.112	-.024	.132	.030	.048	.239	.132	.100
θ_{owd}	.170	.154	.043	.148	.219	.085	.244	.175	.480	.357	.147	.471
E _{pwd}	-.136	-.093	-.127	-.199	-.144	-.130	--	--	--	--	--	--
θ_{pwd}	.081	.098	-.149	-.031	.067	-.003	--	--	--	--	--	--
E _{owv}	-.137	-.086	-.082	-.263	-.161	-.085	-.162	-.021	.123	-.090	.010	.113
θ_{owv}	.132	.158	.044	.018	.097	.273	.120	.055	-.252	-.160	-.138	-.196
E _{pwv}	-.022	-.035	-.055	-.154	-.148	-.139	--	--	--	--	--	--
θ_{pwv}	-.036	-.052	.964	-.007	-.032	.849	--	--	--	--	--	--

From this table, the following facts can be seen;

- 1). In case of throat area and throat width, log converted variables generally show higher correlation coefficients than do the original values of them.
- 2). In case of the direction of throat section, original values of the variables generally show higher correlation coefficients than do the log converted variables.
- 3). Influence of exposure condition to correlation coefficients is not clear in case of both throat area and throat width although it is significant in case of the direction of throat section.

Basing on these findings, it was decided to use log converted variables for the analysis of both throat area and throat width, and original variables for the analysis of the direction of throat section. Details of the analytical results will be shown in the next Chapter.

RESULTS ON THE STEPWISE MULTIPLE REGRESSION ANALYSIS

Multiple regression analysis was performed stepwise on each of the characteristic variables of (1) Whole inlets; (2) Exposed inlets; and (3) Protected inlets. Table 2 shows the regressions obtained by the first step analysis together with those obtained by the final step analysis. In this table, R indicates the multiple correlation of the regression on each characteristic variables, and numerals in each colomun show the partial regression coefficients of the corresponding external variables.

Table 2. Results of multiple regression analysis on the characteristic variables of throat section.

$$Y = C_0 + \sum_{i=1}^m A_i X_i$$

Step	C ₀	P	E _{owd}	θ _{owd}	E _{pwd}	θ _{pwd}	E _{owv}	θ _{owv}	E _{pwv}	θ _{pwv}	V _n	R	Groups
Regressions on throat area; All variables-logarithmic values													
1 st	-.063	.600										.835	Whole
8 th	-.165	.586	-.085	.368	.069	-.261	-.028	.021	-.012			.862	
1 st	-.071	.579										.845	Exposed
8 th	-.189	.564	-.091	.239	.061	-.127	-.187	.008	.058			.865	
1 st	-.001	.655										.824	Protected
Regressions on throat width; All variables-logarithmic values													
1 st	1.188	.405										.843	Whole
2 nd	-.689	.581									-.438	.917	
9 th	-.890	.571	.005	.077	.014	-.004	.021	.029	.001			-.417	.924
1 st	1.202	.400										.873	Exposed
2 nd	-.557	.573									-.411	.933	
9 th	1.292	.573	-.063	.173	.073	.092	.048	.060	-.036			-.407	.945
1 st	1.154	.411										.772	Protected
2 nd	-.842	.569									-.459	.864	
Regression on the direction of throat section; Original values													
1 st	-60.0										.880	.964	Exposed

From this table, the following facts can be found;

A. On the regressions of throat area.

- 1). Tidal prism has been introduced into every regression obtained by the first step analysis. This indicates that tidal prism is the most predominant external variable for throat area.
- 2). The first step regressions are barely improved by introducing additional external variables into the analysis. In case of exposed inlets, R of the first step regression is 0.845. However, R of the eight step regression is only 0.865.

B. On the regressions of throat width.

- 1). Tidal prism is the most predominant external variable for throat width. In case of exposed inlets, R of the first step regression is 0.873.
- 2). Mean rate of tidal flow is the next predominant variable for throat width. The first step regressions are all improved considerably by the introduction of mean rate of tidal flow into the analysis. In case of exposed inlets, R of the second step regression is improved to 0.933 from 0.873.
- 3). Second step regressions, however, are barely improved by the performance of further step analysis. In case of exposed inlets, R of the ninth step regression is improved only to 0.945 from 0.933.

C. On the regression on the direction of throat section.

- 1). Direction of the penetrating wave energy is the most predominant external variable for the direction of throat section.
- 2). The first step analysis gave quite satisfactory regression on the direction of throat section as shown below.

$$\theta_{ts} \text{ (degree)} = -60.0 + 0.88 \theta_{pwv} \text{ (degree)}$$

where R of this regression is 0.964.

Figure 5 shows the relationship between the measured values of throat area of whole inlets and those estimated by the eighth step regression shown

in table 2. In this figure, abscissa indicates the scale for the measured values of throat area, and ordinate the scale for the estimated values of throat area. As it can be seen from this figure, measured values of throat area scatter considerably around the estimated values of them. This fact shows that multiple regression analysis could not derive the satisfactory regression even after the introduction of eight external variables into the analysis.

In figure 6, measured values of throat width are plotted against the corresponding values of throat width estimated by the ninth step regression shown in table 2. In this figure, abscissa shows the scale for measured width and ordinate the scale for estimated width. Measured values of throat width still scatter around the estimated values of throat width. This fact also indicates that ninth step regression on throat width was not satisfactory enough.

Figure 7 shows the result of the first step analysis on the direction of throat section. In this figure, abscissa indicates the scale for the direction of penetrating wave energy and ordinate the scale for the direction of throat section. As it can be seen from this figure, data of θ_{ts} fall fairly close around the first step regression. Standard deviation of θ_{ts} from the regression was 28.4° . This fact indicates that the first step regression on θ_{ts} is quite satisfactory one. Here, some explanation should be added on the magnitude of θ_{pwv} . Figure 8 shows the mutual relationship between θ_{ts} and θ_{pwv} for the various magnitude of θ_{ts} . As it can be seen from this figure, θ_{pwv} becomes greater than 360° when θ_{ts} becomes greater than 260° . In this case, $\theta_{pwv} + 360$ was used for the analysis of θ_{ts} instead of θ_{pwv} .

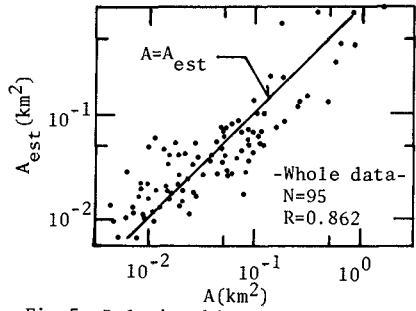


Fig-5. Relationship between A and A_{est} .

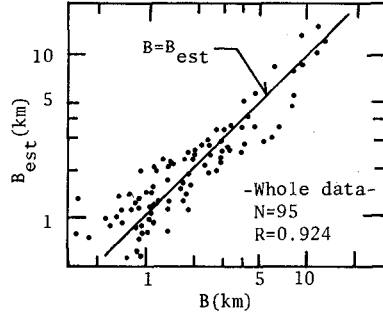


Fig.-6. Relationship between B and B_{est} .

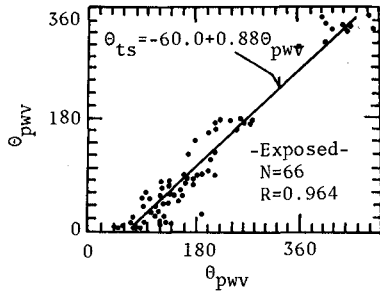


Fig.-7. Relationship between θ_{ts} and θ_{pwv} .

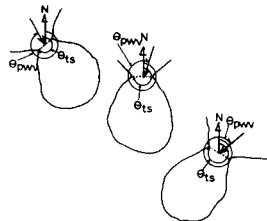


Fig.-8. Measurement of θ_{pwv} against θ_{ts} .

DISCUSSION

In the previous Chapter, the author showed that the first step analysis or the simple regression analysis derived quite satisfactory regression on the direction of throat section. He also showed that satisfactory regressions were not obtained on both throat area and throat width by the performance of multiple regression analysis into which more than eight external variables were introduced.

This may be caused by the effects of the following factors which were not taken into account in the previous analysis;

- 1). Geometrical features of inlets and their backed bays.
 - 2). Geological features around the inlets and their backed bays.
- In these two factors above, geometrical features may control the contribution rate of the external variables to throat section. Thus, tidal inlets with different geometrical features will probably behave differently even if external variables of the same magnitude were induced on them. If this is true, more reliable regressions may possibly be obtained on both throat area and throat width by performing multiple regression analysis on the data of tidal inlets classified by certain parameters representing geometrical features of tidal inlets and their backed bays.

Then, the author provided the following twelve parameters which are all dimensionless;

- 1). r_{as} : Throat area/Mean surface area of backed bay
- 2). r_{bp} : Throat width/Principal axial length of backed bay
- 3). r_{bs} : Throat width/Shore length of backed bay
- 4). r_{es} : l_{es} /Shore length of backed bay
- 5). r_{hna} : Mean depth at throat section/Mean tidal range
- 6). r_{hnb} : Mean depth at throat section/Throat width
- 7). r_{hnp} : Mean depth at throat section/Principal axial length of backed bay
- 8). r_{hxa} : Maximum depth at throat section/Mean tidal range
- 9). r_{hxb} : Maximum depth at throat section/Throat width
- 10). r_{hxp} : Maximum depth at throat section/Principal axial length of bay
- 11). r_{op} : Opening angle of tidal inlet/ 360°
- 12). r_{ps} : Principal axial length/Shore length of backed bay

In these parameters above, l_{es} means the circumference of a virtual circle whose area is equal to mean surface area of backed bay.

On the other hand, the following two variables were provided to measure the reliability or the fitness of the final step regressions on both throat area and throat width which were obtained in the previous Chapter;

$$A_{fit} = A_{est}/A \times 100(\%)$$

$$\text{and } B_{fit} = B_{est}/B \times 100(\%)$$

where A_{est} and B_{est} are the values of throat area and throat width estimated by their final step regressions shown in table 2.

In order to see the influence of the geometrical parameters upon A_{fit} and B_{fit} , correlation analysis was performed among them. Table 3 summarizes the results of analysis. From this table, the following facts can be noticed;

- 1). A_{fit} of both exposed inlets and protected ones has relatively high correlation with r_{as} or the ratio of throat area to mean surface area of backed bay.
- 2). B_{fit} of both exposed and protected inlets has considerably high correlation with r_{hxb} or the ratio of the maximum depth at throat section to throat width.

Table 3. Correlation coefficients between each of A_{fit} and B_{fit} and twelve parameters representing geometrical features of inlets and bays.

Parameters	(Exposed inlets, N=66)						(Protected inlets, N=29)					
	(Both orig)		(Both log)		(Pars log)		(Both orig)		(Both log)		(Pars log)	
	A_{fit}	B_{fit}	A_{fit}	B_{fit}	A_{fit}	B_{fit}	A_{fit}	B_{fit}	A_{fit}	B_{fit}	A_{fit}	B_{fit}
r_{as}	-.463	.216	*.608	.026	-.604	.029	-.574	.127	*.702	.154	-.604	.119
r_{bp}	-.326	-.520	-.427	-.554	-.437	-.519	-.385	-.611	-.498	-.737	-.433	-.729
r_{bs}	-.320	-.560	-.458	-.583	-.420	-.557	-.471	-.437	-.668	-.553	-.622	-.558
r_{es}	.191	.257	.221	.368	.129	.334	.641	.297	.609	.285	.579	.289
r_{hna}	-.403	.217	.526	.324	-.463	.285	-.290	.119	-.596	.387	-.568	.361
r_{hnb}	-.032	*.754	-.054	*.704	-.076	.685	-.027	*.939	-.083	*.954	-.043	*.927
r_{hnp}	-.348	.312	-.398	.137	-.426	.150	-.497	.349	-.609	.395	-.494	.364
r_{hxa}	-.297	.254	.428	.345	-.330	.314	-.298	.143	-.572	.390	-.518	.371
r_{hxb}	.018	.716	.038	*.745	.048	*.734	-.013	*.894	-.036	*.936	.022	*.910
r_{hxp}	-.286	.319	-.344	.174	-.345	.186	-.437	.362	.548	.372	-.412	.350
r_{op}	-.056	-.249	-.036	-.193	-.061	-.196	.025	-.187	.047	-.223	.064	-.219
r_{ps}	.057	.030	-.015	-.000	.073	-.019	-.457	.173	-.470	.211	-.495	.187

Note: (1). Both-orig; Values of A_{fit} , B_{fit} and parameters are original
 (2). Both-log; Values of A_{fit} , B_{fit} and parameters are logarithmic
 (3). Pars-log; Values of parameters are logarithmic although values of A_{fit} and B_{fit} are original

Figure 9 shows the distribution of A_{fit} of both exposed and protected inlets plotted against their corresponding values of r_{as} . From this figure, it can be seen that tidal inlets may be classified into the following three groups due to the magnitude of r_{as} .

- 1). Group in which throat area is always overestimated by the final step regression.
- 2). Group in which throat area is always underestimated by the final step regression.
- 3). Group between the two above.

On the other hand, figure 10 shows the distribution of B_{fit} of both exposed and protected inlets plotted against their corresponding values of r_{hxb} . From this figure, it can be noticed that tidal inlets may also be classified into similar groups due to the magnitude of r_{hxb} .

- 1). Group in which throat width is always overestimated by the final step regression.
- 2). Group in which throat width is always underestimated by the final step regression.
- 3). Group between the two above.

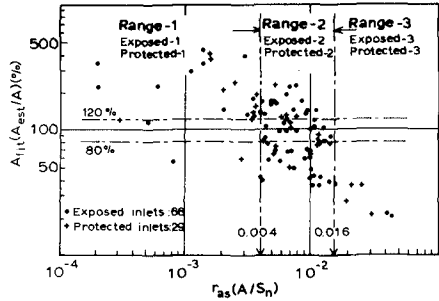


Fig.-9. Relationship between A_{fit} and r_{as} .

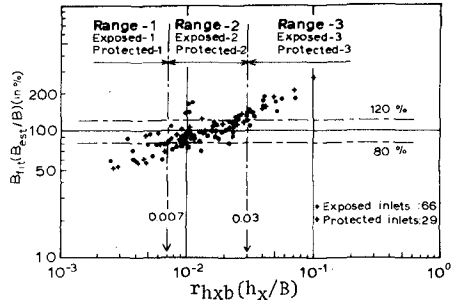


Fig-10. Relationship between B_{fit} and r_{hxb} .

Basing on these findings, tidal inlets were classified into the following groups shown in table 4 for the analysis of throat area.

Table 4. Classification of tidal inlets due to both exposure condition and magnitude of geometrical parameter, r_{as} .

Range of r_{as}	Groups classified	Sample number
$r_{as} < 0.004$	Exposed-1	14
	Protected-1	10
$0.004 \leq r_{as} < 0.016$	Exposed-2	50
	Protected-2	15
$r_{as} \geq 0.016$	Exposed-3	2
	Protected-3	4

For the tidal inlets involved in Groups 1 and 2, stepwise multiple regression analysis was performed on their throat areas. Table 5 summarizes the final step regressions on them.

Table 5. Final step regressions on throat area of the classified inlets due to both exposure condition and geometrical parameter, r_{as} .

$Y = C_0 + \sum_{i=1}^m A_i X_i$												
Step	C_0	P	E_{owd}	θ_{owd}	E_{pwd}	θ_{pwd}	E_{owv}	θ_{owv}	E_{pww}	θ_{pww}	R	Groups
8 th	-1.652	.681	-.103	.902	.375	-1.049	-.012	.707	-.176		.970	Exposed-1
8 th	.181	.831	-.134	.299	.135	.016	-.153	-.022	.039		.945	Exposed-2
1 st	.153	.856									.933	Protected-1
1 st	.430	.819									.976	Protected-2

As it can be seen through the values of R in table 5, the former regressions on throat area were improved significantly by introducing geometrical parameter, r_{as} , into the analysis.

Figure 11 shows the distribution of throat areas of tidal inlets (Exposed-2) estimated by the corresponding final step regression plotted against their corresponding values of measured throat areas. From this figure, it can be noticed clearly that the regressions shown in table 5 are quite reliable ones.

Similar analysis was performed on throat width. Namely, tidal inlets were classified into the following groups due to both exposure condition and magnitude of geometrical parameter, r_{hx} .

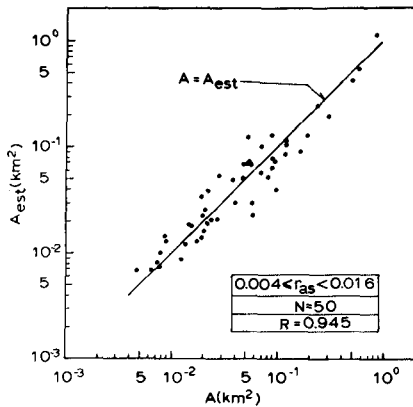


Fig.-11. Relationship between A and A_{est} .

Table 6. Classification of tidal inlets due to both exposure condition and magnitude of geometrical parameter, r_{hxb} .

Range of r_{hxb}	Groups classified	Sample number
$r_{hxb} < 0.007$	Exposed-1	11
	Protected-1	9
$0.007 \leq r_{hxb} < 0.030$	Exposed-2	41
	Protected-2	14
$r_{hxb} \geq 0.030$	Exposed-3	14
	Protected-3	6

For the inlets of each group, multiple regression analysis was performed stepwise on their throat width. Table 7 summarizes the final step regressions on them.

Table 7. Final step regressions on throat width of the classified inlets due to both exposure condition and geometrical parameter, r_{hxb} .

$Y = C_0 + \sum_{i=1}^m A_i X_i$													Groups
Step	C_0	P	E_{owd}	θ_{owd}	E_{pwd}	θ_{pwd}	E_{owv}	θ_{owv}	E_{pwv}	θ_{pwv}	V_n	R	Groups
9 th	-.833	.387	-.225	.540	-.061	-.168	.116	.447	.041	-.077	.999		Exposed-1
9 th	-1.058	.478	-.027	.106	.060	.140	.018	.051	-.023	-.341	.971		Exposed-2
6 th	.341	.583	.241	--	.200	--	-.293	--	.093	-.184	.822		Exposed-3
2 nd	-1.770	.594								-.693	.993		Protected-1
2 nd	-.630	.529								-.395	.983		Protected-2
2 nd	-2.996	.937								-.150	.990		Protected-3

In this analysis, quite high value of multiple correlation was also obtained for each group of tidal inlets except the case of Exposed-3. This fact indicates that former regressions on throat width were improved significantly by introducing geometrical parameter, r_{hxb} into the analysis.

Figure 12 shows the distribution of throat width(Exposed-2) estimated by the corresponding final step regression in table 7 plotted against their corresponding values of measured throat width. From this figure, it can be noticed clearly that the regressions shown in table 7 are quite reliable ones except the regression for Exposed-3.

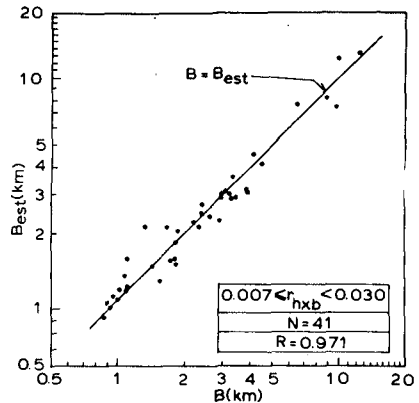


Fig.-12. Relationship between B and B_{est} .

CONCLUSION

Tidal inlets on the Pacific coast of Japan were studied with respect to three characteristic variables of their throat sections:(1) Throat area;(2) Throat width; and (3) Direction of throat section. For each of these three variables, multiple regression analysis was performed stepwise by introducing external variables such as tidal prism, mean rate of tidal flow, wind energy, wave energy and so on one by one into a linear regression model. Exposure condition of throat section to open sea and geometrical parameters of inlets and bays were also introduced into the analysis. As a result, the following facts were found;

- 1). Quite reliable regressions are found between throat area and external variables if the tidal inlets are classified due to the magnitude of geometrical parameter, r_{as} which is the ratio of throat area to mean surface area of the backed bay. These regressions are shown in Table 5.
- 2). Quite satisfactory regressions are found between throat width and external variables if the tidal inlets are classified due to the magnitude of geometrical parameter, r_{hxb} which is the ratio of the maximum depth at the throat section to throat width. These regressions are shown in Table 7.
- 3). Direction of the penetrating wave energy is the most predominant external variable for the direction of throat section, and quite reliable regression shown below is obtained for the exposed inlets.

$$\theta_{ts}(\text{degree}) = -60.0 + 0.88 \theta_{pw}(\text{degree})$$

ACKNOWLEDGEMENT

This is a part of the author's doctoral dissertation submitted to the Graduate Division, University of California, Berkeley in 1975. The author is greatly indebted to Professor J.W. JOHNSON for his continual guidance to the completion of this work.

REFERENCES

1. BRUUN, P. and GERRITSEN, F., "Stability of Coastal Inlets," North Holland Publishing Co., Amsterdam, 1960, p.58.
2. Bureau of Ports and Harbors, Hokkaido Development Agency, "Characteristics of Waves Along the Coast of Hokkaido," March, 1967(in Japanese).
3. JOHNSON, J.W., "Characteristics and Behaviors of Pacific Coast Tidal Inlets," Jour. Waterways and Harbors and Coastal Engineering Division, ASCE, Aug., 1973, pp.325-339.
4. O'BRIEN, M.P., "Estuary Tidal Prism Related to Entrance Area," Civil Engineering, Vol. 1, No. 8, 1931, pp.738-739.
5. O'BRIEN, M.P., "Equilibrium Flow Areas of Tidal Inlets on Sandy Coast," Jour. Waterways and Harbors Division, ASCE, Feb., 1969, pp.43-52.
6. The Economical Planning Agency of Japan, "Geological Maps of Japan," 1967.
7. The Fifth District Port Construction Bureau, Ministry of Transport, Japan, "Wave Table no. 2," March, 1970(in Japanese).
8. The Japan Fishery Agency, "Report on Wave Characteristics at Each Fishery Port of Japan:1965-1968," Dec., 1970(in Japanese).
9. The Fourth District Port Construction Bureau, Ministry of Transport, Japan, "Observation Report of Tidal Range and Wave-No. 8," March, 1972(in Japanese).

10. The Japan Maritime Safety Agency, "Bottom Sediment Charts of the Adjacent Seas of Japan," 1949.
11. The Second District Port Construction Bureau, Ministry of Transport, Japan, "Characteristics of Waves Along the Coast of Japan," March, 1961(in Japanese).
12. The Third District Port Construction Bureau, Ministry of Transport, Japan, "Primary Data for Coastal Construction-Shikoku," Dec., 1962(in Japanese).

CHAPTER 98

TIDAL INLET FLOW DYNAMICS AND SEDIMENT MOVEMENT

J. L. Machemehl, N. E. Bird and A. N. Chambers
Center for Marine and Coastal Studies
North Carolina State University
Raleigh, North Carolina 27607

ABSTRACT

A numerical simulation model for the computation of tidal and fresh water flow exchange through a coastal inlet (developed by Amein¹) was modified and calibrated with field data (current, water surface elevation and bottom topography) for Lockwoods Folly Inlet, North Carolina. The calibrated model was then used to predict the changes in the flow regimes brought about by natural and manmade changes such as storms and dredging, respectively, and to predict the changes in flow regimes caused by the Lockwoods Folly River.

A generalized hypothesis of the patterns of sediment through and bypassing the inlet were formulated from an evaluation of the flow data and from an analysis of the orientation and structure of the bedforms observed in the inlet and on the offshore bar. The bedforms were analysed in the field and from an uncontrolled mosaic made from multi-spectral aerial photographs. Confirmation and refinement of the transport rates and movement patterns during ebb tide were made by introducing 454 kilograms (1000 lbs.) of fluorescent tracer sand in two colors into the inlet channels. The sediment movement through the inlet was established and correlated with the numerical simulation model. Confirmation and refinement of the transport rates and movement patterns during flood tide were made by introducing 680 kilograms (1,500 lbs.) of fluorescent tracer sand in three colors into the surf zone on the updrift beach and on the offshore bar. The sediment movement indicated the existence of bar bypassing (which was the dominant bypassing mechanism) and tidal flow bypassing. The bypassing mechanism of the inlet was found to agree with other atlantic coast inlets.

When used in conjunction with an analysis of bedform and tracer sand data the numerical simulation model was found to be a valid method for monitoring the high energy inlet environment.

INTRODUCTION

Description of the Study Area

Lockwoods Folly Inlet is approximately 10 miles west of the Cape Fear River and 9 miles east of Shallotte Inlet in Brunswick County, North Carolina. Holdens Beach borders the Inlet on the west while

Long Beach borders the Inlet on the east as shown in Figure 1. The beaches are almost east-west in direction. Holdens Beach is approximately 13,400 meters (44,900 ft.) long and has an average width of 490 meters (1600 ft.) while Long Beach is approximately 14,000 meters (46,000 ft.) long and has an average width of 400 meters (1300 ft.). Both the eastern end of Holdens Beach and the western end of Long Beach have been the victim of extensive and severe erosion. The Corps of Engineers² has stated that the eastern 1,800 meters (6,000 ft.) of Holdens Beach has experienced the highest rate of shoreline erosion in Brunswick County. Shoreline positions in the vicinity of the Inlet are shown in Figure 1.

The Atlantic Intracoastal Waterway (AIWW) separates the beaches from the mainland. The Lockwoods Folly River enters the AIWW 2100 meters (6900 ft.) east of the Inlet. In 1672 the Inlet was aligned with the Lockwoods Folly River.

Meterological and Oceanographical Data

On an annual basis the winds blow almost equally onshore and offshore with winds from the east occurring less frequently. During the period of this study the predominant wind was south to southeast at an average speed of 1.9 meters per second (3.7 knots). Wave height and direction data were available from the Corps of Engineers. The waves observed had a period of less than 9 seconds and a height of less than 5 ft. Unusual conditions during the study included a period of squalls and several days of storms.

The mean tidal range at Lockwoods Folly Inlet was 1.3 meters (4.2 ft.). The spring tidal range is 1.5 meters (4.8 ft.). The tides are semi-diurnal. The current velocities in the Inlet channel ranged from 129 to 160 cm/sec. (2.0 to 2.5 knots).

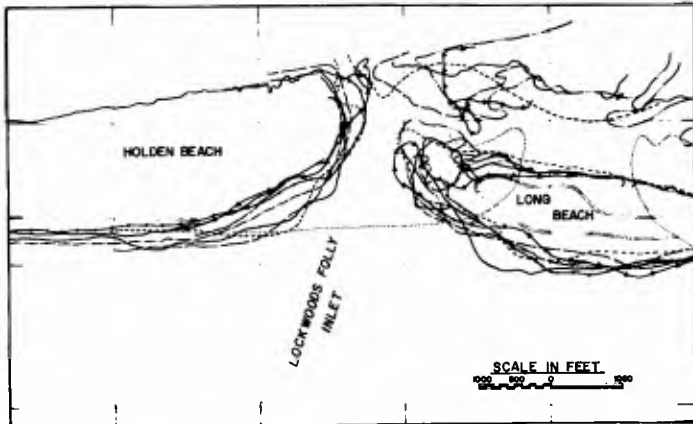
Objectives of Study

Lockwoods Folly Inlet is of particular interest as a study area. The Inlet is included in a proposed Corps of Engineers project for erosion control and hurricane protection of adjacent beaches. The Inlet is very active with strong tidal currents and shoaling sand bars. Wave energy is frequently concentrated near the Inlet due to refraction around the offshore sand bar which tends to aggravate the erosion.

The objectives of this study were:

- (1) To adapt Amein's numerical model to the Inlet,
- (2) To develop a generalized sediment movement pattern for the Inlet, and
- (3) To evaluate the natural bypassing system at the Inlet.

INLET FLOW DYNAMICS



LEGEND

DATE	HIGH WATER SHORELINE
1859
1923	-----
1934	-----
1943	-----
1954	-----
1961	-----
1963	-----
1970	-----
1972	-----

FIGURE 1. Historic Shoreline Positions for Lockwoods Folly Inlet, North Carolina.

Numerical Simulation Model

Flow Computations. Amein's¹ numerical simulation model was modified and adapted to Lockwoods Folly Inlet. The numerical simulation model is based on the equations of unsteady flow with an implicit method for numerical simulation of the flow equations. A system of 28 nonlinear equations were solved using the generalized Newton iteration method.

The equations of unsteady flow are based on the conservation of mass and momentum. For the flow between Section 1-1 and 2-2 as shown in Figure 2, the equations can be written:

$$\frac{\partial Q}{\partial x} + \frac{\partial A}{\partial t} - q = 0 \dots \dots \dots (1)$$

And

$$\frac{1}{A} \frac{\partial Q}{\partial t} + \frac{V}{A} \frac{\partial Q}{\partial x} + V \frac{\partial V}{\partial x} = -g \frac{\partial y}{\partial x} -g \frac{\partial z}{\partial x} -g S_f \dots \dots \dots (2)$$

Where Q is the discharge, q is the point discharge, V is the velocity, g is the acceleration of gravity, y is the depth of flow and s_f is the friction slope.

A non-uniform rectangular grid in the x and t plane as shown in Figure 3 was used to simulate Equations 1 and 2 for numerical solution. The differential equation were simulated for a finite time Δt and a finite distance Δx . Equation 1 is simulated by

$$\frac{Q_{i+1}^{j+1} - Q_i^{j+1}}{\Delta x} + \frac{A_{i+1/2}^{j+1} - A_{i+1/2}^j}{\Delta t} - q_{i+1/2}^{j+1} = 0 \dots \dots \dots (3)$$

where

$$A_{i+1/2} = \int_{x_i}^{x_{i+1}} A(x) \Delta x \dots \dots \dots (4)$$

$A_{i+1/2}$ is approximated by $\frac{1}{2} (A_i + A_{i+1})$

Equation 2 is simulated by

$$\frac{1}{A_{i+1/2}^{j+1}} \frac{Q_{i+1/2}^{j+1} - Q_{i+1/2}^j}{\Delta t} + \frac{1}{(\bar{A}_{i+1/2})^2} \frac{1}{2\Delta x} \left\{ (Q_{i+1}^{j+1})^2 - (Q_i^{j+1})^2 \right\} +$$

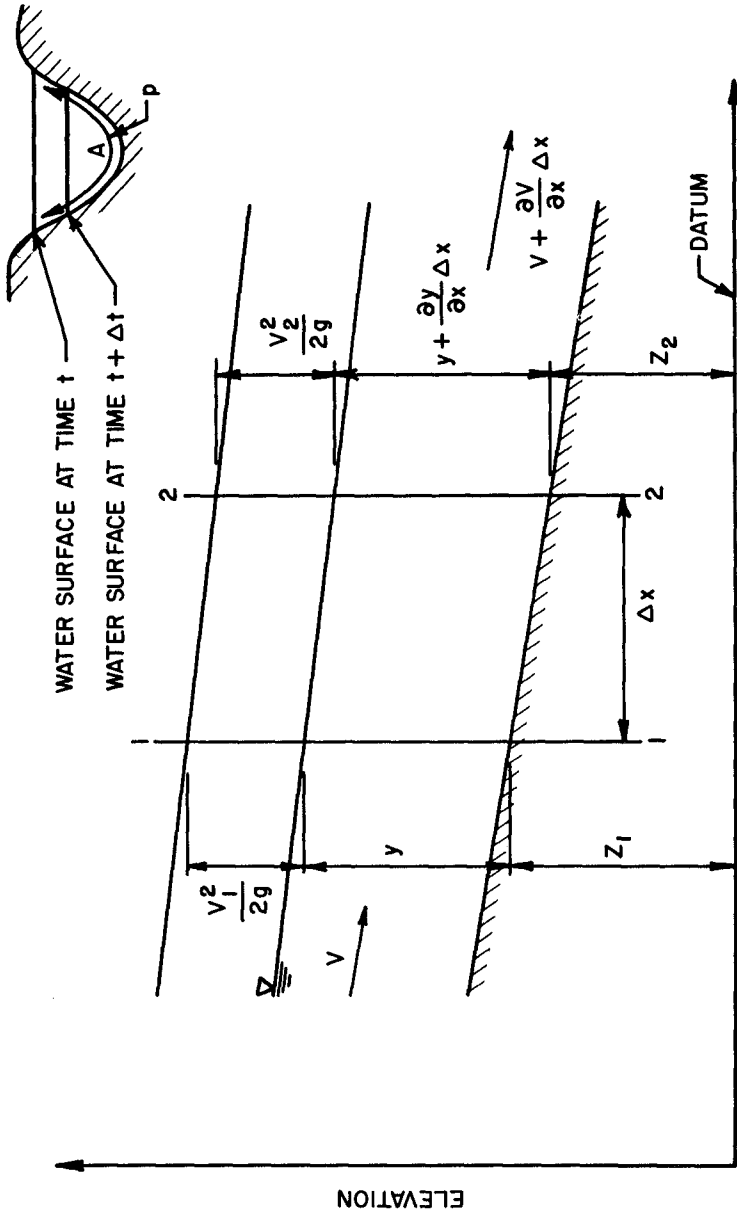


FIGURE 2. Definition Sketch for Open Channel Flow.

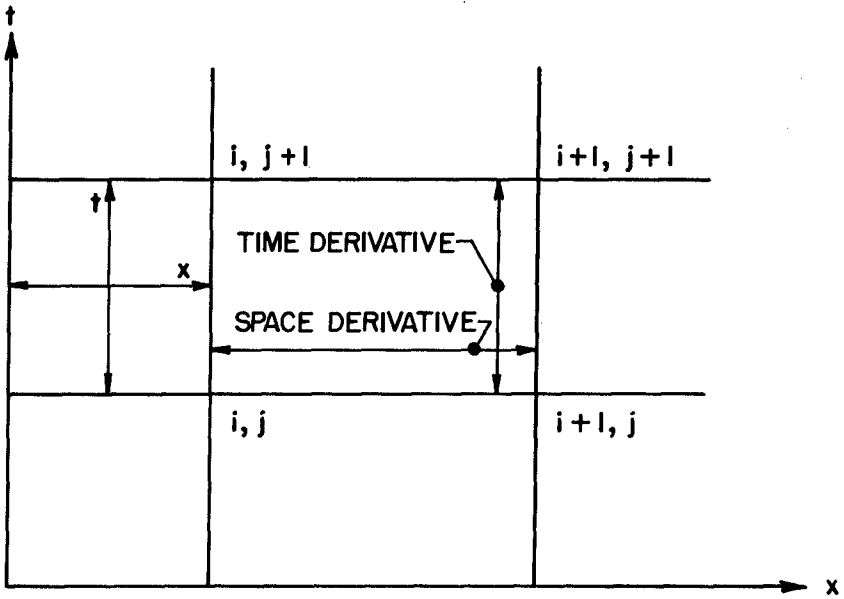


FIGURE 3. Definition Sketch for a Network of Points on the x, t Plane.

$$\frac{1}{2\Delta x} \left\{ \left(\frac{Q_{i+1}^{j+1}}{A_{i+1}^{j+1}} \right)^2 - \left(\frac{Q_i^{j+1}}{A_i^{j+1}} \right)^2 \right\} + g \left[\frac{(y_{i+1}^{j+1} + z_{i+1}) - (y_i^{j+1} - z_i)}{\Delta x} \right] + \bar{S}_{f_{i+1}}^{j+1} = 0 \dots \dots \dots (5)$$

where

$$\bar{Q}_{i+1/2}^{j+1} = \frac{1}{\Delta x} \int_{x_i}^{x_{i+1}} Q(x, t) dx \dots \dots \dots (6)$$

and

$$\bar{S}_{f_{i+1/2}}^{j+1} = \frac{1}{\Delta x} \int_{x_i}^{x_{i+1}} S_f(x, t) dx \dots \dots \dots (7)$$

or

$$\bar{Q}_{i+1/2}^{j+1} = \frac{1}{2} \left\{ Q_{i+1}^{j+1} + Q_i^{j+1} \right\} \dots \dots \dots (8)$$

and

$$\bar{S}_{f_{i+1/2}}^{j+1} = \frac{1}{2} \left\{ S_{f_{i+1}}^{j+1} + S_{f_i}^{j+1} \right\} \dots \dots \dots (9)$$

The approximations of \bar{A} , \bar{Q} and \bar{S}_f are based on a linear assumption, and if Δx is sufficiently small the result would be valid.

The unknown variables in the simulation equations are the ones with the superscripts $(j + 1)$. The independent unknowns are the values of discharge and stage at grid points $(i, j+1)$ and $(i+1, j+1)$. For an inlet system the part of equations with four unknowns can be evaluated because the additional equations obtained from the boundary conditions and channel junctions will result in the same number of equations as there are unknowns.

Application: to Lockwoods Folly Inlet

For problem purposes the inlet was represented by 14 stations as shown in Figure 4. The channel system was divided into five channels with two junctions. The channel sections are:

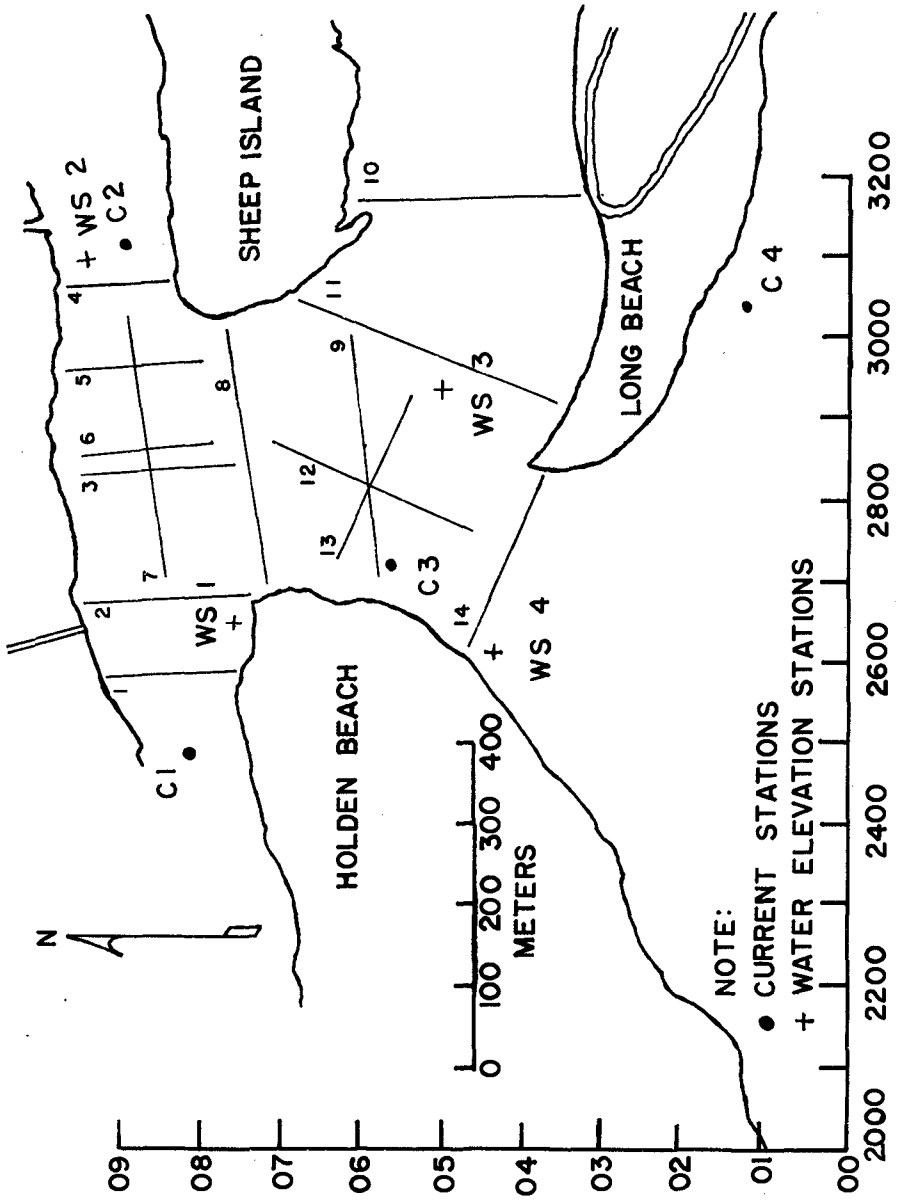


FIGURE 4. Flow Stations.

- 1, 2, 3
- 4, 5, 6
- 7, 8, 9
- 10, 11, 12
- 13, 14

The junctions are:

- 3, 6, 7
- 9, 12, 13

The value of x is taken as zero at junction 9, 12, 13 and increases to seaward. The flow during an ebb tide is in the positive x direction.

The simulated equations of conservation and momentum, Equation 3 and Equation 5 are abbreviated by:

$$F(Q_i, Q_{i+1}, y_i, y_{i+1}) = 0 \dots \dots \dots (10)$$

$$G(Q_i, Q_{i+1}, y_i, y_{i+1}) = 0 \dots \dots \dots (11)$$

$Q_i, Q_{i+1}, y_i, y_{i+1}$ are values of discharge and stage at time $j+1$. Since all unknown quantities are at time $j+1$ that superscript has been omitted. Equations 10 and 11 can be written for each channel section as follows:

Section 1, 2, 3

$$F(Q_1, Q_2, y_1, y_2) = 0 \dots \dots \dots (12)$$

$$G(Q_1, Q_2, y_1, y_2) = 0 \dots \dots \dots (13)$$

$$F(Q_2, Q_3, y_2, y_3) = 0 \dots \dots \dots (14)$$

$$G(Q_2, Q_3, y_2, y_3) = 0 \dots \dots \dots (15)$$

Section 4, 5, 6

$$F(Q_4, Q_5, y_4, y_5) = 0 \dots \dots \dots (16)$$

$$G(Q_4, Q_5, y_4, y_5) = 0 \dots \dots \dots (17)$$

$$F(Q_5, Q_6, y_5, y_6) = 0 \dots \dots \dots (18)$$

$$G(Q_5, Q_6, y_5, y_6) = 0 \dots \dots \dots (19)$$

Section 7, 8, 9

$$F(Q_7, Q_8, y_7, y_8) = 0 \dots \dots \dots (20)$$

$$G(Q_7, Q_8, y_7, y_8) = 0 \dots \dots \dots (21)$$

$$F(Q_8, Q_9, y_8, y_9) = 0 \dots \dots \dots (22)$$

$$G(Q_8, Q_9, y_8, y_9) = 0 \dots \dots \dots (23)$$

Section 10, 11, 12

$$F(Q_{10}, Q_{11}, y_{10}, y_{11}) = 0 \dots \dots \dots (24)$$

$$G(Q_{10}, Q_{11}, y_{10}, y_{11}) = 0 \dots \dots \dots (25)$$

$$F(Q_{11}, Q_{12}, y_{11}, y_{12}) = 0 \dots \dots \dots (26)$$

$$G(Q_{11}, Q_{12}, y_{11}, y_{12}) = 0 \dots \dots \dots (27)$$

Section 13, 14

$$F(Q_{13}, Q_{14}, y_{13}, y_{14}) = 0 \dots \dots \dots (28)$$

$$G(Q_{13}, Q_{14}, y_{13}, y_{14}) = 0 \dots \dots \dots (29)$$

This system consists of 18 equations and 28 unknowns. To find a solution ten additional equations are required. They may be written based on the conditions existing at the boundaries.

At each junction the energy level is the same, so that the energy, represented as $y + z + \frac{v^2}{2g}$, can be equated for each section at a junction. Abbreviating the energy equation as

$$H(Q_i, Q_{i+1}, y_i, y_{i+1}) = 0 \dots \dots \dots (30)$$

the following four equations can be written:

Junction 3, 6, 7

$$H(Q_3, Q_7, y_3, y_7) = 0 \dots \dots \dots (31)$$

$$H(Q_6, Q_7, y_6, y_7) = 0 \dots \dots \dots (32)$$

Junction 9, 12, 13

$$H(Q_9, Q_{13}, y_9, y_{13}) = 0 \dots \dots \dots (33)$$

$$H(Q_{12}, Q_{13}, y_{12}, y_{13}) = 0 \dots \dots \dots (34)$$

The law of conservation of mass at each junction is used to obtain the following two equations:

Junction 3, 6, 7

$$F(Q_3, Q_6, Q_7) = 0 \dots \dots \dots (35)$$

Junction 9, 12, 13

$$F(Q_9, Q_{12}, Q_{13}) = 0 \dots \dots \dots (36)$$

The water surface elevations provided by the tide gauges provide boundary data for four more equations. They are represented

as
 $F(y_1) = 0 \dots \dots \dots (37)$

$$F(y_4) = 0 \dots \dots \dots (38)$$

$$F(y_{10}) = 0 \dots \dots \dots (39)$$

$$F(y_{14}) = 0 \dots \dots \dots (40)$$

The system of Equations 12 through 29 and 30 through 40 provides twenty eight equations and twenty eight unknowns which can be solved by several methods.

Flow Model Input Data

Boundary conditions, bathymetry data, friction coefficient and initial flow rates were used as model input data. The boundary conditions were expressed as water surface elevations as a function of time. The values are listed in Table 1. The channel section parameters of cross sectional area and wetted perimeter are represented by linear algebraic equations as a function of depth *y*, measured from mean low water. The equations are:

$$A = A_0 + A_1 y \dots \dots \dots (41)$$

$$P = P_0 + P_1 y \dots \dots \dots (42)$$

Table 1. Field Boundary Data.

TIME	*WATER SURFACE ELEVATION			
	STATION 1 (M)	STATION 2 (M)	STATION 3 (M)	STATION 4 (M)
0.0	0.12	0.11	0.09	0.06
0.5	0.03	0.02	0.03	0.00
1.0	0.00	0.00	0.00	0.03
1.5	0.02	0.03	0.02	0.08
2.0	0.09	0.11	0.08	0.14
2.5	0.20	0.20	0.18	0.24
3.0	0.30	0.30	0.29	0.35
3.5	0.42	0.43	0.47	0.49
4.0	0.58	0.55	0.61	0.66
4.5	0.72	0.72	0.75	0.81
5.0	0.85	0.88	0.90	0.98
5.5	1.04	1.04	1.05	1.16
6.0	1.16	1.14	1.13	1.30
6.5	1.28	1.25	1.26	1.43
7.0	1.34	1.31	1.28	1.54
7.5	1.34	1.33	1.30	1.49
8.0	1.28	1.28	1.28	1.43
8.5	1.19	1.19	1.19	1.22
9.0	1.07	1.07	1.07	1.05
9.5	0.96	0.94	0.94	0.93
10.0	0.84	0.84	0.81	0.73
10.5	0.73	0.73	0.67	0.61
11.0	0.61	0.61	0.58	0.49
11.5	0.49	0.49	0.47	0.37
12.0	0.37	0.40	0.37	0.26
12.5	0.24	0.27	0.24	0.18

*Above Mean Low Water

The values of A_0 , A_1 , P_0 , P_1 are listed for each station in Table 2. The area coefficients were obtained from the fathometer profiles. Since the channels were wide with respect to their depth, the wetted perimeter was considered to be the channel width. The friction coefficient was estimated and then adjusted until the computed results matched the observed values. The initial flow rates were considered for time zero using the current velocities measured with the current meter. Time zero was the predicted time of low tide. The values are listed in Table 3.

Table 2. Coefficients of Expression for Area and Wetted Perimeter.

STATION	COEFFICIENTS FOR AREA		COEFFICIENTS FOR WETTED PERIMETER	
	A_0	A_1	A_0	P_1
1	330.07	175.41	155.45	20.83
2	388.32	206.37	182.88	20.83
3	388.32	206.37	211.35	2.00
4	410.62	128.59	118.87	22.92
5	451.68	141.45	150.40	2.00
6	451.68	141.45	150.40	2.00
7	650.30	346.07	394.25	2.00
8	650.30	346.07	353.57	29.17
9	650.30	346.07	394.25	2.00
10	47.38	187.83	51.82	177.09
11	55.74	220.98	60.96	208.34
12	55.74	220.98	60.96	2.00
13	869.54	366.71	369.84	2.00
14	869.54	366.71	332.22	27.08

$$\text{Cross Sectional Area} = A_0 + A_1 y$$

$$\text{Wetted Perimeter} = P_0 + P_1 y$$

Table 3. Initial Flow Values.

Station	VALUE OF (M)	*CHANNEL BOTTOM ELEV. (M)	**INITIAL DEPTH (M)	INITIAL FLOW RATE (Cu M/S)
1	-650	-4.72	0.12	148
2	-470	-5.03	0.11	148
3	-290	-5.03	0.10	148
4	-520	-5.03	0.12	169
5	-410	-5.03	0.11	169
6	-290	-5.03	0.10	169
7	-290	-4.57	0.10	317
8	-180	-4.11	0.08	3.7
9	0	-4.11	0.07	317
10	-390	-1.52	0.09	39
11	-170	-1.52	0.08	39
12	0	-4.11	0.07	39
13	0	-4.11	0.07	356
14	190	-4.11	0.06	356

*Below Mean Low Water

**Above Mean Low Water

Flow Model Output Data

The output of the model was average discharge and elevation at each station. The computed results for station 14 (See Figure 4) are plotted along with measured data in Figures 5 and 6.

Flow Channels

The bedforms on the offshore bar were analyzed to determine the pattern of flow across the offshore bar. Figure 7 illustrates the ebb flow patterns (larger arrows indicate higher velocities).

SEDIMENT MOVEMENT

Hypothesis of Sediment Bypassing System

Bedform analysis provided the majority of the data used in the formulation of the preliminary hypothesis. Several areas of the inlet were found to carry the majority of the flow as it moved across the offshore bar. The two major areas included an ebb channel, a few meters offshore of Holden Beach, and another minor channel, when compared to the main inlet gorge, near the grid point 2700 (See Figures 4 and 7). These two areas on the offshore bar were found from bedform analysis to carry the highest velocities of flow. A disordered pattern of flow near grid point 2700 was indicated by the observed orientation of the bedforms, but flow over a large portion of the offshore bar tended to move toward the Holden Beach ebb channel. Bedform analysis showed little tendency of the flow to move seaward except through these two previously indicated ebb channels.

Flow data used in the formulation of the preliminary hypothesis included a wave refraction analysis of the area, current velocity measurements, and bathymetry profiles. Wave refraction analysis provided an idea of the location of areas at which extensive erosion would likely occur. The analysis by the Corps of Engineers² found these areas to be the eastern tip of Holden Beach and the western tip of Long Beach. A typical wave from S 60° W and a period of 8 seconds was used in the analysis. The wave refraction analysis also provided the Corps of Engineers with data used to estimate the amount of energy transmitted to the beach zone. From this data, the Corps of Engineers was able to estimate a net annual littoral drift of 245,000 cubic meters/year (320,000 cubic yards/year) in an easterly direction. Current velocity measurements showed the maximum ebb velocity in the inlet gorge to be 1.2 meters/second (4 feet/second) but this velocity was significantly reduced to 0.77 meters/second (2.5 feet/second) in the inlet gorge off Long Beach. This velocity reduction was due to a combination of the widening of the inlet as well as the passing of large volumes of water over the offshore bar. Bathymetry profiles obtained during the period of study showed a maximum depth of 5 meters (17 feet) in the inlet gorge. A depth of 1.5 to 1.8 meters (5 to 6 feet) covered the offshore bar at the high tide. The depth of the water flowing through the ebb channel along Holden Beach reached a depth of 1.5 meters (5 feet) at high tide.

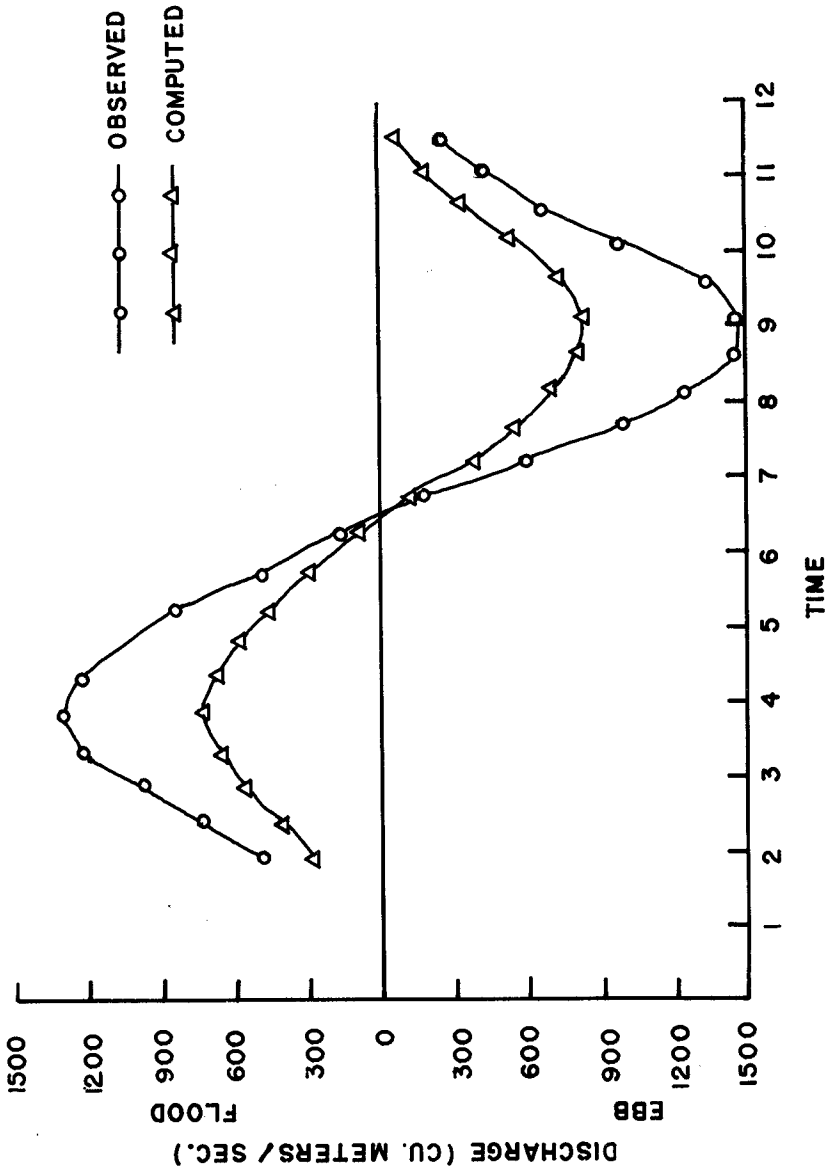


FIGURE 5. Comparison of Computed and Observed Values of Discharge at Station 14.

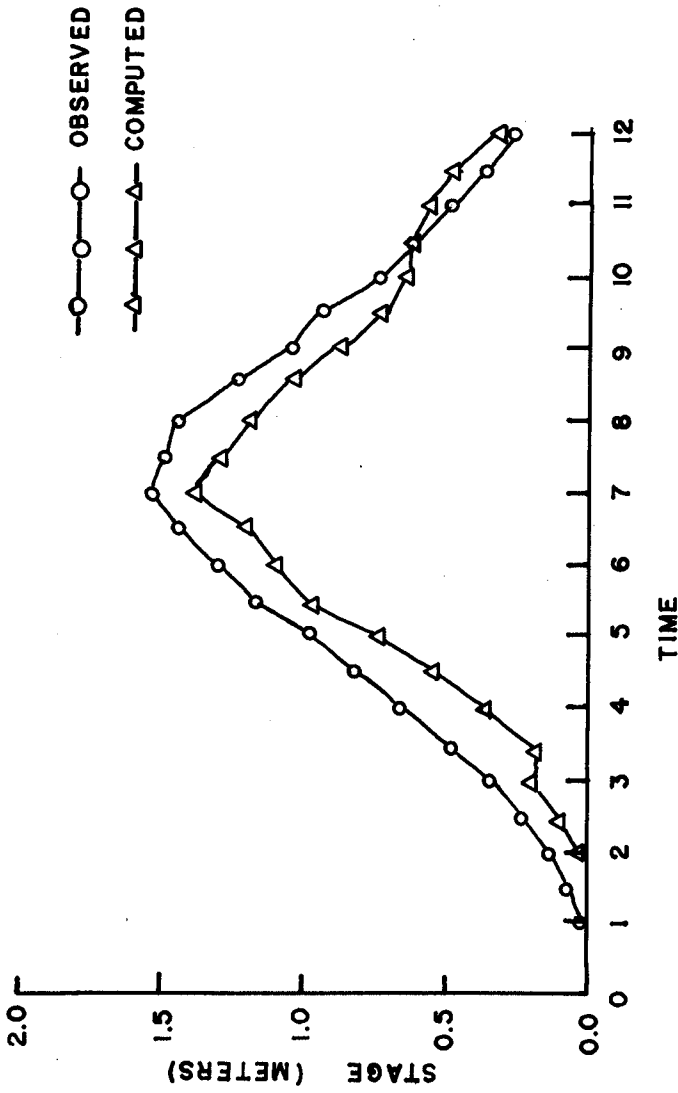


FIGURE 6. Comparison of Computed and Observed Values of Stage at Station 14.

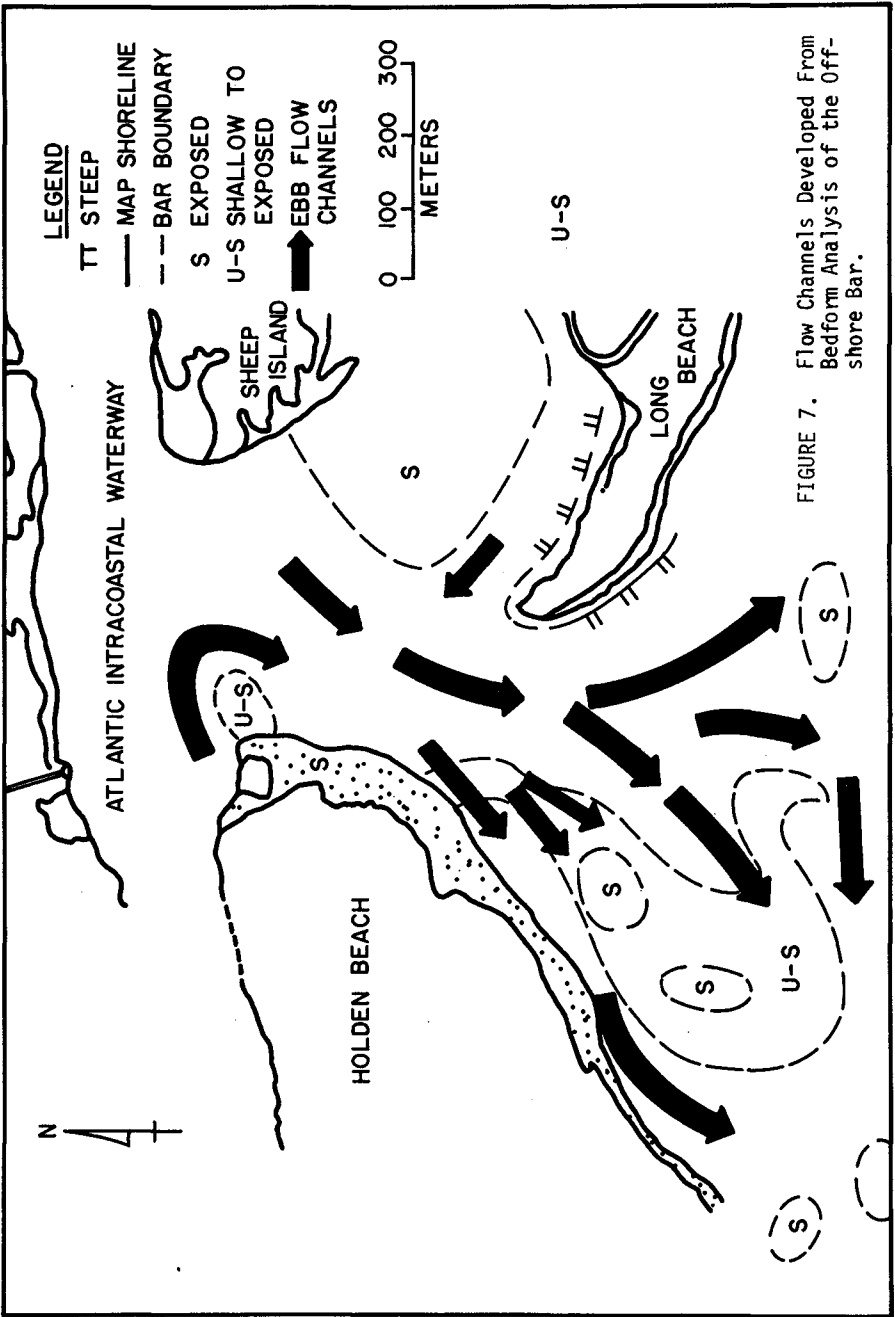


FIGURE 7. Flow Channels Developed From Bedform Analysis of the Off-shore Bar.

From an analysis of this data, a preliminary hypothesis of the bypassing system was developed. Sediment moved either toward the ebb channel near Holden Beach and was swept into the inlet gorge by the high tidal velocities, or else bypassed the inlet by moving across the offshore bar toward the 2700 grid point. This hypothesis was tested by introducing three different colored tracers onto the offshore bar along the 2000 grid line. Tracer tests were conducted during the ebb to flood cycle in an attempt to verify the pattern of movement indicated from the preliminary hypothesis.

Bar Bypassing Tests

The movement of the sediment across the bar was determined by introducing a fluorescent tracer onto the offshore bar in water soluble bags. The water soluble bags released the tracer onto the bar without allowing it to go into suspension in the water column. Signal green and fire orange were released on the offshore bar along grid line 2000. Blaze orange was raked into the beach between low and high tides along grid line 2000.

Core samples were taken during the tidal cycle. The samples were later analyzed by counting the number of tracer grains present in each sample under a long wave ultraviolet light. Samples containing 1-5 grains were considered to indicate a presence of tracer, while those with 6-10 grains indicated a low concentration; 11-20 grains indicated a medium concentration, and a sample containing more than 20 grains was considered to be highly concentrated. Eighty three core samples taken from the offshore bar were analyzed. Fifty percent of the core samples contained 5 or less grains. Six percent of the core samples did not contain any tracer sand, while twenty-two percent contained 20 or more grains.

Sediment Movement Tests

Ebb to Flood Tests. Two hundred twenty seven kilograms (500 lbs.) of signal green and fire orange tracer were released onto the offshore bar along grid line 2000. Blaze orange was raked onto the beach. The tracer sand entered the bar migration pattern. Samples were taken in the grid system between grid lines 2000 and 3000. Tracer was detected in high concentrations near the point of introduction. The tracer pattern was distinguishable along the shoreline of Holden Beach until it reached the Atlantic Intracoastal Waterway. Signal green tracer initially was stagnate at the end of the ebb channel. Within 24 hours the signal green tracer had established a pattern of movement across the bar. Fire orange tracer established two bypassing patterns; one similar to that which blaze orange initially followed, and the other a pattern of movement also across the offshore bar. Fire orange tracer traveled along the Holden Beach shoreline in an easterly direction until being influenced by the tidal currents of the gorge. From tracer analysis, fire orange tracer was found in detectable concentrations on Long Beach, possibly carried by the current of the inlet gorge. From tracer analysis, fire orange tracer was found in detectable concentrations on Long Beach after 24 hours. A second pattern across the offshore bar was established

as was the case with the blaze orange and signal green tracer. Two types of sediment bypassing were evident at the inlet. The first type tidal flow bypassing, was verified by the pattern of movement of fire orange tracer. The fire orange tracer moved across the offshore bar until being influenced by the tidal currents. The second type found at the inlet was bar bypassing, which from stability analysis was found to be the dominant type of bypassing in effect at the inlet.

Transport Rates Across The Offshore Bar

The transport rates were estimated from the tracer data. The actual transport rates were possible higher than the rates estimated. Blaze orange tracer was first detected at the 2600 grid line (considered to be the edge of the bar) 9 hours after its introduction onto the beach. The rate of transport across the offshore bar was estimated to be 1.8 cm.sec./ (0.059 ft./sec.). Neither signal green nor fire orange tracer was detected on the edge of the bar until 24 hours following introduction. The rate of transport for both tracers was computed to be 0.7 cm./sec.). (0.023 ft./sec.). A composite of the locations of the sediment tracer materials in the bar bypassing tests are shown in Figure 8.

CONCLUSIONS

The following conclusions were drawn from the study:

1. The numerical simulation model agreed reasonably well with the measured values for stage and discharge.
2. The sediment movement patterns in the inlet were related to tidal current patterns.
3. Sediment crossed the inlet from east to west.
4. The offshore bar will continue to grow as it traps and bypasses sand.
5. The inner shoal will continue to grow and encroach on the intracoastal waterway, thus necessitating periodic dredging.

ACKNOWLEDGEMENT

This study was partly supported by the North Carolina Coastal Research Program and by the Center for Marine and Coastal Studies.

LIST OF REFERENCES

1. Amein, M., "Computation of Flow Through Masonboro Inlet, N. C.", Sea Grant Publication UNC-SG-73-15, Sea Grant Program, N. C. State University, Raleigh, North Carolina, 1973, pp. 7-35.
2. U. S. Army Corps of Engineers, Wilmington District, General Design Memorandum, Phase I, Hurricane Wave Protection Beach Erosion Control Brunswick County, North Carolina, Beach Projects-Yaupon Beach and Long Beach Segments, July 1973.

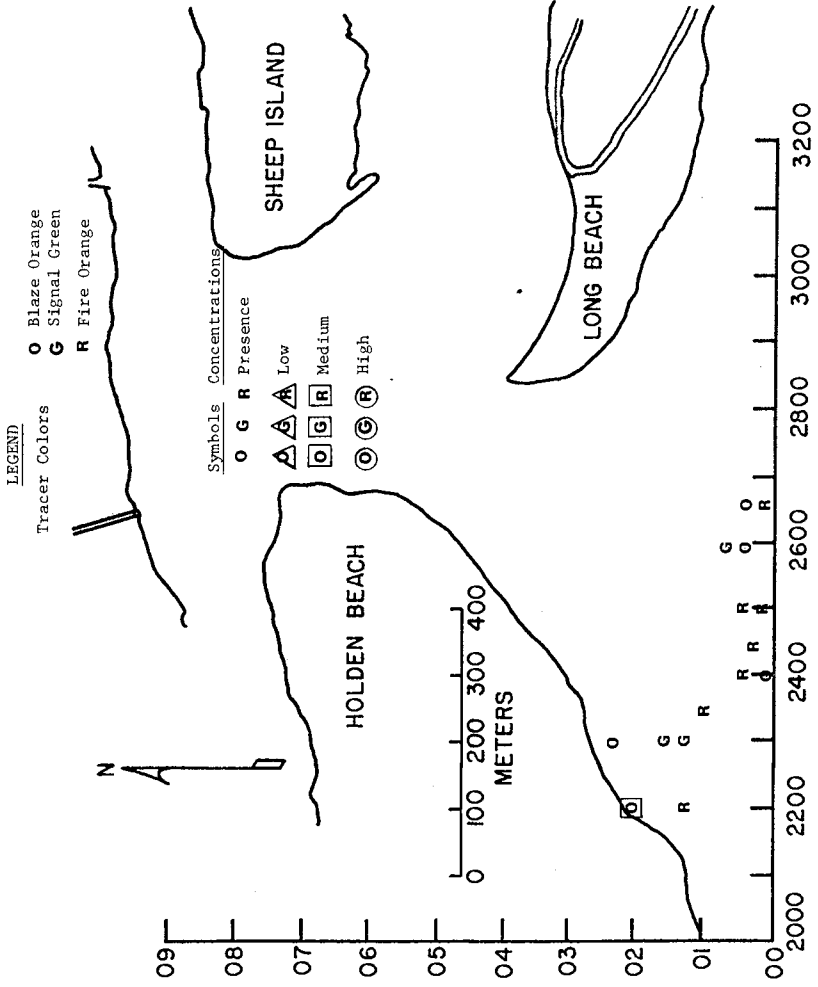


FIGURE 8. Location of Detected Blaze Orange, Signal Green, Fire Orange Trace Sand - AM, 25 August 1974. Note: 24 Hours After Introduction.

CHAPTER 99

MEASUREMENT OF BED FRICTION IN TIDAL INLETS

by

A. J. Mehta¹, R. J. Byrne² and J. T. DeAlteris³

ABSTRACT

The flow characteristics and the stability of a tidal inlet are governed, among other factors, by the channel bed friction. In order to determine the bed shear stress regime and the frictional characteristics, near-bed velocity profiles were obtained at the throat sections of two inlets, John's Pass and Blind Pass, on the Gulf Coast of Florida. A specially designed steel cage with five current meters in a vertical array was used to obtain the profiles in the bottom one meter of the flow.

The profiles were found to be logarithmic but it is noted that, especially near the times of slack water, the effect of inertia becomes significant. However, during the major part of the flood or ebb flow period, frictional effects are dominant. In the fully rough regime of flow, the bed-shear stress - velocity relationship is found to follow the square law, with a constant, characteristic friction factor and Manning's n for each inlet. This friction factor is used in hydraulic formulas, based on uniform, steady open channel flow relationships, to obtain the tidal prism - throat cross-sectional area ratio, which is then compared with that obtained from flow discharge measurements. Agreements and discrepancies in the comparison are discussed. The relationship between the bed shear stress at incipient motion and the grain size at the bed is reviewed, and it is noted that the observed relationship at the two inlets does not agree with the well-known correlation of Shields for uniform sandy beds.

INTRODUCTION

The hydraulic and sedimentary regime of a tidal inlet depends strongly on the friction characteristics of the channel bed. These characteristics are most commonly defined in terms of a friction factor, a Chezy coefficient or a Manning's n . Standard texts on hydraulics give values of these coefficients, particularly Manning's n , for rivers and canals of various geometries and vegetative cover. However, for tidal inlets, information of this sort is limited and is only derived indirectly from measurements of tides and currents, rather

¹ A. J. Mehta, Assistant Professor, Coastal and Oceanographic Engineering Laboratory, University of Florida, Gainesville, Florida 32611.

² R. J. Byrne, Head, Department of Geological Oceanography, Virginia Institute of Marine Science, Gloucester Point, Virginia 23062.

³ J. T. DeAlteris, Graduate Assistant, Virginia Institute of Marine Science, Gloucester Point, Virginia 23062.

than through direct near-bed measurements. Correspondingly, the variation of the bed shear stress with the tidal cycle and its relationship to the motion of the sediment over the bed is also established indirectly.

Experience and observation have established that the most characteristic morphologic feature of a tidal inlet is its throat section, and that flow measurements at this location yield important information on the hydraulics and the stability of an inlet. A significant part of the frictional resistance to the flow occurs at the throat, and the cross-sectional area of the throat, among other parameters, seems to correlate uniquely with the tidal prism through the inlet (O'Brien, 1969, 1976). Moreover, it has been shown that there appears to be a correspondence between this prism-area relationship for stable inlets and the regime equations for rivers and canals in non-silting, non-scouring equilibrium (Mason, 1973, Bruun, 1974), despite the fact that the flow in an inlet is primarily oscillatory. The question arises as to whether the direct measurement of near-bed velocity profiles at the throat can yield a friction factor, or a Manning's n , which may be considered to be characteristic for the inlet in a manner similar to that in a canal. Furthermore, inasmuch as the regime of sediment transport is dependent upon the bed shear stress, the determination of the latter as a function of the stage of tide should correlate with the bed sediment motion at the throat. These considerations led to the planning of the field experiments described in this paper, with the following specific objectives:

- (1) To measure the velocity distribution in the bottom one meter of the flow at the throat section of an inlet.
- (2) To simultaneously record the state of bed motion at the throat.
- (3) To determine characteristic friction coefficients from the measured data.
- (4) To obtain the tidal prism-throat cross-sectional area ratio based on hydraulic formulas involving the above coefficients, and to compare this ratio with that obtained from flow discharge measurements and a survey of the throat.
- (5) To establish the relationship between the critical shear stress for the bed grain motion and the grain size at the throat.

HYDRAULIC RELATIONSHIPS

The simplest method of analysing and testing inlet hydraulic data is that based on the generally accepted correspondence between inlet hydraulics and steady, uniform open channel flows. In the turbulent regime, the logarithmic profile for the flow velocity u is

$$\frac{u}{u^*} = B + \frac{1}{\kappa} \ln \frac{Z}{K} \quad (1)$$

where u^* = friction velocity, κ = Karman constant (= 0.40), $Z = zu^*/\nu$, $K = ku^*/\nu$ (wall Reynolds number), z = elevation above the theoretical bed, k = bed roughness and ν = kinematic viscosity of water. The depth-mean velocity \bar{u} can be

obtained from Eq. (1) for a depth of flow h (assuming $h \gg z_0$)

$$\bar{u} = 2.5u^* \left[\ln \left(\frac{h}{z_0} \right) - 1 \right] \quad (2)$$

and Manning's n and k from

$$n = \frac{1.49h^{1/6}}{g^{1/2}} \frac{u^*}{\bar{u}} \quad (3)^1$$

$$k = (31.6n)^6 \quad (4)^2$$

Finally

$$B = 2.5 \ln \left(\frac{k}{z_0} \right) \quad (5)$$

where z_0 is the value of z at $u = 0$.

It can be shown that the sensitivity of Manning's n to the depth h may be expressed as

$$\frac{\Delta n}{n} = \left[\frac{1}{6} - \frac{1}{\left\{ \ln \left(\frac{h}{z_0} \right) - 1 \right\}} \right] \frac{\Delta h}{h} \quad (6)$$

Here Δn and Δh are small changes in n and h , respectively. The purpose of introducing Eq. (6) is to test the effect of changes in depth due to the tide on the computation of Manning's n . If this variation is small, it would be acceptable to ignore the range of tide in the inlet for the purpose of the hydraulic computations.

The bed shear stress τ_0 ($=\rho u^{*2}$) is defined as

$$\tau_0 = \frac{f}{4} \rho \frac{\bar{u} |\bar{u}|}{2} \quad (7)$$

where, in the fully rough range of flow ($k > 70$), the friction factor f depends solely on the ratio of the bed roughness to the depth of flow (for a wide channel).

$$\frac{1}{\sqrt{f}} = 2.34 + 0.87 \ln \frac{h}{k} \quad (8)$$

The foregoing relationships are strictly applicable to steady, uniform wide open channels only, but Eqs. (1) through (8) should be applicable to tidal inlets with the following characteristics:

- (1) no significant density stratification, i.e. low fresh water discharge relative to the tidal prism

¹The foot-pound-second units are used in the computations throughout this paper; metric units have been used in data presentation only.

²Eq. (4) is also known as Strickler's equation.

- (2) low ratio of tidal amplitude divided by the mean depth of flow
- (3) relatively large width to depth ratio
- (4) negligible wave-induced turbulence
- (5) negligible effect of the inertia of the mass of water in relation to frictional dissipation at the bed.

PRISM-AREA RELATIONSHIP

The tidal P is by definition related to the cross-sectional mean maximum velocity \bar{u}_{max} in an inlet according to

$$P = \frac{\bar{u}_{max} A_c T}{\pi C_K} \quad (9)$$

where A_c = throat cross-sectional area below MWL, T = tidal period and C_K is a coefficient that accounts for the deviation from the sinusoidal variation of the velocity in the inlet (Keulegan, 1967). Keulegan and Hall (1950) found that $C_K = 0.86$ agrees well with most inlet data. In Eq. (7), at $\bar{u} = \bar{u}_{max}$, $\bar{\tau}_o = \bar{\tau}_{o,max}$, and eliminating \bar{u}_{max} with the help of Eq. (9) yields

$$\frac{P}{A_c} = \sqrt{\frac{g}{T\rho}} \sqrt{\bar{\tau}_{o,max}} \frac{T}{\pi C_K} \quad (10)$$

If f , $\bar{\tau}_{o,max}$ and T are measured, P/A_c can be calculated and compared with a corresponding ratio in which P is obtained directly from volumetric flow discharge measurement and A_c determined by a survey.

By assuming a depth as well as width averaged velocity as in an open channel, and a relatively small ratio of the tidal amplitude a_c at the throat divided by the cross-sectional mean depth \bar{h} , Krishnamurthy (1974) obtained

$$\frac{P}{A_c} = 1.25 u_{cr}^* T \left(1 + \frac{2a_c}{\pi h} \right) \left[\ln \left(\frac{10 \cdot 93 \bar{h}}{k} \right) \right] \quad (11)$$

Here it is also assumed that the inlet is in a state of non-silting, non-scouring equilibrium, and that in such an inlet, on the average, the friction velocity $u^* = u_{cr}^*$, corresponding to τ_{ocr} , the critical bed shear stress for the incipient motion of the grains on the bed.

An agreement between the measured P/A_c and that derived from the above two equations, particularly Eq. (10), would clearly point to the relevance of the measured value of the friction factor at the throat.

THE INLETS

Two inlets, John's Pass and Blind Pass, shown in Fig. 1, were selected for the purpose of the measurements. These inlets connect the Gulf of Mexico to Boca Ciega Bay, near Tampa, Florida. Despite their relative proximity, the two inlets have disparate morphological characteristics, as seen from Table 1.

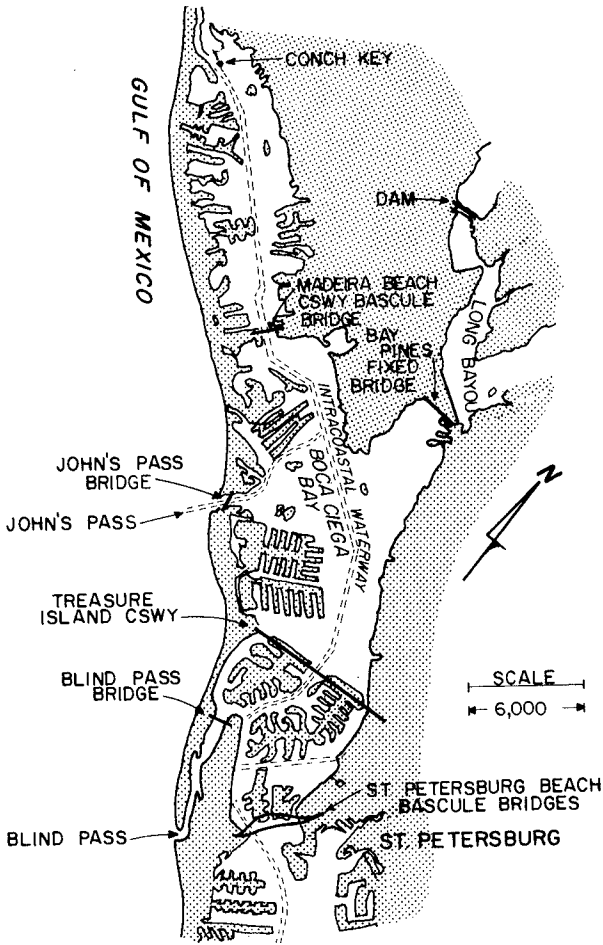


Fig. 1. John's Pass and Blind Pass Connect the Gulf of Mexico to Boca Ciega Bay. The City of Tampa (not shown) is due Northwest.

TABLE 1

Inlet	Mean Depth \bar{h} at the Throat below MWL (ft)	Throat Cross-section A_c below MWL (ft ²)	Length of the Channel (ft)	Jetties	Stability
John's Pass	16.0	9,500	2,200	one	Good
Blind Pass	5.2	440 ³	1,200	two	Intermediate

John's Pass is a stable inlet with no major problem of sedimentation. The 1,200 ft. long Blind Pass channel is followed by another 6,000 ft. long and relatively wider channel which enters Boca Ciega Bay. This second segment of the channel may, however, be considered to be a part of the bay itself, as currents in this channel are relatively low (Sanchez-Diaz, 1975). The inlet cross-section has been decreasing steadily during the past century (Mehta and Adams, in press), and there have been some shoaling problems near the entrance, but the inlet has remained open. Figs. 2 and 3 give a closer look at these inlets, and indicate the locations of the throat sections. The penetration of ocean waves at these sections is minimal. Currents and salinity profiles indicated that the fresh water outflow at these inlets is rather small and that density stratification is not significant. The bed at the throat of John's Pass is laden almost entirely with relatively large pieces of shell. At Blind Pass, shells are found in patches surrounded by relatively fine sand.

EQUIPMENT

The essential equipment consisted of a vertical array of five ducted impeller current meters fitted inside a steel cage which could be lowered at the desired location from a specially designed A-frame on a barge. The following is a brief description of the current meter and the cage.

The current meter (Fig. 2): This consisted of a 3 in. o.d. and 6 in. long stainless steel duct containing an axially mounted impeller with six epoxyglas blades. Two small magnets attached to the tip of two of the blades closed a reed switch mounted on the duct. The circuit was connected through a long insulated wire to a deck unit which could count the actuation caused through the rotation of the impeller. The counts were calibrated to yield the current speed (Byrne and Boon, 1973).

The cage (Fig. 2): This consisted of a framed cube, 4 ft. on the edge, constructed of 1 x 3/16 in. angle iron. For stability at the bottom of the inlet, the base of the cage was weighted with four 75 lb. lead weights fastened, one each, to the bottom corners of the frame. The vane assembly (which helped align the meters along the direction of flow) was fabricated from a 45 in. section of channel aluminum, modified to accept the mounting arms of five current meters, which were installed at 21.6, 36.2, 51.4, 75.6 and 103.6 cm above the base of the cage. Outputs from the current meters were monitored on a barge, anchored at a position close to the cage. A more detailed description of the equipment

³ Based on data obtained in 1974 prior to the construction of new jetties.

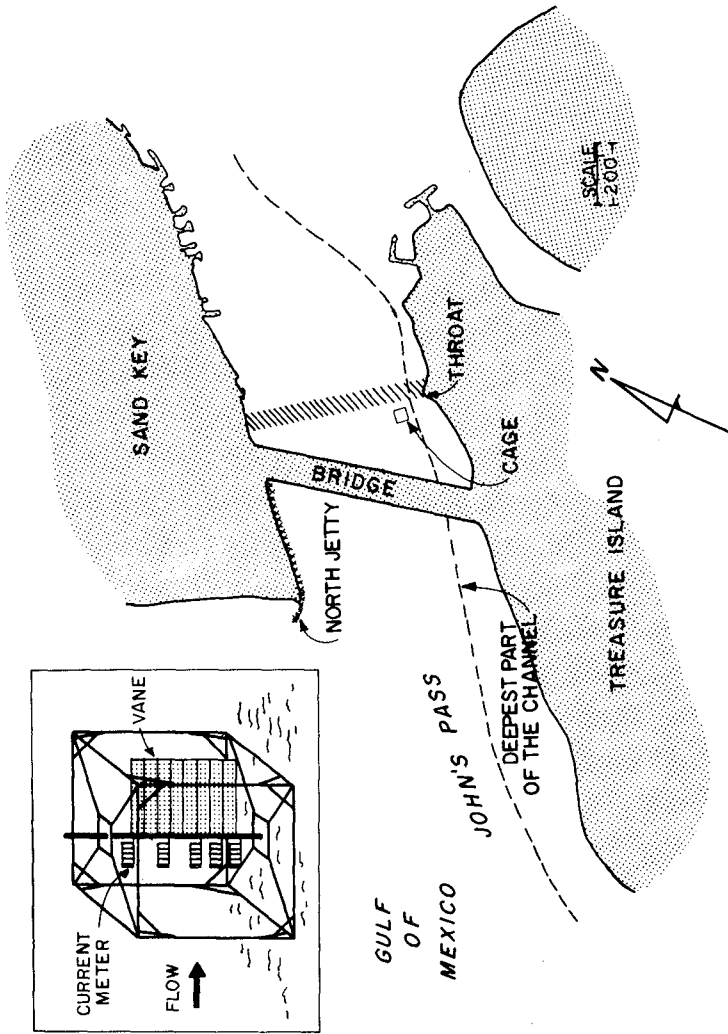


Fig. 2. John's Pass. The Inset Shows the Steel Cage with the Current Meters and the Vane Assembly.

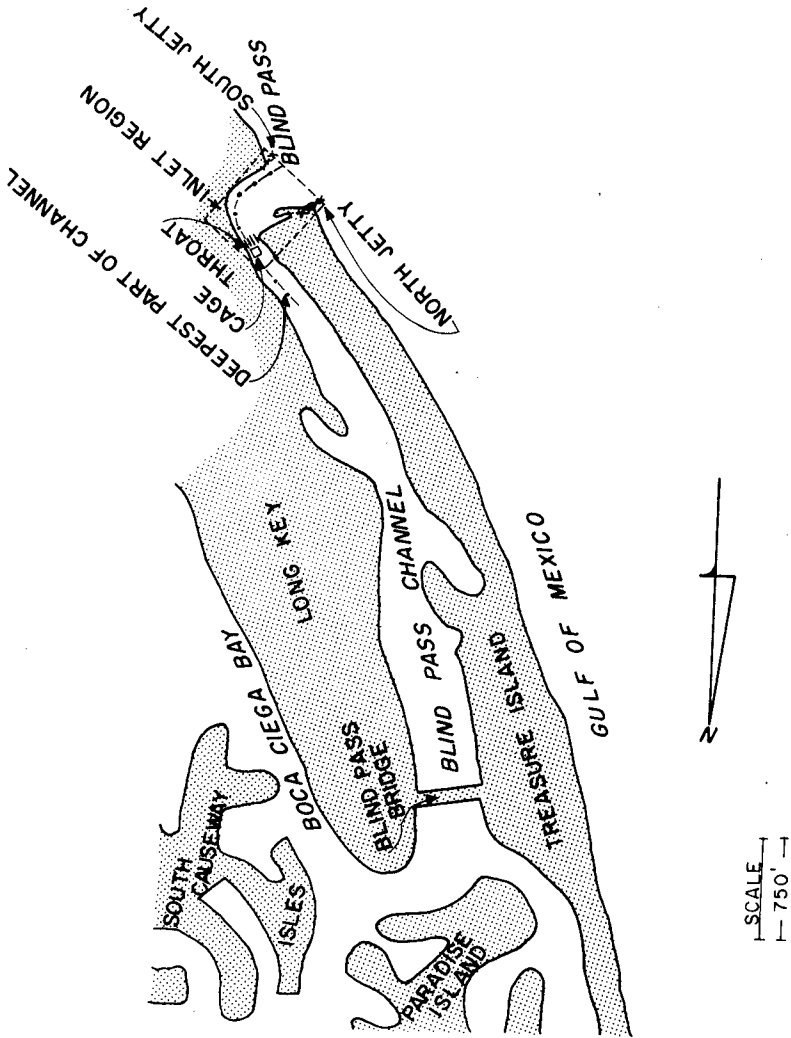


Fig. 3. Blind Pass. Note the Narrow Throat Section.

and its use may be found elsewhere (Mehta, Byrne and DeAlteris, 1975).

FIELD STUDY

The original plan was to obtain near-bed velocity profiles at a number of points across the throat by moving the cage from point to point, but time limitation and the presence of very heavy seaweed concentrations in the flow along certain parts of the channel at John's Pass permitted measurements at one location only, namely at the deepest part of the channel near the throat (Fig. 2). At Blind Pass, due to the narrow throat section, the measurements were also taken at one location only (Fig. 3) close to the deepest channel.

At John's Pass, data were collected on August 5, 6, 7, 8 and 9, 1974, and on August 14 at Blind Pass. On each day, counts corresponding to each of the five current meters were simultaneously recorded from the deck units on the barge every few minutes, for a total time period ranging from slack to slack (one-half tidal cycle). At John's Pass measurements were obtained over floodtides and at Blind Pass over an ebbside. The depth of water below MWL at the site of the cage was 25 ft. at John's Pass and 12 ft. at Blind Pass.

In addition to the near-bed profiles a single current meter at John's Pass obtained a few profiles over the entire depth. At Blind Pass, a current meter was installed near the throat to yield a continuous velocity measurement there. Tides were measured at both the inlets and a set of six stilling wells were installed at Blind Pass to measure the water surface slopes near the throat. Divers made observations on the state of sediment motion at the bed.

DATA ANALYSIS

Due to fouling by seaweed, divers had to clean the meters from time to time. For data analysis, any profile with less than four data points was considered unsuitable. As a result, for example, all the profiles obtained on August 6 had to be eliminated.

Fig. 4 shows examples of the velocity profiles obtained at John's Pass on August 9, and Fig. 5 shows profiles at Blind Pass on August 14. As in these examples, almost all the profiles were found to be logarithmic, according to Eq.(1). The ratios, a_c/h , of the average amplitude of tide to the depth of flow at the cage during the experiment were as follows: .

TABLE 2

Inlet	a_c (ft)	h (ft)	a_c/h (%)
John's Pass	0.76	25	3
Blind Pass	1.36	12	11

Thus at John's Pass, the tidal amplitude was 3% of the depth at the cage and at Blind Pass it was 11%. Using a typical value of $z_0 = 0.007$ ft., and these percent changes in depth, Eq.(6) gives the corresponding $\Delta n/n$ as less than 0.1% at John's Pass and less than 0.2% at Blind Pass. It can be shown likewise, that the percent changes in \bar{u}^2 corresponding to the above changes in depths are also negligible. Thus in Eqs.(3) and (7), the effects of tidal

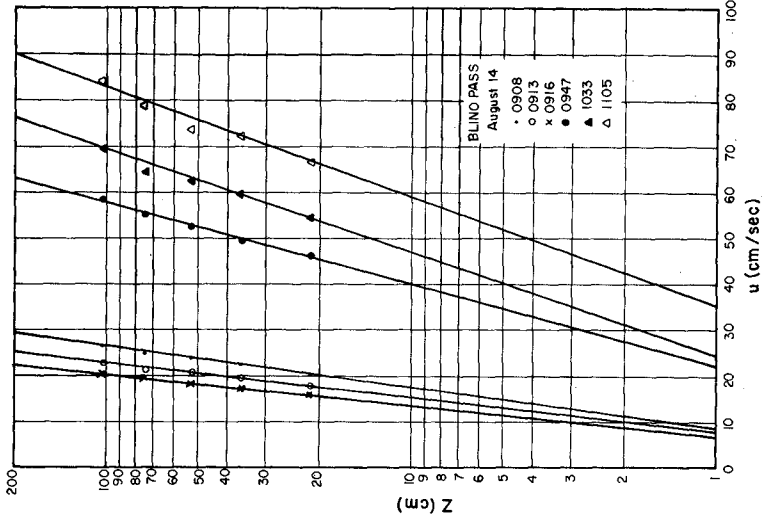


Fig. 5. Typical Examples of Near-bed Velocity Profiles at Blind Pass, August 14, 1974.

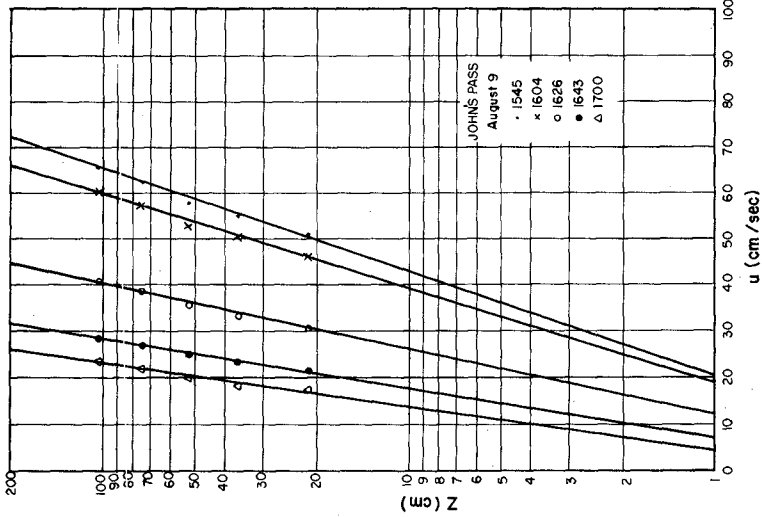


Fig. 4. Typical Examples of Near-bed Velocity Profiles at John's Pass, August 9, 1974.

variation on the value of n and f , respectively, may be ignored. In all computations, therefore, only the depth below MWL at the site of the cage was used.

The question of the effect of inertia was dealt with by observing the behavior of the coefficient M

$$M = \frac{\frac{\partial \bar{u}}{\partial t}}{\frac{f}{8h} \bar{u} |\bar{u}|} \quad (12)$$

which is the ratio of the temporal acceleration term divided by the friction term in the momentum equation.⁴ In Fig. 6, \bar{u} and M are plotted for the floottide on August 9 at John's Pass. From slack to slack, the period of flood is 5 hr. 45 min. It is observed that at times of fluctuation in current speeds M becomes large, but its value is most significant close to times of slack water, where the inertia effect is clearly dominant. Consider for example the time period during which $|M|$ is equal to or greater than unity. Ignoring those times when this occurs for short intervals, and taking only the periods close to slack waters, the total time interval when $|M| \geq 1$ is 45 min., which is only 19% of the flood period. Measurements on other days at John's Pass yielded similar values, and at Blind Pass, on August 14, $|M| \geq 1$ only during 11% of the ebb. These observations tend to indicate that it is not unreasonable to use steady, uniform flow formulas for tidal inlet hydraulics although, clearly, phenomena close to slack water are likely to be strongly influenced by the effects of inertia.

In all calculations, \bar{u} , as computed from Eq. (1), was used instead of one which may be obtained from a measured velocity profile over the entire depth of flow. This is because only a few of the latter were obtained, and it was found that the average velocities obtained from these did not differ to any appreciable extent from those obtained from the near-bed profiles.

RESULTS

Fig. 7 is an example of the variation of the bed shear stress τ_o with time, on August 8, at John's Pass. From recorded diver observations on the state of bed motion, it is possible to determine the corresponding bed shear stress, as indicated on the figure.

In Fig. 8, τ_o is plotted against \bar{u} on logarithmic co-ordinates for all the data points from John's Pass. Of particular importance here is the observance of the square law according to Eq.(7), with a constant friction factor f . The straight line gives $f = 0.027$, Manning's $n = 0.026$ from Eq.(3) and bed roughness $k = 0.31$ ft. from Eq.(4). Fig. 9 shows similar data for Blind Pass, with $f = 0.021$, $n = 0.020$ and $k = 0.07$. A few bed shear stress values obtained from surface slopes at Blind Pass were found to be nearly twice as large as those obtained from the velocity profiles, as these included losses at the channel bend (Fig. 3) as well (Mehta et al., loc. cit.).

In both, Figs. 8 and 9, at low velocities, the data points begin to

⁴The temporal acceleration term is much more significant than the spatial acceleration term in the flow through the channel itself. The flow may therefore be considered to be uniform.

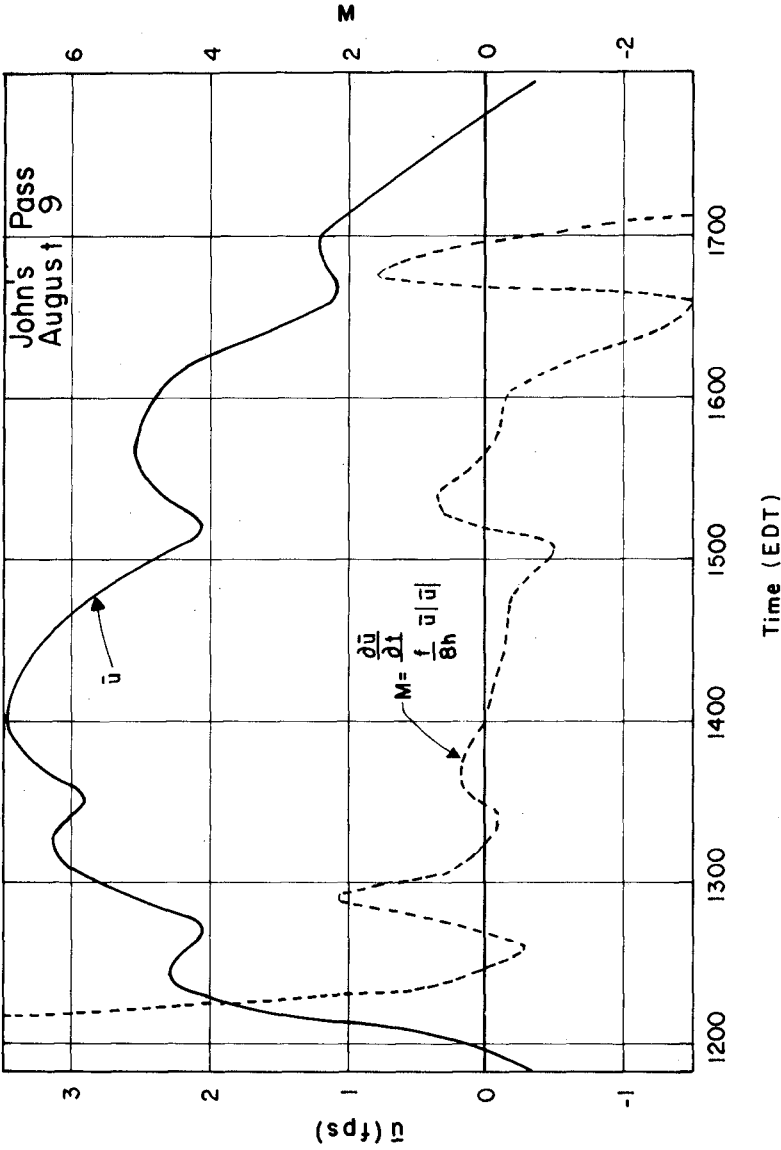


Fig. 6. Effect of Inertia Relative to Friction in Tidal Flood Flow through John's Pass, August 9, 1974.

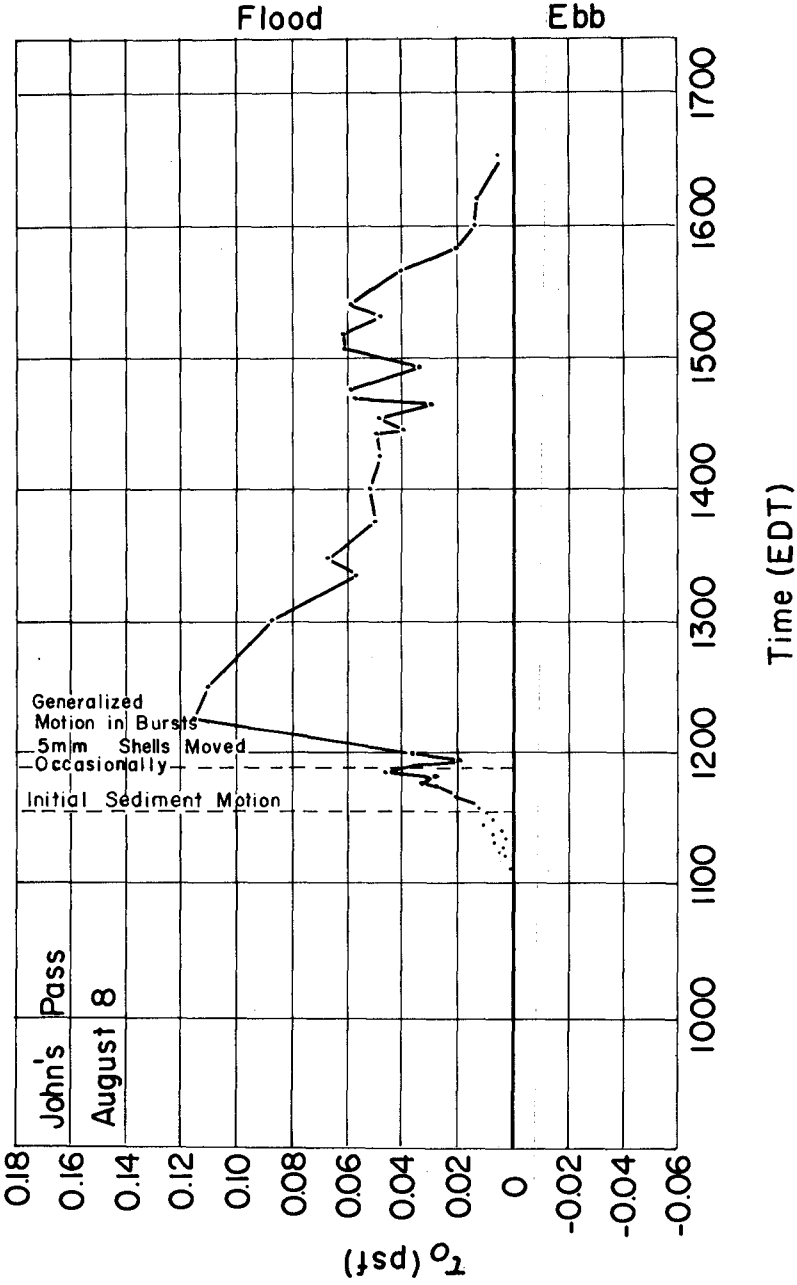


Fig. 7. Time Variation of τ_0 at John's Pass, August 8, 1974.

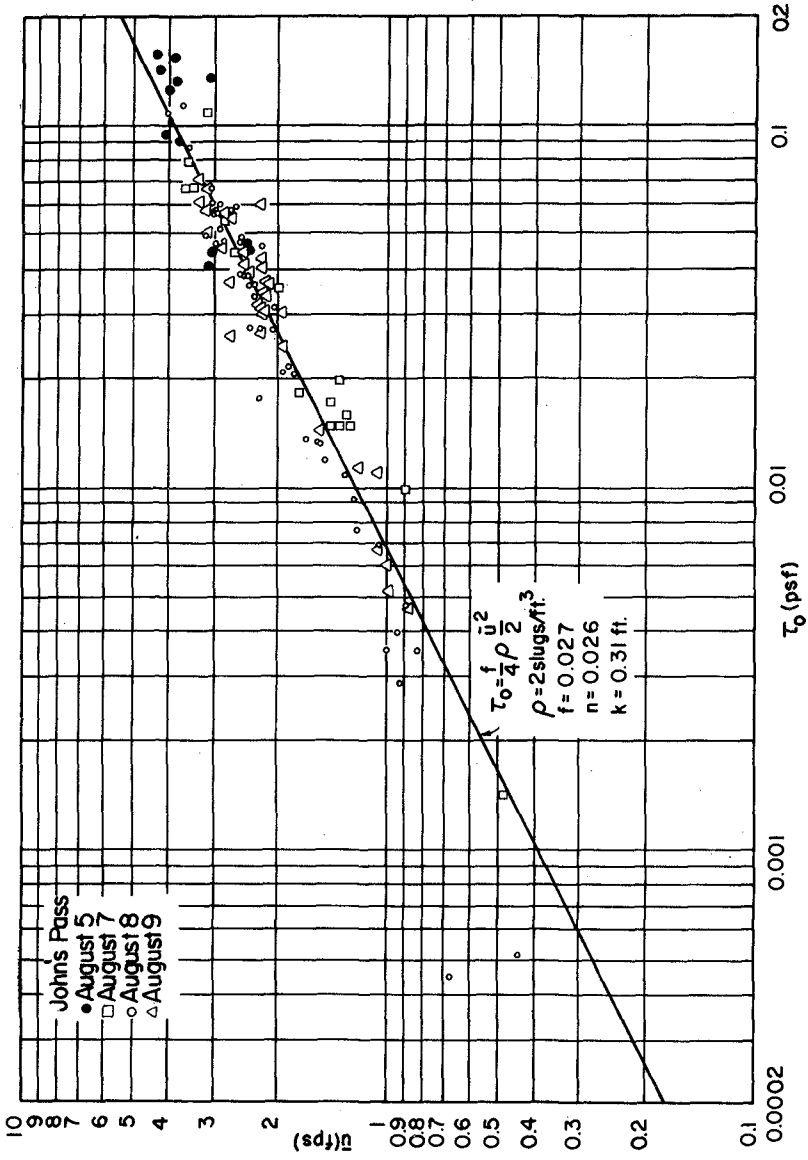


Fig. 8. Relationship between τ_0 and \bar{u} , John's Pass.

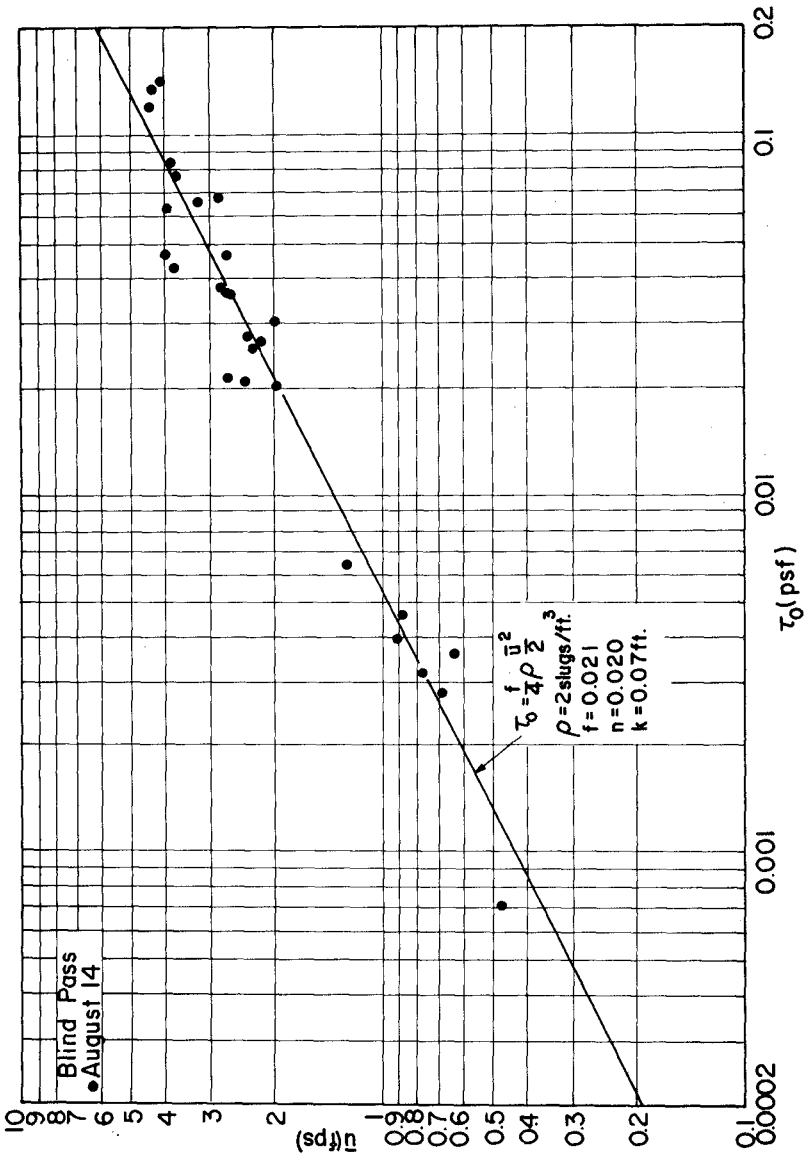


Fig. 9. Relationship between τ_0 and \bar{u} , Blind Pass.

deviate systematically from the straight line, such that the measured shear stress is lower than that predicted by the line. This is, it can be shown, because these data points are in the transition range of flow, with $K < 70$ (Mehta, et al., loc. cit.). The friction factor f initially decreases in this range, as in an open channel, giving lower τ_o values.

At flow velocities near 4 fps and greater, another deviation from the straight line is observed in Figs. 10 and 11. This deviation is such that the measured friction factor f is greater than that predicted by the straight line, and is possibly due to a changing bed roughness associated with a re-orientation of the bed at these high velocities.

In Figs. 10 and 11, the coefficient B of Eq.(1) calculated from Eq.(5) has been plotted against K , for John's Pass and Blind Pass, respectively. A comparison with the well-known experimental relationship obtained by Nikuradse for beds of relatively uniform sand grain roughness shows that the B values from the two inlets are generally higher than those indicated by the curves. Furthermore, for high values of K , B indeed attains a constant value; $B = 8.65$ for John's Pass and 8.60 for Blind Pass, as opposed to 8.50 for the Nikuradse data. These higher values of B are most likely to be due to the non-uniformity of the bed material in the inlets (Yalin, 1972). Thus in the case of John's Pass, where the proportion of shell on the bed is greater than at Blind Pass, the B value is correspondingly larger. This fact is clearly reflected in the values of the bed roughness k as well.

Measured tidal prisms and the tide ranges at the two inlets are given in Table 3. The prism through John's Pass is an order of magnitude larger than that through Blind Pass. Indeed, the former inlet is primarily responsible for the flushing of the northern portion of Boca Ciega Bay.

TABLE 3

Date	Inlet	P (ft ³)	2a _c (ft)
August 5	John's Pass	5.46×10^8	1.97
August 6	John's Pass	4.16×10^8	1.74
August 7	John's Pass	3.74×10^8	1.44
August 8	John's Pass	-----	1.28
August 9	John's Pass	2.44×10^8	1.72
August 14	Blind Pass	3.77×10^7	2.72

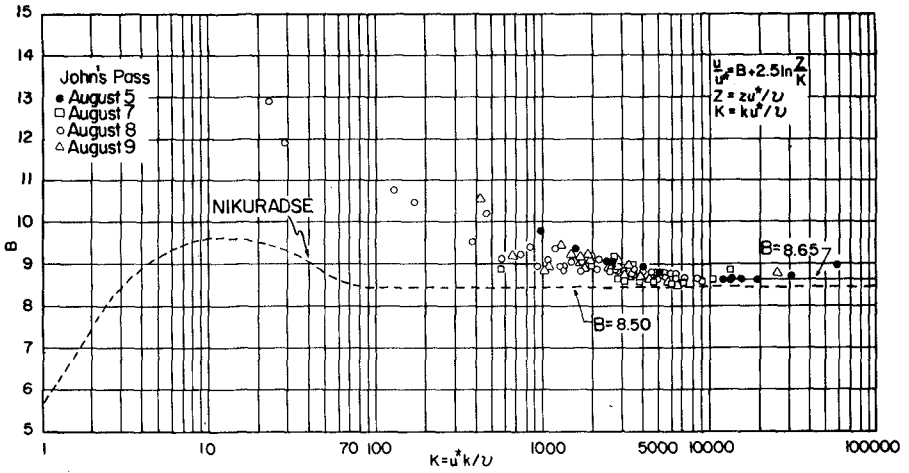


Fig. 10. Coefficient B of Eq.(1) Plotted against Wall Reynolds Number K, John's Pass.

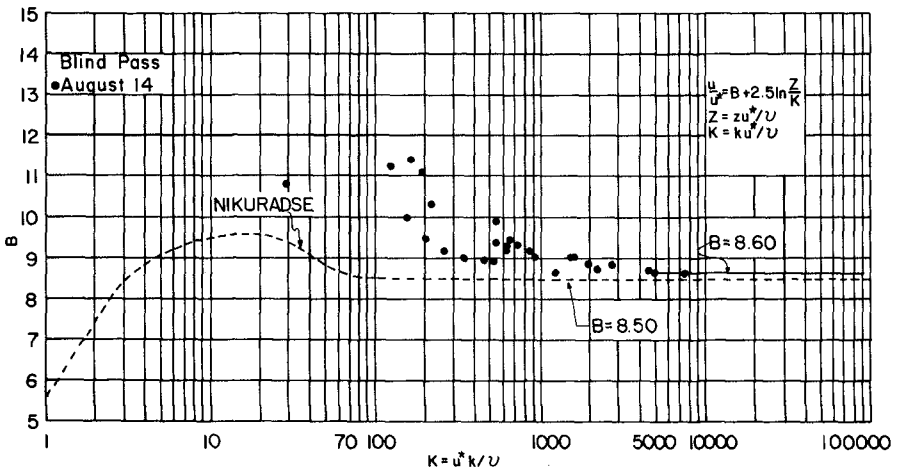


Fig. 11. Coefficient B of Eq.(1) Plotted against Wall Reynolds Number K, Blind Pass.

BED MOVEMENT

The motion of sand and shell was observed by the divers and is summarized in Table 4.

TABLE 4

Observation	τ_o (approx. range) (psf)
No detectable motion	0.000 - 0.010
Incipient motion of individual sand grain	0.010 - 0.015
Creeping motion of sand and "small" shells	0.015 - 0.045
Movement of individual "large" shells	0.045 - 0.060
Movement of the entire shell bed	0.060 -

Ranges of bed shear stress τ_o were determined by matching the times of observation with τ_o in plots such as Fig. 7. Since the diver observations were somewhat subjective, and the sediments in the two inlets are similar (the median, shell free sand diameter is 0.22 mm. at both the inlets), the classification of bed movement in Table 4 ignores any differences in bed motion between the two inlets. In the table, "small" refers to shell pieces less than approximately 5 mm. in diameter, and "large" to pieces larger than 5 mm. in diameter.

Because of the relatively small quantities of fine sand and shell pieces in motion at low flow velocities, attempts to collect the sediment in bed-load traps were not successful. Also, at high velocities, the divers were unable to enter the waters, and therefore could not make observations on the sediment motion when the currents were maximum.

DISCUSSION

A way in which the relevance of the friction factors derived from measurements at the throat may be determined is by testing Eqs.(10) and (11) against P/A_c determined from discharge measurements. Table 5 summarizes the calculations.

TABLE 5

	P/A_c (ft)	
	John's Pass	Blind Pass
Eq. (10)	5.12×10^4	8.81×10^4
Eq. (11)	3.04×10^4	4.26×10^4
Measured	4.08×10^4	8.54×10^4

The ratio for John's Pass represents a four day average ($\tau_{o\max} = 0.16, 0.11, 0.10$ and 0.06 psf at John's Pass and 0.13 psf at Blind Pass). In the estimation of $\tau_{o\max}$, a smooth curve was fitted to each of the τ_o -time curves, and the maximum was selected. A correction to this maximum was applied according to

$$\bar{\tau}_{o\max} = (\bar{u}_{\max} / \bar{u}_{\max}^2) \tau_{o\max} \quad (13)$$

to account for the transverse velocity profile. Here, \bar{u}_{\max} and τ_{\max} are values at the location of the cage, $\bar{\tau}_{\max}$ and \bar{u}_{\max} are the corresponding cross-sectional averages. It was found that $\bar{u}_{\max}/u_{\max} = 0.90$ and 0.86 , at John's Pass and Blind Pass, respectively. Also, measurements gave $C_K = 1.0$ and 0.84 , respectively.

Table 4 indicates that Eq.(10) predicts a P/A_C which is larger than the measured value by 25% at John's Pass and 3% at Blind Pass. This implies that the appropriate value of the friction factor f in Eq.(10) should be 1.56 times the directly measured value (0.027) at John's Pass, but only 1.06 times the measured value (0.021) at Blind Pass.

It is interesting to note that, considering the assumptions involved, Eq.(11) (with $u_{Cr}^* = \sqrt{\tau_{ocr}/\rho} = 0.079$ fps) agrees reasonably with the measurements at John's Pass, but predicts a substantially lower P/A_C at Blind Pass. A possible explanation for this is that Blind Pass is not a very stable inlet. This is reflected by the rather large measured P/A_C value as well.

Another comparison can be made through Eq.(8). This equation gives $f = 0.026$ and 0.022 , which is in excellent agreement with the measurements. These values are obtained by using the local mean depth $h = 25$ ft. and 12 ft., respectively, at the two inlets. If the cross-sectional mean depths \bar{h} from Table 1 are used, $f = 0.030$ and 0.027 respectively, at John's Pass and Blind Pass.

It is worthwhile to compare the observed relationship between the critical stress at incipient motion and the grain size, with the well-known relationship obtained by Shields for channels with sand beds in the fully rough range of flow:

$$\tau_{ocr} = 0.056 (\gamma_s - \gamma) d_{50} \quad (14)$$

where γ_s is the unit weight of the sand grain ($=169$ lbs/ft³), $\gamma = \rho g = 64$ lb/ft³ and d_{50} is the median grain size. Using $d_{50} = 0.22$ mm $= 0.0007$ ft. gives $\tau_{ocr} = 0.004$ psf, whereas the observed value was close to 0.013 psf. It has been shown elsewhere (Mehta and Christensen, 1976) that this discrepancy is due to the presence of a rather large ratio of the bed roughness k to the diameter d_{50} , and also due to the differences in the velocity profiles from that in a channel with a uniform sand grain bed.

CONCLUSIONS

1. The velocity profiles in the bottom one meter of the flow near the deepest part of the channel throat section were found to be logarithmic at John's Pass and Blind Pass.
2. The effect of inertia was found to be important in relation to frictional dissipation near the times of slack water. Elsewhere, this effect may be considered to be relatively insignificant.
3. The bed shear stress and the depth-mean velocity derived from these profiles were found to be related by the square law in the fully rough range of flow, with a characteristic friction factor and a Manning's n for each inlet.
4. The velocity coefficient B was found to vary in a manner similar to that in a wide open channel, but B values were generally higher for the two inlets.

5. The tidal prism-throat cross-sectional area ratio, as determined from a hydraulic relationship, Eq.(10), agreed with the directly measured ratio at Blind Pass, but at John's Pass, there was a difference, indicating that f , as determined from the measurements, was 56% too low.
6. Shields' criterion for the incipient motion of sand grains predicted a critical shear stress which was about one-third of the observed value.

ACKNOWLEDGEMENT

Thanks are due to Dean O'Brien for his help in the planning and execution of the field operation. Dr. Wiseman of the Coastal Studies Institute, L.S.U., provided data on salinity measurements at John's Pass. The assistance of Chris Jones in the computations is acknowledged. The work described here was supported by funds from the Office of Naval Research, Geography Programs, Contract N00014-68-A-0020, Project NR-388-106.

REFERENCES

- Bruun, P., Discussion, J. Waterways, Harbors and Coastal Engr. Div., ASCE, Vol. 100, No. WW4, November, 1974, pp. 403-409.
- Byrne, R. J., and Boon, J. D., "An Inexpensive Fast Response Current Speed Indicator," Chesapeake Science, Vol. 14, No. 3, September, 1973, pp. 217-219.
- Keulegan, G. H., "Tidal Flow in Entrances: Water-level Fluctuations of Basins in Communication with Seas," Committee on Tidal Hydraulics Technical Bulletin No. 14, U.S. Army Corps of Engineers, July, 1967.
- Keulegan, G. H., and Hall, J. V., "A Formula for the Calculation of the Tidal Discharge through an Inlet," U.S. Beach Erosion Board Bulletin, Vol. 4, No. 1, January, 1950, pp. 15-29.
- Krishnamurthy, M., Discussion, J. Waterways, Harbors and Coastal Engr. Div., ASCE, Vol. 100, No. WW2, May, 1974, pp. 165-166.
- Mason, C., "Regime Equations and Tidal Inlets," J. Waterways, Harbors and Coastal Engr. Div., ASCE, Vol. 99, No. WW3, August, 1973, pp. 393-397.
- Mehta, A. J., Byrne, R. J., and DeAlteris, J., "Hydraulic Constants of Tidal Entrances III: Bed Friction Measurements at John's Pass and Blind Pass," Coastal and Oceanographic Engineering Laboratory Technical Report No. 26, University of Florida, Gainesville, March, 1976.
- Mehta, A. J. and Christensen, B. A., "Incipient Motion of Sediment Grains in River Entrances with Shell Beds," Rivers 76 - Symposium on Inland Waterways for Navigation, Flood Control and Water Diversions, Vol. II, Fort Collins, Colo., Aug, 1976.
- Mehta, A. J., and Adams, Wm. D., "John's Pass and Blind Pass: Glossary of Inlets Report," University of Florida Sea Grant Program (in press).
- O'Brien, M. P., "Equilibrium Flow Areas of Inlets on Sandy Coasts," J. Waterways and Harbors Div., ASCE, Vol. 95, No. WW1, February, 1969.
- O'Brien, M. P., "Notes on Tidal Inlets on Sandy Shores," U.S. Army Coastal Engineering Research Center GITI Report 5, February, 1976.
- Sanchez-Diaz, E. S., "A Dye Dispersion Study at Blind Pass, Florida," Dept. of Sciences M.S. Thesis, University of Florida, Gainesville, 1975.
- Yalin, M. S., "Mechanics of Sediment Transport," Pergamon Press, 1972.

CHAPTER 100

MORPHODYNAMICS OF A WAVE-DOMINATED RIVER MOUTH

L.D. Wright
Coastal Studies Unit, Dept. of Geography
University of Sydney
Sydney, N.S.W. 2006 Australia

Abstract

The mouth of the Shoalhaven River on the southeast coast of Australia is subject to direct attack by high energy waves and offers a general model of wave-dominated river-mouth deposition. During river floods seawater is completely flushed from the lower reaches of the channel and significant quantities of sandy bed load and suspended silts are debouched into the Tasman Sea. However, breaking waves cause intense mixing between the effluent and ambient waters while wave-induced mass transport and setup oppose and partially impound outflow. Unusually rapid deceleration and lateral effluent expansion result. Sediments accumulate in the form of a broad crescentic river-mouth bar with its crest situated about 2 channel widths seaward of the outlet and as broad shallow subaqueous levees capped by swash bars. Post-depositional shoreward return of sands by shoaling waves produces a constricted outlet. During low river stage wave setup enhances flood tidal currents and partially inhibits ebb tide outflow. This leads to a gradual shoreward migration of the river-mouth bar, a narrowing of the constricted outlet and to upstream migration of river-mouth sands into the lower reaches of the channel.

Introduction

Recent studies show that river mouth depositional patterns depend on the relative contribution from three primary processes which derive their energy directly from the river outflow and on modifications by marine processes. The three primary processes are: (1) turbulent diffusion, (2) turbulent bed friction; and (3) buoyant expansion. Major modifying processes include those induced by tides and waves. Depositional patterns at many river mouths may be explained largely in terms of one or more of the primary processes. The well-studied mouths of the Mississippi, for example, are dominated by buoyant expansion and experience minimal influence from tides and waves (Wright and Coleman, 1974). In contrast, many river mouths are attacked directly by high wave energy. Wave-current interactions cause pronounced modifications to effluent behavior while waves directly redistribute the river mouth sediments contemporaneously with their initial discharge. Some notable examples of wave-dominated river mouths include the mouths of the Senegal (West Africa); Sao Francisco and Jequitinhonha (Brazil); Magdalena (Columbia); Orange (South Africa); Burdekin (Queensland, Australia); and Shoalhaven (New South Wales, Australia). The process signatures and depositional morphologies of these river mouths show common attributes among themselves but differ markedly from those of river-dominated or tide-dominated river mouths. The high-energy southeast coast of Australia offers excellent examples of wave-dominated river mouths. This paper summarizes 18 months of observations at the mouth of the Shoalhaven River about 150 km south of Sydney, Australia.

Environment of the Study Area

The Shoalhaven River Delta and estuary (Fig.1) are situated near the township of Nowra, New South Wales on the east coast of Australia. By world standards the Shoalhaven is a small river although it is the largest on the south coast of New South Wales. The river's catchment has a total area of 7250 km² and receives an average rainfall of 760 mm. The mean discharge rate at the Nowra Bridge near the head of the delta is only 57.3 m³ sec⁻¹; however, flows of over 5,000 m³ sec⁻¹ occur at a return interval of 10 years. Flows in excess of this magnitude occurred in both 1974 and 1975. The bed load of the river consists of fine to medium sands of angular to rounded quartz, feldspar and rock fragments. During flood the river also transports high concentrations of suspended silts and clays.

The Shoalhaven has built a Recent deltaic plain 85 km² in area, extending from Nowra to the coast. At the present time the discharge of the Shoalhaven enters the sea via 2 outlets; the Crookhaven entrance which is situated in a relatively protected environment in the lee of Crookhaven Heads and the Shoalhaven entrance which is exposed to the full spectrum of wave conditions. The protected Crookhaven entrance provides a low energy "control" example for comparing the behavior of the wave-dominated Shoalhaven entrance. The river debouches into Shoalhaven Bight, a broad, arcuate embayment bordering the Tasman Sea. The nearshore bed, though flatter than that fronting neighboring coastal sectors, is relatively steep, with an average gradient of 0° 45' and a concave-upwards profile. Water depths of 20 metres occur within 1.5 km from the present shoreline.

The tides of the region are semidiurnal with a mean range of 1.2 metres and a spring range of 1.8 metres. The combined tidal prism of the Shoalhaven and Crookhaven estuaries is estimated to be about 23 x 10⁶ m³ during spring tides. This exceeds the base flow by 18 times but is only 1/5 the volume of extreme flood discharge. The river mouth and adjacent coastline are dominated by high energy waves. The region experiences a highly variable wind wave climate superimposed on persistent refracted long period southerly and southeasterly swell. Deepwater wave power averages 178 Watts per cm of crest width and exceeds 1250 Watts cm⁻¹ for 1% of the time. Significant deepwater wave height exceeds 1.5 metres 50% of the time, is greater than 3 metres for 5% of the time and has approached 10 metres several times over the past 2 years.

Field Techniques

This paper is based largely on direct field observations made over the period August 1974 to January 1976. Observations of outflow behavior, estuarine circulation, wave characteristics and resultant morphologic patterns were made over a wide range of hydrologic and marine energy conditions. Bathymetric surveys in the Shoalhaven estuary and offshore were conducted using a Ratheon model DE 731 echo sounder; positions were determined by theodolite and horizontal sextant angles. Autolab salinity-temperature meters were used for S-T profiling and Toho-Dentan direct-reading current meters were used for current profiling. Drogues and dye were employed to determine larger scale flow patterns. Continuous tidal and river stage height data were recorded by means of 5 Bristol recording tide gages maintained by the Shoalhaven Shire Council and by a Stephens water level recorder. Incident deepwater wave characteristics were measured by the Maritime Services Board of New South Wales' offshore wave rider located 5 km seaward of the entrance to Botany Bay (100 km north of the study region).

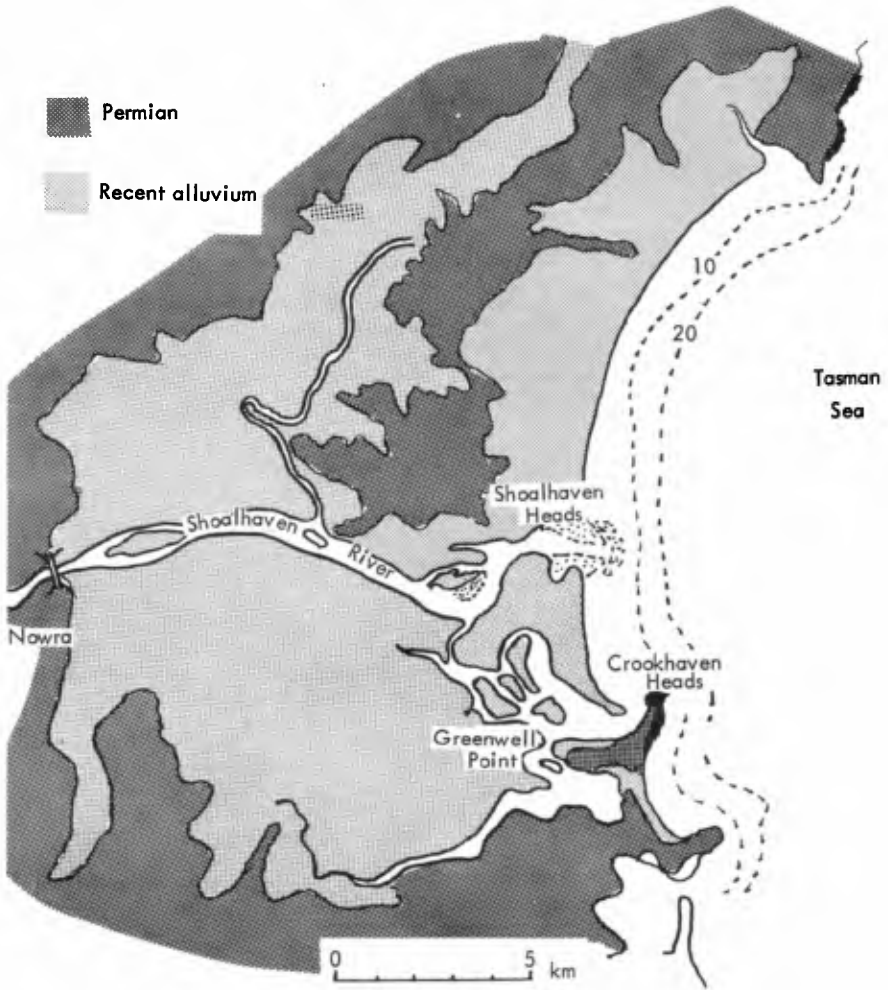


Figure 1: The Shoalhaven Delta

Flood-Stage Outflow

Significant transport and deposition of river-derived sediments at and immediately upstream from the mouth of the Shoalhaven takes place primarily during river flood when seawater is flushed from the estuary. During floods the beach which often seals the Shoalhaven Heads entrance is breached (or widened if the entrance has not been previously sealed) and sands are debouched through the outlet into Shoalhaven Bight. The Shoalhaven experienced extreme flood conditions in August 1974 and again in June 1975. The discharge rates associated with both floods substantially exceeded the 10 year discharge rates: peak discharge associated with the August 1974 and June 1975 floods were $7400 \text{ m}^3 \text{ sec}^{-1}$ and $6900 \text{ m}^3 \text{ sec}^{-1}$ respectively at the Nowra Bridge 13 km upstream from the entrance (Dept. Public Works, N.S.W., 1975). During the August 1974 flood observations were restricted logistically to field reconnaissance; however, field data were obtained during the June 1975 flood.

Figure 2 shows water surface elevation curves from Nowra Bridge and Shoalhaven Heads encompassing the period preceding, during and immediately following the flood (June 19-25, 1976). The portion of the curves for the period June 19-20 indicates the normal low-stage surface behavior and demonstrates the tidal dominance of the lower channel. It is apparent from this low-stage curve that tidal amplitude undergoes only slight attenuation and deformation over the distance from the entrance to Nowra. A tidal lag of about 1 hour 45 minutes is also evident. With the onset of the flood water levels rose abruptly at both the upstream and river mouth stations. A flood peak of 5.09 metres at Nowra (2130 hrs. on June 21) was accompanied by a peak of 2.15 at the Shoalhaven Heads entrance, thus resulting in a maximum water surface gradient of 23 cm km^{-1} in the lower estuary. Flood flow completely obliterated the effects of tidal rise and fall at the Nowra Bridge over the period June 21-26. However, at the mouth tidal influence persisted throughout the flood even though marine waters were completely flushed from both entrances.

Unfortunately it was logistically impossible to obtain direct current observations in the entrance during the flood peak; however, current, salinity-temperature and bathymetric data were obtained immediately following the peak during the period of subsiding stage. Figure 3 shows typical velocity profiles and water density structures in the Shoalhaven Heads entrance during ebbing and flooding tides on June 26-27. The flood-stage river-mouth bar profile is also shown. (In this figure and figures which follow, water density is expressed in units of σ_t which is related to density, ρ , by $\sigma_t = (\rho - 1) \cdot 1,000$ and is calculated from salinity and temperature data.) As the diagram indicates salt water was completely flushed from the entrance and flow was seaward at all depths during both phases of the tide. The influence of tides is strongly evident from a comparison of the ebbing versus flooding currents: outflow was accelerated during ebbing tide and inhibited during flooding tide. The ebb-tide outflow attained surface speeds of over $2 \text{ metres sec}^{-1}$ whereas surface outflow averaged only about $40\text{-}50 \text{ cm sec}^{-1}$ during flooding tide. Strong bed shear accompanied the flood stage outflow on both tidal phases and pronounced seaward transport of bed load was evidenced from the presence of seaward-migrating mega-ripples with amplitudes on the order of 50 to 100 cm.

Vertical density stratification in the entrance throat and over the river-mouth bar was negligible (Fig.3). It has been shown elsewhere that the effectiveness of buoyancy in suppressing effluent turbulence depends

To a large extent on F' , the densimetric Froude number at the outlet (Hazashi and Shuto, 1967, 1968; Wright and Coleman, 1971) where

$$F'_o = U / \sqrt{\gamma gh'}$$

where U is the mean outflow velocity, g is the acceleration of gravity, h' is the depth of the maximum density gradient and γ is the density ratio

$$\gamma = 1 - (\rho_f / \rho_s) \text{ where } \rho_f \text{ and } \rho_s \text{ are respectively the}$$

densities of fresh water and sea water. Throughout the high stage and falling stage period F' exceeded substantially the value of 16.1 regarded by Hayashi and Shuto (1967, 1968) as necessary for fully turbulent effluent diffusion.

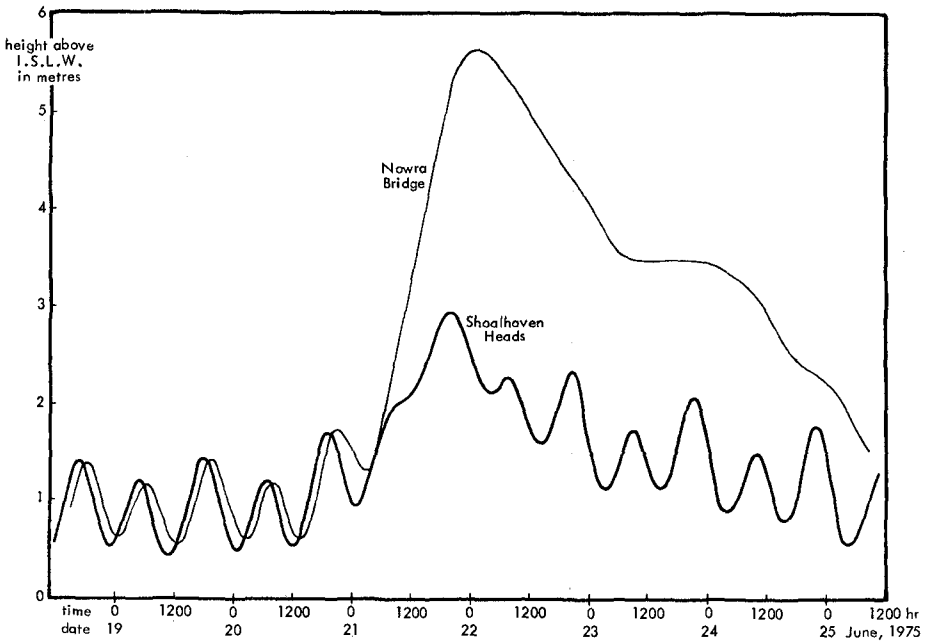


Figure 2: Water Surface Elevation Curves for Shoalhaven Heads and Nowra Bridge, June 19-25, 1975

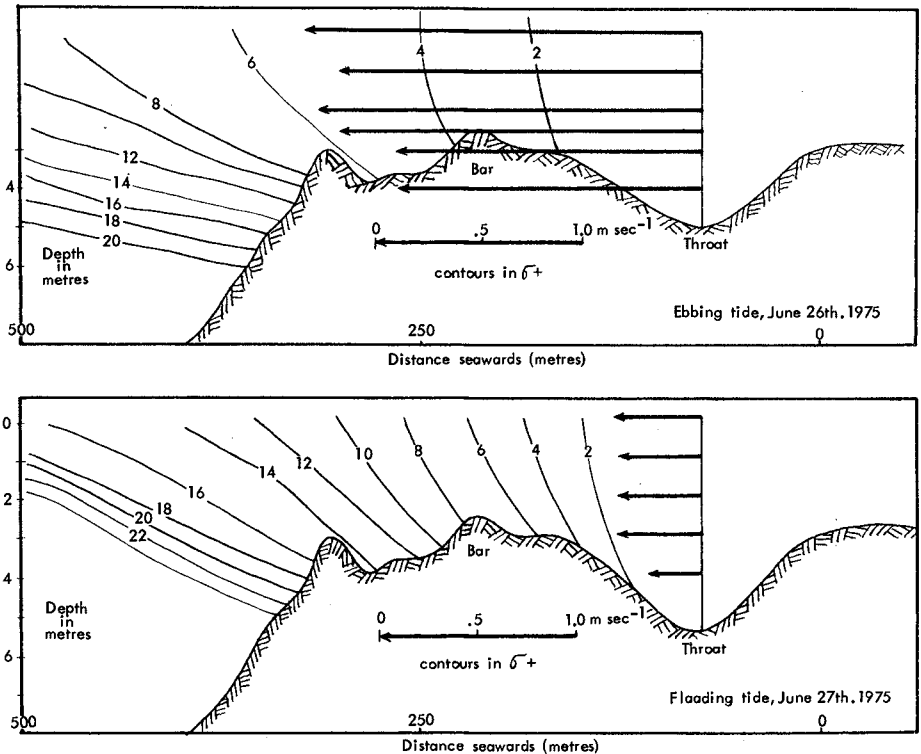


Figure 3: Current and Density Profiles at the Mouth of the Shoalhaven River on Ebbing and Flooding Tides, June 26-27, 1976

It is common on the southeast coast of Australia for increased stream-flow to coincide with the occurrence of powerful southeasterly waves. The floods of August 1974 and June 1975 were associated with lows situated over the coast which also generated high energy waves: the June 1975 flood was accompanied by a significant wave height of 7 metres. The dominant waves associated with the storm arrived from the southeast and had a peak period of 13 seconds. Owing to the direction of incidence of these waves the Crookhaven entrance was comparatively sheltered from extreme energy conditions; however, the Shoalhaven Heads entrance was fully exposed to direct wave attack.

The most conspicuous influences of high wave energy on flood-stage outflow were wave-induced setup and increased effluent diffusion and deceleration. The importance of wave setup on the Shoalhaven Heads entrance is apparent from Figure 4 which shows simultaneous flood-stage water level curves from Shoalhaven Heads and Greenwell Point (situated just upstream from the Crookhaven Heads entrance) together with the significant wave heights for the same period. From the graphs it can be seen that flood-stage water levels were substantially higher at the exposed Shoalhaven Heads entrance than at the more sheltered Crookhaven outlet. At the time of the peak wave height, which preceded the flood crest by about 15 hours, water level at Shoalhaven Heads exceeded that at Greenwell Point by 60 centimetres.

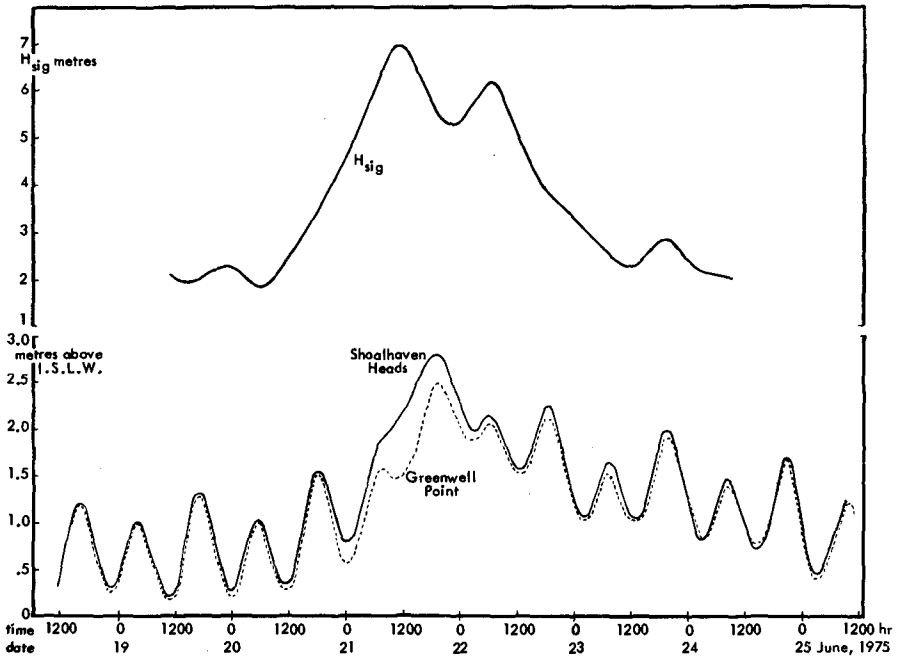


Figure 4: Simultaneous Curves of Significant Wave Height as Recorded by the Botany Bay Offshore Wave Rider and Water Surface Elevations at Shoalhaven Heads and Greenwell Point, June 19-25, 1975

The important role of waves in enhancing effluent mixing and deceleration was evident from a comparison of observations at the two outlets made on June 27 and 28 during falling stage as sea water reentered the extreme lower reaches of the distributaries. At the time of these observations river discharge had decreased to levels insufficient to flush completely the seawater from the channels but still significantly exceeded the tidal prism of the estuary. Conditions such as these have been observed elsewhere to favour strong vertical stratification and salt-wedge intrusion under normal conditions (e.g., Wright, 1971). At highly stratified river mouths such as the mouths of the Mississippi River the outlet densimetric Froude number tends to maintain values near unity and outflow expands largely as a buoyant plume which experiences only gradual deceleration (Wright and Coleman, 1971, 1974). Figure 5 shows the typical density (σ_t) structure and current profile observed at the Crookhaven outlet during falling stage. A close analogy to the Mississippi model is apparent: there was a steep pycnocline, the densimetric Froude number was slightly less than 1 and there was a flow reversal just beneath the pycnocline. Seaward of the outlet the Crookhaven effluent expanded in the shelter of Crookhaven Heads as a buoyant surface layer with minimal lateral and vertical mixing.

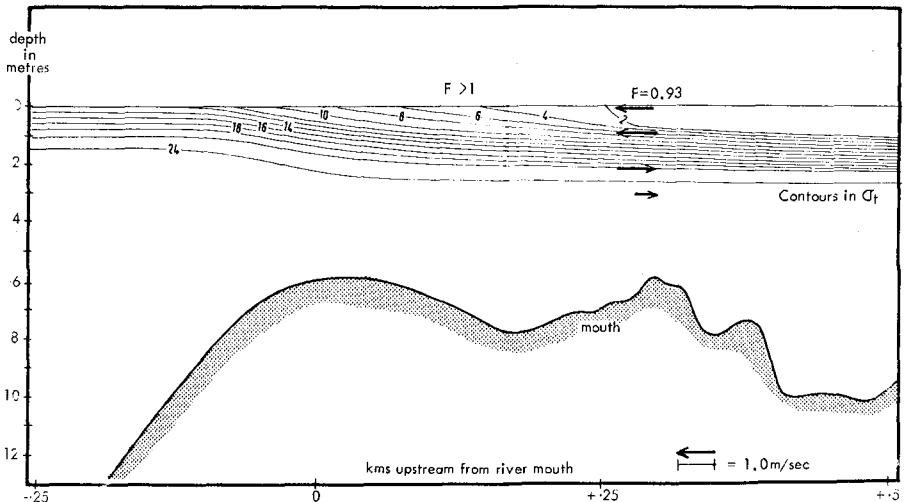


Figure 5: Density and Flow Structure in and Seaward of the Crookhaven Mouth During Falling Stage, June 27, 1975

Outflow patterns at the exposed Shoalhaven Heads entrance during the same period contrasted sharply with those of the Crookhaven. From Figure 6 it can be seen that denser brackish water had intruded a short distance into the Shoalhaven entrance by June 28, 1975. However, unlike the Crookhaven, flow through the Shoalhaven Heads outlet was seaward at all depths and the density structure indicated a vertically well-mixed condition owing to the action of breaking waves. Immediately seaward of the entrance throat breaking waves caused rapid mixing and momentum exchange between effluent and ambient water. In addition to intensified mixing, outflow was opposed by wave-induced shoreward transport of seawater which abruptly converged with the effluent immediately seaward of the seawardmost break point. The combined effect was to cause extremely rapid seaward deceleration of the outflow: maximum velocities decreased from 1.5 m sec^{-1} at the entrance throat to 20 cm sec^{-1} within a distance of 2 channel widths (250 m) seaward. This rate of deceleration was several times greater than that predictable from the theories or observations of fully turbulent or buoyant jets (e.g., Wright and Coleman, 1974) and must be attributable to wave effects.

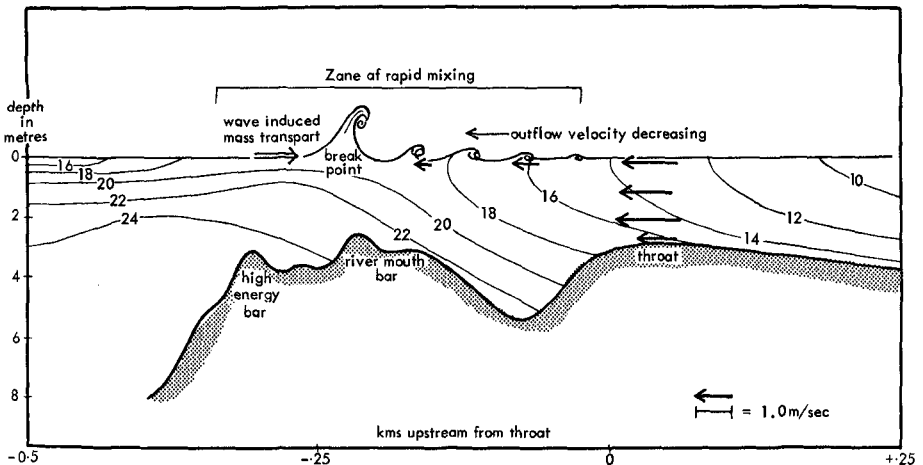


Figure 6: Density and Flow Structure and Two-Dimensional River-Mouth Morphology at the Shoalhaven Heads Mouth During Falling Stage, June 28, 1975.

The plan-view surface outflow patterns associated with flood discharge are illustrated in Figure 7 together with the resultant depositional morphology. Flow patterns shown in this diagram were determined by drogue and dye tracking and from aerial observations. Waves which broke over the crescentic river-mouth bar impeding seaward flow caused the effluent to spread abruptly alongshore. Flow divergence landward of the bar crest was accompanied by shoreward transport and emergence of seawater over the seaward front of the bar. Lateral to the effluent centreline, velocity gradients were extremely steep causing abrupt deposition and shoaling in the form of subaqueous levees.

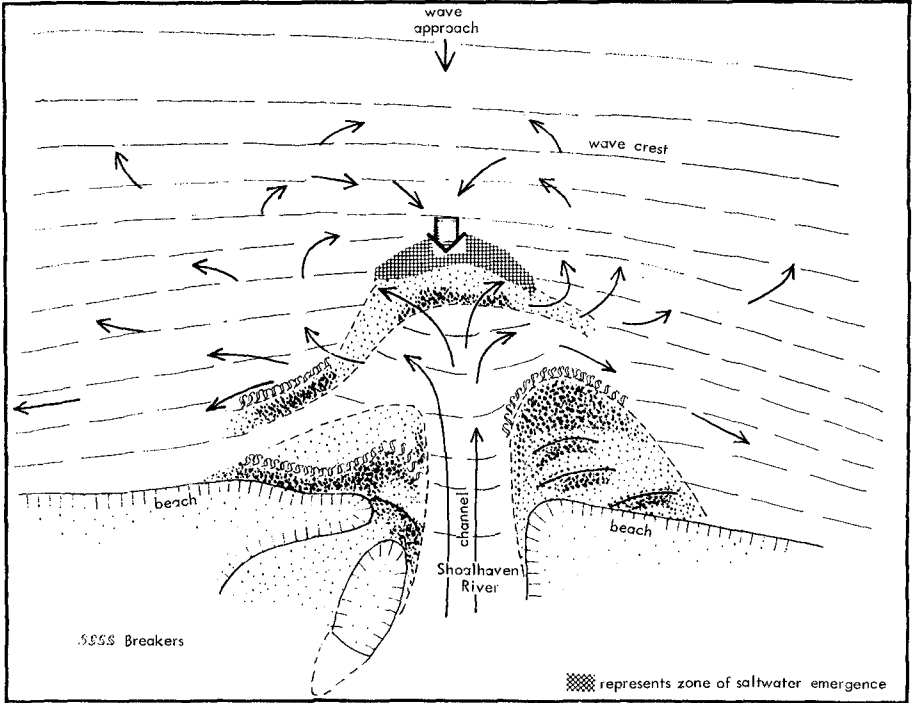


Figure 7: Horizontal Surface Outflow Patterns and Plan-View Morphology at the Shoalhaven Heads Mouth, June 28, 1975 (lengths of arrows not proportional to current speed)

Flood-Stage River-Mouth Morphology

The depoositional morphology produced by the flood stage outflow is shown in profile and plan in Figures 6 and 7. Rapid wave-induced deceleration caused abrupt depoosition of bed load resulting in a conspicuous river-mouth bar at a short distance from the inlet throat. The bar was wide and crescentic in plan-view and was situated at 2 channel widths seaward of the outlet (as compared with 4 to 6 channel widths at the mouth of the Mississippi: Wright and Coleman, 1974). Surveys immediately after the flood in June, 1975, in August, 1975, and in December, 1975 indicated that the bar consistently had 2 crests. The seawardmost bar crest was asymmetrical with a steeper landward face and appeared to be migrating shoreward under the influence of shoaling waves.

In plan, the distinguishing features of the river mouth were: (1) a crescentic and highly regular river-mouth bar; (2) a constricted outlet; and (3) broad subaqueous levees which widen to shoreward and are surmounted by swash bars. The wide subaqueous levees are apparently associated with the combination of steep lateral velocity gradients and post-depositional reworking of river-mouth sands by shoaling waves. These levees were the most extensive depositional unit at the river mouth in terms of both surface area and sand volume. Sediments returned shoreward by wave-induced swash bar migration over the levee/shoals accumulate adjacent to the entrance throat and constrict the mouth until a balance is achieved between the reconcentrated outflow and the waves. The crescentic bar and wide subaqueous levees of the flood-stage Shoalhaven mouth appeared to be analogous in form and function to the terminal lobe and ramp-margin shoals of ebb-tidal deltas (e.g., Hayea *et al.*, 1970; Oertel, 1972).

Low-Stage Outflow

As the river returns to normal or low flow, saltwater quickly intrudes into the lower reaches of the channel. Figure 8 shows the low stage density structure in the lower 15 km of the Shoalhaven estuary. Throughout most of its length the estuary is well mixed by tides. At and immediately upstream from the Shoalhaven Heads entrance marine salinities prevail; salinities decrease progressively upstream becoming fresh a short distance above the Nowra Bridge. Under low stage conditions flow is bidirectional through the two entrances which function essentially as tidal inlets. Tidal influence extends to well above the Nowra Bridge and there is minimal tidal attenuation in the lower 15 km of the channel.

Figure 9 shows a comparison of the low stage tide curves from the Shoalhaven Heads and Crookhaven entrances, and illustrates the continual effects of wave-induced setup on the Shoalhaven Heads outlet. This setup impedes ebb outflow and augments flood tide inflow through the Shoalhaven entrance. Under these low stage conditions waves breaking over the crest of the river-mouth bar impound ebb outflow, causing it to spread laterally along the inshore zone (Fig.10). Sediment-laden efflux trapped in this way ultimately escapes by way of rips which prevail on either side of the large transverse bar, created by the river-mouth bar.

A recent set of 25 hourly observations by C. Brown (Posford, Pavry, Sinclair and Knight Consulting Engineers, 1976) testified to the importance of wave setup in creating tidal transport asymmetry through the Shoalhaven entrance.

The results of these observations are summarized in Table I. The table demonstrates that at the time of the observations (March, 1976) low

stage inflow through Shoalhaven Heads exceeded the outflow by more than 2 times. The excess inflow through Shoalhaven Heads exits together with the base flow of the river by way of the more protected Crookhaven entrance.

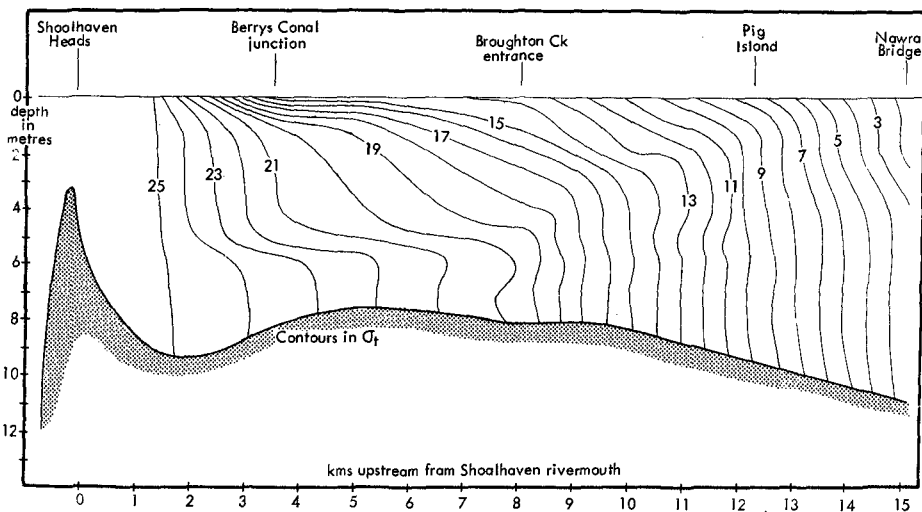


Figure 8: Longitudinal Density Profile of the Lower Shoalhaven Estuary at Low Stage, August 11, 1975

	Main Channel Upstream from Canal	Shoalhaven Heads	Crookhaven Heads
Flood (inflow)	$9.6 \times 10^6 \text{ m}^3$	$11 \times 10^6 \text{ m}^3$	$12 \times 10^6 \text{ m}^3$
Ebb (outflow)	$13.6 \times 10^6 \text{ m}^3$	$5 \times 10^6 \text{ m}^3$	$22 \times 10^6 \text{ m}^3$

Table 1: Mean Flood and Ebb Tidal Discharges Through Shoalhaven Heads and Crookhaven Heads, March 13-14, 1976
(Source: Posford, Pavry, Sinclair and Knight Consulting Engineers)

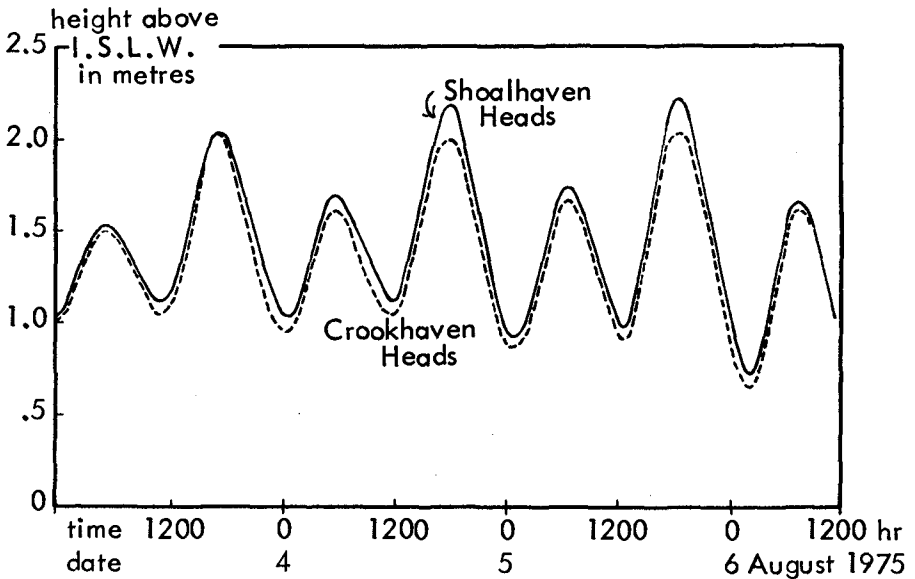


Figure 9: Simultaneous Tidal Curves for Shoalhaven Heads and Crookhaven Heads during Low Stage, August 3-6, 1975

Low-Stage Sediment Transport and Morphology

During prolonged low-discharge periods the combination of shoaling waves, flooding tides and setup results in a net shoreward return of sediment which ultimately reenters the lower reaches of the lower Shoalhaven estuary. Much of this sediment accumulates as a flood-tidal delta just upstream from the entrance throat along the flanks of the channel; however, a significant proportion of the sediment migrates over 5 kilometres upstream and accumulates on tidal point bars and mid-channel islands. Analyses of sediments from the river mouth and lower Shoalhaven channel indicate a mixture of well-rounded quartz typical of offshore and open coast environments and riverine sands consisting of angular rock fragments, feldspars and quartz. The percentage of riverine sand increases upstream from 30% to 50% at the river mouth to 100% at 13 km upstream.

Figure 11 shows the depositional morphology of the Shoalhaven Heads outlet as it appeared in January 1976 following a low-stage period of 5.5 months. By this stage large swash bars had migrated shoreward over the subaqueous levees and entered the mouth as a complex succession of recurved ridges which substantially reduced the width of the outlet. The crescentic river-mouth bar had migrated shoreward while the southern subaqueous levee had become extended across the outlet by dominant southeasterly waves,

causing outflow to be deflected to the north. In profile the double-crested bar form previously described was still apparent. However, both crests had migrated approximately 100 metres shoreward and the outer crest had become more pronounced and 1.5 metres shallower. In addition, the outer bar had increased in longshore width and had assumed a more regular form. Except for an outflow channel across the northeast quadrant the bar extended continuously shoreward to the beach on either side of the outlet. Where the river-mouth bar welded to the beach wide transverse bars surmounted by large emergent swash bars resulted. The transverse bars were flanked on either side by large rips by way of which the wave-impounded river effluent escaped seaward (Fig. 11).



Figure 10: The Mouth of the Shoalhaven During Low Stage, January, 1976
Note Turbid Effluent Water Trapped Inshore of Surf Zone

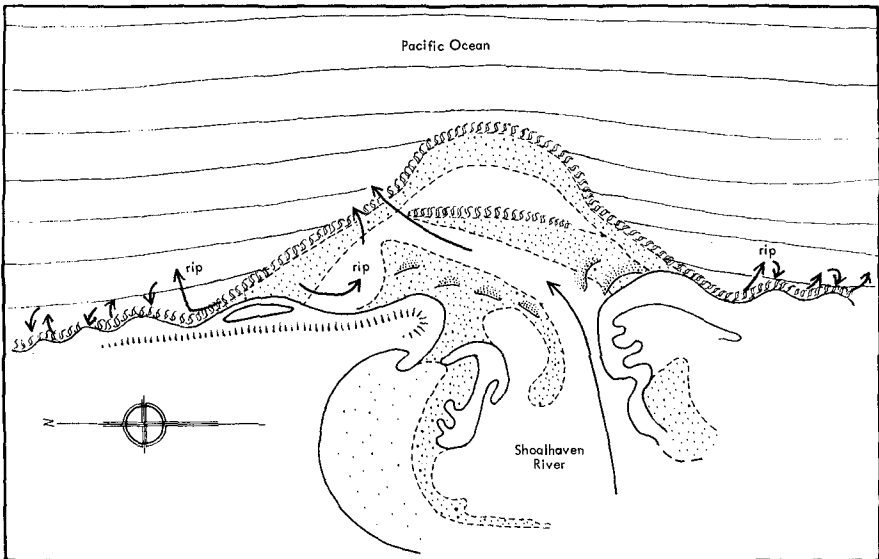


Figure 11: Low Stage Morphology and Outflow Patterns of the Mouth of the Shoalhaven, January, 1976

Inspection of aerial photographs reveals that when conditions of low river flow and wave dominance persist for a prolonged period, bar sands will continue to enter the mouth, narrowing the throat and choking the outlet. This causes discharge to be increasingly diverted through the Crookhaven entrance. Eventually shoreward migration of the bar completely seals off the Shoalhaven outlet. Once sealed, the mouth remains closed until it is breached by the next flood (Fig.12).



Figure 12:

The Mouth of the Shoalhaven as it Appears when Fully Closed Following Prolonged Low Discharge Periods

Summary and Conclusions

The depositional morphologic patterns observed at the mouth of the Shoalhaven contrast drastically with patterns observed at river mouths in low-wave energy environments but are analogous in major respects to those of other wave-dominated river mouths. It is inferred from this study that the distinguishing aspects of the morphology of the mouth of the Shoalhaven River are largely attributable to interactions between the river outflow and high-energy shoaling waves. Waves influence effluent behavior in at least two fundamental ways: (1) wave breaking and associated turbulence enhances mixing, obliterates vertical density gradients and causes more rapid deceleration; and (2) wave-induced mass transport and setup oppose the outflow, causing a local reduction in longitudinal hydrostatic gradient, "trapping" the issuing river water inshore and promoting abrupt lateral spreading of the outflow.

The major morphologic features produced by these wave-effluent interactions include: (1) a broad crescentic and highly regular river-mouth bar located at a short distance seaward of the outlet; (2) broad shallow sub-aqueous levees; and (3) a conspicuously constricted outlet.

Acknowledgments

This study was supported by the Australian Research Grants Committee (ARGC) and by a University of Sydney Research Grant (URG). Able assistance both in the field and the data analysis stage was provided by Mr. P. Cowell and Ms. D. Waddy. Valuable information and cooperation were provided by Mr. C. Brown of Posford, Pavry, Sinclair and Knight Consulting Engineers, and Mr. J. Downey, Shire Engineer, Shoalhaven Shire Council. Wave rider data were provided by Neil Lawson of the Maritime Services Board of N.S.W.

References

- Department of Public Works, N.S.W., 1975, "Shoalhaven Floods: August 1974, June 1975", Hydraulics and Soils Laboratory Report No. 194, 20 pp. + 20 figs.
- Hayashi, J. and N. Shuto, 1967, "Diffusion of Warm-Water Jets Discharged Horizontally at the Water Surface", Internat. Assoc. Hydraulic Res., 12th Congress Proc. 4, pp.47-59.
- _____ and _____, 1968, "Diffusion of Warm Cooling Water Discharged from a Power Plant", Proc. 11th Conf. Coastal Engineering.
- Hayes, M.O., V. Goldsmith and C.H. Hobbs, 1970, "Offset Coastal Inlets", Proc. 12th Conf. Coastal Engineering, pp.1187-1200.
- Oertel, G.F., 1972, "Sediment Transport of Estuary Entrance Shoals and the Formation of Swash Platforms", J. Sed. Petrol., vol.42, pp. 858-863.
- Posford, Pavry, Sinclair and Knight, Consulting Engineers, 1976, Shoalhaven Entrance Study, report submitted to Dept. of Public Works, N.S.W.
- Wright, L.D., 1971, "Hydrography of South Pass, Mississippi River Delta", Am. Soc. Civ. Eng., Proc. Waterways, Harbors and Coastal Engr. Div. No.97, pp.491-504.
- _____ and J.M. Coleman, 1971, "Effluent Expansion and Interfacial Mixing in the Presence of a Salt Wedge, Mississippi River Delta", Jour. Geophys. Res., Vol.76, pp.8649-8661.
- _____ and _____, 1974, "Mississippi River Mouth Processes: Effluent Dynamics and Morphologic Development", Jour. Geol., Vol.82, pp.751-778.

CHAPTER 101

RESULTS OF RIVER MOUTH TRAINING ON THE CLARENCE BAR, NEW SOUTH WALES, AUSTRALIA

Cyril D. Floyd, Late Principal Engineer, Harbours and Rivers,
Department of Public Works, N.S.W., Australia.

Bruce M. Druery, Department of Public Works, N.S.W., Australia

ABSTRACT

A case study is given of river training works at the mouth of the Clarence River. The study spans a period of ninety years. Extensive hydrographic data from the later part of this period is presented and examined in detail.

Prior to 1903 internal training walls had been constructed to stabilise the internal channel and stabilise the bar location at the mouth of the Clarence River. In 1956 construction started on entrance jetties with the aim of deepening the bar. The work was carried out over a period of 16 years. The slow rate of construction has allowed changes in bar depth to be compared with depths estimated by an empirical formula which relates bar depth to tidal flow and channel width. Results have shown that the empirical formula gives a reasonable estimate of bar depths and that bar depth is independent of jetty length.

Results have shown that the behaviour of the bar is strongly affected by floods. Some details of bar volume and movement are presented.

1. GENERAL

The Clarence River is the largest river reaching the coast of New South Wales. It is situated in the north of the state of New South Wales and the entrance lies on the southern fringe of the Australian cyclone area - see fig. 2.1. The Clarence has a catchment area of 8463 square miles (2190 km²).

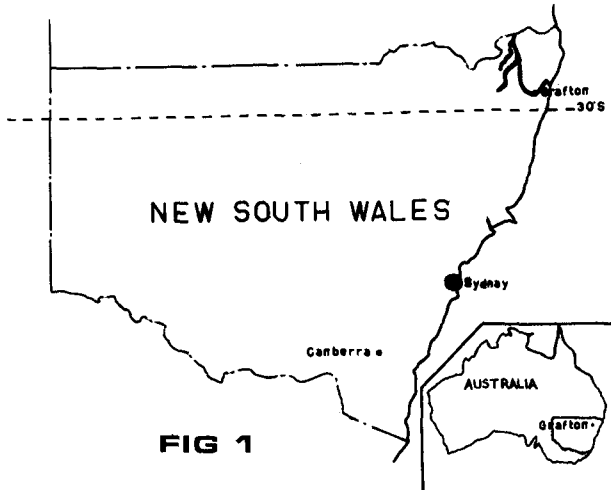


FIG 1

Flow from the catchment is extremely variable. At times the flow can be zero for long periods and in flood, flows of up to 600,000 cubic feet per second (16800 cubic metres per second) have been recorded at Grafton which is 40 miles (64 Km.) from the ocean. Normal fresh water flow is about 4000 cubic feet per second (113 m³/sec.).

Below Grafton a flood plain of about 127,000 acres (51,000 ha.) acts as storage for flood flows so that the maximum flow at the entrance is much reduced and prolonged. Flood flows at the entrance exceeding the normal tidal flow at extreme spring tides are rare.

The river is tidal for a distance of about 60 miles (96 Km.) from the ocean and the area of the tidal reaches is 34,000 acres (13,750 ha.). Tidal range in the ocean is 4.42 feet (1.34m.) for mean spring tides and extreme range is 6.58 feet (1.99m.).

Maximum tidal flow through the entrance for a mean spring tide (4.42 ft. ocean range) is 88,000 cubic feet per second (2.5×10^6 m³ per second) ebb tide and the total volume of flow is about 8×10^8 cubic feet/ (2.26×10^7 m³). The maximum flow occurs at low water with a tide level of about 1 foot above I.S.L.W.

The entrance and lower reaches are in tidal regime. Prevailing swell is from the south east and net annual littoral drift, from south to north, is considered to be of the order of 100,000 cubic yards.

2. HISTORICAL

The mouth of the river was first surveyed in 1845 but details other than the position of mean high water mark are not now available. A report several years later states that the mouth which was 6,800 feet (2060m.) wide consisted of a series of shallow tortuous channels which were not navigable. See fig. 2

In 1860 the entrance had narrowed to 750 feet (228m.) and at this time plans were prepared to construct training walls and jetties to stabilise the location of the channel and the bar crossing. Details of this proposal are shown in figure 3.

Following a series of floods in the years 1860 to 1880 the scheme was modified to that shown in figure 3 (Moriarty's proposals) but the work was abandoned in 1889 when a new scheme was approved as shown in figure 3. At that stage works constructed under the original proposal were as indicated in the same figure.

The internal training walls of the 1889 scheme were constructed but the entrance jetties were not. The work stopped in 1903 and apart from some additions and alterations to the internal walls no further work was carried out until 1956.

Although no effective work was carried out on the entrance jetties other than a short length on the southern one the internal walls resulted in a stable location and a bar which with frequent dredging served reasonably well for coastal shipping until this declined during the war years 1939/45.

3. WORK SINCE 1956

Following on from a Parliamentary decision to establish a port at the mouth of the river, plans were prepared for the construction of jetties to improve bar depths. It is not possible to ascertain with any certainty what bar depth it was hoped to obtain but it seems that a channel depth of 20 feet (6.1m.) below I.S.L.W. was the aim, with apparently a similar bar depth.

The works proposed are shown in figure 3 and consisted of two jetties of unequal length, the northern being the longer. The original plan was not adhered to and during construction the width between the jetties was reduced and the southern jetty lengthened.

Construction started in 1956 and continued until July, 1971 when work ceased. During this period the entrance channel, bar and nearby areas were surveyed at frequent intervals (usually every

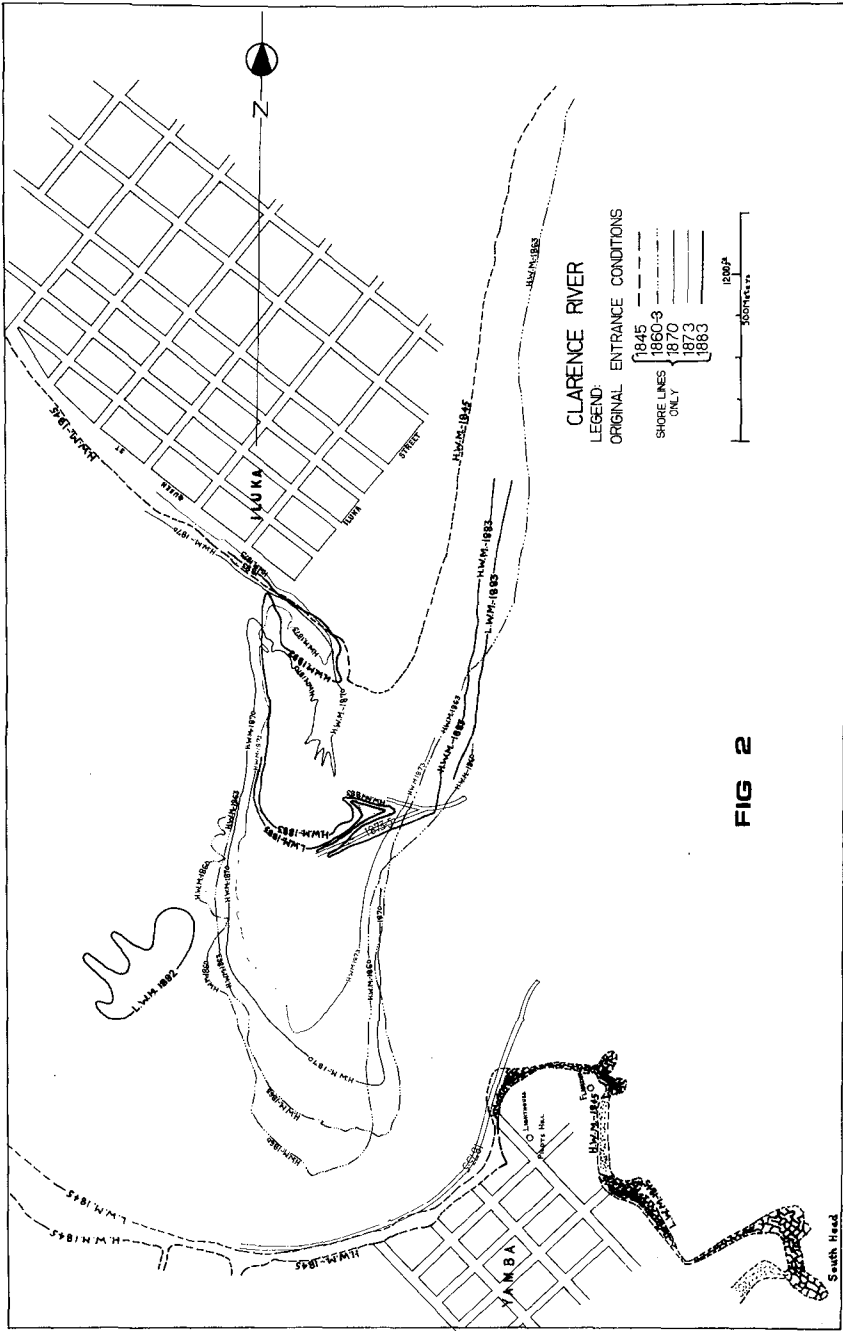


FIG 2

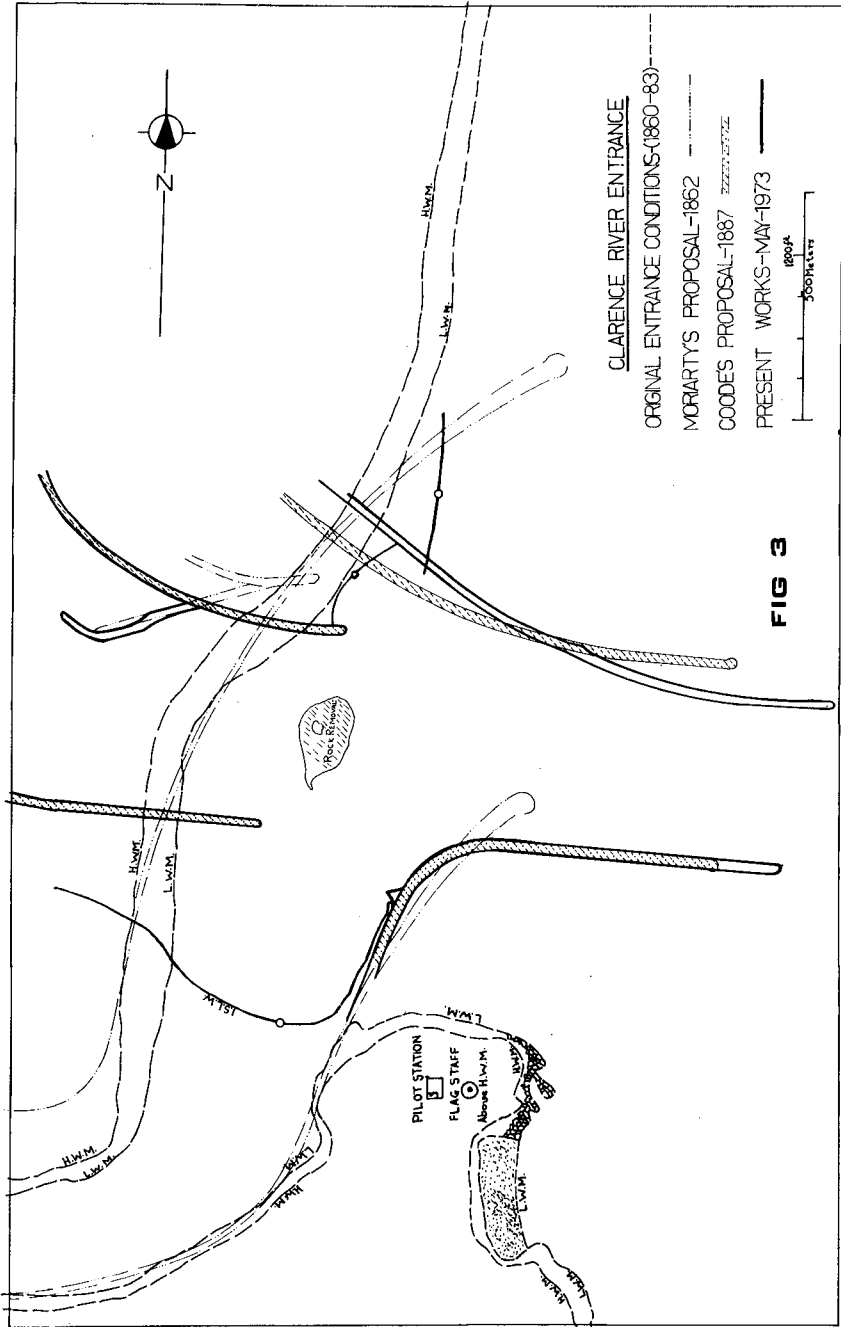


FIG 3

three to six months and quite often monthly).

A rock reef with depths varying from about 23 feet on the south to 8 feet on the north lies between the ends of the old internal training walls. This reef is irregular and causes considerable turbulence at flood and ebb tides as well as during floods. Removal to a depth of about 23 feet below I.S.L.W. over a width of about 500 feet was included in the authorized works but has not been done.

Construction started on the northern jetty and when it reached a distance of 2,150 feet seaward of the end of the old southern training wall (for convenience and also as an approximate indication of effective change in entrance geometry the end of the old southern training wall has been used as a reference point in this paper) work then transferred to the southern jetty which was constructed to an effective length of 2,750 by July, 1964. As this stage work again transferred to the northern jetty and it was extended to its final length of 3,950 feet seaward of the reference point by November, 1968. The final stage was the extension of the southern jetty to an effective length of 3,800 feet by July, 1971.

The old internal training walls had been constructed with centre lines 1450 feet apart at their seaward ends. The new jetties commenced in 1956 were to be 1450 feet apart.

In 1964 an assessment of tidal flow was first made. This indicated that the jetty spacing as authorized would not result in a channel depth of 20 feet below I.S.L.W. if tidal flow was distributed evenly between the jetties. A spacing of 1,200 feet centre to centre was then adopted as a compromise between navigation and flood needs.

4. RESULTS OF WORKS

(a) Bar Formation

Early surveys from 1860 to 1883 show bar depths of from 12 feet to 15 feet below a low water datum (exact definition not known). The alignment of the entrance was due north as shown in fig. 4. Internal channels had ruling depths of about 14 feet.

The original scheme did not progress sufficiently to draw any conclusions on its effects.

The works carried out under the 1889 proposal improved the internal channel depths and alignment and resulted in a stable mouth which was now aligned almost due east. A Symmetrical bar formed with a natural depth of 12 feet below I.S.L.W. see fig. 5. Flow patterns through the entrance were irregular, a result of the reef between the ends of the walls and of the alignment of the internal channels.

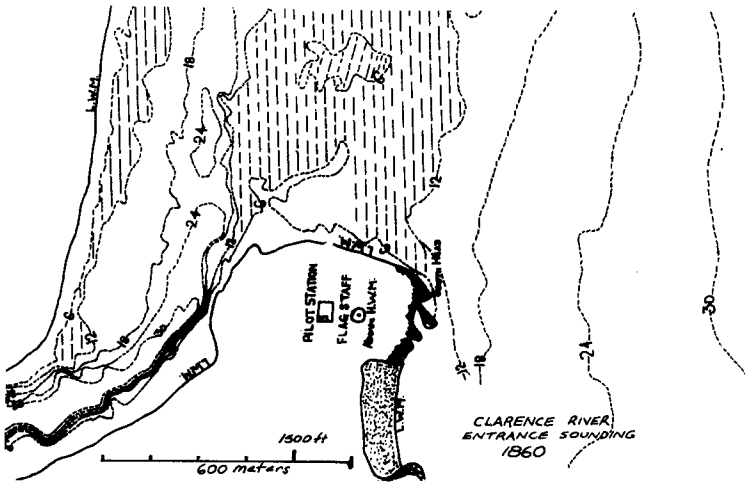


FIG 4

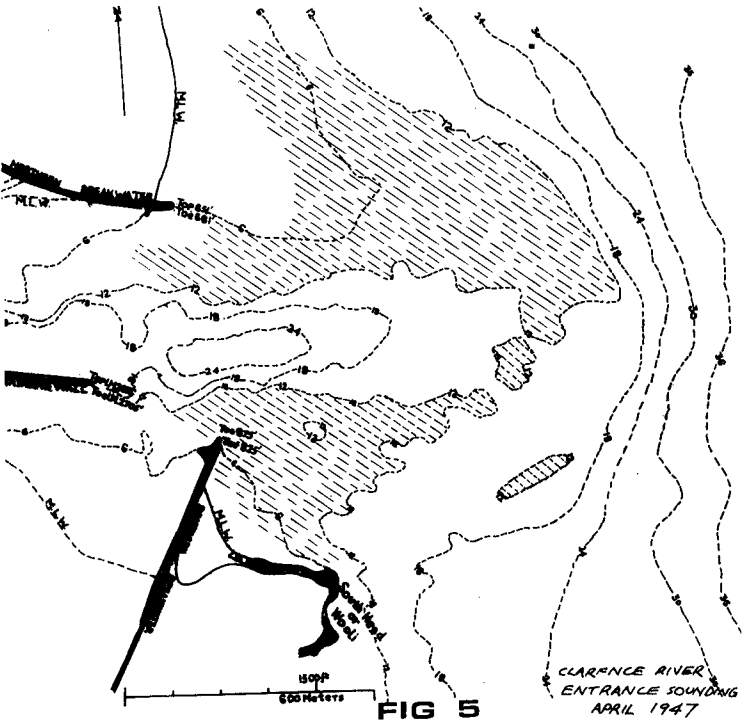


FIG 5

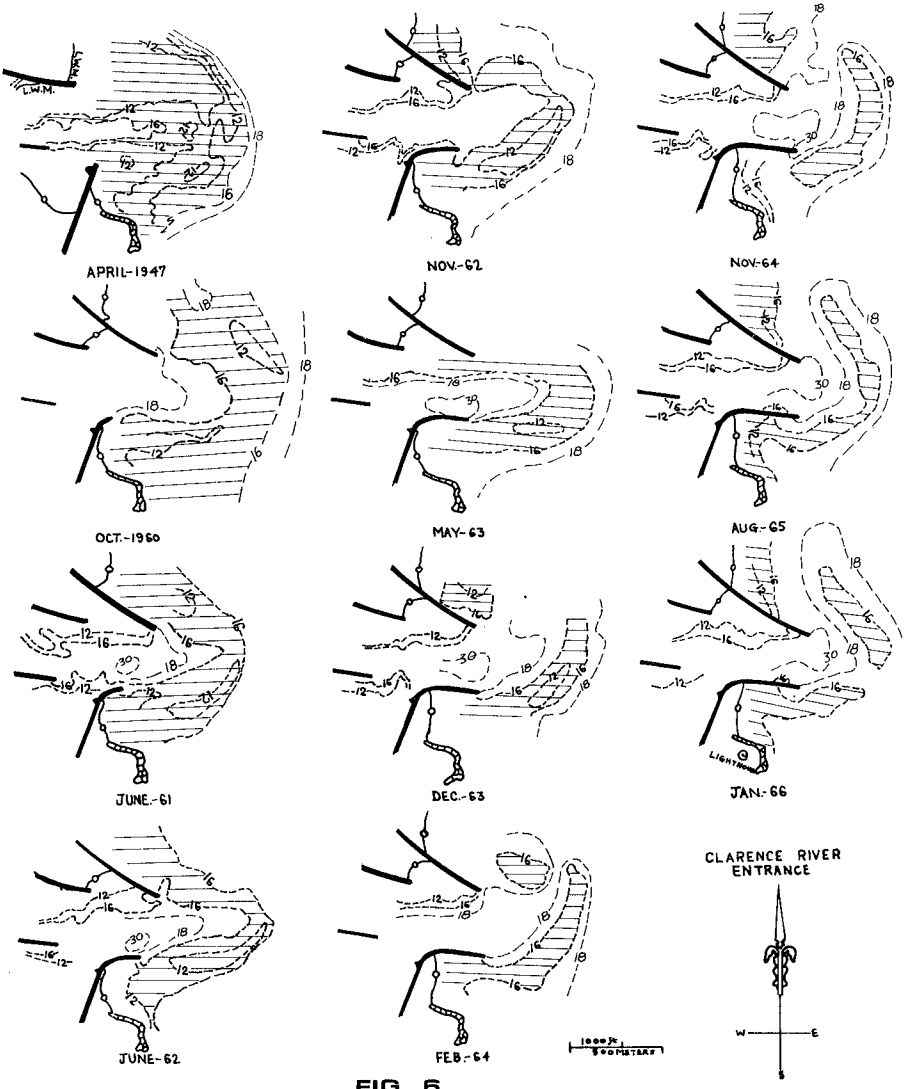


FIG 6

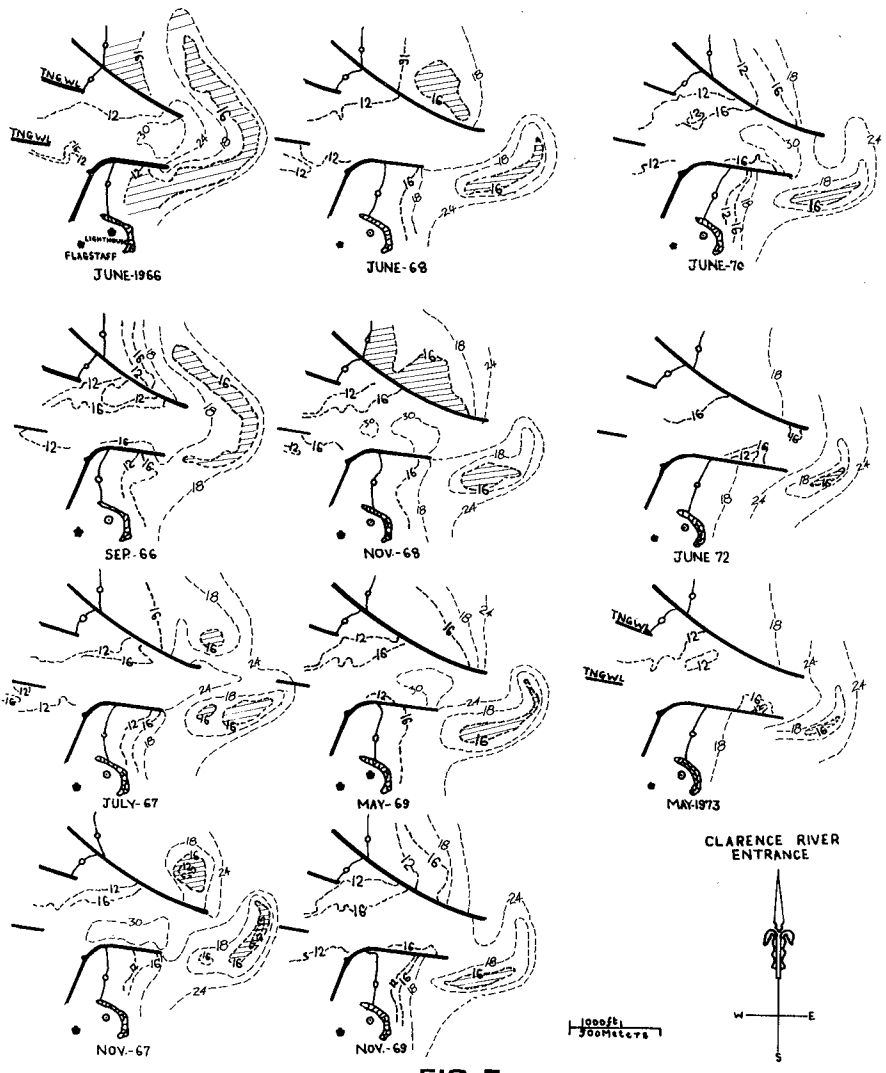


FIG 7

In the period 1956-1959 the northern jetty was built to a point of 2,150 feet seaward of the reference line referred to earlier. At this stage the bar depth was unchanged but the bar was in the form of an isolated shoal with deeper water between the shore and its two ends. The bed of the small bay between the entrance and Wooli Head had deepened by about 10 feet - see fig. 6.

From 1960 to 1965 the northern jetty length was unaltered and the southern one was constructed to 2,750 feet from base. The alignment of the inshore section of the south wall is such that it did not affect ebb flow through the entrance until mid-1961 when its effective length changed from nil to 1,400 feet in a few months. Shortly afterwards the bar became asymmetrical and could almost be considered a half bar (figure 6). This condition continued until mid-1964 when the two jetties projected equal distances and the bar again became symmetrical. The bar was again in the form of a crescent shoal with deeper water shoreward of each end.

With further extension of the northern jetty the bar remained symmetrical until the northern jetty was about 1,200 feet beyond the southern. The bar then again became asymmetrical. Further lengthening of the southern jetty did not alter this and the work ceased in 1970 with the northern jetty 3,950 feet and the southern jetty 3,800 feet seaward of the base line. The last survey in 1973 showed no marked change - see fig. 7.

(b) Bar Movement

Bar movement seems to have been strongly related to at least two factors :-

1. The seaward advance of the jetties
2. The occurrence of floods

Referring to fig. 8, the solid line is a plot of the distance from the end of the southern internal training wall to the seaward extremity of the outer 20 ft. contour of the bar. The broken line is a similar plot for the inner 20 ft. contour. The progress in construction of the entrance jetties is also shown from the same baseline.

On the whole it can be seen that the construction of the entrance jetties to a length of approx. 3900 ft. has caused the outer face of the bar to advance seawards by 1000 ft. and the inner face to advance seawards by 2600 ft. The result has been a progressive decrease in width across the bar.

The abrupt peaks on the graph correspond to the occurrence of

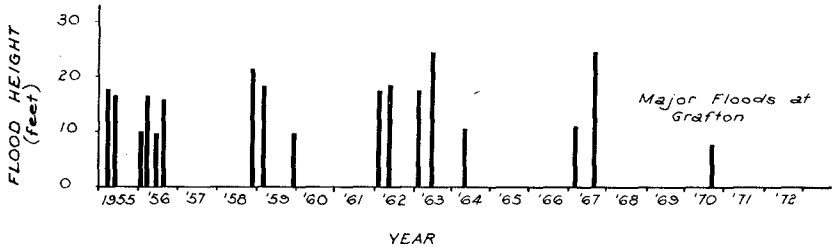
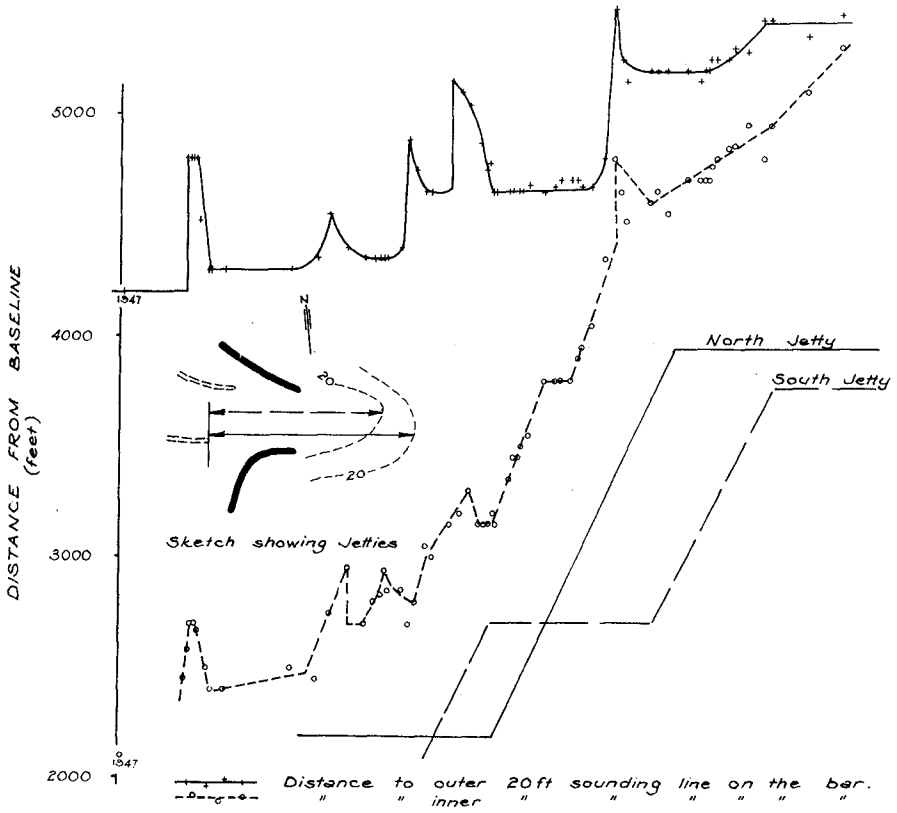


FIG 8

RECORD OF PROGRESSIVE BAR DEPTHS

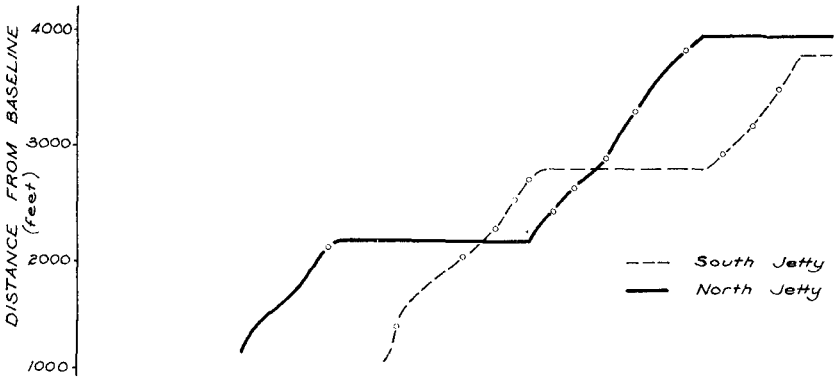
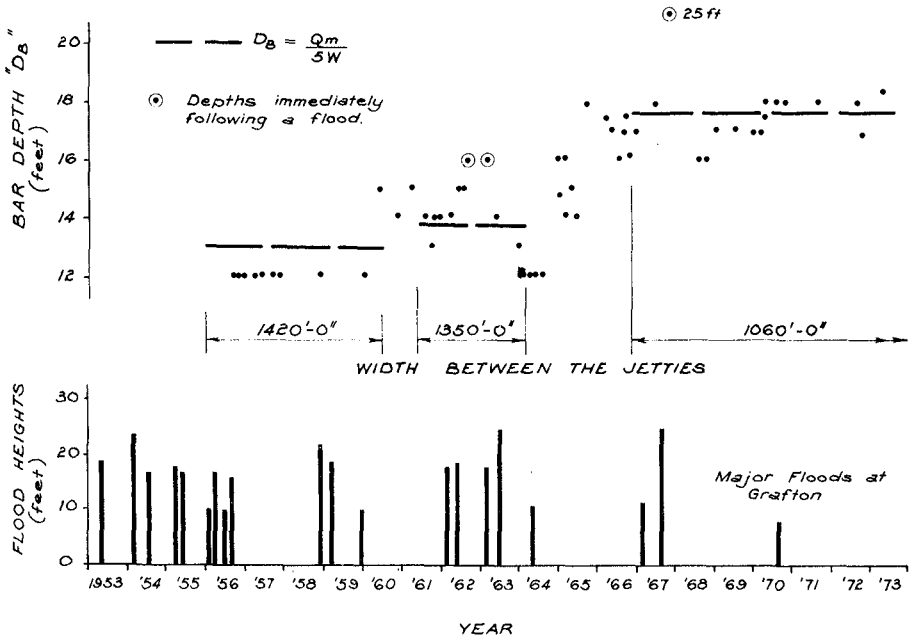


FIG 9

a major flood in the river. During each flood sand in quantities up to 0.6 million cubic yds. (N.B. volumes are discussed under (d)), were deposited on the seaward face of the bar thereby causing it to advance seawards as much as 700 ft. Scouring of the inner face of the bar occurred but the advance was seldom more than half that of the outer face.

During the 12 months immediately after each flood, the outer face of the bar retreated to a new equilibrium position compatible with the position of the advancing jetties. After this 12 month period of adjustment the outer face was very stable and showed very little tendency to move.

(c) Bar Depth

In a paper presented at the 1968 Coastal Engineering Conference (ref. 1) an empirical relationship for prediction of bar depths was derived from results of other river training works.

This was in the form :

$$D_B = \frac{Q_m}{5W}$$

where D_B = depth over bar saddle measured below the surface when maximum ebb flow occurs for a tide of mean spring range.

Q_m = Maximum ebb flow for that tide channel.

W = Surface width when Q_m occurs (all measurements in feet).

In figure 9, D_B is compared with measured bar depths (depths measured below water level for maximum flow during a tide of mean spring range, i.e. 1 foot above I.S.L.W.).

With a full semi-circular bar the depth is taken as the best depth over the bar saddle. With a "half" bar the depth is taken on the centre line of the ebb flow as indicated by bottom contours.

The correlation between bar depth and channel depth found on other entrances could not be checked here because of the turbulence resulting from the reef formation near the ends of internal walls. The bottom contours at all times were very irregular between the jetties.

During the first stage of construction whilst the northern jetty was being built to 2,150 feet the bar was consistently

at a depth of 12 feet or 1 foot less than calculated D_B . In the second stage whilst the southern jetty was being constructed to 2,750 feet bar depths fluctuated between 16 feet and 13 feet. It returned to a depth of 12 feet for a short period as further lengthening of the northern jetty was started. Calculated D_B was 13.75 feet at this time.

With further extension of the northern and southern jetties to their final length bar depths were generally between 0.6 and 1.6 feet less than the calculated value of D_B .

Since the work stopped bar depths have been consistently 0.4 feet deeper than calculated D_B .

The period when bar depths are less than predicted D_B are when the northern jetty projects beyond the southern.

Depths appreciably greater than predicted occur from the time the works first reduced the entrance width until the final width was established.

Such consistent increases in bar depths as occurred followed reductions in the effective width of the channel.

The comparatively small variation in bar depths from the predicted (- 1 3/4 ft. neglecting short term increases in depth due to local guttering by floods) is probably due to the slow rate of construction and the long pauses whilst jetties were brought up to equal lengths. Usually bar depths of as much as twice the predicted can be expected during construction.

(d) Sand Volume

Within the limitations of early surveys, it appears that the volume of sand in the bays to the south of the river mouth, the bar, and the adjacent beaches and dunes has not significantly altered between 1860 and 1960. That is to say the early training works simply re-distributed the entrance bar and shoal with very little change in overall sand volumes.

The results of detailed volume calculations for the period 1962-1972 are shown in fig. 10. The volumes were calculated within a control area bounded by a line joining the ends of the internal training walls, the 42ft. sounding line, 1600 ft. of Iluka Beach to the north and 800 ft. of Yamba Beach to the south.

It can be seen that floods have supplied sediment in quantities up to 0.6 million cubic yards during any one year of floods. The total supply of sediment during 62/72 period was 1.5 million cubic yards.

VOLUME CHANGES ON THE CLARENCE RIVER BAR

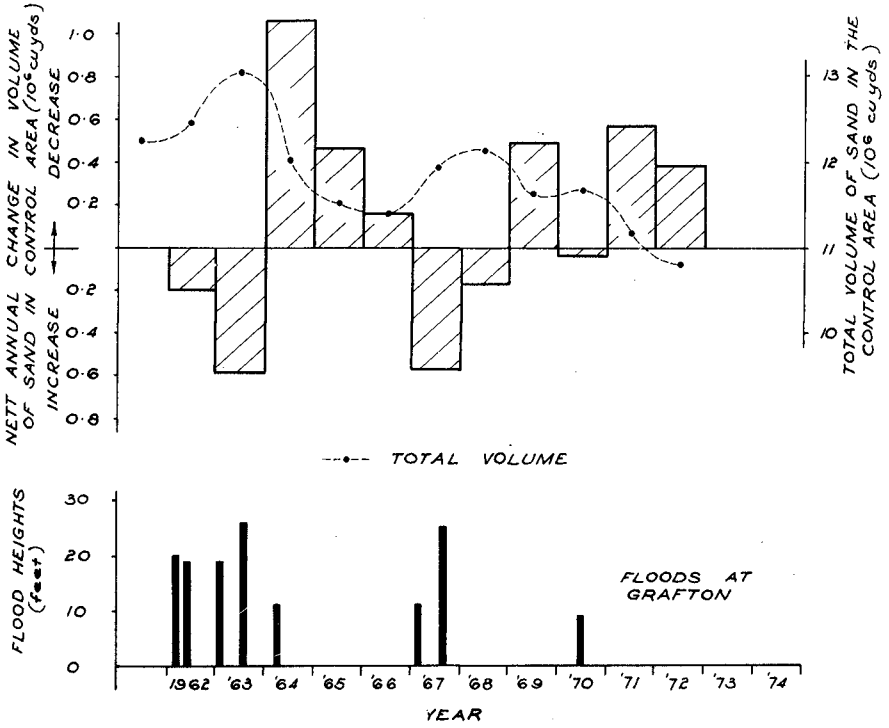


FIG 10

The rate of removal of sediment from the bar system by littoral agencies was greatest immediately following periods of deposition. The maximum loss occurred in 1964 when approx. one million cubic yards was removed from the control area. The gross removal of sediment during the 62/72 period was 3.0 million cubic yards.

There has been some accumulation of sand on Yamba Beach and on the new beach between Woolf Head and the southern jetty. This, however, has been accompanied by a compensatory deepening immediately seaward.

It appears, therefore, that the small littoral drift from the south is deflected by Yamba Head and either enters the bar exchange system to eventually pass to the north or even passes around the bar.

Volume calculations have not been sufficiently extensive to trace the path of the sediment removed from the bar. It is strongly suspected that the majority has moved northwards up the coast.

5. CONCLUSIONS

The results of entrance jetty constructions over a period of sixteen years on this river confirm that bar depth can be related to tidal flow and channel width and is independant of jetty length. It follows that entrance jetties should not be any longer than is necessary to move the bar outside the beach system so that it may be reasonably stable.

In this case jetties just long enough to transition smoothly to the required width would have produced the same bar depth. Possibly because of the sheltered position it might have been possible to obtain a satisfactory result with modification to the existing training walls.

Floods have been an important factor in the behaviour of the Clarence River bar. While the inner face of the bar responded to construction of the entrance jetties by progressively moving seawards, it was found that floods were the necessary catalyst to bring about movement of the seaward face. There is an inference here that if construction of the jetties had been carried out at a considerably greater rate, the bar would have been eliminated for a time until re-established by flood and littoral deposits.

The decrease in sand volume around the entrance would lead to the expectation that with a return of a period of more regular floods, the bar formation will cease to be that of a "half bar" and again assume a semi-circular shape.

TABLE 1

DATE	EFFECTIVE JETTY LENGTH IN FEET*		DISTANCE TO 20' CONTOUR		EFFECTIVE CHANNEL WIDTH IN FEET AT EBB FLOW MAX.	BAR DEPTH IN FEET AT MAX. EBB FLOW MEAN SPRING RANGE	
	MONTH	YEAR	SOUTH	NORTH			INNER
	1947	-	-	2100	4200	1420	12
Aug.	1956	-	-	2450	4800	-	12
Sept.	do	-	2150	2580	4800	-	12
Oct.	do	-	-	2700	4800	-	12
Nov.	do	-	-	2700	4800	-	12
Dec.	do	-	-	2670	4530	-	12
Mar.	1957	-	-	2500	4300	-	12
April	do	-	-	2400	4300	-	12
Aug.	do	-	-	2400	4300	-	12
April	1959	-	-	2500	4300	-	12
Dec.	do	-	-	2450	4350	-	12
April	1960	-	2200	2750	4550	1420	15
Oct.	do	-	2200	2950	4400	-	14
Mar.	1961	1400	2200	2700	4350	1350	15
June	do	1500	2200	2800	4350	-	14
Aug.	do	-	-	2880	4350	-	13
Sept.	do	-	-	2940	4350	-	14
Oct.	do	-	-	2850	4350	-	14
Feb.	1962	1900	2200	2850	4400	-	14
April	do	-	-	2700	4890	-	15
June	do	-	-	2800	4750	-	15
Sept.	do	-	-	3050	4650	-	15
Nov.	do	2100	2200	3000	4650	-	16
May	1963	-	-	3150	5150	-	16
Aug.	do	2250	2200	3200	5100	-	14
Dec.	do	-	-	3300	5040	-	13
Feb.	1964	2550	2200	3150	4875	1350	12
April	do	-	-	3150	4750	-	12
May	do	-	-	3150	4785	-	12
June	do	2700	2200	3200	4650	-	12
July	do	2700	2200	3150	4650	-	12
Nov.	do	-	-	3350	4650	-	16
Dec.	do	-	-	3450	4650	-	16
Feb.	1965	2750	2450	3450	4650	-	14
Mar.	do	-	-	3500	4650	-	15
May	do	-	-	3550	4680	-	14
Oct.	do	2750	2650	3800	4650	-	18
Jan.	1966	2750	2750	3800	4670	1100	17½
Mar.	do	-	-	3800	4700	-	16
June	do	-	2850	3800	4700	-	16
Aug.	do	-	-	3900	4700	-	17
Sept.	do	-	-	3950	4650	-	16
Dec.	do	-	3150	4050	4650	1060	17
April	1967	-	-	4350	4800	-	18
July	do	-	3550	4800	5480	-	25
Sept.	do	-	-	4650	5250	-	-
Nov.	do	-	-	4520	5150	-	-

TABLE 1 (cont.)

DATE	EFFECTIVE JETTY LENGTH IN FEET*		DISTANCE TO 20' CONTOUR		EFFECTIVE CHANNEL WIDTH IN FEET AT EBB FLOW MAX.	BAR DEPTH IN FEET AT MAX. EBB FLOW MEAN SPRING RANGE	
	MONTH	YEAR	SOUTH	NORTH			INNER
June	1968	-	3850	4580	5200	-	16
Aug.	do	-	-	4650	5200	-	16
Nov.	do	2800	3950	4680	5200	-	17
May	1969	2950	-	4700	5200	-	17
Sept.	do	-	-	4700	5150	-	16
Nov.	do	3150	-	4700	5200	-	17
Dec.	do	-	-	4700	5200	-	17
Jan.	1970	-	-	4770	5250	-	-
Mar.	do	-	-	4800	5250	-	18
June	do	3350	-	4850	5250	-	18
Aug.	do	-	-	4860	5300	-	18
Dec.	do	-	-	4950	5280	-	18
May	1971	-	-	4800	5430	1060	18
July	do	3800	3950	4950	5430	-	18
June	1972	-	-	5100	5350	-	18
May	1973	-	-	5200	5450	-	18½

NOTE : * from baseline through end of south training wall.

6. ACKNOWLEDGEMENTS

The permission of Mr. W.J. Hilton, Chief Engineer, Department of Public Works, N.S.W. to present this paper is acknowledged.

The junior author would like to acknowledge the contribution to and inspiration for this paper by the late C.D. Floyd.

7. REFERENCES

1. "RIVER MOUTH TRAINING IN NEW SOUTH WALES" C.D. FLOYD, 1968 CONFERENCE COASTAL ENGINEERING.

CHAPTER 102

SEDIMENTATION PROBLEMS AT OFFSHORE DREDGED CHANNELS

by

A. A. Kadib

Coastal Engineering Specialist, Bechtel Inc.,
San Francisco, California U.S.A.

ABSTRACT

Estimating the rate of sediment deposition and annual maintenance dredging at offshore dredged channels have been two of the most challenging tasks confronting coastal engineers in the past 10 to 15 years. Because of the complexity of the mechanism of sediment-flow interaction and the lack of available practical methods for estimating the sediment transport rate under waves and current action, it is felt that a simple and rational method is needed for describing sediment behavior at offshore dredged channels and estimating accretion rates. It is hoped that this paper contributes to the answer of this problem.

The paper describes the mechanism of sediment deposition and presents a simple method for estimating the rate of annual maintenance dredging. The effect of using a submerged breakwater for relieving the sedimentation problem within the dredged channel is also presented.

INTRODUCTION

Along any reach of coastline where navigation works and other coastal structures exists or are contemplated, patterns and rates of long-term littoral and offshore sand movement and expected accretion are vital information for proper engineering, design and maintenance. Sediment movement along the breaker zone and at the offshore area is controlled mainly by the action of the prevailing waves and currents of these locations. When moving sediment loads encounter a partial obstruction such as a dredged channel, a condition is realized that is conducive to sediment deposition. There are at least three basic types of man-made works at the offshore area which function as sediment barriers (Figure 1). These consist of: (a) dredged navigation channels connecting super-tanker harbors with deep water offshore and up to 25 meter water depth; (b) dredged offshore channels for cooling water intakes for nuclear and liquefied natural gas plants; and (c) dredged offshore areas for open-sea loading and berthing terminals. In a recent study, the question

came up concerning the economical feasibility of such offshore dredging activities and their impact on the overall shoreline processes operative in the project area. In order to answer this question, estimates of the rate of sediment movement and the expected annual maintenance dredging are necessary preliminaries. Unfortunately, there is no proven prediction method of general validity for quantitative estimates of onshore-offshore and longshore sediment transport rates, and designers usually rely on limited field data of questionable accuracy to formulate some feeling for the problem under consideration. Because of the above difficulties and the fact that more accurate field data are usually expensive and difficult to get, it is felt that a simplified method is needed to estimate the rate of sediment movement for water depths of up to at least 20 meters.

The approach described here is based on available theoretical studies(2, 3, 4, 5, 6) and experiences gained with maintenance dredging at the Suez Canal offshore dredged channel, located at Port Said Harbor, Egypt(7, 8, 9). Items considered are: (a) factors contributing to sedimentation; (b) method of estimating deposition rate; (c) effect of using a submerged breakwater for relieving the sedimentation problem, and (d) optimum design for protection against accretion.

FACTORS CONTRIBUTING TO SEDIMENTATION

Consider any section along the offshore part of a dredged channel shown in Figure 2. Assume that both the current and wave climatology in the vicinity of the dredged channel are known. This could be considered either as (1) an average steady current characterized by a velocity U , a wave height H , and a wave period T , or (2) as a known number of storms with a given duration and direction. For the first case, the average currents and wave condition can be used to estimate the annual sediment effect, whereas for the second case, the effect of each storm can be evaluated separately and the annual effect can be obtained by integrating the effects of all expected storms within a given year. In either case the basic flow field is the same. This flow field (Figure 2-a) may be simplified as:

- Steady current with an average velocity U_1 at water depth d_1 . By continuity, this current will have velocity U_2 at depth d_2 .
- Maximum oscillatory current $U_{bed\ max}$ at the bed, due to wave action. This current may be expressed by the equation

$$U_{bed\ max} = \frac{\pi H}{T} \frac{1}{\sinh 2 \pi d/L} \quad (1)$$

where

H = wave height,
 T = wave period,
 L = wave length at water depth d.

It is believed that the above flow velocities are the most important factors contributing to sediment movement in the vicinity of the dredged channel and their contribution may be summarized as follows:

1. Bed Load (Q_b).

Einstein(5), Kalkanis(3) and Abou-Seida(2), proposed the use of a modified unidirectional bed load function, shown in Figure 3, for estimating the rate of bed load movement under wave action. In order to use Figure 3, one has to calculate flow intensity Ψ_* defined as

$$\Psi_* = \xi \frac{\gamma_s - \gamma_f}{\gamma_f} \frac{g D}{U_a^2} \quad (2)$$

where

ξ = "hiding factor" for small particles in a sediment mixture and may be assumed unity for uniform grains,
 γ_s = specific weight of sediment,
 γ_f = specific weight of water,
 g = acceleration of gravity,
 D = sediment size,
 U_a = wave particle velocity at 0.35 D from the boundary.

References (2), (3) and (5) show U_a is the most difficult factor to calculate in equation (2). Analysis of the data reported by Abou-Seida(2) show that U_a can be approximated by

$$U_a = 0.5 U_{bed \max} \quad (3)$$

Now with a known value of flow intensity Ψ_* , the oscillatory bed load intensity ϕ_* can be obtained from Figure 3. The oscillatory bed load rate q_b is given by the equation

$$q_b = \phi_* \gamma_s \left(\frac{\gamma_s - \gamma_f}{\gamma_f} \right)^{1/2} g^{1/2} D^{3/2} \quad (4)$$

The sediment concentration in the bed layer, C_a , is given by Abou-Seida(2) as

$$C_a = \frac{q_b}{2DU_a} \quad (5)$$

and the bed load rate Q_b is given by

$$Q_b = C_a a U_c \quad (6)$$

where

a = thickness of the bed layer, assumed in this study as equal to 2 cm,
 U_c = local current velocity near the bed and including mass transport velocity due to wave action.

2. Suspended Load Q_s

Theoretically speaking, wave motion, other than the breaking wave effect, lacks the existence of turbulence which is responsible for suspended sediment. On the other hand, it has been observed that considerable amounts of sediment move in suspension under the combined action of waves and currents^(4, 7, 11). Therefore, it was decided to attack the suspension problem by assuming that the steady current effect, only, is responsible for suspended sediment distribution within any cross section along the dredged channel.

If it is assumed that bed load takes place within a certain layer, the average concentration within this layer can be computed from equation (5). From this concentration, C_a , at height, a , above the bed, the concentration C_h at a height, h , above the bed can be expressed by the well known relationship (1)

$$\frac{C_h}{C_a} = \left[\frac{(d-h)a}{(d-a)h} \right]^Z \quad (7)$$

in which $Z = \frac{V_s}{0.4U_*}$ with V_s = fall velocity of the sediment grain, U_* = bed shear velocity; and d = the total water depth.

According to Einstein⁽¹⁾, the suspended load Q_s can be written as

$$Q_s = 11.6 U_* C_a a [P I_1 + I_2] \quad (8)$$

where

I_1 and I_2 can be obtained from reference 1.

P is determined from $P = 2.3 \frac{h}{h_o}$ in which

h_o = bed roughness.

From equation (8), the suspended sediment load to the updrift side of the dredged channel and inside the channel can be estimated.

METHOD OF ESTIMATING DEPOSITION RATE

When an offshore channel is dredged, both the flow and sediment patterns, approaching from the updrift side of the channel experience some changes as the flow crosses the dredged channel. This is shown in Figure 2. Consider Figure 2-a where the channel is dredged to depth d_2 below mean sea level, and the natural water depth to the updrift side of the channel is d_1 . Flow approaching the channel has a certain sediment load capacity which could be estimated using equations (6) and (8). As the flow approaches the dredged channel, two main mechanisms will take place:

- The dredged channel will act as a sand trap along most of its length and consequently most of the bed load Q_b approaching the channel will deposit within the channel.
- The suspended load, Q_s , on the updrift side of the channel will reduce to Q_{s2} across the channel. This reduction is caused by a decrease in the steady flow velocity within the dredged channel.

These considerations permit calculation of the rate of sediment deposition per channel unit width, Q_d , according to the following equation

$$Q_d = Q_{s1} - Q_{s2} + Q_b \quad (9)$$

where

Q_{s1} = rate of suspended load reaching the channel/
unit width,

Q_{s2} = rate of suspended load across the channel/
unit width,

Q_b = rate of bed load reaching the channel/unit
width.

Equation (9) can be used for various natural water depths, d_1 , along the channel thus permitting calculation of the total deposition rate along the channel.

As an example consider a dredged channel depth of 20 meters with a natural water depth of 10 meters. The annual rate of sediment deposition, Q_d , is estimated under the following assumed conditions:

average wave height (H) = 2.00 meters;
 average wave period T = 8 seconds;
 average bed material grain size D = 0.10 mm.

Results of the computations are summarized in Table 1.

TABLE 1

Example of Estimating Sediment
 Deposition Along a Dredged Channel Section

<u>Item</u>	<u>Sediment Rate m³/m/Year</u>
Q_b	340
Q_{s_1}	1700
$Q_{total} = Q_b + Q_{s_1}$	2040
Q_{s_2}	940
$Q_{deposition}$	1100

SUBMERGED BREAKWATER EFFECT

Submerged breakwaters have been used successfully for relieving and reducing the sediment deposition along offshore dredged channels. An example is the Suez Canal navigation channel which extends from the Port Said Harbor to natural water depth of about 15 meters. (The Suez Canal Authority is presently deepening the navigation channel to accommodate ships with drafts up to 22 m). Table 2 summarizes the annual maintenance dredging conditions along the offshore navigation channel during the period 1901 to 1966(7, 8).

TABLE 2

Variation of Annual Maintenance Dredging
Along the Suez Canal Navigation Channel
(Port-Said Harbor) During the Period 1901-1966

<u>Period (Years)</u>	<u>Average Depth of Navigation Channel (m)</u>	<u>Mean Annual Dredging (million m³)</u>	<u>Type of Protection Against Accretion (Updrift Side)</u>
1901-1906	9.5	0.65	Full breakwater to water depth of 7.00 meters
1911-1916	11.50	2.25	Full breakwater to water depth of 9.00 meters
1917-1920	12.00	0.35	Partial construction of a submerged breakwater about 4 meters high
1921-1923	12.00	1.25	
1939-1945	12.00	0.600	Submerged breakwater to water depth of 11.5 meters and about 4 meters high above bottom
1951-1955	13.00	1.4	Submerged breakwater to water depth of 11.5 meters
1961-1966	14.00	2.4	

Table 2 shows that: (1) increasing the depth of the navigation channel causes an increase in the annual maintenance dredging; and (2) construction of the submerged breakwater has considerable effect on reducing the annual maintenance dredging.

EFFECT OF SUBMERGED BREAKWATERS ON SEDIMENT AND FLOW PATTERN

Consider a submerged breakwater with average height h above the bed and located to the updrift side of the dredged channel (Figure 5). The use of such a breakwater would have the following principal effects on the sediment and flow conditions in the vicinity of the dredged channel:

- The submerged breakwater could cause the bed load to either go around it or settle to the updrift side of the breakwater.
- Portion of the suspended sediment load of relatively high concentration near the bed would also be partially prevented from reaching the dredged channel.
- The submerged breakwater will generate a longitudinal current along its entire length which will transport sediment in the offshore direction away from the dredged channel.

Quantitative analysis of the effect of submerged breakwaters in relieving the sedimentation problem along the dredged channel is rather difficult. It is believed that a reasonable answer to this problem is given by the rational method developed below.

1. Submerged Breakwater Efficiency η .

Consider a submerged breakwater with variable relative heights $\frac{h}{d}$, where h is the breakwater height above the natural bed and d is the water depth as shown in Figure 5. For any breakwater relative height $\frac{h}{d}$ the breakwater's sediment trapping efficiency, η , may be defined by the equation

$$\eta = \frac{Q_t(h/d)}{Q_d(h/d=0)} \quad (10)$$

where

$$\begin{aligned} Q_t(h/d) &= \text{rate of sediment trapped by the} \\ &\quad \text{breakwater for any relative height} \\ &\quad h/d, \\ Q_d(h/d=0) &= \text{rate of channel deposition without} \\ &\quad \text{the breakwater.} \end{aligned}$$

2. Sediment Risk Factor "R"

Figure 4 shows the definition of the sediment risk factor R . The physical meaning of R may be explained as follows:

- (a) For $h/d = 0$; $R = 1$ and the expected annual dredging to maintain the dredged channel is equal to the annual rate of sediment deposition Q_d .

- (b) For $h/d = 1$; $R = 0$ and expected annual dredging = 0.
- (c) For $h/d = \text{any ratio}$, the expected annual dredging can be approximated by the equation

$$Q_{\text{dredging}} = Q_d \times R \quad (11)$$

where

Q_{dredging} = annual maintenance dredging; and

Q_d = annual rate of channel deposition for $h/d = 0$.

Using the definition of R as shown in Figure 5,

i.e.,

$$R = \frac{\int_a^h \left[\frac{(d-h)a}{(d-a)h} \right] dh \frac{v_s}{0.4} U_*}{\int_a^d \left[\frac{(d-h)a}{(d-a)h} \right] dh \frac{v_s}{0.4} U_*} \quad (12)$$

and considering sediment particle grain size range from 0.075 mm to 0.2 mm and average steady flow velocities between 0.2 m/sec and 1.00 m/sec, the average values of the risk factor R for various h/d ratios are shown in Table 3.

TABLE 3

Average Values by Risk Factor R	
Breakwater Relative Height h/d	Average Value of R
0	1
0.2	0.36
0.3	0.25
0.5	0.125
1.00	0

Using the sediment risk factors obtained in Table 3 as a reduction in the deposition rate for $h/d = 0$ case, and equation (11), the annual rate of deposition for various breakwater relative height can be estimated. The breakwater sediment trapping efficiency, n , can be computed from equation (10).

Using the results of the example given in Table 1, the submerged breakwater efficiency and the estimated annual maintenance dredging is given in Table 4.

TABLE 4

Effect of h/d on % Annual Dredging and Breakwater Efficiency n

h/d	R	Q_d $m^3/year$	Q_t $m^3/year$	n %	% Annual Dredging w.r.t. $h/d = 0$
0	1	1100	0	0	100
0.2	0.36	400	700	64	36
0.3	0.25	275	825	75	25
0.5	0.125	140	960	87	13
1.00	0	0	1100	100	0

It can be observed from Table 4, that submerged breakwaters with relative heights, h/d , between 0.3 and 0.5 would have greater effect in reducing sedimentation problems inside the dredged channel. Figure 5 shows the relationship between h/d and percent annual dredging needed to maintain the dredged channel. The annual dredging is plotted as:

(a) percentage of the total sediment load ($Q = Q_s + Q_b$)

estimated to the updrift side of the breakwater, and (b) percentage of the expected channel deposition rate without the use

of a submerged breakwater ($\frac{h}{d} = 0$).

Examination of the data reported in Table 2 shows that the annual maintenance dredging for the Suez Canal navigation channel (Port Said Harbor) reached 2.25 million m^3 /year during the period 1911-1916. A submerged breakwater ($\frac{h}{d} = 0.4$) was constructed and completed during the period 1939-1945. After the submerged breakwater was completed, annual maintenance dredging reduced to 0.6 million m^3 /year which is

about 25% of the annual dredging without the submerged breakwater. To the writer's knowledge, this is the only field data available on the submerged breakwater effect which could be used to check the theoretical curve shown in Figure 5.

OPTIMUM DESIGN FOR OFFSHORE DREDGED
CHANNEL AND PRACTICAL APPLICATION

The results of studies reported in this paper are useful for feasibility and economical evaluation of offshore dredging projects. In practice the following steps are suggested:

- Step 1. Collect field data on waves and current climatology, and bed material characteristics.
- Step 2. For the proposed dredged channel geometry, estimate annual rate of deposition (which is equivalent to the expected rate of annual maintenance dredging). This can be obtained from equation (9).
- Step 3. Estimate the average annual cost of dredging the dredged channel without the use of any breakwater protection.
- Step 4. Consider submerged breakwater protection schemes with various $\frac{h}{d}$ ratios. For each $\frac{h}{d}$, estimate average annual cost for:
- Breakwater construction.
 - Expected annual maintenance dredging. The rate of maintenance dredging can be obtained from Figure 5.
 - Estimate average maintenance cost for the breakwater. It should be noted that submerged breakwater does not need frequent maintenance as compared with full breakwater.
- Step 5. From step 4, get the average annual cost for various submerged breakwater schemes and plot the data as shown in Figure 6.
- Step 6: From a plotting similar to that shown in Figure 6, one can usually find a design scheme which will minimize the average annual cost. This scheme will give the most economical design.

SUMMARY AND CONCLUSIONS

A rational method is presented to estimate annual maintenance dredging along offshore dredged channels. The method is based on available theoretical studies on the subject of mechanism of sediment transport under wave and current action.

The effect of protecting the dredged channel against accretion is discussed. Efficiency of using submerged breakwaters with various relative height for relieving the sediment deposition rate are analyzed; breakwaters with relative height 0.3 to 0.5 were found to have high efficiency in reducing sediment deposition within the dredged channel.

REFERENCES

- (1) Einstein, H. A., "Bed Load Function for Sediment Transportation in Open Channel Flows," U.S. Department of Agriculture, Tech. Bulletin No. 1026, 1950.
- (2) Abou-Seida, M. M., "Bed Load Function Due to Wave Action," University of California Wave Research Laboratory - H.E.L 2-11, January, 1965.
- (3) Kalkanis, G., "Transportation of Bed Material Due to Wave Action," Technical Memo 2, U.S. Army Coastal Engineering Research Center, February, 1964.
- (4) Horikawa and others, "Suspended Sediment Due to Wave Action," Coastal Engineering Conference, 1963, page 168.
- (5) Einstein, H. A., "Sediment Transport by Wave Action," 13th Coastal Engineering Conference, July, 1972, Vancouver, B.C., Canada.
- (6) Beach Erosion Board, "Turbulent Flow Near an Oscillatory Wall," Technical Memo No. 97, July, 1957.
- (7) Kadib, A. A. "Sediment Motion at Port Said Harbor and Shoaling Problems at the Offshore Navigation Channel," Suez Canal Authority Research Center, Technical Report No. 48, October, 1970.
- (8) Hilaly Nabil, A., "Port Said Harbour and the New Project for the Suez Canal," Suez Canal Authority Research Center, Technical Report No. 41, January, 1969.
- (9) Commission Consultative Internationale for Suez Canal, 1946 Metting Report, Suez Canal Authirty, Egypt.
- (10) Kadib, A. A., "Rate of Littoral Drift Using Fluorescent Tracer," 13th Conference on Coastal Engineering, Canada, July, 1972.
- (11) Cole, C. V. and Vaidyaraman, P. P., "Deepening the Approach Channel to the Port of Cochin," 13 Congress of the I.A.H.R., Proc. Vol. 3, 1969, page 233.
- (12) King, C. A. M., "Depth of Disturbance of Sand on Sea Beaches by Waves," Jour Sed. Pet., Vol. 21, 1951.

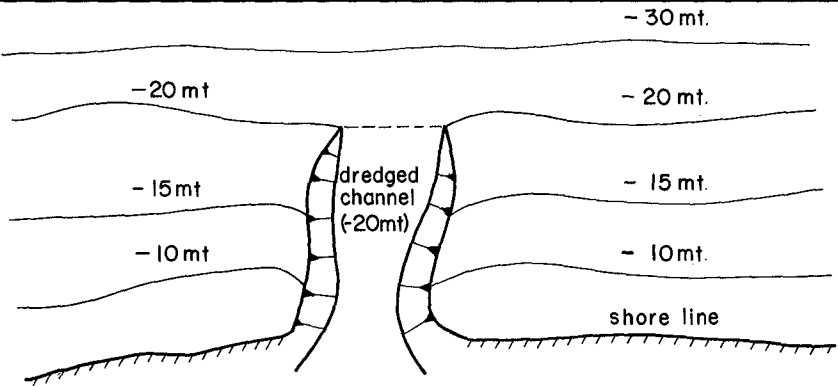


Fig. 1-a DREDGED NAVIGATION CHANNEL

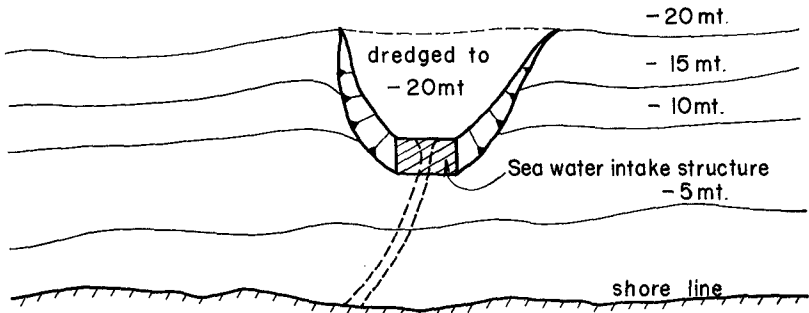


Fig. 1-b OFFSHORE DREDGING FOR COOLING WATER INTAKES

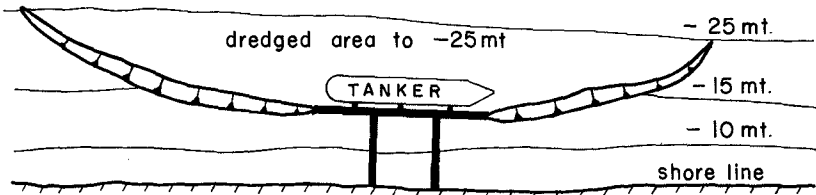
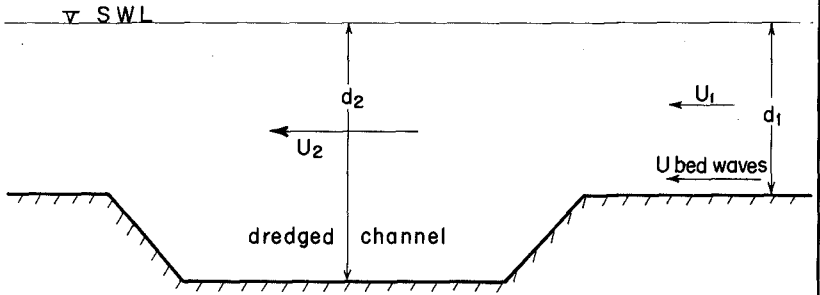
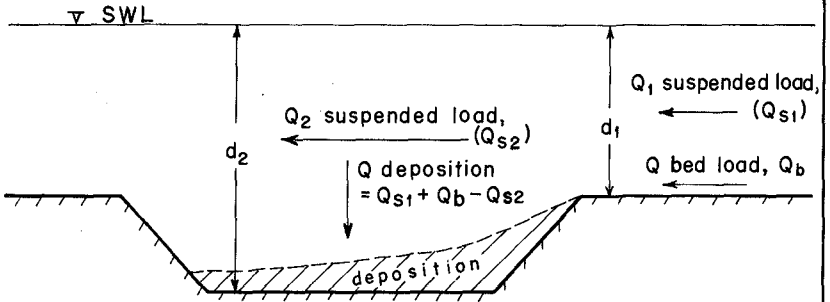


Fig. 1-c DREDGING FOR OFFSHORE LOADING OF SUPER TANKERS

Fig. 1 EXAMPLES OF OFFSHORE DREDGING



a. FLOW VELOCITIES CONTRIBUTING TO SEDIMENT MOVEMENT



b. SEDIMENT PATTERN ACROSS THE DREDGED CHANNEL

Fig. 2 MAIN FACTORS CONTRIBUTING TO SEDIMENT DEPOSITION

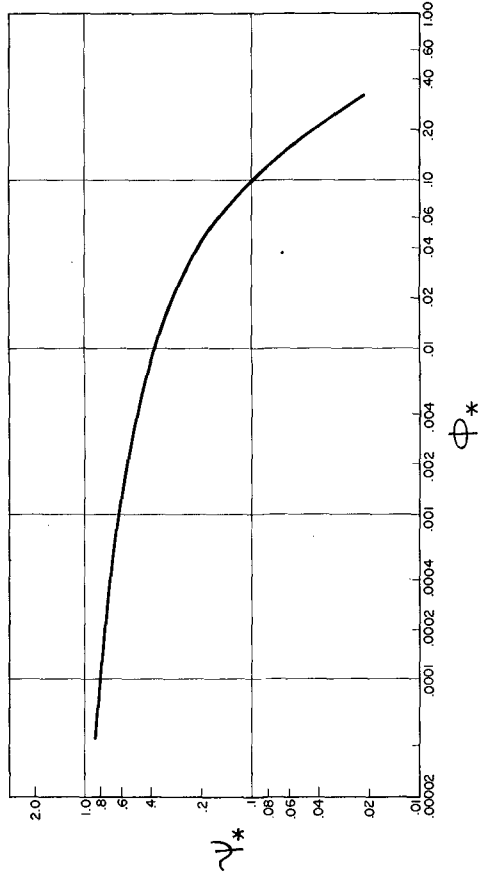
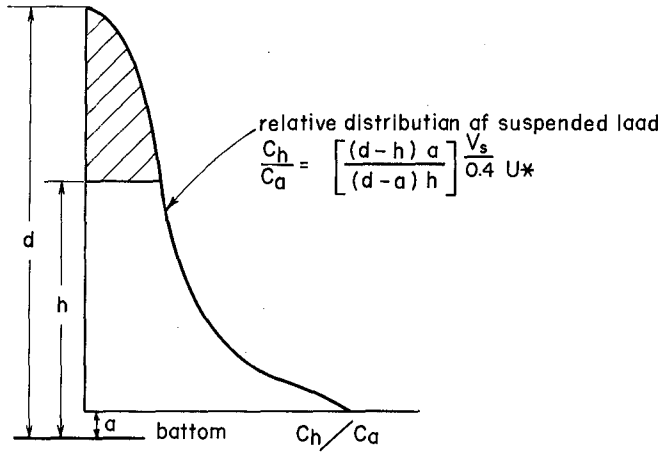


Fig. 3 GRAPHICAL REPRESENTATION OF THE BED LOAD EQUATION, CURVE
(after Kalkanis and Abo Saida)



$$\text{Risk factor } R = \frac{\text{Suspended sediment above height } h}{\text{Total suspended sediment available}}$$

Fig. 4 DEFINITION OF THE RISK FACTOR R

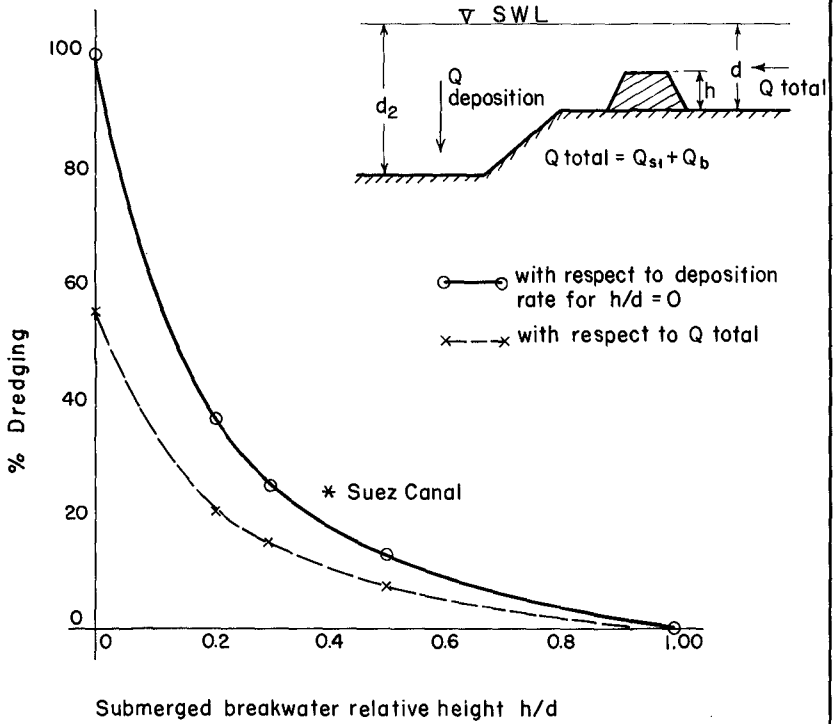


Fig.5 EFFECT OF SUBMERGED BREAKWATER RELATIVE HEIGHT ON MAINTENANCE DREDGING

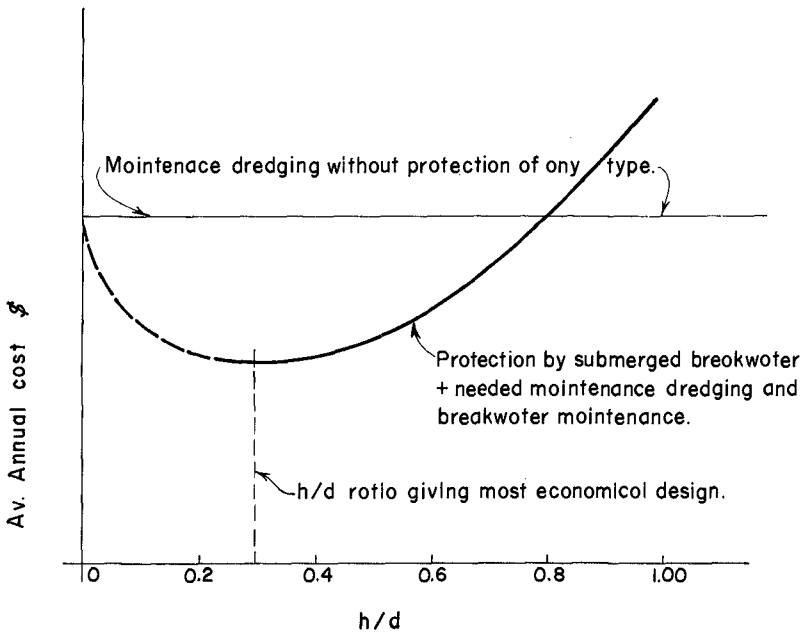


Fig. 6 OPTIMUM ANALYSIS FOR THE MOST ECONOMICAL DESIGN

CHAPTER 103

STABILITY OF TIDAL CHANNELS DEPENDENT ON RIVER IMPROVEMENT

by

Volker Barthel *)

1. Abstract

Many authors have dealt with the migration of sand in front of the German coast of the North Sea. Especially the movement of sand-banks and deep channels in the Weser-estuary was subject-matter of several investigations with different results.

Thorough investigations of selected cross-sections point out, that the movement goes on in some regions. The important shipping channel however has obtained a certain stability during the last 30 - 40 years, because the migration of sand occurs otherwise than in former days.

This phenomenon coincides with the extensive and decisive river improvement measures in the inner part of the Weser-estuary.

Current measurements in the investigation area demonstrate, that concentrated tidal currents in the deep channels guarantee a sufficient clearance for shipping purpose.

It seems to be sure, that for the present no essential shifting of the main channel calls for important measures in the field of shipping, dredging and building of sea-marks.

2. Introduction

The estuaries of the navigable rivers in the Federal Republic of Germany flowing to the North Sea are deep cutting bights with fine sand bottoms.

*) Dipl.-Ing.

Wasser- und Schifffahrtsamt Bremerhaven
Am Radarturm 1, 2850 Bremerhaven, W.-Germany

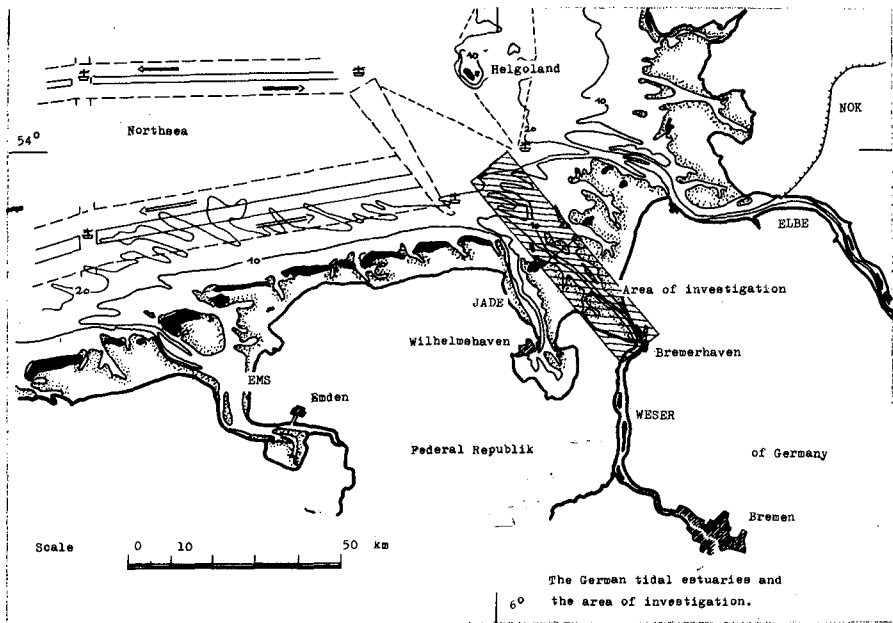


Fig. 1

On Fig. 1 one can see a part of the German bight with the large tidal rivers Ems, Jade, Weser and Elbe. The investigation area, which is to be spoken about, lies inside of the Weser-estuary. A few words of explanation to the situation:

The Outer Weser has a length of about 60 km, extending from the open sea til Bremerhaven, and important port of transshipment of ore, cars, fruit, mixed cargo an with a most important container terminal. About 65 km upstreams lies the city of Bremen with its also important harbour at the lower Weser.

Between Bremerhaven and Bremen the harbours of Nordenham and Brake are situated. Ships with a draught up to 45 feet can go to Bremerhaven, those with a draught up to 35 feet can go til Bremen.

The atlantic tidal wave penetrates in a wide-spread front into the North Sea and it has its largest tidal range on the right side, i.e. at the Scottish coast. The right branch proceeds very fast into southern direction whereas the left branch remains behind. Arriving at the German coast the tidal wave turns aside to the east and now follows the coast-line counter clockwise. The predominant tidal currents go in the same direction in the flood tide, the currents in the ebb-tide have a predominant direction from east to west. Caused by reflection and the deflecting power of the rotation of the earth there are some rotational tides in the North Sea which influence the directions of the tidal currents too. The tidal waves penetrate into the estuaries and are reflected, absorbed and deformed dependent on the morphology of the estuary. But those phenomenons are well known.

3. Morphological changes

The evident north-east directing migration of sand in front of the German coast effected by dominant waves and currents carries material from the North Sea Reservoir and eroded sand from the East Friesian Islands. This material crosses the estuaries and causes permanent shift of the channels and sand banks in the reef region.

On Fig. 2 one can see the migration of channels and sandbanks in two cross-sections in the Outer Weser from 1910 til 1975. The two important tidal and navigable channels with depths down to 20 sometimes 25 m are the "Neue Weser" and the "Alte Weser". The surrounding sand-banks come up to a height of 2.5 m beneath the water surface and the other less important channels are not directly connected with the river - bed of the Weser. The drawing shows the movement of the center or the axis of gravity of the most important banks and channels referring to a fixed line.

MIGRATION OF THE CHANNELS AND SAND-BANKS IN THE OUTER WESER 1910 - 1973

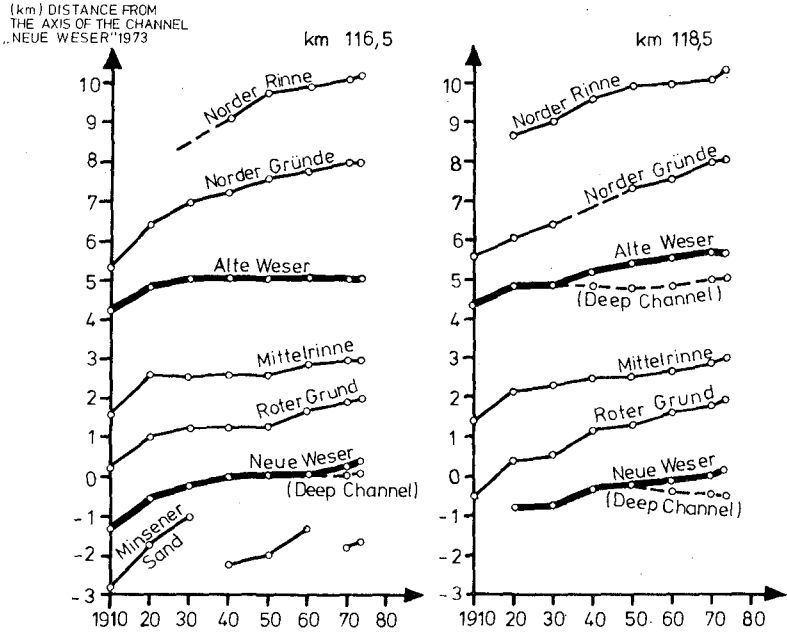
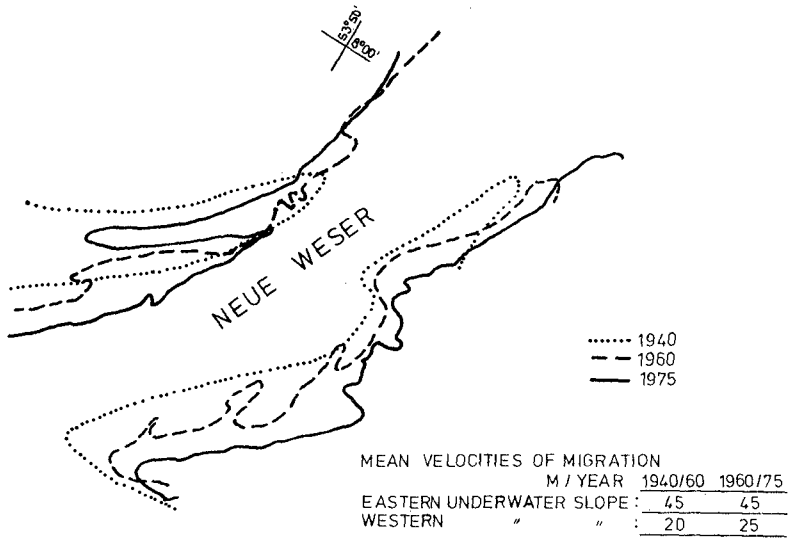


Fig. 2

The movement is also to be seen on a simplified graph in Fig. 3



MIGRATION OF THE 10m-CONTOUR
 IN THE "NEUE WESER" 1940-1975

Fig. 3

You see the contours of the 10 - m - line in the "Neue Weser" in the states of 1940, 1960 and 1975. The mean velocity of migration is

- on the west side: 20 m / year
- on the east side: ~ 60 m / year on an average.

Because of this provable migration the navigable channels, the buoys and the pertinent sea-marks (i.e. light houses, directional beacons etc.) had to be transferred or given up several times in the past.

The laws and regularities of this migration in the reef region have been discussed by several authors until now (Ref. 2,6,7). And there were different results of investigations:

Some of them discovered, that it takes a sand-bank 60 - 70 years to cover the distance to the next sand-bank. Plate (Ref. 6) writes about the "return of similar forms" in the reef region. Göhren (Ref. 2) presents an extensive classification of all these statements and points out a "return of similar states" every 110 - 120 years.

There are maps of the Outer Weser since 1859, which are sufficiently exact for an investigation of the migration in the reef region. Since 1910 the maps are so exact that you can follow the motion of single cross-sections. In an extensive research of the morphological changes from that time until now it was found out, that the migration of sand in the decisive regions happens otherwise today than in former days. This finding seems to be of an eminent importance for navigation, building of sea-marks and dredging.

In former days the penetration of flood in the reef region was delayed by a labyrinth of shallow channels and sandbanks, spread over the whole estuary. The sand migrating from west to east crossed the estuary in large sandbanks and underwater-dunes, the height of which was often only 2 - 3 m beneath the water surface. This undulatory motion seemed to lead to a recurrence of similar states in morphology in a period of 110 - 120 years. This regularity still required a development, which was undisturbed by all artificial influences.

After a thorough investigation of up to 8 cross-sections in the reef-region one can see, that the migration of large sand-banks nearly stops in parts of the cross-sections between 1920 and 1930. In Fig. 2 it is shown, that especially in the "Neue Weser" and in the "Alte Weser" this effect is evident. The increase of the graph of "Neue Weser" and "Alte Weser" comes to zero, while in the time between 1859 and 1920 it was nearly steady. The results of the other cross-sections, show the same trend.

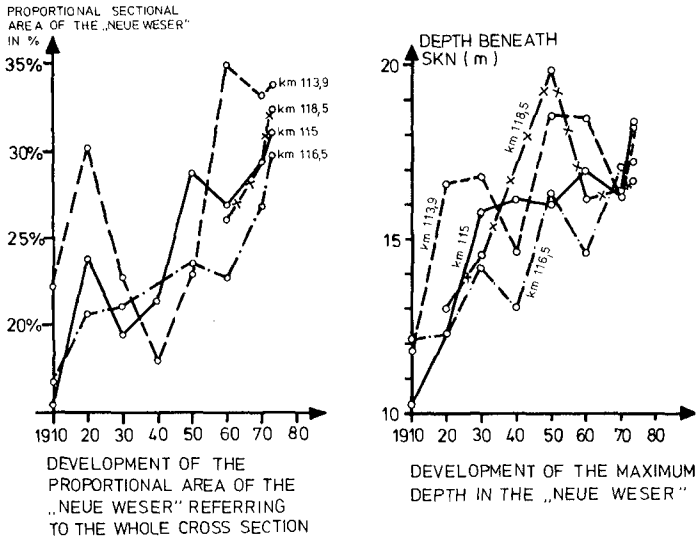
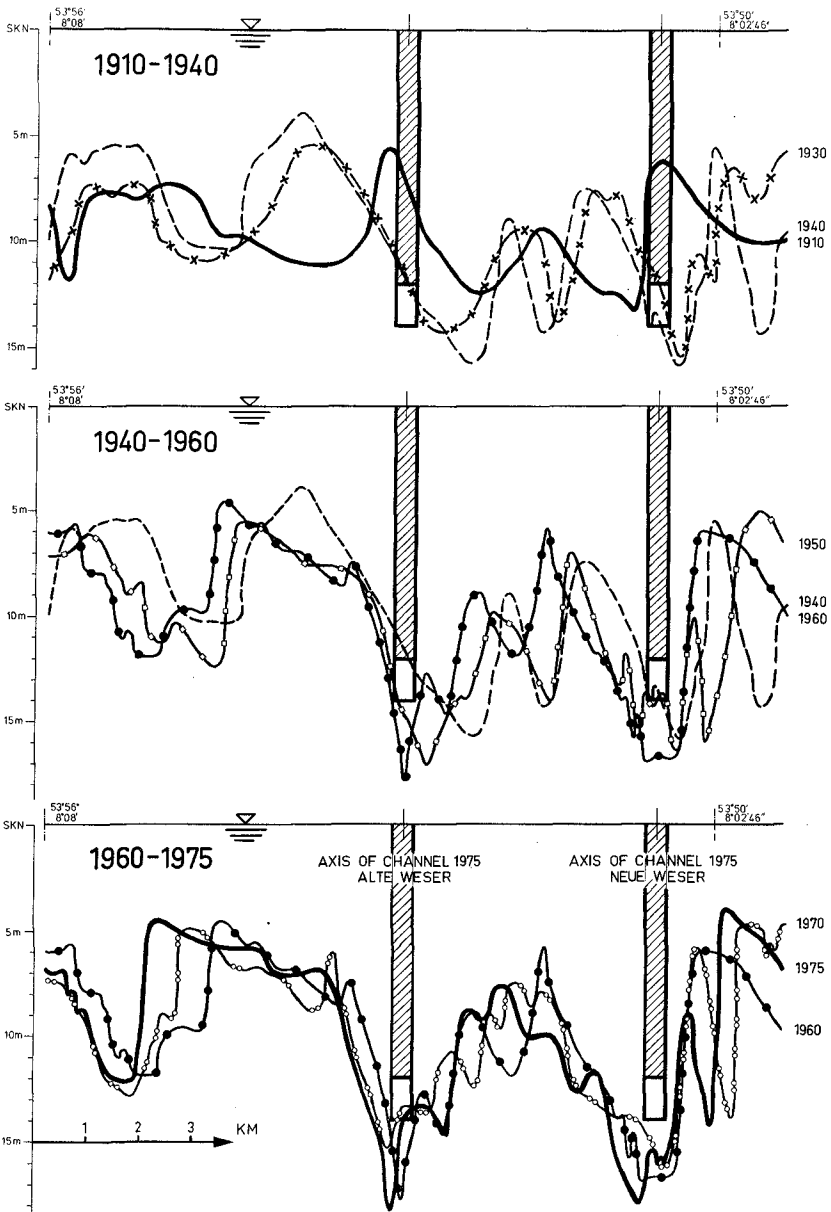


Fig. 4

Fig. 4 presents the development of the channel "Neue Weser" (NW). The left part indicates, that the proportional sectional area of the NW has been growing since 1930 from 21 % to 33 % on an average. The development of the maximum depth in the NW shows an increasing tendency with deviations. That ist not so obvious in the AW.

A careful study of the development of the cross sections in their chronological sequence gave the picture, which is to be explained in Fig. 5 in one cross-section, though it is to be found in nearly all of the analysed ones: Before 1920/30 the large sand-banks cross the estuary as a whole, leading to a permanent alteration of the navigable channels and the banks between them. But then there is a change in behaviour. The underwater - slopes moving from the west become steeper, a small underwater dune is



ALTERATION OF THE CROSS-SECTION KM 115 FROM 1910 - 1975

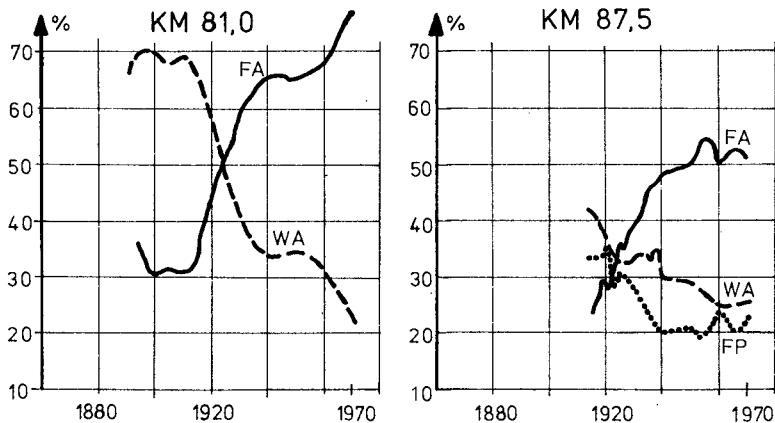
Fig. 5

separated from its origion bank and moves with increasing loss of size down to the bottom of the channel NW where it isn't to be found again.

Where does this behaviour come from?

Already in 1935 it could be proved, that the shift in the reef region had affected the conditions of the shipping channel of the inner part of the Outer Weser. Yet a mutual influence between inner and outer region could not be detected at that time.

Within the period of 1920 - 1930 the large and important improvement measures and dredgings in the middle section of the Outer Weser were carried out and influenced the hydraulic conditions in a good manner. Misplacing of the unfortunate shipping channel into a better position, building of a lot of groynes and training walls and dredging led to a more undelayed penetration of the tidal wave and affected the concentration of tidal currents in a positive way. The further morphological development in the Outer Weser showed, that the river structures in connexion with dredging operations had fully achieved their effect. An extensive study of these facts was carried out in 1970/1972 and was lectured on the 14th CEC in Kopenhagen 1974. It showed that most of these hydraulic and morphological developments began soon after those important improvement measures. (Ref. 5)



DEVELOPMENT OF THE PROPORTIONAL SECTIONAL AREAS F_0 OF THE CHANNELS "FEDDERWARDER ARM" (FA) "WURSTER ARM" (WA) AND "FEDDERWARDER PRIEL" (FP)

Fig. 6

The maximum current velocities grew in parts of the river with 30 %. The distribution of the quantity of flow in those parts of the river, which are divided into two branches, is of a great importance for the hydraulic behaviour. The development of this distribution was also satisfactory, as Fig. 6 shows in one example. Besides the whole river up to Bremen was deepened from 1890 til now (12 m beneath SKN* in the Outer Weser). The mean tidal range in the Lower Weser grew from 0.25 m to 3.5 m.

4. Current measurements

Though there was no opportunity to compare nowadays measurements with elder ones there were carried out a lot of measurements of current velocity and direction in the whole area to support the theory of nowadays behaviour of the reef region. The therefore required instruments are developed especially for an application in shallow water in Western Germany. All current meters were installed about 1,5 m over the bottom to record the currents near the bottom. The evaluation method for the measured values which are photographed by a camera is well - known (Ref. 3). During the interpretation great importance was attached to the ratio

$$\frac{V_e \max}{V_f \max} \quad \text{and} \quad \frac{SV_e}{SV_f}$$

and the maximum and resulting currents (Fig. 7,8)

$$SV_{e,f} = \text{amount of the vector } Fe_{,f}$$

$$V_{e,f} = \int_{K_e}^{K_f} v_i dt$$

The interpretation of all measured values gives the following characteristics of currents in the investigation area:

The maximum currents are situated in the deep channels, especially at the west side of the "Neue Weser". The intensity of the currents, i. e. the amount of velocity with regard to it's time of influence, has it's maximum values in the same region. The time of less transportation of sand ($v \leq 25 - 30$ cm/s) is very short here (1 hour) and is growing with decreasing distance to the east side of the investigation area. (3.5 hours)

* SKN = the German word "Seekartennull" = mean low water of a spring tide

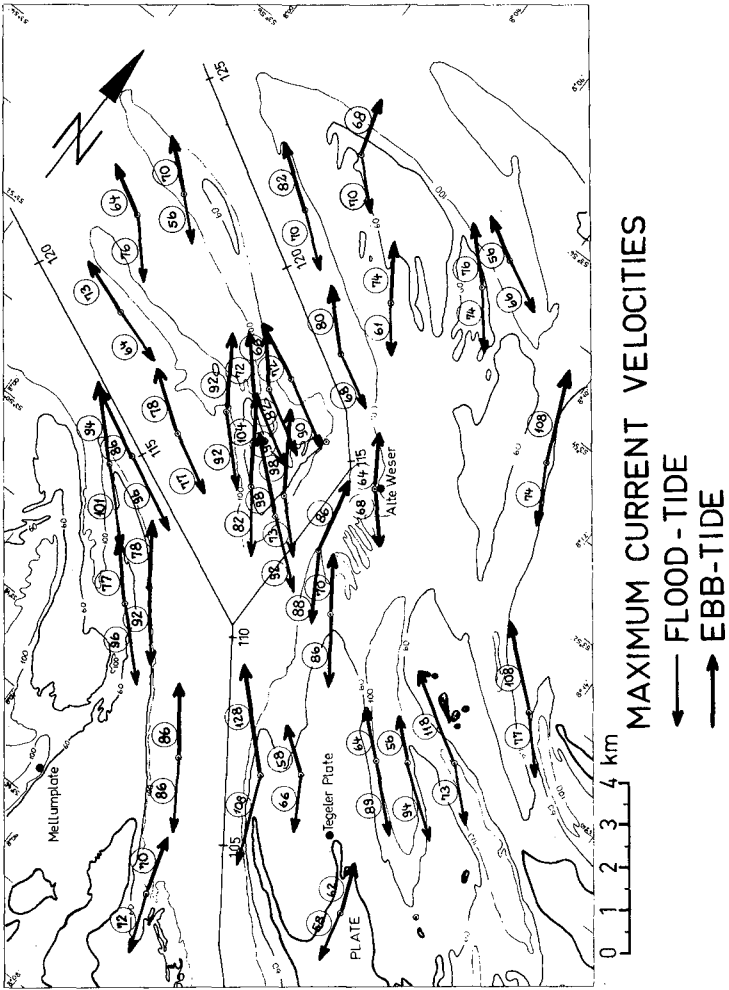


Fig. 7

The directions of the currents, which are affected by wind and rotational tides demonstrate the possible transportation of sand.

The resulting current vector

$$V = \int_{K_e}^{K_e} v_i dt$$

shows the displacement of a water particle during one tide. One can recognize, that the directions of the resulting vectors only in the "Neue Weser" (Fig. 8) correspond with the direction of the channel axis. In the other regions, especially on the sand-banks, there is an enormous displacement to the North-East. The dependence of the resulting vectors' directions on wind-affected tides is very important.

The ratio $\frac{v_e \max}{v_f \max}$ and

$\frac{SV_e}{SV_f}$ finally shows, that there is a

predominance of flood currents in the "Neue Weser" and of ebb-currents in the "Alte Weser".

There is every reason to believe that the migration of sand on the sea-floor is proportional to the fourth power of the current velocities (Ref. 1,4). Therefore the evaluation method includes the computation of the values.

$$\sum_{D_f} \frac{(v_f - v_{gr}) \cdot v_f^3}{D_f} \quad \text{and} \quad \sum_{D_e} \frac{(v_e - v_{gr}) v_e^3}{D_e}$$

v_{gr} = limiting value of velocity for the start of sand-transportation (~ 25 cm/s)

$D_{f,e}$ = period of flood/ebb - current

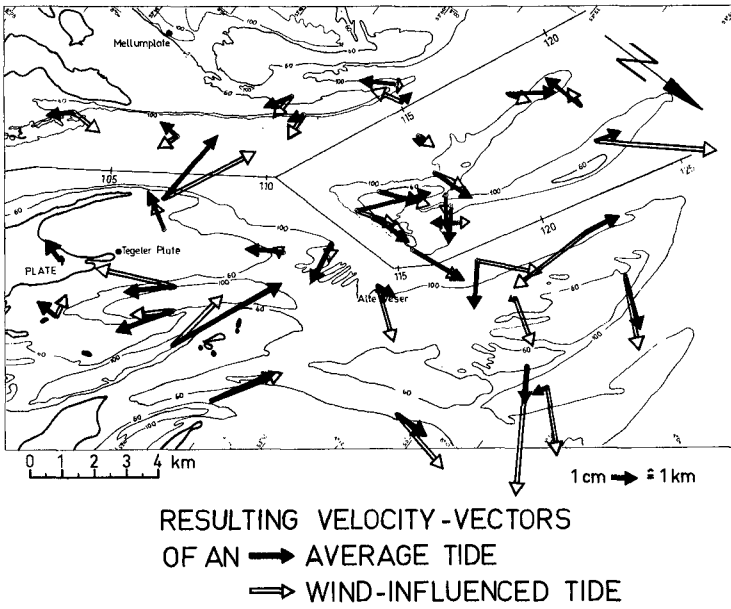


Fig. 8

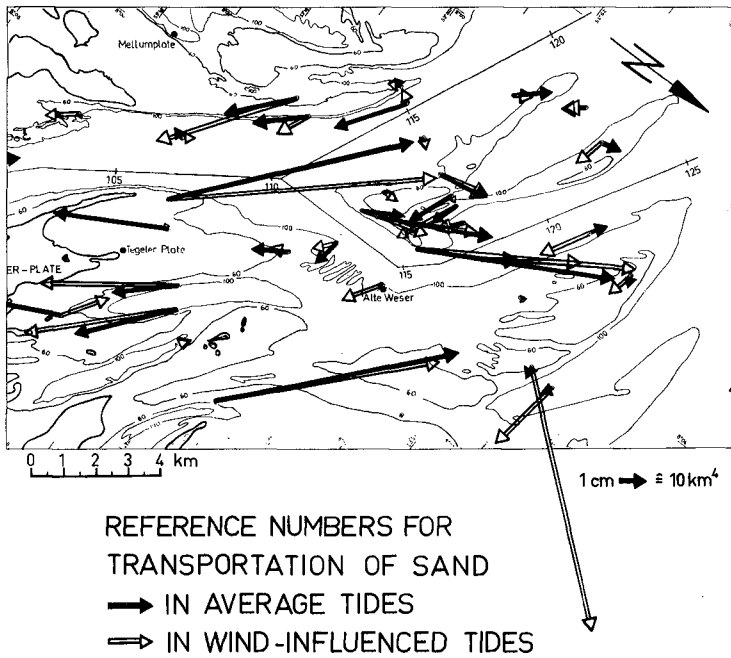


Fig. 9 shows the resulting reference numbers of sand-transportation which give another indication for the direction and amount of the movement of sand.

5. Conclusions

Comparing the results of the current measurements with the view of morphological changes you see the following proceedings in the reef area:

Effectuated by wave motion and tidal currents the sand is eroded at the steep underwater slopes of the NW and AW and crosses the deep channels as giant ripples, which seldom narrow down the required depth. On the back of the extended sand-banks the sand moves on zig-zag course with a resulting North-East direction. The migration in little ripples occurs there as well as the motion of larger underwater-dunes. At some places the underwater slopes come up to a speed of 60 m a year. The average speed is 20 to 30 m a year. Both of the deep channels are changing their form; the crucial deep channel for shipping-especially in the NW is nearly steady however. Beside the tidal currents wave motion has especially on the sand banks an essential part in migration of sand. Therefore the direction of migration depends on the respective wind direction too. It will be the task for the next years, to filter the quantitative part of wave motion in the interaction between waves and currents by measuring.

As a by-product of the investigations the cover-line of the same cross-section in different years (Fig. 5) gives a clue to the kind of material (sedimented or undisturbed) which can be found at dredging.

References:

1. Dillo, H.G. Sandwanderung in Tideflüssen
Heft 17 der Mitteilungen des Franzius-Instituts für Grund- und Wasserbau der TH Hannover, 1960
2. Göhren, H. Beitrag zur Mophologie der Jade-und Wesermündung
Die Küste, Jg. 13, 1965
3. Göhren, H. Meßwertaufbereitung von Dauerstrommessungen mit Hilfe der elektronischen Datenverarbeitung
Deutsche Gewässerkundliche Mitteilungen, Jg. 9 H. 2, 1965
4. Göhren, H. Triftströmungen im Wattenmeer
Heft 30 der Mitteilungen des Franzius-Instituts für Grund- und Wasserbau der TH Hannover, 1968
5. Hovers, G. Morphological Changes in a Fine Sand Tidal Estuary After Measures of River Improvement
Proceedings of the 14 th Coastal Engineering Conf. Copenhagen, Denmark, 1974
6. Plate, L. Forschung als Grundlage für den Ausbau der Außenweser Deutsche Wasserwirtschaft 1935, H. 4
7. Poppen, H. Die Sandbänke an der Küste der Deutschen Bucht der Nordsee, Annalen der Hydrographie Bd. 40 Jg. 1912

CHAPTER 104

CHANGES DUE TO JETTIES AT TILLAMOOK BAY, OREGON

Paul D. Komar¹ and Thomas A. Terich²

ABSTRACT

Bayocean Spit, separating Tillamook Bay from the Pacific Ocean on the north Oregon coast, underwent severe erosion following construction of a north jetty at the bay entrance in 1914-17. This erosion ultimately led to the complete breaching of the spit in 1952. Simultaneous to the spit erosion south of the entrance, the shoreline north of the north jetty advanced seaward by some 600 m (2000 ft). This pattern of erosion and deposition following jetty construction has generally been interpreted as the jetty blocking a large north to south net littoral drift in the area, estimated by a previous study at 620,000 m³/yr (800,000 yd³/yr). Our reexamination of the shoreline changes and patterns of erosion and deposition following jetty construction disagrees with this interpretation, and instead we conclude that all of the changes resulted from local rearrangements of the beach due to the disrupted equilibrium following jetty construction, but at the same time maintaining an overall condition of zero net littoral drift. This interpretation is supported by other evidence that indicates a near-zero net drift on this portion of the Oregon coast. Thus severe coastal erosion can result from jetty construction even in areas of zero net littoral drift.

A new south jetty has been recently completed (1974). The result has been further realignments of the shoreline with accretion and shoreline advance immediately south of the south jetty. This provides further confirmation that a zero net littoral drift exists in the area.

This study also demonstrates the effects of building only a single jetty rather than a pair of jetties. Following construction of the north jetty, the outer bar or ebb-tide delta at the Tillamook Bay inlet grew appreciably in size. Sand deposited there came from erosion of Bayocean

¹School of Oceanography, Oregon State University, Corvallis, Oregon 97331.

²Department of Geography, Western Washington State College, Bellingham, Washington 98225.

Spit further to the south. The shoal growth pushed the main channel at the entrance against the north jetty where it has remained since jetty completion. In the process, the channel became much deeper and narrower than the channel geometry prior to jetty construction.

INTRODUCTION

Bayocean Spit on the northern Oregon coast, about 80 km (50 miles) south of the Columbia River, separates Tillamook Bay from the Pacific Ocean (Figure 1). This spit has had a long history of development and

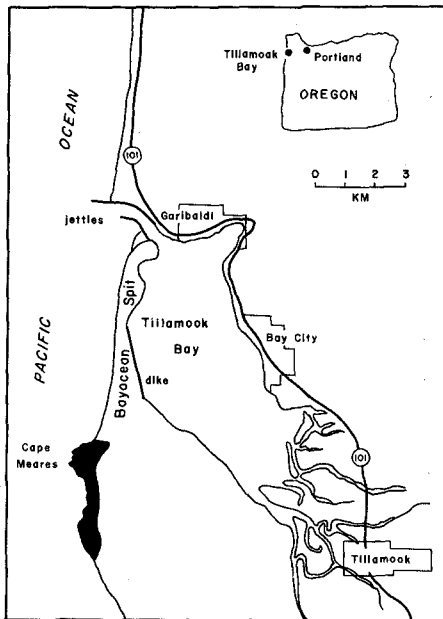


Figure 1: Tillamook Bay and Bayocean Spit.

erosion. The development and ultimate financial failure of Bayocean Park, a resort community built on the spit early in this century, has been discussed by Terich and Komar (1974). The final demise of the community resulted from erosion to the sand spit following construction of a north jetty at the Tillamook Bay entrance in 1914-17. Erosion over some

thirty-five years progressively narrowed the spit, and in 1952 it was breached at its narrowest point. This breach has been subsequently repaired by the construction of a dike, and recently a new south jetty has been constructed. The purpose of the present paper is to analyze the shoreline changes that resulted from the jetty construction and led to the erosion of Bayocean Spit. This example of shoreline erosion resulting from jetty construction is unusual in that, as will be shown, this area of the Oregon coast has a zero or near-zero net littoral drift along its beaches. Thus the shoreline changes and erosion are not the more familiar case of jetties blocking a net littoral drift, causing erosion in the downdrift direction. This study also demonstrates the results of constructing only a single jetty under such conditions, rather than a pair of jetties.

LITTORAL DRIFT ON THE OREGON COAST

With the exception of the section of coast near the mouth of the Columbia River, the Oregon coast is a series of long pocket beaches separated by pronounced rocky headlands. All evidence indicates that these areas are experiencing a seasonal reversal in the sand drift along the beaches, but with a zero or near-zero net littoral drift over a several years time span. This is best demonstrated by the effects of jetty construction on patterns of shoreline erosion and accretion. The study of Komar, et al. (1976) investigated these patterns for all jetty systems on the Oregon coast with the exception of the Columbia River jetties. Our study found that following jetty construction, sand would in general accumulate adjacent to the jetties, both to the north and south, filling in the pockets formed between the jetties and the pre-jetty shorelines which curved inward at the entrances. Our study showed that the amount of deposition adjacent to the jetties depended on the sizes of the pockets formed by the jetty construction. Deposition commonly occurred both north and south of the jetty systems, and the relative amounts of shoreline accretion on opposite sides of the jetties could in no way be taken as inferring a net littoral drift along the coast. Sand for this shoreline advance next to the jetties came from erosion of the coast at greater distances from the jetties.

The shoreline alterations following jetty construction continued until the shoreline became essentially straight and parallel to the prevailing wave crests, at which point zero net sand transport was again achieved and a new equilibrium reached. As will be shown in this paper, this pattern of deposition adjacent to the jetties and erosion at greater distances along the coast also explains the shoreline alterations at the Tillamook Bay entrance that led to the destruction of Bayocean Spit. The pattern of changes there, however, was complicated by the fact that only a north jetty was constructed initially, not a pair of jetties.

Deposition around jetties therefore indicates that, except near the Columbia River, the Oregon coast beaches have, as close as we can determine, a long term zero net littoral drift. This is also supported by observations that there is a seasonal reversal in the general transport directions due to the patterns of storm systems. During the summer months waves prevail from the northwest, causing a southerly sand transport along Oregon beaches. During the winter months the transport is to the north due to waves arriving mainly from the southwest. The wave data is inadequate, however, to actually carry out any calculations of littoral drift rates in an attempt to demonstrate a zero net drift.

Similar to the jetties, the rocky headlands show no indications of blockage of a net littoral drift, there being no accumulations of beach sand either to the north or south sides. What little study that has been done of heavy minerals in the beach sands also indicates that there is no bypassing of littoral sands around these headlands, which is reasonable considering their sizes and that they extend to considerable water depths. It is because of these barriers that the Oregon beaches can be described as pocket beaches of varying size. The only net littoral drift required within a pocket beach is the small amount necessary to redistribute the beach sand away from its sources to the complete stretch of beach. Previous studies (for example, Komar and Rea, 1976) have shown that sea cliff erosion is the primary source of beach sands in most areas, the river sands being trapped within the estuaries. Therefore even a net drift required for sand redistribution within the Oregon pocket beaches will be very small.

Because there is essentially a zero net drift of littoral sands

on the Oregon coast beaches, the erosion of Bayocean Spit following jetty construction clearly is not another example such as the Santa Barbara, California, breakwater, or the Port of Madras, India, where the coastal erosion resulted from blockage of a large net littoral drift by jetty construction.

SHORELINE CHANGES FOLLOWING CONSTRUCTION OF A NORTH JETTY

The principal sources of information on the shoreline changes utilized in this study are: (1) surveys undertaken by the Corps of Engineers, Portland District, before and after jetty construction; (2) aerial photographs from a variety of sources; (3) field studies of old shorelines and other features that are still visible; and (4) the writers' surveys in the case of the more recent construction of the south jetty at Tillamook Bay. In addition to the shoreline changes, once erosion became appreciable on Bayocean Spit, the Corps of Engineers, Portland District, monitored the rates of retreat of the dune bluffs and coastal property on the spit; this data has also been utilized. Since most of the shoreline changes and spit erosion occurred more than twenty-five years ago, we have had to rely primarily on historic data rather than on our own measurements. There is of course a certain amount of uncertainty in doing this.

A north jetty at the entrance to Tillamook Bay was begun in 1914 and completed in 1917. For economic reasons, an accompanying south jetty was not constructed at that time. The most apparent immediate response to the north jetty construction was a shoreline advance to the north of the jetty, documented in Figure 2. The buildout of the shoreline there nearly kept pace with the jetty extension. As in the cases of jetty construction elsewhere on the Oregon coast, and already discussed in this paper, this deposition adjacent to the north jetty occurred primarily so that the pocket formed between the jetty and the pre-jetty shoreline, which curved inward toward the bay entrance, would be filled. The shoreline built outward only until it became parallel to the prevailing wave crests, at which point long term changes ceased. The overall position of the shoreline has changed very little in the

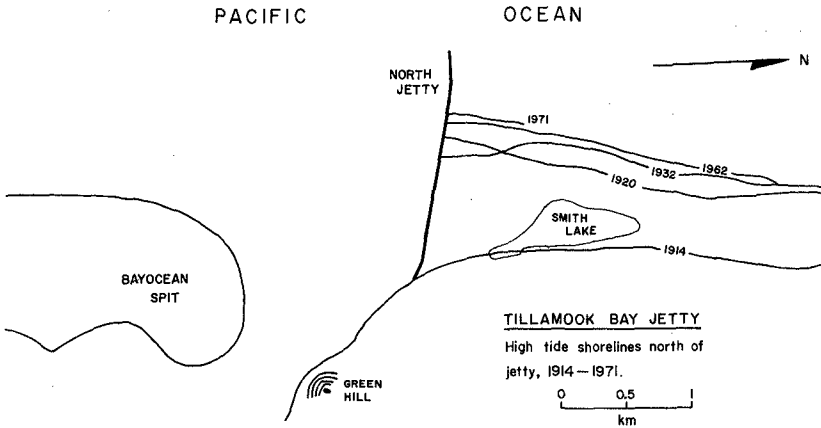


Figure 2: The shoreline advance north of the north jetty at the Tillamook Bay entrance after its completion in 1917. The 1914 shoreline gives a typical pre-jetty location.

past forty-some years, the only alterations being due to partial jetty degradation and reconstruction in the 1930's.

The sand accumulation north of the north jetty amounted to some $6,000,000 \text{ m}^3$ ($8 \times 10^6 \text{ yd}^3$). The second most apparent effect of the north jetty construction was the resulting erosion of Bayocean Spit to the immediate south. Based on this pattern of deposition to the north and erosion to the south, previous studies generally concluded that there must be an appreciable southerly net littoral drift. Based on accumulation rates north of the north jetty, this littoral drift was estimated at $600,000 \text{ m}^3/\text{yr}$ ($800,000 \text{ yd}^3/\text{yr}$) by the Corps of Engineers (1970), but placed at a lower estimate of $140,000 \text{ m}^3/\text{yr}$ ($180,000 \text{ yd}^3/\text{yr}$) by O'Brien (1930). We have already summarized the evidence that argues against such a net littoral drift on the Oregon coast. In the case of the Bayocean Spit and Tillamook Bay area, the pronounced headland Cape Meares exists to the immediate south (Figure 1). If such a large net drift did exist, this cape should also block the transport causing a buildout of the beach there to the north; there is no noticeable buildout, the beach in fact being principally gravel and cobbles; not sand as on the beach

to the north fronting the spit, and the cliffs near Cape Meares are undergoing extensive erosion. As already indicated, the deposition north of the north jetty following its construction can be better interpreted as changes resulting from local rearrangements of the beach due to the disrupted equilibrium caused by the jetty's presence but at the same time maintaining an overall condition of zero net drift.

It is difficult to determine when noticeable dune and property erosion began on the spit itself following construction of the north jetty in 1914-17. O'Brien (1930) indicated that there was considerable erosion at that time just to the north of Cape Meares (Figure 1), off the spit itself. He also mentioned, however, that the spit itself had suffered little change, "although the channel has moved northward against the jetty, probably due to the decreased sand pressure from the north." This channel migration following jetty construction and the growth of the shoal outside the bay entrance will be documented later. The sand deposition at the bay entrance came from erosion of the beach along the length of Bayocean Spit. From O'Brien's comment it would appear that there may have been some beach erosion at that time but the erosion had not yet reached the dunes nor threatened any property in Bayocean Park.

O'Brien (1930) also mentioned that the north jetty had weathered down appreciably. For this reason, the north jetty was reconstructed and lengthened in 1932-33. After this reconstruction erosion on the spit became very apparent. Even while reconstruction was in progress erosion began to undermine the sidewalk fronting the natatorium of Bayocean Park, built close to the beach, and by 1936 the structure's roof had collapsed (Figure 3). Erosion of the spit was progressive, although some winters were more severe than others and caused rapid dune and property retreat. For example, during January 1939 a storm broke a small gap along the narrow southern end of the spit, washing sand and gravel into the bay. The natatorium was finally completely destroyed by this storm (Figure 3). Maximum recession of the top of the dune bluff was 7.5 m (25 ft) with an average recession of 2 m (7 ft). In addition to the loss of the natatorium, four houses were undermined and lost, nine were immediately threatened,



Figure 3: Progressive erosion of the natatorium on Bayocean Spit.

and six had to be moved back for safety.

Washovers of the spit occurred during subsequent winter storms until on 13 November 1952 storm waves together with high tides entirely breached the spit's narrowest southern section, initially removing a 1200 m (4000 ft) long segment of spit. This breach progressively widened, becoming nearly a mile wide at high tide. The breach developed into the natural opening for the bay, the northern entrance with the jetty beginning to shoal and close (Figure 4; 1955 survey). Waves rolled through the breach producing swells within the bay, causing some erosion to farmlands on the bay's edge. For this reason it was decided to close the breach, so in 1956 work was begun on a rubblemound dike, set back within the bay. The construction of this dike and the difficulties in closure are discussed by Brown, et al. (1958). It was anticipated that the

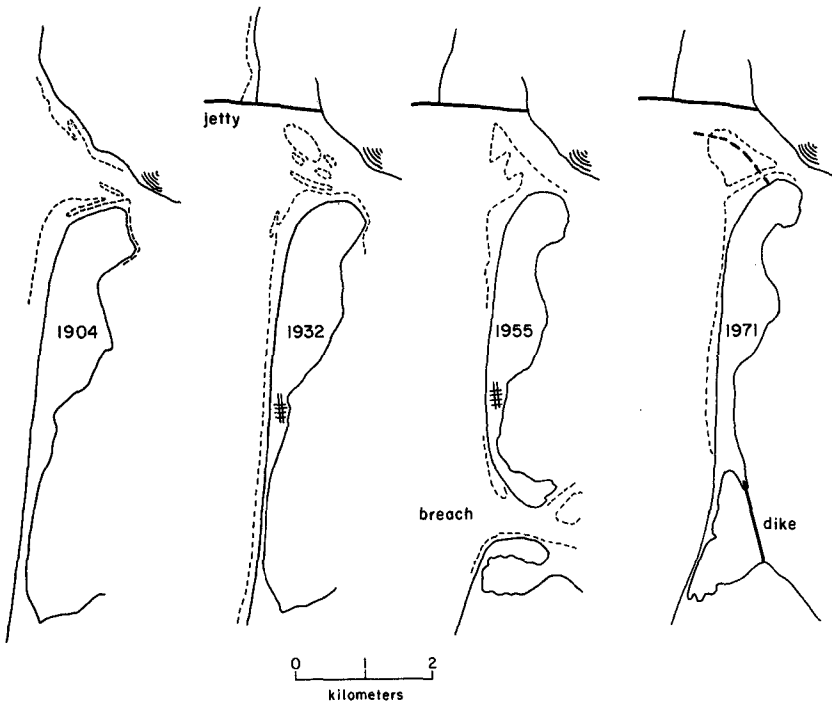


Figure 4: Progressive erosion to Bayocean Spit leading to its breaching in 1952, necessitating the placement of a dike closing the breach.

pocket in the shoreline seaward of the dike would fill and re-establish a sand beach fronting the dike, which it did as can be seen in the 1971 survey of Figure 4.

SHOAL DEVELOPMENT AND CHANNEL CHANGES AT THE BAY ENTRANCE

Although erosion occurred along most of the length of Bayocean Spit following construction of the north jetty, there was some deposition to the immediate south of the jetty (as well as to the north, as already seen). This deposition to the jetty's south at the bay entrance was in the form of a substantial growth to the outer bar or ebb-tide delta. As will be discussed later, it is estimated that some $3.3 \times 10^6 \text{ m}^3$ ($4.3 \times 10^6 \text{ yd}^3$) of sand was added to this shoal following jetty construction.

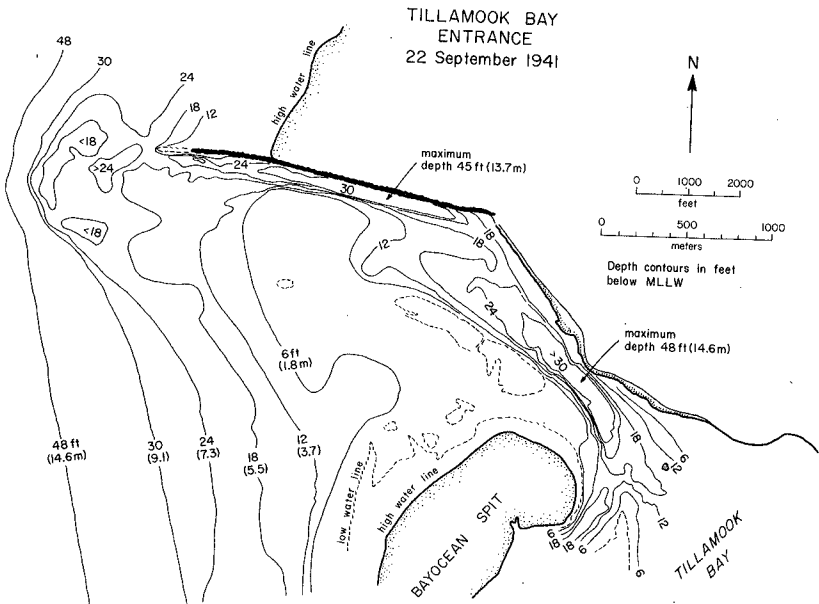
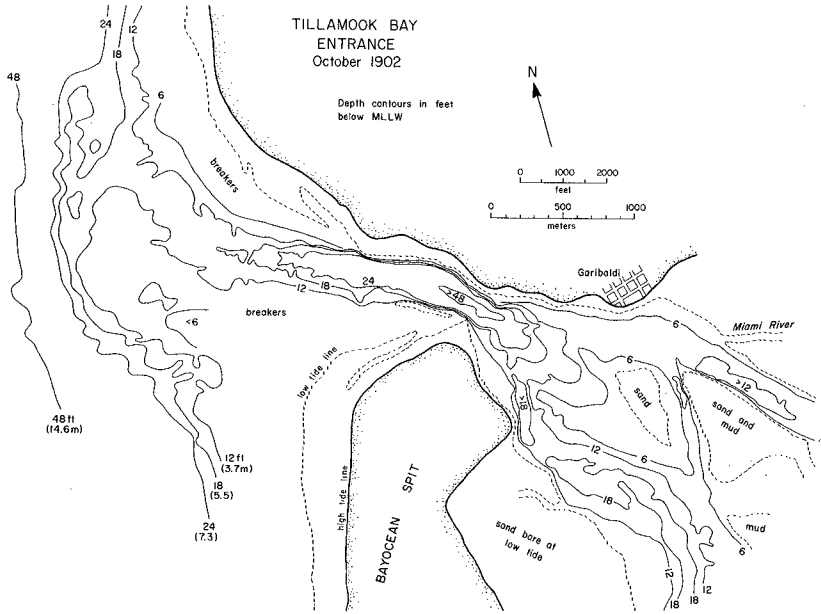


Figure 5: Tillamook Bay entrance before (upper) and after (lower) north Jetty construction in 1914-17.

The changes in the shoal and bay entrance are illustrated by Figure 5, the upper survey showing the entrance prior to jetty construction and the lower being typical of the entrance after construction. It is seen that there was an increase in the overall size of the outer bar shoal and a reduction in water depths. Under moderate to high wave conditions, this shoal became entirely covered by breaking waves and surf, making it a hazard to boats using the entrance.

Figure 5 also shows that the channel leading from the bay entrance was pushed northward against the jetty by the growth of the shoal. The channels at the entrances to the Umpqua and Coquille Rivers on the Oregon coast similarly migrated until they became adjacent to the single jetties that were initially built there (Komar, et al., 1976; Kieslich and Mason, 1976). Such a response to a single jetty rather than a pair of jetties has also been shown to occur on other coasts (Kieslich and Mason, 1976).

In addition to the growth of the outer bar and migration of the main channel following construction of the north jetty at Tillamook Bay, there were changes in the geometry of the channel outside the entrance. This is shown in Figure 6 which compares channel cross-sections before (June 1914) and after (June 1920) jetty construction. It is seen that after jetty development the channel became much deeper and narrower than existed prior to construction. These changes are presumably the response of the channel to the pressure from the south by the shoal growth. However changed in depths and widths, the channels before and after jetty construction did not differ significantly in cross-sectional areas. In addition, the changes in geometry did not extend inward along the channel into the entrance itself. Figure 7 shows a number of channel cross-sections immediately north of the spit at the entrance's narrowest point, some before and some after jetty completion. There are no noticeable effects there due to the addition of the north jetty. Despite the changes in channel geometry just outside the entrance and the growth of the shoal, the entrance itself remained relatively unchanged and bore the same relationship to the tidal prism within the bay according to O'Brien's (1931, 1939) relationship.

Although this study undertook no field investigations of the currents and waves in the area of the entrance, the changes in the channel position and geometry, and the growth of the outer bar shoal can be

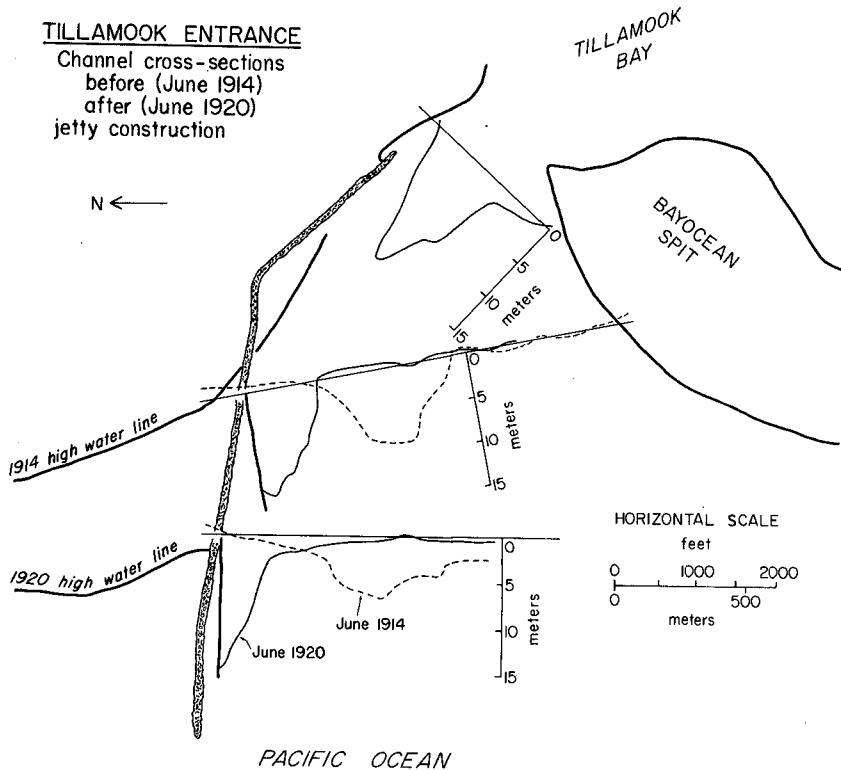


Figure 6: Deepening and narrowing of the channel following construction of a north jetty.

understood in terms of the findings of previous studies of inlets. Processes in the vicinity of inlets are complex in that they are the combined results of tidal-currents, wave action, and possible effects of salinity and thermal stratification resulting in a net inward flow at the bottom of the channel. The main ebb flow currents generally act to carry sand from the bay and nearshore areas to the offshore where it is deposited in the form of a delta, sometimes called the "ebb-tide delta." If located on a coast with a zero net littoral drift, this delta would be symmetrical and arcuate in shape. The existence of a net littoral drift would produce an asymmetry. Although the main ebb flow is directed offshore, currents move inward toward the entrance in the nearshore, from both sides of the inlet. Two eddies or gyres may develop on flanks of the main ebb channel emanating from the inlet; one gyre would be a clockwise flow, the other

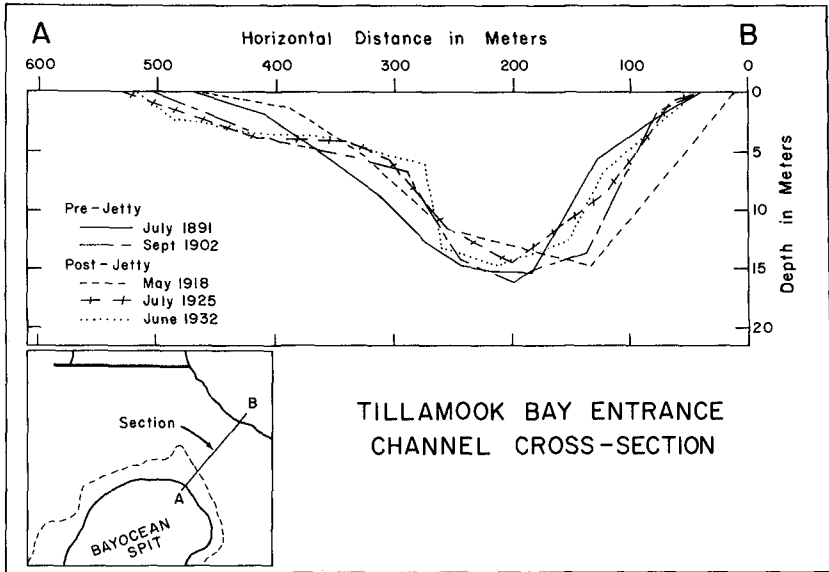


Figure 7: Cross-sections of the Tillamook Bay entrance before and after construction of the north jetty.

counter-clockwise, but both would produce currents directed toward the inlet on their shoreward sides. Lynch-Blosse and Kumar (1976) subscribe to such gyres being important at inlets, and discuss modifications where longshore currents are superimposed due to a general oblique wave approach to the coast. Dean and Walton (1975) point out that the ebb current can be viewed as a jet directed seaward, the high velocities in the central current of the jet transferring momentum outward and entraining adjacent waters, giving rise to the gyres described above. As a result, during ebb flow from the inlet there will be inward moving currents close to the shore, transporting sand toward the inlet and aiding the development of the flanking outer bars or shoals. During tidal flood flows the water converges toward the inlet from all sides, especially in flood channels to the flank of the deeper ebb channel. Thus the flood currents also aid in the development of flanking shoals.

Wave action generally acts to counter growth to the outer bar of the inlet. It does this by transporting sand back onshore to the beaches.

For this reason, on coasts of high wave conditions (like Oregon) the outer bars of inlets tend to be smaller than on coasts of small waves (Dean and Walton, 1975; Walton and Adams, this volume). However, wave refraction over the shoal can also aid in the development of the outer bar, and some studies have suggested that this process may be more important than the current gyres already discussed (Hayes, et al., 1971; Hubbard, this volume). Refraction of the waves around the outer bar causes a longshore current directed toward the inlet from both sides, thus working in concert with any ebb-tide gyres and flood-tide currents acting in the area. With an overall oblique wave approach to the inlet area, the longshore current may be inward toward the inlet on only the updrift side.

As seen in Figure 5 (upper), typical flanking outer bars existed at the Tillamook Bay entrance prior to jetty construction. There was a seaward offset of the northern shoreline which is sometimes taken to indicate a net littoral drift (Hayes, et al., 1971; Lynch-Blosse and Kumar, 1976), but there is no consistency as to whether the shoreline offset is updrift or downdrift of the inlet. The presence of an offset at the Tillamook Bay inlet in an area of zero net littoral drift casts doubts on offset direction as an indicator of net drift direction and on the theories of origin of the offset which rely on the presence of a net littoral drift.

The construction of the single north jetty at the Tillamook Bay inlet provided additional protection from the wave activity. This protection would allow for further growth of the south flanking shoal, the north flanking shoal becoming covered by the shoreline advance to the north of the north jetty. The growth of the south flanking shoal was presumably due to the continuation of an eddy gyre in this region during ebb tide, and perhaps due to wave refraction effects, both described above, but with a decrease in the wave activity that had acted to reduce the size of the shoal. This is partly verified by model studies conducted at the Waterways Experiment Station on the Masonboro Inlet, North Carolina, and reported in Dean and Walton (1975, page 137). Like the Tillamook Bay entrance, the Masonboro Inlet has only a single jetty. The model studies indicated that shoal growth resulted from (a) the jetty's sheltering of the shoal area, thereby creating a sand

trap, and (b) a large eddy or gyre carrying sand toward the inlet on both ebb and flood currents.

It is seen that all factors affected by the installation of a north jetty at Tillamook Bay would act to increase the growth of the south flanking shoal. The shoal growth pushed the channel northward against the jetty, and the pressure from the developing shoal also presumably accounts for the narrowing and deepening of the channel.

INTERPRETATION OF SHORELINE CHANGES AND THE BUDGET OF SEDIMENTS

As already indicated, a closer inspection of the changes following construction of the north jetty does not agree with the interpretation of a large net littoral drift identified by earlier studies (Corps of Engineers, 1970). The overall pattern of erosion and deposition is illustrated schematically in Figure B, and it is seen that the pattern is symmetrical north and south of the jetty, complicated by the fact that only a single jetty was installed. Although erosion occurred along most

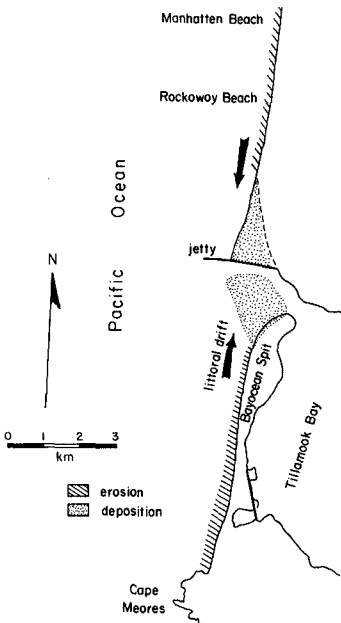


Figure B: Patterns of erosion and deposition following construction of a north jetty but prior to the south jetty development.

of the length of Bayocean Spit, there was a net deposition just to the south of the jetty in the form of growth to the flanking outer bar. Following jetty construction, sand moved northward from most of the length of the spit and accumulated in this shoal growth. As will be shown shortly, the loss of sand from the spit erosion can be approximately balanced by the amount of sand deposited on the shoal plus that carried into the bay during the 1952-56 breach.

To the north of the jetty sand accumulated and the shoreline advanced (Figure 2). Deposition there probably derived its sand from beach erosion further to the north, symmetrical with the northward movement of sand on the spit to the inlet. This overall pattern of deposition adjacent to jetties and erosion at greater distances was shown to occur at other Oregon coast jetty systems (Komar, et al., 1976), and was reviewed earlier in this paper. Erosion to Bayocean Spit was much greater than erosion to the north of the jetty at Manhattan Beach and Rockaway Beach (Figure 8) because of the longer stretch of beach that exists to the north. Only a small amount of sand had to be eroded per unit length of shoreline to supply sand to the accretion area immediately north of the jetty. In contrast, Bayocean Spit is only a small segment between the jetty and Cape Meares on the south (Figure 8) so that a larger amount of sand had to be supplied by each unit length of spit shoreline erosion to support the shoal growth next to the inlet.

We have attempted to put sediment volumes on the patterns of erosion and deposition illustrated in Figure 8 by the development of a budget of sediments. This budget is for changes following the completion of the north jetty in 1917 but before the construction of the south jetty in 1969. Our estimates are given in Figure 9. Deposition to the north of the jetty amounted to some $6 \times 10^6 \text{ m}^3$, which agrees with previous estimates of the fill (Corps of Engineers, 1970). As already indicated, this sand deposition came from beach erosion further to the north; that erosion value is given in Figure 9 in parentheses because we have no actual measure of the erosion other than the supposition that it will balance the deposition north of the jetty. Of course any transfers of sand around the jetty during or after construction would alter this exact balance; unfortunately we have no way to evaluate such a

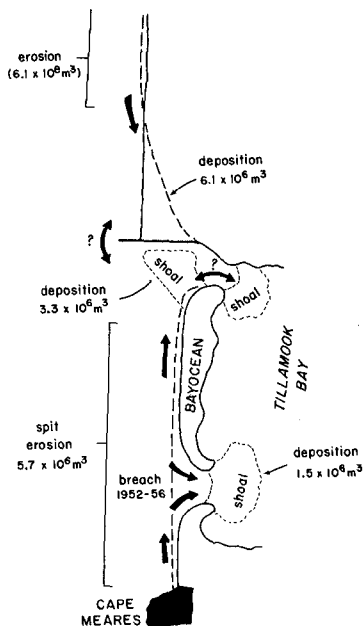


Figure 9: Budget of sediments for areas of erosion and deposition following construction of the north jetty at Tillamook Bay.

transfer around the north jetty, but believe it to be small, especially in comparison with the volume of sand deposited to the north of the jetty. This belief is in part supported by the continued existence of a shoreline offset north and south of the jetties, even after construction of a south jetty. This suggests that the jetties are an effective barrier to longshore movements of sand on the beaches; otherwise sand would presumably transfer from the north to the south beach until they have equal offshore extents.

We estimate that the flanking outer shoal to the south of the jetty increased in volume by $3.3 \times 10^6 \text{ m}^3$ following jetty construction. This estimate is based on comparisons of bathymetric surveys such as those of Figure 5, before and after jetty completion. Our estimate shows reasonable agreement with the results of Walton and Adams (this volume). They place the total volume of the outer bar of Tillamook Bay at $15 \times 10^6 \text{ m}^3$, so the measured growth volume is small in comparison. Of special interest is that Walton and Adams show that outer bars on

coasts with small wave energy are some 23% larger than bars on coasts with large wave energies. If we reason that the growth of the Tillamook inlet outer bar is due to the additional protection offered by the jetty from wave attack, and employ their 23% resulting growth factor, one obtains a volume increase of $3.5 \times 10^6 \text{ m}^3$, almost exactly the same as our measured increase ($3.3 \times 10^6 \text{ m}^3$).

Erosion of Bayocean Spit and the area to its immediate south up to Cape Meares amounted to some $5.7 \times 10^6 \text{ m}^3$ (Figure 9). This estimate is based on measured beach and dune bluff retreats and heights of the dune bluffs and sea cliffs.

The other large transfer of sand in the area was into the bay when the spit breached in 1952 and remained open until 1956. This volume of deposition and loss from the seaward side of the spit is estimated at $1.5 \times 10^6 \text{ m}^3$, and is based on the volume of spit removed by the breaching process (which gives a minimum transfer) and shoaling values within that portion of the bay. This estimated volume is considered to be much poorer than our estimates of spit erosion or deposition near the jetty.

There is also the possibility of some deposition on the inner shoal (flood-tide delta), within the bay at the jettied entrance. The surveys of the entrance area, before and after jetty construction, suggest that deposition within the bay in this area was small, but we could not make satisfactory measurements from the available data.

Altogether there is a reasonable accounting for the transfer of sand from erosion areas to deposition areas in the region of Bayocean Spit and Tillamook Bay following construction of the north jetty. The shoal growth and sand entering the bay through the breach together account for $4.8 \times 10^6 \text{ m}^3$ of deposition. This is close to the $5.7 \times 10^6 \text{ m}^3$ of estimated erosion from the spit. Considering the inaccuracies of these estimates, the results demonstrate that the patterns of erosion and deposition can be accounted for by local rearrangements of nearshore sands following construction of the north jetty, without blockage of an appreciable net littoral drift by the jetty.

CONSTRUCTION OF THE SOUTH JETTY

The hazardous channel conditions which developed due to the growth of the outer bar following construction of the north jetty prompted renewed considerations for construction of a south jetty. Construction of a south jetty was begun in April 1969 and completed in 1974 with a total length of 2000 m (6,500 ft).

Even as the south jetty was being constructed, sand accumulated between it and the curved pre-jetty shoreline, causing a shoreline advance to the south. This accumulation continued until the shoreline became straight and parallel to the prevailing wave crests, the same as described earlier for other jetty systems on the Oregon coast as well as for the earlier construction of the north jetty. This provides further proof for a zero or near-zero net littoral drift in the area.

SUMMARY OF CONCLUSIONS

(1) With the exception of the section of coast near the Columbia River, the Oregon coast is a series of pocket beaches separated by pronounced rocky headlands. There is a zero or near-zero net littoral drift within these pockets. Shoreline changes due to jetty construction are therefore not due to blockage of a net drift.

(2) Following completion of a single north jetty in 1917 at the Tillamook Bay entrance, the shoreline built outward to the immediate north. This accretion occurred to fill the embayment created between the jetty and the pre-jetty shoreline which curved inward toward the bay entrance. Deposition continued until the shoreline became straight and parallel to the prevailing wave crests, at which time a new equilibrium was achieved with a zero net littoral drift.

(3) Bayocean Spit to the south of the Tillamook Bay entrance suffered severe erosion following construction of the north jetty, culminating in its breaching in 1952. Initially, sand eroded from the spit moved northward and was deposited at the entrance in the form of growth to the outer bar (ebb-tide delta). Later when the spit breached, considerable quantities of littoral sediments were also carried into the bay.

(4) Growth of the outer inlet bar or shoal following construction

of a north jetty can be understood in terms of wave and current processes acting at inlets. The single jetty offered increased protection from the waves and perhaps augmented flanking currents flowing inward toward the inlet.

(5) Considerable coastal erosion can result from jetty construction even in coastal areas that are not experiencing a sizeable net littoral drift; blockage of a net drift by jetty construction is not a necessary prerequisite for erosion.

ACKNOWLEDGEMENTS

This work is a result of research sponsored (in part) by the Oregon State University Sea Grant Program, supported by NOAA Office of Sea Grant, Department of Commerce, under Grant #04-6-158-44004.

REFERENCES

- Brown, H.E., G.D. Clark, and R.J. Pope (1958) Closure of the breach in Bayocean Peninsular, Oregon: Jour. Waterways and Harbors Div., ASCE, January 1958, n.WW1, paper 1516, 20p.
- Corps of Engineers (1970) Tillamook Bay, Oregon: Committee on Tidal Hydraulics, U.S. Army Corps of Engineers.
- Oean, R.G., and T.L. Walton (1975) Sediment transport processes in the vicinity of inlets with special reference to sand trapping: Estuarine Research, Vol.II, Geology and Engineering, Academic Press, NY, p.129-149.
- Hayes, M.O., V. Goldsmith, and C.H. Hobbs (1971) Offset coastal inlets: Proc., 12th Coastal Engr. Conf., p. 1187-1200.
- Hubbard, D.K. (this volume) Changes in inlet offset due to stabilization: Proc. 15th Conf. Coastal Engr., Hawaii, July 1975.
- Kieslich, J.M, and C. Mason (1976) Channel entrance response to jetty construction: Proc., Civil Engr. in the Oceans III, ASCE, p. 689-705.
- Komar, P.D., J.R. Lizarraga, and T.A. Terich (1976) Oregon coast shoreline changes due to jetties: Jour. Waterways, Harbors and Coastal Engr. Div., ASCE, v. 102, n. WW1, paper 11933, p. 13-30.
- Komar, P.D., and C.C. Rea (1976) Beach erosion on Siletz Spit, Oregon: Ore Bin, v. 38, n. 8, p. 119-134.
- Lynch-Blosse, M.A., and Naresh Kumar (1976) Evolution of downdrift-offset tidal inlets: A model based on the Brigantine inlet system of New Jersey: Jour. of Geology, v. 84, p. 165-178.
- O'Brien, M.P. (1930) Report on sand movement on the Pacific coast on the United State, Part III: Tidal inlets: Beach Erosion Board unpubl. report.
- O'Brien, M.P. (1931) Estuary tidal prisms related to entrance areas: Civil Engineering, v. 1, n. 8, p. 738-9.

- O'Brien, M.P. (1969) Equilibrium flow areas of tidal inlets on sandy coasts: Jour. Waterways and Harbors Div., ASCE, v. 95, n. WW1, p. 43-52.
- Terich, T.A., and P.D. Komar (1974) Bayocean Spit, Oregon: History of development and erosional destruction: Shore and Beach, v. 42, p. 3-10.
- Walton, T.L., and W.D. Adams (this volume) Capacity of inlet outer bars to store sand: Proc., 15th Conf. Coastal Engr., Hawaii, July 1976.

CHAPTER 105

CHANGES IN INLET OFFSET DUE TO STABILIZATION

Dennis K. Hubbard

Coastal Research Division
Department of Geology
University of South Carolina
Columbia, S. C. 29208

ABSTRACT

Available evidence indicates southward littoral transport through the Merrimack Embayment. In apparent contradiction, the beach on the southern (Plum Island) side of the inlet has built seaward of the updrift beach. This phenomenon is related to a balance between storm and fair weather conditions. Wave observations under a variety of surf conditions show that during storms, sand is transported southward along the face of the nearshore bar fronting Plum Island. During calm periods sand is moved northward along the beach until it is trapped by the southern jetty and removed from the then active tidal current transfer system. Using discharge data and wave measurements from the Merrimack Inlet area, Bruun's bypassing coefficient ($r = Q_{1s}/Q_{max}$, where Q_{1s} is the longshore transport rate in M^3/yr and Q_{max} is the maximum inlet discharge in M^3/sec) was computed for storm and fair weather conditions. During storms, the bar bypassing observed in the field was clearly indicated. During calmer periods tidal current transfer was predicted. This relationship is considered only an approximation as it does not consider many important physical parameters (grain size, nearshore slope, wave type, etc.).

INTRODUCTION

The literature is replete with references concerning bypassing of sand around tidal inlets. Numerous researchers have considered the importance of this process to engineers (Angas, 1960; Bowman, 1960; Bruun and Gerritson, 1960; Caldwell and Lockett, 1965; Dean and Walton, 1975; Herron and Harris, 1967; Hodges, 1955; McDonald and Sturgeon, 1956; Watts, 1962). These studies have generally shown that the type and rate of bypassing that occurs are dependant upon the volume of sediment supplied to the inlet (littoral drift) and the ability of the inlet to flush this material from its throat (related principally to tidal prism). Furthermore, the nature of this relationship will be reflected in the morphology of an individual inlet and its associated sand bodies.

At Murrells Inlet, S. C., (Fig. 1) net longshore transport rate is small and sand tends to reside in the inlet system. The near balance between sand entering and leaving the inlet causes it to be choked with sand. In this case, bar bypassing dominates at the expense of local navigation. At Kiawah Inlet, S. C. (Fig. 2) another type of bypassing, channel abandonment, occurs. Over a period of 10 months, the sand that had accumulated on the updrift side of the inlet was bypassed as the main channel was closed and a path further updrift was initiated (Fig. 2).

Whatever the process responsible for bypassing, introduction of a large structure into the littoral zone (a jetty, for example) results in a significant



Figure 1. Low tide photograph of Murrells Inlet, S. C. Note the large shoal occupying the channel cross-section. This is a result of the near balance of sand moving in and out of the inlet.



Figure 2, Bypassing at Kiawah Inlet, S. C. These photographs show the configuration of the inlet in April, 1975 (A), November, 1975 (B) and February, 1976 (C). Note the abandonment of the main ebb channel between April and November, 1975 followed by swash bar development in February, 1976.

modification of the bypassing process. In most documented cases, the resultant pattern of erosion and deposition is similar to that shown in Figure 3; that is, accretion along the updrift beach at the expense of the eroding downdrift beach.

The Merrimack River Inlet is located in northeastern Massachusetts near the Massachusetts-New Hampshire border (Fig. 4). The inlet separates two active Holocene barriers, Salisbury Beach to the north and Plum Island to the south. A variety of coastal defense structures have been used to stabilize the inlet and retard the rate of erosion along adjacent beaches. Since their construction however, these structures have been responsible for many problems (Hubbard, 1974). The jetties, built in sections since 1912, have effectively stabilized the position of the inlet while causing localized erosion on the nearby beaches and river front. Despite the apparent effectiveness of the jetties as barriers to littoral transport, the downdrift side of the inlet does not show the serious erosion usually associated with structures of this type. In fact, the downdrift beach is presently undergoing rapid progradation. Both field observations and mathematical considerations are presented to explain this phenomenon.



Figure 3. Low tide aerial photograph of the Cape Cod Canal entrance. Note the erosion-deposition pattern resulting from interruption of littoral transport. Sand is moving toward the viewer. Photo by Miles O. Hayes.

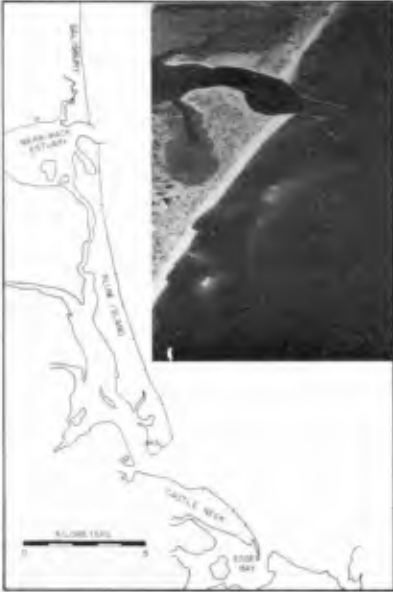


Figure 4. Map showing the location of Merrimack Inlet. The top of the figure follows the Massachusetts-New Hampshire border. The inset is a low tide aerial photograph looking northward over Plum Island (foreground) and Merrimack Inlet. Note the well developed nearshore bar system that extends past the inlet mouth.

Sediment Dispersal

Several lines of geomorphic evidence indicate a southward transport of littoral material through the Merrimack Embayment (Fig. 5). First, the seaward displacement of the 20 meter contour near the southern end of the embayment suggests that Ipswich Bay is a sink for material moving in that direction. Bothroyd (pers. comm.) has observed an accretionary beach at Castle Neck. Also, the southward migration of Plum Island by spit growth on its downdrift end (Farrell, 1969) indicates a sediment supply to the north. Finally, grain-size trends along Plum Island and Castle Neck beaches (Anan, 1971) and on the Merrimack ebb-tidal delta (Hubbard, 1975) also suggest southward littoral transport through the area (Fig. 5).

Morphology and Hydrodynamics

One would expect that under these conditions the beach on the northern side of Merrimack Inlet would be accreting while the southern beach eroded. To the contrary, the downdrift shoreline extends approximately 300 meters seaward of the northern beach. Furthermore, rapid accretion has been observed adjacent to the inlet since the 1967 rehabilitation of the south jetty.

If we consider that this offset is the result of some factor other than the jetties, then the downdrift offset inlet should have persisted when the jetties were absent. Analysis of existing charts of Merrimack Inlet show that although

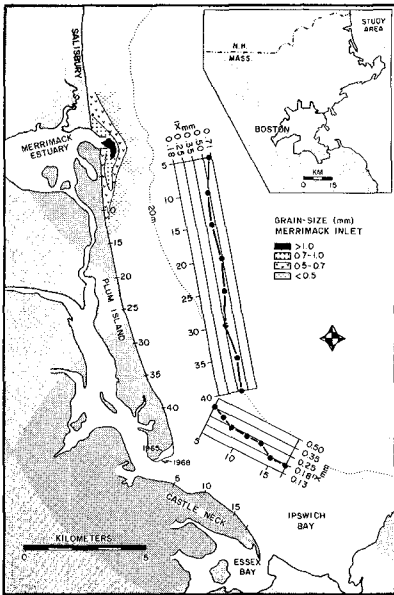


Figure 5. Summary of evidence for southward sand transport in the Merrimack Embayment.

- 1) seaward displacement of the 20 m contour in Ipswich Bay.
- 2) recurve spit growth on the southern tip of Plum Island.
- 3) grain-size trends.

the inlet was offset downdrift in 1741, by 1776 the inlet configuration had changed to that of an updrift offset (Fig. 6). 1809 saw the reestablishment of the downdrift offset. These and other reversals were probably related to the by-passing of sand around the inlet. Under natural conditions, the inlet therefore did not persist as a downdrift offset. The flip-flopping observed between 1741 and 1900 ceased abruptly however after the jetties were built in the early 1900's. A 1940 photograph from Chute and Nichols (1942) shows that the present configuration had already developed at that time (Fig. 7). It seems logical therefore, that the pattern of erosion and deposition observed at Merrimack Inlet is related to the presence of the jetties.

This pattern results from a balance between the dominant northeasterly storm waves and the prevailing southeasterly waves generated during fair weather conditions. It can be seen in Figure 8 that during storms the sediment moves uniformly southward except for a divergence in transport direction occurring immediately downdrift of the inlet. At this point a break in the nearshore bar occurs through which waves pass and break directly on the beach. Immediately updrift of the gap the bar reaches its highest elevation in response to the retardation of sand flow along the shoal. This adjustment of the waves to the topography of the nearshore bar results in northward sand transport during storms along the beach immediately downdrift of the jetty and the retention of sand in this part of the system.

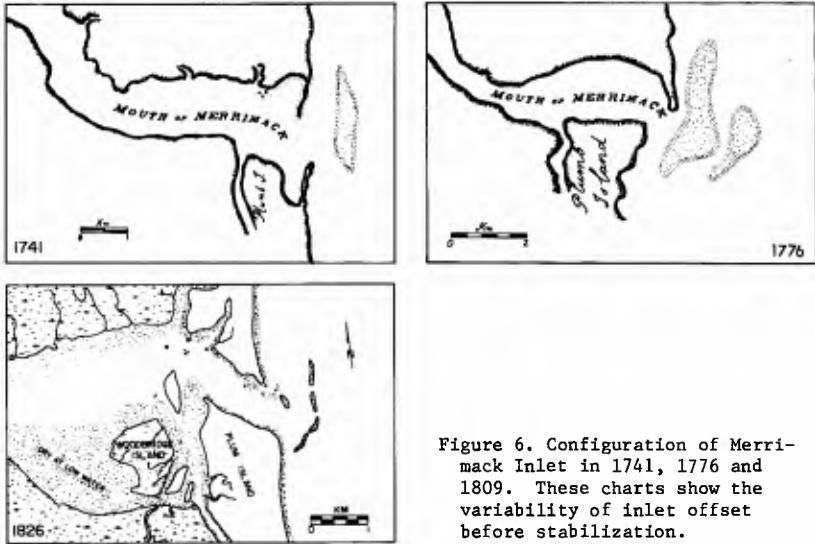


Figure 6. Configuration of Merrimack Inlet in 1741, 1776 and 1809. These charts show the variability of inlet offset before stabilization.



Figure 7. Aerial photograph looking westward across Merrimack Inlet. Note the similarities between this photo and Figure 9. From Chute and Nichols (1942).

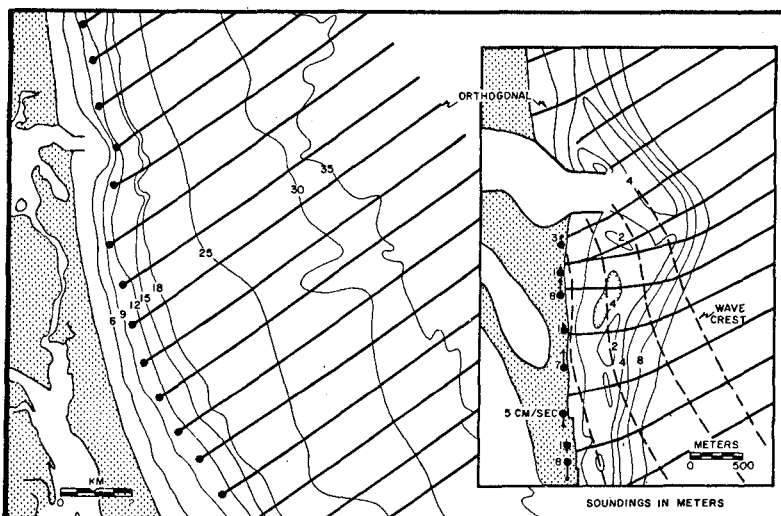


Figure 8. Wave refraction around the Merrimack ebb-tidal delta. The numbers in the inset are longshore current velocities measured during northeast wave approach.

During higher tidal stages, be they astronomical or meteorological, the entire beach comes under severe wave attack. Sand is removed from the beach and moved offshore toward the permanent nearshore bar and to the south (Fig. 9). The bar on the updrift side of the inlet extends nearly to the beach and provides a point of entry for sand into the by-passing system.

During fair weather, sand is moved landward and toward the north under the influence of the prevailing southeasterly waves (Fig. 9). On the south side of the inlet, this landward transport occurs through the migration of entire segments of the permanent nearshore bar onto the beach (Fig. 10). Once on the beach, this sand moves northward until it is trapped by the southern Merrimack jetty.

Bruun (1966) presented a formula to determine whether the movement of littoral material past an inlet would occur by the development of an inlet shoal or by tidal current transfer. Using a ratio between littoral drift (Q_{LS} in M^3/yr) and maximum inlet discharge (Q_{max} in M^3/sec) in twenty-eight inlets, he was able to determine whether tidal current transfer or bar bypassing would dominate in each case. Empirically, r values ($r = Q_{LS}/Q_{max}$) less than 10 - 20 indicated predominant tidal current transfer while values greater than 200 - 300 implied bar bypassing.

Using the maximum spring-tidal discharge of $2500 m^3/sec$ measured in the Merrimack Inlet, a value of $7.5 \times 10^4 M^3/yr$ was calculated as the volume of

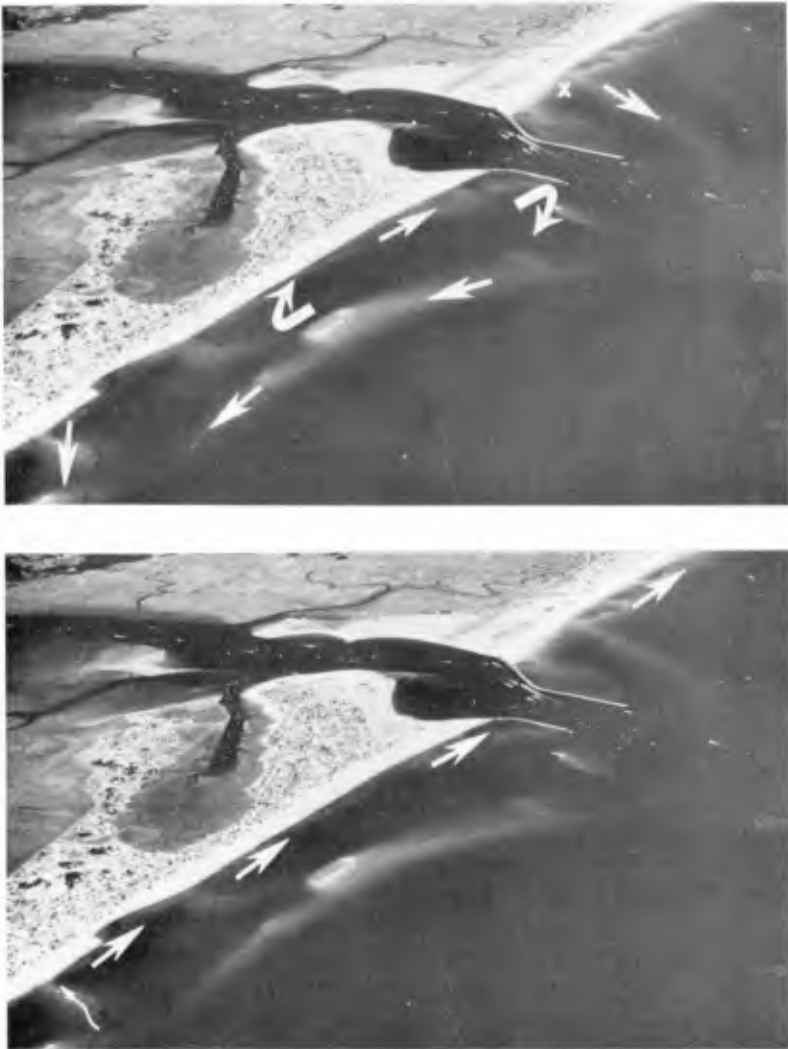


Figure 9. A (above). Sand transport patterns observed during storm conditions. The X indicates the point of attachment of the nearshore bar on the northern side of the inlet.
B (below). Sand transport patterns observed during fair weather.

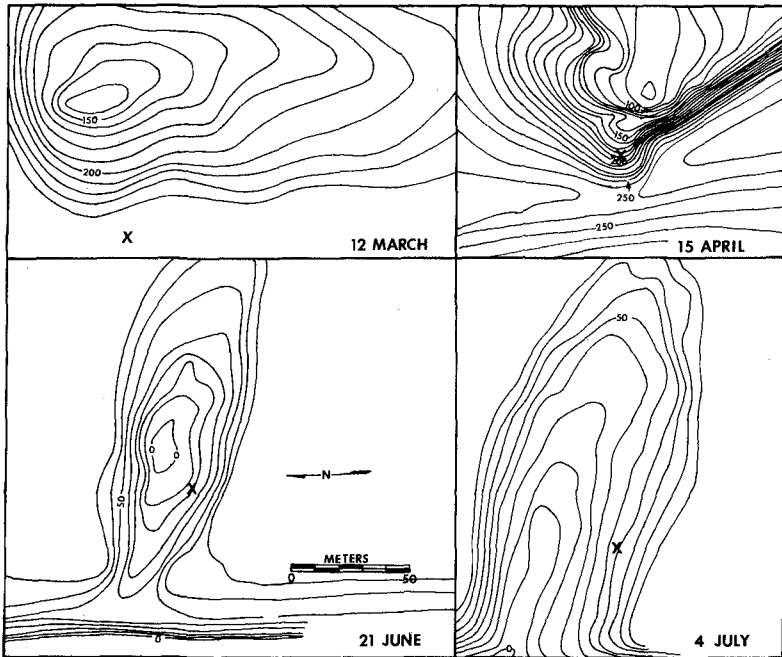


Figure 10. Bar migration under fair weather conditions. Note the transition in morphology from that of a longshore bar on 12 March to a transverse bar on 4 July. The X is in the same location on all maps.

longshore drift necessary to initiate bar by-passing. Using these data and formulas from the Shore Protection Manual (U.S. Army, 1973), longshore transport rates for the Merrimack Inlet area were computed. Using the relationships,

$$P_{1S} = 100.6 (H_b^3/T) \sin \alpha_0 \quad (1) \text{ and,}$$

$$Q = (7.5 \times 10^3) P_{1S} \quad (2)$$

where: P_{1S} = surf zone approximation for the longshore component of wave energy flux
 H_b = breaker height
 T = wave period
 α_0 = angle between deepwater wave crest and shoreline
 Q = longshore transport rate

it was determined that an 8 ft. (2.4 m) wave with a deepwater approach angle between 30° and 45° and a period between 6 and 9 seconds could initiate bar bypassing. Waves observed during northeasters are commonly above this height. Also due to the strong effect of local waves during storms, these periods and angles are representative.

Waves in excess of three meters were observed by Abele (1972) during a northeaster on 19 February 1972. According to the U. S. Army (1973) relationships,

$$Q = (7.5 \times 10^3) P_{1s} \quad (2) \text{ and,}$$

$$P_{1s} = 32.1 H_b^{5/2} \sin 2\alpha_b \quad (3)$$

where α_b = angle between crest of breaker and shoreline, breaking waves with a height of 10.7 ft (3.25 m) and an approach angle of ten degrees (values consistent with Abele's (1972) data) could transport volumes of 8.75×10^5 M³/yr. The corresponding r value of 350 is above the value needed to initiate bar bypassing. Prevailing southeasterly waves during fair weather periods average 1 ft (30 cm) in height and have characteristically small breaker angles. Equations 2 and 3 were used to determine longshore transport rates and subsequent r values for 30 cm waves approaching at various angles. The bypassing coefficient corresponding to a breaker angle of 45 degrees (most breakers approach at angles less than five degrees) was computed as 2.8. This is well below the value of $r = 20$ for tidal current transfer. It should be pointed out that because the nearshore bar is a permanent feature it is both the wave condition and littoral drift volume (which are admittedly related) that determine the mechanism of inlet bypassing in this case. Bruun's relationship is therefore an indication of what is going on rather than an explanation of the process itself.

CONCLUSIONS

- 1) Several lines of evidence indicate net southward littoral transport through the Merrimack Embayment.
- 2) Despite this, the beach south (downdrift) of Merrimack Inlet is presently accreting.
- 3) This phenomenon is the result of a balance between storm and fair weather conditions:
 - a) During storms, sand moves off the beach and southward along the permanent nearshore bar that extends past Merrimack Inlet.
 - b) During fair weather, sand moves landward and toward the north along the beach. Under these conditions, sand is trapped by the southern jetty.
- 4) Bruun's bypassing relationship can be used to at least partially explain this phenomenon. During storms the volume of drift is high enough to bypass the inlet along the nearshore bar face. Under calmer conditions, tidal current transfer which is blocked by the jetties occurs.

ACKNOWLEDGMENTS

This work was done as part of project DACW72-72-C-0032, Coastal Engineering Research Center of the U. S. Army Corps of Engineers, M. O. Hayes, principal investigator.

REFERENCES

- ABELE, R. W., 1972, Detailed analysis of short-term variations in beach morphology (and concurrent dynamic processes) for summer and winter periods, 1971-1972, Plum Island, Massachusetts: Final report for Contract DACW72-71-C-0023, Coastal Engineering Research Center, 166 p.
- ANAN, F. S., 1971, Provenance and statistical parameters of sediments of the Merrimack Embayment, Gulf of Maine: unpub. PhD disser., Geology Department, University of Massachusetts, 377 p.
- ANGAS, W. M., 1960, Shark River Inlet sand bypassing project: Jour. Waterways and Harbors Div., Proc. Am. Soc. Civ. Eng., No. WW 3, pp. 29-47, (Discussion: WW 2, pp. 153-157, 1961).
- BOWMAN, J. R., 1960, Natural bypassing of sand at coastal inlets: Discussion, Proc. Am. Soc. Civ. Eng., Jour. Waterways and Harbors Div., Vol. 86, Paper 2540, No. WW 2, pp. 131-132.
- BRUUN, P. and GERRITSEN, F., 1960, Stability of coastal inlets: Amsterdam, North Holland Publ. Co., 124 p.
- CALDWELL, J. M. and LOCKETT, J. B., 1965, Effects of littoral processes on tide water navigation channels: Chap. 6, Evaluation of present state of knowledge of factors affecting tidal hydraulics and related phenomena, U.S. Army, Corps of Engineers, Com. on Tidal Hyd.; Rept. 3, pp. VI-1 through VI-26 (Originally pub. 1950).
- CHUTE, N. E. and NICHOLS, R. L., 1942, Shoreline changes on Plum Island, Massachusetts: Am. Jour. Sci., V. 40, pp. 349-355.
- DEAN, R. G. and WALTON, T. L., 1975, Sediment transport processes in the vicinity of inlets with special reference to sand trapping: Proc. 2d Int. Estuarine Res. Conf., Myrtle Beach, (L. E. Cronin, ed.), pp. 129-150.
- FARRELL, S. C., 1969, Growth cycle of a small recurved spit, Plum Island, Massachusetts: in Coastal Research Group, Coastal Environments, NE Massachusetts and New Hampshire, (M. O. Hayes, ed.), Cont. No. 1-CRG, Geology Department, University of Massachusetts, pp. 316-336.
- HERRON, W. J. and HARRIS, R. L., 1967, Littoral bypassing and beach restoration in the vicinity of Port Hueneme, Calif.: Conf. Coas. Engr., 10th, Proc., V. 1, pp. 651-675.
- HODGES, T. K., 1955, Sand by-passing at Hillsboro Inlet, Florida: U.S. Beach Erosion Bd. Bull., V. 9, No. 2, Washington, pp. 1-6.

- HUBBARD, D. K., 1974, Tidal inlet morphology and hydrodynamics of Merrimack Inlet, Massachusetts: unpub. MS thesis, Geology Department, University of South Carolina, 144 p.
- HUBBARD, D. K., 1975, Morphology and hydrodynamics of the Merrimack River ebb-tidal delta: Proc. 2d Int. Estuarine Res. Conf., (L. E. Cronin, ed.), Myrtle Beach, S.C., pp. 253-266.
- MCDONALD, T. J. and STURGEON, M. A., 1956, Sand by-passing at a Virginia tidal inlet for nourishment of Virginia Beach: Proc. Am. Soc. Civ. Eng., Jour. Waterways and Harbors Div., V. 82, No. WW 3, Paper 976, pp. 976-1 through 976-14.
- U. S. ARMY COASTAL ENGINEERING RESEARCH CENTER, 1973, Shore Protection Manual: Chapter 4, 180 p.

CHAPTER 106

TOPOGRAPHIC CHANGE RESULTING FROM CONSTRUCTION OF

A HARBOR ON A SANDY BEACH: KASHIMA PORT

by

Norio TANAKA* and Shoji SATO**

* Hydraulics Division

** Head of Marine Hydrodynamics Division

Port and Harbour Research Institute, Ministry of Transport

Nagase, Yokosuka, Japan

ABSTRACT

This paper presents some general properties on topographic change on the shore and sea bed in the vicinity of ports and harbours constructed on the sandy beach, mainly with the case study of Kashima Port. Following three characteristics of the topographic change due to prolongation of breakwaters are discussed; that is,

- i) The shoaling and the change of topography in the area surrounded by breakwaters and shoreline.
- ii) Topographic change of artificial beach in the updrift beach of breakwater having the long oblique part.
- iii) Erosion and accretion of downdrift beach due to the prolongation of the oblique part of breakwater.

INTRODUCTION

Port Kashima, the biggest new industrial port in Japan, has been constructed on the central part of a bow-shape sandy coast of 70 kilometers long facing the Pacific Ocean as shown in Fig. 1 and Fig. 2. Since 1961, before the start of the construction works, many kinds of field investigations and model experiments have been conducted by the Port Construction Office of Ministry of Transport and the Port Construction Office of Ibaragi Prefecture under the continuous co-operation of Port and Harbour Research Institute.

Authors had reported the some results of these investigations on the characteristics of this coast before the beginning of the construction works in the 10th Conference on Coastal Engineering (S. Sato and N. Tanaka, 1966). Furthermore, one of authors had already presented a paper on the topographic change during the early period of the construction works in the 12th Conference



Fig. 1 The location of Kashima Port and other harbours mentioned in this paper.

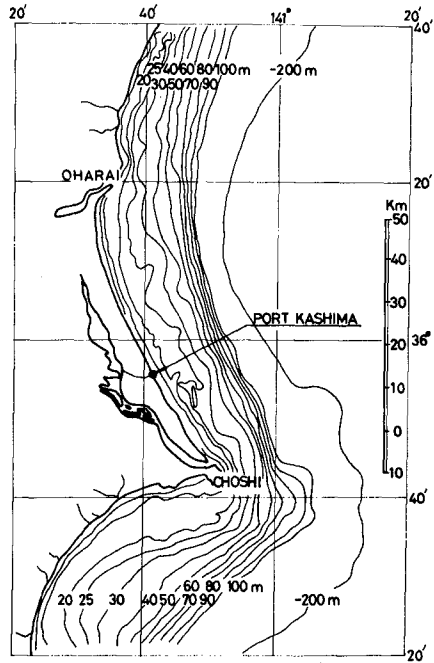


Fig. 2 Kashima Coast and the location of Kashima Port.

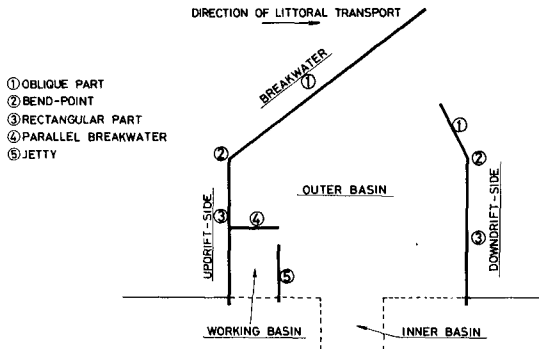


Fig. 3 The terminology in this paper.

on Coastal Engineering (S. Sato and I. Irie, 1970). Therefore, this paper composes a series with these other papers. The terminology employed in this paper is given in Fig. 3.

THE CHARACTERISTICS OF THE COAST AND THE LITTORAL DRIFT OF KASHIMA COAST

The northern portion of Kashima Coast has a narrow beach with the cliff of Kashima Plateau and the Naka River flows out to the sea at the northern end. The southern portion is a part of the alluvion formed by the Tone River and has wide beach with sand dunes. The influence of the discharged materials from these two rivers is restricted in the area near to their river mouth, and it is considered that the source of sand drifted in the central portion should be the coast itself.

The natural topography before the port construction was comparatively simple and stable. At the central portion where Kashima Port is located a sand dune of about 8 meters high above L. W. L. ran along the coast and the backshore was 50 to 80 meters wide and 3 to 4 meters high. There were along-shore bars at 100 to 300 meters seaward from the shoreline which were of 0.5 to 2 meters deep at the crest and of 1.5 to 3 meters deep at the trough. In the offshore area of those alongshore bars, the sea bed topography was very smooth and depth contour lines ran parallel each other until the water depth reaches to 20 meters. But, the area less than 40 meters beyond 20 meters in water depth is very gentle in the bottom slope and reaches to the seaward edge of the submerged terrace and depth contour lines make complex curves. The sea bed slope was about 1/10 to 1/30 in the forshore, about 1/50 to 1/60 in the inshore and about 1/100 to 1/120 in the area shallower than 20 meters depth in the offshore.

Waves approach almost perpendicularly to the coast from the direction of northeast to east-southeast, though the southerly waves exceed the northerly ones a little in summer and the oppsite takes place in winter. The annual predominant direction of waves depends on the frequency of tyoons approached to this coast; in the year when tyoons frequently attack this coast, the southerly waves prevail. The maximum significant wave observed in this coast has been about 6.5 meters in height and almost 10 to 13 seconds in period.

The mean diameter of bottom materials is about 0.15 millimeters in the offshore zone and 0.2 to 0.6 millimeters in the inshore zone. The alongshore littoral transport per year has been estimated to be the order of 600,000 cubic meters both in the southerly and northerly directions, though the southerly transport slightly exceeds the northerly one (S. Sato and N. Tanaka, 1966).

CONSTRUCTION WORKS OF PORT KASHIMA

The general plan of Port Kashima was set in 1962, but it was modified in 1968 according to an increase of ship sizes as shown in Fig. 4.

The construction works began at April 1963 with dumping of rubble stones for the south jetty of the working basin for small crafts. By April 1975, the north breakwater of 1050 meters long, the parallel breakwater of working

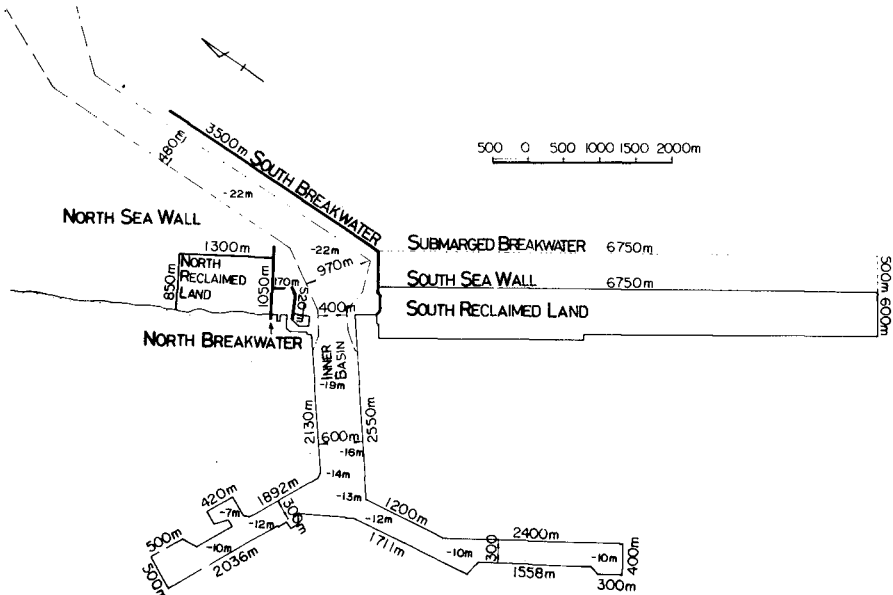


Fig. 4 The general plan of Kashima Port

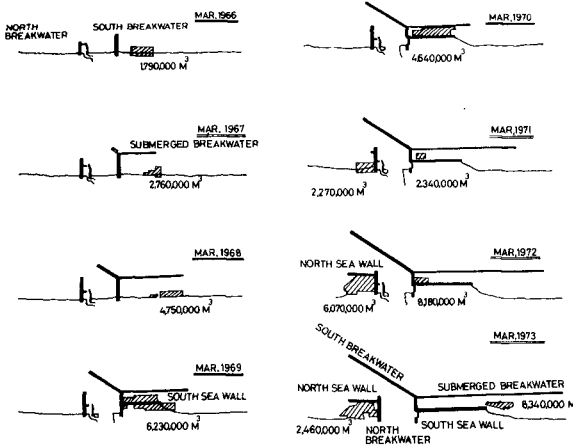


Fig. 5 The process of the construction works of structures and the discharge of dredged sand.

basin and the south breakwater of 4300 meters long have been completed.

In April 1965, the dredging works of the inner basin was begun without disturbing the shoreline in the outer basin by cutter-suction dredgers which entered into the inner basin through the beach of the working basin by cutting it. The shoreline in the outer basin was cut in September 1968 to connect the inner basin to the outer basin. The dredged sand has been dumped on the beaches of both sides of the harbour. In the period from April 1965 to April 1975, the amount of the sand dumped on the beach has reached to about 50 millions cubic meters.

In this period, the bulkheads were constructed for reclaimed land in the both side of the harbour and the submerged breakwater was also built in front of the south man-made beach. The processes of these works are shown in Fig. 5 and Fig. 6.

SHOALING OF THE OUTER BASIN OF HARBOUR FOLLOWING THE PROLONGATION OF BREAKWATERS.

Figure 7 shows sounding maps for each summer in the period from 1963 to 1968, during which the breakwaters were constructed but no dredging works were initiated in the outer basin. In this figure, solid lines indicate the constructed portions of breakwaters and dotted lines denote the portions where only the rubble mound base of caisson was constructed.

The comparison of the sounding maps of 1965 and 1966 indicates that the depth contour lines shallower than 5 meters moved landward at the middle of coast between the south and north breakwater and offshoreward near the both breakwaters, as the rectangular parts of those breakwaters were prolonged. This tendency became much clear with the prolongation of the oblique part of the south breakwater and the depth contour lines took more convex shape. Moreover, the mean direction of the beach in the outer basin became to take more oblique angle to the shoreline of former days, and the most receded point of shoreline was shifting northward with the prolongation of the oblique part of the south breakwater; this can be seen from the comparison of the sounding maps of 1967 to 1968.

On the other hand, the central portion of the outer basin was shoaled, the depth contour lines deeper than 7 meters becoming concave in shape as shown in the maps of 1966 to 1968.

Severe scouring were seen in the vicinity of the tip of the breakwaters when they were in the surf zone, as well as at the inside of the rubble mound. These characteristics of the sea bottom topography around breakwaters are commonly found in other harbours as reported by Sato and Irie (S. Sato and I. Irie, 1970).

Figure 8 indicates the volume change of sand in the outer basin in the same period as that of Fig. 7. Solid lines indicate the change of sand volume in each area shown in the note of this figure as well as that of the total area of the outer basin, while the dashed line is the volume change of the sand dumped on the south coast. In this four years, sand of about 2 millions cubic meters increased in the outer basin in total and the accretion of sand

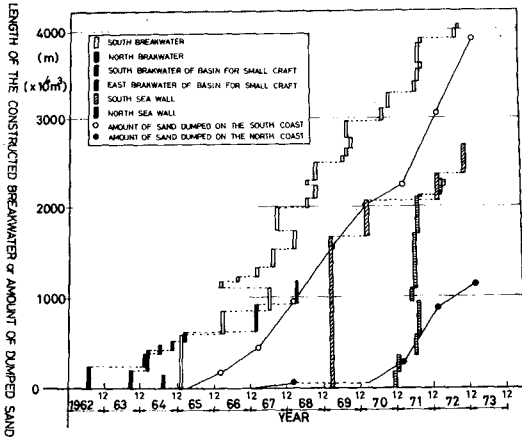


Fig. 6 The length of constructed structures and the amount of dumped sand onto beach.

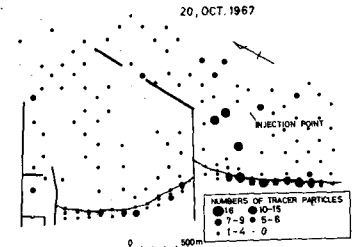
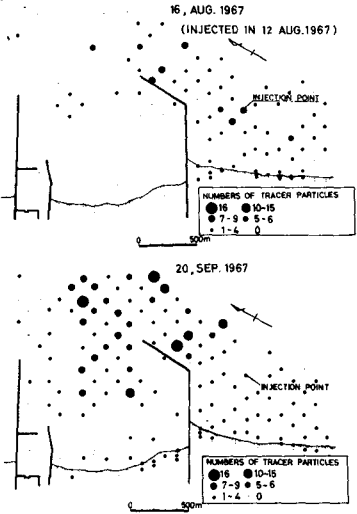


Fig. 9 The distributions of fluorescent tracers.

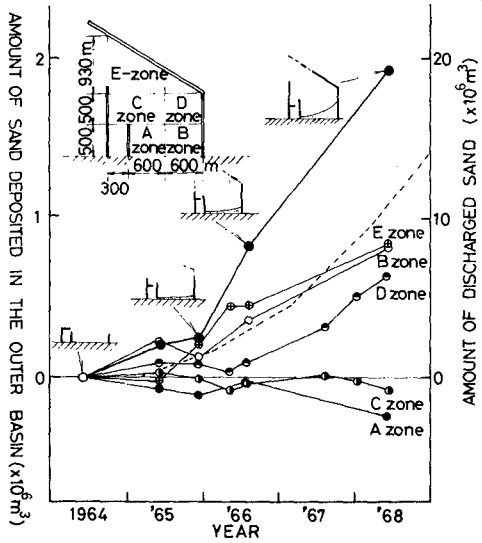
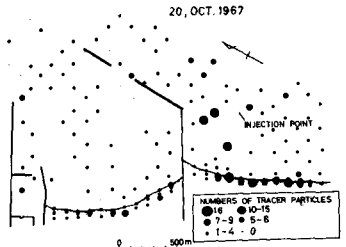


Fig. 8 The volume change of sand in the outer basin (in the period of 1964 to 1968).



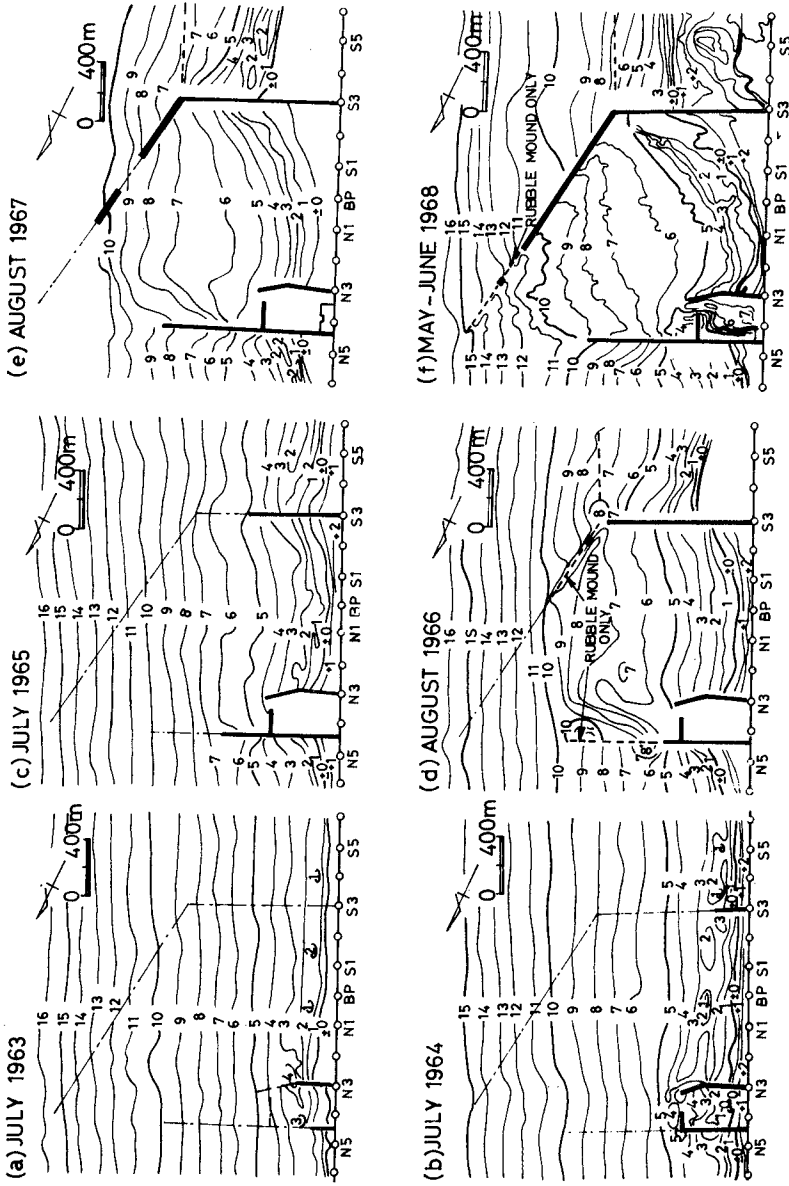


Fig. 7 Sounding maps for each summer from 1963 to 1968

took place in the area B, D and E which are located near the south breakwater. On the other hand, the area A and C were scoured gradually. These pattern of the volume change of sand is considered to be closely related to the diffraction of waves and formation of the counter-clockwise circulating currents in the outer basin as reported by authors (S. Sato and I. Irie, 1970 and N. Tanaka, 1974).

In Fig. 8, the change of the total volume of sand of the outer basin seems to have close correlation with the amount of sand dumped on the south coast. Figure 9 shows the distribution of fluorescent tracers injected in the offshore zone of the south coast on 12th of August, 1967. The result clearly indicates the movement of sands which move offshoreward along the south breakwater and enter into the outer basin going around the tip of the south breakwater.

TOPOGRAPHIC CHANGE OF ARTIFICIAL BEACH CONSTRUCTED USING THE DREDGED SAND

As mentioned above, since April 1965, dredged sands have been discharged onto the south coast and the amount of these sand reached to about 22 millions cubic meters until March 1971. The change of the shore line in this period is shown in Fig. 10. In this figure, the x, y and z axes indicate the alongshore distance from the south breakwater, the distance between the shoreline and the datum line, and the years of survey, respectively. Therefore, the thick solid lines represent the shape of the shoreline at a certain time and the thick dashed-dot lines indicate the change of the distance between the shoreline and the datum line.

The shoreline of the south coast began to advance seaward near the south breakwater due to the discharge of dredged sand, and the beach continued to extend seaward or southward until 1970. But, after the winter of 1970, although discharge of dredged sands was continued, the artificial beach began to be eroded from the neighbourhood of the south breakwater and this erosion was extended southward.

In pace with the change of the shoreline, the beach profiles also changes as shown in Fig. 11. The slope of sea bed in the part shallower than 10 meters deep became steeper gradually with the advancement of the shoreline, but after the beginning of the erosion, the slope returned toward the original one the reverse process of that mentioned above.

Figure 12 indicates the relationship between the advancement of the shoreline and the slope of the sea bed at each water depth. The slope of sea bed became steeper with the advancement of the shoreline and reached to a certain critical slope for the water depth of 10 meters and less. The average values of these critical slopes were as follows:

range of water depth	average value of the critical slope
0 to 2 meters	1/25
2 to 4 meters	1/50
4 to 6 meters	1/60
8 to 8 meters	1/65
8 to 10 meters	1/100

The difference between these critical slope and the natural one before fill is the largest in the area of 2 to 4 meters depth, and it becomes small in both the shallower or deeper area.

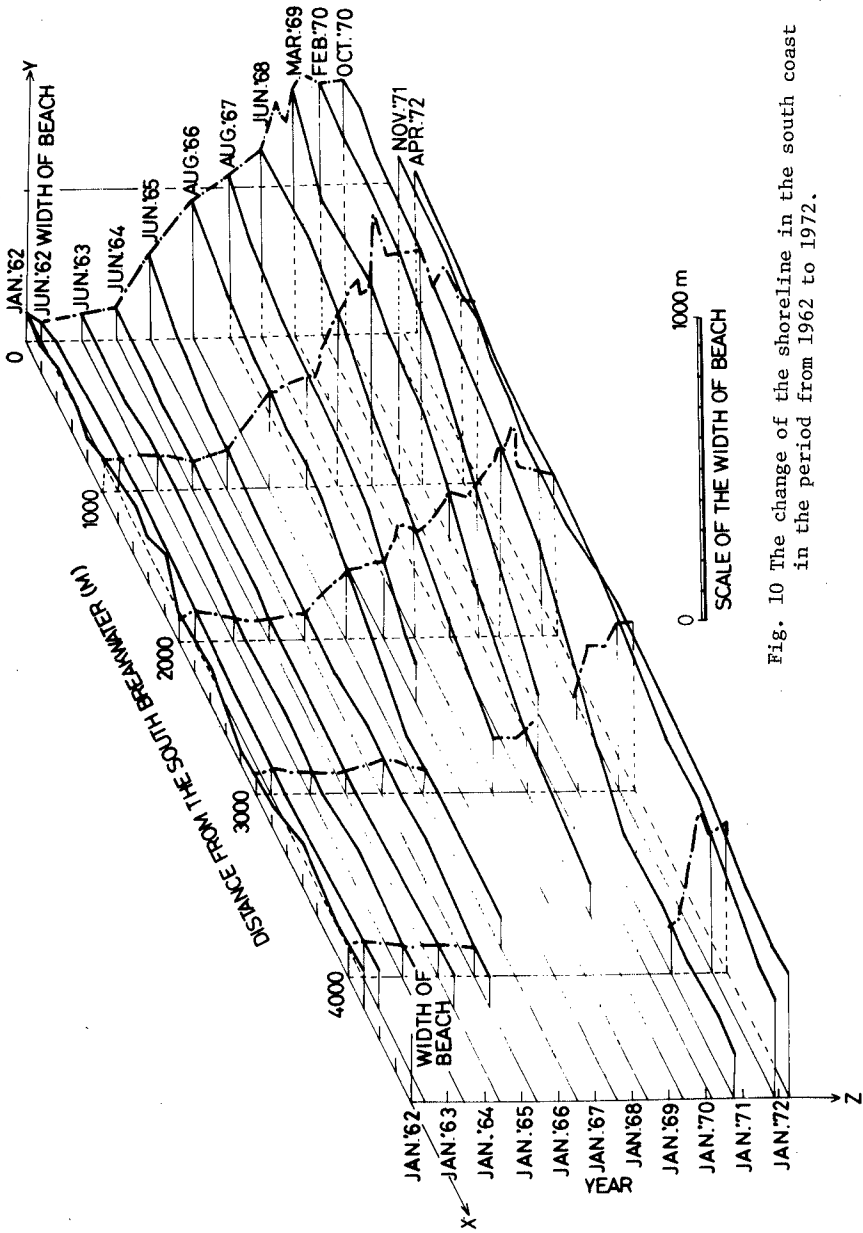


Fig. 10 The change of the shoreline in the south coast in the period from 1962 to 1972.

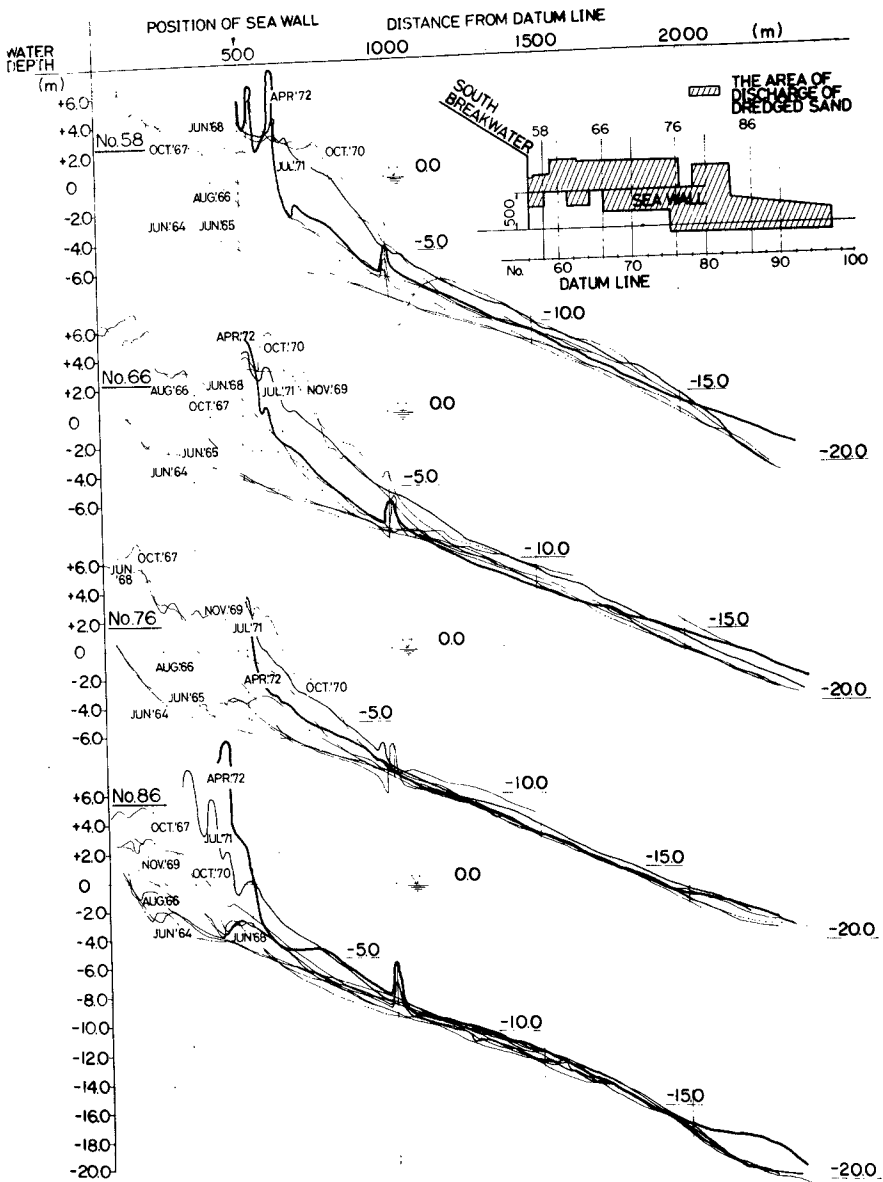


Fig. 11 The change of profiles of the south coast

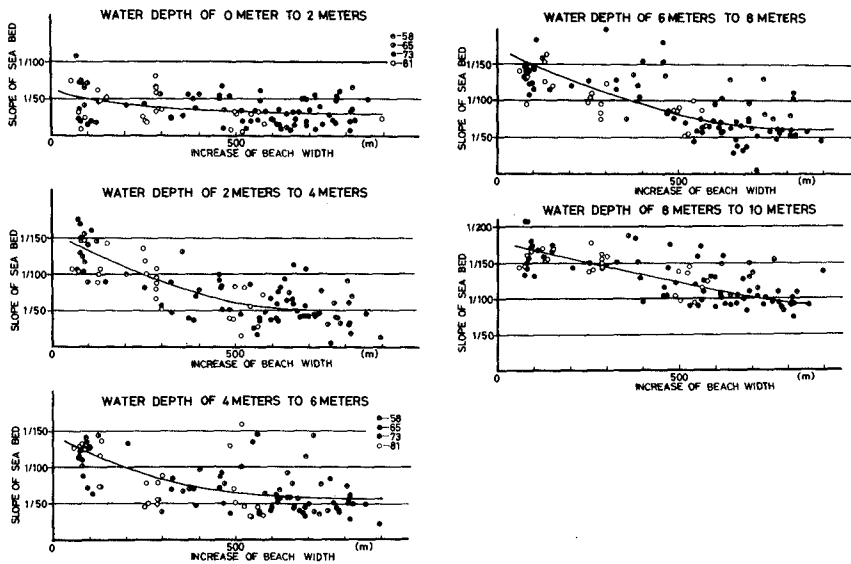


Fig. 12 The relationship between the advancement of the shoreline and the slope of sea-bed.

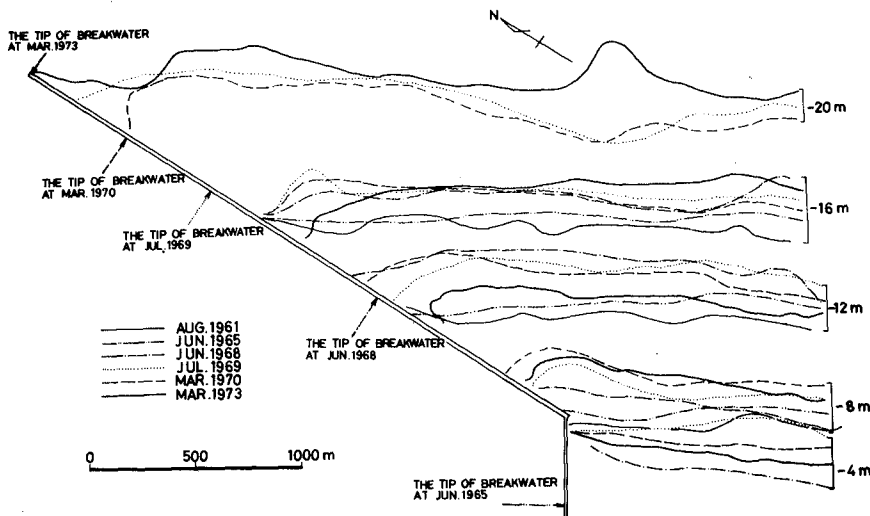


Fig. 13 The change of depth contour lines in the offshore side of the south breakwater.

Some amount of sand discharged onto the south coast was transported by waves and currents to the offshore side of the oblique part of the south breakwater forming a submarine bank along the breakwater. But, after the winter of 1970, this submarine bank was also rapidly scoured. The change of depth contour lines of 4, 8, 12, and 20 meters deep is shown in Fig. 13. In this figure, the attention is called for the fact that the contour lines of 16 and 20 meters deep moved offshoreward even after the beginning of scour of the submarine bank.

Figure 14 is the distribution of the difference of the water depth surveyed in the different years; i. e., the upper figure is the difference of depth in the period of the growth of the submarine bank from April 1965 to August 1970 while the lower one is the difference in the period of scouring of bank from August 1970 to March 1973. In the period of the growth of the submarine bank, the decrease of the water depth was the largest near the bending point of the south breakwater. The area of considerable shoaling extended from that point toward the tip of the breakwater forming a belt within the distance of about 200 meters from the breakwater. On the other hand, in the period of scouring, the scouring was found only around the bending point of the south breakwater, and the extent of scouring was the severest along the foot of the breakwater. The offshore area of this zone was continuously shoaled even after the beginning of the scouring of south coast.

Such the examples of the erosion at the updrift side of a long oblique breakwater are found in many other ports as in the cases of Sendai Harbour and Hachinohe Harbour shown in Fig. 15. These two harbours are located at the end of long sandy beaches facing the Pacific Ocean, where waves from the down drift side are sheltered by a headland. Although updrift side of these harbours are shoaled over the wide area, the erosion of the same pattern as Kashima Port is found near the breakwater of the updrift side.

Such erosion at the updrift side of a long oblique breakwater may be considered to be caused by the currents formed along the breakwater due to waves. Fig. 16 indicates examples of experimental results on the currents due to waves around the breakwater prolonged obliquely. The experiments were conducted using a fixed bed model having the bottom slope of 1/15 in the landward of the shoreline and 1/30 in the seaward of it. Model waves of 4 centimeters in height and 0.8 seconds in period were acted from the direction perpendicular to the shoreline. In this figure, thick solid lines indicate the breakwater, and the origin of the co-ordinate is taken at the point of intersection of the shoreline to the breakwater.

In every case, currents which flow updriftward along the breakwater and the shoreline are formed. These currents turn their direction offshoreward at a certain point, the position of which goes away from the breakwater with the increase of the length and obliquity of the breakwater. The velocities of these currents also increase with the length of breakwater, but the increase of the length in the offshore area of the surf zone is not so effective.

EROSION AND ACCRETION OF DOWNDRIFT BEACH BY THE PROLONGATION OF BREAKWATER.

Figure 17 shows the sounding maps for each winter in the period from 1970 to 1973 in which the oblique part of the south breakwater was prolonged beyond the tip of north breakwater. The dotted lines in each maps represent the

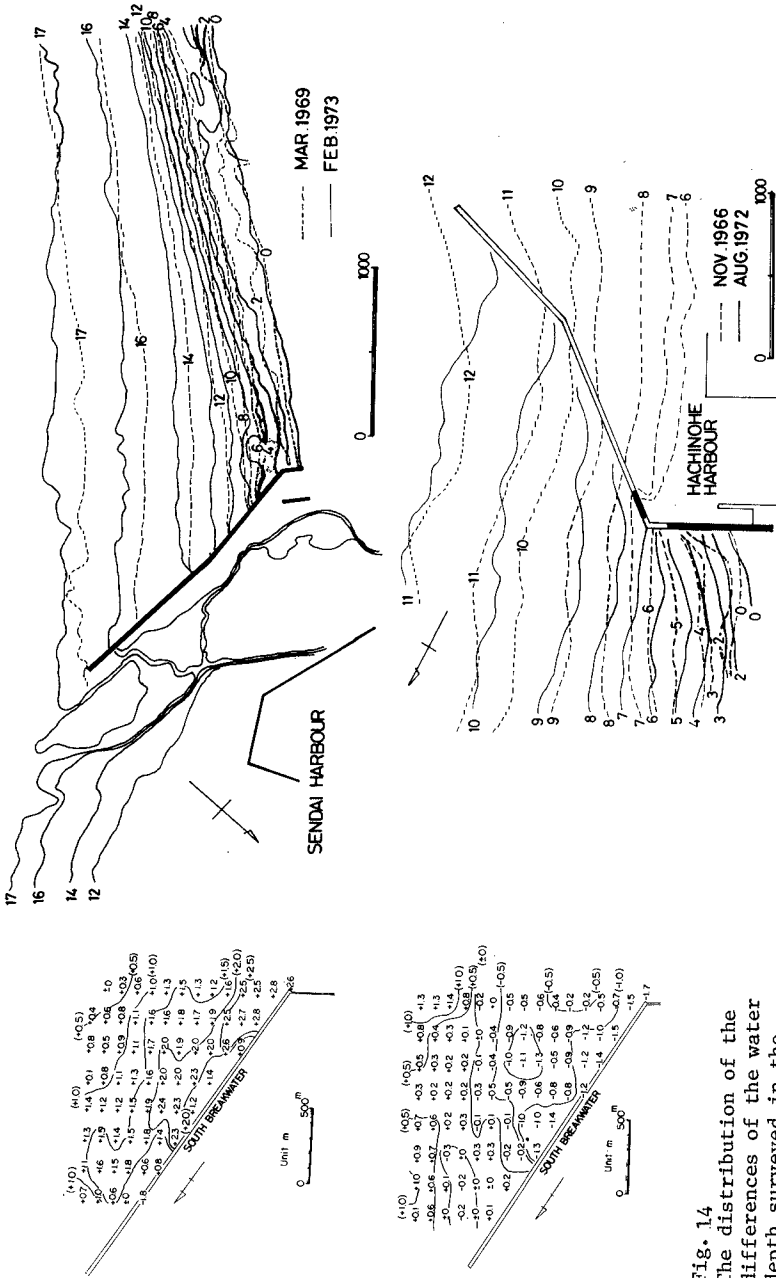


Fig. 15 Examples of the erosion at the updrift side of a long oblique breakwater (Sendai Harbour and Hachinohe Harbour).

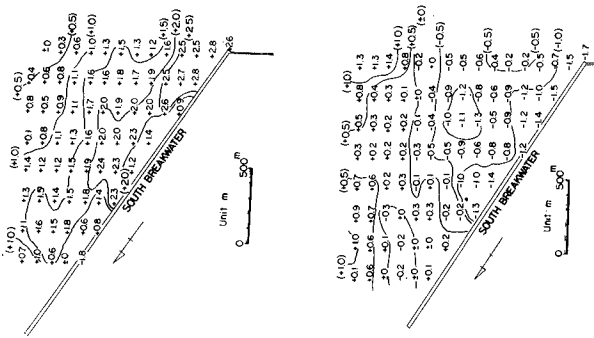


Fig. 14 The distribution of the differences of the water depth surveyed in the different year.

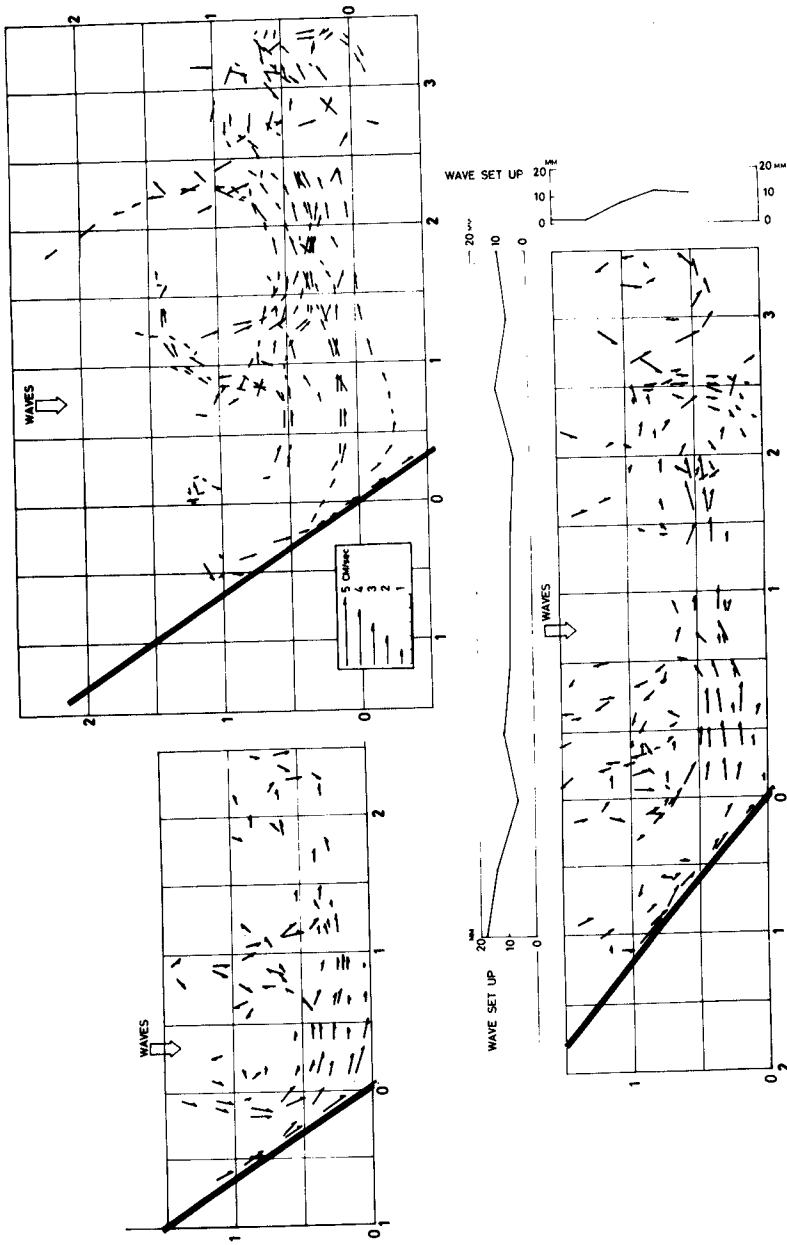


Fig. 16 Examples of results of the model experiment on the currents due to waves along the breakwaters prolonged obliquely (wave height= 4 cm, period= 0.8 sec.).

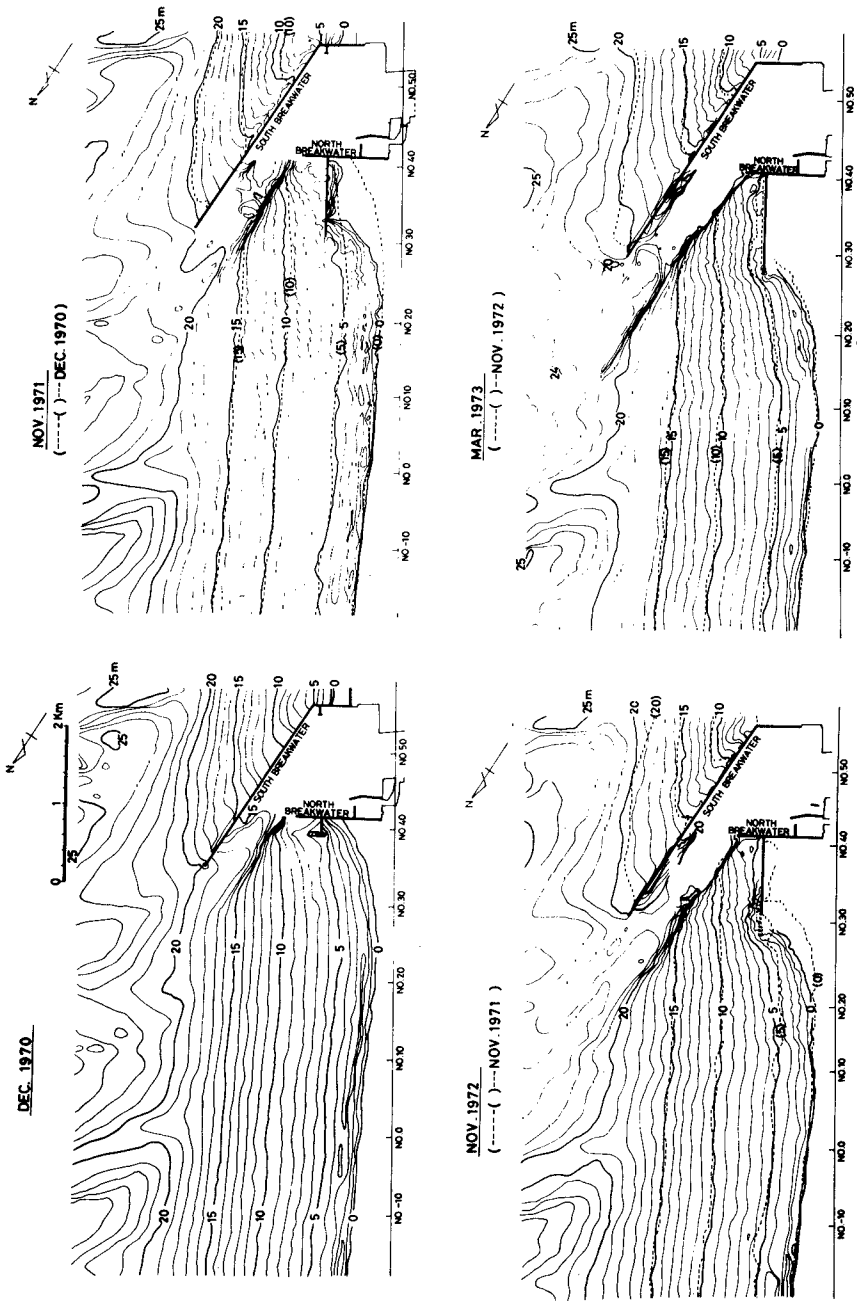


Fig. 17 Sounding maps for each winter in the period from 1970 to 1973.

depth contour lines of one year before.

In the area sheltered by the south breakwater at the outside of the north breakwater, the depth contour lines shallower than 15 meters moved seaward year by year. At the north side of these shoaled area, the zone shallower than 5 meters in depth was eroded. Moreover, these shoaling and erosion zone seem to extend to the north and the deeper area with the prolongation of the south breakwater.

Figure 18 indicates the change of the distance between the shoreline and the datum line measured along the fixed surveying lines in the north coast. At the line of No.27 to 39 located near the north breakwater, the shoreline advanced seaward gradually during the early years and after a certain years the advancement of shoreline was accelerated rapidly. At the lines of No.15 and 21, the shorelines moved seaward or landward slowly during the early years, but after a certain years the shorelines receded suddenly and then advanced again few years after. Furthermore, at the lines of No.3 to 9 located the most far away from the north breakwater, the shorelines were stable or erosive in the early years, but they were eroded rapidly after a certain years. The sudden change of shoreline movement occurred earlier at the line near to the north breakwater than the farther one. This fact means that the boundary between the shoaled area near the north breakwater and the eroded area of north side of it was shifted northward year by year.

Figure 19 indicates the relationship between the position of the tip of the south breakwater and the most eroded place or the north boundary of the accreted area near the north breakwater. In this Figure, dates written along the south breakwater and the shoreline indicate the times when the tip of the south breakwater, the most eroded place, and the boundary of the accreted area were located at respective positions. The thin solid lines and dashed-dot lines are the lines connecting the tip of the south breakwater to the most eroded place and the boundary of the accreted area at the same date, respectively.

In this figure, three solid lines run almost parallel each other, keeping the constant angle of 45 degrees with the predominant wave direction. Likewise, the three dashed-dot lines run parallel, keeping the angle of 30 degrees.

Figure 20 shows the distribution of differences of the water depth between the sounding maps of December 1970 and March 1973 as well as two lines which make the angle of 45 degrees and 30 degrees with the predominant direction of waves at the tip of the south breakwater. It is known from this figure that the area remarkably shoaled in the offshore area is also in the south side of the line of 30 degrees.

The above mentioned pattern of the change of the sea bed topography can be found frequently in other harbours as shown in Fig. 21, which indicates the changes of shorelines measured on aerial photographs. Harbours shown in this figure are located on the sandy beach facing the open sea. In these examples, the angles of the line connecting the tip of the main breakwater and the most eroded place measured from the wave direction are among 40 to 50 degrees. On the downdrift side boundary of accreted area, this angles are among 20 to 30 degrees.

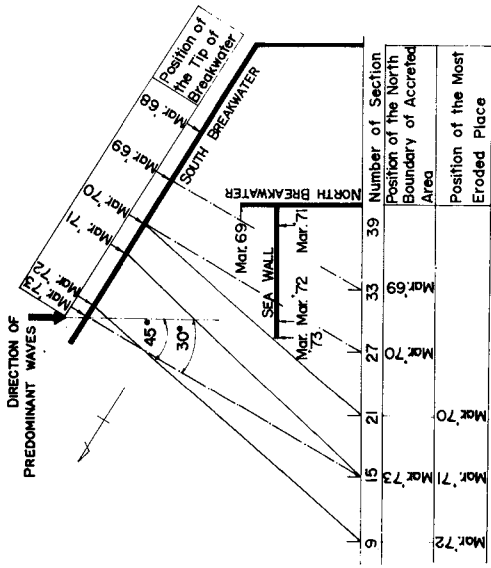


Fig. 19 The relationship between the position of the tip of the south breakwater and the most eroded place of the north boundary of the accreted area.

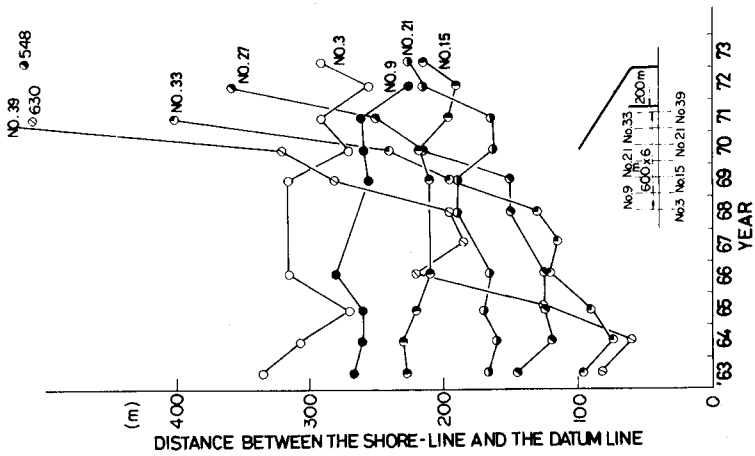


Fig. 18 The change of the distance between the shoreline and the datum line in the north coast.

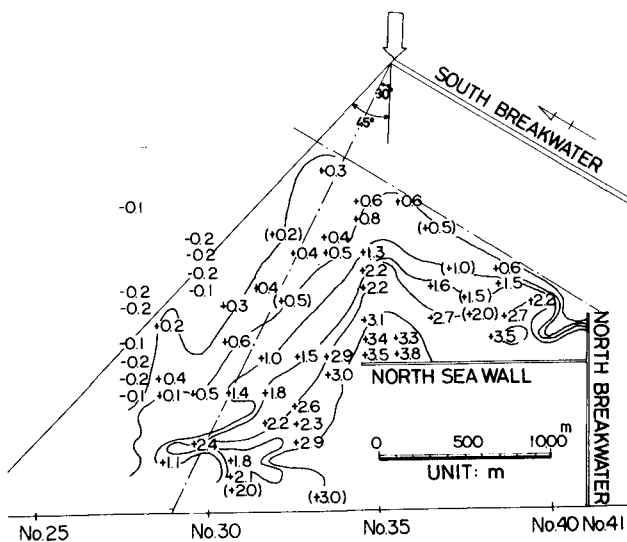


Fig. 20
The distribution of differences of the water depth between the sounding maps of Dec. 1970 and Mar. 1973.

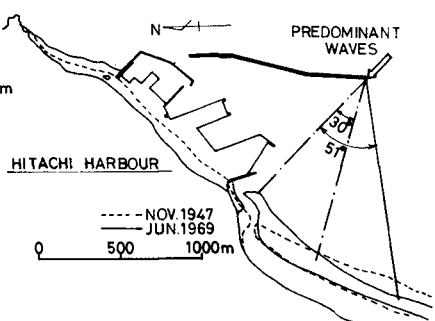
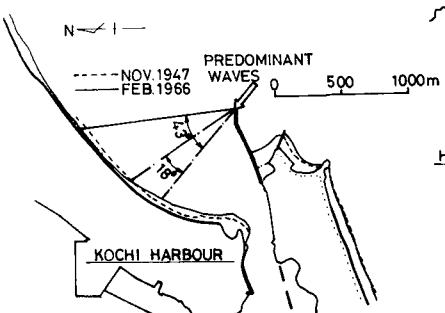
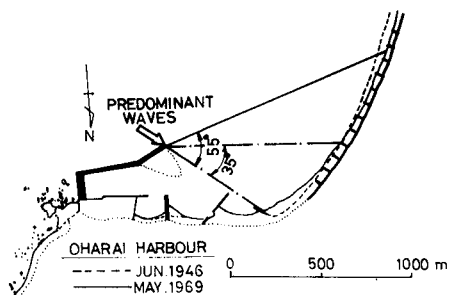
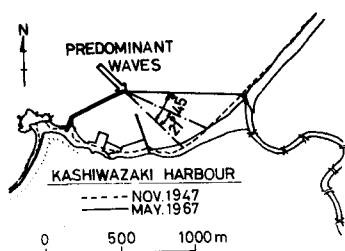


Fig. 21 Examples of the topographic change at the downdrift side of harbours (Kashiwa-zaki Harbour, Oharai Harbour, Khochi Harbour and Hitachi Harbour).

As demonstrated in the example of a model experiment shown in Fig. 22, the cause of this kind of topographic change is considered to be the currents formed in the downdrift side of this harbour due to waves diffracted at the tip of the main breakwater. The experiment was performed in the same model in the former chapter under the same wave condition. Due to wave diffraction, the wave height becomes small behind the breakwater. As the result of this decrease of wave height, the wave set-up also decreases from the open portion toward the sheltered area behind the breakwater as shown in the upper graph of Fig. 22. This alongshore gradient of the wave set-up is considered as the main cause of the currents which transport bed materials toward the sheltered area behind the main breakwater.

CONCLUSION

The following points were made clear as the general properties on the change of the topography of sea bed caused by construction of new ports, that is:

- 1) When the oblique part of updrift side breakwater did not cover the tip of the downdrift side breakwater, the outer basin was shoaled remarkably. Almost all the materials entered into the outer basin were carried by the circulating currents and were deposited behind the updrift side breakwater of at the central portion of the outer basin. The central part of the beach in the outer basin was eroded due to these currents. As the result of these change, the shoreline in the outer basin took convex shape.
- 2) When the shoreline advanced due to the discharge of dredged sands, the profile became steeper gradually and reached to a critical one. But, in the erosion period, the slope of man made beach returned toward the original one taking the reverse process with one in the progressive period.
- 3) After the length of the oblique part of updrift side breakwater reached to about 2,000 meters, the updrift beach of this breakwater was severely eroded due to currents formed along the oblique part of updrift side breakwater.
- 4) Since the time when the oblique part of updrift side breakwater was prolonged beyond the tip of downdrift side breakwater, a certain place of the downdrift beach began to be eroded, and the harbour side of this eroded place was accreted. The position of this eroded place and the boundary of accreted area were shifted with the prolongation of the updrift side breakwater.
- 5) The line connecting the tip of updrift side breakwater with the most eroded place or the downdrift side boundary of the accreted area always kept a constant angle with the predominant wave direction. These angle were about 40 to 50 degrees for the most eroded place and 20 to 30 degrees for the boundary of the accreted area, respectively.
- 6) The cause of this change of sea bed topography is considered to be the currents formed in the downdrift side of the harbour due to waves diffracted at the tip of updrift side breakwater.

REFERENCES

- 1) Shiji SATO and Norio YANAKA; Field investigation on sand drift at Kashima Coast, Proc. of 10th Conf. on Coastal Engineering, Sept. 1966.
- 2) Shoji SATO and Isao IRIE; Variation of topography of sea bed caused by the construction of breakwaters, Proc. of 12th Conf. on Coastal Engineering, Sept. 1970.
- 3) Shoji SATO, Norio TANAKA and Katsuhiro SASAKI; The case history on variation of sea bottom topography caused by the construction works of Kashima Port, Report of P.H.R.I., Vol. 13, No. 4(2), Dec. 1974 (in Japanese)
- 4) Norio TANAKA; Topography change of sea bed around harbours constructed on sandy beach, Proc. of L974 Annual Research Presentations of P.H.R.I., Dec. 1974 (in Japanese)

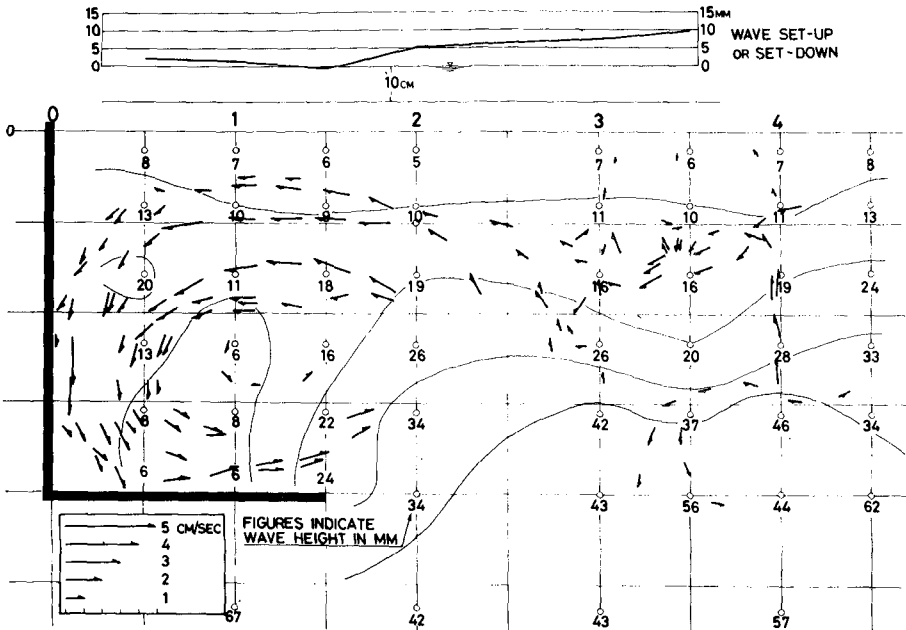


Fig. 22 An example of a model experiment on the currents formed in the downdrift side of the harbour due to waves.

CHAPTER 107

IMPACT OF YACHTING MARINAS ON BEACHES

by

J.P. LEPETIT *

The development of tourism resulted in the construction of very many small yachting harbours along the French mediterranean shore during recent years. Some of them were constructed on the rocky foreland located at the end of sandy beaches. Such beaches being a priori stable, no particular sedimentation investigation was carried out. In several cases, the construction of a port led to rapid evolution of the beach, accretion occuring in the vicinity of the port and erosion elsewhere.

1 - NATURE OF THE PROBLEM

When a port is situated on a sandy shore experiencing significant littoral drift, many precautions are taken to ensure the continuity of sediment transit (by passing) or to remedy the consequences of its interruption.

It is not the same in the case of a sandy beach enclosed between two rocky forelands and apparently stable. Generally there is very little net sand movement from one beach to another past the headlands and the coastal line does not change significantly with time. This can be misleading giving the impression that there is little or no longshore transport of sediment : this however is not the case

* Chef de la Division Hydraulique Maritime - Laboratoire National d'Hydraulique de Chatou - Electricite de France - Chatou - France.

as the resultant littoral drift along a shore is usually a balance between sand movement due to swells from opposing directions which may individually transport very significant quantities of material. Even though the resultant sediment movement due to the two opposing swells produces zero drift on a stable beach between two rocky headlands, a change in only one of the terms can induce spectacular evolution.

To illustrate such a mechanism, let us consider the schematic case of a west-east oriented beach submitted to two swells, having different origins (north-west and north-east, as in fig. 1), but the same frequency. In the natural state, the north-west swell induces a littoral drift eastwards when the north-east swell does the same westwards. On average, they cancel each other out and the shore is stable during a long period of time ; it comes under the influence only of alternated evolutions, generally small, as the continuance of each swell is limited.

Now, let us build a port with an enveloping breakwater at the west end of the considered beach (fig. 2) ; this port will achieve a sheltered zone from the north-west swell, where the transit eastwards becomes zero and where the only transit westwards, due to the north-east swell subsists. The equilibrium is broken and a net littoral drift appears in the sheltered zone ; the sand accumulates at the port entrance and, to satisfy continuity, the rest of the beach erodes. The evolution so induced is therefore doubly harmful : the port access is endangered and the beach disappears.

This mechanism and the consequent beach evolution are very obvious and the explanation of the damage suffered is easy for the specialists in the subject. Unfortunately, the mechanism is less evident a priori and the engineers, having overcome their apprehension about the stability of the shore in its natural state, do not feel the need to get advice from these specialists before designing a project.

2 - AN EXAMPLE OF EVOLUTION VERIFIED IN SITU

A spectacular example is provided by Bormes-les-Mimosas port (fig. 3), which was constructed on a rocky foreland separating two beaches of very fine sand, the first at the north and the second at the south. This port includes a jetty constructed on the rocky foreland oblique to the shore and a breakwater parallel to the shore. The entrance to the port is open to the north beach. The beach experiences swells from the east which are almost parallel to the shore, and produce very little drift, swells from the south-east creating a south-north transport of sediment and north-east swells producing a contrary north-south movement. The port works considerably after the effect of the swells and result in a large zone on the south beach sheltered from the north-east swells and, on the north beach, a zone, as important as the first, sheltered from south-east swells. As a

consequence of the imbalance, more sand is transported along the north beach from north to south than formerly and similarly more sand is transported along the south beach from south to north, producing significant accretion in the vicinity of the port during the course of two or three years.

Figure 4 shows the evolution of the shoreline on each side of the marina during its construction.

On the upper part of the figure, only the south part of the breakwater is built, but it already creates a sheltered zone on the south beach where a beginning of accretion is clearly visible.

In the middle part, the accretion is increasing fastly and propagating to the north like a sand wave. The advancing of the breakwater to the north also induces an accretion on the north beach.

The last picture of figure 4 is a copy of a postcard showing the marina after completion. The accretion on both sides of marina is clearly visible.

Plan views of figure 5 show the initial configuration of the shoreline in 1968 and in 1973 after completion of the marina. There is a uniform recession of the north beach shoreline and it is quite evident that the sand trapped near the marina comes from this beach. But as the volume of sand trapped is greater than the volume lost by the beach, a part of it comes probably from offshore erosion which occurred in front of the breakwater.

Another erosion occurred on the south beach and a groyne was constructed to stop this erosion and its extension to the whole beach.

The advance of the shoreline at the south is more than 100 m, and on the side of the entry channel the accretion necessitates maintenance dredging.

3 - MEANS OF STUDY

For reasons of cost and time allowed, it is not possible to carry out a study on a movable bed model for each yacht-port to be built, but the noted evolutions may be anticipated thanks to simple studies on drawings. Such studies consist of the determination of the direction where the existing in situ swells come from, the establishment for these swells of wave refraction diagrams giving the propagation of swells as well as their angle of incidence with the shore and diffraction diagrams giving the effect of the port on the swells spreading. By reasoning from the results of these calculations or from the operation of a littoral drift mathematical model, it is possible to estimate both the effect on sand transport and the resulting evolution of the shoreline.

4 - POSSIBLE REMEDIAL MEASURES (fig. 6)

In order to avoid such a type of evolution, it is necessary to design ports that don't create sheltered zones from certain swells outside the structures. For that, the pegging out of the port along the shore shall correspond with a maximum possible accuracy to the extent of the zone where the spreading of various swells is disturbed by the presence of the port structures. The best way seems to design a port including two convergent breakwaters, the direction of each of them corresponding to the swells extreme origine. In the case of an asymmetrical port that includes only one breakwater starting from the shore, it seems necessary to build on the other side a groin long enough to allow the sands transit to stop just at the limit of the sheltered zone created by the port.

CONCLUSION

It should not be forgotten that a beach seeming stable is in fact in dynamic equilibrium under the action of various movements of sand that cancel each other out. Therefore, it is enough to change one of these to disturb the general equilibrium and provoke rapid evolution. The construction of a port, even of small importance, in the vicinity of sandy beaches must consequently be preceded by a minimum study by drawings, that will allow an assessment to be made of the future evolution resulting from port construction and the definition of a certain number of safeguards that will be used if the noted evolution is effectively as dangerous as the predicted one.

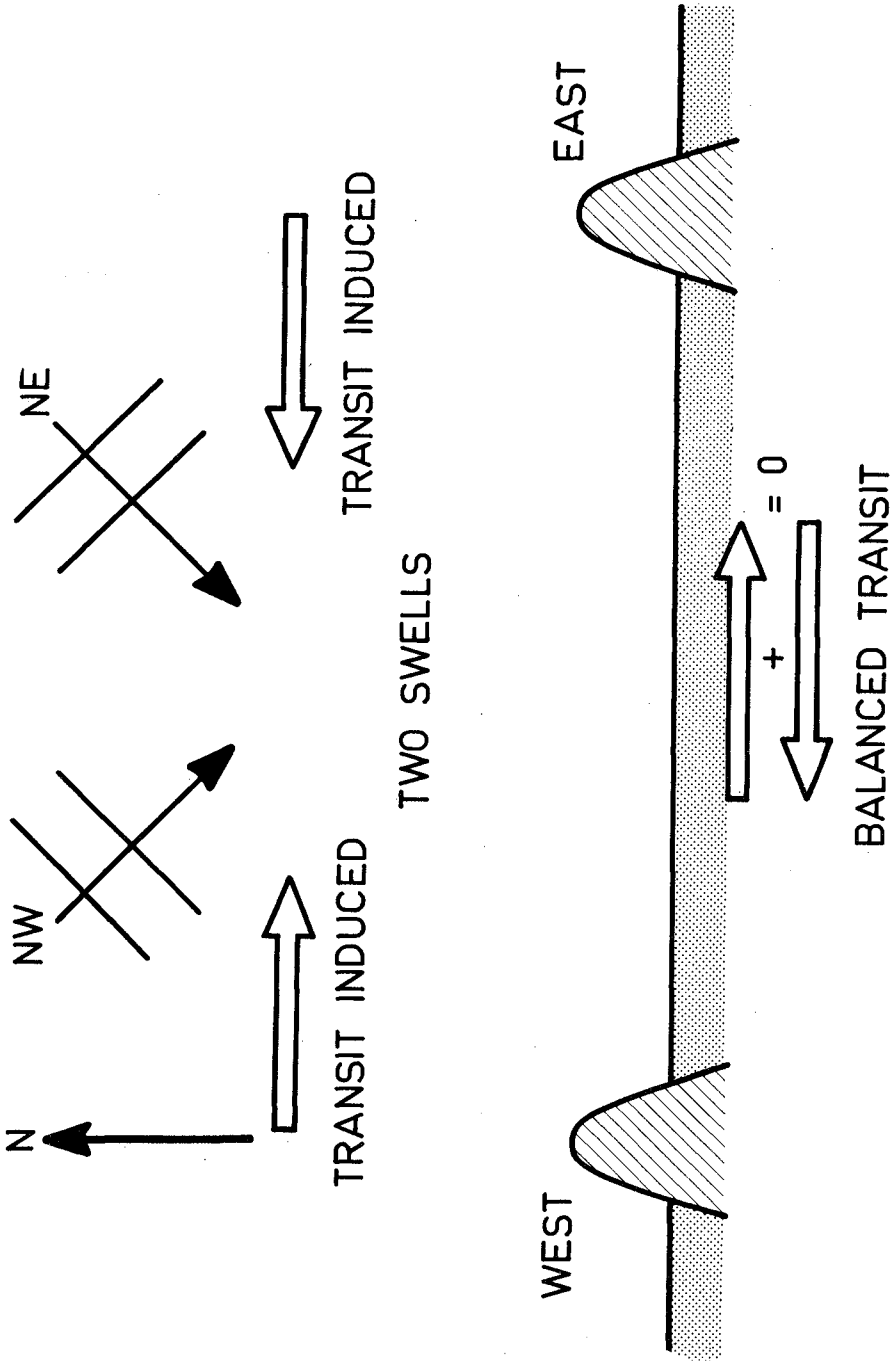
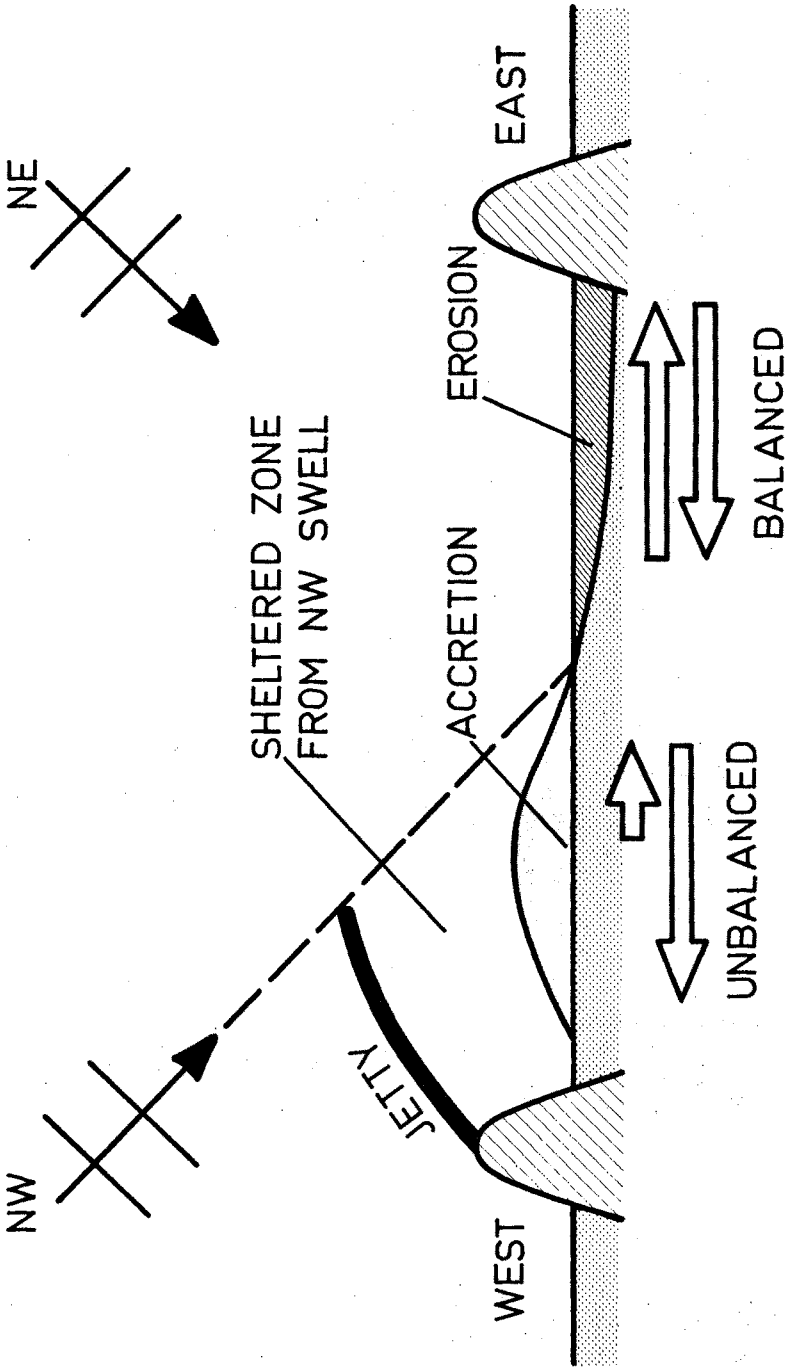


Fig.1 - BEACH IN EQUILIBRIUM IN ITS NATURAL STATE



TRANSIT

Fig.2 - BEACH CHANGES AFTER BREAKWATER CONSTRUCTION

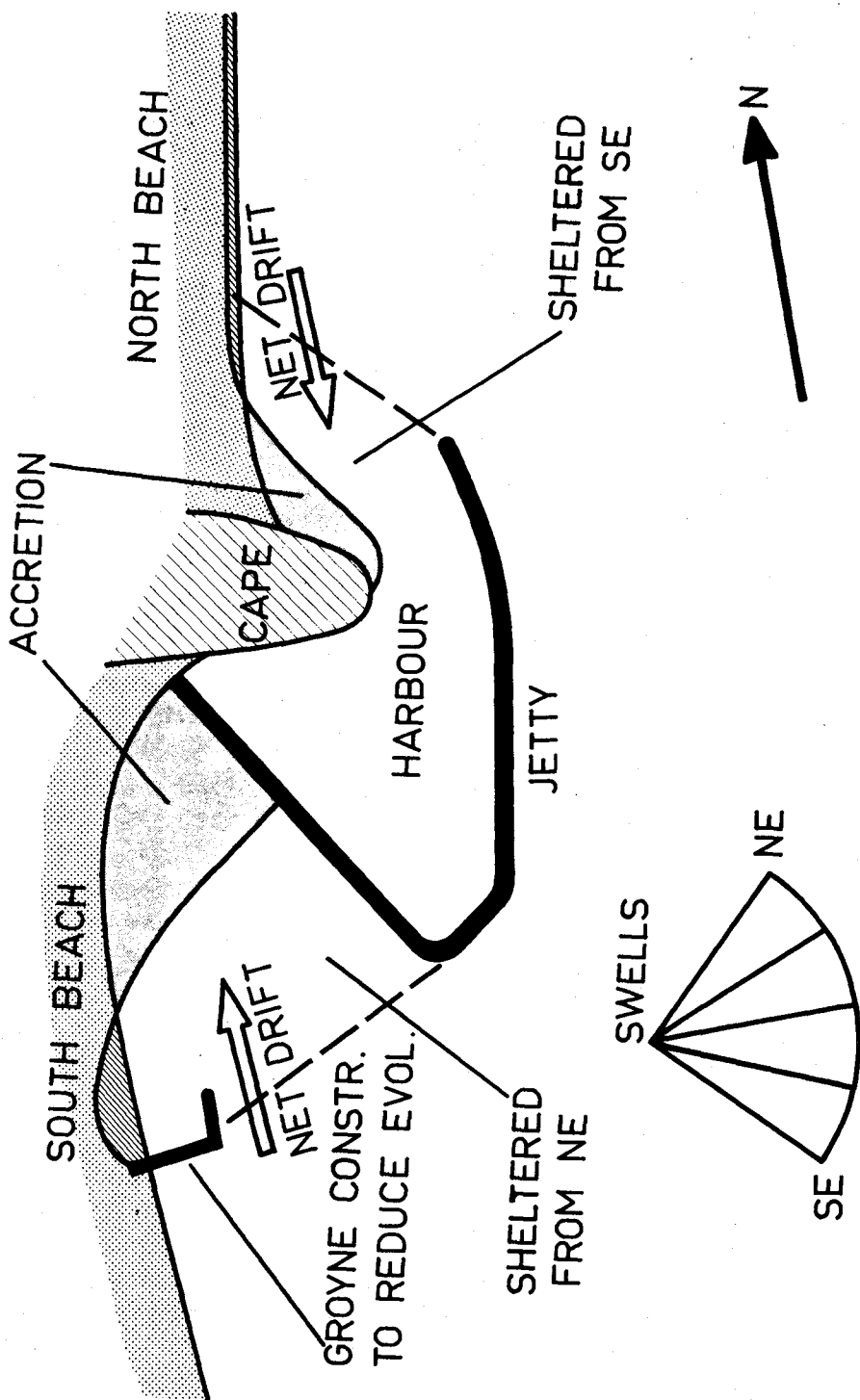
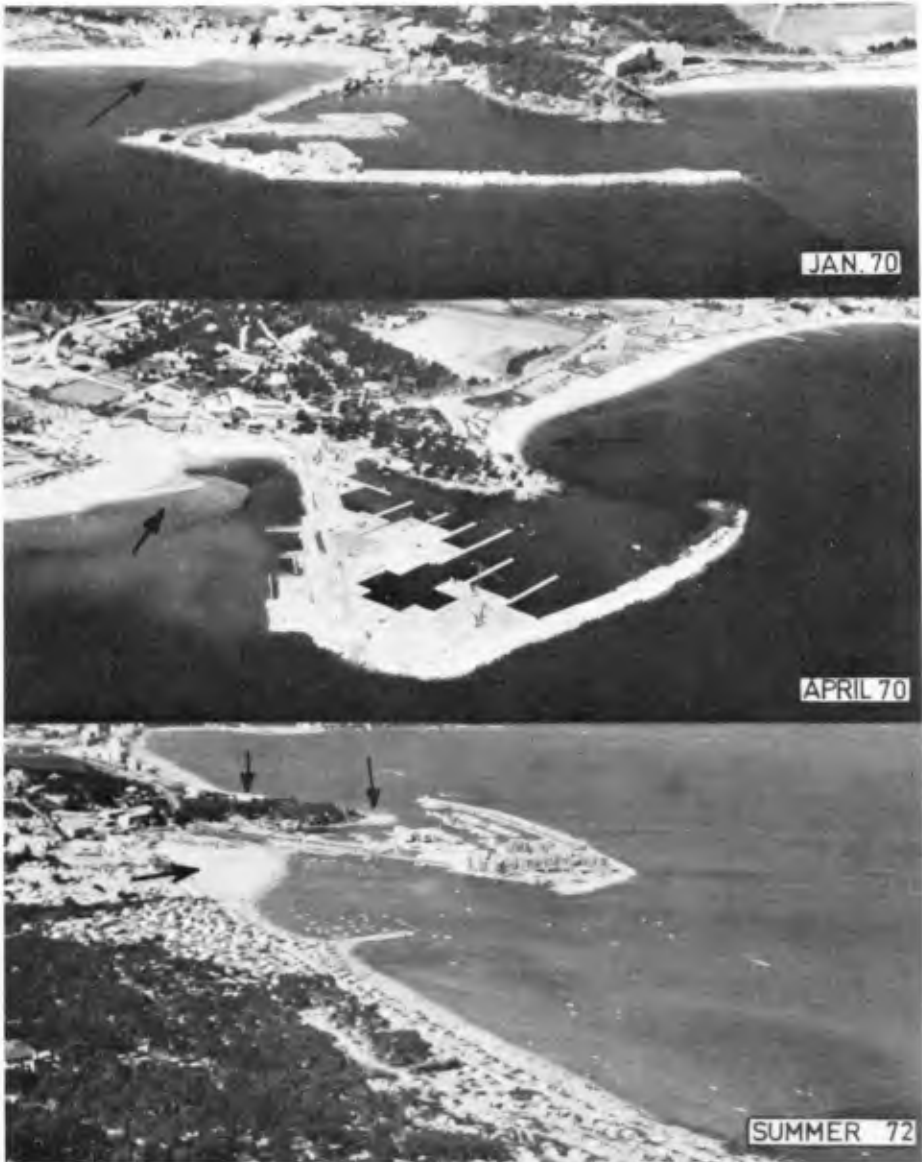


Fig.3 - BORMES LES MIMOSAS PORT

*FIGURES SE RAPPORTANT A L'ETUDE INTITULEE:
THE IMPACT OF YACHTING MARINAS ON BEACHES*

by
J. P. Lepitt



**Fig.4 – EVOLUTION OF SHORELINE DURING
MARINA CONSTRUCTION**

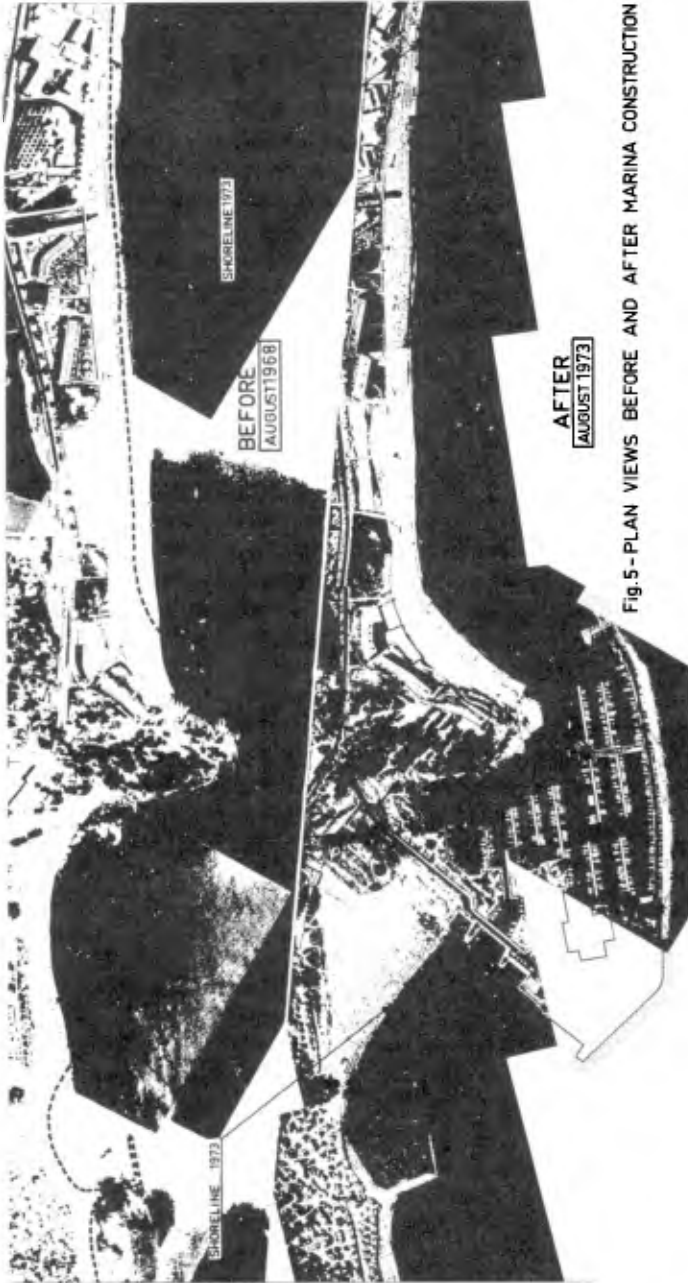
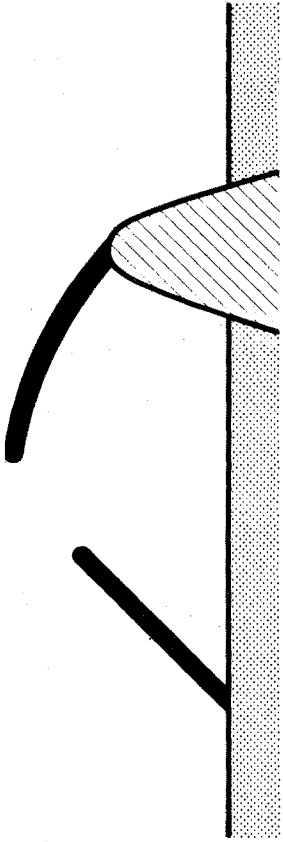
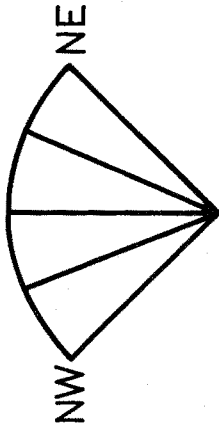


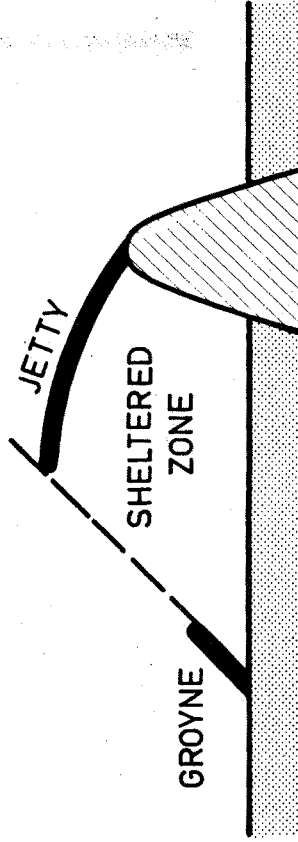
Fig. 5- PLAN VIEWS BEFORE AND AFTER MARINA CONSTRUCTION



a - DESIGN WITH NO SHELTERED ZONE OUTSIDE THE JETTIES



SWELL SECTOR



b - DESIGN WITH GROUYNE TO STOP THE TRANSIT OF SAND

Fig. 6 - DESIGNS REDUCING IMPACT

CHAPTER 108

HARBOUR INLETS ON TIDAL ESTUARIES

Hans Vollmers*

Two important points should be considered if a harbour mouth is planned on a river:

1. The traffic conditions especially the navigation must be considered (i.e. large width of the mouth)
2. The sedimentation should be small (i.e. small width of the mouth)

These conditions are contradictory. Harbour mouths are lateral enlargements. The current doesn't follow these enlargements, a separation sheet forms which is characterized by eddies. A more or less great mass of water is in movement in the enlargement. These rotating movements are called "vortices". One distinguishes "primary vortices", "secondary vortices" etc. depending on the initiating current (Fig. 1).

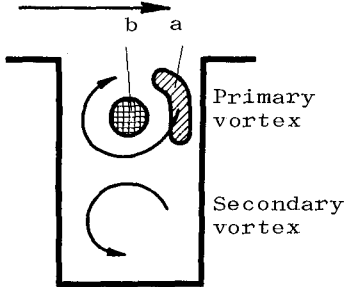


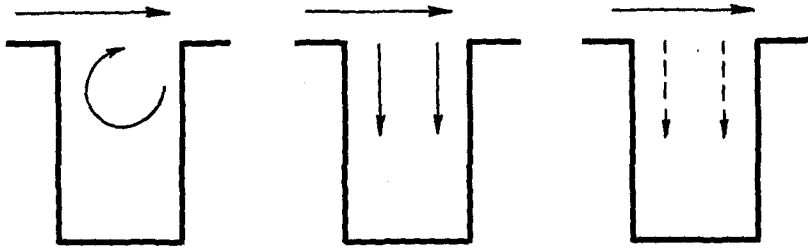
Fig. 1

The deposition of sediment in lateral enlargements depends on the characteristics of the vortices, because the exchange of liquid material has interacted with the exchange of transported material. Normally the coarse material deposits in area a and the fine material in area b (Fig. 1).

Generally one can define the reasons for sedimentation as follows (Fig. 2).

1. Current effect (vortex in the harbour mouth caused by energy exchange)
2. Tide effect (fill up of the harbour basin during the flood tide)
3. Density effect (density current caused by different salinity in the estuary and the harbour entrance)

* Dr.-Ing. Baudirektor, Bundesanstalt für Wasserbau
Hamburg, Germany



a. Current effect b. Tide effect c. Density effect

Fig. 2

The current effect is dominant for the sedimentation in harbour mouths situated on rivers with one-directional flow. If it is possible to influence the primary vortex the sedimentation will be smaller. Fig. 3 shows possible ways to displace or to diminish the primary vortex.

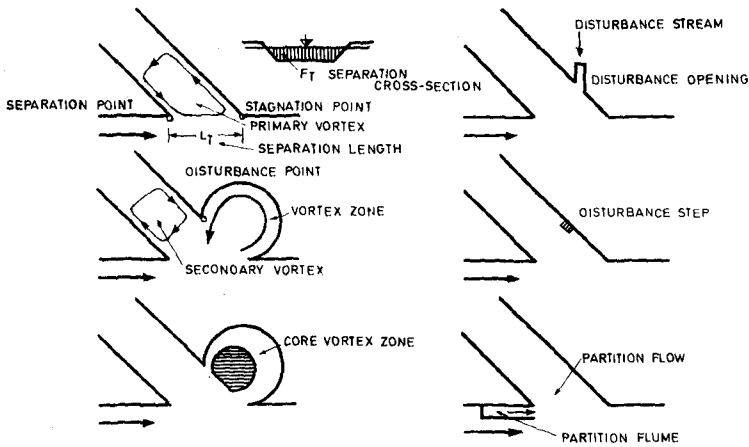
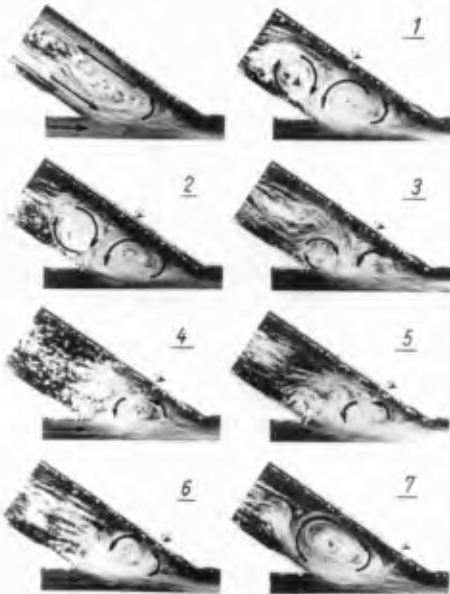


Fig. 3

There is the "vortex zone", the "vortex zone" restricted on the border current (core vortex zone), a so-called "disturbance opening" and a "disturbance step". These methods are based on an alteration of the downstream geometry of the harbour mouth.



It is possible to influence the separation zone i.e. the velocity gradient between the river flow and the vortex area with a so-called "partition flow". The "partition flow" is directly taken from the river flow, but only the upper layer with smaller sediment load.

The influence of the primary vortex with the "disturbance step" may be seen on Fig. 4. The practical use of a "vortex zone" is demonstrated on a harbour at the Rhine River. Above one can see the situation before the alteration of the mouth and below there is the new entrance. Now the deposition zone has been located downstream (Fig. 5).

Fig. 4



In estuaries it is very difficult to find a satisfying solution because the current direction changes rhythmically. Neglecting the density effect, the following happens (Fig.6): During the flood tide, the current effect and tide effect superpose mutually, i.e. the current intensity is very great starting on the stagnation point. During the ebb tide the two effects work against one another. Because vortices are movements with no much energy small currents can destroy the development of a vortex.

Fig. 5

These general considerations were used for a case study in the Ems-Estuary-Model at the Bundesanstalt für Wasserbau in Hamburg.

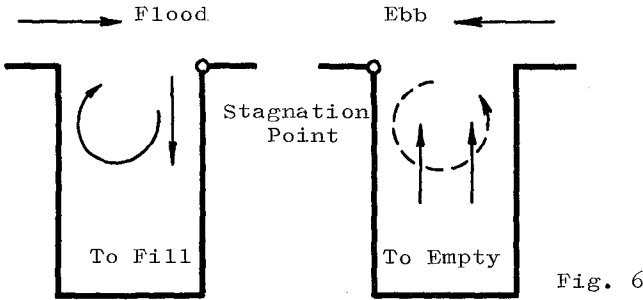


Fig. 6

The model includes the River Ems and has been built as a fixed bed model, with the possibility to also investigate sections with movable bed. The horizontal scale is 1:500, the vertical is 1:100. Since the Ems is a boundary river between the Netherlands and the Federal Republic of Germany a number of problems also arose for the Dutch authorities. The new entrance of the Delfzijl harbour was one of these problems (Fig. 7).

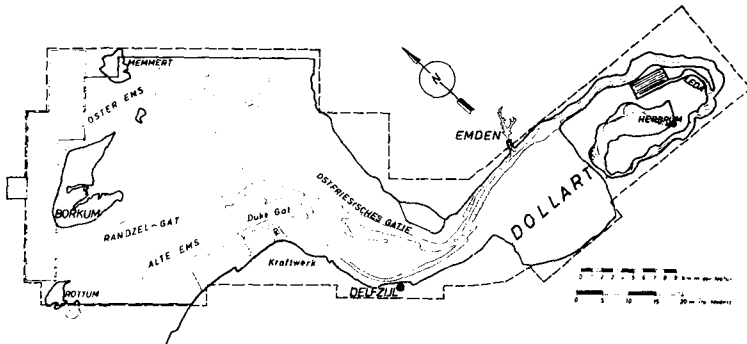


Fig. 7

The general situation of the Delfzijl harbour is shown in Fig. 8. 20 years ago the harbour was only the basin on the left, the bight of Watum was the access channel. Because the sedimentation in the bight of Watum increased, it was necessary to dredge a new access from the main channel Borkum - Emden. The industrial development and the sedimentation in the near field zone of the old entrance led to the enlargement of the basin and the construction of the new entrance. The old entrance will be closed later on. Contrary to usual harbours with vertical

development to the river the Delfzijl harbour is practically only a parallel channel under tidal influence. It could be expected that very bad current conditions would appear if the old entrance was closed. Therefore the model investigations were concentrated to improving the current situation in the new entrance.

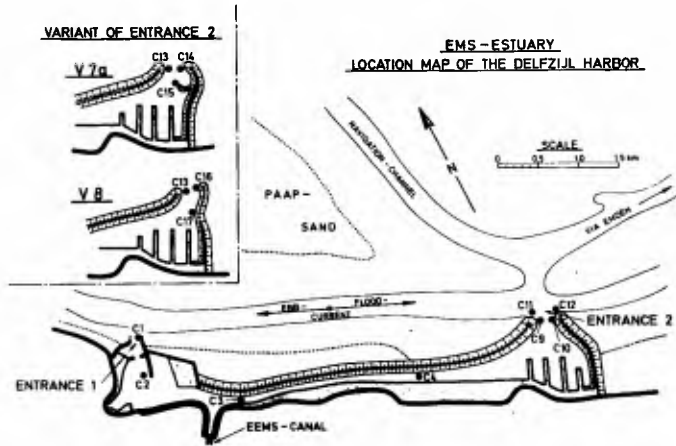


Fig. 8

The estimation of the different investigated variations has been carried out with the aid of the surface current visualised with photographed scraps of paper and with the aid of velocity measurements in a medium water depth at certain points.

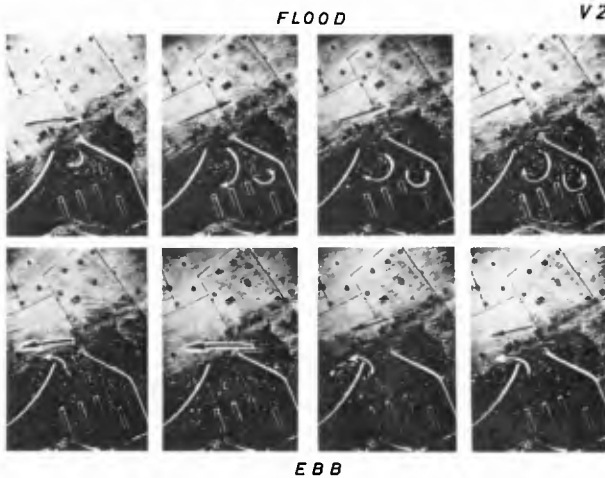


Fig. 9

EBB

The current situation for V2 (new entrance open, old entrance closed) can be gathered from Fig. 9. During the flood tide there is a velocity concentration on the right jetty which produces a large vortex in the main basin. The current effect and tide effect are superposed upon one another. During the ebb tide the tide effect i.e. the outflow from the basin dominates the current effect. There is no rotating flow in the entrance zone. In this case the current effect is especially small caused by the diversion of the upstream jetty.

Fig. 10 shows clearly that using a "vortex zone" there is no possibility to avoid the primary vortex in the harbour mouth. Only in the first flood phase one can see a relatively good velocity distribution in the entrance cross section. Subsequently, large vortices appear.

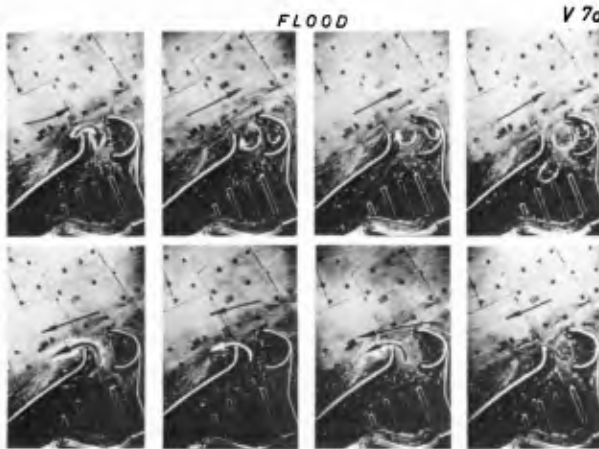


Fig. 10

EBB

Geometrical alterations were not sufficient to suppress the overlapping of current and tide effect. Finally the only possibility was to renounce the closure of the sea-side entrance and to produce a stream against the tide and current effect in the new entrance. For this reason a systematic investigation has been started with different widths (100, 65, 50, 40 m) of the old entrance. The development of the surface current for an inlet width of 100, 65 and 40 m is demonstrated by the following photos. The results of the investigation with three various inlet width are

- a) 100 m(Fig. 11): The energy slope is sufficient to prevent the inflow on the upstream jetty. In the first flood phase there is practically no movement. Later, a uniform outflow appears in the harbour mouth. During

the ebb tide the current enters the harbours on the downstream jetty, a small vortex now turns in the large basin.

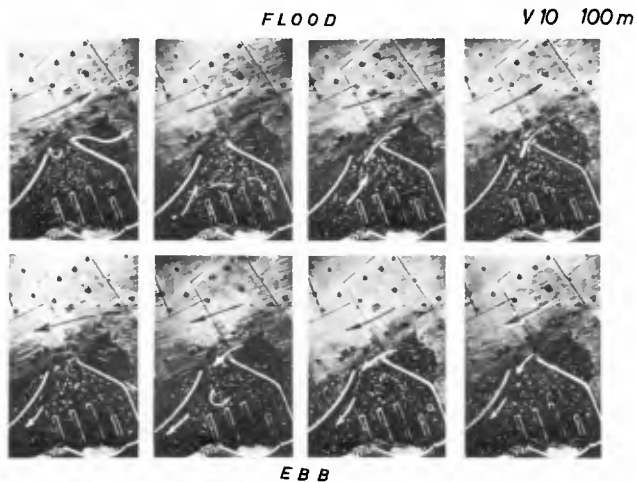


Fig. 11

- b) 65 m (Fig. 12): For an opening width of 65 m one can see nearly the same surface current distribution.

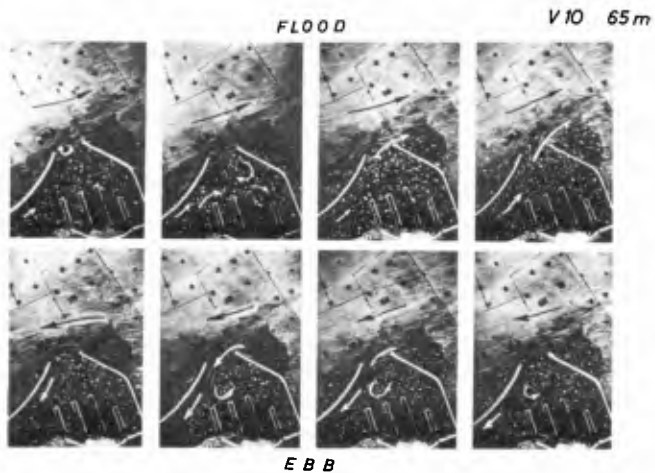


Fig. 12

c) 40 m (Fig. 13): This width is not sufficient to avoid the inflow on the upstream jetty in the first flood phases. Only in phase 4 an outflow occurs.

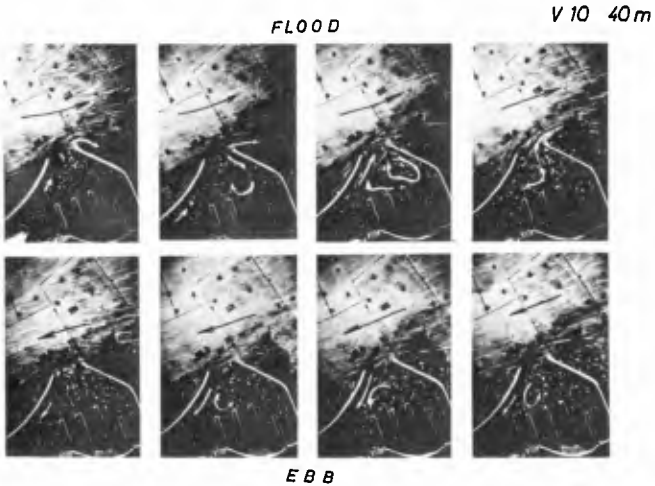


Fig. 13

During the ebb tide the current distribution is nearly the same for all opening widths.

To help confirm the observations of the surface currents, velocity measurements were carried out in medium water depth in certain points. Fig. 8 shows these measuring points. The velocity has been measured either in flood/ebb direction or vertically to it. Fig. 14 may help explain.

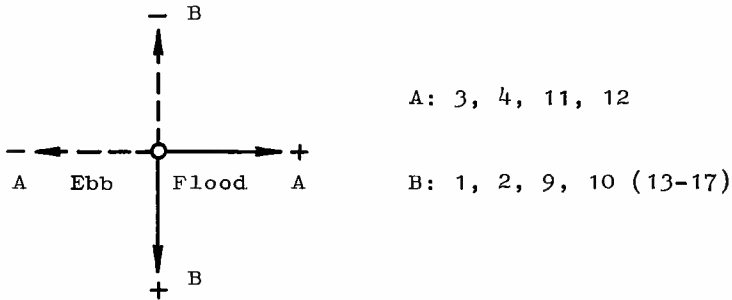


Fig. 14

At the velocities for V 7a und V 8, there are high inflow rates in C 14 and also in C 16. The oscillations in C 15 depend on the position of the current distribution in C 13 has the same characteristic for V 7a and V 8 (Fig. 15).

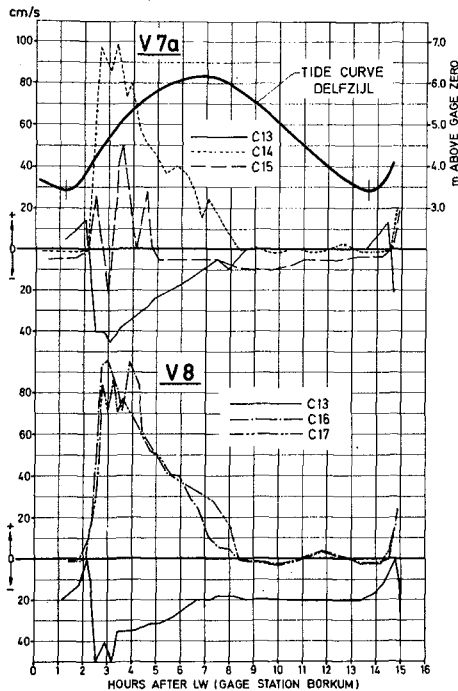


Fig. 15

Fig. 16 to Fig. 19 demonstrate the results of the test series V 10 in comparison with V 1 (old harbour without the new entrance) and V 2 (new harbour, old entrance closed). In C 1 one can see clearly the increase of velocity depending on the width of the old entrance. The decrease of velocity in C 2 in relation to the increased width depends on the situation of C 2 because this point is influenced by the jet-stream (Fig. 16 and Fig. 8).

In the harbour channel the velocity relationship is clear. With decreasing width the velocity also decreases. This clearly appears during the ebb tide in C 4 (Fig. 17).

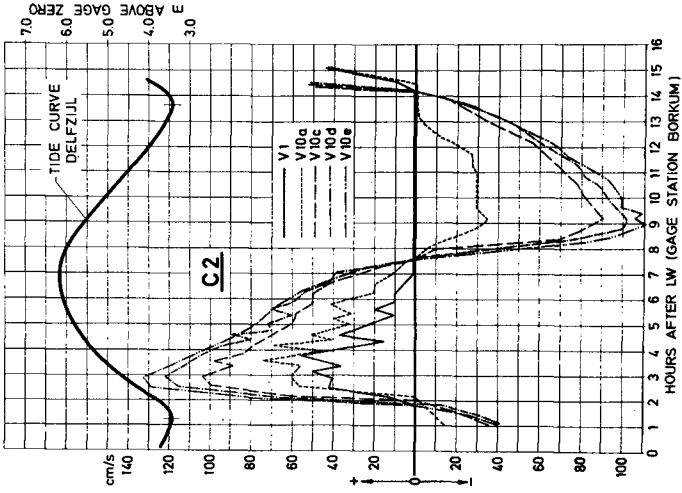


Fig. 16b

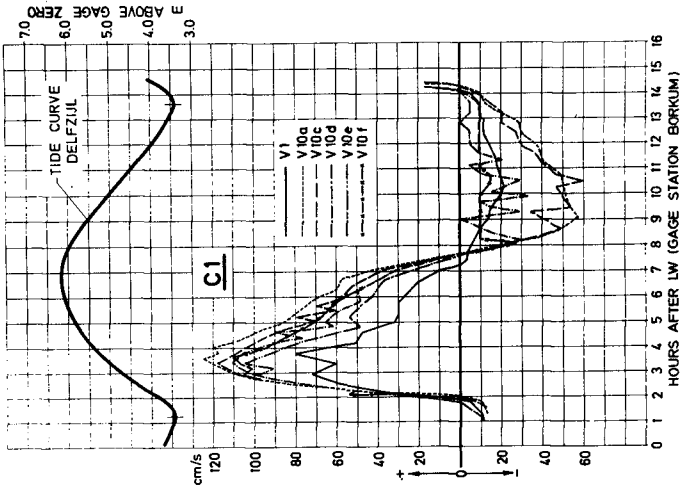


Fig. 16a

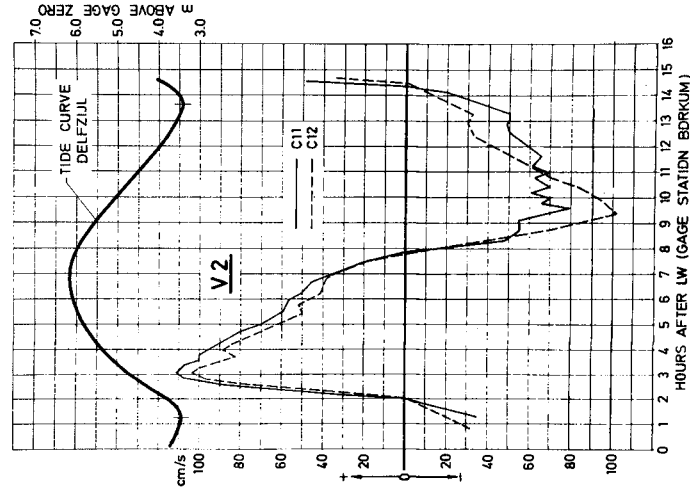


Fig. 18

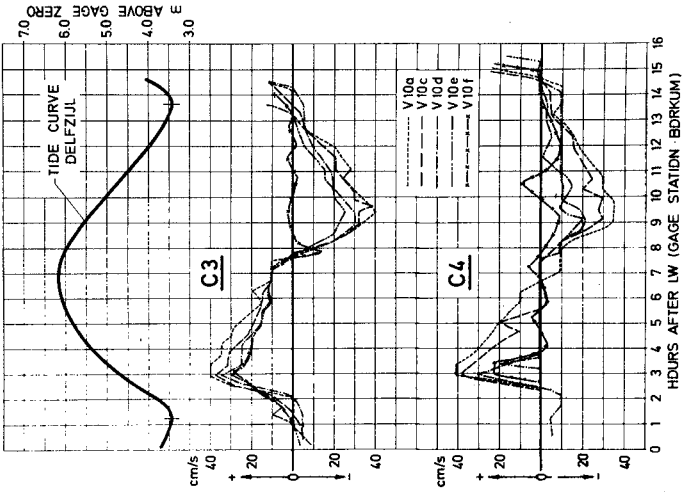


Fig. 17

The points C 11 and C 12 are situated in the main current in front of the new entrance. The distribution is typical for a tide flow. The smaller and oscillating ebb velocities in C 11 are influenced by the upstream jetty and the outflow from the harbour basin (Fig. 18).

In C 10 the difference of the current situation between closed and opened old entrance is clearly recognizable. There is a very high inflow during the flood tide and a small outflow in the ebb tide. In C 9, one can notice a permanent outflow during the whole tide. (flood: vortex in the harbour mouth; ebb: emptying of the harbour) (Fig. 19).

In the test series V 10 the graduation between as well flood and ebb as the width of the old entrance is very good. For V 10 an ebb inflow is not possible because for this test the old entrance has been closed during the ebb.

Following the model tests it was proposed not to close the old entrance and to observe the situation. After finishing the construction in nature a number of velocity measurements were made in the two entrances and in the harbour channel. Up to now the results are not completely analysed.

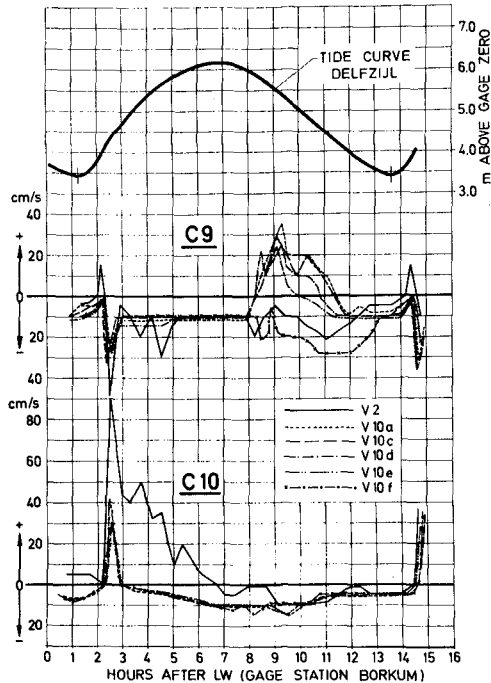


Fig. 19

In general one can say the following:

The model results are in a fair agreement with the nature. But concerning the vertical distribution of velocity there are phenomenon which need special investigations to explain it.

In contrariety to a vortex which is produced by an one-directional flow and which shows a good agreement between surface and bottom current, one observes different rotating systems in lateral enlargements under tidal influence.

Measurements in the entrance to the Kiel-Kanal may explain this phenomenon (Fig. 20). Certainly in this case the density effect is of great importance. In Fig. 21 and 22 the normal velocity distribution during the tide has been measured in the Elbe River in front of the entrance. One can recognize also the displacement of the slack-water. Fig. 21 shows the first flood phase. In the surface area there is a fillstream in the entrance and near the bottom the water flows out. During the ebb tide the distribution of surface and bottom current is also quite different, which is demonstrated by Fig. 22.

References

- DURSTHOFF, 1970, Über den quantitativen Wasseraustausch zwischen Fluß und Hafen, Mitt. des Franzius-Instituts der Technischen Universität Hannover, Heft 34
- v.KROSIGK, 1964, Die Kinematik der Wasserwalzen mit lot-rechter Achse, 153. Arbeit Theodor-Rehbock-Flußbaulaboratorium, Technische Hochschule Karlsruhe
- MAGENS, 1958, Untersuchungen der Ursachen und des Vorgangs der Verschlickung der Schleusenvorhöfen zu Brunsbüttelkoog, Mitt. Blatt BAW Nr. 10
- VOLLMERS, 1964, Ergebnisse systematischer Untersuchungen von Maßnahmen zur Verringerung der Schwebstoffablaagerungen in Binnenhafenmündungen, Die Wasserwirtschaft, Heft 9
- WIERECKY, 1975, Strömungsmessungen in den Vorhöfen Brunsbüttel, Versuchsprotokolle WBA Brunsbüttel (unpublished)

Fig. 21

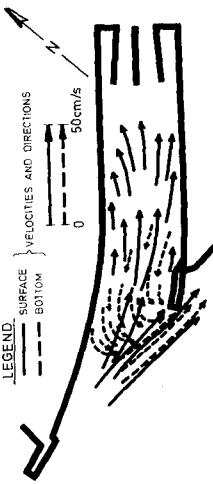


Fig. 22

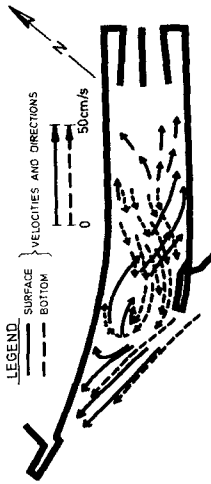
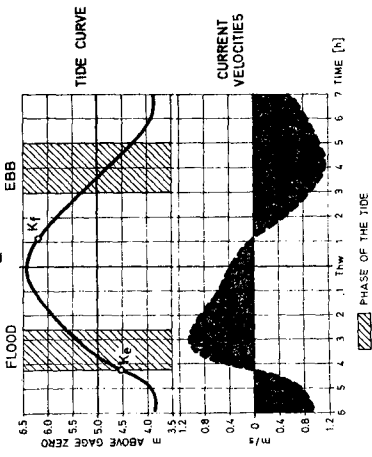
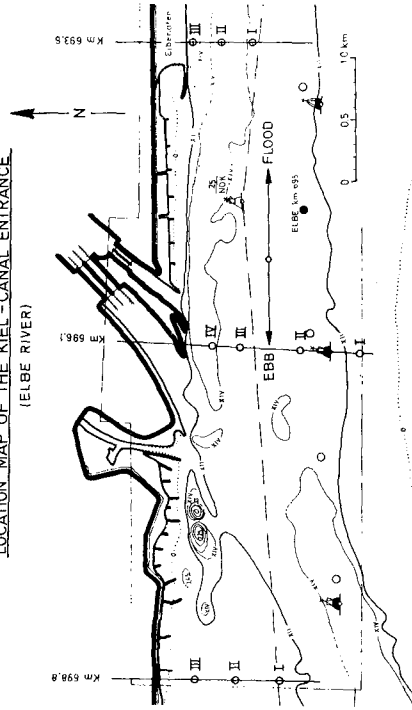


Fig. 20

LOCATION MAP OF THE KIEL-CANAL ENTRANCE
 (ELBE RIVER)



CHAPTER 109

SAND CIRCULATION PATTERN AT PRICE INLET, SOUTH CAROLINA

Duncan M. FitzGerald
Dag Nummedal
Timothy W. Kana

Coastal Research Division
Department of Geology
University of South Carolina
29208

ABSTRACT

A sand circulation pattern has been determined for Price Inlet, South Carolina, using wave refraction diagrams, littoral process measurements, bedform orientations and inlet hydraulic data. The dominant process acting on the ebb-tidal delta is wave swash which impedes the ebb-tidal currents and augments the flood-tidal currents. This produces a net landward transport of sand on the ebb-tidal delta as evidenced by the landward migrating swash bars. Bedform orientations and velocity measurements taken on the swash bars also support this conclusion.

Countering the general landward transport direction is the ebb dominance of the main channel. This dominance can be explained by higher inlet efficiency at low water than at high water. Consequently, bay tide phase lag is larger at high than at low water resulting in a longer flood duration. This causes higher mean ebb-tidal currents and a consequent larger potential net ebb transport of sand. This inlet characteristic explains why little sand is transported inside the inlet, why the throat remains scoured and why sand entering the main channel is carried seaward.

INTRODUCTION

Wave refraction diagrams, littoral process measurement, bedform orientations and inlet hydraulic data were used to determine the pattern of sand movement at Price Inlet, South Carolina. A knowledge of sand transport in the vicinity of inlets is important in understanding ebb-tidal delta morphology and how sand naturally bypasses tidal inlets. This study verified certain conclusions of previous investigations and generated a sand circulation model which is a further development of one proposed by Hine (1975).

Physical Setting

Price Inlet is located 15 km north of Charleston Harbor between two beach-ridge barrier islands of Holocene Age (Fig. 1). The inlet is backed by an extensive system of salt marsh and meandering tidal creeks and is connected to the Intracoastal Waterway. The inlet has no fresh water influx other than local precipitation. The mean tidal range is 1.5 m, and the mean tidal prism is 14 million cubic meters. During spring tides, these parameters may increase to 2.1 m and 20 million m³, respectively. The dominant annual onshore wave energy comes from a northeasterly direction, (FitzGerald, 1976).



Figure 1. Aerial view and location map of Price Inlet, South Carolina. Note the well-developed ebb-tidal delta.

Review of Previous Work

Detailed field investigations of sediment transport patterns in the vicinity of tidal inlets were initiated by Bruun and Gerritsen (1959). Based on studies at Eyerlandse Gat Inlet on the Dutch coast, they recognized the segregation of flood and ebb channels and the resultant sand transport. Oertel (1972; 1975), working on the Georgia coast, observed the importance of breaking waves on swash bars and the interaction between the wave bore and the ebb-tidal currents. He also recognized that ebb-deltas have separate regions of flood and ebb dominance. Dean and Walton (1975) traced the flow pattern during maximum current velocity through Redfish Pass, Florida, and concluded that the lateral transfer of the expanding ebb jet momentum caused entrainment of adjacent waters. Entrainment, in turn, would explain flood dominance of the marginal flood channels. They also stated that the seaward transport of sand was due to tidal currents; whereas, the landward movement of sand was probably due to wave forces. At the Chatham Harbor estuary, Massachusetts, Hine (1975) demonstrated the seaward transport of sand in the main ebb channel and recognized wave-induced landward migrating swash bars.

Ebb-Delta Morphology

The large intertidal and shallow subtidal accumulation of sand that fronts Price Inlet conforms well to the ebb-tidal delta model developed by Hayes (1975), (Fig. 2). The major components of this model are the following: a main ebb channel that ends at the terminal lobe, the seaward dipping lobe of sand; channel margin

linear bars which flank the main ebb channel; swash platforms, shallow sub-tidal sheets of sand located on either side of the main ebb channel; swash bars, intertidal sand bodies occurring on the swash platforms; and marginal flood channels, located between the swash platforms and the adjacent beaches. At Price Inlet, the northern channel margin linear bar is connected to a number of large coalescing swash bars. On the southern part of the ebb delta, the channel margin linear bar is attached to a series of elongate landward-migrating swash bars that parallel the shoreline of Capers Island for almost a kilometer. The main ebb channel and marginal flood channels are well developed at the inlet (Fig. 1).

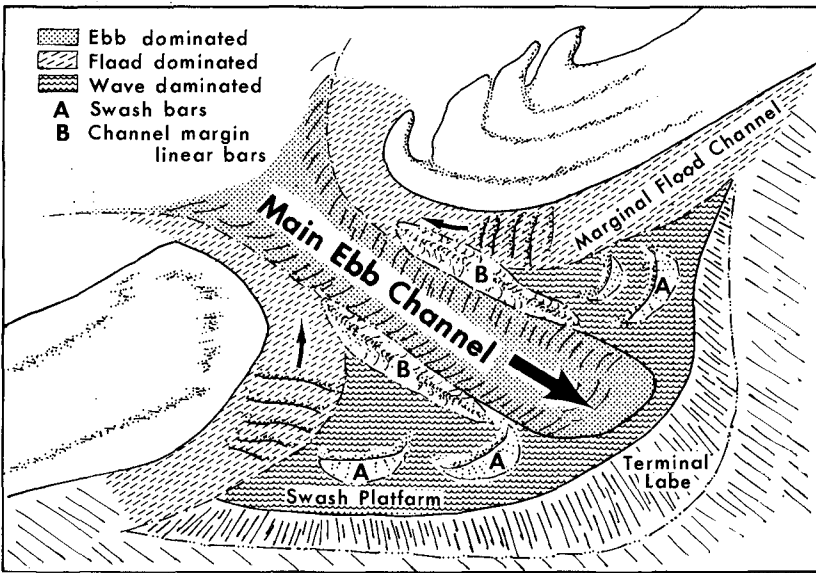


Figure 2. Typical ebb-tidal delta morphology (After Hayes, 1975). The ebb jet maintains a deep central trough, the main ebb channel, flanked by channel margin linear bars and wide arcuate swash platforms. Wave action on the swash platforms generate landward migrating swash bars. Marginal flood channels separate the channel margin linear bars from the adjacent beaches.

Different patterns indicate which areas are dominated by ebb currents, flood currents or waves.

SAND TRANSPORT PATTERNS

Transport to the Inlet

On the central South Carolina coast, there is dominant southward transport of coarse-grained littoral sediment although short term reversals in transport direction do occur. This is determined from wave observations, geomorphic evidence and trends of accretion and erosion (Finley, 1975; Stephens, et al., 1975). Sand enters the ebb-tidal delta complex by longshore transport from the north. Flood-tidal currents and wave bores carry the sand to the marginal flood channels and to the channel margin linear bars. The marginal flood channels constitute pathways for sand transport into the main ebb channel as demonstrated by the flood oriented sandwaves and megaripples which floor these channels. Current measurements in the marginal flood channels also reveal a dominant landward flow (Fig. 3). Wave bores and flood-tidal currents across the swash bar-channel margin linear bar complex probably deliver the bulk of sediment to the main ebb channel. At low tide, wave action transports a portion of the incoming sand in a southerly direction along the periphery of the swash platform.

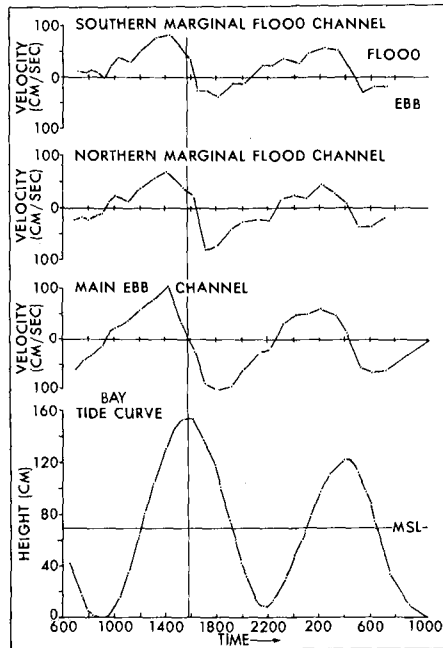


Figure 3. Current velocity curves at Price Inlet, August 15, 1975. Note the dominance of landward currents in the marginal flood channels. Wave bores traveling across the swash bars cause a super-elevation of the water surface in the marginal flood channels, thus augmenting inlet-directed currents.

Transport in the Main Ebb Channel

From high resolution seismic studies of the channel bottom and monitoring of bedform migrations over many tidal cycles, it is evident that no significant amount of sand moves landward through the throat. Therefore, the main channel must be ebb dominated. Seismic profiles made with a 3000 hz EG&G uni-boom system, reveal a gently (3 deg.) seaward dipping surface of probably Pleistocene age (Colquhoun, 1976; pers. comm.) underlying the inlet. At the throat, the channel is scoured to this surface; further seaward, the Holocene ebb-tidal delta wedge gradually thickens to reach a maximum of 6 meters (Fig.4). SCUBA-diving has identified a 10-20 cm thick layer of coarse sand and shell fragments at the throat bed. Bottom traces of the main ebb channel made over a complete tidal cycle indicate that no bedforms migrate across the inlet throat. Also, sandwaves and megaripples which floor portions of the channel bottom remain ebb oriented.

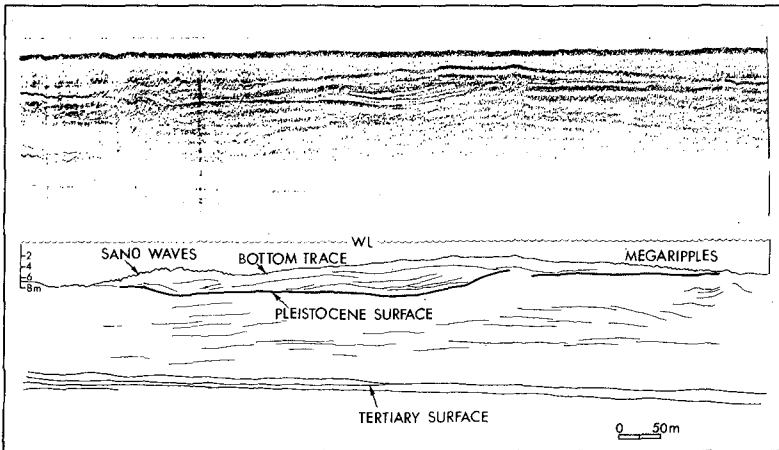


Figure 4. Seismic trace and interpretation through the main ebb channel. The trace runs seaward from the inlet throat (left) where the channel is scoured down to the Pleistocene surface. The Holocene ebb-tidal delta, a wedge of coarse grained clastic sediments, overlies the Pleistocene horizon and reaches a maximum thickness of 6 meters.

It is here proposed that the ebb dominance of the inlet is a function of the hydraulic characteristic of the inlet-marsh system. Keulegan (1967) has defined a repletion coefficient as a measure of the impedance to flow through an inlet. The coefficient is proportional to the quantity A_C/A_B where A_C is cross-sectional area of the inlet throat and A_B is the surface area of the water in the bay. During flooding, A_B increases rapidly as the lower marsh and tidal flats are covered with water. On the other hand, steep banks of the inlet throat cause only minor changes in A_C during the tidal cycle. Consequently, flow through the inlet is much more efficient at low water than at high water, (Table 1).

Table I

Mean Tidal Range (1.52 m)	A_c	A_b	A_c/A_b
Average low water	1002	2,541,000	.00040
Average high water	1093	6,543,000	.00017
Spring Tidal Range (2.1 m)			
Average low water	994	2,347,000	.00042
Average high water	1110	7,563,000	.00015

Note: Areas in square meters
 A_c - inlet cross-sectional area
 A_b - bay area

At ocean high tide, there is a substantial landward surface slope through the inlet as a result of the high impedance. Thus, the inlet will flood during early ocean ebb. Inlet impedance is greatly reduced at low tide, and the lag between ocean and bay lows is insignificant (Fig. 5). This inlet characteristic results in a longer flood duration, an average of 44 minutes at Price Inlet. Boon (1975) and Byrne (1976), working at Wachapreague Inlet, Va., have also documented the same trend, and ascribe the cause to distortions of the tidal curve. Due to the diurnal inequality, successive ebb and flood tidal prisms are not necessarily equal, but the mean ebb prism equals the mean flood prism. Because the ebbing period is shorter than the flooding period, the mean ebb currents are stronger than the mean flood currents.

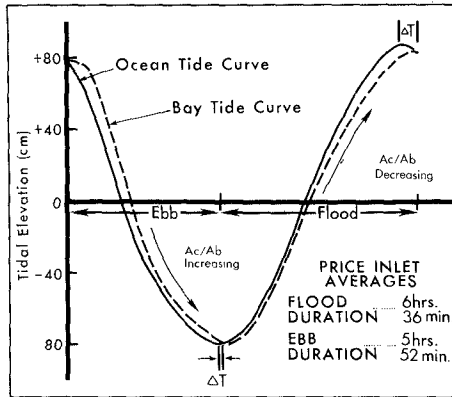


Figure 5. Hypothetical relationship between ocean and bay tides at Price Inlet. As the ocean reaches high water, inlet efficiency, A_c/A_b , the ratio of throat cross-sectional area to the surface area of the bay, is low and the water level inside the inlet lags that of the ocean. Therefore, the inlet floods even after the ocean has begun to ebb. At low tide, inlet efficiency is high, and the bay water level closely follows that of the ocean. This results in a longer flood duration than ebb duration. At Price Inlet, the average difference is 44 minutes.

Maddock (1969), using sedimentation flume data, established that total sediment transport rate is proportional to the cube of the current velocity. His transport equation for a velocity range of .1 to 2 m/sec and a mean grain size range of .3 to .7 mm is:

$$V = 4.03 (L/\rho)^{1/3}$$

where V is velocity, (m/sec), ρ is mass density of the fluid, (kg/m^3), and L is the total sediment load, $\text{kg/m}^2\text{-sec}$. Assuming the validity of the relationship for tidal inlets, Maddock's formula has been used to determine sand transport rates at Price Inlet. Using hydraulic data measured at the inlet, the weight of sand passing through the inlet throat has been calculated for ebb and flood tidal cycles of varying tidal ranges. It is seen in Figure 6 that a fairly close relationship exists between potential load and tidal range, and that ebb currents will transport far more sand than flood currents.

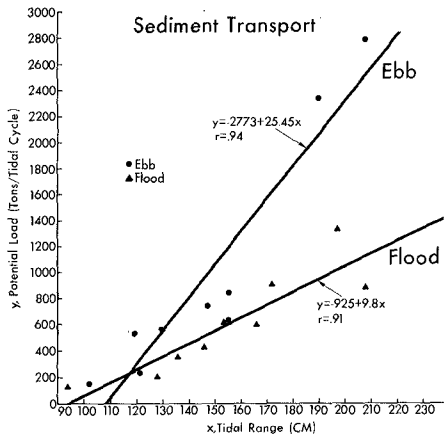


Figure 6. Potential load (tons/tidal cycle) has been determined at the throat section of the main ebb channel using Maddock's (1969) relationship where bedload transport is proportional to the cube of velocity. The individual values were computed from current velocity data measured at Price Inlet for varying tidal phases (neap to spring tides). Except for very low tidal ranges, potential ebb transport predominates.

Sediment transport calculations show a potential net ebb transport rate of 364,000 tons/year through the inlet throat at Price Inlet. A net longshore sand transport rate of 128,000 tons/year toward the inlet was estimated from wave parameters measured on Bull Island just north of the inlet (Kana, 1976).

Consequently, the potential net ebb discharge of sand through the inlet is more than capable of removing sand entering the inlet and keeping the channel scoured.

Effects of Wave Refraction

Sand in the main ebb channel is ultimately carried to the seaward portion of the ebb delta where the mean depth is typically 2 m. The dominant north-east waves breaking in this area at low tide generate a net southward sand transport. Due to wave refraction on the swash platform, a sediment transport reversal occurs just south of the delta. Figure 7 demonstrates a net transport of sediment toward the inlet north of point A regardless of deep water wave approach direction. Inside the swash bars, the transport of sand toward the inlet is augmented by flood-tidal currents. The transport reversal is partly responsible for reintroducing sand into the inlet and in building the beach directly south of the inlet. This mechanism is thought to cause downdrift offsets (Hayes, 1970).

Swash Bar Processes

Swash bar development and migration is a continuous process on the swash platform. Over the past four years, many swash bars have formed in these areas and migrated toward the inlet to form swash bar-channel margin linear bar complexes. Both of these bar complexes have recently increased in volume; the southern one has migrated landward; whereas, the one to the north has remained essentially stable with the bulk of its accretion on the seaward side. During an 8 month period from August 1975 to April 1976, the 1 to 2 m slipface which fronts the entire southern bar complex migrated approximately 100 m. Process measurements on the southern bar complex indicate that its landward migration is related to wave swash (Fig. 8). The bore created by waves breaking on the swash bars impedes the ebb tidal currents but augments the flood tidal currents, resulting in a net landward transport of sand. Bedform orientations, shell alignment and current lineations reflect this landward sand transport (Fig. 9). The most common large scale bedform on the bar complexes are linear and cusped megaripples. The migration of the bar complex will continue until it welds to the beach, causing an increased downdrift offset at the inlet. Aerial photographs document at least five episodes of bar welding at Price Inlet since 1941. A more complete description of ebb tidal delta morphology at Price Inlet and associated shoreline changes is discussed by FitzGerald (1976).

The momentum of the wave bore across the swash bars causes a water level set-up behind the southern bar system. This causes the water to exit through the southern flood channel even during a portion of the ebbing cycle (Fig. 3). This flood dominance was explained as jet entrainment by Dean and Walton (1975), a process which is believed to be minimal at Price Inlet. There is a smaller water level set-up in the northern flood channel due to the attitude of the bar with respect to the updrift beach and the incoming waves (Fig. 1).

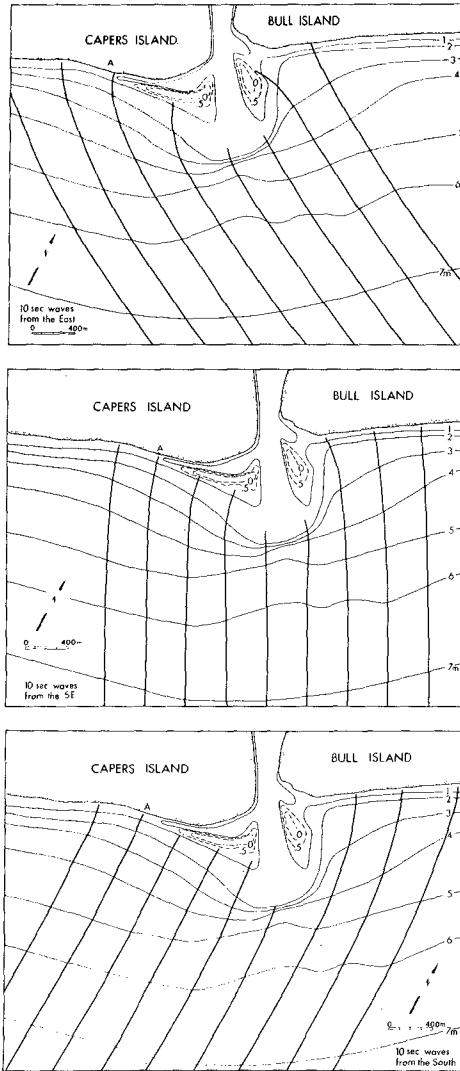


Figure 7. Wave refraction diagrams for 10 sec waves indicate that regardless of wave approach direction, wave refraction around the ebb-delta causes a sediment transport reversal just south of the delta at location A. This mechanism is partly responsible for reintroducing sand into the main channel and for accretion of the downdrift beach.

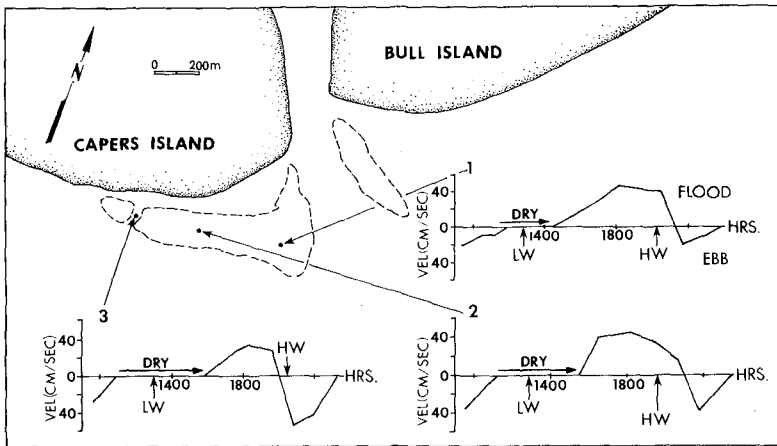


Figure 8. Velocity measurements on the southern swash bar-channel margin linear bar complex on August 20, 1975, show that landward currents predominate. The velocity asymmetry is a result of wave swash retarding the ebb currents and increasing the flood currents.

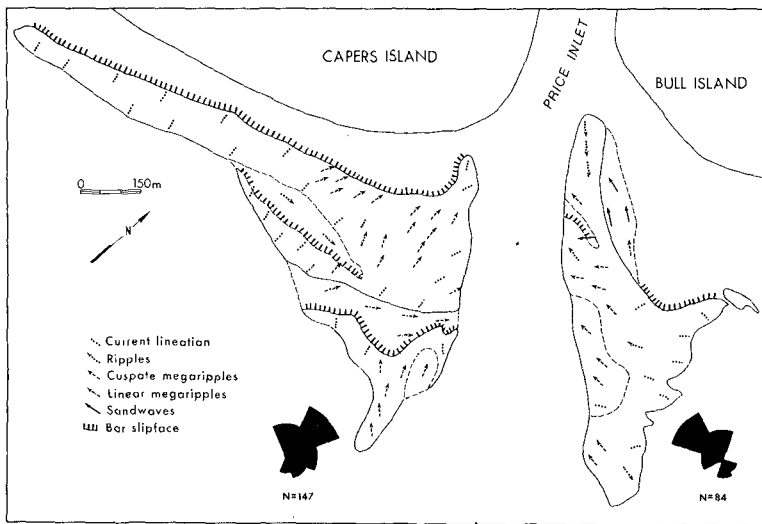


Figure 9. Bedform orientation map of the intertidal portion of the ebb-tidal delta at Price Inlet. Note from rose diagrams that the dominant bedform orientation on either side of the main ebb channel is toward the inlet, indicating landward sand transport.

CONCLUSIONS

1. The sand circulation pattern (Fig. 10) on the ebb-tidal delta of Price Inlet illustrates dominant landward transport except along the periphery of the swash platform where southward transport occurs. Countering this general landward transport pattern is the seaward transport of sand in the main ebb channel.

The ebb dominance of the main channel is explained as a result of greater inlet efficiency at low water than at high water. Landward currents generated by wave bores dominate the swash platform and the swash bar-channel margin linear bar complex. Wave set-up behind the southern bar system augments the inlet-directed currents in the southern marginal flood channel. This process occurs to a lesser extent in the northern flood channel.

Assuming that velocity cubed is proportional to total sediment transport, a potential net ebb transport of 364,000 tons per year was determined for the inlet throat. This value, compared with a net long-shore transport rate toward the inlet of 128,000 tons per year, indicates that all sand entering the main channel will be carried seaward and the throat will remain scoured.

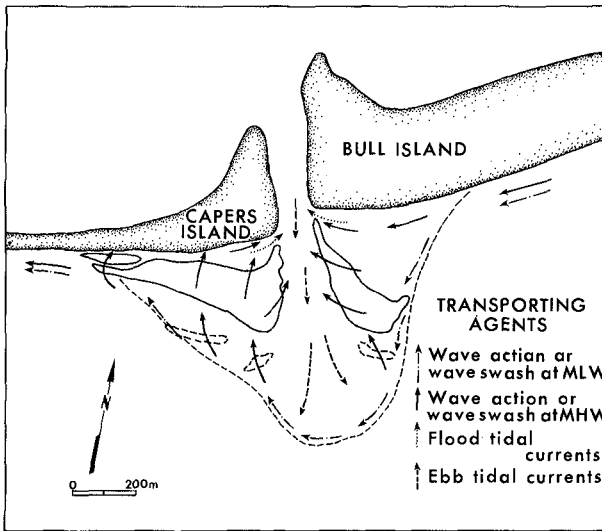


Figure 10. Sand circulation pattern for Price Inlet determined from wave refraction diagrams, littoral process measurements, bedform orientation and inlet hydraulic data. Note the different wave effect at low and high tide, the seaward transport in the main channel due to the dominant ebb-tidal currents, and the landward transport on the ebb delta due to wave swash.

ACKNOWLEDGEMENTS

This study was supported by the U. S. Army Research Office Grant No. DAAG 29-76-G-0111 (Miles O. Hayes and Dag Nummedal Principal Investigators). Jeff Knoth, Ray Levey, Rob Clemens, and Stormy Attaway are gratefully thanked for field assistance. Mrs. Ethel Magwood is thanked for her hospitality in her home at Price Inlet.

REFERENCES

- BOON, J.D., III, 1975, Tidal discharge asymmetry in a salt marsh drainage system: *Limnology and Oceanography*, v. 20, 71-80.
- BRUUN, P., AND F. GERRITSEN, 1959, Natural bypassing of sand at coastal inlets: *Jour. Waterways and Harbors Division, ASCE*, paper 2301, 75-107.
- BYRNE, R. J., 1976, Speculative hypothesis on the evolution of barrier island-inlet-lagoon systems: II, A case study, Wachapreague, Virginia: *Geol. Soc. America, Abstracts with Programs*, v. 8, no. 2.
- DEAN, R. G., AND T. L. WALTON, 1975, Sediment transport processes in the vicinity of inlets with special reference to sand trapping: in CRONIN, L.E., (ed.), *Proceedings of the 2nd International Estuarine Research Federation Conf.*, Myrtle Beach, S. C., 129-150.
- FINLEY, R. J., 1975, Morphologic development and dynamic processes at a barrier island inlet, North Inlet, South Carolina: Unpub. Ph.D. dissertation, Univ. of South Carolina, Columbia, S. C. 269 p.
- FITZGERALD, D.M., 1976, Ebb tidal delta of Price Inlet, South Carolina: Geomorphology, physical processes, and associated inlet shoreline changes: in HAYES, M.O., and T. KANA (eds.), *Terrigenous Clastic Depositional Environments*, AAPG sponsored field course, II-158-171.
- HAYES, M. O., V. GOLDSMITH, and C. H. HOBBS, III, 1970, Offset coastal inlets: *Am. Soc. Civil Engineers, Proc.*, 12 Conference on Coastal Engineering, 1187-1200.
- HAYES, M. O., 1975, Morphology of sand accumulation in estuaries: an introduction to the symposium: in CRONIN, L.E., (ed.), *Proceedings of the 2nd International Estuarine Research Federation Conf.*, Myrtle Beach, S. C., 3-22.
- HINE, A.C., III, 1975, Bedform distribution and migration patterns on tidal deltas in the Chatham Harbor Estuary, Cape Cod, Massachusetts: in CRONIN, L.E., (ed.), *Proceedings of the 2nd International Estuarine Research Federation Conf.*, Myrtle Beach, S. C., 235-252.
- KANA, T. W., 1976, Sediment transport rates and littoral processes near Price Inlet, S. C: in HAYES, M. O., and KANA, T., (eds.), *Terrigenous Clastic Depositional Environments*, AAPG sponsored field course, II-158-171.

- KEULEGAN, G. H., 1967, Tidal flow in entrances. Water level fluctuations of basins in communication with seas: Tech. Bull. No. 14, Committee on Tidal Hydraulics, Corps of Engineers, U. S. Army, Vicksburg, Miss., 100 p.
- MADDOCK, T., JR., 1969, The behavior of straight open channels with movable beds: U. S. Geol. Survey Prof. Paper 622-A, 70 p.
- OERTEL, G. F., 1972, Sediment transport on estuary entrance shoals and the formation of swash platforms: Jour. Sed. Petrology, v. 42, 858-863.
- OERTEL, G.F., 1975, Ebb-tidal deltas of Georgia estuaries: in CRONIN, L. E., (ed.), Proceedings of the 2nd International Estuarine Research Federation Conf., Myrtle Beach, S. C., 267-276.
- STEPHEN, M. F., P. J. BROWN, D. M. FITZGERALD, D. K. HUBBARD, and M. O. HAYES, 1975, Beach erosion inventory of Charleston County, South Carolina: A Preliminary Report: Tech. Rept. No. 4, South Carolina Sea Grant Program, Charleston, S. C., 74 p.

CHAPTER 110

BEACH HAVEN AND LITTLE EGG INLETS, A CASE STUDY

Joseph DeAlteris¹, Thomas McKinney², and James Roney³

ABSTRACT

A comprehensive investigation of coastal processes active within and in the vicinity of Beach Haven and Little Egg Inlets was completed as part of the Coastal Processes Investigation for the proposed Atlantic Generating Station. The suspected complex nature of this dual natural inlet system was documented and a process-response model is presented to relate the more significant physical forcing functions to observed morphologic and hydraulic changes. A rising sea level, a net littoral drift from the north and the sediment scouring power of the flow in the two main channels serving the tidal basins are the principal factors related to the geographic and hydraulic stability of the system. The results of the study can be used to evaluate the potential impact, if any, of the proposed Atlantic Generating Station on the adjacent coastal environment.

INTRODUCTION

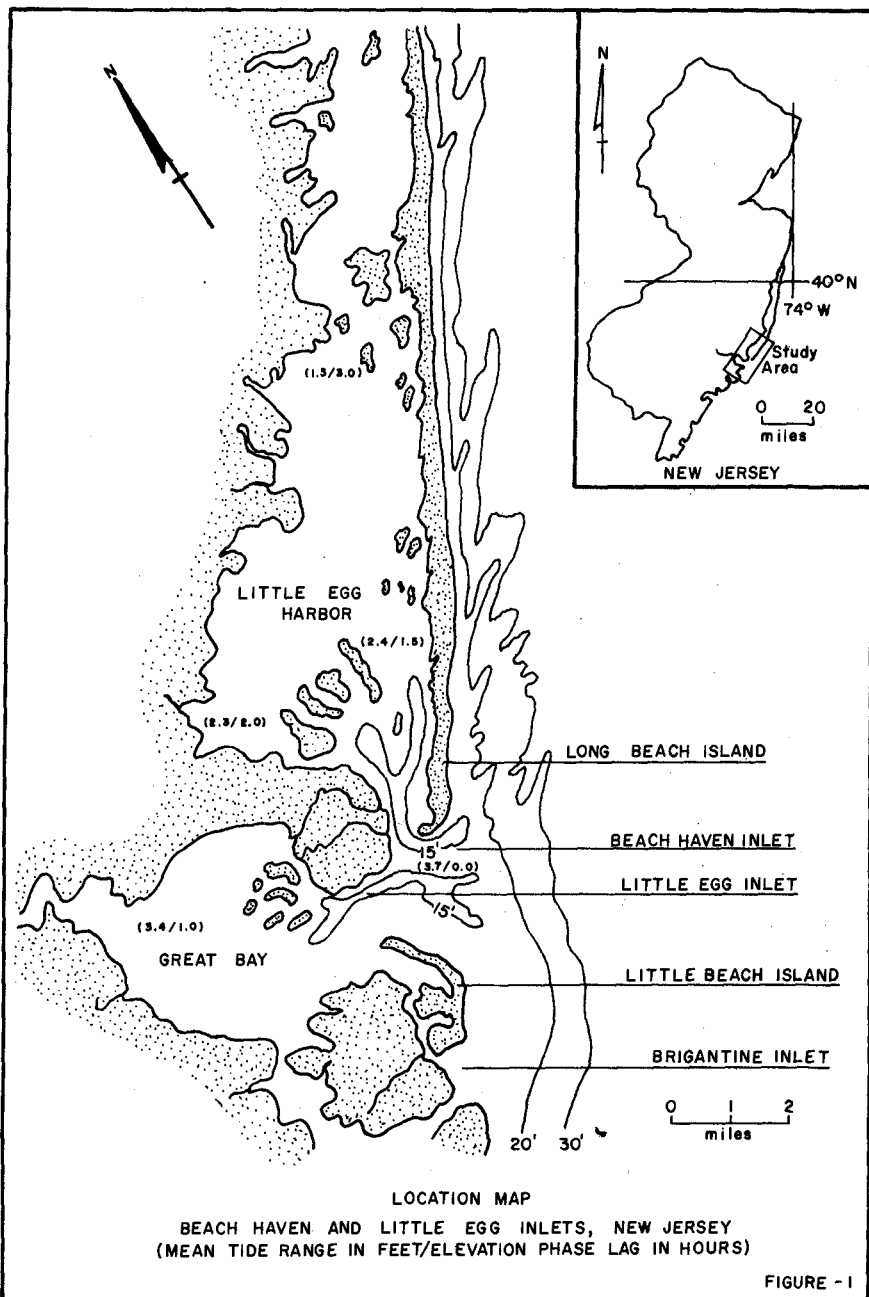
Beach Haven and Little Egg Inlets are juxtaposed natural tidal inlets located midway along the New Jersey Coast, U.S.A. (Figure 1). As part of the Coastal Processes Investigation, for the proposed Atlantic Generating Station, a study was made of these inlets and their adjacent beaches to obtain baseline data on the dynamic nature of this complex natural system. The necessity for a study of this type was noted by the Atomic Energy Commission (1973) in their report on the Workshop for Offshore Nuclear Power Siting. The inlet study included the following task investigations:

1. A study of the recent geomorphic history of the inlet complex using historical shoreline and bathymetric charts dating from 1840 to 1974, site aerial photographs dating from 1933 to 1974, and the biweekly monitoring of beach profiles in the vicinity of the inlet channels.

1 Pandullo Quirk Associates, Wayne, N.J. 07470

2 Dames and Moore, Cranford, N.J. 07016

3 Franklin Institute, Philadelphia, PA 19103



2. A study of the hydraulic characteristics of the inlet complex including analyses of short-term and long-term changes in the cross-sectional areas of the inlet throats, of the storage basin characteristics for each of the inlets, and tide and velocity measurements at the inlet throats.

The purpose of this paper is to present the methodology and results of these individual task studies and a process-response model for the long and short-term evolution of the inlet complex.

Previous studies in this area include the contributions of Shepard and Wanless (1971) which provides a general discussion of the coastal geological features and Charlesworth (1968) which discusses marine sedimentation processes in the inlets. Caldwell (1966) estimates the net littoral drift in this area to be approximately 500,000 cubic yards per year to the south. Fair weather waves in the study area are generally from the SE, are less than 3 feet in height, and have periods of 5 to 6 seconds, (Darling, 1968). Storm generated waves are generally from the NE, are greater than 3 feet in height, and have periods greater than 7 seconds. The mean ocean tide range at Atlantic City Steel Pier (10 miles to the south) is 4.1 feet; the spring tide range is 5.0 feet. The tides are semi-diurnal in nature. The Beach Haven-Little Egg Inlet system is located at a sharp boundary between two distinctly different sediment regimes in the New Jersey coastal sector (McMaster, 1954). The beaches to the north of the inlet system are characterized by medium to coarse sand with an opaque heavy mineral assemblage while the beaches to the south are characterized by fine sands with a hornblende heavy mineral assemblage. DeAlteris and Vespucci (1975) describe the quarternary stratigraphic sequence of the inlet complex based on the results of borings along the transmission line route (Figure 2).

The general limits of the study area included Beach Haven and Little Egg Inlets, their respective storage basins and the beaches adjacent to the inlet (Figures 1 and 2). The Beach Haven Inlet throat channel is located between the southern terminus of Long Beach Island and Sheepshead Marsh. The channel presently reaches a maximum depth of 48 feet (Referenced to MLW). The storage basin served by Beach Haven Inlet includes Little Egg Harbor and Manahawkin Bay. The overall dimensions of these bays are 15 miles long by 3 miles wide. The bays are flanked on the landward side by fringing upland marsh. The average depth of bays is 3 feet (Referenced to MLW). Within this storage basin, there are significant reductions in tidal amplitude and phase lags in the tide curve. Beach Haven Inlet channel is about 2 miles long and has large ebb and flood tidal deltas at each end.

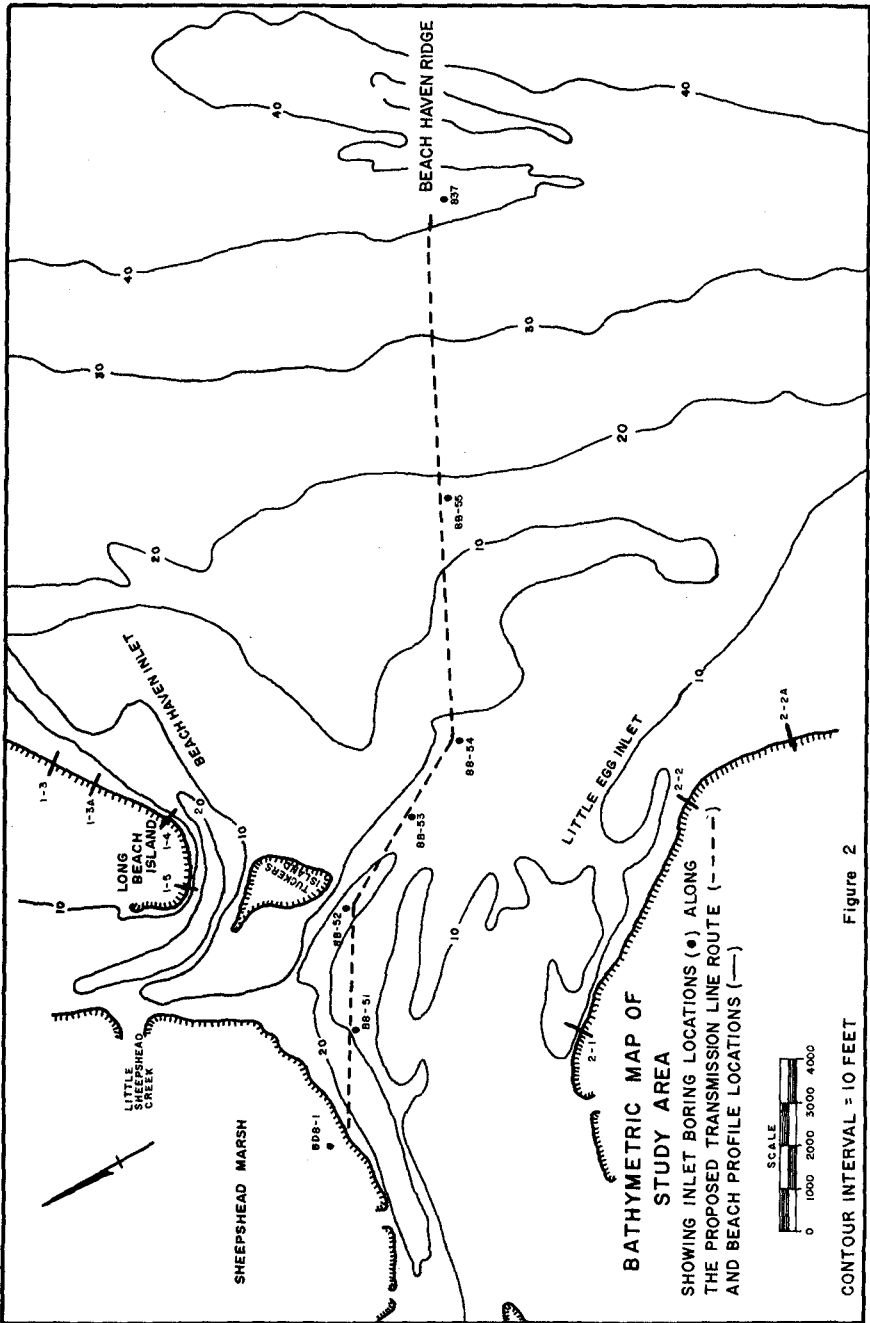


Figure 2

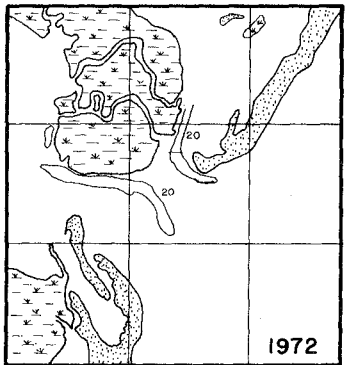
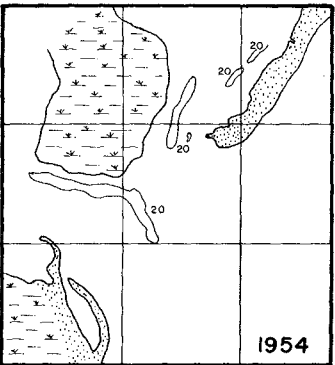
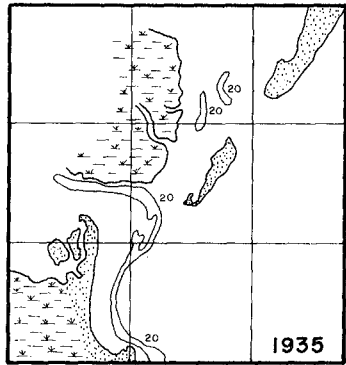
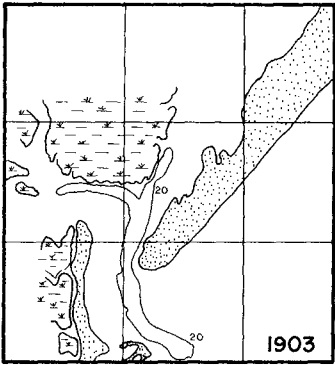
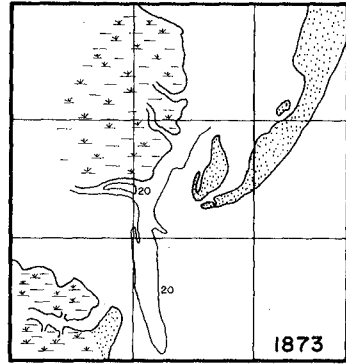
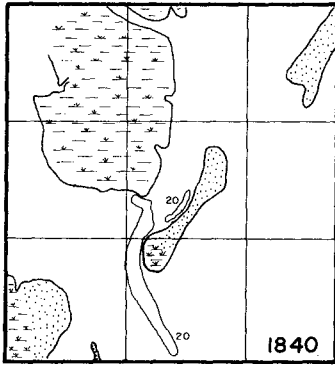
The Little Egg Inlet throat channel is located between the northern flank of Little Beach Island and Sheepshead Marsh. The channel presently reaches a maximum depth of 52 feet (Referenced to MLW). The storage basin served by Little Egg Inlet consists of Great Bay and the lower reaches of the Mullica River. Great Bay is a large open bay, approximately 4 miles in diameter, with an average depth of 6 feet (Referenced to MLW). There are no significant reductions of the tidal amplitude or phase lags in the tide curve within Great Bay. Great Bay is surrounded by fringing salt marsh that periodically floods on spring tides. The lower portion of the Mullica River is tidal in nature and is therefore included in the storage area. The mean annual discharge of the Mullica River is about 0.1% of the mean tidal discharge of the inlet and therefore has not been considered in the tidal hydraulic analysis. The Mullica River is flanked by fringing upland marsh. The outer inlet channels of Beach Haven and Little Egg Inlets are presently separated by Tuckers Island Shoal.

GEOMORPHIC HISTORY OF THE INLET COMPLEX

Using copies of the original hydrographic survey boat sheets available from the National Ocean Survey for the period 1840 through 1954 and the results of a bathymetric survey conducted in 1972 by E G & G, the history of the inlet channels and adjacent beaches was investigated. The individual charts were adjusted to a common scale and grid for comparison purposes and the results of these efforts are summarized in Figure 3.

In 1840, two inlets were present, separated by a large island called Tuckers Island. The primary channel was Little Egg Inlet between Little Beach and Tuckers Islands. The maximum depth of the channel was 59 feet. Some flow also passed between Tuckers and Long Beach Islands, but data are not available on the channel dimensions. Between 1840 and 1873, accretion on the southern end of Long Beach Island caused it to extend southward, overlapping Tuckers Island. Long Beach Island had grown almost 13,000 feet south of its 1840 location. Tuckers Island decreased from about 12,000 feet in length to less than 5,000 feet.

The closure of Beach Haven Inlet's outer channel in the 1870's, had a pronounced effect on the northern limb of the channel at Little Egg Inlet. Tidal flow from Little Egg Harbor was routed through the narrow passage between Tuckers Island and the peninsula to the west. Deep scour occurred over an area extending far into Little Egg Harbor. Depths to 50 feet were present in several places, showing the effect of increased constriction of the channel. By 1903, Long Beach Island had grown more than 7,000 feet and completely absorbed Tuckers Island. At this point, conditions seemed to reach a state of quasi-stability with a



BEACH HAVEN AND LITTLE EGG INLETS
1840 - 1972

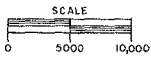
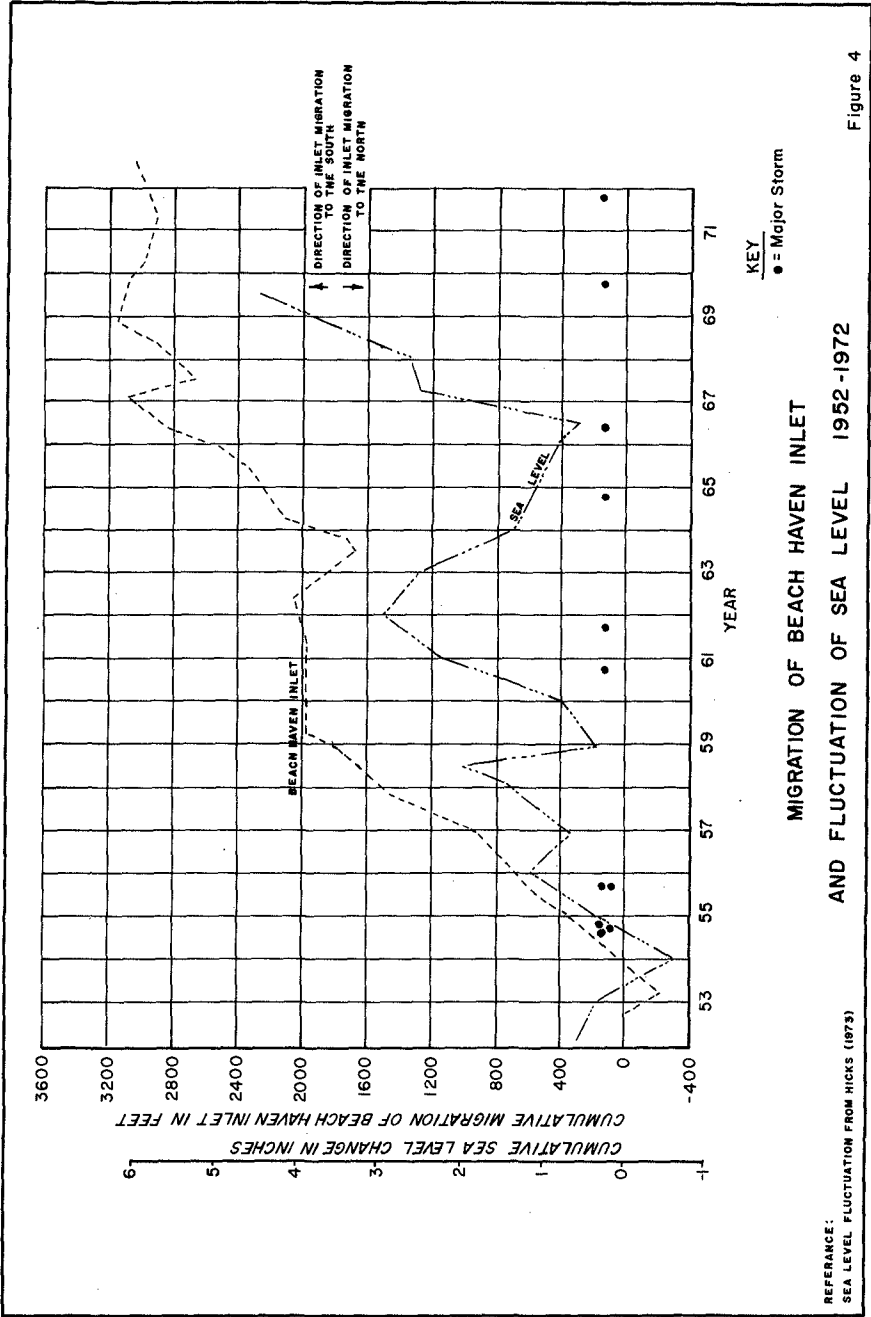


Figure 3

single inlet (Little Egg Inlet) relieving both Great Bay and Little Egg Harbor and with Beach Haven Inlet outer channel temporarily non-existent. With a single channel serving the two basins, tidal velocities were apparently sufficiently high to prevent further deposition or constriction of the channel. This semi-stable condition continued until 1920, with the maximum southerly extent of Long Beach Island occurring in 1915. The effect of the constriction was most apparent in the channel, which was now 3 miles long and had depths in excess of 60 feet.

In 1920, equilibrium was upset and Long Beach Island was breached at a point 20,000 feet north of the 1972 position of Little Egg Inlet. The new inlet established itself rapidly, eroding into Long Beach Island to form a major topographic feature. The previous cycle of southerly migration, closure of the northerly inlet, and subsequent growth to a semi-stable single inlet condition had been completed and the cycle begun anew. The survey of 1935 indicated that Long Beach Island had grown southward several thousand feet, while Tuckers Island had eroded considerably. This survey showed increased scour in the northern portions of Beach Haven Inlet. The inlet was narrower and the channel apparently deepened. Little Egg Inlet to the south, showed signs of shoaling. A deep gorge was maintained, but it was reduced to a very narrow breadth. The northern branch of the channel which lead into Little Egg Harbor had been completely buried. By 1954, Tuckers Island was reduced to an intertidal shoal, and the axes of the two channels were separated by about 7,000 feet at their closest point. By 1972, the separation had reduced to little more than 3,000 feet with Little Egg Inlet remaining in a stationary position. All movement can therefore be attributed to the southerly migration of Beach Haven Inlet.

Using aerial photographs dating from 1933 to the present, a more detailed study of the recent evolution of the inlet complex was accomplished. The most interesting result of this study is shown in Figure 4 and suggests a correlation between the rate of migration of Beach Haven Inlet and fluctuations in the rate of sea level rise and storm action. The sea level curve is taken from Hicks (1973) and the distance of inlet migration was determined by measuring on the aerial photographs from a fixed reference point on the barrier to the inlet channel. The periods of rapid southerly inlet migration correlate with periods of rapid sea level rise; while periods of minimal southerly inlet migration and short-term reversals correlate with periods of minimal sea level rise and lowering of sea level.



REFERENCE:
SEA LEVEL FLUCTUATION FROM HICKS (1973)

MIGRATION OF BEACH HAVEN INLET
AND FLUCTUATION OF SEA LEVEL 1952-1972

KEY
● = Major Storm

Figure 4

In order to provide data on short-term changes on the beaches adjacent to the inlets, a beach profiling program was initiated in the summer of 1973, and continued for a period of 18 months. Using a horizon leveling method adapted from Emery (1961), the beach profiles were measured on a bi-weekly schedule. The area under each profile was represented as cubic feet of sand per linear foot of beach. This was plotted as a time series and a first order regression line calculated for each profile to represent the trend, (Goldsmith and others, 1975). The results of the profiling program (Figures 5 and 6) indicate that the profiles which show the most dramatic trends of erosion and/or accretion are located in and adjacent to the inlets. The profiles located at the distal portions of both prograding spits on Long Beach and Little Beach Islands, (1-3, 1-3A, 1-4, 1-5, 2-1) show accretional or relatively stable trends, suggesting continued inlet-directed drift along these beaches. Seaward of these segments, zones of significant erosional trends are noted on both Long Beach and Little Beach Islands. The exact mechanism of the erosional trend at Profile No. 2-2 on Little Beach Island spit is not clear, but the refraction pattern for waves from the northeast suggest that in addition to the suspected interaction of Little Egg Inlet flow, wave energy concentrations into this zone may also be an important factor. Most of the remaining ocean-facing portions of Little Beach Island show a slight erosional trend during the measuring period. Profile No. 2-2A on the north end of Little Beach shows a high accretional trend. This is also suggested by the shoal in the nearshore area as outlined by the 10 foot contour line (Figure 2). The shoal is elongated parallel to the trend of the outer channel of Little Egg Inlet. The details of the processes controlling this accretional nodal point are also lacking. However, it may represent the confluence of the northerly directed littoral drift derived from the eroding beaches to the south on Little Beach and the tidal ebb flow of Little Egg Inlet. The proximity to the dominantly erosional segment at Profile No. 2-2 also suggests a transport contribution from that source, perhaps aided as well by the tidal flow from Little Egg Inlet. In contrast to these inlet influenced beach profiles, the beach profiles facing the Atlantic Ocean are more subdued in both their short-term changes and long-term accretion/erosion trends. This is attributed to the more uniform wave energy distribution along this section of shoreline.

HYDRAULIC CHARACTERISTICS OF THE INLET COMPLEX

The tidal prism represents the volume of water entering the storage basin in a given tidal cycle. If the basin surface remains horizontal throughout the bay as the tide rises and falls, then:

$$P = \text{Tidal Prism} = H \times A_B \quad (1)$$

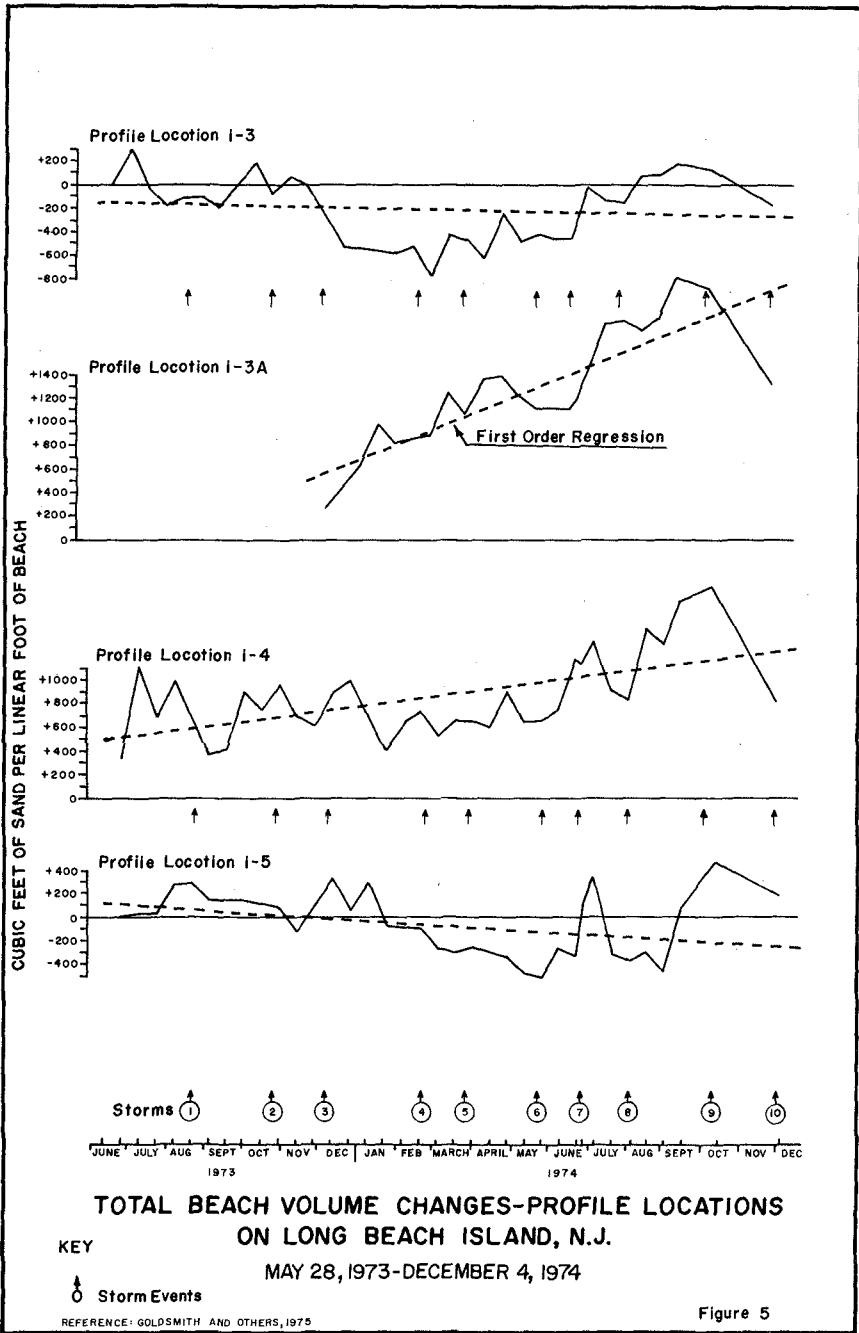


Figure 5

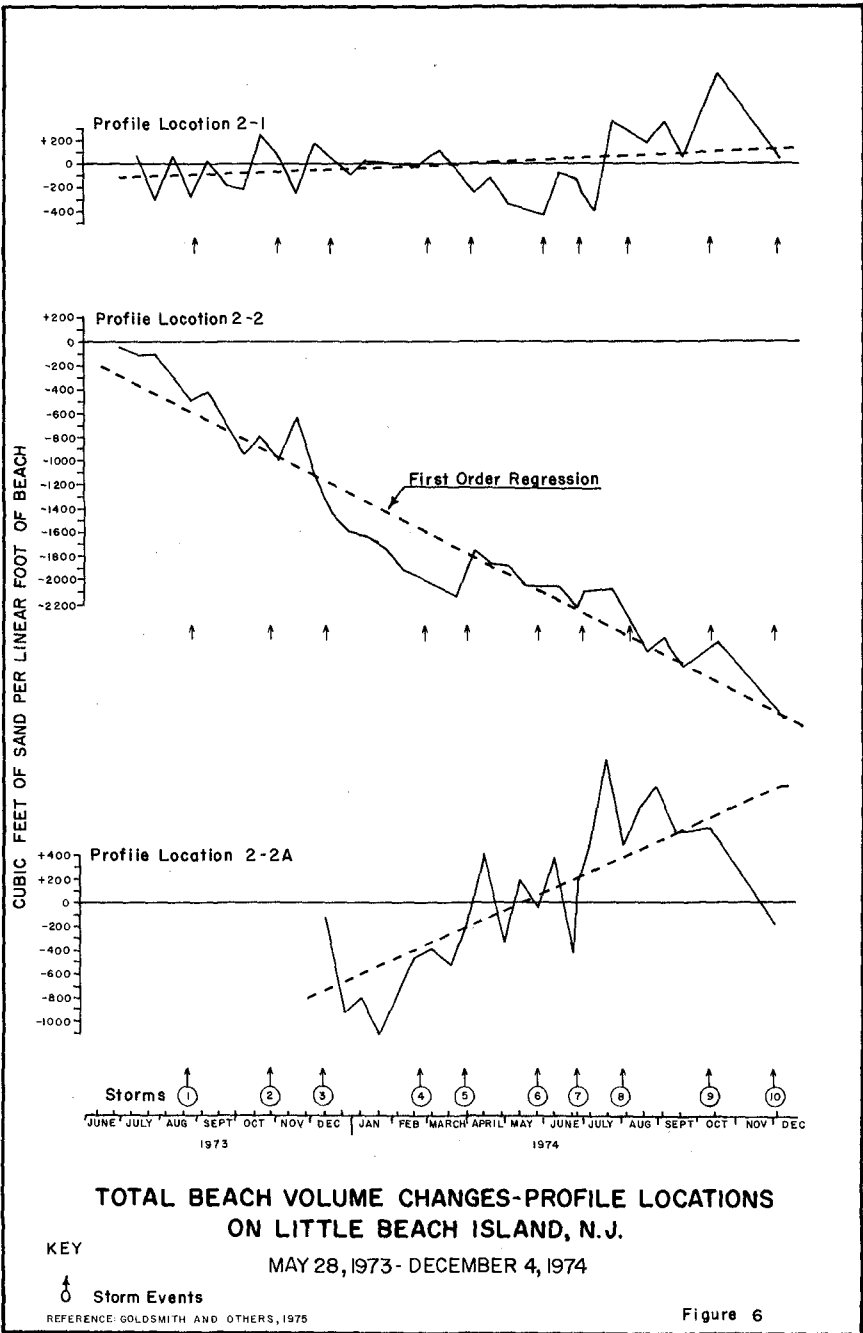


Figure 6

where A_p is the basin area and H is the average difference between high and low tide elevations in the bay. In practice, however, there may be considerable differences in tide range within the bay accompanied by phase lags of several hours. Computation of tidal prism is then considerably more complex and a straightforward prism analysis is possible only by making discharge measurements at the inlet throat.

The tidal prisms for Beach Haven and Little Egg Inlets were first calculated from Equation 1 using average values for mean and spring tide ranges. For Little Egg Harbor, the basin was subdivided into eight sections for which the range was relatively constant and the total prism was taken as the summation of the sectional prisms. The result of this calculation is given in Table 1 for mean and spring tides. It is emphasized that this calculation is only a crude first approximation. There is a significant phase lag in surface elevation within Little Egg Harbor because of the time involved for the tidal wave to proceed up the shallow bay. For Great Bay, the phase lag is on the order of one hour, therefore the volumetric calculation of tidal prism should be reasonable (Table 1). However, for Little Egg Harbor, the phase lag between high water in the inlet and in the upper bay is about three hours and therefore the calculation of tidal prism simply based on storage basin area and tide range may be subject to considerable error.

Analyses of inlet throat discharges were made, based on measured velocity profiles and tide varying channel cross-sectional areas. Velocity data taken at hourly intervals at the surface, mid-depth and near bottom over an entire tidal cycle were obtained from the Corps of Engineers, Waterways Experimental Station. Cross-sectional areas for each section were evaluated from Alpine Geophysical's 1974 bathymetry. The raw current data from each station were plotted as a function of time and smoothed by fitting a sinusoidal type curve to the data. From the velocity data and the channel cross-sections, the channel discharges were calculated. These values were then adjusted to be representative of a spring tide range and are shown in Table 1.

To a good approximation, the hydraulic stability of a "sandy" inlet may be characterized by a unique relationship between the cross-sectional area at the entrance and the spring tidal prism. Based on a wealth of empirical data, O'Brien (1969) postulated,

$$A = (2 \times 10^{-5}) P \text{ spring} \quad (2)$$

	<u>Little Egg Inlet</u>	<u>Beach Haven Inlet</u>
Mean Tidal Prism (Volumetric)	3.1 (10) ⁹ ft ³	1.9 (10) ⁹ ft ³
Spring Tidal Prism (Volumetric)	3.8 (10) ⁹ ft ³	2.3 (10) ⁹ ft ³
Spring Tidal Prism (adjusted discharge)	3.7 (10) ⁹ ft ³	2.4 (10) ⁹ ft ³
Throat Cross Sectional Area, 1974 (Ref MSL)	7.0 (10) ⁴ ft ²	4.3 (10) ⁴ ft ²
Equilibrium Flow Area Based on O'Briens Relationship (Ref MSL)	7.4 (10) ⁴ ft ²	4.8 (10) ⁴ ft ²

HYDRAULIC CHARACTERISTICSTABLE 1

where A = Cross-sectional area at the throat at MSL (ft^2), $P_{3\text{spring}}$ = Volume of tidal prism at spring tide (ft^3).

The implication is that tidal prism or "tidal power" is the forcing mechanism which maintains and determines the entrance channel. The term "stability" does not imply that the inlet will not change over time but rather that the system is in a state of dynamic equilibrium. A "stable" inlet implies a long-term balance between scour capability of tidal currents and depositional potential from littoral drift. Dramatic or permanent changes in storage basin characteristics of a tidal inlet system will then be manifested by a change of the entrance channel cross-sectional area. One such mechanism might be a geomorphic alteration of the storage basin which would change the tidal prism. A stable inlet will adjust to such changes with a new entrance channel which again permits a state of equilibrium.

Many inlets are not in fact totally "sandy". In a given inlet, one might expect to find a wide range of sediments, ranging from cohesive silts and clays on the channel flanks to shells and gravels on the channel bottom. Given some sand, however, it appears that the adjusting mechanism is generally sand transport as sands are most easily eroded (DeAlteris and Byrne, 1973). This explains, in part, why a unique maximum velocity (about 3.5 fps) is approximated in many inlets and a wide range of inlets may be characterized by Equation (2), (O'Brien, 1969). In particular, Little Egg and Beach Haven Inlets are at least partially sandy so that O'Brien's relationship should be a valid interpretation of their "stability".

Given the present spring tidal prism (adjusted discharge, Table 1), the equilibrium cross-sectional areas were computed from Equation (2). These results are shown in Table 1 and are compared with actual sections given by recent bathymetry. The results indicate that the measured cross-sections at Beach Haven and Little Egg Inlets are approximately equal to the "equilibrium cross-sections".

Within the accuracy of O'Brien's relationship and combined with the inaccuracies of the present analysis, one may conclude that Little Egg and Beach Haven Inlets are at present hydraulically in equilibrium or stable type inlets.

Historical changes in the bathymetry of Little Egg and Beach Haven Inlets were studied to gain some insight into the long-term stability or variability of the area. Hydrographic boat sheets showing both inlet channels, were available for 1903 and 1935 and Alpine Geophysical Associates' data for 1972 and 1974. A "throat" was identified for each inlet and the cross-sectional area was computed from the chart bathymetry. The cross-sectional areas of these sections are given in Table 2. Note that while a particular inlet may change drastically (even disappear), changes in the combined inlet area are relatively minor. For 1903 and 1935, the total Beach Haven and Little Egg cross-sectional areas were nearly identical at about 73,000 ft.², compared with recent cross-sections which average about 97,000 ft.². Adjacent geomorphic changes must therefore also be considered. Great Bay was formerly serviced by an additional inlet slightly north of Brigantine Inlet, commonly called Wreck Inlet. Since 1933, Wreck Inlet has migrated some 1,400 feet southward until merging with Brigantine Inlet in 1963. Wreck Inlet serviced Great Bay by means of Great Thoroughfare which is still present, but in a very reduced state. Simultaneously, Brigantine Inlet was narrowed from 3,000 feet in 1940 to its present width of 700 feet. One may conclude, therefore, that at one time, significant quantities of tidal flow were interchanged between the Wreck Inlet-Brigantine Inlet system and the southern portions of Great Bay. Great Thoroughfare is no longer an avenue for significant flow so that Great Bay is almost exclusively serviced by Little Egg Inlet. In view of the previous discussion of hydraulic stability, the changes in total entrance area from 1903-1935 era to present, seems at least qualitatively reasonable. The effective tidal prism for Little Egg Inlet is now considerably larger, encompassing all of Great Bay. As the storage basin area and tidal prism have increased during the last 30 years, the inlet cross-sectional area has increased to preserve hydraulic stability.

Short-term changes of the inlet channel cross-sections were also investigated by periodic bathymetric measurements along five transects across the Beach Haven and Little Egg Inlet channels. The measurements were made using a small boat, a precision fathometer and an electronic range finding device. The raw profiles were corrected to MSL with local tide data. Channel cross-sectional areas were computed using a limited baseline length that included the central channel and its flanks only, not the wide peripheral shoal areas. During the monitoring period, the area changes were minimal (less than 10 per cent of the average area). In all cases, the actual morphologic changes occurred on the seaward

YEAR	AREA AT BEACH HAVEN INLET (ft ²)	AREA AT LITTLE EGG INLET (ft ²)	COMBINED TOTAL (ft ²)
1903 (1)	-----	-----	72,480
1935 (1)	35,860	37,090	72,960
1972 (2)	35,650	58,900	94,550
1974 (2)	36,680	60,800	99,480

(1) From U.S.C.G.S. Boat Sheets, Reference MLW.

(2) From Alpine Geophysical 1974 Bathymetry, Reference MLW.

HISTORICAL INLET CHANNEL CROSS SECTIONAL AREAS

TABLE 2

flank opposite the marsh. This is due to the geology of channel cross-section, that is, sands occur on the seaward or updrift flank while cohesive sediments are found on the channel bottom and on the channel flank adjacent to the marsh.

SUMMARY AND CONCLUSIONS

The results of these inlet studies were directed toward assessments of the geomorphic and hydraulic stability of the inlet channels. Beach Haven Inlet is geographically unstable due to the steady southwestward elongation of Long Beach Island. During the last 20 years, Beach Haven Inlet has migrated southwest at a mean rate of 160 feet per year. Fluctuations in this rate along with mean shoreline recession rate, correspond well to fluctuations in the local rate of relative sea level rise. During the next 50 years, it is speculated that Beach Haven Inlet will merge with Little Egg Inlet forming a single entrance to the sea, after which a new break-thru inlet will form on the northern portion of Long Beach Island. This sequence occurred under identical circumstances between 1873 and 1923. This speculation presumes that there will be no attempt to stabilize this natural system. Hydraulically, Beach Haven Inlet appears stable. That is, during the last 75 years, the cross-sectional area of the inlet throat has remained relatively constant at approximately 36,000 square feet. The measured tidal prism for Beach Haven Inlet when plotted against the throat cross-sectional area, lies reasonably close to O'Brien's curve. Little Egg Harbor, the storage basin for Beach Haven Inlet, is long, narrow and shallow. Within this storage basin, there are significant reductions in tide range and phase lags in the tide curve. In contrast to Beach Haven Inlet, Little Egg Inlet is geographically stable; only the outer inlet channel thru the ebb tidal delta has migrated in the recent past. Little Egg Inlet appears hydraulically stable, that is, the inlet throat cross-sectional area has remained relatively constant. Both the calculated and measured tidal prisms when plotted versus the channel throat cross-sectional area, lie reasonably close to O'Brien's curve. Between the surveys dated 1936 and 1973, the inlet throat cross-sectional area increased from 37,000 square feet to its present size of 59,000 square feet. This increase in cross-sectional area can be related to an increase in tidal prism served by the inlet due to the closure of Wreck Inlet, a former inlet on the south side of Little Beach Island. Hydraulically, Little Egg Inlet is distinctly different from Beach Haven Inlet. There are no significant reductions of the tidal amplitude or phase lags in the tide curve within Great Bay.

REFERENCES

- Atomic Energy Commission, 1973, Offshore Nuclear Power Siting Workshop, Deliberation and Recommendations, A.E.C. Publication, WASH.-1280, 36 pp.
- Caldwell, J.M., 1966, Coastal Processes and Beach Erosion: Journal of the Society of Civil Engineers, V. 53, No. 2 p.142-157.
- Charlesworth, L.J., 1968, Bay, Inlet and Nearshore Marine Sedimentation - Beach Haven - Little Egg Inlet Region, New Jersey: unpublished PhD dissertation, University of Michigan.
- Darling, J.M., 1968, Surf Observations along the United States Coasts: J. Waterways and Harbors, A.S.C.E., V.94, WW 1, p.11-21.
- DeAlteris, J.T. and Byrne, R.J., 1973, A Geological Control of a Natural Tidal Inlet: Abs., N.E.S.M., Geological Society of America, Vol. 5, No. 2 , p.155.
- DeAlteris, J.T. and Vespucci, P., 1975, The Quarternary Stratigraphic Sequence of Little Egg Inlet, N.J.: Abs., N.E.S.M., Geological Society of America, Vol. 7, No. 1, p.129.
- Emery, K.O., 1961, A Simple Method of Measuring Beach Profiles: Limnology and Oceanography, V. 6, p. 90-93.
- Goldsmith, V., Farrell, S.C. and Goldsmith, Y.E., 1975, Shoreface Morphology Study of the South End of Long Beach Island, Little Beach Island and the North End of Brigantine Island, New Jersey: an unpublished report from Coastal Dynamics, Port Republic, N.J. to Dames and Moore, Cranford, N.J.
- Hicks, S.D., 1973 , Trends and Variability of Yearly Mean Sea Level, 1893-1971, N.O.A.A., T.M. No. 12.
- McMaster, R.L., 1954, Petrography and Genesis of the New Jersey Beach Sands: State of New Jersey Department of Conservation and Economic Development, Geol. Series Bulletin No. 63, 239 pp.
- O'Brien, M.P., 1969, Equilibrium Flow Areas of Inlets on Sandy Coasts: J. Waterways and Harbors, A.S.C.E. WW 1, p.43-52.
- Shepard, F.P. and Wanless, H.R., 1971, Our Changing Coastlines: McGraw-Hill, Inc. New York, N.Y., 570 pp.

CHAPTER 111

OFFSHORE SEDIMENTARY PROCESSES AND RESPONSES NEAR BEACH HAVEN-LITTLE EGG INLETS, NEW JERSEY

Thomas McKinney, Joseph DeAlteris,¹
Yung Y. Chao,² Lloyd Stahl, and James Roney³

DAMES & MOORE
Cranford, New Jersey

INTRODUCTION

The offshore region in the vicinity of the Beach Haven and Little Egg Inlets of New Jersey is the site of the proposed Atlantic Generating Station, a floating nuclear power plant to be constructed 2.8 n. mi. offshore by Public Service Electric and Gas Company (Figure 1A). In order to assess the impact of this proposed project on the region, a comprehensive study of the nearshore and offshore region was conducted. A complete synopsis of this study is available in PSE&G (1976). This paper presents the results of the investigations into the sedimentary processes operative in the offshore region. The dynamics and coastal evolution of the nearshore region is summarized in DeAlteris et al., (1976; this conference).

The proposed Atlantic Generating Station (AGS) is located offshore of the complex and transient tidal inlet system of Beach Haven and Little Egg Inlets. These inlets are the major hydraulic connections between the Atlantic Ocean and the Great Bay and Little Egg Harbor estuaries. A large, roughly triangular ebb-tidal delta is present at the mouths of and between the two inlet channels. The major offshore bathymetric feature is a broad linear sand ridge, the Beach Haven Ridge, which trends northeast and reaches a maximum elevation of -28 feet (NLW) (Figure 1A). The AGS site is located on the landward flank of the ridge and partially in the adjacent trough in about 40 feet of water. Landward of the wide, northward-deepening trough, the ocean bottom slopes gently up towards the ebb-tidal delta of Beach Haven and Little Egg Inlets. The offshore zone adjacent to the proposed AGS is separated from an extensive tidal marsh lagoon system by a broken chain of barrier islands, from Long Beach Island on the north to Little Beach and Brigantine Islands on the south.

The Beach Haven Ridge is one of a system of sand ridges which occur on the shelf surface. In recent years the origin of these features has been the subject of a number of studies. Duane et al., (1972) studied the sand shoals on the inner portions of the eastern continental shelf of the United States. Swift et al., (1973) review the question of the ridge and trough topography of the Middle Atlantic Bight. A detailed description of the geomorphic elements of the inner New Jersey continental shelf for this region is presented in PSE&G (1975). Duane et al., (1972) suggested that the shoreface-connected ridges originated in a shallow nearshore environment in response to the interaction of south-trending, shore-parallel, wind-driven currents and waves during winter storms. They suggest that as sea level rises, and the shoreface retreats, the shoals are abandoned and isolated as "relict" features on the shelf surface. This concept was proposed in part by Moody (1964) from studies of the ridge system at Bethany Beach, Delaware.

Duane et al., (1972) recognized two categories of shoreface-connected ridges based on their orientation to the shoreline and their inferred response to the coastal hydraulic regime:

¹Pandullo Quirk Associates, Wayne, New Jersey

²Rutgers University, New Brunswick, New Jersey

³Franklin Institute, Philadelphia, Pennsylvania

Type I Ridges - Ridges with wide angle to the shoreline (over 30°)

Type II Ridges - Ridges with low angle to the shoreline (less than 30°).

Type I ridges are oriented transverse to the wind-driven storm currents and essentially parallel to the direction of wave attack. The Type II ridges would be oriented nearly parallel to the storm-generated currents and normal to the wave attack. During the initial stages of development, the low angle ridges (II) have the morphologic responses of wave-built bars (Duane *et al*, 1972; McHone, 1972). Wide angle ridges, such as those studied by Moody (1964), are more responsive to the coast-parallel storm currents and may migrate to the south. Moody's data showed that for a 42-year period, migration rates were about 10 feet per year. These cases of ridge migration were noted for the shallow segments of the shoreface-connected ridges.

Moody (1964) also suggested that considerations of wave refraction indicated that the wave orthogonals tended to converge over crests, producing nearbottom residual wave currents which would converge obliquely shoreward toward the crests. The wave refraction patterns may also be an important generating mechanism for the shoal topography (Moody, 1964; Goldsmith and Colonell, 1970). Thus, ridges oriented parallel to the prevailing storm wave attack, would produce consistent patterns of wave convergence on the north side of their connections with the shoreline, causing erosion in this area. The ridges would tend to perpetuate themselves by a feedback mechanism during the retreat of the coastline.

The Beach Haven Ridge cannot be classified as a typical shoreface-connected ridge. Duane *et al*, (1972) define the shoreface-connected ridges as those ridges outlined by, but landward of the isobath that defines the shoreface (usually the 30 ft isobath). In the study area, the nearshore profile is dominated by the sedimentary buldge of the tidal delta from the double inlet system (Figure 1B). The Beach Haven Ridge is located adjacent to the basal segments of this progradational feature which has been deposited over the shoreward edge of the ridge system (Figure 1B). Thus, the position of the ridge is comparable to the isolated, "relict" linear shoals elsewhere on the inner shelf and its location adjacent to the rising nearshore profile (shoreface) is due to its proximity to the large inlet system. The Beach Haven Ridge forms a low angle with the shoreline and would be comparable to Type II ridge of the shoreface-connected ridges, suggesting a response comparable to a longitudinal bedform in relation to the inferred controlling processes. Thus, its position beyond the upper shoreface and its orientation, parallel to the storm currents (Type II), both suggest a degree of stability of position and a lower sedimentary transport climate. The studies conducted in the offshore zone tend to substantiate these inferences.

GEOLOGIC FRAMEWORK

The geologic studies carried out in conjunction with soil investigations of the AGS site are presented in detail elsewhere (Stahl *et al*, 1972; PSE&G, 1972). These investigations support previous findings which indicate that the ridges on the inner shelf were formed by nearshore dynamic processes subsequent to the Holocene transgression of the shoreline (Field and Duane, 1976).

In addition, the AGS studies indicate that a backbarrier sand unit is differentially preserved below the sand ridge and that the underlying Holocene lagoonal clay unit below this is locally exposed in the landward trough. The subsurface data thus suggests that during shoreface retreat, the backbarrier unit was differentially eroded from the trough and its residue was deposited in the adjacent ridge (Figure 1B). The preservation of the backbarrier facies below the ridge suggests that, once the ridge formed, it did not migrate substantially and thus protected the underlying backbarrier sandy units from further erosion in this earlier upper shoreface setting. This pattern of long-term stability, suggested from the geologic data, is consistent with the historical analysis of the ridge stability, the studies of short-term stability of the ridge in response to major dynamic events and the assessment of the sediment transport from the monitoring of the hydraulic regime.

SURFICIAL SEDIMENTS

The nearshore area in the vicinity of the AGS site was sampled during the summer of 1974. The location of bottom samples is indicated in Figure 1A. Grain size analysis was conducted on the samples using calibrated 1/4 Phi sieves and where appropriate, hydrometer analysis.

Sieving was conducted on 8-inch diameter sieves using standard techniques as outlined by Folk (1968). Sieves were calibrated with respect to effective openings by using sets of standard glass spheres from the U.S. Bureau of Standards. Calculation of statistical movement measures following Friedman (1961) and plotting of frequency, and cumulative frequency curves was carried out using a computer program.

The grain size parameters which were found most useful in defining the patterns of sediment distribution and dispersal in the nearshore zone were the modal grain size and the percentage of fines (greater than 62 microns). The distribution of these parameters are presented in Figure 2A and Figure 2B.

Previous detailed grain size studies have revealed that in sandy sediments, a central sub-population can be recognized (Moss, 1962, 1963, and 1972; Visher, 1967). This central population is the main component of most sands and appears to represent a saltation population of framework building grains. This central population is a near Phi - normal distribution and is

represented by a central parabola when the frequency distribution is plotted on logarithmic scale (Hald, 1954; McKinney and Friedman, 1970). The parabola-like aspects of the distribution can be seen in the frequency plots listed in Figure 3 and 5B. The modal size was determined as the central grain size of this parabola. From Figures 2A and 2B the distribution of sediment patterns can be delineated.

Figure 3 presents the sequence of frequency curves on logarithmic scale across sampling Profile I to illustrate the nature of the systematic variation and traceability of distinct modal entities and their relationship to the morphologic elements in the nearshore zone.

The modal size shows systematic variation which enables this parameter to be contoured and related to apparent dispersal trends which reflect the transport and depositional processes which resulted in accumulation of these sediments (Figure 2A). The modal size distribution map of primary modes has been constructed using a contour interval of 0.4 Phi units. The following sediment classes of modal sizes have been shaded for additional emphases: a) Modal sizes coarser than 1.0 Phi (includes coarser and very coarse sands). b) Modal sizes 1.0 Phi to 1.8 Phi (medium sand). c) Modal sizes 1.8 Phi to 3.0 Phi (fine sands). d) Modal sizes 3.0 to 3.4 Phi (very fine sands). Note that the boundaries between B and C listed above is not the boundary between medium and fine sands as defined in the Wentworth (1928) classification of grain sizes, but for the purposes of discussion in the context of the contouring of modal sizes discussed above, these subdivisions will be referred to as medium sands and fine sands, respectively. The contoured pattern of modal sizes reveals and outlines three major sedimentary facies:

1. Tidal sand deposits - these sediments are defined by the alternating patterns of fine and medium sand reflecting the onshore-offshore pattern of tidal ebb and flood flow from the double inlet system.
2. The shoreface very fine (and silty) sands.
3. The shelf sand sheet - with modal sizes ranging from coarse to fine sands.

Tidal Sand Facies - Tidal sand facies as mapped by the contours of modal shows a very close relationship to the tidal channel and inlet morphology. Fine sands are deposited on shoal areas between active tidal channels which are characterized by medium sands. Locally, coarse sands characterize the deeper portions of the inlet channels as in the Beach Haven channel system to the north. A general asymmetry to the sizes can be noted within the inlet system with the northern half of the inlet system being characterized by a predominance of medium sand modal sizes, while the southern portion has a greater abundance of fine sand sizes. Charlesworth's (1968) study of sediments and hydraulics of this double inlet system reveal a similar southerly decrease in grain size as defined by trend surface

analysis of mean grain sizes of inlet samples. The variation in modal size also shows a systemic pattern of decreasing sizes down the axis of the inlet channels in an offshore direction. This pattern terminates in bulges in the modal size contours of the fine sand lobes on the upper shoreface. This would seem to indicate and reflect the decreasing sediment transport capacity associated with the flow in the tidal channels offshore and the associated deposition. Fine sand seems also to have accumulated in the shadow zone of the ebb flow seaward of Tucker's Island.

The distal portions of the complex ebb delta system is marked by a slope increase illustrated by the 10- to 15-foot contours. Locally, a flattening is noted on the upper segments on this outer delta front, seaward of the Beach Haven Inlet as outlined by the 5-foot contour. These outer flattened margins of the delta complex are characterized by coarser grain sizes. The flat area off of the Beach Haven delta is characterized by modal sizes of 1.2 to 1.3 Phi. The outer edge of the delta front to the south is characterized by an increase of modal sizes to 1.5 Phi above the surrounding suite of modal sizes which range from 1.8 to 2.1 Phi. These patterns apparently reflect the storm-wave reworking of the outer distal portions of the ebb tidal delta.

Most of the tidal sands within this area are characterized by very low percentage of fine material. In general, there is an increase in the percentage of fine materials at the distal edge of the tidal sand facies corresponding with the sediments in the upper portions of the shoreface zone, where percentages of fines increased to 0.5 to 1 percent of the total sediment (Figure 2B). Locally, a few sampels within the tidal sand facies contain percentages of fines greater than 1 percent as is indicated in Figure 2B.

Shoreface Facies - The modal size distribution reflects a systematic decrease in grain size from the sediments which characterize the outer segments of the tidal sand facies as described above, into the sedimentary suite defined as the shoreface sand. These sands are characterized by a definitive pattern of modal grain sizes which occur within the upper portions of the shoreface morphology as defined by the approximate position of the 15-foot contour.

The sediments within the shoreface zone are characterized by a very uniform pattern of modal sizes over the wide area of this zone which range from 2.9 Phi in the upper portions of the shoreface to 3.2 Phi in the lower portions (Figure 2A and 3). In general, this area is characterized by sizes within the very fine sand modal class.

The distribution of these very fine modal sands is best developed in the central and southern portions of the study area. The shoreface area seaward of Long Beach in the northern segment of the study area does not appear to be characterized by a continuous suite of very fine sands. In this region, corresponding with the location of small-scale ridge and swale morphology, the bottom sediments are characterized by coarser grain sizes

ranging from fine to medium to coarse sands. The distribution in the occurrence of the very fine modal sand class as outlined in Figure 2A also corresponds with those areas characterized by percentage of fine material which are greater than 1 as indicated in Figure 2B.

Thus, the shoreface sands are located within a definitive morphological setting and are characterized by the well-defined and narrow range of modal sizes and increased percentages of fine silty material. The percentage of fine materials increases locally on the lower portions of the shoreface zone to values in the 30 to 40 percent range (Figure 2B).

The shoreface sands have been identified from textural analysis of samples within cores from subsurface material across this zone. Cores through the shoreface suite are characterized by similar modal sizes of very fine sand and similar percentages of fine silty material. Sedimentary structures within the cores are locally characterized by thin laminations of this very fine silty sand material. Except for the occurrence of one sample in the landward trough of the offshore sand facies to be described below, this distinctive modal suite is present only within the narrowly defined limits of the shoreface zone.

Shelf Sand Facies - Beyond the thin distal edge of the shoreface very fine silty sand facies described above, lies the shelf sand sediments. This facies is characterized by predominance of coarse and medium sands. The contour patterns of modal grain sizes for this offshore suite is characterized by a distinctive coast-parallel orientation in contrast with the coast-perpendicular patterns of contours in the tidal sands and shoreface facies.

The northern portions of the shelf sand facies is characterized by very coarse modal sizes, apparently representing the southern distal edge of the reworked fluvial gravel deposits of Schlee and Platt (1970). Frank and Friedman (1971), also identified these coarse sands in similar depth position immediately to the north of the present study area.

The boundary between the offshore distal edge of the shoreface sand and the shelf sand facies is, in general, a very sharp one as indicated by the contours of modal size (Figure 2A), with modal sizes varying from very fine sands to coarse to medium sands within very short distances. In addition, sediments of the shelf sand facies located adjacent to the distal edge of the shoreface sands are characterized by secondary modes of the very fine sand mode of the shoreface suite (Figure 3).

As with the other facies within the study area, there appears to be a regional fining of the grain sizes within the shelf sand facies from coarse on the north to predominantly finer sizes on the south.

The more detailed variations in the distribution of modal sizes can be described within the context of the ridge and swale topography as outlined in the bathymetric chart of the Atlantic Generating Station area

(Figure 1A). The landward trough of the Beach Haven Ridge is characterized by an underlying framework of medium and coarse sand sizes. This suite forms a thin cover over the Holocene lagoonal clay unit as described in corings and borings (Figure 1B). Locally, the clay is exposed at the surface. In addition, during the sampling period, isolated samples of fine sand and one sample of very fine modal sand were present within the landward trough. The medium and coarse sands above the Holocene clay show the presence of secondary modes of fine and very fine sands as admixtures (Figure 3). Locally, higher values of fine material (Figure 2B) correspond with the presence of the very fine sand admixtures in the landward trough.

Thus, the landward trough is characterized by a thin sedimentary cover which represents an admixture of predominantly coarse and medium modal sizes and local admixtures of suspended fine material and secondary modes of fine and very fine sand which locally represent the predominant modal size. Thus, the sorting within these sediments is relatively poor compared to adjacent areas (Figure 3).

The Beach Haven Ridge itself is characterized by the predominance of medium sand sizes along its axial portions. A decrease of modal sizes occurs from the central axial portions of the ridge down the northward sloping axial portions of the ridge from grain sizes of 1.2 Phi to 1.3 Phi to 1.4 Phi in a northerly direction. A central zone of coarse sand is located along the axial portions of the ridge where the lineation aspect of the ridge is clearly defined. The location of this coarse sand zone along the axis of the ridge correlates with the crossing of caustic rays as indicated in the wave refraction diagrams for storm waves from the northeast (PSE&G, 1975). Further to the south of this area, along the continuation of the ridge trend, grain sizes within the ridge proper decrease. In this region, the ridge morphology is not clearly defined and flattens out with a general southward merging with the shoreface morphology.

This flattening of the ridge crest to the south is outlined by the nature of the 30- to 35- foot contours in this area (Figure 1A). Also noted in the ridge morphology in this region, is a broad delta-like fan which occurs on the upper portions of the seaward flank. This is indicated by the outline of the 35- and 40- foot contours. This feature, which occurs opposite a lower area, or swale in the crestal portions of the ridge, is very similar to the fan-like features mapped and discussed by McHone (1972) for a shallow shoreface-connected ridge on the south Virginia coast. The Virginia features are associated with erosional saddles in the ridge crest and have been ascribed to the breaching of the ridge during storms and the deposition of fine sediments in the adjacent sediment lobes on the seaward flanks.

A careful examination of the modal sizes in the area of this fan-like bulge shows that it corresponds to a comparable lobe of finer bottom sizes as indicated by the seaward convexity in the isopleths of modal size that become finer down the axis of the fan. At the base of the fan, immediately seaward of the 35-foot contour, a depocenter of fine sand (modal size 2.2 Phi) is noted.

Superimposed on the general pattern of coarse and medium sands, is the distribution of fine sands in selected areas in the offshore sand facies. A distinctive aerial distribution of such fine sands is encountered on the seaward flank of the Beach Haven Ridge and incorporates the fan-like feature described above.

The modal sizes of the outer shelf fine sands are characterized by a narrow range of modal sizes (2.0 to 2.3 Phi). This is in contrast to the wide range of fine modal sizes noted for the sands of the tidal facies which can be related to the systematic dispersal of sediment from the tidal inlets. The surficial zone of fine sand (2.0 to 2.3 Phi) noted on the seaward flank of Beach Haven Ridge has also been identified from analysis of cores in this area. The core data indicates that the fine sands are 1 to 2 feet thick and overlie medium sands which characterize the core of the ridge. Another ridge-parallel zone of fine sand occurs further seaward of the ridge flank but it is not as clearly defined as the former. To the south, both fine sand units appear to merge to form a broadening zone of fine sand which characterizes the southern inner segments of the shelf sand facies.

The occurrence of the fine sand deposit on the seaward portion of the Beach Haven Ridge also corresponds to a general increase in the percentage of fine material in this area of the offshore facies. Locally, values of percent of fines are greater than 1 and in a few cases very high portions of fine material occur in isolated patches on the outer segments of shelf sand facies (Figure 2B).

BOTTOM STABILITY

An analysis of bathymetric data from 1677, but in detail from 1935 to 1972, reveals the Beach Haven Ridge has maintained its general position for almost 300 years and its overall orientation and shape for at least 35 years, the period when detailed maps were available. Moderate variation in the sea floor over this period are, however, evident.

The landward trough has been the site of alternating periods of infilling and erosion. The periods of infilling can be related to greater influx of sediment from the adjacent inlet system. The correlation of such an event with the passage of Hurricane Agnes in June 1972 suggests that sediment was pumped out of the inlets by the reflux of storm surge that accompanied this event and was deposited at the distal edge of the shoreface. Subsequent remobilization of this fine silty sand during storm events, resulted in the removal of a few feet of this material from the trough surface. At no time, however, did erosion proceed down to and involve the Holocene clay unit which underlies the trough. The overall trend was one characterized by a general erosion of the lower shoreface and the south-trending headward segments of the trough.

The erosive resistance of the Holocene clay which underlies the trough is further documented by a laboratory analysis of the critical shear stress of erosion of this unit that was carried out at the University of

California, Davis (Krone, 1974), samples of cohesive sediment from 20 diver-collected cores were kept moist and shipped immediately to Davis. Testing was accomplished using a rotating cylinder apparatus, modified after Moore and Masch (1962), using both sea water and distilled water. The critical shear stress for surface erosion was found to exceed the capacity of the apparatus, 82 dynes/cm². Occasionally, the presence of small sand lenses and concentrations of shell material, resulted in the falling off of "chunks", even though the rest of the surface did not erode.

Accompanying the patterns observed in the landward trough, were the observations of slight depositional trends ranging to a few feet on the seaward flank of the ridge. Subsequent sediment analysis from cores and surface samples indicate that this depositional trend was also characterized by fine sands. Thus, the differential mobility of the fine sands appears to correlate to the minor variations in the ridge and trough morphology over the measuring period.

A program to evaluate short-term changes in and around the ridge was conducted from the summer of 1973 to the summer of 1974. Bottom elevations were measured by divers on a bi-monthly schedule. Measurements were made with reference to a series of stakes at each field (Figure 4A). The results indicate that there was no significant scour or accumulation at any of the stake fields at any time during the measuring period. Variations noted were on the order of magnitude of the wave ripple heights.

In addition to bottom elevation measurements, the stake field study enabled divers to collect bottom samples over the monitoring period for an analysis of the temporal variations in bottom sediment texture. The statistical parameters for a particular stake field were remarkably consistent during the measuring period. This consistency is reflected in the plots of the size distributions which fall into tight envelopes as plotted on the Phi-probability scale (Figure 4B). The small variations noted may easily reflect the variations expected due to the combined sampling, splitting and analysis operations and/or the variations related to position on a ripple crest or trough. Stake field 5 samples showed the most variability within the stake field and with time for a particular stake. The slight variability at stake field 5 occurs in the fine sand portion of the distributions.

Storm Hydraulics and Effects of December, 1974 Storm - The long-term cumulative effects of erosion and deposition are intergrated and reflected by the changes in the historical bathymetry. Such patterns are responses to the coastal circulation system.

The dynamic aspects of the coastal circulation at the AGS site have been monitored for over two years (E.G.&G. 1974, 1975). This area is characterized by the interaction of tidal current outflow from the inlets and the general pattern of coast-parallel, coastal current circulation. Like other segments of the Middle Atlantic Bight, this coastal region displays a geostrophic coastal current which is driven by the density patterns associated with lighter nearshore waters due to the freshening influence of river runoff and results in a general net south-westerly drift, measured at the site as 5 cm/sec. Although the net and predominant drift is to the south, during

winter months, due to the low runoff and extreme cooling for the inner shelf waters, the density gradients are reversed and the drift can be reversed, to a northeasterly direction. Superimposed on this coastal drift, is a weak (1.5 cm/sec.) quasi-estuarine onshore-offshore circulation; offshore in the surface waters and onshore along the bottom.

The dominant process operative in the offshore area with the potential for differential sediment transport, is the wind-driven circulation associated with major storms. The intensity and directional aspect of the bottom flow regime is directly related to the wind intensity and direction; reversals in the wind direction are accompanied by reversals in the bottom current circulation patterns. The wind patterns associated with storm events generally resulted in coast-parallel circulation particularly to the southwest or downcoast direction in response to "Northeaster" storms which characterize this area. Currents in this direction tended to be characterized by somewhat greater values and were of slightly longer duration than the upcoast bottom currents associated with continental storms. This can be related to the superposition of the downcoast wind-driven circulation with the southwesterly geostrophic drift which characterizes the coastal circulation. However, the data indicates that upcoast storm-driven bottom circulation does occur in response to continental storms and must be considered in the evaluation of the sedimentary processes for the offshore area. This upcoast transport is increasingly important for winter months when the tendency for a northeasterly drift is increased.

The current data (obtained from Savonius Rotor instruments) as summarized for the year 1972, shows that the percentage of occurrence of current values with a potential for bottom transport (velocities greater than 40 cm/sec. near the bottom) was about 3 percent and was associated with the wind-driven circulation from these storm events, mostly in a downcoast direction.

On December 1 and 2nd, 1974, a major northeaster storm passed the site, resulting in strong winds out of the east with unlimited fetch. A maximum observed wave height of 5.6 meters and a maximum significant height of 4.4 meters, recorded on December 1st were the most severe to be encountered during the two year measuring period. This storm was the most damaging coastal storm for the eastern seaboard since the major storm of 1962. Peak flow in the lower meters had an hourly average speed of 62 cm/sec, while the upper flow speeds reached 85 and 95 cm/sec, directed in the downcoast direction. In order to assess the impact of this storm on the bottom configuration and sediment texture of the ridge, a series of bathymetric profiles across the ridge system were measured shortly after the storm (Figure 4A). In addition, stake fields 2 and 5 were measured and bottom sediment samples were collected to compare with earlier data. Comparisons of the pre- and post-storm profiles are presented in Figure 5A. The results indicate that the ridge system was essentially unchanged by the storm. Measurements at stake fields 2 and 5 were unchanged also from the previous measuring period. The post-storm bathymetric profiles do indicate that one to two feet of sediment was eroded from the lower portion of the shoreface and some from the landward trough. There is also the suggestion of a slight zone of accretion

on the seaward flank of the ridge in places. The sediment analysis of the post-storm samples did show an interesting variation at stake field 5; stake field 2 sediments were unchanged. The comparison between a representative size distribution for stake field 5 sediments prior to the December, 1974 storm and the post-storm sediment distribution is presented in Figure 5B. The storm resulted in the addition or admixture of a distinct very fine sand modal component to the earlier sediment distribution. The very fine sand population apparently is derived from the erosion and remobilization of the very fine silty sands of the lower shoreface and landward trough. The storm transport has apparently moved this material from the lower shoreface and trough up onto the landward flank as a thin textural admixture. The process has also enabled the separation of the silty fraction from the shoreface sands as the very fine sand moved offshore as bottom sediment while the fines (< 62 microns) were suspended and apparently travelled further downcoast.

DISCUSSION AND CONCLUSIONS

The distribution of the sediments in the study area and the aerial variations in their compositional and their textural parameters provide insight into the nature and degree of sediment transport processes that have been operative in this region. The modern active processes of sediment transport and deposition are most active in the double-inlet system in the nearshore zones. Here, tidal currents are largely responsible for the sediment patterns observed. The decreasing pattern of grain sizes and increased proportion of fine suspension material of the shoreface zone, represents the distal portions of the modern zone of nearshore sedimentation. The origin of the basic coarse pattern of the sediment distribution and character of the offshore shelf sands cannot be attributed to modern processes. Their general pattern can be related to the reworking of fluvial deposits to the north and the differential erosion of backbarrier Holocene sediments by coast-parallel processes at lower sea levels.

The nature and degree of modern sediment transport in and around the offshore ridge system can be closely related to the distribution of fine sand and suspended material as primary and secondary modal entities in the offshore sands. The landward trough is the distal depo-center for modern very fine sand and silt derived from the nearshore zone. When the influx of this fine silty sand material is high, as perhaps during major storm events which produce a flushing of the inlet system, the trough floor is covered with these fine silty sands over the thin coarser sands which cap the Holocene clay within the trough. Subsequent coast-parallel storm transport, especially by northeasters, may flush out the fine sands from the trough. This appears to reflect the ongoing balance of accretion from, and progradation of, the distal portions of the shoreface zone and the subsequent reworking of these loose silty sands by storms.

The remobilization of the fine sands in this setting at the headward portions of the trough, may thus pass to the south and over the flattened crestal parts of the ridge. Such migration of the mobile fine sand fraction would explain deposition of the fine sands which characterize the gentle seaward flank of the ridge. This sand has accumulated here in the "lee"

of the ridge as a thin coating and relates to data from the historical bathymetry analysis which indicates accretional events in these seaward flanks over various measuring periods.

The base level of the landward trough reworking is clearly the erosion-resistant Holocene clay foundation and its coarse sand capping.

It is the coming and going of the fine silty sands which have characterized the modern sediment transport in and around the ridge system. Elsewhere, away from the main source of this modern fine material, the coarser sediments of the offshore shelf facies only display this finer material as subordinate bimodal admixtures.

The well sorted and unimodal medium to coarse sands of the Beach Haven Ridge crestal zone are an exception. Here storm-wave agitation has apparently kept these transient fine fraction admixtures from accumulating within the crestal ridge sands.

The suggestion that the only significant transport of sediment in the offshore zone, is the fine sands which form the thin and disconnected admixtures into the coarse sands of the offshore shelf facies, is substantiated by sediment analysis of the stake fields. In particular, the post-storm (December, 1974) sediment comparisons for stake field 5 clearly indicated that it is this fine sand only, which has been differentially moved and deposited on the ridge's landward flank.

It is concluded that the Beach Haven Ridge, originated during an earlier sea level stand by an active differential erosion on the upper shoreface. Due to sea level rise, the ridge system is now located out of the zone of active shoreface erosion and within the zone of nearshore deposition. The outflux of sediment in the nearshore zone from the double inlet system is of considerable magnitude and has been capable of covering the shelf sand facies (Figure 1B). This depositional zone thins to a distal edge over the shelf sands to the north, apparently due to the net effect of the transport of the shoreface sands to the southwest in response to the net coastal currents in that direction.

A differential battle at the offshore distal edge of the shoreface depositional zone, between the progradation of this edge, due to the greater sediment influx into this zone, and the regression of the distal edge by the reworking currents and low sediment supply to the offshore zone, appears to characterize the sediment regime in the offshore area. In this battle, fine sands are transported over the ridge system out onto the shelf in a step-like fashion, as a thin coating over the older coarser shelf sediments. The long range pattern, if sea level continues to rise, would be one of the translation of the nearshore shoreface depo-center shoreward, further isolating the ridge system as the distal edge as the shoreface migrates landward.

ACKNOWLEDGEMENTS

This work was performed for Public Service Electric and Gas Co. and we would like to acknowledge the assistance and guidance of Mr. Doug Briggs during this effort.

REFERENCES

- Charlesworth, L.J., 1968, Bay, Inlet and Nearshore Marine Sedimentation; Beach Haven - Little Egg Inlet Region, New Jersey. Ph.D. Dissertation; University of Michigan, 2 Vols.
- DeAlteris, J.T., McKinney, T.F., and Roney, J., 1976, Beach Haven and Little Egg Inlets, A Case Study, 15th International Conference on Coastal Engineering, Honolulu, Hawaii.
- Duane, D.B., Field, M.E., Meisburger, E.R., Swift, D.J.P., and Williams, J.S., 1972, Linear Shoals on the Atlantic Inner Continental Shelf, Florida to Long Island, In: D.J.P. Swift, D.B. Duane, and O.H. Pilkey, (Editors), Shelf Sediment Transport: Process and Pattern, Dowdon, Hutchinson and Ross, Stroudsburg, Pa., pp. 447-498.
- E.G.&G. (Waltham, Mass.), 1974, Summary of Oceanographic Observations in New Jersey Coastal Waters Near 39° 28' N Latitude and 74° 15' W Longitude During the Period May 1972 through April 1973. A Report to Public Service Electric and Gas Co.
- E.G.&G. (Waltham, Mass.), 1975, Summary of Oceanographic Observations in New Jersey Coastal Waters Near 39° 28' N Latitude and 74° 15' W Longitude During the Period May 1973 through April 1974. Report to Public Service Electric and Gas Co.
- Field, M., and Duane, D., 1976, Post Pleistocene History of the United States Inner Continental Shelf: Significance to Origin of Barrier Islands, Geol. Soc. America Bull., V. 87, 691-702.
- Folk, R.L., 1968, Petrology of Sedimentary Rocks, Hemphills, Austin, Texas, 169 p.
- Frank, W.M., and Friedman, G.M., 1973, Continental Shelf Sediments off New Jersey. Jour. Sedimentary Petrology, 43:224-237.
- Friedman, G.M., 1961, Distinction Between Dune, Beach and River Sands from Their Textural Characteristics: Jour. Sedimentary Petrology, V. 31, 514-529.
- Goldsmith, V. and Colonell, J.M., 1970, Effects of Nonuniform Wave Energy in the Littoral Zone, Proc. 12th Coastal Eng. Conf. Amer. Soc. of Civil Engineers, New York, 2:767-785.
- Hald, A., 1952, Statistical Theory, with Engineering Applications. New York, John Wiley and Sons, Inc., 783 pp.
- Krone, R.B., 1974, Letter Report to Dames & Moore: Measurements of Critical Shear Stress for Erosion of Core Samples from the Atlantic Shelf, Sept. 3rd.

REFERENCES (Continued)

- McHone, J.F., Jr., 1972, Morphologic Time Series from a Submarine Sand Ridge on the South Virginia Coast, Unpublished M.S. Thesis, Institute of Oceanography, Old Dominion University.
- McKinney, T.F. and Friedman, G.M., 1970, Continental Shelf Sediments of Long Island, New York. *Jour. Sedimentary Petrology*, 40:213-248.
- Moody, D.W., 1964, Coastal Morphology and Process in Relation to the Development of Submarine Sand Ridges off Bethaney Beach, Delaware. Unpublished Ph.D. Dissertation, John Hopkins University, 160 p.
- Moore, W.C. and Masch, F.D., 1962, Experiments on the Scour Resistance of Cohesive Sediments, *Am. Geophys. Union, J. Geophys. Res.*, V. 67, No. 4.
- Moss, A.J., 1962, 1963, The Physical Nature of Common Sandy and Pebbly Deposits: Part I: *Am. Jour. Sci.* 260:337-373. Part II: 261:297-343.
- _____, 1972, Bed-Load Sediments, *Sedimentology*, 18:159-219.
- Public Service Electric and Gas C., 1972, Preliminary Safety Analysis Report, Atlantic Generating Station, Units 1 and 2.
- _____, 1975, Final Coastal Process Report, Atlantic Generating Station, Appendix D-13, Preliminary Safety Analysis Report.
- Schlee, J. and Platt, R.M., 1970, Atlantic Continental Shelf and Slope of the United States - Gravels of the Northeastern Part. *Geol. Survey Prof. Paper* 529-H.
- Stahl, L., Koczan, J. and Swift, D.J.P., 1972, Anatomy of a Shoreface - Connected Ridge System on the New Jersey Shelf: Implications for the Genesis of the Shelf Surficial Sand Sheet, *Geology*, 2:117-120.
- Swift, D.J.P., Duane, D.B. and McKinney, T.F., 1973, Ridge and Swale Topography of the Middle Atlantic Bight: Secular Response to the Holocene Hydraulic Regime, *Marine Geology*, 15:227-247.
- Visher, G.S., 1969, Grain Size Distributions and Depositional Processes, *Hour. Sedimentary Petrology*. 39:1074-1106.
- Wentworth, C.K., 1922, A Scale of Grade and Class Terms for Clastic Sediments: *Jour. Geology*. 30:377-392.

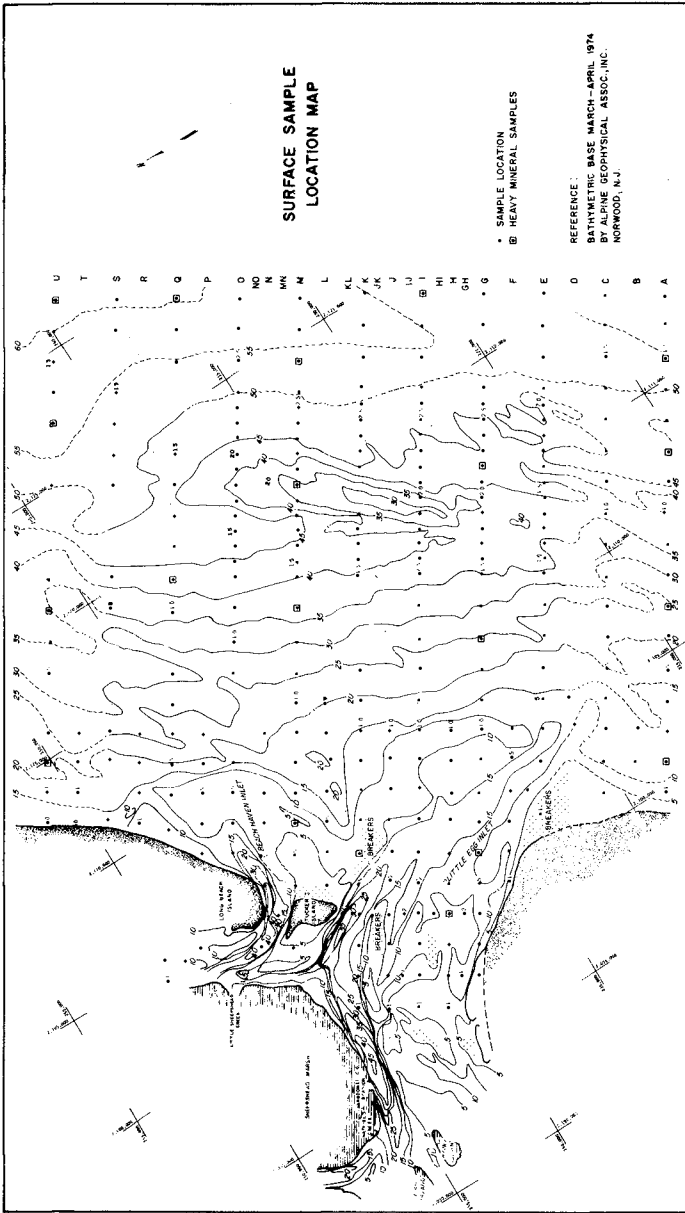


FIGURE 1A

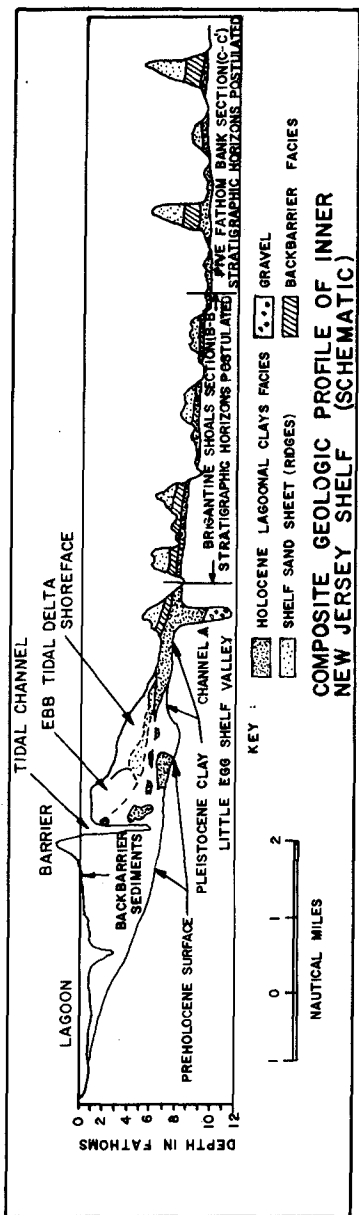


FIGURE 1B

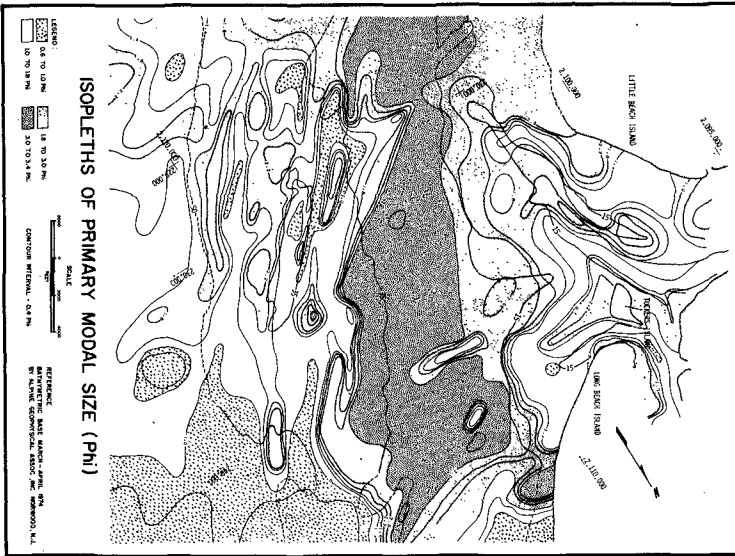


FIGURE 2A

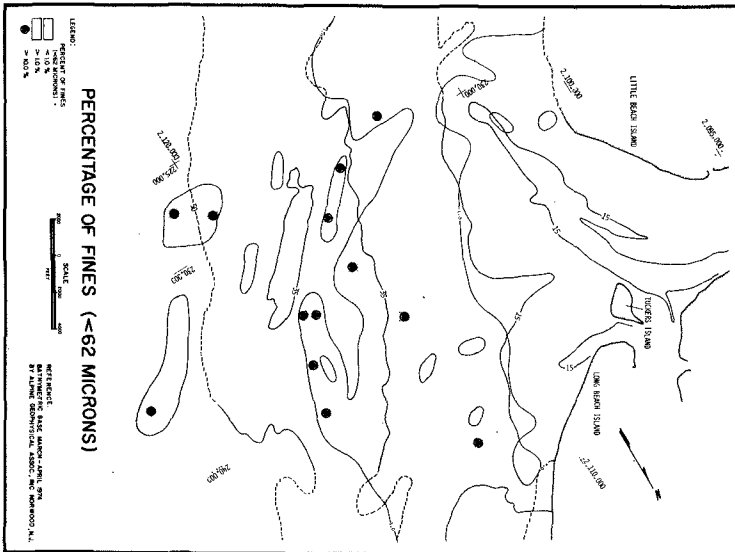


FIGURE 2B

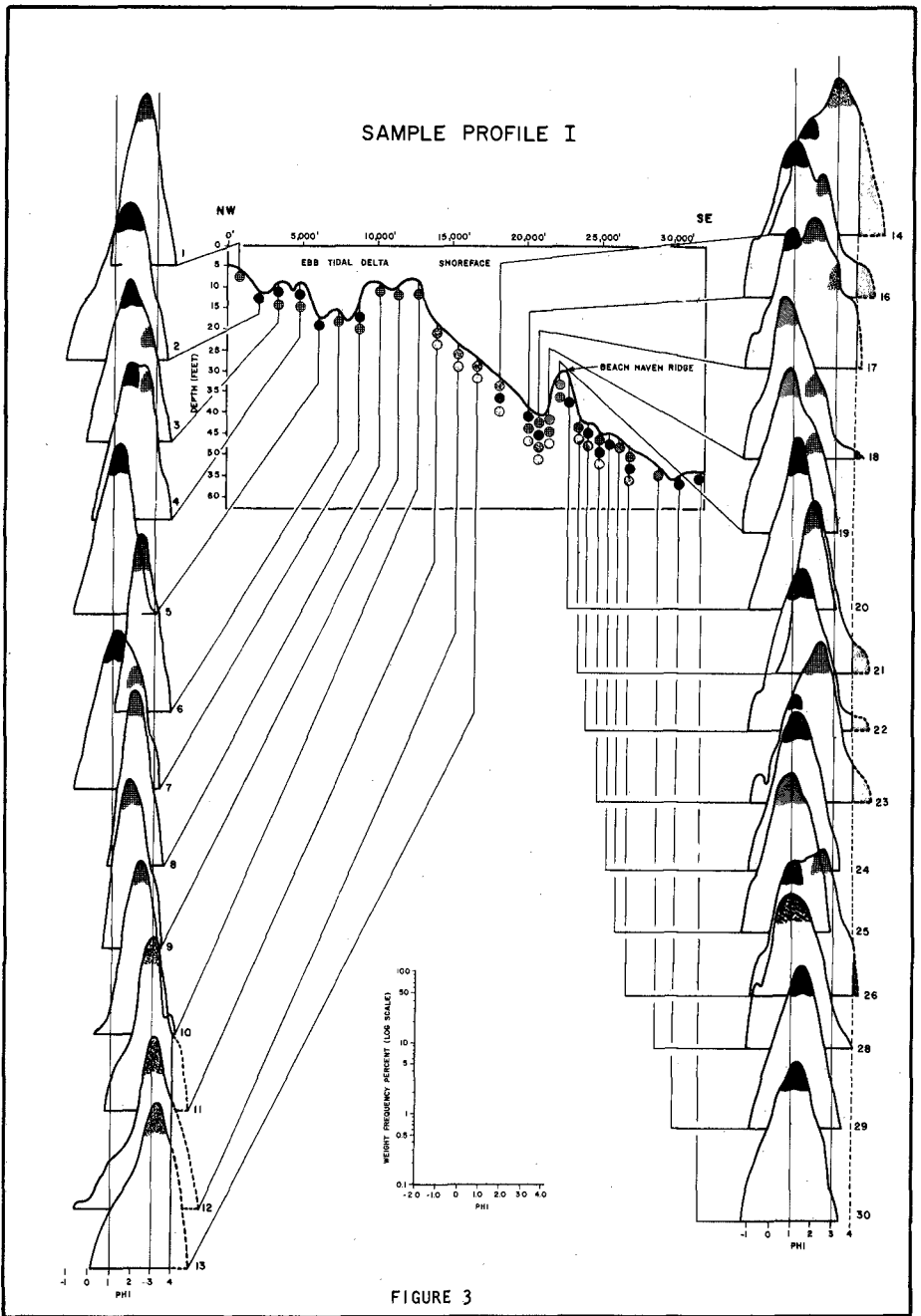


FIGURE 3

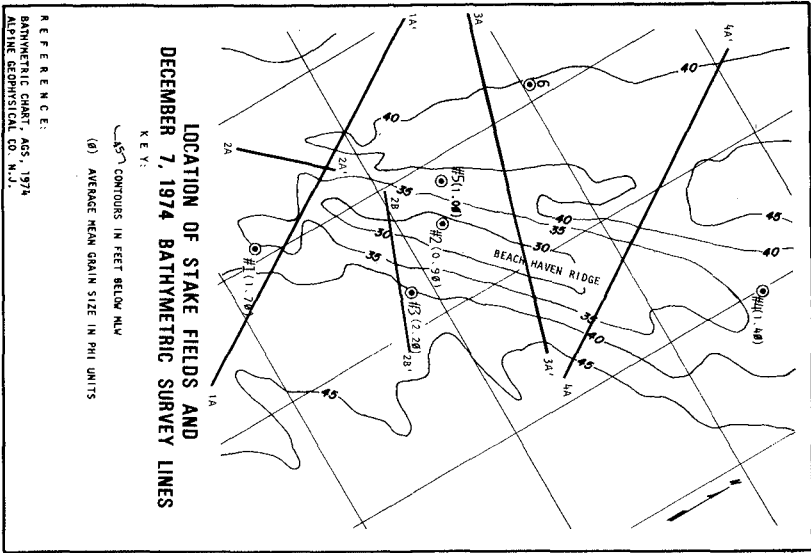


FIGURE 4A

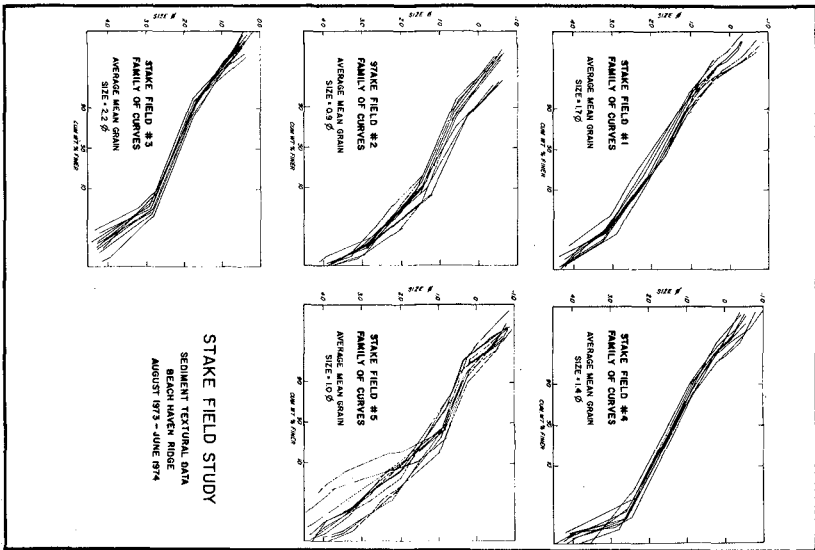


FIGURE 4B

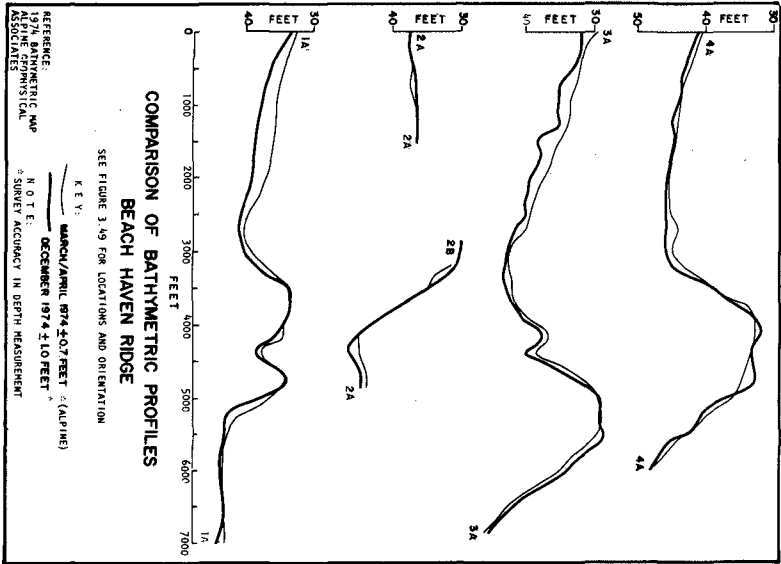


FIGURE 5A

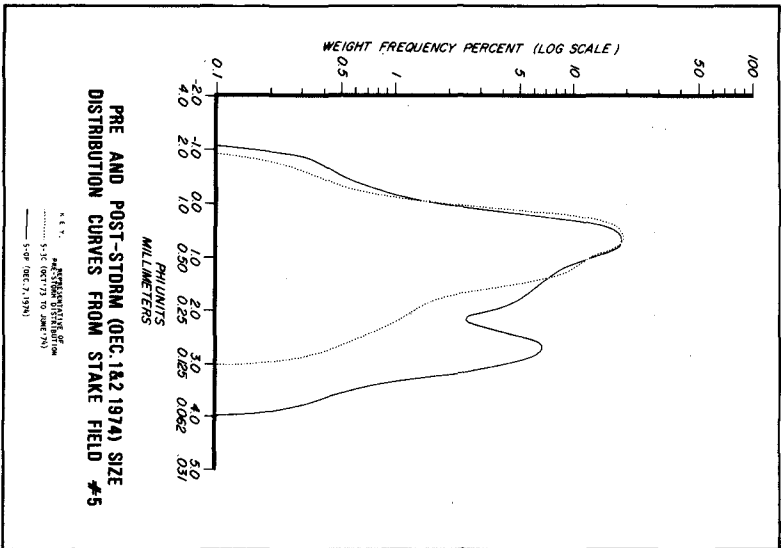


FIGURE 5B

CHAPTER 112

CAPACITY OF INLET OUTER BARS TO STORE SAND

Todd L. Walton, Jr.¹ and William D. Adams²

ABSTRACT

Inlets act as large sand sinks for sand derived from adjacent beaches. An attempt to quantify the amount of sand in an outer bar is made with the major governing parameter of inlet hydraulics, tidal prism. In areas of high wave activity there appears to be a well defined limiting relationship to the amount of sand stored in the offshore bar as a function of tidal prism. In areas where inlets are exposed to lower wave activity, more scatter is noted in this correlation.

Relationships for estimating the equilibrium storage volume of sand in the outer bar/shoal of newly cut inlets on highly exposed, moderately exposed, and mildly exposed coasts (where degree of exposure relates to wave action offshore) are proposed for use in estimating quantities of sand which will eventually be lost to adjacent beaches.

A conclusion of the study is that more sand is stored in the outer bar of a low energy coast than in the outer bar of a high energy coast. An upper limit to outer bar storage in low energy zones may be a function of additional parameters other than tidal prism such as longshore energy flux at the inlet site and inlet history.

INTRODUCTION

A commonly recurring problem of importance to coastal engineers is evaluating the number of inlets which a given length of shoreline can maintain in terms of inlet stability, and the degradation which a given inlet will cause to the surrounding shoreline. A considerable amount of research effort has been placed on the hydraulic aspects of inlet design and is discussed in References (1,2,3,4,5, and 6). Little research though has been done on the effects of inlets on adjacent shorelines (7). It is apparent that these effects are considerable when a correlation of shoreline erosion rates and locations of tidal inlets are made. In Florida, shoreline recession rates in the near vicinity of inlets are one to two orders of magnitude higher (10-70 feet per year) than average shoreline recession rates away from the influence of inlets (1-3 feet per year) (8). It is apparent that these inlets act as sand sinks in their capacity to absorb tremendous quantities of sand in both their outer bars and their inner shoal areas. Unfortunately this sand is derived from adjacent beaches and causes a consequential degradation to those beaches. An idea as to the magnitude of the inner shoal volumes of

¹Assistant Professor - Marine Advisory Program - Coastal and Oceanographic Engineering Laboratory

²Graduate Assistant - Coastal and Oceanographic Engineering Laboratory

sand trapped by an inlet is given in Table 1. The data in this Table are calculated from comparative surveys of the inlets over the period of years noted. It appears that the inner shoals of inlet systems may reach an equilibrium shoaling volume (Reference (10)) after a given period of time, therefore decreasing the erosional influence on adjacent shorelines (assuming no dredging of inner shoals takes place).

It seems reasonable to assume at first that such a process might occur on outer shoal/bars of inlets also. If an inlet is to be cut in a barrier island system, it is desirable to have an estimate of this sand volume which will eventually be lost from the surrounding beaches to the outer bar/shoals and to the inner shoals of the inlet. The present paper discusses a correlation between the amount of sand stored in the outer bar of an inlet and the inlet tidal prism or the inlet channel cross section. Assuming one can properly estimate the inlet hydraulics and equilibrium cross-sectional area which an inlet will take, this correlation should allow a coastal engineer to obtain a rough approximation of the final consequences which the opening of an inlet will have on adjacent shorelines.

METHODOLOGY

Calculation of Sand in Outer Bar/Shoals

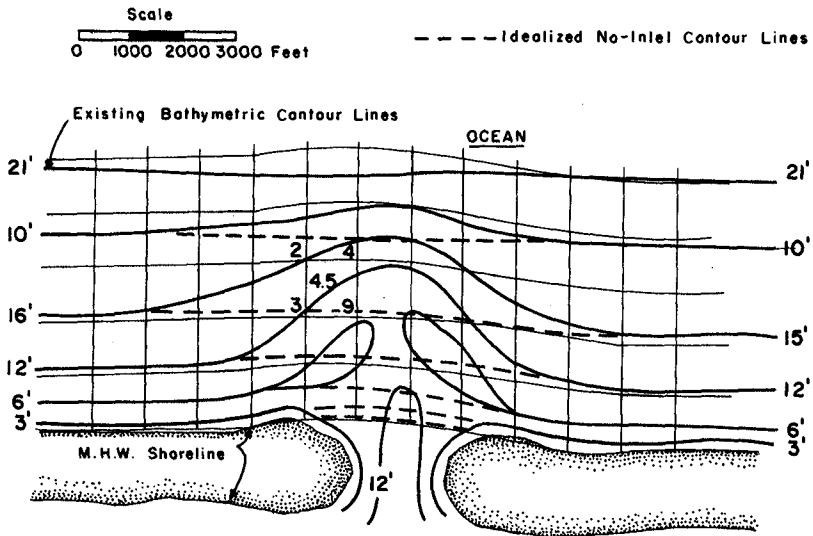
The procedure followed in calculating the volumes of sand residing in the outer bar/shoals of inlets is covered in depth in Reference (7). A summary of the methodology follows.

The parallel contour lines upcoast and downcoast of an inlet away from the influence of the inlet, were assumed as the natural topography of the coast without the inlet. This idealized "no-inlet" hydrography was then superimposed on a chart of the actual hydrography for the inlet. Depth differences between the actual existing bathymetry and the idealized "no-inlet" bathymetry were then calculated at the intersections of a grid system and averaged for each grid square and summed to give a volume of sand in the outer bar. The procedure for calculation is summarized in Figure 1 from Reference (7). As the procedure is somewhat subjective, the total difference in sand volume between the idealized "no-inlet" shoreline and the existing inlet shoreline was calculated two or more times for each inlet system with acceptable answers showing less than 10% deviation in the bar/shoal sand storage volumes calculated. Volumes of sand in outer bar/shoals of inlets on the lower East Coast of Florida were very hard to estimate in this manner due to complicated offshore reef structures in the nearshore zone and in all but one case were eliminated from further consideration. Volumes of sand stored in the outer bar/shoals of 44 inlets around the sandy portion of the United States coastline were calculated in the above manner and are presented in Table 2.

As an indication of how extensive some inlet outer bar/shoal systems are, Figure 2 shows an inlet outer bar/shoal system for St. Mary's River Entrance. St. Mary's River Entrance on the Florida-Georgia border has shoals extending over five nautical miles offshore (from the updrift coastline). This inlet has one of the largest offshore bar/shoal systems

Table 1. Volumes of Material Deposited in Inlet Bay Shoals

<u>Inlet</u>	<u>Calculated Volume of Shoaled Material in Bay Shoals (cubic yards)</u>	<u>Period of Survey</u>	<u>Inlet History</u>
Redfish Pass, Florida	3.75×10^6 (130,000/year)	1879 - 1956	Inlet opened in hurricane in 1926
Fort Pierce Inlet, Fla.	7.49×10^6 (160,000/year)	1879 - 1930	Inlet opened by man in 1921
St. Lucie Inlet, Fla.	7.46×10^6 (210,000/year)	1882 - 1930	Inlet opened by man in 1892
Sebastian Inlet, Fla.	2.58×10^6 (180,000/year)	1882 - 1938	Inlet opened by man in 1924 - has had a history of natural closure
Clearwater Pass Entr., Fla.	5.09×10^6	to - 1950	Inlet historically open
Carolina Beach Inlet, N.C.	4.00×10^6 (235,000/year)	1952 - 1969	Inlet opened in 1952 Reference (9)



Procedure

1. Construct Idealized No-Inlet Contour Lines
2. Impose 1000 foot square grid system on chart and calculate differences between actual depth and idealized no-inlet depth at grid line intersections (see example block)
3. Average depth differences at intersections and record in center of block (see example block)
4. Compute volume of sand in outer shoal by summing averaged block depth differences and multiply by 10^6 feet²

Figure 1. Steps in Calculation of Accumulated Volume of Sand in the Outer Bar. Procedure Illustrated for Idealized Inlet. From Reference (7).

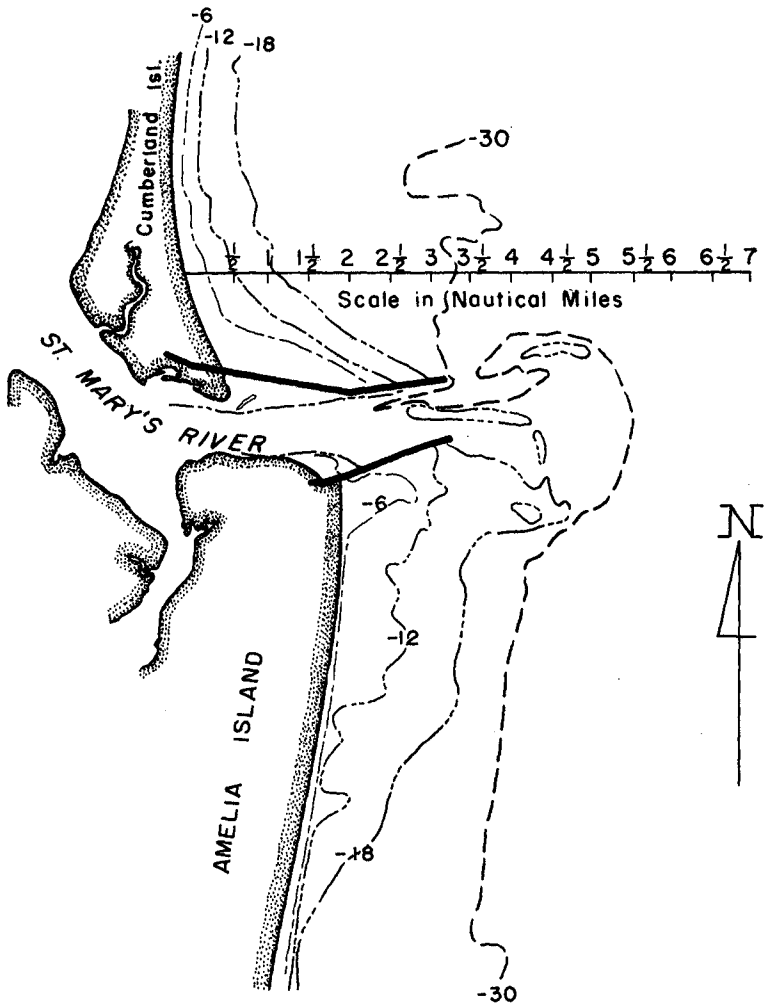


Figure 2. St. Mary's River Entrance.

of inlets investigated in Florida with over 136 million cubic yards of sand stored in it. The heavily developed area to the south of this inlet has historically suffered from erosion.

Tidal Prisms

Tidal prism measurements came from References (11,12,13,14, and 15). In most all of the cases the tidal prisms were either measured from current data taken at the throat of the inlet or by the "cubature method". Jarrett (14) discusses the cubature method in detail. In most all cases the date when the prism was measured corresponded to the survey date from which the estimate of outer bar sand volume was made.

Tidal prisms for the 44 inlets in which sand volumes have been calculated are presented in Table 2.

Channel Cross Section Areas

Channel cross section areas came from References (11,12,13,14, and 15) and from some additional measurements by the authors. In most all cases the cross section used was that at the throat area as defined in Reference (11), and were taken from the same survey as the inlet outer bar. Channel cross sectional areas are presented in Table 2.

Coastal Energy Regime

To suitably classify the data on inlets into some organizational scheme with regard to wave energy acting on the outer shoals of the inlets it was necessary to use some type of coastline parameters which gives a rough quantitative description of the energy potential available to modify the outer shoals of inlets. The parameters chosen were wave height, wave period, and nearshore continental shelf slope. Wave heights and wave periods available were average wave heights from wave gages in the nearshore zone (15 to 20 feet below MLW) from the Coastal Engineering Research Center wave gage program. As these wave heights already have the measure of continental shelf slope implicit in them (energy has been dissipated over the shelf up to the wave gage depth), the basic measure of wave energy used to separate energy environments was the parameter H^2T^2 (wave height² x wave period²). On mildly exposed, moderately exposed, and highly exposed coastlines, this parameter was arbitrarily chosen to range from 0-30, 30-300, >300 respectively. This classification lumps the South Carolina, Texas, and lower Gulf Coast of Florida inlets into the mildly exposed coast range; the East Coast, and Panhandle of Florida (Gulf Coast) inlets into the moderately exposed coast range; and the Pacific Coast coasts into the highly exposed coast range. The (wave energy) parameter H^2T^2 , and the offshore distance to the 5 and 10 fathom depth curves are given for various coastal segments in Table 3.

RESULTS

The data used in the correlations of tidal prisms with outer bar/shoal sand storage volumes are given in Table 2. Correlations were made for three coastal energy level groupings and for all inlets combined using

Table 2. Tidal Prism-Outer Bar Storage Volume Relationship

Inlet	Tidal Prism (ft.)	Measurement Date	Outer Bar Volume (yd.)	Survey Date	Cross Section Area at Throat (above MSL) (ft.)
Little Egg, N.J.	17.2×10^8 (S)	1935	45.0×10^6	*	38.3×10^4
Brigantine, N.J.	5.23×10^8 (S)	1936	6.70×10^6	*	1.22×10^4
Great Egg Harbor Ent., N.J.	20.0×10^8 (S)	1936-37	24.2×10^6	*	7.01×10^4
Hereford, N.J.	11.9×10^8 (S)	1937	25.0×10^6	*	3.57×10^4
Oregon Inlet, N.C.	39.8×10^8 (S)	1965	27.2×10^6	*	6.66×10^4
Beaufort, N.C.	50.5×10^8 (S)	1935-36	45.4×10^6	*	8.66×10^4
Carolina Beach Inlet, N.C.	5.25×10^8 (S)	1967	3.51×10^6	1967	0.76×10^4
Stono Inlet, S.C.	28.6×10^8 (S)	May, 1934	93.2×10^6	*	5.43×10^4
North Edisto River, S.C.	45.8×10^8 (S)	Ref. (12)	216.0×10^6	*	9.95×10^4
Nassau Sound, Fla.	22.0×10^8 (S)	1934	53.2×10^6	1953-54	7.25×10^4
St. Augustine Inlet, Fla.	13.1×10^8 (S)	1957	106.0×10^6	1954-57	2.65×10^4
Barnegat Inlet, N.J.	6.25×10^8 (S)	1936	13.1×10^6	*	1.48×10^4
Indian River Inlet, Del.	5.25×10^8 (S)	1948	3.11×10^6	*	$.966 \times 10^4$
Winyah Bay S.C.	30.2×10^8 (S)	1935	73.6×10^6	*	7.86×10^4
St. Marys, Fla.	47.7×10^8 (S)	1937	136.0×10^6	1954-55	14.4×10^4
St. John's River, Fla.	17.3×10^8 (S)	1958-59	90.2×10^6	1967	5.73×10^4
Jupiter Inlet, Fla.	1.11×10^8 (S)	1967	0.97×10^6	1967	$.291 \times 10^4$

Table 2 (Continued)

Inlet	Tidal Prism (ft ³)	Measurement Date	Outer Bay Volume (yd ³)	Survey Date	Cross Section Area at ₂ Throat (aboveMSL) (ft ⁴)
Bakers Haulover, Fla.	3.6×10^8 (S)	1928	0.29×10^6	1928	$.438 \times 10^4$
Captiva Pass, Fla.	19.0×10^8	Aug. 1960	12.34×10^6	1956	2.87×10^4
Boca Grande, Fla.	126.0×10^8	1959	$175. \times 10^6$	1956	16.6×10^4
Gasparilla Pass, Fla.	4.7×10^8	Nov. 1958	6.90×10^6	1956	1.33×10^4
Midnight Pass, Fla.	2.84×10^8	Mar. 1955	0.63×10^6	1954	$.322 \times 10^4$
New Pass, Fla.	4.00×10^8	Sept. 1953	6.60×10^6	1954	$.637 \times 10^4$
Longboat Pass, Fla.	4.90×10^8	Oct. 1953	7.78×10^6	1954	1.14×10^4
Ponce de Leon, Fla.	5.74×10^8 (S)	1936	19.0×10^6	1924	1.15×10^4
Sarasota Pass, Fla.	7.6×10^8	Mar. 1955	18.7×10^6	1954	2.31×10^4
Pass-a-Grille, Fla.	14.2×10^8	1950	23.5×10^6	1952	3.5×10^4
John's Pass, Fla.	5.03×10^8	1951-52	6.30×10^6	1952	$.886 \times 10^4$
Clearwater Pass, Fla.	6.8×10^8	June. 1951	3.00×10^6	1950	2.23×10^4
Dunedin Pass, Fla.	3.76×10^8	1959	8.5×10^6	1950	1.44×10^4
East (Destin) Pass, Fla.	15.7×10^8	1938	4.90×10^6	1941-47	1.72×10^4
Pensacola Bay Entr., Fla.	94.5×10^8	Apr. 1940	49.1×10^6	1940	11.2×10^4
Mobile Bay Entr., Ala.	$200. \times 10^8$	June. 1935	$1173. \times 10^6$	*	31.5×10^4
Venice Inlet, Fla.	0.74×10^8	May. 1955	0.89×10^6	1954	$.236 \times 10^4$

Table 2 (Continued)

Inlet	Tidal Prism (ft ³)	Measurement Date	Outer Bar Volume (yd ³)	Survey Date	Cross Section Area at Throat (above MSL) (ft ²)
Galveston Entr., Texas	59.4×10^8	1934	$127. \times 10^6$	*	19.7×10^4
Aransas Pass, (Rockport) Texas	17.6×10^8	Ref. (15)	25.9×10^6	*	1.6×10^4
Redfish Pass, Fla.	5.67×10^8	Ref. (15)	4.25×10^6	1956-60	1.19×10^4
San Francisco, Ca.	$510. \times 10^8$	Ref. (12)	$1055. \times 10^6$	*	93.8×10^4
Tillamook Bay, Oregon	21.1×10^8 (D)	Ref. (12)	22.07×10^6	*	3.69×10^4
Grays Harbor, Washington	$170. \times 10^8$ (D)	Ref. (13)	$342. \times 10^6$	*	29.1×10^4
Columbia River, Oregon	$382. \times 10^8$ (D)	Ref. (13)	$1006. \times 10^6$	*	50.8×10^4
Nehalem River, Oregon	5.66×10^8 (D)	Ref. (13)	4.2×10^6	*	$.964 \times 10^4$
Umpqua River, Oregon	22.0×10^8 (D)	Ref. (12)	33.7×10^6	*	4.62×10^4
Coos Bay, Oregon	25.1×10^8 (D)	Ref. (15)	36.2×10^6	*	5.65×10^4

* Outer bar volume computed from Nautical chart of latest issue (Survey date unknown)

(S) Refers to Spring Tidal Prism (D) Diurnal Tidal Prism

Table 3. Classification of Coastline by Offshore Slope and Wave Energy

Coastal Area	Distance to: 5 fathom curve	(in Nautical Miles) 10 fathom curve	Avg. Wave Ht. H (feet) *	Avg. Wave Period T. (seconds) *	$\frac{H^2 T^2}{ft^2 - sec.^2}$
New Jersey/Delaware	$\frac{1}{2}$ - $1\frac{1}{2}$	1 - 3	$1\frac{1}{2}$ - $2\frac{1}{2}$	$6\frac{1}{2}$	169
North Carolina	$\frac{3}{4}$ - $\frac{1}{2}$	10 - 15	2 - 4	5	225
South Carolina	5 - 8	18 - 22	$\frac{1}{2}$ (Georgia)	5	1.6
Upper Florida (East Coast)	$\frac{1}{2}$ - $2\frac{1}{2}$	11 - 17	2	5	100
Lower Florida (Gulf Coast)	2 - 5	11 - 20	1	4	16
Panhandle Florida (Gulf Coast)	$\frac{1}{2}$ - 1	1 - 2	$1\frac{1}{2}$ - 2	4	49
Texas	1 - 3	5 - 8	1 - $1\frac{1}{2}$	4	25
Oregon/Washington	$\frac{1}{2}$ - 1	1 - $2\frac{1}{2}$	3 - 5	9	1296

* These are rough averages from gage(s) located in the nearshore zone of the areas noted and may vary considerably depending on a variety of factors (information from Coastal Engineering Research Center wave gage program).

an equation:

$$V = aP^b \quad (1)$$

where

V = volume of sand stored in the outer bar/shoal of the inlet
(in cubic yards of immersed sand),

P = tidal prism of inlet (in cubic feet),

a, b = correlation coefficients.

Linear regression was used to obtain the coefficient b for the case of highly, moderately, and mildly exposed inlets and for the case of all 44 inlets combined. For these four cases the coefficient b equals:

Highly Exposed Inlets	$b = 1.23$
Moderately Exposed Inlets	$b = 1.08$
Mildly Exposed Inlets	$b = 1.24$
All Inlets	$b = 1.26$

As there was no significant difference in the exponential correlation coefficients, the value $b = 1.23$ corresponding to high energy coast (Highly exposed) inlets was used for the correlations with all inlet groupings. The justification for this somewhat arbitrary fixing of parameters was that a minimum of scatter existed in the correlation of the Pacific Coast Inlets (Figure 3). The minimum scatter in this plot over two orders of magnitude is somewhat surprising in view of the many parameters which should be of importance in inlet outer bar shoaling such as inlet history, available longshore energy flux, and physiography of the inlet-coastal location. The reasons for this minimum scatter in the Pacific Coast inlets studies may be more apparent upon considering the variables causing sand shoaling in outer bars.

The mechanism whereby sand is fed to the outer bar is twofold. Ebb tide flows tend to drive the material offshore which is being fed to the inlet by longshore currents, and wave activity on the outer bar tends to drive the material back to shore while at the same time feeding sand to the inlet in adjacent longshore current systems. The inlet outer bar/shoal is self perpetuating in the sense that longshore currents feed sand to the inlet system which causes the outer bar to grow which in turn causes wave refraction and sheltering effects at the inlet promoting a continued flux of sand toward the inlet over an increasing area (16).

Inlet history is important too. Should the inlet close or the tidal prism be reduced drastically (due to modifications of the inlet inner bay system) much of this material would be driven back to the beaches. The principal author has noted this occurrence in two locations on both the East Coast and Gulf Coast of Florida. In the case of the Pacific Coast inlets studies, all of the inlets have been open over recorded history.

Physiography must play an important part also. The authors have

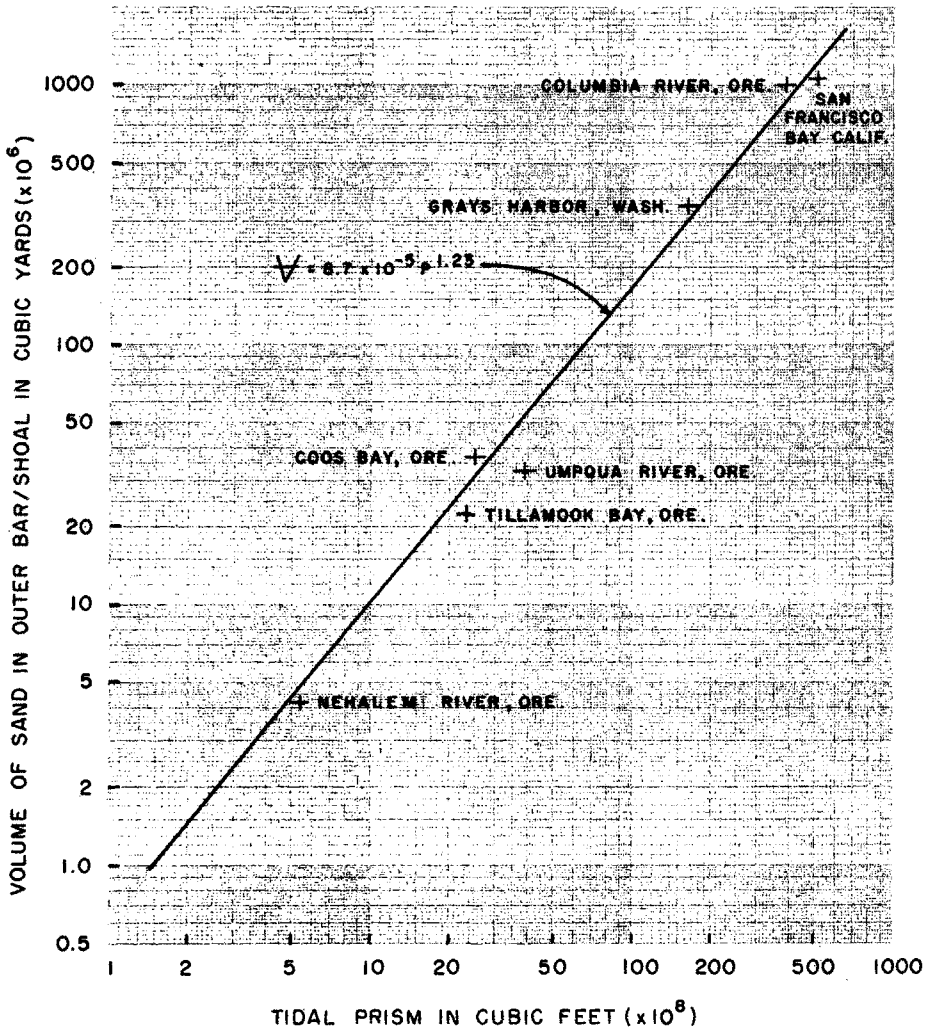


FIGURE 3. Tidal Prism-Outer Bar Storage Relationship for Highly Exposed Coasts.

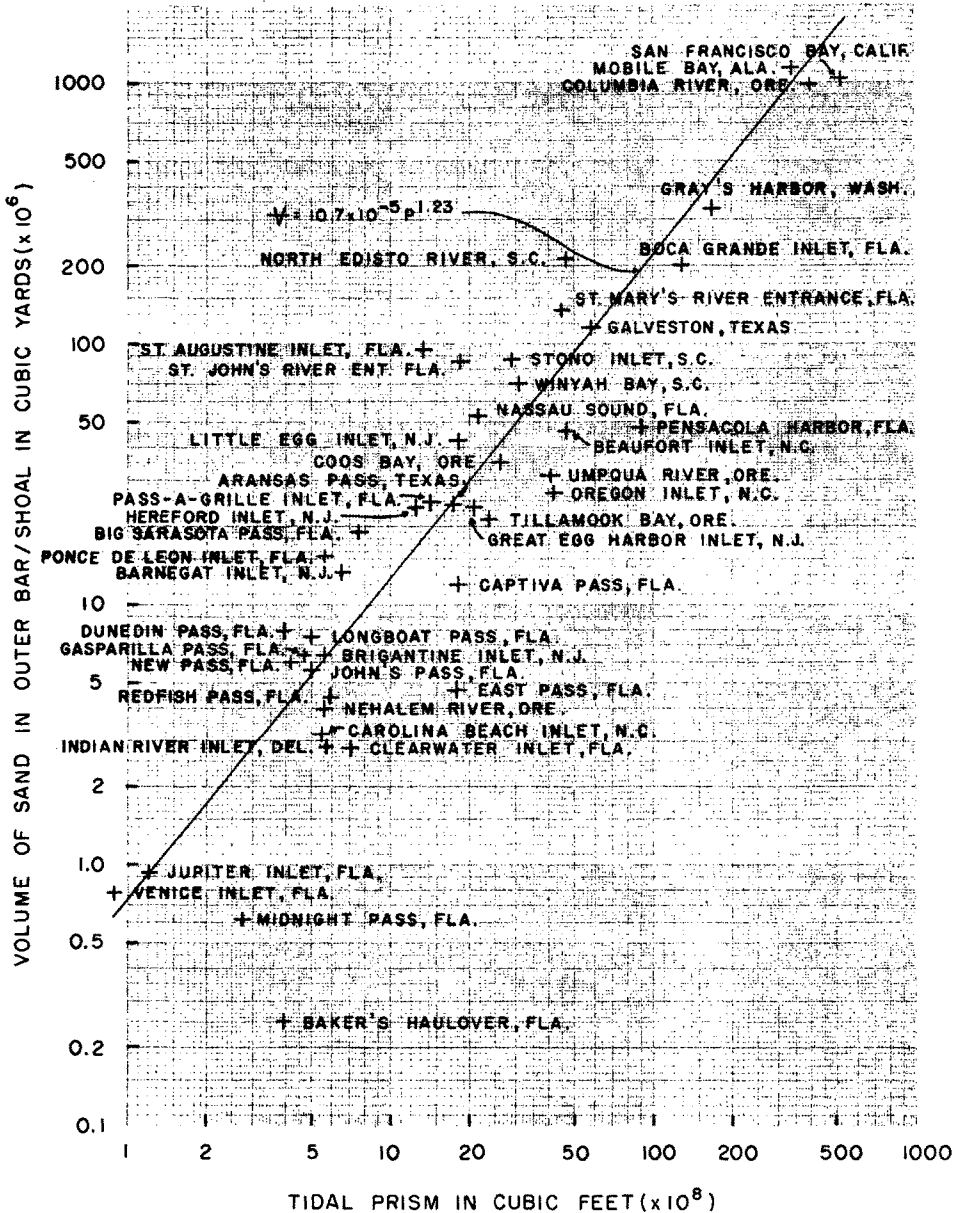


FIGURE 4. Tidal Prism-Outer Bar Storage Relationship for Inlets on Sandy Coasts.

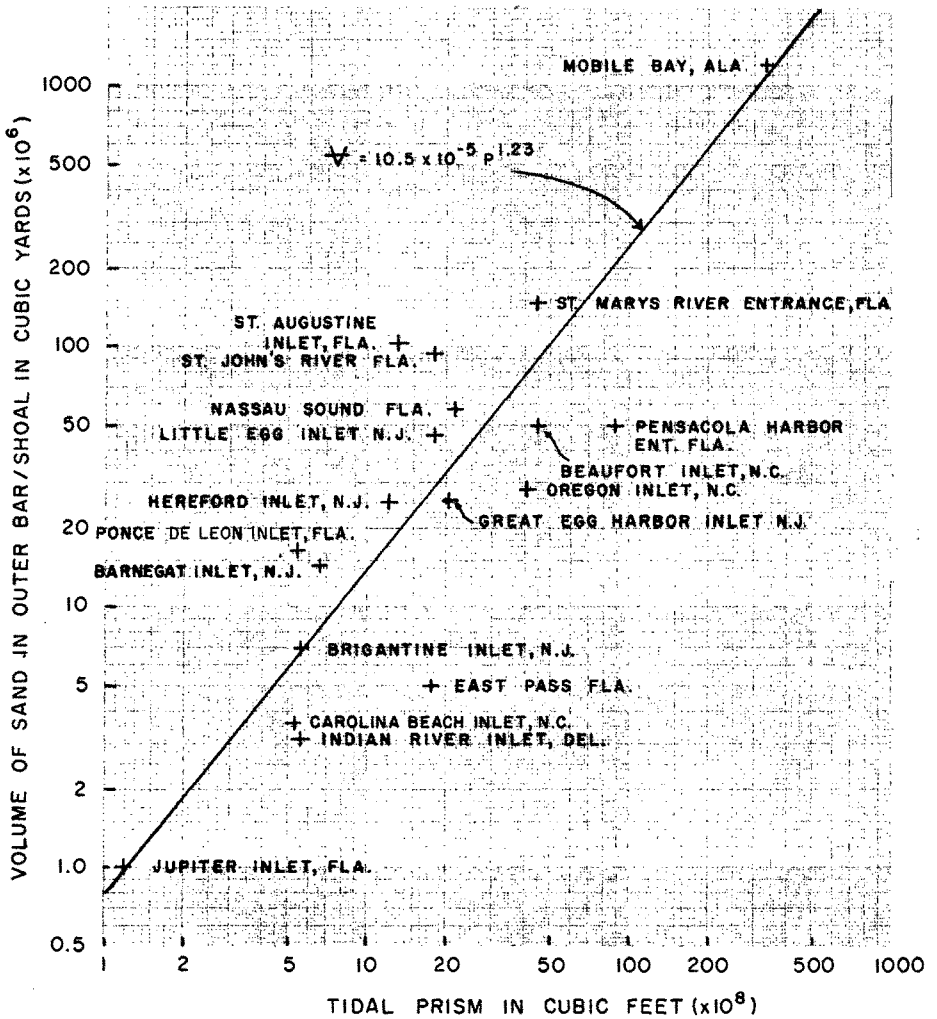


FIGURE 5 . Tidal Prism-Outer Bar Storage Relationship for Moderately Exposed Coasts.

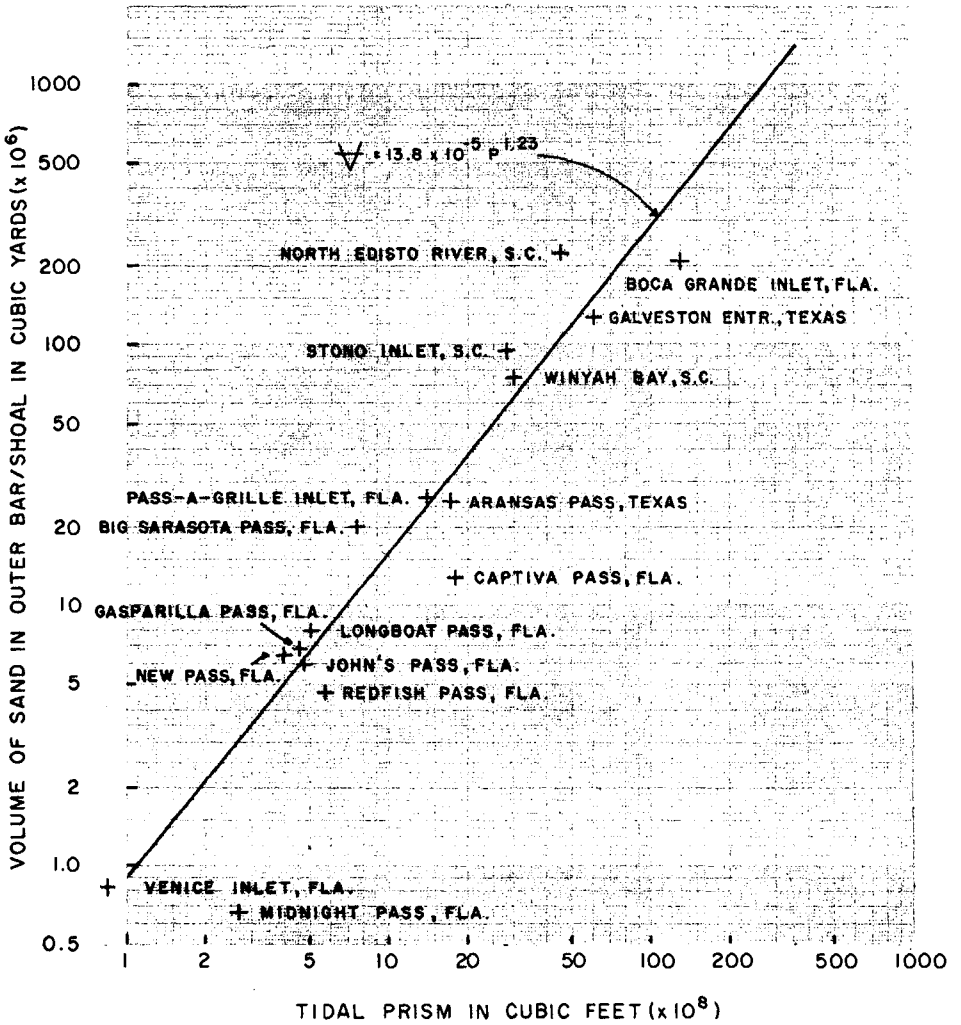


FIGURE 6 . Tidal Prism-Outer Bar Storage Relationship for Mildly Exposed Coasts.

noted that inlets which are estuarine (i.e., estuaries), have significantly smaller inner shoals most likely due to the predominance of ebb flow during landward flooding periods. The Pacific Coast inlets used for the highly exposed coast correlation are alike in that they are estuary systems.

Thus, the Pacific Coast inlets are physiographically similar, historically open, and have similar (in a gross sense) longshore energy flux levels; and, therefore, should experience less scatter.

Using the exponential correlation coefficient $b = 1.23$, analysis was made to determine the correlation coefficient a and the corresponding volume - prism relationship for the three groupings of inlets and for the 44 inlets combined. The corresponding equations are shown below:

Highly exposed coasts (7 inlets)	$\Psi = 8.7 \times 10^{-5} P^{1.23}$	(2)
Moderately exposed coasts (18 inlets)	$\Psi = 10.5 \times 10^{-5} P^{1.23}$	(3)
Mildly exposed coasts (16 inlets)	$\Psi = 13.8 \times 10^{-5} P^{1.23}$	(4)
All inlets (44 inlets)	$\Psi = 10.7 \times 10^{-5} P^{1.23}$	(5)

The plots of the prism-outer bar storage volume for the various inlet groupings are given in Figures 3, 4, 5, and 6. Three inlets were not used in any of the inlet groupings although they were used in the "all inlet" correlation. These inlets and the reasons for non-inclusion in the groupings are shown below:

1. Baker's Haulover Inlet - The inlet was created in 1923 with very short jetties which were destroyed in the hurricane of 1926 along with the occurrence of major modifications on the inlet. The inlet was rebuilt in 1928 shortly before the survey data in Table 2 was taken, therefore the outer bar would be expected to be far below any equilibrium value.
2. Clearwater Pass (formerly Little Pass) see below
3. Dunedin Pass (formerly Big Pass) Major modifications have occurred in the Clearwater Harbor area, drastically changing the inlet hydraulics of Clearwater Pass and Dunedin Pass to the North. The outer bars have responded to the tidal prism changes accordingly but may not as yet have reached an equilibrium for the new tidal prisms of the inlets as changes in the sedimentary structure of an inlet lag changes in tidal hydraulics.

As inlet channel cross-sectional area shows a definite correlation with tidal prism (11, 12) and is an easier quantity to measure than tidal prism, a correlation was also made with the available data for bar volume—~~channel cross-sectional area~~ relationships. Correlations were made for the three coastal energy level groupings and for all inlets combined using an equation:

$$\Psi = a'A^{b'} \quad (6)$$

where

V = volume of sand stored in outer bar/shoal (as before),
 A = inlet channel cross-section area at throat (in square feet),
 a', b' = correlation coefficients

Linear regression was again used to obtain the coefficient b' for all cases and is tabulated below:

Highly Exposed Inlets	$b' = 1.28$
Moderately Exposed Inlets	$b' = 1.23$
Mildly Exposed Inlets	$b' = 1.28$

The value $b' = 1.28$ corresponding to the highly exposed and mildly exposed inlets was used for the correlations with all inlet groupings, and analysis was made for the coefficient a' . The corresponding equations for all inlet groupings are shown below:

$$\text{Highly exposed coasts (7 inlets)} \quad V = 33.1A^{1.28} \quad (7)$$

$$\text{Moderately exposed coasts (18 inlets)} \quad V = 40.7A^{1.28} \quad (8)$$

$$\text{Mildly exposed coasts (16 inlets)} \quad V = 45.7A^{1.28} \quad (9)$$

The plots of the cross sectional area-outer bar storage volume for the various groupings are not shown, but prove to have considerably less scatter than the tidal prism - outer bar storage volume plots. Under a given set of conditions either tidal prism measurements or inlet cross-sectional measurements could be considerably unrepresentative of the "equilibrium" conditions, hence, both the volume - prism and volume-cross section relationships should be considered when obtaining an estimate of the sand storage capacity of an outer bar system.

CONCLUSIONS

The volume of sand stored in the outer bar/shoals of inlets shows a strong correlation with the tidal prism, and also, as would be predicted by the pioneering work of O'Brien (11,12), a strong correlation with cross sectional inlet throat area also.

Although a great deal of scatter exists in the data, the trend of increasing outer bar/shoal storage with increasing tidal prism exists over two orders of magnitude as shown by the included inlet data.

A correlation was made of these parameters and it was found that more material was stored in the outer bar/shoals of low (wave) energy coasts than high (wave) energy coasts. This is because there is more available (wave) energy to drive the sand back to shore in high energy environments after being deposited as a shoal.

A number of parameters other than tidal prism (or cross-sectional area) and wave energy also play a large role in sand trapping on outer bar/shoals. Two important parameters which have not been explicitly considered in the present analysis are longshore energy flux which moves the sand to the inlet where the ebb tidal current can deposit it on the outer bar, and size distribution of littoral material which limits the

ability of the material to movement away from the surf zone. Further research is needed to better define how these parameters control the influence of outer bar sand storage.

Further work is also needed on the inner bay or lagoon shoal storage volumes and on the potential of any given inlet to trap sand in its interior shoal system.

ACKNOWLEDGMENTS

This work is a result of research sponsored by the NOAA Office of Sea Grant, Department of Commerce under the State University System of Florida Sea Grant Project, "Nearshore Circulation, Littoral Drift, and the Sand Budget of Florida."

REFERENCES

1. Brown, E.I., "Inlets on Sandy Coasts," ASCE Trans., Vol. 65
2. Keulegan, G.B., 1967 "Tidal Flows in Entrances" Committee on Tidal Hydraulics Technical Bulletin #14, Corps of Engineers, Vicksburg.
3. O'Brien, M.P. and Dean, R.G., 1972, "Hydraulics and Sedimentary Stability of Coastal Inlets," Proceedings of Thirteenth Coastal Engineering Conference, Vancouver.
4. Escoffier, F., 1975 (to be published in Shore and Beach Magazine), "Tidal Inlets with Inertia".
5. Van de Kreeke, J., "Water-Level Fluctuations and Flow in Tidal Inlets," Journal, Waterways and Harbors Division, ASCE, Vol. 93, No. WW4.
6. Mota, Oliviera, I.B., 1970, "Natural Flushing Ability in Tidal Inlets," Proceedings, Twelfth Conference in Coastal Engineering, pp. 1827-1845.
7. Dean, R.G., Walton, T.L., 1973, "Sediment Transport Processes in the Vicinity of Inlets with Special Reference to Sand Trapping," Proceedings Second International Estuarine Research Conference, Academic Press.
8. U.S. Army Corps of Engineers, 1971, National Shoreline Study, Regional Inventory Report; South Atlantic - Gulf Region, Jacksonville District, Jacksonville, Florida.
9. Vallianos, L., 1970, "Recent History of Erosion at Carolina Beach, N.C.," Proceedings Twelfth Coastal Engineering Conference, Washington D.C.
10. Walton, T.L., 1973, "Glossary of Inlets Report #1-St. Lucie Inlet" Sea Grant Program Publication SUSSG-1, University of Florida.
11. O'Brien, M.P., 1931, "Estuary Tidal Prisms Related to Entrance Areas," Civil Engineering, Vol. 1, No. 8, pp. 738-739.
12. O'Brien, M.P., 1969, "Equilibrium Flow Areas of Inlets on Sandy Coasts," Journal Waterways and Harbors Division, ASCE.
13. Johnson, J.W., 1972, "Tidal Inlets on the California, Oregon, and Washington Coast," University of California, Hydraulic Engineering, Laboratory Report HEL 24-12.
14. Jarrett, J.T., 1974, "Tidal Prism - Inlet Area Relationships:" U.S. Army Waterways Experimental Station, Vicksburg, Mississippi.
15. Bruun, P. and Gerritsen, F. 1966, Stability of Coastal Inlets, Vol. 1 and 2. North-Holland Publishing Company, Amsterdam.
16. Walton, T.L., and Dean, R.G., "Outer Bars as a Source of Beach Nourishment Material," Shore and Beach Magazine (to be published in 1976).

CHAPTER 113

INLET CHANGES OF THE EASTFRISIAN ISLANDS

by

Günter Luck

Research Station for

Island- and Coast-Protection,

Norderney, West-Germany

ABSTRACT

The seven sandy islands of the Eastfrisian group would appear to be initially formed and now continually supplied with sand from the Westfrisian group and the mainland to the west. The inlets between these islands are in dynamic equilibrium with the strong tidal currents of the near 2,5 m range in the area. Hydrographic information dating back to 1650 permits the development of a hypothetical model which explains the historic changes and might predict future trends. The installation of coastal defence structures on the eroding western extremities of some islands in the mid 19th century has greatly influenced the bars by which sand is transported from island to island in an easterly direction.

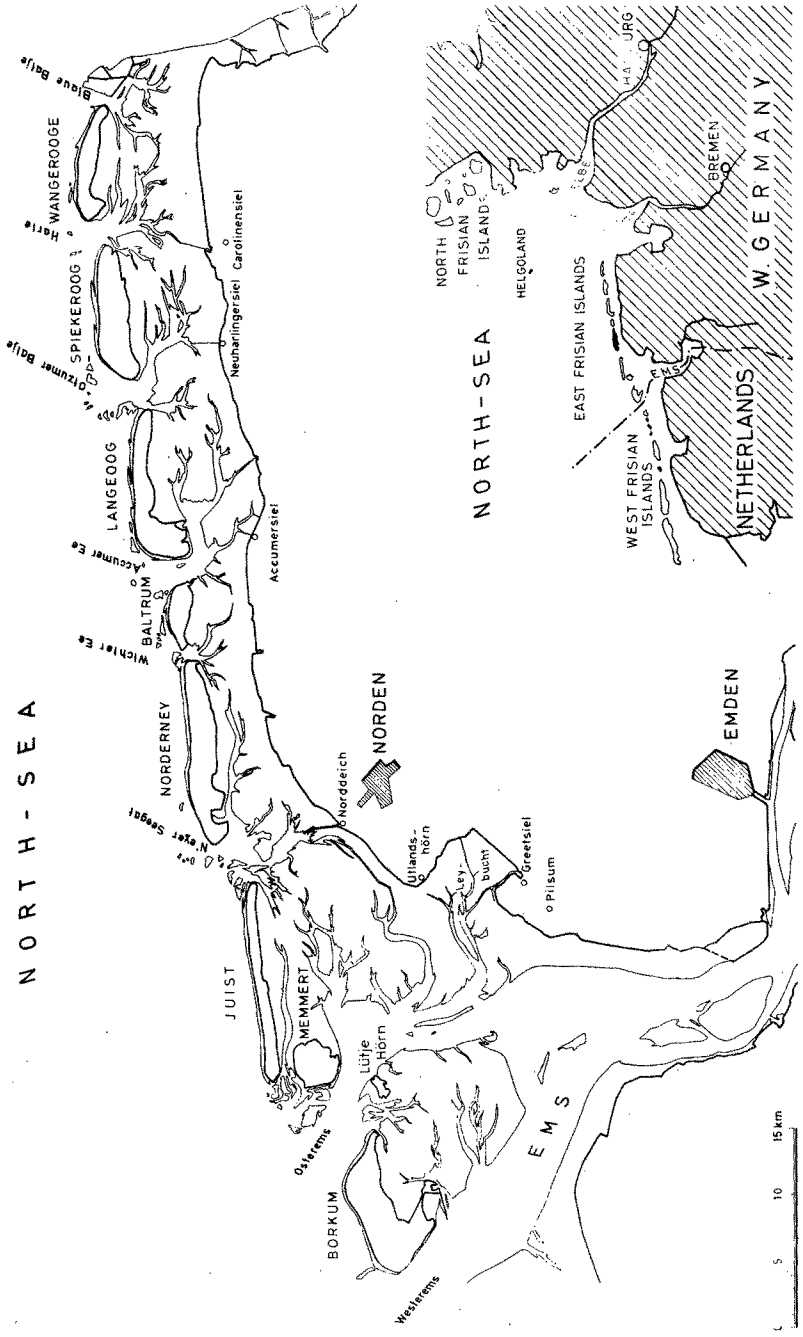
GEOGRAPHY

In front of the southern German North Sea coast between the estuaries of the Jade and Ems Rivers the Eastfrisian Islands are situated; from west to east they are: Borkum, Juist, Norderney, Baltrum, Langeoog, Spiekeroog and Wangerooge (fig. 1). These islands are separated by the tidal inlets Osterems, Norderney inlet, Wichter Ee, Accumer Ee, Otzumer Balje and Harle. Southward, to the coast of the mainland, extend vast tidal flats with sand, silt or mixed soil. The mean tidal range increases from west to east as follows: 2,2 m at Borkum, 2,4 m at Norderney, 2,6 m at Baltrum, 2,7 m at Spiekeroog and 2,9 m at Wangerooge/east.

FORMATION AND AGE OF THE ISLANDS

The islands are completely built of sand and only along their southern borders are more-or-less extensive marsh areas, which have developed by natural siltation. For a long time there have been only very vague notions concerning formation and age of the islands. It was supposed that they were remainders of the former mainland, separated at some stage by storm tides. According to another theory they once belonged to an extended spit of land, which was pierced during a storm tide at several points. However, by the aid of rationalizations, facts and latest findings of the morphological/hydrological processes in the Eastfrisian tidal flats it can be shown, that the islands were formed by the coincidence of current, surf and wind (LÜDERS, 1953).

Fig. 1: EAST FRISIAN ISLANDS



The west to east directed flood current, which is stronger than the ebb current, shifts the sands necessary for the formation of the islands from the Belgian/Dutch coastal area.

Even today the origin of the sands has not been definitely resolved. Mineral explorations prove some sediments are from the big rivers, but also there is erosion material from the British cliffs. More distant sands of the bottom of the North Sea are traceable. These sediments, transported by the tidal currents, are formed into longshore bars by wind and waves and finally the surface is elevated above the high-water-level and is stabilized by vegetation. The influence of plants on the blown sand is to increase the height of the bars until they become dune islands. The constant supply of new sea sands provides the nutrients necessary for a strong and healthy vegetation.

The distance between the mainland and the islands is determined by the tidal range. At little or no tidal range the longshore bars and finally the dune islands are formed closer to the coast.

So far it is not possible to determine the exact age of the islands. However, there are references from Greek sailors which permit the hypothesis, that the islands already existed in 300 B.C. As the Atlantic transgression, which led to the formation of the North Sea, commenced about 10.000 B.C. and was interrupted by several phases

of regression, a geological determination of the age of the shifting sands cannot be performed and therefore a definite estimate of the age of the islands is not possible.

As the sands are powerless against the forces of current, surf and wind, the islands in the past underwent frequent changes of shape, with long-term developments being overshadowed by short-term events. The tidal flats, tidal inlets and islands are in a state of dynamic equilibrium (WALTHER, 1971) and therefore the changes in the islands and tidal inlets affect also the tidal flats. Only by the construction of the protection works on the islands in the middle of the last century was this process interrupted.

ANCIENT REPORTS

The coast and the adjoining tidal flats were first described by the Roman geographers PLINIUS and STRABO at about the birth of Christ. But the first time the islands were named was in 1398. However, the document did not give further details. Since the 16th century the islands are mentioned more frequently in nautical manuals, and recorded in coastal views for navigation purposes. The first comprehensive descriptions of the islands date from the years 1650 and 1657 (cited in THILO, 1953). For the first time the height and location of the dunes were related to sea level. Narrow beach sections and dune erosion were fully described and measurements were recorded. Following upon these

observations inquiries were made as to whether the natural sand supply was sufficient or if there was a necessity to protect beach and dunes by artificial means.

These reports are valuable since. With their aid, supplemented by other ancient reports, it is possible to record the island contours relatively well. They provide also the basis for the Historical Map 1 : 50.000 of the Research Station for Island- and Coast-Protection, Norderney (HOMETIER, LUCK, 1969).

The most remarkable phenomenon of the long-term development of the islands, traceable since about 1650, is the fact that at their western ends they underwent a considerable loss of beach and dunes, whilst they built up in the east. This phenomenon, being interrupted by the construction of the protection works, often has been called the "west-east-migration" of the Eastfrisian Islands. The west to east directed "migration" results from the preponderantly eastward directed forces of wind, tide and surf current. With the aid of numerous investigations in the area of the Eastfrisian Islands the mechanism of this west-east-shift could be interpreted.

THE MAP OF GUITET OF 1708

The first map recording the area of the Eastfrisian Islands well enough to be interpreted was drawn by the Dutch Admiral Mathurin GUITET in 1708 (fig. 2). The then existing contours of tidal flat, islands and tidal inlets are preserved in

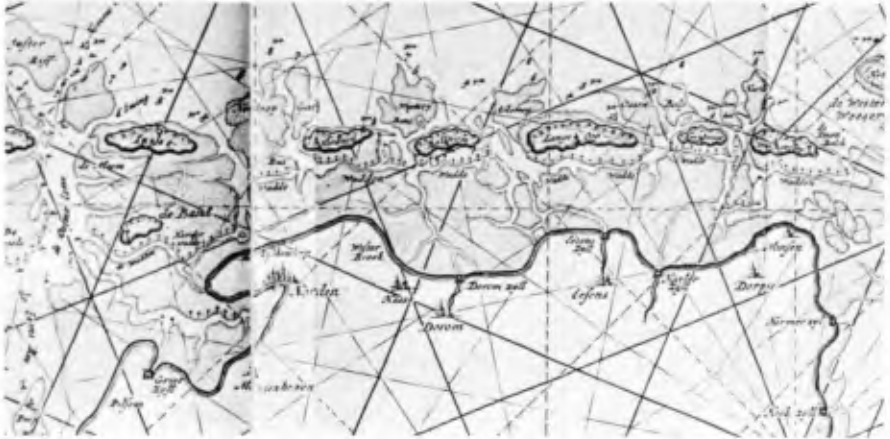


Fig. 2: Wad en buyten-kaart, M. GUITET, Amsterdam 1708/10

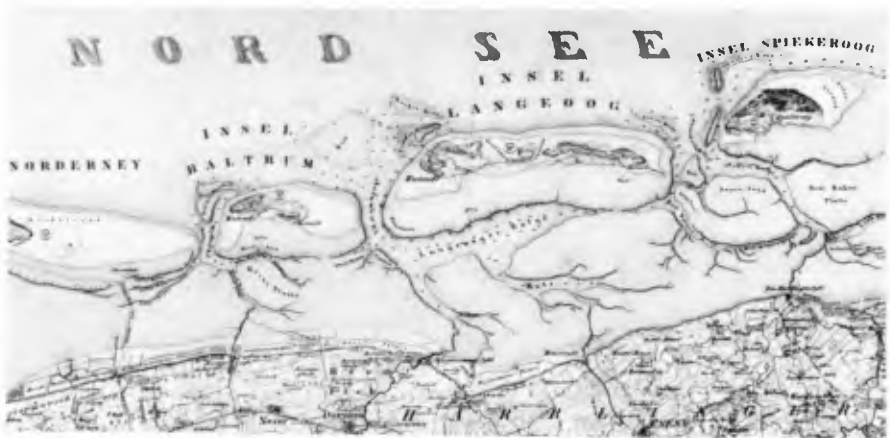


Fig. 3: Eastfrisian coast and islands, A. PAPEN, 1843

this map. However, the length of the islands, width of the tidal inlets etc. cannot be measured due to the map's lack of accuracy in scale. For the coastal research the most remarkable phenomenon at that time was the division of the tidal inlets between the islands into two deep narrow channels, which were separated by middle-sands. The first map of accurate scale from the year 1860 (fig. 3), however, shows tidal inlets with only one deep narrow channel. Consequently in most tidal inlets there must have been an alteration from double to single channel profile.

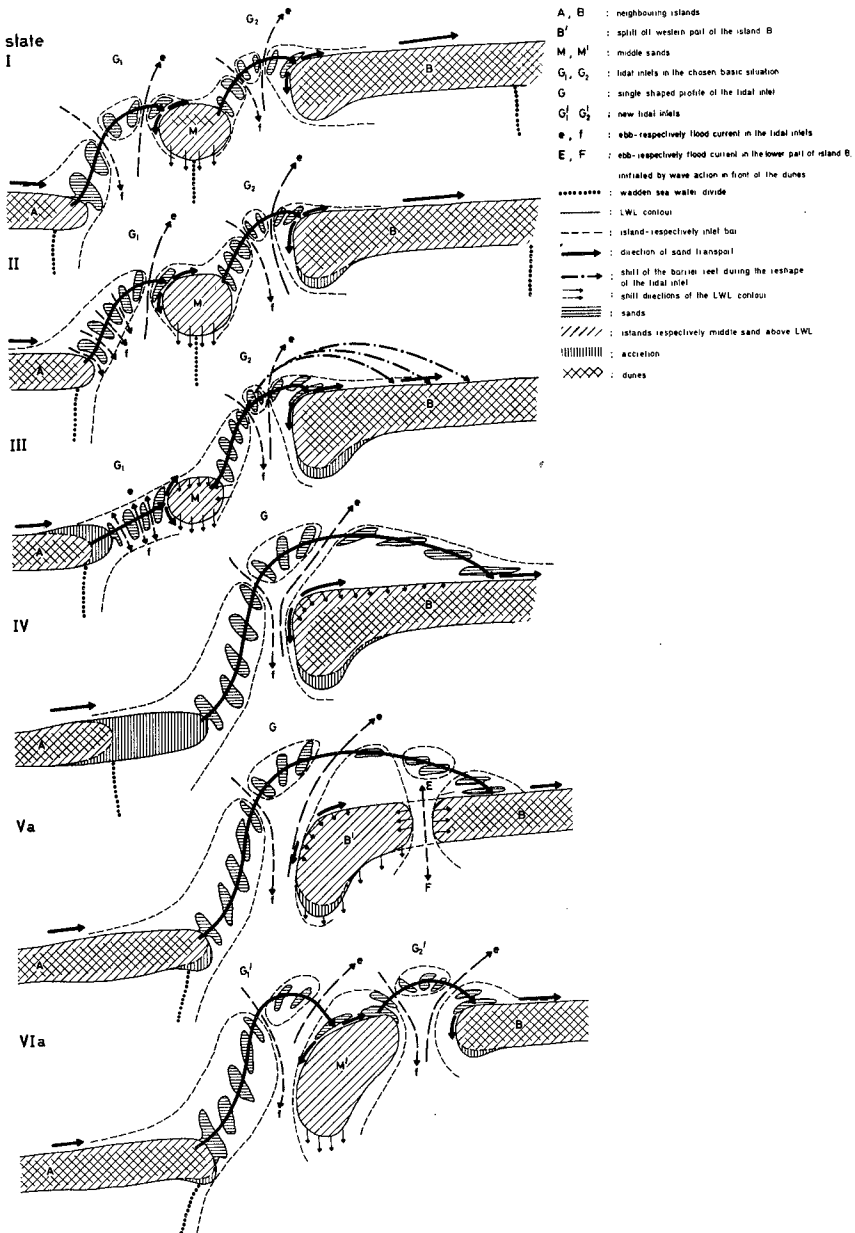
The map of GUITET shows the remains of the once large island Buise, which obviously extended into the present offshore area north of Juist Island. The final phase of the disappearance of this island is recorded relatively well in contemporary maps, discussions, sailing-instructions etc. (LANG, 1955). The well substantiated events in the Norderney inlet, the reduction of the island Buise to a middle-sand and it's final merging at the eastern end of Juist Island, plus the change of the tidal inlet from a double to a single channel profile, made it possible to rationalize these processes on the basis of the findings of modern hydrodynamics. Though the existing information for the other inlets is less comprehensive it is sufficient to prove the applicability of these basic findings.

MODIFICATION OF THE TIDAL INLETS

Though the events in the tidal inlets did not all proceed at the same time, the modifying processes are uniform and can be reproduced in hypothetical models. These explanations can be divided into separate successive stages (fig. 4):

Stage I: The middle-sand M between the islands A and B lies above high-water-level and is being shifted to the south. This southward displacement of M is substantiated by contemporary reports. The tidal inlets G_1 and G_2 , which seem to have been hydraulically equal, are located on both sides of the middle-sand. Each one, G_1 and G_2 , has it's own intake area separated by the topographical water-divide of the middle-sand M. Northward of the tidal inlets are sands, the spatial order of which evoke the optical impression of a bow, for which reason they are called "sand-reef-bow" or simply "reef-bow". The west-east sand transport within the region of the tidal inlets takes place within these reef-bows. Since their widths correlate more-or-less to the dimensions of the adjoining Wadden-Sea intake areas (WALTHER, 1934) (i.e. small intake area = small reef-bow and visa versa) these reef-bows are relatively flat and reach from A to M and from there to B. As M is small and the sand, coming from A, does not find enough room to spread or build dunes, these sand-supplies do not take hold and M undergoes a loss of material. The

Fig. 4: model of longterm reshape of a tidal inlet
(without scale)



north-western end of B, however, is well provided with sand and correspondingly resistant to erosion.

Stage II: Due to the continuing southern movement of M and the east-directed growth of A the reef-bow of G_1 shortens. As the total sand-supply remains constant over a longer period of time the shoals are moved closer together and consequently the water-exchange in G_1 is reduced. These processes are complementary. Although the water-exchange is now increased in G_2 , due to the reduction in G_1 , the arc of the reef-bow is still unchanged and the northwestern end of the island B is still well supplied with sand. At the same time the topographical water-divide of M, still effective in Stage I, is gradually reverted and the formerly two separate catchment areas gradually become one.

Stage III: The processes of Stage II continue and M has now become part of the reef-bow of G_1 . As the entire intake area between the water-divides of the islands A and B remains constant, changing only minimally over a long period of time, the water-exchange shifts increasingly to G_2 . Thus the reef-bow of G_2 is displaced further north and the attachment area of the sands on B is shifted eastward. This produces a sand deficiency on the western end of island B.

Stage IV: The development of the tidal inlet from a double to a single channel profile has been completed. The reef-bow of G has found it's new shape and in the west of island B, which is no longer receiving natural sand-supply, the dunes begin to recede under the influence of the surf. On Norderney Island for instance this state was reached around 1800.

With the Eastfrisian Islands the natural development has not gone beyond Stage IV. The beach and dune erosion, which occurs after termination of Stage IV, was prevented by seawalls and groynes. An uninterrupted development would have allowed the inlets to further change their shape as described in Stage V and Stage VI. In one case, namely on Wangerooge Island, this process has already begun with the formation of a new deep channel (FÜHRBÖTER, LUCK, LÜDERS, 1973).

Stage V: The dunes of island B are eroded by surf and wind; they recede up to the area of sufficient sand-supply (attachment area) and there remains only a beach B'. At elevated high-water-levels the surf erodes a channel close to the dune base, which gradually becomes deep enough to overflow even at normal tides. With this the preconditions for the formation of a new tidal inlet are fulfilled. On Wangerooge Island, the eastern most Eastfrisian Island, such a development started about 1900. The final development of a new channel was

prevented by the construction of a long and heavy groyne (LÜDERS, 1952).

Stage VI: The channel in front of the dune base of island B has developed into a new tidal inlet. The duneless west-beach of the island B is cut off and has become a new middle-sand M'. By this stage a configuration has been reached, which approximates that of Stage I.

The developments, described in this hypothetical model, apply to the islands Juist to Wangerooge. Borkum Island, due to its location in the Ems estuary, is influenced by other parameters, which do not allow a transfer of the concepts to the Ems and Easter-Ems inlets.

The investigations, involving developments since 1650, prove that the transitions of the tidal inlets tend to proceed in cycles from double to single channel profile and back to the double version. An unrestricted extrapolation of these phenomena into the future, however, is not possible without consideration of the secular water rise. Over a longer period of time the secular water rise effected a southward shift of the islands, which will continue. At the moment the possibilities are being studied for including the secular water rise into the present models.

DEVELOPMENT OF LENGTH AND WIDTH OF THE ISLANDS
AND TIDAL INLETS

Since 1650 the total length of the island chain from Juist to Wangerooge remained constant at about 68 to 69 km, provided that the beach accretions of Juist/west and Wangerooge/east (about 3,5 km) are deducted. However, within the row of islands changes on a large scale took place (see Table I).

Table I: Development of the tidal inlets and islands
between the MHW-lines [m]

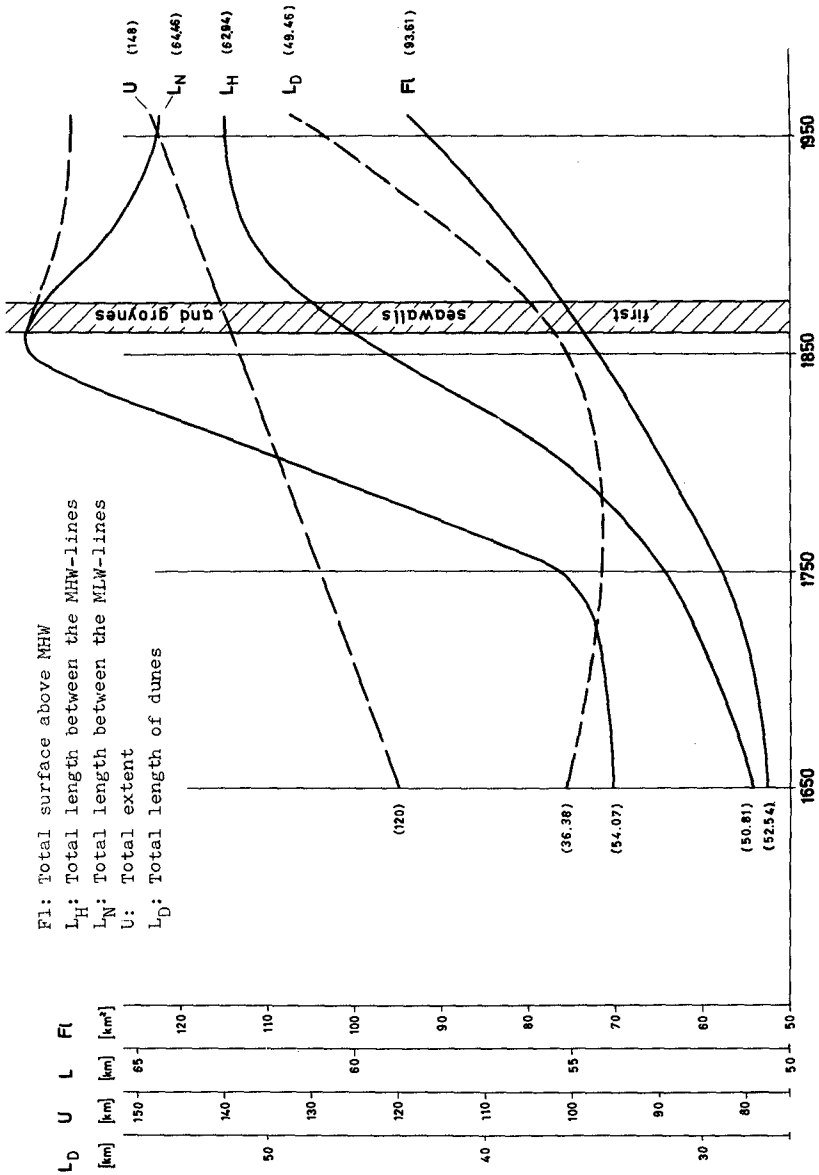
Year	1650	1750	1860	1960
Juist Island	10470	13010	15810	14970
Norderney Inlet	6800	4730	2600	2770
Norderney Island	8070	9440	13470	13870
Wichter Ee Inlet	2170	2030	710	850
Baltrum Island	8170	7560	5460	5050
Accumer Ee Inlet	3150	2480	1360	1710
Langeoog Island	9600	10280	11230	10920
Otzumer Balje Inlet	2440	2400	2440	2410
Spiekeroog Island	5230	5180	5910	9810
Harle Inlet	5800	5670	4810	2000
Wangerooge Island	7300	7400	7950	8320
Total	69200	70180	71750	72680

All tidal inlets narrowed and the islands, except Baltrum Island, became longer. The shortening of Baltrum Island of about 3 km since 1650 was effected by a simultaneous strong eastward growth of Norderney Island. This development was prevented by the construction of protection works on Baltrum Island, which stopped a further transformation of the tidal inlet Wichter Ee and with this the on-going eastward growth of Norderney Island. Without it's strong protection works Baltrum Island finally would have been completely destroyed, similar to Buise Island, and the last remains would have merged into the eastern end of Norderney Island.

Figures 5 and 6 also illustrate the relations between the transformation process in the row of islands and the events in the tidal inlets. Figure 5 shows the curves of the total length of the islands (without tidal inlets) between the low and high water lines, of the dunes, of the total surface and of the total circumference.

Altogether a growth of the islands can be recognized.

Of special interest are the curves of the lengths, which increase slowly in the beginning and then quickly after 1750. At first the construction of the protection works 1860 through 1870 had little effect on the lengths between the high water lines, because the protection works in the beginning were only effective within the reach of the dunes. Therefore at first the MHW lines



F_I : Total surface above MHW
 L_H : Total length between the MHW-lines
 L_N : Total length between the MLW-lines
 U : Total extent
 L_D : Total length of dunes

Fig. 5: Development of the row of islands

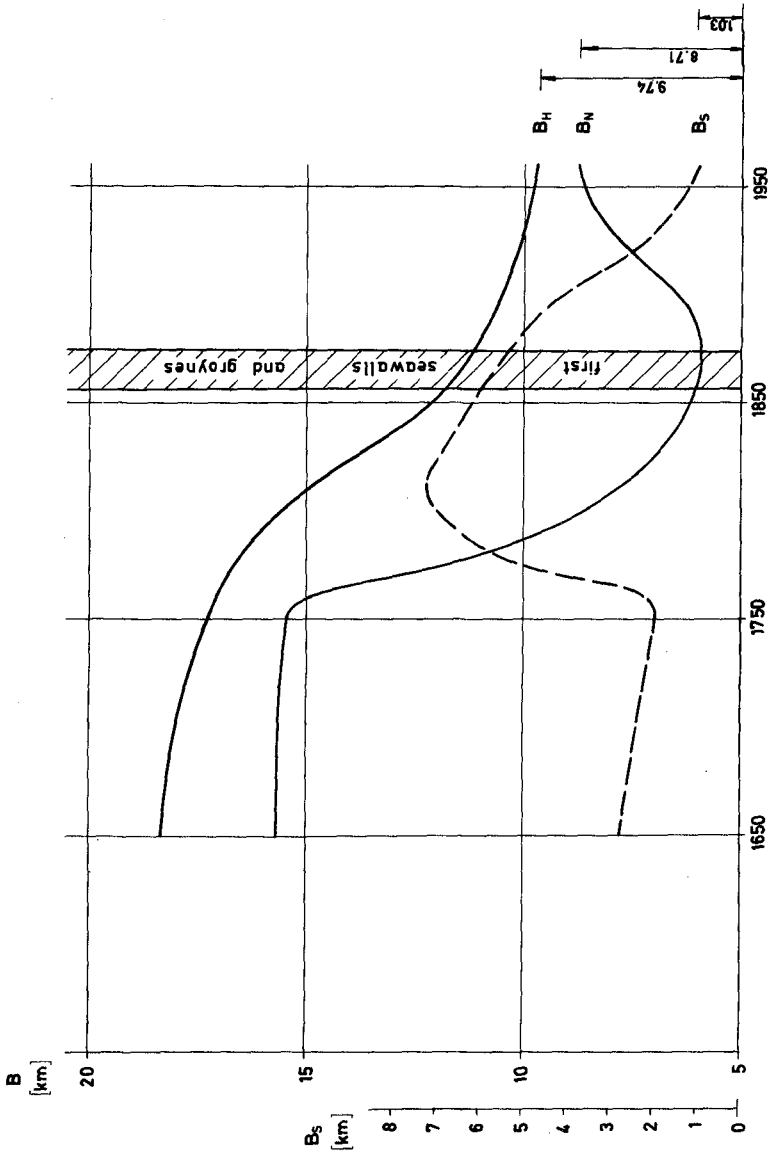


Fig. 6: Development of the width of the tidal inlets km
 B_H : Total width between the MHW-lines; B_N : Total width between the MLW-lines;
 B_S : Width of the beach between MHW and MLW

had still space to shift backward. The curve of the lengths between the MLW lines, however, falls significantly after the construction of the protection works. These reductions in length occurred at the western ends of Juist Island and Wangerooge Island, the latter being displaced southward since the storm tides of 1854/55.

The curves of the total widths of the tidal inlets (fig. 6) show a complementary development. The more the total lengths of the islands increased, the more the tidal inlets became narrow. Here in the beginning the construction of the protection works had no influence on the curve either, as the MHW and the MLW lines first still had enough space to shift. The rise of the MLW curve after 1860 has to be referred to the southward displacement of the duneless westbeach of Wangerooge Island, which has already been mentioned. The seawalls and groynes, constructed after 1874, served as immediate dune protection and left the large westbeach to the forces of waves and current (LÜDERS, WILLECKE, 1951).

CONCLUSIONS

Under natural conditions (i.e. without protective works) the Eastfrisian Islands tend to shift eastward. On the basis of well substantiated long-term events in the Norderney inlet this tendency could be traced back to

morphological events in the tidal inlets and systemized in a hypothetical model. The application of the concepts, gained for the Norderney inlet, to the tidal inlets between Juist Island and Wangerooge Island can be proved by means of old maps, descriptions etc. as well as by consistent reasoning, facts and findings of modern hydrodynamics.

The ancient "west-east-migration" or shift of the Eastfrisian Islands has been effected by the active processes in the tidal inlets, followed passively by the islands. The seawalls and groynes have produced a static condition, which if not present would have been temporary in nature.

REFERENCES

1. FÜHRBÖTER, A.
LUCK, G.
LÜDERS, K. "Gutachten über die Dünen- und Strand-
sicherung im Westen der Insel Wanger-
ooge"
Hannover 1973, not published
2. GUITET, M. "Wad en buyten-kaart"
Amsterdam 1708/10
3. HOMEIER, H.
LUCK, G. "Das Historische Kartenwerk 1 : 50.000
der Niedersächsischen Wasserwirtschafts-
verwaltung als Ergebnis historisch-
topographischer Untersuchungen und
Grundlage zur kausalen Deutung hydro-
logisch-morphologischer Gestaltungs-
vorgänge im Küstengebiet"
Göttingen 1969

4. LANG, A.W. "Juister Watt"
Schriften der Wirtschaftswissenschaftlichen Gesellschaft zum Studium Niedersachsens E.V., Neue Folge, Band 57, 1955
5. LÜDERS, K. "Bilanzbericht über den Inselschutz
WILLECKE, H. auf Wangerooge"
Wilhelmshaven 1951, not published
6. LÜDERS, K. "Die Wirkung der Buhne H in Wangerooge-
West auf das Seegat "Harle"
Die Küste, Heft 1, 1952
7. LÜDERS, K. "Die Entstehung der ostfriesischen Inseln
und der Einfluß auf den geologischen
Aufbau der ostfriesischen Küste"
In: Probleme der Küstenforschung im
südlichen Nordseegebiet, Band 5, 1953
8. THILO, R. "Bilanzbericht über den Inselschutz
auf den ostfriesischen Inseln"
Aurich 1953, not published
9. WALTHER, F. "Die Gezeiten und Meeresströmungen
im Norderneyer Seegat"
Bautechnik, Heft 13, 1934
10. WALTHER, F. "Zusammenhänge zwischen der Größe
der ostfriesischen Seegaten mit ihren
Wattgebieten sowie den Gezeiten und
Strömungen"
Forschungsstelle Norderney, Jahres-
bericht 1971, Band XXIII

CHAPTER 114

BARRIER ISLAND DYNAMICS: OVERWASH PROCESSES AND EOLIAN TRANSPORT

Stephen P. Leatherman¹

Abstract

The northern 5 miles of shoreline at Assateague Island, Maryland are presently being eroded. During storms, swash surges are able to overtop the most landward (storm) berm as overwash with deposition occurring on the barren flats. Where primary barrier dunes still exist, sediment-charged surges are funneled through breaches in the dune field for deposition of the entrained material on the washover fan.

Sediment budget computations show that there has been a small net loss of material at each washover area, in spite of 7 discrete overwash events during a 26 month time interval. The predominant north-west winds effectively eroded the overwash material, transporting the majority of the sand back to the beach. This analysis indicates that there exists a balance between overwash and eolian processes with wind transport being slightly dominant.

Introduction

The impetus that spurred this research was the sharp debate among coastal investigators concerning the importance of overwash in terms of the sediment budget of a barrier island. Dolan (1972) maintained that construction of large barrier dunes in the 1930's along the Outer Banks of North Carolina has had a significant adverse impact on this shoreline's stability. By preventing overwash, material that would have been deposited on the backdune area will either be lost offshore or carried alongshore. The viewpoint of the Corps of Engineers (Shore Protection Manual, 1974) is that island maintenance by overwash is probably only significant within the context of a geologic time frame. The mechanics of barrier island migration by the overwash process have not been previously established by quantitative studies.

Assistant Professor, Department of Geology, Boston University,
Boston, Massachusetts 02215

This investigation was designed to address the question of the short-term sedimentary dynamics of a washover area on Assateague Island.

The concept of a sediment budget was adopted to monitor the amount of sediment transport. The sediment budget is defined for the control volume which includes the washover fan/flats and adjacent barrier dunes, vegetated barrier flats and marsh. The beach is excluded from the control volume since only net changes can be recorded, not the actual quantities and directions of sediment removal, transportation and deposition. Sediment budget calculations should permit determination of the relative importance of overwash as a process shaping the barrier island.

During the past 26 months (February 1973 - April 1975) of continuous study, 7 discrete overwash events were monitored at Assateague Island, Maryland. Field surveying prior to and after an overwash enabled calculation of the total subaerial sediment transport along selected sections of the island. Monthly surveys allowed for the detection of subsequent post-storm reworking and transport of sand on the backdune zone.

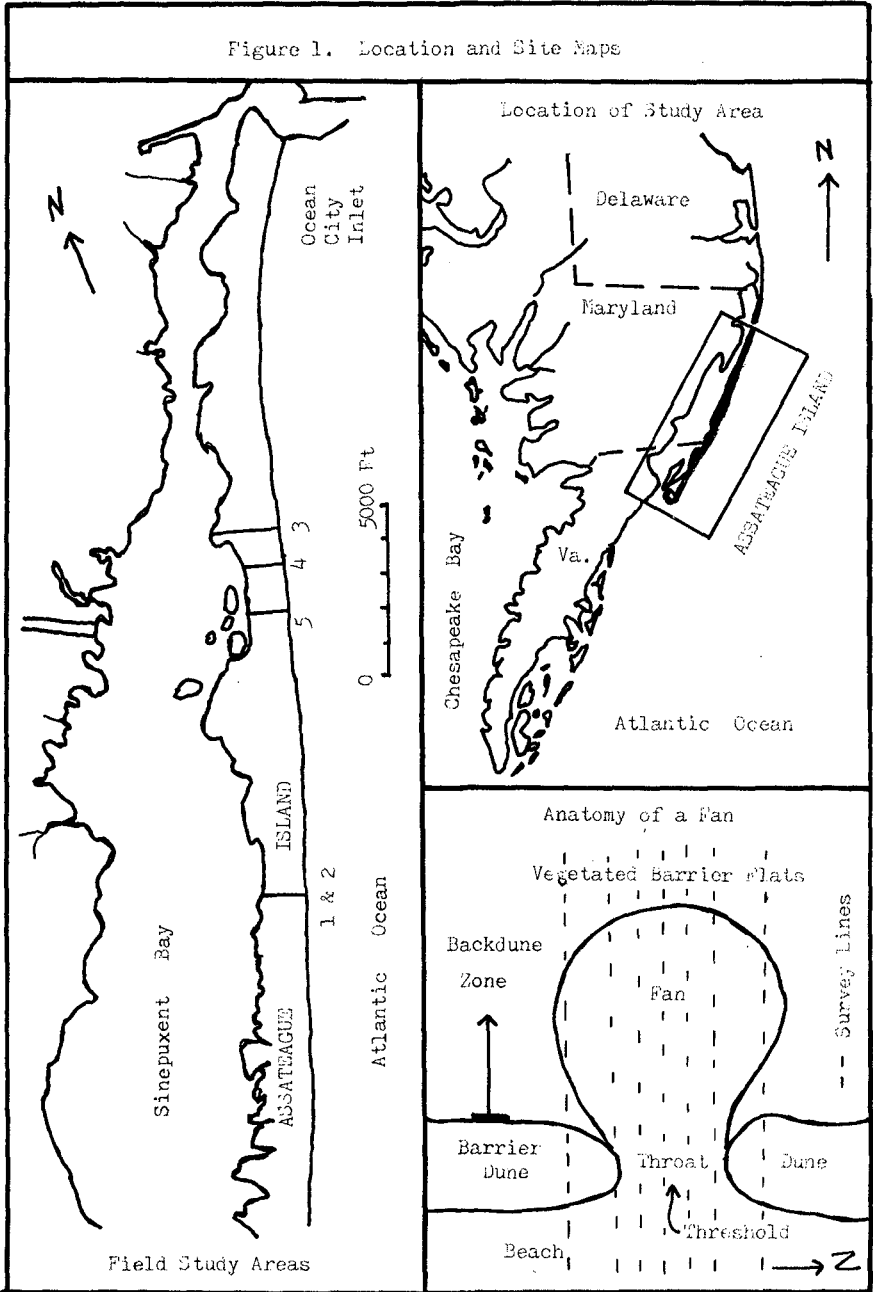
A single washover fan (Site 1) was selected for the initiation of this study (Fig. 1). The dunes are eroded during major storms, and gaps between the dunes force overwash sediments into discrete units enabling study of individual deposits. Site 2 was established in the fan adjacent to that of Site 1 for volumetric comparison on an annual basis. For the final year of field work, 3 additional sites were chosen based on their position along the island and on their physiographic features. Sites 3 and 4 are located in a region of broad washover flats where barrier dunes no longer exist. Site 5 is similar to the primary site (Site 1), except that the dimensions of the fan are much larger.

Previous Research

Overwash has been reported to be a significant process along the Gulf and East Coasts of North America, but little quantitative data is available on its transport potential. In fact, there is a scarcity of data correlating "storm intensity" to the expected amount of shoreline erosion. This type of data has direct application to engineering considerations, but it is difficult to obtain due to the unpredictability of occurrence and magnitude of coastal storms.

Caldwell (1959) compiled data concerning the amount of beach erosion for various storms along the New Jersey shoreline. Everts (1973) and Everts *et al.* (1974) also used surveying programs to determine the amount of erosion associated with single storms for New Jersey and New York beaches. These data sets, along with original field data on beach erosion and overwash deposition from the North Carolina coast, have been summarized by Schwartz (1975).

Figure 1. Location and Site Maps



Overwash Sediment Transport

Storm parameters and overwash deposition for each event monitored by this investigator as well as Schwartz's (1975) data are given in Table 1. Relative measures of storm surges at Assateague Island were obtained by subtracting the predicted tide (U.S. Dept. of Commerce, NOAA Tide Tables) from the recorded tide (NOAA-NOS) for the Indian River Inlet (Bridge) tide gage, located approximately 20 miles north of Ocean City, Md. Significant deep water wave hindcasts were based on the Bretschneider technique. Surf observations of breaker height and wave period were obtained from the CERC Beach Evaluation Program.

The amount of sediment transport for the first two storms re-recorded during this study were reported by Fisher, Leatherman and Perry (1974), and these results will not be reviewed. The March and November 1974 northeasters were sedimentologically insignificant. Field observations for both storms showed that overwash surges represented only a small portion of the total swash, as only the leading edge of water was able to traverse the beach face. The April 1975 northeaster also represented a threshold occurrence. Since none of these storms resulted in any appreciable amount of beach erosion or overwash, no further discussion is warranted.

The December 1, 1974 northeaster was the largest storm to attack these shores during the survey interval, and data is available for all survey sites along the island. Figure 2 shows the transect across Site 1 washover fan from the beach to the barrier flats. The fan gained 217 ft^3 of sediment per foot while the first 60 feet of beach seaward of the dune line was eroded 110 ft^3 per foot for a net gain of $107 \text{ ft}^3/\text{ft}$. The sand plug level indicated that erosion by the overwash surges was confined to the seaward-most (throat) portion of the fan. The total volume of material transported into this single fan was $9,840 \text{ ft}^3$ which corresponded to an effective transport of 221 ft^3 per foot of throat width.

Sites 3, 4 and 5 were also surveyed so that the amount of beach erosion and overwash deposition along these transverse slices of the island would be available for comparison. At Site 3, the lower beach was apparently not eroded by the December northeaster while the storm berm on the backshore was carved away (Fig. 3). The quantity of sand eroded from the storm berm approximately equaled the amount of overwash, except for a small total line loss of $-29 \text{ ft}^3/\text{ft}$. The overwash penetration distance was 800 feet, equal to one-half of the island's width at this location, but only $91 \text{ ft}^3/\text{ft}$ of material was deposited on the flats as overwash.

Site 4, the other line extending across the broad, nonvegetated washover flats, experienced a totally different pattern of sediment redistribution (Fig. 4). The upper beach profile migrated over 80 feet landward with a loss of $64 \text{ ft}^3/\text{ft}$ for the 80 feet of beach surveyed. The major lens of sedimentation occurred from 200 feet to 600 feet landward of the beach for 153 ft^3 of overwash deposition per

TABLE 1. STORM PARAMETERS AND OVERWASH DEPOSITION

<u>Storm Dates</u>	<u>H_o (ft)</u>	<u>H_b (ft)</u>	<u>Storm Surge/ Tide (ft)</u>	<u>Period (sec)</u>	<u>Overwash Deposition (ft³/ft)</u>
February 9-11, 1973 ¹ (Cape Hatteras)	22.5	--	--	--	130
March 22, 1973	17.5	6	1.6/4.3	8-12	50
October 26, 1973	14.0	6	1.3/4.4	10	59
March 30, 1974	10.0	--	no data ²	--	0
November 8, 1974	10.5	--	1.2/3.6	--	0
December 1, 1974	16.5	9	2.7/5.0	7-8	221
March 19-20, 1975	11.5	5.5	1.0/3.3	8-12	29
April 15-16, 1975	11.0	--	--	--	0

¹Schwartz (1975)²Cage inoperative

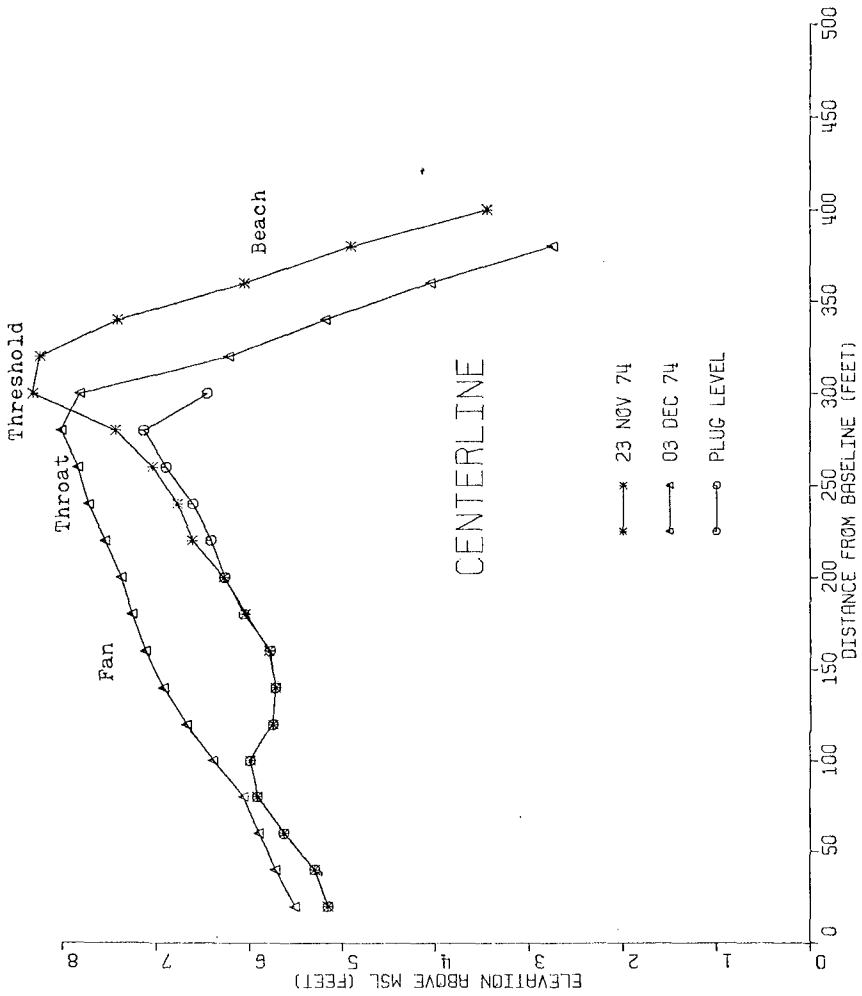


Figure 2. Site 1, Centerline Changes, December 1, 1974 Northeast

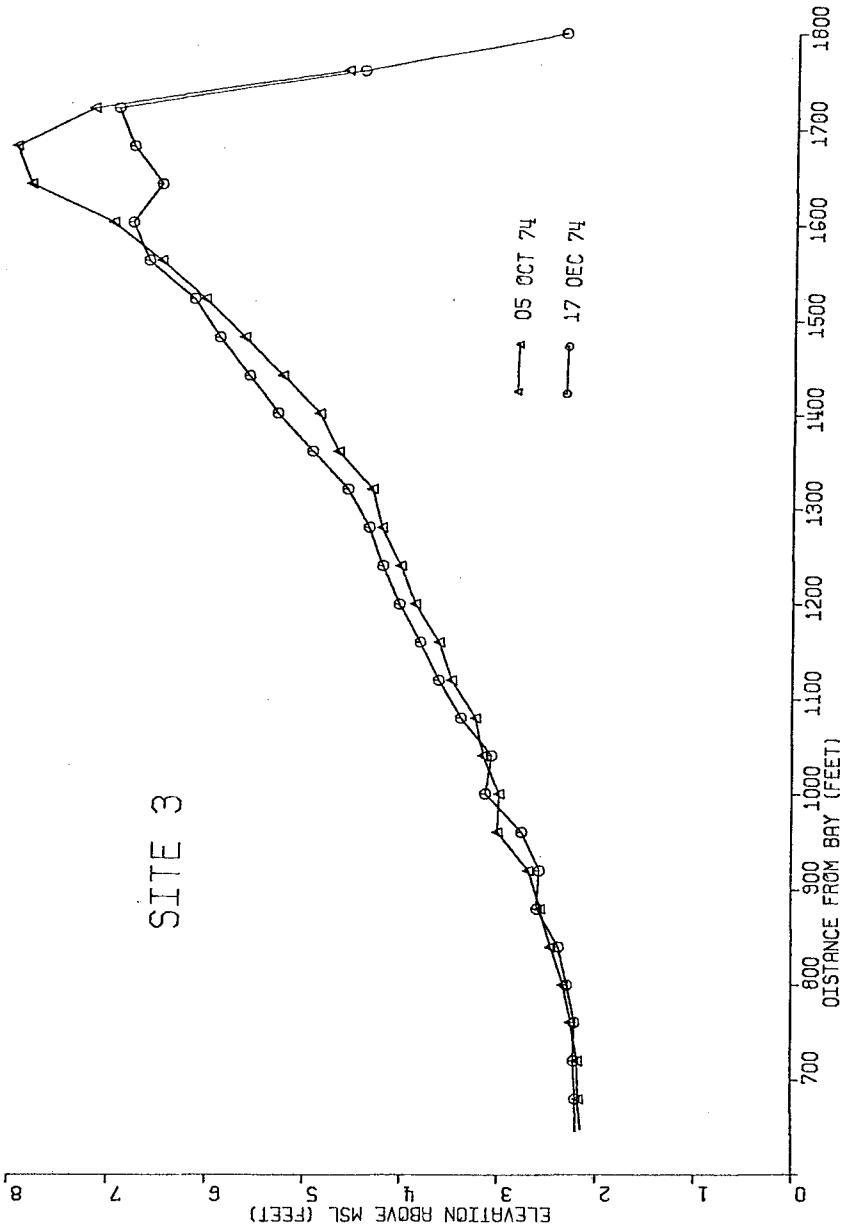


Figure 3. Site 3, December 1, 1974 Storm

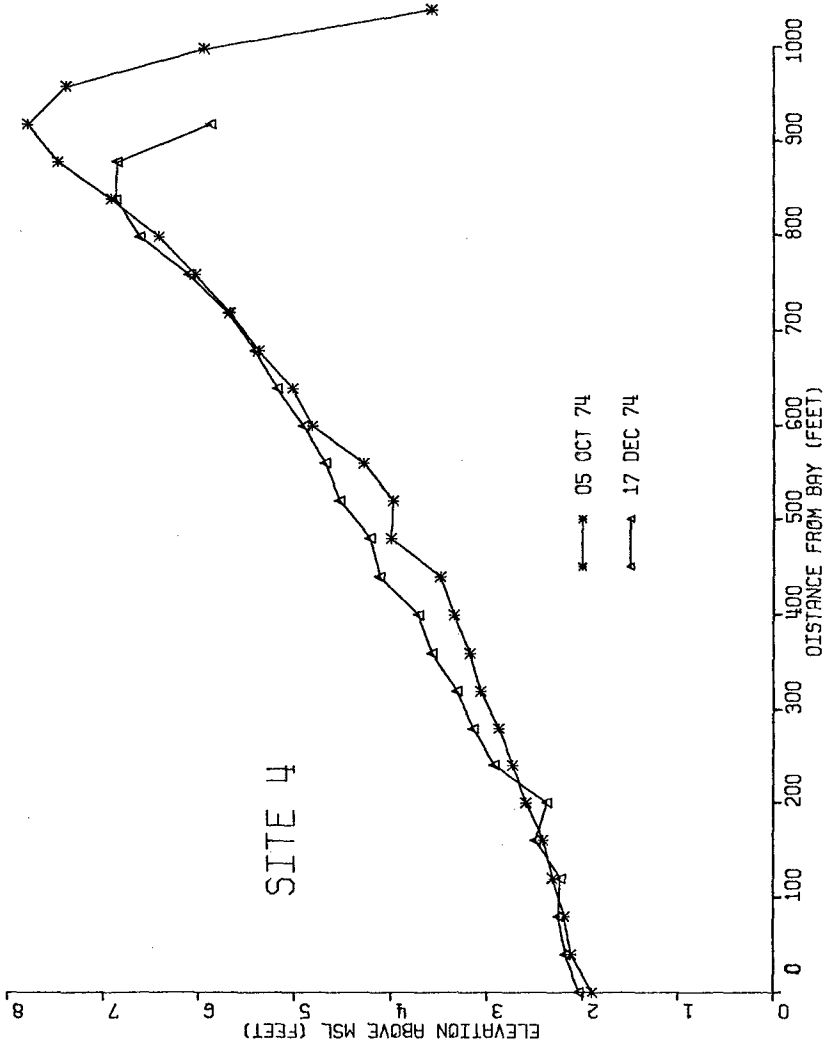


Figure 4. Site 4, December 1, 1974 Storm

foot of beach. Absence of material seaward of this zone of accumulation must be related to the hydraulics of the overwash surges. The overwash surges carried sediment to within 220 feet of the bay where it was deposited as delta foreset beds. Calculations indicate a net gain of sediment across the profile line ($89 \text{ ft}^3/\text{ft}$), but only 80 feet of beach was included in the survey.

The final survey site (Site 5) experienced the greatest amount of deposition. Approximately $300 \text{ ft}^3/\text{ft}$ of new material was deposited along this line as overwash (Fig. 5). As in the previous cases, only the upper backshore of the beach could be surveyed due to high water so that the total amount of beach erosion could not be ascertained. The deposit abruptly terminated at a distance of 250 feet from the bay. The dunes were severely scaped and eroded, but volumetric determinations were not possible at this site.

During the March 1975 northeaster, an electromagnetic current meter was successfully used to measure the overwash surge velocities during the storm event. The mean of the maximum instantaneous velocities was $5.2 \text{ ft}/\text{sec}$ at 1.5 inches off the bottom, while the flow depths averaged 6 inches. During the 4 hour and 40 minute time period bracketing high tide, 121 overwash surges were recorded by the magnetic tape data logger. A comparison of profiles taken hours before the storm and on the following day showed that an average of 29 ft^3 of overwash material was deposited per foot of breach. There was actually a small amount of beach accretion ($9 \text{ ft}^3/\text{ft}$), indicating a net onshore movement of bottom sediment. The barrier dunes were not eroded since the storm tide was quite low (Table 1).

Sediment Budget

Sediment budget calculations indicated the net changes for the washover areas. Overwash was the only significant mechanism of sediment transport to the backdune zone as documented by monthly surveys. Eolian processes were largely ineffective in westward transport, but the strong winter northwest winds resulted in severe deflation of the washover fan/flats between storms.

The net 2 year change at Site 1 has been erosion (Table 2). Survey lines that experienced greatest erosion were the least vegetated along their lengths. Figure 6 shows the net 26 month change along the centerline at this site. The fan elevation has been lowered several feet while the vegetation contact, which appears as a bulge in the survey line, has actually moved seaward during this time interval. The total change for the washover fan and adjacent environs at Site 1 has been a small net loss of material from the fan surface. Slightly over 1000 ft^3 of sand has been lost from the area bounded by the survey grid, not including seaside dune and beach erosion.

The trend for the adjacent washover fan (Site 2) was weighted heavily toward erosion for a net loss of $6,000 \text{ ft}^3$ during this time interval. This fan, however, was sparsely vegetated with an active

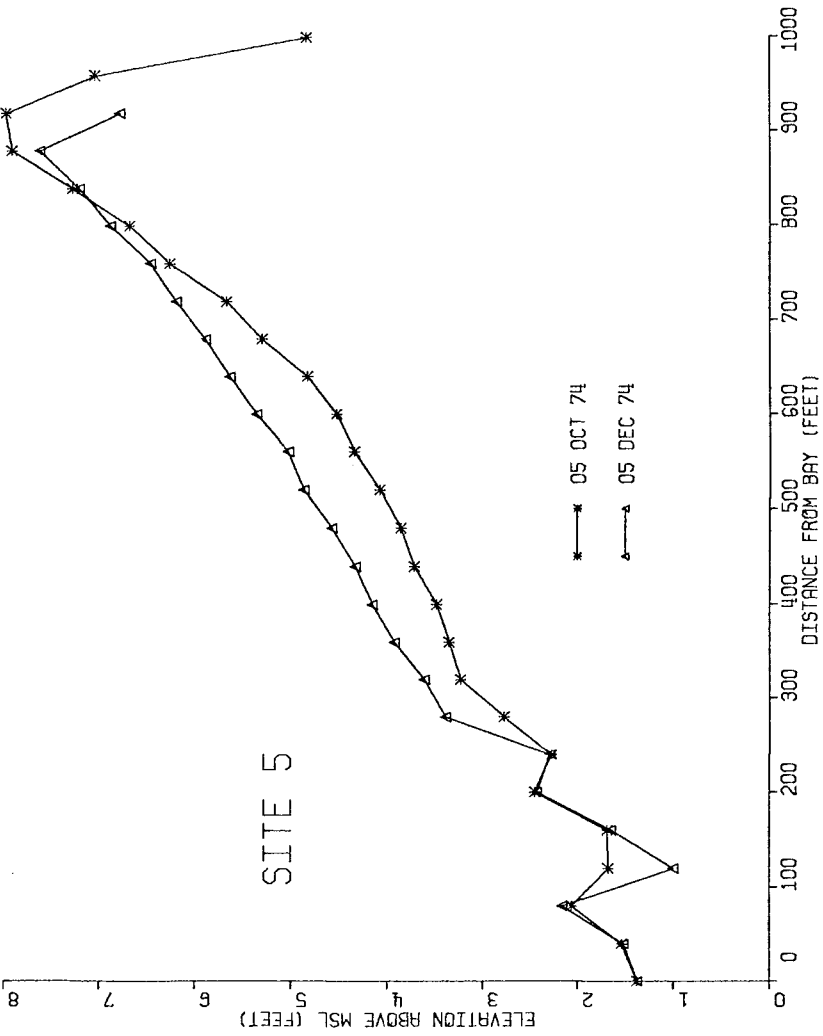


Figure 5. Site 5, December 1, 1974 Storm

TABLE 2. WASHOVER FAN AND BEACH NET CHANGE
(Leatherman, 1976)

<u>Survey Dates</u>	<u>Line</u>	<u>Total Line Change (ft./ft)</u>	<u>Washover Fan (ft./ft)</u>	<u>Beach Change (ft./ft)</u>	<u>Length of Beach Surveyed (ft)</u>
21 Apr 73 - 24 Apr 75	Northline 4 Site 1	+32	-4	+36	100
21 Apr 73 - 24 Apr 75	Northline 2 Site 1	+95	+74	+21	100
6 Apr 73 - 24 Apr 75	Northline 1 Site 1	-187	-86	-101	100
17 Feb 73 - 24 Apr 75	Centerline Site 1	-184	-117	-67	100
6 Apr 73 - 24 Apr 75	Southline 1 Site 1	-263	-122	-141	100
21 Apr 73 - 24 Apr 75	Southline 2 Site 1	-64	+31	-95	100
22 Apr 73 - 24 Apr 75	Southline 4 Site 1	0	+31	-31	60
5 Oct 74 - 24 Apr 75	Site 3	+3	-102	+70	80
5 Oct 74 - 24 Apr 75	Site 4	-67	-45	-50	80
5 Oct 74 - 24 Apr 75	Site 5	-147	-69	-45	80

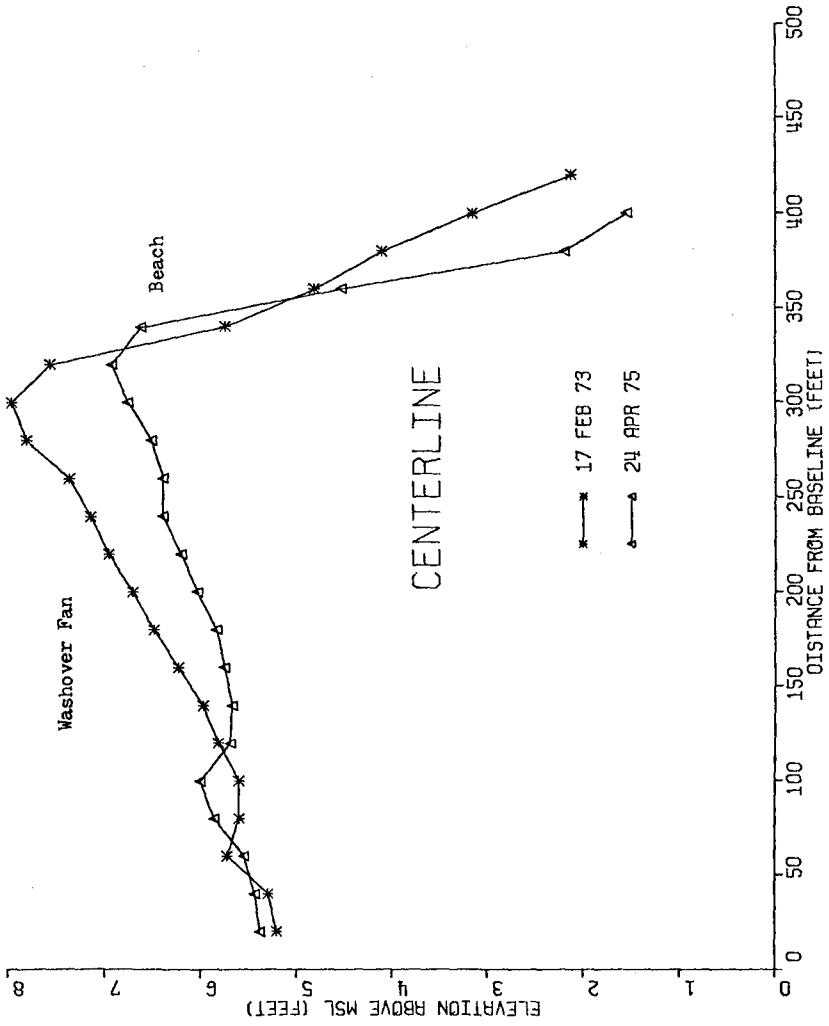


Figure 6. Site 1, Centerline, Net 26 Month Change

blowout on the north dune which flanked the fan. In the absence of any stabilizing agent, the newly-deposited overwash sand was very susceptible to reworking by the predominant northwest winds, resulting in loss of material from the fan surface.

Sites 3, 4 and 5 had similar response patterns during the 1974-75 storm season. In each case there was a zone of eolian action where wind was able to strip away large quantities of sand as shown at Site 4 (Fig. 7) and Table 2. Below an elevation of 4.7 feet, there has been net accretion on all three lines. Sand deposited below this critical elevation will not be reworked. Field observations indicated that this elevation coincided with watertable or semi-saturated conditions.

Discussion

A limiting criterion for the generation of an overwash event can be related to a significant wave hindcast by the Bretschneider method. Deep water waves with heights of 10 to 11 feet represent the minimum conditions necessary for overwash. This condition is generally satisfied by a small northeaster, which generates 24 knot winds for 20 hours or more. For larger events, the deep water wave hindcast is certainly an important index in terms of assessing a storm's impact on the shoreline, but is perhaps not the most important factor.

For this discussion of storm size versus amount of overwash, refer to Table 1. Data for the February 9-11, 1973 northeaster at Cape Hatteras is from Schwartz (1975), and this storm was hindcasted by this investigator for comparative purposes. Unfortunately, other storm parameters, such as amount of surge, are now known. Examination of Table 1 reveals that there is not a clearly definable correlation between storm size, as given by deep water wave height, and amount of deposition. A far more important parameter may be storm surge, in-as-much as the December 1, 1974 northeaster resulted in the largest amount of deposition per breach width, but had the third highest hindcasted deep water wave height. This analysis does not argue against waves as a controlling parameter for overwash but asserts that storm surge may be more important. Large waves and high surge are somewhat coupled systems since both are dependent on some of the same meteorological parameters. Based on this data set, it is suggested that storm surge is the single most important factor in determining the magnitude of an overwash. Since only certain size waves are allowed to reach the shore based on breaking criterion, it is the height of the storm tide that allows the dunes to be directly attacked by storm waves and swash surges to overtop the barrier threshold as overwash.

In attempting to determine if there is a differential amount of sedimentation along the island, only the December 1, 1974 overwash data is available for all survey sites. Sites 3, 4 and 5 showed the greatest amount of variance in deposition (Table 2), but are all con-

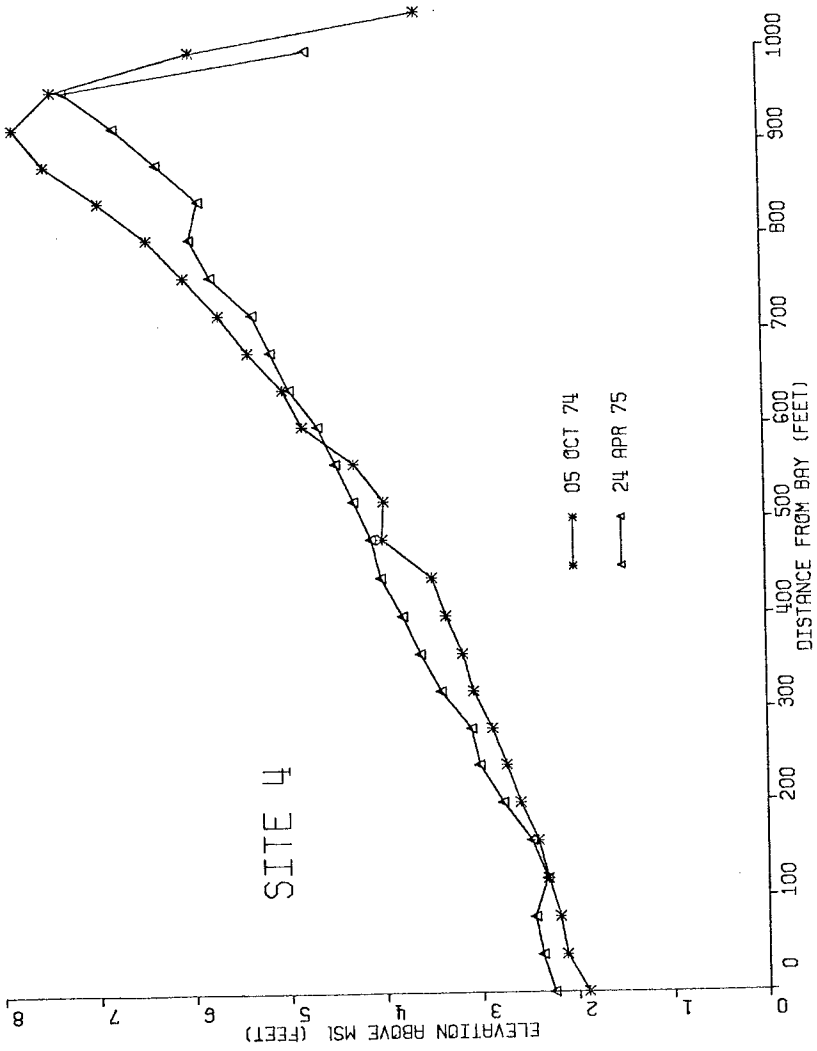


Figure 7. Site 4, Net 1 Year Change

tained within a one-half mile stretch of coast. This differential amount of sedimentation may be linked to local constraints, such as sand availability.

As previously mentioned, overwash deposition at Site 3 almost perfectly matched the amount of storm berm lost plus a small amount of beach erosion. At Site 4, there has been a much greater amount of overwash deposition, and, as reflected by before and after profiles (Fig. 4), probably a greater amount of beach erosion. The length of beach surveyed (80 ft in this case) was a severe limitation in exactly defining this relationship. At Site 5, there was 300 ft³/ft of overwash deposition, which is over three and almost two times greater than that recorded at Sites 3 and 4, respectively. The corresponding amount of beach erosion at Site 5 was quite small in comparison to the large amount of deposition. It should be noted that Site 5 washover fan is bounded by large dunes on each side of the throat which may act as a source of sand. Post-storm field inspection indicated a large amount of seaside dune face erosion associated with its scarping and landward retreat. This analysis indicates that the chief source of material for the overwash surges is the beach backshore and dunes.

A rough calculation of the amount of overwash as compared to beach and dune erosion can be made by using the December 1974 data set at Site 1. The average amount of beach erosion for the first 60 feet seaward of the dune line was 118 ft³/ft. Dune erosion rates were quite variable as recorded by the north and south dune profile lines, so an average value of 52 ft³/ft was used for calculation purposes. The third dimension of the control volume can be defined as half the shoreline distance between fans on each side of the fan monitored. For Site 1 this distance corresponded to 145 feet of dune and 187 feet of beach length as source area or a total of 29,600 ft³ available for net displacement. Total volume calculations for Site 1 showed that 9,300 ft³ of material was effectively transported across the threshold which represented 31 percent of that available in this specified zone of change. The majority of sand removed from this zone was probably transported a short distance offshore to become incorporated into the large storm bar. Undefined amounts of sand are permanently lost offshore, and an imbalance in the longshore transport at any particular point along the shoreline necessitates net erosion or accretion of material.

Conclusions

In spite of contributions from 7 discrete overwash events, there has actually been a small net loss of material from the fan/flats. Sand transport by wind was seen to be of the same order of magnitude as hydraulic transport by overwash. This analysis indicated that there is a balance between overwash and eolian processes with wind transport being slightly dominant. As a result of these two processes, there is a tendency for sediments from different environments of deposition to become homogenized. Since the backshore beach, dune

and overwash sand are almost of the same mean grain size (1.70 ϕ) and standard deviation (0.30 ϕ), there is only a small loss of material associated with their transport and redeposition. Sand from each area can act equally as a source for the other. This interpretation agrees with the long-held concept that dunes serve as sources of sediment (to the beach) in times of need (during storms).

The above indicates that non-vegetated washover fan/flats serve merely as temporary reservoirs for the eventual redistribution of the sand. Wind reworks the deposit with the bulk of the sand being blown back onto the beach face. The result of this sediment exchange process is dune erosion due to seaside scarping, no change on the fan, flats and marsh, and a stable or eroding beach consistent with upstream littoral drift conditions.

Acknowledgements

This study was supported, in part, by the Office of the Chief Scientist, Mid-Atlantic Region, National Park Service, Philadelphia, Pa.

References

1. Caldwell, J. M., 1959, Shore erosion by storm waves, U. S. Army Corps of Engineers, Beach Erosion Board MP 1-59, 17p.
2. Coastal Engineering Research Center, Beach Evaluation Program (BEP), Assateague Island, 1972-1974.
3. Dolan, R., 1972, The barrier dune system along the Outer Banks of North Carolina, a reappraisal, Science, V. 175, p. 286-288.
4. Everts, C. H., 1973, Beach profile changes in Western Long Island, Coastal Geomorphology, Publications in Geomorphology, State University of New York, Binghamton, N. Y., p. 279-301.
5. Everts, C. H., DeWall, A. E. and Czerniak, M. T., 1974, Behavior of beach fill at Atlantic City, New Jersey, Proceedings of the 14th International Conference on Coastal Engineering, Copenhagen, p. 1370-1388.
6. Fisher, J. S., Leatherman, S. P. and Perry, F. C., 1974, Overwash processes on Assateague Island, Proceedings of the 14th International Conference on Coastal Engineering, Copenhagen, p. 1194-1212.
7. Leatherman, S. P., 1976, Quantification of overwash processes, Ph.D. dissertation, University of Virginia, 245p.
8. Schwartz, R. K., 1975, Nature and genesis of some storm washover deposits, CERC Tech. Memo. No. 61, 69p.

9. U. S. Army Corps of Engineers, 1974, Shore Protection Manual, Coastal Engineering Research Center, Ft. Belvoir, Virginia.
10. U. S. Dept. of Commerce, NOAA-NOS tide data, Indian River Bridge Tide Gage, 1973-1975.
11. U. S. Dept of Commerce, NOAA tide tables, Atlantice coast of North America, 1973-1975.

CHAPTER 115

PROCESS AND MORPHOLOGY CHARACTERISTICS OF TWO BARRIER BEACHES IN THE MAGDALEN ISLANDS, GULF OF ST. LAWRENCE, CANADA

by

E. H. Owens

Coastal Studies Institute, Louisiana State University,
Baton Rouge, Louisiana 70803

ABSTRACT

Detailed field investigations of barrier beach morphology and processes at adjacent sites in the Magdalen Islands, Gulf of St. Lawrence, show that the two beaches are in distinctly different morphodynamic environments. The differences are expressed in terms of wave energy levels, sediment dispersal patterns, and nearshore, littoral, and dune geomorphology. The exposed west-facing coast has a steeper offshore gradient, is a zone of sediment bypassing, and has a complex sequence of three nearshore bars. Wave energy levels are lower on the sheltered east coast, and this is a zone of sediment redistribution and deposition with a single, linear nearshore bar. The different morphological characteristics of the two barriers are attributed to the spatial variation in energy levels and to the differences in offshore gradients on the two coasts. Computed wave energy values, derived from data monitored during two study periods (August and November, 1974), indicate that the mean wave energy levels were greater on the west coast as compared to the east coast by factors of 2.25 in summer and 2.95 in winter. This is due primarily to the dominance of winds out of the westerly quadrant throughout the year.

INTRODUCTION

The Magdalen Islands consist of a series of barrier beaches that are oriented northeast-southwest to connect small bedrock outcrops on the shallow central shelf of the southern Gulf of St. Lawrence (Owens, 1975) (Figure 1). This is a microtidal environment (mean tidal range less than 1.0 m) and, as the Gulf is an enclosed sea, the wave climate is dominated by locally-generated wind waves. Winds are dominantly from between southwest and northwest throughout the year, with a higher frequency of storm winds in winter months (Table 1). Limiting factors for wave action on the beach are maximum fetch distances on the order of 300 km and the presence of sea or beach-fast ice for periods up to four months each winter. Littoral processes are dominated by wind waves associated with the west to east passage of low-pressure systems across Atlantic Canada (Table 2). On the west coast of the Magdalen Islands the shoreline is exposed to the dominant and prevailing winds out of the northwest. Maximum wave and breaker height values on the west beach occur at times of maximum wind velocities, independent of wind direction. On the east-facing coast wave characteristics are closely associated with the onshore wind component (Owens, 1977).

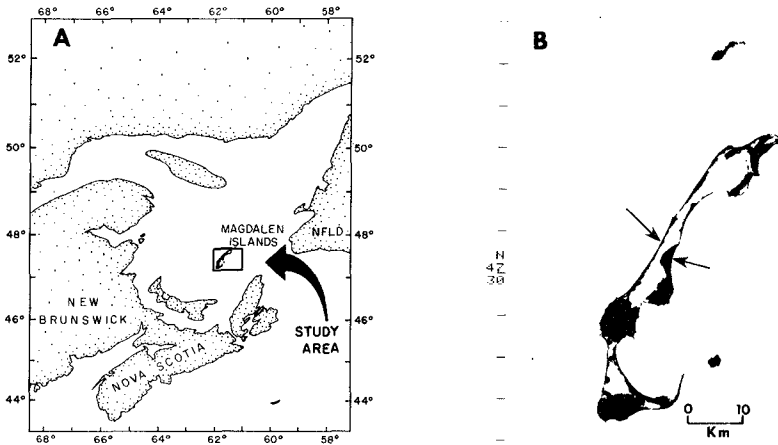


Figure 1. Magdalen Islands study area: A. Location. B. Study sites on the central tombolo.

Table 1. Wind Data, Magdalen Islands (1933-1972)

	Mean Wind Velocity (km/h)	Mean Direction	Mean Hours/Month with Given Wind Velocities		
			88-101 km/h	102-120 km/h	>120 km/h
Jan.	47.2	NW	13.4	2.0	0.1
Feb.	41.4	NW	7.2	1.8	0.4
March	40.6	NW	6.2	0.4	0.4
April	36.2	NW	1.8	0.3	--
May	35.2	NW	0.4	--	--
June	33.3	NW	0.2	--	--
July	30.6	SW	--	--	--
Aug.	30.4	SW	0.7	--	--
Sept.	35.7	NW	1.7	0.4	--
Oct.	41.0	NW	5.0	0.7	--
Nov.	41.7	NW	6.5	1.4	0.7
Dec.	45.7	NW	9.0	2.2	0.2

Table 2. Storm Duration and Frequency, Magdalen Islands

A. Number of Storms with Winds >90 km/h and >115 km/h by Quadrant Over a 40-Year Period					
	>90 km/h	Duration >3 hours	Duration >6 hours	>115 km/h	Duration >3 hours
NW-NNE	256	68	37	15	3
NE-ESE	62	12	3	--	--
SE-SSW	124	15	5	2	--
SW-WNW	120	15	9	8	1

B. Annual Frequency of Storm by Quadrant					
	>90 km/h	Duration >3 hours	Duration >6 hours	>115 km/h	Duration >3 hours
NW-NNE	6.4/yr	1.7/yr	0.9/yr	2 in 5 yr	1 in 13 yr
NE-ESE	1.5/yr	1 in 3 yr	1 in 13 yr	--	--
SE-SSW	3.1/yr	2 in 5 yr	1 in 8 yr	1 in 20 yr	--
SW-WNW	3.0/yr	2 in 5 yr	1 in 4 yr	1 in 5 yr	1 in 40 yr

Mean and maximum wave height values are greater on the west coast in all seasons due to the prevailing onshore winds. A distinct difference in wave energy levels exists between the two study sites (Figure 2). Comparison of computed wave energy values (Table 3), derived from time-series data monitored during two study periods (August and November, 1974), shows that the mean values are greater on the west coast by factors of 2.25 and 2.95 for the summer and winter phases of the study. The same comparison for the computed longshore sediment transport rates (Table 4) shows that the combined hourly rates are greater on the west coast by 2.7 and 2.0 for the summer and winter study periods. The estimated annual gross volume of longshore sediment transport is approximately four times greater on the west-facing barrier.

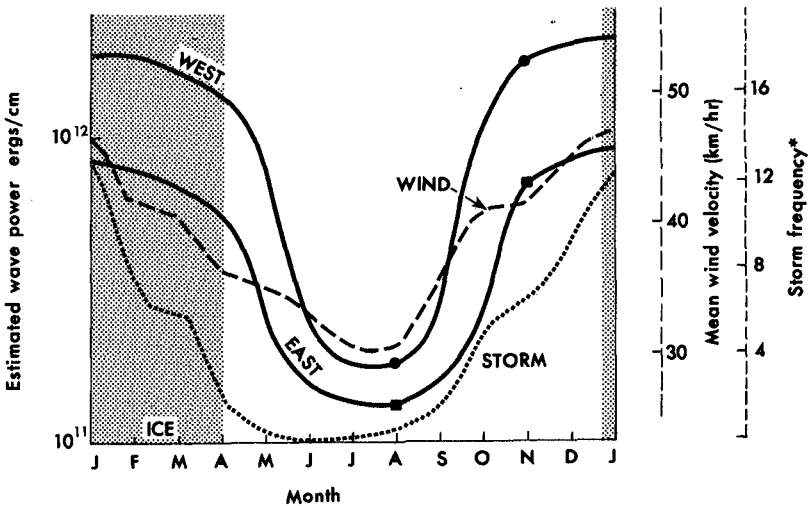


Figure 2. Seasonal variations in (1) estimated wave energy on the east and west barriers, (2) mean monthly wind velocity, and (3) storm frequency. The period of sea-ice cover or beach-fast ice is indicated by the shaded area. Wave energy values are extrapolated. Storm frequency (*) is the number of periods in each month when wind velocities exceed 55 km/h, based on data over a 40-year period.

Table 3. Computed Wave Energy Values (ergs/cm)

		Mean	Minimum	Maximum
Summer	West	2.52×10^{11}	2.12×10^9	1.65×10^{13}
	East	1.12×10^{11}	2.12×10^9	1.10×10^{13}
Winter	West	2.51×10^{12}	1.68×10^{11}	7.38×10^{13}
	East	8.51×10^{11}	3.04×10^{10}	5.89×10^{13}

Table 4. Summary of Computed Longshore Sediment Transport Rates

		West Coast	East Coast
Average Hourly Rate (m^3/h)	Summer	149 to N	53 to N
		95 to S	39 to S
	Winter	631 to N	265 to N
		519 to S	315 to S
Net Daily Rate (m^3/day)	Summer	428 to N	201 to N
	Winter	1,261 to N	962 to S
Estimated Annual (m^3/yr)	Gross	2,059,030	550,943
	Net	233,931 to N	104,112 to S

Owens (1977) has shown that in addition to this spatial variation there is also a distinct temporal variation in energy levels between the two sites that is reflected in littoral zone morphology. On the west coast there is a seasonal variation in wave energy levels that produces a "summer-winter" beach cycle. On the sheltered east coast variations in energy levels due to the passage of low-pressure systems across the region are more important than the seasonal variations. This produces beach cycles of erosion during storms and deposition during the post-storm recovery period (Table 5).

Table 5. Characteristic Differences between the Coastal Environments of the East and West Barriers—Magdalen Islands

	West	East
Wave energy	a. High energy environment	a. Moderate energy environment
	b. Marked seasonal variation in wave energy levels	b. Large short-term variations due to storm-wave activity
Littoral zone morphology	a. "Summer-winter" beach cycle	a. Storm/post-storm beach cycle
	b. Relatively stable morphology in plan and profile	b. Large short-term variations in morphology
Offshore Slope	0°10'	0°05'
Nearshore Slope	0°33'	0°53'

OFFSHORE ZONE

On the shallow shelf adjacent to the west coast of the Magdalen Islands, sediment is being transported landward by present-day processes (Owens, 1975). This is an area of coarse and medium sands (Table 6) and is a non-depositional sedimentary environment, with local reworking and the formation of lag deposits (Loring and Nota, 1973). Sediment that is transported toward the Islands is moved rapidly alongshore in shallow water toward and around the extremities of the barriers. The shelf adjacent to the east coast is sheltered from waves out of the west and is a depositional area of fine-grained sediments (Table 7) (Loring and Nota, 1973).

The nature of the sedimentary environments on the Magdalen Shelf is controlled in part by differences in the wave climate to the west and to the east of the islands that result from the dominance of wind-generated waves out of the west. In the zone of sediment reworking and transportation on the shelf to the west of the Islands the sandstone bedrock is overlain by a thin, discontinuous layer of sand and gravel. In the depositional area to the east of the Islands the bedrock is buried by a continuous cover of well-sorted

Table 6. Sedimentary Environments--Magdalen Islands

	West	East
Offshore	Coarse/medium sands	Fine sands
Nearshore (<5 m)	Medium sand (1.31 ϕ)	Medium sand (1.81 ϕ)
Beach	Medium sand (1.67 ϕ)	Medium sand (1.87 ϕ)
Dunes	Medium sand (1.67 ϕ)	Medium/fine sand (1.95 ϕ)

Table 7. Energy-Morphology Characteristics--Magdalen Islands

		West	East
Sediment dispersal	Offshore	Toward east	Zone of deposition
	Nearshore	Rapid longshore movement	Zone at redistribution and deposition
Subaqueous profile		Relatively steep (1:300)	Relatively flat (1:625)
Frictional attenuation of waves		Low	High
Amount of energy reaching shoreline		High	Low

sands (Loring and Nota, 1973). The gradients of the subaqueous slope off the west- and east-facing barriers are therefore partially controlled by the sediment dispersal pattern that results from the local wave climate.

Wright and Coleman (1972) note that nearshore wave power is a function of the subaqueous slope, due to the effects of frictional attenuation, and that as water depth decreases frictional attenuation rates increase. The offshore profiles adjacent to the two barriers are very different (Figure 3), particularly between the 15-m and 40-m depth contours. The broad, shallow shelf off the east coast has an average gradient of $0^{\circ}05'$ (1:626) from the shoreline to the 20-m contour, approximately half the gradient of the shelf off the west coast ($0^{\circ}11'$, 1:312). Wave periods are usually less than

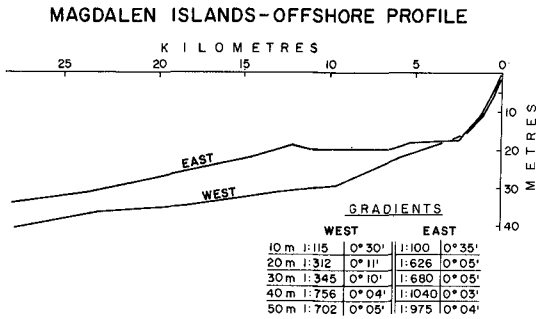


Figure 3. Offshore profiles and gradients--taken on lines perpendicular to the shoreline at the two study sites.

8 seconds in the Gulf, so that although some longer period waves would feel bottom in water depths up to 50 m, the frictional attenuation rates would probably be highest in depths between 30 m and 10 m.

Due to the shallower depths on the east coast the loss of energy by frictional attenuation is much greater than on the west coast. In addition, as the dominant and prevailing winds are out of the west, and locally-generated waves dominate the wave climate, the east coast is a protected environment in which wave heights are lower than on the west-facing barrier (Owens, 1977). The net effect is that (1) more energy is available on the western barriers (Table 3) and (2) a higher proportion of that energy reaches the nearshore zone as compared to the east-facing barrier.

NEARSHORE ZONE

The effects of the difference in the wave energy levels on the two coasts are clearly reflected in the nearshore zones. Surveys on the west study site show a large crescentic bar system that shoals to 5-6 m at 800 m from the beach, a smaller middle crescentic bar, and an intermittent inner bar (Figure 4). Comparison of field surveys in 1974-75 with aerial photographs taken in 1970 indicates that the plan form of the outer bar appears to be constant through time. Small longshore movements of the outer crescentic bar system result in occasional overlapping of the bars in the vicinity

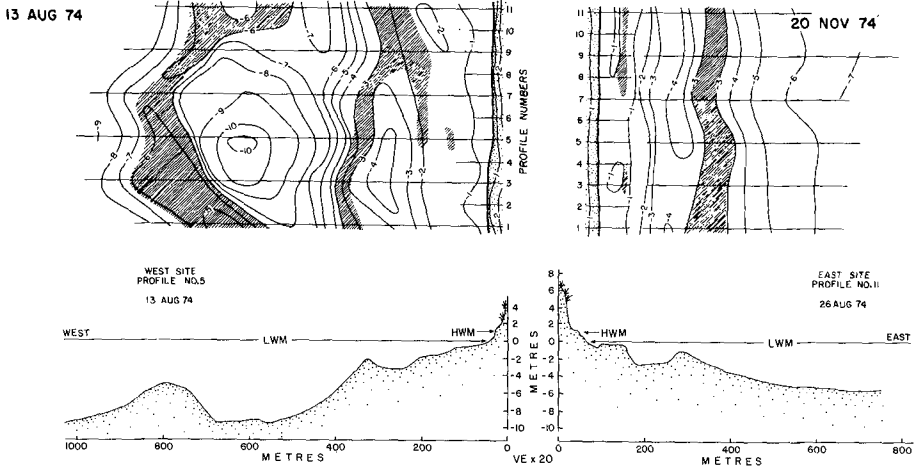


Figure 4. Nearshore profiles and morphology at the west and east coast study sites. The nearshore profiles are spaced at 100-m intervals and shaded areas on the maps indicate the location of subaqueous bars.

of the horns of the crescents. Also, it was found that the apex of the outer bar oscillated perpendicular to the shoreline between 700 and 900 m from the beach (Figure 5). These variations resulted in modification of the crescentic bar form but surveys showed that the basic location and shape of the outer bar did not change over a 9-month period. More variation was observed in the plan form of the two inner bar systems, particularly following periods of storm-generated waves.

By contrast the east-facing barrier is characterized by a single asymmetrical linear nearshore bar that shoals to 1.5-2.5 m at 250 m from the beach (Figure 4). The trough depth on the landward side of the bar varied between 3 and 5 m. Migratory bars were also recorded inshore on the shallow low-tide terrace adjacent to the beach. Although the nearshore bar had a low amplitude rhythmic plan shape following storm-wave activity, the basic linear form of the bar did not change significantly over the 9-month period of the surveys. The plan form of the bars on the low-tide terrace varied considerably, and this has been related to differences in the direction of wave

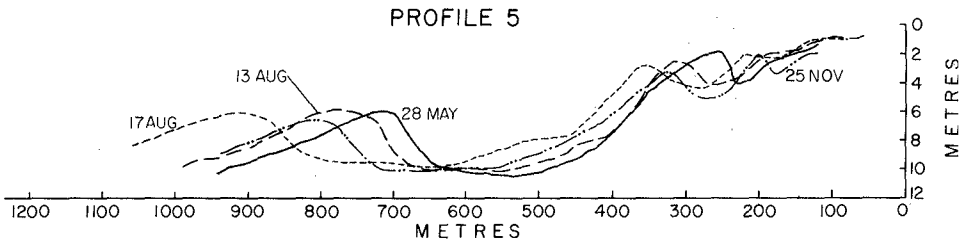


Figure 5. Composite of nearshore profiles surveyed on line 5 on the west study site. The profile is located on Figure 4 (from Owens, 1977).

approach during summer months and to storm-wave activity during the winter season (Owens, 1977).

Although the large differences in wave energy levels on these two barriers clearly affect the character of the nearshore zone, the actual variations in the size and the morphology of the nearshore bar systems could be explained in several ways. If it is assumed that breaking waves control bar formation, then the fact that the bars on the western barrier are farther offshore, in deeper water, and larger than the bar on the east coast would be due simply to higher wave heights on the west coast. But, as the two sets differ so radically in plan form it is difficult to accept that bar formation could result from a simple variation in wave height between the two coasts. On the other hand, it is possible that the variation in the size and spacing of the bars, perpendicular to the shore, could be due to the effects of standing waves generated by the reflection of incident waves from the beach (Bowen and Inman, 1971; Suhayda, 1974). Bowen and Inman suggest that the alongshore plan form of crescentic bars results from the sediment dispersal patterns associated with the formation of edge waves in the surf zone. The absence of a well-defined crescentic bar on the eastern barrier probably results from the consistently oblique wave approach and high breaker angles that generate strong longshore currents, thus preventing the development of rhythmic morphology on the outer bar.

INTERTIDAL ZONE (BEACH)

Sediment size (Table 6) and tidal range are constant between the beaches of the two study sites, so that variability in beach morphology results from differences in wave energy levels or in nearshore topography modifying the incoming incident waves. The beaches of the western barrier are generally narrow (20-30 m) (Photograph 1) with a relatively steep beach-face slope (approximately 1:4) (Figure 6). These beaches are characterized by an overall lowering of beach elevation in winter months, due to increased levels of wave activity during this season. This produces a "summer-winter" beach cycle (Figure 7).

The beaches of the eastern barrier are wider (40-50 m) (Photograph 2) and have a flatter beach-face slope (approximately 1:8) (Figure 6). The dominance of storm-wave activity over seasonal variations in wave energy levels on this coast produces beach cycles that are related to erosion during storms and recovery during post-storm conditions. Although the beach elevation is lower in winter months, as compared to the summer (Figure 7), the short-term variability related to storm-wave activity is more significant (Owens, 1977).

The difference in slope of the beach face at the two sites is a reflection of the different effects of nearshore topography on breaking waves. Waves reaching the beach face on the west coast were predominantly plunging breakers, during both study periods, whereas those on the east coast were predominantly spilling breakers. This difference in breaker type results from the different gradients immediately seaward of the intertidal zone. Water depths and gradients are greater at the west study site (Figure 4) due primarily to the presence of a wide low-tide terrace on the east-facing barrier.

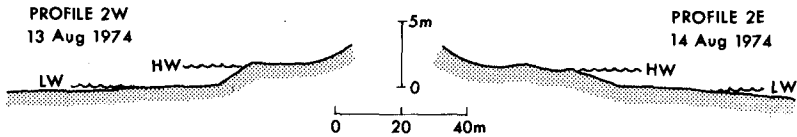


Figure 6. Representative beach profiles for the two study areas.



Photograph 1. West study site beach (May 1975).



Photograph 2. East study site beach (August 1974).

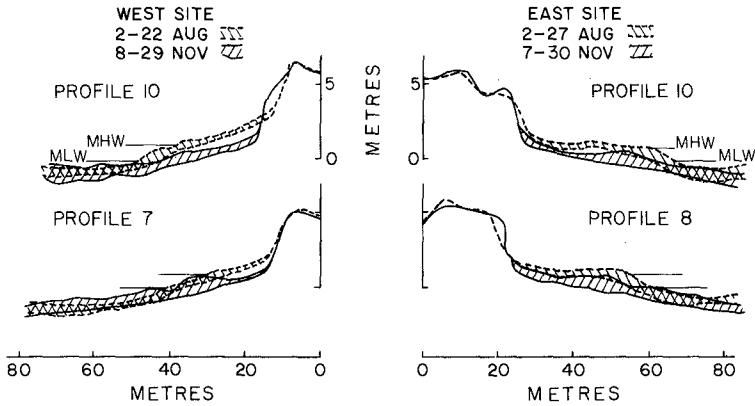


Figure 7. Sweep zone profiles for summer and winter beach profiles at selected locations for the two study sites (after Owens, 1977).

The berm crest was slightly higher on the western beach (Figure 6) as a result of higher wave heights on this coast that lead to a build-up of sand to greater elevations on the berm during high tide periods. Bascom (1954) pointed out that, although storm waves tend to erode the berm, they also create a berm at a greater elevation due to increased wave heights and that they may leave a high, narrow berm that will survive until a larger storm erodes it.

SUBAERIAL ZONE (DUNES)

The dunes on the western barrier are up to 15 m in height, and erosion during major storms produces irregular scarps in the backshore dunes (Photograph 3). During post-storm recovery a new foredune ridge develops adjacent to the beach, leaving an abandoned scarp that is subsequently modified by eolian processes. This pattern of irregular erosion in the backshore, followed by infilling to maintain a regular shoreline, has produced a complex dune topography. The concentration of wave energy at particular locations along the dune barrier is probably a reflection of the effects of the complex nearshore morphology on storm waves.



Photograph 3. Aerial view of dunes at the west study site (August 1974).

The dunes of the east study site are part of a progradational dune-ridge complex (Photograph 4) with a series of parallel ridges that reach 10 m in height adjacent to the beach (Owens and McCann, in preparation). Erosion during storms is relatively constant along this section of barrier, and there is no evidence that the ridges have been breached at any time. This dune-ridge complex is not characteristic of all the east-facing barriers of the Magdalen Islands (Figure 8). Elsewhere dune heights are rarely greater than 5 m and storm-wave erosion causes the development of washover channels that breach the dunes and the development of fan deposits on the lagoonal side of the barrier (Photograph 5).

SUMMARY

The high energy west-facing barriers of the Magdalen Islands are primarily a zone of sediment bypassing. Material that is fed into the nearshore-littoral system is transported rapidly alongshore toward the northeastern and southern extremities. The barriers are relatively stable, with washover deposits occurring only in the updrift sections adjacent to bedrock outcrops



Photograph 4. Aerial view of beach-ridge complex at the east study site (August 1974).



Photograph 5. Washover channels and fan deposits on the east-facing barrier to the north of the east study site (August 1974).

- EROSION
- a **** SEDIMENT OUTPUT > INPUT (SECTIONS OF WASHOVER)
- b ◊ SHELTERED UPDRIFT SITES OF OVERWASH OR
 INLET DEVELOPMENT
- ACCRETION
- c SPITS - TRANSPORT ENDPOINTS
- d ||||| BEACH RIDGE COMPLEXES
- ➔ DIRECTION OF LONGSHORE SEDIMENT TRANSPORT

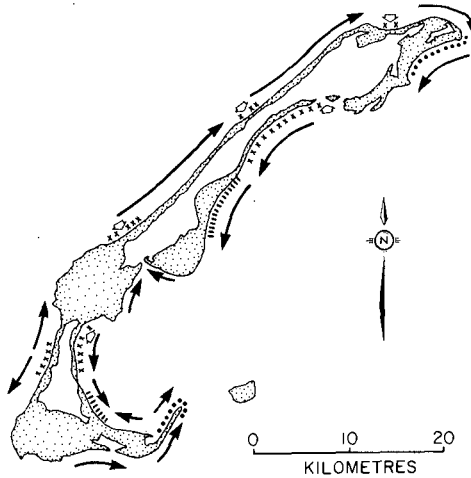


Figure 8. Generalized longshore sediment transport directions and areas of erosion or deposition on the Magdalen Islands barriers.

or, in the case of the southern tombolo, where there is a movement of sediment away from the central section of the barrier (Figure 8). The sheltered, lower energy eastern barriers are both lower and, except for the two beach-ridge complexes, are frequently overwashed. This environment is primarily one of sediment redistribution and deposition, with a net nearshore-littoral transport from northeast to southwest.

These basic mesoscale differences between the two barrier systems are reflected in the morphology and process characteristics of each coast. Spatial variations in offshore, nearshore, beach, and dune morphology can be directly related to the amounts and variability of wave energy levels on the two coasts. The pattern of sediment dispersal in the offshore and nearshore zones is controlled by the dominance of wind-generated waves out of the west (controlling the overall energy levels) and the resulting differences in subaqueous slope gradients (which affect the nearshore wave energy levels).

ACKNOWLEDGMENTS

The research program on the Magdalen Islands was part of a study carried out at the Atlantic Geoscience Centre, Bedford Institute of Oceanography, Dartmouth, Nova Scotia (Geological Survey of Canada Project 740009). Salary support since January 1976 has been provided under a contract with the Geography Programs, Office of Naval Research, Arlington, Virginia 22217. The illustrations were prepared by the Drafting and Illustrations Section of the Bedford Institute and by Mrs. G. Dunn of the Coastal Studies Institute.

REFERENCES

- Bascom, W. H., 1954, The relationship between sand size and beach face slope; *Trans. Amer. Geophys. Union*, 32, 866-874.
- Bowen, A. J., and Inman, D. L., 1971, Edge waves and crescentic bars; *Jour. Geophys. Res.*, 76, 8662-8671.
- Loring, D. H., and Nota, D. J. G., 1973, Morphology and sediments of the Gulf of St. Lawrence; *Fish Res. Board Canada, Bull. No. 182*, 147 p.
- Owens, E. H., 1975, Barrier beaches and sediment transport in the southern Gulf of St. Lawrence; *Proc. 14th Coastal Engr. Conf.*, Copenhagen, June 1974, A.S.C.E., N.Y., 1177-1193.
- Owens, E. H., 1977, Temporal variations in beach and nearshore dynamics; *Jour. Sediment. Petrol.*, v. 47 (in press).
- Owens, E. H., and McCann, S. B., in preparation, The coastal geomorphology of the Magdalen Islands, Quebec.
- Suhayda, J. N., 1974, Standing waves on beaches; *Jour. Geophys. Res.*, 79, 3065-3071.
- Wright, L. D., and Coleman, J. M., 1972, River delta morphology: wave climate and the role of the subaqueous slope; *Science*, 176, 282-284.

CHAPTER 116

GEOMORPHOLOGY OF THE SOUTHERN COAST OF ALASKA

Miles O. Hayes
Christopher H. Ruby
Michael F. Stephen
Stephen J. Wilson

Coastal Research Division
Department of Geology
University of South Carolina
Columbia, S. C. 29208

ABSTRACT

The shoreline of southern Alaska is a narrow coastal plain dominated by large glaciers, periodic earthquake activity, and strong extratropical cyclones. Studies on the coastal geomorphology and sediments carried out in 1969-71 and in the summer of 1975 were directed at defining geological hazards with respect to developing shore facilities for OCS oil exploration activities. Most of the shoreline was found to undergo rapid changes and experience a variety of serious environmental hazards. The safest potential port areas are located inside Icy Bay and Yakutat Bay. The coastal areas in the vicinity of the Malaspina Glacier and the Copper River delta are examples of the two principal shoreline types (glacial outwash plain and deltaic).

The coastal area surrounding the Malaspina Glacier, the largest piedmont glacier in the world, was classified into 5 categories on the basis of its geomorphology, sediments, and local glacial history:

1. Regional retreating coast: This area, which is located at the mouth of Icy Bay, is eroding rapidly (approximately 1.5 km since 1900) as a result of retreat of a glacier (up the bay) a distance of over 40 km since 1900. Consequently, it should not be developed.
2. Prograding spits: Sandy spits that have built into either side of Icy Bay since the retreat of the glacier are also unstable because of the general recession of the shoreline as a result of erosion at the mouth of the bay.
3. Abandoned glacial coasts: These areas, located on the inner eastern shores of Icy Bay and Yakutat Bay, are coastlines of relatively low wave energy composed of abandoned glacial tills, kame terraces, and outwash sediments. These are the most stable and least hazardous areas on the southern Alaska coast.
4. Actively eroding glacial margins: This area, located at Sitkagi Bluffs on the southernmost terminus of the Malaspina Glacier, is an eroding scarp of glacial till jutting into the Gulf of Alaska.
5. Glacial outwash coasts: These shorelines are highly variable and are usually dominated by prograding spits composed of sand and gravel.

The shoreline of the Copper River delta is made up of a complex of six fine-grained mesotidal barrier islands separated by tidal inlets that increase in size in a westerly direction. The islands have undergone major readjustments since the Good Friday earthquake of 1964, which raised the area 3 m. For example,

Egg Island has increased significantly in size; shoreline accretion of 400 m between February 1970 and May 1975 was measured at a site on the updrift end of the island. The patterns of erosion and deposition on the islands conform to those of the barrier island drumstick model developed during studies of the South Carolina coast.

INTRODUCTION

The southern coast of Alaska (Fig. 1) is an exceptionally dynamic area. Intense tectonic activity, large waves, strong tidal currents, highly variable winds, and active glaciation interact to produce one of the most rugged and variable coastlines in the world. The Chugach and St. Elias mountains, an extension of the Cordilleran Mountain system, control the gross orientation of the coastline. Fronting these mountains is a narrow coastal plain consisting of glacial and fluvial deposits undergoing active modification by tectonic, aeolian, and marine processes. Rapid advance and retreat of the numerous glaciers that border the coastal plain has caused sudden and dramatic shifts in loci of erosion and deposition along the beaches.

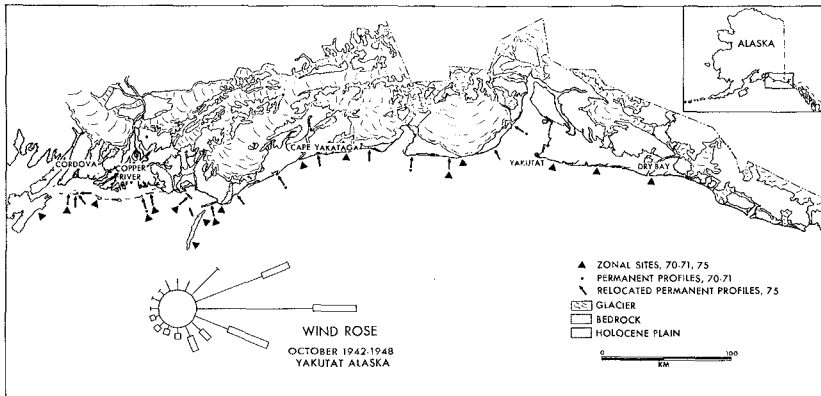


Figure 1. Study area. Note distribution of Holocene coastal plain (max. width = 35 km). Wind rose for Yakutat shows a dominance of easterly winds.

The coastal mountains, formed in response to subduction of the Pacific plate along this collision-type coast, are undergoing rapid uplift. Frequent earthquakes result in large ground displacements. During a single earthquake in 1899, the head of Yakutat Bay was uplifted 15 m. The entire coastal zone of southern Alaska has been subject to modifications resulting from this rapid tectonic activity.

The morphology and sediments of the coastal plain shoreline of southern Alaska were studied on a reconnaissance basis in 1969-71. Fifteen permanent beach profiles were established, 18 detailed specific site studies (zonal studies) were carried out (Fig. 1), and sediment samples were collected at 90 stations,

using a 4 km spacing. The area was revisited in the summer of 1975, during which time the permanent profiles were remeasured, and 99 beach profiling stations were occupied in the central portion of the study area (in the vicinity of the Malaspina Glacier). Using a 15 cm coring tube, sediment samples were taken at 3 stations at each of the 99 profile locations. The samples were then analyzed for grain size with a settling tube. Approximately 10,000 ground and aerial photos were taken. They have been analyzed and compared to photos taken during the 1969-71 studies and also compared with vertical aerial photos from various sources.

Extratropical cyclones that generate southeasterly winds dominate the coastal processes. Wind frequency diagrams for the entire Gulf of Alaska area are shown in Figure 2 (from Nummedal and Stephen, 1976). These winds create wave energy flux patterns that trend from east to west in the study area (Fig. 3), and, consequently, generate a dominant east to west littoral sediment transport pattern (Fig. 4).

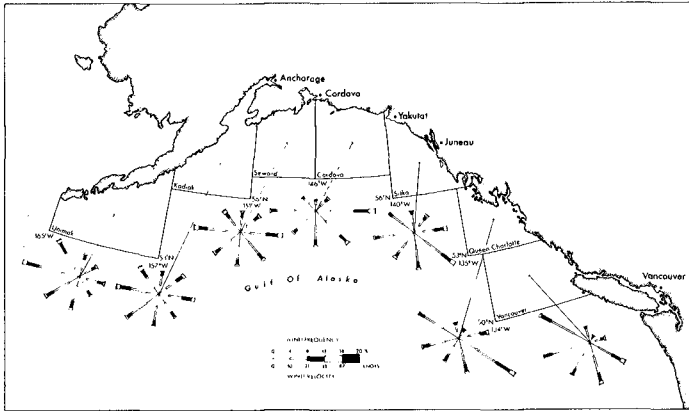


Figure 2. Wind frequency distributions for coastal data squares in the Gulf of Alaska. The diagrams are based on wind observations presented in Summary of Synoptic Meteorological Observations (U.S. Naval Weather Service Command, 1970). The dominant and prevailing winds are generally aligned parallel to the shoreline because of the temperature-induced pressure gradient along the coastal mountains. On the northeast coast of the Gulf, the dominant winds blow toward the northwest; on the northwest coast, they blow toward the east and northeast. (From Nummedal and Stephen, 1976; Fig. 13)

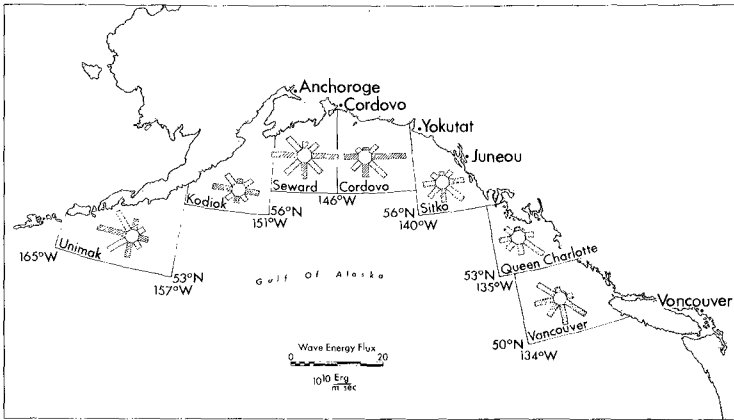


Figure 3. Wave energy flux distributions for the coastal areas of the Gulf of Alaska. The computations are based on deep water wave observations presented in Summary of Synoptic Meteorological Observations (U. S. Naval Weather Service Command, 1970). The wave energy flux is highest out of the southeast for the Vancouver, Queen Charlotte, and Sitka data squares, out of the east at Cordova, and out of the west at Seward, Kodiak, and Unimak. This pattern corresponds closely to that of the winds (Fig. 2). (From Nummedal and Stephen, 1976; Fig. 18)

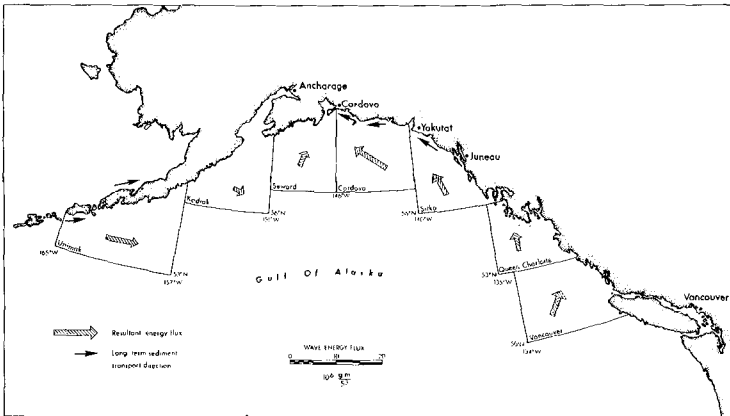


Figure 4. Direction of longshore sediment transportation based on large scale coastal geomorphic features and resultant wave energy flux distribution for the coastal areas of the Gulf of Alaska. Large scale coastal features used in establishing long-term transport directions include spits, inlet offsets, and crescentic embayments. The resultant wave energy flux is determined by vectorial addition of the distributions presented in Figure 3. Note the convergence of wave energy flux toward Prince William Sound. (From Nummedal and Stephen, 1976; Fig. 19)

The coastal morphology consists of (1) an outwash plain shoreline, which is a complex of outwash streams with downdrift beach-ridge plains, and (2) the delta of the Copper River, which has a seaward margin made up of mesotidal barrier islands. It is unusual to find a depositional shoreline of this magnitude (Fig. 1) on a collision coast. It owes its origin to the huge sediment output of glaciers that drain the largest ice field in North America, and to the sediments of the Copper River, which has a mean annual load of $100 \pm \times 10^6$ metric tons (Reimnitz, 1966; see Table 1).

TABLE 1. Annual Sediment Load of the Copper River (Reimnitz, 1966)

WOOD CANYON	Suspended Load: 66.0×10^6 metric tons
	Bed Load: <u>9.9×10^6 metric tons</u>
	Total: 75.9×10^6 metric tons
DELTA	Total Load: $100 \pm \times 10^6$ metric tons
<u>Comparisons:</u>	
COPPER RIVER (at delta)	$100 \pm \times 10^6$ metric tons
MISSISSIPPI RIVER	450×10^6 metric tons
AMAZON RIVER	347×10^6 metric tons

Figure 5 compares the beach sediments of the outwash plain depositional system with the beach sediments of the barrier islands of the Copper River delta. The outwash plain beaches are both texturally and mineralogically immature. All of the samples have very low percentages of quartz, being classified as litharenites (using scheme of Folk, 1974). The samples show a wide range of values of sorting and mean grain size (Fig. 5).

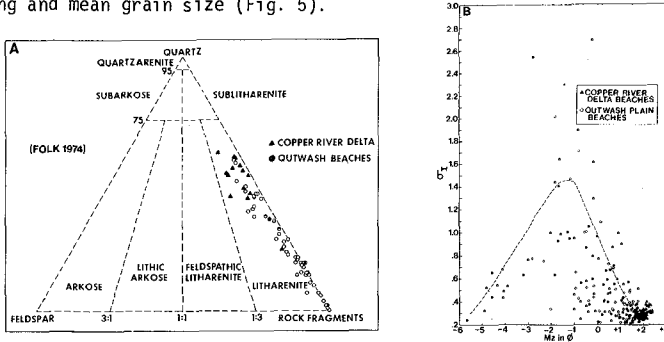


Figure 5. A. Composition of outwash plain and Copper River delta barrier island sediments. All samples are litharenites, with the barrier island sands being more quartz rich. B. Mean grain size (M_z ; Folk, 1974) vs. sorting (σ_T). Copper River delta beaches are moderately sorted medium to fine sand; whereas the outwash plain sediments show a wide range in size and sorting.

MALASPINA AREA

Introduction

Study during the summer of 1975 was focused in the vicinity of the Malaspina Glacier (Fig. 6). The project was designed to provide process information and to continue our study of the coastal morphology and sedimentation. Beach profiles were measured at 3 km intervals over the entire study area (Fig. 6) in order to assess regional trends in beach morphology. The results of these studies allow the subdivision of the coast into five principal geomorphic type areas which are closely related to the local glacial history.

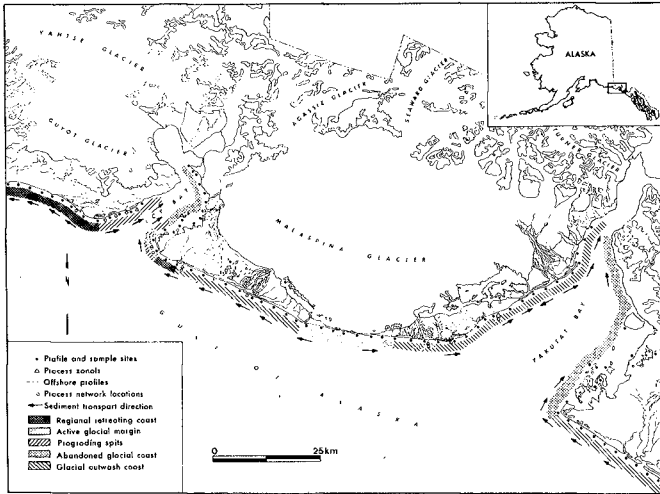


Figure 6. Location of area studied in summer of 1975. Arrows indicate dominant longshore sediment transport direction on the basis of combined morphological and process data. The different classes of shoreline types and location of study sites are also indicated.

Regional retreating coast

This area is located at the mouth of and downdrift of Icy Bay (Fig. 6). The recent retreat of the Guyot Glacier up into Icy Bay resulted in a loss of sediment to this coastal section, causing widespread erosion (approximately 1.5 km since 1900). Beach profiles are generally flat with concave-upward upper beach faces backed by eroding scarps at the spring high-tide swash line (Fig. 7). Sediments are mixed sand and gravel. Heavily forested beach ridges, glacial outwash plains, and till areas on either side of Icy Bay are being cut back severely. Broad overwash terraces are advancing over low-lying areas. This area should be omitted from all considerations for shoreline development.



Figure 7. Regional retreating coast. A. Beach profile and sketch for station DBC-79, which is located approximately 5 km west of the entrance to Icy Bay (Fig. 6). Note the concave upward shape of the profile, the erosional scarp, and the developing washover terrace. LTT = low-tide terrace; A, B, C = sediment sampling localities. B. Station DBC-79 on 14 June 1975.



Figure 8. A. Riou Spit, a prograding sand spit at the eastern entrance to Icy Bay. Photo taken on 4 August 1975. B. Example of abandoned glacial shoreline, eastern margin of Yakutat Bay (Knight Island). Photo taken on 21 August 1975.

Prograding spits

On either side of Icy Bay, sandy spits are prograding into deeper water as the shoreline around the mouth of the bay erodes. The largest, Riou Spit, is located on the east, or updrift, side of the Bay (Fig. 8A). Riou Spit is migrating both alongshore and landward because of recession of the shoreline adjacent to the bay. The beach profiles on the spits are relatively flat with broad berm-top overwash areas. These spit areas are considered to be quite unstable for development purposes because of their rapid rates of change and their exposure to open ocean waves.

Abandoned glacial coasts

These areas, located on the inner eastern shores of Icy Bay and Yakutat Bay, are characterized by deposits of unconsolidated tills, kame terraces, and outwash sediments which supply abundant gravel to the beaches. An example is shown in Figure 8B. Profiles are very steep, short, and often have well-developed multiple cusped berms. High vegetated storm berms indicate infrequent but violent storms. Sediments are predominantly well-sorted and rounded gravel. Sand and gravel spits occur downdrift of till islands in Yakutat Bay. Because of their protected nature and slow rates of erosion and deposition, these are the most favorable areas available for the development of shore facilities.

Actively eroding glacial margins

This area, located at Sitkagi Bluffs, on the southernmost terminus of the Malaspina Glacier, is an eroding scarp of glacial till on the shoreline of the Gulf of Alaska. Beach profiles in front of the Bluffs are extremely short and steep, backed by eroding till scarps (Fig. 9A). Beach material ranges from sand and angular gravels to large erratics left behind as the scarps retreat (Fig. 9B). These retreating scarps, and their adjacent boulder beaches, are virtually inaccessible for any kind of human activity at high tide.

Glacial outwash coasts

These beaches are generally prograding, with abundant mixed sand and gravel spits trailing toward the west, except inside Yakutat Bay, where a major transport reversal occurs. Beach-ridge plains often develop downdrift of the major river mouths. Beach profiles are relatively flat with abundant ridge-and-runnel systems, resulting in a shoreline with a characteristic rhythmic topography. Typical examples of glacial outwash coasts are illustrated in Figure 10. When glacial sources are distant, sediments tend to have a high sand to gravel content. The beaches in these areas are relatively stable and are considered to be the second most desirable areas for shoreline development in southern Alaska.

Process data

Process observations were obtained at two levels during July-August, 1975:

A) Process Network (Fig. 6). Regional process variability was determined by multiple observations during stable meteorological conditions.



Figure 9. Actively eroding glacial margins. A. Field sketch of profile Mal-5, located in front of the Malaspina glacier. B. Station Mal-5 (sketched in A) on 26 July 1970.

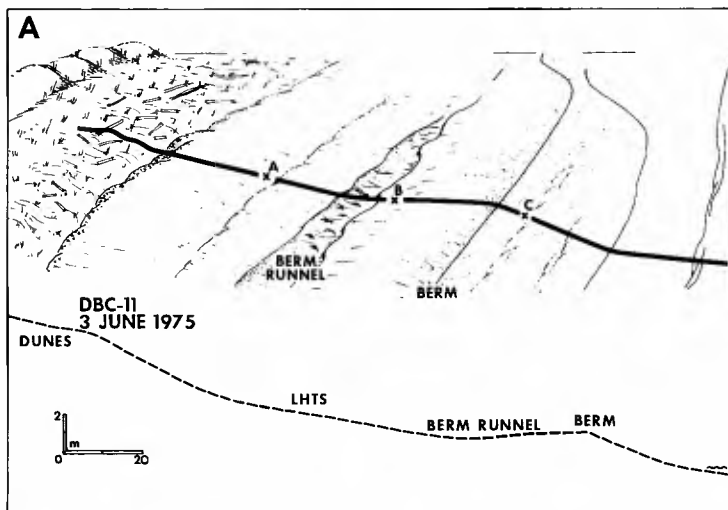


Figure 10. Glacial outwash coasts. A. Field sketch of station DBC-11, a fine-grained (sand dominant) spit on the outwash plain of the Yakutat foreland. B. Station DBC-11 on 3 June 1975. Note welded berm. C. Coarse-grained (gravel dominant) outwash plain near Malaspina Glacier. Photo taken in summer of 1970.

B) Six Process Zonals (Fig. 6). Continuous 48-hour monitoring of meteorological, wave, littoral, and morphological variability was maintained at single sites selected as representative of shoreline segments.

Regional process parameters document littoral transport in directions that correlate with regional morphology. Dominant south and southeast waves yielded sediment transport toward the west away from eroding till cliffs and from the mouths of outwash streams.

Process zonal measurements allowed documentation of the passage of a complete storm cycle. Commonly, two distinct wave trains were monitored. Under such conditions, drift directions and velocities were erratic and strong rip currents were prevalent. Dominant wave approach was a function of the path of low pressure systems moving through the Gulf of Alaska. Southerly waves were characteristic of calm conditions, and southeasterly waves were characteristic of storm conditions.

Breaker heights averaged 1.5 to 2.0 m, with a maximum measured height of 4 m recorded during a storm. Suspended sediment concentrations taken from the bore of plunging waves were as high as 150 gms/liter. Measured beach profiles revealed up to 15 cm of accretion to the beach face during one tidal cycle.

COPPER RIVER DELTA AREA

Introduction

The barrier island shoreline of the Copper River delta was uplifted 3 m by the Good Friday earthquake of March 1964 (Fig. 11). This has brought about many adjustments of the morphology of the islands in response to changes in the level of wave erosion and deposition. The sands of the barrier islands are mineralogically immature, averaging about 50% quartz and 50% metamorphic rock fragments (Fig. 5). They are moderately sorted, medium- and fine-grained sands.

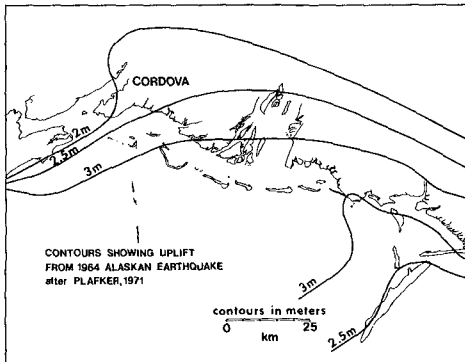


Figure 11. Uplift (in meters) of the Copper River delta area during the Good Friday earthquake of 1964.

Mesotidal barrier islands

A tidal range of 3-4 m places the Copper River delta in the mesotidal class of Davies (1964). As has been pointed out elsewhere (Hayes et al., 1973; Hayes and Kana, 1976), mesotidal barrier islands have two distinctive morphological characteristics:

1. In coastal areas with dominant waves that approach the shoreline at an oblique angle, the tidal inlets commonly show downdrift offsets; that is, the barrier beach downdrift of the inlet protrudes further seaward than the one on the updrift side (Hayes et al., 1970). The tidal inlets of New Jersey, the Delmarva Peninsula, and South Carolina are good examples. The present downdrift offset at Price Inlet, S. C., which has changed from downdrift offset to updrift offset and back to downdrift offset again since 1941, is discussed in detail by FitzGerald (1976).
2. Many mesotidal barrier islands have a drumstick shape, with the bulbous part of the drumstick being located on the updrift side of the barrier (Fig. 12A). Drumstick-shaped mesotidal barrier islands from Alaska, the Netherlands, South Carolina, and Georgia are outlined in Figure 12B.

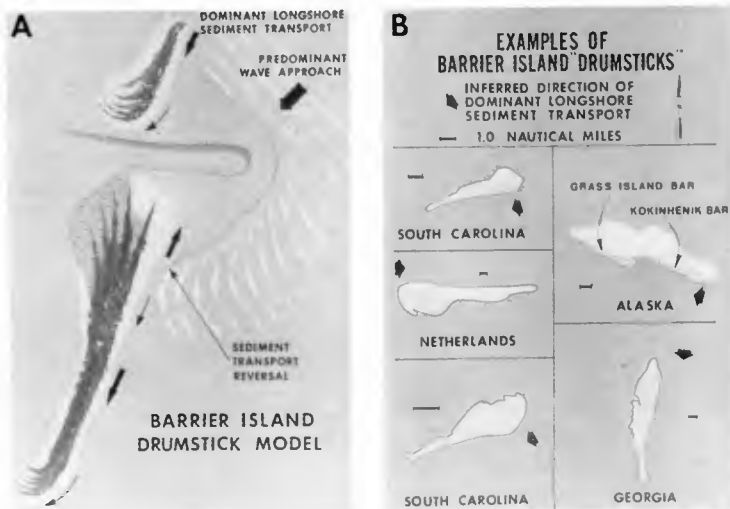


Figure 12. A. Barrier island drumstick model. B. Examples of barrier island "drumsticks" from South Carolina, Georgia, the Netherlands, and Alaska.

Barrier islands of the Copper River delta

The mesotidal barrier islands of the Copper River delta conform well to the drumstick model discussed above. Four systematic east to west changes in the barrier island system are apparent (Fig. 13):

- (1) The downdrift offset increases in an east to west direction, except at the westernmost spit, which is anchored to bedrock;
- (2) The size of the ebb-tidal delta increases from east to west;
- (3) Inlet width increases from east to west; and
- (4) The drumstick shape of the barriers becomes more pronounced in a westerly direction.

These changes are thought to be brought about by two interrelated factors. The river is rapidly filling in the eastern portion of the estuarine system; hence, smaller tidal prisms and smaller ebb-tidal deltas are developed on the east side of the delta. A 20 km long island, Kayak Island (see Fig. 1), is located to the east of the delta, which partially protects the eastern end of the delta from the dominant southeasterly waves. It is, thus, the western part of the delta that is more strongly affected by the oblique wave approach of the dominant waves. Therefore, the effect of wave refraction around the ebb-tidal deltas is greater on the west side of the delta. The drumstick shape of the barriers becomes more accentuated as the wave refraction increases.

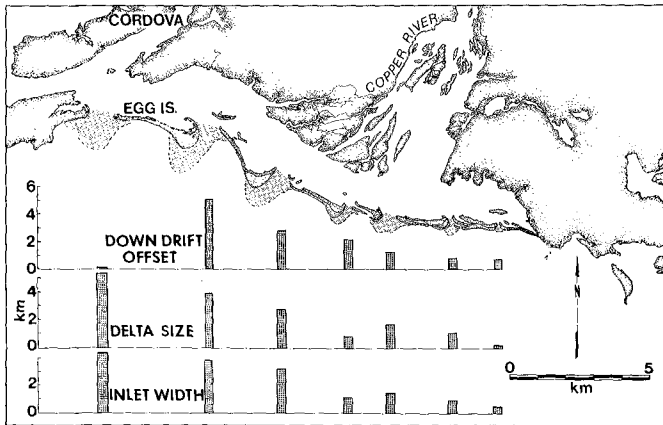


Figure 13. Barrier islands of the Copper River delta.

These barrier islands have undergone some remarkable changes in the past twelve years. They have largely prograded since they were uplifted by the March 1964 earthquake. Data for Egg Island (Figs. 14 and 15) illustrate these changes. A wave-cut scarp on a permanent profile at the east end of the island (EG-1; Fig. 14) eroded 56 m between February 1970 and May 1975. On the other hand, station EG-4, which is located at the widest point of the updrift bulge of the island, prograded 400 m during that same time. This process of overall aggradation of the barrier just downdrift of the inlet accentuated the drumstick shape of the barrier. This process of downdrift accretion is illustrated by the photographs in Figure 15.

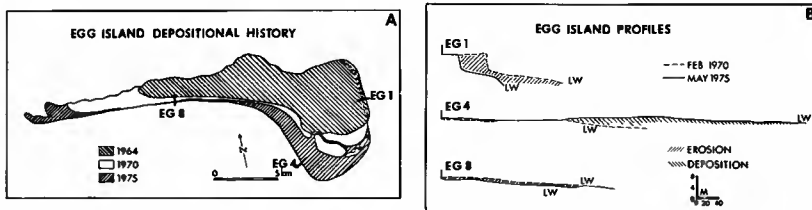


Figure 14. Changes of Egg Island, Copper River delta, Alaska, after the March 1964 earthquake, which raised the delta 3 m. Note continual accentuation of the drumstick shape of the island through time.

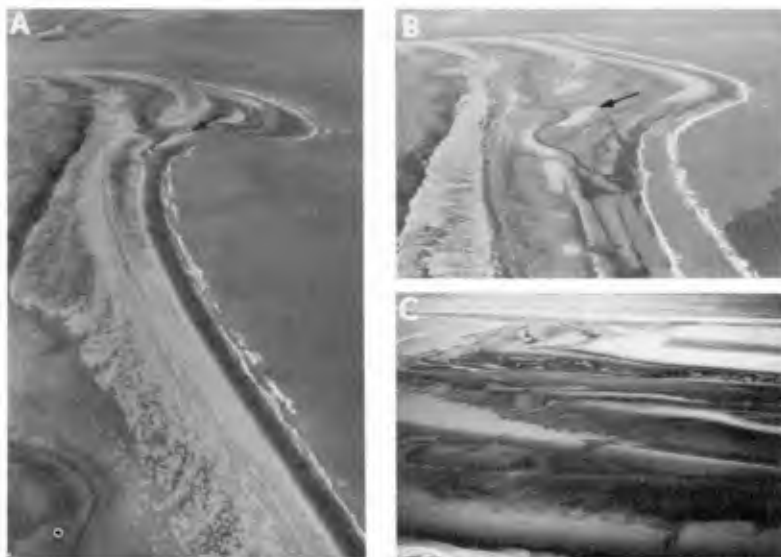


Figure 15. Egg Island, Alaska. A. Low-tide view taken in June, 1971. B. Low-tide view of east end of Egg Island taken in May 1975. Arrow points to same sand bar as the one indicated by the arrow in A. This beach accreted 400 m between February 1970 and May 1975 (see Fig. 14; profile EG-4). C. Multiple intertidal ridges welding on the beach at station EG-4. Photograph taken in the summer of 1969.

These remarkable changes, plus the occurrence of severe storms that overwash the islands, make the barrier islands of the Copper River delta an undesirable place to develop. On the other hand, Cordova, which has a sheltered harbor on Price William Sound, shows considerable promise.

CONCLUSIONS

1. In the Malaspina Glacier area, the most desirable shorelines for coastal development are the stable, sheltered abandoned glacial coasts inside Icy Bay and Yakutat Bay. The least desirable area is the regional retreating coast at the mouth of Icy Bay, which is eroding rapidly.

2. Southeasterly storms (extratropical cyclones) play a primary role in shaping the morphology of the coastal zone.

3. Combination of wave hindcast data, field process measurements, and studies of coastal geomorphology indicate a dominant littoral sediment transport from east to west.

4. The mesotidal barrier islands of the Copper River delta area show characteristics typical of other mesotidal shorelines (downdrift offsets and drumstick shapes).

5. Major changes in the barrier islands have occurred since the area was uplifted during an earthquake in 1964. Changes continue to accentuate the drumstick shape of the islands.

ACKNOWLEDGEMENTS

The earlier phases of this project (1969-71) were supported by the Geography Programs of the Office of Naval Research (Contract No. N00014-67-A-0230-0001, Miles O. Hayes, principal investigator), and the later phases were supported under contract with the National Oceanic and Atmospheric Administration (Contract No. 03-5-022-82; Miles O. Hayes, principal investigator).

REFERENCES CITED

- DAVIES, J.L., 1964, A morphogenic approach to world shorelines: *Zeit. für Geomorph.*, Bd. 8, 27-42.
- FOLK, R.L., 1974, *Petrology of sedimentary rocks*: Hemphills, Austin, Texas, 117 p.
- FITZGERALD, D.M., 1976, Ebb-tidal delta of Price Inlet, South Carolina; Geomorphology, physical processes, and associated shoreline changes: in HAYES, M. O. and KANA, T. W., eds., *Terrigenous Clastic Depositional Environments*, Tech. Rept. 11 - CRD, Dept. Geol., Univ. South Carolina, II-143 - II-157.
- HAYES, M. O., GOLDSMITH, V., AND HOBBS, C. H. III, 1970, Offset coastal inlets: *Am. Soc. Civil Engrs. Proc.*, 12th Coastal Engr. Conf., 1187-1200.

- HAYES, M. O., OWENS, E. H., HUBBARD, D. K., and ABELE, R. W., 1973, The investigation of form and processes in the coastal zone: in COATES, D.R., ed., Coastal Geomorphology, Publications in Geomorphology, Binghamton, N.Y., 11 - 41.
- HAYES, M. O., and KANA, T. W., 1976, Terrigenous clastic depositional environments: some modern examples: Tech. Rept. No. 11 - CRD, Dept. Geol., Univ. South Carolina, 308 p.
- NUMMEAL, O., and STEPHEN, M. F., 1976, Coastal dynamics and sediment transportation, northeast Gulf of Alaska: Tech. Rept. No. 9 - CRO, Geol. Dept., Univ. South Carolina, 148 p.
- REIMNITZ, E., 1966, Late Quaternary history and sedimentation of the Copper River delta and vicinity, Alaska: Ph.D. diss., Univ. Calif., San Diego, 160 p.

CHAPTER 117

TRACING ESTUARINE SEDIMENTS BY NEUTRON ACTIVATION

by

Richard M. Ecker,^{1/} John F. Sustar^{1/} and Cpt. William T. Harvey^{1/}

ABSTRACT

Tracing the movement of dredged sediments in north San Francisco Bay was accomplished jointly by the San Francisco District of the U.S. Army Corps of Engineers, Explosive Excavation Research Laboratory (now the Explosive Effects Division of the Weapon Effects Laboratory, U.S. Army Waterways Experiment Station), and the Stanford Research Institute. The study involved developing a technique which would permit the long-term tracing of fine sediments dredged from Mare Island Strait after disposal at the Carquinez Strait disposal site; application of the tracer; disposal of the tagged sediment for the February-March 1974 dredging of Mare Island Strait; sampling bottom sediments throughout the study area for a 10-month period; and, quantitative analysis of the collected samples.

INTRODUCTION

The continuous maintenance of navigable waterways in a dynamic sediment system such as San Francisco Bay opens many questions regarding the economics of the dredging operation and the sphere of influence that the operation has on the marine environment. Annual maintenance dredging for Federal, local and private facilities in San Francisco Bay is about 10 million cubic yards. The annual sediment inflow into the Bay is also about 10 million cubic yards. Previous studies to determine the dispersion of dredged sediments have been short-term studies, showing the initial distribution of dredged sediments only. Thus, a study was initiated to investigate the long-term dispersion and circulation of dredged sediments disposed of in a portion of San Francisco Bay.

The technique used for tracing dredged sediments was originally developed to trace tagged material emplaced in an underground explosive charge and subsequently released to the atmosphere by detonation of the explosive. The application of the tracing technique involved the fixing of a tracer element onto quantities of dredged sediments, introduction of this tagged material into dredge hoppers prior to disposal, sampling bottom sediments throughout the study area for a 10-month period, and quantitative analysis of the collected samples.

^{1/} Navigation and Coastal Planning Section, U.S. Army Engineer District, San Francisco, California.

STUDY AREA

The study area was located in the northern portion of San Francisco Bay including Suisun Bay, Carquinez Strait, Mare Island Strait and San Pablo Bay shown in Figure 1. Ninety percent of sediment inflow to the Bay comes through Carquinez Strait, the outlet of flows from the Central Valley of California.

The major portion of dredging in this area is the maintenance of the Mare Island Strait channel to a depth of 30 feet mean lower low water, an annual quantity of about 2.5 million cubic yards. Disposal occurs at a designated site in Carquinez Strait, west of the entrance to Mare Island Strait. Other dredging operations are conducted across San Pablo Bay, at oil terminal facilities and in small marinas throughout the area. With exception of San Pablo Bay (Pinole Shoal), dredged sediments are silty-clay with clay contents ranging from fifty to sixty percent.

TRACING TECHNIQUE

The method used for tracing the movement of dredged sediments in the study area was neutron activation. Radioactivity is not involved in this method until after the samples are collected and the tracer element is used at low concentrations. Certain chemical elements, when exposed to thermal neutrons in a nuclear reactor, become radioactive by capturing the neutrons. The radioactive atoms (radionuclides) of the element decay by releasing energy in the form of an electron (beta particle) and one or more gamma rays. The period of time required for the radionuclide to lose 50 percent of its activity is known as its "half-life." If the decay process is accompanied by one or more gamma rays, the gamma rays have a characteristic energy level which is associated with the atomic mass and chemical species of the decaying radionuclide. The neutron-activable elements can be identified by measuring the gamma-ray energies emitted by an activated sample. The quantity of each of the elements in the sample can be calculated if the gamma-ray emission rate and neutron exposure of the sample are known.

In using the neutron activation technique to trace sediment movement, a small amount of a trace material, in very low abundance in the prototype system (at least a factor of five less than that being added), is fixed to a quantity of sediment and introduced at a known concentration into the dredge hopper. The dredged material and tagged material are then released into the study area at the disposal site. After a period of time, bottom sediment samples are taken, processed, neutron activated, and the amount of trace element in the sample determined. Knowing the concentration of trace element fixed to the original sediments and the amount of the tagged sediments added to each hopper load allows the calculation of the percentage of dredged material present in a bottom sample.

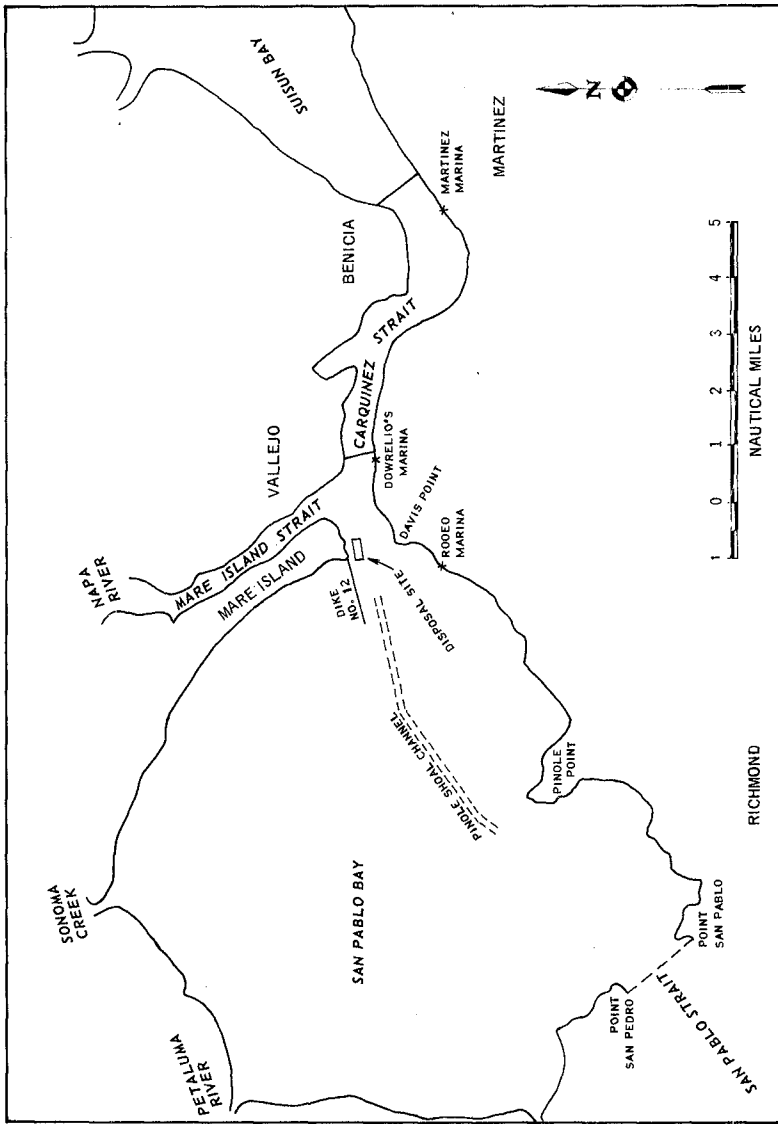


FIGURE 1

STUDY AREA FOR MATERIAL RELEASE INVESTIGATION.

The selection of a trace element to be used with the Mare Island Strait sediments was based on an extensive investigation of chemical element concentrations in sediments from Mare Island Strait and San Pablo Bay and an evaluation of detection limits. Estimates of total sediment movement over a one-year period within the study area ranged from ten to twenty million cubic yards of sediment, which included the quantity dredged, sediment inflow to the study area, and the mixing of sediments in San Pablo Bay, Mare Island and Carquinez Straits, and Suisun Bay.

After an investigation of numerous candidate trace elements, including gold, rhenium, and iridium, it was determined that iridium would be the best tracer element for the following reasons:

a. "The amount of iridium minimizes the mass that must be added to the traced sediment and therefore would least affect particle settling characteristics."

b. "The limit of detection for iridium is a factor of two lower than that for rhenium."

c. "The 74.37 day half-life permits examination of neutron activated samples at significantly long post-irradiation time without significant reduction in signal due to radioactive decay."

The concentration of iridium determined to occur naturally in the study area is 5×10^{-10} grams of iridium per gram of dry sediment.

SEDIMENT TAGGING AND DISPOSAL

The iridium, approximately 22 lbs. (9.9 kg), to be used in the tracing operation was initially purchased in the form of a metal powder and subsequently converted to a soluble iridium salt. The soluble salt was then surface adsorbed to 21,729 lbs. (9.86×10^6 grams) of sediments previously dredged from Mare Island Strait by the Navy and deposited in a landfill site. The resulting concentration of iridium in the tagged sediments was approximately 1.01×10^{-3} gram of iridium per gram of dry sediment.

The chemical and physical properties of the material from the landfill site were investigated and found to be essentially the same as those of sediments taken from dredge hoppers during a previous dredging of Mare Island Strait.

A total of 8,169 gal (30.9 m^3) of tagged material in 5 gal paint cans and 55 gal drums was placed aboard the Corps dredge, CHESTER HARDING, prior to dredging in February 1974. The HARDING is a dual suction dredge having port and starboard variable-depth trailing suction arms and two bottom-dumping hoppers located forward and aft of the mid-ship superstructure.

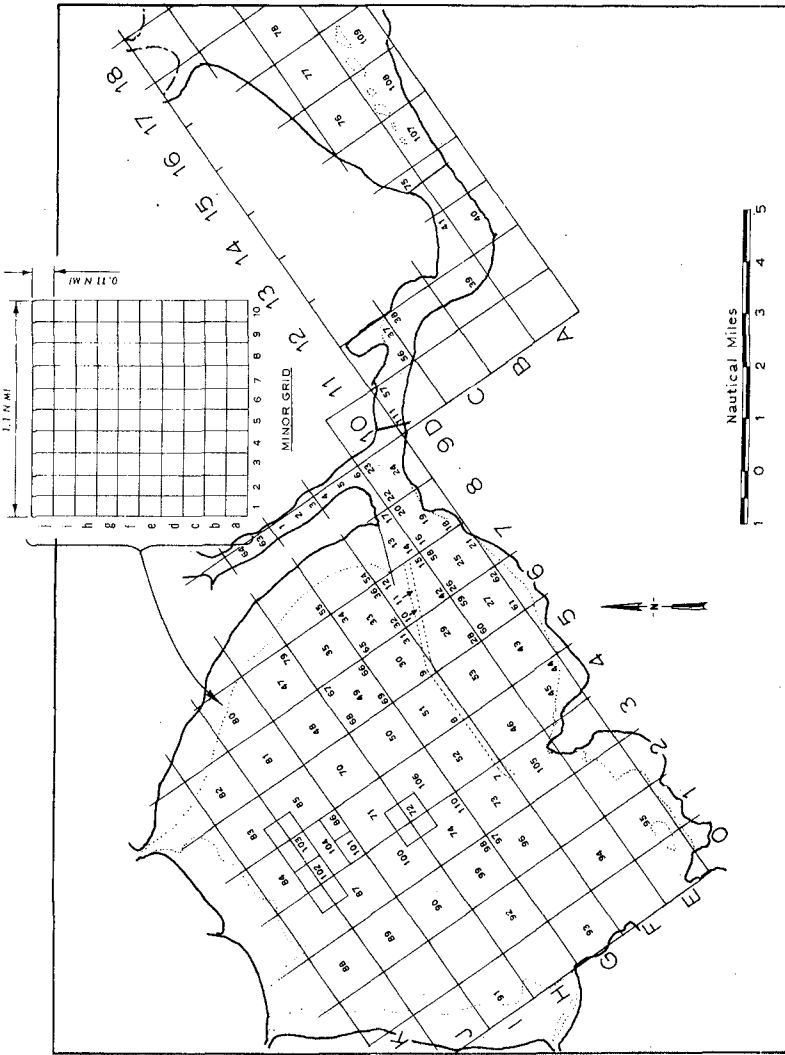
The dredging of Mare Island Strait began on 19 February 1974 and continued until 30 March 1974. Dredging of the Strait was continuous for 12 consecutive days, followed by a 2-day break. A total of 706 trips between the dredging area and the Carquinez disposal area were made during the 35 dredging days. Tagged sediments were introduced into the hoppers on each of these 706 trips. The volume of dredged sediment carried in the dredge hoppers was 2,300 cubic yards per load. A total of 1,624,000 cubic yards of sediment were dredged and disposed of at the Carquinez disposal site during the 35 dredging days. The concentration of iridium in the dredged sediments was 1.95×10^{-8} grams of iridium per gram of dry sediment.

Addition of the tagged sediments to the dredge hoppers was always accomplished after leaving the channel to avoid contamination by hopper overflow. The tagged sediments were added to the dredged material via standpipes located in each hopper.

SEDIMENT SAMPLING

To quantify the deposition and circulation of dredged material, a high percentage of tagged sediment must be accounted for during each of the sampling periods. For this reason, a sampling area encompassing the maximum limits of circulation of the tagged dredged material was desirable. Prior studies indicated that the majority of the dredged sediment released at the Carquinez Strait disposal site during a one-year period will remain in an area encompassed by San Pablo Bay, Carquinez Strait, Mare Island Strait and Suisun Bay.

A grid sampling system was established for the tracer study. Figure 2 shows the grid system established for the study area. The basic grid system consists of grids 1.1 nautical miles square and is oriented 58 degrees East of North. Each basic grid was further subdivided into a minor grid (shown in Figure 2) with 0.11 nautical mile square grids. Samples were taken at the midpoint of each designated grid once per sampling period. A total of 111 sampling locations (shown in Figure 2) were established in the study area. Sampling locations were located in the deep waters of Carquinez Strait; however, due to an inability to penetrate the hard bottom at several locations with the sampling equipment, limited sampling was conducted. This is a good indication that dredged material deposited in the deep channel areas of the Strait probably did not stay there very long. Sampling periods were designated monthly due to the ability of the sampling boat to sample approximately five locations per day. The first sampling period, March 1974, was divided into two periods by sampling approximately 50 locations twice during the month. The remaining sampling periods occurred monthly from April-December 1974 and included sampling of approximately 100 locations per month. In addition to the samples taken at regular intervals in the study area, other sediment samples were taken in an attempt to further define the dredged material circulation. These additional samples were taken from the hoppers of the dredge during the February-March 1974 and October-November 1975 dredging cycles, from selected shoaling areas in Central and South Bays (Figure 3), and from 10 cross sections of the Mare Island Strait shown in Figure 4).



Tracer Program Grid

FIGURE 3

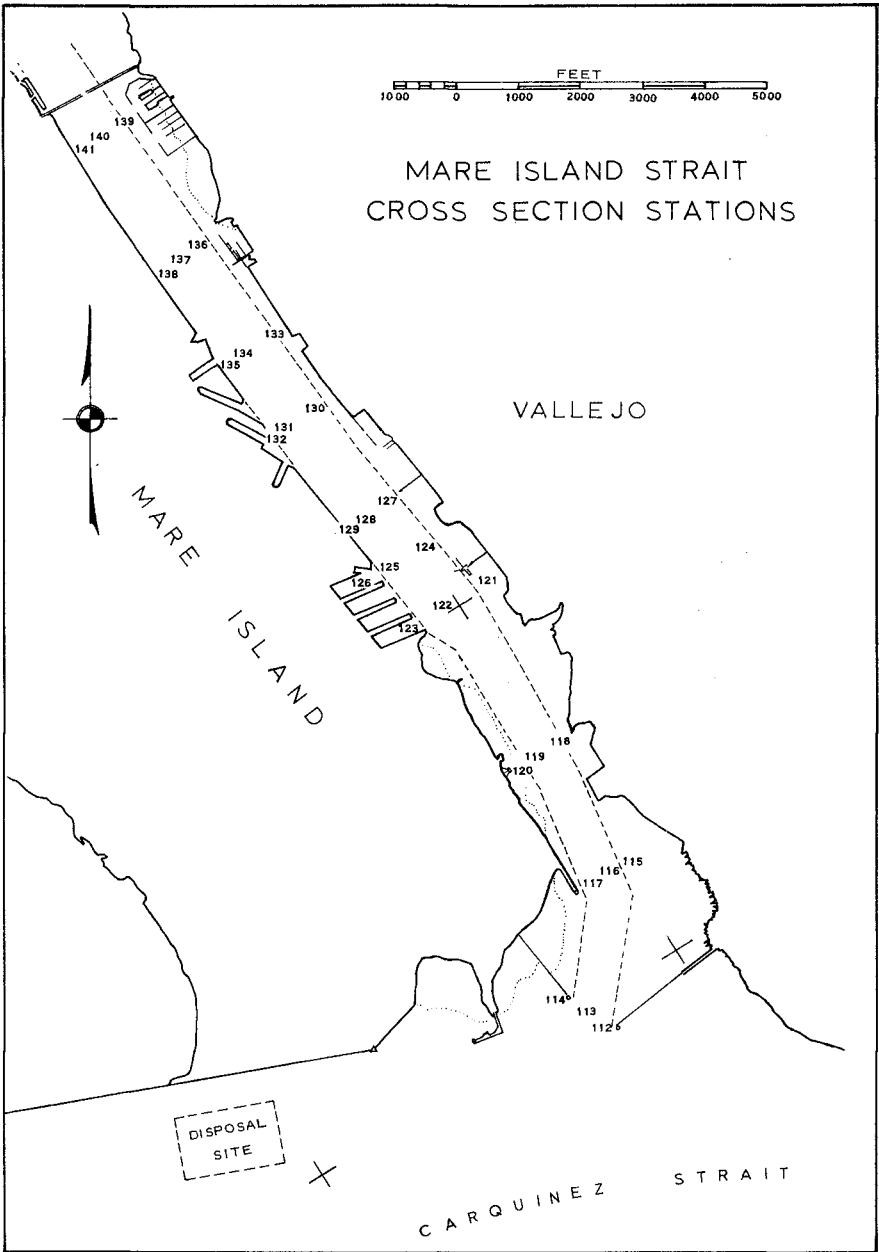


FIGURE 3

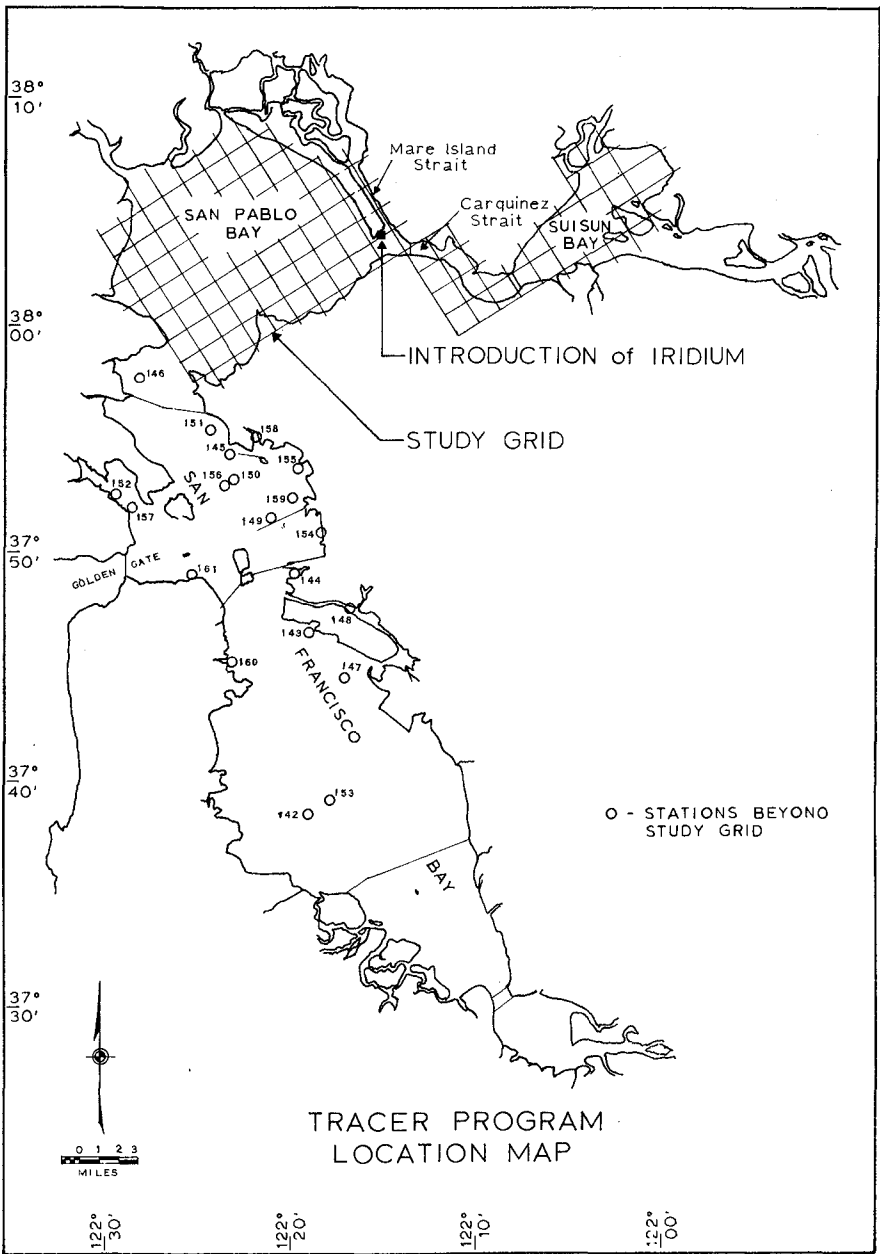


FIGURE 4

The purpose of taking samples along cross sections in Mare Island Strait (Figure 4) was to attempt to determine the extent of movement of dredged material back into the Strait prior to the fall dredging of the Strait from 20 September - 30 October 1974. In late August 1974, 30 core samples were taken along 10 cross sections in the Strait.

The purpose of taking hopper samples was to determine if the dredge was rehandling sediments that were previously dredged and to estimate the return of tagged sediments to the dredged channel. The hopper samples taken during the February-March 1974 dredging were collected on every tenth dredging cycle and prior to the introduction of iridium into the hoppers. The samples were taken by dipping a plastic container into the sediments in the hopper. The samples were subsequently placed in plastic containers. All samples were carefully taken to avoid iridium contamination.

The purpose of sampling shoaling areas in Central and South Bays was to determine if the dredged material disposed in Carquinez Strait contributed significantly to shoaling in these areas. Samples were taken at 20 locations (Figure 3) from September to December 1974.

Horizontal control for the sampling program was provided by three-point sextant triangulation and radar; and, where the water was shallow, sampling locations were marked by stakes. The depth of the top of the samples was referenced to mean lower low water datum by staff gages located at various points in the study area close to the sampling locations.

The sampling program was conducted using a modified World War II landing craft medium (LCM). The cargo deck of the LCM was modified with a well through the deck and hull. A double "A" frame was positioned above the well for raising and lowering of the sampling equipment through the well.

Push-tube vertical core sampling was used for bottom sampling. This method uses a 4-inch pipe casing in which a 2-1/8-inch ID steel push-tube barrel is inserted. The pipe casing was lowered to the bottom from the surface and provided a readily available elevation reference and reentry into the same hole. The push-tube barrel with acrylic liner was then inserted into the pipe casing and pushed into the sediment to obtain a core sample. Core samples up to 30 inches in length could be taken; however, 20-inch samples were normally taken to insure inclusion of the top layer of sediment. Five core samples were normally taken at each sampling location. Each sample was logged and labeled and stored for subsequent processing.

SAMPLE PROCESSING

The daily collection of samples was taken to the Stanford Research Institute facilities at Camp Parks, California, for processing.

The top one inch of sediment from each of the five tubes from a particular location was removed, dried, and the weight of dry sediment recorded. The remaining sediments in one of the five tubes was then selected for further processing, and the sediments were carefully removed in 4-inch increments. Each of these 4-inch increments was also dried and the weight recorded. The remaining four tubes were stored for possible future use.

The five 1-inch increments were combined into one sample and ground and passed through a 20-mesh sieve. These increments were combined to produce a sample large enough to extract a 50-gram aliquot. The 4-inch increments were also ground and passed through the mesh.

A 50-gram aliquot was selected from each incremental layer for determination of iridium content. The iridium content of each aliquot was determined using a fire assay process. Fire assay is a process used in the assay of ores for noble metals. In this process, finely divided ore is mixed with lead oxide, a reducing agent, and fluxing materials. The mixture is heated until it melts, and, upon melting, separates into two liquid phases. The ore stays on top in a slag phase, and the noble metals and a few other elements in the heavy metallic phase go to the bottom. When the mixture cools, the slag and the noble metals are separated and the slag is discarded. The noble metals were then formed into a right cylinder and sealed in an aluminum tube for neutron activation.

The irradiation of the encapsulated metals was performed at the General Atomic TRIGA Mark III reactor at the University of California, Berkeley. After an adequate decay period, the irradiated samples were taken to SRI's Camp Parks facility for gamma ray counting and determination of iridium content.

RESULTS

The large number of samples taken in the study area and processed presented a rather massive problem in data display for analysis purposes. The solution to the data presentation problem was the creation of computer-prepared graphical displays of the percent dredged material data. The graphical displays were produced using the AUTOMAP II computer mapping program developed by the Environmental Systems Research Institute of Redlands, California. The program comprises a computer graphics system written in Fortran IV language, which can produce various types of maps displaying qualitative and quantitative information. The initial work in keypunching the data for use with the AUTOMAP II program and the computer graphics for the study area was accomplished by the Corps of Engineers, Hydrologic Engineering Center in Davis, California.

Graphic displays were produced for each sampling period. However, for the purposes of this paper only certain months will be shown and these will be a composite (weighted average) of samples taken in the first 9 inches of sediment. The displays illustrate the distribution

of percent dredged material over the study area. Table 1 is a legend to go along with the displays, showing the maximum value of percent dredged material, the range of percent dredged material for each map symbol, the frequency of occurrence of percent dredged material for sampled locations, and the percent of the study area covered by the specified map symbols. The graphical displays have been designed such that, upon visual inspection, the darker areas represent greater percentages of dredged material.

April 1974 (Figure 5)

The April sampling period was conducted shortly after cessation of dredging and disposal operations.

As shown in Figure 5, dredged material was dispersed throughout most of San Pablo Bay, Carquinez Strait, Suisun Bay and Mare Island Strait. Localized areas of high percentages of dredged material were found in the northwestern shallows of San Pablo Bay, off Pinole Point and in the southeastern shallows of San Pablo Bay. These areas, representing about eight percent of the total surface areas, had percentages of dredged material ranging from 8 to 40 percent. Twenty-five percent of the total surface area had percentages of dredged material of 4 to 8 percent. These intermediately high areas were found in the southern shallows of San Pablo Bay between Pinole Point and Point San Pablo, the northern shallows of San Pablo Bay, Mare Island Strait, Benicia and Martinez, and the west end of Suisun Bay. Forty-eight percent of the total surface area had percentages of dredged material ranging from 0.5 to 4 percent. About eighteen percent of the total surface areas had percentages of dredged material ranging from 0 to 0.5 percent.

August 1974 (Figure 6)

By the end of August, five months after completion of dredging in Mare Island Strait, very little dredge material was found over the entire 100 square mile study area. The highest percentages of dredge material ranged from 0.5 to 2 percent and was found over approximately fifteen percent of the total surface area. These low percentages were found primarily in the northern shallows of San Pablo Bay, and small areas of Carquinez Strait. Eighty-five percent of the total surface area had percentages of dredge material between 0 and 0.5 percent.

October 1974 (Figure 7)

During the months of September and October the percent dredged material throughout the 100-square-mile area increased. The second dredging cycle in Mare Island Strait took place between 20 September and 30 October 1974. None of the dredge sediment from the second dredging cycle was tagged with the tracer element. All sampling in the month of September was completed before the dredging operations commenced so the increase in dredge material during September cannot be attributed to redredging of sediment that was released in February-March. However,

the increased percentages in October were substantially greater than in September leading one to believe that previously tagged dredged material from the first dredging cycle had found its way back into the Mare Island Strait Channel after disposal at the Carquinez disposal site and was being redredged during the second dredging cycle. However, as the percent dredge material increased in September prior to redredging, the drastic increase in October cannot be solely attributed to the redredging of Mare Island Strait. The increase is a combination of redredging and wind-wave resuspension and deposition of sediments.

Twelve percent of the total surface area during the month of October had percentages of dredged material ranging from 8 to 40 percent. These high percent dredged material areas were found primarily in the eastern southern shallows between Pinole Point and Carquinez Strait and the eastern northern shallows. Isolated areas of higher percentages of dredge material were also found in the natural channel leading to San Pablo Strait and Central Bay and near Martinez in Carquinez Strait. Intermediately high areas, between four and eight percent dredged material, were located around the fringes of the high percentage areas, in the extreme southern end of San Pablo Bay, and along the eastern shore of Suisun Bay. Seventy percent of the total surface area had percentages of dredge material less than two percent. These low percent dredge material areas were found in the northern San Pablo Bay shallows, Carquinez Strait and Suisun Bay.

December 1974 (Figure 8)

By December much of the dredged material that had reappeared in September and October had again disappeared from the top 9 inches. Ninety percent of the total surface area had percentages of dredge material less than two percent. Six percent of the area had percentages of dredged material between two and four percent, and three percent of the area had percentages of dredged material greater than four percent.

TABLE 1
PERCENT OF STUDY AREA WITH PERCENT DREDGED SEDIMENT

Level Number	Symbol	Value Range	Sampling Period											
			April	May	June	July	Aug	Sep	Oct	Nov	Dec			
Low	LLLLL LLLLL	0.0 0.0	0.00	0.00	0.00	0.00	0.00	0.00	0.00	0.00	0.00	0.00	0.00	0.00
1		0.0 0.5	17.78	26.04	59.79	62.89	85.57	71.13	50.51	79.38	70.71			
2	0.5 2.0	28.89	43.75	27.84	27.84	14.43	22.68	19.19	15.46	20.20			
3	2.0 4.0	18.89	19.79	8.25	6.19	0.00	1.03	8.08	3.09	6.06			
4	+++++ +++++	4.0 6.0	20.00	5.21	3.09	1.03	0.00	2.06	3.03	1.03	1.01			
5	/////	6.0 8.0	5.56	2.08	1.03	0.00	0.00	0.00	7.07	0.00	2.02			
6	00000 00000	8.0 10.0	2.22	1.04	0.00	0.00	0.00	0.00	3.03	0.00	0.00			
7	00000 00000	10.0 20.0	5.56	2.08	0.00	1.03	0.00	3.09	7.07	1.03	0.00			
8	00000 00000	20.0 40.0	1.11	0.00	0.00	1.03	0.00	0.00	2.02	0.00	0.00			
9	00000 00000	40.0 80.0	0.00	0.00	0.00	0.00	0.00	0.00	0.00	0.00	0.00			
10	00000 00000	80.0 100.0	0.00	0.00	0.00	0.00	0.00	0.00	0.00	0.00	0.00			
High	HHHHH HHHHH	100.0 100.0	0.00	0.00	0.00	0.00	0.00	0.00	0.00	0.00	0.00			
Highest Value			25.46	16.80	7.72	30.49	1.62	14.82	25.18	12.44	6.46			

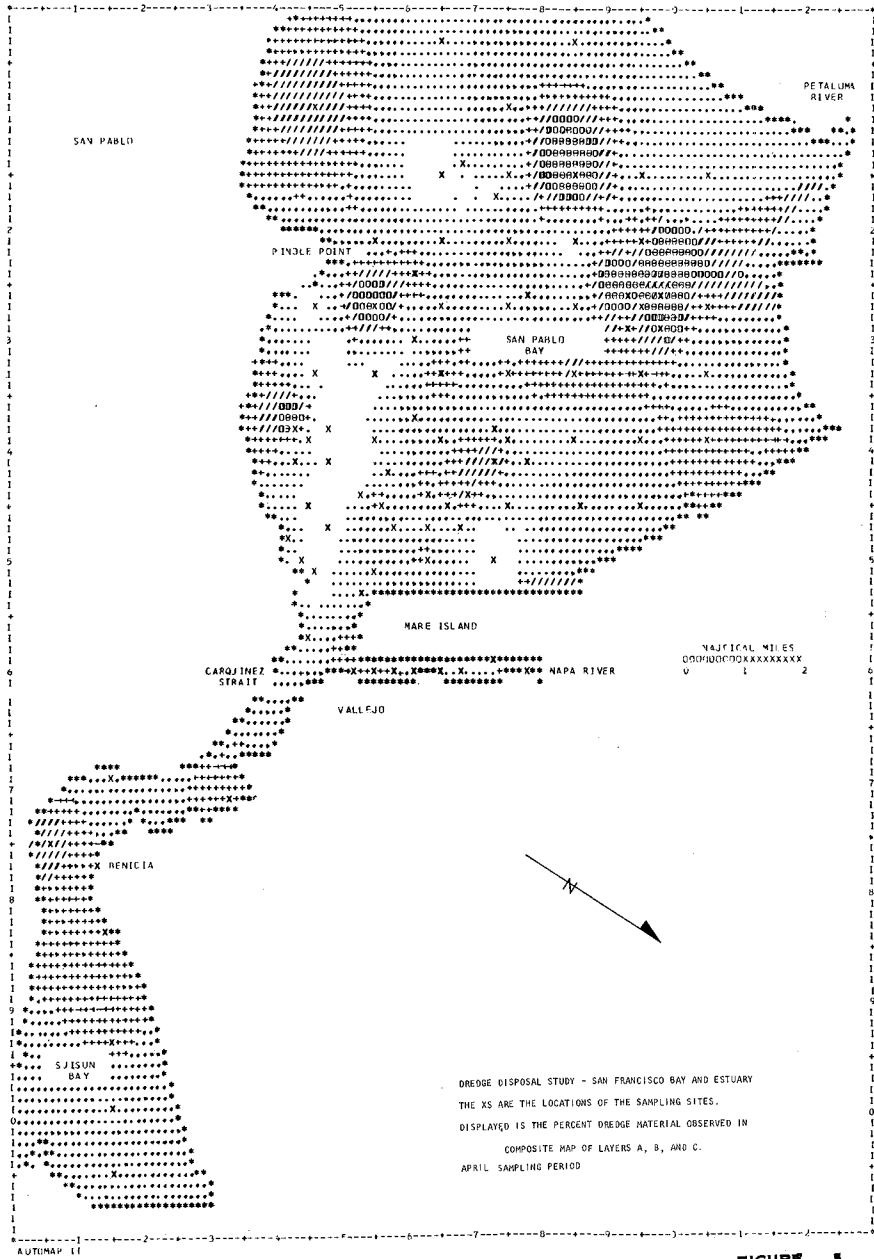


FIGURE 5

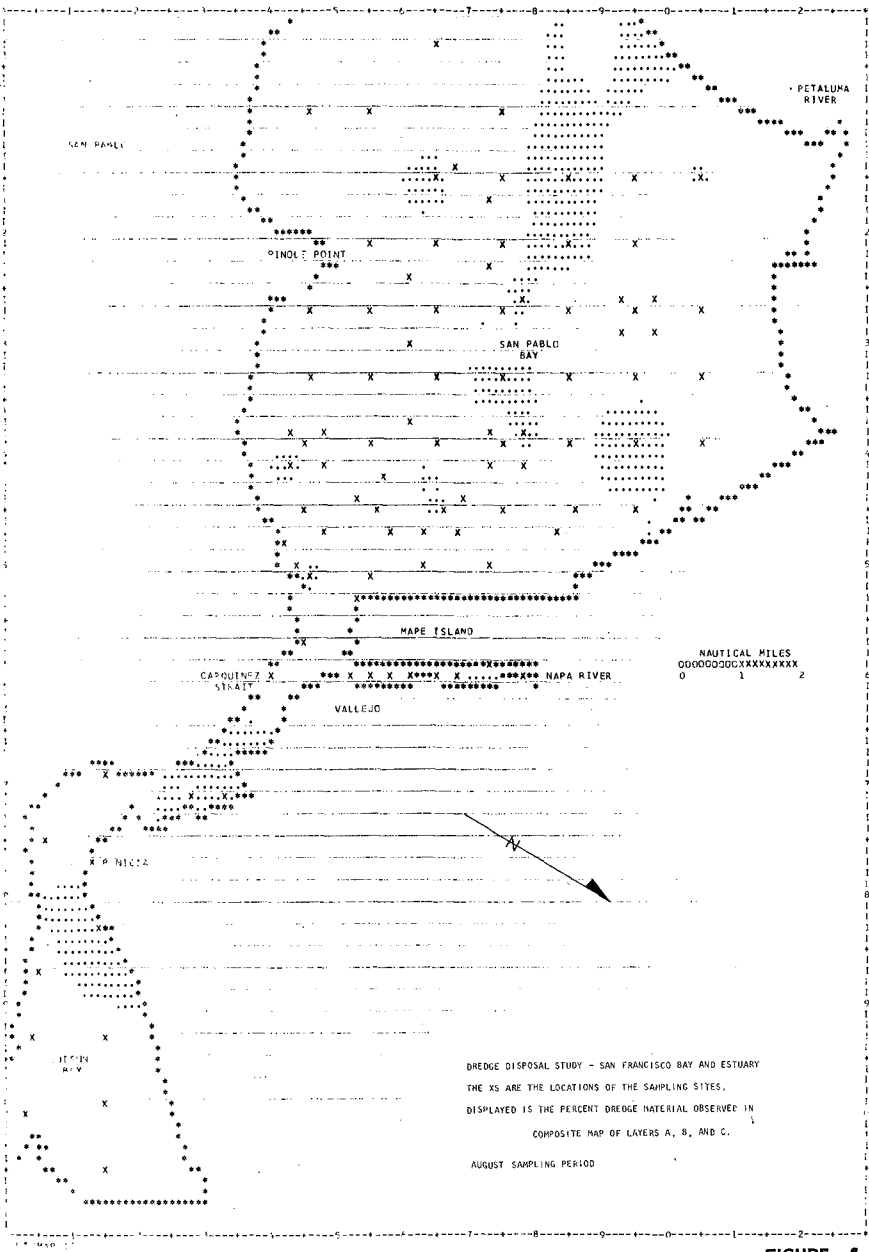
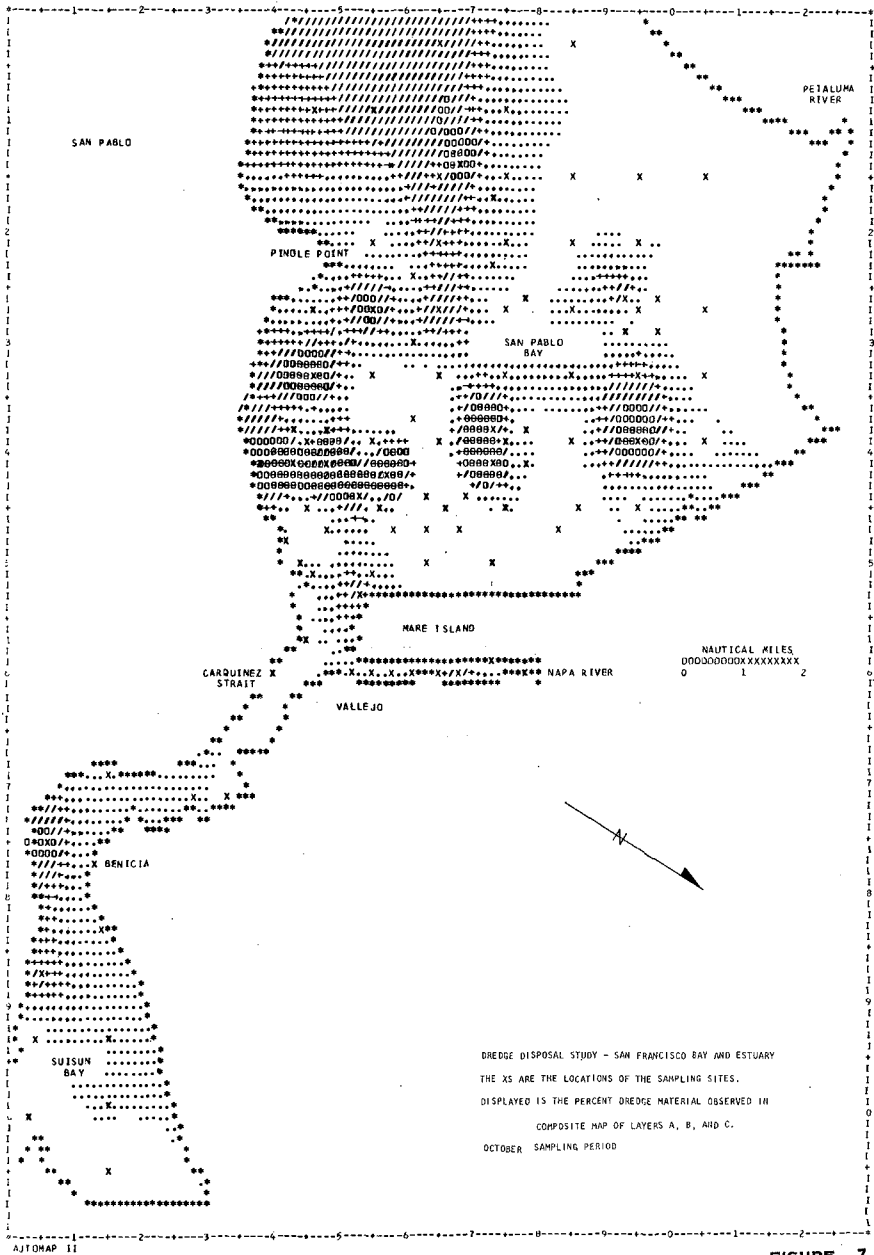


FIGURE 6



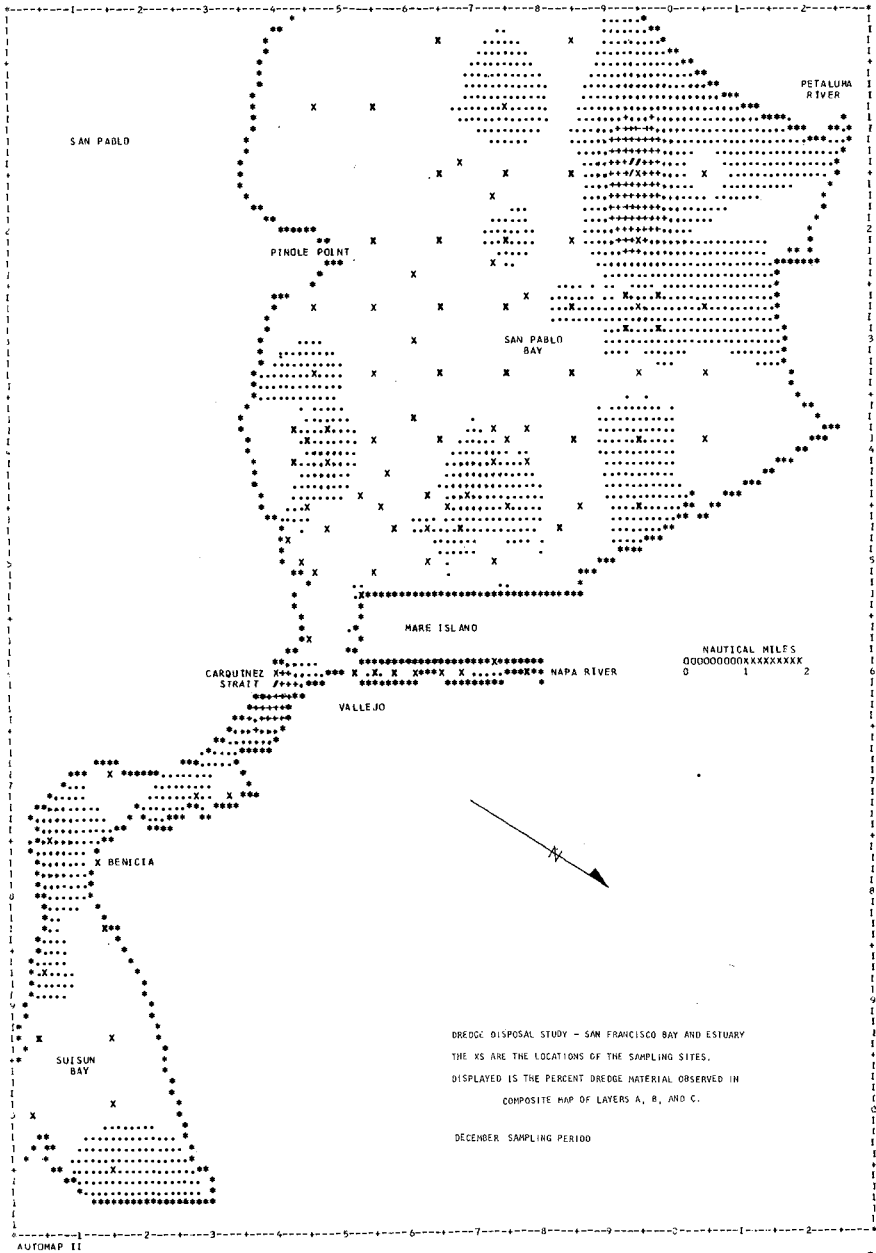


FIGURE 8

CONCLUSIONS

Dispersion of dredged material after disposal at the Carquinez disposal site was very rapid. During the dredging operation dredged sediments make up a large percent of the total sediment in and around the disposal site, including dredged material that had re-entered the dredged channel. After the completion of dredging operations at Mare Island Strait, dredged material was found dispersed in April over a 100-square-mile area including San Pablo Bay, Carquinez Strait and Suisun Bay. Localized areas were found in San Pablo Bay of high percentages of dredged material. By August, five months after completion of dredging, little evidence of dredged material was present in the top 9 inches of sampled sediments over the study area. However, in September tagged dredged material reappeared in the sampled sediments. In October dredged material in the study area increased significantly over that found in September. This increase has been attributed primarily to the estuarine processes which resuspend, circulate, and deposit sediments within the study area. The primary cause of the increase was not attributed to redredging of tagged sediments, although this certainly accounted for some of the increase. By December, two months after the second dredging cycle of Mare Island Strait, most of the dredged material had again disappeared from the top 9 inches of the study area.

The initial movement of dredged material back into Mare Island Strait was estimated to be 10 percent of the total volume dredged, and the long-term movement into the Strait estimated to be no more than 15 percent. These estimates generally agree with those made by other investigators. Limited amounts of tagged sediments were also detected in shoal areas of Central and South Bays indicating that dredged material was leaving the study area and moving seaward. Limited amounts of tagged sediments were also found at depths of approximately 2.5 feet below Bay bottom, indicating that sediments are being mixed either during or after deposition.

ACKNOWLEDGEMENT

The material in this paper is based on observations by the authors during studies by the San Francisco District of the U.S. Army Corps of Engineers of dredged material disposed in San Francisco Bay. Publication of this paper has been approved by the Corps of Engineers but any views, interpretations or conclusions developed are those of the writers only.

CHAPTER 118

SAND MOVEMENT INVESTIGATIONS BY MEANS OF RADIOACTIVE TRACERS IN A HYDRAULIC MODEL AND IN THE FIELD

by

Hans Rohde*)

The Lower and the Outer Elbe constitute the sea-going navigation channel which has the heaviest shipping traffic in the Federal Republic of Germany. In order to obtain and maintain the fairway depth necessary for shipping, river construction works and dredging are applied to an equal extent (5). In order to investigate the practicability of these measures in detail, large hydraulic models of the River Elbe Estuary are available at the Coastal Department of the Federal Institute for Hydraulic Engineering (Außenstelle Küste der Bundesanstalt für Wasserbau) at Hamburg. The problems which result from the displacement of the sands and the fairways, as well as those of sediment transportation, are especially investigated in a model with a moveable bed consisting of granulated polystyrol (5). Details concerning the construction, instrumentation, and questions concerning the scale ratios of this model were given by VOLLMERS during the 13th International Conference on Coastal Engineering 1972 in Vancouver (7). Fig. 1 shows the River Elbe Estuary and the outer boundaries of the model, the length scale of which is 1 : 800 and the depth scale 1 : 100. Fig. 2 shows a view of the model in the direction of the ebb current.

*) Dr.-Ing., Leitender Baudirektor, Bundesanstalt für Wasserbau, Außenstelle Küste, Hamburg, Federal Republic of Germany

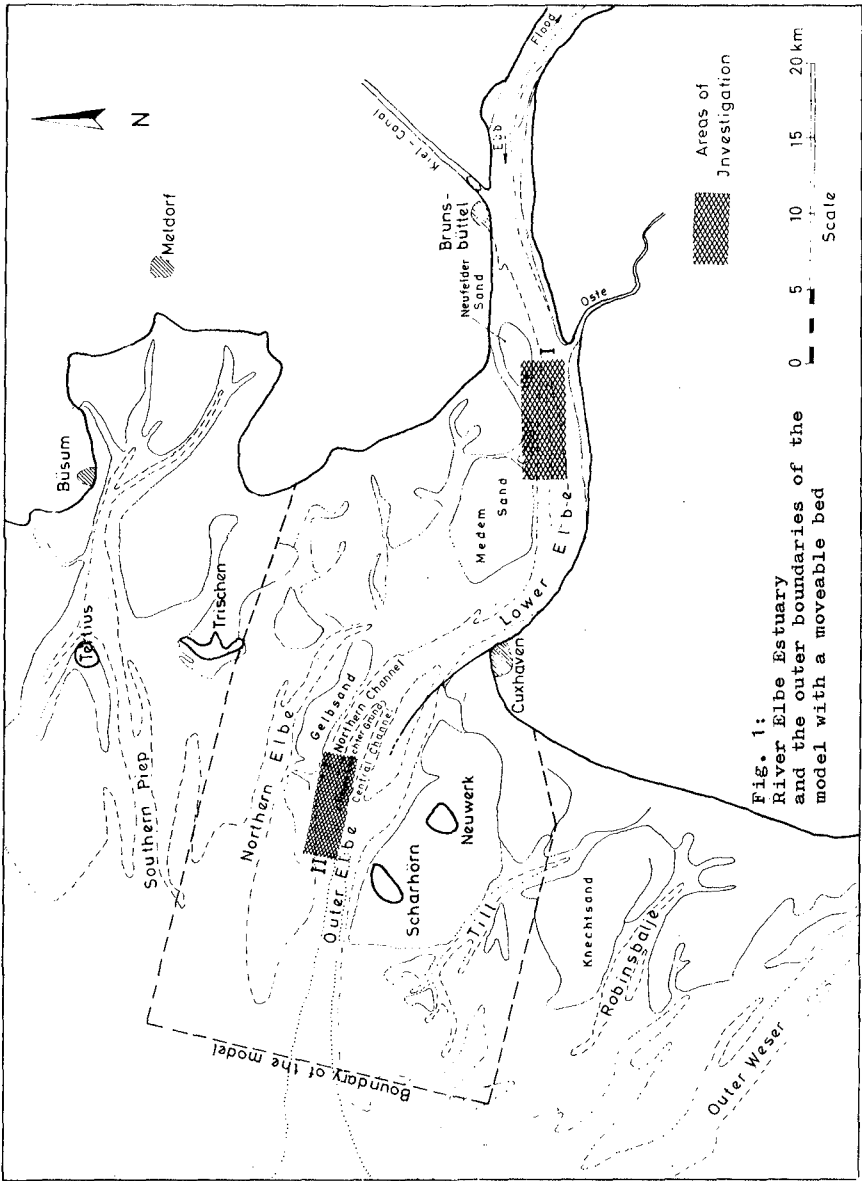


Fig. 1:
River Elbe Estuary
and the outer boundaries of the
model with a moveable bed



Fig. 2: The Elbe model with moveable bed

In 1973 an investigation was first undertaken to measure direct, with the aid of radioactive isotopes, the spreading of the moveable bed material. The aim was to find ideal situations in the River Elbe Estuary where dredged spoil taken from the fairway could be deposited without danger of the material being retransported - owing to the current - to positions where it could again hinder shipping. The hydraulic fill-fields must be accessible to deep-drawing hopper dredgers. In order to investigate the retransportation of the dredger spoil deposited, a small amount of the models bed material was labelled with the isotope Bromine 82 (Br 82 , half-life value 36 hours). From time to time, 25 g with an activity of 10 Mikrocuries (μCi) were placed at different positions in the model, one after the other; and the distribution of the material after a period of 150 tides in each was investigated and then compared with current conditions prevailing at the time. An evaluation for the various dredge spoil hydraulic fill-fields was obtained from that data. Fig. 3 shows the



Fig. 3: Measurement equipment for the investigation of the spreading of radioactive material in the model

the measurement by scintillation counter of the spreading of the radioactive material in the model. The counting equipment hangs on a boom which can be moved transverse to the direction of movement of the mobile measurement bridge which spans the whole of the model. Thereby, every point of the model's surface can be reached by the counting equipment. On the left of the picture, one can see the printer with which the measurement values are registered. VOLLMERS provided details of the model investigations during the 15th IAHR Congress in Istanbul (8).

As yet, the comparison between the isotope measurements in the hydraulic model and corresponding measurements in the field were still not available. For such a comparison two positions were chosen. The position I was situated in the Lower Elbe between Brunsbüttel and Cuxhaven, and II in the Outer Elbe, northeastwards from the Island of Scharhörn (see Fig. 1). This manuscript is intended to provide information concerning those investigations. Nearly 50 similar investigations using radioactive tracers have been carried out in the coastal areas of the North Sea, since 1960, by the Coastal Department of the Federal

Institute for Hydraulic Engineering at Hamburg. The methods of labelling applied thereby, the introduction onto the sea bottom or the river bottom as well as the measurement of the radioactivity and its spreading over the bottom, is comprehensively reported in (1), (3), and (6).

In the case of all hitherto existing investigations, the main point was merely to qualitatively comprehend the sand movements; therefore, to gain evidence about the main direction of movement of the sand. At the present time, there are investigations in operation that will enable quantitative statements to be made in the future; therefore, evidence about the amounts of radioactive materials transported in the various directions. A method for that has been given by MUNDSCHENK (4). For this method, a new, particularly heavy measurement sledge has been constructed by the Coastal Department of the Federal Institute for Hydraulic Engineering. This sledge is illustrated in Figs. 4 and 5. Fig. 4 is a side elevation of the sledge, which - during measurement operations - is dragged over the bed of the waterway behind a tow-boat.



Fig. 4: The new measurement sledge, lateral view



Fig. 5 : The measurement sledge from below

Fig. 5 shows the underside of the sledge, and - at the same time - provides a clear impression of its size. The measuring probe can be seen at the rear end. This measurement sledge has proved itself to be very good. It is extraordinarily stable, and will reriht itself alone if it has tipped over. The distance of the probe from the bottom remains practically always constant, which is of special significance for the comparatability of the measurement values, especially in the case of quantitative investigations. The registration of the measurement values is carried out on board of the towing ship by means of a tape printer. This measurement sledge was also used in the investigations (described in this manuscript) which were carried out in the Lower and the Outer Elbe, although the

spreading of the radioactive sand was to be only qualitatively recorded.

The investigation area I lies westwards of the Neufelder Sand (see Fig. 1). The Medemrinne (Medem Channel), a subsidiary channel of the Lower Elbe, has sufficient depths to be able to be negotiated by deep-draught hopper dredgers. The Channel is separated from the actual navigational channel by a sand ridge. Current measurements gave a rather larger flood stream velocity when compared with that of the ebb stream velocity: on the other hand, the ebb stream duration was larger than that of the flood stream. Fig. 6 shows the tidal curve and the graph of the current velocity at the eastern end of the Medem Channel, as it was measured in the model experiment. On the basis of the current, velocities, nothing can be definitely concluded as to how the sand movements take place. In the model, at the two positions (Point A) at the eastern end of the Medem Channel and 3 km to the East of that (Point B); each time, in succession, 25 g of radioactive bed material was deposited and the spreading was measured after 150 model tides. In Fig. 7, the areas in which radioactive material could be identified are shown as being darker. From this, it could be seen that there was a clear movement in the direction of the extensive sand plate which lies in the direction of the flood - the Neufelder Sand. A sand transportation in the navigational channel was not observed.

In spring 1973, in the immediate vicinity of the model deposition Point A, an amount of 10 kg of sand was introduced on the river bed in the field. This sand was labelled with 3 Curie Scandium 46 (Sc 46, half-life value 84 days). The stratification of the isotope on the surface of the sand grains direct took place by a chemical method (2) without preliminary preparation of the sand with waterglass (Na_2SiO_3). The spreading of the material was measured by

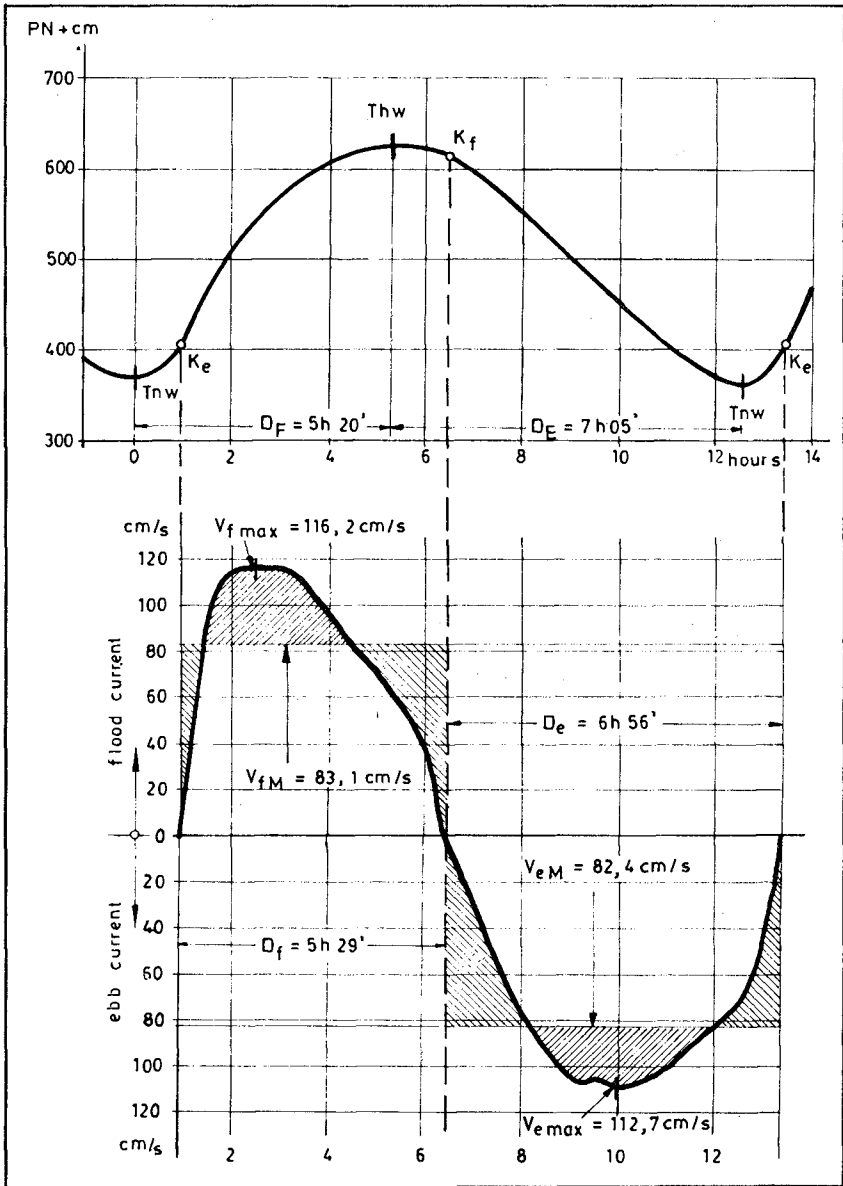
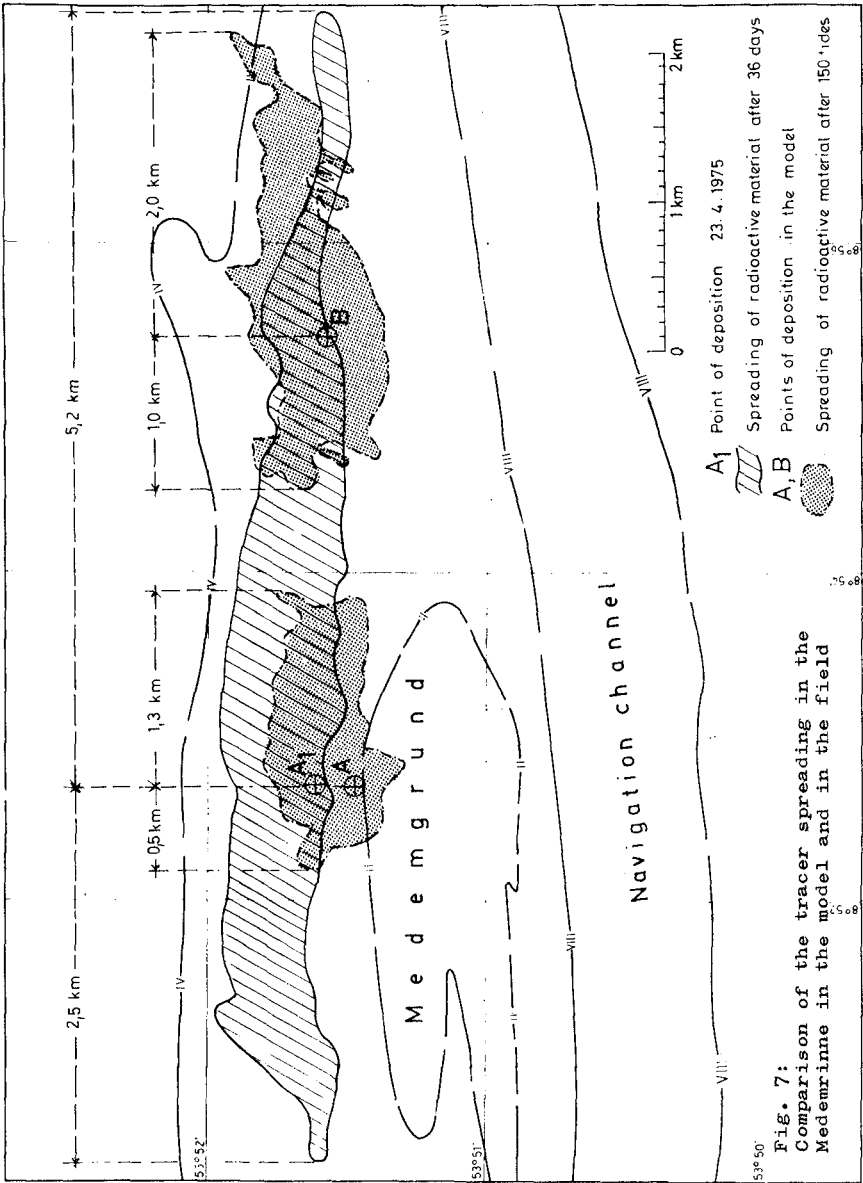


Fig. 6: Tidal curve and graph of the current velocity in the dumping area of the Medemrinne (Model measurements)



means of a scintillation counter. The counting equipment was built into the heavy measurement sledge (shown in Figs. 4 and 5) which was towed by the ship over the bottom. Furthermore, for control and for precise demarcation of the area in which radioactive sand was detectable, extensive bottom samples were taken and were γ -spectrometrically investigated by means of a multi-channel analyzer. The area in which radioactive sand in the field could be detected within 36 days is shown cross-hatched in Fig. 7.

The investigations revealed a good harmony between the spreading direction of the radioactive tracer in the model and in the field. Not only in the field, but also in the model, a predominating transportation in the direction of the flood stream took place in the direction of the Neufelder Sand. No radioactive material was found in the navigational channel. During the whole of the investigation period of 36 days, the activity in the close proximity of the introduction point remained the highest. In comparison, considerable differences in the spreading period in the model and of that in the field could be recognized. To begin with, if one considers the introduction points A and A1: in the model the largest spreading in the flood stream direction measured after 150 tides was 1.3 km; in the ebb stream direction only 0.5 km. The spreading stretch, therefore, was 2.6 times larger in the flood stream direction than that in the ebb stream direction. In the field experiment, the introduction point lay 250 m more northwards. Already, after 36 days or 72 tides, radioactive material was found at a distance of 5.2 km in the flood stream direction and 2.5 km in the ebb stream direction. Therefore, the spreading in the flood stream direction was 2.1 times greater than that in the ebb stream direction.

The model introduction point B was at the eastern end of the spreading area detected in the field. The material deposited here, therefore, spread out in the flood stream

direction double so far as in the ebb stream direction (2.0 km and 1.0 km). The spreading direction was also in good conformity with that established in the field experiment.

Fig. 8 shows the radioactivity as measured in the field (after 3 and 4 weeks) in the longitudinal reach of the spreading. The points are the measurement values calculated on the day of the introduction. The dashed line evens out these values and provides a picture of the distribution of the radioactivity. The logarithmical scale, which is based upon this illustration, is shown on the left of Fig. 8, the dimension is Nanocurie (nCi). The staged curve shows the distribution of the radioactivity in the model experiment, the scale is given on the right of the figure, the dimension is Impulses per Minute. Nanocurie and Impulses per Minute are not to be compared direct, it is intended only to present the form of both distribution curves vis-à-vis to one another in Fig. 8. One can quite clearly recognise that, in both cases, the rise on the left (that is, to the West of the introduction point) is very steep. The maximum is somewhat displaced towards the right. The main body of the radioactive bed material, in the model experiment, had obviously shifted intensely towards the right (East), and a second maximum had built itself up. The more intense shift towards the East, in the direction of the flood current, was also produced by the distribution curve in the field.

The comparison of the experiments revealed that the spreading took place in the field substantially quicker than in the model experiment. The relationship between the extents of the spreading in both the ebb and flood stream directions, indeed, were about the same size both in the model and in the field. However, it was positive that in about half the number of tides in the field the distance from the introduction point in which radioactive

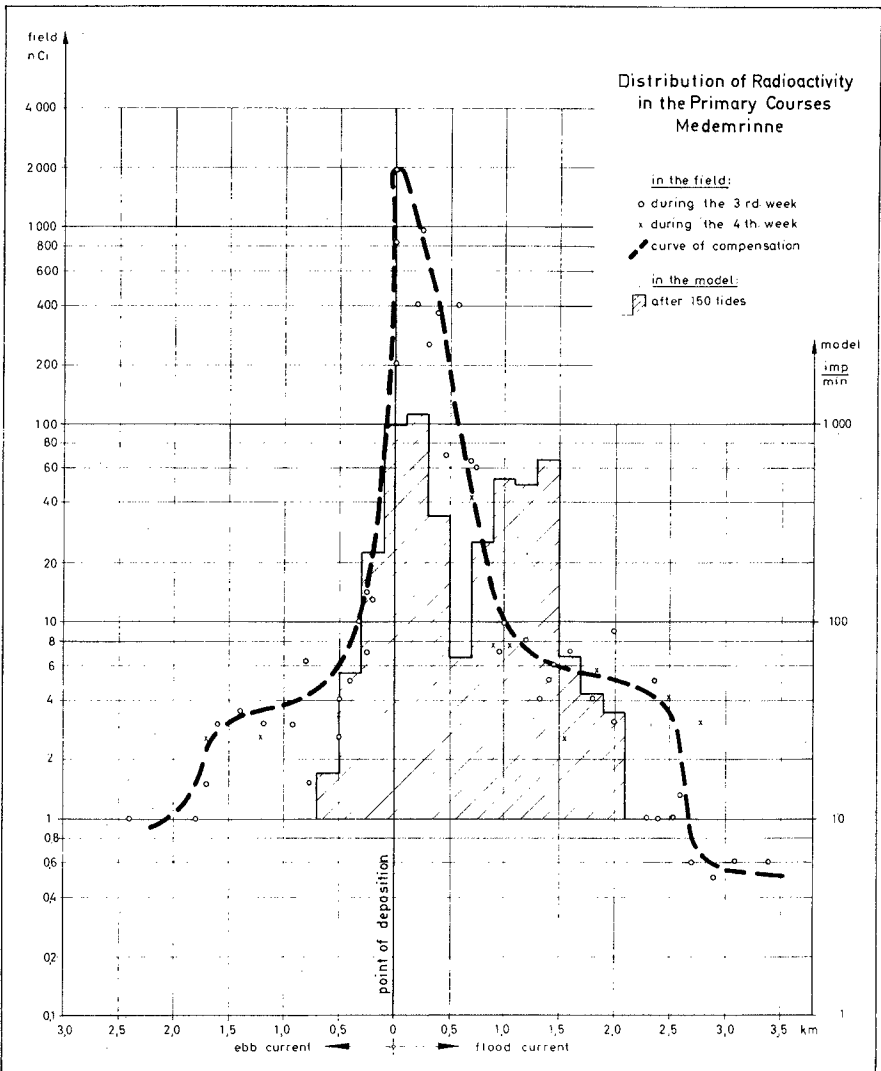


Fig. 8: Spreading of the tracer in the Medemrinne in the model and in the field (Distribution of the radioactivity in the main spreading direction)

material could still be detected was four times greater in the flood stream direction and five times greater in the ebb stream direction, than those in the model experiment. Thereby, one must still bear in mind that, in the so-called morphological Model Time Scale, a model tide represents a larger span of time than a tide in the field. These great differences in the spreading velocity are to be traced back, primarily, to differences between the transportation behaviour of the model bed material and that of the natural sand in the field. The model bed material is transported predominantly as bedload; on the other hand, a larger part of the sand in the field - in suspension. In particular, the radioactive amounts of sand furthest away from the introduction points and which were found only at individual positions, would seem to have reached their deposition location in suspension. Only in a part of the stretch where the sand could be detected as enclosed strips, could the radioactive sand have been transported as bedload, during the relatively short period of observation.

A further investigation in the Outer Elbe was carried out in autumn 1975. The investigation area II lay at the westerly end of the Norderrinne (Northern Channel) which is separated by the Neuen Leuchter Grund from the Mittelrinne (Central Channel) which serves as the main navigational channel (see Fig. 1). Thereby, the deposition point was situated in the vicinity of the introduction point 1 (which is described in (8)) in the model with a moveable bed. In this investigation, the isotope Chromium 51 (Cr 51, half-life value 28 days) was used, and the enrichment was made after previous preparation of the sand with water-glass (1). 100 kg of sand with an activity of 20 Curie was used. Chromium 51 is not so ideally suited for investigations of this type as is Scandium 46, because Chromium 51 has a shorter half-life value and a less energy-rich γ -radiation. As Fig. 9 shows, the ebb stream velocity predominated quite obviously in the vicinity of the introduction

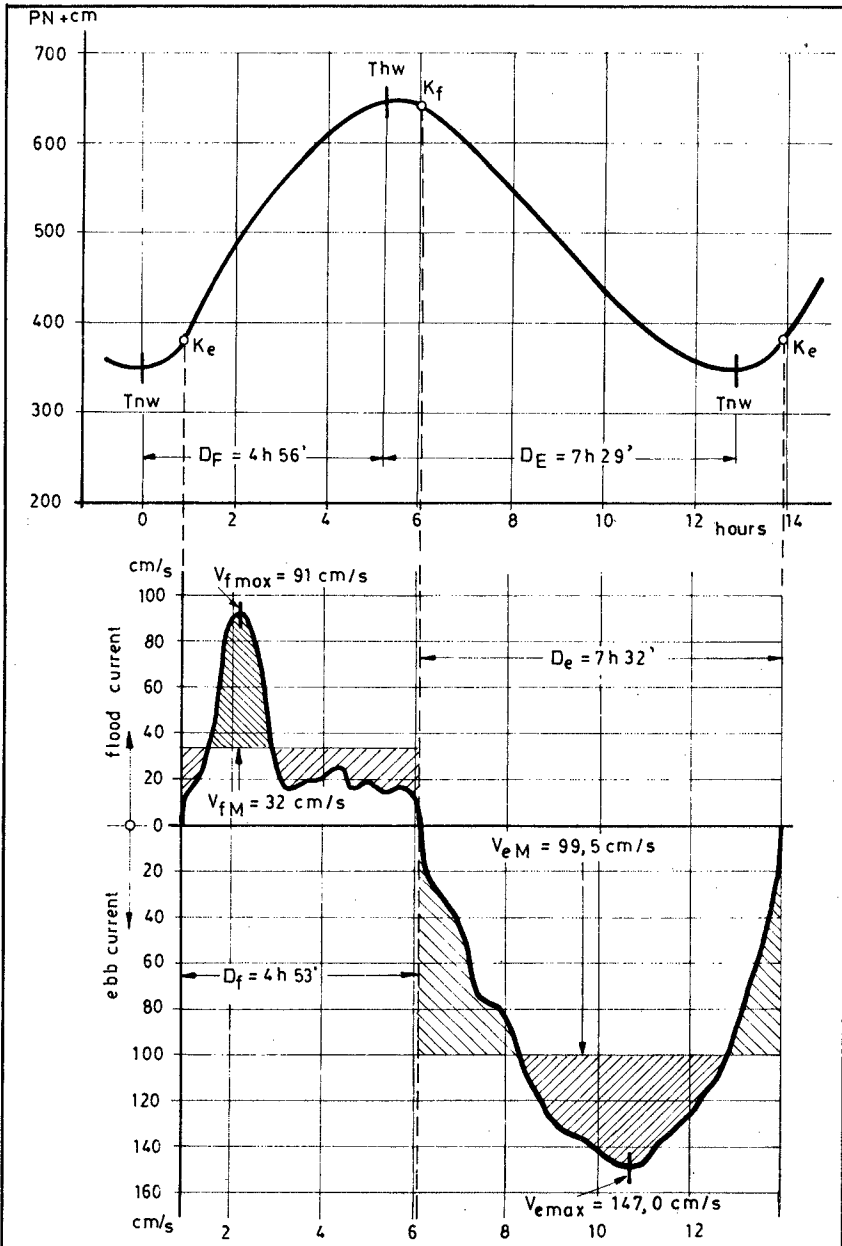


Fig. 9: Tidal curve and graph of the current velocity in the dumping area of the Northern Channel (Model measurements)

point. Correspondingly, a predominant transportation of the sand in the direction of the ebb stream was also to be expected. The spreading of the radioactive bed material, which was measured after 150 model tides, is illustrated in Fig. 10 as dark area. The area where radioactive sand could be detected already five days or ten tides after the introduction in the field, is shown as cross-hatching. Here, also the transportation directions show good harmony, practically no transportation occurred in the flood stream direction. It is particularly interesting that, three weeks after the introduction, a limited spot with heavily increased radioactivity at the edge of the main navigation channel was to be found at 8 km distance from the introduction point. This position is shown in double-hatching in Fig. 10. Sand deposits build up abundantly at this position. The investigations in the Northern Channel of the Outer Elbe confirm the results which were obtained during the investigations in the Medem Channel. Here, also, the spreading in the field occurred very much more quickly than in the model experiment, which is to be traced back to transportation in suspension. The radioactive material which was found at 8 km distance away, must have been transported exclusively in suspension.

The investigations have shown that experiments using radioactive tracers in a model with a moveable bed can give valuable indications concerning the sediment transportation to be expected in the field. In particular, it permits the determination of the direction of main movement. In the field, however, larger transportation distances are attained in a shorter time, because, in part, the transportation takes place in suspension. In the model experiments, the deposition of the whole of the amount of the radioactive material introduced could be recorded exactly. To date, that is not yet possible in investigations carried out in the field. As, in the only qualitative field investigations, however, the same main transportation directions resulted

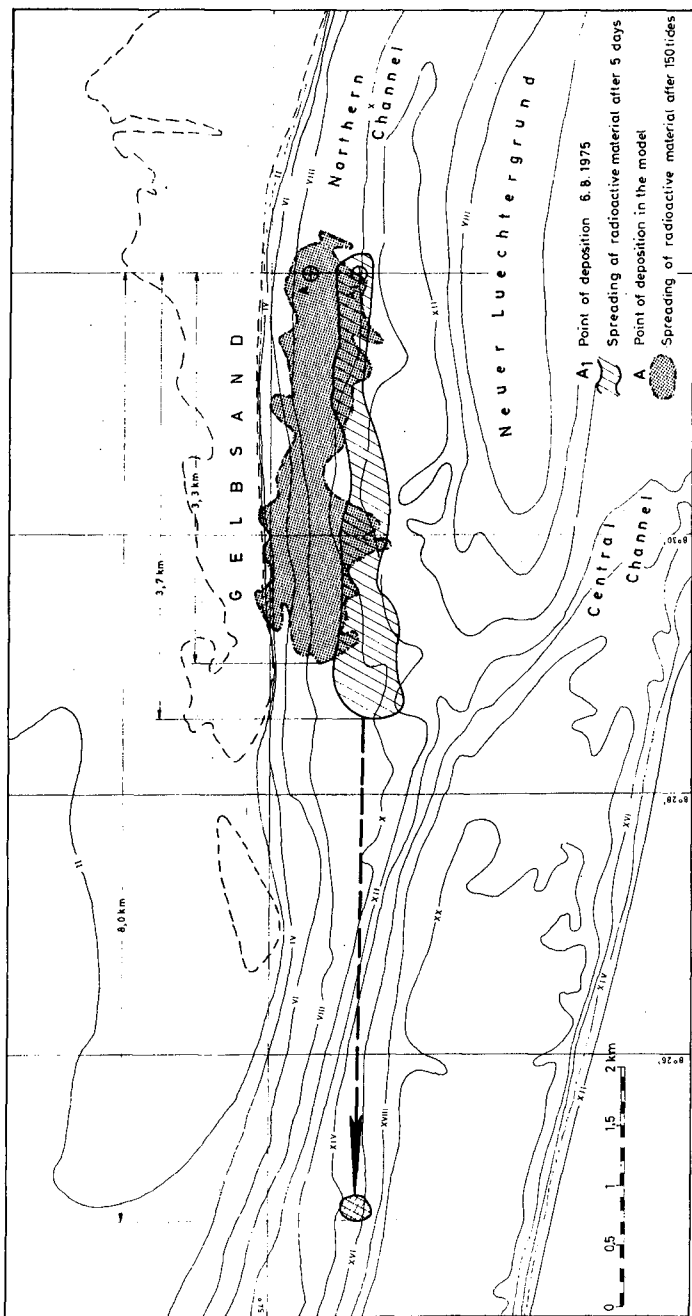


Fig. 10: Comparison of the tracer spreading in the Northern Channel in the model and in the field

as in the model experiment, and as the shape of the distribution curves was also similar, it is to be supposed that thereby an indication is given about the amount transported. In the area in which the higher radioactivity was measured in the field, in spite of the greater possibilities of a mixing and over-enrichment with inactive sands, the heaviest sand transportation is to be expected.

Further comparisons between model experiments and investigations in the field must yet clarify details, especially also the different transportation of the radioactive sand in the field, not only quantitatively but also qualitatively. Such investigations are planned for the future.

References:

- (1) Bundesanstalt für Wasserbau,
Tätigkeitsbericht 1968 - 1969. Teilbericht Außenstelle Küste, Fachgruppe Seebaugrundlagen.
Karlsruhe 1970
- (2) Gütte, H. und Becker, H.,
Verfahren zur Oberflächenmarkierung von natürlichem Sand mit Radionukliden. EURATOM-Bericht 2167.d
1965
- (3) Meyn, G.,
Anwendung radioaktiver Isotope bei der Untersuchung der Sandwanderung. Atomkernenergie Bd. 17, Lfg. 1
1971
- (4) Mundschenk, H.,
Methodische Beiträge zur quantitativen Erfassung von Sedimentbewegungen, Teil II. Deutsche Gewässerkundliche Mitteilungen, Heft 6
1972
- (5) Rohde, H.,
Eine Studie über die Entwicklung der Elbe als Schifffahrtsstraße. Mitteilungen des Franzius-Instituts der TU Hannover, Heft 36
1971

- (6) Schulz, H. und Meyn, G.,
Sandwanderungsuntersuchungen mit radioaktiven Isotopen im deutschen Küstengebiet der Nord- und Ostsee in den Jahren 1961/1962. Deutsche Gewässerkundliche Mitteilungen, Heft 2
1963
- (7) Vollmers, H. und Giese, E.,
Elbe Tidal Model with Movable Bed. Proc. Coastal Engineering, Vol. III, Vancouver
1972 und
Das Tidemodell der Elbe mit beweglicher Sohle.
Die Küste, Heft 24
1973
- (8) Vollmers, H. und Giese, E.,
Measurement of Sediment Transport by Radioactive Tracers in a Tidal Model with Movable Bed.
Proc. XV. IAHR Congress, Vol. I, A. 4, Istanbul
1973

CHAPTER 119

MEASUREMENT OF SUSPENDED SEDIMENT IN THE SURF ZONE

F.A. Kilner *

1. Introduction

The sea is an important source of water for cooling and other industrial purposes. From practical considerations, the water is usually drawn from a zone close to the shore, perhaps within one or two kilometres of the shore line through an intake structure such as a tunnel, pipeline or harbour or some combination of these. If the coast is exposed to strong wave action and the local sea bed is of a sandy nature, sediment will be lifted into suspension by the oscillatory motion induced by the waves, and thus any sea water transported to the shore will contain a sediment load.

This sediment content may have an adverse effect on the operation of the intake structure in various ways. If the water velocity is maintained at a high enough value throughout to avoid deposition, then the sand water mixture will tend to abrade the surface with which it is in contact. If however the water velocity is permitted to fall below the deposition value, sediment accumulation will occur which may be intentional as in a settling basin (requiring regular dredging or other removal) or inadvertent as in a pipe conduit (leading to partial blockage of the pipe).

The writer has been associated with two sea water intake schemes, one on the western coast of South Africa, being a cooling water supply for a nuclear power station with a water consumption of about $100 \text{ m}^3/\text{s}$; the other an intake for the recovery plant of a mining company in Namibia, water capacity about $1 \text{ m}^3/\text{s}$. In both cases, information was needed concerning the variation of sediment concentration with distance above the sea bed, this distribution being measured at selected distances from the shore line. This led to a review of available techniques for determining the sediment content of sea water, and thence to development of new procedures and instruments. The details of these developments are presented in this paper.

2. Laboratory measurements of sediment concentration

There are established methods of measuring sediment concentrations in laboratory channels, either directly by withdrawing a sample of water under conditions of minimum disturbance of the local flow, (with subsequent analysis of the withdrawn sample) or indirectly by measuring the optical, electrical or acoustic properties of a localised water volume, the changes in these properties being related to sediment concentration by calibration.

* Associate Professor, Department of Civil Engineering, University of Cape Town, Rondebosch, South Africa.

For example the electro-optical sediment concentration meter, which senses electrically the loss of light transmission due to the presence of sediments, was first described by Hom-ma and his associates in the period 1962 to 1965 [3, 4 and 5] and subsequently further refined and developed by Kennedy and co-workers in the period 1969 to date, [7, 8, 9 and 15]. In 1969 Hattori [6] introduced a sensor system in which the electrical conductivity of a sediment laden zone enabled the number of grains to be effectively counted. Basinski and Lewandowski [13] introduced a radiation sensor which made use of the principle that the concentration of suspended sediment in water is related to the absorption of gamma radiation. Wenzel [14] described acoustic methods of sediment concentration determination in which either the change in acoustic velocity or the extent of sound absorption could be related to the quantity of solids present.

Such inferential methods for assessing the sediment concentration imply that the instrument is sensitive only to the mass of the sediment in the zone explored. However in most cases it appears that other factors may influence the measurement obtained, for example the size and translucency of the particles and even the speed with which they are moving, thus a series of calibrations may be required.

In uni-directional flow, much attention is paid to the withdrawal of sediment laden water at the rate appropriate to the local flow velocity of the water. However, in wave action, where the velocity vector varies in magnitude and direction, it seems practically impossible to synchronise the rate of water withdrawal with the local velocity. In a laboratory of course, there is at least no difficulty in locating the instrument in the desired sampling position.

3. Field measurement of sediment concentration

There are surprisingly few field measurements of this type, although it is here necessary to distinguish between comparative samplers, such as bamboo tubes which give relative concentrations only [2], and quantitative samplers which give an absolute measurement of sand content in (say) ppm (parts per million by mass). In this latter category Watts [1] made a major contribution by measuring sand concentration at a site on the California coast, using a pump-filter-meter system all components of which appeared to be submersible. His measurements were taken at six stations between 100 and 300 m from the shore line (largely in the surf zone) and sampled mainly within 1 m of the sea bed. These tests identified the concentrations as being of the order hundreds to thousands ppm, and as the sand content was retained in the instrument, size distributions of the sediment could be obtained. The field tests were preceded by laboratory experiments to identify the optimum conditions for water withdrawal which appeared to be a vertical nozzle drawing at a high water speed (about 5 m/s); the resulting quantity of water withdrawn was about 200 litres, over about 5 minutes. The equipment required a

power supply, made use of a convenient pier, and the paper concluded with the comment that "no satisfactory operational procedure has been developed for this sampler which would facilitate the procurement of samples other than from a fixed structure".

Fairchild [10] made use of a similar pier mounted sampler, but modified the system in that only the nozzle was submerged, the pump and receiving tank being tractor mounted to make the system more manoeuvrable. He also used a slightly higher intake velocity, greater than 6 m/s, which could have caused some entrainment with the nozzle positioned at its lowest position of 75 mm from the sea bed.

Hom-ma and Horikawa [3] make reference to an instantaneous horizontal sampler (Fujiki type) as used on tests on the coast of Japan, but give no details of how the sampler operated or was positioned.

Jensen and Sorensen [12] described measurements made in the entrance channel to the port of Karachi in water 11 m deep. They used a steel tripod frame resting on the sea bed, with nozzles attached at various elevations, and water samples were lifted by suction to an anchored surface vessel for subsequent concentration determination. The samples appeared small (2 litres at a time) and as the wave heights were less than 3 m, the zone explored was outside the breaker line.

4. Design criteria

The literature review led to tentative specifications for a versatile sediment sampler for determination of offshore concentrations as follows:-

- a) Indirect sampling methods were rejected for use in the sea on the grounds that organic content and small marine organisms could give spurious information. In addition, the calibration of indirect instruments may be affected by the nature of the sediment as distinct from its mass. Direct sampling implies positive withdrawal of a water sediment mixture.
- b) The water volume sampled should be as large as possible (minimum 100 litres) in order to handle as large a sediment quantity as possible (for example 100 litres of water yields only about 10 g of sediment at 100 ppm concentration). This sampling will take several minutes.
- c) Following from (b) above, the sediment must be extracted and the water rejected (returned to the sea) otherwise the storage capacity required for the instrument would be excessive. This procedure has the added advantage that the sediment load may be examined in detail.

- d) As far as possible, a field test should not involve personnel in or on the sea, otherwise zones of particular interest, such as a breaker line, and occasions of particular interest, such as a period of unusually strong wave action, may in themselves inhibit sampling activity.

5. Pneumatic samplers

From the outset, it was decided to use pneumatic power for any sampler design, based on the ready availability of portable vacuum and compressor equipment.

An elementary form of sampler was used initially, employing commercially available preserving jars, of 2 litre capacity, which are able to withstand a total internal vacuum. When equipped with a modified screw lid, containing a quick release manual valve, it could be used as a hand held sampler, suitable for relatively high concentrations in wading depths. Auxiliary equipment consisted of a portable generator and vacuum pump, which enabled as many bottles as desired to be vacuumised on the beach: when opened under water, a pressure head of about 10 metres is available immediately to fill the bottle, a process which takes about 2 seconds. Although only accurate when concentrations are of the order thousands of ppm, this procedure remains convenient for work close inshore.

For deeper water two compressed air samplers have been designed to fulfill the criteria outlined in paragraph 4, both using conventional 7 litre, 200 atmosphere compressed air cylinders for power supply. Sampler I has been in use for some months, and has proved effective, but requires a helicopter to insert and retrieve it. Sampler II is under development, and attempts to avoid a support vehicle entirely, rather making use of an offshore anchor.

The basic operational component of both these samplers consists of a compressed air cylinder connected to an air motor through a trigger valve. In sampler I this valve is actuated by water inflow into a compartment when the sampler is resting on the sea bed. The air motor has a common shaft with a centrifugal pump which draws sea water through an inlet tube positioned at the desired sampling height above the sea bed. The pump drives the water sample through a water filter and meter and back to the sea. The air cylinder capacity is such that the quantity of water sampled is about 100 litres and takes about 5 minutes to flow through the instrument, although the quantity could be increased easily by using higher pressure cylinders. The complete unit is weighted by a base plate, which also has three radial support arms to permit the sampler to remain stably on the sea bed under wave action. The function of the helicopter is restricted to lifting the prepared sampler off the beach, transporting it to the desired offshore station, lowering it into the water until slack rope indicates the device is on the sea bed, and

then hovering until the sampling is complete, when the sampler is lifted clear of the water and returned to the beach. Once onshore, the empty cylinder is replaced, the water meter reading is taken as a measure of sample size, the nylon mesh filter is removed and replaced, and the process repeated. If desired, the position of the inlet pipe may also be changed. The cycle time for one reading is of the order of 15 minutes, but the strain on the helicopter pilot is considerable, and in practice not more than eight readings have been taken in one day.

Sampler II is designed to avoid the use of the helicopter, which is replaced in effect by an endless rope between the shore line and a heavy offshore anchor, the sampler being attached to the rope and in this way moved into desired station. In this development the sampler is basically buoyant, but when in position an air chamber is flooded by radio signal from the shore, causing the sampler to sink into position and initiate the sample pumping as described above. By means of time switches the air chamber is blown free of water at the end of sampling, the device surfaces and is pulled back to shore again.

The figures and photographs on following pages show the two compressed air samplers in outline and under operating conditions.

6. Conclusion

Subject to the successful operation of sampler II, surf zone sampling may now be accomplished by a shore-based party subject only to the retention of an offshore anchor buoy and sheave to accommodate an endless rope link to the shore. This permits sampling under any conditions of wave action. For isolated samples required from different areas, the helicopter may still be useful for sampler positioning.

Measurements of sediment concentration have been obtained inside and just outside the surf zone under local wave heights up to about 6 metres. Viewed from a helicopter under these conditions, the magnitude of vorticity about a vertical axis occurring naturally appears to outweigh the local vorticity generated by the presence of the instrument, thus it is assumed that the sediment measurement is not being exaggerated by the presence of the device. Further support for this view is not possible, as it is believed that this is the first time sampling has been achieved at all under these wave conditions, and thus comparative measurements are not available. However, very broadly the concentration magnitudes obtained in the present series of tests seem rather low when compared with tests conducted from fixed pier platforms.

7. Acknowledgements

The author is indebted to Mr Neil Heidstra, a postgraduate student, who contributed significantly to the development and field trials of the instruments described in the paper. Generous financial support for this research programme was received from the Electricity Supply Commission of South Africa for which the author expresses appreciation.

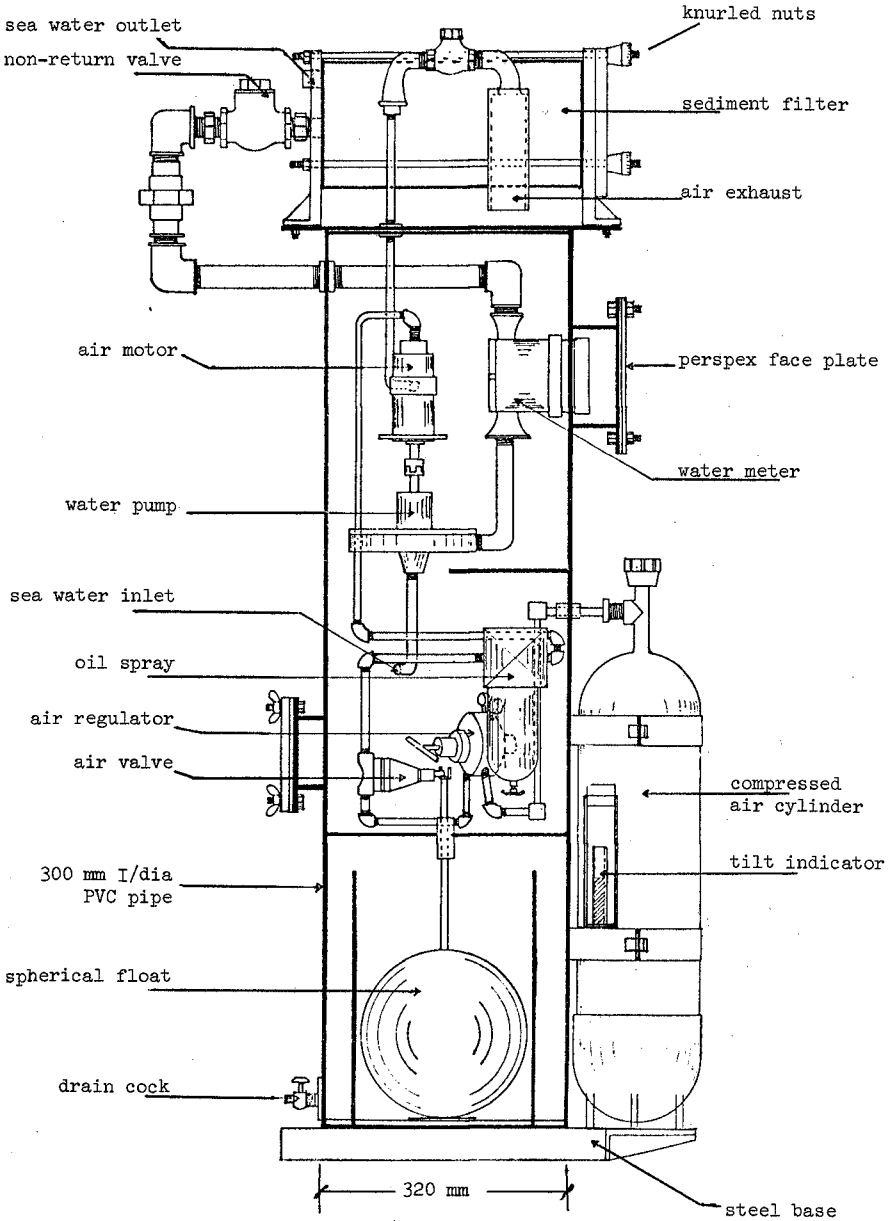
Vacuum sampler system



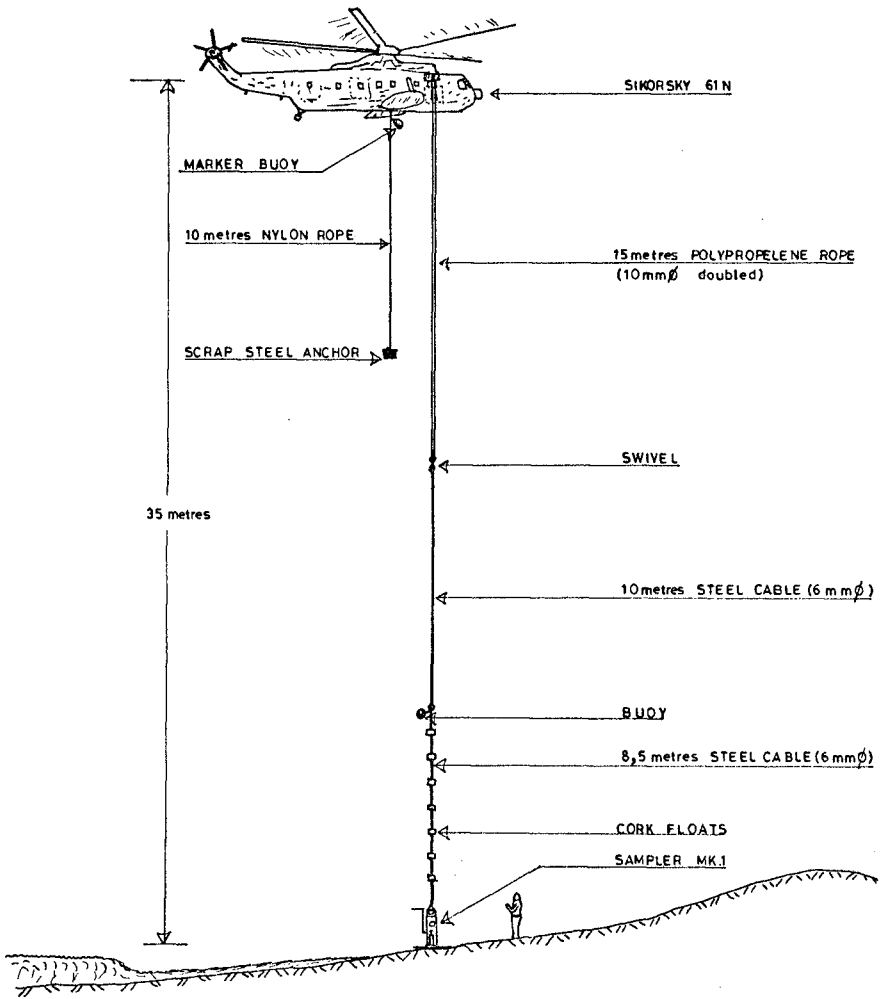
Helicopter sampler (no 1) on beach



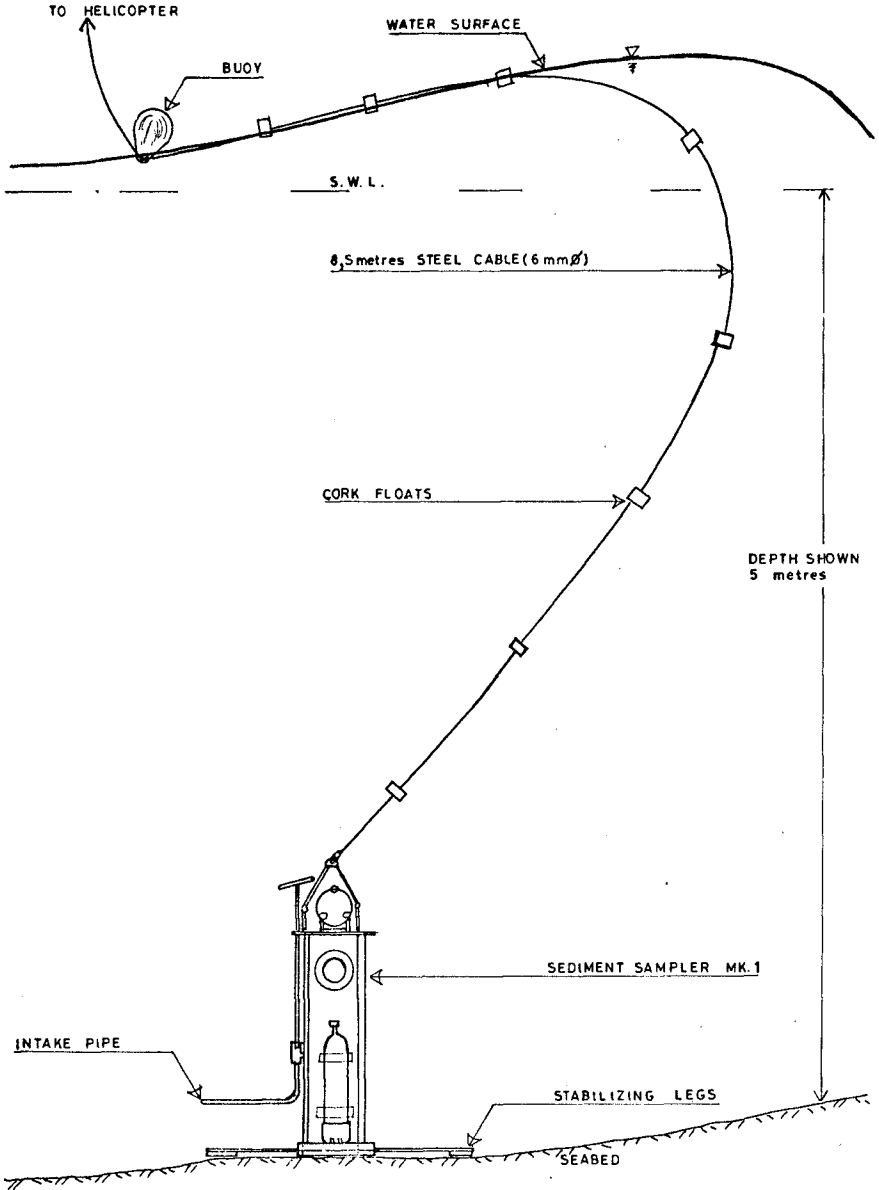
Sampler I
Helicopter supported
Overall height 1,4 m



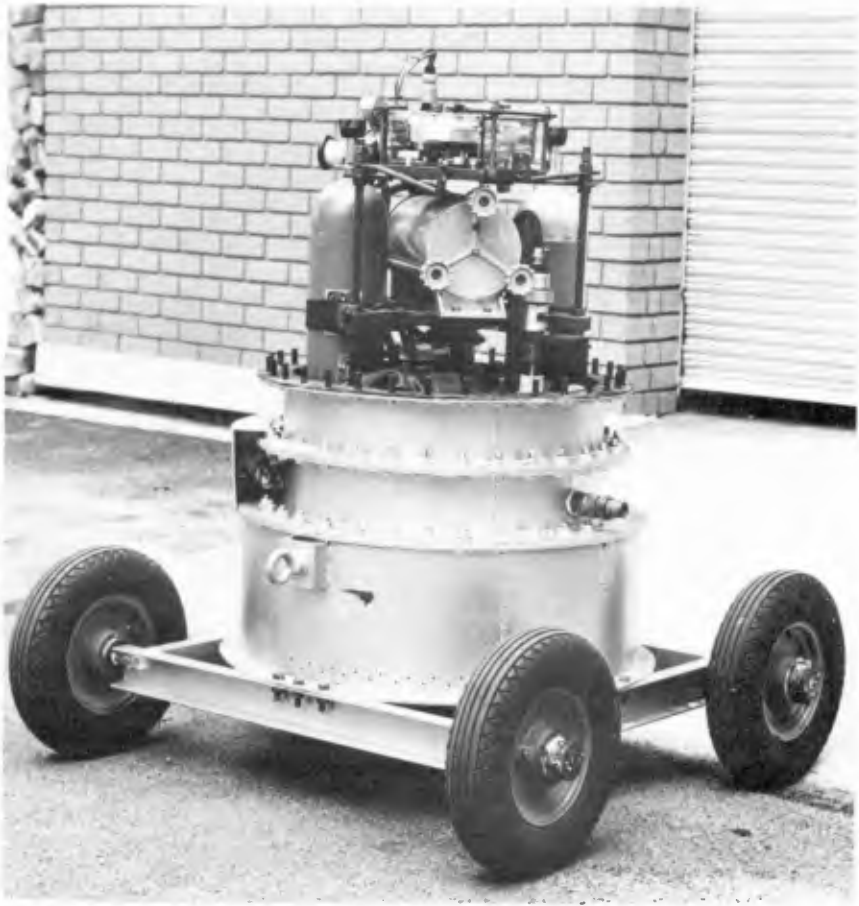
Helicopter sampler (no I)
being prepared on the beach



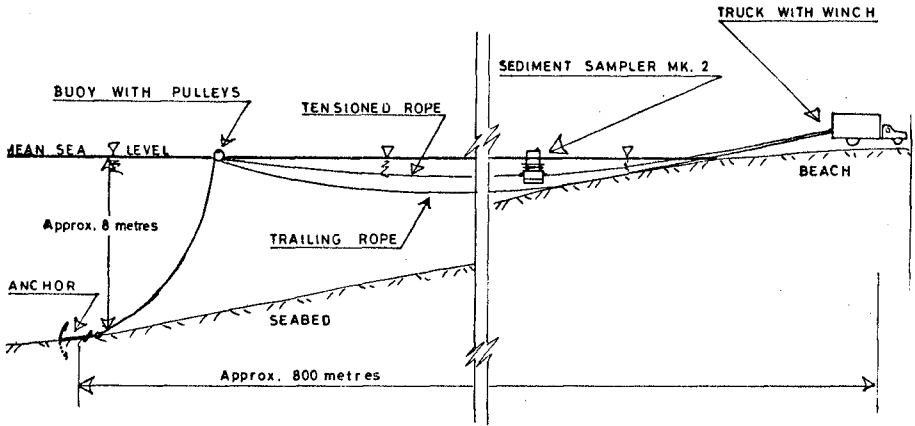
Helicopter sampler (no I)
on sea bed



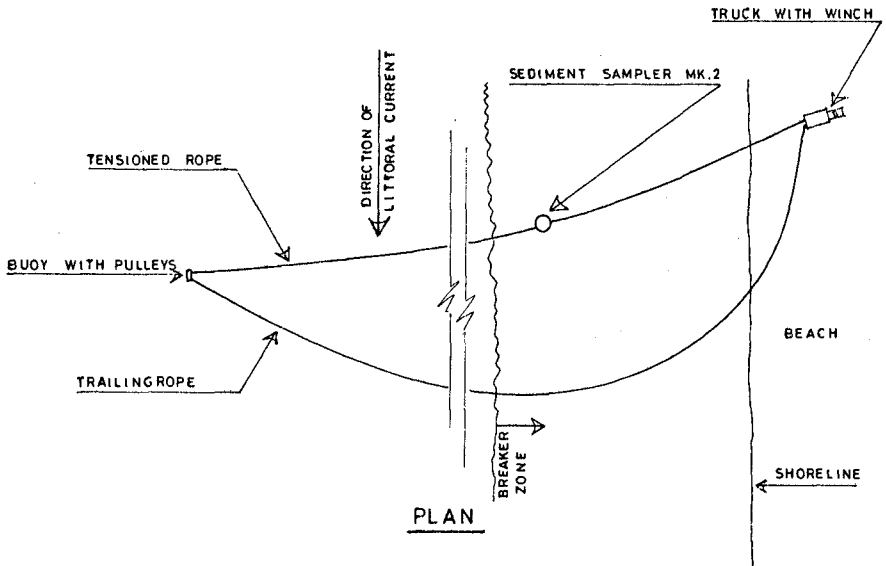
Sediment sampler no II



Operational configuration
for sampler no II

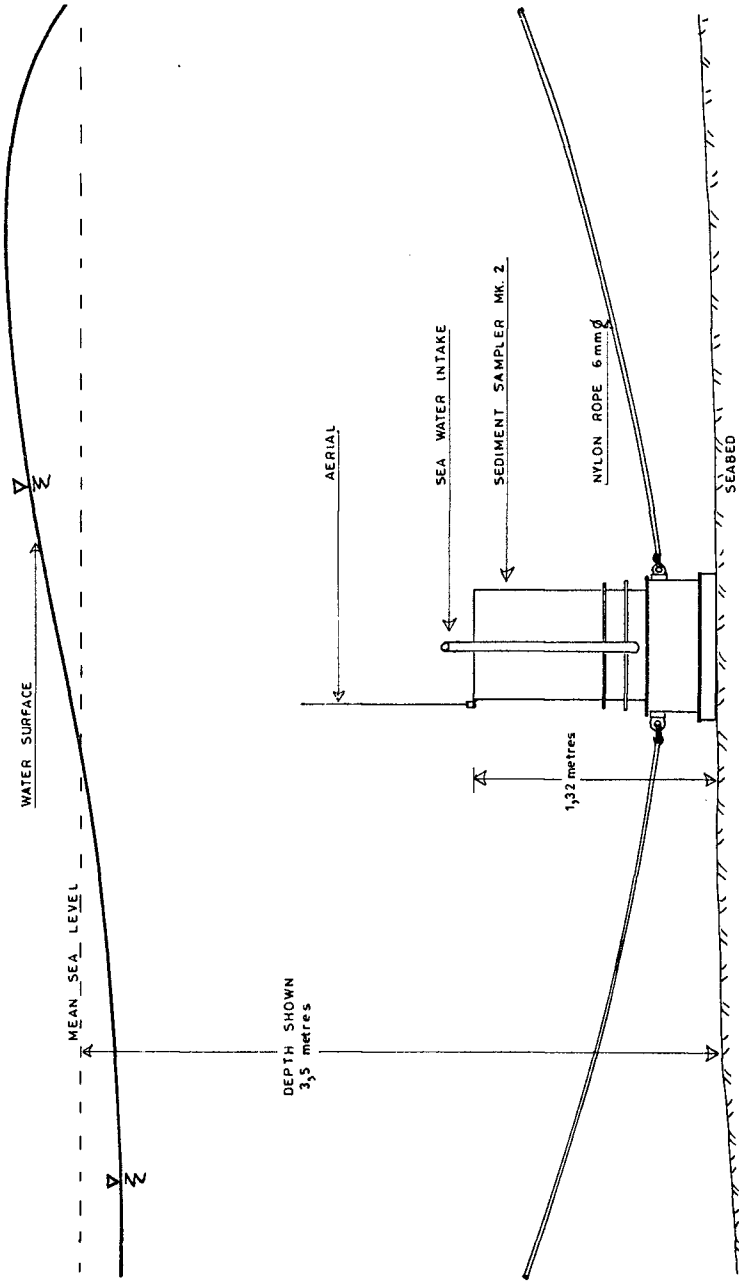


ELEVATION



PLAN

Sediment sampler no II on sea bed



8. References

1. Watts, G.M.,
"Field investigation of suspended sediment in the surf zone".
Proceedings of the 4th Conference on Coastal Engineering,
Chicago, 1953, Chapter 11, pp 181-187.
2. Fukushima, H. and Kashiwamura, M.,
"Field investigation of suspended sediment by the use of
bamboo samplers", Coastal Engineering in Japan, 1959, Vol. 2,
paper 6.
3. Hom-ma, M. and Horikawa, K.,
"Suspended sediment due to wave action", Proceedings of the
8th Conference on Coastal Engineering, Mexico City, 1962.
4. Hom-ma, M. and Horikawa, K.,
"A laboratory study on suspended sediment due to wave action",
Proceedings of the 10th Congress, International Association of
Hydraulic Research, London, 1963.
5. Hom-ma, M., Horikawa, K. and Kajima, R.,
"A study on suspended sediment due to wave action", Coastal
Engineering in Japan, 1965, Vol. 8, paper 7.
6. Hattori, M.,
"The mechanics of suspended sediment due to standing waves",
Coastal Engineering in Japan, 1969, Vol. 12, paper 8.
7. Bhattacharya, P.K., Glover, J.R. and Kennedy, J.F.,
"An electro-optical probe for measurement of suspended
sediment concentration", Proceedings of the 13th Congress,
International Association for Hydraulic Research, Kyoto,
Japan, 1969.
8. Bhattacharya, P.K. and Kennedy, J.F.,
"Sediment suspension in shoaling waves", Proceedings of the
14th Conference IAHR, Paris, 1971.
9. Kennedy, J.F. and Locher, F.A.,
"Sediment suspension by water waves", from "Waves on beaches
and resulting sediment transport", edited by R.E. Meyer,
Academic Press, New York and London, 1972.
10. Fairchild, J.C.,
"Longshore transport of suspended sediment", Proceedings of
the 13th Conference on Coastal Engineering, Vancouver, 1972.

11. Gohren, H. and Laucht, H.,
"Instrument for long-term measurement of suspended matter (silt gauge)", Proceedings of the 13th Conference on Coastal Engineering, Vancouver, 1972.
12. Jensen, J.K. and Sorensen, T.,
"Measurement of sediment suspension in combination of waves and currents", Proceedings of the 13th Conference on Coastal Engineering, Vancouver, 1972.
13. Basinski, T. and Lewandowski, A.,
"Field investigations of suspended sediment", Proceedings of the 14th Conference on Coastal Engineering, Copenhagen, 1974.
14. Wenzel, D.,
"Measuring the sand discharge near the sea-bottom",
Proceedings of the 14th Conference on Coastal Engineering, Copenhagen, 1974.
15. Nakato, T., Glover, J.R., Kennedy, J.F. and Locher, F.A.,
"Characteristics of Iowa sediment concentration measuring system", Proceedings of the 15th Conference on Coastal Engineering, Honolulu, 1976.

CHAPTER 120

IOWA SEDIMENT CONCENTRATION MEASURING SYSTEM

by

Tatsuaki Nakato⁽¹⁾, Frederick A. Locher⁽²⁾,
John R. Glover⁽¹⁾, and John F. Kennedy⁽³⁾,

I. INTRODUCTION

The Iowa Sediment Concentration Measuring System (ISCMS) is an electro-optical instrument developed in 1969 (Glover, Bhattacharya, and Kennedy 1969) for measurement of suspended solid concentrations in unsteady solid-liquid flows. It has been used extensively in laboratory investigations to determine spatial and temporal variations of sediment concentration in a variety of steady, unsteady, uniform, and nonuniform flows (Bhattacharya 1971; Danushkodi 1974). Concurrent measurements of concentration and velocity fluctuations have been used together to obtain estimates of mass transfers in unsteady sediment-laden flows, with the goal of improving the understanding of the underlying mechanisms responsible for sediment entrainment and suspension (Nakato 1974). Interpretation of the data gathered in these experiments pointed out the need for a more thorough understanding of how the optical and electronic components of the ISCMS respond to the passage of individual sediment particles through the optical field of the transducer (Locher *et al.* 1974). An investigation was undertaken to determine the sensitivity of the ISCMS output to the position of a particle in the transducer field; the role of particle velocity in determining the ISCMS output; the effects of particle translucency and size on the output of the system; and the dependency of mean concentration estimates on integration time.

II. THE ISCMS PROBE FIELD

The transducer consists of a 1.55-mm diameter light source (P-N gallium arsenide, type TIL 24) and sensor (NPN planar silicon phototransistor, type TIL 604) separated by a distance of about 3.2 mm with their optical axes co-aligned, as shown in figure 1. Light from the source is attenuated by particles in the probe's optical field and the modulated light signal is transduced to an output voltage by the sensor and electronic circuits. Calculation of the average number of particles present in the transducer field in some wave-induced sediment entrainment studies at The University of Iowa demonstrated that often only one or two particles are present in the field, and highlighted the importance of knowing the effects of particle position and residence time in the space between the source and sensor on the system output.

(1) Research Engineer, Institute of Hydraulic Research, The University of Iowa, Iowa City, Iowa.

(2) Senior Engineer, Bechtel Corporation, San Francisco, California

(3) Director, Institute of Hydraulic Research, The University of Iowa, Iowa City, Iowa

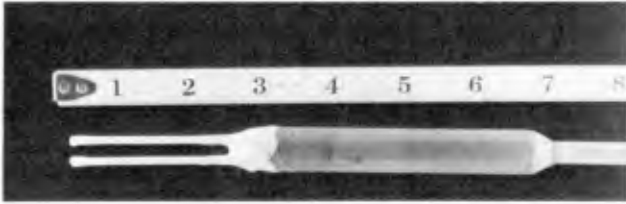


Figure 1. The ISCMS probe.

To investigate the ISCMS sensitivity to particle position, "artificial particles" were made by spattering India ink on a glass slide and then selecting several ink spots with the desired size and shape for detailed investigation. This approach was adopted because there is no means of supporting single glass bead or sand particle within the probe field without introducing additional refraction of the light. The slide with simulated particles was mounted on a microscope traversing mechanism, the ink spots were positioned at various locations along the optical axis of the source-sensor pair, and the corresponding ISCMS outputs were monitored. The results of tests with circular spots with diameters of 0.38, 0.25, and 0.12 mm are summarized in figure 2, in which the system output voltage normalized by the voltage obtained with the particle adjacent to the sensor is plotted versus spot distance from the sensor. It is seen that the ISCMS output voltage initially rises sharply with increasing distance, obtains a peak value at about 1.0 mm from the sensor, and then trails off monotonically until the spot is adjacent to the source where the output is only 50-60 percent as great as when it is adjacent to the sensor. In other words, the ISCMS response is strongly dependent on the position of the particle when traversed on the optical axis within the transducer field.

Tests also were conducted to ascertain the effect of the radial position of a "particle" in the probe field on the system response. These were realized by traversing a spot radially across the probe field in planes that were perpendicular to the optical axes and located at various distances from the sensor. The typical set of results shown in figure 3 depicts the variation in the ISCMS response as the 0.38 mm spot was traversed radially at several sections between the source and sensor. Note that the ISCMS output voltage for each location was normalized with the reading obtained with the particle adjacent to the sensor. These results show that the ISCMS output voltage varies continuously as the particle is moved radially through the optical field. It was found that the diameters of circular cylinders within which the normalized voltage is larger than approximately 0.5 are 0.6 and 1.0 mm for the 0.25 and 0.38 mm particles, respectively. The physical diameter of the source and sensor is 1.55 mm; therefore a substantial portion of the cross-sectional area of the probe field is not highly effective in sensing the particle.

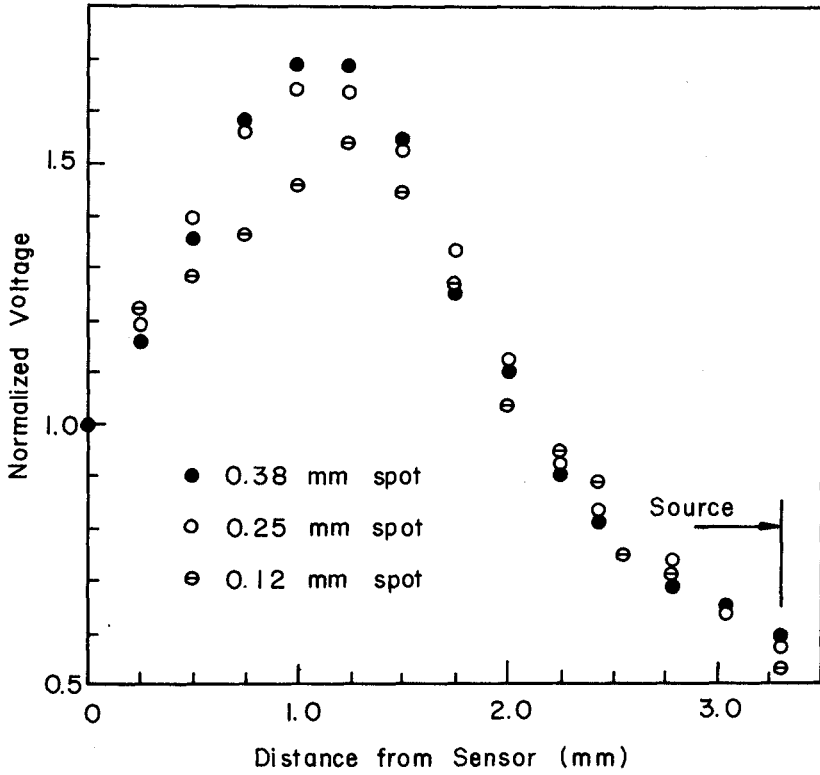


Figure 2. Variation of the ISCMS output for three "artificial particles" traversed along the optical axis of the transducer.

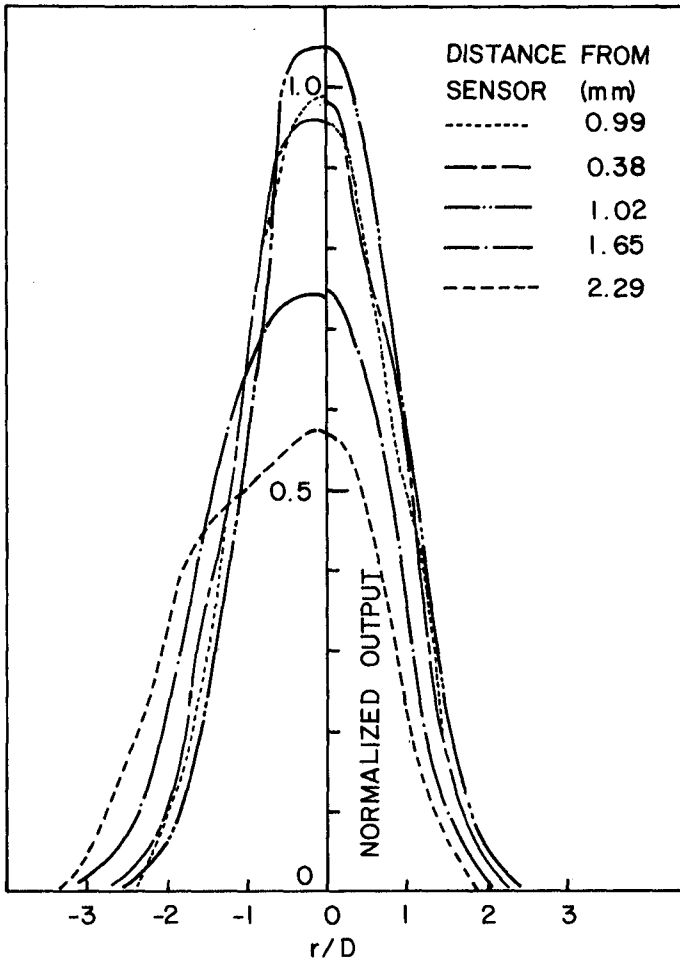


Figure 3. Variation of the ISCMS output along the radial axis of the transducer for the 0.38 mm "artificial particle".

The effects of particle velocity on the ISCMS response were investigated by passing a field of simulated particles through the transducer's sensing volume at different speeds. The "particle field" consisted of 120 0.127-mm diameter drilled holes equally spaced around the periphery of an 8.89-cm diameter circle on a lucite disk. The disk was rotated at various angular speeds about the center of the particle circle, with the simulated particles crossing the optical axis of the source-sensor pair. The rms of the ISCMS output voltage was recorded for several different angular speeds of the disk. The rms output voltages were normalized by the rms voltage obtained at a frequency of 100 particles per second or less; the results from several repetitions are plotted on figure 4. It is seen that there is no attenuation of the amplitude of the ISCMS voltage for frequencies under 100 Hz, but at higher speeds the signal is progressively diminished. This indicates that the upper limit of particle speed for which the instrument is able to measure the concentration corresponding to the passage of an individual particle through the transducer's field is approximately 23 cm/s. However, at a particle speed of 46 cm/s, the normalized rms voltage of the ISCMS output was reduced by only about 8 percent.

III. EVALUATION OF MEAN CONCENTRATION OF SUSPENDED SEDIMENT

To evaluate the effects of particle translucency on the ISCMS output, mean sediment concentrations were measured in suspensions of three different sediments: two quartz sands and crushed walnut shells with median diameters of 0.14, 0.25, and 0.20 mm, respectively. The specific weights of the two materials were 2.65 and 1.33 g/cm³. These tests were conducted in a turbulence jar, in which each sediment was held in suspension in water by means of vertically oscillating grids. During calibrations, samples were withdrawn to obtain reference values of concentration, and the ISCMS output was recorded with the probe at several different elevations. The test results are plotted in figure 5 with $\Delta V/V_0$ presented as a function of $\bar{C}/\gamma D$, where ΔV is the net ISCMS output voltage; V_0 is the output voltage with the light sensor shielded from the source light (approximately 12 volts); \bar{C} is the measured mean concentration in ppm; D is the median diameter of the sediment; and γ is the specific weight of the sediment. It is seen in figure 5 that the calibration curves for the three samples are linear, and the data from the two quartz sands plot almost congruently. However, the slope of the calibration curve for the walnut shells is much larger than that for the quartz sands. This difference was attributed to variations in the opaqueness of the two materials. The walnut shells are less translucent than the quartz sand, and therefore produce stronger attenuation of the transmitted light and larger ISCMS output voltages. During the calibration, photographs of the ISCMS signals for each sample were obtained and their signal characteristics were compared. The results showed that there are far more voltage readings below the zero reference for the quartz sands than for the walnut shells. This effect is the results of light being reflected off the surface of the quartz particles into the sensor as the particle enters or leaves the probe field. The crushed walnut-shell surface does not reflect light as well as the quartz sand, and therefore drops below the reference voltage level were not so prominent. These negative voltages indicate light intensities above the ambient light

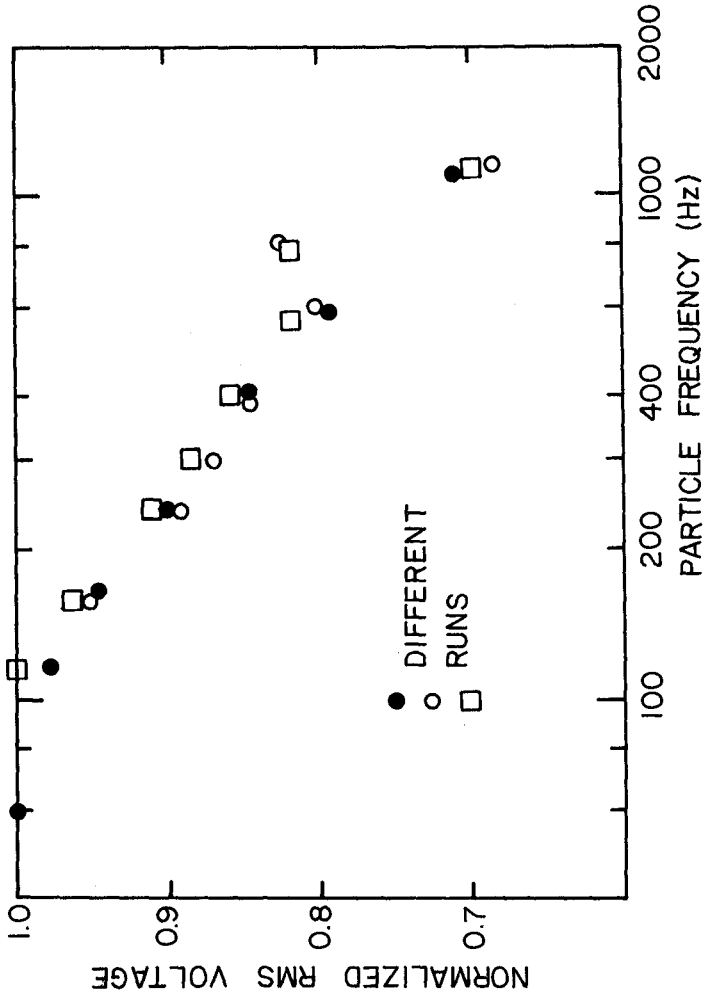


Figure 4. Attenuation of rms voltage as a function of particle frequency (rotating disk test).

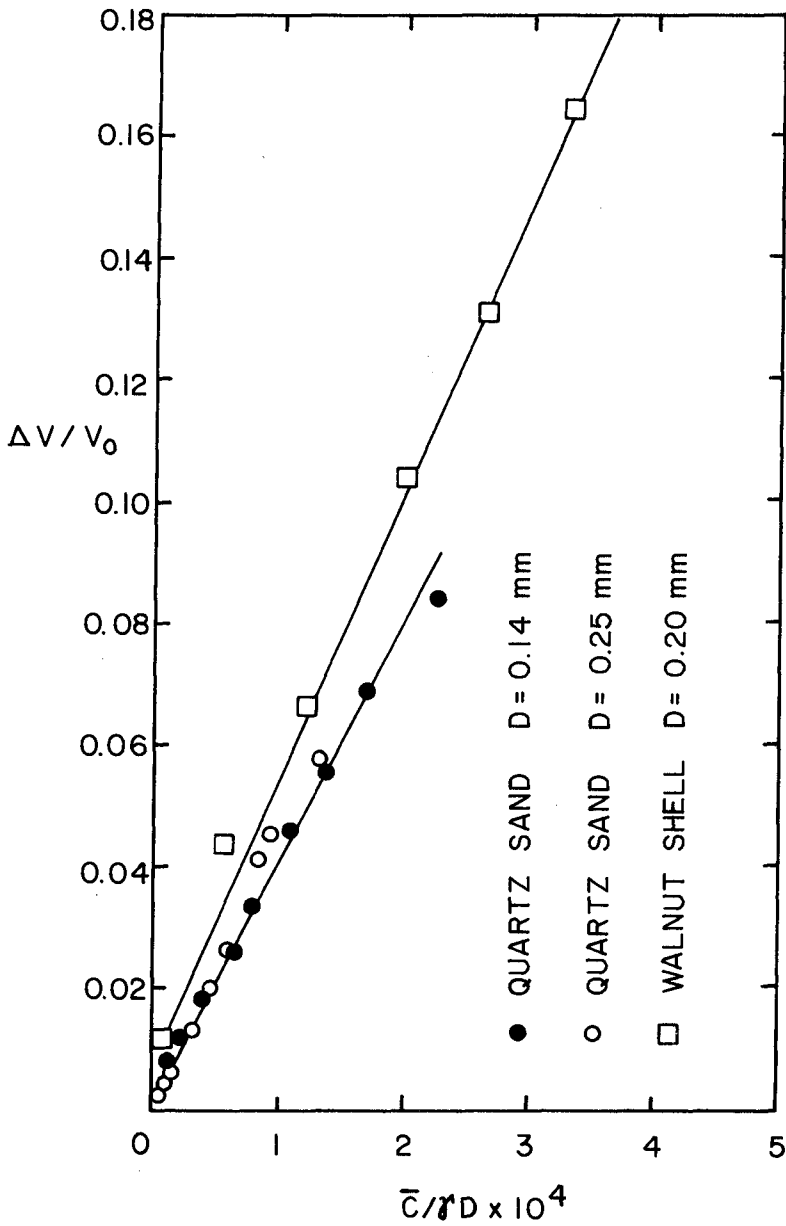


Figure 5. Calibration curve expressing $\Delta V/V_0$ as a function of $\bar{C}/\gamma D$ for quartz sand and walnut shells.

level with no particle in the probe field; therefore these negative voltages have to be discarded through a single polarity integrator in the instrument. The principal conclusion from this phase of the investigation was that the ISCMS must be calibrated for each different sediment material.

Tests to ascertain the sensitivity of the ISCMS to particle diameter also were conducted in the turbulence jar using four different glass beads with median diameters of 0.029, 0.062, 0.100, and 0.200 mm. Calibration data for the four samples are plotted in figure 6. The calibration curves are seen to be linear over the range of concentrations tested: 400 to 16,000 ppm. However, the slopes of the calibration curves are dependent on the diameter, with values of 3.62, 4.87, 7.96, and 12.35 ppm/mV, for the 0.029, 0.062, 0.100, and 0.200 mm beads, respectively. This dependency of calibration-curve slope on particle diameter can be explained as follows. For a fixed concentration, the number of particle present in the sensing volume of the probe increases with reduction in particle diameter. In the case of the finer sediments, some particles hide in the shadows of others, and are not detected by the light sensor. Therefore, at high concentrations the actual particle concentration in the probe field is higher than that indicated by the output.

Tests also were conducted in the turbulence jar to determine the effect of integration time on the measured estimate of mean sediment concentration for the two quartz sands and the walnut shells described above. A series of 200 sequential 10-sec averages of the ISCMS output voltage were obtained for each of these sediments at low, medium, and high mean concentrations ranging from 360 to 11,000 ppm. Successive 10-sec averages were combined to form sets of 20-sec and 50-sec averages, and the effects of averaging time of the confidence intervals of the mean concentration estimates were examined. It was found that increasing the averaging time above 10-sec does not have an appreciable effect on the confidence interval of the mean-concentration estimates. Similar tests also were made in the Iowa Oscillatory-Flow Water Tunnel (Nakato 1974; Locher *et al.* 1974). In these tests a signal-averaging technique (Trimble 1968) was employed to decompose the analog concentration signal into its mean, periodic, and random components. Although the ISCMS response is dependent on the position of the sediment particle in the probe's sensing volume, for a completely random sediment motion the trajectories along which the particles traverse the field tend to be uniformly distributed over the sensing volume. Therefore, the effect of particle position on probe response described above averages out over time, and the signal-averaged measurements of $\bar{C} + C_p$, where \bar{C} and C_p are respectively, the mean and periodic components of the sediment concentration, were judged to be accurate. The period of the oscillatory fluid motion, T , over the 0.14 mm quartz sand bed was 1.8 sec, and the piston stroke was 15.2 cm. The ripples produced on the bed had a mean wavelength of 8.5 cm and a mean height of 1.2 cm. With the probe over the ripple crest, data from 200 wave cycles were obtained, with a sampling interval of 18 milliseconds, and analyzed in groups of 20, 50, and 100 wave cycles. The value of \bar{C} for the data from 200 wave cycles was 3,094 ppm, while the mean concentrations for the data from the first and second 100 cycles were 3,096 and 3,092 ppm, respectively. The values of $\bar{C} + C_p$

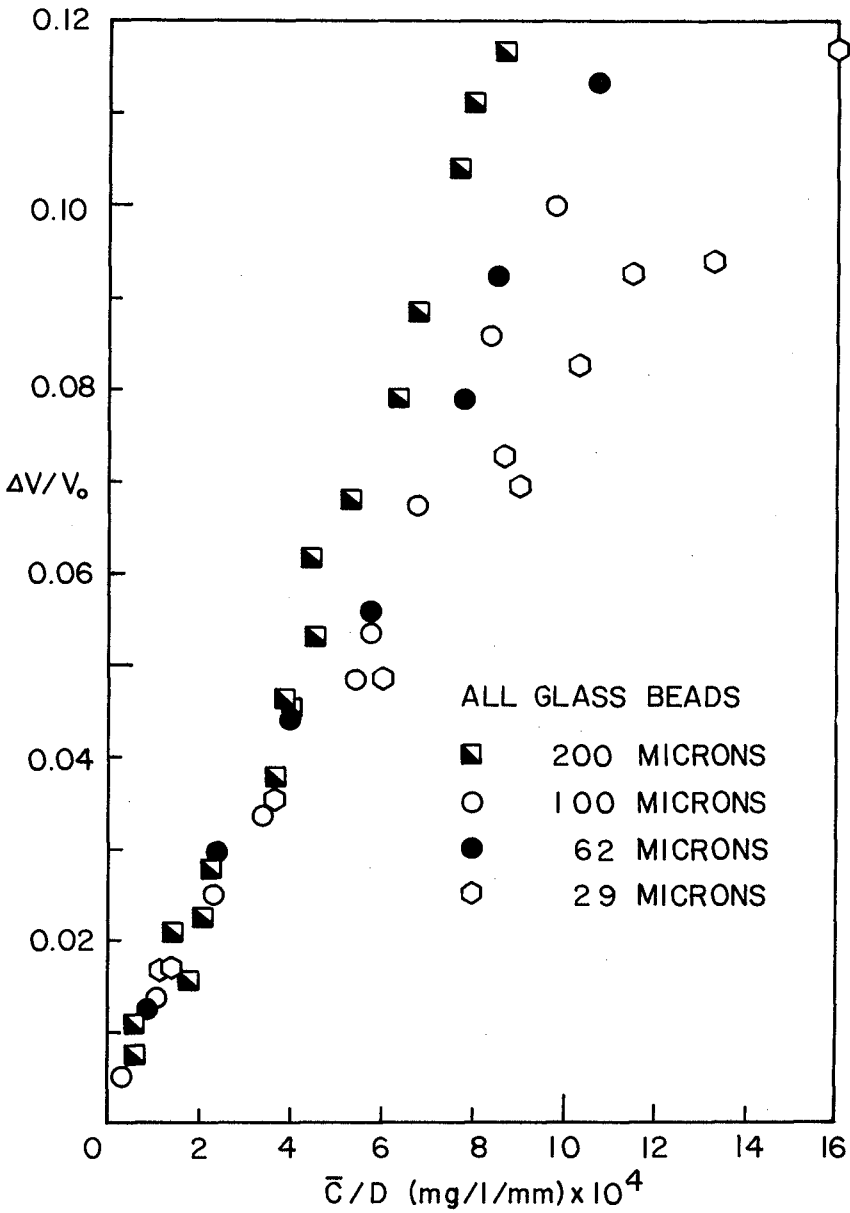


Figure 6. Calibration curve expressing $\Delta V/V_0$ as a function of \bar{C}/D for glass beads.

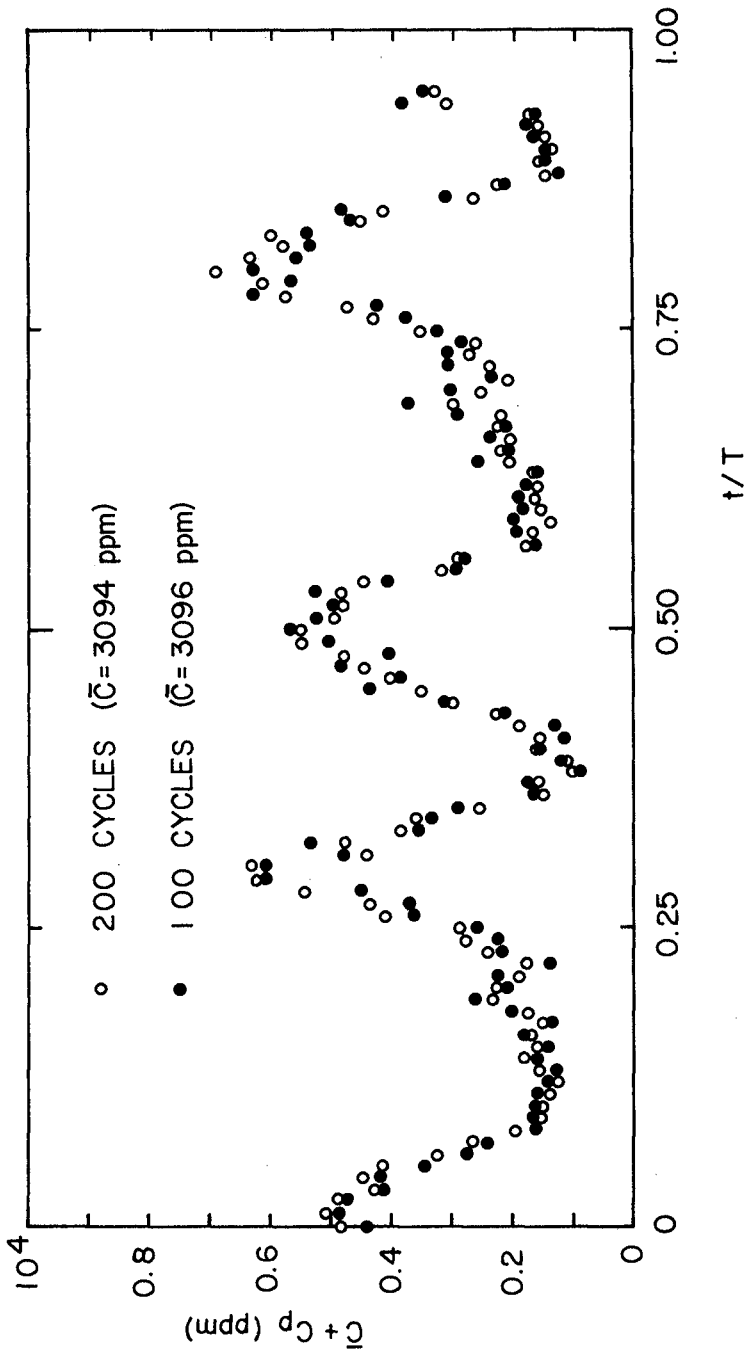


Figure 7. Comparison of estimates of $\bar{C} + C_p$ with 100- and 200-cycle wave data.

calculated from the set of 200-cycle data and the first 100-cycle data are plotted in figure 7. It is seen that there is not much difference in the estimates of $\bar{C} + C_p$ between two sets of data. However, the mean concentrations as well as the periodic components C_p obtained from the sets of 50- and 20-cycle data varied somewhat from that yielded by the 100-cycle data sets. The variations in the \bar{C} estimates were found to be between 2,867 ppm and 3,317 ppm, and 2,746 ppm and 3,521 ppm for the 50- and 20-cycle data, respectively. The plots of \bar{C} and C_p values from the 50- and 20-cycle data also were found to scatter much more widely than those of 100-cycle data. It was concluded, therefore, that at least 100 wave cycles of data are necessary to obtain meaningful estimates of the mean and periodic components of sediment concentration in the suspended sediment field produced by oscillatory motion over a rippled sand bed investigated in this study.

IV. SUMMARY OF RESULTS

The principal results of this investigation may be summarized as follows:

1. The ISCMS response to the single particle depends strongly on the particle position within the probe field. Therefore, the instantaneous output voltage of the ISCMS cannot be correlated with the instantaneous suspended sediment concentration within the probe position.
2. The frequency response of the instrument limits the use of the ISCMS to flows with mean velocities less than approximately 23 cm/s. At a particle velocity of 46 cm/s the rms output is down approximately 8 percent.
3. The ISCMS output voltage varies linearly with mean sediment concentration. However a separate calibration must be obtained for each sediment.
4. An integration time of at least 10 seconds is necessary to obtain reliable estimates of mean sediment concentration when calibrating the ISCMS probe in a turbulent jar. This appears to be a reasonable lower time limit also when the ISCMS is used in steady uniform flows.
5. Approximately 100-cycle wave data are sufficient to obtain quantitative estimates of $\bar{C} + C_p$ in the oscillatory flume used in the present study.

ACKNOWLEDGMENTS

This study was supported primarily by the U.S. Army Corps of Engineers, Coastal Engineering Research Center, under Contract No. DACW-72-73-C-0022, and in part by funds of the Institute of Hydraulic Research, The University of Iowa.

REFERENCES

1. Bhattacharya, P.K., "Sediment Suspension by Shoaling Waves," Ph.D. Thesis, The University of Iowa, 1971.

2. Danushkodi, V., "An Experimental Investigation of the Turbulent Structure of Sediment Suspensions," Ph.D. Thesis, The University of Iowa, 1975.
3. Glover, J.R., Bhattacharya, P.K., and Kennedy, J.F., "An Electro-Optical System for Measurement of Mean and Statistical Properties of Sediment Suspension,": IIHR Report No. 120, Iowa Institute of Hydraulic Research, The University of Iowa, 1969.
4. Locher, F.A., Glover, J.R., and Nakato, T., "Investigation of the Operating Characteristics of the Iowa Sediment Concentration Measuring System," IIHR Report No. 170, Iowa Institute of Hydraulic Research, The University of Iowa, 1974.
5. Nakato, T., "Wave-Induced Sediment Entrainment from Rippled Beds," Ph.D. Thesis, The University of Iowa, 1974.
6. Trimble, C.R., "What is Signal Averaging?", Hewlett-Packard Journal, Vol. 19, No. 8, 1968.

CHAPTER 121

FACTORS INFLUENCING ESTUARY SEDIMENT DISTRIBUTION

by
Mary P. Kendrick¹ and B. V. Derbyshire²

Introduction

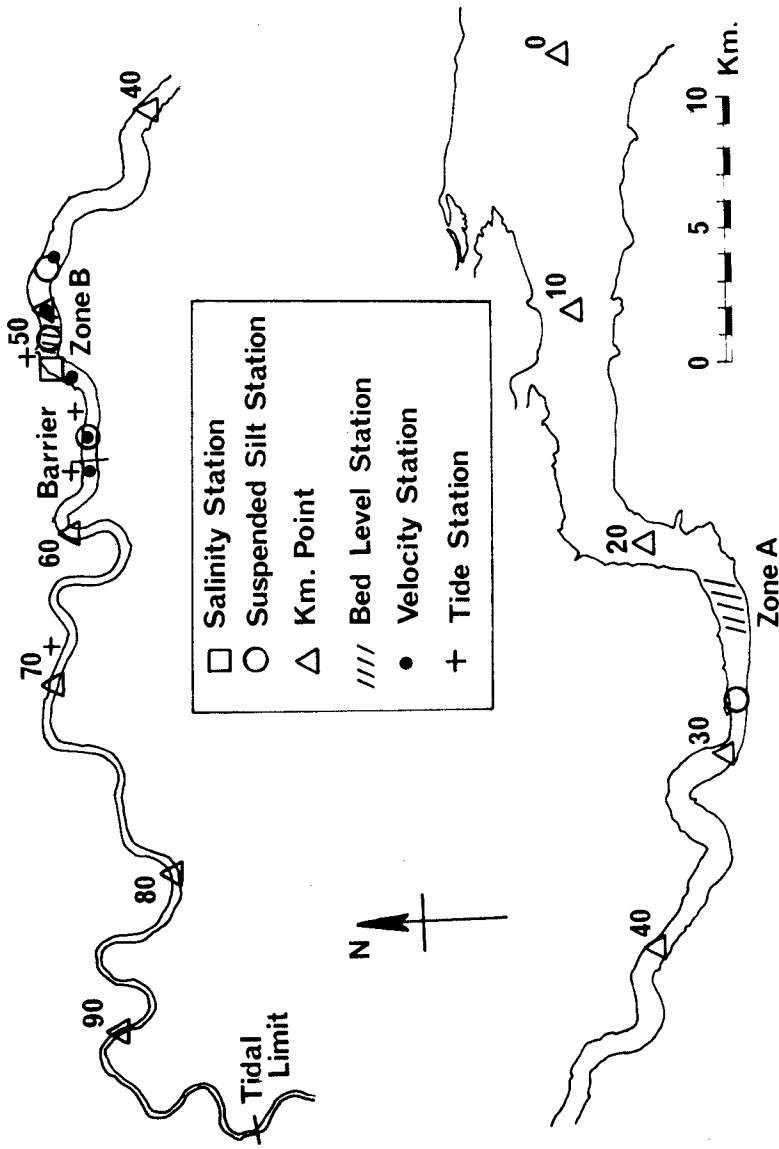
Many factors combine to determine the way in which sediments are distributed throughout an estuary.

Most fundamental are those which produce the natural rhythm of diurnal (or semi-diurnal), bi-monthly and seasonal fluctuations due to predictable variations in tide and weather. This group includes tidal discharge, fresh river flow and the resultant distribution of saline water. When considered together with such factors as the availability and properties of sediments within and beyond the landward and seaward limits of an estuary, they determine how the available material shall be eroded, transported and deposited during the course of the natural cycle.

Superimposed on these regular fluctuations are the effects of other factors which may or may not be predictable, are not necessarily regular in occurrence and may be either natural or man-made.

These include secular trends, such as long-term adjustments in land/sea levels or climatic conditions, which have a small but continuing effect on some of the factors in the first group. They also include sudden, short-term events like earthquakes or hurricanes which impose a shock to the system that may involve the movement of large quantities of material during the subsequent period of readjustment. Sometimes the influence of this group

1. Principal Scientific Officer) Hydraulics Research
2. Senior Scientific Officer) Station, Wallingford,
Oxon, England.



KEY PLAN OF ESTUARY

Fig. 1.

of factors on sediment movement is indirect in that they necessitate the implementation of civil engineering works which, in turn, lead to a redistribution of sediment.

Finally, and most familiar to the coastal engineer, are those factors which create the recurring practical problems confronting him as estuaries are developed more and more intensively to meet the demands of modern industrial society - the construction of new jetties and container berths, channel dredging and training for navigation, sand and gravel winning for industry, the commissioning of water-cooled power stations, the discharge of sewage and industrial effluents, the control of water supply and tidal discharge by hydraulic structures, etc. Such developments usually affect the prevailing distribution of sediment in some way.

The tidal Thames in England (Fig 1) exemplifies a relatively well-documented estuary which for many years has been studied in the field, on physical and mathematical models and through laboratory tests on sediment. Using some of the results of these studies, the authors attempt to demonstrate how the above-mentioned factors interact: (a) in the short-term throughout a single tide, (b) during the slightly longer course of the bi-monthly spring-to-neap cycle, (c) as a result of annual seasonal variations and (d) in the longer term over a period of 30 years or more. Finally the paper illustrates the impact that civil engineering works can have on an estuary whose prevailing sediment distribution is already the result of the combined effect of the factors previously discussed.

Diurnal (or semi-diurnal) effects

Fig 2 depicts events on one (semi-diurnal) spring tide over an 8 km stretch of estuary (Fig 1).

The tidal range, which was 5.53 m at km point 0 (the mouth) about 50 km away, is amplified to 6 m (a), the

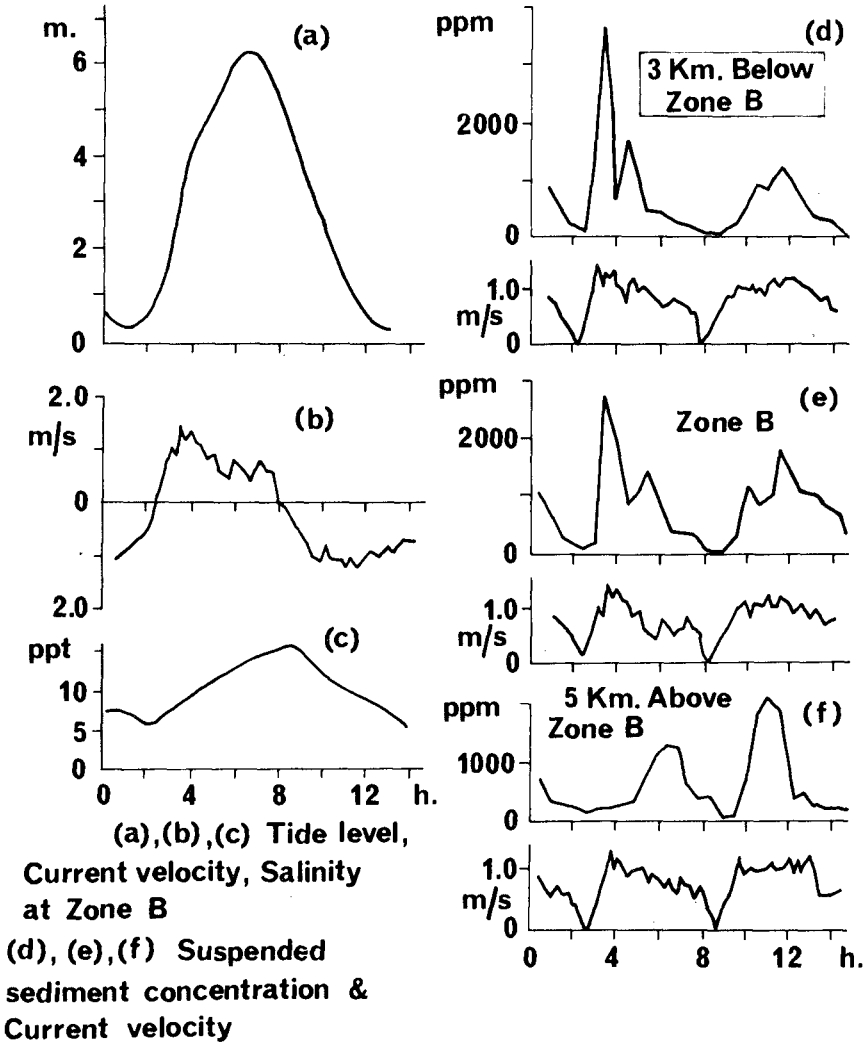


Fig. 2. SEMI-DIURNAL FLUCTUATION IN FACTORS AFFECTING SEDIMENT DISTRIBUTION

slightly shorter flood period giving marginally higher maximum current velocities on the flood than on the ebb (b). The vertically well-mixed conditions produce a rise in salinity of 10 parts per thousand at all depths from slack low tide to slack high tide (c). Because of the difficulties inherent in attempting direct measurement of changes in the level of the surface of a silty bed throughout a tide, measurements of variations in both the concentration of suspended sediment and current velocity at a number of depths at selected stations are used to infer how material is eroded, transported and deposited in a given reach of the estuary.

The records shown on (d), (e) and (f), 1.5 m above the bed, typify the pattern of changes occurring throughout the lower 3 m of flow.

On the flood tide, material at the station 3 km seawards of Zone B (d) is entrained as soon as the critical shear for erosion is reached. The fact that the subsequent sharp decline in sediment concentration is not accompanied by a significant decrease in current velocity suggests that the material passes from the site up the estuary. Some of it deposits before arriving at Zone B, probably in the lee of bends, where flow is slow. If this were not the case, the concentration-time curve at Zone B would provide evidence of its arrival there. Instead, graph (e) shows that conditions at this site are similar to those shown on graph (d), sediment entrainment occurring early on the flood tide followed by a reduction in concentration as material moves away up-estuary.

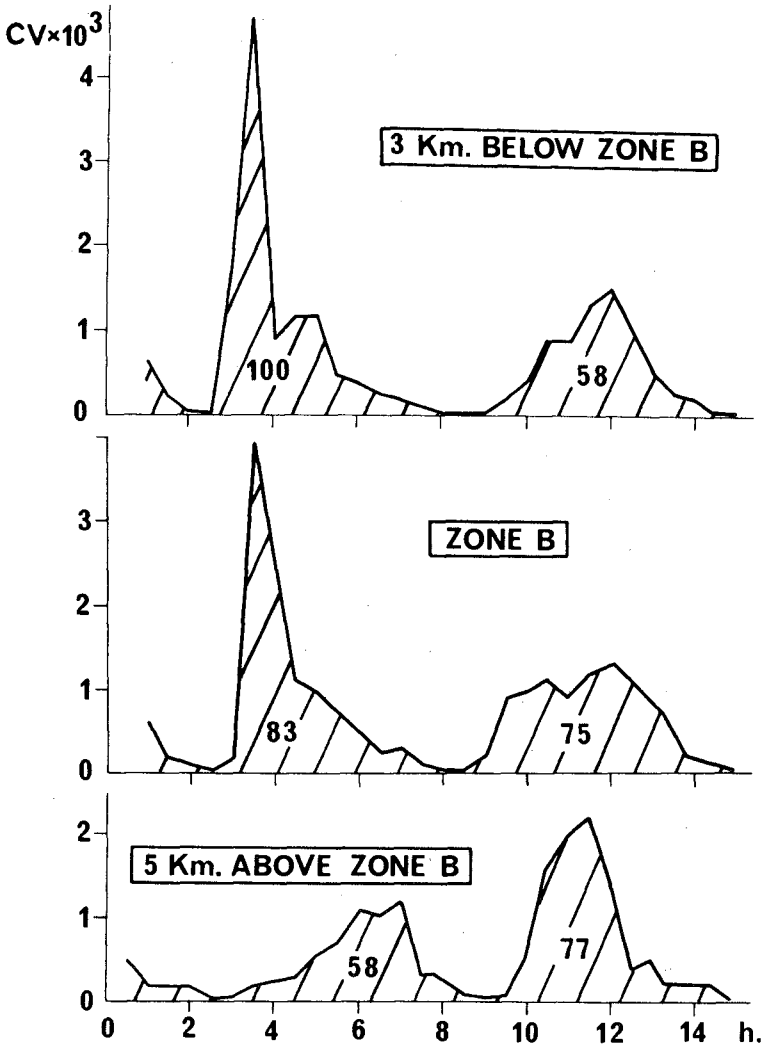
A second, smaller concentration peak occurs at both stations and, assuming that suspended sediment travels at the speed of the water transporting it, the evidence suggests that this material was eroded from the bed at a position more than 3 km below Zone B, passed through the lower

silt station, deposited some of its load on the bed between there and the second station and passed on up the estuary.

At the third station, 5 km above Zone B (f), events are quite different. The suspended sediment concentration remains low even when the current velocity has exceeded 1 m/s, indicating little or no erosion of the bed locally. It is not until between 3 and 4 hours after low water that material arrives from further down the estuary, and the timing suggests that this could have originated at, and upstream of, Zone B. Some of this sediment passes on for a short distance before settling on the bed, the remainder deposits at the station due to the decrease in current velocity associated with the arrival of slack high tide.

On the ebb, concentrations at this station soon exceed 2000 ppm as the deposited sediment is re-entrained, and clearly more sediment passes down the estuary at this point than passed up on the preceding flood tide. The velocity-time curve shows that the sediment is transported seawards, concentrations remaining low for the rest of the ebb tide. At Zone B, conditions at the start of the ebb are similar, material being eroded from the bed as soon as the critical shear is reached. This moves away down-estuary, but halfway through the ebb tide the concentration-time curve (e), peaks suddenly, and this rise coincides with the arrival time of the suspended sediment which created the concentration peak at the station 5 km up-estuary. From this point until slack low water, the concentration at Zone B falls as current velocity falls, material depositing at and below the site.

At the third station 3 km seaward, sediment concentration rises and falls gradually as ebb current velocity increases and decreases (d), reaching only half the maximum value recorded at the other two stations - a further indication of deposition on the bed between here and Zone B.



C = Concentration (ppm) V = Velocity (m/s)

Fig. 3. SEMI-DIURNAL FLUCTUATION IN SEDIMENT FLUX

The data in (d), (e) and (f) are re-plotted on Fig 3 as sediment-flux curves for each of the three stations. These graphs illustrate more clearly the longitudinal sediment redistribution in the study area already inferred from the raw data on Fig 2 since the areas under the curves represent the quantity of sediment per unit area passing each station on each half tide.

To facilitate comparison, the flood tide sediment flux at the seaward station is regarded as 100 units. With this as the reference, Fig 3 demonstrates that within the 8 km of estuary used in the example, the amount of sediment deposited on the bed during the flood tide is more than twice that deposited on the ebb. Furthermore, whereas flood tide deposition is distributed relatively evenly both above and below Zone B, most of the ebb tide deposition occurs at Zone B and seawards. (Clearly the greater the number of measuring points per river section, the more reliable will be the result.)

Bi-monthly (spring-to-neap) effects

Figs 2 and 3 shew how sediment can be redistributed during the course of a single tide under a condition of low river flow. Fig 4 demonstrates the slightly longer-term variations that can occur during the bi-monthly spring-to-neap cycle, employing data collected near to Zone A and Zone B (Fig 1), two areas respectively 25 km and 50 km above the estuary mouth. The data are plotted both for summer (low river flow) and winter (high river flow) conditions. Graph (a) shews the cyclic variation in tidal range and indicates that tidal currents in both summer and winter must be similar since tidal ranges are similar. (River flow has negligible effect on currents at the monitoring stations.) (b) shews the steady, low summer river flow and the fluctuating, higher winter river flow. (c) and (d) shew the bi-monthly variation in mean suspended sediment concentration on both flood and ebb tides.

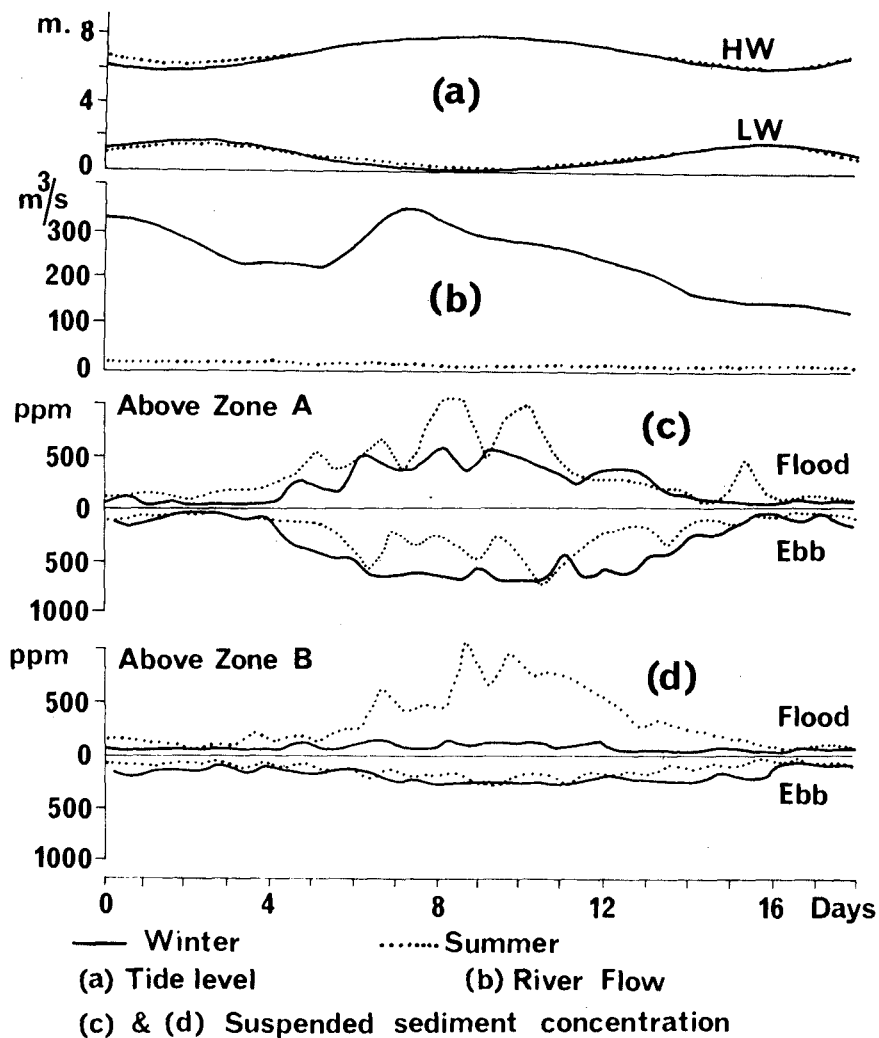


Fig. 4. BI-MONTHLY FLUCTUATION IN FACTORS AFFECTING SEDIMENT DISTRIBUTION

The most significant fact to emerge is that sediment concentration increases and decreases with tidal range, remaining low throughout the period of neap tides and increasing as the range exceeds the mean value. Significant sediment movement is therefore largely confined to spring tides.

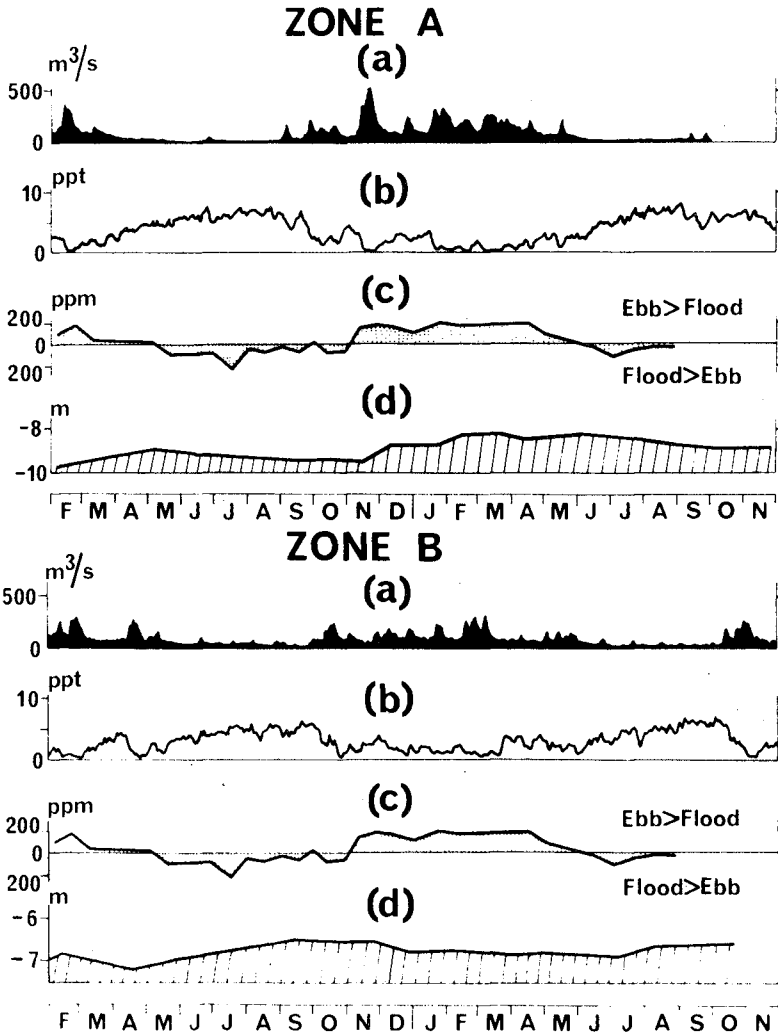
In the summer, spring tide concentrations are higher on the flood than on the ebb at the 2 stations just above Zone A and Zone B, suggesting a net landward movement of material up the estuary during this period. However, flood tide values are similar at the 2 stations indicating no net accretion of the bed between the sites. The transported material must therefore deposit further up the estuary. On the ebb, values are higher near Zone A than near Zone B indicating erosion of the bed between the stations.

In the winter the converse is true. Spring tide concentrations are higher on the ebb than on the flood at both stations, implying net deposition seaward of the lower station (from bed level data this in fact occurs at Zone A). However, at this time of the year both flood and ebb values are much greater near Zone A than Zone B, indicating considerable sediment movement, with deposition occurring between the two sites on the flood and erosion occurring on the ebb.

Annual seasonal effects

Continuing the study by extending the time-scale of cyclic variations from 2 weeks to 2 years, Fig 5 shows the relationship between fresh river flow, water salinity, concentration of suspended sediment and river bed level at Zone A and Zone B. The location of study zones and monitoring stations is given on Fig 1.

The significant feature is that for a given 2-year pattern of variations in river flow, salinity and suspended sediment concentration, bed levels in the two areas react in diametrically opposite ways.



(a) River flow (b) Salinity (c) Suspended sediment concentration (d) Bed level relative to Chart Datum

Fig. 5. SEASONAL FLUCTUATION IN FACTORS AFFECTING SEDIMENT DISTRIBUTION

High river flow (October-April), the consequent low salinity and the subsequent ebb-predominant, suspended sediment concentration result in accretion of the bed at Zone A. On the other hand, a similar combination of factors produces erosion of the bed at Zone B. Low river flow (May-September), the consequent high salinity and the subsequent flood-predominant, suspended sediment concentration result in erosion of the bed at Zone A whilst at Zone B, the result is accretion.

Clearly, material is redistributed seasonally along the estuary, the reduction in salinity associated with a prolonged period of high river flow leading to the release (through a reduction in cation bonding) of deposits at Zone B for transportation down-estuary. Conversely, during the period of low river discharge, the prevailing net landward movement of water and sediment in the lower layers of flow in the seaward reaches results in the gradual up-river transport of sediment.

Effects of secular trends

So far, the paper has described only those regular, largely predictable variations in natural phenomena which affect estuary sediment distribution. It now considers other, less regular, less predictable factors whose continuing effects, though small, can be of considerable significance when superimposed on existing regular fluctuations. The long-term land/sea level adjustment taking place in the southern North Sea provides a useful example.

Following an examination of 50 years of daily records of tide level, salinity and river flow, the authors confirm earlier findings (Ref 1, Ref 2) that mean tide level at the mouth of the Thames and tidal amplitude 70 km up-estuary have risen significantly during this century. In addition they shew this to be accompanied by a rising trend in saline penetration and a falling trend in river flow. Fig 6

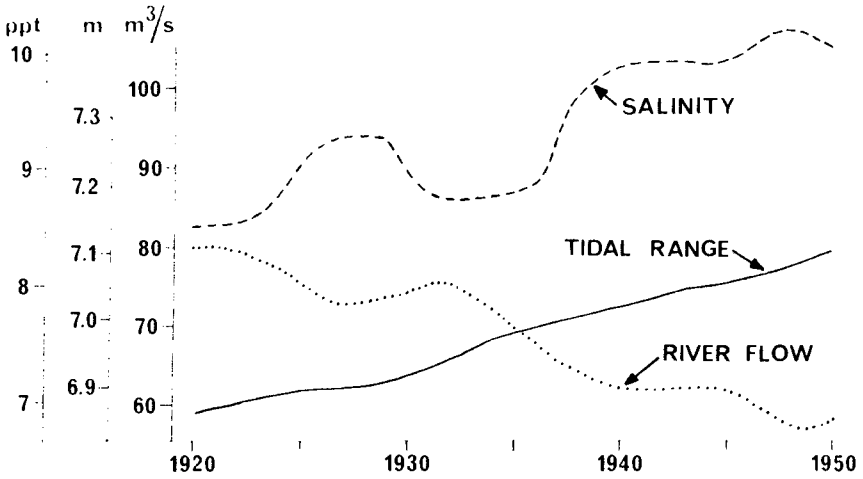


Fig. 6. SECULAR TREND IN FACTORS AFFECTING SEDIMENT DISTRIBUTION

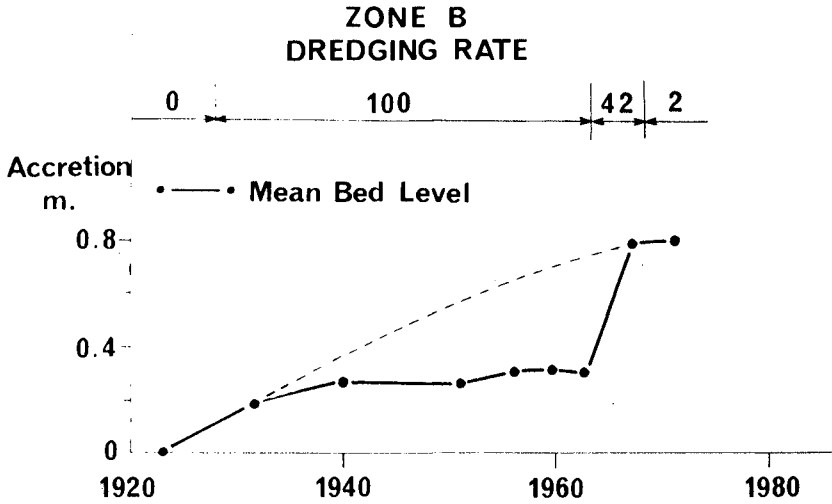


Fig. 7. RESPONSE OF BED LEVELS TO SECULAR TRENDS

illustrates this in the form of 15-year running means for all three parameters for the period 1920-1950.

The relative dependence of saline penetration on tidal range and river flow is currently being investigated. However, for present purposes, the significant fact is that for a period of at least 30 years, the main hydraulic factors controlling sediment movement themselves underwent a gradual change in a constant direction. The net effect on sediment distribution was to increase the thickness of the deposits on the estuary bed in the reaches immediately landward of the major deposition zone of the estuary - Zone B. Civil engineering works, including continuous channel maintenance dredging, masked this effect to some extent during the major part of the period, but when dredging was reduced, the readjustment of the estuary sediment distribution to the changing situation was rapid.

This effect is demonstrated by Fig 7, which shows changes in mean bed level (derived from soundings at approximately 30-m intervals on sections 175 m apart) between 1923 and 1971 for a 4-km - long reach located 3 km above Zone B. Annual dredging during the period of continuous channel maintenance is taken to be 100 units.

Effects of civil engineering works

Up to this point, the paper has been largely confined to a consideration of the interaction of those factors which affect estuary sediment distribution before they have been modified in any way by man's intervention. The authors now go a step further and examine what can happen to the sediment distribution when development schemes are carried out which modify the influence of those factors.

Two examples are cited - one familiar, the other perhaps less so. The first, jetty construction, usually affects only the local area but can be costly in terms of economic efficiency if badly located and ill-designed, as

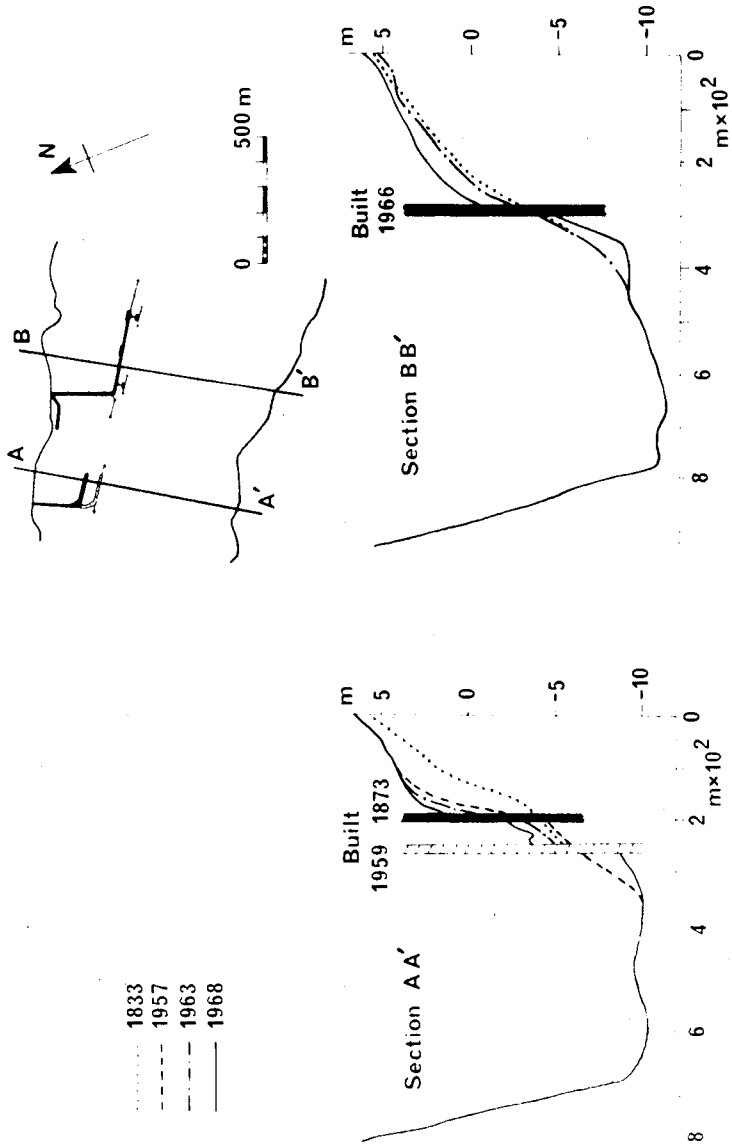


Fig. 8. EFFECT OF JETTY CONSTRUCTION ON SEDIMENT DISTRIBUTION

was often the case in the past and unfortunately still happens today.

Fig 8 demonstrates the response of bed levels in the Thames to the construction and extension of jetties about 35 km above the mouth. The bankside accretion which occurred between 1873 and 1957 following the building of the first jetty (Section A-A') amounted to a riverward movement of the low tide mark of about 80 m. This was relatively local in effect, not extending as far down-estuary as Section B-B' where the bankline had remained as before. However, once a jetty was built at B-B' and associated front face dredging carried out, bankside deposition began there also, and in 2 years (1966-1968) the bankline advanced about 50 m. Meanwhile, back at A-A', an extension into deeper water had been added in 1959 and dredging also undertaken along the front face. Deposition continued - at a reducing rate behind the original 1873 construction, but at a higher rate between it and the new extension.

Why did this deposition occur? Prior to jetty construction sediment was carried into the area on the flood tide, deposited round about slack high water, re-entrained on the ebb and transported seawards. A long-term balance was therefore maintained and bed levels near the side of the estuary changed very little from year to year. Jetty construction had the effect of marginally reducing current velocities near the bank and thus providing a longer period for deposition at high water. Furthermore the ebb current was less efficient in re-entraining sediment and so the former balance between deposition and scour was no longer maintained.

The civil engineering undertaking used as the second example of how such works modify the influence of the hydraulic factors responsible for estuary sediment distribution is tide control (Ref 3). It is more ambitious than

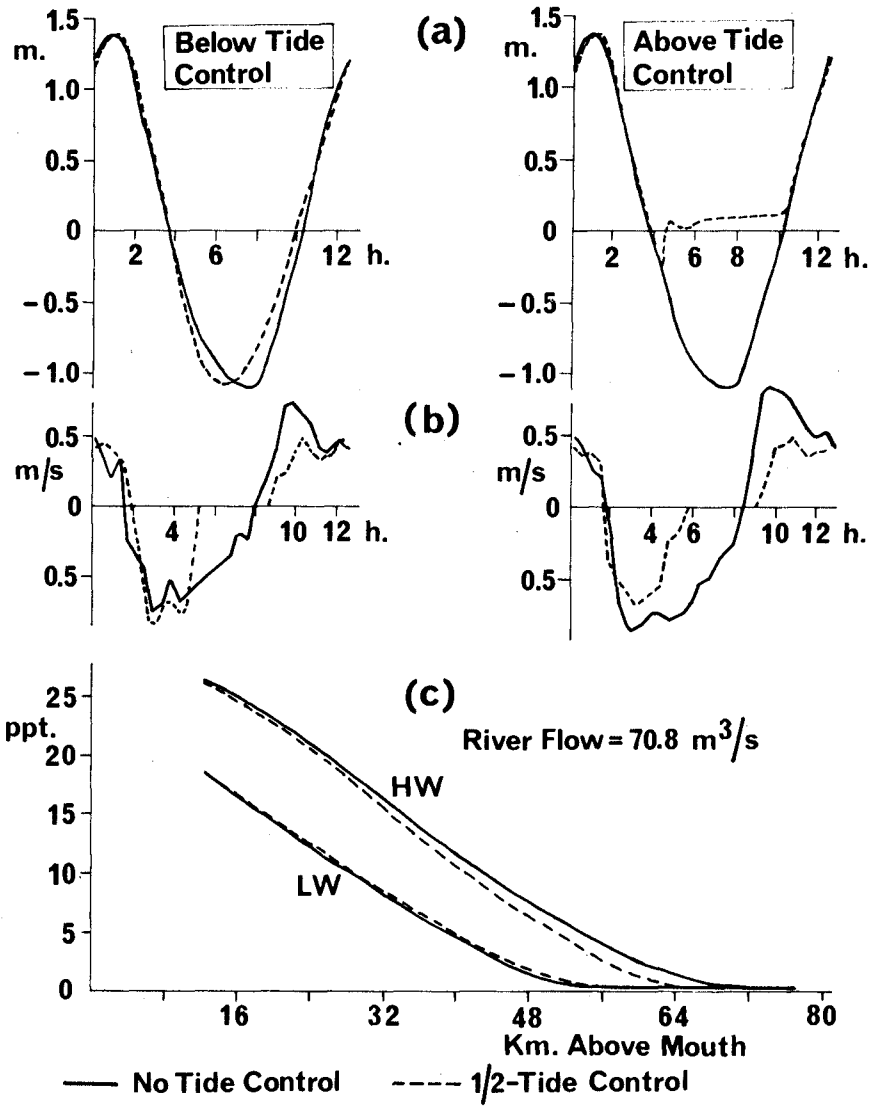


Fig. 9. EFFECT OF TIDE CONTROL ON WATER MOVEMENT

jetty construction, has more far-reaching effects and is therefore much less likely to be carried out without prior investigation into its likely impact on the estuary environment.

Physical and mathematical model studies of various forms of tide control have been made at Wallingford. Using physical model results, Fig 9 shows the effect on water movement of one form - half-tide control by a gated barrier located 55 km above the estuary mouth. The way the system operates is for the gates to be shut halfway through every ebb tide, remain closed throughout the low water period, be re-opened halfway through the following flood tide when water levels on either side of the structure are the same, and remain open throughout the high water period.

The effect is demonstrated by comparing tide levels (a), current velocities (b) and salinity (c) with and without half-tide control at stations above and below the structure. Below the structure, the response to tide control is for the ebb period to be shorter, the flood period correspondingly longer, maximum flood current velocities lower and maximum ebb current velocities higher. Above the structure, once the initial fall in flood tide level following gate closure has occurred, levels increase slowly with incoming river flow until the gates are re-opened: current velocities on both flood and ebb tides are lower. The main effect of half-tide control on the longitudinal salinity distribution is to move the upstream limit of saline penetration about 5 km seawards (Ref 4).

Fig 10 demonstrates how these changes in water movement within the estuary affect the sediment distribution on the bed according to both the physical model (upper diagram) and the mathematical model (lower diagram).

The results take different forms. Those from the physical model are presented in the form of deposition/erosion

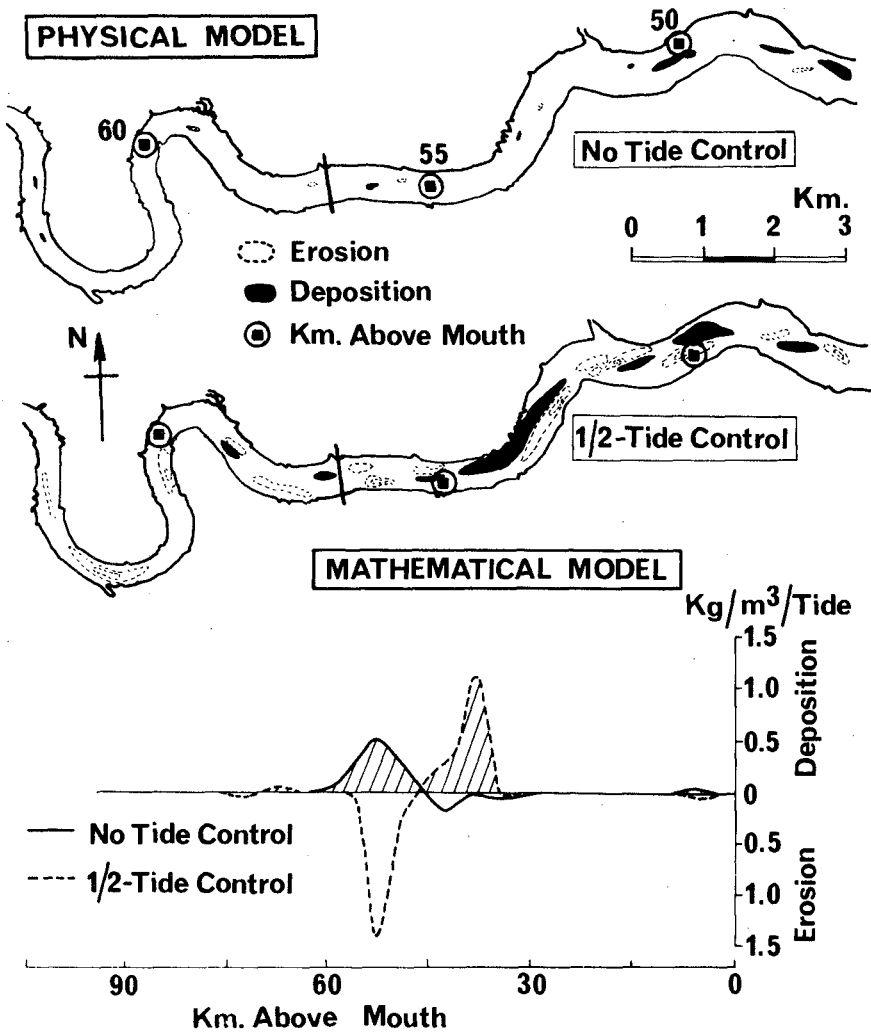


Fig 10. EFFECT OF TIDE CONTROL ON SEDIMENT DISTRIBUTION

charts which compare the negligible change in sediment distribution following construction but before operation of the tide control structure, with the considerable sediment redistribution resulting from continuous half-tide control. The mathematical model results illustrate longitudinal changes in the location of zones of erosion and deposition, indicating that tide control has the opposite effect to that of the rising trend in tidal range in that it produces a seaward migration of the major deposition zone.

Acknowledgements

This paper is published by permission of the Director of Hydraulics Research, Wallingford, England. The authors gratefully acknowledge the cooperation of the Thames Water Authority, the Port of London Authority, the Greater London Council and the National Maritime Museum in making available historical charts and records. They also thank Mr I L Fish, Scientific Officer of the Hydraulics Research Station, for his help in analysing data and preparing illustrations.

References

1. Suthons, C T 1963, Proc. Inst. Civ. Engrs, London. 24, 433.
2. Rossiter, J T 1969, Dock & Harb. Auth. London. 49, 461.
3. Kendrick, M P 1972, Phil. Trans. Roy. Soc. London A. 272, 223-243.
4. Owen, M W & Odd, N V M 1970, Int. Conf. on Utilization of Tidal Power, Halifax Nova Scotia, Dept. of Energy, Mines & Resources, Ottawa.

CHAPTER 122

SEDIMENT TRANSPORTATION AND DEPOSITION MODELS FOR MOBILE BAY, ALABAMA

by

Gary C. April¹
Samuel Ng²
C. Everett Brett³

ABSTRACT

The objective of this study is the application of hydrodynamic and material transport mathematical models for Mobile Bay in predicting sediment transport and deposition profiles within the bay system. Of particular importance are the seasonal variations of sediment distribution which are critically influenced by current patterns within the estuary. Both point and non-point sources of sediment will be included in the analysis.

Results will be presented in two ways. The first or long term variations in sediment distribution will be assessed by correlation with tidal cycle average velocities at various locations within the bay. Calculated distribution patterns will be compared with observed bathymetric data over the past century. The net effect of the construction of the Mobile ship channel on deposition patterns within the bay will also be evaluated. Secondly, short term variations in sediment transport and deposition resulting from man-made and natural disturbances will be analysed using a sediment transport model. This model will include deposition, bulk fluid transport and resuspension characteristics and will be capable of predicting localized, short term sediment patterns from maintenance dredging operations within the bay. Model trend results will be compared with field data collected during recent dredging activities and high altitude photographic data obtained for the bay area.

-
1. Professor of Chemical Engineering, The University of Alabama, Box G, University, Alabama 35486
 2. Graduate Assistant, The University of Alabama
 3. C. Everett Brett, Director, Natural Resources Center, Box 6282, University, Alabama 35486

INTRODUCTION

There is a growing awareness that the natural resources of the world are limited. This fact gives credence and a sense of immediacy to those who are trying to better understand and describe those processes which affect the amount and the quality of these resources. One of the most abundant and most taken-for-granted natural gifts is water. The waters adjacent to coastal regions are some of the most often studied because of their importance to man.

The coastal environment is a vital part of man's daily activity - providing food, recreation, jobs and habitats. Thus the already complex, dynamic natural processes which maintain a balance between fresh water and saline water is further confounded by man-made impacts. To minimize adverse events on these areas, a clear understanding of the properties and behavior of these systems must be established. Plans formulated with technically sound data are far more likely to produce results which are both environmentally and economically sound.

In recent years, studies have been accelerated to better characterize the coastal waters and to better describe the processes which take place in these areas. Studies have included models - both mathematical and physical - as well as the more traditional investigations involving data acquisition - both field oriented and remotely sensed. The interaction of these methods provide techniques for the rapid prediction of changes in the system and the impact that these changes have on water quality and behavior.

This paper summarizes some of the interactive methods used to characterize sediment transport patterns within the Mobile Bay estuary along the coastline of the northeastern Gulf of Mexico. The methods described are part of a continuing effort to develop compatibility between model, ground truth and remotely sensed information for the rapid estimation of estuarine behavior as governed by man-made and natural events.

MOBILE BAY SYSTEM

Mobile Bay receives the discharge of the fourth largest river system in the United States (Figure 1). An average of 5×10^9 kilograms of suspended sediment are transported into the estuary each year. Circulation patterns within the bay are governed by these river discharges, tidal influence from the Gulf of Mexico, wind influence and bay geometry. Seasonal variations due to meteorologic conditions, and shorter term variations due to the diurnal tidal state, result in hydrodynamic and material transport behavior which is complex.

The bay experiences seasonal variations in rainfall, runoff and sediment loading which can be broadly classified as low, medium and high in the following way (Table 1).

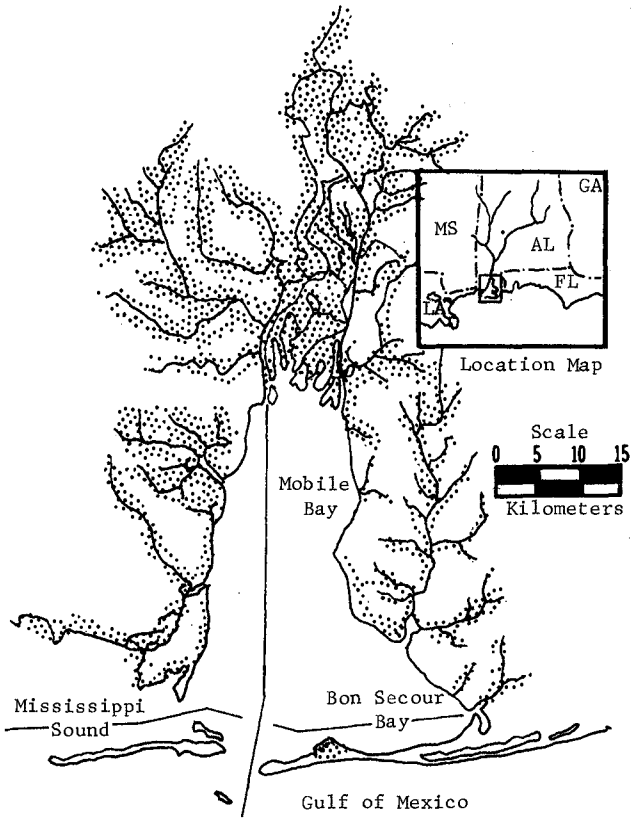


Figure 1.--Mobile Bay Estuarine System.

Table 1. -- Seasonal Average River Flow Rates and Sediment Load for the Mobile Bay System; 1952-1963 (U.S. Corps of Engineers, 1974).

River Flow Rate Classification	Period Covered	Average	Flow Rate	Average Sedi-	Sediment
		Flow Rate m ³ /sec	(Range) m ³ /sec	ment Load Kilograms x 10 ⁻⁶	Load (Range) Kilograms x 10 ⁻⁶
Low	August-November	531	447-700	68	50-107
Medium	May-July	1090	801-1609	215	145-353
High	December-April	2978	1609-3849	673	343-937
	Annual Averages	1609		357	

During the heavy runoff period the bay receiving waters are dominated by the high river flows to the extent that salinity intrusion within the bay is suppressed to the mid and lower sections of the estuary. This condition also results in the most pronounced transportation of sediment within the bay. Conversely, during periods of reduced river flow and sediment loading, bay currents are dominated by the tidal influence. This results in a greater potential to deposit sediment although the total volume is significantly reduced because of the decrease in solids loading during these periods.

Shoaling in the bay has averaged about 0.6m per century. However, there are portions of the bay which are highly stable and other regions which have rates of nearly 3.0m per century. These wide variations are a result of the complex, natural circulation patterns and man-made influences such as channel construction and maintenance dredging activities which exist in the bay (Ryan, 1969). Nearly 1.6×10^9 kilograms of suspended sediment bypass the bay annually. This material discharges into the Gulf through two natural passes in the southwestern area of the estuary. During tidal dominant periods (especially during flood tide cycles) solids can be introduced into the bay from the Gulf. These materials are transported to the bay mouth by the predominantly east to west littoral current which occurs in the northeastern Gulf of Mexico.

The influence of these variations in sediment transport and deposition patterns is analysed in this paper by considering the hydrodynamic behavior of the bay using mathematical modeling methods (Hill and April, 1974; Liu and April, 1975).

MODEL DESCRIPTION

Several mathematical models based on the laws of conservation of mass and momentum have been formulated for Mobile Bay (Table 2). These include two dimensional (depth averaged) models describing the hydrodynamic, conservative and non-conservative species transport behavior within the bay. Solution of the model equations is achieved using finite difference methods on a UNIVAC 1110 digital computer. These models have been used to study the influence of river discharge rate, wind direction and speed and tidal conditions on bay circulation and material transportation. Utilization of these models to investigate long term and short term trends resulting from natural and man-made disturbances on the system is part of an on-going research effort.

MODEL APPLICATION

Examples of methods used to assess sediment behavior are presented for a series of different conditions as dictated by the time frame over which information is being sought. These periods are broadly classified into long range or seasonal events and short range or within tidal cycle events for convenience. Each type will be discussed separately in subsequent sections.

The Effect of Seasonal Variations on Sediment Transport in Mobile Bay

Just as there are settling and scouring events within tidal cycles, there also exist seasonal variations which influence the sediment transportation and deposition characteristics within the bay. The effect of these seasonal events are studied by considering the hydrodynamic behavior of the bay using mathematical modeling methods. In particular, for the purpose of this paper, correlation of the hydrodynamic and sediment transport behavior is made using a tidal cycle average current generated for seasonal average flow conditions. This technique is a convenient method of lumping variables which are difficult to interpret and impossible to obtain over long term periods. The method provides a rapid assessment of those regions more susceptible to high transport and/or deposition of sediment. For Mobile Bay, a value of 0.06 m/sec correlates well with observed long term sediment transportation and deposition trends (i.e. a value < 0.06 m/sec indicates a region of low transportation; a value > 0.06 m/sec indicates a region of high transportation). Areas which have a high transportation potential regardless of river flow rate are indicated by the closed regions (Figure 2). These include the Bay areas adjacent to passes and waters near the Mobile and Tensaw Rivers in the north.

Table 2.--Mathematical Representation and Operational Modes of the Mobile Bay Models (Hill and April, 1974; Liu and April, 1975).

Name	Equation Form	Results	Modes
Continuity	$\frac{\partial Q_x}{\partial x} + \frac{\partial Q_y}{\partial y} + \frac{\partial H}{\partial t} = -(R + E)$	Tidal Height	Tidal Cycle Daily Avg Monthly Avg Seasonal
Momentum x-Component	$\frac{\partial Q_x}{\partial t} + gD \frac{\partial H}{\partial x} = KV^2 \cos \psi - fQQ_x D^{-2} + Q_x (2Ws \sin \phi)$	x-Component of Surface Current	Tidal Cycle Daily Avg Monthly Avg Seasonal
y-Component	$\frac{\partial Q_y}{\partial t} + gD \frac{\partial H}{\partial y} = KV^2 \sin \psi - fQQ_y D^{-2} + Q_y (2Ws \sin \phi)$	y-Component of Surface Current	Tidal Cycle Daily Avg Monthly Avg Seasonal
Species Continuity	$\frac{\partial C}{\partial t} + v_x \frac{\partial C}{\partial x} + v_y \frac{\partial C}{\partial y} = E \left(\frac{\partial^2 C}{\partial x^2} + \frac{\partial^2 C}{\partial y^2} \right) + \frac{E}{D} \left(\frac{\partial C}{\partial z} (z_s) - \frac{\partial C}{\partial z} (z_b) \right) - \frac{1}{D} (Cv_z (z_s) - Cv_z (z_b)) + R_o$	Concentration of Species	
Salinity	$R_o = 0$	Salinity Concentration	Daily Avg Seasonal
Coliform	$R_o = KC$; where $K = f(\theta)$	Coliform Bacteria Concentration	Monthly Avg Seasonal
Sediment	$R_o = K_1 f(v_s) + K_2 f(E) - K_3 f(v_r)$	Suspended Sediment Concentration	Seasonal Tidal Cycle

Note: f in the last equation is a functional representation for those terms listed. For example a modified form of Stokes' Law might be represented by the term $f(v_s)$.

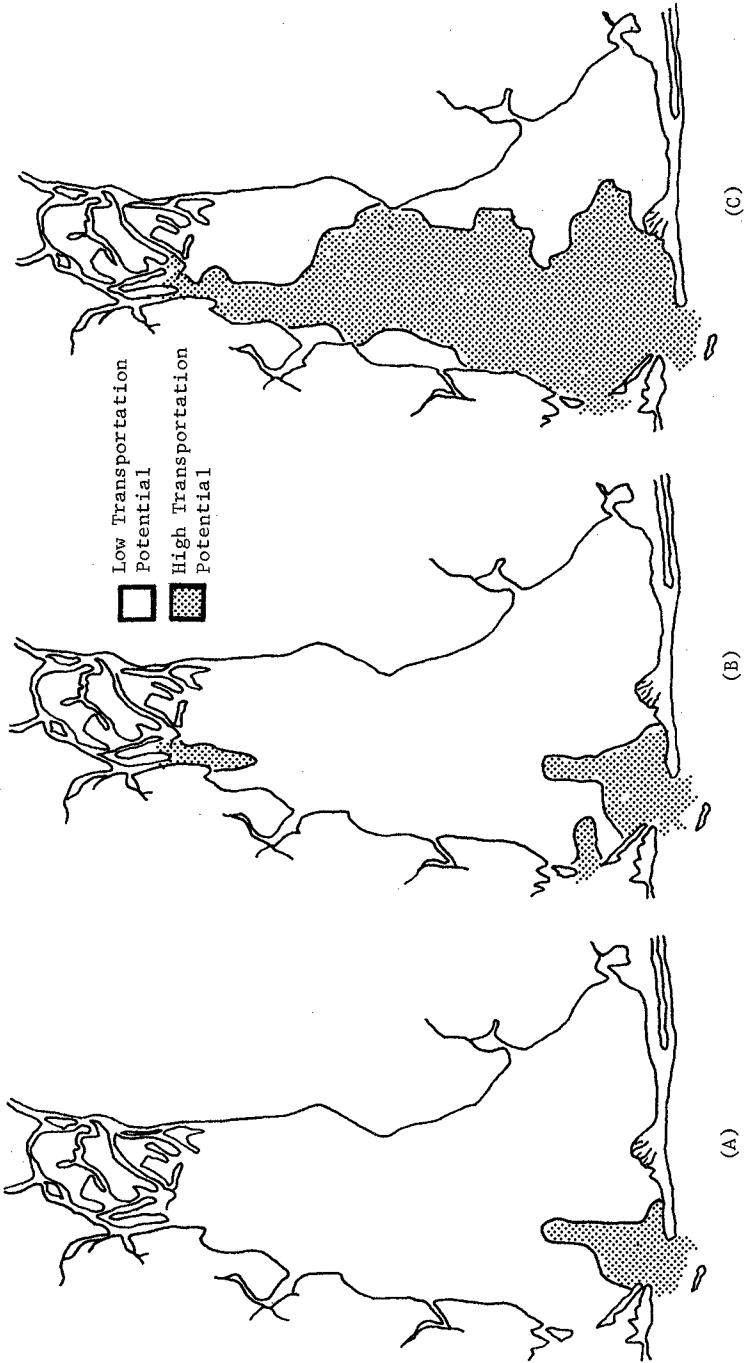


Figure 2.--Schematic Diagram Illustrating the Areas of High Transportation Potential at (A) Low, (B) Medium, and (C) High River Flow Conditions.

The open areas represent regions of low sediment transportation. These areas include the head waters between the Mobile and Tensaw Rivers, the Bon Secour Bay area and regions along the western shoreline. The seasonal variations can be observed by following the progression of the high transportation potential areas from high to low river flow conditions. It is likely that materials deposited during low river flow conditions become re-suspended during high river flow periods. This phenomenon can be traced using the hydrodynamic and material transport model for the bay. Included in this method of analysis are allowances for turbulence as estimated by local dispersion coefficients.

The Impact of Channelization on Long Term Sediment Transport in the Bay

In order to assess the possible long term impact that the Mobile ship channel has had on bay circulation and sediment transportation patterns, the hydrodynamic model was run under two conditions. The first set of conditions was derived from the 1847-1851 bay contour diagram from which bay depths were used as input to the model (Ryan, 1969). The second set of conditions were those including the ship channel in which bay depths and model parameters were adjusted to simulate this modification to the natural system. Both cases were run for a river flow rate of $3510 \text{ m}^3/\text{s}$. Transportation patterns were again determined using the tidal cycle average velocity criteria discussed earlier (Figure 3). A more even transportation pattern is observed over the lower two-thirds of the bay for conditions in which the ship channel is excluded. This condition can be explained by the higher volumetric throughput that occurs as a result of channelization along the west-central bay. A comparison of these results with deposition maps for the periods 1852-1920 and 1920-1973 prepared from bathymetric data supports the general patterns projected by the hydrodynamic model (Figure 4).

Within Tidal Cycle Variations in Mobile Bay Sediment Transport

Short term variations in sediment transportation patterns within the bay are of two varieties; man-made sediment disturbances resulting from maintenance dredging activities, and, naturally occurring sediment disturbances caused by high river flow rates, runoff and wind conditions. The latter cases are of particular interest in that it provides a means of interacting the hydrodynamic model with satellite and high altitude photographic data (remotely sensed) obtained during high sediment load conditions.

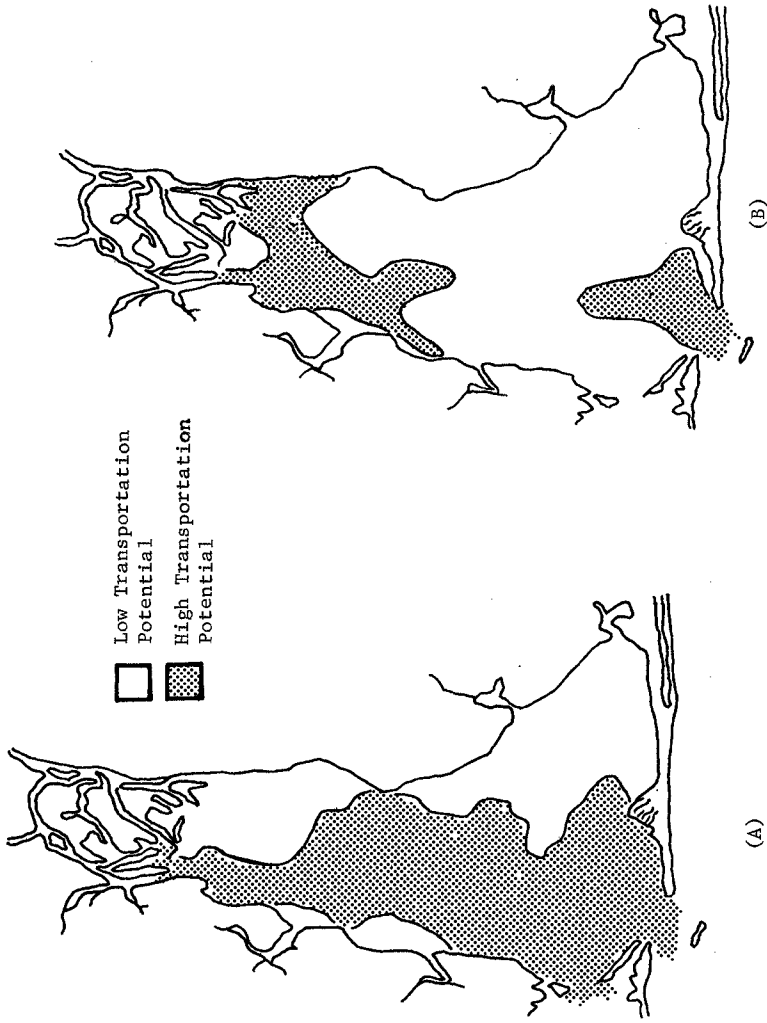


Figure 3.--Schematic Diagram Illustrating the Impact of Channel Construction on Bay Transportation Potential at High River Flow Conditions; (A) No Channel, (B) Channel.

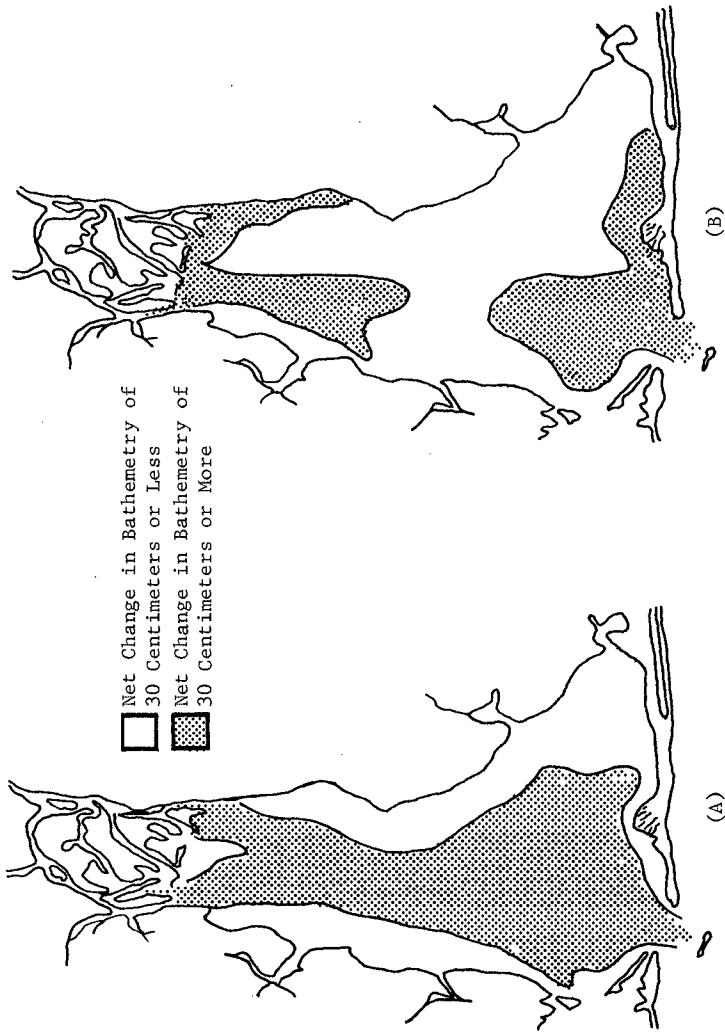


Figure 4.--Sediment Deposition Trends as Reflected by Bay Bathymetric Data for the Periods (A) 1852-1920 and (B) 1920-1973 (Sapp, 1975).

Sediment Transportation Resulting from Maintenance Dredging

Disturbances to the bay system resulting from maintenance dredging activities in areas adjacent to the Mobile ship channel account for the relocation of approximately 7.6×10^6 cubic meters of sediment. Hence, it becomes important to assess the impact that these dredged materials have on bay sediment transport and resettling behavior and the areas affected.

Such an analysis was made using the hydrodynamic model of the bay as a source of current direction and speed, and dispersion coefficient data as a function of tidal state. Subsequently, the material transport model was used for a subsystem (i.e. cell grid dimensions of 0.5 km; reduced from the two km hydrodynamic grid size) defined by the location affected by the dredging operation.

Field data collected in an independent study (Brett, 1975) were used to verify the model results. The field data were collected in May 1972 for the purpose of measuring the extent of sediment transport and deposition adjacent to a dredge discharge line. The dredge location was in the central bay (Figure 5). Comparison of suspended sediment concentrations as a function of distance from the dredge discharge indicates good agreement between the model predicted results and actual field data (Figure 6). There was no noticeable level of sediment in the water column beyond station 5; a distance of 1525 meters from the dredge discharge in a north-northeasterly direction. This is attributed to a change in the bay current pattern from near flood tide to near high water slack in which current velocities decrease rapidly to levels less than 0.06 m/sec. Similar conclusions can be derived by considering the thickness of deposited material along the north-south sampling transect (Figure 6).

As the tide enters high water slack, the sediment transport was shifted from a north-northeasterly direction to a more easterly direction. Similar patterns were observed as those discussed during the flood tide condition. However, because of the low current velocities, the dredging discharge rate becomes an important source of energy for transportation during this period. Thus the nature of the deposition patterns was such that this material was deposited over a shorter distance (Figure 6). These observations are consistent with the lower velocities and shorter period of time that occur during the slack water condition.

Similar patterns to those experienced during flood tide and high water slack conditions were postulated for ebb tide and low water slack. More material will be transported over a longer distance as a consequence of the longer period of high current velocities in the ebb flow direction. During seasonal periods when river flow rates are smaller than the value investigated in this study, a smaller area will be affected as a result of the more uniform ebb/flood tidal relationship. Because of the river inputs, the ebb tide condition is always greater than the flood conditions except during unusual periods.

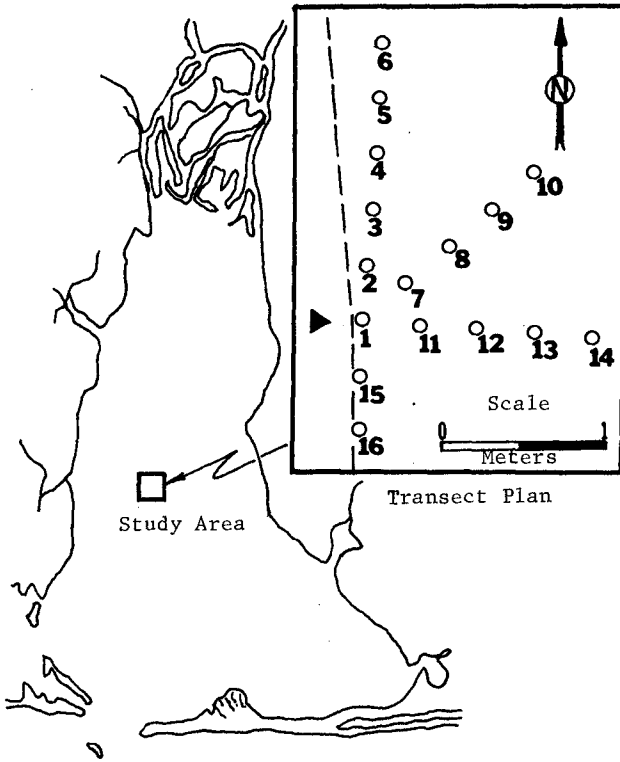


Figure 5.--Location Map and Transect Plan for Maintenance Dredging Program (Brett, 1975).

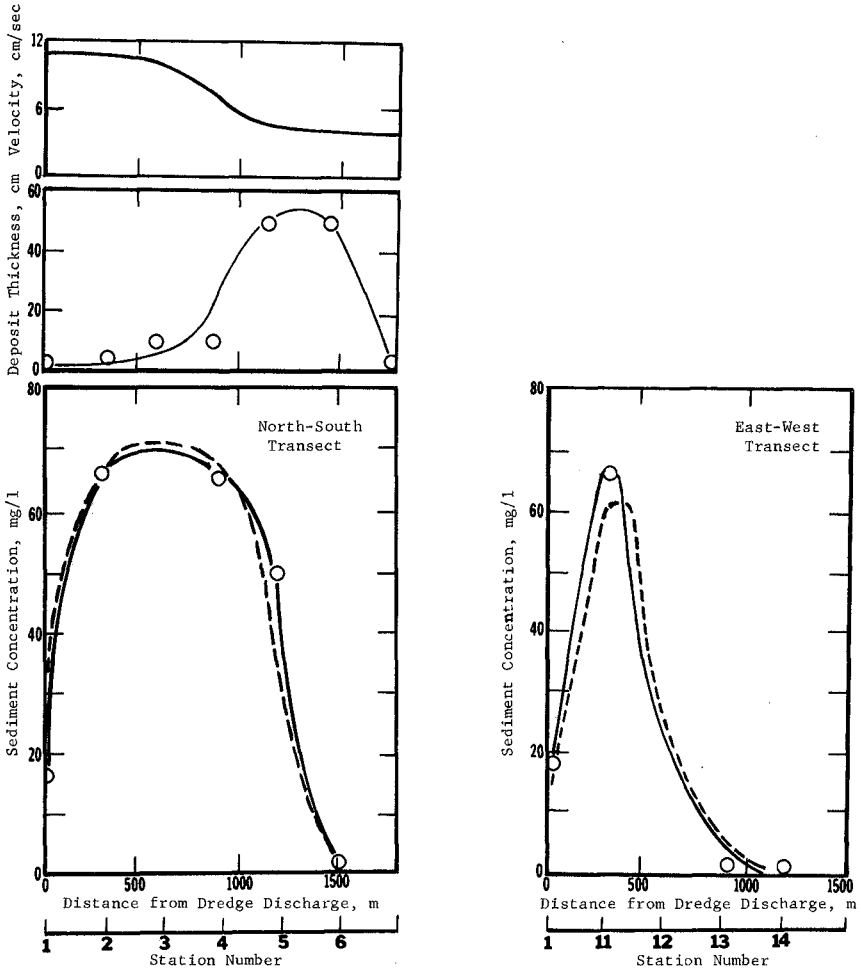


Figure 6.--Comparison of Model Calculated (Dash) and Field Measured (Solid) Results for Maintenance Dredging Program (Brett, 1975).

Naturally Occurring Sediment Transportation Events

The relationship of sediment transportation patterns to the hydrodynamic properties of Mobile Bay is shown by comparing model predicted velocity profiles with satellite photographs (Figure 7). In the case shown the hydrodynamic model was run at the local conditions observed during the photographic mission over the bay. The resulting velocity vectors were then reduced by a density slicing method where the following criteria were applied:

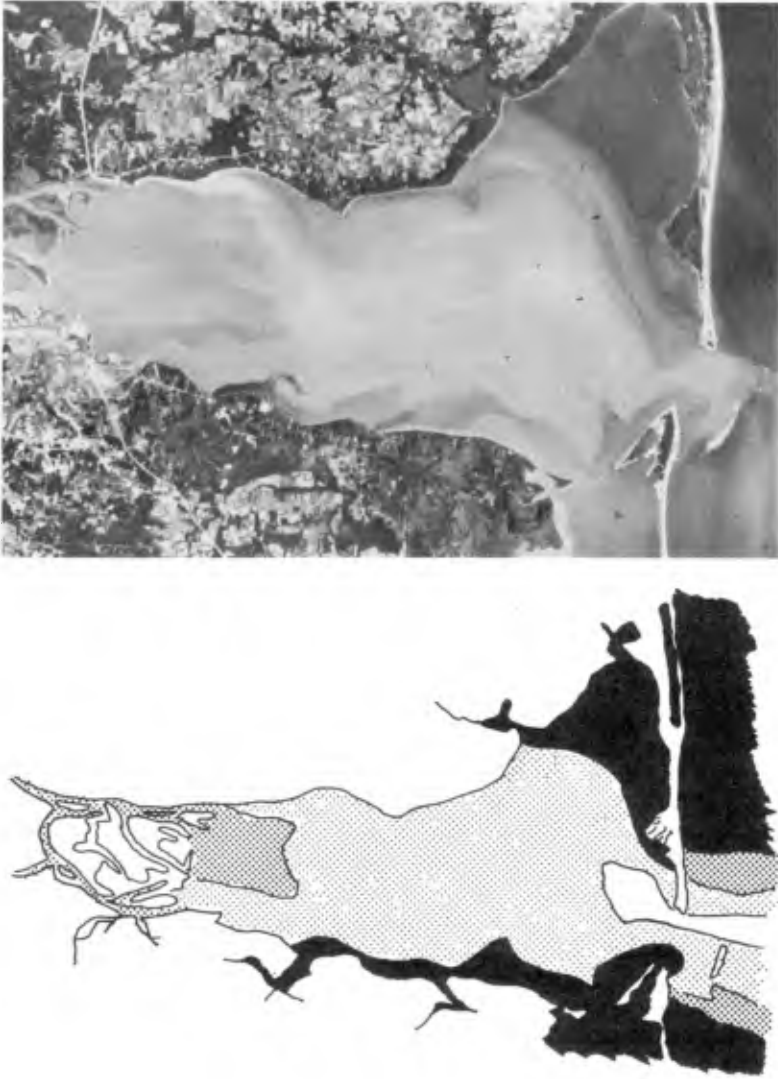
Category	1	2	3	4	5
Velocity Range m/sec	0-0.13	0.13-0.25	0.25-0.45	0.45-0.90	0.90-1.25

It should be noted that this method is highly acceptable when there is high sediment loads within the bay in which hydrodynamic factors constitute the primary driving force. Studies are in progress to better identify and account for those conditions which produce wind and/or bay bottom sediment disturbances.

The comparison shown indicates a first attempt at using remotely sensed data to complement mathematical modeling efforts. It also provides better coverage of bay behavior than what is currently available by either sporadic field data programs and photographic missions, the success of which is dependent on good meteorological conditions.

CONCLUSIONS

The above discussion of ongoing work related to the characterization of natural and man-made disturbances and the impact that they have on bay behavior is intended as a review of methods currently used. Because of the interrelationship of material transport (sediment) and hydrodynamic behavior (current), the use of mathematical modeling methods to predict change and assess impacts on the bay quality and material transport can be made. As seen the techniques can be rather crude such as those long range variations in sediment depositional potential or more refined analyses involving local, within tidal distribution of dredge materials. In either case, the dependency on data to calibrate and verify the results forms the critical step in the method. Once calibrated, however, the model results can be used to supplement data collection programs and provide a broader, more complete coverage than what is currently available. Some success has been shown for high sediment load conditions which are river oriented. Continued efforts to predict disturbances which are wind driven or which result from local bay bottom scouring is important to complete this area of investigation.



(A) (B)
Figure 7.--Comparison of Sediment Transportation Patterns Predicted by the Hydrodynamic Model (A) and Skylab IV photograph taken January 21, 1974 (B).

The knowledge gained from these studies have allowed, in many cases, quantification of results previously considered only in a qualitative sense. Although far from analytical in all cases, these methods provides a basis for assessing trends in behavior caused by natural and man-made disturbances. These methods also point out the need for continued investigations aimed at better descriptions of these complex systems which are vital to man's future.

ACKNOWLEDGEMENT

The authors would like to acknowledgement the support of the National Aeronautics and Space Administration, Marshall Space Flight Center and the United States Corps of Engineers, Mobile District, during certain phases of this study and other related investigations. The University of Alabama, Marine Science Program, is also thanked for their support during the developmental stages of the Mobile Bay modeling projects.

REFERENCES

- Brett, C. E., "Environmental Study of the Effect of Maintenance Dredging on Sediment Dispersion in Mobile Bay, Alabama," The University of Alabama, Tuscaloosa, Al., April 1975, 25 pages.
- Eckenfelder, W. W., Jr., Industrial Water Pollution Control, McGraw-Hill Book Co., New York, N. Y., 1966.
- Hill, D. O. and April, C. C., "A Hydrodynamic and Salinity Model for Mobile Bay," BER Report No. 169-112 (NAS8-29100), May 1974, 339 pages.
- Liu, H. A. and April, G. C., "A Non-Conservative Species Transport Model for Mobile Bay," BER Report No. 185-112 (NAS8-29100), January 1975, 185 pages.
- Ryan, J. J., "Sedimentologic Study of Mobile Bay," Department of Geology, Florida State University, Tallahassee, Fl., June 1969, 110 pages.
- Sapp, C. D., et. al, "Shoreline and Bathymetric Changes in the Coastal Area of Alabama - A Remote Sensing Approach," ALA-ADO-X996-CZMP-02, Geological Survey of Alabama, Tuscaloosa, Al., June 1975.
- U. S. Corps of Engineers, Mobile District, "Summary Printout of Monthly River Discharge Rates for Water Years 1928-1973; Mobile River at Mount Vernon," January 1974, 2 pages.

NOMENCLATURE

C	Concentration of Species in the Water Column, M/L^3
D	Depth of Water in the Bay, L
E	Rate of Mass Transfer by Evaporation, L/T
	Dispersion Coefficient, L^2/T
f	Bay Bottom Friction Factor
	Functional Representation
g	Gravitational Acceleration, L/T^2
H	Height of Water Above a Cell Datum, L
K	Constants
Q	Discharge Rate, L^3/T
R	Rate of Mass Transfer by Rainfall, L/T
	Rate of Disappearance or Appearance of Mass, M/L^3T
t	Time, T
V	Resultant of the Velocity Vector, L/T
v	Local Grid Velocity, L/T
W	Wind Velocity, L/T
x	Distance in the East-West Direction, L
y	Distance in the North-South Direction, L
z	Distance in the Depth Direction, L
∂	Differential Operator
θ	Temperature
ϕ	Wind Direction
ψ	Angle Measurement in the Coriolis Term

SUBSCRIPTS

b	Bottom
o	Source or Sink Term
r	Resuspension
s	Settling
	Surface
x	East-West Direction
y	North-South Direction
z	Depth Direction

CHAPTER 123

WAVE-FORMED RIPPLES IN NEARSHORE SANDS

John R. Dingle¹
Douglas L. Inman²

ABSTRACT

Ripples are generated and modified by wind-generated waves and their profiles are controlled by the nature of the near-bottom wave motion and by the size of the bed material. Wave-formed ripples develop under a definable set of conditions called the ripple regime. The ripple regime is bounded by those conditions that initiate grain motion, low-wave intensity, and by those that cause the disappearance of ripples, onset of sheet flow. Sheet flow occurs when intense wave motion causes several grain layers to be in motion. Three distinct ripple types occur in nearshore areas of fine sand - relict ripples, vortex ripples, and transition ripples. Vortex and transition ripples lie within the active ripple regime, whereas relict ripples do not.

Ripples in fine sand were studied in the field at La Jolla, California, where profiles were obtained using a newly developed high-resolution sonar capable of vertical resolution of the order of one millimeter. Simultaneous profile and wave-pressure measurements permit correlation of the ripple profiles with individual waves and with the wave spectrum. The sonar, with its rapid scan capability (\sim one meter per second), gives instantaneous measurement of the actively changing bed features in nearshore waters. The combination of bottom scans and wave-pressure measurements extends previous wave-ripple studies to include all of the nearshore ripple regime.

The relation between the wave and ripple data from this study is best shown by plotting ripple steepness η/λ against the wave form of the Shields relative stress criterion θ . Vortex ripples ($\eta/\lambda \sim 0.15$) occur for θ values less than 40 but greater than the minimum value which is determined by the onset of grain motion.

The transition from vortex ripples to sheet flow commences at a θ value around 40 and ends at $\theta_c \sim 240$, where θ_c is the critical value for the onset of sheet flow. With transition ripples, the decrease in steepness is caused by a decrease in ripple height, since the ripple wavelength remains essentially constant. Beds that become planar as a result of intense wave conditions ($\theta > 240$) re-ripple in a few wave cycles once the intensity decreases. For this reason, bottom scans taken before equilibrium is reestablished show ripples that have a low steepness.

-
1. U. S. Geological Survey, Menlo Park, CA 94025
 2. Scripps Institution of Oceanography, La Jolla, CA 92093

During some experiments where no sheet flow occurred between scans, migration of transition ripples was measured and found to range between zero and four centimeters per minute, increasing with increasing values of the theoretical bottom wave-drift current. Whenever migration was observed, it was in the direction of wave propagation, i.e., onshore.

Ripple symmetry is the ratio of the horizontal crest-to-trough distance β (in the direction of wave travel) to the ripple wavelength λ . A β/λ value of 0.50 indicates a symmetric ripple. Measured values of β/λ ranged from 0.36 to 0.61 with 74% of the values in the range 0.45 - 0.55, and 55% in the range 0.47 - 0.53.

INTRODUCTION

When progressive surface gravity waves shoal, interactions occur between the oscillating fluid and the bottom sediment. When these interactions become sufficiently intense, ripples develop on bottoms composed of sand. The oscillatory nature of the flow produces ripples that are generally symmetric in cross section, a geometry that is discernible from the distinctly asymmetric ripples formed by unidirectional flows. If the wave conditions remain constant for a long enough period of time, the ripples reach an equilibrium state with constant values of height and wavelength. The equilibrium ripple geometry is a function of the sand size and the character of the wave action above the bottom.

As shoaling progresses the near-bottom orbital velocities become more intense. This produces a ripple regime within which ripple sizes change systematically and within which each ripple is in equilibrium with the waves over it. For time periods of the order of a wave period, the movement of a ripple is characterized by an onshore-to-offshore oscillation of the ripple crest as first the wave crest and then the wave trough pass over the ripple. Any net movement of the ripple over longer time periods is related to differences in the crest and trough orbital velocities that occur in shallow water.

Flow conditions commensurate with the ripple regime occur over much of the nearshore, and the profile of the ripples varies within this region (Figure 1). In deeper water, where the wave action is generally too weak to move the sand, the bed generally contains relict ripples which formed under earlier, more intense wave action and which are gradually reworked by organisms. Ripples form once the wave action is of sufficient strength to move sand. Although the ripple height η and wavelength λ change as the wave intensity increases, the ripple steepness η/λ remains relatively constant (vortex ripples) until the bottom is subjected to the very strong flows that normally occur in relatively shallow water. As the flow strength increases beyond the conditions where vortex ripples occur, the ripples become less steep (transition ripples) until finally the ripples disappear as several grain layers are in motion (sheet flow regime). In deeper water the ripples tend to be relatively short crested, giving the bed a three-dimensional appearance (Inman, 1957). By the time transition ripples develop, ripple crests are quite long and the bed has become markedly two-dimensional in appearance.

Previous Work

Hunt (1882) and Darwin (1883), using laboratory wave tanks, were among the first to show that symmetrical ripples could be produced by oscillatory water motions. The work of Bagnold (1946) quantified the relation between ripple size and flow conditions. Bagnold's work has been extended by subsequent investigators, and now many aspects of oscillation ripples can be predicted with some degree of accuracy.

Bagnold's classic experiments on oscillation ripples demonstrated the relation between orbital diameter and ripple wavelength when flow conditions are near the threshold of grain motion (Figure 2). Once grains begin moving, ripples form and their wavelength is approximately equal to the orbital diameter. Increases in orbital diameter cause an increase in wavelength until a limiting value is reached, and the limiting value is grain size dependent. Over the range of orbital diameters studied by Bagnold, the wavelength was not a function of the period of oscillation. Bagnold did not extend the experiments to more intense flow conditions to determine whether the wavelength remained constant until sheet flow occurred.

Inman (1957), in a comprehensive field study of wave-formed ripples, obtained the ripple wavelengths by marking with grease pencil on clear plastic laid on top of the ripples. The near-bottom orbital displacements were measured in situ, while the wave period was obtained from the record of a fathometer mounted on a small boat. The results of Inman's work are shown in Figure 3. Except for a few points, ripple wavelength generally decreases with increasing orbital diameter. The Inman field data was produced under larger orbital diameters than the Bagnold laboratory data. Combining the two data sets reinforces Bagnold's observation that the ripple wavelength can only increase to a certain point with increasing orbital diameter. Then, rather than remain constant, as might be inferred from Bagnold's data, the wavelength actually decreases again. These aspects of ripple wavelength are integrated into a conceptual model of sedimentary structures by Clifton (1976).

Inman's rough estimates of ripple height gave a steepness value on the order of 0.15 except in the more intense flow regimes where the steepness began to decrease. Carstens, and his coworkers (1969), looking at oscillation ripples on sand beds using a pulsating water tunnel, also observed that the ripple steepness decreased from 0.15 under the most intense flows.

Most nearshore sands are composed of material with density similar to that of quartz (density of 2.65 gm/cm^3). It is important, however, that the variation of ripple form with grain density be studied for application to heavy mineral environments and to movable bed modeling. Mogridge and Kamphuis (1972) showed that variations in ripple height and wavelength can be significant, but that the ripple steepness is only weakly affected by grain density since the height and wavelength variations tend to cancel out. They further state that the importance of grain density diminishes as the wave period increases since fluid accelerations become less important at the longer periods.

Present Study

Previous studies show that the equilibrium ripple wavelength is a function of the grain size of the sediment and of the near-bottom orbital diameter of the oscillating fluid. Some of the earlier studies also suggest that the ripple steepness decreases systematically prior to sheet flow (it is zero at the onset of sheet flow). This study, undertaken as part of a doctoral program at the Scripps Institution of Oceanography (Dingler, 1974), establishes criteria for the limits of the ripple regime and describes the ripple geometry in the transition zone between constant steepness ripples and sheet flow. The lower limit of the ripple regime (onset of grain motion) was studied in a large wind-wave channel using oceanic wave periods and heights (Dingler, 1974). The upper limit (onset of sheet flow) and the ripple profile in the transition zone were determined by field measurement using a newly developed profiler. Most of the experiments were performed in the vicinity of the Scripps pier where the sediment is a well-sorted fine quartz sand.

THEORETICAL CONSIDERATIONS

Wave Relations

The wave and ripple parameters used in this study are sketched in Figure 4. The near-bottom orbital velocity u at any point is related to the maximum velocity u_m and the phase of the wave by

$$u = u_m \cos(\sigma t)$$

where t is time, $\sigma = 2\pi/T$ is the angular frequency of oscillation and T is the wave period (linear wave theory; Airy, [1845]). The maximum velocity, which occurs during crest and trough passage, is given by

$$u_m = \frac{\pi d_o}{T} = \frac{\sigma H}{2 \sinh(kh)} \quad (1)$$

where d_o is the orbital diameter, h is the water depth, H is the wave height, $k = 2\pi/L$ is the wave number and L is the wave length at the point of interest. The value of kh is obtained for a given depth and period by iterative solution of the wave dispersion relation

$$\left(\frac{2\pi}{T}\right)^2 \frac{h}{g} = kh \tanh(kh)$$

where g is the acceleration of gravity. In shallow water ($h/L < 1/20$) deviations from linear theory become significant with the exception that the near-bottom velocities are still reasonably predictable from linear theory (LeMehuate, et al., 1969; May, 1975).

When the wave train consists of waves of varying amplitudes and frequencies, Fourier analysis techniques are used to analyze the time series of the wave record. The technique used in this study follows the procedure of Cooley and Tukey (1965) with the final output being a plot of the mean-square elevation of the water surface $\langle \eta^2 \rangle$ per fre-

quency band Δf . Since the mean energy per unit area of water surface E is related to $\langle \eta^2 \rangle$ by

$$E = \rho g \langle \eta^2 \rangle = 1/8 \rho g H_{rms}^2$$

where H_{rms} is the root-mean-square wave height, $\langle \eta^2 \rangle$ is proportional to the available wave energy given that the fluid weight per unit volume ρg remains essentially constant for sea water. Then, u_m is related to $\langle \eta^2 \rangle$ by

$$u_m = \frac{\sigma (2 \langle \eta^2 \rangle)^{1/2}}{\sinh(kh)}$$

Another commonly used parameter, the significant wave height $H_{1/3}$, is assumed to be given by

$$H_{1/3} = \sqrt{2} H_{rms}$$

Dimensional Analysis

The ripple steepness η/λ is a function of seven independent variables. These seven variables are (1) fluid related: the fluid viscosity μ and density ρ ; (2) sediment related: the grain density ρ_s and grain size D ; and (3) flow related: the near-bottom orbital diameter d_o , the period of oscillation T , and the acceleration due to gravity g (note that grain-shape factors are not included in this analysis, although a completely general analysis would include shape and packing). Since u_m , d_o and T are related in linear theory (Equation 1), only two of these three variables are required to specify the wave conditions. As the immersed weight of the sediment depends on a density difference, the factor converting volume to immersed weight γ_s ,

$$\gamma_s = (\rho_s - \rho)g$$

replaces gravity as an independent variable. The complete dimensional functional relation is given by

$$\eta/\lambda = f(\rho, \mu, \rho_s, D, d_o, T, \gamma_s)$$

and this is non-dimensionalized to give the functional relation

$$\eta/\lambda = \phi \left[\frac{\rho \gamma_s D^3}{\mu^2}, \frac{\gamma_s T^2}{\rho D}, \frac{d_o}{D}, \frac{\rho_s}{\rho} \right]. \quad (2)$$

Equation (2) will be represented in shorthand notation by

$$\eta/\lambda = \phi (X_1, X_2, X_3, X_4).$$

A fifth dimensionless variable, the wave form of the Shields relative stress criterion θ , is obtained by combining X_2 and X_3 .

$$\theta = \pi^2 X_3^2 / X_2 = \rho u_m^2 / \gamma_s D.$$

The dimensionless variable X_1 is equal to Re^2/θ , where $Re = \rho u_m D/\mu$ is a Reynolds number. Although Re and θ include flow parameters, X_1 is formed by the fluid and granular properties only. It therefore reflects the influence of viscosity independent of the stage of the fluid-granular motion, and remains constant throughout the stages of the flow. The dimensionless variable X_2 indicates the influence of wave period. The dimensionless variable X_3 indicates the importance of the drag force F_D to the inertial force F_I in an oscillatory system. Thus,

$$F_D \sim D^2 u^2$$

and

$$F_I \sim D^3 (du/dt).$$

For oscillatory flow

$$du/dt = u_m \sigma \sin(kx - \sigma t).$$

Then

$$\frac{F_D}{F_I} \sim \frac{D^2 [u_m \cos(kx - \sigma t)]^2}{D^3 u_m \sigma \sin(kx - \sigma t)}.$$

Comparing maximum values, even though they are 90° out of phase, yields

$$\frac{F_D}{F_I} \sim \frac{u_m}{D} = \frac{d_o}{2D} = \frac{X_3}{2}.$$

The dimensionless variable X_4 is the "specific mass" and indicates the influence of the mass of grains ρ_s relative to that of fluid ρ . Since ρ_s is associated with inertial forces of the grains, its nondimensional form X_4 may be significant whenever grains are subjected to non-gravitational accelerations.

EXPERIMENTAL PROCEDURE AND DATA ANALYSIS

The results of this study are based primarily on field data as bed forms in the large wind-wave channel at Scripps were influenced by the channel boundaries during intense flow conditions. Most of the study was conducted in the high-energy nearshore environment at La Jolla, California, where flow conditions were sufficient to produce both ripples and a flat bed (Figure 5).

Ripple Profiling

Oscillation ripples on beds of fine sand tend to have elevations of the order of a centimeter and lengths of the order of a decimeter.

Ripple wavelengths can be measured rather accurately in situ with a meter stick, but ripple heights are almost impossible to measure manually because the weight of the meter stick flattens the crests and because constant water motion from the waves disrupts the measurement. To overcome this difficulty, a sediment surface profiler using high frequency sound waves (4.5 MHz) was developed (Dingler, et al., unpublished manuscript). The vertical resolution of the sonar was ascertained to be at least 1 mm. The sonar head was mounted in an open aluminum framework that sat about 25 cm above the bottom (Figure 6). The frame was easily transported and relatively scour free. Visual observations during field experiments under various flow conditions indicated that the flow disturbance caused by the sonar frame did not reach the sand bed.

Procedure

Most of the experiments were undertaken in the vicinity of the Scripps pier. Two Scuba divers entered the water at the end of the pier and the sonar frame with attached pressure sensor was lowered to the divers. The divers carried the sonar away from the pier in order to eliminate effects of the pier on the flow field and oriented the frame on the bottom normal to the ripple crests (Figure 6). A surface sample of sand was collected from each site.

Each experiment lasted at least 8.5 minutes. The procedure was repeated as many as three times at stations spaced about 70 m apart (on-offshore). Often wave intensities were such that sheet-flow conditions extended far enough offshore to permit only one experiment.

Sonar scans occurred about once a minute and each scan required from three to six seconds to complete. Generally, the scans were made to coincide with lulls in wave activity in order to minimize profile errors caused by crest movement during the passage of moderate to large waves. Also, under intense flow conditions, there was sufficient sand in suspension just above the bottom that the sonar responded to the suspended load rather than to the bed forms.

Data Reduction and Analysis

All the data was cabled to a shelf station where it was transmitted to the laboratory via the Shore Process Laboratory SAS system (Lowe, et al., 1972). The data was first digitized at a sample rate of 125 times per second with a 10 bit resolution. Then it was recorded on both strip chart and on magnetic tape. Each ripple profile was plotted from tape on graph paper and the data on the plots reduced by hand. Averages and standard deviations were obtained for ripple height, wavelength and asymmetry, and the averages were used in subsequent calculations. Finally, by following individual ripple crests from profile to profile an estimate of the migration rate for the ripples was obtained.

In some experiments the bed was smoothed by intense flows and subsequently re-rippled. In these cases the use of spectral wave parameters would be inappropriate. Instead, the analog pressure record was

directly analyzed and the wave parameters calculated from a few large waves that occurred before the scan of interest.

RESULTS AND DISCUSSION

Oscillation ripples occur over a range of definable flow conditions. The lower limit is the onset of grain motion and the upper limit is the occurrence of sheet flow. Within these limits the ripples have a cross-sectional geometry that is predictable when the flow intensity and grain size are known. Based on steepness, two types of ripples are found: vortex ripples (ripple steepness ~ 0.15) and transition ripples (ripple steepness < 0.15).

Ripple Geometry

Two data reduction procedures were used on the wave data in this study. In the first procedure the flow parameters were calculated from the wave spectrum and represent the root-mean-square values as recorded over an interval of 8.5 minutes. In the second procedure the near-bottom flow parameters were calculated from a short section of the wave record preceding the sonar scan and represent the "instantaneous" conditions prior to the measurement. In subsequent discussions the latter procedure will be referred to as the "single wave" procedure. It was employed only when flat bed conditions had been observed at some time during the experiment.

The nature of field experimentation generally precludes systematic variation of one dimensionless variable while holding the others constant as can be done in the laboratory. In the dimensionless functional relation

$$\eta/\lambda = \Phi(X_1, X_2, X_3, X_4)$$

the dimensionless variables X_1 and X_4 are independent of the flow conditions. By selecting field locations where the sediment is material of quartz density and where the grain-size variations are small, the effect of the variables X_2 and X_3 can be analyzed independent of X_1 and X_4 . When the data for fine sand is plotted as

$$\eta/\lambda = \Phi_1(X_2^a X_3^b)$$

on log-log paper, values of $a = -1$, $b = 2$ produce a coherent trend to the data. This is not surprising as this combination of the two dimensionless groups is proportional to the relative stress Θ (Equation 3) which is an important variable in many fluid-granular interactions.

Ripple steepness is plotted as a function of relative stress in Figure 7. Although the data shows a consistent trend when plotted in this manner, the steepness values begin to decrease at a lower value of the relative stress than in the studies of Inman and Carstens, et al. This occurs because there is a fundamental difference in analysis procedures. Bed forms for fine sand respond rapidly (i.e., in one or two wave periods) to changes in wave characteristics. The "single wave" procedure, which emphasizes instantaneous conditions, is thus similar to

the constant wave conditions of the laboratory. The spectral analysis procedure, on the other hand, considers waves of varying height and period occurring over a time period of 8.5 minutes. To emphasize the importance of larger waves on the ripple geometry, Inman used an orbital diameter parameter based on the significant wave rather than the root-mean-square wave. When Figure 7 is modified to emphasize the importance of the larger waves on the ripples (Figure 8), correlation is significantly improved for those conditions where the data sets overlap.

Figure 9 is a five minute record of the second experiment of 26 October 1972 at a water depth of 3.4 meters. The top trace is the wave record as measured at the pressure sensor. The second trace shows the output of the sonar head as it sat at the onshore end of the track. The third trace gives time relative to the start of the experiment. The times of the scans are indicated by arrows and the scans are shown in the bottom four traces. At the time of scan 1 the bed was rippled and the steepness value fell on the equilibrium curve of Figure 8. Subsequently, a set of large waves produced sheet flow and a flat bed (scan 2). Following the passage of several smaller waves the bed again was rippled, although the steepness had not yet reached an equilibrium value (scan 3). Before equilibrium was reached a set of two large waves almost re-leveled the bed (scan 4). This series of bed profiles shows that in fine sand the bed responds rapidly to intense flow and a bed can be flattened and re-rippled in a time equivalent to a few wave periods.

The transformation of a fine sand bottom from transition ripples to a flat bed occurs over one or two wave periods. Assume that the bottom is subjected to waves of variable height and of sufficient intensity that transition ripples occur following the passage of intermediate height waves, while the largest waves produce sheet flow and a flat bottom. Once the flat bottom occurs, it persists during periods of the smallest waves because they are not of sufficient intensity to move the sand. As the wave conditions intensify, sediment begins to move and vortex ripples start to form. If these wave conditions were to persist for a sufficient time (minutes), the ripples would eventually reach an equilibrium configuration with a steepness of about 0.15. This wave pattern does not persist for more than a few wave cycles in such a variable system and only transition ripples form.

Transition ripples occur for relative stresses greater than 40, but less than the critical value for sheet flow. The decrease in steepness of the transition ripples is attributable to decrease in ripple height since the experiments show that the ripple wavelength itself remains constant for these flow conditions (Figure 10). At a critical relative stress value of 240 sheet flow prevails and a flat bed again forms. The growth of the ripples from a flat bed to transition ripples is schematized by dashed lines in Figure 8.

The effect on ripple steepness of the dimensionless variable $X_1 = \rho \gamma_s D^3 / \mu^2$ was not determined conclusively because of a lack of good study sites with coarse sand. The only usable information on the importance of larger grain sizes came from some preliminary laboratory experiments and from a few field experiments. All of the laboratory and all

but two of the field data points were for vortex ripples (Figures 7 and 8). The two transition ripple values fall with the fine sand values, which suggests that ripple steepness does not strongly depend on the dimensionless variable X_1 . This is consistent with the findings of Mogridge and Kamphuis (1973).

Because the grain density remained constant for the field experiments, X_4 was not evaluated. Mogridge and Kamphuis state that this variable is not important with respect to the ripple steepness although X_4 does have a significant effect on the ripple height and wavelength.

The criterion for the onset of grain motion under progressive waves has been shown to be

$$\frac{\gamma_s T^2}{\rho D} = 240 \left[\frac{d_o}{D} \right]^{\frac{4}{3}} \left[\frac{\rho \gamma_s D^3}{\mu^2} \right]^{-\frac{1}{9}}$$

when the grain diameter is less than the (theoretical) thickness of the wave-formed boundary layer (Dingler, 1974). Rearrangement of this relationship in terms of the threshold relative stress θ_t gives

$$\theta_t = 0.0027 (\gamma_s^2 / \rho \mu)^{\frac{1}{3}} T. \quad (4)$$

For the case of material of quartz density ($\rho_s = 2.65 \text{ gm/cm}^3$) in a typical nearshore environment ($\rho = 1.0 \text{ gm/cm}^3$, $\mu = 1.1 \text{ centipoise}$), equation (4) reduces to

$$\theta_t = (1.7 \text{ sec}^{-1}) T.$$

In Figure 8 this relation has been superimposed upon the curve for the equilibrium ripple steepness to indicate the lower limit of the ripple regime for various wave periods.

Ripple Migration

Ripple migration under oscillatory flow conditions might be expected to occur when a net fluid flow is superimposed on the oscillations. The bottom wave-drift current has been shown to produce an onshore ripple migration in the laboratory (Inman and Bowen, 1963). Ripple migration is a critical aspect of sediment transport over the shelf since the rate of grain migration is inherently related to the burial and exposure of the grains by the moving ripple form (Inman and Bagnold, 1963). Study of ripple migration for transition ripples is complicated by the occasional destruction or near destruction of the ripples and by the associated high sediment concentrations in sheet flow. The migration rate of the sand thus involves both movement of the ripple form and movement by sheet flow.

The intermittent scanning of the bottom prevented ripple migration measurements for every experiment. Yet in several experiments, the position of individual ripple crests could be traced from scan to scan and the migration rates of these ripples showed a positive correlation

with the theoretical bottom wave-drift current u_0 (Table 1).

$$u_0 = 5/4 u_m^2 T/L. \quad (5)$$

A better understanding of the nature of the bottom wave-drift current over rippled beds is necessary before a more detailed study of ripple migration rates can be attempted.

Table 1

Ripple migration rates obtained from repeated sonar scans. The bottom wave-drift current u_0 is calculated from Equation 5 using rms values from the wave spectral analysis.

Experiment	u_0 , cm/sec	Migration rate cm/min
1	4.7	4.2
6	3.2	1.2
11	2.8	0.5
9	1.2	0.0

Ripple Shape and Variability

Analysis of the ripple profiles included the measurement of the horizontal distance from crest to onshore trough β , which when divided by the wavelength λ , is indicative of the symmetry of the ripple form. The ripple symmetry factor β/λ is 0.50 for a symmetrical ripple, less than 0.50 when the ripple has a steep onshore facing crest, and greater than 0.50 for a steep offshore facing crest. The measured values of β/λ ranged from 0.36 to 0.61 with 74% of the values in the range 0.45 - 0.55, and 55% in the range 0.47 - 0.53. There was no correlation between the symmetry value and the relative stress for the spectrally related ripples, but this can be attributed to the fact that the ripple scans followed specific waves while the relative stress was based on 8.5 minutes of wave record. Even though the ripple height and length do not change with every wave for non-sheet flow conditions, a large wave crest or trough could slightly modify the steepness factor by a slight onshore or offshore movement of the ripple crest. Some uncertainty in the measurement of β due to the flat nature of ripple troughs also contributed to the range of symmetry values. The β/λ values for the "single wave" ripples showed some correlation with the relative stress such that a β/λ value of 0.42 corresponded to the lowest relative stress value and β/λ increased to 0.48 with increasing relative stress.

Standard deviations were calculated for the ripple parameters η , β , and λ . For comparative purposes these values were expressed as the coefficient of variation that is defined as the ratio of the standard deviation to the mean value. For all the data, the values of the coefficient of variation for η and β were generally between 0.10 and 0.25 while for λ they were often less than 0.10. Some of the variation in the ripple elevation is probably due to the fact that the elevations were generally so small that their measurement has a lower relative accuracy than that of the other parameters. The β measurements were

more variable than the λ measurements because of the greater difficulty in determining the exact location of the lowest part of the trough.

CONCLUSIONS

From this study of wave-formed ripples in a high-energy nearshore sand environment these conclusions are drawn:

1. Once ripples form, their steepness is controlled by the relative stress. The steepness remains constant until the relative stress reaches a value of 40, then decreases to zero (flat bed) for sheet flow.
2. Sheet flow, which produces flat beds, commences at a value of the relative stress of 240.
3. Relative stresses greater than 240 cause ripples in fine sand to disappear and the bed to become flat after the passage of one or two large waves. A rippled bed reappears after the passage of a few smaller waves.
4. Ripple migration rates in fine sand range from zero to 4.2 cm per minute. The migration is always onshore and can be correlated with the theoretical bottom wave-drift current.
5. Grain size appears to have negligible effect on steepness of vortex or transition ripples. It should be noted however, that the maximum ripple wavelength and height are grain size dependent.
6. Ripple symmetry ranged from 0.36 to 0.61 with 55% of the values falling in the range 0.47 - 0.53 and 74% in the range 0.45 - 0.55.
7. A sonic bed profiler operating at 4.5 MHz is capable of resolving the ripple elevation to at least 1 mm and works well in both the laboratory and the field.

Acknowledgements

This research was supported by the Sea Grant Program and the Office of Naval Research under contract with the Scripps Institution of Oceanography, University of California, La Jolla, California.

REFERENCES

- Airy, G. B., 1845, "On tides and waves", Encyclopedia Metropolitana, vol. 5, p. 241-396.
- Bagnold, R. A., 1946, "Motion of waves in shallow water; interaction between waves and sand bottoms", Proc. Roy. Soc. London A, 187, p. 1-15. Includes G. I. Taylor, 1946, (16-18).
- Carstens, M. R., F. M. Neilson and H. D. Altinbilek, 1969, "Bed forms generated in the laboratory under an oscillatory flow: analytical and experimental study", U. S. Army Corps of Engineers, Coastal Eng. Res. Center, Tech Memo 28, 105 pp.

- Clifton, H. E., 1976, "Wave-formed sedimentary structures---a conceptual model", SEPM Special Publication, (*in press*).
- Cooley, J. W., and J. W. Tukey, 1965, "An algorithm for the machine calculation of complex Fourier series", Mathematics of Computation, vol. 19, no. 90, p. 297-301.
- Darwin, G. H., 1883, "On the formation of ripple mark in sand", Proc. Roy. Soc. London, Series A, vol. 36, p. 18-43.
- Dingler, J. R., 1974, "Wave formed ripples in nearshore sands", Ph.D. thesis, University of California, San Diego, 133 pp.
- Dingler, J. R., J. C. Boylls, and R. L. Lowe, 1976, "A high-frequency sonar for profiling small-scale subaqueous bedforms", unpublished manuscript.
- Hunt, A. R. 1882, "On the formation of ripple-mark", Proc. Roy. Soc. London, Series A, vol. 34, p. 1-18.
- Inman, D. L., 1957, "Wave-generated ripples in nearshore sands", Beach Erosion Board, U. S. Army Corps of Engineers, Tech. Memo 100, 65 pp.
- Inman, D. L. 1974, Unpublished teaching notes: S10 216 Physics of Sediment Transport, University of California, San Diego, California.
- Inman, D. L. and R. A. Bagnold, 1963, "Littoral processes", The Sea, vol. 3, M. N. Hill, ed., Interscience, New York, 529-553.
- Inman, D. L. and A. J. Bowen, 1963, "Flume experiments on sand transport by waves and currents", Proc. Eighth Conf. Coastal Engng., Amer. Soc. Civil Eng., p. 137-150.
- LeMehaute, B., D. Divoky and A. Lin, 1969, "Shallow water waves: a comparison of theories and experiments", Proc. Eleventh Conf. Coastal Engng., Amer. Soc. Civil Eng., p. 86-96.
- Lowe, R. L., D. L. Inman, and B. M. Brush, 1973, "Simultaneous data system for instrumenting the shelf", Proc. Thirteenth Conf. Coastal Engng., Amer. Soc. Civil Eng., vol. 1, p. 95-112.
- May, J. P., "Ability of various waterwave theories to predict maximum bottom orbital velocities in the shoaling wave zone", Coastal Research Notes, vol. 4, No. 6, p. 7-9.
- Mogridge, G. R., J. W. Kamphuis, 1973, "Experiments on bed form generation by wave action", Proc Thirteenth Conf. Coastal Engng., Amer. Soc. Civil Eng., vol.2, pp. 1123-1142.

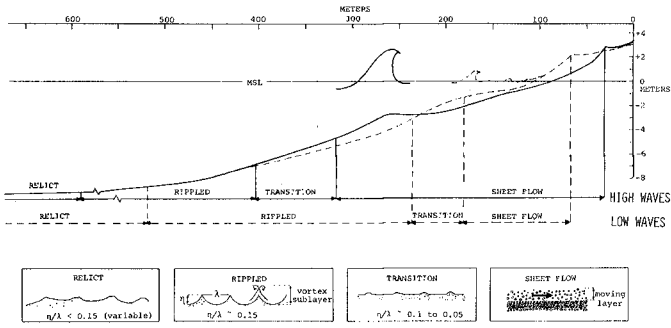


Figure 1. Range in characteristic ripples under varying wave conditions in nearshore waters (modified from Inman, 1974).

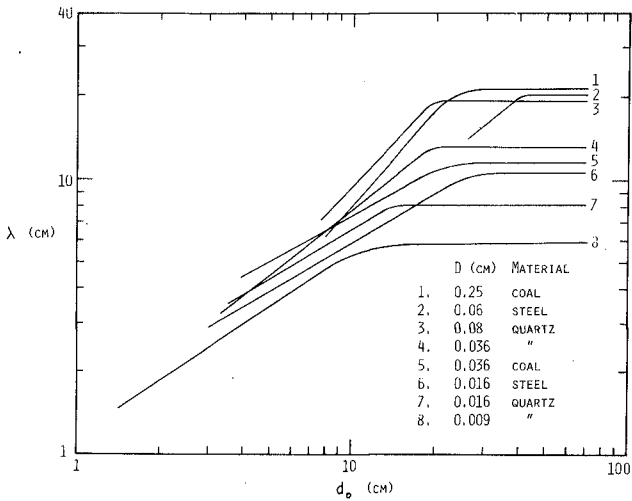


Figure 2. Relation between ripple wavelength λ and orbital diameter d_0 for sand size material of various grain sizes and densities (Bagnold, 1946).

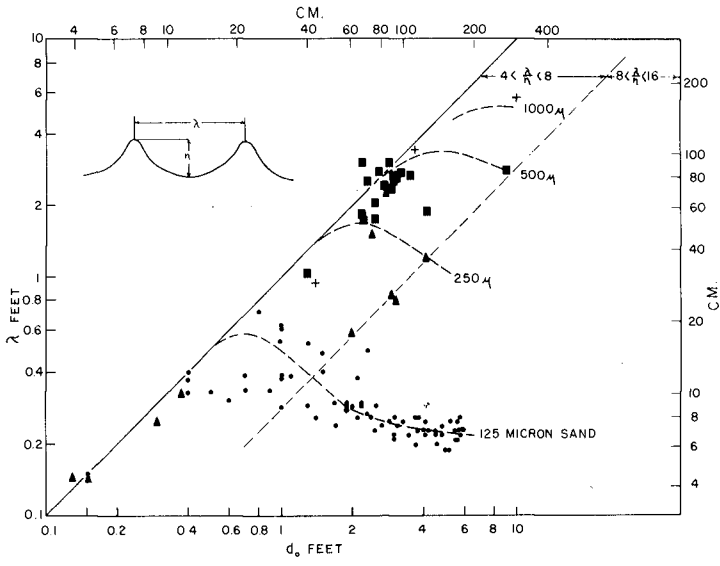


Figure 3. Dependence of ripple wavelength λ on orbital diameter d_0 for ocean waves (Inman, 1957).

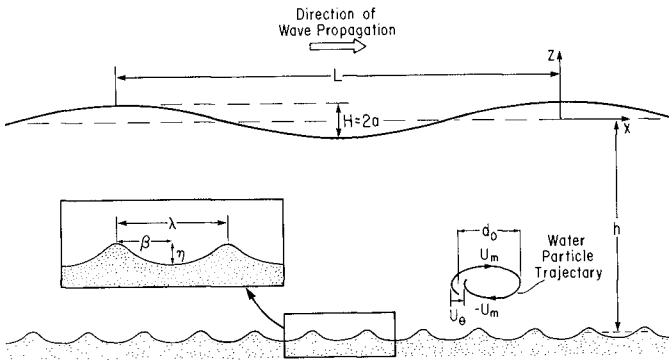


Figure 4. Definition sketch for wave and ripple parameters used in this study.

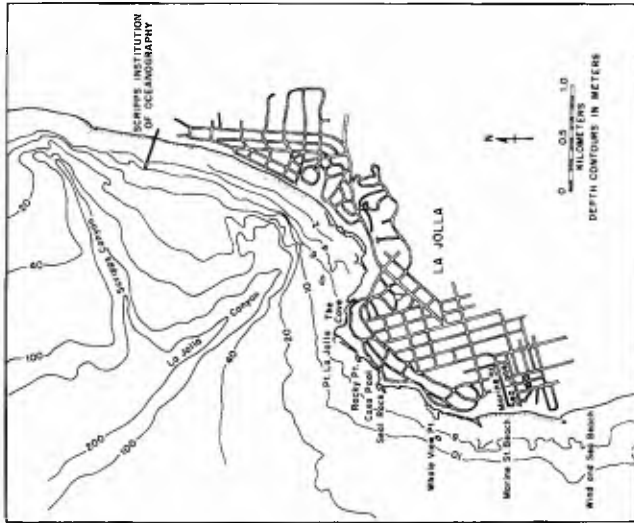


Figure 5. Location map for field sites at La Jolla, California. Experimental sites were: (1) off Scripps Institution of Oceanography pier, (2) outside Casa Pool, and (3) off Marine Street Beach at Sea Lane.

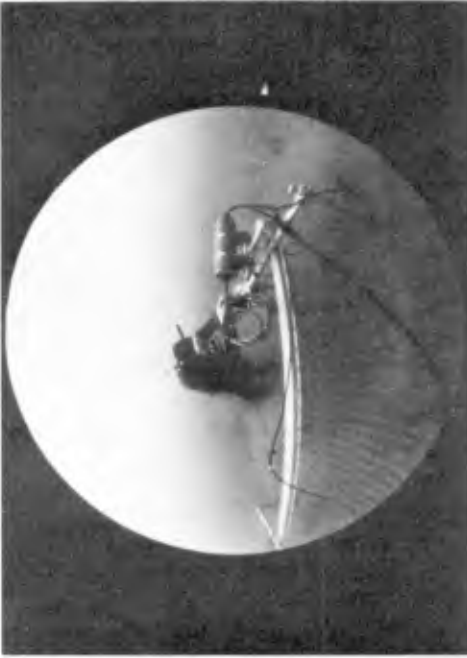


Figure 6. Fish-eye photograph of sonar transducer and mounting frame on site over a fine sand bed (Photograph by Tom Harman).

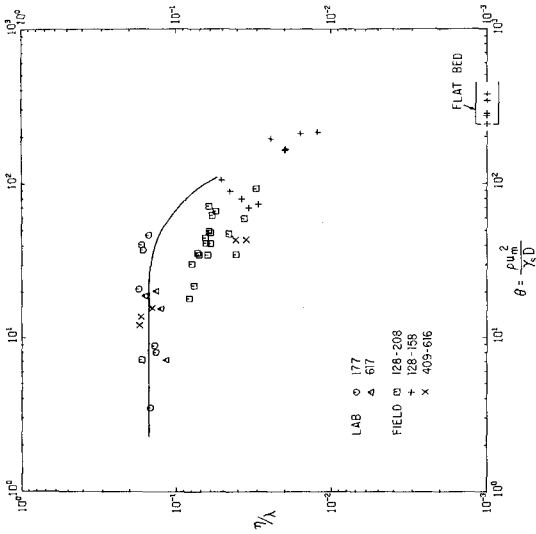


Figure 7. Ripple steepness η/λ as a function of relative stress θ . The solid line shows the mean of earlier data (Inman, 1957; Carstens, et al., 1969). All data are from the present study. Wave computations based on: θ , spectral analysis using H_{rms} ; \circ , Δ , steady amplitude (laboratory); $+$, \times , single wave (field). Median diameter in microns. Values in the box on the abscissa indicate scans where the sonar profiled a flat bed.

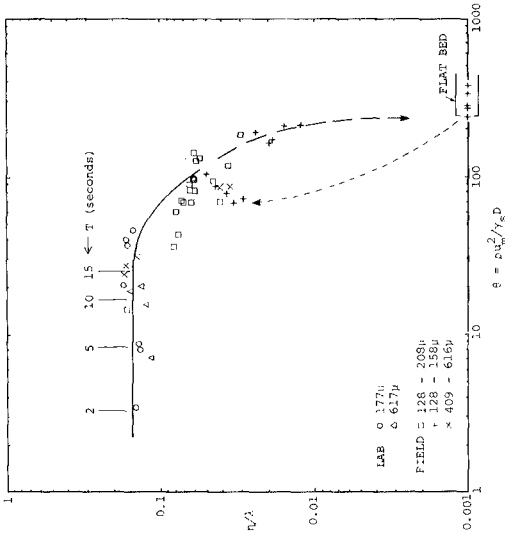


Figure 8. Ripple steepness η/λ as a function of relative stress θ with the spectral analysis wave computations \square converted to $H_{1/3}$. Symbol explanation otherwise the same. Data trends indicated by dashed lines. Short vertical lines give the onset of grain motion for selected wave periods (from Dingle, 1974).

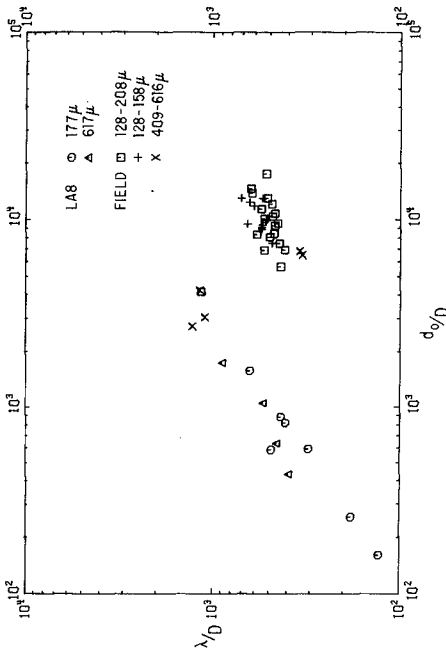


Figure 10. Dependence of relative ripple wavelength λ/D on dimensionless number d_0/D for field experiments in beds of quartz material. Data from the present study.

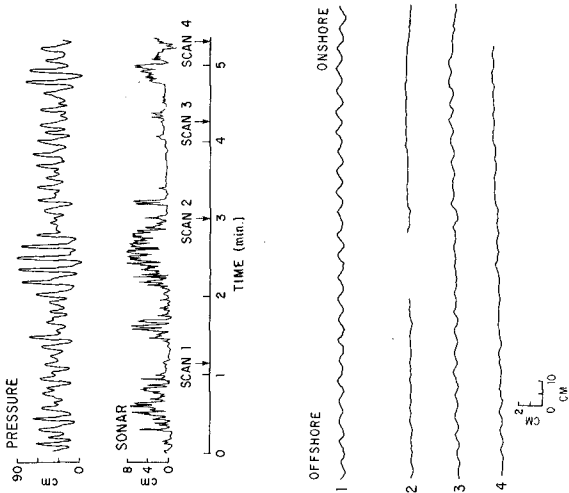


Figure 9. Analog records from field experiment of 23 October 1973 showing pressure and sonar at rest (above) and sonar scans 1-4 (below). Site north of Scripps Institution of Oceanography pier at a water depth of 3.4 meters. Bottom composed of fine sand with a median diameter of 151 μm .

CHAPTER 124

ORIGIN OF SUBMARINE DUNES

by

M.S. Yalin¹

ABSTRACT

The turbulent bursting process is outlined and attention is drawn to the fact that the "coherence distance" of the regenerating macroturbulent eddies is of a magnitude that is much the same as the length of dunes. Consequently it is postulated that the length of dunes is merely the "imprint" of the coherence distance on the deformable surface of a movable bed and the origin of dunes is explained accordingly. It is shown that the frequently observed similarity between tidal and unidirectional dunes is due to the similarity of the tidal transport and the transport corresponding to an intermittent unidirectional flow. The explanations presented herein are expected to be valid for dunes caused by both unidirectional flows and tidal currents.

INTRODUCTION

Measurements carried out in the field indicate that the large scale bed features (dunes, megadunes) produced by tidal currents approximate rather closely to the dunes produced by the equivalent unidirectional flows. Thus in Ref [1] H. Ozasa states that "the dimensions of submarine sand waves (dunes) formed by tidal currents in the Bisan Strait at the Seto inland sea in Japan are approximately equal to the values calculated by Yalin's formula". Similarly, in Ref [2] Per Bruun points out that the dunes on the bottom of the Cook Inlet in Alaska are much the same as those on the bottom of the Mississippi river (where the flow conditions are comparable with those of the Cook Inlet). The data obtained from some parts of the British coast also appear to indicate the resemblance between the two types of dunes (W.A. Price, Hydraulics Research Station, Wallingford - private communication).

The approximate equality of unidirectional and tidal dunes can be explained by the similarity of the mechanisms of their production. Indeed if a tidal current is present then the cyclic velocity and shear stress diagrams (corresponding to a location) can no longer be symmetrical. It will be assumed in the following that the positive part of the τ_0 diagram is higher than its negative part (Fig 1) and that

¹ Professor of Hydraulics, Queen's University, Kingston, Canada.

$$|(\tau_o)_{\max}^+| > (\tau_o)_{cr} \quad \text{while} \quad |(\tau_o)_{\max}^-| < (\tau_o)_{cr} \quad (1)$$

In this case the transport will be present, and dunes will form, only during the time interval θ^+ when the tidal flow is virtually a unidirectional flow. One can say that if (1) is valid, then the dunes are formed by the tidal flow in the same manner as if they were formed by an intermittent unidirectional flow. It should be remembered that the duration (\mathcal{C}) of the development of large size dunes is of the order of several months. Thus \mathcal{C} is much larger than the tidal period T which justifies the expression "intermittent unidirectional flow". Clearly in some cases $|(\tau_o)_{\max}^-|$ can also be larger than $(\tau_o)_{cr}$. This, however, can hardly invalidate the above description in principle, as the presence of the less effective opposite transport during θ^- will merely reduce the efficiency of the "build up" during θ^+ . The reduction of "efficiency" will, of course, lead to the extension of the development duration \mathcal{C} , but this has no bearing on the argument.

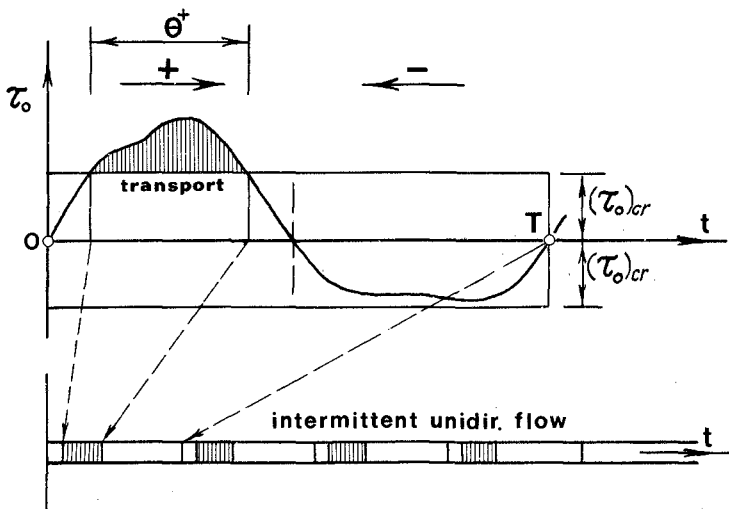


FIG. 1

No dunes have been observed in laminar flows, and the prevailing view is that they are due to turbulence. The author is of the same view. The present paper is his attempt to explain the occurrence of dunes in the light of the new information gained in the field of turbulence research.

Much has changed with regard to the understanding of turbulent flows in the past few years. Recent research (Refs [3] to [8]) has revealed that "turbulence is not as chaotic and random as has been assumed previously", (J. Laufer, Ref [3]). It has been found that turbulence contains in its structure "a certain order" which manifests in the form of an "observable chain of events", even if the elements forming this "chain" exhibit some substantial stochastic deviations from their (definable) average values. The total chain of the events mentioned is referred to as the "bursting process". In the following, first outline information on the bursting process is given, then, using this information, an attempt is made to explain the origin of dunes (i.e., of the sand waves which have the size proportional to the external dimensions of flow). This explanation appears to be clearer than previous ones (Ref [9]).

The descriptions and considerations that follow refer to unidirectional flows. However, as it can be inferred from the earlier part of this Introduction, they should be applicable also to tidal flows (during the time intervals θ^+).

BURSTING PROCESS

1. Consider a developed macroturbulent eddy E transported in the direction of the flow (Fig 2.1). The current formed by the (adverse) velocities of its lower part is referred to as the "sweep". The arrival of a sweep at a location of the flow boundary (bed) slows down the flow contacting the bed at that location. The reduction of the flow velocities leads to a local conversion of turbulent flow contacting the bed into a retarded viscous flow. Since the eddy E is usually three-dimensional (e.g., spheroidal rather than cylindrical) the sweep and consequently the retarded local viscous flow layer, shortly the "low-speed streak", are also three-dimensional (i.e., they have a limited width).
2. The passage of the eddy E further downstream causes appropriate conditions for the "separation" (or the "lift-up") of the low-speed streak (Fig 2.2), and consequently for the formation of a "recirculation cell" C. The separated low-speed streak ("ejected fluid") and the recirculation cell C constitute together the "lifting module" which moves away from the bed and which is transported downstream (by the time average flow).
3. The removal of the lifting module causes the replacement fluid to move instead ("cleansing sweep"). Thus the motion of the lifting module inevitably generates a flow field as shown schematically in Fig 2.3. Note that the recirculation cell C and the cleansing sweep adjacent to its downstream side form a "new" eddy E' which progressively grows in its size when the elevation of the lifting module increases. One can say that the progress of the lift-up is equivalent to the growth of a "newly born" macroturbulent eddy (E').

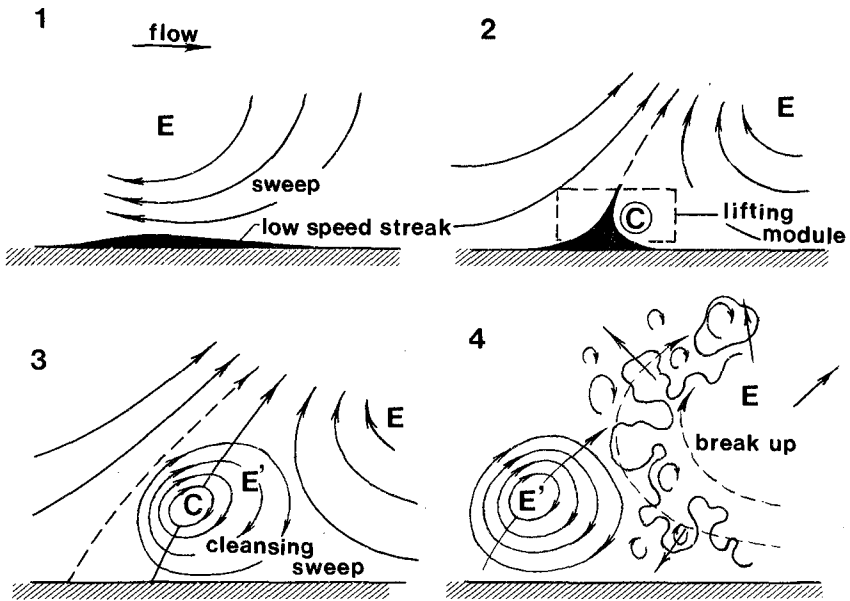


FIG. 2

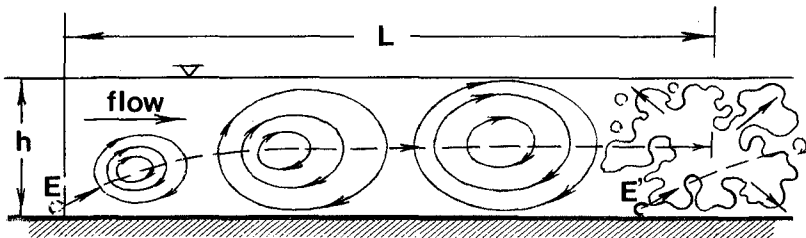


FIG. 3

4. The lifting module E' moves downstream immediately behind the "parent" module E . Since much of the energy of the parent module E was spent for the birth of E' , the module E is in a "weak" state, and therefore the adverse velocity fields of E' and E (Fig 2.4) are likely to destroy the module E by disintegrating it into a multitude of smaller eddies ("break-up phase"). The scattered multitude of smaller eddies manifests itself in the form of high frequency fluctuations (microturbulence) superimposed on the low frequency ones (macroturbulence).

Although the study of the quasi-cyclic events is still only at its beginning, the researchers in the field seem to be in agreement that the bursting process is regenerative, i.e., that the "birth" of one module is associated with the "death" of another, and thus that the path of a module (E) should end at the location where the path of the next module (E') begins (Fig 3). Let L be the average value (expectation) of the possible path lengths L_i . It is clear that the length L , which can be called the average

"coherence length", is yet another linear characteristic determining the internal structure of a turbulent flow (in addition to the eddy sizes ℓ). Since a macroturbulent eddy carried by the flow downstream can maintain its identity or coherence only along a distance L_i comparable with L , a

"signal" transmitted by an eddy, on average, cannot travel farther than L . One can say that the length L signifies the average extent of the longest disturbances that can occur in the longitudinal direction (x) of a turbulent flow. How big are the coherence lengths L_i of macroturbulent eddies? The measurements of M.A. Badri Narayanan and his co-workers (Ref [5]), carried out for a boundary-layer flow, indicate that the distances L_i are "of the order of several boundary-layer thicknesses δ ". Indeed, as can be seen from their plot (Fig 9 (middle) in Ref [5]), the majority of the experimental points are scattered within the interval

$$\approx 4 \delta < L_i < \approx 7 \delta \quad (2)$$

which includes the value $L_i = 2 \pi \delta$. In the case of a two-dimensional flow in an open channel, h must figurate instead of δ and one would expect that the average coherence distance should be close to $2 \pi h$ which is a "standard" for the orientative prediction of the length of dunes. A more detailed prediction of the dune length Λ can be carried out with the aid of Fig 7.28 in Ref [9] which is the graph of the function

$$\Lambda = \phi(X, Z) \cdot h \quad (3)$$

where $\phi(X, Z) \approx 2 \pi$ if $X > \approx 40$ and/or $Z > \approx 10^4$.

If (as is often postulated) the large scale formations on the flow bed (dunes) are caused by the large scale longitudinal disturbances that occur in the velocity field (u) of a turbulent flow, then the effective spectral density function $S(\omega)$ of the stochastic process $u = f(x)$ (which reflects the fluctuations along the flow direction x at a given instant) must be regarded as defined over a "narrow band" which includes the lowest spacial frequencies $\omega = 1/L_i$ only (Fig 4). The frequency $1/L$ is in the midst of the "band", corresponding autocorrelation function being

$$R_x = e^{-\alpha x} \cdot \cos \left(2 \pi \frac{x}{L} \right) \quad (4)$$

As is clear from the (trigonometric) nature of this function, shown schematically in Fig 4, any disturbance of the field u at a section $x = 0$, say, must be accompanied by similar kinds of disturbances (along x) with the intervals L . For example, if the disturbance in the field u at $x = 0$ (e.g., due to an imperfection or discontinuity on the bed surface) is as to produce an "accretion" (+), then the tendency for an accretion will also be present at the sections $x = L, 2L \dots$ etc. (though with a lesser intensity, due to the "damping factor" $e^{-\alpha x}$); at the sections $x = L/2, 3L/2 \dots$ etc., the tendency for an "erosion" (-) will be present. The sequence of alternate accretions and erosions will inevitably deform the flat initial bed surface into a wavy one, the wave length Λ being the same as L .

When concluding this paper it should be mentioned that the average coherence length L of macroturbulent eddies is, in fact, proportional to their maximum size ℓ_{\max} . Since in the case of a unidirectional flow the size of the largest eddies is the same as the thickness of the flow (δ or h) the proportionalities such as $L \sim \delta$ or $L \sim h$ (introduced above) are justifiable. In general, however, $L \sim \ell_{\max}$, and $\Lambda \approx L$ should be regarded as given by

$$\Lambda \approx 2 \pi \cdot \ell_{\max} \quad (5)$$

(if $X > \approx 40$ and/or $Z > \approx 10^4$)

In some cases of a tidal flow the time average value of ℓ_{\max} (during θ^+) may be less than the average flow depth h , and therefore it would be more prudent to consider the length Λ of the tidal dunes as a quantity which "cannot exceed $2 \pi h$ " (if $X > \approx 40$ and/or $Z > \approx 10^4$) rather than as that which is "equal to $2 \pi h$ ".

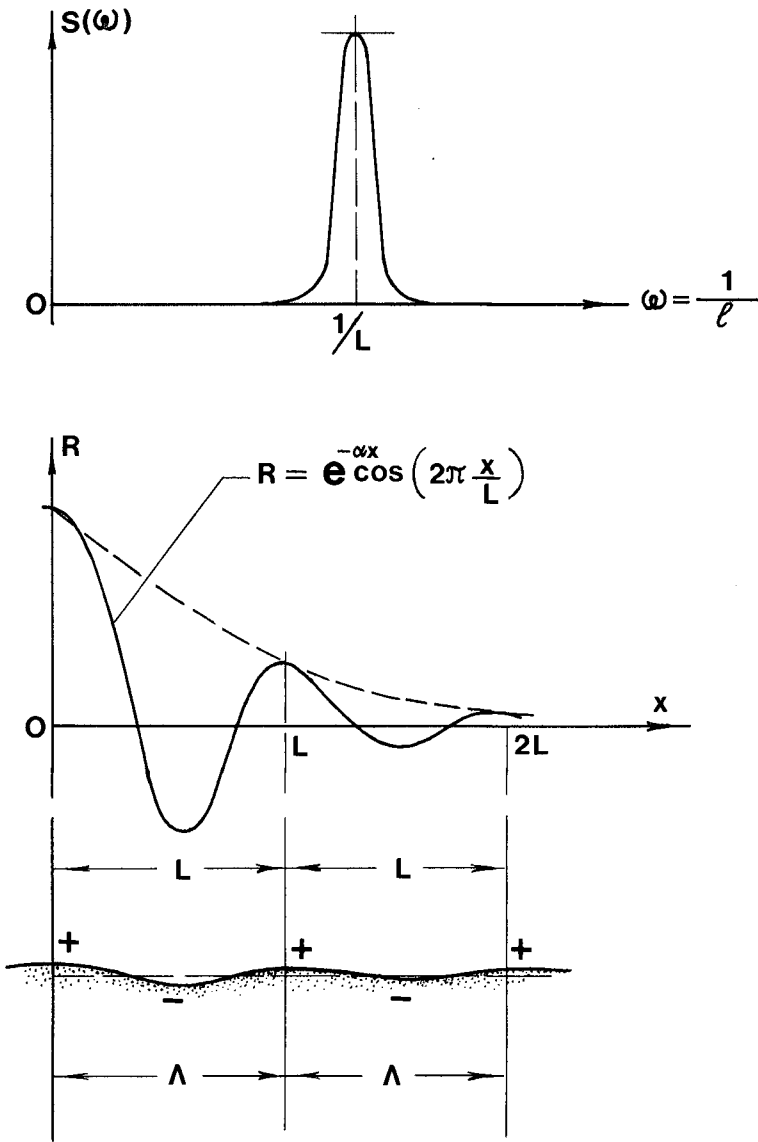


FIG. 4

REFERENCES

1. H. Ozasa: Field investigation of large submarine sand waves. Coastal Engineering in Japan, Vol. 17, 1974.
2. Per Bruun: Port Engineering. Gulf Publishing Co., Houston, Texas, 1973.
3. J. Laufer: New trends in experimental turbulence research. No. 8076, Annual Review of Fluid Mechanics, Annual Reviews Inc., Palo Alto, California, Vol. 7, 1975.
4. G.R. Offen, S.J. Kline: A proposed model of the bursting process in turbulent boundary layers. J. Fluid Mech., Vol. 70, Part 2, 1975.
5. K. Rao, R. Narasimma, M.A. Badri Narayanan: The "bursting" phenomenon in a turbulent boundary layer. J. Fluid Mech., Vol. 48, 1971.
6. G.R. Offen, S.J. Kline: Combined dye-streak and hydrogen-bubble visual observations of a turbulent boundary layer. J. Fluid Mech., Vol. 62, 1974.
7. H.T. Kim, S.J. Kline, W.C. Reynolds: The production of turbulence near a smooth wall in a turbulent boundary layer. J. Fluid Mech., Vol. 50, 1971.
8. S.G. Nychas, H.C. Hershey, R.S. Brodkey: A visual study of turbulent shear flow. J. Fluid Mech., Vol. 61, 1973.
9. M.S. Yalin: Mechanics of Sediment Transport, Pergamon Press, Oxford, 1972.

LIST OF SYMBOLS

t	time
x	direction parallel to the flow
y	direction perpendicular to flow
ρ	fluid density
ν	kinematic viscosity
h	flow depth
δ	boundary layer thickness
u	local flow velocity
τ	local shear stress
τ_0	shear stress acting on the bed
$(\tau_0)_{cr}$	critical value of τ_0 (corresponding to the beginning of sediment transport)
$v_* = \sqrt{\tau_0/\rho}$	shear velocity
D	representative grain size (usually D_{50}) of bed material
$X = v_* D/\nu$	grain size Reynolds number
$Z = h/D$	relative flow depth
Λ	dune length
$\overline{\tau_0}$	duration of the dune development
T	tidal period
θ	part of the tidal period where $\tau_0 > (\tau_0)_{cr}$
L_i	"coherence distance" of an eddy (i)
L	average value (expectation) of the distances L_i

CHAPTER 125

TRANSPORT MECHANISM IN TIDAL DUNES

by Horst Nasner^x

I. Preliminary Remarks

An interesting question arising within the scope of the further development of the German tidal rivers Elbe and Weser, is whether tidal dunes or sand waves will be formed after the navigation channel deepenings and that the success of the development measures will thus be partially or fully undone. In order to be able to better assess the formation and regeneration of these large patterns after dredging, heightened knowledge of the sand transport in a tidal dune field is necessary. A possibility of investigating the sand transport in a tidal river with pronounced tidal dunes in the field, can be realized by measurements with luminaries or tracers. The advantage of investigations in the field is, that all laboratory required scale effects are eliminated. The more difficult measuring comprehension of the course of the test in prototype must be solved through purposefully planned investigation programs.

Subsequent to observations of many years standing, on behavior of four tidal dune areas in the navigation channel of the Weser River estuary (6), investigations were carried out with luminaries above reach 1 (Fig. 1) from September till November 1974. The aim was, to obtain information on the transport mechanism for tidal dunes and heightened knowledge on the causes of regeneration after dredging.

II. Execution of the Investigations in the Field

A. The Investigation Area

The sand wave stretch in the straight section of the lower Weser River between km 27.5 and km 28.0 was fixed for the luminary measurements. As shown by earlier investigations, the large dunes in this area are approximately two-dimensional. Their crests and troughs run perpendicular to the flow direction in the navigation channel (6). The longitudinal profile was determined by the navigation line. In order to be able to undertake the locality determination for the longitudinal soundings required for the waterway survey, double markers have been erected by the Waterways Administration at intervals of about 500 meters on both shores of the Weser. The profile of the Weser bottom in the axis of the navigation channel in the investigation area after various soundings in 1974,

^x) Dr.-Ing., Staff Member in Firm Prof.Dr.Lackner & Partners, Consulting Engineers, GmbH & Co. KG, Bremen, Germany

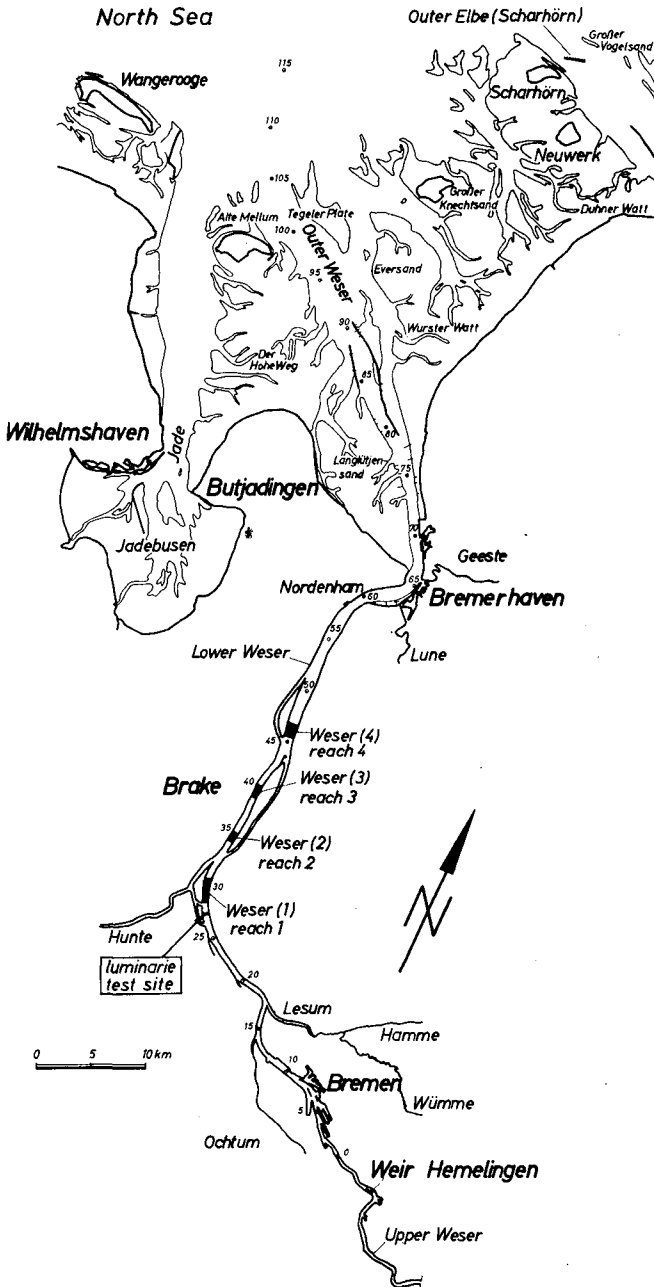


Fig. 1 Weser River with Luminarie Test Site

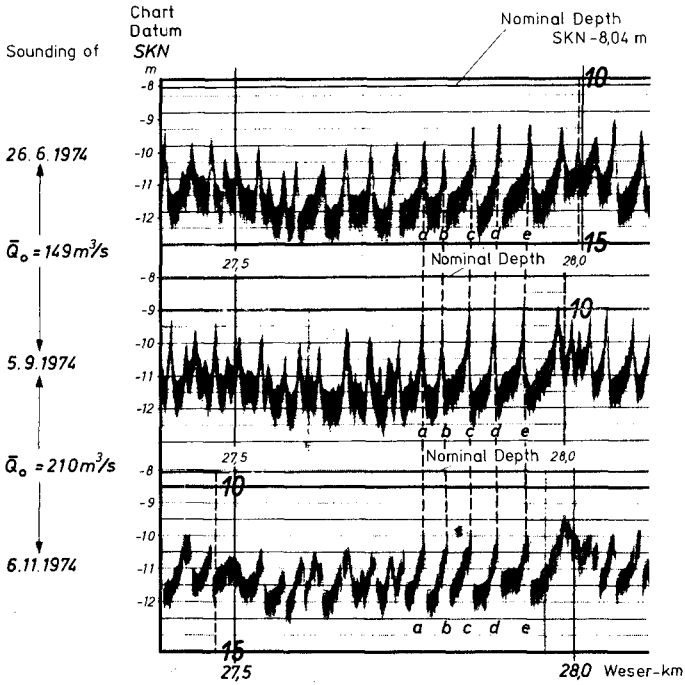
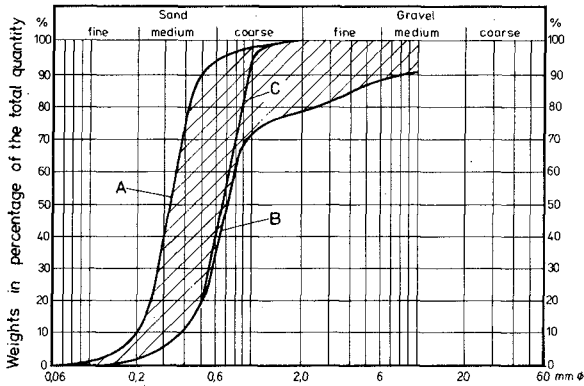


Fig. 2 Echograph Recordings of the Weser River Bottom



A to B: Grain curve strip of care sample 12

C: Grain distribution curve of the test material

Fig. 3 Grain Distribution Curves

is depicted in Fig. 2. In order to facilitate the locating of the sand waves for the measurements, the position of five sand wave crests and six sand wave troughs was additionally fixed by double markers on the shore of the Weser River on 29th August 1974. As the large dunes change their form only insignificantly in the tidal current rhythm and migrate over a long period of time very slowly in ebb current direction, contingent on the fresh water discharge Q_0 of the Weser (the greater Q_0 is, the higher is the transport velocity u (6)), the additional reference markers were of valuable assistance in carrying out the planned soundings.

B. The Investigation Program

On 29th August 1974, about 1 m^3 of sand was taken from the crest zone of sand wave c (Fig. 2) and subsequently prepared for the investigations. A grain distribution curve for the dyed sand has been depicted in Fig. 3. A very uniform sand ($d_{50} = 0.65 \text{ mm}$, $d_{90}/d_{10} = 2.44$) is concerned here. The test material was dyed two different colors (yellow and orange) and packed into sacks of water-soluble material.

On 18th September 1974, the dyed sand was deposited into a grabber on an anchored ship and quickly placed on the luff slopes of sand wave b (orange) and about 40 m below at c (yellow) in the crest zones, in mid-navigation channel (Fig. 4).

As a result of the packing, it was ensured that none of the sand material would enter a state of suspension before reaching the bottom. On the following days (19/9 and 20/9/74), two and four tides later, the first 9 core extractions were carried out from an anchored vessel with a Senkowitsch probe. The core diameter was 7 cm.

In order to disturb the river bed as little as possible in the area of the sand placing points (at b and c) the core samples were taken at sand waves d and e (Fig. 4). The crest of sand wave d was about 40 m from the location where the yellow dyed sand had been placed and about 90 m distant from sand wave crest b (orange). The crest of sand wave e lay a further 50 meters below d.

In order to create as little danger as possible for ship traffic, the soundings at d and e on the 19th and 20th September 1974 were taken up to 8 m beyond the navigation line. On 22nd and 23rd October 1974, 8 further core extractions were executed at sand waves e and d up to about 15 m beyond the navigation line. The taken bed material was investigated sectionwise (5 cm and 10 cm) for the grain composition and luminaries present.

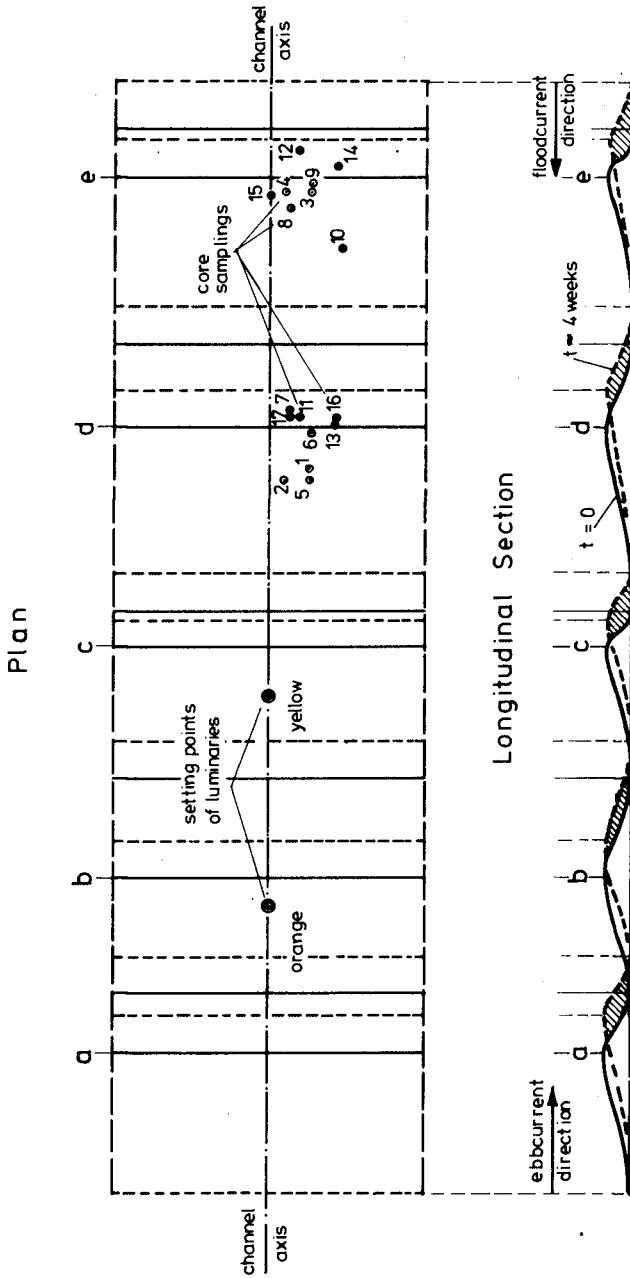


Fig. 4 Location of the placed luminaries and the Core Sampling Points

In a further operation with a soil grabber on 4th November 1974 in a limited investigation area, upstream to Weser-km 25.5 and downstream to Weser-km 30.0, samples were taken in the navigation line from the surface of the Weser bottom. Subsequently, it was ascertained whether and how many luminaries were present in the soil samples.

III. Investigation Results

A. Tidal and Fresh Water Conditions in the Investigation Period

No storm tides occurred during the investigation period. The mean range of tide in the test area is app. 3.35 m, the mean water depth about 10 m and the mean ebb current velocity app. 100 cm/s.

All measuring operations were executed at low tide.

The mean fresh water \bar{Q}_O between the measurings is compiled in the following:

29/8/1974	Taking of the test material
18/9/1974	Start of the investigations
19/20/9/1974	Core sampling (CS 1 to CS 9)
	\bar{Q}_O (29/8 to 18/9/1974) = 131 m ³ /s
22/23/10/1974	Core sampling (CS 10 to CS 17)
	\bar{Q}_O (19/9 to 21/10/1974) = 144 m ³ /s
4/11/1974	Taking of soil samples
	\bar{Q}_O (22/10 to 3/11/1974) = 429 m ³ /s

According to earlier investigations, at such low fresh water as was the case at the end of October 1974, the sand waves migrate in ebb current direction only very slowly (up to about 20 cm/day) (6). The mean migration velocity of the large tidal dunes in the investigation area was about 50 to 70 cm/day for $\bar{Q}_O = 429$ m³/s from 22/10 to 3/11/1974.

Dredging was not carried out in the test field in the period between 29/8/1974 and 4/11/1974.

B. Core Extractions

1. Luminaries

A total of 63 luminaries were found in the up to app. two meter long core extractions (CS 1 to CS 9, Fig. 4), of 19th and 20th September 1974, of which 36 (57 %) were yellow and 27 (43 %) orange. This result was not surprising, as the placing point of the yellow material lay a

sand wave length closer to the extraction position. According to the evaluation of the samples taken on 19th and 20th September 1974, luminaries were found at sand wave d down to a depth of 0.30 m, and 50 m below at sand wave e, to a depth of 0.10 m.

Soundings of the Weser River bottom on 25/9/1972 during a full tidal current period and at a spring tide range of 405 cm, showed a displacement of the sand wave crests of an average 2.0 m in the tide current direction for the Weser area of km 28.4 to km 30.9. The average sand wave height at the time of the turning of the high tide K_f was 11 cm higher in the mean, than at the turning of the low tide K_e . In contrast to laboratory tests (1), the geometry of the tidal dunes in the field remains unchanged during alternating tidal currents (8). The explanation for the height increase of the sand waves in the Weser is, that the steeper lee slope is levelled off by the flood current and the thereby eroded material is deposited on the luff side. The local redistribution of the sand waves during the tidal movement clears up the question, why the luminaries were found in the extracted cores up to 0.3 m below the sand wave surface, one and two days after they had been placed.

The core samples taken on 22nd and 23rd October 1974 were intended to give information on the long-term resultant redistribution of the bed material in ebb current direction. A total of 138 were found in the 8 core samples (CS 10 to CS 17, Fig. 4), of which 80 (58 %) were yellow and 58 (42 %) orange. The number of luminaries found in the samples of only 7 cm diameter is of minor significance as compared to the fact, that the investigation material was found at greater depths in six of eight cores. Luminaries were present in core sample CS 12 down to 1.80 m below the surface of the sand wave. The only explanation for this is, that in the resulting wandering of the sand wave in ebb current direction, the dyed sand was deposited on the lee side. A similar result was brought about by theoretical considerations for directionally steady current (2,3,4), according to which the sand transport is effected in a sand wave field through erosion of the luff slopes and alluvium on the lee side in short distance transport. In Fig. 5, the distribution of the luminaries found at 10 cm intervals in the core sample CS 12 taken from sand wave e, is depicted. The luminaries are spread over the entire length of the core, as was also the case with the other samples. The number of luminaries present in the 10 cm long cylinder pieces, fluctuates between 2 and 8. Conclusions can be drawn only with reservations and without claim to general acceptance, because of the low number. It is therefore conceivable for example, that the section-wise alternating quantity of luminaries, is traceable to differing tidal and current conditions in the time from 18/9/1974 (placing of the material)

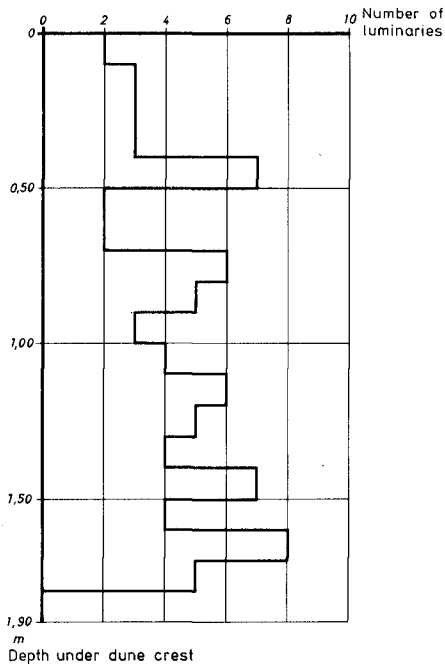


Fig. 5 Luminaries found in a Core Sample taken from Dune Crest app. four Weeks after Start of Tests

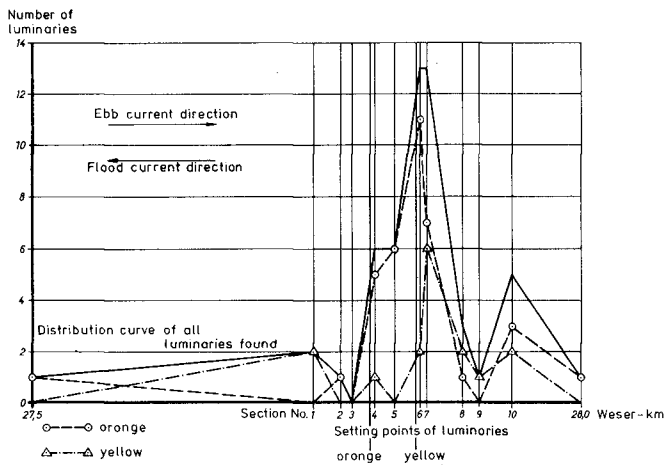


Fig. 6 Luminaries found on the River Bottom app. six Weeks after Start of Tests

up to 22/10/1974 (taking of CS 12). An increased ebb tide current on several days could have led to a stronger alluvium in the lee area of the sand wave and thus to a higher concentration of luminaries in certain extraction depths. The explanation for the presence of the luminaries from the upper surface down to 1.80 m boring depth is, that the material which had been deposited during the ebb tide phase in the lee area, was transported upstream again in part during the following flood tide phase.

As a result of the luminaries at greater depth below the upper surface of the sand waves, the fact is confirmed that the sand transport at tidal sand waves takes place essentially through local redistribution of the bed material.

The extent to which the luminaries had spread on the upper surface in the investigation area about six weeks after their placing on the Weser bottom, was determined by taking soil samples in the axis of the navigation channel between Weser km 25.5 and Weser km 30.0, and in the crest and trough areas of sand waves a to e. No luminaries were found upstream from km 27.5 and downstream from km 28.0. The luminaries found in a limited investigation area have been depicted in Fig. 6. With the exception of the sample in section No. 9 with a total weight of about 220 g, all other soil samples had a total weight of about 1000 g and thus easy to compare.

The result given in Fig. 6 shows clearly, that the investigation material was transported only insignificantly in ebb current direction, even 6 weeks after the start of the field test.

In comparison to the resultant current route in the test reach, the ebb current orientated sand transport in the sand wave field is smaller by decimal powers, as shown by the following. Cross section referred flood and ebb routes " s_f " and " s_e " were determined according to a calculation with mean tide by the Wasser- und Schiffahrtsdirektion Bremen (Waterway and Navigation Authority Bremen) (9). The mean ebb (flood) current velocities v_{em} (v_{fm}) in the discharge cross section result from the integral of the current velocities between the turn of tide points K, divided by the current duration D_f (D_e).

$$v_{fm} = \frac{\int_{K_e}^{K_f} v_f(t) dt}{D_f} ; \quad v_{em} = \frac{\int_{K_f}^{K_e} v_e(t) dt}{D_e}$$

The cross section referred flood (ebb) routes are determined with:

$$"s_f" = \int_{K_e}^{K_f} v_f(t) dt \quad ; \quad "s_e" = \int_{K_f}^{K_e} v_e(t) dt$$

The residual current results from $s_r = "s_e" - "s_f"$. The following values for s_r result for two Weser reaches below the investigation area are of interest here

Weser	Q_0 m ³ /s	s_r km/Tide
km 28.4 to 30.9 reach 1, Fig. 1	100 282 600	3.9 7.1 12.3
km 34.5 to 35.5 reach 2, Fig. 1	100 282 600	3.9 6.9 11.4

At a fresh water discharge of only 100 m³/s, the residual current is already app. 4 km/tide in ebb current direction. The fresh water discharge was $Q_0 = 224$ m³/s in the mean from the beginning of the investigations (18/9/1974) up to the day of the taking of the soil samples (4/11/1974). The short travel distance of the bed material on the surface shows how stable the sand wave covered river bottom is. The investigations with luminaries have shown in total, that the bed material in a sand wave field is transported through local redistribution with the resultant travel velocity of the tidal dunes.

2. The Bed Material

The section-wise executed sieve analyses of the core samples have shown, that the bed material in the interior of the sand waves is not uniform. In Fig. 3, the enveloping grain distribution curves of the analyses of the core samples CS 12 have been depicted (curves A and B). The earlier determined grain distributions of sand wave reaches in the Weser and Elbe Rivers (6), all lie in the medium sand range between enveloping curves A and B.

The tendency is, that the grain distribution curves of the other core samples are similar to those shown in Fig. 3.

The evaluation of the bed material in the soil samples, showed in general with increasing depth, a reduction of the finer components as compared to the coarser material, as also shown by the example of core sample CS 12 (Fig. 7). This result also coincides with earlier investigations on river banks and sand waves, according to which, coarser material is present in the trough areas (5,6,8).

The inconstant distribution in the core samples shows how the transport of fine and coarse bed material, contingent on the time, proceeds over the luff slope of a sand wave to the neighbouring lee slope, as a result of which, the stratification recognizable in Fig. 7 occurs. This time-contingent transport of differing bed material can likewise be responsible, that the number of found luminaries fluctuates in the core sample sections. In order to be able to obtain further information thereon, the grain diameter of the luminaries must also be determined in future measurings.

It must yet be mentioned at this point, that model tests at the Franzius Institute with bed material from sand wave c, have confirmed the alternating stratification of coarser and finer bed material in the interior of the sand wave, despite the changed geometric and hydraulic conditions in the laboratory at stationary current (10).

The fact emerged during the core extractions at sand waves d and e, that beginning at drilling depths which correspond to the elevation of the troughs, a firm clay layer was found. Accordingly, the sand banks in the area under consideration here, migrate over a non-erodable soil, from which no sand waves are formed. This result shows, what importance is attached to objectively executed soundings, before the deepening of a river bottom. It can only then be stated, whether sand wave formation must be figured on after the work is completed, when it is known what type of bed material will be encountered during deepening dredging. If for example, there is a layer of clay present at the trough level of a sand wave reach and a subgrade is created during a deepening through stripping the sand wave, sand waves could only then form after the development measures, if sandy material from outside can penetrate into the deepened river stretch.

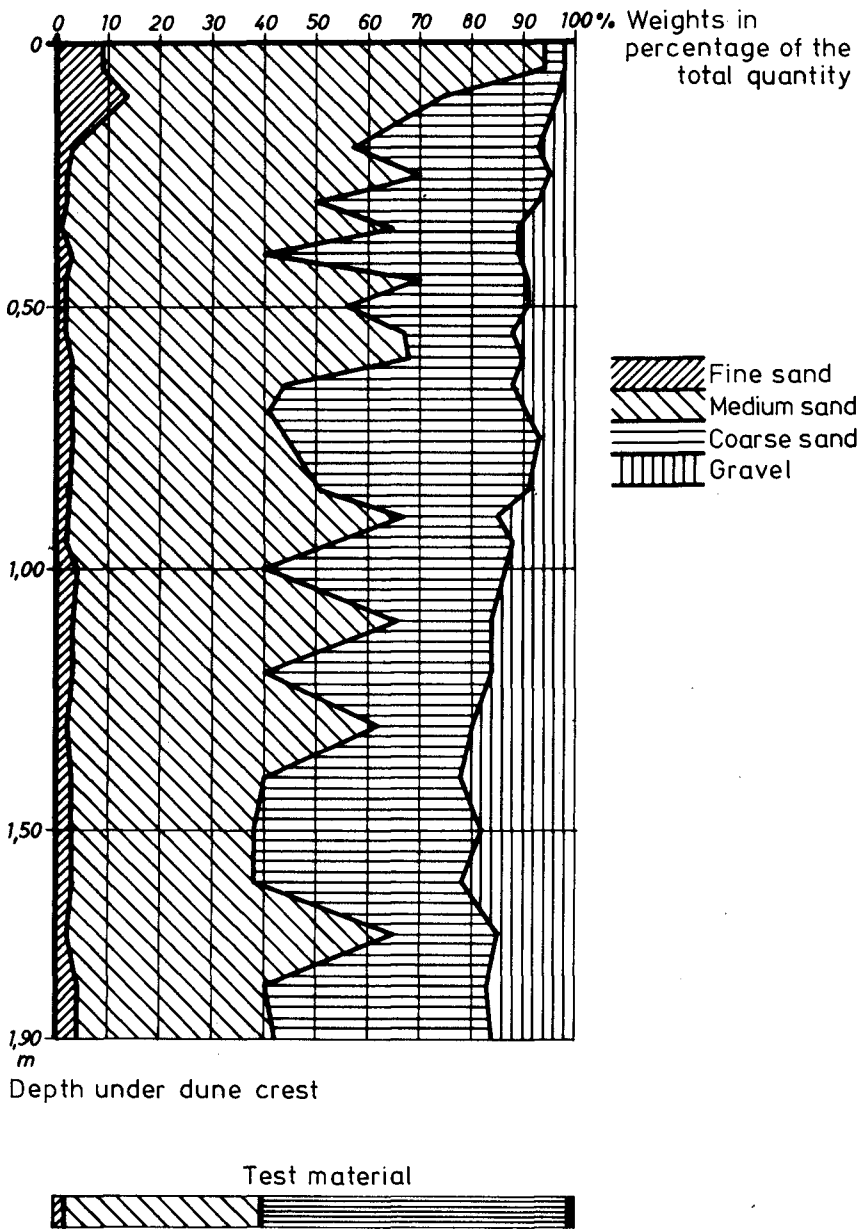


Fig. 7 Core Sample taken from a Dune Crest

IV. Conclusions

The investigations with luminaries in a sand wave reach of the lower Weser River, in good concurrence with theoretical considerations (2,3,4), have shown that the sand transport is effected essentially through local redistribution of the bed material. The resultant sand transport in ebb current direction corresponds to about the migration velocity of the tidal dunes. It emerges from the result, that the regeneration of the sand waves after dredgings and the minimum depths resulting therefrom, are likewise caused by short distance transport. Separate investigations on the regeneration of tidal dunes after dredgings have shown, that the troughs are very stable and that the sedimentation takes place chiefly in the crest area (7). As undesirable water depths are repeatedly encountered also in sand wave reaches of several kilometers length, and the sand transport proceeds only very slowly, the bed material required for the growth of the banks must enter the navigation channel in transverse transport from the embankments and shores. If it could be managed to prevent the continued feeding of bed material from the sides through shore and embankment revetments, it should be possible to considerably lengthen the regeneration time of the tidal dunes solely herefrom.

V. Acknowledgement

The investigations were carried out at the request of the Deutsche Forschungsgemeinschaft (German Research Association) in cooperation with the City of Brake Waterways and Navigation Authority, the Bundesanstalt für Wasserbau (Federal Institute of Hydraulic Engineering) Küste field office in Kiel and the Franzius-Institute of the Technical University of Hanover.

VI. Bibliography

- (1) DILLO, H.G.: Sandwanderung in Tideflüssen.
(Sand Transport in Tidal Rivers)
"Mitteilungen des Franzius-Instituts für Grund- und Wasserbau der Technischen Hochschule Hannover, Heft 17, 1960".
- (2) EXNER, F.M.: Über die Wechselwirkung zwischen Wasser und Geschiebe in Flüssen.
(On the Interaction between Water and Bed Material in Rivers)
"Sitzungsbericht der Akademie der Wissenschaften in Wien, Abt. IIa, Band 134, 1925".

- (3) EXNER, F.M.: Zur Dynamik der Bewegungsformen auf der Erdoberfläche.
(On the Dynamics of Moving Formations on the Surface of the Earth)
"Ergebnisse der Kosmischen Physik, 1. Band, 1931".
- (4) FÜHRBÖTER, A.: Zur Mechanik der Strömungsriffel.
(On the Mechanics of Current Ripples)
"Mitteilungen des Franzius-Instituts für Grund- und Wasserbau der Technischen Hochschule Hannover, Heft 29, 1967".
- (5) HENSEN, W.: Verlauf der Sandwanderung in der Elbe von km 582 bis km 590.
(Course of the Sand Migration in the Elbe River from km 582 to km 590)
"Die Bautechnik, Heft 10/12, 1943".
- (6) NASNER, H.: Über das Verhalten von Transportkörpern im Tidegebiet.
(On the Behavior of Sand Waves in the Tidal Area)
"Mitteilungen des Franzius-Instituts für Wasserbau und Küsteningenieurwesen der Technischen Universität Hannover, Heft 40, 1974".
- (7) NASNER, H.: Regeneration of Tidal Dunes after Dredging,
Proceeding of World Dredging Conference WODCON VII, 1976
World Dredging Association, San Pedro, California
- (8) VOLLMERS, H. and WOLF, G.: Sohlenumbildung im Bereich der Unterelbe.
(Bottom Transformation in Area of the Lower Elbe River)
"Die Wasserwirtschaft, 59. Jg., 1969, Stuttgart".
- (9) WATERWAYS AND NAVIGATION AUTHORITY, BREMEN: Mittlere Strömungsgeschwindigkeiten in der Unterweser für die Oberwassermengen $Q_0 = 100 \text{ m}^3/\text{s}$, $282 \text{ m}^3/\text{s}$ und $600 \text{ m}^3/\text{s}$ bei mittlerer Tide, unveröffentlicht, 1972.
(Mean Current Velocities in the Lower Weser River for the Fresh Water Discharge Amounts $Q_0 = 100 \text{ m}^3/\text{s}$, $282 \text{ m}^3/\text{s}$, and $600 \text{ m}^3/\text{s}$ at Mean Tide, not published, 1972).

(10) ZANKE, U.:

Über den Einfluß von Kornmaterial, Strömungen und Wasserständen auf die Kenngrößen von Transportkörpern in offenen Gerinnen.

(On the Influence of Granular Material, Currents and Water Levels on the Characteristic Magnitudes of Sand Waves in Open Channels).

"Mitteilungen des Franzius-Instituts für Wasserbau und Küsteningenieurwesen der Technischen Universität Hannover, Heft 44, 1976".

CHAPTER 126

SEDIMENTATION STUDIES ON THE NIGER RIVER DELTA

Ramiro Mayor-Mora, D. Eng. (1)
Preben Mortensen, M.Sc. (2)
Jorgen Fredsoe, M.Sc. (2)

1. Introduction

An area of the Niger River Delta was studied from October 1974 to October 1975 in connection with feasibility studies and preliminary design for the development of a deep draught port in the Western portion of the Delta. The provision of a 100-kilometer, 8 or 10 m navigation channel through one of the entrances from the sea, up to new port facilities at Warri required comprehensive hydraulic, hydrographic and sedimentation surveys over such period.

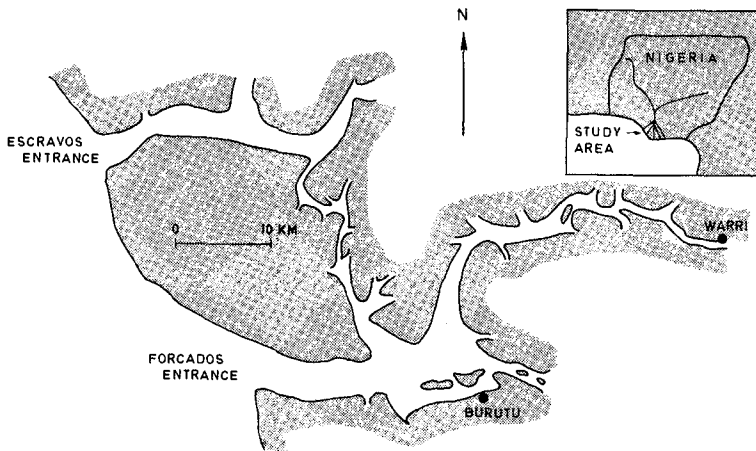


Figure 1. Location Map

- (1) SNC Inc. (Consultants), Montréal, Canada
- (2) Danish Hydraulic Institute, (DHI), Copenhagen, Denmark

The sedimentation studies dealt primarily with the conditions at the entrances. The main entrance to the existing ports of the Western Niger Delta used today by ships of up to 6 m draught is the partly protected entrance of Escravos. At such entrance, two moles were constructed around 1960 following intensive hydraulic studies that included testing on physical models.

However, the sedimentation is concluded to be in the order of 2 million cubic meters per year in the lee of the breakwaters. This sedimentation has been explained and possible solutions discussed.

An unprotected channel through the Forcados Entrance was considered as an alternative to improvement of the Escravos Entrance. Such a channel would be dredged through sand and the sedimentation due to combined current and wave actions was studied.

A theory for sedimentation of suspended load in an unprotected dredged channel in non-cohesive material was developed in connection with the study of Forcados Entrance. This theory is presented herein as an appendix.

2. Escravos Entrance

2.1 Background

The present entrance to the ports of the Western Niger Delta for ships drawing less than 4 to 5 m was chosen following hydrographic and hydraulic studies in the period 1953-1955. The minimum natural depth of Escravos bar was about 4.0 m and those studies concluded that a dredged 6 m deep channel through Escravos Entrance was required and that it had to be protected from sedimentation.

Based on hydraulic model tests, it was decided to construct a breakwater system consisting of a main breakwater (length 9 km) on the southern side of the channel and a detached breakwater (length 1 km) on the northern side of the channel, as illustrated on Figure 2 below.

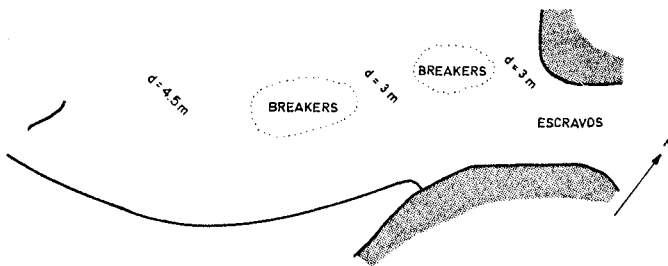


Figure 2. Present Escravos Entrance Protection

The purpose of the breakwater protection was

- to protect the navigation channel from deposition of material coming from the south due to the northgoing littoral drift.
- to guide the main part of the ebb current over the Escravos Bar creating current velocities sufficient for natural maintenance of the dredged channel.

The model studies concluded that the flow had to be concentrated further by means of an island breakwater, whereas the last 2 to 3 km of the dredged channel beyond the tip of the main breakwater were suggested to be left unprotected.

2.2 Monitoring of Sedimentation

One of the main objectives of the study was to investigate and explain the heavy siltation that was known to take place in lee of the breakwaters.

After a maintenance dredging carried out in November-December, 1974, a field investigation program including frequent soundings on the bar was initiated and continued until August, 1975. The monitoring yielded definitive answers to the important questions of where and when sedimentation occurs and which kind of material is depositing in the channel.

It was calculated that if the dredged channel had been constantly maintained with a navigation depth of 6.0 m, the annual maintenance dredging would be in the order of 2.0 million cubic meters depending on the assumptions made (frequency of dredging, over-dredging, etc.).

Apparently, sedimentation in the channel in the lee of the breakwater takes place throughout the year. It is difficult to calculate any seasonal variation of the sedimentation based on the results of the monitoring, since a depth close to the natural depth was achieved about half a year after completion of the dredging. But it is assumed that the sedimentation rate is constant throughout the year, since no significant change is found from the period December to March (when the fresh water season ends) to the period April to May (when the rough-wave season starts).

The sediments deposited in the dredged channel were found to consist of extremely fine, silty materials.

2.3 Sedimentation Mechanism

An explanation to the heavy siltation in the channel in the lee of the mole is found through a study of the current patterns through the Escravos Entrance, which are strongly dominated by the tides.

During the ebb current, the flow is concentrated at the mouth of the Escravos River. At some distance seawards from the mouth, the depth in the main channel decreases, the current velocities increase slightly and a flow out of the channel into the shallow area north of the channel is found.

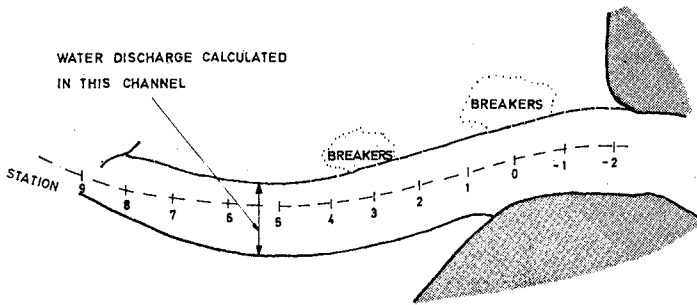
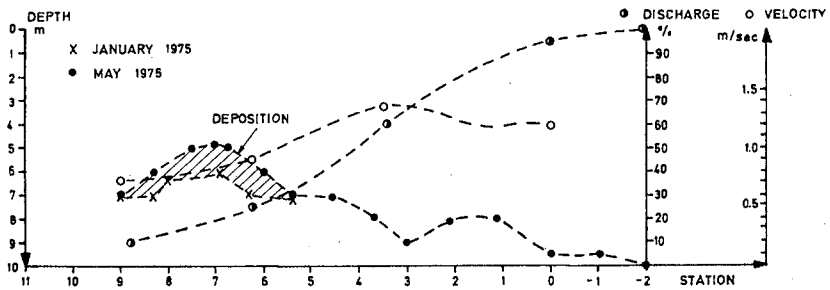


Figure 3. Sedimentation and Ebb Discharges in the Lee of the Breakwater

It is evident that a major part of the flow turns north before reaching the tip of the breakwater, especially in the area between the breakers and the island breakwater. The resulting effect is a decrease in current velocity east of the tip of the breakwater.

Figure 3 shows a characteristic ebb discharge across a section along the navigation channel in percentage of the total water discharge leaving the mouth of the Escravos River. It can be seen that only about 10% of the total discharge passes over the sedimentation area.

It is therefore concluded that the breakwaters do not create the desired effect, except for a local increase in current velocities between the breakwaters which does occur. The region of heavy siltation is found in the lee of the main breakwater, where current velocities decrease.

It should be emphasized that the clay and silt depositing in the channel do not necessarily originate directly in the Escravos River. North of the channel the bed consists of silt and clay exposed directly to wave action, the magnitude of sediment concentrations at the river mouth being very close for either the rough or the mild wave seasons. Therefore, considerable quantities of suspended silt and clay are being brought into the Escravos River during the flood current and out again during ebb current. The sedimentation in the channel may therefore be considered a transport from one area of the Escravos Entrance to another due to the difference in the current patterns during flood and ebb.

2.4 Possible Improvements

The most straightforward way to reduce sedimentation would be to construct a northern breakwater which should run more or less parallel to the existing main breakwater and be connected to the coast north of the Escravos Entrance as shown on Figure 4. This new arrangement would reduce the quantity of fine material being brought into the system from the north and at the same time, because of the flow concentration, create a scouring effect between and beyond the breakwaters.

By confining the navigation channel between two breakwaters the flow conditions between them would be similar to those at the mouth of the Escravos River in the present situation:

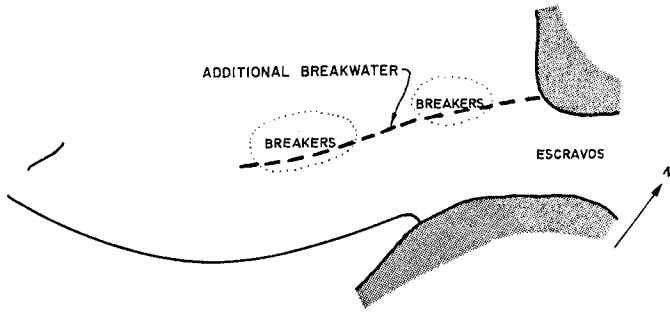


Figure 4. Escravos Entrance Improvement

During ebbing the flow acts as a jet and during flooding its behaviour is similar to that characteristic of a drain. Hence, in order to avoid sedimentation or significantly reduce it in the new navigation channel, the tip of the new breakwater should necessarily be placed at such a distance from the coast that the erosion zone beyond the new mouth extends across the whole of the present bar region in order to obtain sufficient natural depths throughout that shallow region.

The difference in flow pattern between ebb and flood currents would, along with other mechanisms, be able to generate erosion of the bed to a new natural depth similar to the present depth at the mouth of Escravos River (11 m).

3. Forcados Entrance

3.1 Proposed Navigation Channel

A navigation channel through the Forcados Entrance was studied because a route through Forcados to Burutu and to Warri would be much shorter and involve much less capital dredging within the estuary than a waterway to the same ports through the Escravos Entrance (see Figure 1).

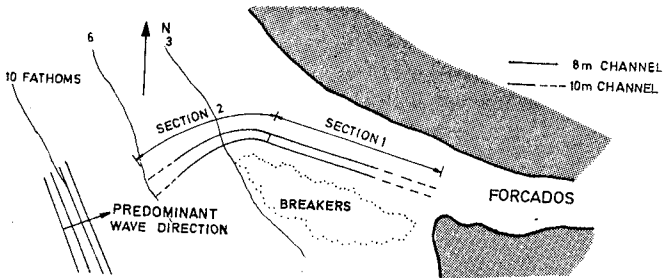


Figure 5. Navigation Channel through the Forcados Entrance

The outermost part of the channel has a direction perpendicular to the depth contours in order to minimize capital dredging.

3.2 Present Conditions

At the Forcados Entrance the present natural depth of the bar at the threshold is about 4.8 m according to soundings made in September 1975. The depth of 4.8 m is about equal to the natural depth on the Escravos Bar before construction of the breakwaters.

The main difference between the entrances of Escravos and Forcados is the vast breaker zone south of the Forcados entrance channel that creates an asymmetrical configuration of the entrance.

The breaker zone, reaching more than 10 km into the sea, is exposed to direct wave attack.

The ebb currents concentrate along the area north of the breaker zone with typical velocities of about 1.0 m/sec. at the mouth of the river. The current velocities have been found to decrease only slightly before reaching the Forcados Bar.

While flooding, the Forcados Entrance acts like a drain. The incoming currents just north of the breaker zone are very weak compared to the outgoing currents. Most of the tidal volume going in through the Entrance while flooding passes through the breaker zone.

In general, the bottom configuration in the Forcados Entrance area is found to be rather stable, charts covering a period of 100 years showing little change in the same configuration. But the vast southern area directly exposed to wave action and the interaction between northgoing and westgoing sand transports results in fluctuations of the bottom configuration around the breaker zone.

3.3 Sedimentation Mechanisms

On Figure 5, the navigation channel has been divided into two sections which, from a sedimentation point of view, are different since the principal mechanisms causing sedimentation are different.

Section 1 of the channel runs from the mouth of the Forcados River to the eastern side of threshold of Forcados Bar. Within section 1, the main sedimentation mechanism will then be flattening of the channel sides due to currents parallel to the channel alignment.

Section 2 of the channel is exposed to direct wave action, and the predominant current directions are perpendicular to the channel alignment.

In the channel where the bed consists of fine sand the concentration of suspended sediments is determined by the waves and the currents. Concentrations a few centimeters from the bottom are determined by the wave action (wave height and wave period) while the distribution of the concentration from the thin bottom layer to the surface is determined by the current.

The bottom concentration determined by the waves will, in general, decrease as the depth increases.

As the current passes over the side slope of the dredged channel, the concentration profile determined by the waves and the current will change, and in principle a quantity of suspended sediment corresponding to the difference in concentration profiles will settle in the dredged channel.

This sedimentation mechanism is dominating in section 2 of the navigation channel through Forcados Entrance. However, the mechanisms described for section 1 have also some effect although in a modified manner.

3.4 Calculated Sedimentation Rates

In section 1 of the entrance, the future sedimentation rates are calculated on the basis of the theory developed in Ref. 1 Levelling of Side Slopes in River Navigation Channels.

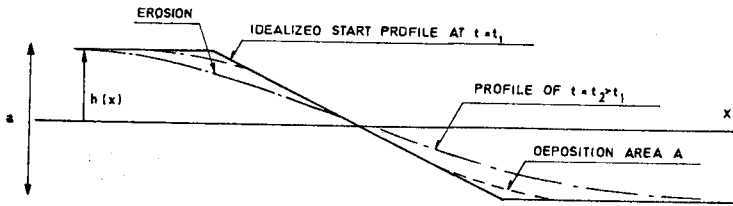


Figure 6.

The depositing volume per meter of channel (deposition area A shown on Figure 6 above) is found as the difference between the profile $h(x)$ at the time $t = t_2 > t_1$ and the profile at the time $t = t_1$:

$$A = a \frac{\sqrt{v}}{\sqrt{\pi}} \cdot (\sqrt{t+t_1} - \sqrt{t_1})$$

This general solution to the problem of instability of a transverse slope in an unidirectional flow yields the deposition volume at the bottom of the slope as a function of the time t after a certain start condition at time t_1 .

v is a function of the longitudinal bed-load transport rate.

In section 1 of the channel sedimentation rates of about 50 cubic meters per meter channel per year were found.

In section 2 of the channel the main sedimentation process is the one described in the Appendix, Changes in the Profile of Concentrations Due to Changes in Water Depth.

The general expression for the sedimentation rate in the dredged channel is:

$$q_r = \left\{ q_{10} \left(1 - \exp \frac{-W}{\epsilon} \frac{W}{V_b} \frac{D_1}{D_2} \frac{B}{\cos \alpha} \right) - q_{20} \left(1 - \exp \frac{-W}{\epsilon} \frac{W}{V_b} \frac{B}{\cos \alpha} \right) \right\} \cos \alpha.$$

where

- q_{10} = transport of suspended sediments, equilibrium conditions at depth D_1
- q_{20} = transport of suspended sediments, equilibrium conditions at depth D_2
- W = settling velocity of the sand grains
- ϵ = current eddy viscosity
- V_b = "slip" velocity
- B = total channel width
- α = angle between current direction and the perpendicular to the channel alignment
- D_1 = present depth
- D_2 = dredged depth

From the expression above, it is seen that the relative rate of sedimentation (the expression inside the main bracket) increases as the width of the channel B and the current angle α increase, and that the rate decreases as the current velocity V increases.

In the present case it was found that more than 95% of the material, corresponding to the difference in equilibrium transport at water depth D_1 and equilibrium transport at water depth D_2 would settle in the channel.

For the calculation of the equilibrium transport the concentration of suspended load in a reference level 5 cm above the bottom, C_a , was determined from experiments in an oscillating flume.

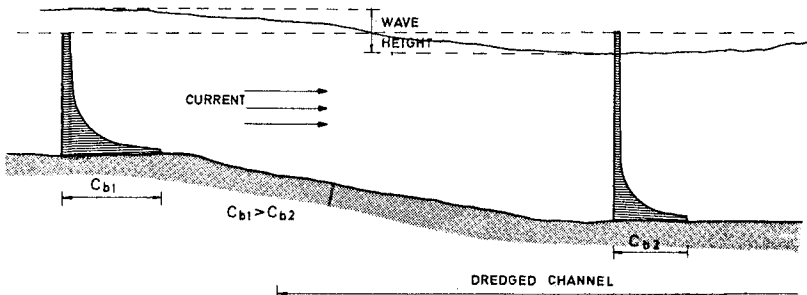
The sedimentation rates in section 2 of the channel were calculated to be in the order of 1000 cubic meters per meter channel per year (conservative estimate).

APPENDIX

Changes in the Profile of Concentrations of Suspended Material
Due to Changes in Water Depth.

A1 Introduction

In the following discussion a flow over the side slope of a dredged channel is considered. The bed beyond the slope is assumed horizontal and the width of the horizontal channel bottom is assumed to be of infinite length, as shown in the sketch below.



As the flow passes the side of the channel, its velocity changes and therefore the total sediment load, carried as bed load and suspended load, changes accordingly.

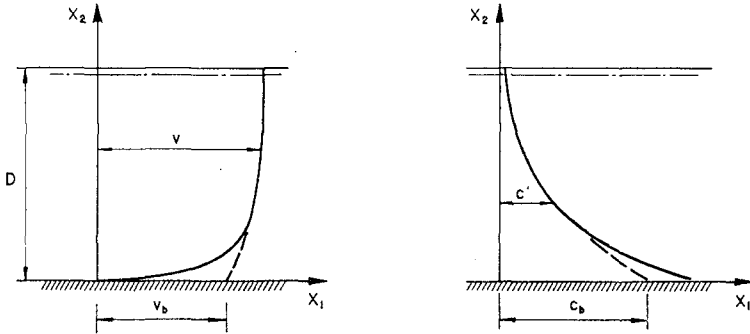
While the bed load is able to respond very quickly to changes in the flow, changes in the suspended load take place over a period of time due to the finite settling velocity of the suspended grains.

The purpose of this appendix is to describe how the concentrations of suspended material respond to the change in depth conditions. The theory is developed in two steps:

- In the first step the equilibrium concentration profile is determined by the bottom concentration only. The latter decreases as the depth increases, but the shape of the upper part of the concentration profile does not change.
- The shape of the concentration profile changes as the depth increases. The profile is stretched due to the divergence of the stream lines as the flow passes over the channel side.

A2 The Calculation Model

The calculation model is based on the "slip-velocity" method, described in Refs. 2 and 3. The basic idea behind this calculation method is to assume that the current eddy viscosity ϵ is constant over the depth (rather than decreasing to zero at the bottom). This method (or approximation) makes it necessary to introduce a finite velocity at the bottom, the so-called "slip-velocity".



In the following introduction to the basic equations, x_1 is the horizontal coordinate and x_2 is the vertical coordinate. The vertical distribution of concentration is considered in two situations.

In the steady, uniform condition the vertical distribution of the concentration c_0 is determined by the equilibrium between settling and diffusion.

$$Wc_o + \epsilon \frac{dc_o}{dx_2} = 0 \quad (A2.1)$$

where W is the settling velocity of the grains.

The solution to equation A2.1 is

$$c_o = c_{bo} \cdot e^{\left(-\frac{W}{\epsilon}x_2\right)} \quad (A2.2)$$

where c_{bo} is a nominal bottom concentration and ϵ is the current eddy viscosity.

In the non-uniform situation the distribution of concentration of suspended material is determined by an equilibrium between settling, diffusion and convection:

$$\frac{dc}{dt} = W \frac{\partial c}{\partial x_2} + \epsilon \nabla^2 c \quad (A2.3)$$

As mentioned above the theory will be developed in two steps. In both steps the approximation is made that the current field is steady and uniform, while the distribution of concentrations of suspended sediments is steady but non-uniform in the x_1 -direction. Using this approximation equation A2.3 may be written

$$v \frac{\partial c}{\partial x_1} = W \frac{\partial c}{\partial x_2} + \epsilon \left(\frac{\partial^2 c}{\partial x_1^2} + \frac{\partial^2 c}{\partial x_2^2} \right) \quad (A2.4)$$

Introducing the "slip-velocity" method the variation in the velocity v over the depth may be neglected, the velocity is constant, equal to the "slip-velocity", v_b .

A3 General Solution to the Problem

a) First Step

On the horizontal bed before reaching the side of the channel ($x_1 = 0$), the concentrations are considered to be stationary and uniform, and accordingly the concentration profile is given by equation A2.2. As the depth increases on the side of the channel the bottom concentration changes and equation A2.2 has to be modified in order to satisfy the non-uniform condition.

In order to find a general solution to equation A2.4 the distribution of concentrations is written as

$$c = c_1 \cdot e^{-\frac{W}{\epsilon}x_2} + f(x_2) e^{-\lambda x_1} \quad (A3.1)$$

where c_1 and λ are constants and $f(x_2)$ an unknown function of x_2 .

Substituting c in equation A2.4 for the expression for c in equation A3.1 we find:

$$\frac{d^2 f}{dx_2^2} + W \frac{df}{dx_2} + (\epsilon \lambda^2 + V \lambda) f = 0 \quad (A3.2)$$

The solution for equation A3.2 is

$$f(x_2) = \alpha_1 \cdot e^{(-\frac{W}{\epsilon} + \frac{\epsilon}{W}(\lambda^2 + \frac{\lambda V}{\epsilon}))x_2} + \alpha_2 e^{-\frac{\epsilon}{W}(\lambda^2 + \frac{\lambda V}{\epsilon})x_2} \quad (A3.3)$$

The constants α_1 , α_2 and λ are determined from the boundary conditions as follows:

On the horizontal bed on top of the slope ($x_1 = 0$) the boundary condition is determined by equation A2.2.

$$c = c_{b1} e^{-\frac{W}{\epsilon}x_2} \quad \text{for } x_1 = 0$$

At an indefinite distance from $x_1 = 0$ a new uniform solution, corresponding to equation A2.2 but with a different bottom concentration, is found:

$$c = c_{b2} e^{-\frac{W}{\epsilon}x_2} \quad \text{for } x_1 = \infty$$

The only set of equations that satisfies the first boundary condition is:

$$\frac{W}{\epsilon} = \frac{\epsilon}{W} (\lambda^2 + \frac{\lambda V}{\epsilon})$$

$$\alpha_1 = 0$$

$$c_{b1} = c_1 + \alpha_2$$

The second boundary condition is satisfied by

$$c_1 = c_{b2}$$

From these four equations the unknown constants in the solution to equation A3.1 are found:

$$\alpha_1 = 0, \alpha_2 = c_{b1} - c_{b2}, \lambda = \frac{W^2}{\epsilon v}$$

yielding the solution

$$c = c_{b2} e^{-\frac{W}{\epsilon}x_2} + (c_{b1} - c_{b2})e^{-\frac{W}{\epsilon}x_2} \cdot e^{-\frac{W^2}{\epsilon v}x_1} \quad (\text{A3.4})$$

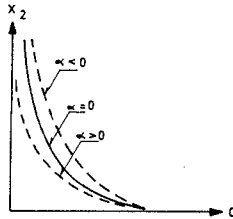
when W^2/v^2 tend to zero, that is $W \ll v$.

b) Second Step

In the previous step the calculation was made under the assumption that the concentration profile was in equilibrium with a certain bottom concentration changing as the depth increased but the "shape" of the profile was unchanged.

In the second step it is assumed that the concentration profile is stretched due to the divergence of the streamlines as the flow passes over the channel side.

A simple exact solution to the problem of this step is not possible but the effects of the stretched profile may be described by changing the boundary conditions.



If the first boundary condition is given by the equation

$$c = c_{b1} e^{-\frac{W}{\epsilon}(1-\alpha)x_2} \quad x_1 = 0,$$

this condition will be fulfilled by equation A3.3, if

$\alpha_1 = 0$, $\alpha_2 = c_{b1}$ and $\lambda = (1-\alpha)\frac{W^2}{\epsilon v}$, considering $W \ll v$.

That is, for $c = c_{b1} e^{-\frac{W}{\epsilon}(1+\alpha)x_2} \cdot e^{-(1+\alpha)\frac{W^2}{v}x_1}$ (A3.5)

To this solution, a solution

$c_2 = f(x_1) e^{-\frac{W}{\epsilon}x_2}$ (A3.6)

to equation A3.4 that satisfies the boundary conditions

$c_2 = c_{b2} d^{-\frac{W}{\epsilon}x_2}$ for $x_1 = \infty$

$c_2 = 0$ for $x_1 = 0$

has to be added. This solution is

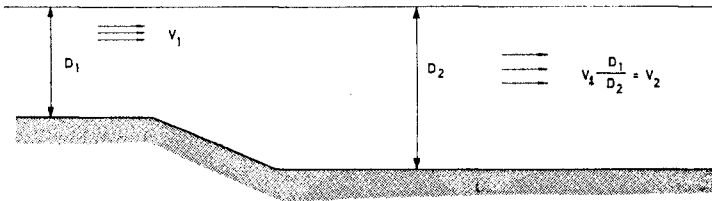
$c_2 = c_{b2} e^{-\frac{W}{\epsilon}x_2} (1 - e^{-\frac{W^2}{\epsilon v}x_1})$ (A3.7)

Therefore the total solution to the problem presented in the two steps is

$c = c_{b1} e^{-\frac{W}{\epsilon}(1+\alpha)x_2} \cdot e^{-\frac{W^2}{\epsilon v}(1-\alpha)x_1} + c_{b2} e^{-\frac{W}{\epsilon}x_2} (1 - e^{-\frac{W^2}{\epsilon v}x_1})$ (A3.8)

A4 Application of the General Solution

For the present application of the theory developed above, a situation determined by a combination of waves and a moderate current is considered.

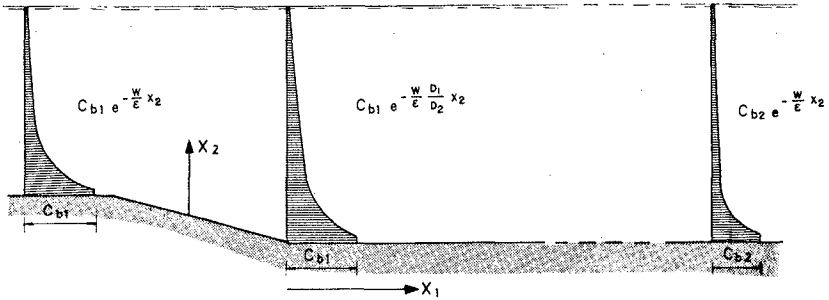


The undredged depth is called D_1 , and the corresponding current velocity V_1 . The depth in the channel is called D_2 and the corresponding current velocity V_2 .

The concentration of suspended material in a bottom layer a few centimeters thick (bottom concentration) is determined by the wave action, as the bed shear stress due to the wave action is much greater than the current shear stress, whereas the vertical distribution of the concentrations from the bottom to the surface is governed by the currents.

The bottom concentration on the horizontal bed beyond the side slope is called c_{b1} and the vertical distribution of concentration is described by

$$c_{b1} \cdot e^{-\frac{W}{\epsilon} x_2} \tag{A4.1}$$



At the toe of the side slope of the channel the approximation is made that the bottom concentration is unchanged, but the concentration profile is stretched with the same ratio as the depth is changed, i.e. $\frac{D_1}{D_2}$. Therefore the concentration is given by

$$c_{b1} \cdot e^{-\frac{W}{\epsilon} \frac{D_1}{D_2} x_2} \tag{A4.2}$$

At an indefinite distance from the channel side a new equilibrium profile is reached. The bottom concentration is given by c_{b2} and the concentration profile is accordingly given by

$$c_{b2} \cdot e^{-\frac{W}{\epsilon} x_2} \tag{A4.3}$$

Keeping in mind that the eddy viscosity is assumed to be constant and that the current velocity in the applied calculation model may be replaced by the constant "slip-velocity", the transport of suspended material q may be easily calculated as

$$\int_0^D (c \cdot v) dx_2 \tag{A4.4}$$

At the un-dredged depth D_1 , the sediment transport q_{10} is

$$q_{10} = \int_0^{D_1} c_{b1} e^{-\frac{W}{\epsilon} x_2} \cdot v dx_2 \approx v_{b1} \cdot \frac{\epsilon}{W} c_{b1} \cdot (1 - e^{-\frac{W}{\epsilon} D_1}) \tag{A4.5}$$

In the case of sand particles (high W),

$$q_{10} = v_{b1} \cdot \frac{\epsilon}{W} c_{b1} \tag{A4.6}$$

At an infinite distance from the side slope ($x_1 = \infty$), the sediment transport is given by

$$q_{20} = \int_0^{D_2} c_{b2} \cdot e^{-\frac{W}{\epsilon} x_2} \cdot v dx_2 \approx v_{b2} \frac{\epsilon}{W} c_{b2} \tag{A4.7}$$

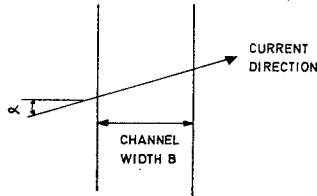
The sediment transport $q_2(x_1)$ between the two boundaries is given by an integration of equation A4.4

$$\begin{aligned} q_{20} &= \int_0^{D_2} \left\{ c_{b1} \cdot e^{-\frac{W}{\epsilon} \frac{D_1}{D_2} x_2} e^{-\frac{W}{\epsilon} \frac{W}{v} \frac{D_1}{D_2} x_1} - c_{b2} e^{-\frac{W}{\epsilon} x_2} \right. \\ &\quad \left. \cdot (1 - e^{-\frac{W}{\epsilon} \frac{W}{v} x_1}) \right\} \cdot v \frac{D_1}{D_2} dx_2 = \\ q_{10} \cdot e^{-\frac{W}{\epsilon} \frac{W}{v} \frac{D_1}{D_2} x_1} - q_{20} (1 - e^{-\frac{W}{\epsilon} \frac{W}{v} x_1}) \end{aligned} \tag{A4.8}$$

The overall aim of the above calculation is to evaluate the rate of sedimentation between the two boundary conditions corresponding to the two equilibrium situations at $x_1 = 0$ and $x_1 = \infty$. The rate of sedimentation as well as the distribution of sedimentation is found by subtracting the sediment transport $q_2 = q_2(x_1)$ from the sediment transport at $x_1 = 0$. The rate of sedimentation $q_Y(x_1)$ is given by

$$q_{10} - q_2 = q_Y(x_1) = q_{10} \left(1 - e^{-\frac{W}{\epsilon} \frac{W}{v} \frac{D_1}{D_2} x_1}\right) - q_{20} \left(1 - e^{-\frac{W}{\epsilon} \frac{W}{v} x_1}\right) \quad (\text{A.4.9})$$

If the current crosses the channel at an arbitrary angle α , the following sedimentation rate q_x per meter of navigation channel length is found:



$$q_x = \left\{ q_{10} \left(1 - e^{-\frac{W}{\epsilon} \frac{W}{v} \frac{D_1}{D_2} \frac{B}{\cos \alpha}}\right) - q_{20} \left(1 - e^{-\frac{W}{\epsilon} \frac{W}{v} \frac{B}{\cos \alpha}}\right) \right\} \cos \alpha \quad (\text{A4.10})$$

This general expression has been developed for application to sand bed material (non-cohesive materials only).

4. Acknowledgement

The results of the studies have been published with the permission of the Controller of Engineering, Nigeria Ports Authority, Lagos, Nigeria.

Director, T. Sorensen of the Danish Hydraulic Institute has contributed by interpretations of the sedimentation mechanisms and by inspiring discussions.

5. References

1. Fredsoe, J., Levelling of Side Slopes in River Navigation Channels. Progress Report No. 38. Institute of Hydrodynamics and Hydraulic Engineering, Technical University of Denmark.

2. Engelund, F., Flow and Bed Topography in Channel Bends.
Journal Hydraulic Division,
ASCE, Vol. 100, HY11, Nov. 1974.
3. Engelund, F., Instability of Erodible Beds,
Journal Fluid Mechanics,
42, part 2, 1970.

CHAPTER 127

GENERATION OF TROUGHS BY DENSITY CURRENTS

Hans Speekenbrink *

Abstract

Along the northern bank of the so-called "Maasgeul" scour has occurred, causing a trough. It is concluded from field measurements that the trough development is induced by density currents along the slope of the bank. The stratified flow system is dealt with mathematically. The calculated results are compared with the field measurements and agree fairly well. Trough development can be avoided by flattening the slope or by a bottomprotection.

Introduction

Since early 1970 scour has occurred along the northern boundary of the so called "Maasgeul", the dredged shipping route to the "Europoort" and Rotterdam harbours (see fig. 1), over a distance of about two miles. By this scour a trough has developed (see fig. 2 and 3) with a depth of 5 to 10 m below the bed of the navigation channel (M.S.L. - 24 m) with slopes of about 1 : 3 (see fig. 4). The surrounding sea bed has a depth of M.S.L. -16 m at the eastern- and of M.S.L. -19 m at the western end of the trough.

The material eroded from within the trough sedimentates south of it in the channel, from where it has to be removed right away in order to keep the guaranteed navigational depth at all times.

Widening of the trough in easterly direction possibly can endanger the stability of the end of the northern harbour mole.

*Rijkswaterstaat, Department for Coastal and Sea Research,
The Netherlands

Investigations have now been carried out into :

- a. The mechanism, that causes the generation of the trough
- b. The future equilibrium profile of the trough
- c. Possible measures to avoid or reduce trough development.

Trough development

Scouring has occurred along the northern bank of the "Maasgeul" from about 300 m west of the end of the northern harbour mole to about 4 km west of this mole. This section of the "Maasgeul" may be considered as a transition zone between open sea and the mouth of the river Rhine, which discharges its water via the "Rotterdam Waterway".

In January 1970 scouring started about 500 m west of the end of the mole over a distance of about 50 m and widened to the east (150 m) and to the west (200 m) in 4 months time. Some months later scouring was observed about 2 - 3 km west of the first trough over a distance of 1000 m. This trough widened in easterly direction to join the first trough although a small ridge remained between the two trough sections (see fig. 3).

Trough developments were first observed by routine echo soundings made to guard the navigational depth. In August 1974 with scour still continuing it was decided to carry out echo soundings more frequently. Every month, if possible in respect of weather conditions, echo soundings were carried out in lanes perpendicular to the trough axis at distances of 250 m. Until now scouring still continues almost linear in time (see fig.5), although it seems that scouring in summer is slightly greater than in wintertime.

The slopes of the northern bank steepened from about 1:10-15 to 1:3 in the first two years of trough development (see fig. 6). This slope has been rather stable since, although periodically slopes up to 1:1 were observed. The slopes of the southern bank have steepened to a value of about 1:4.

The northern bank remained very stationary but the southern bank moved in a southerly direction over an average distance

of about 15 m in two years time.

No significant widening of the trough in easterly nor in westerly direction could be distinguished during the last two years of observations.

The mechanism, causing trough generation

To find an explanation for the generation of the trough, surveys were carried out into the vertical distribution of the current velocities and directions and of the salt concentrations and temperatures. The measurements were related to the vertical tidal movement in Hook of Holland. The situations of the measuring points are indicated on fig. 2.

All measurements showed stratification during low tide. Differences in current direction up to 90° were found in upper and lower layer. In the upper layer the less saline water, discharged from the "Rotterdam Waterway" flows in a westerly direction, parallel to the channel axis (see fig. 7). Velocities reach values of 0.5 - 0.8 m/s at this tidal stage. The flow in the lower region shows a more southerly direction, almost perpendicular to the channel axis, corresponding to the direction of the tidal stream along the Dutch Coast at low tide. The velocities in this layer are about 0.5 - 0.6 m/s at the measuring point north of the trough, 0.8 - 1.0 m/s at the trough and about 0.5 - 0.6 south of it.

From these measurements of current velocities and density distributions it was concluded that density currents occur at low tide. A sketch of the stratified flow system is given in fig. 8.

The heavier underflow accelerates beneath the discharged, less saline river water, becoming critical at the upper edge of the bank of the trough and supercritical further down along the slope due to the steepness thereof.

Supercritical flow occurs at internal Froude-numbers F_i greater than 1.

$$F_i = \sqrt{\frac{u_i}{\epsilon g a_i}} \quad i = 1, 2 \quad (1)$$

in which u =velocity; $\epsilon = (\rho_2 - \rho_1) / \rho_2$; ρ =density;
 g =gravitation acceleration; a =layer depth; and subscripts 1 and
 2 = upper and lower layer respectively.

The increasing velocities will cause erosion and thus steepening of the bank. In this bank there is a clay layer with a thickness of about 3m. The top of this layer is found at a depth of about M.S.L. - 18 m at the eastern end of the trough and about M.S.L. - 20 m at the other end. The clay is very stiff and is resistant to scour, thus limiting erosion to the foot of the bank. When the slope steepens more than the natural slope of the bed material, the clay layer is undermined causing a slide down and thus an intermittent shift of the bank in a northerly direction. Although this shift can not be determined from the echo soundings it may be derived from core samples taken at the trough in 1974 that a local slide down of the clay layer occurred.

This clay layer may also be responsible for the fact that scouring did not start before 1970 and only after deepening the navigation channel to a level below this layer.

The foot of the bank may be regarded as a so called plunge-pool from which also sediment is removed.

The current measurements show that the flow is supercritical at the trough in the navigation channel. The conversion will take place via an internal hydraulic jump at the southern bank of the trough. Downstream this jump the current velocities will be too low for erosion and even sedimentation occurs, causing a ridge along the trough.

Mathematical model for two-layer stratified flow

A mathematical model may be derived for the flow across the trough. The following assumptions were made: (1) the flow is steady; (2) the flow in each layer is one dimensional i.e. there is a constant velocity and density at each cross section in each layer; (3) stratification is stable; there is a sharp interface between the layers and there is no entrainment across

the interface; therefore the density is also constant longitudinally in each layer; (4) shear stresses are acting along the bottom and the interface and are proportional to the velocity differences across the boundaries.

North of the trough the bottom has a gentle slope and the water surface and the interface are assumed to have gentle slopes too. The vertical accelerations may be neglected so the water pressure can be considered hydrostatic. The following equations, as given by Schijf and Schonfeld [1] may be applied.

The equations of motion for the upper and lower layers can be written as :

$$\frac{da_1}{dx} + \frac{da_2}{dx} + \frac{u_1}{g} \frac{du_1}{dx} + \frac{f_i |u_1 - u_2| (u_1 - u_2)}{ga_1} + S_b = 0 \quad (2)$$

and

$$(1-\epsilon) \frac{da_1}{dx} + \frac{da_2}{dx} + \frac{u_2}{g} \frac{du_2}{dx} - \frac{f_i |u_1 - u_2| (u_1 - u_2)}{ga_2} + \frac{f_b |u_2| u_2}{ga_2} + S_b = 0 \quad (3)$$

respectively, in which x = longitudinal coordinate taken as positive from north to south; f_i = friction factor at the interface; f_b = friction factor at the bed; S_b = bottom slope.

The continuity equations read :

$$\frac{dq_i}{dx} = 0 \quad i = 1, 2 \quad (4)$$

in which q = au = discharge per unit width.

Substituting the continuity equations in the equations of motion to eliminate du_i/dx and da_i/dx and neglecting u_i^2 in relation to $a_i g$ according to the field measurements, the resulting equation may be written as :

$$\frac{da_2}{dx} = \frac{(u_1^2 - \epsilon g a_1) a_2 S_b + (1 - \epsilon) f_i (a_1 + a_2) |u_1 - u_2| (u_1 - u_2) - f_b a_1 |u_2| u_2}{u_2^2 a_1 + u_1^2 a_2 - \epsilon g a_1 a_2} = 0 \quad (5)$$

$$\begin{aligned} \frac{da_2}{dx} = & \frac{q_1^2 - \epsilon g a_2^3 S_b + (1 - \epsilon) f_i (a_1 + a_2) (a_2 q_1 - a_1 q_2) |a_2 q_1 - a_1 q_2|}{(q_2^2 a_1^3 + q_1^2 a_2^3 - \epsilon g a_1^3 a_2^3)} + \\ & + \frac{-f_b a_1^3 |q_2| q_2}{(q_2^2 a_1^3 + q_1^2 a_2^3 - \epsilon g a_1^3 a_2^3)} \end{aligned}$$

At the upper edge of the northern bank of the trough critical flow will occur if the denominator equals zero :

$$q_2^2 a_1^3 + q_1^2 a_2^3 - \epsilon g a_1^3 a_2^3 = 0 \quad (6)$$

Deriving the total depth at the edge from echo soundings and vertical tide measurements, the discharges from flow measurements and ϵ from salinity and temperature measurements the depth of the interface at the edge may be computed from equation (6). With this depth as boundary condition the flow north of the trough may be calculated from the upper edge of the bank in negative x-direction using equation (5).

The northern bank has a steep slope and the flow in the lower layer will accelerate. It is assumed that the shear stresses in the lower layer are negligible and the energy equations are applied.

The energy equations for the lower and the upper layer may be written as

$$H = \frac{\rho_1}{\rho_2} a_{1x} + a_{2x} + a_{3x} + \frac{1}{2g} u_{2x}^2 \quad (7)$$

and

$$H_u = a_{1x} + a_{2x} + a_{3x} + \frac{1}{2g} u_{1x}^2 + h_x \quad (8)$$

respectively, in which H = energy head elevation relative to the trough floor; a_3 = bed surface elevation relative to the trough floor; index x refers to the distance along the bank; index u refers to the upper edge and h_x = inertia losses.

Assuming that the inertia losses h_x equal the drop in velocity head of the upper layer, thus

$$h_x = \frac{u_{1u}^2}{2g} - \frac{u_{1x}^2}{2g} \quad (9)$$

and substituting equation (9) in equation (8) yields

$$a_1 + a_2 + a_3 = \text{constant} \quad (10)$$

Differentiating equation (7) and using equation (4) and (10) the resulting equation may be written as

$$\epsilon S_b + \left(\frac{\epsilon g a_2^3 - q_2^2}{g a_2^3} \right) \frac{da_2}{dx} = 0 \quad (11)$$

Now the flow on the northern bank can be calculated from the upper edge of the bank in positive x -direction using equations (6) and (11).

The calculations may be simplified by assuming constant friction factors and constant slopes at both sides of the upper edge of the bank.

Calculations were carried out, taking $f_i = 0.001$ and $f_b = 0.004$. The boundary conditions q_2 , q_1 , ϵ and the slopes at both sides of the edge were derived from field measurements. As an example a calculated interface depth is given in figure 10 as well as the measured depth. As may be seen there is a fair agreement. The discharges used as boundary conditions in this example were derived from the velocity measurements in figure 7. The density profiles were derived from salinity and

temperature measurement at the same time (see fig. 11).

At the southern bank an internal hydraulic jump will occur. The flow system in this section is very complicated and has to be investigated by means of hydraulic model tests, which have not been made so far.

Future equilibrium profile

Erosion of the trough floor probably will continue until the hydraulic jump will be submerged. At what depth of trough this will occur has to be investigated in a hydraulic model.

A further widening of the trough is not expected. The longitudinal stability of the trough may be explained at the eastern end by the presence of a bottom protection around the toe of the northern harbour mole. At the western end the density difference decreases due to longitudinal mixing. Besides the steepness of the bank slope is much less (about 1 : 40) as well as the difference in depth between the channel and the surrounding sea bed. Due to these reasons the velocities along the bank are less too.

Measures to be taken to reduce or avoid trough development

To restrain the erosion a bottom protection on the trough floor and the banks may be considered. On the northern bank drag forces and gravity act in the same direction. The critical velocity for stability of loose grained material, as for instance shingle, on slopes can be compared with the critical velocity on a horizontal bed according to

$$u_{cr,s} = \sqrt{\cos S_b} \sqrt{1 - \frac{\tan S_b}{\tan \theta}} u_{cr,h} \quad (12)$$

in which u_{cr} = critical velocity for initiation of movement of bed material; θ = natural slope of the bed material; and subscripts s and h referring to slope and horizontal bed respectively. Using the Shields diagram and taking $\theta = 45^\circ$ it can be calculated that the minimum required grain diameter for the trough bank protection is about 3 cm. At the trough floor the

minimum grain diameter may be even more due to the strongly curved flows here.

Another possible measure to restrain the erosion is reducing the high current velocities and avoiding supercritical flow on the bank by flattening the slope. The flow in the lower layer will not accelerate when $da_2/dx \geq 0$. Using equation (5) and taking $da_2/dx = 0$, the equation for the critical slope, $S_{b,cr}$, may be written as

$$S_{b,cr} = \frac{f_b a_1^3 q_2^2 + (1-\epsilon) f_i (a_1 + a_2) (a_2 q_1 - a_1 q_2)^2}{a_2^3 (q_1^2 - \epsilon g a_1^3)} \quad (13)$$

Assuming $q_1 = 0$ and critical flow on the bank (equation (6)) the equation may be rewritten as

$$S_{b,cr} = f_b - (1-c) f_i \left(\frac{a_1 + a_2}{a_1} \right) \quad (14)$$

From this equation it may be derived that the critical slope is about 1 : 150. Due to possible variations in the main parameters, the friction factors, the critical slope must be considered of the order of 1 : 100 to 1 : 250. These flat slopes involve more than about $4 \cdot 10^6 \text{ m}^3$ to be dredged.

By flattening the slope the upper edge of the bank is shifted in a northerly direction and may become situated outside the surface front of the discharged less saline water. Due to this the flow in the lower layer will stay subcritical.

Because sand is needed in the near future for beach nourishment immediately north of the northern harbour mole, it is considered now to flatten the northern wall of the trough to a slope of about 1 : 50. For this measure a quantity of about $1.600.000 \text{ m}^3$ has to be dredged. Plans are being worked out now and dredging activities will probably be carried out in autumn 1976. The outcoming clay (about 600.000 m^3) will be dumped in the trough as refillment. The effect of this measure will be closely watched by making echo soundings every month, if possible in respect of weather conditions.

Summary and conclusions

Along the northern bank of the "Maasgeul" scour has occurred due to density currents induced by density differences between the discharged river water and the heavier sea water. Stratified flow occur at low tide.

The flow accelerations along the slope, causing trough generation, may be dealt with mathematically. The results of the mathematical model agree fairly well with field data.

The trough development, increasing the amount of maintenance dredging and endangering the stability of the northern harbour mole may be reduced by a bottom protection or by flattening the slope. The latter possibility will be carried out in the near future.

Acknowledgements

The author is much indebted to Mr. H.N.C. Breusers (Delft Hydraulics Laboratory) for his valuable suggestions.

References

[1]

Schijf, J.B., and Schonfeld, J.C., "Theoretical Considerations on the Motion of Salt and Fresh Water", Proceedings of the Minnesota International Convention, I.A.H.R. and A.S.C.E., pp 321-333, 1953.

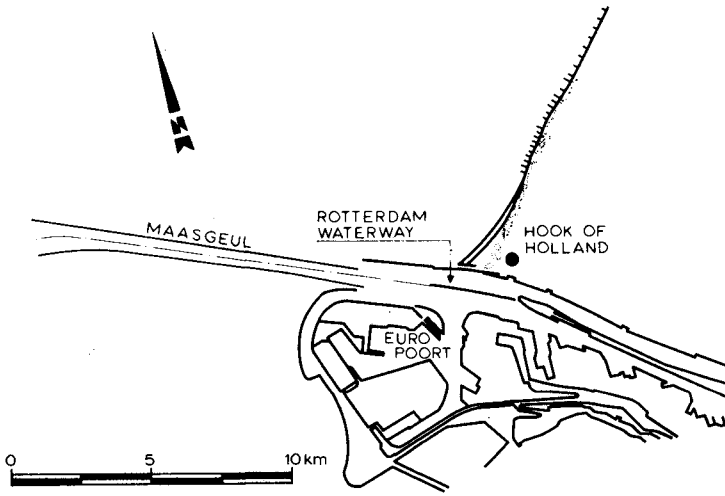


FIG 1 THE MAASGEUL NAVIGATION CHANNEL TO EUROPOORT

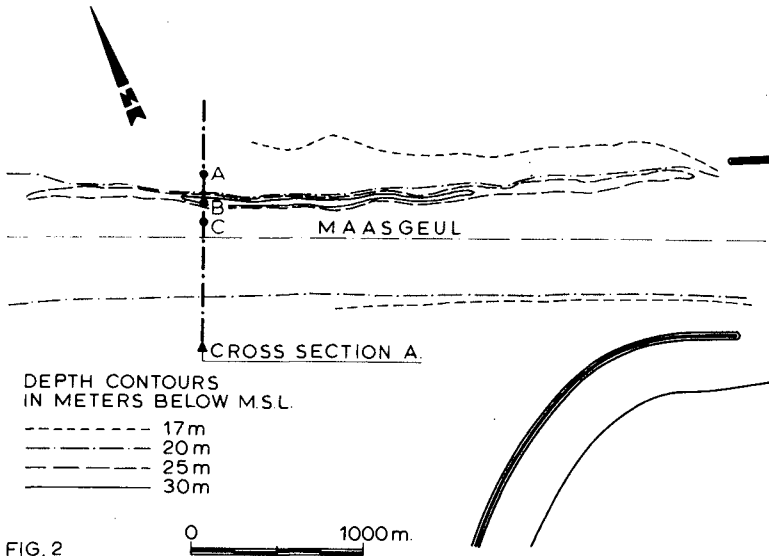


FIG. 2 TROUGH IN THE MAASGEUL ALONG NORTHERN BOUNDARY

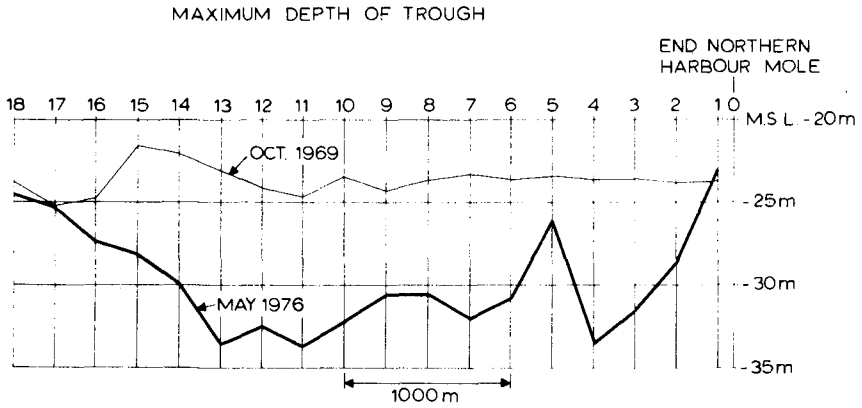


FIG. 3

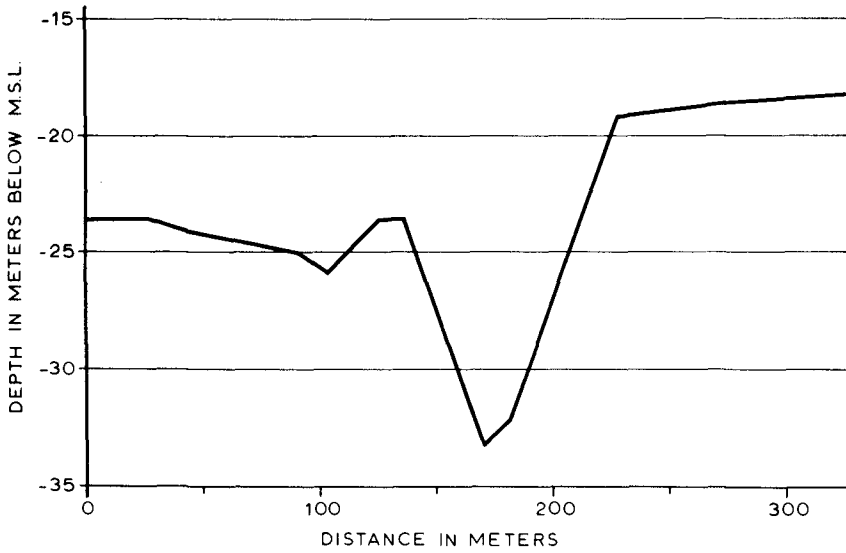


FIG. 4 CROSSSECTION A. OF TROUGH



FIG. 5 INCREMENT OF MEAN DEPTH OF TROUGH AS FUNCTION OF TIME

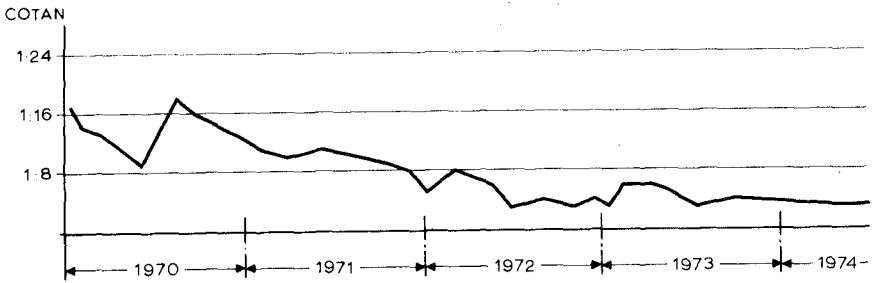


FIG. 6 CHANGE OF SLOPE OF NORTHERN TROUGH BANK IN TIME

DISPLACEMENT IN m¹ OF SOUTHERN WALL AS FUNCTION OF TIME

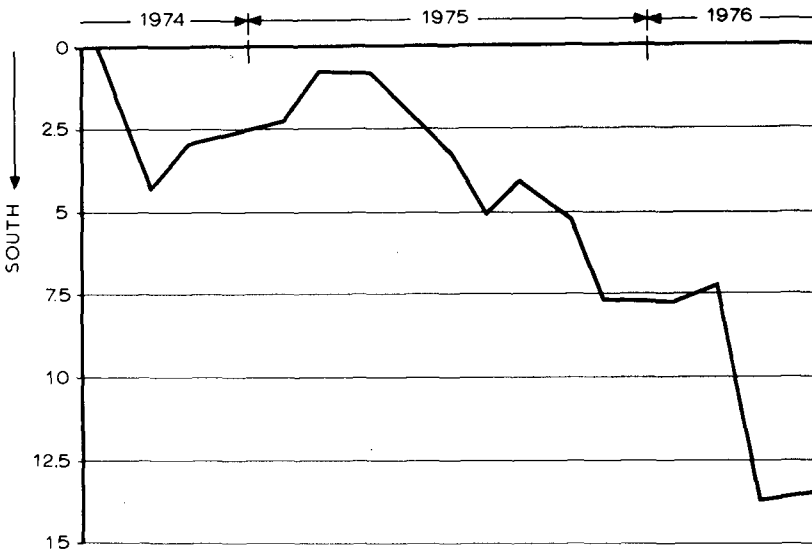


FIG. 7a

DISPLACEMENT IN m¹ OF NORTHERN WALL AS FUNCTION OF TIME

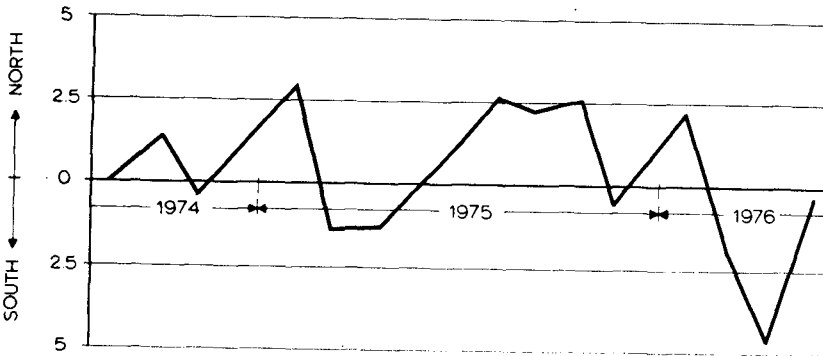


FIG. 7b

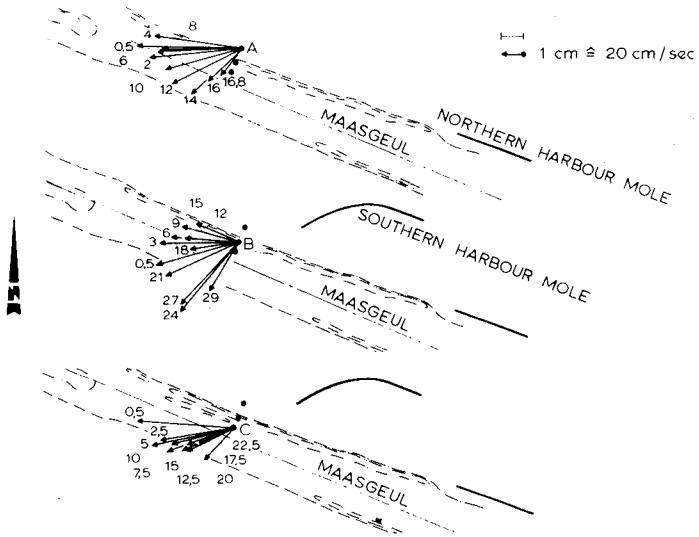


FIG 8 CURRENT VELOCITIES AND DIRECTIONS ON DIFFERENT DEPTHS AT LOW WATER AT POSITIONS IN THE TROUGH, NORTH AND SOUTH OF THE TROUGH.

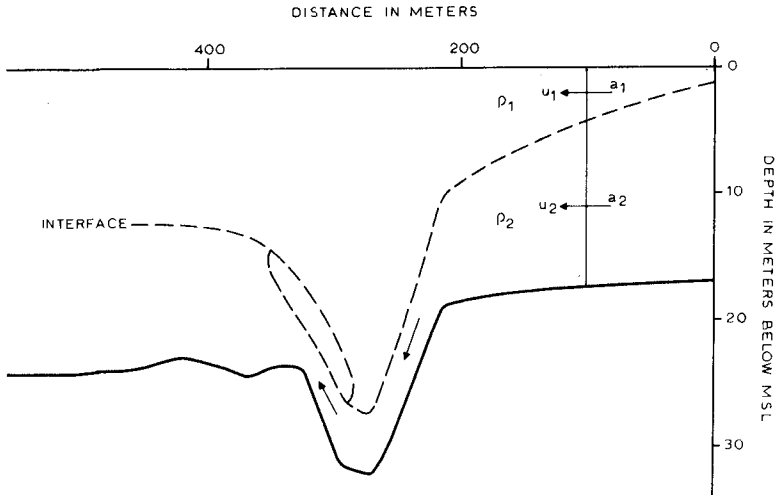


FIG 9 DEFINITION SKETCH STRATIFIED FLOW ACROSS TROUGH

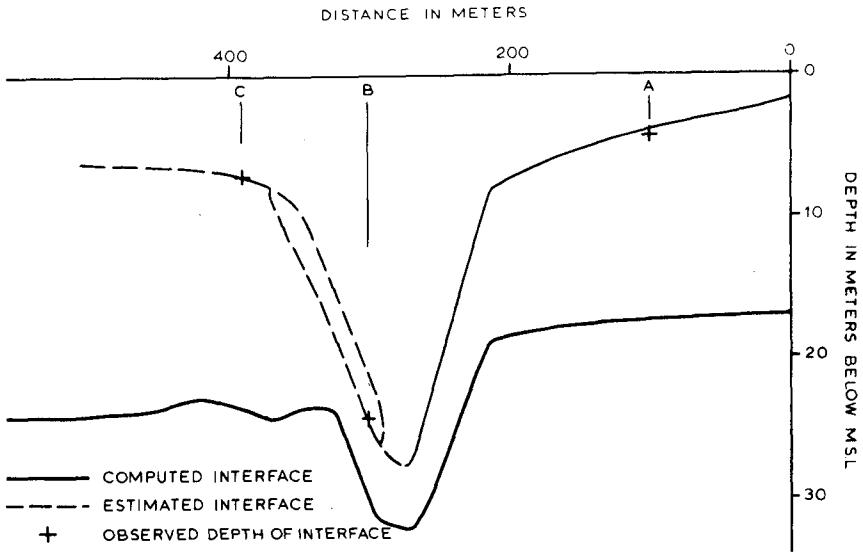


FIG. 10 DEPTH OF INTERFACE

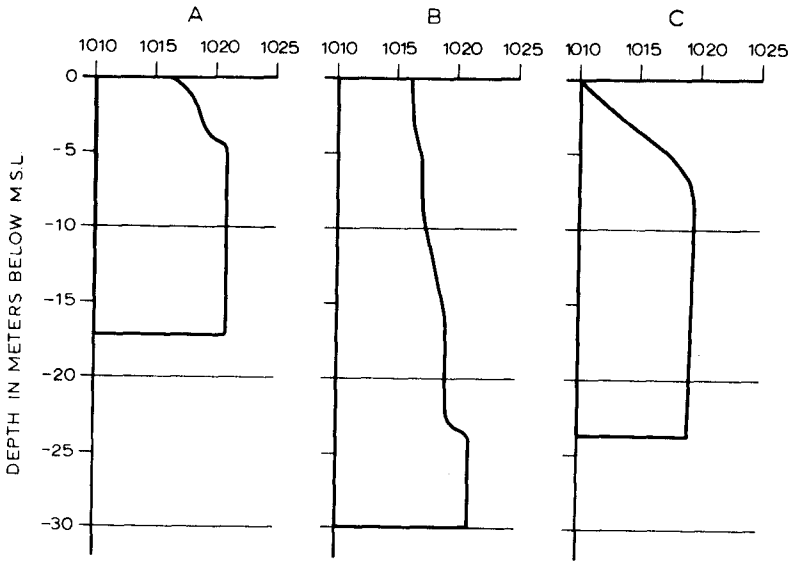


FIG. 11 DENSITY PROFILES AT POSITIONS A, B AND C.

CHAPTER 128

CONCEPT OF MINIMUM SPECIFIC ENERGY AND ITS RELATION TO NATURAL FORMS

by

Gordon R. McKay^{*}, B.Eng., Ph.D. (Liverpool)

and

Ahad K. Kazemipour^{**}, B.Eng.(Tehran), M.Eng.Sc.(NSW)

It is proposed to show in this paper that there is a solution to the problem of non-uniform flow and this solution not only explains in detail many land forms which occur naturally, but thereby, yields a definition of 'form' loss.

If a channel, in which the transverse distribution of specific energy is uniform, converges and/or diverges, and the bed changes so that the flow will be critical at all cross-sections at the same time, the channel appears to be close to being hydraulically smooth.

Many natural forms, particularly estuaries, are readily explicable in this way. The most obvious one is the bar at the mouth of a river. It follows, if the river enters the sea with reasonable uniform grade, which most rivers do, the bed must rise as the flow loses the restricting influence of the banks (i.e. the width increases) if constant specific energy is to be maintained.

It is possible to calculate with considerable accuracy the dimensions of useful structures based on this concept. A large number of full size but nevertheless experimental structures have been built making use of the resultant benefits which develop:- low turbulence, accurate differential water levels and a clearly defined flow pattern, allowing very considerable savings to be made by eliminating expensive protective works.

* Professor of Civil Engineering, University of Queensland, Australia.

** Iranian Government Postgraduate Research Fellow in Hydraulic Engineering, University of Queensland, Australia.

INTRODUCTION

For more than two centuries, the calculation of open channel flow, steady or unsteady, uniform or non-uniform, has been based on the concept of a long uniform channel in which the boundary shear in some way determines the total head loss. Euler-Bernoulli principle (1700-1782), Chezy's (1718-1798), Poiseuille's (1799-1869), Darcy-Weisbach's (1803-1871), Bazin's (1829-1917) and Manning's (1816-1897) formulas, all of which are in regular use today, are based on the concept of such a long uniform channel. Adaptation of the relatively modern Karman-Prandtle's (1930-32) theory of boundary layer and velocity distribution to open channels is also based on the concept of the long uniform channel.

This assumption was reasonable in the past for artificial channels since most of the channel works (sewers and storm drains) were constructed so that the cross-section of the channel was often semi-circular and therefore the distribution of the shear stress around the boundary could be considered more or less uniform.

There is strong evidence in the literature^{1*} that the studies of energy losses in open channels have been closely related to the phenomena of the boundary layer. For fully developed flow in a uniform channel of any size, the boundary layer will occupy all of the channel, but in partly developed turbulent flow, the energy loss due to frictional resistance is related to the stage of the development of the boundary layer. Again, past research on boundary layer has been concentrated on flow through circular pipes and past flat plates parallel to the stream.

The practising engineer may rightly question the above philosophies and assumptions, but what alternative has been possible? From Report of Task Force on Friction Factors in Open Channels¹ - "*At least, it could be hoped there would be made available something similar to the resistance diagrams now used for steady flow in uniform pipes and for frictional resistance of ships. It should be stated at the beginning that these hopes cannot be realised at this time. Principle obstacles are the wide range of surface roughness sizes and types encountered in practical channels (from smooth concrete linings to boulder-stream canyons), the effect of bed movement in unlined channels, and the numerous bends and structures that prevent the attainment of steady, uniform, fully developed flow*".

In order to allow a solution to the apparently simple problem of determining the flow capacity of a bridge opening or culvert, the U.S. Bureau of Public Roads² publishes a manual of 90 pages of tabulated data. If the bridge type and flow pattern can be reasonably compared with one of those in the manual, a solution can be assessed. Such techniques do little to validate the basic principle.

* Numbers refer to the references in the Appendix.

In deriving and applying the basic formulae and principles of uniform flow to open channels, a quantity 'hydraulic radius', R , representing the channel geometry, is used. Diameter of the pipe, D , is replaced by $4R$. This substitution carries with it the assumption that the distribution of shear stress around the boundary of the channel is uniform. It is well known now that in open channels, especially with non-circular cross-sections, such uniformity of shear stress is a false assumption. This fact clearly points out the failure of hydraulic radius to be the sole geometric quantity representative of the channel cross-section. The effect of cross-sectional shape must be taken into account in the analysis and prediction of the energy losses in open channels. Such studies have been made by some investigators in recent years, among whom are F. Engelund (1964)³, H. Rouse (1965)⁴, E.O. Macagno (1965)⁵, C.C. Shih and N.S. Grigg (1967)⁶, E. Marchi (1967)⁷, N. Narayana Pillai (1970)⁸ and C.L. Yen and D.E. Overton (1973)⁹. The results of these investigations are yet inconclusive. According to H. Rouse⁴, "*the effect of change in shape upon the resistance function is actually twofold. On the one hand, it produces a change in the wetted perimeter, P , per unit cross-sectional area, A , the reciprocal of which is designated by the hydraulic radius, R . On the other hand, it produces a change in the distribution of velocity and shear; as a result, the shear will generally vary from point to point of the perimeter. Both effects are thus involved in the equilibrium relationship between the gravitational motive force and the surface resistance which the flow entails*". He supports the validity of the hydraulic radius concept, but concludes that the effect of cross-sectional shape is related to the variation in the hydraulic radius and two coefficients of a semi-logarithmic resistance function. He also refers to the importance of the aspect ratio in the analysis in relation to the effect of cross-sectional shape.

The junior author in another work* has proposed other parameters as being more representative of the cross-sectional shape on flow resistance in smooth channels. This method offers a far more rational solution than methods previously proposed by others.

If the flow takes place in a natural stream with erodible bed and banks, the calculations which are at all possible do little to determine the proportions of any change which is likely to occur and in fact hardly assist in allowing predictions of even the general form of the change. Because of the ever varying shape and size of the channel cross-section and unavoidable irregularities in channel alignment, the flow is rarely uniform in natural streams.

It should be appreciated that open channel formulae based on observations of pipe experiments or from small scale physical models of channels and canals or rivers, cannot and do not represent natural situations because :

* Under preparation for publication.

- (i) The dimensions and proportions of natural rivers are completely different from those of the pipes for which energy losses have been determined experimentally. In practice the pipes are almost invariably round, ranging in diameter from 1cm to about 10m. The cross-sectional shape of a natural watercourse is quite indeterminate; the width can vary from a few centimetres to many kilometres, while the depth varies from a few millimetres to a very limited amount compared with the width.
- (ii) It is quite impossible to represent all the detailed features and irregularities of a river on the model. We cannot truly conform to the laws of similarity.

Any researcher using large area landscape type models soon appreciates that such models are far too smooth although boundary shear relationships say they should be far too rough.

In small scale models, losses due to boundary shear will always be relatively large because of the effect of scale on both the size and velocity in Reynolds number. However, to assume these losses represent the total energy loss must lead to serious error.

All energy losses will be represented as turbulence. Eddy size is largely a function of the size of the solid boundary generating the eddy. The velocity will determine the number of eddies. Eddies from boundary shear are small and because of their size, dissipate quickly. In contrast eddies generated by channel irregularities and changes in cross-section will be large and will persist downstream adding considerably to the apparent roughness. The reaction of movable boundaries in natural streams to locally generated turbulence cannot be joined with the overall average conditions.

Often the energy losses due to boundary roughness, cross-sectional shape and the boundary irregularities have been confused with one another. For example, H.A. Einstein and N.L. Barbarossa (1951)¹⁰ separated the total energy loss of the natural flow into frictional losses and form losses. Frictional losses were defined as those due to grain roughness and form losses those due to size, shape and spacing of the individual irregularities and presence of sand ripples and dunes. L. Bajorunas¹¹, in the discussion of the same paper states that: the roughness factor that reflects the channel irregularities decreases and approaches zero with increasing flow. On the other hand in V.A. Vanoni and Li San Hwang's (1967)¹² results, the bed roughness due to form of the ripples and dunes is the major part of the total roughness and does not approach zero with increasing flow. In the discussion of Einstein and Barbarossa's paper, Sir. C. Inglis¹³ categorises the total losses into (i) those due to textural roughness; (ii) those due to ripple roughness; and (iii) those caused by form drag resulting from the major irregularities of the banks, bed, islands and sandbanks. Inglis does not believe in combining groups (ii) and (iii) because of a different time scale by which they change.

The question is, what constitutes the total energy loss in natural rivers and how much of the total loss is due to boundary shear and how much is due to form?

CONDITION FOR NO FORM LOSS

It is proposed to show in this paper that there is a solution to the problem of non-uniform flow and this solution not only explains precisely many land forms which occur naturally, but thereby yields a definition of 'form' loss.

The only channel which gives truly no 'form' loss is of rectangular section. In any other channel the specific energy must vary across the channel. This would generate turbulence not associated with boundary shear. The elements of flow across the section can be shown to respond in different ways to an overall change in section shape.

B.A. Bakhmeteff (1932)¹⁴ showed that if the flow in a channel is tranquil and the channel converges slowly, the surface will fall, the velocity will increase and, if the channel then diverges slowly to its original width, the flow will return virtually without extra loss, to its original uniform flow pattern; i.e. the 'form' loss is zero. If, however, the convergence continues, the flow will ultimately become critical (i.e., the depth y_c will be $2/3(y_o + v_o^2/2g)$ when y_o and v_o are the depth and velocity in the initial channel, g is the acceleration due to gravity and y_c is the critical depth). Any further convergence will lead to a rise in level upstream of the constriction and a corresponding head loss through it.

Similarly, it was shown that if in a uniform rectangular channel a smooth hump is introduced, the water surface level falls, the velocity increases and the depth decreases. The height of the hump for no 'form' loss is limited to that which creates critical conditions at the hump; i.e.

$$y_c = 2/3 \left[(y_o + v_o^2/2g) - \Delta z \right]$$

Δz being the height of the hump. If the height of the hump is increased beyond this limit, the upstream level will rise and a 'form' loss occurs at the restriction.

There is, however, in addition to these particular cases, a condition which offers a wide range of cross-section proportions which will offer no 'form' loss.

If $v_c^2/2g + y_c = H_o + \Delta z$ everywhere, and the transition is as before reasonably slow, there will be no 'form' loss.

H_0 is the initial specific energy = $v_0^2 / 2g + y_0$

Δz is now the change in level of the bed

v_c is the critical velocity

both H_0 and Δz have the same sign and for convenience are measured positively down from the total energy line.

In many natural channels the 'form' loss is the major portion of the total head loss. It is then possible, by building a non-uniformity to this concept to create useful structures which cause no afflux. Any increase in boundary shear loss due to increased velocities can be offset by a reduction in 'form' loss.

The proposition was not determined initially as a result of a theoretical or laboratory research. It arose from the successful solution of a number of ad hoc problems.

DESIGNED SMOOTH TRANSITION STRUCTURES

The City of Redcliffe is a satellite town of Brisbane, the capital of Queensland. It has extensive if quite beaches on Moreton Bay and is the nearest seaside holiday resort to Brisbane. The road pattern is just about 45° to the natural drainage lines. One of these drainage lines - Humpy Bong Creek - literally splits the centre of the town in two. In 1958 the sole crossing of this creek was a narrow wooden bridge joining the shopping centre to the south, with the municipal buildings to the north. The shopping centre was along the beach promenade. There were just about enough parking places for the shop assistants' cars. Shopping on any Saturday in the holiday season was quite an adventure.



FIG.1. GENERAL VIEW OF REDCLIFFE AND PROPOSED IMPROVEMENT ON THE CREEK

The flow in the creek was largely sullage water. The banks were steep, ragged and overgrown. Altogether it was a smelly, unpleasant area. It was therefore proposed that a multipurpose improvement be made. (Fig. 1).

- (i) Build a weir to raise the fresh water level in the creek to cover the ragged steep banks and allow the area to be dressed, grassed and easily maintained as a park. At the same time the weir would exclude the tide and eliminate the smell of rotting vegetation.
- (ii) Culvert the creek to remove access problems and create an extensive car park on and adjacent to the culvert. The car park would serve the shops and public offices by day and in addition the proposed Civic Centre and R.S.L. Hall by night.
- (iii) To alleviate flooding of the shops and adjacent area.

An admirable proposal, but how to do it? - particularly at a price the town could afford. The catchment of the creek was rapidly urbanizing and the estimated maximum flow was 910 cusecs ($25.8 \text{ m}^3/\text{sec}$). The general level of the land adjoining, and hence flood level, at the creek mouth was R.L. 8.0 ft (2.440m) L.W.O.S.T. This would preferably also be the level of the car park. High tide was R.L. 4.5 ft (1.370m) L.W.O.S.T. and experience had shown that any outlet with an invert below high tide became stuffed with sand in the dry winter season. It was also necessary that the standing water level in the lake should not be less than R.L. 5.25 ft (1.600m) L.W.O.S.T. to cover all the trash growth on the vertical banks and allow easy maintenance. At that time the whole area flooded at least once every two years and by traditional hydraulics the problem appeared to be unsolvable as the length of the culvert was some 600 ft (180m).

The Department of Civil Engineering, University of Queensland, suggested the solution illustrated in Fig. 2. The logic of this solution was :- The discharge is 910 cusecs ($25.8 \text{ m}^3/\text{sec}$) flowing upstream of the weir at a level of R.L. 8.0 ft (2.440m). If we neglect the velocity head we can take R.L. 8.0 ft (2.440m) as the level of the total energy line at the weir. The weir level was set at R.L. 5.25 ft (1.600m) to give satisfactory pondage conditions. The maximum available specific energy at the weir is 2.75 ft (838mm). Thus the critical depth is $\frac{2}{3} \times 2.75 = 1.83 \text{ ft}$ (558mm). The maximum flow per foot width of weir is thus 14.2 cusecs ($1.327 \text{ m}^3/\text{sec}/\text{m}$ width), so the minimum width of the weir is 64 ft (19.5 m). The culvert barrel was 18.0 ft (5.480m) wide, a Queensland Main Roads' Department standard width. The flow per ft width must be 50.51 cusecs ($4.7 \text{ m}^3/\text{sec}/\text{m}$) so the minimum (critical) depth is 4.30 ft (1.304m). The corresponding velocity head is 2.15 ft (652mm), so total specific energy is 6.45 ft (1.956m). Therefore the level of the culvert invert at entrance is R.L. 8.0 ft, less boundary shear fall, less 6.45 = approximately R.L. 1.43 ft (440mm).

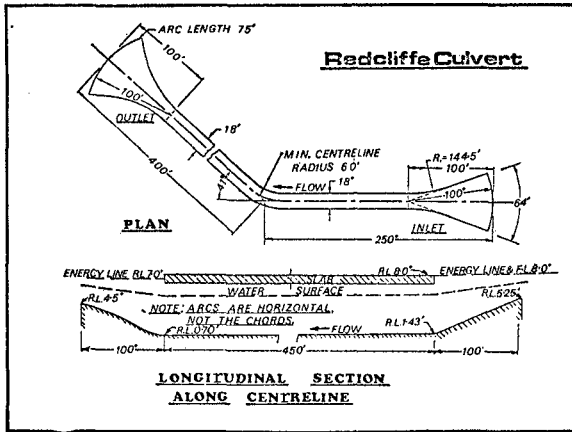


FIG.2. DETAILS OF REDCLIFFE CULVERT

An arbitrary assumption was made that there would be 1.0 ft (305mm) of head loss due to boundary shear so the level of the energy line at the outlet is R.L. 7.0 ft (2.130m). The high tide level is R.L. 4.5 ft (1.370m) L.W.O.S.T. so the available specific energy is $7.0 - 4.5 = 2.5$ ft (762mm). The minimum depth is $\frac{2}{3} \times 2.5 = 1.67$ ft (509mm) and the maximum flow per ft width at outlet is 12.25 cusecs ($1.139 \text{ m}^3/\text{sec/m}$) so minimum outlet width is 74.3 ft (22.620m).

In plan the inlet weir was joined to the culvert with an arbitrary shape and the culvert to the outlet weir likewise. The inlet and outlet floors were designed so that everywhere we had critical flow. The culvert slab fitted very conveniently between R.L. 8.0 ft (2.440m) and the water surface to give ample freeboard. Despite much critical comment the Department was commissioned to build a model. A very big model $1'' = 1 \text{ ft}$ (1:12) was built. Very quickly we learned that the inlet and outlet had to be part of flow nets. With this single modification the model performed perfectly. There was an amazing correlation between the calculated and model water levels, everywhere within 0.01 ft (3mm on the model). There was apparently no difficulty in imposing this flow system.

The culvert was built. No flow measurements have been taken but no flooding whatsoever has occurred since, although there have been at least three occasions when the design flow has probably been exceeded. This includes 1974 when Brisbane suffered devastating flooding, both from the local creeks and the Brisbane River.

Some years later we were asked to investigate the augmentation of the water supply for a small town, Clermont, in Central Queensland. With this request was attached a very odd condition - that any weir in the river must not cause flooding at a lesser flow than at present nor at more frequent intervals. There was good reason for this condition. Clermont lies in the junction of two streams, the Belyando River and Rocky Creek. Typical of western Queensland the highest land for some miles around is the river bank. Once the flood breaks out it spreads through the town and over the adjacent

country. In 1916 a major flood peaked on a Saturday night and nearly one hundred people were drowned. Naturally Clermont is now a little sensitive to flooding.

There is always a minimum storage below which storage has little purpose. This minimum storage determines the minimum weir height and, in this case, the required weir was relatively high compared to the banks of the river. The whole region is alluvium and consequently maintaining the weir in the river was also an equally difficult problem. Having tried a whole array of strange shapes and arrangements, we failed to satisfy these conditions and reported accordingly.

However, reflecting on the Redcliffe outfall, there were second thoughts. If this culvert were cut in two and placed end to end, it gave a system of weir without afflux. The bank full flow could be taken as the design flow, Q . The slope of the water surface at this stage is known. The velocity, V , is Q/A when A is the cross-sectional area at 'bank full'. The energy line will then be $V^2/2g$ above and parallel to the bank full-flow surface. The height of the weir crest; i.e. Storage Level, is already determined. The difference between storage level and the energy line level is the specific head. Forthwith the critical depth, the maximum flow per unit width and the minimum length (width) of the crest can be calculated. This crest width was very much wider than the river itself. By choosing an arbitrary plan shape, the height at any other transverse section of the weir can be readily calculated and the longitudinal profile determined; alternatively a profile of the weir can be chosen and the widths calculated.

The Clermont Weir (Fig. 3) was 20 ft (6m) high, 350 ft (106.8 m) wide along the crest. The bank slopes were, of necessity, flat to obtain a smooth transition. The problem now was not the adequacy of the design but how to build it. The only possible solution for such a big volume structure was somehow to build the bulk of it in earth.



FIG.3. PHOTOGRAPH OF CLERMONT WEIR

This was done (not without incident) and the earth protected by a filtered concrete slab. No other protection to bed and banks was found

necessary. Again no measurements have been made but there have been many flows over the weir and at least there have been no complaints in the twelve years of its existence. A much larger but similar weir has since been built. This second weir (Fig. 4) is at Chinchilla, South-West Queensland. It is 40 ft (12.2 m) high and has a crest of 750 ft (228.300m). It stores 7,500 acre feet ($3 \times 10^6 \text{ m}^3$) and the crest is actually level with the adjacent bank contour. A bank six feet high ties the end of the weir to higher ground some distance away. When the flow starts to overtop this bank; i.e. when flooding commences upstream, the flow is some 35,000 cusecs ($1000 \text{ m}^3/\text{sec}$) and the measured afflux was 4.0 inches (100 mm). Below the design flow the excess energy is dissipated in a single roller on the face of the weir. No other protective works are provided. Above the design flow, all trace of the weir disappears.

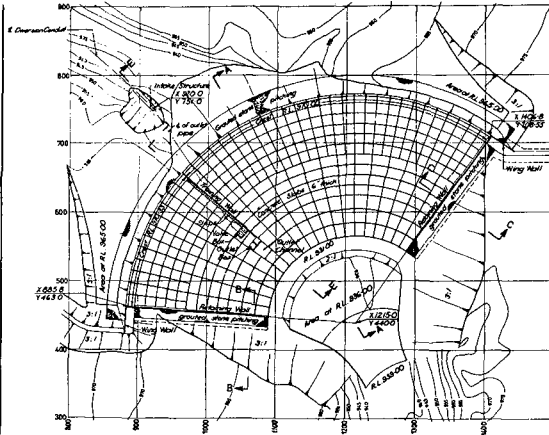


FIG.4. PLAN OF CHINCHILLA WEIR

The strangely smooth turbulent free flow over these weirs posed the question, was the concrete protection necessary? Eventually the opportunity arose to build an earth weir protected only by grass. It was designed to have no effect at a level at which the flow would cause flooding or nuisance if exceeded - not the maximum flow. It has been completely successful. The earth formation was completed on the 5th November, 1967. The bank was sown with Greenleaf Sudan - a fast growing sorghum and sprigged with Kikuyu. The first flow over it occurred exactly five weeks later. In January, 1968, two months after completion, the weir was submerged completely early on a Saturday evening and remained completely submerged until Tuesday mid-day. The photo (Fig. 5) was taken on the Wednesday. The growth was adequate protection and the weir has survived ever since. In order to secure these weirs in the early vulnerable period before the grass is established they have been reinforced with a cheap plastic mesh.

As grass had proved completely adequate as protection in these smooth flow structures, they became far more attractive cost-wise, despite the strange shape, than more traditional designs. A number of smaller but identical weirs have been built and protected by grass only. The cost is \$50-\$100 per million gallons stored ($500-1000 \text{ m}^3$ per dollar). This type



FIG.5. PHOTOGRAPH OF YULEBA WEIR

of weir makes possible extensive storage at sites which have previously been discarded. The optimum site is the *widest, shallowest*, and hence highest part of the river bed.

The farm dams were not high, averaging 5 ft (1.5 m); the highest has been nine feet (2.74 m). At small overflows the bank is subjected to velocities close to \sqrt{gh} when h is the height of the dam. Even at a height of five feet, this amounts to over 12 ft/sec (4m/sec). There was never suspicion of scour.

The calculations associated with these designs are indeed simple. The accuracy of the calculations is very good and the performance completely predictable. The confidence gained from these successes enabled much more exotic structures to be designed and built to achieve solutions not previously possible, in particular culverts and bridges without afflux but discharging at high velocities so that the span is minimized.

Typical is the Nudgee Road Bridge over the Kedron Brook in Brisbane. At the point of the crossing the natural stream channel had completely degenerated having left its well defined steep watercourse and entered the coastal swamp. Long since the area had been drained by a small canal-like waterway to a well defined tidal inlet some miles away. This channel could not even carry the annual flow. The design flood of 30,000 cusecs (850 m³/sec) spread over a width of 1320 ft (404m) increasing downstream. The road crossed the swamp on a low embankment rising to a short timber bridge over the canal, and the floods rose over the embankment and cut the traffic.

A major shopping complex had been built upstream of the crossing but still within the swamp zone. The council had required a considerable portion of their area to be retained as a flood relief channel and the remainder had had to be filled to a considerable depth. The area had continued to develop and Nudgee Road became a major traffic route and at this point the timber bridge failed. The situation required the immediate construction of a new two-lane all-weather crossing (subsequently to be four-lane). There could be no raising of the flood level for fear of damage in the shopping complex; the 1967 flood having risen to within 1 ft (300 mm) of the floor levels. The difference in cost of embankment

to bridge structure was \$1000 per ft length.

The constant energy design gave certainty of calculation and the absolute minimum span. The ground (bed) level was determined by the lowest level at which it was possible to grow grass - the area being tidal. This was taken at R.L. 7.5 ft (2.280m) L.W.O.S.T. The design flood (30,000 cusecs) level was R.L. 15.6 ft (4.750m); the existing ground level was R.L. 10.0 ft (3.047m). The slope is surface fall only and in flood, amounts to less than 1 foot per mile. The approach, being so wide, was considered rectangular.

Approach velocity = $30,000 / (1320 \times 5.6) = 4.0$ ft/sec (1.22m/sec)

R.L. Energy line is 15.85 ft (4.830m)

For ground level at R.L. 10.0 ft (3m), $y_c = 3.9$ ft (1.19m) and critical unit flow $q_c = 43$ cusecs ($4m^3/sec/m$), so flow can be restricted to 688 ft (210m) width only. Under bridge the available specific head $H_s = 8.1$ ft (2.470m), $y_c = 5.4$ ft (1.645m) and $q_c = 71$ cusecs/ft ($6.6 m^3/sec/m$), therefore the minimum width is 423 ft (129m). The bridge was built with 9 x 50 ft (9 x 15.26m) spans with round piers.

The lip of inlet fan was 400 ft (122m) above the bridge. The shape of the fan is shown in Fig. 6. A model scale 1:48 gave results which agreed with the computed results to within 0.2 ft (61mm). These models must be truly three-dimensional as it is no longer possible to study a 'representative' longitudinal section. The model showed that if the approaches were not depressed with the 450 ft (137m) wide opening, the

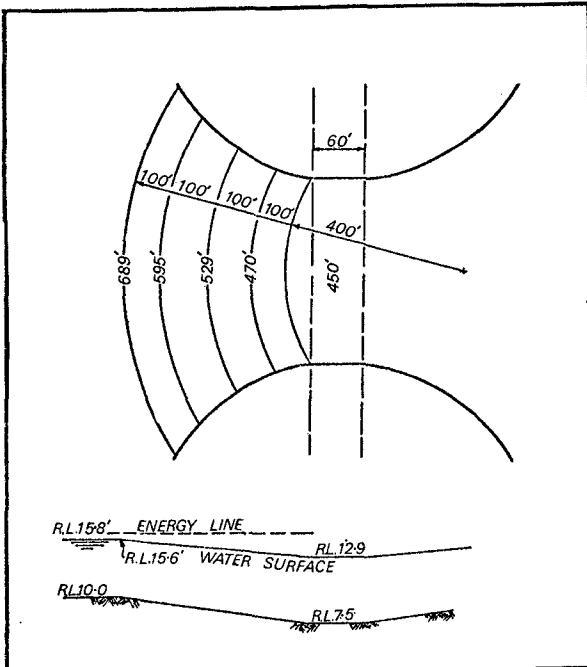


FIG. 6. NUDGEE ROAD BRIDGE INLET

flood level rose above R.L. 18.5 ft (5.650m), the minimum road embankment level, and overtopping occurred. The minimum span to pass the flood at ground level R.L. 10.0ft (3m) was 688 ft (210m). The model again showed the remarkably smooth turbulent free flow and as a result grass only was used as protection on the inlet and outlet fans even though the velocity exceeds 13 ft/sec (3.96 m/sec). The outlet fan was an exact image of the inlet fan.

The cost of the earthworks in the fans was \$10,000, the saving on the bridge about \$240,000.

The design procedure was used in different circumstances in Stawell, Victoria, Australia, by N. Cottmann, Shire Engineer. A bridge on the Stawell-Newington road had a capacity of 800 cusecs (22.62 m³/sec) before the road overtopped - which happened in every flood. The bridge approaches were redesigned so that the same bridge could carry 5,000 cusecs. Fig. 7 shows the bridge carrying 4,300 cusecs (122 m³/sec) in February, 1975. Although the water level under the bridge was well below the approach level it recovered the level and passed through virtually without afflux. Again, despite 15 ft/sec (4.57 m/sec) velocity and minimal protection, no scour occurred.



FIG.7. STAWELL BRIDGE CARRYING 4300 CUSECS (122 m³/sec) IN 1975

The concept lends itself to use in dual or multipurpose structures, in particular the combination of flood alleviation with stream crossings. The South East Freeway out of Brisbane was deliberately routed through the valley of the Norman Creek in order to minimize the number of houses it was necessary to resume. But the valley was free of houses because the area was subject to severe short floods from the adjoining urban areas. Retardation basins in the form of playing fields had been established along much of the length of the creek. The freeway not only crossed the creek on numerous occasions but the embankment occupied a significant portion of the available retardation basin area.

Because of the certainty of the calculation, minimum energy culverts were used throughout. The inlet fan to each culvert was so arranged as to act as a minimum energy weir and to discharge a particular flood at a particular level; i.e. the highest possible. (Fig. 8). The flow through one culvert is not affected by the backwater of the culvert/weir



FIG.8. PHOTOGRAPH OF CULVERT ENTRANCE

downstream. The loss of detention area was amply compensated by the increased depth made available.

A different version of this same theme, flood alleviation and a stream crossing, is that at Settlement Shores, Macquarie, N.S.W. This is a very popular holiday area conveniently situated north of Sydney. The Hasting River flows out of the ranges and meanders in a large loop through the coastal swamps. Even in small floods the area presented was flooded and is unsuitable for development.

A large channel will be built to short circuit the loop but at the lower end a minimum energy weir is to be built high enough to prevent egress of the tide. At the same time the weir allows the free discharge of the flood water virtually without head loss at a lower level and thus frees the area from danger of inundation. Immediately below the weir a very rapid convergence allows economic convenient bridging as access to

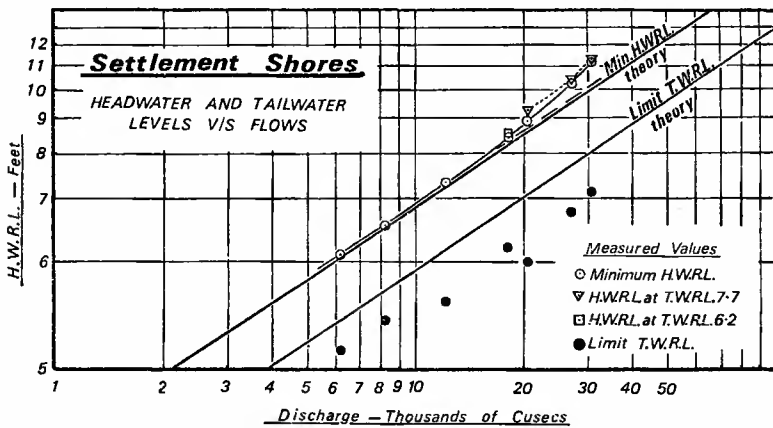


FIG.9. SETTLEMENT SHORES - HEAD-DISCHARGE RELATIONSHIP

the area. Fig. 9 shows the relationship between the calculated and measured head water/tail water on the model. From our experience, the prototype losses will be relatively far less.

NATURAL SMOOTH TRANSITIONS

It became increasingly clear that each of these structures had counterparts in nature. The Redcliffe tidal outfall is surely an idealized and miniaturized river bar formation. If a river enters the sea with reasonably uniform energy, then as the river loses the constricting influence of the banks, the bed must rise to maintain constant energy. If the divergence of the banks is uniform the bar is in fact curved. If the banks are curved the bar is straight. In the days of sail, it was always said that 'ships sailed up-hill over the bar', and how true this could be. Equally it is claimed, again with some truth, that it is always choppy over the bar.

It makes no difference whether the tide is ebbing or flooding, the same shape is demanded by the concept of constant energy. It is not surprising that C.D. Floyd (1968)¹⁵ reports on river mouth training in New South Wales, Australia to the Public Works Department. *"A summary is given of the results of training sixteen rivers in an endeavour to increase bar depths. The bars are of simple crescent formation fed by littoral drift.*

Whilst the training works have improved conditions for navigation, they have not resulted in any appreciable increase in bar depths.

Despite the complex mechanisms involved in bar formation a consistent simple relationship is found to exist between channel and bar depths. This correlation seems to apply to all rivers and inlets with simple bar systems and extends over a range from a bar depth of two feet to 60 feet!

The majority of the work (the training) was carried out in the period 1880 to 1910 with minor changes and additions in the period 1910 to 1930. Commencing in the 1950's, a major training scheme was started on the Clarence River and also a programme of development of small river entrances for fishing craft."

The inlet and outlet features of the culverts are surely the corresponding scour so often appended by nature to man-made structures. A perfect fan completely formed naturally is given in Fig. 10. This is below a small portal bridge over a gravel bed stream after a short sharp fresh flow. The complete culvert form is the shape which always develops between the tidal lagoon and the ocean. This is so well illustrated by Per Bruun (1966)¹⁶. He writes of 'the gorge' and the 'shoals' and illustrates it profusely when he is searching for a relationship for the stability of this strange shape which is deeper in its middle than at either end. (Fig. 11). The entrance to San Francisco Bay, both inside and out, is a perfect major example of this form (Fig. 12).

That this complete culvert shape is a not uncommon geological feature, many arch dam builders have found to their cost. The Gordon River in Tasmania, Australia, is typical. The gorge narrows to provide the perfect abutments but the solid floor is a long way below that at the entrance to the gorge. Of world renown because it is so well advertised, is that mysterious gorge on the River Aare in Switzerland. At places



FIG.10 FAN AT BLYTH CREEK - ROMA

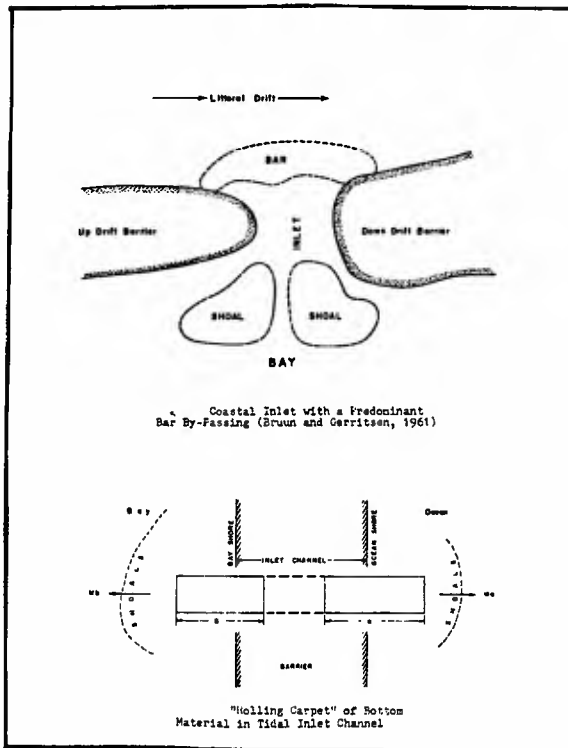
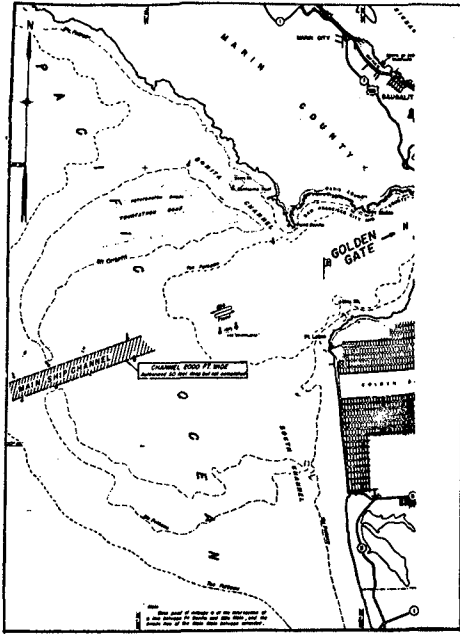


FIG.11. TIDAL LAGOON - (FROM REF. 16)



The Golden Gate and its Ocean Shoals (U.S. Corps of Engineers Annual Report, San Francisco District, 1952).

FIG.12. SAN FRANCISCO BAY - (FROM REF. 16)

this is little more than a meter wide and its depth is a hundred metres below the river bed at each end.

"The Gorge of the Aare near Meiringen (by Professor Dr. P. Arbenz (Berne)). Half an hour beyond Meiringen the Haslital is blocked in the whole of its breadth by a barrier, on the steep walls of which grey chalk is everywhere to be seen. It is not the result of a landslip, nor is it a moraine, but rather a crossbar of rock, a small mountain range in the valley, abounding in small peaks and valleys and a labyrinth of wooded indentures and defiles. The river Aare pierces through this rocky obstacle in the famous Gorge of the Aare. It has eaten its way through the rock at so great a depth, that the fall on its way through the gorge is but slight. A level path leads to Innertkirchen on the other side of this rocky crossbar."

How else could a 'blind' channel be formed across half tide sand banks in an estuary?

The earth weirs arise in the central reaches of many rivers where a well formed channel suffers a change of grade, widens and shoals quite

severely to form pools in low flow periods - the silt banks of Australian streams - below which the stream will converge again to a well-defined channel. These are the sites to be chosen for farm dams and far from scouring, many of the grassed weirs are actually growing.

A very good example of accidental minimum energy culvert must surely be the old London Bridge (Fig. 13). As little as 25% of stream area was available to the tide passing through the bridge. The tidal range is high but up to high tide the plan shape is ideal and the Thames mud was no doubt duly scoured to give the correct profile. This bridge survived from 1209 to 1825 A.D. For five centuries it was the only bridge.



FIG.13. OLD LONDON BRIDGE

Obviously if a form persists there must be some mechanism by which it becomes self sustaining and able to resist any destructive forces. The concept of minimum energy is just such a mechanism. Minimum energy introduces critical velocities; i.e. the maximum velocity which can exist at that energy condition or for that flow per unit width. It is wrong to assume that critical velocities are high, they can be so small that they are unable to move even sand particles. The concept allows the velocity to diminish without reducing the total discharge. Thus the natural fan shape at both inlet and outlet becomes quite stable and self sustaining.

As the velocity of the flow in the connecting deeper channel is always greater than the approaching flow, any bed load is carried through the deeper section. Any floating material will move much easier in the deeper channel so anything which is carried in will be carried out. If the total flow increases for some reason, the inlet fan will erode back to a higher, longer lip. The central section will either become deeper or wider and the eroded material will be carried up the outlet fan to deposit there again to form a higher, longer lip.

The concept does not restrict a river, alluvial or otherwise, to one particular shape so much sought by many researchers - G. Lacey (1930)¹⁷, T. Blench (1957)¹⁸, F.M. Henderson (1963)¹⁹, D.B. Simons and M.L. Albertson (1960)²⁰. Any rectangular shape is acceptable. Provided there is everywhere

the right relationship between width and depth the energy grade will be uniform. The river can become narrower if it deepens or can become wider provided it shallows. The actual cross-sectional shape is a function of the material of the bed and banks. If you add the hypothesis of L.B. Leopold and W.B. Langbein (1966)²¹, that meanders are curves of minimum energy in bending (and there are any number of suitable curves for any situation), then a river has almost complete choice of cross-section and position and can still satisfy the overall concept.

CONCLUSIONS

- 1 - There is no doubt that the concept of minimum and constant energy unfolded here does allow the quantitative determination of smooth transitions in open channels and these transitions can have useful applications.
- 2 - It was shown that in addition to the previously known applications of specific energy, there is a condition which offers a wide range of cross-section proportions without additional 'form' loss. This condition is the reduction of ground (bed) level to satisfy a further convergence of the flow; i.e. to reduce span or to drop the water surface to increase headroom.
- 3 - A solution was offered to the problem of non-uniform flow and an explanation was given for the occurrence of many land forms in nature, such as formation of a river bar and estuaries.
- 4 - The transition shapes are essentially self sustaining. They are 'smooth' with no 'form' loss. There is no energy change and there is no turbulence, hence no scour. As any other shape would require more energy to convey the flow, there is also no deposition.
- 5 - To impose an unacceptable change on such a system is courting disaster as is evidenced by the many vain attempts to change estuarine conditions which are essential to the estuary's very survival. Equally futile is to attempt to rid rivers of the 'bar'. We can learn much by studying the natural shapes.
- 6 - By simply using constant energy rather than constant discharge, we can accurately predetermine the dimensions of the appropriate shape and this shape will be without 'form' loss. Structures can be built to other forms but they will have to be defended, to retain their form, by solid protection or continual maintenance.
- 7 - Always the shape is the same - a strange fan shape. The shape of a scour hole below a culvert. The shape of the old London Bridge. The shape of a tidal inlet to a lagoon. The shape outside San Francisco Bay; of a channel very much deeper than the lakes it connects or the channel through a sandy estuary. All these shapes are, we are sure, conforming to the concept of $v_c^2/2g + y_c = H_0 + \Delta z$.

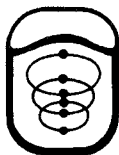
APPENDIX - REFERENCES

1. Progress Report of the Task Force on Friction Factors in Open Channels of the Committee on Hydromechanics of the Hydraulic Division, "Friction Factors in Open Channels", J. of Hydraulic Division, Proc. ASCE, Vol. 89, No. HY2, March, 1963, pp. 97-143 + Discussions.
2. "Capacity Charts for the Hydraulic Design of Highway Culverts", U.S. Bureau of Public Works, Hydraulic Engineering Circular No. 10, March, 1965.

3. F. Engelund, "Flow Resistance and Hydraulic Radius", Acta Polytechnica Scandinavica, Civil Engineering and Building Construction Series No. 24, 1964, pp. 1-23.
4. H. Rouse, "Critical Analysis of Open Channel Resistance", J. of Hydraulic Division, Proc. ASCE, Vol. 91, No. HY4, July 1965, pp. 1-25.
5. E.O. Macagno, "Resistance to Flow in Channels of Large Aspect Ratio", J. of Hydraulic Research, Vol. 3, No. 2, 1965, pp. 41-57.
6. C.C. Shih and N.S. Grigg, "A Reconsideration of the Hydraulic Radius as a Geometric Quantity in Open Channel Hydraulics", Proc. 12th Congress, I.A.H.R., Vol. 1, (Paper A36), Sept., 1967, pp. 288-296.
7. E. Marchi, "Resistance to Flow in Fixed-Bed Channels with the Influence of Cross-sectional Shape and Free Surface", Proc. 12th Congress, I.A.H.R., Vol. 1, (Paper A5), Sept., 1967, pp. 32-40.
8. N. Narayana Pillai, "On Uniform Flow through Smooth Rectangular Open Channels", J. of Hydraulic Research, Vol. 8, No. 4, 1970, pp. 403-417.
9. C.L. Yen and D.E. Overton, "Shape Effect on Resistance in Flood-Plain Channels", J. of Hydraulic Division, Proc. ASCE, Vol. 99, No. HY1, Jan., 1973, pp. 219-238.
10. H.A. Einstein and N.L. Barbarossa, "River Channel Roughness", J. of Hydraulic Division, Trans. ASCE, Vol. 77, Separate No. 78, July, 1951, pp. 1121-1146.
11. L. Bajorunas, Discussion of "River Channel Roughness" - Reference 10.
12. V.A. Vanoni and Li San Hwang, "Relation Between Bed Forms and Friction in Streams", J. of Hydraulic Division, Proc. ASCE, Vol. 93, No. HY3, May, 1967, pp. 121-144.
13. Sir C. Inglis, Discussion of "River Channel Roughness" - Reference 10.
14. B.A. Bakhmeteff, "Hydraulics of Open Channels", McGraw-Hill, 1932.
15. C.D. Floyd, "River Mouth Training in New South Wales, Australia", Proc. 11th Conference on Coastal Engineering, London, England, Vol. 2, Part 4, Chapter 80, Sept., 1968.
16. P. Bruun, "Tidal Inlets and Littoral Drift - Vol. 2, of Stability of Coastal Inlets", Universitets forlaget, Trondheim, 1966.
17. C. Lacey, "Stable Channels in Alluvium", Proc. Institution of Civil Engineers, Vol. 229, Part 1, 1930.
18. T. Blench, "Regime Behaviour of Canals and Rivers", Chapter 3, Civil Engineering Handbook, Butterworth's Scientific Publications, London, 1957.
19. F.M. Henderson, "Stability of Alluvial Channels", Trans. ASCE, Vol. 128, Part 1, 1963, pp. 657-686 + Discussion.
20. D.B. Simons and M.L. Albertson, "Uniform Water Conveyance Channels in Alluvial Material", Proc. ASCE, Vol. 86, No. HY5, May 1960, pp. 33-71.
21. L.B. Leopold and W.B. Langhein, "River Meanders", Scientific American, Vol. 214, No. 6, June, 1966, pp. 60-70.

PROCEEDINGS
OF THE

Fifteenth
Coastal Engineering
Conference



July 11-17, 1976 • Honolulu, Hawaii

Sponsored by the
State of Hawaii
University of Hawaii
American Society of Civil Engineers
through its Coastal Engineering Research Council
American Shore and Beach Preservation Association



Published by the American Society of Civil Engineers
345 East 47th Street, New York, N.Y., 10017

Price \$50.00

ACKNOWLEDGMENTS

The following served as the Organizing Committee for the Fifteenth International Conference on Coastal Engineering:

Charles L. Bretschneider
(Chairman)
Department of Ocean Engineering
University of Hawaii

J. Thomas O'Brien
J.K.K. Look Laboratory of
Oceanographic Engineering
University of Hawaii

Harold P. Brown
Conference Center
University of Hawaii

David S. D. Chung
U. S. Naval Facilities
Engineering Command
Pearl Harbor, Hawaii

Ada Marie B. O'Brien
Honolulu, Hawaii

S. Joseph Amaki
Department of Transportation
State of Hawaii

Howard A. Schirmer
Dames and Moore, Engineers
Honolulu, Hawaii

Karl V. Keller
Pacific Division, Corps of
Engineers, U. S. Army
Honolulu, Hawaii

Frederick A. Zobrist
Neighbor Island Consultants

Appreciation is expressed to the Department of Planning and Economic Development of the State of Hawaii and the Hawaii Visitors Bureau for providing the many photographs appearing on the title pages for the various parts of the proceedings.

CONTENTS

PART III

COASTAL STRUCTURES AND RELATED PROBLEMS

Chapter 129	
CONCEPTS OF DESIGN OF COASTAL STRUCTURES	
Casimir J. Kray	2209
Chapter 130	
WAVE ACTION ON LARGE OFF-SHORE STRUCTURES	
C. J. Apelt and A. Macknight	2228
Chapter 131	
TSUNAMI HAZARD AND DESIGN OF COASTAL STRUCTURES	
George Pararas-Carayannis	2248
Chapter 132	
NUMERICAL CALCULATION OF WAVE FORCES ON STRUCTURES	
B. D. Nichols and C. W. Hirt	2254
Chapter 133	
WAVE FORCES ON SQUARE CAISSONS	
G. R. Mogridge and W. W. Jamieson	2271
Chapter 134	
WAVE PRESSURES ON LARGE CIRCULAR CYLINDRICAL STRUCTURES	
Hiroshi Nakamura	2290
Chapter 135	
FORCES ON ROUGH-WALLED CIRCULAR CYLINDERS IN HARMONIC FLOW	
Turgut Sarpkaya	2301
Chapter 136	
HIGH REYNOLDS NUMBER OSCILLATING FLOW BY CYLINDERS	
Tokuo Yamamoto and John H. Nath	2321

CONTENTS

Chapter 137	
FLOW SEPARATION, WAKE VORTICES, AND PRESSURE DISTRIBUTION AROUND A CIRCULAR CYLINDER UNDER OSCILLATORY WAVES	
Yuichi Iwagaki and Hajime Ishida	2341
Chapter 138	
CYLINDRICAL CAISSON BREAKWATER: STRAIN MODEL TESTS	
Helge Gravesen, Finn P. Brodersen, Jørn S. Larsen, and H. Lundgren	2357
Chapter 139	
NEAR-BOTTOM WATER MOTION UNDER OCEAN WAVES	
Robert A. Grace	2371
Chapter 140	
WAVE FORCES ON SUBMERGED OBJECTS	
Suphat Vongvisessomjai and Richard Silvester	2387
Chapter 141	
FORCES ON A SPHERE UNDER LINEAR PROGRESSIVE WAVES	
Scott A. Jenkins and Douglas L. Inman	2413
Chapter 142	
NEW DESIGN PRINCIPLES FOR RUBBLE MOUND STRUCTURES	
Per Bruun and Ali Riza Günbak	2429
Chapter 143	
DESIGN AND CONSTRUCTION OF HUMBOLDT JETTIES, 1880 to 1975	
Orville T. Magoon, Robert L. Sloan, and Nobuyuki Shimizu	2474
Chapter 144	
DESIGN OF MAIN BREAKWATER AT SINES HARBOUR	
John Dorrington Mettam	2499
Chapter 145	
EXPERIMENTAL STUDIES OF STRESSES WITHIN THE BREAKWATER ARMOR PIECE "DOLOS"	
Omar J. Lillevang and Wayne E. Nickola	2519
Chapter 146	
EFFECT OF BROKEN DOLOSSE ON BREAKWATER STABILITY	
D. Donald Davidson and Dennis G. Markle	2544

CONTENTS

Chapter 147	
ARMOUR BLOCKS AS SLOPE PROTECTION	
A. F. Whillock and W. A. Price	2564
Chapter 148	
LARGE SCALE MODEL TESTS OF PLACED STONE BREAKWATERS	
Charles K. Sollitt and Donald H. DeBok	2572
Chapter 149	
DESIGN AND CONSTRUCTION OF PROTECTIVE STRUCTURE FOR NEW REEF RUNWAY, HONOLULU INTERNATIONAL AIRPORT	
Wilfred D. Darling	2589
Chapter 150	
RESPONSE OF SEADYKES DUE TO WAVE IMPACTS	
A. Führböter, H. H. Dette, and J. Grüne	2604
Chapter 151	
PERMEABLE SEAWALL WITH RESERVOIR AND THE USE OF "WAROCK"	
Takeshi Ijima, Enzoh Tanaka, and Hideaki Okuzono	2623
Chapter 152	
LABORATORY STUDY ON PERVIOUS CORE BREAKWATERS	
Hideo Kondo, Satoshi Toma, and Kenji Yano	2643
Chapter 153	
WAVE TRANSMISSION THROUGH TRAPEZOIDAL BREAKWATERS	
Ole Secher Madsen and Stanley M. White	2662
Chapter 154	
QUAY WALL WITH WAVE ABSORBER "IGLOO"	
Naofumi Shiraishi, Robert Q. Palmer, and Hiroshi Okamoto	2677
Chapter 155	
SLIT-TYPE BREAKWATER; BOX-TYPE WAVE ABSORBER	
Shoshichiro Nagai and Shohachi Kakuno	2697
Chapter 156	
METHOD OF ANALYSES FOR TWO-DIMENSIONAL WATER WAVE PROBLEMS	
Takeshi Ijima, Chung Ren Chou, and Akinori Yoshida	2717

CONTENTS

Chapter 157	
WAVE OVERTOPPING EQUATION	
J. Richard Weggel	2737
Chapter 158	
OVERTOPPING OF RUBBLE-MOUND BREAKWATERS BY IRREGULAR WAVES	
Yvon Ouellet and Pierre Eubanks	2756
Chapter 159	
FLOATING BREAKWATER PERFORMANCE	
Bruce H. Adee	2777
Chapter 160	
DESIGN, ANALYSIS AND FIELD TEST OF A DYNAMIC FLOATING BREAKWATER	
D. J. Agerton, G. H. Savage, and K. C. Stotz	2792
Chapter 161	
PROTECTION OF MARITIME STRUCTURES AGAINST SHIP COLLISIONS	
Kazuki Oda and Shoshichiro Nagai	2810
Chapter 162	
ADDED MASSES OF LARGE TANKERS BERTHING TO DOLPHINS	
Taizo Hayashi and Masujiro Shirai	2830
Chapter 163	
SUBHARMONIC COMPONENTS IN HAWSER AND FENDER FORCES	
J. H. van Oorschot	2840
Chapter 164	
LOW-COST SHORE PROTECTION OF THE GREAT LAKES: A DEMONSTRATION/RESEARCH PROGRAM	
John M. Armstrong	2858
Chapter 165	
LOW-COST SHORELINE PROTECTION	
B. L. Edge, J. C. Housley, and G. M. Watts	2888
Chapter 166	
RECENT APPLICATIONS OF ARTIFICIAL SEAWEED IN THE NETHERLANDS	
Henk G. H. Ten Hoopen	2905



Nawiliwili Harbor, Island of Kauai

PART III

COASTAL STRUCTURES AND RELATED PROBLEMS

Ala Wai Marina, Honolulu, Oahu



CHAPTER 129

CONCEPTS IN DESIGN OF COASTAL STRUCTURES

Casimir J. Kray*

Timber Structures

Certain design of the existing and proposed coastal structures for lateral loading in the United States is presently based upon the use of timber which is structurally inefficient in the elastic range. Figure 1, for example, indicates the plan of timber pile structure. This is a low-capacity dolphin composed of 19 piles, where piles in line of load carry two times axial load and three times larger shear than next piles in line of load.

A relatively small load will be conducive to yield in the tension or compression members. Repetitive loading will gradually cause collapse of such structure.

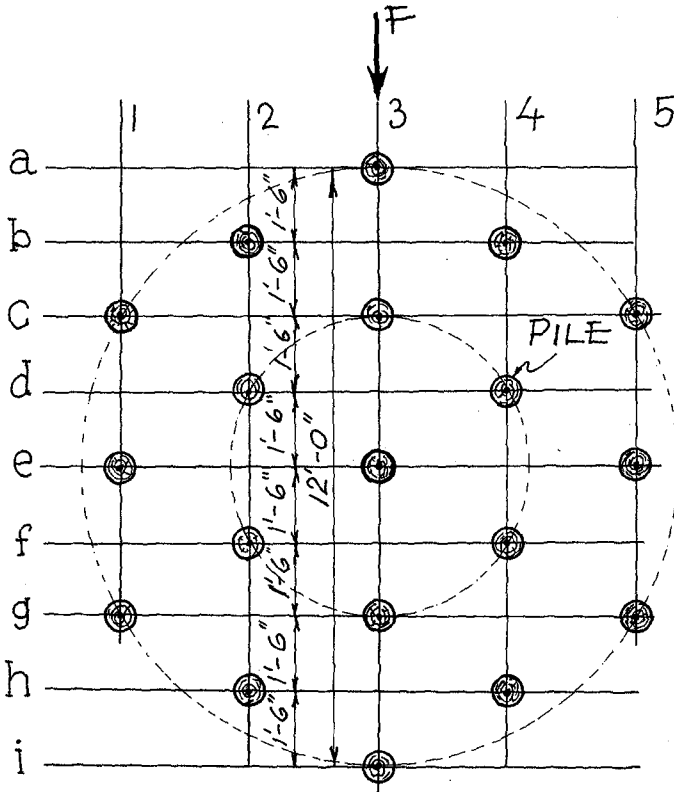
Being inefficient in the elastic range, timber structures may nevertheless, be adequate to provide safety for condition of shallow water, moderate wind pressures, moderate tides, and for moderate cross and reversing currents. However, such factors as: traffic safety, the possibility of marine borer attack, the location of structures in greater water depths, where they are exposed to waves, currents, tides, winds, and floating objects, indicate a need for larger capacity, more reliable and functional coastal structures consistent with the growing requirements.

Alternate Materials and Structural Considerations

The other type of coastal, rigid type structures, using reinforced concrete or structural steel with extensive bracing or with batter piles, are expensive and unyielding. This stiffness may be a reason for inflicted damages to the vessels and to structures themselves upon contact. These rigid structures are also prone to catastrophic failures during earthquakes.

*Consultant, Waterfront Structures, Naval Facilities Engineering Command, Alexandria, VA

By reason of the foregoing shortcomings of timber structures in general and rigidity of reinforced concrete, there is a trend in the Navy to high strength steel tubular sections, to be used singularly, or in groups for resilient type structures, see fig. 2.



PILES 2-3 & i-3 CARRY TWICE LARGER LOAD & THREETIMES LARGER SHEARS THAN PILES C-3 & g-3, REF 1.

FIG 1 - PLAN OF TIMBER PILE STRUCTURE

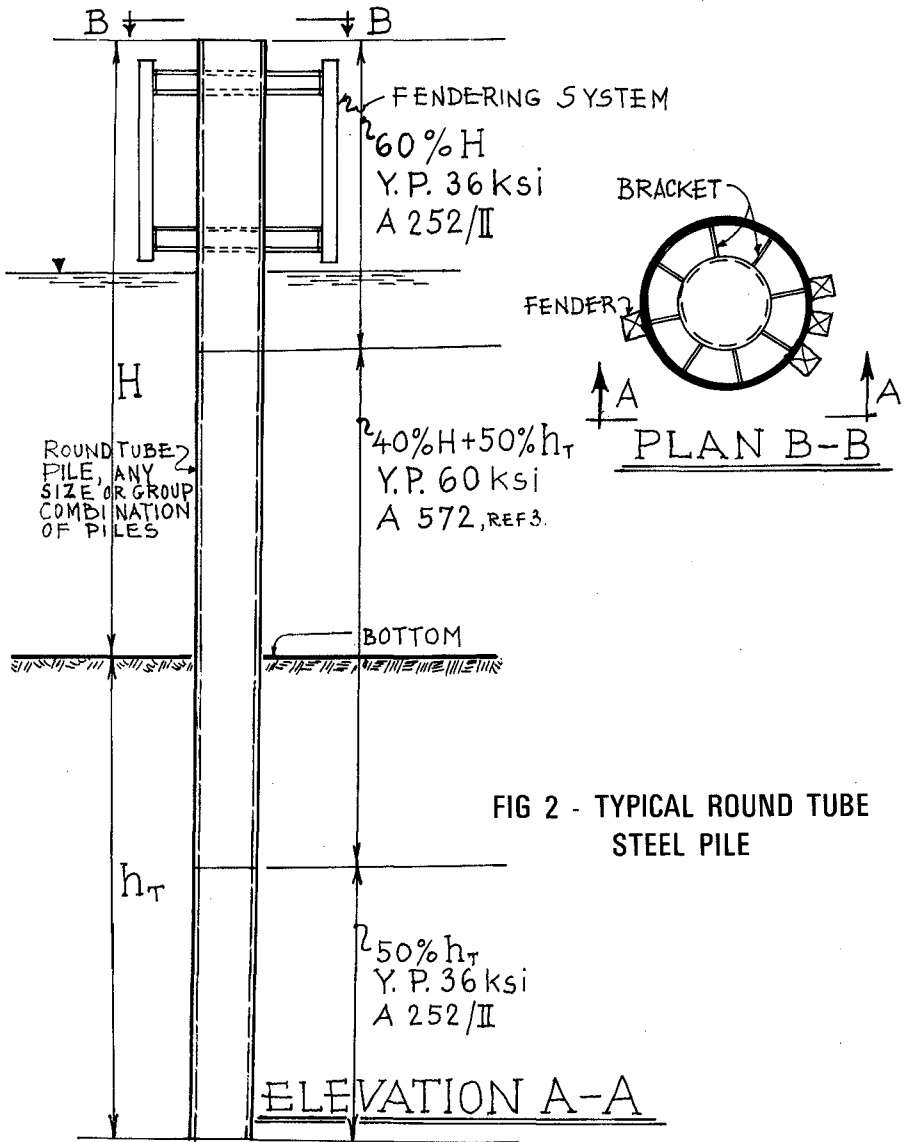


FIG 2 - TYPICAL ROUND TUBE STEEL PILE

COHESIONLESS FOUNDATION SOIL			
PILE SIZE Φ-IN t-IN	EMBEDMENT DEPTH ft	FORCE F KIPS	ENERGY E FT-KIPS
36 x 3/4	40	27	30
48 x 3/4	48	48	45
60 x 3/4	72	74	65
60 x 1	76	100	97
60 x 1 1/4	79	125	131
60 x 1 1/2	82	153	167
72 x 3/4	80	106	84
72 x 1	84	143	130
72 x 1 1/4	88	180	175
72 x 1 1/2	91	212	222

NOTE:

1. $f_y = 60 \text{ KSI} \cdot \gamma_s = .05 \text{ K/FT}^3 \cdot f = 7 \text{ K/FT}^3 \cdot K_p = 3$
2. FORCE APPLICATION $H = 50 \text{ FT}$
ABOVE THE COHESIONLESS BOTTOM

FOUNDATION SOIL	CHARACTERISTIC LENGTH	DEPTH OF EMBEDMENT FOR LONG PILE BEHAVIOR
COHESIONLESS	$T = \sqrt[5]{EI/f}$	MIN. $h_T = 3T$
COHESIVE	$T = \sqrt[4]{4EI/K}$	MIN. $h_T = 2T$

EI - FLEXURAL RIGIDITY OF PILE (MODULUS OF ELASTICITY K/FT^2 × MOMENT OF INERTIA OF PILE SECTION FT^4)

f - COEFFICIENT OF HORIZONTAL FOUNDATION MODULUS K/FT^3

K - " " " " " " " " " " " " " " " " K/FT^2

FIG 3 - CAPACITIES OF VARIOUS SIZE ROUND TUBE STEEL PILES

Such steel piles will provide:

- a. Improved pile to soil transfer of forces.
- b. More efficient sharing of centric and eccentric forces by all piles; also better resistance to torsional forces, and better mobilization of torsional strains, to enable high energy storage.
- c. Possibilities of larger deflections, for high energy absorption in bending, because the flexural elastic strain energy for steel is very high. Grade of steel can be varied in each pile, during the fabrication process.
- d. Far greater efficiency in torsion, remarkably more than that in bending.

This is because the torsional shear stress is the same around the circumference of the pile and along its length. That advantage should be distinguished from bending stresses, which vary from zero at neutral axis, to a maximum at extreme fibers of the cross section; and from zero at the top of the pile to the maximum at the bottom.

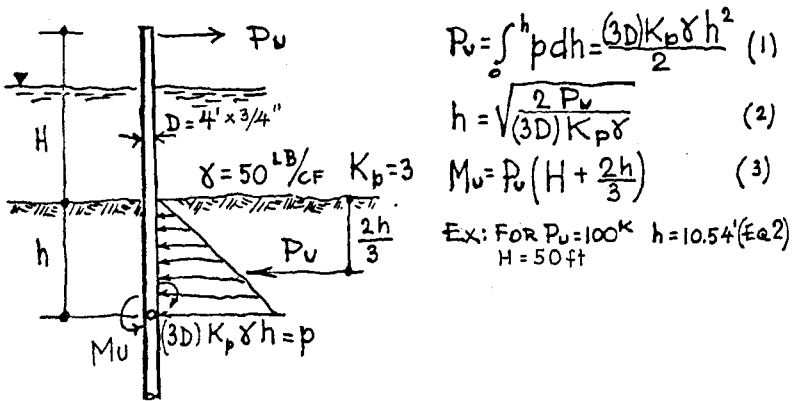


FIG 4 - ULTIMATE LOAD CONDITIONS FOR A PILE

Some assumptions made for design of resilient structures with tubular, round steel piles are:

- a. Slope changes at upper ends of group of two piles (or more) should not be constrained, which is particularly important in weak soils.

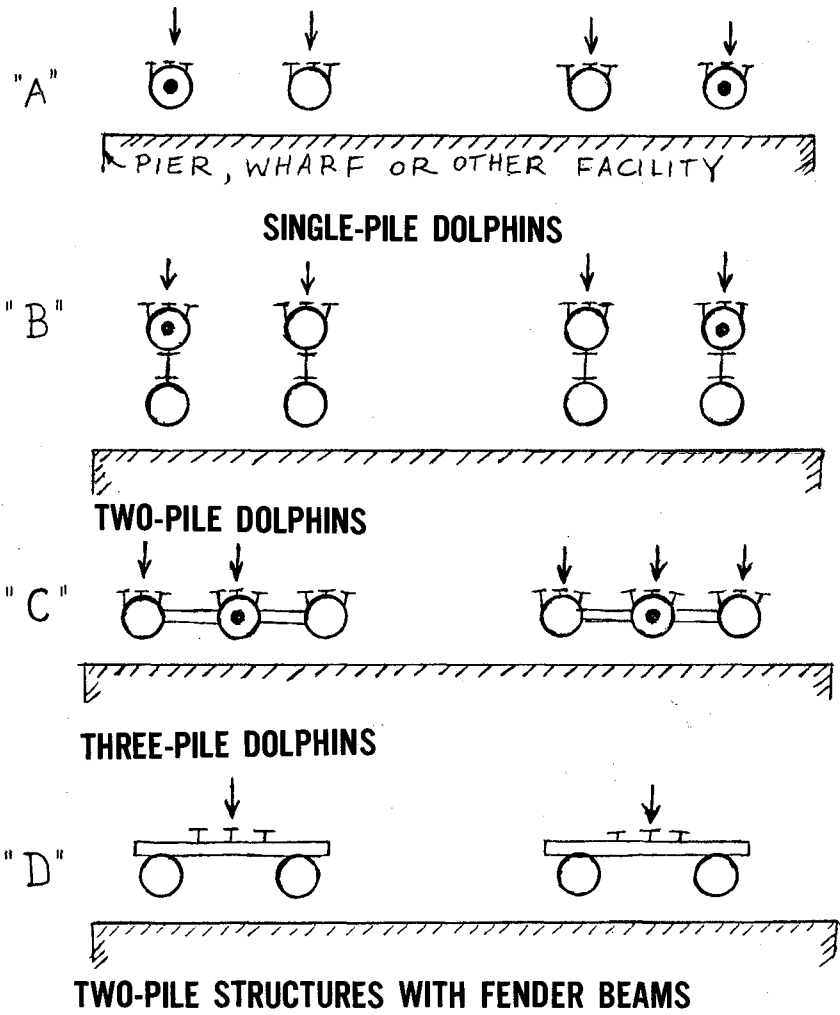
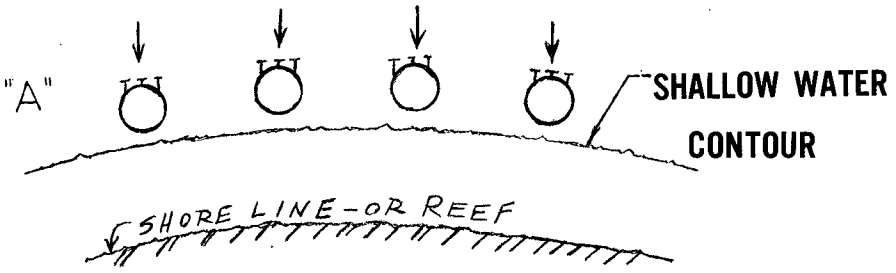
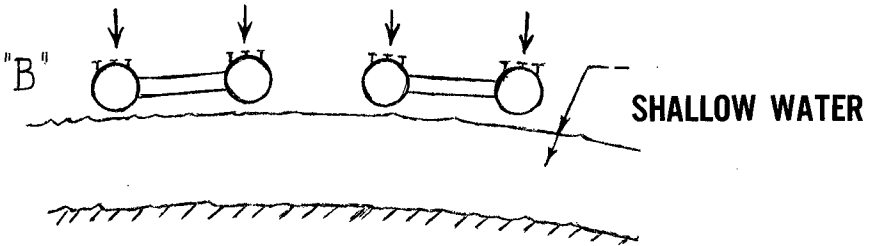


FIG 5 - VARYING CAPACITY PROTECTIVE STRUCTURES
ALTERNATIVE CONFIGURATIONS

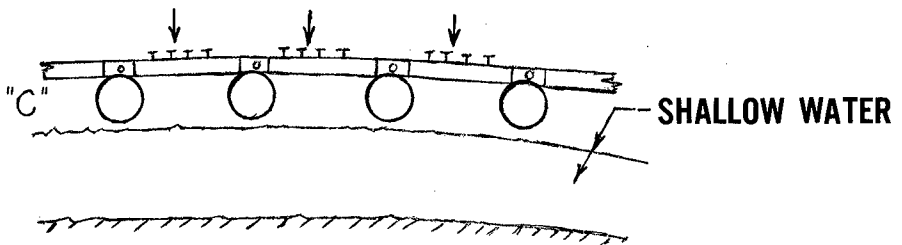


SINGLE-PILE ACTION



DOUBLE-PILE ACTION

(Connected in pairs)



MULTIPLE-PILES ALTERNATIVE

(Connected continuously)

FIG 6 - VARYING RESPONSE SAFETY STRUCTURES

- b. 50% of yield point in piles is used for mooring and for berthing forces.
- c. 75% of yield point is used for energy absorption.
- d. 1/8" wall thickness is provided additionally, for effects of corrosion.

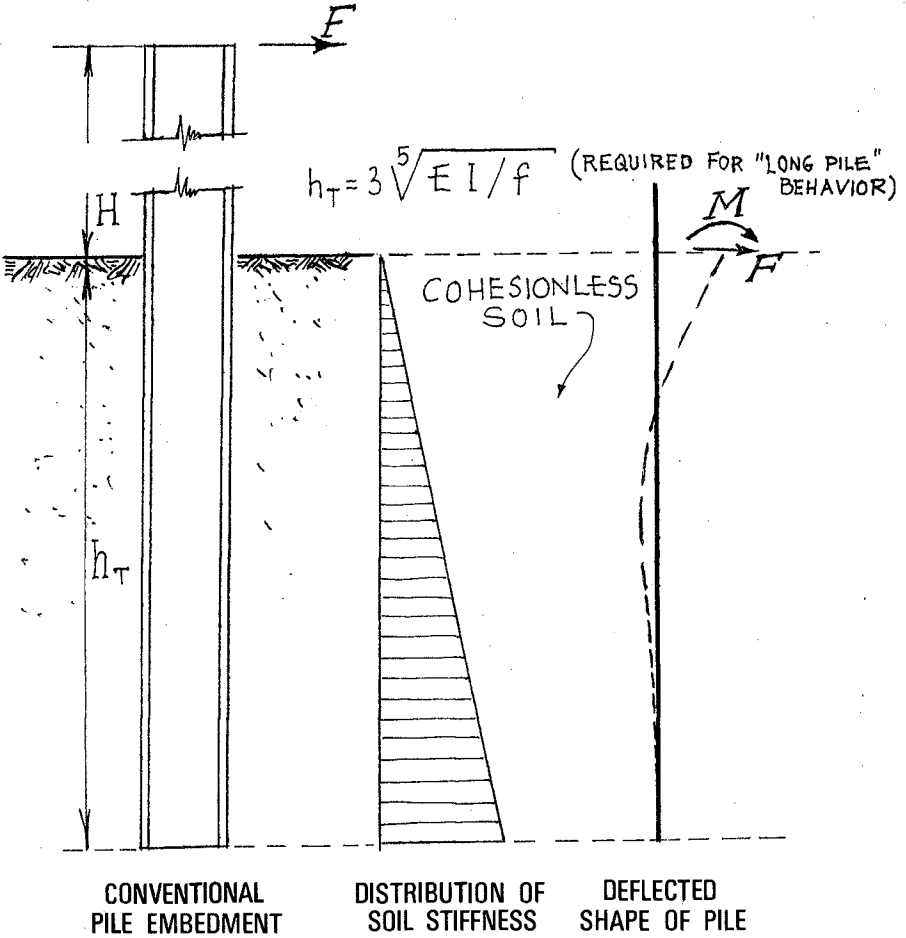


FIG 7 - PILE-SOIL INTERACTION

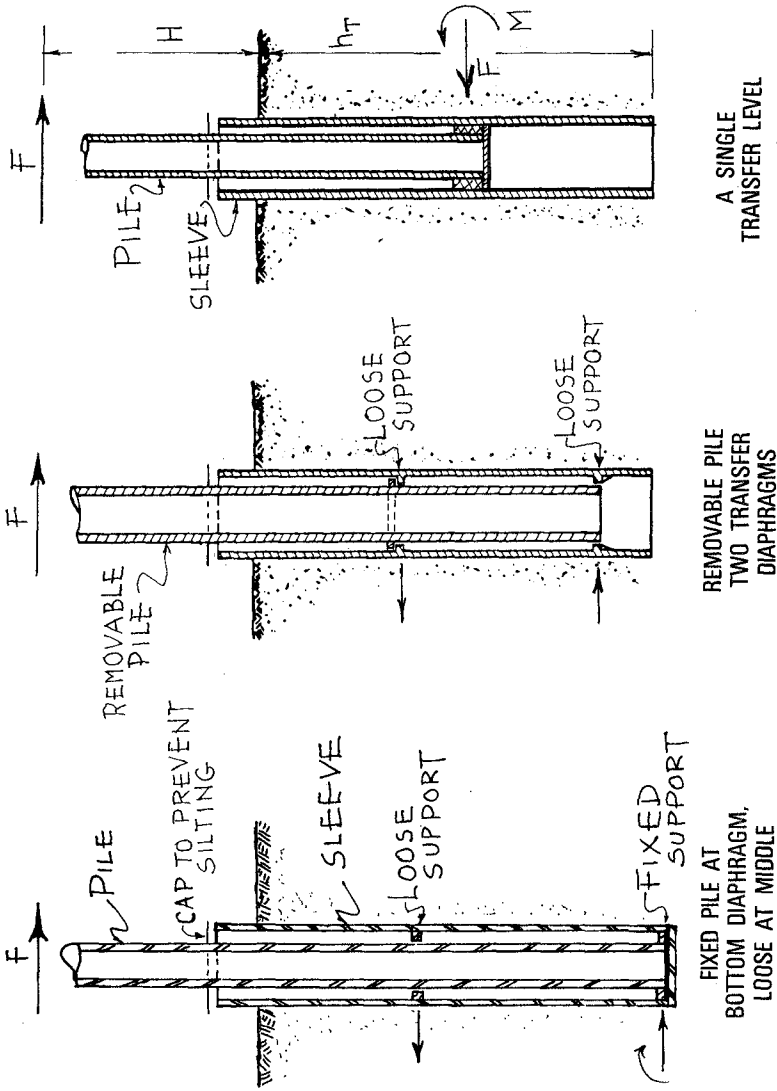


FIG 8 - ALTERNATE USE OF SLEEVE - VERTICAL SECTION
 PILE TO SLEEVE FORCE TRANSFER, REF. 2.

For illustration, figure 3 lists static force and energy absorbing capacities of various size tubular steel piles in cohesionless subgrade soil for forces applied at 50 ft from the bottom of the sea.

In consideration of the above-described items, there might be circumstances in which it would be desirable to transfer lateral forces acting on coastal structures into the soil through piles in bending, without the severe constraints to such bending which are imposed by soil behavior.

Regarding soil pile interaction, see figure 4 for the ultimate load capacity of a pile in cohesionless soil. It is assumed in figure 4, that the pile reaches its ultimate load condition, when a yield hinge develops at a certain depth. This is a commonly used approximation for interaction with cohesionless subgrade soil. In such a case, passive soil pressure counteracts the horizontal force action. Yield moment in the pile resists bending moment, caused by the horizontal forces.

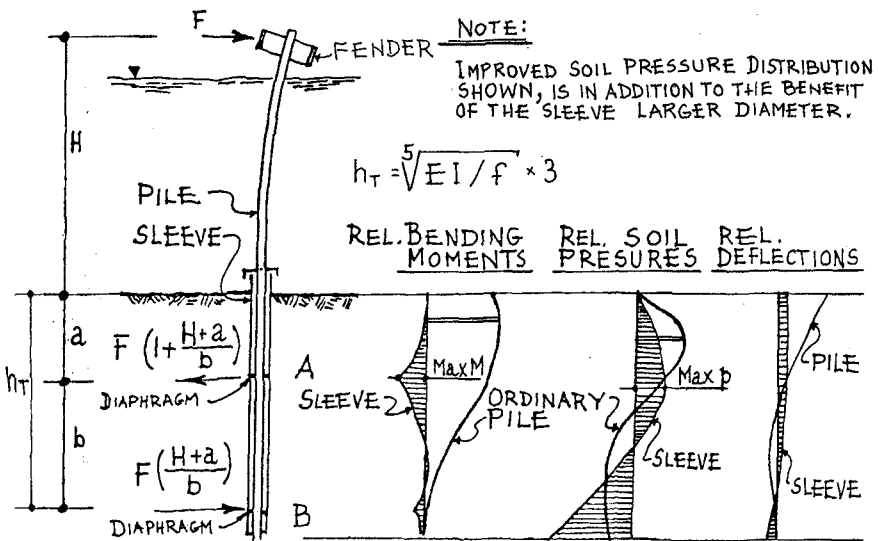


FIG 9 - RELATIVE-BENDING MOMENTS & SOIL PRESSURES

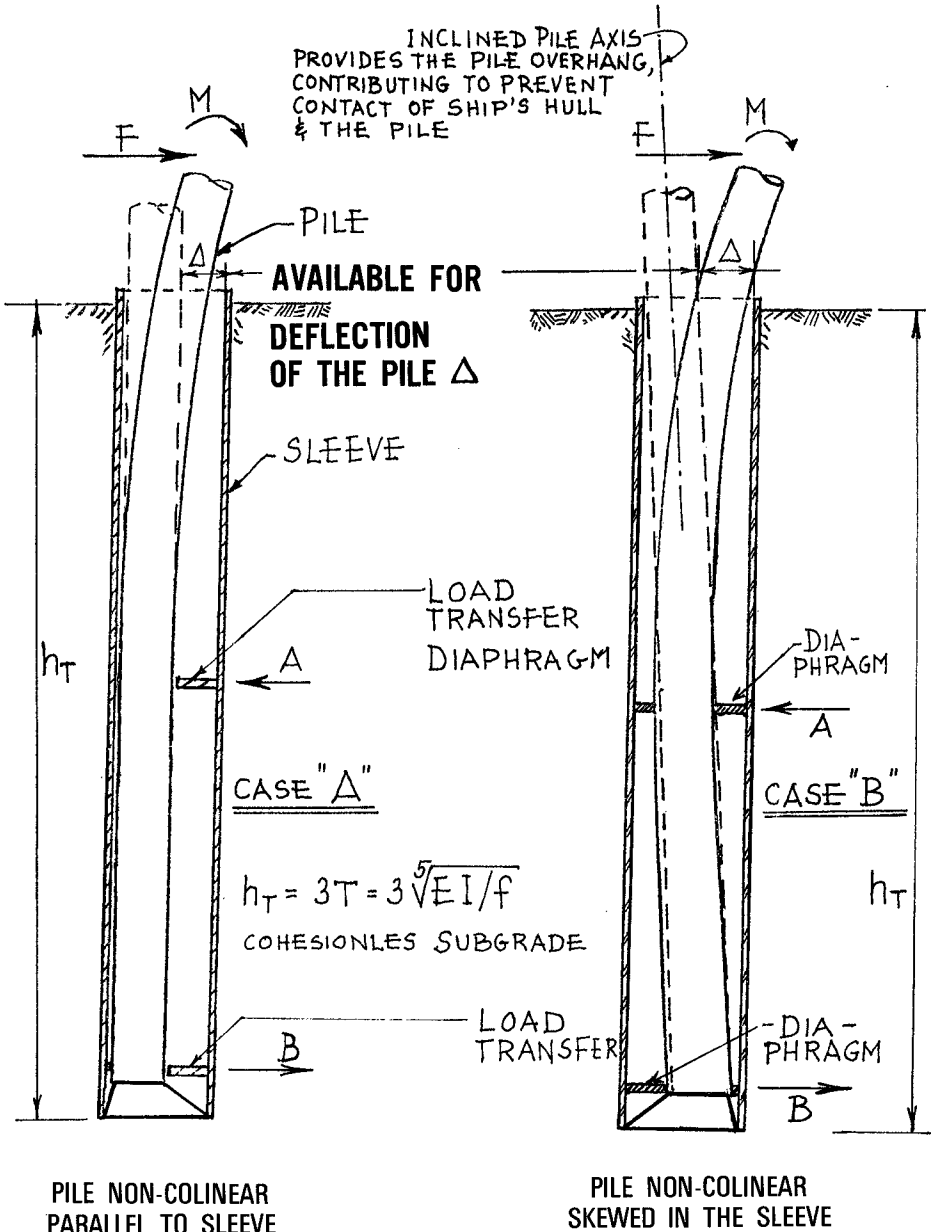
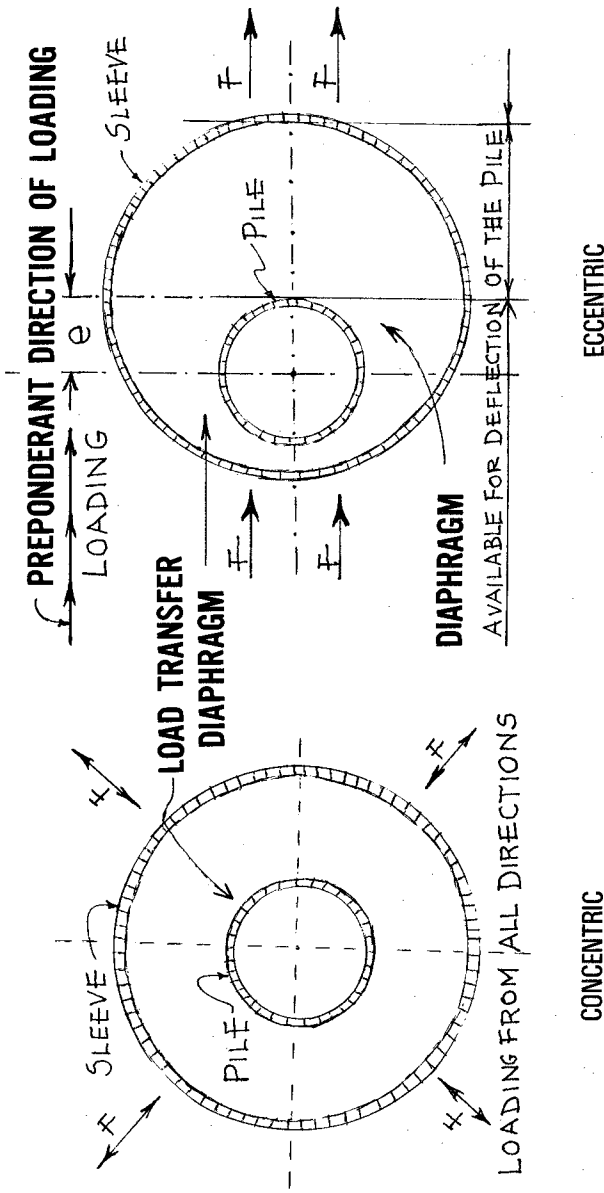


FIG 11 - VERTICAL SECTION - PILE IN THE SLEEVE FOR MAXIMUM DEFLECTION



ECCENTRIC

CONCENTRIC

FIG 10 - LOCATIONS OF PILE IN THE SLEEVE - PLAN

After deciding on the kind of piles most suitable for field conditions, next it will be the intent of the designer to optimize the structure-to-ground interface, for improved structural response to lateral loading.

Design Concepts in Development

Such structures which resist lateral load by pile bending, rather than by axial forces in piles, batter piles, or in the bracing; can absorb large amounts of energy, a major consideration in case of contact with floating objects propelled by wind, current, tides, and wave action. In the exploitation of this advantageous characteristic of piles in bending for coastal structures, it would be desirable to use structural steel- round tubular piles, preferably of high-yield strength.

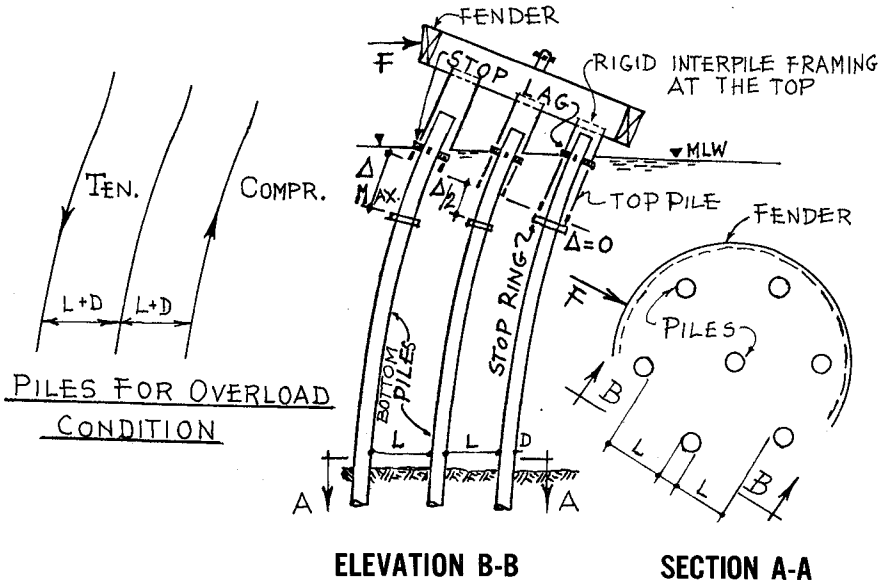


FIG 12 - SLIP JOINTED PILES' CLUSTER ELEVATION

Figure 5 shows structures composed of single, two pile and three pile dolphins, for protection of other vulnerable coastal installations or vessels from damage upon contact. Also, often they supplement lateral resistance of piers, wharves or quay walls, themselves not capable of supporting larger lateral loads. Figure 6 is an arrangement in plan of piles for various response, used for the single, double, and multiple pile action.

However, piles of such structures develop large shear and bending moment at the seabed elevation and imply lateral soil pressures which may well be above the elastic capability of many soils.

The loading, moments and forces are concentrated at the upper end of embeddings where the soil is least resistant, see figure 7.

Therefore, certain improvisations are possible in order to provide for greater efficiency and safety in the applications of structural steel piles in coastal structures. For examples, the following could be done:

NOTE: IN A PILE CLUSTER
PROVISION FOR TORSION
MAY BE NEEDED FOR ONE
OR TWO PILES ONLY.

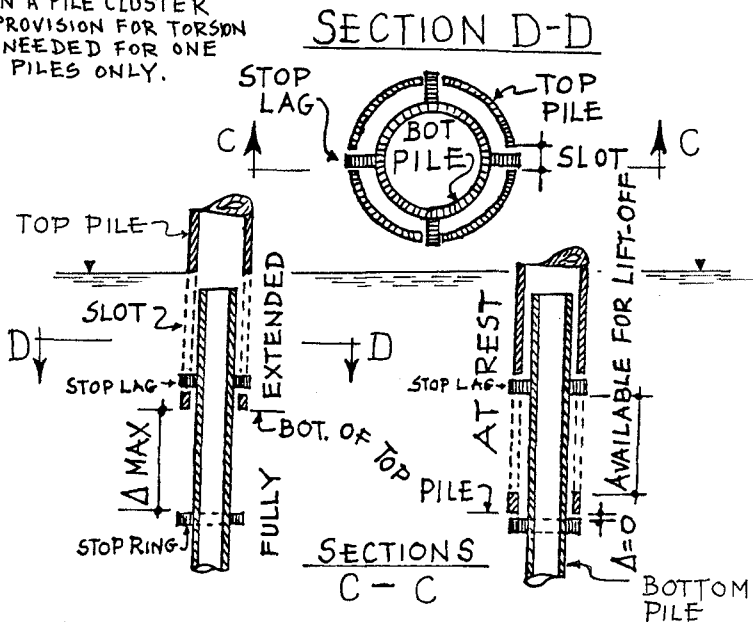


FIG 13 - DETAIL OF SLIP JOINT IN PILES

EXAMPLE : 7 PILES 36" PP X 0.75" ; $f_y = 50$ ksi
 ASSUME RATED CAPACITY AT $f_s = 28$ ksi
 --" SLIP-JOINT CLOSURE AT $f_g = 36$ ksi

	At Rated Capacity	At Joint Closure
DOLPHIN FORCE, F	191,000 LBS	245,000 LBS *
FORCE DISPL., Δ	16.8 INCHES	21.6 INCHES
ABSORBED ENERGY	133,700 LB-FT	229,000 LB-FT
MAX PILE SHEAR, AT SEABED	29,500 LBS	39,400 LBS
" " MOM., "	167,000 LB-FT	209,000 LB-FT
" " VERT. LOAD	≈ SHARE OF SELF-WT.	≈ SHARE OF SELF-WT.
SLIP-JOINT TRAVEL	7.5 INCHES	9.7 INCHES

*After joint closure there is substantial additional force capacity (†modest additional energy capacity) as the pile pull-out capacity is mobilized.

FIG 14 - PERFORMANCE OF PILES' CLUSTER

The Sleeve Concept

In case of large shear and bending moment together with poor soil condition, the desired flexibility can be achieved by isolating the upper portion of the embedded section of pile from the soil contact by driving it through a pipe sleeve of larger diameter, see figure 8, which sketches three arrangements for transfer of forces from pile to sleeves. Mud-line force F and moment M react through load transfer diaphragms in the sleeve, as concentrated forces, at depths where soil resistance is greater. The sleeve of larger diameter than the pile delivers in turn the load to the soil.

Figure 9 depicts the comparison of moments, soil pressures and deflections for pile without sleeve, and for the sleeve action. Obvious smaller moments and better distribution of soil pressures as well as deflections result. Figure 10 illustrates two alternate relations between the pile and the sleeve as to location: concentric or eccentric. Figure 11 indicates two possible eccentric locations of the pile in the sleeve in vertical sections: with parallel axes of the pile and sleeve or skewed pile axis with respect to vertical sleeve. One case A is with constant eccentricity throughout the depth of embedment, the second case B with varying eccentricity, respectively.

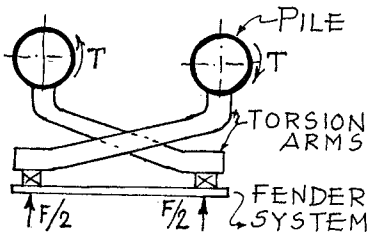
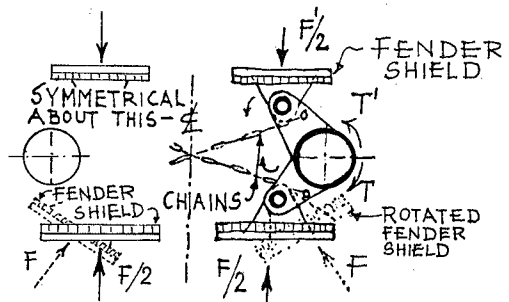


FIG 15 - TORSION ACTION PLAN



TO BE MORE EFFECTIVE, RATIO OF BRACKET ARM LENGTH TO WATER DEPTH MUST BE SUBSTANTIAL

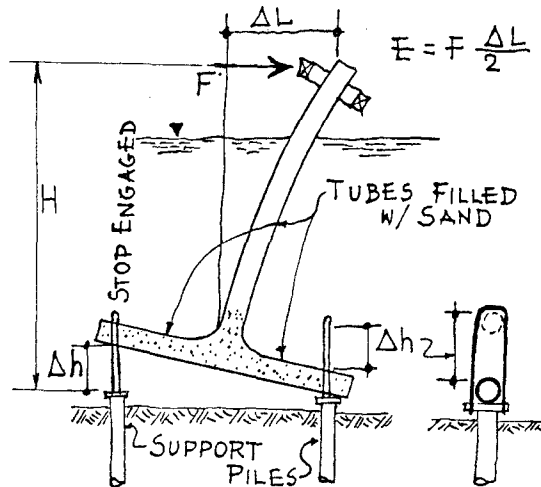
FIG 16 - TORSION BRACKETS - PLAN

This concept has also utilization potential in columns for alleviating earthquake distress or permit thermal expansion of horizontal overhead members carried by such columns.

The Elongation of Tension Piles

To introduce in the outer piles of structure slip joints which would preclude pile axial tension forces until the prepositioned joint stops are engaged; see figure 12. This figure shows seven parallel piles supporting rigid deck platform with slip joints in piles, permitting their elongation without inducing moments at the connection with platform, until stop lag is engaged by the bottom of top pile.

Such slip joints in piles are relatively simple, and capable to transmit pile torsion, as well as, pile bending moment. See also figure 13 for slip joints in cluster of piles. At the bottom in section C-C and on the top section D-D, detail of slip joints are shown. At the right is a pile at rest and at the left in fully extended position. Outer piles are permitted to lengthen under loading without inducing moments in piles until stops in piles are engaged. Then axial forces are induced and moment, thus augmenting load carrying capacity of the structure. Figure 14 represents an example of such a structure performance.



**FIG 17 - TETRAPOD - GRAVITY BALANCED
ELEVATION**

Torsion - Mode Piles

This concept utilizes vertical tubular piles fitted with torque arms on which the outside forces act, causing torsional and bending stresses in the piles. This increases their deflection and energy absorption, see figure 15, which indicates plan of torsion action induced in piles by loading the projecting arms rigidly connected to piles.

(SAND-FILLED LOWER TUBES) EXAMPLE

(1) ALL TUBES PP 36" X 1.25" ($f_y = 50$ ksi; Max $f_s = 30$ ksi)

<u>L</u> <u>(FT.)</u>	<u>LEG</u> <u>(FT.)</u>	<u>WEIGHT</u> <u>(LBS.)</u>	<u>F</u> <u>(LBS.)</u>	<u>ENERGY (LB-FT)</u>	
				<u>5' HOR. DISPL.</u>	<u>10' HOR. DISPL.</u>
60	33	103,000	28,500	142,000	268,000
70	32	105,000	24,300	121,000	218,000

(2) ALL TUBES PP 48 X 2.50 ($f_y = 50$ ksi; Max $f_s = 30$ ksi)

<u>L</u> <u>(FT.)</u>	<u>LEG</u> <u>(FT.)</u>	<u>WEIGHT</u> <u>(LBS.)</u>	<u>F</u> <u>(LBS.)</u>	<u>ENERGY (LB-FT)</u>	
				<u>5' HOR. DISPL.</u>	<u>10' HOR. DISPL.</u>
60	41	277,000	95,000	475,000	890,000
70	40	280,000	78,000	390,000	700,000

Note: Max vert. force on one support point is equal to the above tabulated weight.

Max hor. force on one support is twice the dolphin capacity, F, tabulated above.

FIG 18 - PERFORMANCE OF A GRAVITY BALANCED TETRAPOD

Figure 16 depicts the other arrangement of torsion brackets for loads acting on either side of structure, as the case may be. Fender shields rotate on vertical pins thus being able to accept loads coming at an angle to the structure.

Tetrapod Concept

The idea utilizes a gravity-balanced tetrapod principle for a structure, consisting of a single-vertical pile, rigidly connected to three horizontal round steel tubular members in the seabed area.

Figure 17 is an example of tetrapod action in exaggeration. Lift of one of the legs on the side of the load is indicated.

The collision energy from floating objects is absorbed by bending of tubular elements. At large loads there is a lift-off at one of the three support points, rarely of two, and energy is absorbed by overcoming weight of steel members and sandfill in tubes - until stop is engaged for extra large load, see figure 17.

Figure 18 gives an example of tetrapod structures with tubular legs filled with sand in 60 ft and 70 ft of water depth for 36" and 48" diameter piles.

Acknowledgement

The above-discussed concepts suggest a number of design innovations which promise greater efficiency and performance for coastal structures. These ideas are in the experimental or development stage, currently being studied and investigated, by the Naval Facilities Engineering Command, with assistance from Hansen, Holley and Biggs Structural Engineers.

Reference

1. Bureau of Yards and Docks, Department of the Navy "Analysis and Design of Dolphins", Contract No. NBy37595, 1963
2. M.J. Holley, Jr. and C.J. Kray, "Sleeved Piles for Offshore Structures under Lateral Loading" Proc. Offshore Technology Conference, Houston, Texas, Paper No. OTC 1897, 1973
3. Naval Facilities Engineering Command, Department of the Navy "Design Standards for Structural Steel Dolphins in Cohesionless Soil", Contract No. N00025-71-C-023, 1973

CHAPTER 130

WAVE ACTION ON LARGE OFF-SHORE STRUCTURES

C.J. Apelt (1) and A. Macknight (2)

SYNOPSIS

The paper describes investigations carried out in order to design for the wave action, both wave force and scour, on large off-shore berthing structures sited approximately 1.3 miles (2.1 km) off-shore near Hay Point, North Queensland, in 56 feet (17 m) of water at low tide, the tidal range being 20 feet (6 m). The region is a cyclone area and the structures must be capable of withstanding attack from maximum predicted waves with period of 8.25 seconds and amplitude of 24 feet (7.3 m).

The main units in the berthing structures are concrete caissons sunk on to the ocean bed and the largest of these have plan dimensions of approximately 150 feet (46.7 m) by 135 feet (41.4 m) with four columns approximately 40 feet (12.2 m) square projecting through the water surface. No theoretical method available at the time of the investigation was capable of accurate calculation of wave forces on these structures. A scale model was tested to obtain wave forces and the paper compares results from the model with those of numerical methods and discusses the application of the results to the design functions. Scour effects were also modelled and the results used as the basis for design of scour protection.

1. INTRODUCTION

Hay Point is an exposed rocky headland on the northern Queensland coast approximately 750 miles north of Brisbane. The Great Barrier Reef offers a degree of protection but fetch distances within the Barrier still allow the development of large wave heights during cyclonic disturbances. The port at Hay Point consists of two berths to cater for 100,000 dwt bulk carriers exporting coal to Japan; the annual throughput being some 20 million tons per annum (mtpa). The berths are sited 1.3 miles (2.1 km) offshore where 56 feet (17 m) of water is provided at low tide. The first berth, a conventional piled structure, was commissioned in 1971 and has a throughput capacity of approximately 10 mtpa. Studies of ship turn round times, tidal restriction and other factors showed that upgrading of the first berth, even with the provision of 2 shiploaders, would still leave it incapable of handling the output from the one or two additional mines proposed. Accordingly the decision was made to construct a second berth.

Once the location and alignment of the second berth had been chosen, several types of construction were considered. In the event, concrete caissons which could be constructed at a remote site, floated to and grounded at Hay Point were selected since they provided, inter alia, the following advantages:-

- * the maximum of work could be carried out in the sheltered conditions of the construction site, leaving a minimum to be completed at the exposed site.
- * minimisation of risk to shipping and of disruption of port operations during the construction period.

(1) Reader in Civil Engineering, University of Queensland.

(2) Partner, Rendel & Partners, Brisbane, Australia.

Figure 1 illustrates the site and the alignment of the two berths. The layout and structures of the new berth are illustrated in Figure 2, which also indicates the scour protection. The cross sections of a concrete berth caisson and of the large columns penetrating the water surface are shown in Figure 3, which also provides details of the scour protection system and of the foundation preparation adopted. Figure 4 shows a completed berth caisson grounded at Hay Point.

2. WAVE CLIMATE

Hay Point is located on latitude 21°S and is subject to cyclonic activity concentrating primarily through the months of December to April. The Great Barrier Reef is located to the East and is an effective barrier to storm waves originating in the Coral Sea. The longest uninterrupted fetch lies to the East with water depths varying between 6 and 30 fathoms. To the North, East and S.E. of Hay Point, fetch distances are largely broken up by islands and by shallow water.

Characteristically the wave climate predominates from the S.E., being influenced largely by storm activity in the Tasman Sea, but interposed with random and irregular cyclonic activity usually generated in the Coral Sea. Refraction of waves arriving from S.E. tends to concentrate long period waves from an East and E.S.E. direction, periods of at least 20 seconds having been recorded from the East. Extensive investigations into the wave climate were conducted and these are summarised in Figure 5. Figure 5 is a plot of measured data on wave height, and from this the following probabilities for deep water waves were obtained:-

Occurrence interval (years)	1	10	100
Significant wave height (feet)	10.5	13.5	17.5

The steepness of the waves is such that breaking conditions would not be expected. Directional distributions showed that most waves approached the site from the S.E. quadrant, the directions E.S.E. and S.E. being particularly dominant.

A special examination of potential cyclone activity was undertaken using hindcast techniques and 4 possible cyclones were simulated. Potential deep water waves of greater than 20 ft were generated with periods of the order of 8 seconds. The determination of the probability of such a cyclone occurring is quite difficult and even more so at a given location. However, at Hay Point the probability was considered to be of the order of 1 in 300 to 1 in 500 years and for the waves generated to occur at high water the probability is 1 in 600 to 1 in 1000 years. In general, most of the higher waves consistent with a prediction of a significant wave height of 20 feet would either be unstable because of large steepness or would have shoaled and, therefore, only a few could be expected to reach the structure in a 6 hour period and, then, only at high tide. The probability of a cyclone occurring with a maximum wave of 24 feet generated is estimated as approximately 1 in 50 years and, at high tide, 1 in 100 years. It was estimated that such waves could be expected to reach the structure 40 to 60 times in any 6 hour period of wave persistence. It was considered reasonable therefore to adopt a maximum design wave of 24 feet with a period of 8.25 seconds from which to determine the forces on the structure due to waves, the forces being subject to load factors as discussed below.



FIG. 1 Hay Point bulk coal loading Berths

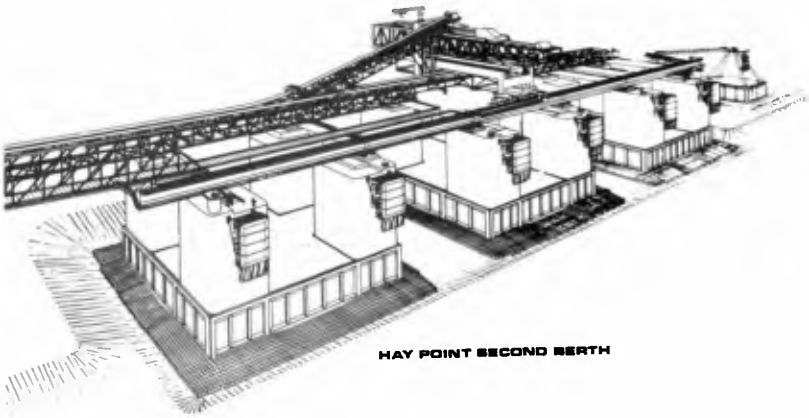


FIG. 2 New Berth structures at Hay Point

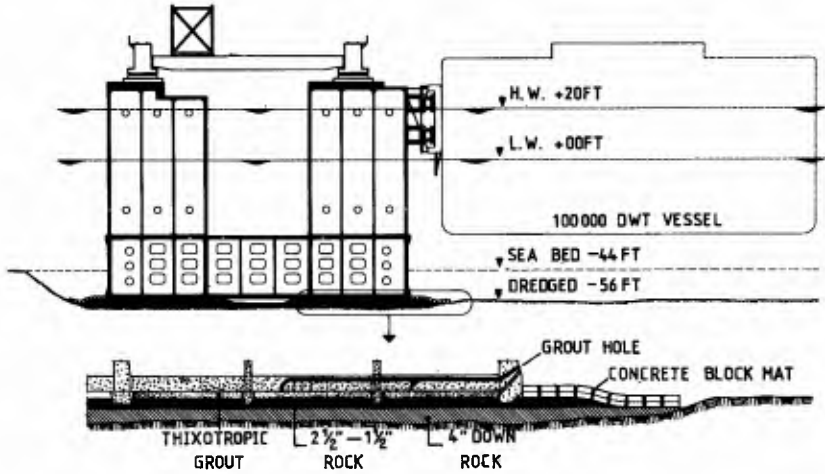


FIG. 3 Main Berth Caisson; structure and foundations

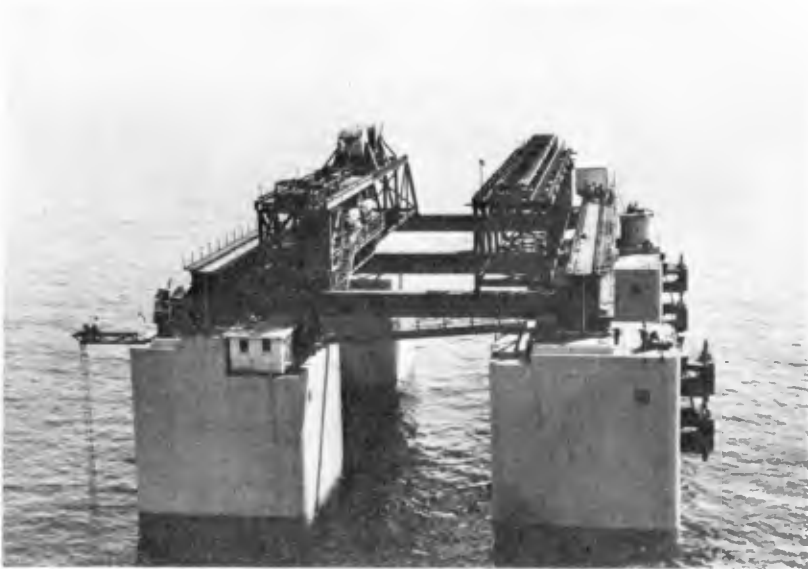


FIG. 4 Main Berth Caisson grounded at Hay Point

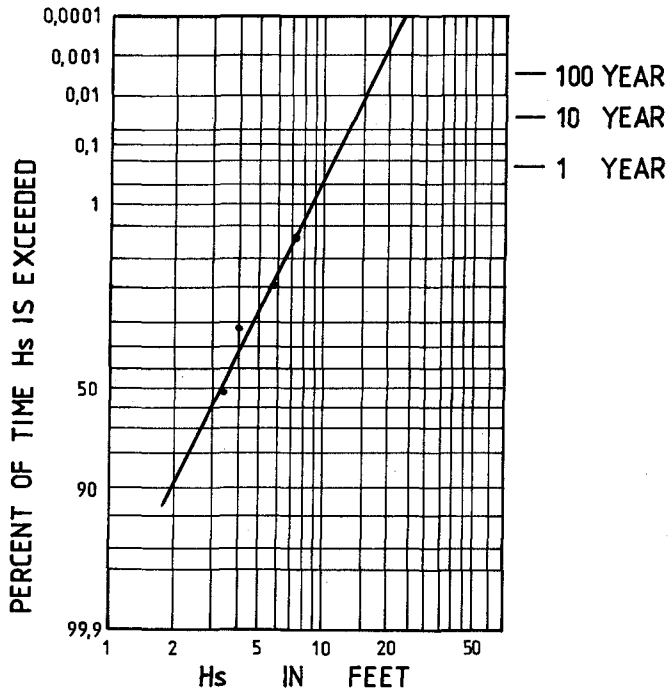


FIG. 5 DEEP WATER SIGNIFICANT WAVE HEIGHT.

3. PRINCIPAL DESIGN REQUIREMENTS

The size of an individual column on one of the caissons is approximately 40 feet (12.2 m) square, the theoretical wave length of the design wave is approximately 350 feet (107 m) and for the more frequent waves the wave length is about 200 feet (61 m). Thus, methods of calculating wave forces such as those developed by Morrison (Ref. 1) or by Sainflou (Ref. 2) are inappropriate since they are based on the assumption that the characteristic structure dimension is either very small or very large (i.e. a bluff body) compared to the incident wave length. In the first instance, therefore, a numerical method based on linear diffraction theory (Ref. 3) was used to give estimates of wave forces to allow the design process to commence and proceed. Simultaneously, measurements of wave pressures were made with a physical model of a complete caisson with its four columns, to include interaction effects from adjacent columns, the influence of a porous foundation and of the geometry of the bottom of the caissons which formed a cruciform gap under the central part of the base.

It was the intention that the caissons should be a gravity design and that they should be stable when grounded without additional securing or ballast. Therefore, an accurate picture of variations with time of wave forces on the columns and on the overall structure was

essential. In addition to the overall stability requirements, the value of the moment at the base of the column together with the positive and negative pressure history on a column during the passage of a wave were required to ensure the competence of the structural elements forming the columns.

In the case of scour protection the quantitative assessment of requirements could be achieved only by model analysis. The two principal types of caissons, the large berth caissons and the smaller approach caissons, both required modelling. The chief problem in the case of the berth caisson was to derive a suitable weight for the type of protection considered the most suitable from a construction viewpoint. In the case of the approach caissons it was not clear at the design stage whether or not the foundation should be recessed below the level of the surrounding sea bed or whether the foundation could be constructed directly on it and, so, both these arrangements were modelled.

4. WAVE FORCE ANALYSIS

The numerical calculations of wave forces were carried out by Dr. C.J. Garrison (Ref. 3). Since the dimensions of the structures are not small compared to the wave length, linear diffraction theory was used. All the cases analysed with this numerical model were for incident waves of height 23.6 feet (7.2 m) and period 8.25 seconds at high tide. Wave forces on the exposed surfaces of a main berth caisson of plan dimensions 150 feet (46.7 m) by 135 feet (41.4 m) were computed for incident wave directions normal to the longer and to the shorter faces, in a mean water depth of 78 feet (23.7 m). Wave forces were also computed for a single approach caisson in mean water depth of 70 feet (21.3 m), for a wave direction normal to one face. The total forces and moments on the exposed surfaces of the main berth caisson calculated for the case of waves approaching in the direction normal to the longer face are shown in Figure 6. Some results from the physical model are included for comparison. These are discussed in Section 6.

The wave forces calculated by linear diffraction theory gave estimates which enabled design to commence and proceed. However, the theoretical model is not accurately applicable in this case since it implies that all motions are very small, which is not a good approximation for the large waves involved, for which the ratio of wave height to water depth is approximately 1:3. Further, the theoretical calculations do not take into account effects due to separation of flow past the vertical columns nor can they predict the pressure fluctuations on the underside of the caisson. These limitations of the numerical model made it necessary to conduct extensive measurements of wave effects on a scale model.

5. WAVE FORCE MODEL

Transient pressures on the surfaces of a scale model of a berth caisson were measured under the action of both "cyclone" waves and of "design waves" at High Water and at Low Water. The incident wave characteristics adopted for the model tests on the basis of the data available on wave climate were as follows:-

Cyclone Wave:- Height (H_{max}), 24 feet (7.3 m); Period, 8.25 secs.
Design Wave:- Height ($H_{1/3}$), 12 feet (3.7 m); Period, 6.0 secs.

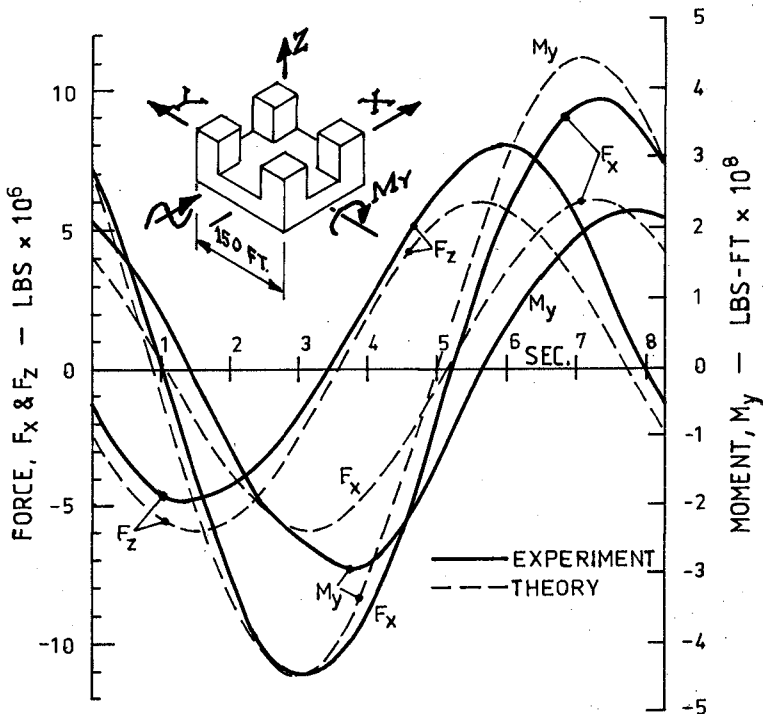


FIG. 6 WAVE FORCES FROM EXPERIMENT AND THEORY.

Wave roses obtained at the site indicated that the dominant direction for incident waves is from ESE, but that waves could be expected from virtually any direction within the range SE to NW. The compressed time period in which the model studies had to be carried out made it impossible to conduct tests for all possible directions of incident wave. Consequently, the tests were limited to the study of waves approaching normally to the berth line (wave crests parallel to the longer side of the caissons) and of waves approaching from the dominant ESE direction (wave crests at an angle of $52\frac{1}{2}^\circ$ to the longer side of the caissons). The tide levels adopted gave water depths above the foundation level of the caisson of 76 feet (23 m) at High Water and of 56 feet (17 m) at Low Water.

The berth caissons are founded on four pads, one at each corner, 40 feet x 40 feet in plan. The foundation pads are set on prepared base material, as shown in Figure 3, and it is considered that the water pressures applied to the under side of the foundation pads will be those corresponding to the current tide level without any significant effect from wave action. However, the cruciform area on the under side of the caisson between the foundation pads will be subjected to pressure variations caused by wave action because it communicates directly to the sea through the gaps between the foundation pads along each side of the caisson. The effects of wave pressures on this region

of the underside of the caisson were found to be very significant in the overall stability of the caisson. Consequently, wave pressures on the underside of the caisson were measured for two conditions, viz:- (i) the gaps along each side of the base were unobstructed, (ii) 90 percent of each gap was closed, the remaining 10 percent of opening being distributed uniformly over the length of the gap.

5.1 Experimental details

Wave Basin: All of the tests were carried out in a wave basin 10 feet (3 m) wide and 48 feet (15 m) long at the University of Queensland. The wave generator was of paddle type, the throw at top and bottom of the paddle being capable of independent adjustment. A spending beach of crushed rock at a slope of 1 in 10 was placed at the opposite end of the basin from the wave generator in order to eliminate wave reflection. The models were located approximately half way along the basin. The incident waves from the wave generator, as measured at this location, were free of any significant higher harmonics and there was no significant reflection off the spending beach.

Model: The model of the main berth caisson was constructed to a scale of 1:60 from clear perspex (lucite) sheet. It can be seen in Figure 7. A total of 135 pressure tapping points was built into the model for measurement of pressures on all external surfaces, including the under-side of the caisson. This large number of tapping points was dictated by the need to measure the pressure distribution in sufficient detail for the purposes of structural design. The pressure tappings were 0.062 inch (1.57 mm) in diameter and they were connected to the pressure recording system through rigid nylon tubing of 0.127 inch (3.22 mm) internal diameter. It was not possible to locate the available pressure transducers inside the model; instead it was necessary to connect the pressure tappings to the externally located transducers by carrying the connecting tubing out from the model through the tops of the four columns and it was physically impossible to fit more tubes into the columns. Because of this restraint, only one column was fitted with tappings, ten in each vertical face. For tests in which the waves were approaching normally to the structure, it was possible to measure the complete pressure distribution over the base caisson in one set-up, since measurements were needed over only one half of the base on account of symmetry. For this same set-up the pressures were measured on the one instrumented column in the front position and then the model was rotated through 180 degrees so that pressures could be measured on the column in the rear position. For tests in which the waves approached the caisson other than normally, it was necessary to set the model in four orientations in order to obtain the complete pressure distribution over the base caisson and over the four columns.

Pressure Measurement: The pressure tappings at the surface of the model were connected through rigid nylon tubing to pressure transducers with a range ± 10 inches (254 mm) of water. These consist essentially of a metal bellows which deflects under pressure and displaces an armature. The movement of the armature induces strain in unbonded strain gauge elements which form the arms of a Wheatstone bridge. The voltage output from the Wheatstone bridge was amplified by carrier amplifiers and the amplified signal was recorded on a pen recorder. The model wave periods were 0.775 sec. and 1.065 sec. for the Design



FIG. 7 Model Berth Caisson and instrumentation

wave and Cyclone wave respectively. The natural frequency of the pressure transducers (dry) is in excess of 300 Hz and the response of the pen recorders is flat up to 40 Hz. The pressure transducers were of differential type and the case reference pressure used was the ambient atmospheric pressure in order to prevent the occurrence of zero shift, which would otherwise be caused by changes in atmospheric conditions. In order to achieve consistent, repeatable performance over long periods of time, it was found necessary to ensure that the air in the cases of the transducers was completely dry. All of the elements of the instrumentation system can be seen in Figure 7. Full details are given by Apelt (Ref. 4).

Wave Profile Measurement: The wave profile was recorded by means of a capacitance type wave probe, the electrical output from the probe being recorded on the pen recorder.

Experimental Procedure: The instrumentation available for the tests comprised three pressure transducers and associated carrier amplifier systems, one wave recorder and two twin channel pen recorders. One recorder channel was used always to register the incident wave profile and the other three channels were used to record the outputs from the three pressure transducers which were connected to pressure tapping points in groups of three until all had been monitored. Synchronisation of the four separate signals was achieved by activation of the event marker pen on each recorder with a signal generated from a relay on the wave generator. The signal was pulsed once for each period of the wave generator and this provided an accurate time base as well as synchronisation. The pressure history at each tapping point was recorded for at least three successive wave periods in order

to average out the effects of any small variations in the incident waves. Provision was made in the circuitry to permit purging of the tubing under pressure in order to clear any air or blockage from the tubes at the beginning of each test and at any other time, if the need arose. The pressure transducers were also connected to a calibrating chamber so that static calibrations of the total pressure recording system could be carried out at the beginning and end of each measurement session.

Dynamic Calibration of Pressure Recording System: The inertia of the large volume of water in the tube connecting to the pressure transducer greatly modified the frequency response of the pressure measuring system. A preliminary series of tests established that it was necessary to adjust the length of the connecting tube to achieve satisfactory response characteristics at the different wave periods. For a wave period of 0.775 seconds the optimum length of the connecting tube was found to be 9 feet and for a wave period of 1.065 seconds it was found to be 15 feet. Even with this arrangement it was not possible to achieve a response which was completely free of amplitude modulation. Consequently, the pressure recording system was calibrated dynamically at the frequencies corresponding to the design wave and to the cyclone wave so that the appropriate conversion factor could be applied to the static calibrations carried out regularly throughout the programme of measurement. Details of the procedure used for dynamic calibration are given by Apelt (Ref. 4). At a wave period of 1.065 seconds the dynamic response was found to be amplified 1.13 times compared to the static response and at a wave period of 0.775 seconds the dynamic response was found to be attenuated by a factor of 0.80 compared to the static response.

6.0 RESULTS OF WAVE PRESSURE MEASUREMENTS

Only selected results which are thought to have some general interest beyond the specific design study are presented here. The full set of wave pressures and of wave forces are given in Apelt (Ref. 4). Forces and moments on elements of the caisson and on the caisson as a whole due to wave action were computed by numerical integration of the measured wave-induced pressures. The coordinate and sign conventions used are the standard conventions of calculus, as illustrated in Figure 6. The origin of coordinates is located at the centre of the caisson base at foundation level and moments have generally been computed with reference to this origin. However, moments on the columns have been computed about axes in the base of the column at the level of the upper surface of the caisson base.

In some tests the gaps along the lower edges of the Caisson base were left unobstructed, and this condition is referred to as "FULL OPENINGS", while for cases in which these gaps were closed for 90 percent of their length, the condition is referred to as "TEN PERCENT OPENINGS". In all of the model tests, water was allowed to enter the space inside each column through two holes, located one in each inward-facing side of the column. Scaled to prototype dimensions, each hole was 0.75 feet in diameter and was located 5 feet above the top surface of the Caisson base, on the centre-line of the face of the column. The depths of water inside the columns were inferred from the pressures recorded at the tapings inside the columns in the top surface of the Caisson base, and the water surface inside each column varied

significantly from the still water level throughout the wave period. The contributions to vertical components of forces and to moments due to these variations in water levels within the columns are included in all of the results, except where otherwise noted. Since it should be possible to achieve a virtually constant water level within the columns, corresponding to still water level, by reduction of the size of the openings through the sides of the columns, the effects of such a modification on maxima of forces and moments have been computed. Quantities calculated for the conditions when the water level inside each column is constant at still water level are indicated by a prime, i.e., $\Sigma Fz'$ and $\Sigma My'$.

6.1 Maximum forces and moments due to waves approaching in direction normal to berthline: The maximum forces and moments on the Berth Caisson due to waves approaching in the direction normal to the berthline are set out in Table 1. The largest horizontal and vertical forces are caused by 24 feet waves at High Water but the largest moments, in most cases, are caused by 12 feet high waves at Low Water. For the latter case the vertical forces are relatively small and the maximum variations in foundation stresses, both positive and negative, are caused by 24 feet high waves at High Water.

The effects produced by maintaining the water level inside the columns constant at still water level can be assessed from the data in Table 1. For example, this modification causes reductions in vertical forces but increases in moments for the case of 24 feet high waves at High Water, both for FULL OPENINGS and for TEN PERCENT OPENINGS.

The benefits derived from restriction of the openings along the bottom edges of the Caisson are clear from the data in Table 1. For three of the four test conditions the case of TEN PERCENT OPENINGS has smaller maxima for all forces and moments than does the case of FULL OPENINGS UNDER.

6.2 High Water: 24 feet high waves approaching in direction normal to berthline: The details of forces and moments experienced by a Berth Caisson and by components of it, for the case of 24 feet waves approaching normally to the longer face at High Water are shown in Figures 8a to 8d. The total forces and moments for the whole Caisson are shown in Figure 8a and the separate contributions of the base and columns to horizontal and vertical components of force are shown in Figures 8b and 8c respectively. The significant effects on vertical forces caused by partial closure of the gaps along the bottom edges of the Caisson are evident in Figures 8a and 8c. The columns contribute the largest component to the horizontal force on the Caisson, as can be seen from Figure 8b.

The details of moments experienced by the columns are shown in Figure 8d; it can be seen that the columns are subjected to very large moments and, in fact, the columns make the largest contribution to the moments experienced by the Caisson as a whole.

The time histories of forces and moments in Figures 8a to 8d display marked departures from symmetry which are due to a number of effects, including the large wave height (the ratio of wave height to water depth is approximately 1:3), separation of flow past the columns and interactions between the columns. It is of interest to note that, whereas the maximum total horizontal force is larger than the maximum

TABLE 1 - RANGES OF FORCES AND MOMENTS ON BERTH CAISSON
FOR WAVES APPROACHING IN DIRECTION NORMAL TO BERTH-LINE

Units of Force:- lbs x 10⁶; Units of Moment:- lbs-feet x 10⁶

WAVE HEIGHT:-	24 feet	24 feet	12 feet	12 feet
TIDE STATE:-	HIGH WATER	LOW WATER	HIGH WATER	LOW WATER
ΣF_x ; MAX +ve	9.53	7.10	1.28	4.91
ΣF_x ; MAX -ve	-11.07	-4.94	-1.01	-4.78
FULL OPENINGS:-				
ΣF_z ; MAX +ve	7.75	4.59	2.16	2.76
ΣF_z ; MAX -ve	-7.93	-4.88	-2.26	-2.86
ΣM_y ; MAX +ve	242	224	163	363
ΣM_y ; MAX -ve	-321	-97	-141	-342
$\Sigma F_z'$; MAX +ve	7.09	4.59	1.66	2.88
$\Sigma F_z'$; MAX -ve	-6.03	-4.77	-1.88	-2.98
$\Sigma M_y'$; MAX +ve	265	219	148	343
$\Sigma M_y'$; MAX -ve	-371	-92	-115	-328
TEN PERCENT OPENINGS:-				
ΣF_z ; MAX +ve	5.58	3.63	1.71	0.24
ΣF_z ; MAX -ve	-4.43	-3.91	-2.38	-1.33
ΣM_y ; MAX +ve	233	112	153	353
ΣM_y ; MAX -ve	-271	NO -ve	-136	-326
$\Sigma F_z'$; MAX +ve	5.11	3.53	1.22	0.32
$\Sigma F_z'$; MAX -ve	-2.72	-3.81	-1.99	-1.20
$\Sigma M_y'$; MAX +ve	256	112	137	333
$\Sigma M_y'$; MAX -ve	-321	NO -ve	-110	-306

of any partial contribution to it, the maximum of total moment is less than the maximum contribution from the columns, a result of the complex phase relationships between the several contributions to the total effect. The maximum of total vertical force is approximately the same as that on the top surface alone for the case of FULL OPENINGS, but is smaller for the case of TEN PERCENT OPENINGS.

6.3 Low Water: 12 feet high waves approaching in direction normal to berthline: The total forces and moments experienced by a Berth Caisson under these conditions are shown in Figure 9. This case is included for comparison with the results for the 24 feet wave at High Water and it can be seen that the maximum moments in Figure 9 are larger than those in Figure 8a. The large total moments in Figure 9 are almost entirely the consequence of large moments on the base of the Caisson which, in turn, result from the fact that the contributions from the top and underneath surfaces of the Caisson are nearly in phase. In contrast, the large total moments in Figure 8a arise from the very large moments experienced by the columns.

6.4 Effects of Wave direction on Column Moments: The tests with waves approaching in the direction normal to the berthline showed that the columns would be subjected to very large forces and moments under the

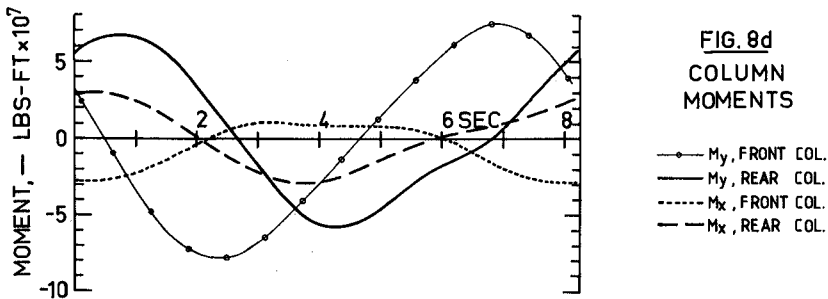
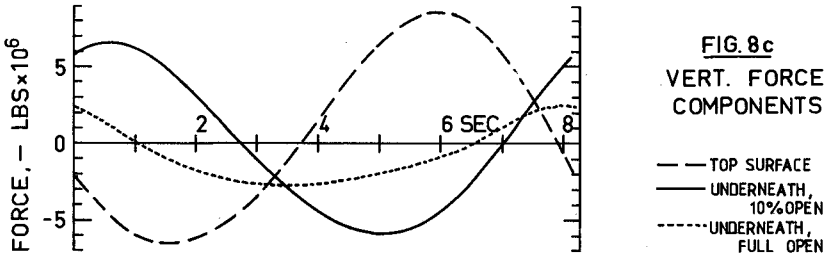
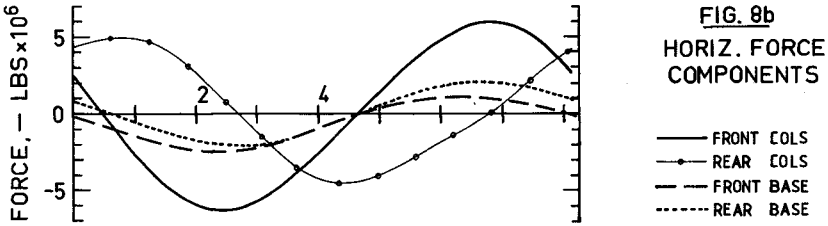
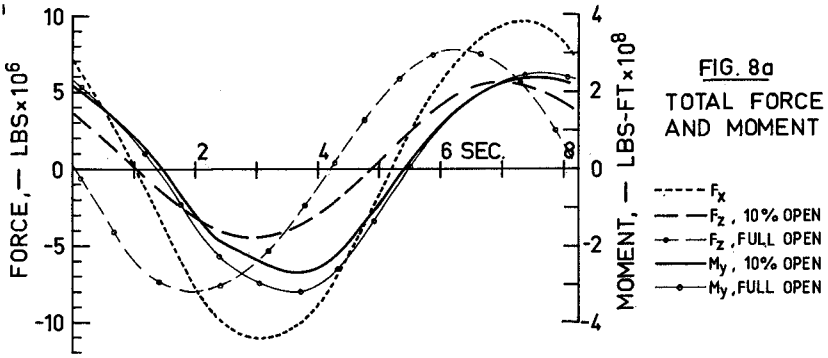


FIG. 8 WAVE FORCES ON BERTH CAISSON; 24 FT WAVES AT H.W.

action of 24 feet high waves at High Water. A series of tests was completed to determine the forces and moments experienced by the columns for the same wave and tide conditions except that the waves were approaching from the dominant ESE direction. It was found that the maximum bending stresses due to moment under these conditions will be developed in the rear leading column in the presence of neighbouring caissons. This also proved to be the worst of all cases tested, giving bending stresses 22 percent higher than for the worst case for waves approaching normal to the berthline. The moments experienced by the rear leading column in these angled waves are shown in Figure 10, which includes results obtained with and without neighbouring caissons. It can be seen that the presence of neighbouring caissons causes the maximum moments on the column to be increased almost twofold. The presence of neighbouring caissons also resulted in increases of approximately 25 percent in the maxima of moments on the front leading column. However, in the case of both "down-wave" columns the presence of neighbouring caissons had only small effects on the maxima of the moments.

7. COMPARISON BETWEEN EXPERIMENT AND THEORY

The forces and moments produced by calculations of Garrison (Ref.3) based on linear diffraction theory, are compared with the results derived from experimental pressure measurements in Figure 6. The conditions for which the comparison is possible are those of High Water with cyclone waves approaching in the direction normal to the longer side of the Berth Caisson and, although the conditions used for theoretical calculations and experimental studies are very closely similar, they are not identical. The depth of water in the experimental studies was 76 feet (23 m) and the wave height was 24 feet (7.3 m). The corresponding values in the theoretical calculations were 78 feet (23.7 m) and 23.6 feet (7.2 m) respectively. The wave period was 8.25 seconds in each case.

The quantities compared in Figure 6 are total Moment, Horizontal and Vertical forces due to wave action on the exposed surfaces of the Caisson. The effects of wave induced pressure variations on the underside of the Caisson and inside the columns are not included in the comparison. The results obtained from the two approaches display significant differences. Whereas all three curves derived from linear diffraction theory are nearly symmetrical, all curves obtained from measured pressure distributions display large departures from symmetry. These departures from symmetry are considered to be due to the significant non-linearity of the incident wave and to the effects of flow separation about the vertical columns. The lack of symmetry in the curves derived from experimental results shows most clearly in the different magnitudes for positive and negative peak values. The two sets of results also show significant and complex differences in the phase relationships between the three quantities, F_x , F_z and M_y . The ratios of the peak values of the three quantities are given in Table 2.

TABLE 2 - RATIOS OF EXPERIMENTAL MAXIMA TO THEORETICAL MAXIMA

F_x		F_z		M_y	
+ve	-ve	+ve	-ve	+ve	-ve
1.60	1.85	1.36	0.81	0.50	0.64

The differences are least for vertical forces, F_z . The experimental

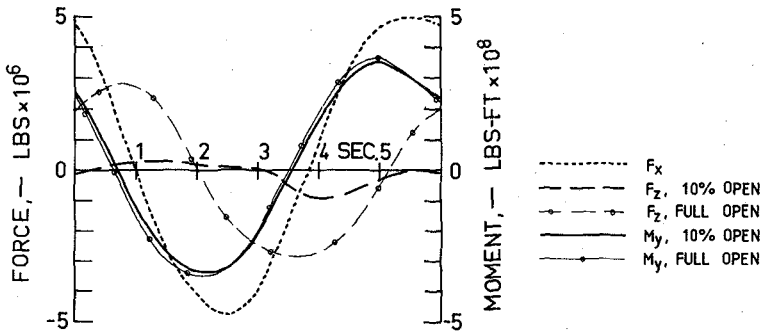


FIG.9 WAVE FORCES ON BERTH CAISSON; 12FT WAVES AT L.W.

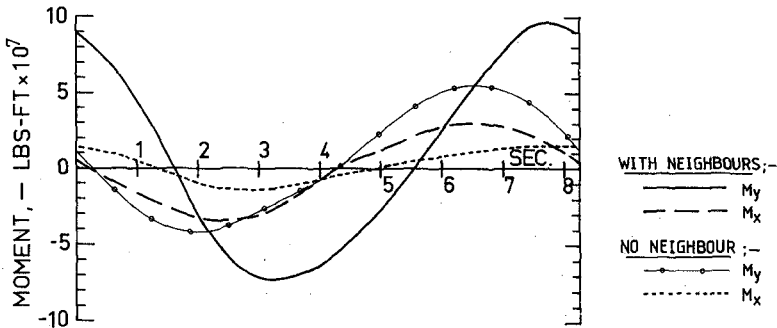


FIG.10 COLUMN MOMENTS; 24FT WAVES AT H.W. FROM E.S.E.

values of horizontal force F_x are much larger than those predicted by linear diffraction theory but, in spite of this, the experimental values of moments are only approximately one half those predicted by the theory. The explanation of the latter result is that the total moment is the summation of contributions from the four columns, from the vertical faces of the base of the caisson and from its top surface; the combination is considerably smaller in magnitude than some of the individual contributions and the phase relationships between the individual contributions are of very great significance in determining whether effects are additive or whether they cancel each other.

8. APPLICATION OF RESULTS

Pressure readings derived from the model study were converted directly to the equivalent head of water acting on the surface. The maximum loading condition on the column faces for the passage of waves was extracted from the readings and applied directly as a loading to the column for bending moment and shear force calculation on the column as a whole.

The exterior walls of the columns were designed for two methods of behaviour, viz:- as two dimensional panels and as horizontally spanning

beams of unit width. In the latter case it was necessary to analyse the entire circumference of the column as a continuous member and to apply the instantaneous pressure loading on the circumference. This loading varied from a maximum positive pressure of 25 feet of water to a maximum negative pressure of 15 feet. The method used ensured that the axial loading in the walls from the pressure distribution was also determined. The water level inside the columns was tidal and found to vary during the passage of the waves. The loading on the walls could vary from positive (inwards) to negative (outwards) as the water level rose and fell above tide level. This introduced a reversing load of compression and tension into the interior walls. The walls were designed for the worst case of tension and compression combined with bending moment induced by uneven external wall loading together with fatigue conditions.

The overall stability criteria were established prior to the present formal recommendations of Federation Internationale de la Precontrainte and Det Norske Veritas and were as follows:

(i) For loadings derived from numerical analysis

- * horizontal and vertical wave loads - load factor 1.4
- * wind loads load factor 1.4
- * dead loads load factor 1.0

In this case the worse combination of horizontal and vertical wave loads was adopted.

(ii) For loadings derived from physical modelling, the same load factors were used and, in this case, the combination of vertical and horizontal loads used was that conforming with the observed phase difference.

The somewhat unusual feature of taking the dead load factor as 1.0 in lieu of 0.9 is justified since the caissons, in floating, were effectively weighed to within 1 percent.

Stability criteria of 1.0 on overturning and 0.7 on sliding were adopted for both these load factors. In the event, the stability criteria adopted conformed to both Federation Internationale de la Precontrainte and Det Norske Veritas requirements.

9. STUDY OF SCOUR NEAR CAISSONS DUE TO WAVE ACTION

The ocean bed at the site of the berth is covered with fine sand. The berth area is dredged to a general depth of 56 feet below low water and the berth caissons are founded on an area of crushed rock, consisting of sizes passing a 4 inch screen, which has been levelled off to R.L. -56 feet (See Fig. 3). Scour tests were carried out at a linear scale of 1:60 in order to safeguard the structures against erosion resulting from wave action. The model of the main berth caisson which was used for pressure measurements was also used in the scour tests. At a scale of 1:60 the corresponding maximum size of foundation material for the model is 0.07 inch. The material used to represent the prototype foundation material in the scour studies was prepared from finely crushed rock, by rejection of all sizes not passing a No. 7 sieve and by washing from the remainder the sizes passing a No. 25 sieve.

Interaction between the incident waves and the berth structures will produce significant velocities in the vicinity of the caissons and

these induced velocities provide the most important mechanism for erosion of the foundation material. It is very difficult to assess the relative importance of viscous action in the complex phenomena involved in generation of the currents by interaction between incident waves and structures and in movement of the foundation material by these currents. However, the induced velocities are of the same order as the maximum orbital velocities in the incident wave and the Reynolds number based on bed material size is of order 1000 in the model. It is considered that this Reynolds number is large enough to ensure that scale effects in the model will not be so large as to invalidate the general results of the scour studies. The results of the scour studies are considered to be qualitatively correct but no estimate can be made concerning quantitative accuracy.

9.1 Wave scour near main berth caisson: For studies of wave scour near the main berth caisson, the model of the caisson was mounted on a 2 inch thick layer of the crushed rock fines. All wave scour tests were run continuously for one hour, which corresponds to 7.75 hours of prototype time reckoned according to Froude number scaling. However, as noted above, the uncertainty associated with different viscous effects in model and prototype makes scaling between elapsed times for the model and prototype approximate only. Further, the tide level varies continuously so that a continuous test at low water imposes conditions which are equivalent to a much longer interval of elapsed time with regard to scour development in the prototype.

No Protection: The first studies were carried out with no scour protection in place in order to determine the extent of the problem. The worst scour developed under the action of 24 feet high waves at Low Water. Deep scour and undermining developed along each edge of the caisson for waves approaching normally to the berthline; deep scour holes developed at each corner of the caisson for waves approaching from E.S.E. The scour hole developed at one of the "side" corners in this latter test is shown in Figure 11. Similar scour patterns were observed for 24 feet high waves at High Water and, although they were not as deep or extensive as those observed at Low Water, they were still quite significant. Waves 12 feet high caused some small localised scour when approaching normally to the berthline at Low Water but not otherwise.

Scour Protection: The protection developed during the model tests consisted of a skirt of woven plastic fabric, fixed to the bottom edges of the caisson and extending horizontally for a distance of 15 feet to provide a barrier between the erosive water currents and the foundation material. The fabric was to be held in place by concrete slabs, 7'6" square and having a net weight under water of 50-60 pounds per square foot. The slabs were to cover the fabric completely, and it was planned that they would be linked together at their edges by simple hinged connections. The protective fabric was to be of sufficiently open weave to permit rapid equalization of pressures above and below it, but the weave was to be close enough to prevent loss of any but the finest rock particles through it. In the tests on the model of the main berth caisson, an open weave soft plastic fabric was used to simulate the protective fabric and the slabs were simulated with square sheets of aluminium, 1.5 inch x 1.5 inch x 0.1 inch thick. The weight under water of the corresponding full size slabs is 56.8 lbs per sq.ft and,

if concrete slabs, the required thickness is 8.25 inches. This small discrepancy in thickness of the slabs is of no significance in the context of these studies. In the model studies the model slabs were not linked together so that any tendencies for the slabs to be moved about would be shown up more readily.

The series of tests with the scour protection in place showed that it was completely satisfactory for protection against 12 feet high waves. Waves 24 feet high caused varying amounts of movement of the protective slabs. The greatest movements of slabs were observed when these large waves approached from E.S.E. at low water and they occurred at the "side" corners of the caisson. The conditions at the same side corner as shown in Figure 11 after one hour of testing at these most severe conditions can be seen in Figure 12. Pumping action through the woven fabric resulted in some slight displacement of the foundation material.

9.2 Wave Scour at Approach Caisson: The approach structures linking berth to shore are supported on caissons which are 55 feet (17 m) square in plan. Two possible treatments of the foundations for the approach caissons were considered. In the "lowered" foundation a hole 90 feet (28 m) square is dredged to a depth approximately 5 feet (1.5 m) below the general bed level and partly back-filled with a layer of crushed rock, approximately 2 feet (0.6 m) thick. In the "raised" foundation the layer of crushed rock is placed directly on the sea-bed and the caisson founded on this raised layer. The same scour protection as had been developed for the main berth caissons was proposed for the approach caissons.

The scour studies on the approach caisson demonstrated clearly that the "lowered" foundation is very much to be preferred over the "raised" foundation. In the tests on the "raised" foundation, the wave-induced currents were so strong near the base of the caisson that the scour protection was attacked violently and its effectiveness was completely destroyed. On the other hand, in the case of the "lowered" foundation, the scour protection was found to be satisfactory even under the worst conditions but only if the cruciform-shaped gap under the caisson between its foundation pads is closed off. When this gap was left open a very strong pumping action with significant scour capacity developed beneath the caisson under wave action.

The conditions after one hour of testing on the "lowered" foundation with the gaps closed, under attack from 24 feet high waves at Low Water can be seen in Figure 13. The foundations of the caisson have been protected satisfactorily. The general erosion of the sea-bed down-wave from the caisson is caused by a strong streaming motion in this region which results from the interaction between the incident waves and the caisson.

10. CHOSEN METHOD OF SCOUR PROTECTION

The simulated scour protection devised for the tests was later considered too involved for actual construction and a form of flexible matting was devised as indicated on Figures 2 and 3. This consisted of a mat of concrete blocks approximately 15 feet square, each block being approximately 1'7" square in plan and 1'3" thick and cast on wire ropes running in two directions which allow flexibility and ready handling. The gaps between the blocks were maintained at 1½" to act as a filter

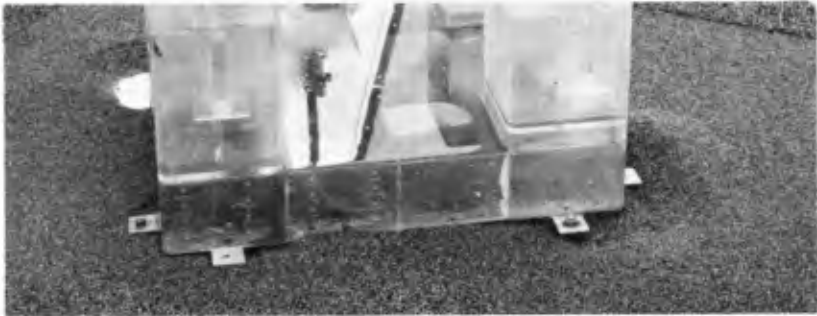


FIG. 11 Scour near Berth Caisson - 24 ft Waves from E.S.E. at L.W.



FIG. 12 Scour protection - 24 ft Waves from E.S.E. at L.W.

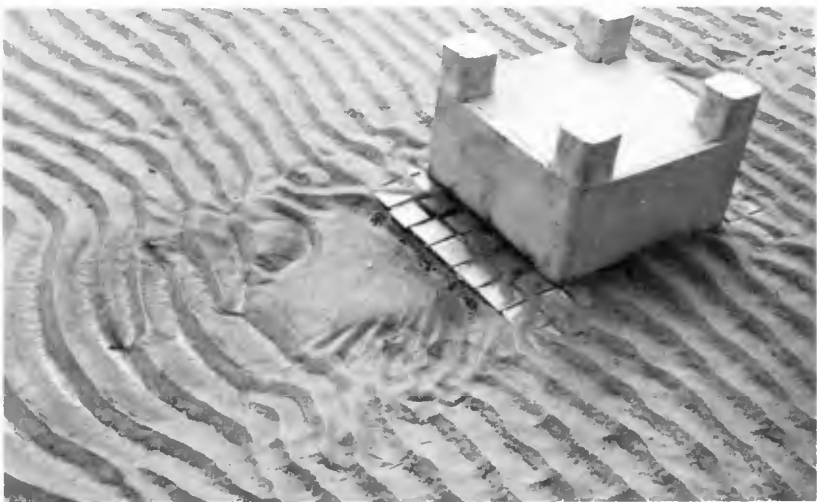


FIG. 13 Scour near Approach Caisson - 24 ft Waves at Low Water.

to prevent the removal of foundation rock during periods of intense wave action. The weight of the matting chosen was equivalent to 90 lbs/sq ft under water, which is nearly twice the model weight, but it was considered that the remedial work that might be required after severe scour could be very serious and therefore a conservative approach was adopted. Figure 14 illustrates the operation of laying 'scour mats and shows their inherent flexibility. Laying of the units was controlled by divers.

11. PERFORMANCE OF PROTOTYPE

The prototype has been in operation since July 1975 and the Queensland coast experienced 8 cyclones in the 1975-6 cyclone season. A wave-rider buoy has recently been installed by the Department of Harbours and Marine, approximately 19 miles (30 km) to the N.E. of Hay Point in 84 feet (26 m) of water, and a maximum wave height of 14.5 feet (4.4 m) was recorded during the most severe of these cyclones. Only one cyclone passed near Hay Point. This cyclone (code name David) necessitated full emergency precautions at the berth. When operations were closed down, the sea had risen to about 12 feet waves. Recording devices have not yet been placed on the structure and no further observations were possible. Examination of the structure and of the foundation after the cyclone revealed no signs of damage.

12. ACKNOWLEDGEMENT

The authors thank Utah Development Company, owner of the Berth, for permission to publish this paper.

13. REFERENCES

1. Morison, J.R., O'Brien, M.P., Johnson, J.W. and Schaaf, S.A. "The force exerted by surface waves on piles", *Petrol. Trans.* 189, 1950.
2. Sainflou, M. "Treatise on vertical breakwaters", *Annales des Ponts et Chaussées, IV*, trans. by W.J. Yardoff, U.S. Corps of Engs., 1928.
3. Garrison, C.J. "Report on wave forces on ocean caissons for extension to Hay Point Terminal - UDC", Naval Postgraduate School, Monterey, California, Jan. 1973.
4. Apelt, C.J. "Hay Point Off-Shore Berth Structures. Forces and Scour due to Wave Action", Report No CH/18-76, Dept. of Civil Engineering, University of Queensland, Jan., 1976.



FIG. 14 Laying of scour mat

CHAPTER 131

TSUNAMI HAZARD AND DESIGN OF COASTAL STRUCTURES

George Pararas-Carayannis

Director, International Tsunami Information Center

P. O. Box 3650

Honolulu, Hawaii 96811

Abstract

Damage of coastal structures by tsunamis results by the direct and indirect action of hydrostatic and dynamic pressures, foundation failures, overtopping and flooding. Reliable assessment of the potential tsunami hazard at a coastal site and adequate engineering design of critical structures require analysis and understanding of all aspects of a tsunami system leading to its terminal behavior. Description of the space-time history of tsunami waves generated by impulsive disturbances require consideration of events and processes in the following regimes: (a) generation; (b) propagation and dispersion; and (c) termination. Processes and events in each regime during the development of a tsunami are under their own unique hydrodynamic constraints but are dependent on what has preceded. In predicting tsunami wave characteristics at some distance from the generating source, the error structure may be pyramidal. Essential to any method of tsunami prediction at a distant or a nearby coast will be the full consideration and study of tsunami generative mechanisms. If the tsunami generation mechanics cannot be deduced with a reasonable degree of accuracy, it is not likely that the tsunami terminal aspects will be reliably predicted. Prediction of tsunami height at a distant or at a nearby coast requires knowledge of the magnitude and type of ground displacements in the tsunami generating area and of the characteristics of the surface waves resulting from such action. Although all mechanisms involved during tsunami generation are not fully understood, it is possible to obtain a suitable tsunami initiating function through the use of experimental data, historical data, and established empirical relationships, for each type of generating mechanism. Reliable computation of the tsunami propagation effects over and across the ocean can be obtained with proper modeling to provide an adequate description of the tsunami energy flow through the use of physical and numerical studies. Similarly, the terminal aspects and nearshore modification of the tsunami wave system can be approximated to provide the engineering criteria necessary for the assessment of the potential tsunami hazard at a coastal site.

Introduction

Increasing pressure for the construction of large coastal installations, such as power plants, and superport terminals, and the increasing residential development of coastal zones, have emphasized recently the need for more accurate estimates of the terminal effects of tsunamis. Questions that most often arise deal with such subjects as the frequency of catastrophic tsunamis at a given coastline; the maximum expected runup from a tsunami for a given site; the dynamic forces that can be expected; and finally how to design structures to withstand the forces and effects of a possible tsunami.

The answers are not simple. Attempts to solve these problems may become involved in numerous complex mathematical solutions which require numerous approximations and simplifications, to the point that the accuracy of these solutions becomes doubtful. In addition, theoretical and analytical solutions often assume a smooth transmission of tsunamis to the coast without taking into account the effects of obstacles (islands, seamounts, reefs, etc.) which complicate the phenomenon. At the mouths of rivers, in estuaries, and generally in bays or other irregular coastlines, tsunamis undergo such alterations and changes of their characteristics, that theoretical appraisal of tsunami height, runup, velocities, or forces on coastal structures often are invalid. In such instances, historical and statistical data, visual observations, and other empirically-derived data become the sole guide in evaluating the maximum possible height, runup, and effect of tsunami waves on coastal structures.

Unfortunately, historical and statistical data on tsunamis is non-existent for certain coasts, or the historic record may be of very short duration to permit a suitable analysis. Therefore, there is always the danger in designing coastal structures that potential tsunami effects may be either ignored, underestimated, or overestimated. If the tsunami potential danger is underestimated or ignored, the design of the coastal structure will not be adequate. If the tsunami potential danger is overestimated, overdesign of the coastal structure results, causing excessive financial expenditure for the project. In spite of all these difficulties, a combination of historical observations, laboratory experiments, and theoretical studies, provide assurances of a more accurate evaluation of a probable maximum tsunami at the coast. Such studies require time and expenditures which cannot be reasonably justified unless the coastal structures are important and will serve a critical function (i.e., protection of nuclear power plant).

Interaction of Tsunamis with Coastal Structures: Damage of coastal structures by tsunamis may be by the direct action of hydrostatic and dynamic pressures on the face of a structure, resulting in foundation failure due to erosion, or overtopping and flooding. The forces on the face of the structure are caused by the rapid water motion in the form of gravity waves or in the form of irregular violent motions. The hydrostatic and dynamic pressures of gravity waves on structures depend basically on the height, direction, period, and velocity of the waves, the design of the coastal structure, and a number of other factors.

The most adverse interaction of tsunamis with a coastal structure exists when the directional approach of the waves is perpendicular to the longitudinal axis of the structure because the pressure is exercised in the direction of least resistance of the structure. However, this is true if we consider only the water pressures on the structure and not other direct or indirect effects of a tsunami, which could be of greater danger, regardless of direction, or height. For example, there could be instances when the direction of water movement may not be perpendicular to the longitudinal axis of the structure and yet the water motion may result in strong currents which may undermine the structure by eroding the material near its foundation with subsequent failure.

The period of the tsunami is another factor which could influence the effect of these waves on a coastal structure. This may affect degree of flooding and permissible overtopping. Tsunami period is usually of 15-30 minute duration. Therefore, it is expected that when a tsunami arrives at an open harbor, it floods progressively both the outer and inner sides of coastal protective works of the harbor, without causing significant pressure differentials on opposite sides of structures. A small pressure differential on the two sides of a coastal protective structure may occur at the arrival of the tsunami waves due to the dynamic momentum of the moving water. This pressure effect is a function of the velocity of the tsunami and will be more pronounced if the harbor has a narrow entrance, if the tsunami approaches at high speeds, or if a bore is formed.

Hydrodynamic Pressures of Local Earthquakes on Coastal Structures: The design of coastal structures usually requires consideration of different loads which include those caused by wind waves, the weight of the structure itself, the seismic forces acting on the structure, and the permanent or moving loads resting or interacting with the structure. Although the seismic effects are often adequately considered, the hydrodynamic forces which could develop in the water from an earthquake and which interact with the structures, are often ignored.

Seismically-generated hydrodynamic pressures acting with a sloping breakwater, for example, are directly related to seismic accelerations, the depth of the water in front of the structure, and the slope of the structure's face. During a local earthquake, the hydrodynamic pressure on the structure ranges alternately from zero to a maximum value on both sides of the structure. It has an alternating direction in phase always with the direction of the seismic ground accelerations. It can be concluded that considerable hydrodynamic pressures can develop on the faces of coastal structures during a local earthquake and such forces should be considered in the design. These forces will be particularly critical in the design of high breakwaters, or of structures with a vertical face, if these structures will be constructed in areas where large and frequent earthquakes occur. A local earthquake may result also in oscillations of the waters of a bay or a harbor which could excite the natural mode of oscillation of a basin resulting in greater runup and damage to coastal structures within that basin. Such resonance effects are not always adequately considered in designing coastal protective works.

Engineering Guidelines

Runup height, terminal velocity and periodicity are the three most important terminal parameters of a tsunami of concern to engineers in designing coastal structures. Tsunami runup height and terminal velocity are the most difficult to estimate without knowledge of what has preceded. For a complete understanding of the problem and for the development of the spacetime history of tsunami waves generated by impulsive disturbances, consideration should be given to events and processes in the regimes of generation, propagation and termination. Processes and events in each regime during the development of a tsunami are under their own unique hydrodynamic constraints but are dependent on what has preceded.

Tsunami Generation: Prediction of tsunami height at a given coastal site requires knowledge of the magnitude and type of ground displacements in the tsunami generating area and of the characteristics of the surface water waves resulting from such action. Understanding of the disturbances responsible for tsunami generation is limited. Very little work has been done in relating tectonic or other impulsive disturbances to ocean surface effects. Most of the laboratory studies completed to date have investigated tsunamis resulting from simplified displacements under restrictions of analytical conditions which bear limited resemblance to processes in nature.

Although all mechanisms involved during tsunami generation are not fully understood, it is possible to obtain a suitable tsunami initiating function through the use of experimental data, historical data, and established empirical relationships for each type of tsunami generating mechanism. For example, the type and extent of crustal displacements associated with tsunamigenic earthquakes can be approximated. These displacements will depend on earthquake magnitude, depth of focus, epicenter location, geologic trends in the area, length of rupture, orientation, and type of ground motions.

In evaluating the runup at a specific coastal site, or the safety of a critical coastal structure (i.e. a nuclear power plant) for a tsunami generated from a distant or a local earthquake, consideration should be given to the nature, characteristics, and mechanism of the largest possible seismic event that can give rise to a maximum tsunami. It is proposed that the term of Maximum Probable Tsunami (MPT) be adopted in designating such a source event, and that criteria be developed to describe such design tsunami.

In planning or designing important coastal structures teleseismic and potentially tsunamigenic source areas should be identified geographically in relation to the site of interest. Tectonic structures and trends of each region should be identified. Historic information should be provided on depth, frequency, density, distribution, and magnitude of earthquakes, together with records of tsunami generating activity for each potentially tsunamigenic region. Following preliminary assessment of such data, a tsunamigenic source should be selected which would be most critical to the site of interest. Conservative values of seismic parameters should be assigned

to a hypothetical earthquake which can produce the maximum initial tsunami function. For example, a magnitude of 8.5 on the Richter Scale may be assigned to a hypothetical, shallow-focus earthquake, having a rupture of 1,000 km, a total displacement area of 150,000 square kms, involving vertical displacements along the rupture of at least 3 meters, and having a critical orientation towards the proposed site.

Using critical seismic parameters of the source, empirical relationships, current theories, and other historic or experimental data, an initial tsunami function should be reasonably developed which should be consistent with ground displacements, coupling mechanisms, and source dimensions.

Tsunami Propagation: The initial tsunami wave and subsequent waves should be propagated from the source taking into consideration interactions, resonances, and boundary modifications, in order to obtain the maximum possible tsunami runup at site of interest.

Finite difference numerical computer programs have been developed for the propagation of tsunami waves across the deep ocean to the edge of the continental shelf and have been used for verification using data of historical tsunamis (Wilson and Torum, 1964; Hwang and Divoky, 1970; Hwang, Butler and Divoky, 1972; Houston and Garcia, 1974). Such computer programs take into consideration the sphericity of the earth in solving the linearized long wave equation of motion and continuity. The finite difference methods permit uplift deformation of the water surface at the selected tsunami source to be used as an initial condition. A time history of water surface information conforming to the bathymetric features of the ocean, is propagated away from the source and a transfer function is provided at the edge of the continental shelf. To propagate a tsunami across the continental shelf, other analytical solutions of the linearized long wave equation have been developed. Although numerical models exist which can propagate tsunami wave across the shelf, the necessity for large systems and the computer storage and routine requirements are great and make such solutions expensive. Often simple two dimensional analytic solutions are used to propagate standing waves over the Continental shelf, based on theoretical solutions for tides in canals. These studies do not necessarily produce very correct results, but they are better than no studies at all.

Tsunami Termination: The probable maximum height of tsunamis at a coastline is difficult to estimate. There is no simple or exact method or numerical model which can be used for estimating tsunami runup. Most of the coastlines where tsunami runup estimates are required are irregular. Interactions of tsunami waves with an irregular coastline may result in the trapping and resonance of tsunami wave energy and may result in higher-than-expected runup. As mentioned earlier, large bays and harbors may have resonant periods which may coincide with the peak of the tsunami spectrum and such resonance could result in an increase of wave height and runup. Tsunami runup calculations for such irregular coastlines must first take into consideration the increase of wave height by resonance, then use this estimate as input in calculating total runup. Also, ambient conditions and cumulative effects should be considered. Numerical models applicable to

runup estimates of long waves have been developed which can be valid for waves of the tsunami frequency. In using these models, care should be exercised in selecting the proper boundary conditions.

The water velocity of the tsunamis that flow into a coastal area is difficult to estimate because it depends on many such factors, as the topography, the direction of approach, and the length of the waves. Because of the complexity of flow conditions, the velocity of the water can only be roughly approximated. An erroneous assumption often used in estimating terminal velocity is treating the tsunami as a bore -- something which in reality does not occur frequently.

Finally, since all the factors which contribute to tsunami runup are not fully understood, tsunami inundation cannot be computed entirely from theoretical analysis. For coastlines where historical information on runup is available, a statistical approach can be used to predict future events. This method does not require a complete understanding of the hydrodynamic considerations involved, but examines the magnitude and frequency of occurrence of historical tsunami runup. Such frequency analysis has been commonly used for the study of rainfall and stream flow records (Foster, 1935). Gumbel, (1941, 1942) applied an extreme value probability distribution to flood flows. Similar frequency studies of extreme events have been made ranging from rainfall to floods, to drought, to water quality and to ocean wave studies. In general, frequency analysis is a useful analytic tool for the study of randomly occurring events, such as large tsunamis.

References

- Foster, H.A., Duration Curves, Trans. Am. Soc. Civil Engrs., Vol. 99, pp. 1213-1235, 1935.
- Gumbel, E.J., The Return Period of Flood Flows, Am. Math. Statist., Vol. XII, No. 2, pp. 163-190, June, 1941.
- Gumbel, E.J., Statistical Control Curves for Flood Discharges, Trans. Am. Geophys. Union, Vol. 23, pp. 489-500, 1942.
- Houston, J.R. and A.W. Garcia, "Type 16 Flood Insurance Study: Tsunami Predictions for Pacific Coastal Communities," Techn. Rept. H-74-3, U.S. Army Engineer Waterways Experiment Station, Vicksburg, Ms., May, 1974.
- Hwang, L.S., Butler, H. Lee and D.J. Divoky, "Tsunami Model: Generation and Open Sea Characteristics," Bull. of Seism. Soc. of Amer., Vol. 62, No. 6, pp. 1579-1596, Dec., 1972.
- Hwang, L.S. and D.J. Divoky, "Tsunami Generation," Journal of Geophysical Research, Vol. 75, pp. 6802-6817, Nov. 20, 1970.
- Wilson, B.W. and A. Torum, The Alaskan Tsunami of March 1964: Engineering Evaluation Tech. Memo. No. 25, Coastal Eng. Research Center, Corps Engrs., U.S. Army, Wash., D.C., 401 pp+, 1968.

CHAPTER 132

NUMERICAL CALCULATION OF WAVE FORCES ON STRUCTURES*

B. D. Nichols and C. W. Hirt**

I. INTRODUCTION

A finite-difference technique for solving the Navier-Stokes equations for an incompressible fluid is used to calculate transient wave forces experienced by fixed and moving bodies. The numerical technique is based on the Marker-and-Cell (MAC) method developed by Harlow and Welch (1965). This new technique uses an especially simple solution algorithm that is designed for persons with little or no experience in numerical fluid dynamics. Originally conceived as an instructional tool, it has proven to be an extremely useful and versatile calculational method. Many useful calculations are possible with the publicly available code, SOLA-SURF, which is briefly described in Sec. II; however, the outstanding feature of this numerical scheme is the ease with which it can be modified to handle more complex problems. Reported here, in Sec. III, are examples to illustrate the utility of this new calculational tool for investigating the dynamic interactions between ocean waves and coastal structures.

II. THE NUMERICAL TECHNIQUE

The solution algorithm contained in SOLA-SURF solves the Navier-Stokes equations for an incompressible fluid. A stationary network of rectangular cells is used to divide the calculational region into a finite number of elements with which the fluid variables are associated. The primary field variables are the velocity components and the pressure. Each of the velocity components is specified at the center of the cell face to which it is normal and the pressure is specified at the cell center.

*This work was performed jointly under the auspices of the United States Energy Research and Development Administration and the Office of Naval Research, ONR Task #NR 062-455.

**The authors are members of the Fluid Dynamics Group (T-3), Theoretical Division, Los Alamos Scientific Laboratory, Los Alamos, NM 87545.

The fluid motion is numerically determined by advancing the fluid configuration through a series of small time increments. During each time step the solution to the momentum equation is obtained in two phases. First, the velocities and pressures from the previous time step are used to determine the fluid velocities in each cell, with the initial conditions used for the first time step. This explicit calculation does not necessarily ensure incompressibility; therefore, in the second phase the tentative velocity field is adjusted through changes in the pressure field. The pressure in each mesh cell is adjusted to drive to zero the velocity divergence in that cell. The pressure and velocity distributions must be obtained by iteratively adjusting these velocities in each cell in the mesh. This solution algorithm and other features of the technique are described in detail in a report by Hirt et al. (1975).

Free or curved rigid surfaces are permitted across the top and bottom of the computational mesh. The surfaces are defined by single valued functions of the height above the bottom of the computational mesh and are specified at the center of each vertical column of cells. The change in the free surface elevation is determined kinematically by the local fluid velocities, i.e., by the vertical component of the fluid motion plus the horizontal convection of the surface elevation from adjacent cell columns.

The free surface boundary conditions require that the normal and tangential velocities immediately outside the surface be chosen to ensure a zero transfer of momentum through the surface. A good approximation to these conditions is to set the velocities normal to the surface to satisfy the incompressibility condition in the cells in which the free surface is located and to set the tangential velocities in the cells immediately outside the fluid equal to the adjacent interior velocities. The pressure in surface cells is determined by a linear interpolation or extrapolation between the pressure in the fluid cell immediately below the surface cell and a specified pressure at the surface.

The pressure in each cell in which a rigid surface is located is derived under the constraint that the velocity normal to the surface be zero. This requires a variation in the Newton-Raphson type solution method used to obtain pressures for interior fluid cells. The velocity boundary conditions for these rigid boundaries are free-slip, i.e., the normal velocity and tangential velocity gradient are zero at the boundary, which makes them identical to the free surface boundary conditions. In addition, these rigid surface boundary conditions can be easily inserted in SOLA-SURF to create rigid, curved bodies at any location in the computational mesh. A special boundary condition section has been designated in the code to facilitate these types of modifications.

A copy of the SOLA-SURF code is available from the Argonne Code Center. The address is Argonne Code Center, Argonne National Laboratory, 9700 South Cass Avenue, Argonne, Illinois 60439.

III. THE CALCULATION OF WAVE FORCES ON STRUCTURES

We present four brief studies to illustrate the areas in which the ocean engineer may find SOLA-SURF to be a useful tool. The first two calculations, i.e., solitary wave run-up on a vertical wall and on a sloped beach, are good examples of what can be done with the relatively simple SOLA-SURF code without modification. The remaining calculations require the addition of special boundary conditions to create stationary or moving interior structures.

1. Reflection of a Solitary Wave

In this first example, a solitary wave travels over a fluid of constant depth, runs up a vertical wall, and reflects from the wall. The calculational region was resolved by 75 horizontal by 10 vertical cells, with cell dimensions of 0.5 horizontally and 0.2 vertically, and a time step of 0.1 was used. (The units in this calculation were non-dimensional.) All the wall boundaries were specified to be rigid, free-slip boundaries and the fluid is nearly inviscid. Laitone's second order approximation was used to initially define the free surface profile and velocity field of the solitary wave, as presented by Weigel (1964). The pressure field was initially set to hydrostatic pressure. Figure 1 shows the free surface profile and the velocity field, represented by velocity vectors drawn from cell centers, at times 13, 18, 20, and 26. The integrity of the wave profile and the velocity field remains excellent as the wave propagates down the channel and reflects from the wall.

To compare with the experiment of Camfield and Street (1967), the numerical calculation was repeated several times with initial wave heights ranging from 0.1 to 0.6, and with an undisturbed fluid depth of 1.0. A comparison of the computed maximum wave run-up with the experimental results is shown in Fig. 2. The abscissa is the ratio of the initial wave height, H_0 , to the undisturbed fluid depth, d , and the ordinate is the ratio of the maximum wave run-up on the vertical wall, R , to d . As the plot shows, the SOLA-SURF calculated data are in excellent agreement with these experimental data for a wide range of initial wave heights.

2. Solitary Wave on a Sloping Beach

Solitary waves are often used as the initial wave shape to simulate shoaling, breaking, and run-up of large, long waves on a beach. SOLA-SURF cannot handle breaking waves because of the restriction that the free surface slope be less than the mesh cell diagonal. This restriction can be removed by using the more complicated surface marker particle treatment as described, for example, by Nichols and Hirt (1971). However, we have calculated the solitary wave running up a sloped beach and measured the variation in maximum amplitude with depth. The rigid bottom slope was $1/20$, with the ratio of wave height to fluid depth of 0.1.

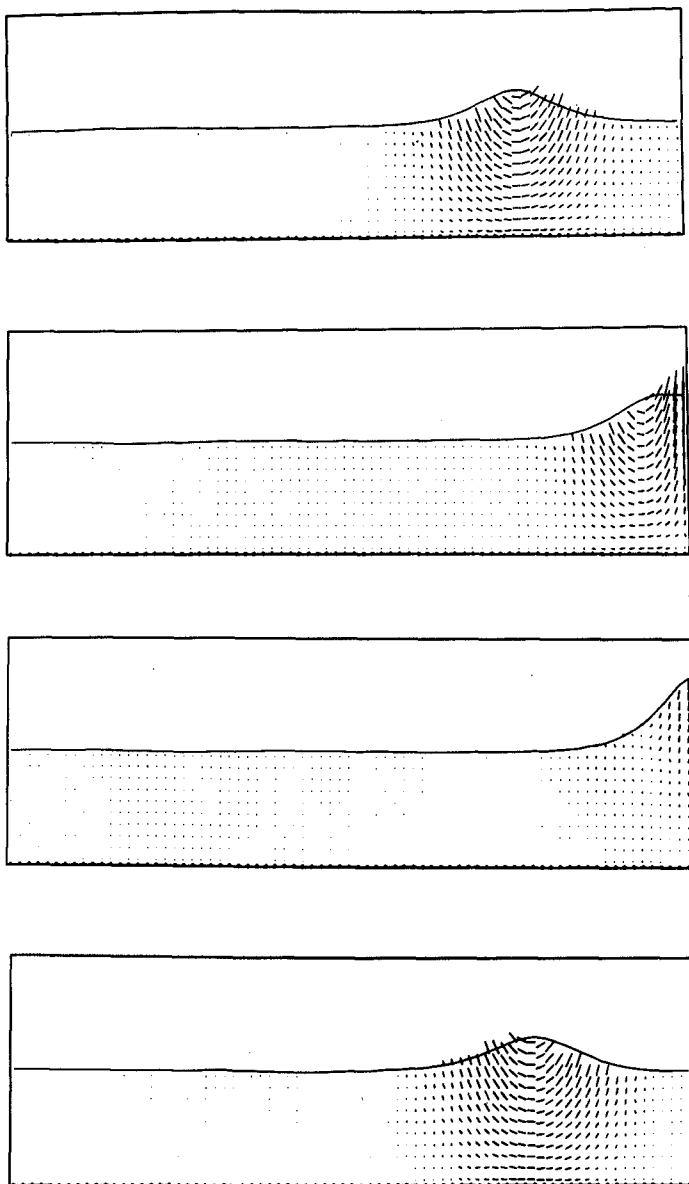


Fig. 1. Free surface profiles and velocity vector plots of solitary wave run-up on a vertical wall at times 13, 18, 20, and 26.

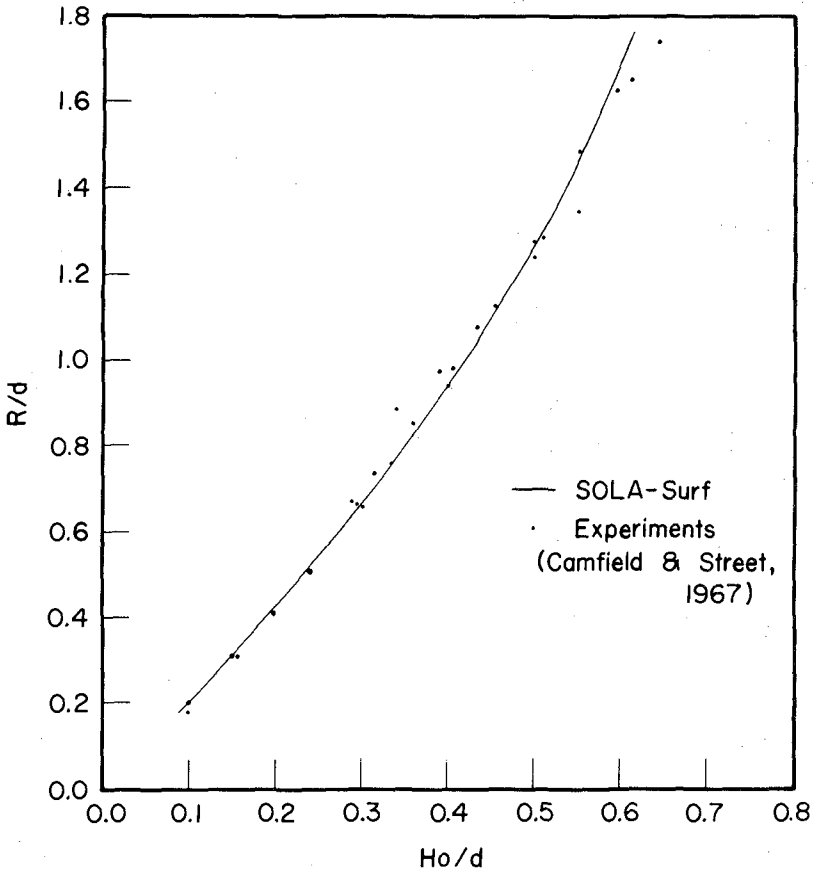


Fig. 2. A comparison of the computed maximum wave run-up, R , with experimental values for many initial wave heights, H_o .

Again, Laitone's second order approximation was used to initially define the solitary wave. Free-slip boundary conditions were specified for all rigid boundaries. A mesh of 90 horizontal by 18 vertical cells was used with cell dimensions of 0.5 horizontally and 0.1 vertically. The mesh length was chosen to accommodate the solitary wave totally over the horizontal section of the mesh bottom. SOLA-SURF does not have provisions to treat the intersection of the variable top and bottom boundaries in a cell. To allow the solitary wave to run farther up the beach without reflecting from the vertical wall, a shelf two and one-half cells beneath the undisturbed fluid surface was incorporated into the bottom boundary configuration. This is shown in Fig. 3, along with the free surface profile and the velocity field at times 0, 9, 22, and 28. At the later times, steepening of the wave front and growth of the wave height is obvious. Indeed, the calculated variation in maximum amplitude with depth compares very well with previous calculations, as shown in Fig. 4. In this plot, we compare the computed variation in maximum wave amplitude at different fluid depths with the theories of Peregrine (1967) and Madsen and Mei (1969). The numerical calculation of Chan and Street (1970) are virtually the same as the SOLA-SURF results. Peregrine derived equations of motion for long waves in water of varying depth that are extensions of the Boussinesq equations and that include nonlinear terms and a term to account for the effects of the vertical acceleration of the water on pressure. These equations were solved numerically for a solitary wave on a beach of uniform slope. Madsen and Mei treated the same problem with slightly different, but equivalent, equations. One difference, however, between the calculations is that Peregrine located the crest of the solitary wave immediately above the toe of the slope. The effect of this is seen in the comparison plot. Peregrine's calculation starts with $H/H_0 = 1.0$ at $d/d_0 = 1.0$, where H is the wave amplitude, H_0 is the initial wave amplitude, d is the undisturbed fluid depth at the horizontal location corresponding to the wave crest, and d_0 is the undisturbed fluid depth over the horizontal section of the bottom surface. The Madsen and Mei and SOLA-SURF calculations, which start with the wave initially over the flat bottom, show the ratio of the wave height at the toe of the slope to the initial wave height is greater than 1.0. The SOLA-SURF calculations are in good agreement with the other calculations. The effect of the shelf in our calculation is evident. The wave height does not continue to grow as the wave front reaches the shelf and, consequently, the value of H/H_0 falls slightly below values calculated without the shelf at low values of d/d_0 .

3. Forces on Submerged Structure

The determination of forces on submerged structures in the presence of gravity waves is of practical engineering importance. The SOLA-SURF code was used to calculate the horizontal and vertical forces on a submerged, rectangular structure resulting from a train of regular surface waves. This rectangular structure was created midway between the free surface and the mesh bottom by setting to zero the velocities on all faces of cells that make up the structure. These are set in the special boundary condition section of the code. The horizontal and vertical forces on the structure were determined by integrating the pressures acting on the surfaces of the structure. The dimensions of the submerged structure were chosen to compare with the experimental data of Brater et al. (1958).

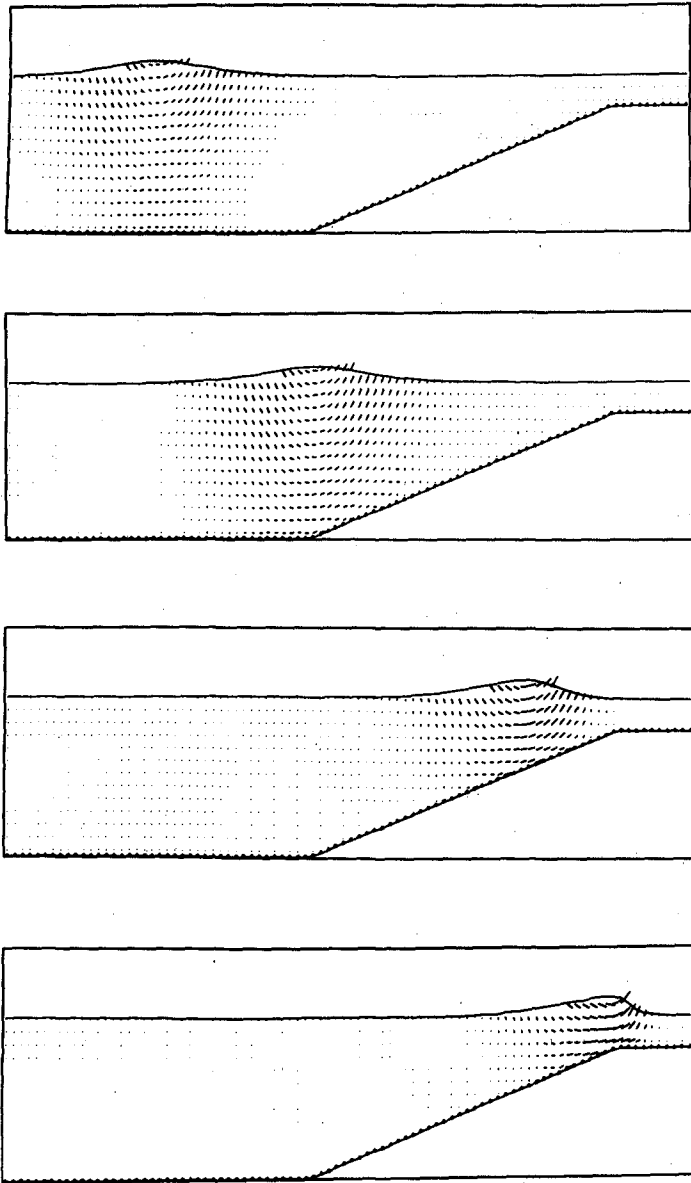


Fig. 3. Free surface profiles and velocity vector plots of solitary wave run-up on a 1/20 sloped beach at times 0, 9, 22, and 28.

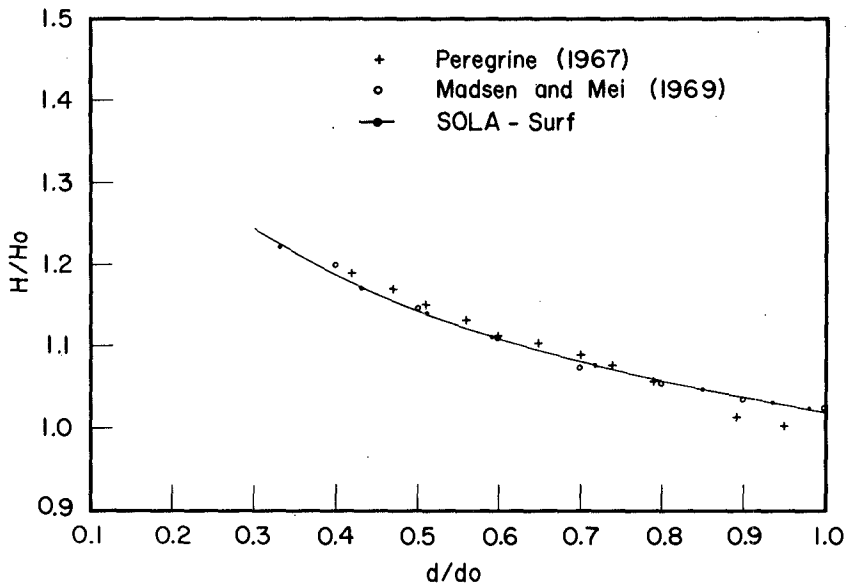


Fig. 4. A comparison of the computed variation in maximum wave amplitude, H , at different fluid depths, d , with other calculations.

The surface wave train was generated at the boundary of the computational mesh by setting the time dependent wave height and velocity components in the fictitious column of cells at the left side of the mesh. The mesh was 120 horizontal by 16 vertical cells, and the obstacle was 2 by 5 cells. Figure 5 shows the computer generated free surface profile, velocity field, and obstacle at times 0, 1.50, 3.25, and 4.25. The wave form is not perfectly sinusoidal; however, this is expected because an approximate shallow water expression was used to generate the wave form and, of course, the leading wave is distorted as it travels into still water. The exact form of the waves used in the experiment is not known.

Our computed data are compared with the experimental data in Fig. 6. The wave forces, normalized by wave height, are plotted as the vertical coordinate and the location of the center of the structure ($Y_b + d_o$), normalized by d_o , is plotted as the horizontal coordinate, where Y_b is zero at the free surface and d_o is the undisturbed fluid depth. The computed horizontal forces are in very good agreement with the experimentally determined forces of Brater et al. (1958). However, the

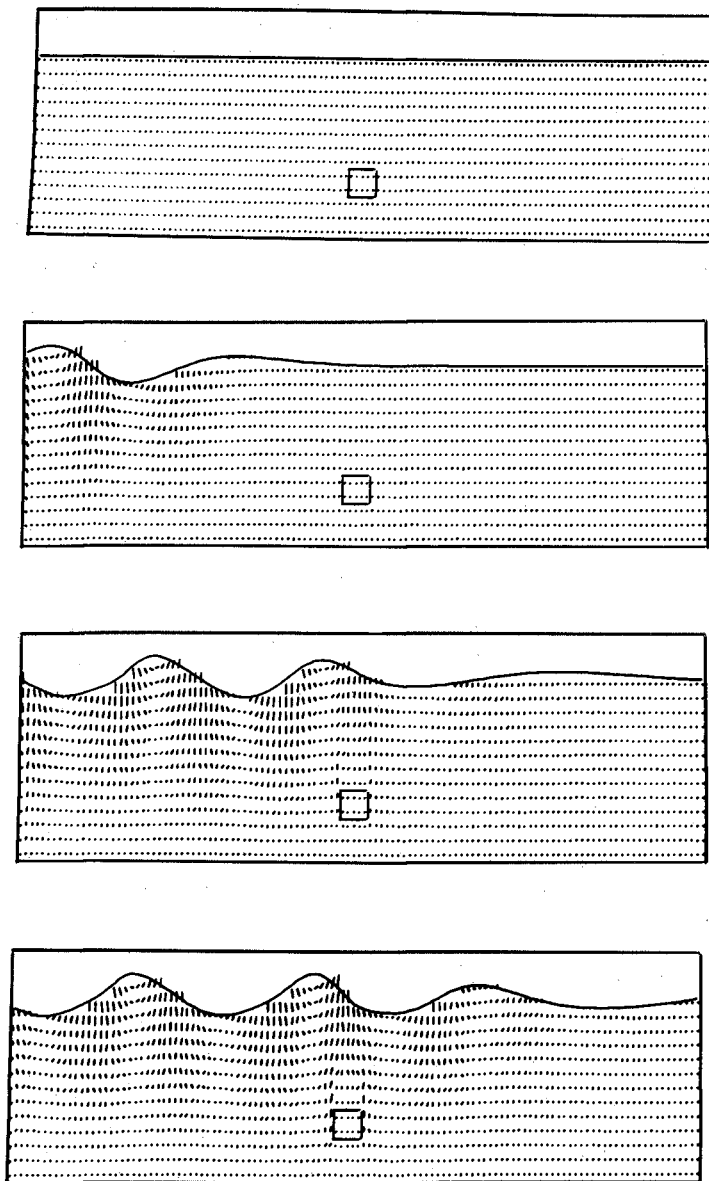


Fig. 5. Free surface profiles and velocity vector plots resulting from the propagation of a sinusoidal wave over a submerged structure at times 0, 1.50, 3.25, and 4.25.

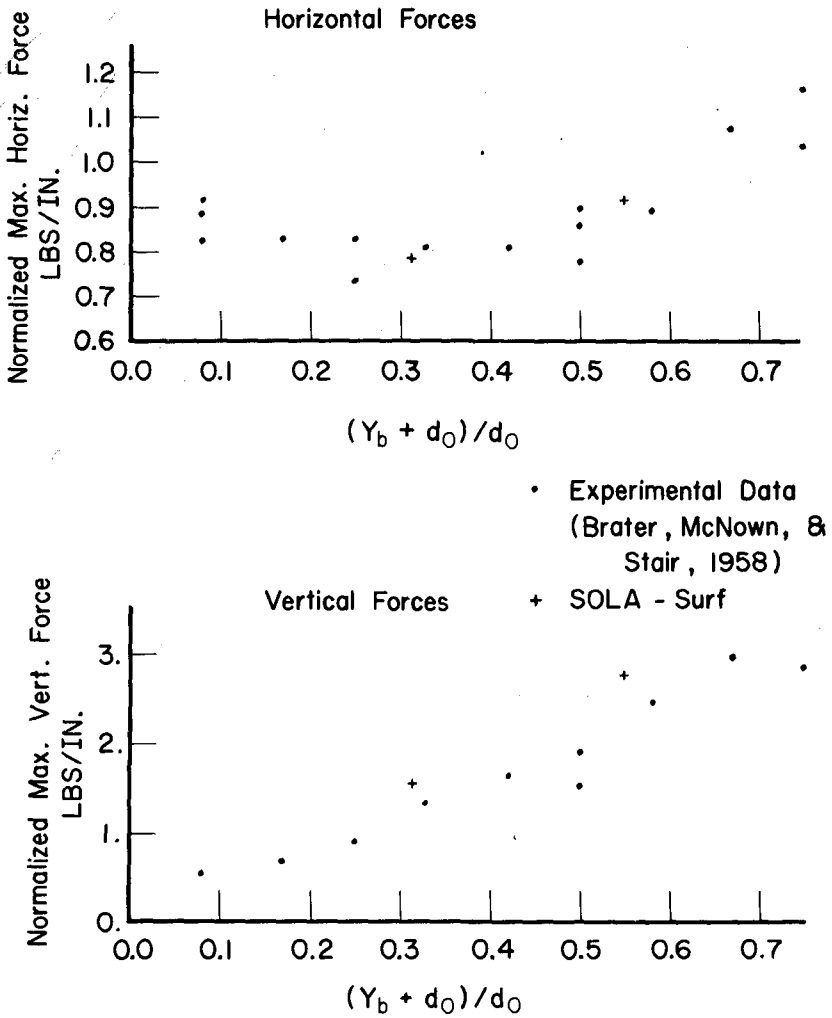


Fig. 6. A comparison of computed forces on a submerged structure with experimental data.

vertical forces calculated are about 20% larger than the experimental data. The accuracy of the numerical calculation was tested by increasing the temporal and spatial resolution and tightening the pressure iteration convergence criterion. These tests confirmed the originally calculated results, indicating that numerical accuracy is not the source of disagreement. Since the vertical force is very sensitive to the wave form, we may not be correctly modeling the experimental waves.

4. Forces on Floating Bodies

Hydrodynamic forces exerted on partially submerged, floating bodies are of interest to naval architects and ocean engineers. Different types of fluid motion may be generated to study these forces. Here we report on calculations for bodies undergoing forced harmonic oscillations in an otherwise quiescent fluid. In particular, we have studied heave forces on two-dimensional cylinders with rectangular and triangular cross sections and sway forces on a triangular or wedge shaped cylinder.

Pure heaving motions produce only vertical forces, which, for low amplitude motions, may be described by their amplitude and phase relative to the forced harmonic motion. These forces are due to buoyancy, inertial (added mass), and energy dissipation (wave generation) effects. In this study added mass and damping coefficients are computed and compared with the experimental work of Vugts (1968).

These calculations used mesh sizes that varied from 100 to 250 cells in the horizontal direction, depending on the period of motion, and 20 to 30 cells in the vertical direction. Typical calculation times on the CDC-7600 were 0.20 ms/cycle/cell. For the rectangular body, the mesh cell size was 0.1 horizontally and 0.2 vertically. Five cells were used to resolve the half-width of the body, which was located at a plane of symmetry at the left mesh boundary. Figure 7 shows the location of the rectangular body and the velocity field after approximately 2.5 periods of oscillation. To model the harmonic motion of the rectangular cylinder, special boundary conditions had to be added to the SOLA-SURF code. At the rigid bottom boundary of the rectangular body, the cell pressure is derived under the constraint that the normal fluid velocity be equal to that of the body. Because the SOLA-SURF boundary conditions restrict the surface slope to be less than that of a cell diagonal, we had to eliminate this restraint at the vertical side of the cylinder by aligning the side with a cell boundary line. Then boundary conditions were added to set zero velocities normal to the side of the cylinder.

The added mass coefficient, μ , and the damping coefficient, λ , are given by

$$\mu = \frac{\gamma \cos \beta}{\omega^2 a}$$

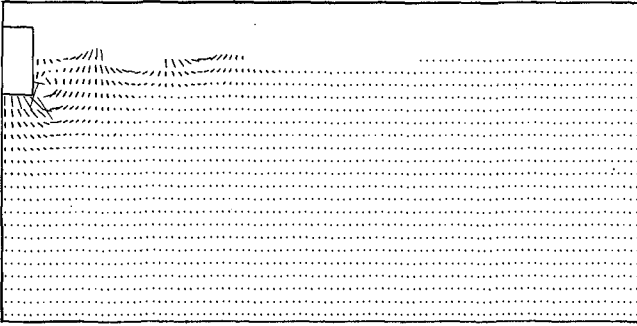


Fig. 7. Velocity vector plot of the fluid in which a rectangular cylinder is in forced heave at the left mesh boundary after 2.5 periods.

and

$$\lambda = \frac{\gamma \sin \beta}{\omega a} ,$$

where a is the amplitude of motion, ω is the frequency of motion, and γ is the amplitude of the assumed harmonic pressure force on the body. The phase shift β was obtained by comparing plots of the body displacement and pressure force acting on the rectangular body as functions of time and measuring the shift in phase. A detailed description of the determination of these coefficients is given by Nichols and Hirt (1975). These calculated added mass and damping coefficients are compared with experimental data in Fig. 8. The coefficients are normalized by ρA and $\sqrt{B/2}g$, where ρ is the fluid density, A is the mean submerged area, B is the rectangular body beam, and g is the acceleration of gravity. The calculations were for $B/T = 2.0$, where T is the rectangular body draft at its mean location. The amplitudes of motion, normalized by B , were 0.025 and 0.05. Vugts' experiments were conducted in fluid depths, normalized by B , varying from 4.50 to 5.625. The normalized depth was 4.0 for the calculated results. The calculated data generally agrees very well with the experimental data. The discrepancy in the calculated damping coefficient at the normalized frequency of 1.25 is probably due

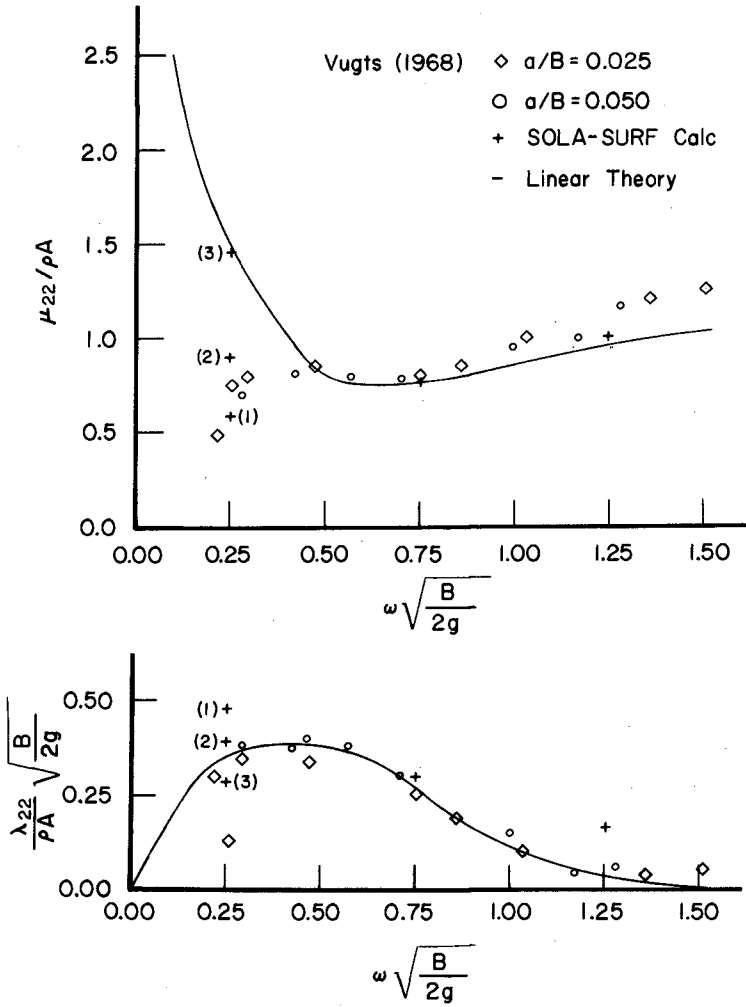


Fig. 8. A comparison of numerically computed and experimental values of added mass (top) and damping (bottom) coefficients from a rectangular cylinder in forced heave for $B/T = 2.0$.

to inaccuracies in determining the phase shift β , since it is very small at this beam width and frequency. To check this, another calculation was made, which is not plotted in Fig. 8, for $B/T = 8$ and $\omega\sqrt{B}/2g = 1.25$. In this case the phase shift is much larger, and the added mass coefficient agrees closely with the experimental data. The calculated damping coefficient in this case is very close to the experimental data, lying between the linear theory and the experimental data.

There is a discrepancy between the experimental data and linear theory for the added mass coefficient at normalized frequencies below 0.5. Vugts explains this as being caused by experimental inaccuracies. With a normalized fluid depth of 4.0, the calculated coefficient at a frequency of 0.25 is slightly higher than that of the experiments. (This is the middle point marked (2) in Fig. 8 at this frequency.) However, calculations with a fluid depth of 2.0, marked (1), and a fluid depth of 8.0, marked (3), show clearly that the finite depth is the cause of the disagreement with the linear theory. The added mass coefficient for the shallower fluid depth is slightly less than the experimental data, but with the normalized depth of 8.0 the calculated coefficient agrees with the linear theory, which assumes an infinite depth.

We next extended this capability to calculate the added mass and damping coefficients of a 60° wedge in sway. The coefficients, normalized as described above, were calculated for normalized frequencies ranging from 0.5 to 1.25 and with $B/T = 1.155$. An amplitude of motion, normalized by B , of 0.05773 was used. As shown in Fig. 9, the numerical data is in very good agreement with linear theory, but agrees less well with the experimental data. Expecting closer agreement with experimental data, we were concerned about possible numerical inaccuracies and tested for these in various ways. We tightened up the convergence criterion, increased by a factor of two the spatial and temporal resolution, used a new second order differencing scheme, and made various tests on the wedge interface boundary conditions. In addition, the calculations were performed in a moving reference frame attached to the body, as well as in the laboratory frame. However, all calculations were consistent to within a few per cent, thus, we believe the calculations are accurate.

Nonlinear effects were expected to have a greater influence. For example, secondary flow formed at the wedge tip is expected to increase the damping coefficient somewhat. This secondary vortex is shown in Fig. 10, which shows the velocity field and free surface configurations at times 0.50, 2.25, and 4.50. It should be noted that Vugts concluded that the generated eddy hardly disturbs the pressure distribution over the wedge surface. He explained the disagreement of his results with the linear theory as "a small systematic error at the higher frequencies of motion, where high demands are imposed on the structural set-up." We have shown that Vugts' tentative conclusions were correct and that linear theory does accurately predict the added mass and damping coefficients for the wedge in sway at this amplitude. Of course, at higher amplitudes for the forced sway, nonlinear effects must eventually enter.

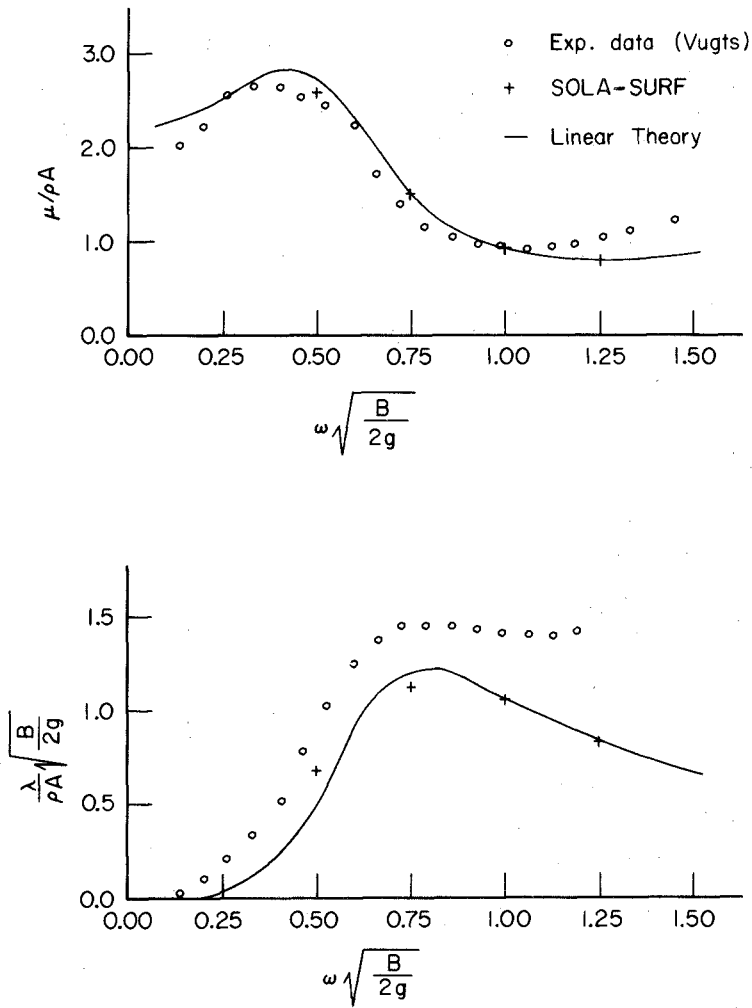


Fig. 9. A comparison of numerically computed and experimental values of added mass (top) and damping (bottom) coefficients from a 60° wedge in forced sway for $B/T = 1.155$.

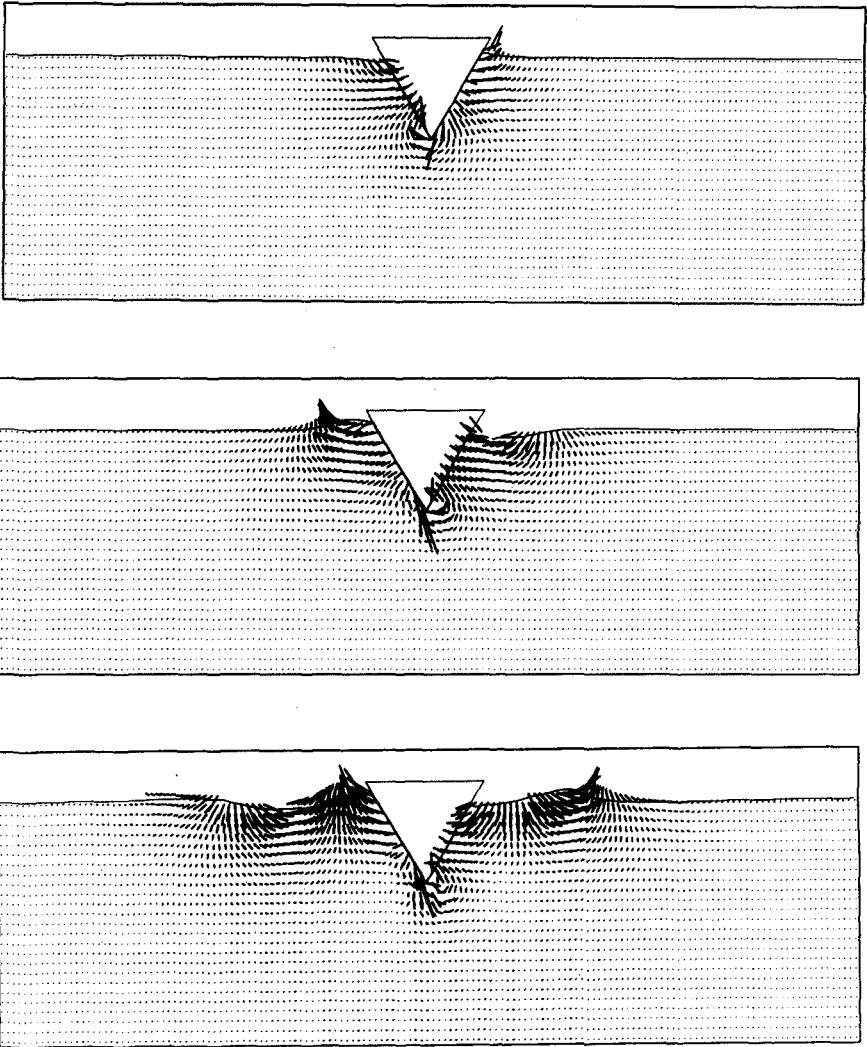


Fig. 10. Free surface profiles and velocity vector plots resulting from a 60° wedge in forced sway at times 0.50, 2.25, and 4.50.

REFERENCES

- Brater, E. F., McNow, J. S., and Stair, L. D., "Wave Forces on Submerged Structures," J. Hydraulics Division, ASCE, 84, Proc. paper 1833 (1958).
- Camfield, F. E. and Street, R. L., "An Investigation of the Deformation and Breaking of Solitary Waves," Stanford University Technical Report No. 81 (1967).
- Chan, R.K.-C. and Street, R. L., "SUMMAC - A Numerical Model for Water Waves," Stanford University Technical Report No. 135 (1970).
- Harlow, F. H. and Welch, J. E., "Numerical Calculation of Time-Dependent Viscous Incompressible Flow of Fluid with Free Surface," Phys. Fluids 8, 2182 (1965).
- Hirt, C. W., Nichols, B. D., and Romero, N. C., "SOLA - A Numerical Solution Algorithm for Transient Fluid Flows," Los Alamos Scientific Laboratory report LA-5852 (1975).
- Madsen, O. S. and Mei, C. C., "The Transformation of a Solitary Wave over an Uneven Bottom," J. Fluid Mech., 39, 781 (1969).
- Nichols, B. D. and Hirt, C. W., "Improved Free Surface Boundary Conditions for Numerical Incompressible-Flow Calculations," J. Comp. Phys., 8, 434 (1971).
- Nichols, B. D. and Hirt, C. W., "Methods for Calculating Multi-Dimensional, Transient Free Surface Flows Past Bodies," Proceedings of the First International Conference on Numerical Ship Hydrodynamics, Gaithersburg, MD (1975).
- Peregrine, D. H., "Long Waves on a Beach," J. Fluid Mech., 27, 815 (1967).
- Vugts, J. H., "The Hydrodynamic Coefficients for Swaying, Heaving, and Rolling Cylinders in a Free Surface," International Shipbuilding Progress, 15, 251 (1968).
- Wiegel, R. L., Oceanographical Engineering, Prentice Hall, Englewood Cliffs, New Jersey (1964).

CHAPTER 133

WAVE FORCES ON SQUARE CAISSONS

by

G.R. Mogridge* and W.W. Jamieson*

ABSTRACT

The forces and overturning moments exerted by waves on large vertical square-section caissons have been measured in the laboratory. Each model caisson extended from the bottom of a wave flume through the water surface and was oriented either with one side perpendicular to the direction of wave propagation or turned through an angle of forty-five degrees to this position. For a given orientation, each model was tested for a range of wave heights (up to the point of breaking) for various wave periods and water depths. A digital computer was used for the acquisition, processing, plotting and storage of the experimental data.

In addition to the experimental work, an approximate theoretical method is presented which allows the wave loadings on a square caisson to be estimated by means of a simple desk calculation. The experimental data shows that this simple method of calculation is reasonably accurate over a wide range of wave conditions and caisson sizes.

INTRODUCTION

In recent years, considerable research has been carried out to estimate the wave loads on various shapes of monolithic offshore structures; however, very little information is available in the literature concerning wave loadings on large vertical square-section caissons resting on the ocean bottom and extending through the water surface. Hogben and Standing (3) describe a numerical method which can be used for the solution of wave loads on large bodies including square caissons. The same method was previously used by Garrison and Chow (2), Milgram and Halkyard (7), and numerous others. Although numerical methods can be used for shapes

* Assistant Research Officers, Hydraulics Laboratory, National Research Council of Canada, Ottawa, Ontario, Canada, K1A 0R6.

for which closed form solutions do not exist, programming is time consuming and computation costs can be high. Hogben and Standing presented a few results of wave loads measured on a model of a square caisson. The experimental data was compared with the numerical solution (4) and also an approximate solution (3) based on the diffraction theory of MacCamy and Fuchs (6). For most of the range of relative caisson sizes tested, the results fitted both solutions reasonably well. Ijima, Chou and Yumura (5) have presented a numerical method for calculation of wave scattering by isolated breakwaters of arbitrary shape. Wave height distributions about rectangular breakwaters were calculated and were found to compare favourably with distributions measured in the laboratory. Although wave forces were not measured on the model breakwaters, they were calculated using the known velocity potentials at the boundaries of the breakwaters.

In this presentation it is assumed that in general terms, the wave forces on a square caisson or cylinder occur in a similar manner to the wave forces on a circular cylinder. That is, if the size of the square cylinder is small relative to the wave length, the cylinder does not deform the incident wave and the wave force on the cylinder consists of the sum of the inertial and viscous forces. However, if the size of the cylinder or caisson is large relative to the incident wave length, it causes reflection and diffraction of the incident waves and the viscous drag forces are negligible in comparison to the inertial forces.

This paper presents an approximate theory which can be used to estimate the wave forces and moments on large vertical square caissons. The theory, based on the linear diffraction theory of MacCamy and Fuchs (6), has been simplified so that only three graphs need be used to obtain the complete solution. Force and moment measurements on models of square caissons show that the approximate theory gives a satisfactory solution over a large range of caisson sizes and wave conditions.

THEORETICAL METHOD

It is assumed that the wave force on a large square-section cylinder or caisson can be expressed as an inertial force if the coefficient of mass used includes the effects of wave reflection and diffraction. Thus the horizontal force per unit length of the caisson is expressed as

$$f_x = C_{ms} \rho b^2 du/dt \quad (1)$$

where C_{ms} is the coefficient of mass for the square-section caisson, ρ is the mass density of the fluid, b is the side length of the caisson and du/dt is the horizontal component

of the water particle acceleration. Substituting into Eq. 1 the expression for du/dt from linear wave theory gives

$$f_x = C_{ms} \frac{2\pi^2 \rho b^2 H}{T^2} \frac{\cosh k(y+d)}{\sinh kd} \cos(kx - \sigma t) \quad (2)$$

where H is the incident wave height, T is the wave period, d is the water depth, σ is the wave frequency, $\sigma = 2\pi/T$, k is the wave number, $k = 2\pi/L$, L is the wave length and t is the time. The coordinates are chosen so that x is positive in the direction of wave propagation and y is positive in the upward direction. The origin of these coordinates is at the still water level where the water surface elevation plotted against x has a maximum negative slope (Fig. 4). By equating the inertial force per unit length on a square caisson to that on a circular caisson of diameter D_e ,

$$C_{ms} \rho b^2 du/dt = 0.25 C_m \rho \pi D_e^2 du/dt \quad (3)$$

it is found that the diameter of an equivalent circular cylinder is

$$D_e = 2b (C_{ms}/\pi C_m)^{\frac{1}{2}} \quad (4)$$

If it is assumed that $C_{ms} = C_m$, then,

$$D_e = 2b/\pi^{\frac{1}{2}} \quad (5)$$

The force per unit length on the equivalent circular cylinder is obtained using the diffraction theory of MacCamy and Fuchs (6):

$$f_x = \frac{2\rho gH}{k} \frac{\cosh k(y+d)}{\cosh kd} A(ka_e) \cos(\sigma t - \alpha) \quad (6)$$

where $A(ka_e) = \left[J_1'^2(ka_e) + Y_1'^2(ka_e) \right]^{-\frac{1}{2}}$

and $\alpha = \tan^{-1} \left[\frac{J_1'(ka_e)}{Y_1'(ka_e)} \right]$

g is the acceleration due to gravity, a_e is the radius of the equivalent circular cylinder, and J_1 and Y_1 are Bessel functions of the first and second kind respectively, both of the first order. Eq. 6 is equated to Eq. 2 for $x = 0$ to give the expression for the coefficient of mass C_{ms} for a square caisson:

$$C_{ms} = \frac{L^2}{\pi^2 b^2} A(ka_e) \frac{\cos(\sigma t - \alpha)}{\cos \sigma t} \quad (7)$$

A modified coefficient of mass C_{ms}^* is defined as

$$C_{ms}^* = \frac{L^2}{\pi^2 b^2} A(ka_e) \quad (8)$$

such that,

$$C_{ms} = C_{ms}^* \frac{\cos(\sigma t - \alpha)}{\cos \sigma t} \quad (9)$$

The coefficient of mass C_{ms} is a function of time and varies through a wave cycle while C_{ms}^* is only a function of b/L (Fig. 3). C_{ms} is equal to C_{ms}^* when α is approximately zero, that is, for b/L approaching zero or equal to 0.52. The phase angle α plotted as a function of b/L is shown in Fig. 4.

The total force in the x direction is obtained by integrating the force per unit length as given by Eq. 2 for $x = 0$, through the depth of water from the bottom to the still water level:

$$F(t) = C_{ms} \frac{\rho \pi b^2 H L}{T^2} \cos \sigma t \quad (10)$$

Substituting the expression for C_{ms} given by Eq. 9 into Eq. 10 gives

$$F(t) = C_{ms}^* \frac{\rho \pi b^2 H L}{T^2} \cos(\sigma t - \alpha) \quad (11)$$

The maximum force occurs when $\sigma t = \alpha$:

$$F_{\max} = C_{ms}^* \frac{\rho \pi b^2 H L}{T^2} \quad (12)$$

The overturning moment about the base of the cylinder is

$$M(t) = \int_{-d}^0 f_x(y + d) dy \quad (13)$$

Substituting the expression for f_x from Eq. 2 and C_{ms} from Eq. 9 and carrying out the integration gives

$$M(t) = C_{ms}^* \frac{\rho g b^2 H L}{4\pi} [kd \tanh kd + \operatorname{sech} kd - 1] \cos(\sigma t - \alpha) \quad (14)$$

The maximum overturning moment occurs when $\sigma t = \alpha$:

$$M_{\max} = C_{ms}^* \frac{\rho g b^2 H L}{4\pi} [kd \tanh kd + \operatorname{sech} kd - 1] \quad (15)$$

Figs. 3, 4 and 5 give the solutions to the above equations. Fig. 3 gives C_{ms}^* by the solution of Eq. 8 so that the maximum horizontal force may be calculated by Eq. 12. The maximum overturning moment can then be obtained directly from Fig. 5 since C_{ms}^* is known. The phase angle α is plotted in Fig. 4 and allows the determination of $F(t)$ and $M(t)$ as given by Eqs. 11 and 14.

EXPERIMENTAL METHOD

The square caisson (Fig. 1) used in the experiments was 12 in. by 12 in. in cross section and was constructed of 1/4 in. thick plexiglass. It was supported 1/8 in. above the flume bottom by a rigid 3 in. diameter steel tube clamped to a steel frame above the wave flume. A force meter was contained within the caisson and consisted of two 3/4 in. diameter stainless steel strain rods 12 in. long. The wave force on the caisson was transferred to the top strain rod through a horizontal steel bar and to the bottom strain rod through a steel base plate (Fig. 1). Foil strain gauges glued on the strain rods were aligned so that total horizontal forces could be measured in the direction of wave propagation and normal to the wave direction to give longitudinal and transverse forces, respectively. The photograph in Fig. 1 shows two brass bushings on the strain rods which make the fixed connection to the supporting 3 in. diameter steel tube. The steel plate connects the free end of the bottom strain rod to the caisson, and the steel bar which passes through apertures in the supporting tube connects the free end of the upper strain rod to the caisson. Using the two bridge outputs from the strain rods, it was possible to measure total forces and to calculate the corresponding total overturning moments. A more detailed description of the wave force meter and its calibration is given by Pratte et al. (9). From the calibration curves of the force meter, its error band was estimated to be less than $\pm 2\%$ over the range of forces measured. The natural frequency of vibration of the caisson in the maximum depth of water was approximately 11 Hz.

Wave profiles in the flume were measured using a non-contacting capacitive wave transducer suspended above the water surface midway between the cylinder and the flume wall. The wave flume was approximately 6 ft. wide, 4.5 ft. deep and 220 ft. long.

A limited number of tests were conducted using a square caisson 2 ft. by 2 ft. in cross section to obtain force and moment data for larger values of the relative size b/L . The model caisson was suspended from a force meter in a wave flume 12 ft. wide, 4.5 ft. deep and 162 ft. long. The force meter (Fig. 2) consisted of three aluminum strain members 3 in. in diameter. The strains in these members caused by wave loads were measured using semiconductor strain gauges forming six Wheatstone bridges. Three bridges measured strain due to bending and gave outputs proportional to longitudinal, transverse and vertical forces. Three bridges measured strain due to torque and gave outputs proportional to the moments about the three coordinate axes. A detailed description of this force meter is given by Funke (1).

Preliminary tests in the 12 ft. wave flume were carried out with a 12 in. square-section caisson (Fig. 2) to confirm experiments already conducted in the 6 ft. flume.

Wave heights were measured using a capacitive rod wave gauge at the location of the model but without the model in the flume. Thus, a different method of measuring incident wave heights was an additional check on the 6 ft. flume results.

Monochromatic waves were generated in five water depths ranging from 9.7 to 29.0 in. and nine wave periods were tested from 0.77 to 2.58 sec. For each water depth and period tested, a number of wave heights were generated ranging from small amplitude waves to those that were on the point of breaking. Each model caisson was tested with two faces parallel to the incident wave fronts ($\beta = 0^\circ$) and also at 45° to this position ($\beta = 45^\circ$). A digital computer was used for the acquisition, processing, plotting and storage of data. Sampling of the data was commenced after the waves passing the model reached steady state conditions. For each test, the wave profile and the corresponding wave forces were sampled every one hundredth of a second for a total of six seconds. Total forces and overturning moments were computed and automatically plotted along with the measured wave profile. Experimental results were also printed and data was stored on magnetic tape. Although it has not been possible to include all the experimental data in this paper, the results presented are representative of the complete testing program. A comprehensive presentation of the experimental results may be found in Mogridge and Jamieson (8).

EXPERIMENTAL RESULTS

The number of waves in each test record varied depending on the wave period because of the fixed sampling time of six seconds. Any test with a variation in wave height or maximum force measurement within the record of more than 5% was discarded. From the test records, total forces and overturning moments were taken as average absolute maximum values of positive and negative measurements, for which the variation was normally less than 5%. The forces and corresponding moments measured in the transverse direction were negligible and are not included in the presentation of experimental results.

Using the measured absolute maximum forces with known values of wave height, length, period and caisson size, C_{ms} was calculated for varying values of b/L and then plotted on the theoretical curve in Fig. 3. Dimensionless moments were also calculated using the known values of C_{ms} and were plotted on the theoretical curve in Fig. 5. The experimental data shows good agreement with the theory for b/L between 0.092 and 0.399 and also for d/L between 0.063 and 0.786. The results shown for b/L and d/L greater than 0.09 were obtained by averaging all the test results with wave steepnesses less than 0.09. For b/L and d/L less than 0.09, only data for wave steepnesses of less than 0.01 were used. Even with this restriction on the data used, there is still some

deviation of the C_{ms} data in Fig. 3, but the moment data in Fig. 5 shows good agreement. It is concluded that the approximate theory can be used for situations where b/L and d/L are both greater than approximately 0.09. Although there is no data presented in this paper defining the d/L limit, experiments were conducted for d/L approximately equal to 0.09 and b/L greater than 0.09 for which the experimental data agreed with the linear theory. Additional data for d/L equal to 0.08 and b/L greater than 0.09, did not fit the theoretical curve, thus defining d/L of approximately 0.09 as the limit for the theory.

To examine the variation of the forces and moments with wave steepness, they have been expressed non-dimensionally and plotted against H/L in Figs. 6 to 8. The experimental results for b/L and d/L greater than 0.09 (Figs. 6 and 7) show reasonable agreement with the theoretical curves for wave steepness up to 0.09. Fig. 8 shows data for which there is a reasonable comparison with the theoretical curves only for very low wave steepness because b/L is less than 0.09. For close agreement at high wave steepness, it is necessary for both b/L and d/L to be greater than 0.09. The largest deviation between the theory and the experimental results is approximately 85% and occurs for the moment measurement for $\beta = 45^\circ$, $b/L = 0.047$ and $H/L = 0.032$. The large differences from the linear theory for b/L and d/L less than 0.09 and large H/L are believed to be due to non-linearity of the waves and the effect of viscosity introducing drag forces of considerable magnitude. For b/L and d/L larger than 0.09, these effects are apparently negligible although at values of d/L approaching 0.09, the waves were obviously non-linear and there was flow separation at the corners of the caisson under all wave conditions.

There are two factors which are evident in the experimental results from which the data in Fig. 8 has been obtained. Firstly, the absolute values of positive and negative wave loads are no longer approximately equal. They differ from their average values by as much as 30% for the data in Fig. 8 for which $b/L = 0.047$ and $\beta = 45^\circ$. Secondly, the phase angles between wave load records and wave profiles do not correspond to the theoretical values for α given by Eq. 6. To illustrate this, results which compare well with the theory have been plotted in Fig. 9 and results for b/L equal to 0.047 which do not compare well with the theory have been plotted in Fig. 10. In Fig. 9, positive and negative forces are approximately equal and for all wave steepnesses the measured phase difference between the force records and the wave profiles are approximately equal to the theoretical value of $\alpha = 8.8^\circ$. Although the theoretical phase difference for the results in Fig. 10 is $\alpha = 1.3^\circ$, the measured phase difference increases to almost 50° with increasing wave steepness. This is characteristic of an increasing drag force. However, the increasing phase angle

can also be due to the non-linearity of the waves because the maximum acceleration of the fluid no longer occurs at the still water level.

Although most of the experimental results described above were obtained in a 6 ft. wide flume, some experiments were conducted in a 12 ft. flume using different equipment and techniques. Since the results are intermixed, it is necessary to show how the measurements in the two wave flumes compared. The comparison is made by repeating the same tests in each wave flume using 12 in. square caissons. The first comparison shown in Fig. 11 is for $b/L = 0.184$, $d/L = 0.445$ and $\beta = 0^\circ$. The second comparison (Fig. 11) is for a series of tests where there are large deviations from the theory, that is, for $b/L = 0.047$, $d/L = 0.115$ and $\beta = 0^\circ$. In both cases the data obtained in the two flumes agree closely, giving an added degree of confidence to the experimental results.

CONCLUSIONS

An approximate method (Figs. 3, 4 and 5) based on the diffraction theory of MacCamy and Fuchs (6) has been developed to give the solution for the wave loads on a square caisson piercing the water surface. The method has been found to be satisfactory for relative caisson sizes of b/L from 0.09 to 0.40, for relative water depths of d/L from 0.09 to 0.79 and wave steepnesses up to 0.09. For b/L and d/L less than 0.09, the theoretical method cannot be used except for waves of very low steepness, because viscous drag forces and non-linearity of the waves become important. The above limits of applicability for the theory are the same whether the alignment of the square caisson is beam on to the waves, $\beta = 0^\circ$, or turned through an angle of 45° to this position.

ACKNOWLEDGEMENT

This project was funded in part by the Department of Public Works, Canada.

REFERENCES

1. Funke, E.R., "A Six Degree of Freedom Dynamometer for the Measurement of Wave Forces on Models of Offshore Structures", National Research Council of Canada, Hydraulics Laboratory, Laboratory Technical Report No. LTR-HY-54, 1976.

2. Garrison, C.J, and P.Y. Chow, "Wave Forces on Submerged Bodies", Proc. ASCE, Vol. 98, No. WW3, August, 1972, pp. 375-392.
3. Hogben, N. and R.G. Standing, "Wave Loads on Large Bodies", International Symposium on the Dynamics of Marine Vehicles and Structures in Waves, edited by R.E.D. Bishop and W.G. Price, Mechanical Engineering Publications Limited, London, 1975, pp. 258-277.
4. Hogben, N. and R.G. Standing, "Experience in Computing Wave Loads on Large Bodies", Seventh Offshore Technology Conference, Houston, Paper No. OTC 2189, May, 1975, pp. 413-431.
5. Ijima, T., C.R. Chou and Y. Yumura, "Wave Scattering by Permeable and Impermeable Breakwater of Arbitrary Shape", Proc. Fourteenth Coastal Engineering Conference, Copenhagen, Vol. 3, Chap. 110, June, 1974, pp. 1886-1905.
6. MacCamy, R.C. and R.A. Fuchs, "Wave Forces on Piles: A Diffraction Theory", U.S. Army, Beach Erosion Board, Technical Memorandum No. 69, December, 1954, 17 pp.
7. Milgram, J.H. and J.E. Halkyard, "Wave Forces on Large Objects in the Sea", Journal of Ship Research, Vol. 15, No. 2, June, 1971, pp. 115-124.
8. Mogridge, G.R. and W.W. Jamieson, "A Design Method for the Estimation of Wave Loads on Square Caissons", National Research Council of Canada, Hydraulics Laboratory, Laboratory Technical Report No. LTR-HY-57, 1976.
9. Pratte, B.D., E.R. Funke, G.R. Mogridge and W.W. Jamieson, "Wave Forces on a Model Pile", First Canadian Hydraulics Conference, Edmonton, May, 1973, pp. 523-543.

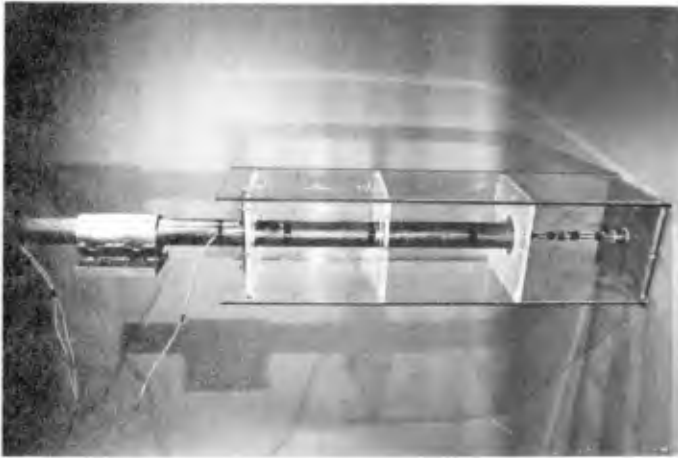
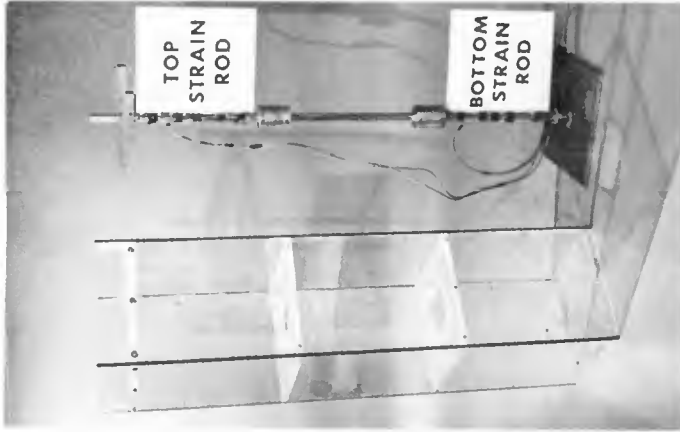


FIG.1 MODEL CAISSON AND FORCE METER (6 FT WAVE FLUME)

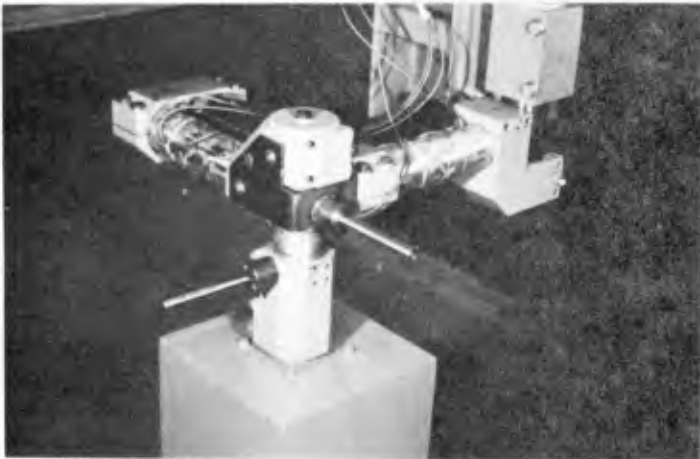


FIG.2 MODEL CAISSON AND FORCE METER (12FT WAVE FLUME)

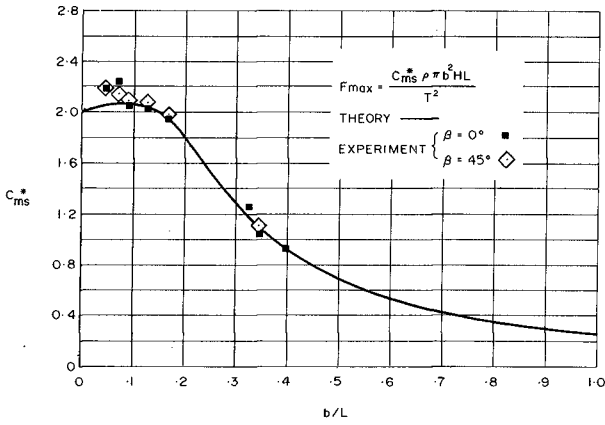


FIG. 3 C_{ms}^* AS A FUNCTION OF b/L

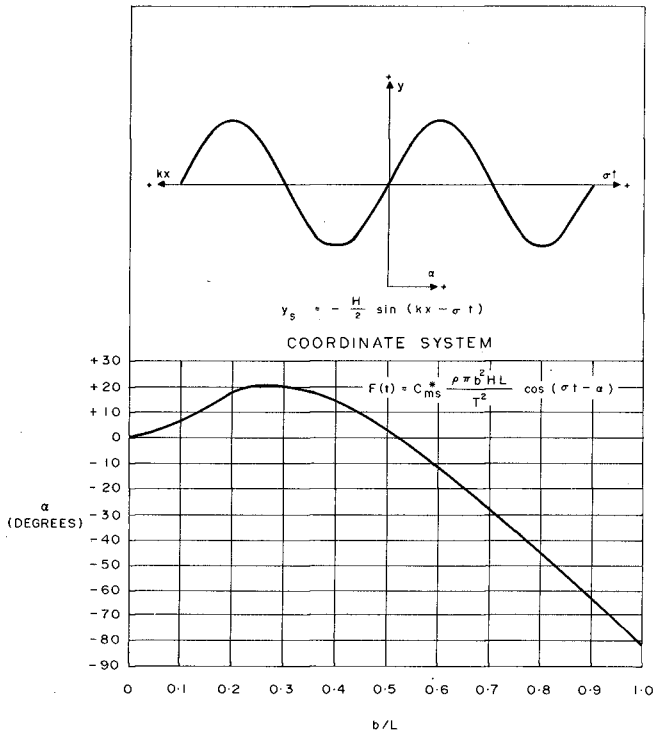


FIG. 4 PHASE ANGLE AS A FUNCTION OF b/L

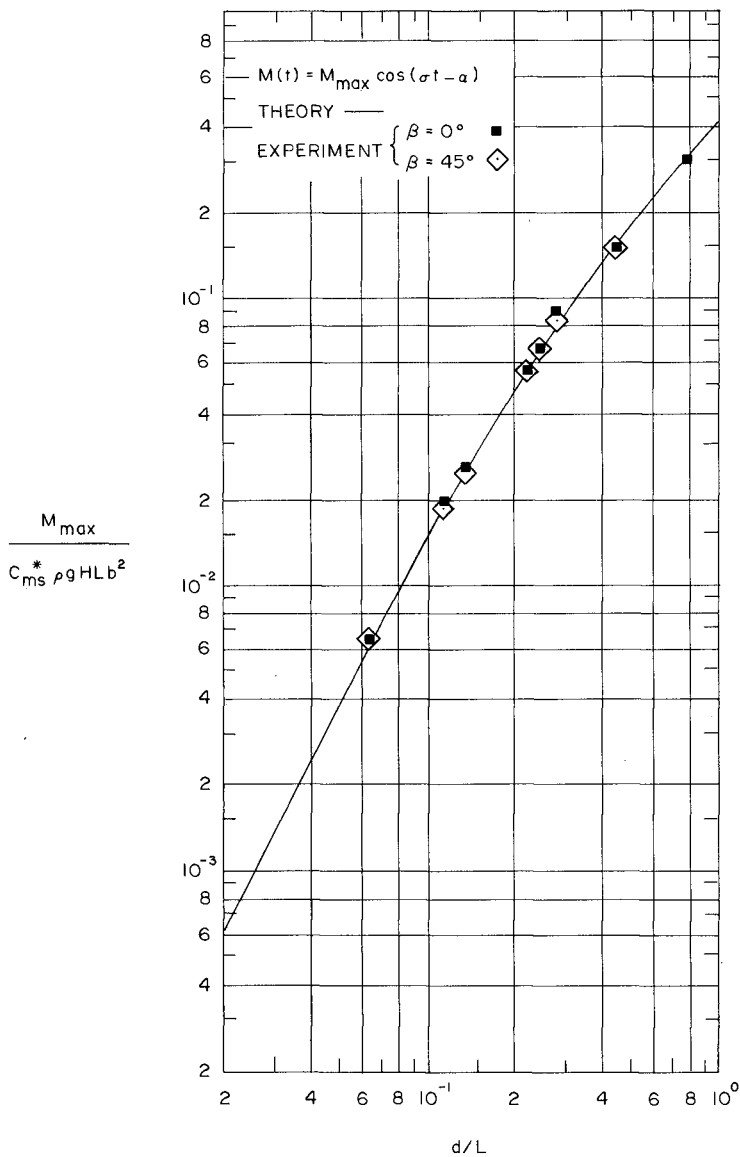
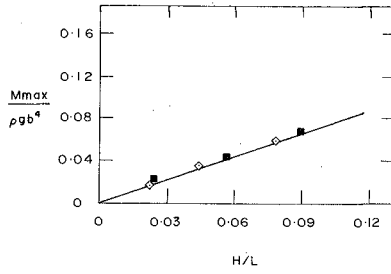
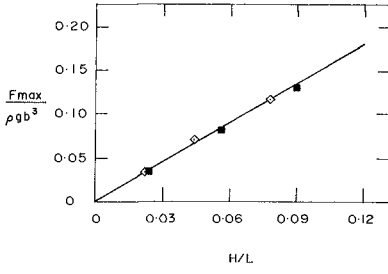
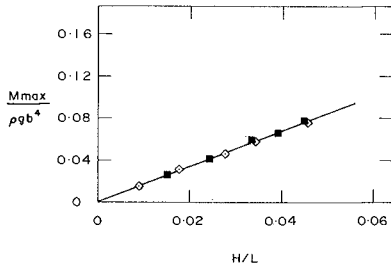
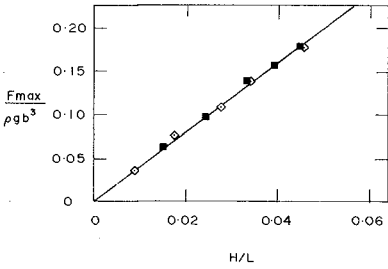


FIG. 5 DIMENSIONLESS OVERTURNING MOMENT AS A FUNCTION OF d/L

EXPERIMENTAL $\left\{ \begin{array}{l} \beta = 0^\circ \\ \beta = 45^\circ \end{array} \right. \begin{array}{l} \blacksquare \\ \diamond \end{array}$
 MacCAMY AND FUCHS —
 Fmax, Mmax: AVERAGE OF MAXIMUM FORCES AND
 MOMENTS IN POSITIVE AND NEGATIVE DIRECTIONS



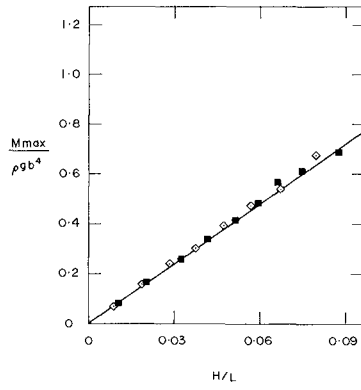
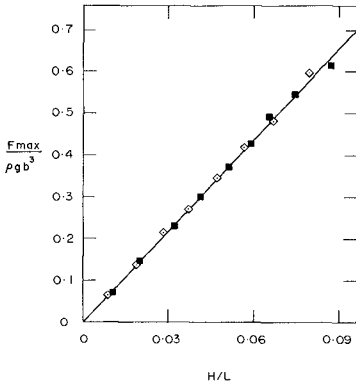
$$\frac{b}{L} = 0.345, \quad \frac{d}{L} = 0.280$$



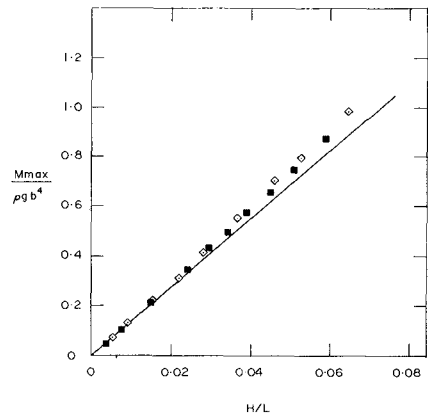
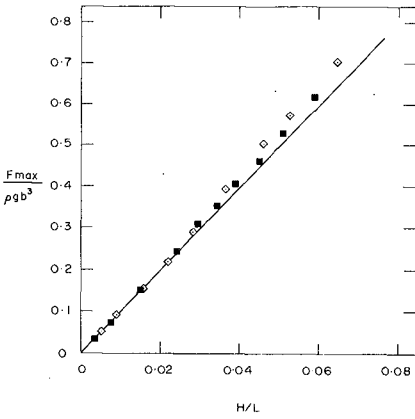
$$\frac{b}{L} = 0.168, \quad \frac{d}{L} = 0.137$$

FIG. 6 DIMENSIONLESS MAXIMUM FORCES AND OVERTURNING MOMENTS ON A SQUARE CAISSON

EXPERIMENTAL $\left\{ \begin{array}{l} \beta = 0^\circ \quad \blacksquare \\ \beta = 45^\circ \quad \diamond \end{array} \right.$
 MacCAMY AND FUCHS —
 F_{max}, M_{max} : AVERAGE OF MAXIMUM FORCES AND
 MOMENTS IN POSITIVE AND NEGATIVE DIRECTIONS



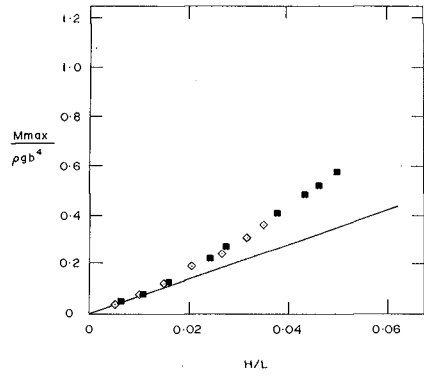
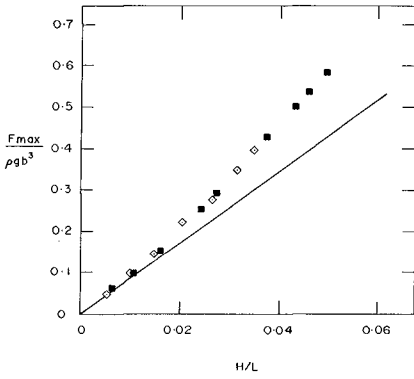
$$\frac{b}{L} = 0.128, \quad \frac{d}{L} = 0.246$$



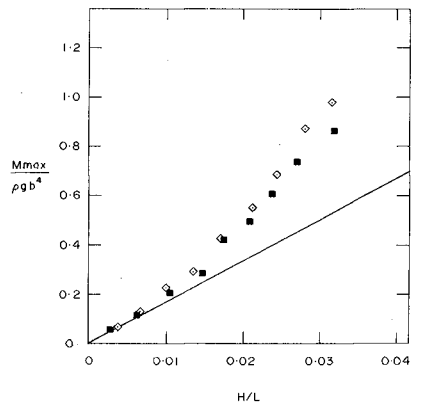
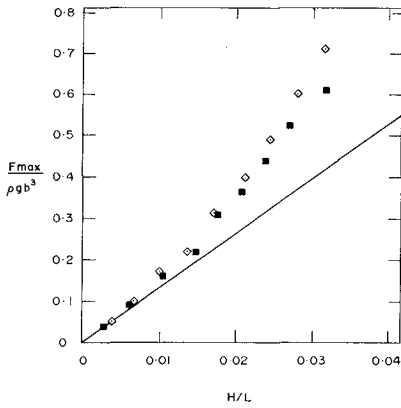
$$\frac{b}{L} = 0.092, \quad \frac{d}{L} = 0.222$$

FIG. 7 DIMENSIONLESS MAXIMUM FORCES AND OVERTURNING MOMENTS ON A SQUARE CAISSON

EXPERIMENTAL $\left\{ \begin{array}{l} \beta = 0^\circ \quad \blacksquare \\ \beta = 45^\circ \quad \diamond \end{array} \right.$
 MacCAMY AND FUCHS ———
 F_{max}, M_{max} : AVERAGE OF MAXIMUM FORCES AND
 MOMENTS IN POSITIVE AND NEGATIVE DIRECTIONS



$$\frac{b}{L} = 0.073, \quad \frac{d}{L} = 0.116$$



$$\frac{b}{L} = 0.047, \quad \frac{d}{L} = 0.115$$

FIG. 8 DIMENSIONLESS MAXIMUM FORCES AND OVERTURNING MOMENTS ON A SQUARE CAISSON

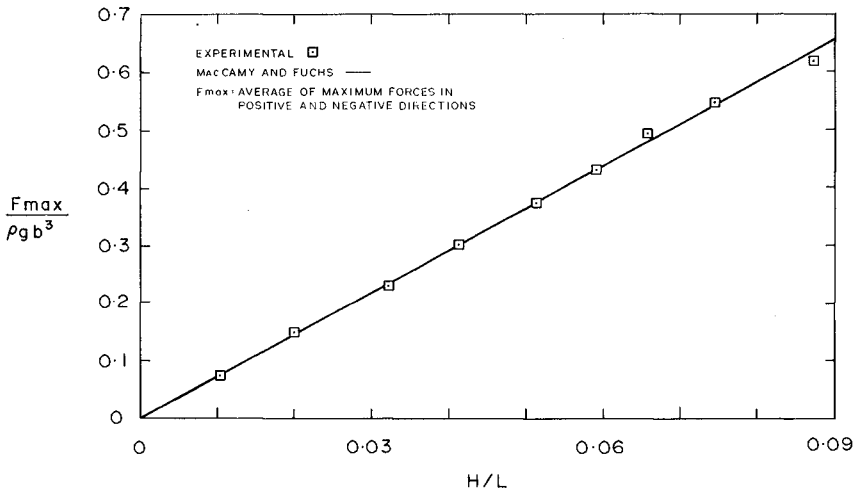
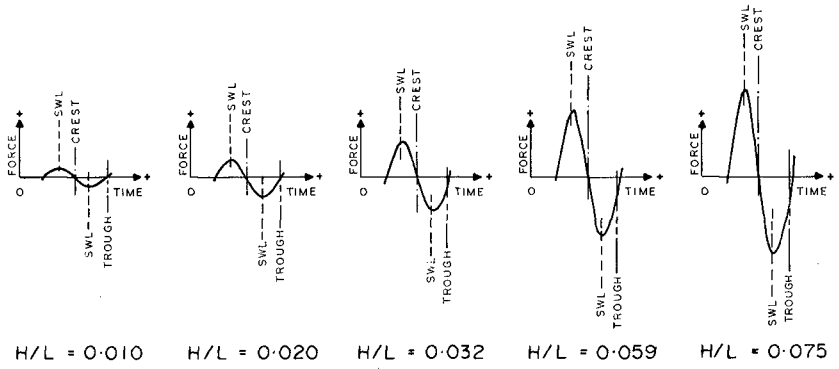


FIG. 9 PHASING BETWEEN WAVE PROFILES AND FORCE RECORDS FOR INCREASING WAVE STEEPNESS

$$\left(\frac{b}{L} = 0.128, \frac{d}{L} = 0.246, \beta = 0^\circ \right)$$

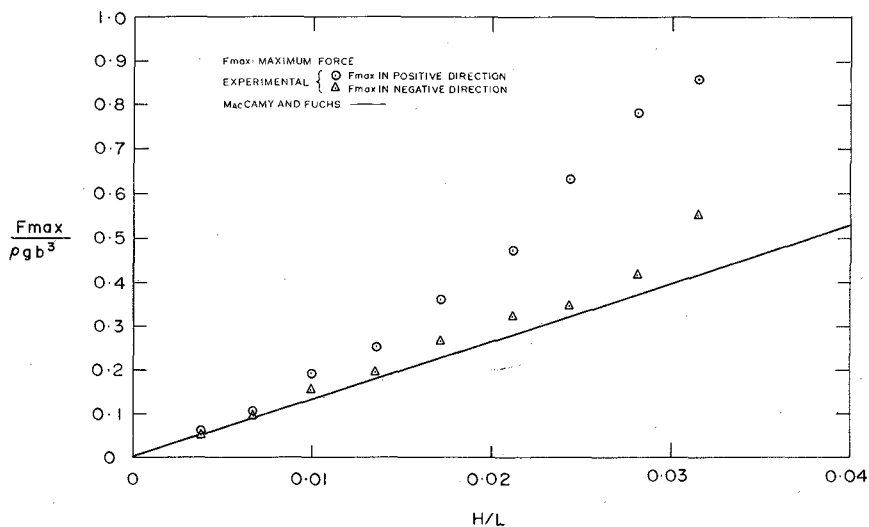
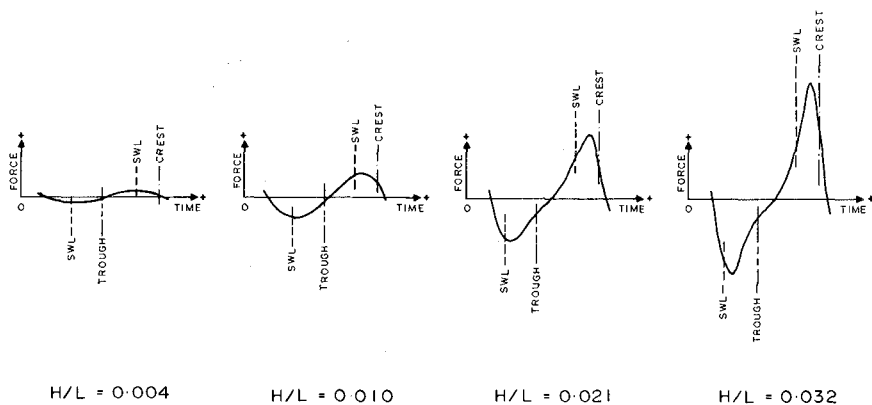
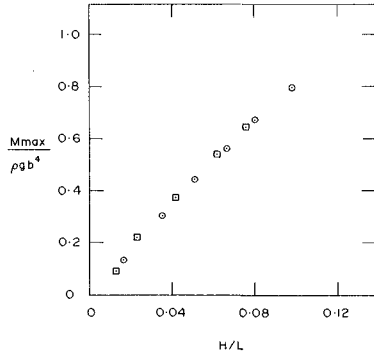
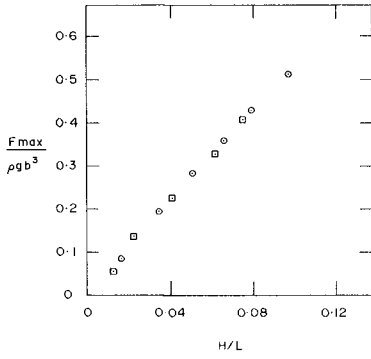


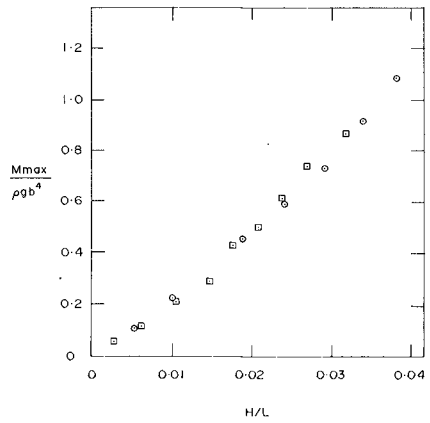
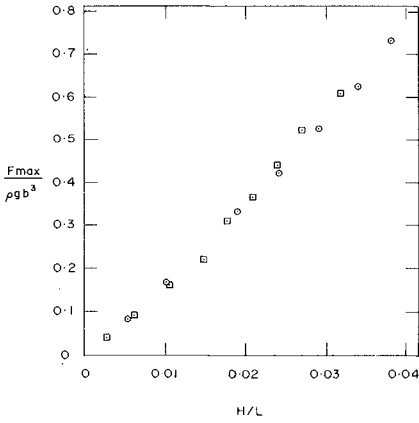
FIG. 10 PHASING BETWEEN WAVE PROFILES AND FORCE RECORDS FOR INCREASING WAVE STEEPNESS

$$\left(\frac{b}{L} = 0.047, \frac{d}{L} = 0.115, \beta = 45^\circ \right)$$

6 FT WIDE FLUME □
 12 FT WIDE FLUME ○
 Fmax, Mmax - AVERAGE OF MAXIMUM FORCES AND
 MOMENTS IN POSITIVE AND NEGATIVE DIRECTIONS



$$\frac{b}{L} = 0.184, \quad \frac{d}{L} = 0.445, \quad \beta = 0^\circ$$



$$\frac{b}{L} = 0.047, \quad \frac{d}{L} = 0.115, \quad \beta = 0^\circ$$

FIG.II COMPARISON OF TEST RESULTS USING DIFFERENT EXPERIMENTAL METHODS

CHAPTER 134

WAVE PRESSURES ON LARGE CIRCULAR CYLINDRICAL STRUCTURE

by Hiroshi Nakamura
Civil Engineering Laboratory, Central Research Institute
of Electric Power Industry, Chiba, Japan

ABSTRACT

The field observations on wave pressures on large circular cylindrical structures are performed at the cooling water intake structure for Hamaoka nuclear power plant, which is located at the coast of Pacific Ocean. In this report, the results of the field observation on wave pressures are compared with the results of the calculation by small amplitude wave theory considering wave diffraction around the cylinder.

1. Introduction

There are many researches on wave forces on circular cylinder. If the diameter of circular cylinder is small in comparison with wave length, we can neglect the deformation of wave by cylinder and express wave forces as the sum of drag force and inertial force in accordance with Morison's formula. But if the diameter of circular cylinder is large, Morison's formula become invalid, and we must consider deformation of wave around the cylinder.

Wave forces on large circular cylinder are studied by Laird,¹⁾ McCamy and Fuchs,²⁾ Bonnefille,³⁾ Nagai and others,⁴⁾ Chakrabatri,⁵⁾ Watanabe and Horikawa,⁶⁾ Yamaguchi and Tsuchiya⁷⁾ and so on. Most of these studies are theoretically or experimentally in the laboratory. Field observations on wave forces or pressures on large circular cylindrical structure are very rare.

Though it is not easy to measure all factors governing the phenomena in field observation, we can confirm the results of theoretical calculations and experiments in laboratory.

In this paper, the results of the field observations on wave pressures acting on large circular cylindrical structure are compared with the results of the calculation.

Observations were performed at the cooling water intake structure for Hamaoka nuclear power plant. It is sited at the coast of Pacific Ocean in Japan (See Fig. 1)

Cooling water intake structure is 600 m from shoreline. The water depth at this site is about 9 m and bottom slope is 1/100. The diameter of the

structure is 16 m, and its height above the bottom is 11.2 m. (See Fig. 2)

Since the diameter of this structure is large, the inertial force is rather predominant than the drag force in all wave condition if we assume that $C_M = 2.0$ and $C_D = 1.0$. So it is possible to calculate the wave pressures on the structure by McCamy and Fuchs's formula.

Intake structure has six intakes, and there is a circular projection below the intakes, and there are fenders above the still water level. So it is not simple circular cylinder. And its height above the still water level is low in order to avoid breaking wave forces. But here it is assumed that the structure is circular cylinder, and the effect of wave overtopping is neglected. Thus we compared measured pressures with calculated pressures. Of course measured pressures are due to irregular waves, and calculated pressures are due to replaced regular waves.

2. Theory

(1) Wave pressures by small amplitude wave theory.

Wave pressures around the large circular cylinder is expressed as Eg. 1., if we consider the cylindrical co-ordinate shown in Fig. 3.2)

$$\frac{P}{wH} = - \frac{1}{\pi^2 \left(\frac{D}{L}\right)} \frac{\cosh kh \left(1 + \frac{Z}{h}\right)}{\cosh kh} \cdot f\left(\theta, \frac{D}{L}\right) e^{i\sigma t} \dots (1)$$

$$f\left(\theta, \frac{D}{L}\right) = \frac{1}{H_0^2 \left(\frac{\pi D}{L}\right)} + 2 \sum_{n=1}^{\infty} (i)^n \frac{\cos n\theta}{H_n^{(2)} \left(\frac{\pi D}{L}\right)} \dots (2)$$

in which w is unit weight of water, p is wave pressure, H is height of progressive wave, L is wave length, k is wave number, σ is wave angular frequency, h is water depth, D is diameter of cylinder, $H_n^{(2)}$ is derivative of Hankel function of the second kind of orders n , n is positive integer.

(2) Dimensional analysis of wave pressure on large circular cylinder.

It is known a priori that wave pressure acting on large circular cylinder depends on the next parameters, if the roughness of structure surface is neglected,

$$\frac{P}{wH} = f_1 \left(\frac{D}{L}, \frac{h}{H}, \frac{H}{D}, \frac{\nu}{D\sqrt{gD}}, \frac{Z}{h}, \theta \right) \dots (3)$$

in which ν is coefficient of kinetic viscosity, g is acceleration of gravity.

The fourth parameter on the right-hand side of Eg. 3 may be considered to represent the ratio of the Froude number to Reynolds number. It may be disregarded as it seems to be small.

Thus the dimensionless wave pressure acting on the side of circular cylinder could be written as

$$\frac{P}{wH} = f_2 \left(\frac{L}{D}, \frac{h}{H}, \frac{H}{D} \right) \dots (4)$$

In analysis of the results of field observation, the effects of parameters in right-hand side of Eg. 4 on the value of P/wH are investigated.

3. Outline of observation

Field observations have been performed for about two years from September in 1972. (See Fig. 4)

Eight pressure gauges were attached to the side of intake structure shown in Fig. 5. Pressure gauges are strain-gauge type ones, and their range is from 0 to 2 kg/cm^2 .

Wave gauge is set up in the offing. Its distance from the shoreline is 950 m, and water depth at the wave gauge site is about 13 m. Wave heights and pressures were often observed simultaneously, and about 170 data on the vertical and horizontal pressure distributions were recorded.

Each datum was recorded for twenty minutes and we obtained highest pressures, significant pressures and so on from the records for twenty minutes.

The analysis of the results of the observations is performed on the data that the highest wave height is more than 1 m. The range of the values of the highest wave height H_{max} , wave period T_{max} , water depth h , and dimensionless parameters shown in right-hand side in Eg. 4 are as follows:

H_{max}	: 1.0 - 8.9 m	D/L_{max}	: 0.11 - 0.34
T_{max}	: 6.0 - 16.0 sec	h/H_{max}	: 1.1 - 16
h	: 8.4 - 10.0 m	H_{max}/D	: 0.06 - 0.56

in which L_{max} is a wave length of highest wave as small amplitude wave.

4. Results

In order to compare the observed values with calculated values by Eg. 1, it is assumed that the highest pressure P_{max} acting on the structure depend on the highest wave height, and the relations between dimensionless wave pressures and the dimensionless numbers shown in the right-hand side of Eg. 4 are investigated.

In obtaining above-mentioned dimensionless numbers from field data, we assume as follows :

- a. The incident waves come shown in Figure 4. In other words, point No. 2 and 4 are at $\theta = 0$.
- b. Progressive wave height at the site of intake structure equals to wave height obtained by wave gauge.
- c. Water depth at the site equals to one obtained from the tide curve at the Omaezaki Harbour, where is 8 km from the power station.

(1) Relations between D/L_{max} and $P_{\text{max}}/wH_{\text{max}}$

Relations between D/L_{max} and $P_{\text{max}}/wH_{\text{max}}$ are investigated from the field data at all pressure measured points. The relations at the point No. 2 and No. 4 are shown in Fig. 6. The curves in Fig. 6 are calculated

from Eg. 1. Upper curve corresponds to the case of observed minimum water depth, and lower curve corresponds to the case of observed maximum water depth.

The results of comparison of observed dimensionless pressures with calculated ones are as follows:

- a. Most of observed values are smaller than calculated ones at the deep part, but there are many observed values larger than calculated ones near the still water level.
 - b. In case of small values of D/L_{max} , observed values of P_{max}/wH_{max} are scattered above and below the calculated values. But in case of large values of D/L_{max} , most of observed values of P_{max}/wH_{max} are smaller than the calculated values.
- (2) Relations between h/H_{max} and P_{max}/wH_{max}

Relations between h/H_{max} and P_{max}/wH_{max} in case of $D/L_{max} \neq 0.15$ (0.14 - 0.16) and 0.20 (0.19 - 0.21) at the point No. 2 and No. 4 are shown in Fig. 7. In this figure, calculated values of P_{max}/wH_{max} are shown as solid line.

In case of small values of h/H_{max} , observed values of P_{max}/wH_{max} are smaller than calculated values. This is due to nonlinearity of wave, as pointed out by Yamaguchi and Tsuchiya.⁷⁾

In case of large values of h/H_{max} , observed values are larger than calculated ones. This reason is not clear. But it is considered that the observational error is large if the wave height is small, and that the fenders near the still water level have influence to the observed wave pressures.

- (3) Relations between H_{max}/D and P_{max}/wH_{max}

Relations between H_{max}/D and P_{max}/wH_{max} in case of $D/L_{max} \neq 0.15$ and 0.20 at the point No. 2 and No. 4 are shown in Fig. 8. In this figure, calculated values of P_{max}/wH_{max} are shown as solid line. The observed values of P_{max}/wH_{max} become smaller, as the value of H_{max}/D become larger, and in case of small values of H_{max}/D , observed values of P_{max}/wH_{max} are larger than calculated values.

- (4) Vertical and horizontal distributions of wave pressures

In case of $D/L_{max} \neq 0.15$ and 0.20, vertical distributions of observed and calculated wave pressures at $\theta = 0$ are shown in Fig. 9. Horizontal distributions of observed and calculated maximum wave pressures at the slightly lower points than still water level are shown in Fig. 10. As shown in these figures, the observed values coincide fairly well with the calculated values, or the formers are smaller than the latters in case of $h/H_{max} < 4$.

Fig. 11 shows the horizontal distributions of observed and calculated wave pressures as maximum pressures occur at $\theta = 0$. In this figure the observed values are larger than calculated values at the rear side of structure. This reason is not clear. But it is perhaps due to the waves passing through the intakes.

(5) Applicable range of Eg. 1

From the applicable point of view, it is necessary to know the applicable range of Eg. 1. Comparing all field data with the results of theoretical calculation, the applicable range is investigated. Broken lines in Fig. 7 and 8 show the upper limit of observed values of $P_{max}/\eta H_{max}$. Such limits are obtained at the another measuring points, and applicable range of Eg. 1 shown in Fig. 12 is obtained.

(6) Wave pressures on very large circular cylinder

Calculations of wave pressures on large circular cylinder by small amplitude wave theory are not so precise, as it is described already. Recently calculations of wave pressures by finite amplitude wave theory are presented, but these calculations are very complicated. So if we can use Eg. 1, it is very convenient.

The results of the calculation by Eg. 1 for the side of circular island, which has a very large diameter, are shown in Fig. 13.

REFERENCES

1. Laird, A.D.K. : A model study of wave action on a cylindrical island. Trans. of AGU, Vol. 36, No. 2, pp 270 - 285, 1955.
2. MacCamy, R.C. and R.A. Fuchs : Wave forces on piles : A diffraction theory, Tech. Memo. No. 69. B.F.B. Corps of Eng., pp. 1 - 17, 1954.
3. Bonnefille, R. and P. Germain : Wave action on isolated vertical cylinders of large dimensions, IAHR Congress, London, pp. 311 - 318, 1963.
4. Nagai, S. : Wave forces on structures, Advances in Hydrosience Vol. 9, pp. 254 - 324, 1973.
5. Chakrabatri, S.K. : Nonlinear wave forces on vertical cylinder, Proc. of A.S.C.E., Vol. 98 No. HY 11, pp. 1895 - 1909, 1972.
6. Watanabe, A. and K. Horikawa : Breaking wave forces on a large diameter cell, 14th International Conference on Coastal Engineering, Chap. 102, 1974.
7. Yamaguchi, S. and Y. Tsuchiya : Nonlinear effect of wave on wave pressure and wave force on a large cylindrical pile (in Japanese), Proc. of Japan Society of Civil Engineering, No. 229, pp. 41 - 53, 1974.

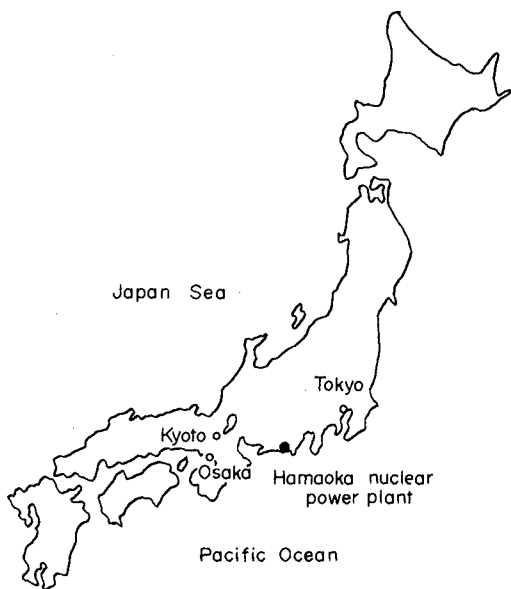


Figure 1. Location of Hamaoka nuclear power plant.

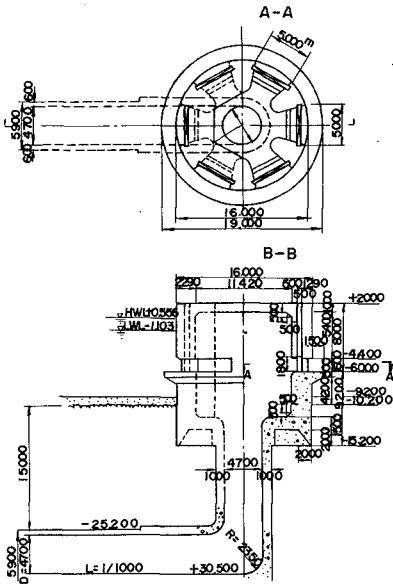


Figure 2. Intake structure of Hamaoka nuclear power plant

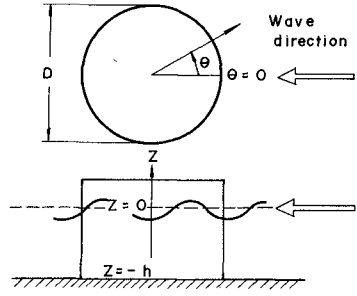


Figure 3. Cylindrical Coordinate

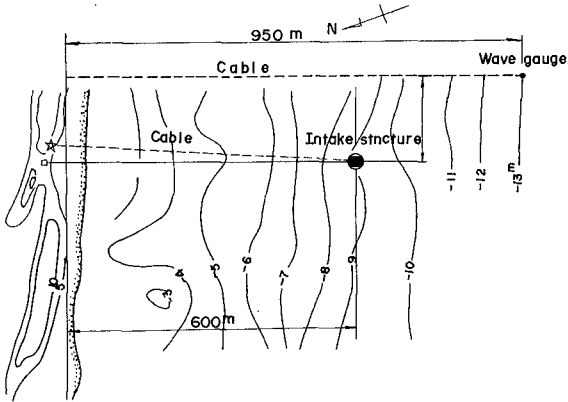


Figure 4. Position of intake structure

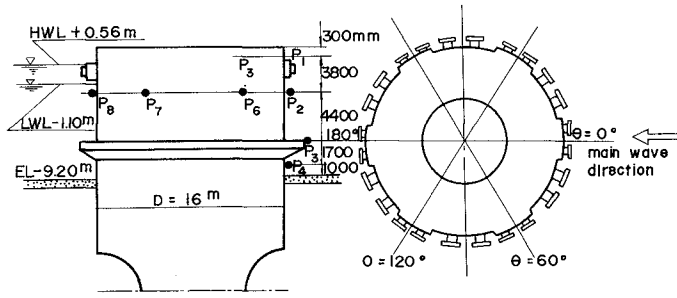


Figure 5. Position of pressure gauges

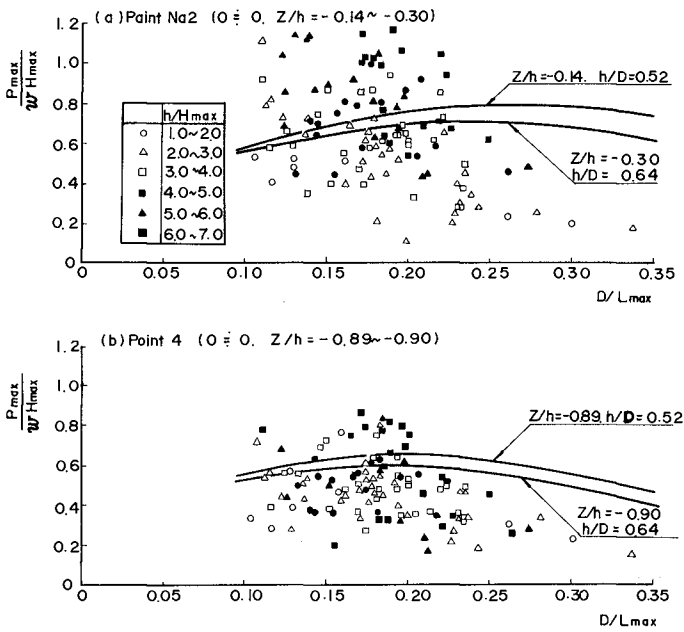


Figure 6. Relation between D/L_{max} and P_{max}/wH_{max}

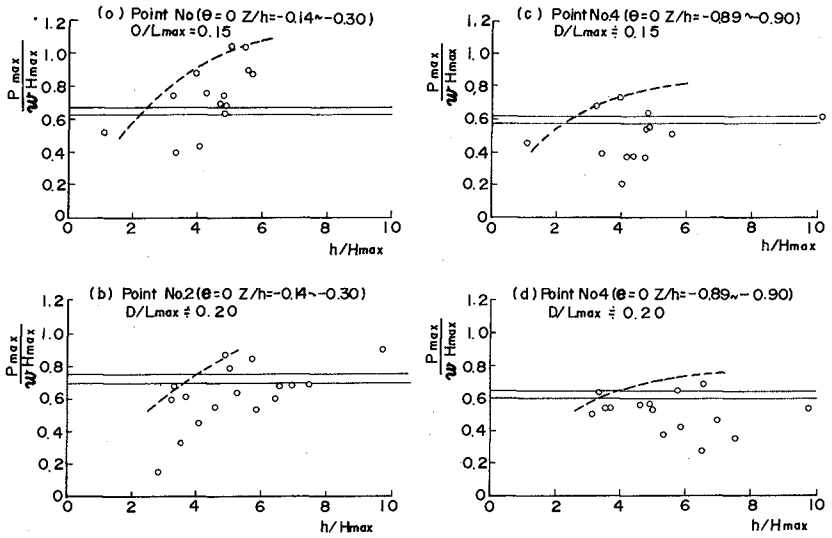


Figure 7 Relation between h/H_{max} and P_{max}/wH_{max}

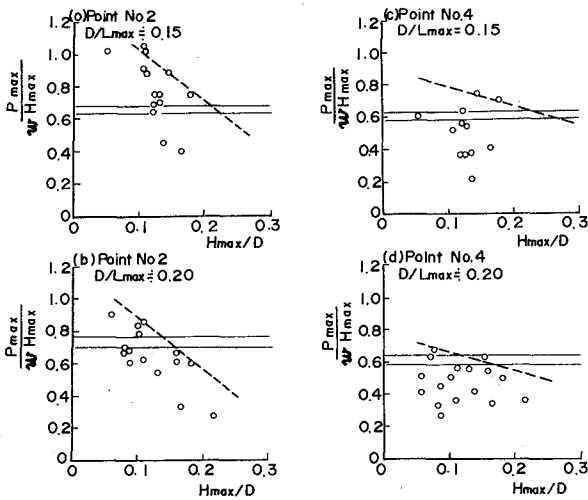


Figure 8, Relation between H_{max}/D and P_{max}/wH_{max}

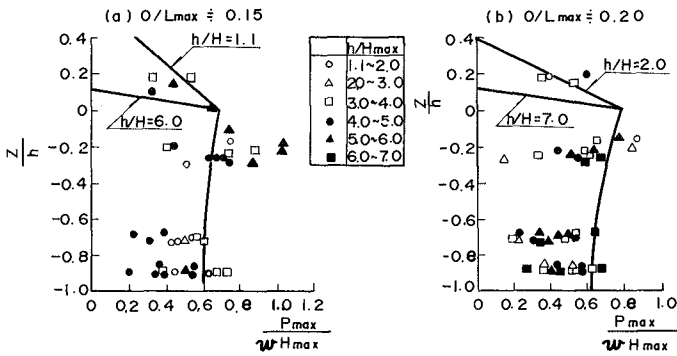


Figure 9. Vertical distribution of wave pressures

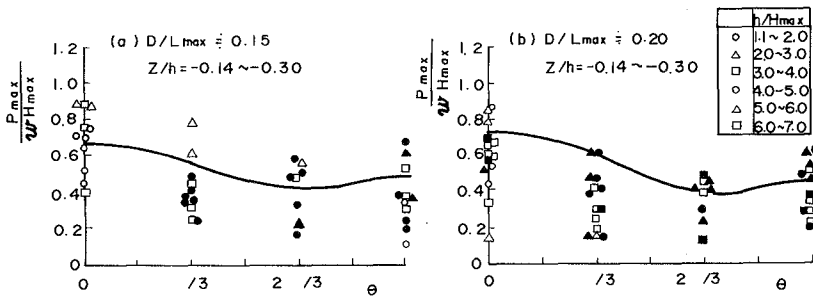


Figure 10. Horizontal distribution of wave pressures

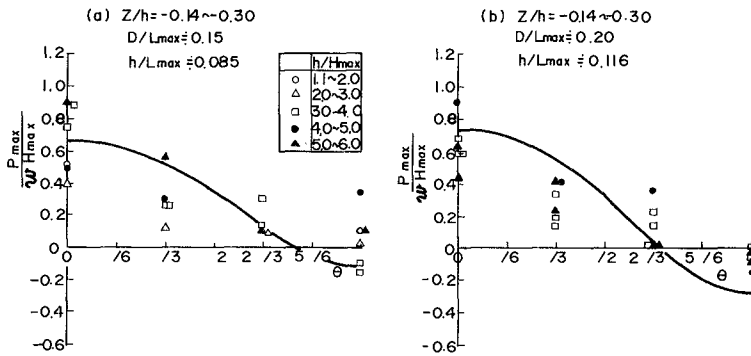


Figure 11. Horizontal distribution of wave pressures as maximum pressure occurs at $\theta = 0$

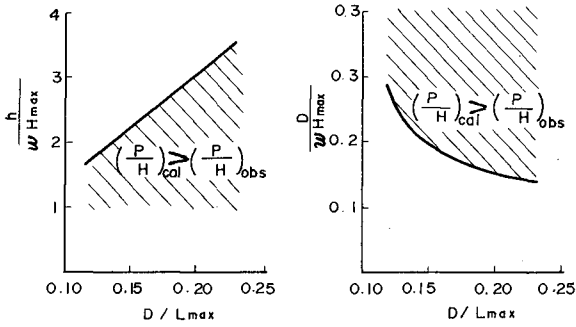


Figure 12 Applicable range of equation (1)

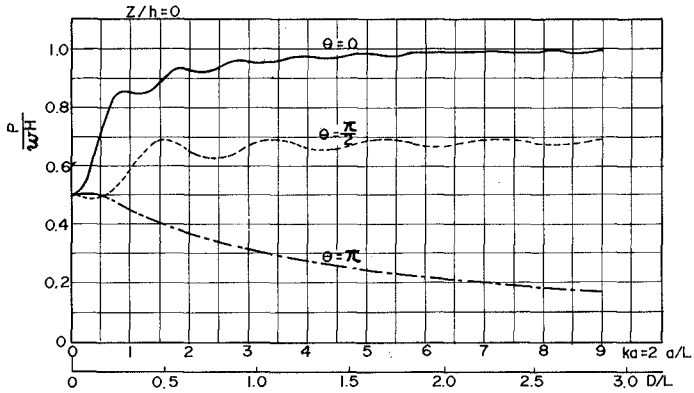


Figure 13 Relation between D/L and P/wH

CHAPTER 135

FORCES ON ROUGH-WALLED CIRCULAR CYLINDERS

IN HARMONIC FLOW

by

Turgut Sarpkaya

Distinguished Professor of Mechanical Engineering
Naval Postgraduate School, Monterey, California

ABSTRACT

This paper presents the results of an extensive experimental investigation of the in-line and transverse forces acting on sand-roughened circular cylinders placed in oscillatory flow at Reynolds numbers up to 1,500,000, Keulegan-Carpenter numbers up to 100, and relative roughnesses from 1/800 to 1/50. The drag and inertia coefficients have been determined through the use of the Fourier analysis and the least squares method. The transverse force (lift) has been analysed in terms of its maximum and root-mean-square values. In addition, the frequency of vortex shedding and the Strouhal number have been determined.

The results have shown that all of the coefficients cited above are functions of the Reynolds number, Keulegan-Carpenter number, and the relative roughness height. The results have also shown that the effect of roughness is quite profound and that the drag coefficients obtained from tests in steady flow are not applicable to harmonic flows even when the loading is predominantly drag.

INTRODUCTION

The prediction of the forces generated by waves and currents remains as a basic problem in marine hydrodynamics. The complexity of the problem stems partly from the difficulty of accurately defining the kinematics of the flow field, partly from the difficulty of accounting properly for the effects of time-dependent separation and vortex shedding, and partly from the difficulty in extrapolating the laboratory findings to various conditions of the marine environment where three-dimensional effects and reduced spanwise coherence play important roles.

The methods based on diffraction theory and classical hydrodynamics are applicable only to relatively simple cases, irrespective of the size and shape of the structure, where separation does not play an appreciable

role. It is a well-known fact that the shear-layer instability and the non-linear interaction between the shear layers lead to vortex shedding in steady flow past bluff bodies. The general characteristics of this shedding mechanism are fairly well understood through measurements, flow visualization, and numerical experiments for various bluff bodies, in particular for a circular cylinder held normal to the ambient flow. Any effect, such as the periodicity of flow, which interferes with the production of vorticity, position of the separation points, shear-layer instability, and the feedback mechanism causes additional time and history dependent non-linear interactions. The net effect of these interactions is to change the vortex shedding and hence the vortex-induced oscillations in both the forces and structure in both the in-line and transverse directions. The problem is not yet amenable to mathematical analysis and requires experiments of high intrinsic quality for at least a partial understanding of its many perplexing aspects.

Much of the present knowledge on separated harmonic flows has been obtained by means of model tests at Reynolds numbers generally two to three orders of magnitude smaller than prototype Reynolds numbers. These model tests have relied heavily on the so-called Morison formula for expressing the force as the sum of a drag and inertia force. The values of the drag and inertia coefficients to be used in the Morison equation became the subject of many experimental studies in the last twenty years. The correlation of these coefficients with the relative amplitude of the waves (or the Keulegan-Carpenter number, hereafter referred to as K) has been generally inconclusive [1]. Furthermore, lift forces which are associated with vortex shedding have received relatively little attention. It thus became clear that much is to be gained by considering plane oscillatory flow about cylinders at high Reynolds numbers in order to isolate the influence of individual factors such as relative amplitude, Reynolds number, relative roughness, spanwise correlation, wall-proximity, etc. on vortex shedding and resistance. It is with this realization that a broad research program was undertaken to study the characteristics of periodic flow about bluff bodies.

The results obtained with smooth cylinders in two U-shaped water tunnels have been previously reported by Sarpkaya [2-6]. The preliminary results obtained with rough-walled cylinders for one particular value of K , ($K = 50$), through the use of various types of distributed roughness elements (sand, sand paper, and polystyrene beads) have also been reported in [3] and [4].

The present paper deals with in-line and transverse forces acting on sand-roughened circular cylinders in harmonic flow in the range of Reynolds numbers from 10,000 to 1,500,000; K values from about 4 to 100; and relative sand roughnesses from 1/800 to 1/50.

BACKGROUND ON THE EFFECTS OF ROUGHNESS

Of the scores of papers dealing with fluid loading on offshore structures (see the reviews by Grace [7] and Hogben [8]), none seems to have treated the effect of roughness on the force-transfer coefficients. Yet it is a fact that the structures in the marine environment become gradually covered with rigid as well as soft excrescences. Thus, the fluid loading due to identical ambient flow conditions may be significantly different from that experienced when the structure was clean partly because of the 'roughness effect' of the excrescences on the flow and partly because of the increase of the 'effective diameter' of the elements of the structure.

In the absence of any data appropriate to the harmonic or wavy flows, it has been assumed that "the drag coefficients obtained from tests in steady flow" over artificially - or marine-roughened cylinders "are applicable to wave flows at least when the loading is predominantly drag" [9].

It is not generally appreciated that the consequences of all "nearly steady flows" are not always identical to those of "steady flows." The case in point is the harmonic flow under consideration. Even for large amplitudes of oscillations, there is only a finite vortex street comprised of vortices of nearly equal strength due to the "nearly steady" nature of the flow. As the flow reverses, the situation is not that of a uniform flow (with or without free stream turbulence) approaching a roughened cylinder but rather that of a finite vortex street approaching a rough-walled cylinder. Such a flow cannot be regarded identical to steady flow with some turbulence of fairly uniform intensity and scale as the present results show.

It is instructive to briefly review the salient features of the influence of roughness on the cross-flow around a cylinder in steady flow in order to delineate the differences between the steady and harmonic flow about rough-walled cylinders.

Among others, primarily the experiments of Fage and Warsap [10], Achenbach [11], Szechenyi [12], and Güven et al. [13] have shown that roughness in steady flow about a cylinder precipitates the occurrence of 'drag crisis' and gives rise to a minimum drag coefficient which is larger than that obtained with a smooth cylinder. This is partly because of the transition to turbulence of the free shear layers at relatively lower Reynolds numbers due to disturbances brought about by the roughness elements and partly because of the retardation of the boundary-layer flow by roughness (higher skin friction) and, hence, earlier separation. Evidently, the drag crisis in steady flow about a roughened cylinder is a state even more precarious than that for a smooth cylinder for the occurrence of a laminar-separation and turbulent reattachment bubble is hastened by the retardation of the flow by roughness. It is also evident that the Reynolds number must be sufficiently high for a given roughness to bring about a drag crisis.

The conditions leading to the occurrence of the drag crisis are therefore quite important. Not only the relative size of the roughness elements but also their shape and distribution may be quite important in addition to the parameters characterizing the ambient flow about an otherwise smooth bluff body. It is in fact partly for the difficulty of uniquely specifying the 'roughness' and partly for the differences in other test conditions (free stream turbulence, relative length of the cylinder, end gaps, etc.) that there are considerable differences between the data reported by various workers, particularly in the drag crisis region. For example, the effective surface roughness may be larger or smaller than the nominal relative roughness based on the geometric size of the roughness element depending on the shape and arrangement of the roughness elements [14]. Also, a higher turbulence level precipitates the drag crisis. Thus, the critical range is wider for higher free stream turbulence [13]. Attempts have been made [14] to experimentally determine an equivalent sand-grain roughness through the use of uniform flow in a channel. An equivalent roughness determined in this manner may not necessarily give a meaningful measure of the effect of roughness as far as the boundary layer flow over a circular cylinder is concerned.

In the supercritical and transcritical regions, the drag coefficient for a roughened cylinder is considerably larger than that for a smooth cylinder primarily because of the larger wake which is brought about by the earlier separation due to the retardation of the boundary layer. Several facts are worth noting. Firstly, the transcritical drag coefficient depends on both the character of the flow and the surface condition of the cylinder. In other words, the particular value of the transcritical drag coefficient in steady flow over a roughened cylinder is not necessarily identical to that for a time-dependent flow over the same cylinder. Experiments with steady flow over roughened cylinders show that the drag coefficient in the transcritical region returns more or less to its steady sub-critical value. Other flows may exhibit a similar behavior provided that the spanwise coherence is maintained. In other words, the subcritical value of the drag coefficient for a given flow may give an indication of its transcritical value for the same flow over a roughened cylinder. Evidently, what is specified here is the functional dependence of velocity on time and not the magnitude of the characteristic velocity.

Secondly, the larger the effective roughness, the larger is the retardation of the boundary layer. This leads to earlier separation and larger drag coefficient. Thirdly, the pressure distribution about the cylinder is affected not only by the location of the separation point but also by the development of the retarded boundary layer ahead of separation [13]. This in turn is affected not only by all the parameters characterizing the roughness but also by the character of the ambient flow (time-dependence, angle of attack, shear, turbulence, just to name a few of the parameters).

It seems from the foregoing that the disturbances generated by the roughness elements cause an incalculable change in the critical region of

the flow and that a more thorough examination of the one-parameter characterization of roughness, k/D , is required in order to understand the effect of roughness, because the packing, size distribution, and shape may be important. Although, wind- and water-tunnel experiments on flow past rough-walled cylinders have been made for about 50 years, there is still a lack of precision in the definition of even the roughness let alone the force and pressure coefficients. The purpose of this paper is not to study this question but rather to show, among other things, that different types of roughness elements (sand paper, polystyrene beads, sand) can give rise to different drag-coefficient curves in the critical region appropriate to the particular flow. It is in fact partly for this reason that it has been thought advisable to investigate afresh the effect of roughness on cylinders in harmonic flow using only sand of uniform size and packing rather than three different types of roughness [3].

IN-LINE AND TRANSVERSE FORCES AND GOVERNING PARAMETERS

The in-line force which consists of the drag force F_d and the inertia force F_i is assumed to be given by [15]

$$F = F_d + F_i = 0.5C_dLD\rho|U|U + 0.25C_mLD^2\pi\rho.dU/dt \quad (1)$$

in which C_d and C_m represent respectively the drag and inertia coefficients and U the instantaneous velocity of the ambient flow. For an oscillating flow represented by $U = -U_m\cos\theta$, with $\theta = 2\pi t/T$, the Fourier averages of C_d and C_m are given by Keulegan and Carpenter as [16]

$$C_d = -0.75 \int_0^{2\pi} (F_m \cos\theta / \rho U_m^2 LD) d\theta \quad (2)$$

and

$$C_m = (2U_m T / \pi^3 D) \int_0^{2\pi} (F_m \sin\theta / \rho U_m^2 LD) d\theta \quad (3)$$

in which F_m represents the measured force.

The method of least squares consists of the minimization of the error between the measured and calculated forces. This procedure yields [5]

$$C_{dls} = -(8/3\pi) \int_0^{2\pi} (F_m |\cos\theta| \cos\theta / \rho DLU_m^2) d\theta \quad (4)$$

and $C_{m|s} = C_m$. Evidently, the Fourier analysis and the method of least squares yield identical C_m values and that the C_d values differ only slightly.

The transverse force has been expressed in terms of the maximum lift coefficient defined by

$$C_L = (\text{maximum amplitude of the transverse force in a cycle}) / (0.5\rho DLU_m^2) \quad (5)$$

In addition, the frequency of the oscillations of the transverse force and the Strouhal number have been evaluated.

It is recognized that the coefficients cited above are not constant throughout the cycle and are either time-invariant averages or peak values at a particular moment in the cycle. A simple dimensional analysis of the flow under consideration shows that the time-dependent coefficients may be written as

$$F/(0.5DL\rho U_m^2) = f(U_m T/D, U_m D/\nu, k/D, t/T) \quad (6)$$

in which F represents the in-line or the transverse force. Equation (6), combined with Eq. (1), assuming for now that the latter is indeed valid, yields

$$C_d = f_1(K, Re, k/D, t/T) \quad (7)$$

$$C_m = f_2(K, Re, k/D, t/T) \quad (8)$$

in which $K = U_m T/D$ and $Re = U_m D/\nu$, and k/D represents the relative roughness. Evidently, it is assumed that the effect of roughness may be characterized by the parameter k/D alone, with k defined as the average grain size. Experiments necessary to obtain an equivalent sand height or some other representative length are costly and time consuming and are not available for the oscillating flow data analysed here.

There is no simple way to deal with Eqs. (7) and (8) even for the most manageable time-dependent flows. Another and perhaps the only other alternative is to eliminate time as an independent variable and consider suitable time-invariant averages as given by Eqs. (2), (3), and (4). Thus, one has

$$[C_d, C_m, C_L, \dots] = f_i(K, Re, k/D) \quad (9)$$

It appears, for the purposes of Eq. (9), that the Reynolds number is not the most suitable parameter involving viscosity. The primary reasons for this are that the effect of viscosity is relatively small particularly for $Re < 20,000$ and that U_m appears in both K and Re . Thus, replacing Re by $\beta = Re/K = D^2/\nu T$ in Eq. (9), one has

$$C_i(\text{a coefficient}) = f_i(K, \beta, k/D) \quad (10)$$

in which $\beta = D^2/\nu T$ and shall be called the 'frequency parameter.'

From the standpoint of dimensional analysis, either the Reynolds number or β could be used as an independent variable. Evidently, β is constant for a series of experiments conducted with a cylinder of diameter D in water of uniform and constant temperature since T is kept constant in a U-shaped oscillating flow tunnel. Then the variation of a force coefficient with K may be plotted for constant values of β . Subsequently, one can easily recover the Reynolds number from $Re = \beta K$ and connect the points, on each $\beta = \text{constant}$ curve, representing a given Reynolds number.

From the standpoint of the laminar boundary layer theory, β represents

the ratio of the rate of diffusion of vorticity through a distance δ (the boundary layer thickness) to the rate of diffusion through a distance D . This ratio is also equal to $(D/\delta)^2$ and, when it is large, gradients of velocity in the direction of flow are small compared with the gradients normal to the boundary, a situation to which the boundary layer theory is applicable. It should also be noted in passing that β is of special importance even for oscillations at very low Reynolds numbers. For example, for a cylinder or sphere undergoing harmonic oscillations without separation in a fluid otherwise at rest, the added mass and drag coefficients are uniquely determined in terms of β [17, 18].

A re-analysis of the data given by Keulegan and Carpenter [16] through the use of β , K , and Re in the manner just described clearly shows [3, 4] that (a) C_d depends on both K and Re and decreases with increasing Re for a given K ; and that (b) C_m depends on both K and Re for K larger than approximately 15 and decreases with increasing Re . A similar analysis of Sarpkaya's data [2] also shows that C_d and C_m depend on both K and Re and that C_m increases with increasing Re . Notwithstanding this difference in the variation of C_m between the two sets of data, these results put to rest the long standing controversy regarding the dependence or lack of dependence of C_d and C_m on Re and show the importance of β as one of the governing parameters in interpreting the data, in interpolating the K values for a given Re , and in providing guide lines for further experiments as far as the ranges of K and β are concerned.

BRIEF DESCRIPTION OF THE EXPERIMENTAL ARRANGEMENT

The oscillating flow system consisted of a large U-shaped vertical water tunnel with a 3 ft by 3 ft test section. The cross-section of the two vertical legs is twice that of the test section. The two corners of the tunnel were carefully streamlined to prevent flow separation. The auxiliary components of the tunnel consisted of plumbing for hot and cold water, butterfly-valve system, and the air-supply system. Oscillations in the tunnel were obtained through the use of the butterfly valves (mounted on top of one of the legs of the tunnel) and a rack and pinion system actuated by an air-driven piston and a three-way control valve. The fluid oscillated smoothly with a period of $T = 5.500$ seconds. The elevation, acceleration, and the in-line and transverse forces were monitored continuously by means of appropriate transducers. The analogue traces were absolutely free from secondary oscillations so that no filters were used between the outputs of the transducers and the recording equipment (see sample trace in Fig. 1).

Circular cylinders with diameters ranging in size from 2 inches to 6.5 inches have been used in this study. The cylinders were turned on a lathe from aluminum pipes or plexiglass rods. The length of each cylinder was such that it allowed 1/32 inch gap between the tunnel wall and each end of the cylinder. A doubleball precision bearing was inserted at each end of the cylinder in aluminum housings which sealed the cylinder air tight.

In view of the discussion concerning the one-parameter characterization of the roughness in terms of k/D , it was decided to use only one type of roughness element. The possible use of sandpaper, glass beads, wire screens, etc. was disregarded for they would have exhibited different packing as well as different size distribution characteristics. Clean sand was sieved through the use of standard ASTM sieves in order to obtain a given grain size.

Each cylinder was mounted horizontally on a specially constructed, manually operated, rotating apparatus and covered with a thin layer of air-drying epoxy resin using a brush. When the epoxy coating reached a certain degree of consistency, then the finely pre-sieved sand was transferred into a slightly larger sieve and sprinkled over the rotating cylinder. Within about 10 minutes, the epoxy hardened and the cylinder was left alone for the epoxy to cure. Then the cylinder surface was cleaned to remove excess sand and extra sand particles that at times attached to each other forming an easily breakable spike. This procedure has been followed for all cylinders and has invariably resulted in cylinders of roughness with perfect uniformity. A sample photograph of the rough surface, taken with a scanning electron microscope, is shown in Fig. 2.

In order to determine the variation of the force coefficients with Reynolds number for a given Keulegan-Carpenter number and relative roughness, all cylinders were tested at the same relative roughnesses ($k/D = 1/800, 1/400, 1/200, 1/100,$ and $1/50$), and the experiments were carried out at three or four water temperatures.

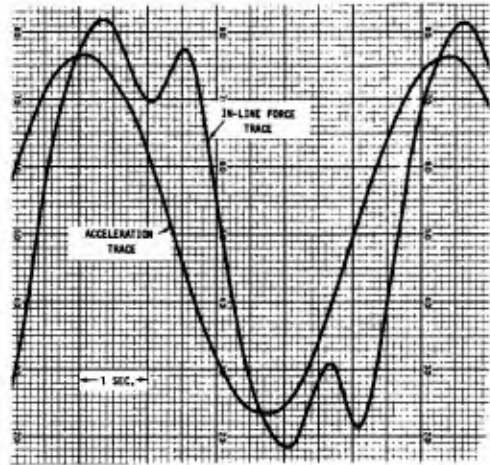


Fig. 1 Sample in-line force and acceleration traces.

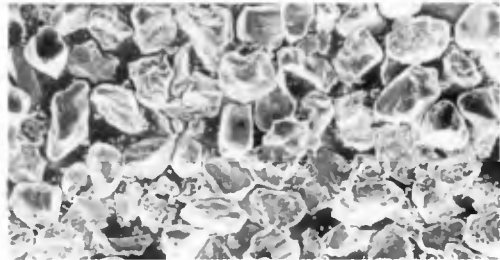


Fig. 2 Distribution of sand particles, ($k = 0.0055$ inch).

Two identical force transducers, one at each end of the cylinder, were used to measure the instantaneous in-line and transverse forces. The gages had a capacity of 500 Lbf with an overload capacity of 200 percent. The deflection of the gages under 500 Lbf load was 0.01 inch. For the largest cylinder and amplitude encountered in the experiments, the maximum load was less than 200 Lbf, and the deflection of the beam was less than 0.008 inches.

The in-line and transverse forces were simultaneously recorded with the instantaneous acceleration on two two-channel Honeywell recorders running at a speed of 10 divisions per second. The amplitude of the transverse force, instantaneous value of the in-line force, and the flow characteristics such as $U_m T/D$ and Re were determined from these traces. The root-mean-square value of the lift force was determined for each cycle by reading the force at every division or 0.1 second intervals.

Three transducers were used to generate three independent d.c. signals, each proportional to the instantaneous value of the elevation, velocity, and acceleration. These transducers were calibrated and their linearity checked before each series of experiments. In addition, the velocity at the test section was directly measured with a magnetic velocity meter. Suffice it to say that all four methods gave nearly identical results and yielded the amplitude, velocity, or acceleration, to an accuracy of about two percent relative to each other. These comparisons, as well as the perfectly sinusoidal and noise-free character of all pressure and force traces, speak for the suitability of the unique test facility used in this study. The additional details of the apparatus and procedure are given in Ref. [3].

DISCUSSION OF THE RESULTS

The drag and the inertia coefficients, obtained through the use of equations (2) and (3) have been plotted for each cylinder and relative roughness as a function of K for various constant values of β . Then the Reynolds number for a particular value of K has been calculated simply through the use of $Re = K\beta$. As described earlier, such a procedure enables one to express C_d or C_m as a function of the Reynolds number for a given K and k/D . In view of the fact that each coefficient depends on at least three independent parameters (Re , K , and k/D), it is not possible to show on two-dimensional plots the variation of either C_d or C_m for all values of Re , K , and k/D . However, this difficulty is alleviated by the fact that the variation of a given force coefficient for a given Re and k/D is not very strong from one K to another. Thus it has been decided to choose five representative K values, namely $K = 20, 30, 40, 60,$ and 100 , to present the variation of C_d and C_m with Re .

Figures 3 through 12 show C_d and C_m for five values of K as a function of the Reynolds number. Each curve on each plot corresponds to a particular relative roughness. Also shown on each figure is the corresponding drag or inertia coefficient for the smooth cylinder at the corresponding K value.

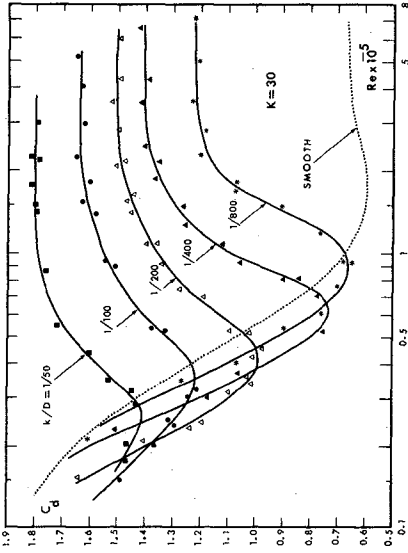


Fig. 5 C_d versus Re for $K = 30$.

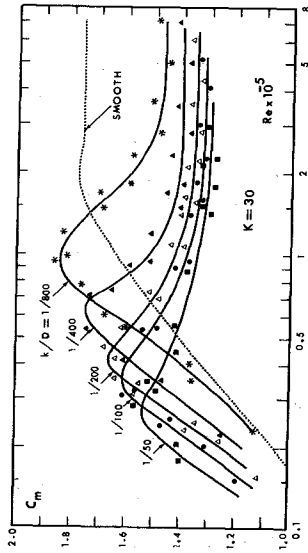


Fig. 6 C_m versus Re for $K = 30$.

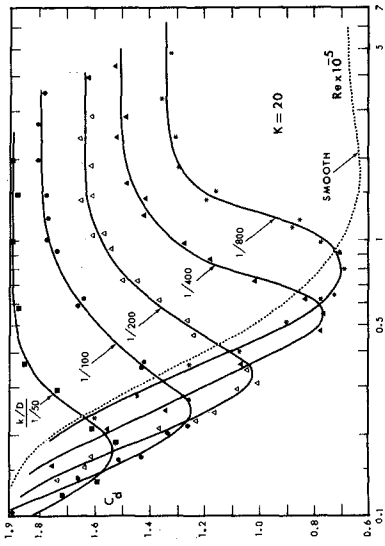


Fig. 3 C_d versus Re for $K = 20$.

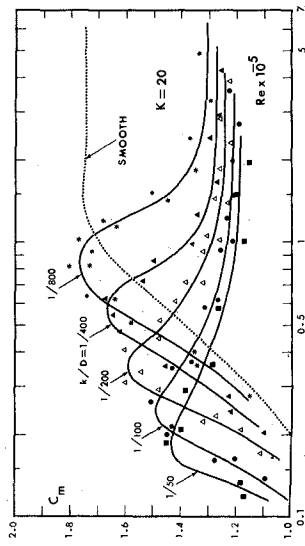


Fig. 4 C_m versus Re for $K = 20$.

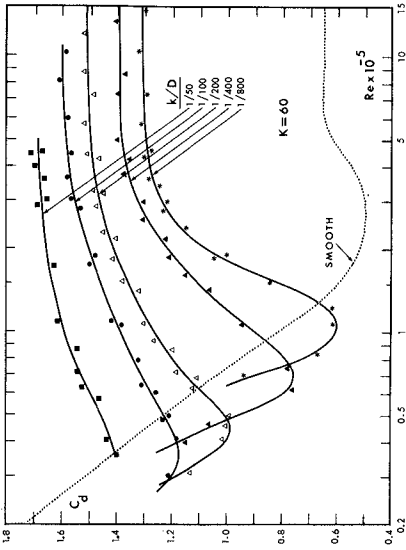


Fig. 9 C_d versus Re for $K = 60$.

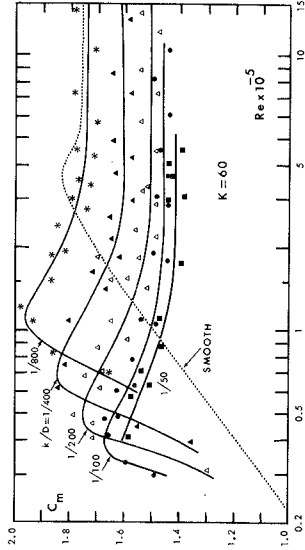


Fig. 10 C_m versus Re for $K = 60$.

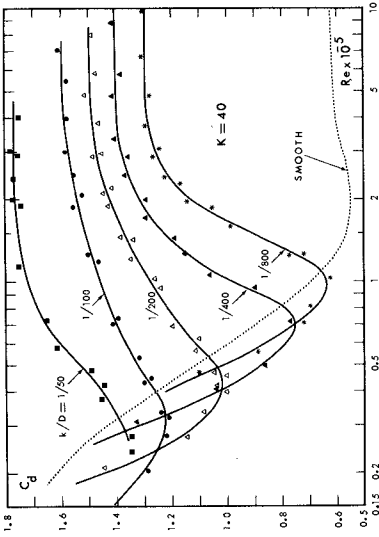


Fig. 7 C_d versus Re for $K = 40$.

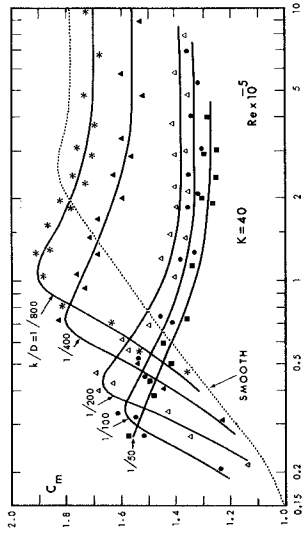


Fig. 8 C_m versus Re for $K = 40$.

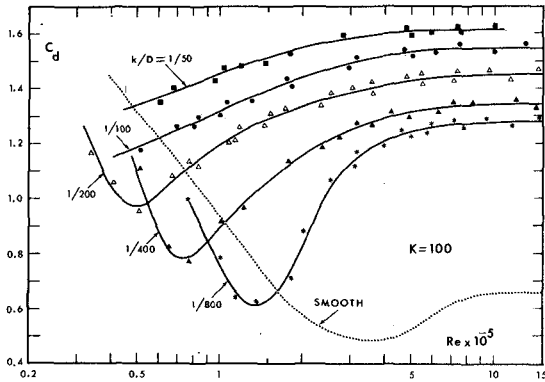


Fig. 11 C_d versus Re for $K = 100$.

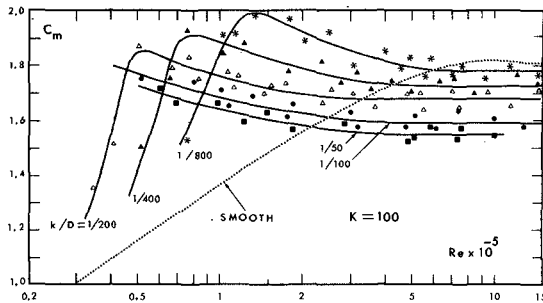


Fig. 12 C_m versus Re for $K = 100$.

The $k/D = \text{constant}$ curves on each C_d plot are quite similar to those found for steady flow about rough cylinders [10-13]. For a given relative roughness, the drag coefficient does not significantly differ from its smooth cylinder value at very low Reynolds numbers. As the Reynolds number increases, C_d for the rough cylinder decreases rapidly, goes through the region of drag crisis at a Reynolds number considerably lower than that for the smooth cylinder and then rises sharply to a nearly constant transcritical value. The larger the relative roughness the larger is the magnitude of the minimum C_d and the smaller is the Reynolds number at which that minimum occurs. However, there appears to be a minimum Reynolds number below which the results for rough cylinders do not significantly differ from those corresponding to smooth cylinders. In other words, the Reynolds number must be sufficiently high for the roughness to play a role on the drag and

flow characteristics of the cylinder.

The figures for the drag coefficient also exhibit a few other interesting features. First, even a relative roughness as small as $1/800$ can give rise to transcritical drag coefficients which are considerably higher than those for the smooth cylinder. Secondly, the asymptotic values of the drag coefficient for roughened cylinders (e.g., $k/D = 1/100$), within the range of Reynolds numbers encountered, can reach values which are considerably higher than those obtained with steady flows over cylinders of similar roughness ratios. In other words, it is not safe to assume that the transcritical drag coefficient in harmonic flows will be identical to those found in steady flows and will not exceed a value of about unity. On the basis of the present results it may be said that such a conjecture is not accurate even for K values as large as 100 (corresponding to a wave height-to-diameter ratio of about 30). It is therefore important to remember that the effect of roughness depends not only on the relative size of the roughness element but also on the characteristics of the ambient flow as well as on the body about which this flow takes place. The characteristics of the ambient flow determine to a large extent the state of the flow (subcritical, critical, and transcritical) during a given cycle of oscillation. The geometry of the body dictates, together with the flow, the variation with time of the separation points. It is therefore not easy to draw a parallel between the behavior of steady flow and that of harmonic flow over a smooth and rough cylinder. In fact, the steady as well as the oscillating flow results for rough cylinders show that, in either case, the transcritical drag coefficient nearly returns to its subcritical values.

The Reynolds number at which the drag crisis occurs gives rise to an 'inertia crisis.' In other words, for a given relative roughness, C_m rises rapidly to a maximum at a Reynolds number which corresponds to that at which C_d drops to a minimum. At relatively higher Reynolds numbers, C_m decreases somewhat and then attains nearly constant values which are lower than those corresponding to the smooth cylinders. It is also apparent from the inertia coefficient curves that the smaller the relative roughness the larger is the maximum inertia coefficient. For relatively smaller roughnesses such as $k/D = 1/800$, the terminal value of C_m is nearly equal to that of a smooth cylinder. The behavior of C_m is not entirely unexpected. It has long been noted [16] that whenever there is a rise in the drag coefficient, there also is a decrease in the inertia coefficient.

Before closing the discussion of the drag and inertia coefficients, it is necessary to point out the remarkably consistent behavior of the data points, particularly for C_d . Perhaps it would not have been too surprising had the data been obtained for one relative roughness through the use of only one cylinder. In the present investigation, the use of several cylinders and several temperatures for a given cylinder always provided data for nearly identical k/D , Re , and K values. For instance, the C_d and C_m values obtained at a given K , Re , and relative roughness k/D ,

using a 5 inch cylinder at a low temperature corresponds to the C_d and C_m values using a 4-inch cylinder at a high temperature. Remembering the fact that not only the actual size of the cylinders but also the size of the sand grains differed in order to obtain the same k/D , and the fact that the experiments were carried out at different temperatures and times, one fully realizes that the correlation of the data and the relatively small scatter are indeed quite remarkable. This is due not only to the repeatability of the tests but also due to the vibration-free operation of the entire tunnel system.

The correlation length along the cylinders was not directly measured. However, one series of experiments was conducted with a 2.18-diameters (12 inches) long, centrally located, section of a 5.5 inch cylinder which 'floated' on the ends of the force transducers with small gaps (1/32 inch) between the section and the rest of the rigidly supported 12-inch long sections. The floating and the dummy sections were coated with sand for a relative roughness of $k/D = 1/100$. The comparison of the lift, drag, and inertia coefficients obtained with the short section with those obtained with the longer section spanning the entire test section has shown (at least for five Reynolds numbers, five K values, and one k/D) that the two sets of coefficients are nearly identical. Evidently, the force-cancelling effects of phase shifts which may have been brought about by three-dimensional effects were either insignificant or non-existent. Thus, it is concluded that both the three-dimensionality effects and the boundary-layer effects play very little or no role in the present experiments. However, the comparison of the results shown in Figs. 3 through 12 with the previously reported [4, 6] preliminary results for $K = 50$ alone indicates the effect, particularly in the drag-crisis region, of the type of roughness element used on the variation of the force-transfer coefficients with the Reynolds number. Previously, sand paper, sand, and polystyrene beads were used as roughness elements for a given cylinder in order to achieve the desired relative roughness in a given Reynolds number range. A detailed study of the effective roughness of each type of roughness element and the discussions with the manufacturer have shown that the effective roughness of the sand paper is larger than the height of the mean sand particles applied on it. Furthermore, the gluing of the sand paper on the cylinder invariably resulted in a 'joint' along the cylinder which might have generated larger disturbances and promoted earlier transition. The polystyrene beads, on the other hand, present an effective-roughness height which is often smaller than their actual size [14]. In spite of these differences in the 'effective roughness' of various types of roughness elements, however, the terminal values of the drag coefficients in the transcritical region remained practically the same for a given actual effective relative roughness whether the data were obtained with sand alone or with a combination of other roughness elements. Evidently, it will be most interesting and desirable to carry out similar experiments with cylinders roughened in the ocean environment. The testing of such cylinders with steady uniform flow [9] is not sufficient for the purposes under consideration, namely the determination of the fluid loading on offshore structures.

APPLICABILITY OF MORISON'S EQUATION

Since its inception, questions have been raised regarding the applicability of Morison's equation to time-dependent flows in general and to wavy flows in particular. It has been known that the equation predicts quite accurately the in-line force for both very small values of K (K smaller than about 10) and for large values of K (K larger than about 20). For intermediate values of K , differences have been observed between the measured and calculated values. These differences have been attributed either to the imprecise measurement of the kinematics of the flow or to the shortcomings of the equation. It is now realized that not only these two factors (namely the heuristic nature of the equation and the difficulty of measuring the local velocities and accelerations) but also the three-dimensional nature of the wavy flows and decreased spanwise coherence must be partly responsible for the differences between the measured and calculated forces. In fact, it would have been extremely difficult to draw meaningful conclusions concerning the applicability of Morison's equation through the use of the field data. It is only through the use of carefully conducted two-dimensional harmonic flow experiments that one can ascertain the degree of applicability of Morison's equation.

Figure 13 shows the calculated and measured forces normalized by $0.5\rho D L U_m^2$ together with the normalized velocity and the difference between the measured and calculated forces for a relatively large value of K . It is evident that there is often a remarkable correspondence between the measured and predicted forces particularly for K values larger than about 20. This is also true for K values smaller than about 10. In the disturbance-sensitive region of vortex formation, the onset of asymmetry ($K \approx 4.5$) and the subsequent growth and shedding of single or alternating vortices have profound effects not only on the measured in-line force but also on the coefficients calculated. Morison's equation assumes that the in-line force F is an odd harmonic function, i.e., $F(\theta) = -F(\theta+\pi)$, for a flow represented by $U = -U_m \cos\theta$. Thus, the drag and inertia coefficients calculated through the use of an in-line force for which $F(\theta) \neq -F(\theta+\pi)$ are not quite correct. Thus, it is clear that part of the reason for the larger differences between the measured and calculated forces even in two-dimensional harmonic flows is due to the use of the force-coefficient expressions [Eqs. (2) and (3)] which are derived by assuming the in-line force to be given by an odd harmonic function. In the range of K values from about 10 to 20, particularly for low values of Re , this assumption is not quite correct as evidenced by the present experiments [3, 4, 6].

The reason for the asymmetry in the magnitude of the in-line force and the differences between the measured and calculated forces is primarily the fractional shedding of vortices and vortex induced oscillations in the in-line force. It is a well-known fact that in steady flow the vortex shedding causes a gradient of fluctuating pressure across the body and gives rise to periodic force fluctuations in the in-line force. In harmonic flow, the fully grown vortices move back and forth about the cylinder and do not necessarily shed alternately. Thus, it is possible that the oscillations in the in-line force due to eddy shedding are relatively larger than those in steady flow. The effect of these oscillations may be incorporated into Eq. (1) as follows,

$$F/(0.5\rho DLU_m^2) = (\pi^2 D/U_m T) C_m \sin\theta - C_d |\cos\theta| \cos\theta - \eta C_L \cos(St.K.\theta - \phi) \quad (11)$$

in which η represents a coefficient, ηC_L the amplitude of the normalized difference between the measured and calculated forces, St the Strouhal number defined by fD/U_m with f as the frequency of lift oscillations, and ϕ the phase angle. In the range of K values from 10 to about 15, $St.K$ should be taken equal to 3. For larger values of K , $St.K$ may be taken equal to $0.20K$. Extensive calculations through the use of appropriate values of the parameters cited above with $\eta = 0.1$ have shown that the above equation considerably reduces the difference between the measured and calculated in-line forces. These calculations will not be reproduced here for their purpose was simply to demonstrate that the eddy-induced in-line oscillations can account for most of the error in the predictions of the Morison equation in the range of K values from 10 to about 20. For larger K values, the predictions of the Morison equation are indeed excellent as evidenced by Fig. 13.

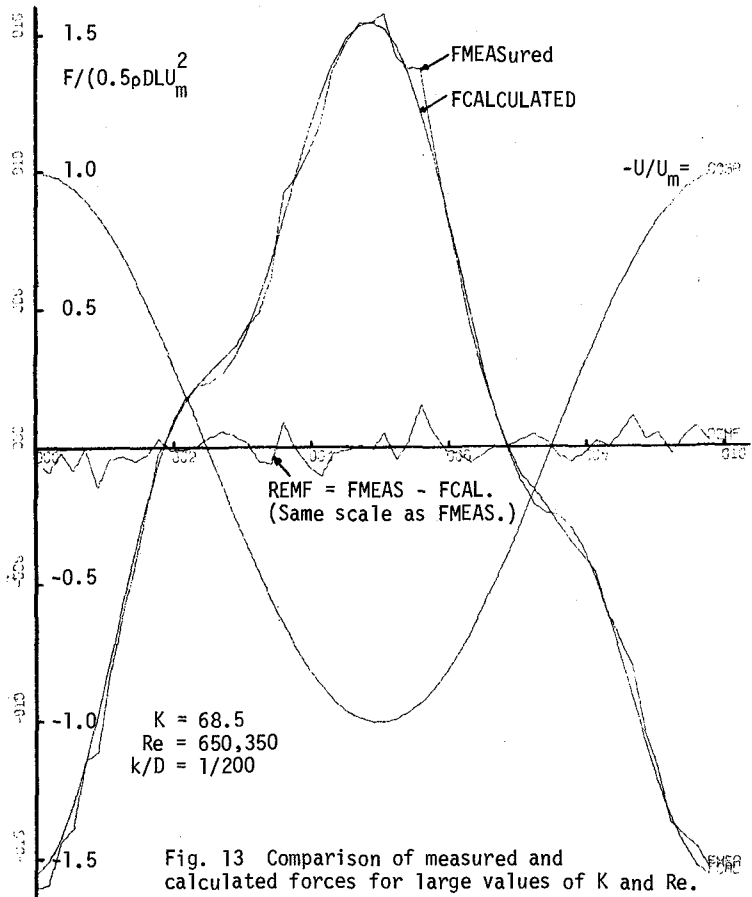


Fig. 13 Comparison of measured and calculated forces for large values of K and Re .

In considering the relevance of the coefficients presented herein and of the equation devised by Morison to wave induced loads on offshore structures, it is of course important to take into account the differences between uniform two-dimensional harmonic motion and the wave motion where the velocity vector both rotates with time at a point and decays in magnitude with depth. The spanwise variations of the flow in general lead to reduced spanwise coherence. It is safe to assume that both the three-dimensionality of the flow and the reduction of the correlation length along the cylinder, in an ocean environment, tend to increase the base pressure and thus give rise to transcritical drag coefficients which are smaller than those obtained with purely two-dimensional flows. The drag coefficients presented herein obviously represent their maximum possible values since they have resulted from a uniform, two-dimensional flow where the instantaneous wake of the cylinder has the highest possible degree of spanwise coherence. The similarity between the reduced drag coefficient due to lack of spanwise coherence in wavy flows and the drag coefficient in steady flows (both for roughened cylinders) is pure coincidence and certainly the wrong reason in arriving at the right value. It is rather unfortunate that even the experiments with wavy flows cannot be expected to isolate the effect of reduced spanwise coherence since such experiments surely bring in other factors whose influence is combined in a complex way with that of the reduced correlation. Thus, the value of the results presented herein lies in the fact that the designer now knows the maximum possible value of the coefficients under consideration, if not the values which might be more appropriate to the conditions under which the structure must survive and function. These conditions might include, among other things, currents and wave induced oscillations. Under these circumstances, the coefficients obtained either with two-dimensional harmonic flows or with waves without a current superimposed on them cannot be expected to apply to the design of the structures. Furthermore, the equation proposed by Morison needs major changes to accommodate the existence of the currents.

TRANSVERSE FORCE

The transverse force coefficients for smooth cylinders have been presented in Refs. [3, 4, 6]. The results for the rough cylinders are presented in Fig. 14 as a function of K for various values of β and one particular value of k/D . Additional details and data may be found in [19].

Evidently, C_L does not vary appreciably with either β or Re . The data presented in [19] for other values of k/D show that C_L does not vary with k/D also within the range of the parameters encountered. If there is some variation with these parameters (Re and β), it is certainly masked by the scatter in the data. The transverse force coefficient inevitably exhibits a larger scatter than that for the in-line force coefficients because of the somewhat random nature of the shedding of the vortices. Consequently, it is not too uncommon to obtain a variation of 20-25% for a given K value. This fact is of importance in discussing the effect of the Reynolds number on the lift coefficient.

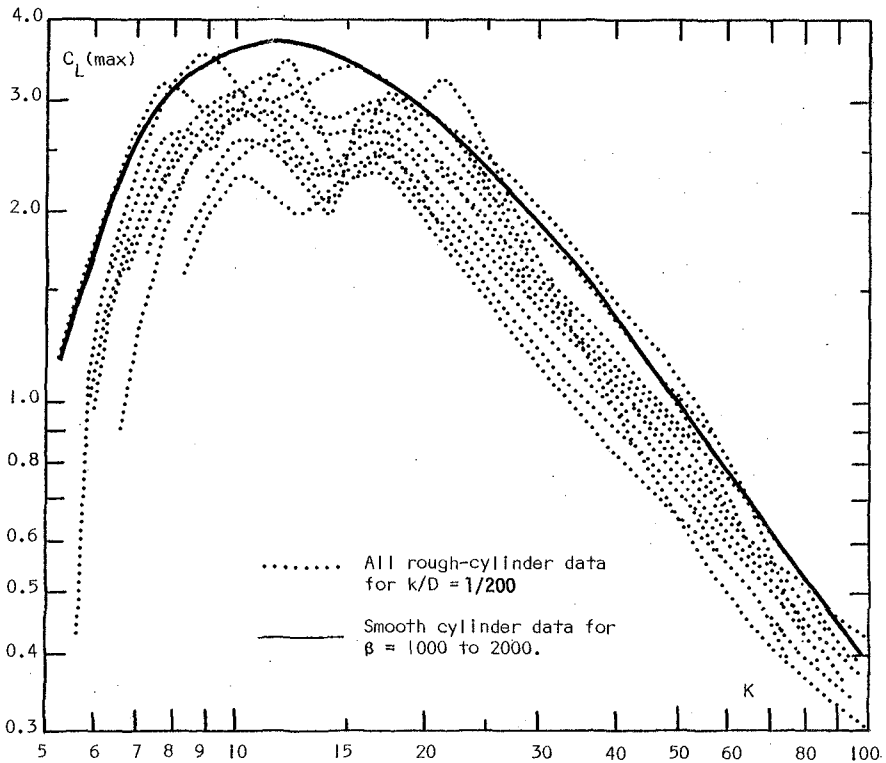


Fig. 14 Transverse force coefficient for various values of β for $k/D = 1/200$.

Also shown in Fig. 14 is the lift coefficient for smooth cylinders for β in the range 1000 to 2000. It is rather surprising that the smooth cylinder data at relatively low values of β form more or less the upper limit of the rough cylinder data. In other words, the lift coefficient for rough cylinders does not depend on Re and become almost identical with those for smooth cylinders at very low Reynolds numbers. The consequences of this observation for model testing purposes are rather obvious.

As noted earlier, the alternating nature of the transverse force is as important as its magnitude. It is for this reason that the frequency of the alternating force has also been calculated [14]. A close examination of the frequency ratios shows that f_v/K remains essentially constant at a value of about 0.22. To be sure, there are variations from one cylinder to another and from a given combination of Re and K to another one. Nevertheless, the Strouhal number ($St = f_v D/U_m = f_v/K$) is fairly constant for all roughnesses, relative amplitudes, and Reynolds numbers larger than about 20,000. This fact is of special importance in determining the in-line and transverse vibrational response of the elements of a structure to wave-induced transverse forces. Once again it should be kept in mind that the spanwise coherence along a vertical cylinder in the ocean environment is reduced by the variation of the velocity vector with time and depth and that the coefficients presented herein represent the maximum possible values of the transverse force.

CONCLUSIONS

The extensive investigation of the in-line and transverse forces on roughened circular cylinders in harmonic flow warrants the following conclusions:

1. The drag and inertia coefficients depend on Re , K , and k/D . The effect of size distribution and packing of the grains has been minimized by using only sand and applying it as uniformly as possible over the test cylinders;

2. The drag coefficient undergoes a 'drag crisis' depending on the relative roughness and rises to an asymptotic value within the range of Reynolds numbers tested. The asymptotic values of the transcritical drag coefficient are larger than those corresponding to the smooth cylinder case. Furthermore, the larger the relative roughness the larger is the asymptotic value of the drag coefficient;

3. The inertia coefficient also undergoes an 'inertia crisis' at Re values corresponding to the 'drag crisis' at which C_m reaches a maximum value and then asymptotically decreases. The terminal values of C_m depend, as in the case of C_d , on K and k/D ;

4. The predictions of the Morison's equation through the use of the Fourier-averaged drag and inertia coefficients are in excellent agreement with the measured forces in the range of K values smaller than about 10 and larger than about 20;

5. Within the range of parameters tested, C_L does not depend on Re . Its distribution is, surprisingly enough, very close to that obtained with the smooth cylinders at very low Reynolds numbers. The Strouhal number for rough cylinders remains nearly constant for all Reynolds numbers at about 0.22 with the possible exception of those at very low Reynolds numbers.

ACKNOWLEDGMENTS

The results presented herein were obtained in the course of research supported by a grant from the National Science Foundation. This support and the assistance of Messrs. N. J. Collins, S. Evans, and P. Henning, students at the Naval Postgraduate School, are gratefully acknowledged.

REFERENCES

1. Wiegel, R. L., Oceanographical Engineering, Prentice Hall, Inc., Englewood Cliffs, N. J., 1964, pp. 257-260.
2. Sarpkaya, T., "Forces on Cylinders and Spheres in a Sinusoidally Oscillating Fluid," Journal of Applied Mechanics, ASME, Vol. 42, No. 1, March 1975, pp. 32-37.
3. Sarpkaya, T., "Vortex Shedding and Resistance in Harmonic Flow about Smooth and Rough Circular Cylinders at High Reynolds Numbers", Naval Postgraduate School Tech. Report No. NPS-59SL76021, Feb. 1976, Monterey.
4. Sarpkaya, T., "In-Line and Transverse Forces on Cylinders in Oscillatory Flow at High Reynolds Numbers", OTC Paper No: 2533, May 1976.
5. Sarpkaya, T., "Vortex Shedding and Resistance in Harmonic Flow about Smooth and Rough Circular Cylinders", Proceedings of the Conference on The Behaviour of Offshore Structures, August 1976, pp: 220-235, Trondheim.
6. Sarpkaya, T., "Forces on Cylinders Near a Plane Boundary in a Sinusoidally Oscillating Fluid", Fluid Mechanics for Petroleum Industry, ASME, 1975.
7. Grace, R. A., "Wave Forces on Submerged Objects", Mis. Report No. 10, Univ. of Hawaii Look Lab-M-10, July 1974.
8. Hogben, N., "Fluid Loading of Offshore Structures, A State of Art Appraisal: Wave Loads", Maritime Tech. Monograph, No. 1, RINA, 1974.
9. Miller, B. L., "The Hydrodynamic Drag of Roughened Circular Cylinders", Trans. RINA, presented at the Spring Meeting, April 1976, (to be published)
10. Fage, A. and Warsap, J. H., "The Effects of Turbulence and Surface Roughness on the drag of a Circular Cylinder", ARC R and M 1283, 1929.
11. Achenbach, E., "Influence of Surface Roughness on the Cross-Flow Around a Circular Cylinder", JFM, Vol. 46, Pt. 2, 1971, pp. 321-335.
12. Szechenyi, E., "Supercritical Reynolds number Simulation for Two-Dimensional Flow Over Circular Cylinders", JFM, Vol. 70, Pt. 3, 1975, pp. 529-542.
13. Guven, O. et al., "Surface Roughness Effects on the Mean Flow Past Circular Cylinders", Iowa Inst. of Hyd. Res., Report No. 175, May 1975, Iowa City.
14. Schlichting, H., Boundary-Layer Theory, McGraw-Hill Book Co., N. Y., 1968.
15. Morison, J. R., et al., "The Force Exerted by Surface Waves on Piles", Petroleum Trans., Vol. 189, 1950, pp. 149-157.
16. Keulegan, G. H. and Carpenter, L. H., "Forces on Cylinders and Plates in an Oscillating Fluid", J. of Res. National Bureau of Standards, Paper No. 2857, Vol. 60, No. 5, May 1958.
17. Rosenhead, L. (Ed.) Laminar Boundary Layers, Oxford Press, 1963, p. 393.
18. Stokes, G. G., Trans. Camb. Phil. Soc. 9, Pt. II, 8-106.
19. Collins, N. J., "Transverse Forces on Smooth and Rough Cylinders", Thesis, Naval Postgraduate School, Monterey, Calif., June 1976.

CHAPTER 136

High Reynolds Number Oscillating Flow by Cylinders

by

Tokuo Yamamoto¹

and

John H. Nath²

ABSTRACT

In order to determine the added mass, drag and lift coefficients of a smooth cylinder at various distances from a plane boundary, the forced cylinder oscillation tests at high Reynolds number 10^5 to 10^6 and the wave force tests at moderate Reynolds number 10^4 to 10^5 have been carried out at the Wave Research Facility at Oregon State University.

It is found that the drag, lift and added mass coefficients are all strongly Reynolds number dependent. The effect of the near by plane boundary is to increase all of the force coefficients two to four times as compared to the free stream flow values. This is a most important factor to be aware of for design purposes.

1

Assistant Professor
Department of Civil Engineering
Oregon State University
Corvallis, Oregon

2

Professor of Mechanical Engineering/Oceanography
Director of Environmental Fluid Dynamics Laboratory
Oregon State University
Corvallis, Oregon

INTRODUCTION

Fluid forces on submerged cylinders are important to ocean engineers who have to design pipe-like structures which are subjected to environmental fluid-dynamic loads. Some typical structures are submerged oil pipelines, ocean outfalls, offshore drilling rigs, submerged oil storage tanks and mooring cables. Although this subject has been investigated by many investigators for several years, the problem has not been completely understood because of the very complicated nature of the flow. These forces are influenced by Reynolds number, cylinder roughness, angle of skew, free stream turbulence, formation and collapse of the wake and the proximity of the free surface, the ocean bottom and other cylinder members.

This subject is a continuing study at Oregon State University. Rigid cylinders subjected to flow that is perpendicular to the central axis are considered as a beginning investigation to more general conditions. An extensive literature review was made early in the study (8). The influence of a plane boundary was first treated analytically in (8, 9). The theory has been extended to a group of cylinders (7) and applied to various types of engineering problems (10, 11).

Experimental verification of the theory was made for the simple case of a cylinder near a plane boundary (3,4,7,8,11). An excellent agreement between theory and experiment was obtained for the case when wake formation is small ($A/D < 1.5$ where A = the double amplitude of water particle displacement relative to the cylinder, and D = cylinder diameter). For the cases of large wake formation ($A/D > 1.5$) the experimental results deviate considerably from potential flow theory.

The above results suggest that the real fluid oscillatory flow around rigid cylinders can be classified into two major flow situations; 1) the potential flow, and 2) wake flow. The classification of these two flow situations is discussed briefly in the following.

Potential Flow. If the thickness δ of the boundary layer on the cylinder is small compared to the cylinder diameter and if the boundary layer does not separate, the flow around the cylinder can be essentially modeled with the potential flow theory. The thickness of the laminar boundary layer on the cylinder may be given by

$$\delta = C \sqrt{\frac{v}{\omega}} \quad (1)$$

in which

C is a constant slightly dependent on the diameter of cylinder (for a flat plate $C = 2\pi$, Ref. 12)

ν = kinematic viscosity

$\omega = 2\pi/T$ where T = period of oscillation.

The relative boundary layer thickness may be defined as

$$\delta^* = \frac{\delta}{D/2} = 2C \sqrt{\frac{\nu}{\omega D^2}} = \frac{4\pi}{D} \sqrt{\frac{\nu}{\omega}} \quad (2)$$

Sarpkaya (4) claims that $D^2\omega/\nu$ (which he calls the β - parameter) is very important in oscillatory flow, without physical explanation. From Eq. (2), β is related to δ^* as

$$\delta^* = 4\pi \sqrt{\frac{1}{\beta}} \quad (3)$$

The ranges of the oscillation period for ocean waves and for earthquake ground motions are about 1 to 15 sec. and .1 to 1 sec., respectively. According to Eq. 1, the boundary layer thickness ranges from 2.43 to 9.35 mm for ocean waves and .76 to 2.42 mm for earthquakes. This is small compared to the diameter of structural members for offshore structures which range from about 100 to 2000 mm. However, the boundary layer effect may not be negligible for small size models of offshore structures in laboratory experiments.

Due to the oscillatory nature of the flow, the boundary layer on the cylinder surface does not separate (or the wake formation after separation is small) if the amplitude of water particle displacement to the cylinder diameter is $A/D < 1.5$.

The authors have derived a closed form analytical solution for the hydrodynamic forces on any number of cylinders which may move in any manner as shown in Ref. (7). Several practical examples were solved (9, 10, 11).

Wake Flow. If the amplitude of the water particle displacement is large compared to the cylinder diameter, or $A/D > 1.5$, the boundary layer separates from the cylinder surface and a wake forms. The characteristics of the wake depend on the maximum Reynolds number, $U_m D/\nu$, as well as the wake parameter, A/D , where U_m = maximum water particle velocity relative to the cylinder. Since no complete theory is available for the prediction of hydrodynamic forces on cylinders in the wake flow situation, they must be determined experimentally.

The data in the open literature to date are limited to the lower values of $U_m D/\nu$ and A/D and only for the free stream flow condition (1,6). The present investigation considerably extends the range of the parameters to higher values and generates information for various values of e/D for the first time (e = the gap between the cylinder and a near by plane boundary).

An experiment specially designed to generate the hydrodynamic force coefficients at high Reynolds numbers (1×10^5 to 1.05×10^6) and large wake parameters is reported on herein. Newly generated wave force data with moderate Reynolds numbers (1×10^4 to 1×10^5) are also presented.

OSCILLATING CYLINDER EXPERIMENTS

In order to investigate the oscillatory flow around cylinders with a large wake formation at high Reynolds numbers, the experiments were conducted at the Wave Research Facility at Oregon State University. The facility has a wave and towing basin which is 104m long, 3.66m wide and generally 4.57m deep. The overall view of the experimental setup is shown in Fig. 1. The 30cm (12 in) diameter test cylinder, which nearly reaches across the width of the wave basin, (3.66m) was forced to oscillate in a large mass of water which is otherwise still. The wave board, with a 150 horsepower motor and piston, was used to move the cylinder through a cable linkage as shown. A dam was constructed to keep the wave board dry. The motion of the wave board was amplified and transmitted to the test cylinder through the wire ropes and sheaves. Wire ropes were anchored on the amplifier sheaves to avoid any possible slips and were tensioned by spring pulleys. The maximum amplitude of cylinder motion was 6m. The cylinder was located 2m from both the basin bottom and the free surface and 12m from the dam, to best approximate the free stream flow condition.

To investigate the effect of a near by plane boundary, a movable concrete false bottom covering the 12m section below the cylinder was located at various distances from the cylinder. The test cylinder is detailed in Fig. 2. The 76cm long test section is suspended between two dummy sections by two elastic bars on which strain gages were attached to measure the horizontal and vertical component of forces. Two accelerometers were attached to the inner cylinder to measure the horizontal acceleration of the cylinder. The total amplitude, A , of cylinder displacement was measured by eye.

Four amplitudes were studied, i.e. $A/D = 20, 15, 10$ and 5 . For each amplitude, the frequency of oscillation was varied to cover the maximum cylinder velocity, U_c , from $.3$ to 4.27 m/sec. The horizontal accelerations together with the wave board displacement were simultaneously recorded on a photosensitive strip chart recorder.

It should be noted that the flow past a stationary object is hydrodynamically equivalent to the flow due to the same object moved in the otherwise still fluid as long as the fluid is incompressible. The only difference is that the object in the moving fluid experiences an extra force, which is equal to the displaced mass of the fluid times the ambient fluid acceleration, due to the pressure field necessary to accelerate the fluid.

WAVE FORCE EXPERIMENTS

In order to investigate the oscillatory flow around cylinders in a large wake flow situation at moderate Reynolds numbers (1×10^4 to 1×10^5), wave force experiments were also made at the Wave Research Facility. A 76mm diameter horizontal cylinder was instrumented and mounted at various distances from a false bottom in 2m water. The horizontal and vertical forces, together with the water surface fluctuation, were recorded simultaneously. Since the detail of similar experimentation has been reported in our previous paper (Ref. 4), it will not be repeated here again.

ANALYSIS OF EXPERIMENTAL DATA

The analysis of the data from the oscillating cylinder tests and the wave force tests was based on the Morison equation. The horizontal force $F_x(t)$, on a cylinder undergoing sinusoidal motion may be given in the form of the Morison equation as

$$F_x(t) = C_D \frac{1}{2} \rho D L |\dot{x}(t)| \dot{x}(t) + (C_M \frac{1}{4} \rho \pi D^2 L + M) \ddot{x}(t) \quad (4)$$

wherein $x(t)$ is the cylinder displacement from the neutral position and $\dot{}$ and $\ddot{}$ on x designate d/dt and d^2/dt^2 respectively, ρ = density of fluid, C_D = drag coefficient, C_M = added mass coefficient and L = the length of test cylinder, M = mass of test cylinder.

For a sinusoidal motion, $x(t)$, $\dot{x}(t)$ and $\ddot{x}(t)$ are given as

$$x(t) = \frac{A}{2} \sin \omega t \quad (5)$$

$$\dot{x}(t) = \frac{A\omega}{2} \cos \omega t \quad (6)$$

$$\ddot{x}(t) = -\frac{A\omega^2}{2} \sin \omega t \quad (7)$$

From Eq. 6, the maximum velocity U_m is

$$U_m = \frac{A\omega}{2} \quad (8)$$

The maximum acceleration \dot{U}_m is given as

$$\dot{U}_m = \frac{A\omega^2}{2} \quad (9)$$

For a sinusoidal motion $\ddot{x}(t)$ vanishes when $\dot{x}(t)$ is maximum and vice versa. In a very simple analysis, C_D and C_M is often evaluated by measuring the horizontal force F_D at the instant of maximum ambient velocity and the force F_M at the instant of maximum acceleration.

For the simple approach,

$$C_D = \frac{F_D}{\frac{1}{2} \rho D L U_m^2} \quad (10)$$

and

$$C_M = \frac{F_M}{\frac{1}{4} \rho \pi D^2 L U_m} - \frac{M}{\frac{1}{4} \rho \pi D^2 L} \quad (11)$$

The measured cylinder motion was fairly sinusoidal. The maximum horizontal force at $A/D = 15$ and 20 occurred at the instant of maximum velocity. This indicates that there is no phase lag between the drag force and the ambient velocity. Thus, the simple approach was used in this paper. Some data from the forced cylinder oscillation tests were also recorded in digital form on magnetic tapes. If time and opportunity permit in the future, the least squared time average method used in Refs. 1 and 6 will be applied to the digital data to see the difference in the values C_D and C_M determined by the two methods.

The lift coefficient, C_L , is defined from the maximum vertical force, F_L , and the maximum velocity, U_m , as

$$C_L = \frac{F_L}{\frac{1}{2} \rho D L U_m^2} \quad (12)$$

In Eqs. 10, 11 and 12, U_m was computed from the measured value of A and ω and Eq. 8, and U_m was directly obtained from the measurement. The error between the measured value of U_m and the computed value from Eq. 9 using measured values of A and ω was usually small. For each run (which included several oscillations) the ensemble average of four to six samples was used to determine the force coefficients.

From wave force data, C_D and C_L were also evaluated based on Eqs. 10 and 12 utilizing the Airy wave theory and measured wave height and frequency.

EXPERIMENTAL RESULTS

Experiments were carried out for the following combinations of the parameters, e/D , A/D and $U_m D/v$:

Oscillating Cylinder Tests (D=30cm)

e/D : 6, 1, 0.5, 0.25, 0.083

Oscillating Cylinder Tests (D=30cm) continued

A/D : 20, 15, 10, 5

 $\frac{U_m D}{v} \times 10^{-5}$: 10.5, 7.88, 5.25, 2.63, 1.31Note: The maximum value of $\frac{U_m D}{v}$ depends on A/D.Wave Force Tests (D=7.62cm)

e/D : 3, 1, .5, .33, .063

A/D : 3.5 to 33

 $\frac{U_m D}{v}$: 10^4 to 10^5

Example Data. Typical force, acceleration and displacement records from the cylinder oscillation tests are shown in Fig. 3 for $e/D = 6$, $A/D = 10$ and $U_m D/v = 5.25 \times 10^5$, and in Fig. 4 for $e/D = 0.083$, $A/D = 10$ and $U_m D/v = 5.25 \times 10^5$. The cylinder acceleration is fairly sinusoidal and has practically no phase lag with the wave board displacement. This is a good indication that the actual cylinder motion was approximately sinusoidal. (Because of small cable slack, the motion of the cylinder cannot be exactly sinusoidal.) The high frequency noise at about 8 Hz is due to the natural vibration frequency of the test cylinder in water.

Compare the vertical forces for $e/D = 6$ and $.083$. For the free stream flow condition, $e/D = 6$, the lift force fluctuates equally up and down at six times the oscillation frequency for this particular condition. This is due to the alternating vortex shedding. However, for the near-bottom flow condition, $e/D = .083$, the lift force is toward the boundary or downward during a very short period where the velocity is small, but for the remainder of the flow cycle, where the velocity is significantly large, the lift force is away from the boundary, or upward. The explanation for this is that due to the oscillatory nature of the flow, there is a moment where the wake does not clearly exist, so the force is toward the boundary as for the potential flow condition. But as soon as the wake is clearly formed, the force becomes upward, due to the asymmetric flow due to the near by boundary. For this case, the lift force always fluctuates at twice the flow oscillation frequency.

This effect of a near by boundary may be important with regard to the design of submerged pipelines.

The force coefficients, C_D , C_M and C_L , are plotted versus the Reynolds number, $U_m D/\nu$, with the wake parameter, A/D , and the relative gap, e/D , as parameters, and are discussed in the following section.

Drag Coefficient. The plots of the drag coefficient versus the Reynolds number for the "free stream" flow condition are shown in Fig. 5. Actual values of e/D are 6 and 3 for oscillating cylinder tests and wave force tests, respectively. The general trends of the oscillatory cylinder data and the wave force data match continuously. This may be a good indication of the physical similarity between the two flow conditions. The oscillatory flow data (1,6) and the steady flow data (5) available in the literature are also shown for comparison.

The oscillatory flow results from the three investigations agree fairly well. For the range of the wake parameter studied, i.e., A/D from 3.5 to 33, C_D from oscillatory flow varies gently as $U_m D/\nu$ varies from 10^4 to 10^6 . This is distinguishably different from the well known steady state data which has an abrupt transition of the high subcritical value of C_D to the low supercritical value.

Does the oscillatory flow value of C_D approach the steady state value as A/D approaches infinity? This question still remains to be answered.

The plots of C_D vs. $U_m D/\nu$ for the near boundary flow condition ($e/D = .083$ for the oscillating cylinder tests and $e/D = .063$ for the wave force tests) are shown in Fig. 6. The general tendency is similar to that of the free stream flow case except that the value of C_D for this case is considerably higher than that for the free stream flow. The steady flow data by Jones (2) happens to give a lower limit of the oscillatory flow data shown.

Similar plots for three intermediate values of e/D were made but are not shown here because of space limitation. The general trends are similar to those in Figs. 5 and 6 but the value of C_D varies depending on e/D .

The plots of C_D versus $U_m D/\nu$ at the largest $A/D = 20$ are shown in Fig. 7. As noted before, the general trends are the same for all e/D . The value of C_D decreases until it reaches the minimum at $U_m D/\nu =$ about 3×10^5 , then it increases gradually as $U_m D/\nu$ increases from 10^4 to 10^6 . The absolute value of C_D increases as the cylinder approaches the boundary. The value of C_D for the near boundary flow ($e/D = .083$) is about two times as large as that for the free stream flow. This is probably due to the flow blockage effect of the plane boundary.

Added Mass Coefficient. The added mass coefficient, C_M , obtained from the oscillating cylinder tests is plotted versus $U_m D/\nu$ for the free stream flow condition ($e/D = 6$) in Fig. 8. The data from the present study are compared with the data by other investigators. Again, all

of the data agree fairly well. The value of C_M increases gradually until it reaches the maximum at about $U_m D/\nu = 3 \times 10^5$, then it decreases gradually as $U_m D/\nu$ increases from 10^4 to 10^6 . The experimental value of C_M is always smaller than the theoretical value ($C_M = 1.0$). This is due to the wake effect which strongly depends on the Reynolds number, $U_m D/\nu$. The effect of A/D on C_M is not so clear.

Similar plots for the near boundary flow condition ($e/D = .083$) are shown in Fig. 9.

The plots of C_M versus $U_m D/\nu$ at $A/D = 20$ are shown for various values of e/D in Fig. 10. The theoretical value of C_M , which is independent of $U_m D/\nu$, increases from 1.0 to 2.3 as the cylinder approaches from the free stream to the plane boundary. The experimental value of C_M increases by the same order of magnitude as e/D decreases, but is strongly dependent on the Reynolds number.

Lift Force Coefficient. Plots of C_L versus $U_m D/\nu$ for the free stream flow condition ($e/D = 6$ for the oscillatory cylinder tests and $e/D = 3$ for the wave force tests) are given in Fig. 11. The OSU data are compared with the data in Ref. 6. The data from the two investigations agree very well at all values of A/D . The value of C_L increases as A/D decreases in the range of A/D 5 to 20. For a given A/D , C_L decreases gradually as $U_m D/\nu$ is increased. For the free stream flow condition the lift force fluctuates many times up and down in a half cycle of oscillation due to alternating vortex shedding as shown in Fig. 3. The fluctuation frequency depends on A/D .

The plots of C_L versus $U_m D/\nu$ for the near boundary flow condition ($e/D = 0.83$ for the oscillating cylinder tests and $e/D = .063$ for the wave force tests) are shown in Fig. 12. As explained before, the lift force for this case is not due to the vortex shedding but due to the flow asymmetry. Therefore, the lift for this case is always at twice the oscillation frequency of the flow and independent of A/D .

The plots of C_L versus $U_m D/\nu$ at $A/D = 20$ are shown for various values of e/D in Fig. 13. The positive lift force increases significantly as e/D decreases. The value of C_L for $e/D = .083$ is about four times larger than C_L for the free stream flow condition for the entire range of $U_m D/\nu$. The dependence of the negative lift force on e/D is not as clear as that of the positive lift force.

PRACTICAL APPLICATIONS

Real design oscillatory flows such as ocean waves and earthquakes should be classified into either the potential flow situation ($A/D < 1.5$) or the wake flow situation ($A/D > 1.5$) according to the wake parameter.

For the potential flow situation, such as earthquake problems, a closed form solution for the hydrodynamic forces on any number of cylinders is available in Ref. 7. The calculated force coefficients for one, two and three cylinders near a plane boundary (11) and for a 4x4 cylinder arrays (10) are also available.

For the wake flow situation, such as wave force problems, the experimental data of drag, lift and added mass coefficients covering the Reynolds number, U_D/ν , of from 10^4 to 10^6 , the wake parameter, A/D , from 3.5 to 33, the relative gap between the cylinder and a plane boundary, e/D , from .065 to 6.0, are presented herein for the design of pipelines, offshore platforms and other pipe structures.

CONCLUSIONS

To determine the added mass, drag and lift coefficients of a smooth cylinder at various distances from a plane boundary, the forced cylinder oscillation tests at high Reynolds numbers 10^5 to 10^6 and the wave force tests at moderate Reynolds numbers 10^4 to 10^5 have been carried out at the Wave Research Facility at Oregon State University. The following conclusions are drawn from the results.

1. The data from the forced cylinder oscillation tests matched continuously with the data from the wave force tests. This indicates the physical similarity between the two flow situations.
2. The drag, lift and added mass coefficients are all strongly Reynolds number dependent. Unlike steady flow, C_D from oscillatory flow for $A/D = 5$ to 20 decreases gradually from a high value until it reaches a minimum at about $U_D/\nu = 3 \times 10^5$ and then increases gradually as the Reynolds number increases from 10^4 to 10^6 . The value of C_L monotonically decreases as the Reynolds number increases. The value of C_M has a maximum at about $U_D/\nu = 3 \times 10^5$. This is true for all values of e/D .
3. The drag and lift coefficients are generally higher for the smaller values of A/D . Both C_D and C_L become fairly independent of A/D when this parameter becomes as large as 15 or 20. The influence of A/D on C_M is less clear. This tendency is true for all values of e/D .
4. The effect of a near by plane boundary is to increase all of the force coefficients. At $A/D = 20$, C_D increased about two times, C_L about four times and C_M about two times as e/D decreases from 6 to .083. This may be due to the blockage effect of the near by plane boundary. *This is a most important factor to be aware of for design purposes.*

5. The wake characteristics are completely different between the free stream flow and the near boundary flow conditions. In the free stream flow, many alternate vortexes shed during a half cycle of oscillation. The numbers of vortexes varies depending on the value of A/D . Near a plane boundary, the vortex shedding is suppressed. The flow changes from the potential flow situation to the wake flow situation during a half cycle. So the lift force also changes from negative to positive during the half cycle. This frequency characteristic of lift force near a plane are independent of the value of A/D as long as $A/D > 1.5$.

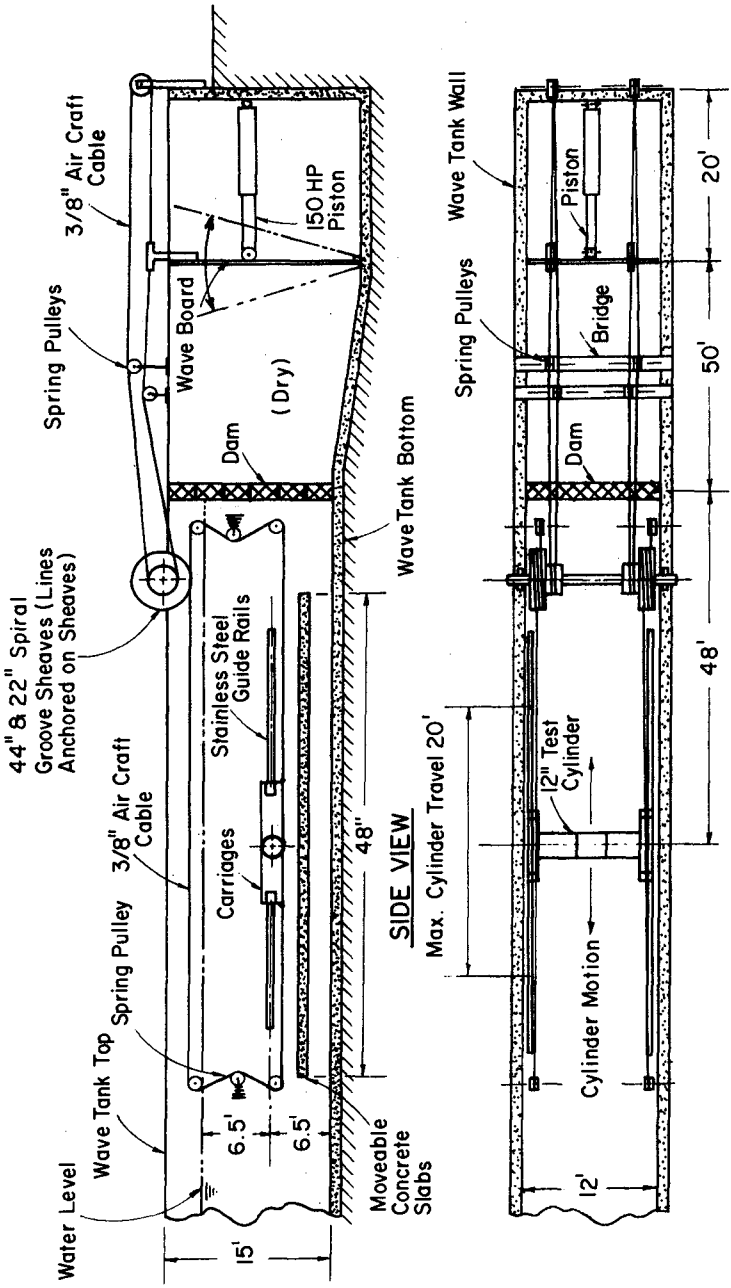
ACKNOWLEDGEMENT

The forced cylinder oscillation study was supported by the National Science Foundation under contract ENG75-06901. The wave force study was supported by the National Oceanic and Atmospheric Administration (maintained by the U.S. Department of Commerce) Institutional Sea Grant contract 04-6-158-44004 at Oregon State University. Y. W. Chan assisted in conducting the experiments.

REFERENCES

1. Garrison, C. J., "Drag and Inertia Coefficients in Oscillatory Flow about Cylinders," Preprint of ASCE National Water Resources and Ocean Engineering Convention, Preprint 2693, April 1976.
2. Jones, W., "Forces on a Transverse Circular Cylinder in the Turbulent Boundary Layer of a Steady Flow," Ph.D Thesis, Rice University, 1970.
3. Nath, J. H. and Yamamoto, T., "Forces from Fluid Flow Around Objects," Proceedings of 14th Coastal Engineering Conference, Copenhagen, Ch. 106, June 1974.
4. Nath, J. H., Yamamoto, T. and Wright, J. C., "Wave Forces on Pipes Near the Ocean Bottom," Proc. of Offshore Technology Conference, OTC 2496, Houston, May 1976.
5. Roshko, A., "Experiments on the Flow Past a Circular Cylinder at Very High Reynolds Numbers," Journal of Fluid Mechanics, Vol. 10, 1961.
6. Sarpkaya, T., "Vortex Shedding and Resistance in Harmonic Flow About Smooth and Rough Circular Cylinders at High Reynolds Numbers," Technical Report NPS-59SL76021, Naval Postgraduate School, Monterey, CA, February 1976.
7. Yamamoto, T., "Hydrodynamic Forces on Multiple Circular Cylinders," ASCE Hydraulic Division Journal, September 1976.

8. Yamamoto, T., Nath, J. H. and Slotta, L. S., "Yet Another Report on Cylinder Drag or Wave Forces on Horizontal Cylinders," Bulletin No. 47, Engineering Experiment Station, Oregon State University, April 1973.
9. Yamamoto, T., Nath, J. H. and Slotta, L. S., "Wave Forces on Cylinder Near Plane Boundary," Journal of Waterways, Harbors, and Coastal Engineering Division of ASCE, WW 4, November 1974. And discussions by 1) Chakrabarti and Cotter, and 2) Grace, R. A. in WWHCE Journal, WW 3, August 1975.
10. Yamamoto, T., and Nath, J. H., "Hydrodynamic Forces on Groups of Cylinders," Proceedings of Offshore Technology Conference, Houston, 1976.
11. Yamamoto, T. and Nath, J. H., "Preprints of ASCE National Water Resources and Ocean Engineering Convention, Preprint 2633, April 1976.
12. Yamamoto, T., Nath, J. H. and Smith, C. E., "Longitudinal Motions of Taut Moorings," ASCE WWHCE Journal, February 1974.



TOP VIEW

FIG. 1 The experimental setup for the forced cylinder oscillation tests.

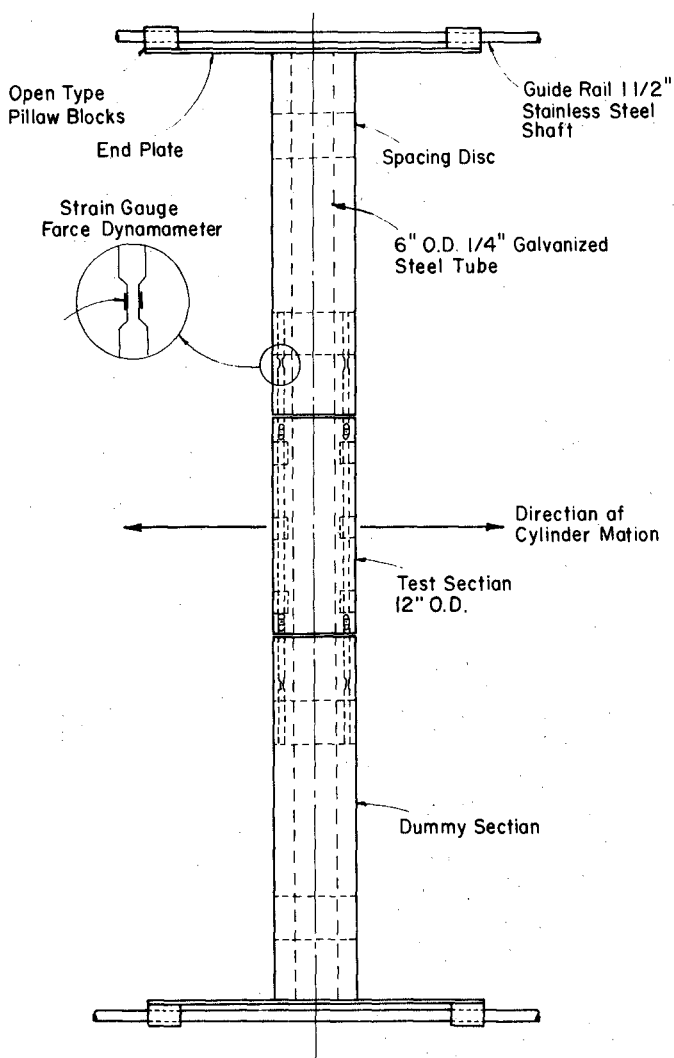


FIG. 2 Test cylinder for Forced Cylinder Oscillation Tests.

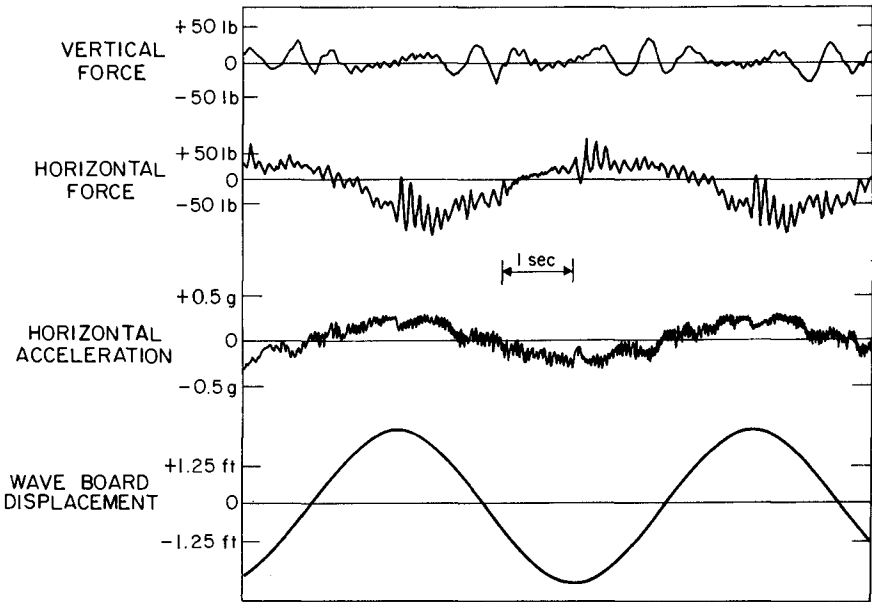


FIG. 3 Example Data for $e/D = 6$, $A/D = 10$ and $U_m D/\nu = 5.25 \times 10^5$, Oscillating Cylinder Tests.

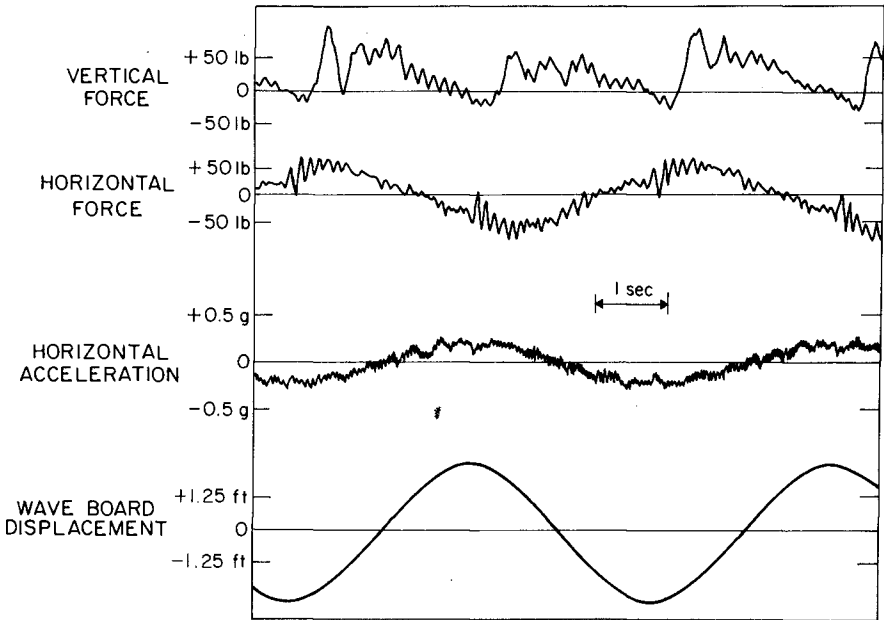


FIG. 4 Example Data for $e/D = .083$, $A/D = 10$ and $U_m D/\nu = 5.25 \times 10^5$, Oscillating Cylinder Tests.

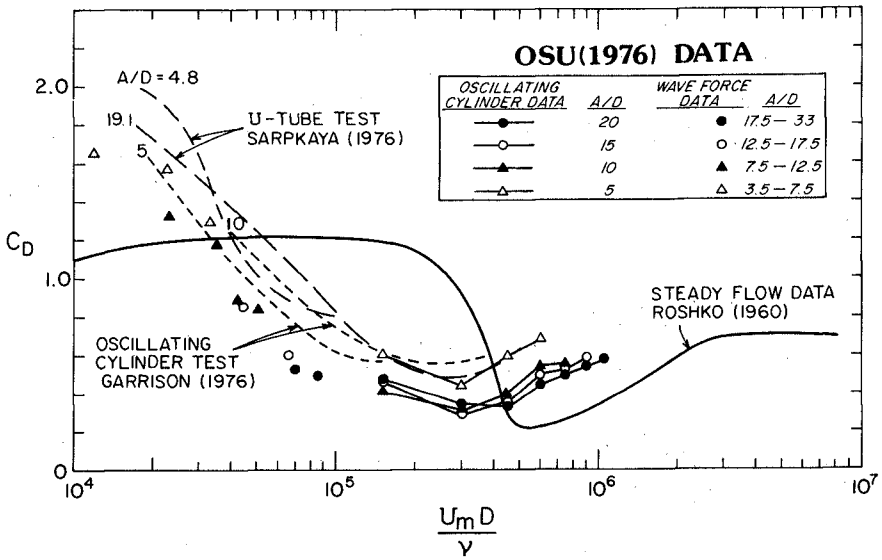


FIG. 5 Drag coefficient vs. Reynolds Number for Free Stream Flow condition, ($e/D = 6$ for oscillating cylinder data and $e/D = 3$ for wave force data.)

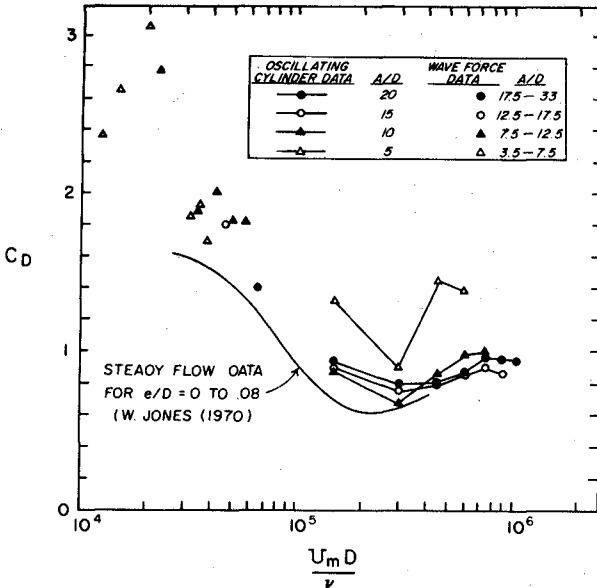


FIG. 6 Drag coefficient vs. Reynolds Number for Near Boundary Flow condition ($e/D = .083$ for oscillating cylinder tests and $e/D = .063$ for wave force data.)

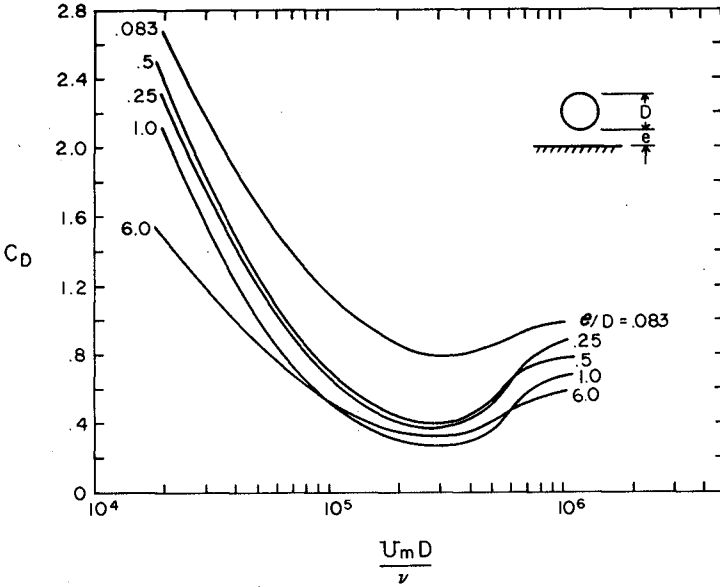


FIG. 7 Drag coefficient vs. Reynolds Number for various values of e/D at $A/D = 20$.

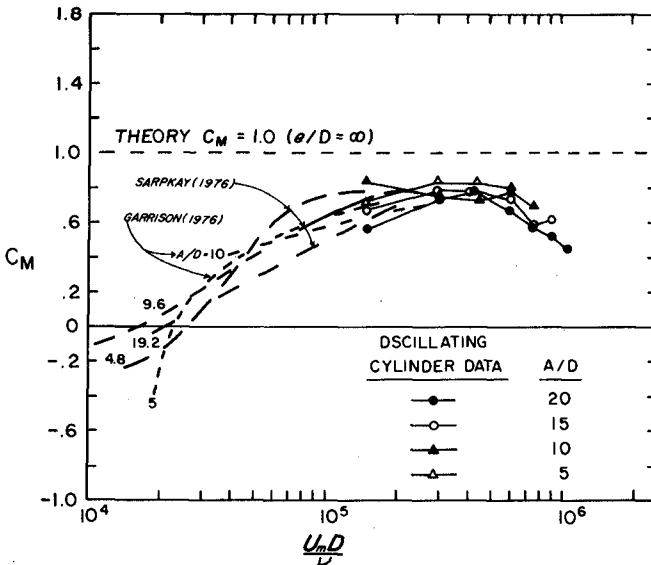


FIG. 8 Added Mass coefficient vs. Reynolds Number for Free Stream Flow condition.

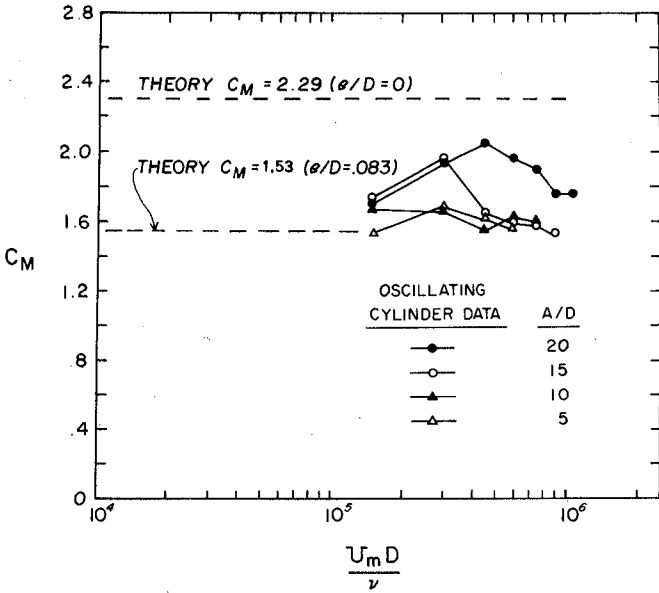


FIG. 9 Added Mass coefficient vs. Reynolds Number for Near Boundary Flow condition.

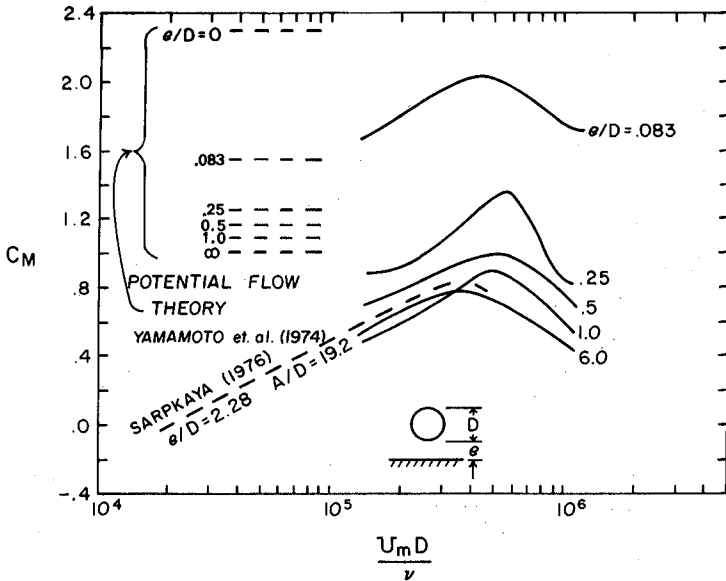


FIG. 10 Added Mass coefficient vs. Reynolds Number for various values of e/D at $A/D = 20$.

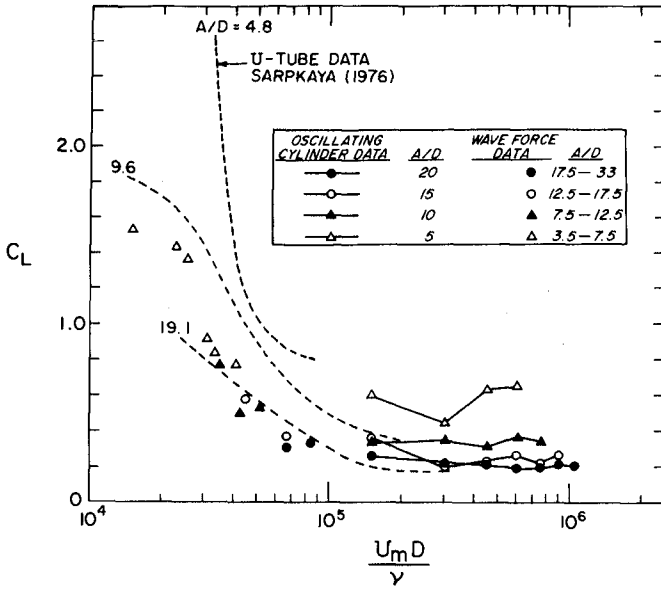


FIG. 11 Lift Coefficient vs. Reynolds Number for Free Stream Flow condition.

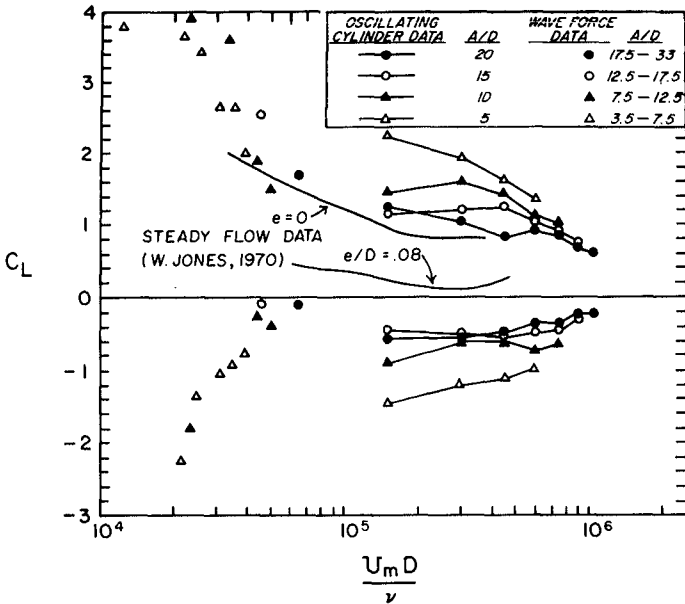


FIG. 12 Lift Coefficient vs. Reynolds Number for Near Boundary Flow condition.

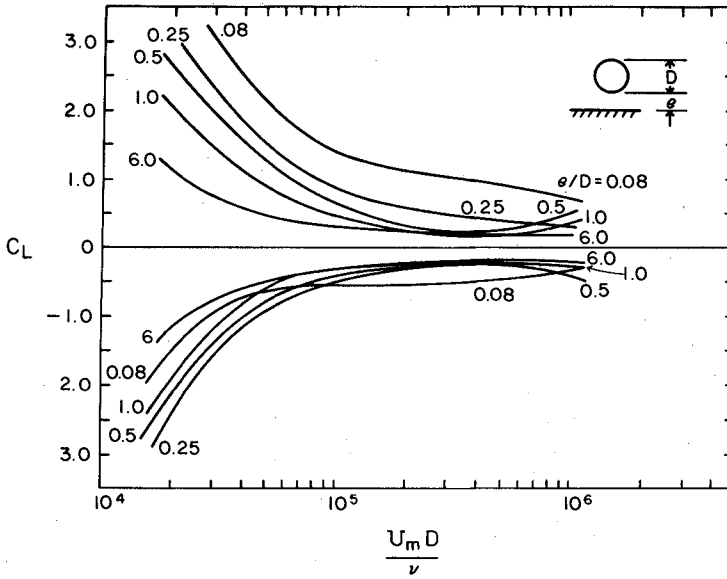


FIG. 13 Lift Coefficient vs. Reynolds Number for various values of e/D at $A/D = 20$.

CHAPTER 137

FLOW SEPARATION, WAKE VORTICES AND PRESSURE DISTRIBUTION AROUND A CIRCULAR CYLINDER UNDER OSCILLATORY WAVES

Yuichi Iwagaki
Professor

and

Hajime Ishida
Research Assistant

Department of Civil Engineering
Kyoto University
Kyoto, Japan

ABSTRACT

Flow separation of a laminar boundary layer on the surface of a circular cylinder developed by monochromatic waves has been investigated both theoretically and experimentally, and next, characteristics of vortex formation and shedding have been discussed with Keulegan-Carpenter's number and Reynolds number, and finally, local depressions of the wave pressure around the cylinder induced by wake vortices have been examined in the experiment.

INTRODUCTION

A number of studies have been made with respect to wave forces on marine structures, especially on a circular cylinder. However, in order to estimate the wave forces more correctly, it is necessary to make clear the mechanism of wave force action. For this purpose, it is important, as the first step, to investigate the transformation of waves by the circular cylinder and induced flow along the cylinder, and next, to evaluate the magnitude of pressures acting on the cylinder exerted by such an affected wave field.

In case of steady flow, it has already been ascertained that both the behavior of fluid around a cylinder and forces on it are principally subject to Reynolds number $Re = UD/\nu$, in which U :flow velocity, D :diameter of cylinder and ν :dynamic viscosity. Son and Hanratty^{1),2)} indicated that in the range of lower Reynolds number the position of separation point moves forward from the back stagnation point with increase in Reynolds number. For instance when $Re = 500$, the angle of separation point from the front stagnation point θ_s is about 95° , and when Re increases between 4000 and 100000, it becomes about 80° .

Then it is well known that such a separation causes wake vortices and their configurations are also subject to Reynolds number; that is, a pair of symmetric and stable vortices is formed at values of Re lower than 40 and Karman vortex street appears at values of Re between about 70 and 2500³⁾. In this case, the frequency of vortex generation is known by using Strouhal number determined by Reynolds number⁴⁾.

Hereupon, corresponding to such patterns of fluid motion, the distributions of pressure and shearing stress around a cylinder are determined. Among the fluid forces on the cylinder, the drag force due to the shearing stress is predominant in the range of lower Reynolds number. However, with increase in Reynolds number, another kind of drag force becomes predominant owing to depression of pressure induced by wake vortices at the rear part of the cylinder. It is too familiar to state that these results are shown by a figure in text books as the relationship between the drag coefficient and Reynolds number⁴⁾.

On the other hand, in case of wave fields, the separation point, the behavior of wake vortices and the pressure distribution have not been made so clear that there exist unknown facts about the correspondence of the drag and inertia coefficients to the conditions of fluid motion.

From this point of view, in the present study, general characteristics of the flow separation of a laminar boundary layer on the surface of a circular cylinder developed by monochromatic waves are shown by using the theory presented by the authors in the previous paper⁵⁾, and then, experimental results of the separation point obtained by taking photographs using the method of flow visualization are compared with the theoretical ones, and next, vortex formation and shedding are investigated by means of successive photography. Finally, wave pressure distributions around the cylinder are measured by using a small pressure gauge and depressions of the pressure induced by wake vortices are discussed.

FLOW SEPARATION

1. THEORY

The coordinate system is shown in Fig.1. Denoting the water particle velocity in the boundary layer along the cylinder in the polar coordinate (θ, r, z) or in the boundary layer coordinate (x, y, z) by u , the separation point of a streamline in the boundary layer is generally determined by the condition that

$$\partial u / \partial r |_{r=R} = 0 \quad \dots\dots\dots (1)$$

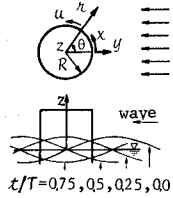


Fig.1 Coordinate system.

The authors have already obtained the second approximate solution of the water particle velocity in the boundary layer in the following dimensionless form by means of the boundary layer approximations and the perturbation method in the previous paper⁵⁾:

$$u_{2nd} = u_0 + \epsilon_1 u_1, \quad \dots\dots\dots (2)$$

$$u_0 = \zeta_0^+ u_0 e^{i\sigma t}, \quad \dots\dots\dots (3)$$

$$u_1 = (\epsilon_2 / \epsilon_1) \zeta_1^+ u_0 e^{i\sigma t} + \zeta_{1a}^- (u_0 \hat{u}_{0x} + \hat{w}_0 \hat{w}_{0z}) e^{2i\sigma t} + \zeta_{1d}^- (u_0 \hat{w}_{0z} - \hat{w}_0 \hat{u}_{0z}) e^{2i\sigma t} + \zeta_{1b}^- \{ (\hat{u}_0 \hat{u}_{0x} + \hat{u}_0 \hat{u}_{0x}) + (\hat{w}_0 \hat{u}_{0z} + \hat{w}_0 \hat{u}_{0z}) \} + \zeta_{1c}^- \{ (\hat{u}_0 \hat{u}_{0x} - \hat{u}_0 \hat{u}_{0x}) + (\hat{u}_0 \hat{w}_{0z} - \hat{u}_0 \hat{w}_{0z}) \} + \zeta_{1e}^- \{ (\hat{u}_0 \hat{w}_{0z} + \hat{u}_0 \hat{w}_{0z}) - (\hat{w}_0 \hat{u}_{0z} + \hat{w}_0 \hat{u}_{0z}) \}, \quad \dots\dots\dots (4)$$

$$\epsilon_1 = \pi H / L, \quad \epsilon_2 = \sqrt{\nu T} / 2\pi R, \quad \dots\dots\dots (5)$$

$$\left. \begin{aligned} \zeta_0^+ &= 1 - e^{-(1+i)\eta^+}, & \zeta_1^+ &= \frac{1}{\sqrt{2}} \eta^+ e^{-(1+i)\eta^+}, \\ \zeta_{1a}^- &= -\frac{i}{2} e^{-\sqrt{2}(1+i)\eta^-} + \frac{i}{2} e^{-(1+i)\eta^-} + \frac{1-i}{2} \eta^- e^{-(1+i)\eta^-}, \end{aligned} \right\} \dots\dots\dots (6)$$

$$\left. \begin{aligned}
 \zeta'_{1d} &= \frac{7i}{4}e^{-\sqrt{2}(1+i)\eta'} + \frac{3i}{2}e^{-(1+i)\eta'} + \frac{1-i}{2}\eta'e^{-(1+i)\eta'} + \frac{i}{4}e^{-2(1+i)\eta'}, \\
 \zeta'_{1b} &= \frac{3}{4} + \frac{1}{4}e^{-2\eta'} + e^{-\eta'} \left(\frac{1}{2}\cos\eta' + 2\sin\eta' \right) - \frac{\eta'}{2}e^{-\eta'} (\cos\eta' - \sin\eta'), \\
 \zeta'_{1c} &= \frac{3}{4} - \frac{1}{4}e^{-2\eta'} + e^{-\eta'} (\cos\eta' - \frac{1}{2}\sin\eta') + \frac{\eta'}{2}e^{-\eta'} (\cos\eta' + \sin\eta'), \\
 \zeta'_{1e} &= \frac{1}{2} + e^{-\eta'} \left(\frac{1}{2}\cos\eta' + \sin\eta' \right) - \frac{\eta'}{2}e^{-\eta'} (\cos\eta' - \sin\eta'),
 \end{aligned} \right\} \dots\dots\dots (6)$$

$$\eta' = ky\sqrt{Re^*/2}, \dots\dots\dots (7)$$

in which, ϵ_1 :very small quantity of the order of the wave steepness in magnitude, ϵ_2 :very small quantity of the order of the ratio of the boundary layer thickness to the radius of cylinder in magnitude, σ :angular frequency, H :wave height, L :wave length, T :wave period, R :radius of cylinder, k :wave number, $Re^*(= c/vk)$:convenient Reynolds number using the wave celerity c instead of the fluid velocity, and U_0 and W_0 :amplitudes of dimensionless velocities derived by eliminating both the dimensional part $\pi H/T$ and time variation part $e^{i\sigma t}$ from the water particle velocities of diffracted waves on the surface of cylinder in the direction of the coordinates x and z respectively. Suffixes x and z indicate differentiations with respect to x and z respectively, and \wedge and \vee indicate real and imaginary parts respectively.

By applying this velocity u_{2nd} to the velocity u in Eq.(1), Eq.(1) is rewritten as follows:

$$\partial u_{2nd}/\partial \eta' |_{\eta'=0} = \partial u_0/\partial \eta' |_{\eta'=0} + \epsilon_1 \partial u_1/\partial \eta' |_{\eta'=0} = 0. \dots\dots\dots (8)$$

Using Eq.(3) and Eq.(4), $\partial u_0/\partial \eta' |_{\eta'=0}$ and $\partial u_1/\partial \eta' |_{\eta'=0}$ are expressed as follows:

$$\begin{aligned}
 \partial u_0/\partial \eta' |_{\eta'=0} &= (1+i)U_0e^{i\sigma t}, \dots\dots\dots (9) \\
 \partial u_1/\partial \eta' |_{\eta'=0} &= (\epsilon_2/\epsilon_1) \frac{1}{\sqrt{2}}U_0e^{i\sigma t} \\
 &+ (1-\frac{1}{\sqrt{2}})(1-i)(U_0\hat{u}_{0x} + W_0\hat{u}_{0z})e^{2i\sigma t} + (\frac{5}{2}-\frac{7\sqrt{2}}{4})(1-i)(U_0\check{w}_{0z} - W_0\check{u}_{0z})e^{2i\sigma t} \\
 &+ \frac{1}{2}\{(\hat{u}_0\hat{u}_{0x} + \hat{u}_0\hat{u}_{0z}) + (\check{w}_0\hat{u}_{0z} + \check{w}_0\hat{u}_{0z})\} - \frac{1}{2}\{(\hat{u}_0\check{u}_{0x} - \hat{u}_0\check{u}_{0z}) + (\hat{u}_0\check{w}_{0z} - \hat{u}_0\check{w}_{0z})\}. \dots (10)
 \end{aligned}$$

It is impossible to express the separation point θ_s explicitly from Eq.(8) so that the separation point is obtained as the point that the sign of left hand side of Eq.(8) is just changed in varying θ by 1° in computations.

2. COMPUTATIONS AND DISCUSSIONS

Fig.2 shows an example of the time variation of the water particle velocity in the boundary layer u_{2nd} . In this case, Keulegan-Carpenter's number ($[K.C.]_m = U_{max}T/D$) is 6. The water particle velocity at $\theta = 150^\circ$ denoted by a dotted line becomes negative value after t/T is about 0.125, which means the occurrence of flow separation behind the cylinder and the generation of subsequent reverse current. On the other hand, the water particle velocity at $\theta = 30^\circ$ denoted by a solid line becomes positive during the phase of wave trough, which also means the occurrence of flow separation. The shadow regions in this figure show the duration and intensity of these reverse currents.

Fig.3 shows an example of the time variation of flow separation point with a parameter of Keulegan-Carpenter's number (hereafter, it is denoted as K.C. number for abbreviation). As the water particle velocity varies in magnitude with the wave phase, the separation

point proceeds from behind of the cylinder to front of the cylinder with increase in t/T during the phase of wave crest and its reverse movement is seen during the phase of wave trough. Especially when K.C. number is small, for example 3, the separation point varies quickly in the wide range, and this phenomenon is peculiar to flow separation under oscillatory waves. The reason may be explained by the fact that the phase of the water particle velocity in the boundary layer proceeds faster than the phase of ambient velocity. On the other hand, when K.C. number is large, for example 15, the separation point does not vary so widely, which is similar to the flow separation in steady flow.

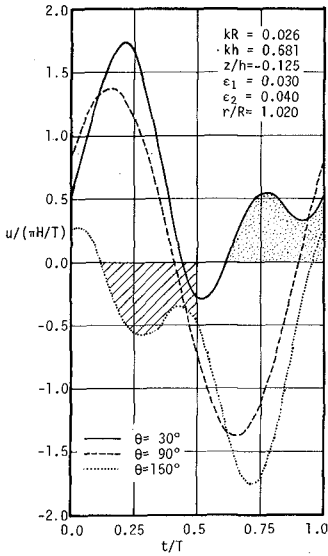


Fig.2 Variation of water particle velocity u_{2nd} in boundary layer with time.

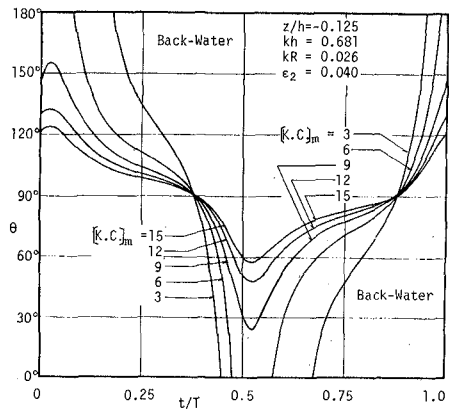


Fig.3 Variation of flow separation point with time.

Fig.4 shows the shift of separation point due to K.C. number, in which the phase t/T is fixed to 0.25 and kR is taken as a parameter. In this figure, for example, when kR is 0.01, the flow separation does not occur if K.C. number is smaller than 2, and with increase in K.C. number, the separation point moves from 180° toward 90° . And finally it approaches to a definite point asymptotically for each kR . If K.C. number is constant, it is found that the smaller kR , the smaller angle of separation point; that is, the wake region behind the cylinder becomes wider. In this calculation, it is also found that Reynolds number $U_{max}D/\nu$ and the relative water depth kh do not much affect the separation point.

Fig.5 shows the vertical distributions of separation point. If we consider the case that $h = 40$ cm, $D = 3$ cm and $\nu = 0.01112$ cm²/sec, the wave period of each curve becomes 0.5 sec \sim 5.0 sec as shown in the figure. In this calculation, K.C. number at the position where $z/h = -0.1$ is 6. In the figure, when the wave period is as short as 0.5 sec or 0.7 sec, the flow separation occurs only near the water surface. On the other hand, when the wave period is as long as 2 sec or 5 sec, the separation point does not change vertically so much. This is caused by the vertical distributions of water particle velocity of the main flow, which means vertical change of K.C. number.

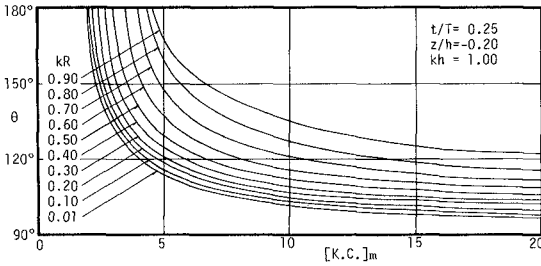


Fig.4 Shift of flow separation point.

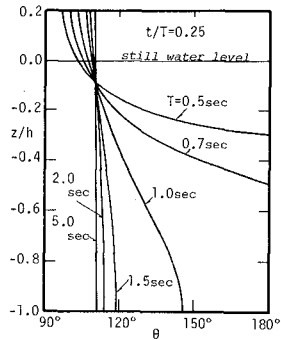


Fig.5 Vertical distributions of flow separation point.

3. EXPERIMENTS AND CONSIDERATION

In the experiment of flow separation, a circular cylinder made of Lucite with a diameter of 3 cm was installed in the center of a wave tank, which is 27 m long, 50 cm wide and 70 cm deep. As shown in Fig. 6, from this cylinder surface, a platinum wire with a diameter of 0.05 mm was stretched horizontally, and trains of hydrogen bubbles were generated from the platinum wire by using a pulse generator, and photographs were taken through the glass bottom. As the cylinder was made rotatable around the vertical Z-axis in Fig. 1, the separation point was examined by rotating the cylinder every 5° in the range of angle from 90° to 160° during the phase of wave crest.

The water depth h was 40 cm and the measuring point z_p was 5 cm below still water level, and the correspondence of experimental cases to the wave characteristics is shown in Table 1, in which $Re_m = u_{max}D/\nu$.

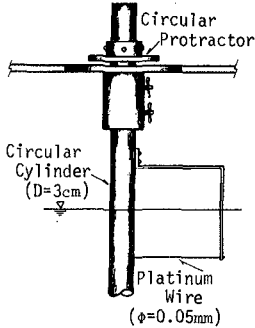
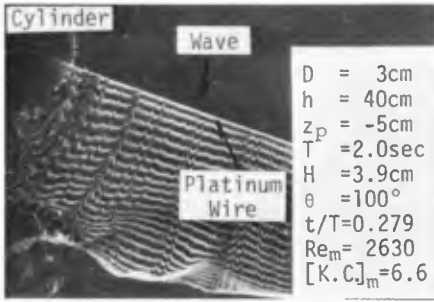


Fig. 6 Sketch of experimental apparatus for flow separation.

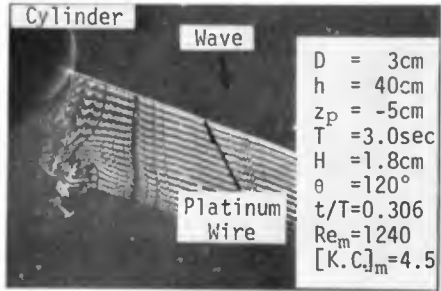
Table 1 Experimental condition for flow separation.

Case	T(sec)	H(cm)	$h=40$ cm, $z_p=-5$ cm	
			[K.C.] _m	$Re_m \times 10^{-3}$
I-1	2.0	1.5~1.6	2.5~2.7	1.02~1.09
I-2	2.0	2.4~2.6	4.1~4.4	1.64~1.77
I-3	2.0	3.3~3.4	5.6~5.7	2.25~2.32
I-4	2.0	3.7~3.9	6.2~6.6	2.49~2.63
I-5	2.0	4.9~5.1	8.3~8.6	3.30~3.44
I-6	2.0	5.7~5.8	9.6~9.8	3.84~3.91
I-7	3.0	1.0~1.1	2.5~2.8	0.69~0.76
I-8	3.0	1.8~2.0	4.5~5.0	1.24~1.38
I-9	3.0	2.5~2.7	6.2~6.7	1.73~1.87
I-10	3.0	3.5~3.8	8.7~9.5	2.42~2.63
I-11	3.0	4.5~4.9	11.2~12.2	3.11~3.39

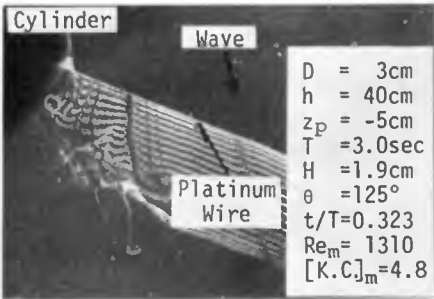
Some examples of photographs taken about flow separation are shown in Photo. 1(a), (b) and (c). Photo. 1(a) shows that when $t/T = 0.279$, the flow is not separated yet at the position of the platinum wire where $\theta = 100^\circ$, in which K.C. number is 6.6. Photo. 1(b) is an example of such a critical condition that the flow is just separated at the position of platinum wire, in which $t/T = 0.306$, $\theta = 120^\circ$ and K.C. number is 4.5. Photo. 1(c) is the case when $t/T = 0.323$ and the position of the platinum wire, $\theta = 125^\circ$, is in the region of reverse current because of flow separation, in which K.C. number is 4.8.



(a) Not separated.



(b) Critical.



(c) Separated.

Photo.1 Visualization of flow separation.

Fig.7 shows the comparison between theoretical separation points and experimental values. In this figure, experimental data are divided into three flow conditions by the photographs; that is, at the intersection point of the platinum wire and the cylinder surface, the separation has not occurred yet, just occurred and already occurred as shown in Photo.1(a), (b) and (c) respectively. This figure indicates that the experimental values agree well with the theoretical ones except Cases I-6, I-10 and I-11, in which K.C. numbers are so large that the vortices generated before a half period of waves in front of the cylinder become to disturb the boundary layer during their shedding along the cylinder surface toward the rear part of the cylinder by the return flow.

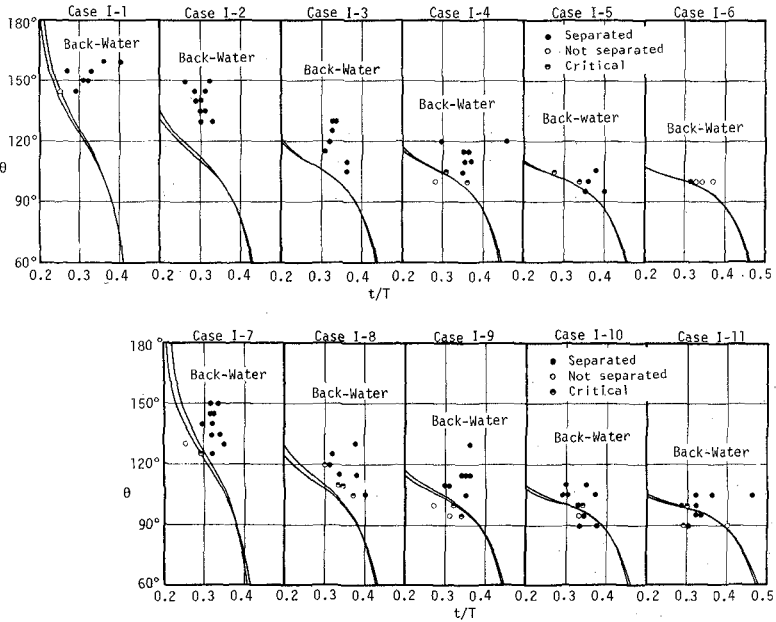


Fig.7 Comparison of theoretical flow separation point with experimental data.

WAKE VORTICES

1. EXPERIMENT

In the experiment of wake vortices, platinum wires were stretched horizontally from the cylinder surface at the angles of about 90° and 270° , and photographs of hydrogen bubble lines were taken successively with an interval of about 0.25 sec by using a motor driven camera. Other experimental apparatus were same as in the case of flow separation. Experimental conditions were as follows: $h = 40$ cm, $z_p = -5$ cm, $v = 0.01141$ cm²/sec, and the wave period T in the range from 1 sec to 8 sec and the wave height H from 1.5 cm to 7.5 cm were used in this experiment.

Examples of successive photographs showing the time process of vortex formation and shedding are shown in Photo.2 and Photo.3, which are an example of a pair of symmetric vortices and that of extremely asymmetric vortices or almost Karman vortex street respectively.

From Photo.2, it is recognized that after flow separation, a new pair of vortices begins to form behind the cylinder at the phase $t/T = 0.30$ and is growing up symmetrically till $t/T = 0.50$, in which another pair of vortices at the right side of each photographs is an old one generated in front of the cylinder before a half period of waves and transported by main flow, and that as the main flow changes its direction after $t/T = 0.5$, the vortices are transported toward the front of the cylinder at each side of the cylinder. In this case, K.C. number is 7.4.

On the other hand, it is recognized from Photo.3 that a pair of small vortices appears slightly at the phase $t/T = 0.15$, but only one vortex at the lower side of the cylinder in the photographs is growing large till $t/T = 0.23$ and begins to shed at $t/T = 0.31$, and the other vortex at the upper side of the cylinder in the photographs is growing till $t/T = 0.51$. In this case, K.C. number is as large as 19.8, and hydrogen bubble lines are quite turbulent because of the remaining effects of some vortices generated before a half period of waves.

2. DISCUSSION OF RESULTS

The relationship between vortex configurations and both Reynolds number Re_m and K.C. number $[K.C.]_m$ is shown in Fig.8(a). The explanation of each symbol is shown in Fig.8(b), in which dotted lines show the path of vortices in return flow. In this figure, it is found that the vortex configurations are generally transformed by K.C. number; that is, when K.C. number is smaller than 2, flow separation does not occur both theoretically and experimentally, and when K.C. number is smaller than about 7.5, a pair of symmetric vortices appears. With increase in K.C. number, a pair of vortices becomes asymmetric, especially when K.C. number is larger than 15, it becomes extremely asymmetric as shown in Vortex-Pattern C, and finally, when K.C. number reaches about 20, vortices become similar to Karman vortex street.

It is apparent that such transformations of vortex configuration are caused by the characteristics of vortex generation and shedding. The former is closely related to the characteristics of flow separation and the latter is due to the sweeping effect of a main flow and the stability of vortices. In other words, when K.C. number is small, the flow separation does not continue so long time as to form vortices, and even when Reynolds number is high to some extent, the wake vortices may not be formed so easily in the wave field as in the steady flow. On the other hand, as the angle of separation point becomes smaller with increase in K.C. number and does not vary so quickly with the wave phase which means that the wake region becomes larger for a longer time, the generation and shedding of wake vortices in the wave field become similar to those in steady flow.

It is considered that the state of vortex shedding in the wave field may be known by using the relationship between Reynolds number and Strouhal number obtained in the case of steady flow⁶). Denoting the frequency of vortex shedding, the wave frequency and Strouhal

$D=3\text{cm}$, $h=40\text{cm}$, $Z_p=-5\text{cm}$, $T=4.9\text{sec}$, $H=1.9\text{cm}$, $Re_m=1220$, $[K.C.]_m=7.4$

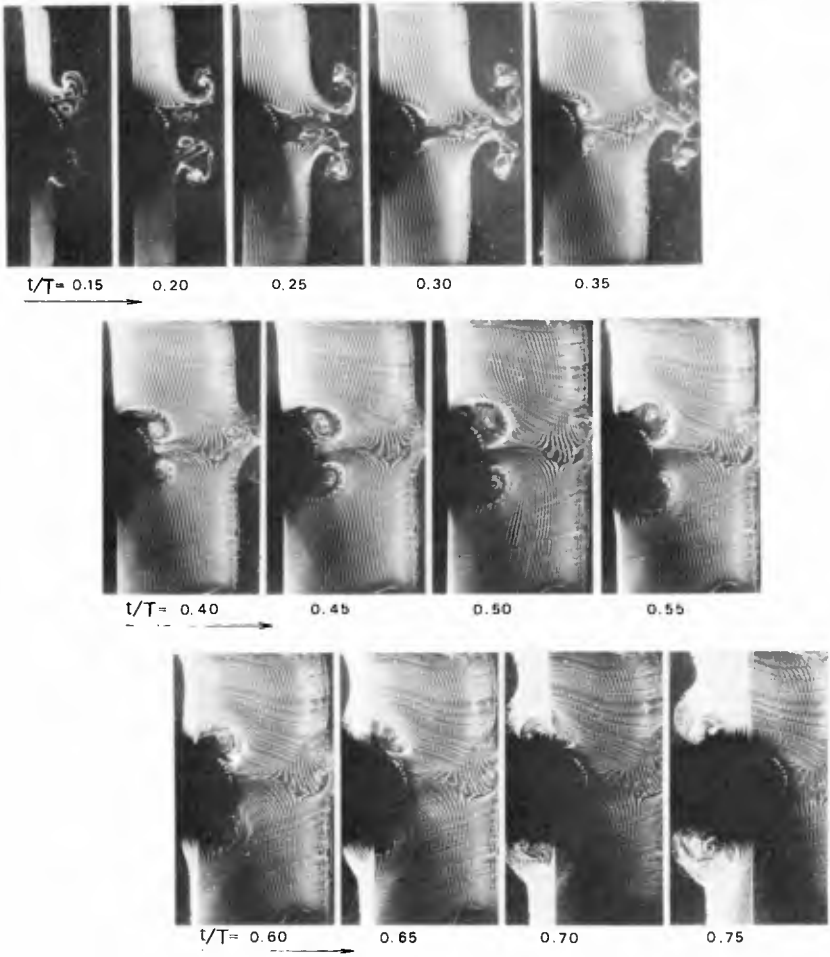
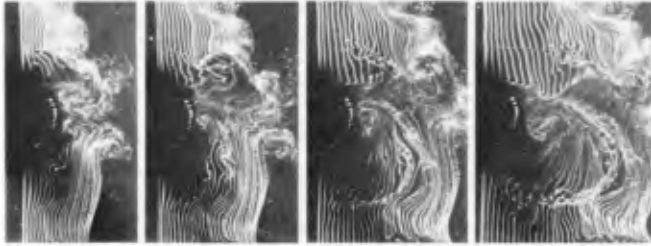
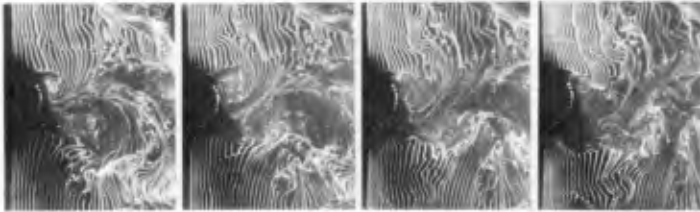


Photo.2 Time variation of wake vortices in case of a pair of symmetric vortices.

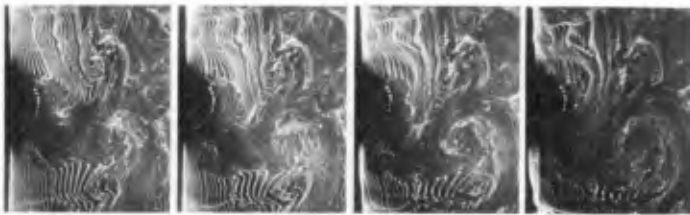
$D=3.2\text{cm}$, $h=10\text{cm}$, $Z_0=-1.5\text{cm}$, $T=7.2\text{sec}$, $H=3.2\text{cm}$, $Re_{D1}=2110$, $K.C._{D1}=110$



$t/T = 0.15$ 0.19 0.23 0.27



$t/T = 0.31$ 0.35 0.39 0.43



$t/T = 0.47$ 0.51 0.55 0.59

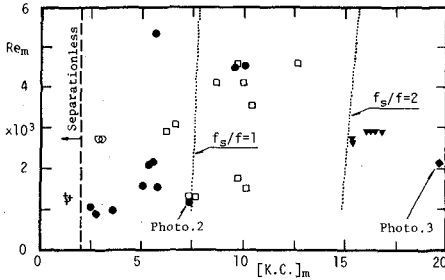
Photo.3 Time variation of wake vortices in case of Karman vortex street.

number by f_s , f and S respectively, the value of f_s/f means the number of shedding vortex during one wave period, which is estimated by the following equation:

$$f_s/f = (Re/Re_m) \cdot S \cdot [K.C.]_m, \dots\dots\dots(11)$$

in which the validity of Eq.(11) is easily confirmed by substituting $Re = UD/v$, $Re_m = U_m D/v$, $S = f_s D/U$ and $[K.C.]_m = U_m/(Df)$ into the right hand side of Eq.(11).

Therefore, $f_s/f = 2$ corresponds to the condition that a pair of vortices are generated during a half period of wave and the direction of flow in the wave field is reversed just before a subsequent vortex appears, which is considered to be similar to the configuration of Vortex-Pattern C. The dotted line denoted by $f_s/f = 2$ in Fig.8(a) shows the condition in the case of applying the average value of Re during a half period and the value of S corresponding to Re_m , which corresponds well to Vortex-Pattern C appearing when $[K.C.]_m$ is about 16.



(a)

Fig.8 Variation of vortex-pattern behind cylinder with K.C. number and Reynolds number.

Symbol	Flow Pattern	Note
+		Without separations and without vortices.
○		Separations but without vortices.
●		Vortex-Pattern A; A pair of symmetric vortices.
□		Vortex-Pattern B; A pair of asymmetric vortices.
▼		Vortex-Pattern C; A pair of extremely asymmetric vortices.
◆		Vortex-Pattern D; Pseudo Karman vortex street.

(b)

PRESSURE DISTRIBUTION

1. EXPERIMENT

In the experiment of wave pressure measurements, a wave tank which is 17.5 m long, 1.5 m wide and 75 cm deep was used, in which, a circular cylinder consisting of three parts, as shown in Photo.4, with a diameter of 3 cm and a total length of 85 cm was installed vertically at the position of 9 m and 25 cm apart from the wave generator paddle and the side wall respectively. A very small pressure gauge with a diameter of 2.8 mm shown in Photo.5 was attached to the surface of the middle cylinder part at the position A shown in Fig.9, and its linearity was confirmed to be very well.

Distributions of wave pressure were measured by rotating this cylinder intermittently around the center axis, and then, the water depth h was 40 cm and the measuring point Z_p was 5 cm below still water level. In Table 2, wave height H , wave period T , K.C. number, Reynolds number and the angle of separation point calculated theoretically at the wave phase $t/T = 0.25$ are shown correspondingly to each experimental case.

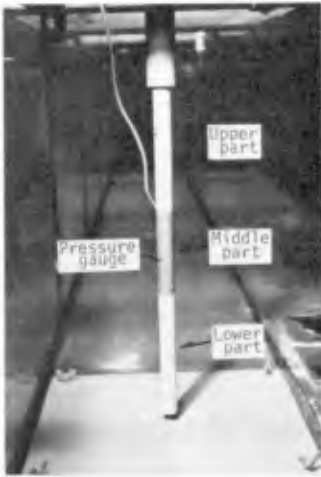


Photo.4 Experimental apparatus for wave pressure.



Photo.5 Mini-sensor of pressure gauge.

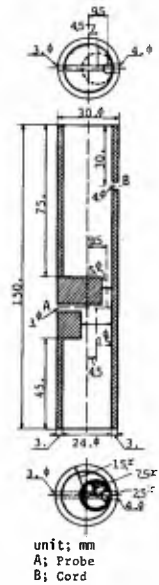


Fig.9 Cross section of middle part of cylinder.

Table 2 Experimental condition
for wave pressure.

Case	T(sec)	H(cm)	[K.C.] _m	Re _m × 10 ⁻³	θ _s
					(t/T=0.25)
III-1	0.7	3.5	2.6	2.77	147°
III-2	0.7	7.5	5.3	5.80	115°
III-3	1.0	3.8	3.5	2.71	128°
III-4	1.0	8.7	8.0	6.25	106°
III-5	1.5	3.3	4.2	2.21	120°
III-6	1.5	6.5	8.6	4.43	105°
III-7	2.0	3.0	5.1	2.01	115°
III-8	2.0	7.9	13.3	5.30	100°
III-9	2.5	3.0	6.1	1.96	110°
III-10	2.5	6.0	12.5	3.90	100°

2. DISCUSSION OF RESULTS

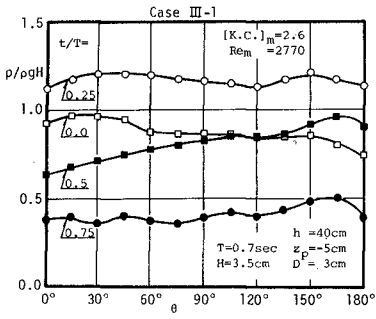
In the analysis of experimental data, it is assumed that the wave conditions are constant even if the angle of measuring point is changed, and the value of wave pressure at each angle is determined by averaging the data during three cycles of successive waves.

Some examples of pressure distributions around the cylinder at the wave phases $t/T = 0, 0.25, 0.5$ and 0.75 are shown in Fig.10(a) and (b), and correspondingly, time variations of wave pressure at the angles $\theta = 30^\circ, 90^\circ$ and 150° are shown in Fig.11(a) and (b). In each figure, (a) and (b) show the results of Cases III-1 and III-7 respectively.

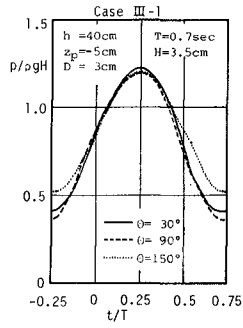
In Case III-1, Reynolds number is 2770 and K.C. number is as small as 2.6. In this case, flow separation occurs but any wake vortex does not appear distinctly, and therefore, pressure distributions are roughly smooth as shown in Fig.10(a) and time variations of pressure are almost sinusoidal as shown in Fig.11(a), corresponding to the water level variation.

In Case III-7, Reynolds number is 2010 and K.C. number is 5.1. In this case, a pair of symmetric vortices appears and causes local depressions of wave pressure; that is, in Fig.10(b), the pressures at the angles $\theta = 120^\circ$ and 60° are extremely decreased by each wake vortex at the wave phases $t/T = 0.25$ and 0.75 respectively. And moreover, it is found in Fig.11(b) that the time variation curve of wave pressure at $\theta = 150^\circ$ fluctuates near $t/T = 0.25$, which is also regarded as the effect of wake vortices.

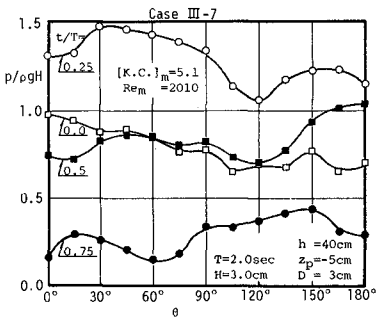
It is understood from these examples that wake vortices cause the local depressions of wave pressure and induce the drag force, and moreover, it is considered that if wake vortices neither vanish nor shed soon and remain near $\theta = 0^\circ$ or 180° even when $t/T = 0$ or 0.5 respectively, the inertia force tends to decrease due to their vortices. This phenomenon may occur in the case of Vortex-Pattern C.



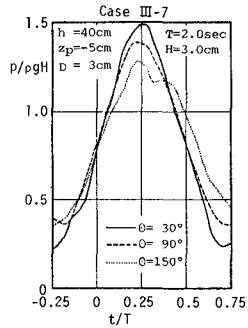
(a)



(a)



(b)



(b)

Fig.10 Pressure distribution around cylinder.

Fig.11 Pressure variation with time.

CONCLUSION

As a process of making clear the generation mechanism of wave forces acting on a circular cylinder, following the previous study of the water particle velocity in the laminar boundary layer, the characteristics of flow separation, wake vortices and wave pressure have been investigated, and the results obtained are as follows:

1. The separation point of the laminar boundary layer developed by wave motion on the cylinder is mainly varied with the wave phase and K.C. number. When K.C. number is small, apparent flow separation occurs so that the separation point varies quickly in short time. However, when K.C. number becomes large, the variation of separation point with the wave phase becomes more gradual and characteristics of flow separation become similar to those in steady flow.
2. Experimental values of separation point agree well with the theoretical ones in the case when K.C. number is smaller than about 9. However, when K.C. number becomes larger, the difference between both values becomes noticeable by the reason that wake vortices generated before a half period of waves disturb the boundary layer during their reverse shedding.
3. Within the range of this experiment, the configuration of wake vortices is successively transformed from a pair of symmetric vortices to asymmetric ones and finally Karman vortex street with increase in K.C. number. Generally speaking, the configuration of wake vortices is subject to the ratio of the frequency of vortex generation to the wave frequency, which may be determined by K.C. number, Reynolds number and Strouhal number.
4. Wave pressures around a cylinder are affected by wake vortices and the dynamic pressure in addition to the static pressure caused by water level variation. Wake vortices induce local pressure depressions in the wave field as well as in steady flow, and therefore, it is considered that fully developed vortices may cause to not only increase the drag force but also decrease the inertia force.

ACKNOWLEDGEMENT

The authors wish to express their gratitudes to Mr. W. Kioka and Mr. Y. Motoyama for their assistances through the experiments. This work was partly supported by Scientific Research Funds from the Ministry of Education.

REFERENCES

- 1) Son, Jaime S., and Thomas J. Hanratty: Velocity gradients at the wall for flow around a cylinder at Reynolds numbers from 5×10^3 to 10^5 , Jour. Fluid Mech., Vol. 35, Part 2, pp. 353-368, 1969.
- 2) Son, Jaime S., and Thomas J. Hanratty: Numerical solution for the flow around a cylinder at Reynolds numbers of 40, 200 and 500, Jour. Fluid Mech., Vol. 35, Part 2, pp. 369-386, 1969.
- 3) Batchelor, G.K.: An Introduction to Fluid Dynamics, Cambridge University Press, pp. 343-353, 1967.
- 4) Schlichting, H.: Boundary Layer Theory, McGraw-Hill, 1968.
- 5) Iwagaki, Y., and H. Ishida: Laminar boundary layer around a circular cylinder under oscillatory waves, Proc. 14th Coastal Eng. Confer. ASCE, Vol. 3, pp. 1848-1862, 1974.
- 6) Keulegan, G.H., and L.H. Carpenter: Forces on cylinders and plates in an oscillating fluid, Jour. Res. Nat. Bur. Stand., Vol. 60, No. 5, pp. 423-440, May 1958.

CHAPTER 138

CYLINDRICAL CAISSON BREAKWATER: STRAIN MODEL TESTS

Helge Gravesen¹, Finn P. Brodersen²,
Jørn S. Larsen², H. Lundgren³

ABSTRACT

The distribution of *shock pressures on a vertical face breakwater* is so random from one shock to the next that the determination of the *internal forces in a thin-walled reinforced-concrete structure* is difficult even when a large number of pressure cells is used in a model test. Therefore a technique has been developed that allows the direct determination of the internal stresses by means of strain gauges.

The new technique has been applied to a breakerwater consisting of a series of cylindrical caissons. The results show that a strain gauge model is more advantageous than a pressure cell model because of its simpler data analysis and better determination of the quantities required for design.

1. INTRODUCTION

It is well known that *vertical face breakwaters* may be exposed to heavy shock forces of short duration. Such impacts have often resulted in the *sliding* of individual breakwater caissons, see for example Refs. 2 and 8, where the slidings/nonslidings of breakwaters in Japan have been used for the evaluation of various wave pressure formulae. Because of the large inertia of the masses involved in rotation, it is much less frequent that breakwaters have been damaged due to insufficient stability against *overturning*. A third effect of the shock pressures is the production of *internal stresses* in thin-walled caissons of reinforced concrete.

A distinction may be made between *ventilated*, *hammer* and *compression shocks*, see Ref. 5, 6 or 7. While it is advisable by the design of the cross section to avoid hammer and compression shocks, there are many cases where ventilated shocks are inevitable. The development of a ventilated shock is described in Refs. 6 and 7.

The influence of the *geometry of the front face* on the magnitude of the shock forces is described in Refs. 6 and 7, the latter giving ranges of dimensionless coefficients in the formulae for forces and pressures.

¹Senior Research Engineer, Danish Hydraulic Institute (DHI), Agern Allé 5, DK-2970 Hørsholm, Denmark.

²Hydraulic Engineer, DHI.

³Professor of Marine Civil Engineering, Institute of Hydrodynamics and Hydraulic Engineering, Technical University of Denmark, Building 115, DK-2800 Lyngby, Denmark. — Consultant, DHI.

The various *types of caissons* (rectangular, cylindrical, diaphragm, multicellular) are discussed in Ref. 7.

In comparison with traditional rectangular caissons, breakwaters of caissons containing *cylindrical, reinforced-concrete shells* are highly economical structures for three reasons:

- (a) The cylindrical shell is better capable of resisting the wave forces and the pressure from sand fill, resulting in smaller thickness of the outer walls, less cracking, less weight and less steel.
- (b) Transverse walls can be given a larger spacing (diaphragm type) or completely eliminated (cylindrical type), depending upon the method of construction (Ref. 7), thus resulting in smaller weight of the caisson, as well as less concrete and steel.
- (c) The stability is improved because of the delay in development of shock pressures from the front generatrix to the reentrant corner, as described in Refs. 6 and 7. This effect is pronounced in the cylindrical type, but of little importance in the diaphragm type.

Investigations during the last 16 years of breakwaters containing cylindrical shells have also led to a series of *developments in model testing techniques*:

- (1) The first application of large-diameter cylindrical shells to breakwaters was for the Hanstholm harbour, Denmark, for which the model tests took place in 1960 (Ref. 4). While, previously, the forces on vertical face breakwaters had been measured by pressure cells only, the stability of the Hanstholm breakwater was investigated by measuring on the model caisson the *total horizontal and vertical forces*, as well as the overturning moments. In subsequent investigations a three-component strain gauge dynamometer has been used. For the Hanstholm breakwater shock forces could be almost entirely eliminated by the introduction of a *top face sloping 30°* with the horizontal, starting from about still water level (Ref. 4), because at Hanstholm there is little variation of the water level for all western gales.
- (2) The next step in the development of testing technique was a method for *generation of wave trains of natural shape* directly from wave records, thus producing shock pressures in a flume only 15 m long. At the same time a method was devised for the determination of the *re-reflection from the generator* by measuring the energy in the flume during the test. These methods, which are described in Ref. 3, were first used in 1971 in tests for the breakwater of the Brighton marina, U.K. (Refs. 1 and 7).
- (3) Because of the random and complex distribution of shock pressures on cylindrical caisson breakwaters, as much as *20 pressure cells* have been applied in model tests (Refs. 6 and 7), with a view to the determination by computer programs of the internal forces in the shells.
- (4) The stability and strength designs require that the forces and pressures measured in model tests be extrapolated to rare situations as statistical parameters. A method of *statistical analysis* combining the statistics of the wave climate with the statistical distributions of the model data has been developed.

Because of the difficulties of extrapolating complex and random pressure distributions to rare situations, Danish Hydraulic Institute felt the necessity of developing a model technique by which the *strains* (and hence also the stresses), induced in the cylindrical shell by the wave pressures, are *directly determined by means of strain gauges*.

This technique was developed in cooperation with the Institute of Hydrodynamics and Hydraulic Engineering and the Structural Research Laboratory, Technical University of Denmark.

The present paper gives a description of this technique, as well as a comparison between the directly measured internal forces and the forces calculated by a computer program from pressure cell recordings.

2. STRAIN GAUGE MODEL

The model (Figs. 1 and 2) is geometrically similar to the prototype. The model material is *araldite* with $E = 3.2 \text{ GN/m}^2$, which is about twice as much as required for dynamic similarity at a model scale 1:20. This deviation from dynamic similarity is without significance, however, because the inertial forces of the prototype concrete shell are negligible even for the fastest shocks.



Fig. 1 Strain gauge model placed in a 600 mm wide flume

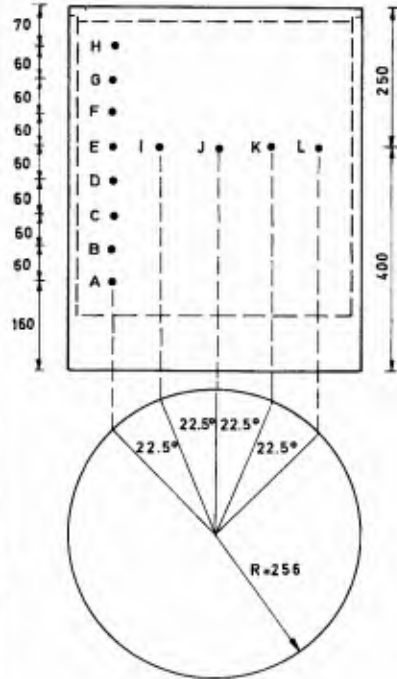


Fig. 2 Strain gauge model (dimensions in mm)

The determination of the *complete stress situation at one point* of the shell requires two rosettes (outside and inside), each containing 3 strain gauges. The rosettes on the outside are embedded so as to give a minimum insulation of 100 MΩ.

The rosettes A-H (Fig. 2) are placed along one vertical line on the cylinder. In order to determine the full stress distribution in the shell, the cylinder is rotated 22.5° between one test series and the next one. For this reason rosettes I-L are mounted at the same level as E in order to give reference time values for the initiation of a shock pressure at the front generatrix.

Normal forces are considered positive as tension in the shell. Bending moments are positive when there is tension on the inside.

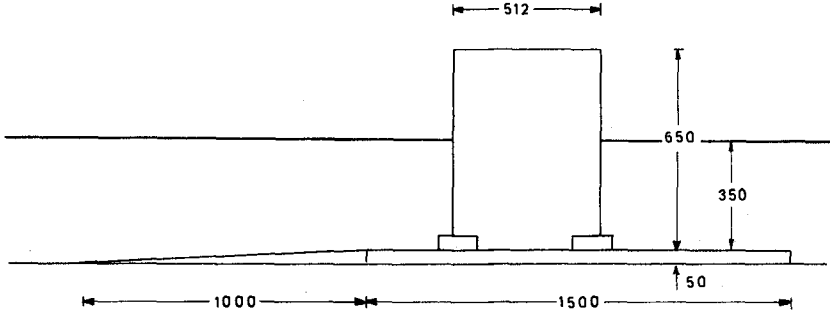


Fig. 3 Longitudinal section of the cylinder in the flume

The model has a diameter of 512 mm, a height of 650 mm, and a thickness of 15 mm. It is placed in 350 mm of water (Fig. 3) inside a 600 mm wide flume that is part of a 4 m wide flume (Fig. 4), in which the undisturbed generated waves can be recorded.

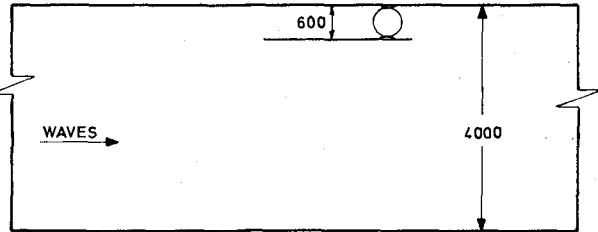


Fig. 4 Plan showing cylinder in the 600 mm flume inside the 4 m flume

The median values of the strains recorded in 10 repeated tests at a specified time for a specific shock wave have been calculated for comparison with the stresses computed from the pressure cell model mentioned below. The *standard deviation* is estimated to be about 10%.

3. PRESSURE CELL MODEL

The pressure cell model has the same diameter and height as the strain gauge model. 16 or 14 pressure cells are used. Fig. 5 shows to the left the arrangement of cells for the measurement of shock

pressures around the front generatrix and, to the right, the arrangement determining shock pressures in the corner between two caissons.

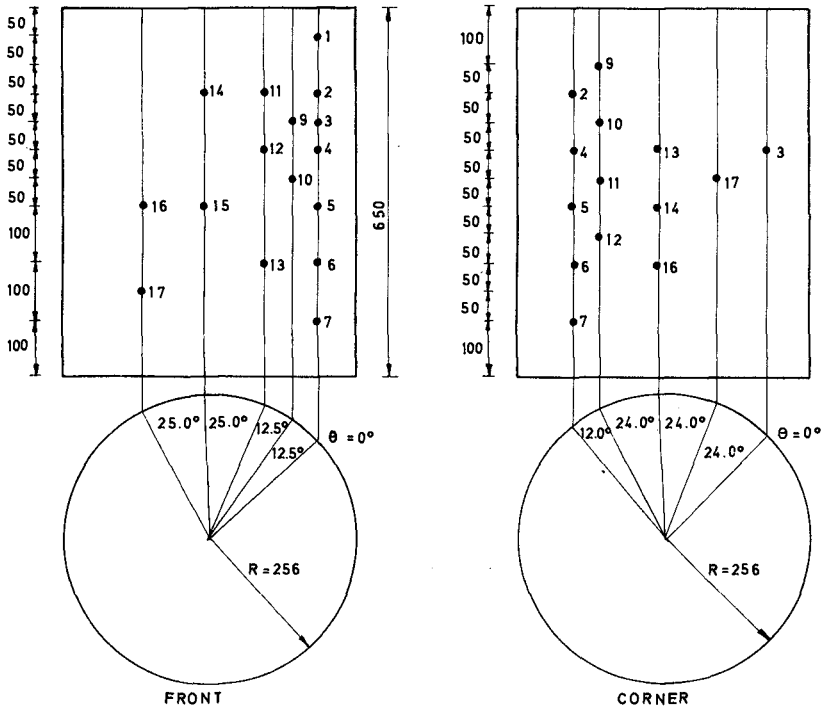


Fig. 5 Pressure cell model

For 10 repeated tests median values of the pressures have been used as input in a *computer program* for the calculation of the internal forces in a circular cylindrical shell of constant wall thickness and elastic material.

The program BAC, developed at the Structural Research Laboratory of the Technical University of Denmark, has been chosen. This program is based upon the development of the load in fourier terms $\cos n\theta$ and $\sin n\theta$ with $n \leq 9$. In the vertical direction the shell is divided into a large number of equidistant horizontal rings. With the use of finite elements in the vertical direction, the program calculates the internal forces (and the deformations) at these equidistant levels.

Because of the limited number of pressure cells and the large gradients exhibited by shock pressures, the actual pressure distribution is poorly defined. In addition, the limited number of terms in the fourier series are unable to give an exact representation of the recorded pressures.

As an illustration of the *approximations involved*, the dotted line in Fig. 6 shows the pressure distribution as defined by pressure cells

spaced 22.5° along the most exposed horizontal section in the model tests for the Brighton marina breakwater (scale 1:22), at a moment where the shock pressure on the front generatrix is particularly high. It will be seen that the maximum fourier series load (the full line) is much lower than the recorded pressure. It is estimated that this discrepancy results in a standard deviation of about 10% for the internal forces.

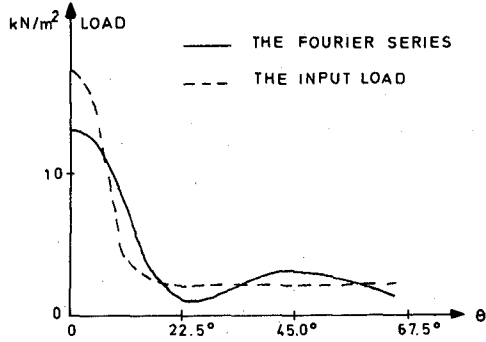


Fig. 6 Shock pressure distribution along horizontal section

Including the large scatter of the pressure distributions in 10 repeated tests, the total *standard deviation* is estimated to be 15% on the median values of bending moments, with a maximum scatter of about 30%.

The fourier series in Fig. 6 represents 10 terms, $n = 0-9$, which give the contributions shown in Figs. 7 and 8, respectively, to the normal force N_θ and the bending moment M_θ in the vertical section through the front generatrix, as well as to the normal force N_x and the bending moment M_x in the horizontal section.

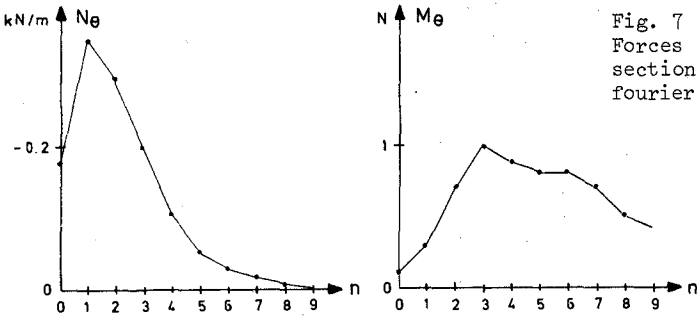


Fig. 7 Forces in vertical section from fourier terms $\cos n\theta$

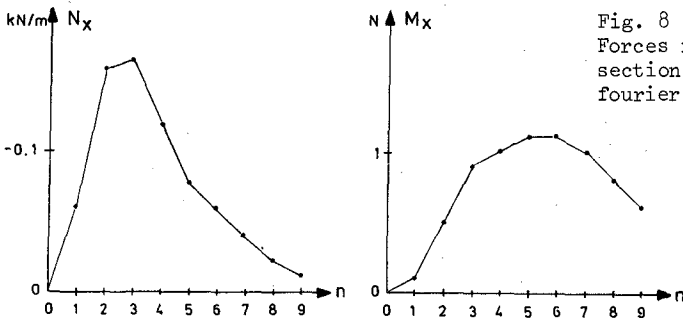


Fig. 8 Forces in horizontal section from fourier terms $\cos n\theta$

It appears that the values for $n > 9$ would have contributed essentially to the bending moments had the computer program been extended to higher terms. (It may be mentioned that the computational error increases with the order of the term.)

4. COMPARISON OF THE RESULTS FROM THE TWO MODELS

The median values of the normal forces and bending moments are presented in Fig. 9 at the instant when a large shock wave hits the front of the caisson, and in Fig. 10 at the slightly later instant when the same wave hits the corner between two caissons. The results from the strain gauge model are shown as dots, while the forces computed from the pressure cell model appear as full curves.

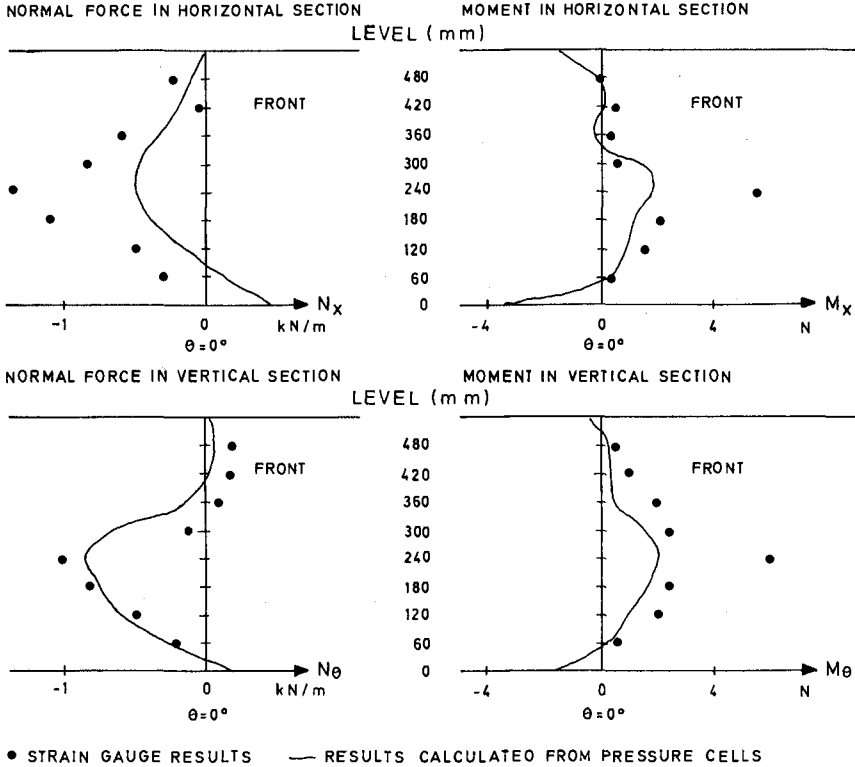


Fig. 9 Internal forces along the front generatrix

When the two sets of results are compared, the following circumstances should be borne in mind:

- (a) For the pressure cell model the load is defined by a number of cells that is small compared to the irregular variation of the shock load. Between the cells the pressures have been estimated by linear interpolation.

- (b) For the pressure cell model it has been assumed that the load is symmetrical around the plane through the middle of the flume. Because of the sensitivity of the shock pressures to small disturbances, the full curve in Fig. 9 may be slightly incorrect.
- (c) The times chosen for the analysis of data from the two models may not correspond exactly to each other.

The comparison shows large differences between the two models at the most exposed points of the cylinder (level 240 mm in Fig. 9 and level 360 mm in Fig. 10). The discrepancy in the bending moments might be the result of a smaller extent of the highest pressures than inherent in the linear interpolation mentioned under (a) above.

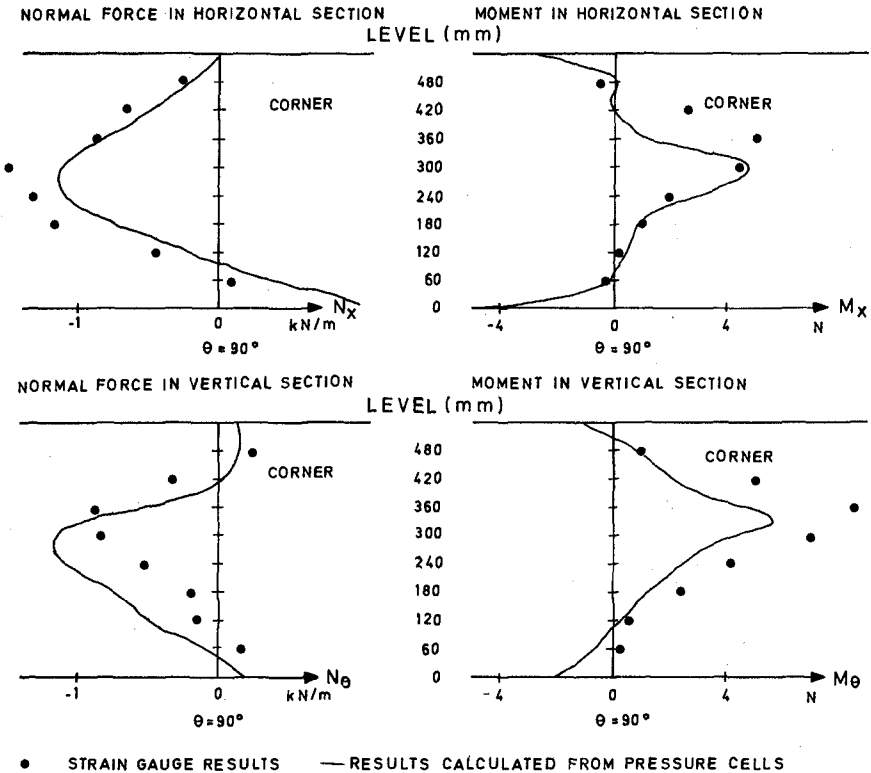


Fig. 10 Internal forces along the corner generatrix

5. COMPARISON OF PRESSURE CELL AND STRAIN GAUGE MODELS

As a result of this investigation it is concluded that a strain gauge model (SGM) is more advantageous than a pressure cell model (PCM). This conclusion is based upon the following comparison of the two techniques:

(a) Construction of Model

A PCM is less expensive than an SGM because the former need to have only the correct outside shape while the latter must be moulded out of a special material of good elastic properties. In addition, the wall thickness of the SGM should not deviate too much from geometric similarity with the final design.

(b) Instrumentation of Model

The acquisition of a large number of pressure cells with amplifiers and equipment for simultaneous recording of many channels is expensive. On the other hand, the same instrumentation may be used for several breakwater projects.

The number of rosette gauges required for an SGM is considerably larger than in the investigation reported in this paper, because the cylinder cannot be rotated due to its structural connection with the neighbouring caissons. Qualified workmanship is a prerequisite for the installation of the gauges. However, the costs of the gauges and their installation add little to the costs of the investigation. Simultaneous recording of 6 channels (two rosettes) is an absolute minimum, because two rosettes are required for the determination of the complete stress situation at one point.

(c) Test Runs

If sufficient pressure cells are available the PCM requires only one test run for a given wave train, while the SGM requires many runs to give records from, say, 20-30 rosettes. The repetitive runs, however, is a matter of routine that can be performed by one technician.

(d) Adequacy of Information

While the SGM gives complete information for the design of the reinforcement at each rosette point, the information from the PCM is insufficient because of the difficulties of defining the shock pressure distributions in connection with the large local pressure gradients. As a consequence of this, the results from the PCM may also depend upon the shell computer program applied, cf. Figs. 7-10.

(e) Data Analysis

For the SGM the analysis of the distribution functions for the strain maxima under the heaviest shocks is relatively simple, cf. Fig. 11 below. Also, the extrapolation to rare situations with due consideration of the wave climate can be done with reasonable accuracy, see Figs. 12-15 below.

For the PCM it does not seem feasible to carry out the stress analysis by computer program for so many load situations that the distribution functions for the stresses at the various points can be determined with sufficient accuracy. Hence, it is necessary to extrapolate the pressure distributions to rare situations and to apply the computer program for a few loads only. Thus, it is hardly possible to take sufficient regard to the wave climate, and the indirect determination of the design stresses may become somewhat problematic.

6. STRAIN DISTRIBUTION FUNCTIONS

For each zero-crossing period T_z and significant wave height H_s , the strains may be assumed to be *exponentially distributed*. The distribution functions have been determined for a number of combinations of T_z and H_s by means of trains of 1000 waves reproduced as described in Ref. 3.

As an example, Fig. 11 shows the distribution functions from one test run for point D on the front generatrix of the cylinder (Fig. 2). The abscissa PN is the so-called *probability number*, i.e. the relative occurrence per wave for which the strains shown are exceeded. The ordinate is the strain with the unit microstrain μS , where $1 \mu S = 10^{-6}$.

For each value of PN the 6 strains plotted are simultaneous values from the records. The strains measured are arranged after the peak order of ϵ_{ho} , i.e. the horizontal strain on the outside of the shell. Thus, the extreme value $\epsilon_{ho} = -22 \mu S$ recorded for 1000 waves is exceeded with a probability number of $PN = 0.55 \cdot 10^{-3}$ per wave, while the next value $\epsilon_{ho} = -21 \mu S$ is exceeded $1.5 \cdot 10^{-3}$ times per wave.

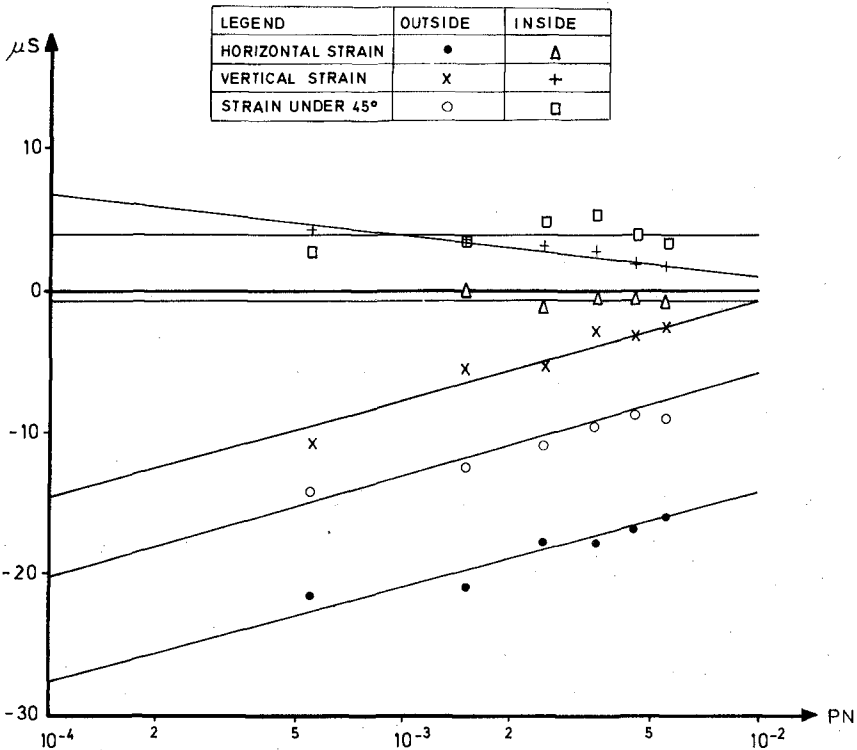


Fig. 11 Strain distribution functions at point D for $T_z = 1.52$ s and $H_s = .134$ m

Except for the inside diagonal strain (under 45°), the arrangement after the peak order of ϵ_{ho} also gives nearly monotonous arrangements of the other simultaneous strains. Thus, the result of this test run may be expressed by the following linear relationships:

$$\text{Outside horizontal strain} = \epsilon_{ho}$$

$$\text{Outside vertical strain} = \epsilon_{vo} = \epsilon_{ho} + 13 \mu\text{S} \quad (1)$$

$$\text{Outside diagonal strain} = \epsilon_{do} = \epsilon_{ho} + 8 \mu\text{S} \quad (2)$$

$$\text{Inside horizontal strain} = \epsilon_{hi} = -1 \mu\text{S} \quad (3)$$

$$\text{Inside vertical strain} = \epsilon_{vi} = (\epsilon_{ho} + 11 \mu\text{S}) \cdot (-0.4) \quad (4)$$

$$\text{Inside diagonal strain} = \epsilon_{di} = +4 \mu\text{S} \quad (5)$$

The fact that the rare strains are not proportional indicate that the shell carries the high shock pressures in different ways, with little variation of the strains on the inside.

7. STATISTICAL STRAIN ANALYSIS

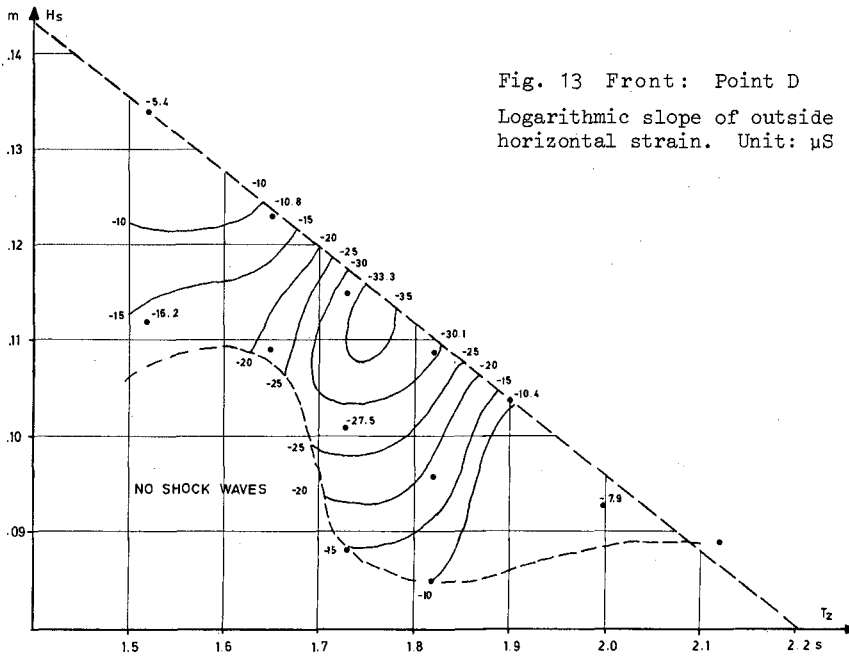
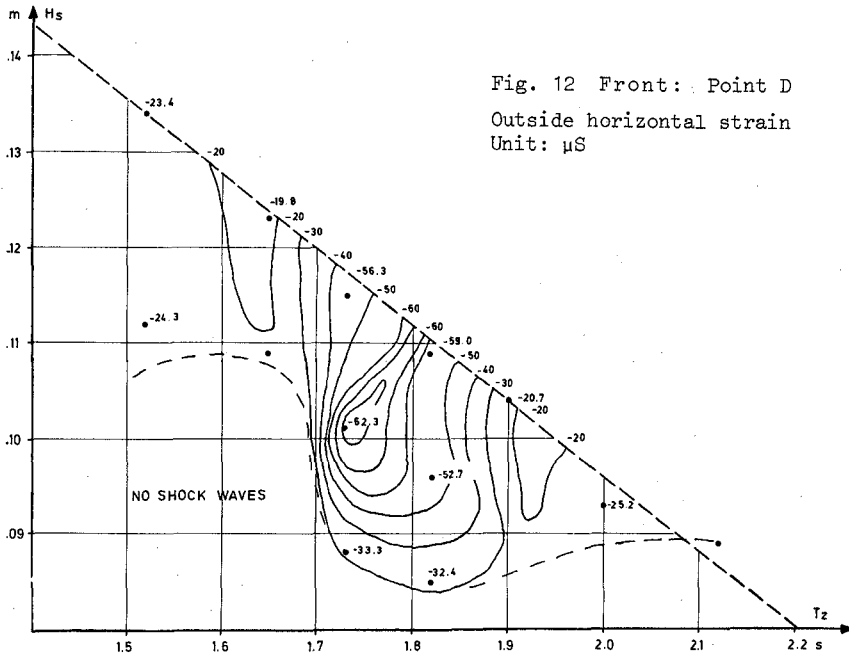
For the design of the shell it is necessary to know the *stress conditions* that are exceeded only once in, say, 100 years, with appropriate choice of the factors of safety for steel and concrete.

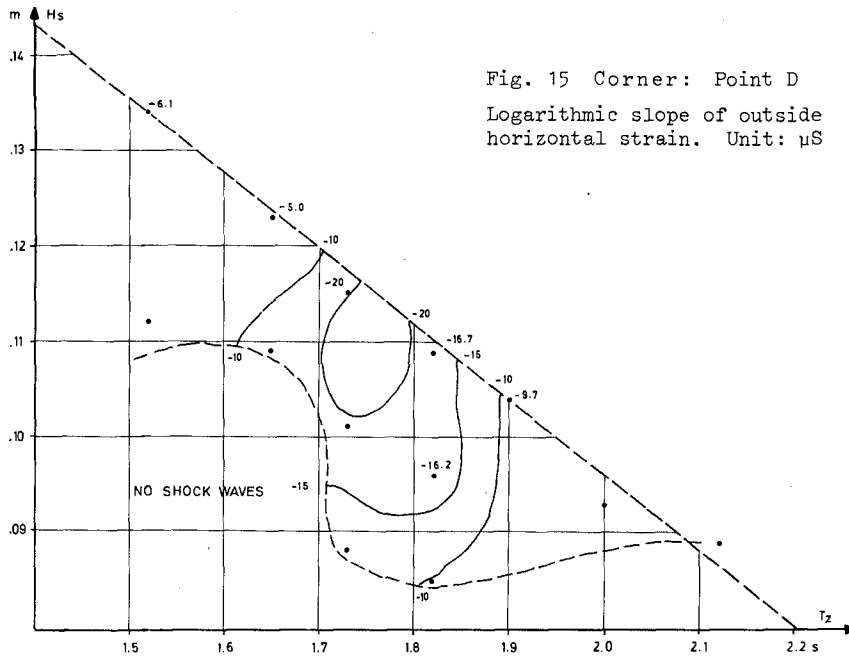
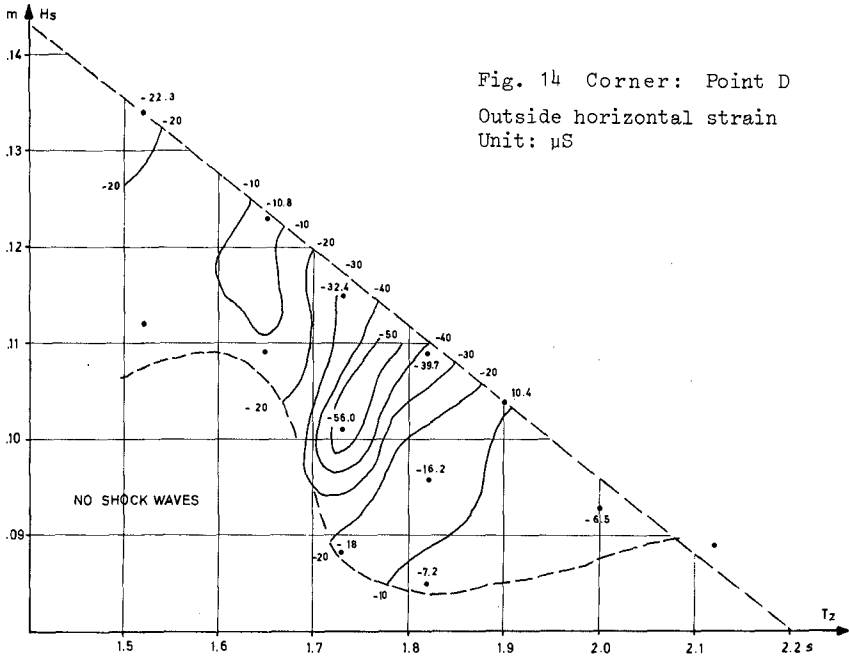
The *purpose* of the statistical analysis of the strains is to find the annual number of waves, ANWS, that exceed various strain values S . If the distribution function ANWS is plotted against S and extrapolated to the value $\text{ANWS} = 10^{-2}$, the corresponding value of S will occur once in 100 years.

In principle, the statistical analysis should be based upon the *probability density function* $p(T_z, H_s, WL, WD)$, i.e. the wave climate expressed as a function of zero-crossing period T_z , significant wave height H_s , water level WL and wave direction WD. Evidently, it is necessary to know the density function only for the larger values of H_s . In addition, if the wave direction deviates more than, say, 20° from the normal to the breakwater alignment, the shock forces are much reduced. Thus, in practice it is usually possible to introduce several simplifications in the complete statistical analysis.

As an *illustration* of the application of the results of the strain gauge model tests, Fig. 12 shows, for $\text{PN} = 0.55 \cdot 10^{-3}$ per wave, the outside horizontal strain ϵ_{ho} at point D along the front generatrix (Fig. 2) as a function of T_z and H_s . (The dotted straight line represents the limitation of wave conditions that could be generated in the flume.)

In order to find ANWS_{ho} as a function of ϵ_{ho} one could consider the areas within the curves where ϵ_{ho} takes the values $-40 \mu\text{S}$, $-50 \mu\text{S}$ and $-60 \mu\text{S}$, respectively. For each of these areas a summation is performed of the density function $p(T_z, H_s)$ for the determination of ANWS_{ho} that exceed the corresponding strains. For this calculation it is useful to know the logarithmic slope of the exponential distribution of ϵ_{ho} , which is plotted in Fig. 13.





After $ANWS_{ho}$ has been found for the three values of ϵ_{ho} mentioned, the approximately exponential distribution function $ANWS_{ho}$ is extrapolated to the value 10^{-2} . The corresponding value of ϵ_{ho} is used for the calculation of the remaining 5 strains by means of linear relationships such as (1) - (5) above.

Figs. 14 - 15 give the statistics of ϵ_{ho} for a corner point, in analogy to Figs. 12 - 13 for a front point.

It will be seen from Figs. 12 and 14 that the highest strain values occur within a rather narrow interval of mean period T_z . Hence, it is an important conclusion of the present investigation that the shock loads seem to depend considerably on the wave period. This result will have a significant influence on the test programs for future projects.

8. DESIGN OF REINFORCEMENT

During heavy shock loads the fine cracks always occurring in reinforced concrete will open (and close again). This phenomenon cannot be represented in a purely elastic strain model or in the calculation by a computer program. Because of the plasticity inherent in the opening of cracks, it is permissible to distribute the reinforcement much more uniformly than indicated by force diagrams such as Figs. 9 - 10.

REFERENCES

1. Cohen, H.L., D. Hodges, and F.L. Terrett, 'Brighton marina: Planning and design,' Proc. Symp. Marinas and Small Craft Harbours, Southampton 1972, Southampton Univ. Press, 1973, pp. 397-419.
2. Goda, Y., 'New wave pressure formulae for composite breakwaters,' Proc. 14th Coastal Engrg. Conf., Copenhagen 1974, Am. Soc. Civ. Engrs., New York, 1975, Vol. 3, pp. 1702-1720.
3. Gravesen, H., E. Frederiksen, and J. Kirkegaard, 'Model tests with directly reproduced nature wave trains,' 14th Coastal Engrg. Conf., Copenhagen 1974, Am. Soc. Civ. Engrs., New York, 1975, Vol. 1, pp. 372-385.
4. Lundgren, H., 'A new type of breakwater for exposed positions,' Dock & Harbour Auth., London, 1962, Vol. 43, No. 505, pp. 228-231.
5. Lundgren, H., 'Wave shock forces: An analysis of deformations and forces in the wave and in the foundation,' Proc. Symp. Research on Wave Action, Delft 1969, Vol. 2, Paper 4, 20 pp.
6. Lundgren, H., 'Coastal engineering considerations,' Proc. Symp. Marinas and Small Craft Harbours, Southampton 1972, Southampton Univ. Press, 1973, pp. 77-104.
7. Lundgren, H., and H. Gravesen, 'Vertical face breakwaters,' Proc. 6th Int. Harbour Conf., Antwerp 1974, Paper 2.11, 11 pp.
8. Nagai, S., and K. Kurata, 'Investigations of wave-pressure formulas due to damage of breakwaters,' Proc. 14th Coastal Engrg. Conf., Copenhagen 1974, Am. Soc. Civ. Engrs., New York, 1975, Vol. 3, pp. 1721-1740.

CHAPTER 139

NEAR-BOTTOM WATER MOTION UNDER OCEAN WAVES

by

Robert A. Grace*

SUMMARY

A two-year ocean experiment involving wave-induced forces on a test pipe mounted on the sea floor [Grace and Nicinski (1976)] involved the measurement of various quantities other than the pipe forces per se. A pair of these involved surface wave characteristics and wave-induced water motion at the level of the pipe centerline but off to one end of the pipe. These wave-kinematics data have been combined, and the results of this work make up this paper in which the emphasis is on the deterministic approach to data interpretation. Presented are comparisons of the velocity and acceleration data with the predictions of Airy and stream function theories plus discussion of the dispersion of the field data. The primary intent of the paper is to suggest to designers of bottom-laid structures, such as pipes, how values of the peak velocity and maximum acceleration of the water motion associated with a non-breaking design wave of specified characteristics can be chosen.

TEST SITE AND WAVE CONDITIONS

A site was chosen on a moderately level area of coral rock bottom 1400 feet from the reclaimed shoreline near Kewalo Basin, the fishing and tour boat harbor for Honolulu, where the water depth was 37 feet. Peak-to-trough tidal variations in Hawaiian waters are in the 1-to-2-foot range, so that the depth can be considered constant for all practical purposes.

We installed at this test site various structures. The major one related to the topic of this paper consisted of a heavy base composed of steel I beams and a wave mast bolted to it. This mast consisted of two parts; the lower one remained vertical and occupied approximately half the water column, whereas the upper one tilted down when not deployed and vertically upwards when a buoyancy chamber mounted permanently on it was blown. Both 3-inch and 2-inch-diameter steel pipe were used in the mast. The graduated upper part of the mast in part resembled the mast of a sailboat. A line over a pulley enabled us to pull the top of a 15-foot-long, wire-wound electrical wave staff to the summit; an acme thread bracket well down the tilting mast portion permitted us to then tighten the staff parallel to the mast. A cable ran from an oscillator at the top of the staff over the water to the project boat where suitable power supply and recording instrumentation were available. The boat, incidentally, was a 31-foot-long catamaran with 12-foot beam, an excellent work platform for our purposes.

A ducted-impeller velocity sensor was attached, by means of U bolts, to a small pipe cantilevered out from the end of the base for the 16-inch test pipe. The sensor was always located 15 inches from the bottom and 38 1/2 inches from

*Professor of Civil Engineering, University of Hawaii, Honolulu, Hawaii.

the end of the test pipe. The latter dimension was a compromise (for the pipe force work) between having the sensor close enough to represent the water motion incident upon the test pipe and yet far enough away not to be influenced by water motion around the end of it. A cable extended from the current meter up to associated d.c. power supply and recorder in the instrument shack on the boat.

We gathered concurrent data for waves and associated water motion on twelve different occasions, and the peak wave height measured overall was about 12 1/2 feet. However, we did encounter waves too big to measure accurately; one of these, a fluke, overtopped everything by quite a margin, severely bent the wave mast even though stiffened by a stout line from its top, and gave us all a fright; another snapped off the whole (repaired) mast at the base, along with all five stays set seaward, and wrote an end to wave-measuring for the remainder of the project.

Our test waves arrived between March and September of 1975 and 1976. The origin of these swells was in the Southern Hemisphere chiefly in the Tasman Sea as well as in the Pacific and Great Southern Ocean east of New Zealand. Swell from the latter source is generally the larger in Hawaii. Measured periods ran from 7 to 19 seconds, but by far the bulk of the observations lay in the range between 12 and 17 seconds.

PAST RELATED WORK

We were by no means the first to carry out at-sea measurements of waves and wave-induced water motion in the sea. Various types of field investigations have been run, and these are typified by Inman and Nasu (1956), Shonting (1967a, b) and Thornton and Krapohl (1974). A considerable amount of laboratory research has also been carried out on wave-induced water motion. Perhaps the most significant of such studies was the work of Goda (1964), and a particularly relevant part of his data, as far as this project is concerned, is shown in Tables 1 and 2. These data were kindly supplied to the writer by Goda for re-working.

The variables shown in Tables 1 and 2 are as follows: \bar{H} is the average and s_H the unbiased standard deviation of a sample of ten ostensibly identical waves of period T ; d is the water depth; g is the acceleration due to gravity; c_{Airy} and L_{Airy} are the wave celerity and wave length predicted by Airy wave theory; $u_{c_{\text{Airy}}}$ and $u_{c_{\text{s.f.}}}$ are the peak horizontal flow speeds under the waves, for a measurement location off the bottom of 0.13 times the depth, predicted by Airy and stream function theories; \bar{U}_c and s_u are the mean and standard deviation of the sample of ten measured peak flow velocities for each wave, and r_{HU} is the product-moment correlation coefficient between measured wave heights and velocities.

Table 1: Characteristics of Selected Waves from Goda (1964)

<u>Test No.</u>	\bar{H} (cm)	\bar{H}/d	\bar{S}_H (cm)	<u>T (sec)</u>	$T\sqrt{g/d}$	c_{Airy} (cm/sec)
44	36.1	0.24	0.6	2.38	6.09	316
45	52.7	0.35	1.0	2.36	6.04	315
46	58.5	0.39	1.1	2.43	6.21	318
47	34.6	0.23	0.7	2.98	7.62	340
48	55.9	0.37	0.8	3.14	8.03	344
49	28.6	0.19	0.2	4.15	10.61	361
50	47.0	0.31	0.3	4.16	10.64	361
51	64.5	0.43	0.6	4.17	10.66	361
52	57.3	0.38	0.8	5.77	14.76	372
53	64.3	0.43	0.6	7.89	20.18	377
54	77.2	0.51	1.2	7.90	20.20	377

Table 2: Peak Velocity Data of Selected Waves from Goda (1964)

Test No.	d/L_{Airy}	$u_{c,Airy}$ (cm/sec)	$u_{c,s.f.}$ (cm/sec)	\bar{u}_c (cm/sec)	s_u (cm/sec)	$\bar{u}_c/u_{c,Airy}$	r_{HU}	$s_{u/c}$ $u_{c,Airy}$
44	0.20	30.0	31.8	39.0	1.2	1.30	0.20	0.0039
45	0.20	43.4	44.7	49.7	2.1	1.14	0.17	0.0067
46	0.19	49.7	50.6	55.7	1.7	1.12	0.33	0.0055
47	0.15	34.3	36.0	37.4	1.7	1.09	-0.58	0.0051
48	0.14	57.1	57.9	66.8	3.3	1.17	-0.41	0.0096
49	0.10	32.3	37.9	35.7	1.6	1.11	0.04	0.0045
50	0.10	53.2	62.1	62.9	2.9	1.18	0.36	0.0081
51	0.10	73.1	78.8	80.0	2.1	1.10	0.56	0.0057
52	0.07	68.9	84.4	73.8	5.2	1.07	-0.29	0.0139
53	0.05	79.6	98.6	84.0	4.3	1.06	-0.06	0.0113
54	0.05	95.6	111.4	99.7	2.4	1.04	0.10	0.0063
Average	--	--	--	--	--	1.12	0.04	0.0073

Goda's data appear to show clearly that the predictions of the stream function theory [Dean (1965, 1974), Dalrymple (1974)] are too high when long waves are involved. Le Méhauté *et al* (1968) have concluded, on the basis of laboratory experiments, that the Airy theory provides the best estimate of near-bottom peak velocity of a number of classical theories.

BACKGROUND TO DATA

The pulse output of the velocity sensor and the stepped history of the wave staff were recorded on the same d.c. chart recorder. We found it easier to calibrate the staff against the graduated wave mast than by noting readings on the digital readout which was updated at a rate of ten per second. There were various problems with the wave staff but by and large these were compensated for in some way - e.g. by using the staff in a potentiometer arrangement, by reading trough values from the mast in cases when there were aberrations in wave staff behavior, and in reading crest levels from the mast when a particularly large wave went above the top of the staff.

The velocity history, a series of pulses whenever one blade magnet of the three-bladed impeller passed a reed switch enclosure on the side of the duct, was translated into a velocity history as follows. A sequence of between-pulse times was first lightly smoothed. The starting point for the translation of pulse history into a velocity trace was at the shortest interval or intervals within a trough or crest where the steady-state calibration of the sensor should be best represented. The rectangular-area rule was used until the between-pulse time changed. From then on the trapezoidal-area rule was followed - until the last (or first) pulse before (after) the change in flow direction. Points worked forward in time from a trough and backwards in time from a following crest were joined with a smooth curve whose maximum slope provided our best estimate of the peak acceleration under the wave.

The major advantage to the ducted meter is that it works - and one can see easily whether it is working or not. However, one pays a price for this. First, there is the time-consuming translation of the pulse history into a smooth velocity trace as outlined above. A second problem could concern off-angle use of the ducted meter. However, we oriented our meter directly into the approaching swell (as judged by the feel of the water motion and the movement of sand along the sea floor) and so there should be a minimal problem of this nature.

There are mixed emotions about the electromagnetic current meter. Some researchers feel that it is a first-class measuring device and various others are diametrically opposed. On one occasion we borrowed an electromagnetic sensor (spherical) and its owner-operator in order to compare the output of the ducted and electromagnetic types. I mounted these two meters side by side myself. Subsequently, the ducted meter ran perfectly; the electromagnetic meter yielded a trace that was very much in step with the output of the ducted meter but one that had nothing to do with the supposed calibration of the instrument.

VELOCITIES: DETERMINISTIC APPROACH

The comparisons between theoretical and measured kinematics data are shown in Figures 1 through 4. The sample size for the velocity data is 236, for the acceleration data 171.

During the final month and a half of the project, much of the higher velocity information in Figures 1 and 2 was obtained. Before these data were gathered and processed, it appeared that Airy theory provided predictions that were not only very good but also superior to those of the stream function theory. However, it is clear from Figures 1 and 2 that Airy theory tends to underestimate the high speeds while the stream function theory overestimates them. The Airy theory still provides the lower standard error of estimate, s_e (0.43 versus 0.54 fps), for the data, but such a measure of fit is of course biased by whatever data constitute the sample - i.e. high or low speeds.

Even if the data for higher flow speeds (Figure 1) were to lie along the line as for the lower speeds, it is still obvious that the peak flow speed for any particular wave can exceed that predicted by Airy theory by approximately up to 40%. In the past it was suggested [e.g. Grace and Rocheleau (1973)] that a powerful approach to the prediction of extreme peak flow speeds would be to use the Airy theory predictions and then to tack on a probabilistically-chosen residual. It was suggested that the distribution of residuals be considered Gaussian with zero mean and a standard deviation given by 0.007 times the Airy theory celerity of the wave. Although the number 0.007 was based on field work, the same figure applies in an average sense to the data of Goda (1964) in Table 2.

Figure 1 indicates, however, that for ocean swell approaching those used in design the above approach may be unworkable. For this reason, since the stream function theory predictions provide a vague upper boundary for the velocity data (Figure 2), it is suggested that the predictions of this theory be used as the best theoretical estimate of U_{\max} , the value near the top of the distribution for the true peak horizontal, near-bottom flow speed. An alternate approach would be to use 1.4 times $u_{\max, \text{Airy}}$.

ACCELERATIONS

The standard errors of estimate for the acceleration predictions of Airy theory (Figure 3) and the stream function theory (Figure 4) are respectively 0.56 and 0.48 ft/sec². It is clear from the Figures that both theories underestimate \dot{U}_{\max} for the higher waves, a failing of some considerable import in engineering design situations. A line given by the equation $\dot{U}_{\max} = 2.5 \dot{u}_{\max, \text{Airy}}$ provides an upper envelope to the Figure 3 data, and it is provisionally

suggested that non-breaking wave near-bottom accelerations for design (\dot{U}_{\max}^{\max}) be adopted by using this equation when $0.05 \leq d/L_{\text{Airy}} \leq 0.10$.

Graphical differentiation of the near-bottom ($S/d = 0.05$) velocity plots in Iwagaki and Sakai (1970) have resulted in the data shown in Table 3.* There is substantial scatter in these data due to the double-humped nature of some of the waves and conceivably also to the technique used by the researchers in linking forward-flow and rearward-flow parts of the hot film anemometer velocity traces. But it is fairly clear that there is a general tendency for R to grow with increasing d/L_{Airy} and that the numbers obtained largely mirror those found in this field investigation.

VELOCITIES: STOCHASTIC APPROACH

Consider three ocean waves with the same gross characteristics of height, period and water depth. Classical wave theory predicts the same near-bottom peak flow velocity and acceleration for all three waves.

There is virtually an infinity of possible water surface configurations that could exist between vertical constraints (wave height) and horizontal constraints (wave length, inferred from wave period and water depth), and there is no reason to suppose that three real waves of identical gross characteristics would have the same near-bottom maximum flow velocity and acceleration. See Figure 5.

A sample of n waves with the same H , T and d would give n values of U_{\max} and n values of \dot{U}_{\max} . This dispersion can be accounted for with a deterministic wave model either by taking account of the actual surface profile (rare, and not applicable in design) or by using the theoretical prediction as an initial estimate and then adding on a probabilistically-chosen residual as remarked earlier.

The standard modern method for accounting for dispersion, however, involves the use of a probabilistic approach, the so-called Gaussian wave model. An infinity of independent, infinitesimal-mean-square sinusoids is assumed to be propagating in the same direction. A Gaussian distribution then applies to the overall surface wave ordinate; the same probability density function also applies to the (horizontal, near-bottom) flow speeds and accelerations due to the linear relationship between such quantities and the wave ordinate according to the Airy theory which applies to sinusoidal waves.

*Other laboratory data such as those of Elliot (1953) (referenced in Wiegel (1964)), Le Méhauté *et al* (1968) and Tsuchiya and Yamaguchi (1972) do not yield near-bottom accelerations.

Table 3: Iwagaki and Sakai (1970)
Acceleration Data and Airy Theory Predictions

(d = 16.0 cm, S = 0.8 cm)

\underline{H} (cm)	\underline{T} (sec)	$\underline{H/d}$	$\underline{d/L_{Airy}}$	$\underline{U_{max}}$ (cm/sec ²)	$\underline{u_{maxAiry}}$ (cm/sec ²)	$\underline{R^{**}}$
6.72	1.03	0.42	0.138	132.7	127.7	1.04
6.86	1.30	0.43	0.104	144.5	113.3	1.28
6.04	1.58	0.38	0.084	164.0	85.9	1.91
7.21	1.83	0.45	0.072	105.3	90.8	1.16
7.05	2.08	0.44	0.063	133.8	79.4	1.69
4.89	2.39	0.31	0.055	47.6	48.3	0.99
5.06	2.63	0.32	0.049	104.3	45.8	2.28
4.13	2.84	0.26	0.045	101.0	34.9	2.89
4.11	3.07	0.26	0.042	69.2	32.0	2.16
3.66	3.40	0.23	0.038	86.3	25.9	3.33

** $R = \frac{U_{max}}{u_{maxAiry}}$

The mean-square spectral density, commonly called the spectrum, of surface wave ordinate displays the absolute amounts of mean-square value contributed by the different-frequency components in the sea surface. Such a measured spectrum can be transformed analytically into one for the near-bottom water particle flow speed by using the (frequency-dependent) Airy theory transformation factor.

In Figure 6 a surface wave ordinate spectrum is presented. In addition, there are two near-bottom flow speed spectra shown, one theoretical and the other measured. It is clear that the theoretical curve has only about half the mean-square content of the measured one; in addition the theoretical peak is about 25% less than that for the measured data. Thus, although the probabilistic wave model yields dispersion, its predictions for relatively shallow water swell are out of line with reality, at least according to our results.

ACKNOWLEDGEMENTS

The National Oceanic and Atmospheric Administration, National Sea Grant Programs, provided the basic funding for this project. Matching funds were provided by the State of Hawaii. I am very grateful for this financial support and for the physical support of the following project members: Henry Ho; Frederick Casciano; Steven Nicinski; Arthur Shak; Wilfred Ii; Elizabeth Leis; Sylvia Khong; Kent Reinhard; Gabriel Zee; Charles Schuster; James Sands; Shepard Williams; Edward Noda; Michael Rayfuse; Joseph Castiel; Edgar Bilderback. Jacques Legrand assisted in processing data from other sources.

REFERENCES

- Dalrymple, R. A., "A Finite Amplitude Wave on a Linear Shear Current," Journal of Geophysical Research, Vol. 79, 1974, pp. 4498-4504.
- Dean, R. G., "Stream Function Representation of Nonlinear Ocean Waves," Journal of Geophysical Research, Vol. 70, 1965, pp. 4561-4572.
- Dean, R. G., "Evaluation and Development of Water Wave Theories for Engineering Application," U.S. Army, Corps of Engineers, Coastal Engineering Research Center, Fort Belvoir, Virginia, Special Report No. 1, November, 1974, 2 Vols.
- Elliot, J. G., Interim Report, California Institute of Technology, Pasadena, California, Hydrodynamics Laboratory, July, 1953.
- Goda, Y., "Wave Forces on a Vertical Circular Cylinder: Experiments and a Proposed Method of Wave Force Computation," Port and Harbour Technical Research Institute, Yokosuka, Japan, Report No. 8, August, 1964.
- Grace, R. A., and Nicinski, S. A., "Wave Force Coefficients from Pipeline Research in the Ocean," Proceedings, Eighth Annual Offshore Technology Conference, Houston, Texas, May, 1976, Vol. 3, pp. 681-694.

- Grace, R. A., and Rocheleau, R. Y., "Near-Bottom Velocities under Waikiki Swell," University of Hawaii, Honolulu, Look Laboratory of Oceanographic Engineering, Technical Report No. 31, October, 1973.
- Inman, D. L., and Nasu, N., "Orbital Velocity Associated with Wave Action Near the Breaker Zone," U.S. Army, Corps of Engineers, Beach Erosion Board, Washington, D. C., Technical Memorandum No. 79, March, 1956.
- Iwagaki, Y., and Sakai, T., "Horizontal Water Particle Velocity of Finite Amplitude Waves," Proceedings, Twelfth Coastal Engineering Conference, Washington, D. C., September, 1970, pp. 309-326.
- Le Méhauté, B., Divoky, D., and Lin, A., "Shallow Water Waves: A Comparison of Theories and Experiments," Proceedings, Eleventh Conference on Coastal Engineering, London, England, September, 1968, pp. 86-107.
- Shonting, D. H., "Measurements of Particle Motions in Ocean Waves," Journal of Marine Research, Vol. 25, No. 2, 1967a, pp. 162-181.
- Shonting, D. H., "Observations of Particle Motions in Ocean Waves," Naval Underwater Weapons Research and Engineering Station, Newport, Rhode Island, Technical Memorandum No. 377, July, 1967b, 2 Vols.
- Thornton, E. B., and Krapohl, R. F., "Water Particle Velocities Measured under Ocean Waves," Journal of Geophysical Research, Oceans and Atmospheres, Vol. 79, 1974, pp. 847-852.
- Tsuchiya, Y., and Yamaguchi, M., "Horizontal and Vertical Water Particle Velocities Induced by Waves," Proceedings, Thirteenth International Conference on Coastal Engineering, Vancouver, Canada, 1972, Vol. 1, pp. 555-568.
- Wiegel, R. L., Oceanographical Engineering, Prentice-Hill Book Co., Englewood Cliffs, New Jersey, 1964.

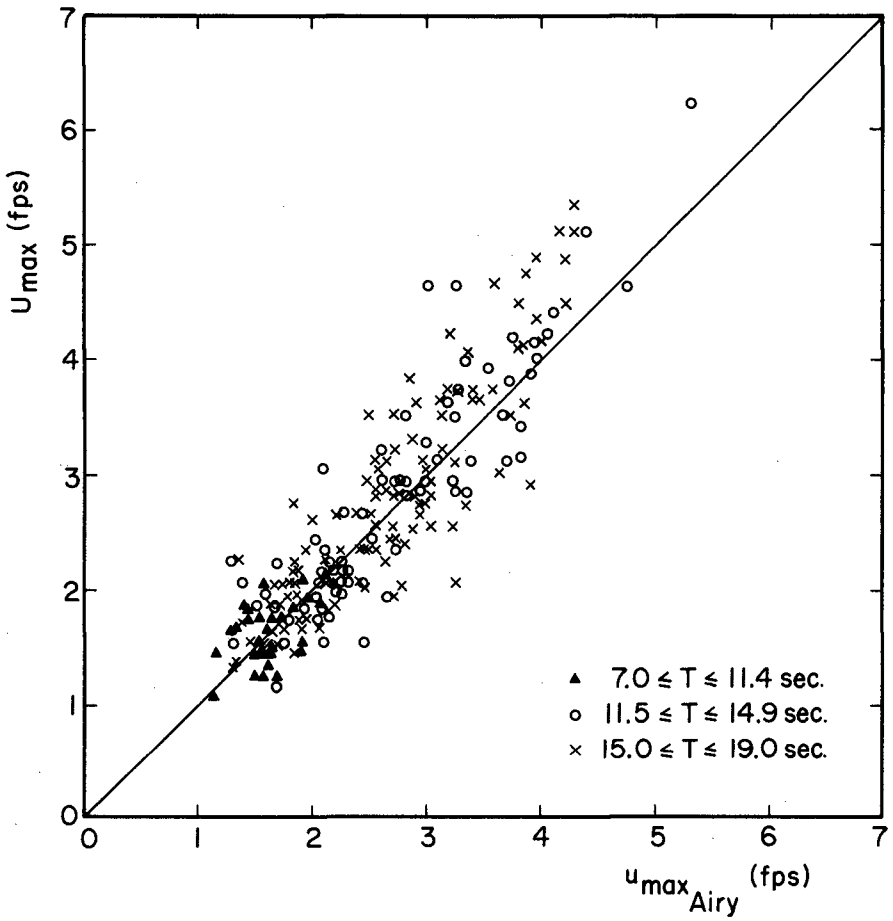


Figure 1: Comparison of Measured Velocity Data with Airy Theory Predictions

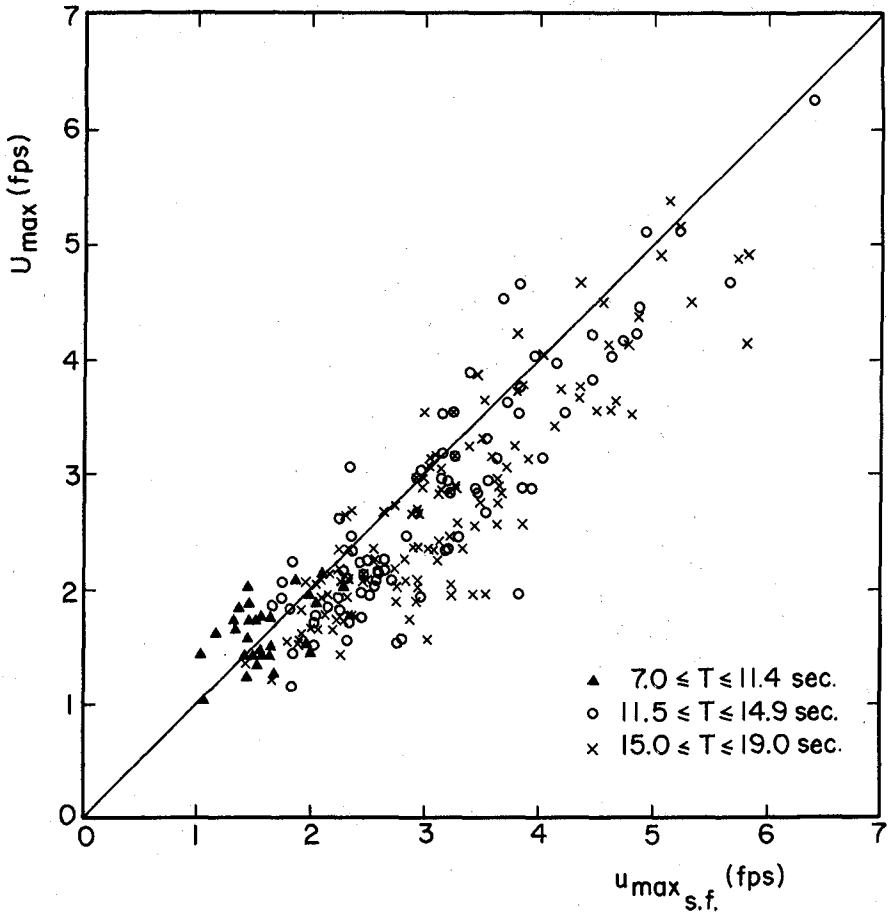


Figure 2: Comparison of Measured Velocity Data with Predictions of Stream Function Theory

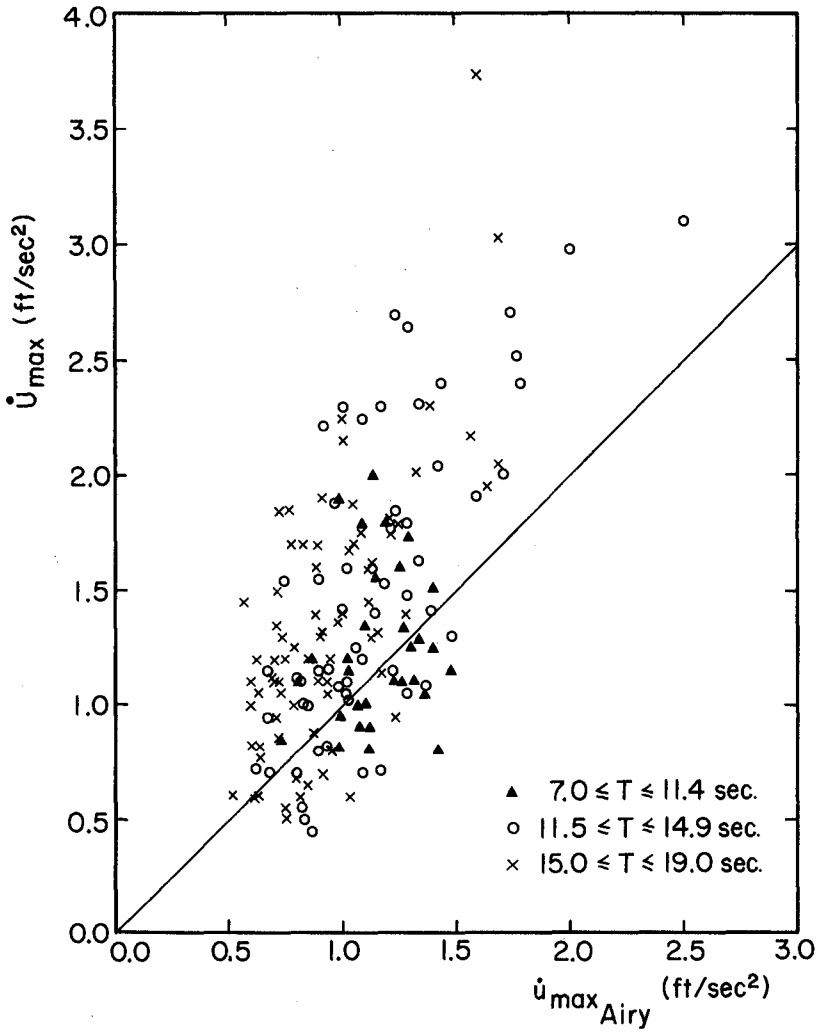


Figure 3: Comparison of Measured Acceleration Data with Airy Theory Predictions

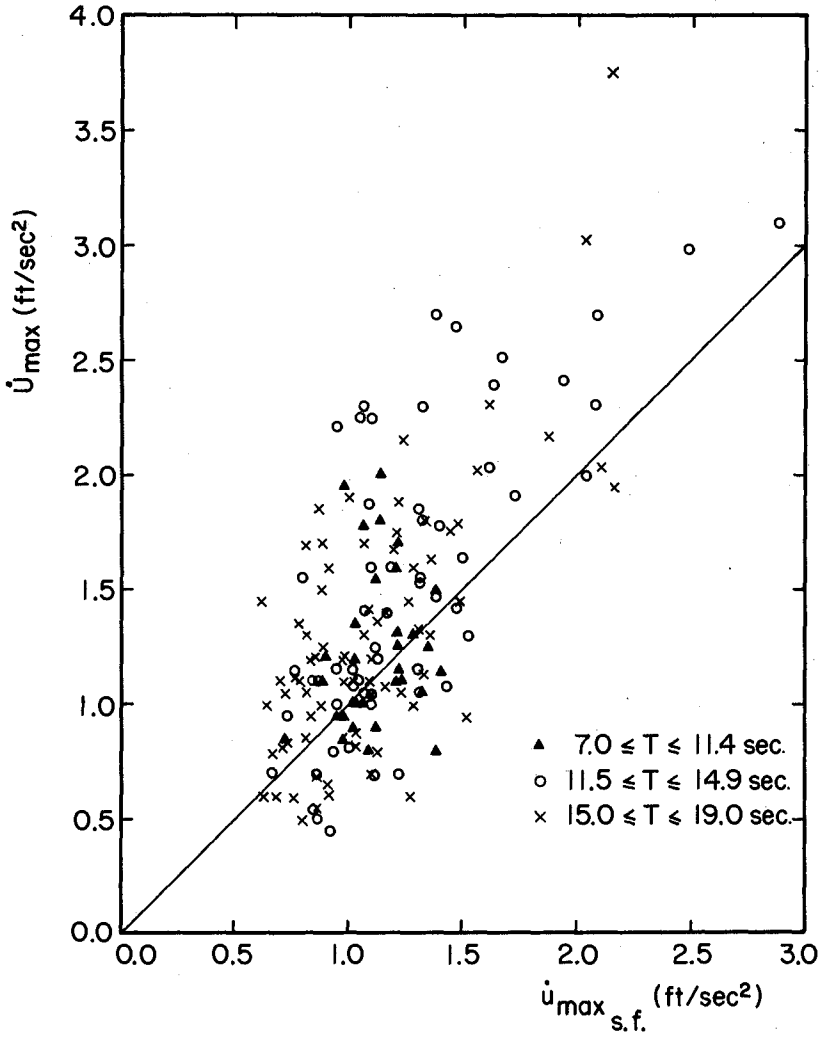


Figure 4: Comparison of Measured Acceleration Data with Predictions of Stream Function Theory

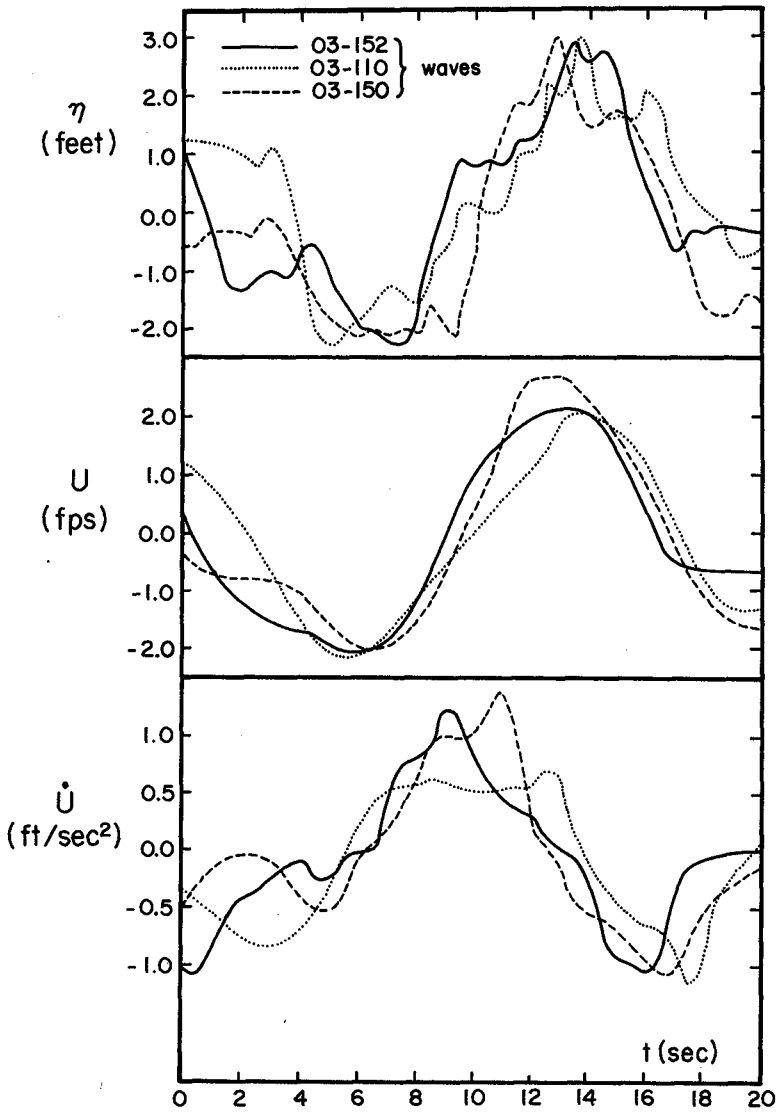


Figure 5: Measured Ordinate, Velocity and Acceleration Traces for Three 'Identical' Waves

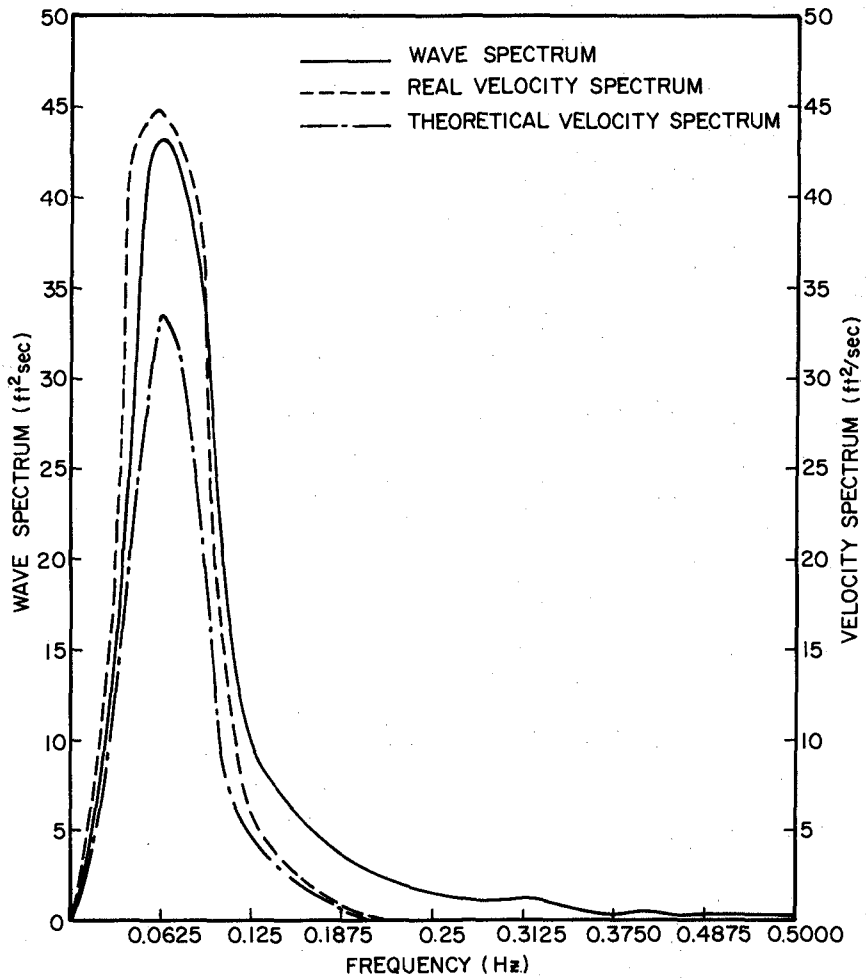


Figure 6: Example Comparison of Measured and Gaussian Wave Model Spectra

CHAPTER 140

WAVE FORCES ON SUBMERGED OBJECTS

by

Suphat Vongvisessomjai
Asian Institute of Technology
Bangkok, Thailand

and

Richard Silvester
Department of Civil Engineering
University of Western Australia

ABSTRACT

Limitations of the Morison equation for computing wave forces on small submerged structures have encouraged the use of dimensionless relationships containing only height, period and water depth. However in dividing the force by the theoretical drag force or inertia force a relationship can be found with the Keulegan parameter ($U_{im} T/D$) over a wide range of conditions and different types of wave. The U_{im} value can be determined from empirical and theoretical data for all depths and wave steepnesses. The relating coefficients for various dimensions and shapes of submerged object are predictable from potential theory or modified slightly because of viscous and such other forces induced by bottom and free surface boundaries.

For computing wave forces on a submerged object which is large compared to the wave length, the Morison equation is replaced by the Diffraction theory. Criteria for selecting the latter theory are presented.

INTRODUCTION

Much work has been carried out in recent years on wave forces exerted on submerged structures (1) (2) (3) (4) (5) (6) (7). Work prior to 1974 has been summarised by Hogben (8). The bodies studied have included cylinders, spheres, blocks and other symmetrical shapes. The more complex units being employed as gravity structures in the oil exploration industry (9) are being equated to these simple forms and also tested individually in flumes (10). There is a dire need to further this work and rationalise the whole procedure (8).

The original achievements in this topic were made by Morison et al (11) whose relationship in equation 1, has been used for a number of decades,

$$F_{Ti} = \frac{1}{2} \rho C_{Di} A_i |U_i| U_i + \rho C_{Mi} \psi dU_i/dt \quad (1)$$

where the symbols are as listed in the notation at the end of the paper.

Equation 1, is the addition of a drag and inertial component, whose validity is being questioned on a number of counts. Apart from the necessary assumption that the object must be small compared to the incident wave length (e.g. D/L small), there are a number of limitations to Morison's approach, as follows:

- (i) the summation infers the addition of two terms that reach their peak at different times during the wave cycle. The proportions of the drag component to the inertial component vary with the wave conditions making it difficult to assess such a maximum force.
- (ii) the velocities and accelerations of water particles must be known in a prototype situation in order to compute the force. These kinematic variables must be calculated from the specified wave characteristics using either linear theory or a more sophisticated approach. It has been pointed out (12) (13) that no theory can presently predict the vertical distribution of water-particle velocities. The linear theory appears to be accurate (14) for $h/L > 0.3$ but for shallower depths an empirical approach will be presented later. There is much more work required to completely solve this problem of velocities and accelerations of fluid particles.
- (iii) each term on the RHS of equation 1, contains a coefficient, the values of which have ranged widely and wildly in the literature (15). This constant, relating force to wave conditions, is specific to the object shape and dimension. Normally linear theory has been employed to determine velocities and accelerations in flume tests. It may be the inappropriateness of this application in the shallower conditions that has caused such confusion in this matter. On some occasions values from unidirectional flow have been applied but more recently (4) tests with oscillating tunnels have produced consistently good results.

- (iv) in spite of the improving quality of coefficient assessment under laboratory conditions, the operative values in complex prototype situations need full-scale verification. Some oil exploration structures are being instrumented for this purposes but some simple full-sized objects need to be installed in the sea and tested, as suggested by Hogben (8).
- (v) the summation in equation 1, does not allow for any interaction of the two terms. For example, the influence of acceleration on the drag force in such a way as to produce a maximum value when the velocity is not at its peak.
- (vi) once the structure assumes proportions that commence to modify the incident wave the Morison equation is no longer valid. This may be due to the member itself being large or adjacent members influencing the water motions. Whilst theory may account for wave scattering at some limiting condition there is a vast transition range in which the wave/structure interaction has not been determined.

Because of the difficulties outlined above some workers have recently by-passed the need for computing the velocity and acceleration, and the concomitant coefficients, by relating the maximum force measured to the basic wave variables of height and period in a specified water depth (1) (7) (16). These have been related by dimensionless parameters which appear to follow consistent curves.

Whilst it is proposed to promote the use of velocity terms rather than basic characteristics of waves the case of objects extending through large proportions of the depth needs special attention. Since different levels of the structure, say a vertical cylinder, are receiving differing pressures it is extremely difficult to integrate them into some peak value. Such integration has been suggested (17) using linear theory but as noted already this does not apply for $h/L < 0.3$ which is normally the case. In this event it is better to relate a maximum measured force to some dimensionless parameter made up of H , T and h (16). This approach has been used by Silvester (13) in his suggested computation of forces on piles, using data and coefficients given by Goda (18).

VARIABLES EMPLOYING VELOCITY

The Morison equation (1) in nondimensionalized form gives

$$\frac{F_{Ti}}{\rho V (dU_i/dt)_m} = C_{Mi} \sin \sigma t + \frac{C_{Di}}{4\pi} \frac{U_{im} T}{(V/A_i)} |\cos \sigma t| \cos \sigma t$$

$$= f_n [C_{Mi}, D_{Di}, \frac{U_{im} T}{(V/A_i)}, \frac{t}{T}] \quad (2)$$

for an inertia formulation; and,

$$\begin{aligned} \frac{2F_{Ti}}{\rho A_i U_{im}^2} &= 4\pi C_{Mi} / \left[\frac{U_{im} T}{(W/A_i)} \right] \sin \sigma t + C_{Di} |\cos \sigma t| \cos \sigma t \\ &= f_n [C_{Mi}, C_{Di}, \frac{U_{im} T}{(W/A_i)}, \frac{t}{T}] \end{aligned} \quad (3)$$

for a drag formulation.

Alternatively, by dimensional analysis factors can be derived which include orbital velocities of water particles. These are

$$\frac{F_{Tim}}{\rho V (dU_i/dt)_m} = f \left[\frac{D}{L}, \frac{U_{im} T}{D}, \frac{U_{im} D}{v}, \frac{U_{im}}{\sqrt{g(h-d)}} \right] \quad (4)$$

for an inertia formulation;

$$\text{or} \quad \frac{F_{Tim}}{\rho A_i U_{im}^2} = f \left[\frac{D}{L}, \frac{U_{im} T}{D}, \frac{U_{im} T}{v}, \frac{U_{im}}{\sqrt{g(h-d)}} \right] \quad (5)$$

for a drag formulation. Relative roughness can also be introduced as an independent variable, as has been done by Sarpkaya (19).

The inclusion of the orbital velocity term, preferably the maximum value (U_{im}) at the centre line of the body, is preferred over the wave parameters for the following reasons:

- (i) the force is directly dependent upon the water motion which varies throughout the water depth in a complicated manner not amenable to any current theory, except linear for $h/L > 0.3$.
- (ii) utilization of the velocity retains a link with other phenomena such as flow separation, vortex generation and wake formation.
- (iii) limits of applicability for drag and inertial terms can be determined, in terms of velocity or amplitude of water excursion proportional to dimensions of the object. This is preferable to ratios of object size to wave height alone which does not consider other conditions such as wave steepness and depth ratio.
- (iv) inclusion of velocity in the dimensionless parameters permits the assessment of Reynolds number ($U_{im} D/v$). This might be disregarded for clear water conditions of $20 \times 10^3 > R_D > 10^3$. However, suspended sediment may so alter the apparent kinematic viscosity in prototype conditions that this parameter may have to be considered. Correlations of Reynolds number with force coefficients have met with little success (5) (20) (21). Only at very high Reynolds numbers

($R_D > 20 \times 10^3$) the drag coefficient shows the trend to decrease with increased R_D , whereas the inertia coefficient exhibits the opposite trend [Sarpkaya, 19].

- (v) the Froude number in equations (4) and (5) ($\frac{U_{im}}{\sqrt{g(h-d)}}$), which includes the velocity term, will influence the force as the object gets closer to the bottom. The effect of e/D on the inertia coefficient of submerged cylinders has been computed from potential flow theory and verified experimentally (3). As the object gets closer to the surface the Froude number, $\frac{U_{im}}{\sqrt{g(h-a-e)}}$, or the ratio $(h-a-e)/D$ are sufficiently sensitive to detect surface effect.

- (vi) the term $U_{im} T/D$ in equations (2) - (5) is commonly called the Keulegan parameter. It is the ratio of drag to inertia force, but is equally the ratio of excursion length ($2\pi\xi$) of the fluid particles in progressive waves to the transverse dimension of the object (D). This has been shown by Keulegan and Carpenter (20) to correlate better with forces averaged over a wave cycle than the other factors in equations (4) and (5). Sarpkaya (4) has displayed a similar correlation for the sphere and cylinder. Even forces on discs (21) can be related to $\frac{dU_i}{dt} D/U_{im}^2$ which is equivalent to $2\pi/(U_{im} T/D) = 1/(\xi/D)$. There is little doubt (22) that this parameter is the dominant variable to which non-dimensional forces should be correlated. Such correlations are illustrated in Fig. 1 for submerged cylinders, where their dependencies are explicitly shown.

WATER PARTICLE VELOCITIES

Any assessment of forces, be they drag or inertial in character, must rely finally on an accurate determination of velocity or acceleration. Tests by Le Méhauté et al (12) have indicated that no single theory predicts the velocity distribution throughout depth as recorded in flume tests. Silvester (13) has placed eleven theories in order of accuracy, as judged by these experimental results, for motions at the surface, still water level (SWL), and the bed. For the latter two, or the main body of water, the modification of the Airy theory by Goda (18) proved closest to the measured data. For surface velocities the solitary wave theory by Boussinesq, as reported by Munk (23), was nearest to experiment. Overall, Goda's empirical formula was assessed number one and Stokes second order theory least accurate. Reference (13) should be inspected to see the order of other theories.

The report by Goda (18) contains results of an extensive series of

flume tests from which maximum horizontal velocity (U_{xm}) at the SWL was listed over a wide range of h/L and H/h ratios. Silvester (14) plotted $(U_{xm})_{SWL}/\sqrt{gh}$ against HL/h^2 and found the points aligned parallel to 1st order theoretical lines of varying h/L . For constant $HL/h^2 = 1$, it was shown that

$$\frac{(U_{xm})_{SWL}}{\sqrt{gh}} = \frac{2}{3} \frac{h}{L} \quad (6)$$

which indicated a complete relationship of

$$\frac{(U_{xm})_{SWL}}{\sqrt{gh}} = \frac{2}{3} \frac{h}{L} \frac{HL}{h^2} = \frac{2}{3} \frac{H}{h} \quad (7)$$

Replotting of $(U_{xm})_{SWL}/\sqrt{gh}$ versus H/h verified equation (7). For greater depths (i.e., $h/L > 0.3$) the 1st order Airy theory matched the experimental data extremely well. This can be expressed, for $HL/h^2 = 1$ as

$$\frac{(U_{xm})_{SWL}}{\sqrt{gh}} = 1.255 \frac{H}{h} \left[\frac{h}{L} \right]^{0.5} \quad (8)$$

Horizontal velocities at the bed were also measured from the vertical distribution graphs supplied by Goda (18). These were plotted as percentages of SWL values and were found to follow the linear theory down to $h/L = 0.14$. For smaller ratios the experimental points deviated below those predicted by linear theory.

It can be seen from equations (6) and (8) for constant HL/h^2 that $(U_{xm})_{SWL}/\sqrt{gh}$ varies only with h/L , as depicted in Fig. 2. The linear theory is shown for SWL and bed elevations, as also the curves from Goda's experiments (18). It is seen that at small depth ratios these two empirical lines tend towards the hyperbolic theory for SWL and bed velocities as given by Iwagaki and Sakai (25). The break from the theoretical curve occurs at $h/L = 0.3$ for SWL values and at $h/L = 0.14$ for bed velocities. Note the maximum for the latter at $h/L = 0.25$. The two scales of HL/h^2 and $(U_{xm})_{SWL}/\sqrt{gh}$ are necessary to obviate wave breaking at $H/h = 0.78$ approximately.

To obtain percentage values of horizontal velocity at other depths a graph of $[U/U_{SWL}]_m$ % was graphed versus h/L . For $h/L > 0.3$ linear theory could be used. For $h/L < 0.04$ the hyperbolic theory (25) could assist. For transitional depths the cnoidal theory as modified by Mejlhede (26) could be of assistance. Smooth transitions from deep to shallow water should be expected for any proportional depths, from which percentages of U_{xm} at SWL as given by equation (7) can be derived. These are contained in the lower parts of Fig. 3 and Table I.

Velocities at levels above SWL are much more dependent on H/h than those within the body of water. Goda's modified Airy theory for maximum horizontal velocity at the crest is

$$(U_{xm})_c = \frac{\pi H}{T} \sqrt{1 + \alpha \left[\frac{H}{h}\right]^{1/2} \left[\frac{Z}{h}\right]^3 \frac{\cosh 2\pi \frac{Z/L}{h/L}}{\sinh 2\pi \frac{Z/L}{h/L}}} \quad (9)$$

where α is a factor dependent on h/L

Z is height from the bed, such that at the crest

$$\frac{Z}{h} = 1 + 0.885 \left[\frac{H}{h}\right]^{1.275} \quad (10)$$

Goda provides graphs for SWL and surface values versus h/L for a range of H/h . Ratios of $[U_c/U_{SWL}]_m$ were obtained and plotted in Fig. 3, and included in Table I. The theoretical curves so derived have been modified slightly from the experimental trends recorded by Goda (18). The two percentage scales in Fig. 3 to the right and left of $h/L = 0.1$ have been used to improve the accuracy of the diagram.

The procedure thus suggested is that U_{xm} at SWL be determined by equation (7), which applies for $h/L < 0.2$. U_{xm} Values at SWL for $h/L > 0.2$ and other depths for all depth ratios can be computed by the percentage values.

Once an acceptable value of U_{xm} is available at any particular level maximum horizontal amplitude $x_m(\xi)$ and maximum acceleration (dU_x/dt) can be determined from linear theory as follows

$$\xi = \frac{U_{xm} T}{2\pi} \quad \text{and} \quad \left[\frac{dU_x}{dt}\right]_m = \frac{2\pi U_{xm}}{T} \quad (11)$$

until suitable modification is suggested from experiment.

Values of vertical maxima of velocity, acceleration and amplitude of water motion, based upon linear theory, are all given by the simple ratio $\tanh 2\pi Z/L$. Table II provides percentages over a range of h/L and Z/h , those at the bed being zero.

The values given in the tables and graphs of this paper will no doubt be refined as further experimental data and theoretical analyses become available, but they are believed to be the closest approximation to this data. It is submitted that the large fluctuations in coefficients of drag and inertia derived from flume tests in the past have occurred due to calculation of velocities etc. from linear theory when this was inapplicable for the depth ratios tested. More recent evaluations by water tunnel tests (4) have provided more consistent and realistic results.

APPLICATION OF PARAMETERS

It has been shown above that Reynolds and Froude numbers can be ignored over a wide range of prototype conditions, leaving the pre-dominant parameters of D/L and $U_{im} T/D = 2\pi \xi/D = 2\pi \left[\frac{dU_i}{dt} D/U_{im}^2\right]$.

It is thus convenient to discuss the application of relevant theories within ranges of D/L and $2\pi\xi/D$.

When $D/L < 0.2$ the diffraction theory gives $C_{Mx} = C_{Mp}$ as from Figs. 4 to 6 for various shapes of objects. This relative size serves as an upper bound value for selecting the Morison equation. On the contrary when $D/L > 0.2$ the incident wave is scattered and the action changes the flow field in the vicinity of the boundary. Though the Morison equation may become unreliable, it does not necessarily call for the application of the diffraction theory because this size factor does not necessarily ensure negligible viscous effects or predominance of inertia. Such condition is gauged from the relative magnitude of the drag to inertia force or the total force to the drag force. This is dictated by the value of the Keulegan parameter above $[U_{xm} T/D = 2\pi\xi/D]$ as seen in Fig. 7.

In this figure can be seen the predominance of inertia when $U_{xm} T/D < 3$. It is in this region that diffraction theory should be used for force calculation. Between 5 and 12 for this parameter both drag and inertial components make up the total drag. It is to be noted that for the same region the phase difference between F_{Txm} and U_{xm} change by 90° due to the alteration in major force. Between 12 and 25 is a transition region to the predominantly drag force condition. Beyond $U_{xm} T/D = 25$ the dimensionless force and hence the coefficient C_D remains essentially constant even though the ratio of drag to inertia increases continually.

In the section (b) of Fig. 7 the actual coefficients C_{Mx} and C_{Dx} are compared with the potential flow value C_{Mp} and the steady flow value C_{Ds} respectively, at similar Reynolds numbers (27). For $U_{xm} T/D < 3$ it can be observed that $C_{Dx} = C_{Ds} = 0$ and that $C_{Mx}/C_{Mp} = 1.0$. At the other extreme of $U_{xm} T/D > 25$ constant coefficients exist, namely $C_{Mx}/C_{Mp} = 0.75$ and $C_{Dx}/C_{Ds} = 1.5$. The major difference in the theoretical and experimental coefficients in the transition zone are to be noted, with maxima or minima at $U_{xm} T/D = 12$ or $\xi/D \approx 2$.

USE OF COEFFICIENTS

By employing only the $U_{im} T/D$ term on the RHS of equations (2) - (5) as independent variable the U_{im} force equation can be written as

$$\frac{2F_{Tim}}{\rho A_1 U_{im}^2} = f\left[\frac{U_{im} T}{D}\right] \quad (12)$$

This is the ratio of measured force to the theoretical drag force at the same U_{im} value. Data of several workers listed in Table III have been utilized according to this equation (12) as in Figs. 8, 9, 10a and 10b. The data have been collected mainly for $U_{im} T/D < 3$ and $D/L < 0.32$ for

different types of objects. Some have been conducted in flumes (6) (19) (28) (29) (30) (31) (32) (33) whilst others have involved the use of tunnels with oscillating flow (4). The measurement of velocity in the latter is direct, whereas in the former it is computed from the wave characteristics through some theory. As already noted this can introduce some error, the magnitude of which varies with both H/h and h/L .

The plots from Figs. 8 to 10 indicate the dimensionless force to vary inversely with $U_{im} T/D$ for small values of this parameter for all shapes of objects used and different wave types. When the relationship in equation (12) is algebraically manipulated it can be written as

$$\frac{F_{Tim}}{\rho V (dU_i/dt)_m} = \text{constant} \quad (13)$$

The constant in equation (13) is then the experimental coefficient of inertia (C_{Mi}) which can be compared with the theoretical potential values C_{Mp} as drawn in Figs. (8) - (10) (and also Fig. 1). Thus the relationship between the dimensionless forces, Keulegan parameters, and inertia coefficient from potential flow theory can be fairly established in this range of $U_{im} T/D < 3$; both for the objects laid on the bottom, $e/D = 0$, and lifted from the bottom, $e/D \neq 0$.

When the cylinder is half a diameter lifted from the bottom as in Fig. 9, $e/D = 0.5$, the inertia coefficient is not deviated much from potential value ($C_{Mp} = 2$ for no boundary effect); but due to bottom effect, $e/D = 0$, C_{Mp} is modified from value of 2 to that of about 3.3.

The relative effect of the free surface is distinctly seen in Fig. 5 for shell structure (35). For half cylinder, Table III indicates that with $(h-e-a)/D > 1.0$ or $(h-e-a)/D > 0.944$ the free surface effect has not come to change the coefficient values (see Fig. 10 b). As the object is nearer to the surface, $(h-e-a)/D < 0.5$, change in value of the coefficient is clearly seen (see Fig. 6).

CONCLUSION

1. Fundamental formulation of Morison equation gives rise to a number of practical limitations mainly confined within the inability to determine accurately the velocity and acceleration of fluid particles.
2. Through interaction of theory and empiricism, means to obtain more accurate velocity is given for all depth ratios and wave steepness.
3. Morison equation is appropriate for computing forces when the size of the submerged object $D/L < 0.2$. The equation is replaced by the Diffraction theory when $D/L > 0.2$ and $U_{im}T/D < 3$.
4. Proper choices of forms of non-dimensional forces and independent variables are shown to give good correlations and links with either potential flow or steady flow, over a practical range of dependent variables.
5. Both the non-dimensional inertia and drag formulations are shown to correlate with the Keulegan parameter well for varieties of object shapes and wave types.
6. Effects of bottom and free surface are found to be relatively influential at $e/D < 0.5$ and $(h-a-e)/D < 0.5$ respectively.

NOTATION

(i) Variables

A	:	projected area
a	:	radius of cylinder or sphere
C	:	coefficient
D	:	diameter of the cylinder or sphere
d	:	submergence depth
d	:	differential
e	:	vertical space between object and bed
F	:	force
g	:	gravitational acceleration
H	:	wave height
h	:	depth of water
L	:	wave length
ℓ	:	transverse length of object
R_D	:	Reynolds number
α	:	factor in equation (9)
T	:	period
t	:	time
U	:	fluid velocity at centroid of object
Z	:	height above bed
ρ	:	fluid density
ν	:	kinematic viscosity
σ	:	wave angular velocity
V	:	displaced volume
ξ	:	horizontal excursion length from mean position
ψ	:	phase difference

(ii) Subscripts

c	:	crest of wave
D	:	drag
M	:	inertia
m	:	maximum
p	:	potential flow
s	:	steady state
SWL	:	still water level
T	:	total
x,z,i	:	horizontal, vertical and any i-directions respectively of forces or coefficients or velocity
y	:	lateral direction

REFERENCES

1. Chakrabarti, S.K. and R.A. Naftzer, "Non-linear wave forces on half cylinder and hemisphere", Proc. ASCE 100(WW3), 1974, 189-204.
2. Yamamoto, T., J.H. Nath and L.S. Slotta, "Wave forces on cylinder near plane boundary", Proc. ASCE 100(WW4), 1974, 345-359.
3. Nath, J.H. and T. Yamamoto, "Force from fluid flow around objects", Proc. 14th Conf. Coastal Eng. 3, 1974, 1808-1827.
4. Sarpkaya, T., "Forces on cylinders and spheres in a sinusoidally oscillating fluid", ASME J. App. Mech., 1975, Paper No. 75 - APMW-27.
5. Tsuchiya, Y. and M. Yamaguchi, "Total wave force on a vertical circular cylindrical pile", Proc. 14th Conf. Coastal Eng. 3, 1974, 1789-1807.
6. Vongvisessomjai, S., "Wave force on submerged structure", Proc. 1st Aust. Conf. on Coastal Eng., 1973, 174-181.
7. Garrison, C.J., F.H. Gehrman and B.T. Perkinson, "Wave forces on bottom-mounted large-diameter cylinder", Proc. 101(WW4), 1975, 343-356. [See also, Discussion by Vongvisessomjai, WW3, 1976, in press].
8. Hogben, H., "Fluid loading of offshore structures, a state of the art appraisal: Wave loads", J. Roy Inst. Naval Arch., 1974.
9. McPhee, W.S., "Drilling and production platforms for the oil industry", Proc. I.C.E. Conf. Off-shore structures, 1975, 189-196 (Discussion 197-206).
10. Hogben, N. and R.G. Standing, "Wave loads on large bodies", Proc. Inter. Symp. Dyn. Mar. Vehicles and Struct., 1974, 258-277.
11. Morison, J.R., M.P. O'Brien, J.W. Johnson and S.A. Schaaf, "The forces exerted by surface waves on piles", Petrol. Trans., Am. Inst. Min., Metal and Petrol. Engrs., 189, 1950, 149-154.
12. Le Méhauté B., D. Divoky and A. Lim, "Shallow-water waves: a comparison of theories and experiments", Proc. 11th Conf. Coastal Eng. 1, 1968, 86-107.
13. Silvester, R., Coastal Engineering Vol. I, Elsevier Publ. Co., 1974, Chapt. IV, p. 176.
14. Silvester, R., "Water particle orbits in deep - to - shallow-water waves", Proc. 5th Aust. Conf. Hyd. and Fl. Mech., 1974, 310-316.
15. Wiegel, R.L., K.E. Beebe and J. Moon, "Ocean wave forces on circular cylindrical piles", Proc. ASCE 83(HY2), 1957, 89-119.

16. Paape, A. and H.M.C. Breusers, "The influence of pile dimension on forces exerted by waves", Proc. 10th Conf. Coastal Eng. 2, 1966, 840-849.
17. Dean, R.G. and D.R.F. Harleman, "Interaction of structures and waves", Estuarine and Coastline Hydrodynamics, McGraw Hill, N.Y. (Ed. A.T. Ippen), 1966, 341-403.
18. Goda, Y., "Wave forces on a vertical circular cylinder: experiments and a proposed method of wave force computation", Port Harbour Tech. Res. Inst. Rep. No. 8, 1964.
19. Sarpkaya, T., "Vortex shedding and resistance in harmonic flow about smooth and rough circular cylinders", Proc. - Seminar on Behaviour of Offshore Structures, 1976, 220-235.
20. Keulegan, G.H. and L.H. Carpenter, "The forces on cylinders and plates in an oscillating fluid", U.S. Nat. Bur. Std. Rep. 4821, 1958.
21. Sarpkaya, T. and C.J. Garrison, "Vortex formation and resistance in unsteady flow", Trans. ASME, 30, Ser. E(1), 1963, 16-24.
22. Iversen, H.W. and R. Balent, "A correlating modulus for fluid resistance in accelerated motion", J. App. Phys. 22, 1951, 324-328.
23. Chakrabarti, S.K., A.L. Wolbert, and W.A. Tam, "Wave forces on vertical circular cylinder", Proc. ASCE 102(WW2), 1976, 203-221.
24. Munk, W.H., "The solitary wave theory and its application to surf problems", Ann. N.Y. Acad. Sc. 51, 1949, 376-424.
25. Iwagaki, Y. and T. Sakai, "Horizontal water particle velocity of finite amplitude waves", Proc. 12th Conf. Coastal Eng. 1, 1970, 309-326.
26. Mejlhede, N., "Cnoidal waves on arbitrary depth", Inst. Hydrodyn. and Hyd. Eng. Tech. Univ. Denmark, Prog. Rep. 36, 1975, 11-20.
27. Hoerner, S.F., Fluid Dynamic Drag, Publ. by author, Midland Park, N.J. 1965.
28. Crooke, R.C., "Re-analysis of existing wave force data on model piles", U.S. Beach Erosion Board, Tech. Memo No. 71, 1955.
29. Schiller, F.C., "Wave forces on submerged horizontal cylinder", M. Eng. thesis, Naval Postgraduate School, Monterey, Calif., Rep. AD 727 691-1971.
30. Shank, G.E. and J.B. Herbich, "Forces due to waves on submerged structures", Texas A & M Univ. Rep. SG-70-212, Coastal Eng. Rep. 123, 1970.

31. Garrison, C.J. and V.S. Rao, "Interaction of waves with submerged objects", Proc. ASCE 97(WW2), 1971, 259-278.
32. Brater, E.F., J.S. McNown and L.D. Stair, "Wave forces on submerged structures", Proc. ASCE 84(HY6), 1958, 1-26.
33. Brater, E.F. and R. Wallace, "Wave forces on submerged pipe lines", Proc. 13th Conf. Coastal Eng. 3, 1972, 1703-1722.
34. Goda, Y. and T. Yoshimura, "Wave force on a vessel tied at offshore dolphins", Proc. 13th Conf. Coastal Eng. 3, 1972, 1723-1742.
35. MacCamy, R.C. and R.A. Fuchs, "Wave forces on piles: a diffraction theory", Tech. Memo. 69, Beach Erosion Board, 1954.
36. Lebreton, J.C. and P. Cormault, "Wave action on slightly immersed structures, some theoretical and experimental consideration", Proc. Symp., Research on Wave Action 4, Delft Hyd. Lab., 1969.

TABLE I Percentage of U_{xm}/U_{SML} at Various Depths and Depth Ratios

h/L	.01	.02	.04	.06	.08	.1	.15	.2	.3	.4	.5	.6	.7	.8
h/L_0	.0007	.0025	.01	.022	.037	.056	.11	.17	.286	.395	.498	.599	.7	.8
H/h=0.8	175	182	190	194	197	200	208	212	229	252	276	305	328	351
0.7	160	164	171	175	177	190	208	212	229	252	276	305	328	351
0.6	146	145	148	152	156	160	185	212	229	252	276	305	328	351
0.5	134	133	135	138	142	145	166	186	229	252	276	305	328	351
0.4	126	125	125	125	127	130	141	156	193	246	276	305	328	351
0.3	120	118	117	117	118	119	124	133	162	203	251	305	328	351
0.2	116	114	112	110	110	109	112	117	136	161	189	234	281	351
0.1	112	109	106	105	104	103	104	108	119	137	154	178	198	224
Z/h	100	100	100	100	100	100	100	100	108	120	132	146	156	168
1.0(SWL)	98	96	93	91	90	88	85	80	74	68	63	59	54	50
0.75	96	92	88	86	84	81	73	65	48	36	28	23	19	16
0.5	94	89	84	82	78	75	66	57	38	24	16	11	8	6
0.25	92	86	81	77	73	69	60	51	32	19	11	7	4	2
0 (bed)														

Note: Percentages underlined indicate broken waves.

TABLE II Vertical Maxima of Velocity, Acceleration and Amplitude as Percentage of Horizontal Values (Values at bed are zero)

h/L	.01	.02	.04	.06	.08	.1	.15	.2	.3	.4	.5	.6	.7	.8
Z/h														
1.0(SWL)	7	13	25	36	47	55	73	84	95	99	100	100	100	100
0.75	5	10	18	27	36	44	61	72	83	90	94	96	100	100
0.5	4	6	12	18	24	30	44	57	75	85	90	93	97	100
0.25	2	3	6	9	12	16	23	32	48	60	69	76	82	90

TABLE III Sources of Data and Experimental Range of Some Parameters for Cylinders and Spheres

Data Sources	Object	Direction of force/object orientation	Types of waves; P=progressive S=standing W=water tunnel generated wave	Figure	Symbol	Relative size D/L	Relative distance from bottom e/D	Relative distance from free surface (h-e-a)/D
Garrison & Rao (1971)	hemi-sphere	Hor.	P	6	Define in Fig.	0.0414-0.2387	0	0.125, 0.25, 0.5, 1.0, 1.5
Crooke (1955)	cyl. cyl. cyl. sphere	Hor./Hor. Ver./Hor. Hor./Ver. Hor.	P P P P	8a	▲ ■ ● +	0.0134-0.0362 0.0129 0.0072-0.0365 0.0083-0.0360	- - - -	- - - -
Vongvisessomjai (1973)	cyl.	Hor./Hor.	P S	8b	▲ △	0.0223-0.3183	0.635-1.0 1.365-5.5
Keulegan & Carpenter (1958)	cyl.	Hor./Hor.	S	8c	△	0.0026-0.0159	5.41-34.93	3.28-19.69
Sarpkaya (1975) Sarpkaya (1975)	cyl. sphere	Hor./Hor. Hor.	W W	8c 8c	△ +	- -	- -	- -
Schiller (1971)	cyl. cyl.	Hor./Hor. Ver./Hor.	P P	9	▲ ■	0.0280-0.3126 "	0.0, 0.1, 0.2, 0.5	1.5-2.5 "
Shank & Herbich (1970)	half-cyl.	Hor./Hor.	P	10b	▲	0.0675-0.2646	0	0.944, 1.5, 2.167

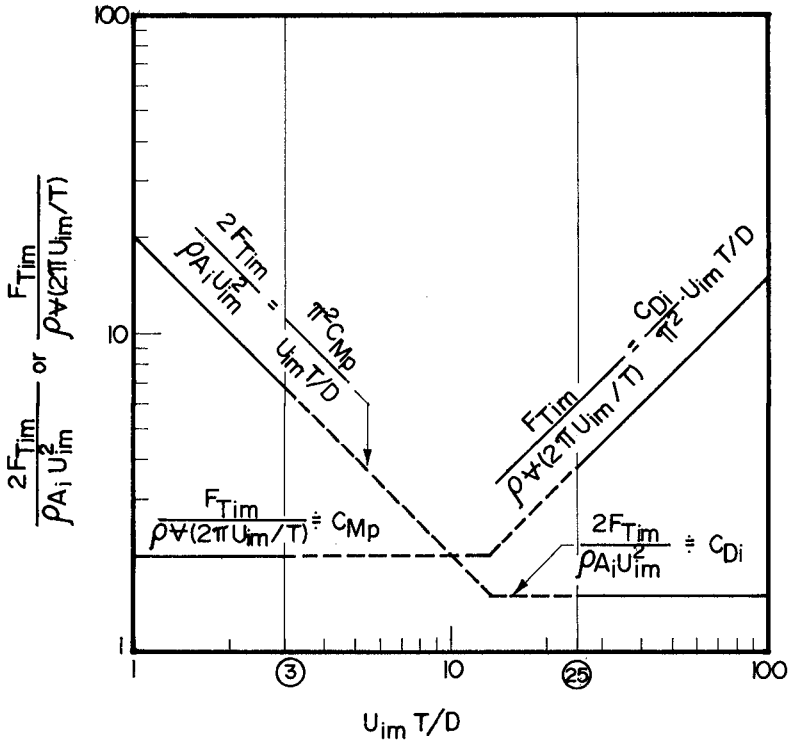


Fig.1 Asymptotes of Dimensionless Wave Forces on Submerged Cylinders

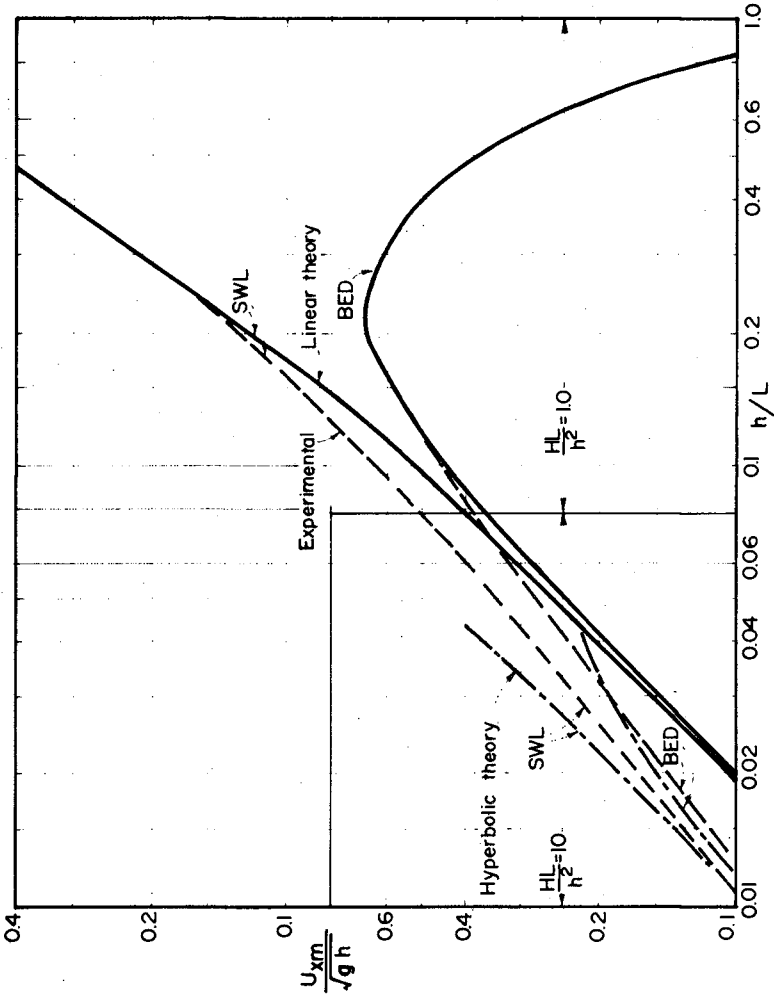


Fig. 2 Variation of velocity parameter with h/L for constant values of HL/h^2

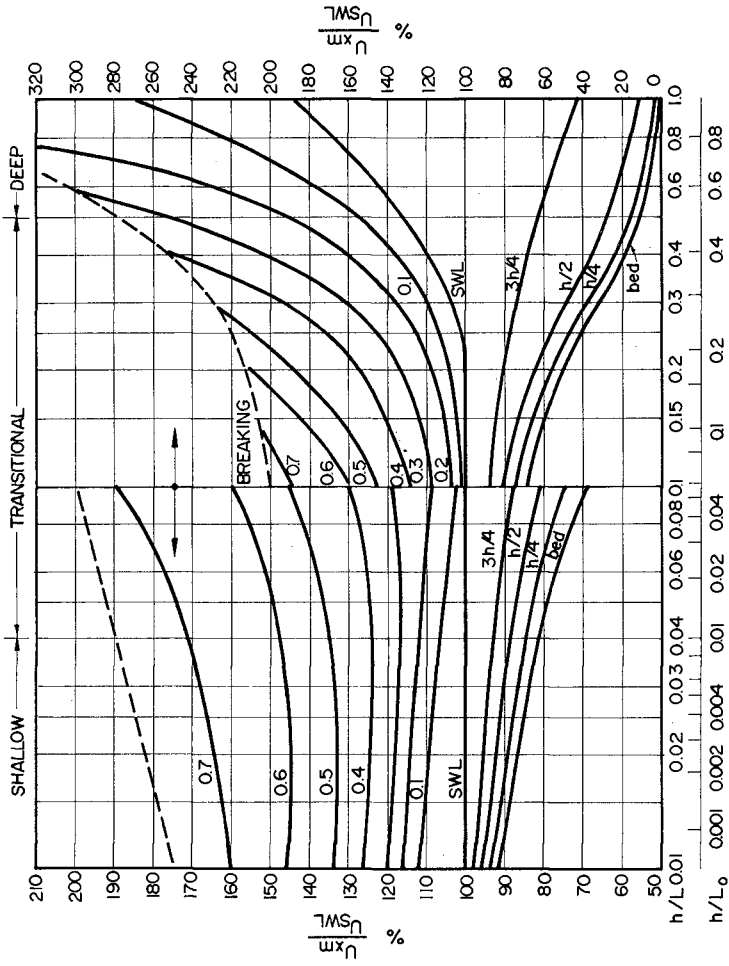


Fig. 3 Vertical distribution of U_{xm}/U_{sWL} versus h/L . Curves below SWL cover range of depth. Curves above SWL are surface values over range of H/h . Note two scales for $\% U_{xm}/U_{sWL}$ each side of $h/L = 0.1$

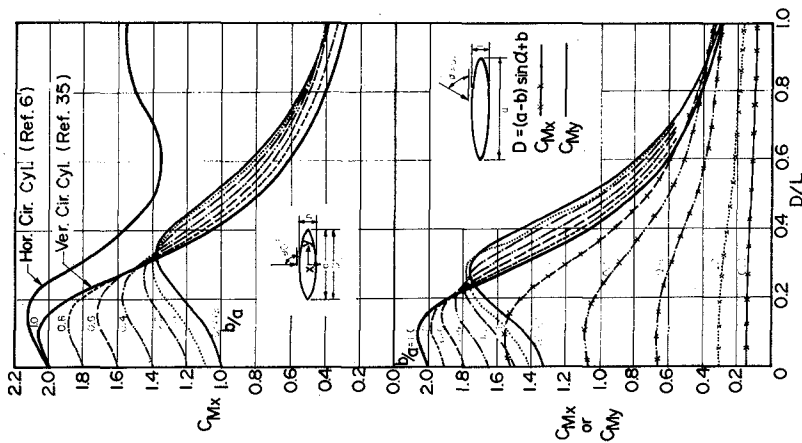


Fig.4 Inertia Coefficients of Vertical Elliptical Cylinders of Different aspect ratios, b/a , and angles of attack, α (Ref. 34)

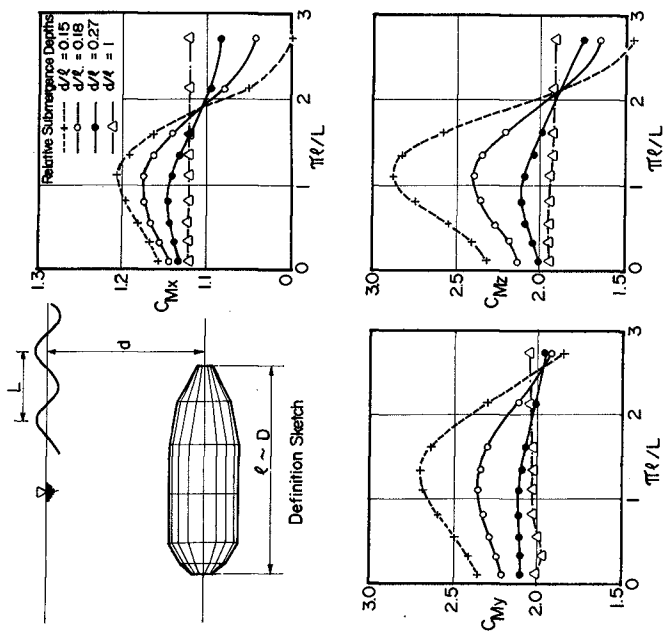


Fig. 5 Inertia Coefficients of a Shell at Different Relative Submergence Depths (Ref.36)

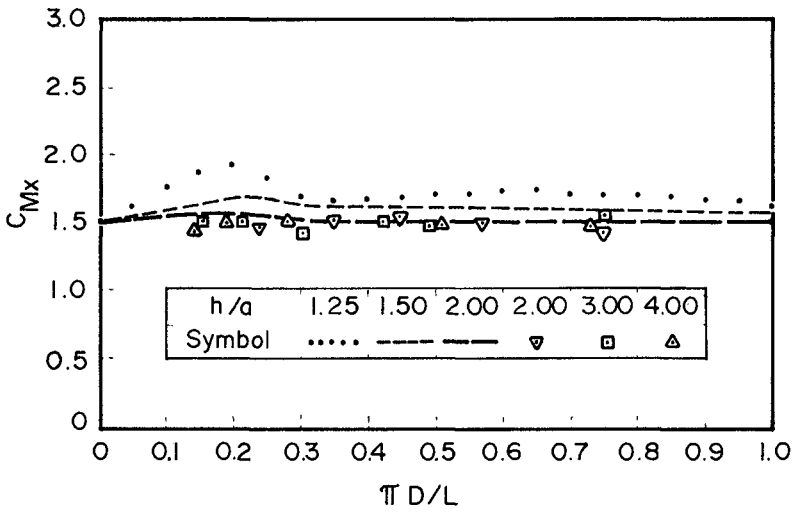
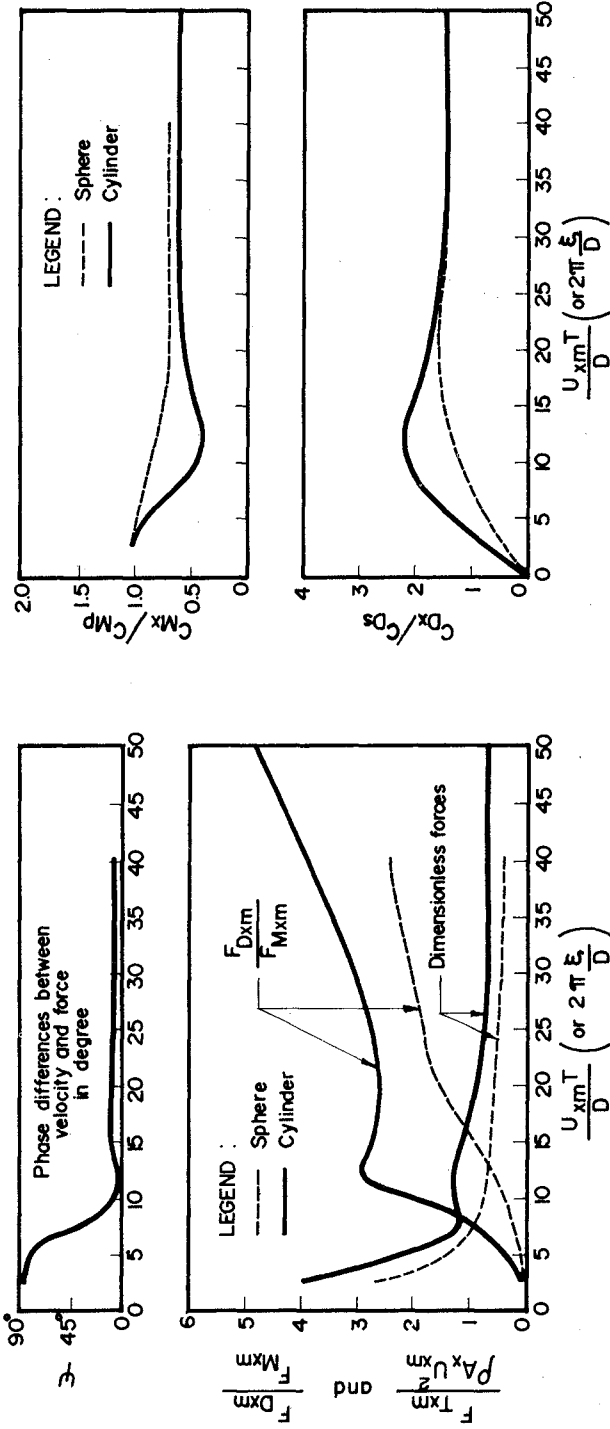


Fig. 6 Inertia Coefficient of a Hemisphere Laid on Bottom (See Data Source in Table III)



7a) Plots of total dimensionless force, relative magnitude of drag and inertia, and phase angle.

7b) Plots of relative inertia and drag coefficients

Fig. 7 Correlation of forces and coefficients with Keulegan parameter

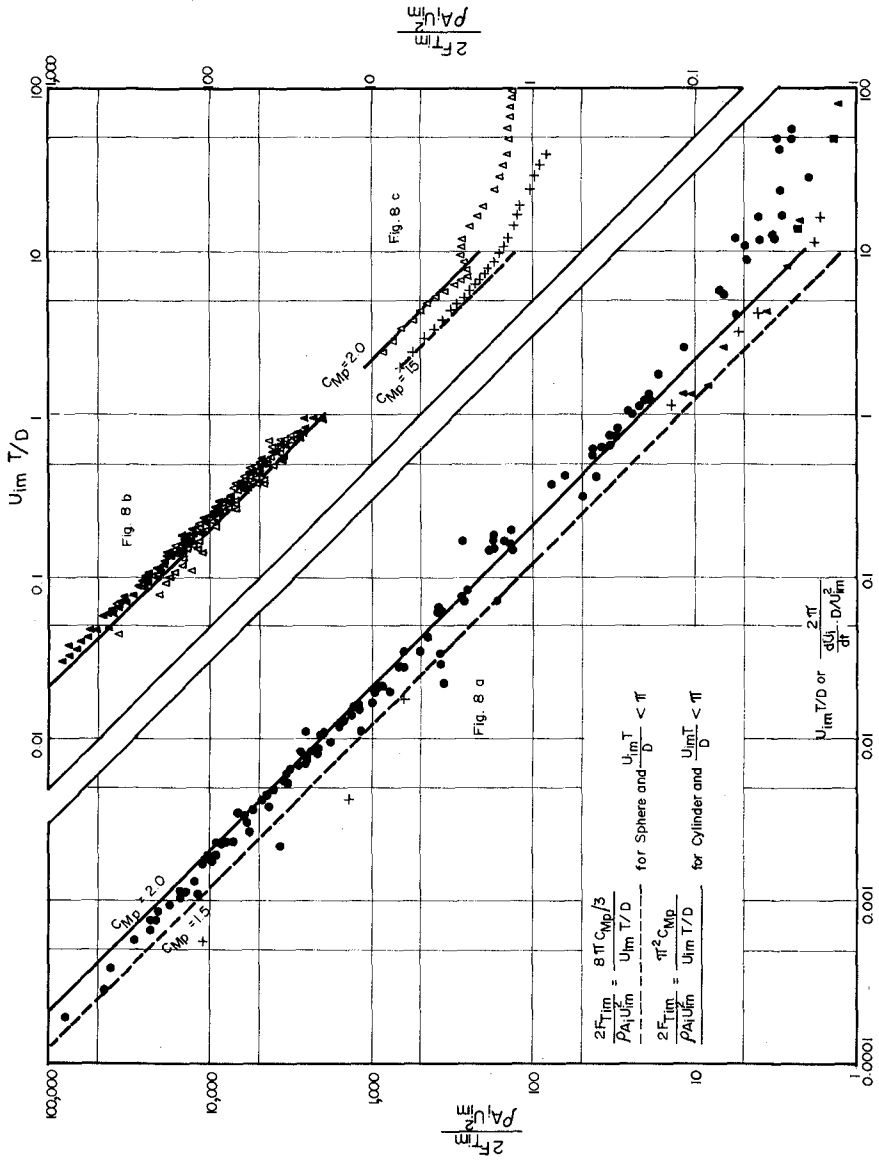


Fig. 8 Relationship between dimensionless forces, Keulegan parameter, and potential flow inertia coefficients for submerged objects (See Table III for definition of symbols)

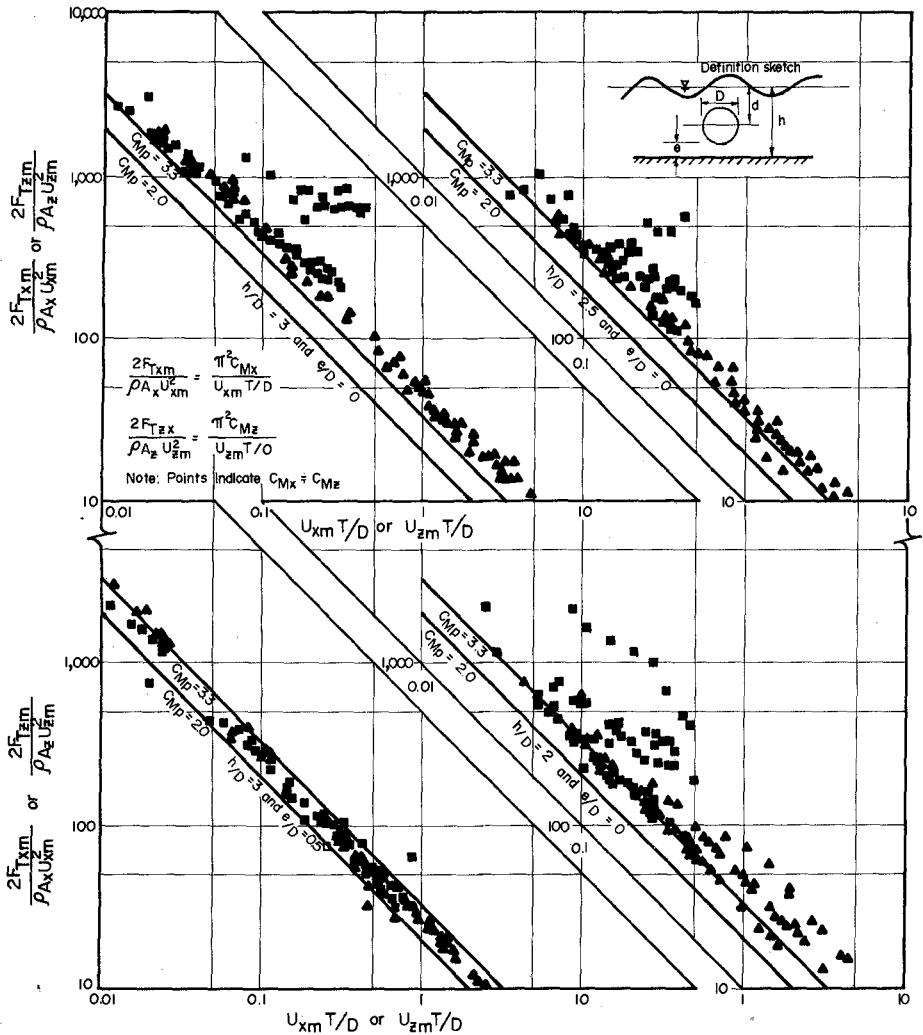


Fig. 9 Relationship between dimensionless forces in horizontal (and vertical) direction, and Keulegan parameters for varying relative distance from floor, e/D , and relative depth h/D of large object (See Oaka Source in Table III)

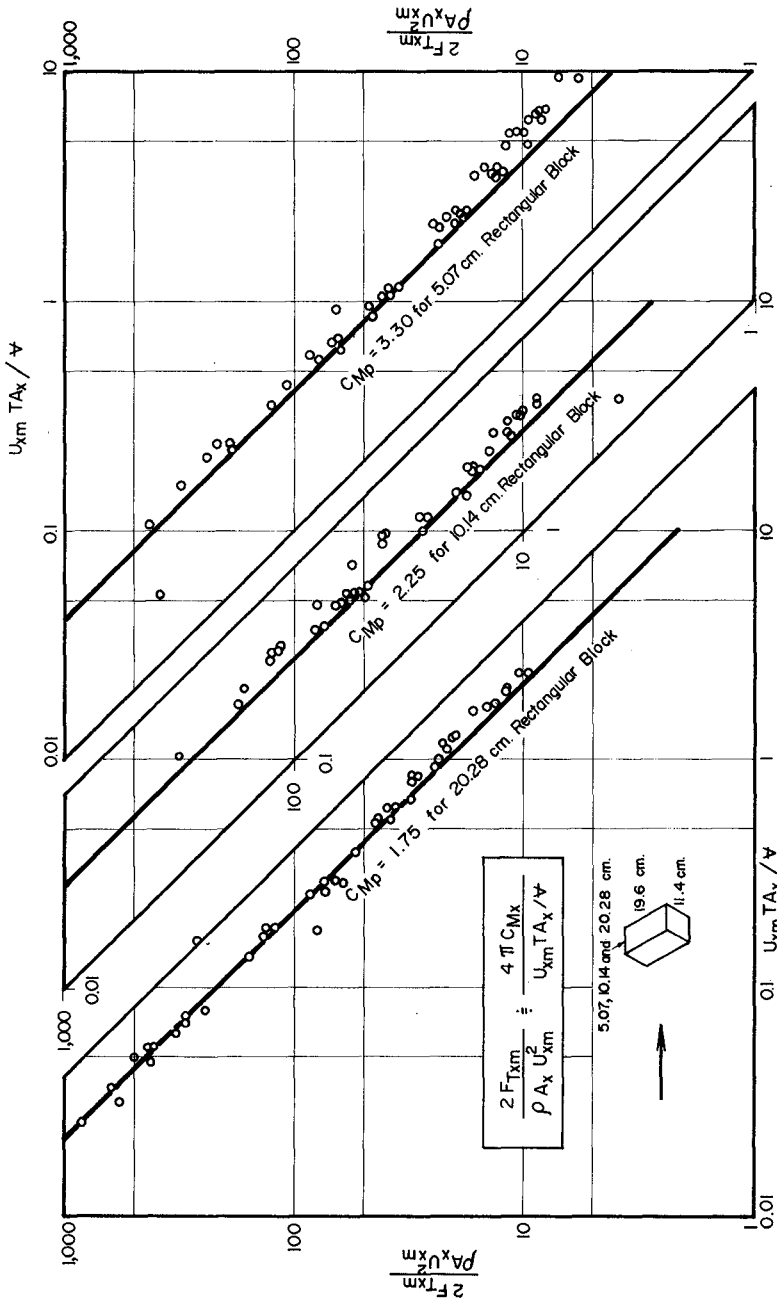


Fig. 10a. Plotted points showing asymptotics of inertia coefficient, C_{Mx} , to its potential value, C_{Mp} , on the plot of the dimensionless forces and Keulegan parameter for rectangular blocks

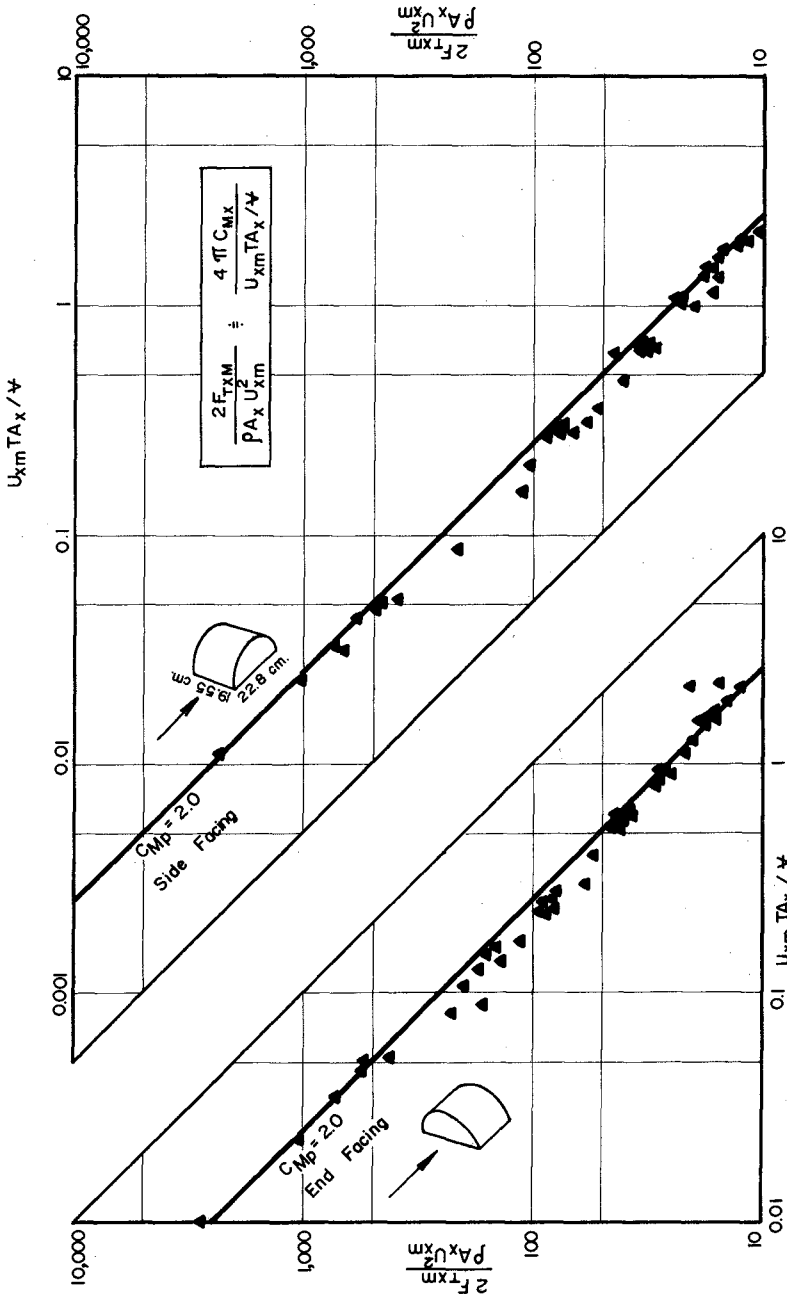


Fig. 10b. Plotted points showing asymptotics of inertia coefficient, C_{Mx} , to its potential value, C_{Mp} , on the plan of the dimensionless forces and Keulegan parameter for different exposed configuration of half - cylinders (See Table III for Data Source)

CHAPTER 141

FORCES ON A SPHERE UNDER LINEAR PROGRESSIVE WAVES

Scott A. Jenkins and Douglas L. Inman
Scripps Institution of Oceanography, University of California
La Jolla, California 92093

ABSTRACT

The rms horizontal forces which result from the action of a linear, deep and intermediate water, laboratory scale waves were measured on submerged spheres removed several diameters from the free surface. The study focuses on unseparated flows encountered at small values of (d_0/D) , where d_0 is the orbital diameter and D is the sphere diameter. Under these conditions, a steady streaming around the vertical equator of the sphere was observed, giving rise to a circulation in the sense of rotation of the orbital motion. This phenomena was found to diminish the resultant of the wave pressure on the sphere predicted by potential theory. In approaching the onset of separation, the drag coefficients were found to compare in size with those reported for similar motions in steady unidirectional flow.

INTRODUCTION

Much of the experimental work addressing the problem of wave induced forces on submerged circular bodies have used in-line oscillatory flows; where the motion is simply back-and-forth and $w_{\infty}/u_{\infty} = 0$ (as in Keulegan and Carpenter, 1956; Seymour, 1974; and Sarpkaya, 1975). While the conditions of these experiments may approximate the flows encountered under shallow water waves, it is not clear whether these data are appropriate to the design of offshore structures encountering intermediate or deep water waves, under which the motion is orbital and $w_{\infty}/u_{\infty} = \tanh k(z + h)$, after linear theory.

Previous experiments in which progressive waves have been used to create oscillatory motion (O'Brien and Morison, 1952; and Grace and Casciano, 1969) have involved separated local flow over spheres usually in close proximity to the bottom. Under waves, unseparated motions are a consequence of vorticity being confined by small particle orbits to the immediate neighborhood of the body, when $d_0/D < 1$, despite the fact that large Reynolds numbers may prevail. The unseparated flow regime has not yet received thorough experimental scrutiny, particularly for orbital motion, and this lack of information is critical in the design of submerged structures whose cross-sectional dimension may exceed the amplitude of the water motion.

The following study explores these areas by providing measurements of the wave loads on a smooth sphere which result from the orbital motions under linear, intermediate and deep water laboratory scale surface waves, when the local flow is unseparated.

Force Estimates

Instead of pursuing estimates of the wave force time history, we seek estimates of rms values of the force from Morison's equation as useful "engineering numbers". In this way, the time invariant coefficients of the drag and

inertial terms are physically plausible as time averaged values. With these coefficients, only a spectrum of the free surface is required to establish the relative size of horizontal rms values of the drag to the inertia forces at a given frequency by the following

$$\frac{F_f}{F_m} = \frac{c_f \rho A_0 (u_\infty |u_\infty|)_{\text{rms}}}{c_m \rho V_0 (\dot{u}_\infty)_{\text{rms}}} = \frac{3\sqrt{3}}{8} \frac{c_f}{c_m} \left(\frac{d_0 \text{ rms}}{D} \right)$$

where $d_0 \text{ rms} = H_{\text{rms}} \frac{\cosh k(h-b)}{\sinh kh}$

The anticipated Strouhal dependence arising from a ratio of convective to unsteady inertial terms is equivalent for linear waves to a ratio of the size of the undisturbed particle orbits to the body, (d_0/D). Thus, under the condition for which unseparated motions are found, namely ($d_0/D < 1$), the inertia force appears as the larger component of the wave load.

The inertia force can be estimated with a scattering description under the hypothesis of potential flow for a sphere submerged at least one diameter, D , under linear deep water waves. The inertia force is the resultant of the local wave pressure,

$$F_{mi} = \iint \rho \frac{\partial \phi}{\partial t} n_1 dS$$

where three independent wave profiles combine linearly to give ϕ on the surface of the sphere. The first of these is the undisturbed incident wave, ϕ_∞ . Thus, if $kD \ll 1$, the undisturbed incident wave acts to accelerate the sphere into orbital motion like an equivalent volume of water, and contributes $\rho V_0 \dot{u}_\infty$ to the inertia force, giving a time independent value of unity for the inertia coefficient. However, the undisturbed incident wave cannot alone meet the condition of no flow through the sphere, and so a disturbance, ϕ_s , due to the presence of the sphere is added. This disturbance or scattered wave is determined so that the normal velocity over the surface of the sphere is zero

$$\frac{\partial}{\partial r} (\phi_\infty + \phi_s) = 0 \quad \text{at} \quad r = D/2$$

There is an additional pattern of disturbances, Froude waves, as a consequence of the proximity of the sphere to the free surface. However, if the sphere is at rest, and, if the depth of submergence is taken to be D , where $d_0/D < 1$, then the Froude number is $O(\epsilon d_0/D)^{1/2}$ and it may be verified that any contribution to the force by Froude waves is altogether negligible after first order linear theory due to Havelock (1952) and after complete second order theory due to Kim (1969).

Expanding the spatially dependent parts of the incident and scattered waves into a series of tesseral spherical harmonics, Lamb (1932, art 86 and 106) as,

$$\exp(kz + ikx) = \exp(kr \sin\theta \sin\omega + ikr \cos\theta) = \sum_n \sum_s A_n^s P_n^s(\cos\theta) \cos s\omega$$

yields a scattering formulation which does not rely on the plane wave approximation as for acoustic scattering, or for scattering of surface waves by a vertical cylinder. The orthogonality on a spherical surface of the set of surface harmonics,

$$P_n^S(\cos\theta) \cos s\omega$$

taken with the condition of no flow through the sphere and the radiation condition,

$$\phi = \phi_\infty + \phi_\infty (D/2x)^{\frac{1}{2}} (|\phi_r = D/2|/|\phi_\infty|)$$

as $x \rightarrow \infty$ yields the coefficients, A_n^S , for the incident and scattered waves. These have been evaluated in Havelock¹ (1954) and specify the pressure over the surface of the sphere resulting in the following expressions for the horizontal and vertical components of the inertia force

$$F_{m_x} = \frac{1}{4} \rho g D^2 (2\pi)^{3/2} \frac{H}{2} e^{-kb} (1 + 1/2)(kD/2)^{-1/2} J_{3/2}(kD/2) \sin(-\sigma t)$$

$$F_{m_z} = \frac{1}{4} \rho g D^2 (2\pi)^{3/2} \frac{H}{2} e^{-kb} (1 + 1/2)(kD/2)^{-1/2} J_{3/2}(kD/2) \cos(-\sigma t)$$

Normalizing the amplitudes of the horizontal and vertical components by the amplitudes of $\rho V_0 u_\infty$ and $\rho V_0 w_\infty$ respectively gives the following time independent inertia coefficient for both components

$$c_m = \frac{3}{2} (1 + c_a)(kD)^{-3/2} J_{3/2}(kD/2)$$

where $c_a = 1/2$ and is plotted in Figure 1. When the sphere becomes small in relation to the wave length, c_m is found to converge to 1.5, the value for a sphere in an unbounded uniformly accelerating fluid, and thereby supporting assumptions made in this regard in the early work of O'Brien and Morison (1952). Furthermore the horizontal and vertical components are found to lead the wave profile in time by constant phase angles of $\pi/2$ and π respectively. However, once $kD/2 \gg 1$, c_m becomes small and oscillating as

$$c_m = \frac{g}{4} \sqrt{\frac{2}{\pi}} (kD/2)^{-2} \cos(kD/2 - \pi)$$

for $kD/2 \gg 1$. As a result, the phase of the inertia force relative to the incident wave profile varies rapidly with wave number, since the incident wave is now leaking around a very large obstacle. The lack of a dependence in c_m on the depth of submergence is a consequence of neglecting the effects of Froude waves by limiting the analysis to the case where $b > D$.

If the sphere is subjected to shallow water waves, then $w_\infty/u_\infty^2 \neq 0$ and the acoustic plane wave approximation appears admissible. Scattering of plane waves by a spherical obstacle is treated in Lamb (1932, art no 296) and results in an inertia coefficient which converges in the small body limit, $kD/2 \ll 1$, to 1.5 as

$$c_m = 1 + \frac{2 + (kD/2)^2}{4 + (kD/2)^4}$$

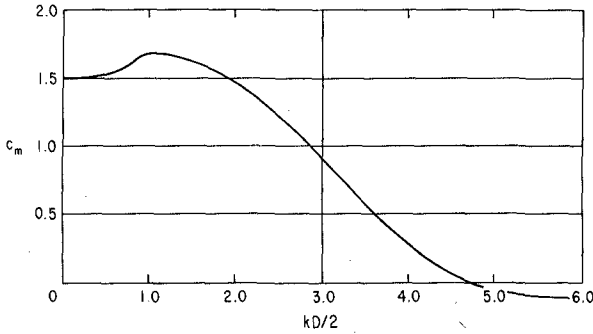


Figure 1. Spherical deep water scattering solution for the inertia coefficient, c_m , after Havelock (1954), where k is the wave number = $2\pi/\text{wave length}$; D is the sphere diameter.

Experiment

The horizontal component of the wave load was measured for polished spheres of 10 cm and 20 cm diameters subjected individually to discrete frequency waves of 0.2, 0.4, 0.6 and 0.75 Hz and heights of 5, 10, 15, and 20 cm, for a total of 32 separate experiments in the 2.5 meter wide wind and wave channel in the Scripps Institution Hydraulics Laboratory. The spheres were situated at mid-depth in 154 cm of water. This choice of experimental parameters limited the investigation to be consistent with the previously stated assumptions and regimes of interest by insuring negligible Froude wave effects ($0.012 < F_r < 0.11$), orbital motion, ($0.24 < w_\infty/u_\infty < 0.93$), and thorough coverage of the regime of small amplitude motion up to the onset of separation ($0.053 < d_0/D < 3.5$). The study however was limited to examination of the small body limit ($0.017 < kD/2 < 0.216$) due to the problem of cross channel waves when attempting to generate waves which are shorter than the sphere diameter in a channel which must necessarily be significantly wider than D .

The measured horizontal force, F , was resolved in the frequency domain into the drag and inertia components of the Morison estimator, \hat{F} , by a harmonic analysis technique adapted from Seymour (1974), involving minimizing the mean squared error in $\langle (F - \hat{F})^2 \rangle$ where

$$\hat{F} = c_1 u_\infty |u_\infty| + c_2 \dot{u}_\infty$$

$$c_1 = \rho C_f A_0$$

$$c_2 = \rho C_m V_0$$

$$\begin{aligned} \langle (F - \hat{F})^2 \rangle = & \langle F^2 \rangle + c_1^2 \langle (u_\infty |u_\infty|)^2 \rangle + 2c_1 c_2 \langle u_\infty |u_\infty| \dot{u}_\infty \rangle + c_2^2 \langle \dot{u}_\infty^2 \rangle - 2c_1 \langle F u_\infty |u_\infty| \rangle \\ & - 2c_2 \langle F \dot{u}_\infty \rangle \end{aligned}$$

If the incident waves are linear, then

$$\langle u_\infty | u_\infty | \dot{u}_\infty \rangle = 0$$

Expressing the covariance and variance in terms of the cospectral and spectral estimates, $\langle xy \rangle = C_{X,Y}$ and $\langle x^2 \rangle = S_X$, and taking $\partial/\partial c_i \langle (F - F)^2 \rangle = 0$, solving for c_1 and c_2 gives

$$c_f = \frac{8 C_{F, u_\infty | u_\infty}}{\rho \pi D^2 S_{u_\infty | u_\infty}}$$

and

$$c_m = \frac{6 C_{F, \dot{u}_\infty}}{\rho \pi 0^3 S_{\dot{u}_\infty}} = \frac{6 C_{F, X}}{\rho \pi 0^3 \sigma^2 S_X}$$

To arrive at c_f and c_m using this scheme each individual experiment was repeated four times during which time histories of horizontal force and free surface elevation were sampled and stored on magnetic tape using an IBM 1130 computer system. As much frequency resolution as possible was desirable. However, a limit of 2048 samples per record was imposed by the 1130 system and a need for as many samples per wave cycle as possible to adequately define the wave profiles led to the compromise of sampling at 20 Hz to allow each run a duration of 102.4 sec and a frequency resolution of 0.0097 Hz. After transforming these time series using Fast Fourier transform routines, the Fourier coefficients for the horizontal particle position required to construct S_X and $C_{F,X}$ were obtained from those of the free surface through phase shifting $\pi/2$ by reversing the cosine and sine coefficients, changing the sign of the cosine coefficient and then multiplying by

$$\frac{\cosh k(h - b)}{\sinh kh}$$

after linear theory. The Fourier coefficients for $u_\infty | u_\infty |$ were obtained by taking derivatives (slopes) of the free surface time series, squaring, and then transforming to the frequency domain. The resulting Fourier pairs representing the square of the vertical velocity at the free surface were then phase shifted by $\pi/2$ as before and attenuated to the depth of submergence as;

$$\left(\frac{\cosh k(h - b)}{\sinh kh} \right)^2$$

The drag and inertia coefficients realized in this way from the principle frequency band of each run were then averaged among the set of quadruplicate runs comprising each separate experiment.

Because this method relies heavily on the average time dependence of u_∞ being zero, care was taken to minimize seiche and reflection in the wave channel by submerging a tethered floating breakwater at the beach end. In addition, only wave forms of small steepness were used, with $0.008 < \epsilon < 0.22$. To minimize generation of a free second harmonic due to the paddle motion, the

paddle throw was adjusted to a flapper mode for the deep water waves and to a semi-piston/flapper mode for the intermediate water waves.

Results of the Force Experiment

An example of the grouped spectra of horizontal force and the free surface when unseparated local flow persists is found in Figure 2, using a 10 cm sphere under a 0.75 Hz, 20 cm wave. The linear character of the incident waves is evidenced by the negligible energy appearing at harmonics above the driving frequency. The second harmonic in the force spectra is two orders of magnitude below the peak at the driving frequency where a phase difference of $\pi/2$ with the free surface is seen, indicating the predominance of the inertia force.

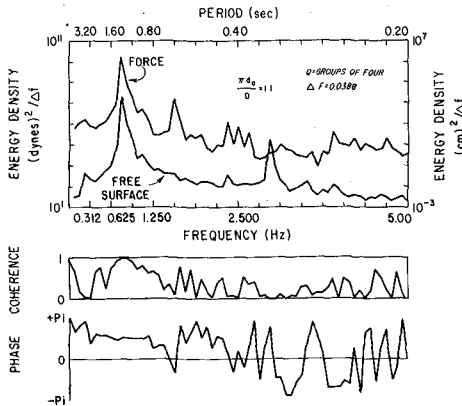


Figure 2. Grouped spectra of the free surface and horizontal force for unseparated orbital motion.

Flow visualization using dye injection from three parts embedded in the spheres at 90° increments around the horizontal equator demonstrated as in Figures 3-5 that the local flow is both laminar and unseparated for $\pi d_0/D < 3.2$. Surprisingly, the dye streaks from the forward and aft ports produced by several cycles of motion show in Figures 3 and 4 a steady streaming close to the surface of the sphere, superposed on the local particle motion, causing a circulation around the vertical equator in the sense of rotation of the orbital motion, despite the linear character of the incident waves. Similarly, dye released from the side port in Figure 5 circulates in multiple cycles as laminar streaming around latitudinal belts in the vertical plane. As $\pi d_0/D$ exceeded 3.2 and the orbits became increasingly flattened the circulation became turbulent as seen in Figure 6, in response to adverse pressure gradients imposed by the wave field prior to each flow reversal. By $\pi d_0/D = 7$ the onset of separation was observed when portions of the dye plume would break away from the sphere at the moment of reversal of the local flow, disrupting the turbulent circulation.



Figure 3. Dye streak produced by two cycles of motion showing circulation proceeding over the top of the sphere at $\pi d_0/D = 3.2$. Waves progressing from left to right.

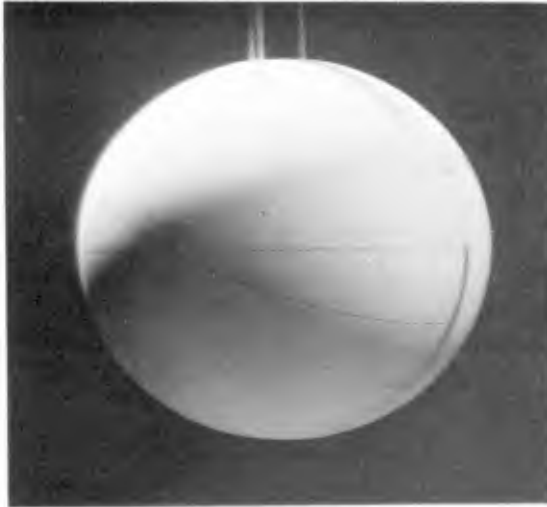


Figure 4. Circulation carries dye 6 cm in two cycles from rear port towards the underside of the sphere at $\pi d_0/D = 0.32$. Waves progressing from left to right.



Figure 5. Dye spreading in a spiral from the side port towards the vertical equator at $\pi d_0/D = 1.1$. Waves progressing from left to right.

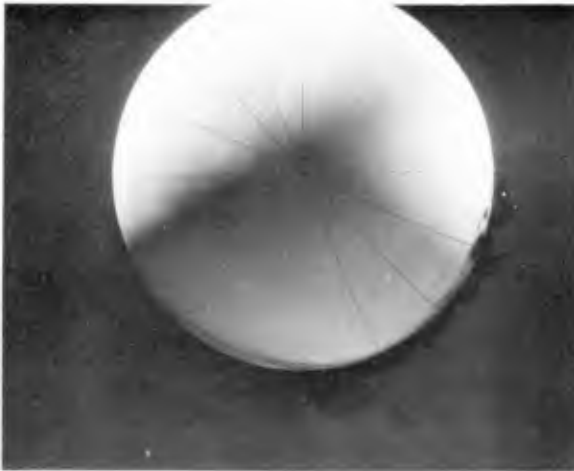


Figure 6. Turbulent circulation carrying dye plume from the rear port around the bottom of the sphere for $\pi d_0/D = 4.0$.

The drag coefficients measured in this investigation were found to vary systematically with the Keulegan-Carpenter form of the Strouhal number as shown in Figure 7. For $\pi d_0/D < 3.2$, the sizes of the drag coefficients were typical of those for unseparated steady unidirectional flow around a sphere at low Reynolds number ($0.6 < R < 25$). In the range $3.2 < \pi d_0/D < 7$ where turbulent circulation was observed, c_f was found to be comparable to values measured for steady unidirectional flow when closed streamlines behind a separation bubble are found for $25 < R < 150$. Indeed the turbulent circulation may evolve as a separation bubble formed near flow reversal and then convected around the sphere under the influence of orbital motion. When $\pi d_0/D > 9$ and the onset of separation is clearly developed the values of c_f measured here are found to compare in size with those reported for a sphere in steady translation with fully separated flow and open-ended streamlines at about $R = 10^4$. The range of Reynolds numbers covered in this study was from 0.5×10^4 to 4×10^4 , based on the amplitude of the horizontal velocity component.

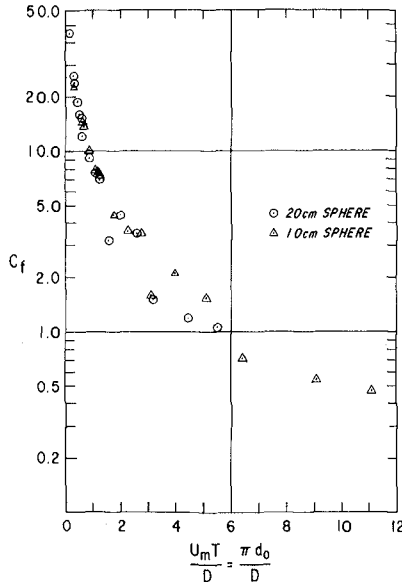


Figure 7. Measured drag coefficients, c_f , against the inverse of the Strouhal number, $u_m T/D = \pi d_0/D$, where u_m is the maximum horizontal particle velocity in the undisturbed wave; T is the wave period and d_0 is the orbital diameter.

The measured inertia coefficients, c_m , Figure 8, defy explanation in terms of the results of the scattering problem. To find the values all less than unity is particularly surprising, and, since the sphere is so small in relation to the incident wave length, the pressure of the undisturbed wave

alone should result in an inertia coefficient of unity. Any scattering of the incident wave would add to this. The circulation, which could not be generated in the absence of viscosity for simple harmonic motions appears to be the only physical explanation for these values.

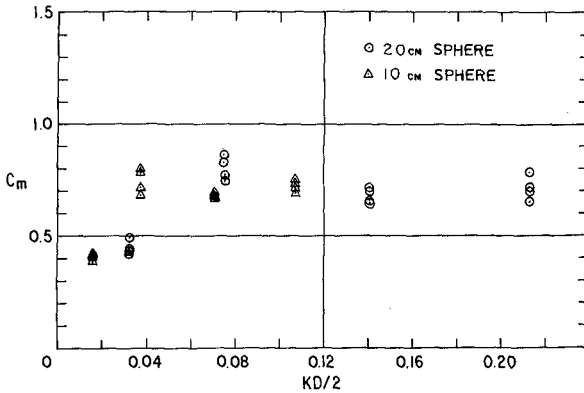


Figure 8. Measured inertia coefficients, C_m , against $kd/2$.

Circulation Streaming

Nonlinear free-surface effects as considered in Kim (1969) for a submerged sphere do not appear a likely mechanism for generating the circulation observed in this study due to the remoteness of the sphere from the free surface ($3.8 D < b < 7.7 D$) and the small size of the sphere with respect to the incident wave length. Furthermore, the streaming appears most intense near the surface of the sphere. Therefore, the boundary layer does seem a likely mechanism.

Schlichting (1966) has treated the problem of steady streaming as developed by a circular cylinder executing small amplitude oscillations in still water. Photographic evidence of similar streaming near a cylinder due to acoustic waves in air may be found in a paper by Holtsmark, et al (1954). However, the streaming developed by these in-line oscillatory flows does not result in a net circulation because the streaming flows away from the cylinder along the axis in line with the oscillations, and towards it at locations transverse to these oscillations.

Streaming over a flat bottom under the orbital motion of progressive waves, "bottom wind", has been treated in Longuet-Higgins (1953) and shown to be a consequence of the retarding influence of the boundary layer being greater for that portion of the orbit in closest proximity to the wall. Consider, then, in Figure 9, the solid path lines of deformed, closed orbits in the vicinity of a submerged sphere under linear inviscid, irrotational waves when $kd/2 \ll 1$. There is negligible decay in the amplitude of the motion vertically over one sphere diameter, and no net time independent motions result. But if viscosity and the formation of boundary layers is allowed in the model,

then the orbits can no longer remain closed and a "bottom wind" results around the sphere to give rise to a time independent circulation in the sense of rotation of the orbital motion. Considerably more vigorous streaming may be realized around a sphere than over a flat bottom, because in diffracting around the sphere the local velocities and orbital diameters are increased relative to those in the undisturbed field, with diffraction velocities approaching $3/2 u_\infty$ for $kD/2 \ll 1$.

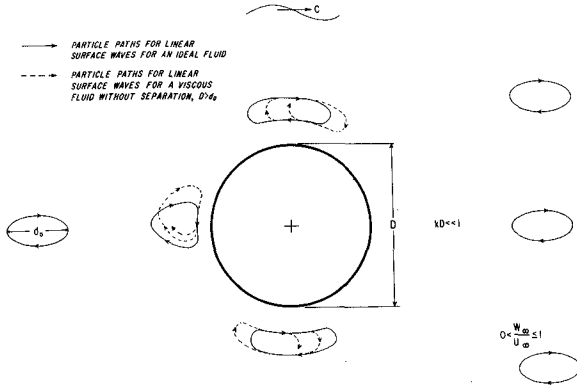


Figure 9. "Bottom wind" around a sphere as a mechanism for circulation streaming.

The streaming velocities around the vertical equator were estimated for each wave condition in the force experiments by measuring the progress of the leading edge of a dye streak for an integral number of wave cycles. The dye was released from the rear port from where it proceeded around the bottom of the sphere and was thus not perturbed by the small diameter sting used to support the sphere from the surface. The circumferential streaming velocity $\langle u_\theta \rangle$, was found to be almost linear with $(d_0 W_\infty / \pi D)$ as shown in Figure 10. At large values of $(d_0 W_\infty / \pi D)$ the streaming was more difficult to measure due to turbulence, but tended to decay and then quickly degenerate with the onset of separation. These results demonstrate that for a given wave height the circulation will be most intense for a deep water wave and diminishes as the wave becomes shallow water in character, and cease altogether once the motion is merely back-and-forth, assuming separation has not yet set in.

With such a circulation added to the diffracting velocity field, the action of fluid inertia must result in a force historically termed as lift, F_L , which acts normally to the instantaneous far field velocity and will therefore rotate through 2π in a wave cycle. Because the circulation is in the sense of rotation of the orbital motion, and because the phase of the inertia force lags the wave profile in space by a constant $\pi/2$ when $kD/2 \ll 1$, the lift opposes the inertia force at any given wave phase as illustrated schematically in Figure 11. Because the streaming is generated at the top of the ac boundary layer, $O(\nu/\sigma)^{1/2}$, it is assumed that the Kutta-Joukowski theorem is appropriate to estimate rms values of the horizontal

component of lift. This presupposes that the streaming velocity $\langle u_\theta \rangle$, decays as $(1/r)$ and this has not yet been verified. In addition, the circulation distribution from the vertical equator to the sides transverse to the waves must be specified. The expanding spiral shaped dye streak issued from the side port in Figure 5 show that the streaming diminishes towards the sides of the sphere. If an assumption of solid body rotation is applied to the region within the vortex tube which results from the circulation around the vertical equator, then the streaming velocity $\langle u_\theta \rangle$, decays from the vertical equator to zero at the sides as $\cos\omega$. The rms value of the horizontal component of lift can then be estimated from only knowing the streaming around the vertical equator, $\langle u_\theta \rangle$ and from $w_{\infty rms}$ by

$$F_{l rms} = \frac{2}{3} \rho \pi D^2 \langle u_\theta \rangle (w_{\infty})_{rms}$$

where the vertical motion gives rise to the horizontal component of lift. Because the horizontal component of F_l opposes the horizontal component of the inertia force, its rms values can be normalized by $\rho V_0 (\dot{u}_{\infty})_{rms}$, and then added to the measured values of, c_m in Figure 6, thereby subtracting the viscous effects due to circulation to give apparent inviscid values for the inertia coefficient plotted in Figure 12. Many of these values are comparable in size with the expectations of the scattering solution. However, due to the approximations in computing $F_{l rms}$, these are presented here only to illustrate that the circulation can augment the inertia force at least to an extent that can account for the very small values of c_m measured in this study.

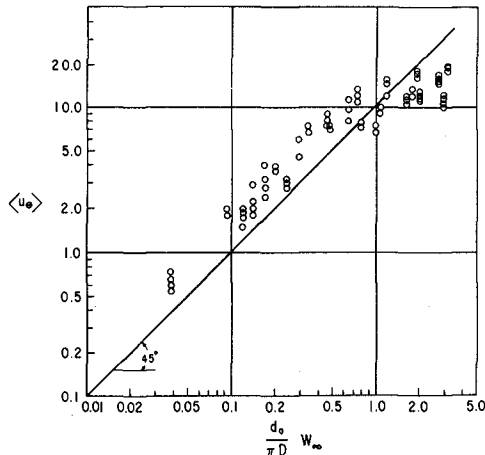


Figure 10. Streaming velocities $\langle u_\theta \rangle$, measured around the vertical equator of the sphere against $(d_0 w_\infty / \pi D)$ where w_∞ is the amplitude of the vertical particle velocity in the undisturbed wave. Velocities are expressed in units of cm/sec.

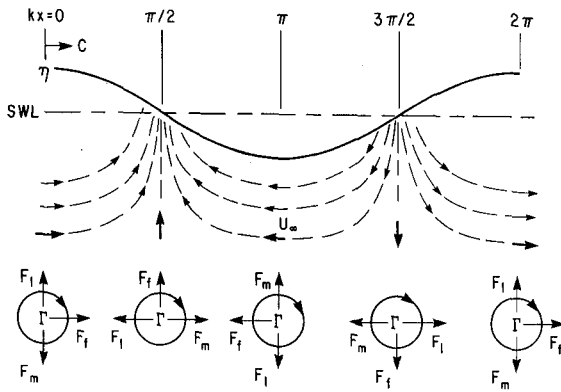


Figure 11. Phase relationships between drag, F_f , the inertia force, F_m , and lift, F_l , relative to the wave profile when a circulation, Γ , in the sense of the orbital motion is present.

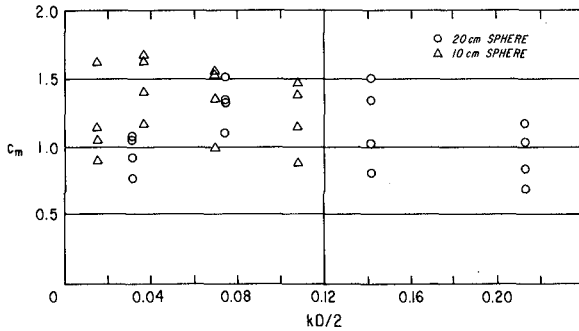


Figure 12. Apparent inviscid inertia coefficients, c_m , obtained by correcting measured values of c_m for the horizontal component of lift.

Conclusions

Even when the gross viscous effects associated with separation are avoided, the smaller viscous effects which prevail in unseparated orbital motion and give rise to circulation streaming are sufficiently important to render potential theory as a rather poor description of the problem of forces induced by linear progressive waves. Because the circulation phenomena cannot be accounted for by in-line oscillatory flow, such studies are inappropriate to the design of circular members which exceed the amplitudes of the motions under deep and intermediate water waves.

Symbols

A_n^s	solid harmonic coefficient
A_o	frontal area of a sphere = $\pi D^2/4$
b	depth of submergence
c_a	added mass coefficient
c_f	drag coefficient = constant in the time domain
c_m	inertia coefficient = constant in the time domain
C_{xy}	cospectral estimate
D	sphere diameter
d_o	orbital diameter in the undisturbed wave
F_f	drag force
F_l	lift force
F_m	inertia force
F_r	Froude number = u_ω/\sqrt{gb}
\hat{F}	Morison estimator
g	acceleration of gravity
H	wave height
h	water depth
$J_{n+1/2}$	Bessel function of the first kind and half odd integral order with argument = $kD/2$
k	wave number
n_i	direction cosine

P_n^s	Legendre function of order s and degree n with argument $= \cos \theta$
r	radial coordinate
R	Reynolds number
s	order
S	spherical surface area
S_x	spectral estimate
t	time variable
V_0	volume of the sphere $= \pi D^3/6$
u_∞	horizontal particle velocity in the undisturbed wave $= \partial \phi_\infty / \partial x$ at the depth of submergence of the sphere
\dot{u}_∞	horizontal particle acceleration in the undisturbed wave at the depth of submergence of the sphere
u_θ	circumferential velocity component
V_0	volume of the sphere $= \pi D^3/6$
w_∞	vertical particle velocity in the undisturbed wave, $= \partial \phi_\infty / \partial z$ at the depth of submergence of the sphere
x, y, z	Cartesian coordinates with the x -axis in the direction of wave advance, the y -axis transversely, and the z -axis positive upwards
Γ	circulation
ϵ	wave steepness $= kH/2$
ϕ	local velocity potential $= \phi_\infty + \phi_s$
ϕ_∞	velocity potential of the undisturbed incident deep water waves $= (H\sigma/2k) \exp(kz) \sin(kx - \sigma t)$
ϕ_s	velocity potential of the scattered wave
ρ	fluid density
σ	radian frequency $= 2\pi/\text{wave period}$
θ	angular coordinate in the xz plane
ω	angular coordinate in the xy plane
$ $	absolute value
$\langle \rangle$	time average

References

- Grace, R. A. and F. M. Casciano, 1969, "Ocean wave forces on a subsurface sphere", Jour. Waterways and Harbors Div., Proc. Amer. Soc. Civil Eng., WW3, Paper no 6722, p 291-317.
- Havelock, T. H., 1952, "The moment on a submerged solid of revolution moving horizontally", Quart. Jour. Mech. Appl. Math., vol 5, p 129-36.
- Havelock, T. H., 1954, "The forces on a submerged body moving under waves", Quart. Trans. of Inst. of Naval Arch., January, and in The Collected Papers of Sir Thomas Havelock on Hydrodynamics, ONR/ACR-103, pp 590-96.
- Holtmark, J., I. Johnsen, T. Sikkeland and S. Skavlem, 1954, "Boundary layer flow near a cylindrical obstacle in an oscillating incompressible fluid", Jour. Acoust. Soc. Amer., vol 26, p 102.
- Keulegan, G. H. and L. H. Carpenter, 1956, "Forces on cylinders and plates in an oscillating fluid", Nat. Bureau of Standards, Report No 4821, 57 pp.
- Kim, W. D., 1969, "Nonlinear free-surface effects on a submerged sphere", Jour. Hydronautics, vol 3, no 1, p 29-37.
- Lamb, H., 1932, Hydrodynamics, Cambridge University Press, 738 pp.
- Longuet-Higgins, M. S., 1953, "Mass transport in water waves", Phil. Trans. Roy. Soc. London, Series A, no 903, vol 245, p 535-581.
- O'Brien, M. P. and J. R. Morison, 1952, "The forces exerted by waves on objects", Trans. Amer. Geophys. Union, vol 33, no 1, p 32-8.
- Sarpkaya, T., 1975, "Forces on cylinders and spheres in a sinusoidally oscillating fluid", Jour. Applied Mech., Trans. Amer. Soc. Mech. Eng., vol 42, no 1, p 32-7.
- Schlichting, H., 1966, Boundary Layer Theory, McGraw-Hill Inc., New York, 747 pp.
- Seymour, R. J., 1974, "Resistance of spheres in oscillatory flows", Ph. D. Dissertation, Scripps Institution of Oceanography, University of California, San Diego, 86 pp.

Acknowledgements

This research was sponsored by NOAA, Office of Sea Grant, U. S. Department of Commerce, under Grant Number USDC 04-3-158-22.

CHAPTER 142

NEW DESIGN PRINCIPLES FOR RUBBLE MOUND STRUCTURES

by
Per Bruun and Ali Riza Günbak
The Norwegian Institute of Technology

Abstract

This paper describes the effect of wave period on the stability of rubble mound breakwaters. Introductorily wave run-up and run-down on smooth slopes and on rubble mounds were measured, and breaker types were observed and recorded for different incoming wave and slope characteristics. The surf similarity

parameter, $\xi = \frac{tg\alpha}{\sqrt{H/L_0}} = \sqrt{\frac{g}{2\pi}} \cdot \frac{tg\alpha}{\sqrt{H}} \cdot T$ was found practical for

description of breaker type, run-up and run-down on both smooth and permeable slopes. Pressure measurements along the smooth slopes and in the core of a rubble mound were undertaken with two different core materials. It was shown that the most dangerous condition for the stability of rubble mounds occurs at the so-called "resonance condition". Resonance refers to the situation that occurs when run-down is in a low position and collapsing-plunging wave breaking takes place simultaneously and repeatedly at or close to that location. This corresponds to a range of ξ values in between 2 and 3. Photographic instrumentation was introduced and tested to quantify the initial damage on a rubble mound.

This paper is a 1/3 abstract of a thesis for the Dr. Eng. degree by Ali Riza Günbak.

WAVE PROPAGATION TOWARDS A SLOPING STRUCTURE

GENERAL

Waves that propagate from deep water towards a beach will change characteristics due to shoaling. If the beach slope is not very mild and the deep water wave steepness (H_0/L_0) is not too small, the wave will finally break somewhere on or in front of the beach. The condition before breaking is called the "non-breaking wave" condition; the condition at the point of breaking is the "breaking wave" condition, and the condition towards the shore is the "broken wave" condition. In this paper only waves that are "non-breaking" until they reach the structure are studied.

TYPES OF BREAKERS REFLECTION

The main types of breakers are described by Galvin (20) as "collapsing", "plunging" and "spilling". For a fixed slope, breakers will change form from collapsing towards spilling as steepness increases. Battjes (3) described the transition from one breaker type to the other on smooth slopes based on Galvin's data. Using the so-called "offshore surf parameter",

$$\xi_0 = \frac{\text{tg}\alpha}{\sqrt{H_0/L_0}} \quad \text{breaker types and limiting criteria are listed}$$

below:

<u>Breaker Type</u>		<u>Limiting Criteria</u>
Surging or Collapsing	if	$3.3 < \xi_0$
Plunging	if	$0.5 < \xi_0 < 3.3$
Spilling	if	$\xi_0 < 0.5$

Replacing ξ_0 by ξ_b the surf parameter defined as $\xi_b = \frac{\text{tg}\alpha}{\sqrt{H_b/L_0}}$

one has:

<u>Breaker Type</u>		<u>Limiting Criteria</u>
Surging or Collapsing	if	$2.0 < \xi_b$
Plunging	if	$0.4 < \xi_b < 2.0$
Spilling	if	$\xi_b < 0.4$

These breaker types are shown in Fig. 1, from which it is seen that the distance between the breaker point and the mean water line varies. Battjes (3) estimated this distance (x_b) roughly as

$$\frac{x_b}{\frac{1}{2}T\sqrt{gd_b}} \cong 0.8 \xi_b^{-1} \quad (1)$$

where $x_b = d_b \cot\alpha$ and $H_b = d_b$ (shallow water).

Observations (3) showed that this estimate was qualitatively correct, but quantitatively about 20% higher than experimental values.

The reflection coefficient, $r = \frac{H_r}{H_1}$ is given for waves breaking on a slope ($\xi < 2.5$) as:

$$r = 0.1 \xi^2 \quad \text{where} \quad \xi = \frac{\text{tg}\alpha}{\sqrt{H/L_0}} \quad (2)$$

and H is the incoming wave height in front of the structure. For non-breaking waves, r can be taken as one.

RUN-UP IN RELATION TO TYPE OF BREAKING

Theoretical run-up calculations for breaking waves mainly investigate the behaviour of a bore on a slope. Most of the theories (15, 26, 57) describe the breaking phenomenon by a non-linear long wave theory. In this respect they use the method of characteristics for integration which was first introduced by Stoker (52).

According to the above-mentioned theories, the height of a bore approaches zero near the water line, and run-up starts beyond this level. The highest run-up that can be obtained corresponds to the velocity head $R_u = \frac{u^2}{2g}$ of the flow at the water line when the bore is at that point.

Theoretical investigations by Daubert and Warluzel (15) showed that run-up on a dry slope by the first incoming wave is higher than run-up for the following waves, which run up against down-rushing water from the preceding wave. This is in agreement with experimental results (24).

The run-up theory for bores refers to the situation for a fully developed bore. It is not concerned with an intermediate phase in the form of a spilling breaker, which occurs on mild slopes. This intermediate phase is given by Le Méhauté's "Non-Saturated Breaker Theory" (38). It is based on a semi-theoretical account of the energy balance for a spilling breaker. This theory includes the friction (f) and bottom slope characteristics (s) where it is assumed that:

$$f = 14.6 \frac{n^2}{d^{1/3}} \quad n = \text{Manning Coefficient} \approx 0.02$$

$$d = \text{Water Depth (ft)}$$

$$s = \text{bottom slope}$$

With the above assumptions it is concluded that:

1. If $s < 0.37 f$, waves never break. All energy is dissipated by bottom friction and no run-up takes place.
2. If $0.37 f < s < 0.37 f + 0.01$, waves break as spilling breakers, and the rate of energy dissipated by the breaker increases as the bottom slope increases. All the wave energy is dissipated before the waves reach the beach. There is practically no run-up. Wave set-up, however, occurs as a result of mass transport and momentum in the breaker. The set-up can be calculated by the available methods (5, 42).
3. If $s > 0.37 f + 0.01$, a fully developed bore occurs. The run-up may be calculated by means of run-up theories for bores (15, 26, 38, 57).

Run-up of breaking waves may be evaluated by the method of characteristics (52). To obtain a solution, many assumptions, including the initial bore characteristics, must be made.

Long mathematical calculation procedures are needed for each incidental case, and they do not provide a direct method for calculating run-up on a slope from the properties of swells far from the shore. Empirical calculations of run-up of breaking waves are therefore usually preferred. The change of wave characteristics from deep to shallow water, needless to say, should be considered in calculating the wave height occurring before run-up (21, 33, 41, 56, 58).

UPRUSH OR UPRUN

Investigation by Inoue (30) on smooth slopes, demonstrated that $\frac{R_u}{H_0}$ maximizes when the value of $\frac{d}{H_0}$ is approximately one, which means that wave breaking may take place at the toe of the structure or right in front of it (21). Fig. 2 is a characteristic result by Inoue (30) demonstrating the effect of water depth on wave run-up, which increases with decreasing $\frac{d}{H}$ until it equals about 1.

The effect of water depth on wave run-up was investigated by Saville (13), who concluded that the depth effect is negligible when $\frac{d}{H} > 3$ for all steepnesses. Hunt in (28), using the available experimental data on wave run-up, gives an empirical equation for calculation of run-up on continuous smooth slopes for waves breaking on the slope,

$$\frac{R_u}{H} = \left(\frac{2.3 \operatorname{tg} \alpha}{\sqrt{H/T^2}} \right)$$

where H is the incoming wave height in front of the structure in feet. Using the ξ parameter the above formula reduces to

$\frac{R_u}{H} = \xi$ for $\xi < \xi_{br} = 2.3$. Fig. 3 relates Hunt's formula to various experimental results.

Battjes and Roos (4) conducted experiments on smooth slopes $\left(\frac{1}{3} < \cot \alpha < \frac{1}{7}; 0.54 < \xi < 1.97 \right)$. They found the following expressions: Maximum velocity

$$V_{\max} = \sqrt{gh} (0.5 \text{ to } 0.75) \xi \text{ for } \frac{x}{\sqrt{HL_0}} < 0.6 \quad (3)$$

Average run-up front velocity above SWL

$$C = gH \cdot 0.6 \xi^2 \quad (4)$$

Run-up time

$$t_u = T \cdot 0.7 \xi^{-1/2} \quad (5)$$

where x is defined in Fig. 4.

Regarding uprush on slopes with friction elements, the reader is referred to (8) and (54).

Permeability decreases wave run-up relative to smooth impervious slopes. The effect increases as the slope angle decreases and the relative run-up (R_U/H) increases with increasing ξ values. The trend of the increase is getting milder with higher ξ values. Savage's (45) results contradict the above conclusion, but his results referred to beaches with uniform grain size and not to a typical breakwater slope

Uprush on composite slopes is dealt with in ref's. (8, 10, 24, 28, 46, 47, 54). Wave set-up and set-down both have minor effects on run-up/run-down, as mentioned later (3, 16, 29, 40, 48).

DOWNRUSH OR RUN-DOWN

Run-down (R_D) is defined as the vertical distance between the SWL and the water level at the lowest point of water recession on the slope. It can therefore be positive as well as negative. A positive quantity of run-down means that run-down cannot be completed. The slope is continuously under water below SWL, and the run-up meets the water which remained from the previous run-down and accordingly decelerates considerably. The importance of different run-up/run-down conditions on the beach formation has already been shown by Kemp (35, 36), who also measured uprush and downrush velocities (37). Semi-theoretical approaches to down-rush velocities are mentioned in ref's. (6, 7, 9). Battjes and Roos (4) conducted experiments for wave run-down on smooth slopes. ($\text{Cot}\alpha = 3.0, 5.0, 7.0, 10.0$) ($0.02 < H/L_0 < 0.03$). The above experiments refer to waves breaking on the slope. ($0.3 < \xi < 1.9$). They define run-down:

$$R_D = R_U(1 - 0.4 \xi) \quad (6)$$

From the above-mentioned it is known that breaking occurs for $\xi < 2.3$. For $\xi = 2.3$, R_U is always positive. This means that if the above formula is applicable for all ranges of breaking waves ($\xi < 2.3$) on smooth slopes, then run-down cannot be completed in full for the waves breaking on the slope and run-up and run-down are always going to interact above SWL. The existence of the above flow condition is analysed by assuming the movement of a water mass along the slope under the action of the gravity only. With such an assumption one has (fig. 4):

$$\sqrt{H} \overline{L_0} / \cos\alpha = 0.1 \cdot g \cdot \sin\alpha \cdot t^2$$

Using $L_0 = \frac{g}{2\pi} T^2$ one obtains,

$$\frac{t}{T} = \sqrt{\frac{1}{\pi} \cdot \frac{1}{\cos\alpha} \cdot \frac{1}{\sqrt{\xi}}}$$

Assuming that $\cos\alpha \approx 1$, which is true for slopes less than 1 in 3 with an error of maximum 5%, one has:

$$\frac{t}{T} = 0.564 \xi^{-\frac{1}{2}} \quad (7)$$

Equation (7) gives the relative time of travel of a water particle from the maximum run-up position, down to SWL. Therefore this is the shortest time that run-down can reach SWL. Equation (7) predicts the run-up time experimentally. For regular waves, the relative time t_1/T left for the wave front to retreat back down to SWL without interacting with the new run-up is then:

$$\frac{t_1}{T} = 1 - \frac{t_u}{T} = 1 - 0.7 \xi^{-1/2} \quad (8)$$

From equations (7) and (8) it may be noted that on smooth slopes, for $\frac{t}{T} > \frac{t_1}{T}$ run-up and run-down always interact above SWL. Actually during run-down, pressure forces and boundary resistance will all retard the run-down. Therefore, the question of interaction of run-down and run-up for breaking waves on smooth slopes ($\xi < 2.3$) remains to be checked experimentally.

Fig. 5 shows the variation of run-up and run-down with ξ on Dolos covered rubble-mound breakwater slopes. The data is taken from ref. (25) for 1/73.7 scale model tests. Although there is scattering of data in fig. 5, it shows a trend of increasing run-up values with increasing ξ values. If a regression line is drawn from these data, run-up will become nearly constant for high ξ values ($\xi > 4.0$).

Run-down also increases with increasing ξ values and becomes nearly constant at high ξ values ($\xi > 4.0$). Data in fig. 5 show higher run-down values for $\text{Cot}\alpha = 3.0$ than for $\text{Cot}\alpha = 2.0$ at the breaking range when $\xi < 3.0$. This may be due to the fact that the water running up and down on the 1 in 3 slope travels a longer distance than on the 1 in 2 slope. This may cause a higher possibility of penetration of water deep into the breakwater body and will therefore cause deeper run-down on the 1 in 3 slope.

Fig. 6, 7, 8 and 9 show the relative run-up and run-down variation with ξ on a permeable breakwater slope of 1 in 1.5. Data are from Dai & Kamel's tests (14) on rough quarrystones, smooth quarrystones, rough quadripods and smooth quadripods. It should be noted that these data were obtained on three different model scales. All data are included in the above figures. The water depth to deep water wave height ratio (d/H_0) is not always > 3.0 and run-up and run-down is as indicated above affected by depth. Although the above-mentioned may cause increase of the scatter (data are only available for $\xi > 2.0$), the general remarks made for run-up and run-down on rubble-mound breakwater slopes with increasing ξ values hold qualitatively for these data.

Based on the above review it may therefore be concluded that relative run-up (R_u/H) and relative run-down (R_d/H) on rubble-mound slopes show a trend with ξ values for $d/H_0 > 3.0$. Both increase from spilling breakers, towards plunging, collapsing and surging breakers and assume approximately a constant value for surging breakers when $\xi > 4.0 - 5.0$.

THE STABILITY
OF RUBBLE-MOUND BREAKWATERS

GENERAL

Today, the most frequently used formula for breakwater design is the Irribaren formula which was modified by Hudson (27) and given by:

$$W = \frac{\gamma_r H^3}{K_D \left(\frac{\gamma_r}{\gamma_w} - 1 \right)^3 \text{Cotg} \alpha} \quad (9)$$

where

$$\begin{aligned} \gamma_r &= \text{specific weight of stone} \\ \gamma_w &= \text{specific weight of water} \\ \frac{1}{K} &\sim K_D = \text{stability coefficient} \end{aligned}$$

Its popularity comes from the extensive tabulation of the K_D values by scale model tests. They are given for regular waves, for no overtopping conditions and for certain specific breakwater cross-sections. Much criticism has been raised against this formula and its background (1, 2, 9, 10, 11, 18, 19, 20, 21, 22, 23). Ref. (55) states that different laboratories in the world list different K_D values for determining the initial damage. These differences are caused by lack of consideration to the effects of water depth, porosity of and friction between units and to the fact that tests were conducted at different ranges of these parameters. Ref.'s (10, 11) give a detailed analysis of the effect of porosity and friction on the stability of rubble-mounds. Due to the scarcity of data and the wide range of variables, it is not possible at this time to give quantitative figures for these parameters.

Accepting the hydrodynamic nature of the phenomena (flow causing drag and inertia forces), it is not logical to ignore the different flow characteristics occurring on the breakwater by assuming a constant stability coefficient K_D for the whole range of wave periods. Therefore a hypothesis was developed which includes the effect of wave period on the stability, using the knowledge of flow characteristics explained above.

THE IMPORTANCE OF WAVE PERIOD ON THE STABILITY OF SLOPES

The importance of wave period on the formation of beach profiles was, as already mentioned, investigated by Kemp (35, 36) who found that "the phase-difference was the dominant factor in the relation between waves and geometry of beach profile". He defined the phase-difference as the ratio of the run-up time (t_u) to the wave period (T). The run-up time (t_u) has a different meaning than the one used here. It is defined as the time needed for the water front to advance from the breaking

point up to maximum run-up. Kemp also mentions the occurrence of vortexes at the sea bottom due to the interaction of run-down water with the incoming breaker (fig. 3 of ref.(35)).

His experiments showed that for low phase differences ($\frac{t_u}{T} \leq 0.3$) a step profile and for high phase differences ($\frac{t_u}{T} \geq 1.0$) a bar profile developed. A transition from step to bar profile exists when t_u/T is in between 1.0 and 0.3.

Bruun in (10) and (11) compares step profiles from beaches with stabilized breakwater profiles. The stable breakwater profiles are cross-sections of some prototype breakwaters which finally obtained a stable cross-section. The step beach profiles are taken from experimental data and converted to prototype scale using model laws. From comparisons it is concluded that a stable breakwater profile assumes a cross-section similar to a step profile of a beach. This together with Kemp's results brings out the fact that flow characteristics affect breakwater stability, and a phase difference smaller than 1.0, as defined above, is responsible for the stable breakwater profile.

Sigurdsson (50) measured slope parallel and normal forces using spheres as armour units. His tests were performed on 1 in 1 and 1 in 3 slopes. From his measurements Sigurdsson categorizes the forces acting on the armour units based on different flow conditions as shown in table (1) in reference to fig. 10.

TABLE (1) CLASSIFICATION OF HYDRAULIC FORCES

Force Category	Resulting Extreme Values			
	Parallel Maximum	Force Minimum	Normal Maximum	Force Minimum
Incipient breaker preceded by outflow	x		x	
Incipient breaker preceded by backflow	x		x	
Flow into the breakwater				x
Flow out of the breakwater		x	x	
Changes in the buoyancy force	x	x	x	x
Impact	x	x		x
Uprush	x			
Backflow		x		

The following is part of his conclusion:

- i - "The most important hydraulic forces occur under the toe of an advancing breaker or when water is flowing out of the breakwater".

- ii - "The lowest level of wave retreat is an important factor in determining the distribution of hydraulic forces with depth".
- iii - "Considerable impact forces occur when the breaker front strikes the capstones in a rubble-mound breakwater. These forces are directed upward and parallel to the breakwater face. They are strongest for flat breakwater slopes".

Sandström (44) conducted experiments similar to Sigurdsson's. His tests were run for constant wave height of $H = 7$ cm, with wave periods of $T = 0.8$ sec and $T = 1.0$ sec. The steepest test slope was 1 in 1.5. This corresponds to a ξ value lower than 3.15 which indicates that for continuous slopes wave forces occurring with plunging breakers were relatively close to resonance, and the plunging breaker hit a barren slope. Sandström also mentions maximizing of normal forces on armour units below SWL due to the sudden turning of the flow resulting from the interaction of the run-down with the incoming breaker. For armour blocks above SWL run-up is more decisive for slope gradients 1 in 3 and 1 in 4.

Hedar (23) expressed this much earlier and insists that breakwater stability is different for run-up and run-down. He introduced two stability equations for the two different phases of flow. Analysis of his formulae together with the given experimental coefficients show that the design for slopes steeper than 1 in 3 must be based on the run-down formula.

Carstens et al (12), from their experiments with regular waves, showed a relation between wave run-up and the stability of rubble-mound breakwaters. Run-up and run-down, however, are closely related.

RESONANCE CONDITION

The resonance phenomenon was first mentioned in ref.'s (10,11). On page 20 of ref. (10) the occurrence of this phenomenon is defined: "Such a situation may occur if the uprush-downrush period or what may be termed the downrush period is equal to the wave period, assuming that downrush is at its lowest position at the toe of the breaking wave so that every downrush meets a breaking wave at the lowest position of the downrush." It was indicated that, at resonance, the hydrostatic pressure from the core structure would also be maximized causing uplift forces on the armour blocks. Attempt was not made to define resonance condition more specifically in terms of structure and wave characteristics.

With reference to fig. 11 the time history of the wave front along the slope above still water level (SWL) is drawn. Three different conditions may occur in all ranges of slope and wave characteristics, in other words, in all ranges of ξ .

Fig. 11a shows the condition at which run-down will never come below SWL, and run-up and run-down always interact above SWL. This condition occurs for $\xi < 1.60$. This range of ξ values includes plunging and spilling breakers. On rubble-mound slopes the condition described in fig. 11a may only occur at ξ values much lower than 1.60, due to permeability.

Fig. 11b represents the interaction of run-up and run-down at SWL. On smooth slopes this corresponds to a ξ value of 1.60 or somewhat higher. On permeable slopes this will be a much lower ξ value (fig.'s 5-8). Fig. 11c demonstrates how run-down may reach below SWL. It may then be completed before the arrival of the next wave, or it may interact with the run-up below SWL. On smooth slopes this corresponds to $\xi > 1.60$. Fig. 11d gives the description of the resonance condition as defined above, in terms of time history plots where point "B" refers to the breaking point and the dotted line shows the wave profile at the maximum run-up position. In this study, the breaking point refers to the point at which the wave front becomes vertical as shown in fig. 11d.

From the above-mentioned, it is known that waves break when $\xi < 2.5$. This, together with the above deductions, restricts the resonance condition to the range of $1.60 < \xi \leq 2.5$ for smooth slopes and to $\xi \leq 2.5$ for permeable slopes.

Analysis of fig.'s 5-9 shows that run-down on rubble-mounds does not reach its maximum value at $\xi \leq 2.5$. Therefore, the earlier definition of resonance had to be changed to "the condition that occurs when run-down is in a low position and wave breaking takes place simultaneously and repeatedly at that location". The verification of the above definition and its point (range) of occurrence in the ξ spectrum, referring to smooth and permeable slopes, was looked further into by experiments.

The importance of "resonance" is its relation to maximum forces on sloping structures. This is due to the kinematic conditions occurring below the breaker causing lift forces. Strong drag and inertia forces also occur on the armour blocks due to the high run-up and run-down and the accompanying large scale turbulence. The impact forces on the blocks also seem to maximize around the resonance condition. At the same time the mean water table elevation in the core rises due to the high run-up, causing an outward pressure on the armour blocks, as mentioned later. This effect will become even more significant when it is combined with the set-down of the mean water table outside the breakwater (22, 34).

Iversen (31) measured the velocities under a breaking wave, and Kemp and Plinston (37) velocities in the uprush and downrush zone. Wiegel (59) calculated the horizontal accelerations occurring in and under a breaking wave using the data given in ref. (31). Fig. 12 shows the kinematic conditions under two breaking waves with equal breaker heights (H_b) on 1 in 10 and 1 in 50 slopes. It may be observed that the backflow due to

run-down water in front of the breaker is higher for 1 in 10 slope than 1 in 50 slope. High horizontal forward velocities exist directly under the breaking wave crest. When high run-down velocities interact with the high forward velocities in the toe, they cause rotating flows under the sloping front of the breaking wave (fig. 12). During this rotation, velocities and accelerations normal to the slope occur. On a rubble-mound breakwater, the rotating flow causes high drag and inertia forces on armour blocks trying to pull them out of their place. This force corresponds to the lift forces measured by Sandström (44) and by Sigurdsson (50) under ideal assumptions.

Impact forces on the slope also maximize around the resonance condition. With reference to fig. 13, this may be explained as follows:

Assuming that a water mass plunges from the crest of a breaking wave with a velocity of $C_{br} = \sqrt{g(H_b + z)}$ and travels a distance " X_p " along the slope under the action of gravity only (neglecting air resistance). For $\gamma \approx 0$, the fall time " t_b " for this mass can be written:

$$t_b = \sqrt{\frac{2(H_b + z - X_p \sin\alpha)}{g}} \quad (10)$$

The horizontal distance this mass can travel may be written as:

$$X_p \cos\alpha = C_{br} t = \sqrt{g(H_b + z)} \sqrt{\frac{2(H_b + z - X_p \sin\alpha)}{g}} \quad (11)$$

Solving equations (10) and (11) for X_p , one obtains:

$$X_p = (H_b + z) \left\{ \frac{\sqrt{\sin^2\alpha + 2\cos^2\alpha} - \sin\alpha}{\cos^2\alpha} \right\} \quad (12)$$

Assuming $H_b = \gamma_b \cdot X_B \sin\alpha$ and replacing this in (34),

$$X_p = \left(\gamma_b \cdot X_B + \frac{z}{\sin\alpha} \right) f(\alpha) \quad (13)$$

where

$$f(\alpha) = \frac{\sin\alpha (\sqrt{\sin^2\alpha + 2\cos^2\alpha} - \sin\alpha)}{\cos^2\alpha}$$

The values of $f(\alpha)$ are given in table (2) below for some slope angles (α):

TABLE (2)
SLOPE CONSTANTS FOR PLUNGE DISTANCE

α°	$\text{Cot}\alpha$	$f(\alpha)$
38.66	1.25	0.660
33.69	1.5	0.598
26.57	2.0	0.500
21.80	2.5	0.428
18.43	3.0	0.373
15.95	3.5	0.331
14.04	4.0	0.297
11.31	5.0	0.246

Equation (13) needs information on "z", " X_B " and " γ_b " values. It is known that γ_b is the maximum for plunging-collapsing breakers (ξ value around 2.5). On smooth slopes it can be assumed to be about 1.2. Inserting this value of γ_b in equation (13) together with an assumed value of $z = \frac{1}{2} X_B \text{Sin}\alpha$, one obtains:

$$X_p = 1.7 f(\alpha) X_B \quad (14)$$

Solving equation (14) for $f(\alpha)$ when $X_p = X_B$, one finds $f(\alpha) = 0.588$.

The above calculations show that a plunging water mass will always hit below SWL for slopes less than 1 in 1.5 (table 2). If it was assumed that the run-down prediction given by equation (6) was true for $\xi = 2.5$, run-down would only penetrate below SWL at $\xi > 2.5$, which means that a plunging water mass always hits a layer of water remaining from the previous run-down on slopes less than 1 in 1.5. This water-pad will act as an absorber and decrease the strength of impact forces on the slope. Therefore, it is much more likely to obtain high impact forces on steep slopes with ξ values close to the resonance condition.

The maximum water flow velocity may occur at the impact point. This is point "p" in fig. 13. The magnitude of the velocity at point $p_1 (V_p)_1$ can be calculated in reference to fig. 13 from the energy equation assuming negligible energy loss as:

$$\frac{1}{2} m V_p^2 = \frac{1}{2} m C_{Dr}^2 + mg(H_b + z - X_p \text{Sin}\alpha) \quad (15)$$

where datum line was passed from the impact point "p" in fig. 13. In the above equation "m" refers to the water mass which plunges. Solving equation (15) for V_p :

$$V_p = \sqrt{C_{Dr}^2 + 2g(H_b + z - X_p \text{Sin}\alpha)} \quad (16)$$

From equation (11) one can write:

$$g X_p^2 \text{Cos}^2\alpha = 2(H_b + z - X_p \text{Sin}\alpha) \quad (17)$$

Using equation (17), equation (18) becomes:

$$V_p = \sqrt{C_{br}^2 + \left(\frac{g X_p \cos \alpha}{C_{br}} \right)^2} \quad (18)$$

Equation (18) shows that $V_p > C_{br}$. Therefore, maximum flow velocity will occur at the impact point. The orientation of this velocity vector " V_p " at the moment of impact may influence the stability. As the magnitude of this component parallel to the slope is bigger, it will cause more overturning moments on the blocks trying to move them out of their place.

In order to define resonance condition in terms of structure and wave characteristics and to observe the nature of the destructive forces at this condition, experiments were performed on smooth impermeable slopes and on rubble-mounds.

TESTS ON UPRUSH/DOWNRUSH

Tests were run on smooth slopes, 1 in 2, 1 in 3 and 1 in 5. Resistance wires were used for recording run-up and run-down. Wave heights between 4 cm $\leq H \leq$ 15 cm were used with periods 0.8 sec $\leq T \leq$ 2.43 sec, wave steepnesses thereby $H/L_0 < 0.1$. This corresponds to average prototype conditions covering the 1.33 $< \xi < 7.96$ range, which include all types of breakers except spilling. During the tests water depth was constantly 0.5 m. In the experimental range, this corresponds to $d/H_0 > 3.0$ at which wave run-up is not affected by the water depth.

The results are plotted in fig.'s 14 and 15. Breaker types are also shown using different symbols for each breaker type. Another set of experiments was conducted with wave heights of $H = 9.0$ cm and 13.0 cm only, but for different wave periods. Breaking points (B) of the waves were recorded visually only on 1 in 2 and 1 in 3 slopes. Data were converted to $(x_E/H) \sin \alpha$ and plotted in fig. 15 together with run-down data.

Fig. 14 shows a trend in run-up with ξ . It may be seen that R_u/H increases sharply with ξ reaching a maximum at $2.0 < \xi < 3.0$ and decreases again with further increase of ξ . It attains approximately a constant level for high ξ values ($\xi > 4.0$). Types of breakers as also indicated in fig. 14 show that plunging breaking occurred until $\xi = 3.19$ and collapsing breaking until $\xi = 3.42$. For $1.0 < \xi < 2.5$ only plunging breakers were observed. From $\xi = 2.5$ to $\xi = 3.2$ plunging and collapsing breakers became mixed. At $3.20 < \xi < 3.40$ collapsing and surging were mixed, and after $\xi = 3.40$ only surging waves occurred. This observation of breaking conditions was very similar to the results mentioned above except that breaking might occur up to $\xi \approx 3.40$ instead of at $\xi \approx 2.5$. The value $\xi \approx 2.5$ is a theoretically obtained figure referring to a situation halfway between breaking and non-breaking. Hunt's run-up prediction, which was mentioned above ($R_u/H = \xi$), seems to hold for these data also at $\xi < 3.0$. The above results show that for the range of $2.2 < \xi < 3.2$, wave run-up on smooth slopes obtain maximum

values. This result should be considered in designing the crest elevation of any impermeable sloping wave protection structure. Data on overtopping were not considered in this study. The reader is referred to ref.'s (3, 8, 13, 32, 43, 53, 54 and 55). Wave run-down data have less scatter than wave run-up data. Fig. 15 shows these data together with breaking point data and demonstrates that wave run-down increases continuously with ξ and assumes approximately a constant value for high ξ values ($\xi > 4.0$). The mean curve crosses the SWL roughly at a ξ value of 2.2. For $\xi < 2.2$ run-down cannot take place below SWL and run-up and run-down always interact. The model developed above (22) gave $\xi \approx 1.60$ for the run-down penetrating down to SWL. The difference between these two results is undoubtedly caused by neglect of the effects of friction and pressure forces on the flow.

Analysis of breaking point data and run-down data showed that true resonance can hardly ever be achieved. There will always be a run-down "tongue" remaining from the previous wave in front of the breaking wave. Also, for this reason, the resonance condition defined earlier should be changed to "the condition that occurs when run-down is in a low position and wave breaking takes place simultaneously and repeatedly close to that location".

PRESSURE MEASUREMENTS

Pressure measurements were conducted on slopes 1 in 2 and 1 in 3. The combination of wave height, period and slope angle was arranged so that data were obtained for different types of breakers. Fig. 16 is an example of the variation of dynamic pressures along the slope. From this figure, it may be seen that the impact pressures (maximum dynamic pressures) and the suction pressures (minimum dynamic pressures) penetrate deeper on the slope with increasing ξ values.

Analysis of fig.'s 17 and 18 show that the impact pressures and the suction pressures maximize in the range of $2.0 < \xi < 3.0$, that is, close to the resonance condition. The sudden increase of the impact pressures at the resonance condition supports the hypothesis on impact pressures introduced above. Indeed, if the mathematical formulation of the plunge distance given by equation (13) is used together with fig. 15, some quantitative results may be obtained. Calculating the plunge distance for $\text{Cot}\alpha = 2.0$

$$x_p = \left(\gamma_b \cdot x_B + \frac{z}{\text{Sin}\alpha} \right) f(\alpha)$$

Assuming $z = \frac{1}{2}x_B \text{Sin}\alpha$ and inserting the value of $f(\alpha) = 0.5$ from table (2), x_p becomes

$$x_p = 0.5 x_B (\gamma_b + \frac{1}{2})$$

At $\xi = 3.0$ with a plunging breaker, the value of γ_b can be assumed 1.2. The value of x_B can be calculated using fig. 14 as:

$$x_B = 1.40 H \frac{1}{0.447} = 3.13 H$$

For a wave height of $H = 9.0$ cm,

$$x_p = 0.5 \cdot 3.13 \cdot 9(1.2 + 0.5) = 23.94 \text{ cm}$$

and

$$x_B = 28.17 \text{ cm}$$

For this reason the maximum point upslope where the plunging water crest may cause an impact would be $(28.17 - 23.94) = 4.23$ cm below SWL. If the maximum run-down value is checked for this case from fig. 15, it will be 22.13 cm. Therefore, the plunging wave crest will undoubtedly hit the bare slope and therefore cause a high impact. If similar calculations are made for $\xi = 1.5$, one finds that the maximum upslope point where the plunging wave crest may cause an impact would be 4.53 cm below SWL. From fig. 15 one can see that $\xi = 1.5$, run-down ends 6.35 cm above SWL. Therefore, the plunging wave will always hit a layer of water remaining from the previous run-down and cause less impact pressures. As mentioned below, fig.'s 17 and 18 support the result of the above analysis. Some Russian data (49, 51) on impact pressures also support the above hypothesis. Popov (51) made some experiments on 1 in 4 smooth slope with different incoming wave steepnesses for waves breaking on the slope. During the test he used constant wave height and changed the wave period. His results show (22) that impact pressures on the slope increase with increasing ξ values or periods. The linear increase may be due to decreasing water layer thickness which the plunging wave crest hits. Selivanov (49) made some prototype measurements on smooth slopes. He (also) concluded that the maximum impact pressures occur with deep run-down.

From fig.'s 17 and 18 it may be seen that suction pressures are highest at the resonance condition, that is, close to $\xi = 3.0$. On fully impervious slopes the static head of the wave will tend to compensate this suction pressure and no buoyancy forces are exerted upon the cover layer. In rubble-mounds, armour blocks which are submerged are subjected to buoyancy forces which will decrease the weight of the block and thereby its resistance to uplift. Therefore, the combined suction forces on a rubble-mound may be able to lift (suck) blocks out of the mound. As mentioned above, the breaking wave and wave run-up/run-down conditions are similar on smooth impermeable slopes and permeable slopes. It may, therefore, be assumed that force patterns would tend to be similar on permeable and on smooth impermeable slopes, although various degrees of permeability and roughness may cause more turbulence, therefore also more scatter on the permeable rough slope.

TESTS ON FLUCTUATIONS
OF WATER TABLE IN THE MOUND
IN RELATION TO UPRUSH/DOWNRUSH

Wave run-up and run-down were measured using resistance wires. Synchronized water table fluctuations in the core and in the filter were recorded by Sand-Born recorders simultaneously with the run-up/run-down time history on the rock slope. Measurements in the core by resistance wires were obtained 5 cm inside the core from the filter. Another wire system was stretched on the armour stone surface along the slope for uprush/downrush recording.

Tests were conducted with a constant water depth of 50 cm. The wave heights were ranged between $3.8 \text{ cm} < H < 16 \text{ cm}$ and the wave period between $0.8 \text{ sec} < T < 2.43 \text{ sec}$. Breakwater slope was 1 in 2.5. The range of ξ was $1.37 < \xi < 4.77$. A synchronization signal was transmitted and marked on all channels using a push-button system.

Relative wave run-up (R_u/H) and run-down (R_d/H) on the breakwater were plotted against ξ values as shown in fig. 19. It may be seen that wave run-up and run-down increase with increasing ξ values. The relative wave run-up and run-down at the filter layer and in the core are given in fig.'s 20 and 21. Fig. 22 shows a variety of wave run-up data derived from tests plotted in fig.'s 3, 14, 19 and others (22). The lower values of Hudson's data in fig. 22 is a result of the approximation $H \sim H_0$.

Fig. 22 shows that wave run-up on a rubble-mound breakwater and on a smooth slope do not assume a constant ratio for all ξ ranges. A ratio of 0.5 seems to be valid for the maximum run-up on smooth slopes and maximum run-up on rubble-mound breakwater slopes.

Fig. 19 shows that wave run-down increases continuously with ξ in the test range. From fig.'s 6, 7, 8 and 9, it is apparent that wave run-down on breakwater slopes assumes a constant value for $\xi > 5.0$. Therefore a constant level of relative run-down (R_d/H) may be expected at fig. 19 for $\xi > 5.0$. A comparison between wave run-down on smooth slopes and on rubble-mound breakwaters reveals some differences. For $\xi < 2.20$, run-down on smooth slopes does not penetrate below SWL. On rubble-mound slopes, it does. This difference is mainly due to inflow of water into the breakwater body causing lower run-up and higher run-down values on breakwaters. For $1.5 < \xi < 4.0$, wave run-down on smooth slopes increases much faster than on rubble-mound breakwaters. This undoubtedly is due to the friction forces which retard the run-down on breakwaters and the outflow from the breakwater body which feeds the run-down. Both of these effects decrease the run-down on rubble-mound breakwaters. From data on the type of breakers occurring at different ξ values, it may be concluded that wave breaking on rubble-mounds ceases at smaller ξ values than on smooth slopes. Plunging breakers occur until $\xi \approx 2.0$. Around $2.0 < \xi < 2.60$ plunging and collapsing breakers become mixed. Collapsing breakers occur until $\xi \approx 3.10$. It was observed that the type of breaker also depends

on the height of the incoming wave. At the same ξ value a higher wave may cause a plunging breaker while a lower wave breaks collapsing on the rubble-mound. Although there will not be much change in the above transition values given for breakers on rubble-mounds, a higher wave than the maximum wave used during the tests may shift the breaker transitions somewhat towards higher ξ values.

Fig.'s 20 and 21 show the maximum and minimum elevations of the water table inside the filter and core respectively for different ξ values. It may be noted that until $\xi \approx 3.0$ the maximum water level in the filter stays much lower than maximum run-up on the slope. After $\xi \approx 3.0$ the water table in the filter follows wave run-up values. This means that inflow cannot be completed for small ξ values. The minimum water table elevation in the filter stays very close to SWL for $\xi < 2.5$. For $\xi > 2.5$ it goes below SWL and decreases (comes further down) with increasing ξ values.

A similar trend of water table fluctuations inside the core may be seen from fig. 21. For $\xi \leq 3.0$ the water level does not go below SWL in the core and all fluctuations remain above it. This causes an extra head above SWL which undoubtedly affects the stability. It may be seen that for small ξ values, water level fluctuations inside the core become very small. This means that for small ξ values, the water table fluctuations take place around a certain point inside the core close to the filter layer (22). This result refers mainly to the finer core materials. For high ξ values the water level fluctuations inside the core increase. Tests demonstrate that for $\xi < 4.0$ the water table in the core remains above SWL at the run-down position of the water profile on the breakwater. Fig. 23 shows the approximate quasi-stationary water table profiles at three different ξ values at the run-down position on the breakwater. Data from the tests were used to plot these figures. It may be seen that for small ξ values, flow into the core is not completed when run-down occurs on the breakwater. Fig. 23 also shows that a force inside the breakwater caused by the sloping water surface at the quasi-stationary state, may be transferred to the armour rock in the form of an added buoyancy force. Pressure measurements were conducted inside the breakwater on a horizontal plane 20 cm below SWL for the two different core materials used. The time history of the pressure was drawn with 0.2 sec intervals using linear interpolation in between the discrete points. The main difference between the pressure measurements with two different core materials is a relative increase of the build-up of pressures in the finer material. This effect of permeability causes that the maximum and minimum pressure fluctuations are shifted up with finer core material. For details, the reader is referred to (22).

Fig. 24 shows the mean pressure gradients in fine and coarse core at $\xi = 3.0$. It is drawn using detailed results and linear interpolation in between the discrete readings. Maximum mean pressures occur at $P_2 - P_3$ or between $(P_2' - P_3')$ causing concave

mean pressure distribution curves as shown in fig. 24. These mean pressure gradients ($d\bar{p}/dx$) occurring inside the core reveal the existence of a force acting from inside the core towards the slopes. In the range of the experimental pressure measurements a similar pattern of the $d\bar{p}/dx$ distribution is observed inside the core for two different permeabilities. This means that in the distance $P_1 - P_1'$ the force acting in the core does not show much difference with the core permeability, but it is likely that this build-up of pressure head inside the core will act upon the highly permeable filter or armour layer due to pressure gradients in the core close to filter layer. It may therefore be concluded that the difference in pressures inside the core will be maximum close to the filter layer, which may be seen from fig. 24, where filter and armour layers are shown at -20 cm elevation. The forces occurring inside the core due to the build-up of hydrostatic head are directed towards the filter layer and the armour rock. Due to the complex flow situation, nothing can be said about the actual magnitude and distribution of this force which attempts to push the rocks outward. It may therefore be interpreted as an extra bouyancy force indirectly caused by the waves. This force increases with decreasing permeability. For a constant wave height the build-up of pressures inside the core increases with increasing wave period or ξ value. This increase develops faster with finer core material and has a sharp increase with ξ for $\xi < 3.0$, but increases less after this value. In addition, it should be noted that wave set-up on a slope diminishes with increasing ξ values. Indeed Fairchild (17) mentioned that in the experiments with smooth slopes of 1 in 3 and 1 in 6 no set-up could be measured, but only set-down occurred. A similar conclusion may be transferred to a rubble-mound breakwater which means that set-sown in front of a breakwater increases with increasing ξ values. This makes another contribution to increase of outward pressure, thereby to reduction of armour stability (16, 17).

OVERALL STABILITY OF ARMOUR

The dislocation of the armour stone on the breakwater is a result of the existence of various forces which may join in combinations that cause maximum destructive forces. From the above-mentioned it is known that wave run-up and run-down increase with increasing ξ values and assume a constant level approximately for $\xi > 5.0$. This may cause higher run-down velocities on the breakwater for increasing ξ values acting on the armour blocks as drag and inertia forces. It is therefore more probable that damage will occur with the longest period waves when ξ is less than 5. It is mentioned above that the maximum impact forces on the armour blocks occur at or close to the resonance condition. The suction forces occurring under a breaking wave due to the interaction between the breaker forward velocities and run-down velocities generally also maximize close to or at the resonance condition.

Maximum impact and suction forces seem to occur under breaking waves for $2.0 < \xi < 3.0$. The increase in core pressures and

run-down drag forces is relatively small for $\xi > 3.0$. In this range no wave breaking occurs. Therefore, it may be assumed that the first dislocations of the armour stones on the breakwater will occur around the ξ values between 2 and 3 where wave breaking still takes place. After the dislocation of some stones from the breakwater surface, the armour blocks may roll down due to the run-down forces which may be highly turbulent. This means that for the advancement of the damage, long period waves which surge up on the breakwater are as responsible as the waves at the resonance condition. For advance of damage waves occurring in the wave spectrum with $\xi > 2.0$ therefore are all critical.

The above-mentioned general conclusions are supported by tests undertaken at the Coastal Engnerg Research Center (1, 2) in 1974. These tests were performed in a wave flume 193.5 m long, 4.57 m wide and 6.1 m deep. Wave heights of $0.55 \text{ m} \leq H < 1.83 \text{ m}$ with periods $2.8 \text{ sec} < T < 11.3 \text{ sec}$ were tested. They were conducted at a constant water depth of 4.57 m. A rip rap covered breakwater was tested with slopes of 1 in 2.5, 1 in 3.5 and 1 in 5.0. Test results were presented in terms of the zero damage wave height "H_{ZD}". Zero damage wave height was defined as the highest wave height which will create no damage to the structure. A 10% increase of this wave height will cause damage. Wave heights were measured in front of the structure. The original data obtained from these tests are plotted in fig. 25 in terms of zero damage stability number "N_{ZD}" versus ξ where N_{ZD} and ξ were defined as,

$$N_{ZD} = \frac{H_{ZD}}{\left(\frac{W_{50}}{Y_r}\right)^{\frac{1}{3}} (S_r - 1)} \quad (19)$$

and

$$\xi = \frac{\text{tg} \alpha}{\sqrt{H_{ZD}/L_0}} \quad S_r = \frac{Y_r}{Y_w}$$

When equation (19) is compared with equation (9), N_{ZD} is equivalent to $(K_D \text{ Cot} \alpha)^{\frac{1}{3}}$. Results of tests of earlier date (1959) are also presented in fig. 25, which clearly shows the effect of wave period on the stability of rubble-mound breakwaters. When the range of breakwater and wave characteristics covered are considered, they verify the above conclusions for the stability of rubble-mound breakwaters, which were based on the hydrodynamic analysis of the phenomenon.

Fig. 25 shows that the stability number N_{ZD} depends on the slope angle much more than expressed by ξ . In fig. 26, curves were drawn from the lowest zero damage stability numbers of each slope. This shows that the minimum stability point shifts from a ξ value around 2 to a ξ value of around 3 with increasing slope angle. It also shows the effect of ξ on stability and demonstrates that minimum stability occurs for $2.0 < \xi < 3.0$.

It may be questioned whether results from tests on rip rap can be transferred to rubble-mounds as rip rap would tend to be a little denser than rubble-mounds. The answer undoubtedly is that it is possible, as nothing has changed in the overall hydrodynamic situation, but due to turbulence spreading may be more pronounced with rubble-mounds. The instrument mentioned in the next section confirmed the general validity of a "transfer".

THE OPTICAL BREAKDOWN DEVELOPMENT SENSOR

This instrument (the OBDS) was developed to quantify the breakdown by measuring the actual movements in a mound, thereby replacing the earlier procedures of counting blocks "which moved out of place" or "rolled down the slope" - a very subjective method by "figures and facts".

The OBDS is a photographic instrument. Its main item is a "Mamiya Universal" camera with accessories. Its principle is called "solarization" or "bas-relief" effect in photography. It is based on the trick of applying a negative film to mask out all highlights passing through a positive film. A Polaroid Type 105 Positive/Negative Pack Film was used. First a picture of the test section was taken. The negative of this film was inserted into the camera in such a way that negative film masked all highlights coming from the structure. This alignment of the negative film with the structure may be achieved by slight axial and rotational movements of the camera. The camera is set at this position and a photocell connected to an amplifier is put on to the eyepiece of the camera. Any change on the original test structure will affect the alignment of the negative and the structure, and more light will come to the photocell. This will cause a deflection on the amplifier.

The above described working principle necessitates the use of high contrast colours on the test object. For this purpose, it was decided to paint the test object in partial black and white. The light coming on to the test object should be very uniform. The calibration of the system is done by causing some known amount of deflection in the test object or on the camera and observing the corresponding deflections on the amplifier. In the ideal case, if the test object can be painted as a chess-box, this calibration procedure may be done easily. Fig. 27 is a schematic view of the masking procedure for a chess-box-like test object. It represents the condition where the negative completely masks the highlights coming to the photocell causing minimum deflection on the amplifier. At this position the amplifier is set to "zero" deflection. Then the camera is tilted until maximum deflection is observed on the amplifier. This corresponds to one square deflection "L" on the test object shown in fig. 27 because all the lights will pass the negative due to

the ordered pattern of the test object. Assuming the linearity of the system in between the maximum deflection "D" and the zero deflection, a calibration coefficient "c" can be calculated as,

$$c = D/L \quad (\text{deflection/length})$$

and any deflection occurring on the amplifier "d" can be converted to the test objects deflection "l" from the relation,

$$l = d/c \quad \text{for } l < L$$

The above calculation of the deflection assumes that movement of the test object as a whole is in one direction. It also has a condition that this deflection should be less than a square size. If the test object is a rubble-mound, movement may be measured similarly. To make recording clearer, stones may be painted white and black. Calibration and actual use of the instrument is described in (22) and will be published in detail in the near future as a separate paper (ASCE, Waterways, Harbors and Coastal Engineering Division).

Fig. 28 is an example of rock movements recorded by OBDS for different wave characteristics. It includes data for all wave periods tested and for wave heights which cause dislocation. As it could be expected, movements of stones increase for increase of wave heights. The start of major movements takes place when $H \geq 11$ cm.

Fig. 29 shows the effect of ξ on movements. For $H = 11.8$ cm, movements are bigger than for $\xi = 2.3$, as well as for $\xi = 1.45$ and $\xi = 3.32$. This is in agreement with the maximization of damaging forces at or close to the resonance condition mentioned in the earlier sections of this paper.

SUMMARY

The main goal of the paper was to determine the flow conditions which maximize destructive wave forces occurring on a sloping wave-protection structure. It includes both impermeable as well as permeable structures. Special emphasis is put on the latter.

The study only covers the wave protection structures at $d/H \geq 3.0$ where flow patterns occurring on the structure are not affected by the depth. The slope (α), the wave height (H) and the wave period (T) are main parameters. The flow characteristics occurring with different combinations of α , H and T are explained with the "surf similarity parameter", $\xi = \text{tg}\alpha/\sqrt{H/L_0}$. The effect of any other parameter on the flow characteristics is included by inserting empirical coefficients into the system.

Wave breaking and wave run-up/run-down characteristics were first summarized from the available literature. The result of these investigations is analysed relative to ξ and most of the data are re-plotted against ξ . This showed that wave breaking and wave run-up/run-down on sloping structures may be described in terms of ξ .

A theory was developed about the maximization of forces on the slope based on the flow characteristics. It suggests that forces maximize at $2.0 < \xi < 3.0$. Run-up/run-down and pressure experiments on smooth slopes are described. It was found that on smooth slopes wave run-up has a maximum at $2.0 < \xi < 3.0$, where plunging and collapsing breakers are mixed on the slope. Wave run-down cannot go below SWL for $\xi < 2.20$, and run-up and run-down always interact. Run-down increases continuously with increasing ξ values until $\xi \approx 5.0$ and assumes a constant value after this. It is shown that maximum impact pressures on the slope occur at $2.0 < \xi < 3.0$ when a plunging breaker crest strikes the bare slope

Run-up/run-down and core pressure tests on a rubble-mound breakwater are also described. It was found that wave run-up and run-down increase continuously with increasing ξ and assume a constant value approximately at $\xi > 5.0$. A build-up of hydrostatic head occurs inside the core due to the existence of the waves and exerts an outward force on the armour stones mainly due to high pressure gradients in surface layers and filters. This build-up of hydrostatic head inside the mound increases with increasing ξ values for $\xi < 4.0$. It was shown that decreased core permeability causes increased build-up of hydrostatic pressure. Maximum destructive forces acting on an armour unit trying to dislocate it seem to occur around $2.0 < \xi < 3.0$. This was verified by actual stability experiments. Due to the desire of obtaining more exact (quantitative) recordings, an instrument (the OBDS) was developed. It is described briefly and is subject to further testing.

A summary of the flow conditions and forces occurring on smooth impermeable and rubble-mound breakwater slopes are given in

tables (A) and (B). The tables describe the conditions in terms of ξ parameter. The limits indicated in these tables differentiating various phases of the characteristic parameters relative to ξ are not yet rigid boundaries, but indicate approximate transition values only. It is believed that in the very wide range of structure and wave characteristics these tables may be useful for a preliminary design of wave protection structures.

TABLE (A) A SUMMARY OF WAVE ACTION ON SMOOTH IMPERMEABLE CONTINUOUS SLOPES BASED ON ξ VALUES

$\xi = \frac{tga}{\sqrt{H/L_0}}$	0.1	0.5	1.0	1.5	2.0	2.5	3.0	3.5	4.0	4.5	5.0	5.5
	Breaking											
Breaker Type ¹⁾	Spilling	Plunging		Plunging		Plunging		Plunging		No Breaking		
Breaker Index (γ_b) ²⁾	0.8	1.0	1.1	1.2		Plunging		Collapsing		Surging		
Number of Waves in the Surf Zone ²⁾	6-7	2-3	1-2	0-1	0-1							
Reflection Coefficient ²⁾	$r = 0.1 \xi^2$											
³⁾ Set-Up Predominant ----- Run-Up/Pre-Down Predominant Wave Run-Up ⁴⁾ Increases with ξ ----- Maximizes ----- Decreases Slightly Relative Run-Up (R_u/H) ⁵⁾ ----- $R_u/H = \xi$ ----- Scatters around a constant value Wave Run-Down ⁶⁾ ----- Increases with ξ ----- Penetrates Below SWL ----- Scatters around a constant value Relative Run-Down (R_d/H) ⁶⁾ ----- Cannot Penetrate Below SWL ----- Penetrates Below SWL ----- constant value Maximum Wave Set-Up (η_{max}) ⁷⁾ $\eta_{max} = 0.5\gamma_b H_b$ ----- $R_d/H = \xi - 0.45 \xi^2$ ----- Breaking Point (B) ⁶⁾ goes deeper with increasing ξ												
Impact Pressures due to Breaking Waves ⁸⁾	Plunging crest hits on a layer of water impact press. increases with ξ Impact pressures maximize somewhere in this region											
1) Based on experimental results given in fig.'s 14 and 15 2) Taken from ref. (3) 3) Shown in fig. 22 4) Shown in fig. 3 5) Shown in fig. 15 6) Shown in fig. 15 7) Shown in fig. 31 of ref. (22) 8) Shown in fig.'s 17 and 18												

TABLE (B) A SUMMARY OF WAVE ACTION ON RUBBLE-MOUND BREAKWATERS BASED ON ξ VALUES

$\xi = \frac{t g \alpha}{\sqrt{H} L_0}$	0.1	0.5	1.0	1.5	2.0	2.5	3.0	3.5	4.0	4.5	5.0	5.5
	Breaking											
Breaker Type ¹⁾	Spilling	Plunging	Plunging	Plunging-Collapsing	Plunging-Collapsing	Plunging-Collapsing	Plunging-Collapsing	Plunging-Collapsing	Plunging-Collapsing	Plunging-Collapsing	Plunging-Collapsing	Plunging-Collapsing
Breaker Index (γ_b) ²⁾	0.8	1.0	1.1	1.2								
Main Energy Dissipation	due to Wave Breaking											
Wave Run-Up ³⁾	Increases with increasing ξ values											
Wave Run-Down ³⁾	Increases with increasing ξ values											
Breaking Point $[\bar{B}]^4)$	Goes deeper with increasing ξ											
Build-Up of Hydrostatic ⁵⁾ Head Inside the Core	Increases with increasing ξ values											
Suction Pressures ⁶⁾	Increases with ξ											
Impact Pressures ⁷⁾	Increases with ξ											
Zero Damage ⁸⁾	Decreases with ξ											
Stability Number (NZD)	Decreases with ξ											

1) Based on experimental results on 1 in 2.5 slope breakwater. Data is given in Appendix IV.
 2) Transferred from smooth slope results. No data is available.
 3) Shown in fig.'s 5, 6, 7, 8, 9 and 22.
 4) Transferred from smooth slope results. No data is available.
 5) Shown in fig.'s 68, 69, 70, 71 and 72 of ref. (22)
 6) Deducted from smooth slope measurements presented by fig.'s 17 and 18. No data is available.
 7) Transferred from smooth slope measurements. No data is available.
 8) Shown by fig.'s 25 and 26.

CONCLUSION

The conclusion given in twelve points below only covers sloping structures at a relative water depth of $d/H > 3.0$ where non-breaking wave conditions occur until the structure is reached. They are mostly applicable to wave-protection structures with steep continuous sloping faces, permeable as well as impermeable. They refer to monochromatic wave conditions.

- i) Most of the overall flow characteristics like breaking, run-up, run-down may be defined by single parameter $\xi = \text{tg}\alpha/\sqrt{H/L_0}$.
- ii) On smooth slopes in the range of $0.5 < \xi < 2.0$, wave run-up may be predicted using Hunt's formula $R_u/H = \xi$.
- iii) On smooth slopes, maximum wave run-up occurs for waves breaking on the slope in the range of collapsing - plunging breakers. This corresponds approximately to $2.0 < \xi < 3.0$.
- iv) On rubble-mound breakwaters, wave run-up increases continuously with ξ until ξ approximately equals 5. From there on run-up assumes a constant level.
- v) Wave run-down on slopes increases with increasing ξ values until ξ approximately equals 5.0. From there on it assumes a constant level.
- vi) Wave run-down on smooth slopes cannot penetrate below SWL for $\xi < 2.20$, and run-up and run-down always interact above SWL.
- vii) Maximum impact pressures on smooth slopes occur at $2.0 < \xi < 3.0$ where the breaking wave crest hits the bare slope.
- viii) A build-up of hydrostatic pressure occurs inside a rubble-mound due to wave uprush. It increases with decreasing permeability and with increasing ξ values for $\xi < 4.0$.
- ix) Stability of rubble-mound breakwaters is also affected by the wave period. Forces trying to dislocate the armour maximize with deep run-down occurring simultaneously and repeatedly with collapsing - plunging wave breaking. This corresponds to $2.0 < \xi < 3.0$ at which the initial stability of the rubble-mound is most critical.
- x) With reference to fig. 2 and similar plottings (30), results for $d/H < 3.0$ will undoubtedly show a similar trend even if adjustments on ξ and ξ ranges are likely. This is subject to further research as are scaling and checking of the OBDS instrument that was developed to quantify rock movement in a reliable way.
- xi) As seen from tables A and B, the $\xi = \frac{\text{tg}\alpha}{\sqrt{H/L_0}}$ parameter is useful for description of a great many single phenomena included in wave action on sloping structures.
- xii) Finally - and as already expressed in ref 11:

"The significance of wave period is clearly demonstrated. This underlines the necessity - demonstrated with much pain in many practical mishaps - of designing rubble-mounds and other sloping structures based on design criteria which includes wave period. It is not enough to select a "design wave" and a "proper" K_{Δ} value based on some more or less realistic laboratory experiments. It is also not enough to select a "design storm" or a specific "design spectrum". The design wave or the design spectrum gives a "load" which is sometimes regarded as the maximum exposure that can occur. This could be far from the truth, however. A much more reliable, scientifically as well as practically, better reasoned design procedure is first to select one from a technical and economical view attractive design. The next step is to examine a number of actual wave spectra from the site including analyses of extreme events (11) and trains of approximately regular waves with special reference to the correlation between succeeding waves as described in ref.'s 23 and 27. Tests should then concentrate on irregular waves and on combinations of certain waves and periods that occur in the actual spectra with particular reference to conditions that produce the most dangerous resonance phenomena. This confirms actual experiences from a great number of actual observations in the North and Arctic seas and also the inadequacy of design-formulas that ignore wave period and spectral characteristics as well."

REFERENCES

1. Ahrens, P.J.: Large Wave Tank Tests of Riprap Stability
Tech.Mom.No. 51, May 1975, U.S. Army Corps of Engineers
2. Ahrens, P.J. et al: "Wave Period Effect on the Stability of Riprap", Civil Engineering in the Ocean, Univ.of Delaware,1975.
Printed by the ASCE.
3. Battjes, J.A.: Computation of Set-Up, Longshore Currents, Run-up and Overtopping due to Wind Generated Waves
Delft. Publ. 74-2, 1974.
4. Battjes, J.A. and Roos, A.: Characteristics of Flow in Run-up of Periodic Waves
Delft Publ. 1974.
5. Bowen et al.: Wave Set-Down and Set-Up
Journal of Geophysical Research, 73 (8), april 15, 1968.
6. Brandtzæg, A. and Tørum, A.: A Simple Mathematical Model of Wave Motion on a Rubble Mound Breakwater Front
10th Coastal Eng. Cong., 1966.
7. Brandtzæg, A. and Tørum, A.: Velocities in Downrush on Rubble Mound Breakwaters
11th Coastal Eng. Conf., 1968, London.
8. Bruun, P.: Breakwaters for Coastal Protection
18th Int. Now. Congress, Rome, Section II, Question I, 1953.
9. Bruun, P.: Discussion to "Damage Function of Rubble Mound Breakwaters
Proceedings of the American Society of Civil Engineers, Journal of Waterways and Harbors Division, Vol. 96, WW2, May 1970.
10. Bruun, P. and Johannesson, P.: A Critical Review of Hydraulics of Rubble Mound Structures
Division of Port and Ocean Eng., Univ. of Trondheim Publ., Inst. Rep. R3-1974.
11. Bruun, P. and Johannesson, P.: Parameters affecting Stability of Rubble Mounds
Proceedings ASCE, Journal of the Waterways Harbors and Coastal Engineering Division, Vol. 102, No. WW2, 1976.
12. Carstens et al.: The Stability of Rubble Mound Breakwaters against Irregular Waves
Proc. of 10th Conf. on Coastal Eng., Tokyo, Japan, Sept. 1966, Vol. II.

13. Coastal Protection Manual
U.S. Army Coastal Eng. Research Center, Department of the Army Corps of Engineers, 1973.
14. Dai, Y.B. and Kamel, A.M.: Scale Effect Tests for Rubble Mound Breakwaters
Research Report H-69-2 of U.S. Army Eng. Waterways Experiment Station, Corps of Engineers, Vicksburg, Mississippi, Dec. 1969.
15. Daubert, A. and Warluzel, A.: Modèle Mathématique non lineaire de la propagation d'une houle et de sa reflexion sur une plage
I.A.H.R., Vol. 4, Sept. 1967.
16. Dorrestein, R.: Wave Set-Up on a Beach
Univ. of Florida, Publication 1962.
17. Fairchild, J.C.: Model Study of Wave Set-Up Induced by Hurricane Waves at Narragansett Pier, Rhode Island
The Annual Bulletin of the Beach Erosion Board, Department of the Army Corps of Engineers, Vol. 12, July 1958.
18. Font et al.: Stability of Rubble Mound Breakwaters Subjected to Breaking Waves
Summaries of the 14th Int. Conf. on Coastal Eng., Copenhagen 1974.
19. Font, J.B.: Damage Functions of Rubble Mound Breakwater
Proceedings of the 12th Conf. on Coastal Engineering, Washington, 1970.
20. Galvin, C.J.: Breaker Type Classification on Three Laboratory Beaches.
Journal of Geophysical Research, Vol. 73, No. 12, 1968.
21. Galvin, C.J.: Breaker Travel and Choice of Design Wave Height
Proceedings of American Society of Civil Engineers, Journal of the Waterways and Harbors Division, Vol. 95, WW2, May 1969.
22. Günbak, A.R.: The Stability of Rubble Mound Breakwaters in Relation to Wave-Breaking and Run-down Characteristics and to the $\xi = \text{tg}\alpha/\sqrt{H/L_0} \sim \frac{\text{tg}\alpha}{\sqrt{H}} T$ number.
23. Hedar, P.A.: Stability of Rock-fill Breakwaters
Doktorsavhandlingar vid Chalmers Tekniska Högskole, No. 26, 1960.

24. Herbich, J.B., Sørensen, R.M. and Willenbrock, J.H.:
Effect of Berm on Wave Run-up on Composite Beaches
Proc. of American Society of Civil Engineers, Journal of
Waterways and Harbors Division, Vol. 89, WW2, May 1963.
25. High Island Water Scheme - Hong Kong
Wallingord Publ., Oct. 1970, EX 532.
26. Ho, D.V. and Meyer, R.E.: Climb of a Bore on a Sloping
Beach, Part 1
Journal of Fluid Mech., Vol. 14, 1962.
27. Hudson, R.Y.: Laboratory Investigation of Rubble Mound
Breakwaters
Proc. of the Amer. Soc. of Civ. Eng., Journal of the
Waterways and Harbors Division, Vol. 85, No. WW3, Sept. 1959.
28. Hunt, I.A.: Design of Seawalls and Breakwaters
Proceedings of American Society of Civil Engineers, Journal
of Waterways and Harbors Division, Vol. 85, WW3, Sept. 1959.
29. Hwang Li-San: Wave Set-Up of Nonperiodic Wave Train and
Its Associated Shelf Oscillation
Journal of Geophysical Research, Vol. 75, No. 21, 1970.
30. Inoue, M.: Effects of Wave Height and Sea Water Level on
Wave Overtopping and Wave Run-Up
Coastal Eng. in Japan, Vol. 8, 1965.
31. Iversen, H.W.: Discussion of Results from Studies of Wave
Transformation in Shoaling Water, Including Breaking
Univ. of Calif. Publ., Series No. 3, Issue No. 331, March 1952.
32. Iwagaki et al.: On the Effect of Wind on Wave Overtopping
on Vertical Seawalls
Bull. Dis. Prev. Res. Inst., Kyoto Univ., 16, No. 104, Part 1,
Sept. 1966.
33. Jonsson, I.G.: A New Proof of an Energy Equation for Surface
Gravity Waves Propagating on a Current.
Basic Res. Prog. Rep. 23, 11-19, Coastal Engineering Lab.
and Hydraulic Lab., Tech. Univ. Denmark, 1971.
34. Jonsson, I.G. and Jacobsen, T.S.: Set-Down and Set-Up in a
Refraction Zone
Prog. Rep. 29, pp. 13-22, Aug. 1973, Inst. of Hydrodyn. and
Hydraulic Eng., Tech. Univ. of Denmark.

35. Kemp, P.H.: The Relation Between Wave Action and Beach Profile Characteristics
Proc. of 7th Int. Conf. on Coastal Eng., The Hague, 1960, Vol. 1.
36. Kemp, P.H. and Plinston, D.T.: Beaches Produced by low Phase Difference
Proceedings of American Society of Civil Engineers, Journal of Hydraulics Division, Vol. 94, HY 5, Sept. 1968.
37. Kemp, P.H. and Plinston, D.T.: Internal Velocities in the Uprush and Backwash Zone
Proceedings of the 14th Int. Conf. on Coastal Engineering, Copenhagen 1974, Vol. 1.
38. LeMéhauté, B.: On Non-Saturated Breakers and the Wave Run-up
Proc. 8th Coastal Eng. Conf., 1962, Mexico City.
39. LeMéhauté, B. and Webb, L.M.: Wave Set-up and the Mass Transport of Cnoidal Waves
National Eng. Science Co., Interim Report No. 3, 1966.
40. LeMéhauté, B.: A Synthesis on Wave Run-up
Journal of Amer. Soc. of Civil Engineers, Feb. 1968.
41. Longuet Higgins, M.S. and Stewart, R.W.: The Changes in Amplitude of Short Gravity Waves on Steady Non-Uniform Currents
Journal of Fluid Mechanics, Vol. 10, 1961.
42. Longuet Higgins, M.S. and Stewart, R.W.: Radiation Stress and Mass Transport in Gravity Waves, with Application to "Surf Beats"
Journal of Fluid Mechanics, Vol. 13, 1962.
43. Rottinghaus et al.: Shore Protection Study for a Selection of U.S. Interstate Highway 35 in Duluth, Minnesota
Proc. of the First Int. Conf. on Port and Ocean Eng. Under Arctic Conditions, Vol. II, 1971, Norway.
44. Sandström, Åke: Wave Forces on Blocks of Rubble Mound Breakwaters
Bulletin No. 83, Hydraulics Lab., Royal Inst. of Tech., Stockholm, Sweden 1974.
45. Savage, R.P.: Wave Run-Up on Roughened and Permeable Slopes
Proc. of the American Society of Civil Engineers, Journal of Waterways and Harbors Division, Vol. 84, WW3, May 1958.

46. Saville, T.: Wave Run-up on Shore Structures, Transactions of the American Society of Civil Engineers, Vol. 123, 1953.
47. Saville, T.: Wave Run-up on Composite Slopes Proc. of 6th Int. Conf. on Coastal Eng. 1957.
48. Saville, T.: Experimental Determination of Wave Set-up Proc. of 2nd Tech. Conf. on Hurricanes, 242, 1961.
49. Selivanov, L.V.: Discussion of Construction Norms: Determination of Wave Loads on Sloping Structures Hydrotechnical Construction, No. 5, May 1972.
50. Sigurdsson, Gunnar: Wave Forces on Breakwater Capstones Proceedings of the Am. Soc. of Civ. Eng., Journal of the Waterways and Harbors Division, Vol. 88, WW3.
51. Skladnev and Popov, I. Ya.: Studies on Wave Loads on Concrete Slope Protections of Earth Dams Proc. of the Symposium Research on Wave Action, Vol. II, Delft, The Netherlands, July 1969.
52. Stoker: Water Waves Pure and Applied Mathematics, Vol. IV, Interscience Publ., 1957.
53. Straumsnes, A. and Bruun, P.: Comparison Between Spray and Splash at Some Typical Permeable Coastal Structures and the Influence of Ice Floes Deposited on These Structures on Spray and Splash Quantities First Int. Conf. on Port and Ocean Engineering Under Arctic Conditions, Vol. 1, 1971.
54. Technical Advisory Committee on Protection Against Inundation, Wave Run-up and Overtopping Rijkswaterstaat, The Hague, 1974.
55. Wang Hsiang: Synthesis of Breakwater Design and Design Review Procedures Ocean Eng. Rep. No. 1, Oct. 1974, Department of Civil Engineering, Univ. of Delaware.
56. Weggel, C.R.: Maximum Breaker Height Proceedings of the American Society of Civil Engineers, Journal of the Waterways and Harbors Division, Vol. 98, WW4, Nov. 1972.

57. Laboratory Wave Generating Apparatus
written by Biesel et al in French, translated by Meir Pilch,
St. Anthony Falls Hydraulics Lab., Univ. of Minnesota,
Rep. No. 39, 1954.
58. Whitham, G.B.: Mass, Momentum and Energy Flux in Water
Waves
Journal of Fluid Mechanics, Vol. 13, 1962.
59. Wiegel, R.L. and Skjei, R.E.: Breaking Wave Force Prediction
Proceedings of the American Society of Civil Engineers,
Journal of Waterways and Harbors Division, Vol. 84, No. WW2,
March 1958.

NOTATION

B	Berm length (L)
c	Wave celerity (L/T)
\bar{c}	Run-up front velocity (L/T)
C_g	Wave group velocity (L/T)
D	Characteristic length of stone (L)
D_m	Equivalent diameter of stone or grain of which m percent of the weight is contributed by stones or grains of lesser weight (L)
d	Water depth (L)
d_b	Water depth at the breaking point (L)
d_B	Water depth at the berm section (L)
E	Wave energy density (FL/L ²)
F	Force (F)
f	Bottom friction
g	Gravitational acceleration (L/T ²)
H	Wave height in front of the structure (L)
H_b	Wave height at the breaking point (L)
H_0	Deep water wave height (L)
H_0'	Unrefracted deep water wave height (L)
H_{ZD}	Zero damage wave height (L)
h_c	Structure crest elevation (L)
K_R	Refraction coefficient
k	Wave number in front of the structure (rad/L)
k_0	Deep water wave number (rad/L)
L	Wave length in front of the structure (L)
L_0	Deep water wave length (L)
m	Water mass (FT ² /L)
n	Manning's coefficient
P	Porosity (%)
p	Pressure (F/L ²)
\bar{p}	Mean pressure averaged for one wave period (F/L ²)
\bar{q}	Time averaged mean overtopping volume (L ³ /L)
r	Reflection coefficient
R_u	Wave run-up (L)
R_d	Wave run-down (L)

$R_{u\beta}$	Wave run-up under oblique wave attack of β degrees (L)
R_{uf}	Maximum filter water table elevation (L)
R_{df}	Minimum filter water table elevation (L)
R_{uc}	Maximum core water table elevation (L)
R_{dc}	Minimum core water table elevation (L)
S	Radiation stress (FL/L^2)
S_x	Radiation stress along x direction (FL/L^2)
T	Wave period (T)
u	Water particle velocity under a wave (L/T)
v	Water particle velocity on the slope (L/T)
\bar{W}	Average armour stone weight (F)
W_{50}	Median armour stone weight at which m percent of the total weight of armour gradation is contributed by stones of lesser weight (F)
α	Slope angle with the horizontal (degrees)
β	Angle of incidence of waves (degrees)
γ_w	Specific weight of water (F/L^3)
γ_r	Specific weight of rock (F/L^3)
γ_b	Breaker index
μ	Coefficient of friction between the stones
ϕ	Angle of repose (degrees)
ξ	Surf similarity parameter
$\bar{\eta}$	Mean water table elevation (L)

Note: Notations in paranthesis show the dimension of each parameter where
 F = Force (ton, kilo or gram)
 L = Length (meter, cm or mm)
 T = Time (second)

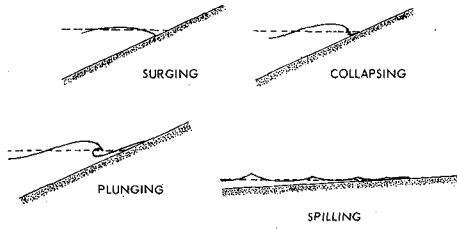


Fig 1 Breaker Types (3)

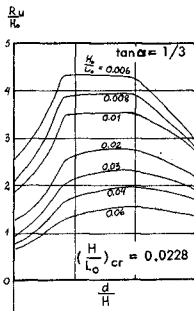


Fig 2 Effect of Water Depth on Wave Run-up (24)

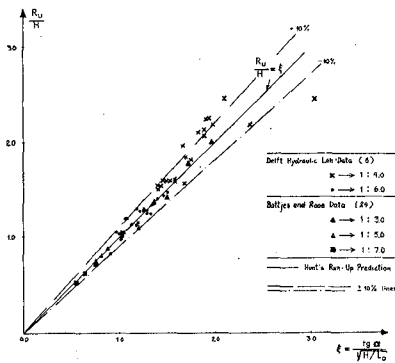


Fig 3 Wave Run-up on Smooth Slopes ($d/H_0 > 3.0$)

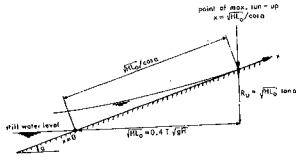


Fig 4 Run-up Characteristics for Wave Breaking on the Slope (4)

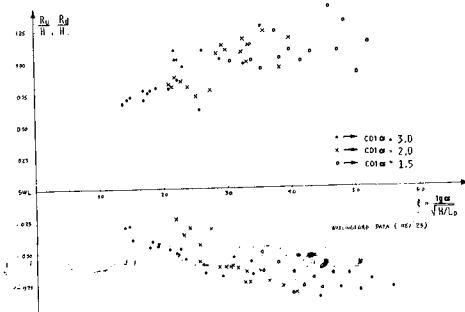


Fig 5 Variation of Wave Run-up/Run-down with ξ for Dolos Cover Breakwater Slopes of 1 in 1.5, 1 in 2.0 and 1 in 3.0

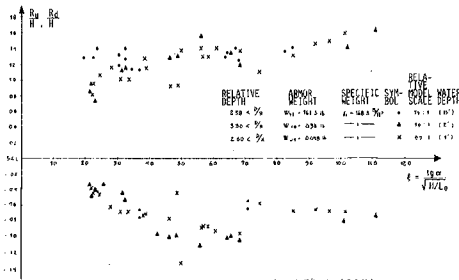


Fig. (20) Variation of Wave Run-up/Run-down with ξ for Rough Quarrystone Cover Breakwater Slope of 1 in 1.5

Fig 6 Variation of Wave Run-up/Run-down with ξ for Rough Quarrystone cover Breakwater Slope of 1 in 1.5

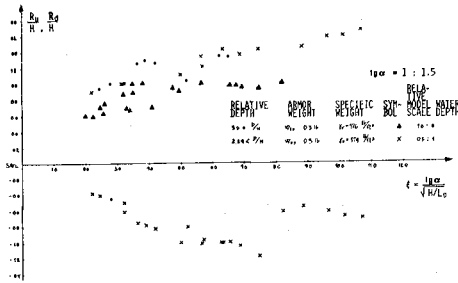


Fig 7 Variation of Wave Run-up/Run-down with ξ for Smooth Quarrystone Cover Breakwater Slope of 1 in 1.5.

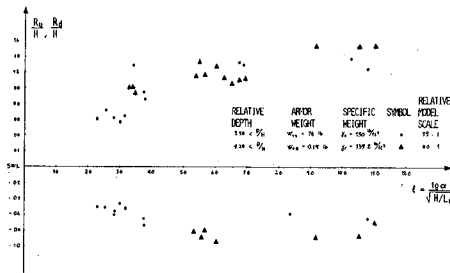


Fig 8 Variation of Wave Run-up/Run-down with ξ for Rough Quadripod Cover Breakwater Slope of 1 in 1.5

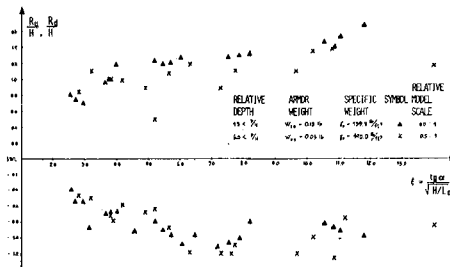


Fig 9 Variation of Wave Run-up/Run down with ξ for Smooth Quadripod Cover Breakwater, Slope 1 in 1.5

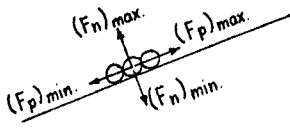


Fig 10 Nation used in Table 1 for Force Components on an Armour Block (50)

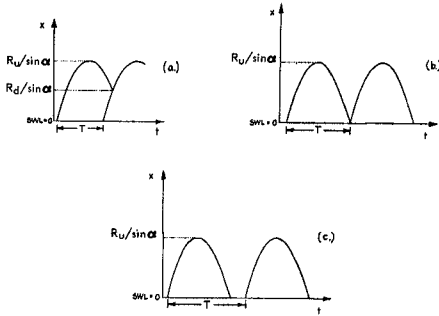


Fig 11a, b, c Time History of the Wave Front along the Slope about SWL

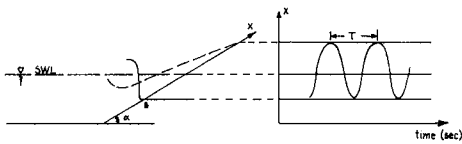


Fig 11d Resonance Condition

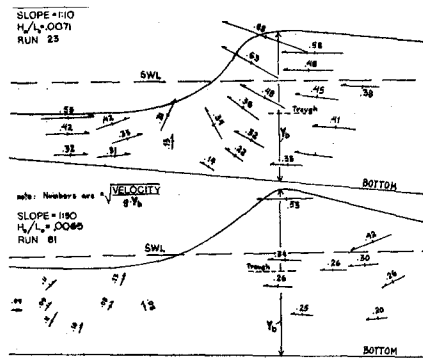


Fig 12 Kinematics of a Breaking Wave (31)

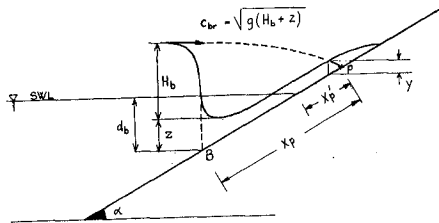


Fig 13 Computation of the Plunge Length on a Slope

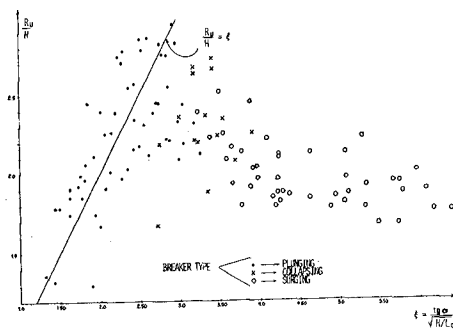


Fig 14 Wave Run-up on Smooth Slopes

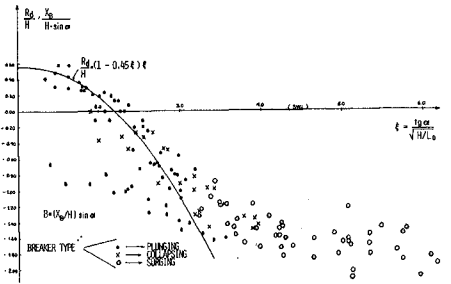


Fig 15 Wave Run-down and Breaking Point Data on Smooth Slopes

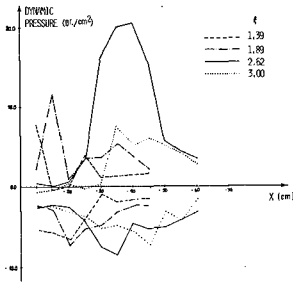


Fig 16 Distribution of Maximum and Minimum Dynamic Pressures along the Smooth Slope (cotg $\alpha = 3.0$ $H = 9.0$ cm)

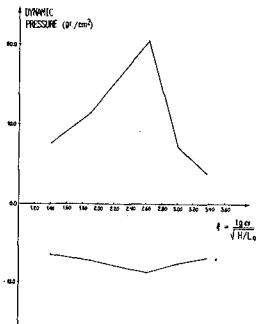


Fig 17 Variation of Maximum and Minimum Dynamic Pressures with ξ for Smooth Slope, 1 in 3.0, $H = 9.0$ cm

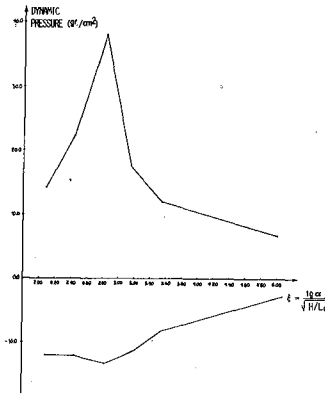


Fig 18 Variation of Maximum and Minimum Dynamic Pressures with ξ for Smooth Slope ($\cot\alpha = 2.0$ $H = 9.0$ cm)

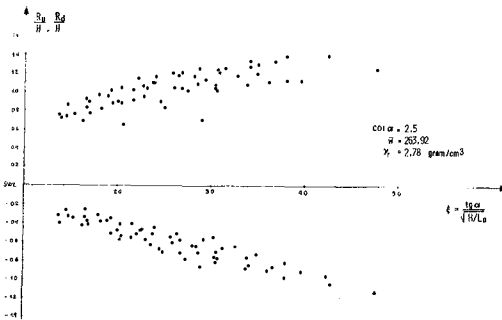


Fig 19 Wave Run-up/Run-down on Rubble Mound Breakwater

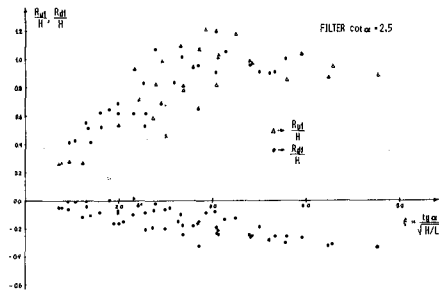


Fig 20 Maximum and Minimum Water Table Elevations, R_{uf} and R_{df} , along the Boundary between Filter and Core

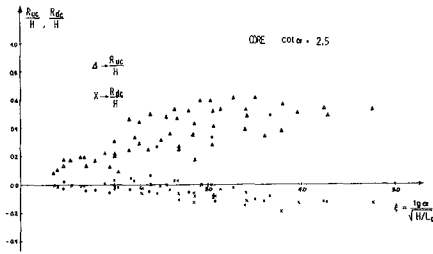


Fig 21 Maximum and Minimum Water Table Elevations (R_{UC} and R_{DC}) along a Plane, parallel to the Breakwater Surface 5 cm inside the Core

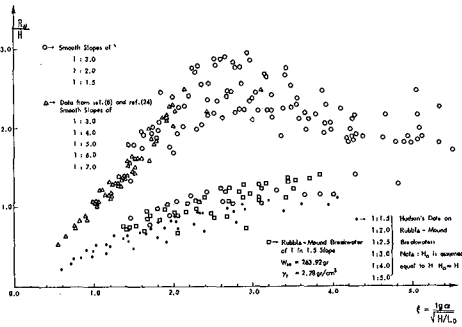


Fig 22 Wave Run-up Spectrum ($d/H_0 > 3.0$)

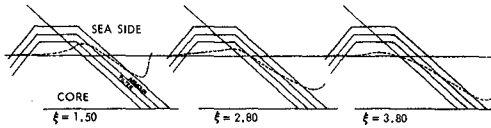


Fig 23 Schematic Representation of the Water Table in the Breakwater at Run-down Position

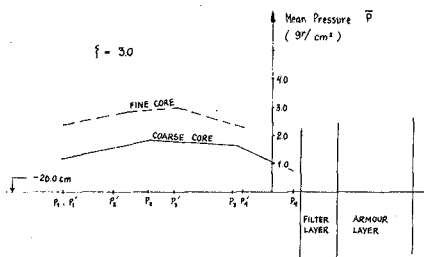


Fig 24 Mean Pressure Gradients inside the Core

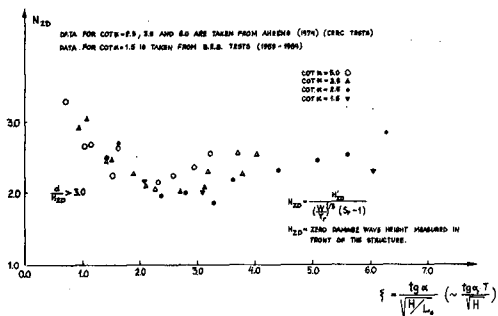


Fig 25 Zero Damage Stability Number versus ξ

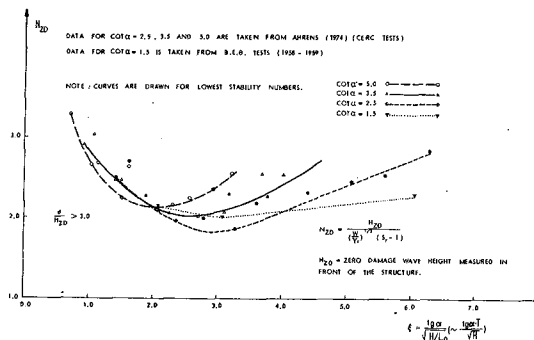


Fig 26 Zero Damage Stability Number versus ξ

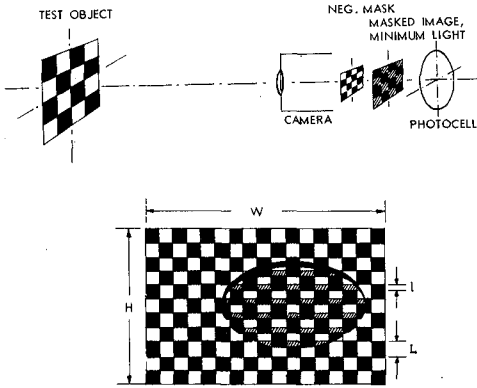


Fig 27 I-II Schematic View of Minimum Light Condition in the OBDS Partial Deflection on the Test Object

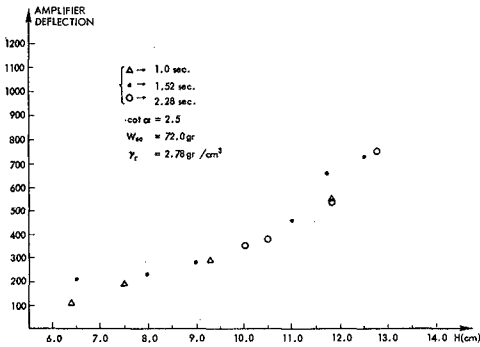


Fig 28 Rock Movements recorded by the OBDS for different Wave Characteristics

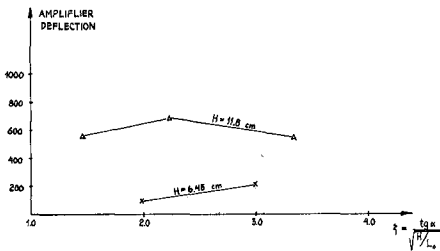


Fig 29 Effect of Wave Period on Rock Movements measured by the OBDS

CHAPTER 143

DESIGN AND CONSTRUCTION OF HUMBOLDT JETTIES, 1880 to 1975

by

Orville T. Magoon¹, M. ASCE

Robert L. Sloan², M. ASCE

Nobuyuki Shimizu³

ABSTRACT

In the Chief of Engineers annual report of 1877, it was concluded that "The only way...in which a safe entrance could be obtained into this harbor would be by the construction of two parallel jetties, of very heavy stone, about 500 yards apart, from the north and south spits at the entrance."

In 1882, a special Board of Engineers concluded that the "occupation of the south breaker spit by a structure...carried to low water and running from the south head (spit) in a north-westerly direction..." be built. Construction of the south jetty began in 1889 and of the north jetty, subsequently authorized, in 1891.

Due to the severe wave action, a number of rubble-mound construction techniques including stone, concrete cubes, tetrahedrons, and finally dolos armor units have been used. A description will be given of the construction and associated results. Experience with the reinforced and unreinforced concrete dolosse units will also be discussed.

INTRODUCTION

A 19th-century Corps of Engineer report contains a description of the Humboldt Bay entrance area by the San Francisco District Engineer as follows:

-
1. Civil Engineer, U. S. Army Engineer Division, South Pacific, San Francisco, California, Chief, Coastal Engineering Branch, Planning Division
 2. Civil Engineer, U. S. Army Engineer District, San Francisco, California, Assistant Chief, Water Resources and Urban Planning Branch, Engineering Division
 3. Civil Engineer, U. S. Army Engineer District, San Francisco, California, Chief, Foundations and Materials Branch, Engineering Division

"It has been reported by masters of vessels that no such heavy seas have been encountered elsewhere in the world, unless perhaps south of the Cape of Good Hope and Cape Horn. Waves have been seen to break in 8 or 10 fathoms of water. It was originally believed that no jetties or such construction could possibly withstand the forces brought to bear by waves during storms, so that the improvement was undertaken with great misgiving."¹

A very vivid description indeed of the severe wave conditions encountered by navigators and those engaged in attempting to provide a stable entrance to Humboldt Bay.

The Humboldt Jetties are two of the oldest manmade structures on the Pacific coast subjected to extreme wave attack. Inasmuch as these structures have been constructed and maintained over a long span of time and have used a variety of design and construction techniques, they represent a significant coastal engineering case history. The material presented here represents a summary of all known information on these jetties; however, any additional information on this subject from readers of this paper would be welcomed by the authors.

GENERAL DESCRIPTION

Humboldt Bay, a land-locked harbor on the coast of Northern California, is about 420 kilometers (225 nautical miles) north of San Francisco and about 290 kilometers (156 nautical miles) south of Coos Bay, Oregon. The entrance is protected by two rubble-mound jetties, which are about 0.7 kilometers (0.5 mile) apart and extend from the ends of two long and narrow sand spits separating the bay from the ocean. The width of the bay varies from 0.8 kilometers (0.5 mile) to about 6.5 kilometers (4 miles), and the length is 23 kilometers (14 miles). The southern portion of Humboldt Bay extends about 6.5 kilometers (4 miles) south from the entrance, widening gradually from 0.8 kilometers (0.5 mile) to 3.6 kilometers (2.25 miles) in width. A dredged channel extends for some 3 kilometers (2 miles) from the entrance to Fields Landing, which lies about midway along the east side of the South Bay. Humboldt Bay is shown on Figure 1.

The entrance is dredged to a 12.2 meters (40 feet) depth. Inside Humboldt Bay north of the entrance, a fairly deep natural channel closely follows the north spit. A 10.7 meters (35 feet) channel is dredged for almost 3 kilometers (2 miles) along the waterfront of the City of Eureka.

The tides are semidiurnal with a range between mean lower low water and mean higher high water of 1.95 meters (6.4 feet) at the south jetty and 2.04 meters (6.7) feet at Eureka. The entrance channel is exposed to high waves generated by local coastal storms accompanied by high winds, and to high waves or swell produced by offshore, distant, Pacific Ocean storms, unattended by high winds. Both types of waves generally occur during the period from November through April

with the critical area of approach being from southwest through northwest. More detailed information on Bathymetry and wave climate is given in Magoon and Shimizu,² and in model studies by the Waterways Experiment Station in Vicksburg, Mississippi, U.S.A.³ There is also a paper on channel shoaling by Noble.⁴

The initial Federal investigation of Humboldt Bay looking toward a possible improvement of the entrance by jetties was made in 1878.⁵ This report states:

"This bay affords fine shelter after vessels have once got into it, but it is a bar-harbor, the bar being composed of shifting sands, with heavy breakers even in moderate summer weather.

To give an idea of the great height of waves rolling over this bar, we will state that when the Board of Engineers for the Pacific Coast arrived off the bar, in the Coast Survey steamer Hassler, the weather was very moderate, with only the usual summer wind from the northwest, yet, although there was 20 feet of water on the bar at the time, the pilot refused to take in the Hassler, drawing only 12 feet of water at the time, stating that he could not do so without running the risk of the vessel striking bottom and her possible loss in the breakers.

The shores on both sides of the entrance are low and sandy, and there is no stone in the immediate vicinity.

The only way, as it appears to the Board, in which a safe entrance could be obtained into this harbor would be by the construction of two parallel jetties of very heavy stone, about 500 yards apart, from the north and south spits at the entrance.

If such jetties were built, the very large area of the inner bay would probably afford sufficient tidal prism to keep open a deep channel over the bar, against all drifts from the action of sea-waves. But such construction would be attended with immense difficulties and enormous expense. It is a question even, with the members of the Board, whether such construction would be physically possible, and one, too, upon which we dare not express an opinion without a searching examination of all the contingencies upon which the stability or instability of such works would hinge. We have not, therefore, made any plan or estimate of cost for a breakwater at this place, deeming it, if not impossible of execution, highly improbable that a breakwater or jetties will be attempted here at the present time."

This report correctly identifies the major problems that have continued until the present: "shifting sands", "high waves", "lack of stone in the immediate vicinity", and lack of understanding of structure stability. The report also notes that if two jetties could be built, there would probably be sufficient tidal prism to keep the jetties open.

Jetty layout and construction on the Pacific Coast is mentioned by Symons⁶ in 1893 who indicates that the Humboldt Jetties were designed to be high tide jetties and that their construction was similar to that at other Pacific Coast harbors, but was "done by single broad gauge track" rather than the double narrow gauge track. He also expresses his desire to see the construction of a "single curved jetty, concave to the channel, instead of a pair of nearly parallel jetties, with the hope that a good and satisfactory channel would be developed, as along the concave bank of a river." The concept of a single "reaction breakwater" which would develop the potential energy of the ebb currents, rendering them kinetic, and applying them locally on the crest of the bar where they are needed for scour was discussed in detail by Haupt in 1899.⁷ Perhaps because of the above subsequently stated interest in the single jetty concept, the Chief of Engineers recommended the construction of a single jetty at the Humboldt Bay south spit—a low enrockment (rising to the level of ordinary low water) of rubble stone. A length of 6000 feet and a depth of 6 feet were assumed to be necessary (73,000 tons of stone) in addition to "an enlargement of the sea head" and beach and shore protection (17,000 tons of stone). The report also notes that from 1851 to 1882, the entrance channel had varied in width from 2200 to 4200 feet and in depth from 21 feet to between 10 to 12 feet.

INITIAL CONSTRUCTION

The initial contract for construction of the south jetty was let in 1888.⁸ By 1890 it was realized that the southern end of the north spit was eroding rather than holding firm and providing a deep entrance. The Chief of Engineers Annual Report of 1891⁹ states:

"In October, 1890, a Board of Engineers was convened to consider and report upon a project for the improvement of Humboldt Bay. The board met at Eureka on December 11, 1890. After study of the subject, it was decided to modify the existing project so as to embrace shore protection work on the north spit, and the construction of a jetty starting from there and running seaward nearly parallel to the jetty on the south spit, both jetties to extend out to the 18-foot contour and be raised to the plane of high water, thus confining the tidal flow within definite bounds and securing the full benefit of its scouring capacity."

It was also apparently concluded that the jetties would have to extend to "high water."

By late 1891 an additional contract had been completed, and the south jetty was about 4000 feet long, and the north jetty about 1500 feet long. This latter contract used 28,000 cubic yards of brush mattresses and 100,000 tons of stone.

The jetties were built from a timber trestle which was constructed with an overhanging pile-driver revolving on a turntable. The trestle

consists of four-pile bents sixteen feet apart supporting two standard gauge tracks of forty-pound T rails and is designed to last only long enough to complete the jetty beneath it. A typical pile bent is shown in Figure 2.

Filter material used was a layer of brush mattresses approximately forty-four feet wide.

"A mattress is built upon two piles swung under the trestle by wire cables made fast to the cap timbers. First is laid upon these sling-piles a grillage of poles bound at every intersection with strong wire. Upon the grillage are placed in successive layers bundles of brush about twelve feet long, the bundles in each layer being at right angles with those of the next. When the brush has a thickness of about six feet, another grillage is placed on the top. The two grillages are made to compress the brush to two-thirds of its original volume by means of long screws extending through the mattress. The grillages are then bound together by numerous wires, previously brought up through the brush from the bottom. The screws are removed, and the mattress is ready.

Cars filled with small rock are brought, and a layer of stone is thrown by hand upon the mattress to serve as ballast. Six men are stationed on the cap timbers. They stand with uplifted axes ready to cut the lashings and free the cable ends. Others stand by the car doors ready to release the rock. The word is given. With a cracking and a crash, the mattress strikes water. In a second a rattling volley of rock drives it out of sight to the bottom."⁸

These jetties resulted in a fixed channel, at least 700 feet wide and 25 feet deep until 1905. As the jetties deteriorated from lack of maintenance, the channel shoaled and by 1907, the outer ends of the jetties were completely buried in the sand.

REBUILDING OF JETTIES

Between 1911 and 1915 the south jetty was reconstructed. Between 1915 and 1925 the north jetty was rebuilt. The new jetties were built on the foundations derived from the old structures. Due to the inability of driving piles for a new trestle through the old stone "foundation," the new structures were built by the "cap method." The crane that was used has a capacity of 20 tons at a 35-foot radius, with a maximum reach of 50 feet. The crane operates in a 17-foot gauge track, placed on wooden ties imbedded usually in about 18 inches of concrete cap. In the original reconstruction, no parapet stones were used on the jetty.

"The concrete cap method has proved a success. While used as an incident of construction to prevent the tracks from being washed away,

it was found, as anticipated, to retard the action of the sea in tearing down the jetty structure. The average cost of the concrete cap, 22 feet wide and 18 inches deep, was about \$20 per linear foot, including tracks and foundation of stone. No forms were used after 1914.

The plant for concrete mixing consists of one standard-gauge flat car and a Foote batch mixer of 21-cubic-foot capacity, end discharge, and steam-operated. The concrete is placed by a foreman and four laborers, the regular stone unloading crew. A section of this concrete cap is usually built in two hours, including the leveling of the foundation and placing of ties and standard-gauge rails. Difficulty is experienced during rough weather in protecting fresh concrete from being washed out by the waves. This condition was improved by placing a parapet of larger stone seaward of it, and covering the fresh concrete with canvas and boards weighted down with old rails.

When the south jetty was completed in 1915, a concrete monolith weighing about 1,000 tons was built at the end for the protection of the jetty head, the most exposed and vulnerable part. The concrete block was 30 by 30 by 14 feet, with the base at five feet above mean lower low water. It is reinforced with old 60-pound steel rail made fast with old cables and U-bolts. When the work of reconstruction was completed, the depth of water at the sea end was 31 feet, instead of 18 feet as before. The bottom of the block was laid at about high-water elevation. The top of the block was at an elevation of 19 feet above low water. The concrete block has proved a success in protecting the sea end."

The next phase of construction of the north jetty began in late 1915. Armor stones were from 6 to 20 tons and the larger stones were placed in the upper layer on a slope of 1 on 2 on the exposed side and 1 on 1-1/2 on the protected side. The crest was raised to about 19 feet above mean lower low water, and a reinforced concrete monolith 32 feet wide, 14 feet thick (above high water), and 32 feet in length. Steel reinforcing consisted of old railroad rails. Seaward of the monolith a 7 foot thick by 32 foot wide by 30 feet long slab was placed, and large stones were placed around the slab and monolith. A typical section of the north jetty is shown in Figure 3.

LATER CONSTRUCTION ACTIVITIES

Due to the adverse sea conditions at the site, floating equipment could not be utilized for construction or repairs of the jetties, thus all work was conducted from the jetty crest. With these limitations the sizes of stones or shape that could be placed in the jetties were limited to the capacity of the available equipment or additional other methods were improvised to place larger armour protections. Generally, the structures could not be built from the seaward toe upward. Prior to 1970, the weights of stones and shapes were limited to about 20 tons. Since units of sufficient sizes to provide the required protection could not be placed effectively, the jetties at Humbolt Harbor have required constant maintenance during the past years. Sources of

stone over the years have been generally located in surrounding areas of fairly close proximity, however, stone has been brought in from as far away as Oregon. A record of the maintenance work conducted at the jetties is presented in Table 1 at the conclusion of this report.

The north and south jetties were completed to their full lengths in 1925 and 1927, respectively. During this period the parapet wall was constructed and the concrete cap was placed on the crest of the jetties. Concrete was also placed on the channel-side slope of the jetties to hold the armour stones together.

When construction was completed, the side slopes of the jetties were approximately 1 vertical to 1.5 horizontal with a crest width of approximately 20 feet. The elevation of the crest varied from about 12 feet to 19 feet msl at the seaward end. The parapet walls were located on the south sides of the jetties and were about 4 feet in height and 6 feet in width. Above msl elevation the armour stones of the side slopes were imbedded in concrete. The parapet walls were located on the south sides of the jetties due to predominant waves from the southwesterly direction and the wide channel being approximately 3,000 feet in width.

Emergency repairs and periodic maintenance works were required during 1930 and 1957. Primarily, work consisted of using mass concrete to fill the eroded areas in the crest and imbedding the armour stones on the side slopes and the replacement of armour stones in areas that were breached or washed out. To provide the necessary protection, concrete blocks weighing over 100 tons were used as early as 1932. These blocks measured 11 by 11 feet and were cast on the crest at the site of the repair work on greased or oiled sheet board. The jetty side of the sheet platform was picked up and the blocks were launched by compressed air into washed-out areas of the slope. Actual placement of these blocks could not be accomplished due to lack of equipment that would handle these size units. It should be noted that many of these 100-ton blocks broke when they hit the water. They did not appear to break as often, however, when they struck other blocks or stone. In the 1930s and 1940s 12-ton tetrahedrons were also used for repairs. These units were considerably smaller than we would now consider stable.

During the winter of 1957-1958, severe storms deteriorated the north and south jetties to such an extent that repair work constituted a major construction project. The repairs of the north jetty commenced in 1960 and were completed in 1961. The south jetty was repaired during 1962 and 1963. The trunk portions of the jetties were repaired by mass concrete and 12-ton stones were placed on 1 vertical to 1.5 horizontal slopes in the eroded areas. The heads of the jetties were varied to about elevation 25 feet. Construction of the heads was accomplished by using 20-ton blocks for perimeter forming and placing mass concrete within block forms. The concrete was reinforced with large reinforcing bars and track rail. The heads were protected with 12-ton stones placed on 1 vertical to 1.5 horizontal side slopes with a cover layer

of 100-ton cubic concrete blocks. Most of the 100-ton blocks were washed away during the winter storms of 1964-65. Both the north and south jetties progressively deteriorated due to wave action. By 1970 the heads of the jetties were totally destroyed and another major rehabilitation work was required.

Extensive model studies were conducted for this rehabilitation work. Various concrete shapes were investigated. The adopted design consisted of placing 42 and 43-ton dolosse on 1 vertical to 5 horizontal slopes against the heads of the jetties. The placement slope was dictated by the existing conditions around the jetty heads which were covered with stones and concrete blocks from the jetties. The dolosse were to be placed a maximum of 230 feet from the heads of the jetties in two layers, placed at random with 11 dolosse per 1,000 square feet of slope area. The dolos units were to be placed from the toe to the head in two layers.

The rehabilitation work² on the south jetty was accomplished in 1971 and the north jetty in 1972. The Model VC 4600 Monitowac Crane, "Ringer," was used for the placement of the dolosse. Prior to construction, the Contractor made scale models of the dolos to study the placement of the dolos. Then the locations for each dolos to be placed to provide the necessary coverage were plotted and predetermined. The boom angle of the crane provided the distance from the head and the deflection of the boom from a given line provided the exact location for each dolos. The dolosse were picked up in the center of the trunk by a wide two-prong claw, lifted, the boom was moved to the deflection and lift angles, and the dolosse were lowered and placed. When placed the dolosse of the lower layer were positioned to locate the standing fluke seaward and the trunk in line with the direction of the waves where possible. The dolosse in the upper layers were placed and positioned to provide the greatest interlocking stability.

The dolosse have been in place for 5 and 4 years for the south and north jetties, respectively, and although there has been some breakage of the dolos units¹⁰ and settlement of perhaps 5 feet at portions of the south jetty head, the structural integrity of the jetties is not endangered.

The following tabulation presents a historical summary of the quantities of stone placed for new construction and maintenance (including concrete and special concrete armor units) from initiation of construction activities in 1889 to the present time. These records have been obtained from annual reports prepared by the Office, Chief of Engineers, U. S. Army, dating from 1891, and from early reports.

Table 1
SUMMARY OF NEW WORK AND MAINTENANCE QUANTITIES,
1889 - 1973

YEARS	NEW WORK		MAINTENANCE		REMARKS
	Quantity (tons)	Concrete (c.y.)	Quantity Stone (tons)	Concrete (c.y.)	
1889-1899	1,150,000	—	—	—	North and south jetties, including shore protection.
1911-1921	855,713 ^{1/2}	473	132,979	—	Includes provision of 950-ton reinforced concrete monolith at the seaward head of the south jetty in 1915-16.
1922-1931	196,393 ^{1/2}	—	442,612	10,221	Includes reinforced concrete monolith at the seaward end of the north jetty, completed in 1925 and weighing 1050 tons.
1932-1941	—	—	10,340	68,729 (plus 43,853 tons)	Includes restoration of jetty ends with mass concrete and placement of precast concrete blocks on slopes.
1942-1951	—	—	—	40,693	Includes placement of 100-ton blocks on both jetties
1952-1961	—	—	34,205	3,142	Includes six 100-ton blocks
1962-1971	—	—	232,839	20,919	Excludes 225 20-ton concrete-form blocks, 116 100-ton concrete form blocks, 2,259 42- & 43-ton concrete dolosse & 5,257 20-ton concrete form blocks.
1971-1973	—	—	64,622	2,740	Excludes 2,533 42- & 43-ton concrete dolosse and 95 20-ton concrete form blocks.

^{1/2}Although the major jetty rebuilding activities of this period were classified as "new work," the quantities could be considered as maintenance figures since the original jetty structures had long since been completed.

CONCLUSIONS

Engineering decisions made over a period of nearly a century by competent people in search of solutions to the Humboldt Bay entrance problem have shown that corrective actions are available and can be applied with an increasing degree of confidence given today's technology. The design of protective structures for severe wave climate areas such as Humboldt Bay is a difficult and challenging, but certainly not insurmountable, task.

ACKNOWLEDGEMENT

Acknowledgement is gratefully made to the Corps of Engineers, U. S. Army, for access and permission to use this study material. The views of the authors do not purport to reflect the position of the Corps of Engineers, Department of the Army, or Department of Defense. Acknowledgement is also made to the staff of the American Society of Civil Engineers headquarters for permission to reprint all photographs and plates from referenced ASCE transaction papers.

LIST OF REFERENCES

1. Whittemore, George F., "Construction of the Humboldt Bay Jetties," *The Military Engineer*, Vol. XVIII, No. 97, January-February 1926.
2. Magoon, O. T., and Shimizu, N., "Use of Dolos Armor Units in Rubble Mound Structures, e.g. For Conditions in the Arctic," *Proceedings, First International Conference on Port and Ocean Engineering under Arctic Conditions*, Vol. II, pp. 1089-1108, 1971.
3. Davidson, D. D., "Proposed Jetty Head Repair Sections, Humboldt Bay, California," *Technical Report H-71-8*, U. S. Army Waterways Experiment Station, Vicksburg, Mississippi, November 1971.
4. Noble, R. M., "Shoreline Changes Humboldt Bay, California," *Hydraulic Engineering Laboratory, College of Engineering, University of California, Berkeley, California*, February 1971.
5. House of Representatives, Ex. Doc. No. 22, 45th Congress, 3d Session, printed January 15, 1879.
6. Symons, Thomas W., "Jetty Harbors of the Pacific Coast," *Transactions, ASCE Vol. XXVIII*, March 1893, pp. 156-184, and discussion Vol. XXVIII, May 1893.
7. Haupt, Lewis M., "The Reaction Breakwater as Applied to the Improvement of Ocean Bars," *Transactions, ASCE Vol. XLII*, December 1899, pp. 465-546.
8. Dennison, W. E., "Humboldt Bay and Its Jetty System," *Overland*, October 1896, Vol. 28, pp. 381-91.
9. Chief of Engineers Annual Report, 1891, part 5, pp. 3120 to 3128.
10. Magoon, O. T., Sloan, R. L., and Foote, G. L., "Damages to Coastal Structures," *Proceedings, 14th Coastal Engineering Conference*, Copenhagen, Denmark, June 1974.



Figure 1. Humboldt Bay.

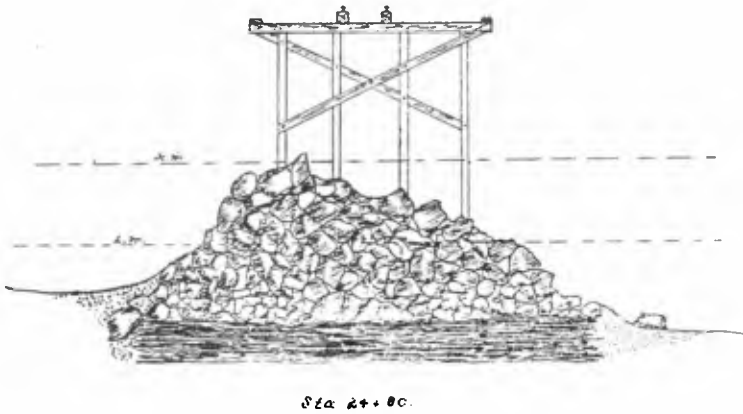


Figure 2. Typical pile bent.

The Military Engineer

Vol.



Figure 3. Typical section of the north jetty.



Figure 4. Jacoby Creek Quarry



Figure 5. Monitor at Jacoby Creek Quarry



Figure 6. Locomotive crane switching car—Jacoby Creek Quarry.



Figure 7. Hauling stone to ferry.



Figure 8. Landing stone at north jetty.



Figure 9. Typical pile driver.

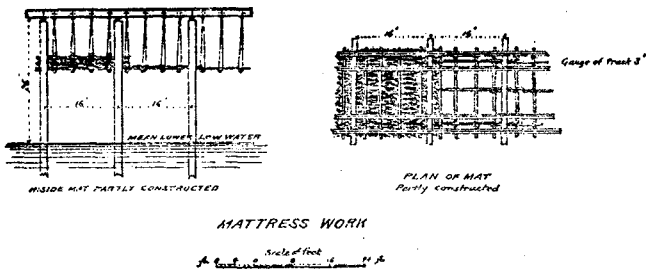


Figure 10. Construction of mattress.

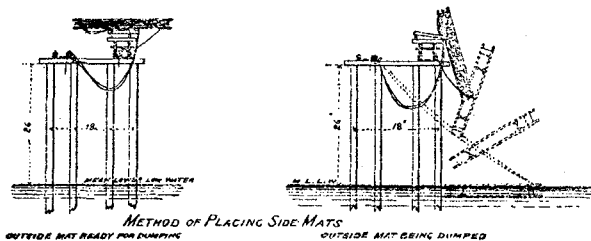


Figure 11. Placement of side mats.

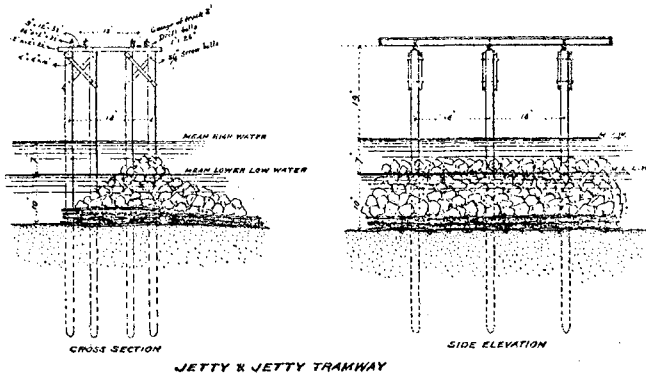


Figure 12. Jetty tramway.

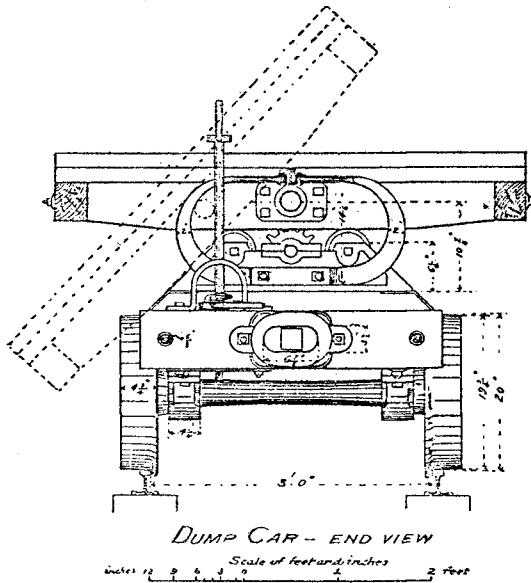


Figure 13. End view of dump car.



Figure 14. Constructing brush mattresses.



Figure 15. Compressing the mattress.



Figure 16. Dropping mattress.



Figure 17. Lifting stone.



Figure 18. Jetty construction.

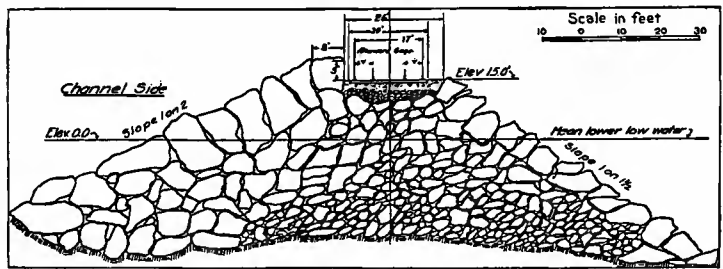


Figure 19. Typical section of north jetty with concrete cap.



Figure 20. Placing stone from cap.



Figure 21. Truck delivery of stone and concrete.



Figure 22. Sea face of south jetty with 20-ton pre-cast concrete blocks (1932).

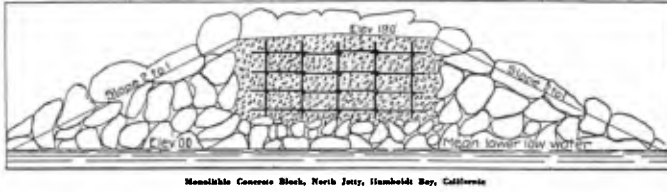


Figure 23. Monolithic concrete block, north jetty



Figure 24. Monolith form blocks.



Figure 25. Pouring monolith.



Figure 26. Preparing to launch 100-ton cubes.

CHAPTER 144

DESIGN OF MAIN BREAKWATER AT SINES HARBOUR

John Dorrington Mettam*

Introduction

In March 1972 the author's firm in association with two Portuguese firms of consulting engineers, Consulmar and Lusotecna, were appointed by the Portuguese Government agency Gabinete da Area de Sines to prepare designs for the construction of a new harbour at Sines on the west coast of Portugal. The location is shown in Figure 1.

The main breakwater, which is the subject of this paper, is probably the largest breakwater yet built, being 2 km long and in depths of water of up to 50 m. It is exposed to the North Atlantic and has been designed for a significant wave height of 11 m. Dolos units invented by Merrifield (ref. 1) form the main armour.

The project programme required that studies be first made of a wide range of alternative layouts for the harbour. After the client had decided on the layout to be adopted, documents were to be prepared to enable tenders for construction to be invited in January 1973. This allowed little time for the design to be developed and only one series of flume tests, using regular waves, was completed during this period. Further tests in the regular flume were completed during the tender period and a thorough programme of testing with irregular waves was commenced later in the year, continuing until August 1974 when the root of the breakwater was complete and the construction of the main cross-section was about to start.

The model tests, which were carried out at the Laboratorio Nacional de Engenharia Civil in Lisbon, were reported by Morais in a paper presented to the 14th International Coastal Engineering Conference in 1974. (ref. 2)

Layout

Sines was selected as the most suitable place on the whole Portuguese coastline for development of a maritime industrial complex served by a new deepwater harbour.

The first phase of the project was to be a new oil refinery with a harbour handling tankers up to 500,000 DWT. Later development would include provision for tankers up to 1,000,000 DWT as well as a wide range of other berths to serve other industries.

* Partner in the firm of Bertlin and Partners, Consulting Engineers of Redhill, Surrey, U.K.

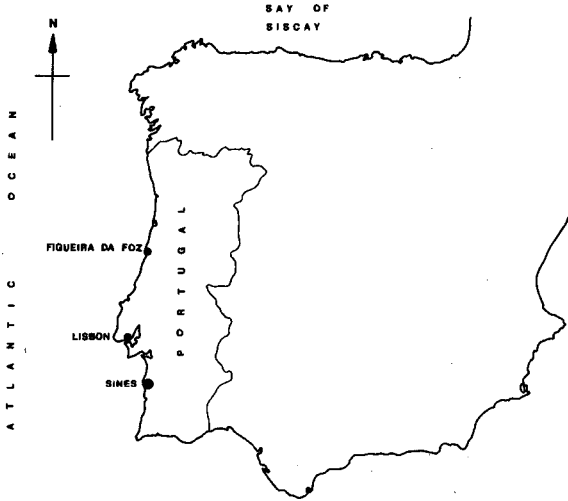


FIG. 1 SITE LOCATION

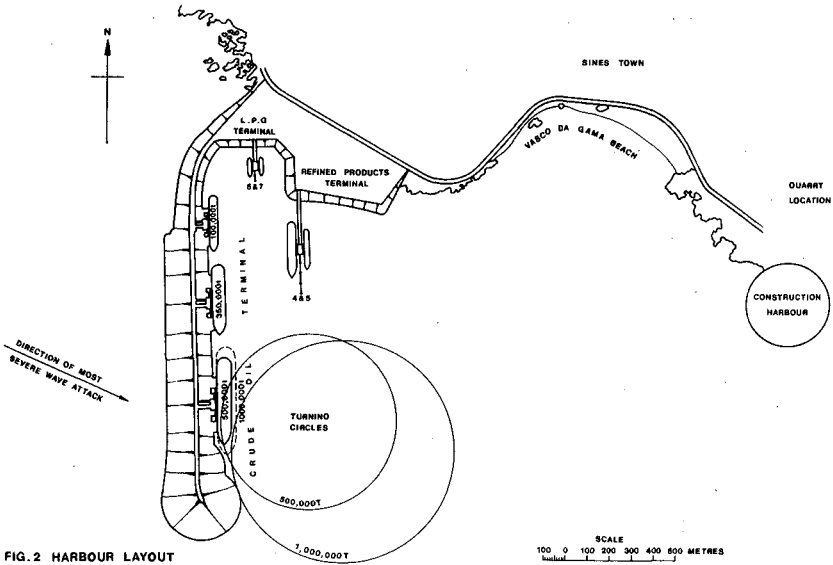


FIG. 2 HARBOUR LAYOUT

The layout of the first phase of the West Breakwater is shown in Fig. 2. Details of the adjacent berths are given in Table 1.

Upgrading of Berth 1 to handle ships of 1,000,000 DWT would require strengthening of the breasting dolphins, and some dredging to enlarge the turning circle.

Table 1 - Details of Berths 1 - 7

Berth No.	Commodity	Max. Ship Size (DWT)	Draft (m)	Depth at Berth (m. below chart datum)
1	Crude oil	500,000 (1,000,000)	28 (33)	39 (see note 1)
2	Crude oil	350,000	25	28
3	Crude/Products	100,000	15	18
4	Products)	45,000	12	19
5	Products)	(100,000)	(15)	(see note 2)
6	L. P. G.)	3,000	6	7
7	L. P. G.)			

Note

(1) It is envisaged that a second berth for 1,000,000 DWT could be provided by a southward extension of the breakwater.

(2) Berths upgraded to 100,000 DWT in Phase 2.

Other berths for dry bulk commodities, general cargo etcetera would form a separate complex adjacent to the South Breakwater, the precise layout of which has not yet been decided. Construction of this complex will be by stages to suit development of industries.

A construction harbour near the South Breakwater was included in the contract near the quarry site to assist the contractor to handle the enormous volume of rock required for breakwater construction. This will finally be used for harbour craft, fishing vessels and coastal shipping.

Design Wave Height

A wave recorder had been installed at Sines in September 1971, as soon as it had become clear that this site would be selected for the harbour. This however had only yielded records for one winter when design of the breakwater started, and for two winters when the final decision had to be made on the weight of armour unit. To supplement this record an analysis was made (ref. 3) to assess the probable wave climate at Sines from some earlier detailed observations made at Figueira da Foz (ref. 4) over a period of 7 years.

In view of the uncertainty regarding the best method of extrapolating extreme values from short period records four different methods were used. No method gave consistently better fit to the available data and no conclusion could be drawn regarding relative reliability. The method of calculation of waves at Sines from those at Figueira da Foz was considered likely to give slightly too high a value - because of the difficulty of allowing for the fact that Sines is further from the main storm areas. Equal weight was therefore given to the shorter period of records at Sines even though these gave a lower result. Table 2 gives the results of the various methods of extrapolation together with the value of significant wave height finally adopted.

Table 2 - Extrapolation of Extreme Waves (Significant Height)

Source	Method of Extrapolation	Return Period (years)			
		1	10	30	100
Figueira da Foz	Gauss	6.5	9.8		14.0
	Weibull	6.3	8.6		11.0
	Weibull Modified(ref.5)	6.5	8.7		11.0
	Exponential	6.5	8.8		11.2
	Mean	6.5	8.9		11.8
Sines Waverider	Gauss	7.8	9.2		11.5
	Weibull	6.1	7.0		8.0
	Weibull Modified (ref.5)	5.8	6.5		7.2
	Exponential	7.0	8.8		10.4
	Mean	6.7	7.9		9.3
Adopted Value for Design		6.5	8.5	9.5	11.0

For the irregular wave flume tests damage criteria were established on the lines proposed by Ouellet (ref. 6). These are shown in Table 3, which also includes overtopping criteria. The wave spectrum used was the Pierson - Moskowitz, based upon site storm records.

Table 3 - Breakwater Design Criteria

Storm Return Period (Years)	Significant Wave Height H_s (m)	Dolos Movement	Overtopping
1	6.5	Nil	Begins with H_{max} individual 10 - 11 m
10	8.5	Oscillation only	-
30	9.5	Beginning of displacement	Severe overtop with 15-16 m H_{max} individual
100	11.0	1% Damage	-

When testing with regular waves the same criteria were applied as far as practicable using wave periods corresponding to a fully risen sea. Wave heights and periods are given in Table 4.

Table 4 - Wave Periods for Regular Wave Flume

Height (m)	8	9	10	11	12	13	14	15
Period (sec.)	11.5	12.3	12.9	13.5	14.2	14.8	15.3	15.8

Development of Design for Main Cross-Section

In the initial design stages consideration was given to a range of possible solutions. The main choice was between rubble mound construction and composite construction with a vertical face structure founded on a rubble mound.

Some preliminary tests of the composite section showed that very large wave forces would be exerted on the vertical structure even if it was founded as deep as -20 m CD. Such forces could probably have been much reduced by the introduction of a perforated face construction. Even so, with the construction problems on such an exposed site it was decided that a rubble mound design would be more economical.

In this decision the availability of a suitable rock, in very large quantities, was of course a major consideration.

With the great depths at the site it was important to adopt a form of armouring which allowed the seaward face to be as steep as practicable, to reduce the volume of rubble core, and to restrict the reach required for the cranes placing heavy armour units.

Discussions with Mr. Merrifield convinced the designers that Dolos units would be the best solution currently available. Comparative studies of dolos and tetrapods during the first phase of regular wave flume tests confirmed this view. Attendance by the author at the 13th International Coastal Engineering Conference in Vancouver in 1972 was also most helpful and the author is indebted to the many people at that conference with experience in research on dolos, and in their use, who generously shared their knowledge.

In preparing breakwater designs it is the author's view that preliminary designs based upon past experience must always be fully tested by flume testing using the precise conditions of waves and topography for the site. This is particularly important when dolos are being used because classic design formulae such as Hudson's (refs. 7 & 8) developed initially for rock armouring, do not allow properly for the type of interlock displayed by these units which alters the importance of slope and specific gravity. Such formulae also omit the effect of wave period, which must be a major factor in determining the wave forces particularly at Sines where wave periods are longer than at many other sites.

For this reason the design was mainly developed by flume testing, first on the regular wave flume and later on the irregular wave flume. The initial design submitted to contractors for tendering, Fig. 3, was based on the first series of tests in a regular wave flume.

This design would in any case have been subject to change when further flume tests were completed. In addition the successful tenderer (Societa Italiana per Condotte d'Acqua S.p.A) submitted an alternative design which was accepted in principle by the Client subject to model testing, Fig. 4. The purpose of the change was twofold; to widen the breakwater crest to provide space for the oil pipelines which would otherwise have required a separate structure; and to provide more space for constructional equipment. This design was considerably modified after carrying out irregular flume tests, the final cross-section being shown in Fig. 5.

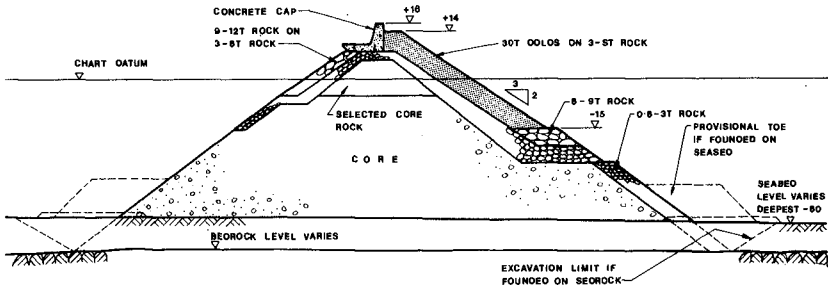


FIG.3 TENDER DESIGN

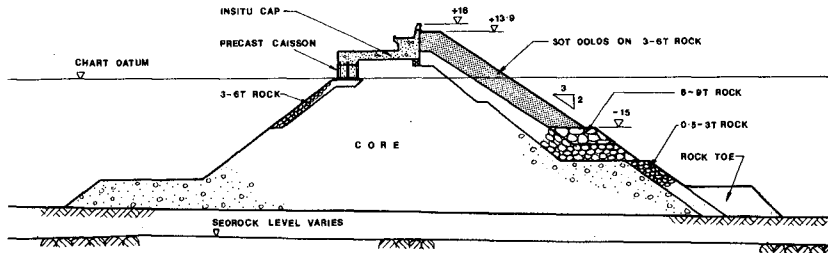


FIG.4 CONTRACTOR'S ALTERNATIVE DESIGN

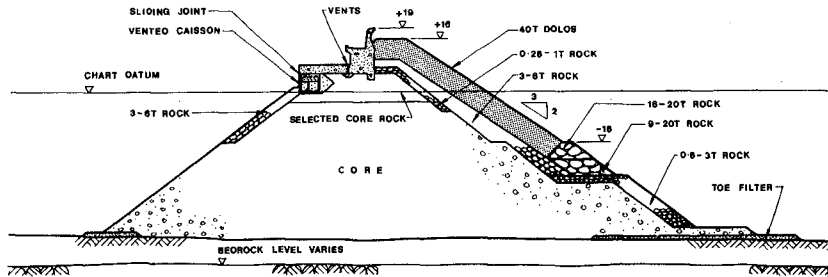
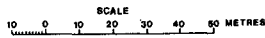


FIG.5 FINAL DESIGN



The main changes resulting from the irregular wave tests were:-

- 1) Increased crest height on wave wall.
- 2) Adoption of curved profile wave wall.
- 3) Increased width of dolos armouring in front of wave wall.
- 4) Increased weight of capping and introduction of sliding joint at junction with caissons at back.
- 5) Introduction of heavier armour (16-20t) at toe of dolos slope.

The weight of dolos armouring, which had been changed from 30t to 40t nominal (actually 42t) as a result of the second series of regular wave tests was confirmed by the irregular flume tests.

The final design is discussed, section by section, below.

Foundation

The main length of the breakwater is founded, in depths varying from 30m to 50m, on granular deposits overlying shaley mudstone. The deposits consist of sand and gravel in thicknesses of up to 12m.

Site investigations completed after tenders were invited, showed that these deposits were sufficiently dense to support the breakwater. Calculations were made to check the stability under surcharge loadings of up to 60 m of rubble filling. Detailed consideration was also given to the possibility of liquefaction under earthquake conditions (ref. 9) and under the reversal of pressure resulting from severe wave attack. It was concluded that it would not be necessary to remove any bed material before placing the rubble mound.

To guard against scour a toe protection was provided consisting of a 1 m thick filter layer of 5 mm to 100 mm graded stone on which a 2-m thick layer of core material was placed. A narrower strip of filter material under the back slope of the breakwater guards against leaching of the foundation material through the toe of the rubble core.

Rubble Core

The main rubble core was obtained from a quarry sited close to the shore near the site of the construction harbour. Borings showed massive rock, with unbroken cores up to 3 m long. The rock, which has a specific gravity of 2.9, consists of gabbro and diorite.

Two grades of core material were specified. The principal grade complies with the following: "Core material shall not contain overburden or any clayey organic or other deleterious material. It shall consist of rock evenly graded from 1 kg to 3,000 kg. It may contain broken rock fines under 1 kg not exceeding 5% by weight. The quantity of rock under 10 kg in weight shall not exceed 15% of the total weight."

The 'selected' grade, used in the main cross section only above level -2.5 m CD and in the root of the breakwater is similar but the finer material under 10 kg is restricted to between 5% and 10% by weight.

Placing of most of the core material is by dumping from 1,000 t hopper barges. Up to -20 m CD there is no restriction on placing but above this level core construction is not allowed more than 50 m ahead of the secondary armour, which itself is not allowed more than 50 m ahead of the dolos. The purpose of this is to restrict the amount of work at risk during storms. (Fig. 6). The upper part of the core is tipped from 70 t lorries running on top of the core which is at level +5.5 m CD (c.f. high water level +3.8 m CD)

Settlements are being recorded during construction and concreting of the cap is not allowed until 3 months after placing of the core by which time the main settlement has taken place.

The effect of earthquakes on the breakwater was checked using the analysis suggested by Newmark (ref. 10) and developed by Goodman and Seed (ref. 11). This analysis, which is a dynamic method of approach, is used to determine the displacement of the breakwater during the passage of the design earthquake.

Under an earthquake of intensity between 7 and 8 on the modified Mercalli scale, which is expected with a return period of 100 years, a settlement of about 0.5 m is expected.

Rock Armouring and Underlayers

Secondary armour of 3 t to 6 t rock is provided under the main armouring of dolos units. The size is determined partly by the size of the main armour - so that it cannot be drawn through the gaps in between the dolos - but also by the requirement that it should resist attack by 3m to 4m waves during construction.

This secondary armour should be able to retain the core material, after fines have been leached out of the surface of the core. However a tertiary layer of $\frac{1}{2}$ t to 1 t stone was added in the most vulnerable zone to reduce the amount of fines leached out of the core near the seawall. This material can only withstand minor wave attack and must be placed just before the 3 t to 6 t stone.



Fig. 6 Breakwater under construction

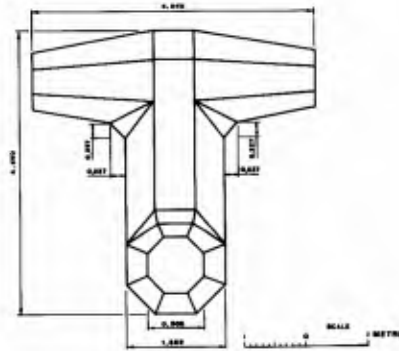


Fig. 7 40 tonne dolos



Fig. 8 Dolos moulds

At the toe of the dolos face irregular wave tests showed that draw down under severe wave attack caused damage with 6 t to 9 t rock as originally provided. Stone of 16 t to 20 t weight, supported on 9 t to 20 t rock proved sufficiently stable, but only with the revised shape shown in Fig. 5. This toe armour rests on 0.5 t to 3 t rock which also extends down the seaward face.

On the rear face armour is only provided to a depth of 15 m below low water. Rock of 3 t to 6 t weight proved adequate because overtopping water is thrown clear of the vertical back face of the cap and its energy is dissipated in water.

The 3 t to 6 t armour is also required to resist waves running along the back of the breakwater due to direct attack in southerly storms which are infrequent and diffracted waves from more westerly storms.

Main Dolos Armour

The main dolos armour units have a volume of 16.56 cu m and with a concrete specific gravity of 2.53 weigh approximately 42 t.

The dimensions, shown in Fig. 7, provide a waist: leg ratio of 0.35. Fillets at the junction of the legs have a dimension of 5% of the leg length. Tests by Lillevang (ref. 12) show that this size of fillet greatly reduces the stress concentration compared with a sharp corner but that a better stress pattern is obtained with a radius. When these results were made available to us the moulds had already been fabricated and units had been cast which showed little or no tendency for cracking at this corner, and it was decided not to alter the design.

Consideration was given to providing reinforcement but it was not done. The benefit from reinforcing this type of unit is very doubtful and the potential danger of damage due to corrosion of the steel is more serious. Instead it was decided to provide a high strength concrete - 400 kg/sq cm at 28 days - made with a low heat pozzolanic cement. The contractor's design for moulds, shown in Fig. 8, is considered a very good one. The arrangement of casting with the trunk vertical allowed concrete to be placed and vibrated carefully in the critical area at the corners between the legs and trunk. A compressible joint in the moulds reduced the tendency for shrinkage to put the trunk into tension.

Time did not permit photoelastic analysis of stresses in the dolos. Some comparisons were however made between concrete stresses (ignoring the notch effect of sharp corners) in these and earlier units. These are presented in Tables 5, 6, and 7 in terms of static and dynamic stresses under loads equal to the dolos unit weight.

Table 5 - Comparison of dimensions of Dolos units

Project	East London	Sines	Ratio $\frac{\text{Sines}}{\text{East London}}$
Weight	20 U. S. tons	41.9 metric tonnes	2.31
Volume (cu. m)	7.55	16.56	2.19
Overall Length (m)	3.693	4.540	1.23
Waist Thickness (m)	1.108	1.589	1.43
Waist Ratio	0.30	0.35	1.17

Table 6 - Comparison of maximum static tensile stress in Dolos units

Note (1) Applied load = self weight of 1 Dolos unit

(2) All stresses are in tonnes/sq. m.

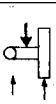

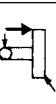




Load Case	1	2	3	4	5	6	7
Loading Condition							
East London Dolos	93 (100%)	80 (100%)	193 (100%)	243 (100%)	112 (100%)	205 (100%)	287 (100%)
Sines Dolos	84 (90%)	63 (80%)	186 (97%)	173 (71%)	104 (92%)	131 (64%)	200 (70%)

Table 7 - Relative dynamic stresses in Dolos units

Load Case	1	2	3	4	5	6	7
East London Dolos	100%	100%	100%	100%	100%	100%	100%
Sines Dolos	100%	89%	108%	79%	102%	71%	78%

The design of the armour face was based upon the recommendations of Zwamborn and Beute (ref. 13) and 155 units were specified per 1,000 sq. m of armour face. To ensure maximum interlock it was required that the complete face be built in a single operation rather than in separate layers.

This method has also been specified for placing rock armour (ref. 14) and is no more difficult than proper placing of separate layers. Hydraulic model tests showed that the number of dolos required could be placed in three separate layers but comparative tests confirmed at a very early stage that the specified method of placing in one operation gave a much more stable face. No comparisons were made with the thinner, two layer, armouring recommended by Waterways Experimental Station (ref. 8) but the author considers that detailed comparisons would show that the two layer system would require heavier dolos to give equal stability.

The specified method of placing is particularly advantageous in assisting interlocking on steep slopes, such as the $1 : 1\frac{1}{2}$ slope adopted at Sines, and it is considered that there would be little if any improvement in stability if a flatter slope were adopted because interlock during placing would be reduced.

Full records of damage during placing have not yet been made available to the designers, who are not responsible for site supervision, but it is reported that breakages of the order of 2-3% have occurred. Broken units are removed unless they are so interlocked that removal is impracticable. This rather high rate of damage no doubt stems from the use of floating cranes, already available to the contractor from another project, instead of cranes mounted on the breakwater. On such an exposed site this involves placing dolos with waves of up to 1 m and even so there is considerable down-time even during summer months.

Concrete Capping

The capping carries a road and pipelines. Its width reduces beyond each oil berth as fewer pipelines are required. To avoid damage to the pipelines the rubble mound is allowed to settle for 3 months before concreting commences. Despite this precaution the slab is heavily reinforced to resist stresses induced by settlement which may be expected to continue particularly during storms or earthquakes. Some damage to pipelines and minor structures during extreme storms and severe earthquake is of course acceptable provided that the main structure survives.

Fig. 9 shows the capping proposed by the contractor which model tests indicated would not be satisfactory, even after incorporating the vents shown in Fig. 10. The tests showed that it is important to have a sliding joint between the capping slab and the small caissons at the rear of the breakwater. Details are shown in Fig. 11. The difference in type of failure is illustrated in Figs. 12 and 13. Without a joint the cap tends to lift and rotate about the back corner of the caisson causing a local failure at the back of the rubble mound. With the joint the cap slides over the caisson and the cut off at the front of the cap tends to dig into the top of the rubble. Provided the cut off is sufficiently strongly reinforced, failure can only occur by a deep shear through the main body of the rubble mound.

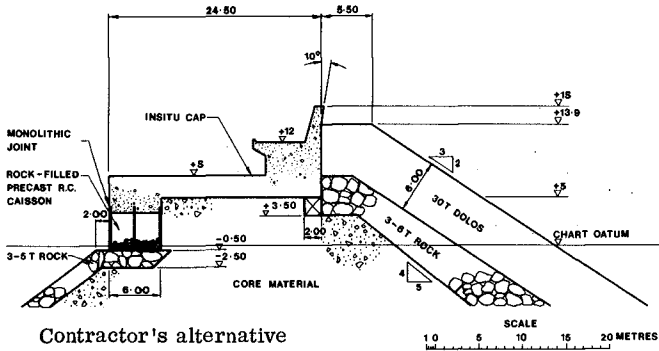


Fig. 9 Contractor's alternative capping design

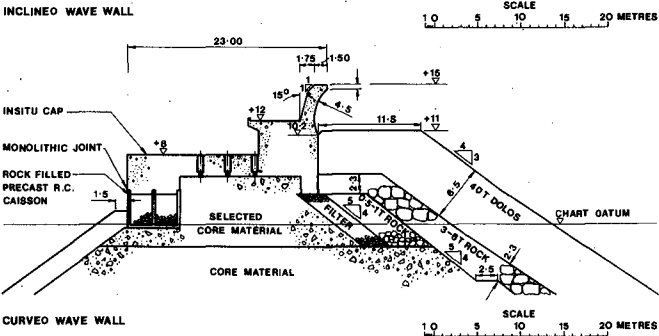
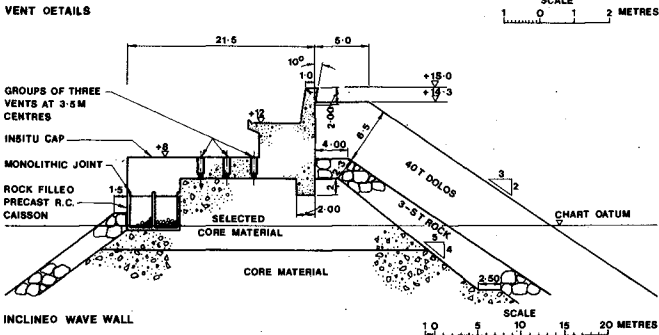
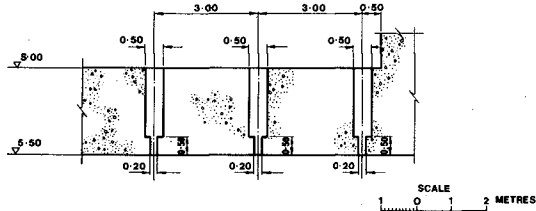


Fig. 10 Model test on contractor's alternative capping design

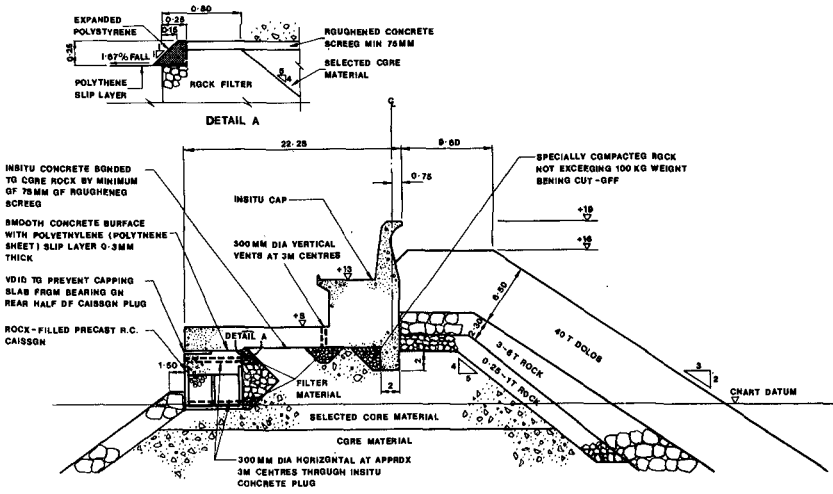


FIG. 11 FINAL DESIGN CAPPING DETAIL

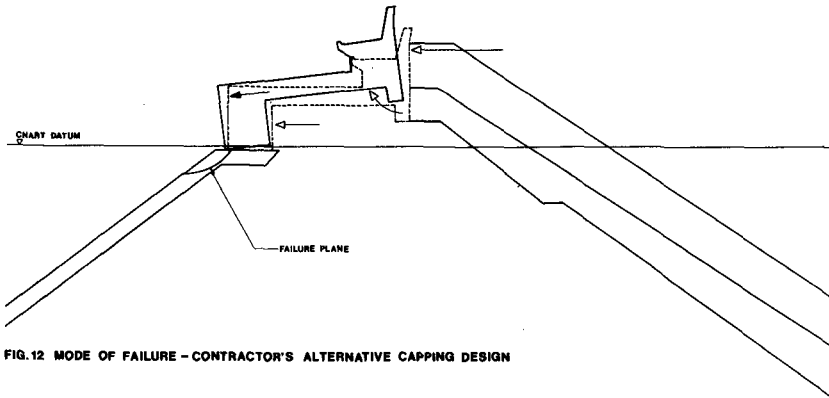


FIG. 12 MODE OF FAILURE - CONTRACTOR'S ALTERNATIVE CAPPING DESIGN

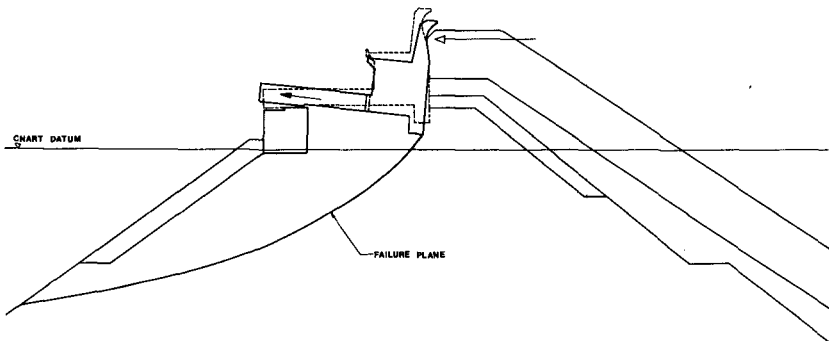


FIG. 13 MODE OF FAILURE - FINAL CAPPING DESIGN

Model tests on the alternative wave walls shown in Fig. 10 showed the value of curving the front of the wall, above the top of the dolos, to throw back the stream of water which comes over the dolos, thereby delaying the onset of overtopping. The proportions are based upon extensive research by Vera-Cruz at the LNEC hydraulic laboratory in Lisbon. Tests were made to determine the bending moments due to wave forces on the upper part of the wall which are of course very substantial. (Fig. 14)

The cap is cast in lengths of 15 m between joints. The total weight of each bay (excluding pipelines and the caisson below the sliding joint) ranges from 4,000 t to 5,000 t. The total wave force with the maximum individual wave in the 100 year storm is calculated to be 60 t/m, producing a bending moment at the base of the wave wall of 200 t f-m/m. Measurements on a model of the section of wave wall above road level gave a maximum prototype bending moment of 180 t f-m/m. Reinforcement in the cut off is designed to transfer a force of 160 t/m or 2,400 t/bay.

The vents in the cap, which are designed to minimise uplift pressures from water movements in the rubble core, are 300 mm diameter and are provided at 3 m centres. The bottom of each vent pipe is surrounded by a filter of 50 mm to 100 mm size rock to prevent leaching out of fine material. The vents have been observed to pass a mixture of air and water during a storm with maximum individual wave less than 10 m.

The joint between the capping slab and the small caisson is formed by a very careful steel float finish to the concrete which is covered by polythene sheeting to ensure a free sliding joint. Expanded polystyrene, as shown in Fig. 11, prevents any possible transfer of shear forces through stones being caught between the slab and the caisson. The sliding joint is formed only over half the top of the caisson. The other half, near the harbour, is covered with sand which is subsequently flushed out to leave a 100 mm gap. This is to ensure that vertical loads are applied to the caisson in a way which gives the most favourable distribution of stress on the foundation.

Root of Breakwater

The topography of the site is such that there is a clearly defined section of breakwater on shallow rock foundations before the bed drops steeply into deep water where the main cross-section, already described, is required.

The root section is not only protected by shallow water but also by a number of rocks to seaward so that waves are depth limited and tend also to be divided. The length closest in-shore is armoured with natural rock. Fig. 15 shows the design for a typical length of the root section in a depth of about 4 m at low water where the armour is 15 t dolos. It will be seen that the wave wall design is more closely related to the contractor's alternative cross-section (Fig. 4) for the main breakwater but the crest height and cut off arrangements were modified in light of the model test results for the main cross-section. No model tests

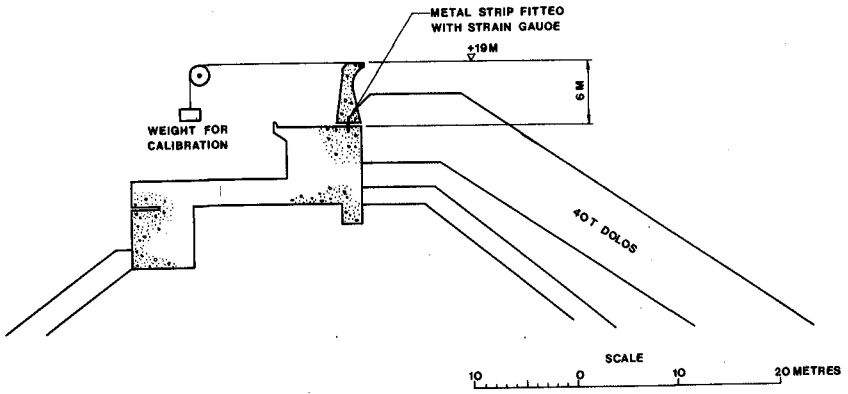


Fig. 14 Final design model study of forces on wave wall

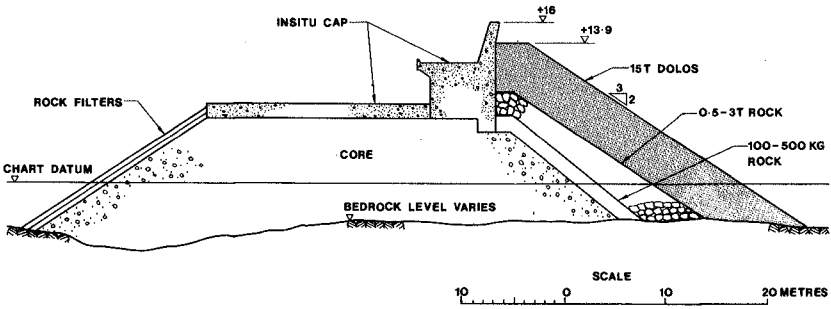


Fig. 15 Root of breakwater

were made for the root section because the broken nature of the sea bed makes any flume tests unrealistic.

Breakwater Head

The design of the head of the breakwater is still being studied on a wide flume at the LNEC in Lisbon. The original intention was to use a caisson head in the form of a vertical cross wall founded at about -24 m CD. This design would have had the advantage that future extension is very easy.

At this site it is necessary to design for earthquake forces and the worst wave attack is from WNW. Both factors require any caisson to be very wide to resist heavy forces from the shoreward side making this design more costly than a round head armoured with dolos.

Since the need for further extension, which would provide a second berth for ships of 1,000,000 DWT, appears to be very remote it has been decided to adopt a roundhead design.

Acknowledgements

This paper is produced with the kind permission of the Gabinete da Area de Sines which is gratefully acknowledged. Thanks are due to Mr. Berry of Bertlin and Partners who helped in the preparation of this paper. The author wishes to acknowledge the kind help of Mr. Merrifield who invented the dolos unit and generously made it freely available.

He also thanks many others interested in research on the behaviour of dolos units and in their use who have exchanged information privately and through papers and discussions at the 13th and 14th International Coastal Engineering Conferences.

References

1. Merrifield, E.M. "Dolos - a new breakwater and coastal protection block". The Dock and Harbour Authority, April 1970.
2. Morais, C. Campo "Irregular wave attack on a Dolos breakwater" 14th Conference on Coastal Engineering, Copenhagen, 1974.
3. Castonho, J.P. Carvalho and Vera-Cruz "Estudo da agitacao maritima no futuro porto de Sines" Lisbon 1972.
4. Carvalho, J.R. and Barcelo "Agitacao maritima na costa oeste de Portugal Metropolitano" Memoria no. 290 do Laboratorio Nacional de Engenharia Civil, Lisbon, Portugal, 1966.
5. Battjes, J. A. "Long term wave distribution at seven stations around the British Isles". N.I.O. Internal Report No. A.44, July 1970.
6. Ouellet, Y. "Considerations on factors in breakwater model tests" 13th Conference on Coastal Engineering, Vancouver, 1972.
7. Hudson, R. Y. "Laboratory investigation of rubble mound breakwaters" Proc. A.S.C.E., Waterways and Harbours Division, Sept. 1959.
8. Hudson, R. Y. "Concrete armor units for protection against wave attack - Report of ad hoc committee on artificial armor units for coastal structures" U.S. Army Engineer Waterways Experimental Station, Vicksburg, 1974.
9. Bjerrum, L. "Geotechnical problems involved in foundations of structures in the North Sea" Geotechnique 23, No. 3, 1973.
10. Newmark, N.M. "Effects of earthquakes on dams and embankments" 5th Rankine Lecture, Geotechnique 15, No. 2, 1965.
11. Goodman, R. E. and Seed "Earthquake-induced displacements in sand embankments". Proc. A.S.C.E. Vol. 92, SM2, March 1966.

12. Lillevang, O "Experimental studies of stresses within the breakwater armor piece "Dolos"." 15th Conference on Coastal Engineering, Honolulu, 1976 and private communications.
13. Zwamborn, J. A. and Beute "Stability of dolos armour units." ECOR Symposium, Stellenbosch, 1972.
14. Mettam, J. D. "Larnaca : new port for Cyprus." The Dock and Harbour Authority, June, 1969.

CHAPTER 145

EXPERIMENTAL STUDIES OF STRESSES WITHIN THE BREAKWATER ARMOR PIECE "DOLOS "

Omar J. Lillevang,* F.ASCE and Wayne E. Nickola**

Introduction

Stresses induced within the breakwater armor piece "Dolos", when it is subjected to loads, are not reliably inferred from the two-dimensional techniques of analysis used in conventional design of structures. Other methods that take the solid geometry of the dolos into consideration are available, and comprehensive application of one of them, three-dimensional photoelastic stress analysis, is reported here.

Breakage of Dolosse

Breakage experienced at 15 projects throughout the world, where nearly 150,000 dolosse ranging from 3 to 42 short tons (2,000 pounds or 907 Kg.) in weight are in use on breakwaters, is digested for the reader by Table I. It has been impressively low. With the exception of one project, Humboldt Bay, none of those dolosse are reinforced.

It is well known that most of the breakage of pre-cast armor pieces takes place during the manufacture and storing and during the construction of the breakwater. Table I illustrates it. Several details within the table that stand out are commented upon in the following notes, each note being identified by the line number from the table:

Line 3. According to the owner's report, the relative high breakage during manufacture stems from 100°F air temperatures during casting, which contributed to development of shrinkage stresses and minute cracking.

A wave storm during construction rolled numerous dolosse that were not yet nested in the armor matrix and they suffered impact fractures.

Breakage in service is attributed by the owner's report to battering during severe storms by loose large quarrystones.

Line 4. Most of the in-service breakage occurred when a localized area of the foundation eroded, and an abrupt subsidence into the pit caused 10 dolosse to break.

* Consulting Engineer, Los Angeles, California

**Manager of Applications Engineering, Photolastic, Inc., Malvern, Pennsylvania

TABLE I

DIGEST OF BREAKAGE OF DOLOSSE AT 15 LOCATIONS WORLDWIDE

Line	Project	Year	Number	Short Tons	Per Cent Broken		
					Making	Building	In Service*
1	Cap Aux Meules	'70	7,418	4	1.0	1.0	"Limited Number"
2		'70	3,934	6			
3	Crescent City	'74	246	40	2.4	6.5	2.8
4	East London	'64	2,000	19.75	0.15	0.5	0.25
5	Gaansbaai	'70	2,786	5	←---4.0---→		0.5
6		'70	865	13.5			
7		'70	928	18.5			
8	High Island	'73	6,619	27.5	"Insig."	0.8	0 ?
9	Hirtshals	'72	2,600	9.6	0.3	0.3	0.04
10	Honolulu	'74	13,692	4	0	1.4	0.2
11		'74	4,317	6	0	1.5	
12	Humboldt Bay	'71	4,794	42	0.02	0.02	0.75
13	Mossel Bay	'69	3,423	3	1.0	1.2	1.0
14		'69	2,634	6			2.0
15	Port Elizabeth	'67	14,266	3	4.0	"Neglig."	"Neglig."
16		'67	13,790	3	0.15		
17	Richards Bay	'72	28,084	5.5	0.3	0.8	"Insig."
18		'72		16.5			
19		'72		22.1			
20		'72		33.2			
21	Riviere au Renard	'72	7,921	5	3.3	0.6	"A Few"
22		'72	1,552	14	2.5	0.5	
23	Sandy Point	'69	500	7	←-----1.0-----→		
24	Table Bay	'69	5,900	3.4	0.6	0.14	0.01
25		'69	11,700	6.7	0.3	0.07	
26	" "	'71	3,000	3.4	←-----1.0-----→		0
27		'71	1,500	6.7			
28		'74	400	11.2			
29	Thorlakshórn	'75	2,600	9.9	0.4	1.2	1.0

* Includes breakage during consolidation of the structures, e.g. during first storms.

- Lines 5, 6, 7. Extensive litigation over the project has made factual discussion of breakage unavailable, but subsequent to consolidation of the structure it appears breakage has been nominal.
- Line 12. All but 26 of the dolosse contained steel bar reinforcement. The owner's representative reports the unreinforced versions were placed in low areas after completion of the armoring, and were thus "not integrated with other units". Of the 36 dolosse broken, 9 were not reinforced.
- Lines 13, 14. Owner's representative reports manufacturing breakage was reduced by halting cold-weather pours and changing the cementing ingredients, from 50/50 Portland cement/"slagment" to all Portland cement, during cold-weather pours.
- All the dolosse were made with "all-in", pit run sandstone aggregate, resulting in concrete that was sometimes over-sanded and sometimes under-sanded. Cement was 50% Portland and 50% "Slagment", blast furnace slag.
- Line 14. In-service breakage can be separated into 1.7% initial consolidation fractures caused by insufficient fitting, and by some abrupt localized downslope adjustments, and 0.3% breakage since the consolidations during the first storms.
- Line 15. Contractor tried to use a form made of concrete for the lower half of these dolosse. Those unyielding form surfaces proved to be warped and bulged, and tended to lock in the newly cast dolosse. Excessive force was needed to remove them. When the problem was diagnosed, new fabricated steel forms were substituted and breakage immediately was all but eliminated.
- Lines 21, 22. Heavy breakage during manufacture was attributed to removal of forms when castings were only 4 hours old.
- Line 29. Contractor surmises breakage relates to steam heating of the new castings while still in the forms.

The various projects listed in Table I include many variations in materials, in quality control during manufacture, in strength of concrete and in dimensional proportions. Thus it would be surprising if there were systematic relationships between breakage intensity and size, and there is none to be seen in the table.

Popov (4) and Danel, et al (1) have shown that armor pieces of different sizes but identically similar shape, and made of the same material, will break on impact with an unyielding surface from the same height of fall. The theory and Danel's experiments with dropping 295 tetrapods, of from 20 ounces to 25 tons weight, suggest design

loads for impulsive forces on the dolos would be the same for any size piece. With other types of loads, however, steady ones or dynamic forces less severe than impacts, stresses sustained by a dolos under design conditions may be larger or smaller as the size and weight of the piece is larger or smaller. In that case there would be reason to modify the larger pieces with stress reducing measures that smaller dolosse would not require.

Three approaches toward stress management which could be combined, or be mutually exclusive, are discussed in this paper. They are:

1. Incorporating steel bars to take the tensile stress;
2. Reduction of force moments by thickening the shank, and consequently shortening the flukes;
3. Reduction of stress concentrations at critical parts of the dolos by minor geometric modifications, viz. at the intersections of the flukes with the shank, to keep stresses below the modulus of rupture of the concrete.

The photoelastic tests indicate that, to have any useful effect toward preventing fracture of a dolos at its intersections of flukes with the shank, steel bar reinforcement would have to be placed so close to the skin of the piece that loss of the steel by corrosion in a short time would be unavoidable; the cost of such steel thus would be wasted and its effect would be ephemeral.

The tests suggest some stress reduction does result from thickening of the shank, but not significantly when the extent of thickening is kept below sensible limits that are proposed by the dolos' conceptor, Eric M. Merrifield. It is his view, expressed in personal communications with the senior author, that thickness of shanks in excess of 36 per cent of the height of the dolos would cause undesirable losses of interlocking characteristics.

Modifying the intersections between flukes and shank showed significant reductions of stress concentrations in the test pieces. Making dolosse of all sizes in future with a small curved fillet at those corners is proposed, not only to reduce stress concentrations but also to minimize concrete imperfections that often occur at sharp corners during pouring of concrete.

Photoelastic Stress Analysis

Among methods of experimental stress analysis that have been developed and proved is the photoelastic study of loaded two-dimensional plastic models. Either reflection or transmission of polarized light from or through various plastic materials yields light interference patterns that are rationally related to stresses within the plastic. Knowledge of this phenomenon is not new. It has been available with use of two-dimensional models for a century, and has been in widening use since the 1930's. Beginning with discoveries made in 1936, three-dimensional plastic models of complicated geometry have been loaded in

laboratory ovens, at temperatures above the softening point of the model material. In this temperature range the material does soften but remains linear and deforms elastically under the applied loads. After being held under load at carefully controlled specific elevated temperatures, the oven heat is systematically and very slowly withdrawn until the model piece has reached room temperature. During this cooling phase of the "stress-freeze" process, which may take several days, the loads on the model are sustained. When the model has reached room temperature the loads can be removed, but the stress patterns persist within the plastic. The model can then be cut into thin slices at any planes of interest, and polished. When polarized light is transmitted through those slices and examined with appropriate optical equipment each one shows the stress patterns that were induced along that plane by the test loads. Calibrations and rational computation procedures relate the patterns to definitive stress values. These techniques are commonly relied upon by industry. Complicated forgings, castings, fabrications, pressure vessels, struts, bearing housings and a host of other shapes and devices have been evaluated by this method. Except for some work that may have been done in England, it apparently has not been used before on a breakwater armor piece.

Description of Models

Sixteen three-dimensional models of dolosse for the present tests were cast from photoelastic thermal-setting plastic. All were made with the dimension h equal to 6 inches, which is 15.24 centimeters. As will be seen in several figures in this paper, the dimension h is present in two ways in the dolos. It is the overall height from tip to tip of two adjoining flukes, and is also the overall length of the piece, measured parallel to the axis of the shank. Half the models were made with shank thickness 32 per cent of h and the other half with 35 per cent. For each thickness ratio, four different versions were cast that varied the geometric details at the intersection of the fluke with the shank. The traditional dolos, with sharp intersections between fluke planes and the planes forming the shank, was tested at both thickness ratios. Those specimens were identified by codes 32HS and 35HS, the letter S identifying the sharp intersection characteristic for pieces with shanks 32 per cent as wide and 35 per cent as wide, respectively, as the height. Other versions of corner geometry, also tested for both 32 and 35 per cent shank thickness, had chamfers created by planes (32HC and 35HC), a small-radius circular fillet (32HF and 35HF), and a larger-radius circular fillet (32H ϕ and 35H ϕ).

In the stress-freeze tests, stresses frozen into the model dolosse were produced with two different loading patterns. In the "Tension" series, equal forces that were all directionally parallel with the shank's axis were applied at the ends of the four flukes. Pairs of forces were oppositely directed, in a normal sense placing the shank in tension; therefrom the "Tension" term for describing those tests. In the "Torsion" series, equal forces were again applied at the ends of the four flukes, but acting in planes perpendicular to the axis of the shank and directed to twist the shank; therefrom the "Torsion" term for that series. Sixteen models were made and stressed. Fifty-eight sections were sliced from various parallel or intersecting planes, to find the stress characteristics within the dolosse resulting with

all the variations that were involved. Figure 1 shows and compares the four details of the corner that were studied, being cross-sections in

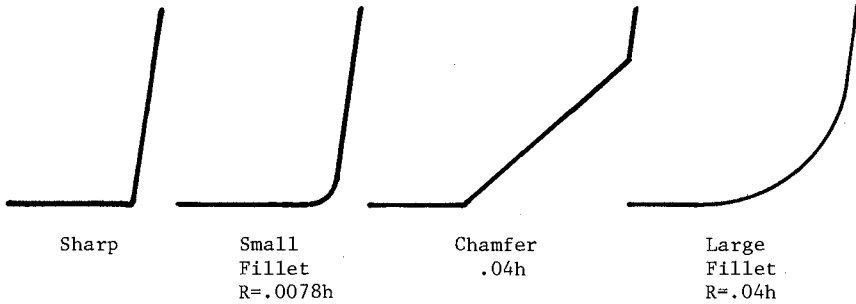


Figure 1

the plane common to both the fluke axis and the shank axis. As illustrated in Figure 2, the chamfer tapered to a point in the corners between planes either side of the ones cut for the profiles that are shown in Figure 1. The circular fillets in those same two flanking corners had to have radii 1.5 times as long as those in the central corner, because the angle of intersection of planes adjoining ac is larger than the angle of intersection along ab. The circular fillets did not taper to a conical point.

All the models were made with flukes whose cross-sections normal to their axes were not symmetrical octagons. The left side of Figure 3 shows the awkward geometry that develops at the intersections of flukes with the shank if a symmetrically octagonal fluke is made. To eliminate the intersection problem a slab of constant thickness, S, should be taken off the whole octagonal side of the fluke, above the shank at the intersection ab. If the maximum breadth of the octagon at the tip of the fluke is the commonly used .20h, and t is the thickness or breadth of the shank octagon, then the thickness of the slab to be removed, shown at the right side of Figure 3, is:

$$S = \frac{0.12132(.2t/h - t^2/h^2)}{(t/h)\tan 22.5^\circ - 1} (h)$$

The models with chamfered and filleted corners, consistently for comparison values, also were made with flukes of asymmetrical cross-sections.

Rubber moulds for casting all the photoelastic models were formed by pouring a silicone rubber compound around a precisely machined acrylic resin master dolo that had sharp corners. To modify the master in order to make moulds for the chamfer and fillet versions, pattern maker's beeswax was hand-tooled into the corners of the master pattern. At the scale of these models, the corners of the hand-molded chamfer planes were not as sharp as one would expect intersections to be in the prototype, where structural steel plate is the likely material from which such forms would be fabricated. Because the

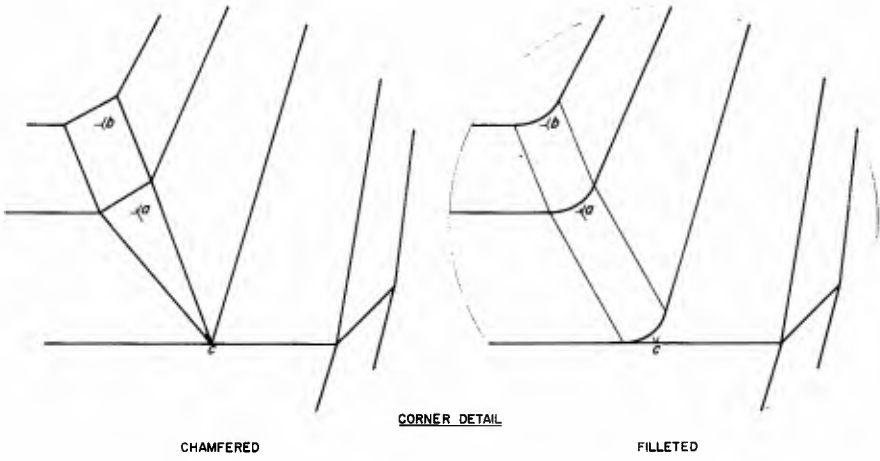


Figure 2

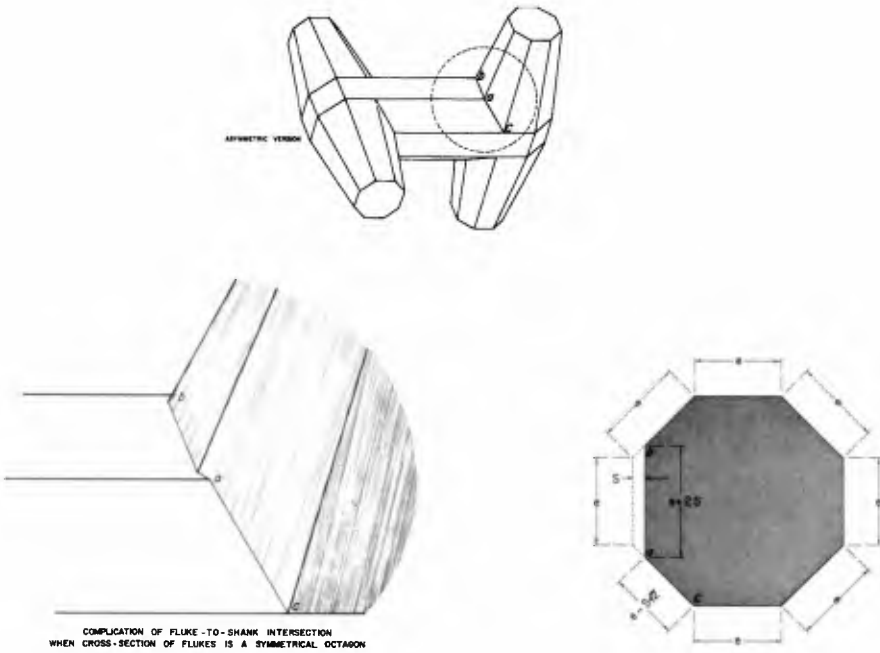


Figure 3

chamfer intersections probably were slightly rounded, the stress concentrations shown by the photoelastic models with the chamfered corners probably are less severe than they would be at prototype size, or than they would have been had the model chamfers been precisely machined instead of being hand formed of beeswax on the master pattern.

The theory of photoelastic stress analysis is well covered in reference works that are readily available in technical libraries, so there is no development of the theory in this paper. However, the laboratory techniques employed in the present tests and the analytical procedures that were followed deserve description.

A reconnaissance test program was carried out before the stress freeze models were made, to compare at least qualitatively the effects of six different arrangements of loading. For the reconnaissance, a specially compounded aluminum-filled epoxy resin was selected, and model dolosse cast from it were clad with a thoroughly bonded bi-refractive coating material. The bond was made with an epoxy-based reflective cement. A reflection polariscope was used to view the model while it was under each loading arrangement. Elastic deformations induced by the loads were transferred from the dolos to the cladding by shear forces developed at their interface. When polarized light was reflected from the surface of the model through the bonded layer, the coating exhibited patterns of birefringence which were quantitatively analyzed. Out of those preliminary tests it was concluded that the "Tension" and "Torsion" loading patterns previously described would best develop the internal stress information that was wanted from the stress-freeze photoelastic procedures.

Internal Stress Data, Quasi-Dimensionless Form

Stresses that were shown in the photoelastic models were reported in quasi-dimensionless form, to enable easy calculation of stresses in prototype dolosse of any size and for any selected value of the moment and shear producing forces. Stresses in the prototype were related to stresses in the model by:

$$\sigma_p / \sigma_m = (F_p / F_m) (h_m / h_p)^2$$

Where σ_p , σ_m = Stress in prototype and model, respectively
 F_p , F_m = Load on prototype and model, respectively
 h_p , h_m = Corresponding dimensions of prototype and model, respectively.

If F_p is expressed in units of the total dead weight of the prototype dolos, and ρ is the unit weight of the concrete from which the prototype dolos is made, and V is the volume of the dolos, then

$$\sigma_p / \sigma_m = (n V \rho / F_m) (h_m / h_p)^2$$

where n is the number of units of the dolos' weight, a convenient way to express the design load. All models were six inches high, i.e. $h = 0.5$ feet. Thus, for models where the shank thickness t is 32 per cent of h , and Volume consequently equals $.1550h^3$,

$$\sigma_p = .03875 h_p \rho n (\sigma_m / F_m)$$

For the models with $(t/h) = 0.35$ the volume is

$$V = .1739h^3,$$

So for those models it can similarly be shown that

$$\sigma_p = .043475 h_p \rho n (\sigma_m / F_m)$$

The test results for surface stresses then could be presented as the parameter $\sigma/\rho h$, and for internal stress components on the plane of each slice as $(\sigma_1 - \sigma_2)/\rho h$. In all cases, the numerical values of the parameter were calculated with n equal to 0.5, that is to say they are stresses induced by two forces whose sum is the dead weight of the dolos. Multiplying the numerical values of the stress parameters by the unit weight of concrete intended for a prototype dolos, in pounds per cubic foot, and the product by the height of that dolos in feet, yields stress in the prototype in pounds per square inch.

Presentation of Results

Figures 4, 5 and 6 are examples of the forms in which stress analyses from most of the 58 slices in the complete test program were reported. Figures 4 and 5 are examples of reports on those slices that presented "Tension" test results and Figure 6 is for a "Torsion" test.

At upper right on Figures 4 and 6 the dimensions of the dolos are shown and the loading patterns of the forces F are displayed.

At top center of all sheets like Figures 4 and 6 is shown where the reported-upon slice was cut from the stress-freeze three-dimensional model.

In the photoelastic examination of each slice the optical system presented the lines of constant stress, the isochromatic fringe patterns $(\sigma_1 - \sigma_2)$, at full model size. It also projected the slices at ten times model size. The enlarged projections were examined to identify the locations of maximum stress concentrations at the surface and the direction of steepest gradient of stress variation within the dolos. That part of each slice was reproduced as a line drawing at the lower left of all the sheets like Figures 4 and 6, showing the surface lines of the fluke and of the shank and the intersection profile and the "contours" of the stress parameter $(\sigma_1 - \sigma_2)/\rho h$. These slice displays were oriented to place the direction of the visually determined transect of steepest gradient of stresses parallel with the horizontal direction of the data sheet.

The diagram at lower right on all the sheets like Figures 4 and 6 is a direct projection, from the left, of the stress values at the surface of the dolos, and illustrate the rate of stress increase toward

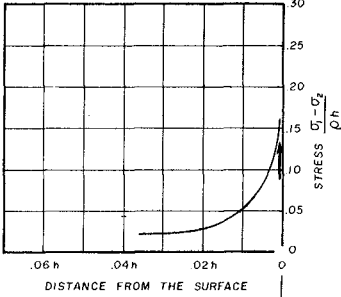
SURFACE AND INTERNAL STRESS PATTERNS
IN THE BREAKWATER ARMOR PIECE "DOLOS"

SHARP CORNER ; $t/h = 0.32$

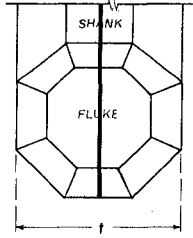
ANALYSIS OF SLICE A

TENSION TEST, NO. 32.HSIA

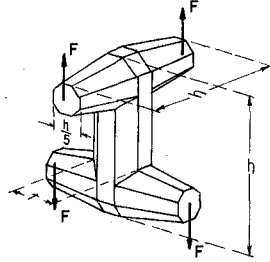
INTERNAL STRESS
ALONG THE TRANSECT



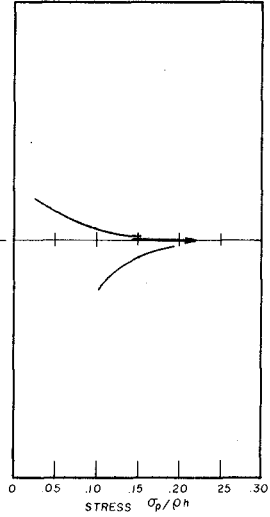
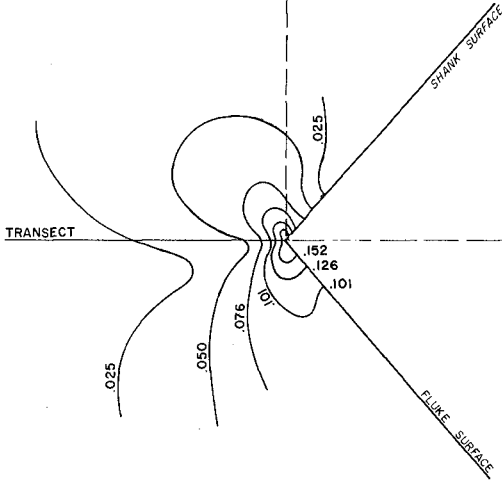
LOCATION OF THE SLICE



LOADING PATTERN



UNIT WEIGHT, ρ
WEIGHT, $W = \rho V$
VOLUME, $V \approx 0.679 t^{1.297} h^3$



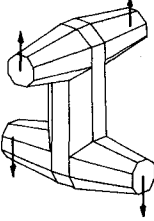
CONTOURS OF EQUAL STRESS
WITHIN THE DOLOS
NEAR THE JUNCTION OF SHANK & FLUKE
($\frac{\sigma_1 - \sigma_2}{\rho h}$, $F = \frac{W}{2}$)

STRESS AT THE SURFACE
OF THE DOLOS

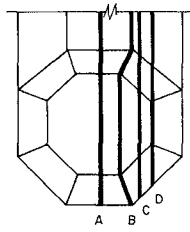
Figure 4

CONTOURS OF INTERNAL STRESSES, $\sigma_1 - \sigma_2$
 IN THE BREAKWATER ARMOR PIECE "DOLOS"
 "TENSION" LOADING
SHARP CORNERS

LOADING PATTERN



LOCATION OF SLICES

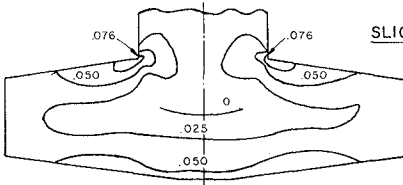


TEST NO. 32 HS I

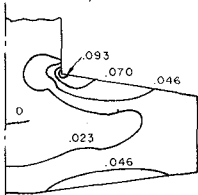
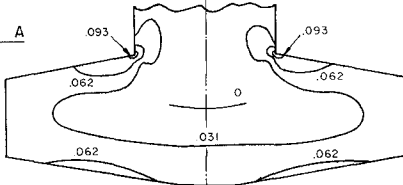
$t/h = 0.32$

TEST NO. 35 HS I

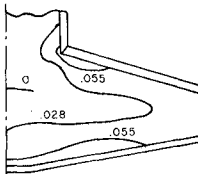
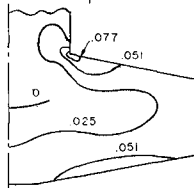
$t/h = 0.35$



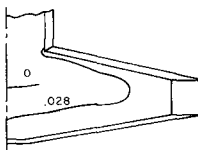
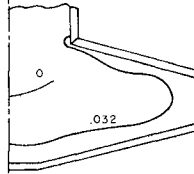
SLICE A



SLICE B



SLICE C



SLICE D

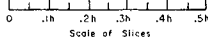
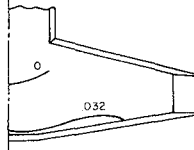


Figure 5

SURFACE AND INTERNAL STRESS PATTERNS
IN THE BREAKWATER ARMOR PIECE "DOLOS"

SHARP CORNER ; $t/h = 0.32$

ANALYSIS OF SLICE B

TORSION TEST, NO. 32 HSB

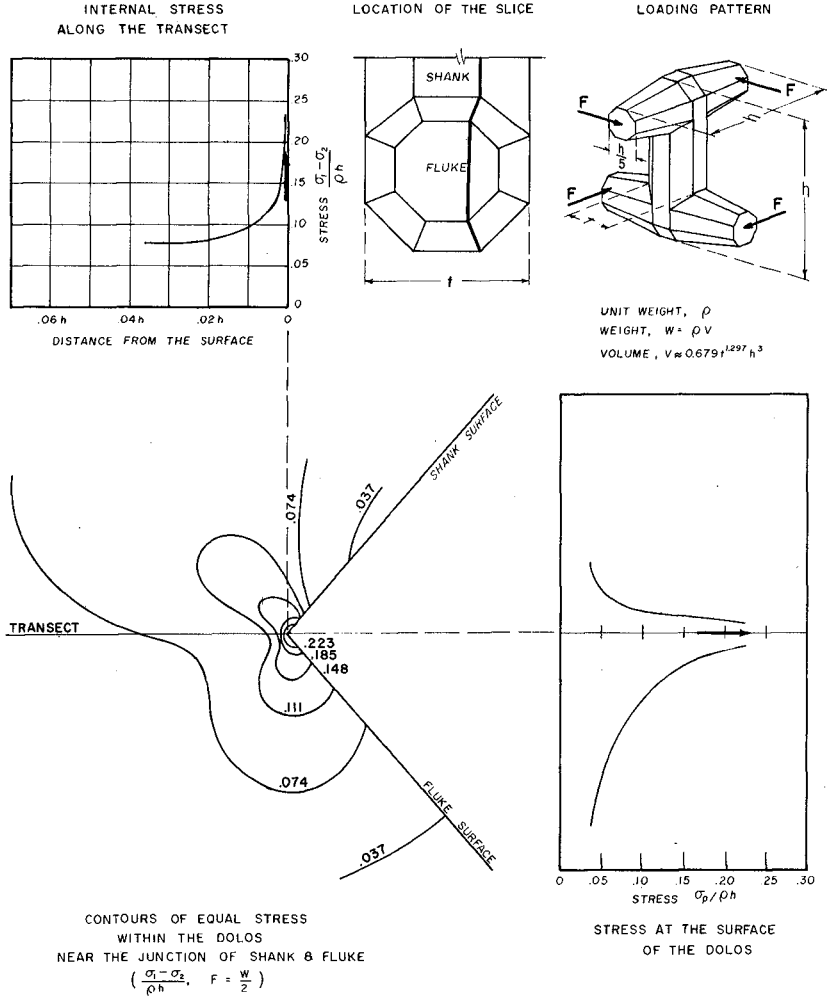


Figure 6

the maximum concentration at the corner. These values at the surface are the tensile stress, because σ_2 must be zero at a free surface and the load pattern is such that σ_1 in this case must be tensile.

At top left, the internal stress variation along the transect of steepest gradient was projected upward from the cross-section at lower left.

Stress gradients in the sharp cornered dolosse were extremely steep at the surface, and absolute determination of values at the corners was not possible. This is indicated on all plots of surface stress and of internal stress for sharp cornered pieces by small arrows, emphasizing that the value of $\sigma/\rho h$ was not determined, and the curves stop short of joining on the Surface Stress graph and of reaching the $h = 0$ abscissa on the Internal Stress graph. In fact, if it were possible to make an absolutely sharp corner, the $h = 0$ line would be the vertical asymptote of the internal stress curve.

Four slices were taken from each "Tension" model for analysis. In models with sharp corners and with chamfered corners and with small radius filleted corners the slices were all taken at the planes described at the upper right of Figure 5. The lower parts of Figure 5 show the equal stress contours for each of the whole slices of the Tension Tests for Sharp Corners, not just the enlarged detail close to the corners that were reproduced on Figures 4 and 6. As before, numerical values for the maximum concentration of stress in the corners could not be shown, but the analysts estimated they would be on the order of 0.30 to 0.32. The rapidity with which stresses reduce, as one considers planes removed from the shank's shoulder at Slice B, is apparent when one examines the stress patterns on Figure 5 of slices C and D at successively greater offsets from the axis of the piece.

There were three slices removed from each "Torsion" test model that had sharp or chamfered or short-radius filleted corners. Two of the locations are shown at the upper right on Figure 7 and the third, a surface slab containing the corner and called Slice A, is shown on the sketch at upper left. Stress contours for all three slices are shown as before, and orthogonal trajectories of the principle stresses in Slice A are also shown. The solid orthogonals indicate the direction of the maximum tensile stress, and the dashed ones indicate the direction of the maximum compressive stress. These stress trajectories are not to be confused with the lines of constant stress, isochromatic fringe patterns ($\sigma_1 - \sigma_2$), referred to as "stress contours" before in this paper. The stress trajectories represent the force flow lines of principal stress direction and are of variable stress intensity along the trajectory. Data sheets similar to Figure 7 were prepared for the Torsion tests of the chamfered and of the small radius filleted corners, but are not reproduced here.

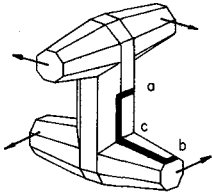
When all data were available from testing the first three variants, with sharp, chamfered and small-radius filleted corners, comparisons were made that suggested yet another corner variation should be investigated. Table II shows maximum stress values at the surface in the corners of the three variants, all expressed as fractions of the stress

STRESS TRAJECTORIES AND CONTOURS OF TORSION INDUCED INTERNAL STRESSES, $\sigma_1 - \sigma_2$ IN THE BREAKWATER ARMOR PIECE DOLOS

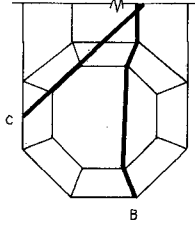
SHARP CORNER; $t/h=0.32$

TORSION TEST NO. 32 HS

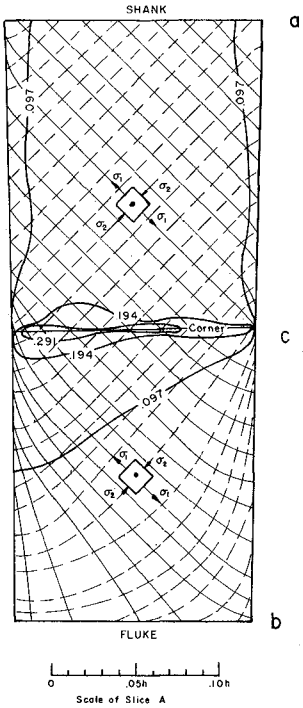
LOADING PATTERN AND LOCATION OF SLICE A



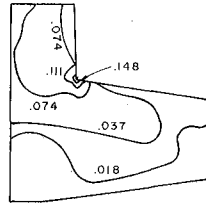
LOCATION OF SLICES B & C



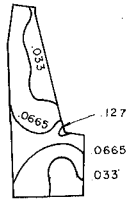
SLICE A



SLICE B



SLICE C



DEVELOPED VIEWS OF THE SLICES

Figure 7

analysts' best estimate of the corner concentration stresses in the sharp cornered models, which is 0.30 ϕ h.

TABLE II

RELATIVE MAGNITUDES OF SURFACE STRESS CONCENTRATIONS

		<u>Sharp Corners</u>	<u>Small Fillet Corners</u>	<u>Chamfered Corners</u>
t/h = 0.32	"Tension"	1.00	0.73	0.63
t/h = 0.32	"Torsion"	1.00	0.80	0.63
t/h = 0.35	"Tension"	1.00	0.67	0.67
t/h = 0.35	"Torsion"	1.00	0.87	0.49

Considering the analysts' view, that imprecise moulding of intersections of the chamfer planes with the fluke and shank planes tended toward understatement of stresses by the chamfered models, it appeared that the minute-radius fillet reduced stresses essentially as well as did the chamfer.

Guided by published stress reduction factors for details of common structures, a judgment was made that a dolos with circular fillets of a radius equal to 4 per cent of the dimension h should be tested. With larger radii, the published factors suggested, incremental reduction of stress concentrations became less significant. There was a concern, lest the fillet become so large that the very desirable nesting or tangling characteristic of dolosse in an armor matrix should be impaired. New stress-freeze model dolosse were made, with circular fillets of .04h radius on the corner labelled ab in Figures 2 and 3 and of 1.5 x .04h on the side corners, ac of Figures 2 and 3. As before their h dimension was 6 inches and the same Tension and Torsion loads were applied.

There were models, also as before, where the shank thickness was 32 per cent of h (t/h = .32) and where it was 35 per cent. Figures 8, 9, 10 and 11 show the results, and are directly comparable with Figures 4-7 inclusive. The pattern of slices taken from "Tension" models in these experiments was modified, as can be seen by comparing the descriptive drawing at the upper right of Figures 5 and 9. By cutting Slice C from the large fillet models on a plane radial to the fluke axis it became possible to identify the inclination and direction of the plane through the crotch of the dolos where all stress gradients were of maximum steepness. The new slice E_A was then cut along that plane. As can be seen on the slice E_A stress contour plot, at the bottom of Figure 9, the stress magnitudes are negligible along that plane. Thus, recognizing that the E_A plane is perpendicular to the A slice, and nominally coincident with the maximum gradient transect lines of the A and B slices, it is practical and conservative to use the internal stress values from slices A and B as indicative of the maximum principal stress σ_1 (tension) rather than the principal stress difference $\sigma_1 - \sigma_2$.

In certain instances it is desirable to know the shear stress magnitude in concrete. This information is readily available from the

SURFACE AND INTERNAL STRESS PATTERNS
IN THE BREAKWATER ARMOR PIECE "DOLOS"

ENLARGED FILLET CORNER; $t/h = 0.32$

ANALYSIS OF SLICE A

TENSION TEST, NO. 32Hφ1A

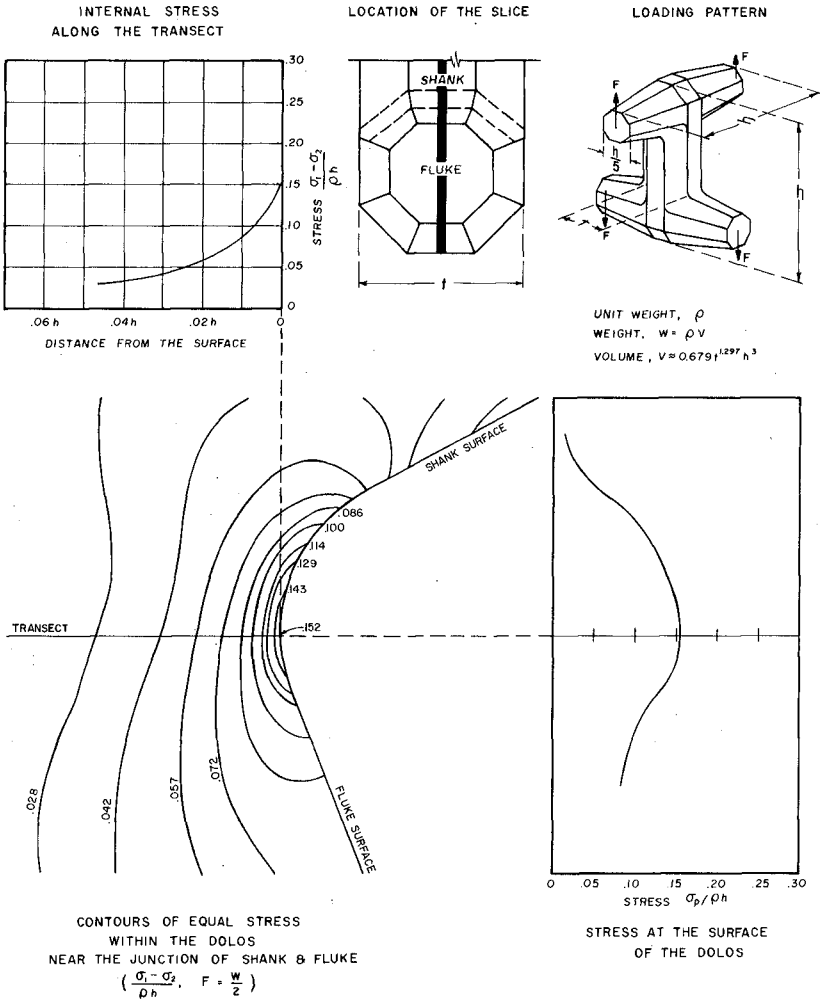


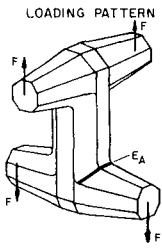
Figure 8

CONTOURS OF INTERNAL STRESSES, $\sigma_1 - \sigma_2$

IN THE BREAKWATER ARMOR PIECE "DOLOS"

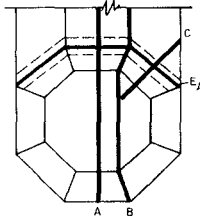
"TENSION" LOADING

ENLARGED FILLET CORNER; $t/h = 0.32$ & 0.35

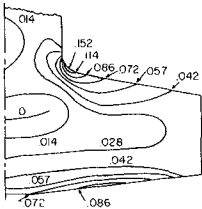


$t/h = 0.32$

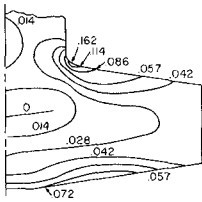
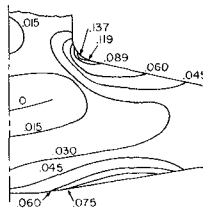
LOCATION OF SLICES



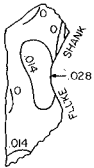
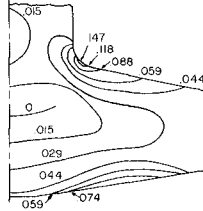
$t/h = 0.35$



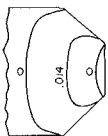
SLICE A



SLICE B



SLICE C



SLICE E_A

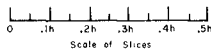
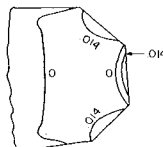


Figure 9

SURFACE AND INTERNAL STRESS PATTERNS
IN THE BREAKWATER ARMOR PIECE "DOLOS"

ENLARGED FILLET CORNER; $t/h = 0.32$

ANALYSIS OF SLICE B

TORSION TEST, NO. 32H48

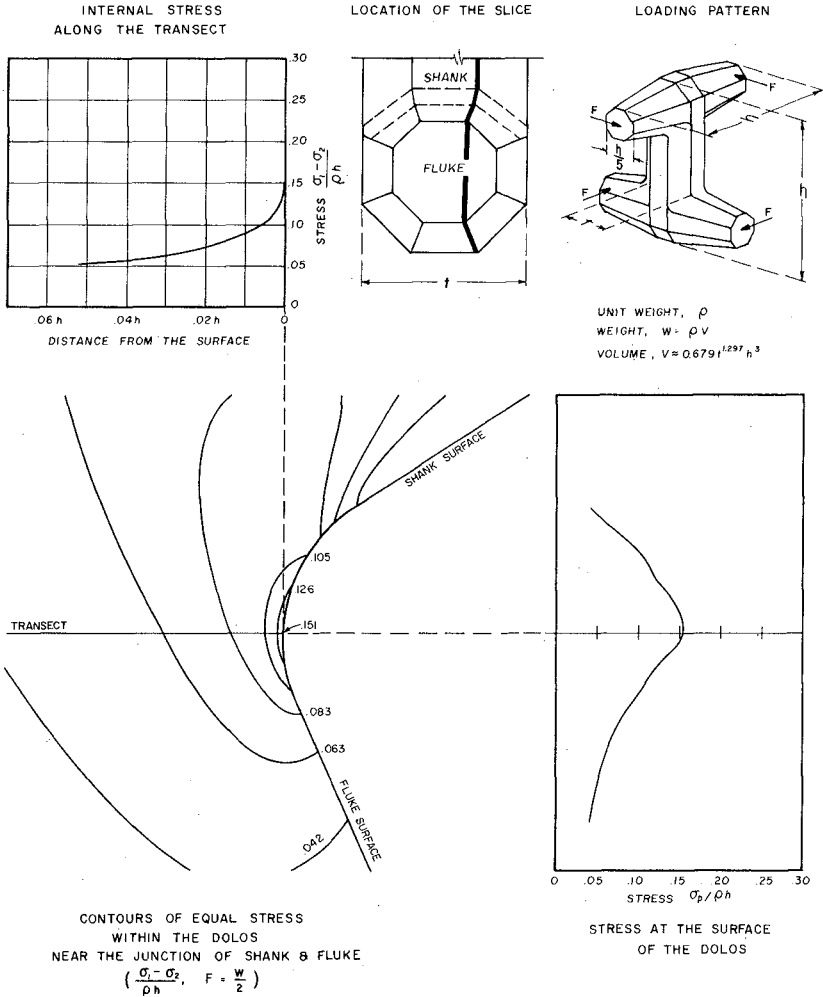


Figure 10

CONTOURS OF INTERNAL STRESSES, $\sigma_1 - \sigma_2$
 IN THE BREAKWATER ARMOR PIECE "DOLOS"
 TORSION LOADING

ENLARGED FILLET CORNER; $t/h = 0.32$ & 0.35

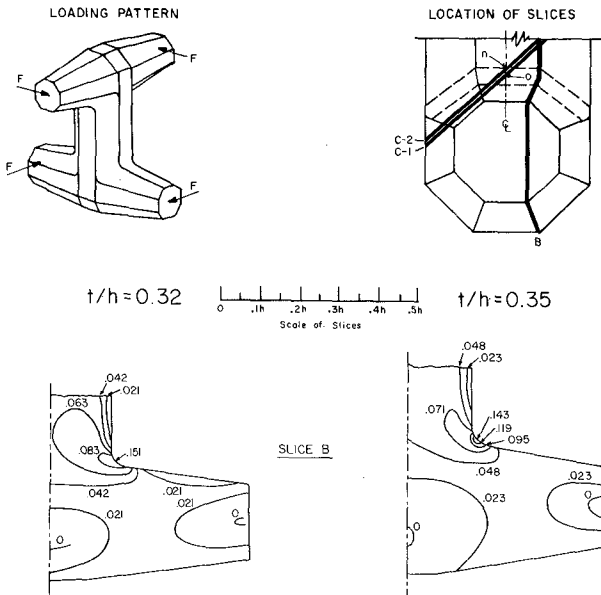


Figure 11

stress contours. The contours as shown are for the difference of principal stresses ($\sigma_1 - \sigma_2$). From Mohr's Circle the maximum shear stress τ_{\max} is:

$$\tau_{\max} = (\sigma_1 - \sigma_2)/2$$

and the contours truly display $2 \tau_{\max}$ as shown.

Figures 12 and 13 each summarize and provide direct visual comparison of the internal stress gradients for all sixteen of the models that were tested. Figure 12 compares the effects of corner details and shows, to the immediate right from each graph, the numerical value of the stress parameter at the surface for each of the three corners that were not square. Recalling the analysts' estimate, that the sharp cornered dolosse had surface stress values between .30 and .32 ρh , it appears the circular fillet with radius of .04h would reduce the critical stress in the corners by 50 per cent, at least, of the sharp cornered stress value.

Figure 13 presents the same curves as Figure 12, but arranged to evaluate the effect of varying the ratio of shank thickness to dolos height, t/h .

EFFECTS ON STRESS OF THREE
FLUKE-TO-SHANK CORNER DETAILS

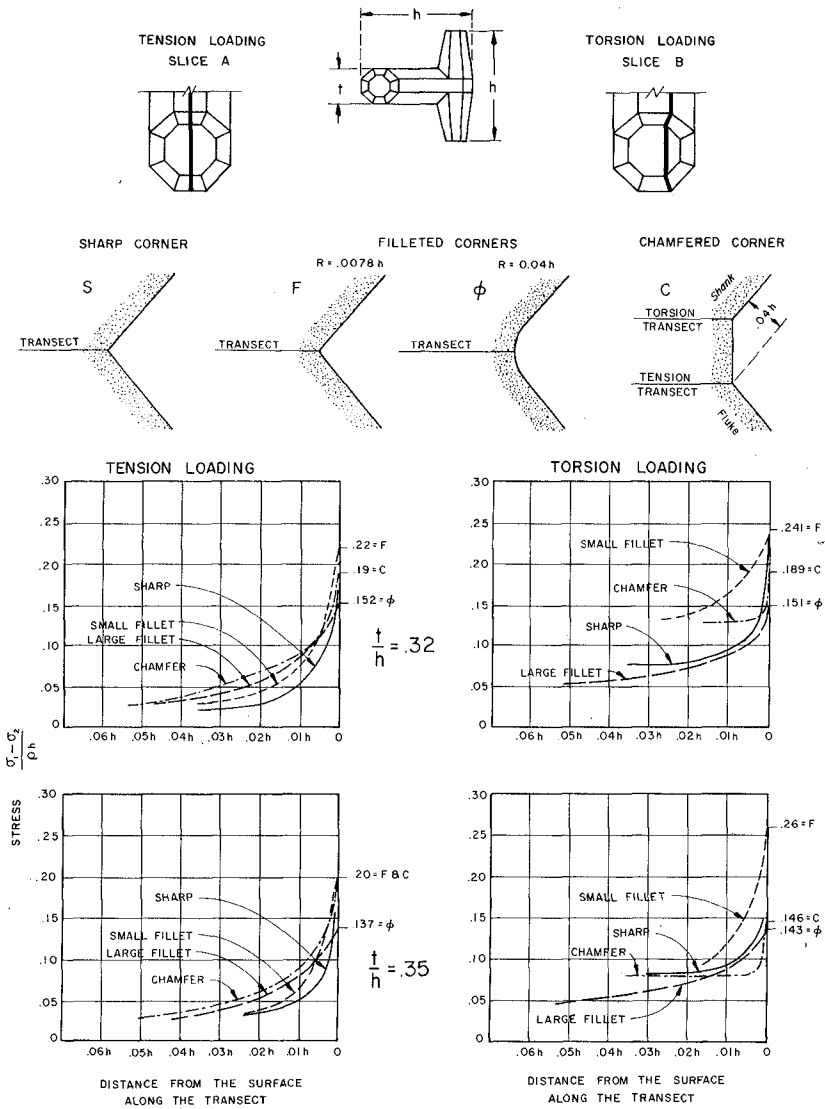
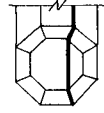
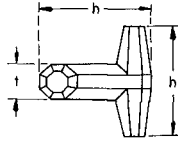
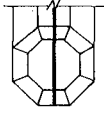


Figure 12

EFFECTS ON STRESS OF VARYING THE SHANK THICKNESS, t

TENSION LOADING
SLICE A

TORSION LOADING
SLICE B



TENSION LOADING

TORSION LOADING

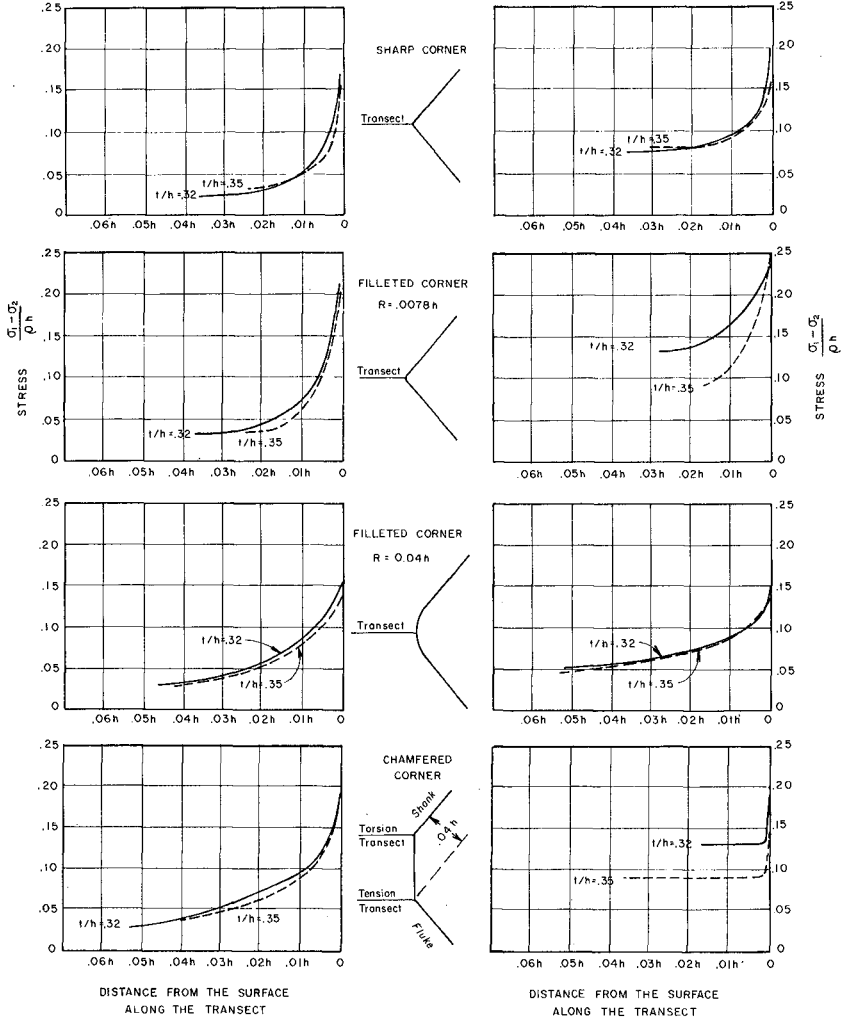


Figure 13

Flexural Strength of Concrete

In 1957 Paul Klieger (3) presented data from comprehensive flexural tests of concretes that are remarkably systematic and are useful in considering fracture stresses in the dolos.

Beams 6 by 6 inches and supported over 18-inch spans were loaded to failure, and the tensile strengths of their concretes were calculated as the Modulus of Rupture. Strengths were determined for ages varying from one day to one year. Six-inch cubes were prepared from the ends of the broken beams and tested as compression specimens. A sufficient number of standard 6-inch diameter by 12-inch length standard cylinders also were cast from the same batches of concrete made for the beams, and they also were broken in compression. That permitted developing a reliable factor for converting cube compressive strengths to standard cylinder compressive strengths. It was determined that, for the aggregate being used, the ratio of 6" by 12" cylinder compressive strength at all ages of test specimens to the compressive strength of 6-inch modified cubes was 0.93.

One of the experimental series dealt with a concrete typical of marine structures, made with ASTM Type II cement and with air entrainment of 4.5%. One hundred forty-three test beams of ages ranging from one day to one year were tested in flexure. There is very little scatter of data from the straight line $R = 1.1 (f_c)^{.75}$, where

R = Modulus of Rupture, the flexural tensile stress in pounds per square inch at the beams' extreme fibre at loads producing failure;

f_c = compressive strength of a standard cylinder at the age of the flexural test specimen.

Figure 14 comes from another arrangement of Klieger's data (points not plotted), to show how the Modulus of Rupture in his tests was found to vary with age of the concrete. It can be put to good practical use when making judgments as to how soon after casting a dolos one can handle it, with acceptable risks of damage to its structural integrity.

Concrete for dolosse has commonly been specified with a minimum acceptable compressive strength at 28 days of 5,000 pounds per square inch, roughly 350 Kg/cm². The Modulus of Rupture at age 28 days for that specified compressive strength could be estimated from the Krieger experiments at 650 pounds per square inch, or 46Kg/cm². At one day, according to Figure 14, that same concrete might have a flexural strength of 200 pounds or more per square inch, or 15 Kg/cm².

A project being planned in the United States will use dolosse of the unprecedented weight of 62 short tons, which is just over 56 metric tons. If made from concrete with a specific gravity of approximately 2.4, their h dimension will be 17.5 feet, or 5.33 meters. On the same project smaller dolosse also will be placed, weighing 40 and 11 short tons. Respectively, their h dimensions would be 15.1 and 9.8 feet. Table III has been calculated from the transect curves of Figures 12

VARIATION IN MODULUS OF RUPTURE WITH TIME

TYPE II CEMENT CONCRETE WITH 4.5% AIR ENTRAINMENT
 FABRICATED AT VARIOUS TEMPERATURES, 73°F TO 105°F
 (Journal ACI, Vol. 29 No. 12, June 1958)

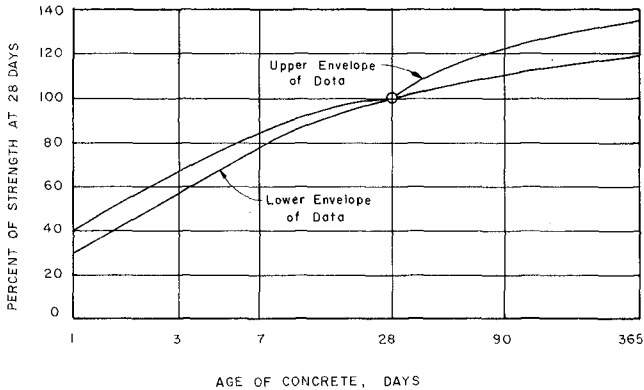


Figure 14

and 13 to illustrate the stress magnitudes, under the loads F of the photoelastic experiments, at various depths in the three sizes of dolosse for the planned project.

Good practice in reinforced concrete design for hydraulic structures, particularly for a sea water environment, requires that there be substantial thickness of dense, hard, sound concrete between embedded steel and the water that surrounds or splashes the concrete. A 3-inch cover, which is 7.5 cm, commonly is required and 4 inches, nominally 10 cm, or more is required by some.

The stresses displayed in Table III suggest the reason for the low breakage experience with dolosse at existing projects that achieved uniformly high quality concrete and that were faithfully built in compliance with appropriate breakwater designs. The largest existing dolosse with sharp corners are those at East London, South Africa, and weigh just under 20 tons each. Larger ones at Hong Kong's High Island East Cofferdam (27.5 tons), Richards Bay, South Africa (33 tons), Crescent City, California (40 tons), Humboldt Bay, California (42 and 43 tons) and Sines, Portugal (44 tons) all are chamfered. Under the loading conditions used in calculating the Table III stresses, all would have surface maximum stresses of less than 650 pounds per square inch. At 4 inches depth, the closest to the surface many experienced

TABLE III

FLEXURAL STRESS AT THE PEAK SURFACE CONCENTRATION POINT
AND σ_1 - σ_2 AT DEPTHS, NEAR THE PEAK POINT

$$t/h = 0.32; \rho = 150\#/cu.ft.; F = 0.5W.$$

(Pounds Per Square Inch)

Position	Corner Treatment	Dolos Size & Mode of Loading					
		11 Tons h=9.8'		40 Tons h=15.1'		62 Tons h=17.5'	
		Tension	Torsion	Tension	Torsion	Tension	Torsion
Surface	Sharp	440?	440?	680?	680?	790?	790?
Peak	Sml.Fillet	325	355	500	550	580	635
Stress	Chamfered	280	280	430	430	500	495
	Lge.Fillet	235	220	360	340	420	395
<hr/>							
2"	Sharp	50	125	105	215	140	255
From	Sml.Fillet	75	210	155	360	200	440
Surface	Chamfered	115	195	205	300	250	350
	Lge.Fillet	95	115	185	195	230	235
<hr/>							
4"	Sharp	30	110	65	180	80	215
From	Sml.Fillet	40	195	95	310	125	370
Surface	Chamfered	55	195	150	300	190	350
	Lge.Fillet	55	90	120	160	155	190

engineers want reinforcing steel placed in concrete immersed in or splashed by sea water, the stresses shown in Table III are so low that the effect of steel bar reinforcement on crack prevention might not be discernible. Such steel then would be redundant at best, because it could only act if some mortal blow striking the dolos opened a crack the bars would be incapable of preventing. For some time, the bars in such a cracked dolos might stop separation into fragments, but probably only so long as oxygenated sea water seeping to the bars through the crack had not yet completed corroding the bars to the point of severing or to exerting swelling stresses on the surrounding concrete that typically makes it spall away and create failure by that condition. It appears that reinforcing steel in dolosse must be an economic waste. However, a possibly stronger reason for not burying them within the piece is a concern such bars could induce shrinkage cracks, during hydration of cement in the freshly poured concrete.

The authors are persuaded that large dolosse, say 30 tons and heavier, need to have eased corners between flukes and shank to reduce stress concentrations to prudent maximum levels. The use of central fillets of radius .04h and side fillets of .06h radius is seen as the best means for easing those corners, because important collateral benefits in concreting derive. Other easing geometries that are almost as effective in stress reduction do not provide as clear a concreting

advantage. The relative simplicity of incorporating the fillet details when fabricating steel forms suggests it will be useful to have filleted corners in dolosse of all sizes, the concrete placing advantages being the justification.

The viewpoints expressed in the foregoing paper and conclusions reached are those of the authors. The photoelastic testing that made the paper possible were performed for Public Service Electric and Gas Company, of Newark, New Jersey. Their permission to publish the test data for the benefit of practicing engineers is acknowledged, with appreciation.

References and Bibliography

1. Danel, P., Chapus and Dhaille, "Tetrapods and Other Pre-cast Blocks for Breakwaters", ASCE Waterways and Harbors Journal, Sept. 1960.
2. Hetenyi, M., "Handbook of Experimental Stress Analysis", John Wiley and Sons, Appendix II.
3. Klieger, P., "Effect of Mixing and Curing Temperature on Concrete Strength", Journal American Concrete Institute, June 1958, Proceedings Vol. 54, p. 1063.
4. Langhaar, H. L., "Dimensional Analysis and Theory of Models", John Wiley and Sons.
5. Popov, E. P., "Introduction to Mechanics of Solids", Prentice-Hall, Inc. 1968.
6. Redner, S., "Encyclopedia of Polymer Science and Technology", John Wiley and Sons, Vol. 9, pgs. 590-610.

CHAPTER 146

EFFECT OF BROKEN DOLOSSE ON BREAKWATER STABILITY

by

D. Donald Davidson¹ and Dennis G. Markle²

Introduction

Although the use of rubble-mound structures for protection of coastal areas is common throughout the world and considerable hydraulic design data have been developed to aid the designer, very little data are provided on the structural integrity of individual armor units and the effect of broken units on the stability of such structures. The forces to which such structures are subjected are complicated and vary with type and geometry of the structure, depth of water, bottom configuration seaward of the structure, water level relative to the crown of the structure, and wave dimensions. Since all of these parameters are involved, accurate determination of wave forces cannot be calculated; and although it is not impossible to model the structural strength of armor units or measure forces on individual armor units, there are physical limitations which make the tasks extremely difficult. There is one way, however, that a breakwater stability model, as it exists today, can provide useful information on this subject and that is to purposely break given numbers of armor units and observe the effect on the overall stability of the structure. Such tests have been conducted at the U. S. Army Engineer Waterways Experiment Station for the Atlantic Generating Station (AGS) Breakwater in which specific answers were desired; thus, the data are limited to the dolos armor unit. The data do provide, however, significant indications regarding the type and extent of breakage (cluster or random) that is most detrimental to the overall stability of the structure; whether costly reinforcing steel is warranted to assure reduced armor breakage; and where necessary, data from this type study can be used as a basis for setting maintenance criteria that will prevent deterioration of the breakwater due to armor unit breakage.

Background

The AGS Breakwater is a 104-ft high, horseshoe-shaped, rubble-mound breakwater proposed for construction about three miles off the coast of New Jersey in about 30-40 ft of water (Figure 1). The purpose of the breakwater is to provide protection for two floating nuclear power plants. Initial tests conducted with unbroken dolosse indicated that for a selected condition of 16-sec, 40-ft waves at a still water level of +16.3-ft mean low water (mlw), 37-ton and 62-ton dolosse would be completely stable (practically no movement) on the trunk and heads of the breakwater, respectively. The broken-unit tests evolved from the question that if for some reason (i.e., reinforcing steel were not used,

¹Chief, Wave Research Branch, USAE Waterways Experiment Station.

²Research Hydraulic Engineer, USAE Waterways Experiment Station.

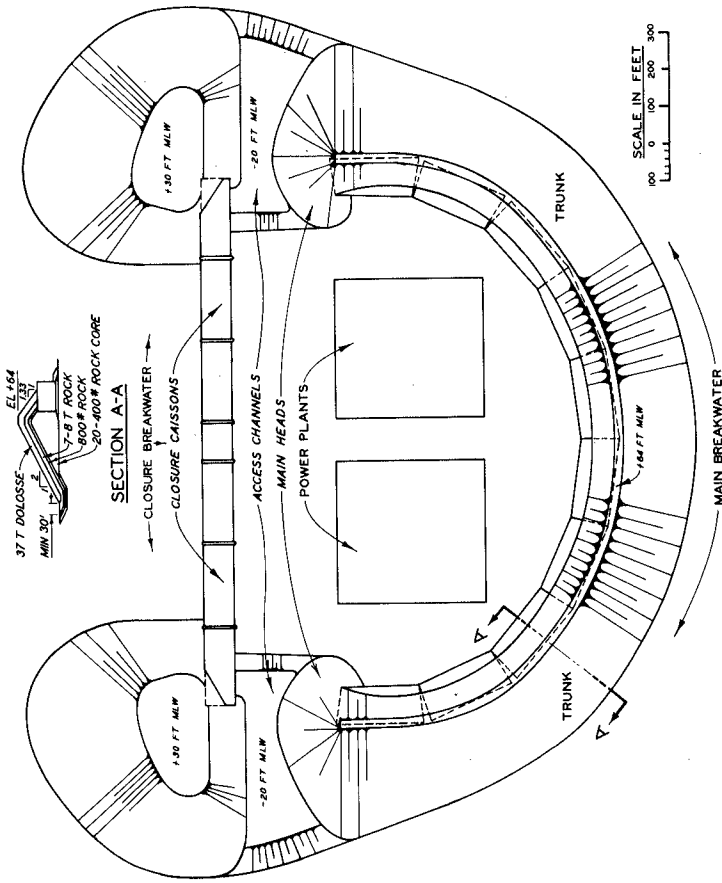


Figure 1. Layout of the Atlantic Generating Station

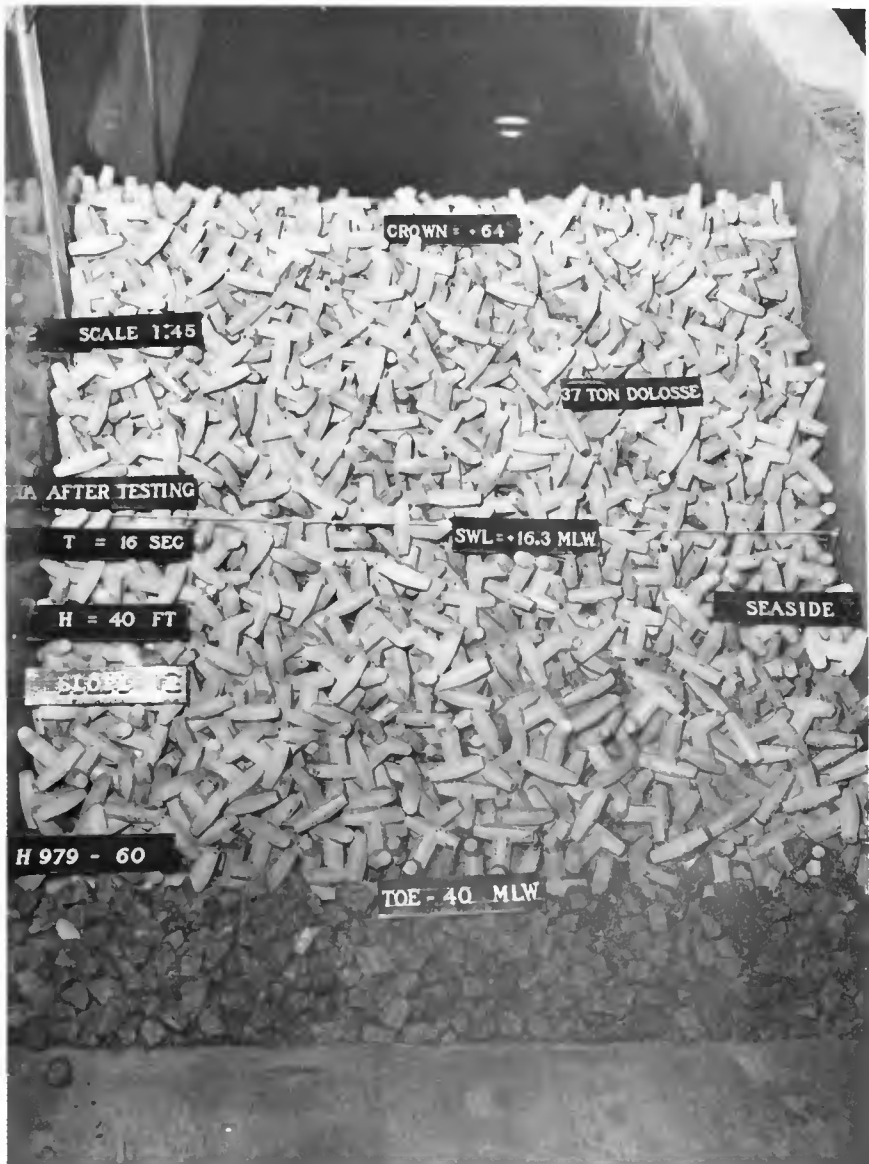
higher storm conditions, etc.), the armor units experienced breakage, what number of dolosse could be broken without having a detrimental effect on stability of the breakwater. Actual field experience for most projects throughout the world indicates that not over 2 percent of the total number of primary armor units are broken during the process of armor curing, placement of armor units, and exposure to wave attack not exceeding the design conditions. Therefore, if it can be shown that a significantly higher percentage of the armor units can be broken without deteriorating the stability of the structure, there is no need to use costly reinforcing steel to prevent breakage; or if the breakage should approach the critical percentage predicted by the model, proper maintenance can be initiated to preclude serious damage to the structure.

Two-Dimensional Model Tests

Normal Design Condition, Uniform Breakage

Several set of broken unit tests were conducted for the AGS Breakwater; however, only two sets of these tests are addressed in this paper--normal design conditions and extreme wave conditions. Both sets of tests used, for their respective water levels, the worst breaking wave condition that could occur on the structure. The first set of two-dimensional broken unit tests were conducted at an undistorted scale of 1:45 for the 16-sec, 40-ft wave condition at a swl of +16.3 ft mlw (condition for which model tests had already determined that unbroken 37-ton dolosse were completely stable on the trunk section of the structure, see Photograph 1). Using the unbroken unit test results as a base condition, up to 25 percent (in 5-percent increments) of the top layer of dolosse were broken and uniformly distributed (represents random breakage) over the test section.

The test section was constructed in the model in the same manner as two-layer unbroken unit test sections were constructed, which on the average requires about 55 percent of the total number of dolosse in the bottom layer and about 45 percent in the top layer. Once the unbroken unit test section was completed and the number of dolosse in the top layer determined, the number of broken dolosse specified for that test was determined and randomly placed in the top layer by removing an unbroken dolos and dropping a whole dolos in two parts in its place. Individually broken dolosse were never represented by more than two pieces. It is believed the model procedures used yield conservative results, since the disruptive action of replacing the unbroken armor unit with pieces does not occur in the prototype (i.e., most unbroken armor units simply break in place). Tests of each percent broken dolosse were conducted at least twice and sometimes three times with each repeat test verifying the original results. Test waves for all the tests were monochromatic and were subjected on the test sections in specific cycles (i.e., given time duration of about 30-sec increments with about 7-10 minutes between cycles to eliminate wave reflection effects). Each breakwater section was tested until stabilization (no progressive damage with time) or until damage had progressed to an unacceptable level.



Photograph 1. Test section of whole dolosse after testing with a design condition of 16-sec, 40-ft waves at a swl of +16.3 ft mlw.

Results

Observed results of the 5 and 10 percent broken unit tests indicated that individual dolosse were not displaced or did not move in place any more than that which occurred with a test section of whole dolosse. Photograph 2 shows an after testing view of a test with 10 percent of the top layer of dolosse broken and uniformly distributed (dots on the photo represent the breakage density). Tests with 15 percent of the top layer of dolosse broken indicated that there was a slight readjustment of a few of the units in the top layer of dolosse (Photograph 3). This readjustment was not significant to the overall stability, but one could tell some reneesting had occurred. It is believed that 15 percent uniform breakage is the upper limit in which this type breakage can be allowed without initiating small areas of spot damage. After testing, results of the tests with uniform breakage of 20 percent (Photograph 4) and 25 percent (Photograph 5) substantiates this belief in that spot damage tends to increase with breakage above the 15 percent level. During the 5 to 15 percent uniformly distributed broken dolos tests, it was observed that the individual broken pieces of dolosse were not significantly displaced up and down the slope but tended to nest into the void areas nearest their initial position. As the broken percentage increased (20-25 percent breakage), the half pieces reached such numbers that they began to break down the interlocking characteristics of the whole units and displacement of both the whole and half dolosse was more evident.

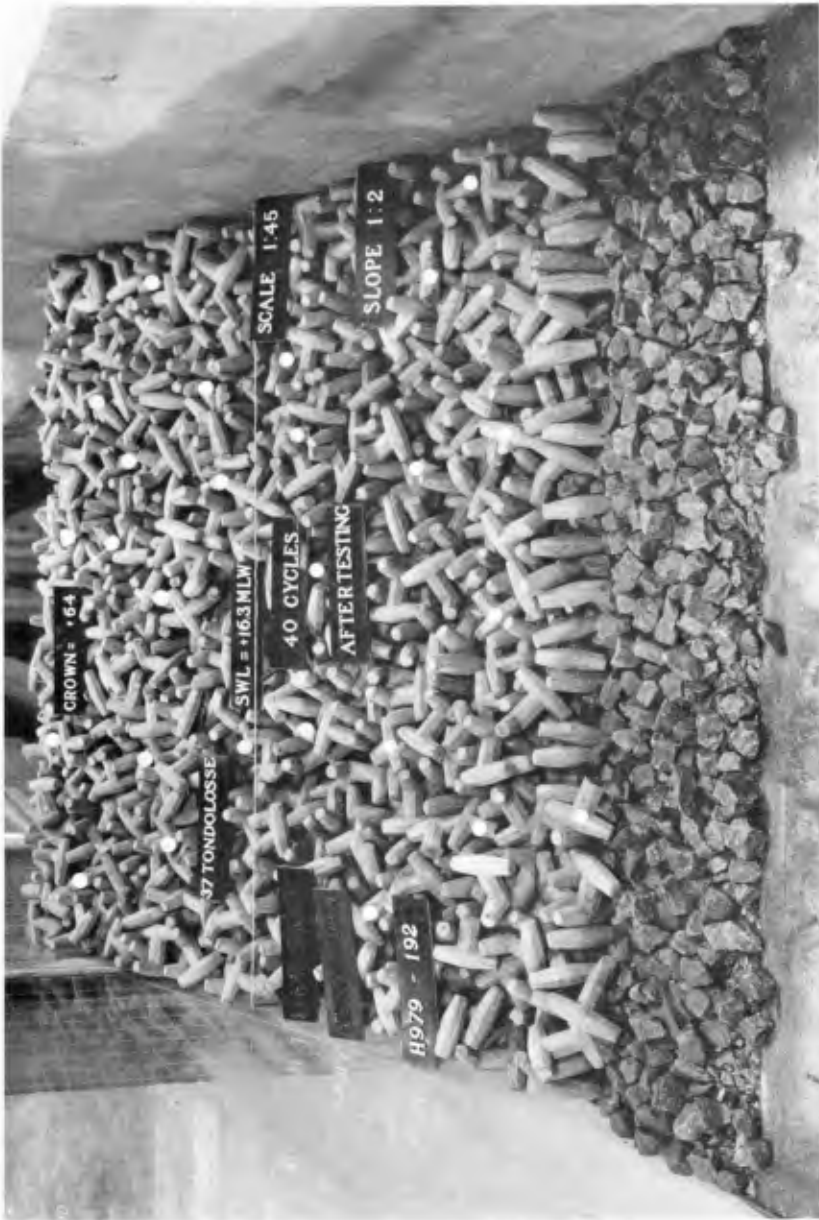
Extreme Wave Conditions, Uniform Breakage

The second set of two-dimensional broken dolos tests, in which only 10 and 15 percent of the top layer of dolosse were broken and uniformly distributed, were conducted at the 1:45 scale to compare with the same basic armor protection provided in test series one (whole 37-ton dolosse) but with an extreme storm condition* of 15-sec, 48-ft waves at a swl of +27.4 ft mlw. In this series, both the whole dolos and uniformly distributed broken dolos tests accrued a higher degree of damage than test series one (16-sec, 40-ft waves), but neither progressed beyond repairable damage.

Results

Photographs 6, 7, and 8, respectively, show a whole dolos test section, a test section with 10 percent of the top layer broken and uniformly distributed, and a test section with 15 percent of the top layer broken and uniformly distributed after testing with the extreme wave conditions. Again, the results show that uniformly distributed breakage up to about 15 percent of the top layer of dolosse did not show significant change in stability relative to that for unbroken units.

* The extreme wave condition described herein was a first estimate of a Probable Maximum Hurricane that could occur in this area but was deemed unreasonably high and subsequently has no relation on the selection of the final design condition.



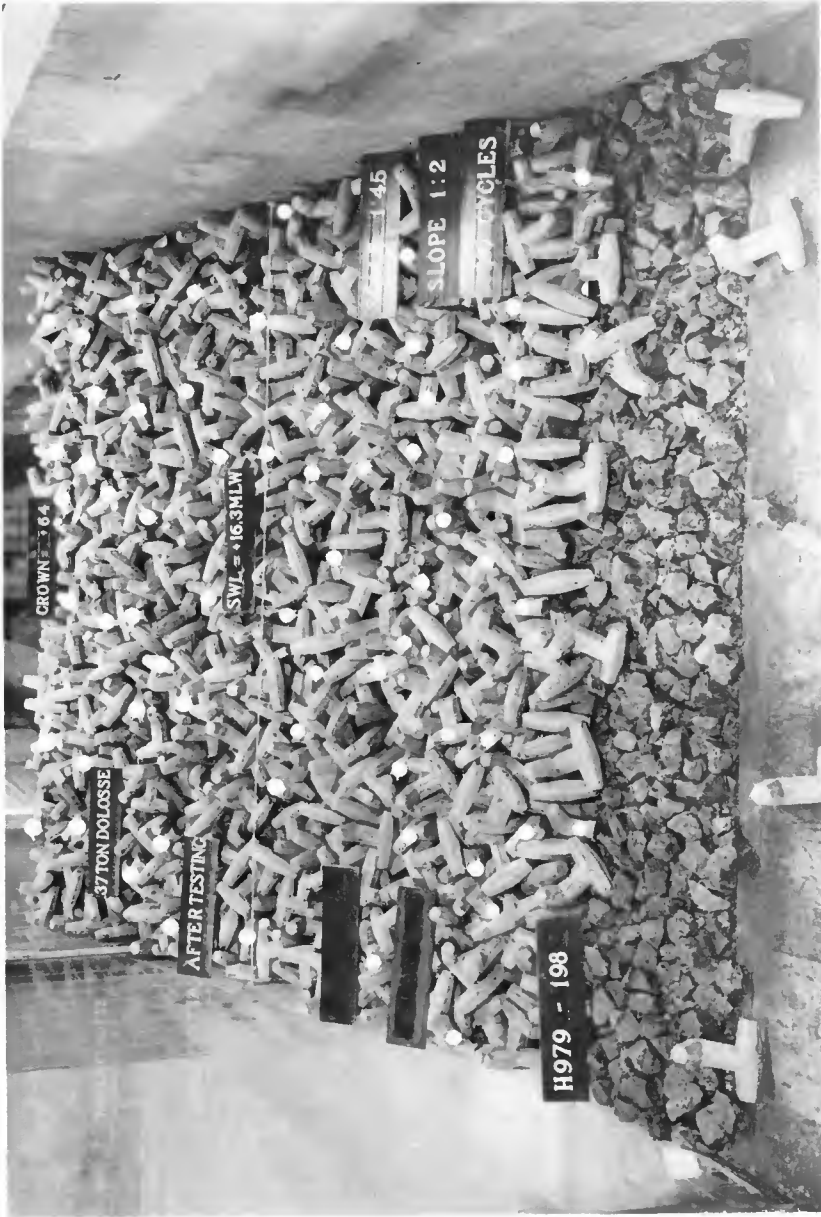
Photograph 2. Test Section with 10 percent of the top layer of dolosse broken and uniformly distributed after testing with a design condition of 16-sec, 40-ft waves at a swl of +16.3 ft mlw.



Photograph 3. Test section with 15 percent of the top layer of dolosse broken and uniformly distributed after testing with a design condition of 16-sec, 40-ft waves at a swl of +16.3 ft mlw.



Photograph 4. Test section with 20 percent of the top layer of dolosse broken and uniformly distributed after testing with a design condition of 16-sec, 40-ft waves at a swl of +16.3 ft mlw.



Photograph 5. Test section with 25 percent of the top layer of dolosse broken and uniformly distributed after testing with a design condition of 16-sec, 40-ft waves at a swl of +16.3 ft mlw.



Photograph 6. Test section of whole dolosse after testing with an extreme wave condition of 15-sec, 48-ft waves at a swl of +27.4 ft mlw.



Photograph 7. Test section with 10 percent of the top layer of dolosse broken and uniformly distributed after testing with an extreme wave condition of 15-sec, 48-ft waves at a swl of +27.4 ft msl.



Photograph 8. Test section with 15 percent of the top layer of dolosse broken and uniformly distributed after testing with an extreme wave condition of 15-sec, 48-ft waves at a swl

Extreme Wave Conditions, Cluster Breakage

Since prototype armor breakage could occur in concentrated numbers as well as randomly, two-dimensional tests of the extreme wave condition were extended to include units broken in clusters. These tests consist of 10, 5, and 3 dolos units broken in a cluster. For each set of cluster breakage, individual broken clusters were positioned on the structure at the swl, about halfway between the swl and the toe of the structure, and about halfway between the swl and the structure crown (Photograph 9). Similar to the uniform breakage construction procedure, it is believed these tests present a certain amount of conservatism since the test sections were constructed with unbroken dolosse, then for each cluster the respective number of dolosse were removed through both layers and the correct number of broken dolosse dropped into the hole. Even though this was done as gently as possible, these procedures could not help but disrupt the interlocking action of the armor units.

Results

Results of this type of cluster breakage indicate that clusters of 10 broken units would allow deterioration of the cover layers (Photograph 10, dashed circles represent initial positions of clusters) and could, with extended storm duration, cause major damage that might or might not be repairable. The results of tests using the 5 broken unit clusters also indicate deterioration (Photograph 11); however, it is not as severe and takes longer for the damage to occur, thus the more likelihood the area influenced by the cluster breakage can readjust to interlocking. During the 5 and 10 broken unit cluster tests, the failure of the breakage area seemed to occur in the following manner. The first few waves settled the broken units into rather tight clusters and the unbroken dolosse surrounding the clusters did not have any place to interlock; consequently, the unbroken dolosse around the clusters were displaced. This caused a loosening of the armor units in the area of the cluster until such time that the broken units had no "pocket protection" and were themselves displaced, which added to deterioration of the cover layer. Test results for the cluster of 3 broken units (Photograph 12) do not show this characteristic; and, in fact, indicate that clusters with three broken units are similar in stability to that of the unbroken dolos tests.

Three-Dimensional Model Tests

Extreme Wave Conditions, Uniform Breakage

Although the data are limited, a three-dimensional stability test (waves at an angle of 60 degrees to the trunk and end portions of the breakwater) using 15 percent of the top layer of dolosse broken and uniformly distributed was conducted at a 1:55 scale to compare with the results of similar unbroken unit tests. This particular test, which was conducted twice, used 62-ton dolosse on the heads of the breakwater which had been determined by previous tests to meet the no-damage stability criterion for the normal design condition (16-sec, 40-ft waves). As



Photograph 9. Test section indicating the positioning of the cluster breakage used in the two-dimensional tests.



Photograph 10. Test section with 10-unit clusters broken after testing with an extreme wave condition of 15-sec, 48-ft waves at a swl of +27.4 ft mlw.



Photograph 11. Test section with 5-unit clusters broken after testing with an extreme wave condition of 15-sec, 48-ft waves at a swl of +27.4 ft mlw.



Photograph 12. Test section with 3-unit clusters broken after testing with an extreme wave condition of 15-sec, 48-ft waves at a SWL of +27.4 ft MLW.

indicated earlier, it was expected that both the whole dolosse test section and the 15 percent broken unit test section would sustain damage for the extreme wave condition (Photographs 13 and 14, respectively). However, the point to be made is that the results show that similar damage occurred for both the broken unit condition and the whole unit condition. This is in agreement with the two-dimensional tests and indicates that if the breakage is uniformly distributed, up to 15 percent of the top layer of dolosse can be broken without having a detrimental stability effect over that obtained using unbroken units under similar conditions.

Conclusions

Based on the findings of this study, it is concluded that:

- a. Concentrations of broken dolosse are more detrimental to stability of the breakwater against wave attack than uniform or random breakage.
- b. If the uniform or random breakage exceeds 15 percent of the number of dolosse in the top layer and the cluster breakage exceeds 3 dolosse in a cluster, the stability of the breakwater will be less than that exhibited by a breakwater composed of unbroken dolosse.
- c. For the type of movement indicated by the no-damage criterion used in this study, the value of using reinforcing steel to reduce potential breakage of armor units is highly questionable.

Acknowledgments

The hydraulic model tests described in this paper were conducted intermittently by the U. S. Army Engineer Waterways Experiment Station (WES) for Public Service Electric and Gas Company (PSE&G), Newark, New Jersey, during the period May 1973 through August 1974 in the Wave Dynamics Division (Dr. R. W. Whalin, Chief) of the Hydraulics Laboratory (Mr. H. B. Simmons, Chief). Technical Director of WES was Mr. F. R. Brown. The tests were conducted by Mr. D. G. Markle, Research Hydraulic Engineer, with the assistance of Messrs. C. Lewis and W. G. Dubose, Engineering Technicians, under the immediate supervision of Mr. D. D. Davidson, Chief of the Wave Research Branch. Most of the contents of this paper are extracted from the final project report presently being prepared by Messrs. Davidson and Markle.

The support of PSE&G in funding the investigation reported herein and in granting permission for publication of this paper is gratefully acknowledged. Special acknowledgment is due all the managerial personnel of PSE&G and in particular Messrs. F. Brandt and B. Johanson.

The Office, Chief of Engineers is gratefully acknowledged for granting permission to conduct the study and for authorizing publication of this paper.



Photograph 13. Three-dimensional test section of whole units after testing with an extreme wave condition of 15-sec, 48-ft waves at a swl of +27.4 ft mlw.



Photograph 14. Three-dimensional test section with 15 percent of the top layer of dolosse broken and uniformly distributed after testing with an extreme wave condition of 15-sec, 48-ft waves at a swl of +27.4 ft mlw.

CHAPTER 147

ARMOUR BLOCKS AS SLOPE PROTECTION

By

A F. Whillock¹ and W. A. Price²

Introduction

Dolosse blocks were first described in 1966 by Merrifield and Zwamborn in a paper to the 10th Coastal Engineering Conference held in Tokyo. They reported a block whose design weight was one-fifth to one-sixth that of natural stone to resist the same wave height. The reaction of the profession was surprise and perhaps a little disbelief that the new block could have such a high K_D value. A considerable amount of testing followed in a number of hydraulic laboratories. Quite a lot of work was done at the Hydraulics Research Station at Wallingford and some interesting points came to light. The paper discusses how wave period and angle of attack affect block stability and suggests a way in which engineers might approach the problem of design of breakwaters.

The effect of wave period

The equation normally used to describe the performance of armout units is the Hudson equation:-

$$W = \frac{w_r H^3}{K_D (S_r - 1)^3 \cot \theta}$$

-
- | | |
|---|---|
| 1. Senior Scientific Officer |) Hydraulics |
| 2. Senior Principal Scientific Officer) | Research Station,
Wallingford, Oxon,
England. |

- W = weight of armour units in lbs
 w_r = unit weight of armour unit lbs/ft³
H = design wave height - ft
 S_r = specific gravity of armour unit relative to water
 θ = angle of breakwater to horizontal
 K_D = stability coefficient

The Hudson equation does not include any allowance for wave period. During an investigation carried out for the design of Dolosse for the High Island Breakwater in Hong Kong, various slopes of breakwater were subjected to waves of different periods. Having selected a wave period the wave height was increased until failure occurred. A definite influence of wave period was observed and this is illustrated in Fig 1, which refers to tests carried out with 5.7 ton Dolosse on a 1:2 slope. Although more experiments are necessary, enough has been done to show that the observed period dependence is real and a possible explanation for it is as follows. As the wave period increases the wave tends to surge on to the protective layer rather than break. This sets up high velocities over the surface layer. It is suspected from watching many tests with Dolosse that although they are very stable to plunging breakers acting normal to the slope, their weakness lies in their inability to resist the drag caused by this surface flow.

Type of failure

The advantage of a properly designed tipped-stone breakwater is that as the wave heights build up, the extent of the damage will occur gradually. This is not the case with Dolosse. Approaching the state of serious damage small changes in wave height will produce large changes in damage - considerable rebuilding rather than repair being necessary to the breakwater.

An attempt has been made in Fig 2 to illustrate the difference in behaviour of Quarry stone, Dolosse and Tetrapods. It demonstrates that what would be acceptable damage for Quarry Stone would be very serious damage for a Dolosse breakwater; Tetrapods occupying an intermediate position. (It should be noted that strictly comparative data was not available to make the analysis - averaged values from a number of sources were therefore used.) The indications are that any increase of stability which can be brought about by an open form of block with a high voids ratio and designed to interlock will result in a reduction of the margin of safety as failure is approached.

Engineers when they design breakwaters are faced with the choice between a number of blocks and rightly suspect that the performance is adequately described by one number. It would help if all results were reduced to a common form as we have attempted to do here. The correct block for a particular situation could then be chosen.

Fig 2 also shows that the K_D ratios (Dolos/rock) decrease as the percentage of damage is increased. At failure, when the movement of large numbers of blocks is involved, the assembly is fluidised by the passage of water through the layers and the benefit of interlocking and friction disappear. The only restraint to block movement is then the weight. It follows that sophisticated blocks should only be used with a large factor of safety. Keep well away from the serious failure situation by designing a block weight which gives little damage at extreme wave heights. Even so, the advantages of a high K_D factor will still be available to give an economical design.

The effect of angle of attack

It is commonly assumed that breakwaters are more stable to oblique wave attack since the wave heights are reduced by refraction and the armour units are effectively on a reduced slope. Experiments with quarry stone support this view. There is reason to believe that such an improvement in stability might not occur with blocks that are susceptible to drag forces. To check the possible effects a short series of tests were carried out in a wave tank (Fig 3).

The Dolosse breakwater which was constructed on a framework could be readily turned at angles to the direction of wave approach. Regular waves were increased in steps at each angle until the number of removals was such that failure was imminent. Fig 3 shows that the overall stability of the blocks decreased up to an angle of 60° and then improved dramatically.

The explanation is similar to the one given earlier for period dependence. In breaking at an angle to the slope some flow takes place along it and this coupled with velocities up the slope due to the wave break or surge causes high velocities and hence high drag. The increase in stability found above 60° is due to adverse effects of surface flow being overtaken by the benefit of wave height reduction. The rapid improvement again stresses that the difference in wave attack between acceptable damage and failure can be small.

Conclusions

- (a) Tests have shown that wave period affects the stability of Dolosse.
- (b) The way in which failure builds up should be an important factor in design.

- (c) The angle of attack of waves significantly affects the stability of a breakwater armoured with open type blocks having high drag coefficients.
- (d) Serious consideration should be given to adopting a uniform method of presenting test results so that direct comparisons can be made between various types of block.

Acknowledgements

This paper is published with the permission of the Director of the Hydraulics Research Station, Wallingford.

References

1. Hydraulics Research Station. Unpublished report EX 532 Oct 1970. High Island Water Supply Scheme. A study of the use of dolos armour units.
2. Information on Tetrapods given by:
 - (a) Merrifield E M and Zwamborn J A The economic value of a new breakwater armour unit, Dolos. Chapter 51 Proc. 10th Conf on Coastal Engineering Tokyo 1966.
 - (b) Font J B Damage functions for a rubble mound breakwater under the effect of swells. Chapter 96 Proc. 12th Conf on Coastal Engineering Washington 1970.
 - (c) Oullet Y Laval University Civil Engineering Dept. Report T-18.
3. Hydraulics Research Station. Report INT 159 Dec 1976 The Stability of Dolos Blocks under Oblique Wave Attack.

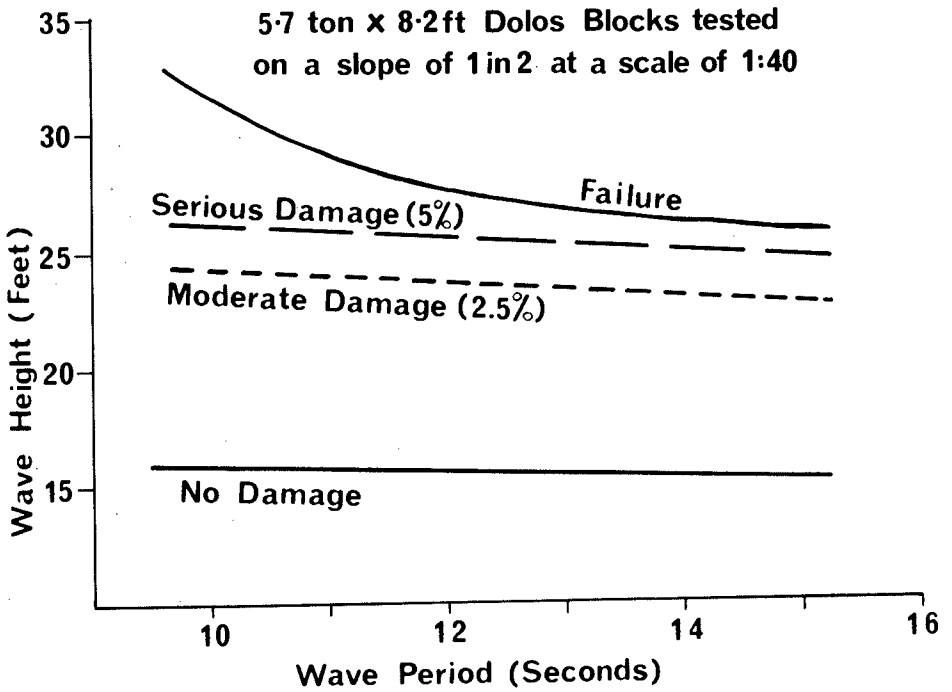


FIG. 1 Effect of Wave Period

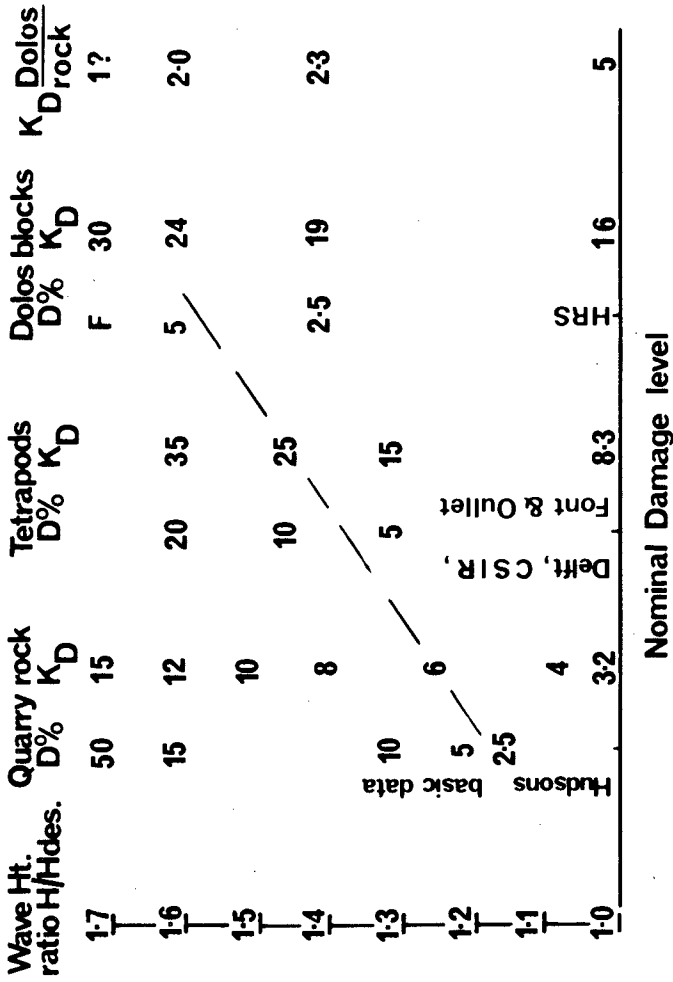


FIG. 2 COMPARISON OF DAMAGE TO ARMOUR BLOCKS

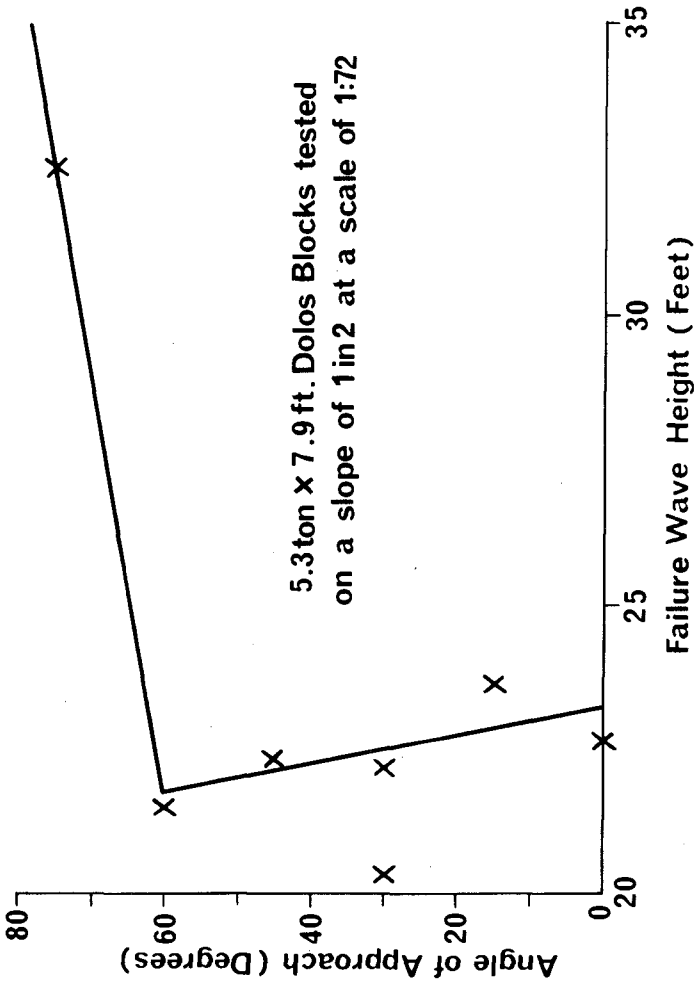


FIG.3 Effect of Angle of Approach

CHAPTER 148

LARGE SCALE MODEL TESTS of PLACED STONE BREAKWATERS

by

Charles K. Sollitt
Asst. Prof. of Civil Engineering
Oregon State University
and

Donald H. DeBok
Lieutenant, U.S. Coast Guard
National Data Buoy Office

Abstract

Large scale model studies reveal that Reynolds scaling can affect the apparent stability and wave modifying properties of layered breakwater structures. Results of a study for a breakwater configuration designed to protect offshore power and port facilities in water depths to 60 feet are presented and discussed. The armor layer of this structure is formed from quarried rock of irregular rectangular parallelepiped shape, individually placed perpendicular to 1:2 seaward slope and crest. The resulting armor layer is relatively smooth, densely packed and very stable. Model studies of similar configurations were studied at 1:10, 1:20 and 1:100 scale ratios. Stability, runup, rundown and reflection were measured for a variety of water depths, wave heights and periods. Analysis of the large scale test results establish that the placed stone armor is approximately as stable as dolos armor units. Runup, rundown and reflection respond similar to rough, impermeable slopes. Comparison of large and small scale results demonstrate that relative increases in drag forces at lower Reynolds numbers decrease stability and runup in small scale models.

Introduction

The challenge of offshore power production and deep draft port facilities has stimulated interest in large protective breakwater structures. Some elegant wave attenuation schemes have been proposed and a variety of artificial armor unit shapes are being investigated. There are, however, many offshore locations where natural rock structures are the most economical alternative for protective breakwaters. One method of stone or rock construction which has received little attention is the placed stone construction technique. This method has been used with considerable success for two decades along the Pacific Northwest coast of the continental United States and yet the advantages of this type of breakwater construction have not been carefully studied.

A unique feature of this specific construction technique is that rock is quarried for an approximately rectangular parallelepiped shape with one major axis. Then the rock is individually placed on the breakwater surface with the long axis perpendicular to the slope. A single layer of armor units placed in this manner provides a densely packed, relatively smooth surface with stability approaching that of dolos armor units.

This construction technique was studied superficially in 1961 (Jackson, 1963). Although the tests indicated that placed stone was more stable than random stone, an increase in the stability coefficient was not recommended because of the limited number of tests. However, the outstanding maintenance record of jetties along

the coasts of Oregon and Washington indicate that these structures have been conservatively designed. In order to compensate for the lack of sound design information, this study was undertaken to investigate the overall hydraulic behavior of placed stone armor breakwaters. Included in the study are runup, rundown, reflection and stability.

The specific design being considered is a 100 foot high structure which is proposed for use in relatively deep water (50 ± 10 feet) to protect offshore nuclear power plants and superports. A cross section of the structure is presented in Fig. 1. The crest of the structure is 35 feet wide. It slopes at 2:1 on the seaward face to MLLW where it breaks to a slope of 1.5:1. The back face falls away quickly at 1.25:1 and encounters a concrete caisson at MHHW. The caisson provides a working platform for constructing the breakwater and maximizes mooring area on the leeward side of the structure. The placed stone armor material is represented by the A+, A and B designation in the figure. All other materials are barge dumped or randomly placed. The largest armor, A+ (25-35 tons) extends from ten feet below MLLW to ten feet above MHHW. This is considered to be the region which experiences the largest wave impact loads.

The study was conducted at a large scale to minimize scale effects. It is known that drag forces are an important mechanism for retarding runup, dissipating energy and loading armor units so that, in general, Reynolds similarity cannot be neglected in breakwater modeling. Since drag coefficients increase at low Reynolds Number, one would expect small models to produce relatively high drag

PROTOTYPE BREAKWATER SECTION

DIMENSIONS IN FEET

<u>MATERIAL</u>	<u>SIZE (TON)</u>
A+	25-35
A	15-25
A-	10-15
B	6-12
B-	3-6
C	0-3

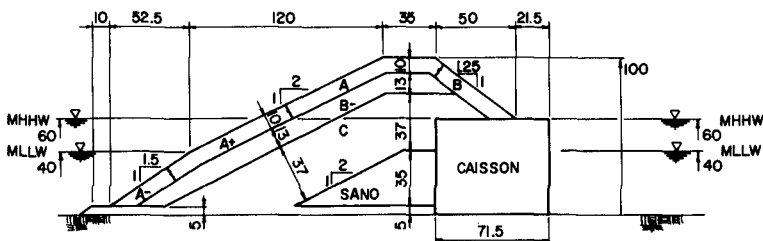


Fig. 1. Prototype Breakwater Cross Section

forces and therefore less runup, less reflection and less stable conditions. Therefore, extrapolating small model results to prototype scale could yield an uneconomical, overdesigned armor unit and an underdesigned crest elevation.

In order to quantify the scale effect, this study was conducted at three scale ratios: 1:10, 1:20 and 1:100. Froude similarity was used to dimension each model, and model results expressed in dimensionless form were compared. The hypothesized scale effects were found to occur and to be significant in the small model.

The structure was found to behave like a rough, impermeable slope in terms of runup and rundown. The placed stone armor units were found to be extremely stable, with stability coefficients approaching that of dolos.

Test Conditions and Procedures

A test program of monochromatic wave excitation was conducted at the Oregon State University Wave Research Facility. The wave channel is 342 feet long, 12 feet wide, 15 feet deep and has a 290 foot test section. The wave board is of the flap type variety which is hinged at the bottom in a section which has a total depth of 18 feet. The board is controlled by a 150 HP, 3500 psi pump with an attached hydraulic servomechanism activated by an electronic function signal generator. The installation is unique in that it has water on only one side of the wave board. This scheme reduces the power requirements of the wave generator by one-half and eliminates the need for a dissipative media behind the wave board. The facility has the capability of producing solitary waves, periodic waves and random waves for modeling ocean wave spectra. Breaking waves up to five feet high can be generated and the useful frequency range is from 0.2 to 2.0 hertz.

Three model scales were tested, 1:10, 1:20 and 1:100. Each scale was exposed to prototype waves periods of 9, 13.5 and 16 seconds. Wave heights were increased from prototype heights of approximately 15 feet to breaking wave heights which exceeded 45 feet for the two longer wave periods. Each wave condition was continued until 500 waves had been produced or significant damage had occurred.

Two bottom slope conditions were modeled during the test. The model itself was supported on concrete slabs approximately five feet above the bottom of the test channel. A "flat" bottom was created by extending the false bottom horizontally to an equivalent prototype distance of 1000 feet from the toe of the structure. A "sloped" bottom was created by shoaling the bottom at a 1:12 slope from 40 feet (prototype) in front of the structure to a greater depth 520 feet seaward. The bottom proceeded horizontally from that point. Tests of all three scales were conducted using the flat bottom configuration first, followed by the sloping bottom. The flat bottom limited wave heights due to breaking of finite amplitude partial standing waves in the vicinity of the breakwater. The sloping bottom permitted sustained large amplitude waves during stability tests.

In addition to varying bottom slope, wave height and period, three different still water depth conditions were investigated; 40, 50 and 60 feet. Each test run proceeded by establishing the slope, depth and wave period and incrementally increasing the wave height relative to the previous run at the same period. The waves were allowed to interact with the structure until a quasi-steady state wave environment was established. Then, each of the following parameters were measured: incident and reflected wave height and period, runup, rundown and damage.

Incident and reflected wave heights were resolved using the wave envelope method. The partial standing wave envelope was profiled using an acoustic wave gauge mounted on a moving carriage. Incident and reflected wave heights were solved from the sum and difference of antinode and node amplitudes. Runup and rundown were quantified relative to elevation gradelines on the channel walls adjacent to the model. Average values across the width of the model were recorded. Damage was recorded as it occurred by stopping the test and noting the number of stones and surface area affected. Progressive damage was evaluated by continuing the tests without repairing the damaged area until catastrophic failure was imminent or 500 waves had passed.

Interpretation of Results

Runup

Runup is the vertical distance above still water attained by a wave rising on some prescribed surface. Its magnitude is a function of both the wave and surface properties. Runup is an essential design parameter for ocean and coastal structures if overtopping is to be minimized or avoided.

It is common to express runup relative to the offshore wave height which produced this condition. This measure of relative runup allows a design engineer to proceed directly from offshore wave forecasting to runup calculations at the structure if refraction does not alter the wave form. Local wave conditions probably dominate the runup process, however, it may be very difficult to calculate local modifications caused by wave interaction with a complex structure. Attempts to predict runup analytically have generally not been successful except for conditions of simple, mild, impermeable slopes (Le Mehaute, *et. al.*, 1968). In the absence of dependable runup predictions, experimentally determined values of runup have been an essential recourse.

Runup data collected in the context of this study have been assembled to facilitate comparison with other studies. Accordingly, relative runup (runup divided by deepwater wave height, R_u/H_0) is presented graphically as a function of a deepwater wave steepness parameter (H_0/T^2). According to linear wave theory deepwater wave steepness is:

$$\begin{aligned} \text{steepness} &= \text{wave height/wave length} \\ &= H_0/L_0 = 2\pi H_0/gT^2 \end{aligned}$$

where g = gravitational acceleration
and T = wave period.

The constant, $2\pi/g$, had been dropped from this expression for numerical expediency. The resulting steepness parameter is dimensional, with units of ft/sec².

The data are presented in Figures 2 through 5. Flat and sloped bottom results are combined at the 1:10 and 1:20 scales (Figs. 2 and 3) and separated at the 1:100 scales (Figs. 4 and 5). Note that depth and period identities have been retained for clarity by utilizing a uniform symbol notation as indicated in the legend on each figure.

Mean trends interpreted from these figures indicate that relative runup increase with:

- 1) increasing wave steepness
- 2) increasing wave period
- 3) increasing bottom slope
- 4i) increasing depth on flat bottoms
- 4ii) decreasing depth on sloping bottoms.

This behavior is a significant contrast to that depicted in popular design resources, such as the *Shore Protection Manual* (U.S. Army, 1973), wherein period and depth dependence are often difficult to resolve. Curves represented by the dashed lines in Figs. 2-5 serve to illustrate this apparent dichotomy. Both curves were taken from the *Shore Protection Manual*; curve B represents runup on a graded riprap, 1:2 impermeable slope while curve C represents runup on a rubble, 1:2 permeable slope. The curves are presented as a synthesis of data for combinations of wave periods, heights and water depths. One would interpret from these curves that relative runup decreases for increasing values of $H_0/T^2 > 0.1$. In contrast, consider the 9 second period data in Figure 4. Here it is clearly shown that relative runup increases with wave steepness for a given constant value of wave period and water depth. The same behavior can be observed in the 1:10 scale results in Fig. 2. The reason for this behavior is a strong dependence on wave period. In all of the figures, the short wave periods occur below and to the right while the long wave periods occur above and to the left. For a given wave steepness, the shorter period waves are not as high and propagate at a slower speed than longer waves. Therefore, less power is available for conversion to runup, and less runup occurs. Viewed as an entire collection of data, the mean trends follow the dashed lines because for a given range of design wave heights, the steeper waves are dominated by short periods while the less steep waves are dominated by long periods.

The reference lines, B and C, in each of Figs. 2-5 reveal additional information about general runup characteristics on this structure. In Fig. 2 it is apparent that the large scale data tends to group around line B indicating that the densely packed, placed stone surface responds to runup similar to an impermeable riprap slope. Line C, representing a permeable rubble slope, yields less runup because surging flow on this surface can penetrate the interstices of the relatively porous rubble. The response at the 1:20 scale in Fig. 3 is similar to the 1:10 scale. However, at the 1:100 scale, (Figs. 4 and 5) essentially all data points fall below reference line B, indicating less overall runup at smaller scales. This concurs with the anticipated scale effect, i.e., flow at low Reynolds number in the small model produces higher drag forces relative to the inertia of the surging fluid, thereby retarding runup to a greater degree than at large scale and at prototype conditions. Because the 1:20 and 1:10 scale data is so similar, it would appear that the Reynolds number at these two scales is high enough to yield a nearly constant surface drag coefficient. Since this drag coefficient should also be suitable for all larger Reynolds numbers, it is to be concluded that the 1:20 and 1:10 scale results are also representative of prototype conditions. The 1:100 scale results, however, tend to underestimate prototype runup by approximately 20%.

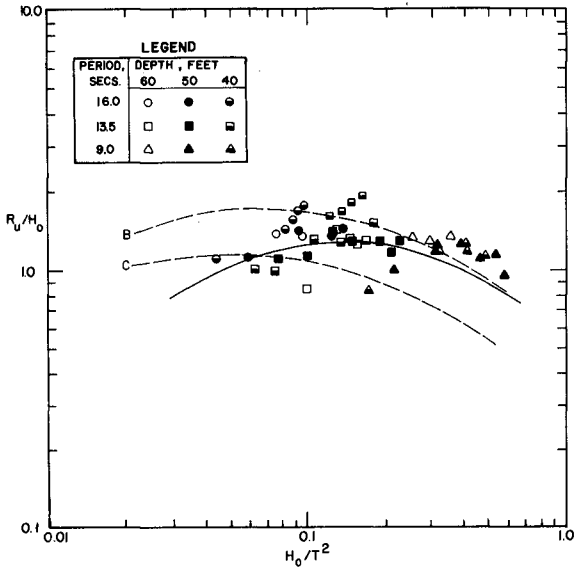


Fig. 2. Relative Runup, 1:10 Scale, Sloped and Flat Bottom

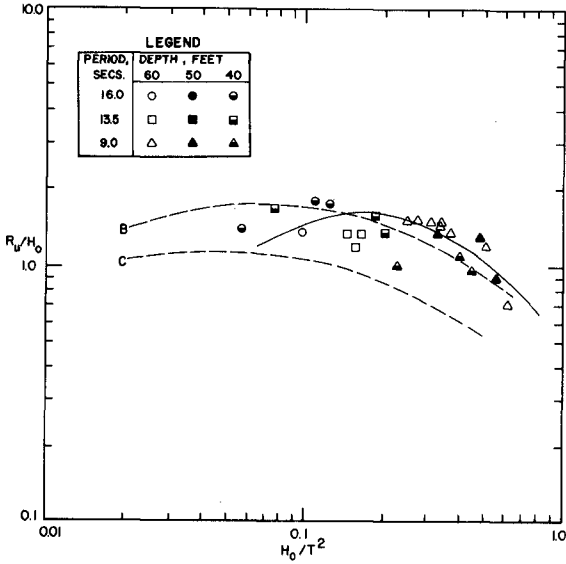


Fig. 3. Relative Runup, 1:20 Scale, Sloped and Flat Bottom

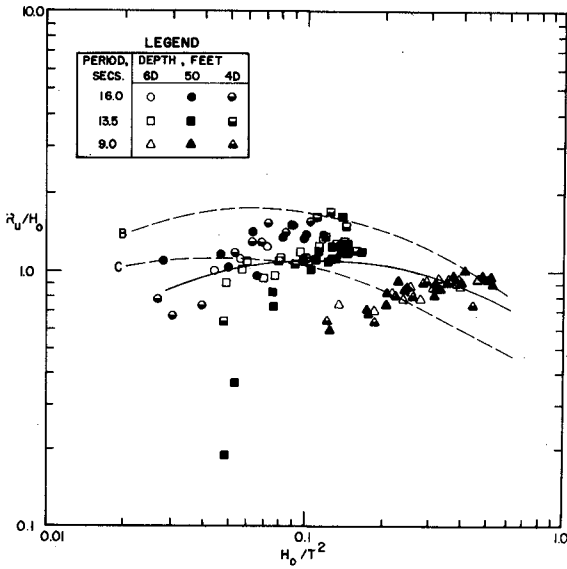


Fig. 4. Relative Runup, 1:100 Scale, Sloped Bottom

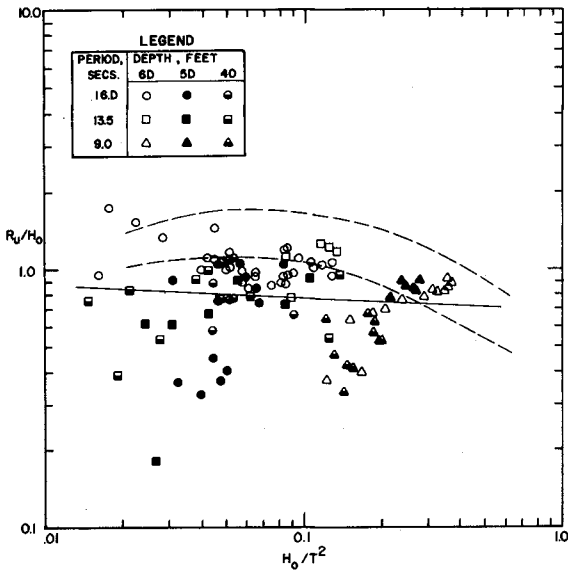


Fig. 5. Relative Runup, 1:100 Scale, Flat Bottom

Comparing Figs. 4 and 5 indicates that flattening the bottom slope in front of the breakwater tends to reduce runup. This behavior is to be anticipated and has been demonstrated in other studies as well. The flat bottom imposes a depth restriction on the finite amplitude partial standing waves seaward of the structure. The waves break within one wave length on the flat bottom reach if the superimposed incident and reflected wave heights exceed approximately one still water depth. This breaking limitation does not develop on the sloping bottom until the incident wave height alone exceeds the depth at some point along the slope. Thus, the flat slope combined with reflection from the breakwater surface protect the structure from very high incident waves.

Wave period and water depth dependence may be separated graphically by non-dimensionalizing runup in terms of water depth rather than deepwater wave height. This is accomplished in Figs. 6 and 7 where the data for the 1:10 scale model and the 1:100 scale model are presented. Least square exponential fit lines are drawn through the data at indicated constant values of d/T^2 . Note that d/T^2 is proportional to the water depth divided by deepwater wave length. The effect of wave period is evident in both figures with long period data on the left and short period data on the right. For a given value of wave steepness and depth, the short period waves always produce less absolute runup. The effect of water depth also separates well on these graphs. It is readily apparent within each group of constant period data that water depth increases from left to right. Therefore, for a given wave period and steepness, shallower water produces more runup relative to the depth. This simply demonstrates that the shoaling effect is more pronounced in shallow water.

Rundown

Rundown is the vertical distance between the still water level and the minimum elevation attained by a wave on a specified surface. Rundown is an important design parameter because it identifies the minimum elevation exposed to large wave impact loads and large local velocities. The region between maximum runup and rundown requires the greatest care in the selection and placement of breakwater armor material. Placement of armor to some depth less than maximum rundown may initiate failures at the toe of the structure which later propagate up the slope.

Rundown data for the 1:10 and 1:100 scale models are presented in Figs. 8 and 9, respectively. The dashed line in each figure is reproduced from the Shore Protection Manual and represents relative rundown on an impermeable, graded riprap, 1:2 slope. Interpretation of the data on these curves reveals that relative rundown increases with:

- 1) increasing depth
- 2) increasing period
- 3) decreasing steepness
- 4) decreasing model size.

Although not presented in this discussion, the flat bottom tends to increase rundown relative to the sloping bottom at the 1:100 scale.

Comparison of runup and rundown dependence on depth and steepness suggests a useful analogy to wave profile distortions resulting from finite amplitude effects. Waves of finite height tend to develop higher crests and shallower troughs as wave steepness increases and as the ratio of water depth to wave length decreases. Similarly, runup increases with increasing steepness and decreasing depth while rundown decreases under the same conditions. Thus, the ratio of rundown/runup re-

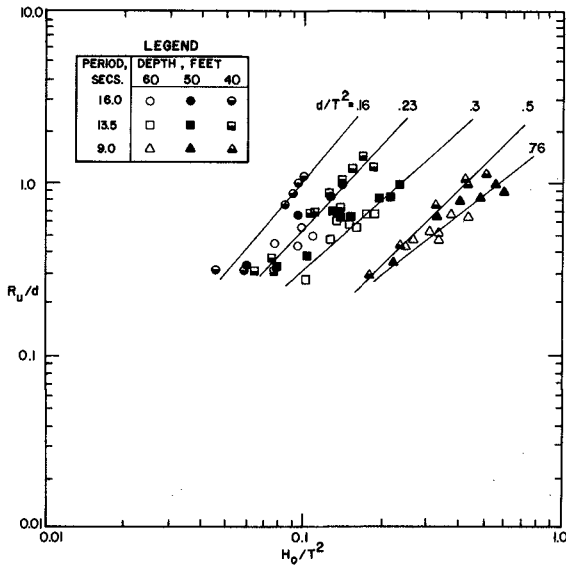


Fig. 6. Runup Divided by Depth, 1:10 Scale, Sloped and Flat Bottom

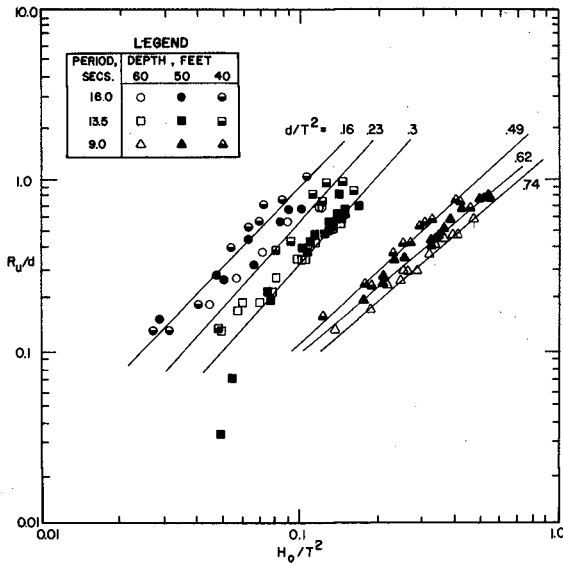


Fig. 7. Runup Divided by Depth, 1:100 Scale, Sloped Bottom

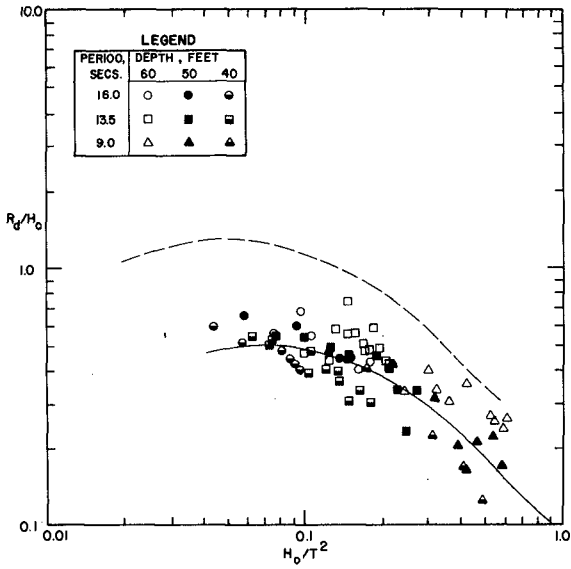


Fig. 8. Relative Rundown, 1:10 Scale, Sloped and Flat Bottom

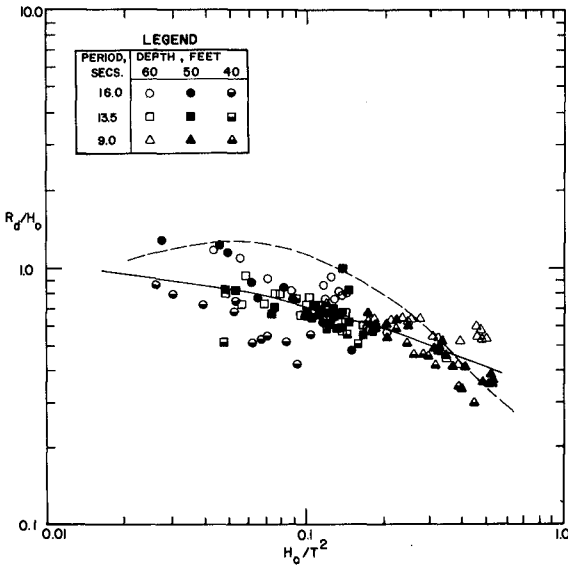


Fig. 9. Relative Rundown, 1:100 Scale, Sloped Bottom

sponds as the ratio of trough amplitude/crest amplitude to similar changes in depth and steepness.

The scale effect also produces opposite changes in runup and rundown. Small scale models tend to reduce relative runup due to increased friction. Comparing Figs. 8 and 9, however, indicates that rundown increases in the small model. This response can be explained in terms of the cyclic behavior of runup and rundown. Each event repeats once each wave period so that if a greater portion of a period is required for runup, then less time will be available for rundown before the next runup cycle begins. In large models, relative runup is increased and a greater fraction of the wave period is required for maximum runup to be attained. A reduced fraction of the wave period remains for rundown, hence, maximum rundown is reduced in large models. Conversely, small models take less time for reduced runup so more time is available to yield increased rundown. The scale effect is accentuated in rundown, as evidenced by the least squares, best fit, solid line through the data at both scales. The 1:100 rundown results are approximately 40% larger than the 1:10 rundown results.

Reflection

The reflection coefficient is defined as the ratio of the reflected wave height to the incident wave height. Reflection is important because the resulting partial standing wave condition can impose a limit on marine traffic activity in the vicinity of the structure and influence adjacent sediment shoaling patterns.

Reflection coefficient (C_r) data for the 1:10 and 1:100 scale models are presented in Figs. 10 and 11, respectively. The solid line through the data represents a least squares, best fit average for the entire collection. An examination of these figures discloses that reflection increases with:

- 1) decreasing depth
- 2) increasing period
- 3) decreasing steepness
- 4) increasing model size.

Although not presented in this discussion, the reflection coefficient behavior is not significantly different for flat bottom configuration when compared to similar conditions on a sloping bottom.

The response to period and steepness is consistent with energy dissipation considerations along the breakwater surface. Surface drag is a nonconservative force which increases with the square of local velocities. Wave particle velocities increase with increased wave steepness and reduced period. These changes induce higher drag forces, more energy dissipation and therefore consume energy available for generating the reflected wave. Conversely, a reduction in wave steepness or increase in period causes a reduction in local velocities and energy dissipation, thereby increasing reflection as observed in Figs. 10 and 11. The observed scale effect also follows this trend. Low Reynolds number flow in the small model causes proportionately higher drag and reduces reflection by up to 10%.

Stability

Stability is a measure of the ability of breakwater armor to resist damage from wave attack. Ultimately, the integrity of the entire structure is dependent upon design considerations which adequately account for stability requirements. Several definitions for stability are currently in use, some more elegant than

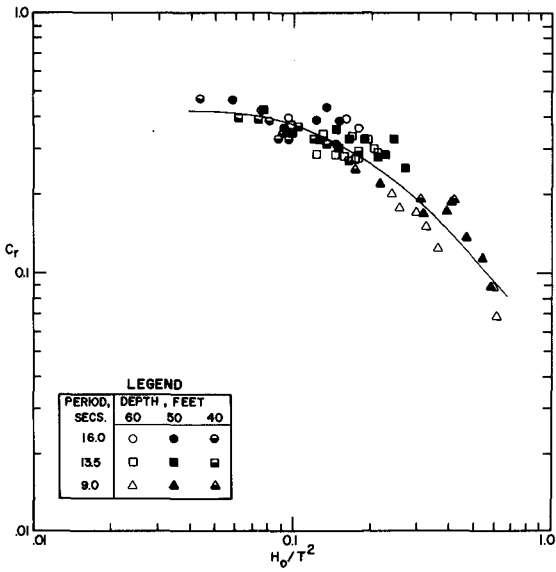


Fig. 10. Reflection Coefficient, 1:10 Scale, Sloped and Flat Bottom

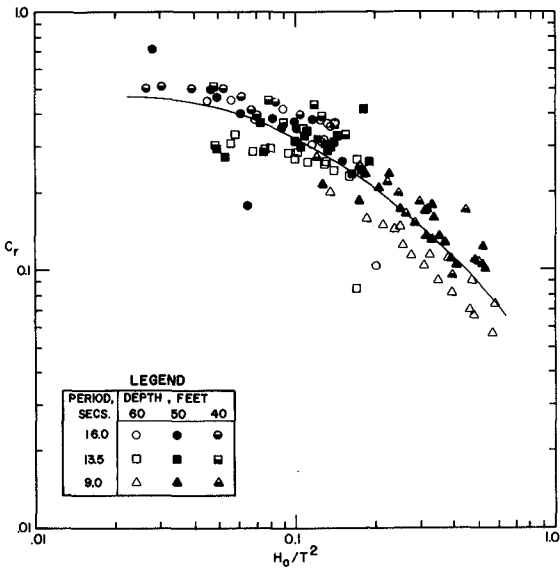


Fig. 11. Reflection Coefficient, 1:100 Scale, Sloped Bottom

others. The one definition which is subject to the least confusion quantifies stability as that wave height which causes an "acceptable" level of damage to a particular structure under specified conditions of water depth and wave period. "Acceptable" damage is most always less than 5% of the seaward armor surface area, usually less than 1%. This limiting wave height has been found to be weakly dependent on water depth and wave period. Attempts to develop a dimensionless stability coefficient for comparison of alternative armor units have led to a variety of expressions which are proportional to the zero damage wave height divided by the cube root of the armor unit volume. Hudson's formula (Hudson, 1953), was developed to quantify stability of units which rely only on their submerged weight for stability. Although it was not intended for use in describing units which have interlocking strength, Hudson's stability coefficient is still the most widely used standard for armor unit comparison.

No damage is often an uneconomical and unnecessary design requirement. Paul and Baird (1971) have attempted to identify alternative failure modes for more flexible design requirements. These modes or failure zones are:

- Zone 1: No movement of armor units
- Zone 2: Local movement but no displacement
- Zone 3: Few units displaced
- Zone 3a: Damage stops before 10 units are displaced per 100 lineal feet of breakwater
- Zone 4: Continuous damage will ultimately destroy armor layer
- Zone 5: Immediate, complete failure of the armor layer.

This failure mode analysis was used to identify levels of failure in the placed stone study. Results for the 1:10 and 1:100 scale models are presented in Figs. 12 and 13, respectively. Damage to A and A+ armor materials are summed in these figures.

The failure mode analysis indicates a slight dependence on relative depth. This results from long waves at shallow depths (high T^2/d) attacking the A- layer below MLLW. Smaller wave heights can damage this layer in shallow water. Higher waves are required to cause the same damage in water of greater relative depth (low T^2/d). At both scales, increasing wave heights cause increasing levels of damage. However, proportionately higher prototype waves are required to cause the same level of damage in the large model. Zone 4 could not be achieved at the 1:10 scale because equivalent prototype wave heights in excess of 55 feet could not be generated.

Levels of damage can also be quantified in terms of the percent of the armor surface area experiencing displaced units after exposure to 500 design waves. This data is presented in Fig. 14, for all three scales and all combinations of wave period and water depth. Least squares, best fit lines have been extended through the data at each scale. Again, larger waves cause more damage. The scale effect is readily apparent in this figure. The 1:100 scale model indicates that comparable damage will be caused by a wave height which is less than 80% of that indicated by the 1:10 scale results. Zero damage wave heights (H_{ZD}) extrapolated from Fig. 14, provide the following estimates for Hudson's stability coefficient (K_D) at each scale:

Scale	H_{ZD}	K_D
1:10	35'	29
1:20	35'	29
1:100	28'	23

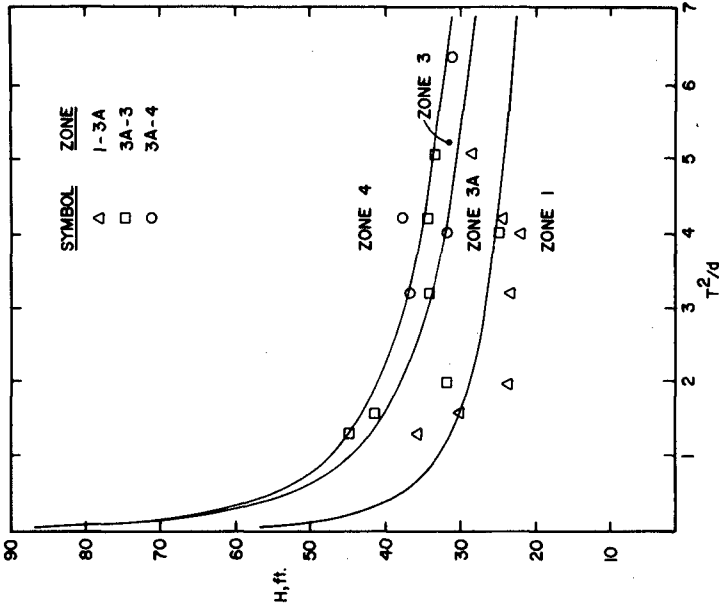


Fig. 13. Failure Mode Zones, 1:100 Scale

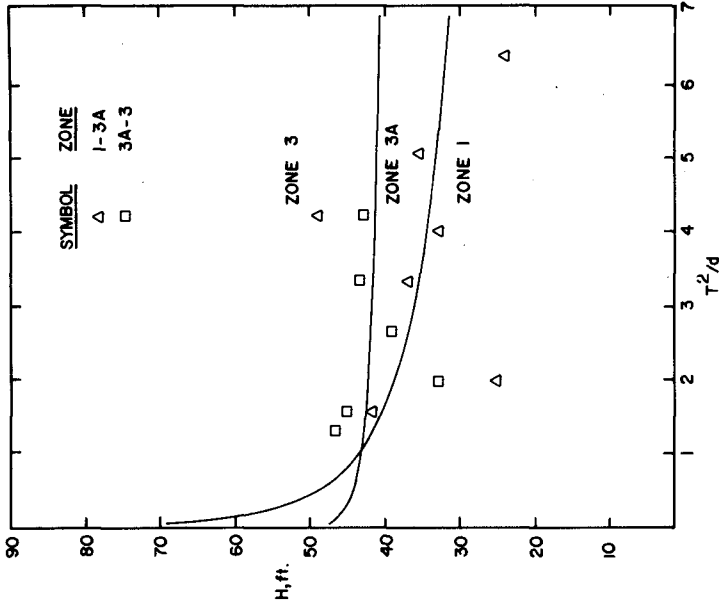


Fig. 12. Failure Mode Zones, 1:10 Scale

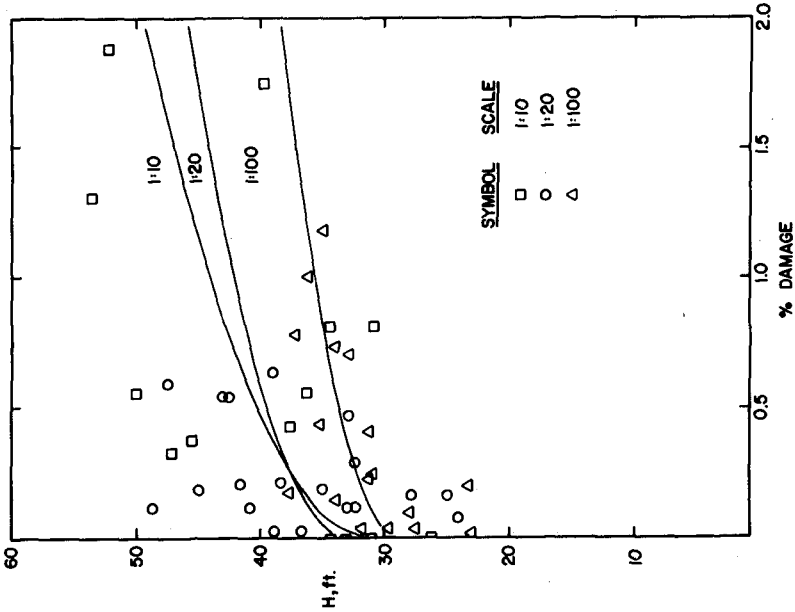


Fig. 14. Area I Damage versus Wave Height

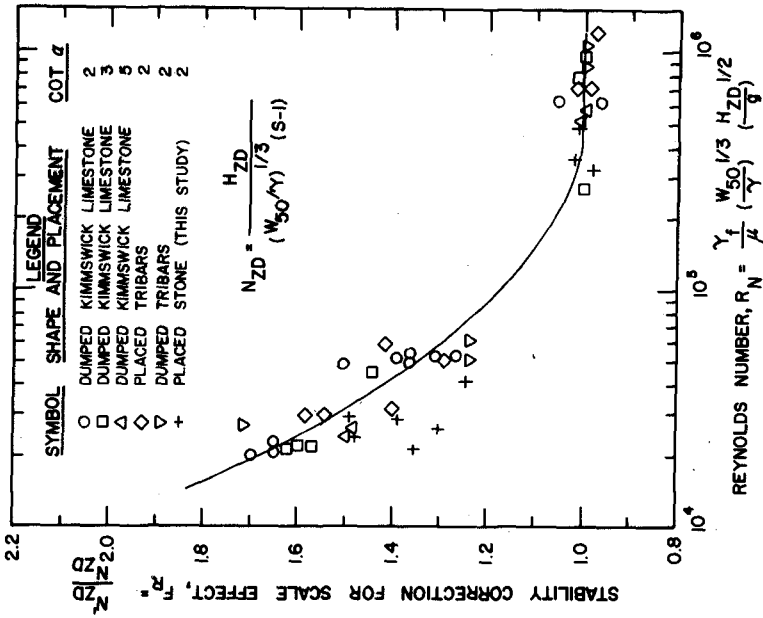


Fig. 15. Stability Scale Effect

Stability scale effects have been investigated by Thomsen, et.al. (1972), for several armor unit shapes. The results are summarized in Fig. 15. In this study, a zero damage stability coefficient, N_{ZD} , and Reynolds number, R_N , have been defined as presented on the figure, wherein:

- H_{ZD} = zero damage wave height (Zone 3-a or less)
- W_{50} = average armor unit weight
- γ = material specific weight
- S = material specific gravity
- γ_f = fluid specific weight
- μ = fluid dynamic viscosity.

The scale effect is defined as the ratio of the large scale stability coefficient, N_{ZD} , divided by a smaller scale stability coefficient, N_{ZD} . Data from the placed stone study are superimposed on the results of Thomsen, et.al., as indicated in the legend. Thomsen concluded that Reynolds numbers in excess of $3 \cdot 10^5$ must be achieved to avoid scale effects. Also, the no damage wave height will be overestimated by approximately 60% if the scale is reduced by another factor of five. The results from the present study support this conclusion. The 1:20 scale model occurs at the limiting Reynolds number and shows no significant scale effect. The 1:100 scale model is one-fifth of the limiting Reynolds number size, and a 40% reduction in stability is indicated, as shown in Fig. 15. Thus, small models underestimate prototype stability due to the magnification of drag forces at low Reynolds number.

Summary

The results of this study provide research and design information about the total hydraulic behavior of placed stone armor breakwaters. The armor surface responds to runup similar to an impermeable, graded riprap slope. Rundown, however, is reduced. Reflection coefficients are relatively low, compared to a smooth, impermeable reflecting surface. The structure is extremely stable, similar to that of dolos armor. Comparison of large and small model results indicate that scale effects distort small model results by decreasing runup, reflection and stability while increasing rundown.

Acknowledgements

This study was sponsored by the Umpqua Division of Bohemia Corporation, Eugene, Oregon and conducted at the Oregon State University Wave Research Facility.

References

- 1) Hudson, R.Y., "Wave Forces on Breakwaters," Transactions of ASCE, Vol. 118, 1953, p. 653.
- 2) Jackson, R.A., "Stability of South Jetty Siuslaw River, Oregon," Technical Report No. 2-631, U.S. Army Engineer Waterways Experiment Station, Corps of Engineers, Vicksburg, Mississippi, July 1963.
- 3) Le Mehaute, B., R.C. Koh and L.S. Hwang, "Synthesis on Wave Runup," J.W.W.H., Proceedings of ASCE, Vol. 94, No. WW1, February 1968, pp. 77-92.
- 4) Paul, M.W. and W.F. Baird, "Discussion of Breakwater Armor Units," The First International Conference on Port and Ocean Engineering Under Arctic Conditions, Vol. II, August 1971, p. 1-27.

- 5) Thomsen, A.L., Wohlt, P.E. and Harrison, A.S., "Riprap Stability on Earth Embankments Tested in Large and Small Scale Wave Tanks," Technical Memo No. 37, U.S. Army Coastal Engineering Research Center and Missouri River Division, June 1972.
- 6) U.S. Army Coastal Engineering Research Center, Shore Protection Manual, Vol. II., U.S. Govt. Supt. Doc., 1973

CHAPTER 149

DESIGN AND CONSTRUCTION OF PROTECTIVE STRUCTURE FOR NEW REEF RUNWAY HONOLULU INTERNATIONAL AIRPORT

by

Wilfred D. Darling, F. ASCE*

ABSTRACT

This paper describes the design and construction of the protective structure for a new Reef Runway at the Honolulu International Airport with special emphasis on the use of dolosse concrete armor units.

INTRODUCTION

A 12,000-foot long runway located parallel to and 6,700 feet south (seaward) of the existing 12,380-foot runway 8L-26R, which will permit increased capacity, noise abatement, and increased safety to downtown Honolulu and its suburbs, is nearing completion at the Honolulu International Airport as shown in Figure 1. The Reef Runway and associated taxiways are located on land created by over 19 million cubic yards of dredged coral placed on an existing reef. In order to protect the land fill from erosion by wave action, a 16,100 foot long protective structure has been built out of stone and 18,000 dolosse concrete armor units. The protective structure, which has a top elevation varying from plus 4.0 feet to plus 20.0 feet msl, is located approximately 1,000 feet south (seaward) from the centerline of the Reef Runway.

DESIGN STUDIES

Initial hydraulic model studies were made under contract with the University of Hawaii Look Laboratory under the Department of Ocean Engineering (1). Extensive three-dimensional and two-dimensional hydraulic model studies were

*Consultant on Coastal Engineering during the project, The Ralph M. Parsons Company, Honolulu, Hawaii.

made to facilitate design of the protective structure. The three-dimensional model was used initially to obtain storm wave information at the protective structure location to be used in two-dimensional studies, and later to study tsunami waves for possible interaction effect between the proposed structure and the adjacent harbors and shore properties and to measure run-up on the protective structure. Computer refraction studies were made to provide input for the three-dimensional study. The major conclusion resulting from the model study and refraction study was that the water depth fronting the proposed structure determines the design wave, which is a breaking wave, the size of which is dependent on the water depth at the seaside toe of the structure and bottom slope. The water depth on the reef along the protective structure varies from slightly below zero elevation msl at the shallow end to as much as 27 feet below zero msl at the deep end. A still water level of plus 3.0 feet msl was adopted for design resulting in design breaking waves of over 25 feet in part of the deep water section. The shallow water section of the structure is protected by a fringing coral reef that varies in width from 400 to over 2000 feet.

The two-dimensional study by Look Laboratory was completed to develop design criteria for overtopped and non-overtopped sections subjected to breaking waves. Armor units tested consisted of quarry stone and tribars. Subsequent to completion of the above mentioned initial studies, Tetra Tech, Inc., of Pasadena, California, was engaged to design the protective structure (2,3). Additional two-dimensional hydraulic model studies were made to develop overtopped and non-overtopped structure sections subjected to breaking waves. Quarry stone and dolosse armor units were tested. In addition to conventional side slopes, a seaside berm section was tested. Design parameters were adopted for use in design of the structure based on the above mentioned testing plus information available from previous studies by the U. S. Army Corps of Engineers (4), and the Port of East London, South Africa (5,6). For the dolosse the stability factor, K_p , as used in the Hudson formula, was based on a certain percent damage, namely 2% and 4%, resulting in K_p factors of 32 and 64, respectively, for the two conditions. This was considered acceptable in view of the infrequent occurrence of design storms. A layer coefficient K_d , of 1.3 was used resulting in a requirement for 75 4-ton dolosse for each 1,000 square feet of area covered and 55 6-ton dolosse for each 1,000 square feet. The design as completed for advertising included five alternates for the seased armor for the westerly 4,650 lineal feet of the deep water portion of the structure. The five alternates were as follows: 4 and 6-ton dolosse; a combination of stone and 4 and 6-ton dolosse; 8, 12, and 24-ton tribars; a combination of stone and 12 and 24-ton tribars; and all stone with a seaside berm 200-feet wide with top

elevation at minus 12 feet msl. The low bidder, Hawaiian Dredging and Construction Company, chose the dolosse alternate. For the shallow water reach the section consisted of ledge coral protected on the seaside by 2 layers of basalt armor stone with sizes varying from 250 lb nominal size at the shallowest end to 3000 lb in the deeper water. For the deep water portion of the structure, the first 1,650 lineal feet consisted of quarry run core stone with 2 layers of basalt underlayer stone protected by 2 layers of 5-ton armor stone, with the westerly 4,650 lineal feet protected by 4 or 6-ton dolosse armor. On the land side armor stone varied from 1300 lb to 8-ton size at the head section, with the majority of the land side armor stone being 5-ton size.

Figure 2 shows the typical non-overtopped section of the deep water portion of the structure on coral foundation with dolosse armor. The structure has a 15-foot top width, with 1 vertical to 1.5 horizontal side slopes on both sides except for the head section where the slopes are 1 vertical to 2.25 horizontal. Two layers of 2000 lb underlayer stone were used underneath the 4-ton dolosse while 2 layers of 3000 lb underlayer stone were used underneath the 6-ton dolosse. The land side apron shown on figure 3 was used in 3 reaches where overtopping during design storms is expected. The seaside foundation stone blanket shown was not included in the original contract but was added after construction was started when substantial areas of sand, with depths as much as 14-feet, were discovered in the foundation as a result of an underwater survey using a jet probe. Six reaches required the protective stone blanket under the dolosse armor with a total length of 870 lineal feet.

QUARRY OPERATIONS

Over 800,000 tons of stone was required for the core, underlayer, and armor of the protective structure. Twelve different sizes of stone were specified for use varying from quarry run core stone to 8-ton armor. The majority of the stone, 88%, was obtained from a quarry on the Island of Molokai, a distance of about 60 miles from the project location. The remainder of the stone was obtained from the Island of Oahu, including 51% of the 5-ton armor stone. The quarry at Molokai included andesite and basalt with the latter being the most predominant type of stone present. Investigations at the quarry were accomplished by percussion drilling only, no cores were obtained, thus very little was known of spacing of natural fractures in the formation. As it turned out the majority of the area opened up had quite closely spaced fractures, both vertically and horizontally, thus only a small percentage of the large size stone could be produced from any one blast.

In addition there were numerous areas where cinders and residual soil were encountered which resulted in the handling of a large quantity of waste material to permit recovery of acceptable stone. The specifications for the quarry run core stone permitted not more than 10% smaller than 4-inch size and required at least 10% exceeding 18-inch size. Because of the high percentage of small spalls and residual soil present, it was necessary to install a screening plant to scalp the core stone in order to meet the 10% maximum minus 4-inch requirement. Figure 4 is a view of the screening plant; after the large stone was picked from each blast, the quarry run material was hauled from the quarry floor to the top of bank and dumped into the hopper at the screening plant where the excess objectionable fines were removed.

Hauling of stone from the quarry to the wharf at Kaunakakai, Molokai, was done with 5 semi-trailer trucks, each carrying 2 20-ton steel containers which were picked up and dumped into barges by a crane. Figure 5 shows one of the trucks with the steel containers, while figure 6 shows the crane dumping one of the containers into a barge at the wharf. Five and six barges were generally used in the haul from Molokai to the project site with capacities varying from 600 to 1800 tons of stone per trip. The two smaller barges with 600 ton capacity were bottom dump barges used in hauling core stone for the deep portion of the structure.

CASTING OF DOLOS ARMOR UNITS

Casting of 6-ton dolos was started during October 1973. There were a total of 29 forms available. Forms for the 4-ton dolos were available in January 1974, from that time the normal daily casting included 80 4-ton and 29 6-ton dolosse. Special steel hinged forms were fabricated in Portland, Oregon, for the project. Figure 7 shows part of a row of forms with the traveling conveyor depositing concrete into one of the forms. Figure 8 shows a form opened for cleaning after removal of the dolos cast the previous day. Consolidation of the concrete was accomplished by the use of a form vibrator located under the horizontal section of the dolos form, as well as by the use of a cylindrical hand held vibrator which was inserted from the top of the vertical leg. The forms were filled each day with crews reporting on an early shift to remove form bolts and open the forms so that a fork lift could remove the dolosse cast the previous day and place them in storage where membrane curing compound was sprayed on the concrete. Forms were immediately cleaned and re-oiled and closed so that filling could start again. Figure 9 shows a form opened with the dolos ready for removal. Figure 10 shows the fork-lift carrying the dolos to the storage area.

CONSTRUCTION OF THE PROTECTIVE STRUCTURE

Construction was started at both ends. The bottom dump barges were used to dump core stone along the centerline at the west end with alignment provided by a laser beam. Also a floating crane was used to unload core and underlayer stone from non-dump barges at the deep end. At the east end ledge coral existed in a thin layer, 6 to 12 inches thick in the safety areas, where it was ripped by a D-9 tractor and loaded by drag line on trucks for hauling to the structure alignment. After the seaside slope was completed, a clamshell crane followed along and placed two layers of the size armor specified for the area involved. Armor stone which was off-loaded at a temporary wharf at the east end was hauled by truck and dumped on the adjacent work road on the landward side which is part of the safety area fill; the work road was kept at elevation plus 2 to 3 feet msl. A gradall and a crane were both used for placing the 250 and 550 lb stone; cranes only were used for the larger sizes of armor stone. At station 149+00, 6,400 feet from the west end of the structure, the transition to the deep section was started and core stone was trucked from the temporary wharf and end dumped to continue the work. Two layers of underlayer stone were placed by crane and another crane followed up after a short interval placing two layers of 5-ton armor stone. This continued for 1,750 lineal feet where the seaside armor changed to dolosse. Four-ton dolos were used for a total of 3,550 lineal feet, 13,692 were placed, while 6-ton dolos were used for a total of 1,100 lineal feet, including the head section, 4,317 were placed. The underlayer and back side armor for a major portion of the deep section of the structure was initially placed by one or two floating cranes, however, a great deal of work was required by cranes working on top of the structure, 7 to 9 feet below final crest, in straightening the sections to conform to plans. Batter boards were installed at regular intervals to assist the crane operators in placing the stone to line. Even with the use of batter boards it was noted that below the water surface a few feet the tendency was for the slope to steepen from 1 vertical to 1.5 horizontal specified since the natural angle of repose of the stone was steeper than the required slope. In order to check the seaside toe of the core, underlayer, and mark the toe for the dolosse, an offset centerline was established by divers on the sea bottom by anchored cables 25 or so feet seaward of the final structure toe. This facilitated locating the toe line for each item. Floats were placed for each toe line in turn which guided the crane operators in placing stone and dolosse.

DOLOSSE PLACING

Placing of dolosse concrete armor units was started during October 1974. A Manitowac 3000 crane equipped with special steel tongs was used for handling the dolos. At first the dolosse were loaded by fork lift truck on flat bed semi-trailors and hauled along the work road to the location where needed. Six 4-ton dolosse were hauled per load while four 6-ton dolosse were hauled per load. Figure 11 shows a load of 4-ton dolosse which have been delivered to the unloading point with the crane ready to lift a dolos prior to placing in the structure. The placing rate averaged about 20 dolosse per hour. Later a small barge with a capacity to haul 70 4-ton dolosse was used as shown in figure 12, however, because of the time required to load the barge and tow it from the east end temporary wharf out to sea and around the west end of the structure to a location behind the structure, placing of dolosse was limited to 70 per day, or less when swells would not permit the small tow boats to operate in the open sea. The use of flat bed semi-trailer trucks was resumed for hauling dolosse from the storage area to the structure and placing continued intermittently until the project was completed. One crane worked ahead on preparation of underlayer stone to final line for the dolosse, however, it could not keep ahead of dolosse placement so that at times two cranes worked on underlayer, and when 100 feet or so was approved dolosse placement would resume. Figure 13 shows a crane placing dolos as well as a view from the sea side showing a portion of completed dolosse armor. Figure 14 is a view of completed dolosse from the back side prior to placement of back-up stone.

Breakage of dolosse during placing operations amounted to 1.4% of the unreinforced units handled. Although the design specified two layers of dolosse, the requirement to place 75 4-ton and 55 6-ton dolosse for each 1,000 square feet of area to be protected resulted in a three-layer cover. A large percentage of the breakage resulted from trying to fit the top layer of dolosse in place. Data resulting from studies by the Waterways Experiment Station, U. S. Army Corps of Engineers, completed subsequent to design of this project, indicate that a layer coefficient, K_{Δ} , of 1.0 rather than 1.3 could be used to provide a two-layer cover without any loss of stability (7). Using this lower value would result in a requirement of 51 4-ton and 39 6-ton dolosse per 1,000 square feet of area protected, a considerable reduction from the number used on this project. This should be considered for future projects. Another interesting item on this project based on sections adopted where dolosse armor were used and unit prices for the stone and dolosse, is that protection by the 6-ton dolosse cost less than protection by the 4-ton dolosse, amounting to nearly \$1500 less cost for each 1,000 square feet of area protected by the 6-ton dolosse, as compared with the 4-ton dolosse. This is impor-

tant to consider when design contemplates accepting a percentage damage of dolosse armor. It could be less costly to design for no-damage with larger units than to accept damage of smaller units. Although the present structure was designed based on accepting 2% and 4% damage of the dolosse armor units, a calculation of the actual stability factors, K_D , along the structure based on actual depths of water at the seaward toe and slope of ocean bottom indicates that for a majority of the area stability factors fall well below the no-damage range as shown in the U. S. Army Corps of Engineers Shore Protection Manual (7). The Manual does recommend minimum slopes of 1 vertical to 2 horizontal for dolos armor until further test data is available*. However, the Reef Runway Protective Structure is designed for breaking waves throughout, thus there should be no question of adequacy of the present design where stability factors are below the values considered adequate for the no-damage condition.

ACKNOWLEDGEMENT

Acknowledgement is gratefully made to the State of Hawaii, Department of Transportation, Airports Division, for permission to present this paper.

*Dr. Robert Whalin, Chief, Wave Dynamics Division, U. S. Army Waterways Experiment Station, Corps of Engineers, indicated during the conference that additional testing of dolosse armor units has indicated that slopes of 1 vertical to 1.5 horizontal are stable and the Shore Protection Manual will be revised accordingly.

REFERENCES

1. J.K.K. LOOK LABORATORY, Department of Ocean Engineering, University of Hawaii, Hydraulic Model Study, Proposed Reef Runway, Honolulu International Airport, November 20, 1970.
2. COLLINS, J. IAN, Tetra Tech, Inc., Model Tests of the Reef Runway Protective Structure for Honolulu International Airport, August 1972.
3. COLLINS, J. IAN, Tetra Tech, Inc., Design Analysis for the Protective Structure for the Proposed Reef Runway at Honolulu International Airport, August 1972.
4. COASTAL ENGINEERING RESEARCH CENTER, U. S. Army Corps of Engineers, Technical Report No. 4, 1966.
5. MERRIFIELD, E. M. and ZWAMBORN, J. A., The Economic Value of a New Breakwater Armour Unit "Dolos", Volume 2, Proceedings of the 10th Conference on Coastal Engineering, September 1966.
6. MERRIFIELD, E. M., Dolos Concrete Armor Protection, Civil Engineering, December 1968, pages 38-41.
7. COASTAL ENGINEERING RESEARCH CENTER, U. S. Army Corps of Engineers, Shore Protection Manual, Volume II, 1973.

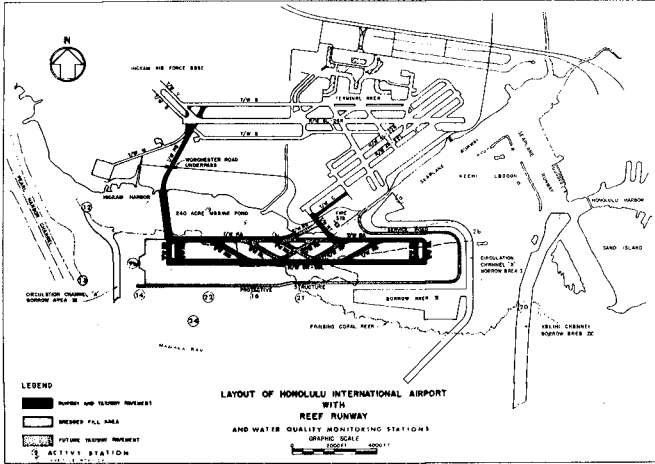


FIGURE 1 Layout of Honolulu International Airport with Reef Runway.

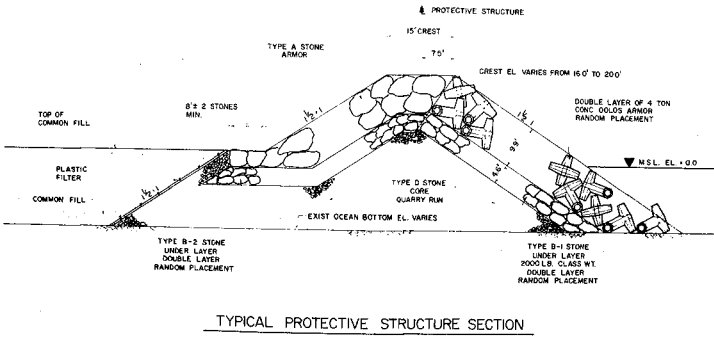


FIGURE 2 Non-overtopped Protective Structure Section.

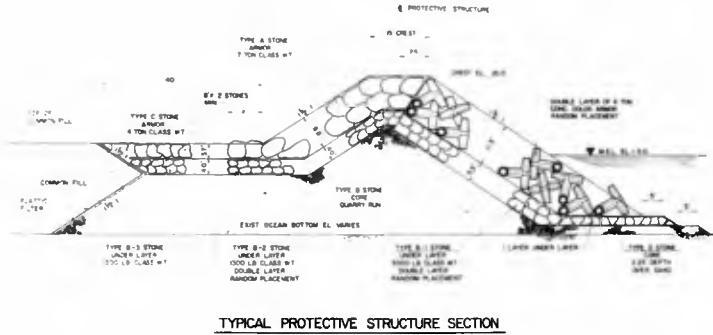


FIGURE 3 Over-topped Protective Structure Section.



FIGURE 4 Molokai Quarry - Screening Plant



FIGURE 5 Molokai Quarry - Stone Hauling Truck.



FIGURE 6 Kaunakakai, Molokai Wharf - Crane Loading Barge.



FIGURE 7 Casting Concrete Dolos



FIGURE 8 Dolos Form Open



FIGURE 9 Fork lift removing dolos from form



FIGURE 10 Fork lift placing dolos in storage yard



FIGURE 11 Dolosse on flat bed truck



FIGURE 12 Dolosse on barge



FIGURE 13 Crane placing dolos - Showing a view from ocean of completed dolosse armor.



FIGURE 14 View along backside of structure showing dolosse in place prior to placing back up armor stone.

CHAPTER 150

RESPONSE OF SEADYKES DUE TO WAVE IMPACTS

A. Führböter¹⁾, H. H. Dette²⁾ and J. Grüne³⁾

ABSTRACT

Damages on seadykes and revetments are mainly caused by wave impacts due to breaking waves. These impact forces act on small areas for a very short time and cause crater-like formations, when the forces are transmitted instantaneously to the side-walls of cracks in the cover of dykes or through joints into and below revetments.

In this paper the results of investigations on impact forces are presented. A comparison of field data and laboratory data proves considerable differences, which must be explained mainly by the different air entrainment for prototype and small-scale conditions in the breaking waves. Both the data from field and small-scale model emphasize, that the slope of the dyke or revetment is responsible at first for frequency and magnitude of the impact forces.

Furthermore the effect of impact forces is demonstrated by the results of investigations on the stability of stone revetments with joints.

1) Prof. Dr.-Ing., 2) Oberingenieur Dr.-Ing., 3) Dipl.-Ing.,
Leichtweiss-Institut für Wasserbau of the Techn. Univ. Braunschweig,
Germany, Div. of Hydrodyn. and Coastal Eng. and members of Sonder-
forschungsbereich 79 of the Techn. Univ. Hannover

INTRODUCTION

The wave impact force due to breaking wave is the main factor causing damages on seadykes and revetments at a level around the highest storm surge stillwater level.

These impact forces occur, when the water particles of the breaker tongue are stopped abruptly by the outer layer of dykes or revetments. The impacts stand out for very high pressures during a very short time (10^{-2} to 10^{-3} seconds) on small areas. This cause consequences, which are like detonations of the surface materials of seadykes. The effects of impacts are presented schematically in Figure 1 for different types of seadykes and revetments.

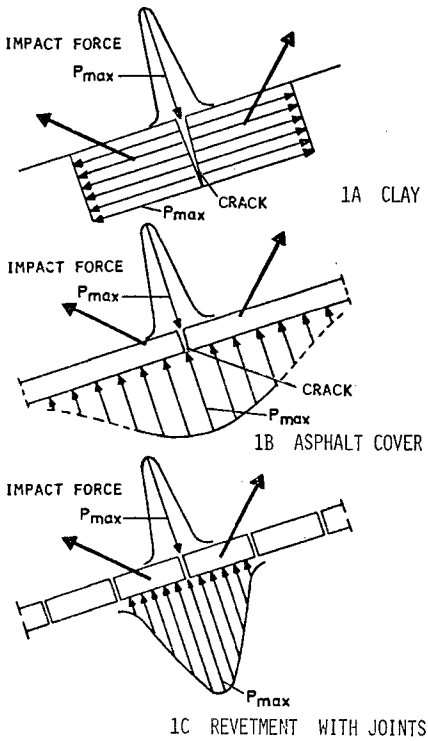


Fig. 1 Effects of wave impacts on seadykes and revetments

On dykes made from or covered with clay, a crater-like formation can be caused, when the impact force hits directly upon a crack in the clay surface (Fig. 1 a). Even more dangerous effects may occur, when these impact forces act on cracks of asphalt covered sand core dykes. The total force is transmitted instantaneously to the side-walls of the cracks and into the sand core beneath the asphalt cover. In combination with thixotrope effects of this water-saturated sand, also caused by the impacts, a sudden destruction of the dyke may be possible (Fig. 1 b).

Similar effects occur on revetments made from artificial concrete blocks with joints (Fig. 1 c).

The above mentioned effects occurring on the outer layer of dykes or revetments will become even more complicated when these covers are placed on natural or artificial filter layers.

Figure 2 and Figure 3 show some typical damages in the field caused by impact forces during heavy storm surges. Fig. 2 gives an example for a crater-like formation. The diameter was about 6.0 m, the depth about 2.0 m. The significant wave height during the attacking storm surges in 1973 has been hindcasted to 0.75 m.

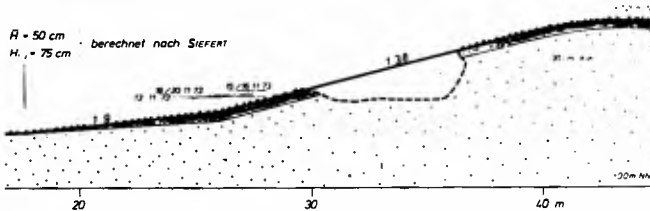


Fig. 2 Damage of clay-covered sand dyke due to wave impacts (after Forschungs- und Vorarbeitenstelle Neuwerk)



Fig. 3 Damage of a stone revetment due to wave impacts

First investigations of BAGNOLO 1939 (1) and DENNY 1951 (3) proved, that the occurrence of impact forces only can be described statistically. DENNY 1951 (3) showed, that by using regular waves the frequency distribution can be described with the normal distribution. This distribution even for regular waves is affected by the random effect of the breaking process itself. In prototype additionally the random effect of the breaker point due to random waves takes part, so that two random effects are superimposed to the occurrence of impacts.

INVESTIGATIONS ON IMPACT FORCES

In Germany in recent years some investigations on this phenomena have been carried out: FÖHRBÜTER 1966(4,5) simulated the impact forces of breakers in laboratory; results of field investigation and small-scale model tests are described by FÖHRBÜTER 1971 (6) and BOELKE, RELOTIUS 1974 (2).

FULL-SCALE LABORATORY TESTS

The laboratory tests of FÖHRBÖTER 1966(4,5) were carried out in prototype scale. This has been done by simulation only of the breaker tongue collapsing on the dyke surface. Figure 4 shows the principle of the simulation.

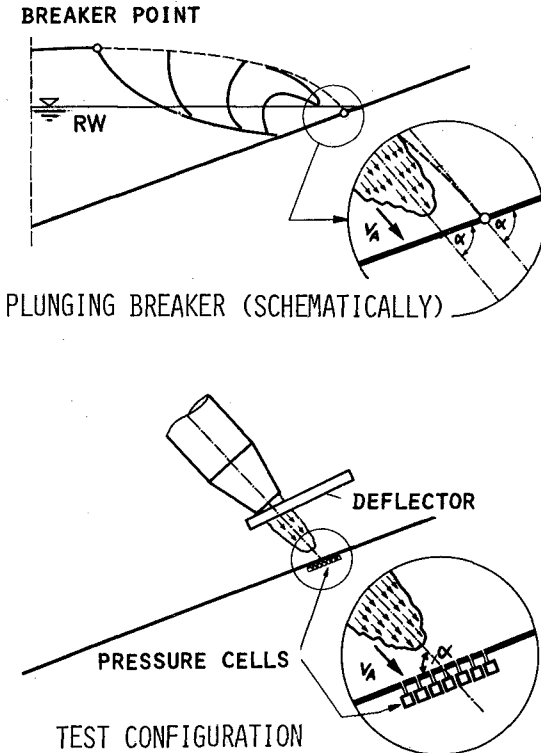


Fig. 4 Principle of the full-scale laboratory simulation of wave impacts (FÖHRBÖTER 1966)

The test equipment consisted of a pipe with a deflector for simulation of the breaker tongue and a surface with pressure cells for simulation of the dyke. The test conditions corresponded to wave heights of 1 to 3 m.

In Figure 5 as an example of the test results the frequency distribution of the maximum pressures

p_{max} has been plotted, in the lower part as an histogram, in the upper part as a log-normal distribution. The essentials of these tests were at first the verification of a normal distribution for occurrence of impact forces and secondly the demonstration that already a thin water-sheet due to the backflow of the preceding wave is damping the impact force magnitude (Fig. 6). For a thickness of the water-sheet of 0.1 m no more impact forces have been observed.

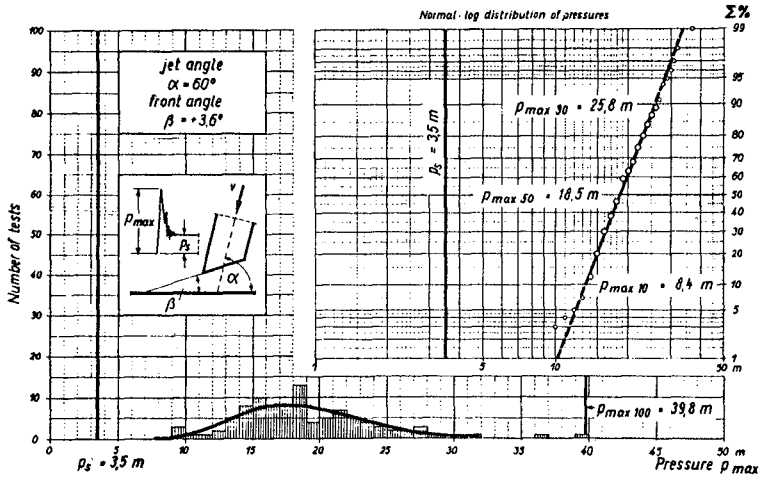


Fig. 5 Frequencies of maximum pressures p_{max}
 (FÜHRBÜTER 1966)

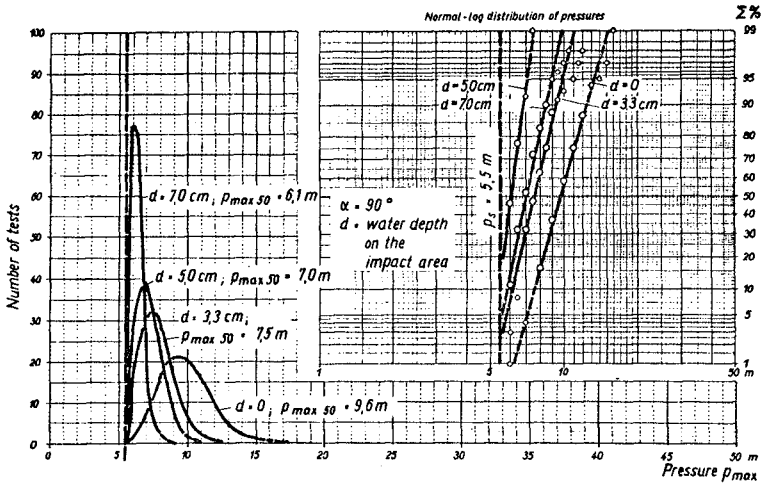


Fig. 6 Damping effect of a water-sheet
 (FÜHRBÜTER 1966)

FIELD INVESTIGATIONS

Field investigations have been carried out at the storm surge barrage of the Eider-river in Germany. At one adjacent asphalt covered sand dyke, which has a slope of 1 to 6, an additional testsection with a slope 1 to 4 has been added for research purpose (Figure 7). On both slopes pressure cells have been installed in steps of 0.25 m in vertical direction.



Fig. 7 Asphalt covered sand dyke of the Eider storm-surge barrage with test section (pressure cells before fitted in the asphalt cover)

Fig. 8 shows the time history of the occurrence of impact forces during one of the heavy storm surges of 1973 for both slopes. The influence of the slope comes out very clear as well for the total number of the impact forces as for the magnitude.

More distinct this effect comes out in Figure 9, which shows a comparison of the field data of three storm surges.

For a slope 1 to 4 a further comparison of laboratory and field data is

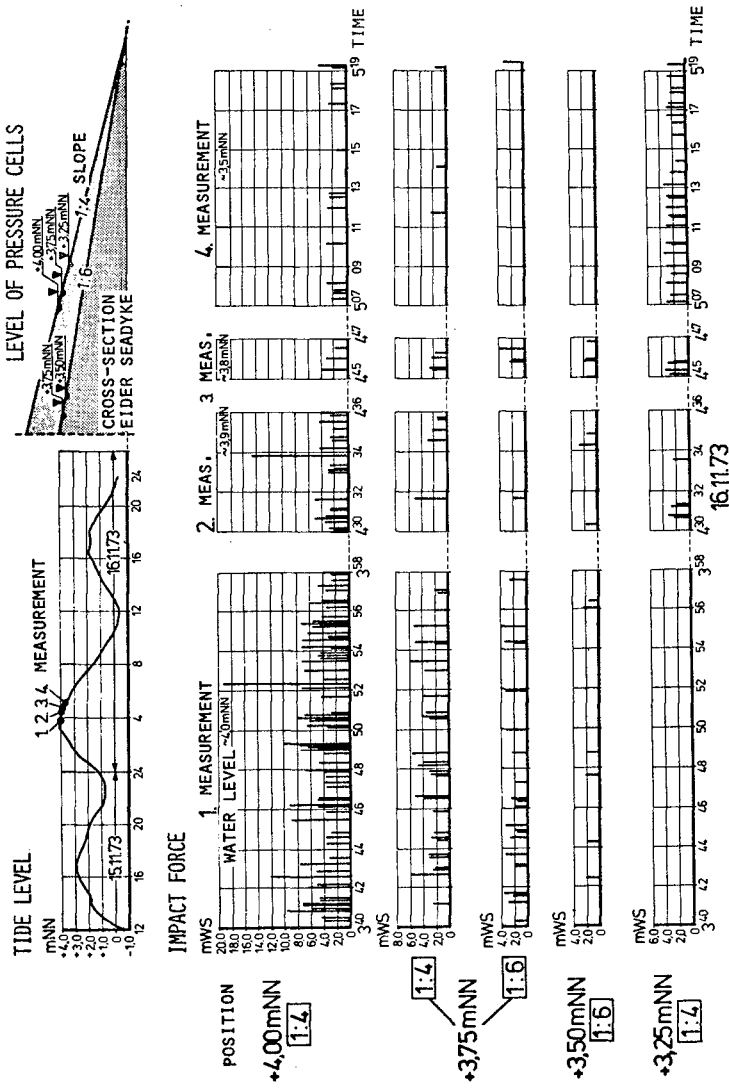


Fig. 8 Time history of impact forces during the storm surge of 16.11.73 (BOELKE, RELOTIUS 1974)

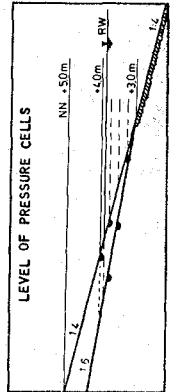
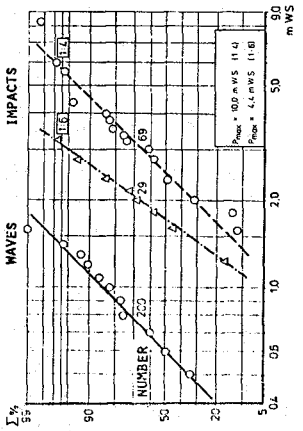
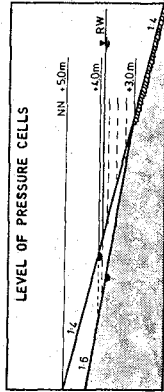
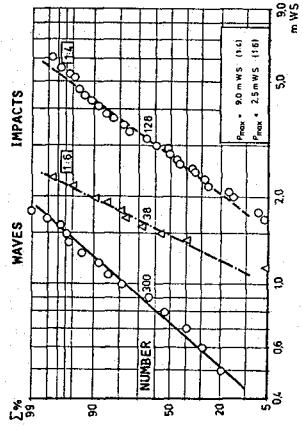
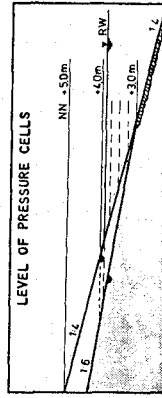
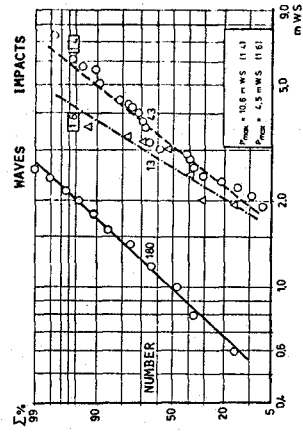


Fig. 9 Field data of three different storm surges (BOELKE, RELOTIUS 1974)

plotted in Fig. 10. The impact force distributions have been plotted as a multiple value compared to significant wave height H_s . The smallscale model tests were carried out with waveheights of about 0.2 m (approximately a scale 1 to 10 compared to field data); the field data were obtained for wave heights of 0.9 to 1.8 m and the prototype scale simulation in laboratory, which is mentioned before, corresponded to wave heights of about 1.0 to 3.0 m. This comparison confirmed theoretical treatments, that the impact forces cannot be reproduced in magnitude of transferred quantitatively for prototype conditions due to the different air entrainment in dependence of the absolute magnitude of waveheight.

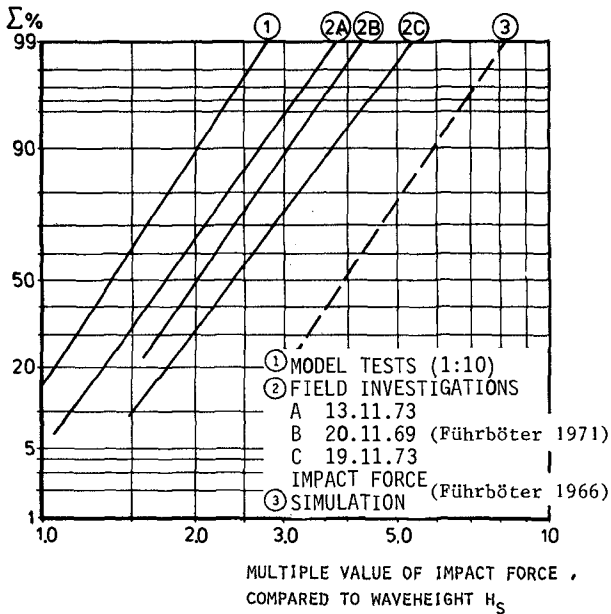


Fig. 10 Comparison of results for investigations on impact forces (slope 1:4) (BOELKE, RELTIUS 1974)

MODEL TESTS

Additionally to the field investigations further feedback model tests were carried out in order to know at which horizontal distances $\pm \Delta h$ from the

still water level impact forces do occur.

For different slopes 1 to 4, 1 to 5 and 1 to 6 Figure 11 shows the results.

On the horizontal axis $\pm \frac{\Delta h}{H_s}$ is equal the vertical distance of the impact

attack from the still water level referred to the significant wave height H_s .

The number of impacts within a sequence of 100 waves is defined as multiple

value of H_s ranging from $k = 1$ up to 2. It was found that the main impact

forces can be expected approximately in the range of Δh equal half the

significant wave heights H_s below the still water level.

Furthermore secondary-impact forces occur additionally around the still water

level and above. This can be explained by the effect, that the water particles

on the dyke surface are elevated due to the collapsing breaker tongue and

plunged down again on the surface.

INVESTIGATIONS ON THE STABILITY OF REVETMENTS

The results of impact force investigations have been confirmed by investigations on the stability of revetments made from concrete stones.

With regard to economical considerations heavy quarry stone revetments on seadykes which are stable due to their weight are more and more replaced by various types of light-weight concrete slabs and blocks which are different by the kind of interlocking and by the kind of surface roughness.

During heavy storm surges in 1973 and 1976 damages occurred on the concrete block revetment of a new seadyke in the Elbe-estuary. It was observed that the damage started due to the uplifting of single blocks out of the cover layer. This was continued by the washing-out of gravel which was used as filter layer and finally resulted in a damage of the revetment with holes having diameters of several meters (Fig. 12).

In order to explain the reasons for damages the revetment was rebuilt in model and attacked by waves as they have been observed during the storm surge. With the model-scale 1 to 5 it was found that the damage pattern in model was similar to that in nature so that this test series could be regarded as a calibration reference for further and more detailed investigations with regard to the selection of different filter layers.

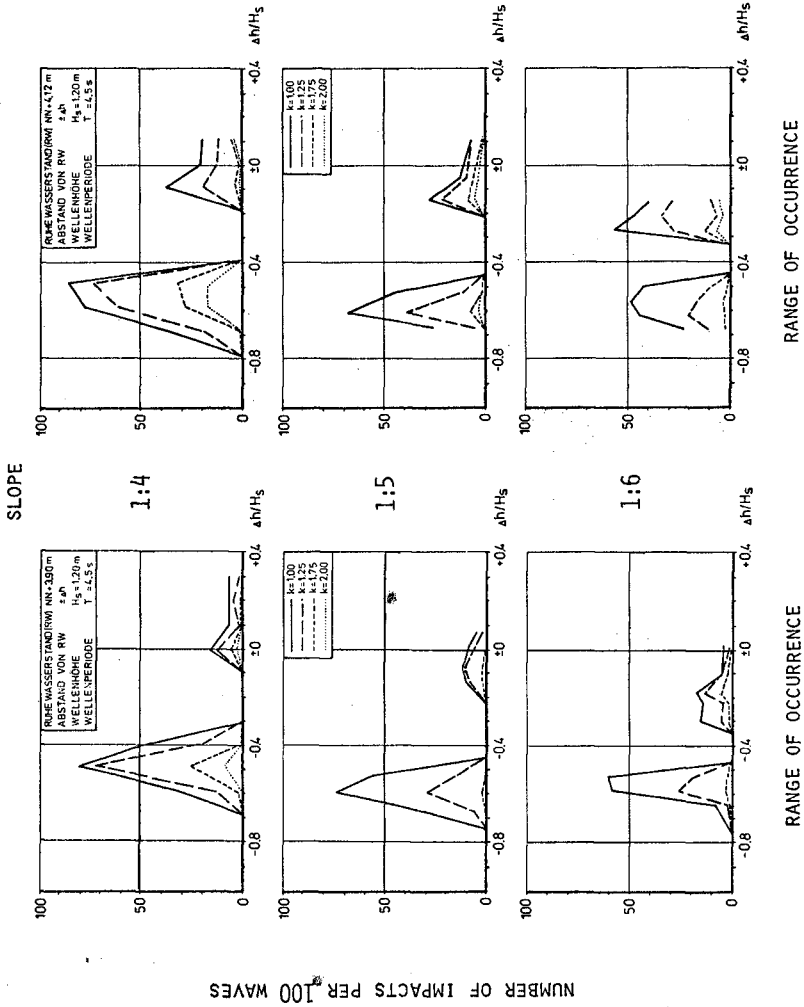


Fig. 11 Results of model tests on the occurrence range of wave impacts (BOELKE, RELOTIUS 1974)



Fig. 12 Typical damage of stone revetments due to wave impacts

One type of concrete stones (type HARINGMAN, prototype size: 0.5 x 0.5 x 0.15 m) which have been tested, were arranged in three different kinds on the seadykes with a slope of 1 to 3:

- revetment I: the stones are positioned on a 0.15 m thick (in prototype) layer of gravel (three-dimensional filter) and a nylon filter mat below the gravel for the protection of the sand core
- revetment II: the stones are positioned on a 0.05 m thick (in prototype) layer of gravel (three-dimensional filter), which lies on clay
- revetment III: the stones are directly fitted on concrete or asphalt

Fig. 13 shows a plan view of the revetment I and II, where the detached stones have been marked. For each test both revetments side by side have been attacked simultaneously by the same waves. These tests confirmed the occurrence

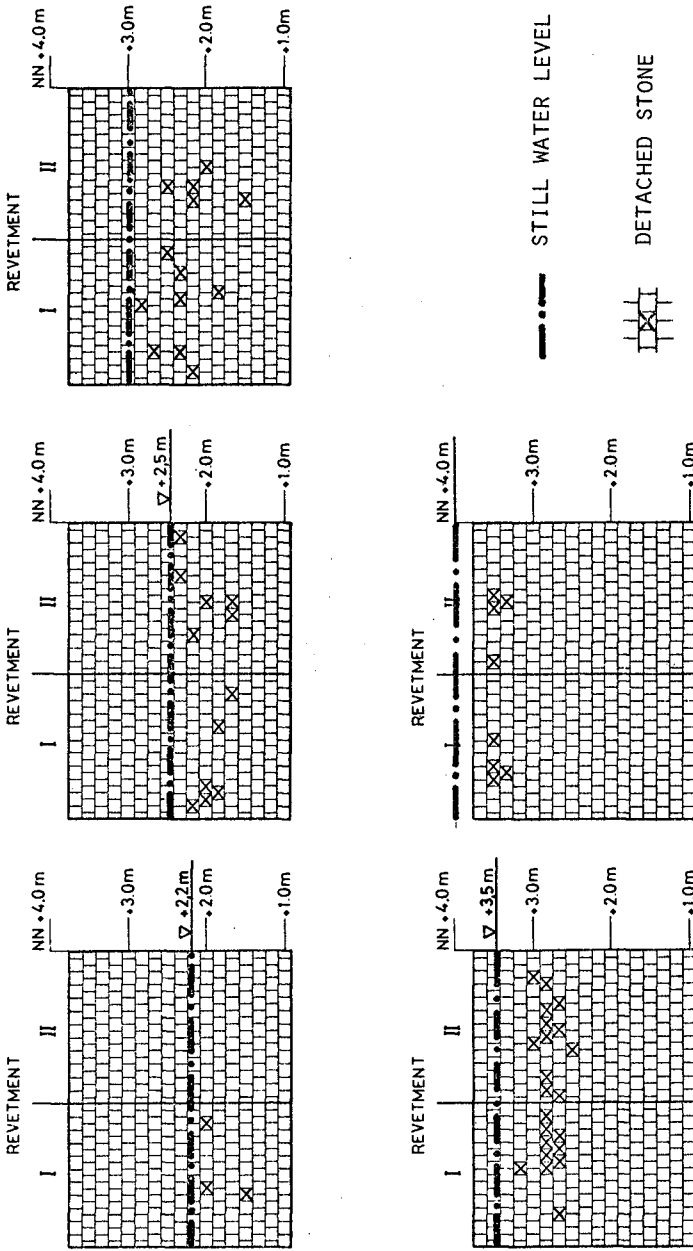


Fig. 13 Plan view of the revetment I and II with detached stones as an example for the range of the occurrence of detached stones

range of impact forces found in the model tests mentioned before. Fig. 14 shows an example of the damaged revetments in the model tests.



Fig. 14 Damaged revetment I and II after wave attack

In Fig. 15 and 16 the total number of detached stones is plotted as a function of the number of waves for the three revetments.

Damages occurred for all these arrangements. This can easily be explained by the effect of the impact forces, as the total force is transmitted instantaneously through the joints into the gravel layer.

The worst results were obtained for revetment II with a filter thickness of only 0.05 m (Fig. 15). For the 0.15 m thick gravel layer (revetment I)

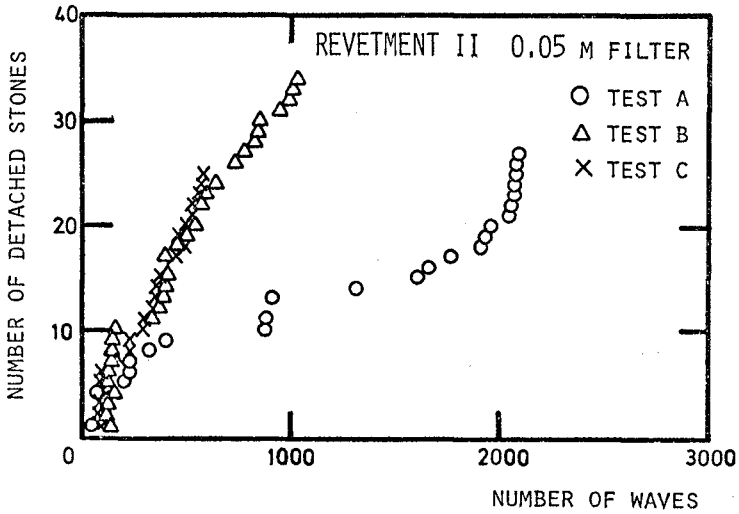
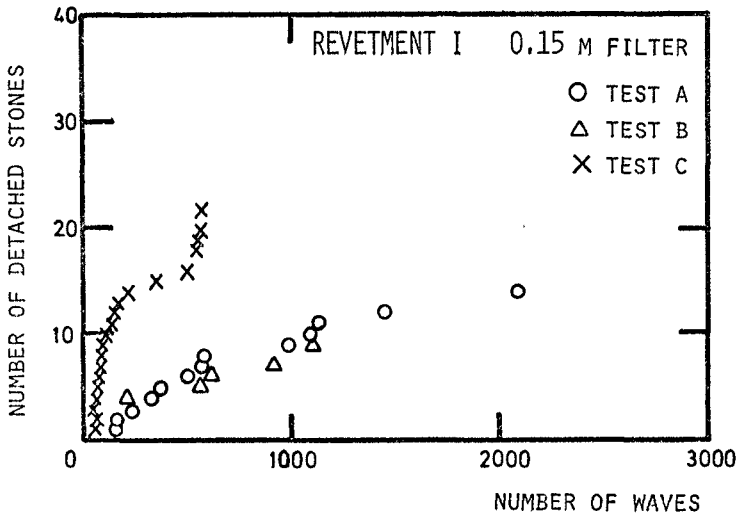


Fig. 15 Detached stones as a function of the number of waves

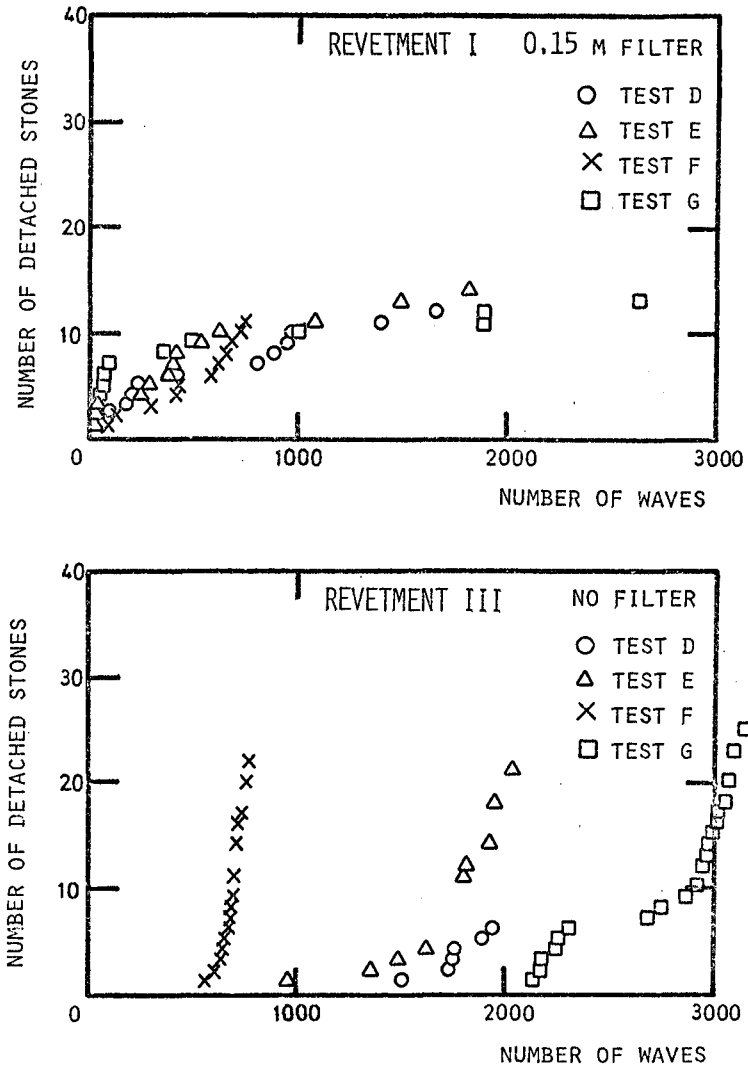


Fig. 16 Detached stones as a function of the number of waves

stabilisations of some damages have been observed, due to a gliding of the stones into the holes of the gravel layer and a guying there. For both gravel filters it was observed, that in addition to the damages due to impacts further damages occurred in that moment, when during the wave trough the water level in the filter was higher referred to the actual level of the wave. This is caused by the less faster draining of the water in the filter layer through the joints of the revetment in dependence of the wave movement. By this effect stones loosened by impact forces were uplifted and then slid down to the bottom of the revetment.

A comparison of revetment I and revetment III shows Fig. 16. The significant result is, that in the first stage of the wave attack there was no damage for revetment III (which has no filter), but after the first damages due to impact forces only this process preceded faster compared to the other types of revetments.

The important influence of filters has been tested for another type of concrete stones (type TERRAFIX, prototype weight 45 kg). In combination with a thin filter mat (two-dimensional filter) these blocks resisted more than 12.000 waves (H_s in prototype 1.6 m) with no damage.

The above mentioned investigations showed the complex behaviour of different filter layer types. It can be pointed out that filter layers cannot be selected independently of the type of the revetment; there are strong interactions between the different parameters. Further investigations on this subject will be carried out by the authors.

REFERENCES

1. BAGNOLD, R. A. 1939 Interim report on wave-pressures research
Journal of the institute of civil engineering,
London, 1939

2. BOELKE, S. and RELOTIUS, P. C. 1974 Über die wellenerzeugten Druckschlagbelastungen von Seedeichen im Böschungsbereich zwischen 1:4 und 1:6
Mitt. des Leichtweiss-Instituts der Techn. Universität Braunschweig, 1974
3. DENNY, D. F. 1951 Further experiments on wave pressures
Journal of the institution of civil engineers, Vol. 35, 1951
4. FOHRBÖTER, A. 1966 Der Druckschlag durch Brecher auf Deichböschungen
Mitt. des Franzius-Instituts der Techn. Universität Hannover, Heft 28, 1966
5. FOHRBÖTER, A. 1969 Laboratory investigation of impact forces
Proc. of Symposium on wave action
Vol. II. 1969, Delft
6. FOHRBÖTER, A. 1970 Air entrainment and energy dissipation in breakers
Proc. 12th Intern. Conf. on Coast. Eng., Sept. 1970, Washington
7. FOHRBÖTER, A. 1971 Zufallsprozesse bei der Belastung durch brechende Wellen,
SFB 79, Jahresbericht 1970
8. FOHRBÖTER, A. 1974 Modellversuche für ein Deckwerk aus Betonformsteinen
DETTE, H. H.
BOELKE, S.
RELOTIUS, P. C.
Bericht Nr. 266 des Leichtweiss-Instituts der Techn. Universität Braunschweig, 1974
(unpublished)

CHAPTER 151

PERMEABLE SEAWALL WITH RESERVOIR AND THE USE OF "WAROCK"

by

Takeshi IJIMA*, Enzoh TANAKA** and Hideaki OKUZONO***

Abstract

Interesting facts that a uniformly permeable seawall of vertical faces with appropriate reservoir has remarkable characteristics of absorbing wave energy even for long period waves in the same degree of usual sloped-face seawall and that these characteristics appear most clearly for permeable seawall of trapezoidal cross-section with backward-sloped reservoir wall are found theoretically and experimentally. Moreover, it is shown that a perforated wall with reservoir has similar characteristics to those for uniformly permeable wall with reservoir.

"Warock" is a type of concrete blocks which was invented in order to realize the wave absorbing seawall in practical works. Several examples of ever constructed wave absorbing seawalls, quaywalls and breakwaters by means of "Warock" in Japan are introduced.

I Introduction

A type of seawall with reservoir has been investigated by Jarlan (1961), Boivin(1963), Cote(1964), Terrett(1968), Marks(1968), Sawaragi (1973,1975) and others. And, they are concerned solely with perforated, thin wall and the effect of the width of the perforated wall in relation to the width of reservoir is entirely ignored. However, the width of permeable wall plays an important role to absorb the incident wave energy. In this paper, we are concerned with wide wall of uniform porosity and of perforated wall, and not only with permeable wall of vertical faces but also of sloped faces.

Since the ability for seawall to absorb incident wave energy is represented by the reflection coefficients, we are limited to the consideration on them. Moreover, since the wave absorbing ability appears clear-

* Professor: Faculty of Engineering, Kyushu University, Fukuoka, JAPAN

** Head: Wave Research Laboratory, Sansei Construction Co. Ltd.

Hakata-Ekimae, Hakata-Ku, Fukuoka 812, JAPAN

*** Research Assistant, Kyushu University, Fukuoka, JAPAN

ly for relatively long period waves, we first introduce a simple analysis for vertical-face reservoir seawall of uniform porosity by long wave theory and then a precise numerical analysis for seawall of arbitrary cross-section by means of the authors' method proposed in the paper entitled "A Method of Analyses for Two-Dimensional Water Wave Problems", which is submitted to this Conference. Finally, comparing the perforated wall with uniformly permeable wall experimentally, we introduce "Warock" as a practical tool to realize the reservoir seawall in actual field.

II Theory and Experiment on The Vertical-Face Seawall with Reservoir

In Fig.2-1, suppose that ABCD is a vertical wall of uniform porosity with width ℓ , placed in front of impervious wall EF with reservoir space d and on bottom FDB of constant water depth h . The origin of coordinate system is taken at still water surface on foreshore face AB and x-axis is in horizontal, z-axis is vertically upwards. The incident wave is assumed to be long wave with frequency ω .

Dividing the fluid region into three parts (0) ($x \geq 0$), (I) ($0 \geq x \geq -\ell$) and (II) ($-\ell \geq x \geq -(\ell+d)$) and indicating the quantities in these regions by subscripts 0, 1 and 2, respectively, the mass and momentum equations and the resulting horizontal fluid velocity u and surface displacement ζ by long wave assumption are as follows:

Region (0):

$$\frac{\partial \zeta_0}{\partial t} = -h \frac{\partial u_0}{\partial x}, \quad \frac{\partial u_0}{\partial t} = -g \frac{\partial \zeta_0}{\partial x} \quad (2.1)$$

Assuming incident wave of unit amplitude and reflected wave with complex reflection coefficient ψ_0 , the surface displacement ζ_0 is written as Eq.(2.2). Then, the fluid velocity u_0 and wave number k_0 are derived from Eq.(2.1) as Eq.(2.3) and (2.4).

$$\zeta_0 = (e^{ik_0x} + \psi_0 e^{-ik_0x}) e^{i\omega t} \quad (2.2)$$

$$u_0 = -\frac{gk_0}{\omega} (e^{ik_0x} - \psi_0 e^{-ik_0x}) e^{i\omega t} \quad (2.3)$$

$$\lambda_0^2 = \omega^2 h / g \quad \text{where} \quad \lambda_0 = k_0 h \quad (2.4)$$

Region (I):

Denoting the porosity as V , the linearized drag force coefficient for the porous material as μ and the mass force coefficient as \mathcal{E} , the mass

and momentum equations are as follows:

$$\frac{\partial S_1}{\partial t} = -\frac{h}{V} \frac{\partial u_1}{\partial x}, \quad \frac{1}{V} \frac{\partial u_1}{\partial t} = -g \frac{\partial S_1}{\partial x} - \frac{\mu}{V} u_1 - \frac{\varepsilon(1-V)}{V} \frac{\partial u_1}{\partial t} \quad (2.5)$$

Taking the surface displacement S_1 as Eq.(2.6), the fluid velocity u_1 and wave number K_1 are derived as Eq.(2.7) and (2.8).

$$S_1 = a_1 [e^{iK_1(\lambda+t)} + \psi_1 e^{-iK_1(\lambda+t)}] e^{i\omega t} \quad (2.6)$$

$$u_1 = -\frac{\sigma \nabla a_1}{k_1 h} [e^{iK_1(\lambda+t)} - \psi_1 e^{-iK_1(\lambda+t)}] e^{i\omega t} \quad (2.7)$$

$$\lambda_1^2 = [1 + \varepsilon(1-V) - i \frac{\mu}{\sigma}] \frac{\sigma^2 h}{g} \quad \text{where } \lambda_1 = k_1 h \quad (2.8)$$

Region (II):

Eq.(2.1) is valid here, and putting the surface displacement S_2 as Eq.(2.9), the fluid velocity u_2 is provided by Eq.(2.10).

$$S_2 = a_2 [e^{iK_0(\lambda+l+d)} + \psi_2 e^{-iK_0(\lambda+l+d)}] e^{i\omega t} \quad (2.9)$$

$$u_2 = -\frac{g K_0 a_2}{\sigma} [e^{iK_0(\lambda+l+d)} - \psi_2 e^{-iK_0(\lambda+l+d)}] e^{i\omega t} \quad (2.10)$$

On the boundary EF ($x = -(\ell+d)$), horizontal fluid velocity u_2 must vanish, so that we have

$$\psi_2 = 1, \quad S_2 = a_2 [e^{iK_0(\lambda+l+d)} + e^{-iK_0(\lambda+l+d)}] e^{i\omega t} \quad (2.11)$$

On the boundary CD ($x = -\ell$) and OB ($x = 0$), horizontal velocity and surface displacement should be continuous.

$$\begin{aligned} S_1 &= S_2 & \text{and} & & u_1 &= u_2 & \text{at } x = -\ell \\ S_1 &= S_0 & \text{and} & & u_1 &= u_0 & \text{at } x = 0 \end{aligned} \quad (2.12)$$

Accordingly, we have

$$a_1(1+\psi_1) = a_2(e^{iK_0 d} + e^{-iK_0 d}), \quad \alpha a_1(1-\psi_1) = a_2(e^{iK_0 d} - e^{-iK_0 d}) \quad (2.13)$$

$$1+\psi_0 = a_1(e^{iK_1 \ell} + \psi_1 e^{-iK_1 \ell}), \quad 1-\psi_0 = \alpha a_1(e^{iK_1 \ell} - \psi_1 e^{-iK_1 \ell}) \quad (2.14)$$

where $\alpha = \frac{V \Gamma}{\lambda_0 \lambda_1}$ and $\Gamma = \sigma^2 h / g$ (2.15)

From Eq.(2.13) and (2.14), ψ_0 is obtained as follows:

$$\Psi_0 = \frac{1 - \alpha^2 - \gamma(1 + \alpha)^2 + 4\alpha e^{-2ik_r d}}{(1 + \alpha)^2 - \gamma(1 - \alpha^2)} \quad (2.16)$$

where

$$\gamma = e^{-2ik_r d} + e^{-2ik_r l} - e^{-2i(k_r d + k_r l)}$$

The reflection coefficient K_r is given by the absolute value of Ψ_0 .

$$K_r = |\Psi_0| \quad (2.17)$$

Fig.2-2 is the calculated and measured reflection coefficients for various reservoir width d , when the permeable wall width l is equal to water depth h and the incident wave frequency $\alpha^2 h/g$ is 0.25 (the depth to wave length ratio h/L is 0.083). Horizontal axis shows the ratio of total width $X (= l + d)$ to depth h or to wave length L .

The model wall in experiments is made by armor blocks of 500 cm³ with porosity $V = 0.63$ in wave flume of length 22 m with water depth $h = 50$ cm. The reflection coefficients are measured by Healey's method with incident wave height of 5 ~ 7 cm. Calculated values are obtained by Eq.(2.16)(2.17) with $\xi = 0$, $V = 0.40$ and $\mu/\rho = 1.1$.

From the figure, it is found that the reflection coefficient decreases with the increase of total width X and reaches the minimum 0.1 at $X \approx 2.2h$ or $X \approx 0.18L$ and then increases gradually.

Fig.2-3 is the one for $l = h$ and $\alpha^2 h/g = 0.5$ ($h/L = 0.123$).

Fig.2-4 is for $l = 0.5h$ and $\alpha^2 h/g = 0.50$ ($h/L = 0.123$).

In both cases, the tendency of the change of reflection coefficient with the increase of reservoir width (or increase of total width X for fixed width of permeable wall) is entirely similar to each other and to the one in Fig.2-2, and the minimum coefficient appears at $X = 0.18L$ in every cases.

From above results, it is clear that if a vertical permeable wall is equipped with a reservoir behind it, the reflection coefficient decreases remarkably and reaches minimum at an appropriate width of reservoir. And the total width of seawall at that most effective wave absorbing ability is about 0.18 times the wave length, when the width of permeable wall is half or equal to the water depth, more generally, when the width is the same order of water depth.

Above-described analysis is based on the long wave assumption. As for general waves, the problem has been analyzed by the author(1972) by the method of continuation of velocity potentials. Fig.2-5 is an example

of calculated results by above method for $\ell = h$ and $\alpha^2 h/g = 0.25, 0.50, 1.0$ and 2.0 , taking $V = 0.5$, $\mu/\rho = 2.0$ and $\xi = 0$. From this figure, it is clear that the minimum reflection coefficient appears to each $\alpha^2 h/g$ but the minimum value itself is smaller for smaller $\alpha^2 h/g$, that is, for longer wave length. That is to say, the effect of reservoir to wave absorbing ability appears clearer for longer period waves than for shorter waves.

These minimum values of reflection coefficients are the same order of those which are attained by usual sloped-face seawall. That is, the permeable seawall with reservoir has a same degree of ability for absorbing incoming energy as sloped-face seawall, though it is limited to some particular period wave, corresponding to the width of permeable wall and reservoir.

Above results of theoretical and experimental investigations are summarized as follows:

(i) Permeable vertical seawall without reservoir cannot absorb incoming wave energy effectively, even if the wall is sufficiently wide, that is, the wave absorbing ability of vertical seawall without reservoir is unsatisfactory for ordinary period waves and it is impossible to expect the same degree of absorbing effect as permeable sloped seawall, especially for long period waves. This is due to the fact that on general sloped surface the incident wave deforms gradually or abruptly due to sudden decrease of water depth on the slope and accelerates the fluid velocity or otherwise breaks and dissipates the greater part of the energy, but on the contrary, for vertical permeable wall the incident wave penetrates partly into the wall without deformation or breaking, so that only a part of the energy is lost solely by turbulence in permeable wall. Consequently, in order to induce an effective energy dissipation in permeable wall, it is necessary to accelerate the fluid velocity inside the wall. The reservoir behind the permeable wall plays a role of accelerating the fluid flow across the permeable wall for ordinary or even for longer period waves. This situation is as follows: When a wave crest comes, the permeable wall dams up the flow of incoming wave in front of the wall and the reservoir stores the inflow water. And the water level in the reservoir rises up gradually with some lag following to the rising up of outside water level. When a trough comes, the situation is reversed. Such a difference of water levels along inside and outside faces of permeable wall and therefore,

the surface slope of flow in permeable wall is always steeper than the one for flow without reservoir. This is the reason why the reservoir accelerates the flow across the wall and induces a large amount of energy loss. And, there exists the most effective width of reservoir for given width of permeable wall, wave period and water depth to induce the maximum amount of energy loss.

(ii) For ordinary or longer period waves, the reflected wave is minimized when the total width of seawall with reservoir (the permeable wall plus the reservoir width) is about 0.18 times the wave length, when the width of permeable wall is the same order of water depth. This total width is considerably shorter than the one for perforated, thin wall. Sawaragi(1973) has shown that the total width for the latter to provide the minimum reflection coefficient is $0.25L$, that is, one-fourth of wave length. This is due to the fact that in case of thin, perforated wall the reflected wave from the backwall of the reservoir (EF in Fig.2-1) constitutes a standing wave system with the incident wave and the maximum horizontal fluid flow appears at nodal point (at the point of $L/4$ from EF) and that the maximum energy dissipation is induced by this flow through perforated wall. Therefore, the reservoir in this case does not play any particular role to accelerate the fluid flow through perforated wall.

(iii) The reflection coefficient attained by the reservoir seawall of above total width is sufficiently small in the same degree as the one by permeable sloped-face seawall. And at the same time, the surface wave elevation along the foreside face of wall is much smaller than the one for vertical permeable wall without reservoir, which results in the smaller amount of overtopping waves than the latter.

III Generalized Analysis for Reservoir Seawall of Arbitrary Cross-Section

In Fig.3-1, suppose that AA'B'B is a uniformly permeable wall of arbitrary cross-section placed on impervious sea bottom CB'A'O' with variable water depth. The origin of coordinate system is taken at still water surface and is sufficiently distant from the seawall at constant water depth h . x-axis is in horizontal and z-axis is vertically upwards. Then, fluid region is divided into four parts (O), (I), (II) and (III).

Assuming that the drag force for the porous material in region (II) is linearized to be proportional to fluid velocity, the fluid motion in region (II) has a velocity potential.

Then, the velocity potential in each region is represented in the form of Eq. (3.1) with potential function ϕ_c , $\phi^{(1)}$, ϕ^* and $\phi^{(3)}$, denoting the incident wave amplitude as S_c and frequency as ω .

$$\bar{\Phi}(x, z, t) = \frac{\gamma S_c}{\gamma} \phi(x, z) e^{i\omega t} \tag{3.1}$$

After the same manner as the method proposed in our separate paper "A method of Analyses for Two-Dimensional Water Wave Problems", the boundary-values and its normal derivatives of potential functions for region (I), (II) and (III) are in the following relations, where potential functions on the boundaries are defined as shown in Fig.3-1:

Region (I):

On \overrightarrow{OA} : $\bar{\Phi}_1^{(1)} = \Gamma \Phi_1^{(1)}$ where $\Gamma = \frac{\rho^2 h \gamma}{\rho}$ (3.2)

On $\overrightarrow{AA'}$: $\bar{\Phi}_2^* = \bar{\Phi}_2^{(1)}$, $\Phi_2^* = \frac{1}{\beta} \Phi_2^{(1)}$ where $\beta = \frac{\alpha}{\bar{\nu}}$ (3.3)

On $\overrightarrow{A'O'}$: $\bar{\Phi}_3^{(1)} = 0$ (3.4)

On $\overrightarrow{O'O}$: $\bar{\Phi}_c = i\lambda_c(1-\psi)A(RZ)$, $\Phi_c = (1+\psi)A(kZ)$ (3.5)

Region (II):

On \overrightarrow{BA} : $\bar{\Phi}_1^* = \alpha \Gamma \Phi_1^*$ where $\alpha = 1 + \varepsilon(1 - \bar{\nu}) + i\mu/\rho$ (3.6)

On $\overrightarrow{AA'}$: Same as Eq. (3.3) (3.7)

On $\overrightarrow{A'B'}$: $\bar{\Phi}_3^* = 0$ (3.8)

On $\overrightarrow{B'B}$: $\bar{\Phi}_4^* = \bar{\Phi}_3^{(3)}$, $\Phi_4^* = \frac{1}{\beta} \Phi_3^{(3)}$ (3.9)

Region (III):

On \overrightarrow{BC} : $\bar{\Phi}_1^{(3)} = \Gamma \Phi_1^{(3)}$ (3.10)

On $\overrightarrow{CB'}$: $\bar{\Phi}_2^{(3)} = 0$ (3.11)

On $\overrightarrow{BB'}$: Same as Eq. (3.9) (3.12)

Thus, the Green's identity formula for every region are as follows:

(i) Region (I)

$$\begin{aligned}
 & -\Phi^{(1)}(i) + \sum_{j=1}^{N_1^{(1)}} (\bar{E}_{ij} - \Gamma E_{ij}) \Phi_i^{(1)}(j) + \sum_{j=1}^{N_2^{(1)}} [\bar{E}_{ij} \Phi_2^{(1)}(j) - E_{ij} \bar{\Phi}_2^{(1)}(j)] + \sum_{j=i}^{N_3^{(1)}} \bar{E}_{ij} \Phi_j^{(1)}(j) \\
 & + \psi \sum_{r=1}^M G_{ir} A(kZ_r) = - \sum_{r=1}^M G_{ir}^* A(kZ_r) \\
 & \quad (i = 1 \sim N_1^{(1)}, 1 \sim N_2^{(1)}, 1 \sim N_3^{(1)}, (0, Z_p) \text{ on } \overrightarrow{O'O}) \tag{3.13}
 \end{aligned}$$

(ii) Region (II)

$$\begin{aligned} \phi^{*(i)} + \sum_{j=1}^{N_1^*} (\bar{E}_{ij}^* + \alpha \Gamma E_{ij}^*) \phi_i^*(j) + \sum_{j=1}^{N_2^{(i)}} \left[\frac{1}{\beta} \bar{E}_{ij}^* \phi_2^{(i)}(j) - E_{ij}^* \bar{\phi}_2^{(i)}(j) \right] \\ + \sum_{j=1}^{N_3^*} \bar{E}_{ij}^* \phi_3^*(j) + \sum_{j=1}^{N_3^{(3)}} \left[\frac{1}{\beta} \bar{E}_{ij}^* \phi_3^{(3)}(j) - E_{ij}^* \bar{\phi}_3^{(3)}(j) \right] = 0 \end{aligned}$$

$$(i = 1 \sim N_1^*, 1 \sim N_2^{(i)}, 1 \sim N_3^*, 1 \sim N_3^{(3)}) \quad (3.14)$$

(iii) Region (III)

$$-\phi^{(i)} + \sum_{j=1}^{N_1^{(3)}} (\bar{E}_{ij} - \Gamma E_{ij}) \phi_i^{(3)}(j) + \sum_{j=1}^{N_2^{(3)}} \bar{E}_{ij} \phi_2^{(3)}(j) + \sum_{j=1}^{N_3^{(3)}} [\bar{E}_{ij} \phi_3^{(3)}(j) - E_{ij} \bar{\phi}_3^{(3)}(j)] = 0$$

$$(i = 1 \sim N_1^{(3)}, 1 \sim N_2^{(3)}, 1 \sim N_3^{(3)}) \quad (3.15)$$

The notations used in above equations are the same as those in our separate paper (1976).

Eq. (3.13) (3.14) (3.15) are $(N_1^{(i)} + 2N_2^{(i)} + N_3^{(i)} + N_1^* + N_3^* + N_1^{(3)} + 2N_3^{(3)} + N_2^{(3)} + 1)$ linear equations with respect to the same number of unknown quantities $\phi_i^{(i)}$, $\phi_2^{(i)}$, $\bar{\phi}_2^{(i)}$, $\phi_3^{(i)}$; ϕ_i^* , ϕ_3^* ; $\phi_i^{(3)}$, $\phi_2^{(3)}$, $\phi_3^{(3)}$, $\bar{\phi}_3^{(3)}$ and ψ . Solving above equations simultaneously, we obtain all of the unknowns and the potential values at points in every region are calculated by Green's theorem. The reflection coefficient K_r is given by the absolute value of ψ . In addition, the surface wave profiles are calculated as follows:

$$\text{From C to B: } S_3(j)/S_0 = -i \phi_1^{(3)}(j) e^{i\sigma t}, \quad j = N_1^{(3)} \sim 1 \quad (3.16)$$

$$\text{From B to A: } S^*(j)/S_0 = -i \phi_1^*(j) e^{i\sigma t}, \quad j = 1 \sim N_1^* \quad (3.17)$$

$$\text{From A to O: } S_i(j)/S_0 = -i \phi_1^{(i)}(j) e^{i\sigma t}, \quad j = N_1^{(i)} \sim 1 \quad (3.18)$$

Above method is applied to reservoir seawall with various cross-sections, where the permeable wall is of rectangle, trapezoid and inverse trapezoid, and the backwall of reservoir is vertical or sloped, as shown in Fig.3-2. The width of rectangular wall is taken as $h/2$ and those of trapezoidal wall at still water level, half depth and bottom are taken as $h/4$, $h/2$ and $3h/4$, respectively, so as to be of the same cross-sectional area as the rectangle. The slope of the backwall is taken as $\pm 60^\circ$ to the horizontal bottom.

In Fig.3-2, the type (A) is of vertical backwall, the type (B) is of backward-sloped backwall and the type (C) is of forward-sloped backwall. As shown in later, since the characteristics of the reservoir are represented by its width at still water level, the representative width of the seawalls

is better to be taken as X , which is the distance from the half-depth point on the foreside face of permeable wall to the water line of the backwall of reservoir.

In numerical calculations, we take the geometrical surface OO' at the distance $3h$ from the seawall and $N_1'' = 15$, $N_2'' = 10$, $N_3'' = 12$, $M = 21$ for region (I), $N_1^* = 5$, $N_2^* = 5$ for region (II). As for the region (III), we take $N_3^{(3)} = 10$, and $N_1^{(3)}$, $N_2^{(3)}$ are taken as $6 \sim 10$, according to the variable width of the reservoir. The porosity V is taken as 0.7 and the coefficient μ/ρ is as 0.9, \mathcal{E} is 0.

Fig.3-3 is the calculated reflection coefficients of the type (A) with respect to the ratio of total width X to the water depth or the ratio to the wave length L , for $\alpha^2 h/g = 0.50$ ($h/L = 0.123$). It is seen that in every wall, the minimum reflection coefficient appears at $X = 1.5h$ or $X = 0.18L$ and that the wave absorbing ability of the inverse trapezoidal wall is inferior to those of the others. Therefore, it will be reasonable to exclude the inverse trapezoidal wall from further considerations.

Fig.3-4 shows the calculated reflection coefficients for the type (B) and (C), excepting the inverse trapezoidal wall, in comparison with the one for rectangular wall with vertical backwall. It is found that in every wall the minimum reflection coefficient appears at nearly the same value of X as before, and that for smaller values than that X , the type (B) provides lower reflection coefficients than those of the type (C). Therefore, it will be reasonable to conclude that the rectangle or trapezoidal wall of the type (B) is better, of which the trapezoidal wall will be the most preferable, because of the smallest volume of the reservoir.

Above characteristics for various types of reservoir seawall based on the calculated results are proved by experiment.

Fig.3-5 shows the measured reflection coefficients for the type (A). The model walls are made by quarry stones of mean diameter 5 cm with porosity $V = 0.53$ in wave flume with water depth $h = 50$ cm and length 22 m, and reflection coefficients are measured by Healey's method for incident wave height $H = 6.7$ cm. From the figure, it is clear that the minimum reflection coefficient appears at the same value as the one calculated before, and that the inverse trapezoidal wall shows the highest reflection coefficient.

Fig.3-6 is the measured reflection coefficient for the type (B). This shows that the rectangular or trapezoidal wall is better.

Above results for various types of seawall are summarized as follows:

(i) As for the cross-section of permeable wall, the rectangular or trapezoidal wall is better than the inverse trapezoidal wall. As for the back-wall of reservoir, the backward-sloped one is better and forward-sloped one is to be avoided.

(ii) The reservoir is characterized not by the volume but by its free surface width. And, the total width for the seawall to provide the minimum reflection coefficient is about 0.18 times the wave length and the value at that width is the same order of the one attained by permeable sloped-face seawall.

IV Characteristics of the Perforated, Wide Wall with Reservoir

In the uniformly permeable wall, the energy dissipation is induced by the turbulence of flow inside the wall. While, in the perforated wall, the energy is dissipated mainly by jet flow turbulence through the wall. Therefore, the situation seems to be quite different. However, the experiments on the perforated wall show that the wave absorbing characteristics of the permeable and perforated walls quite resemble to each other.

Fig.4-1 is the measured reflection coefficients of perforated walls with reservoir, where the water depth h is 50 cm, wave frequency $\omega^2 h/g$ is 0.50 ($h/L = 0.123$) and incident wave height is $H_i = 4 \sim 6$ cm. The diameter of the circular holes of the wall is kept as $D = 5.0$ cm, average porosity is $V = 0.33$ and the width of the wall is varied as 4, 10 and 20 in cm, that is, $l/h = 0.08, 0.20$ and 0.40 .

From the figure, it is found that the minimum reflection coefficient appears at $X/L = 0.25$ for $l/h = 0.08$, at $X/L = 0.20$ for $l/h = 0.20$ and at $X/L = 0.18$ for $l/h = 0.40$, that is, for wide wall the total width for minimum reflection coefficient is nearly $0.18L$, which is the same value as the one for uniformly permeable wall and for thin wall the total width for minimum reflection coefficient approaches to $L/4$, which is also the same value as permeable wall.

Fig.4-2 is the measured reflection coefficients for constant width of perforated wall $l = 10$ cm. Water depth is 50 cm and wave frequency is $\omega^2 h/g = 0.50$, the incident wave height is $4 \sim 6$ cm. The diameter of horizontal holes varies as 3.2 cm, 5.0 cm and 8.0 cm, with average porosity $V = 0.33$. From this figure, it is seen that the reflection coefficients for larger diameter than incident wave height are higher than those for smaller

diameter but the minimum values for every diameter appear at nearly the same value of $X/L = 0.20$.

From above results, it will be estimated that the perforated wall has similar characteristics on wave absorbing ability to the one of the uniformly permeable wall, though the situation of energy dissipation is quite different from each other. Therefore, it seems to be reasonable to replace the uniformly permeable wall by perforated wall without loss of the characteristics on wave absorption.

V The Use of "Warock" for Wave Absorbing Structures

The "Warock" is a type of concrete blocks to construct the seawall with reservoir. As shown in Fig.5-1 and Photo.5-1, it consists from the fore-side part of hexagon column with franges at both ends and the rearside part of vertical slab, which are connected by horizontal beam. Placing the block in a row along the shoreline and piling up in several columns to the required height, a seawall with reservoir is constructed, where the foreside parts of blocks constitute the perforated wall of average porosity 0.48 and the rearside parts provide the backwall, between which we have reservoir of porosity 0.75 because of the existence of horizontal beams. Photo.5-2 shows a "Warock" hanged by crane in construction of a wave absorbing quay-wall in actual place. The weight of this block is 20 tons, the length is 4.5 m, width is 2.0 m and the height is 1.7 m.

In order to oppose several period waves in various water depth, we have three sizes of blocks. The size A is 3.5 m in length, 1.6 m in width, 1.4 m in height and 10 tons in weight; the size B is as shown in Photo.5-2 and the size C is 6.0 m in length, 2.4 m in width, 2.0 m in height and 40 tons in weight.

Photo.5-3 shows the quaywall under construction by "Warock", piling up in four columns. The rightside of the figure constitutes vertical retaining wall, that is, the backwall of reservoir and leftside constitutes a perforated wall and between them is the reservoir. Photo.5-4 shows the front view of a part of the quaywall.

In this way, various types of seawall, quaywall and breakwater with wave absorbing ability are constructed by "Warock".

Fig.5-2 is the cross-section of quaywall constructed at water depth 10.4 m at Muroran Harbour, in Hokkaido. "Warock" of 20 tons are placed in three columns on the foundation by cellar block and rubble mound.

Fig.5-3 is the quaywall of depth 3.0 m constructed at Ushibuka Harbour in Kyushu with four columns of "Warock" of 10 tons in weight. Fig.5-4 is the breakwater at depth 4.5 m, constructed against wave period 5.0 seconds and height 1.20 m at Odo Marina in Fukuoka City, by 20 tons "Warock" in three columns. Fig.5-5 is the breakwater of double rows in three and four columns of 20 tons and of 10 tons "Warock", constructed at depth 7.0 m at Hiakari harbour in the Port of Kita-Kyushu at North Kyushu. The outside face of the breakwater is against the open sea waves of period 5.2 seconds and height 1.70 m and the inside face is to absorb the induced waves in harbour.

The use of the "Warock" for reservoir seawall is limited to the place where water depth is less than about 6 m and wave period is shorter than about 6 seconds. For larger depth and longer period waves, the seawall is better to be prefabricated in one body, transported by crane berge and placed on the site.

Fig.5-6 is the cross-section of breakwater by prefabricated reservoir seawall, constructed at depth 3.0 m at Tannawa Marina in Osaka Bay, against wave period 6.1 seconds and wave height 1.9 m. Photo.5-5 is the prefabricated body on the shore, whose length is 6.0 m, width is 5.6 m, height is 7.0 m and weight is 260 tons. Fig.5-7 is the seawall constructed at depth 7.0 m at the north coast of Kashima Harbour against open ocean waves of period 9.11 seconds and height 6.0 m. Photo.5-6 is the prefabricated body, whose widths of perforated wall and reservoir are 5.0 m and 6.0 m, respectively, the total width is 13 m, length is 13 m, height is 11 m and weight is 1800 tons.

VI Conclusions

The characteristics of the seawall with reservoir are summarized as follows:

- (i) The uniformly permeable wall with reservoir has the best ability of wave absorption when the total width is about 0.18 times the wave length, if the width of permeable wall is the same order of water depth. If the permeable wall is thin, the total width of best ability approaches to $L/4$.
- (ii) The most effective cross-section for the permeable wall with reservoir to absorb wave energy is thought to be of trapezoidal wall with backward-sloped backwall of reservoir.
- (iii) The perforated wall with reservoir has similar characteristics on

wave absorption to the uniformly permeable wall with reservoir.

(iv) The permeable or perforated wall with reservoir in total width of about 0.18 times the wave length has the same degree of wave absorbing ability as the permeable sloped-face seawall, even for long period waves.

(v) Such a seawall with reservoir is realized by means of "Warock" for actual field. For larger depth and longer period waves, it can be realized by prefabricated perforated wall.

References

- Jarlan, G.E. (1961): "A Perforated Vertical Wall Breakwater", The Dock and Harbour Authority, 1961, April
- Boivin, R. (1963): "Comments on Vertical Breakwaters with Low Coefficients of Reflection", The Dock and Harbour Authority, 1963, June
- Cote, G.J. and G.H. Simard (1964): "The Breakwater Quay at the Bay of Comeau", The Dock and Harbour Authority, 1964, April
- Terrett, F.L., J.D.C. Osorio and G.H. Lean (1968): "Model Studies of Perforated Breakwater", Proc. 11th International Conf. Coast. Eng. A.S.C.E.
- Marks, W. and G.E. Jarlan (1968): "Experimental Studies on a fixed Perforated Breakwater", Proc. 11th International Conf. Coast. Eng. A.S.C.E.
- Sawaragi, T. and K. Iwata (1973): "Some Considerations on Hydraulic Characteristics of Perforated Breakwater Quay", Proc. J.S.C.E. No. 220
- Sawaragi, T. and K. Iwata (1975): "Wave Dissipating Effect of a Horizontal Slit-Type Breakwater and Some Considerations of its Construction in the Field", Proc. J.S.C.E.
- Ijima, T., H. Okuzono, Y. Yumura and H. Sakai (1972): "Vertical Permeable Breakwater and Quaywall with Reservoir", Proc. Japanese Conf. Coast. Eng. 1972, Nov.
- Ijima, T., C.R. Chou and A. Yoshida (1976): "A Method of Analyses for Two-Dimensional Water Wave Problems", Proc. 15th International Conf. Coast. Eng. A.S.C.E.

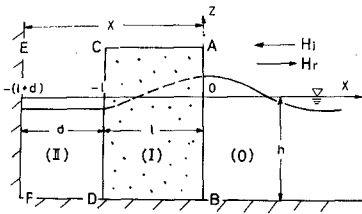


Fig.2-1 Permeable Seawall with Reservoir

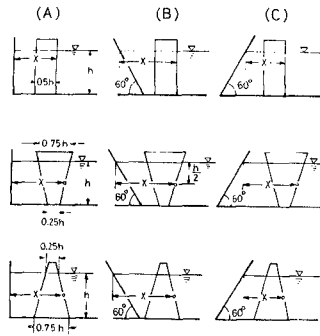


Fig.3-2 Various Types of Reservoir

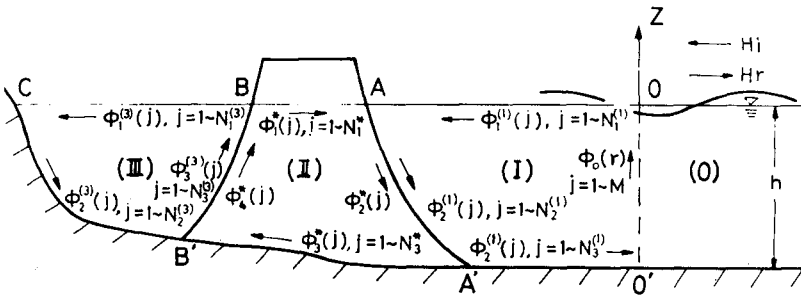


Fig.3-1 Definition Sketch for Reservoir Seawall

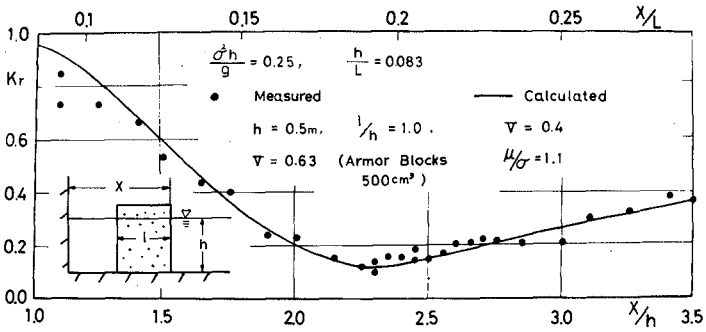


Fig.2-2 Ref. Coeff. for Reservoir Seawall

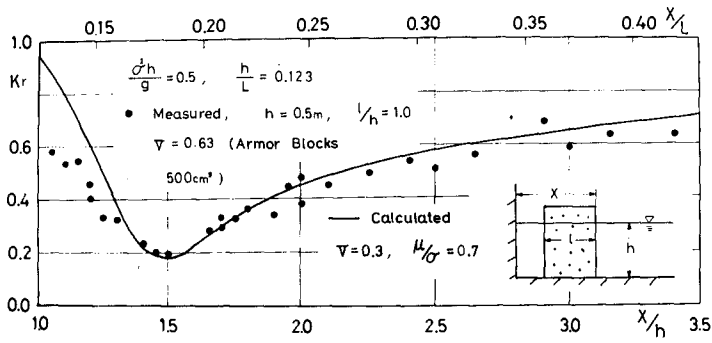


Fig.2-3 Ref. Coeff. for Reservoir Seawall

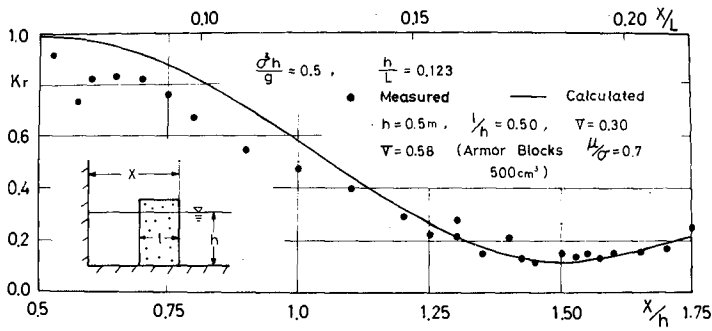


Fig.2-4 Ref. Coeff. for Reservoir Seawall

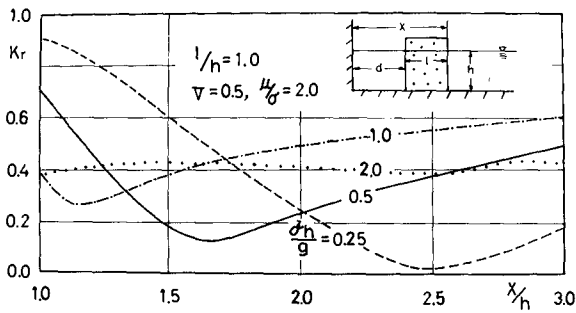


Fig.2-5 Reflection Coefficient for Uniform Type Wall

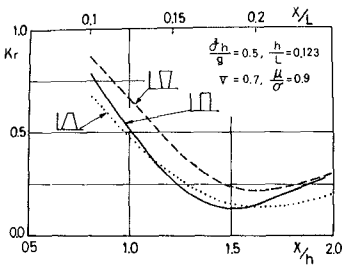


Fig.3-3 Ref. Coeff. for Vertical Back Wall (Type A)

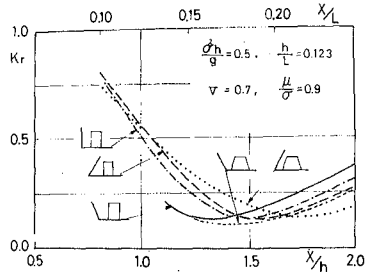


Fig.3-4 Ref. Coeff. for Sloped Back Wall

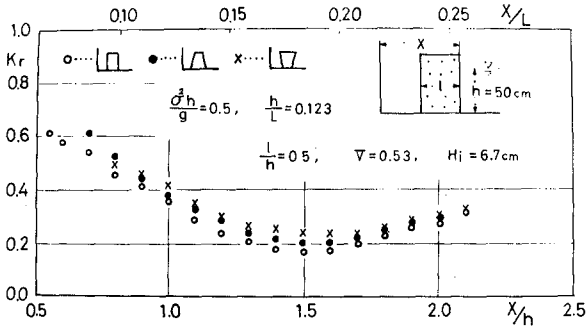


Fig.3-5 Ref. Coeff. for Vertical Back Wall (Measured)

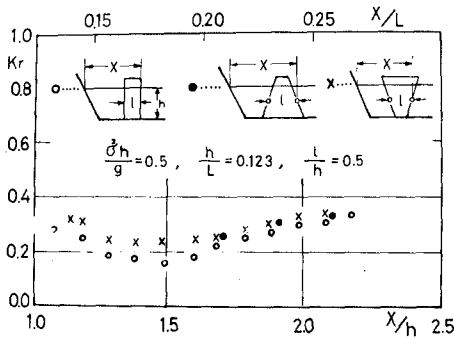


Fig.3-6 Ref. Coeff. for Sloped Back (Measured)

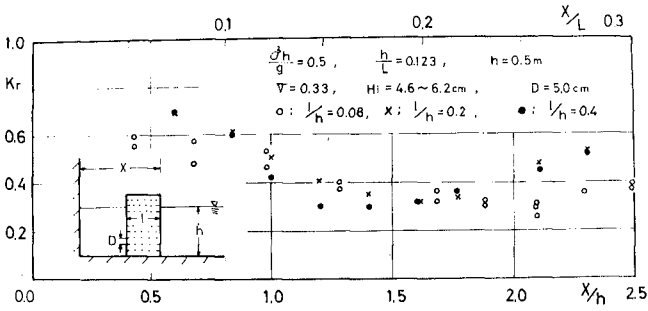


Fig.4-1 Ref. Coeff. for Solid Wall with Horizontal Holes

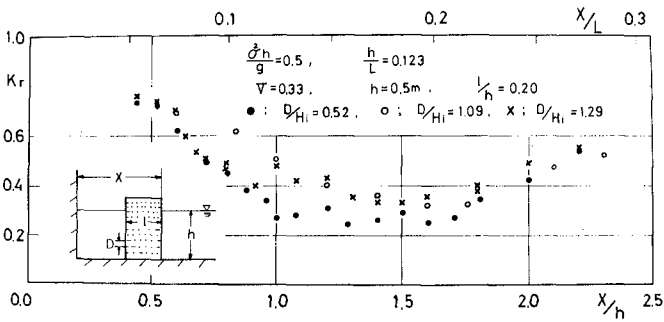


Fig.4-2 Ref. Coeff. for Solid Wall with Horizontal Holes

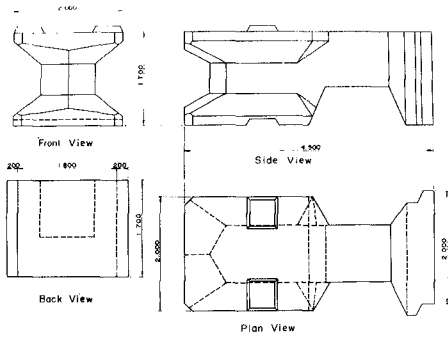


Fig. 5-1 Scheme of a "Wrench" (20 tons) 15Steel in Material

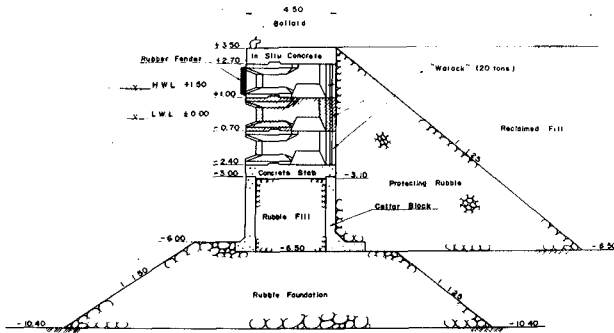


Fig. 5-2 Cross-Section of Quaywall by "Warock" at Majuro Harbour
(Sizes in Meters)

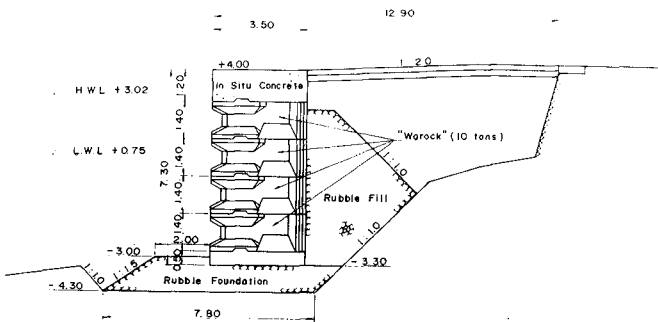


Fig. 5-3 Cross-Section of Quaywall by "Warock" at Ushibuka Harbour
(Sizes in Meters)

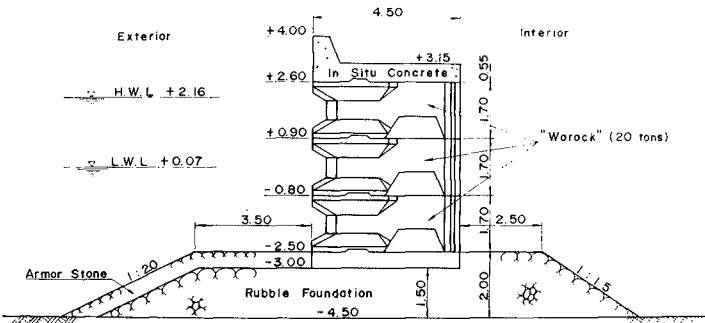


Fig. 5-4 Cross-Section of Breakwater by "Warock" at Odo Marina
(Sizes in Meters)

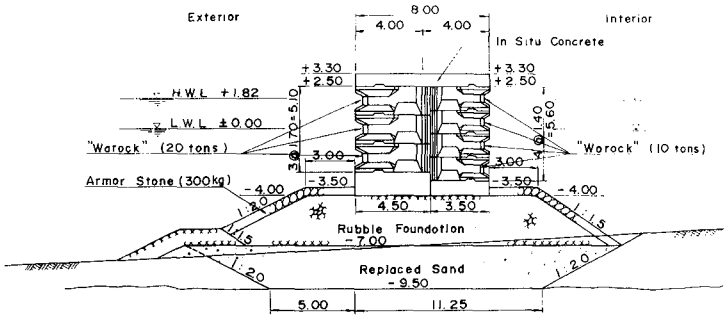


Fig. 5-5 Cross-Section of Breakwater by "Warock" at Hiakari Harbour
(Sizes in Meters)

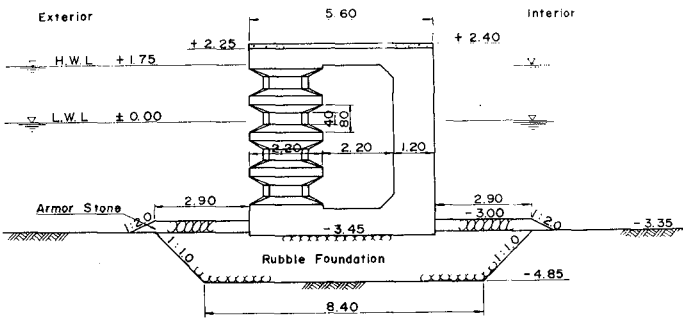


Fig. 5-6 Cross-Section of Breakwater by Prefabricated Reservoir Seawall
at Tan-nawa Marina (Sizes in Meters)

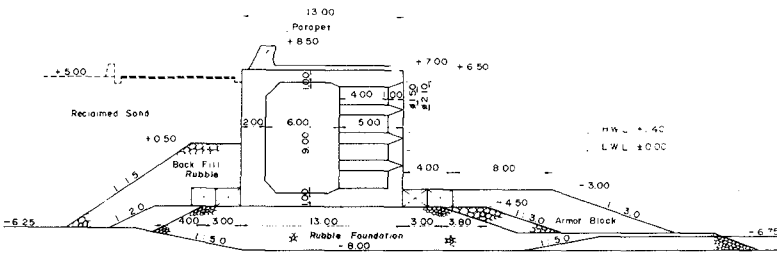


Fig. 5-7 Cross-Section of Seawall by Prefabricated Reservoir Seawall
at the North Coast of Kushima Harbour (Sizes in Meters)



Photo.5-1: A "Warock"



Photo.5-3: Quaywall under Construction



Photo.5-2: A "Warock" hanged by Crane

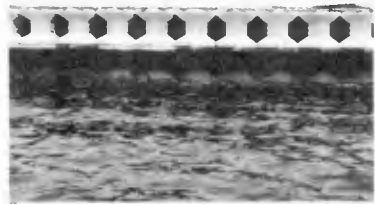


Photo.5-4: Front View of Quaywall



Photo.5-5: Prefabricated Body of Breakwater at Tannawa Marina



Photo.5-6: Prefabricated Seawall at Kashima Harbour

CHAPTER 152

LABORATORY STUDY ON PERVIOUS CORE BREAKWATERS

by

Hideo KONDO, Professor

Satoshi TŌMA, Assistant Professor

Kenji YANO, Research Assistant

Department of Civil Engineering
Muroran Institute of Technology
Muroran, 050, Japan

ABSTRACT

Effects of permeable core layer installed in trapezoidal and rectangular breakwaters have been studied experimentally and analytically. As the materials for armour and core use of the lattice composed of circular cylinders was made in addition to rocks. Perforated plates were also applied as a kind of very thin core.

Experimental results show that the reflected wave heights from breakwater could be reduced considerably by locating the core layer shoreward within it while core thickness controls the transmitted wave heights in the protected water area. Harmonic analysis about the water surface in lattice armour reveals that the second harmonic waves take a pattern of standing wave distribution having a node at the seaward face of breakwater. Thin perforated plates work successfully for reducing the transmitted wave heights when they are installed at the rear face of breakwater.

An analytical approach to predict the transmission and the reflection coefficients is applied for the present experimental data and shown to be useful.

INTRODUCTION

It is well understood by coastal engineers that pervious breakwaters bring less seaward reflective wave energy and wave run-up than impervious ones do, as observed in several laboratory and field experiments.

However they have disadvantage of allowing shoreward wave energy penetration which results in the transmitted waves behind it.

In order to obtain less transmitted wave energy without precluding the merits stated, for instance, a rubble-mound breakwater usually has a permeable core layer which has less permeability compared with armour ones, or it is said to be composed of pervious multi-layers. Effects of hydraulic characteristics of pervious cores on wave transmission and reflection have not been known despite their importance

in functional design of pervious breakwaters. The present study deals with fundamental effects of pervious cores installed within porous breakwaters based on experiments on model breakwaters as well as analytical approach.

EXPERIMENTAL FACILITIES AND PROCEDURE

Experiments were performed on horizontal bottom in a wave channel of 18.5 meter long, 0.4 meter wide and 1.0 meter deep. Waves were generated with a regular and flap type generator. Parallel wire wave gages were used to measure water surface fluctuations. Fig. 1 presents arrangement of experimental equipments.

Cross sectional configurations of model breakwaters were of rectangular and trapezoid as shown in Fig. 2.



Photo. 1 Trapezoidal Breakwater Made of Lattice (No Core)

Table 1 Hydraulic Coefficients of Breakwater Materials

		Porosity λ (%)	Diameter D (cm)	Turbulent Coefficient C_3	(Turbulent Frictional Slope) / v^2 $\left(\frac{\Delta h}{l}\right) t \frac{1}{v^2}, (\text{sec}^2 \cdot \text{m}^{-2})$
Armour	Lattice ($\phi 34$)	60.7	3.4	0.11	2.0
	Rock A	44.8	3.8	0.4	30.0
Core	Lattice ($\phi 11$)	60.7	1.1	0.11	6.0
	Rock C	43.0	2.9	0.3	36.0

Three kinds of the core thickness tested were 13, 20 and 26 cm for the core location at center of breakwaters. With thickness of 20 cm, the core location was varied in three ways, i.e., the front, center and rear, respectively. Distance between the center core and the front or the rear cores was 20 cm. Main armour material of

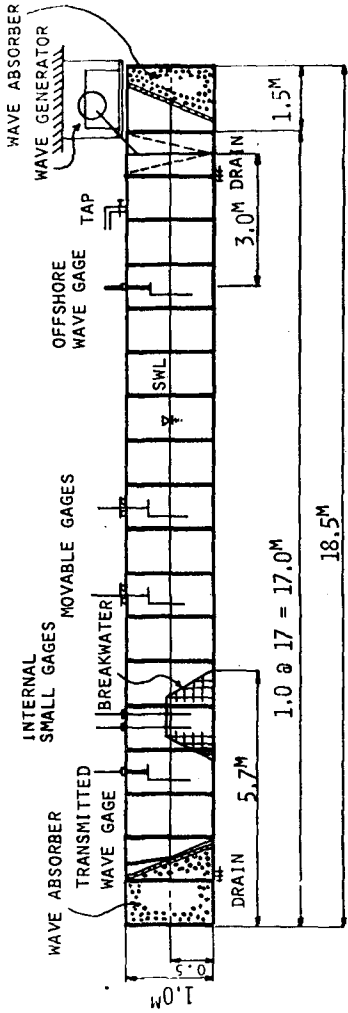


Fig. 1 Arrangement of Experimental Equipment

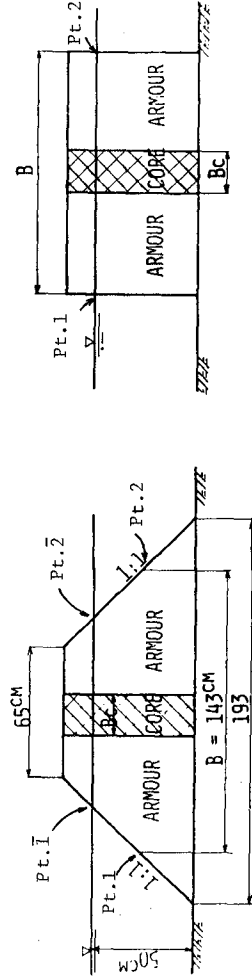


Fig. 2 Cross Section of Model Breakwaters

breakwaters was the lattice of $D = 3.4$ cm (Photo.1), and the core ones were the another lattice of $D = 1.1$ cm and the rock of the median diameter (D_m) = 2.9 cm. Hydraulic characteristics of the lattice were discussed in detail previously¹⁾. Some of the hydraulic properties are cited in Table 1. Coefficient C_3 in the table is of one to turbulent resistance, and is related to the frictional slope as in the following equation.

$$\frac{\Delta h}{\ell} = \frac{V^2}{2g\lambda^5 D} \cdot \left[\frac{C_2}{(DV/\nu)} + C_3 \right], \quad (1)$$

where V , g , ν , and C_2 are steady discharge velocity, acceleration of gravity, kinematic viscosity, and another coefficient for laminar flow resistance, respectively. The turbulent frictional slope, denoted $(\Delta h/\ell)_t$, is defined as that neglecting the laminar term in Eq.1, and is expressed as,

$$\left(\frac{\Delta h}{\ell} \right)_t = \frac{C_3 V^2}{2g\lambda^5 D}. \quad (2)$$

The ratio of the turbulent frictional slope of the lattice armour to that of core is 1:3 for the lattice core, and it is 1:18 for the rubble core. The ratio for a typical rubble mound breakwater²⁾ having artificial concrete blocks of $\lambda = 0.5$ and $C_3 = 0.67$ as armour and rock of $\lambda = 0.4$ and $C_3 = 0.4$ as core¹⁾, is 1:15 provided weight of the core unit is 1/200 of the armour one, which is close to 1:18.

Uniformly perforated steel plates were also employed since they were expected to represent one of the thin cores. The plates with circular holes of 1.2 and 2.0 cm in diameter and of porosity of 20 and 34 % were tested. The rock as armour material was used mainly with the plates.

The incident wave height H_I and the reflected one H_R were determined by moving one or two gages to measure amplitudes at loops and nodes, and adding or subtracting the latter to the formers. The transmitted wave height through breakwater H_T was measured at location about one quarter wave length shoreward from the point of the rear face which intersects with the still water surface.

The transmission coefficient and reflection coefficients are defined as H_T/H_I and H_R/H_I , and denoted hereafter K_T and K_R , respectively.

The internal water surface fluctuations of lattice armour were measured by inserting small gages vertically into voids between cylinders. Dimensions of experimental waves were the ranges shown below. while the water depth h was kept constant of 50 cm.

Incident wave heights $h = 1 - 10$ cm, Wave periods $T = 0.7 - 2.2$ sec.

RESULTS AND DISCUSSIONS

In the statement followed results about trapezoidal breakwaters will be mainly presented except for the ones with plates. Rectangular breakwaters will be discussed in comparison with the trapezoidal ones in a few sections.

1) Comparison of K_T and K_R between No-core and With-core Breakwaters

First of all, function of the core installed in a porous breakwater has been investigated. Fig. 3 shows the case of lattice core,

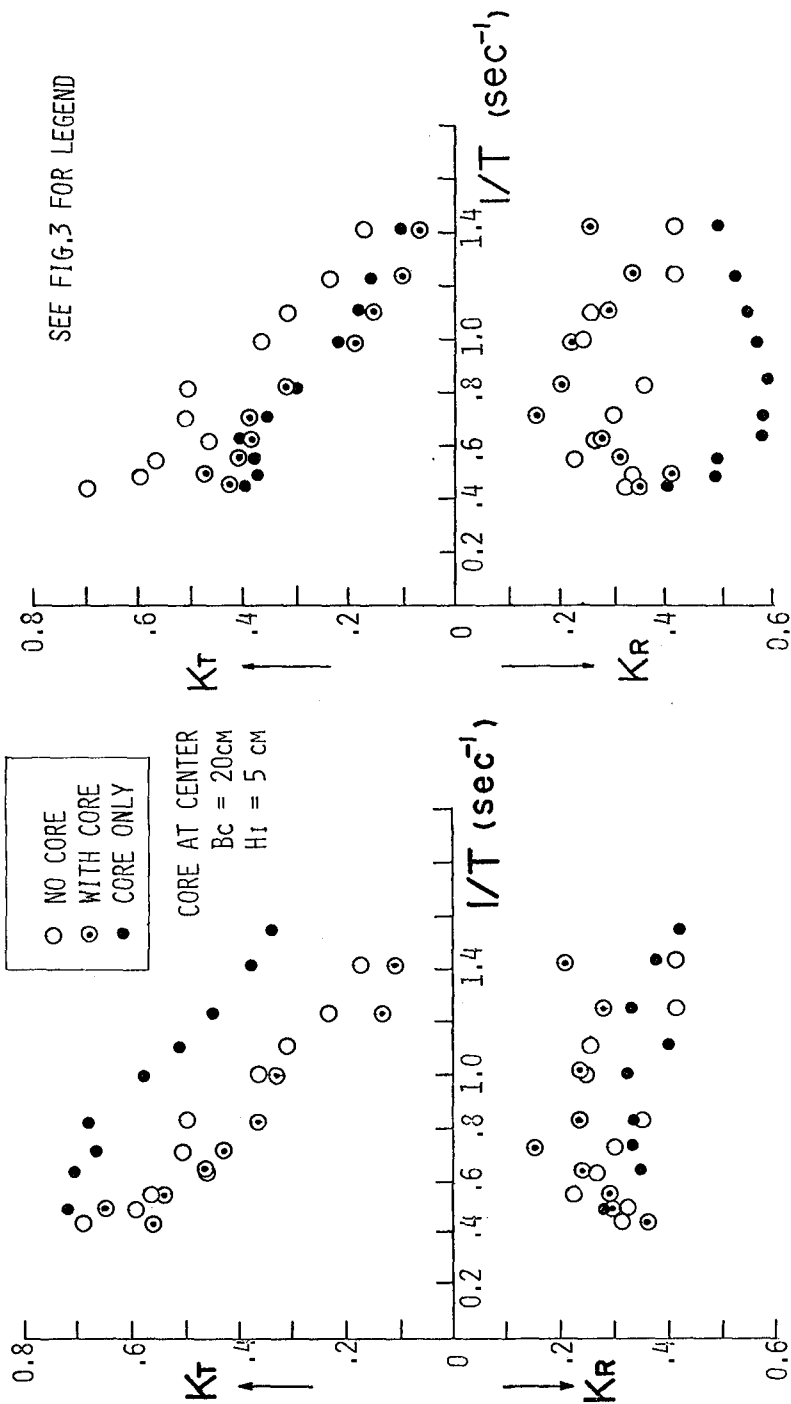


Fig. 3 Effect of Lattice Core on K_T and K_R

Fig. 4 Effect of Rubble Core on K_T and K_R

in which the ordinate is taken as the transmission coefficient upward and as the reflection coefficient downward, and the abscissa is frequency. K_T of the with-core breakwater is nearly the same as no-core one. In this case the core doesn't work effectively since the frictional slope of the core is only three times that of armour. Fig. 4 presents the case of rubble core, in which K_T of with-core is dominated by the core and almost coincides with that of the case of core layer only. K_R of with-core, however, is considerably smaller than that of the core only, and approaches to that of no-core and is a little smaller than it as a whole. This suggests that installing a suitable core layer possibly decreases K_R besides K_T .

2) Effect of Core Thickness on K_T and K_R

Effect of the thickness of core on decreasing K_T is greater for the rubble core than for the lattice core as expected. K_T and K_R for cases of rubble core are shown in Fig. 5 for three kinds of thickness. In the figure, relative width of breakwater B/L which has been known as one of the most important parameters to determine K_R for single layer breakwaters¹⁾ and to wave pressures on the impervious wall behind the permeable absorbers³⁾. The thickness, however, doesn't give appreciable change of K_R , especially for the rubble core.

3) Effects of Core Location on K_T and K_R

With a kind of core, the location of core in a armour greatly affects K_R but scarcely does K_T , an opposite trend to the effect of thickness. Fig. 6 presents the case that a rubble core is installed at three different locations in lattice breakwater of trapezoidal cross section. It shows that the breakwater with the rear core gives considerably smaller K_R than the others do for waves of the relative width B/L less than 0.7. Most of prototype breakwaters and waves are satisfied with the above B/L condition. To the contrary, K_T hardly depends upon the core location.

Fig. 7 is an example to explain effect of the relative wave height H_I/h on the transmission and reflection coefficients, with location as parameter. K_T decreases as H_I/h increases, irrespectively of core location. Meanwhile K_R decreases slightly with H_I/h in the range of experiment, H_I/h less than 0.14.

4) Wave Height Distribution in and around Breakwaters

Fig. 8 exhibits wave height distributions measured at seaward and shoreward water areas of breakwaters, and in the armour layers of lattice, too. The case of rear core has another maximal wave height in addition to the one appearing near the seaward face of breakwater. The latter maximal of the rear-core breakwater is remarkably smaller than those found for the front-core and no-core ones. Behind the location of the rear-core, the two wave heights of cases with core are almost the same and scarcely depends upon the core location.

Inspecting the distribution characteristics, it may be assumed that the reflected waves appearing in front of breakwater with core are composed of the two reflective waves, namely, the one from seaward face of armour and the another from seaward face of core. Accordingly, a larger distance between the two faces contributes to obtain less reflected wave energy and consequently lower K_R because of a greater phase difference between the two reflected waves at the seaward water area. On the other hand, the transmitted waves may be approximated with the one kind wave which penetrates through the breakwater and

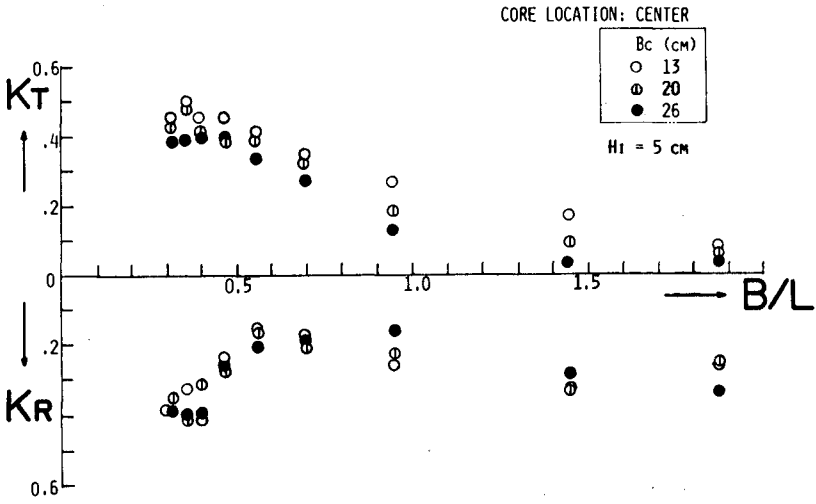


Fig. 5 Effect of Core Thickness on K_T and K_R (Rubble Core)

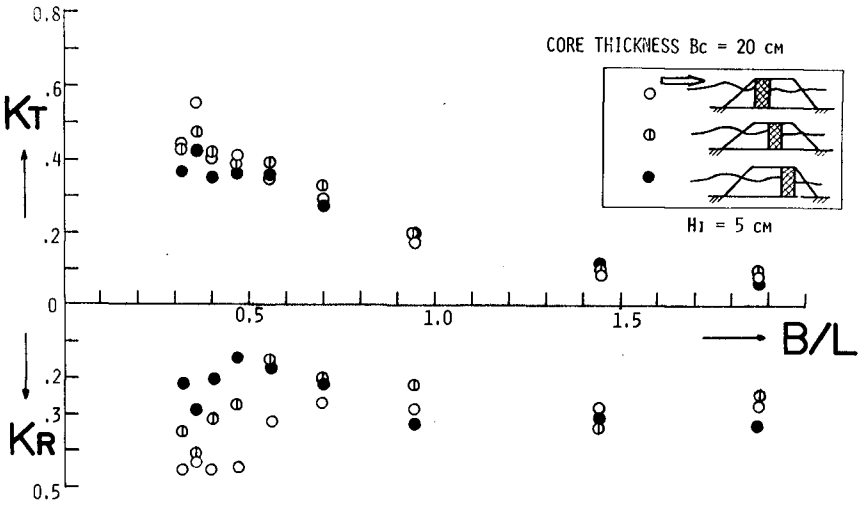


Fig. 6 Effect of Core Location on K_T and K_R (Rubble Core)

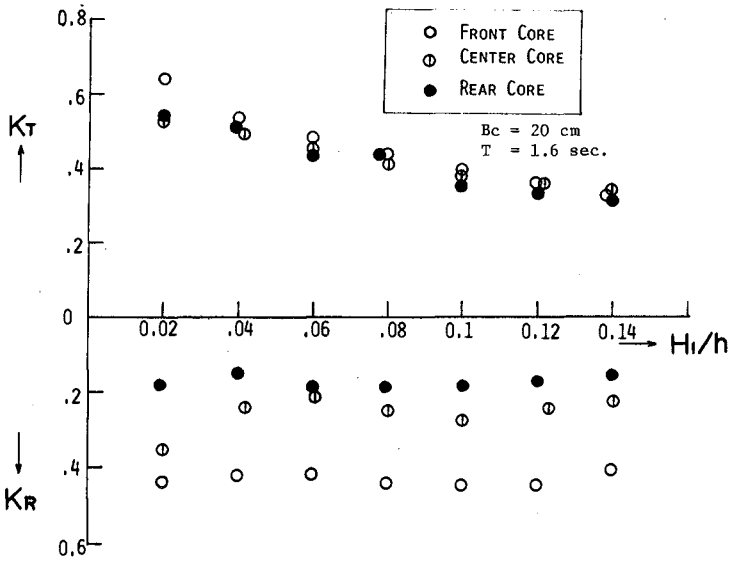


Fig. 7 K_T and K_R versus H_I/h for Rubble Core

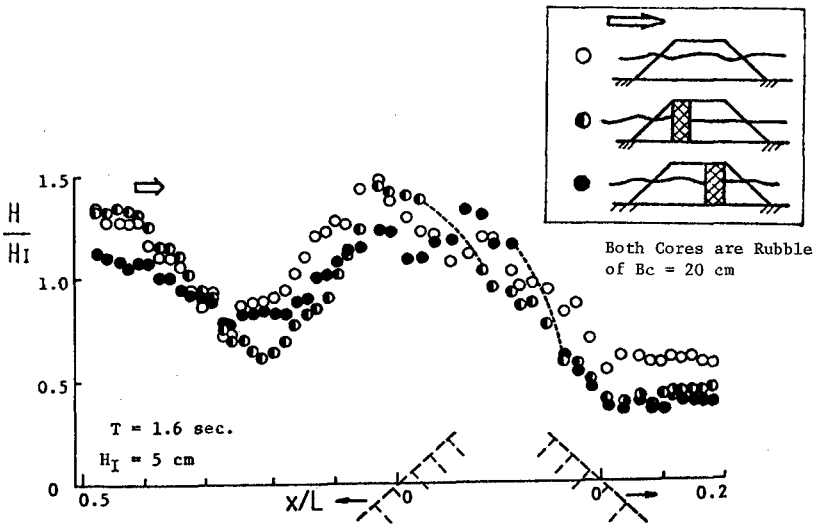


Fig. 8 Wave Height Distribution in and near Breakwaters

appear in the shoreward water area.

The following several figures show the results of harmonic analysis of water surface fluctuations in and around various kinds of breakwater. They bring wave height distribution of higher harmonics other than that of fundamental one whose period is that of the incident wave, as seen in Figs. 9-14. Wave height distribution of fundamental harmonic almost coincides with the directly determined height of crest to trough from the recorded profile, depicted with triangles in the figures. Types of standing wave prevail in front of structures and progressive wave pattern do behind them for the two waves.

Dimensionless wave heights, H_N/H_1 in the figures, for slit walls made of single row or double rows of cylinders are less than 0.2 everywhere for 2nd and 3rd harmonics. The case of two rows is shown in Fig. 9 in which distribution of the higher harmonics looks like a standing wave too and the size is nearly the same to that found for incident waves.

Inside of the single layer breakwater made of lattice, 2nd harmonic has nodes at the front and the rear faces of breakwater (See Fig. 10). The higher harmonics are considered to be generated due to the quadratic loss of internal flow within breakwaters ⁴). As for the rubble core layer itself, 2nd harmonic gives a clear pattern of standing wave in the seaward water area, especially for longer waves, which suggests the higher harmonics are generated in the case due to abrupt change of water particle velocity.

The wave height distribution of 2nd harmonics for the rubble core breakwaters of $B_c=20\text{cm}$ was investigated in the armours of both sides of core. In the seaward armour, it has usually a node near the front face, but at the rear face of armour it doesn't necessarily has a loop. The latter trend possibly relates to that the fundamental or the directly determined waves do not necessarily take a loop at the rear face of armour. In the shoreward armour behind core, however, it has always nodes at the both faces, while the fundamental ones have loops at the front face and nodes at the rear face.

Heights of 2nd harmonic in armours are relatively greater for rectangular ones. The cause of this trend can be sought in the fact that a kind of resonance which brings large difference of horizontal velocity within breakwater, likely occurs for rectangular one than for trapezoidal one.

5) Comparison Between Rectangular and Trapezoidal Breakwaters

K_T and K_R of trapezoidal breakwaters are compared with those of rectangular ones which have the width B that coincides with the mean width below the still water of the trapezoidal ones. K_T is larger for the trapezoidal ones, as expected. K_R of rectangulars oscillates more sharply with B/L than that of trapezoids. Distribution of K_R plotted against B/L gives different trends for the two cases, which suggests a difference of location of reflective planes between the two structures. Discrepancy of the two K_R becomes smaller as the core location moves shoreward, as seen in Figs. 15 and 16.

6) Analytical Prediction of K_T and K_R

Several analytical approaches to estimate K_T and K_R for porous breakwaters have been proposed recently ⁵⁾⁻⁸⁾. But they deal with essentially breakwaters made of one kind of materials and take no account of the effect of core location as found hitherto.

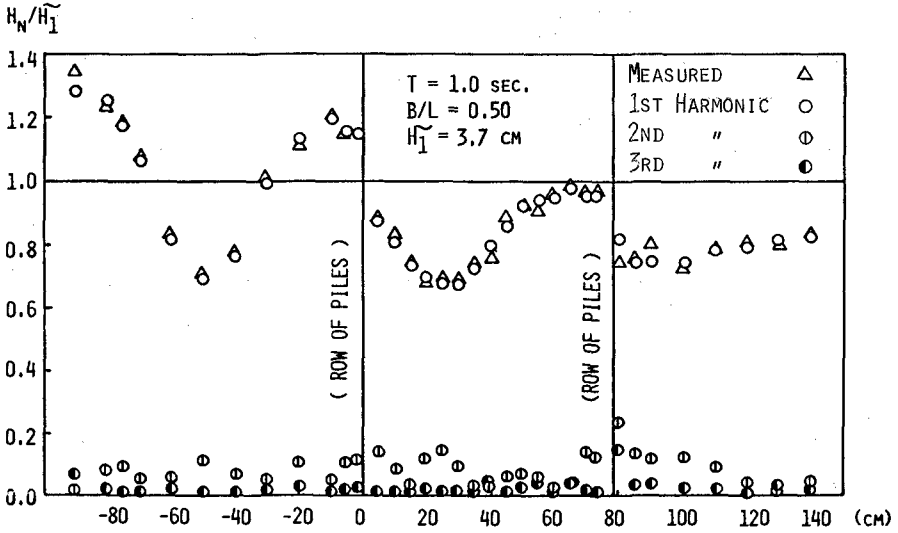


Fig. 9 Wave Heights of 1st - 3rd Harmonics (Two Rows of cylinders)

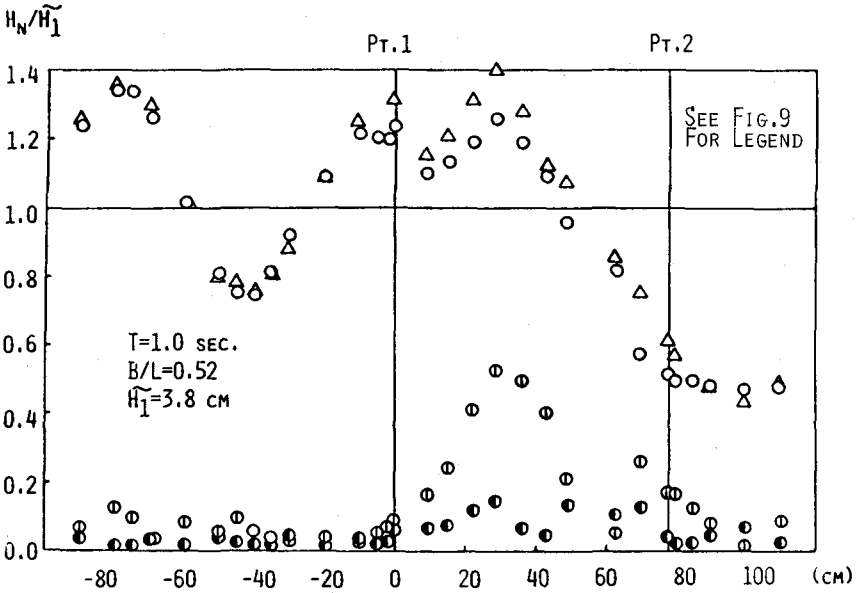


Fig. 10 Wave Heights of 1st - 3rd Harmonics (Rectangular Lattice of No Core)

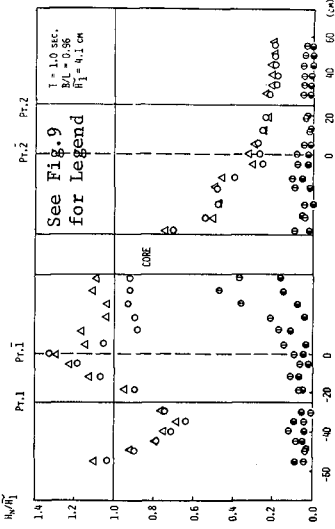


Fig. 11 Wave Heights of 1st - 3rd Harmonics (Rectangular Center-Core)

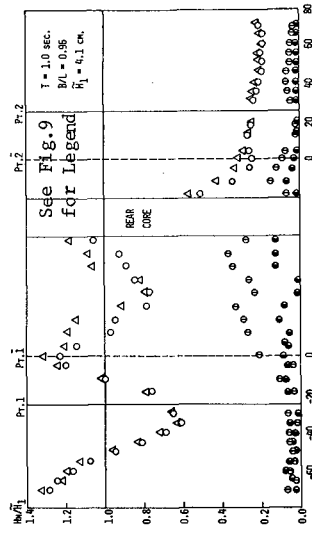


Fig. 12 Wave Heights of 1st - 3rd Harmonics (Trapezoidal Center-Core)

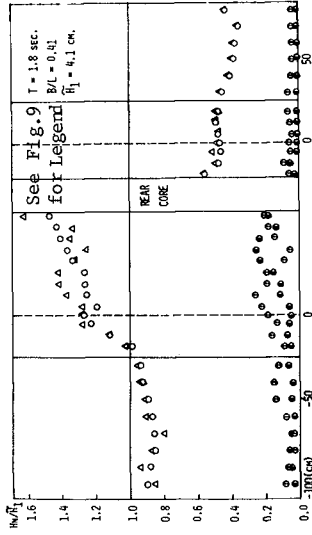


Fig. 13 Wave Heights of 1st - 3rd Harmonics (Trapezoidal Rear-Core)

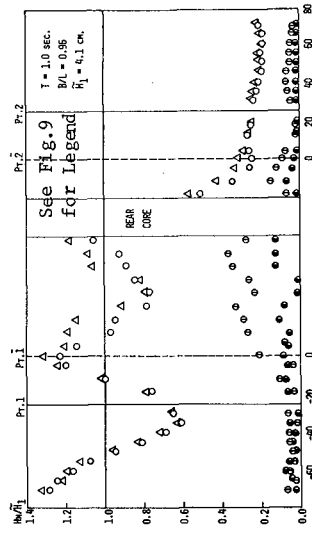


Fig. 14 Wave Heights of 1st - 3rd Harmonics (Trapezoidal Rear-Core)

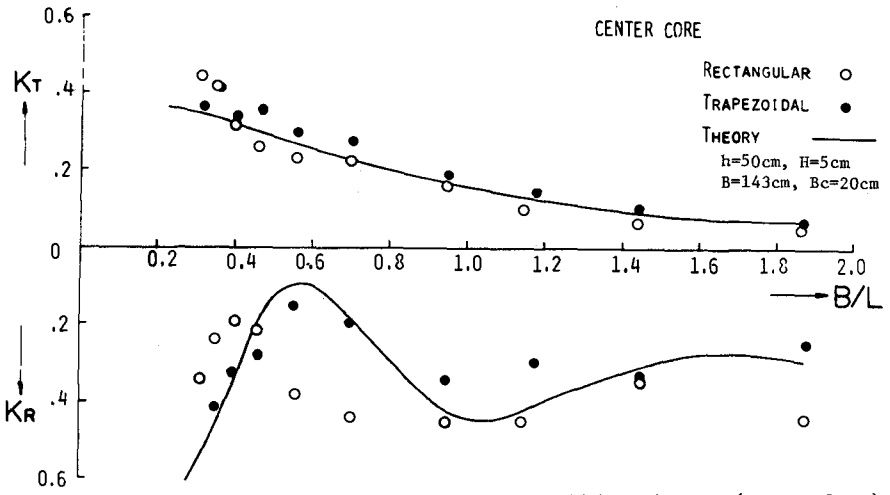


Fig. 15 Comparison Between Rectangular and Trapezoidal Breakwaters (Center Core)

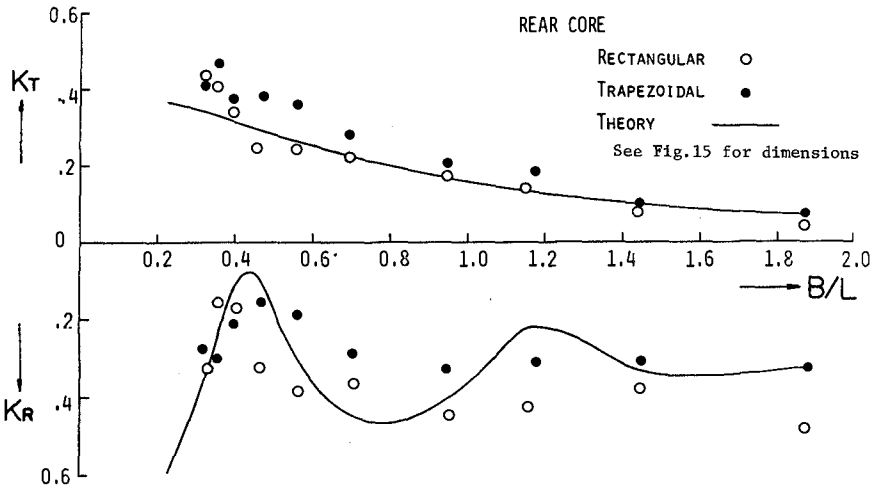


Fig. 16 Comparison Between Rectangular and Trapezoidal Breakwaters (Rear Core)

Problems of wave transmission and reflection coefficients for multi-layered porous breakwaters may be solved as one of boundary value problems as performed by a few researchers for single layer pervious breakwaters^{6), 7)}. But such a solution will become extremely cumbersome as number of layers increases for multi-layered breakwaters.

A simplified approach to estimate K_T and K_R for multi-layered porous breakwaters has been proposed⁹⁾, whose summary is presented in APPENDIX. It is applied for the experimental data, which seems to be useful for K_T of both rectangular and trapezoidal breakwaters and K_R of trapezoidal ones, as we can see in Figs. 15 and 16.

K_T and K_R of three kinds of prototype breakwater, namely, center-core, rear-core and no core ones, are calculated for cases $H_I = 1.0$, and 5.0 meter with varying T . The result is shown in Figs. 17 and 18. K_T can be successfully reduced by installing a core, while K_R can be lowered by locating the core shoreward in breakwater.

7) Perforated Plate Breakwaters

Employment of pervious core for porous breakwaters can be expected to reduce the transmitted wave height. One of the simplified pervious cores may be thin plates or slab with pores and/or slits. Several studies have been disclosed about perforated wall breakwaters with chambers, but not with those filled with granular materials. Perforated steel plates with circular holes were used as thin cores. Breakwaters of rectangular cross section were only tested (Photo. 2). One to three plates were installed at the front and the rear faces of, and at the center of breakwaters

K_T and K_R of the plate breakwaters are shown in Figs. 19 and 20. The plate installed at the rear face of breakwater works successfully for reducing K_T especially for longer waves. Breakwaters having the two plates at the both faces bring higher K_R than the cases of rear plate only and no plate, though they can lower K_T considerably.



Photo. 2 Rubble Breakwater with Perforated plates

CONCLUSIONS

- 1) Pervious core layers installed in porous breakwaters effectively decrease the transmitted wave height, and possibly reduce the reflected wave height too provided they being placed shoreward in breakwaters.
- 2) The simplified analytical approach is confirmed to be useful to predict the transmission and reflection coefficients for pervious core breakwaters.
- 3) Thin perforated plates set at the rear face of pervious breakwa-

ters are effective to decrease K_T without increasing K_R . They may replace the cores made of granular materials in prototype breakwaters if practically feasible.

ACKNOWLEDGEMENTS

This study has been carried out with the science research grant offered by the Ministry of Education in the period of 1973 - 75.

The writers would like to acknowledge Professor Yuichi Iwagaki of Kyoto University, who had organized a nationwide research project to which the present study belonged.

The writers wish to express their gratitudes to former research assistant, Katsuei Kasai, and former students, Hidetoshi Sōma, Etsurō Yamada, Shigeru Kobiyama and Ryūichi Satou of Department of Civil Engineering, Muroran Institute of Technology, for their co-operation given during the course of study.

REFERENCES

- 1) Kondo, H. and S. Tōma: Reflection and Transmission for a porous structure, Proc. of XIIIth Coastal Eng. Conf., Vol. III, pp. 1847-1866, 1972.
- 2) U.S. Army Coastal Engineering Research Center: Shore Protection Manual, 2nd Edition, 1975.
- 3) Kondo, Hideo: Wave pressures on vertical wall with porous absorbers, Proc. of Japan Society of Civil Engineers, No. 223, pp. 85-97, 1974.
- 4) Mei, C. C., P. L-F Liu, and A. T. Ippen: Quadratic loss and scattering of long waves, Jr. of the Waterways, Harbors and Coastal Eng. Div., Proc. of ASCE, WW3, pp. 217 - 239, 1974.
- 5) Kondo Hideo: An analytical approach to wave transmission through permeable structures, Coastal Engineering in Japan, Vol. 13, pp. 31 - 42, 1970.
- 6) Ijima, T., Y. Eguchi and A. Kobayashi: Study on pervious breakwaters and quay walls, Proc. of 18th Conf. on Coastal Eng. of JSCE, pp. 121 - 130, 1971 (in Japanese).
- 7) Sollitt, C. K. and R. H. Cross: Wave Reflection and Transmission at permeable breakwaters, Rt. No. 147, R. M. Parsons Lab., MIT, 1972.
- 8) Madsen, Ole Secher: Wave transmission through porous structures, Jr. of the Waterways, Harbors and Coastal Eng. Div., Proc. of ASCE, WW3, pp. 169 - 188, 1974.
- 9) Kondo, H., S. Tōma and K. Kasai: An analytical approach to predict the transmission and reflection coefficients for multi-layered porous breakwaters, Memoirs of the Muroran Institute of Technology, Science and Engineering, Vol. 9, No. 1 (to be published in 1976, in Japanese).
- 10) Kondo, H. and S. Tōma: Breaking wave transformation by porous breakwaters, Coastal Engineering in Japan, Vol. 17, pp. 81 - 91, 1974.

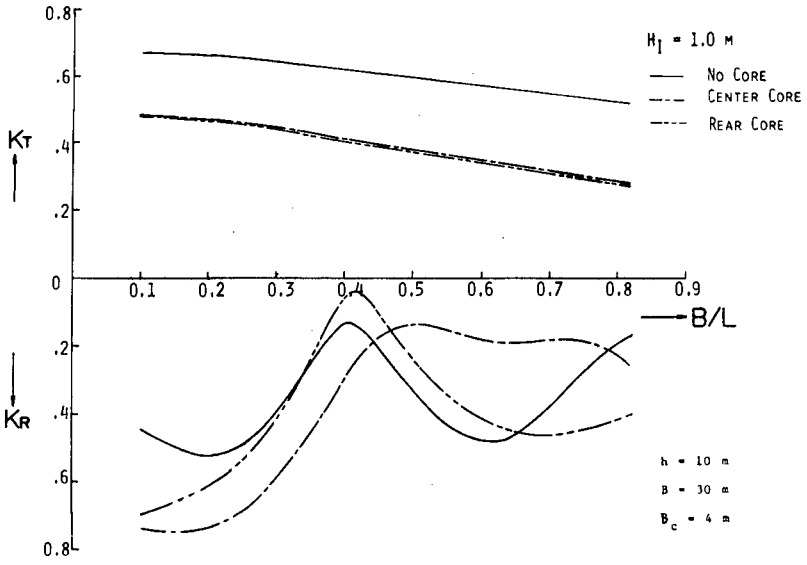


Fig. 17 Prediction of K_T and K_R for Prototype Breakwaters

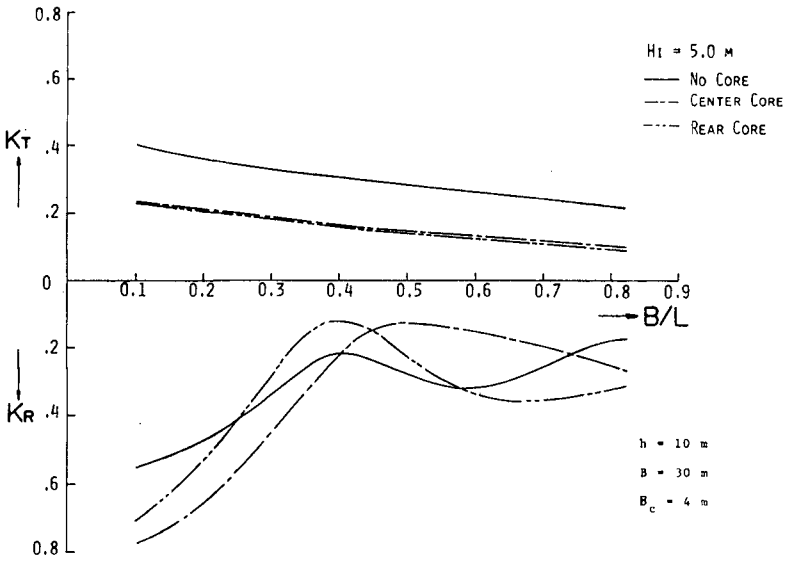


Fig. 18 Prediction of K_T and K_R for Prototype Breakwaters

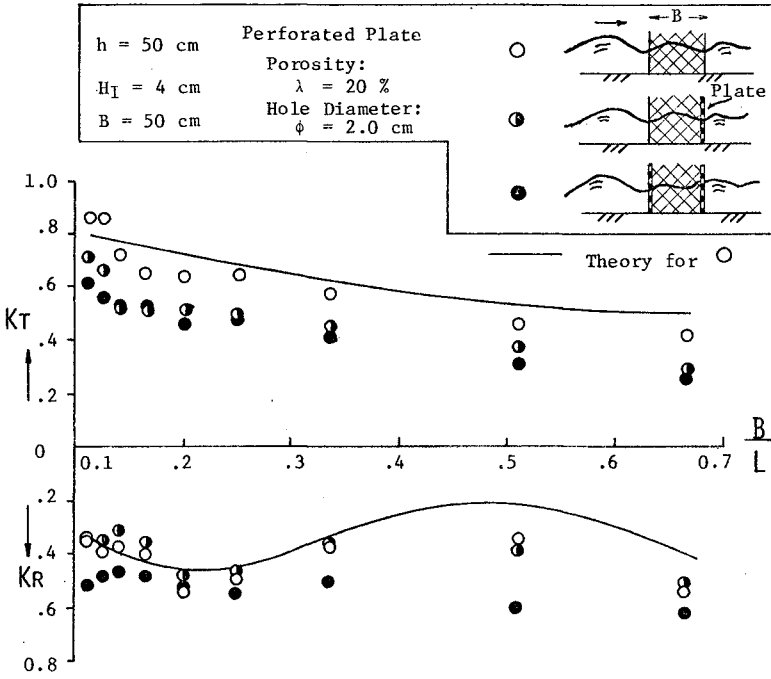


Fig. 19 K_T and K_R of Lattice Breakwaters with Perforated Plate

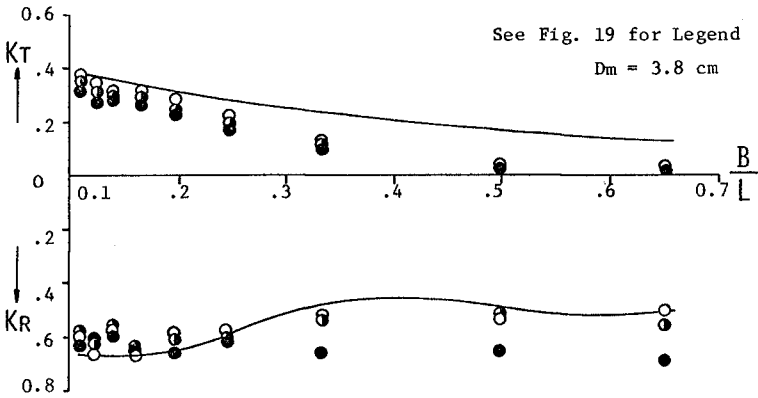


Fig. 20 K_T and K_R of Rubble Breakwaters with Perforated Plate

APPENDIX

AN APPROACH TO PREDICT TRANSMISSION AND REFLECTION COEFFICIENTS FOR MULTI-LAYERED POROUS BREAKWATERS 9)

The present approach is derived on the basis of linearized Forchheimer's law for the frictional loss in breakwaters provided waves are of shallow water, which is in accordance with the line of the previous approach for single layer one^{5),1),10)}.

Besides, the following assumptions are made.

- (1) Breakwaters are composed of rectangular layers, and the boundaries between layers are vertical.
- (2) The transmitted waves appearing in the protected water area are the one component waves to which the incident waves develop after passing through all the layers consecutively. The components come to the area after reflected back once or more are neglected.
- (3) The reflected waves are sum of the waves reflected one time only, each of which is generated when the incident waves of (2) pass a boundary between adjacent two layers.

According to the above assumptions, the transmission coefficient K_T of a breakwater composed of N layers (See Fig. 21), are given by,

$$K_T = K_{t,1} \cdot K_{t,2} \dots K_{t,J} \dots K_{t,N} \cdot K_{t,N+1} \cdot \exp[-(n_1 B_1 + n_2 B_2 + \dots + n_J B_J + \dots + n_N B_N)], \quad (3)$$

where n_J is the damping factor of wave height while advancing in the J layer of the width B_J , and $K_{t,J}$ is the transmission coefficient when waves penetrates into the layer $J+1$ from J passing through the boundary J 5),1).

The equation of the water surface for the resultant reflected waves, η_R , is expressed as the sum of reflected waves, $\eta_{r,J}$ original-

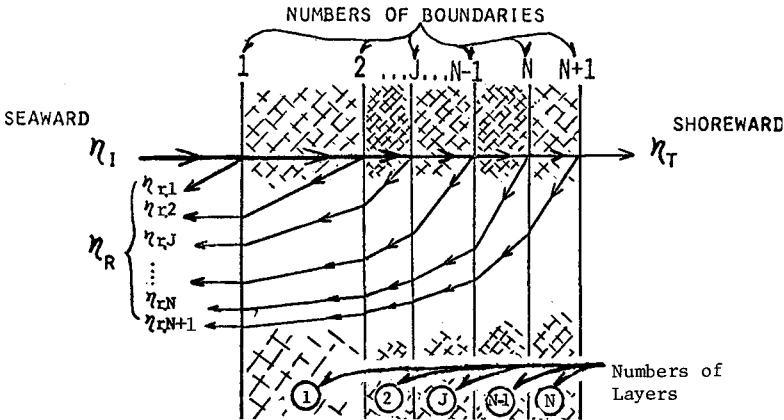


Fig. 21 Scheme of Wave Transformation by Multi-Layered Breakwater

ly generated at the boundary J, (J = 1, 2,N, N+1), as

$$\eta_R = \eta_{r,1} + \eta_{r,2} + \dots + \eta_{r,J} \dots + \eta_{r,N} + \eta_{r,N+1} , \quad (4)$$

where,

$$\begin{aligned} \eta_{r,1} &= \frac{H_I}{2} \cdot K_{r,1} \cdot \sin(\sigma t + m_0 x + \alpha_{r,1}), \quad m_0 = 2\pi/L, \\ &\vdots \\ \eta_{r,J} &= \frac{H_I}{2} \cdot K_{t,1} \cdot K_{t,2} \dots K_{t,J-1} \cdot K_{r,J} \cdot K_{tb,J-1} \dots K_{tb,1} \cdot \exp[-(n_{i,1} + n_{r,1})B_1 + (n_{i,2} + n_{r,2})B_2 \dots + (n_{i,J} + n_{r,J-1})B_{J-1}] \cdot \sin[\sigma t + m_0 x - (m_{i,1} + m_{r,1})B_1 - \dots - (m_{i,J-1} + m_{r,J-1})B_{J-1} + \alpha_{t,1} \dots \alpha_{t,i-1} + \alpha_{r,J} + \alpha_{tb,J-1} + \dots + \alpha_{tb,1}], \\ &\vdots \\ \eta_{r,N+1} &= \frac{H_I}{2} \cdot K_{t,1} \cdot K_{t,2} \dots K_{t,J-1} \dots K_{t,N} \cdot K_{r,N+1} \cdot K_{tb,N} \dots K_{tb,1} \cdot \exp[-\sum_1^N (n_{i,J} + n_{r,J})B_J] \cdot \sin[\sigma t + m_0 x - \sum_1^N (m_{i,J} + m_{r,J})B_J + \sum_1^N \alpha_{t,J} + \alpha_{r,N} + \sum_1^N \alpha_{tb,J}], \end{aligned}$$

where m_j is the wave number in the J layer and α is a phase angle. Subscript i, r and t for m, n, K_t , K_r , α and η correspond to the incident, reflected and transmitted waves, respectively. That denoted tb corresponds to the waves transmitting back seaward after reflected at one of the boundaries.

Consequently, the reflection coefficient is obtained as,

$$K_R = [A_1^2 + A_2^2 + \dots + A_{N+1}^2 + 2\{A_1 A_2 \cos(\beta_1 - \beta_2) + A_1 A_3 \cos(\beta_1 - \beta_3) \dots + A_J A_N \cos(\beta_J - \beta_N) \dots + A_N A_{N+1} \cos(\beta_N - \beta_{N+1})\}]^{1/2} , \quad (5)$$

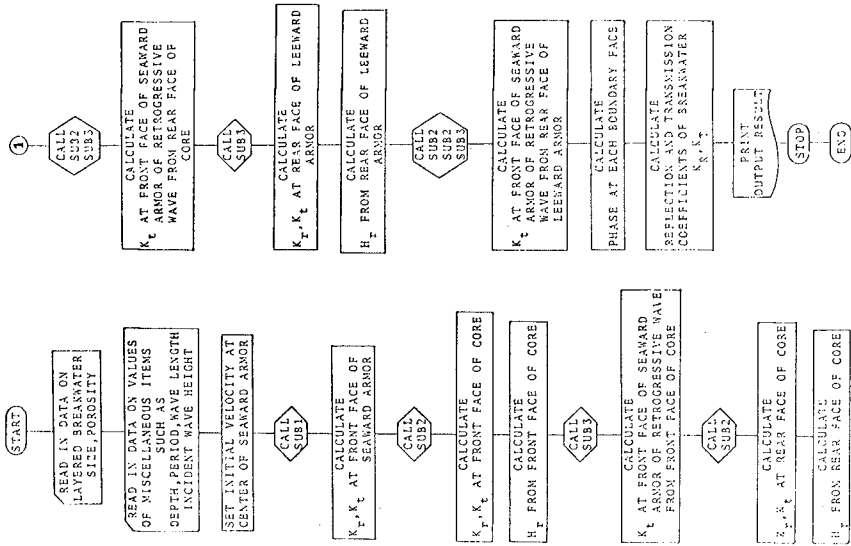
where,

$$\begin{aligned} A_1 &= K_{r,1}, \quad A_2 = K_{t,1} \cdot K_{r,2} \cdot K_{tb,1} \cdot \exp[-(n_{i,1} + n_{r,1})B_1], \dots \\ A_J &= K_{t,1} \cdot K_{t,2} \dots K_{t,J-1} \cdot K_{r,J} \cdot K_{tb,J-1} \dots K_{tb,1} \cdot \exp[-(n_{i,1} + n_{r,1})B_1 + \dots + (n_{i,2} + n_{r,2})B_2 + \dots + (n_{i,J} + n_{r,J})B_J], \dots \\ A_{N+1} &= K_{t,1} \cdot K_{t,2} \dots K_{t,J} \dots K_{t,N} \cdot K_{r,N+1} \cdot \exp[-(n_{i,J} + n_{r,J})B_J]. \end{aligned}$$

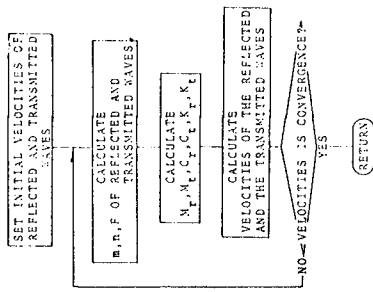
Also,

$$\begin{aligned} \beta_1 &= \alpha_{r,1}, \quad \beta_2 = -(m_{i,1} + m_{r,1})B_1 + \alpha_{t,1} + \alpha_{r,2} + \alpha_{tb,1}, \dots \\ \beta_J &= [-\{(m_{i,1} + m_{r,1})B_1 + (m_{i,2} + m_{r,2})B_2 + \dots + (m_{i,J} + m_{r,J})B_J\} + \alpha_{t,1} + \alpha_{t,2} + \dots + \alpha_{t,J-1} + \alpha_{r,J} + \alpha_{tb,J-1} + \dots + \alpha_{tb,1}], \dots \\ \beta_N &= [-\sum_1^N (m_{i,J} + m_{r,J})B_J + \sum_1^N \alpha_{t,J} + \alpha_{r,N+1} + \sum_1^N \alpha_{tb,J}]. \end{aligned}$$

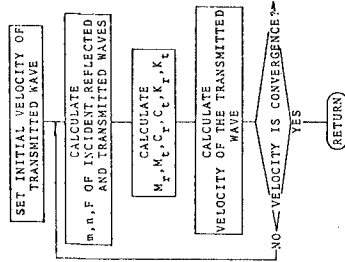
A Flow Chart of computer program for the previous core breakwaters, i.e., for the case of N = 3, is presented in Fig. 22.



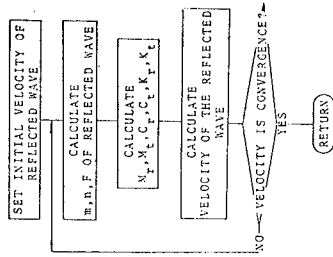
MASTER FLOW CHART



FLOW CHART - SUB2



FLOW CHART - SUB1



FLOW CHART - SUB3

FIG. 22

FLOW DIAGRAM FOR TRANSMISSION AND REFLECTION COEFFICIENTS OF PERVIOUS CORE BREAKWATERS.

CHAPTER 153

WAVE TRANSMISSION THROUGH TRAPEZOIDAL BREAKWATERS

by

Ole Secher Madsen ⁽¹⁾, M.ASCE and Stanley M. White ⁽²⁾, A.M. ASCE

Introduction

Previous publications resulting from this study dealt with certain aspects of the interaction of normally incident waves with a porous structure. Madsen and White (1976a), hereafter referred to as (I), developed a semi-empirical procedure for the prediction of reflection coefficients of rough impermeable slopes. Madsen (1974) with discussion by Kondo (1975) and Closure by Madsen (1976), collectively referred to as (II) hereafter, developed an explicit solution for the transmission and reflection coefficients of homogeneous rectangular crib-style breakwaters. When viewing the interaction of incident waves with a trapezoidal, multilayered breakwater as a problem of energy dissipation, the problem treated in (II) may be regarded as an idealized analysis accounting for the internal dissipation of energy within the structure, whereas (I) may be regarded as an idealized analysis of the energy dissipation on the seaward face of the breakwater, i.e., the external energy dissipation. The present paper presents a synthesis of the results obtained in (I) and (II) into an approximate procedure for the prediction of wave reflection from and transmission through trapezoidal, multilayered breakwaters.

The present paper presents only the major points of the approximate procedure. Thus, extensive references to (I) and (II) are made and only the determination of the hydraulically equivalent breakwater is presented in some detail. For a presentation of the entire development of this model for the reflection and transmission characteristics of trapezoidal, multilayered breakwaters the reader is referred to Madsen and White (1975) or Madsen and White (1976b) where detailed numerical examples of the use of the procedure may also be found.

Description of the Approximate Procedure

The basic assumptions of the approximate procedure are, of course, those inherent in the analyses and procedures developed in (I) and (II):

(1) Associate Professor of Civil Engineering, R.M. Parsons Laboratory, Massachusetts Institute of Technology, Cambridge, MA 02139

(2) Design Civil Engineer, J. Ray McDermott Company, New Orleans, LA 70160 (formerly Research Assistant, R.M. Parsons Laboratory, Massachusetts Institute of Technology)

- (a) Relatively long normally incident waves which may be considered adequately described by linear long wave theory.
- (b) The incident waves do not break on the seaward slope of the breakwater, so that the external energy dissipation may be considered mainly due to bottom frictional effects.
- (c) The cover layer on the seaward slope of the breakwater consists of natural stones, so that the empirical relationships developed in (I) may be considered valid.

With these assumptions stated the following procedure is suggested as being physically realistic although approximate in nature.

For most multilayered trapezoidal breakwaters the stone size in the layer under the cover layer of the seaward slope is small relative to the stone size of the cover layer. As a first approximation the structure may therefore be regarded as resembling an impermeable rough slope. Thus, with the incident wave characteristics and the stone size of the cover layer as well as the seaward slope of the trapezoidal breakwater specified, the procedure developed in (I) may be used to account approximately for the energy dissipation on the seaward slope, i.e., the external energy dissipation may be estimated. This energy dissipation accounts approximately for the dissipation of energy associated with the top layer of stones in the cover layer. The remaining wave energy may be expressed as the energy associated with a progressive wave of amplitude

$$a_I = R_I a_i \quad (1)$$

in which a_i is the amplitude of the actual incident wave and R_I is the reflection coefficient determined by the procedure developed in (I).

With the energy dissipated on the seaward slope accounted for, the remaining energy is partitioned between reflected, transmitted and internally dissipated energy. This partition of energy is the problem dealt with in (II), and it is evaluated by regarding the remaining energy as an equivalent wave of amplitude a_I normally incident on an equivalent homogeneous rectangular breakwater. The role of this homogeneous rectangular breakwater is to reproduce the internal energy dissipation associated with the trapezoidal, multilayered breakwater, i.e., the two breakwaters should in this sense be hydraulically equivalent. A rational method for obtaining a homogeneous, rectangular breakwater which is hydraulically equivalent to a trapezoidal, multilayered breakwater is developed in the following section based on steady flow considerations. By employing the procedure developed in (II) the partition of the remaining wave energy among reflected, transmitted and internally dissipated energy is therefore approximately evaluated by determining the reflection coefficient, R_{II} , and the transmission coefficient, T_{II} , of the hydraulically equivalent homogeneous rectangular breakwater subject to an equivalent incident wave of amplitude a_I .

Having now accounted for the external as well as for the internal energy dissipation, the amplitude of the reflected wave is found to be

$$|a_r| = R_{II} a_I = R_I R_{II} a_i \quad (2)$$

and the transmitted wave amplitude is

$$|a_t| = T_{II} a_I = R_I T_{II} a_i \quad (3)$$

The approximate values of the reflection and transmission coefficient, R and T , of a trapezoidal, multilayered breakwater are therefore

$$R = \frac{|a_r|}{a_i} = R_I R_{II} \quad (4)$$

and

$$T = \frac{|a_t|}{a_i} = R_I T_{II} \quad (5)$$

It should be emphasized that the approximate procedure outlined above is predictive in the true sense of the word, i.e., no other information than what may be expected to be available is needed.

Determination of the Equivalent Rectangular Breakwater

From the description given of the approximate method for obtaining the reflection and transmission coefficients of a trapezoidal, multilayered breakwater, the missing link for carrying out this analysis is the determination of the hydraulically equivalent homogeneous rectangular breakwater.

In Madsen and White (1976b) it was shown that a simple analysis, which essentially neglected unsteady effects, gave transmission and reflection coefficients equal to those obtained from the more complete analysis for structures of small width relative to the incident wavelength (II, eqs. 32 and 33). This observation suggests that a rational and reasonably simple determination of the hydraulically equivalent breakwater may be based on steady flow considerations. Therefore, a hydraulically equivalent breakwater is taken as the homogeneous rectangular breakwater which gives the same discharge, Q , as the discharge through the trapezoidal, multilayered breakwater. This definition will, according to the simple analysis presented in (II), preserve the equality of transmission coefficients for the two structures and hence essentially give the same internal dissipation. This definition of the equivalent breakwater is illustrated schematically in Figure 1.

Figure 1 shows schematically a trapezoidal, multilayered breakwater consisting of several different porous materials. These porous materials

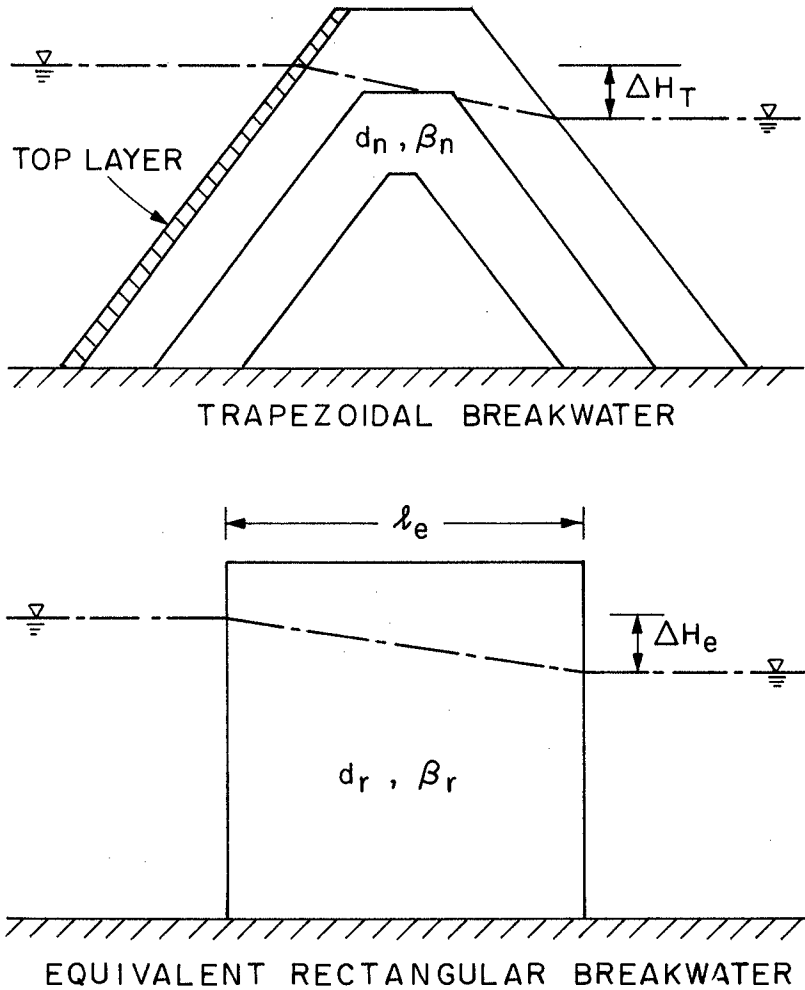


Figure 1. Definition Sketch of Trapezoidal Multilayered Breakwater and Its Hydraulic Equivalent Rectangular Breakwater.

are identified by their stone size, d_n , and their hydraulic characteristics, β_n , in the flow resistance formula (II, eq. 18). To keep the following determination of the equivalent breakwater reasonably simple, the flow resistance is assumed to be purely turbulent although in principle it is possible to perform the determination of the equivalent breakwater based on the more general form of the Dupuit-Forchheimer resistance formula. Since the energy dissipation associated with the top layer of stones on the seaward slope has been accounted for in the determination of the external energy dissipation, the rectangular homogeneous breakwater which accounts approximately for the internal dissipation should be hydraulically equivalent to the trapezoidal, multilayered breakwater with the top layer of cover stones removed.

The homogeneous rectangular breakwater consists of a reference material of stone size, d_r , and hydraulic characteristics, β_r . The reference material should be taken to be representative of the porous materials of the multilayered breakwater. In keeping with the assumption of long waves the flow is assumed to be essentially horizontal and the horizontal discharge velocity is found from

$$\rho g \frac{\Delta H_e}{l_e} = \rho \beta_r U^2 \quad , \quad (6)$$

in which l_e is the width of the equivalent breakwater and ΔH_e is the head difference defined in Figure 1, ρ is the fluid density and g is the gravitational acceleration. The discharge per unit length is therefore obtained from equation (6) to be

$$Q = U h_o = \left\{ \frac{g \Delta H_e}{\beta_r} \right\}^{1/2} \frac{h_o}{\sqrt{l_e}} \quad (7)$$

in which h_o is the depth of water.

To evaluate the discharge per unit length of the trapezoidal, multilayered breakwater a horizontal slice of height, Δh_j , is shown schematically in Figure 2. This horizontal slice consists of segments of the different porous materials of lengths l_n . From the assumption of purely horizontal flow it follows that the discharge velocity of the slice considered, U_j , must be the same in all segments and the total head loss across the breakwater must be equal to ΔH_T , the head difference shown in Figure 1. From this it is seen

$$\Delta H_T = \sum_n (\Delta H_n) \quad . \quad (8)$$

in which ΔH_n is the head loss associated with the segment of length, l_n ,

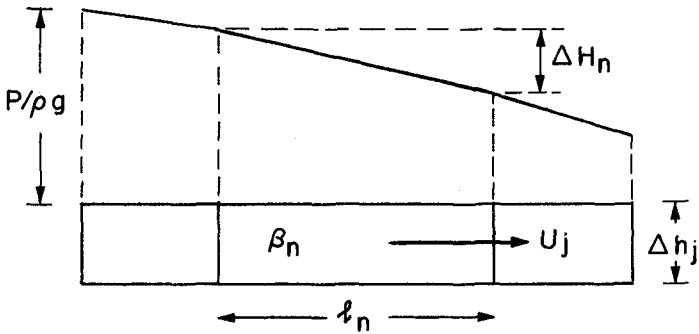


Figure 2. Horizontal slice of thickness, Δh_j , of multilayered breakwater. and hydraulic characteristics, β_n . From equation (6) it is seen that

$$\Delta H_n = \beta_n l_n \frac{U_j^2}{g} = \beta_r \frac{U_j^2}{g} \left(\frac{\beta_n}{\beta_r} l_n \right) \quad (9)$$

in which β_r is the hydraulic characteristic of the reference material. Equation (8) may therefore be written:

$$\Delta H_T = \beta_r \frac{U_j^2}{g} \sum_n \left(\frac{\beta_n}{\beta_r} l_n \right) \quad (10)$$

in which the summation is carried out over the n different porous materials of the horizontal slice of thickness, Δh_j .

From equation (10) the discharge associated with the slice of thickness Δh_j is found to be

$$\Delta Q_j = U_j \Delta h_j = \left\{ \frac{g \Delta H_T}{\beta_r} \right\}^{1/2} \frac{\Delta h_j}{\left\{ \sum_n \left(\frac{\beta_n}{\beta_r} l_n \right) \right\}^{1/2}} \quad (11)$$

and by adding the contributions from all horizontal slices of the trapezoidal breakwater one obtains

$$Q = \sum_j \Delta Q_j = \left\{ \frac{g \Delta H_T}{\beta_r} \right\}^{1/2} h_o \sum_j \left\{ \frac{1}{\left[\sum_n \left(\frac{\beta_n}{\beta_r} \lambda_n \right) \right]^{1/2}} \frac{\Delta h_j}{h_o} \right\} \quad (12)$$

Thus, requiring that the discharges per unit length given by equations (7) and (12) be identical, the width, ℓ_e , of the equivalent rectangular breakwater is

$$\ell_e = \left\{ \sum_j \left(\frac{1}{\left[\sum_n \left(\frac{\beta_n}{\beta_r} \lambda_n \right) \right]^{1/2}} \frac{\Delta h_j}{h_o} \right)^2 \right\} \left(\frac{\Delta H_e}{\Delta H_T} \right) \quad (13)$$

This equation shows that the width of the equivalent breakwater may be determined from knowledge of the configuration of the trapezoidal, multilayered breakwater and the corresponding head differences, ΔH_e and ΔH_T .

As described in the previous section the equivalent breakwater is subject to an equivalent incident wave of amplitude a_I given by equation (1). A simplified analysis of the interaction of incident waves and a rectangular homogeneous breakwater of small width relative to the length of the incident waves was presented in (II). This simplified analysis essentially neglected unsteady effects and any phase difference between the incident, reflected, and transmitted waves. The runup on the seaward slope of the hydraulically equivalent rectangular breakwater is taken as a representative value of the head difference, ΔH_e , across the equivalent breakwater. With this assumption, which neglects the influence of a transmitted wave of small amplitude, one obtains

$$\Delta H_e = (1 + R_{II}) a_I = (1 + R_{II}) R_I a_i \quad (14)$$

in which R_{II} is the reflection coefficient of the equivalent breakwater, determined by the procedures developed in (II).

The value of the head difference across the trapezoidal breakwater, ΔH_T , is in accordance with the argument presented for the equivalent rectangular breakwater taken as the runup on the seaward slope of the trapezoidal breakwater. This runup may in principle be determined by the procedure developed in (I). However, there is reason to believe that such an estimate, which would correspond to an impermeable slope, would be somewhat on the high side. In general one may, however, take

$$\Delta H_T = 2R_u a_i \quad (15)$$

where R_u is the best estimate available for the ratio of the runup to the

incident wave height $H_i = 2a_i$ for given slope characteristics. If R_u is taken as determined from Figure 3 in (I) the estimate of ΔH_T is expected to be conservative.

Equations (14) and (15) show that the ratio

$$\frac{\Delta H_e}{\Delta H_T} = \frac{(1 + R_{II})R_I}{2R_u} \quad (16)$$

is a function of the reflection coefficient, R_{II} , of the equivalent breakwater. Since this reflection coefficient cannot be determined until the width of the equivalent breakwater, l_e , is known one is faced with a tedious iterative procedure. However, in most cases a sufficiently accurate estimate of R_{II} may be obtained by assuming initially that $\Delta H_e/\Delta H_T$ is unity and use this estimate along with the best estimate of R_u to obtain a new value of $\Delta H_e/\Delta H_T$ from equation (16).

To evaluate Equation (13) the hydraulic characteristics, β_n , of the various layers must be known. Since β_n in general is unknown the use of empirical relationship suggested in (II, eq. 40) is necessary. This relationship

$$\beta = \beta_o \frac{1-n}{n} \frac{1}{d} \quad (17)$$

is strongly dependent on the value of the porosity, n , which must be assumed. Since this empirical relationship is valid only for natural stones, in fact it is established for sands, its use is limited to rubble-mound breakwaters. The empirical, dimensionless constant β_o is a function of stone shape, etc., and $\beta_o = 2.7$, as suggested in (II) seems to be a reasonable value. Since equation (13) depends on the relative value of β_n/β_r the value of β_o is immaterial so long as it may be assumed the same for all layers.

Computation of Transmission and Reflection Coefficients for Trapezoidal, Multilayered Breakwaters

To apply the approximate method outlined in the preceding sections it is assumed that the incident wave characteristics are known, i.e., $H_i = 2a_i$, h_o , T or L are given. The procedure is therefore

a. Determination of the External Dissipation. The first step is to estimate the external energy dissipation on the seaward slope using the procedure developed in (I). To perform this analysis the necessary information, in addition to the incident wave characteristics, is

$$\text{Surface Roughness} = d_r ; \text{ Seaward Slope} = \tan\beta_s \quad (18)$$

This information is sufficient for carrying out the procedure developed in (I) for the determination of the reflection coefficient of impermeable rough slopes, R_I . Since the rate of energy dissipation on a rough impermeable slope is related to its reflection coefficient this step in the analysis may be viewed as an approximate evaluation of the energy dissipation on the seaward slope of a trapezoidal, multilayered breakwater.

The empirical relationships for the frictional effects established in (I) are valid only for slopes whose roughness is adequately modeled by gravel, i.e., natural stones, which is reflected in the previously stated assumption, (c).

b. Determination of the Internal Dissipation. Having determined the energy dissipation on the seaward slope, the remaining wave energy is equivalent to an equivalent incident wave of amplitude a_I given by equation (1). The partition of the remaining energy among reflected, transmitted and internally dissipated energy is estimated from the procedures developed in (II). To perform this analysis the hydraulically equivalent breakwater is determined as outlined in the previous section. The information necessary for the determination of the hydraulically equivalent rectangular, homogeneous breakwater is

Breakwater Geometry;
 Material Properties (including porosity); (19)
 Runup on trapezoidal breakwater.

The use of equation (17) to estimate the hydraulic characteristics of a porous material reduces the necessary information to generally available quantities except for the porosity and the runup on the seaward slope in order for equation (13) to be evaluated. Use of $n = 0.4$ seems reasonable in conjunction with $\Delta H_e / \Delta H_T = 1$ for preliminary calculations.

With these assumptions the equivalent breakwater is readily determined and the explicit procedure developed in (II) may be used to obtain an estimate of the partition of the remaining energy among reflected, transmitted and internally dissipated energy, i.e., the reflection and transmission coefficients R_{II} and T_{II} , respectively, of the equivalent breakwater may be obtained.

c. Determination of the Transmission and Reflection Coefficient of Trapezoidal, Multilayered Breakwaters. From the results obtained in steps a and b it is now possible to estimate the transmission and reflection coefficient of a trapezoidal, multilayered breakwater since the external as well as the internal energy dissipation has been accounted for. From the description of the procedure given previously it follows that the transmitted and reflected wave amplitudes, $|a_t|$ and $|a_r|$, are given by

$$|a_t| = T_{II} a_I = T_{II} R_I a_i \quad (2)$$

and

$$|a_r| = R_{II} a_I = R_I R_{II} a_i \quad (3)$$

The transmission coefficient, T, and reflection coefficient, R, are therefore obtained from

$$T = \frac{|a_t|}{a_i} = T_{II} R_I \quad (4)$$

and

$$R = \frac{|a_r|}{a_i} = R_I R_{II} \quad (5)$$

Comparison Between Predicted and Observed Transmission and Reflection Coefficients of a Trapezoidal, Multilayered Breakwater

The preceding section has illustrated the use of the approximate method for the determination of transmission and reflection coefficients of trapezoidal, multilayered breakwaters. This procedure was followed choosing values of the incident wave characteristics and breakwater characteristics corresponding to the laboratory experiments performed by Sollitt and Cross (1972), and the predictions may therefore be compared directly with the experimentally observed values of the transmission and reflection coefficients given by Sollitt and Cross (1972, App. G). This comparison between predicted and observed transmission and reflection coefficients is shown in Figure 3, where the values of T and R are plotted against the incident wave steepness, H_i/L , corresponding to a value of $h_o/L = 1/12$, i.e., relatively long waves as assumed throughout this paper.

From the comparison presented in Figure 3 the predicted reflection coefficients are in excellent agreement with the observed reflection coefficients for lower values of the incident wave steepness. For larger values of the incident wave steepness the predicted reflection coefficient is seen to increase slightly whereas the observed reflection coefficients exhibit a decreasing trend with increasing wave steepness. As discussed by Madsen and White (1975 and 1976b) this trend of the experimental reflection coefficients is generally observed and may be partly due to experimental errors in the determination of the reflection coefficient. This was discussed briefly in (I) and in detail in Madsen and White (1975 and 1976b).

The transmission coefficients predicted based on the assumption $\Delta H_e/\Delta H_T = 1$ are seen to be lower than the experimentally obtained values. This, of course, is the expected type of discrepancy since the runup on the seaward slope of the trapezoidal breakwater is almost certain to exceed the runup on the equivalent rectangular breakwater. Adopting the theoretical value of the runup, R_u , on the trapezoidal breakwater predicted by the procedure developed in (I) is expected to give transmission coefficients

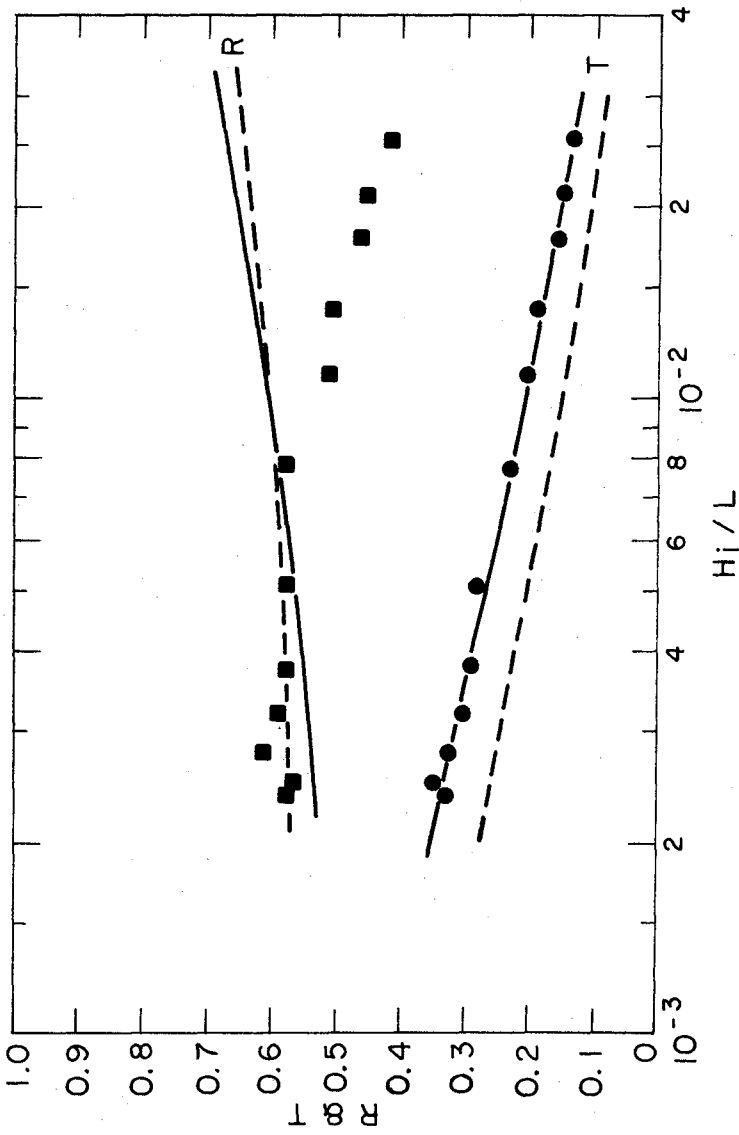


Figure 3. Comparison of predicted and observed reflection and transmission coefficient of trapezoidal, multilayered breakwater tested by Sollitt and Cross (1972, App. G, kh = 0.5).
 ■ Experimental reflection coefficient, ● experimental transmission coefficient,
 — prediction based on $\Delta H_e/\Delta H_T = 1$, --- prediction based on $\Delta H_e/\Delta H_T$ given by equation (16)

slightly on the high side. This anticipated behavior is not exhibited by the predicted transmission coefficients plotted in Figure 3. In fact, the agreement between observed and predicted transmission coefficients is excellent.

A slightly different estimate of the runup on the seaward slope of a trapezoidal breakwater may be obtained by adopting, for example, the results obtained by Jackson (1968), who reported values of R_{11} approximately equal to unity for test conditions similar to those of Sollitt and Cross (1972). In the present case this value of R_{11} would result in a slightly lower prediction of the transmission coefficient than the prediction indicated by the full line in Figure 3.

The procedure developed here for the prediction of transmission and reflection coefficients of a trapezoidal, multilayered breakwater did not rely on the experimental data shown in Figure 3 to obtain a "good fit." The overall comparison between predicted and observed transmission and reflection coefficients, which is analogous to the comparison given by Sollitt and Cross (1972, Fig. 4-14), must therefore be considered very good.

Summary and Conclusions

This paper presents the synthesis of the results of an analytical study of the reflection and transmission characteristics of porous rubble-mound breakwaters. An attempt was made at making the procedures entirely self-contained by introducing empirical relationships for the hydraulic characteristics of the porous material (II) and by establishing experimentally an empirical relationship for the friction factor that expresses energy dissipation on the seaward slope of a breakwater, (I).

The results are presented in graphical form and require no use of computers, although the entire approach could be programmed. The procedures were developed in such a manner that the information required to carry out the computations can be expected to be available. Thus, for a trapezoidal, multilayered breakwater subject to normally incident, relatively long waves the information required is:

- (a) Breakwater configuration: breakwater geometry and stone size and porosity of the breakwater materials
- (b) Incident wave characteristics: wave amplitude, period, and water depth.

Only the porosity of the breakwater materials may be hard to come by. It is recommended that the sensitivity of the results to the estimate of the porosity, n , be investigated.

The hydraulic flow resistance in the porous medium is expressed by a Dupuit-Forchheimer relationship and empirical formulas are adopted. The investigation shows that reasonably accurate results are obtained by taking

$$\beta_0 \approx 2.7$$

$$\alpha_0 \approx 1150$$

(20)

in equation (40) of (II). To estimate reflection and transmission characteristics of a prototype structure only the value of β_0 needs to be known. For laboratory experiments the value of the ratio, α_0/β_0 is important in assessing the influence of scale effects. In a laboratory setup it is possible to determine the best values of α_0 and β_0 from the simple experimental procedure used by Keulegan (1973). Thus, it was found that the porous materials tested by Sollitt and Cross (1972) showed a value of $\alpha_0 = 2,700$, a better value than that given by equation (20). However, the important thing to note is that the analysis carried out in (II) presents a method for assessing the severity of scale effects in hydraulic models of porous structures. The empirical relationships for the flow resistance of porous materials have been demonstrated to be fairly good for porous materials consisting of gravel-size stones, diameter less than 2 inches (5 centimeters), which is a considerable extension of the conditions from which they were derived (sand-size). The use of the formulas for rubble-mound breakwaters is, however, a further extension and caution is recommended.

The energy dissipation on a rough, impermeable slope was investigated in (I). The experimental investigation revealed the need for an accurate method for the determination of reflection coefficients from experimental data. The simple procedure of seeking out the locations where the wave amplitudes are maximum and minimum, respectively, may lead to reflection coefficients which are much too low, unless the recorded surface elevation is analyzed and only the amplitude of the first harmonic motion is used to determine the reflection coefficient. Accurately determined reflection coefficients for slopes with roughness elements consisting of gravel led to an empirical determination of the friction factor (I, eqs. 32 and 34) expressing the energy dissipation on a rough slope due to bottom friction. Adopting this empirical relationship a procedure for estimating the reflection coefficient of rough impermeable slopes was developed. This procedure was quite accurate in reproducing the experimentally obtained reflection coefficients in a separate set of experiments. The procedure for the determination of the reflection coefficient of rough impermeable slopes is limited to slopes having roughness elements consisting of natural stones. To make the procedure generally applicable, empirical relationships for the friction factor should be determined for slopes whose roughness elements consist of models of concrete armor units.

The synthesis of the investigation presented in this paper, is the development of an approximate procedure for the prediction of the reflection and transmission characteristics of trapezoidal, multilayered breakwaters. This procedure is entirely self-contained and yields excellent results when compared with the model scale experimental results obtained by Sollitt and Cross (1972).

It is emphasized that the analytical model for the reflection and transmission characteristics of trapezoidal, multilayered breakwaters developed here needs further verification before it can be used with complete confidence. However, the good agreement between predictions and observations exhibited in Figure 3 is encouraging and does indicate that a simple analytical model which may be used for preliminary design of rubble-mound breakwaters has been developed.

To improve the physical realism of the approximate model for the interaction of waves and porous structures a more accurate description of the flow over the sloping seaward face of the porous breakwater should be developed. Development of such an analytical model is presently being pursued and should lead to improved results, in particular, in the prediction of runup on the permeable seaward slope. In addition an experimental investigation is called for to resolve the problem of whether or not the discrepancy between predicted and observed reflection coefficients, exhibited in Figure 3, is due mainly to experimental errors.

Acknowledgment. This work is a result of research sponsored by the United States Coastal Engineering Research Center under Contract DACW72-74-C-0001. Funds to present and prepare this paper were provided through a National Science Foundation Grant ENG 7608982 under which further research into this topic will be performed.

References.

- Jackson, R.A., "Design of Cover Layers for Rubble-Mound Breakwaters Subjected to Nonbreaking Waves," Research Report No. 2-11, U.S. Army Engineer Waterways Experiment Station, Vicksburg, Miss., 1968.
- Keulegan, G.H., "Wave Transmission through Rock Structures," Research Report No. H-73-1, U.S. Army Engineer Waterways Experiment Station, Vicksburg, Miss., 1973.
- Kondo, H. (1975), Discussion of "Wave Transmission through Porous Structures," by Madsen (1974), Journal of the Waterways, Harbors and Coastal Engineering, Vol. 101, WW3, pp. 300-302.
- Madsen, O.S. (1974), "Wave Transmission through Porous Structures," Journal of the Waterways, Harbors and Coastal Engineering, Vol. 100, WW3, pp. 169-188.
- Madsen, O.S. (1976), Closure to "Wave Transmission through Porous Structures," by Madsen (1974), Journal of the Waterways, Harbors and Coastal Engineering, Vol. 102, WW1, pp. 94-97.
- Madsen, O.S. and S.M. White (1975), "Reflection and Transmission Characteristics of Porous Rubble-Mound Breakwaters," Technical Report No. 207, R.M. Parsons Laboratory, Department of Civil Engineering, Massachusetts Institute of Technology.

Madsen, O.S. and S.M. White (1976a), "Energy Dissipation on a Rough Slope," Journal of the Waterways, Harbors and Coastal Engineering, Vol. 102, WW1, pp. 31-48.

Madsen, O.S. and S.M. White (1976b), "Reflection and Transmission Characteristics of Porous Rubble-Mound Breakwaters," Miscellaneous Report No. 76-5, U.S. Army Engineer Coastal Engineering Research Center, Fort Belvoir, Virginia.

Sollitt, C.K. and R.H. Cross (1972), "Wave Reflection and Transmission at Permeable Breakwaters," Technical Report No. 147, R.M. Parsons Laboratory, Department of Civil Engineering, Massachusetts Institute of Technology.

CHAPTER 154

QUAY WALL WITH WAVE ABSORBER "IGLOO"

Naofumi Shiraishi,* Robert Q. Palmer,** Hiroshi Okamoto***

ABSTRACT

This report summarizes the results of the research on a gravity type quay wall comprising several layers of concrete blocks with a special shape called "Igloo" as shown in Photograph-1.

INTRODUCTION

The recent trend for higher utilization of the basin in the ports and harbors by using the vertical wall as the facilities for berthing and cargo handling presents extreme difficulties for securing the calmness within the ports as the vertical wall would keep on reflecting the invading waves and increase the wave energy. Much research has been conducted on the vertical wave absorbing structure in Japan in recent years.

Research has proved that a vertical wave dissipating structure had an optimum wall depth which absorbs waves most effectively in accordance with the incident wave period.^{1), 2)} This report is an article on the gravity type structure which is contrived to actual application with the best wave dissipating effect, and is made of concrete blocks.

Our first step is to conduct a two dimensional model test look into the relationship between inci-



Photograph-1

* Dr. Eng., Senior Managing Director, Nippon Tetrapod Co., Ltd.

** President, Tribars Incorporated

*** Engineer, Development Section, Nippon Tetrapod Co., Ltd.

dent wave period and dissipating effect, and then to conduct a three dimensional model test where we will investigate how the vertical wave dissipating structure calms the basin.

WAVE DISSIPATING PRINCIPLES OF IGLOO SYSTEM

The principles of the Igloo wave dissipating system are shown on the illustrations (Fig-1) and are summarized as follows:

The horizontal plate converts the vertical wave movement into the horizontal flow, then induces the water to enter the block which rotates the water inside cylindrical chambers and reduces the energy through the friction with the wall surface through the forced diversion and merging of the flows.

Further in detail, the column shaped front wall lets the waves into the block smoothly, hardly reflecting the waves. The horizontal plate converts the vertical movement of the waves (the circular movement, to be more precise) into a horizontal flow. In physical terms, the potential wave energy is converted to kinetic energy. The converted water causes friction alongside the wall surface in the block chambers and diverts and merges as it rotates, thus losing the energy. The loss ratio of water energy that flows in a void encountering resistance is the subject of studies in various universities. It has been found that the ratio is proportionate to 2nd or 3rd power of the velocity. That is, the more distance the water flows at a faster velocity, the more energy is lost.

Igloo system is contrived for the water to flow the longer distance at the faster speed. When the Igloos one piled together, the chambers formed by these blocks take a circular shape with a narrow entrance and a wider inside. Thus shaped blocks impart

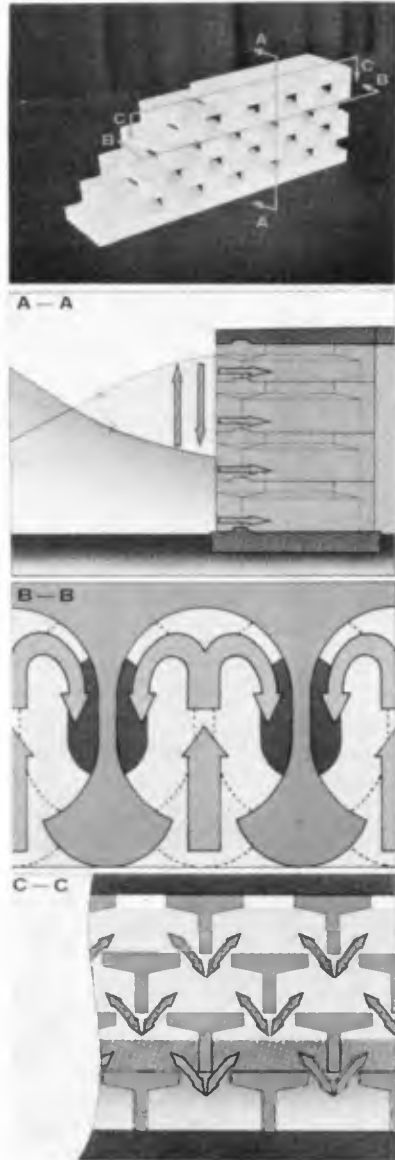


Fig-1

faster velocity to the mass of water and induce the water into the chambers. The water advances directly into the innermost part of the chamber and then separates into two, and rotates alongside the walls. When the water rotates, the distance of the water flow increases. Even though the chamber space may be limited, the water revolves within the chambers at a high velocity and the energy thus lost is quite big.

As the phase between the water level in front of the seawall and that of the chambers is quite different, the water level in front of the seawall lowers, causing energy loss when the water is discharged from the chambers.

TWO DIMENSIONAL MODEL TEST

The model tests of this structure were carried out in the laboratory to investigate the hydraulic properties.

1. Test Facilities

Two dimensional wave channel with a wind tunnel owned by the Hydraulic Research Center of Nippon Tetrapod Co., Ltd. was used.

Dimensions of the channel:

Length 49.0m, Height 1.0m, Width 1.0m (50cmx2)

Wave generator

Flap type (hydraulic system, irregular waves)

Wave high: 25 cm Max

Period: 0.6~3.0 sec

Blower: Suction type, propeller system (Wind volume, 600 m³/min.)

2. Test Model

We used a mortar-made 1:25 scale model of Igloo blocks and its specific weight was 2.3 ton/m³, which is the same weight of actual Igloo blocks. The model is 15.2~26.0 cm in depth, 12 cm in width and 4.4~6.8 cm in height; their actual block size is 3.8~6.5 m in depth, 3.0 m in width and 1.1~1.7 m in height.

3. Test Method

(1) The wave measuring method:

The reflection coefficient is measured by the method provided by Healy, and the variation of the water level is checked by a volmetric wave meter. The change in the electric volume caused by the change in the water level is converted into an electric current, amplified by an amplifier and recorded by an oscillograph.

(2) Wave generation method:

Sinoidal waves made by the function generator send the wave to the wave making control device, which generates regular waves with the required periods and heights.

4. Test Conditions

The cross section of the tests is shown in Fig-2. Test conditions are shown in Table-1.

5. Test Results

Non-dimensional factors affecting Igloo's wave dissipation include B/L: the ratio of wall depth against wave length, hc/H: the ratio of Igloo crown height above still water level against wave height, i: bottom slope, h/L: relative water depth, h/H: the ratio of wave height against water depth, H/L: wave steepness and others.

If the design conditions are limited to $h/H > 2, 3 < T < 10$ sec, $0.3 < H < 2$ (m) in case of actual application, influence of non-dimensional factors such as h/L, H/L, and others are not so great. Out test condition is always set at $i=1/30$. The remaining non-dimensional factors such as B/L and hc/H will play an important role. Therefore we summarized the test results concerning reflection coefficient KR which is shown in Fig-3 (a)~(e) with B/L on the horizontal axis of coordinates and with hc/H as a parameter.

The following were made clear.

(1) In all tests, wave dissipating

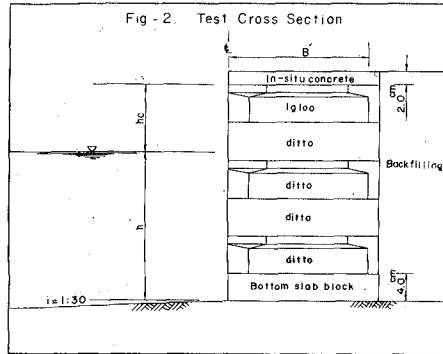


Table-1 Test Conditions

B (B') (cm)	h (cm)	T (sec)	Lo (cm)	h/Lo	h/L	L (cm)	H (cm)	hc (cm)	B'/L	h/H	hc/H	H/L
15.2 (13.6)	16.0	0.8	100	0.018	0.055	83	2.0	2.0	0.039	2.67	0.5	0.006
~ 0.164												
0.047												
~ 0.198												
0.058												
22.0 (20.4)	~ 22.0	~ 2.4	~ 900	~ 0.220	~ 0.242	~ 349	~ 6.0	~ 8.0	~ 0.246	~ 11.0	~ 4.0	~ 0.072
26.0 (24.4)	0.070											
~ 0.294												
34.0 (32.4)	0.093											
~ 0.390												

List of Notation

- B: Igloo depth
- B: Effective depth of Igloo
- h: Water depth at the toe of the seawall
- T: Wave period
- Lo: Wave length in deep water
- L: Wave length of progressive waves at the toe of seawall
- H: Height of progressive waves at the toe of seawall
- hc: Distance from still water level to the crown height of Igloo (i.e, clearance)

effect gives the best result when $B/L=0.14\sim 0.19$.

(2) Under the condition of $hc/H < 0.5$, Igloo's performance is not satisfactory.

The above two conclusions are almost enough in designing Igloo system. Namely, in compliance with the local wave conditions, Igloo wall depth B will be set at $B/L=0.14\sim 0.19$. The crown height of Igloo should be designed high enough to enable berthing and cargo handling. It is particularly important to set hc at $hc < \frac{1}{2}H$ for the designed wave height H .

It has been previously indicated that the reflection coefficient becomes minimized when B/L is given a certain value. This is worth noting and can be explained as follows:

The extreme example of long wave is shown in "Seiche", in that the longer the period, the bigger the reflection coefficient becomes. The water level ascends and descends very slowly. The same can be said for the Igloo chambers where the water level that ascends and descends requires exactly the same length of time. Regardless of the shape of Igloo void, the waves reflect completely against the rear wall.

Conversely, if the incident wave period is too short, the reflection coefficient becomes larger. Such phenomenon can be explained as

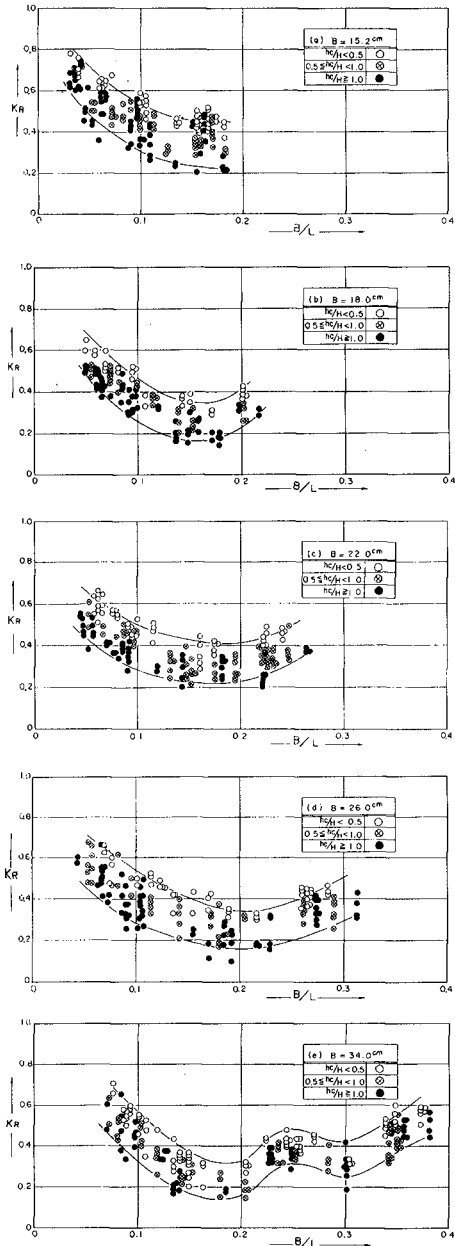


Fig-3 Reflection Coefficient of Igloo

the responsive characteristics of water surface in the chambers. Depending upon the volume and shape of the Igloo void, the water in the void is composed of a responsive system with natural frequency. If water movement in front of Igloo system is considered as an external force and the frequency of this external force increases extremely, the Igloo system can hardly respond to the external force. In other words, despite the violent up-and-down motion of the waves in front of the Igloo system, the water in the void is almost tranquil. In this case, the waves reflect against the system as if it were a vertical wall.

Where there is a certain gap between the frequency of the external force and the natural frequency of the Igloo, the wave energy is most effectively reduced in the chambers. Also, the energy dissipates due to disturbances in front of the wall where two types of waves with different phases cause turbulence in order to keep the continuity of water surface. In our experiments, scattering waves with extremely short length were observed within the one wave length in front of the structures. We have to provide the theory behind this observation.

THREE DIMENSIONAL MODEL TEST

1. Reflection coefficient of incident waves from an oblique direction

Wave dissipating effect of incident waves from a right angle is obtained in the two dimensional test, but that from an oblique direction will be found in the three dimensional test. The measuring method of reflection coefficient for the incident waves from an oblique direction can be obtained by Hadly's theory. But due to the scattering waves against the wave dissipating structure, accurate measurement is difficult. Therefore, we use the indirect method to obtain reflection coefficient of incident waves from an oblique direction.

The calmness in the water basin using various types of center line structure is measured by changing boundary conditions (equivalent to reflection coefficients) through a computer's mathematical simulation method and the results will be compared with the hydraulic tests. The reflection coefficient is obtained from the boundary conditions where the two results coincide with one another. This is the exact opposite of the common method. Although some questions remain as to whether the given boundary conditions are accurate and yet reflection coefficient of the structure is correctly reflected. Considering the recent improvements made in the accuracy of the mathematical simulation method and the relative comparison with traditional vertical walls being the focal point of discussions, this method is considered to be reasonable.

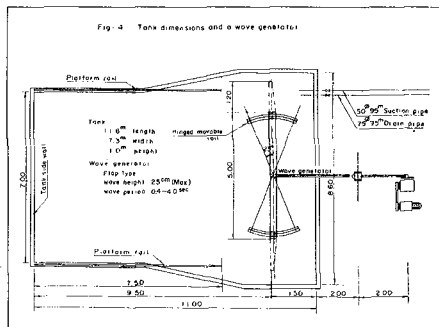
2. Experimental Facilities

Three dimensional wave tank owned by Hydraulic Research Center of Nippon Tetrapod Co. was used. Fig-4 shows the tank dimensions and a wave generator.

3. Experimental method and conditions

Fig-5 shows one of the structure models. The water depth of the wave generator is 56 cm and that of the structure is 16 cm. And the slope is three to one. Small gravel and film wastes are placed around the side walls of the tank in order to avert reflection waves from the side walls.

The vertical wall model is made of mortar. The Igloo model is made of hard rubber 6 cm in width, 2.8 cm in height, 9.0 cm in depth, which is equivalent to 1:50 scale model. The regular waves in this experiment are 2.0 cm in height, 0.71 sec and 1.13 sec in period at the place where the water depth is 56 cm. Fig-6 shows the center line of the model and Table-2 shows test conditions.



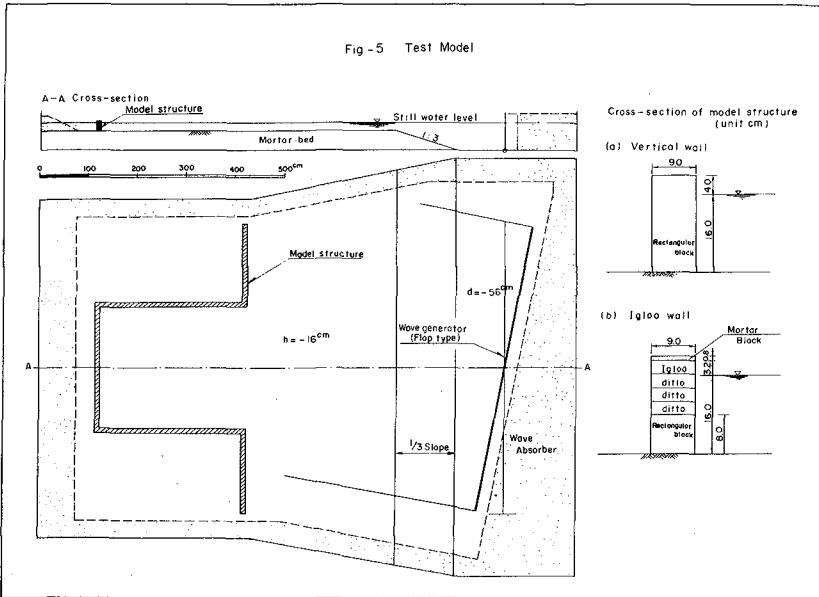
The wave height in front of the structure are measured by a capacitance probe type wave meter placed under a movable platform across the tank. This meter reads wave height at the points distributed with 20 cm intervals length-wise and cross-wise.

4. Results

Some cases are shown in Fig-7 through 9. Fig-7(a) (b) show the waves at a 45° angle on the center line of the structure. Vertical wall produced a net-like wave pattern in the basin because the crests of incident waves and reflected waves mix with one another. Amplitude at this point is two times that of incident wave height and more than two times at the wall. Those points of intersection run along the model front with the waves. Crests at even interval seem to run along the wall. Actual crest speed will be 5m/sec~10m/sec with waves of 10 sec in period at 45° angle. These waves cause overtopping, exert an unfavorable influence upon ships.

Igloo will absorb most of the crests of reflection waves. Crests of the incident waves run along the Igloo wall, when water level in the chambers rises shortly afterwards causing chain reaction in the adjacent chamber. Eddies and turbulences arisen will then diminish the wave energy. Photograph-2 shows the wave conditions of the Igloo wall.

Fig-8(a), (b) show an experiment concerning the waves on V-shaped center line. The effect of the Igloo wall will be more distinct than that of a straight center line. Vertical wall will produce the standing waves from the three direction such as incident waves and reflec-



ted waves from two different directions. In this experiment, wave amplitude is five times more than the incident wave height where amplitude is highest. Amplitude in the Igloo wall will be only twice that of the incident wave on the same spot. Photograph-3 shows the wave manners on the vertical wall and Igloo wall.

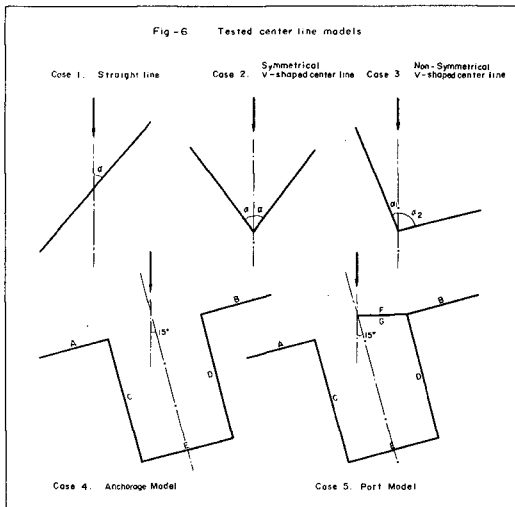
Photograph-4 shows the waves in the basin between the two wharfs. In the case of conventional vertical wall, a net-like wave pattern is seen in the basin. The pyramidal waves at the intersections of the net becomes several times higher than the incident waves. Excessive overtopping is observed at a quay wall. On the otherhand, in the case of Igloo wall, results of the test showed that waves in the basin presented the similar appearance to those of the incoming waves as though there were no structure.

Fig-9(a), (b) show the experiment of a port model. Vertical wall in the innermost part of the ports shows the same wave height as those of incident wave. But through the proper placement of a wave absorbing structure, reflection waves in the port decrease. In coming waves from the open sea diffract into the port, but wave heights in the innermost part of the port becomes smaller.

Table - 2 Test Conditions

Case No.	Center line shape	Center line angle	Type of wall	Incident wave period	Case No.	Center line shape	Center line length (cm)	Type of wall	Incident wave period
1	Straight line	$\alpha = 30^\circ$	(I)	0.71	4	Anchorage model	A = 175	A~E (I)	0.71
			(II)	0.71			B = 170	(I)	1.13
		$\alpha = 45^\circ$	(I)	0.71			C = 310	A~E	0.71
			(II)	0.71			D = 310	(II)	1.13
		$\alpha = 60^\circ$	(I)	0.71			E = 225	A, B, D (I)	0.71
(II)	0.71		C, E (II)	(II)	1.13				
2	Symmetrical V-shaped center line	$\alpha = 30^\circ$	(I)	0.71	5	Port model	A = 175	A~G	0.71
			(II)	0.71			B = 170	(I)	1.13
		$\alpha = 45^\circ$	(I)	0.71			C = 310	A~G	0.71
			(II)	0.71			D = 310	(II)	1.13
		$\alpha = 60^\circ$	(I)	0.71			E = 225	A, B, D, G (I)	0.71
(II)	0.71		C, E (II)	(II)	1.13				
3	Non-symmetrical V-shaped center line	$\alpha_1 = 60^\circ$ $\alpha_2 = 30^\circ$	(I)	0.71	Type of wall (I) Conventional vertical wall (II) Igloo wall				
			(II)	0.71					
		$\alpha_1 = 75^\circ$ $\alpha_2 = 15^\circ$	(I)	0.71					
			(II)	0.71					
		$\alpha_1 = 75^\circ$ $\alpha_2 = 45^\circ$	(I)	0.71					
			(II)	0.71					
		$\alpha_1 = 90^\circ$ $\alpha_2 = 30^\circ$	(I)	0.71					
			(II)	0.71					
		$\alpha_1 = 90^\circ$ $\alpha_2 = 60^\circ$	(I)	0.71					
			(II)	0.71					

Tested Waves	Scale	Wave period (T)	Wave depth h	Wave height H ₀	Deepwater wave length L ₀	Nondimensional parameter		Wave length L (cm)	
						H ₀ /L ₀	H ₀ /L		
A-Wave	Model	1	0.71	1.65m	2.0 ^{cm}	7.8 ^{cm}	0.205	0.229	7.0 ^{cm}
	Proto	50	√50	5.0	8.0 ^m	1.0 ^m	3.5 ^m		3.5 ^m
B-Wave	Model	1	1.13	1.65m	2.0 ^{cm}	2.0 ^{cm}	0.080	0.123	1.3 ^{cm}
	Proto	50	√50	8.0	8.0 ^m	1.0 ^m	1.0 ^m		6.5 ^m



5. Comparison with a Mathematical Simulation Model

Wave height distribution of the basin can be obtained by the mathematical model using the same conditions as the physical model. Experimental results of each mathematical model using various boundary conditions with the same reflection coefficient as the structure can be compared with the experimental results of the physical model to find out the values of boundary conditions where two results coincide most closely. This is the method to identify the reflection coefficient of oblique incident waves. The mathematical model does not include the nonlinear wave effect, while the physical model does. So that amplitude of the mathematical model should be modified accordingly.

Tajbakhsh and Keller's three dimensional approximation formula shows the standing wave as follows:

$$\eta' = \left[1 + \frac{\varepsilon^2}{256} (9\omega_0^{-8} + 6\omega_0^{-4} - 15 + 8\omega_0^4) \right] \cos x$$

$$+ \frac{1}{8} \varepsilon (\omega_0^{-2} + 3\omega_0^{-6}) \cos 2x$$

$$+ \frac{3}{256} \varepsilon^2 (9\omega_0^{-12} + 6\omega_0^{-6} + 30\omega_0^{-4} - 16 + \omega_0^{-4} + 2\omega_0^8) \cos 3x$$

$$\varepsilon = ka$$

$$\omega_0 = gk \tanh kh$$

$$k = 2\pi/L$$

$$\eta' = a^{-1} \eta$$

a : amplitude of standing waves in deep water .

η : crest height at a certain water depth

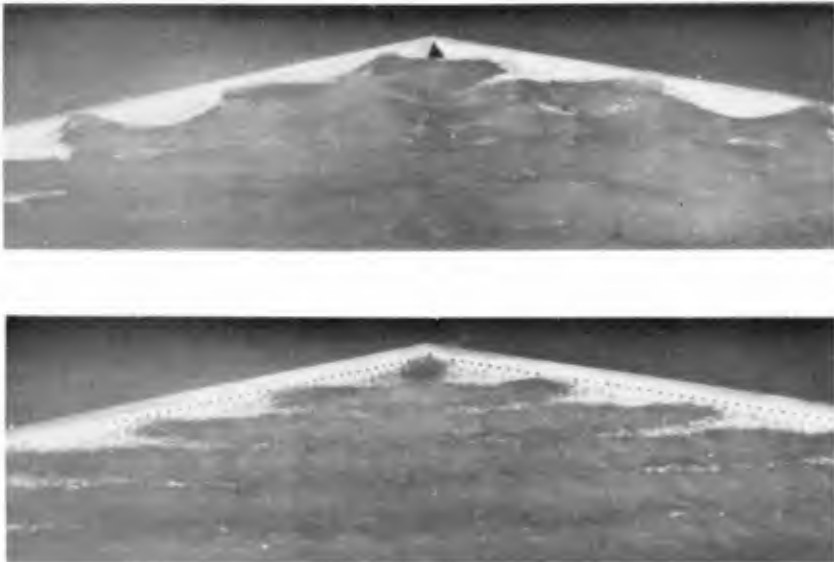


Photograph-2

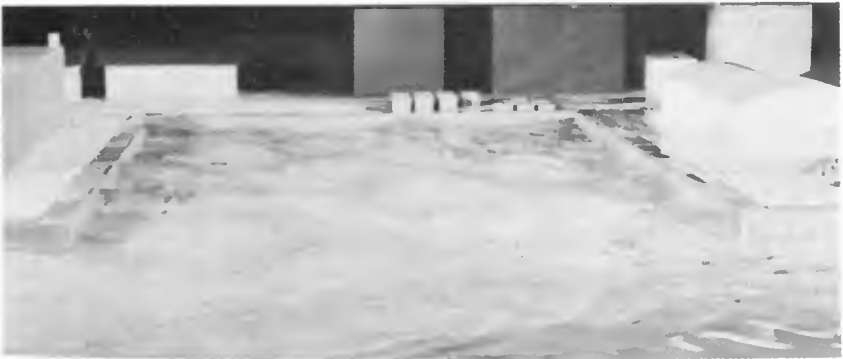
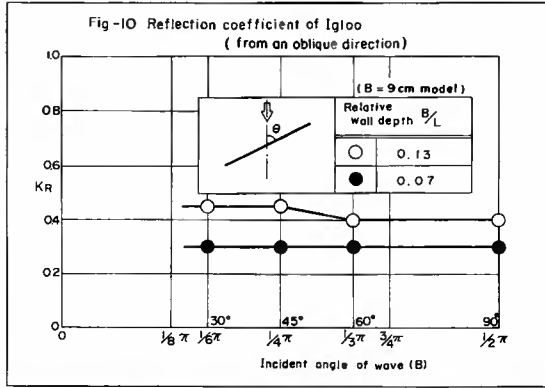
Fig-8(c), (d) show the experimental results of the mathematical model and they can be compared with those of the physical model. Given an incident wave angle of 45° , the values of the physical model coincided closely with those of the mathematical model in which boundary conditions are 30% of reflection coefficient.

Fig-10 shows the reflection coefficients acquired by comparing the physical model with the mathematical model concerning many incident angles. The tests proved that reflection coefficient of Igloo hardly varied according to incident angles.

Fig-9(c), (d) show the mathematical model tests conducted under proper boundary conditions. These results coincide with one another so that the mathematical model is considered to be a useful method in estimating the wave height distributing in a port. It will be effectively used in the layout of a port including wave absorbing structures.



Photograph -3



Photograph-4

CONCLUSIONS

1. The wave dissipating characteristics of Igloo are shown in Fig-3. The best results are obtained at $B/L=0.14\sim 0.19$.
2. The reflection coefficient at $B/L=0.14\sim 0.19$ showing the minimum value can be explained in the responsive characteristics of Igloo system.
3. We confirmed by the three dimensional model test that Igloo helped improve calmness of a port.
4. Through the use of mathematical simulation model with the proper boundary conditions, the wave height distribution chart in the port was compared to that of the physical model. Then, we confirmed that the two results coincided with one another.
5. Fig-10 shows the summarized reflection coefficient values from the physical and mathematical model tests for oblique incident waves. The reflection coefficient of oblique incident waves does not vary according to the angle of incident waves.

ACKNOWLEDGEMENT

We obtained very useful advice from Dr. K. Horikawa, Professor of Tokyo University, and Dr. S. Sato, Head of Marine Hydrodynamics Division, Port and Harbour Research Institute of Ministry of Transport, and received guidance from Mr. H. Kato, Chief engineer, Hydraulic Research Center of Nippon Tetrapod Co., Ltd., in composing a Mathematical Simulation method, to whom we are most grateful.

REFERENCES

- (1) Yoshizo Nagao, Hisanori Kato, "Several experimental studies concerning vertical wall dissipating structure" (Papers presented to the 17th Conference of Coastal Engineering in Japan).
- (2) Takeshi IJIMA, Yasuhiko EGUCHI and Akira KOBAYASHI, "Theory and Experiment on Permeable Breakwater and Quay Wall" Technical Report No.3 Coastal Engineering Department, Kyushu University, Fukuoka Japan, April 1971.

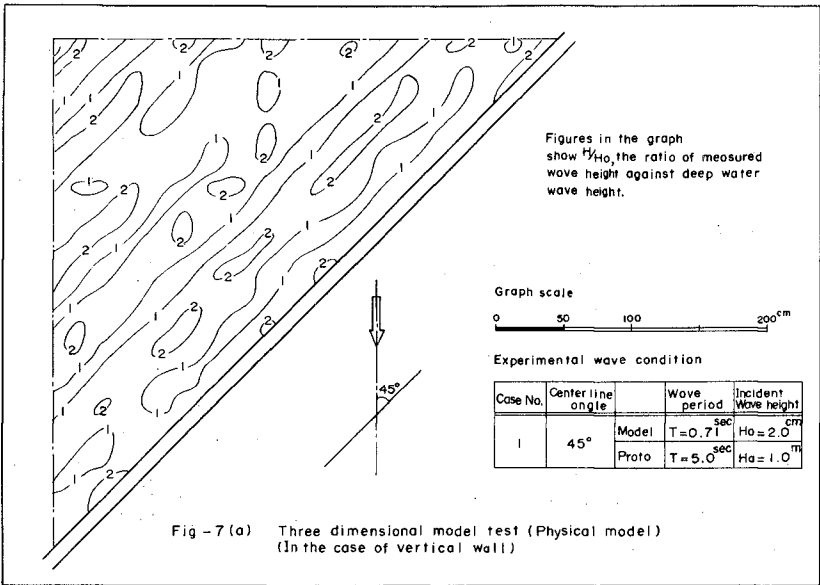


Fig-7(a) Three dimensional model test (Physical model)
(In the case of vertical wall)

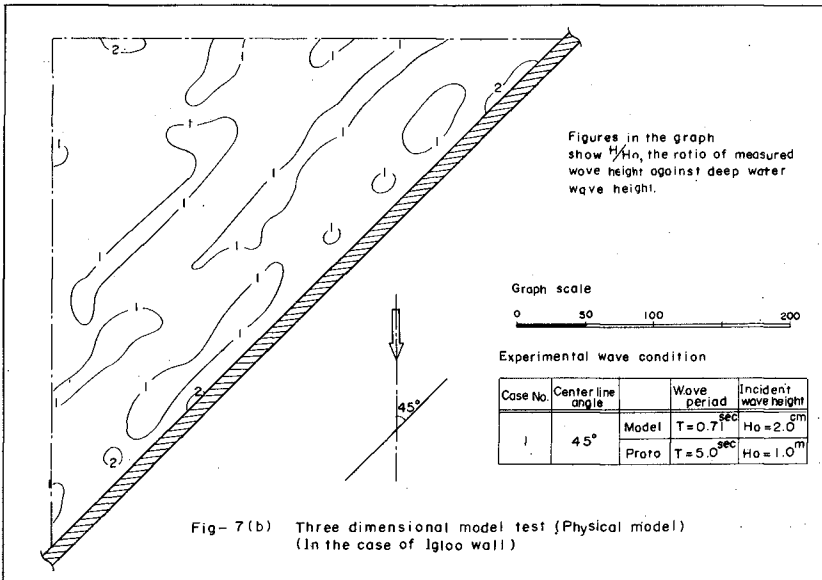


Fig-7(b) Three dimensional model test (Physical model)
(In the case of Igloo wall)

Fig - 8(a) Three dimensional model test (Physical model)
(In the case of vertical wall)

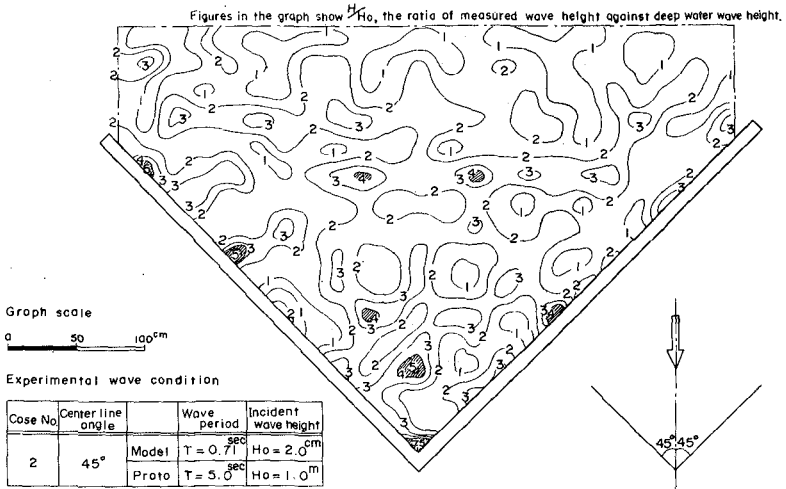


Fig - 8(b) Three dimensional model test (Physical model)
(In the case of Igloo model)

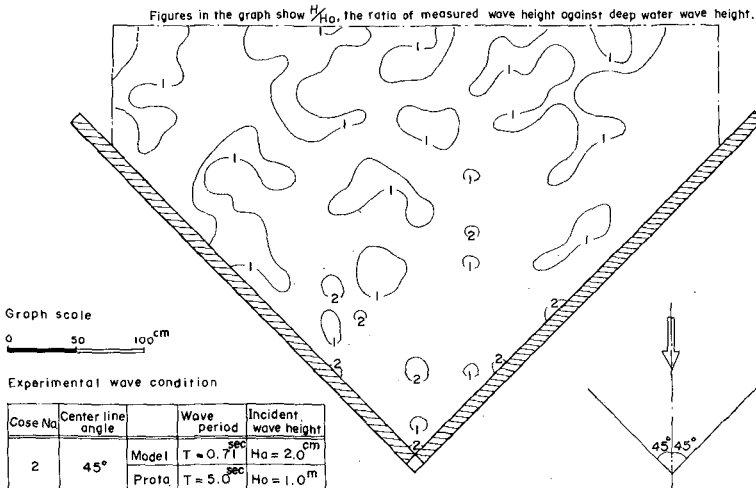


Fig-8(c) Three dimensional model test (mathematical model)
In the case of vertical wall (KR=0.9)

Figures in the graph show H/H_0 , the ratio of calculated wave height against deepwater wave height.

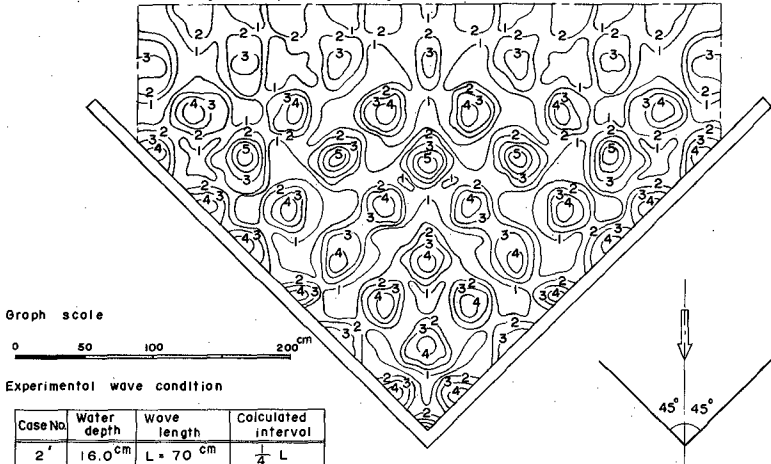
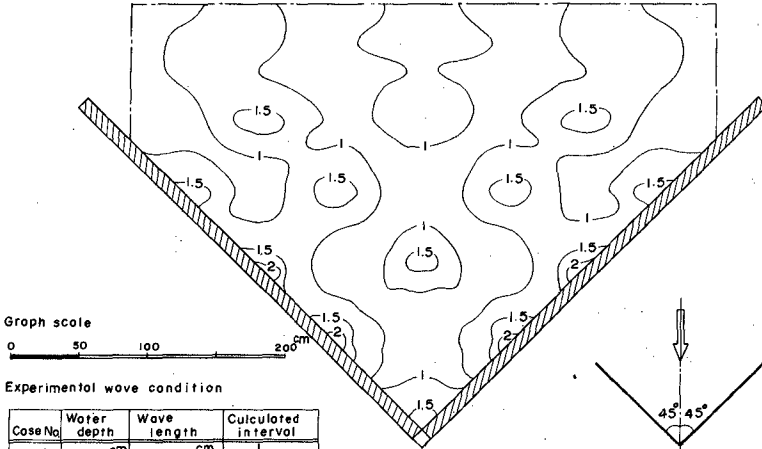
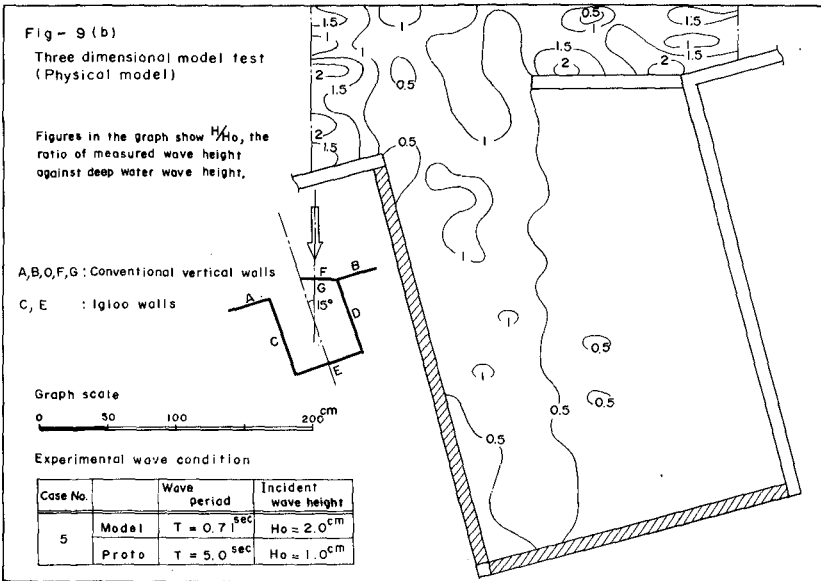
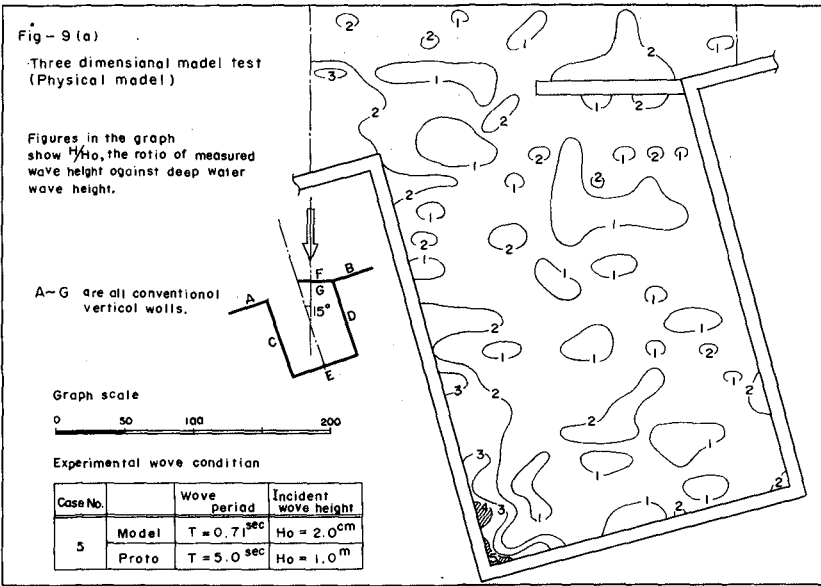
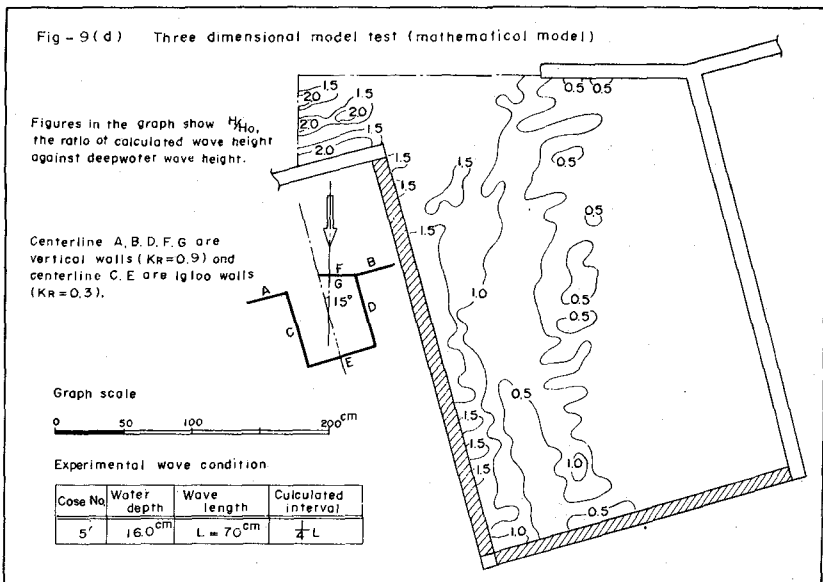
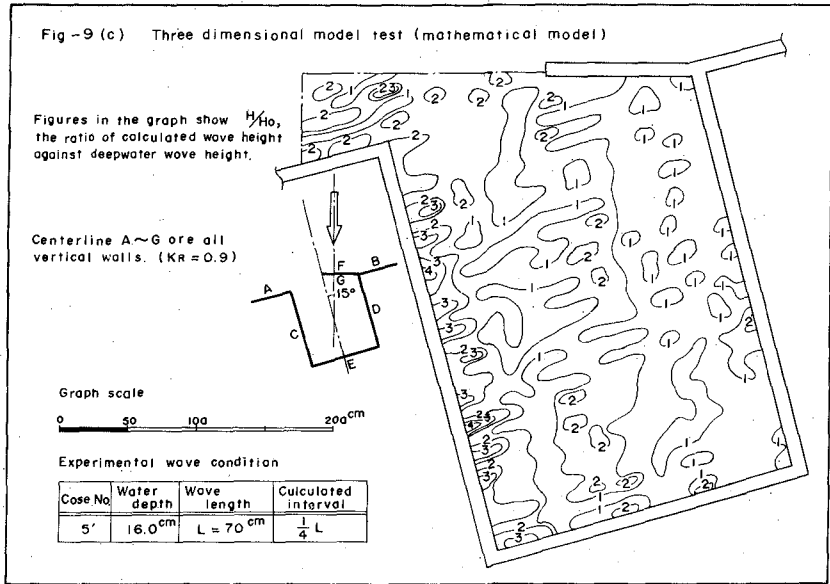


Fig-8(d) Three dimensional model test (mathematical model)
In the case of Igloo wall (KR=0.3)

Figures in the graph show H/H_0 , the ratio of calculated wave height against deepwater wave height.





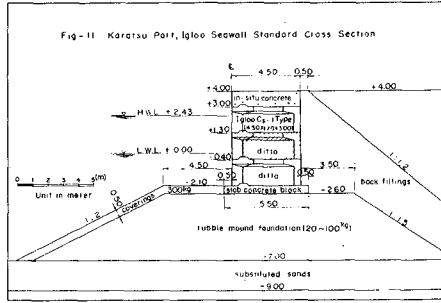


APPLICATION

Igloo walls have been actually constructed and are going to be installed in several ports. Examples are given to show a standard type cross-section.

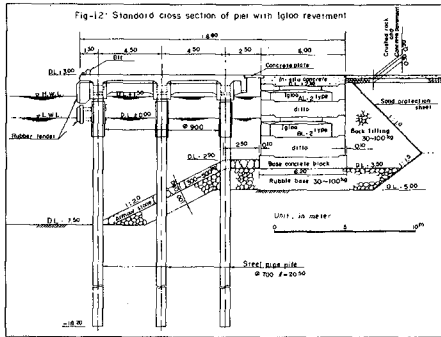
- (a) As a revetment for a reclaimed land in a port (Fig-11)

Waves from the outer sea do not directly invade into the port. This wave dissipating structure is designed against the waves of short period and of high frequency as they are undesirable for navigation. Igloo wall was less expensive than the inclined armour block structures such as Tetrapod and Doloss.



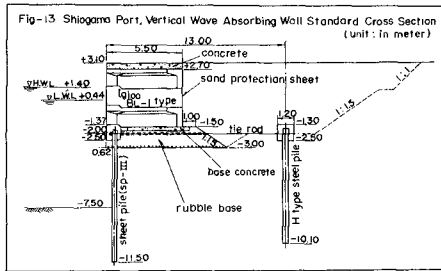
- (b) As a revetment for a pier (Fig-12)

Out of many sectional profiles of deep-water mooring facility, pier structure was selected. And Igloo was planned as revetment for the pier to keep calm the port.



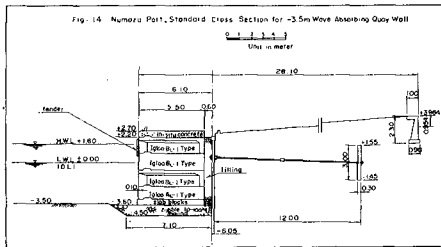
- (c) Igloo wall on sheet piles (Fig-13)

We could use a dry method in constructing mooring facilities in a port which is expanded into the land. And Igloo wall was constructed on the sheet-piles as a quay wall because of its advantages in economics and construction work.



- (d) Igloo wall in front of an existing quay wall (Fig-14)

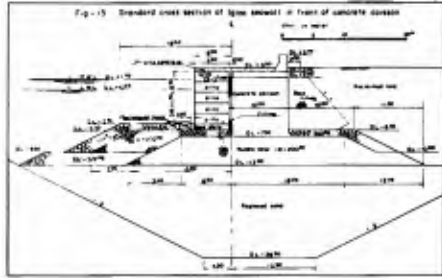
The old sheet-piles quay wall was re-constructed by placing Igloo in front of the existing quay wall on the excavated ground making the water depth from 3 to 3.5m. This wall also helped calm the port. An extra safety measure was taken by providing a provisional sheet-pile in front of the existing sheet-pile wall during the construction period.



(e) As a revetment for a fishing area (Fig-15)

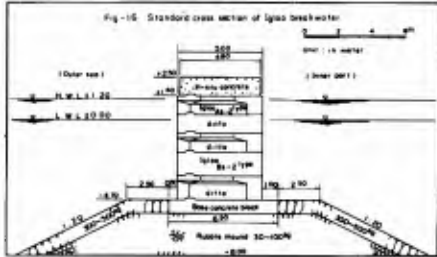
Igloo wall was planned in front of the existing breakwater made of concrete caisson with three fold objectives: preventing overtopping and reflection waves and providing a fishing area for the community people.

The Igloo wall seemed to become comfortable dwellings for small fish, as other type of wave absorbing structures such as Tetrapod and Doloss. But the latter are not suitable for fishing.



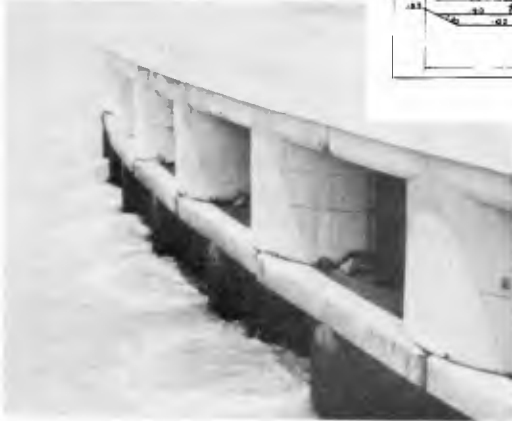
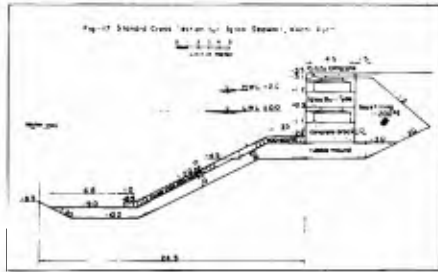
(f) As a wave absorber for bay with narrow entrance or for lake (Fig-16)

Igloo wall is planned as a wave absorbing breakwater because wind waves produced in the lake are less 1.5m in height and reflection waves from breakwater are harmful to fishing and fish culture.



(g) As a revetment for a waterway to prevent reflection waves (Fig-17)

As the port entrance is narrow and a number of ships pass this waterway, Igloo wall was constructed because it could dissipate invading waves from the outer sea as well as waves from navigating ships. The wall harmoniously matched with the aesthetics of nearby beach.



Photograph-5

CHAPTER 155

Slit-type Breakwater; Box-type Wave Absorber

by

Shoshichiro Nagai* and Shohachi Kakuno**

ABSTRACT

A box-type wave absorber, which is composed of a perforated vertical front-wall and a perforated, horizontal bottom-wall, has been proved by a number of experiments to show lower coefficients of reflection and more distinguished reduction of wave pressures than the perforated vertical-wall breakwater.

A breakwater of composite-type, which is 1500 m long and to be built at a water depth of 10 to 11 m below the Datum Line in the Port of Osaka, is being designed to set this new type of wave absorber in the concrete caissons of the vertical-walls which is named "a slit-type breakwater". The typical cross-section of the breakwater and the advantages of the slit-type breakwater are presented herein.

INTRODUCTION

Since the papers of a perforated vertical wall breakwater were published by Jarlan (1961)¹ and Boivin (1964)² on the Dock and Harbour Authority, some papers on the perforated breakwater and quay-wall have been published in Britain³ and Japan⁴.

However, the physical principles in the wave attenuation of the perforated vertical breakwater has not been made clear, therefore, decisive relationships between the characteristics of incoming waves and the optimum width of the chamber have not been obtained.

EXPERIMENTAL EQUIPMENT AND PROCEDURES

All experiments concerning the basic studies of the box-type wave absorber and the comparisons of reflection coefficient between the box-type wave absorber and the perforated vertical wall breakwater were

* Professor of Hydraulic Engineering, Faculty of Engineering, Osaka City University, Osaka, Japan.

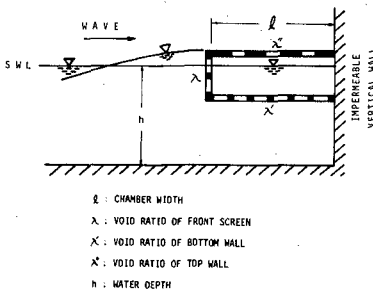
** Research Associate of Hydraulic Engineering, Faculty of Engineering, Osaka City University, Osaka, Japan.

carried out on a model-to-prototype scale of 1/25 in a 50 m-long wave channel of 1 m-width and 1.65 m-height with one side of glass wall at the Harbour and Coastal Engineering Laboratory of Osaka City University.

The height of an incident wave, H_I , and those of composite waves, H_C , generated in front of the box-type wave absorbers and the perforated vertical wall breakwaters were measured by visual observation through the glass wall and by wave-recorders. The reflection coefficients were calculated by means of the expression $K_R = (H_C - H_I)/H_I$. Each test was repeated several times to make sure of the results. The fluctuations of the water level inside the chamber were measured by two wave-gauges and the horizontal and vertical velocities of water particles at the perforations (circular holes of 6 cm-diameter) were measured by current-meters of photo-transister-type.

The depth of water was constant 94 cm in most of the experiments in the 50 m-long wave channel, and only when the effects of the water depth and the water level on the reflection coefficient of the composite waves were investigated, the water depth was changed $h = 59$ cm, 72 cm, 78 cm, 86 cm, 94 cm, and 102 cm. Two groups of $H_I \cong 3$ cm to 6 cm and $H_I \cong 10$ cm to 14 cm were used for the incident wave height, but the period of the incident wave was widely changed $T_I = 0.8$ sec, 1.0 sec, 1.2 sec, 1.4 sec, 1.6 sec, 1.8 sec, 2.0 sec, 2.2 sec and 2.4 sec.

The width of the 1/25-model of box-type wave absorber, l , was changed from 16 cm to 80 cm, shown in Fig. 1. In most of the experiments the height of the models were constant 24 cm and the vertical front-wall had two rows of the perforations as shown in Fig. 1. The models of perforated vertical wall breakwaters and box-type wave absorbers were made of 4 cm-thick plywood, and most of the perforations used in the experiments were circular holes of 6 cm-diameter after the tests of the effect of the shape on the reflection coefficient, K_R .



MODEL	l	λ	λ'	λ''
MODEL 1	16 cm	0.24	0.29	0.29
MODEL 2	22 cm	0.22	0.26	0.26
MODEL 2-1	22 cm	0.22	0.17	0.26
MODEL 3	30 cm	0.22	0.25	0.25
MODEL 3-1	30 cm	0.22	0.17	0.25
MODEL 4	40 cm	0.26	0.26	0.26
MODEL 4-1	40 cm	0.26	0.13	0.26
MODEL 5	54 cm	0.22	0.25	0.25
MODEL 5-1	54 cm	0.22	0.15	0.25
MODEL 6	60 cm	0.22	0.25	0.25
MODEL 6-1	60 cm	0.22	0.15	0.25
MODEL 7	70 cm	0.22	0.26	0.26
MODEL 7-1	70 cm	0.22	0.13	0.26
MODEL 8	80 cm	0.22	0.25	0.25
MODEL 8-1	80 cm	0.22	0.13	0.25

Fig. 1. Kinds of box-type wave absorber used in the experiments

The void ratio of the perforated vertical front-wall, λ , and that of the perforated bottom-wall, λ' , were widely changed from 0.00 to 0.47 to investigate the effects of λ and λ' on the K_R , but in most of the experiments λ was kept nearly constant 0.22, and $\lambda' \cong 0.13$ or 0.15 and 0.25, as shown in Fig. 1. The small void ratios of $\lambda' = 0.13, 0.15$ and 0.17 were made by closure of the seaward half of the perforated horizontal bottom-wall of $\lambda' = 0.25$ or 0.26.

The chamber width of the perforated vertical wall breakwater was changed $l = 30$ cm, 40 cm and 80 cm, and the void ratio of the vertical wall was kept constant $\lambda = 0.23$.

The experiments of the slit-type breakwaters which took advantage of the box-type wave absorber have been conducted on a scale of $1/15$ in a 100 m-long wave channel with a wind blower, 2 m-deep and 1.2 m-wide at the laboratory, the one side of the walls of which is made of 2 cm-thick glass plate to be able to make visual observation of the waves in front of and inside of the breakwater. The wave pressures were measured at several points of the perforated front-wall and the vertical solid back-wall of the slit-type breakwaters, as shown in Fig. 2, to be compared with the wave pressures on the solid vertical wall of the conventional composite-type breakwaters, and also the uplift pressures were measured at the bottom-wall of the box-type wave absorber. The widths of the box-type wave absorber of the slit-type breakwater, l , were changed 5.50 m and 3.75 m in prototype. The models were made of iron plates. The void ratio of the perforated vertical front-wall was $\lambda = 0.22$, and that of the perforated bottom-wall $\lambda' = 0.14$.

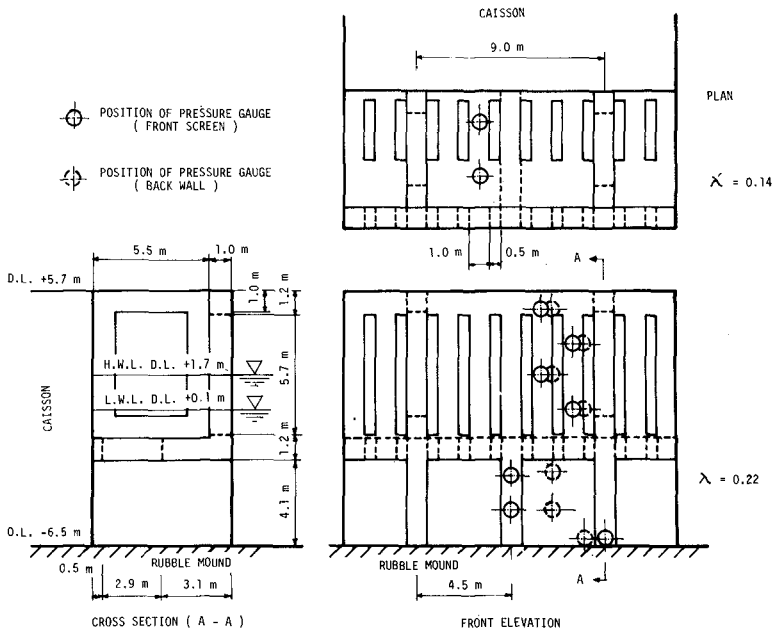


Fig. 2. Location of the wave pressure gauges

PHYSICAL PRINCIPLE OF WAVE ATTENUATION

According to the experiments and theory, which have been carried out in our laboratory, it may be stated that the wave attenuation in the perforated vertical wall breakwater is fundamentally and mainly due to the phase difference between the wave motion outside the chamber and the

fluctuations of the water level inside. As the phase difference increases, larger mass of incoming waves plunge into the chamber as jets which dissipate the energy of the waves due to turbulence inside the chamber. Energy loss due to friction created by passage of the jets through the perforations may be stated negligible small. Therefore, the shape and thickness of the wall of the perforation have few effects on the wave attenuation. But it is naturally important to select an adequate value of the percentage of the void of the perforated wall. As the coefficient of transmission, γ_T , of the perforated vertical wall or the perforated front-wall of the box-type absorber approaches to 0.62, the coefficient of reflection, K_R , of the composite waves generated in front of the perforated vertical wall or the box-shape wave absorber decreases toward zero.

If standing waves predominate in the waves in front of the perforated vertical wall, the water particles move only upward and downward or toward the sea and the land, reciprocally, but there is no mass transport which can create strong jets diffusing into the chamber. From the viewpoint of wave dynamics, it is definitively necessary that progressive waves are always predominant in front of the perforated vertical wall in order to create strong jets diffusing into the chamber. For this purpose the extension of the perforated vertical wall to the bottom or deeper portion of the water depth should be avoided lest standing waves should be predominant in the waves in front of the perforated vertical wall, and moreover it becomes much expensive in its construction cost as the depth of water becomes deep at a given site.

If a box-shape absorber composed of a perforated vertical front-wall and a perforated horizontal bottom-wall is attached near the sea surface to the impermeable vertical wall, as shown schematically in Fig. 1, incoming waves can plunge into the chamber of the box-shape absorber as a progressive wave, creating strong jets diffusing through the perforations into the chamber. Moreover, if adequate devices are made for the perforation of the horizontal bottom-wall of the box-shape absorber, the phase of the fluctuations of the water level inside the chamber would be possible to be delayed up to about 90° from the wave motion outside the chamber.

The width of the chamber, l , is also an important factor to reduce the reflection coefficient, K_R . When the ratio of l to the length of an incoming wave, L , that is l/L , is adequately selected, K_R of the composite waves in front of the perforated vertical wall or the box-shape absorber shows the minimum value. According to the experiment and theory, the perforated vertical wall breakwater showed the $(K_R)_{\min}$ for $l/L = 0.18$, and the box-type absorber for $l/L = 0.15$ to 0.18 .

The large phase difference, the adequate values of γ_T and l/L would be the fundamentally important factors for the box-type wave absorber.

The advantages of this wave absorber in the low coefficient of reflection and the distinguished attenuation of shock pressures exerted by breaking waves have been proved by extensive experiments.

DIFFERENCES BETWEEN THE BOX-TYPE WAVE ABSORBER AND THE PERFORATED VERTICAL WALL BREAKWATER

Although both progressive waves and partial standing waves are generated at the seaward domain of the box-type wave absorbers, the for-

mer are always predominant and plunge against the absorbers. In the box-type wave absorbers of Model 8 which has $l = 80$ cm, $\lambda = 0.22$ and $\lambda' = 0.25$ and Model 8-1 which has $l = 80$ cm, $\lambda = 0.22$ and $\lambda' = 0.13$, the wave motions outside the chamber, the fluctuations of the water levels at the sea-side and land-side inside the chamber, the horizontal velocities in the circular holes (middle hole) of the perforated vertical front-wall and the vertical velocities in the circular holes (landside) of the perforated horizontal bottom-wall were measured for various incident waves of $H_I = 5$ cm to 14 cm and $T_I = 1.4$ sec to 2.4 sec. The measured values for an incident wave of $T_I = 1.8$ sec and $H_I = 12.9$ cm are shown in Figs. 3 (a) and (b). Fig. 3 (a) shows the wave motion outside the chamber (thick full line), the fluctuation of the water level at the sea-side (dotted line) and that at the land-side (broken line), and the horizontal velocity of water particle in the circular hole located at the middle part of the perforated vertical front-wall (thin full line). Fig. 3 (b) shows the vertical velocity of water particle in the circular hole located at the land-side in the chamber (thin full line).

According to Fig. 3, it is known that the fluctuation of the water level at the sea-side in the chamber of Model 8-1 is delayed to a large extent from the wave motion outside the chamber. The maximum horizontal velocity of water particle of the incident wave calculated is $(u_c)_{\max} = 24$ cm/sec, and that passing through the circular hole is estimated $(u'c)_{\max} = (u_c)_{\max}/0.22 = 109$ cm/sec, which is comparable with the measured maximum horizontal velocity $u'_{\max} = 120$ cm/sec in Fig. 3 (a). The maximum vertical velocity of water particle of the standing wave of $2H = 20$ cm generated on the vertical wall is calculated $(v_c)_{\max} = 28$ cm/sec, and that passing through the circular hole of the horizontal bottom-wall of Model 8 is estimated $(v'c)_{\max} = (v_c)_{\max}/0.25 = 112$ cm/sec, which is close to the measured vertical velocity in the circular hole at the land-side in the chamber, $v'_{\max} = 120$ cm/sec, shown in Fig. 3 (b).

It is also seen from Figs. 3 (a) and (b) that the maximum horizontal velocity measured at Model 8-1 ($\lambda = 0.22$) is $u'_{\max} = 130$ cm/sec, which is larger than $u'_{\max} = 120$ cm/sec measured at Model 8 ($\lambda = 0.22$), and the maximum vertical velocity measured at Model 8-1 ($\lambda' = 0.13$), $v'_{\max} = 80$ to 110 cm/sec, is smaller than $v'_{\max} = 120$ cm/sec at Model 8 ($\lambda' = 0.25$). The fluctuations of the water level at the land-side in the chamber at Model 8-1 decrease considerably compared with those at Model 8.

These facts indicate that at Model 8-1 which closes the sea-side half of the perforated horizontal bottom-wall to make $\lambda' = 0.13$, the wave motion at the loop of the standing wave generated at the vertical (non-perforated) wall is controlled considerably, and this means the suppression of the energy of the standing wave at the vertical wall which results in the increase of the horizontal velocities of the incoming wave, causing large discharges of the incoming waves plunging into the chamber, with strong jets diffusing into the chamber through the perforations. Due to this, the coefficient of reflection, K_R , of Model 8-1 decreases to 0.20 to 0.34 for larger incident waves of $H_I = 10$ cm to 14 cm, and moreover the values of K_R are levelled over a wide range of wave periods of 1.6 sec to 2.4 sec, as shown in Fig. 4. These characteristics of Model 8-1 would be most desirable advantages for wave absorber.

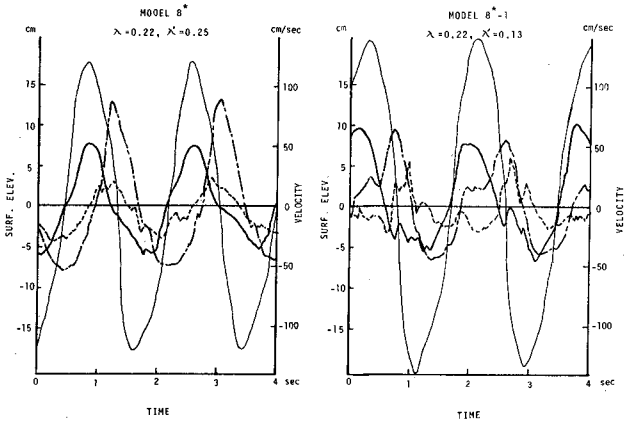


Fig. 3 (a). Horizontal velocities at the perforated horizontal front-wall

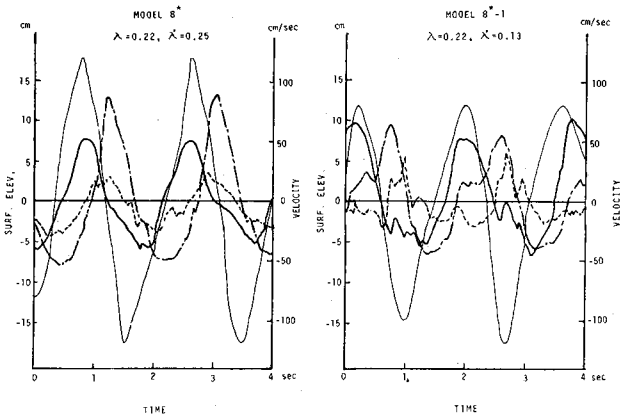


Fig. 3 (b). Vertical velocities at the perforated horizontal bottom-wall

Fig. 3. Fluctuations of the water levels inside the chamber and the curves of velocities through the circular holes

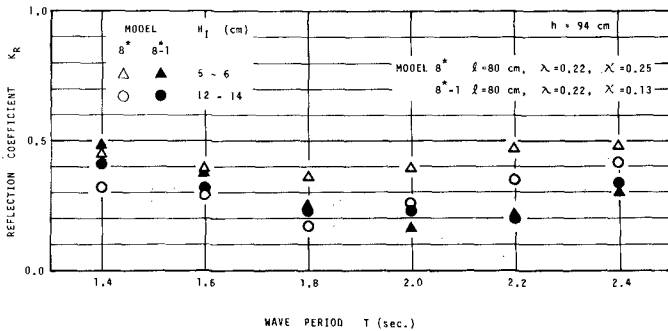


Fig. 4. Coefficients of reflection of box-type wave absorber Models 8 and 8-1

In most cases of perforated vertical wall breakwaters, standing waves with a loop at the solid vertical wall are generated at the sea-side of the perforated walls, therefore the waves do not progress towards the breakwaters, and the waves moves upwards somewhat earlier than the rising of the water level inside the chamber. This phase difference is considerably smaller than that at the box-type wave absorber described above. The horizontal velocities of water particles passing through the circular holes of the perforated vertical wall measured at the experiments were close to those calculated of standing waves generated at the solid vertical wall, and the water particles passed through the perforations towards the land and the sea, reciprocally, every a half period of the standing wave. Therefore it was observed that the discharges of the mass of the waves flowing into the chamber were smaller than those of the box-type wave absorbers, and the jets diffusing the chamber were weaker than those of the box-type absorbers. These facts resulted in larger values of $K_R = 0.42$ to 0.46 for incident waves with heights of $H_I = 12$ cm to 14 cm and periods of $T_I = 1.6$ sec to 2.4 sec in the Model 80 of perforated vertical wall breakwater which had a chamber width of $l = 80$ cm.

Fig. 5 shows the behaviours of the wave motion outside the chamber as well as the jet diffusion and strong wave spray inside the chamber when an incoming wave with $H_I = 13$ cm and $T_I = 1.8$ sec plunged against the Model 6-1 of box-type wave absorber which had chamber width of $l = 60$ cm, $\lambda = 0.22$, and $\lambda' = 0.15$. Fig. 6 shows the behaviours of the wave motion outside the chamber and the standing wave at the vertical wall when the same incoming wave as that of Fig. 5 came to the Model 80 of perforated vertical wall breakwater.



Fig. 5. Jet diffusion and wave spray in a box-type wave absorber



Fig. 6. Standing wave outside and inside the wave chamber of a perforated vertical wall breakwater

EFFECT OF THE VOID RATIO OF PERFORATION
ON THE COEFFICIENT OF REFLECTION

(1) The void ratio of the perforated front-wall

The coefficients of reflection, K_R , for the periods $T_I = 1.4$ sec to 2.4 sec of incident wave are shown in Fig. 7 when the void ratios of the perforated vertical front-wall were changed $\lambda = 0.12, 0.22, 0.30$ and 0.47

at Model 8-1 which had the chamber width $l = 80$ cm and the constant void ratio of the perforated horizontal bottom-wall of $\lambda' = 0.13$. It is seen from Fig. 7 that K_R are at minimum values of 0.1 to 0.2 and 0.2, respectively, for $\lambda = 0.22$ and 0.30.

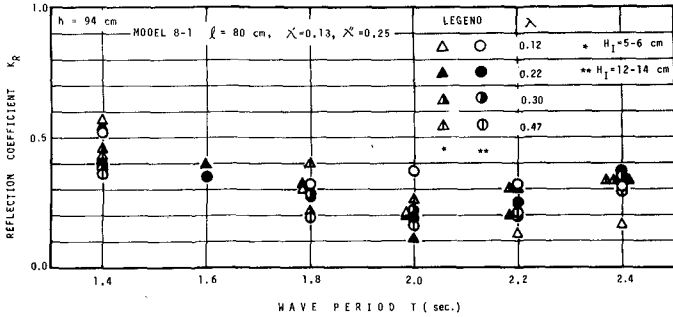


Fig. 7. Coefficients of reflection of Model 8-1 with variable λ

Fig. 8 shows the values of K_R for the different values of $\lambda = 0.00$, 0.22, 0.34 and 0.47 at Model 3 which has $l = 30$ cm and the constant value of $\lambda' = 0.25$. It is known that K_R also shows minimum values 0.20 to 0.24 and 0.18 to 0.37, respectively, for $\lambda = 0.22$ and 0.34.

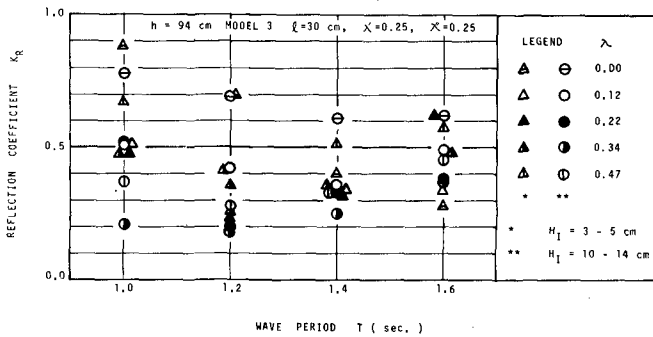


Fig. 8. Coefficients of reflection of Model 3 with variable λ

(2) The void ratio of the perforated bottom-wall

In order to investigate the effect of the void ratio of perforated horizontal bottom-wall on the coefficient of reflection, a large number of experiments were carried out by changing the values of the void ratio $\lambda' = 0.00$ to 0.43 at Model 2, 3, 4, 5, 6, 7 and 8 which all had a constant value of $\lambda = 0.22$. The experimental results showed that K_R were at minimum values of 0.10 to 0.20 for $\lambda' = 0.13$ to 0.17 where were made by closing the sea-side half of the perforated bottom-wall, Figs. 4 and 9 show the experimental results of two models of Model 8 and Model 3, respectively.

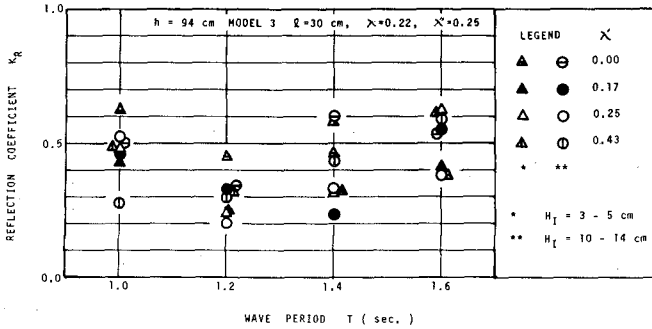


Fig. 9. Coefficients of reflection of Model 3 with variable λ'

(3) The void ratio of the top-wall

The experiments showed that the void ratio of the perforated horizontal top-wall, λ'' , had no effect on the coefficient of reflection if the top-wall had sufficient perforations so that it would not considerably control the upward motion of the water level inside the chamber.

THEORY

The perforated front-wall of the box-type wave absorber or the perforated vertical wall of the breakwater is situated at $x = 0$, shown in Fig. 10, and the vertical solid back-wall is located at $x = l$ which defines the width of the wave chamber. The incident waves incoming in the positive x direction normally on the perforated vertical wall are written

$$\eta_I = a \sin (kx - \sigma t), \tag{1}$$

in which a = wave amplitude, k = wave number = $2\pi/L$, L = wave length, $\sigma = 2\pi/T$ and T = wave period.

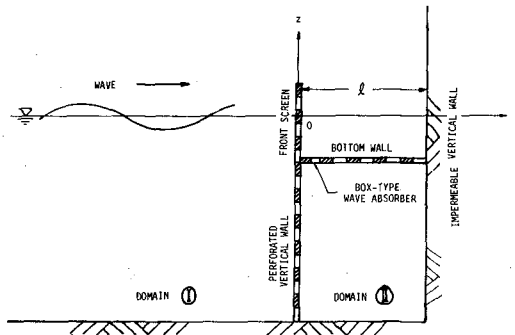


Fig. 10. Definition sketch

If the coefficient of reflection and the coefficient of transmission of the perforated vertical front-wall are denoted by γ_R and γ_T , respectively, the reflected and transmitted waves of the front-wall are written

$$\eta_R = -\gamma_R \cdot a \sin (kx + \sigma t) \quad (2)$$

and

$$\eta_T = \gamma_T \cdot a \sin (kx - \sigma t) \quad (3)$$

From the law of the conservation of mass the following relation is obtained

$$\gamma_R + \gamma_T = 1 \quad (4)$$

If η_T is supposed to be totally reflected from the solid back-wall at $x = l$ without any structure between $x = 0$ and $x = l$, the reflected wave η_{TR} is written

$$\eta_{TR} = -\gamma_T a \sin (kx + \sigma t - 2kl) \quad (5)$$

In the cases when the incident waves transmit the box-type wave absorber or the perforated vertical wall breakwater, the phase of the reflected waves from the back-wall is delayed as if a length Δl were added to the length l by passing through the perforations, and the reflected waves can be given by

$$\eta_{TR} = -\gamma_T a \sin \{ kx + \sigma t - 2k (l + \Delta l) \} \quad (6)$$

Then the composite waves generated at the sea-side of the wave absorber (shown as domain \textcircled{D} in Fig. 10) can be given by

$$\begin{aligned} \eta_C &= \eta_I + \eta_R + \gamma_T \cdot \eta_{TR} \\ &= a \sin (kx - \sigma t) - \gamma_R a \sin (kx + \sigma t) \\ &\quad - \gamma_T^2 a \sin \{ kx + \sigma t - 2k (l + \Delta l) \} \end{aligned} \quad (7)$$

Eq. 7 can be written

$$\eta_C = a \sqrt{A} \sin (\sigma t + \beta_1), \quad (8)$$

in which

$$\begin{aligned} A &= \gamma_T^4 + \gamma_T^2 - 2\gamma_T^3 \cos 2k (l + \Delta l) + 2 (\cos 2kx + 1) \{ 1 - \gamma_T \\ &\quad + \gamma_T^2 \cos 2k (l + \Delta l) \} + 2\gamma_T^2 \sin 2k (l + \Delta l) \sin 2kx \end{aligned} \quad (9)$$

Eq. 9 can be rewritten

$$\begin{aligned} A &= \gamma_T^4 + \gamma_T^2 - 2\gamma_T + 2 + 2\gamma_T^2 (1 - \gamma_T) \cos 2k (l + \Delta l) \\ &\quad + 2 [\gamma_T^4 + \gamma_T^2 - 2\gamma_T + 1 + 2\gamma_T^2 (1 - \gamma_T) \cos 2k (l + \Delta l)]^{1/2} \\ &\quad \times \sin (2kx + \beta_2) \end{aligned} \quad (10)$$

A takes the maximum value at $x = x_0$ where the condition of $\sin (2kx_0 + \beta_2) = 1$ is satisfied, and then $A = A_0$ is

$$\begin{aligned} A_0 &= [\{ \gamma_T^4 + \gamma_T^2 - 2\gamma_T + 1 + 2\gamma_T^2 (1 - \gamma_T) \cdot \cos 2k (l + \Delta l) \}^{1/2} \\ &\quad + 1]^2 \end{aligned}$$

thus

$$\sqrt{A_0} = \{ \gamma_T^4 + \gamma_T^2 - 2\gamma_T + 1 + 2\gamma_T^2 (1 - \gamma_T) \cos 2k(1 + \Delta l) \}^{1/2} + 1 \tag{11}$$

The reflection coefficient, K_R , of the composite waves in the domain ① in Fig. 10 can be obtained by

$$K_R = \frac{a\sqrt{A_0} - a}{a} = \sqrt{A_0} - 1 = \{ \gamma_T^4 + (1 - \gamma_T)^2 + 2\gamma_T^2 (1 - \gamma_T) \cdot \cos 2k(1 + \Delta l) \}^{1/2} \tag{12}$$

Fig. 11 shows the relationships between K_R and l/L which are obtained with the parameters of $\Delta l/L$ and $\gamma_T = 0.77$ (constant). It can be seen that as the values of $\Delta l/L$ increase from 0 to 7/100, 1/10 and 1/8, the points where minimum value of K_R occurs approach from $l/L = 0.25$ to 0.125. Fig. 12 shows the relationships between K_R and l/L when the values of γ_T are varied from 0.1 to 0.9 at the constant value of $\Delta l/L = 1/10$. It is known that as γ_T increases from 0.1 to 0.6, K_R decreases to 0 at $\gamma_T \approx 0.62$, and on the contrary, K_R increases again as γ_T increases from 0.62 to 0.90.

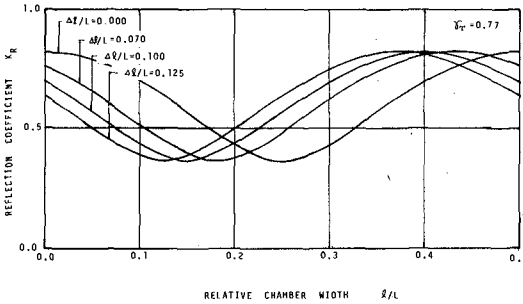


Fig. 11. Relationships between K_R and l/L with a parameter of $\Delta l/L$

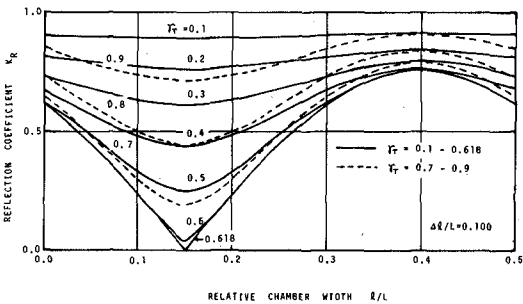


Fig. 12. Reflection coefficient dependence on γ_T

From Figs. 11 and 12, it is known that since the value of $1/L$ where $(K_R)_{min}$ occurs decreases as the value of $\Delta l/L$ increases, it may be stated that such a wave absorber as can give as large value of $\Delta l/L$ as possible would be most favourable. Thus the maximum value of $\Delta l/L$ which can be expected as the wave absorber is obtained from the condition

$$2k (1 + \Delta l) = \pi \tag{13}$$

$$\left(\frac{\Delta l}{L} \right)_{max} = \frac{1}{8} \quad \text{for} \quad \frac{\Delta l}{L} = \frac{1}{L} \tag{14}$$

It may therefore be concluded that the objectives of the wave absorber are

- i. the transmission coefficient γ_T should approach to 0.62, and
- ii. the value of $\Delta l/L$ should approach to $1/8$.

Fig. 13 shows the values of K_R for the various values of $1/L$ measured in Models 30 ($l = 30$ cm), 40 ($l = 40$ cm) and 80 ($l = 80$ cm) of perforated vertical wall breakwater ($\lambda = 0.23 = \text{constant}$). The full line in Fig. 13 is a theoretical line obtained by Eq. 12, in which γ_T is taken 0.77, an average value of γ_T measured in Model 80.

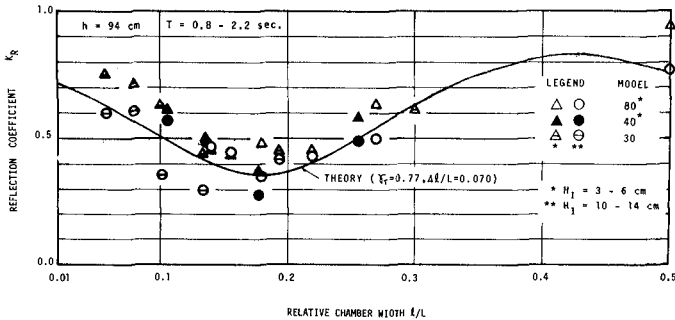


Fig. 13. Reflection coefficient dependence on l/L (perforated vertical wall breakwater)

Fig. 14 shows the values of K_R for the various values of $1/L$ measured in Models 1 to 8 of box-type wave absorber, in which λ' , the void ratio of the perforated bottom wall, are 0.13 to 0.17 except $\lambda' = 0.29$ of Model 1. The full, broken, and chain lines are all theoretical lines obtained by Eq. 12. The full line is obtained by the use of $\gamma_T = 0.70$ and $\Delta l/L = 0.10$, and it may be stated that the full line would show the average of the experimental values of K_R when $1/L \leq 0.15$. The chain line obtained by $\gamma_T = 0.70$ and $\Delta l/L = 0.07$ may be said to show the average of the experimental values of K_R when $1/L > 0.15$, and the broken line, obtained by $\gamma_T = 0.63$, the average value of γ_T measured in Model 8-1, would represent the smallest values of K_R in the vicinity of $1/L = 0.15$.

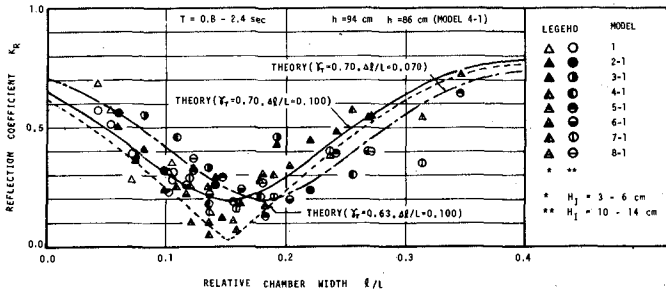


Fig. 14. Reflection coefficient dependence on $1/L$ (box-type wave absorber)

SLIT-TYPE BREAKWATER

How to attach the box-type wave absorber to the seaward side of the caisson of breakwater and what kind of perforation would be best for the construction and structure of the caisson were discussed from the viewpoint of practical harbour engineering, and finally slits were decided as the perforations of the vertical front-wall and horizontal bottom-wall to be attached to the caisson as shown in Fig. 15.

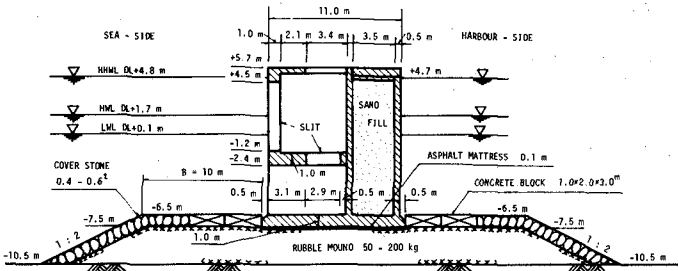


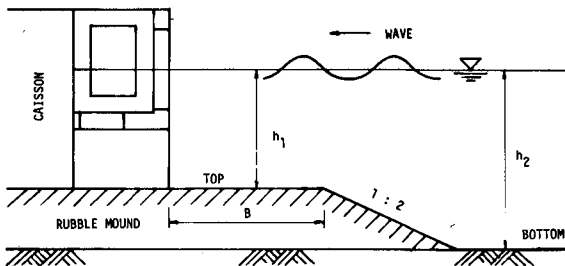
Fig. 15. Slit-type breakwater to be built in the Harbour of Osaka

All experiments to measure wave pressures exerted on the slit-type breakwaters have been carried out by generating breaking, non-breaking and standing waves by the use of models of $1/15$ scale in the 100 m-long wave channel. Some of the cross-sections of the breakwaters and the characteristics of the waves used in the experiments are shown in Tables 1 and 2.

At the outset of the experiments it was confirmed that the $1/15$ -scale model had the same values of reflection coefficients as those in the $1/25$ -scale model, that is, K_R showed a minimum value of about 0.20 at waves of $T = 5$ sec for the breakwater of $l = 5.50$ m, and at $T = 4$ sec for the one of $l = 3.75$ m.

Table 1. Models of slit-type breakwater

Base rubble-mound			Water depth	
Top D.L.	Bottom D.L.	Top width B	h_1	h_2
- 6.5 m	- 10.5 m	10.5 m	6.6 m	10.2 m
			8.2 m	12.2 m
			9.7 m	13.7 m
- 5.0 m	- 10.5 m	10.5 m	5.1 m	10.6 m
			6.7 m	12.2 m
			8.2 m	13.7 m
- 5.0 m	- 10.5 m	15.0 m	5.1 m	10.6 m
			6.7 m	12.2 m
			8.2 m	13.7 m



Cross-section of the slit-type breakwater model

Table 2. Characteristics of incident waves used in the experiments

Period T(sec)	Height H(m)	Length L(m)	H/L	Wind velocity V(m/sec)
10.0	4.4	95	0.046	30
8.0	4.1	72	0.057	30
7.0	4.0 to 4.3	61 to 66	0.065 to 0.069	30
7.0	3.7 to 4.3	61 to 66	0.061 to 0.065	0
6.0	3.3 to 3.4	49 to 52	0.065 to 0.067	0

The experimental results have proved that the wave pressures exerted on the slit-type breakwaters by breaking waves remarkably reduce to be less than 60 % of those on the conventional breakwaters with solid vertical caisson, and the reduction of the wave pressures becomes larger as the intensity of the shock pressure becomes higher. The upward pressures exerted on the horizontal bottom-walls are also very small. The physical reasons of the considerable reduction of wave pressures may be considered as follows.

(1) When a wave recedes from the vertical wall of the breakwater to the lowest level, the water in the chamber of the box-type wave absorber would be empty or nearly empty. Since the void ratio of the slotted bottom-wall, $\lambda' = 0.14$, is smaller than that of the slotted vertical front-wall, $\lambda = 0.22$, the phase of rising of the water level inside the chamber is delayed from the upward moving of the incoming wave outside the chamber. The shock pressure which would be exerted on the vertical front-wall by the attack of the crest of the breaking wave is remarkably reduced by diffusing through the slits into the chamber due to this retardation.

(2) Then the water level inside the chamber rises and jets diffusing through the slits of the front-wall dissipate large part of their energy by turbulence in the water inside the chamber and reduce substantially their horizontal velocities. This results in the remarkable reduction of the wave pressures on the solid vertical back-wall.

There has been no case when shock pressures were exerted by breaking waves on the front-walls and solid vertical back-walls of slit-type breakwaters even at conventional breakwaters in which shock pressures of so high intensities as 12.0 t/m^2 to 14.0 t/m^2 exerted on the vertical walls.

The wave pressures exerted on the slit-type breakwaters by standing waves were almost same as those on the conventional breakwaters with solid vertical wall.

(3) The upward pressures exerted on the horizontal slotted bottom-wall by the waves transmitted underneath the wave absorber are also as small as 1.1 t/m^2 to 2.5 t/m^2 due to the dissipation of the wave energy through the slits.

Fig. 16 and Table 3 show the comparisons of the maximum simultaneous pressures on a conventional composite-type breakwater and a slit-type breakwater.

$P_e \text{ max}$ (slit) in Table 3 defines the sum of the resultants of the maximum simultaneous wave pressures exerted on the slotted vertical front-wall and that on the solid vertical back-wall. There is actually a little time difference in their occurrences, but for the safety the two maximum resultant pressures were considered to be occurred at the same time. $P_c \text{ max}$ is the maximum resultant pressure calculated by the wave pressure formulas⁵.

Table 3. Comparisons of max. wave pressures exerted on conventional composite-type and slit-type breakwaters

(a) Chamber width $l = 5.50$ m, Top of base rubble-mound D.L. - 6.5 m, Top width of base rubble-mound $B = 10.5$ m

Water depth h_2 (m)	Incident wave			H/L	Composite wave height		Coeff. of refl.		Max. result. wave pressures*			Ratios of wave pressure		Upward pressure P_u (t/m^2)
	Period T(sec)	Height H(m)	Length L(m)		H_c (m)		K_R		Solid wall		Slit-type	P_e max (slit)		
					Solid	Slit	Solid	Slit	P_e max (t/m)	P_c max (t/m)	P_e max (t/m)	P_e max / P_e max	P_c max / P_c max	
10.6	7.0	4.0	61	0.066	7.0	5.2	0.70	0.30	47.6*	39.1**	22.0	0.46	0.56	2.0 ~ 2.4
	7.0	3.7	61	0.061	6.5	4.7	0.78	0.29	20.4	27.1	19.1	0.93	0.70	1.8 ~ 2.2
	6.0	3.3	49	0.067	5.8	4.2	0.74	0.27	14.9	22.0	14.7	0.99	0.67	1.4 ~ 1.9
12.2	7.0	4.3	64	0.067	7.3	5.5	0.74	0.31	28.1	36.9	25.2	0.90	0.68	1.8 ~ 2.3
	7.0	4.1	64	0.064	7.1	5.3	0.75	0.31	23.8	34.9	21.5	0.90	0.62	1.8 ~ 2.1
	6.0	3.3	51	0.065	5.7	4.6	0.73	0.35	18.1	24.3	17.9	0.99	0.74	1.2 ~ 1.5
13.7	7.0	4.3	66	0.065	7.0	5.6	0.61	0.32	27.0	37.3	28.2	1.05	0.76	1.9
	7.0	4.3	66	0.065	6.8	5.3	0.64	0.25	24.6	37.3	26.1	1.06	0.70	1.5 ~ 1.6
	6.0	3.4	52	0.065	5.8	4.8	0.66	0.39	18.5	25.5	21.3	1.15	0.83	1.2 ~ 1.4

* : indicates measured pressure by a breaking wave

** : indicates pressure calculated by the wave pressure formulas for breaking waves

(b) Chamber width $l = 5.50$ m, Top of base rubble-mound D.L. - 5.0 m, Top width of base rubble-mound $B = 10.5$ m

Water depth h_2 (m)	Incident wave			H/L	Composite wave height		Coeff. of refl.		Max. result. wave pressures*			Ratios of wave pressure		Upward Pressure P_u (t/m^2)
	Period T(sec)	Height H(m)	Length L(m)		H_c (m)		K_R		Solid wall		Slit-type	P_e max (slit)		
					Solid	Slit	Solid	Slit	P_e max (t/m)	P_c max (t/m)	P_e max (t/m)	P_e max / P_e max	P_c max / P_c max	
10.6	7.0	4.0	61	0.066	6.8	5.2	0.64	0.31	48.8*	49.7**	19.4	0.40	0.39	2.0 ~ 2.4
	7.0	3.7	61	0.061	6.2	5.0	0.60	0.34	36.3*	43.5**	17.5	0.48	0.40	1.8 ~ 2.2
	6.0	3.3	49	0.067	6.2	4.3	0.82	0.30	18.9	19.1	13.4	0.84	0.70	1.4 ~ 1.8
12.2	7.0	4.3	64	0.067	7.2	5.5	0.64	0.27	46.5*	45.5**	28.3	0.61	0.62	1.9 ~ 2.1
	7.0	4.1	64	0.064	7.0	5.2	0.71	0.29	40.6	31.0	22.8	0.56	0.73	1.6 ~ 2.0
	6.0	3.3	51	0.065	5.8	4.5	0.75	0.38	22.7	22.1	20.9	0.92	0.94	1.3 ~ 1.5
13.7	7.0	4.3	66	0.065	7.3	5.7	0.63	0.28	25.5	35.1	27.9	1.09	0.79	1.8 ~ 2.1
	7.0	4.3	66	0.065	7.2	5.7	0.66	0.35	25.4	35.1	24.9	0.98	0.71	1.8 ~ 2.0
	6.0	3.4	52	0.065	5.9	4.5	0.72	0.35	17.7	24.9	19.8	1.12	0.79	1.0 ~ 1.2

* : indicates measured pressure by a breaking wave

** : indicates pressure calculated by the wave pressure formulas for breaking waves

Table 3. Comparisons of max. wave pressures exerted on conventional composite-type and slit-type breakwaters

(c) Chamber width $l = 5.50$ m, Top of base rubble-mound D.L. - 5.0 m, Top width of base rubble-mound $B = 15.0$ m

Water depth h_2 (m)	Incident wave			H/L	Composite wave height H_C (m)		Coeff. of refl. K_R		Max. result. wave pressures			Ratios of wave pressure		Upward pressure P_u (t/m^2)
	Period T (sec)	Height H (m)	Length L (m)		Solid	Slit	Solid	Slit	Solid wall		Slit-type	P_e max / P_e max	P_c max / P_c max	
									P_e max (t/m)	P_c max (t/m)	P_e max (slit) (t/m)			
10.6	7.0	4.0	61	0.066	7.1	5.6	0.77	0.31	59.8*	61.1**	33.0	0.55	0.54	2.2 ~ 2.8
	7.0	3.7	61	0.061	6.2	5.1	0.66	0.39	47.0*	54.0**	18.5	0.39	0.34	1.8 ~ 2.4
	6.0	3.3	49	0.067	5.9	4.3	0.81	0.33	19.6	44.7**	11.7	0.60	0.26	1.3 ~ 1.8
12.2	7.0	4.3	64	0.067	7.2	5.6	0.64	0.30	45.6*	62.5**	24.2	0.53	0.39	1.8 ~ 2.1
	7.0	4.1	64	0.064	6.9	5.3	0.67	0.31	26.7	31.0	20.5	0.77	0.66	1.5 ~ 1.9
	6.0	3.3	51	0.065	5.9	4.7	0.72	0.38	16.7	22.1	19.0	1.14	0.86	1.3 ~ 1.5
13.7	7.0	4.3	66	0.065	6.9	5.6	0.58	0.33	26.7	35.1	28.7	1.08	0.82	1.5 ~ 1.9
	7.0	4.3	66	0.065	6.6	5.7	0.50	0.34	28.6	35.1	25.9	0.90	0.74	1.5 ~ 1.8
	6.0	3.4	52	0.065	5.6	4.5	0.64	0.36	17.6	24.9	20.6	1.17	0.83	1.1 ~ 1.4

* : indicates measured pressure by a breaking wave

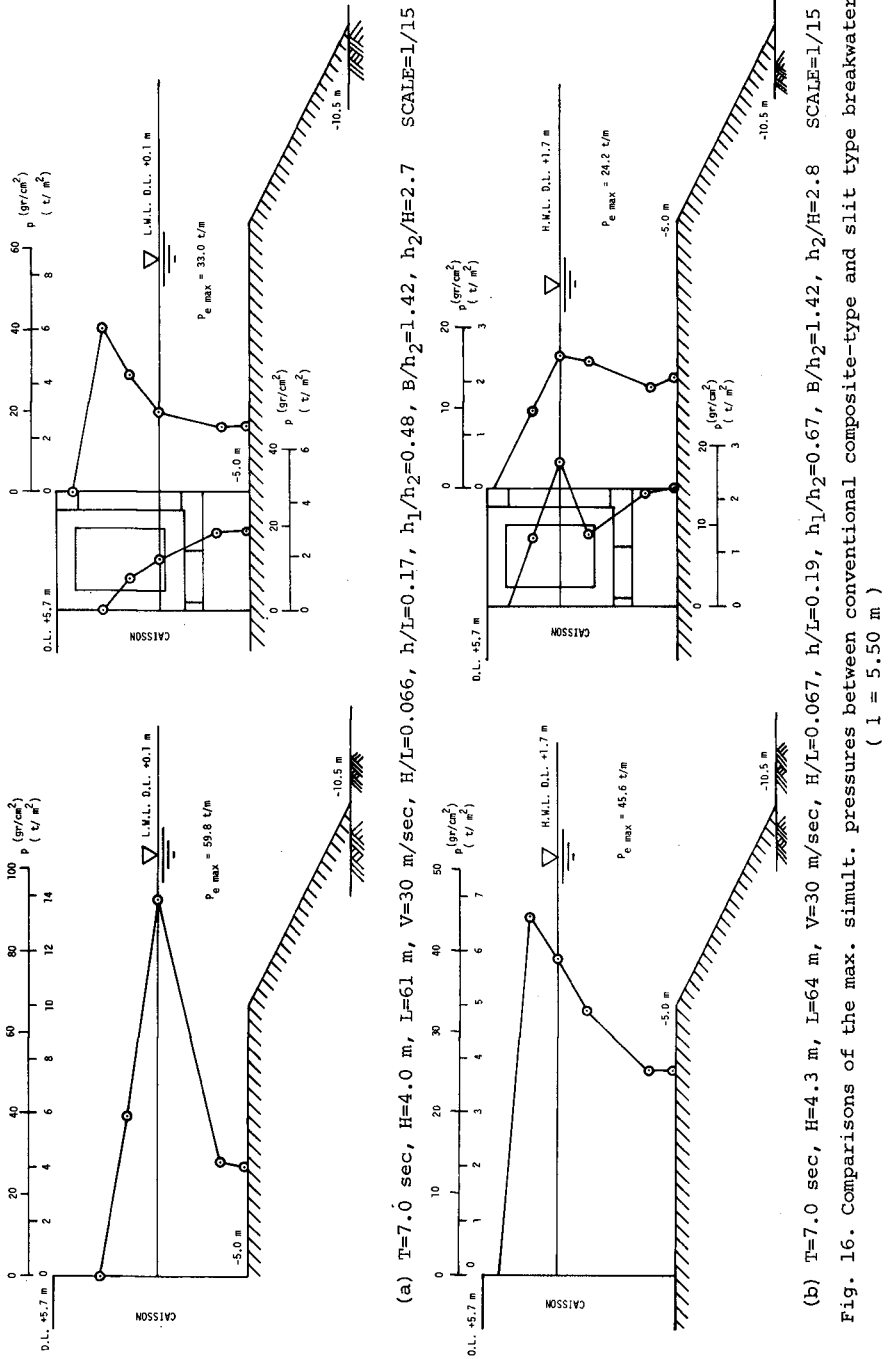
** : indicates pressure calculated by the wave pressure formulas for breaking waves

(d) Chamber width $l = 3.75$ m, Top of base rubble-mound D.L. - 6.5 m, Top width of base rubble-mound $B = 10.5$ m

Water depth h_2 (m)	Incident wave			H/L	Composite wave height H_C (m)		Coeff. of refl. K_R		Max. result. wave pressures			Ratios of wave pressure		Upward pressure P_u (t/m^2)
	Period T (sec)	Height H (m)	Length L (m)		Solid	Slit	Solid	Slit	Solid wall		Slit-type	P_e max / P_e max	P_c max / P_c max	
									P_e max (t/m)	P_c max (t/m)	P_e max (slit) (t/m)			
10.6	10.0	4.4	95	0.046	7.2	6.8	0.64	0.55	36.8	49.9	30.6	0.83	0.61	2.4
	8.0	4.1	72	0.057	7.6	6.3	0.85	0.42	52.4*	40.4**	29.4	0.56	0.73	2.3
	7.0	4.2	61	0.069	7.5	5.5	0.79	0.31	48.2*	41.6**	27.7	0.56	0.67	2.2
	7.0	4.0	61	0.066	7.0	5.3	0.70	0.34	47.6*	39.1**	20.0	0.42	0.51	1.9
	7.0	3.7	61	0.061	6.5	4.8	0.78	0.35	20.4	27.1	19.2	0.94	0.71	1.7
	6.0	3.3	49	0.067	5.8	4.5	0.74	0.43	14.9	22.0	13.2	0.89	0.60	1.5
12.2	7.0	4.3	64	0.067	7.3	6.2	0.74	0.42	28.1	36.9	26.4	0.94	0.72	1.9
	7.0	4.1	64	0.064	7.1	5.6	0.75	0.35	23.8	34.9	22.7	0.95	0.65	1.7
	6.0	3.3	51	0.065	5.7	4.7	0.73	0.44	18.1	24.3	16.2	0.90	0.67	1.2
13.7	7.0	4.3	66	0.065	7.0	6.0	0.61	0.40	27.0	37.3	30.5	1.13	0.82	1.8
	7.0	4.3	66	0.065	6.8	5.8	0.64	0.38	24.6	37.3	29.4	1.20	0.79	1.7
	6.0	3.4	52	0.065	5.8	4.6	0.66	0.38	18.5	25.5	20.4	1.10	0.80	1.1

* : indicates measured pressure by a breaking wave

** : indicates pressure calculated by the wave pressure formulas for breaking waves



REFERENCES

1. Jarlan, G. E., " A Perforated Vertical Wall Breakwater ", The Dock and Harbour Authority, April, 1961, London.
2. Boivin, R., " Comments on Vertical Breakwaters with Low Coefficients of Reflection ", The Dock and Harbour Authority, June, 1964, London.
3. Terrett, F. L., Osorio, J. D. C., and Lean, G. H., " Model Studies of a Perforated Breakwater ", Proc. of the 11th Conf. on Coastal Engineering, Vol. II, Sept., 1968, London.
Marks, W., and Jarlan, G. E., " Experimental Studies on a Fixed Perforated Breakwater ", Proc. of the 11th Conf. on Coastal Engineering, Vol. II, Sept., 1968, London.
4. Nagao, G., and Kato, H., " Experimental Studies on Permeable Vertical Breakwaters ", (in Japanese), Proc. of the 17th Conf. on Coastal Engineering in Japan, 1970.
Sawaragi, T., and Iwata, K., " Some Considerations on Hydraulic Characteristics of Perforated Quay Wall ", Proc. of the Japan Society of Civil Engineers, Vol. 220, Dec. 1973.
5. Nagai, S., and Otsubo, T., " Pressures by Breaking Waves on Composite-type Breakwaters ", Proc. of the 11th Conf. on Coastal Engineering, Vol. II, Sept., 1968, London.
Nagai, S., " Pressures of Standing Waves on Vertical Wall ", Journal of Waterways and Harbours Div., Proc. of ASCE., WW1, Feb., 1969.
Nagai, S., " Pressures of Partial Standing Waves ", Journal of Waterways and Harbours Div., Proc. of ASCE., WW3, Aug., 1968.

CHAPTER 156

METHOD OF ANALYSES FOR TWO-DIMENSIONAL WATER WAVE PROBLEMS

by

Takeshi IJIMA*, Chung Ren CHOU** and Akinori YOSHIDA**

Abstract

One of the most powerful tools to analyze the boundary-value problems in water wave motion is the Green's function. However, to derive the Green's function which satisfies the imposed boundary conditions is sometimes difficult or impossible, especially in variable water depth. In this paper, a simple method of numerical analyses for two-dimensional boundary-value problems of small amplitude waves is proposed, and the wave transformation by fixed horizontal cylinders as an example of fixed boundaries, the wave transformation by and the motion of a cylinder floating on water surface as example of oscillating boundaries and the wave transformation by permeable seawall and breakwater as example of permeable boundaries are calculated and compared with experimental results.

I Introduction

The author (1971) has investigated the problem of wave transformation by permeable breakwater and seawall with vertical faces by the method of continuation of velocity potentials. Sollitt (1972) has also calculated the same problem by the similar method to the author's and recently Madsen and White (1976) have investigated the problem with long wave assumption. Such a problem can be analyzed theoreticall when the structure is of vertical faces, but as for the sloped-faces, it is possible only to estimate under several conventional assumptions.

The problem on wave transformation by and the motion of floating rectangular body in constant finite water depth area has been analyzed by one of the authors (1972) by the method of continuation of velocity potentials. Such a problem for floating cylinder with arbitrary cross-section shall be solved by means of Green's function, being derived by John (1950). However, the process is rather complicated and can not be applied to the case

* Professor: Faculty of Engineering, Kyushu University, Fukuoka, JAPAN

** Master of Engineering, Graduate Student at the Kyushu University

of variable water depth.

The proposed method in this paper is not to use Green's function but to use logarithmic function of the distance between the point on the boundary and the inner point of fluid region, according to Green's theorem. By means of our method, above-described problems concerning to the sloped-face permeable structures, the floating body in variable water depth area and so on are easily formulated and numerically analyzed. In the followings, the formulations and numerical evaluations for small amplitude waves are described and compared with experimental results.

II Green's Theorem and Identity Formula

We assume that a potential function $\phi(x, z)$ is defined in a closed domain enclosed by a curve D in (x, z) plane as shown in Fig.2-1. Indicating the point on the boundary curve D by (ξ, η) , the outward normal by ν , the distance between the point (ξ, η) and a point (x, z) in the domain by r , that is, $r = \sqrt{(\xi - x)^2 + (\eta - z)^2}$, and the constant reference length to the geometrical size of the domain by h_0 , it follows by Green's theorem that the potential value at point (x, z) is provided by the potential values $\phi(\xi, \eta)$ and its normal derivatives $\partial \phi(\xi, \eta) / \partial (\nu / h_0)$ on the boundary curve as follows:

$$\phi(x, z) = \frac{1}{2\pi} \int_D \left[\phi(\xi, \eta) \frac{\partial \log(r/h_0)}{\partial (\nu/h_0)} - \frac{\partial \phi(\xi, \eta)}{\partial (\nu/h_0)} \log(r/h_0) \right] \frac{dS}{h_0} \quad (2.1)$$

If the point (x, z) lies on the boundary at (ξ', η') , Eq.(2.1) leads to the Green's identity formula as follows:

$$\phi(\xi', \eta') = \frac{1}{\pi} \int_D \left[\phi(\xi, \eta) \frac{\partial \log(R/h_0)}{\partial (\nu/h_0)} - \frac{\partial \phi(\xi, \eta)}{\partial (\nu/h_0)} \log(R/h_0) \right] \frac{dS}{h_0} \quad (2.2)$$

where $R = \sqrt{(\xi - \xi')^2 + (\eta - \eta')^2}$

In Eq.(2.1) and (2.2), the integration denotes the line integral along the curve D. Then, dividing the boundary curve into N small elements by N points and indicating the length and the central point of the j-th element as ΔS_j and (ξ_j, η_j) , as shown by Fig.2-2, Eq.(2.1) and (2.2) are approximated by the following summation equations, respectively.

$$\phi(x, z) = \frac{1}{2} \sum_{j=1}^N [\bar{E}_{xj} \phi(j) - E_{xj} \bar{\phi}(j)] \quad (2.3)$$

$$\phi(i) = \sum_{j=1}^N [\bar{E}_{ij} \phi(j) - E_{ij} \bar{\phi}(j)] \quad (2.4)$$

where

$$\phi(j) = \phi(\xi_j, \eta_j), \quad \bar{\phi}(j) = \partial\phi(\xi_j, \eta_j)/\partial(\nu/h_0) \quad (2.5)$$

$$E_{xj} = \frac{1}{\pi} \int_{\Delta S_j} \log\left(\frac{r_{xj}}{h_0}\right) \frac{dS}{h_0}, \quad \bar{E}_{xj} = \frac{1}{\pi} \int_{\Delta S_j} \frac{\partial}{\partial(\nu/h_0)} \log\left(\frac{r_{xj}}{h_0}\right) \frac{dS}{h_0} \quad (2.6)$$

$$E_{ij} = \frac{1}{\pi} \int_{\Delta S_j} \log\left(\frac{R_{ij}}{h_0}\right) \frac{dS}{h_0}, \quad \bar{E}_{ij} = \frac{1}{\pi} \int_{\Delta S_j} \frac{\partial}{\partial(\nu/h_0)} \log\left(\frac{R_{ij}}{h_0}\right) \frac{dS}{h_0}$$

E_{xj} , \bar{E}_{xj} , and E_{ij} , \bar{E}_{ij} are integrated values over the j -th element referring to the point $x = (x, z)$ and $i = (\xi_i, \eta_i)$, respectively, and they are calculated numerically as follows:

$$E_{ij} = \frac{1}{\pi} \log\left(\frac{R_{ij}}{h_0}\right) \cdot \frac{\Delta S_j}{h_0}, \quad \bar{E}_{ij} = \frac{1}{\pi} \left(\log \frac{\Delta S_i}{2h_0} - 1\right) \cdot \frac{\Delta S_i}{h_0} \quad (2.7)$$

$$\bar{E}_{ij} = \theta_{ij}/2\pi, \quad \bar{E}_{ii} = 0$$

where θ_{ij} is the subtending angle of the point $i = (\xi_i, \eta_i)$ to the j -th element, and

$$R_{ij} = \sqrt{(\xi_j - \xi_i)^2 + (\eta_j - \eta_i)^2}, \quad \Delta S_j = \sqrt{(\Delta \xi_j)^2 + (\Delta \eta_j)^2}$$

$$\Delta \xi_j = \frac{1}{2}(\xi_{j+1} - \xi_{j-1}), \quad \Delta \eta_j = \frac{1}{2}(\eta_{j+1} - \eta_{j-1})$$

E_{xj} , \bar{E}_{xj} are calculated, replacing the point $i = (\xi_i, \eta_i)$ by $x = (x, z)$ in Eq. (2.7).

Eq. (2.1) or (2.3), the Green's theorem, states that the potential function at any point in the domain is determined by its boundary-values and normal derivatives. In other words, to solve a boundary-value problem is equivalent to determine the boundary-values and its normal derivatives of the interested potential function.

Eq. (2.2) or (2.4), the Green's identity formula, states that the boundary-values $\phi(\xi, \eta)$ and its normal derivatives $\bar{\phi}(\xi, \eta)$ are in linear

relationships which are defined by the geometrical shape of the domain.

This is the first set of relations between ϕ and $\bar{\phi}$ on the boundary.

Therefore, if another set of relations between ϕ and $\bar{\phi}$ is provided, it follows that they should be determined by solving the two set of relations, simultaneously. And, in our problems, this second relation is given by dynamical or kinematical boundary conditions on the boundaries of the interested domain.

III Wave Transformation by Fixed Cylinder

As an example of fixed boundaries, we consider the wave transmission through and wave forces to the semi-immersed cylinder with arbitrary cross-section in variable water depth area. In Fig.3-1, the origin O of the coordinate system is at still water surface, x- and z- axis are horizontal and vertically upwards, respectively. We assume that CDC' is a fixed cylinder at variable depth area, where the depth at sufficiently distant from the cylinder is constant h to the right and constant h' to the left and that the incident wave of frequency σ and amplitude S_0 comes from the right. We take the geometrical boundaries AB and A'B' at $x = \ell$ and $- \ell'$, where the depths are h and h', respectively, and divide the fluid region into three parts (O), (I) and (O') as shown in the figure.

The fluid motion is assumed to have velocity potential with potential function $\phi(x, z)$ as shown by Eq. (3.1).

$$\bar{\phi}(x, z; t) = \frac{g S_0}{\sigma} \phi(x, z) e^{i\sigma t} \quad (3.1)$$

where g is gravity acceleration and t is time. The potential functions in region (O), (I) and (O') are denoted by $\phi_0(x, z)$, $\phi(x, z)$ and $\phi'_0(x, z)$, respectively. Then, since region (O) and (O') are of constant depth and so far from the cylinder that the scattering waves are damped to be vanished, the potential functions for them are expressed simply by Eq. (3.2) and (3.3) without scattering terms.

$$\phi_0(x, z) = [e^{iK(x-\ell)} + \psi e^{-iK(x-\ell)}] A(KZ) \quad (3.2)$$

$$\phi'_0(x, z) = \psi' e^{-iK'(x-\ell')} A(R'Z) \quad (3.3)$$

In Eq. (3.2), the first term is for the incident wave and the second term is for reflected wave with complex reflection coefficient ψ . Eq. (3.3) is for transmitted wave with complex transmission coefficient ψ' .

The functions $A(kz)$ and $A(k'z)$ are given by Eq.(3.4) with wave numbers k and k' for region (O) and (O'), which are determined by Eq.(3.5). The reflection- and transmission coefficient K_r and K_t are provided by Eq.(3.6).

$$A(kz) = \frac{\cosh k(z+h)}{\cosh kh} \quad A(k'z) = \frac{\cosh k'(z+h')}{\cosh k'h'} \quad (3.4)$$

$$kh \tanh kh = \frac{\sigma^2 h}{g} \quad k'h' \tanh k'h' = \frac{\sigma^2 h'}{g} \quad (3.5)$$

$$K_r = |\psi| \quad K_t = |\psi'| \quad (3.6)$$

Now, we consider the dynamical or kinematical conditions on the boundaries of fluid region (I).

On the free surface AC, C'A' at $z = 0$, we have Eq.(3.7).

$$\frac{\partial \phi}{\partial z} = \frac{\sigma^2}{g} \phi \quad \text{or} \quad \bar{\phi} = \frac{\partial \phi}{\partial(\nu/h_0)} = \Gamma \phi \quad \text{where} \quad \Gamma = \frac{\sigma^2 h_0}{g} \quad (3.7)$$

and h_0 is taken as the distance between point A and B'.

On the immersed surface of fixed cylinder CDC' and on bottom BB', we have Eq.(3.8) because of the impervious boundaries.

$$\frac{\partial \phi}{\partial \nu} = 0 \quad \text{or} \quad \bar{\phi} = \frac{\partial \phi}{\partial(\nu/h_0)} = 0 \quad (3.8)$$

Finally, on the geometrical boundaries AB ($x = \ell$) and A'B' ($x = -\ell'$), we have from Eq.(3.2) and (3.3)

$$\phi_0 = (1 + \psi) \cdot A(kz), \quad \bar{\phi}_0 = h_0 \frac{\partial \phi_0}{\partial x} = i\lambda_0 (1 - \psi) \cdot A(kz) \quad (3.9)$$

$$\phi'_0 = \psi' \cdot A(k'z), \quad \bar{\phi}'_0 = -h_0 \frac{\partial \phi'_0}{\partial x} = -i\lambda'_0 \psi' \cdot A(k'z) \quad (3.10)$$

$$\text{where} \quad \lambda_0 = kh_0 \quad \lambda'_0 = k'h_0 \quad (3.11)$$

As shown in Fig.3-2, we divide the boundaries AC, CDC', C'A' and BB' into N_1 , N_2 , N_3 and N_4 elements, respectively and geometrical boundaries AB, A'B' into M and M' elements, and denote the potential functions on them by $\phi_1, \phi_2, \phi_3, \phi_4$ and ϕ_0, ϕ'_0 , respectively. Then, substituting the relations (3.7) ~ (3.10) into the Green's identity

formula (2.4) for the fluid region (I), the following simultaneous linear equations with respect to the potential functions on the boundaries and coefficients ψ and ψ' are provided:

$$\begin{aligned}
 -\phi(i) + \sum_{j=1}^{N_1} (\bar{E}_{ij} - \Gamma E_{ij}) \phi_1(j) + \sum_{j=1}^{N_2} \bar{E}_{ij} \phi_2(j) + \sum_{j=1}^{N_3} (\bar{E}_{ij} - \Gamma E_{ij}) \phi_3(j) \\
 + \sum_{j=1}^{N_4} \bar{E}_{ij} \phi_4(j) + \psi \sum_{r=1}^M G_{ir} A(kz_r) + \psi' \sum_{s=1}^{M'} G'_{is} A(k'z_s) \\
 = - \sum_{r=1}^M G_{ir}^* A(kz_r)
 \end{aligned} \quad (3.12)$$

where

$$G_{ir} = \bar{E}_{ir} + i\lambda_0 E_{ir}, \quad G'_{is} = \bar{E}_{is} + i\lambda'_0 E_{is}, \quad G_{ir}^* = \bar{E}_{ir} - i\lambda_0 E_{ir} \quad (3.13)$$

In above equations, the first term $\phi(i)$ should be written as follows, according to the position of point (i):

$$\begin{aligned}
 \text{For } i = 1 \sim N_1, \quad \phi(i) = \phi_1(j) \quad ; \quad i = 1 \sim N_2, \quad \phi(i) = \phi_2(i); \\
 i = 1 \sim N_3, \quad \phi(i) = \phi_3(j) \quad ; \quad i = 1 \sim N_4, \quad \phi(i) = \phi_4(i);
 \end{aligned} \quad (3.14)$$

For point (i) on AB and A'B', putting $i = (\ell, z_p) = (p)$, $i = (-\ell', z_q)$ = (q), we take

$$\phi(i) = (1 + \psi) \cdot A(kz_p), \quad \phi(i) = \psi' A(k'z_q) \quad (3.15)$$

Eq.(3.12) yields $(N_1 + N_2 + N_3 + N_4 + 2)$ linear equations with respect to the same number of unknown quantities. Solving these equations, all of the unknowns are determined and by means of Eq.(2.3), the potential function at any point in fluid region is calculated, and at the same time those of regions (0) and (0') are obtained by Eq.(3.2) and (3.3).

The fluid pressure at point (j) = (ξ_j, η_j) on the immersed surface of the cylinder is given as

$$\frac{p(j)}{\rho g S_0} = -i \phi_2(j) e^{i\alpha t} \quad (3.16)$$

Consequently, the horizontal and vertical resultant forces P_x and P_z and the resultant moment T around the point (x_0, z_0) are calculated as follows:

$$\frac{P_x}{\rho g S_0 h_0} = -i e^{i\omega t} \sum_{j=1}^{N_2} \phi_2(j) \cdot \frac{\Delta \zeta_j}{h_0} \quad (3.17)$$

$$\frac{P_z}{\rho g S_0 h_0} = i e^{i\omega t} \sum_{j=1}^{N_2} \phi_2(j) \cdot \frac{\Delta \xi_j}{h_0} \quad (3.18)$$

$$\frac{T}{\rho g S_0 h_0^2} = i e^{i\omega t} \sum_{j=1}^{N_2} \left(\frac{\xi_j - x_0}{h_0} \cdot \frac{\Delta \xi_j}{h_0} + \frac{\zeta_j - z_0}{h_0} \cdot \frac{\Delta \zeta_j}{h_0} \right) \phi_2(j) \quad (3.19)$$

The first calculated example is a semi-immersed circular cylinder whose center is fixed at still water surface on constant water depth area and whose diameter D is 0.8 times the water depth h . The geometrical surface AB and $A'B'$ are taken at $x = 3h$ and $-3h$, respectively. The numbers of calculation points on the boundaries are taken as $N_1 = 20$, $N_2 = 14$, $N_3 = 20$, $N_4 = 30$ and $M = M' = 20$. The second example is double cylinders whose diameters are the same as above and whose centers are apart by three times the diameter D .

Fig.3-3 shows the calculated and measured transmission coefficients with respect to the non-dimensional frequency $\sigma^2 h/g$ or to the ratio of diameter to wave length D/L for the first and second examples, where the solid line and open circles are for single cylinder and the broken line and solid circles are for double cylinders. From the figure, it is seen that the transmission coefficient for single cylinder decreases gradually and the one for double cylinders decreases rapidly with increasing frequency and that the measured values are somewhat lower than the calculated values for higher frequencies but the tendencies of both are in good agreement. The discrepancies between measured and calculated values are thought to be due to the non-linear effect of measured waves. (The experiments were carried out in wave flume of length 22 m with water depth $h = 40$ cm and incident wave amplitude $S_0 = 3 \sim 4$ cm.)

IV Wave Transformation by and the Motion of Floating Cylinder

In Fig.4-1, it is assumed that a cylinder of cross-section $CDD'C'$ with gravity center at (\bar{x}_0, \bar{z}_0) and center of buoyancy at (x_b, z_b) in equilibrium condition is moored by spring lines DE and $D'E'$ with spring constant K on the variable sea bottom $B'E'EB$, and is subjected to the incident wave of frequency σ and small amplitude S_0 from the right. Then, the position of

the gravity center of the cylinder (x_0, z_0) and the rotation angle δ of the cylinder around gravity center at any time t in motion are expressed by the complex amplitude of horizontal and vertical displacements X, Z and of the rotation angle Θ as follows:

$$x_0 = \bar{x}_0 + X e^{i\omega t}, \quad z_0 = \bar{z}_0 + Z e^{i\omega t}, \quad \delta = \Theta e^{i\omega t} \quad (4.1)$$

Similarly to the previous section III, the velocity potential is expressed by Eq. (3.1) and the potential function in region (O), (O') are by Eq. (3.2), (3.3) with reflection and transmission coefficients ψ and ψ' . And also, the potential function at free surface and at bottom in fluid region (I) are in the relation of Eq. (3.7) and (3.8), respectively. However, on the oscillating surface CDD'C', the normal derivatives of the potential function ϕ_2 is given by the following expression, due to the kinematical boundary condition:

$$\bar{\phi} = i \Gamma \left[\frac{X}{S_0} \frac{dz}{ds} - \frac{Z}{S_0} \frac{dx}{ds} - \frac{\Theta a}{S_0} \left\{ \frac{x - \bar{x}_0}{a} \frac{dx}{ds} + \frac{z - \bar{z}_0}{a} \frac{dz}{ds} \right\} \right] \quad (4.2)$$

where a is a reference length to the horizontal size of the cross-section, for example, a is taken as half width for rectangular cylinder and as radius for circular cylinder. (x, z) is the coordinate of point on the surface CDD'C' and s is the length measured along CDD'C'.

The complex amplitudes X, Z and Θ in Eq. (4.2) can be expressed by the potential function ϕ_2 on the immersed surface of cylinder, taking account of the following equations of motion of the cylinder:

$$M \frac{d^2 x_0}{dt^2} = P_x + F_x, \quad M \frac{d^2 z_0}{dt^2} = P_z + P_s + F_z \quad (4.3)$$

$$I_0 \frac{d^2 \delta}{dt^2} = T_\theta + T_s + M_\theta$$

where M is the mass of the cylinder; I_0 is the moment of inertia around the gravity center; P_x, P_z, T_θ are the resultant horizontal and vertical fluid forces and moment around gravity center due to the fluid pressure acting to the immersed surface; P_s, T_s are the restoring force and moment for vertical displacement and rotation of cylinder due to statical fluid pressure; F_x, F_z, M_θ are the mooring forces and moment by the mooring lines induced by the motion of the cylinder.

Indicating the fluid density by ρ , the draught in mooring condition

by qh ($l > q > 0$), the mass M , the moment of inertia I_θ and the immersed volume of the cylinder V are expressed with positive constants ν_1 , ν_2 and ν_3 as follows:

$$M = \nu_1 \int a q h, \quad I_\theta = \nu_2 \int a^2 (q h)^2, \quad V = \nu_3 a q h \quad (4.4)$$

Since the fluid pressure on the immersed surface is expressed by Eq. (3.16), P_x , P_z and T_θ are given as follows:

$$\begin{aligned} P_x &= -i \rho g \zeta_0 e^{i\sigma t} \int_S \phi_2(x, z) dz \\ P_z &= i \rho g \zeta_0 e^{i\sigma t} \int_S \phi_2(x, z) dz \\ T_\theta &= i \rho g \zeta_0 e^{i\sigma t} \int_S \{ (x - \bar{x}_0) dx + (z - \bar{z}_0) dz \} \phi_2(x, z) \end{aligned} \quad (4.5)$$

where integrations are taken along the surface CDD'C'.

Denoting the length of water line as $2l_0$, P_S and T_S are given as

$$P_S = -2 \rho g l_0 Z e^{i\sigma t}, \quad T_S = -\rho g V \left\{ \frac{3}{2} \frac{l_0^3}{V} - (\bar{z}_0 - Z) \right\} \Theta e^{i\sigma t} \quad (4.6)$$

For simplicity, we assume that the cross-section of the cylinder and the mooring condition are symmetrical with respect to the vertical line through the gravity center. Taking the angle of mooring line with horizontal as β and the mooring point on the cylinder as (a_0, b_0) and $(-a_0, b_0)$, the mooring forces and moment to the cylinder F_x , F_z and M_θ are expressed as follows:

$$\begin{aligned} F_x &= -2K(X - S\Theta) \cos^2 \beta e^{i\sigma t}, \quad F_z = -2K \sin^2 \beta e^{i\sigma t} \\ M_\theta &= 2KS(X - S\Theta) \cos^2 \beta e^{i\sigma t} \end{aligned} \quad (4.7)$$

where

$$S = b_0 - \bar{z}_0 - (a_0 - \bar{x}_0) \tan \beta$$

Substituting Eq. (4.1) (4.4) (4.5) (4.6) and (4.7) into Eq. (4.3), it follows that X , Z and Θ are expressed by $\phi_2(x, z)$.

$$\frac{X}{S_0} = \frac{i}{\delta} \int_S \phi_2(x, z) \cdot \left\{ k_{x\theta} \frac{x - \bar{x}_0}{a} \frac{dx}{a} + (k_{z\theta} \frac{z - \bar{z}_0}{a} - \alpha_3) \frac{dz}{a} \right\} \quad (4.8)$$

$$\frac{Z}{S_0} = \frac{i}{\alpha_2} \int_S \phi_2(x, z) \frac{dx}{a} \quad (4.9)$$

$$\frac{\partial a}{S_0} = \frac{i}{\gamma} \int_S \phi_2(x, z) \left\{ \alpha_1 \frac{x - \bar{x}_0}{a} \frac{dx}{a} + \left(\alpha_1 \frac{z - \bar{z}_0}{a} - k_{x0} \right) \frac{dz}{a} \right\} \quad (4.10)$$

where

$$\begin{aligned} \gamma &= \alpha_1 \alpha_3 - k_{x0}^2, & \alpha_1 &= k_{xx} - \nu_1 \frac{qh}{h_0} \Gamma, \\ \alpha_2 &= k_{zz} - \nu_1 \frac{qh}{h_0} \Gamma + \frac{2l_0}{a}, & \alpha_3 &= k_{00} - \nu_2 \frac{(qh)^2}{a h_0} \Gamma \\ &+ \frac{2}{3} \left(\frac{l_0}{a} \right)^3 - \nu_3 \frac{qh}{a} \frac{\bar{z}_0 - z_b}{a}, & k_{xx} &= \frac{ZK}{\rho g a} \cos^2 \beta \\ k_{zz} &= \frac{ZK}{\rho g a} \sin^2 \beta, & k_{00} &= \frac{ZKS^2}{\rho g a^3} \cos^2 \beta, & k_{x0} &= \frac{ZKS}{\rho g a^2} \cos^2 \beta \end{aligned} \quad (4.11)$$

Introducing Eq. (4.8) (4.9) (4.10) into Eq. (4.2), $\bar{\phi}_2$ on the immersed surface of cylinder is written by ϕ_2 as follows:

$$\bar{\phi}_2(x, z) = \Gamma \int_S \phi_2(u, v) \cdot F(x, z; u, v) \quad (4.12)$$

where

$$\begin{aligned} F(x, z; u, v) &= \left[\left(\frac{1}{\alpha_2} + \frac{\alpha_1}{\gamma} \cdot \frac{u - \bar{x}_0}{a} \cdot \frac{x - \bar{x}_0}{a} \right) \frac{dx}{ds} - \frac{1}{\gamma} \left(k_{x0} - \alpha_1 \frac{z - \bar{z}_0}{a} \right) \cdot \right. \\ &\cdot \left. \frac{u - \bar{x}_0}{a} \frac{dz}{ds} \right] \frac{du}{a} + \frac{1}{\gamma} \left[\left(\alpha_1 \frac{v - \bar{z}_0}{a} - k_{x0} \right) \frac{x - \bar{x}_0}{a} \frac{dx}{ds} + \left\{ \left(\alpha_3 - \right. \right. \right. \\ &\left. \left. \left. k_{x0} \frac{z - \bar{z}_0}{a} \right) - \left(k_{x0} - \alpha_1 \frac{z - \bar{z}_0}{a} \right) \frac{v - \bar{z}_0}{a} \right\} \frac{dz}{ds} \right] \frac{dv}{a} \end{aligned} \quad (4.13)$$

where (x, z) and (u, v) are the coordinates of the points on the immersed surface. Indicating the calculation points on the surface as (ξ_j, ζ_j) and (ξ_m, ζ_m) , corresponding to (x, z) and (u, v) , Eq. (4.12) is written as follows:

$$\bar{\phi}_2(j) = \Gamma \sum_{m=1}^{N_2} F(j, m) \cdot \phi_2(m) \quad (4.14)$$

Similarly to the preceding section III, applying Eq. (3.7) (3.8) (3.9) (3.10) and (4.14) to the Green's identity formula (2.4) for the fluid region (I), we have linear simultaneous equations with respect to the potential functions ϕ on the boundaries and ψ, ψ' . They are written by replacing the term $\sum_{j=1}^{N_2} \bar{E}_{ij} \Phi_2(j)$ in Eq. (3.12) by $\sum_{m=1}^{N_2} \sum_{j=1}^{N_2} [\delta_{jm} \bar{E}_{ij} - \mathcal{P} E_{ij} F(j, m)] \Phi_2(m)$, where δ is Kronecker's delta and $\delta_{jm} = 0$ ($j \neq m$): $= 1$ ($j = m$).

Solving the equations, we can obtain all of the boundary-values of potential function of region (I) and the transmission-, reflection coefficient, similarly to the section III. Then, the amplitudes of motion of cylinder are calculated by Eq. (4.8) (4.9) (4.10) and also the mooring force F to the wave-side mooring line DE is calculated as follows:

$$\frac{F}{S_o K} = \left[\frac{X}{S_o} + \frac{Z}{S_o} \tan \beta - \frac{D a}{S_o} \frac{S}{a} \right] \cos \beta \cdot e^{i \omega t} \quad (4.15)$$

The mooring force F' to the lee-side line D'E' is given by replacing β by $-\beta$ in above expression.

As an example, we consider the case when a circular cylinder is moored on constant water depth h . The diameter $D = 2a$ is $0.914h$, the draught is $0.67h$ ($q=0.67$), the mooring points on the cylinder are ($\pm 0.486h, -0.114h$) and $\nu_1 = 1.467, \nu_2 = 0.670, \nu_3 = 1.646$. The cylinder is of uniform density 0.584 and the center is at $0.114h$ below still water surface. The spring constant $K/\rho g a$ is 0.227 and mooring angle β is 33° . Fig.4-2 is the calculated (solid line) and measured (open circles) transmission coefficients with respect to the non-dimensional frequency or to the ratio of diameter to the wave length D/L . Experiments were carried out in wave flume with water depth $h = 35$ cm and a circular cylinder of diameter $D = 32$ cm, whose center was at depth 4.0 cm below still water level in equilibrium condition. The figure shows that the calculated and measured values are in good agreement. Moreover, it shows an interesting fact that the incident wave is perfectly intercepted even by floating cylinder, if the frequency $\omega^2 h/g$ is 0.42 and 1.74 , that is, D/L is 0.10 and 0.26 . Fig.4-3 is the calculated reflection coefficient and amplitudes of motion of cylinder.

V Wave Transformation by Permeable Seawall and Breakwater

In Fig.5-1, suppose that ABC is a permeable seawall placed on impervious bottom BCO'. The geometrical boundary is taken at OO', which is sufficiently distant from the seawall and of constant water depth h. Dividing the fluid region into three regions (O), (I) and (II), the velocity potentials in region (O) and (I) are assumed to be expressed in the form of Eq.(3.1) with potential functions $\phi_0(x,z)$ and $\phi(x,z)$, respectively. In permeable region (II), indicating the quantities by superscript *, the mass and momentum equations are written with horizontal and vertical fluid velocities u^* , w^* and fluid pressure p^* as follows:

$$\begin{aligned} \frac{\partial u^*}{\partial x} + \frac{\partial w^*}{\partial z} &= 0 \\ \frac{1}{V} \frac{\partial u^*}{\partial t} &= -\frac{1}{\rho} \frac{\partial p^*}{\partial x} - \frac{\mu}{V} u^* - \frac{\varepsilon(1-V)}{V} \frac{\partial u^*}{\partial t} \\ \frac{1}{V} \frac{\partial w^*}{\partial t} &= -\frac{1}{\rho} \frac{\partial p^*}{\partial z} - g - \frac{\mu}{V} w^* - \frac{\varepsilon(1-V)}{V} \frac{\partial w^*}{\partial t} \end{aligned} \quad (5.1)$$

where ρ is the fluid density, V is porosity of the seawall, μ is the coefficient of drag force to the porous material which is linearized to be proportional to the fluid velocity and ε is the added mass force coefficient to the material. The fluid motion represented by Eq.(5.1) has velocity potential, which is expressed by Eq.(5.2) with potential function Φ^* , and fluid velocities, pressure and surface profile are provided by Eq.(5.3).

$$\Phi^*(x,z;t) = \frac{gS_0}{\sigma} \phi^*(x,z) e^{i\sigma t} \quad (5.2)$$

$$u^* = \partial \Phi^* / \partial x, \quad w^* = \partial \Phi^* / \partial z, \quad p^* / \rho g S_0 = -i\beta \phi^*(x,z) e^{i\sigma t} \quad (5.3)$$

$$S^*/S_0 = -i\beta \phi^*(x,0) e^{i\sigma t}, \quad \beta = \frac{\alpha}{V}, \quad \alpha = 1 + \varepsilon(1-V) + i\mu/\sigma$$

The potential function ϕ_0 in region (O) is given by Eq.(3.2), so that the boundary conditions of fluid region (I) are provided by Eq.(3.7) on \vec{OA} , by Eq.(3.8) on $\vec{OO'}$ and by Eq.(3.9) on $\vec{O'O}$. As for the conditions on \vec{AC} , since the mass flux and energy flux through the boundary AC should be continuous, it follows from Eq.(3.16) and (5.3) that

$$\bar{\phi}^* = \bar{\phi}, \quad \phi^* = \frac{1}{\rho} \phi \quad (5.4)$$

As for the porous region (II), we have Eq.(5.5) on free surface \vec{AB} from the kinematical condition, and Eq.(5.6) on impervious boundary BC.

$$\frac{\partial \phi^*}{\partial Z} = \alpha \frac{\rho^2}{g} \phi^* \quad \text{or} \quad \bar{\phi}^* = \alpha \Gamma \phi^*, \quad \Gamma = \frac{\rho^2 h_0}{g} \quad (5.5)$$

$$\frac{\partial \phi^*}{\partial Z} = 0 \quad \text{or} \quad \bar{\phi}^* = 0 \quad (5.6)$$

As shown in Fig.5-2, denoting the potential functions on the boundaries \vec{OA} , \vec{AC} , \vec{CO}' and $\vec{O}'\vec{O}$ by ϕ_1 , ϕ_2 , ϕ_3 , ϕ_0 and on the boundaries \vec{BA} , \vec{AC} and \vec{CB} by ϕ_1^* , ϕ_2^* and ϕ_3^* , dividing these boundaries into N_1 , N_2 , N_3 , M and N_1^* , N_2^* , N_3^* and taking the outward normal for region (I) and inward normal for region (II), and applying the boundary conditions (3.7) (3.8) (3.9) to the Green's identity formula (2.4) for region (I) and conditions (5.4) (5.5) and (5.6) to Eq.(2.4) for region (II), we have the following equations:

(i) For fluid region (I):

$$\begin{aligned} & -\phi(\omega) + \sum_{j=1}^{N_1} (\bar{E}_{ij} - \Gamma E_{ij}) \phi_1(j) + \sum_{j=1}^{N_2} [\bar{E}_{ij} \phi_2(j) - E_{ij} \bar{\phi}_2(j)] \\ & + \sum_{j=1}^{N_3} \bar{E}_{ij} \phi_3(j) + \psi \sum_{\gamma=1}^M G_{i\gamma} A(kZ_\gamma) = - \sum_{\gamma=1}^M G_{i\gamma}^* A(kZ_\gamma) \end{aligned} \quad (5.7)$$

($i = 1 \sim N_1, 1 \sim N_2, 1 \sim N_3$ and $(0, Z_p)$ on $O'O$)

(ii) For porous region (II):

$$\begin{aligned} & \phi^*(\omega) + \sum_{j=1}^{N_1^*} (\bar{E}_{ij}^* + \alpha \Gamma E_{ij}^*) \phi_1^*(j) + \sum_{j=1}^{N_2^*} \left[\frac{1}{\rho} \bar{E}_{ij}^* \phi_2(j) \right. \\ & \left. - E_{ij}^* \bar{\phi}_2(j) \right] + \sum_{j=1}^{N_3^*} \bar{E}_{ij}^* \phi_3^*(j) = 0 \end{aligned} \quad (5.8)$$

($i = 1 \sim N_1^*, 1 \sim N_2, 1 \sim N_3^*$)

Eq.(5.7), (5.8) are $(N_1 + 2N_2 + N_3 + N_1^* + N_3^* + 1)$ linear equations with respect to the same number of unknowns ϕ_1 , ϕ_2 , $\bar{\phi}_2$, ϕ_3 , ψ , ϕ_1^* and ϕ_3^* . Consequently, solving these equations simultaneously, we can determine all of the unknowns, from which the potential values at points in fluid region are calculated by Eq.(2.3).

The surface wave profiles are calculated as follows:

$$\begin{aligned} \text{From B to A: } S^*(j) &= -i\beta \phi_i^*(j) e^{L\sigma^2 t} & j &= 1 \sim N_1^* \\ \text{From A to O: } S(j) &= -i \phi_i(j) e^{i\omega t} & j &= N_1 \sim 1 \end{aligned} \quad (5.9)$$

Fig.5-3 and 5-4 are the calculated and measured reflection coefficients with respect to non-dimensional frequency $\sigma^2 h/g$ for model seawall of 1:1 slope and of vertical face, respectively, made by quarry stones of mean diameter 6 cm with porosity $V = 0.43$ in constant water depth $h = 40$ cm. The widths of both seawalls at still water level are equal to twice the water depth h . The solid lines in figures are calculated values, taking $V = 0.5$, $M/\sigma = 1.0$ and $\xi = 0$ for all frequencies. The measured and calculated values are almost in good agreement.

Wave transformation by permeable breakwater is analyzed in the similar manner. In Fig.5-5, solid line, solid circles and broken line, solid triangles are the calculated and measured reflection and transmission coefficients, respectively, for model permeable breakwater with 1:1.5 sloped faces and the width at still water level h . Other conditions are the same as the seawall. The calculated values are somewhat different from measured values but the tendencies are nearly in agreement. Fig.5-6 is for permeable breakwater model with rectangular cross-section of width $2h$. The measured and calculated values are in good agreement.

Fig.5-7 is the calculated distribution of equi-potential lines (solid lines) and its orthogonals (broken lines) for permeable breakwater in Fig. 5-5 at $\sigma t = 0^\circ, 30^\circ, 60^\circ$ and 90° , when the incident wave crest approaches to the breakwater.

VI Conclusions

It is clear that the proposed method provides a convenient and simple analysis for two-dimensional boundary-value problems of small amplitude waves. And, if the difficulties arising in solving simultaneous equations of so many unknown quantities were overcome, this method is extended directly to the problem of three-dimensional waves and also to the finite amplitude wave problems by means of perturbation method.

References

- Ijima, T., Y. Eguchi and A. Kobayashi (1971): " Permeable Breakwater and Sea-Wall ", Proc. 18th Japanese Conf. Coasta. Eng. J.S.C.E.
- Ijima, T., Y. Tabuchi and Y. Yumura (1972): " Scattering of Surface Waves and the Motion of Rectangular Body in Waves of Finite Water Depth", Proc. J.S.C.E., No. 202
- John, F. (1950): " On the Motion of Floating Bodies, II", Comm. Pure and Applied Mathematics, Vol. III
- Madsen, O.S. and S.M. White (1976): " Reflection and Transmission Characteristics of Porous Rubble-Mound Breakwater ", Miscellaneous Rept. No. 76-5, Coast. Eng. Res. Center, U.S. Army, Corp. of Eng.
- Sollitt, C.K. (1972): " Wave Transmission through Permeable Breakwater ", Proc. 13th International Conf. Coast. Eng. A.S.C.E.

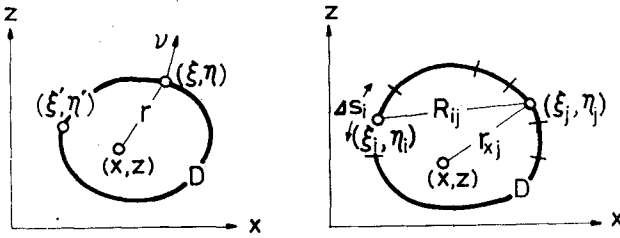


Fig.2-1 Definition Sketch Fig.2-2 Definition Sketch

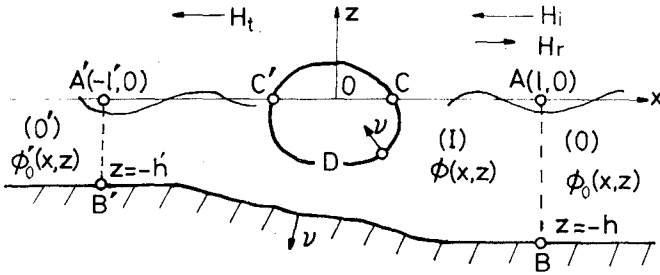


Fig. 3-1 Definition Sketch for Fixed Cylinder

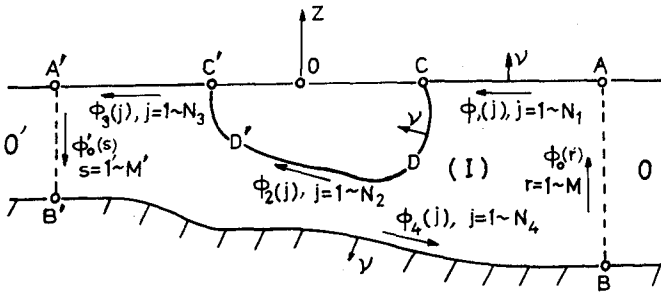


Fig.3-2 Definition of Potential Functions

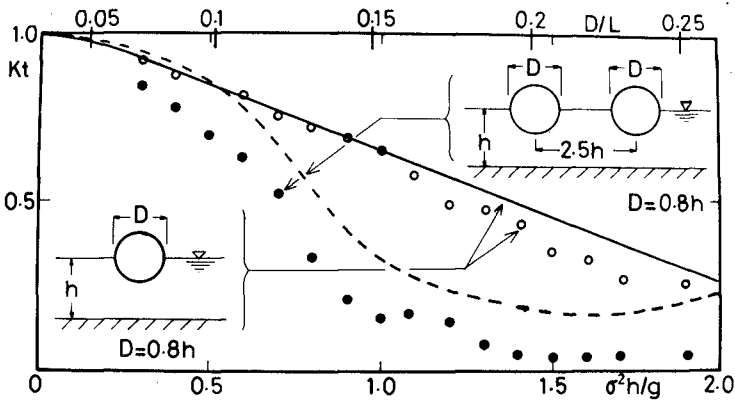


Fig.3-3 Transmission Coefficient of Single and Double Cylinders

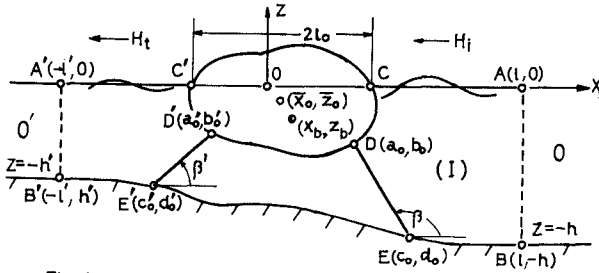


Fig.4-1 Definition Sketch

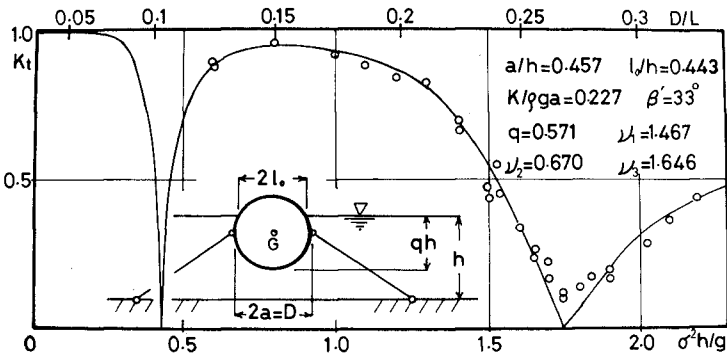


Fig.4-2 Transmission coefficient of moored floating cylinder

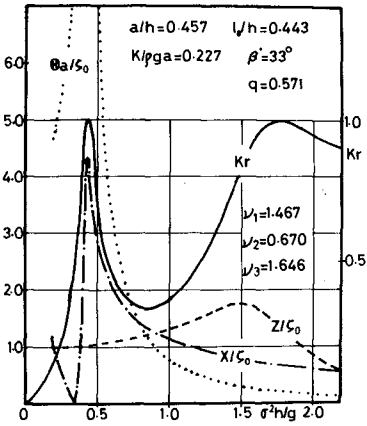


Fig. 4-3 Amplitude of motions and Reflection coefficient

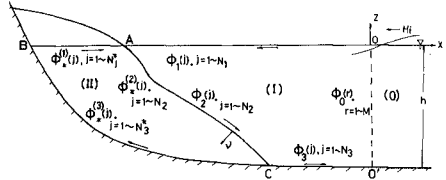


Fig. 5-1 Definition Sketch for Permeable Seawall

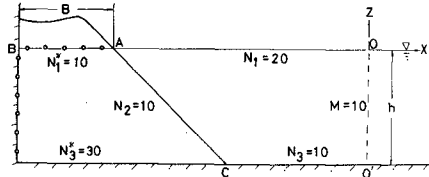


Fig. 5-2 Calculated Cross-Section of Permeable Seawall

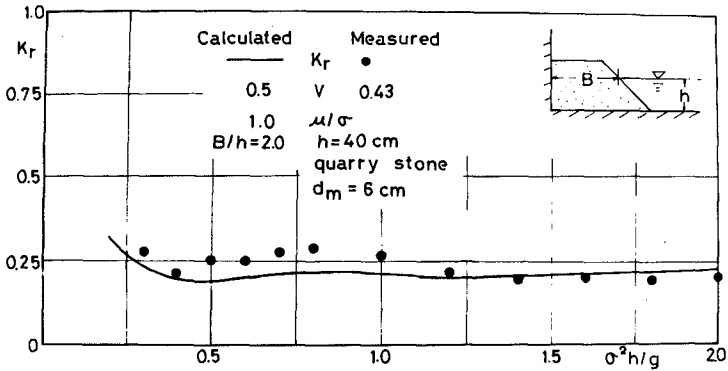


Fig. 5-3 K_r for Sloped-Face Seawall

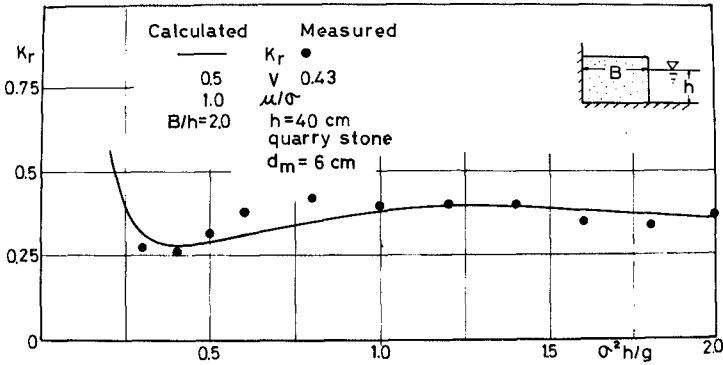


Fig. 5-4 K_r for Vertical-Face Seawall

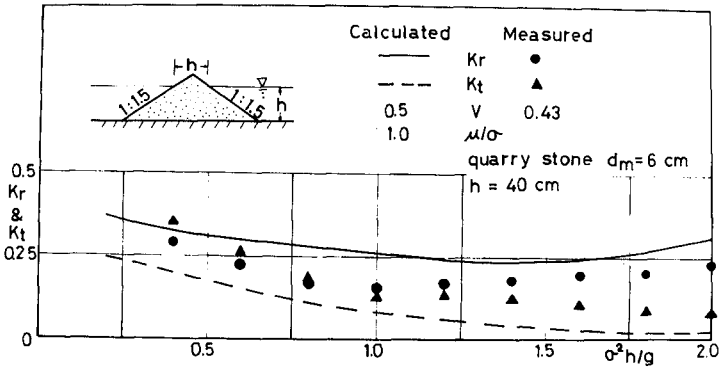


Fig. 5-5 K_r and K_t for Breakwater with Sloped Faces

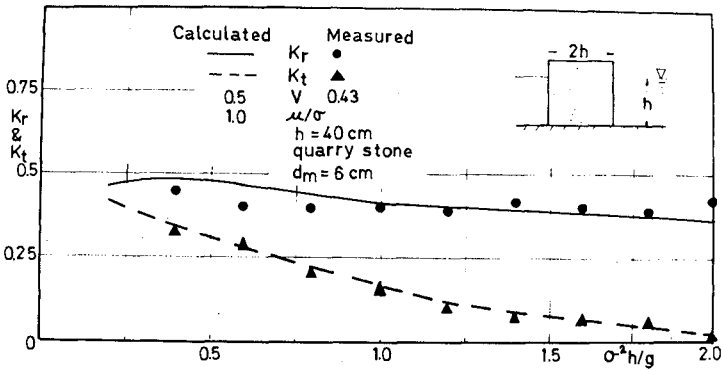
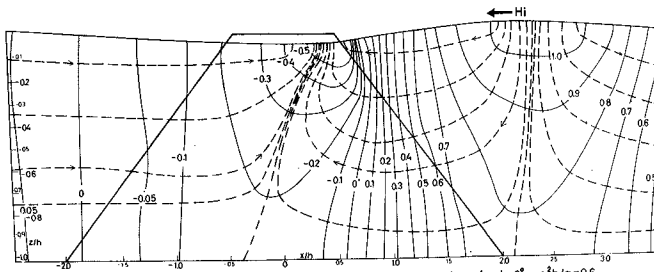
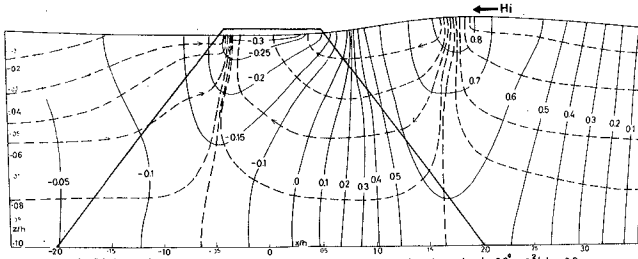


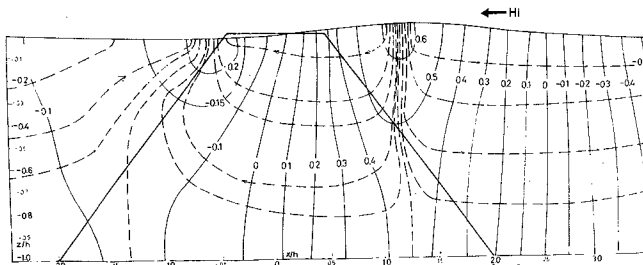
Fig. 5-6 K_r and K_t for Vertical-Face Breakwater



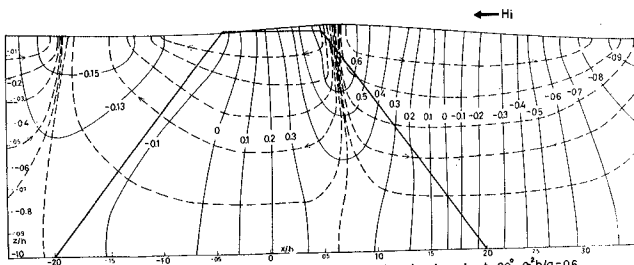
a Distribution of Velocity Potentials for Type A Breakwater at $\alpha t = 0^\circ$, $\alpha^2 h/g = 0.6$



b Distribution of Velocity Potentials for Type A Breakwater at $\alpha t = 30^\circ$, $\alpha^2 h/g = 0.6$



c Distribution of Velocity Potentials for Type A Breakwater at $\alpha t = 60^\circ$, $\alpha^2 h/g = 0.6$



d Distribution of Velocity Potentials for Type A Breakwater at $\alpha t = 90^\circ$, $\alpha^2 h/g = 0.6$

Fig. 5-7

CHAPTER 157

WAVE OVERTOPPING EQUATION

by

J. Richard Weggel¹

INTRODUCTION

In the early 1950's the Corps of Engineers' Jacksonville District initiated a series of laboratory tests to investigate the overtopping of proposed levee sections for Lake Okeechobee, Florida. For economic reasons, the alternative to build levees with crest elevations that were at times below the limit of wave runup was investigated and the quantities of water carried over the structures for various freeboard allowances, structure slopes and wave conditions determined. The initial tests were conducted at the Waterways Experiment Station (WES) in Vicksburg, Mississippi for the Jacksonville District at what was taken to be a 1 to 30 model scale. Model wave heights varied from 4.05 cm to 12.2 cm (0.133 to 0.40 ft). In order to expand the range of test conditions investigated, the Beach Erosion Board, currently the Coastal Engineering Research Center (CERC), commissioned an expanded series of tests that considered the overtopping of riprap faced, curved and stepped seawalls as well as the overtopping of "smooth" slopes. These tests, also conducted at WES, were considered to be at a 1 to 17 scale with model wave heights ranging from 5.36 cm to 21.5 cm (0.176 to 0.706 ft). A number of tests were subsequently conducted in CERC's large wave tank to determine the influence scale effects might have on overtopping. These tests are referred to as 1 to 2 1/2 scale tests. The model wave heights investigated ranged from 48.8 cm to 140.2 cm. (1.60 to 4.60 ft).

¹Special Assistant, U.S. Army Coastal Engineering Research Center, Fort Belvoir, VA 22060

Much of the overtopping data obtained during these tests has been presented by Saville (2)* and by Saville and Caldwell (1) and summarized in CERC's TR-4 (3); however, in this latter publication the data were presented in dimensional form making their general application difficult. In keeping with the decision to present information in CERC's Shore Protection Manual (4) in dimensionless form whenever practicable, the overtopping data was reanalysed and an empirical expression derived. The broad range of model scales used in the overtopping experiments also provide an opportunity to investigate the effect of model scale on test results. A summary of overtopping test conditions investigated is given on Table 1.

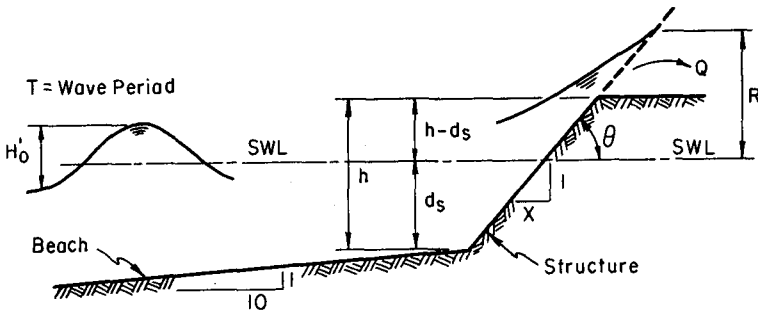


Figure 1. Definition of terms.

* Numbers in parentheses correspond to references listed in Appendix I.

TABLE 1 - SUMMARY OF OVERTOPPING TEST CONDITIONS

"Scale" of Test	Structures Investigated	Flume Dimensions	Type of Generator	Range of Wave Heights (Model Values)	Range of Wave Periods (Model Values)
1 to 30	1 on 3 smooth slope 1 on 6 smooth slope Composite slope Slope with berm	21.3 m long At generator 1.22 m wide 0.88 m deep At test section 0.39 m wide 0.49 m deep	Flep type	4.05 to 12.2 cm	0.822 to 1.28 sec
1 to 17	Smooth vertical wall 1 on 1-1/2 smooth slope 1 on 3 smooth slope 1 on 1-1/2 stepped slope 1 on 1-1/2 riprap faced slope Curved wall Recurved wall	36.6 m long 1.52 m wide 1.52 m deep	Plunger type	5.36 to 21.5 cm	0.717 to 3.64 sec
1 to 2-1/2	1 on 3 smooth slope 1 on 6 smooth slope	193.5 m long 4.57 m wide 6.10 m deep	Bulkhead type	48.8 to 140.2 cm	0.386 to 10.12 sec

TABLE 2

AGREEMENT BETWEEN MEASURED AND CALCULATED OVERTOPPING RATES
(Using SPM published values of d and Q_o^* , based on 1 to 17 scale data)

Structure Type	Number of Points	Correlation Coefficient
Smooth Face		
Vertical	56	0.980
1 on 1-1/2 slope	93	0.996
1 on 3 slope	83	0.992
Riprap Face		
1 on 1-1/2	43	0.998
Stepped Face		
1 on 1-1/2	60	0.990
Galveston Curved Wall		
on 1 on 10 beach	33	0.995
on 1 on 25 beach	33	0.998
Recurved Wall		
on 1 on 10 beach	5	0.999

DIMENSIONAL ANALYSIS

The variables describing the overtopping of a given structure are depicted on figure 1. They include:

H'_0 = deepwater wave height	[L]
T = wave period	[T]
g = gravitational acceleration	[L] [T] ⁻²
Q = overtopping rate (volume per unit time per unit crest length)	[L] ² [T] ⁻¹
R = runup height measured vertically from the still water level (SWL) (e.g. the height to which the water would runup if the structure were high enough to preclude overtopping)	[L]
d_s = water depth at the structure toe	[L]
h = height of the structure crest above the bottom	[L]
ν = kinematic viscosity	[L] ² [T] ⁻¹
θ = structure slope	[dimensionless]

plus any other geometric parameters necessary to describe the various structure types. A dimensional analysis of the preceding 9 variables having 2 dimensions gives the following dimensionless terms:

$$d_s / H'_0 = \text{relative water depth at the structure toe}$$

$$H'_0/gT^2 = \text{wave steepness parameter}$$

$$F = (h-d_s)/H'_0 = \text{relative height of structure crest above SWL}$$

$$F_0 = R/H'_0 = \text{relative runup or height of structure crest required to preclude overtopping}$$

$$Q^* = Q^2/gH'_0{}^3 = \text{relative overtopping rate}$$

$$\theta = \text{structure slope, and}$$

$$R_e = \frac{H'_0{}^2}{\nu T} = \text{a Reynolds' number.}$$

The phenomenon is scaled primarily according to Froude similarity; however, the Reynolds' number serves as a measure of any scale effects. Other formulations of R_e are possible, the present one having been adopted for its simplicity.

Generally it is not permissible to eliminate dimensionless terms by combining them unless an analytic or empirical relationship between two of the variables is known. If it is assumed that such a satisfactory relationship is available for the runup R , the overtopping rate can be expressed in terms of R and the ratio $F/F_0 = (h-d_s)/R$ can be substituted for F and F_0 . The preceding dimensionless terms are obviously not the only combinations of terms possible; however, they were selected after considerable trial and error because they provided the greatest possibility for keeping dimensionless variables constant and investigating the variation of Q^* with individual parameters.

DATA ANALYSIS

For a given structure and set of incident wave conditions (e.g. constant d_s/H'_0 , H'_0/gT^2 and θ), the dimensionless overtopping rate, Q^* was plotted against the dimensionless crest height, $F/F_0 = (h-d_s)/R$.

A typical plot showing two data sets differing only in model scale, is shown in figure 2. Generally, all data sets when plotted semi-logarithmically exhibited a linear variation of Q^* with F/F_0 for small values of F/F_0 ; also, the value of Q^* must approach zero as the relative crest height, F/F_0 approaches 1.0 (i.e., as the crest of the structure approaches the limit of wave runoff). The curve therefore approaches $F/F_0 = 1.0$ asymptotically on the semi-logarithmic plot. The hyperbolic tangent function exhibits identical behavior; hence, an equation of the form,

$$\frac{F}{F_0} = \alpha \tanh \left[\log \frac{Q^*}{Q_0^*} \right] \quad (1)$$

was used to approximate the data. Here α and Q_0^* are empirical coefficients to be established by comparing the equation with the data. The value of α generally establishes the shape of the curve since it is the slope of the curve at $F/F_0 = 0$. Q_0^* represents the value of Q^* for a structure with its crest elevation at the SWL. Figure 3 depicts equation 1 for various values of α . To establish values of α and Q_0^* a transparent template was made of figure 3 and used as an overlay to Q^* vs F/F_0 data plotted at the same scale on semi-logarithmic graph paper. By moving the template vertically until one of the curves coincided with the trend of the data, the value of α could be directly determined. The value of Q_0^* was determined by reading the value of Q^* where the α curves intersected $F/F_0 = h-d_s/R = 0.0$ on the data plot. Thus, by overlaying the template to each data set, values of α and Q_0^* were established for each structure type and set of incident wave conditions. Interestingly, the form of equation 1 is such that it could be used to describe the overtopping of all of the structures for which data were available; consequently, figures similar to figure 4 could be prepared for each structure type. Such figures, which give α and Q_0^* as functions of d_s/H_0 and H_0'/gT^2 for a given structure type, are presented in the SPM (4) for other structure slopes and types.

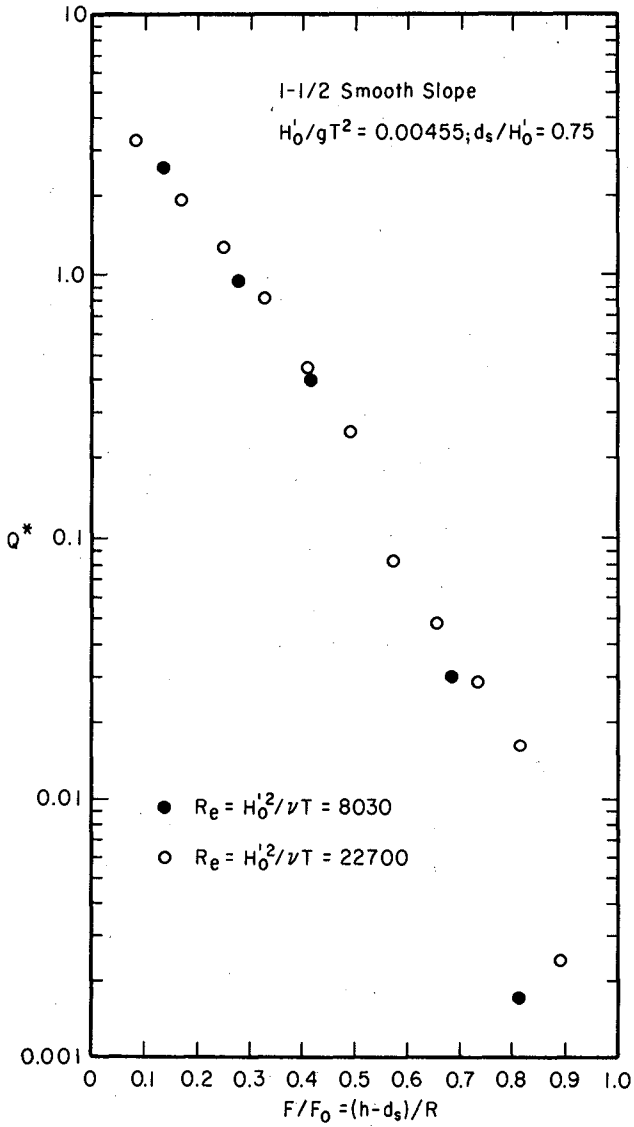


Figure 2. Typical data plot, 1 on 1 1/2 smooth slope, $H_0'/gT^2 = 0.00455$;
 $d/H_0' = 0.75$.

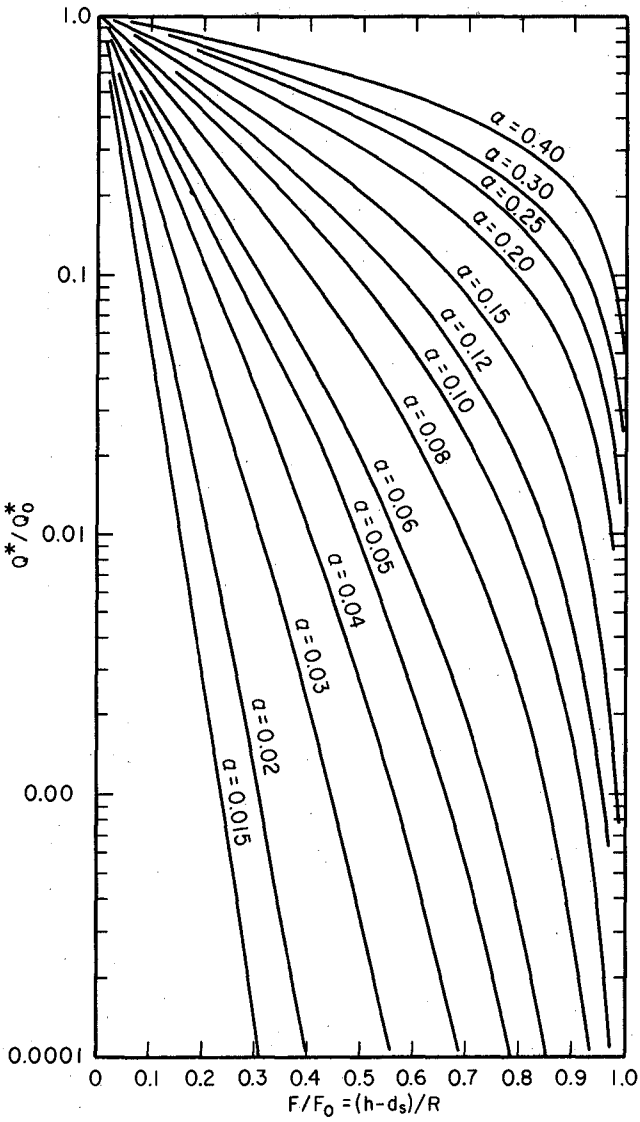


Figure 3. Presentation of equation 2 for various values of α .

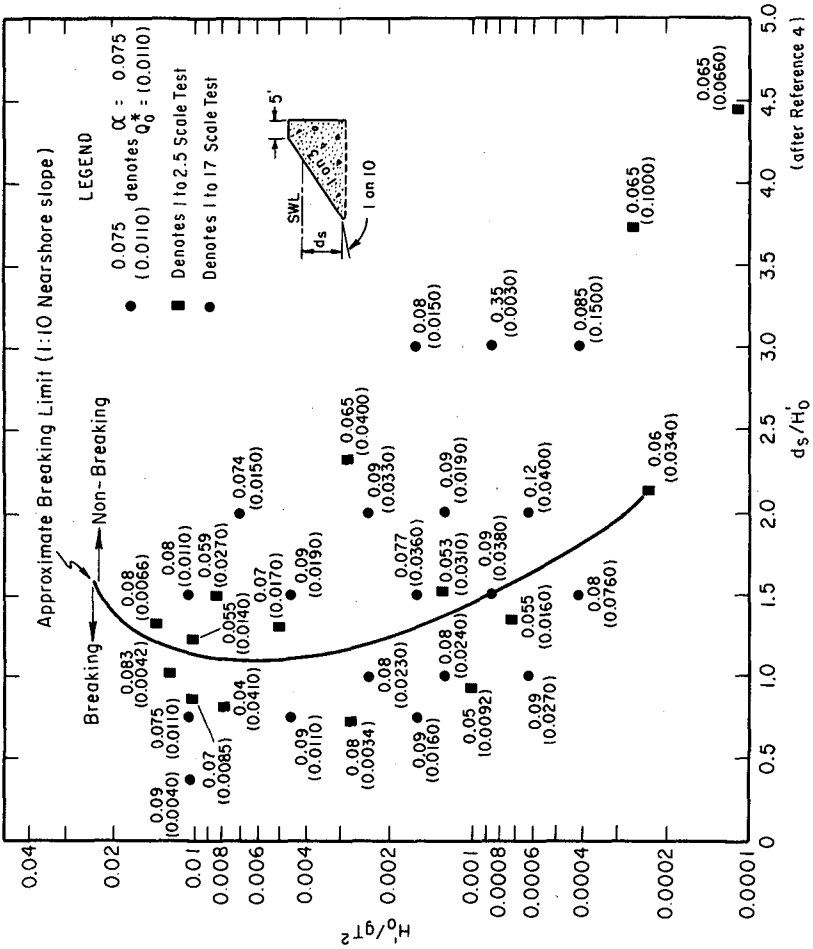


Figure 4. Variation of α and Q_0^* with incident wave conditions - initial data analysis, 1 on 3 smooth slope.

By substituting the dimensionless variables into equation 1 and solving for Q , one finds,

$$Q = \left(g Q_o^* H_o^3 \right)^{1/2} \exp \left\{ - \frac{0.217}{\alpha} \tanh^{-1} \left[\left(\frac{h-d}{R} \right) \right] \right\} \quad (2)$$

or equivalently, since $\tanh^{-1} \left(\frac{a}{b} \right) = \frac{1}{2} \log_e \left(\frac{b+a}{b-a} \right)$,

$$Q = \left(g Q_o^* H_o^3 \right)^{1/2} \exp \left\{ - \frac{0.217}{2\alpha} \log_e \left[\left(\frac{R+h-d}{R-h+d} \right) \right] \right\} \quad (3)$$

Either equation 2 or 3 can be used in conjunction with figures such as figure 4 to determine overtopping rates.

To evaluate the ability of equation 2 or 3 to predict the overtopping rates measured in the experiments, the values of α and Q_o^* as published in the SPM, were used with equation 2 and computed overtopping values compared with measured values. Table 2 presents the correlation coefficients found in the analysis. In general, agreement was excellent; the worst case was for the vertical wall data with $r = 0.980$. (The small number of data points for the recurved wall make the correlation analysis for that structure inconclusive).

Subsequent to publication of the SPM, further analysis of the data for smooth slopes was undertaken in an attempt to relate α and Q_o^* to incident wave conditions and structure slope. For a given slope, the variability of α with incident wave conditions was relatively small, suggesting that an average α could be used and the data reanalysed to establish the Q_o^* value that best fit the data for the average α . The average value, $\bar{\alpha}$, is shown on figure 5 for four smooth structure slopes with data obtained at three different scales.

The effect of decreasing model scale seems to result in a more rapid drop-off of the overtopping rate with increasing structure height. (see figure 2). This effect is also related to the value of R used to compute F/F_o , however, an expression relating $\bar{\alpha}$ with structure slope (smooth

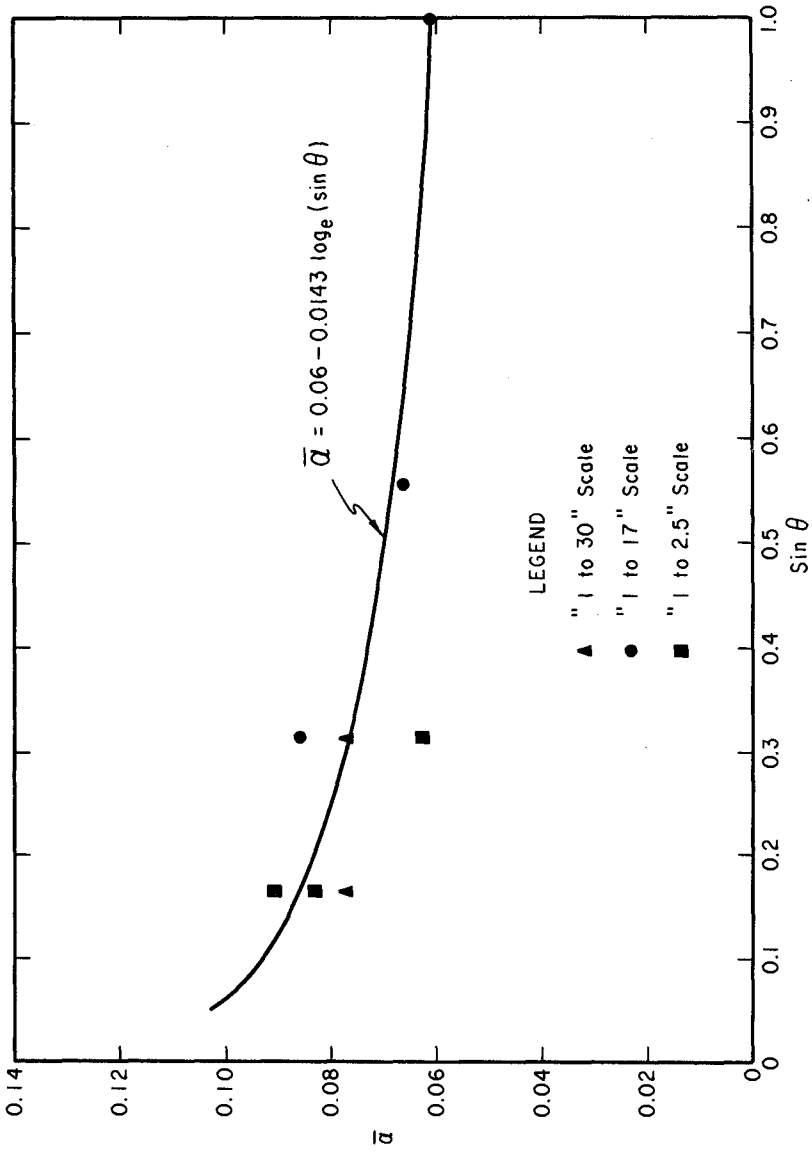


Figure 5. Average values of α as a function of structure slope.

slopes only) is given by,

$$\bar{\alpha} = 0.06 - 0.0143 \log_e (\sin \theta) \quad (4)$$

The data for smooth slopes was reanalysed using the values of α given by equation 4 for each slope and appropriate best fit values of Q_o^* selected. These Q_o^* values could then be compared with an expression calculated as an upper bound on Q_o^* .

Physically, the value of Q_o^* corresponds to the dimensionless quantity of water transported over the structure if the structure crest were at the SWL (i.e., $F/F_o = 0$). For waves that do not break before hitting a structure, the volume of water above the SWL in a wave profile will define an approximate upper limit for Q_o^* . Defining the volume of water above the SWL as V ,

$$V = \epsilon HL \quad (5)$$

where H = wave height, L = wave length and ϵ = a dimensionless factor depending on the shape of the wave profile. For a sinusoidal wave, $\epsilon = 1/(2\pi)$, while for various cnoidal wave profiles, ϵ can be obtained from figure 6 if the appropriate value of the modulus of the complete elliptic integral k^2 is known. (see Reference 5). Then, the overtopping rate is given by,

$$Q = \frac{V}{T} = \frac{\epsilon HL}{T} \quad (6)$$

Recalling that Q_o^* is defined by,

$$Q_o^* = \frac{Q^2}{gH_o^3}$$

and using linear wave theory expressions for H/H_o' and L/L_o' ,

$$Q_o^* = \frac{\left[\frac{\epsilon}{2\pi} \right]^2 \left[\frac{H'}{H_o} \right]^2 \tanh^2 \left[\frac{2\pi d}{L} \right]}{H_o'/gT^2} \quad (7)$$

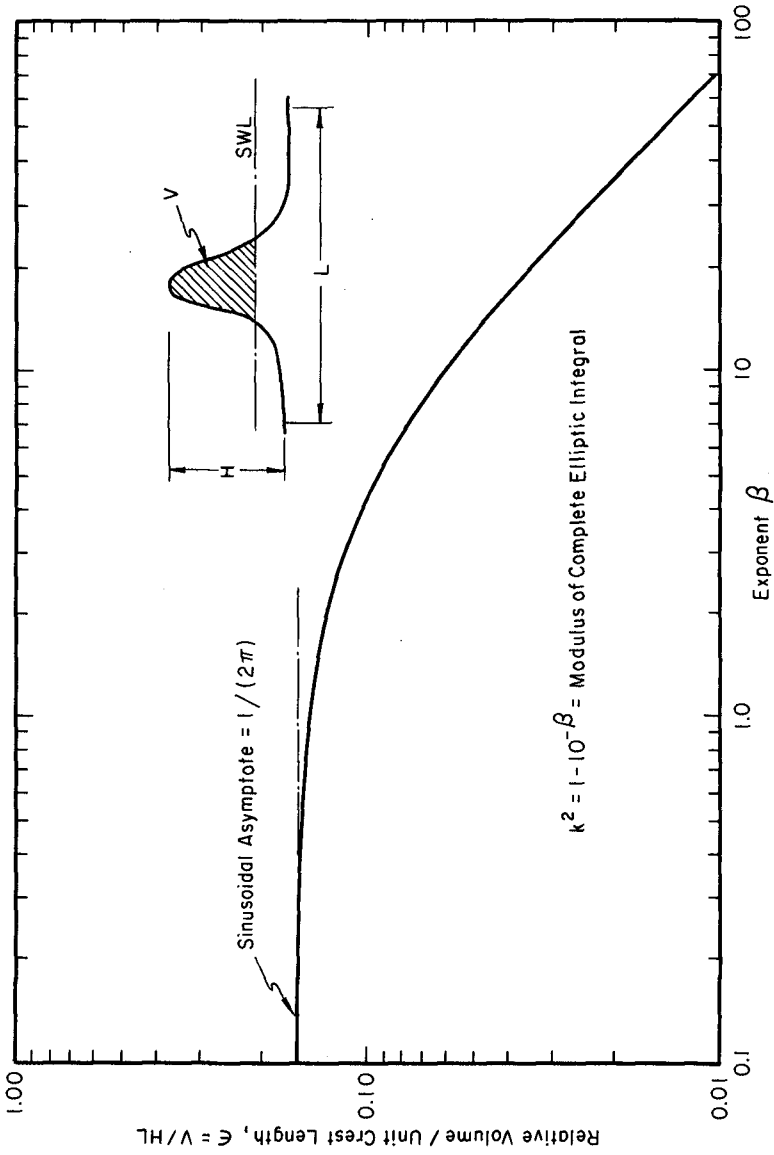


Figure 6. Dimensionless fluid volume per unit crest length above the SWL for cnoidal waves.

Equation 7 is plotted on figure 7 for both $\epsilon = 1/(2\pi)$ (labelled linear theory) and for ϵ values determined from cnoidal wave theory. Also shown on figure 7 are the Q_o^* values determined by the analysis for constant \bar{a} described above. In general, data from the 1 to 17 scale tests falls well below the cnoidal wave curves for all slopes for which data were available. Data from the 1 to 2 1/2 scale tests (squares on figure 7), however, are in general conformance with the cnoidal curves when $d_s/H_o' > 1.5$ (non breaking waves). Agreement appears best for long waves of small steepness. Steeper waves, and waves that break have considerably lower values of Q_o^* than predicted by the linear theory or cnoidal theory curves.

SCALE EFFECTS

Scale effects arise because of an inability to model all aspects of a phenomenon simultaneously, usually because of the limited range of fluid properties practically achievable; hence, to achieve both Froude and Reynolds' similarity in a model, the model fluid viscosity would have to vary as the scale ratio to the 3/2 power times the prototype fluid viscosity. Therefore, if as is usually the case, the same fluid is used in both model and prototype, only one similarity law can be satisfied at the expense of the other. If surface tension is also a factor, the problem is even more complex. Since the wave overtopping phenomenon is dominated by wave motion, a Froude modelling law governs; however, turbulent and viscous dissipation also influence overtopping; thus Reynolds' effects must also influence the phenomenon. If viscosity is included in the original dimensional analysis, a Reynolds' number arises from the analysis and serves as a "scale factor" or as a measure of scale effects. The formulation of the Reynolds' number adopted to investigate scale effects was, $R_e = H_o'^2/\nu T$.

The influence of R_e on an individual data set for which all other dimensionless variables are constant is shown in figure 2. Both sets of points on the figure are from what were termed 1 to 17 scale tests; however, the wave height in the one test was 10.76 cm (solid circles, $R_e =$

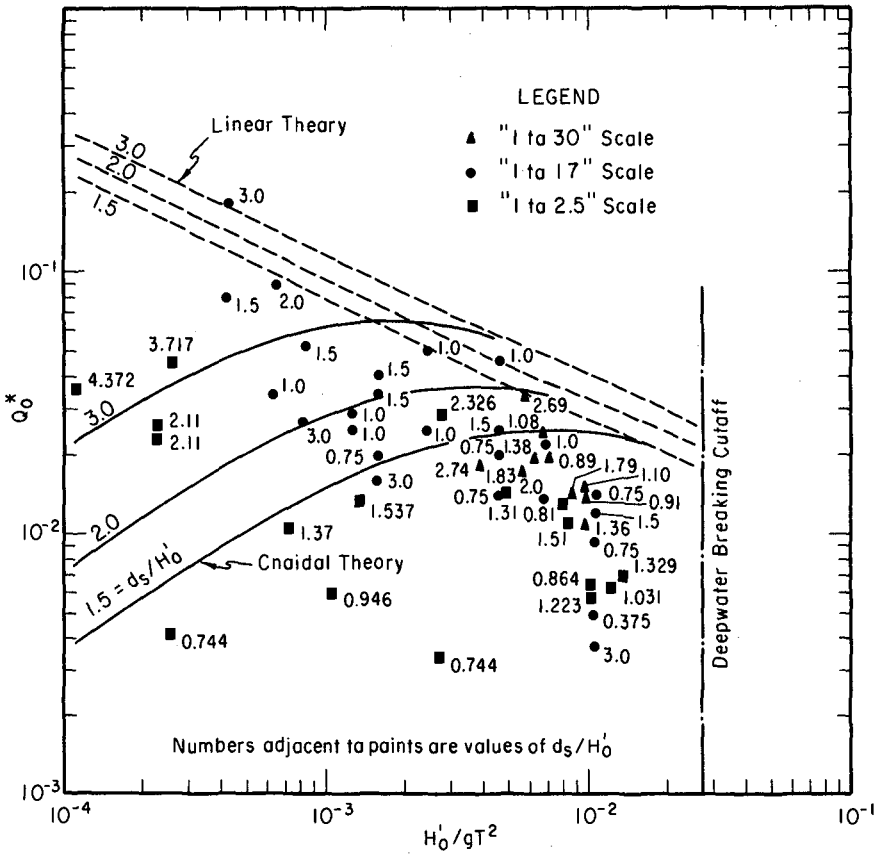


Figure 7. Comparison between measured and predicted values of Q_o^* (Based on reanalysis of data with constant $\alpha = 0.0765$, 1 on 3 smooth slope).

8030) while in the other test, the wave height was 21.52 cm (open circles, $R_e = 22700$). The greatest influence of scale appears when the structure crest is near the limit of wave runup (e.g. at the tail of the curve near $F/F_0 = (h-d_s)/R \rightarrow 1.0$). It is in this relatively thin layer of fluid that viscous effects can be expected to increase in importance. Inasmuch as it is the shape of the curve that is affected, it is the value of α that is, to a limited extent, influenced by scale. This slight dependence of α on scale is shown on figure 8. For the 1 on 3 slope, the SPM values of α are plotted against R_e for a broad range of d_s/H_0' and H_0'/gT^2 values. While it is difficult to draw firm conclusions regarding scale effects from figure 8 since d_s/H_0' and H_0'/gT^2 varied, there appears to be a decrease in α with increasing R_e . Note that the test designated as the 1 to 30 scale (triangular points) when characterized by $R_e = H_0'^2/vT$ as a "scale factor" are actually not at a smaller scale than the 1 to 17 scale tests (circles) since the smaller wave heights also had correspondingly smaller wave periods.

The effect of scale on Q_0^* appears to be negligible since no systematic variation of Q_0^* with R_e could be found. Since Q_0^* represents the dimensionless overtopping rate for a structure with its crest at the SWL, a relatively thick layer of flow, insensitive to viscous effects, tends to minimize any dependence of Q_0^* on R_e for smooth slopes.

In general, it appears that the primary influence of scale on the overtopping of smooth sloped structures is through scale effects manifest in the runup phenomenon. In the data analysis described herein, the actual measured or "correct" runup was used; consequently, the influence of scale effects on the runup was not considered. Other investigators have demonstrated that small scale runup experiments tend to significantly underpredict runup at larger scales. The observed effect of scale on overtopping itself appears to be relatively small; thus if the runup values used in equations 2 or 3 are corrected for scale effects, the predicted overtopping rates (using appropriate α and Q_0^* values) will provide good estimates of prototype overtopping rates.

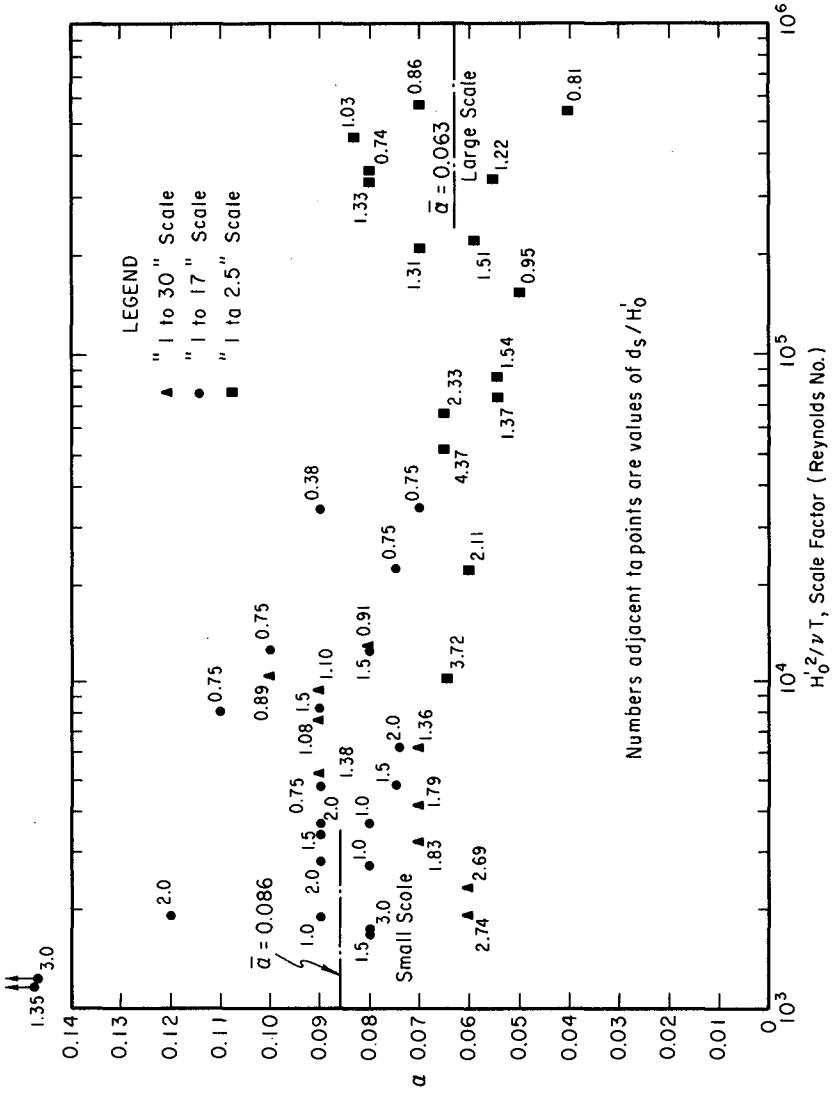


Figure 8. Variation of α with Reynolds' number (scale factor).

EXAMPLE

A levee is constructed with a 1 on 3 slope to just preclude overtopping by a wave 1.05 m high when the water depth at the structure toe is 1.5 m deep. If the design wave period is 5 sec, determine the rate at which water is carried over the structure by the design wave if a storm surge of 0.6 m occurs. The unrefracted deepwater wave height can be estimated from the linear theory; $H/H'_0 = 1.073$ for $d_s/L_0 = 0.0384$; hence, $H'_0 = 1.05/1.073 = 0.98$ m. From reference 4, the relative runup is $R/H'_0 = 2.2$, which, when corrected for scale effects, becomes $R/H'_0 = 2.2(1.12) = 2.464$. Thus, $R = 2.464(0.98) = 2.41$ m and the height of the structure crest above the bottom is $h = 1.5 + 2.41 = 3.91$ m. To determine the overtopping rate, calculate $d_s/H'_0 = (1.5 + .6)/0.98 = 2.14$ and $H'_0/gT^2 = 0.98/9.81(5)^2 = 0.0040$. From figure 4, interpolating, $\alpha = 0.08$ and $Q^*_0 = 0.024$. From equation 2,

$$Q = \left[(9.81)(0.024)(.98)^3 \right]^{1/2} \exp \left\{ \frac{0.217}{0.08} \tanh^{-1} \left[\frac{(3.91-2.1)}{2.41} \right] \right\}$$

$$Q = 0.471 \exp \left\{ -2.713 \tanh^{-1} (0.751) \right\}$$

$$Q = 0.471 \exp \left\{ -2.713 (.975) \right\}$$

$$Q = 0.0334 \text{ m}^3/\text{sec-m}$$

If the average α value (equation 4) had been used with the cnoidal curves of figure 7, the value of α would have been 0.0765 and $Q^*_0 = 0.033$. Using these values in equation 2 gives $Q = 0.0347 \text{ m}^3/\text{sec-m}$.

CONCLUSIONS

1. Equation 2 or 3 along with the empirically established values of α and Q^*_0 of reference 4 can be used to predict overtopping rates for various structure slopes and structure types if accurate predictions of runup are available.

2. Alternatively, for smooth slopes, if conservative (high) estimates are desired, equation 2 or 3 can be used with the average α given by equation 4, and the value of Q_o^* given by equation 7 with ϵ determined from figure 6. This corresponds to using the Q_o^* values given by the cnoidal curves of figure 7.

3. Scale effects in overtopping tests arise primarily in modifying the runup. If scale effect corrected values of runup are used in equations 2 or 3, the predicted overtopping values will have been corrected for most viscosity induced scale effects.

ACKNOWLEDGEMENTS

Much of the original data analysis discussed herein was performed while the author was in the Design Branch, Engineering Development Division at CERC under the general supervision of Robert A. Jachowski. Philip N. Stoa performed the initial data reduction and analysis and Harold McClung assisted in the computer runs associated with the analysis. Their assistance is gratefully acknowledged.

The research described herein was conducted under the Civil Works Program of the Corps of Engineers. Permission to publish this material is appreciated.

APPENDIX I - REFERENCES

- (1) Saville, Jr., T. and J.M. Caldwell, "Experimental Study of Wave Overtopping on Shore Structures," Proceedings, Minnesota International Hydraulics Convention, Minneapolis, Minnesota, September 1-4, 1953.
- (2) Saville, Jr., T. "Laboratory Data on Wave Runup and Overtopping on Shore Structures," Technical Memo #64, Beach Erosion Board, October, 1955.
- (3) US Army Coastal Engineering Research Center, "Shore Protection Planning and Design," Technical Report #4, Washington, D.C., 1966.
- (4) US Army Coastal Engineering Research Center, "Shore Protection Manual," US Government Printing Office Stock #0822-00077, Vols 1-3, 1973.
- (5) Wiegel, Robert L., Oceanographical Engineering Prentice-Hall, Inc, Englewood Cliffs, New Jersey, 1964.

CHAPTER 158

OVERTOPPING OF RUBBLE-MOUND BREAKWATERS BY IRREGULAR WAVES

by Yvon Ouellet* and Pierre Eubanks**

ABSTRACT

This paper describes the results of an experimental study on the effect of waves on rubble-mound breakwaters, wave transmission subsequent to wave overtopping, the stability of the three sides subjected to wave action and the effect of the breakwaters on waves. Two different rubble-mound breakwaters were tested, i. e. one with a rigid impermeable crest and the other with a flexible permeable crest. Tests were performed with both regular and irregular wave train systems. To obtain the simulated irregular wave trains, four theoretical spectra were chosen: Neumann, Bretschneider, Moskowitz, and Scott. Results obtained from tests with irregular wave trains were compared to those obtained from tests with regular wave trains. It was found that more information was obtained on the behaviour of the structure when it was submitted to the attack of irregular waves than when submitted to regular waves, and that the use of irregular wave trains gave more interesting results.

1. INTRODUCTION

In some cases, it is not necessary to protect completely the lee side of a breakwater and some overtopping is allowed. An example of this is the use of an overtopped breakwaters for the partial protection of the Pilgrim Nuclear Power Station⁽⁶⁾. Some research works have been made on the overtopping effect, of which the following ones have been consulted: Cross and Sollitt⁽³⁾, Hiroyoshi

* Associate professor, Department of Civil Engineering, Laval University

** Graduate student, Department of Civil Engineering, Laval University

and Tsugio⁽⁵⁾, Lording and Scott⁽⁶⁾, Ouellet⁽⁹⁾, Shiraishi, Numata and Endo⁽¹³⁾, Tsurata and Goda⁽¹⁵⁾, and the U.S. Corps of Engineers⁽¹⁶⁾. Most of the experimental works have been done under regular wave conditions.

It was then intended to establish an experimental programme to study the effect of irregular wave overtopping on structures as well as the effect of structures of waves. Although the stability of the structures and the wave overtopping are part of the study, the wave transmission subsequent to wave overtopping was mainly concerned.

2. THEORETICAL CONSIDERATIONS

Transmission Coefficient - The transmission of regular wave trains past a structure may be described in terms of the transmission coefficient, K_t , which is defined as the ratio of the height of the wave transmitted past the structure to the height of the wave incident on the structure

$$K_t = \frac{H_t}{H_i} \quad (1)$$

Transfer Function - When a structure is submitted to the attack of irregular trains, the characteristics are best described in terms of its transfer function⁽¹⁾. If $x(t)$ and $y(t)$ are, respectively, the incident and transmitted wave profiles, and $X(f)$ and $Y(f)$ are, respectively, the Fourier transforms of $x(t)$ and $y(t)$, then the transfer function may be defined as:

$$H(f) = \frac{Y(f)}{X(f)} \quad (2)$$

where $X(f)$ and $Y(f)$ are respectively the Fourier transform of $x(t)$ and $y(t)$:

$$\left. \begin{aligned} X(f) &= \int_{-\infty}^{\infty} x(t) e^{-i2\pi ft} dt \\ Y(f) &= \int_{-\infty}^{\infty} y(t) e^{-i2\pi ft} dt \end{aligned} \right\} \quad (3)$$

in which f = the frequency, in Hertz. In fact, we know that the transfer function is the Fourier transform of the system to a unit impulse.

In practice, however, the following relation is used to determine the transfer function:

$$H(f) = \frac{S_{yx}(f)}{S_{xx}(f)} = \frac{X^*(f) Y(f)}{X^*(f) X(f)} \quad (4)$$

in which $S_{yx}(f) = Y(f) X^*(f)$ represents the cross power spectral density function of $y(t)$ with respect to $x(t)$, $S_{xx}(f) = X(f) X^*(f)$ represents the auto power spectral density function of $x(t)$, and $X^*(f)$ represents the complex conjugate of $X(f)$. This procedure makes it possible to retain the phase information without the need of having to synchronize the two signals.

Coherence Function - The preceding equations are based upon linear systems. Even if, in practice, linear systems do rarely occur, the use of the constant parameter linear system is often justified. In order to judge the applicability of the linear model it is possible to estimate the accuracy of the transfer function by means of the coherence function

$$\gamma_{xy}^2(f) = \frac{|S_{xy}|^2 / S_{xx}^2}{S_{yy} S_{xx}} = \frac{S_{xy} S_{xy}^*}{S_{yy} S_{xx}} = \frac{|S_{xy}|^2}{S_{yy} S_{xx}} \quad (5)$$

which represents the ratio of the magnitudes of the response function obtained, respectively from the cross-spectral density function and from the input and output density spectra. The coherency for an ideal system with no noise in measured input and output is unity. The presence of noise or the nonlinearity of the system reduces the coherence function. The coherence function is then an indicator of the system behavior in showing those parts of the output not correlated with the input over the frequency range.

3. TEST PROCEDURE

Wave Flume - A sketch of the wave tank layout is shown in Fig. 1. The channel is 111 ft (36 m) long, 6 ft (1.86 m) wide, and 4 ft (1.3 m) deep. The distance between the wave paddle and the model breakwater (center of crest) is about 65 ft (21 m).

The wave generator consists of a paddle operated by a hydraulic piston, the movements of which are controlled by an electric signal from a programming device capable of generating regular and irregular wave trains. A wave filter which absorbs, to some extent, waves reflected by the model is in front of the wave generator.

The flume was divided into two sections, i.e., the front one of 3.5 ft (1.1 m) and the back one of 2.5 ft (0.76 m). The front section was used as the test section whereas the back section was used to measure the incident wave characteristics. This arrangement made possible the measurement of the incident, reflected and transmitted wave profiles.

Wave heights and periods were measured with resistance type wave gages. A first gage, located in the smaller section of the flume where reflection is almost eliminated by a wave absorber placed at the end of the flume, was used to measure the incident wave characteristics. A second gage, placed behind the structure in the larger section of the flume measured the transmitted wave characteristics, while a third movable gage, placed in front of the structure, measured the incident and reflected wave characteristics. Measurements taken on the third gage, which also included the envelope of the incident and reflected waves, were only used to perform some verifications in cases of experiments with regular waves.

Wave data were analysed using a Fourier Analyzer model HP-5451A, a product of Hewlett Packard Company⁽⁴⁾. Fig. 2 shows an overview of the analyzer system

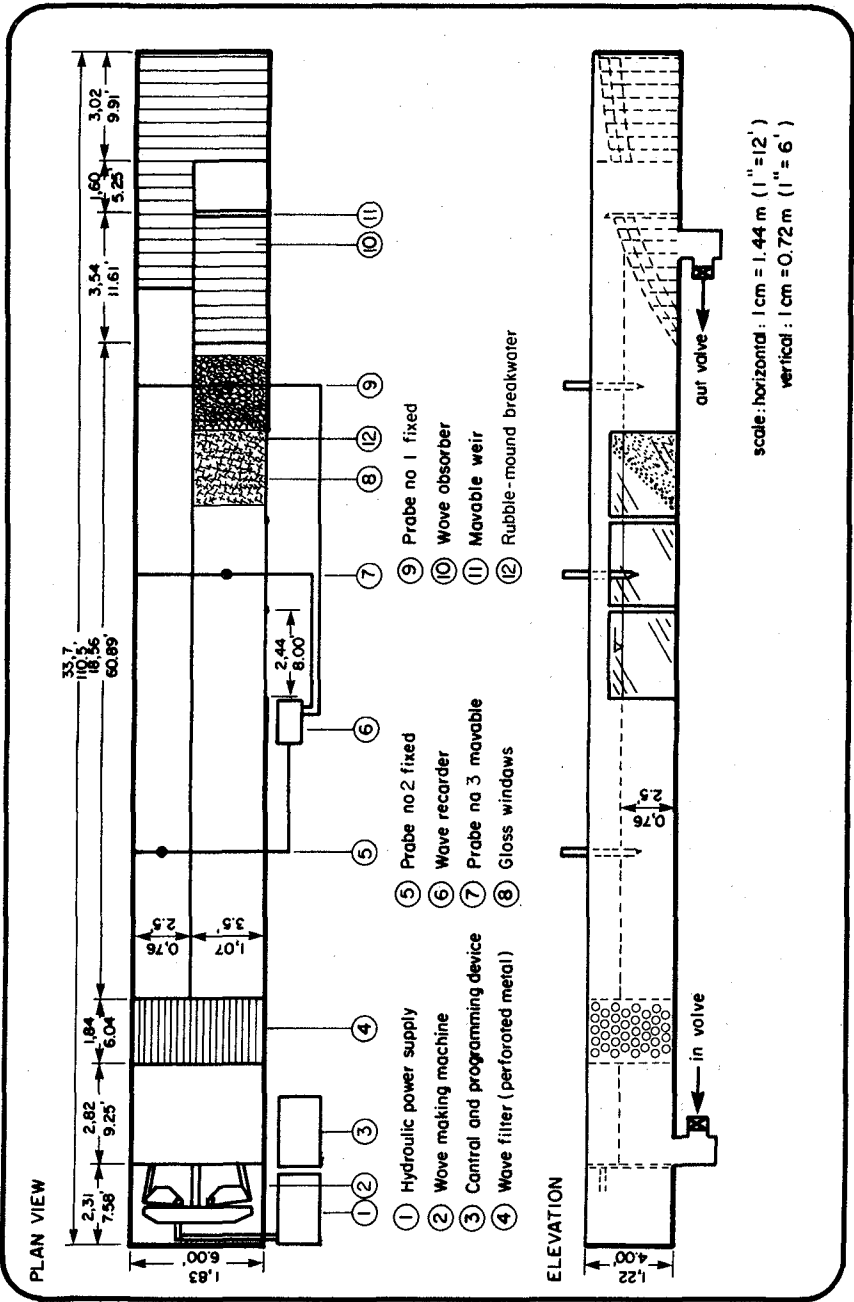


Fig. 1 — SKETCH OF WAVE TANK LAYOUT.

and details of its operation are available in user manuals furnished with the instruments.



Fig.2—FOURIER ANALYSER SYSTEM.

Description of Models - A simplified sketch of the cross-section of the two models studied is shown in Fig. 3. The first model consists of a rubble-mound breakwater formed by two layers of dolos armor units seaside, two layers of rubble on the lee side, and a thick concrete cap crest. The second structure is similar to the first differing only at the crest; the crest of the latter is formed by two layers of dolos armor units. Because both models were placed behind observation windows, the observation of certain characteristics, such as overtopping height, was made possible.

Test Conditions - In order to verify the models and to make possible further comparisons, both models were first tested under regular wave attack. All tests were carried out at four different water depths varying both the wave height and

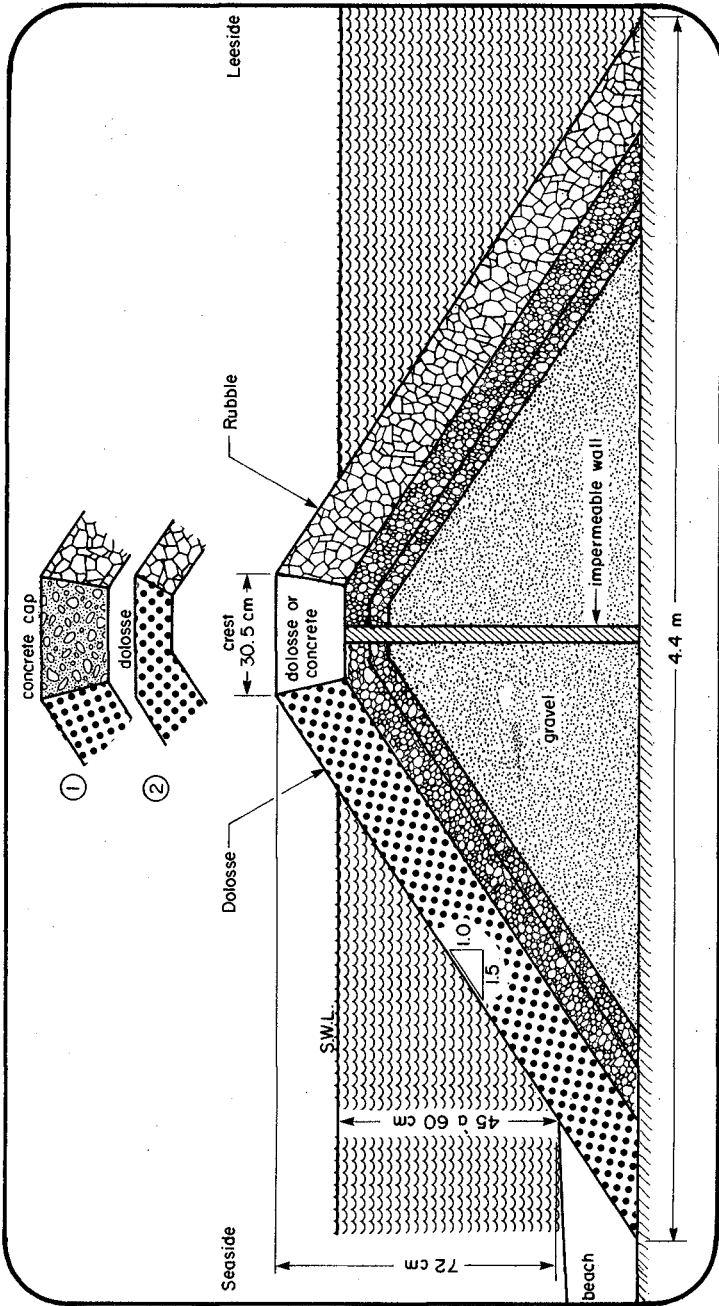


Fig. 3 — SKETCH OF RUBBLE-MOUND BREAKWATER.

the frequency. Typical results of these tests are shown in Fig. 4 and 5, respectively for the concrete cap breakwater and the breakwater covered with dolosse. The transmission coefficient, expressed as a percentage, is plotted versus the frequency. The transmission coefficient was also represented as a function of the relative depth, but for the present paper only the frequency is used.

The two models were also submitted to the attack of irregular wave trains which were produced by adjusting the variable amplitudes and phases of the 20 different harmonic components of the programming device. As in the case of regular wave tests, the water depth varied from 45 cm to 60 cm. In order to make even further comparison possible, four different types of wave spectra were simulated on the model on a scale of 1:16. These consist of Neumann⁽⁸⁾, Bretschneider⁽²⁾, Moskowitz^(7,11) and Scott⁽¹²⁾ which are shown in Fig. 6, with the corresponding wind velocities used. The related equations are the same as those in previous studies^(9,10), from which simulated spectra were obtained (Fig. 7).

4. TESTS RESULTS AND ANALYSIS

Fig. 8 and 9 show typical examples of recorded surface profiles of incident and transmitted waves, and the results of the spectral analysis of the above signals in the case of a simulated Neumann spectrum. Fig. 8 corresponds to the concrete cap breakwater with the depth $h = 60$ cm and the simulated significant wave height $H_s = 4.25$ m (13 ft). Fig. 9, on the other hand, corresponds to the other structure for the same values of h and H_s .

By means of spectral analysis^(1,14), the following results were obtained and plotted for all tests involving irregular wave trains: the incident wave spectrum, S_I , from which the significant wave height may be obtained; the transmitted wave spectrum, S_T , from which the transmitted significant wave height

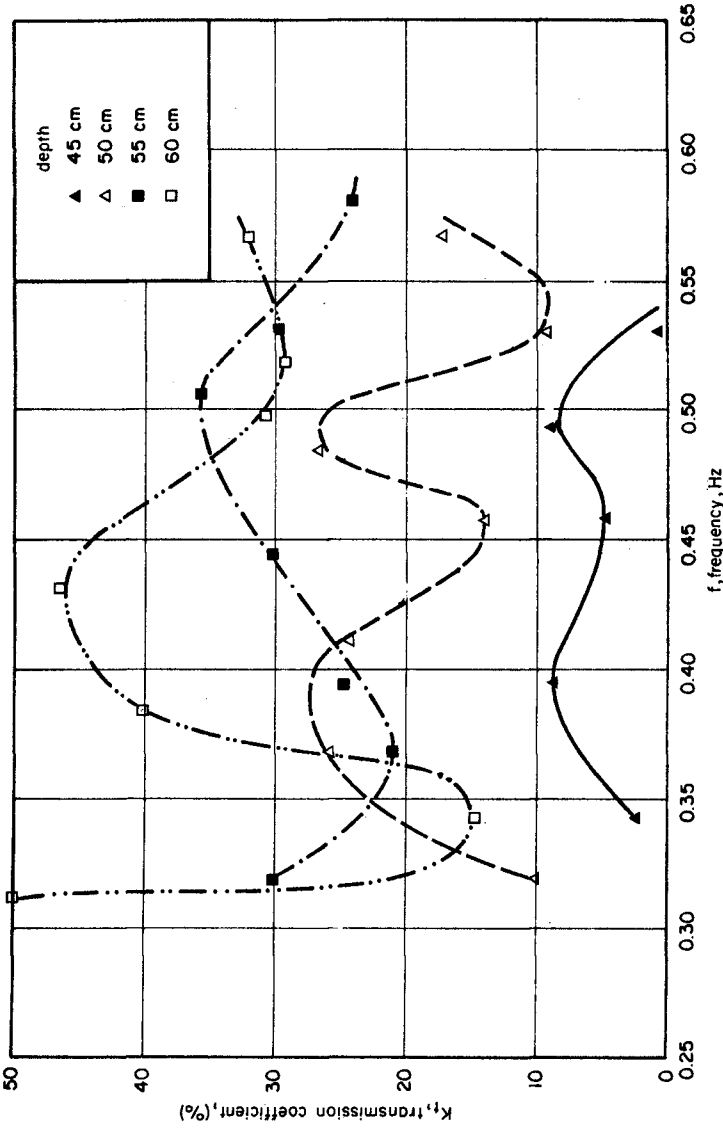


Fig. 4— TRANSMISSION COEFFICIENT AS A FUNCTION OF FREQUENCY, (REGULAR WAVES).
(amplitude: SKT 7, crest: concrete)

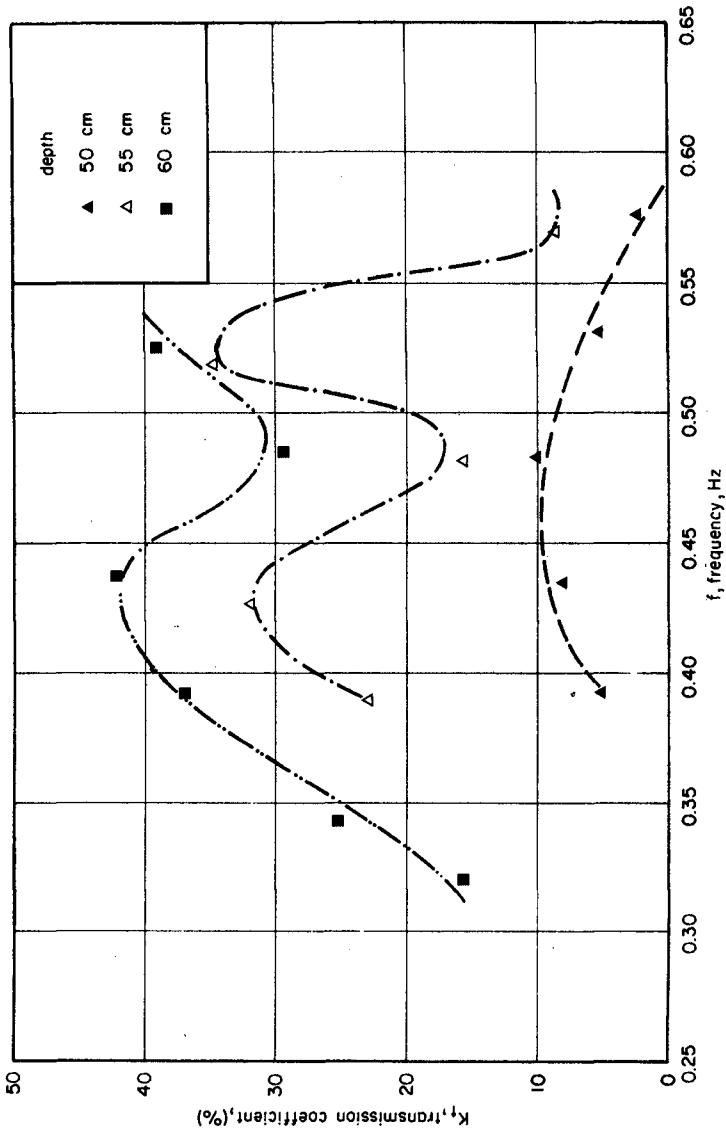


Fig. 5—TRANSMISSION COEFFICIENT AS A FUNCTION OF FREQUENCY, (REGULAR WAVES).
(amplitude: SKT 7, crest : dolosse)

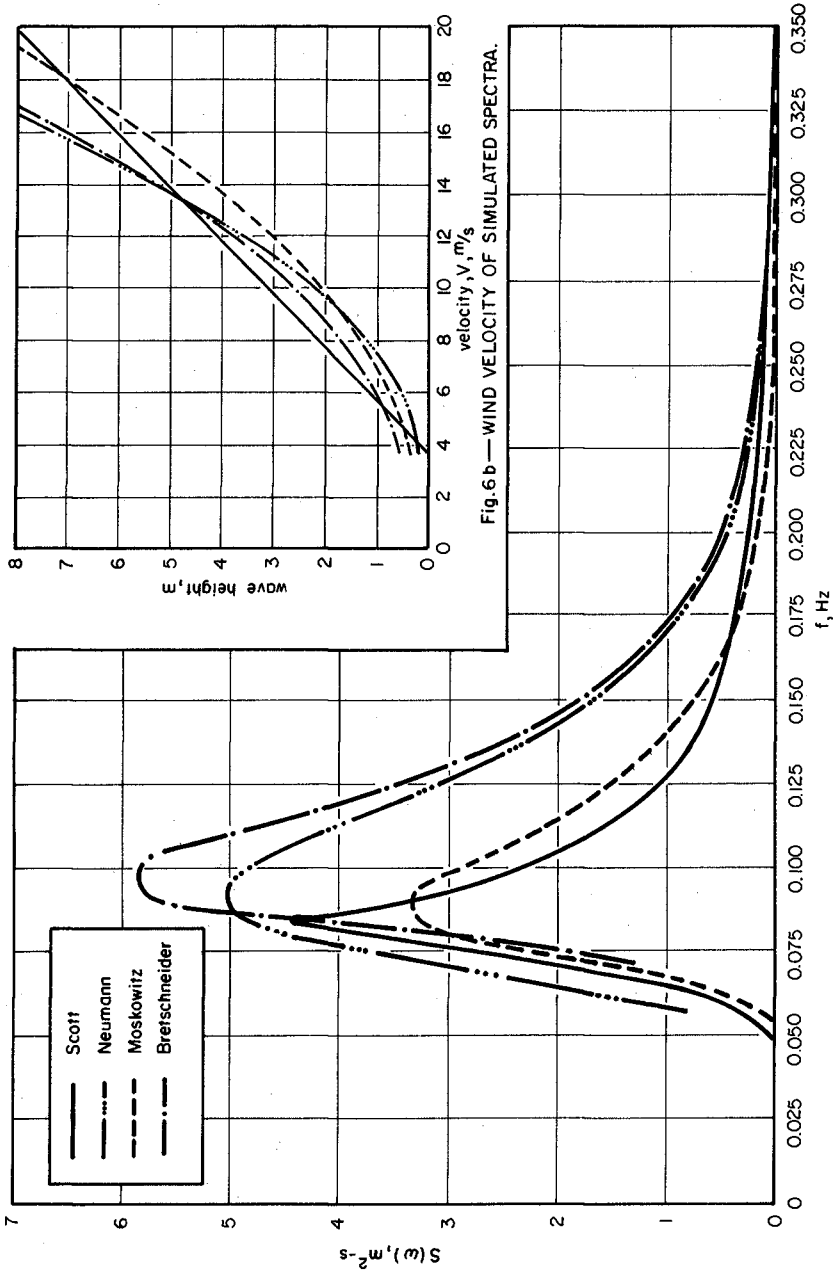


Fig. 6 b — WIND VELOCITY OF SIMULATED SPECTRA.

Fig. 6 a — THEORETICAL WAVE SPECTRA.

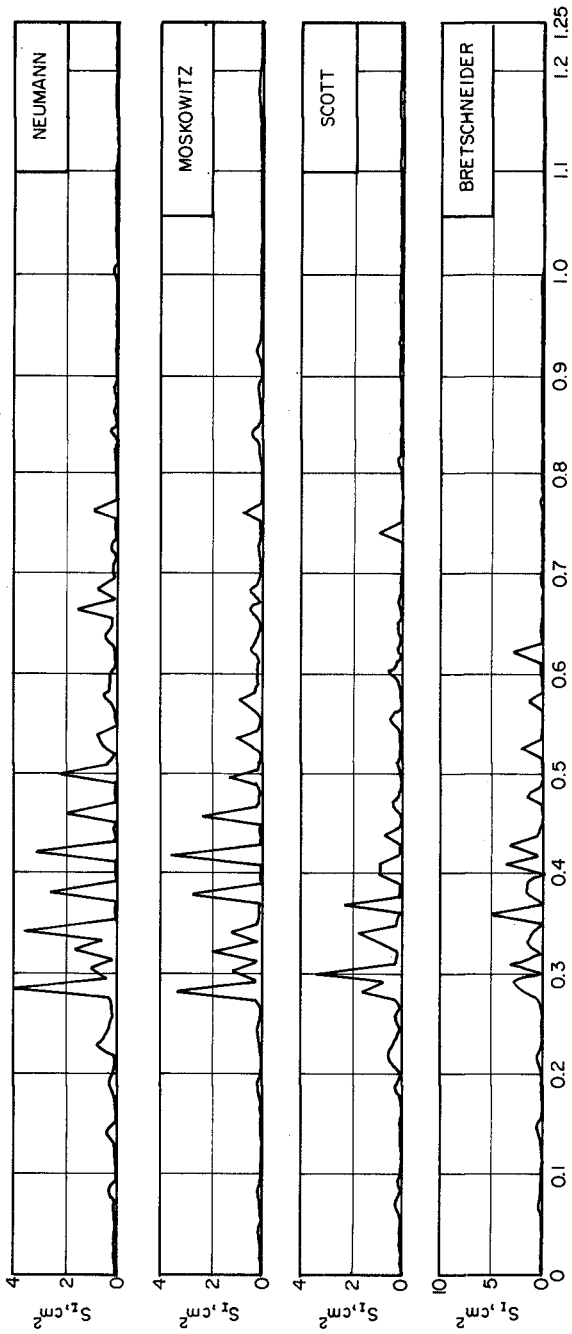


Fig. 7 — SIMULATED WAVE SPECTRA.

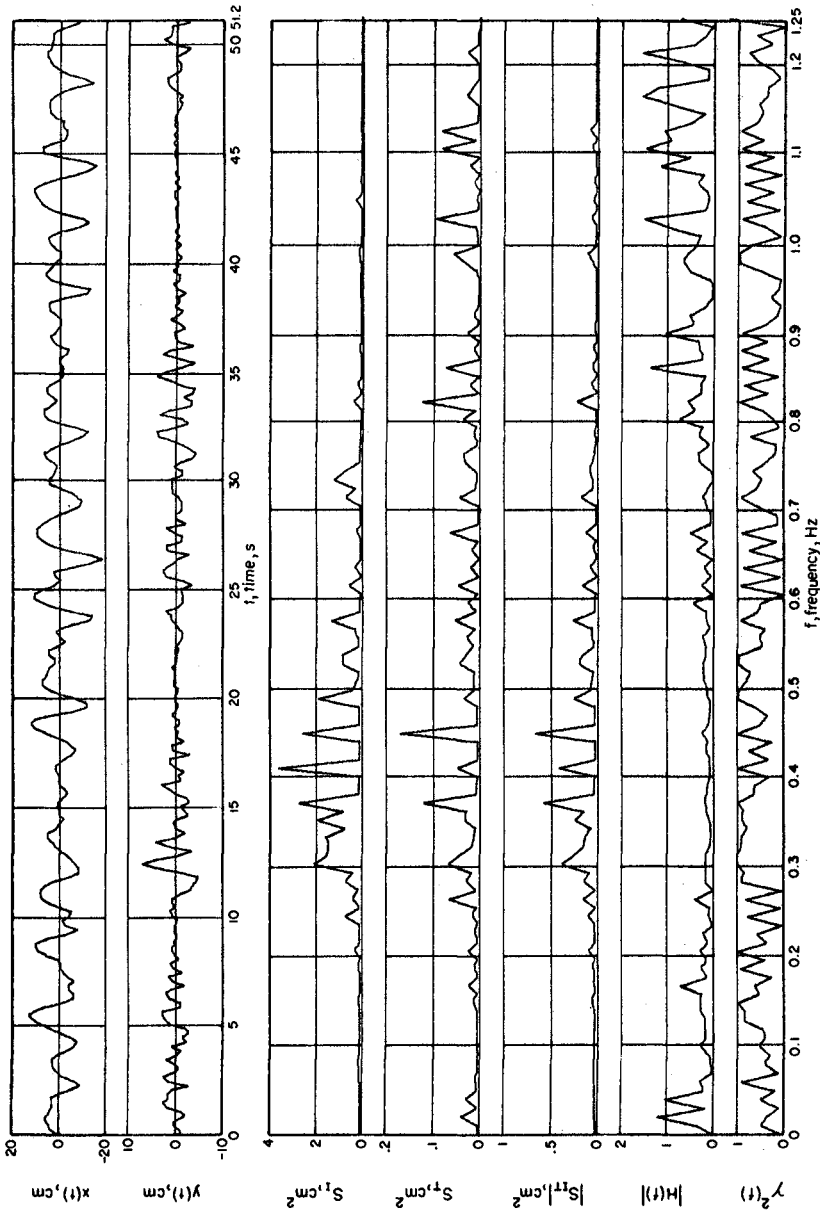


Fig. 8—IRREGULAR WAVES: NEUMANN SPECTRUM.
N-13-60-CB

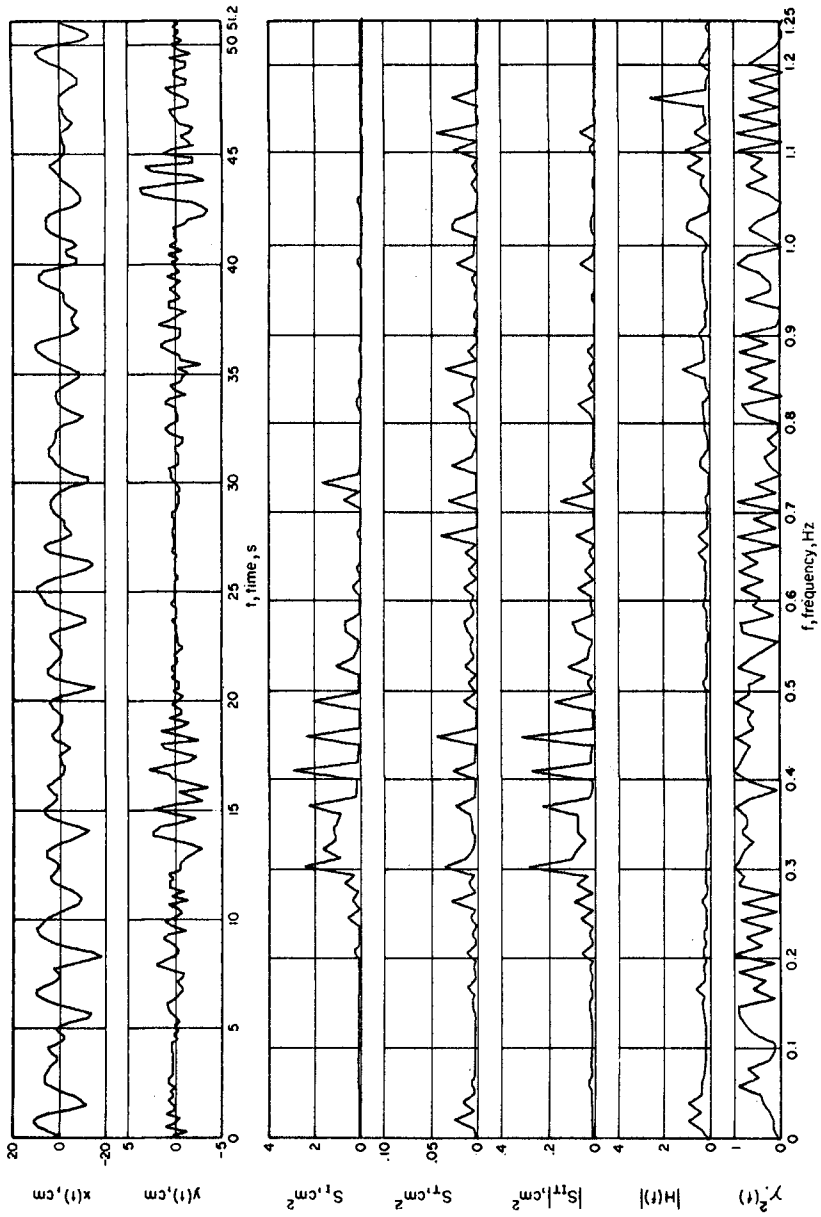


Fig. 9 ——— IRREGULAR WAVES: NEUMANN SPECTRUM.
N-13-60-D

may be obtained; the magnitude of the cross power spectrum, $|S_{IT}|$; the magnitude of the transfer function, $|H(f)|$; and the coherence function $\gamma^2(f)$. Both structures were submitted to the same tests under similar conditions using all four simulated wave spectra. The results were analyzed individually and then compared to each other as well as to regular wave tests. Under the test conditions examined, the following results were found to be the most interesting:

1° Single test analysis

- a) The incident wave energy, S_I , is much greater than the transmitted wave energy, S_T ; consequently the incident significant wave height is also greater than the transmitted significant wave height.
- b) The magnitude of the transfer function, $|H(f)|$, is weak, showing there is very little energy transmitted over the structure.
- c) At frequencies containing energy the coherence function γ^2 generally varies from 0.8 to 1.0, meaning the output signal is affected very little by the presence of noise or the nonlinearity of the signal.

2° Comparison between spectra

- a) When the incident energy spectra were reverted to significant wave heights it was found that only the Neumann and Bretschneider spectra gave values corresponding to the simulated wave height; Moskowitz and Scott with smaller energies gave wave heights about 1 m smaller than the simulated wave height.
- b) For equivalent values of incident energy disregarding the actual wave height as compared to the simulated height, it was found that the transmitted energy varies very little between different spectra.

3° Comparison between structures

- a) The concrete cap breakwater is much more stable than the dolos

crest breakwater, yet the former allows more overtopping than the latter.

- b) Damage tends to occur at almost the same overtopping wave heights for both structures.

4° Comparison with regular wave tests

- a) Observations allowed to establish that 3 or 5 out of every 20 waves would overtop the structure with irregular waves whereas all 20 would overtop the structure with regular waves.
- b) Damage occurs at a faster rate with regular waves than with irregular waves.
- c) The ratio $H_t/H_i(K_t)$ was as high as 50% whereas the ratio H_{ts}/H_{is} only reached 28%.

Figs. 10a and 10b show the relationship between significant wave height and overtopping wave height for all four spectra respectively for the concrete and dolos crest breakwater in 60 cm depth. The same relationship was also found in the case of regular wave trains as shown in Fig. 11a, for the concrete cap and in Fig. 11b for the dolos crest breakwater. Other depth curves have been added on these figures but without the measured points in order not to overcharge the figures. The dispersion of the points is approximately the same for the ones given.

The slope of the curves are approximately the same for the different water depths the difference being only in the ordinate at the origin. Furthermore, visual observations allowed to establish at which overtopping height the breakwater was damaged or destroyed completely. These observations were made for all three exposed faces. Having established that an incident wave height and an equivalent significant wave height have almost identical overtopping heights,

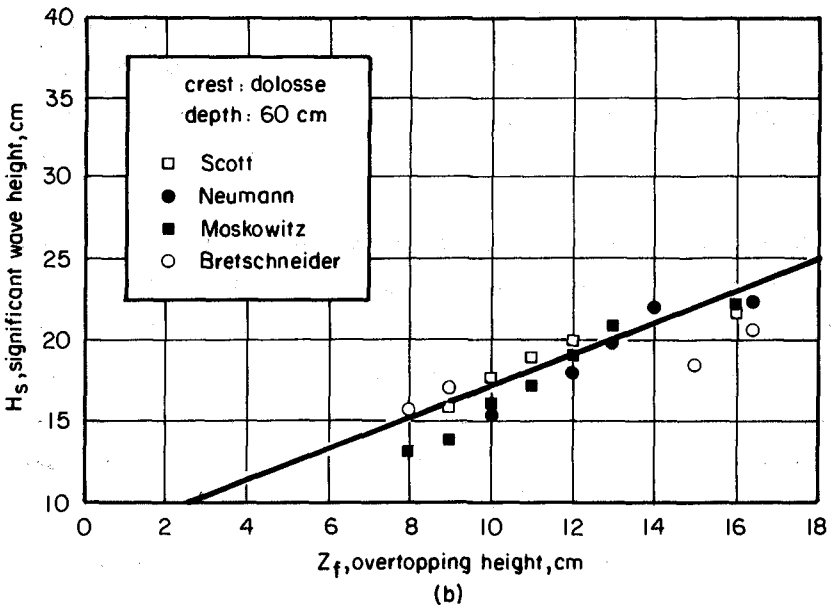
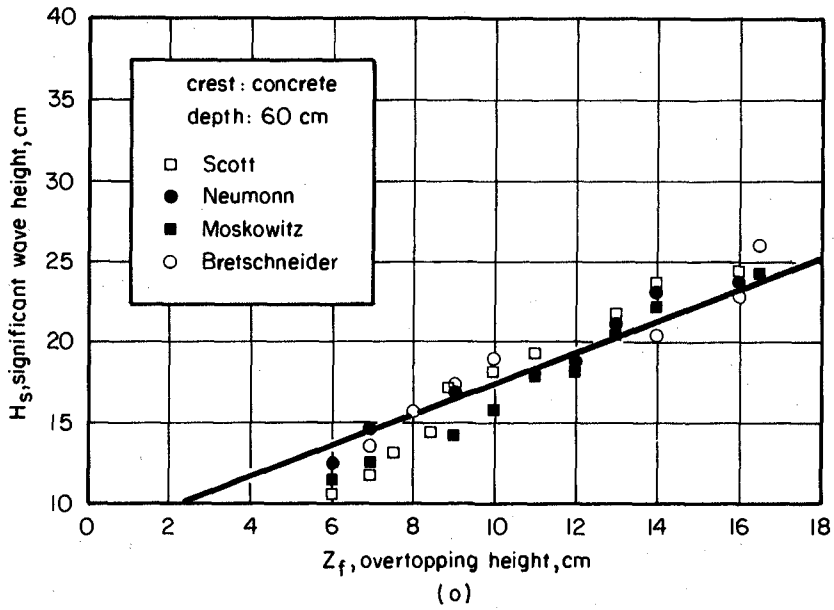


Fig.10 — SIGNIFICANT WAVE HEIGHT VS OVERTOPPING HEIGHT, IRREGULAR WAVES.

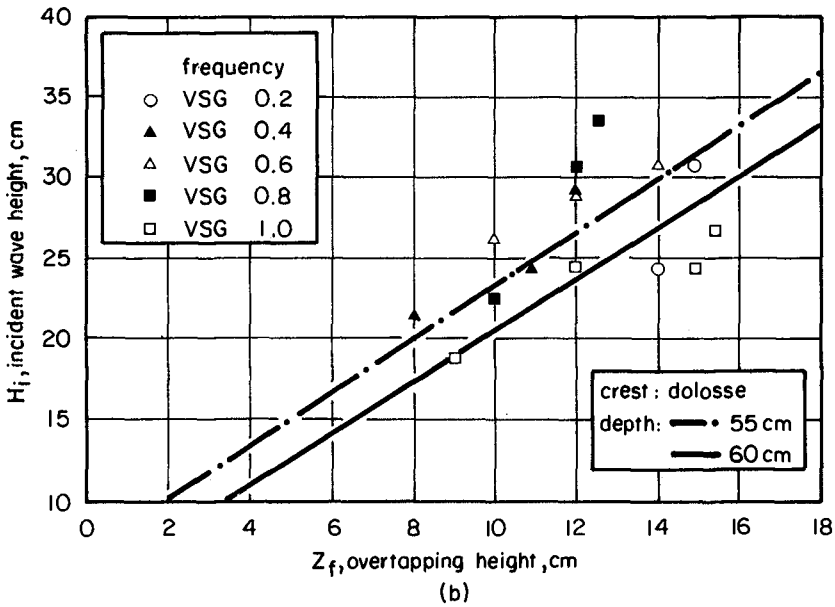
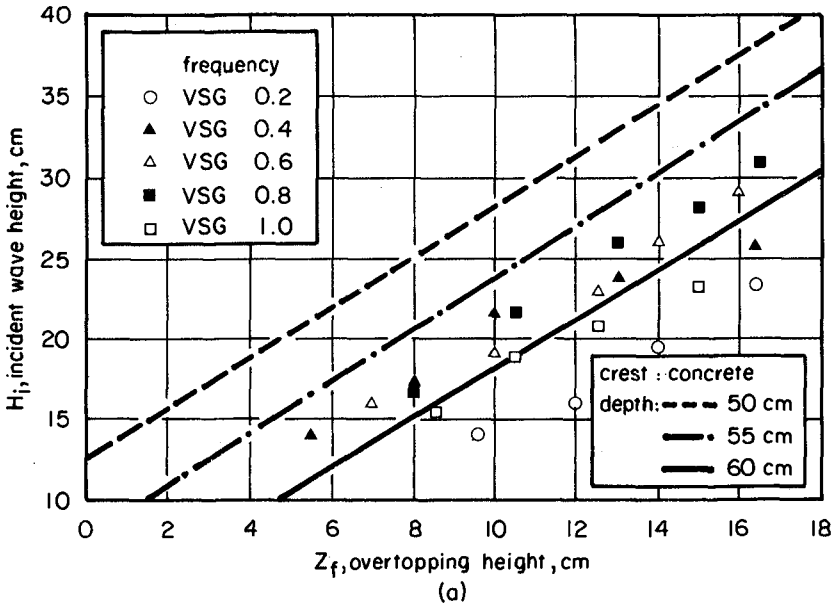


Fig.11 — WAVE HEIGHT VS OVERTOPPING HEIGHT, REGULAR WAVES.

it would be possible to predict at which significant wave height the structure will be damaged, using only regular wave trains, the main difference being the quantity of damage.

A comparison between the results obtained for the concrete cap breakwater and the dolos protected breakwater shows that on one hand the former is much more stable than the latter, whereas, on the other hand, the concrete cap structure allows more energy to be transmitted than the dolos protected structure. These differences are primarily due to the difference in the shape of their respective crests.

In order to estimate the relative efficiency of either structure, the ratio of the transmitted significant wave height to the incident significant wave height has been calculated. The characteristic wave height,

$$H_{m_0} = 4\sigma = \sqrt{\int_0^{\infty} S(f) df} \quad (6)$$

σ^2 being the variance of the process, has been used to represent the significant wave height from which the ratio of the transmitted wave height to the incident wave height has been determined. From the results it has been found that, for the concrete cap breakwater, the maximum values of this ratio vary between 0.06 [h = 45 cm ; H = 4.25 m Bretschneider spectrum] and 0.28 [h = 60 cm ; H = 4.25 m ; Neumann spectrum] while the corresponding values for the dolos crested breakwater vary from 0.04 [h = 45 cm ; H = 4.25 m ; Bretschneider spectrum] to 0.19 [h = 60 cm ; H = 4.25 m ; Neumann spectrum]. It should be remembered, however, that this parameter does not take into account the frequency which is an important factor in such a study.

5. CONCLUSIONS

The described tests have shown that the response of a structure gives more information when submitted to the attack of irregular waves than regular

waves. However, the zone of damage caused by given overtopping wave heights is the same regardless of the type of waves used, which implies the predictability of damages. Furthermore, such parameters as the quantity of damage, the rate of wave overtopping, and the total energy of overtopping, and the total energy of overtopping waves are always of greater magnitude when the structure is submitted to regular wave trains.

All the tests with regular waves have been carried out varying the frequency by a small amount at each step. It was noticed that, for one reason or another, the transmission coefficient curves show an oscillating tendency as a function of frequency. Furthermore, the same tests pointed out that the incident wave height curves versus frequency are also oscillating. However, the fact that the incident wave heights may oscillate does not explain entirely the transmission coefficient oscillation; this is subject to further research.

The magnitude of the transfer function shows how the two breakwaters examined are efficient when submitted to irregular wave tests. From the results obtained it can be seen that these breakwaters will, beyond the slightest doubt, prevent or reduce to a minimum energy transmission from the seaside to the lee-side of the structure. Further, to support this affirmation, it has already been seen that the maximum ratio of transmitted significant wave height to incident significant wave height was 0.28.

Results have also shown that the structures are quite stable up to 12 cm (1.9 m prototype) of wave overtopping, major damage begins to occur between 12 and 14 cm of wave overtopping depending on the structure, and total destruction occurs for overtopping heights beyond 16 cm (2.6 m prototype).

REFERENCES

1. BATH, M., "Spectral Analysis in Geophysics", Elsevier Scientific Publishing Company, Amsterdam, Oxford, New York, 1974.
2. BRETSCHNEIDER, C.L., "Revisions in Wave Forecasting: Deep and Shallow Water", Proc. 6th Conference on Coastal Engineering, Houston, Council on Wave Research, University of California, 1958.
3. CROSS, R.H., and SOLLITT, C.K., "Wave Transmission by Overtopping", Journal of the Waterways, Harbors and Coastal Engineering Division, Proceedings of the American Society of Civil Engineers, pp. 295-308, August 1972.
4. HEWLETT-PACKARD, "System Operating Manual", Fourier Analyser System, Hewlett-Packard, April 1972.
5. HIROYOSHI, Shi-igai and TSUGIO, Kono, "Analytical Approach on Wave Overtopping on Levees", Coastal Engineering, pp. 563-573.
6. LORDINC, P.T. and SCOTT, J.R., "Armor Stability of Overtopped Breakwater", Journal of the Waterways, Harbors and Coastal Engineering Division, Proc. ASCE WW2, May 1971.
7. MOSKOWITZ, L., "Estimates of the power Spectrums for Fully Developed Seas for Wind Speeds of 20 to 40 Knots" Journal of Geophysical Research 69, no. 24, pp. 5161-5180, December 1964.
8. NEUMANN, G., "On Ocean Wave Spectra and a New Method of Forecasting Wind-Generated Seas", U.S. Army Corps of Engineers Beach Erosion Board, Tech. Memo. 43, December 1943.
9. OUELETT, Y., "Effect of Irregular Wave Trains on Rubble Mound Breakwaters", Journal of the Waterways, Harbors and Coastal Engineering Division, Proc. ASCE, vol. 98, WW1, pp. 1-14, Feb. 1972.
10. OUELETT, Y. and MORIN, Y., "Effect of Structures on Irregular Waves Compared to Regular Waves" Journal of the Waterways, Harbors and Coastal Engineering Division, Vol. 101, no. WW3, pp. 231-246, August 1975.
11. PIERSON, W.J. and MOSKOWITZ, L., "A Proposed Spectral Form for Fully Developed Wind Seas Based on the Similarity Theory of S.A. Kitaigorodskii", Journal of Geophysical Research 69, no. 24, pp. 5181-5190, December 1964.
12. SCOTT, J.R., "A Sea Spectrum for Model Tests and Longterm Ship Prediction", Journal of Ship Research, December 1965.
13. SHIRAIISHI, N., NUMATA, A. and ENDO, T., "On the Effect of Armour Block Facing on the Quantity of Wave Overtopping", Coastal Engineering, pp. 853-869.
14. THORNTON, E.B. and CALHOUN, R.J., "Spectral Resolution of Breakwater Reflected Waves", Journal of the Waterways, Harbors and Coastal Engineering Division, Proc. ASCE, WW4, November 1972.
15. TSURATA, S. and GODA, Y., "Expected Discharge of Irregular Wave Overtopping", Coastal Engineering, pp. 833-852.
16. U.S. CORPS OF ENGINEERS, "Shore Protection Manual" U.S. Army Engineering Research Center, Department of the Army, Corps of Engineers. 1973.

CHAPTER 159

FLOATING BREAKWATER PERFORMANCE

by

Bruce H. Adee*

INTRODUCTION

The Pacific Northwestern United States contains large areas of protected waters with abundant recreational boating opportunities. The area also supports many commercial fishermen who use small boats in their fishing operations. As a result, there is a large demand for sheltered moorage for all these vessels. Traditionally, this demand has been accommodated by constructing rubble-mound breakwaters for marina protection. At present, most of the sites where rubble-mound breakwater construction is economically feasible have been used. Conditions at many of the remaining areas for marina development are unsuitable for traditional techniques of marina construction. In general, the cost is too great because the water is too deep, or the environmental degradation resulting from marina development is unacceptable. To satisfy the demand for moorage, while at the same time overcoming the other restrictions, floating breakwaters have been employed at many new marina facilities.

In order to optimize the configuration of floating breakwaters and to overcome the problems which have been encountered with their use, the University of Washington has undertaken a continuing program of research. The aim of this research has been to monitor the performance of existing breakwaters and to develop a theoretical model to predict performance. Using the theoretical model supplemented with appropriate model-scale tests, a series of parametric variations will be tested to determine the effects of these variations on breakwater performance.

At present, several comparisons of the theory with model tests and full-scale performance have been reported by Adee (1975a, 1975b, 1976). This report is a continuation of this effort incorporating data obtained at the Friday Harbor, Washington floating breakwater.

FLOATING BREAKWATER OPERATION

A floating breakwater is illustrated in Figure 1. An incident wave approaches the breakwater. Part of the energy contained in the incident wave is reflected, part passes beneath the breakwater, and some is lost through dissipation. Another part of the incident wave energy excites the motions of the breakwater. These motions are restrained by the mooring system. The oscillating breakwater in turn generates waves which travel away from the breakwater in the direction of the reflected and transmitted waves. The total transmitted wave is the sum of the component which passes beneath the breakwater and the components generated by the breakwater

* Associate Professor, Department of Mechanical Engineering,
University of Washington, Seattle, Washington

motions. The total reflected wave is composed similarly.

To assess the performance of a floating breakwater one single parameter which has been widely used is the transmission coefficient. This is found by dividing the transmitted wave height by the incident wave height. In conducting field experiments or in developing theoretical models the variables affecting performance which need to be measured include:

- (1) Total transmitted and reflected waves (in theoretical predictions the individual components should be predicted).
- (2) Wave forces on the breakwater.
- (3) Motions of the breakwater.
- (4) Forces on the mooring lines.

FIELD MEASUREMENTS

From the outset, obtaining data on the field performance of floating breakwaters was an important component of the research program. A suite of instruments designed to record breakwater performance data was designed and installed at a floating breakwater in Friday Harbor, Washington.

The breakwater at Friday Harbor forms an L shape with the shorter leg extending from a fixed dock connected to shore. The shorter leg is 227 feet and the longer leg 627 feet. The topography at the site offers relatively good protection to the marina and breakwater. Prevailing southwest winds approach almost parallel to the neighboring shore perpendicular to the short leg. The fetch is about one mile in this direction. The most serious exposure is in the northeast direction through a channel affording about a 1.7 mile fetch. Although storms with winds from this direction are not common, a few severe storms of this type may be expected during a Winter storm season. The layout of the breakwater and marina are shown in Figure 2.

Although the original plan was to instrument the longer leg of the breakwater, it became necessary to alter plans and place the instruments in a position to monitor the shorter leg. Several large barges were tied to the longer leg to prevent a recurrence of damage which had occurred in previous severe storms with winds from the northeast.

Figure 2 also shows the instrument locations. Included in the instrument suite were:

- (1) Incident wave measuring buoy.
- (2) Wave buoy located in incident and reflected wave field.
- (3) Two transmitted wave measuring staffs.

- (4) Four load cells in the anchor lines.
- (5) One horizontally mounted accelerometer.
- (6) Two vertical accelerometers mounted near the seaward and shoreward sides of the breakwater.

The horizontal accelerometer provided surge acceleration directly while the average of the vertical accelerometers and the difference yielded heave and roll accelerations, respectively.

A more detailed description of the equipment is provided by Christensen and Richey (1976).

THE FRIDAY HARBOR BREAKWATER

The Friday Harbor floating breakwater is constructed quite differently from other floating breakwaters. This breakwater has a continuous structure whereas most other floating breakwaters have been constructed using discrete modules connected together.

Figure 3 shows a cross section of the Friday Harbor breakwater. The stringers provide continuous lengthwise support for the decking. The breakwater pontoons are made from a centrifugally molded polyolefin. Each pontoon is about 10 feet long and 5 feet wide but very irregular in shape. A view of the breakwater under construction without decking is given in Figure 4. Ballast is required to insure that the breakwater floats at the design water level. This is provided by 1.5 feet of water in each pontoon.

The breakwater is held in position by mooring lines on the seaward and shoreward side at about 50 foot intervals. The mooring line is chain extending about 45 feet below the breakwater. The next portion of each mooring line is double-braided nylon rope followed by another section of chain which connects to piling driven into the bottom.

Further information on this breakwater may be found in Adee (1975b).

THEORY

When one considers the myriad possible breakwater configurations which have been proposed to date and the different conditions which prevail at each potential breakwater site, the number of required model tests and the attendant expense of selecting a configuration becomes very large. To avoid this expense and also to permit parametric studies aimed at obtaining optimum breakwater configurations, a theoretical model was developed. The goal was to theoretically predict the performance which could be measured in laboratory studies or at prototype installations.

The initial restriction imposed on the theoretical model was to consider only two-dimensional conditions. Under this restriction the breakwater is assumed to be very long in one direction with long-crested waves

approaching so that their crests are parallel to the long axis of the breakwater. At most breakwaters where the wave climate results from wind-generated waves, this condition would rarely be approached. However, experiments performed using a boat wake to generate incident waves on the beam and at an angle to a breakwater indicate larger breakwater motions and larger transmitted waves when the incident wave crests approach parallel to the long axis of the breakwater. As a design tool, a two-dimensional theory provides information on the worst conditions which might be expected to occur. In addition, the information available from extensive two-dimensional wave-channel experiments provide the data needed to test the theoretical model.

The approach used here has been to employ the techniques which naval architects have developed to deal with ship-motion problems. Mathematically, the hydrodynamic equations are formulated in terms of a boundary-value problem for the velocity potential. Solution of this complete problem is presently impossible because the free-surface boundary condition is non-linear. An approximate solution may be obtained if restrictions are imposed on the boundary-value problem, and the procedure of linearization is applied. The restrictions limit the applicability of the solution to cases of small incident wave amplitude and small motion response of the breakwater.

Once the equations have been linearized, the performance of the breakwater may be obtained. The calculation procedure is illustrated in the block diagram of Figure 5.

Results obtained using the theory are in good agreement with laboratory and field data (Adee, 1975b, 1975c, 1976). The theory also provides an indication of the influence of fixed-body transmission, and of sway, heave and roll motions on the transmission coefficient at varying values of the beam to wavelength ratio.

RESULTS FROM FRIDAY HARBOR BREAKWATER

The instruments were placed at the Friday Harbor breakwater and a great deal of data was obtained during the Winter season of 1975. While no extreme storm event occurred during the time of observation, there were many occurrences of storms with mean wind speeds on the order of 20 miles per hour. It is interesting to note that when the transmission coefficient is plotted as a function of frequency the results are very consistent.

Because of the great similarity of the results, one record (FH 7-8) was selected for presentation. In this case the wind was nearly perpendicular to the short leg of the breakwater and the average wind speed was 22.9 miles per hour. The average tidal elevation was 5.3 feet above mean lower low water.

The measured and theoretically predicted transmission coefficient as a function of frequency is shown in Figure 6.

The field data was high-pass filtered with a cutoff frequency of 0.05 Hertz in order to remove the influence of tidal variations or wave buoy

motions. After initial processing the data were directly transformed using fast Fourier transformation procedures and smoothed by averaging adjacent raw spectral components. The complete details of data analysis are contained in Adee, Richey and Christensen (1976).

Extensive comparisons between theory and experiment have shown that the hydrodynamic theory is excellent so long as roll motions are small. In the frequency regions where the theory predicts higher roll motions the transmission coefficient may be in error. This is because nonlinear damping is an important factor in determining roll motion. Nonlinear damping is not included in the theory but may be artificially approximated. Experience has shown that by arbitrarily doubling the calculated hydrodynamic damping, better agreement is produced. Damping has been doubled for the theoretical prediction presented in Figure 6.

One advantage of the theory is that it doesn't simply produce a transmission coefficient, but produces sufficient information to determine what factors have an effect on the wave transmission. For the Friday Harbor floating breakwater as for other floating breakwaters the very low frequency waves are unaffected by the structure's presence yielding a transmission coefficient of nearly unity. The first trough in the transmission coefficient at about 0.3 Hertz results from heave- and roll-generated waves cancelling the fixed-body wave transmission. This transmission coefficient is well below the transmission coefficient which would be obtained with the breakwater rigidly restrained and only fixed-body transmission waves passing through. As frequency increases, there is a peak at about 0.38. At this point, the heave-generated wave has almost vanished, and the fixed-body transmission is also small. The larger predicted transmission coefficient is primarily the result of a roll-generated wave with a smaller component resulting from sway motion. The next trough at 0.43 occurs as the heave motion-generated wave increases and cancels the roll and sway motion-generated components. The fixed-body transmission is very small at 0.43. As frequency increases above 0.43 the transmitted wave is almost totally a result of the sway motion of the breakwater.

Another result of great interest to the designer is the force in the mooring lines. In presenting this data a mooring force coefficient is used which is defined as the amplitude of the force oscillation divided by the incident wave amplitude times the weight per unit length of the breakwater.

The mooring-force coefficient for the seaward mooring line of the Friday Harbor breakwater is shown in Figure 7. Here again, the field data has been high pass filtered to eliminate tidal effects and also a low frequency spike which occurs in the mooring-force spectrum. The theoretical prediction is based on computing the spring constants for the three degrees of freedom, multiplying these by the motions and summing force components. From the designers standpoint, the theory predicts the trends accurately and the overprediction at the peak would add to the margin of safety.

The main conclusion which should be reached from these results is that it is possible to measure the performance of floating breakwaters in

the field and that the theory which has been developed predicts the trends of the data and can play a very useful role in design.

PROBLEM OF COMPARISON

The floating breakwater at Friday Harbor, Washington represents one type of breakwater which provides protection by reflecting the energy contained in the incident wave. Other, more compliant breakwaters have been proposed which provide protection by dissipating this energy or by setting up waves which "interfere" with the incident wave. Still other proposed breakwaters attempt to reduce the energy in the incident wave by forcing it to break over some obstacle. Because these concepts are quite different and because few have been tested at prototype scale, a rational comparison of performance is quite difficult with the data presently available. Clearly, from a users point of view, the breakwater offering the best performance for the least cost would be the most attractive.

To present the performance of various types of floating breakwaters in terms of performance per dollar is very difficult. There has been a great variation in the cost of the floating breakwaters constructed to date, even among those of the same type. Besides, with the diversity of materials available and the rapid fluctuations in their prices which has recently taken place, such information would rapidly become obsolete.

In the course of the study of floating breakwaters at the University of Washington, we have often used beam divided by wavelength as the parameter which characterizes the size of the breakwater. This seems to work well so long as the discussion is centered on breakwaters which protect primarily by reflection. When different types such as the reflecting and tethered float breakwater are to be compared using beam to wavelength is inadequate.

An alternative procedure which seems to have merit is to use the square root of the underwater volume per unit length divided by the wavelength as the independent variable. If we are to ever be able to draw fair general comparisons among proposed floating breakwaters, a consistent scheme for presenting performance data should be developed.

NONLINEAR BEHAVIOR

Figure 8 shows a recorded time history of the mooring forces measured at the Tenakee, Alaska floating breakwater. Looking at this figure one can observe an oscillation with a period of about 60 seconds superimposed on the expected shorter period oscillations.

The linear theoretical model permits the system to respond only at the frequency of the incident wave. In order to explain the presence of these long-period oscillations, nonlinearities must be included in the analysis. To perform a mathematically complete analysis including all nonlinear effects is beyond the present state of the art. However, in the case of the floating breakwater, one can show that if two incident waves are considered and second-order terms are retained, then an exciting force is present at the difference between the frequencies of the incident waves. Normally, this

small exciting force would have little effect. Since the structure is only lightly restrained in sway, the natural period is very long for sway motion. The existence of a small exciting force at the sway natural frequency could explain the large oscillation in mooring force.

Because the mooring lines are critical to floating breakwater survival in extreme storm conditions, further research effort on the long-period oscillations is justified.

ACKNOWLEDGEMENT

Financial support for floating breakwater research at the University of Washington has been provided by the U.S. Army Corps of Engineers Coastal Engineering Research Center and through the National Oceanic and Atmospheric Administration Sea Grant Program. Their support is gratefully acknowledged.

REFERENCES

- Adee, B.H., "Analysis of Floating Breakwater Performance," Proceedings of the Symposium on Modeling Techniques, San Francisco, Calif., 3-5 September 1975a.
- Adee, B.H., "Floating Breakwater: An Idea Whose Time Has Returned," IEEE-MTS Annual Meeting, Ocean '75, San Diego, Calif., September 1975b.
- Adee, B.H., "Floating Breakwater Mooring Forces," Ocean Engineering Mechanics, Am. Soc. of Mechanical Engineers, New York, 1975c.
- Adee, B.H., "A Review of Developments and Problems in Using Floating Breakwaters," Offshore Technology Conference, Houston, Texas, May 1976.
- Adee, B.H., Richey, Ep., Christensen, D.R., "Floating Breakwater Field Assessment Program, Friday Harbor, Washington," Final Contract Report submitted to U.S. Army Corps of Engineers Coastal Engineering Research Center, July 1976.
- Christensen, D.R., Richey, E.P., "Prototype Performance Characteristics of Two Floating Breakwaters," Offshore Technology Conference, Houston, Texas, May 1976.

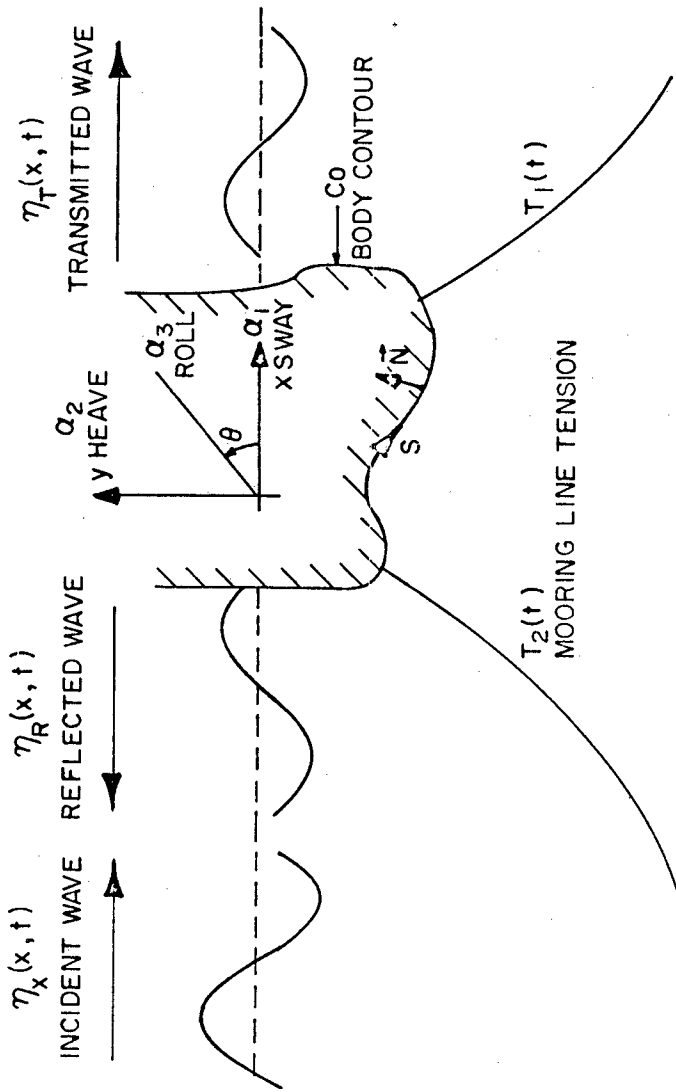


Figure 1. A two-dimensional floating breakerwater.

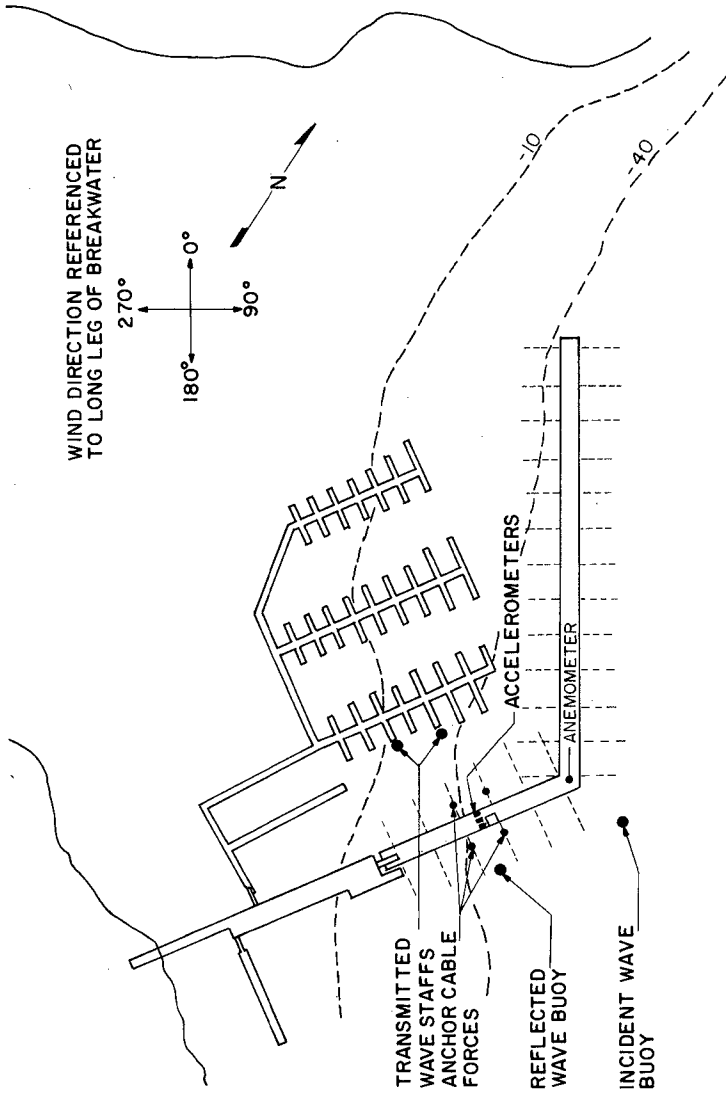


Figure 2. Instrumentation location plan, Friday Harbor breakwater.

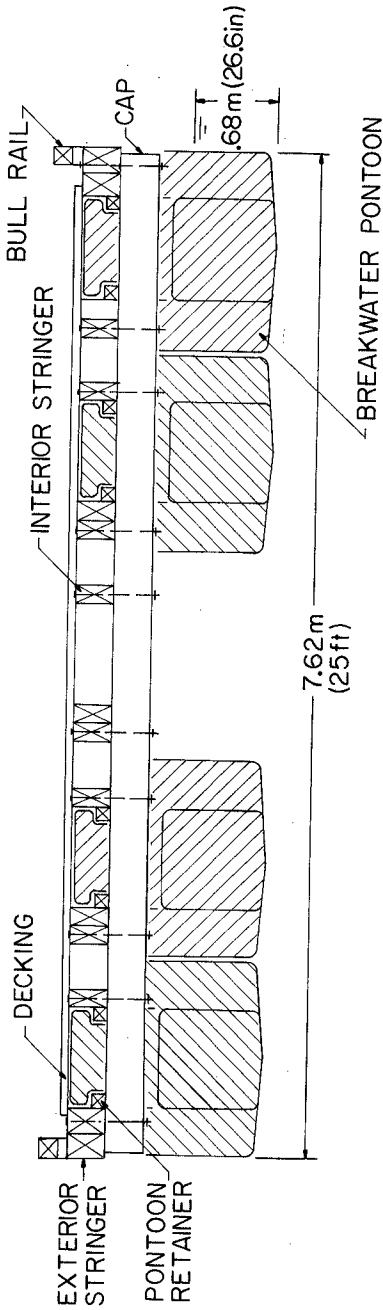


Figure 3. Cross section of Friday Harbor breakwater.



Figure 4. Friday Harbor breakwater before installation of decking.

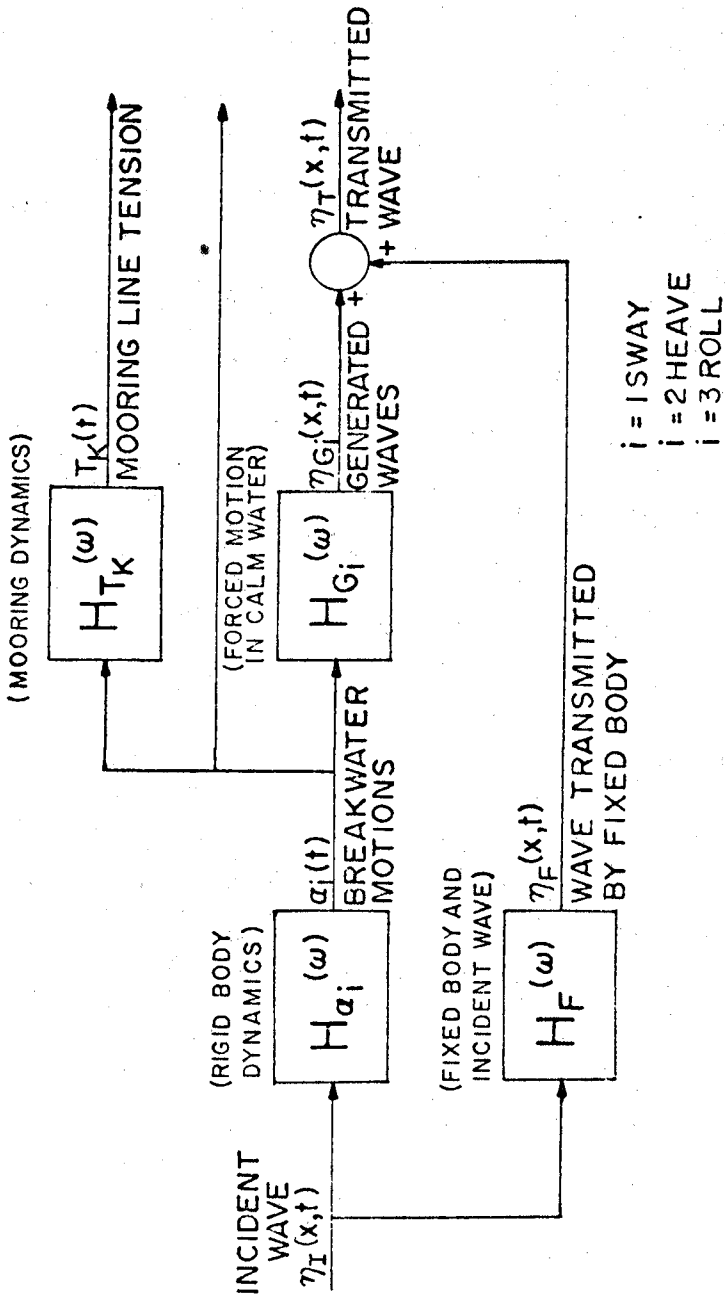


Figure 5. Linear system representation of a floating breakwater.

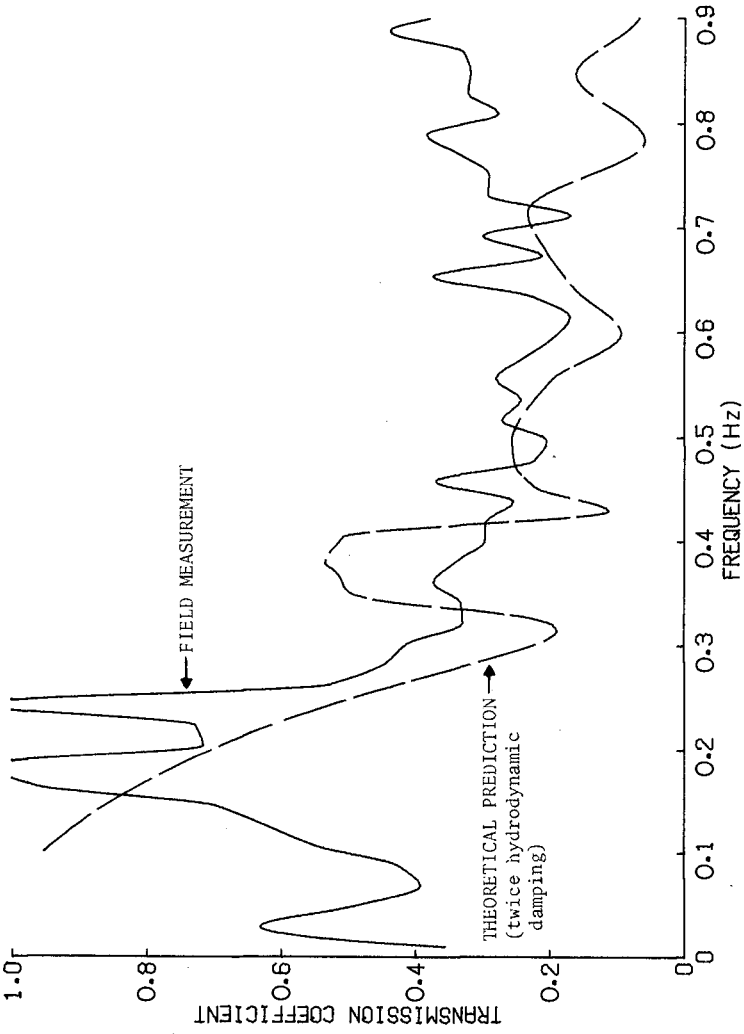


Figure 6. Transmission coefficient for Friday Harbor breakwater (record FH 7-8).

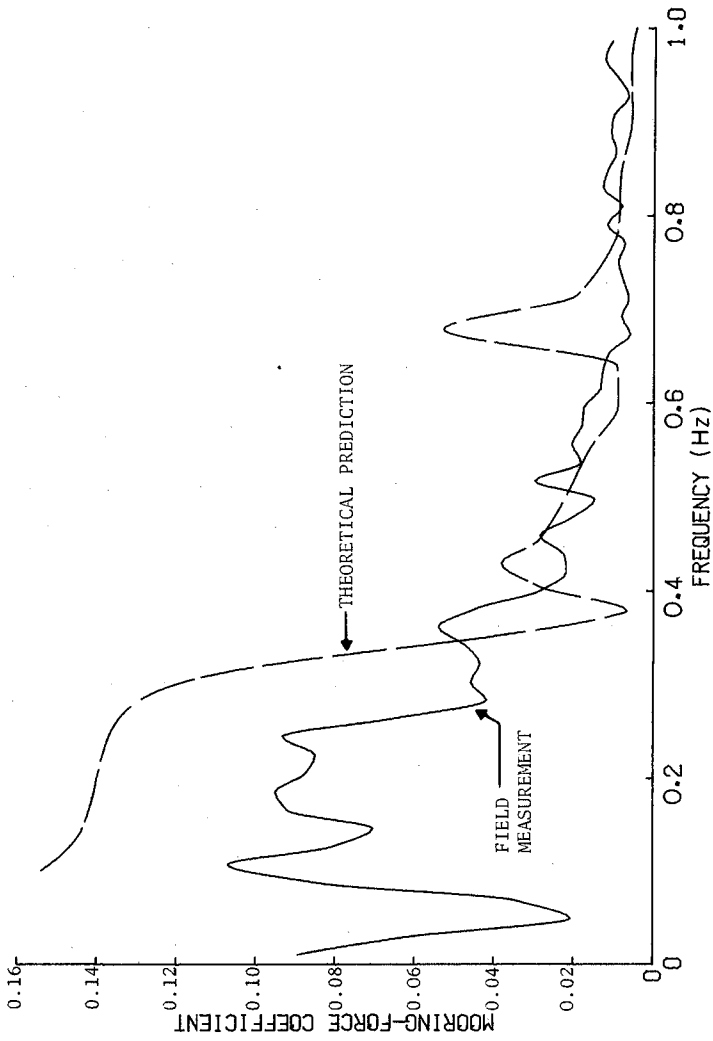


Figure 7. Seaward mooring line mooring-force coefficient, Friday Harbor breakwater (record FH 7-8).

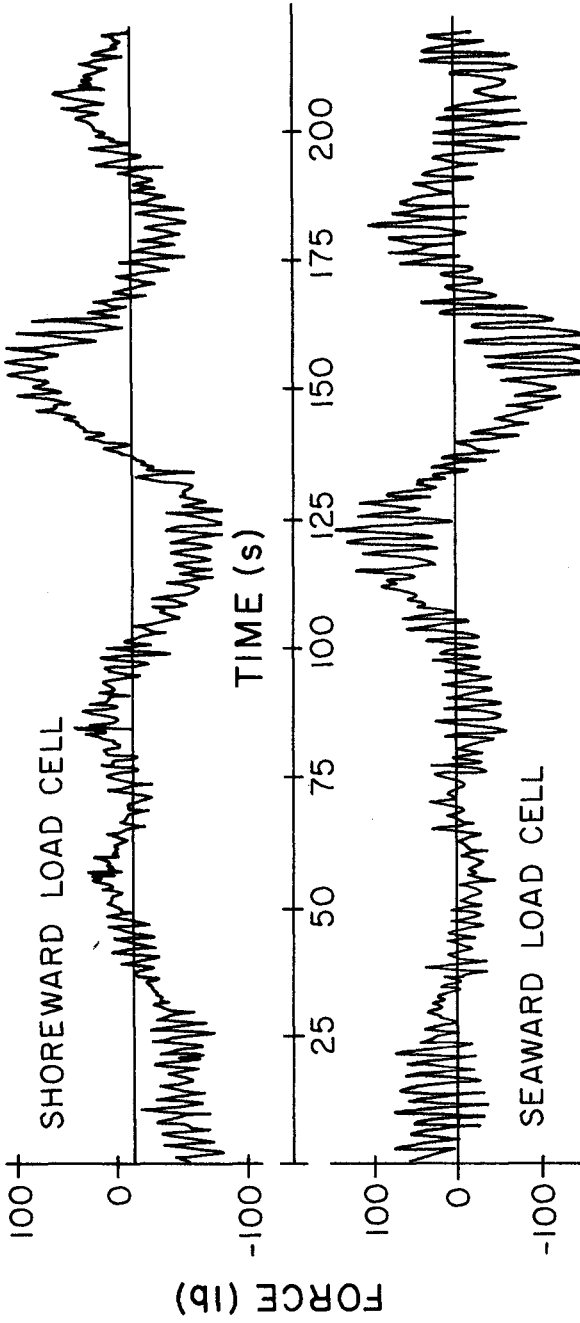


Figure 8. Time history of mooring line load cells, Tenakee breakwater (record TK 7-23).

CHAPTER 160

DESIGN, ANALYSIS AND FIELD TEST OF A DYNAMIC FLOATING BREAKWATER

D. J. Agerton¹, G. H. Savage², K. C. Stotz³

Interest in floating breakwaters has been generated in recent years because the concept offers the potential of providing a less expensive alternative to traditional, solid wall type barriers for providing permanent wave protection to the thousands of new recreational boat harbors and marinas that have been built in the past 20 years. Also, they may be able to provide temporary, mobile wave protection during construction and installation of offshore facilities for oil transfer and production operations, defense facilities and other offshore structures in deeper water (depths exceeding 50 to 100 feet).

The engineering director of one of the largest and most active offshore oil producing companies recently stated that they would be willing to pay up to \$6 million for a mobile, floating breakwater that had the proven capability to significantly reduce risks due to wave action during offshore erection in the North Sea or elsewhere. Considering the investment in just one deep water oil production platform already exceeds \$100,000,000, the worth of such a reusable, wave protection system during the critical erection period of a platform should be large.

The tethered float concept - a dynamic breakwater: In 1974, Seymour and Isaacs (1) introduced the concept of a submerged, tethered float breakwater, an approach that shows promise of being able to attenuate long period, large, deep-water, storm waves at a sufficiently low cost to be feasible. The system is made up of an array of independently moored, spherical buoys submerged just below the water surface (See Fig. 1). Seymour and Isaacs (1) proposed that, with proper specification of tether length and buoy size, each buoy would have a resonant frequency near that of the anticipated predominant waves for a given location. Owing to their dynamic response, it seemed possible to cause the buoys to pendulate back and forth in the incoming waves out of phase with the wave orbital motions; thus the name: Dynamic Breakwater. The effect of this wave excited buoy motion would be to transform wave energy into water turbulence and then heat in the wake of the buoy.

¹Engineering Ph.D. Candidate, University of New Hampshire.

²Professor of Engineering, University of New Hampshire.

³Associate Professor of Electrical Engineering, University of New Hampshire.

Additions and modifications to the tethered float concept: Before and during Isaacs's and Seymour's work Savage and others (2,3,4) had been investigating solid rubber filaments for various buoy mooring applications, and suggested that the use of such moorings would improve the survivability and longevity of such a floating breakwater. Follow-up of this idea soon presented the possibility of significantly increasing the wave attenuation efficiency of the Isaacs-Seymour system. A buoy tether's spring constant might be chosen so it resonated with the predominate wave frequency in the vertical as well as in the horizontal direction. Thus, each buoy could be expected to create more turbulence and dissipate more energy than an inelastically-tethered one. Wave tank model studies of this approach with a single elastically-tethered buoy in 1974 confirmed the possibility of achieving orbital buoy response out of phase with the orbital water particle motion, and encouraged us to proceed.

Research objectives and scope: The three aspects of our investigation were:

- 1) to compare the dynamic response and wave attenuation by tethered buoys with different tether elasticities, float shapes, spacings, and levels of submergence in a wave tank,
- 2) to develop predictive mathematical models of buoy response and wave attenuation in wave tank and field tests,
- 3) to conduct a large enough lake scale model test so that the Reynolds number and period parameter would be large enough for fully turbulent wake conditions to be developed in the buoy field; a condition that we expected to prevail in a full scale system.

The last objective seemed the most significant because successful achievement of fully turbulent flow conditions in a model would permit model results to be used to predict full scale breakwater performance. At the time no other field tests had been carried out for a tethered float array.

WAVE TANK TESTS

The wave tank tests were conducted in the ship model towing facility of the Massachusetts Institute of Technology, Cambridge, Massachusetts. One set of tests measured the dynamic response of a single buoy to sinusoidal wave of various heights and frequencies. Several different shapes of buoys and tethers with different spring constants were used. Buoy response was recorded by means of an optical displacement follower which could continually track the oscillating buoy using only light and no instruments in direct contact with the buoy or its tether. The three float shapes tested were a sphere, a sphere with a concentric disk around its girth (a "Saturn ring"), and an egg. The scale size of the buoy was assumed from Seymour and Isaacs (1) work with a sphere which had shown that "reasonable diameters for the breakwater will be of the same order as the significant wave height".

The buoy shape and tether selected were a sphere with a tether with a low spring constant so that the buoy response to the significant waves in our model sea state and water depth was a near circular orbit (See Fig. 2). The preliminary mathematical model of the system had indicated that such an orbital response would result in the greatest energy dissipation due to form drag for a single buoy. The spherical buoy shape was selected over the other two tested because it was the shape that gave significant vertical as well as horizontal response; *i.e.* near-circular buoy motion.

We then constructed arrays of both wire and elastically-tether buoys across the wave tank and subjected these model dynamic breakwaters to both regular and irregular seas (See Fig. 3). The incident and attenuated waves were measured and recorded and the respective wave energies were calculated. These wave tank breakwater model tests gave results that supported the validity of our first analytical prediction models that elastically-tethered floats dissipated more energy than wire-tethered ones. Other results are shown in Fig. 4.

MATHEMATICAL MODELING

Modeling an elastically-tethered dynamic breakwater requires four steps: (a) writing equations of motion for a tethered buoy in two dimensions; (b) solving those equations for buoy relative velocity; (c) computing the rate of energy dissipation (drag power) of a row of buoys; (d) compounding the drag power row-by-row through the array. In light of the two-dimensional nature of the problem and the complexities introduced by elastic tethers, we did not rely solely on the simplified linear-model approach of Seymour (5). Solution to the non-linear, coupled problem is detailed in a dissertation by Agerton (6) and summarized below. It is a solution of the general case; not restricted to a wire-tethered system.

Modeling wave forces: Force on a fixed object in one-dimensional oscillatory flow can be formulated by the Morison equation as the sum of nonlinear drag and inertial components (7). Frontal area A and flow coefficients C_D and C_M are considered constant.

$$F = F_D + F_I \quad (1)$$

$$F = \frac{1}{2} \rho A C_D |u|u + \rho V_o (1 + C_M) \dot{u} \quad (2)$$

In one-dimensional oscillatory flow, the only dimensionless parameter correlated with drag and mass coefficient is period parameter (8,9) defined as:

$$PP = U_m \tau / d = 2\pi a / d \quad (3)$$

where a is the amplitude of water motion relative to the object. However, the relationship between flow parameters, object dimensions, and flow-force coefficients is not well understood, particularly in two-

dimensional oscillatory flow as would occur in waves in a field experiment. Furthermore, if the amplitude to diameter ratio were the only important parameter, then the scaling of drag forces would present no problem. We have heard no investigator propose that to be the case.

Complexity of the problem increases for two-dimensional flow problems -- as occur for waves acting on a submerged tethered sphere or horizontal cylinder parallel to the wave crests. In such cases, the turbulent wake would appear to rotate around the object during the wave cycle. The vector force can be written by the Morison formulation. Area presented to the flow is the same from all directions. Also, it is assumed C_D and C_M do not change with direction.

$$\vec{F} = \vec{F}_D + \vec{F}_I \tag{4}$$

$$\vec{F} = \frac{1}{2} \rho A C_D |\vec{r}| \vec{r} + M_W (1 + C_M) \ddot{\vec{r}} \tag{5}$$

where \vec{r} is the relative velocity of the fluid and $\ddot{\vec{r}}$ is its relative acceleration. Both can be resolved into horizontal and vertical components. The one and two-dimensional formulations are compared below:

Two-dimensional formulation

One-dimensional formulation

$$F_x = D u \sqrt{u^2 + v^2} + N \dot{u}$$

$$F_x = D |u| u + N \dot{u} \tag{6}$$

$$F_y = D v \sqrt{u^2 + v^2} + N \dot{v}$$

$$F_y = D |v| v + N \dot{v} \tag{7}$$

If only maximum force predictions are of interest, both formulations give the same result. However, when considering wave-force history and energy dissipation, the two-dimensional problem should be formulated as such or justifiably de-coupled into a pair of one-dimensional equations.

By computing the drag work during a wave cycle, one finds that about 15% less energy is dissipated by the one-dimensional formulation. A similar comparison for an elastically tethered sphere is not as simply accomplished because the object has both horizontal and vertical relative velocity whose magnitudes are not necessarily equal. However, the 15% difference in calculated dissipation represents the maximum.

Coefficients of mass and drag: Data on which to base estimates of drag and mass coefficients for spheres in waves are neither plentiful nor consistent. Seymour (5) was first to estimate flow coefficients for tethered spheres in irregular waves in both the laboratory and the ocean. He concluded that at values of rms a/d greater than 0.80, the average C_D was constant. This indicated to him that the flow was fully turbulent -- that is, the wake was fully developed. He further observed that C_M decreased in a gradual linear fashion with increasing a/d ratio, so assuming a single value over a particular excitation spectrum was an acceptable approximation. When the sphere was less rigidly restrained, Seymour observed that C_D increased almost two-fold. He hypothesized that lateral vibration increased the width of the wake and, therefore, the form drag. Laird (10) made similar observations for cylinders. Sarpkaya (9) recently calculated C_D and C_M over a range of period para-

meters in one-dimensional oscillatory flow. The sphere was not rigidly restrained. At a/d ratios greater than about 3.0, C_D was constant at about 0.75, much higher than Seymour had measured. Below 3.0, it decreased in an almost linear fashion. In an ocean experiment, Seymour (5) inferred values of 0.35 and 0.25 for C_M and C_D respectively for a tethered sphere in two-dimensional flow. These were about 70% higher than those calculated in laboratory experiments, a difference he attributed to transverse vibration. Values of flow coefficients estimated by Seymour in the field were initially adopted to carry out the design of our experiments because he had made the only large-scale measurements in two-dimensional flow.

Modeling buoy response and energy dissipation: Fig. 5 depicts the geometry of an elastically-tethered sphere in waves. Based on wave tank observations and on the analysis of elastic tethers, articulation and catenary were assumed negligible (4,11). The working range of the elastic tether is approximately linear (11). Depending primarily on the thickness of the tether, drag forces on the mooring may be substantial. Formulating drag force on a differential section of tether whose free end moves with the velocity of the buoy \dot{x} , and integrating over the length yields:

$$F_{Dt} = \frac{1}{6} \rho A_t C_{Dt} |\dot{x}| \dot{x} \quad (8)$$

Buoyancy, acceleration, wave, and tether forces on the tethered buoy can be resolved into horizontal and vertical components, summed, and algebraically re-arranged to yield non-linear coupled equations of motion.

$$M_x \ddot{x} + D_x |\vec{r}| (\dot{x} - u) + D_t |\dot{x}| \dot{x} + T \sin(\theta) = N_x \dot{u} \quad (9)$$

$$M_y \ddot{y} + D_y |\vec{r}| (\dot{y} - v) + T \cos(\theta) - F_B = N_y \dot{v} \quad (10)$$

$$\text{where } u = a w e^{-kz} \cos(\omega t - kx) \quad v = -a w e^{-kz} \sin(\omega t - kx) \quad (11)$$

Drag power is written:

$$P_{D_x} = \frac{1}{2} \rho A C_D |\vec{r}| u_r^2 \quad P_{D_y} = \frac{1}{2} \rho A C_D |\vec{r}| v_r^2 \quad (12)$$

$$\text{where } u_r(t) = \dot{x}(t) - u(t) \quad v_r(t) = \dot{y}(t) - v(t) \quad (13)$$

$$\text{Total drag is then: } P_D = P_{D_x} + P_{D_y} \quad (14)$$

Integrated over a wave period τ , the drag power and wave power are compared to yield the proportion of wave energy dissipated by a single row of buoys. This is adjusted for buoy packing density β .

$$\lambda_1(\omega_1 a_1) = \beta \frac{\int_0^{\tau} P_D dt}{\int_0^{\tau} P_W dt} \quad (15)$$

It is assumed that the amplitude reduction is completed a short time after the buoy and water have interacted. Therefore the attenuated amplitude is the incident wave amplitude for the second row of buoys.

Through compounding successive simulations, attenuation by an array of buoys can be modeled. However, because dissipation by each row is small, large error is not incurred by assuming all rows are equally effective (6). Dissipation by an array of n rows can therefore be estimated as:

$$a_n^2/a_1^2 = (1-\xi)^n \quad (16)$$

Solving for the number of rows to provide a particular level of dissipation requires solving the equations of motion.

Solution by simulation: The IBM Continuous System Modeling Program (CSMP) was used to simulate the response of an elastically-tethered buoy. Simulation in regular waves permitted calculation of frequency response, energy dissipation, and spatial plotting of the orbiting buoy. Results indicated that elastically-tethered elements could be more effective than comparable wire-tethered elements even though the former required deeper submergence to avoid broaching the surface. Although dissipation in the horizontal direction was actually less, this reduction was more than compensated for by an increased contribution in the vertical dimension. To simulate the response of the tethered element in irregular waves, we used the sum of thirteen randomly phased Fourier components as measured in a lake for the excitation. At a selected time interval, data was written to disk file for subsequent spectral analysis.

The previously discussed one and two-dimensional drag-force formulations were compared through simulation. C_D and C_M were assumed constant for each direction. Linear elongation of the elastic tether was varied over a range of values from 4% to 200%. Regardless of the elastic constant selected, response and dissipation varied no more than 10% in all cases tested; therefore, using the simpler, one-dimensional drag force formulation is an acceptable approximation for a linear model.

To discuss the relationship in irregular waves between relative velocity and energy dissipation requires a linearized model of dissipation so the phenomenon can be treated as a sum of Fourier components (6). Furthermore, complete linear analysis permits more design insight than the trial and error approach of simulation.

Linear analysis: The restoring forces in the equations of motion can be decoupled and linearized. Expressions for the water particle kinematics in a deep-water Airy wave can be simplified by assuming the spatial movement of the buoy will not substantially affect the water velocities and accelerations adjacent to the buoy.

Seymour (5) extended Jacobsen's (12) damping linearization to broadband irregular flows using a statistical approach and minimizing the difference in dissipation calculated by linear and non-linear models. The linearized drag term for the buoy drag is of the form DU_0u_r . U_0 is the "characteristic" relative velocity:

$$U_0 = 16\sigma_{u_r}/3\sqrt{2\pi} \quad (17)$$

where σ_{u_r} is the square root of the variance of relative velocity in one dimension. Seymour's approach was applied to linearizing the drag

of the tether. The linearized tether drag is of the form $D_t U_t \dot{x}$ where:

$$U_t = 16\sigma_x / 3\sqrt{2\pi} \quad (18)$$

Equations 9 and 10 in linearized form are written:

$$M\ddot{x} + [D'_x + D'_t]\dot{x} + K_x x = D'_x u + N\dot{u} \quad (19)$$

$$M\ddot{y} + [D'_y]\dot{y} + K_y y = D'_y v + N\dot{v} \quad (20)$$

where $D'_x = D_x U_0$ and $D'_t = D_t U_t$ (21)

$$K_x = (\rho V_0 - M_s)g/l_0 \quad K_y = k_t \quad (22)$$

Equations 19 and 20 are analogous; only operations on the first will be discussed. Lumping linearized drag terms ($D'' = D'_x + D'_t$) and taking the Laplace transform of each side of the Eq. 19, yields the transfer function of the buoy in the horizontal dimension:

$$H_x(s) = \frac{X(s)}{P(s)} = \frac{D's + Ns^2}{Ms^2 + D's + K_x} \quad (23)$$

The transfer function of relative velocity is:

$$H_{u_r}(s) = \frac{(N-M)s^2 - D_t's - K_x}{Ms^2 + D''s + K_x} \quad (24)$$

Changing from the Laplace transform to a Fourier transform, the predicted spectrum of horizontal relative velocity is:

$$S_{u_r}(\omega) = S_u(\omega) |H_{u_r}(\omega)| \quad (25)$$

where $S_u(\omega)$ is the spectrum of horizontal water particle velocity. The variance of relative velocity is calculated as:

$$\sigma_{u_r}^2 = \int_{-\infty}^{\infty} S_{u_r}(\omega) d\omega \quad (26)$$

The three previous equations are solved iteratively using estimates of the variances of buoy velocity \dot{x} and buoy relative velocity u_r to initiate the double transcendental solution.

Average drag power of a buoy over a frequency band is:

$$\bar{P}_{D_x}(\omega) = \frac{1}{2} D'_x U_r^2(\omega) \quad (27)$$

Therefore, $\bar{P}_{D_x}(\omega) = \frac{1}{2} D'_x S_{u_r}(\omega)$ (28)

Drag dissipation due to the tether is relatively small and therefore, neglected. Energy dissipation by a row of buoys is modeled over each averaged frequency band as the sum of the dissipation by Fourier components in each dimension.

$$\bar{x}(\omega) = \frac{1}{2} \beta \frac{[D'_x S_x u_r(\omega) + D'_y S_y v_r(\omega)]}{P_w(\omega)} \quad (29)$$

Knowing the transcendental solution to each equation, one can calculate the resonant frequencies of the system. Natural frequencies for a tethered buoy whose mass is small and respect to the displaced water and whose tether is a linear spring are written:

$$\omega_{nx} = \sqrt{g/(C_m l_o)} \quad \text{and} \quad \omega_{ny} = \omega_{nx} \sqrt{l_o/(l_o - r_o)} \quad (30)$$

where r_o is the unstretched tether length and l_o is its stretched length. Damping ξ is calculated as $D/2M\omega_n$. Resonant frequency is calculated according to the equation:

$$\omega_r = \omega_n \sqrt{1 - \xi^2} \quad (31)$$

The linearized model provides the analytical tool for matching the system response to predicted wave frequency by indicating the proper tether length and spring constant. The analysis indicates that vertical resonance will always be at a higher frequency than horizontal resonance. One possibility for altering this relationship may lie in using an ellipsoidal buoy so that the area exposed to the flow and the flow co-efficients are different in the horizontal and vertical dimensions.

FIELD TEST

The field test model was designed for installation about 100 yards off the northwest shore of Diamond Island in Lake Winnepesaukee, the largest lake in New Hampshire (See Fig. 6). The storm winds from the northwest had a six to nine mile fetch over which to build wave energy to test the system. We anticipated a maximum of three to four-foot significant waves with a three second peak period based upon the historical observation of long-time residents in the area.

The dynamic breakwater array: The breakwater float array was moored by a level steel frame anchoring grid designed by Vidal (13) with adjustable legs to level it on the bottom like a multilegged table. Buoys were then tethered to their anchoring frame so each tether was the same length. Such an anchoring system would not be practical for a working prototype system, but was used here because it provided an immobile base and simplified the subsequent analysis. It also focused the project on the effects of the elastic tethers and the floats. Such an anchoring frame was also consistent with the installation equipment, funds and talents available to us. The anchoring surface of the frame was 21 feet below the mean

free water surface after installation. The bottom sloped from approximately 27 feet to 35 feet from the shore side to the weather side of the frame.

The 90 floats in the array were 22 inch diameter plastic, inflatable, near-spherical floats. They were tethered with two parallel, one inch diameter solid rubber filaments as shown in Fig. 7. From previous work done by Savage (2,3) and our own tests of the spring constant for available solid rubber filaments, we had specified a filament with a linear spring constant of 15 lbs/foot elongation after initial loading to 120 pounds. However, the material we finally received did not meet specification by a wide margin. Its spring constant was about 35 lbs/foot elongation; so we were unable to obtain the desired magnitude of vertical response of the buoys in even the highest sea states. After discussions with several large manufacturers of rubber we have concluded that knowledge of rubber creep and elastic properties is not sufficiently complete to provide consistent and predictable material properties of the kind we have been seeking.

The array and instrumentation: Fig. 8 shows the plan and side views of the breakwater array that was installed at Lake Winnepesaukee and the location of wave staffs to measure the incident and attenuated waves. Details of the design of these transmission line wave staffs will be available in a publication by Winn, Stotz and Delano (14). As indicated in Fig. 8, one tether was instrumented to permit measurement of buoy motion response. Data from this buoy provided a check on our analytical models of dynamic response.

The effects of diffraction were not directly addressed in this experiment, but we believe such effects were not significant because our breakwater was not a thin, impervious wall. Also, the wave staff measuring the attenuated waves behind the breakwater was located in the middle and close to the breakwater as shown in Fig. 8. It would therefore have received the minimum possible energy transmitted by diffraction if there was any at all.

The greatest difficulty in the field experiment arose from the excessive creep of the rubber tethers that caused some of the floats to come to the surface, and these had to be pulled back down with shortened tethers to maintain design depth. It was here that the lack of quality control on the delivered rubber filaments showed up to seriously hinder the project, but the problem was overcome at the expense of greatly increasing the spring constant of the tethers which altered the breakwater vertical response from the original design.

RESULTS AND DISCUSSION OF THE FIELD EXPERIMENT

The least controllable aspect of the field experiment was the weather. Moderate cold fronts during the fall brought waves only as high as 2.0 feet significant height. A week before winter ice set in, waves 2.5 feet in significant height were recorded. The energy dissipation by the breakwater averaged over nine five-minute records from December 18, 1975 was 51%. Averaged over five records from November 5, it was 53%.

Several adjacent records from each day were selected for detailed analysis and modeling. Averaged incident and attenuated wave spectra measured over a ten-minute interval are shown in Fig. 9. Assuming rows were equally efficient, then each row dissipated about 8% of its incident wave energy.

Modeling buoy response and dissipation: In general, the measured horizontal buoy response was about five times greater than the vertical -- less than we had sought due to the undesirably high tether modulus.

C_D and C_M were estimated by matching the model results to the measured response of a wire-tethered buoy which was switched temporarily into the array so buoy response data with minimum cable drag could be acquired. The best correspondence between measured and modeled buoy motions was for a $C_D = 0.42$ and $C_M = 0.50$. These high values, coupled with the estimated rms a_T/d ratio of 0.65, indicated that the buoy wake was not fully developed as we had expected.

C_D and C_M of 0.42 and 0.50 respectively also yielded the closest fit between measured and modeled response for the elastically-tethered buoy. Fig. 10 compares the measured and modeled frequency response for several averaged records from December 18, and Fig. 11 makes the same comparison for the spectrum of horizontal relative velocities.

From horizontal and vertical spectra of relative velocity, the linearized drag power was computed over each frequency band in each spectrum. Results are compared with those measured in the field in Fig. 12. The lines of least-squares fit correspond in the region of highest energy density. Discrepancies at high frequencies may be due to breakdown of the model in that region. The results of the linear model correspond reasonably well with those of the coupled non-linear model.

CONCLUSIONS

From further investigation of the linear and non-linear models, it appears that their results are within 10% of one another for tether elongations from 0% to 30%, the measure of tether compliance used in our work. At 100% elongation, it appears most elastically-tethered systems can be more effective than their wire-tethered counterparts. However, their performance advantage is marginal because the buoys with more compliant tethers must be submerged deeper to avoid broaching the surface. Also the elastic tether is many times thicker than its wire counterpart and adds damping to the horizontal response; thereby reducing the energy dissipation by the buoy. Finally, it appears that a fully-developed wake (analogous to supercritical, steady flow) is not a necessary condition for maximum energy dissipation. Assuming that $C_D = 0.25$ and $C_M = 0.35$ characterize fully turbulent flow and that $C_D = 0.42$ and $C_M = 0.50$ characterize sub-critical turbulent flow, the models indicate that maximum dissipation by a tethered sphere system could be the same for each flow regime. However, the optimum tether length would be different for a given buoy operating in one flow regime or the other.

In summary, we found it was possible to remove 50% of the wave energy using a nine-row array of tethered buoys, and that we could model the

energy dissipation fairly accurately. Our test of the performance advantage of elastic tethers was not conclusive because of manufacturing problems and present state-of-the-art limitations. Our understanding of relationships between wake development and buoy size relative to wave parameters over a range of scales in two-dimensional oscillatory flow is incomplete.

ACKNOWLEDGMENTS

The principal support for this project from the National Sea Grant Program (Grant No. 04-5-158-50) is gratefully acknowledged. Valuable information and contributions were also received from previous related research, notably the Office of Naval Research Contract No. N00014-67-A-0158-0004 and the United States Coast Guard Research and Development Contract No. 4-20050-000.

REFERENCES

1. Seymour, R. J., and J. O. Isaacs, Tethered float breakwaters, Proceedings of First Int'l. Conf. on Floating Breakwaters, Univ. of Rhode Island, Newport, R.I., April, 1974.
2. Savage, G. H., and J. B. Hersey, Project Seaspider, Reference No. 6842, Woods Hole Oceanographic Institution, Woods Hole, Mass., June, 1968.
3. Savage, G. H., Testing rubber band filaments as buoy moorings for some test navigation buoys, Engineering Design and Analysis Laboratory Report, Univ. of New Hampshire, Ourham. Letter Report to United States Coast Guard Research and Development Center, Contract No. 4-20050-000, November 9, 1973.
4. Demos, S. E., G. A. Stewart, and R. W. Corell, A computer study of the hydrodynamic loading of a compliant taut-wire mooring, EOAL Tech. Rpt. #109, University of New Hampshire, July, 1970.
5. Seymour, R. J., Resistance of spheres in oscillatory flows, Ph.D. Dissertation, Univ. California, San Diego, 1974.
6. Agerton, O. J., The design, analysis and field test of a dynamic floating breakwater. Ph.D. Dissertation, Univ. of New Hampshire, Ourham, Dec. 1976.
7. Morison, J. R., J. W. Johnson, M. P. O'Brien, and S. A. Schaaf, The forces exerted by surface waves on piles, Petroleum Trans., Vol. 189, TP2846, 1950.
8. Keulegan, G. H., and L. H. Carpenter, Forces on cylinders and plates in an oscillating fluid, J. Res. National Bur. Standards, 60, 5, May, 1958.

9. Sarpkaya, T., Forces on cylinders and spheres in a sinusoidally oscillating fluid, J. Applied Mechanics, ASME, March, 1975.
10. Laird, A. D. K., Water forces on flexible oscillating cylinders, J. Waterways Harbors Div., Proc. ASCE, Vol. 88, WW3, August, 1962.
11. Stotz, K. C., D. O. Libby, and G. H. Savage, Computer model and data interpretation for a rubber cable tethered wave amplitude measuring buoy, Proc. Ocean 75 Conf., IEEE and MTS, San Diego, 1975.
12. Jacobsen, L. S., Steady forced vibration as influenced by damping, Trans. ASME, Vol. 52, no. APM 52-15, 1930.
13. Vidal, D. A., Design, analysis, construction, and installation of a floating breakwater anchoring system and related structures. Master of Science Project Report, Univ. of New Hampshire, 1975.
14. Winn, A. L., Stotz, K. C., Delano, J. R., The design and field operation of a transmission-line wave staff. (In preparation), University of New Hampshire.
15. Winn, A. L., G. H. Savage, and R. R. Hickman, Design and instrumentation of a shore-recording wave amplitude measuring buoy, Proc. Ocean 75 Conf., IEEE and MTS, San Diego, 1975.

NOMENCLATURE

a	amplitude	r_0	unstretched tether length
A	area	$S_z(\omega)$	spectrum of z
a_r	amplitude of buoy displacement relative to water particle displacement	s	Laplace operator
B	constant	T	tension in tether
D	Lumped drag constant of form $\frac{1}{2} \rho A C_D$	t	time
D'	Lumped drag constants of form $\frac{1}{2} \rho A C_D U_0$	U_r, V_r	horizontal and vertical relative velocity respectively
D''	Lumped linearized drag constant including buoy and tether drag	U_0, V_0	"characteristic" relative velocity - linearization constants
d	diameter	u, v	water particle velocity
F_B	force of buoyancy	\dot{u}, \dot{v}	water particle acceleration
g	acceleration of gravity	U_m	maximum relative velocity
H	wave height	V_0	displaced volume
$H_x(\omega), H_y(\omega)$	linearized transfer functions	x, y	horizontal and vertical displacements respectively
k_x, k_y, k_z	lumped restoring force constant	z	depth of submergence
k	wave number	z (subscript)	refers to horizontal water particle position
k_t	spring constant for tether	β	buoy packing density (#/ft.)
l_0	tether length for buoy at rest	λ	energy dissipation per row
M	lumped mass constant: $M_b + M_s$	ρ	density of water
M_s	mass of sphere	ξ	damping coefficient
M_w	mass of displaced water	ω	frequency (radians/sec)
N	lumped mass constant: $M_w(1+\mu)$	ω_n, ω_r	natural and resonant frequency
n	number of rows	θ	angle of tether from vertical
P_D	drag power	σ^2	variance
P_W	wave power	$\langle \cdot \rangle$	average value
R	stretched tether length	$\{ \cdot \}$	absolute value
\vec{r}	vector relative velocity		

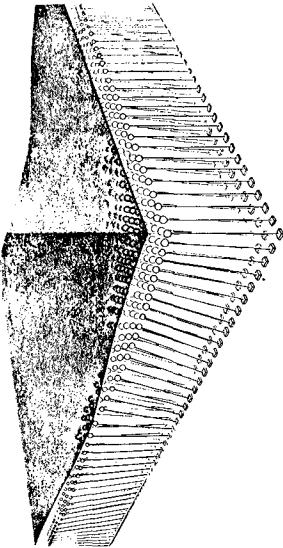


Fig. 1 Seymour and Isaacs tethered float breakwater (1).

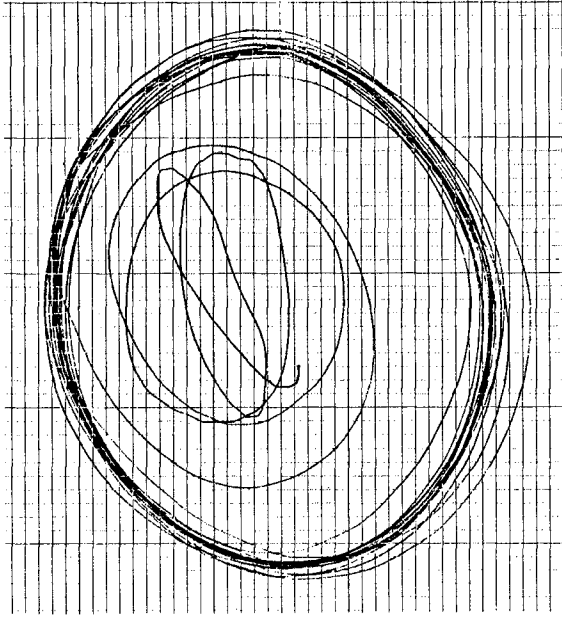


Fig. 2 Orbit of elastically-tethered buoy as tracked by optical instrumentation in wave tank tests.

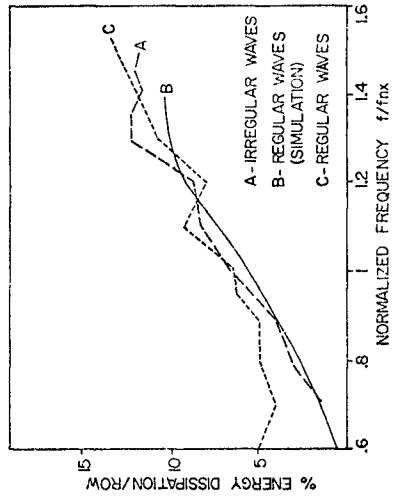


Fig. 4 Measured and modeled performance of scale model elastically-tethered array.

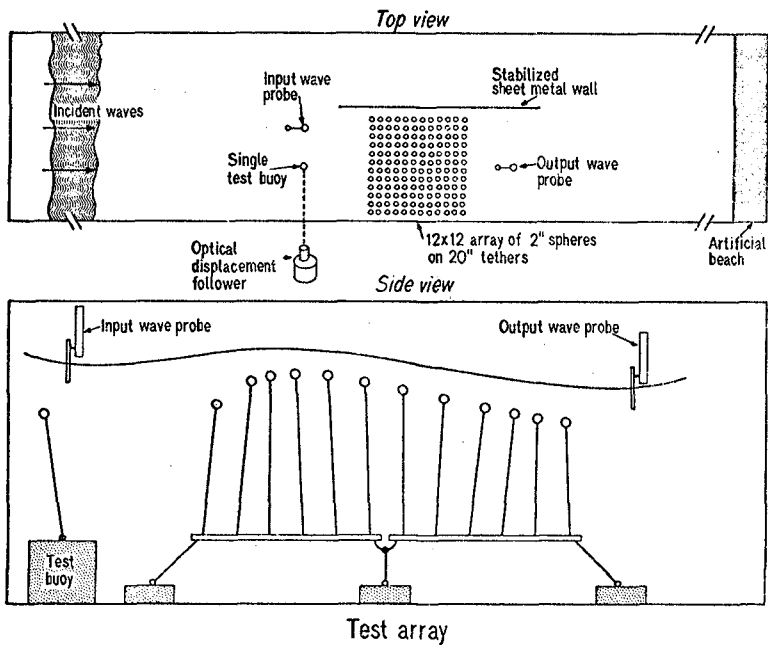


Fig. 3 Top and side views of wave tank tests.

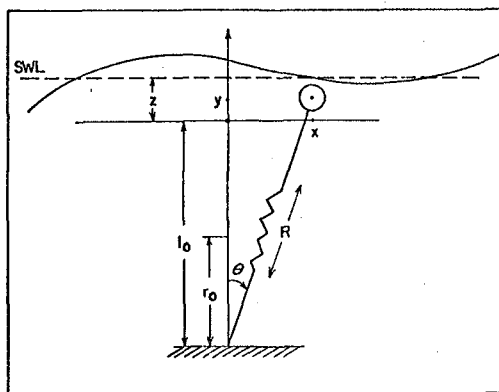


Fig. 5 Geometry of elastically-tethered buoy.

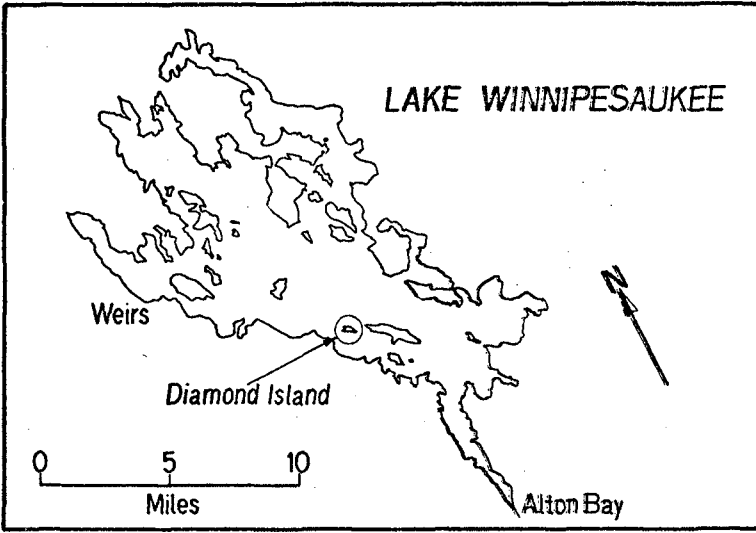


Fig. 6 Diamond Island, site of the field experiment.

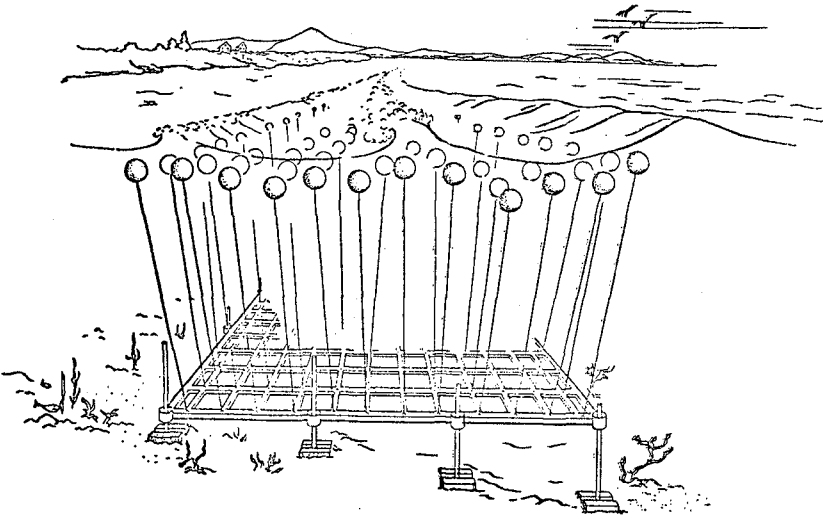
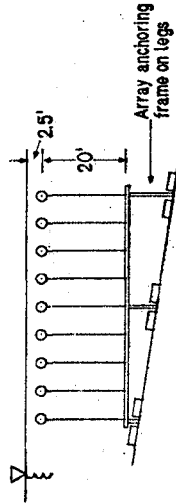
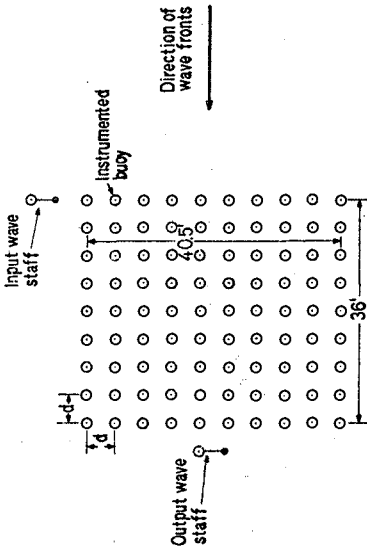


Fig. 7 Elastically-tethered test array for lake field test.



Breakwater array:
 Number of rows: 9
 Number of columns: 10
 Buoy diameter: 2'
 Spacing (d): 4.5'

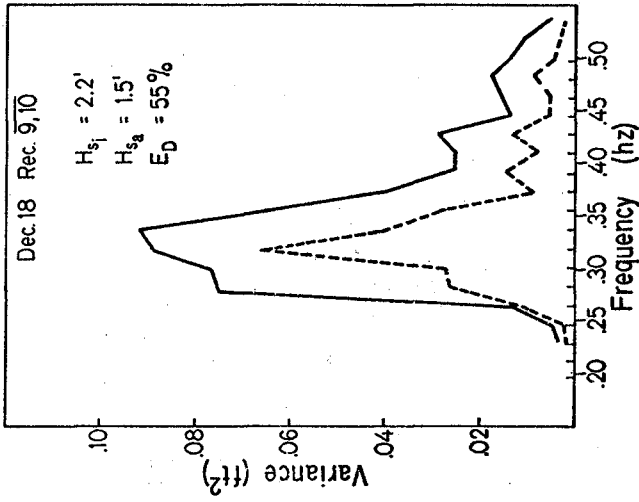


Fig. 9 Measured incident and attenuated wave spectra.

Fig. 8 Layout of field-test array and instrumentation.

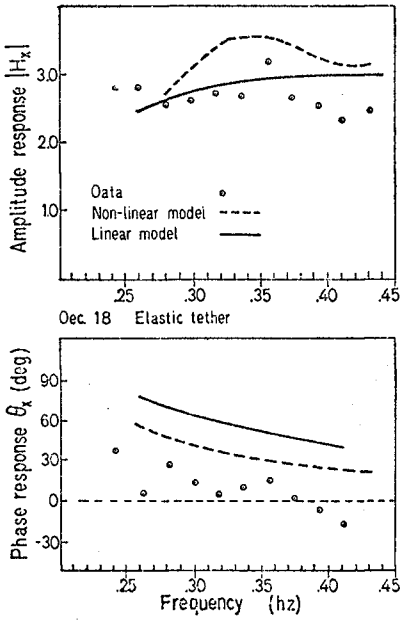


Fig. 10 Horizontal frequency response.

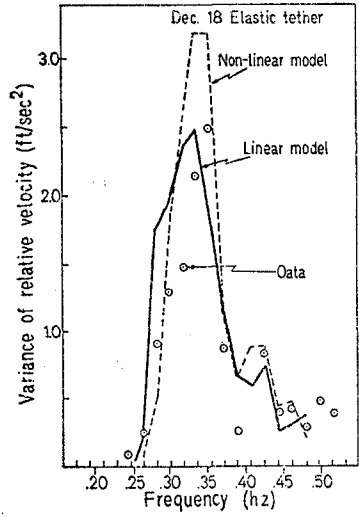


Fig. 11 Spectra of horizontal relative velocity.

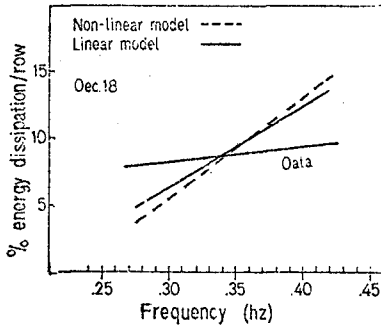


Fig. 12 Breakwater performance.

CHAPTER 161

PROTECTION OF MARITIME STRUCTURES AGAINST SHIP COLLISIONS

by

Kazuki Oda* and Shoshichiro Nagai**

ABSTRACT

This paper deals with the analytical and experimental studies on a new device to prevent the accidents of ship collisions with maritime structures. The practical protection device was designed on the basis of this study and it has been in use for the prevention of ship collisions of a class of 1,000 G/T with a boring tower for the geological survey of the sea beds of a narrow straits in which quite a many ships navigate.

INTRODUCTION

For the recent several years, maritime structures such as drilling platforms, intake towers of cooling water for thermal and/or nuclear power plants and also bridge piers have been constructed nearshore and offshore throughout the world. When they are constructed in seas or straits where many ships navigate, there exists a great possibility of ship collisions with such maritime structures.

In the case of Japan in which several long bridges are being constructed to span the narrow straits with strong tidal currents and quite a many navigation ships, this problem has been considered to be very serious from the points of view of safety navigation as well as the protection of the bridge pier from ship collisions. Even during the terms of the preliminary geological survey of the sea beds at the projected construction sites of the piers of the long bridges, there have been already a lot of accidents of ship contacts with the boring towers for the geological survey. Therefore, it has been urgently needed to find ways for prevention of the accidents of contacts and collisions with erection jackets during the construction of the piers and the piers themselves after the completion of the bridges.

As a result, a new protection device capable of turing securely the original course of approaching vessels to the piers in front of them was proposed by our laboratory and the Honshu-Shikoku Bridge Authority. It consists of three large buoys anchored to the sea bottom and two pressure pneumatic rubber tubes-lines which are tightened with the restoring forces of mooring buoy system and float on the water surface as shown in Fig.1.

* Assistant Professor of Hydraulic Engineering, Faculty of Engineering, Osaka City University, Osaka, Japan.

** Professor of Hydraulic Engineering, Faculty of Engineering, Osaka City University, Osaka, Japan.

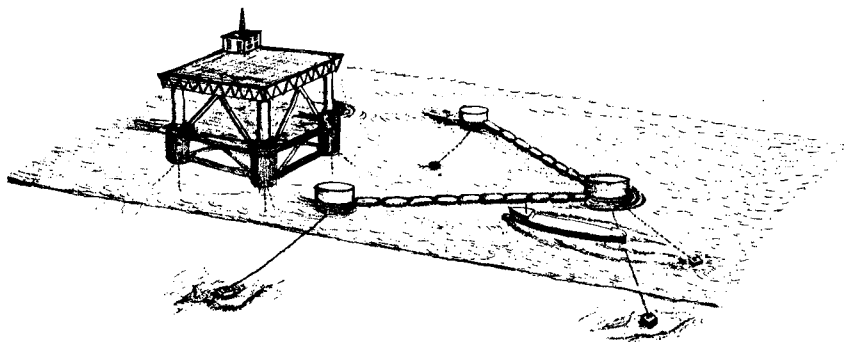


Fig.1. Schematic diagram of the protection device

The analytical and experimental studies were carried out in the hydraulics laboratory of Osaka City University to examine the effect of the proposed protection device and to predict the tensions of the mooring lines of the buoys and the rubber tubes-lines.

APPROACHING CONDITIONS OF SHIPS TO THE DEVICE

(1) Gross tonnages of ships

The results of the investigation on ships passing through the Akashi Straits, the Eastern Bisan Straits and the Kurushima Straits in the Seto Inland Sea, which was conducted by Kobe Mercantile Marine College and Maritime Safety Agency of Japan in July of 1971, are shown in Figs.2, 3 and 4 respectively.

According to these figures, the average number of ships per day passed through is more than 1,000 in every straits. Especially in the Akashi Straits, it comes up to more than 2,000. It will be noted, however, that more than 80% of total ships, including almost all of passenger boats, ferry boats and fishing boats, are smaller ships than 500 G/T while large ships greater than 3,000 G/T are very few in every straits.

It is considered to be quite difficult to protect the piers from the collisions of ships greater than 10,000 to 20,000 G/T by the aid of the device proposed here because of their much larger momentum. For the protection of piers against the collisions of such larger ships, the another way using a steel jacket fender system fixed on the pier is being examined now.

Consequently, it was decided that the gross tonnages of ships considered here to be approaching vessels were 1,000 to 2,000 G/T.

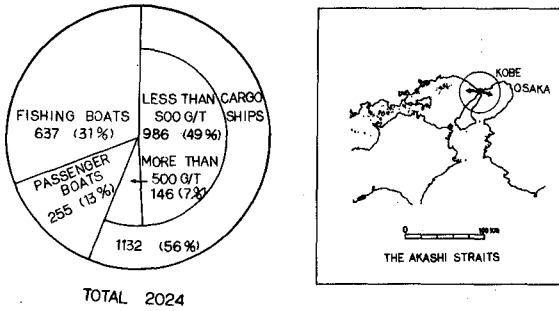


Fig.2. Statistics of ships per day passed through the Akashi Straits

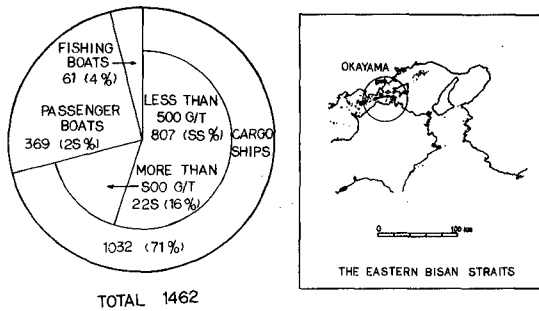


Fig.3. Statistics of ships per day passed through the Eastern Bisan Straits

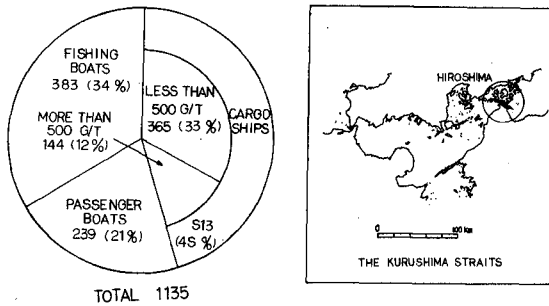


Fig.4. Statistics of ships per day passed through the Kurushima Straits

(2) Approaching speeds and heading angles

According to an annual report "Statistics of Vessels in 1970" published by Ministry of Transportation, 83 to 87% of vessels between 1,000 to 3,000 G/T travel with a speed of 10 to 14 knots.

Since the traveling speeds of ships, however, will be decelerated by the captain in emergency, it may be considered that the approaching speeds into the protection device are less than the usual traveling speeds. As a result, the approaching speeds of ships of a class of 1,000 to 2,000 G/T into the protection device were decided to be 8 to 10 knots in this study.

In general, ships are steered to be almost paralleled to the seaways regulated in narrow straits. Accordingly, the approaching heading angles into the device were taken to be 10 to 15 degrees to the direction of seaway.

THEORETICAL ANALYSIS

1. Basic equations of motion of a ship

A set of co-ordinate axes, x_G, y_G with the origin fixed at the center of gravity of a ship as shown in Fig.5 is used to set up basic equations of motion of a ship. The x_G - and y_G - axes represent the longitudinal and transverse horizontal axes of the ship respectively.

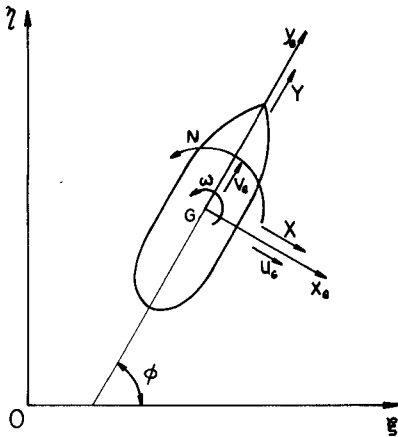


Fig.5. Co-ordinate system

By reference to these co-ordinate axes, equations of motion of the ship in horizontal plane can be written as follows.

$$\left. \begin{aligned} m(\dot{u}_G - \omega v_G) &= X && \text{(sway)} \\ m(\dot{v}_G + \omega u_G) &= Y && \text{(surge)} \\ I_{ZZ}\dot{\omega} &= N && \text{(yaw)} \end{aligned} \right\} (1)$$

where: m = mass of the ship

I_{ZZ} = moment of inertia about the vertical axis through the center of gravity of the ship

u_G, \dot{u}_G = components of the ship velocity and acceleration in x_G -axis direction

v_G, \dot{v}_G = components of the ship velocity and acceleration in y_G -direction

$\omega, \dot{\omega}$ = angular velocity and acceleration about the vertical axis
 X, Y and N = total external forces and moments including hydrodynamic and other non-hydrodynamic forces and moments

The effects of waves and winds are not considered in this treatment. The effects of the coupling roll, pitch, and heave motions into horizontal motion are assumed negligibly small.

The components of external forces X, Y and moments N are expressed as follows for the case of zero rudder angle in linear theory:

$$\left. \begin{aligned} X &= X_u u_G + X_{\dot{u}} \dot{u}_G + X_v v_G + X_{\dot{v}} \dot{v}_G + X_{\omega} \omega + X_{\dot{\omega}} \dot{\omega} + f_x \\ Y &= Y_u u_G + Y_{\dot{u}} \dot{u}_G + Y_v v_G + Y_{\dot{v}} \dot{v}_G + Y_{\omega} \omega + Y_{\dot{\omega}} \dot{\omega} + f_p + f_y \\ N &= N_u u_G + N_{\dot{u}} \dot{u}_G + N_v v_G + N_{\dot{v}} \dot{v}_G + N_{\omega} \omega + N_{\dot{\omega}} \dot{\omega} + f_{\phi} \end{aligned} \right\} \quad (2)$$

where f_x, f_y and f_{ϕ} are the components of non-hydrodynamic external forces and moments. f_p is propulsive forces. $X_{\dot{u}}, X_{\dot{v}}, X_{\dot{\omega}}, Y_{\dot{u}}, Y_{\dot{v}}, Y_{\dot{\omega}}$, and $N_{\dot{u}}, N_{\dot{v}}, N_{\dot{\omega}}$ are hydrodynamic coefficients concerning added masses. $X_u, X_v, X_{\omega}, Y_u, Y_v, Y_{\omega}$ and N_u, N_v, N_{ω} are hydrodynamic coefficients concerning damping forces.

On the assumption that the ship is symmetric with respect to the longitudinal and transverse centerline plane, and that the center of gravity of added mass is coincident with that of the ship, $X_v, X_{\dot{v}}, X_{\dot{\omega}}, Y_u, Y_{\dot{u}}, Y_{\dot{\omega}}, N_{\dot{u}}$ and $N_{\dot{v}}$ can be regarded as zero.

Furthermore, neglecting the effect of damping forces and moments except the damping term $Y_v v_G$ in the surge motion and using nonlinear damping forces $C v_G^2$ instead of linear damping forces $Y_v v_G$, Eq.(2) may be simplified as follows.

$$\left. \begin{aligned} X &= -m_x \dot{u}_G + f_x \\ Y &= -m_y \dot{v}_G - C v_G^2 + f_p + f_y \\ N &= -J_{ZZ} \dot{\omega} + f_{\phi} \end{aligned} \right\} \quad (3)$$

where: $-m_x = X_{\dot{u}}$ added mass in X_G -axis direction
 $-m_y = Y_{\dot{v}}$ added mass in Y_G -axis direction
 $-J_{ZZ} = N_{\dot{\omega}}$ added moment of inertia about the vertical axis
 $C =$ dimensional coefficient of total ship resistances

2. Equations of motion of the ship after contact with the protection device

(1) Co-ordinate system

The co-ordinate system and the symbols used in the theoretical analysis concerning the protection device are shown in Fig.6.

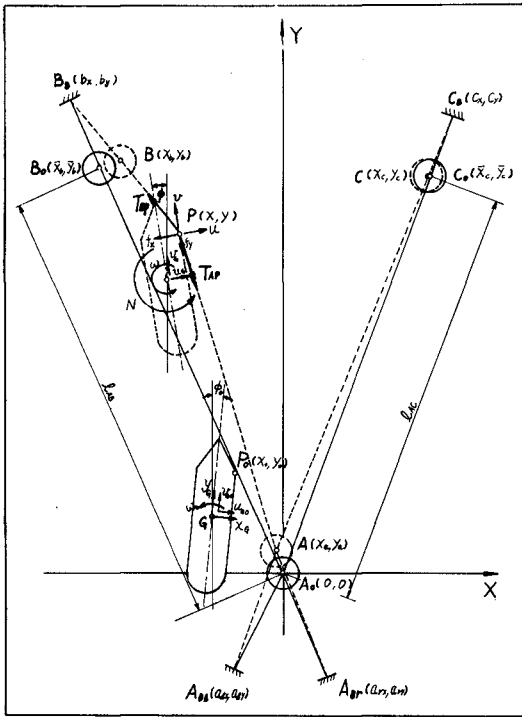


Fig.6. Co-ordinate system and definition sketch of the protection device

The definitions of the symbols in Fig.6 are as follows.

X, Y = co-ordinate axes fixed on the earth with the origin at the center of the main buoy

x_G, y_G = co-ordinate axes with the origin at the center of gravity of the ship

A_{B1}, A_{Br}, B, C = anchor points of each buoy

l_{AB}, l_{AC} = initial distances between the main buoy and the sub-buoy

A, B, C = center points of each buoy

p = contact point with the rubber tubes-line

u_G, v_G = components of the ship velocity in the directions of x_G - and y_G -axes at the center of gravity G

u, v = components of the ship velocity in the directions of x_G - and y_G -axes at the contact point p

ω = angular velocity about the vertical axis of the ship

ϕ = heading angle of the ship to the Y-axis

f_x, f_y = components of the reaction forces on the contact point exerted by the deflection of the rubber tubes-line

The subscript 0, herein, denotes the quantities at the initial time.

(2) Basic assumptions

The following assumptions are introduced to simplify the theoretical analysis on the protection device.

- (a) The movements of the main buoy A are negligibly small.
- (b) Therefore, the movements of the rubber tubes-line AC of the opposite side to the line AB contacting with the ship can be also neglected.
- (c) The configurations of the mooring lines of every buoy can be regarded as straight without any slack.
- (d) The elongations of the mooring lines of the buoys and the rubber tubes-line can be neglected.
- (e) The hydrodynamic forces induced by the movement of the sub-buoy and the rubber tubes-line may be neglected.
- (f) The frictional forces between the rubber tubes-line and the ship hull are minor.
- (g) While the ship is in contact with the rubber tubes-line, the propulsive forces of the ship is constant and the rudder angles is stationarily zero.
- (h) The point of the ship in contact with the rubber tubes-line is stationarily on the bow shoulder of the ship.

(3) External forces and moments on the ship

On the above assumptions, the external forces and moments acting on the ship in contact with the rubber tubes-line are obtained as follows.

Referring to Fig. 7, components of the reaction forces, f_x and f_y on the contact point exerted by the deflection of the rubber tubes-line from the original straight line can be expressed as follows.

$$\left. \begin{aligned} f_x &= - \{ T_{BP} \sin(\theta_{BP} - \phi) - T_{AP} \sin(\theta_{AP} - \phi) \} \\ f_y &= - \{ T_{AP} \cos(\theta_{AP} - \phi) - T_{BP} \cos(\theta_{BP} - \phi) \} \end{aligned} \right\} \quad (4)$$

where: T_{AP}, T_{BP} = tensions of the segments AP and BP of the rubber tubes-line respectively

θ_{AP}, θ_{BP} = angles between the segments AP, BP of the rubber tubes-line and Y-axis respectively

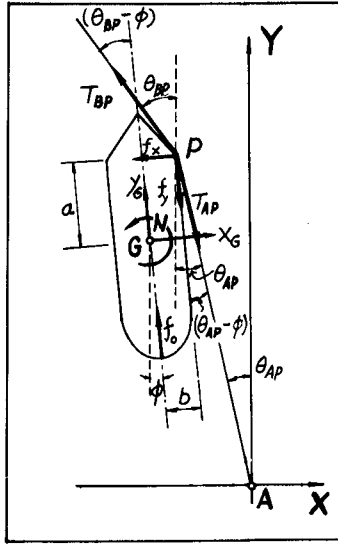


Fig. 7. Definition sketch of the external forces and moments

Since the assumption (f) yields $T_{AP} = T_{BP}$, Eq. (4) can be rewritten as follows.

$$\left. \begin{aligned} f_x &= -T_{AB} \{ (\sin\theta_{BP} - \sin\theta_{AP}) \cos\phi - (\cos\theta_{BP} - \cos\theta_{AP}) \sin\phi \} \\ f_y &= -T_{AB} \{ (\cos\theta_{AP} - \cos\theta_{BP}) \cos\phi + (\sin\theta_{AP} - \sin\theta_{BP}) \sin\phi \} \end{aligned} \right\} \quad (5)$$

where T_{AB} , which is used in place of T_{AP} and T_{BP} , is the tensions of the rubber tubes-line.

From the geometrical relations shown in Fig. 8, the following equations are derived.

$$\left. \begin{aligned} \sin\theta_{AP} &= -\frac{x}{\sqrt{x^2 + y^2}} \\ \cos\theta_{AP} &= \frac{x}{\sqrt{x^2 + y^2}} \\ \sin\theta_{BP} &= \frac{x - b_x}{\sqrt{(x - b_x)^2 + (y - b_y)^2}} \\ \cos\theta_{BP} &= -\frac{y - b_y}{\sqrt{(x - b_x)^2 + (y - b_y)^2}} \end{aligned} \right\} \quad (6)$$

Substituting Eq. (6) into (5), Eq. (7) is obtained.

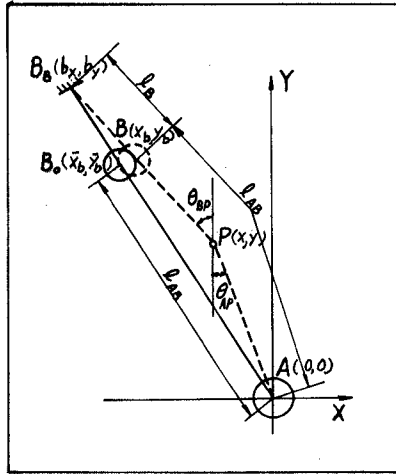


Fig.8. Geometrical relations of the rubber tubes-line

$$\left. \begin{aligned}
 f_x &= -T_{AB} \left\{ \left(\frac{x - b_x}{\sqrt{(x - b_x)^2 + (y - b_y)^2}} + \frac{x}{\sqrt{x^2 + y^2}} \right) \cos\phi \right. \\
 &\quad \left. + \left(\frac{y - b_y}{\sqrt{(x - b_x)^2 + (y - b_y)^2}} + \frac{y}{\sqrt{x^2 + y^2}} \right) \sin\phi \right\} \\
 f_y &= -T_{AB} \left\{ \left(\frac{y - b_y}{\sqrt{(x - b_x)^2 + (y - b_y)^2}} + \frac{y}{\sqrt{x^2 + y^2}} \right) \cos\phi \right. \\
 &\quad \left. + \left(\frac{x - b_x}{\sqrt{(x - b_x)^2 + (y - b_y)^2}} + \frac{x}{\sqrt{x^2 + y^2}} \right) \sin\phi \right\}
 \end{aligned} \right\} \quad (7)$$

External moments f_ϕ around the vertical axis through the center of gravity of the ship induced by these forces f_x , f_y are given by Eq.(8).

$$f_\phi = - (af_x - bf_y) \quad (8)$$

where a and b are the lengths of moment arms of f_x and f_y around the center of gravity of the ship shown in Fig.7 respectively. According to the assumption (h), these lengths are considered to be constant while the ship contacts with the line.

On the other hand, from the equations of equilibrium of the forces acting on the point B and the geometrical relations shown in Fig.9, the tensions T_{AB} of the rubber tubes-line in Eq.(7) can be written as follows.

$$T_{AB} = \{w_0 A_B (h_B - \sqrt{S_B^2 - l_B^2}) - W_B\} \frac{l_B}{\sqrt{S_B^2 - l_B^2}} \quad (9)$$

where: w_0 = specific weight of water

A_B = area of waterplane of the sub-buoy

W_B = weight of the sub-buoy

S_B = length of the mooring line of the sub-buoy

l_B = horizontal distance between the sub-buoy and its anchor point given by Eq.(10)

$$l_B = \sqrt{x^2 + y^2} + \sqrt{(x - b_x)^2 + (y - b_y)^2} - l_{AB} \quad (10)$$

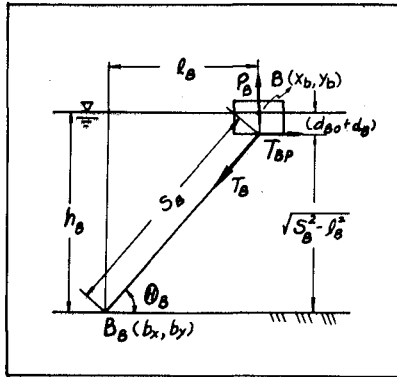


Fig.9. Definition sketch of the forces on the sub-buoy

(4) Total ship resistances and propulsive forces

In general, total ship resistances R_T consisting of frictional resistances and residual resistances which include wave making resistances and eddy resistances are given by Eq.(11).

$$R_T = C v_G^2 \quad (11)$$

where: v_G = velocity of a ship in the direction of the longitudinal axis

C = dimensional coefficient of total ship resistances expressed by Eq. (12)

$$C = (C_f + C_r) \frac{1}{2} \rho S$$

where: ρ = density of water

S = area of wetted surface of the ship hull

C_f = coefficient of frictional resistances

C_r = coefficient of residual resistances

Assuming that a ship approaches into the protection device with a constant speed, the propulsive forces can be considered to equal to the total resistances of the ship traveling with the constant approaching velocity v_G in the direction of the longitudinal axis. Thus, the propulsive forces of the ship can be written as follows.

$$f_p = C v_G^2 \quad (13)$$

where f_p is the propulsive forces.

(5) Tensions of the mooring lines of the buoys

From the equations of equilibrium of the forces acting on the point A and the geometrical relations shown in Fig.10, the tensions of two mooring lines of the main buoy are given by the following equations respectively.

$$\begin{aligned} T_{Ar} &= \sec \theta_{A0} \operatorname{cosec} 2\alpha_0 \{ T_{AB} \sin(\alpha_0 - \theta_{Ap}) + (T_{AC})_0 \sin(\alpha_0 - \beta_0) \} \\ T_{Al} &= \sec \theta_{A0} \operatorname{cosec} 2\alpha_0 \{ T_{AB} \sin(\alpha_0 - \theta_{Ap}) - (T_{AC})_0 \sin(\alpha_0 + \beta_0) \} \end{aligned} \quad (14)$$

where: T_{Ar} , T_{Al} = tensions of the mooring lines AA_r and AA_l respectively

T_{AB} = tensions of the rubber tubes-line AB

$(T_{AC})_0$ = initial tensions of the rubber tubes-line AC

θ_{A0} = initial vertical angle of inclination of the mooring line of the main buoy

$2\alpha_0$, $2\beta_0$ = initial horizontal angle between the two mooring lines of the main buoy and initial angle between the two rubber tubes-lines respectively

In the same way, by references to Fig.9 again, the tensions of the mooring line of the sub-buoy are obtained as follows.

$$T_B = \{ w_O A_B (h_B - \sqrt{S_B^2 - l_B^2}) - W_B \} \frac{S_B}{\sqrt{S_B^2 - l_B^2}} \quad (15)$$

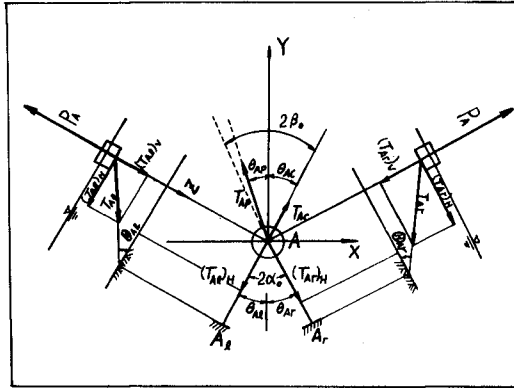


Fig.10. Definition sketch of the forces on the main buoy

(6) Equations of motion of the ship

Substituting Eq.(3) into Eq.(1), equations of motion of the ship after contact with the rubber tubes-line of the protection device can be expressed as follows.

$$\left. \begin{aligned} (m + m_x) \dot{u}_G &= m\omega v_G + f_x \\ (m + m_y) \dot{v}_G &= -m\omega u_G - C v_G^2 + f_p + f_y \\ (I_{ZZ} + J_{ZZ}) \dot{\omega} &= f_\phi \end{aligned} \right\} \quad (16)$$

Using the velocity components u and v of the point of the ship in contact with the rubber tubes-line in the directions of X- and Y-axes fixed on the earth as shown in Fig.11, the velocity components u_G and v_G of the center of gravity of the ship in x_G - and y_G -axes directions can be denoted as follows.

$$\left. \begin{aligned} u_G &= u \cos\phi + v \sin\phi + a\omega \\ v_G &= v \cos\phi - u \sin\phi - b\omega \end{aligned} \right\} \quad (17)$$

Substituting Eq.(17) into Eq.(16), the final equations of motion of the ship after contact with the rubber tubes-line can be written as follows.

$$\left. \begin{aligned} \dot{x} &= u, \quad \dot{y} = v, \quad \dot{\phi} = \omega \\ u &= -\left\{ \frac{\cos\phi}{M_x} + \frac{a}{I_Z} (a \cos\phi + b \sin\phi) \right\} f_x \end{aligned} \right\}$$

(to be continued to the next page)

$$\begin{aligned}
 & + \left\{ \frac{\sin\phi}{M_y} + \frac{b}{I_z} (a \cos\phi + b \sin\phi) \right\} f_y \\
 & - \frac{\sin\phi}{M_y} \{ f_p - C(v \cos\phi - u \sin\phi - b\omega)^2 - \omega v \\
 & + m\omega \left\{ \frac{\cos\phi}{M_x} (v \cos\phi - u \sin\phi - b\omega) + \frac{\sin\phi}{M_y} (u \cos\phi + v \sin\phi + a\omega) \right\} \\
 & \dot{v} = \left\{ \frac{\sin\phi}{M_x} + \frac{a}{I_z} (a \sin\phi - b \cos\phi) \right\} f_x \\
 & + \left\{ \frac{\cos\phi}{M_y} - \frac{b}{I_z} (a \sin\phi - b \cos\phi) \right\} f_y \\
 & + \frac{\cos\phi}{M_y} \{ f_p - C(v \cos\phi - u \sin\phi - b\omega)^2 + \omega u \\
 & + m\omega \left\{ \frac{\sin\phi}{M_x} (v \cos\phi - u \sin\phi - b\omega) - \frac{\cos\phi}{M_y} (u \cos\phi + v \sin\phi + a\omega) \right\}
 \end{aligned} \tag{18}$$

where: $M_x = m + m_x$, $M_y = m + m_y$, $I_z = I_{zz} + J_{zz}$

Eq.(18) is six simultaneous non-linear differential equations and can be solved by means of numerical analysis using the Runge-Kutta-Gill method.

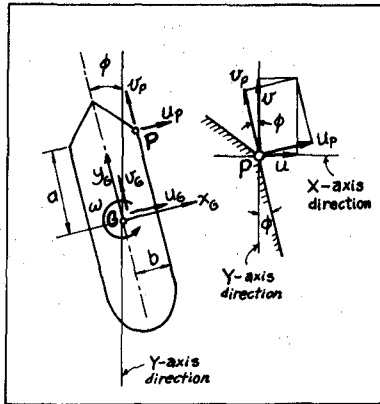


Fig.11. Definition sketch of the velocities

MODEL EXPERIMENTS

Model experiments were conducted on a 1 to 50 model scale in the wave basin which is 42 m long, 12 m wide and 0.75 m deep as shown in Fig.12. A radio-controlled model ship corresponding to 880 G/T cargo ship in prototype was used in the experiments.



Fig.12. Wave basin used in the experiments

The arrangement and dimension of the model of the protection device are shown in Fig.13.

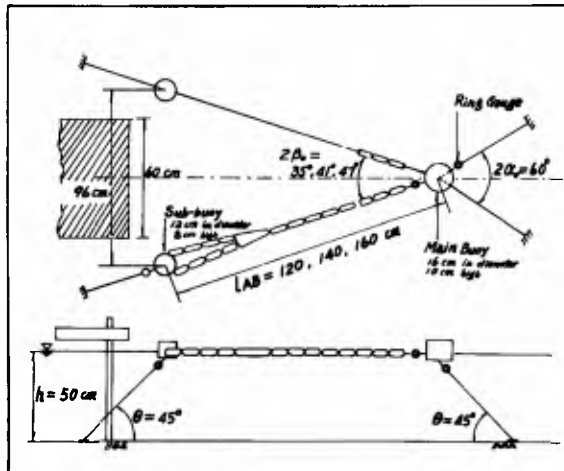


Fig.13. Arrangement and dimension of the model of the protection device

The variable quantities measured in the experiments are the approaching speeds v_{G_0} and the heading angles ϕ_0 of the model ship to the rubber tubes-line, the distances p_0 between the center A of the main buoy and the initial contact point P_0 , the lateral displacements δ_B of the sub-buoy in the X-axis direction, the tensions T_{Ar} , T_B of the mooring lines of the main buoy and the sub-buoy and the tensions T_{AB} of the rubber tubes-line as shown in Fig. 14.

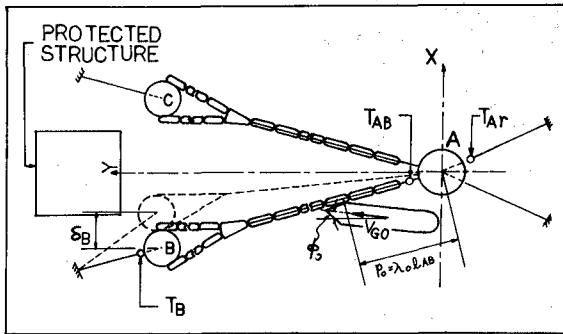


Fig.14. Variable quantities measured in the experiments

The tensions were measured with sensitive ring-gauges made of brass which straingauges are mounted on both sides. Custom-made mini-turnbuckles were used to facilitate the adjustment of the initial tensions of the rubber tubes-lines.

The horizontal motions of the ship and the displacements of the sub-buoy were measured by analyzing 16 mm movies taken from a tower 6 m high above the water level. Fig.15 shows an example of frame-photographs of the 16 mm movies. Fig.16 shows the model ship approaching to the rubber tubes-line and going forward contacting with the line.

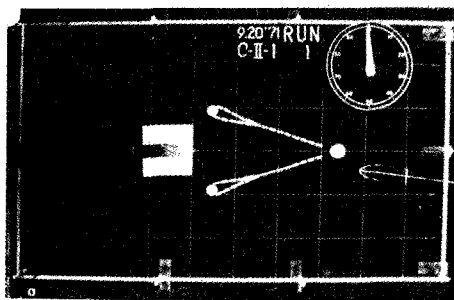


Fig.15. A frame-photograph of 16 mm movies

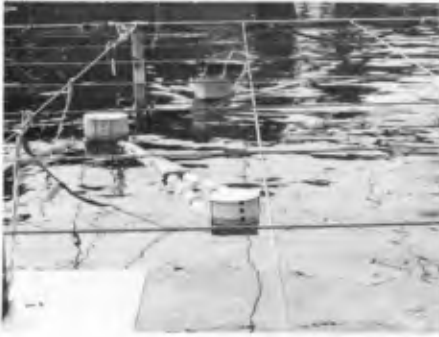


Fig.16(a). The model ship approaching to the rubber tubes-line



Fig.16(b). The model ship going forward contacting with the line

COMPARISON BETWEEN THEORY AND EXPERIMENTS

The theoretical values obtained by means of numerical analysis of the maximum tensions $(T_{AB})_{max}$ of the rubber tubes-line, the maximum tensions $(T_{Ar})_{max}$, $(T_B)_{max}$ of the main buoy and sub-buoy, and the maximum lateral displacements $(\delta_B)_{max}$ of the sub-buoy, were compared with the experimental ones as shown in Figs.17, 18, 19 and 20 respectively.

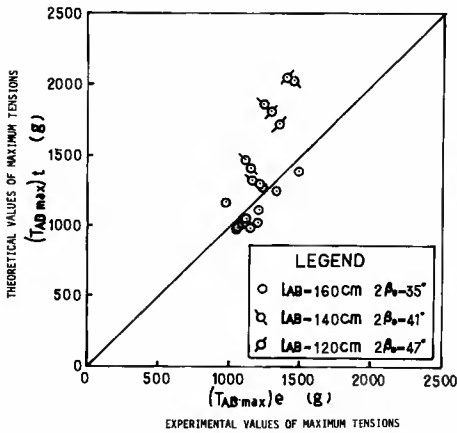


Fig.17. Comparison between the theoretical and experimental values on $(T_{AB})_{max}$

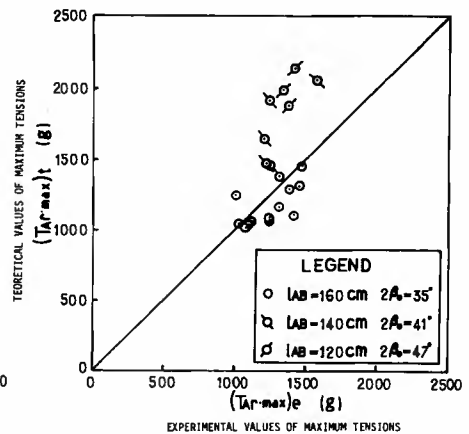


Fig.18. Comparison between the theoretical and experimental values on $(T_{Ar})_{max}$

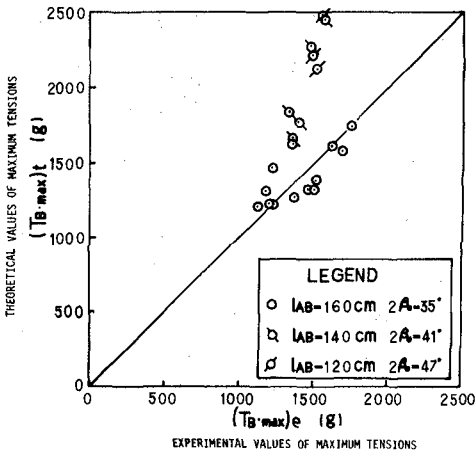


Fig. 19. Comparison between the theoretical and experimental values on $(T_B)_{\max}$

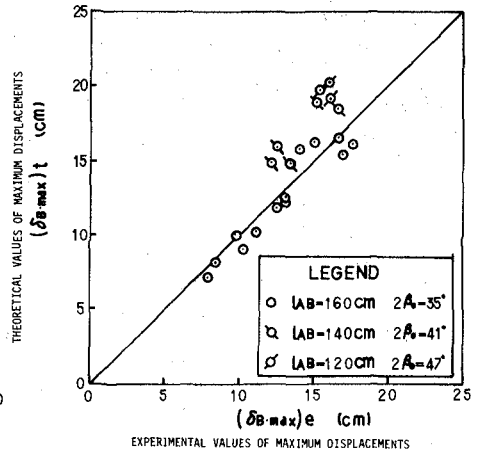


Fig. 20. Comparison between the theoretical and experimental values on $(\delta_B)_{\max}$

These figures show that the agreement between the theoretical and experimental values concerning $(T_{AB})_{\max}$, $(T_{Ar})_{\max}$, $(T_B)_{\max}$ and $(\delta_B)_{\max}$ is good for the case of $l_{AB} = 160$ m, $2\beta_0 = 37^\circ$ but poor for the case of $l_{AB} = 140$ m, $2\beta_0 = 41^\circ$ and $l_{AB} = 120$ m, $2\beta_0 = 47^\circ$.

Namely, it may be said that the theoretical values reasonably agree with the experimental ones for the case of longer distances between the main buoy and the sub-buoy and smaller angles between the rubber tubes-lines, however, the theoretical values much deviate from the experimental results for the case of shorter distances and larger angles.

The major reasons for the much deviation may be considered as the followings.

In general, since the heading angles of the ship relative to the rubber tubes-line are larger in the case of larger angle between the two tubes-lines, the ship contacts with the rubber tubes-line near the bow end in such cases. In addition, in the case of shorter distances between the main buoy and the sub-buoy, the lateral motions of the sub-buoy and the rubber tubes-line tend to be quicker than in the case of longer distances. Therefore, it may be considered that the assumptions (e) and (h) are no longer reasonable for such cases.

From the comparison between the theoretical and experimental results, it may be concluded that the theory is limited to its application for the case of $l_{AB}/L_{pp} \geq 1.3$, $\psi_0 \leq 25^\circ$. Herein, L_{pp} is the length between perpendiculars of the ship and ψ_0 is the initial heading angle relative to the rubber tubes-line.

APPLICATION FOR PRACTICAL USE

A practical protection device for prevention of ship collisions of a class of 1,000 G/T against the floating drilling platform with the deck 43 m by 43 m shown in Fig.21, was designed under the following practical conditions;

gross tonnage of the approaching ship:	1,000 G/T
distance between the main buoy and sub-buoy:	$l_{AB} = 100 \text{ m}$
angle between two rubber tubes-lines:	$2\beta_0 = 36.5^\circ$
horizontal angle between two mooring chains of the main buoy:	$2\alpha_0 = 36.5^\circ$
vertical angles of the mooring chains:	$\theta_0 = 45^\circ$
area of water plane of the sub-buoy:	$A_B = 40 \text{ m}^2$
water depth (effects of the tidal range were taken into consideration):	$h = 50 \pm 1.0 \text{ m}$
approaching speed of the ship:	$v_{G0} = 10 \text{ kt}$
initial heading angle of the ship:	$\phi_0 = 0^\circ$
nondimensional initial contact position ($\lambda_0 = p_0/l_{AB}$):	$\lambda_0 = 0.5$
initial tensions of the rubber tubes-line at Mean Water Level:	$(T_{AB})_0 = 50 \text{ t}$



Fig.21. Picture of the floating drilling platform

The essential results of the numerical calculations for the practical device are summarized in Table 1.

Table 1. Essential Results of the Numerical Calculations for the Practical Device

Essential quantities	At Low Water Level	At High Water Level
Initial values		
$(T_{AB})_0$ (t)	21.2	88.3
$(T_B)_0$ (t)	30.0	125
$(T_{AR})_0$ (t)	21.2	88.3
Maximum values		
$(T_{AB})_{max}$ (t)	157	186
$(T_B)_{max}$ (t)	210	253
$(T_{AR})_{max}$ (t)	179	221
$(\delta_B)_{max}$ (m)	12.9	10.8

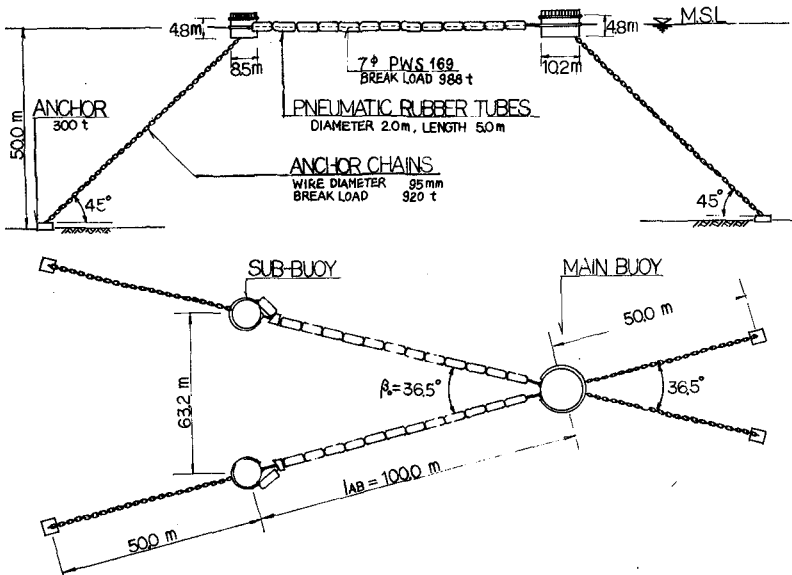


Fig.22. Schematic diagram of the practical protection device

Fig.22 shows the schematic diagram of the practical protection device designed on the basis of the above results of the numerical calculations.

The rubber tubes-line is composed of fourteen pressure pneumatic rubber tubes each 2 m in diameter and 5 m long with a steel pipe along the central axis and a parallel wire rope 105 mm in diameter with a break load of 988 t.

The main buoy is 10.2 m in diameter and 4.8 m high and the sub-buoy 8.5 m in diameter and 4.8 m high.

Anchor chains 95 mm in wire diameter with a break load of 920 t are used for the mooring line of the main-buoy and sub-buoy, and specially moulded cast iron sinkers 300 t in weight in the air were used for the anchors of the buoys.

The initial tensions of the rubber tubes-line can be arbitrarily adjusted by changing the buoy draft by means of pulling up the mooring chains into the buoy using an oil pressure jack equipped on the buoy deck.

Fig.23 shows the practical protection device set in front of the floating drilling platform in the Akashi Straits.



Fig.23. Picture of the practical protection device

CONCLUSION

The new device to protect maritime structures from ship collisions proposed here was proved in experimental and theoretical ways to be very useful to prevent the collisions of ships up to 1,000 to 2,000 G/T with usual traveling speeds of 10 to 14 knots.

The tensions of the rubber tubes-line and the mooring lines of the main buoy and sub-buoy, and the lateral displacements of the sub-buoy can be completely predicted by solving the equations of motion of the ships after contact with the rubber tubes-line by means of numerical calculations using the Runge-Kutta-Gill method.

CHAPTER 162

ADDED MASSES OF LARGE TANKERS BERTHING TO DOLPHINS

By

Taizo Hayashi¹ and Masujiro Shirai²

ABSTRACT

The added masses of large tankers berthing to dolphins are studied both theoretically and experimentally. The movements of large vessels in shallow water in the directions normal to their planes of symmetry cause counter-flows of appreciable velocities under the hulls. The inertia of these counter-flows is shown to have an important effect on the added masses of the vessels. A theoretical formula is derived to determine the mass factor of an ocean vessel in shallow water as a function of the ratio Draught/Water-depth, the Froude number of the vessel and the coefficient of head loss of the counter-flow under the hull.

Experiment is made to determine the mass factor. Comparison between the theory and the experiment shows a good agreement.

INTRODUCTION

The size of tankers has remarkably been increasing. For the design of the dolphins to which large tankers are berthed the accurate estimation of added masses of these vessels is essential.

When the depth of water is sufficiently large in comparison with the draught of a vessel, the added mass of the vessel can be estimated by the use of the formulae derived in the case of deep water [1, 2]. However, in consequence of the remarkable increase of the size of tankers, the depth of water in front of dolphins is usually not very large in comparison with the draught of a large tanker, and sometimes the latter ranges to as much as 80 percent, or even more, of the water depth in front of dolphins.

In the case when the clearance between the hull of a vessel and the bottom of water is small the added mass of the vessel is supposed to differ considerably from that in deep water. The purpose of this paper is to determine theoretically and experimentally the added masses of large tankers in shallow water.

THEORETICAL CONSIDERATION

When a large tanker is navigated with a constant speed in a normal

- 1 Professor, Hydraulic Laboratory, Department of Civil Engineering, Chuo University, Tokyo
- 2 Director of Department of Basic Engineering Research, Technical Research Institute, Taisei Corporation, Tokyo

direction toward dolphins by a tug-boat, it is theoretically supposed, from the consideration based on the equation of continuity of flow of water across the vertical plane in front of the hull of vessel, that the motion of the vessel toward the dolphins causes a counter-flow of an appreciable velocity under the hull bottom.

Figure 1 shows the flow of water caused by the steady movement of a model hull in an experimental flume. The flow was visualized by the use of

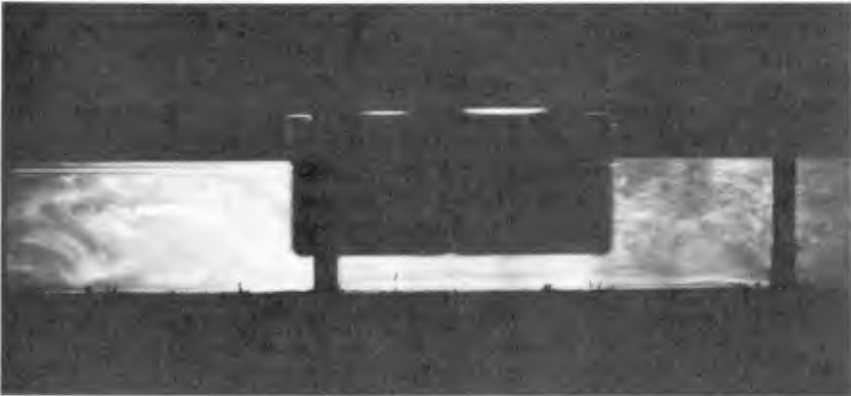


Fig. 1. Flow of water caused by the steady movement of a model hull.

aluminium flakes. The model was pulled with the fine wire, which is seen in the figure. We can clearly notice the counter-flow under the hull. Since the velocity of the counter-flow was appreciable, a vortex filament was induced in front of the hull by the counter-flow, this vortex filament being seen in the figure. The Froude number of the movement of this model hull was 0.0285.

In the steady motion of a vessel (Fig. 2) the equation of continuity for the flow around the vessel may be written as

$$D v_0 = C h' v_0' \tag{1}$$

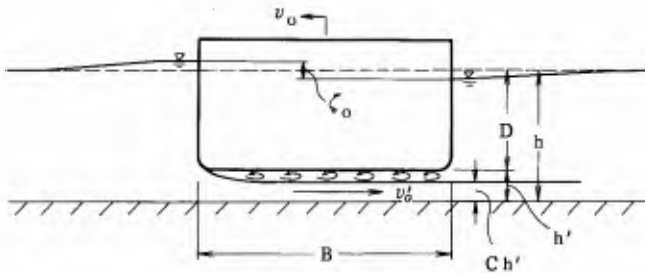


Fig. 2. Steady movement of a vessel and the counter-flow.

where v_0 and v_0' are the steady velocities of the vessel and the counter-flow, respectively, D is the draught of the vessel, C the coefficient of contraction of the counter-flow, and h' the clearance of water under the hull.

When the vessel comes to be in contact with a dolphin, its velocity begins to be decelerated. It is to be noted, however, that even after the instant when the vessel comes to be in contact with the dolphin, the counter-flow under the hull tends to maintain its own velocity owing to its inertia. Consequently, due to the continuity of flow of water, the water level on the dolphin side of the hull goes down forming a negative surge, and the water level on the sea-side goes up forming a positive surge (Fig. 3), until the counter-flow will have eventually been ceased by the negative

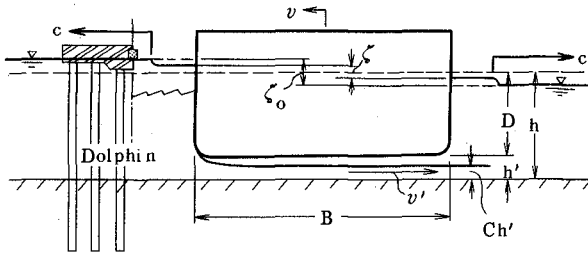


Fig. 3. Negative and positive surges formed in consequence of the deceleration during the movement of a vessel. (ζ decreases as t increases.)

hydraulic gradient, the hydraulic gradient formed by $\zeta < 0$, acting on the counter-flow. Due to the difference of water levels on the both sides of the hull thus brought about, hydrostatic pressure acts on the hull in the direction of the dolphin, hence the force of impact of the vessel is increased. Since this increase of impact of the vessel is caused by the inertia of the counter-flow under the hull of the vessel, we can understand that the inertia of the counter-flow has an important effect on the added mass of the hull.

With all this in mind we make the theoretical analysis, which is shown in the next Chapter.

THEORETICAL ANALYSIS

First, the dynamic equation of the vessel per its unit length is given by

$$\rho D B \dot{v} = -k x - \rho g D \zeta - \tau B \quad (2)$$

Here, ρ is the density of sea-water, B the beam of the vessel, v the instantaneous velocity of the vessel, k the elasticity constant of the system consisting of the mooring structure, intermediate object and the vessel, as a whole, x the total elastic deformation of the same system, g the acceleration of gravity, ζ the instantaneous value of the difference of the

water levels on the both sides of the hull, and τ the shearing stress acting on the bottom of the hull. The second term in the right member expresses the hydrostatic pressure acting on the hull owing to the difference of water levels on the both sides of the hull.

The τ is expressed as

$$\tau = \frac{1}{2} \rho (v + v')^2 C_f \quad (3)$$

where C_f is coefficient of friction and v' is the instantaneous velocity of the counter-flow. We approximate this equation by the following equation.

$$\tau = \beta (v + v') \quad (4)$$

Here, β is a parameter.

As for the elastic deformation, x , it is related with the movement of the vessel as

$$\dot{x} = v \quad (5)$$

The equation of continuity of flow across the vertical plane in front of the hull is given by

$$D v - C h' v' = -c \frac{1}{2} (\zeta_0 - \zeta) \quad (6)$$

in which c is the celerity of surge and ζ_0 is the initial value of ζ . The term in the right member expresses the rate of discharge of water supplied to the counter-flow by the lowering of the water level on the dolphin side of the hull.

The dynamic equation for the counter-flow existing under hull bottom is

$$\rho B \dot{v}' = \rho g \zeta - h_f \quad (7)$$

Here, h_f is the head loss of the counter-flow. This h_f can be expressed as

$$h_f = \lambda v'^2 / 2g \quad (8)$$

in which λ is a coefficient. The above equation is approximated by the following equation

$$h_f = \alpha v' \quad (9)$$

where α is a parameter.

In the six equations, (2), (4), (5), (6), (7) and (9), we have six unknown quantities, v , v' , ζ , x , τ and h_f . Therefore, we can solve these equations. Eliminating v , v' , ζ , τ and h_f from these six equations we obtain

$$\begin{aligned} & \frac{c \rho D B^2}{g (2 C h' + c \alpha)} \ddot{x} + \left[\frac{B (2 \rho g D^2 + c \beta B)}{g (2 C h' + c \alpha)} + \rho D B \right] \dot{x} \\ & + \left[\frac{B c k}{g (2 C h' + c \alpha)} + \frac{2 \rho g D^2 + c \beta B}{c} - \frac{2 D (2 \rho g C D h' - c \beta B)}{c (2 C h' + c \alpha)} \right] x \\ & + k x = \rho g \zeta_0 \left[\frac{2 \rho g C D h' - c \beta B}{g (2 C h' + c \alpha)} - \rho D \right] \end{aligned} \quad (10)$$

which is an ordinary differential equation for x of the third order.

As illustrated in Fig. 4, although the time-variation of x is to be

quite unsymmetrical with respect to T_1 , the time of the maximum deformation of the elastic system, it may approximately be assumed that the variation of x for the range $0 \leq t \leq T_1$ is sinusoidal, namely,

$$x \propto \exp(i\sigma t) \text{ for } 0 \leq t \leq T_1$$

Then, (11)

$$\ddot{x} = -\sigma^2 x \tag{12}$$

Therefore, in Eq. (10) the first term having \ddot{x} can be combined with the third term having \dot{x} to give the damping force. Hence, the term which expresses the inertia force of the vessel is the second term having \dot{x} .

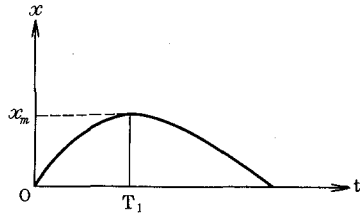


Fig. 4. Time-variation of x .

Obviously, the two terms within the square brackets of the second term in Eq. (10) may be interpreted as the added mass per unit length of the vessel, M , and the mass per unit length of the vessel, M_0 , namely

$$M = B (2 \rho g D^2 + c \beta B) / g (2 C h' + c \alpha) \tag{13}$$

$$M_0 = \rho D B \tag{14}$$

In Eq. (13) two parameters, α and β , are present, which parameters are to be expressed in terms of λ and C_f , respectively. The calculation for this is as follows:

As described previously, Eq. (9) is an approximate expression to Eq. (8) (Fig. 5). In order to determine α definitely, let us take α in such a way that the work done against the h_f given by Eq. (9) during the period $0 \sim T_1$ becomes equal to the work done against the h_f given by Eq. (8) during the same period. Therefore,

$$\int_0^{T_1} \lambda \frac{v'^2}{2g} \cdot v' dt = \int_0^{T_1} \alpha v' \cdot v' dt \tag{15}$$

Furthermore, we approximately assume

$$v' = v_0' \sin \frac{\pi}{2T_1} t \tag{16}$$

Then, substitution of Eq. (16) into Eq. (15) yields the following relation.

$$\alpha = \frac{4\lambda}{3\pi} \frac{v_0'}{g} = \frac{8}{3\pi} h_{f0} \tag{17}$$

in which h_{f0} is the initial value of h_f .

By a similar procedure β can be determined in terms of C_f as

$$\beta = \rho C_f (v_0 + v_0') \frac{8}{3\pi} = \frac{8}{3\pi} \tau_0 \tag{18}$$

where τ_0 is the initial value of τ_0 . Substituting the approximate relation,

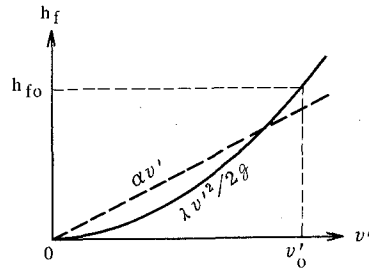


Fig. 5. Approximation of h_f .

$v_o' = v_o D / C h'$; into Eqs. (17) and (18), we obtain the following equations.

$$\alpha = \frac{4\lambda}{3\pi} \frac{v_o}{g'} \frac{D}{C h'} \tag{19}$$

$$\beta = \frac{8}{3\pi} \rho C_f v_o \left(1 + \frac{D}{C h'} \right) \tag{20}$$

Denoting the water depth by h , the celerity of the surge is given by

$$c = \sqrt{g h} \tag{21}$$

Substitution of Eqs. (19), (20) and (21) into Eq. (13) yields the following equation.

$$\frac{M}{M_o} = \frac{D}{C h'} \frac{1 + \frac{4}{3\pi} C_f F_r \frac{B h}{D^2} \left(1 + \frac{D}{C h'} \right)}{1 + \frac{2}{3\pi} \lambda F_r \frac{h}{D} \left(\frac{D}{C h'} \right)^2} \tag{22}$$

Here, F_r is the Froude number of the vessel defined by

$$F_r = v_o / \sqrt{g h} \tag{23}$$

Since

$$\begin{aligned} O(C_f) &= O(10^{-2}), & O(F_r) &= O(10^{-2}), \\ O(\lambda) &= O(1), & O(Bh/D^2) &= O(1), \\ O(D/h) &= O(1), & O(D/C h') &= O(1) \sim O(10), \end{aligned}$$

the above equation may be approximated as

$$\frac{M}{M_o} = \frac{D}{C h'} \left/ 1 + \frac{2}{3\pi} \lambda F_r \frac{h}{D} \left(\frac{D}{C h'} \right)^2 \right. \tag{24}$$

This equation is written as the following equations.

$$\frac{M}{M_o} = \frac{C h'}{D} \left/ \left(\frac{C h'}{D} \right)^2 + \frac{2}{3\pi} \lambda F_r \left(1 + \frac{h'}{D} \right) \right. \tag{25}$$

$$= C \left(\frac{h}{D} - 1 \right) \left/ C^2 \left(\frac{h}{D} - 1 \right)^2 + \frac{2}{3\pi} \lambda F_r \frac{h}{D} \right. \tag{26}$$

The effect of friction on the mass factor is obvious. In the ideal case of no friction, λ disappears, and Eq. (26) is reduced to the following equation.

$$\frac{M}{M_o} = 1 / C \left(\frac{h}{D} - 1 \right) \tag{27}$$

Accordingly, the value of mass factor tends to infinity as the draught, D , approaches to the water-depth, h .

In actual fluid, however, friction has an important effect on the mass factor. In view of Eq. (8) λ can be assumed for practical purposes as

$$\lambda \sim 1 \tag{28}$$

Equation (26) for the values $\lambda = 1$ and $C = 0.5$ is drawn to scale in Fig. 6.

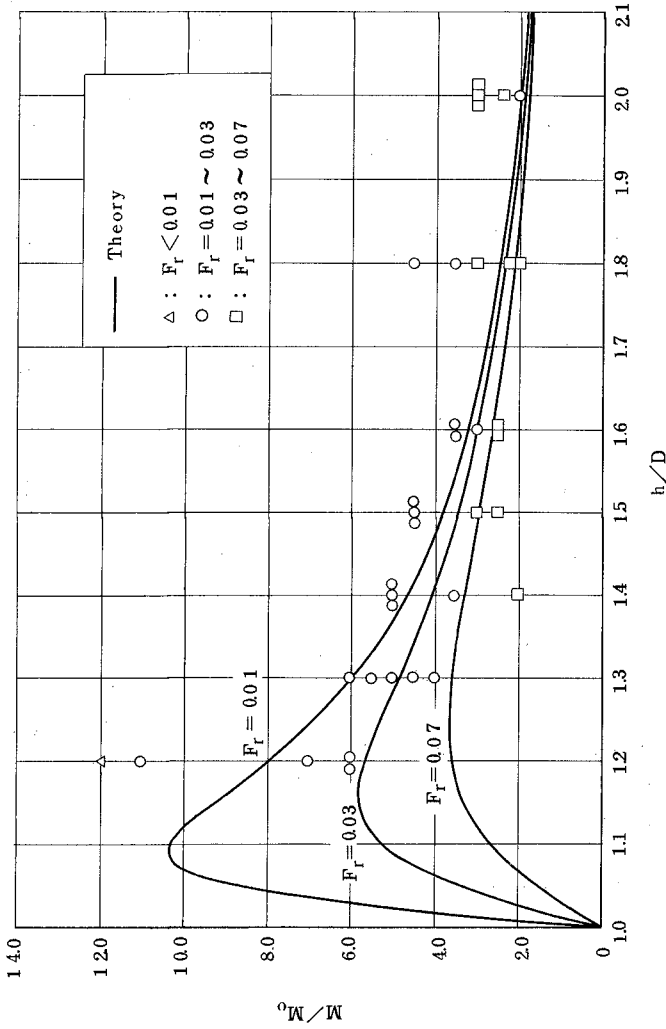


Fig. 6. The ratio Added Mass/Displaced Mass of the large tanker in shallow water.

Owing to the presence of friction the mass factor for a constant value of Froude number has a maximum with respect to the ratio, h/D .

In the calculation for Fig. 6, C has been assumed 0.5. The value of C during deceleration period of the vessel becomes smaller than that during the period of steady motion. In view of this, this value has been taken for C in this analysis.

EXPERIMENT

In order to check the validity of Eq. (26) the authors made laboratory experiment. It was conducted in a two-dimensional flume 30m long, 80cm wide and 90cm high in its side walls. A two-dimensional model of a part hull of a vessel was made (Fig. 7). The model extends to the whole width of the flume, and its dimensions are shown in Fig. 8.

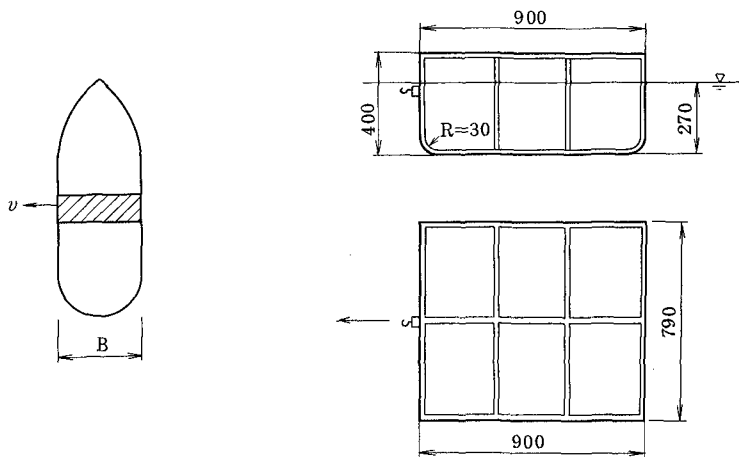


Fig. 7. A part hull.

Fig. 8. The dimensions of the model (in mm).

The model hull was steadily pulled by the fine wire having a weight at its other end (Fig. 9). The model makes a steady motion until the weight touches a table installed downwards. During the steady motion the weight, W , is balanced with the sum of the frictional force exerted by fluid, ϵv^2 , and the friction of the side plates of the vessel moving along the side walls, F , namely,

$$W = \epsilon v^2 + F \tag{29}$$

Since F is the friction of solid bodies, few change of the value of F was observed for various values of v .

At the instant when the weight comes to be in contact with the table, the pulling force of the weight suddenly disappears, and the deceleration

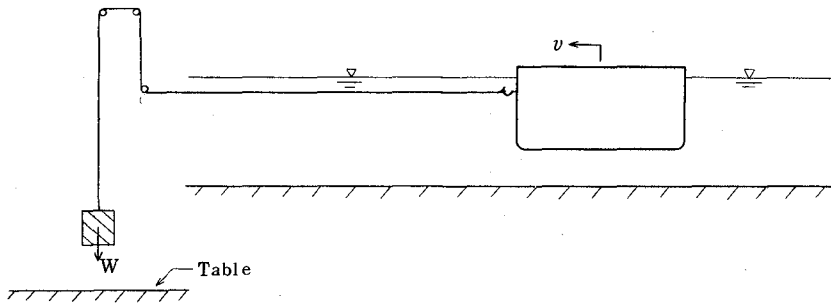


Fig. 9. Device for pulling the model steadily for a while and removing the pulling force suddenly.

of the model hull begins. The balance of forces after the pulling force has disappeared is expressed as

$$(M_0 + M) \frac{dv}{dt} = -\epsilon v^2 - F \quad (30)$$

With the initial condition, $v = v_0$ for $t = 0$, the above equation can be integrated to give

$$v = \frac{\sqrt{\frac{\epsilon}{F}} v_0 - \tan\left(\frac{\sqrt{\epsilon F}}{M_0 + M} t\right)}{\frac{\epsilon}{F} v_0 \tan\left(\frac{\sqrt{\epsilon F}}{M_0 + M} t\right) + \sqrt{\frac{\epsilon}{F}}} \quad (31)$$

Further, this equation is integrated to

$$x = \frac{M_0 + M}{\epsilon} \ln \left\{ \cos\left(\frac{\sqrt{\epsilon F}}{M_0 + M} t\right) + \sqrt{\frac{\epsilon}{F}} v_0 \sin\left(\frac{\sqrt{\epsilon F}}{M_0 + M} t\right) \right\} \quad (32)$$

The decelerating motion of the model hull was recorded by the use of a 8mm motion-picture camera. Measuring the time-variation of the position of the model in this way and also the values of ϵ and F from preliminary experiment, we calculated the added mass, M , from Eq. (32).

Experiment was made for the range $h/D = 0.2 \sim 1$ and $F_r = 0.007 \sim 0.07$. The result of the experiment is shown in Fig. 6. The agreement between the theory and the experiment is pretty good, as a whole, and validity of the present theory is confirmed.

CONCLUSIONS

The movements of large tankers in shallow water in the directions normal to their planes of symmetry cause counter-flows of appreciable velocities under the hulls. The inertia of these counter-flows has an important effect on the added masses of the vessels.

The mass factor, M/M_0 , of large tankers in shallow water can be

determined by Eq. (26).

ACKNOWLEDGEMENT

The authors are grateful to Messrs. Banji SUZUKI, Yasuharu TERUI, Shigeki YASUDA and Shunichi HASHIMOTO, Then-Students at Chuo University, for their earnest assistance and cooperation in conducting the experiment.

REFERENCES

1. Grim, O., *Das Schiff und der Dalben*, Schiff und Hafen, 1955.
2. Vasco Costa, F., *The berthing ship*, The Dock and Harbour Authority, May 1964.

CHAPTER 163

SUBHARMONIC COMPONENTS IN HAWSER AND FENDER FORCES

by

J.H. van Oorschot *

ABSTRACT

Forces in mooring lines and fenders of a moored vessel exposed to waves have a mixed harmonic and a subharmonic character. The subharmonic oscillations, with periods well beyond the range of wave periods, may cause forces that are as large as, or even larger than the forces associated with the harmonic oscillations.

The origins of the subharmonic oscillations are discussed and it is shown that in model testing, the correct reproduction of both the mooring arrangement and the irregular wave motion is essential.

The subharmonic motions, and consequently the total forces, can be partially reduced by specially adapted mooring arrangements as tests on various mooring systems have shown.

1. INTRODUCTION

During the past few decades there has been a rapid development in ship sizes, accompanied by the advent of highly specialised ships, such as LNG carriers, container vessels, etc.. This development has created many challenging problems, not only for nautical engineers in designing the vessels, but also for harbour engineers in providing adequate berthing facilities.

The increase in ship size led to the design and construction of loading and unloading facilities at more and more exposed locations in order to limit the dredging work and the costly construction of protection dams in deep water. Although at these exposed locations the docking itself will still be of importance for the actual design, the behaviour of the moored ship in waves has become an important, and often a determinative, parameter.

On the other hand, special mooring arrangements may be required, even in more or less protected areas, because the tolerable ship motions can be extremely small. For example container transshipment cannot take place if the motions of the container ship are appreciable, and LNG loading arms cannot follow very large ship motions.

The mooring and berthing facilities have to be designed so that the requirements regarding the allowable ship motions, and acceptable downtime, are met at tolerable forces. Wave forces on a ship may easily reach to thousands of tons, even in mild wave conditions. A certain amount of flexibility should,

* Head Maritime Structures Branch, Delft Hydraulics Laboratory, the Netherlands

therefore, be built in to prevent prohibitively large forces in the mooring lines and fenders.

Clearly the optimum between the dynamic behaviour of the ship and the loads in the mooring system has to be assessed for each situation.

In addition to these developments, the expansion of activities offshore should be mentioned, where drilling, construction and transshipment operations are taking place in extremely hostile conditions, using installations for which the wave-excited forces and motions are extremely important.

In the present study, which is primarily focussed on the problem of a moored vessel, the character of the wave-excited motions of a vessel and the corresponding forces in the mooring system are dealt with. However, the conclusions may also largely apply to any other form of anchored floating object.

2. SHIP OSCILLATIONS

In studying the response of a moored ship to a random wave motion, the following types of oscillation can be observed:

- a. Harmonic oscillations.
- b. Superharmonic oscillations.
- c. Subharmonic oscillations.

Ad a. The harmonic motions are the oscillations of the ship (6 components) with frequencies in the range of the wave frequencies. The harmonic wave forces and the harmonic ship motions of a freely-floating ship are generally fairly well linearly related to the wave amplitude. This is even so for the small keel clearances that are usually present at the berths, if only moderate wave amplitudes are considered. As an example one is referred to Figure 1 where the transverse motions (combined roll and sway) at about deck level of an ore carrier at a water depth 17% in excess of the draught are presented. The wave height of the regular waves ranged between about 1.0 m and 2.5 m, and the mooring system was linear. However, if the ship is tightly moored in a non-linear mooring system, the linear approach may no longer be justified.

Ad b. For particular elastic characteristics of the mooring system, oscillations with frequencies higher than the exciting wave frequency (superharmonics) may occur.

Ad c. Finally, subharmonic motions can be observed. These subharmonics have frequencies much smaller than those of the exciting waves. The subharmonic component in the motion or the force often forms a substantial part of the total motion or force. The subharmonic character can even become predominant, and is therefore clearly of importance for practical designs. In Figure 2, derived from Reference 1, some typical recordings are presented of springline and fender forces for a conventional mooring system, containing appreciable subharmonic components.

The subharmonic motions can have the following origins:

- The non-linear and asymmetric elastic character of mooring lines and fenders. Regular harmonic excitation of a mass in a non-linear and asymmetric spring system leads to frequencies different from the excitation frequency, also lower ones. If instead of one single excitation frequency, two discrete frequencies are applied, the resulting motion can also contain so-called combination tones (Ref. 9). In an actual sea condition, with a wave-energy spectrum covering a certain frequency band, these combination tones will show up as well.
- The second order slowly varying wave drift force. Due to this wave drift force subharmonic motions will occur, also with a strictly linear mooring system. However, only in irregular waves. Figure 3 shows an example of a model ship subjected to head waves, where the surging motion contains a predominant subharmonic component.
- Long periodic waves, like seiches and surf beats, may cause subharmonic motions,

particularly if the harbour configuration tends to amplify these phenomena (Ref. 8).

As the slowly varying wave drift force is an important parameter (and often the dominant one in this respect), this drift force will first be discussed.

3. THEORETICAL DESCRIPTION OF WAVE DRIFT FORCE

The study of the wave drift force was originally tuned to the determination of the wave-induced resistance of ships, but in recent years, the computations have been expanded to determine the behaviour of moored vessels. Havelock in the early 1940's published an approximative calculation of the steady drift force (Ref. 4). His computation was based on the observation that the drift force is most predominant near the natural periods of oscillation. It was shown that interaction between first-order effects, which in themselves are purely periodic, may through phase differences give rise to steady drift forces. For head waves:

$$F_D = \frac{1}{2}k(P.z \sin \beta_z + Q.\psi \sin \beta_\psi), \quad (1)$$

where P and Q are amplitudes of buoyancy and pitching moment, z and ψ are amplitudes of heaving and pitching, and β_z and β_ψ are phase lags. Comparable expressions have been derived by others for beam waves.

According to Reference 14 the interaction as described by Havelock only partly explains the steady drift force. The effects of interaction between the waves diffracted by the ship and the incoming waves, as well as the effect associated with the energy dissipation due to outgoing wave radiation resulting from forced ship motions, should be added. To obtain a less complex approach, Hsu and Blenkarn (Ref. 5) developed a description of the drift force, based on the same concept as the radiation stress. The conservation of wave momentum requires that if a wave train is reflected from an obstacle, there is a force exerted on that obstacle equal to the rate of change of wave momentum. The expression for the average drift force on a ship per unit length in regular beam waves becomes:

$$F_D = \frac{\rho g a^2}{2} \left\{ 2(Q-1) \left[1 + \frac{z}{a} \cos(\beta_z + kX_1) \right] - Q \frac{z}{a} \left[\cos(\beta_y + kX_1) + \frac{z}{a} \cos(\beta_y - \beta_z) \right] \right\}, \quad (2)$$

where $Q = [2 \cosh k(d-T)] / \cosh kd$ and X_1 is the average position of the leeward side of the vessel with respect to the centre line. It is assumed that all wave momentum between the free surface and the keel is reflected (at the average position of the ship side) and that the wave field below the keel is not disturbed. Similarly, Maruo (Ref. 6) in an earlier paper applied the wave momentum analysis on a control surface at a great distance from the ship to find the wave resistance in head waves. This computation is also approximative, as the boundary condition at the surface of the ship does not enter the analysis. Moreover, the expressions derived are for deep water.

The most recent description of the wave drift force, introducing the actual boundary conditions at the ship's surface, is from Pinkster (Ref. 12). The total hydrodynamic force in k-direction on the ship (which is allowed to make small amplitude motions about the mean position) is:

$$F_k = \iint p \cdot n_k \cdot dS \quad (3)$$

The pressure p follows from the Bernoulli equation:

$$p = -\rho gZ - \rho \phi_t - \frac{1}{2}\rho(\nabla\phi)^2 \quad (4)$$

The various parameters are then expanded to the second order using a small parameter ϵ (no higher orders, as the low frequency motions are supposed to be generated by the second-order force), so

$$\phi = \epsilon \phi^{(1)} + \epsilon^2 \phi^{(2)}$$

and

$$F_k = \iint \left(p^{(0)} + \epsilon p^{(1)} + \epsilon^2 p^{(2)} \right) \bar{n}_k dS + \iint \left(p^{(0)} + \epsilon p^{(1)} \right) \epsilon n_k^{(1)} dS + \iint p^{(0)} \epsilon^2 n_k^{(2)} dS + O^{(3)} \quad (5)$$

This integration can be carried out for the complete wetted surface S. After elaboration for the horizontal force in longitudinal direction (no roll, no sway) this expression gives:

$$F^{(1)} = \iint_{S_o} -\rho \phi_t^{(1)} \bar{n}_1 dS \quad (6)$$

$$F^{(2)} = \frac{1}{2} \rho g \oint_L \eta_r^{(1)} \bar{n}_1 dS + \psi^{(1)} \iint_{S_o} -\rho \phi_t^{(1)} \bar{n}_3 dS + \iint_{S_o} -\frac{1}{2} \rho (\nabla \phi^{(1)})^2 \bar{n}_1 dS + \iint_{S_o} -\rho \phi_t^{(2)} \bar{n}_1 dS - \rho g z_o^{(1)} \psi^{(1)} A_{wL} + O^{(3)} \quad (7)$$

Apparently the ship motions need only to be known to the first order, unlike the velocity potential. Also the actual wave elevation along the hull (η_r) should be known. Pinkster concludes therefore that a proper calculation for a practical case is for the time being too complex to be carried out.

In regular waves the drift force is of a constant value. As can be seen in Figure 5, which applies for a model ship in beam waves, the ship drifts away after the waves start to grow, and subsequently attains a constant offset. If the wave amplitude varies, the drift force will vary more than proportionally, and the ship will perform a forced oscillation at a frequency equal to the wave frequency and at a frequency matching the frequency of the wave groups (see also Figure 5).

Various investigators have tried to assess the wave drift force and the resulting motion in the general case of irregular waves, on the basis of the steady drift force as measured in regular waves. Hsu and Blenkarn (Ref. 5) computed the slowly varying drift force in irregular waves by assuming that the irregular sea can be characterised by a sequence of waves, each with a defined height, period and steady drift force, and that each wave acts on the ship as if it was one wave out of a sequence of regular waves. This can be written for a narrow-band spectrum in a general form (Refs. 10, 11) as:

$$\bar{F}_D = \rho g \int_0^\infty S_{\eta\eta}(\omega) R^2(\omega) d\omega \quad (8)$$

and

$$S_{FF}(\mu) = 2 \rho^2 g^2 \int_0^{\infty} S_{\eta\eta}(\omega) S_{\eta\eta}(\omega+\mu) R^4(\omega+\mu/2) d\omega \quad (9)$$

However, it has been shown that, particularly for larger vessels, this will yield incorrect results (Refs. 7, 10), because:

- a. The mean drifting force can be shown to be only dependent on the first-order potential, whereas the slowly-varying drifting force contains contributions of both the first- and second-order term of ϕ .
- b. The effect of the dimensions of the vessel relative to the "wave length" of the wave group is not negligible.

Rye et al. (Ref. 13) show that, indeed, already different results are obtained if R is determined in regular waves or in wave groups with constant wave and group period. The same can be seen in Figure 5, where the subharmonic motions are much larger than would follow from the regular wave tests (the amplification due to the response of the ship is only 1.24). It is also pointed out in Reference 13 that the extreme values of the forces or motions are liable to be underestimated if they are derived from the spectrum values S_{FF} , as the distribution, due to the quadratic character of the drift force, is far from normal.

4. EXPERIMENTAL STUDY

4.1 Model set-up

In order to study various aspects of the subharmonic behaviour from a practical point of view, a variety of tests has been made with a model of an ore carrier, in an 8 m wide wind-wave flume at the Delft Hydraulics Laboratory. The wave flume is provided with a flap-type wave generator with the flap being driven by two electronically-controlled hydraulic actuators. The steering signal is random (not a summation of a finite number of components) but can be reset, after which the same sequence of random waves is repeated. The required input signal is obtained by filtering so-called pseudo-random noise (Ref. 8). For the generation of regular waves, a normal function generator is used.

Ship

The data of the ship were:

V	=	320,000	m^3
L_{oa}	=	350	m
L_{pp}	=	330	m
B	=	55	m
T	=	20.5	m
d	=	24	m
C_B	=	about 0.85	m

The model (length) scale was 1 to 100.

Mooring system

The mooring systems used are shown in Figure 4. Due to the use of a high pretension and long linear springs, no slack occurred and the system was purely linear and symmetric (apart from the head waves for system A). The elasticities were chosen so as to coincide reasonably with the overall elasticity of fenders and mooring lines of a conventional mooring system.

Waves

The waves applied were regular and irregular long-crested waves, both beam-on and head-on. The regular waves had periods between 8 and 20 secs, the wave heights ranged be-

tween 1 m and 2.5 m.

The irregular wave had also significant wave heights between 1 m and 2.5 m. The periods corresponding to the peak of the wave energy spectrum were 12, 15 and 18 secs. At 15 secs a narrower and wider spectrum was also used (see Fig. 8).

4.2 Measurements in regular waves

In the tests with regular waves, the constant drift force has been measured, with the symmetric mooring systems, and the results are shown in Figures 6, 7. Particularly for the beam waves there is a considerable scatter. This is partly due to the small values of the drift force and the inherent measuring inaccuracies, but mainly to the fact that the springs were connected above the center of rotation, at the actual application point of mooring lines and fenders. Consequently there were some secondary effects in the force measurements due to the rolling motion, in spite of the long lines used. Nevertheless, a pronounced increase of the drift force can be observed for beam waves in the period range of 14 to 16 secs (natural periods of roll and heave), obviously due to the interaction between the harmonic ship motions and the wave-excited forces, as mentioned in Section 3. Corresponding results have also been presented in Reference 3.

In head waves the drift force increases with increasing wave period, without any distinct maximum in the period range applied. The harmonic motions (surge, pitch and heave) also increase with longer periods in the corresponding frequency band. Clearly, when studying the subharmonic behaviour of a floating object much attention should be given to the correct reproduction of the mooring system.

Together with the steady drift forces, the harmonic motions have been recorded. From these motions and the proper values for the added mass and the damping, the harmonic wave-exciting forces have been computed. The averaged results for the various tests are also shown in Figures 6 and 7. The steady drift force in regular waves appears to be barely a few percent of the harmonic wave force. For instance, for a wave amplitude of 1 m, the drift force for beam waves is only 2-4%, whereas for head waves in that case the drift force is even less than 1%.

Finally the transferfunctions between the line forces and the waves have been determined for the mooring system A (Fig. 4).

4.3 Measurements in irregular waves

Comparison with regular waves, and influence of wave height and period

Additionally to the measurements with regular waves, measurements have been carried out with irregular waves, both head-on and beam-on. In order to demonstrate the limited applicability of the linear transfer functions, and the regular wave tests in general, the 1% exceedance values of the wave-induced forces have been determined from the irregular wave tests, and compared with the 1% values that are obtained applying a linear transfer function $T_{(\omega)}$ between waves and forces. The results have been plotted in Figures 9 and 10, and some typical spectra, applied for both the computations and the measurements, in Figure 8. The differences between the computed and measured values are fairly well proportional to H^2 , as could be expected theoretically. This also means that the shape of the statistical distribution curve does not change significantly for different wave heights. The differences also increase with increasing wave period, and are particularly for $T_p = 18$ sec very pronounced. The computed 1% values followed from:

$$S_{FF}(\omega) = S_{\eta\eta}(\omega) \cdot T_{(\omega)}^2$$

and according to the Rayleigh distribution,

$$F_{1\%} = 3.0 \sqrt{M_{OF}} \quad \text{where} \quad M_{OF} = \int_0^{\infty} S_{FF}(\omega) d\omega$$

From some of the recordings with irregular waves, spectra of the ship motions (sway for beam waves and surge for head waves) and the waves have been made (see Fig. 12). The spectra of the motions shown on this Figure are typical. They contain two distinct maxima, one in the harmonic range and one in the subharmonic range, where there is no wave energy. The energy content of this subharmonic part M'_{OF} has been determined for all tests and normalised by the square of the total energy of the wave motion m_{on}^2 , according to the supposition expressed in (9).

The M'_{OF}/m_{on}^2 can then be supposed to be a function of the peak frequency of the wave spectrum and the energy distribution (shape of the spectrum) for a particular situation. The test results are plotted in Figure 14. It is interesting to note that the value M'_{OF}/m_{on}^2 is a fairly smooth function of the peak frequency of the spectrum. This is particularly surprising for sway, as the value of R in (9) varies very strongly with the wave period (Fig. 6). The spectrum width has not a large influence on this parameter. For beam waves the narrow spectrum results in the largest motions, as opposed to the situation with head waves. The same can be observed in Figures 9, 10 with respect to the subharmonic component of the 1% wave-induced force.

Influence of mooring system

The steady drift force in regular waves has been shown to be only a few percent of the harmonic wave forces. Although the regular-wave tests tend to underestimate the drift forces, the slowly-varying drift force in an actual case with irregular waves is still of second order. So the reason for the large subharmonic motions can only be found in the occurrence of a resonance type of motion of the vessel in its mooring system.

The conditions for resonance are available, as the natural frequencies of oscillation are within the band-width of the slow drift excitation and, moreover, the damping (both linear and quadratic) is extremely small in the low-frequency range (see Fig. 11^{*}). If the low damping is partly responsible for the large subharmonics, it may be expected that improvements can be obtained if special elastic characteristics of mooring lines and fenders are used. In particular if some energy dissipation is applied. With regard to this, some tests have been carried out with other than linear mooring systems. Some typical recordings are presented in Figure 15 together with the wave recordings. For each test the same motion control programme for the wave machine has been applied. Apart from minor details, the wave recordings were similar. The mooring system was changed in each test. The upper curve (System I) shows a subharmonic surging motion, which is reduced for System II where some energy dissipation was built in. In System III the restoring force at positive displacements was constant at a value of 400 tf (average of forces recorded for System I), moreover an appreciable energy dissipation was built in. Nevertheless, the subharmonic motion increased dramatically, but only for parts of the recording. In the remaining parts the subharmonics were of the same order as, or smaller than those for System I.

It is surprising that there was no direct correlation between the occurrence of these extremely large subharmonics and those for System I, as also can be seen in Figure 15. So the adverse effect is not only very large, but also fairly unpredictable. This is the more important, as System III is a type of system that may be found in practice, applying the widely-used constant tensioning winches,

* The damping and added mass coefficients have been derived from data for a ship which is only slightly smaller, and are expected to be accurate within 10%.

with different pull-in and pay-out loads. In Figure 13 the energy spectra of the motions are given for the various mooring systems. In beam waves, the motions for System III became so large that they were beyond the range of the displacement transducers, and could not be analysed.

Influence of a steady force

Not only will the elastic properties of the mooring system depend on the particular types of lines and winches applied, but they may also vary for a particular lay-out as a result of an extra "pretension" caused by a steady wind or current. The effect on the ship motions can be quite significant, as shown by Hsu and Blenkarn (Ref. 5). The wind- and current forces, if present, should therefore always be reproduced in the model experiments. Due to the subharmonic motion, the relative speed of the wind or the current will vary, which may also affect the subharmonic motion in another way. Let U be the permanent velocity of wind or current, and \dot{x} the momentaneous ship velocity, the resistance is then,

$$F_R = \frac{1}{2} \rho C_d A (U - \dot{x})^2 = \frac{1}{2} \rho C_d A (U^2 + \dot{x}^2) - \rho C_d A \dot{x} U$$

if U is a constant, the last term at the right hand side has the character of a linear damping, $2F_R \dot{x}/U$. Due to the higher value of U this virtual damping will for the wind generally be rather small. However, for a steady current this term may be of the order of magnitude of the linear damping in the subharmonic range as shown in Figure 11. In that case it will be required to reproduce not only the steady current force, but the whole current pattern.

5 CONCLUSIONS

Subharmonic components form, particularly in more exposed locations, a substantial part of the total horizontal ship motions or mooring forces. The second order slowly varying wave drift force is an important parameter in this respect.

The slowly varying drift force and consequent subharmonic motions occurring in irregular waves are larger than follow from the steady drift force in regular waves. Moreover, the so-called combination tones in irregular waves may introduce subharmonic motions that will not be found in the case of regular waves.

The second-order drift force in regular waves depends strongly on the harmonic ship motions, as a result of interactions between incident, diffracted and radiated waves.

As opposed to the harmonic motions, subharmonics can to some extent be reduced by applying special elastic characteristics for the mooring system, or more particularly energy dissipating devices. The effect of a variation of the elastic properties, however, seems to be fairly unpredictable.

In irregular waves the subharmonic components increased proportional to H_s^2 . They also continuously increased with increasing peak period of the energy spectrum (T_p), for both sway and surge.

LIST OF SYMBOLS

A	- area	p	- pressure
A_{WL}	- area of water plane	$R_{(\omega)}$	- transfer function
a	- amplitude of wave	S_{xx}	- energy density of x
B	- breadth	T	- wave period; draught
C_B	- block coefficient	$T_{(\omega)}$	- transfer function
C_d	- resistance coefficient	t	- time
c	- spring constant	U	- wind or current velocity
d	- depth of water	X	- horizontal coordinate
F_D	- drift force	x	- surging motion
F_k	- force in k-direction	y	- swaying motion
F_R	- resistance	z	- heaving motion
f	- frequency	Z	- vertical coordinate
g	- acceleration of gravity	β	- phase lag
H_s	- significant wave height	ϵ	- small parameter
k	- wave number = $2\pi/\text{wave length}$	ϕ	- velocity potential
L_{oa}	- length over all	η	- surface elevation
L_{pp}	- length between perpendiculars	ρ	- mass density
M_{oF}	- total energy of harmonic force	ψ	- pitching motion
M'_{oF}	- total energy of subharmonic force	ω, μ	- angular frequency
$m_{o\eta}$	- total energy of wave motion		
n_k	- directional cosine of surface element in k-direction		

LIST OF REFERENCES

1. Bunt, J.D. van den, Model Study on Mooring Forces due to Regular and Irregular Waves, Paper presented at the NATO Advanced Study Institute on Analytical Treatment of Problems in the Berthing and Mooring of Ships, Wallingford, England, May 1973.
2. Danzell, J.F., Cross-Bi-spectral Analysis: Application to Ship Resistance in Waves, Journal of Ship Research, Vol. 18, No. 1, 1974.
3. Eda, H., Dynamic Positioning Control of Drilling Ships, Proc. of the 3rd International Ocean Development Conference, Tokyo, 1975.
4. Havelock, T.H., The Drifting Force on a Ship Among Waves, Philosophical Magazine, Vol. 33, 1942.
5. Hsu, F.H., and Blenkarn, K.A. Analysis of Peak Mooring Forces Caused by Slow Vessel Drift Oscillations in Random Seas, Society of Petroleum Engineers, No. 4, 1972.
6. Maruo, H., Wave Resistance of a Ship in Regular Head Seas, Bulletin of Fac., of Engineering, Yokohama National Univ., Vol. 9, March 1960.
7. Newman, J.N., Second Order Slowly Varying Forces on Vessels in Irregular Waves, International Symposium on the Dynamic of Marine Vehicles and Structures in Waves, Univ. College, London, 1974.
8. Oorschot, J.H. van and Koopmans, F., Random Wave Generation for Research on Immersed Marine Vehicles, Proc. 11th Symposium on Naval Hydrodynamics, London, 1976.

9. Oortmerssen, G. van, The Motions of a Moored Ship in Waves, Doctor's Thesis at the Delft University of Technology, 1976.
10. Pinkster, J.A., Low Frequency Phenomena Associated with Vessels Moored at Sea, Paper SPE 4837, presented at the SPE - European Spring Meeting, Amsterdam, 1974.
11. Pinkster, J.A. and Remery, G.F.M., The Role of Model Tests in the Design of Single Point Mooring Terminals, Paper OTC 2212, presented at the 7th Annual Offshore Technology Conference, Houston, 1975.
12. Pinkster, J.A., Low Frequency Second Order Wave Forces on Vessels Moored at Sea, Proc., 11th Symposium on Naval Hydrodynamics, London, 1976.
13. Rye, H., Rynning, S. and Moshage, H., On the Slow Drift Oscillations of Moored Structures, Paper OTC 2366, presented at the 7th Annual Offshore Technology Conference, Houston, 1975.
14. Wen-Chin Lin and Reed, A.M., The Second-Order Steady Drift Force and Moment on a Ship Moving in an Oblique Seaway, Proc. 11th Symposium on Naval Hydrodynamics, London, 1976.

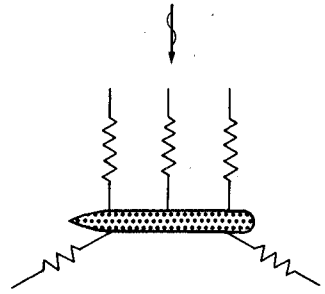
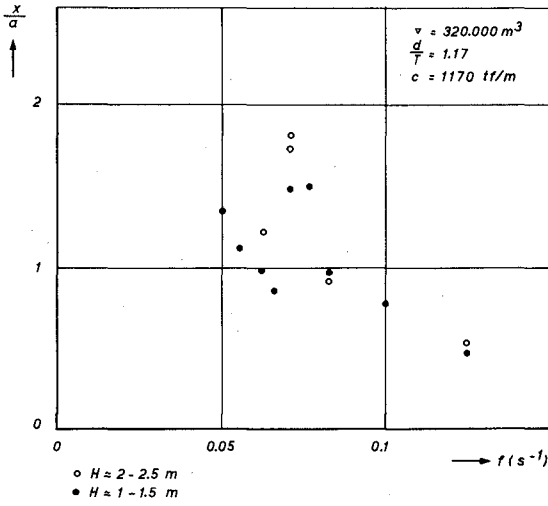


FIG. 1 HORIZONTAL MOTION OF SCHIP SIDE AT 5 m ABOVE WATER-LINE, IN IRREGULAR BEAM WAVES

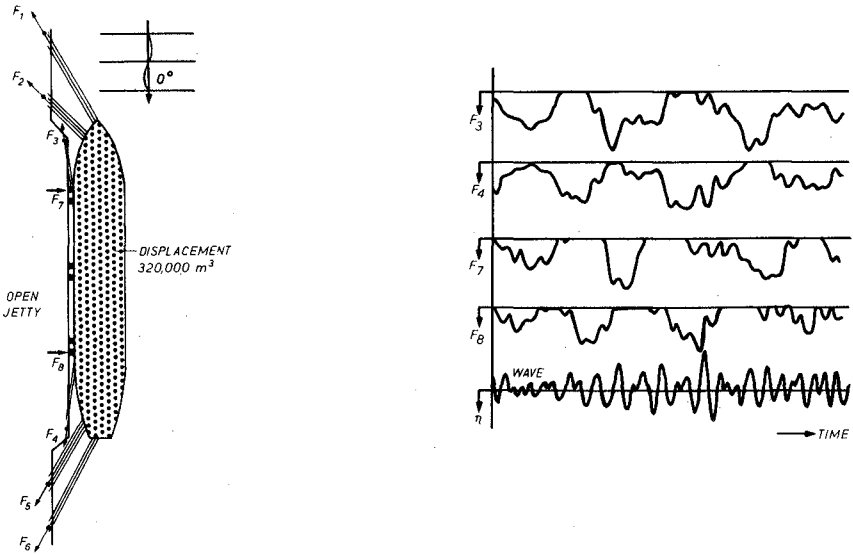


FIG. 2 IRREGULAR WAVES, TYPICAL FORCE RECORD

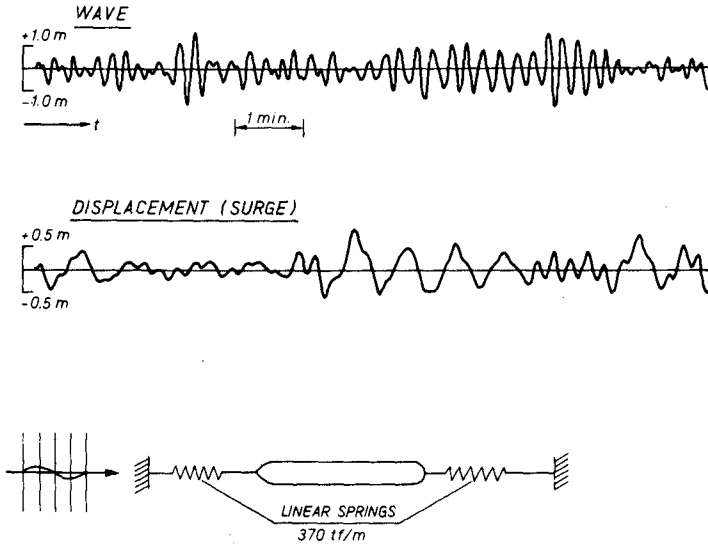


FIG. 3 TYPICAL SURGE RECORD FOR IRREGULAR HEAD WAVES

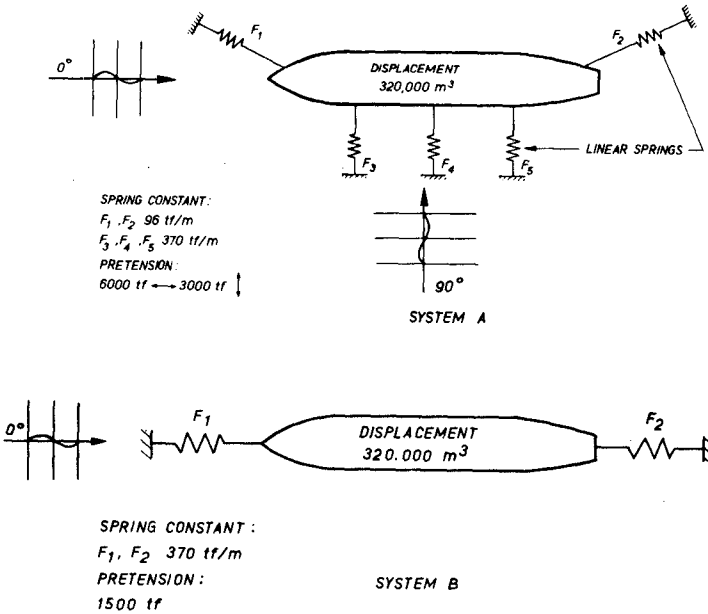


FIG. 4 MODEL SET-UP

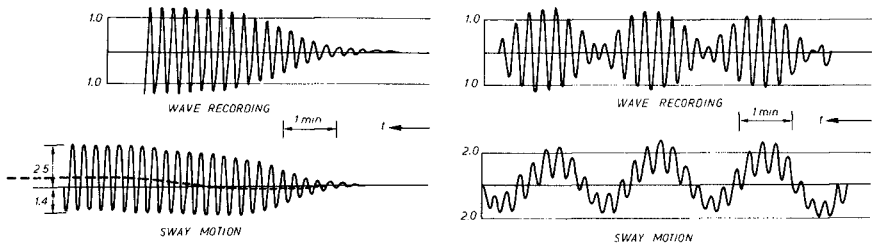


FIG. 5 SWAY MOTION IN REGULAR WAVES AND REGULAR WAVE GROUPS

MOORING SYSTEM A
BEAM WAVES

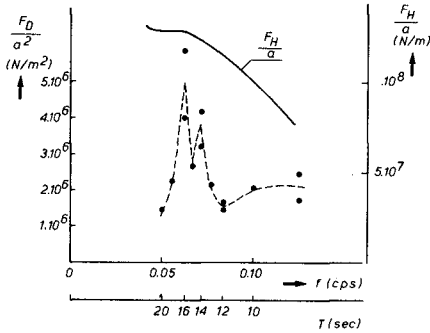


FIG. 6— WAVE DRIFT FORCE FOR SWAY, FROM REGULAR WAVE TESTS (F_D)
— HARMONIC WAVE FORCE FOR SWAY (F_H)

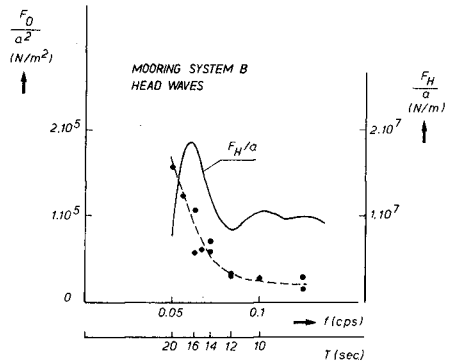


FIG. 7— WAVE DRIFT FORCE FOR SURGE, FROM REGULAR WAVE TESTS (F_D)
— HARMONIC WAVE FORCE FOR SURGE (F_H)

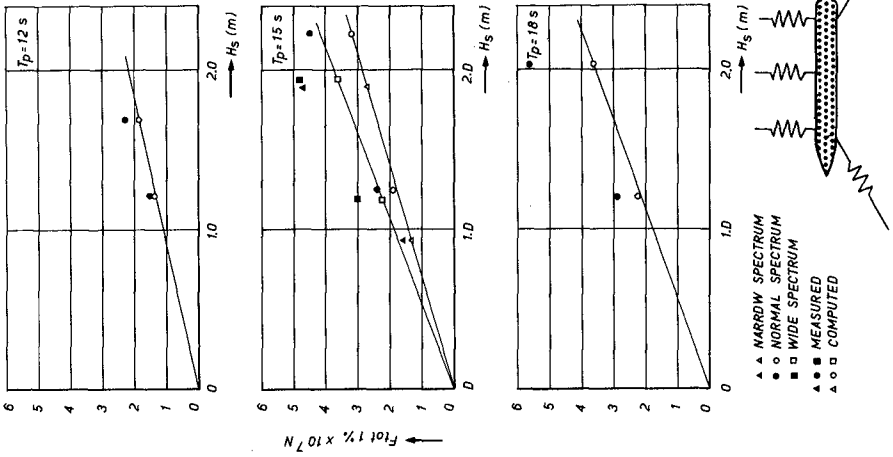


FIG. 9 TOTAL WAVE INDUCED FORCE VERSUS WAVE HEIGHT BEAM WAVES

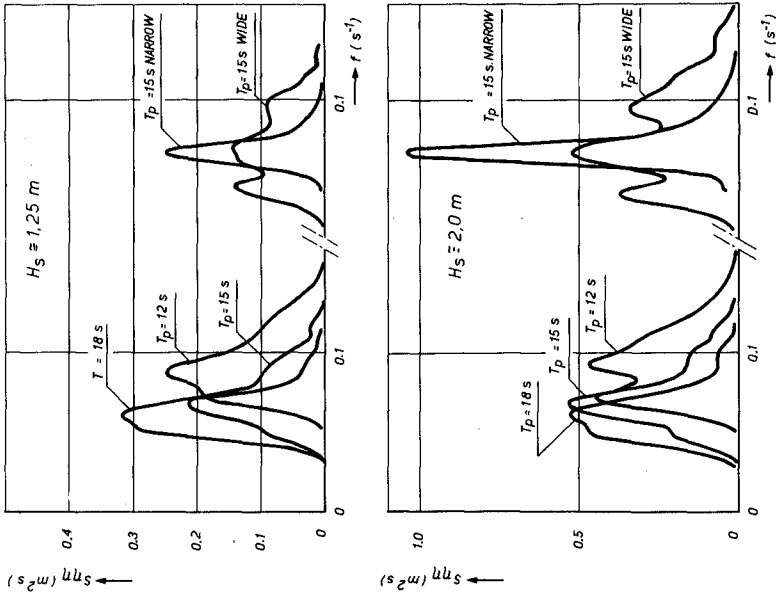


FIG. 8 TYPICAL WAVE SPECTRA FOR COMPUTATION AND MEASUREMENT OF WAVE INDUCED FORCES

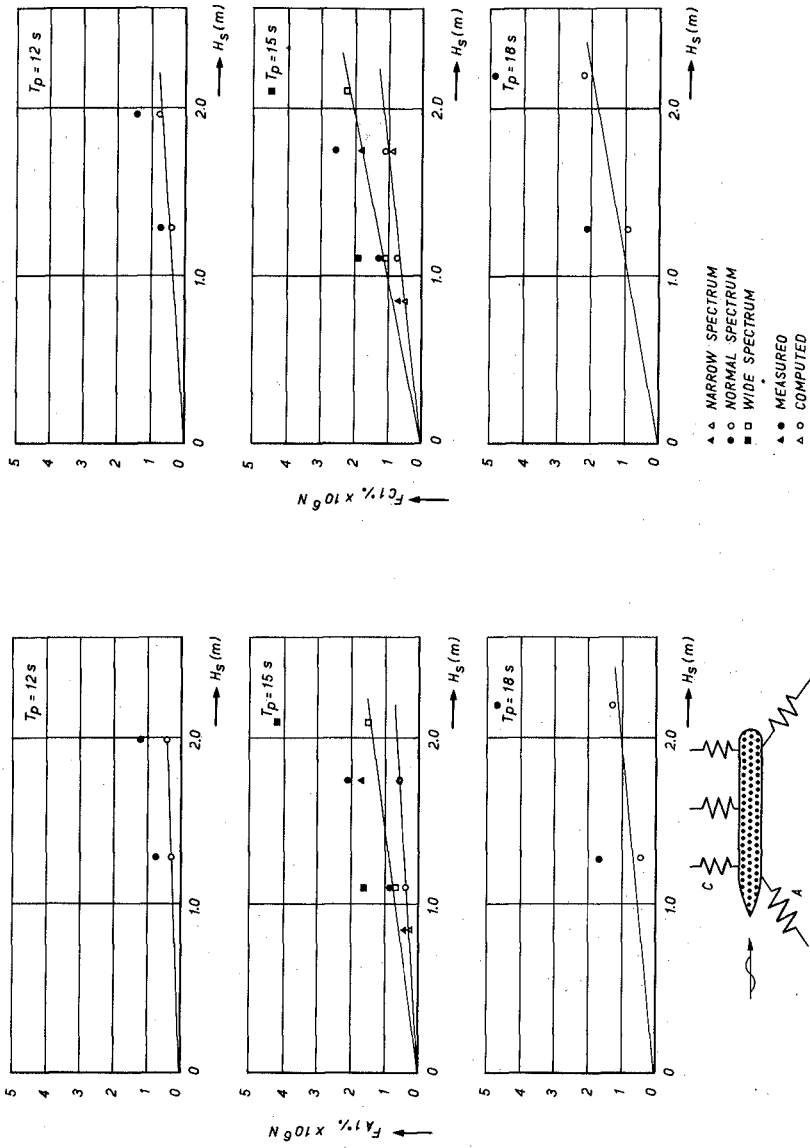


FIG. 10 TOTAL WAVE INDUCED FORCE VERSUS WAVE HEIGHT, HEAD WAVES

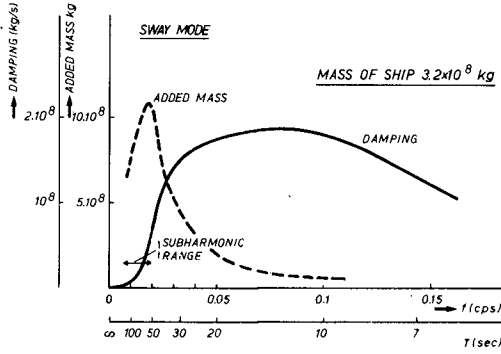
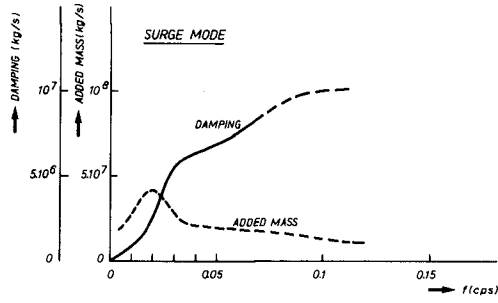


FIG. 11 ADDED MASS AND DAMPING FOR MODEL SHIP DEPTH/DRAUGHT = 1.17

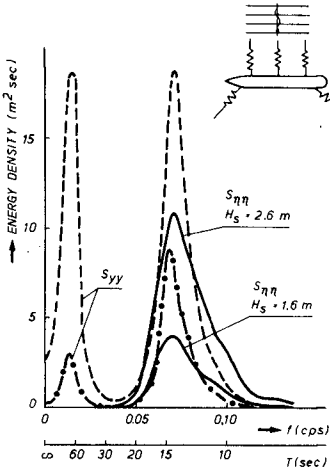


FIG. 12 ENERGIE SPECTRA OF WAVES AND SWAY MOTION

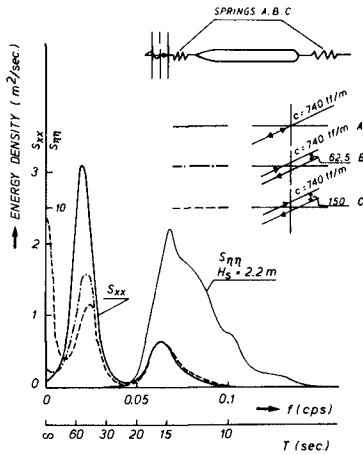


FIG. 13 ENERGY SPECTRA OF WAVES AND SURGE MOTION

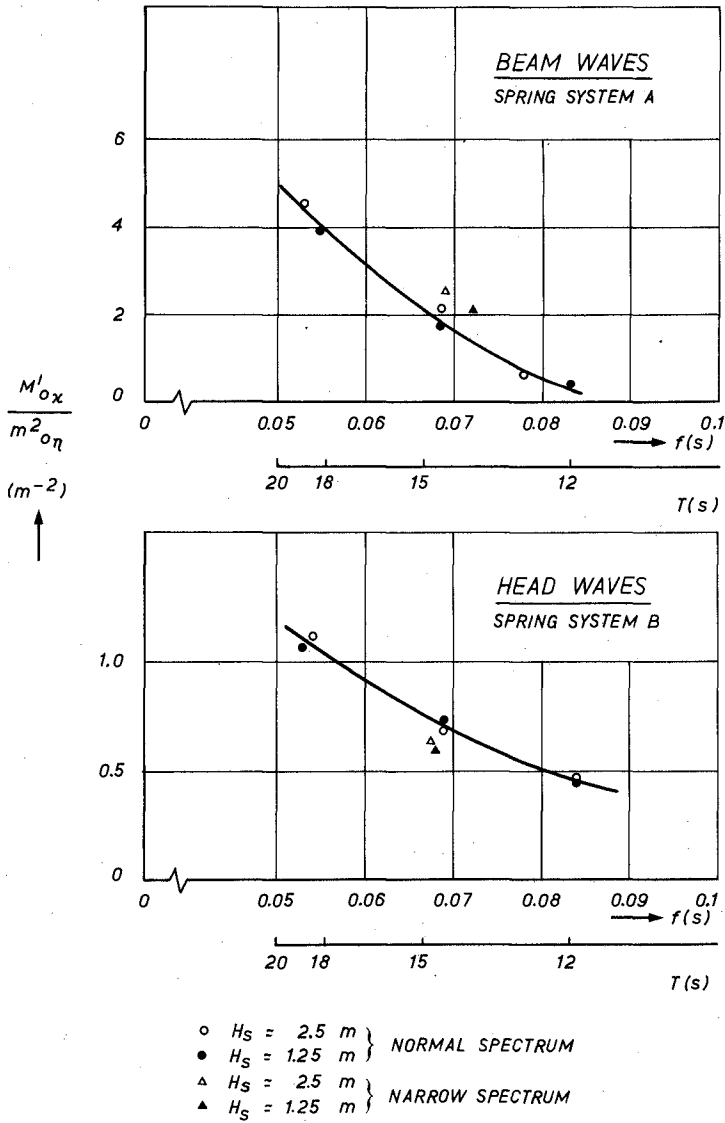


FIG. 14 NORMALISED ENERGY OF SUBHARMONIC MOTION



FIG. 15 SURGE RECORDINGS AT SAME PLACES IN WAVE SEQUENCE

CHAPTER 164

LOW-COST SHORE PROTECTION ON THE GREAT LAKES: A DEMONSTRATION/RESEARCH PROGRAM

by

Dr. John M. Armstrong

Associate Professor, Department of Civil Engineering
and
Director, Coastal Zone Laboratory
The University of Michigan
Ann Arbor, Michigan

BACKGROUND

Shore erosion is currently causing millions of dollars of damage to shoreline property along the Great Lakes (1,2). Erosion is caused by the energy of waves and currents which are produced by large wind storms.

The erosion process on the Great Lakes is most severe when lake levels are near the top of their 6-foot (1.8 meter) range for several years as is currently being experienced. The severe erosion process continues even after lake levels fall, as the bluffs have become unstable and waves from intense storms can still attack them. In order to alleviate the erosion damages to beaches and bluffs, shoreline owners must rely on shore protection methods.

Effective methods of shore protection are designed to slow or stop the erosion process by dissipating wave energy and/or preventing bluff attack. However, the most effective methods are very expensive, costing over \$200 per foot (\$656 per meter) of shoreline. (Costs are calculated, for the purposes of this study, as the length of shoreline which is expected to be protected by the shore protection methods. For sites utilizing revetments, artificial nourishment, and seawalls, the length is the stretch of shoreline actually covered by the method. For locations utilizing groin systems and breakwaters, the system was designed to protect the entire length of the sites; the costs have been calculated on that basis. Whether these systems actually protect that length of shoreline is to be determined by this study.) Shoreline homeowners are usually not able to meet such expenses, and often resort to less efficient and costly alternatives. Private shoreline owners need accurate, reliable information about effective low-cost shore protective methods in order to reduce or alleviate the severe erosion damages to their shoreline.

INTRODUCTION

In response to the urgent need described above, 19 sites were selected along the coast of Michigan in 1973 for the examination of methods of shore protection. The objective of this program was to select, design, install, and evaluate a series of low-cost shore

protection systems. The test sites were distributed around the state in areas which experienced severe erosion. Sites were selected on public land where erosion processes were active and typical. Table 1 lists and Figure 1 shows the test site locations. Site selections were in part determined by the willingness of local agencies to share expenses and by the value of the property being threatened.

Methods of shore protection were chosen to demonstrate the effectiveness of well-known, as well as innovative, concepts. Each project was documented and evaluated with respect to the reduction of erosion rates, cost, construction problems, and durability. A particular effort was made to find reasonable effective and low-cost methods which the homeowner could personally utilize. Emphasis was placed on providing sufficient information to shoreline owners for comparing costs of protective structures against reasonable chances for effective protection.

The selection of the method of shore protection to be used at each site was based upon several criteria. The first criterion corresponds to the stated objective of the program in testing shore protection procedures suitable for use by shoreline owners. It was necessary to stay within an acceptable cost range for property owners. This range had risen over the past 20 years from \$25 per foot (\$82 per meter) of shoreline to \$100 per foot (\$328 per meter) based on previous interactions with homeowners. All of the structures were intended to be in the "low-cost" category, defined for study purposes as costing less than \$100 per foot (\$328 per meter) of shoreline protected. The average cost of methods selected for examination was approximately \$50 per foot (\$164 per meter) of frontage, a desired goal of the study. This cost constraint limited the design options severely. For example, a structure which would be expected to provide protection for all but very rare storms, such as 25- or 50-year frequency storms, would cost from \$200 to \$400 per foot (\$656 to \$1,312 per meter). The low-cost designs used in the demonstration projects can be expected to suffer damage from much less severe storms, such as 5- to 10-year frequency storms.

The second criterion involved testing innovative ideas and procedures with the objective of keeping costs low while maintaining reasonable effectiveness. Innovative, yet untested, methods were important aspects of the program as it was as essential to demonstrate to the homeowner what not to do as well as to show proper shore protection methods. Methods which reflected strong public interest and offered hope for permanence and low-cost effectiveness were also examined for potential testing. Shore protection methods were not included, however, which could adversely affect the environment or degrade the aesthetic qualities of the shoreline. This excluded from the study poorly designed structures and such attempts as the placement of discarded automobiles or straw and hay on the bluff.

The methods of shore protection included in the study are artificial nourishment, groins, revetments, offshore breakwaters, and "seawalls." (The term seawalls as used in this paper does not refer to the traditional concept of seawalls. The term applies to structures which combine the characteristics of seawalls and revetments, yet which resemble neither in the traditional sense.) Materials used in the projects vary from sand to reinforced concrete walls.

Artificial nourishment consists of adding sand to a nearshore area. This raises the beach bottom profile enough to cause waves to break and lose their energy before reaching the former shoreline. This method is aesthetically pleasing as it preserves the beach in its natural condition. It is also an excellent means of shore protection.

Groins are protective structures, similar to a wall, built approximately perpendicular to the shore, which trap sand from the littoral drift. A groin is anchored in the toe of the bluff and extends into the water. Groins used in the study were constructed of wood piling, steel piling, asphalt mastic, rock-filled timber cribs, gabions, giant sandbags, and Longard tubes. (Giant sandbags are nylon bags which can be pumped full of sand. Two of the sizes referred to as "giant" are 2 feet by 5 feet by 10 feet [1.6 meters by 1.5 meters by 3.0 meters] and 1.5 feet by 6 feet by 20 feet [1.46 meters by 1.8 meters by 6.1 meters]. Longard tubes consist of high density polyethylene casings lined with low density polyethylene. These casings are filled with sand to form tubes). The sand trapped by the groin raises the beach profile and protects the bluff. Regular spacing of groins along the shoreline enhances their effectiveness in building up the beach.

Revetments are protective blanket-type structures built at the toe of a bluff. The bluff is graded to a stable slope of three or two to one, horizontal to vertical, before placement of the revetment. Rock, asphalt mastic, and preformed concrete rings were used for the construction of revetments. Any material utilized must be strong enough to resist wave attack and built high enough to prevent overtopping. The toe of the revetment should be protected from undercutting as wave energy during storms accelerates erosion at the toe. Revetments are very effective in areas where groins cannot be constructed. They also often leave a portion of the beach available for recreational activities.

Seawalls are built in front of a bluff and backfilled so that the bluff is continuous to the wall. The purpose of a seawall is to prevent wave energy from reaching the bluff. However, due to the violent turbulence created when waves strike the structure, erosion is greatly accelerated in front of the wall. This undercutting combined with the pressure of saturated soil on the land side, often leads to structure failure. Seawalls were constructed of Longard tubes and giant sandbags. Seawalls traditionally are not suitable methods of shore protection in recreational areas due to the difficulty of water access and the development of deep water in front of the walls. Seawalls are useful in areas where

no other means of protection will work and/or the bluff requires support (the seawall becomes a retaining wall). Caution must be exercised to properly design the seawall which can be expensive.

Offshore breakwaters are walls installed in the water parallel to the shoreline. They attenuate wave energy and depending on their distance from shore the reduced turbulence immediately behind the breakwater enhances the deposition of sand. Offshore breakwaters were built with precast concrete panels and Longard tubes.

To evaluate the effectiveness and durability of the shore protection examined as well as their effect on the nearshore environment, a field monitoring program was established. This involved photographic and subaerial/subaqueous surveys of the sites to obtain profiles of the bluff and beach. The procedure for surveying seawalls, revetments, breakwaters, and nourishment projects consisted of establishing profile lines. Profiles originated inland behind the top of the bluff and extended into the water (limited to the depth a man could wade). These profile lines were established 25 feet (7.6 meters) apart over the length of a project. Groins also were surveyed using profile lines as described above. These profiles, however, were located along the centerline of the structure, immediately adjacent to it, as well as 10 and 25 feet (3.0 and 7.6 meters) on both sides.

Data was collected during and immediately after construction and additionally during the year to provide further site observations. During the first year of study, the surveys were conducted after major storms so that surveys could be conducted at optimum times in terms of checking a structure's effectiveness. Such a storm was defined as one that will be equalled or exceeded on an average of three or four times each year. Initially, major storms were described only by onshore wind speeds and duration because winds play an important role in wave formation. Later, major storms were described by wave size: a 6-foot (1.8 meter) breaking wave at the site was established as the criterion. In subsequent years, sites were surveyed in the spring and fall. It was possible to record the major storms between surveys and still obtain the desired information.

In summary, the 19 locations were monitored utilizing the photographic reviews and conventional surveying techniques described previously. This monitoring program collected data regarding structure effectiveness and durability as well as the feasibility of shoreline owners employing these methods themselves. The following section describes some sites in detail and provides preliminary observations.

SITE DESCRIPTION AND ANALYSIS

Sites 1-4, 16, and 19 were evaluated using photographs and will not be discussed at further length. However, Tables 2 and 4 provide summary information concerning these sites. The remaining sites were surveyed using the conventional surveying techniques previously discussed. Summary information for these sites

can be found in Tables 2 and 3. Complete and reliable data regarding structure effectiveness and durability will be available only after a number of years. Evaluations are based on the structure's performance over time and in various storm conditions. However, general observations of the effectiveness of some of these structures can be made after the first two years of study. Data have been collected continuously since installation. This paper includes all data collected through the fall of 1975.

Site 6, Sanilac 26

A roadside park 4 miles (6.4 kilometers) south of Port Sanilac in Sanilac Township was selected for testing six different groin types. This location has high steep clay bluffs and a tough clay lake bottom. These bluffs have been eroding over the years. The clay lake bottom makes the driving of any type of piles difficult. Thus, the groins selected for this site were designed to rest on the lake bottom. An important aspect of this project was the 200-foot (61.0 meter) spacing between each of the groins. Groins are usually spaced two to three times the length of the groin extending into the lake (3). The distance between the study groin systems was three to four times their length. Table 5 describes the various groin systems installed as well as costs incurred for construction. The structures are listed in successive order from the north end of the site progressing south. Four of the structures can be seen in Figure 2. A plan view of the site is shown in Figure 3. Discussions of each structure's performance will be followed by observations of the entire system's effectiveness.

Two 40-Inch (101.6 cm) Diameter Longard Tubes. These tubes are 100 feet (30.5 meters) long and were installed in the fall of 1973 at a cost of \$30 per foot (\$98 per meter) of shoreline. A third tube was planned to be stacked on those two in a pyramid fashion. Storm interruption during construction prevented placement of the third tube. The two tubes installed were monitored and were found to be trapping sand. This groin appears to be working well. Although some settlement has occurred along both tubes (particularly the southern tube), this movement has not hurt the groin's performance. The tubes have helped to build up the beach and thus resist wave attack. Recession at the top of the bluff has been about 10 feet (3.0 meters) in the immediate vicinity and some slumping has occurred. This could be due to terrestrial processes or the movement of the slope to reach a more stable position.

One 69-Inch (175.3 cm) Diameter Longard Tube. This tube is 50 feet (15.2 meters) long and was installed in the spring of 1974 at a cost of \$25 per foot (\$82 per meter). It was expected to trap sand more effectively than the 40-inch (101.6 cm) diameter tube because it has more freeboard. Freeboard is the height of a structure above the still waterline. However, as of the last survey both groins have performed equally well. Only minor settlement was experienced with this tube. The lack of settlement indicates that this structure can be placed directly on the lake bottom

(without a supporting foundation) in areas where the soil is clay. This tube has effectively trapped sand and prevented direct wave attack on the bluff, although minor recession rates have been recorded in the immediate area.

Gabion Groin. The gabion groin installed at this site in the spring of 1975 is 70 feet (21.3 meters) long and costs \$30 per foot (\$98 per meter) to construct. It has not been under examination long enough to provide significant data. It is in very good condition and has trapped sand as expected. Despite the beach build-up, slumping of the bluff has occurred. This may be due to natural processes other than wave attack.

Giant Sandbag Groin. The giant sandbag groin was installed in the late fall of 1973 and suffered major damage in the first year. The length of the groin is 60 feet (18.3 meters) and costs \$30 per foot (\$98 per meter) to install. Nearly 15 feet (4.6 meters) of sandbags were lost at the lake end of the groin. Vandalism is probably not the cause since the lost bags are at the lakeward end of the structure. No further sandbag loss has been detected, but some bags have shifted since April 1975. The structure appears to be effectively trapping sand despite the damage. Preliminary conclusions as to its effectiveness and durability indicated that sandbag groins could only offer temporary protection. After further study under mild storm activity, it appears that the bags can offer more than just temporary protection. However, they are not as durable as other structures. With annual replacement of damaged bags and protection against tearing, sandbag groins could function effectively for several years.

Asphalt-Mastic Groin. This asphalt-mastic groin was completed in the fall of 1973. Design and construction supervision of this groin was provided by The University of Michigan's Coastal Zone Laboratory. The successful installation of this structure demonstrated that asphalt mastic could be placed through deeper water than previously documented. The asphalt-mastic groin is 60 feet long (18.3 meters) and was installed at a cost of \$45 per foot (\$146 per meter). To date the structure has performed very well. Large amounts of sand have been trapped, providing a protective beach. No movement of the groin has been visible at all; however, there has been minor damage to the north edge. A section of the mastic and underlying rock was broken off at the lake edge. Minor recession and slumping of the bluff has occurred, probably due to terrestrial processes. This type of structure has proven stable and effective although it lacks the aesthetic qualities of other methods. The lack of maintenance requirements indicated that only an initial expense for building will be incurred. This structure has performed as well as the more expensive conventional layered rock with armor stone groin, and is a good example of successful low-cost shore protection.

Timber Crib Groin. Very few data are available for the timber crib groin installed at the extreme south end of the site in the fall of 1975. It extends 50 feet (15.2 meters) and costs \$30 per

foot (\$98 per meter) to install. To date it has remained in excellent condition.

In general, the wider spacing between the different groins has proven effective. Minor bank recession has been recorded for small stretches of the shoreline. However, as stated earlier, this could be completely due to terrestrial processes. Of the six groins studied at Sanilac 26, the asphalt-mastic groin has been the most stable. The sandbag groin has suffered the most damage. The Longard tube groins are performing adequately. Both the gabion and the timber crib groins are in excellent condition.

Site 7, Sanilac 11

Site 7 is located about 1.5 miles (2.42 kilometers) north of Site 6 and has the same high clay bluff shoreline. Two 69-inch (175.3 cm) diameter Longard tubes were installed here as a seawall rather than as the groin system utilized at Site 6. The tubes were placed end-to-end at the toe of the bluff parallel to the shoreline, extending 400 feet (121.9 meters). Cost of construction was \$65 per foot (\$213 per meter) of shoreline at the time of installation in the early fall of 1974. Figure 4 shows the condition of the site in the spring of 1975. While the tubes appear to have performed well at this location, there has been minor shifting and damage. Some sand has been lost at the center of the structure where the tubes meet. The north end of the seawall has moved lakeward by more than 5 feet (1.5 meters), but the entire structure has, in general, resisted back pressure from the slumping bluff. Only slight vertical settlement of the tubes has been detected. The one major storm experienced at this site had no effect on the seawall's performance.

Site 8, Tawas City

Tawas City Park was selected for the examination of a sand nourishment project. The site is sheltered by Tawas Bay and has a sand shoreline with no bluff. Sand nourishment was the selected method of shore protection due to its aesthetic qualities and the site's sheltered location. There is an existing pier (jetty) at the southwest end of the project area. Tawas City installed a timber crib groin at the northeastern limit of the site, which was not included in the study. Installation of the sand fill began in the fall of 1973 and was completed by the spring of 1974. Four hundred linear feet (122.0 meters) of shoreline (between the groin and jetty) was protected with 4,350 cubic yards (3,328 cubic meters) of sand fill. The fill sand used had a size distribution similar to the natural beach sand. The nourishment project costs \$20 per foot (\$66 per meter). (As some sand would probably have been lost without the addition of the timber groin, total cost including the groin is \$80 per foot [\$262 per meter] of shoreline.) After some initial shifting the sand remained relatively stable through the spring of 1975. Minor shifting was again detected upon completion

of the fall survey of that year. The timber crib groin and pier have helped to hold the fill sand in place as well as trap additional sand. However, only minor storm activity has been experienced, so further evaluation of this project is required to determine overall effectiveness. To date the nourishment project has been very successful and inexpensive at this site. This project requires minimal maintenance, thus its long-term effectiveness is high.

Site 9, East Tawas

East Tawas City Park in Tawas Bay was selected as another test site. The same shoreform is found at this site as at Tawas City and a similar method of shore protection was examined. Sand nourishment was used, but without any groins or jetties for protection, at a cost of \$15 per foot (\$48 per meter). Three thousand cubic yards (2,295 cubic meters) of sand fill were placed along 400 feet (121.9 meters) of shoreline in the spring of 1974. For nearly a year the sand nourishment remained stable. During the winter of 1974-75 much of the sand was dispersed. By the fall survey of 1975, some sand had shifted back into the area of the original nourishment. This site experienced the same storm activity as Site 8, yet had much more sand movement. This suggests that stabilization of sand nourishment by a groin system will maintain the initial fill over a longer period of time.

Site 10, Tawas Point Coast Guard Station

A rock revetment was selected for testing at this site and was constructed in the summer of 1974. The shoreline is exposed to direct wave attack and has 10-foot (3.0 meter) sand bluffs. To install the 400-foot (121.9 meter) revetment, a foundation layer of rock (4- to 10-inch [10.6 to 24.4 cm]) was graded to a 3:1 slope 30 feet (9.1 meters) wide. At the top of the revetment a 3 by 5 foot (.9 meter to 1.5 meter) trench was dug and filled with smaller rock (1 to 3 inch [2.5 to 7.6 cm]). This would prevent erosion in back of the revetment caused by wave overtopping. Only the north half of the structure was capped with medium size armor stone (11 to 16 inch [27.9 to 40.6 cm]). Total cost of construction was \$50 per foot (\$164 per meter) of shoreline.

The revetment has been effective in preventing further bluff recession. Although only minor storm activity has been experienced, slight slumping and shifting of the rock is evident. Further rock movement may occur if major storms are experienced. While this structure is very effective in protecting the shoreline, it lacks any aesthetic qualities. This method of shore protection should not be installed in areas where beach use, such as swimming, is allowed.

Site 11, Michiana

This site in the Village of Michiana is an open coast area with 30-foot (9.1 meter) sand bluffs. North and south of the project area there is an existing seawall on a narrow beach. This shoreline is exposed to long fetches from the west and northwest and has been undergoing severe erosion for many years. A new concept in revetment construction on the Great Lakes was chosen for testing at this site. An inexpensive European technique using rock and asphalt mastic (a mixture of sand, mineral filler, and asphalt) was adapted for constructing the revetment. The structure was installed at an expense of \$70 per foot (\$230 per meter) in the fall of 1973 and is 400 feet (121.9 meters) long.

During the first year of study the structure performed very effectively and withstood four major storms. The revetment is shown in Figure 5. However, a storm in the spring of 1975 which produced breaking waves of about 7 feet (2.1 meters) for a duration of 24 hours caused most of the structure to collapse. The damage can be seen in Figure 6. The long duration of the storm rather than the wave heights had the most damaging effect. The storm was so severe that the steel seawall at the top of the bluff was threatened. Damage to the revetment resulted in a change of its slope from a ratio of 2 to 1 to 4 to 1. This left the backside 3 feet (.9 meters) lower after the storm. The underwater region immediately offshore had been severely eroded. The deeper water permitted waves larger than the revetment was designed to withstand to reach the shore. This contributed to the loss of sand behind the structure. Undermining of the revetment was probably caused by scour at the toe and overtopping. The asphalt-mastic revetment was more effective than the seawall as it was able to protect the bluff (and the road) even in its damaged condition.

It appears that the asphalt-mastic revetment performs quite well during most storm activity. The damage to the revetment from the unusually long storm also may have been caused by wave reflection off the steel wall at the north end. This is supported by the fact that 75 feet (22.9 meters) of revetment closest to the wall suffered severe slumping whereas the next 75 feet (22.9 meters) was hardly damaged.

Until it failed, the revetment was able to withstand all wave attacks. Even in its collapsed position, it provides a small level of protection from minor storms. The revetment has remained unchanged since the spring storm. Bluff recession has continued, however, and the road at the top of the bluff is threatened.

Site 12, Lincoln Township

Lincoln Township Park was the site selected for this project and is located near Stevensville. The shoreline is unprotected with a narrow beach backed by 20-foot (6.1 meter) sand dunes. An

existing steel seawall marks the southern border of the site and a concrete wall forms the northern border.

The shore protection structures installed at this site consist of a groin system with two groins 240 feet (73.2 meters) apart. Two types of groins were used: a 40-inch (101.6 cm) diameter Longard tube, 120 feet (36.6 meters) long, and a 90-foot (27.4 meter) long timber pile groin. The two structures are shown in Figure 7.

The Longard tube was the first structure installed at this site in the spring of 1973 at a cost of \$30 per foot (\$98 per meter). The tube was torn by construction equipment during installation of the timber pile groin.

Despite the initial tear, the Longard tube has suffered only moderate damage. The lake end of the tube (approximately 30 feet [9.1 meters]) has been lost and the whole structure has settled about 3 feet (.9 meters) along the centerline. It is very possible that the tube would have settled in this locale even without the influence of the heavy equipment. The rate of settlement increased again in the fall of 1975 after remaining relatively stable for about a year. It has not been determined if this is due to sand washing out of the tube from the lakeward end or by settlement. The tube still acts successfully as a groin in trapping sand and protecting the bluff. Design modifications could be incorporated, such as placing the tube on a foundation (preferably rubble) and covering the tube with an armored protective coating. This modified groin would be a good low-cost method of shore protection, though not as inexpensive as the present design. The present method of placing a 40-inch (101.6 cm) diameter Longard tube on a sandy lake bottom will only serve as a temporary method of erosion control.

The timber pile groin was completed while working through the ice in the winter of 1973 at a cost of \$50 per foot (\$164 per meter). This structure has performed well and shows no sign of any deterioration, thus providing additional evidence that wood is an excellent material for groin construction. An impervious timber pile groin is an old and proven means of shore protection in areas where there is adequate littoral drift.

The wide spacing between groins has proven quite successful and the entire system has worked very effectively in protecting the site by trapping sand and raising the beach profile. Both structures are still stabilizing the bluff although it has slumped somewhat. This slumping is probably due to factors other than wave attack, such as terrestrial processes or heavy human traffic on the bluff, as the beach profile is still raised around the groins and immediately adjacent to the bluff.

Site 14, Pere Marquette Township

This site is located 1 mile (1.6 kilometers) south of the Pere Marquette navigation structure. The shoreline consists of 20-foot (6.1 meter) sand bluffs and a narrow beach. A new concept in breakwater design was selected for testing at this site. The breakwater consists of precast, reinforced concrete panels bolted together to form zig-zag walls. Two 70-foot (21.3 meter) walls and one 56-foot (17.1 meter) wall were constructed. The zig-zag walls were placed offshore parallel to the shoreline with 50-foot (15.2 meter) spacings between structures. The panels were originally to be placed at a water depth giving 1 foot of freeboard. Depth increased so rapidly that panels were placed only 50 feet (15.2 meters) from shore. Such a short distance causes high-water velocities between the bank and breakwater which accelerates erosion. Cost per foot (per meter) of shoreline "protected" equalled \$70 (\$230) when installed in the fall of 1973.

The breakwater system performed quite effectively in building up a beach and preventing bluff recession for the first year. Figure 8 shows the structure in the spring of 1974. Eight major storms were experienced at this site. A major storm with 6- to 10-foot (1.8 to 3.0 meter) waves in the winter of 1975 caused extensive damage to the structure and bluff. All three structures were damaged by settlement and panel breakage. The north section lost two entire panels and settled over 3 feet (.9 meters). It is now completely submerged; this can be seen in Figure 9. One panel was lost off of the center section which also settled and tilted radically. The remaining walls are badly chipped and cracked and have tilted toward shore. Major bluff recession has continued, up to 30 feet (9.1 meters) during the second study year. The bathhouse protected by the breakwater has been completely destroyed.

This experimental use of precast zig-zag walls was intended for onshore use only. Unless redesigned, this type of structure should not be used as an offshore breakwater. Necessary design modifications, however, would eliminate this system from the low-cost category. The private homeowner could not install this structure himself because heavy construction equipment is required. This is not a recommended method of shoreline protection as used in this program. Other breakwater designs, although very expensive, should be used if site conditions require that method of shore protection.

Site 15, Ludington State Park

Ludington State Park was selected for testing two steel pile groins. The low, wide sand beach in front of high dunes was suitable for this method of protection. The groins were installed 125 feet (38.1 meters) apart to stabilize the beach. The north groin is 100 feet (30.5 meters) long and the south groin is 70

feet (21.3 meters) long. It is not possible to determine the final costs of construction as some materials and labor were provided at no charge. Improper anchoring and tie back into the beach has prevented the north groin from performing well. This groin was flanked shortly after construction and deep holes scoured in the lake bottom. This scour caused some shifting of the groin and the breaking of the vales. Repairs had to be made to the north groin. The lake portion had to be pulled out, straightened, and redriven. Above normal maintenance and sand fill has been required for these structures. With the additional filling the groins have successfully prevented beach erosion and protected an adjacent parking area. Since the original construction related problems, the groins have remained stable.

The problems experienced at this site illustrate that good design, when improperly installed, may fail. Steel sheet piling groins are normally effective shore protective structures.

Site 17, Empire

Recession rates as high as 30 feet (9.1 meters) a year have been experienced at the Village Park in Empire Village. This open coast area with 3-foot (.9 meter) sand bluffs was selected for testing a 40-inch (101.6 cm) diameter Longard tube utilized as a seawall. The 300-foot (91.4 meter) tube was laid on a filter cloth foundation parallel to shore at a cost of \$30 per foot (\$98 per meter) of shoreline. The tube can be seen immediately after it was installed in the fall of 1973 in Figure 10. Shortly after construction, the tube was attacked by 5-foot (1.5 meter) breaking waves for a 14-hour period. Probable maximum wave height was 11 feet (3.4 meters). Due to the shoreline configuration, waves pounded directly against the structure. The single tube was unable to withstand this wave attack and was destroyed. The damage can be seen in Figure 11. If the tube had been sewn to the filter cloth, it may have been more effective.

Site 18, Moran Township

This site is located along U.S. 2 in Moran Township. The 30-foot (9.1 meter) sand bluffs found here have been severely eroded. Two styles of seawalls were selected for testing. Three 40-inch (101.6 cm) diameter Longard tubes were installed in a pyramid configuration (one on top of two) on filter cloth parallel to the shoreline within 10 feet (3.0 meters) of the waterline. The tubes extended for 300 feet (91.4 meters). The second structure consisted of giant sandbags placed in four different stacking patterns at the toe of the bluff, parallel to the shoreline, for 250 feet (76.2 meters). The different stacking sequences were incorporated to test their relative effectiveness. All Longard tubes were installed in the fall of 1973. At the east end of the tubes, the sandbag structure was installed in the spring of 1974. A view of this site can be seen in Figure 12. The costs of construction

per foot (meter) of shoreline for each was \$60 (\$197). Five major storms have since been experienced but only minor problems have been experienced. The top Longard tube shifted out of position due to back pressure from the slumping bluff and had to be shimmed up. The western 50 feet (15.2 meters) moved lakeward about 3 feet (.9 meters). The lower tube is now covered with sand, apparently from sand washing in and around it (no vertical movement of the tube has occurred). The condition of the structures in the fall of 1975 is shown in Figure 13. Despite this, the tubes have retained their original effectiveness. The top of the bluff behind the structures has continued to recede and slump. This occurred because the sand bluff was not in a stable position. The most dramatic bluff loss has occurred behind the sandbags and between the two structures. The sandbag structure, despite some bag loss due to vandalism, has remained stable and performs effectively. Both structures have effectively protected the bluff from major erosion damage (although the shoreline adjacent to the structures has also only experienced minor recession). There is a wider expanse of beach in front of the Longard tubes than the sandbags. This appears to be more of a natural phenomenon than an indication of relative structure effectiveness.

Tables 2, 3, and 4 present summary details of the research effort. A brief description of all the sites is included in Table 2 along with method of protection. Table 3 reports the number of major storms at the surveyed sites since the time of construction as well as the condition of the structure and near-shore environment. Table 4 gives structure and nearshore environment condition for the sites studied utilizing photographic methods.

CONCLUSIONS

The durability of shore protective structures depends on the number of major storms that occur, their intensity and duration as well as on soil type, geologic structure of the lake bottom, topography of the shoreland, etc. These site specific variables prevent broad comparisons of structure effectiveness. Long-term effectiveness of the installations cannot be judged until more time has passed. Some of the test sites have not been exposed to a number of major storms common to the Great Lakes. This makes it difficult to evaluate the structure's performance as a form of low-cost shore protection. The ongoing nature of this study is designed to gather the data necessary to fully evaluate the test methods.

Over the short period of the program, the methods of shore protection at East Tawas, Michiana, and Empire have been lost. The breakwaters at Pere Marquette Township and the Longard tube at Lincoln Township have been damaged and the effectiveness of these structures has been substantially reduced. Sandbags have been lost from the Sanilac 26 and Moran Township projects. The loss documents the necessary replacement of sandbags on a yearly basis.

The shore protection methods used at the remaining project sites have experienced only minor changes.

The following observations can be made based on the two years of study:

-- Artificial nourishment projects are very effective methods of shore protection, especially in areas with limited littoral drift which eliminates the use of groins. (Artificial nourishment should not be used in areas with strong littoral currents which rapidly remove the sand.) Groins may be used in conjunction with this method to help hold the sand in place. Nourishment is also aesthetically pleasing as it preserves the beach in its natural state.

-- Groin systems are appropriate methods of shore protection in areas with ample littoral drift. If a groin system is installed where there is not ample littoral drift, sand nourishment may be required to make the system functional. The longer spacing used between groins at Sanilac 26 shows no adverse effects on the performance of the groin system. Longard tubes can be effectively used as groins; however, in sandy areas they may settle and eventually require replacement. Sandbag groins will require yearly replacement of bags. Gabions, asphalt-mastic, and timber crib groins have been stable at the Sanilac 11 site and pile groins, both timber and steel, are generally effective.

-- When site conditions require, revetments and seawalls may be utilized effectively. However, they experience accelerated destruction when overtopped by waves as shown at Michiana and Empire. Longard tubes used at Moran Township and Sanilac 11 as well as the sandbags used at Moran Township, to date, have been suitable methods of shore protection. The rock revetment installed at Tawas Point Coast Guard Station also has been successful.

-- Offshore breakwaters have traditionally been an expensive, yet effective, method. However, as shown by the breakwater system used at Pere Marquette Township, low-cost breakwaters are not suitable shore protection systems.

The data derived from this project have given insight into the possible solutions for preventing shoreline erosion. Only further years of study will provide the data necessary to properly build effective low-cost methods of shore protection. The general conclusions of two years of study presented in this paper contribute to the development of proper methods of shoreline protection from erosion damages.

REFERENCES

1. U.S. Department of the Army Corps of Engineers, North Central Division, National Shoreline Study: Great Lakes Region Inventory Report, Vol. V, 1971, 221 p.

2. U.S. Department of the Army Corps of Engineers, North Central Division, Preliminary Draft: Summary Report of Pilot Study Program of Great Lakes Shoreland Damage Study, undated, unpublished, 100 p.
3. U.S. Department of the Army Corps of Engineers, Coastal Engineering Research Center, Shore Protection Manual, Vol. 2, 1973, 529 pp.

TABLE 1
IDENTIFICATION OF TEST SITES

Site Name	Site Number	Lake
Little Girls Point	1	Superior
Keweenaw Peninsula	2	Superior
Marquette	3	Superior
Whitefish Township	4	Superior
Lakeport State Park	5	Huron
Sanilac 26	6	Huron
Sanilac 11	7	Huron
Tawas City	8	Huron
East Tawas	9	Huron
Tawas Point Coast Guard Station	10	Huron
Michiana	11	Michigan
Lincoln Township	12	Michigan
Charles Mears State Park	13	Michigan
Pere Marquette Township Park	14	Michigan
Ludington State Park	15	Michigan
Big Sable Point	16	Michigan
Empire	17	Michigan
Moran Township	18	Michigan
Manistique	19	Michigan

TABLE 2
PROJECT DESCRIPTION

PROJECT NUMBER	PROJECT LOCATION	SITE DESCRIPTION	METHOD OF PROTECTION:	TEST CONSTRUCTION COST ¹	
				(\$ per foot)	(\$ per meter)
LAKE SUPERIOR					
1	Little Girls Point	Open coast area with 20-foot (6.1 meter) high, predominantly clay bluffs with little to no beach.	"Nami Rings" (2.5 foot by 1 foot [.8 meter by .3 meter] concrete rings weighing 265 lbs. [120.2 kg]). Part of this structure was placed on filter cloth, part on a rock foundation, the remainder was not placed on a foundation. Some of the rings were fastened together.	35	114
2	Keweenaw Peninsula	Open coast area with 15-foot (4.6 meter) sandy bluff with narrow beach.	Revetment using waste wine rock in a size smaller than normally accepted for a revetment of this type.	20	66
3	Marquette	Partially sheltered coast area with a low sand bluff, partially "protected" with broken concrete rubble, little to no beach.	Dredge sand with a large percentage of fines and a steel sheet pile groin.	*	*
4	Whitefish Township	Predominantly sheltered coast area with a low (about 3-foot [.9 meter]) sandy loam bluff, no beach.	Rock revetment with groins "tying" the revetment to the land area behind.	45	148
LAKE HURON					
5	Lakeport State Park	Open coast area with high sand bluff, low foredunes and some beach.	40-inch (101.6 cm) diameter Longard tube installed on bar to form an offshore breakwater.	25	82
6	Sanilac 26	Open coast area with 30-foot (9.1 meter) clay bluffs and no beach.	An experimental groin system with a spacing between groins of about 200 feet (61.0 meters) consisting of:		
			2 40-inch (101.6 cm) diameter Longard tubes, 100 feet (30.5 meters) long	30	98
			69-inch (175.3 cm) diameter Longard tube, 50 feet (15.2 meters) long	25	82
			Cabion baskets, 70 feet (21.3 meters) long	30	98
			Giant sandbags, 60 feet (18.3 meters) long	30	98
			Asphalt mastic, 60 feet (18.3 meters) long	45	148
			Timber crib, 50 feet (15.3 meters) long	30	98
7	Sanilac 11	Open coast area with 35-foot (10.7 meter) clay bluffs and no beach.	Seawall of 69-inch (175.3 cm) diameter Longard tube.	65	213

TABLE 2
PROJECT DESCRIPTION

PROJECT NUMBER	PROJECT LOCATION	SITE DESCRIPTION	METHOD OF PROTECTION:	TEST CONSTRUCTION COST	
				(\$ per foot)	(\$ per meter)
8	Tawas City	Sheltered sand coast area with no bluff and an existing pier (jetty) at the southwest end of the project area and a newly constructed timber pile groin at the northeast limit of the project area.	Nourishment project between a jetty and wood groin. Fill sand has a size distribution similar to the natural beach sand.	20	66
9	East Tawas	Sheltered sand coast area with no bluff.	Nourishment project using fill sand which has a size distribution similar to the natural beach sand.	15	49
10	Tawas Point Coast Guard Station	Open coast area with 10-foot (3.0 meter) sandy soil bluff, no beach.	Layered (staged) rock revetment, half "capped" with armor stone of medium size (11 to 16 inch [27.5 to 40 cm]).	50	164
LAKE MICHIGAN					
11	Michiana	Open coast area with 30-foot (9.1 meter) sand bluff. Shoreline immediately north and south of project area have seawall construction and narrow beach.	Revetment composed of rock and asphalt mastic (a European technique new to the Great Lakes).	70	230
12	Lincoln Township	Open coast area with a 20-foot (6.1 meter) sand dune and a narrow beach.	Groin system with 2 groins 240 feet (73.2 meters) on center composed of:	30	98
			40-inch (101.6 cm) diameter Longard tube, 120 feet (36.6 meters) long Timber pile, 90 feet (27.4 meters) long	50	164
13	Charles Mears State Park	Open coast area with low sandy beach area in front of high dunes. Study area is immediately north of Pentwater navigation structure	Groin system with 3 groins about 150 feet (45.7 meters) on center. Each groin is composed of gabions in beach area and giant sandbags in the water area.	*	*
14	Pere Marquette Township	Open coast area with 20-foot (6.1 meter) sand bluff and narrow beach. The Pere Marquette navigation structure (jetty) is 1 mile (1.6 km) north of the site.	3 precast reinforced concrete, zig-zag breakwaters about 70 feet (21.3 meters) long with 50-foot (15.2 meter) gaps between structures.	70	230

TABLE 2
PROJECT DESCRIPTION

PROJECT NUMBER	PROJECT LOCATION	SITE DESCRIPTION	METHOD OF PROTECTION:	TEST CONSTRUCTION COST	
				(\$ per foot)	(\$ per meter)
15	Ludington State Park	Open coast area with low, wide sand beach in front of high sand dunes.	2 steel pile groins, 125 feet (38.1 meters) on center to stabilize beach. Groins are periodically filled with sand removed from an adjacent parking area.	*	*
16	Big Sable Point	Open coast area with 10-foot (3.0 meter) sand dunes and an existing damaged seawall; no beach.	Tie backs installed on existing seawall; return and cutoff gabion groins constructed from existing seawall landward. Land area behind the seawall and between return walls and cutoff walls sand filled.	*	*
17	Empire	Open coast area with 5-foot (1.5 meter) sand bluff and little to no beach. This area has been experiencing extremely high (30 feet/yr [9.1 meters/yr]) recession rates.	40-inch (101.6 cm) diameter Longard tube placed on filter cloth parallel to the shoreline near the waterline.	30	98
18	Moran Township	Open coast area with 30-foot (9.1 meter) sand bluff and narrow beach.	3 40-inch (101.6 cm) diameter Longard tubes placed pyramid fashion (1 on top of 2) on filter cloth parallel to the shoreline near the waterline. Giant sandbags placed in 4 different stacking patterns parallel to the shoreline along the waterline.	60	197
19	Manistique	Open coast area with 5-foot (1.5 meter) sand bluff and narrow beach.	Gabion mats placed over bluff face in revetment fashion.	20	66
Note:	Cost figures given are determined over the length of shoreline the structure was designed to protect.				
*	Exact cost figures are not available.				

TABLE 3
PROJECT RESULTS THROUGH FALL, 1975 FOR SITES UTILIZING SURVEYS

PROJECT	NUMBER OF STORMS (BREAKING WAVE OF 6 FEET [1.8 METERS] OR GREATER) AT THE SITE SINCE TIME OF CONSTRUCTION (INCLUDES ALL MONTHS)	STRUCTURE CONDITION	NEARSHORE ENVIRONMENT CONDITION
Site 5, Lakeport 40-inch (101.6 cm) diameter Longard tube on bar	3	Unchanged.	Beach area has increased greatly in the vicinity of the tube (unrelated to the tube's performance) to such an extent that it is no longer a breakwater. This site is no longer part of the extended field program since the tube is not required for shore protection.
Site 6, Sanilac 26 2 40-inch (101.6 cm) diameter Longard tubes.	1	Minor differential settlement in tubes.	Sand has been trapped by the groin. Recession at top of bluff is about 10 feet (3.0 meters) in the immediate vicinity of this groin. This recession could be caused by factors other than wave attack.
69-inch (175.3 cm) diameter Longard tube	2	Unchanged.	This groin has been effectively trapping sand, particularly to the north. Top of bluff recession has been minimal.
Gabion	1	Unchanged.	Sand is being trapped, especially on north side of groin.
(Site 6 continued)			
Sandbags	2	Approximately the outer 15 feet (4.6 meters) of this structure have been lost through bag destruction.	Sand has been trapped by this structure. Top of bluff recession has been minimal.
Asphalt mastic	2	Small section (about 3 feet by 3 feet [.9 meter by .9 meter]) of groin has broken off at outer end.	Sand has been trapped by structure. Minimal top of bank recession has been recorded.
Timber crib	1	Unchanged (installed late summer 1975).	No data available.
General		Spacing between groins has been effective to date.	Some areas of localized top of bluff recession.
Site 7, Sanilac 11 69-inch (175.3 cm) diameter Longard tube	2	Structure has remained stable. The center section of the structure has lost sand.	Area of minor bluff recession.
Site 8, Tawas City Sand nourishment	1	Only minor shifting of the sand nourishment.	No change.
Site 9, East Tawas Sand nourishment	2	Totally dispersed.	No apparent effect from sand.

TABLE 3
PROJECT RESULTS THROUGH FALL, 1975 FOR SITES UTILIZING SURVEYS

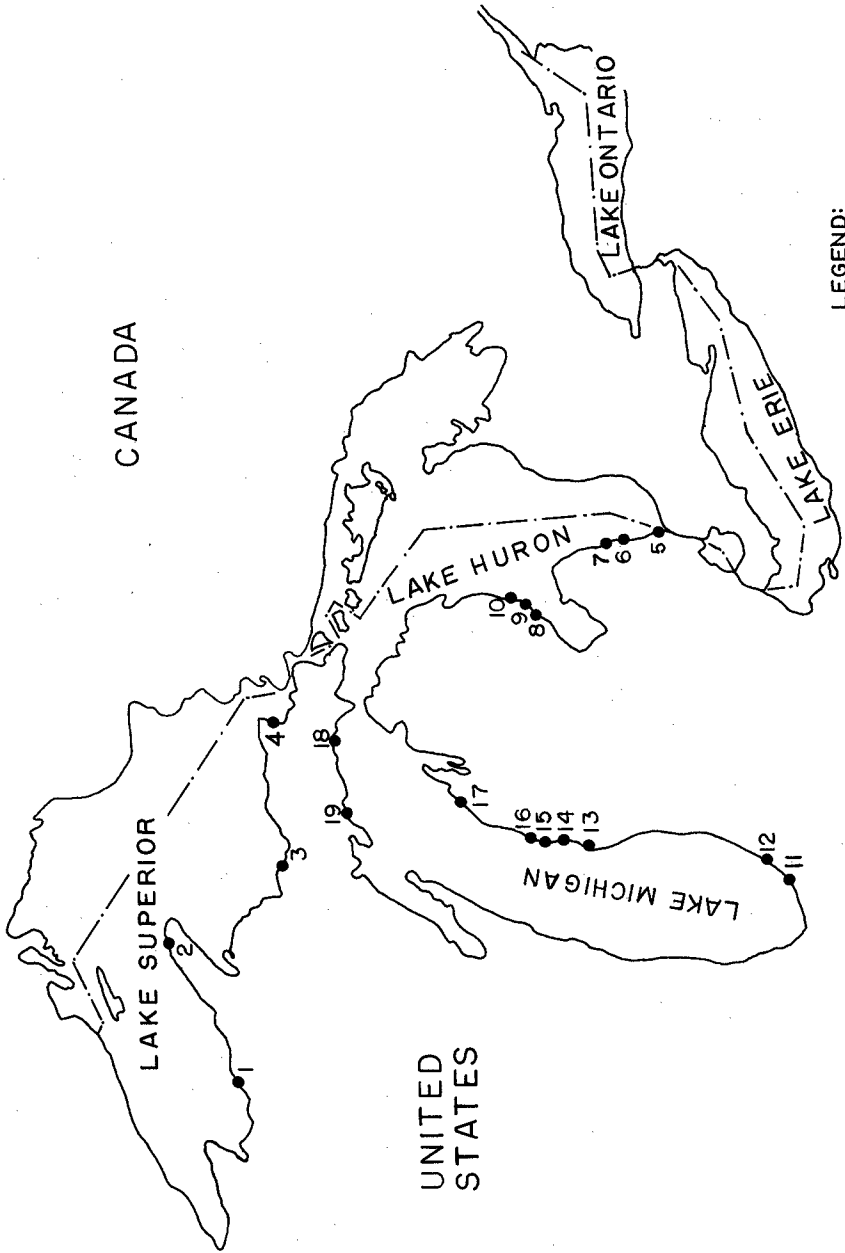
PROJECT	NUMBER OF STORMS (BREAKING WAVE OF 6 FEET [1.8 METERS] OR GREATER) AT THE SITE SINCE TIME OF CONSTRUCTION (IN- CLUDES ALL MONTHS)	STRUCTURE CONDITION	NEARSHORE ENVIRONMENT CONDITION
Site 11, Michiana Asphalt mastic revetment	5	Revetment collapsed on beach after 5 critical storms. The sand behind the revetment's slope has been flattened. Small portions of the revetment are completely destroyed.	Bluff erosion has continued. Remaining revetment is an inconvenience to bathers at this beach.
Site 12, Lincoln Township 40-inch (101.6 cm) diameter Longard tube	18	Outer portion (1/3 of tube) has been lost. The remainder of the tube has settled from 0-2 feet (0-.6 meter).	Tube has trapped and held sand. Slope on dune near tube has flattened to some extent.
Timber pile	18	Unchanged.	This groin has trapped and held sand. Slope on dune near this groin has flattened to some extent.
General			Structures have protected site by trapping sand and raising the beach profile.
Site 13, Charles Mears State Park Gabion and sandbag groins	13	Some settlement detected in all groins. One or 2 sandbags lost from each structure.	System has helped stabilize beach area with artificial nourishment added each spring.
Site 14, Pere Marquette Township Precast concrete breakwater	18	All three structures have settled about 1 foot (.3 meter). Two panels have been lost off the north end of the north section and 1 panel has been lost off the south end of the center section.	Bluff recession has continued. Bathhouse that this installation was meant to protect has been destroyed.
Site 15, Ludington State Park Steel pile groins	14	North groin had to be repaired once (lake portion pulled, straightened, and redriven).	Deep holes have scoured in the lake bottom around the outer edge of the groin. System has required periodic sand maintenance.
Site 17, Empire 40-inch (101.6 cm) diameter Longard tube	-	Destroyed within 1 month.	Rapid bluff recession has continued.
Site 18, Moran Township 40-inch (101.6 cm) diameter Longard tubes	8	Some minor differential settlement. The top tube had to be wedged in place to avoid being pushed off due to back pressure from sliding sand.	Sand bluff has flattened some.
(Site 18 continued) Sandbags	8	A number of sandbags have been lost, partly due to vandalism. Some differential settlement has been detected.	The sand bluff has slumped in some areas.

TABLE 4
PROJECT RESULTS THROUGH FALL, 1975 FOR SITES UTILIZING PHOTOGRAPHIC MONITORING ONLY

PROJECT NUMBER	PROJECT LOCATION	STRUCTURE CONDITION	NEARSHORE ENVIRONMENT CONDITION
1	Little Girls Point	Some change in revetment position due to sliding clay. Rings have filled with sand and small rock.	Some sliding of clay bluff.
2	Keweenaw Peninsula	Unchanged.	Unchanged.
3	Marquette	Groin has remained unchanged; as expected a large amount of sand has shifted.	No apparent effect from structures.
4	Whitefish Township	Unchanged.	Stable.
10	Tawas Point Coast Guard Station	Some shifting in the rocks is evident.	Unchanged.
16	Big Sable Point	(Construction problems were experienced at this site which hampered the study.) All the sand filled behind the wall has been washed out, exposing improperly installed tie backs. The south return wall which was poorly installed has failed.	In spite of these failings, the original seawall is still in place. Bluff recession has continued at a very low rate.
19	Manistee	Structure has been "paved" over and area is now a parking lot.	No longer applicable.

TABLE 5
GROIN SYSTEMS INSTALLED AT SANILAC 26

Type	Structure Length		Test Construction Cost	
	Feet	Meters	Per Foot	Per Meter
2 40-inch (101.6 cm) diameter Longard tubes	100	30.5	\$30	\$98
1 69-inch (175.3 cm) diameter Longard tube	50	15.2	\$25	\$82
Gabion	70	21.3	\$30	\$98
Giant sandbags	60	18.3	\$30	\$98
Asphalt mastic	60	18.3	\$45	\$148
Timber crib	50	15.2	\$30	\$98



LEGEND:
● PROJECT SITE
SCALE: NONE

FIGURE 1
SITE LOCATIONS



Figure 2 Sanilac 26 April 27, 1975

The sandbag groin can be seen in the foreground with the gabion, 69-inch (175.3 cm) diameter Longard tube and the two 40-inch (101.6 cm) diameter Longard tube groins in succession behind it. The group of structures in the far background are not part of this project.

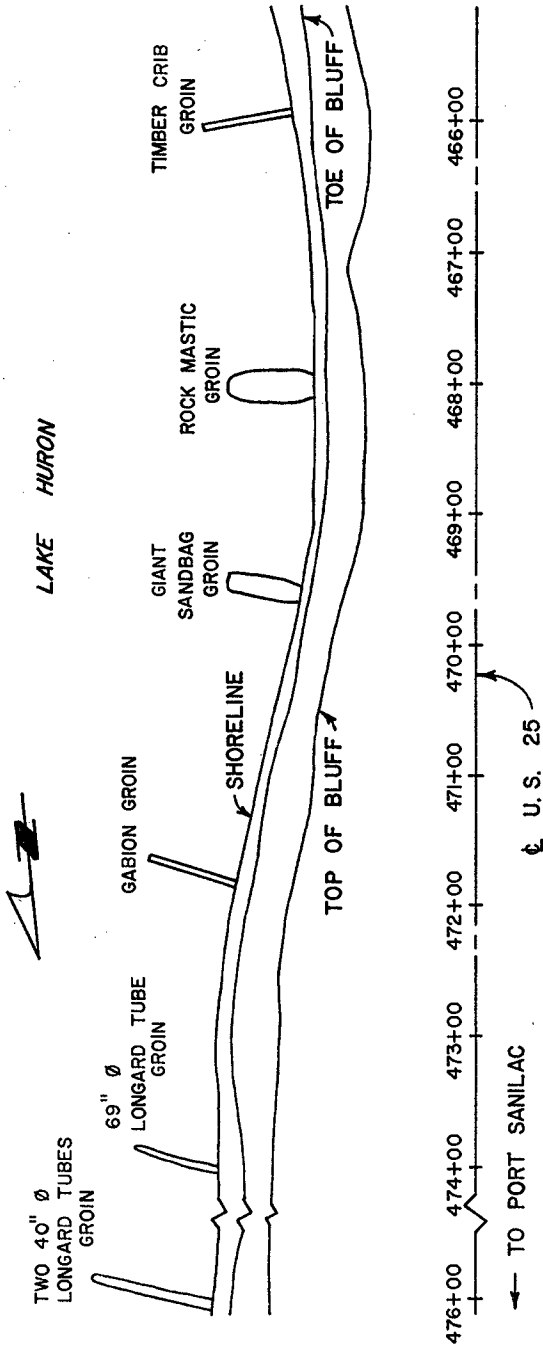


FIGURE 3

PLAN VIEW OF SANILAC 26

SANILAC TWP., MICHIGAN



Figure 4 Sanilac 11 April 27, 1975

This view shows the 69-inch (175.3 cm) diameter Longard tube used as a seawall at Sanilac 11. The very active and slumping clay bluff is evident in the photograph.



Figure 5 Michiana September 23, 1973

The revetment can be seen one month after completion of construction in the fall of 1973.



Figure 6 Michiana October 20, 1975

Large portions of the sand behind the structure have been washed out causing the structure to collapse. Despite its collapsed condition the revetment has maintained its integrity. Emergency fill operations are evident at the south end of the project near the concrete seawall. The entire beach area has been eroded as is evident by the exposed steel pile foundation beneath the concrete seawall.



Figure 7 Lincoln Township April 20, 1974

The timber pile groin, installed in the winter prior to this photograph, is evident in the foreground. Part of the Longard tube, constructed the previous fall, can be seen in the background (near the tripod). Settlement in the tube is particularly evident at the shoreline.



Figure 8. Pere Marquette Township April 29, 1974

This view shows the south and north set of panels (looking north) shortly after construction. The center panels were installed in the fall of 1973. The newer set of panels were placed at a higher elevation (with more freeboard) than the center section. As is evident, these panels were initially very effective in trapping sand.



Figure 9 Pere Marquette Township October 12, 1975

In this photograph (looking north) it is evident that the north and south sets of panels have settled considerably. Effectiveness of the structures has been reduced and the bluff behind the structures (not shown) has been considerably damaged by storms.



Figure 10 Empire November 3, 1973

This picture was taken shortly after construction was completed. The filter cloth foundation and the low sand bluff to be "protected" by the tube is evident.



Figure 11 Empire March 7, 1974

As evident in this photograph, a large portion of the structure has settled out of site. Bluff recession has continued at a high rate.



Figure 12 Moran Township November 4, 1973

The Longard tube structure and one of the stacking patterns of the sandbag structure, both used as seawalls, are shown here. The short stub groin protruding lakeward from the Longard tubes was removed. The active sand bluffs to be protected by the seawalls are evident.



Figure 13 Moran Township October 12, 1975

This is a view of the site two years later. Many sandbags have been lost and the tube has remained stable. Recession activity is evident as shown by the number of trees and vegetation scattered along the face of the bluff. This action is a result of erosion damage prior to the installation of the test projects. The shoreline in front of these structures has stabilized as well as the shoreline in the adjacent areas (no cause and effect relationship is apparent).

CHAPTER 165

LOW-COST SHORELINE PROTECTION

Billy L. Edge,¹ John G. Housley,² and George M. Watts³

ABSTRACT

As the public interest in low-cost, self-installed solutions to shoreline erosion continues to grow, the involvement of private enterprise in developing solutions intensifies. Now that low-cost devices are identified as a salable commodity as goods or services, the number of inventors, creative engineers, agronomists, and foresighted planners producing potential designs are rapidly growing. Over two hundred devices, both proven and untested devices, have been cataloged as a part of the National Shoreline Erosion Demonstration Program. This program calls for the Corps of Engineers to plan, establish, and conduct for a period of five years a shoreline erosion control development and demonstration program including physical and vegetative devices.

INTRODUCTION

There is no need to recount the tales of the thousands of miles of eroding shoreline around the United States as well as throughout the world; the National Shoreline Study adequately covers the discouraging situation around the coastline of the United States. Little else needs to be said to emphasize that without adequate protection, in the broadest sense, a very significant part of our coastline falls prey to the ravages of the sea, and, of course, to man himself. Adequate protection against these forces comes normally by constructing monumental structures, such as the San Francisco seawall (O'Shaunessy), which render the land-sea-air interface permanent. It is definitely not in the best interest of the nation to provide this degree of protection at other than very valuable property at an extremely high wave energy site.

¹Associate Professor of Civil Engineering, Clemson University, Clemson, South Carolina 29631 and Vice-Chairman Shoreline Erosion Advisory Panel.

²Civil Engineer, Planning Division, Directorate of Civil Works, Office of Chief of Engineers, U.S. Army Forrestal Building, Washington, D.C. 20314.

³Chief, Engineering Development Division, U.S. Army Coastal Engineering Research Center, Fort Belvoir, Virginia 20060.

At the opposite extreme of the cost scale is the institutional type of protection. Through appropriate legislation and other forms of institutional arrangements, loss of man-made structures along the shoreline is prevented. By restricting development to behind the third row of dunes (McHarg), man-made structures are protected from falling to the forces of the sea, at least for several years, and at the same time with adequate control the dune structure is maintained for the last line of defense. There is much to be said for this form of protection in an area that is not already fully or even overdeveloped. In the latter case it makes pitifully little sense to legislate shoreline protection. Rather, recognizing that there is little man can do to completely stop erosion, attention must be given to providing erosion protection in the form of a new beach equilibrium--a form which does not match the energy of the ocean against the inertia of a coastline but a form which enhances the resistance of the shore to erosion.

Within the context of the philosophy sketched here shoreline protection can be a reality and not a dream. Moreover, within the broad spectrum of solutions available, from laws to monuments, there is a place for low-cost protection.

Whenever major erosion threatens public property, astute elected officials generally call upon state or federal government to help solve the problem. On the other hand, when the property is private, help is seldom available and the owner is forced to provide his own defense. This requirement often results in many thousands of dollars being wasted by construction of ill-conceived projects. Sometimes the owner goes to a coastal engineer for help; but, more frequently, they design their own protection with the "good advice" of a brother-in-law, uncle, or helpful neighbor. Unfortunately, even if the private landowner does come to a coastal engineer, he seldom receives the kind of inexpensive advice for which he is looking. This is not necessarily the fault of the coastal engineer since the type of protection with which he is normally concerned is of the more glamorous, permanent, and expensive variety. So the home owner, dejected by the exorbitant costs of the traditional shore protection works, is faced with paying more than he can or is willing to afford, selling his property to an unsuspecting buyer, or developing his own solution.

More recently, significant interest has arisen in the governmental and industrial sectors to provide help for the private landowner with an eroding shoreline. Some research has been sponsored by state and federal government, although not at a level commensurate with the problem. A major demonstration and testing program has been undertaken by the Michigan Department of Natural Resources (Brater, Armstrong, and McGill, 1974, 1975). The demonstration projects are designed to provide data on various devices, methods of construction, and costs. Close evaluation of the results of this study will provide extremely useful information on effectiveness and durability of each of these shore protection devices.

Significant efforts have also been made to educate the public about not only devices suitable and available but more fundamentally about the

basic phenomena that cause erosion problems (Brater). These publications range from brochures or "roadmaps" (Arno) to thorough treatments in the language of the intended user (Habel). This self-help literature has been distributed widely in the Great Lakes area and less completely in the Atlantic, Gulf, and Pacific areas with the hope of improving on the landowners self-design.

Industry is responding to the need for low cost solutions through their own research and development which is providing the coastal engineer with many new and innovative ideas that "might" fall into the category of low cost.

Before going further, a few words of clarification are in order. It is not implied that a "low-cost" solution is acceptable or even available for most erosion situations; rather the emphasis of this paper is on eroding areas that are not necessarily amenable to the more-costly, traditional forms of control. Moreover, it must be pointed out that too often the inexpensive methods of protection are not "low-cost" at all.

To evaluate the new concepts and ideas for low-cost protection and to disseminate the results to the owners of eroding shorelines, the U.S. Congress created the National Shoreline Erosion Demonstration Program.

Section 54 of the "Shoreline Erosion Control Demonstration Act of 1974," directed the Secretary of the Army, acting through the Corps of Engineers to establish and conduct for a period of five years a national shoreline erosion control and demonstration program. The intent of the program is to develop and demonstrate to the public and technical community methods for "low-cost" shore protection. Specifically, these methods are to be developed and demonstrated in "sheltered waters." Sheltered waters are defined as those areas where the design breaking wave is less than six feet. In addition, the Act specifically calls for widespread dissemination of the results of this program.

In the following sections, proven methods and devices for low-cost protection is discussed. Next, several of the new and innovative and yet untried concepts are presented. The National Shoreline Erosion Demonstration Program is presented in terms of direction, accomplishments, and goals.

What constitutes low-cost shore protection? This question is addressed here to provide the framework needed for further discussion. Low-cost shore protection is shore protection for sheltered or inland areas which fulfills one of the following criteria:

- a. Cost less than \$50 per front foot for materials and can be constructed without the use of heavy construction equipment.
- b. Cost less than \$125 per front foot for materials plus placement using heavy construction equipment.

These cost figures are intended to provide a degree of protection to the shore for approximately a 10-year period with a minimum of maintenance assuming that a storm exceeding a 1 in 25 year severity is not encountered during the 10-year interval with the severity being measured in terms of a combination of violence and duration.

This definition now raises the question, what is a sheltered area? For the purpose of low-cost protection it is defined as follows. A "sheltered" or "inland" site is an area which falls under one or more of the following conditions:

Coastal shores. Those shores receiving wave attack from waves generated on the open or semi-open waters of the Atlantic, Gulf, Pacific, Bering Sea, or Arctic Ocean, but which waves are attenuated by refraction, diffraction or friction in such a manner that the significant wave height of waves breaking on these shores never exceeds six feet in height.

Tidewater shores. Those shores fronting on the inland tidal waters connected with the Atlantic, Gulf, Pacific, Bering Sea, or Arctic Ocean.

Great Lakes shores. All shores fronting on the Great Lakes plus the shores of all bays connected directly with one of the Great Lakes and standing at the same water levels as the parent Great Lake.

DEVICES AND METHODS WITH POTENTIAL FOR SUCCESS

This section is devoted to describing devices and methods which, if used in the field, would result with a high probability of success. This description is not intended to be all inclusive but rather to present those concepts and established devices which have a probable chance of success. Devices can be categorized as follows:

- Revetments
- Seawalls
- Bulkheads
- Breakwater
- Beach fills
- Groins
- Vegetation
- Institutional

There is one extremely important factor concerning the successful behavior of all gravity, and to some extent cantilevered, type structures in the above list. This factor involves an adequate foundation and toe (most seaward portion) protection for the structure. The successful behavior of any gravity structure whether it be semi-flexible or rigid is very much dependent on the adequacy of foundation materials on which the structure is placed. If the foundation is inadequate or under-designed, a high degree of movement of structural components can be expected with resultant failure of the integrity of the structure. A properly designed and constructed foundation for the overlying structure can result in a satisfactory performance equal to or greater than the desired life of the installation, assuming, of course, the structural components of the main element of the structure are properly designed.

Revetments

Substantial data are available to verify that a graded rip-rap type revetment can be very successful as a shore stabilization structure. Of course, the stone size distribution in the revetment, including the foundation material, must be commensurable with expected wave forces on the structure.

In geographic areas where the cost of placing suitable rip-rap material (stone) exceeds acceptable limits, consideration could be given to the placement of precast concrete armor units on a proper foundation. Most all of the presently used precast armor units are described in the CERC Shore Protection Manual. The use of precast concrete units is generally associated with large coastal structures subjected to very large wave forces. However, there are no apparent technical reasons why small precast concrete armor units, would not be equally effective in a low wave energy environment.

There are other alternative materials and approaches for construction of revetments which exhibit potential success; however, presently available performance data in regard to upper limit of stability are meager and

this lack of information is influential in establishing the relative probability of success if the structure is tested in the demonstration program. These alternatives include the precast concrete interlocking and semi-interlocking units placed on a proper foundation and appropriate toe protection provided. Also, included is a step-type revetment consisting of cribbing units which are interlocking and filled with proper graded stones, all placed on an adequate foundation with toe protection provided in front of the first step. However, one factor of concern for the crib type revetment involves a prediction of the durability of the cribbing units if low-cost constraints are adhered to for its structural make-up.

Seawalls and Bulkheads

The primary function of a seawall is to protect the area behind it from direct wave attack and the structure may or may not be subjected to backfill pressures. Bulkheads' functions are to retain backfill and are subjected to direct wave attack. The functional difference between a seawall and a bulkhead is, therefore, sometimes difficult to delineate, but for purposes of application in moderate to low wave energy environments, they may be considered to serve the same function with seawalls and, therefore, would generally be more massive than bulkheads.

There are a number of existing designs of precast concrete type seawalls, if placed on an adequate foundation, that would be promising for success. Most of these designs would require heavy equipment to handle and place the concrete segments. Promising results could also be obtained for a seawall constructed of cribbing filled with stones with the structure placed on a proper foundation and toe protection provided. However, the factor concerning structural durability of the cribbing for the seawall would be similar to that cited for the cribbed type revetment mentioned earlier.

The presently available technical guidance on bulkhead design is somewhat substantial, therefore, installation of a standard steel, concrete, or timber sheetpile bulkhead as a low-cost structure would most likely be successful. Appropriate measures to prevent excessive wave induced bottom scour in front of the sheetpile is necessary or desirable for most installations. There are alternative sheetpiling materials that would be considered for the bulkheading and depending on local environmental conditions (mainly physical). These may prove to be cost effective and exhibit a high probability of success. Examples of such materials are aluminum, asbestos, fiberglass, and many variations of synthetics. The use of lightweight steel or special additives to concrete to reduce weight but maintain strength, and thus reduce material costs of the sheetpiling, would also seem appropriate to consider.

Breakwaters

There has been limited use of breakwaters in the United States for strictly shore protection purposes. Since these structures are located offshore at depths commensurable with desired beach and shore responses, they are subjected to greater wave forces and structural components must

be stronger or larger than for those structures located in the foreshore or beach zone. An offshore breakwater of proper design will dissipate incident wave energy, thus, the shores within the "lea or shadow" of the breakwater will be protected, and in this context the overall functional behavior of the structure could be considered as promising with regard to success. There are two basic or standard techniques to constructing offshore breakwaters, both of which could be considered as resulting in a high probability of success if constructed in the demonstration programs. The first involves the use of rubble with an armor layer of stone or precast concrete units, depending on economics; and, the second involving the use of semi-interlocking precast concrete segments. Each technique requires provision for an appropriate foundation to support the super-structure, including toe protection which will remain stable under design wave forces. Relatively heavy-duty equipment and possibly certain marine plants are required for most breakwater construction and since the structure is located offshore, it is apparent that construction practices and procedures are more difficult and involved as compared to construction of a similar structure on the shore zone. This is particularly important to keep the project within the low-cost category.

Considerable attention has been given to the use of portable or floating breakwaters to attenuate wave energy. There are currently no devices of this type that do not become less efficient in wave energy attenuation as the wave length of the incident wave increases. The fact that low-cost solutions generally will be confined to sheltered waters does introduce an attraction to utilize floating breakwater devices as short wave periods would normally prevail.

Beach Fill

The use of beach fill as a low-cost structure would result in a probable chance of success provided the placed fill was of suitable size characteristics. Periodic nourishment for the initially placed fill would be required or should be anticipated. The predominance of short period waves breaking on the beach fill means that direct offshore transport will dominate. No beach recovery can be expected by onshore transport since, in general, there would be no, or minimal, occurrences of long period waves; thus, periodic nourishment to balance the losses to the offshore zone would be necessary to maintain desired project dimensions in the study area. Depending on local conditions, terminal structures (groins) may be needed at one or both ends of the eroding segment, as well as, artificial headlands.

Groins

An accurate determination of the littoral material movement of the site specific is essential to the use of groins as a low-cost structure. A moderate amount of alongshore transport of littoral materials must prevail in the area or a groin or groin system will not function properly. Assuming the prevailing littoral material transport conditions are favorable for the functional aspects of a groin system, there are several materials from which the groins can be constructed and successful results

expected. Constructing the groin of rubble has several desirable features in regard to wave energy dissipation and retention of the impounded sand. This assumes the structure has a proper foundation and distribution of stone throughout the groin cross-section. The use of steel, concrete or timber sheetpiling with stone protection around the outer end is also a well-proven and acceptable method for groin construction. Pre-fabricated segments (concrete) which have an interlocking or semi-interlocking design and founded on a proper foundation can also be structurally effective. If the material components of a crib type structure (crib units filled with stone) will be durable for the life of the structure, there is no reason to believe this type of groin would not also be effective.

If the site conditions are favorable for testing of a groin system, the most effective structure would be a rubble design. The performance of a sheetpile design with rubble placed around the outer end of the groin should be comparable to a prefabricated segmented design (interlocking or semi-interlocking) placed on proper foundation materials.

Vegetation

Very little information and guidance are presently available in regard to the effectiveness of vegetation to directly dissipate incident wave energy. Its effectiveness in a high wave energy environment is probably very limited. On the other hand, the use of vegetation to impound or retain aeolian sand in the foredune area of the coastal zone is well proven and these stabilized or created foredunes are of tremendous value in terms of shore protection.

Fairly adequate data are available on species adaptation and on establishment and maintenance on the Atlantic and Gulf Coasts. On the Great Lakes, Pacific and Alaskan coasts, considerably less is known. Although vegetation is the only generally accepted method to feasibly stabilize dunes, few quantitative estimates are available on the degree of protection provided. Dahl et al. gives a very complete literature review. Recent successes using panic grass (Panicum amarum) along the North Carolina Coast in dune stabilization is given by Seneca, Woodhouse and Broome. In addition to panic grass, American beachgrass, european beachgrass, and sea oats are some of the more successful vegetation used in dune building and stabilization.

The intertidal zone has not yet received the same degree of success. However, vegetation appears to offer considerable promise for the more protected site. Considering that many thousands of miles of shoreline are now well protected by natural marsh grass, it is obvious that the most likely technique for stabilizing the shoreline in a sheltered area is to simulate the protection provided by nature. With some assistance by man through planting sufficient numbers of plants or seeds, at the proper time, the invasion of natural marsh species can be hastened. Most of the work done in the intertidal zone has been with smooth cordgrass (Spartina alterniflora). This plant thrives well in the intertidal salt marshes of the Atlantic and Gulf Coasts. In the more brackish waters the following grasses are being considered: three-square (Scirpus Americanus), needle rush grass (Juncus roemerianus), and saltmeadow cordgrass (Spartina patens). Very little

has been written on the degree of protection that this method can provide although there is much current research in this area. Webb and Dodd show how smooth cordgrass has been used in Galveston Bay. It appears though that marsh vegetation in conjunction with some form of physical temporary protection, such as a floating breakwater, offer much opportunity for low-cost shoreline protection at a very attractive cost.

Institutional Devices

Intangible devices are much more difficult to identify except in a generic sense. Moreover, the actual cost of institutional devices are ill defined. Conceptually, the ideas that can be considered in this category include zoning, permitting, taxing and such other regulatory powers that government - local, state, and federal - can use. The institutions in themselves are indeed low-cost; however, the cost of implementing the regulation to the property owner can be quite costly. For example, if a land owner were experiencing a rapid rate of erosion he would want to quickly install some device to slow or stop the process. However, if a coastal zone authority does not permit the use of structures within fifty feet of the mean high water line then the land owner will not be allowed to protect his property and thus his cost will in no way be low. Yet, the cost to the coastal zone authority is minimal. In brief, there are few, if any, institutional devices that could qualify, to the individual homeowner, as low-cost shoreline protection.

INNOVATIVE DEVICES

As the public interest in low-cost, self-installed solutions to shoreline erosion continues to grow, the involvement of private enterprise in developing solutions intensifies. Now that low-cost devices are identified as a salable commodity as goods or services, the number of inventors, creative engineers, agronomists, and foresighted planners producing potential designs are rapidly growing. This energy has and continues to lead to very innovative designs that may be functionally and structurally successful and may be low-cost. As a part of the National Shoreline Erosion Demonstration Program, known devices and methods which have been used or tested in various degrees, or just proposed, have been tabulated. The list is limited to just those items which might be classified as low-cost. A page from that list is included as Figure 1. The devices have been categorized as shown below along with the number of devices in each category.

Revetments	37
Bulkheads and seawalls	35
Groins	39
Offshore breakwaters	24
Floating breakwaters	18
Beach fills	9
Coastal vegetation	27
Other	8

From this compilation of devices, the Shoreline Erosion Advisory Panel (which will be described later in this paper) has recommended that from this list of devices at least the following should be field tested.

- Aluminum bulkheads
- Bins or cribs (concrete, steel, aluminum, or wood)
- Gabions (rusting of mesh container a problem)
- Longard tubes (sand-filled plastic tubes)
- Nami rings (upright concrete culvert pipe)
- Interlocking concrete block (with filter cloth)
- Stone rip-rap (with gravel or plastic filters or mastic binder)
- Plastic bags (sand filled or concrete filled)
- Precast concrete sheet piling (possibly pre-stressed)
- Rubble mound groins and breakwaters
- Concrete pipe groins
- Z-wall offshore breakwaters (steel or concrete)
- Scrap tire floating breakwater
- Tethered floating mat plastic breakwaters

It was further recommended that existing installations of the following devices should be monitored.

- Sand-grabber (cinder blocks)
- Shore-protector (slat breakwater)
- Beach-builder (flap valve breakwater)

Figures 2-9 show examples of several forms of low-cost structures that have been proposed or used in the field. Some of these devices hold great promise while others do not appear as attractive.



Figure 2. The "Sandgrabber" in Lake Erie



Figure 3. Campbell's precast breakwater units



Figure 4. Gobi blocks in the large wave tank at CERC



Figure 5. "Goodyear" type floating breakwater, Cranston, Rhode Island



Figure 6. Sand filled bags as a revetment in conjunction with an asbestos bulkhead and dune vegetation at Seabrook Island, South Carolina



Figure 7. Institutional low-cost measures



Figure 8. Bolsaroca, large, reinforced, synthetic bags filled with mortar or concrete in sites



Figure 9. The Shoreprotector, at Virginia Beach, Virginia

SHORELINE EROSION CONTROL DEMONSTRATION PROGRAM

The Congress finds that because of the importance and increasing interest in the coastal and estuarine zone of the United States, the deterioration of the shoreline within this zone due to erosion, the harm to water quality and marine life from shoreline erosion, the loss of recreational potential due to such erosion, the financial loss to private and public landowners resulting from shoreline erosion, and the inability of such landowners to obtain satisfactory financial and technical assistance to combat such erosion, it is essential to develop, demonstrate, and disseminate information about low-cost means to prevent and control shoreline erosion. It is therefore the purpose of this section to authorize a program to develop and demonstrate such means to combat shoreline erosion.

Thus on March 7, 1974, the President signed into law Section 54, Public Law 251, 93rd Congress -- the Shoreline Erosion Control Demonstration Act of 1974. The Act calls for the Chief, U.S. Army Corps of Engineers, to plan, establish, and conduct for a period of five years a national shoreline erosion control demonstration and development program. The program consists of planning, constructing, maintaining, evaluating and demonstrating prototype shoreline erosion control devices, both physical and vegetative. The Act is silent on institutional devices and these are, therefore, omitted from the program.

Although the Corps of Engineers is administering the project, they are cooperating with the Department of Agriculture, vis-a-vis the Soil Conservation Service, particularly with respect to vegetative means of preventing and controlling shoreline erosion.

The actual demonstration projects developed under this program emphasize the development of low-cost erosion control devices on sheltered or inland waters. These demonstration projects are being constructed with at least two sites each on the shorelines of the Atlantic, Gulf, and Pacific Coasts, the Great Lakes, and the State of Alaska, and with six sites at serious erosion sites in the State of Delaware along Delaware Bay. These demonstration projects can be built on private or public lands as long as a non-federal sponsor can pay at least 25 percent of the construction costs and assume operation and maintenance costs upon completion of the project.

The Act directed the Chief of Engineers to establish the Shoreline Erosion Advisory Panel. The Panel is charged with providing general guidance and expert technical advice to the Chief on the establishment, conduct, and evaluation of results of the program. The Panel consists of 15 members, selected as individuals who are knowledgeable with respect to various aspects of shoreline erosion problems. Representatives from various geographical areas, institutions of higher education, professional organizations, state and local government and private organizations serve on the Panel. Specifically, the Panel is to:

- (a) advise the Chief of Engineers generally in carrying out provisions of this Act;
- (b) recommend criteria for the selection of development and demonstration sites;
- (c) recommend alternative institutional, legal, and financial arrangements necessary to effect agreements with non-Federal sponsors of project sites;
- (d) make periodic reviews of the progress of the program pursuant to this section;
- (e) recommend means by which the knowledge obtained from the project may be made readily available to the public; and
- (f) perform such functions as the Chief of Engineers may designate.

To carry out this program, Congress has authorized appropriations, over the five-year life of the program, not to exceed \$8,000,000.

A demonstration site is a shore frontage occupied by shore protection works consisting of one or more installations or devices to be monitored and evaluated under the SEAP program. The site shall include the area containing the installation or installations, plus adjacent shore fronts likely to be significantly affected by them within ten years of the date of installation. It is further recognized that three types of sites may be used.

- (a) SEAP Site - A site on which installation of protective works are initiated under the SEAP program.
- (b) Joint Site - A site bearing existing shore protection works constructed by others but which are repaired, modified, or supplemented under the SEAP program.
- (c) Existing Site - A site containing existing shore protection works or devices installed by others, but selected for study and evaluation under the SEAP program.

The Panel has developed and adopted a set of criteria for site selection evaluation which considers legal criteria, social and public relations criteria, environmental criteria, and economic criteria. The Panel has also developed and adopted a procedure for site selection; this procedure involves identifying candidate sites and ranking them in order of value as regional demonstration sites, and then matching these sites with a priority listing of methods and devices which the Panel believes worthy of testing. The result is a program of test installations scheduled as to costs and year of installation; the recommended program has been sent by the Panel to the Chief of Engineers with recommendations for construction.

The enabling Act requires that when a demonstration project is installed on non-Federal property, that part of the expense be borne by an agency or individual other than the Federal government. The Panel has prepared a set of recommendations on institutional arrangements which will be forwarded to the Chief of Engineers in October 1976. Among the questions considered in the institutional arrangements are: access to demonstration site by the interested public; liability of Federal government and land-owners for damage to other persons or other property; duration of demonstration testing at the particular site; removal of unsuccessful devices at the end of demonstration period.

The Panel has also addressed the question of monitoring the demonstration sites once the devices have been installed. As a result of its deliberations, the Panel has a draft of guidelines for use in monitoring test installations. The draft guidelines include coverage of such subjects as the proper balance between the number and type of monitoring observations against the expense of the monitoring program, and whether or not a device will be repaired or modified, and to what extent, if it is found to be failing in its intended protective action.

In accordance with the Act, the Chief of Engineers has announced the following sixteen sites (including six in Delaware Bay) where demonstration projects will be constructed.

Kotzabue, Alaska	Slaughter Beach, Delaware
Unalaklett, Alaska	Basin Bayou State Park, Florida
Alameda, California	Stuart-Jensen Causeways, Florida
Bowers, Delaware	Geneva State Park, Ohio
Broadkill Beach, Delaware	Bulls Island, South Carolina
Kitts Hummock, Delaware	Sand Point, Texas
Lewes, Delaware	Oak Harbor, Washington
Pickering Beach, Delaware	Port Wing, Wisconsin

This list includes private, local, state, and federal lands. Moreover, it includes sandy, clay, and cobble beaches, coasts with bluffs and those with dunes, beaches with moderate wave energy and beaches with low wave energy, and beaches frequented by ice. These sites are representative of the U.S. coastline.

The success of this program will do much to bring realistic, workable, low-cost shoreline protection solutions into the hands of local government and most importantly the private landowner.

ACKNOWLEDGEMENTS

The authors wish to acknowledge those members of private industry, the Soil Conservation Service, the Corps of Engineers, and especially the members of the Shoreline Erosion Advisory Panel who have significantly contributed to the concepts and activities described in this paper. This paper reflects only the views of the authors and is not intended to represent the position of any body or institution.

REFERENCES

- Armstrong, J. M. "Demonstration Project for Low-Cost Protection," Proceedings Fifteenth Coastal Engineering Conference, ASCE (1976).
- Arno, N. "Help Yourself: A Discussion of the Critical Erosion Problems on the Great Lakes and Alternative Methods of Shore Protection," U.S. Army Corps of Engineers, North Central Division, Chicago (1973).
- Brater, E. F. "Low-Cost Shore Protection for the Great Lakes," Lake Hydraulic Lab, University of Michigan, Ann Arbor, reprinted in 1975 (1952).
- Brater, E. F., J. M. Armstrong and M. McGill "Michigan's Demonstration and Erosion Control Program: Update Evaluation Report - August 1975," Coastal Zone Lab, University of Michigan, Ann Arbor (1975).
- Combe, A. J., III and D. W. Berg "Guidelines for Monitoring Shore Protection Structures in the Great Lakes," U.S. Army Corps of Engineers, Coastal Engineering Research Center, Working Paper (1974).
- Dahl, B. E., et al. "Construction and Stabilization of Coastal Foredunes with Vegetation; Padre Island, Texas," MP 9-75, U.S. Army Corps of Engineers, Coastal Engineering Research Center (1975).
- Davis, J. H., Jr. "Stabilization of Beaches and Dunes by Vegetation in Florida," Report No. 7, Florida Sea Grant Program, Gainesville (1975).
- Habel, J. F. "Shore Protection in California," Department of Navigation and Ocean Development, State of California, Sacramento (1976).
- McHarg, I. "Best Shore Protection: Nature's Own Dunes," Civil Engineering, September (1972).
- O'Shaughnessy, M. M. "Ocean Beach Esplanade, San Francisco, California," Transactions, ASCE (1924).
- Seneca, E. D., W. W. Woodhouse, Jr., and S. W. Broome "Dune Stabilization with Panicum Amarum Along the North Carolina Coast," MR 76-3, U.S. Army Corps of Engineers, Coastal Engineering Research Center (1976).
- Soil Conservation Service "Vegetative Tidal Bank Stabilization," U.S. Department of Agriculture, College Park, Maryland (1968).
- Webb, J. W. and J. D. Dodd "Vegetation Establishment and Shoreline Stabilization: Galveston Bay, Texas," TP 76-13, U.S. Army Corps of Engineers, Coastal Engineering Research Center (1976).
- Woodhouse, W. W., E. D. Seneca, and S. W. Broome "Propagation of Spartina Alterniflora for Substrate Stabilization and Salt Marsh Development," TM 46, U.S. Army Corps of Engineers, Coastal Engineering Research Center (1974).

CHAPTER 166

RECENT APPLICATIONS OF ARTIFICIAL SEAWEED IN THE NETHERLANDS

by Henk G.H. ten Hoopen.^{*}

ABSTRACT

This paper deals with the effects and the method of laying of some recent emplaced artificial seaweed fields in the Netherlands. The weed is placed on the bottom in coastal waters to promote accretion or at least to prevent erosion along beaches and in gullies. The results of the three field trials, and some of the conditions that govern the successful application of the seaweed, which will be discussed.

INTRODUCTION

For ages measures for coastal protection, such as the construction of groynes, dikes and toe-protection of the dunes have been carried out along the sandy coasts of the Netherlands.

However, fixed structures of this kind, because of the secondary effects on the adjacent unprotected beaches, did not invariably turn out to be the ultimate solution to prevent coastal erosion. It is for this reason that other more flexible methods of coastal

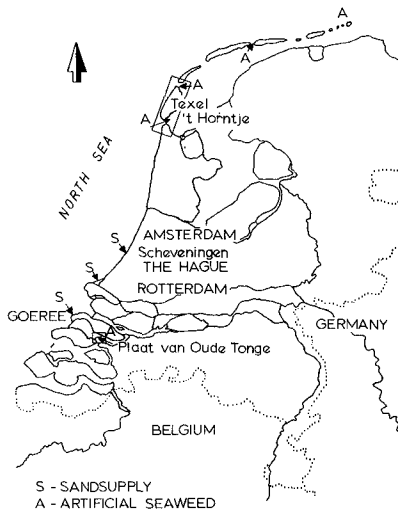


Fig. 1. Map of the Netherlands showing the sites where sand-supplies have been provided and artificial seaweed has been applied.

* Rijkswaterstaat, Den Haag, The Netherlands.



Fig. 2. Artificial seaweed.

protection such as artificial beach nourishment, have been tried out at certain locations. One of the largest trials was carried out at the west coast of the isle of Goeree (see fig. 1), where about 3.5 million m^3 of sand were placed in position (see proceedings of the 14th International Conference on Coastal Engineering). In addition to sandsupplies, tests were carried out with artificial seaweed to prevent erosion of banks in tidal waters (estuaries).

The beds of artificial seaweed consist of rows of light weight foamed polypropylene tapes (0.2 grammes/cm^3) with an anchoring system that consists of a hollow seam ($\emptyset 150 \text{ mm}$) at one end of the weed tapes filled with a heavy material such as gravel. (see fig.2). Successive anchoring tubes, each having a length of 1.5 or 2 m, are joined up lengthwise, thus forming a row. The distance between parallel rows is less or the same as the weedlength (1.5 - 2 m). When placed on the seabottom the purpose of the weed is to promote accretion. Compared with an unprotected bottom, the bottom transport of the sediment will decrease as part of the bottom shear stress will be absorbed by the seaweed. Since 1966 The Dutch Public Works Department has carried out a number of field trials along the Dutch coast. The results were quite variable, depending on local circumstances such as wave-climate and currents.

RESULTS OF SOME RECENT TRIALS WITH ARTIFICIAL SEAWEED.

Seaweed beds around the isle of Texel.

One of the Dutch Wadden islands, situated at the north-western part of the Netherlands called Texel (see fig. 1 and 3), was eroding at its south east side ('t Horntje). A deep gully,

crossing the western shallows, was developing under the influence of tidal currents. This caused damage to the eastern bank of Texel, the erosion was mainly occurring during the ebb tide. The discharge through this gully is in the order of 1000 million m^3 /tide. The velocities during low tide are more than 1m/sec. The average tidal difference is about 1.34 m. Because this location is fairly well protected from the North-Sea swell wind waves generated on the shallows prevail. These waves vary in height between 3 and 5 m. Initially fascine mattresses were laid to stop the erosion. However the erosion continued in the area adjacent

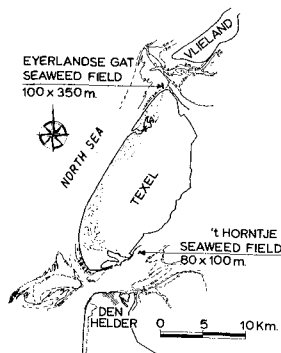


Fig. 3. Position of seaweed fields at "Texel".

to the mattresses. In 1972 it was decided to extend the area covered by mattresses with an artificial seaweed field. The first part of this trial concerned area A (see fig. 4). The weed was put down on an inclined bottom (1:5) at a depth of 5 to 15m below M.S.L. and covered an area of 80 m x 120 m. It was positioned from a pontoon and not dropped at random as was done in previous years in other areas. Because positioning according to the earlier method was not very accurate at greater depths, a more exact method was developed. An iron beam of about 30 m length on which up to

twenty anchoring tubes were laid along its length, was lowered from the pontoon. At a depth of approximately 1 m above the sea bottom the beam was tipped over and the seaweed slipped from the beam. Emplacement of the weed could be continued during the ebb or flood tide until the tidal current reached 1 m/sec. Depending on the depth of water every 3 to 7 minutes a length of about thirty meters of seaweed screen was laid. The pontoon was then moved 1.5 m in a direction opposite the tidal current and the next row was laid. In this way it took about 24 hours to cover an area of about 1000 m^2 . The results of this field trial are shown in fig. 4. Within a few weeks of putting down the weed, there was an accumulation of sand about 35 cm thickness. Till

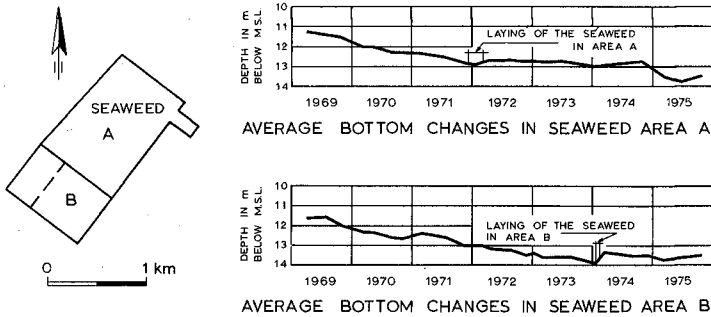


Fig. 4. Average bottom depth in the seaweed area at 't Horntje (Texel).

about the end of 1974 the bottom in area A never scoured below the depth observed immediately prior to the emplacement of the weed. However in 1975 soundings showed a bottom depth below its position at the start of the measures early in 1972. To find out the reason for this anomaly, divers collected some samples of the artificial seaweed, which was now about four years old. Laboratory tests revealed that an increase in specific weight had occurred caused by the filling of the pores in the material by water. Due to this filling the specific weight reached a value of about four times the original value of 0.2 g/cm^3 . Growth of organic material on the weed has been negligible. However especially near the top end of the plastic tapes inorganic deposition had occurred. This was not the cause of the increase in specific weight. Further investigations are in progress to improve the material. After the laying of the weed in area A at the beginning of 1972 the adjacent area B (see fig. 4) however kept degrading. For this reason this area has also been covered in the beginning of 1974. In this instance the laying of the weed was done in a more advanced manner than used before: A $21 \times 2 \text{ m}^2$ "container beam" which could carry eighty four seaweed sections, could be lowered with the aid of a derrick mounted on a pontoon. At a distance of about 2 m above the sea-bottom part of the lower half of the beam was opened by means of a special hinged valve construction. This had the result that about one third of the total load of weed sections

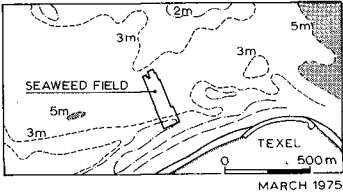
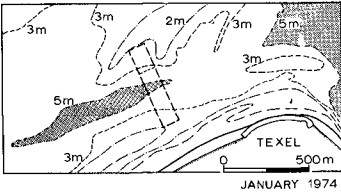


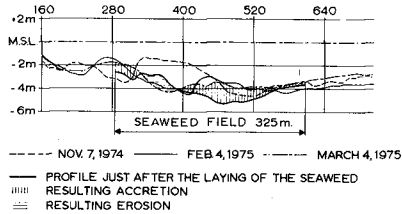
Fig. 5. Position of seaweed field at Eijerlandse Gat. Depth contours 1974 and 1975.

In addition to the erosion problems at the south-east coast of Texel Island, the development of a gully north of Texel, just in front of a dune protection (see fig. 1,3 and 5). It was feared that a connection would develop between this gully and a deeper part of the shallows situated to the east. If this connection did develop, it was quite likely that, because of the higher stream velocities that have to be expected, the gully would extend towards the shore, causing damage to the coastal defence works. Although the conditions in this area are quite different from 't Horntje (the area is subject to strong wave attack); it was decided to lay a strip of seaweed 8 m wide perpendicular to the axis of the developing gully. The favourable results obtained with the weed elsewhere, justified this new trial. In this relatively shallow water, with a maximum depth of about 5.5 m below M.S.L., the weed was put in position in a way different from the one described before.

Fig. 6. Changes of the bottom profile in the seaweedfield Eijerlandse Gat.

carried out. Then the pontoon moved over about 1.5 m to drop another third of the load, and so on. After this the "beam" had to be refilled again above waterlevel. In this way it was possible to cover in the same time three times as much of the bottom than in the method with a single beam mentioned before. Since the laying of this weed-field, there has been sand-accumulation in location B up till the present time (see fig. 4).

Nov. 7, 1974



At shallow depth (e.g. close to the low-water line) the weed was dumped from a pontoon during high tide. At greater depths, use was made of a special pontoon equipped with eight P.V.C. tubes (diameter 35 cm) which at one end could pivot about a fixed point on the bottom (see fig. 7). After lowering the free end of the tubes to the sea-bottom, the weed is put on to the other end and slides to the bottom. The pontoon is then moved over the length of a seaweed section and the filling resumed. In this way the weed can be laid without losing time by lowering a beam, an additional advantage is the working undependent of the tide.

In the past, the depth contours in this area used to move frequently and unpredictably. Since the weed has been "planted", the gully has not developed any further (see fig. 5). It appears therefore, that the presence of the weed has had a beneficial effect. However looking at fig. 6, it is evident that the accumulation of sand in the field cannot only be caused by the weed, as at some places there is an accretion of more than 2 m which cannot possibly derive from the action of the weed. In view of the unpredictability of the bottom movement, insufficient time has elapsed to consider the evidence obtained so far as conclusive in this respect.



Fig. 7. Pontoon with the eight P.V.C. tubes in horizontal position.

Seaweed field at Plaat van Oude Tonge (Delta region).

In the Delta region, situated in the southern part of the Netherlands, the position of some old gullies has recently become very unstable as result of the closure of some estuaries. Between 1958 en 1965 the dam in the Grevelingen estuary, between Goeree and Schouwen, was built. As a consequence considerable morphological changes took place. At Plaat van Oude Tonge for instance (see fig. 1 and 8) a considerable change in direction of the gully "Krammer" occurred, which in future could result in severe damage to protective works in the neighbourhood.

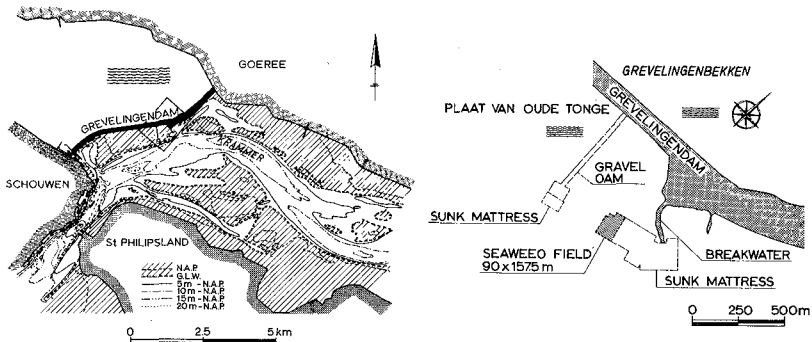


Fig. 8. Position of seaweed field at Plaat van Oude Tonge.

The axis of the gully concerned changed from N - S to NE - SW. As a consequence of the ebb-stream through the gully the Plaat van Oude Tonge eroded heavily. Since 1958 the 2.5 m below M.S.L. depth contour has moved 900 m in the direction of the Grevelingendam, and the gully increased in depth from 8m to 21 m (-M.S.L.). The slope of the western bank changed from 1:22 to 1:3.5. Measures had to be taken to prevent further erosion of this bank in front of the dam. In 1969 fascine-mattresses were placed round the end of an old breakwater over an area of 70,000 m², and 600 m to the west of this breakwater a 500 m long.

A submerged dam was constructed to keep the current as far as possible from the Grevelingendam. However in 1971 and 1972 bank-slides occurred. Extra mattresses were laid, without success

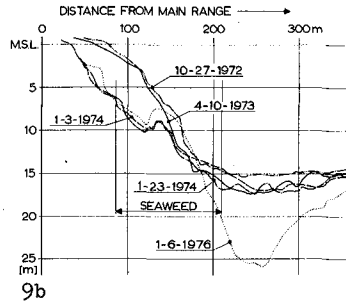
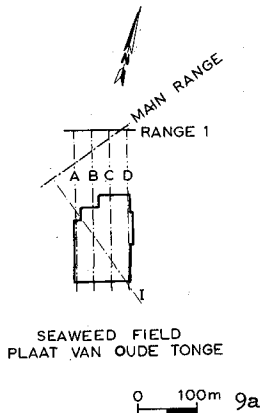


Fig. 9a and b. Profile I (see fig. 9a) before and after the laying of the weed.

however as the slides continued. Because of the similarity to the conditions at 't Horntje (same wave climate and current velocities) it was decided to "plant" a seaweed bed. This was done at the beginning of 1974.

The situation that has developed since then is shown on fig 9b and fig. 10, which show the observations from October 1972 up to Februari 1976. It is obvious that significant changes in the development of the gully and the banks, since the placing of the weed, have been occurred. Nearest the Grevelingendam erosion has come to a standstill and some accretion has taken place. Only along the edge of the weed-field (deepest part) there has been erosion because of secondary effects. The unprotected gully however has deepened considerably. Bankslides have not occurred up till the present but can be expected if the slopes along the edge are getting to steep.

CONCLUSIONS.

From the results mentioned above, it can be concluded that artificial seaweed can be applied successfully in gullies where high flow velocities occur. Accumulation is to be expected when there is little orbital motion near the bottom. However secondary effects along the edge parallel to the stream

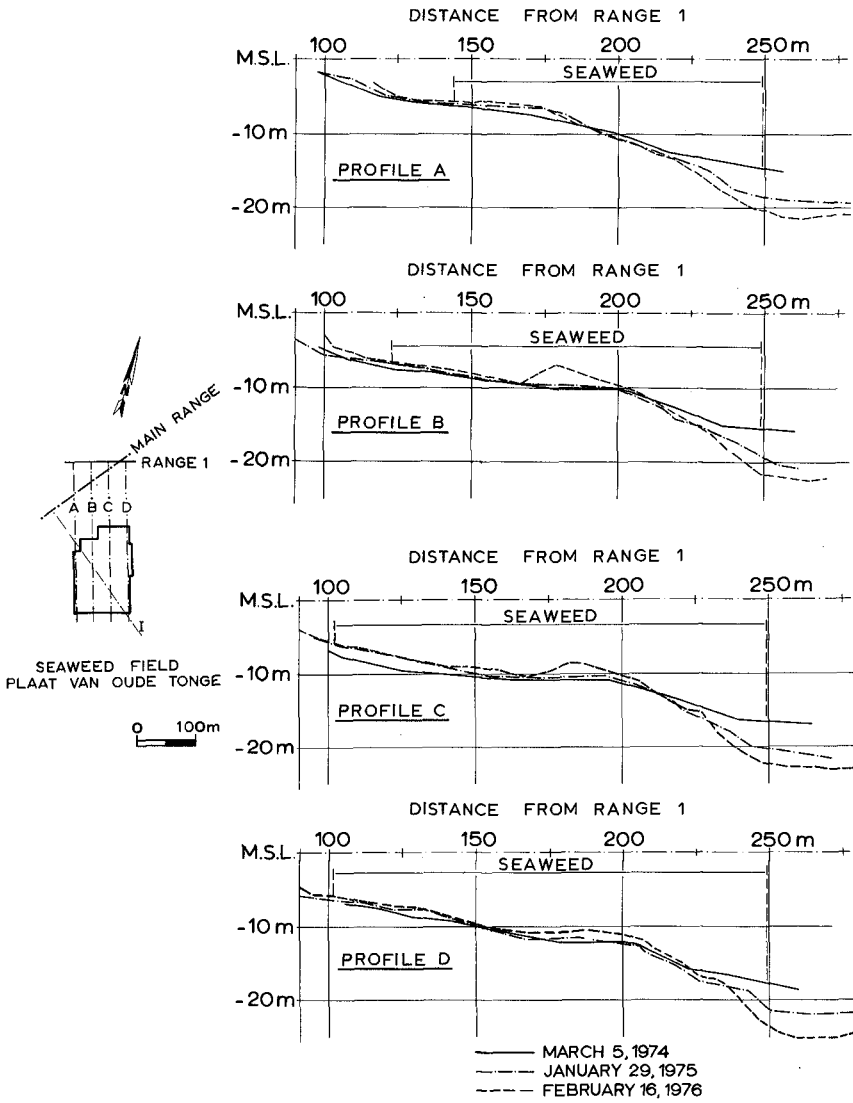


Fig. 10. Changes of bottom profiles at Plaat van Oude Tonge after the seaweed had been put in position.

can be expected. With bigger wave heights prediction of the results is less certain. The costs of the material and of the emplacement of the weed are rather low. They amount to about one fourth of the conventional bottom protection. With investigations to improve the material proceeding it is difficult to predict what will be the lifetime of the artificial seaweed.

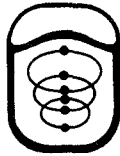
REFERENCES.

- 1 Bakker, W.T., Bax, J., Grootenboer, D., Tutuarima, W.H.:
Artificial Seaweed, Coastal and submarine - pipeline
protection studies with stretched polypropylene foam
strands. ("de Ingenieur" 1972 no 48).
- 2 Guyot, G.: Diffusion turbulente au-dessus et à l'intérieur
d'un couvert végétal: application à l'étude des flux de
chaleur et de masse. (La Houille Blanche, 1969, no 4).
- 3 Price, W.A., Tomlimon, K.W. and Hunt, J.H.:
The effect of artificial seaweed in promoting the build-up
of beaches. Proc XIth Conf. on Coastal Eng., London,
September 1968.
- 4 Artificial weed as bed protection.
Report on model investigation, M 1162, February 1973, Delft
Hydraulics Laboratory.
- 5 Several measure reports of the study service bureaus Hoorn
and Zierikzee of the Rijkswaterstaat of the Ministry of
Transport and Public Works.

#4

RAD

PROCEEDINGS
OF THE
Fifteenth
Coastal Engineering
Conference



July 11-17, 1976 • Honolulu, Hawaii

Sponsored by the
State of Hawaii
University of Hawaii
American Society of Civil Engineers
through its Coastal Engineering Research Council
American Shore and Beach Preservation Association



Published by the American Society of Civil Engineers
345 East 47th Street, New York, N.Y., 10017
Price \$50.00

ACKNOWLEDGMENTS

The following served as the Organizing Committee for the Fifteenth International Conference on Coastal Engineering:

Charles L. Bretschneider
(Chairman)
Department of Ocean Engineering
University of Hawaii

J. Thomas O'Brien
J.K.K. Look Laboratory of
Oceanographic Engineering
University of Hawaii

Harold P. Brown
Conference Center
University of Hawaii

David S. D. Chung
U. S. Naval Facilities
Engineering Command
Pearl Harbor, Hawaii

Ada Marie B. O'Brien
Honolulu, Hawaii

S. Joseph Amaki
Department of Transportation
State of Hawaii

Howard A. Schirmer
Dames and Moore, Engineers
Honolulu, Hawaii

Karl V. Keller
Pacific Division, Corps of
Engineers, U. S. Army
Honolulu, Hawaii

Frederick A. Zobrist
Neighbor Island Consultants

Appreciation is expressed to the Department of Planning and Economic Development of the State of Hawaii and the Hawaii Visitors Bureau for providing the many photographs appearing on the title pages for the various parts of the proceedings.

CONTENTS

PART IV

COASTAL, ESTUARINE, AND ENVIRONMENTAL PROBLEMS

Chapter 167	
DESIGN PROCEDURES FOR OCEAN OUTFALLS	
Jeffrey A. Layton	2919
Chapter 168	
DESIGN CONSIDERATIONS FOR THE SAND ISLAND AND BARBERS POINT OUTFALLS	
Robert C. Y. Koh, Norman H. Brooks, and Floyd Louis Vuillemot . . .	2941
Chapter 169	
BUOYANCY-DRIVEN GRAVITATIONAL SPREADING	
Robert C. Y. Koh	2956
Chapter 170	
NEGATIVELY BUOYANT SLOT JETS	
D. M. Shahrabani and J. D. Ditmars	2976
Chapter 171	
GUIDELINES FOR DESIGN OF AIR BUBBLE SYSTEMS	
Nabil Ismail	2994
Chapter 172	
COASTAL ENVIRONMENT AND A NUCLEAR POWER PLANT	
Ralph A. De La Parra	3014
Chapter 173	
FIELD STUDIES OF SUBMERGED-DIFFUSER THERMAL PLUMES WITH COMPARISONS TO PREDICTIVE MODEL RESULTS	
A. A. Frigo, R. A. Paddock, and J. D. Ditmars	3038
Chapter 174	
THERMAL DISCHARGES: PROTOTYPE VS. HYDRAULIC MODEL	
Gary C. Parker, C. S. Fang, and Albert Y. Kuo	3049

CONTENTS

Chapter 175	
FLOW FIELD NEAR AN OCEAN THERMAL ENERGY CONVERSION PLANT	
D. M. Sheppard, G. M. Powell, and I. B. Chou	3068
Chapter 176	
ADAPTABILITY OF PREDICTION METHOD OF HYDRAULIC MODEL	
EXPERIMENT FOR THERMAL DIFFUSION	
Masanobu Kato and Akira Wada	3082
Chapter 177	
HORIZONTAL DIFFUSION IN TIDAL MODELS AND SCALING CRITERIA	
FOR THERMAL-HYDRAULIC MODEL TESTS	
Gerd Flügge	3097
Chapter 178	
DYNAMICS OF A LONGITUDINALLY STRATIFIED ESTUARY	
Jorg Imberger	3108
Chapter 179	
INTERFACIAL INSTABILITY IN STRATIFIED FLOW	
Richard H. French	3124
Chapter 180	
NUMERICAL MODELING OF DISPERSION IN STRATIFIED WATERS	
George C. Christodoulou and Jerome J. Connor	3138
Chapter 181	
DETERMINATION OF INTERFACIAL EDDY DIFFUSION COEFFICIENT	
OF HIGHLY STRATIFIED ESTUARY	
Yu-Hwa Wang	3158
Chapter 182	
FRICITION AT INTERFACE OF TWO-LAYERED FLOWS	
Nobuyuki Tama	3169
Chapter 183	
TIDAL RESPONSE OF TWO-LAYERED FLOW AT A RIVER MOUTH	
Shizuo Yoshida and Masakazu Kashiwamura	3189
Chapter 184	
EVALUATION OF AIR-SEA INTERFACE HEAT FLUX	
Robert L. Street and A. Woodruff Miller, Jr.	3208

CONTENTS

Chapter 185	
STATE ESTIMATION OF ESTUARINE CIRCULATION AND WATER QUALITY BY NUMERICAL SIMULATION AND OBSERVATION	
J. J. Leendertse and S. K. Liu	3223
Chapter 186	
NUMERICAL MODELLING--AN AID TO ASSESSING FIELD DATA	
H. P. Riedel and F. L. Wilkinson	3243
Chapter 187	
WIND-DRIVEN CIRCULATION OF SAGINAW BAY	
James H. Saylor and Larry J. Danek	3262
Chapter 188	
PREDICTION OF POLLUTANT DISTRIBUTION IN ESTUARIES	
A. Y. Kuo and J. P. Jacobson	3276
Chapter 189	
NUMERICAL MODEL FOR DENSITY CURRENTS IN ESTUARIES	
Karsten Fischer	3295
Chapter 190	
ENERGY DISSIPATION IN TIDAL ESTUARIES	
Hans-Werner Partenscky and Günther Barg	3312
Chapter 191	
ALGORITHM FOR VERTICAL DIFFUSION	
Søren Peter Kjeldsen	3321
Chapter 192	
DISPERSIVE TRANSPORT IN RIVER AND TIDAL FLOWS	
R. B. Taylor	3336
Chapter 193	
TIDAL STREAM FLOW SOLVED BY GALERKIN TECHNIQUE	
L. H. Smith and R. T. Cheng	3358
Chapter 194	
MODEL VERIFICATION FOR TIDAL CONSTITUENTS	
R. W. Whalin, F. C. Perry, and D. L. Durham	3377

CONTENTS

Chapter 195	
FINITE ELEMENT MODEL FOR ESTUARIES WITH INTER-TIDAL FLATS	
Bruno Herrling	3396
Chapter 196	
CALIBRATION OF BRANCHED ESTUARY MODELS	
James P. Bennett	3416
Chapter 197	
MOVABLE BED TIDAL INLET MODELS	
Subhash C. Jain and John F. Kennedy	3435
Chapter 198	
CHURCHILL RIVER SALT-WATER TIDAL MODEL	
Bruce D. Pratte	3445
Chapter 199	
ANALYSIS OF TIME CONDITIONS FOR HYBRID TIDAL MODELS	
Klaus-Peter Holz	3460
Chapter 200	
PLANFORM INFLUENCE ON FLUSHING AND CIRCULATION IN SMALL HARBORS	
Ronald E. Nece, Roger A. Falconer, and Toshiro Tsutsumi	3471
Chapter 201	
COASTAL PROBLEMS IN SRI LANKA	
Frans Gerritsen and Summa R. Amarasinghe	3487
Chapter 202	
ENVIRONMENTAL IMPACTS ON AN ISLAND COMMUNITY	
Gordon A. Chapman	3506
Chapter 203	
STUDY OF AN ARTIFICIAL ISLAND	
J. P. Lepetit and S. Moreau	3526
Chapter 204	
WAVE INDUCED OSCILLATIONS OF HARBORS WITH VARIABLE DEPTH	
F. Raichlen and E. Naheer	3536

CONTENTS

Chapter 205

PROBABLE UTILIZATION LEVEL FOR A BARGE HARBOR

Martin T. Czerniak and Choule J. Sonu 3557

Chapter 206

APPLICATION OF CERC SPECIAL REPORT NO. 2

James W. Dunham 3570

SUBJECT INDEX 3573

AUTHOR INDEX 3633



Kahului Harbor, Island of Maui

PART IV

COASTAL, ESTUARINE, AND ENVIRONMENTAL PROBLEMS

Lahaina, Island of Maui



CHAPTER 167

DESIGN PROCEDURES FOR OCEAN OUTFALLS

by

JEFFREY A. LAYTON*

ABSTRACT

This paper discusses procedures for designing ocean outfalls and offers the coastal engineer a practical design guide outlining the necessary steps required to plan, design, and construct an outfall. The design steps reviewed in this paper include site location considerations, environmental studies, outfall and diffuser hydraulics, pipe materials selection, pipe support systems design, and construction techniques.

INTRODUCTION

Wastewater disposal systems typically involve three components: collection, treatment, and disposal. The design of collection systems for domestic sewage and industrial wastes is generally a simple process. More difficult, but still relatively routine, is the design of primary and secondary treatment facilities to reduce the pollution impact of the wastewater. However, final disposal of the collected and treated wastewater effluent is not a routine design problem. Few disposal options are available; most are limited to land disposal, advanced wastewater treatment (AWT), or discharge to a water body. Land disposal is impractical in many regions due to poor soils and insufficient land availability. AWT is costly and consumes much energy in the treatment process. Effluent discharge to a water body, on the other hand, generally consumes little energy and requires little land. Further, the natural assimilative capacity of many water bodies is high enough to absorb wastewater discharges with no detrimental consequences. Because of these advantages, effluent disposal to the marine environment has become common practice.

Subaqueous effluent discharge occurs in four basic water bodies: river, lake, estuary, or ocean. Of these, the ocean is the ultimate receiving water. An outfall is a mechanism through which effluent is directly discharged to the ocean. The complex process a coastal engineer employs to design and construct an ocean outfall is described in this paper. The same process is applicable to outfalls in rivers, lakes, and estuaries.

OUTFALLS AND DIFFUSERS

An outfall is an underwater pipeline that discharges wastewater into a receiving water. Although the wastewater may have received extensive treatment, it is still desirable, and often necessary, to disperse the effluent to minimize possible impairment to the quality of the receiving waters near the point of discharge. This is accomplished by using a diffuser.

A diffuser is a section of the outfall, usually the deepest, most seaward portion, with relatively small holes or ports along its length (figure 1). These ports discharge the wastewater in numerous small quantities, as opposed to the entire flow being discharged at one point (figure 2). Diffuser ports may be

*Ocean Engineer, CH2M HILL, 1500 - 114th Avenue SE, Bellevue, Washington 98004

simple holes in the outfall pipe wall or short tubes (risers) extending from the pipe. The type of port used depends on the particular conditions of the final installation.

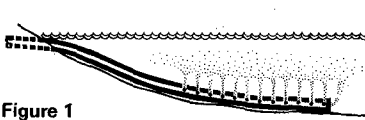


Figure 1
Outfall Diffuser

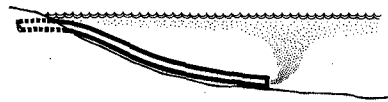


Figure 2
Outfall Without Diffuser

Designing an outfall diffuser system requires the same considerations as designing other types of underwater pipelines. However, the mechanism of discharging the effluent from the outfall to the receiving water requires additional design effort. The various elements of the outfall design process are discussed below.

OUTFALL DESIGN PROCESS

The design of an ocean outfall system is not a simple process. The design engineer must consider many factors to ensure that the outfall survives as a structural system in the ocean environment and also meets water quality requirements. The major components of the outfall design process are:

- Site selection
- Outfall hydraulics
- Dilution and mixing
- Diffuser port design
- Pipe design
- Pipe support systems
- Construction methods

Each of the above components must be evaluated during the design of an outfall. The design is normally phased into four elements: feasibility study, predesign, preliminary design, and final design. Each phase addresses the above outfall design components with increasing detail such that final design results in the preparation of construction plans and specifications. A flow diagram illustrating how the various design components and phases are integrated is in figure 3. Subsequent discussion will elaborate on each factor comprising the design process.

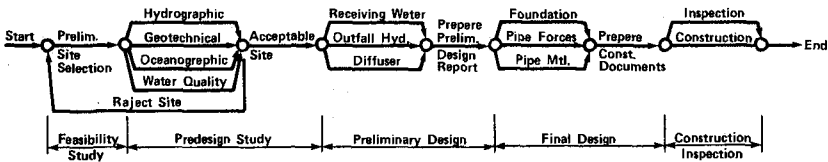


Figure 3
The Ocean Outfall Design Process

Site Selection

A discharge point for an outfall is usually located in proximity to its companion wastewater treatment plant. Therefore, the first step in the outfall site selection process is to determine the feasibility of linking the treatment plant to the nearest receiving water. This process consists of studying existing topographic maps and hydrographic charts, reviewing known literature concerning coastal processes (tides, waves, currents, geology) characteristic to the site, and obtaining available water quality data related to the proposed receiving water. If the existing information suggests that, from a construction cost and water quality viewpoint, one or more outfall routes is feasible, then additional predesign engineering studies are commenced to select a final route. If no routes are judged feasible, then relocation of the treatment plant or alternative disposal systems must be considered.

For sites judged feasible, the following outfall siting criteria are considered in detail in the predesign phase:

- Bottom topography and surf zone
- Physical oceanography
- Water quality
- Underwater soils and geology

Topography

A hydrographic survey of the general area of a proposed outfall alignment is required. An electronic recording echo-sounding device coupled with a horizontal positioning system (electronic or transit) usually produces a sufficiently accurate bottom survey. Surveys within the surf zone, however, are often difficult due to continuous wave action and often require special equipment such as helicopters to act as sounding platforms.

When reviewing the sounding data, various profiles of the bottom topography are plotted. Analysis of the profiles will reveal potential outfall routes. It is desirable to have the outfall line on a continually declining grade. This prevents potential sludge buildup in low points and accumulation of air at high points, both of which can reduce the hydraulic capacity of the outfall.

There is no ideal slope for locating the diffuser; however, a relatively flat slope is desirable. It is also desirable to have essentially equal discharge from each of the diffuser ports to facilitate equal dilutions. With a density difference between the receiving waters and the discharged effluent, a mild slope is beneficial in achieving uniform port discharge. However, a long diffuser on a steep slope can adversely modify the diffuser hydraulics. Not only will the diffuser discharge unequally from all ports, but at low flows, some ports will not flow at all.

If the topography is relatively steep, consideration must also be given to the stability of the final system. The pipeline must be secured from sliding down the slope, either slowly due to unstable soil conditions or suddenly due to natural occurrences.

Since it normally is not economically or technically feasible to significantly modify the general underwater topography of an area, the outfall must be routed and designed in accordance with the natural conditions.

Surf Zone

Penetrating the surf zone is often the most difficult and costly phase of constructing an ocean outfall. The trauma of continuous wave attack in shallow water usually limits construction to a short period during milder summer conditions. Even then, sporadic storms can shut down construction operations or damage the outfall pipe and construction equipment. Therefore, it is desirable to select outfall sites with minimum surf action. Potential sites at headlands or points of land jutting into the sea generally should be avoided because wave refraction will concentrate wave energy on these features. To minimize working in harsh conditions, surf zones extending more than about 1,000 feet offshore should be avoided if possible. Coastlines with sharp bottom dropoffs are preferable for outfall sites because the pipeline can be installed quickly in the narrow surf zone.

Physical Oceanography

Measuring water mass movements at a proposed outfall discharge site is required early in the design process. This knowledge is important because it allows the designer to predict effluent transport under all offshore current conditions. Two methods are commonly employed to measure ocean current systems: drogues and electronic current meters.

Drogues consist of a drag body positioned below the water surface with a line attached to a surface float. Movement of drogues, and therefore currents, is tracked by observing buoy movement. Current meters do not move with the water but remain fixed at a point, measuring the rate and speed of water particles as they flow past. Either system can be used to measure ocean currents, but for most ocean outfall locations both techniques are used to complement each other.

Current measurements are normally conducted over a sufficient time period to develop a comprehensive understanding of water mass movements over the outfall discharge site. This knowledge is vital so the outfall designer can predict where the effluent will be transported under all conditions. Specific monitoring periods can range from a few tidal cycles to long-term observations covering several years at sites subject to seasonal current shifts and upwelling of deep ocean waters. Careful consideration in developing a current monitoring program must be given early in the design process to allow sufficient time to conduct the studies and analyze the results.

During ocean current monitoring, physical properties of the water column, such as temperature and salinity, are also measured to calculate water density as a function of depth. Density profiles indicate the absence or presence of stratification, which can affect the dilution performance of the diffuser.

In addition to the above physical oceanographic measurements, field studies designed to measure the ocean water's natural diffusion characteristics are

often conducted. Dye studies, usually employing a fluorescent tracer such as Rhodamine WT dye, help determine the ability of a potential outfall site's receiving waters to disperse and assimilate wastewater.

Measurements of ocean wave heights and periods are also desirable for outfall sites. Knowledge of the frequency and amount of wave energy passing over the pipeline route is vital to ensure its integrity as a structural system. However, measurements of wave parameters are often difficult to obtain and designers frequently rely on wave forecasting techniques to predict design wave conditions.

Water Quality

The purpose of an outfall diffuser is to disperse effluent to minimize the pollution impact on the receiving water. No matter how efficient the diffuser is in diluting effluent with ambient seawater, some change will occur in the local marine environment around the diffuser. It is a vital element of the outfall design process to accurately predict these changes, both short-term and long-term. However, to predict water quality changes due to outfall discharges, the existing water quality conditions of the receiving water must be known.

Establishing a baseline of water quality conditions within the receiving waters of a proposed outfall often requires extensive environmental monitoring. During the site selection process, it is typically found that the potential ocean outfall site has, at best, a limited record of existing water quality data. Thus, to establish a proper data bank of predischage conditions, a water quality monitoring program is required. Baseline monitoring programs can range from a minimum of collecting one set of water samples at one location to sampling multiple stations at weekly intervals for periods of 1 to 2 years. The parameters sampled, which can also vary widely, mainly depend on composition of the effluent. The minimum parameters that should be considered for a domestic sewage outfall monitoring program are:

Water Column

Dissolved oxygen
pH
Conductivity/salinity
Temperature
Oil and grease
Fecal coliform bacteria
Nutrient content
Heavy metal content
BOD/COD

Benthic

BOD/COD
Heavy metal content
Nutrient content
Biological organisms

Location and number of sampling stations should be carefully established to maximize data acquisition while minimizing costs. Results of physical oceanographic studies should be used to establish sampling stations within the expected water transport zones. A sampling station within the immediate dilution zone of the diffuser is a minimum requirement.

Underwater Soils and Geology

Identifying the geological conditions and their uniformity along a proposed outfall alignment is important since many of the criteria considered in outfall design depend on geologic conditions and soil types. As with most underwater soils investigations, gathering soils data for outfall design is difficult and often costly. However, the investigation must be sufficient to develop design criteria and identify the existing conditions.

Marine geophysical techniques, such as reflection and seismic profiling, are commonly used to determine subbottom stratigraphy. However, interpretation of this type of data is difficult. There is no substitute for obtaining *in situ* soil samples for laboratory analysis. The best results usually are obtained from barge-mounted drilling rigs, but soil sampling with remote or diver controlled subsurface devices has been successful (Noorany, 1971).

Analysis of Site Selection Data

Upon completion of the basic studies outlined above, one particular outfall site is normally chosen as most suitable. The next step in the outfall design process is the preliminary hydraulic design of the pipeline, including diffuser dilution and mixing characteristics.

Outfall Hydraulics

The hydraulic design of an outfall results in determining design flows, selecting pipe diameters for the outfall conduit and diffuser sections, and selecting diffuser port size and spacing.

Design Flows

Outfall design flows depend upon upstream conditions. Daily flow through a domestic sewage treatment plant can vary considerably, while most industrial discharges are more constant. Massive loads to sewer collection and treatment facilities also occur during rainy periods when runoff enters the collection system either directly (combined sanitary and storm sewers) or indirectly through infiltration (leakage at pipe joints and manhole covers). During either event, flow to an outfall can be dramatically increased. If the outfall system is not properly sized, the flow will be restricted, resulting in the backup of effluent in the outfall and possible flooding of onshore facilities.

Ocean outfalls should be designed to discharge peak flows with a gravity system. However, if the hydraulic head between the ocean and the outfall headworks is minimal, discharge of design flows through the outfall may not be possible with a gravity system. Consideration must then be given to the use of pump stations. Unfortunately, pumped outfall systems present new problems--increased costs for continual maintenance of pumps and perpetual use of energy for pumping. A sometimes satisfactory solution to both problems is the combined use of gravity and pump system. During normal flows, the gravity system handles the discharge, while during peak flow periods a pumping system augments the gravity system.

Diffuser Hydraulics

In conjunction with selecting conduit size for the outfall, the diffuser system must also be designed. The size and spacing of the diffuser's ports are determined through a series of complex iterative hydraulic calculations based upon the following parameters:

- Design flows
- Pipe diameter
- Pipe slope
- Frictional resistance of pipe material
- Effluent density
- Receiving water density
- Discharge depth
- Operating head

A computer program is typically employed to solve the manifold hydraulics problem. The program takes into account the discharge characteristics of the individual port and does a numerical integration of the hydraulic conditions port by port with a trial and error optimization of port sizes considering the various factors listed above. A complete description of diffuser hydraulic design has been reported by Rawn, Bowerman, and Brooks (1961) and the basic hydraulic requirements as reported in their paper are summarized below:

Flow Distribution. The division of outflow between the various ports should be fairly uniform. For diffusers laid on a sloping sea bottom, uniform port discharge for all rates of flow is impossible. In such cases, the diffuser should be designed for uniform distribution at low to medium flows. For higher flows, the deeper ports should be allowed to discharge more flow than the average port to prevent possible clogging of the deep end of the diffuser.

Velocity in Diffusers. The flow velocity in all ports of the diffuser should be high enough to prevent gross deposition of sludge or grease. For settled sewage, minimum velocities of 2 to 3 feet per second are required.

Prevention of Seawater Intrusion. All ports should flow full to prevent intrusion of seawater into the pipe.

Dilution and Mixing

A diffuser disperses wastewater by breaking it up into a number of smaller flows and spreading it over a large area. In essence, a diffuser changes a point-source discharge into a line-source discharge. The resulting discharge plume mixes within the receiving water to produce a diluted effluent.

The processes that cause mixing and dilution when effluent is discharged by a diffuser into receiving waters are complex, but primarily involve mixing due to kinetic energy of the initial discharge velocity, mixing caused by buoyant forces due to the density difference of the effluent and receiving waters, and, finally, mixing caused by horizontal cross currents of the receiving waters (Brooks and Koh, 1965). Normally, all three of the above processes act on the discharged effluent to produce the overall mixing and dilution.

Mixing caused by the kinetic energy occurs close to the point of discharge and is primarily a function of discharge velocity. Due to the density and viscosity of water, the energy is dissipated rapidly. Dilution is generally less than two parts of seawater to one part of effluent and occurs within a few feet of the point of discharge.

When the kinetic energy is dissipated, a mixture of effluent and receiving water exists. If the density of the effluent is less than the density of the receiving water at the point of discharge, the mixture will also have a density less than the surrounding receiving waters. This difference in density creates a buoyant force that causes the effluent mixture to rise in the receiving waters. As the mixture rises, it continues to mix with, and therefore be diluted by, receiving water.

If the receiving water is of equal density at all depths, the mixture density will always be less than the density of the surrounding waters and will continue to rise and be diluted (figure 4). Under this condition, the dilution achieved is a function of port diameter, discharge velocity, relative density, and depth of discharge.

If the density of the receiving water decreases with decreasing depth, there will be a depth when the density of the rising effluent mixture is equal to the density of the surrounding receiving waters and less than the density of overlying waters. When this occurs, the effluent mixture will not rise further and is considered trapped (figure 5). In this situation, the dilution achieved is controlled by the height of rise that, in turn, is a function of the density variations of the receiving waters. Entrapment of the effluent plume below the surface is usually a desirable objective for ocean outfall design because it helps prevent possible health and aesthetic problems common to discharges rising to the water surface.

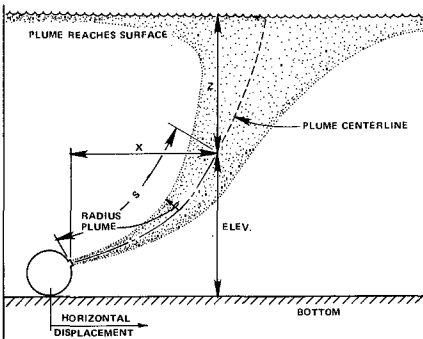


Figure 4
Effluent Plume Characteristics
for Nonstratified Water

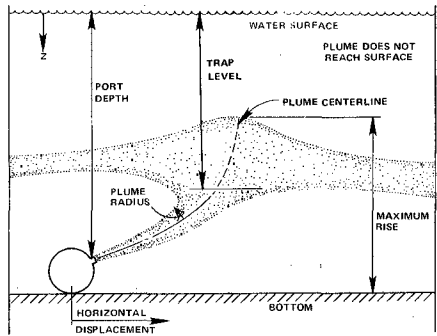


Figure 5
Effluent Plume Characteristics
for Stratified Water

The previous discussion assumes that there are no horizontal currents in the receiving water. Horizontal currents will carry the effluent away from the point of discharge and cause rapid mixing and dilution. Port diameter, discharge velocity, and relative density will have little effect on the dilution achieved (Roberts, 1976). The velocity of the horizontal currents will control the dilution. Because the effluent is diluted and carried away rapidly, the effluent mixture will have little opportunity to rise, regardless of the density of the effluent or receiving waters.

Predicting diffuser plume characteristics is essential in outfall design. Computer programs are typically used to examine various discharge and receiving water conditions and predict height of rise and associated dilution. Baumgartner, Trent, and Byram (1971) have developed such a model which is used in outfall design.

Diffuser Port Design

Orientation

The flow direction of receiving water currents dictates the orientation of the diffuser. There are three basic diffuser orientations (figure 6):

- Current parallel to shore
- Current perpendicular to shore
- Variable current direction

The diffuser should be located perpendicular to the net current to maximize dilution. However, for currents that shift direction, "Y" shaped diffusers are employed to offer the greatest chance for keeping the diffuser perpendicular to the current.

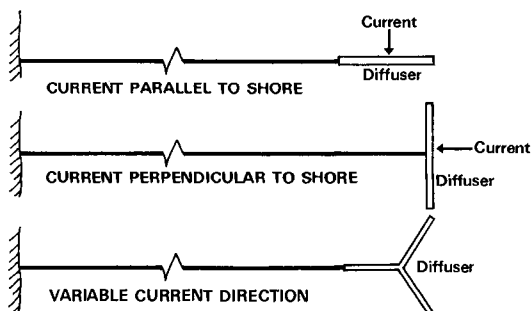


Figure 6
Alternative Diffuser Arrangements

Port Types

The two basic types of diffuser ports are pipe wall port and riser tube (figures 7 and 8). A pipe wall port system consists of holes in the wall of the pipe, at or slightly above the pipe's spring line. To prevent the pipeline filling with bottom sediments, this type of diffuser port requires that the pipe be laid on the ocean bottom rather than buried.

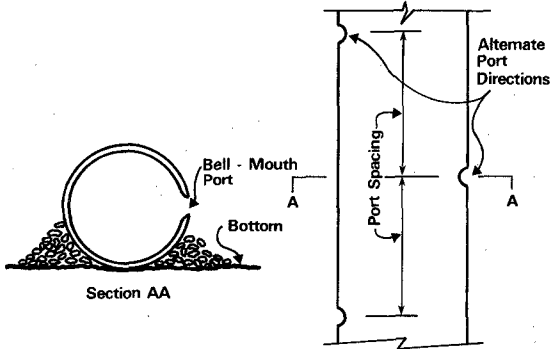


Figure 7
Pipe Wall Port Diffuser

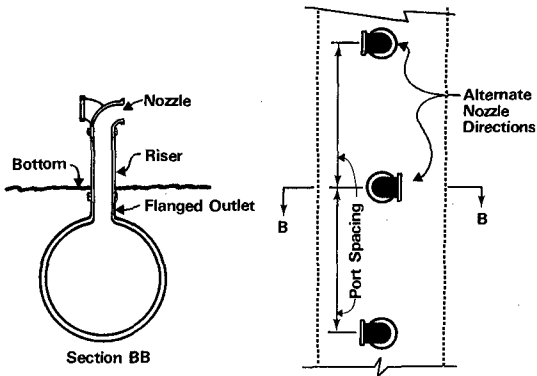


Figure 8
Riser Port Diffuser

Riser tubes are used when the diffuser pipeline must be buried (usually to prevent damage by wave action). Riser tubes project upward from the crown of the buried pipe, penetrating above the ocean bottom. The small, cross sectional area of the risers minimizes exposure to waves and current forces. However, because the riser tubes project above the bottom, they can become vulnerable to impact forces. A typical hazard common to risers--breaking of the rigid tube due to impact forces and subsequent filling of outfall pipe with bottom soils--is shown in figure 9. A satisfactory solution to this problem is the use of flexible riser tubes (figure 10). The rubber pipe wall section allows the tube to absorb impact through deflection. If the impact force is too great, the rubber section fails before the steel, allowing the pipe tube to shear off above the mud line. This type of failure minimizes the chances of filling the pipe with bottom soils and results in simple repair work.

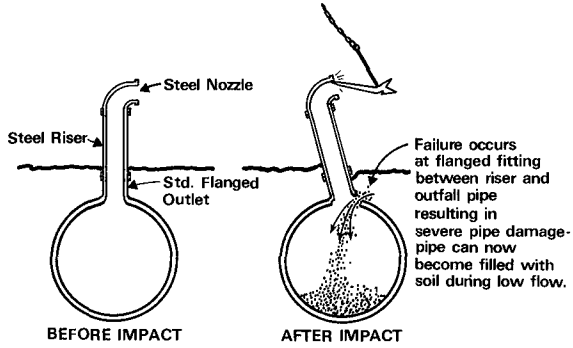


Figure 9
Rigid Diffuser Riser

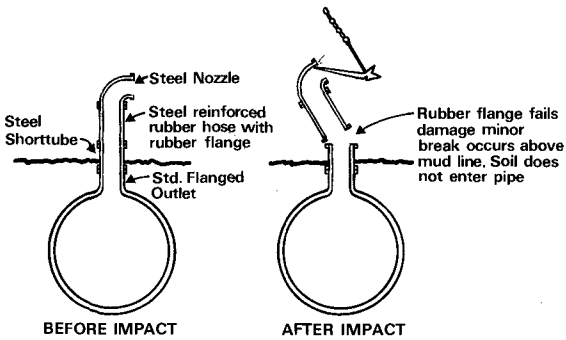


Figure 10
Flexible Diffuser Riser

Onshore/offshore and longshore drift of bottom soils must also be considered in diffuser port designs. Pipe wall ports and riser tube ports must be of sufficient height above the bottom to prevent filling of the diffuser with shifting bottom materials during low flows.

Pipe Design

Completion of the site selection process and preliminary hydraulic design results in establishing the basic outfall pipe parameters--alignment, slope, pipe length and diameter, and diffuser port sizes and spacing. The next element of the design process considers the final design of the pipeline. For ocean outfalls, the following final pipe design components must be considered:

- Foundation requirement
- Pipe forces
- Hydraulic flow properties
- Corrosion resistance
- Pipe material selection
- Pipe anchoring
- Construction methods

Foundation Requirements

Much of the actual pipe design itself depends on the soil conditions. The amount of support along the length of a pipe will influence the type of pipe that is to be used. A change in the support along a pipe will also change the type of pipe used. Some types of pipe can tolerate substantial settlement while other pipes, perhaps with closely spaced joints, would come apart if the settlement is excessive. Although soft sediments most often contribute to pipe settlement, scour and erosion from beneath a pipe can also contribute to loss of support. The support along a pipe in an ocean outfall needs to be continuous just as it does for pipes on land. Since pipes laid on rock under water may not have continuous support beneath them, the pipe may actually span two points on the rock. This can also occur in gravelly soils. Under some conditions, shifting ocean bottom materials (longshore drift) and sedimentation can contribute to the actual load on top or along the side of the pipe. In addition, consideration must be given to outfalls penetrating the surf zone where seasonal changes in beach profile will alternately scour and fill bottom materials over the pipe.

Excavation and Backfill

Outfall pipes generally need to be buried for at least part of their alignment. This requires that the conditions of excavation and backfill be evaluated. The difficulty of excavation, depth of excavation, stability of the open trench, and difficulty of actually placing the pipe in the trench all must be considered in the excavation phase. Many times the excavation must continue through a soft layer down to a firm layer. This requires that the depth of the soft layer be known and that the uniformity of the depth along the alignment be known. The disposition of the excavated material can sometimes be a problem. Most often, it will have to be loaded aboard barges and disposed of, perhaps at some distance from the excavation. It is seldom that the excavated material can also be

used for backfill. Trenches excavated in loose sands or granular material often will not stand open for a long period of time since the sides will slough and material will be brought into the trench by currents and waves. In firm granular material, the trenches generally stand open well and narrow trenches can be used. Support for the pipe along the trench is important. Uniform support is often provided by placing a layer of coarse gravel in the bottom of the trench. Unless the excavated material is exceptionally clean, backfill material will usually have to be imported. Generally, coarse granular material is used for backfilling. Any material with a majority of fines in it will generally cause turbidity problems and be unsuitable. Generally, only the larger particles will reach the trench.

Pipe Forces

Outfalls must be designed to resist both internal and external forces. The internal forces are a result of hydraulic pressure imposed on the line through flow of liquid. Operating pressures in outfalls are typically low and seldom affect the structural design of the pipe. Further, since outfalls discharge at depth, there is no requirement to design the pipe to resist the hydrostatic head of the water column above the pipe. External forces include the dynamic action of waves, force from currents, impact from foreign bodies, and overburden support.

The flow of fluid around a cylinder, such as an exposed pipeline, will induce drag forces on the pipe (Priest, 1974). See figure 11. The resultant force can displace an unanchored pipe horizontally, creating large bending and shear stress within the pipe and at its connection with the shore. If the pipe is anchored or pile supported, the horizontal drag force will then be transmitted to the pipe anchor. Close spacing of the supports may be required to prevent pipe overstress due to bending. Also, closer spacing of supports may be required to eliminate vertical pipe oscillations resulting from the resonate response of the pipe to the current.

The passage of a wave over the pipe can develop large dynamic pressures on the pipeline when it is supported above the bottom (figure 12). The pressures result from drag forces as well as inertial or impact forces caused by the moving fluid. Dynamic pressure can be minimized by locating the pipe in water deep enough so that it is not significantly influenced by the orbital motion of waves. However, the pipe should be buried in the surf zone to a depth sufficient to protect the line from damage.

Impact forces resulting from foreign objects striking the pipeline must also be considered. Impact from a ship's anchor and commercial fishing gear (figure 13) can result in severe damage to an outfall. Locating outfalls in anchorage zones or bottom trawling fishing grounds should be avoided. However, if the outfall alignment must be located in regions with a high probability of occurrences such as dragging anchors, the pipeline should be buried. The minimum pipe cover should be in excess of plow depth of the anchors.

Even though the main pipeline is protected from impact damage, the diffuser riser must extend above the mud line and become exposed. In such cases, the flexible riser systems should be considered as discussed above (figures 9 and 10).

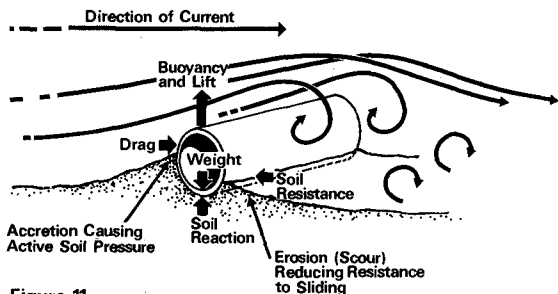


Figure 11
Current Forces

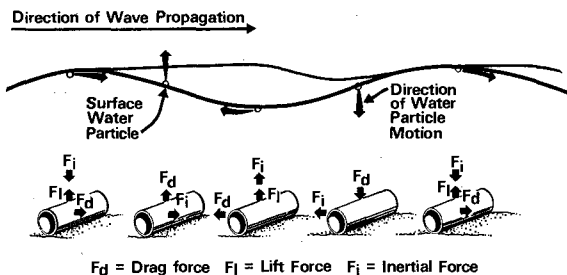


Figure 12
Wave Forces

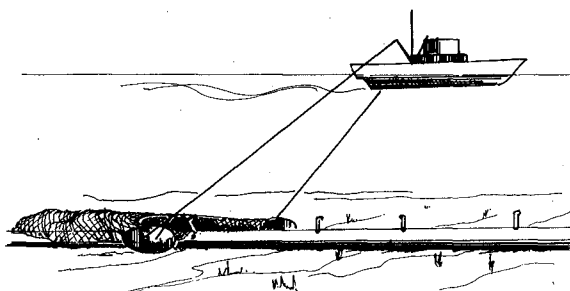


Figure 13
Impact Forces

Hydraulic Properties

An important characteristic of a pipe is its ability to transport the fluid. Various pipe materials can have substantially different frictional characteristics. Some materials, such as cast iron and steel, are subject to internal corrosion that will increase the friction and thus reduce the flow-carrying capacity over a period of time.

The range of friction factors normally applied to pipe materials commonly used for outfall construction is not sufficient to control the selection of materials or allow a reduction in outfall diameter. Since the pipeline materials cost is usually a small part of total project costs, a conservative selection of friction factors and pipe diameters is the normal procedure.

Corrosion Resistance

Saltwater can be a corrosive element for some pipe materials. The bottom sediments may also exhibit a corrosion potential so that the combination can be devastating. The technology exists to protect almost any material from excessive corrosion. The protection provided should be consistent with the design life of the facility and the protection provided associated structures. The costs for this protection are usually minimal. Therefore, corrosion is normally not a controlling factor in the selection of outfall pipe materials.

Pipe Material

A variety of pipe materials are available for ocean outfalls (table 1):

- Reinforced concrete
- Steel
- Concrete cylinder
- Corrugated metal
- Cast iron
- Ductile iron
- Fiber-reinforced plastic
- High-density polyethylene

The most common pipe material used on ocean outfalls is reinforced concrete pipe, which is a heavy and rigid pipe material that is capable of supporting large overburden loads and resisting current and wave movements. Corrosion resistance of reinforced concrete is good in the saltwater environment.

Pipe Joints

A variety of pipe joints ranging from welded to dresser couplings are available for linking outfall pipe sections together. Probably the most common is bell and spigot with a retained rubber gasket. Normally, up to 3 to 5 degrees of deflection are allowed. For greater deflections (up to 15 degrees), ball and socket joints can be used.

Outfall pipe joints are typically equipped with thrust-ties to secure the pipe joint from displacement. A bolted connection at the pipe spring line links each pipe section and restrains the joint from separating due to external forces. Stainless steel bolts are usually used in saltwater. Metallic bond straps electrically linking each pipe section together are also common features of an ocean outfall joint. Bond straps allow external electric currents to be applied to the entire pipeline to control electrolysis.

Pipe Support Systems

The wide range of pipe support systems available to the outfall designer is illustrated in figures 14 through 20. The following is a summary of each system.

Bottom Exposure. For environmental conditions with minimal current, wave, and impact potential, the outfall pipe can be laid directly on the bottom (figure 14). For this condition, only a bedding layer may be required to support the pipe. Where some current or wave action exists, an exposed outfall can be secured to the bottom with concrete anchor blocks or embedment anchors (figure 18).

Bottom Exposure With Armor. Where the pipe is subject to moderate wave attack or strong currents, it is desirable to armor a pipe laid on the bottom. Armoring usually consists of riprap and is designed in similar fashion as breakwaters (figure 15).

Buried Trench Section. Sites with heavy wave action usually require complete burial of the outfall pipe. The trench must be deep enough to ensure that scour action will not expose the pipe. Often, the pipe zone material is riprapped at the surface to reduce scouring potential (figure 16).

Table 1. CONSTRUCTION PROPERTIES OF OCEAN OUTFALL PIPE MATERIALS

Outfall Pipe Material	Composition	Range of Diameter	Nominal Length	Joint Type	Seawater Corrosion Protection	Notes
Reinforced Concrete	Concrete embedded with steel rods or fabric	12 to 120+ inches	10 feet	Bell and Spigot with thrust tie	Bond strap linking each pipe section together for induced electric currents	Very heavy and rigid pipe material; impact resistance high
Steel	Thin plates of steel welded together	Variable	Variable to 100 feet	Welded or mechanical	Pipe typically lined inside and out with mortar	Flexible pipe material; moderate impact resistance
Concrete Cylinder	Prestressed steel barrel with mortar coating and lining	12 to 40+ inches	32 feet	Bell and Spigot with thrust ties	Bond strap	Semirigid pipe material
Corrugated Metal	Rolled and bolted steel sheets, flexed or corrugated to increase stiffness	6 inches to 21 feet	12 feet	Steel band	Steel galvanized and embedded with asbestos felt, bituminous lining	May have limited use in marine environment due to corrosion potential
Cast Iron	Molded gray iron centrifugally cast on a metal mold	12 to 36+ inches	18 feet	Mechanical or ball and socket	Bond strap	Impact resistance low-- brittle failure
Ductile Iron	Chemically altered cast iron	12 to 36+ inches	18 feet	Mechanical or ball and socket	Bond strap	More resistant to impact loads than cast iron
Fiber-reinforced	Fiberglass filaments bonded by resin	12 to 60+ inches	40 feet	Bell and Spigot	None. Can carry caustic effluents	Pipe is lightweight and deflects considerably under earth loads
High-density Polyethylene	Manufactured of Polyethylene resin through a continuous extrusion process	12 to 48+ inches	Pipe can be continually extruded to any desired length	Butt fusion or mechanical joints	None required	Pipe is buoyant in seawater and flexible. Conforms easily with nonlinear bottom topography. Pipe wall easily punctured by sharp objects

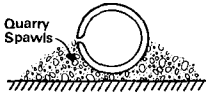


Figure 14
Bottom Exposure

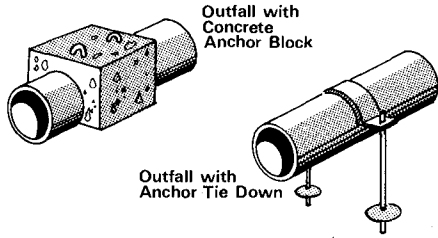


Figure 18
Alternative Pipe Anchoring Methods

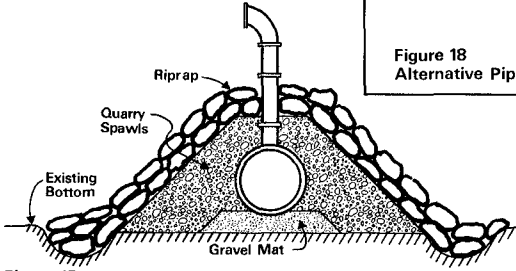


Figure 15
Bottom Exposure With Armor

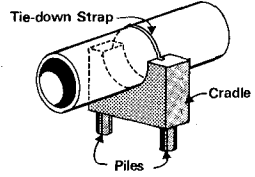


Figure 19
Pile-Supported Outfall

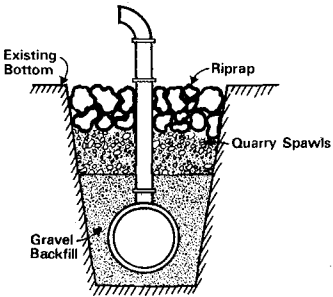


Figure 16
Buried Trench Section

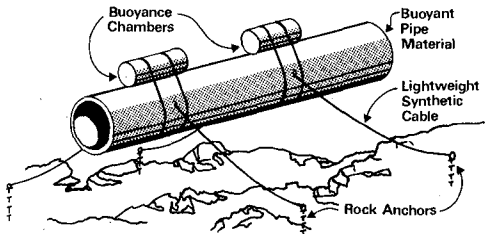


Figure 20.
Floating Outfall -
Rough and Irregular Bottom

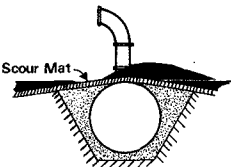


Figure 17
Shallow Trench
With Scour Mat

For some locations, scour mats can be used to eliminate the need for deep trenching. A scour mat consists of a pre-formed concrete mat that is laid over the entire exposed pipe with sufficient width to prevent undermining at its edges (figure 17).

Pile-Supported System. In some instances, the ocean bottom is composed of soft sediments, providing little, if any, bearing support for the pipe. Laying a rigid pipe material directly on the bottom in such conditions is hazardous because of potential dissimilar settlements. A common solution is the use of a pile-supported pipeline (figure 19). Piles are driven to firm bearing and a cap is attached to the pile tops. The pile caps function as a cradle for the pipe, while a tiedown strap prevents vertical pipe movements due to current-induced oscillations or positive buoyance of the pipe such as air trapped in the pipeline.

Semi-Floating Outfall. For some ocean sites, none of the previously mentioned systems is practical. An example might be a site that has minimal current action but a rough and irregular bottom (submerged coral reef). Furthermore, environmental regulations could prevent blasting a trench into the bottom. Laying the pipe directly on the bottom is not desirable because it would be damaged by sharp projections. Driving piles may be prohibitively expensive. However, floating the pipe above the bottom is a possible alternative (figure 20). A semi-floating outfall can act as a suspension bridge in reverse, keeping the pipe suspended above the problem area but below the ocean surface. Pipe material should be lightweight or, at best, buoyant. Additional buoyance chambers may be required to provide vertical uplift. Anchors and anchor cables should be sized to secure the pipe from lateral and longitudinal movements due to minor current or wave action.

Construction Methods

During the pipe design of the outfall, the designer must also consider the various construction methods available to an offshore contractor. Failure of the designer to understand outfall construction procedures can result in a difficult and costly pipe installation.

For ocean outfalls, there are three different zones that the contractor must contend with during construction: onshore, surf, and offshore. Each zone can require different construction methods. The four commonly used construction methods of outfall installation are barge lay, trestle lay, string float, and bottom pull.

With the barge lay method, the pipe is laid in relatively short lengths from a barge to the trench or bottom, similar to onshore sewer construction. The barge lay method is generally used in the offshore zone. Divers must join each pipe length to the previously installed pipe (figure 21). The cost of this method increases tremendously with increase in water depth.

The trestle lay method involves the construction of a pier through the surf zone (figure 22). The pier replaces the barge as a work platform, isolating the pipe-laying equipment from wave action. Usually steel sheeting is driven into the bottom to act as a cofferdam for the pipe trench. Pipe is laid in the trench in a similar matter as a barge lay.



John Goode Photograph

Figure 21. Diver Supervising Pipe Joint Assembly During Barge Lay Operation.



CH2M HILL Photograph

Figure 22. Outfall Construction from Trestle Through Surf Zone.



Figure 23. Launching Outfall by String Float Method.



CH2M HILL Photograph

Figure 24. Offshore Tug Preparing for Bottom Pull of Outfall.

The string float method involves floating the entire pipeline into place on the surface and then sinking the line into place on the bottom (figure 23). To provide the buoyancy necessary to float the line, the pipe and diffuser are temporarily sealed while full of air. When the line is floated into place on the water surface, the air is replaced with water, causing the line to sink. The rate of submergence can be controlled by the rate of air release.

This method is most commonly used with lightweight, flexible, plastic pipes. Additional weight is added to these lines, usually by concrete ballast collars, to provide the negative buoyancy needed to sink the line and hold it in place on the bottom. The feasibility of using this method depends on many factors, including weather and water conditions. Rough water or strong currents are of particular concern.

The bottom pull method involves pulling the line into place along the ocean bottom through the surf zone and offshore areas (figure 24). Large stresses are placed on the joints and pipe and must be considered in design and materials selection. The pipe is joined onshore and pulled seaward as assembly proceeds. A specially constructed sled is used to allow the line to be pulled without damaging the pipe material. In addition to providing a means of attaching the pulling cables, the sled will also provide a grading effect on the soils. Depending on the soils and topography, additional sleds or other supports may be needed along the pipe.

All of the above construction methods will require underwater work during installation. In all cases, diver time is required for inspection of the final installation. To ensure proper monitoring of underwater construction, the use of engineering divers as inspectors rather than commercial divers is recommended (Layton, 1976).

The appropriate method of construction for an outfall line depends on many factors, primarily soils, pipe material and size, environmental conditions, depth of construction, contractor's available equipment, and final design conditions. All of these factors are involved in determining the cost of the final installation.

Perhaps the major factor relating to costs is the amount of underwater work required, particularly work performed in deep water. Difficulty, time required, and, therefore, costs increase greatly as the depth of water increases.

OUTFALL MAINTENANCE

During the design of an outfall, provisions for inspection and maintenance of the diffuser should be considered. Even carefully designed diffusers will require occasional cleaning to remove accumulated grease, slime, and grit (Rawn, Bowerman & Brooks, 1961). These accumulations can reduce flow by increasing frictional resistance. Cleaning can be accomplished by flushing or by pulling a ball through the line.

In addition to cleaning operations, an annual diving inspection of the outfall is recommended. The purpose of the inspection is to check the outfall for structural damage to pipe and diffuser risers, pipe corrosion, changes in biological activity around diffuser, and plugging of diffuser ports due to longshore drift.

Further, it is recommended that an inspection hatch be built into the end of the outfall diffuser to facilitate flushing operations and allow divers access to the outfall's interior for removing obstructions. Also, for long outfalls, several inspection hatches should be located along the conduit and diffuser sections for easy diver access.

SUMMARY

This paper discusses the major components of the complex ocean outfall design process: site selection, outfall hydraulics, dilution and mixing, diffuser port design, pipe design, pipe support systems, and construction methods. All of these components must be evaluated throughout the design process to provide a structurally sound outfall system that meets water quality requirements.

REFERENCES

- Baumgartner, D. J., Trent, D. S., and Byram, K. V., "User's Guide and Documentation for Outfall Plume Model," Working Paper No. 80, Environmental Protection Agency, Corvallis, Oregon, May 1971.
- Brooks, N. H., and Koh, R. C. Y., "Discharge of Sewage Effluent from a Line Source into a Stratified Ocean," International Assoc. for Hydraulic Res., Proc. XI Congress, Leningrad, September 1965, Paper 2.19.
- Layton, J. A., "Underwater Reconnaissance and Construction Inspection by the Diving Engineer," Proceedings of the Fifteenth Coastal Engineering Conference, ASCE, Honolulu, Hawaii, July 1976.
- Noorany, I., "Underwater Soil Sampling and Testing: A State-of-the-Art Review," Symposium for Underwater Soil Sampling, Testing, and Construction Control, ASTM, Atlantic City, New Jersey, June 1971.
- Priest, T. P., "Wave Forces on Pipelines," Pipelines in the Ocean, ASCE, New York, New York, 1974.
- Rawn, A. M., Bowerman, F. R., and Brooks, N. H., "Diffusers for Disposal of Sewage in Sea Water," Trans. ASCE, Vol. 126, Part III, 1961.
- Roberts, P. J. W., "Dispersion from Finite Length Outfall Diffusers", Proceedings of the Fifteenth Coastal Engineering Conference, ASCE, Honolulu, Hawaii, July 1976.

CHAPTER 168

DESIGN CONSIDERATIONS FOR THE SAND ISLAND AND BARBERS POINT OUTFALLS

Robert C. Y. Koh¹
Norman H. Brooks¹
Floyd Louis Vuillemot²

INTRODUCTION

The design and construction of a major ocean outfall and diffuser system for disposal of wastewater effluents is a complex process involving an interplay of requirements originating from various disciplines. These include, among others, considerations of physical oceanography, mixing and dispersion, treatment processes, regulatory requirements, marine geology, economics and construction. The recently completed Sand Island Outfall and the newly designed Barbers Point Outfall are both on the southern coast of the island of Oahu, Hawaii, and are designed for treated sewage effluents from the densely populated portion of the City and County of Honolulu. In this paper, some design considerations of these outfalls will be examined. The emphasis in this paper is on the hydrodynamics, although other design aspects are also discussed briefly.

The design of a large submarine outfall must consider two basic objectives. First, the design must assure the physical integrity of the structure when subjected to the sometimes violent environment. Second, the mixing, dispersion and transport of the effluent must be such that environmental degradation is acceptably small and that water quality requirements are met. In addition, the design process also includes considerations of economics, overall system compatibility, and construction.

The Sand Island Outfall was constructed in 1975-1976 while construction of the Barbers Point Outfall began in 1976. The cost of the Sand Island outfall was 13.7 million.

DESCRIPTION OF THE DESIGN

The Sand Island Outfall is 84 inches in diameter and extends 12,500 ft offshore to a depth of approximately 230 ft. The last 3384 ft of the outfall (the diffuser section) contains 282 ports on the sides of the pipe varying in diameter from 3 to 3.53 inches. The Barbers Point Ocean Outfall is 78 inches in diameter and extends 10500 ft offshore to a depth of 200 ft. The last 1752 ft of the outfall contains 146 ports varying in diameter from 3.41 to 3.74 inches. The design ranges of flow are 32 to 194 mgd for the Sand Island Outfall and 14 to 112 mgd for the Barbers Point Outfall. Figures 1 and 2 show plan views of the two outfalls.

Considerations of forces from hurricane-generated waves and seismic loadings resulted in each pipeline being buried in a trench in the ocean bottom out to a depth of approximately 70 ft where it then gradually emerges from the sea floor and rests on the bottom, being anchored and protected by armor stones. The size and gradations of the stones and the cross sections of the ballast are chosen so that they are stable under the design wave or the design earthquake.

The offshore bathymetry beyond 70 feet depth showed rock and cemented coral outcrops dotting an underwater landscape of sand and coral rubble. The alignments of the outfalls were chosen to avoid these outcrops. The bottom slopes are also quite steep. The alignments of the diffuser sections are chosen to lie essentially on a level to ensure nearly uniform flow distribution along the diffuser for the full

¹Calif. Inst. of Tech., Pasadena, Calif., and consultant to R. M. Towill Corp., Honolulu, Hawaii.

²R. M. Towill Corp., Honolulu, Hawaii.

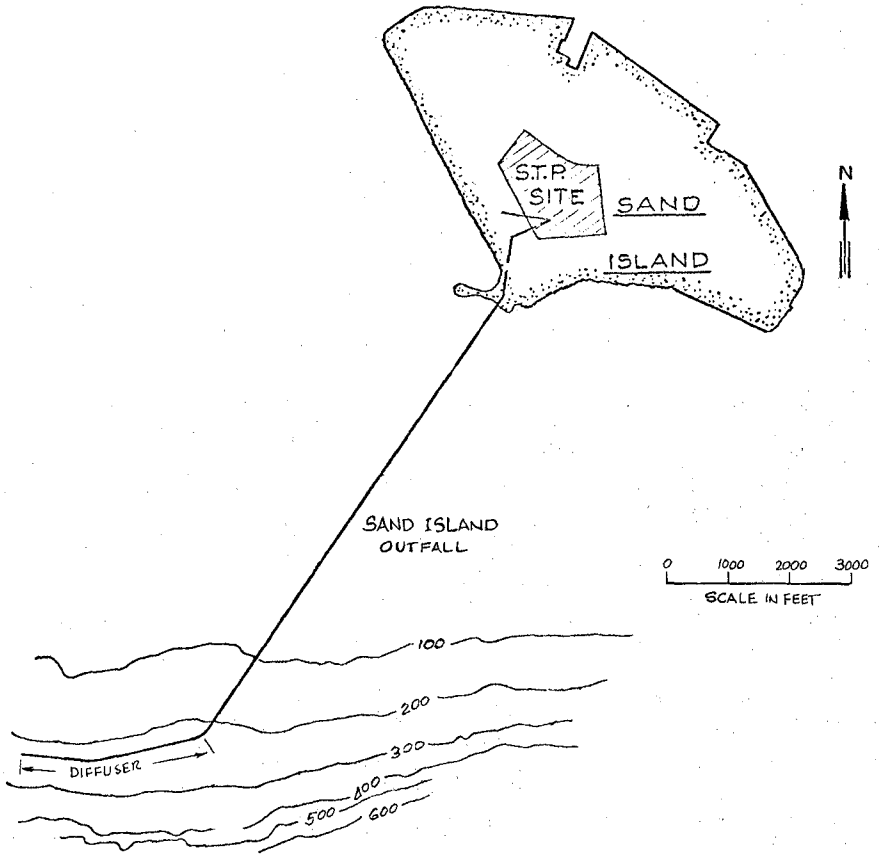


Fig. 1. Schematic Plan of Sand Island Outfall.

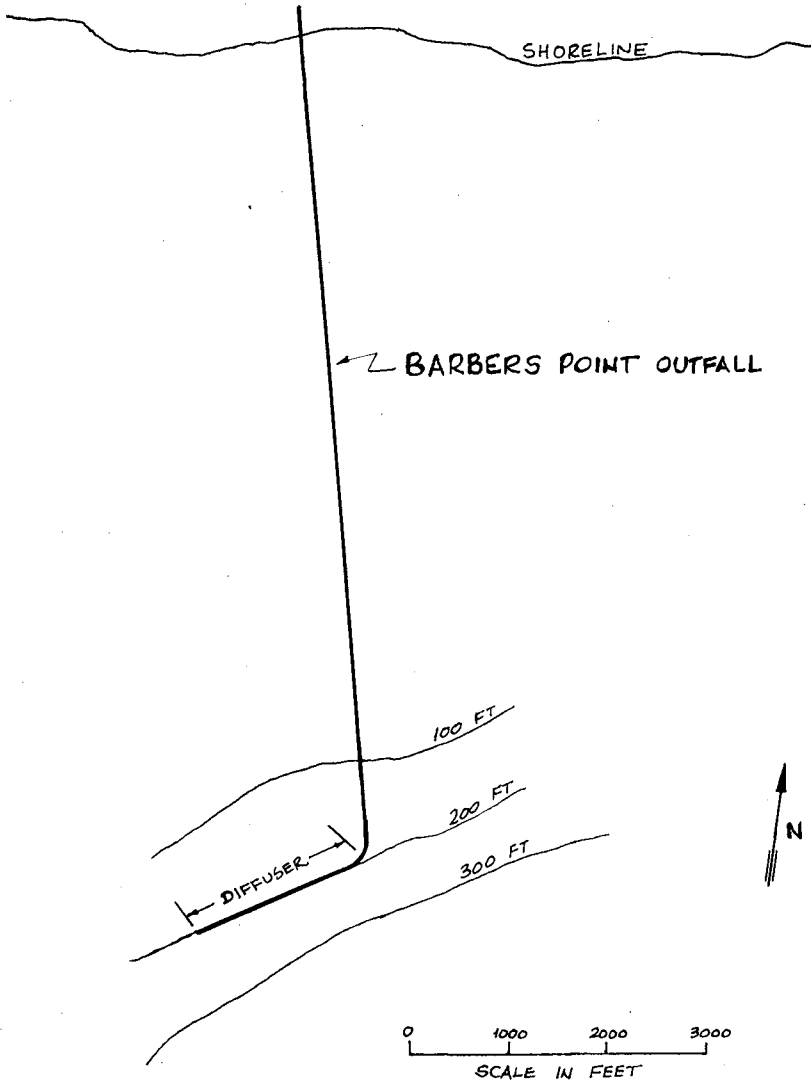


Fig. 2. Schematic Plan of Barbers Point Outfall.

range of discharges. The diffuser pipe sections were ballasted to prevent down-slope rolling or sliding.

The lengths and depths of diffusers for the outfalls have been designed to ensure that the sewage effluent is diluted rapidly with ambient ocean water. Typical values of dilution are on the order of a few hundred. For part of the time, particularly during the summer, the diluted effluent plumes are submerged due to the existence of density stratification in the ambient sea. In the design process, however, high dilution was considered more important than submergence of the sewage field both from environmental as well as from construction and economic considerations.

MIXING AND DISPERSION OF THE EFFLUENT IN THE OCEAN

Initial Dilution and Sewage Field Submergence

When sewage effluent is discharged through a submarine outfall diffuser, it undergoes basically three stages of turbulent mixing processes. First it rises as a buoyant plume, entraining (and mixing with) the ambient ocean water. This first phase of mixing carries the diluted effluent either to the surface or to a terminal level below the surface in the event there is sufficient ambient density stratification. The second phase of transport is that of horizontal spreading. The sewage field, being either buoyant at the surface or more homogeneous at a submerged level, tends to spread out horizontally. This second phase of the establishment of a sewage field is followed by the third phase of dynamically passive turbulent diffusion and advection in the ocean. This last phase of mixing is dependent only on the ambient ocean turbulence and currents. Proper design of an ocean outfall diffuser must take into consideration all these processes although only the first is under the direct control of the design engineer.

One of the recent advances in the technology for ocean sewage disposal is the utilization of the natural ocean density stratification to achieve submergence of the sewage field. The sewage effluent, when mixed sufficiently with the denser seawater below the pycnocline, may not reach the surface since the much diluted effluent becomes denser than the surface seawater. The probability of submergence depends not only on the diffuser design but also on the natural density stratification in the ocean at the disposal site. In particular, if there is no density stratification between the depth of the diffuser and the surface, then the sewage field can never be made to stay submerged no matter how long a diffuser is used.

Predicted dilution and submergence characteristics of the Sand Island Outfall is shown in Figure 3 for various density profiles as determined to be representative of typical conditions during the year (Figure 4). It may be noted that for a given flow, the submergence and dilution are inversely related, i.e., deep submergence is accompanied by lower dilutions. The analysis techniques used in obtaining these results are detailed in Refs. I, II, and IV. Blocking by currents were considered.

During the design process, a variety of different diffuser lengths and depths were investigated as to their performance in terms of initial dilution and sewage field submergence characteristics. For each combination of length and depth, a dilution vs. submergence graph such as shown in Figure 3 could be prepared. It is found that, as displayed in Figure 3, the dilution and submergence are interrelated. For deep submergence due to a strong ambient density gradient, the dilution obtained is low. Sometimes increasing the diffuser depth (for the same diffuser length) may actually decrease dilution if the increased depth places the diffuser in a region with stronger stratification. On the other hand, for the same diffuser depth, lengthening the diffuser always increases dilution. The choice of the diffuser design represents a compromise between achieving high dilution and submergence most of the time but without excessively deep submergence and hence too low dilution. For the case of deep submergence with attendant lower dilutions, the sewage field

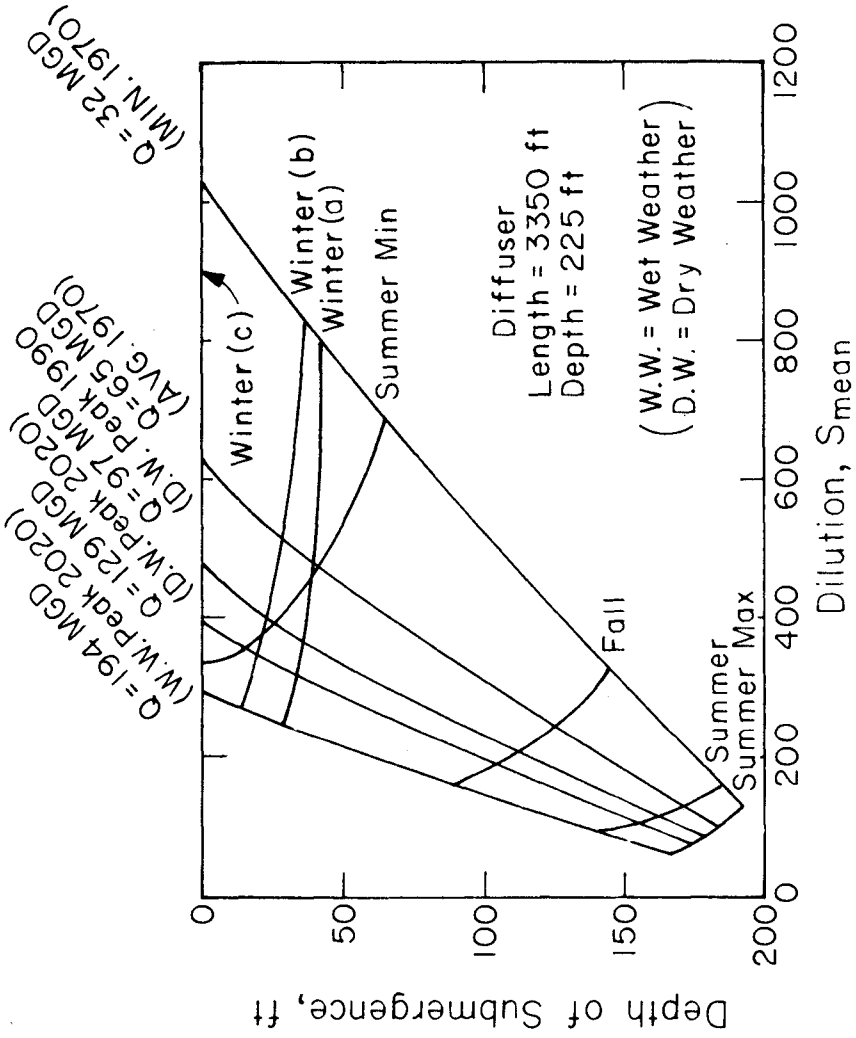


Fig. 3. Dilution and Submergence Characteristics for Sand Island Outfall.

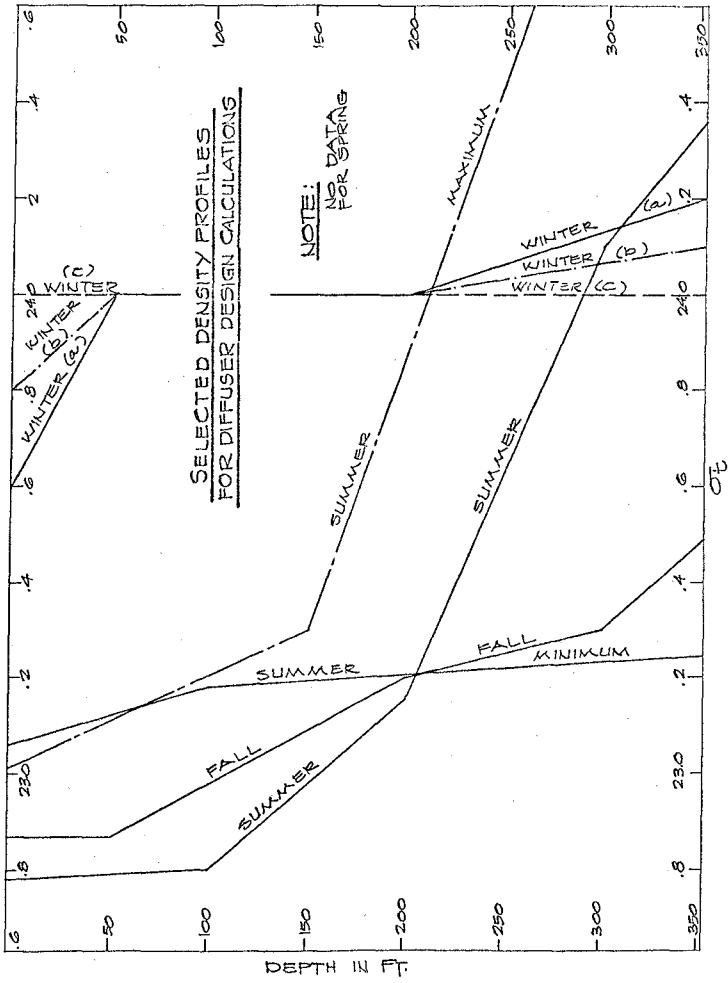


Fig. 4. Design Ocean Density Profiles for Sand Island Outfall.

would be subjected to somewhat slower natural assimilation and potentially higher impact.

Subsequent Transport and Diffusion

The advective transport of the diluted sewage effluent in the ocean environment was investigated by utilizing current meter measurements at the site in combination with statistical analyses, resulting in estimates of the probability of reaching shore as functions of time. Available ocean current data were obtained and analyzed to obtain streaklines for the sewage field advected according to the measured currents. The streaklines were then analyzed to obtain the statistics of transport to two lines designated reef line and recreation line. The reef line is a piecewise linear line which is essentially tangent to the offshore extent of the coral reef. The recreation line is displaced 1000 ft seaward of the reef line. These lines and an example segment of the streakline are shown in Figure 5 for the Sand Island Outfall location. The result of such an analysis is shown in Figure 6 where the probabilities of transport to either of the two lines are shown as a function of time of travel. It is seen that there is little chance of reaching the reef line in less than four hours. Since the bacterial dieoff rate tends to be very rapid in the tropical waters off Hawaii, health hazard due to sewage discharge from the new outfalls is very low.

During the subsequent transport of the sewage field following initial dilution, it will continue to mix with seawater by virtue of turbulent diffusion. This is generally a much less effective means of mixing for typical large plumes. For example, in four hours travel time, the additional mixing achieved by turbulent diffusion is only about a factor of two. For the Sand Island Outfall it is found that the probability of transport to shore within four hours is virtually non-existent. The probability of transport to shore in 24 hrs is no more than a few percent under tradewind conditions and only 10 to 30% during periods interspersed by Kona storms. Results for the Barbers Point Outfall are similar.

INTERNAL HYDRAULICS

The basic premise of a long multiport diffuser is to distribute the sewage effluent over a large area to ensure the availability of large quantities of diluting sea water so that the initial dilution is sufficiently high (on the order of 200 or 300 to 1). Thus it is necessary that the diffuser be designed in such a manner that effluent is discharged nearly uniformly through the many ports.

The quantity of effluent flowing in the diffuser pipe decreases along the diffuser toward the seaward end due to the continual discharge. On the other hand, the flow velocity in the pipe should be maintained sufficiently high to prevent gross deposits of grease or sludge. This fact necessitates decreasing the diffuser pipe diameter toward the seaward end and the provision of a flap gate at the end which can be opened for occasional flushing if and when required.

A hydraulically well-designed diffuser should also be such that i) the pumping head requirements be reasonable, ii) no sea water intrusion occurs, and iii) remain hydraulically insensitive to age. These considerations lead to a choice of relatively small port sizes so that the port densimetric Froude number is relatively high, and certainly larger than two; and to bell mouthed ports which minimize clogging and whose discharge coefficients are high and will remain constant.

In the hydraulic design of the San Island and Barbers Point Outfall diffusers, these requirements were all taken into consideration. In addition, the effect of the density difference between the sewage effluent and sea water, coupled with any change in elevation along the diffuser introduces density head differences which must be taken into account in the hydraulic analysis.

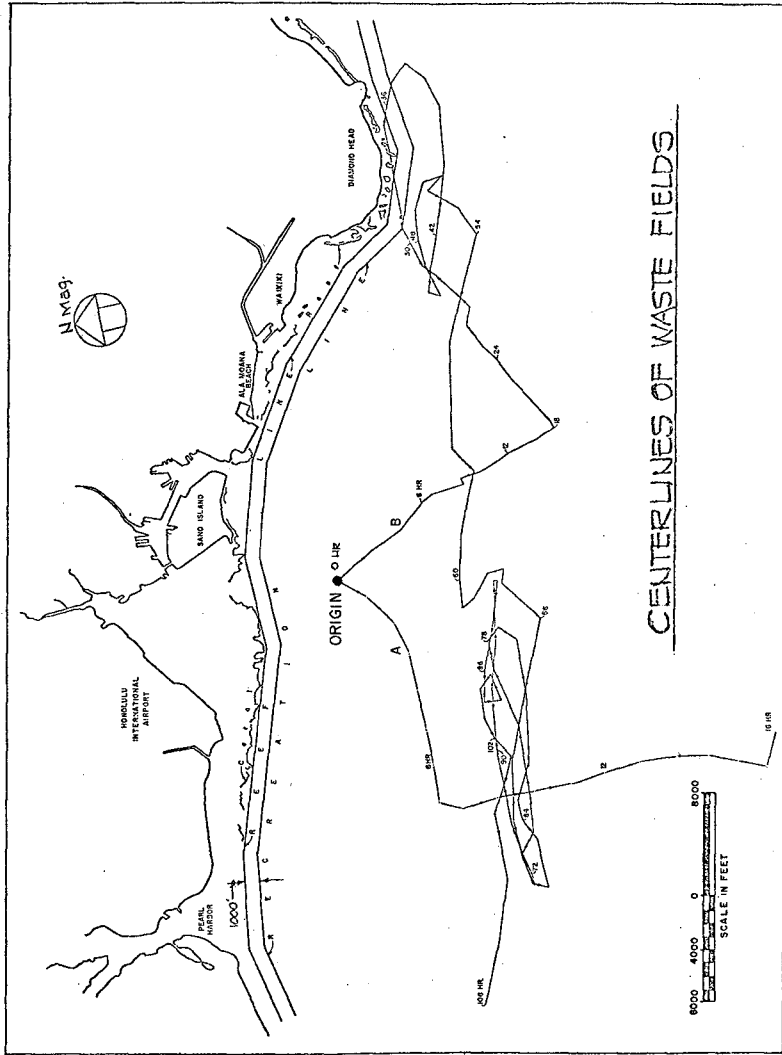


Fig. 5. Definition Sketch and Example Streaklines for Evaluation of Ocean Transport (Sand Island Outfall).

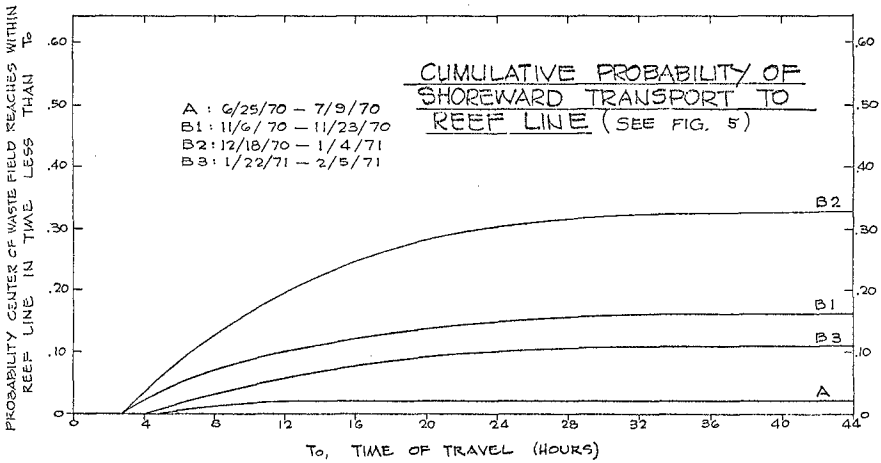
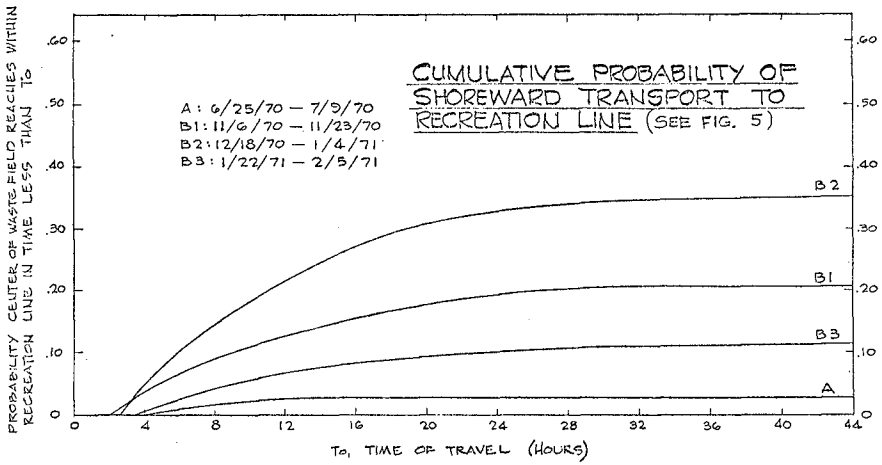


Fig. 6.

The hydraulic analysis of a multiport diffuser is basically a problem in manifold flow. The procedure for the hydraulic calculations has been documented by Rawn, Bowerman and Brooks (1951) and is used in the design. It should be noted that if the diffuser is not placed along a constant elevation, then the phenomenon of density head makes it impossible for the discharge to be uniformly distributed along the diffuser for all flows. In the particular case of the Sand Island Outfall diffuser, the design is such that the discharge is essentially uniform for medium flow rates. At high flow rates, representing the more critical case from the point of view of submergence and dilution, the deeper ports are the ones discharging more.

Figure 7 shows the distribution of port discharge in the pipe along the diffuser for the Barbers Point Outfall for a friction coefficient (Manning n) of 0.015. This is shown as an example. A range of values of the friction coefficient were evaluated in the design process.

While the diffuser pipes in the Sand Island and Barbers Point Outfalls are reduced in steps to maintain a reasonable flow velocity along the pipe, some deposition may still accumulate in the diffuser particularly towards the end. Thus the ends of these diffusers are equipped with flat gates which can be opened to let the flow flush out the system (at most only once every few years, and perhaps never). When the diffuser is operated in this manner, a significant portion of the flow is discharged through the end of the diffuser. However, the bulk of the flow still occurs through the many ports along the diffuser. Figure 8 shows the calculated velocity in the diffuser pipe for the Barbers Point Outfall diffuser when operated in the flushing mode.

OTHER DESIGN CONSIDERATIONS

It is not possible in this brief technical paper to treat all the facets in the design of a major ocean outfall structure. The reader is referred to the two design reports (Ref. I and II) for further details.

In the design process, consideration was also given to: a) geophysical factors such as nature of the ocean bottom and subbottom, and earthquake forces; b) physical factors such as storm waves, currents, and tsunami forces on the structure; c) system hydraulics and pumping requirements; d) economic factors.

The Barbers Point Outfall system also includes a 9166-ft land outfall between the Honouliuli Treatment Plant (elev. 32 ft) and the shoreline. During all but the higher flow rates, the land outfall will not flow full. The vertical alignment chosen for the land outfall consists of a hydraulically steep portion near the plant followed by a mild portion. In this way, critical flow in the land outfall is avoided. Excess energy is dissipated by friction and a hydraulic jump near the upper end of the land outfall. The chosen alignment assures that 1) the hydraulic jump is never more than a few hundred feet downstream of the change in slope, and 2) a long reach of tranquil flow exists before the pipe flows full to avoid significant air entrainment.

CONSTRUCTION OF THE SAND ISLAND OUTFALL

Construction of the Sand Island Outfall began with excavation of the 15-foot deep and 13-foot wide trench at the end of the trestle, 2,500 feet offshore and in water 20 feet deep. The contractor (Morrison-Knudsen) laid pipe downhill to the end of the diffuser. When the trestle was finished, a double bell connection was made at the end of the trestle and pipe was then laid back to the junction box on shore.

Starting from shore, the material on Sand Island was easy to dig since it was old fill material. Along the trestle, hard coral rock was encountered which made it very difficult to drive the two rows of sheet piling extending 2,500 from shore. Beyond the trestle, the bottom slopes gradually downward to where the pipe from the trench exits onto the ocean floor. This trench soil was highly variable,

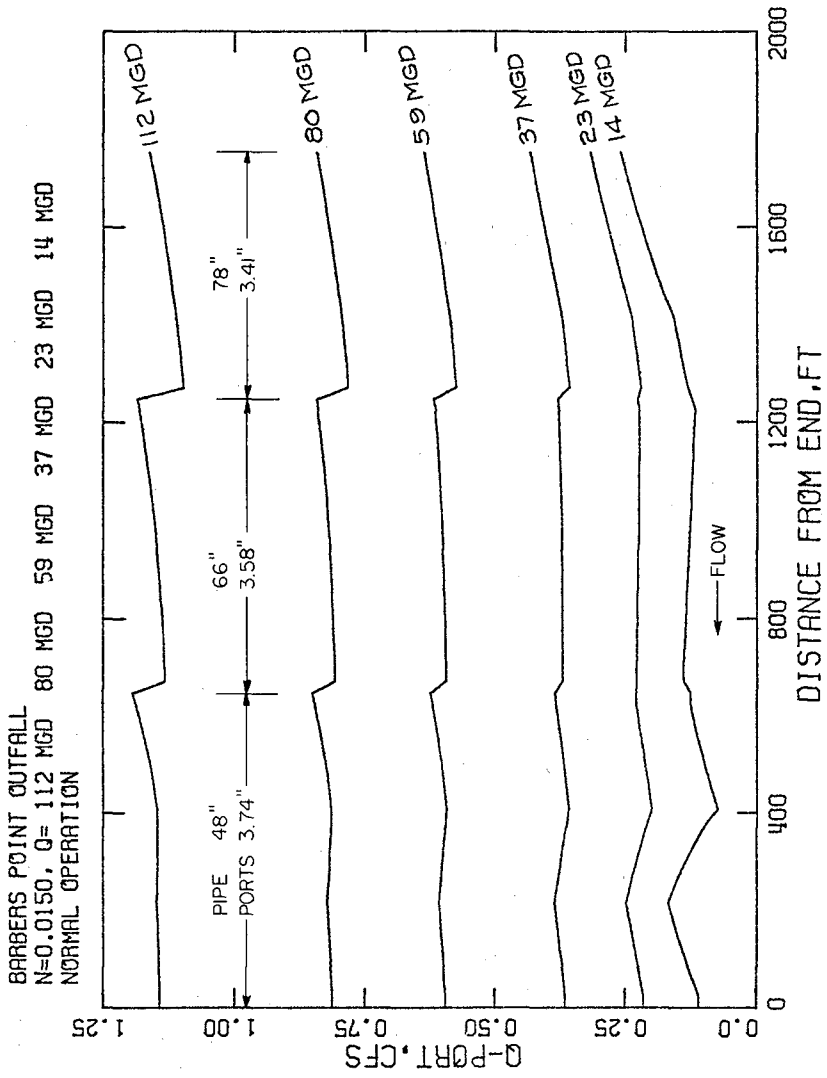


Fig. 7. Distribution of Port Discharge Along Diffuser of Barbers Point Outfall.

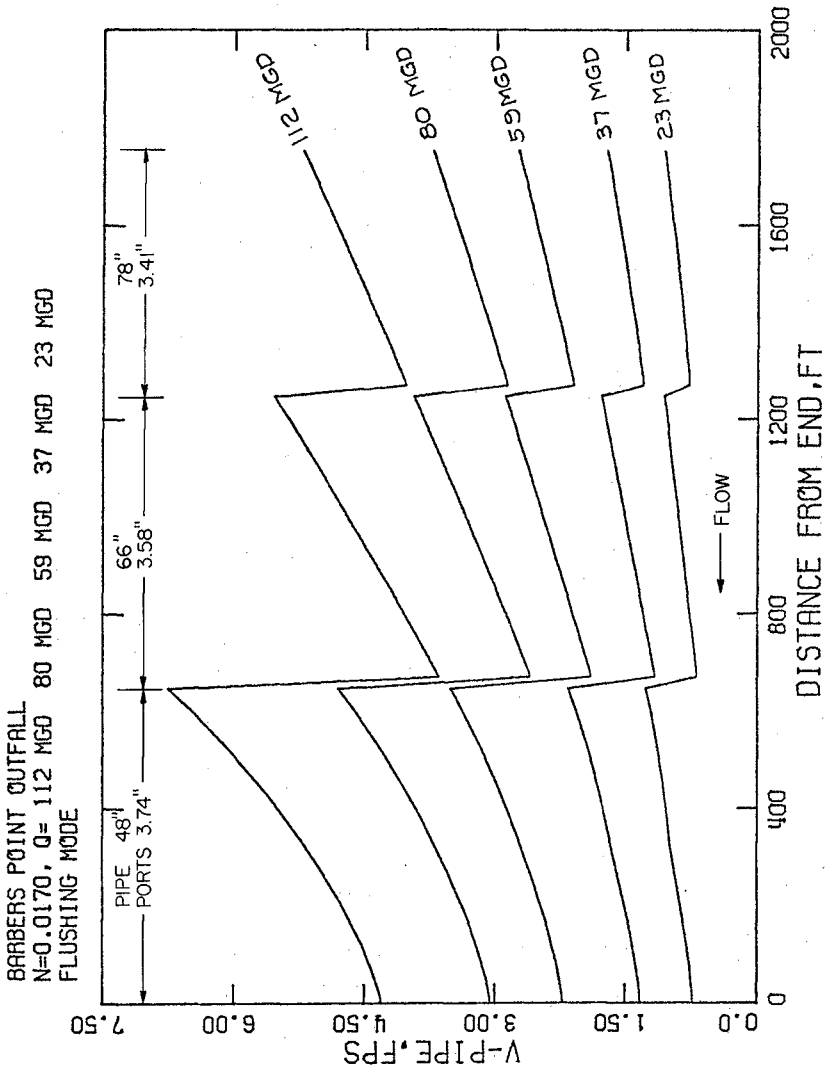


Fig. 8. Distribution of Velocity in Pipe Along Diffuser of Barbers Point Outfall.

changing often from sand to coral of varying hardness. The contractor used 500 lb. charges of dynamite (in 25-pound sacks) repeatedly along the trench, using many charges in the process. The trench excavation was especially difficult in the deeper sectors. Beyond the trench sections, the pipe was placed directly onto the ocean bottom and the work moved quickly to completion, with rock protection being used to stabilize the pipe all the way to the flap gate at the end.

The construction site is on the leeward side of the island so the contractor had a relatively calm working area. Several Kona storms interrupted the work and, on many occasions, the summer swells from the southern hemisphere stopped work because of the difficulty of loading pipe from the pipe barges onto the pipelaying barge. The contractor had allowed 3 months of downtime for weather and sea state and used up most of it during the 18-month period of construction.

The trestle was 2,500 feet long and made of steel H-pipes and beams. High speed carriers moved on the two rails to carry cranes and supplies of sheet piles and pipe. The heavy double bell section proved very difficult to connect to the pipe spigot already in place, because of the water swells in the shallow 20-foot depth. It is interesting to note that the contractor for the Barbers Point Outfall (almost identical to this one) plans to make his connection in much deeper water where the wave forces should be minimal at the joint location.

The pipelaying barge, called the "Davy Crockett", has been used on a number of outfall jobs. It is a converted World War II Liberty Ship, rigged with large anchor winches on each quarter (see Figure 9). The large crane in the center picks up the pipes and places them in a magazine until ready for laying. It then picks one of them up with a so-called "horse", places it on the ocean bottom and pushes it home into the bell of the previous pipe. Figure 9 also shows the complex pipe placing structure, called the "horse", which can pick up a pipe section and then stand on the ocean floor with its 4 legs near the previous pipe in place. Hydraulic controls, moving in 3 dimensions, carefully insert the spigot into the bell of the previous pipe. Once in place the pipe joint is tested with hydrostatic pressure. It is then rocked into position before the horse relaxes its grip on the pipe and is withdrawn. A diving bell is located near the joint. The contractor's diver is on one side, observing the joint make-up and talking by wire line to the horse operator up on the barge. The other side of the bell has a City Inspector, also observing and reporting on the adequacy of the underwater work. In some parts of the excavated trench, the trench width was so wide that the "horse's" legs were too narrow and it had to be extensively modified to straddle the trench.

Many barge loads of heavy armor stone were put in place to protect the pipe from the 46-foot design wave which was predicted as possible during the next 50 years. The initial design called for a thick concrete blanket over the pipe throughout the trench length because large rock was not available. After the job began the local quarry operator decided to make the investment in the equipment required to produce well-graded rock in five different classes ranging in nominal diameter from 1/2-foot to 2-1/2-foot. Divers controlled the placing of rocks around and on top of the pipe in the trench. Smaller size stones were placed near the pipe. This was later topped with armor stone varying up to 2-1/2-foot nominal diameter. The armor stones are of strong basalt with a specific gravity of 2.6. The well-graded mix was not easy to achieve. The City Inspectors sampled batches of these stones at random at the quarry. Each batch was separated. Then each stone of the batch was weighed and set aside into the five weight categories to validate the gradation. It proved to be a very tedious but worthwhile specification, ensuring well-graded armor protection for the pipe.

ACKNOWLEDGMENTS

The outfalls described herein were designed by the R. M. Towill Corporation under contracts for the City and County of Honolulu. The first two authors



Fig. 9. Pipelaying Barge Used in Construction of Sand Island Outfall.

(R. C. Y. Koh and N. H. Brooks) were engaged as special hydraulics consultants by the Towill Corporation for the projects. The authors acknowledge their contributions as well as others involved in the project.

REFERENCES

- I. "Final Design Report, Sand Island Outfall System, City and County of Honolulu," R. M. Towill Corp., Sept. 27, 1972.
- II. "Design Report Barbers Point Ocean Outfall System, Honolulu, Oahu, Hawaii," R. M. Towill Corp., July 1976.
- III. Rawn, A. M., Bowerman, F. R., and Brooks, N. H., "Diffusers for Disposal of Sewage in Sea Water," Trans. ASCE, Vol. 126, Part III, 1961.
- IV. Koh, R. C. Y. and Brooks, N. H., "Fluid Mechanics of Waste-Water Disposal in the Ocean," Ann. Rev. of Fluid Mech., Vol. 7, 1975.

CHAPTER 169

BUOYANCY-DRIVEN GRAVITATIONAL SPREADING

by

Robert C. Y. Koh¹

Introduction

It frequently occurs in environmental fluid mechanics that a mass of less heavy fluid spreads horizontally on top of a heavier one or a more homogeneous parcel of fluid spreads within a stratified one. Examples of such phenomena include spreading of diluted sewage effluent either at the surface or in a submerged layer, the spreading of heated effluent discharged from power plants, and the spreading of oil on the surface of the sea. The general problem is rather complex, being influenced not only by the buoyancy but also by momentum, ambient turbulence and flow, surface tension, waves, wind and other complicating factors. This paper attempts to examine gravitational buoyancy-driven flow in a homogeneous otherwise motionless ambient by casting it in the form of an initial value problem. Several assumptions are made and two empirical coefficients are introduced which must be determined from experiments. Experimental data are also presented, compared with the results of the analysis and the empirical coefficients determined. Previous investigations on similar problems include Sharp (1969, 1971), Koh and Fan (1968, 1969, 1971), and Koh and Chang (1973).

Formulation of the Problem

The fluid dynamic problem which will be considered in this paper is the time dependent spreading of one fluid on top of a heavier fluid. Both the two-dimensional and the axisymmetric cases will be examined. In each geometrical configuration, both the instantaneous and the continuous discharge cases will be investigated. The derivation will be detailed only for the two-dimensional case. Results for the axisymmetric case will be presented without detailed derivations.

Consider that at time $t=0$, a mass of buoyant fluid of volume A , linear dimensions characterized by a and b and density $\rho_0 - \Delta\rho$ is released from a state of rest on the surface of a deep reservoir containing fluid of density ρ_0 (see Fig. 1). It will be assumed that there is little mixing between the two fluids and that the shape of the buoyant fluid remains similar from one instant to another while it spreads. One expects that b will increase with time and a will decrease with time. For the moment, it will be convenient to assume that the motions in the heavier fluid is insignificant.

Figure 2 shows half of the buoyant fluid mass which will be considered as a free body. Assuming for the moment that the pressure distribution is hydrostatic, the buoyancy is seen to induce a net horizontal force of

$$\frac{1}{2} g' a^2 = \frac{1}{2} g \frac{(\rho_0 - \rho) a^2}{\rho}$$

In actuality, the pressure distribution is not hydrostatic. The departure of the pressure distribution from being hydrostatic will be accounted for by a horizontal force term which resembles that for hydrodynamic form drag and will be written

$$- \frac{C_D}{2} \rho a \left(\frac{db}{dt} \right)^2$$

the negative sign to indicate that the force is in opposition to the motion. There is another horizontal force tending to retard the spreading fluid, namely,

¹Research Associate in Environmental Engineering Science, California Institute of Technology.

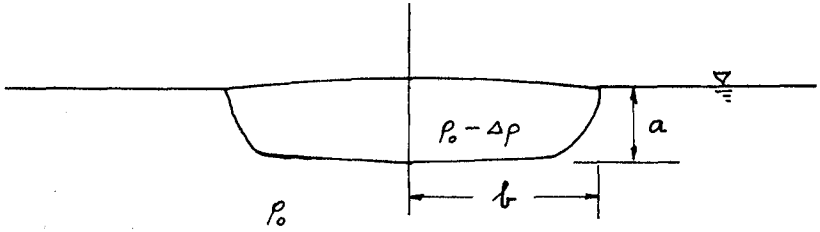


Figure 1. Definition Sketch.

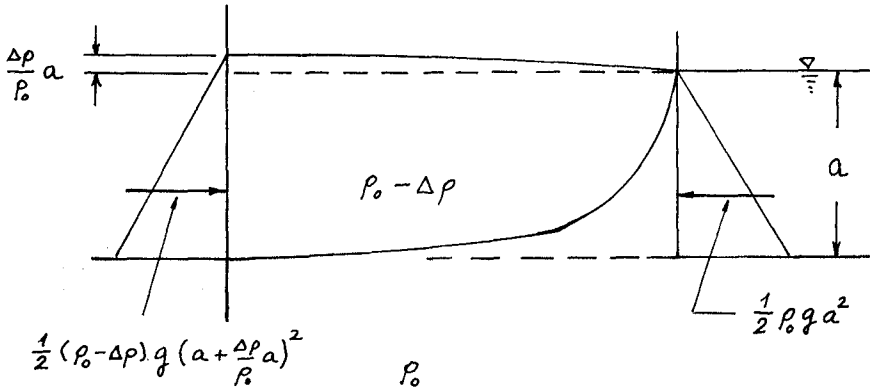


Figure 2. Pressure Forces on Half a Spreading Element.

that on the interface between the two fluids similar to a skin friction. It will be assumed that this force is

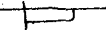
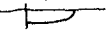
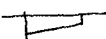
$$- \nu C_F \frac{b}{a} \frac{db}{dt}$$

The net imbalance of these forces must be equal to the net rate of change of momentum of the free body. Thus the equation of motion is

$$\frac{d}{dt} [(C_{ab}) \frac{d}{dt} (C_g b)] = \frac{1}{2} g' a^2 - C_D \frac{g}{2} \left(\frac{db}{dt}\right)^2 - C_F \nu \frac{b}{a} \frac{db}{dt} \tag{1}$$

where C_{ab} is the cross-sectional area of the free body and $C_g b$ is the distance from the origin to the center of mass of the cross-section. These quantities C_a, C_g are coefficients which depend only on the geometrical shape of the cross-section. By the assumption of similarity in shape, they will be constants. Table 1 gives values for C_g and C_a for several shapes.

Table 1

Shape	Geometry	C_g	C_a
rectangle		1/2	1
ellipse		4/3π	π/4
truncated trapezoid		4/9	3/4

For the case of no mixing between the two fluids, the equation for conservation of mass is simply

$$C_a ab = A = \text{constant} \tag{2}$$

for the case of instantaneous release. For a continuous discharge, it is

$$C_a ab = qt \tag{3}$$

where q is the discharge rate which accounts for half of the spreading layer. It should be noted that mixing can be allowed in this formulation by properly modifying the equations. Also, an apparent mass coefficient could have been introduced on the left-hand side of the equation. Neither will be done herein for simplicity. The derivation including these effects can be found in Koh and Chang (1973).

For definiteness, the shape of the spreading layer will be taken to be elliptical so that the coefficients C_a , and C_g are $\pi/4$ and $4/3\pi$ respectively. Equation 1 then becomes, after using either (2) or (3),

$$\frac{d^2 b}{dt^2} = \frac{6}{\pi} \frac{g'A}{b^2} - \frac{3}{2} \frac{C_D}{b} \left(\frac{db}{dt}\right)^2 - \frac{3\pi^2}{16} \frac{C_F \nu}{A^2} b^2 \frac{db}{dt} \tag{4}$$

and

$$\frac{d}{dt} \left(t \frac{db}{dt} \right) = \frac{6}{\pi} g' q \frac{t^2}{b^2} - \frac{3}{2} C_D \frac{t}{b} \left(\frac{db}{dt}\right)^2 - \frac{3\pi^2}{16} \frac{C_F \nu}{q^2} \frac{b^2}{t} \frac{db}{dt} \tag{5}$$

for the instantaneous release and continuous discharge respectively.

In the axisymmetric case, defining the shape of the spreading fluid to be half an ellipsoid of revolution, the equations analogous to (1), (2) and (3) are readily deduced to be

$$\frac{d}{dt} \left\{ \frac{\pi ab^2}{16} \frac{db}{dt} \right\} = \frac{g'a^2 b}{3} - C_D \frac{ab}{4} \left(\frac{db}{dt}\right)^2 - C_F \nu \frac{b^2}{a} \frac{db}{dt} \tag{1a}$$

$$\frac{2\pi}{3} ab^2 = v \quad (2a)$$

$$\frac{2\pi}{3} ab^2 = Q_0 t \quad (3a)$$

From these equations, one can derive the equations analogous to (4) and (5) to be

$$\frac{d^2b}{dt^2} = \frac{8g'v}{\pi^2} \frac{1}{b^3} - \frac{8C_D}{\pi} \frac{1}{b} \left(\frac{db}{dt}\right)^2 - \frac{64\pi}{9v^2} C_F v b^4 \frac{db}{dt} \quad (4a)$$

and

$$\frac{d}{dt} \left[t \frac{db}{dt} \right] = \frac{8g'Q}{\pi^2} \frac{t}{b^3} - \frac{8C_D}{\pi} \frac{t}{b} \left(\frac{db}{dt}\right)^2 - \frac{64\pi}{9Q^2} C_F v \frac{b^4}{t} \frac{db}{dt} \quad (5a)$$

Equations (4), (5), (4a) and (5a) will form the basis of the investigation in the remainder of this paper.

Normalization

The equations (4), (5), (4a), and (5a) will be normalized by choosing characteristic length b_0 and characteristic time t_0 so as to make the resulting dimensionless equations as simple as possible. This leads to the choices for b_0 and t_0 as tabulated in Table 2. The dimensionless equations which result become

Table 2

	Two-dim. instantaneous	Two-dim. continuous	Axisymmetric instantaneous	Axisymmetric continuous
t_0	$\left(\frac{16A^2}{3\pi^2 v}\right)^{3/7} \left(\frac{\pi}{6g'A}\right)^{2/7}$	$\left(\frac{16q^2}{3\pi^2 v}\right) \left(\frac{\pi}{6g'q}\right)^{2/3}$	$\frac{512vq'}{9\pi v}$	$\left(\frac{\pi^2}{8g'Q}\right)^{1/2} \left(\frac{9Q^2}{64\pi v}\right)^{1/2}$
b_0	$\left(\frac{16A^2}{3\pi^2 v}\right)^{2/7} \left(\frac{6g'A}{\pi}\right)^{1/7}$	$\left(\frac{16g^2}{3\pi^2 v}\right) \left(\frac{\pi}{6g'q}\right)^{1/3}$	$\left(\frac{\pi^2}{8g'v}\right)^{1/4}$	$\left(\frac{\pi^2}{8g'Q}\right)^{1/8} \left(\frac{9Q^2}{64\pi v}\right)^{3/8}$

$$\frac{d^2\zeta}{dt^2} = \frac{1}{\zeta^2} - \frac{3}{2} C_D \frac{1}{\zeta} \left(\frac{d\zeta}{dt}\right)^2 - C_F \zeta^2 \frac{d\zeta}{dt} \quad (6)$$

$$\frac{d}{dt} \left(t \frac{d\zeta}{dt} \right) = \frac{t^2}{\zeta^2} - \frac{3}{2} C_D \frac{t}{\zeta} \left(\frac{d\zeta}{dt}\right)^2 - C_F \frac{\zeta^2}{t} \frac{d\zeta}{dt} \quad (7)$$

$$\frac{d^2\zeta}{dt^2} = \frac{1}{\zeta^3} - \frac{8C_D}{\pi} \frac{1}{\zeta} \left(\frac{d\zeta}{dt}\right)^2 - C_F \zeta^4 \frac{d\zeta}{dt} \quad (6a)$$

$$\frac{d}{dt} \left(t \frac{d\zeta}{dt} \right) = \frac{t^2}{\zeta^3} - \frac{8C_D}{\pi} \frac{t}{\zeta} \left(\frac{d\zeta}{dt}\right)^2 - C_F \frac{\zeta^4}{t} \frac{d\zeta}{dt} \quad (7a)$$

where $\zeta = b/b_0$, $t = t/t_0$, corresponding to (4), (5), (4a), and (5a) respectively. Once the solution $\zeta(t)$ is obtained, the thickness a (or dimensionless $\eta = a/a_0$,

with appropriately chosen a_0) can be obtained from the continuity equation (2), (3), (2a), and (3a).

Each of the equations (6), (7), (6a), and (7a) will give solutions in the form $\zeta(t; C_F, C_D, \zeta_0, \zeta_0')$ where the four quantities $C_F, C_D, \zeta_0, \zeta_0'$ are parameters needed to specify the solution. Here ζ_0 and ζ_0' are the values of ζ and $d\zeta/dt$ at $t=0$. It is possible to have included C_F in the normalizing factors b_0 and t_0 . This is not done to allow the effect of C_F to show up more clearly and also allow comparison with experiments to be more meaningful.

Approximate Solution for Small Time

From physical reasoning, it can be expected that for small time, the term involving C_F would be unimportant since ζ would be small. Moreover, for the instantaneous release cases (eqs. 6 and 6a), the term involving C_D would also be insignificant for small t since $d\zeta/dt$ would be small. Thus, for small t , the equations 6 and 6a can be written

$$\frac{d^2\zeta}{dt^2} = \frac{1}{\zeta^2}$$

and

$$\frac{d^2\zeta}{dt^2} = \frac{1}{\zeta^3}$$

subject to the initial conditions $\zeta(0) = \zeta_0, \zeta'(0) = 0$. The solutions can be obtained by quadratures. For example, for the continuous release case,

$$\zeta = \zeta_0 \sqrt{1 + t^2/\zeta_0^4}$$

This represents the transient start-up period. The solution for the instantaneous case is more complex and will not be displayed.

Approximate Solution for Intermediate Time

For times not too large, physical considerations again lead to the approximation of ignoring the term involving C_F in the equations (6), (7), (6a) and (7a). It is now fruitful to examine solutions of the form $\zeta = Bt^\alpha$. Substituting this into each of the equations (ignoring the C_F terms) results in the following values for α , and the resulting time dependence for ζ (width) and η (thickness).

	2-dim. inst.	2-dim. cont.	axisym. inst.	axisym. cont.
α	2/3	1	1/2	3/4
$\zeta \propto t$	$t^{2/3}$	t	$t^{1/2}$	$t^{3/4}$
$\eta \propto t$	$t^{-2/3}$	1	t^{-1}	$t^{-1/2}$

These represent the circumstance when inertia balances the buoyancy driving force.

Approximate Solution for Large Time

For large time, ζ becomes very large, thus making the term involving C_F dominant. Physically this means that the interfacial shear is the dominant resistive force. If one now balances the driving force by this term (i.e., ignore the left-hand side as well as the C_D term in equations (6), (7), (6a), and (7a)), and seek solutions of the form $\zeta = B_1 t^{\alpha_1}$, one finds

		2-dim. inst.	2-dim. cont.	axisym. inst.	axisym. cont.
$\alpha_1 =$		1/5	4/5	1/8	1/2
$\zeta \propto$	$t^{1/5}$	$t^{1/5}$	$t^{4/5}$	$t^{1/8}$	$t^{1/2}$
$\eta \propto$	$t^{-1/5}$	$t^{-1/5}$	$t^{1/5}$	$t^{-1/4}$	1

These represent the circumstance when interfacial shear balances the buoyancy driving force. It is worth noting that the behavior of η (thickness) as function of t (time) is fundamentally different between the two-dimensional and axisymmetric cases for continuous discharge. Whereas $\eta \sim t^{1/5}$ in the two-dimensional case, η tends to a constant value in the axisymmetric case. Physically, this means that the thickness will continue to grow ad infinitum in the former while it would not in the latter case.

Overall Solutions

From the above discussion it is seen that after a brief start-up period, the solution for the extent of the spreading layer can be represented in each case by a power law in time where the power changes from one value to a second value as time progresses. It should be noted that the above results could have been obtained from simple dimensional arguments. The purpose for extracting them herein is to provide more insight into the relationships among the various phenomena represented by the various terms in the equations.

In general, the equations (6), (7), (6a), (7a) including all the terms can only be solved numerically. This has been done using a fourth order Range Kutta algorithm. The results for example cases for equation (6) is shown in Figure 3.

Comparison with Experiments

The results of the analysis will now be compared with laboratory experiments. The writer wishes to acknowledge Messrs. C. Almquist, P. J. W. Roberts and J. C. Chen who actually performed these experiments. While these individuals have performed a larger number of experiments, only example runs are presented herein for comparison purposes. The experimental data used for comparison in the following are shown tabulated in Table 3.

Two-Dimensional Instantaneous Release

These experiments were performed by C. Almquist (1973) as a term project for a course in the Environmental Engineering option at California Institute of Technology. The laboratory tank used was 5 inches wide by 18 inches deep by 16 feet long. It is filled with salt water (sp. gr. ≈ 1.020). A trough at the surface at one end of the tank containing less dense dyed water in hydrostatic equilibrium with the water in the tank is released at $t = 0$ by removal of a partition (see Figure 4a). The subsequent motion of the spreading layer is then timed. The density difference and the amount of the released fluid was varied over a factor of 4 and 9 respectively resulting in a total of twenty experiments. Figure 5 shows the data for four example runs together with the predictions from equation (4). In obtaining this comparison, the initial conditions were chosen to be the values of b and db/dt (dimensional values) at the beginning of the data. The values of C_D and C_F are chosen to obtain a good fit between the prediction and the experiment. However, the same value for C_D and the same value of C_F were used in all four comparisons. This comparison indicates that the predictions are quite good. Moreover, the values for C_D and C_F (0.85 and 0.4 respectively) are what might be expected being of order unity.

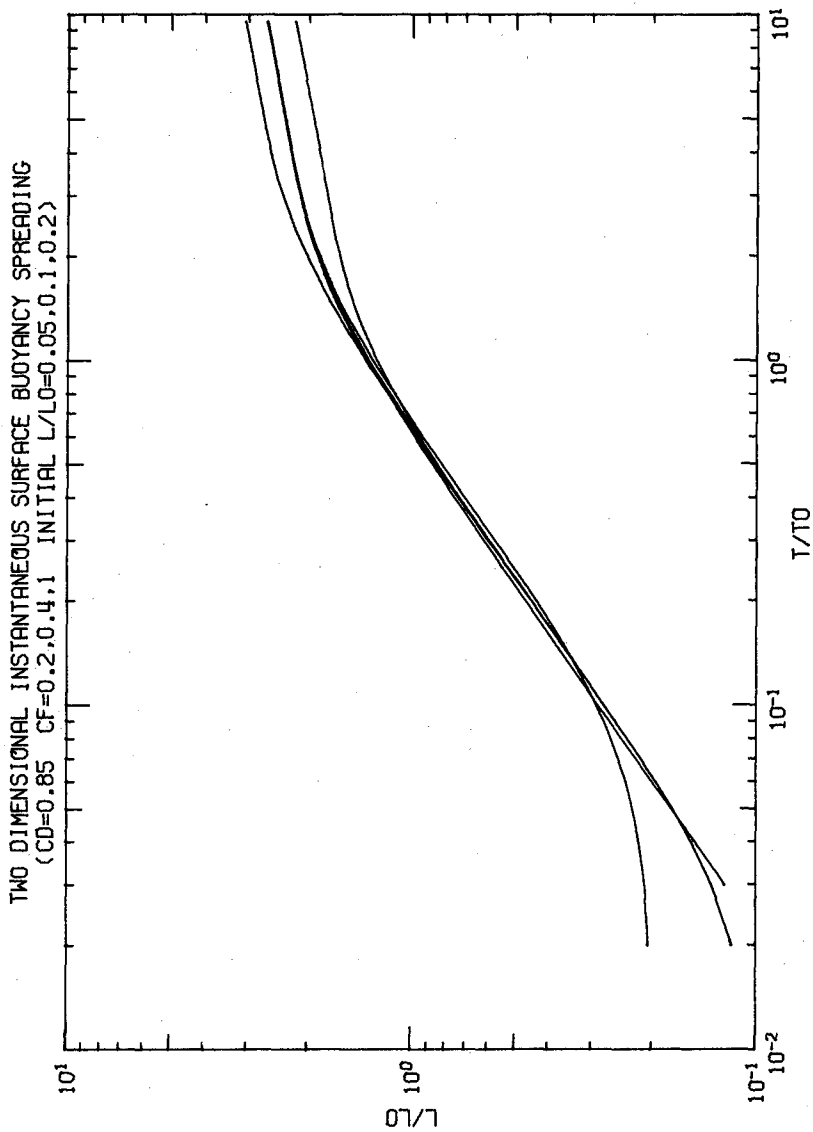
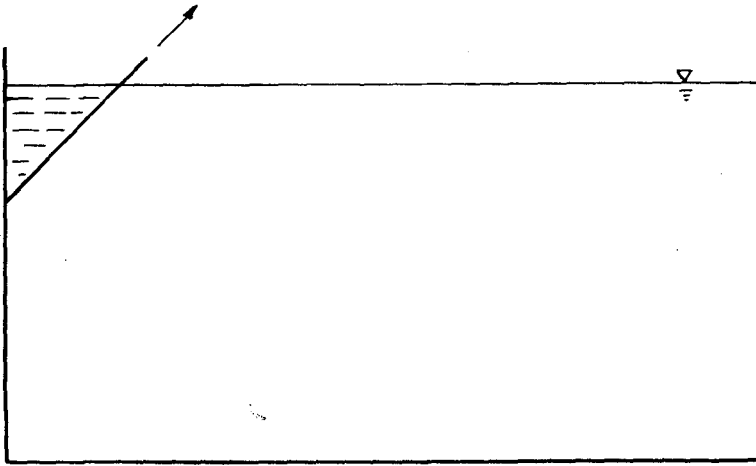
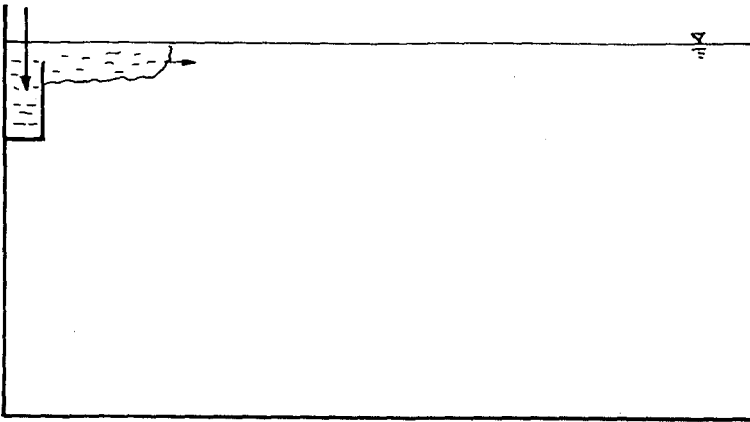


Figure 3.



(a) instantaneous release



(b) continuous release

Figure 4. Schematic of Laboratory Set-Up for Two-Dimensional Surface Release Experiments.

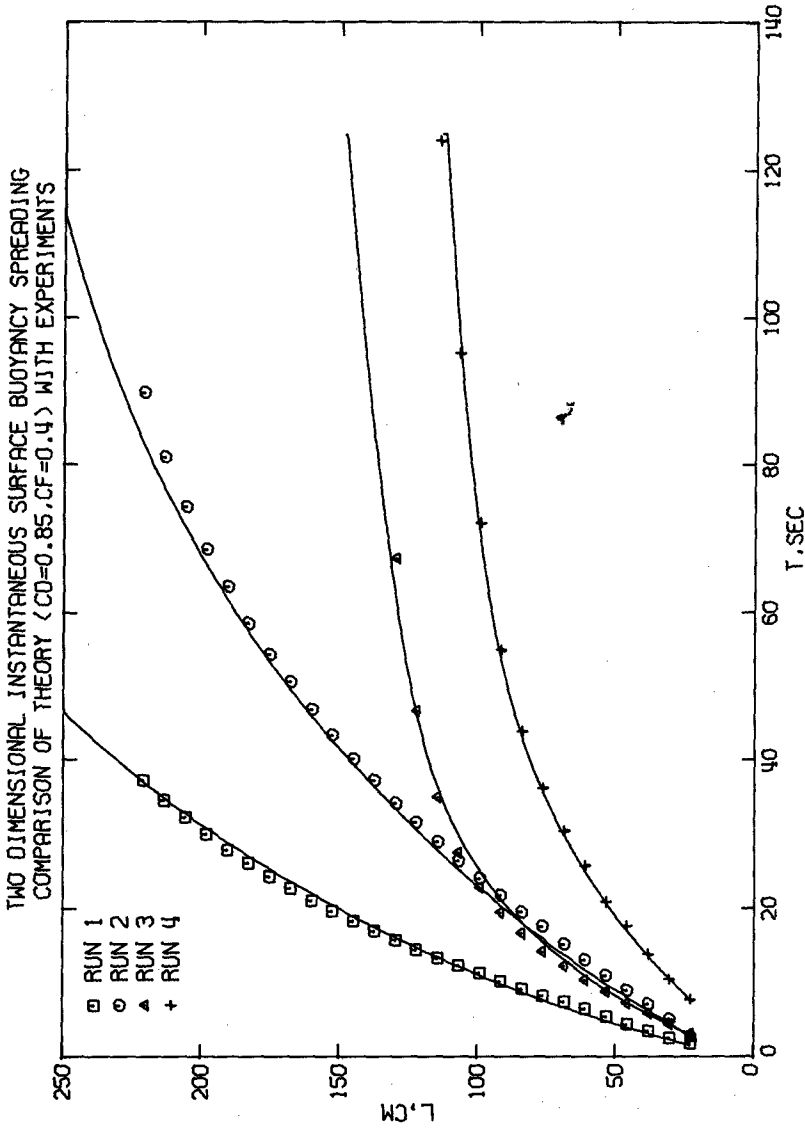


Figure 5.

Table 3

Basic Experimental Parameters

(a) Two-Dimensional Instantaneous Release			(b) Two-Dimensional Continuous Release		
Run No.	A (cm ²)	$\Delta\rho/\rho$	Run No.	q (cm ² /sec)	$\Delta\rho/\rho$
1	116.	0.016	1	2.09	0.0036
2	116.	0.004	2	4.33	0.0038
3	29.	0.016	3	4.06	0.0066
4	29.	0.004	4	3.92	0.0145

(c) Two-Dimensional Submerged Continuous Release			
Run No.	q cm ² /sec	$\Delta\rho/\rho$	Depth cm
1	0.108	0.0240	16.3
2	0.189	0.0252	16.1
3	0.344	0.0244	8.1

(d) Axisymmetric Submerged Continuous Release			
Run No.	Q cc/sec	$\Delta\rho/\rho$	Depth cm
1	41.6	0.051	11.7
2	37.5	0.013	23.4
3	13.5	0.066	5.9
4	13.5	0.022	5.9
5	13.5	0.017	5.9

The same data are shown plotted in Figure 6 in non-dimensional form. The curve shown is for $C_D = 0.85$ and $C_F = 0.4$ obtained as the solution to equation (6) (in dimensionless variables). The initial start-up period is ignored in this solution hence the lack of fit for small t . It should also be pointed out that the initial conditions used in the predictive solution, as a consequence, is independent of the data. From this comparison, it is seen that the analyses does, in fact, conform to the data quite well.

Two-Dimensional Continuous Surface Release

These experiments were also performed by C. Almquist under the same circumstances in the same tank. The only difference in the procedure is in the mode of introduction of the buoyant fluid. In this case, the buoyant fluid is allowed to be discharged continuously at the surface at one end of the tank from a structure as shown in Figure 4b. The supply of the buoyant fluid is via a constant head tank. Comparison of the results of four of the experiments are shown in Figure 7 where the curve is obtained by solving equation (7) using $C_D = 0.5$, and $C_F = 5$.

Two-Dimensional Continuous Submerged Release

These experiments were performed by P. J. W. Roberts in a much larger tank than the previous experiments. The buoyant fluid is now introduced at the bottom of the tank, allowed to rise to the surface and then spread horizontally on the surface. A schematic of the experimental setup is shown in Figure 8. It should be pointed out that while equation (7) is still applicable to this case, interpretation of the coefficients C_D and C_F must be viewed somewhat differently. Whereas in the surface release case, the water depth in the tank is much larger than the thickness of the spreading layer, this is no longer true in the submerged case. More importantly, in this case, mixing occurs during the rise of the buoyant water from the discharge point at the bottom to the surface. An entrainment undercurrent is set up whose direction is opposite to that of the spreading layer. One must, therefore, expect both C_D and C_F to be larger than in the previous experiments. In the case when the entrainment is significant, one expects C_D to be larger by a factor of approximately 3 for the case when the spreading layer is approximately 1/3 of the total depth z as was observed to be the case. Comparison of these experiments with the solution to eq. (7) with $C_D = 2.5$ and $C_F = 14.5$ is shown in Figure 9 where again the data appears to confirm the analysis.

Axisymmetric Continuous Submerged Release

These experiments were performed by J. C. Chen in the same laboratory basin as the two-dimensional submerged release experiments. A 6 mm diameter round orifice is placed at the bottom of the basin. Injection is started and overhead photographs taken at discrete times to record the spread of the dyed buoyant fluid. The normalized variables ζ and t for five of these experiments are shown in Figure 10 together with the analytical results ($C_D = 0.2$, $C_F = 0.05$). The comparison is seen to be reasonable.

It should be noted here that in the submerged release cases, the buoyant discharge undergoes a certain amount of dilution before reaching the surface and spreading. Thus the value of the discharge rate is actually larger than the discharge from the orifice by a factor equal to the average dilution. The buoyancy flux, of course, is still unchanged. In plotting the experimental points in Figures 9 and 10, the discharge rates have been calculated on the basis of simple plume theory with S_a given by

$$S_a = 0.38 \frac{y(g_o' q_o)^{1/3}}{q_o}$$

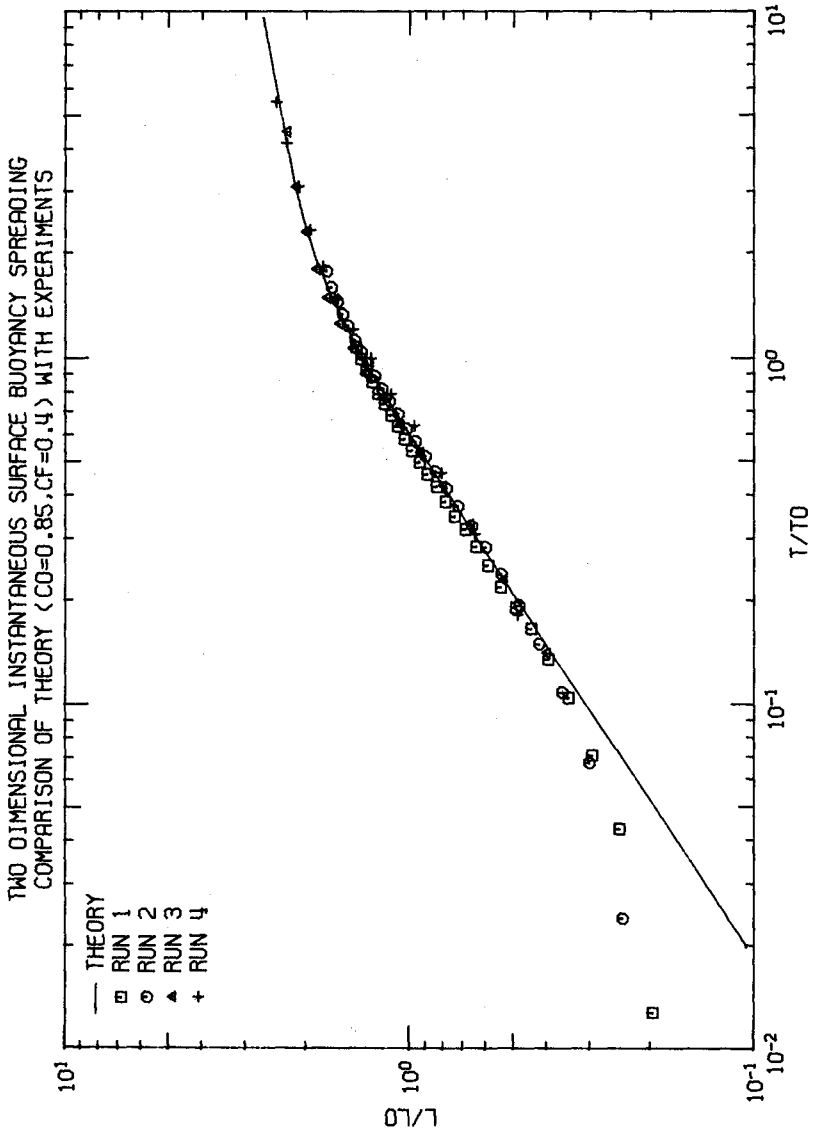


Figure 6.

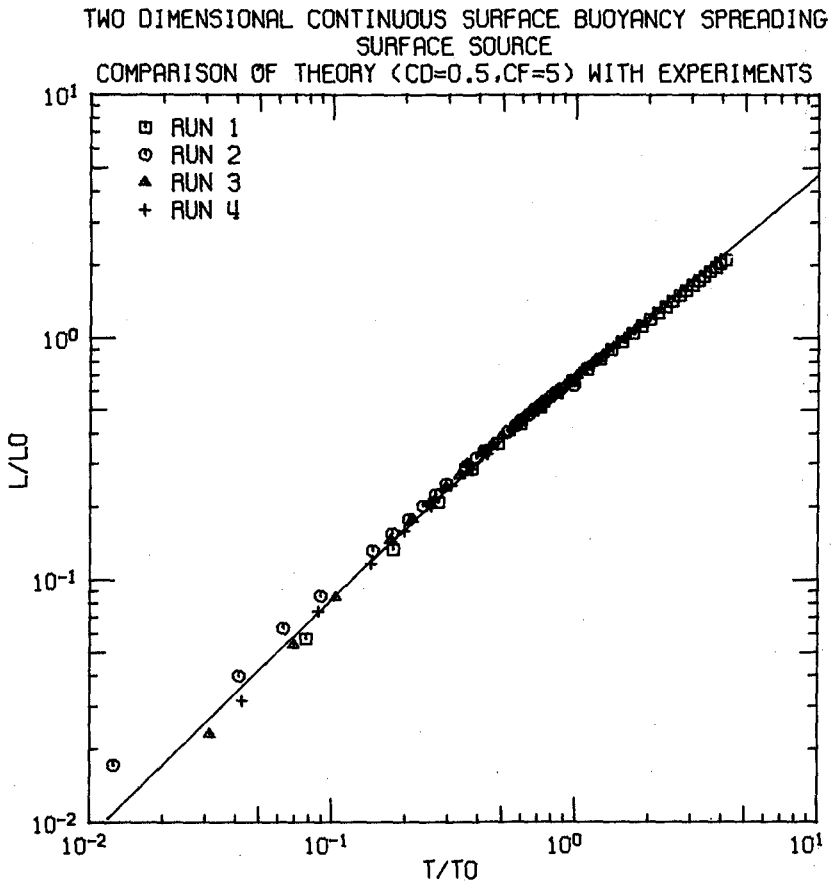


Figure 7.

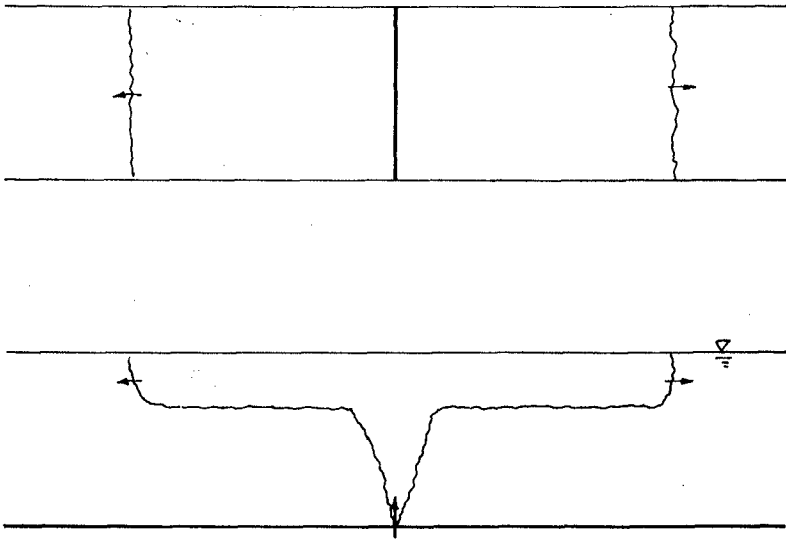


Figure 8. Schematic of Laboratory Set-Up for Two-Dimensional Continuous Submerged Release Experiments.

TWO DIMENSIONAL CONTINUOUS SURFACE BUOYANCY SPREADING
SUBMERGED SOURCE
COMPARISON OF THEORY ($CD=2.5, CF=14.5$) WITH EXPERIMENTS

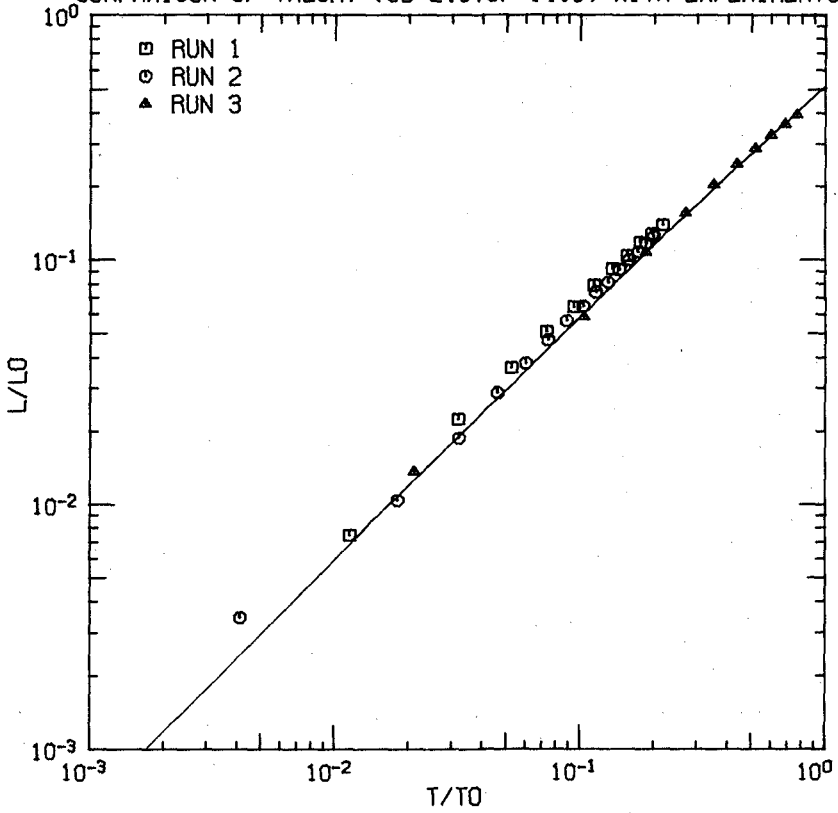


Figure 9.

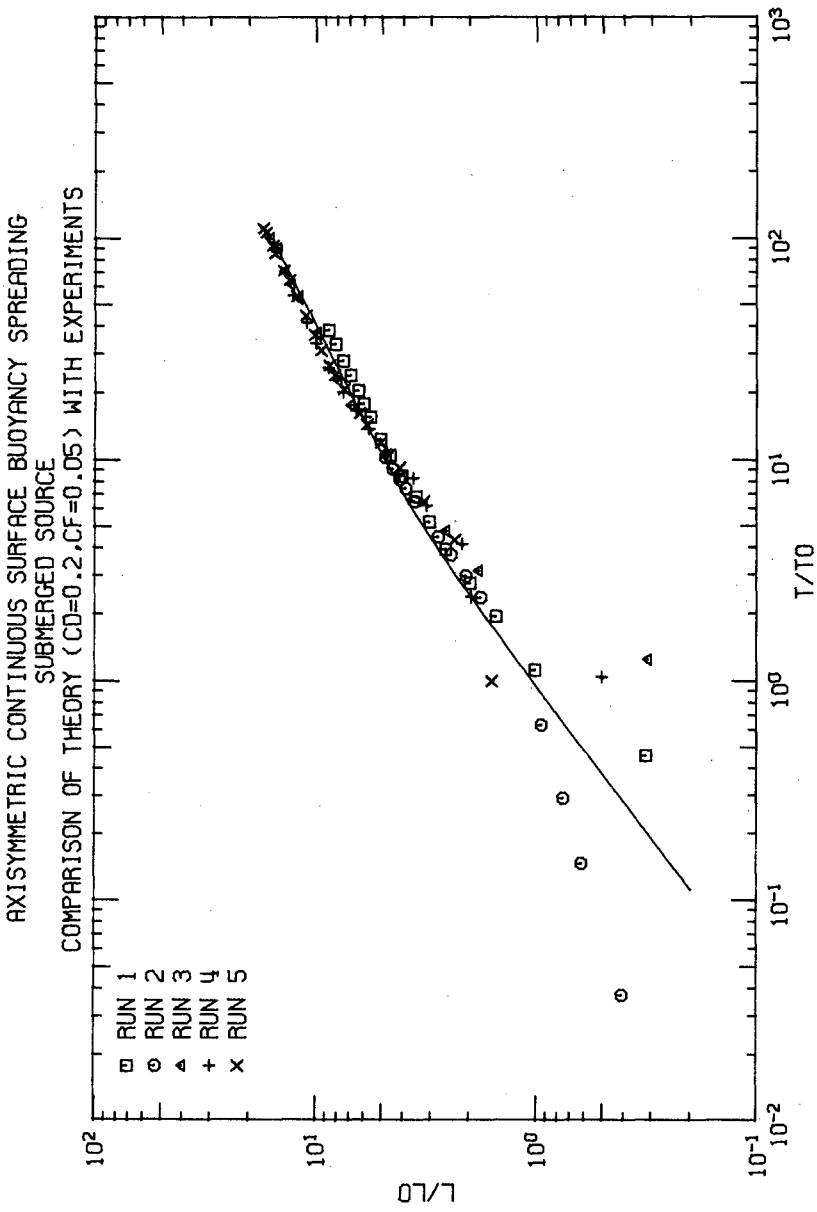


Figure 10.

$$S_a = 0.16 \frac{y^{5/3} (g'_0 q_0)^{1/3}}{q_0}$$

(S_a = average dilution).

Practical Applications

It appears at first glance that the results obtained in the previous sections are of little practical value since in practice, neither two-dimensionality nor axial-symmetry obtains. It will be shown in this section how the results can be utilized to deduce some properties of the flow field which are of great practical value.

(a) Thickness of surface sewage field.

Major coastal discharges of sewage effluent into the ocean frequently employ long diffusion structures (on the order of several thousand feet long) at a depth of approximately 200 ft. Many small ports along the diffuser discharges the effluent in such a way as to approximate a long line source of effluent. It has been found experimentally that, in the event where the ocean is uniform in density and motionless, simple line plume theory gives good predictions of dilution factors (see e.g., Koh and Brooks, 1975). The centerline dilution, S_c according to that theory is simply

$$S_c = 0.38 \frac{(g'_0 q_0)^{1/3} y}{q_0} \quad (8)$$

The average dilution S_a is $\sqrt{2} S_c$. Here $(g'_0 q_0)$, q_0 , and y are the buoyancy flux and discharge per unit length, and vertical distance from the diffuser ($g'_0 = g(\rho_0 - \rho)/\rho$; g = gravitational acceleration, ρ = density of effluent, ρ_0 = density of sea water). Referring to Figure 11, there is seen to be an uncertainty in application of equation (8) in that one does not know what value of y to use. Whereas buoyant plume theory is developed for an infinite fluid, the presence of the ocean surface deflects the sewage field to spread on the surface. The value of y to be substituted into equation (8) to obtain the surface dilution should logically be $(d-a)$ where d is the depth and a the thickness of the sewage field (see Figure 11). The thickness of the surface field a will now be estimated from the results of analyses in this paper. It should first be noted that the thickness $a(t)$ defined in the two-dimensional continuous release case analyzed previously is the quantity of interest. As a function of time, it starts at zero, grows to a constant value, remains constant until interfacial shear forces become important, whereupon it grows as $t^{1/5}$ without limit. For practical problems, the $t^{1/5}$ growth is of little significance since by the time this would occur, the two-dimensionality assumption breaks down. (It may be noted that in the three-dimensional continuous release case, the thickness tends to a constant.) Given that shear is unimportant, one may write equation (5) as

$$\frac{d}{dt} \left(t \frac{db}{dt} \right) = \frac{6}{\pi} (g'q) \frac{t^2}{b^2} - \frac{3}{2} C_D \frac{t}{b} \left(\frac{db}{dt} \right)^2 \quad (9)$$

with solution

$$b = \gamma t \quad (10)$$

where

$$\gamma = \left[\frac{6}{\pi} \frac{g'q}{1 + \frac{3}{2} C_D} \right]^{1/3}$$

but

$$qt = \frac{\pi}{4} ab \quad (11)$$

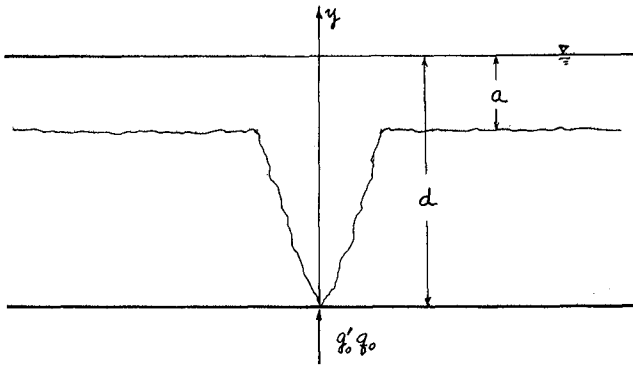


Figure 11. Definition Sketch.

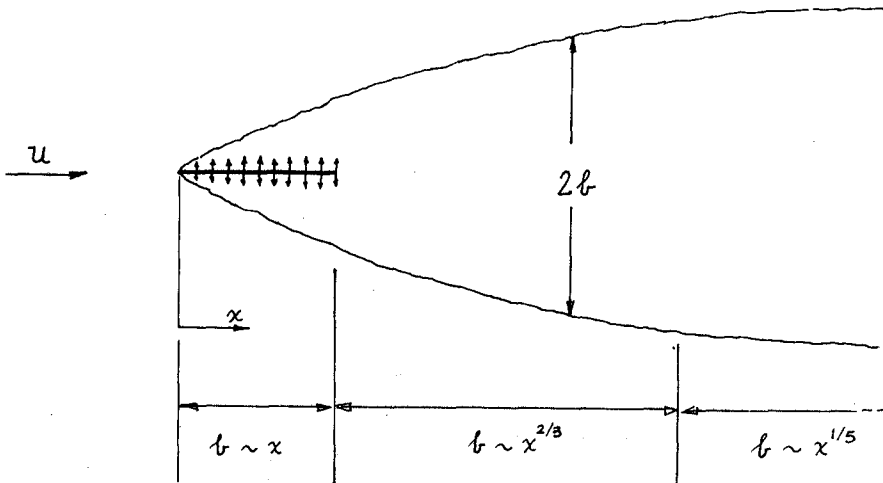


Figure 12. Schematic Plan View of Wastewater Plume.

so that

$$a = \frac{4q}{\pi \gamma} = \frac{4q}{\pi} \left[\frac{1 + \frac{3}{2} C_D}{\frac{6}{\pi} g'q} \right]^{1/3} \quad (12)$$

It may be seen that, in the present case, $g'q = g'_0 q_0 / 2$, and $q = S_a q_0 / 2$ where the factor 2 is to account for the fact that only half the discharge goes to either side. Noting that

$$S_a = \sqrt{2} \cdot 0.38 \frac{(g'_0 q_0)^{1/3} (d-a)}{q_0} \quad (13)$$

and substituting into equation (12) yields

$$a = \frac{4}{\pi} \frac{\sqrt{2} \cdot 0.38 (g'_0 q_0)^{1/3} (d-a)}{2} \frac{1 + \frac{3}{2} C_D}{\frac{6}{\pi} g'_0 q_0 / 2}$$

from which

$$\frac{a}{d} = \frac{\delta}{1 + \delta}$$

$$\text{where} \quad \delta = \frac{2\sqrt{2} \cdot 0.38}{\pi} \left[\frac{1 + \frac{3}{2} C_D}{\frac{3}{\pi}} \right]^{1/3} = \frac{2\sqrt{2} \cdot 0.38}{\pi} \left[\pi \left(\frac{1}{3} + \frac{C_D}{2} \right) \right]^{1/3} \quad (14)$$

From experiments (see Figure 9), $C_D = 2.5$, hence $\delta = 0.40$ and

$$\frac{a}{d} = 0.29$$

In other words, the thickness of the sewage field should be 29% of the total depth. The depth of water available for mixing is $d-a$ and is therefore 71% of the total depth. It is interesting to note that $0.71 \times \sqrt{2} \approx 1$ so that one may use the full depth d for y in equation (8) provided one interprets the result as average instead of centerline dilution.

(b) Shape of surface plume in a parallel current.

An overhead view of the spreading surface field from a long submerged diffuser might be as shown in figure 12 for the case where an ocean current of speed U flows parallel to the diffuser. Assuming that the fluid all travels at speed U , a Galilean transformation (moving with the current) indicates that $b(\frac{x}{U})$ should behave similar to $b(t)$ in the solution presented previously. For x less than L , the length of the diffuser, the continuous injection case applies while for x larger than L , the instantaneous injection case applies. For the case interfacial shear is unimportant in the region $x < L$, $b(x)$ should be proportional to x . For $x > L$, $b(x)$ should be proportional to $x^{2/3}$. For very large x , (interfacial shear becomes important), $b(x)$ should be proportional to $x^{1/5}$. Thus the horizontal extent of the surface field can be obtained by using this approximation in the case when a Galilean transformation is permitted. For low ocean current speed, the surface field would actually extend upstream and in that region, the approximation is no longer valid.

Summary and Conclusions

In this paper, the time dependent spreading of a buoyant fluid on the surface of a heavier fluid is investigated by casting the problem in the form of an initial value problem. By assuming that the shape of the spreading layer remains geometrical similar from one instant to the next, differential equations were derived for two-dimensional and axisymmetric configurations in both the instantaneous and continuous release cases. Laboratory experiments were compared with the analysis and the results were found to compare favorably. Similar analysis can also be performed for the submerged case of spreading in a density stratification.

The results of this analysis should prove of value in environmental fluid mechanics such as the spreading of wastewater or thermal effluent on the sea surface. A fundamental important finding from the analysis is that in the two-dimensional continuous release case, the thickness of the spreading layer would tend to infinity as time tends to infinity while in the axisymmetric case, the thickness tends to a constant. The extra dimension available for spreading in the three-dimensional case is apparently sufficient to prevent complete blocking of the flow (or inundation of the source). In an actual submerged discharge of wastewater from a long diffuser in an otherwise stagnant ambient, the thickness of the spreading layer could probably be represented by the value indicated by assuming $C_F = 0$ in the equation (5). This thickness is deduced to be 29% of the depth. The results of the analysis can also be applied to estimate the horizontal area covered by the surface field in the case of a parallel current.

Acknowledgment

The writer wishes to acknowledge the financial support of NSF (Grant ENG 75-02985) and EPA (Grant T900137-03-2). Thanks are also due Messrs. C. Almquist, P. J. W. Roberts, and J. C. Chen for permitting the use of some of their experimental data.

References

- Almquist, C., "The Two-Dimensional Surface Spreading of a Buoyant Fluid into an Infinite Stagnant Environment," Student Lab Report for Env 112, Caltech, 1973.
- Koh, R. C. Y. and Chang, Y. C., "Mathematical Model for Barged Ocean Disposal of Wastes," EPA-660/2-73-029, Dec. 1973.
- Koh, R. C. Y. and Fan, L. N., "Prediction of the Radioactive Debris Distribution Subsequent to a Deep Underwater Nuclear Explosion," Tetra Tech Report TC129, 1968.
- Koh, R. C. Y. and Fan, L. N., "Further Studies on the Prediction of the Radioactive Debris Distribution Subsequent to a Deep Underwater Nuclear Explosion," Tetra Tech Report TC-154, 1969.
- Koh, R. C. Y. and Fan, L. N., "Mathematical Models for the Prediction of Temperature Distributions Resulting from the Discharge of Heated Water into Large Bodies of Water," EPA 16130 DWO 10/70, 1970.
- Koh, R. C. Y. and Brooks, N. H., "Fluid Mechanics of Waste-Water Disposal in the Ocean," Ann. Rev. of Fluid Mech., Vol. 7, 1975.
- Sharp, J. J., "Spread of Buoyant Jets at the Free Surface," J. Hyd. Div., Proc. ASCE, May 1969.
- Sharp, J. J., "Unsteady Spread of Buoyant Surface Discharge," J. Hyd. Div., Proc. ASCE, Sept. 1971.

CHAPTER 170

NEGATIVELY BUOYANT SLOT JETS

by

D. M. Shahrabani¹ and J. D. Ditmars²

Abstract

The behavior of negatively buoyant slot jets discharged from near the bottom of stagnant and flowing receiving-water environments of uniform density was studied in laboratory experiments. In particular, the locations of the maximum height of rise and maximum horizontal displacement were determined as well as the centerline dilutions at those points. Experiments in stagnant environments were conducted for discharges at angles of 30°, 45°, 60°, and 90° from the horizontal and with discharge densimetric Froude numbers of 10, 20, 30, 40 and 50. For flowing environments, discharges at angles of 45° and 90° for the same range of densimetric Froude numbers were directed into uniform currents with discharge to ambient velocity ratios of 15 and 25. The reattachment eddy formed between the jet and bottom boundary was found to have significant effects on the slot jet trajectories and dilutions. Dilutions at the maximum height of rise and maximum horizontal displacement were less than those predicted for slot jets far removed from the influence of the bottom boundary. The strictly two-dimensional discharges studied provide lower bounds on the dilutions to be expected for the cases of slots of finite length or merged multiport diffuser discharges in which the reattachment eddy is not as well developed.

Introduction

Negatively buoyant discharges are those with densities greater than the density of the receiving-water environment into which they are injected. The residual effluents from coastal desalting plants are brines which are negatively buoyant relative to the source waters. The warm surface water used to provide the heat of vaporization in LNG plants is cooled and negatively buoyant upon return to the surface waters. Industrial effluents, particularly those containing acids or acid-salts, are sometimes negatively buoyant despite having temperatures greater than those of the receiving water.

Slot jets or two-dimensional jets are created by the discharge of an effluent into a receiving-water body from a single orifice of slot

¹Pandullo, Quirk Associates, Wayne, New Jersey, USA.

²Argonne National Laboratory, Argonne, Illinois, USA (on leave from the University of Delaware, Newark, Delaware, USA).

geometry or by the lateral merging of adjacent round jets from a multiport diffuser. Negatively buoyant slot jets sink due to the gravity force acting on them. Because sites for the continuous disposal of negatively buoyant effluents are usually located offshore, near-surface discharges are not often possible, and the discharge structure is located on or near the bottom. Consequently, the effluent is discharged upward into the receiving water at some angle from the horizontal. The initial jet momentum carries the effluent upward so that mixing occurs before the gravity force brings the diluted effluent back to the bottom as indicated in Figure 1. The characteristics of a negatively buoyant slot jet of particular interest are the geometric coordinates and dilutions at the maximum height of rise of the jet and at the point of bottom impingement. The former is important to assure that the jet remains completely submerged, and the latter is of concern in the assessment of the impact on benthic communities.

The results of laboratory experiments with turbulent negatively buoyant slot jets discharged into stagnant and flowing receiving waters of uniform density are reported. For these experiments the discharge is two-dimensional; that is, the slot extends completely across the receiving-water body. Also the jet remains fully submerged below the free surface. Attention, in these experiments, was focused on the jet characteristics at the maximum height of rise and the region of bottom impingement. The applicability of the results to slot discharges of finite length and to merged jets from multiport diffusers is discussed.

Review of Round Negatively Buoyant Jet Behavior

Although no published data on the behavior of negatively buoyant slot jets are known, work has been reported on the behavior of negatively buoyant round jets in both stagnant and flowing receiving water environments of uniform density.

Turner¹ performed experiments with negatively buoyant round jets discharged vertically upward into stagnant environments and determined an expression for the maximum height of rise of such jets. Zeitoun et al.² performed similar experiments for negatively buoyant round jets discharged at a variety of angles from the horizontal and for several discharge conditions. They found that the dimensionless maximum height of rise of the jet, Y_m/D , and the centerline dilution at that point, $S(Y_m)$, could be expressed as functions of the discharge densimetric Froude number, F_r , and the discharge angle, θ_0 , as follows:

$$\frac{Y_m}{D} = C_1 F_r, \quad (1)$$

and

$$S(Y_m) = C_2 F_r, \quad (2)$$

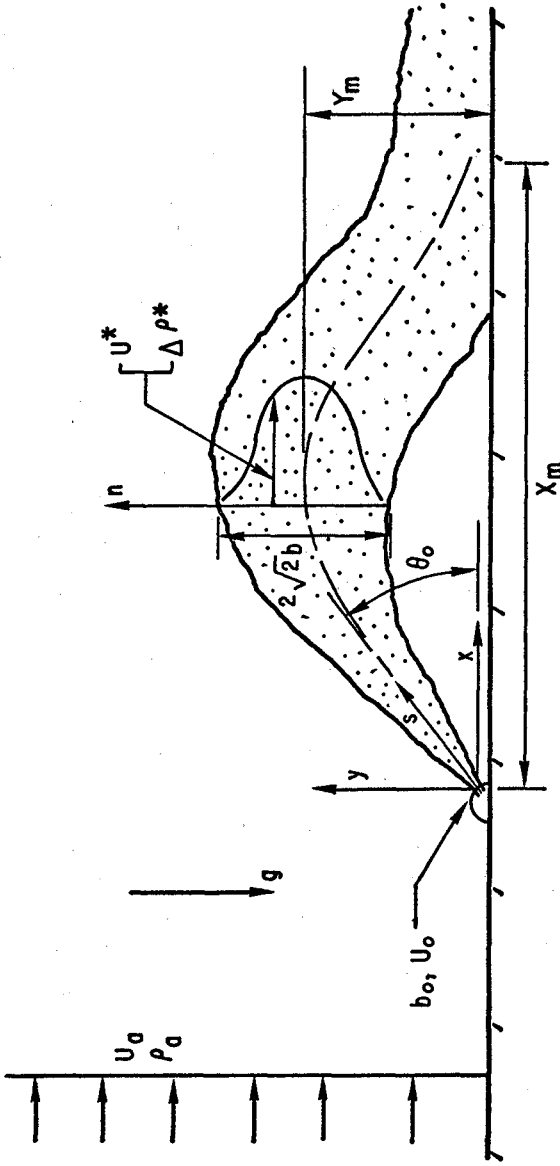


Fig. 1. Schematic Diagram of a Negatively Buoyant Slot Jet

where

$$F_r = \frac{U_o}{\left(\frac{\Delta\rho_o}{\rho} g D\right)^{1/2}}$$

Y_m = maximum height of rise above the discharge

D = discharge diameter

$\frac{\Delta\rho_o}{\rho}$ = discharge density difference divided by a reference density

$S(Y_m)$ = centerline dilution at Y_m

C_1, C_2 = coefficients which are constant for a given angle of discharge, θ_o .

The results of the experiments of Zeitoun *et al.* for θ_o values of 30°, 45°, 60°, and 90° indicate that, for a given discharge angle and no interaction with the free surface, the maximum height of rise and the dilution at that point increase monotonically with increases in the discharge Froude number (as indicated in Eq. (1) and (2)).

Morton³ and Abraham⁴ have presented analyses of the case of a negatively buoyant round jet discharged vertically upward which employ the integral-similarity approach often used in analyses of positively buoyant jets. Predictions for this particular case are difficult to match with experimental results because the jet falls back on itself and the similarity assumption becomes tenuous. Zeitoun *et al.*² applied an integral-similarity analysis with a variable entrainment coefficient to the non-vertical discharge case and found reasonably good agreement between predictions and their experimental data for trajectories and dilutions.

Experiments on negatively buoyant round jets discharged upward into flowing environments of uniform density and velocity have been reported by Holly and Grace⁵ for a vertical discharge and by Pincince and List⁶ for a discharge inclined at 60° from the horizontal and in the direction of flow. Anderson *et al.*⁷ conducted experiments for a variety of discharge angles, discharge densimetric Froude numbers, and ratios between the discharge and crossflow velocities. The crossflow acted to bend the jet trajectory downward which resulted in a decrease in the dilution at the maximum height of rise over the equivalent case in a stagnant environment. The dilution in the region of bottom impingement, however, was found to increase due to the elongation of the trajectory over that in a stagnant case. Anderson *et al.* were able to effect agreement between an integral-similarity model and the experimental results by varying the entrainment coefficient with the discharge densimetric Froude number and velocity ratio.

Slot-Jet Experiments

The experiments for negatively buoyant slot jets in stagnant and flowing environments were conducted in a flume 5.5 m long, 0.33 m wide, and 0.46 m deep. The jet was discharged from a slot in a small (1.27 cm radius) half-cylinder mounted on the flume bottom and extending across the entire width of the flume. Slots of different opening sizes and angles to the horizontal were employed. The receiving-water depth was maintained large enough to avoid any interaction of the jet with the free surface. The receiving water flow was turbulent, in the cases of flowing environments, and the negatively buoyant jets were all turbulent with a minimum discharge Reynolds number (based on slot width) of about 2000.

The discharge effluent was a saltwater solution and the receiving water was fresh with the discharge density and flow rate adjusted to produce the densimetric Froude number desired. Since a saltwater solution was used as the effluent, conductivity probe measurements in the jet were used to infer concentrations and density and thus to determine dilution values. Dye injected into the discharge and a grid on the transparent flume wall were used for photographic records of the jet trajectory. The conductivity measurements were concentrated in the regions of the maximum height of rise and the bottom impingement of the plume. Receiving-water velocities for the flowing cases were measured with a hot-film anemometer and appeared to be quite uniform over the cross-section, except for small regions near the side and bottom boundaries.

Detailed descriptions of the experimental equipment and techniques are given in Reference 8.

Results of Slot-Jet Experiments — Stagnant Environment

Dimensional analysis of the discharge of a negatively buoyant slot jet into a stagnant environment indicates that the dimensionless trajectory coordinates, y/B and x/B , and centerline dilution, S , are functions of the slot discharge densimetric Froude number, F_s , and the angle of discharge from the horizontal, θ_0 , where,

$$F_s = \frac{U_0}{\left(\frac{\Delta\rho_0}{\rho} g B\right)^{1/2}}$$

and

B = discharge slot width.

Experiments were performed in which the Froude number had values of 10, 20, 30, 40, and 50 for each of the discharge angles of 30°, 45°, 60°, and 90°. The results of these experiments are given in terms of the maximum height of rise of the jet centerline above the discharge, Y_m , the maximum horizontal displacement of the jet centerline away from the

discharge in the region of bottom impingement, X_m , and the centerline dilutions at those points, $S(Y_m)$ and $S(X_m)$, respectively.

The data for the normalized maximum height of rise as a function of Froude number for discharge angles 45° , 60° , and 90° are shown in Figure 2. The data for $\theta_0 = 30^\circ$ are not shown as those discharges interacted so quickly with the bottom that trajectory and dilution measurements were difficult. With results similar to those for negatively buoyant round jets, the normalized maximum height of rise varied directly with the discharge Froude number. Contrary to the data of Zeitoun *et al.* for round jets, for which the $\theta_0 = 60^\circ$ case produced the largest value of the coefficient C_1 in Eq. (1), the slot jet data indicate that that coefficient increases monotonically as θ_0 increases from 0° to 90° . Figure 3 indicates that the normalized maximum horizontal displacement increases with discharge Froude number for a given θ_0 and that $\theta_0 = 45^\circ$ results in the greatest horizontal displacement.

The dissimilarity between round and slot jet behavior becomes even more apparent from the centerline dilution data. The centerline dilution at the maximum height of rise is given as a function of Froude number and discharge angle in Figure 4. The dilution increases monotonically with discharge Froude for all angles, similar to round jet experience in Eq. (2), for Froude numbers less than about 30. For discharge Froude numbers greater than about 30, the dilution at the height of maximum rise decreases with increases in Froude number. Similar behavior was found for the dilution at the maximum horizontal displacement, shown in Figure 5. The decrease of the dilution for increases in discharge Froude number appears to be due to the reattachment eddy formed between the sinking slot jet and the bottom boundary and to reentrainment by the jet. The reattachment eddy, shown schematically in Figure 6, acts to pull the jet toward the bottom because of the pressure field established and to enhance reentrainment of the discharged effluent into the jet. The entrainment of this diluted effluent, instead of fresh receiving water, decreases the dilution and decreases the local jet densimetric Froude number.

Analytical-Model Predictions for the Stagnant Case

The effects of the reattachment eddy are manifested in the attempt to predict negatively buoyant slot jet behavior with a model which ignores the presence of the bottom boundary. An integral-similarity model for an unbounded, stagnant receiving water with uniform density was employed. The governing equations were similar to those developed by Fan and Brooks⁹ for positively buoyant slot jets for the cases of the discharge conditions which existed in the experiments. The entrainment coefficient and spreading coefficient were set at 0.16 and 0.89, respectively, and the predictions were corrected for the zone of flow establishment.

Figures 7 and 8 indicate the model predictions of trajectory and dilutions at the maximum height of rise and the maximum horizontal displacement and the experimental values for these parameters for two discharges inclined at 60° from the horizontal. Both cases show that

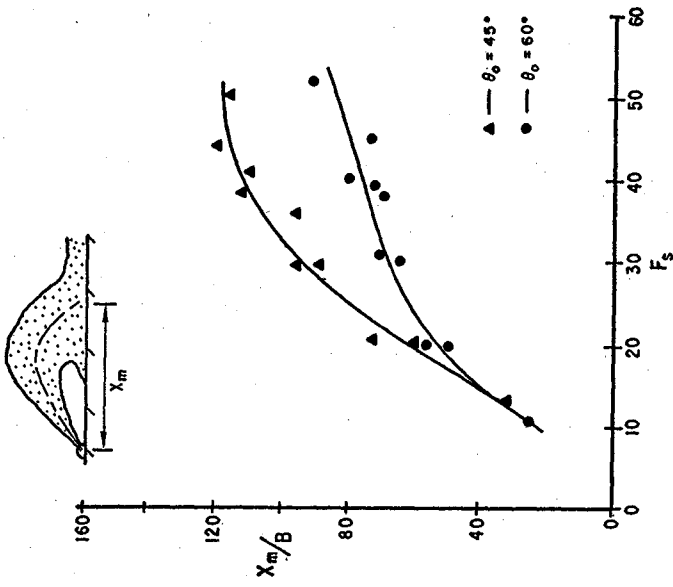


Fig. 3. Normalized Maximum Horizontal Displacement for Stagnant Environment

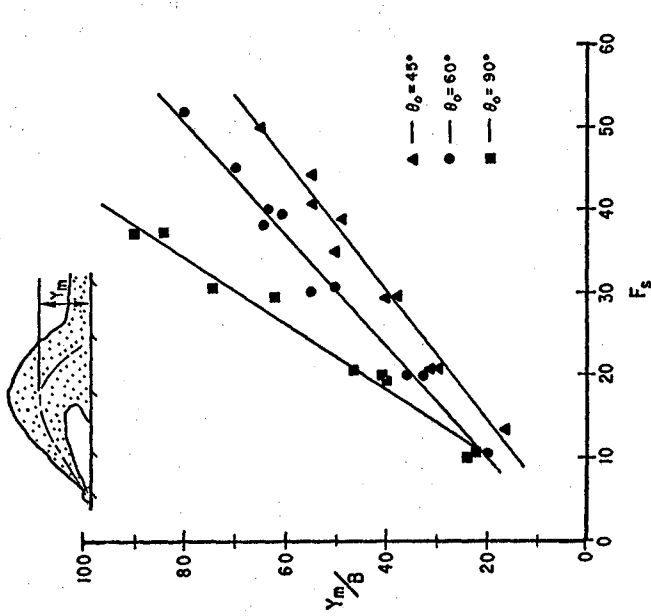


Fig. 2. Normalized Maximum Height of Rise for Stagnant Environment

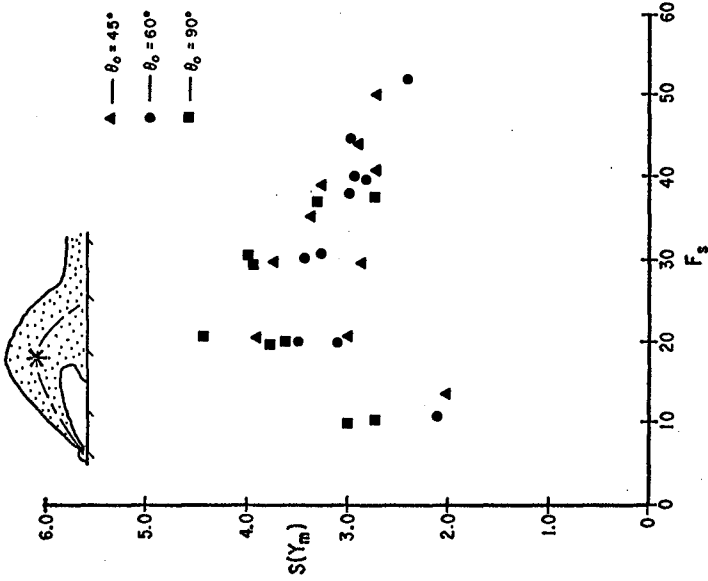


Fig. 4. Centerline Dilution at Y_m for Stagnant Environment

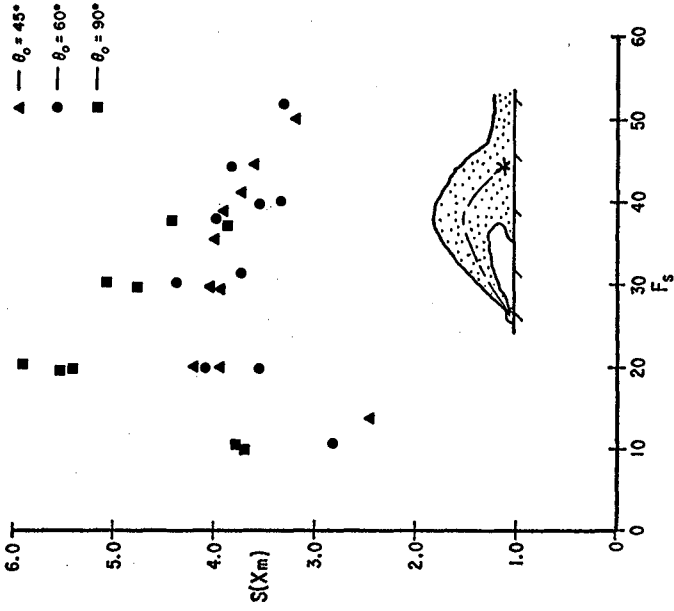


Fig. 5. Centerline Dilution at X_m for Stagnant Environment

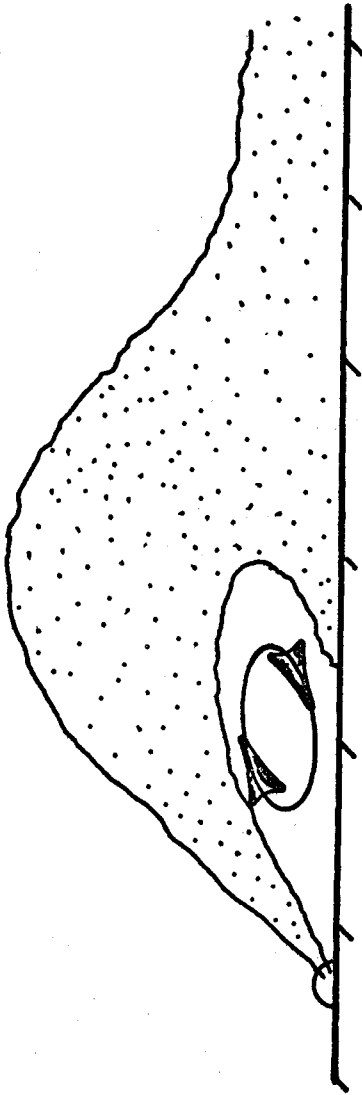


Fig. 6. Schematic Diagram of Reattachment Eddy

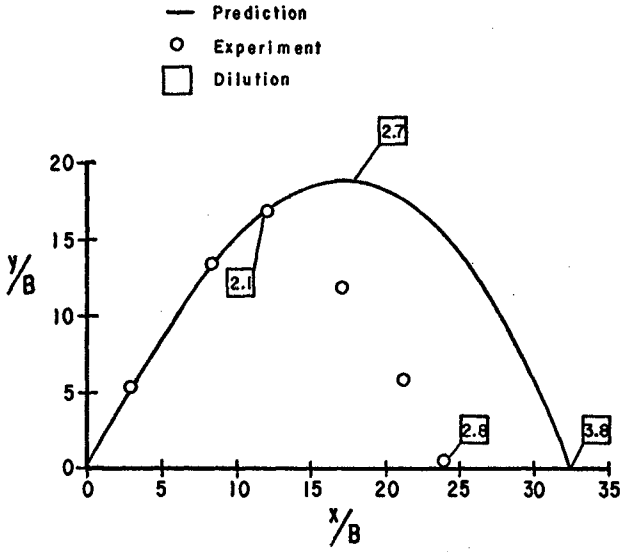


Fig. 7. Comparisons of Predictions and Measurements of Trajectory and Dilution for $\theta_0 = 60^\circ$ and $F_s = 10.4$

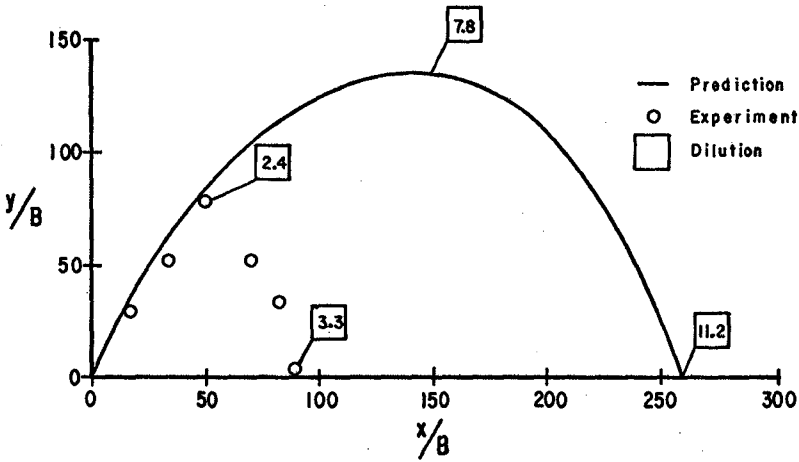


Fig. 8. Comparison of Predictions and Measurements of Trajectory and Dilution for $\theta_0 = 60^\circ$ and $F_s = 52.4$

the experimental trajectories were shorter and lower and that the measured dilutions were lower than the predictions. The disparity between predictions and measurements becomes greater for larger discharge Froude numbers (Figure 7 versus Figure 8). Additional comparisons⁸ indicate that the model for an unbounded receiving water, in general, predicts that the dilution at the maximum height of rise is a monotonically increasing function of Froude number without the decreases in dilution found in the experimental data (Figure 2). A large discharge densimetric Froude number implies relatively large discharge momentum, and consequently, for such a case, more intense reattachment eddies than for the case of a small discharge Froude number.

The failure of the model to predict the negatively buoyant slot jet behavior is directly related to the fact that the bottom boundary and its effects on the flow are neglected in the model. Although the values of the entrainment coefficient and the spreading coefficient are not well-established for the unbounded case, sensitivity studies with variations in these parameters indicated that agreement between predictions and experimental data could not be forced. This simply confirms the fact that the proximity of the bottom boundary is the important feature governing the jet behavior.

Results of Slot-Jet Experiments — Flowing Environment

Dimensional analysis for the case of a deeply-submerged negatively buoyant slot jet in a flowing environment yields an additional governing parameter, K , the velocity ratio,

$$\text{where } K = \frac{U_o}{U_a},$$

and U_a = uniform ambient velocity.

Thus, the governing parameters for the behavior of negatively buoyant slot jets discharged into flowing environments are F_s , θ_o , and K . Experiments were performed for the cases of discharge angles of 45° and 90° for the range of F_s used for the stagnant cases (10 to 50) for K values of 15 and 25.

The normalized maximum height of rise and the normalized maximum horizontal displacement for the $\theta_o = 45^\circ$ case are shown as functions of F_s and K in Figures 9 and 10, respectively. The stagnant case ($K = \infty$) is shown for reference. Figure 9 shows that the jet is bent downward by the ambient current as expected. Figure 10 indicates that the relatively smaller ambient current ($K = 25$) acts to extend the jet downstream farther than in the stagnant case, yet the larger current ($K = 15$) apparently intensifies the reattachment eddy for $F_s > 20$ and lessens the downstream extent of the impingement. The dilutions at Y_m and X_m for $\theta_o = 45^\circ$ are shown in Figures 11 and 12, respectively. The decrease in dilution for large Froude numbers found for the stagnant case appears again in the flowing cases. The bending downward of the jet trajectory due to the

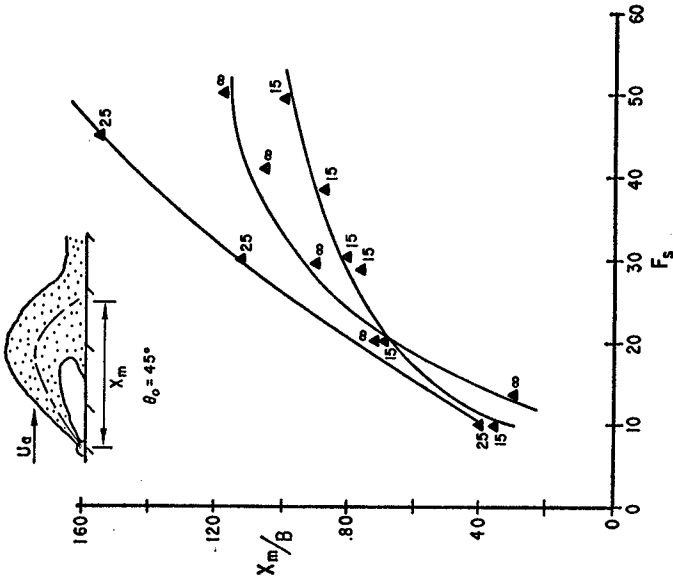


Fig. 10. Normalized Maximum Horizontal Displacement for Flowing Environment, $\theta_0 = 45^\circ$

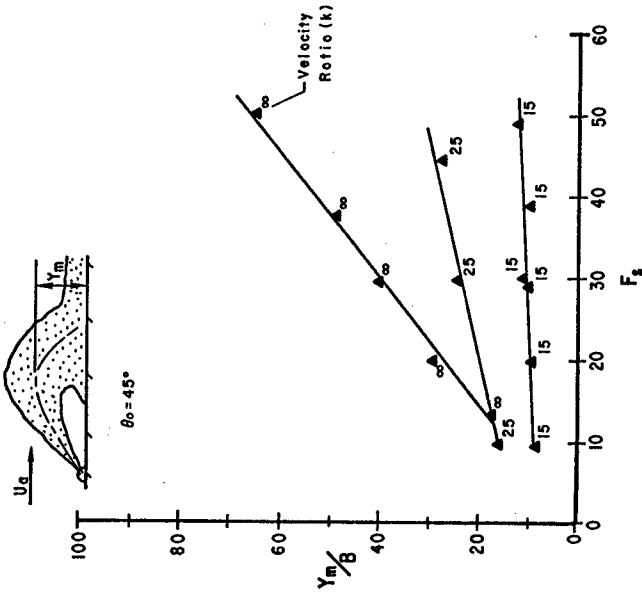


Fig. 9. Normalized Maximum Height of Rise for Flowing Environment, $\theta_0 = 45^\circ$

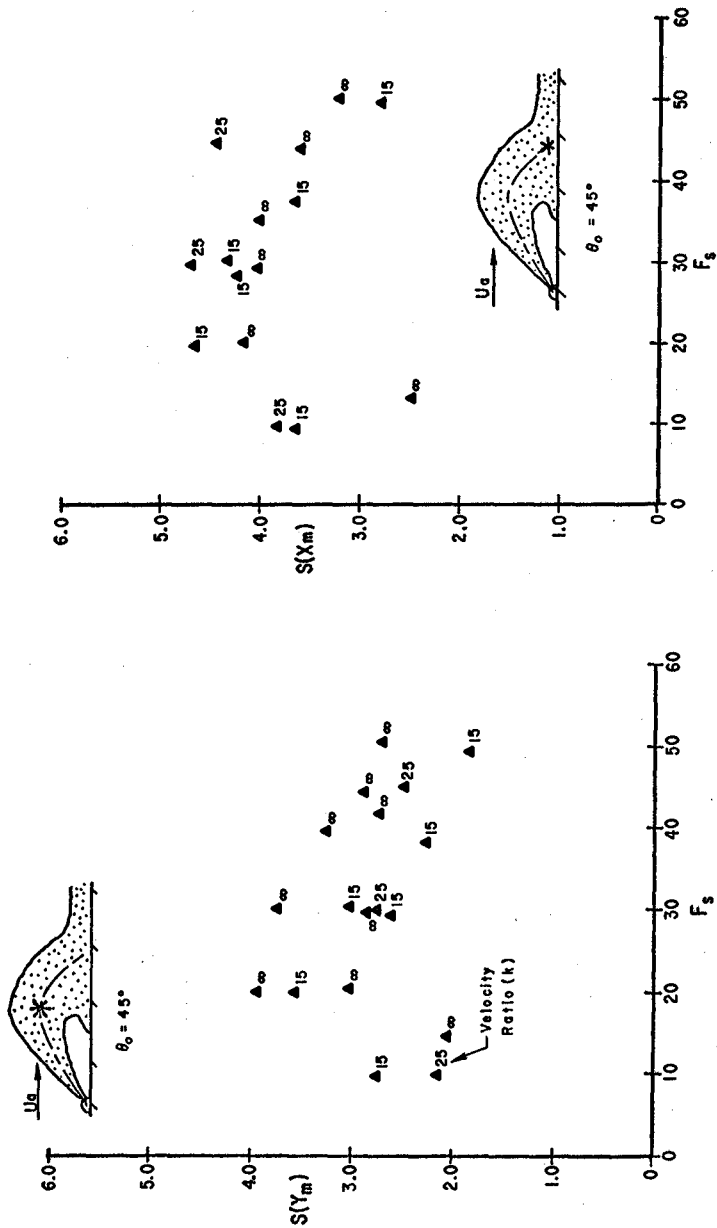


Fig. 11. Centerline Dilution at Y_m for Flowing Environment, $\theta_0 = 45^\circ$

Fig. 12. Centerline Dilution at X_m for Flowing Environment, $\theta_0 = 45^\circ$

current generally results in smaller dilutions at Y_m than in the stagnant case as shown in Figure 11 and larger dilutions at X_m due to elongation of the trajectory before bottom impingement, as shown in Figure 12. However, the data for $S(X_m)$ suggest that the higher current case ($K = 15$) may result in dilutions at X_m about equal to those for the stagnant case due to joint effects of entraining horizontal momentum from the current and of the reentrainment of dense fluid due to the reattachment eddy. Subsequently, counter to the experience with round jets in a current, where the current acted to extend the plume and to enhance mixing before bottom impingement, the slot jet in a current is greatly influenced by the reattachment eddy and enhanced downstream dilution may not be realized.

The normalized maximum height of rise and the normalized maximum horizontal displacement for the $\theta_0 = 90^\circ$ case, a vertical discharge, are shown as functions of F_s and K in Figures 13 and 14, respectively. The stagnant case does not provide the greatest Y_m/B values (Figure 13) because, in that instance, the effluent falls back on itself and, in the flowing case, the bending of the jet causes it to impinge downstream of the slot as shown in Figure 14. That difference between the stagnant and flowing cases is shown again in the dilution data at Y_m in Figure 15, where dilutions for the flowing cases are larger than for the stagnant case. Similar results are shown in Figure 16 for $S(X_m)$. One would expect that for values of K smaller than examined in these experiments (larger relative currents), the discharge would be bent over so much that dilutions at X_m would decrease below those for the stagnant case as occurred in the results for the $\theta_0 = 45^\circ$ discharge (Figure 12)

Applicability to Discharges Which Are Not Two-Dimensional

The results of this study apply strictly to the case of a slot discharge located at the bottom of the receiving water and extending completely across the receiving water (strict two-dimensionality). It has been shown that the reattachment eddy downstream of the discharge has a pronounced effect on the jet behavior. Because the existence and strength of that eddy depend on the physical situation studied, caution is necessary in the application of the results found to discharge situations which are physically different.

A slot discharge on the bottom of and extending across a river or stream clearly resembles the case studied. However, a slot discharge elevated some distance above the bottom would permit entrainment flow to the lower side of the slot and weaken or possibly eliminate the reattachment eddy. In such a case, it is expected that the integral-similarity model predictions would more readily reflect the jet behavior than the experimental results reported here. Likewise, a slot discharge of finite length, not extending entirely across the receiving water body, could induce flow inward along the axis of the slot for entrainment and diminish the strength of the eddy. The merging of adjacent round jets of a multiport diffuser to form a slot jet may also constitute a different physical situation. Although an "equivalent" slot for a multiport diffuser discharge is easily calculated, the flow between the initial round jets would probably result in a weaker reattachment eddy than would be formed had the initial discharge geometry been a slot.

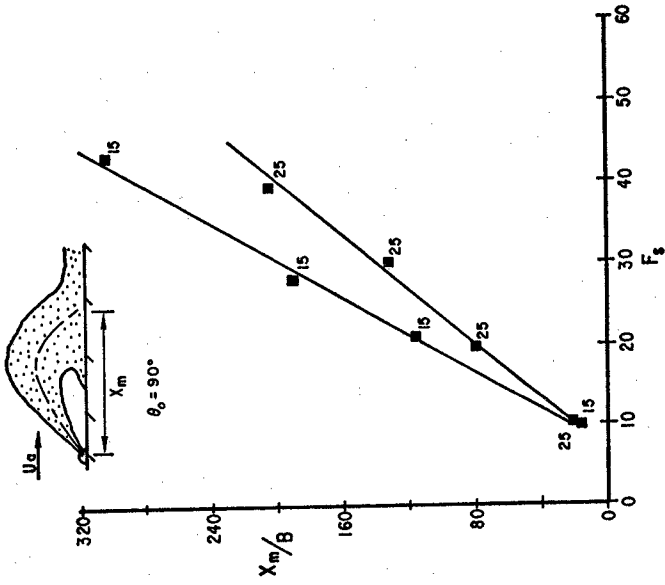


Fig. 14. Normalized Maximum Horizontal Displacement for Flowing Environment, $\theta_0 = 90^\circ$

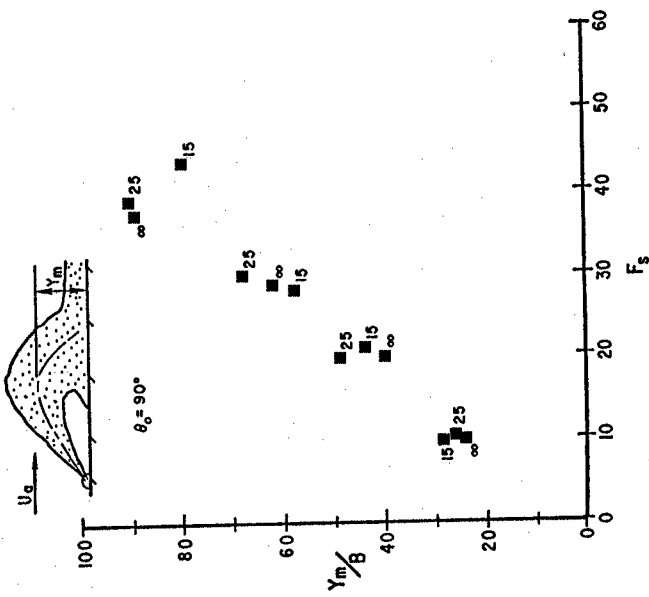


Fig. 13. Normalized Maximum Height of Rise for Flowing Environment, $\theta_0 = 90^\circ$

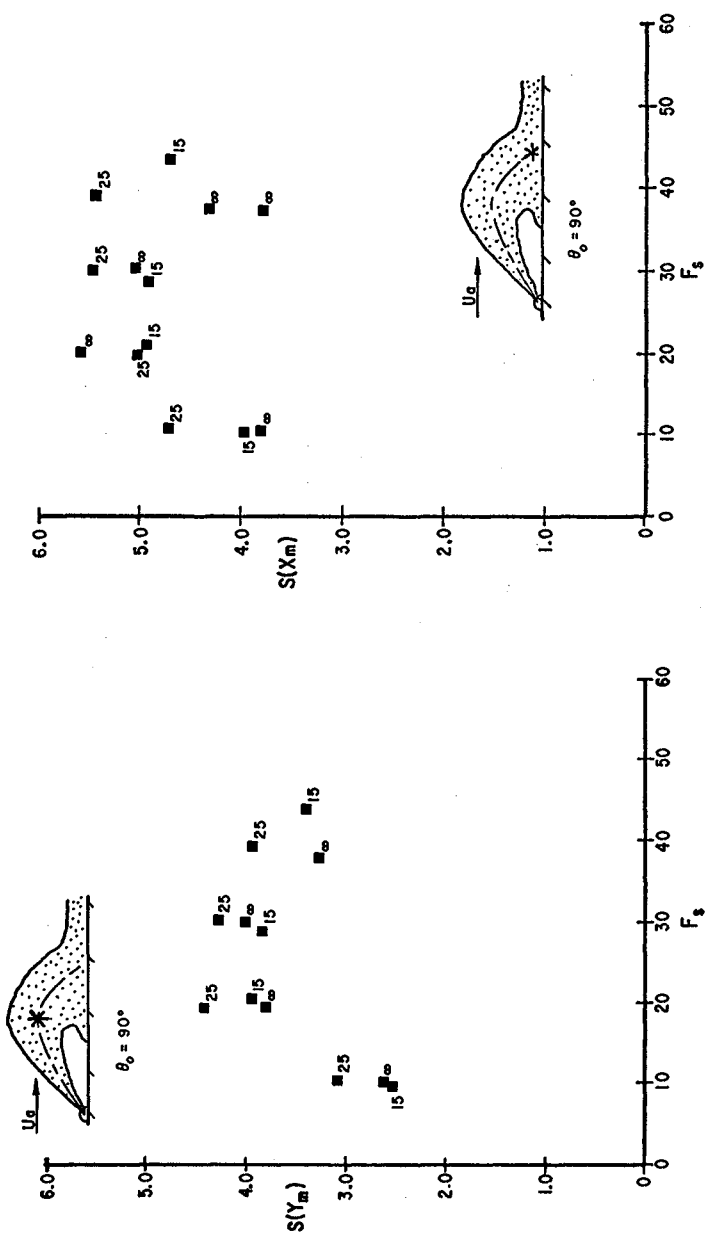


Fig. 15. Centerline Dilution at Y_m for Flowing Environment, $\theta_0 = 90^\circ$

Fig. 16. Centerline Dilution at X_m for Flowing Environment, $\theta_0 = 90^\circ$

All of the physical situations mentioned above result in the possibility that the reattachment eddy may be weakened and hence that the dilution may be increased over that predicted by the experimental data reported for this study. The sensitivity of the results to these factors and the degree to which dilution predictions can be increased remains to be studied. The results for the two-dimensional case reported here do, however, provide the lower-bound or "worst case" on the mixing to be realized from a slot or slot-like discharge of a negatively buoyant effluent. The upper bound would be that behavior predicted by the model for receiving-water environment with no boundary interference.

Conclusions

The behavior of submerged negatively buoyant slot jets discharged near the bottom of the receiving water is influenced by the reattachment eddy created between the jet and the bottom. The trajectories of such jets in stagnant and flowing environments are lower and flatter than would be predicted in the absence of the bottom boundary. Centerline dilutions at the maximum height of rise and the maximum horizontal displacement are reduced considerably relative to predictions for the unbounded case. Contrary to experience with negatively buoyant round jets discharged near the bottom, the dilution at the maximum height of rise for a given discharge angle does not increase monotonically with increases in the discharge densimetric Froude number. The existence of the reattachment eddy in the slot discharge case results in the dilution at that point decreasing for Froude numbers greater than about 30. The strictly two-dimensional case studied provides a lower bound for dilution and trajectory predictions for cases of discharges from finite-length slots and discharges from multiport diffusers which merge to form slots.

References

1. Turner, J. S., "Jets and Plumes with Negative or Reversing Buoyancy," J. Fluid Mechanics, 26, 779-792, 1966.
2. Zeitoun, M. A., et al., "Conceptual Designs of Outfall Systems for Desalting Plants," Research and Development Progress Report No. 550, Office of Saline Water, U.S. Dept. of Interior, Washington, D.C. May, 1970.
3. Morton, B. R., "Forced Plumes," J. Fluid Mechanics, 5, 151-163, 1954.
4. Abraham, G., "Jets with Negative Buoyancy in Homogeneous Fluid," J. Hydraulic Research, 5, 235-248, 1967.
5. Holly, F. M. and Grace, J. L., "Model Studies of Dense Jets in Flowing Fluid," J. Hydraulics Div., Proc. Amer. Soc. Civil Engr., 98, 1921-1933, 1972.
6. Pincince, A. B. and List, E. J., "Disposal of Brine into an Estuary," J. Water Pollution Control Fed., 45, 2335-2344, 1973.
7. Anderson, J. L., et al., "Negatively Buoyant Jets in a Cross Flow," Environmental Protection Technology Series, EPA-660/2-73-012, U.S. Environmental Protection Agency, 1973.
8. Shahrabani, D. M, and Ditmars, J. D., "Negatively Buoyant Slot Jets in Stagnant and Flowing Environments," Ocean Engineering Report No. 8, Dept. of Civil Engineering, University of Delaware, Newark, Delaware, June 1976.
9. Fan, L.-N. and Brooks, N. H., "Numerical Solution of Turbulent Buoyant Jet Problems," W. M. Keck Lab. for Hydraulics and Water Resources, Report No. KH-R-18, Calif. Institute of Tech., Pasadena, January 1969.

CHAPTER 171

GUIDELINES FOR THE DESIGN OF AIR BUBBLE SYSTEMS

By

Nabil Ismail*, Graduate Student
Hydraulic Division, University of California
Berkeley, California, U.S.A.

ABSTRACT

Based on a literature review of theoretical and experimental work on air-bubble systems, guidelines for the ideal design of submerged distributors discharging air into water are presented.

A comprehensive study of gas-liquid dispersions was carried out to find out the effect of physical properties, distributor arrangement, and the air flow rate, on the flow pattern within the jet. This review revealed that the distributor arrangement largely influences the characteristics of the dispersion within the zone of flow establishment. Also, upon analyzing the experimental results of air-water systems, it was found that the zone of flow establishment extends to greater distances of the water depth than that in the case of one-phase turbulent plumes. Furthermore, the experimental results showed that the efficiency of air bubble plumes can be increased by the proper design of the distributor.

Recommendations for the distributor design are given, which include, diameter of orifices and their spacings, pressure drop across orifices, number of manifolds, and the maximum air flow rate.

*On a Study Leave from Civil Engn. Dept., Alexandria University, Alexandria, A. R. Egypt.

INTRODUCTION

Air-bubble systems have been used extensively for a variety of purposes, such as pneumatic breakwaters, prevention of ice formation, as barriers against salt water intrusion in rivers and locks, as barriers to reduce silt intrusion into estuaries, for stopping the spreading of oil spills on the water surface, for reduction of under water explosion waves, and for agitation, mixing, cooling, in process industries.

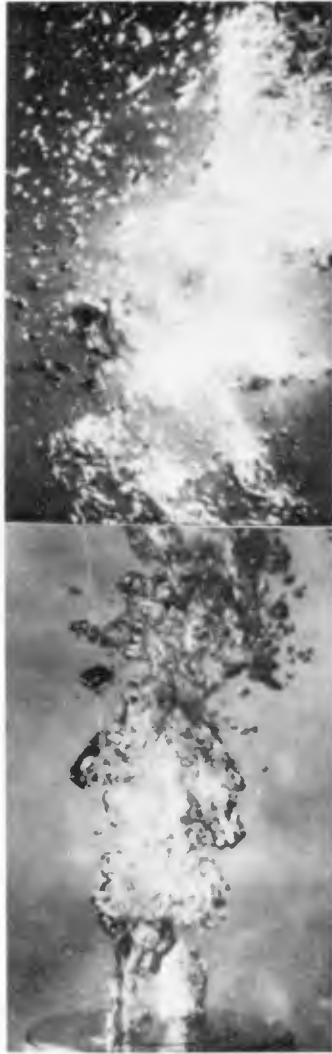
Based on the results of both small and large scale tests, and prototype tests, applied for use as pneumatic breakwaters, there has been a controversy for the past 30 years among investigators of the effect of the air distribution system on the efficiency of bubble systems. In addition, despite the wide range of practical applications, no theory has been developed to give a satisfactory description of the hydrodynamics of air-bubble systems. However, with a better understanding of the physical mechanism of this kind of plumes, there is some hope that the behavior of the air-bubble systems may be analyzed sufficiently well for design purposes.

Therefore, the fundamentals of disintegration of gas jets into liquids, and the subsequent upward motion have received consideration in the present work. This together with analyzing the previous theoretical and experimental work, provide us with some guidelines for the proper design of these bubble systems and necessary information to improve the present theoretical models.

DISINTEGRATION OF GAS JETS INTO LIQUIDS

In the range of air flow rates employed in most of the practical applications, the air issuing from a nozzle or an orifice quickly expands according to the sudden pressure drop across the nozzle, and eventually breaks up due to the instability of the jet. In other words, the continuous air stream disintegrates into series of closely spaced large irregular bubbles after it has travelled some distance from the air source. These irregular bubbles finally disintegrate into smaller ones and begin to rise through the water column. Normally, coalescence of bubbles occurs between bubbles of different sizes, and bubbles, during their rise, might coalesce depending upon their size distribution. Fig. 1 shows the disintegration of an air jet into water of depth 4.5 ft.

The flow pattern of one-phase turbulent jets can be divided into distinct zones. The boundary between the zones of flow establishment and established flow, can be defined



After Abdel-Aal (1)

Fig. (1). Dynamic Behavior of The Air-Water Jet

in the terms of the variation in the velocity and concentration. The extent of the ZFE either for the velocity or for the concentration is just few times the width of the slot.

In the case of a two-phase jet it is rather difficult to determine such boundaries between the different zones of the air-bubble flow. Generally the lateral spreading of the bubbly flow is less than that of the plume. With respect to the air stream, the flow can be divided into the following zones.

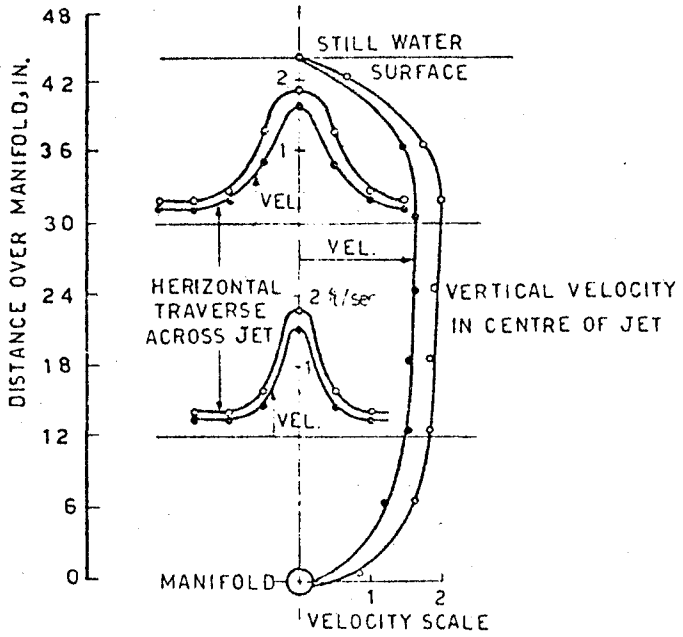
(a) Zone of Flow Establishment (ZFE): This zone can be subdivided:

- i) the initial zone where the air stream is still stable at the end of this zone, the air disintegrates into closely spaced large bubbles.
- ii) the transition zone, where the irregular large bubbles break up into discrete bubbles of various sizes.

and (b) Zone of Established Flow (ZEF): Regarding the gross behavior of the jet, all the previous experimental studies reveal that the center-line velocity reaches an almost constant value, and the velocity profiles become similar, with respect to a virtual source, at some distance above the air source. This defines the region of the jet, where the flow becomes fully developed. In this region, the air-water stream will rise with a velocity which depends on the bubble size distribution and concentration. All the previous experimental work indicates that this distance is comparable to the submergence of the air source which distinguishes this kind of jets from one-phase turbulent jets. Figure 2 shows a typical velocity traverses in a rising air-water jet.

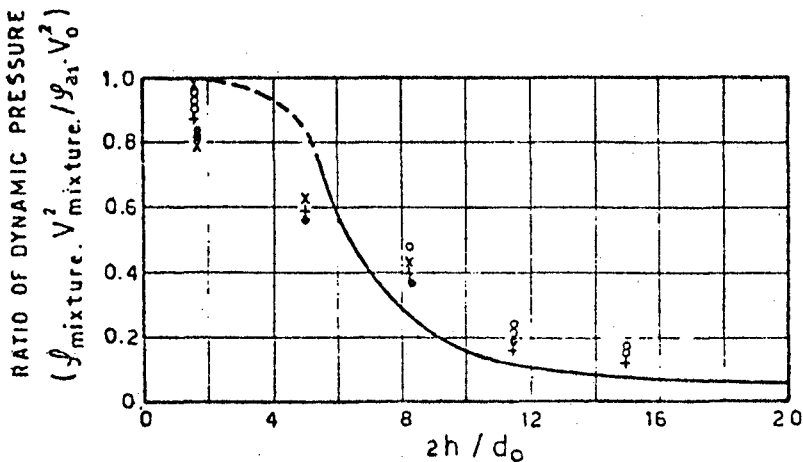
In this kind of turbulent jet, most of the kinetic energy of the air leaving the manifold is rapidly dissipated in the turbulent shearing of the liquid and generation of new surface area (1). Therefore, it is a good assumption to consider that only the potential energy of the bubbles, which is converted to the kinetic energy of the water jet. This is evident, as is shown in Fig. 3. The momentum flux increases due to the buoyancy terms which grow logarithmically with distance above the air source (12 and 13).

Most of the conventional theoretical treatments of one-phase turbulent jets and plumes have considered only the main region of the jet, on the assumption that the extension of the zone of flow establishment is very small compared to the submergence of the jet. The integral technique, used in these treatments has been applied recently, by Cederwall and Ditmars (8), to study the gross behavior of air-bubble plumes over the whole depth of the air-source submergence. The predictions of their model do not represent well the



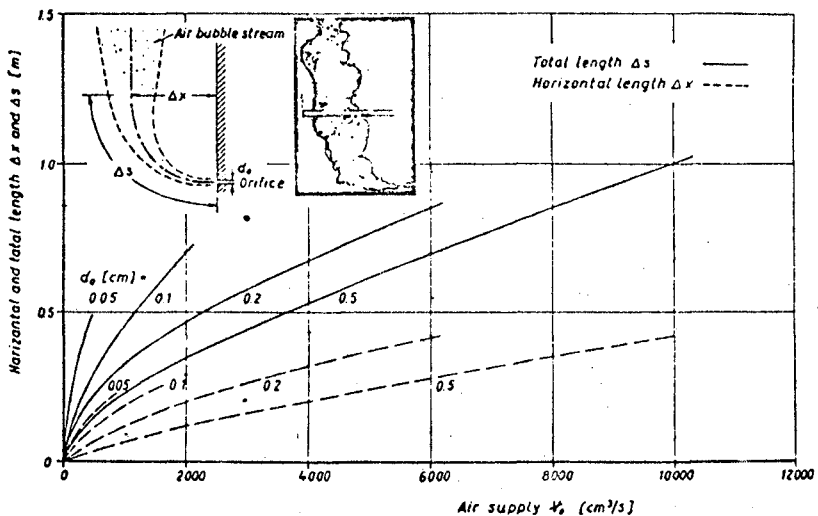
After Charlton (9)

FIG. (2) VELOCITY TRAVERSES IN THE RISING JET SHOWING THE EFFECT OF BUBBLE SIZE AT AN EQUAL AIR - FLOW OF $0.036 \text{ FT.}^2/\text{SEC.}$



After Abramovich (3)

FIG. (3) THE VARIATION IN DYNAMIC PRESSURE ALONG THE AXIS OF A JET GENERATED BY THE DISCHARGE OF AIR IN WATER.



After Kobus (13)

Fig. (4) Extent of Initial Region

actual behavior of the plume. However, a more satisfactory model necessitates a full knowledge of the complex details of the flow conditions in the zone of flow establishment to provide a proper mathematical formulation.

ZONE OF FLOW ESTABLISHMENT

Figure 4 shows the experimental results of Kobus (13) regarding the extent of the zone of flow establishment. It seems from this figure that the length of this zone is proportional to both the air flow rate per orifice and the pressure drop across the orifices. This would suggest that such correlation from these results could be applied to the case of multiple orifice pipe if the individual jets do not merge before disintegration. This could exist if the spacing between orifices is equal to the mean jet diameter at the point of disintegration.

Silberman (21) derived an equation which gives the mean jet diameter, J , by the end of the initial zone which he verified experimentally.

$$J = \left(\frac{q_1}{0.81 \pi^2 g} \right)^{1/5} \quad \text{in ft} \dots (1)$$

where q_1 = the volumetric air flow rate measured at the pressure and temperature in the liquid at the orifice ft^3/sec .

g = the acceleration of gravity ft/sec^2 .

ZONE OF ESTABLISHED FLOW

All the previous theoretical work such as that of Kurihara (14), Charlton (9), Ismail (12), Cederwall and Ditmars (8), have revealed that the potential energy of bubbles is more effectively used for generating an air-water jet by minimizing the relative velocity between the two-phases. In the following, the fundamentals of the bubble-liquid interaction are presented in order to reveal the effect of the various factors such as the physical properties, distributor design, and gas flow rate on the relative velocity of the air stream. The review can be generally classified into two parts. The first is concerned with the disintegration of the air jet while the second deals with the motion of the bubble stream.

Bubble Formation

Leibson et al (15), and Abdel-Aal (1) described in detail the complex breakup of the air-jet in the turbulent region. The turbulent region, where most of the applications of air-bubble systems exist is when the orifice Reynolds number, R_{eo} , exceeds 2100.

The experimental results of Leibson et al, for the case of single orifices, are shown in Fig. 5. This figure shows that as turbulence becomes fully developed (i.e., $2,100 < R_{eo} < 10,000$) the effect of orifice size and Reynolds number on the bubble diameter could be expressed as:

$$d_b = 0.18 d_0^{1/2} R_{eo}^{1/3} \quad \text{in inches} \quad \dots \quad (2)$$

where d_0 is the orifice diameter in inches. This correlation falls closely to the experimental results of Davidson (10) for the same flow conditions. The results also indicate that there is no noticeable effect of orifice diameter d_0 on the bubble size, d_{bvs} , in the fully turbulent region. The bubble size d_{bvs} is defined as the diameter of a bubble whose ratio of volume to surface is equivalent to that of the bubble size distribution. For the air-water system, Leibson et al obtained the following experimental equation which fits the data for orifice Reynolds number greater than 10,000:

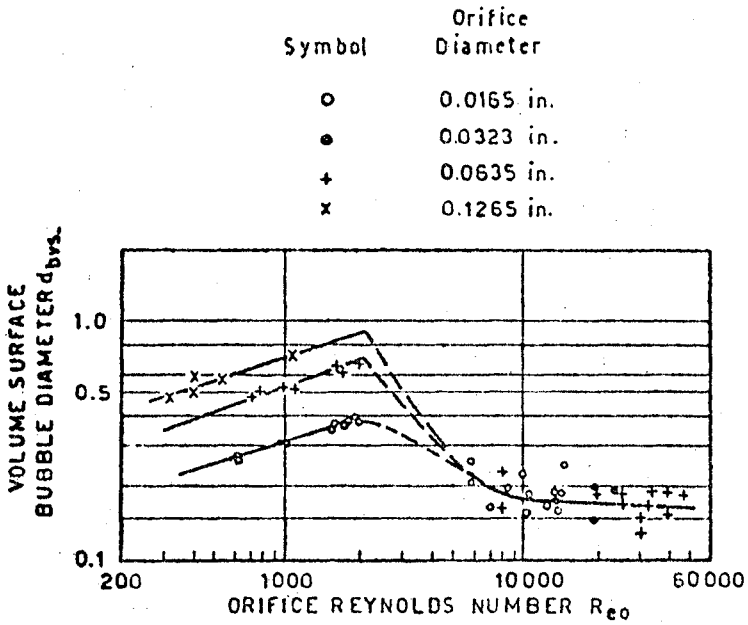
$$d_{bvs} = 0.28 (R_{eo})^{-0.05} \quad \text{in inches} \quad \dots \quad (3)$$

It is important to notice that these results give the bubble size just after jet disintegration. Therefore by increasing the air flow rate within the turbulent region, the bubble size is expected to increase by the end of the transition zone, due to the coalescence of bubbles caused by their increasing proximity (7).

For the case of multiple orifices, the mean bubble size after jet disintegration is given by Calderband (7) for turbulent conditions ($R_{eo} > 2,100$) as

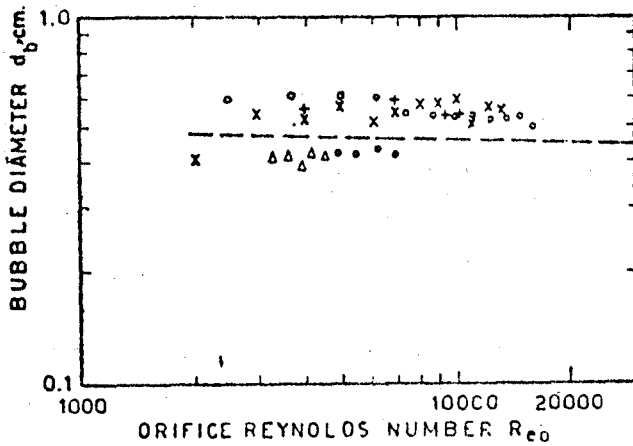
$$d_b = 0.713 (R_{eo})^{-0.05} \quad \text{in inches} \quad \dots \quad (4)$$

This equation is comparable with Leibson's equation for single orifices in the fully developed turbulent regime. These results agree with the findings of Rennie and Evans (20), which are shown on Fig. (6).



After Leibson(15)

FIG. (5) BOTTOM-ENTRANCE FLOW MEAN BUBBLE DIAMETER VERSUS ORIFICE REYNOLDS NUMBER.



After Rennie and Evans (20)

FIG. (6) BUBBLE DIAMETER AGAINST ORIFICE REYNOLDS NUMBER.

In addition to the previous mentioned effect of high gas flow rates on the proximity of bubble, which could be shown in the experimental results of Silberman (Fig. 7), there is another factor affecting coalescence. Normally coalescence of bubbles occurs between bubbles of different sizes. At low gas rates and intensities of turbulence the ranges of bubble sizes normally encountered is not very great. By increasing the gas flow rate or the pressure drop across orifices, turbulence will increase and the size distribution will spread, thus increasing the rate of coalescence. Therefore, in situations where it is desired to attain maximum interfacial area, it is advantageous not to exceed the orifice Reynolds number greater than 10,000.

In this respect Silberman (21) derived an equation by which the size of the largest bubble formed from jets may be predicted and he confirmed it by experiments: the mean bubble diameter is given by

$$d_{bl} = 1.41 \left(\frac{q_1^2}{g} \right)^{1/5} \quad \text{in ft. ...} \quad (5)$$

where q_1 is the volumetric air flow rate evaluated at the orifice in $\text{ft}^3/\text{sec.}$, and g is the acceleration of gravity.

The above equation still holds for the case of multiple orifices as long as the individual jets do not merge before disintegration. It is worthwhile to show the effect of distributing the same air flow rate over many orifices on the mean bubble size. This effect is shown when comparing the bubble sizes in Fig. 7-b and Fig. 8 where the size in the latter figure is smaller due to the decrease of the air flow rate per orifice.

In case where porous pipes are used, the size of bubbles produced depends upon both the size of the pores and the pressure drop across them. For every type of porous pipes, the manufacturer suggests a working limit for gas flow rate (18), after which serious coalescence will occur. Table 1 gives this limiting gas flow rate for various types of porous pipes.

Bubble Motion

In the zone of established flow the rise of bubble swarms is more complicated than the case of single bubbles. This is caused by the interaction of bubbles among themselves. However the motion of single bubbles in stagnant water still provides an instructive conceptual picture of the motion of bubble streams (11).

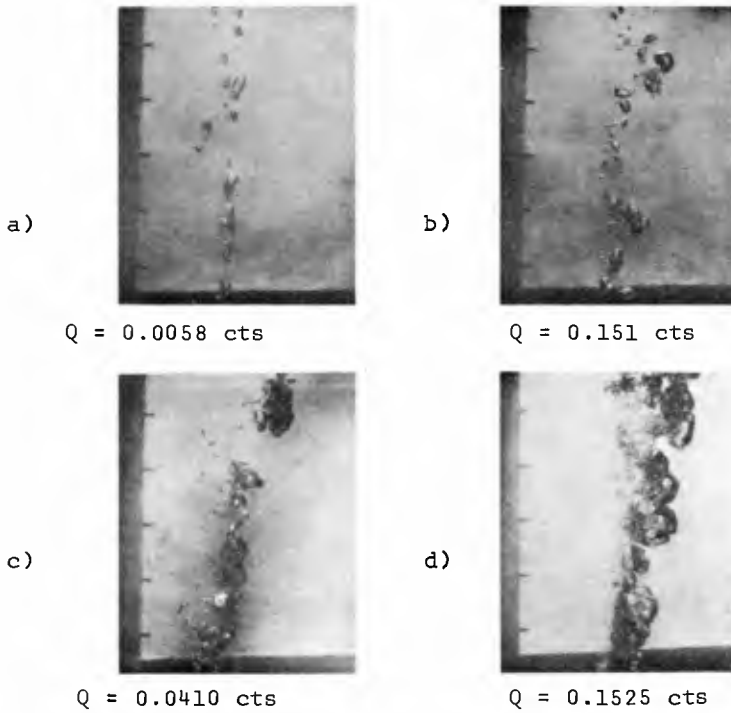


Fig. (7). Effect of Air Flow Rate on Bubble Size in the Transition Zone



Photographs after
Silberman (21)

Fig. (8). Jets from 9, 1/32-in. Circular Orifices
Total Discharge = 0.0108cfs

TABLE (1) : Characteristics of Porous Septa

Grade	AVG % porosity	AVG pore diam.	Air-permeability data	
			Diaphragm thick in. water	Air flow cu.ft/(sq.ft)(min.)
Al and um porous alumina				
P 236	34	240	1	40
P 216	..	720	2	110
National porous carbon				
25	48	120	2	13
Filters porous silica				
Coarse	34.5	250	1.5	31 - 59
Extra	36.5	300	1.5	60 - 100
Porous plastics				
Kel-F	...	15	0.125	138
Micro Metallic porous stainless steel				
D	50	65	0.125	1.38
C	55	165	0.125	27.7

After Perry [18]

Therefore the fundamentals of bubble-liquid motion in stagnant water have been collected together on Fig. 8, which shows the various factors affecting the related aspects of bubble motion (12).

These aspects include the shape of the bubble, its rise path, the drag exerted by the liquid on it, and its rise velocity.

The effect of turbulence on the relative bubble velocity of rise is not yet well defined. The only available data (5) is shown in Fig. 9. This figure shows that for a bubble size larger than 0.3 cm the relative velocity remains relatively constant at approximately 25 to 27 cm/sec., until an equivalent diameter of about 0.9 cm is reached beyond which the slip velocity slightly increases.

DISCUSSION

In the various applications of air-bubble systems there are two descriptions of efficiency which can be applied to an air-water jet. For mixing purposes, the interest is the mass transport capacity of the system, and the efficiency is represented by the ratio of total entrained water to the air flow rate. For pneumatic breakwaters, the criteria of the wave stopping power is the energy of the surface current, and the efficiency is measured by the ratio of the kinetic energy of the surface current to the potential energy available in the air jet leaving the manifold.

The air-bubble systems have proved to be a very efficient means of entrainment water. Table 2 lists entrainment ratios for a wide-world experimental work. On the other hand pneumatic breakwaters have been demonstrated by model tests and full scale tests in U.S.A., England, Japan, and Germany, to be only feasible to attenuate seas of length/water depth up to 5 and periods up to 5 sec. (12). For swell the Japanese experience suggests using parallel multiple air distributors, spaced four times their submergence, when there is an adequate air supply, which imposes limitations for using air-bubble systems to attenuate swell (14).

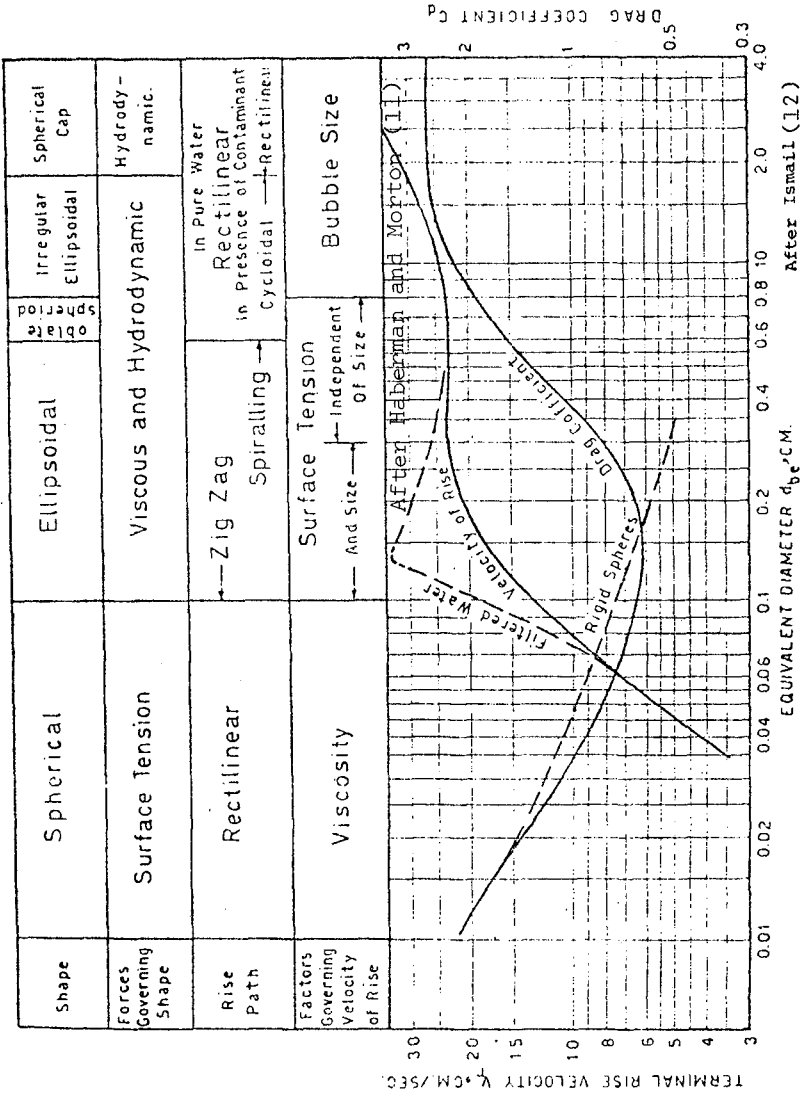
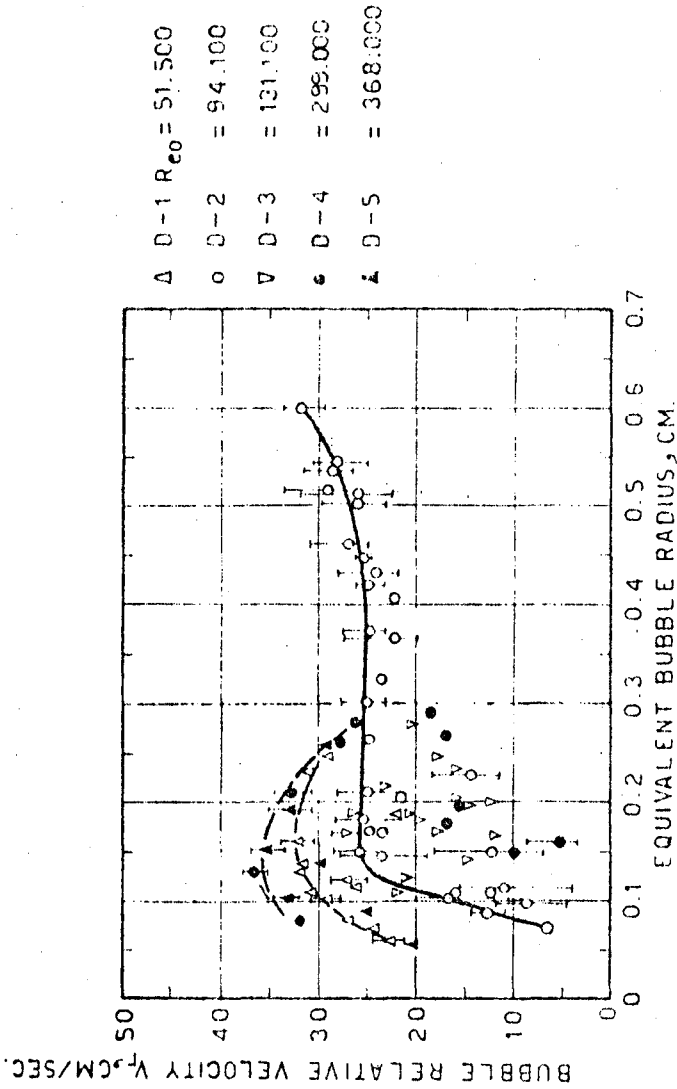


FIG. (9) FUNDAMENTALS OF BUBBLE - FLUID INTERACTION



After Baker and Chao (5)

FIG. (10) VARIATION OF BUBBLE RELATIVE VELOCITY WITH EQUIVALENT RADIUS OF DEMINERALIZED WATER.

Table (2)
Entrainment Ratios of Air-Bubble Systems

Investigator	Water Depth	Air Discharge	Entrainment Efficiency
Baines and Hamilton (1959)	5.5 ft	1 ft ³ /min	123
Bulson (6) 1961	25.5	0.18 ft ³ /sec/ft	75
Bulson	34 ft	0.05 ft ³ /sec/ft	132
Kobus (13)		3000 cm ³ /sec/m	65
Kobus 1968	4.0 ms	6200 " "	85
Kobus		10000 " "	125
Kurihara (14) 1958	8.3 ms	13 lit/sec/m	50
Kurihara	162 ms	20 lit/sec/m	110

In order to reduce the power requirements of operating pneumatic breakwaters, researchers all over the world have investigated the effect of the distributor arrangements on the efficiency of the system. However, there has been a controversy for the last 30 years among the researchers upon this effect.

Bulson (6) reported that when the same quantity of air passed through a variety of orifice diameter and spacings, there was no significant difference in the velocity profile across the jet. Also, he found that results for a single manifold were not noticeably different from those when two or more adjacent manifolds were delivering the same total quantity of air. When using porous pipe as air distributor he found no significant difference in the resulting surface current velocity.

Kurihara (14) attributed the high efficiency obtained in the Japanese experiments to having a very fine dispersion. The air distribution system used in their experiments either in the full scale tests or model tests was distinguished by having a large number of holes. Both a single pipe and a

ladder type of pipe were used. The latter was used to attenuate shallow water waves.

On the contrary, the experiments of the U.S. Army (25) showed that a single discharge manifold produces greater efficiency than do multiple manifolds separated by some distance.

The experimental results of Kobus (13) did not show any effects of the distributor arrangements on the jet-pattern.

In fact Bulson's data do not agree with his conclusions. His data are extrapolated to calculate the values of entrainment and energy efficiencies. This led to the conclusion that there is a positive effect of the distributor arrangements on the efficiency of air-bubble jet, even the range of variation in the arrangements was small. Bulson* agreed about the results of analyzing his data. The reason behind the lower performance he obtained than that of the Japanese experiments is due that the air flow rate per orifice is very large, which resulted in the formation of large air slugs. Also the pressure drop across orifices was very high, which had an adverse effect on the efficiency. This excessive pressure drop is the reason for the low velocity performance in the experimental work of Kobus (13).

On the other hand, decreasing the pressure drop across the orifices resulted in a high efficiency as the experimental results of both Kurihara and the U.S. Army showed.

Regarding the disappointing results which Bulson obtained, when using porous pipes, the type of porous pipe used in his experiments was not the proper one for discharging the high air flow rate employed in his experiments.

For those investigators who used multiple manifolds in order to attain a higher efficiency, the low efficiency obtained in some of their experiments had resulted from the improper design of the spacing between manifolds. This led to a low concentration of the air bubbles within the plume.

CONCLUSIONS

It is concluded that in order to obtain the best efficiency of an air bubble sytem: for a given air flow rate

*Special correspondence with P. S. Bulson, M.E.E., Christchurch, England, 1971.

i) The air flow rate should be distributed over a large number of orifices. This number is determined by calculating the air flow rate per orifice based on the designed maximum bubble size in the dispersion.

ii) The diameter of the orifices should be designed in a way that the orifice Reynolds number is in the fully turbulent region (10000), also the pressure in the manifold should be just sufficient to cause the air to be released.

iii) The minimum spacing between orifices should be equal to the mean jet diameter at the point of air disintegration, to allow disintegration before merging of the individual jets without serious coalescence.

iv) If the above conditions cannot be satisfied by using one manifold, different manifolds could be used. The spacing between them should be designed by model tests in order to achieve an optimum value of air concentration.

v) Porous pipes are preferable provided that we are working within their maximum air flow rate. The maximum limit of using them can reach up to $990 \text{ ft}^3/\text{ft}^2/\text{min}$ which makes the porous pipes utilizable for practical applications.

ACKNOWLEDGMENTS

This paper extends work which was done in 1971 at the Civil Engr. Dept., Alexandria Univ. Egypt. The author is greatly indebted to Professor H. Hammad and Professor I. Ebeido for their interest and continual guidance throughout that work. The valuable discussions of Professor A. El-Taweel, Chemical Engr. Dept., at that time made possible the completion of that work.

I would like to thank Professor R. L. Wiegel, Hydraulic Div., Univ. of Calif., Berkeley, for his critical review and comments on this paper.

REFERENCES

1. Abdel-Aal, H. K., G. B. Stiles and C. D. Holland
"Formation of interfacial area at high rates of gas flow through submerged orifices" A.I.Ch.E. Journal 13, 174, 1966.
2. Abraham, G., "Jet Diffusion In Stagnant Ambient Fluid", Delf Hydr. Lab., No. 29, July 1963.
3. Abramovich, G. N. "The theory of Turbulent Jets" M.I.T. Press, Cambridge, Mass. 1963.

4. Baines, W. D., and Hamilton, "On the Flow of Water Induced by a Rising Column of Air Bubbles". Int. Ass. Hydr. Res., 8th Congress, Montreal, August 1959.
5. Baker, J. and Chao, B. T., "An Experimental Investigation of Air Bubble Motion in a Turbulent Water Stream", A.I.Ch.E Journal, Vol. II, No. 2, 1965.
6. Bulson, P. S. "Currents produced by an air curtain in deep water" Dock and Harbour Authority, XLII, No. 487, 1961.
7. Calderbank, P. H., "The Inter-Dispersion of Immiscible Fluid Phases", Brit. Chem. Eng., Vol. I, 1966, pp 206-209 and 267-274.
8. Cederwall, K., and Ditmars, "Analysis of Air-Bubble Plumes", W. M. Keck Lab., Division of Engineering and Applied Science, Calif. Int. Tech., KH-R-24, Sept. 1970.
9. Charlton, J. A., "The Two-dimensional water flow induced by air rising from a submerged source" British Hydromechanics Research Association Report RP 684, 1961.
10. Davidson, L. Amick, JR, E.H., "Formation of Gas Bubbles at Horizontal Orifices", A.I. Ch. E Journal, Vol. 2, 1956.
11. Haberman, W. L., and Morton, R. K., "An Experimental Study of Bubbles Moving in Liquids, Trans. A.S.C.E., Vol. 121, 1956, pp. 227.
12. Ismail, N. M., "Factors Affecting the Efficiency of Pneumatic Breakwater", M. S. Thesis, Transportation Eng. Div., Alexandria Univ., 1971.
13. Kobus, H.E., "Analysis of the Flow Induced by Air-Bubble System" Coastal Eng. Conf. Vol. II, London, 1968.
14. Kurihara, M., "On the study of a penumatic breakwater in Japan" Coastal Engineering in Japan, 8, 1965.
15. Leibson, I., et al, "Rate of Flow and Mechanics of Bubble Formation from Single Submerged Orifices", A. I. Ch. E Journal, Vol. 2, 1956.
16. List, E., and Imberger, J., "Turbulent Entrainment in Buoyant Jet and Plumes", J. Hydr. Div., Proc., A.S.C.E., Spet. 1973.

17. Morton, B. R., Taylor, G. I., and Turner, J. S., "Turbulent Gravitational Convection from maintained and Instantaneous Source, Pro. Roy. Soc., Vol. A236, 1956.
18. Perry, J. H., et al, editors, "Chemical Engineers' Handbook", 4th editions, McGraw-Hill, 1963.
19. Rayleigh, Lord, "The Theory of Sound", Dover, New York, 1945.
20. Rennie, J., and Evans, E., "The Formation of Froths and Foams above Sieve Plate", Brit. Chem. Eng., Vol. 7, 1962, pp. 498.
21. Silberman, E., "Production of Bubbles by the Disintegration of Gas Jets in Liquid", Pro., 5th Midwestern Conf. on Fluid Mech., Univ. of Mich., 1957.
22. Stefan, H., et al, "Flow Establishment and Initial Entrainment of Heated Water Surface Jets", EPA-660/3-75-014, May 1975.
23. Straub, L. G., E. C. Bowers and Z. S. Tarapore, "Experimental Studies of pneumatic and hydraulic breakwaters" Univ. of Minnesota, St. Anthony Falls Lab. Tech. Paper No. 25, Series B, 1959.
24. Taylor, Sr. G. "The action of a surface current used as a breakwater" Proc. Roy. Soc., A231, 466, 1955.
25. U.S. Army, Trans. Res. Command, Fort Eustis, Virginia, "Offshore Discharge (Pneumatic Wave Attenuation Full Scale Tank Tests)", TREC Technical Report 60-26, December 1960.

CHAPTER 172

COASTAL ENVIRONMENT AND A NUCLEAR POWER PLANT

by

RALPH A. DE LA PARRA

ENGINEER, SOUTHERN CALIFORNIA EDISON COMPANY

INTRODUCTION

Regulatory requirements and social constraints make it necessary to evaluate the environmental effects of a project and to incorporate into the design features to minimize adverse environmental impacts. This paper presents a case history of efforts to meet these requirements for a coastal power plant in southern California.

Southern California Edison Company and San Diego Gas & Electric Company are jointly now constructing two additional units to the existing San Onofre Nuclear Generating Station. Being added are Units 2 and 3. The site, about 84 acres (34 ha.), is located within Camp Pendleton, a United States Marine Corps Base, about halfway between San Diego and Los Angeles, California.

The site (See Figure 1) is situated on the edge of a narrow coastal plain that extends from the coastline to a range of low hills, two miles inland, that have a maximum elevation of 1,725 feet (525 m) above sea level. The plain terminates at the beach in a line of wave-straightened cliffs, extending 60 to 80 feet (18 to 24m) above a narrow sandy beach. Numerous ravines are cut into the cliffs as a result of erosion by storm runoff from the coastal plain.

Oceanographic features at the San Onofre site include a sandy bottom which slopes gradually to a depth of 60 feet (18 m) at about 10,000 feet (3,000 m) offshore. Mean maximum summer surface water temperature is about 73°F (23°C). During the fall and winter the water column is usually thermally homogeneous with a minimum temperature of approximately 56°F (13°C).

Ocean currents at the site are chiefly tidally induced, although large scale low velocity circulation patterns are generally present. Very near to the southern California coast, local currents are influenced primarily by a combination of wind, tide, and local topography. The total current is ordinarily the sum of components due to wind, tide, and perhaps large-scale ocean circulations. Speed of the total current measured at San Onofre typically ranges from 0.10 to 1.75 knots, but averages 0.2 knots.

San Onofre, Units 2 and 3 are being constructed southeast of, and immediately adjacent to existing Unit 1. Both the existing and the units under construction generate electrical power by using pressurized water nuclear reactors. Unit 1 has a capacity of 450 MWe and began commercial operation in 1968. Units 2 and 3 will each have a rated electrical output of 1,100 MWe. Commercial operation of Unit 2 is scheduled to begin in October 1981, and Unit 3 in January of 1983.



San Onofre Nuclear Generating
Station Units 2&3
Construction Site

August 2, 1976

Figure 1

Both the existing and the proposed units use sea water in a once through system for cooling the main condensers. Each of the new units will have a completely separate once through cooling system with a flow rate of 1,850 cfs (3,100 m³/min). The temperature rise of the seawater across the condensers is approximately 20°F (11°C).

EFFLUENT LIMITATIONS

Under the Environmental Protection Agency's (EPA) effluent guidelines and standards for steam electric power generating facilities, Units 2 and 3 are classified as "generating units" and are subject to a "no discharge of heat" limitation. The EPA has approved an exception to the "no discharge of heat" limitation for Units 2 and 3 on the basis that insufficient land is available to construct a recirculating cooling system (cooling towers). Because of this exception, the thermal components of the discharges from Units 2 and 3 are subject only to regulation by the "Water Quality Control Plan for Control of Temperature in the Coastal and Interstate Waters and Enclosed Bays and Estuaries of California" (Thermal Plan). Under the Thermal Plan the applicable guidelines are as follows:

- (1) The temperature of the discharge shall not average more than 20°F (11.1°C) above that of the incoming ocean water.
- (2) The discharge of elevated temperature waste shall not result in increases in the natural water temperature exceeding 4°F (2.2°C) at (a) the shoreline, (b) the surface of any ocean substrate, or (c) the ocean surface beyond 1000 feet from the discharge system. The surface temperature limitation shall be maintained at least 50% of the duration of any complete tidal cycle.

Southern California Edison Company requested and the California Regional Water Quality Control Board, San Diego Region, granted an exception to the specific water quality objectives of the Thermal Plan for the purpose of heat treatment to control marine fouling organisms in the cooling water system. The State Water Resources Control Board conditionally approved the exception to the Thermal Plan for heat treatment purposes contingent upon the Company completing studies which would permit the Regional Board to set precise limits on the frequency, temperature, and duration of heat treatments. These studies are described under "Environmental Impact of Plant Operation" below.

The Thermal Plan requires that exceptions be granted only in accordance with Section 316(a) of the Federal Water Pollution Control Act of 1972 and subsequent federal regulations. Section 316(a) requires the discharger to demonstrate that the proposal would assure the protection of aquatic communities in the receiving waters. EPA has approved the scope of the heat treatment studies being conducted for the State of California as being consistent with the requirements of 316(a) and as therefore being acceptable as a 316(a) demonstration.

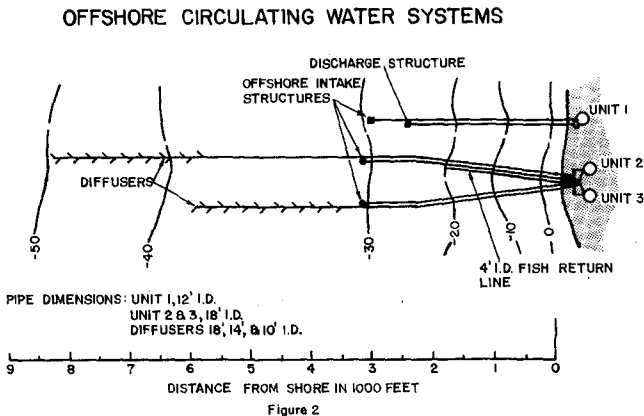
A problem involved in measuring the thermal dispersion from a coastal power plant is that there could be significant natural temperature

variability. At San Onofre, temporal variations in the ocean surface temperature of the order of 2°F can occur over a period of several minutes, and fluctuations over 5 days or so can be as great as 10°F .¹ Spatial variations in ocean surface temperatures of 2°F and greater are numerous over distances of just a few miles.

A paper in the Journal of Geophysical Research² presented the results of time series analyses of several years of coastal ocean temperature records. The records were analyzed using digital filtering, covariance and spectral analysis. The low-frequency component of the temperature signal showed a strong seasonal component in southern California. A period of midwinter warming was apparent in southern California. Intermediate frequency components showed strong correlations in southern California with the presence of distinct and substantial temperature events occurring almost simultaneously over distances of the order of 125 miles (200 km). High-frequency components have a large standard deviation in summer (1.4°F) and a low standard deviation in winter (0.7°F). These components are uncorrelated at stations even a few miles apart.

DESIGN FEATURES TO COMPLY WITH ENVIRONMENTAL REQUIREMENTS

A plan of the offshore circulating water system for Units 2 and 3 is shown in Figure 2. Both of the cooling water intakes will be located about 3,100 feet (945 m) offshore at a depth of about 30 feet (9 m). The outfall for Unit 2 will extend approximately 8,200 feet (2,500 meters) and for Unit 3 approximately 5,900 feet (1,800 meters) from the shoreline. The intake and discharge conduits will utilize 18 foot (5.5 m) ID reinforced concrete pipe.



Each discharge utilizes a diffuser system designed to provide the necessary dilution to meet the California thermal regulatory requirements given above. Each discharge structure consists of a diffuser about 2,500 feet (760 m) in length containing 63 discharge nozzles, or diffuser ports, at the seaward end of the discharge conduit. The diffuser ports will be spaced approximately 40 feet (12 m) apart and will have a nominal throat diameter of approximately 2 feet (0.6 m). The nozzles, shown in Figure 3, will be oriented at a vertical angle of 20° above the horizontal and are aligned to direct the discharge offshore alternately at angles of 25° to the right and 25° to the left of the diffuser section centerline.

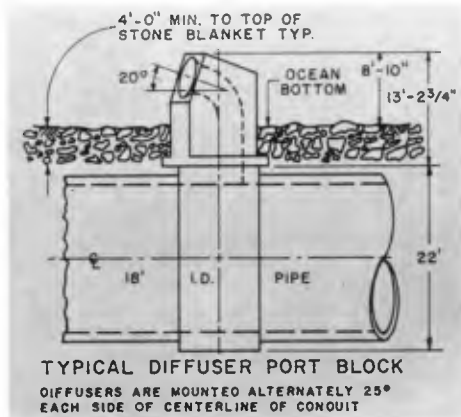


Figure 3

Physical model studies at the California Institute of Technology were used to develop the diffuser design³. A number of different experimental investigations were performed in the course of developing the conceptual design for Units 2 and 3 discharge diffusers. Final confirming tests were conducted in order to provide a model evaluation of the system as finally designed.

The physical model studies predicted a surface delta T not greater than 2.5°F (1.4°C), 1000 feet (300 m) from the diffusers under the most adverse current conditions. The area studied was approximately 2×1.7 miles (3.2×2.7 km). The smallest delta T isotherm definable completely within the area studied was the 1.5°F (0.8°C) isotherm. The 1.5°F (0.8°C) delta T is about the lowest isotherm that can be measured with accuracy in the field because of the ambient surface temperature variations that exist at San Onofre.

The diffuser design produces a general offshore drift, one result of which is to minimize if not completely negate the problems of reentrainment and recirculation. The offshore drift is superimposed on the longshore current. When the tide reverses, this technique provides greater protection against reentrainment of previously discharged water into the plume.

The intake of fish at offshore intake structures is an unavoidable consequence of using seawater for cooling. Past developments have significantly reduced the number of fish entrapped. Continuing studies have resulted in incorporation into the circulating water system design, some unique features to further reduce fish mortality.

The cooling water intake structures for all coastal power plants in the Southern California Edison Company system utilize a velocity cap to reduce fish entrainment. The velocity cap (See Figure 4) is a concrete slab horizontally suspended by columns above the vertical intake pipe. The use of a velocity cap is based on modeling and prototype studies conducted by the Company in the late 1950's⁴ The velocity cap forces water to enter as a horizontal flow rather than a vertical flow. The studies demonstrated that fish are better able to detect, or resist, a vertical flow than a horizontal flow and could therefore avoid being entrained into the cooling water intake structure. The intake of fishes was reduced 90% at stations fitted with the the prototype velocity cap.

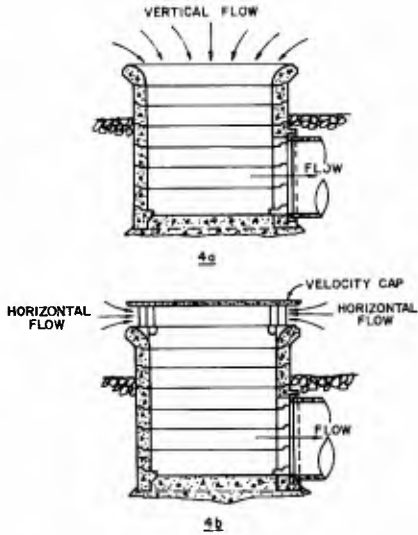
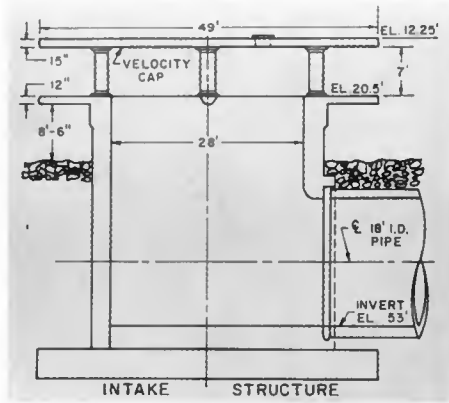


Figure 4.- CONVENTIONAL INTAKE STRUCTURE 4a WITHOUT VELOCITY CAP & 4b WITH VELOCITY CAP

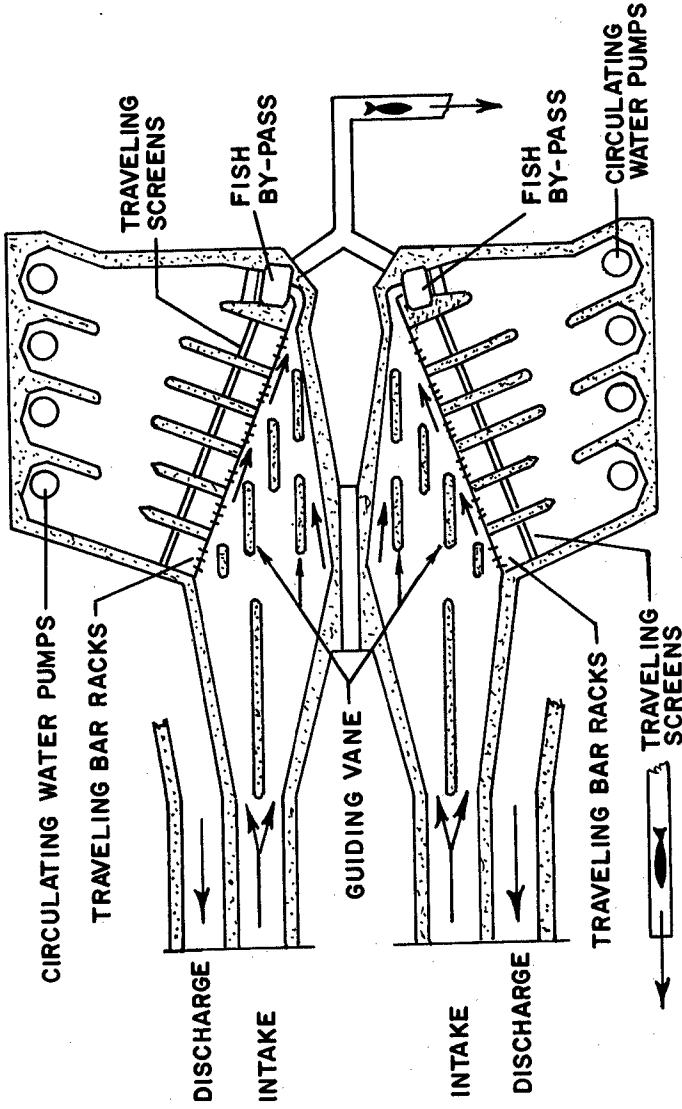
Since the cooling water requirement for San Onofre, Units 2 and 3, is much greater than other plants, it was deemed necessary to develop further means of reducing fish mortality. In 1972, the Company sponsored additional studies to minimize fish entrainment at offshore intake structures and to safely remove fish already entrained into the generating stations' screen wells⁵.



San Onofre Units 2&3

Figure 5

These later studies resulted in a slightly modified velocity cap design for San Onofre, Units 2 and 3, Figure 5. The Units 2 and 3 velocity cap design provides a lip extending out about 8 feet (2.5 m) from the vertical riser and a lower intake velocity.



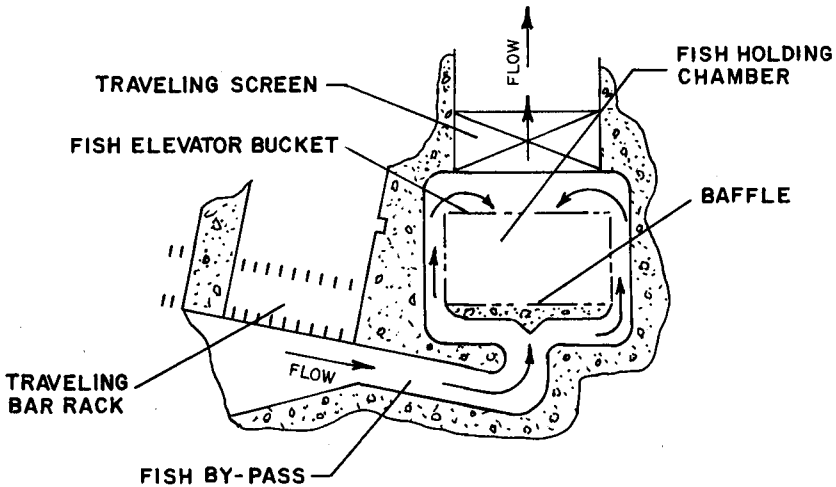
SAN ONOFRE SCREEN WELL CONCEPT

Figure 6

This geometry provides a uniform flow profile across the entrance. Water enters the structure at a velocity of approximately 1.7 feet per second (1/2 m per second) through the circumferential opening.

The fish conservation studies done in 1972 also resulted in a fish conservation system being incorporated into the design of the circulating water system for Units 2 and 3. A plan of the screen wells is shown in Figure 6. Each unit's screen well has a guiding system, fish collecting chamber and fish elevator. The screen well incorporates a system of traveling bar racks and screens to prevent large objects from entering the pump well. It was found that the design most effective for conserving fish was a concept that set the screen well at an angle to the flow stream. The first line of trash removal, trash bars, is positioned at an angle to the flow. Tests showed that all species of fish could be guided with trash bars at right angles to the frame and the frame set at an angle of 30° or less to the flow.

Fish that have entered the circulating water system are guided into the fish collecting chamber, a still water area, shown in Figure 7. A constant flow of water enters the chamber and flows through the screens at the back of the chamber, but fish are prevented from going further. Fish hover over the fish elevator bucket at the bottom of this chamber. The elevator (Figure 8) is a bucket which is periodically raised carrying fish, in water, out of the structure and deposits them into a gravity-flow sluicing channel. A common 4 foot (1.2 m) ID fish return conduit returns entrapped fish, unharmed, to the ocean. The velocity in the fish return conduit is about 5.3



**FISH BY-PASS
AND HOLDING CHAMBER**

Figure 7

feet per second (1.6m per second). Only one fish return conduit is required to serve both units, since each system will operate only a few times per day.

The fish outfall, shown in Figure 9, is in about 15 feet (5 m) of water and is approximately 2000 feet (610 m) offshore. The plan view of the circulating water system, in Figure 2, shows the location of the fish outfall. It is estimated that the fish conservation system, together with the velocity cap will reduce fish loss by more than 99%.

CONSTRUCTION

Site preparation for Units 2 and 3 began in the first quarter of 1974. As of August 1, 1976, construction of this facility was approximately 22% complete. In connection with site preparation for the new units, approximately 2,350,000 cubic yards (1,795,400 cubic meters) of spoil material was excavated from the bluffs. The surface terrace deposit material was disposed of at designated inland sites. The remaining material excavated from the underlying, very dense, fine to coarse sand, consisting of approximately 350,000 cubic yards (267,400 cubic meters), was deposited along the beach in front of the plant site to be redistributed by natural wave action for replenishment of the beaches in the area.

Figure 1 shows an offshore pad, constructed to serve as a laydown area and to allow the construction of the shore portion of the circulating water system and its interface with the offshore conduits, in the dry. The pad is about 1000 feet (300 m) long and extends

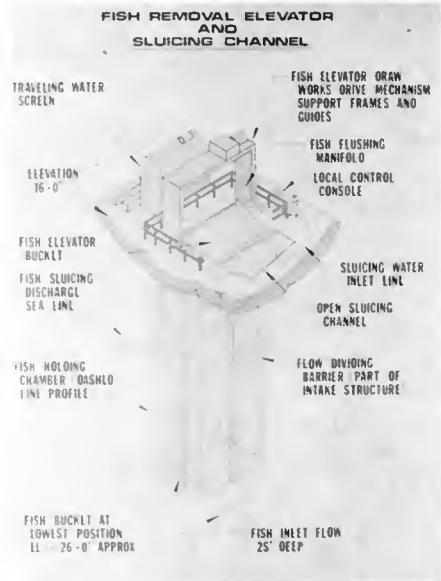
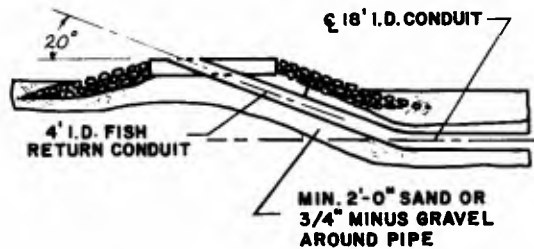


Figure 8



FISH OUTFALL STRUCTURE

Figure 9

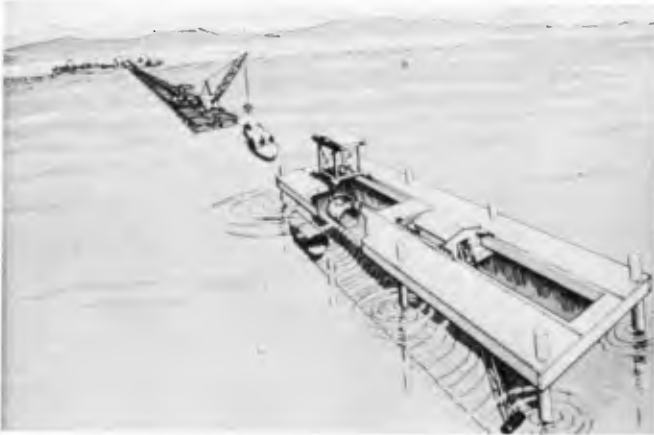
about 300 feet (90 m) offshore. It was constructed by depositing sand from the site excavation offshore, and then driving sheetpiling around the area. One can see that the pad acts as a groin and sand has built up on the northerly end. After the construction is complete the sheetpile wall will be removed and the shoreline will revert back to its normal configuration.

This was the same method used for the construction of Unit 1. From our experience with Unit 1, it is estimated that the shoreline will regain its original alignment with a somewhat wider beach within two years and within 5 years will be back to its original location.

Figure 10 is an artist rendering of the offshore conduit construction. A tressel will be utilized out to about 3000 feet (900 m) offshore, from there a jack-up barge will be used. The dimensions of this barge are about 100 x 300 feet (30 x 90 m). The 18 foot (5.5 m) ID pipe will be layed in 24 foot (7.3 m) sections, buried beneath the ocean bottom, with approximately a 4 foot (1.2 m) cover.

ENVIRONMENTAL IMPACT OF CONSTRUCTION

Extensive environmental monitoring is being conducted during construction to measure the effects of this activity. The monitoring programs include periodic examination of local beaches, intertidal cobble beds, established benthic stations and local kelp beds. The



Laying of 18' ID Cooling Water
Conduits Offshore of San Onofre

Figure 10

monitoring programs are designed to monitor mainly the effects of the construction dewatering discharge into the ocean, the offshore conduit construction and the disposal of sand on the beach. The programs include the following: (1) Water samples of the discharge into the ocean from the construction dewatering and hydrotesting operations are taken and analyzed weekly; (2) Aerial photographs are taken to record the areal extent of visual turbidity present in the ocean and to record placement of sand spoil on the beach; (3) Monthly, beach profiles are taken and bi-monthly intertidal cobble beds in the area are surveyed to determine the amount of inundation, and subsequent re-exposure, of the rocky substrate from sand disposal and from natural conditions; (4) Quarterly, marine biologists conduct intertidal, benthic and local kelp bed surveys.

To date, no irreversible effect upon the local biota can be attributed to the construction activity.

ENVIRONMENTAL IMPACT OF PLANT OPERATION

Heat treatment is the method used by the Southern California Edison Company for the control of fouling organisms within the offshore conduits. Coastal power plants presently heat treat approximately every 5 to 6 weeks by raising the temperature of the discharge to approximately 115° to 125°F (46° to 52°C). Presently, a study, as mentioned above under "Effluent Limitations", is being conducted to determine the optimum mode of heat treatment to control fouling organisms while minimizing adverse effect on marine life. This study consists of the following:

- (1) Fouling organism temperature tolerance and growth rate studies.
- (2) Data collection on fish and macroinvertebrates lost during heat treatment operation at Unit 1.
- (3) Receiving water plankton study.
- (4) Heat treatment plankton mortality study.
- (5) Investigations of alternate methods for controlling marine fouling.
- (6) Heat treatment thermal plume assessment.
- (7) Report on method to minimize nekton entrainment.

These studies will permit the Regional Water Quality Control Board to set precise limits on the frequency, temperature, and duration of heat treatments. The heat treatment study is in progress and will continue through December of 1978. Preliminary data indicates that it may be possible to reduce the frequency, temperature and/or duration of the heat treatments, while still providing protection against excessive marine fouling growth.

An evaluation of the effect on the marine environment of operation of San Onofre Unit 1, and predictions of the effect from Units 2 and 3, is made possible by the San Onofre Unit 1 marine monitoring program in existence since 1963. The monitoring program includes both oceanographic and marine biological studies, and is independent of the monitoring being done for the construction. This program, conducted by consultants, is presently being carried out for Southern California Edison Company, by the Lockheed Ocean Laboratory of San Diego, California. An analysis of the environmental monitoring programs and the predicted thermal addition, show that there will be no adverse effects on the environment from the thermal discharge of Units 2 and 3 and that protection of the beneficial uses of the receiving waters at San Onofre is assured.

In addition to the above monitoring programs, a completely independent program is required as part of the permit process for San Onofre, Units 2 and 3 by the California Coastal Zone Conservation Commission. This program, as were the ones previously mentioned, is an extensive study of the marine environment in order to predict and eventually measure the effects of the proposed new generating units. This work, presently in progress, emphasizes the zooplankton and larval organisms, as well as evaluates compliance with regulatory requirements of state and federal water quality agencies.

It was specified that the California Coastal Zone Conservation Commission program should be designed and conducted under the direction of an independent Marine Review Committee consisting of 3 persons with professional experience in marine biology; one to be chosen by Southern California Edison Company, one to be chosen by opponents of the project, and one to be chosen by the Commission.

The Marine Review Committee program plan has been developed around two elements. The first is a comprehensive definition of the marine ecosystem as it now exists offshore in the vicinity of San Onofre. The second is the development of a predictive model that will utilize data from a special biological program, along with data from the operation of San Onofre Unit 1, to predict the perturbations that will be caused by Unit 2 and 3.

The special biological program has been developed to cover the main ecological elements of the offshore communities and to emphasize those groups that were expected to be the impacted most by plant operation. The biological program covers 6 major study areas:

- (1) Determination of the area of ocean affected by the power plant cooling water intake system.
- (2) Fish population dynamics as influenced by the cooling water system.
- (3) Thermal effects on the structure of benthic ocean communities.
- (4) Fish entrapment.

- (5) Planktonic organisms entrainment into the intake.
- (6) Development of mathematical models using data from the above elements to identify important relationships, test hypothesis, and redirect the program.

Results have not yet been obtained from these studies. The cost of these independent studies will be borne entirely by Southern California Edison and San Diego Gas & Electric Companies.

CONCLUSION

The greatest impact of "borrowing" ocean water for power plant cooling purposes occurs in altering the marine ecosystem immediately around the cooling system's intake and discharge structures. One of the principal environmental concerns in the design of intake systems is possible entrainment of marine organisms. In the design of discharge systems, acceptable limitations of waste heat additions to the receiving water bodies and the rapid dissipation of heat at the discharge outfall should be the main considerations. These considerations and efforts to mitigate adverse effects to the coastal environment have resulted in some unique design features for Units 2 and 3.

Marine monitoring programs, which are part of the project, provide ongoing surveys of the effect of all phases of plant construction and operation. Monitoring programs concerned with temperature dispersion and ecosystem changes indicate that the San Onofre, Units 2 and 3, outfall structures will have little impact upon the San Onofre area. The information obtained can be applied to the siting and design of future power facilities, and will serve as a contribution to basic biological and oceanographic research.

San Onofre Nuclear Generating Station Units 2 and 3 will make it possible to meet the growing public and industrial demand for power, while meeting the legal and social constraints related to environmental concerns.

REFERENCES

1. Koh, R.C.Y., and List, E. J., "Report to Southern California Edison Company on Further Analysis Related to Thermal Discharges at San Onofre Nuclear Generating Station", Hydraulics Consultants, Pasadena, California, September, 1974.
2. List, E. J., and Koh, R.C.Y., "Variations in Coastal Temperatures on the Southern and Central California Coast", Journal of Geophysical Research, Vol. 81, No. 12, April 20, 1976.
3. List, E. J., and Koh, R.C.Y., "Interpretations of Results from Hydraulic Modeling of Thermal Outfall Diffusers for the San Onofre Nuclear Power Plant", Report No. KH-R-31, W. M. Keck Laboratory of Hydraulics and Water Resources, Division of Engineering and Applied Science, California Institute of Technology, Pasadena, California, November, 1974.
4. Weight, R. H., "Ocean Cooling Water System for 800 MW Power Station," Journal of the Power Division, Proceedings of the American Society of Civil Engineers, Paper 1888, December, 1958.
5. Schuler, V. J., and Larson, L. E., "Improved Fish Protection at Intake Systems," Journal of the Environmental Engineering Division, ASCE, Paper No. 11756, December, 1975.

CHAPTER 173

FIELD STUDIES OF SUBMERGED-DIFFUSER THERMAL PLUMES WITH COMPARISONS TO PREDICTIVE MODEL RESULTS

by

A. A. Frigo, R. A. Paddock, and J. D. Ditmars*

Abstract

Thermal plumes from submerged discharges of cooling water from two power plants on Lake Michigan were studied. The system for the acquisition of water temperatures and ambient conditions permitted the three-dimensional structure of the plumes to be determined. The Zion Nuclear Power Station has two submerged discharges structures separated by only 94 m. Under conditions of flow from both structures, interaction between the two plumes resulted in larger thermal fields than would be predicted by the superposition of single non-interacting plumes. Maximum temperatures in the near-field region of the plume compared favorably with mathematical model predictions. A comparison of physical-model predictions for the plume at the D. C. Cook Nuclear Plant with prototype measurements indicated good agreement in the near-field region, but differences in the far-field occurred as similitude was not preserved there.

Introduction

Submerged discharges and multiport diffusers are finding wider use as means of disposing of waste heat from once-through condenser cooling-water systems for power plants. These discharges appear to be superseding surface shoreline discharges for large power plant applications. A reason for employing submerged discharges is that they may create greater initial dilution of the effluent than surface discharges.

The Federal Water Pollution Control Act of 1972 targets heat as a pollutant and hence prohibits its discharge into navigable waterways such as the Great Lakes. However, Section 316(a) of the Act allows for rescinding the no-discharge requirement when it can be demonstrated that the discharge of waste heat will not result in damage to the aquatic environment. It authorizes, on a case-by-case basis, the easing of any thermal limitation that is more stringent than necessary "to assure the protection and propagation of a balanced, indigenous population of shellfish, fish, and wildlife" in the receiving water. This may mean that the surface temperature rise and the extent of the plume will have to be limited — hence the use of high-velocity submerged discharges. One of

*Energy and Environmental Systems Division, Argonne National Laboratory, Argonne, Illinois, 60439, USA.

the requirements for obtaining a 316(a) exemption will probably be a prediction of the spatial and temporal characteristics of the thermal plume from a power plant. Before a plant begins operation, analytical and physical (hydraulic) models must be used for prediction. After operation has begun, actual prototype field measurements can be made.

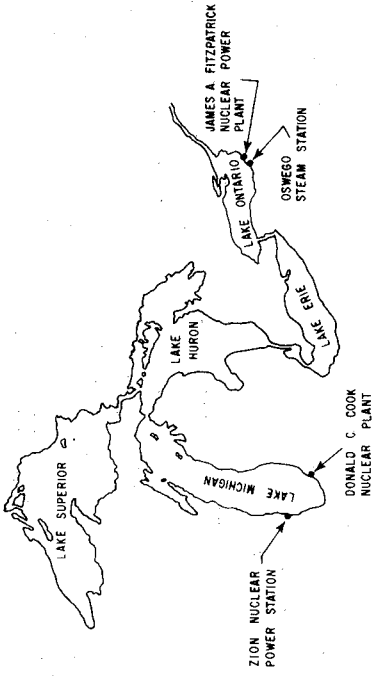
Few predictive models have been verified at prototype scales, and little is known regarding the limitations and applicability of many models. The evaluation of predictive techniques, through prototype-model comparison, is one of the main objectives of the program of which a portion is discussed in this paper.

Argonne National Laboratory (ANL) has been studying the effects of power-plant waste-heat discharges into the Great Lakes since 1970. The initial effort involved the study of thermal plumes from power plants employing shoreline surface discharges. A review of analytical and physical modeling techniques for predicting the fate of waste heat in large lakes was carried out.¹ In addition, a review of available prototype data on thermal plumes was conducted.² This review indicated a paucity of field data describing these plumes under various environmental conditions. Because it was clear that detailed field data of good quality were needed to evaluate the various predictive techniques, ANL began an extensive field program to measure the physical phenomena related to surface shoreline waste-heat discharges into the Great Lakes. Approximately 75 sets of thermal-plume data along with related physical parameters such as lake currents, ambient diffusivities, and meteorological conditions were measured at six different discharge sites on Lake Michigan.^{3,4,5} The results of the thermal-plume measurements were analyzed and compared with model predictions. This four-year effort culminated in a comprehensive critical evaluation of mathematical modeling techniques for surface discharges in which many models were examined and eleven of the most promising models were reviewed in detail.⁶

In response to recent interest in high-velocity submerged discharges, ANL began a study of the physical aspects of these discharges similar to the program carried out for surface discharges. Again, there is a lack of detailed prototype data of good quality for thermal plumes from submerged discharges. This study includes field measurements of the three-dimensional structure of thermal plumes from submerged discharges on the Great Lakes and an evaluation of physical and mathematical models for submerged discharges.

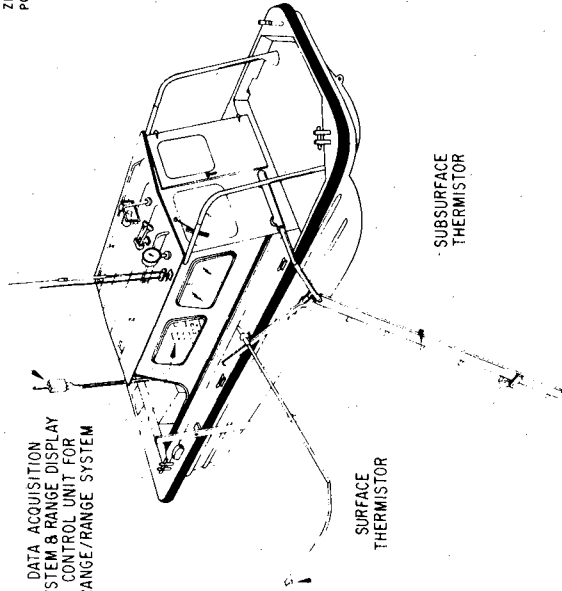
Field studies have been conducted at four power plants with submerged discharges located on the Great Lakes. The power plants being studied include the Zion Nuclear Power Station and Donald C. Cook Nuclear Plant on Lake Michigan and the Oswego Steam Station Unit 5 and James A. FitzPatrick Nuclear Power Plant on Lake Ontario (Fig. 1). Ten sets of thermal-plume data have been collected at the Zion site, nine sets at Donald C. Cook site, three sets at the Oswego Unit 5 site, and four sets at the James A. FitzPatrick site. In addition to thermal-plume temperature data, related information such as limnological, meteorological, and plant operating data have been collected for the times of the thermal-plume surveys. Results of some of the surveys at the Zion and Donald C. Cook plants are discussed in References 7 and 8, respectively.

Fig. 1. Sites of Submerged Discharges Under Study by ANL



RECEIVER/TRANSMITTER FOR RANGE/RANGE SYSTEM

DATA ACQUISITION SYSTEM & RANGE DISPLAY CONTROL UNIT FOR RANGE/RANGE SYSTEM



SURFACE THERMISTOR

SUBSURFACE THERMISTOR

Fig. 2. Schematic Diagram of Survey Boat

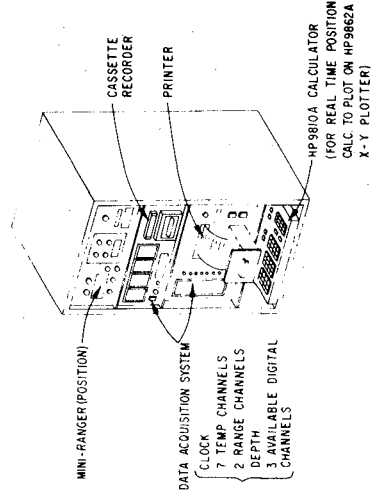


Fig. 3. Schematic Diagram of Data Acquisition System

In this paper, the equipment and techniques used by ANL to collect and handle thermal-plume and related data are discussed. In addition, some results are presented for the case of two adjacent submerged discharges with thermal plumes which effect each other. Comparisons are made between ANL prototype data and pre-operational mathematical- and physical-model predictions.

Field Measurements and Data Handling System

A measurement and data-acquisition system for relatively rapid measurement of the three-dimensional temperature structure of thermal plumes from submerged discharges was developed at ANL. The system was designed for use aboard a small (7.5 m) boat (Fig. 2). The acquisition system (Fig. 3) was interfaced with seven thermistors, a navigational ranging system, a depth sounder, and a real-time boat-position plotting system. The thermistors were mounted at 0.5-m intervals on a 3-m long aluminum bar with streamlined cross section which is towed through the water from the boat. Temperature data at seven depths along with water-depth data are recorded by the system as a function of time and boat position on both paper tape and magnetic-tape cassettes. In addition, the aluminum bar can be replaced with a towed thermistor chain which was developed to allow the measurement of water temperatures in water columns of depths to 10 m. The sampling time interval is variable; typically, data were acquired at eight-second intervals. The data acquisition system allows the collection of data at approximately 1000 points over a linear distance of 10 km in one hour. The real-time plotting system permits the boat operator to know the boat location at any time and, therefore, to adjust the boat's course so as to map completely and in varying detail the study area. The plume data, originally recorded on the magnetic-tape cassettes, are transcribed onto computer-compatible magnetic tapes. These tapes, along with calibration data, are used by a computer program to produce plots of the water temperature and bathymetry as a function of position for each of the depths of measurement. Isotherms and plume centerlines for each level are then drawn by hand on these plots. Figures 5 and 6 are examples of plume isotherm plots at the surface obtained using these techniques. In addition to horizontal plots, vertical cross sections through the plume can also be obtained. The small dots in the figures are the actual temperature values at the location indicated and hence also represent the boat path. The temperature values accompanying the bold dots are representative temperatures corresponding to particular locations.

An ambient water temperature survey is conducted before each plume mapping. Upcurrent from the power plant, the boat is moved from a location offshore to a location as close to the shoreline as possible along a line perpendicular to the shoreline. Ambient water temperatures at the surface and six depths are recorded at about 100 locations during this survey. Ambient lake currents are measured from the boat at fixed locations with a ducted-impeller current meter. In addition, for the duration of the field study, current speed and direction are measured along with lake temperatures at a fixed position and depth by an in-situ current meter/thermograph package. These data are recorded by digital, cassette tape recorder. Wind speed and direction, air temperature, relative humidity, and lake surface conditions are monitored during each thermal-plume field study. Plant operating data and records of wind

speed and direction and air temperature from utility meteorological stations are obtained from the utility records. In addition, thermographs which have been calibrated along with the ANL data acquisition system, are installed in the plant to measure cooling water intake and discharge temperatures to insure temperature data consistency.

Measurements at the Zion Nuclear Power Station

The Zion station is located in northeastern Illinois on the western shore of Lake Michigan about 5.1 km south of the Illinois-Wisconsin state line (Fig. 1). It consists of two units (Unit 1 to the south, Unit 2 to the north) employing pressurized water reactors. Each unit is capable of a gross generating capacity of 1100 MWe. Each unit has its own discharge structure located 232 m from shore, about 47 m on either side of the plant centerline, in about 4.5 m of water (Fig. 4a.). Each discharge structure consists of a rectangular box with 14 ports on the offshore and outboard edges. The ports are 0.9 m high and 1.6 m wide and are oriented at 45° to the box centerline. The discharge flow rate at full power operation is about 50 m³/s for each unit and the average velocity at the outlet ports is 2.4 m/s. The nominal temperature rise of the cooling water is 11 C°.

Plumes were surveyed at the Zion site on ten occasions. On eight occasions cooling water was discharged from only one discharge structure. In most cases, the ambient current was approximately shore-parallel, and thus was either in the direction of the discharge or in a direction opposite to the discharge. An example of the surface isotherms for a single discharge in the direction of the ambient current is shown in Fig. 5. Subsurface isotherms also indicate the same general orientation of the plume. The surface isotherms for a single discharge opposed to the ambient current are shown in Fig. 6. The plume is bent in the direction of the ambient current in the far field, and the near-field surface dilutions are decreased below those for the case of discharge in the direction of the ambient current. Again, subsurface isotherms indicate that the plume far field has been bent in the direction of the ambient current. The case of discharges from both units, one plume with and the other plume opposed to the ambient current, is shown in Fig. 7. While two plumes can be distinguished on this surface isotherm plot, the far-field region is a combination of plumes from both discharges.

One basis for describing and comparing thermal plumes is an isotherm-surface-area plot. The area refers to the surface area enclosed within an isotherm of particular temperature or normalized temperature. The isotherms here are characterized by the excess-temperature ratio, θ/θ_0 , that is, the ratio of the difference between the actual isotherm temperature and the ambient water temperature and the difference between the discharge and ambient water temperatures. Figure 8 shows the results from the surveys at the Zion site for single discharges opposed to the ambient current, and for discharges from both units. The envelope about each average line reflects the range of values determined from the measurements. This scatter appears due to variations in discharge conditions and ambient current magnitude and direction which resulted in variation in values of the discharge densimetric Froude number, F_s , and velocity ratio, K , where,

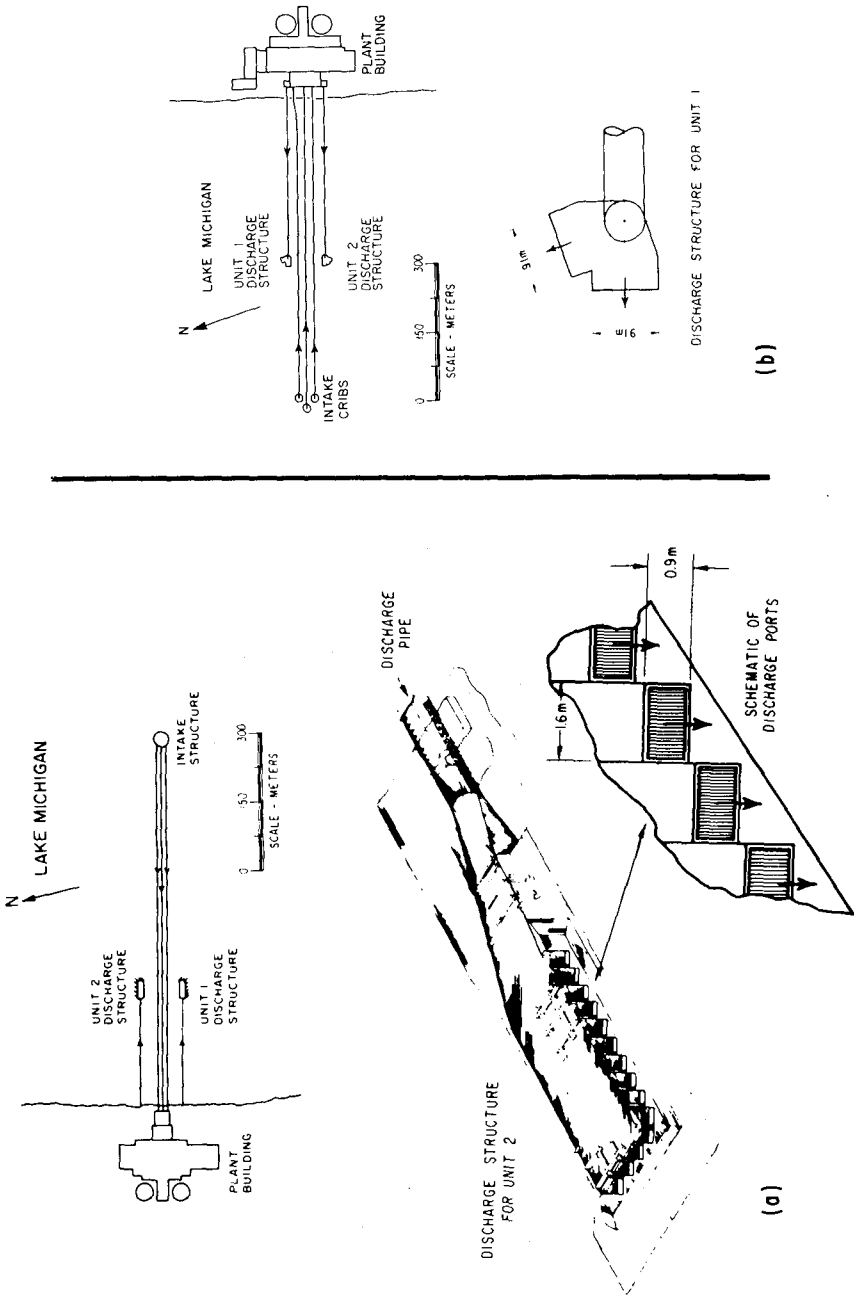


Fig. 4. Schematic Diagram of Cooling-water System and Discharge Structures: (a) Zion Nuclear Power Station and (b) Donald C. Cook Nuclear Plant

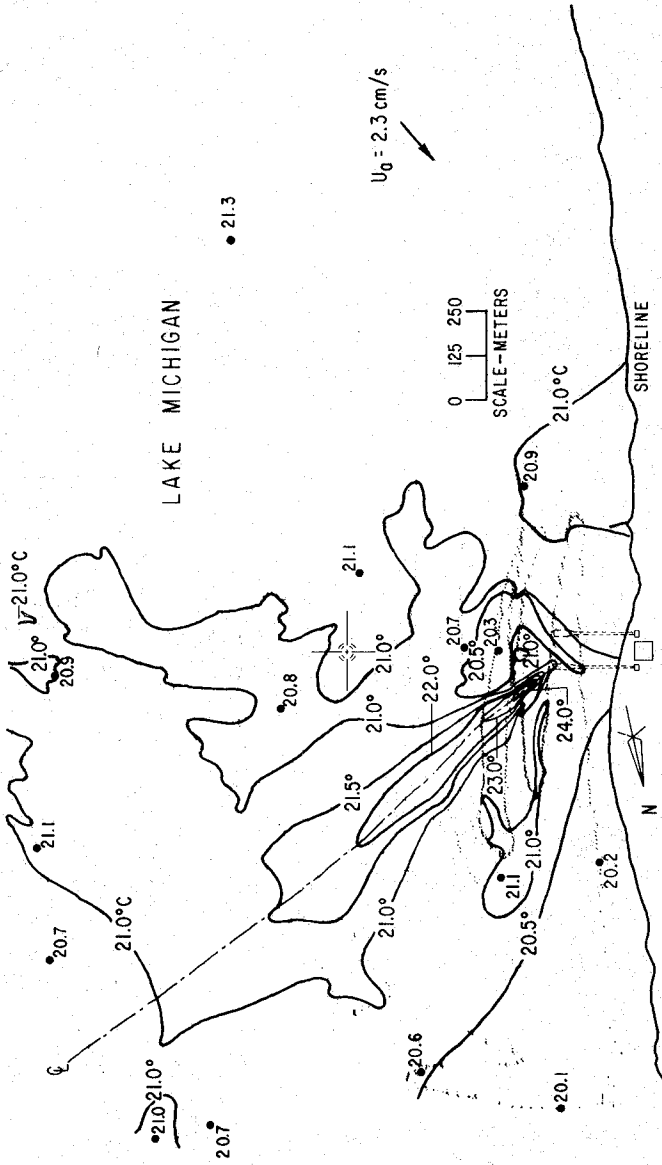


Fig. 5. Thermal Plume at Surface for Zion: July 9, 1975, 1152-1537 hr CDT; Discharge Temperature 28.6°C for Unit 2

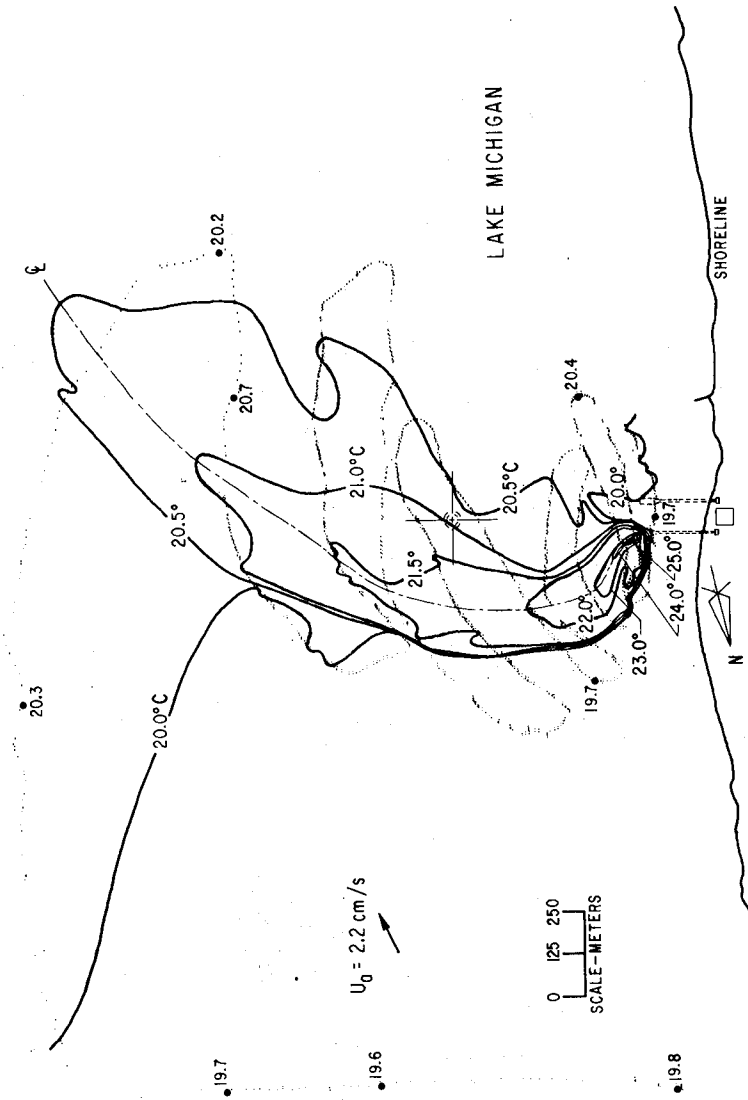


Fig. 6. Thermal Plume at Surface for Zion: July 10, 1975, 1040-1214 hr CDT; Discharge Temperature 28.7°C for Unit 2

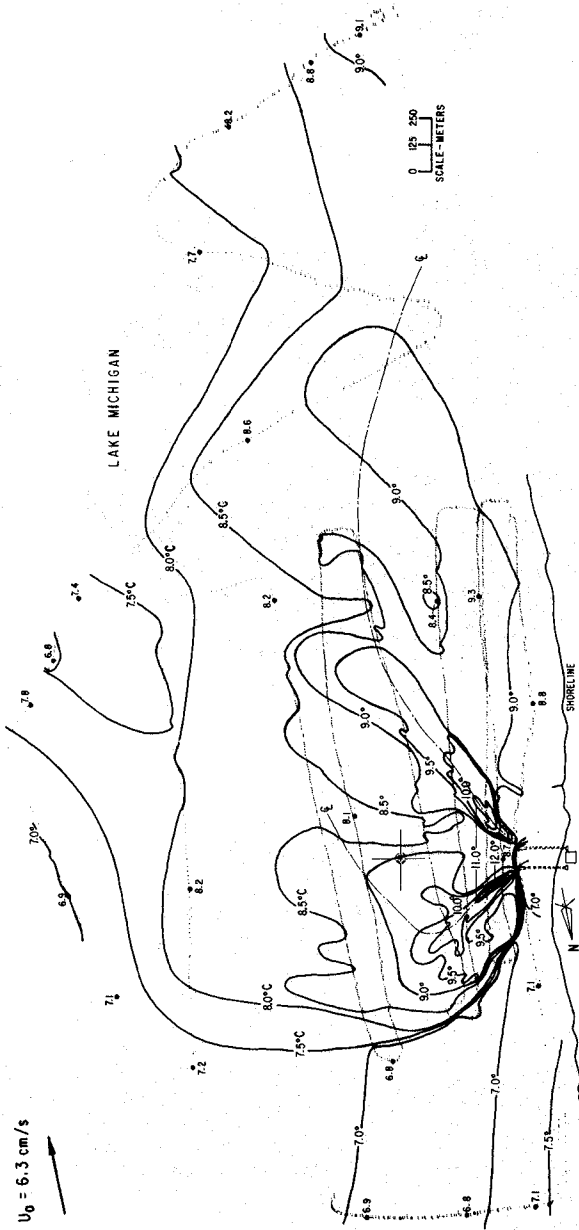


Fig. 7. Thermal Plume at Surface for Zion: May 1, 1975, 1010-1300 hr CDT; Discharge Temperature 16.2°C for Unit 1 and 17.4°C for Unit 2

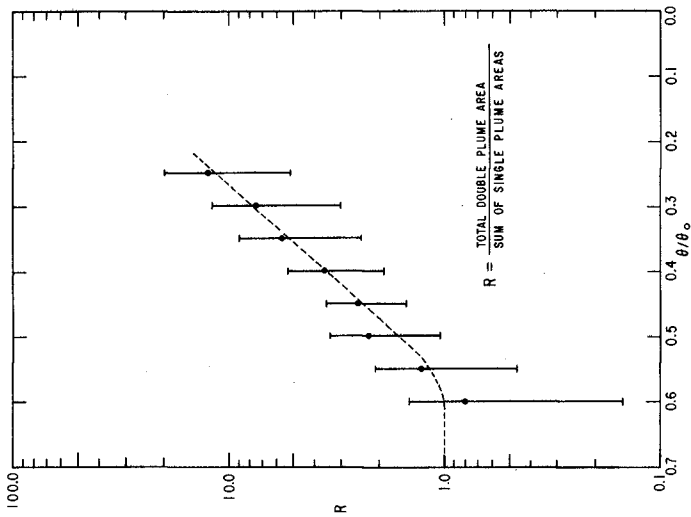


Fig. 9. Ratio of Double-discharge Plume Surface Isotherm Areas to the Sum of Single-discharge Plume Areas

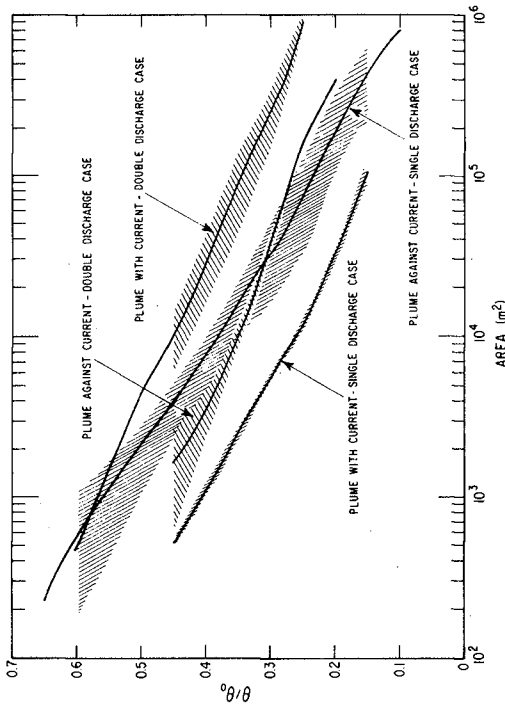


Fig. 8. Comparison of Near-surface Isotherm Areas for Single and Double Discharges, With and Against the Ambient Current

$$F_s = \frac{U_o}{\left(\frac{\Delta\rho_o}{\rho} g B\right)^{1/2}}$$

U_o = slot discharge velocity,

U_a = ambient current velocity,

B = slot width,

and $K = \frac{U_o}{U_a}$;

$\frac{\Delta\rho_o}{\rho}$ = discharge density difference.

The ranges of variation of F_s and K are shown in Table 1.

Table 1

Variations of Parameters for ANL Studies
at the Zion Nuclear Power Station

	<u>With Current</u>	<u>Against Current</u>	<u>Double Discharge</u>
F_s Range	17.0 - 17.5	14.0 - 23.0	22.6 - 25.2
K Range	83 - 100	10 - 111	38 - 45

Single discharges opposite to the ambient-current direction result in larger areas for given isotherm excess-temperature ratios than single discharges in the direction of the ambient current. In the case of discharges from both units (double discharge), Fig. 8 indicates that the plume of the discharge opposed to the ambient current has an isotherm-area relationship similar to that of a single discharge opposed to the current. However, that plume of the pair, with the discharge in the direction of the ambient current, has larger surface areas associated with a given isotherm than a single discharge with the ambient current. It appears that interaction or interference between the adjacent discharge plumes is responsible for the increased areas or decreased dilution in the downcurrent plume of the pair. Entrainment of the heated water from the upcurrent plume into the second plume and thus the blocking of cool ambient water on the upcurrent side results in increased temperature elevations in the downcurrent plume over those experienced by a single discharge in the direction of the ambient current.

The degree of interaction between the plumes in the case of discharges from both units at the Zion site is manifested further by the following comparison. Consider a prediction of the isotherm-area relation for the double-discharge situation at the Zion site which neglects any interaction between the two discharges. In such a case, the total surface area associated with a given excess-temperature-ratio isotherm would be the sum of the corresponding areas for two single-discharge plumes, one discharged with the ambient current and one discharged opposite to the ambient current. A comparison of measured total surface areas for double plumes and the areas resulting from the linear super-

position of single-plume areas is reflected in the ratio, R , shown as function of θ/θ_0 in Fig. 9. If the superposition were valid and interactions were thus negligible, the ratio, R , would be 1.0. However, as shown in Fig. 9, measurements of double plumes indicated far-field areas as much as ten times larger than simple superposition would predict. The ranges in R values for a given value of θ/θ_0 reflect the envelopes of results, and the dots represent mean values.

The double-discharge measurements at the Zion site point out an interesting feature of the design and evaluation scenarios associated with the environmental assessment of thermal discharges. The often postulated idea that the critical situation for surface temperature fields occurs under conditions of small or zero ambient currents appears valid at the Zion site for single discharges but not for double discharges. Relatively small ambient currents appear to result in significant interaction between plumes for the double-discharge case with increases in surface areas affected over those which would be predicted for two non-interacting plumes discharged into a stagnant environment.

Predictive mathematical models applied to the thermal plumes at the Zion site are of two types: a site specific model developed by Pritchard and general models for thermal discharges in shallow water developed at MIT.

Pritchard⁹ made predictions of plume temperatures and geometry for full power operation prior to construction based on a model similar to an earlier model for surface discharges. This modeling effort considered the case of no ambient lake currents and no significant interaction between plumes. Subsequently, on the basis of field observations, the model was modified and refined to include the case of bending of the plume into shallow water by currents.^{10,11} Predictions for this case reflect the effects of reduced entrainment from below the plume, recirculation of heated water through the cooling water intake, and reentrainment of heated plume water following a current reversal. Direct comparison between the Pritchard single plume predictions and the ANL field measurements is not possible as the predictions are for seasonal "worst cases." However, a comparison of the isotherm-area predictions for the fall/spring cases of bent and unbent plumes with the average of the ANL data for single discharge against the current indicates good agreement for $\theta/\theta_0 < 0.5$ and conservative predictions for $\theta/\theta_0 > 0.5$.

No general models for submerged discharge are strictly applicable to the Zion site and discharge geometry. Integral-similarity models for buoyant plumes, such as those reported by Fan and Brooks,¹² are not appropriate for the shallow submergence (depth is only 4.2 slot widths) of the Zion discharge structure. Adams¹³ studied the behavior of horizontal thermal discharges from long, multiport diffusers into shallow water with current directed over the discharge. This model accounts for the acceleration of the flow downstream from the diffuser due to the addition of the discharge momentum and predicts the dilution of the discharge in a well-mixed region downstream of the discharge. Although the proximity of the Zion discharge structure to the shoreline does not conform strictly to the idealized unbounded flow field of the model and the well-mixed region geometry is not predicted by the model, dilution predictions in the well-mixed region were found to be about 1.45 (or

$\theta/\theta_0 = 0.7$) for single discharge conditions at the Zion site. Jirka and Harleman¹⁴ provided a more detailed study of submerged diffuser discharges in shallow water based on a two-dimensional analysis of a long slot-type discharge in a channel with no ambient currents. Several regimes of flow were found possible depending on the hydraulics of the heated water flow on the surface away from diffuser and the entrainment flow on the bottom toward the diffuser. The range of parameters for the horizontal Zion discharge result in the prediction of a flow instability or "full-mixing" region near the diffuser. The uniform vertical temperatures measured at the Zion site in the near-field region confirm that this is approximately the case there. The Jirka-Harleman model gave predictions of the discharge dilution in this "full-mixing" region to be about 1.8 (or $\theta/\theta_0 = 0.6$) for single-discharge conditions at the Zion site.

Although the models of Adams and of Jirka and Harleman are not strictly applicable to the Zion discharge and although temperature measurements do not indicate the extensive, well-defined "full-mixing" region postulated for the models, comparisons of model predictions were made with near-field surface centerline temperatures for eight single plumes measured by ANL. The location of the point of the highest surface temperature on the centerline occurred between 40 and 100 m from the discharge with an average of 70 m, and the corresponding surface excess-temperature ratios ranged from 0.49 to 0.73 with an average of 0.59. There is remarkably good agreement with the model predictions. However, the fact that vertically well-mixed conditions actually exist in the near-field region is probably the primary factor responsible for the good agreement with the effects of finite diffuser length and boundary geometry being of secondary importance.

In addition to preoperational mathematical-model predictions of the thermal-plume characteristics at the Zion site, physical model studies were performed.¹⁵ These studies employed an undistorted model with geometric scale reduction of 1:25 and Froude and densimetric Froude number similitude. The model boundaries appeared to influence the model results significantly. Comparison of model predictions for single discharges, with and against the ambient current, with the ANL field measurements in terms of centerline temperatures and isotherm-area plots indicate that the model results underestimate the initial near-field dilutions.

Detailed discussion of the comparisons between the field data from the Zion site and the predictions of plume characteristics from mathematical and physical modeling techniques is found in Ref. 7.

Measurements at the Donald C. Cook Nuclear Plant

The Donald C. Cook Nuclear Plant is located near Bridgman, Michigan on the southeastern shore of Lake Michigan, about 18 km south of Benton Harbor (Fig. 1). The two D. C. Cook nuclear reactors are nearly identical, pressurized-water units. Each is capable of a gross generating capacity of 1090 MWe. During 1975, only Unit 1 was operational. The Unit 1 discharge structure is located 365 m offshore, in about 5.7 m of water. The cooling-water discharge from Unit 1 is through two horizontal slots each 9.1 m wide by 0.6 m high, about 0.5 m above the

lake bottom (Fig. 4b). One slot is directed offshore while the other is set at 70° to the offshore direction. The discharge flow rate is $48 \text{ m}^3/\text{s}$ and the average discharge velocity is about 4.3 m/s . The nominal temperature rise for the condenser cooling water is about 12 C° .

Plumes were surveyed at the D. C. Cook site on nine occasions during the spring and summer of 1975 by ANL. Comparisons of field data with model predictions require careful examination of all prototype data over a range of conditions. However, as an example, a limited portion of the available data for plumes at the D. C. Cook site is presented here.

Preoperational physical-model studies were undertaken by Alden Research Laboratories¹⁶ for prediction of the characteristics of the thermal plumes due to the discharges from both of the proposed units of the D. C. Cook plant. An undistorted hydraulic model with geometric scale reduction of 1:75 was employed and resulted in an area modeled which extended about 2300 m along the shoreline and about 1100 m offshore. Temperatures and velocities were scaled to preserve both Froude and densimetric Froude numbers. Near-surface temperatures in the model were measured using a fixed grid of 137 thermocouples for a variety of submerged discharge designs and of discharge and ambient receiving water conditions. Examples of the model-study predictions of near-surface isotherms for the case of cooling-water discharge from the final design Unit 1 slots only are shown in Figs. 10 and 11.¹⁷ These figures indicate, in prototype dimensions, the excess-temperature-ratio isotherms for the case of a constant temperature ambient receiving water, uniform, shore-parallel ambient currents in a northerly direction, and maximum cooling-water flows with full-power-generation discharge temperatures about 11.7 C° above ambient water temperature. The magnitude of the ambient current is 6.1 cm/s for the case shown in Fig. 10 and 15.2 cm/s for the case in Fig. 11.

Comparison of prototype data with the physical-model results requires that dynamically similar conditions be found among the prototype surveys. In regard to the near-field dilution of the plume, that requires that the same densimetric Froude number, F_s , and velocity ratio, K , exist. For the model cases reported above, the densimetric Froude number is about 27 for both cases and the velocity ratios are 65 and 26 for Figs. 10 and 11, respectively. For the small relative discharge submergence (water depth to slot width) of 8.5 and large densimetric Froude number, laboratory experiments and analysis¹⁴ indicate that "full mixing" conditions may exist in the near-field region, similar to those found at the Zion site discussed above. The physical-model studies for the D. C. Cook discharge show a vertically well-mixed region in the near field for the range of conditions investigated. Prototype temperature measurements confirm the existence of this near-field feature. Analysis, and to a degree laboratory experiments,¹⁴ indicate that the dilution of the discharge in the near-field "full mixing" region is independent of densimetric Froude and is dependent primarily on the relative submergence. Since scaling of the relative submergence is assured by geometric similitude between model and prototype, dilutions in "full-mixing" regions in the near field should be comparable in model and prototype for cases of similar ambient-current direction and velocity ratio, K . Plume characteristics in the intermediate and far-field regions, however, are not likely to scale so simply. In the

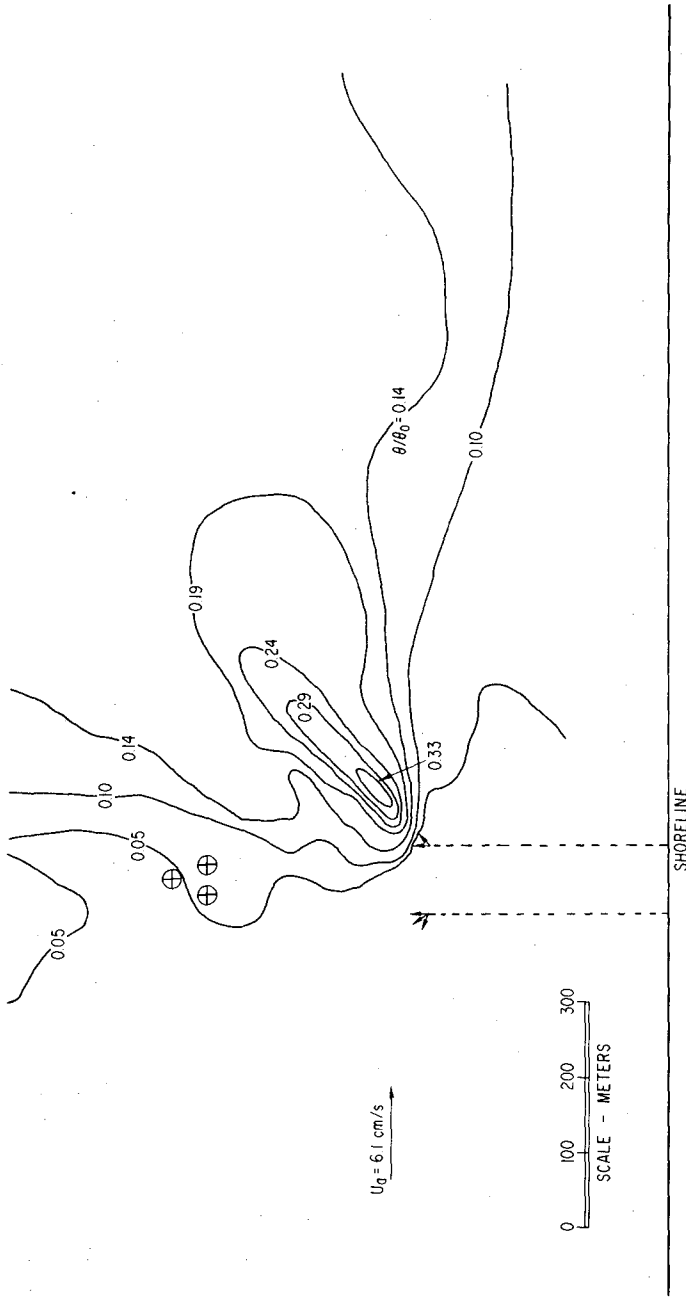


Fig. 10. Surface Excess Temperature Ratio Isotherms From Physical-model Study for D. C. Cook Unit 1 with an Ambient Current of 6.1 cm/s

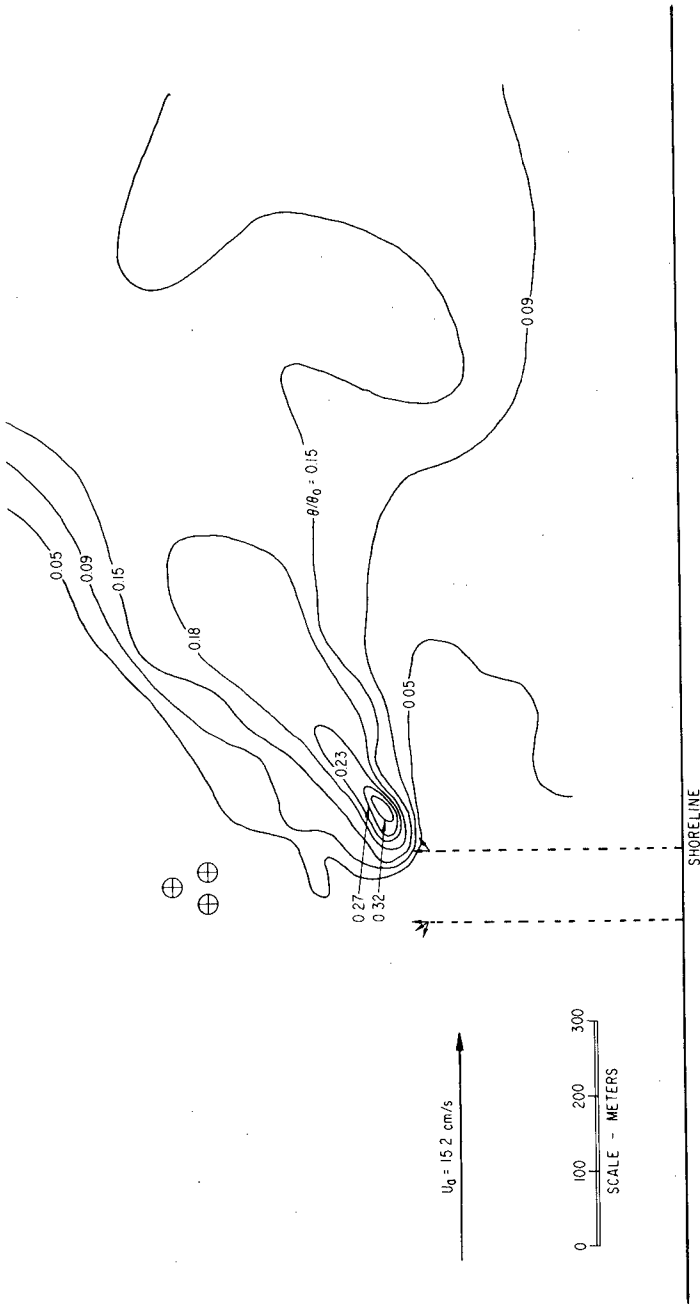


Fig. 11. Surface Excess Temperature Ratio Isotherms from Physical-model Study for D. C. Cook Unit 1 with an Ambient Current of 15.2 cm/s

intermediate region, beyond the "full-mixing" region, preservation of local densimetric Froude number is probably important to produce proper gravitational spreading in the surface region. However, in the intermediate and in the far-field regions interfacial friction should also be scaled properly, and it is not clear that that is possible in an undistorted model of this scale.¹⁸ Moreover, the far-field mixing is primarily governed by ambient mixing processes which may not be scaled properly in the model. Thus, complete similitude between a single model and prototype plume temperatures is unlikely over the range of regimes from the near field to the far field. For the undistorted model studies conducted, the comparison between model predictions and prototype measurements is most appropriate in the near-field region.

An example of prototype surface-temperature measurements at the D. C. Cook site made under conditions providing a degree of similarity is shown in Fig. 12. The ambient lake temperature was uniform, and a plant power generation at about 80% of capacity resulted in a discharge-temperature elevation of 7.4 C° above ambient. The depth-averaged ambient current (measured upcurrent and offshore of the discharge) had a magnitude of 5.8 cm/s and was directed at about 40° from north or about 20° from being shore-parallel as in the model studies. These conditions produce a discharge densimetric Froude number of about 54 and a velocity ratio of about 75. The Froude number associated with the prototype case is about twice as large as that for the model tests mentioned above. However, the prototype Froude number is large enough to indicate "full-mixing" conditions in the near-field region, and such conditions are observed in the near-field temperature data. Thus, as argued above, near-field mixing should be independent of the exact value of densimetric Froude number, and, for similar values of velocity ratio, model and prototype similarity should exist. Comparison of Figs. 10 and 12 indicates reasonable agreement between the near-field surface excess-temperature ratios ($\theta/\theta_0 > 0.27$). However, the general surface-isotherm pattern of the prototype resembles that for the model case with larger ambient current ($K = 26$) shown in Fig. 11. The offshore isotherms in the prototype case are more closely spaced than in either model case and do not indicate the proximity to the intake structures shown in the model case of $K = 65$ (Fig. 10). The comparison between prototype and model plume centerline excess-temperature ratios is shown in Fig. 13. Isotherm-area plots for the prototype and model cases are given in Fig. 14. The agreement for these gross plume characteristics is good, although the prototype data indicate slightly larger centerline temperatures and areas.

Several explanations are possible for the differences between the model and prototype surface-isotherm patterns. The prototype ambient lake current in the vicinity of the discharge did not appear to be shore-parallel as in the model study. The current had a component in the onshore direction. Moreover, the wind was from the west in an onshore direction and, with the current, may have contributed to the close spacing of the prototype offshore isotherms. This effect is not, however, realized on the inshore side of the plume. The difference in power generation levels, as manifested by lower discharge temperature excess in the prototype case, may not be significant in the near-field region but certainly affects the intermediate- and far-field spreading. Since these regions of the model plumes contain larger temperature

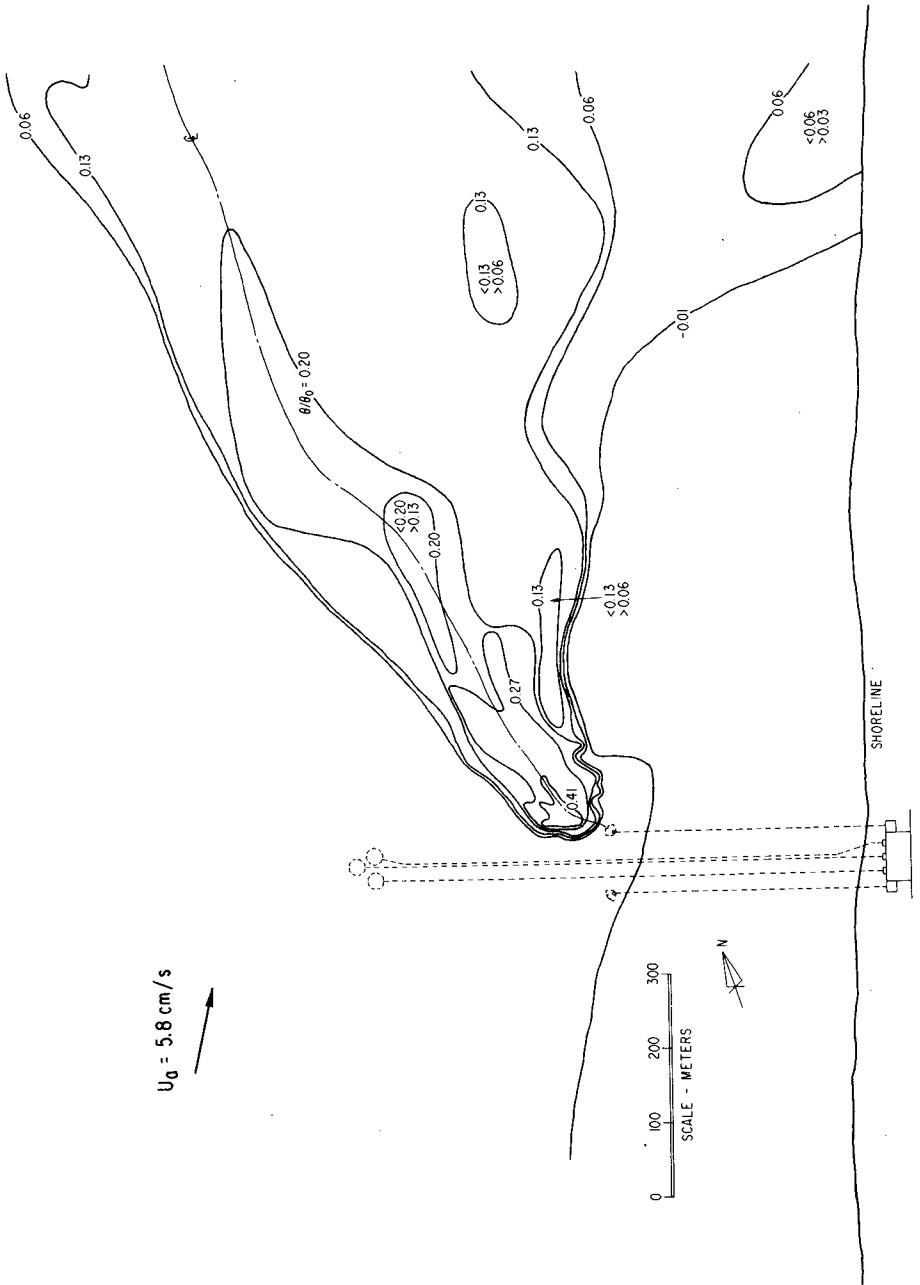


Fig. 12. Surface Excess Temperature Ratio Isotherms from ANL Field Measurements at D. C. Cook: May 14, 1975, 1158-1318 hr CDT. Ambient Current = 5.8 cm/s.

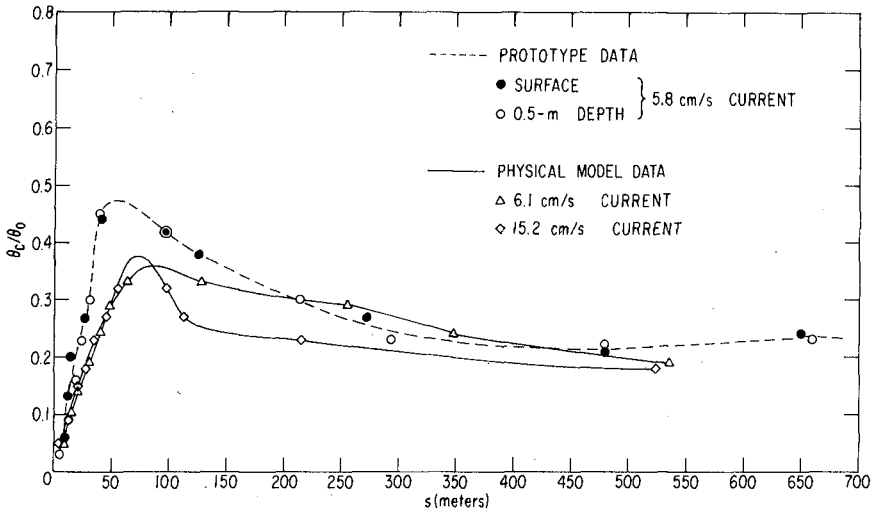


Fig. 13. Comparison of Centerline Temperature Decay from Physical-model and Prototype Data for D. C. Cook Unit 1

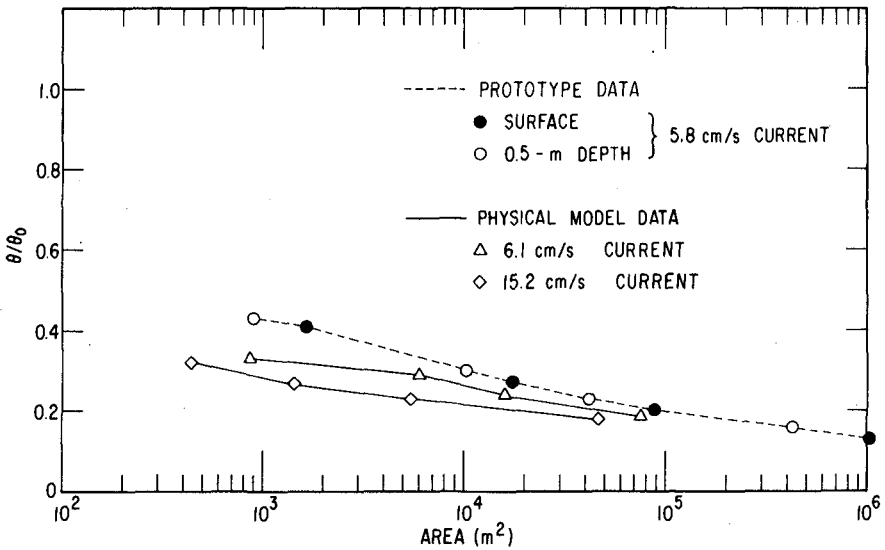


Fig. 14. Comparison of Isotherm Areas from Physical-model and Prototype Data for D. C. Cook Unit 1

excesses than the prototype plume, larger lateral gravitational spreading would be expected in the model cases than in the prototype case. The offshore, far-field region of the model may also be affected by the presence of the model boundary. The offshore model boundary is indicated by the end of the offshore isotherms in Figs. 10 and 11. Its proximity to the plume may result in reduced transport of heat in the downcurrent direction and an increase in temperature in that region.

Evaluation of a physical-model prediction on the basis of a single prototype condition, dynamically similar or not, is hardly proper. The comparison presented is for the purpose of demonstrating the problems associated with such model and prototype comparisons. A comprehensive evaluation requires a set of such comparisons for all the prototype data obtained.

Conclusions

The examples of comparisons between model predictions and prototype measurements demonstrate that while predictions of maximum near-field temperatures may be reasonably good for these cases, prediction of other plume characteristics is not so straight-forward. The cases considered have been relatively simple; that is, ambient receiving-water stratification and ambient current shear have been negligible. Measurements at the Zion site indicated that the direction of the ambient current was an important parameter governing plume dilution and extent. The interaction between plumes from the two discharges at the Zion site resulted in heated surface areas as much as ten times larger than would be predicted by models assuming the superposition of two independent discharges. The example of temperature measurements at the D. C. Cook site indicates the difficulty of obtaining dynamic similarity for comparisons between physical models and prototype cases. The need for prototype measurements at submerged discharge sites is clear. Evaluation of predictive mathematical and physical models requires detailed measurements of the temperature field produced as well as carefully monitoring of ambient conditions. Comparisons between model predictions and prototype measurements require a reconciliation of the idealizations necessary for model predictions and the complex nature of the prototype conditions and an appreciation of the capabilities and limitations of the modeling techniques. Only continued comparisons of model predictions with carefully gathered and interpreted prototype data will enhance the value of either technique for design or environmental assessment.

Acknowledgments

The work reported has been carried out at Argonne National Laboratory for the U.S. Energy Research and Development Administration under Contract No. W-31-109-Eng-38. The assistance of utility personnel at the Zion and D. C. Cook plants is gratefully acknowledged. C. Tome, L. Van Loon, W. Orvosh, and D. L. McCown of ANL were active participants in the development of equipment and the collection and handling of the field data.

References

1. Policastro, A. J., and Tokar, J. V., "Heated Effluent Dispersion in Large Lakes: State-of-the-Art of Analytical Modeling: Part 1. Critique of Model Formulations," Argonne National Laboratory Report ANL/ES-11, January 1972.
2. Tokar, J. V., "Thermal Plumes in Lakes: Compilation of Field Experience," Argonne National Laboratory Report ANL/ES-3, August 1971.
3. Frigo, A. A., and Frye, D. E., "Physical Measurements of Thermal Discharges into Lake Michigan: 1971," Argonne National Laboratory Report ANL/ES-16, October 1972.
4. Frigo, A. A., Frye, D. E., and Tokar, J. V., "Investigations of Heated Discharges from Nuclear Power Plants on Lake Michigan: 1972," Argonne National Laboratory Report ANL/ES-32, March 1974.
5. Tokar, J. V., Zivi, S. M., Frigo, A. A., Van Loon, L. S. Frye, D. E., and Tome, C., "Measurements of Physical Phenomena Related to Power Plant Waste Heat Discharges: Lake Michigan, 1973 and 1974," Argonne National Laboratory Report ANL/WR-75-1, March 1975.
6. Dunn, W. E., Policastro, A. J., and Paddock, R. A., "Surface Thermal Plumes: Evaluation of Mathematical Models for the Near and Complete Field," Argonne National Laboratory Report ANL/WR-75-3, 1975.
7. Paddock, R. A., Frigo, A. A., and Van Loon, L., "Thermal Plumes from the Submerged Discharges at the Zion Nuclear Power Station: Prototype Measurements and Comparisons with Model Predictions," Argonne National Laboratory Report ANL/WR-76-5, July 1976.
8. Frigo, A. A., Paddock, R. A., and McCown, D. L., "Field Studies of the Thermal Plume from the D. C. Cook Submerged Discharge with Comparisons to Hydraulic-Model Results," Argonne National Laboratory Report ANL/WR-75-4, June 1975.
9. Pritchard-Carpenter Consultants, "Predictions of the Distribution of Excess Temperature in Lake Michigan Resulting from the Discharge of Condenser Cooling Water from the Zion Nuclear Power Station," Ellicott City, Maryland, April 1970.
10. Pritchard-Carpenter Consultants, and Hydrocon, Inc., "The Distribution of Excess Temperature from the Zion Generating Station on Lake Michigan: Fall Study Period (December, 1973)," Reference 114, Baltimore, Maryland, July 1974.
11. Pritchard-Carpenter Consultants, and Hydrocon, Inc., "The Distribution of Excess Temperature from the Zion Generating Station on Lake Michigan: Summer Study Period (July 1974)," Reference 118, Baltimore, Maryland, May 1975.
12. Fan, L.-N. and Brooks, N. H., "Numerical Solution of Turbulent Buoyant Jet Problems," W. M. Keck Lab. for Hydraulics and Water Resources, California Institute of Technology, Report No. KH-R-18, 1969.
13. Adams, E. E., "Submerged Multiport Diffusers in Shallow Water with Current," S. M. Thesis, Civil Engineering, Massachusetts Institute of Technology, Cambridge, Massachusetts, June 1972.
14. Jirka, G. and Harleman, D.R.F., "The Mechanics of Submerged Multiport Diffusers for Buoyant Discharges in Shallow Water," Report No. 169, Ralph M. Parsons Laboratory for Water Resources and Hydrodynamics, Massachusetts Institute of Technology, Cambridge, Massachusetts, March 1973.
15. Lantz, C. H. and Lisauskas, R. A., "Zion Discharge Model Study, Zion Station, Commonwealth Edison Company of Illinois," Alden Research Laboratories, Worcester Polytechnic Institute, Holden, Massachusetts, January 1971.
16. Smith, P. J. and Hecker, G. E., "Hydrothermal Model Study, Lake Cooling Water Structures, Donald C. Cook Nuclear Plant, American Electric Power Service Corporation," Alden Research Laboratories, Holden, Mass., October 1973.
17. Markowsky, J., American Electric Power Service Corp., New York, private communication, June 1975.
18. Brooks, N. H., Koh, R.C.Y., List, E. J., and Wolanski, E. J., "Hydraulic Modeling of Thermal Outfall Diffusers for the San Onofre Nuclear Power Plant," W. M. Keck Lab. for Hydraulics and Water Resources, Calif. Inst. of Tech., Report No. KH-R-30, 1974.

CHAPTER 174

THERMAL DISCHARGES: PROTOTYPE vs. HYDRAULIC MODEL

Gary C. Parker*
C. S. Fang*
Albert Y. Kuo*

ABSTRACT

Data on physical parameters in the James River around the condenser cooling water discharge of the Surry Nuclear Power Plant, taken prior to and during plant operation, were analyzed to determine the physical effects of the thermal discharge on the area and to compare the prototype distribution of excess temperature to predictions based on hydraulic model experiments.

The results of this investigation indicated that the increase in water temperatures due to the thermal discharge did not represent a significant alteration of the physical environment outside the mixing zone. The thermal discharge experienced turbulent mixing and entrainment near the out-fall and temperatures decreased rapidly in this region.

Field data on temperature distributions around the discharge, when compared to predictions based on hydraulic model experiments, indicate that the model predictions were conservative.

INTRODUCTION

The generation of electrical energy from a steam source results in an energy loss as described by the laws of thermodynamics. The thermal energy not utilized is rejected from the process in the form of heat transferred to the water circulating through the condensers of a power station. This heat is ultimately transferred to the atmosphere by conduction and evaporative cooling either in closed-cycle systems, e.g. cooling towers, or in once-through systems, from the surface of the receiving water body.

Decisions dealing with methods for transferring the rejected heat to the atmosphere must be based upon a thorough understanding of hydro-thermal dynamics and the effects of excess temperature on indigenous populations of aquatic life.

*Scientists, Virginia Institute of Marine Science,
Gloucester Point, Virginia U.S.A.

The Virginia Institute of Marine Science has been conducting a hydrothermal monitoring program since 1971 at the site of the VEPCO Nuclear Power Plant on the James River (Fig. 1).

The objectives of this investigation have been:

- 1) Compare pre- and post-plant operation data to determine the physical effects of the thermal discharge on the survey area.
- 2) Compare field results with predictions of temperature distributions made with the James River hydraulic model to determine the applicability of the hydraulic model to field temperature predictions.

The Surry Nuclear Power Plant consists of two 788 MW nuclear reactors, the first of which began commercial operation in December 1972, the second in March 1973. The power plant uses the once-through cooling method. Water is drawn into the intake canal on the downstream side of Hog Point, pumped through the condensers and out through the discharge structure into the James River estuary, upstream from Hog Point. The shoreline distance between intake and discharge points is about 9.17 km and the intake canal is about 2.74 km long.

Each unit requires 52,987 liters/second of river water to supply condensing and service water needs. The maximum temperature rise through the condensers is 8.3°C.

FIELD STUDY RESULTS

A detailed description of the study sampling program was given by Parker and Fang (1975) and Fang and Parker (1976). A moving boat sampling scheme was used. The parameters measured were water temperature at depths of 0.15, 0.9 and 1.8 m, air temperature at 0.9 and 1.8 m above the water surface and dew point temperature. These data, along with salinity and dissolved oxygen samples taken at fixed stations and meteorological data from nearby Ft. Eustis, were deemed sufficient to identify natural variations in river conditions and to isolate thermal effects of the heated water discharge.

AREA WITHIN ISOTHERMS

After isothermal plots of a survey run were drawn, a planimeter was used to measure the area within the isotherms

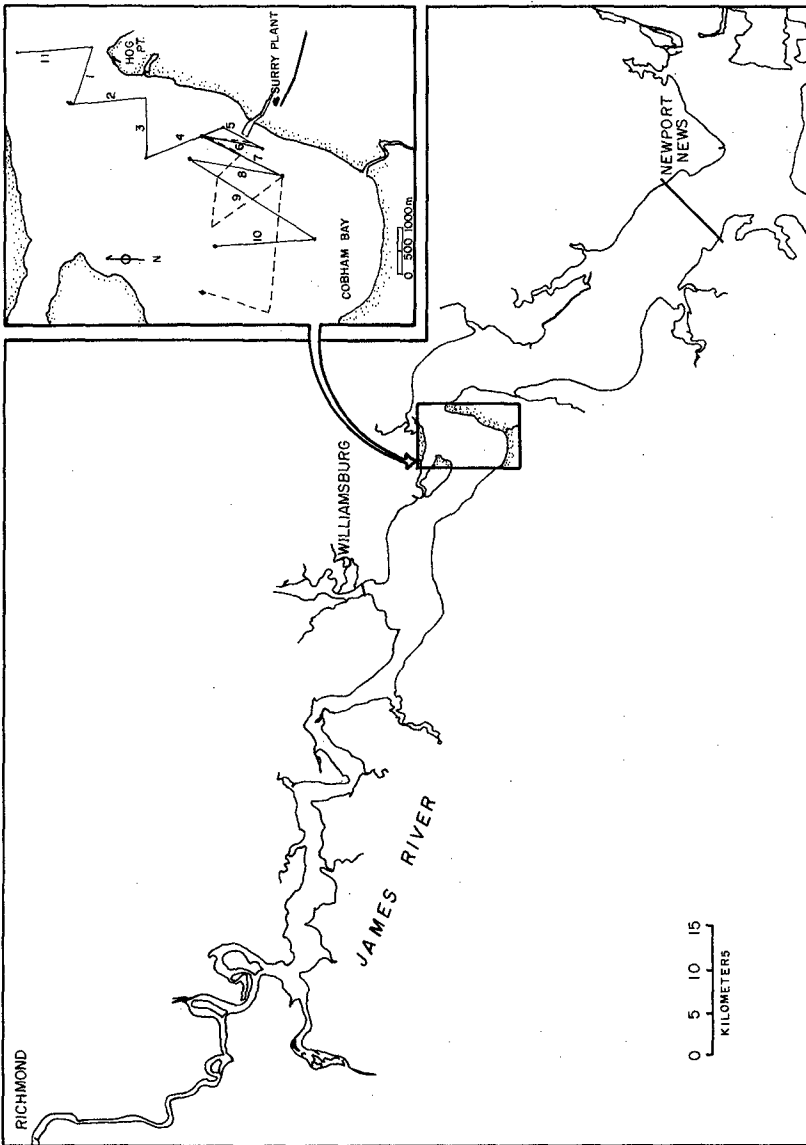


Figure 1. Location of the Surry Nuclear Power Station Site Inset: 1975 transects (solid), 1974 (dashed). Transects 11, 1, 2, 3, 4 same for both years.

which were "closed" around the outfall.

A graph of the area within excess temperature isotherms as a function of fractional excess temperature, Figure 2, indicates that the area (A) within the isotherms generally increases logarithmically with decreasing fractional excess temperature (θ/θ_0). An approximation to a straight line fit to the data is represented by the line:

$$A = (5.6 \times 10^6)e^{-6.8 (\theta/\theta_0)}$$

The data plotted in Figure 2 represent data for plumes with plant operation at greater than 90% capacity. When the data are separated into low and high slack water plumes, as shown in Figure 2, it appears that the low slack water plumes were slightly larger than high slack plumes, although the differences were not significant.

The area data from 1975 indicate as a rough estimate that as the value of θ/θ_0 approaches zero, the area within the excess temperature isotherm, θ , approaches $5.6 \times 10^6 \text{m}^2$, which represents the maximum surface area affected by the plume.

CENTERLINE TEMPERATURE DECAY

In 1975, plume centerline temperature decay was determined from isothermal plots for ten selected survey runs in August and September. The selection process was based upon the ease of determining plume centerlines from the isothermal plots. Plume centerlines were drawn subjectively, and distance and temperature along the centerline were recorded.

A graphical presentation of the data, Figure 3 indicates an exponential centerline temperature decay approximately represented by the equation:

$$\theta/\theta_0 = e^{-.0002d}$$

where d is the distance along the plume centerline. Fractional excess temperatures at centerline distances less than 45 m from the outfall show much less variation than those at greater distances.

The graph indicates that generally θ/θ_0 reaches a value of 0.5 within 1050 m of the outfall, indicating that a major portion of initial plume mixing with ambient water occurs within 1050 m from the outfall.

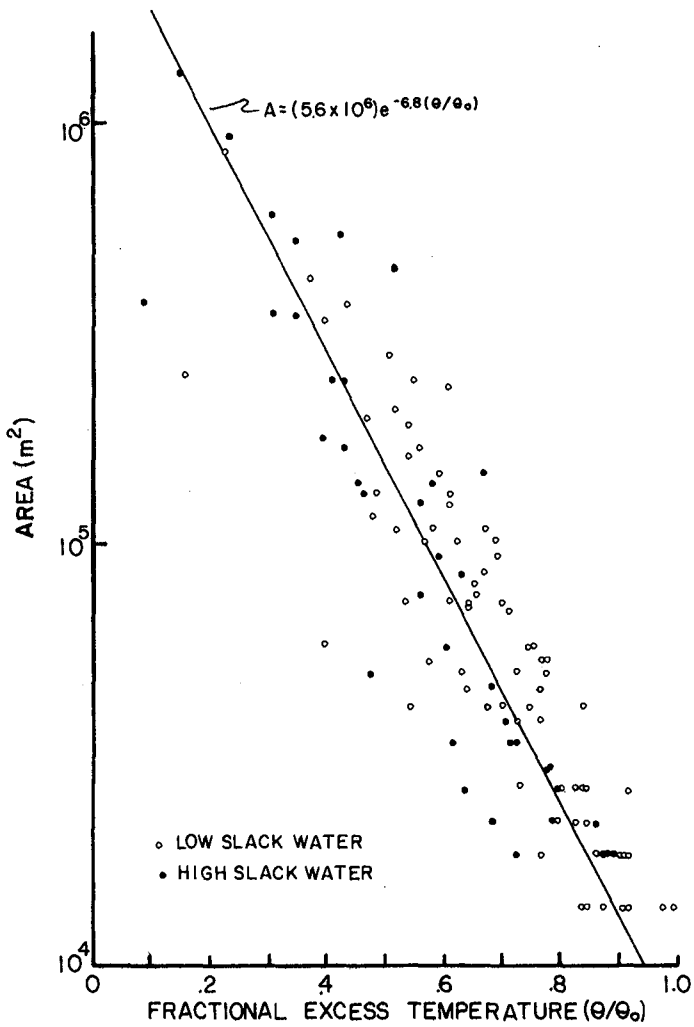


Figure 2. Area within excess temperature isotherm versus fractional excess temperature (θ/θ_0), 1975 data.

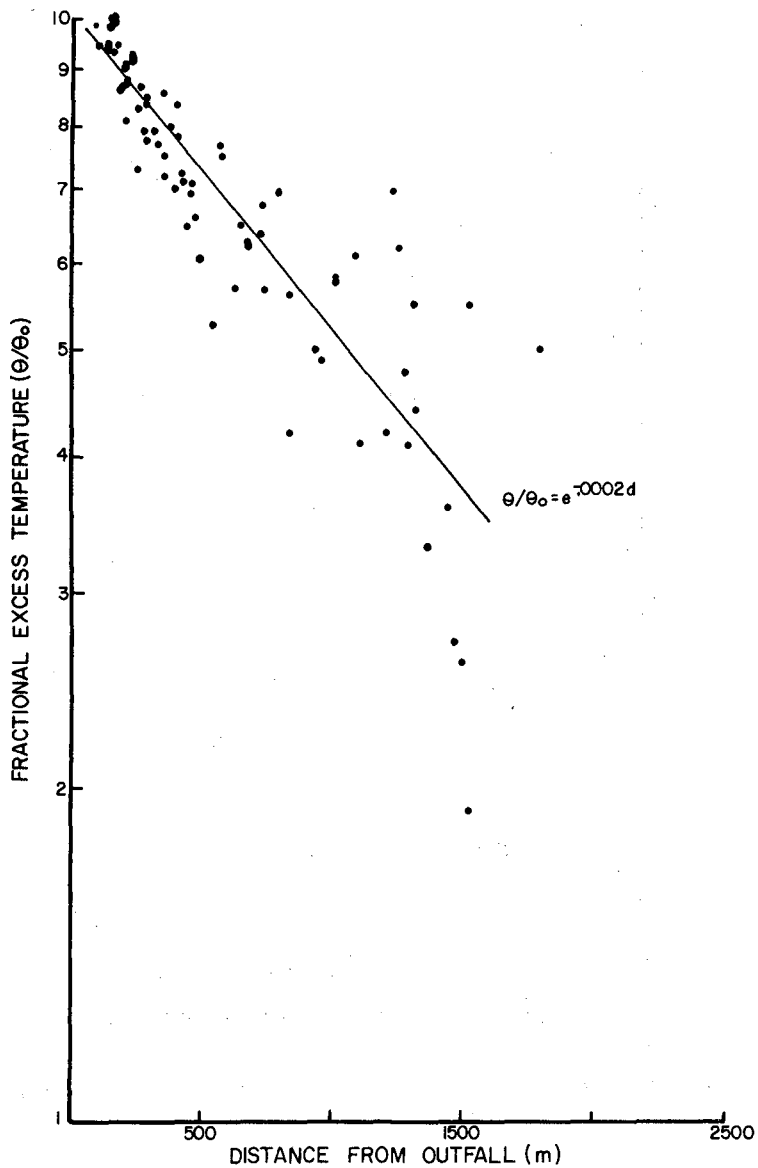


Figure 3. Plume centerline temperature decay, August and September 1975 data.

VERTICAL TEMPERATURE STRATIFICATION

Figure 4 shows a portion of the isothermal plot for August 21, 1975, at high slack water. On this date the plant power production was 1487 MW, winds were SE at 11-12.8 kph. Four transects, AA', BB', B'C, and DD', have been shown in vertical cross section to the maximum sample depth of 1.8 m in Figure 5.

Transects AA' and BB' show a maximum stratification of approximately 1.1°C over 1.8 m. Transect B'C, across the mouth of the outfall, shows a hot core of 37.8°C water at 0.9 m depth at the outfall. The maximum stratification along this transect is approximately 2.8°C over the 1.8 m depth. The plot of transect B'C also shows a sharp temperature gradient on the downstream (B') side of the plume, with a more gradual gradient on the upstream side. Transect DD', 365 m offshore and parallel to B'C, shows that plume temperatures at the centerline have dropped to 35°C. The strongest areas of stratification are on the extreme upstream (D') and downstream (D) ends of the transect. Figure 4 shows that these regions are near sharp temperature gradients at the surface. In these regions the temperature gradient is a maximum 3.3°C over 1.8 m of depth.

COMPARISON OF AREAS WITHIN ISOTHERMS

Areas within excess temperature isotherms for August 1974 and 1975 are compared in Figure 6. Water temperatures are generally at their peak during August, and as mentioned previously, August 1975 power production was continuously higher than 90% of capacity. These factors suggest that August 1975 data would represent conditions under maximum temperature loading for the river. The figure indicates that excess temperature isotherms enclosed larger areas during 1975 than during 1974 and that the differences were greater for low values of fractional excess temperature. The line drawn in Figure 6 shows an approximate best fit line for the 1975 area data; this line represents an approximation for the isotherm area versus fractional excess temperature relationship under equilibrium conditions at the Surry plant. The equation for the line shown in Figure 6 is given by:

$$A = (8.2 \times 10^6) e^{-7.2(\theta/\theta_0)}$$

where A is the area within fractional excess temperature θ/θ_0 . This equation and the line representing it were not calculated mathematically and are given only as approximations. An exact equation for such a relationship obviously does not exist and for this reason, approximations were deemed

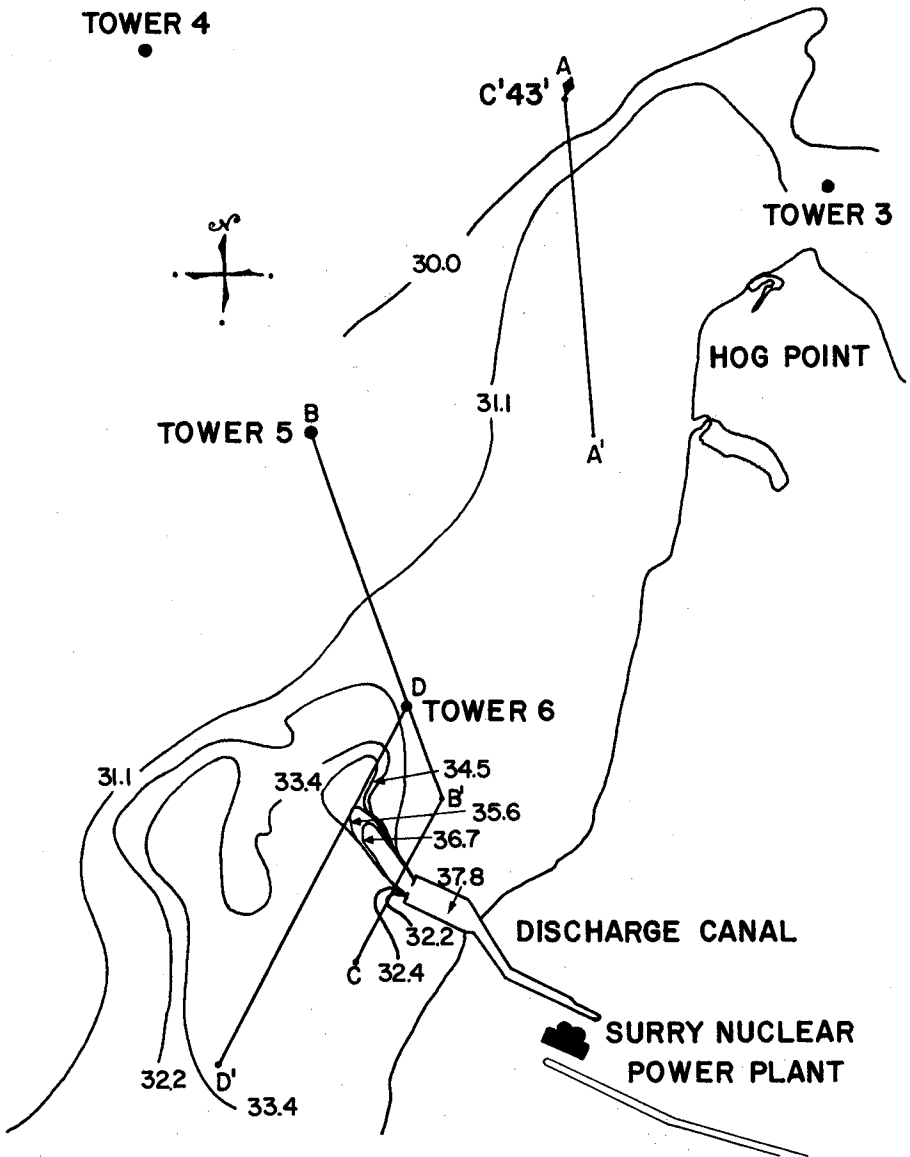


Figure 4. Thermal plume on August 21, 1975.

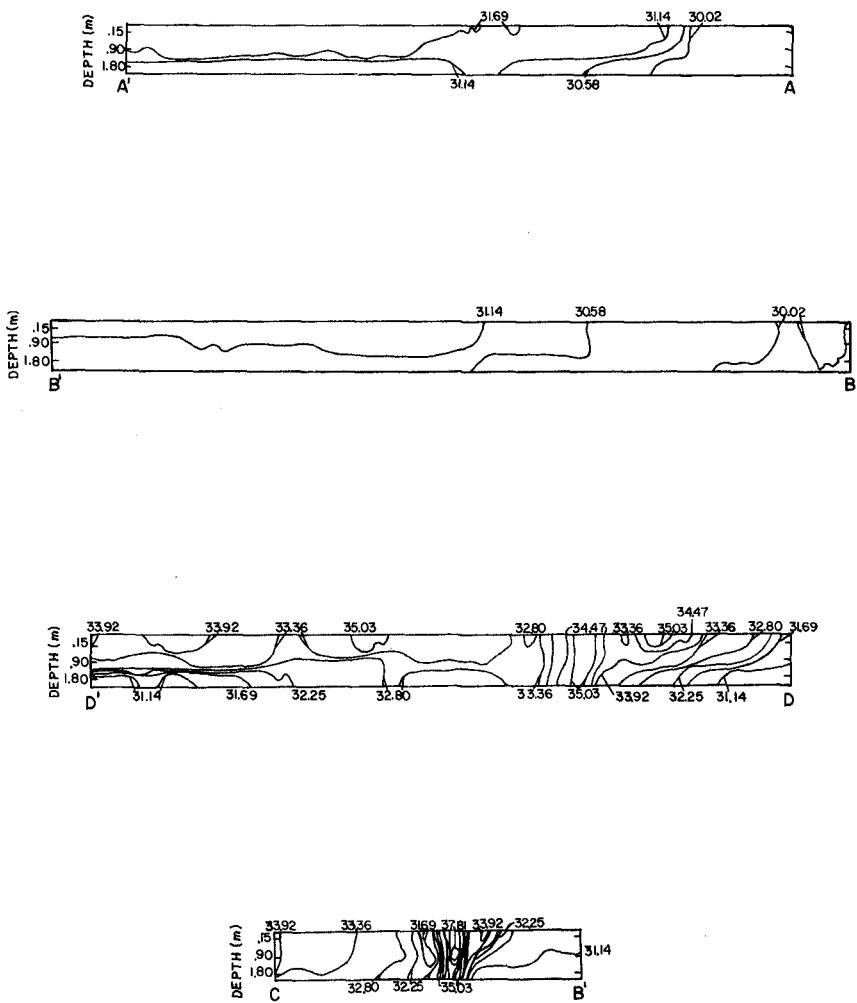


Figure 5. Vertical sections AA', BB', B'C, DD'.

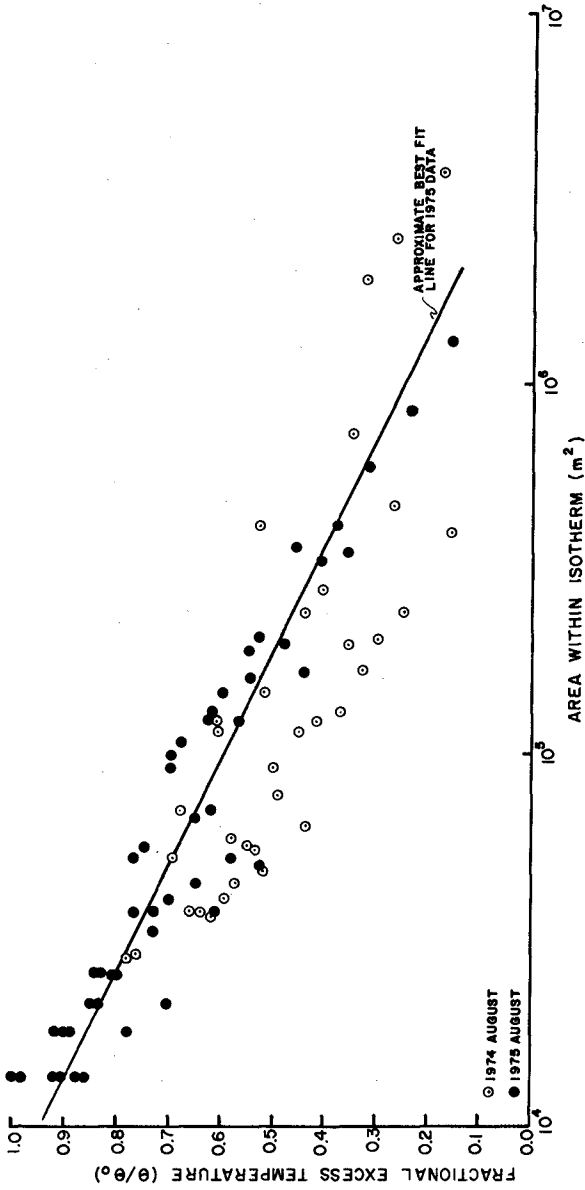


Figure 6. Comparison of areas within excess temperature isotherms for August 1974 and August 1975, power production greater than 1400 MW.

sufficient for the analysis. The equation indicates that as θ/θ_0 approaches zero, the area within the excess temperature approaches 8.2×10^6 square meters. This area represents the maximum area affected by the thermal discharge under equilibrium conditions, with close to maximum (>90%) power production.

HYDRAULIC MODEL PREDICTIONS

Studies conducted by Carpenter and Pritchard (1967) on the hydraulic model of the James River estuary resulted in predictions of excess temperature distributions resulting from the discharge of waste heat by the Surry Nuclear Power Station. One purpose of the present study was to compare these predictions to actual temperature distributions observed in the field in order to determine the reliability of hydraulic modeling as a method of predicting the effects of thermal discharges into an estuary.

The hydraulic model of the James River estuary, located at the U. S. Army Corps of Engineers Waterways Experiment Station, Vicksburg, Mississippi, covers the tidal waterway from Richmond to the mouth and has a horizontal scale of 1:1000, and a vertical scale of 1:100.

Two separate sets of experiments were run on the hydraulic model. In the first set the model was run for a total of 475 tidal cycles, corresponding to approximately 246 days of prototype time. During this set of experiments the river discharge at Richmond was at a simulated 56.6 cms. In the second set of experiments, river discharge at Richmond was at 169.9 cms and the model was run for a total of 784 tidal cycles.

During both sets of experiments a model thermal plant, releasing a simulated 12×10^9 BTU-hr⁻¹ of waste heat into the river, was operating at a location corresponding to the Surry Nuclear Power Plant site.

Temperatures in the model were measured using a rapid response thermistor head mounted on a trolley which ran across the model on a 4.9 meter unit beam. The beam could be moved to the desired transect and the thermistor sensor run across the model to obtain a plot of temperature versus lateral distance made on a strip chart recorder.

The hydraulic model was designed to reproduce the prototype velocity and salinity distribution. The relative pattern of excess temperature should be the same for model and prototype; however, the model was subject to different heat exchange coefficients than prevailed in the natural

environment. It was, therefore, necessary to adjust the excess temperature distributions observed in the model to take into account the difference in the surface exchange coefficients between the model conditions and prototype conditions.

The correction procedure used by Carpenter and Pritchard was:

$$(A_{\theta})_p / (A_{\theta})_m = 1, \theta \geq 0.5 \theta_0$$

$$(A_{\theta})_p / (A_{\theta})_m = 0.9 \frac{\gamma_m}{\gamma_p}, \theta \leq 0.15 \theta_0$$

where $(A_{\theta})_p$ and $(A_{\theta})_m$ were areas within excess temperature isotherm θ for the prototype and model, respectively, and γ_m and γ_p were the heat exchange coefficients for the model and prototype, respectively. The initial excess temperature at the discharge canal (θ_0) determines the regions in which the two relationships were applied. For $0.15\theta_0 < \theta < 0.5\theta_0$, the relationship was assumed to have a linear variation between the two given ratios.

The results of these experiments were presented as a series of excess temperature isothermal plots. Figure 7 shows two of these plots, for high slack water (tidal hour 0), and for slack water (tidal hour 6).

For comparison purposes, prototype data had to be selected so that heat rejection was as close as possible to the modeled heat rejection. As mentioned previously, hydraulic model tests were run for 56.6 and 169.9 cms river discharges at Richmond. This factor should also be taken into account for the comparisons, but it was considered secondary when compared to heat rejection. The prototype data which had the maximum heat rejection also had river discharges in the range 56.6-198.2 cms so that differences between model and prototype due to river discharge differences were minimal. This conclusion is justified since it has been previously shown that river discharge has little direct effect on tidal currents and excess temperature except for periods of extreme river discharge.

The average values of ambient water temperature, wind speed, and heat rejection for the prototype data selected for comparison with the model were 27.6°C, 9.8 kph, 11.2×10^9 BTU-hr⁻¹ respectively. These values are relatively close to the modeled values of 26.7°C, 8.0 kph, and 12.0×10^9 BTU-hr⁻¹. For the purposes of this investigation, the

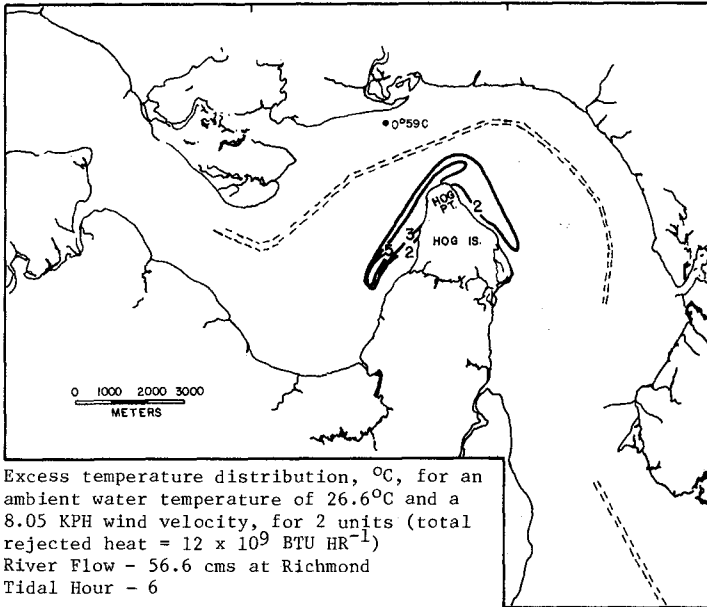
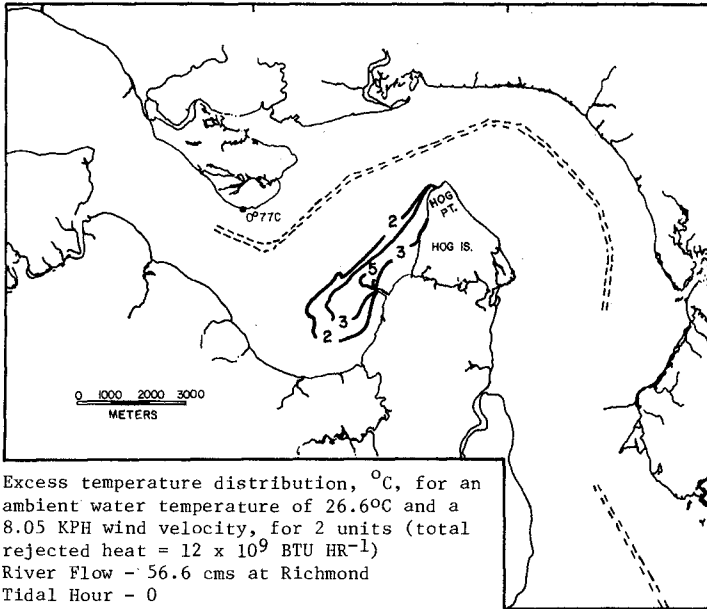


Figure 7. Typical excess temperature isotherms as predicted by the hydraulic model (from Carpenter and Pritchard, 1967).

effects of the differences between ambient water temperature and wind speed for the model and the prototype are considered negligible when compared to the effects due to the difference in rejected heat.

Areas within each excess temperature isotherm were determined from isothermal plots of the appropriate survey runs in 1973 through 1975 using a compensating polar planimeter. These areas, along with the areas within the excess temperature isotherms presented in the results of Carpenter and Pritchard's report, were plotted and are shown in Figure 8.

The figure indicates that the lower limit of the model data approximately coincides with the upper limit of the prototype data. There are only a few data points which lie above the lower limit of the model data. To determine whether the difference between the model and prototype data was statistically significant, the means and 95 percent confidence intervals of the means were calculated for the area within the 2.0°C, 3.0°C, and 5°C excess temperature isotherms in both model and prototype. In the prototype the area within the 2°C and 3°C isotherms were obtained by linear interpolation between the area within next higher and next lower whole degree isotherms.

The means of the area and the 95 percent confidence interval of these means are presented in Figure 9. The fact that the confidence intervals do not overlap for any of the model and prototype data indicates that the differences between the data were significant. The model enclosed areas were significantly greater than the corresponding prototype enclosed areas in all three cases. For the 2°C excess temperature isotherm, the model predictions were greater than prototype data by a factor of five, while for the other two isotherms, model predictions were greater than prototype data by an order of magnitude or more.

The prototype data indicate that the excess heat dissipated more rapidly than was predicted by the hydraulic model. The model predictions for the area with the 2°C excess temperature isotherms were more accurate than those for the higher excess temperatures. Qualitatively, the temperature distributions in the field, as a function of tidal phase, were similar to those predicted by the model.

Lower heat rejection in the prototype was partially responsible for the smaller areas within each excess temperature isotherm. Heat rejection on the days compared with the hydraulic model predictions were from 8-14 percent lower than the modeled heat rejection. It is assumed that at full plant capacity the areas in the prototype would be

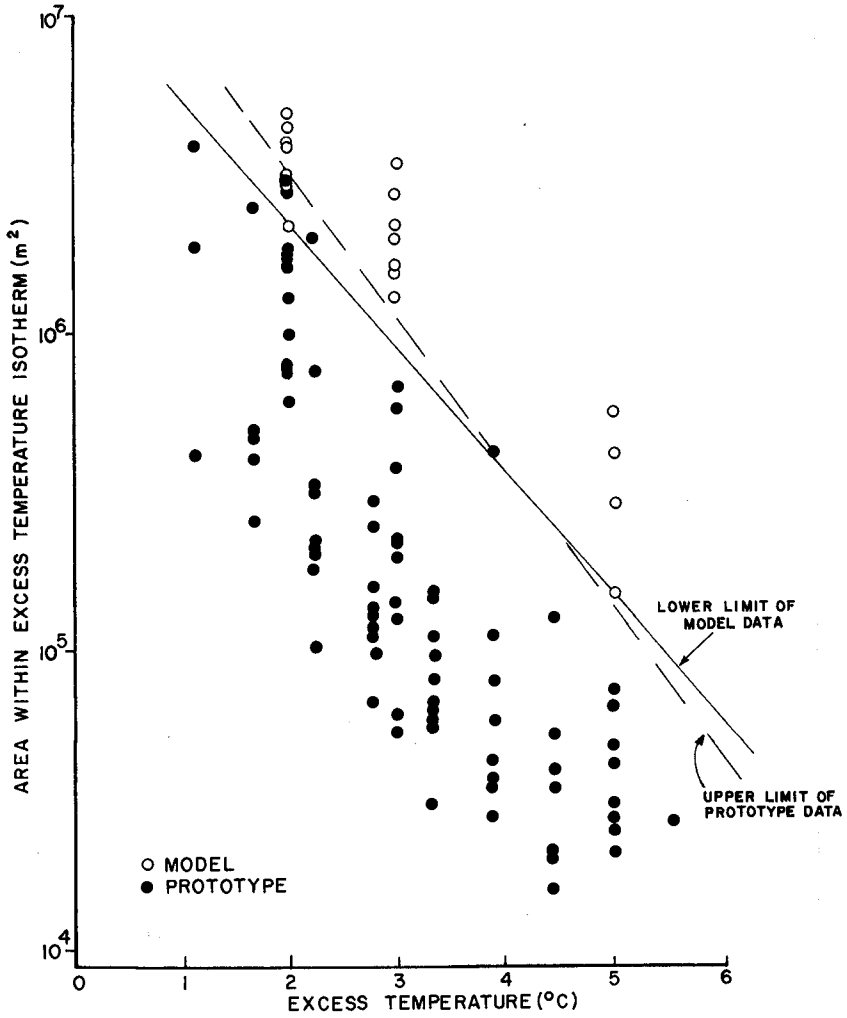


Figure 8. Comparison of areas within a given excess temperature isotherm for the hydraulic model and the prototype.

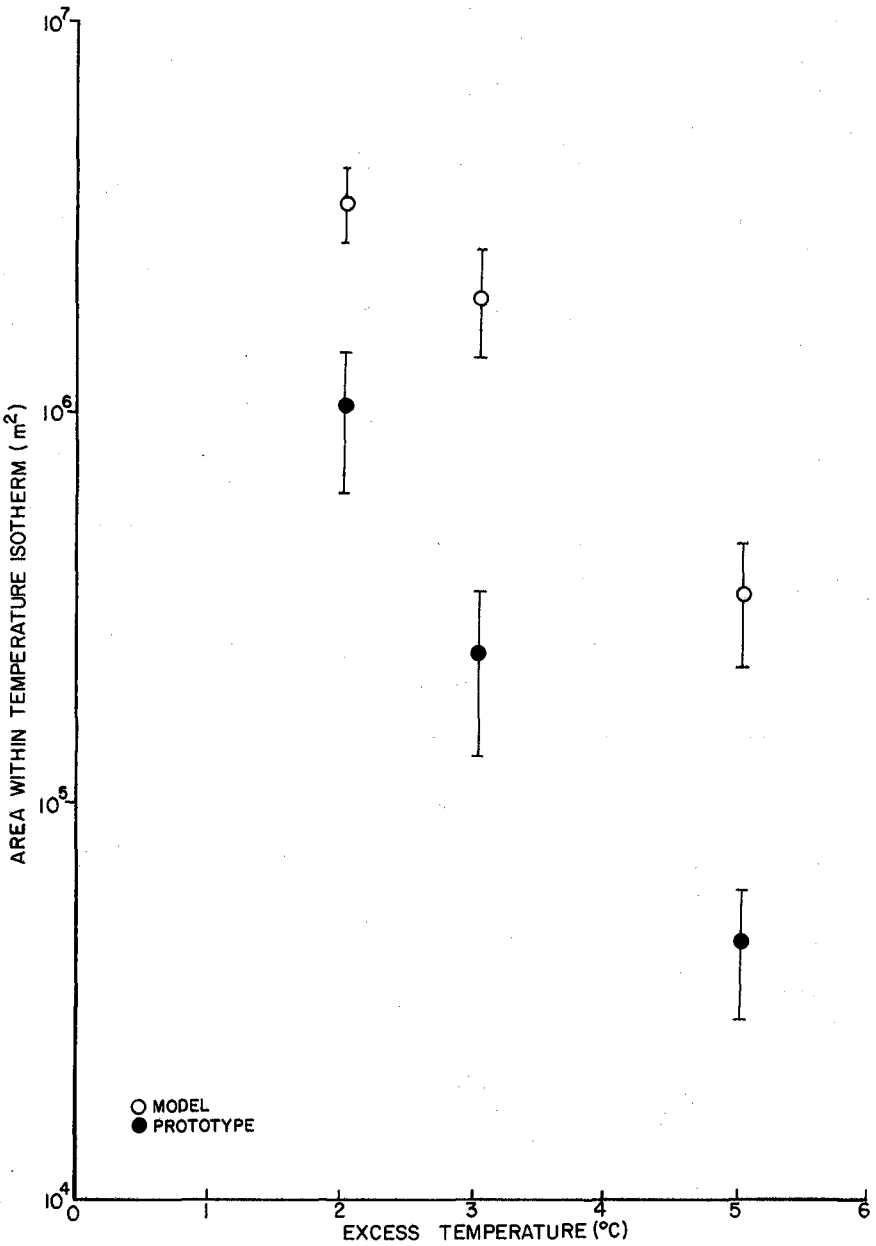


Figure 9. Comparison of mean areas and 95 percent confidence intervals for the hydraulic model and the prototype.

10-20 percent larger, which is probably an over-estimation, the differences between the model predictions and the prototype would still be significant.

Carpenter and Pritchard assumed that in the near field region, which they define as $\theta > 0.5\theta_0$, cooling has had little time to act. To reflect this, the correlation factor applied to this area, $(A_\theta)_p / (A_\theta)_m$, had a value of unity. With an average value of θ_0 of approximately 6.7°C , the field data indicate that for values of $\theta > .50\theta_0$, the ratio $(A_\theta)_p / (A_\theta)_m$ had a value of approximately 0.1.

For the region removed from the outfall, with values of $\theta < 0.15\theta_0$, Carpenter and Pritchard applied the correction factor $(A_\theta)_p / (A_\theta)_m = 0.9 (\gamma_m / \gamma_p)$. The field data indicate that the ratio $(A_\theta)_p / (A_\theta)_m$ had a value of 0.2 for values of $\theta = .33\theta_0$. Since the field data were compared to the corrected model results, the actual correction factor should have been of the form

$$(A_\theta)_p / 0.9 \left(\frac{\gamma_m}{\gamma_p} \right) (A_\theta)_m = 0.2$$

which reduces to

$$(A_\theta)_p / (A_\theta)_m = 0.18 \left(\frac{\gamma_m}{\gamma_p} \right)$$

It would appear, then, that a more accurate set of correction factors than those used by Carpenter and Pritchard have the form

$$(A_\theta)_p / (A_\theta)_m = 0.1, \quad \theta > 0.50\theta_0$$

$$(A_\theta)_p / (A_\theta)_m = 0.18 \left(\frac{\gamma_m}{\gamma_p} \right), \quad \theta < 0.33\theta_0$$

with a linear variation for intermediate values of θ .

The inability of the hydraulic model to predict the areas within the higher excess temperature isotherms to the same order of magnitude was most probably due to scale distortion. In a discussion of hydraulic modeling, Silberman and Stefan (1970) indicate that it is necessary to model three regions: near field, the joining region, and far field, in order to completely model a given plume. In the near field region near the outfall, entrainment of ambient fluid is the major process to be modeled. In the

joining region, entrainment is still important, but buoyancy, surface cooling, and convection are also important. Surface cooling, dispersion, and convection are the most significant processes in the far field. The different physical phenomena involved within each region mean that in most situations these regions cannot be combined in one hydraulic model.

One of the most important considerations when modeling parts of the plume separately is the placement of the proper boundary condition on the separate models. As an example, in a far field model, the initial thickness and momentum of the plume are determined by the end conditions in the joining region.

Carpenter and Pritchard (1967) have attempted to model all three regions of the thermal plume using a distorted model. The model does not accurately model entrainment in the near field and joining region. Field data indicate that the heat dissipation was higher in the near field than predicted by the model, indicating that entrainment was lower in the model than in the prototype. The correction factors used by Carpenter and Pritchard did not account for this entrainment in the near field, which resulted in predictions which were factors of five to ten time greater than the observed field conditions. The modified correction factors, derived from field data and model comparisons, can be applied to other sites or to other hydraulic models, provided that the discharge geometries and velocities are similar and the hydraulic model has the same scale distortion.

ACKNOWLEDGEMENTS

Funding for the study which was provided by the U. S. Energy Research and Development Administration is greatly appreciated.

REFERENCES

- Fang, C. S. and G. C. Parker. 1976. Thermal Effects of the Surry Nuclear Power Plant on the James River, Va. Part VI. Results of Monitoring Physical Parameters. Special Rept. No. 109 in Applied Marine Science and Ocean Engineering of the Va. Inst. of Marine Science.

- Parker, G. C. and C. S. Fang. 1975. Thermal Effects of the Surry Nuclear Power Plant on the James River, Va. Part V. Results of Monitoring Physical Parameters During the First Two Years of Plant Operation. Special Rept. No. 92 in Applied Marine Science and Ocean Engineering of the Va. Inst. of Marine Science.
- Pritchard-Carpenter, Consultants. 1967. Temperature Distribution in the James River Estuary which will Result from the Discharge of Waste Heat from the Surry Nuclear Power Station. A report prepared for VEPCO, Richmond, Va. 79 p.
- Silberman, E. and H. Stefan. 1970. Physical Modeling of Heat Dispersion in Large Lakes: A Review of the State of the Art. Argonne Nat. Lab. Special Rep. ANL/ES-2, 112 p.

CHAPTER 175

FLOW FIELD NEAR AN OCEAN THERMAL ENERGY CONVERSION PLANT

by

D. M. Sheppard⁽¹⁾, G. M. Powell⁽²⁾, I. B. Chou⁽³⁾

The flow field in the vicinity of an Ocean Thermal Energy Conversion (OTEC) Plant is extremely complex. The plants will normally be located in an area of relatively high surface currents and the location must also be such that a large temperature difference exists between the lower layers and the surface. Locations that demonstrate this characteristic can in many cases be modeled as a two layer fluid as shown in Figure 1. A number of different designs for the OTEC plants are being considered, but they all have one thing in common, a large vertical cold water pipe. This pipe extends from near the surface to some point in the cold water layer (see Figure 1). In some designs this pipe is as large as 40 m in diameter and 460 m in length.

Having such a large object penetrating the interface between the two temperature layers in the presence of a shear flow can significantly alter the character of the interface. The highly turbulent wake downstream from the pipe can drastically effect the mixing across this density interface.

A conventional heat engine cycle is used in the plant with the high temperature source being the water in the upper layers and the low temperature reservoir being the water from the lower depths. Since the temperature difference is small for this type of plant (20° max.), vast quantities of both high and low temperature water must be used. The intake and discharge for the warm water as well as the cold water discharge will be in the upper layer; the intake for the cold water will be in the lower layer at or near the end of the cold water pipe.

The flow problem is thus one of a vertical cylinder in a two layer stratified shear flow with sources and sinks located along the cylinder.

Since the integrity of the temperature profile is of the upmost importance to the successful operation of the plant, an understanding of the flow field is essential. In addition, the possible alterations

(1) Associate Professor of Coastal and Oceanographic Engineering Laboratory and Engineering Sciences, University of Florida, Gainesville, Florida.

(2) Graduate Research Assistant, Coastal and Oceanographic Engineering Laboratory, University of Florida, Gainesville, Florida.

(3) Graduate Research Assistant, Coastal and Oceanographic Engineering Laboratory, University of Florida, Gainesville, Florida.

of the environment could be significant especially if a number of OTEC plants are located in the same area. This paper addresses itself to only part of this problem and even then only illustrates the need for more work. The part considered deals with the wake downstream from a cylinder in a two-layer stratified shear flow. A physical model of a typical cold water pipe was placed in a stratified flow facility and measurements were made just above the interface in the wake region.

The mixing across a density interface (thermocline) is believed to be a function of the turbulent energy present at or near the interface (Long). Although this subject is not completely understood at this time, the work of Long¹, Kato and Phillips² and others indicates that the erosion velocity U_e is proportional to U_1^3 where U_1 is the RMS of the turbulent velocity fluctuations near the interface. This relationship should hold provided the other parameters such as the density jump across the interface and the turbulent length scales remain constant. In the undisturbed ocean, the primary source of turbulence is the air-sea interaction at the surface. The intensity of the turbulence decreases with depth. This is perhaps the reason for the depth limits on the thermocline. The introduction of a source of turbulence at or near the thermocline can, as this paper shows, have a significant effect on the level of turbulent energy in this region.

It is difficult, if not impossible, to model all the significant dimensionless groups for a problem such as this. The groups that are of primary importance here are 1) interfacial Froude number, $\frac{\Delta V}{\sqrt{\frac{\Delta \rho}{\rho_2} gh}}$,

2) pipe diameter to interface thickness ratio, $\frac{D}{h}$, and 3) Reynolds number based on the pipe diameter, $\frac{VD}{\nu}$, where ΔV is the difference in the mean

velocities between the upper and lower layers, $\Delta \rho$ the difference in mass density between the upper and lower layers, g the gravitational acceleration, h the thickness of the interface, ρ_2 the mass density of the lower layer, D the diameter of the pipe, V the velocity of the upper layer and ν the kinematic viscosity of the water. The first two groups were held constant for the model and prototype, but this was not possible in the case of Reynolds number. In fact, the Reynolds numbers for the prototype and model were quite different, approximately 10^6 for the prototype and approximately 10 for the model. This must be kept in mind when drawing conclusions about the prototype from the experimental results.

The experiments were performed in a stratified flow facility 24.5 m long, 1.22 m high and .61 m wide (for a complete description of the facility see Ref. 3). Sodium chloride was used as the stratifying agent for these experiments. The lower .61 m of the tank was filled with salt water (dyed red to aid in the flow visualization) and the upper .61 m filled with fresh water. Specific gravity and Brunt Väisälä frequency profiles are shown in Figures 2 and 3. A pump in the 30 cm diameter pipe connecting the ends of the tank is used to circulate the upper layer and create the shear flow velocity profile shown in Figure 4. Salt water was continuously

added at the bottom of the tank and fresh water drawn from the top during the experiments to maintain the interface at approximately the same location. A crosswire hot film probe for measuring y and z components of the velocity and velocity fluctuations, a high resolution electrical conductivity probe for measuring mass density and a glass beaded thermistor for measuring temperature. Were attached to a vertically and horizontally traversing probe support. The four transducer outputs plus a signal giving the location of the probes were digitized and recorded on magnetic tape. The data was reduced on an IBM 370 Mod 65 computer.

The experimental procedure was as follows: The pump was started and allowed to run for approximately one and one-half hours so that the flow could reach an equilibrium condition. A constant speed vertical traverse was made to obtain a mass density profile and locate the position of the interface. A stepped vertical traverse was then made to obtain a time averaged velocity profile. Next the probes were placed approximately 1 cm above the interface and turbulence measurements were made. The cylinder was then put in place and turbulence data taken at the positions shown in the definition sketch.

Constant speed traverse were also made during and at the completion of the turbulence measurements to precisely locate the interface.

The results are given in Table 1 and Figures 5-9. The erosion velocity (velocity at which the interface recedes) is believed to vary as the cube of the RMS velocity near the interface¹. Figure 5 is a graph of the ratio of the erosion velocity with the cylinder to the erosion velocity without the cylinder at the cross sections of the wake shown in Figure 1.

Although more data points are needed to obtain a complete picture the results clearly indicate a substantial increase in the turbulent energy present at the interface. The vastly increased mixing was visible to the eye and was recorded on movie film (shown at conference). Energy density spectra for the horizontal and vertical components of velocity are shown both without (Figures 6 and 7) and with (Figures 8 and 9) the cylinders. Note the overall higher turbulent energy level in the wake. The vortex shedding frequency is also clearly visible in Figures 8 and 9. It should be pointed out again that the Reynolds number based on the pipe diameter for the model is much lower than for the prototype. At higher Reynolds numbers, however, the turbulent energy will undoubtedly be higher and thus the mixing in the wake of the prototype would be ever greater.

No attempts to integrate the erosion velocity over the wake region was made since with the large difference in Reynolds numbers the results cannot be directly applied to the prototype. The results do however indicate that this problem should be investigated further.

REFERENCES

1. Kato, H., and Phillips, O.M., "On the Penetration of a Turbulent Layer into a Stratified Fluid", J. Fluid Mech., Vol. 37, pp. 643, 1969.
2. Long, R.R., "The Influence of Shear on Mixing Across Density Interfaces," J. Fluid Mech., Vol. 70, Part 2, pp. 305-320, 1975.
3. Sheppard, D.M., Shemdin, O.H., and Wang, Y.H., "A Multipurpose Internal Wave Facility," TR-019, Coastal and Oceanographic Engineering Laboratory, University of Florida, Gainesville, Florida, 1973.

Point No.	X (cm)	Y (cm)	ξ (cm)	\bar{u}	RMS u	RMS v	$\sqrt{u_{rms}^2 + v_{rms}^2}$	$\frac{UeTube}{Ue}$	NOTES
1	0.75	12.38	0.83	--	--	--	--	--	Velocity too small
2	2.02	12.38	0.88	2.132	0.489	0.271	.560	20.9	
3	3.29	12.38	0.98	2.23	0.332	0.129	.356	5.39	
4	4.56	12.38	0.93	2.26	0.187	0.052	.194	0.873	
5	0.75	26.19	1.08	2.23	0.301	0.190	.356	5.39	
6	2.65	26.19	1.12	2.46	0.328	0.178	.374	6.25	
7	4.56	26.19	1.21	2.48	0.203	0.095	.224	1.34	
8	5.83	26.19	1.16	2.39	0.208	0.055	.215	1.19	
9	0.75	40.00	1.27	2.37	0.256	0.133	.289	2.88	
10	2.65	40.00	1.30	2.45	0.241	0.140	.279	2.60	
11	4.56	40.00	1.32	2.47	0.247	0.106	.268	2.30	
12	7.10	40.00	1.35	2.47	0.207	0.054	.214	1.17	
13	0.75	65.56	1.39	2.31	0.163	0.078	.180	0.67	
14	2.65	65.56	1.41	2.31	0.202	0.087	.220	1.27	
15	5.83	65.56	1.44	2.35	0.168	0.068	.182	0.72	
16	8.37	65.56	1.46	2.34	0.147	0.047	.154	0.44	
--	0.75	16.98	0.72	2.895	0.220	0.035	.223	--	Without Tube
--	0.75	16.98	1.74	3.256	0.175	0.054	.183	--	Without Tube

With Tube

Without Tube

Without Tube

Without Tube

Diameter of Tube = 1.9 cm

$\Delta p = 0.024$ grams/cm³

$\rho = 1.024$ grams/cm³

Table 1

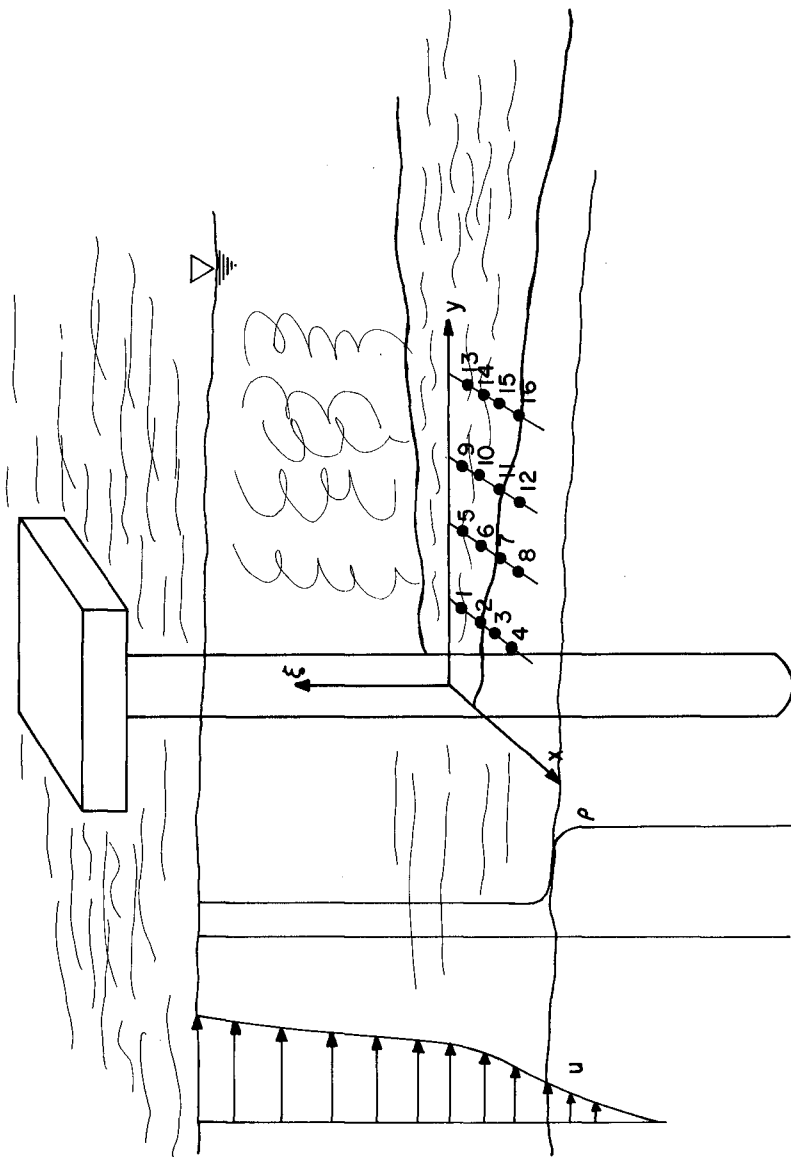


Figure 1 Definition Sketch.

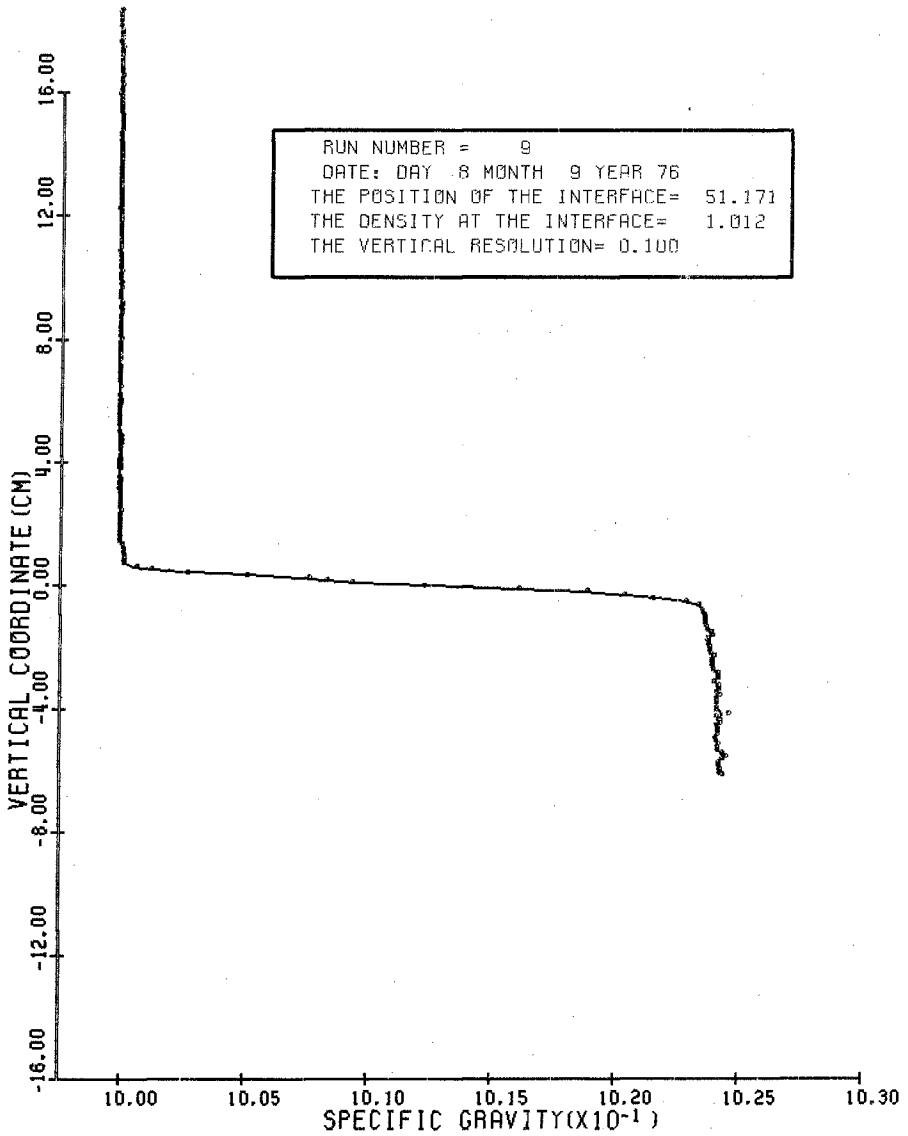


Figure 2 Specific Gravity Profile.

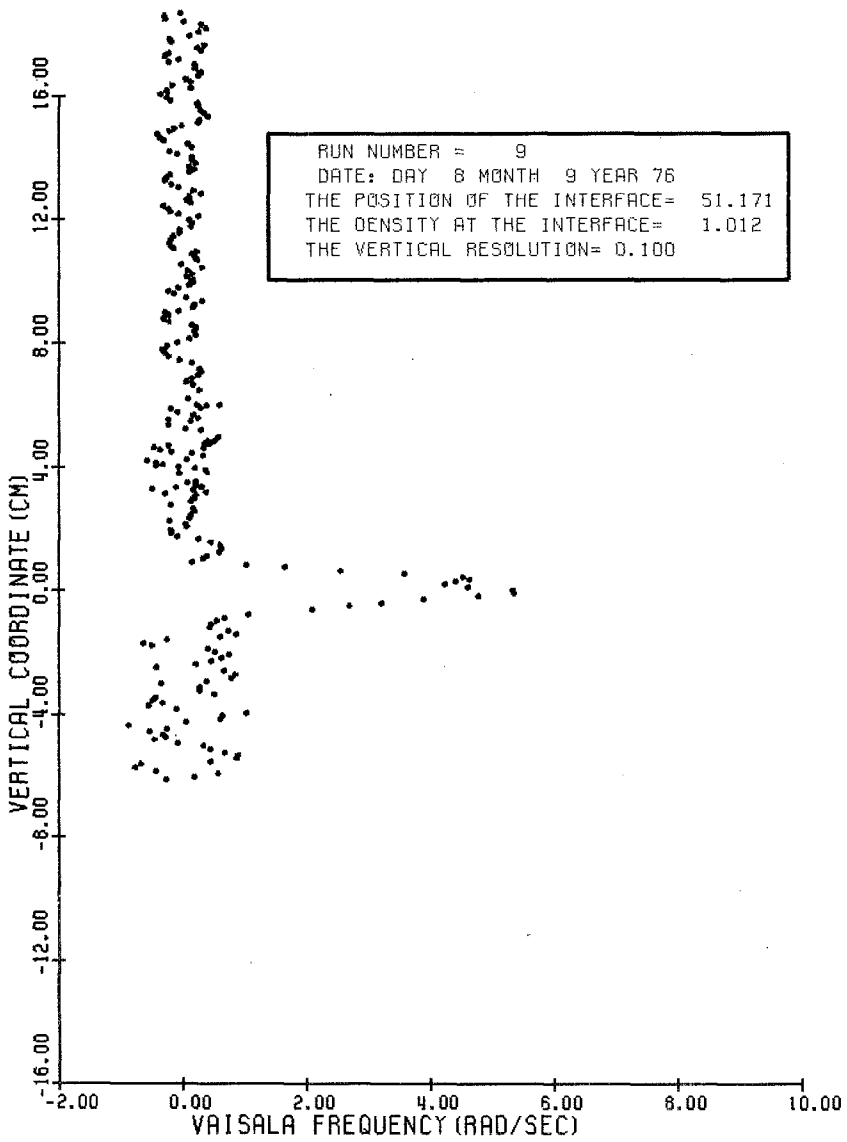


Figure 3 Väisälä Frequency Profile.

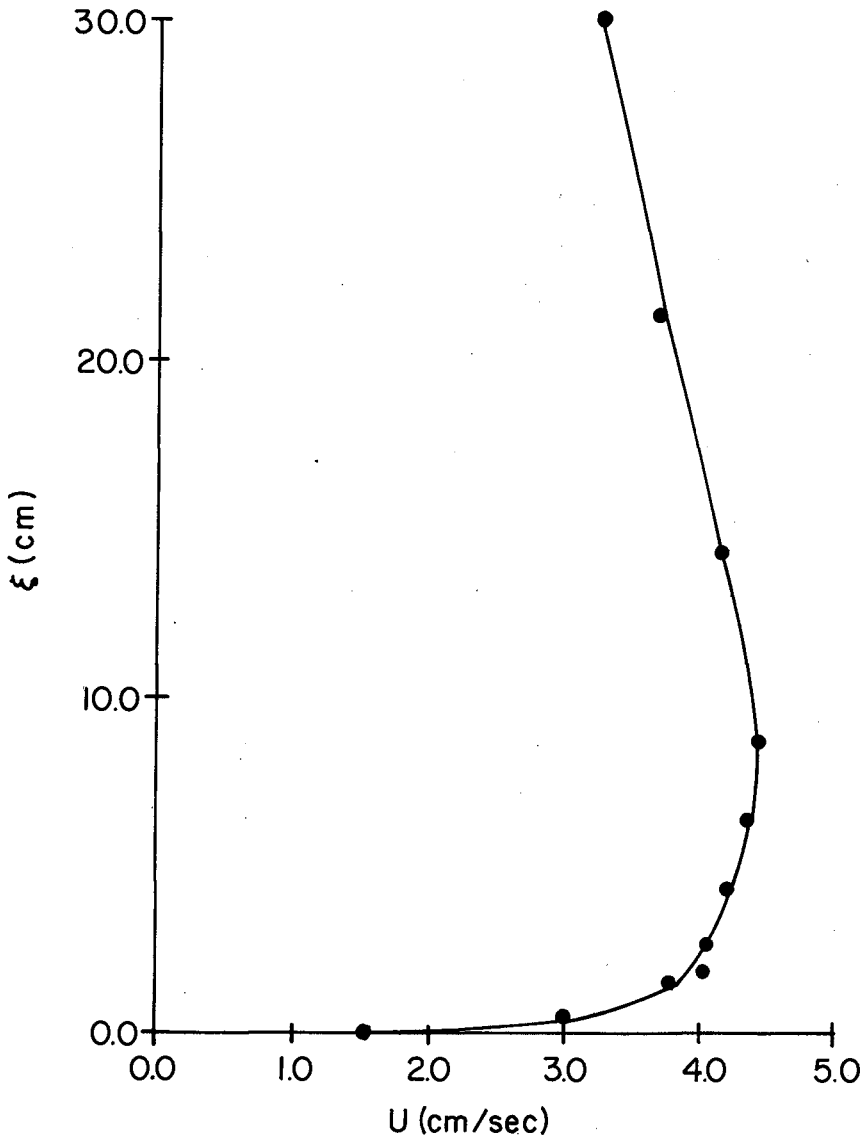


Figure 4 Mean Velocity Profile.

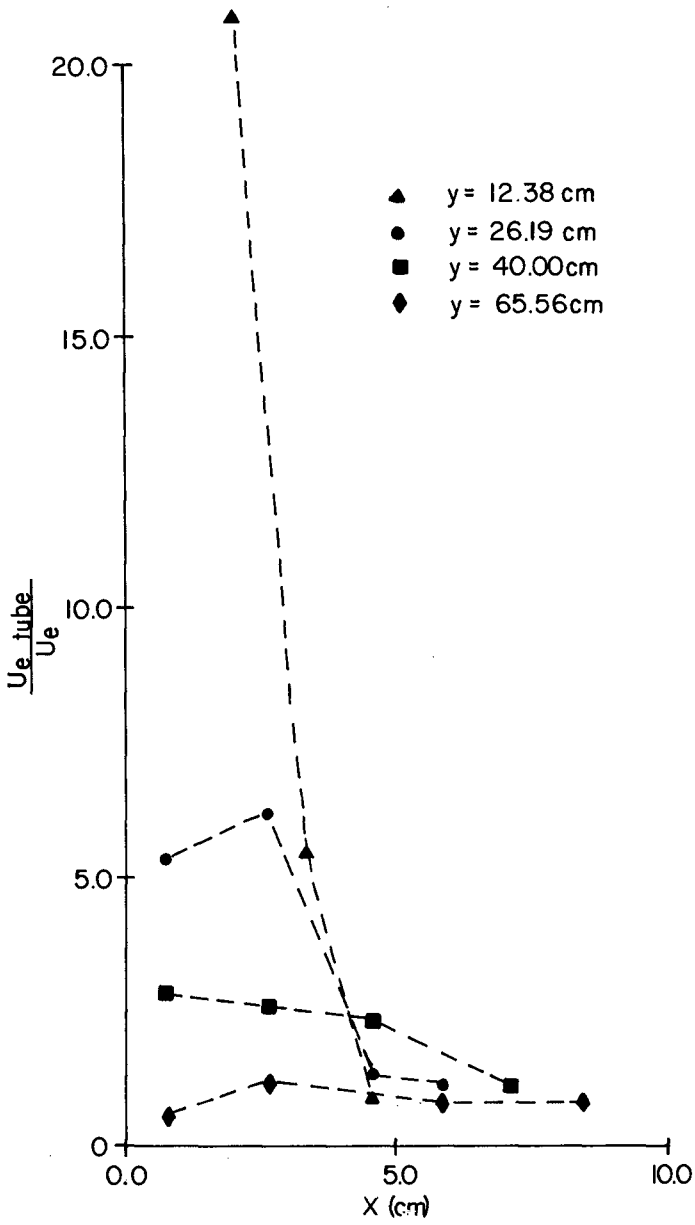


Figure 5 Erosion Rate Ratio.

JULY 6, 1976

RUN #303

POSITION= 53.88 CM

MEAN VELOCITY= 3.256 CM/SEC

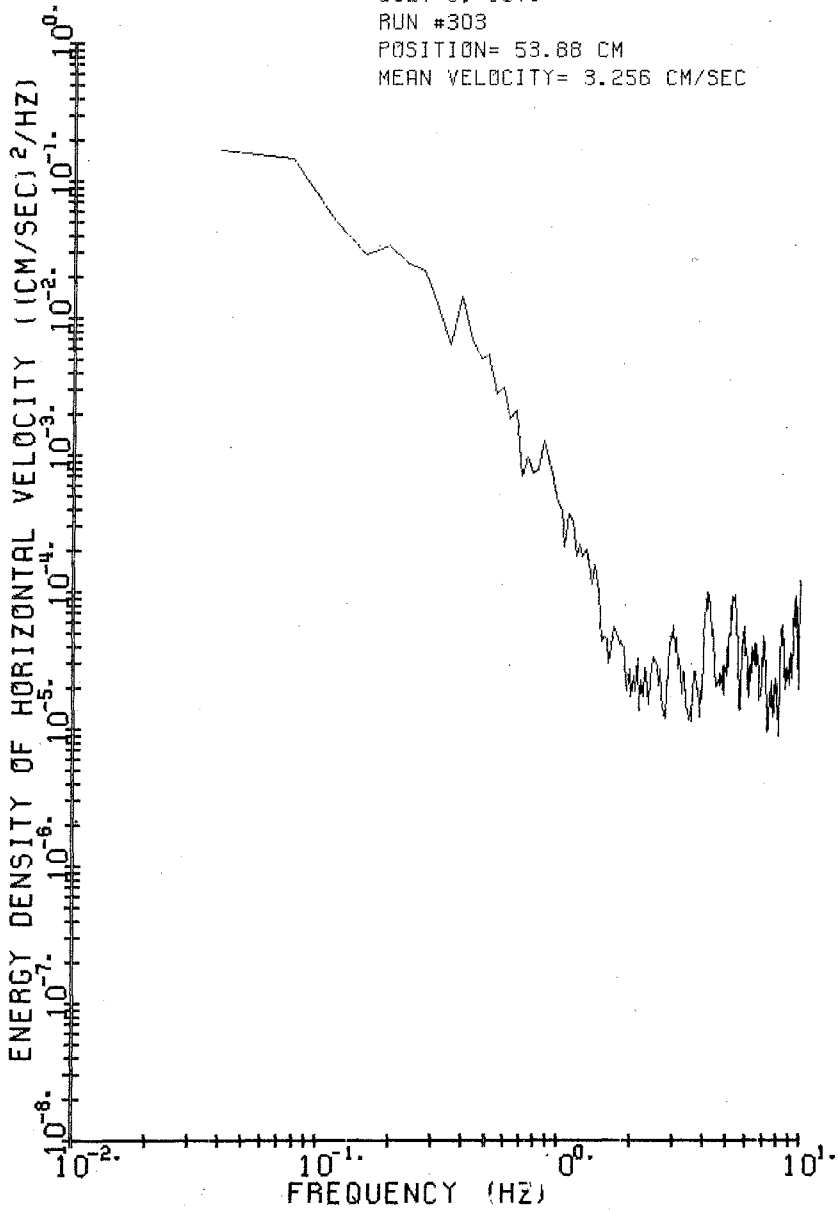


Figure 6 Energy Density without Cylinder.

JULY 6, 1976
 RUN #303
 POSITION= 53.88 CM
 MEAN VELOCITY= 3.256 CM/SEC

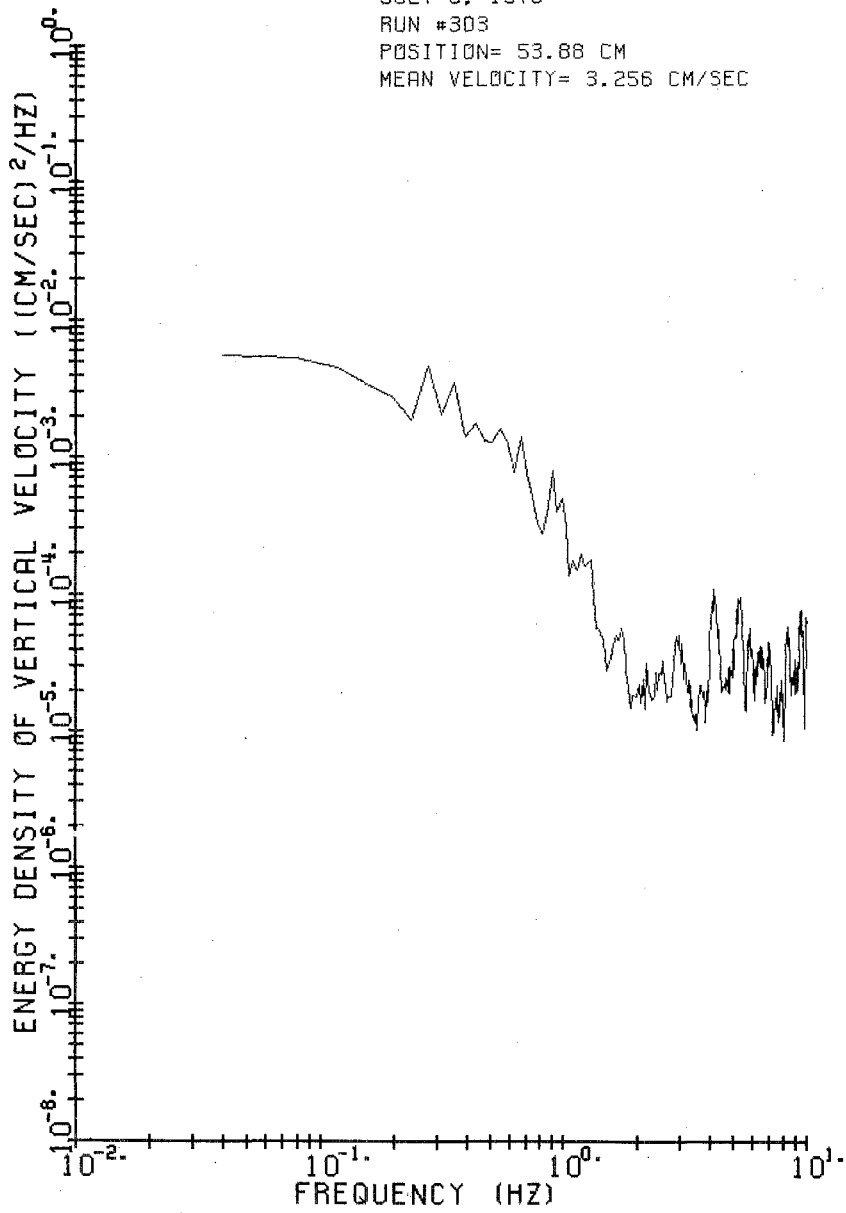


Figure 7 Energy Density without Cylinder.

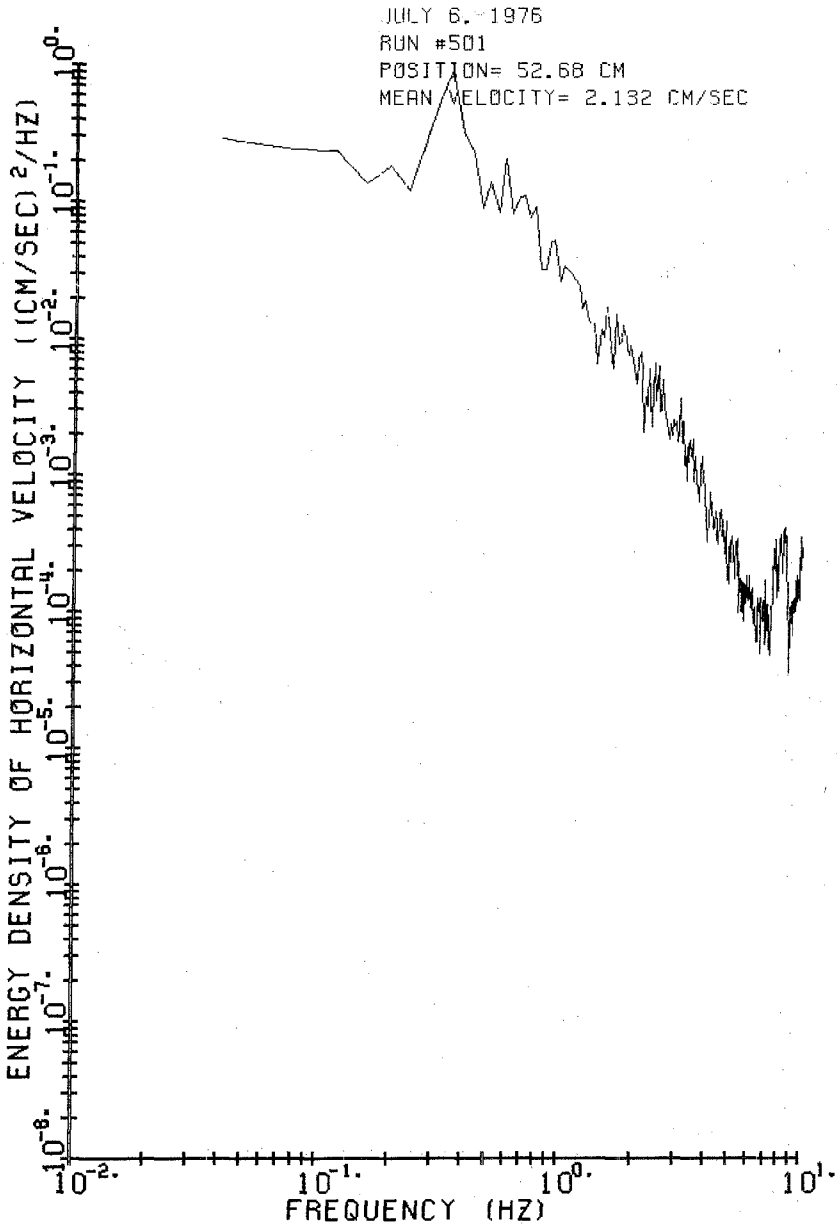


Figure 8 Energy Density with Cylinder.

JULY 6, 1976
RUN #501
POSITION= 52.68 CM
MEAN VELOCITY= 2.132 CM/SEC

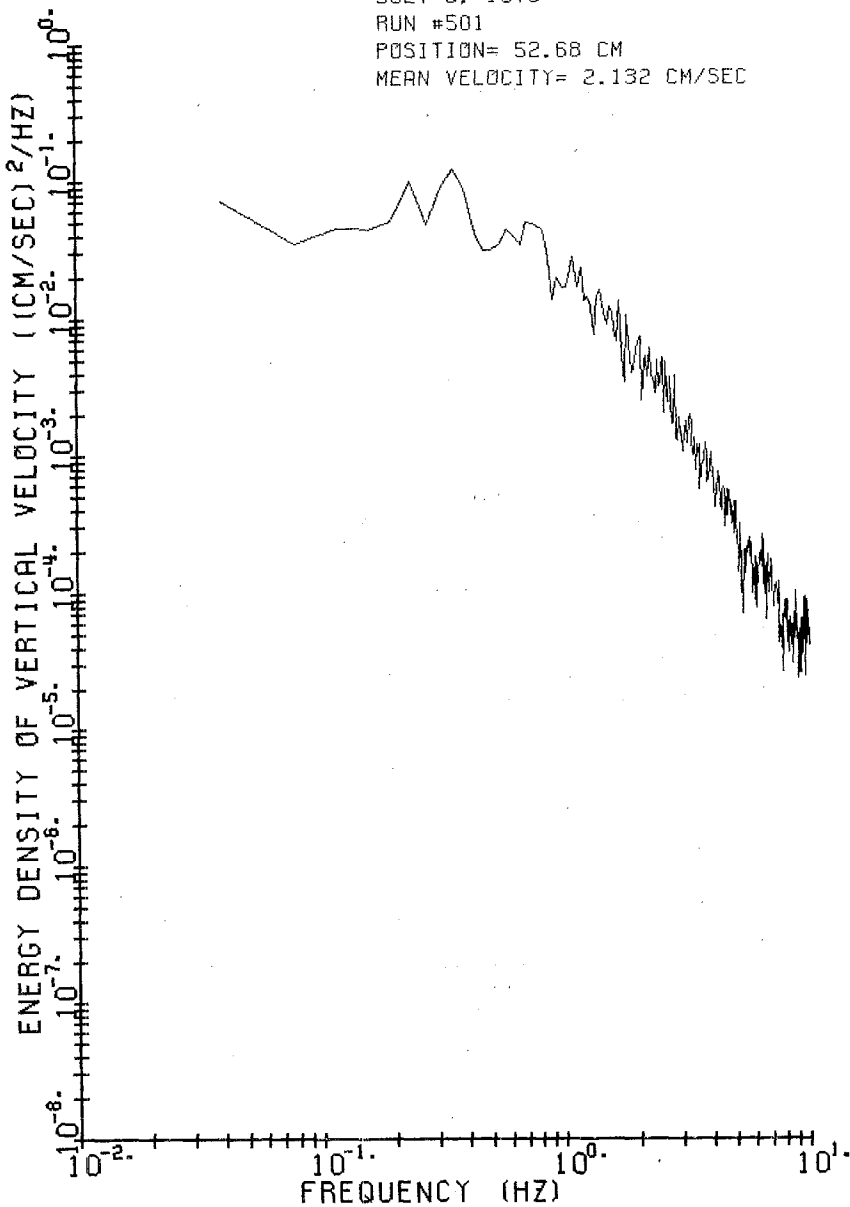


Figure 9 Energy Density with Cylinder.

CHAPTER 176

ADAPTABILITY OF PREDICTION METHOD OF HYDRAULIC MODEL EXPERIMENT FOR THERMAL DIFFUSION

1) 2)

By Masanobu Kato and Akira Wada

1. INTRODUCTION

In formation processes of the region of water temperature rise caused by the cooling water discharge from thermal and nuclear power stations located on the site facing the ocean, flow of discharged cooling water itself, current and turbulence existing in the sea region play an important role.

Their motions are predominant in the horizontal direction in the sea region. The horizontal scale of thermal extent is, therefore, extremely larger than the vertical scale of thermal extent.

Therefore, whenever the diffusion experiments of discharged warm water in the far field are conducted by hydraulic model method, the model which has a difference in the geometrical reduced rate between the horizontal and vertical directions, what is called, the distorted model must be used, so that the effects of the viscosity and the surface tension on the experimental model can be avoided.

In such a model, the horizontal scale is determined by the relation between the size of the experimental water basin and the surface area of the sea region to be reproduced.

But, there is no clear method of choosing the vertical scale, though there are some suggestions about it.

For example, the similarity of the $4/3$ power law of the diffusion coefficient gives a relation between the vertical scale and the horizontal scale of the hydraulic model.

On the other hand, the similarity of the surface heat exchange coefficient gives another relation between the vertical scale and the horizontal scale of hydraulic model if the surface heat exchange coefficients of hydraulic model and prototype are not same.

Therefore, it is better to give some allowance in the determination of the vertical scale of the hydraulic model within the range where the reproducibility of the diffusion phenomena can be conserved.

To clarify sure the relations between the distortion rate and the reproducibility of the phenomena in the model, experiments on the diffusion of discharged warm water were conducted by using three kinds of tidal hydraulic models having different distortion rates.

1), 2) Ocean Environment Section, Hydraulic Department,
Central Research Institute of Electric Power Industry
Abiko Chiba, Japan.

The selected site as prototype is Takasago Point located in the north-eastern part of Harima of the Seto Inland Sea in Japan, where the semi-diurnal tidal current is predominant and two thermal power stations in operation are located adjacently.

In this paper the loci of tidal current, the horizontal turbulence of meso-scale and far field temperature distributions obtained in the three hydraulic models having different distortion rates are compared with those of field measurements in prototype.

From these results, same problems of adaptability for the technique of distorted hydraulic model experiment for predicting the diffusion extent of thermal discharge are discussed.

2. RESULTS OF PROTOTYPE INVESTIGATIONS

The selected site as prototype is Takasago Point located in the north-eastern part of Harima of the Seto Inland Sea, where are two thermal power stations in operation adjacently.

Figure 1 shows the site map of Takasago Point.

One is Takasago Thermal Power Station of Kansai Electric Power Company (total output 900 MW, maximum volume of cooling water 33.5 m³/sec.) and the warmed cooling water is discharged into the sea region in front of the power station.

The other is Takasago Thermal Power Station of Electric Source Development Company (total output 500 MW, maximum volume of cooling water 21.8 m³/sec.) and the warmed cooling water is discharged into the inlet beside the power station.

The temperature rise of the discharged cooling water from both power stations is about 7°C above the ambient sea water temperature.

To examine the characteristics of flow in this sea region, the auto-correlations and the energy spectra of the flow observed for 15 days running at 3 m below the sea surface in the 1 km and 3 km offing of the outlet are calculated.

Figure 2 shows the autocorrelation coefficients of the flow which were observed at station - 2 in Takasago Site.

The autocorrelation of the flow velocity which is parallel to coast oscillates periodically and its period of the oscillation is nearly equal to the period of the semi-diurnal tidal current.

Figure 3 shows the energy spectra of the flow which were observed at station - 2 in Takasago Site.

The energy spectrum of the flow velocity which is parallel to coast has a maximum energy concentration at the frequency equivalent to the period of the semi-diurnal tidal current.

Judging from these figures, it is evident that the semi-diurnal tidal current is predominant in this sea region. It runs north-westward during flood tide and south-eastward during ebb tide.

The amplitude of the semi-diurnal tidal current is about 30 cm/sec. during spring tides.

The actual measurement of the discharged warm water diffusion range in the sea region near Takasago Power Station was carried out by Kansai Electric Power Co., Ltd. from January 22nd to February 3rd, 1972, and also by Water Temperature Survey Corporation from February 15th to 22nd, 1973.

The field surveys were conducted at the time of the spring tide both in 1972 and in 1973; and the amplitude of the semi-diurnal current was

approximately 30 cm/sec.

The environmental water temperature in the sea region was about between 9°C to 11°C and the marine condition was mild.

According to the results of the actual measurement, the area of 1°C rise above ambient sea water temperature extended about 2 - 2.5 km along the coast on both sides from the outlet and extended about 2 km toward the offing from the outlet.

The area of 2°C rise above ambient sea water temperature extended about 1 - 1.5 km along the coast on both sides from the outlet and extended about 1 km toward the offing from the outlet.

3. SIMILITUDE RULE OF HYDRAULIC MODEL EXPERIMENT

(1) Diffusion Process of Discharged Warm Water in the Coastal Sea Region

Although the diffusion phenomenon of discharged warm water is extremely complicated and the factors which affect the diffusion process are various and numerous, the main process can generally be considered as follows:

In the sea region near the outlet, the main process is the entrained mixing between the discharged warm water and ambient water.

The discharged warm water itself flows toward to offing through the process of mixing, and gradually the flow and turbulence of the discharged warm water become smaller than those in the sea region.

In this sea region, the diffusion process affected by the flow and turbulence of the sea controls the formation process of the water temperature distribution. Accordingly, for the purpose of predicting the diffusion of discharged warm water on the basis of the hydraulic model experiment, it is essential to make actual measurement investigations into the diffusion characteristics in the coastal sea region and to verify each factor which controls the diffusion phenomena in each case, and finally to discover the similitude rules for reproducing these factors on the model.

(2) Near Field

In the hydraulic experiment on the water temperature distribution formed in the sea region near the outlet, the entrained mixing phenomena should be reproduced in the model.

Under the condition that we should correspond the internal Froude number of the model with that of the prototype, this phenomenon can be expected to be reproduced.

This condition gives following equations. m means the model and p means the prototype,

$$\begin{aligned}
 F_{ip} = F_{im} &= \frac{U_{op}}{\sqrt{\frac{\rho_{sp} - \rho_{op}}{\rho_{op}} \cdot g \cdot h_{op}}} \\
 &= \frac{U_{om}}{\sqrt{\frac{\rho_{sm} - \rho_{om}}{\rho_{om}} \cdot g \cdot h_{om}}} \dots\dots\dots (1)
 \end{aligned}$$

where

- Fi : internal Froude number
- Uo : outfall velocity
- ρ_s : density of the environmental water
- ρ_o : density of the discharged water
- g : acceleration of gravity
- ho : depth at the outlet

In the hydraulic model where the Froude Similitude Rule is applied, the next relation can be obtained.

$$\frac{\rho_{sp}}{\rho_{op}} = \frac{\rho_{sm}}{\rho_{om}} \dots\dots\dots (2)$$

That is to say, the equation described above shows the condition that we should correspond the environmental water density and the discharged water density of the prototype with those of the model.

However, as it is difficult to grasp the three dimensional phenomena concerning the entrained phenomena near the outlet, more detailed examination of the similitude rule for reproducing the phenomena is considered necessary.

(3) Far Field

In this sea region, the flow and turbulence of the sea play an important role in the formation process of water temperature distribution.

This process is also affected by the heat exchange process between the atmosphere and the sea surface.

The average flow conditions such as the current trace and the topographical current are supposed to be very important factors which play a main role as the advective effects to change the diffusion pattern of the discharged warm water.

After integrating the equation of motion in the vertical direction, neglecting the stress which acts on the water surface and taking into consideration of the stress acting on the sea bed expressed by the help of the friction coefficient, the following relations to reproduce the average flow conditions may be obtained.

$$\frac{U_p}{U_m} = \frac{V_p}{V_m} = \left(\frac{Z_p}{Z_m}\right)^{1/2} \dots\dots\dots (3)$$

$$\frac{t_p}{t_m} = \left(\frac{X_p}{X_m}\right) \left(\frac{Z_p}{Z_m}\right)^{-1/2} \dots\dots\dots (4)$$

$$\frac{C_p}{C_m} = \left(\frac{X_p}{X_m}\right)^{-1} \left(\frac{Z_p}{Z_m}\right) \dots\dots\dots (5)$$

where,

- U, V : vertically averaged velocities in X and Y directions
- t : time

C : friction coefficient
 X, Z : length scales in horizontal and vertical directions.

The equations (3) and (4) can be transferred to the following equation.

$$\frac{U_p}{\sqrt{g Z_p}} = \frac{U_m}{\sqrt{g Z_m}} = Fr \dots\dots\dots (6)$$

where,

Fr : Froude number.

The equation (6) shows the similitude rule of Froude.

It is considered that the average flow condition such as the tidal current trace or the topographical flow can be reproduced by corresponding the Froude number of the model with that of the prototype.

On the other hand, the mechanism and characteristics of the turbulence which play a very important role in the diffusion process in the sea region can be obtained by statistically analyzing the results of long term continuous observation on the flow velocity fluctuations. They can be clearly expressed in the autocorrelation functions and the energy spectrum functions.

According to the results that were obtained using the distorted model on the reproducibility of the horizontal turbulence which exists in the tidal current, it is shown that the statistical characteristics and mechanism of the horizontal turbulence which are expressed in the autocorrelation and the energy spectrum can almost be reproduced in the model by applying the similitude rule of Froude. However, as far as the reproducibility of horizontal turbulence is concerned, it seems that some restrictions are given by the Reynolds number and topographical features at the site to be investigated for the experiment.

Accordingly, in order to reproduce the diffusion process in the sea region far from the outlet on the model, it is necessary to adopt the similitude rule of Froude, and it is also important to check the reproducibility of the average flow condition and the horizontal turbulence by comparing the results of the model with those of the actual measurements in prototype.

The heat balance between the atmosphere and the sea surface is determined by the short wave radiant energy coming from the sun and the sky, the long wave radiant energy from the atmosphere and the water surface, the transfer of the sensible heat energy and the latent heat energy, and by the additional heat energy caused by the discharge of warm water.

The factors which affect the surface heat exchange are the wind velocity, the water temperature, the atmospheric temperature, the humidity, the cloudiness and so on.

The rate of the surface heat exchange is usually expressed by introducing the surface heat exchange coefficient.

The relation of the surface heat exchange coefficient ratio can

be obtained from the equation of thermal diffusion which is integrated in the vertical direction and from the similitude rule of Froude, as follows.

$$\frac{K_{Tp}}{K_{Tm}} = \left(\frac{X_p}{X_m}\right)^{-1} \left(\frac{Z_p}{Z_m}\right)^{3/2} \dots\dots\dots (7)$$

where, K_T : surface heat exchange coefficient

This relation shows that the model must be given distortion if the surface heat exchange coefficient of the model is the same as that of the prototype. Actually however, the former is different from the latter and the coefficient heat exchange in the model is generally presumed to be smaller than that in the prototype because no consideration is given to the effects of the wind.

If a correct coefficient of the heat exchange in the model as well as in the prototype is obtained, the equation (7) provides a means of determining the distortion ratio. However, it is very difficult at the present stage to apply the similitude condition regarding the effect of heat balance in the hydraulic experiment because of difficulty in obtaining the coefficient of surface heat exchange.

4. EXPERIMENTAL METHOD AND MODELING RATIO

The diffusion basin used for the hydraulic model experiment is 20 m x 10 m x 1 m, and the tide production equipment is installed at the end of the basin. This air pressure system can produce the change of the water level and the flow in the model basin by alternating the air pressure in the air-tight chamber. (See Figure 4)

Water temperature, current speed and their variations in the basin were measured by using thermistors and a supersonic currentmeter connected to a data-logger.

The average flow conditions such as the loci of tidal current were measured by photographing the movements of float in the basin from the upper part.

The horizontal length ratio was chosen as 1/1,000 to reproduce the prototype area of 15 km along the coast by 6 km offshore in the experimental basin.

The vertical length ratio was chosen as 1/50, 1/100 and 1/200, so three models having different distortion rates were constructed.

The relations between the values of the prototype (P) and the values of three models (m) are shown in the following table.

Table 1. Summary of Modeling Ratios for the Experiment

		Case I	Case II	Case III
Horizontal length	$X_p/X_m = Y_p/Y_m$	1000	1000	1000
Vertical length	Z_p/Z_m	200	100	50
Distortion rate	$(X_p/X_m)/(Z_p/Z_m)$	5	10	20
Horizontal velocity	$U_p/U_m = V_p/V_m$	14.14	10	7.07
Flow rate	$Q_p/Q_m = (X_p/X_m)(Z_p/Z_m)^{3/2}$	2.83×10^6	10^6	3.54×10^6
Time	$t_p/t_m = (X_p/X_m)(Z_p/Z_m)^{-1/2}$	70.71	100	141.42

5. EXPERIMENTAL RESULTS

(1) Reproducibilities of Average Flow Conditions and Horizontal Turbulence

Before the experiment of the thermal diffusion, the reproducibility of the average flow conditions such as the loci of tidal current and the reproducibility of the horizontal turbulence of meso-scale which play an important role in the diffusion phenomena in the sea were examined.

Figure 5 shows the loci of tidal current during ebb tide obtained in three models having different distortion rates.

In this figure, the experimental results are indicated as the values of the prototype values, and they are compared with the loci of tidal current obtained in the field surveys.

From this figure, it is considered that the average flow conditions such as the tidal current trace obtained in three models having different distortion rates are not influenced so remarkably by the variation in distortion rate, and it is also confirmed that the results of the field surveys are reproduced in these models.

The average flow conditions at the time of flood tide are also reproduced in the models.

S. Hayami et al²⁾ proposed the similitude to give the distortion rate for the model of tidal current, considering the bottom friction in the laminar flow regime, as follows.

$$\frac{C_p(\text{Rep})^{1/2}}{1.328} \cdot \left(\frac{X_p}{X_m}\right)^{1/2} = \left(\frac{Z_p}{Z_m}\right)^{5/4} \dots\dots\dots (8)$$

They conducted the hydraulic model experiments by the use of three models of horizontal length ratio 1/500, distortion rates of 2, 4 and 8.

From the experimental results, they concluded that the flow patterns of the field surveys were reproduced better in the model having distortion rate of 2, which satisfied the relation of equation (8).

But it is considered to be difficult to determine the distortion rate using the relation of equation (8), owing to the fact that the value of the Reynolds number varies with space and time.

Judging from the results of author's experiments and the previous works done by others, it may be concluded that the average flow conditions, such as the loci of tidal current, can be reproduced in the distorted Froude model not influenced so remarkably by the variation in distortion rate.

But careful attention must be paid to the fact that large distortion rate makes the flow in the model basin three dimensional.

The characteristics and mechanism of the horizontal turbulence are represented remarkably by the energy spectrum which can be obtained by statistic analysis of the results of long term continuous observation of fluctuations in flow velocity.

For the purpose of examining the reproducibility of the horizontal turbulence, long term continuous measurements of fluctuations in flow velocity were conducted at the same point as the field survey spot.

The energy spectrum of fluctuations in flow velocity obtained by the experiments performed in the tidal hydraulic models having three different kinds of distortion rates is shown in Fig. 6. The point of measurement is St. 2 shown in Fig. 1.

The energy spectrum shown in this figure is obtained by excluding the oscillating current component in the model which corresponds to the semidiurnal current component. And in the case of the prototype, the spectrum is obtained by excluding the semidiurnal current and the diurnal current. The values of the model are indicated as the values of the prototype according to the similitude rule of Froude.

The energy spectra of the flow parallel to coast show the same energy level as the level of the prototype in both high and low frequency ranges.

But the energy spectrum obtained in the model of distortion rate of 20 shows a larger peak at the frequency equivalent to the period of 6 hours in comparison with those of other two models and prototype.

On the other hand, the energy spectra of the flow normal to coast obtained in three models having different distortion rate are about the same as those of prototype in the high frequency range, but in the low frequency range the energy levels of spectra obtained in two models of distortion rate of 5 and 20 are lower than that of prototype.

Due to the results mentioned above, it has been recognized that the horizontal turbulence having a fluctuation period of less than several hours can be reproduced in the model without being remarkably influenced by the difference in distortion rate. But as far as the horizontal turbulence having a long fluctuation period is concerned, the energy level of the flow normal to coast is lower than the level of the prototype, and the isotropy in the horizontal direction is lost by the effects of the distortion rate of the model, the topographical characteristics of the investigated site, the scale of the experiment and so forth.

(2) Reproducibilities of Diffusion Phenomena of Discharged Warm Water

After examining the reproducibilities of the average flow conditions

like the tidal current trace and the horizontal turbulence, experiments on the diffusion of discharged warm water were conducted.

From the experimental results, the reproducibility of diffusion phenomena and the effect of distortion on the reproducibility were examined.

The diffusion patterns of discharged warm water obtained in the tidal hydraulic models alternate in accordance with change of the tidal current.

The range of water temperature rise spreads toward the north-western sea region during flood tide and it spreads toward the south-eastern sea region during ebb tide.

As regards the diffusion patterns of discharged warm water at each tidal time obtained both in the hydraulic model and prototype, some similar diffusion patterns are recognized, but many different kinds of diffusion patterns are also recognized.

This is due to the fact that the natural phenomena are extremely complicated and have lots of random characteristics. On the other hand, the model keeps the so-called regularity comparatively well as it is simplified in order to reproduce the main factors in the diffusion process of the prototype.

Also it is due to the fact that there is no simultaneity between the data of the field survey because it takes a long time to measure one diffusion pattern.

Accordingly, in examining the reproducibility of diffusion phenomena by comparing the experimental results with the field survey results, it is more reasonable to compare the diffusion range as the envelope of all the patterns than to compare the each individual diffusion patterns.

Figure 7 shows the comparison between the actual measurement results of 1°C and 2°C rise in the surface layer and the enveloped range of 1°C and 2°C in the surface layer obtained in the hydraulic experiments conducted under the conditions corresponding to the conditions at the time of the actual measurement.

From the experimental results on diffusion area of the discharged warm water obtained in the two models with distortion rate of 5 and 10, there was no remarkable difference between them. The diffusion areas of the actual measurements in prototype were reproduced in each experimental result.

On the other hand, as far as the diffusion area of the discharged warm water obtained in the model with distortion rate of 20 is concerned, it was found that the variation in the distortion rate gives greater effects on the reproducibility of diffusion phenomena as compared with the results obtained in other two models and in the field surveys.

It is considered that these results are attribute to the fact that the flow volume of the discharged warm water in the model experiment increases as the distortion rate in the model becomes larger.

In order to determine the flow volume of the discharged warm water in the model having a large distortion rate, therefore, it is not enough to apply Froude similarity rule only.

H. Higuchi et al ³⁾ proposed the similitude to give the distortion rate for the model of turbulent diffusion considering the 4/3 power law of the horizontal diffusion coefficient, as follows.

$$\frac{Z_p}{Z_m} = \left(\frac{X_p}{X_m}\right)^{2/3} \dots\dots\dots (9)$$

This relation requires a distorted model having distortion rate of 10 if the horizontal length ratio is chosen as 1/1000.

But as far as the results of author's experiments are concerned, the diffusion phenomena of discharged warm water are reproduced even in the model having distortion rate of 5 which does not satisfy the relation of equation (9).

6. CONCLUSIONS

Judging from above mentioned results, in order to conduct the diffusion experiment of discharged warm water by using the distorted hydraulic model applying Froude similarity rule, the distortion rate of model should be smaller than 10 within the range where the effects of the viscosity and the surface tension can be neglected.

REFERENCES

- 1) Kato, M. and A. Wada, (1973) : Hydraulic model experiment on thermal diffusion due to tidal current (II), Technical report 73007, Central Research Institute of Electric Power Industry, (in Japanese)
- 2) Hayami, S., H. Higuchi and K.H. Yoshida (1958) : On the similitude of hydraulic models involving tidal motion, Disaster Prev. Res. Inst. Annuals of Kyoto Univ., No. 2, 83 - 95 (in Japanese).
- 3) Higuchi, H. and T. Sugimoto (1968) : On the hydraulic model experiment on the diffusion due to the tidal current (II), Disaster Prev. Res. Inst. Annuals of Kyoto Univ. No. 11 B, 447 - 461 (in Japanese).

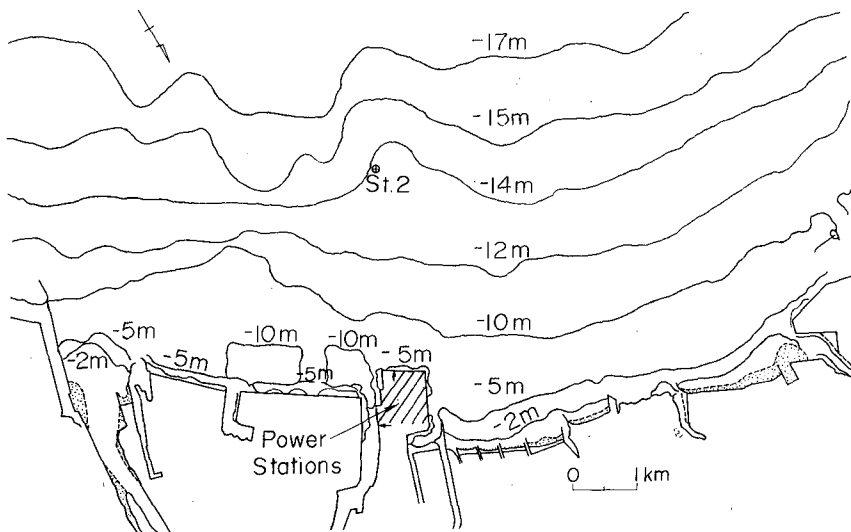


Fig.1 Site map of TAKAGO POINT

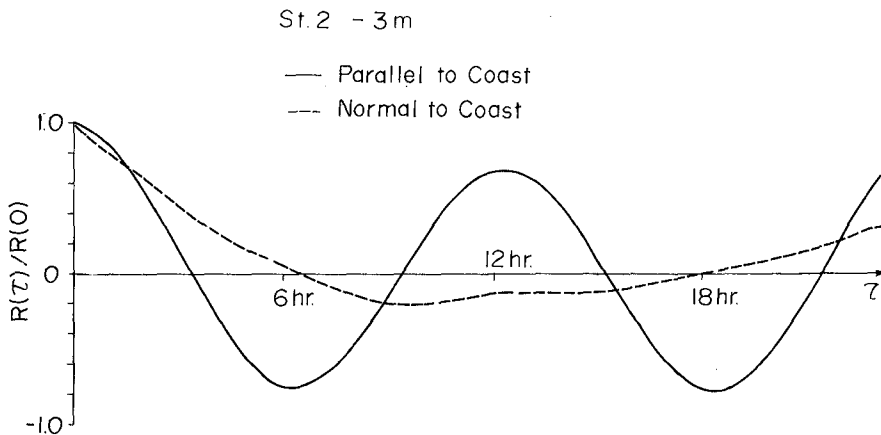


Fig. 2 Autocorrelations of flow velocity (Prototype)

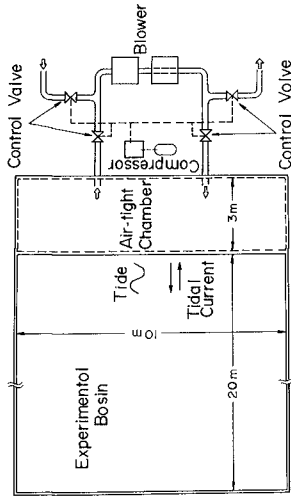
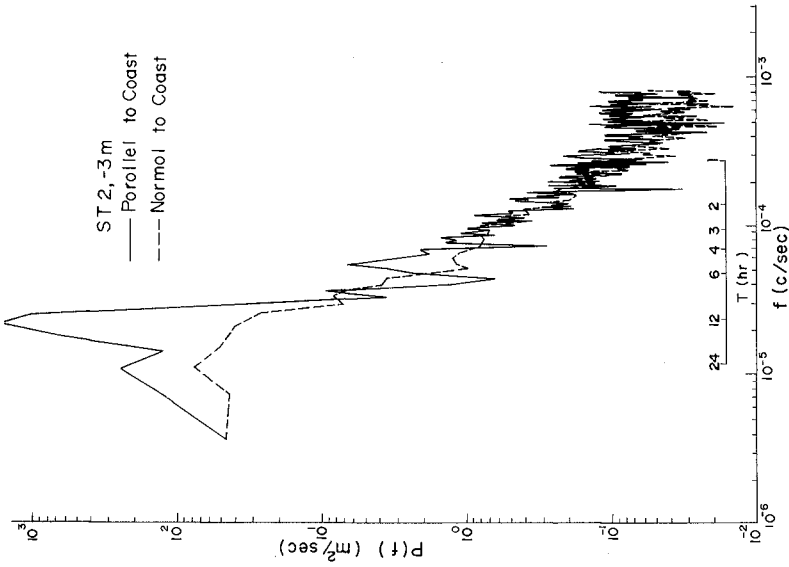


Fig. 4 Tide generation system

Fig. 3 Energy spectra of flow velocity (Prototype)

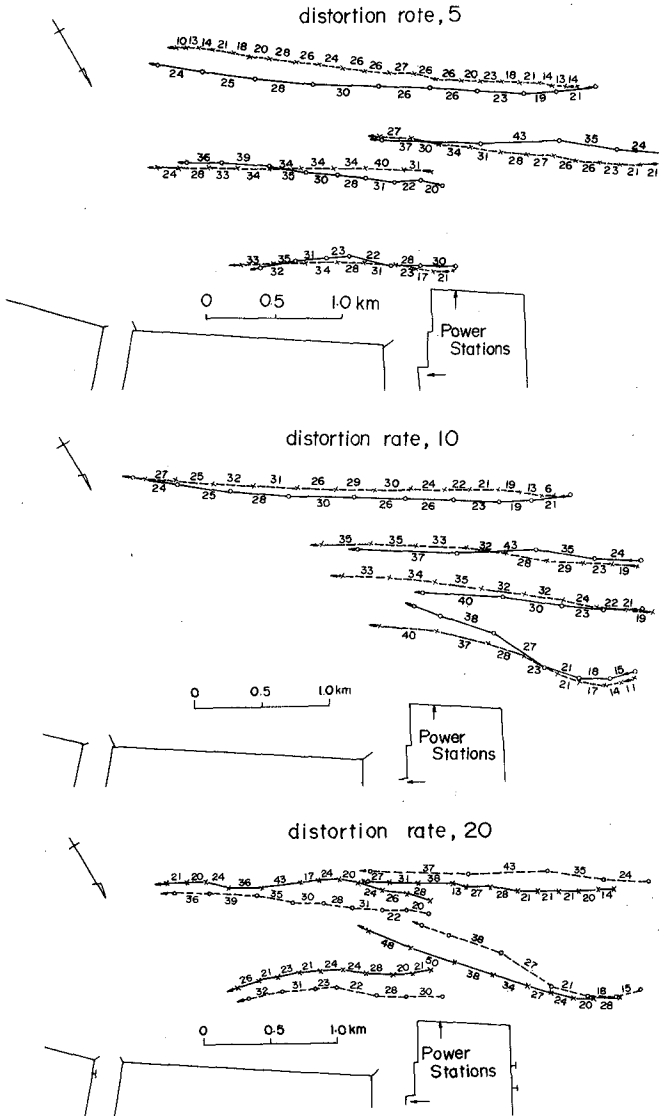
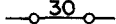
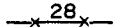


Fig. 5 Comparison between model and prototype loci of tidal current.
(Ebb tide)

	Prototype } Numerals mean prototype Model } velocity in cm/sec
	

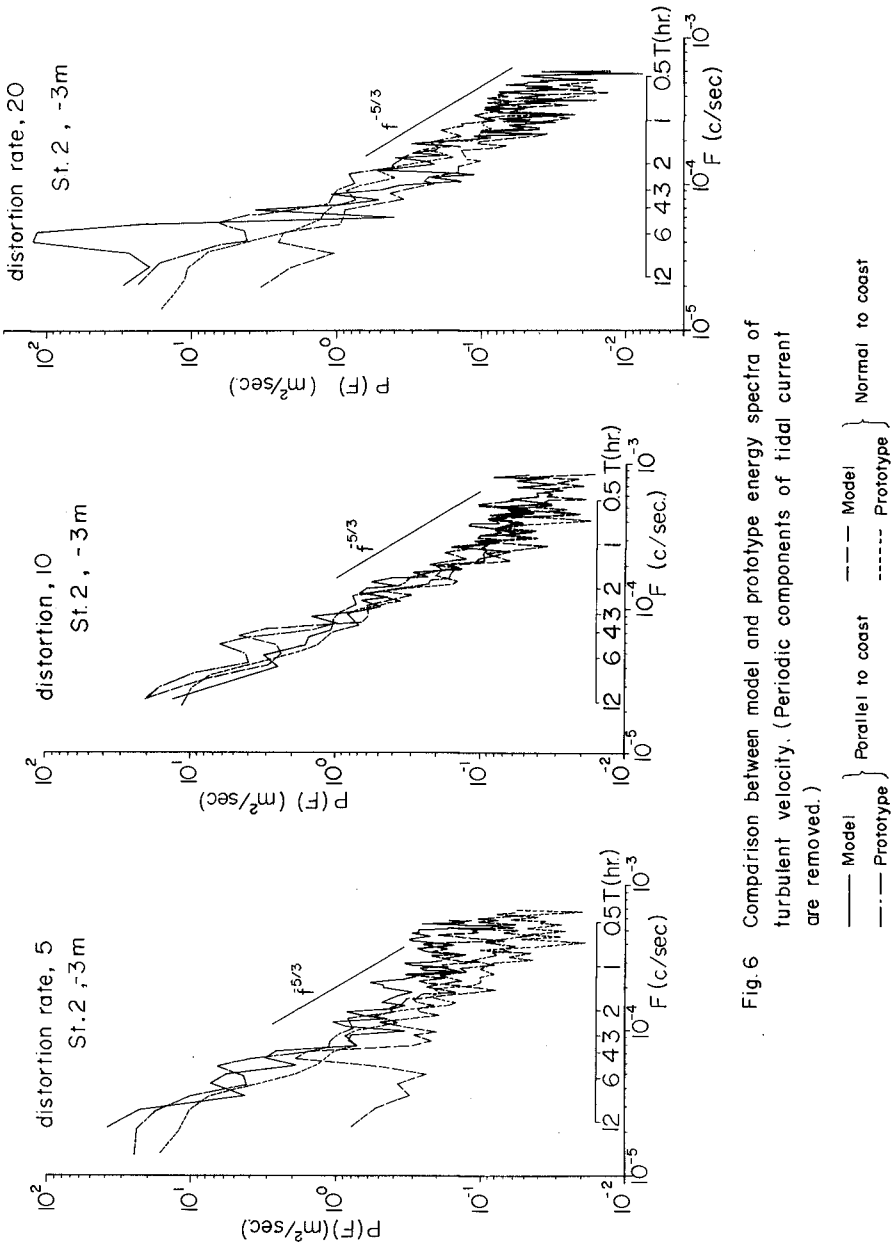


Fig. 6 Comparison between model and prototype energy spectra of turbulent velocity. (Periodic components of tidal current are removed.)

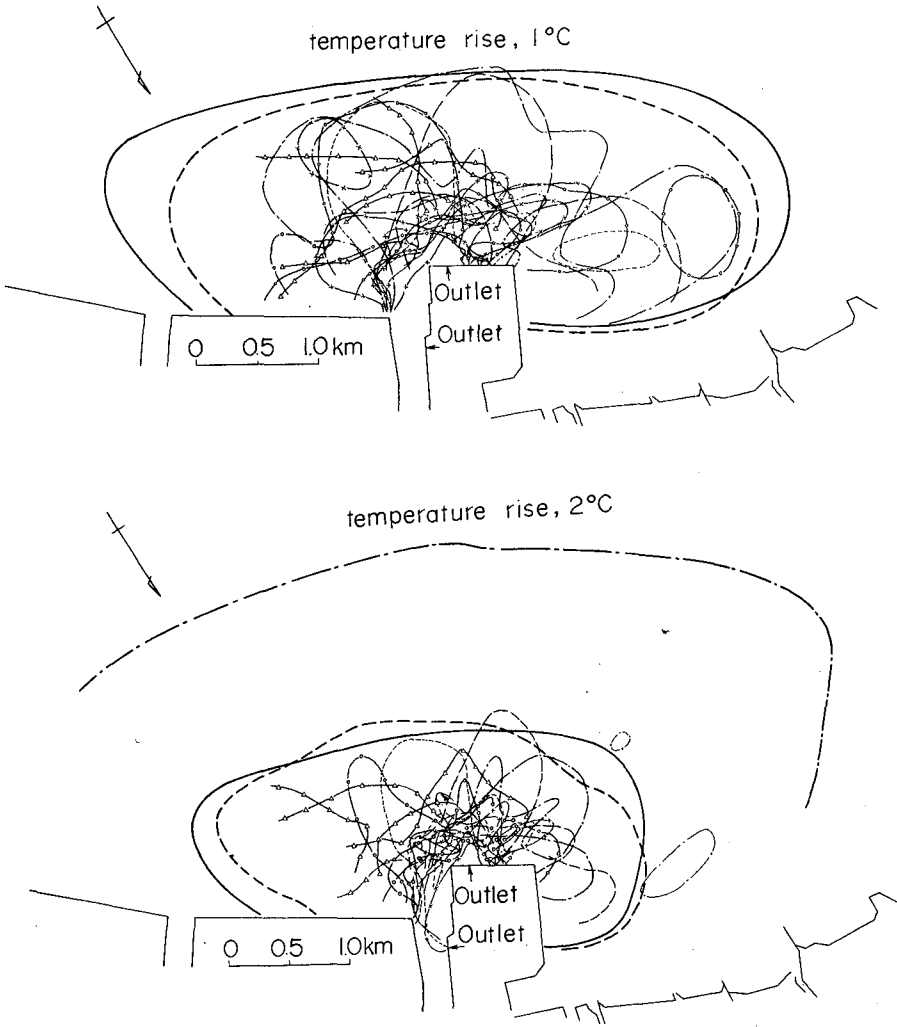


Fig. 7 Comparison between model and prototype diffusion areas.
 (Diffusion areas of model show the areas in which the thermal extents
 at various tidal phases are enveloped.)

- | | | |
|--|-----------------|--|
| <ul style="list-style-type: none"> --- distortion rate, 5 — distortion rate, 10 - - - distortion rate, 20 | } model results | other line : Actual measurements
in prototype |
|--|-----------------|--|

CHAPTER 177

HORIZONTAL DIFFUSION IN TIDAL MODELS AND SCALING CRITEREA FOR THERMAL-HYDRAULIC MODEL TESTS

by
Gerd Flügge^{†)}

INTRODUCTION

Near Brokdorf at the lower Elbe river (West Germany) a nuclear power plant is projected. The electric energy output shall be 1300 MWe; therefore the waste heat output will be about 2600 MWe. The maximum allowed temperature rise in the condenser amounts to 10 K. Accordingly the cooling water discharge is about $61 \text{ m}^3/\text{s}$ in case of the provided once through cooling.

For the purpose of the mixing and spreading of the discharged cooling water by

mean tidal conditions and storm-tide conditions

model tests have been carried out at the Franzius-Institut of the Technical University of Hannover.

SCALING CRITEREA FOR THERMAL-HYDRAULIC MODEL TESTS

With regard to the environmental impact and ecological aspects the temperature distribution has to be determined.

Therefore the whole far-field region is reproduced in the distorted model with a vertical scale of 1:100 and a horizontal scale of 1:300.

The scales of the far-field model were selected with regard to the reproduction of the turbulent diffusion and with re-

†) Dipl.-Ing., Scientific Assistant, Franzius-Institut of the Technical University of Hannover, Germany

gard to the heat exchange at the water surface due to the following scaling criteria for the heat exchange

$$k_r = \frac{K_N}{K_M} = \frac{\lambda_V^{1.5}}{\lambda_H} \quad (\text{as outlined in reference (3)})$$

where K is the heat exchange coefficient in $W/m^2 \cdot K$ and λ_V the vertical scale and λ_H the horizontal scale.

In the laboratory (without wind effects) heat exchange coefficient K_M of about $15 W/m^2 \cdot K$ were measured. For the German estuarine areas one assumes significant mean low heat exchange coefficients of about $50 W/m^2 \cdot K$, hence the value of k_r in the above mentioned model study is 3.33.

In regard to the reproduction of the turbulent diffusion in the model the Reynolds number should be large enough to satisfy that the turbulence is sufficiently well developed.

The scale of the Reynolds number r is given by this relationship

$$r = \frac{Re_N}{Re_M} = \lambda_V^{1.5}$$

where λ_V is the vertical scale, index N indicates prototyp dimension and index M model dimension.

A special near-field model was built for the purpose of cooling water discharge currents, the waste heat recirculation, the dilution and dispersion influenced by the outlet design.

In the near-field region physical effects such as buoyancy, density currents, stratified flows, jet-diffusion and the advective and diffusive heat transport processes are predominant. Therefore a scale of 1:50 and no distortion were selected for the near-field model.

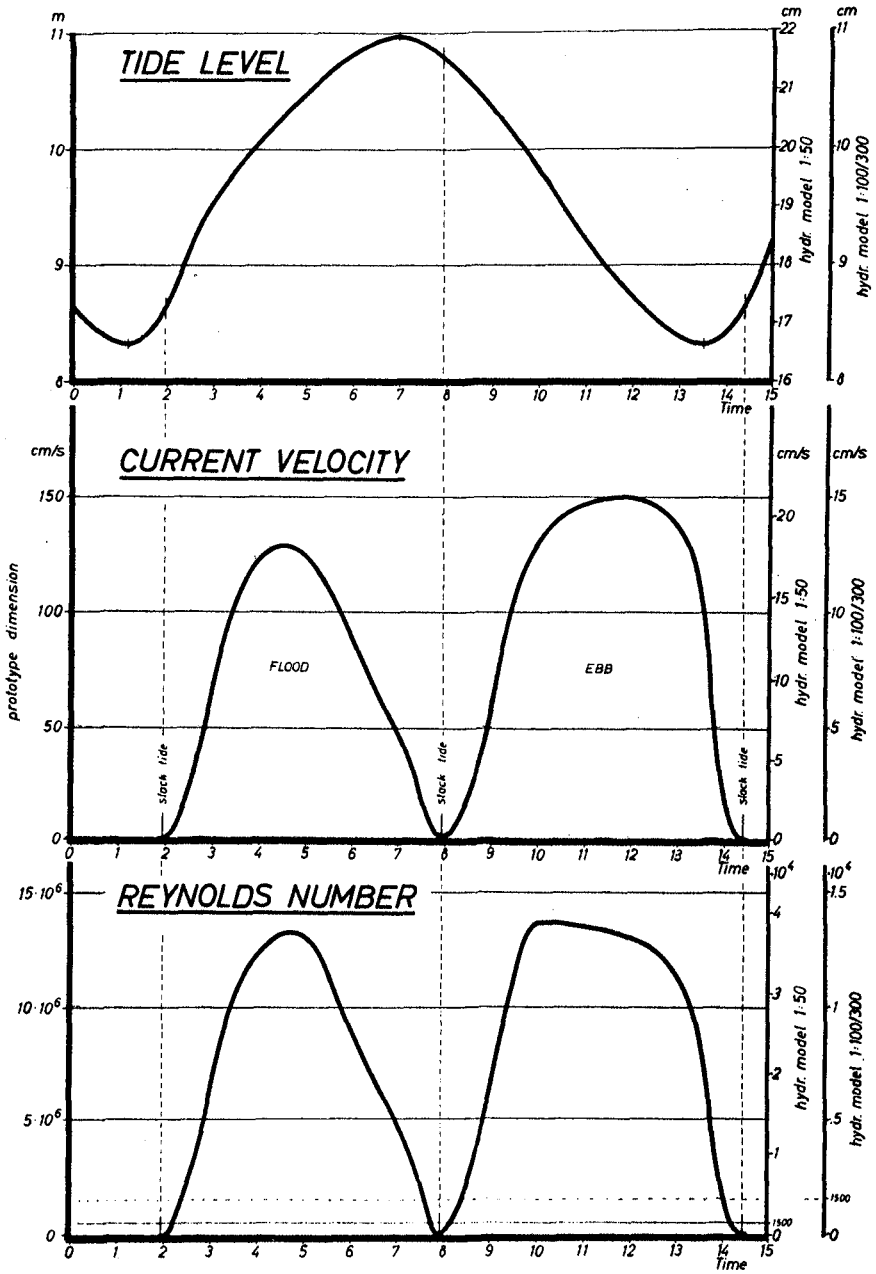


Figure 1

Figure 1 shows the characteristic values for the water depth (tidal level), the current velocity and the Reynolds number as a function of time. On the left hand the prototype dimension and on the right side the values for the undistorted near-field model with a scale of 1:50 and the three times distorted far-field model are represented.

The diagram shows that only during a short time before and after slack tide the Reynolds number of onethousandfivehundred is not satisfied. The dotted line belongs to the far-field model.

DIFFUSION AND TURBULENCE PHENOMENA IN TIDAL MODELS

The model tests showed a characteristic behavior of the horizontal diffusion coefficient D_z during the tidal cycle (Fig. 2).

During the well developed tidal current the horizontal diffusion coefficient is nearly constant. But a short time before and a short time after slack tide the horizontal diffusion coefficient becomes a maximum.

This result leads to the question: What kind of physical effects induces this behavior of the horizontal diffusion?

Theoretical considerations lead to the following statement:

The turbulence is mainly generated through large eddies, the energy of which is a function of the mean flow velocity. The large eddies transfer their energy to smaller eddies until the eddies become so small that they are dissipated by viscosity effects (1).

In turbulence theory distinction is made between:

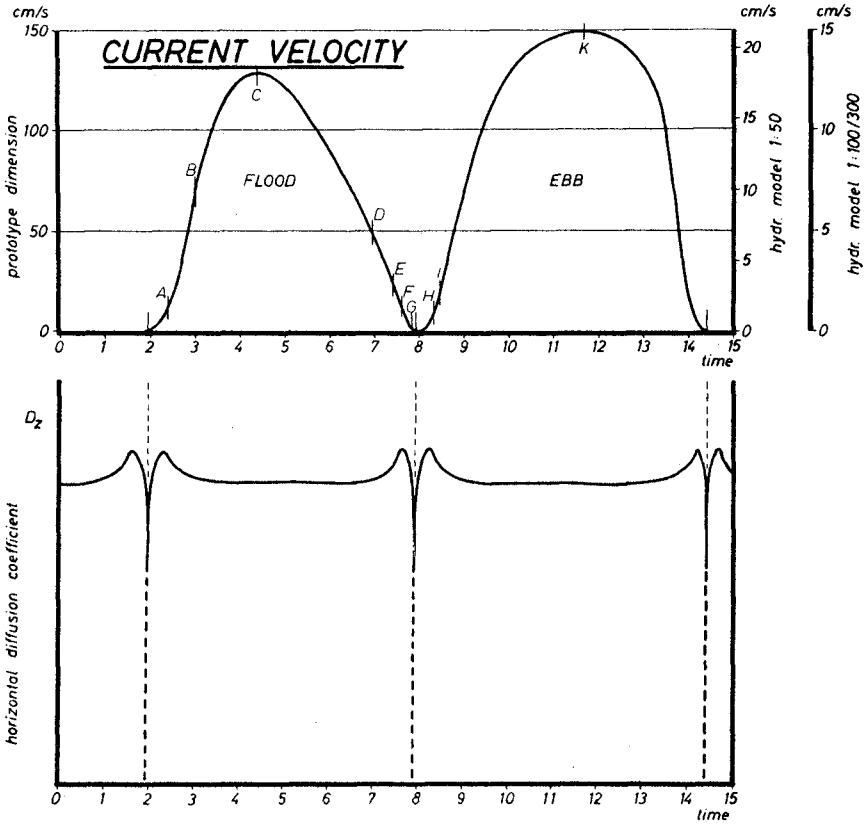


Figure 2

$$\text{integral scale } \Lambda \quad (\text{a macro scale}) \quad \Lambda :: L \quad (1)$$

$$\text{Taylor scale } \lambda \quad (\text{a micro scale}) \quad \lambda :: v \frac{\sqrt{u'^2}}{\epsilon} \quad (2)$$

$$\text{Kolmogoroff scale } \eta \quad (\text{a micro scale}) \quad \eta :: \left(\frac{v^3}{\epsilon}\right)^{1/4} \quad (3)$$

where L : characteristic dimension of length (for example: water depth)

ϵ : energy dissipation per unit mass and unit time

v : coefficient of cinematic viscosity

u' : turbulent velocity fluctuation

The turbulent energy induced by the bottom shear in the fluid motion per unit mass amounts to:

$$E :: \frac{\tau_b \cdot L^2 u}{\rho L^3} :: \frac{f_b \cdot u^3}{L} \quad (4)$$

where τ_b = bottom shear stress ($\tau_b = \frac{1}{8} f_b \cdot \rho \cdot u^2$)
 f_b = bottom shear coefficient

Assuming that a state of equilibrium exists between induced turbulent energy and energy dissipation.

$$E = \epsilon \quad (5)$$

From this condition, we derive (Abraham (2)) the following relationship between the Reynolds number and the scales of turbulence:

$$\frac{\eta}{L} :: Re^{-3/4} \quad (6)$$

$$\frac{\lambda}{L} :: Re^{-1/2} \quad (7)$$

where the Reynolds number is defined as follows:

$$Re = \frac{\bar{u}L}{v}$$

Equation 6 and 7 lead to the following conclusion:

With decreasing Reynolds numbers the size of the eddies which are dissipated by viscosity (Kolmogoroff scale, Eq. 6) increases. The size of eddies of which only a small fraction is dissipated by viscosity (Taylor scale, Eq. 7) increases also with decreasing Reynolds numbers.

These theoretical arguments lead to the statement, that - a short time before and a short time after slack tide, when the horizontal diffusion coefficient D_z increases, the turbulence spectrum of the flow contains mainly large eddies.

Therefore the next step of research was to investigate the behavior of the turbulence spectrum during the tidal cycle - in both models.

Figure 3 shows in the upper diagram the characteristic current velocity as a function of the tidal process and the turbulence spectra at the marked points of time in the upper diagram. The full-line represents the results of the undistorted model, scaled 1:50, and the dotted line represents the results of the distorted model, scaled 1:100/1:300.

The ordinate indicates the velocity fluctuation.

Diagram A points out, that a short time after low water slack the turbulence is not fully developed - in both models. The frequency is smaller than two Hertz, that means only large eddies exist.

At time B the turbulence spectrum in the near-field model is more developed.

That means the turbulence spectrum contains also small eddies. The predominant eddy size is indicated by the maximum of the

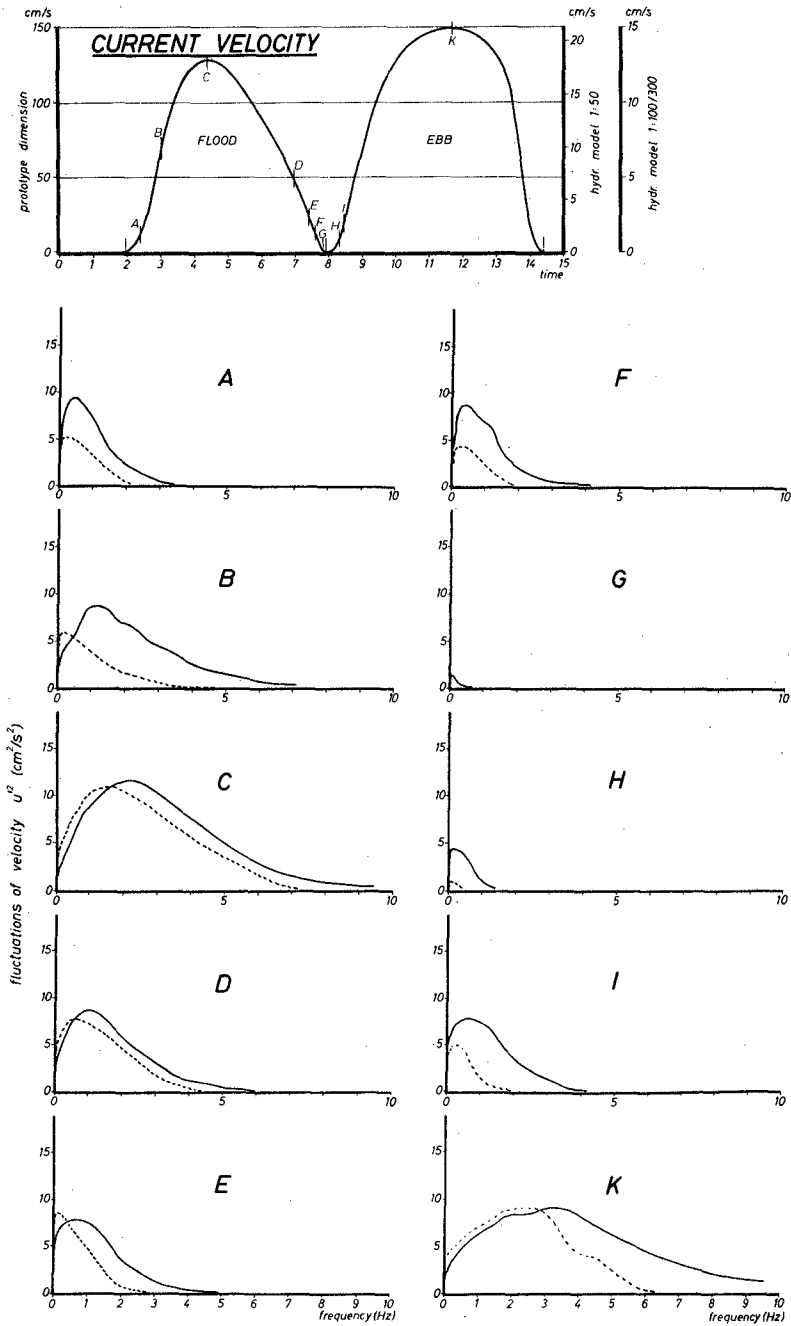


Figure 3

curve. The dotted line shows that - at the same tidal point - in the distorted model the turbulence is not well developed. Only a small fraction of small eddies represented by the higher frequency exists.

At C the turbulence is fully developed. In both models the spectrum has nearly the same shape. In comparison to B the fraction of large eddies decreases; but the fraction of small eddies increases. The total of turbulence intensity - with other words the integral of the curve - becomes a maximum.

At D the turbulence intensity decreases. Mainly the small eddies are filtered out by viscosity effects - or with other words the range of higher frequencies is dissipated. The range of low frequencies has not changed importantly.

At E and F the intensity of turbulence decreases more and more. One can observe that the smaller eddies, that means the range of the higher frequencies of the spectrum, in this case from four to two Hertz, are filtered out. With other words the size of the existing eddies becomes more and more uniform.

At G that means at slack tide there is no turbulence in the far-field model (1:100/300). In the near-field model only a very small fraction with low intensity of turbulence exists.

At H the development of the turbulence has started again. But at this time only a small intensity of turbulence exists. Only large eddies - indicated by low frequencies - are generated.

At I one can confirm a further development of the turbulence spectrum. The spectrum contains mainly large eddies with frequencies to about two Hertz.

At K a fully developed turbulence spectrum exists. In comparison to G, H, I one can confirm that at first the larger eddies are generated and with increasing intensity more and more smaller eddies are produced until the turbulence is fully developed - as shown in diagram K.

CONCLUSION

The statement, that the maximum of the horizontal diffusion coefficient D_z a short time before and a short time after slack tide is caused by the effects of turbulence - that means the turbulence spectrum becomes more and more uniform containing only large eddies - seems to be verified by the investigations in both models.

As well known the turbulence is of a statistically manner.

Therefore the transportation process is also a statistically process - and one can imagine, that the efficiency of the transport process is also influenced by the rate of uniformity of the eddy size.

And in regard to the mentioned behavior of the horizontal diffusion coefficient, it seems that the increase of the eddy size and the uniformity of the eddies after my opinion cause this phenomenon. But to get sure information about this effect and about the magnitude of this effect for prototype conditions field investigations about the variation of the turbulence spectrum during the whole tidal cycle will be done as soon as possible.

REFERENCES

1. HINZE, J.O.: Turbulence
Mc Graw Hill (1959)

2. ABRAHAM, G.: Methodologies for Temperature Impact Assessment
European Course on Heat Disposal from Power Generation in the Water Environment, Delft (1975)
3. SCHWARZE, H.
FLÜGGE, G.: Similarity conditions for thermal-hydraulic model tests of tidal estuaries. 14th Coastal Engineering Conference (1974), Volume III

CHAPTER 178

DYNAMICS OF A LONGITUDINALLY STRATIFIED ESTUARY

by

Jorg Imberger*

1. Introduction.

A partially stratified estuary is defined as one which possesses a quite definite longitudinal salinity gradient from the mouth to the head of the estuary, but only a very weak vertical or transverse salinity structure. For an estuary to exhibit such characteristics it must possess a source of fresh water near the head of the estuary, sufficient vertical mixing to overcome the potential energy associated with such a fresh water inflow and be very much longer than its width to reduce transverse variations.

If the estuary is very shallow (a few meters) then wind generated turbulence is often sufficient to eliminate most or all the vertical structure. Deeper, or very sheltered, estuaries require additional strong tidal shears to break up the vertical density gradients. However, in both cases the mixing is usually not sufficient to completely homogenize the estuary longitudinally and it is found that these estuaries display a near linear salinity gradient along the principle axis of the estuary throughout most of the spring and summer months.

Such a density gradient drives a gravitational circulation within the estuary which leads to a net transport of salt from the sea mouth to the head of the estuary. Two dimensional theories (see for instance Rattray and Mitsuda (1974)) have been established, but in general these greatly underestimate the longitudinal transport found in such estuaries and three dimensional circulation effects must be considered.

Fischer (1972) was the first to recognise this fact and he carried out a first order analysis which pointed to a greatly increased longitudinal dispersion. However, Fischer (1972) carried out his analysis only to first order, not explaining how the transverse pressure field, set up by the first order velocity field convecting the longitudinal density gradient, is balanced. It is the purpose of this paper to give a rigorous foundation to Fischer's (1972) hypothesis that it is the transverse variations in velocity which yield the greatest contribution to any longitudinal transport of the density or any passive pollutant. Furthermore, the presented theory is applied to a local Western Australian estuary which is ideally suited for such a comparison complying strictly to the assumptions of the theory.

In order to facilitate the theoretical work the experimental apparatus described in Imberger (1974) was modified and used to visualize the flow. An insulated, completely enclosed perspex tank possessing a triangular section and containing water was heated

*Senior Lecturer, Departments of Mathematics and Mechanical Engineering, University of Western Australia, Nedlands, 6009, W.A.

at one end and cooled at the other. The dimensions of the tank were 2.58 meters long, 0.45 meters wide and 0.05 meters deep at one side and of zero depth at the other. The flow was visualized by the thymol blue technique and the temperature was measured with small thermistors.

The motion was in general difficult to quantify because of its three dimensional nature. However, two features were common to all the motions observed. Firstly, in the central sections of the tank, away from the end walls, the motion was confined to vertical planes, parallel to the longitudinal axis. The warm fluid at the top flowed towards the cold end and the colder undercurrent flowed towards the warmer end wall. In the shallow sections the net flow was towards the cold end wall, while in the deeper parts the net flow was towards the warmer end wall. Secondly, the temperature structure was approximately independent of the transverse coordinate and dependent only on the distance along the longitudinal axis and the depth below the upper surface.

Hence, the experiments indicated that the dominant force balance of such a flow is

$$\epsilon_z \frac{\partial^3 u}{\partial z^3} + \frac{g}{\rho_0} \frac{\partial \rho}{\partial x} = 0, \text{ where } u \text{ is}$$

the longitudinal velocity, ρ is the density, ρ_0 is a reference density, ϵ_z is the vertical mixing coefficient for vorticity, g is the acceleration due to gravity and x and z are the horizontal and vertical coordinates. This balance yields a scale for the velocity u in terms of the longitudinal density gradient $\frac{\partial \rho}{\partial x}$ and a non-dimensionalizing of the full flow equations, based on this force balance, is shown in section 2 to admit a consistent perturbation solution very similar to that described by Cormack, Leal and Imberger (1974).

2. Gravitational circulation in a triangular shaped basin

Consider half of an idealized estuary as shown in figure 1, filled with water which is kept in motion by a longitudinally applied buoyancy flux. The basin is assumed to possess a cover in contact with the water. This is not an essential assumption and a non-conducting free surface could be treated just as easily. The result with regard to the final mass transport is quite insensitive to this boundary condition, yet the pressure field is simplified reducing the algebra somewhat. All sides and top surfaces are considered to be non-conducting and the emphasis will be on investigating the flow in the central sections of the basin where the flow is essentially in the vertical plane. The end regions where the flow is turned are neglected.

From the experiments described in the introduction the following scales are apparent;

$$\text{Density: } \frac{\rho - \rho_0}{\rho_0} = O(\Delta\rho),$$

$$\text{Horizontal length: } x = O(L)$$

$$\text{Transverse length: } y = O(B)$$

$$\text{Vertical length: } z = O(H)$$

$$\text{Horizontal velocity: } u = O\left(\frac{Gr \epsilon_z}{L}\right)$$

$$\text{Transverse velocity: } v = O\left(\frac{B Gr \epsilon_z}{L^2}\right)$$

$$\text{Vertical velocity: } w = O\left(\frac{H Gr \epsilon_z}{L^2}\right),$$

where $\Delta\rho$ is the applied density variation, Gr is the effective Grashoff number $g\Delta\rho H^3/\epsilon_z^2$, ϵ_z the vertical vorticity diffusion coefficient assumed to be constant and g is the acceleration due to gravity.

This suggests introducing the non-dimensional variables:

$$u^* = \frac{u}{\frac{Gr \epsilon_z}{L}}; \quad v^* = \frac{v}{\frac{B Gr \epsilon_z}{L^2}}; \quad w^* = \frac{w}{\frac{H Gr \epsilon_z}{L^2}}; \quad p^* = \frac{p}{\frac{\epsilon_z^2 \rho_0 Gr}{H^2}}$$

$$\theta^* = -\frac{\rho - \rho_0}{\rho_0 \Delta\rho}; \quad x^* = \frac{x}{L}; \quad y^* = \frac{y}{B}; \quad z^* = \frac{z}{H}$$

Interest here centres on very shallow, long estuaries with aspect ratios

$$A_1 = \frac{H}{L}, \quad A_2 = \frac{H}{B} \quad \text{and} \quad A_3 = \frac{B}{L}$$

all being very small. However, for a perturbation scheme to be applicable, these must be ordered. The most realistic limit is obtained by setting

$$A_2 = A, \quad A_1 = \alpha A^2 \quad \text{and} \quad A_3 = \alpha A \quad \text{where}$$

α is the ratio B^2/LH as $H \rightarrow 0, L \rightarrow \infty$. The Boussinesque approximation to the full equations of motion for the mean components of the velocity may thus be written:

$$\alpha^2 A^4 \text{Gr}(u u_x + v u_y + w u_z) = -p_x + \lambda \alpha^2 u_{xx} + \lambda \Lambda^2 u_{yy} + u_{zz}, \quad (1)$$

$$\alpha^4 A^6 \text{Gr}(u v_x + v v_y + w v_z) = -p_y + \alpha^4 \lambda \Lambda^6 v_{xx} + \alpha^2 \lambda A^4 v_{yy} + \alpha^2 A^2 v_{zz}, \quad (2)$$

$$\alpha^4 A^8 \text{Gr}(u w_x + v w_y + w w_z) = -p_z + \theta + \alpha^4 \lambda A^8 w_{xx} + \alpha \lambda^2 A^6 w_{yy} + \alpha^2 A^4 w_{zz}, \quad (3)$$

$$\alpha^2 A^4 \text{GrPr}(u \theta_x + v \theta_y + w \theta_z) = \lambda \alpha^2 A^4 \theta_{xx} + \lambda^2 A^2 \theta_{yy} + \theta_{zz}, \quad (4)$$

$$u_x + v_y + w_z = 0, \quad (5)$$

where $\lambda = \frac{\epsilon_y}{\epsilon_z} = \frac{\epsilon_x}{\epsilon_z}$, $\text{Pr} = \frac{\epsilon_z}{\kappa_z}$ and all asterisks have been dropped.

The scaling has captured the dominant physical processes and an appropriate solution may be sought in the form,

$$\phi(\underline{x}; \Lambda) = \phi_0 + A^2 \phi_2 + \Lambda^4 \phi_4 + \dots, \quad (6)$$

where ϕ represents the variables u, v, w and p .

Substituting this expansion into the above and expanding terms leads to:

$$O(\Lambda^0): \quad p_{0x} - u_{0zz} = 0, \quad (7)$$

$$p_{0y} = 0, \quad (8)$$

$$p_{0z} - \theta_0 = 0, \quad (9)$$

$$\theta_{0zz} = 0, \quad (10)$$

$$u_{0x} + v_{0y} + w_{0z} = 0, \quad (11)$$

$$O(\Lambda^2): \quad p_{2x} - u_{2zz} = \lambda u_{0yy}, \quad (12)$$

$$p_{2y} = \alpha^2 v_{0zz},$$

$$p_{2z} - \theta_2 = 0,$$

$$\theta_{2zz} = -\lambda \theta_{0yy},$$

$$u_{2x} + v_{2y} + w_{2z} = 0,$$

$$O(A^4): \quad p_{4x} - u_{4zz} = -Gr\alpha^2 (u_{00x} + v_{00y} + w_{00z}) + \lambda\alpha^2 u_{0xx} + \lambda u_{2yy}, \quad (17)$$

$$p_{4y} = \lambda\alpha^2 v_{0yy} + \alpha^2 v_{2zz}, \quad (18)$$

$$p_{4z} - \theta_4 = \alpha^2 w_{0zz}, \quad (19)$$

$$\theta_{4zz} = \alpha^2 PrGr (u_{00x} + v_{00y} + w_{00z}) - \lambda\alpha^2 \theta_{0xx} - \lambda\theta_{2yy}, \quad (20)$$

$$u_{4x} + v_{4y} + w_{4z} = 0. \quad (21)$$

The solution to the problem may now be carried out in stages. Consider the zeroth order problem.

Equation (10) implies

$$\theta_0 = f_1(x,y)z + f_0(x,y),$$

but at $z = 0$, $\theta_{0z} = 0$ which requires that $f_1 = 0$.

Also equation (9) together with equation (8) prohibit f_0 to be a function of y . Hence

$$f_0 = f_0(x), \quad (22)$$

where f_0 must be determined from higher order equations and the end boundary conditions.

Eliminating the pressure from equations (9) and (7) yields

$$u_{0zzz} = f_{0x}, \quad (23)$$

which allows u_0 to be determined

$$u_0(y,z) = \frac{h^3}{12} f_{0x} \left(\frac{2z^3}{h^3} + \frac{3z^2}{h^2} + \frac{z}{h} \right) - \frac{6U_0}{h} \left(\frac{z^2}{h^2} + \frac{z}{h} \right), \quad (24)$$

where h is the local depth equal to $-y$ and U_0 is the net volume flux towards the lighter end of the basin. This may be determined from equations (8) and (7) which require

$$u_{0zzy} = 0. \quad (25)$$

The total net flux over the triangular section shall be assumed to be zero, thus substituting equation (24) into equation (25) leads to

$$U_0(y) = \frac{1}{30} \frac{\partial f_0}{\partial x} y^3 \left(1 + \frac{5}{4} y\right) \quad (26)$$

Equation (15) and the no flux boundary at $z = 0$ require that

$$\theta_2 = f_2(x, y), \quad (27)$$

where $f_2(x, y)$ must still be determined.

Integrating equation (20) from $-h$ to zero with respect to z yields

$$-\theta_{4z}(z = -h) = \alpha^2 \text{PrGrf} U_{0x} U_{0x} - 2\alpha^2 f_{0xx} h - \lambda \theta_{2yy} h, \quad (28)$$

which is only possible if

$$f_0 = kx, \text{ where } k \text{ is a}$$

constant - determined by the flow in the end regions. For the two dimensional analogue Cormack, Leal and Imberger (1974) solved the end regions to show that k could itself be expanded in a power series of A . Here k will be taken as experimental data since the three dimensional motion in end regions where the flow turns is far too complex to solve in closed form.

The heat flux $\theta_{4z}(z = -h)$ is strictly non-zero since

Phillips (1970) type boundary layer always exist at a sloping wall in a stratified fluid. However, the heat flux necessary to drive such a layer at small angles is very small, certainly not an appreciable proportion of the flux convected by U_0 and θ_{4z} may thus in the first instance be set to zero at

$z = -h$. If desired a wall boundary layer could be added with small modifications resulting to the main flow.

Setting $\theta_{2y}(y = -1) = 0$ and $\theta_2(y = -\frac{4}{5}) = 0$ completely determines the second order temperature field.

$$\theta_2(y) = -\frac{\alpha^2 \text{PrGr} k^2}{1440\lambda} (3y^5 + 4y^4 + y + 0.1446) \quad (29)$$

Eliminating the pressure from equations (13) and (14) and substituting equation (29) into the resulting equation yields,

$$v_0(y, z) = -\frac{\text{PrGr} k^2}{288\alpha^2} \left(\frac{y^4}{4} + \frac{4}{15} y^3 + \frac{1}{60} \right) (2z^3 - 3z^2y + zy^2) \quad (30)$$

Equation (11) allows a streamfunction $\psi_0(x, y)$ to be defined such that

$$v_0 = \psi_{0z} \quad \text{and} \quad w = -\psi_{0y}$$

From equation (30) ψ_0 may thus be determined

$$\psi_0(y, z) = -\frac{\text{PrGr} k^2}{576 \alpha^2} z^2 (y - z)^2 \left(\frac{y^4}{4} + \frac{4}{15} y^3 + \frac{1}{60} \right). \quad (31)$$

The flow represented by equation (31) is depicted in figure 2 and it consists of two opposing eddies.

Eliminating the pressure from equations (12) and (14) and substituting for u_0 allows u_2 to be determined.

$$u(x, z, y) = \frac{k}{36} (2z^3 - 3z^2y + 2y^2) + \frac{6U_2(x, y)}{y^3} (z^2 - zy) \quad (32)$$

and U_2 may be determined from equations (12) and (13):

$$U_2(y) = \frac{ky^3}{72} \left(y + \frac{4}{5} \right). \quad (33)$$

Finally, substituting u_0 , θ_0 and θ_2 into equation (20) allows the determination of the 4th order temperature field:

$$\theta_4(z, y) = \frac{\alpha^2 \text{PrGr} k^2}{24} \left\{ \left(\frac{z^5}{5} - \frac{z^4 y}{2} + \frac{z^3 y^2}{3} - \frac{y^5}{60} \right) + \frac{z^2}{2} \left(y + \frac{4}{5} \right) (z - y)^2 \right\}, \quad (34)$$

where the integration constant has been chosen so that $\theta_4 = 0$, $z = \frac{1}{2}y$ and $y = -\frac{4}{5}$.

The quantities so far determined allow the mass transfer to be computed correct to $O(A^4)$. Higher order terms may however easily be derived.

3. Longitudinal mass transfer

The convective mass transfer in the x direction is given by

$$\begin{aligned}
 q &= \int_{-B}^0 \int_{-h}^0 \theta u \, dz \, dy = \frac{HBGr\epsilon_z \Delta\rho}{L} \int_{-1}^0 \int_y^0 \theta^* u^* \, dz^* \, dy^* \\
 &= \frac{HBGr\epsilon_z \Delta\rho}{L} \int_{-1}^0 \int_y^0 \{ (\theta^* u^*)^2 + (\theta^* u^*)^4 \} \, dz^* \, dy^* \quad (35)
 \end{aligned}$$

Substituting from section 2 for $\theta_0, u_0, \theta_2, u_2$ and θ_4 and carrying out the integration yields

$$q = - HB D k^3, \quad (36)$$

where

$$D = \frac{\kappa_z \Delta\rho}{L} \frac{\alpha^2 Pr^2 Gr^2 A^2}{\lambda} \{ 1.286 \times 10^{-7} + 6.81 \times 10^{-5} A^2 \lambda + \}.$$

So far the flow has been considered steady, but since there is a net flux from the estuary mouth to the head of the estuary the salinity will build up there. In line with Taylor's (1954) argument it will be assumed that the time scale of this change is large compared to the flow establishment time. Furthermore, if it is also assumed (again following Taylor (1954) that the gradients of $f_0(x)$ are small enough for the above theory to hold, at least, locally, then a mass balance, averaged across any cross-section yields the relationship

$$\frac{dq}{dx} = - \frac{HB}{2} \frac{\partial \theta_0}{\partial t}. \quad (37)$$

Substituting equation (36) into (37) yields an equation for $\theta_0(x)$

$$\frac{\partial \theta_0}{\partial t} = 6D \left(\frac{d\theta_0}{dx} \right)^2 \frac{d^2 \theta_0}{dx^2}, \quad (38)$$

which may be viewed to the equivalent to Taylor's (1954) mean diffusion equation, the only difference being that the tracer here is the salinity itself which also drives the motion. The exact analogy for the two dimensional flow is discussed in more detail in Imberger (1974).

The exact solution of equation (38) is difficult to obtain for a bounded domain $0 < x < L$. For comparison with experimental work it is sufficient to note that equation (38) admits a self similar valid in the unbounded domain

$$\theta = \theta \left(\frac{x^2}{\sqrt{DE}} \right), \quad (39)$$

yielding a time scale for salinity adjustments at the end of an enclosed estuary of the order of

$$T = \left(1.3 \times 10^7 \frac{\Delta\rho L^2 \lambda}{\kappa_z Pr^2 Gr^2 A^2} \right)^{1/3}. \quad (40)$$

4. Application to the Harvey Estuary

The Harvey estuary situated about 80 km south of Perth is a long, shallow coastal lagoon, behind and parallel with the late Pleistocene dunes. Fig. 3 shows the general bathymetry of the basin and indicates the suitability of the Harvey for testing the above theory. The principle axis of the basin is oriented along the direction of the major wind system which blew consistently from the south with a mean velocity of between 6 and 10 km/hr for most of the study period.

The measurements were initiated in July 1974 when the fresh water inflow for the season was at its maximum. The stations at which the salinity and temperature were measured are indicated on fig. 3 and the actual values recorded are listed in table 1. All measurements were recorded from a small dinghy with a standard induction salinometer.

Figure 4 shows the average salinity plotted against distance from station 140 for the period July to April. The fresh water inflow had ceased almost completely by October 1974. Table 2 shows that the variations with depth are indeed small past station 150 consistent with the assumption of a well stirred lagoon. Table 2 lists the comparison of the experimental findings with those predicted from the above theory. All the assumed values of constants are shown and it is seen that the response time for salinity variations at the southern extreme (station 180 and 190) due to applied changes at Station 140 are predicted quite well. Careful probing of the deepest depressions along the central trough showed evidence of pools of saltier water (usually 1 or 2‰ higher) of about 5 to 10 cm thickness underlying the well mixed water above. This indicates that the 1.5 meter depth is on the limit of wind mixing and salt replenishment by salt wedge underflow does take place on the more calm days. It was very difficult to estimate the magnitude of the contribution to the salt transport by this later mechanism as little is known about the entrainment across a density interface under surface waves. However, the lateral extent was no more than 300 meters i.e. 1/10 of the width. Assuming a fully active layer

of thickness $h_0 = 5$ cm with a velocity $(\Delta\rho gh_0)^{1/2} = 0.02$ m sec⁻¹ and a salinity gradient $\Delta\rho/L = 5.5 \times 10^{-8}$ leads to a flux of $O(h_0^2 u_0) = 8.75 \times 10^{-9}$ compared to 1.9×10^{-6} m²sec⁻¹ for the slow circulation mechanism.

4. Acknowledgement

The author would like to thank Mr. Ron Black, Western Australian Institute of Technology, for helping in the collection of the physical data.

References

- Cormack, D.E., Leal, L.G., Imberger, J. 1974
J. Fluid Mech. Vol. 65, pt 2, pp 209 - 229.
- Fischer, H.B., 1972
J. Fluid Mech. Vol. 53, pt 4, pp 671 - 687.
- Imberger, J. 1974
J. Fluid Mech. Vol. 65, pt 2, pp 247 - 260.
- Ratray, M., Mitsuda, E. 1974
Estuarine and Coastal Marine Science, Vol. 2, pp 375 - 394.
- Phillips, O.M. 1970
Deep-Sea Res. 17, 435-43 p 244.
- Taylor, G.I. 1954
Proc. Roy. Soc. of London 223 pp 446 - 468.

Station Distance km		140 0.00		150 3.35		152 4.90		160 11.05		180 14.20		190 17.80	
Date	Depth	Temp °C	Sal ‰	Temp °C	Sal ‰	Temp °C	Sal ‰	Temp °C	Sal ‰	Temp °C	Sal ‰	Temp °C	Sal ‰
10th July 1974	0.0	13.7	7.0					13.2	5.0			15.0	1.3
	Average	13.7	7.0					13.2	5.0			15.0	1.3
13th Oct 1974	0.00	18.5	13.4	17.6	11.6			17.9	8.9	17.8	7.7		
	1.00	18.4	14.0	17.6	11.6			17.9	8.9	17.8	7.7		
	1.50	18.2	15.0	16.9	13.6			17.9	8.9	17.8	7.7		
	Average	18.36	14.13	17.3	12.2			17.9	8.9	17.8	7.6		4.8
13th Nov 1974	0.00	22.5	17.0	21.2	13.6	21.2	13.0	22.4	12.4	22.8	11.9	23.2	11.2
	0.50	22.5	17.0	20.0	13.5	20.6	12.8	21.2	12.4	22.2	17.2	21.8	17.2
	1.00	22.0	17.2	19.5	13.6	19.6	13.02	20.5	13.0	21.3	12.6	21.0	12.3
	1.50	21.7	17.6	19.2	14.2	19.6	14.5	20.5	13.0	20.6	12.6	20.6	12.4
	Average	22.1	17.2	19.9	13.7	20.2	13.3	21.15	12.7	21.7	13.5	21.6	12.2
7th Jan 1975	0.00	-	31.6	22.5	30.5			21.3	26.5	21.0	26.5	21.1	26.2
	0.50			22.5	30.5			21.3	26.5	21.0	26.5	21.2	26.3
	1.00			22.5	30.5			21.3	26.5	21.0	26.5	21.2	26.3
	1.50			22.5	30.5			21.3	26.8	21.0	26.5		
	Average		31.6	22.5	30.5			21.3	26.5	21.0	26.5	21.1	26.2
20th Jan 1975	0.00					27.0	31.3	21.8	30.3	21.7	29.6	23.0	29.3
	0.50					21.9	31.5	21.6	30.3	21.5	30.1	22.5	29.3
	1.00					21.3	32.0	21.2	30.4	21.4	30.5	22.4	29.3
	1.50					21.2	32.2	21.1	30.7	21.3	30.5	21.8	29.6
	Average					22.8	31.7	21.4	30.4	21.4	30.1	22.4	29.3
23rd Apr 1975	0.0	18.0	38.1					18.0	37.6			21.0	36.9
	Average	18.0	38.1					18.0	37.6			21.0	36.9

Table 1.

Assumed constants

Length L	= 18 km	
Depth H	= 1.5 m	
Half width B	= 1.5 km	
Aspect ratio A_1	= 8.3×10^{-5}	
Aspect ratio A_2	= 10^{-3}	
Aspect ratio A_3	= 8.3×10^{-2}	
Ratio α	= 83	
Applied density difference $\Delta\rho/\rho_0$		= 10^{-2}
Vertical vorticity exchange coefficient ϵ_z		= $10^{-3} \text{ m}^2 \text{ sec}^{-1}$
Ratio of horizontal to vertical exchange coefficient λ		= 80
Turbulent Prandtl number		Pr = 1
Turbulent Grashoff number		Gr = 3.7×10^5
Predicted time response		T = 34 days
Observed time response		T = 1-2 months

Predicted magnitude of

$$\begin{aligned} \text{vertical salinity variations} & O\left(\alpha^2 \text{PrGrk}^2 \times 10^{-3} \frac{\Delta\rho}{\rho_0}\right) A^4 \\ & = 2.5 \times 10^{-5} \text{ }^\circ/\text{oo} \end{aligned}$$

Predicted magnitude of

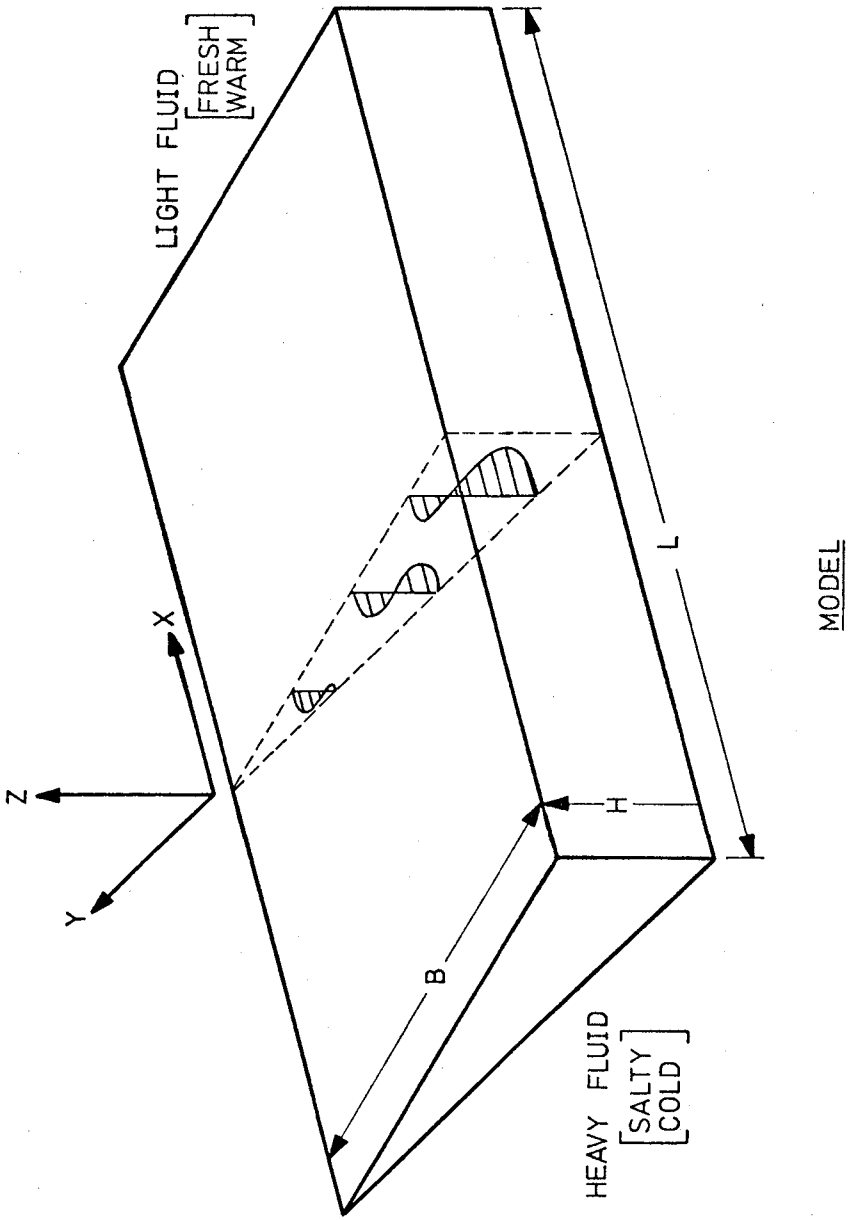
$$\begin{aligned} \text{horizontal salinity variation} & O\left(\frac{\alpha^2 \text{PrGrk}^2}{\lambda} \frac{\Delta\rho}{\rho_0} A^2 10^{-3}\right) \\ & = 0.32 \text{ }^\circ/\text{oo} \end{aligned}$$

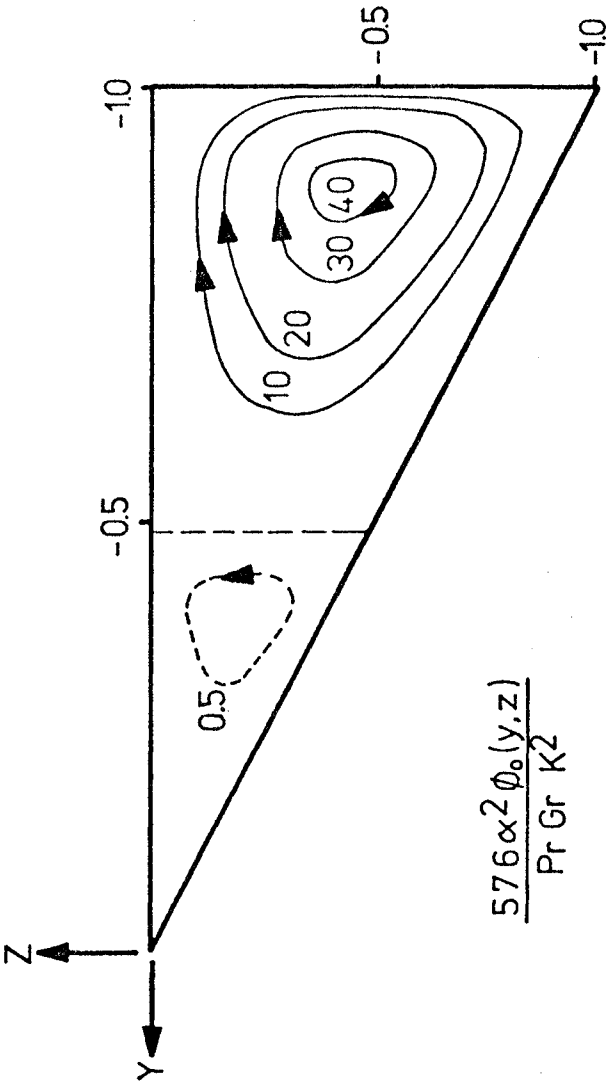
Predicted maximum net flow along principle

$$\text{axis } Q(y = -1) = 0.03 \text{ m}^2 \text{ sec}^{-1}$$

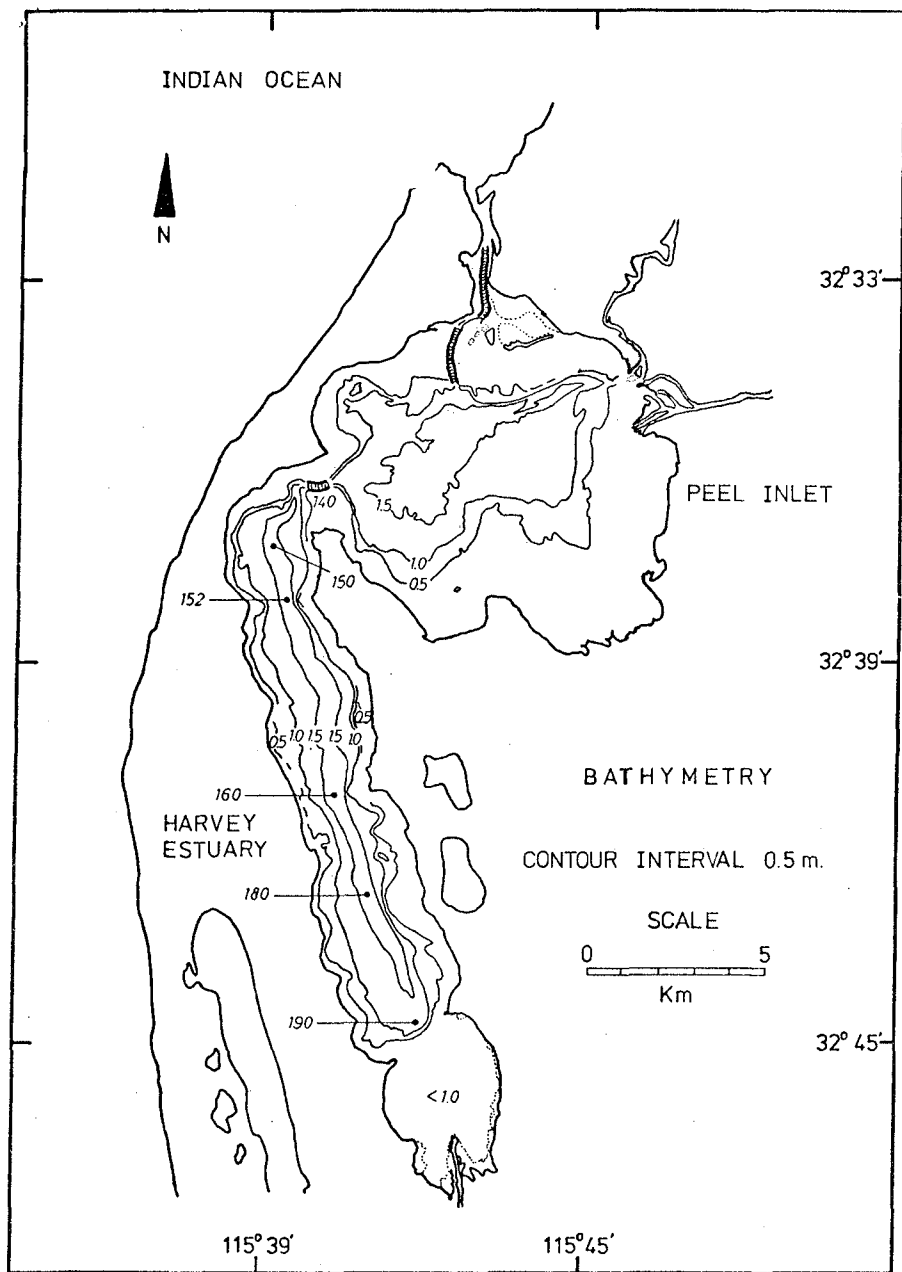
Note: The last three quantities were not measurable.

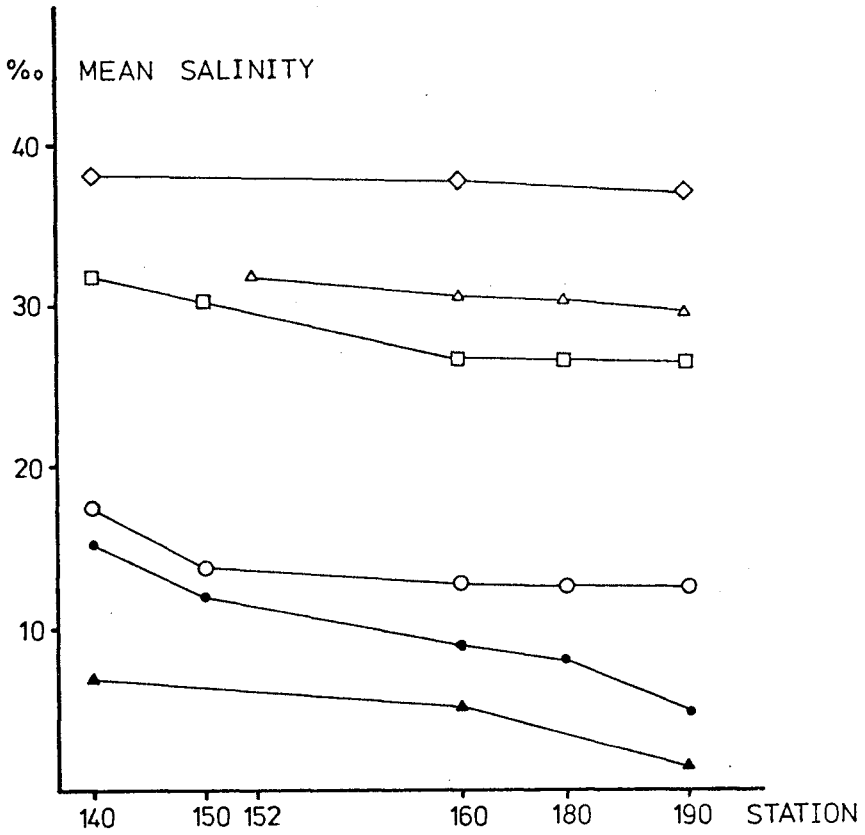
Table 2.





$$\frac{576\alpha^2\phi_0(y,z)}{\text{Pr Gr } K^2}$$





- ◇ 23-06-75
- △ 20-01-75
- 07-01-75
- 13-11-74
- 13-10-74
- ▲ 10-01-74

CHAPTER 179

INTERFACIAL INSTABILITY IN STRATIFIED FLOW

by

Richard H. French*

I. INTRODUCTION

When heated water from a thermal power plant is discharged onto the free surface of an estuary or river, a density stratified flow consisting of superposed layers of hot and cold water is established. Such a flow is characterized by an initially stable interface at which there is zero velocity difference and a decaying density difference. Since it is known that after the density difference has decayed sufficiently the interface will be destroyed by turbulent eddies generated at the bottom boundary, it is pertinent to inquire if the point of interfacial stability can be easily located. It is the purpose of this paper to examine the question of interfacial stability in the presence of boundary generated turbulence and in the absence of interfacial shear.

Although the problem of interfacial stability has been previously investigated, scant attention has been given to the case of a two layer flow without shear in the presence of boundary generated turbulence. Keulegan (1949) investigated a turbulent current of fresh water moving over a quiescent pool of saline water. He concluded that the stability of the interface could be adequately described by a single dimensionless parameter, the "Keulegan" number:

$$K'_U = \frac{\bar{u}^3}{\nu g \frac{\Delta\rho}{\bar{\rho}}} \quad (1)$$

where \bar{u} is the mean velocity of the upper layer and since the lower layer was at rest, \bar{u} is also the velocity difference across the interface, ν the kinematic viscosity of the lower fluid, $\Delta\rho$ the density difference across the interface, $\bar{\rho}$ the density of the upper, flowing fluid, and g the local acceleration of gravity. Interfacial instability was defined as the point at which the rate of mixing suddenly increased; the critical value of K'_U was found to be 180.

Maxwell, et al (1975) studied arrested thermal wedges and arrested cold water intrusions. They concluded that for arrested thermal wedges an increase in bed roughness caused a corresponding increase in the interfacial friction factor; but in the case of arrested cold water intrusions changes in bed roughness had no effect on the interfacial friction factor. Although others have investigated the problem of interfacial instability; e.g., Sherenkov (1971) and

*Assistant Professor, Hydraulic and Water Resources Engineering, Vanderbilt University, Nashville, Tennessee.

Plate and Friederick (1975), the results have not been conclusive.

In the case of Keulegan's investigation, the critical value of K' should not be viewed as a constant; rather, it is a variable dependent not only on fluid viscosity but also on the turbulence present in the two fluids. Turner (1973, p. 118) has indicated that boundary generated turbulence may cause an interface to become wavy; a condition which leads to interfacial instability at values of K' substantially lower than Keulegan's critical value. Plate and Friederick (1975) have noted that field data demonstrates that in some cases buoyant plumes from thermal power plants are not observed upstream of the outlets even though the densimetric Froude number for the flow is less than one. Destruction of the interface by boundary generated turbulence could account for these observations.

The conclusions of Maxwell, et al (1975) verifies the conclusions of Turner (1973, p. 116-118) regarding the mechanisms of mixing in stratified flows. For an arrested thermal wedge, the mixing is controlled by turbulence generated at the bottom boundary, while in the case of an arrested cold water intrusion, the lower layer is stationary relative to the bottom and no turbulence is generated at the boundary. In the former case, boundary generated roughness is important while in the latter case it is unimportant.

Although these previous investigations have aided in understanding the mechanisms of turbulence generation in layered, stratified flow, they have dealt with arrested wedges rather than the environmentally important case of discontinuous vertical density profiles and continuous vertical velocity profiles. In this case, there is no shear at the interface, and interfacial stability is dependent on the stratification and the turbulence generated at the bottom boundary. In the particular case of a decaying density difference across the interface, an interface which is initially stable may at some point become unstable; and, presently, the literature offers no practical criterion for determining the point of instability.

II. EXPERIMENTS

The experiments for this research were performed in a glass flume 12.2 meters long, 1.2 meters deep, and 0.4 meters wide at the Richmond Field Station of The University of California, Berkeley. The experimental apparatus is shown schematically in Figure 1. The upstream end of the flume was connected to a mixing chamber into which fresh and saline water were injected by diffuser pipes. At the downstream end, there was a vertical slotted weir.

Saline water was injected at the entrance beneath the splitter plate by a 15.2 cm. diffuser pipe which was connected to a constant head tank. This water, which originated in San Francisco Bay, was first pumped to a holding pond (capacity 378 cubic meters), and from the holding pond to the constant head tank. The maximum sustainable saline water flow rate was 0.028 m³/s. Fresh water, supplied by a 10.0 cm. city water main to the fresh water constant head tank, was injected above the splitter plate by a diffuser identical to the one used for the saline water. The maximum sustainable fresh water flow rate was 0.071 m³/s. Within the mixing chamber directional vanes and fine mesh screening were used to damp initial turbulence. Additionally, the walls of the chamber and contracting

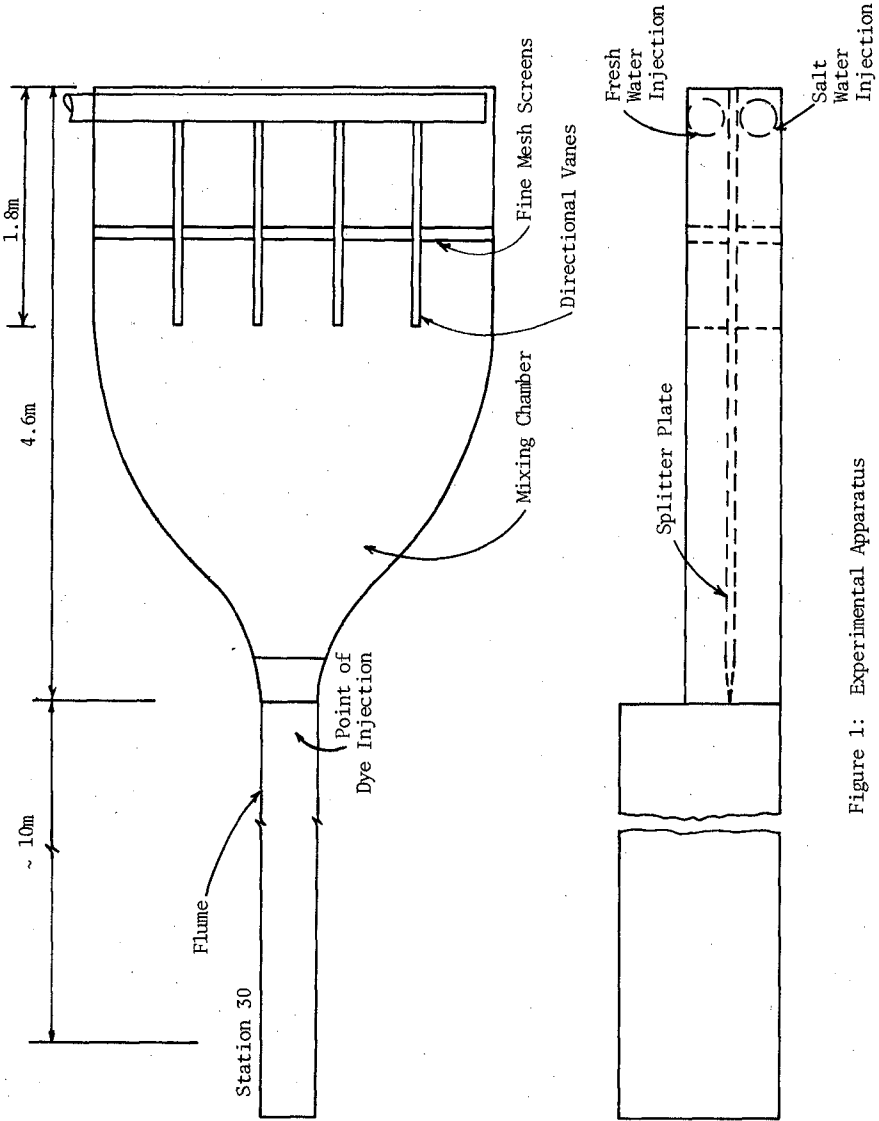


Figure 1: Experimental Apparatus

section were brought to glass like smoothness by repeated applications of epoxy paint.

Once a steady flow was established, the fresh water layer was dyed at the flume entrance to identify the position of the interface. At Station 30, ten meters downstream of the flume entrance, a visual determination of interfacial stability was made, and the results were documented by photographing the interface. The photographs were taken with a Hasselblad 500 EL camera using a Zeiss Distagon wide angle lens ($f = 50$ mm.). In addition, vertical salinity and velocity data were gathered at Station 30, and the water surface slope was determined.

Velocities were measured by a pitot-static tube connected to a PACE P7D differential pressure transducer, and the amplified signal of the transducer was recorded on a strip chart for later analysis. A vacuum system attached to the pitot-static tube was used to collect water samples, and the conductivities of these water samples were determined with a Beckman RC-19 conductivity bridge. The conductivities were converted to salinities by interpolation in a table relating temperature and conductivity to salinity, Tiphane (1962); the salinities were converted to densities by the empirical formulas of Eckart (1958).

The bottom boundary shear velocity, u_* , which was considered a direct measure of the turbulence generated at the bottom boundary, was computed by

$$u_* = \sqrt{gRS_f} \quad (2)$$

where R is the hydraulic radius and S_f the slope of the energy grade line. Since the bottom of the flume was horizontal, S_f was taken as the slope of the free surface. Although the sides of the flume were glass, the bottom was roughened by placing angular stones, approximately $2.5 \times 1.2 \times 1.2$ cm, by hand in a single layer of uniform surface height. The value of u_* calculated by Equation (2) was adjusted by the method of Vanoni and Brooks (1957) to account for the fact that the boundary roughness was not uniform; i.e., while the bottom boundary was hydraulically rough, the side walls were hydraulically smooth.

A wide range of depths and salinities were used; the input salinity was limited to a maximum of 20 ‰, because the source of the saline water was San Francisco Bay which never became more saline. The minimum salinity was 2 ‰ because at lower salinities the mixing was so strong that the flow quickly became homogeneous.

III. EXPERIMENTAL RESULTS

Before describing the experimental results, three terms must be defined in the context of this research.

Stable Interface (Figure 2): A density interface between two homogeneous fluids of different densities across which little or no mixing takes place. In Figure 2, the interface is seen as a sharp line crossed by no noticeable eddies. In this situation, the interface will remain sharp, and the flow will remain layered.

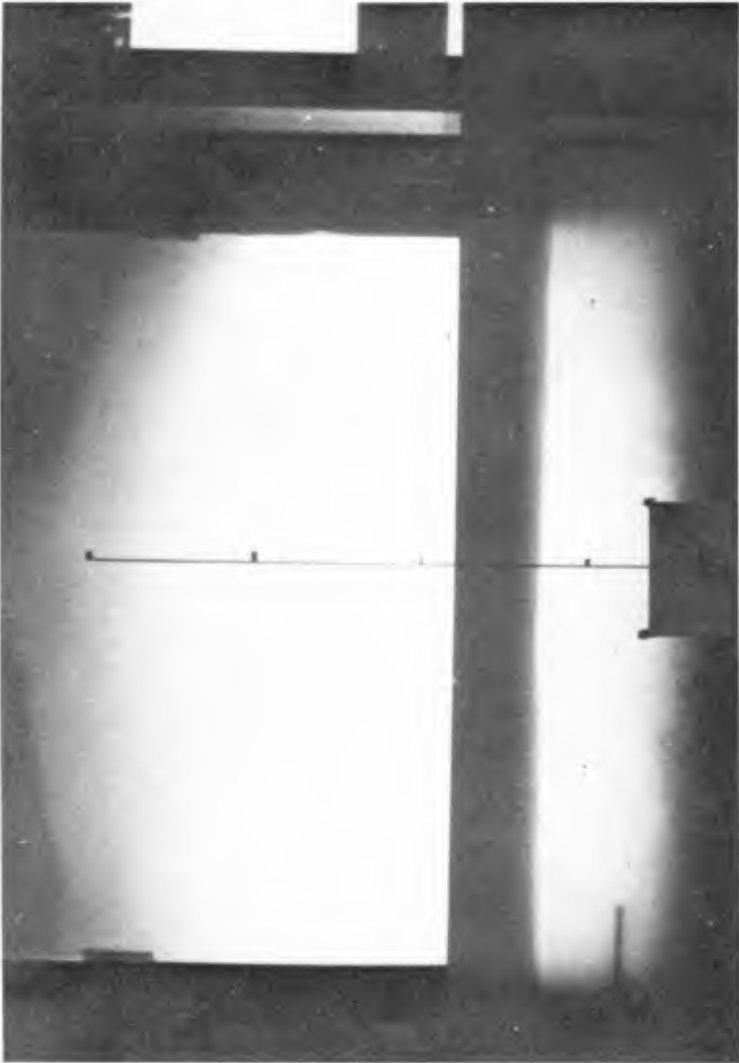


Figure 2: Stable Interface

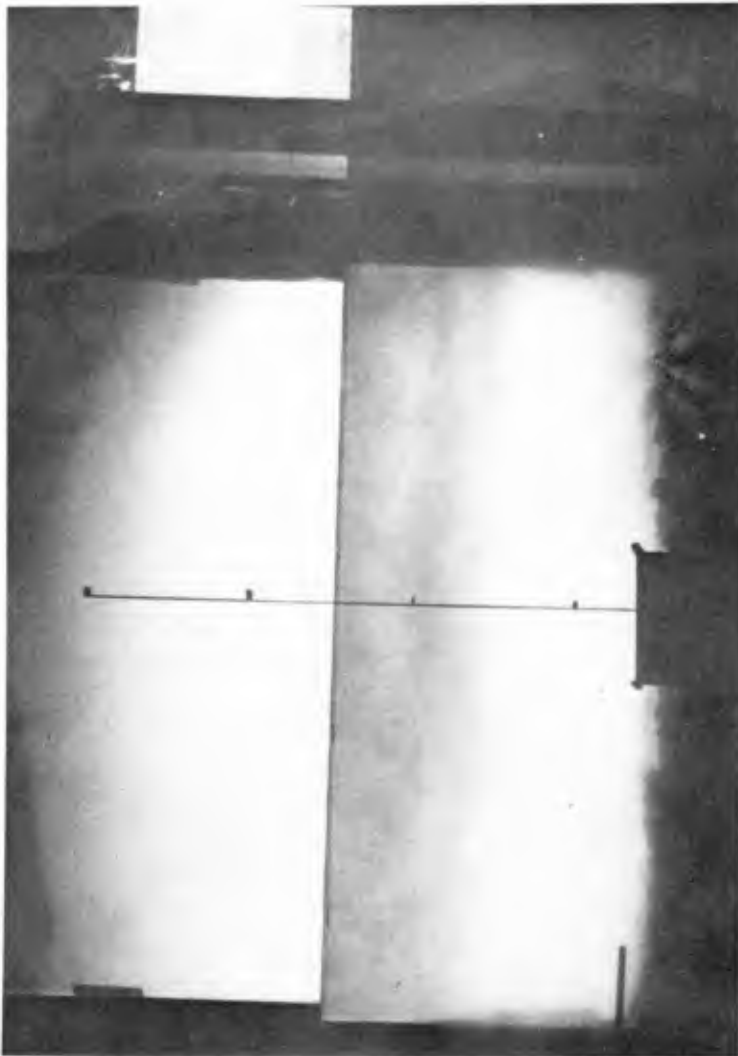


Figure 3: Unstable Interface

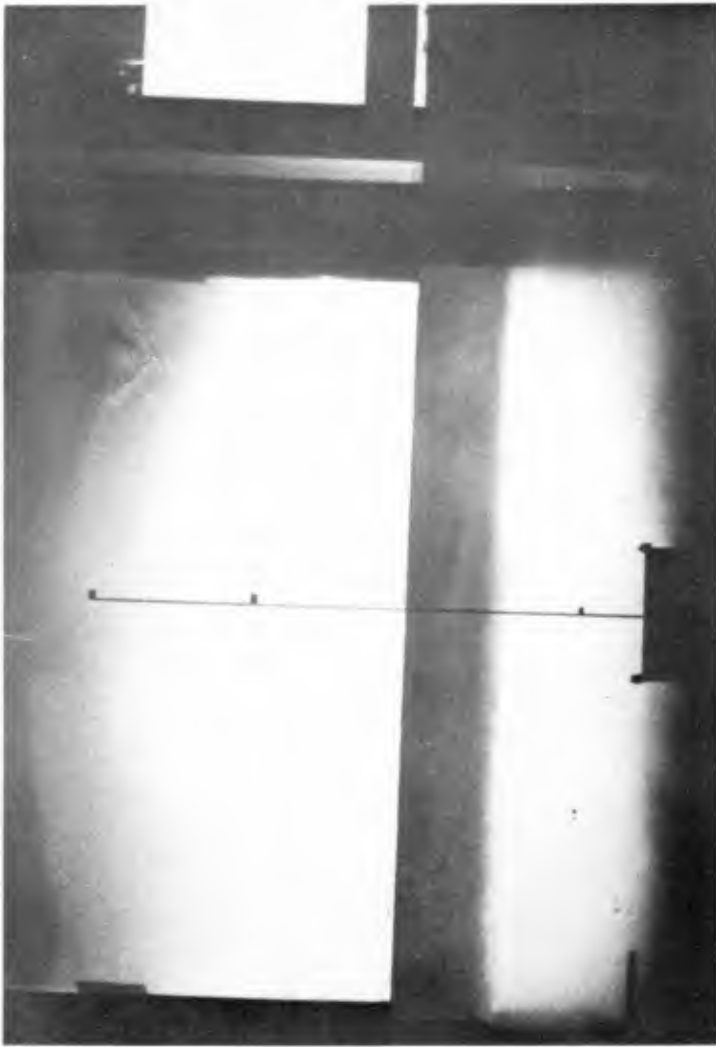


Figure 4: Transition Interface

Unstable Interface (Figure 3): This term specifies a density interface across which there is active mixing. In Figure 3, there are large, violent eddies crossing the interface in both directions; and after a finite period of time, the sharp interface will be destroyed and a continuous system of stratification established.

Transition Interface (Figure 4): This term specifies the case where the interface can be considered neither stable nor unstable. In Figure 4, although there are eddies crossing the interface, they are neither as large nor as violent as those in Figure 3; and it is not clear that the turbulence is of sufficient magnitude to completely destroy the interface.

It was assumed that in a stratified, two layer flow where the turbulence was primarily generated at the bottom boundary the stability of the interface was a function of $(u_*, \bar{u}, D, g \frac{\Delta\rho}{\rho}, \nu)$ where u_* is the corrected bottom boundary shear velocity, \bar{u} the average velocity of the flow, D the total depth of flow, g the acceleration of gravity, $\frac{\Delta\rho}{\rho}$ the maximum change in density across the flow, $\bar{\rho}$ the average density of the flow, and ν the kinematic viscosity of the flow. From this array of variables, the Buckingham Π - theorem states that three dimensionless groups can be formed:

$$R_0 = \frac{g \frac{\Delta\rho}{\rho} D}{u_*^2} \tag{3}$$

$$K_u = \frac{\nu g \frac{\Delta\rho}{\rho}}{\bar{u}^3} \tag{4}$$

and

$$\frac{u_*}{\bar{u}} \tag{5}$$

R_0 is the ratio of the fractional change in buoyancy across the flow and the depth of flow to the turbulent energy generated at the bottom boundary. As defined by Equation (4), the Keulegan number, K_u , is the inverse product of a Reynolds number, $RR = \frac{\bar{u}D}{\nu}$, and a densimetric Froude number, $FF_D^2 = \frac{\bar{u}^2}{g \frac{\Delta\rho}{\rho} D}$; i.e.,

$$K_u = \frac{1}{RR FF_D^2} \tag{6}$$

TABLE I
Experimental Data Summary

Run No.	$\bar{\rho}$ gm/cm ³	$\Delta\rho$ gm/cm ³	D cm	\bar{u} cm/s	u_{*b} cm/s	R_o	$K_u \times 10^6$	f_w	f_b	Class.
6/11/1	1.01095	0.00332	36.0	19.7	2.9	13.6	2.2	0.02	0.18	U
6/11/3	1.01095	0.00540	43.8	12.1	3.4	19.8	15.9	0.03	0.63	U
6/11/4	1.01064	0.00488	50.2	27.9	4.4	12.2	1.2	0.02	0.20	U
6/11/5	1.00976	0.00547	53.8	28.5	3.3	27.8	1.2	0.02	0.10	U
6/11/6	1.00995	0.00502	46.4	31.7	3.6	17.8	0.8	0.02	0.10	U
6/11/7	1.01019	0.00511	41.7	22.2	3.1	21.9	2.4	0.02	0.15	U
6/11/8	1.00989	0.00512	38.0	19.6	3.6	14.9	3.6	0.02	0.26	U
6/12/1	1.01179	0.00938	31.7	14.4	3.4	25.7	16.3	0.03	0.43	U
6/12/2	1.01362	0.00948	27.1	9.0	2.2	51.2	66.7	0.03	0.47	U
6/12/3	1.01439	0.00963	34.2	16.3	3.4	26.9	11.6	0.03	0.36	U
6/12/4	1.01331	0.01012	40.6	11.6	2.6	57.1	34.3	0.03	0.41	S
6/12/5	1.01249	0.01085	44.0	17.3	1.6	175.9	11.1	0.02	0.07	S
6/12/6	1.01236	0.01053	46.6	24.0	2.4	81.1	4.0	0.02	0.08	S
6/12/7	1.01327	0.01036	49.5	24.1	3.9	32.3	3.6	0.02	0.21	S
6/13/1	1.01623	0.01288	41.9	15.3	2.6	78.2	18.5	0.02	0.22	S
6/13/2	1.01379	0.01278	47.5	24.7	3.2	57.0	4.4	0.02	0.14	S
6/13/3	1.01391	0.01254	54.0	28.8	4.5	31.7	2.7	0.02	0.20	S
6/13/4	1.01392	0.01221	56.6	33.9	4.5	33.5	1.6	0.02	0.20	U
6/13/5	1.01343	0.01311	45.7	29.8	4.6	26.9	2.6	0.02	0.14	U
6/13/6	1.01447	0.01354	40.5	27.3	2.9	64.7	3.4	0.02	0.09	T
6/13/7	1.01555	0.01161	35.5	19.3	2.9	46.6	8.3	0.02	0.18	T
6/13/8	1.01568	0.01305	33.9	17.6	1.4	218.1	12.4	0.02	0.05	T
6/13/9	1.01627	0.01366	31.2	15.7	2.2	83.5	18.1	0.02	0.16	S
6/13/10	1.01126	0.00125	23.1	14.8	1.9	7.5	2.0	0.03	0.14	S
6/14/1	1.01257	0.01045	47.1	20.8	2.6	72.7	5.8	0.02	0.12	U
6/14/2	1.01326	0.00983	51.3	18.5	4.2	28.3	7.9	0.03	0.40	S
6/14/3	1.01282	0.00952	54.2	20.0	4.8	21.5	6.0	0.03	0.47	T
6/14/4	1.01290	0.00956	38.7	21.7	2.3	67.7	4.7	0.02	0.09	T
6/14/5	1.01231	0.00958	35.2	18.6	2.9	38.3	7.5	0.02	0.20	T
6/14/6	1.01203	0.00769	30.0	10.5	1.6	93.1	33.1	0.03	0.18	S

TABLE I
(Continued)

Run No.	$\bar{\rho}$ gm/cm ³	$\Delta\rho$ gm/cm ³	D cm	\bar{u} cm/s	U_{*b} cm/s	R_0	$K_u \times 10^6$	f_w	f_b	Class.
6/15/1	1.01120	0.00691	45.6	23.3	2.4	51.3	2.8	0.02	0.09	T
6/15/2	1.01200	0.00692	41.9	13.8	3.0	30.2	13.4	0.03	0.39	T
6/15/3	1.01158	0.00586	39.3	11.5	2.6	33.1	19.7	0.03	0.41	S
6/15/4	1.01158	0.00586	42.1	10.9	1.8	72.2	23.2	0.03	0.23	S
6/15/5	1.01142	0.00611	39.2	9.2	1.8	72.4	39.8	0.03	0.30	S
6/15/6	1.01094	0.00597	49.0	12.0	2.9	34.0	17.4	0.03	0.46	S
6/15/7	1.01173	0.00588	45.6	13.4	1.8	80.2	12.5	0.02	0.14	S
6/15/8	1.01115	0.00586	48.6	12.5	1.9	76.4	15.3	0.02	0.19	S
6/15/9	1.01115	0.00586	52.9	20.8	6.1	8.0	3.3	0.03	0.70	S
6/25/1	1.01573	0.01459	46.2	40.5	3.2	63.1	1.1	0.02	0.05	U
6/25/2	1.01606	0.01427	38.4	29.8	2.0	133.5	2.7	0.02	0.04	U
6/25/3	1.01503	0.01450	34.7	25.8	2.0	117.8	4.3	0.02	0.05	T
6/26/1	1.00960	0.00357	44.1	18.7	2.6	23.5	2.8	0.02	0.15	S
6/26/2	1.00940	0.00362	39.2	13.4	1.7	48.8	7.6	0.02	0.12	U
6/26/3	1.00942	0.00357	38.1	11.0	1.7	44.6	13.6	0.03	0.19	S
6/26/4	1.00966	0.00264	29.5	17.0	3.2	7.4	2.7	0.03	0.28	U
6/26/6	1.00979	0.00032	20.7	13.7	0.8	9.5	0.6	0.02	0.03	U
6/26/7	1.01015	0.00361	39.5	6.6	1.9	39.6	63.1	0.03	0.62	S
6/26/8	1.01018	0.00362	45.8	13.8	2.7	21.6	7.0	0.03	0.30	T
7/26/1	1.01080	0.00497	41.0	19.3	2.4	33.5	3.5	0.02	0.13	T
7/26/2	1.01040	0.00512	47.5	20.8	3.3	21.3	2.9	0.02	0.21	U
7/26/3	1.01040	0.00437	33.2	21.6	1.2	94.6	2.2	0.02	0.03	T

The experimental data are tabulated in Table 1. It should be noted that in most cases the friction factor associated with the bottom, f_b , was substantially larger than the friction factor associated with the glass walls, f_w . It is also noted that f_b varied over a wide range of values, apparently as a function of the Reynolds number; however, the correlation between f_b and R is very low. Thus, it is hypothesized that the variation in f_b must be either due to random experimental error or the effects of the stratification.

Interfacial stability is plotted in Figure 5 as a function of R_b and K_u . In this figure, the "line" delineating the zone of unstable interfaces from the zone of stable interfaces -- the line is the zone of transition interfaces -- is well-defined and slopes downward from left to right. In addition, three points extracted from field data gathered by Motz and Benedict (1971) downstream from the Widows Creek (Alabama) Steam Plant are plotted. The first point is near the point where the thermal plume enters the Tennessee River, and the third point is approximately one mile downstream. Point one clearly represents either a stable or transitional interface and at point three sufficient heat has been lost that the interface is unstable.

Figure 6 demonstrates the dependence of the results on the parameter $\frac{u^*}{\bar{u}}$; i.e., the data plotted in Figure 5 consists of a family of curves with a separate curve for each value of $\frac{u^*}{\bar{u}}$. In Figure 6, small values of $\frac{u^*}{\bar{u}}$ are seen to correspond to relatively large values of K_u , and large values of $\frac{u^*}{\bar{u}}$ correspond to small values of K_u . Thus, the zone of transition interfaces is a band intersecting the $\frac{u^*}{\bar{u}}$ curves.

IV. CONCLUSION

When the bottom boundary is the primary source of turbulence, Figure 5 demonstrates that it is possible to classify the stability of density interfaces between homogeneous fluids on the basis of two dimensionless parameters, R_b and K_u . This system includes the densimetric Froude number, which has previously been the sole criteria of interfacial instability, and a term which accounts for the generation of turbulence at the bottom boundary. Field verification of the results presented here is presently being sought, and it is hoped that once this is accomplished these results will be of use in analyzing the effects of non-conservative stratifying agents discharged into the environment.

Figure 5: Interfacial Stability as a Function of K_U and R_0

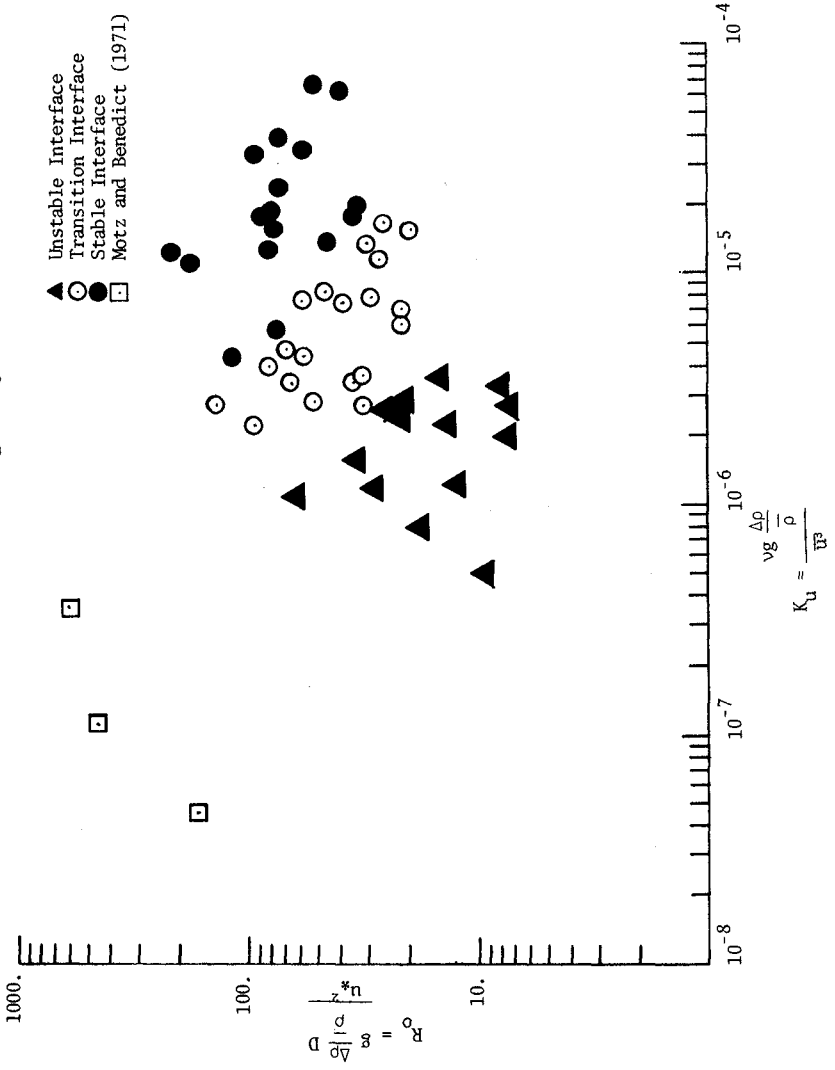
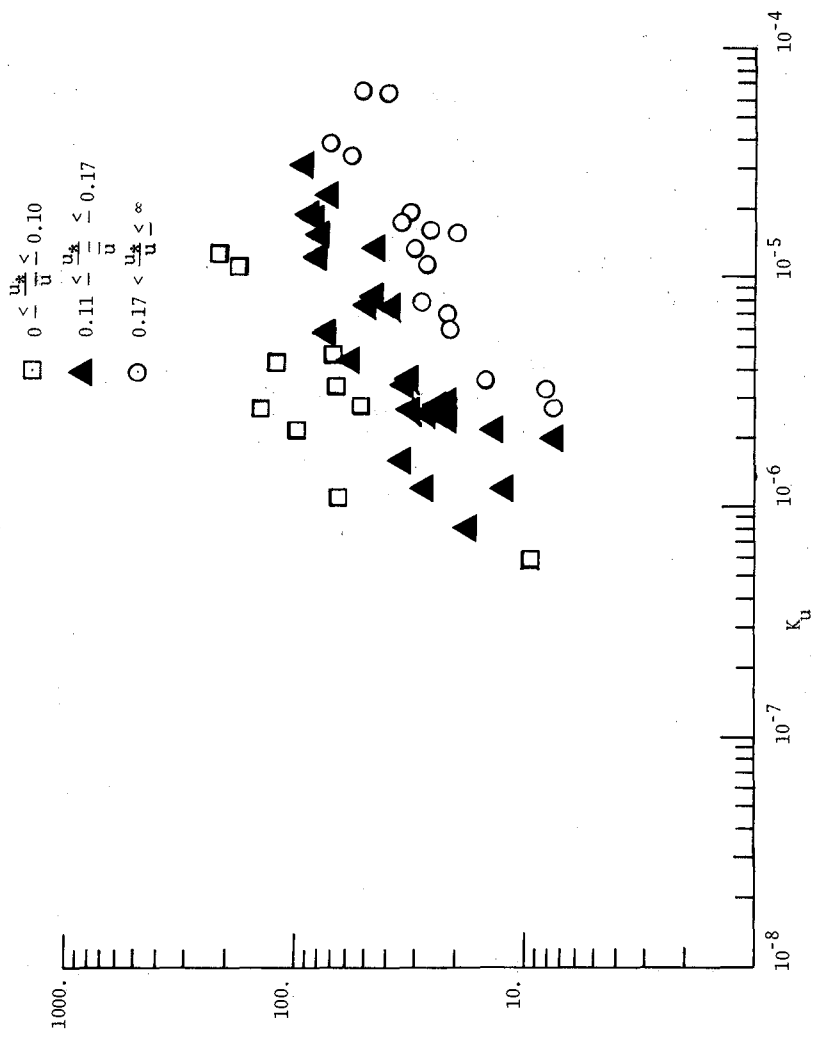


Figure 6: Dependency of Interfacial Stability on $\frac{u_*}{u}$



REFERENCES

- Eckart, Carl, "Properties of Water II - The Equation of State of Water and Sea Water at Low Temperatures and Pressures," American Journal of Science, Vol. 256, April, 1958, pp.225-240.
- Keulegan, G.H., "Interfacial Instability and Mixing in Stratified Flows," Journal of Research of National Bureau of Standards, Vol. 43, November, 1949, pp.487-500.
- Maxwell, W.H.C., Holley, E., Lin, Chi-Yu and Tekeli, Sahin, Study of Stratified Overflows and Underflows, University of Illinois at Urbana-Champaign Water Resources Center, Research Report No. 98, February, 1975.
- Motz, L.H. and Benedict, B.A., "Heated Surface Jet Discharged Into a Flowing Ambient Stream," Water Pollution Control Research Series, U.S. Environmental Protection Agency, 16130 FDQ, March, 1971.
- Plate, E.J. and Friedrich, R., "The Stability of an Interface in Stratified Channel Flow," Proceedings of the XVth Congress of the International Association for Hydraulic Research, Sao Paulo, Brazil, 1975.
- Sherenkov, I.A., Netzkarlo, A.P., and Telezhken, E.D., "Research Investigation of Transfer Process in Two Dimensional Stratified Flow," Proceedings of the XIVth Congress of the International Association for Hydraulic Research, Paris, France, 1971.
- Tiphane, Marcel and St. Pierre, Jacques, "Tables for Sea Water Salinity Determination by Electrolytic Conductivity," Faculte' des Sciences, Universite' de Montreal, Montreal, Quebec, Canada, April, 1962 (also issued as Beckman Publication No. 29.067D).

CHAPTER 180

NUMERICAL MODELING OF DISPERSION IN STRATIFIED WATERS

by

George C. Christodoulou¹

Jerome J. Connor²

ABSTRACT

A numerical model is developed for the quantitative description of the dispersion process in a two-layer system which represents an approximation for a natural coastal water body during the summer season when a distinct thermocline usually exists. The formulation is based on the convection-diffusion equation, vertically integrated between the layer boundaries. Layer velocities and thicknesses are assumed to be obtained from a separate hydrodynamic model. The quantification of the physical processes of entrainment and mixing through the density interface as well as the horizontal dispersion mechanisms is discussed.

The finite element method is chosen for numerical implementation because of its flexibility in grid layout and easier handling of spatial and temporal variability. Triangular elements with linear interpolation functions are used for the spatial discretization, while a simple implicit iterative scheme based on the trapezoidal rule is employed for time integration. The method is shown to be unconditionally stable, for an arbitrary grid and both one- and two-layer problems, when there is no iteration and the parameters are constant. General convergence criteria required by the iteration procedure are developed and expressed in terms of the basic parameters of the problem and are subsequently confirmed by numerical experiments. Verification of the model is performed by comparison with analytical solutions derived for counterflow conditions. Finally the model is applied to a particle dispersion experiment carried out recently in the Massachusetts Bay and comparisons with field data are presented.

¹Research Assistant, Ralph M. Parsons Laboratory for Water Resources and Hydrodynamics, M.I.T., Cambridge, Mass., U.S.A.

²Professor of Civil Engineering, Department of Civil Engineering, M.I.T., Cambridge, Mass., U.S.A.

INTRODUCTION

Coastal dispersion problems have received considerable attention in recent years, due to the rapid growth in the development of the coastal zone and the increasing concern for the impact on the coastal environment. Mathematical models of the hydrodynamic processes involved have been developed in the past based on the assumption that flow parameters and concentrations are approximately uniform over the water column, resulting in a depth-averaged treatment of the problem. This approach is justified to some extent by the characteristic shallowness of coastal water bodies, as compared to their horizontal dimensions. However, the assumption of uniformity is no longer valid during the summer season, when a significant stratification usually exists.

The presence of a strong thermocline suggests the idealization of the flow field as a two-layer system. This is the simplest stratified case and it is felt that it has to be studied prior to proceeding to a multilayer approach, for understanding the fundamental physical behavior of dispersion in a layered system. Multilayer or quasi-three dimensional models of the transport of constituents are presently being incorporated into large multipurpose computer codes [1, 8, 9] utilizing finite difference techniques. Such models will require difficult and costly verification studies and extensive field data (especially boundary conditions) for their proper application to a given area. A simpler two-layer model needs less "tuning" and is much more economical, while still providing a good approximation to the actual conditions when a distinct thermocline exists.

In this paper, problems associated with properly describing the dispersion of matter in a two-layer system are investigated. First, the mathematical formulation is presented and the modeling of the physical processes involved is discussed. Then, the details of the finite element method are examined and, in particular, its stability requirements in this class of problems are established. Lastly, the applicability of the numerical model to real world problems is addressed.

MATHEMATICAL FORMULATION

The present model is intended to describe the dispersion of an arbitrary constituent, possessing vertical mobility, in a two-layer coastal water body of variable bottom topography and boundary geometry. The velocity field in both layers as well as the layer thicknesses will be assumed known, presumably

obtainable through a separate hydrodynamic model. By uncoupling the hydrodynamic and dispersion models, the same flow pattern can be used to investigate very economically the spreading of several different substances and to experiment with different source locations, loading strategies, parameter values, etc. However, this can only be done provided that the constituent of interest does not affect significantly the flow field or the density structure.

The mass balance of a constituent is expressed by the 3-D convection-diffusion equation:

$$\frac{\partial c}{\partial t} = - \frac{\partial}{\partial x} (uc+q_x) - \frac{\partial}{\partial y} (vc+q_y) - \frac{\partial}{\partial z} ((w-w_s)c+q_z) + p \tag{1}$$

where

- u, v, w are the water velocities in the x,y,z directions
- w_s is the particle settling velocity, positive downward
- q_x,q_y,q_z are diffusive fluxes in the x,y,z directions
- p represents generation or decay of the constituent

Integrating between the layer boundaries (Figure 1) and using Leibnitz's rule, one obtains for the top layer

$$\begin{aligned} \frac{\partial c}{\partial t} \int_{-h_1}^{\eta} cdz = & - \frac{\partial}{\partial x} \int_{-h_1}^{\eta} (uc+q_x) dz - \frac{\partial}{\partial x} \int_{-h_1}^{\eta} (vc+q_y) + \int_{-b_1}^{\eta} pdz \\ & + [c(\frac{D\eta}{Dt} - w+w_s) - q_s]_{\eta} + [c(\frac{Dh_1}{Dt} + w-w_s) - q_i]_{-h_1} \end{aligned}$$

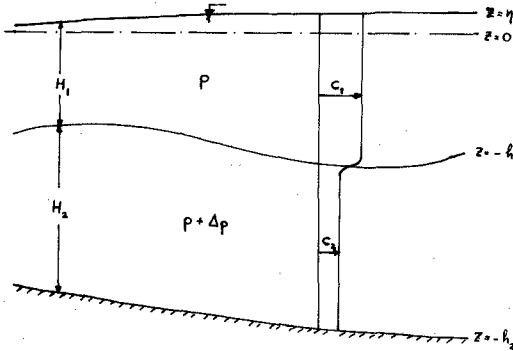


Figure 1: The Two-Layer Idealization

The terms in brackets represent fluxes through the free surface and interface, respectively. The kinematic condition at the surface requires

$$\left[\frac{D\eta}{Dt} - w \right]_{\eta} = 0$$

However, the interface, defined as the position of steepest density gradient, is not necessarily a material surface. We may write in general

$$\left[w + \frac{Dh_1}{Dt} \right]_{-h_1} = w_e$$

and refer to the relative velocity, w_e , of the water particles with respect to the layer boundary as "entrainment" velocity. This is considered positive when directed upward, indicating net water motion from the bottom to the top layer. The other component, q_i , of the interfacial transport is a diffusive flux and can be expressed in terms of the difference in concentration between the layers. Approximating the concentration at the interface as the average value of the two layers, the overall transfer is expressed as:

$$Q_{21} = (w_e - w_s) c_{-h_1} - q_i = (w_e - w_s) \frac{c_1 + c_2}{2} + \alpha(c_2 - c_1) \quad (2)$$

In large water bodies, the erosion of the quiescent lower layer by the upper layer, moving under the influence of wind or other driving mechanism, is explained by the one-way transport of water toward the turbulent layer.

In coastal areas, both layers are quite turbulent and possess velocities of the same order of magnitude, hence water exchange both ways through the interface should be anticipated. Denoting the respective volumetric rates per unit area by m_{21} and m_{12} (Figure 2), the net transfer of material is:

$$Q_{21} = m_{21}c_2 - m_{12}c_1 \quad (3)$$

By comparing Equations (2) and (3) it is evident that

$$w_e = m_{21} - m_{12} \quad (4a)$$

$$\alpha = (m_{21} + m_{12})/2 \quad (4b)$$

Several experimental and theoretical investigations in 1-D two-layer systems have been carried out in the past mostly with one layer quiescent, as reviewed in [3, 15, 11]. The one-way rate of transport, usually measured by the thickening of the moving layer, has been expressed with different velocity and length scales so that at first only a qualitative agreement between them is evident. Upon careful examination, however, it may be seen [5] that a rather general expression in terms of the mean flow characteristics can be given, as follows:

$$m_{ji} = \frac{10^{-3} U_i}{Ri_o} \quad i, j = 1, 2 \quad (5)$$

where the overall Richardson number for a 2-D flow is defined as

$$Ri_o = \frac{g \frac{\Delta \rho}{\rho} H}{(\bar{u}_i - \bar{u}_j)^2}$$

where H is the average layer thickness, i.e., half the depth.

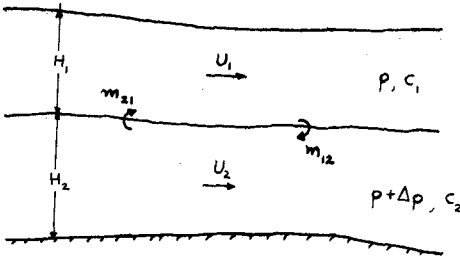


Figure 2: Schematization of Interfacial Transport

We introduce now the following notation

$$C_1 = \int_{-h_1}^{\eta} c dz = \bar{c}_1 H_1$$

$$u = \bar{u} + u'', v = \bar{v} + v'', c = \bar{c} + c''$$

where the overbar denotes layer average value and the double prime spatial deviation from that average. Then, Equation 2 takes the form

$$\frac{\partial C_1}{\partial t} + \frac{\partial}{\partial x} (\bar{u}_1 C_1) + \frac{\partial}{\partial y} (\bar{v}_1 C_1) = - \frac{\partial}{\partial x} Q_{x_1} - \frac{\partial}{\partial y} Q_{y_1} + P_1 \tag{6}$$

where P_1 includes source, decay and interfacial flux terms, and the total dispersive fluxes Q_{x_1}, Q_{y_1} are approximated as follows:

$$Q_{x_1} = - \int_{-h_1}^{\eta} (u'' c'' + q_x) dz = H_1 (E_{xx_1} \frac{\partial \bar{c}_1}{\partial x} + E_{xy_1} \frac{\partial \bar{c}_1}{\partial y}) \tag{7a}$$

$$Q_{y_1} = - \int_{-h_1}^{\eta} (v'' c'' + q_y) dz = H_1 (E_{yx_1} \frac{\partial \bar{c}_1}{\partial x} + E_{yy_1} \frac{\partial \bar{c}_1}{\partial y}) \tag{7b}$$

The dispersion coefficients

$$\underline{E} = \begin{bmatrix} E_{xx} & E_{xy} \\ E_{yx} & E_{yy} \end{bmatrix} = \underline{E}^d + \underline{\epsilon}$$

comprise a second order tensor consisting of a shear-dispersion part and an eddy diffusivity part. The analogy of the effective horizontal spreading due to nonuniformity of the velocity profile to the turbulent diffusion process has

been shown initially by G.I. Taylor [14] for flow through a pipe and later by Elder [7] for flow in an open channel. By extending their arguments to the case where both u and v velocity components are present, one may prove the validity of Eqs.(7a, b) with shear dispersion coefficients given by [5]:

$$E_{xx}^d = \frac{1}{H} \int_0^H \frac{1}{\epsilon_x} \left[\int_0^H u'' d\zeta \right]^2 dz \quad (8a)$$

$$E_{yy}^d = \frac{1}{H} \int_0^H \frac{1}{\epsilon_z} \left[\int_0^H v'' d\zeta \right]^2 dz \quad (8b)$$

$$E_{xy}^d = E_{yx}^d = \frac{1}{H} \int_0^H \frac{1}{\epsilon_z} \left[\int_0^H u'' d\zeta \right] \left[\int_0^H v'' d\zeta \right] dz \quad (8c)$$

where ϵ_z is the vertical eddy diffusion coefficient.

The horizontal turbulent diffusion term accounts for mixing due to horizontal eddies. Based on the theory of locally isotropic turbulence, the well-known 4/3 law is derived. According to [12]

$$\epsilon = b e^{1/3} L^{4/3} \quad (9)$$

where

e is the rate of energy input

L is a length scale and

b is a numerical constant of order 0.1.

As the cloud size increases, larger scale motions are being incorporated into the diffusion term, explaining the length dependence of the diffusion coefficient. It should be clear, however, that this depends on the detail of specification of the advection processes. In the case that the velocity field is specified at certain grid points and the cloud increases beyond the level of discretization, internal mixing is now (partly) described by the advection terms, and hence the length scale of Equation (3) should be related to the grid size.

An alternative expression for ϵ , based on mixing length arguments, is [2,6]:

$$\epsilon = L^2 \sqrt{\phi} \quad (10)$$

where

$$\phi = 2 \left(\frac{\partial \bar{u}}{\partial x} \right)^2 + 2 \left(\frac{\partial \bar{v}}{\partial y} \right)^2 + \left(\frac{\partial \bar{u}}{\partial y} + \frac{\partial \bar{v}}{\partial x} \right)^2$$

This has the advantage of using the readily available mean velocity gradients instead of the energy input. According to [6], the sub-grid scale eddy coefficient is modeled by a length scale an order of magnitude smaller than

the grid size. However, the resolution of the flow field description associated with spatial averaging in the hydrodynamic model employed has to be taken into account and the coefficient increased accordingly.

THE FINITE ELEMENT METHOD

For each layer, the governing equation has the form (6). The boundary conditions are (Figure 3)

- 1) Essential, i.e., the concentration is specified on the boundary segment S_c : $C = C^*$
- 2) Natural, i.e., the normal concentration gradient, or, equivalently, the normal dispersion flux, is specified on the boundary segment S_q :

$$Q_n = Q_n^*$$

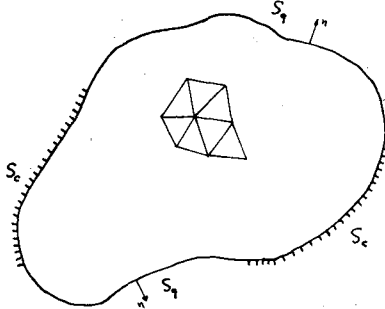


Figure 3: Solution Field and Boundary Conditions

In seeking an approximate solution, the partial differential equation and the flux boundary condition are multiplied by a weighting function (w) and the residual R over the domain is required to vanish:

$$R = \iint_A \left\{ \frac{\partial C}{\partial t} + \frac{\partial(\bar{u}C)}{\partial x} + \frac{\partial(\bar{v}C)}{\partial y} + \frac{\partial}{\partial x} Q_x + \frac{\partial}{\partial y} Q_y - P \right\} w dA + \int_{S_q} (Q_n^* - Q_n) w dS = 0 \quad (11)$$

Employing partial integration, this is rewritten as

$$R = \iint_A \left[\left\{ \frac{\partial C}{\partial t} + \frac{\partial}{\partial x}(\bar{u}C) + \frac{\partial}{\partial y}(\bar{v}C) - P \right\} w - Q_x \frac{\partial w}{\partial x} - Q_y \frac{\partial w}{\partial y} \right] dA + \int_{S_q} Q_n^* w dS = 0 \quad (12)$$

It should be mentioned that the trial function C is required to satisfy the essential boundary condition and the weighting function to satisfy the homogeneous form, i.e., $w = 0$ on S_c .

Expression (12) is called the symmetrical weak form and involves only first derivatives of both trial and test functions, which can therefore be chosen from the same solution space. In the finite element method the domain is subdivided into elements and the total residual is evaluated as the sum of element residuals. By introducing interpolation functions within each element, the continuous problem is transformed to a discrete one, with the concentrations at the nodal points as unknowns. Triangular elements with linear interpolation functions are used herein, as in the one layer model [10]. Setting

$$C = \underline{N} \underline{C}^e \quad w = \Delta C = \underline{N} \Delta \underline{C}^e$$

the element residual becomes:

$$\underline{R}^e = (\Delta \underline{C}^e)^T \left(\underline{M}^e \frac{d \underline{C}^e}{dt} - \underline{P}^e \right) + (\Delta \underline{C}^e)^T \underline{F}^{be} \quad (13)$$

where

$$\underline{M}^e = \iint_A \underline{N}^T \underline{N} dA \quad (14a)$$

$$\underline{P}^e = \iint_A \left[\underline{N}^T \left(P - \frac{\partial}{\partial x} (\bar{u}C) - \frac{\partial}{\partial y} (\bar{u}C) + \frac{\partial \underline{N}^T}{\partial x} Q_x + \frac{\partial \underline{N}^T}{\partial y} Q_y \right) \right] dA \quad (14b)$$

$$\underline{F}^{be} = \int_{S_q} \underline{N}^{bT} Q_n^* dS \quad (14c)$$

Carrying out the summation over all elements for each layer results in:

$$\underline{R} = \sum_e \underline{R}^e = (\Delta C)^T (\underline{M} \dot{C} - \underline{P} + \underline{F}^b) = 0$$

and since ΔC is arbitrary,

$$\underline{M} \dot{C} = \underline{P} - \underline{F}^b = \hat{\underline{P}} \quad (15)$$

This constitutes a set of linear ordinary differential equations and is integrated by using an implicit iterative trapezoidal scheme, as follows:

$$\underline{C}_{1,t+\Delta t}^{(i+1)} = \underline{C}_{1,t} + \frac{\Delta t}{2} \underline{M}^{-1} (\hat{\underline{P}}_{1,t+\Delta t}^{(i)} + \hat{\underline{P}}_{1,t}^{(i)}) \quad (16a)$$

$$\underline{C}_{2,t+\Delta t}^{(i+1)} = \underline{C}_{2,t} + \frac{\Delta t}{2} \underline{M}^{-1} (\hat{\underline{P}}_{2,t+\Delta t}^{(i)} + \hat{\underline{P}}_{2,t}^{(i)}) \quad (16b)$$

Since the geometrical matrix \underline{M} is time-invariant it has to be inverted only once. By lumping all other terms in the $\hat{\underline{P}}$ vector, maximum flexibility in handling time variability of any or all of the relevant parameters and loadings is achieved. In addition, any non-linear relations of the various terms to the concentrations can be readily handled in this way. In practice, the iteration

continues until either the change in concentration between current and previous values is below a specified tolerance or the number of iterations reaches an imposed upper limit.

STABILITY ANALYSIS

Expanding the \hat{P} vector leads to the following form of the matrix equation for each layer

$$\tilde{M}\tilde{C} + \tilde{A}\tilde{C} + \tilde{K}\tilde{C} + \tilde{D}\tilde{C} = \tilde{S} \quad (17)$$

where \tilde{A} is associated with advection, \tilde{K} with dispersion, \tilde{D} with decay and \tilde{S} includes sources and boundary conditions. The trapezoidal integration rule is expressed as follows

$$\begin{aligned} \left[\tilde{M} + \frac{\Delta t}{2}(\tilde{A} + \tilde{K} + \tilde{D}) \right] \tilde{C}_{n+1} &= \left[\tilde{M} - \frac{\Delta t}{2}(\tilde{A} + \tilde{K} + \tilde{D}) \right] \tilde{C}_n \\ &+ \frac{\Delta t}{2}(\tilde{S}_n + \tilde{S}_{n+1}) \end{aligned} \quad (18)$$

To investigate the stability of the scheme, we consider the homogeneous case, i.e., $\tilde{S}_n = \tilde{S}_{n+1} = 0$, and assume the various matrices are constant over the time step. We note that the geometrical, decay, and dispersion matrices, being composed of individual symmetric positive definite sub-matrices, also have these properties. Continuity considerations and the compatibility of inter-element velocity expansions [5], leads to:

$$\tilde{A}\tilde{C} = -\tilde{A}^T\tilde{C} + \int_{S_q} u_n N^b N^b dS \tilde{C}^b \quad (19)$$

where the superscript b denotes boundary quantity and u_n is the velocity normal to the boundary (positive outwards). Writing the advection matrix as the sum of a symmetric and a skew-symmetric part

$$\tilde{A} = \tilde{A}_s + \tilde{A}_{ss}$$

it is seen that the former usually vanishes since normally S_q refers to land boundaries where the normal velocity is zero.

By writing

$$\tilde{C}_{n+1} = a \tilde{C}_n \quad (20)$$

where a is the amplification matrix, one may set

$$\tilde{C}_n = \lambda^n \phi \quad (21)$$

where λ is an eigenvalue of a .

The necessary condition for stability is

$$||a|| < 1 \text{ or } |\lambda| < 1$$

Substituting (21) into the homogeneous form of (18), premultiplying by $\tilde{\Phi}^T$ and noting that, according to the above discussion

$$\begin{aligned}\tilde{\Phi}^T \tilde{M} \tilde{\Phi} &= m > 0 \\ \tilde{\Phi}^T \tilde{K} \tilde{\Phi} &= \kappa > 0 \\ \tilde{\Phi}^T \tilde{D} \tilde{\Phi} &= d > 0 \\ \tilde{\Phi}^T \tilde{A} \tilde{\Phi} &= ia_{ss}\end{aligned}$$

we obtain for λ

$$\lambda \left\{ m + \frac{\Delta t}{2} (\kappa + d + ia_{ss}) \right\} = m - \frac{\Delta t}{2} (\kappa + d + ia_{ss})$$

or,

$$\lambda^2 = \frac{\left[m - \frac{\Delta t}{2} (\kappa + d) \right]^2 + a_{ss}^2}{\left[m + \frac{\Delta t}{2} (\kappa + d) \right]^2 + a_{ss}^2} < 1 \quad (22)$$

This indicates that the scheme is unconditionally stable for an arbitrary grid.

However, the time step is always limited by the desired detail of description of the time variability of inputs or parameters of the problem. When the matrices \tilde{K} , \tilde{D} , \tilde{A} are actually variable, it becomes uneconomical to form and invert matrices of the form $\tilde{M} + \frac{\Delta t}{2} (\tilde{A} + \tilde{K} + \tilde{D})$ every time-step. This is a basic reason for resorting to the iteration procedure discussed earlier, which may be written in expanded form:

$$\tilde{C}_{n+1}^{(i+1)} = \left[\tilde{M} - \frac{\Delta t}{2} (\tilde{A} + \tilde{K} + \tilde{D}) \right] \tilde{C}_n - \frac{\Delta t}{2} (\tilde{A} + \tilde{K} + \tilde{D}) \tilde{C}_{n+1}^{(i)} \quad (23)$$

For convergence of the iteration, however, a restriction on the time step is required. The general sufficient condition

$$\left| \left| \tilde{M}^{-1} \frac{\Delta t}{2} (\tilde{A} + \tilde{K} + \tilde{D}) \right| \right| < 1 \quad (24)$$

leads to

$$\Delta t < \frac{2}{\left| \left| \tilde{M}^{-1} (\tilde{A} + \tilde{K} + \tilde{D}) \right| \right|}$$

or, the more restrictive condition:

$$\Delta t < \frac{2}{\left| \left| \tilde{M}^{-1} \tilde{A} \right| \right| + \left| \left| \tilde{M}^{-1} \tilde{K} \right| \right| + \left| \left| \tilde{M}^{-1} \tilde{D} \right| \right|} \quad (25)$$

Unfortunately, (25) is not practical in this form, since one does not have an explicit relation between the time step and the parameters of the problem. An approximation to it can be obtained by considering a single element only, forming the matrices and evaluating their norms, i.e., their eigenvalues. For uniform velocity U , isotropic dispersion E and decay rate k , the resulting expression for an equilateral triangle of size Δs is [5]:

$$\Delta t < \frac{1}{\sqrt{\frac{3}{2}} \frac{U}{\Delta s} + \frac{8E}{\Delta s^2} + \frac{k}{2}} \quad (26)$$

This was obtained using the average eigenvalue of the $\underline{M}^{-1}\underline{K}$ matrix. The same result is arrived at for a right triangle, when the flow is parallel to one of the legs of the right angle, of size Δs . The conclusions reached at the element level can be conservatively generalized for the whole domain, provided the "worst case" element is considered.

A similar analysis for the two-layer problem shows that the time integration scheme is again unconditionally stable, with no iteration. The latter requires a restriction on the time step analogous to (25). Another term has now to be added in the denominator to account for interfacial mixing, i.e., $||\underline{M}^{-1}\underline{E}||$. Evaluating this term for a single triangle results in the addition of $\alpha'/2$ in the denominator of (26), where α' is the interfacial mixing rate normalized by the layer thicknesses. This term is usually small and consequently the time step is essentially governed by the "worst" layer.

Experimental confirmation of condition (26) was attempted by means of test runs carried out in the 1-D grid shown in Figure 5. The contribution of the decay term was of the order of 1% and thus neglected. For each run, a point was plotted on the plane of the non-dimensional coordinates $(U\Delta t/\Delta s, E\Delta t/\Delta s^2)$. These points are shown in Figure 4 along with the theoretical bound (26). The symbols used are defined in Table 1. It is seen that runs corresponding to points within the "safe" area always converge well, while outside the theoretical boundary more or less significant errors are present, eventually leading to instability a little further outside. Further, the line $E/U\Delta s = 1/2$ is seen to exactly separate runs with and without significant upstream negatives and spatial oscillations due to the approximation of steep concentration gradients. This condition, analogous to finite difference schemes, was derived theoretically [5] and earlier empirically [10]. Thus, accuracy considerations actually reduce the acceptable area to a fraction of the safe region for iteration convergence. Additional runs, carried out in 2-D test grids, as well as grids of natural water bodies, compiled in [5], show the theoretical limit to be still approximately valid.

VERIFICATION AND APPLICATIONS

To test the correctness of the model structure, comparisons with analytical solutions are desirable. However, the availability of analytical solutions is restricted to very simple flow conditions. In Figure 6, the numerical model is compared with the solution for an instantaneous point source in the top layer of a 1-D counterflow. A unit load is distributed between the three nodes at $x = 0$

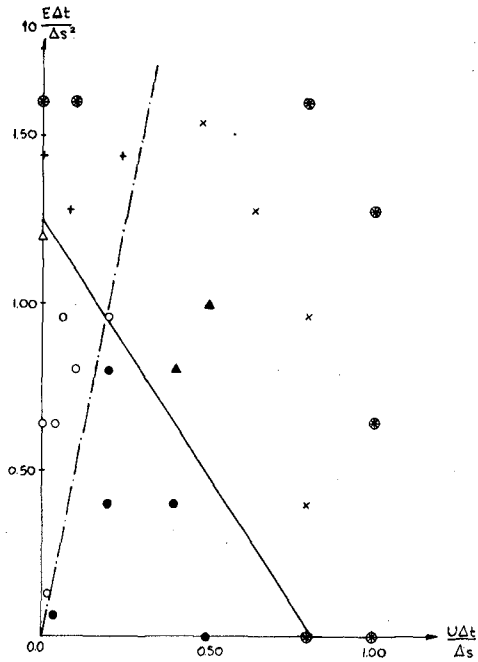


Figure 4 Comparison of Theoretical Bound on the Time Step with 1-D Runs

Table 1
Definition of Symbols used in Figure 4

Symbol	Error after 10 Iterations	Negatives as Percent of Peak	Remarks
o	< 1%	< 10%	Good, smooth solution
●	< 1%	> 10%	Iteration converges well, but result exhibits oscillations
Δ	< 10%	< 10%	Iteration error goes down rapidly as time proceeds
▲	< 10%	> 10%	
+	> 10%	< 10%	It. Error does not always decrease rapidly (some may eventually blow up)
x	> 10%	> 10%	
⊙	—	—	Blows up

of the grid of Figure 5, and the results adjusted to yield values per unit width of the channel. A unit depth is assumed for each layer. Zero concentration is specified at the ends of the grid and zero flux is prescribed along the side boundaries. The parameters used are

$$\begin{aligned}U_1 &= -U_2 = 0.05 \text{ m/sec} \\E_1 &= E_2 = 0.01 \text{ m}^2/\text{sec} \\ \alpha &= 5 \times 10^{-4} \text{ m/sec} \\ \kappa &= 0\end{aligned}$$

It may be observed from Figure 6 that the lower layer concentrations are two orders of magnitude smaller than those of the top layer. This supports to some extent the treatment of the interface as a barrier. However, it may not hold for longer time periods and is certainly not valid for substances possessing vertical mobility. Irrespective of that, it should be clear that a great advantage of the two-layer treatment is the more detailed description of the velocity field. In this particular counterflow case the depth-average velocity is zero, implying a stationary peak of the depth-averaged concentration distribution located at the origin. As shown in Figure 6, this is far from the actual depth-averaged concentration distribution of the two-layer system. Further verification studies can be found in [5].

To establish confidence in the predictive capability of the model and the degree of its applicability under natural conditions, further verification, consisting of comparisons to real-world cases, is necessary. For this purpose a dispersion experiment was carried out by M.I.T., sponsored by the Boston Edison Co., in the vicinity of the Pilgrim Nuclear Power Station (PNPS) on the Massachusetts coast (Figure 7) in August 1975. Five hundred pounds of small fluorescent sphalerite (ZnS) particles were introduced into the water and their motion subsequently monitored for 5 days by boat and by helicopter. Also, two current meter stations had been installed prior to the experiment as indicated in Figure 7 by dots.

The finite element grid used was the same as in the previous applications of one-layer models to the Bay. The value of the dispersion coefficient, $30 \text{ m}^2/\text{sec}$, and the difference in tidal amplitude between the ends of the open boundary, were kept the same as established for the one-layer models [13]. The circulation model used to obtain velocity inputs is that of Wang and Connor [16]. Since it requires both layers to extend over the whole domain, some nodal depths had to be increased

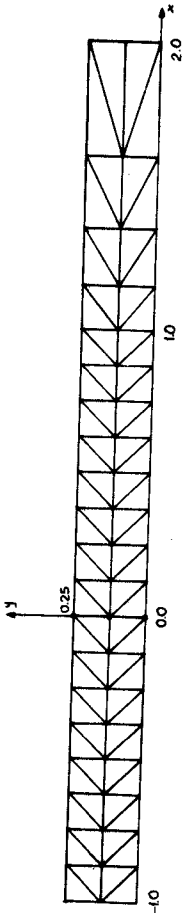
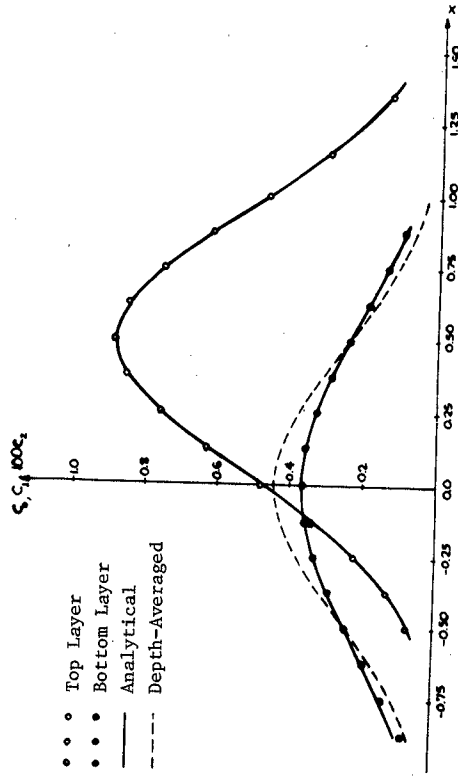


Figure 5 One-dimensional Finite Element Test Grid

Figure 6 1-D Distribution at $t=10$ sec. after an Instantaneous Injection

to at least 15 m in order to avoid intersection of the interface with the bottom. The position of the interface was set at 8 meters as initial condition, consistent with available information [4]. However, much more detailed data are needed for the specification of interface motion along the ocean boundary. In view of lack of such data at present, the interface was assumed to be linear along the boundary and various cases, e.g. remaining fixed over the tidal cycle or moving with the same amplitude as the free surface, were examined. Actual time-varying wind data were used in the computations.

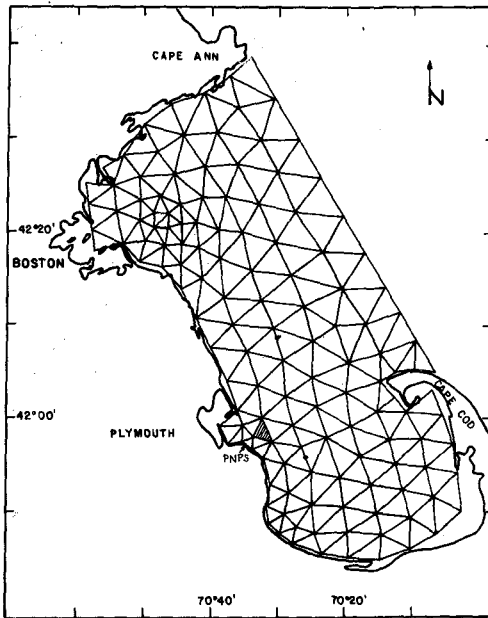


Figure 7 Mass. Bay Finite Element Grid and Location of the MIT Experiment

The experimental results were reduced to layer-average concentrations by averaging together samples taken above and below the thermocline to yield a single representative value for each layer. The resulting plots, in particles/lt, are shown in Figures 8 and 9 corresponding to 2 and 3 days after the dumping took place. The plume is seen to move slowly to the southeast, approximately parallel to the shore and later extending to the east.

In the dispersion simulations the shaded triangle was loaded over a period of three timesteps. The area of the triangle is quite large in comparison to the actual source and as a consequence one should expect unrealistically large plume areas for short times. The interfacial mixing rate is set at 10^{-5} m/sec and the settling velocity at 7.3×10^{-5} m/sec, based on an average particle size of 7 microns. The computed concentrations 2 and 3 days after the injection are shown in Figures 10 and 11. Taking into account the initial spreading of the source, good qualitative agreement with respect to the size and location of the plume as well as the peak values is observed.

CONCLUSION

The objective of this study was to investigate the problem of dispersion in coastal water bodies under conditions of strong stratification. The two-layer idealization was adopted as a useful extreme case and, at the same time, the easiest to handle mathematically. The ability of the two-layer treatment to handle transport between the layers is important, whether or not the constituent of interest has some vertical mobility, in providing a refined picture of the distribution over the depth. A further advantage of the two-layer formulation, evident from both ideal and real-world applications, lies in the more detailed description of the velocity field. However, the sensitivity of the results to variations in the flow field points out the necessity for using realistic current input.

Additional fundamental research is needed for better understanding the turbulent mixing processes in stratified environments. Also, field monitoring programs are required to provide reliable inputs, primarily on the behavior of the interface along open boundaries of the domain under consideration. It is believed that the present two-layer model, providing an extreme-case picture of the response of the physical system, can be a useful tool in coastal dispersion studies.

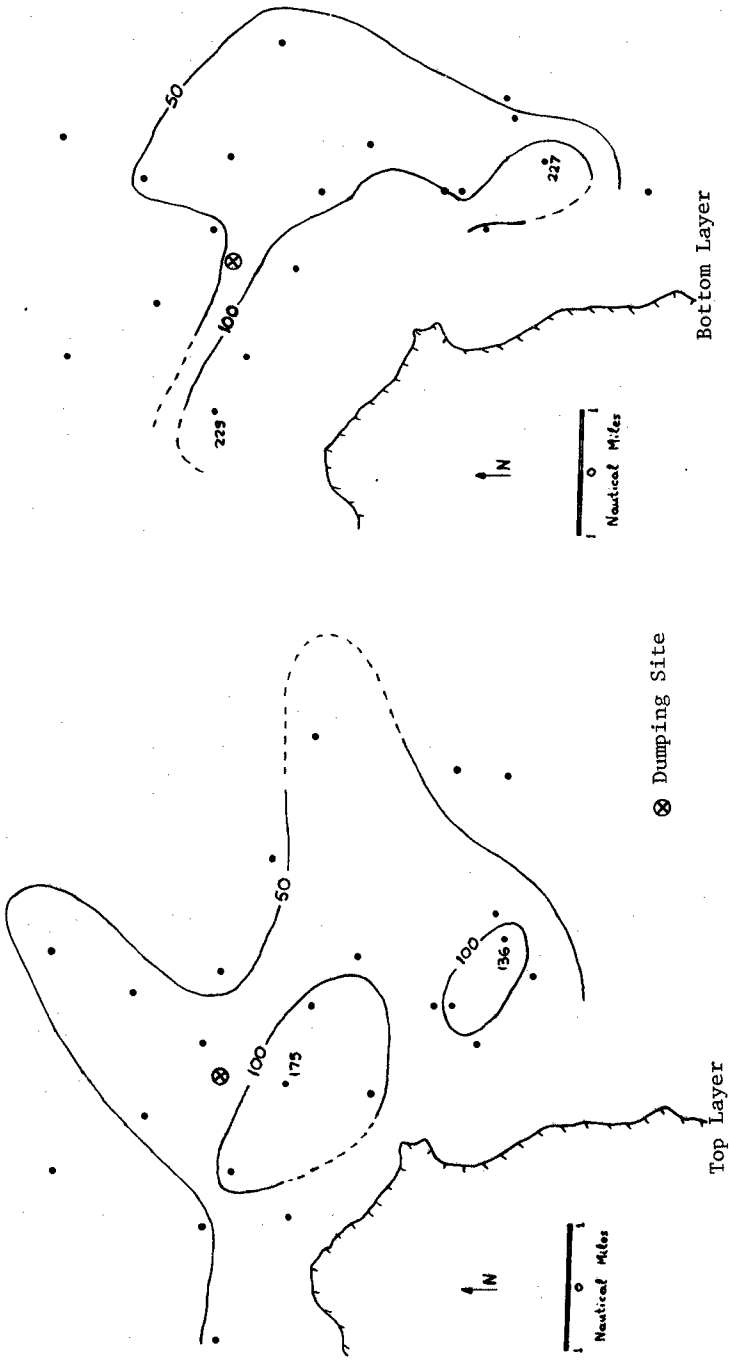


Figure 8 Experimental Results at Day D+2

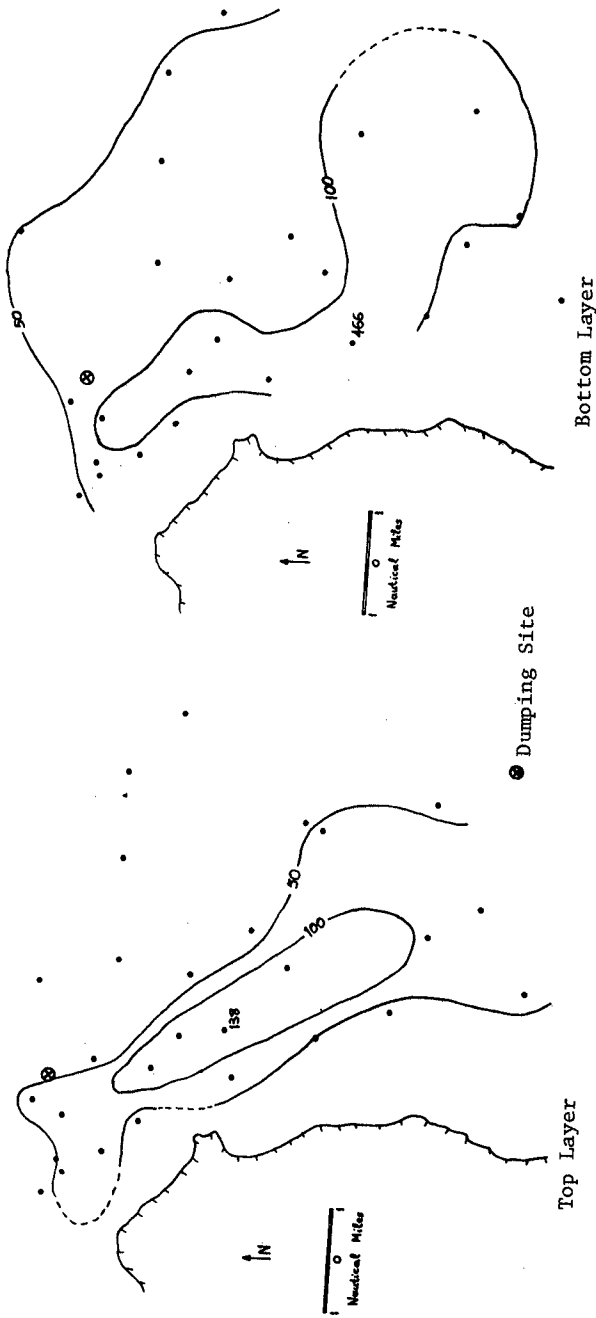


Figure 9 Experimental Results at Day D+3

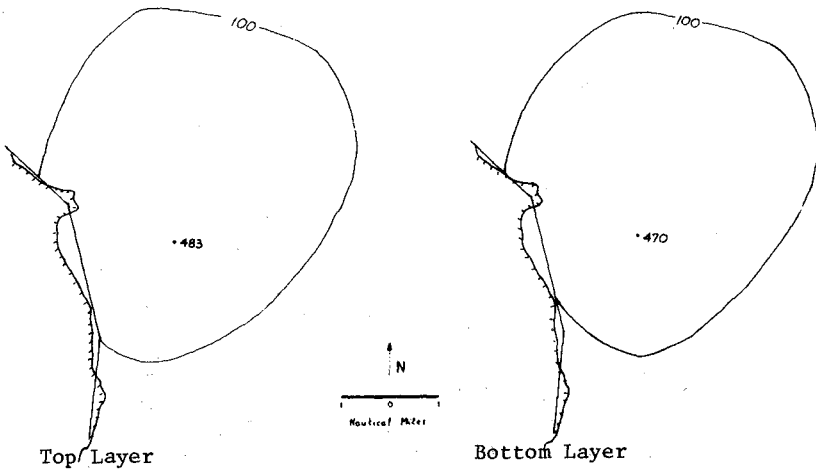


Figure 10 Computed Concentrations at Day D+2

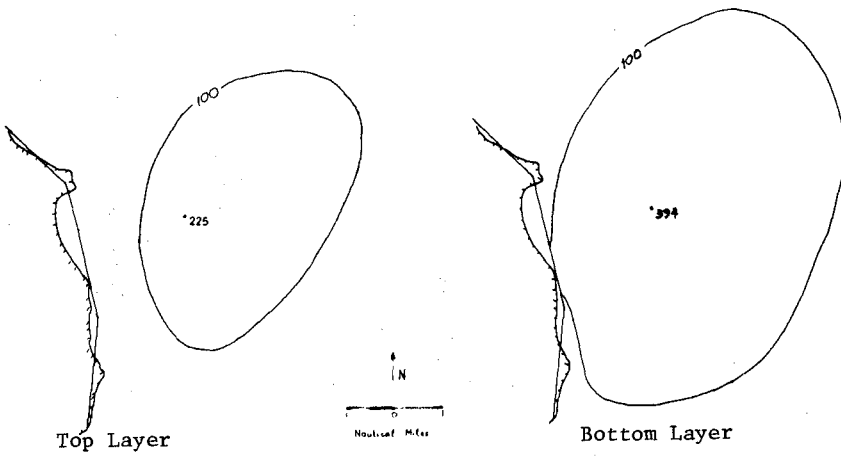


Figure 11 Computed Concentrations at Day D+3

REFERENCES

1. Abbott, M.B. et al, "Systems Modeling of Stratified Fluids", Symposium on Modeling Techniques 'Modeling 75', San Francisco, September 1975
2. Boericke, R.R. and Hall, D.W., "Hydraulic and Thermal Dispersion in an Irregular Estuary", J. Hydraulics Div., ASCE, Vol. 100, HYL, January 1974
3. Breusers, H.N.C. (ed.), "Momentum and Mass Transfer in Stratified Flows", Literature Study, Delft Hydraulics Lab Report R880, December 1974
4. Bumpus, D.F., "Review of the Physical Oceanography of Massachusetts Bay", Woods Hole Oceanographic Inst. Report 74-8, February 1974
5. Christodoulou, G.C., "Mathematical Modeling of Dispersion in Stratified Waters", Sc.D. Thesis, Dept. of Civil Engineering, M.I.T., September 1976
6. Deardorff, J.W., "On the Magnitude of the Subgrid Scale Eddy Coefficient", J. Computational Physics, Vol. 7, Part 1, 1971
7. Elder, J.W., "The Dispersion of Marked Fluid in Turbulent Shear Flow", J. Fluid Mechanics, Vol. 5, Part 4, May 1959
8. Laevastu, T., "Multilayer Hydrodynamical Numerical Models", Symposium on Modeling Techniques 'Modeling 75', San Francisco, September 1975
9. Leendertse, J.J. and Liu, S.K., "A Three-Dimensional Model for Estuaries and Coastal Seas: Vol. II, Aspects of Computation", Rand Co., June 1975
10. Leimkuhler, W.F. et al, "Two-Dimensional Finite Element Dispersion Model", Symposium on Modeling Techniques 'Modeling 75', San Francisco, September 1975
11. Long, R.R., "The Influence of Shear on Mixing Across Density Interfaces", J. Fluid Mechanics, Vol. 70, Part 2, July 1975
12. Osmidov, R.V., "On the Turbulent Exchange in a Stably Stratified Ocean", Izv. Acad. of Science USSR, Atmospheric and Oceanic Physics, Vol. 1, No. 8, 1965
13. Pearce, B.R. and Christodoulou, C.C., "Application of a Finite Element Dispersion Model for Coastal Waters", Proceedings of XVI I.A.H.R. Congress, Sao Paulo, 1975
14. Taylor, C.I., "The Dispersion of Matter in Turbulent Flow through a Pipe", Proc. Royal Society of London, Ser. A, Vol. 223, 1954
15. Turner, J.S., "Buoyancy Effects in Fluids", Cambridge Univ. Press, 1973
16. Wang, J.D. and Connor, J.J., "Finite Element Model of Two Layer Coastal Circulation", Proceedings of XIV International Coastal Engineering Conference, Copenhagen, 1974

CHAPTER 181

DETERMINATION OF THE INTERFACIAL EDDY DIFFUSION COEFFICIENT OF A HIGHLY STRATIFIED ESTUARY

by

Yu - Hwa Wang*

INTRODUCTION

Estuaries may be sequentially classified into highly stratified, moderately mixed and vertically homogeneous. An important difference between moderately stratified or vertically homogeneous estuaries, and highly stratified estuaries (salt wedges) is that, in the former, tidal currents are sufficient to cause turbulent mixing of fresh water and sea water over the full depth of the estuary. In the latter, a distinct interface or interfacial layer exists which separates the two nearly homogeneous layers. The vertical advection of salt in this two-layer flow is the dominant process in maintaining the salt balance. This paper presents an analytical model describing this process. Experiments have been conducted in the laboratory to compare with the developed theory.

A large number of publications concerning estuarine dynamics are available for moderately mixed and vertically homogeneous estuaries. Relatively little information, however, is available for highly stratified estuaries. In an earlier work Keulegan (1949) defined the critical velocity of the upper layer at which the entrainment of the salt water layer starts. A summary of Keulegan's work may be found in Chapter 11 of the book, "Estuary and Coastal Hydrodynamics" edited by Ippen (1966). Recently Partheniades *et. al.* (1975) reviewed Schijf-Schonfeld's analytical work and Keulegan's experimental data with regard to the length, shape and shear stresses of a saline wedge. Wang (1975) compared his laboratory measurements of interfacial stresses with Lock's Theory.

THEORETICAL DEVELOPMENT

For a steady, incompressible, viscous, two-layer, stably stratified estuarial type flow, the governing equations are:

$$u \frac{\partial u}{\partial x} + v \frac{\partial u}{\partial y} = \nu \frac{\partial^2 u}{\partial y^2} \quad \text{Bottom Layer (1)}$$

*Assistant Professor of Coastal Engineering, University of Florida, Gainesville, Florida, 32611

$$u \frac{\partial u}{\partial x} + v \frac{\partial u}{\partial y} = v_2 \frac{\partial^2 u}{\partial y^2} \quad \text{Top Layer (2)}$$

$$\frac{\partial u}{\partial x} + \frac{\partial v}{\partial y} = 0 \quad \text{Continuity (3)}$$

The salt balance equation is:

$$u \frac{\partial c}{\partial x} + v \frac{\partial c}{\partial y} = E \frac{\partial^2 c}{\partial y^2} \quad (4)$$

The symbols and coordinates are referred to in the following sketch. V is the velocity in the y -direction and E the eddy diffusion coefficient. Subscripts 1 and 2 refer to the bottom and top layers.

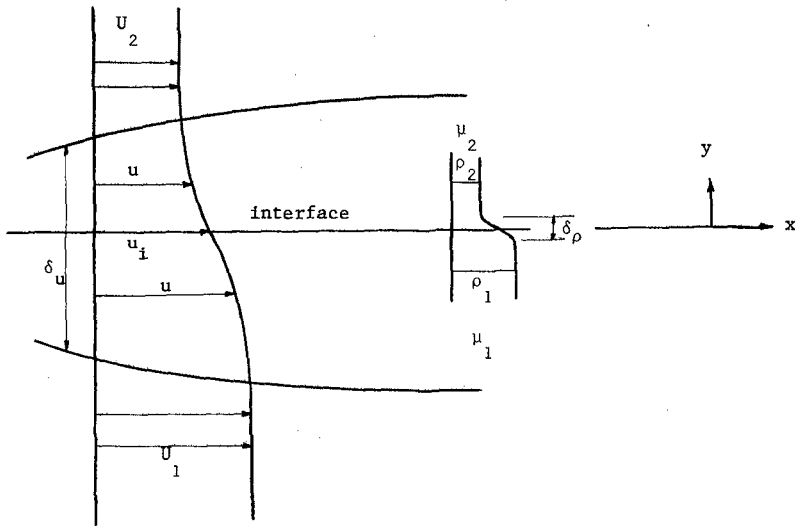


Figure 1. Definition Sketch

From laboratory observation, a highly stratified estuarial flow can be maintained if the flow of both layers are fairly uniform. However, this does not exclude turbulence from the vicinity of the interface due to the instability of the interface and the breaking of interfacial wavelets (Browand and Wang, 1972; Rumer, 1974; Wang 1975). It seems justified to assume self-similarity of velocity profiles such that:

$$\frac{u}{U_1} = \phi \left(\frac{y}{\delta_1} \right) = \phi (\eta_1) \quad (5)$$

where ϕ is a function to be determined, and δ_1 is a vertical length scale such as the thickness of the viscous layer at the interface. This self-similarity assumption is analogous to the case of approximate self-similarity of the velocity profiles in turbulent wakes and boundary layers discussed by Townsend (1956). The observed self-similarity of concentration profiles facilitates the integration of the salt balance equation (4).

With equation (5), the interfacial shear stress is given by:

$$\tau_1 = \mu_1 \left(\frac{\partial u}{\partial y} \right)_{y \rightarrow 0} = \frac{\mu_1}{\delta_1} U_1 \phi_1' \quad (6)$$

the interfacial friction factor is defined as (Lock 1951)

$$f_1 = \frac{\tau_1}{\rho_1 U_1^2} \sqrt{\frac{U_1 x}{v_1}} \quad (7)$$

Eliminating τ_1 between equation (6) and (7), we have

$$\left. \frac{\partial u}{\partial y} \right|_{y \rightarrow 0} = \frac{1}{\mu_1} \left(f_1 \rho_1 U_1^2 \sqrt{\frac{v_1 x}{U_1}} \right) \quad (8)$$

Let

$$\eta_1 = \phi_1 \left(\frac{y}{\delta_1} \right) = y \sqrt{\frac{U_1}{v_1 x}}$$

integrating equation (8) and applying the condition

$$u \rightarrow u_1 \text{ when } y \rightarrow 0-$$

We obtain

$$u = f_1 U_1 \eta_1 + u_1 \tag{9}$$

The continuity equation (3) implies

$$v = \int \left(- \frac{\partial u}{\partial x} \right) dy = \frac{1}{4} f_1 U_1 \eta_1^2 \sqrt{\frac{v}{U_1 x}} \tag{10}$$

substituting (9) and (10) into the salt balance equation (4) and applying the chain rule we have

$$\frac{\partial^2 c}{\partial \eta^2} + \frac{v}{E} \left(f_1 \frac{\eta^2}{4} + \frac{u_1}{U_1} \frac{\eta}{2} \right) \frac{\partial c}{\partial \eta} = 0 \tag{11}$$

Let

$$P = \frac{\partial c}{\partial \eta}, \quad P = \frac{\partial^2 c}{\partial \eta^2}$$

the equation (11) may be solved,

$$P = A_0 \text{ Exp} \left[-f_1 \frac{1}{4} \frac{v}{E} \frac{\eta^3}{3} - \frac{u_1}{U_1} \frac{v}{E} \frac{\eta^2}{4} \right]$$

Integrating to get

$$C = A_0 \int_0^\eta e^{-\left(f_1 \frac{1}{4} \frac{v}{E} \frac{\xi^3}{3} + \frac{u_1}{U_1} \frac{v}{E} \frac{\xi^2}{4} \right)} d\xi + A_1 \tag{12}$$

Near the interface

$$\xi < 1 \text{ and } f_i \ll 1.$$

Therefore,

$$\left| f_i \frac{1}{4} \frac{v}{E} \frac{\xi^3}{3} \right| \ll \left| \frac{u_i}{U_1} \frac{v}{E} \frac{\xi^2}{4} \right|$$

Neglecting the cubic term, we have

$$C = A_0 \int_0^\eta e^{-\left(\frac{u_i}{U_1} \frac{v}{E} \frac{\xi^2}{4} \right) \beta \xi} + A_1. \quad (13)$$

The conditions are:

$$C(\eta = -\infty) = C_1 \text{ implies } A_1 = C_1$$

$$C(\eta = +\infty) = A_0 \int_0^\eta e^{-\beta \xi^2} \beta \xi + C_1 = A_0 \sqrt{\frac{\pi}{\beta}} + C_1$$

Where

$$\beta = \frac{1}{4} \frac{u_i}{U_1} \frac{v}{E}$$

Then,

$$A_0 = -(C_1 - C_2) \sqrt{\frac{\beta}{\pi}}$$

Substituting β , A_0 and A_1 into equation (13), we obtain the concentration distribution

$$C = -(C_1 - C_2) \sqrt{\frac{\beta}{\pi}} \int_0^\eta e^{-\beta \xi^2} d\xi + C_1 \quad (14)$$

The concentration gradient at the interface is obtained by differentiating equation (14) with respect to y .

$$\frac{\partial C}{\partial y} \Big|_{y \rightarrow 0} = -(C_1 - C_2) \sqrt{\frac{u_1}{4\pi E \chi}} \quad (15)$$

For a given station from the river mouth, E is ready to be determined if the concentration gradient and velocity at the interface are known.

EXPERIMENTAL RESULTS AND DISCUSSION

Two streams of salt water of different concentrations $C_1 > C_2$, are brought to the open channel entrance to form a two-layer type flow field. The velocities of both layers are adjusted by control valves. For a given concentration difference $\Delta C = C_1 - C_2$, the degree of mixing at the interface is proportional to the velocity differential $\Delta U = U_1 - U_2$. For this experiment, the ΔU is maintained in such a way that the interface is sharp. The bottom layer is dyed red for visual observations. A standard TSI hot-film probe is used for velocity measurement. Variations in electrical conductivity is used to detect the variations in concentration. Both hot-film sensor and conductivity probes are mounted together in the same probe holder. The velocity profile and concentration profile at various x -stations are obtained simultaneously by traveling these two probes slowly across the interface. The interfacial velocity u_1 and the concentration gradients are obtained from the velocity and density profiles.

The theoretical concentration distribution is compared to the measured profile in Figure (2). The theory gives a less steep slope at the interface than was actually measured. The discrepancy may be explained as the following:

In the process of integration a common vertical scale length is used. This means the theory is developed under the consideration that viscous layer thickness δ_u and diffusion layer thickness δ_ρ is of the same order of magnitude

$$\frac{\delta_u}{\delta_\rho} \approx 1$$

A close examination of the measured data reveals that in the experiment

$$\frac{\delta_u}{\delta_\rho} \gg 1$$

The viscous layer thickness δ_u is plotted against longitudinal x-axis in Figure (3), and the diffusion layer thickness δ_ρ versus x is shown in Figure (4).

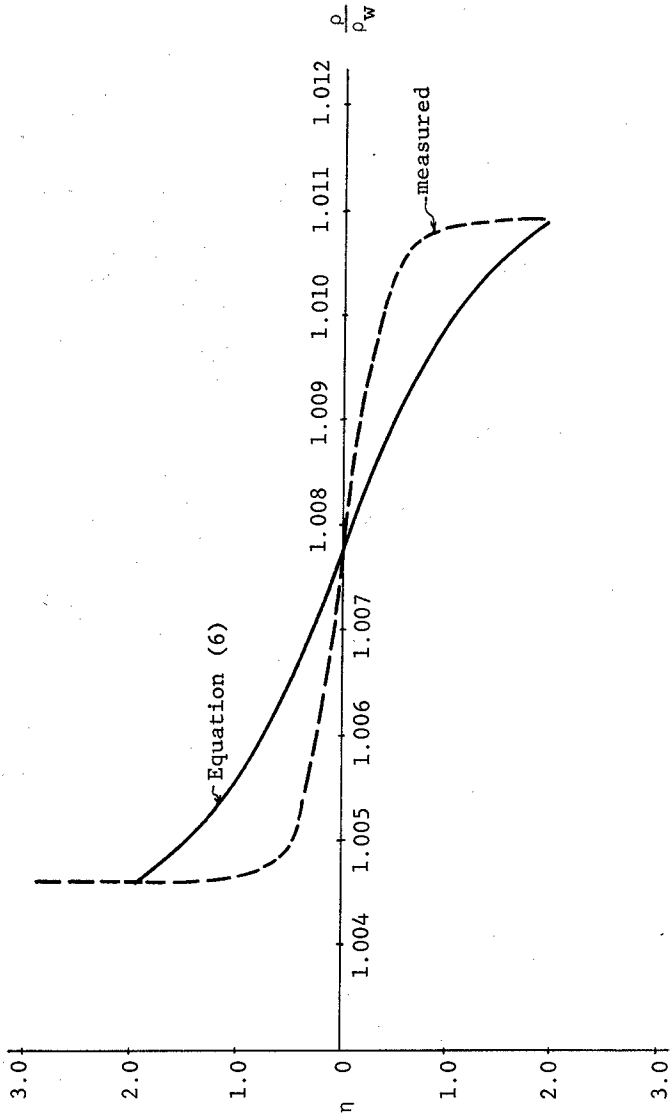
For a given x-station, equation (15) indicates that the eddy diffusion coefficient E is inversely proportional to the square of the concentration gradient at the interface. For this experiment run,

$$\frac{E_{\text{theory}}}{E_{\text{measured}}} = 6.2$$

It may be concluded that the relative size of the viscous layer thickness and diffusion layer thickness is important in determining the eddy diffusion coefficient. The developed theory herein predicts concentration distribution and eddy diffusion coefficient E for $\delta_u = \delta_\rho$. The theory gives larger E values and less steep slopes of the concentrations profile at the interface when $\delta_u > \delta_\rho$, smaller E values and steeper concentration profile slopes at the interface when $\delta_u < \delta_\rho$.

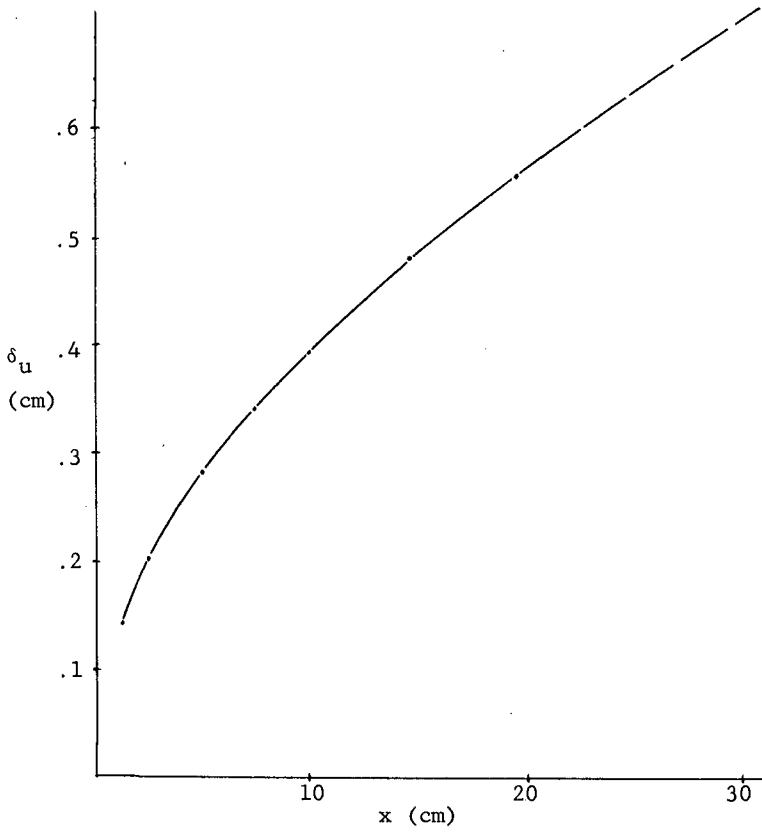
REFERENCES

- 1) Browand, F.K. and Wang, Y.H. (1972), "An Experiment on the Growth of Small Disturbances at the Interface Between Two Streams of Different Densities and Velocities," International Symposium on Stratified Flows, Novosibirsk, USSR.
- 2) Keulegan, G.H. (1949), "Interfacial Instability and Mixing in Stratified Flows," J. Res. National Bureau of Standards, Vol. 43, pp. 487-500.
- 3) Keulegan, G.H. (1966), "The Mechanism of An Arrested Saline Wedge," Chapter 11, Estuary and Coastline Hydrodynamics," Edited by A.T. Ippen, McGraw-Hill.
- 4) Lock, R.C. (1951), "The Velocity Distribution in the Laminar Boundary Layer Between Parallel Streams," Quart. J. Mech. Appl. Math., Vol. 6, part 1, pp. 42-63.
- 5) Partheniades, E., et.al (1975), "On the Shape and Interfacial Resistance of Arrested Saline Wedges," Proceedings XVI Congress IAHR, Vol. 1, pp. 157-164.
- 6) Rumer, R.R. (1973), "Interfacial Wave Breaking in Stratified Liquids," J. of Hydraulic Div. ASCE, Vol. 99, No. HY3, pp. 509-524.
- 7) Townsend, A.A. (1956), "The Structure of Turbulent Shear Flow," Cambridge University Press, U.K.
- 8) Wang, Y.H. (1975), "The Interfacial Stress in a Strongly Stratified Estuary," Proceedings XVI Congress IAHR, Vol. 1, pp. 108-115.
- 9) Wang, Y.H. (1975), "An Experimental Study of the Instability of a Stably Stratified Free Shear Layer," J. of Fluid Mechanics, Vol. 71, part 3, pp. 563-575.



VERTICAL DENSITY DISTRIBUTIONS - A COMPARISON OF THEORY AND MEASURED PROFILE.

Figure 2



THE VISCOUS LAYER THICKNESS δ_u VS. X-AXIS

Figure 3

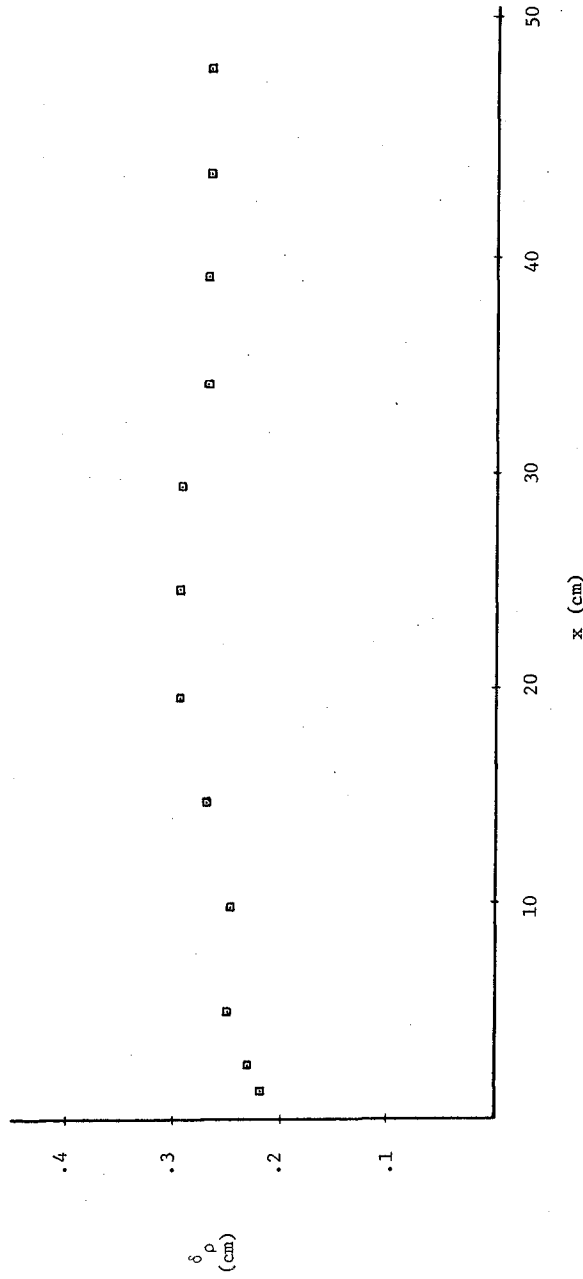


Figure 4. The Diffusion Layer Thickness δ_ρ Vs. X-axis

CHAPTER 182

FRICITION AT THE INTERFACE OF TWO-LAYERED FLOWS

by

Nobuyuki Tamai

Associate Professor
Department of Civil Engineering
University of Tokyo, Tokyo, Japan

ABSTRACT

Viscous perturbed velocity field induced by interfacial waves is solved to the first order in terms of wave amplitude for sharply stratified flows described in a curvilinear coordinate system assuming that the external velocity is uniform and constant along the interface. A new type of formula for the interfacial friction coefficient is proposed based on the theoretical result on viscous dissipation in the boundary layer along the interface. The interfacial friction coefficient is supposed to be inversely proportional to the square root of the product of the Reynolds number of a moving layer and the densimetric Froude number to the fifth. The new formula agrees with observed data better than the best empirical law does especially in the range of large Reynolds number. It is found out, however, that the proportional constant may be affected by stability of the two-layered flow system concerned.

INTRODUCTION

The behavior of saline wedges is directly concerned with the municipal, industrial or agricultural utilization of estuarine waters. The form of the interface and the length of arrested saline wedges have been analyzed by the one-dimensional scheme as the case of varied flows in open channels. However, we have to estimate the value of the interfacial friction coefficient from the bulk hydraulic parameters to perform the prediction in a closed calculation scheme.

One of remarkable flow patterns observed in a two-layered flow system is the generation of interfacial waves and its existence for a relatively wide range of flow conditions. Therefore, the flow regime changes from laminar to turbulent via stable transition zone with interfacial waves. When a whole flow system reaches turbulent condition we have another flow pattern, that is, well mixed estuaries which have density gradient not in vertical direction but in horizontal direction. Although the

flow regime in the upper layer (fresh water) is turbulent, the flow regime near the interface is considered in the transition zone due to the suppression of turbulence by the sharp density gradient. In this analysis mixing between two layers is assumed very weak or none. If there exists moderate mixing between two layers, it is supposed that the density distribution may change and the thickness of the mixed zone will develop along the interface. In this case the flow system develops to a different condition from what was assumed initially. Thus we are concerned especially with the case of abrupt interface with stable infinitesimal interfacial waves at the interface as the first approximation of the fresh-salt interface.

Theoretical approaches are classified into two types. One is to consider the energy dissipation of the formation of interfacial waves. This way of approach was initiated by Keulegan (1949) for inviscid fluids. He derived an expression for the interfacial friction coefficient assuming that the dissipation took on the same value as for surface waves in contact with air. He also formulated the additional shearing resistance due to the mixing. Since the liquid crossing the interface is initially at rest and after crossing the interface it acquires the velocity of the current, the current must suffer momentum loss.

Shi-igai (1965) extended the Keulegan's approach to a fresh-salt two-layered flow system. He expressed the flow field by means of the velocity potential. However, interfacial waves were considered to suffer from viscous dissipation. Thus, a virtual shear flow was considered in his analysis. Summarizing the characteristics of interfacial waves, he proposed that the interfacial friction coefficient was inversely proportional to ψ where $\psi = R_e F_d^2$. Here R_e is the Reynolds number of a moving layer and F_d is the densimetric Froude number.

Hamada (1966) calculated the dissipation of infinitesimal waves formed on the interface of viscous stratified fluids. He utilized the theoretical results of the Rayleigh-Taylor instability problem. His final result is summarized that the interfacial friction coefficient is inversely proportional to the square root of ψ . However, the theory is built up on the basis of no external flow field, which disagrees with the real situation of salt-water wedges.

Another theoretical approach treats with skin friction and momentum loss due to entrainment of fluid particles from a stationary layer. If we consider the laminar condition for a stationary saline wedge, we can theoretically derive a velocity distribution for both layers and calculate shearing stress of the type of skin friction. In the laminar flow the interfacial friction coefficient is inversely proportional to the Reynolds number of a flowing layer.

Valembois (1963) considered the shearing stress at the interface as the sum of a laminar part and a turbulent part. The turbulent part is expressed by the mixing velocity across the interface. Although he obtained the order of magnitude of these components by utilizing four among forty six experimental data of Lofquist (1960), he did not mention the general behavior of the mixing velocity any further.

Recently Pedersen (1972) investigated the mechanism of entrainment in two-layer stratified flows. With the use of the momentum and work energy equations, both with respect to the net entrainment, the interfacial friction coefficient is found to be equal to the non-dimensional entrainment velocity. The details of the entrainment velocity, however, remained vague with respect to hydraulic parameters of a flowing layer since the

interfacial friction coefficient appeared to be a minor objective in his paper.

As was briefly reviewed there are several components which contribute to the friction at the interface of a stratified flow. Referring to the proposed functional relationship it is said that when the Reynolds number is very large and the stratification is stable, which is encountered in saline wedges in estuaries, the magnitude of laminar friction is much smaller than that of the friction due to interfacial wave formation. In addition, as long as we consider a two-layered flow system the mixing between two layers remains weak. Therefore, it is supposed that the friction due to the mixing does not play a dominant role in sharply stratified flows with which we are concerned in this paper. The objective of this paper is to construct a more advanced theory on the interfacial friction under the existence of interfacial waves. Main flow is divided into two parts, that is, an inviscid part and a viscous perturbed part so as to improve previous theories. Then, boundary layer along the wavy interface is analyzed and the interfacial friction coefficient is derived from viscous dissipation in the boundary layer.

THEORETICAL CONSIDERATIONS

The definition sketch of a two-dimensional two-layered flow system is given in Fig. 1. The coordinate system (x, y) is a moving frame with the celerity of interfacial waves, c . We have stable infinitesimal interfacial waves at the interface. The velocity distribution in the upper layer is assumed uniform. This is because the flow of the upper layer is considered turbulent, though the flow regime near the interface is in the transition due to the suppression of turbulence by the density difference. Since the relative importance of skin friction with the resistance due to interfacial waves diminishes as the Reynolds number becomes high, the velocity distribution is not essential in this analysis. The salt-water layer is assumed stationary. If we consider this motion as a relative motion, the situation is general.

The coordinate system (x, y) is transformed into a curvilinear coordinate system (ξ, η) by utilizing a conformal mapping.

$$\zeta = \xi + i\eta = z - ia e^{ikz} \quad (1)$$

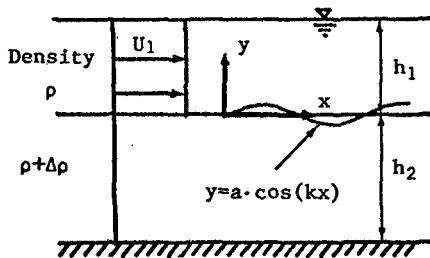


Fig. 1. Definition sketch of a two-layered flow

where $z=x+iy$, a is the amplitude of an infinitesimal interfacial wave, and k is the wave number. From Eq. (1) we obtain

$$\xi = x + a e^{-ky} \sin kx, \quad \eta = y - a e^{-ky} \cos kx \quad (2)$$

Jacobian of the transformation is calculated as

$$J = 1 + 2ak e^{-ky} \cos kx + O(a^2) \quad (3)$$

The interface is expressed by $\eta=0$ if we neglect the effect of the order of a^2 .

The vorticity transport equation for a steady motion is expressed by

$$\mathbf{u} \cdot \nabla \boldsymbol{\omega} - \boldsymbol{\omega} \cdot \nabla \mathbf{u} = \nu \nabla^2 \boldsymbol{\omega} - \nabla(1/\rho) \wedge \nabla p \quad (4)$$

where \mathbf{u} and $\boldsymbol{\omega}$ are velocity and vorticity vectors, respectively, ν the kinetic viscosity of the fluid, ρ the density of the fluid, p the pressure, ∇ a gradient operator, \cdot inner product, and \wedge vector product. Equation of continuity for an incompressible fluid is explained by

$$\nabla \cdot \mathbf{u} = 0 \quad (5)$$

Equation (5) is an exact expression for the equation of continuity even in the case of slight density variation due to a solute and is a passable expression to the first order approximation under the density variation caused by both temperature and concentration (Yih, 1965). The equation of continuity in the curvilinear coordinate transformed by Eq. (1) is

$$J \left\{ \frac{\partial}{\partial \xi} (J^{-1/2} u) + \frac{\partial}{\partial \eta} (J^{-1/2} v) \right\} = 0 \quad (6)$$

where u and v are ξ and η components of velocity, respectively. Equation (6) is satisfied by the stream function, X , defined by

$$u = J^{1/2} \frac{\partial X}{\partial \eta}, \quad v = -J^{1/2} \frac{\partial X}{\partial \xi} \quad (7)$$

In a two-dimensional problem vorticity has just one component perpendicular to ξ - η plane. Therefore we can treat vorticity as a scalar denoting $|\boldsymbol{\omega}| = \omega$. Further, the second term of the left-hand side of Eq. (4) vanishes in case of a two-dimensional problem. Because a sharply stratified flow is considered in this analysis, density gradient and pressure gradient are parallel each other. Therefore, the second term of the right-hand side of Eq. (4) also vanishes in this case. Equation (4) is thus rewritten as in Eq. (8).

$$-J^{1/2} \frac{\partial X}{\partial \xi} \cdot J^{1/2} \frac{\partial \omega}{\partial \eta} + J^{1/2} \frac{\partial X}{\partial \eta} \cdot J^{1/2} \frac{\partial \omega}{\partial \xi} = \nu J D^2 \omega \quad (8)$$

where $\omega = -J D^2 X$ and $D^2 = \partial^2 / \partial \xi^2 + \partial^2 / \partial \eta^2$.

Now perturbation method is applied to solve Eq. (8). Stream function defined in Eq. (7) is expanded in power series as shown in the next equation.

$$X = X_0 + \epsilon X_1 + \epsilon^2 X_2 + \dots \quad (9)$$

where the suffix of X stands for the order of a perturbed representation and $\epsilon = ak$. We assume the external flow is inviscid. Therefore, X_0 is obtained by the inviscid theory. X_1 is composed of a wave component, X_{1w} , which is also calculated by the inviscid theory and a viscous component, X_{1v} . Substitution of Eq. (9) into the definition of vorticity yields

$$\begin{aligned} \omega &= -JD^2X = \omega_0 + \epsilon\omega_1 + \epsilon^2\omega_2 + \dots \\ &= -(1 + 2\epsilon e^{-k\eta} \cos k\xi + O(\epsilon^2)) \cdot (D^2X_0 + \epsilon D^2X_1 + \epsilon^2 D^2X_2 + \dots) \\ &= -\epsilon D^2X_1 - \epsilon^2 (D^2X_2 + 2e^{-k\eta} \cos k\xi \cdot D^2X_1) + O(\epsilon^3) \end{aligned} \quad (10)$$

Since X_0 is derived from the inviscid theory, it provides irrotational motion. Thus the perturbed expression for vorticity begins with the first order in terms of ϵ .

The equation in ϵ is obtained as follows by substitution of Eqs. (9) and (10) into Eq. (8).

$$-\frac{\partial X_0}{\partial \xi} \frac{\partial}{\partial \eta} D^2X_1 + \frac{\partial X_0}{\partial \eta} \frac{\partial}{\partial \xi} D^2X_1 = \nu D^2(D^2X_1) \quad (11)$$

According to the Kelvin-Helmholtz problem, the inviscid solution of the stream function is given by

$$\begin{aligned} \Psi &= (U_1 - c)y + \frac{(U_1 - c)a}{\sinh kh_1} \sinh k(y - h_1) \cos kx \\ &= (U_1 - c)\eta + (U_1 - c)ae^{-k\eta} \cos k\xi + \frac{(U_1 - c)a}{\sinh kh_1} \sinh k(\eta - h_1) \cos k\xi \\ &\quad + O(a^2) \end{aligned}$$

where Ψ is the stream function, U_1 the velocity of the upper layer, and h_1 the depth of the upper layer. The stream function defined by Eq. (9) is thus obtained up to the order of ϵ as

$$\begin{aligned} X_0 &= (U_1 - c)\eta \\ \left\{ \begin{aligned} X_1 &= \frac{1}{k}(U_1 - c)e^{-k\eta} \cos k\xi + \frac{U_1 - c}{k \sinh kh_1} \sinh k(\eta - h_1) \cos k\xi + X_{1w} \\ &= X_{1w} + X_{1v} \end{aligned} \right. \end{aligned} \quad (12)$$

Following Eq. (12) we obtain $\partial X_0 / \partial \xi = 0$. Therefore, we can simplify Eq. (11) further as

$$(U_1 - c) \frac{\partial \omega_1}{\partial \xi} = \nu D^2 \omega_1 \quad (13)$$

In addition length scale along the interface is considered much larger than that of the direction perpendicular to the interface. Hence $\partial / \partial \xi \ll \partial / \partial \eta$ and $\partial^2 / \partial \xi^2 \ll \partial^2 / \partial \eta^2$ may hold to reduce the governing equation as in the following expression.

$$(U_1 - c) \frac{\partial \omega_1}{\partial \xi} = \nu \frac{\partial^2 \omega_1}{\partial \eta^2} \quad (14)$$

where $\omega_1 = -\partial u_1 / \partial \eta$. Here u_1 is the first order component of perturbed velocity.

Now the velocity component along the interface is developed in power series through Eq. (7).

$$\begin{aligned} u &= u_0 + \epsilon u_1 + \epsilon^2 u_2 + \dots \\ &= \frac{\partial X_0}{\partial \eta} + \epsilon \left\{ \frac{\partial X_1}{\partial \eta} + (U_1 - c) e^{-k\eta} \cos k\xi \right\} + O(\epsilon^2) \end{aligned} \quad (15)$$

Boundary conditions under which Eq. (14) is to be solved are determined as follows. As was previously mentioned the interface is expressed by $\eta=0$ to the order of ϵ . Fundamental scheme on the velocity of this paper is that we allow velocity gap in the external flow but we impose no-slip condition for perturbation velocities. Therefore, we have

$$u_1 = 0 \quad \text{at } \eta = 0, \quad u_1 = \frac{\partial X_{1W}}{\partial \eta} \quad \text{at } \eta = \infty$$

The second condition shows that viscous effect vanishes as the distance from the interface increases. If we denote wavy and viscous parts in the perturbed velocity separately, we obtain the following expression from Eqs. (12)₃ and (15)₂.

$$\begin{cases} u_1 = u_{1W} + u_{1V} + (U_1 - c) e^{-k\eta} \cos k\xi \\ u_{1W} = \partial X_{1W} / \partial \eta, \quad u_{1V} = \partial X_{1V} / \partial \eta \end{cases} \quad (16)$$

Thus we obtain the boundary conditions in terms of the first order viscous perturbed velocity, u_{1V} .

$$\begin{cases} u_{1V} = (U_1 - c) \coth kh_1 \cos k\xi & \text{at } \eta = 0 \\ u_{1V} = 0 & \text{at } \eta = \infty \end{cases} \quad (17)$$

The governing equation (14) is again rewritten in terms of u_{1V} .

$$(U_1 - c) \frac{\partial^2 u_{1V}}{\partial \xi \partial \eta} = \nu \frac{\partial^3 u_{1V}}{\partial \eta^3} \quad (18)$$

Integration with respect to η produces Eq. (19).

$$(U_1 - c) \frac{\partial u_{1V}}{\partial \xi} = \nu \frac{\partial^2 u_{1V}}{\partial \eta^2} + H(\xi) \quad (19)$$

Integration constant $H(\xi)$ is considered pressure gradient referring to a momentum equation.

The solution to Eq. (19) is obtained with boundary conditions of Eq. (17) for the case of $H(\xi)$ equals zero, which represents constant external velocity. This is the case that the interface is parallel to the water surface and would be the first approximation even for the case of slightly inclined interface.

$$u_{1v} = (c-U_1) \coth kh_1 e^{-\beta\eta} \cos(k\xi + \beta\eta) \quad (20)$$

where

$$\beta = \sqrt{(c-U_1)k/2\nu} \quad (21)$$

Vorticity is thus calculated up to the first order.

$$\begin{aligned} \omega &= \varepsilon\omega_1 = -\varepsilon\partial u_1/\partial\eta \\ &= \beta(c-U_1)ak \coth kh_1 e^{-\beta\eta} \{\cos(k\xi + \beta\eta) + \sin(k\xi + \beta\eta)\} \end{aligned} \quad (22)$$

In order to obtain a real value for β in Eq. (21), the condition $c \geq U_1$ must be hold. The interfacial wave propagating downstream satisfies this condition. A more detailed description will be given as follows. Let us denote $\Delta\rho = \rho_2 - \rho_1$ and $g' = g \cdot \Delta\rho / \rho_1$, where $\Delta\rho$ is the density difference between upper and lower layers and g is the acceleration of gravity. For the case of a stationary lower layer and of a slight density difference, which is treated in this paper, the condition $c \geq U_1$ can be rewritten on use of the inviscid theory as

$$g' \geq kU_1^2 \coth kh_2 \quad (23)$$

where h_2 is the thickness of the lower layer. For long waves we can approximately express $\coth kh_2 = 1/kh_2$. Thus Eq. (23) reduces to

$$(1/F_d^2)(h_2/h_1) \geq 1 \quad (24)$$

where

$$F_d = \frac{U_1}{\sqrt{\frac{\Delta\rho}{\rho_1} gh_1}} \quad (25)$$

is the densimetric Froude number. The value of F_d is less than unity in density currents like as saline wedges. Therefore, the condition of Eq.(24) is ordinarily satisfied unless the thickness of the lower layer is extremely small. For deep water waves we can put approximately $\coth kh_2 = 1$. Then we obtain the relationship for the wave length λ

$$\lambda \geq 2\pi h_1 \cdot F_d^2 \quad (26)$$

Equation (26) shows that interfacial waves whose wave length is shorter than that given by Eq. (26) are unstable. Since we can expect to have real values for β for usual hydraulic conditions as shown in Eqs. (24) and (26), we can accept Eq. (22) as a basis for further investigation.

Viscous energy dissipation is generated in the boundary layer, the thickness of which is the order of $1/\beta$, along the interface. In this analysis the boundary layer is only considered along the upper surface of the interface. This may be acceptable under the assumptions adopted in this analysis that the lower layer is stationary, the density profile is discontinuous at the interface and the amplitude of interfacial waves is infinitesimal. The mean energy dissipation per unit area is given by

$$\dot{E} = -\mu \int_0^{\delta} \overline{\omega^2} d\eta \quad (27)$$

where δ is the thickness of the boundary layer and overbar denotes the

average over a wave length. Substituting Eq. (22) into Eq. (27) we obtain

$$\dot{E} = -(1/2)\mu\beta(c-U_1)^2 a^2 k^2 \coth^2 kh_1 \quad (28)$$

where the outer edge of the boundary layer is approximated by $\eta=\infty$.

This energy dissipation must be fed by the mean flow of the upper layer. The resistance stress to the upper layer, τ , is thus obtained by dividing the rate of energy dissipation by the mean flow velocity of the upper layer and turning the sign following the definition of the resistance stress.

$$\tau = -\dot{E}/U_1 \quad (29)$$

Interfacial friction coefficient, f_i , defined by

$$\tau = (1/2) f_i \rho U_1^2 \quad (30)$$

is then obtained on use of Eqs. (28), (29), and (30).

$$f_i = \frac{1}{\sqrt{2}} R_e^{-1/2} \left(\frac{c}{U_1} - 1\right)^{5/2} (kh_1)^{1/2} a^2 k^2 \coth^2 kh_1 \quad (31)$$

where

$$R_e = \frac{U_1 h_1}{\nu} \quad (32)$$

is the Reynolds number of the upper layer. It is noted that in this analysis the energy dissipation is not caused by the maintenance of interfacial waves but by the viscous perturbed velocity field which is induced by the presence of interfacial waves.

It is found out that the interfacial friction coefficient is inversely proportional to the square root of the Reynolds number of the moving layer. In order to study the dependence on the densimetric Froude number we have to specify the magnitude of interfacial wave celerity which is obtained by the inviscid theory.

$$c = \frac{U_1 \coth kh_1 + \{g'(\coth kh_1 + \coth kh_2)/k - U_1^2 \coth kh_1 \coth kh_2\}^{1/2}}{\coth kh_1 + \coth kh_2} \quad (33)$$

For a real value of β only plus sign of the square root is considered. This expression can be simplified in two extreme cases of long waves and deep water waves. Further analysis on the frictional coefficient is developed for these cases.

(a) *The case of long waves:* We can put approximately $\coth kh_1 = 1/kh_1$, and $\coth kh_2 = 1/kh_2$. From Eq. (33) we obtain

$$\frac{c}{U_1} = \frac{h_2 + \{F_d^{-2} h_2 (h_1 + h_2) - h_1 h_2\}^{1/2}}{h_1 + h_2}$$

(i) $h_2 \gg h_1$

In this case Eq. (31) reduces to

$$f_i = 0.707 (R_e F_d^5)^{-1/2} (kh_1)^{1/2} a^2 k^2 \coth^2 kh_1 \quad (34)$$

(ii) $h_2 \approx h_1$

In this case Eq. (31) is rewritten as

$$f_i = 0.125 R_e^{-1/2} (\sqrt{2F_d^{-2}-1} - 1)^{5/2} (kh_1)^{1/2} a^2 k^2 \coth^2 kh_1 \quad (35)$$

For very small values of F_d , Eq. (35) reduces to the same type of formula as Eq. (34).

$$f_i = 0.297 (R_e F_d^5)^{-1/2} (kh_1)^{1/2} a^2 k^2 \coth^2 kh_1 \quad (36)$$

(b) *The case of deep water waves:* In this case $\coth kh_1$ and $\coth kh_2$ are approximated to be unity. From Eq. (33) we obtain

$$c/U_1 = (1/2) \{ 1 + \sqrt{\lambda / (\pi h_1 F_d^2)} - 1 \}$$

Substitution of the above expression into Eq. (31) yields

$$f_i = 0.125 R_e^{-1/2} \{ \sqrt{\lambda / (\pi h_1 F_d^2)} - 1 \}^{5/2} (kh_1)^{1/2} a^2 k^2 \coth^2 kh_1 \quad (37)$$

A few remarks on Eq. (37) are added. For the shortest waves that satisfies Eq. (26) f_i reduces to zero. In that case the celerity of the interfacial wave is identical to the mean flow velocity. Thus the upper layer does not suffer from the energy dissipation. The longest wave that satisfies the deep water condition is written as $\lambda = 2h_1$. For this wave we can simplify Eq. (37). If we assume the densimetric Froude number F_d is much smaller than unity, Eq. (37) gives the relationship $f_i \propto (R_e F_d^5)^{-1/2}$.

COMPARISON WITH MEASURED DATA AND DISCUSSION

There have been several experimental works and field observations on saline wedges. Reported data of the interfacial friction coefficient are rearranged on the light of a newly developed formula. Referring to Eqs. (34), (35) and (37), the frictional coefficient depends on the wave characteristics even in specified cases. However, none has been reported explicitly about the wave length, the amplitude, and the celerity of interfacial waves. Therefore whichever formula we choose, certain magnitude of scattering of data around the estimated relationship will be inevitable.

Previous formulae claim the type of relationship

$$f_i = \alpha \psi^{-n} \quad (38)$$

where α and n are constants and $\psi = R_e F_d^2$. Because no observational result explains the amplitude and the wave length of interfacial waves as mentioned above, we have to simplify Eq. (31) in order to compare the theoretical result with reported data. The newly derived formula is approximated as in Eq. (39) excluding the effect of the characteristics of interfacial waves.

$$f_i = m (R_e F_d^5)^{-1/2} \quad (39)$$

where m is a proportional constant. This type of formula is chosen in connection with Eqs. (34), (35) and (37). Note that for very small F_d Eqs. (35) and (37) reduces to the same type of relation as Eq. (34).

The observed data are shown in Fig. 2 in the relationship between f_i and $R_e F_d^5$. Detailed values of f_i , R_e , and F_d of each data are listed in Table 1. A full line in Fig. 2 shows Eq. (39) in which $m=0.085$. The au-

thor's experiment (Tamai, 1964) was performed in a flume 15cm wide and 420 cm long and interfacial profiles of stationary saline wedges were recorded for a bottom slope of 1.27/100. Values of the interfacial friction coefficient were selected to produce the best fit interfacial profile by the numerical integration of a one-dimensional open channel equation for two-layered flows. The determined interfacial friction coefficient is thus considered the average value over the interface. The Reynolds number of the upper layer remains constant even for an inclined interface because of the constant discharge per unit width. The representative depth of the upper layer to calculate F_d is chosen at the mid-point of intruded saline wedges.

Lofquist (1960) performed his experiment in a horizontal flume 23.3cm wide and 30m long. In his experiment a heavier salt-water layer moved underneath a stationary fresh-water layer. Mean shear stress with respect to width at the interface were calculated from the slope of the interface, bed shear stress, and velocity gradient. Although friction coefficient is given with respect to the maximum velocity in the paper, the conversion to the definition of Eq. (30) is available utilizing the listed quantities.

Nakamura and Abe (1970) observed the behavior of a saline wedge in the Kuzuryu River. Values of the interfacial friction coefficient were calculated by the equation

$$f_i = 2 F_d^{-2} \frac{h_1}{h_1+h_2} \left\{ -(1-F_d^2) \frac{\Delta h_1}{\Delta x} + \frac{U_1^2}{(\Delta \rho / \rho_1) g B} \frac{\Delta B}{\Delta x} \right\} \quad (40)$$

Here we assume a stationary lower layer and B is the width of a channel. Symbol Δ explains finite difference in the marked quantities and x is a coordinate axis taken to the direction of fresh-water flow. It is noted that the resulted interfacial friction coefficient through Eq. (40) is considered a local value at a certain position in two-layered flows.

Suga and Takahashi (1971) performed a field observation in the Tone River and experiments in two flumes. One is 80cm wide and 100m long and the other is 30cm wide and 30m long. Values of the interfacial friction coefficient were computed by Eq. (40). Other data reported previously cannot be rearranged in Fig. 2 because the data are tabulated only with the value of ψ which is the sole parameter in the existing formula, Eq. (38). Thus the value of R_e and F_d cannot be obtained separately.

In f_i versus ψ diagram the best fit empirical formula was the case that $\alpha=0.2$ and $n=1/2$ in Eq. (38). But the value of n to explain the trend of the data measured in the Tone River that is one of the largest rivers in Japan is about 6/5. Therefore, the empirical formula fails to explain the behavior of the interfacial friction coefficient in the largest range of ψ . The trend of the data obtained in the Tone River which are indicated in solid circles in Fig. 2 seems to follow a line

$$f_i = 0.025 (R_e F_d^5)^{-1/2} \quad (41)$$

The trend agrees with what the new formula, Eq. (39), predicts, though the magnitude of coefficient is different from other groups of data.

Generally speaking scattering around the solid line

$$f_i = 0.085 (R_e F_d^5)^{-1/2} \quad (42)$$

in Fig. 2 is smaller than that shown in f_i versus ψ diagram by previously proposed formulae. The data reported by Lofquist (1960) illustrated by sol-

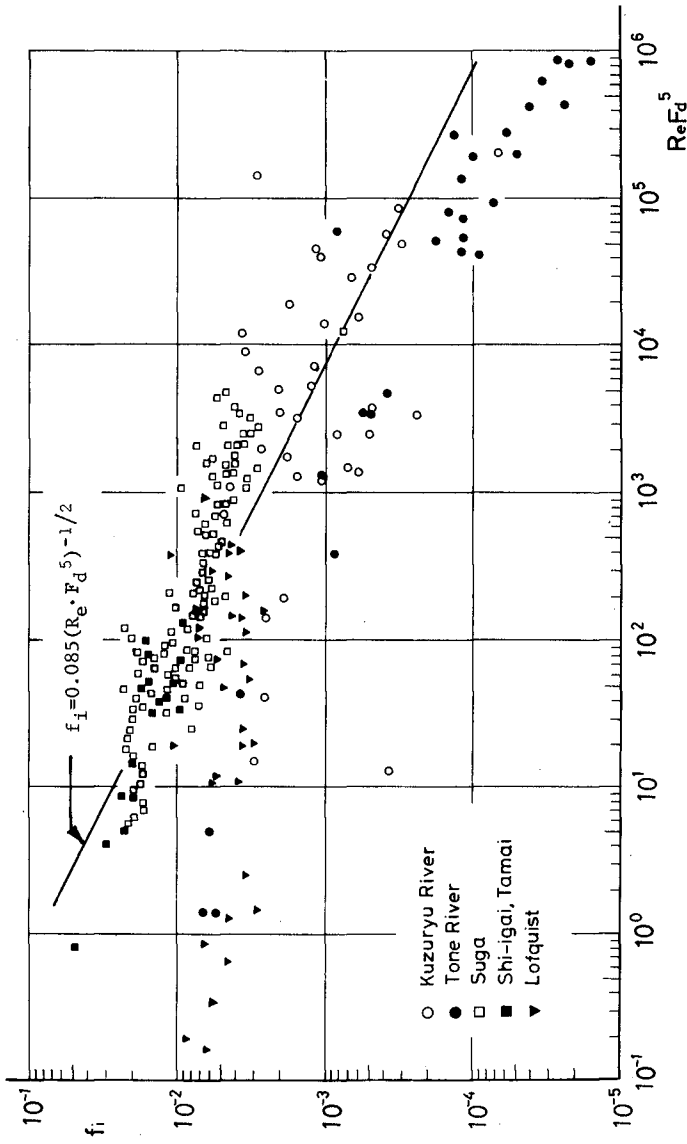


Fig. 2. Interfacial friction coefficient vs. $Re F_d^5$

id reversed triangles in Fig. 2 behave differently from others. Previously only four cases in forty six of Lofquist's experimental results were reported by Valembos(1963). Present analysis revealed that the different relationship held for a set of all forty six data. The magnitude of the interfacial friction coefficient remains almost unchanged regardless of the value of the abscissa. This is partly because Lofquist performed his experiments with a moving denser fluid while a lighter upper layer remained stationary and therefore the results might be affected more strongly by bottom shear. Although the trend is not so clear as Lofquist's data, the data obtained in the Kuzuryu River expressed by open circles in Fig. 2 shows nearly the same feature.

The measured data follow the trend explained by Eq. (42) on the whole. As mentioned above, however, there is a more appropriate formula like Eq. (41) for a special group of data. The variety of the magnitude of coefficients of the derived formulae is discussed from the standpoint of the stability of a two-layered flow system. Equation (43) is an interpretation of the reciprocal of the Keulegan number by Turner(1973).

$$\theta = \left(\frac{\rho U_1^2}{\Delta \rho g \delta} \right) \left(\frac{U_1 x}{v} \right)^{1/2} \quad (43)$$

Here δ denotes the thickness of the boundary layer and x is the length of contact of two layers along the interface. In field observation like the case of the Tone River the length of the contact of interface measured from the saline wedge toe may be much larger than that encountered in experimental flumes. Thus the Keulegan number observed in natural streams is expected much smaller than the critical value if it exists at all. Therefore, the stability of field data may be higher than that obtained in experiments.

The amplitude of the lowest internal mode obtained by Phillips(1969) is expressed for $n \ll N_m$ by

$$a^2 k^2 = \left(\frac{N_m}{n} \right)^{-2} J^{-1}$$

where n is the frequency of an internal wave mode, N_m the maximum Brunt-Väisälä frequency ($N \equiv \{-(g/\rho)(\partial \rho / \partial y)\}^{1/2}$), J the local Richardson number. Substitution of this expression into the derived relationship, Eq. (34), yields

$$f_1 = 0.707 (R_e F_d^5)^{-1/2} (kh_1)^{-3/2} (n/N_m)^2 J^{-1} \quad (44)$$

This suggests that the higher the stability of a two-layered flow system is, the lesser the magnitude of the interfacial friction coefficient will be, which explains the feature of the observed data qualitatively.

One more comment on the field data is added. Values of the interfacial friction coefficient were calculated by Eq. (40) which was applicable only to steady motions. Since tidal motion affects the behavior of saline wedges continuously, we would have measured various hydraulic quantities under unsteady conditions in reality. This discrepancy from the assumed condition may explain the scattering of field data.

CONCLUSIONS

An advanced theory on the interfacial friction of sharply stratified two-layered flows is developed. Because the magnitude of laminar friction is much smaller than that of the friction due to interfacial wave formation in case of the large Reynolds number, the theory is formulated under the existence of interfacial waves. The solution to a governing equation is obtained to the first order in terms of wave amplitude by perturbation method. No-slip condition is imposed for the first order solution and external flow velocity is assumed uniform and constant. In this theory it is considered that the energy dissipation is caused by the viscous perturbation velocity field which is induced by the presence of interfacial waves.

Based on the theoretical result a new type of formula for the interfacial friction coefficient is proposed discarding the detailed properties of interfacial waves which have not been reported in available form. It is said that the agreement between the proposed relationship, that is, f_i is proportional to $(ReF_d^3)^{-1/2}$, and the observed data is better than that demonstrated by the best empirical formula, $f_i \propto (ReF_d^2)^{-1/2}$. Scattering of data may be attributed to the stability of two-layered flows. It is pointed out that the proportional constant in the new formula decreases its magnitude as the stability increases.

This study has explained the hydrodynamic feature of the interfacial friction coefficient under the existence of interfacial waves with no mixing between two layers. In order to determine the more detailed feature of the derived expression, it is still needed to obtain reliable data from which we can specify the interfacial wave characteristics and to develop a more refined theory which can take account of the effect of viscosity even in the zeroth order principal velocity or of the acceleration of the external flow.

ACKNOWLEDGMENTS

The author wishes to express his gratitude to Professor Tosio Iwasaki at Tohoku University for his promotion and valuable suggestions to this study. Cordial assistance offered by Mr. Hiroshi Nakamura of Central Research Institute of Electric Power Industry and by Mr. Kyoza Suga of Public Works Research Institute is also appreciated. Rearrangement of field data would not have been performed without their cooperation of providing the details of their observation data.

REFERENCES

- Hamada, T. (1966) "On density currents(1)", Proc. 13th Japanese Conf. on Coastal Eng., JSCE, 259-262 (in Japanese).
- Keulegan, G.H. (1949) "Interfacial instability and mixing in stratified flows", J. of Research, Nat. Bureau of Stands., Vol.43, 487-500.
- Lofquist, K. (1960) "Flow and stress near an interface between stratified liquids", The Physics of Fluids, Vol.3, 158-175.
- Nakamura, H. and N. Abe (1970) "Salt-water wedge in the Kuzuryu River estuary", Rept. of 2nd Tech. Lab., Central Res. Inst. of Electric Power Industry, No.70519 (in Japanese).
- Pedersen, F.B. (1972) "Gradually varying two-layer stratified flow", J. Hy. Div., Proc. ASCE, Vol.98, HY-1, 257-268.

- Phillips, O.M.(1969) "The Dynamics of the Upper Ocean", Cambridge Univ. Press, 168.
- Shi-igai, H.(1965) "On the resistance coefficient at the interface between salt and fresh water", Trans. JSCE, No.123, 27-31.
- Suga, K. and A. Takahashi(1971) "A study on the salt-water wedge by a large flume", Proc. 26th Annual Meeting, JSCE, Sec. II, 137-140 (in Japanese).
- Tamai, N.(1964) "An experimental study on saline wedges", Graduation Thesis, Dept. of Civil Eng., Univ. of Tokyo, 95pp. (in Japanese).
- Turner, J.S.(1973) "Buoyancy Effects in Fluids", Cambridge Univ. Press, 108.
- Valembois, J.(1963) "Courants de densité: tension tangentielle à l'interface, Essai d'interprétation des résultats de Lofquist", Bulletin du Centre de Recherches et d'Essais de Chatou, No.5, 37-40.
- Yih, C.-S.(1965) "Dynamics of Nonhomogeneous Fluids", Macmillan, 152-154.

Table 1 - Interfacial Friction Coefficient

$$\epsilon = \Delta\rho/\rho_1$$

Experiment, Reporter: Tamai						c.g.s. unit	
Run	h_1	U_1	$v \cdot 10^2$	$\epsilon \cdot 10^2$	$Re \cdot 10^{-3}$	F_d	$f_1 \cdot 10^2$
1	7.1	4.47	1.240	1.05	2.56	0.523	1.67
2	7.2	4.26	1.275	1.00	2.42	0.508	1.60
3	7.1	4.21	1.275	1.00	2.35	0.505	1.45
4	7.2	3.99	1.275	1.00	2.26	0.474	1.58
5	7.1	3.90	1.275	1.00	2.18	0.468	1.58
6	7.1	3.76	1.275	1.00	2.10	0.451	1.34
7	6.6	3.89	1.240	1.05	2.07	0.472	1.74
8	5.6	4.64	1.312	1.15	1.99	0.584	0.93
9	5.7	4.23	1.312	1.15	1.84	0.528	0.96
10	5.7	3.98	1.312	1.15	1.73	0.498	1.07
11	5.7	3.84	1.312	1.15	1.67	0.480	1.20
12	5.7	3.51	1.312	1.05	1.61	0.459	1.50
13	5.5	3.69	1.312	1.15	1.55	0.470	0.98
14	6.7	2.87	1.275	1.00	1.51	0.354	2.00
15	6.8	2.65	1.275	1.00	1.42	0.324	2.32
16	5.5	2.91	1.210	0.95	1.32	0.407	2.08
17	5.2	2.65	1.240	0.95	1.11	0.381	2.46
18	5.1	2.33	1.275	0.95	0.934	0.338	3.18
19	4.7	1.70	1.275	0.90	0.630	0.264	4.82

Experiment, Reporter: Lofquist						c.g.s. unit	
Run	h_1	U_1	$v \cdot 10^2$	$\epsilon \cdot 10^2$	$Re \cdot 10^{-3}$	F_d	$f_1 \cdot 10^3$
3	7.13	3.54	0.952	1.18	2.65	0.375	10.7
4	7.02	4.83	0.956	1.11	3.55	0.538	7.44
6	7.27	5.41	0.928	1.07	4.24	0.618	11.3
7	6.47	1.55	0.928	1.19	1.08	0.180	8.95
8	7.10	2.38	0.904	1.19	1.87	0.204	4.58
9	7.19	3.42	0.900	1.20	2.73	0.371	4.67
10	7.21	4.59	0.902	1.17	3.67	0.504	7.20
11	7.47	4.96	0.889	1.13	4.17	0.545	7.12
12	6.92	2.52	0.842	2.08	2.07	0.211	6.77
13	6.84	3.86	0.835	2.09	3.16	0.326	3.90
14	6.93	4.98	0.828	2.08	4.17	0.408	4.99
15	7.22	5.70	0.849	2.10	4.85	0.466	7.31
16	7.25	6.72	0.844	2.04	5.77	0.555	5.47
17	6.92	2.49	0.870	3.00	1.98	0.173	5.77
18	7.13	4.64	0.855	3.02	3.87	0.316	5.58
19	6.96	6.20	0.872	2.89	4.95	0.438	4.29
20	7.11	6.94	0.864	2.92	5.71	0.483	4.58
21	7.27	7.71	0.860	2.88	6.52	0.535	6.01
22	7.37	8.27	0.856	2.86	7.12	0.570	6.75
23	6.90	2.51	0.875	3.92	1.98	0.153	6.35
24	6.90	5.04	0.857	3.97	4.06	0.305	5.92
25	7.10	7.05	0.849	4.01	5.90	0.418	5.55

Table 1 (continued)

Run	h_1	U_1	$\nu \cdot 10^2$	$\epsilon \cdot 10^2$	$R_e \cdot 10^{-3}$	F_d	$f_i \cdot 10^3$
26	7.15	8.08	0.869	4.18	6.65	0.468	4.38
27	7.25	8.75	0.863	3.94	7.35	0.517	4.61
28	7.17	9.03	0.853	3.75	7.59	0.551	4.67
29	7.51	4.01	0.896	4.80	3.36	0.210	4.47
30	7.01	7.20	0.881	4.73	5.73	0.394	3.32
31	6.97	8.50	0.867	4.65	6.83	0.471	2.68
32	7.19	9.05	0.880	4.72	7.39	0.490	3.66
33	7.14	10.01	0.873	4.60	8.19	0.552	3.56
34	7.32	10.20	0.872	4.68	8.56	0.550	4.57
35	7.06	4.74	0.920	5.74	3.64	0.232	3.34
36	7.09	6.95	0.924	5.61	5.33	0.346	3.69
37	7.04	8.31	0.905	5.67	6.46	0.404	3.63
38	7.12	9.13	0.922	5.67	7.05	0.453	2.90
39	7.23	9.75	0.914	5.64	7.71	0.481	3.36
40	7.32	10.45	0.900	5.32	8.50	0.528	4.05
41	7.12	4.62	0.945	7.55	3.48	0.211	2.80
42	6.88	7.50	0.937	7.55	5.51	0.326	3.11
43	6.88	9.88	0.925	7.40	7.35	0.434	3.48
44	7.21	10.60	0.927	7.68	8.25	0.446	3.66
45	7.27	12.47	0.911	7.60	9.95	0.525	3.92
46	7.37	13.71	0.887	6.86	11.39	0.605	6.69

Kuzuryu River, Reporter: Nakamura

c.g.s. unit

Run	h_1	U_1	$\nu \cdot 10^2$	$\epsilon \cdot 10^2$	$R_e \cdot 10^{-5}$	F_d	$f_i \cdot 10^4$
1	120	32.5	0.869	2.06	4.49	0.660	3.94
2	130	20.7	0.861	2.06	3.13	0.404	2.46
3	135	17.5	0.842	2.06	2.81	0.335	45.0
4	175	26.2	0.841	2.06	5.45	0.441	35.0
5	177	19.0	0.841	1.96	4.00	0.326	6.16
6	180	19.1	0.842	2.06	4.08	0.317	15.5
7	272	33.4	0.964	1.96	9.42	0.462	27.2
8	185	34.0	0.928	1.96	6.78	0.570	10.8
9	170	31.8	0.907	2.06	5.96	0.543	6.78
10	182	21.8	0.892	1.57	4.45	0.412	12.8
11	225	25.6	0.907	2.06	6.35	0.380	20.8
12	134	26.3	0.960	1.96	3.67	0.519	10.3
13	148	20.3	0.963	1.96	3.12	0.381	5.10
14	135	19.0	0.950	1.77	2.70	0.393	8.44
15	135	38.8	0.960	1.96	5.46	0.762	29.2
16	185	20.2	0.960	1.96	3.89	0.339	18.6
17	188	31.9	1.063	2.15	5.64	0.507	17.8
18	66	27.5	1.098	2.19	1.65	0.731	4.96
19	124	10.5	1.105	2.18	1.18	0.204	26.8
20	131	8.9	1.105	2.15	1.06	0.170	31.4
21	135	9.0	1.072	2.30	1.13	0.163	3.82
22	130	10.4	1.075	2.23	2.35	0.364	7.04
23	125	23.0	1.075	2.26	2.67	0.437	15.6

Table 1 (continued)

Run	h_1	U_1	$v \cdot 10^2$	$\epsilon \cdot 10^2$	$Re \cdot 10^{-5}$	F_d	$f_1 \cdot 10^4$
24	82	31.5	1.140	2.27	2.27	0.738	3.06
25	90	26.5	1.145	2.26	2.08	0.594	6.00
26	110	18.2	1.147	2.24	1.75	0.371	10.9
27	105	16.2	1.147	2.16	1.48	0.344	49.8
28	120	12.5	1.143	2.01	1.31	0.257	26.2
29	125	24.9	1.140	2.25	2.73	0.474	27.8
30	150	23.8	1.137	2.25	3.14	0.414	4.92
31	156	14.0	1.135	2.05	1.92	0.250	19.7
32	195	40.5	1.188	1.96	6.65	0.662	3.22
33	205	35.5	1.179	1.97	6.17	0.564	11.7
34	253	24.2	1.188	1.97	5.15	0.346	20.4
35	324	37.2	1.510	2.30	7.98	0.435	37.8
36	254	31.2	1.425	2.21	5.56	0.420	12.0

Tone River, Reporter: Suga

c.g.s. unit

Run	h_1	U_1	v	ϵ	$Re \cdot 10^{-5}$	F_d	$f_1 \cdot 10^5$
1	245	17.0	/	/	4.17	0.315	104
2	305	23.0	/	/	7.02	0.347	66
3	335	24.0	/	/	8.04	0.337	60
4	365	22.0	/	/	8.03	0.602	12
5	385	24.5	/	/	9.43	0.346	38.6
6	410	16.0	/	/	6.56	0.227	89.4
7	240	52.0	/	/	12.5	0.922	2.66
8	300	53.0	/	/	15.9	0.798	4.20
9	315	56.0	/	/	17.6	0.862	1.58
10	330	39.0	/	/	12.9	0.594	7.3
11	350	31.0	/	/	10.9	0.524	9.2
12	140	39.0	/	/	5.46	0.955	2.4
13	230	45.0	/	/	10.4	0.901	3.4
14	260	34.5	/	/	8.97	0.792	6.0
15	290	37.0	/	/	10.7	0.712	10.0
16	320	40.0	/	/	12.8	0.639	12.0
17	350	34.5	/	/	12.1	0.530	18.0
18	50	58.0	/	/	2.9	0.924	5.0
19	240	49.0	/	/	11.8	0.928	2.2
20	290	49.0	/	/	14.2	0.656	13.2
21	330	43.0	/	/	14.2	0.563	14.8
22	355	38.0	/	/	13.5	0.560	11.7
23	380	41.5	/	/	15.8	0.508	11.7
24	160	11.0	/	/	1.76	0.509	84
25	310	11.0	/	/	3.41	0.167	386
26	350	5.0	/	/	1.75	0.124	620
27	410	6.0	/	/	2.46	0.090	688
28	450	6.0	/	/	2.70	0.088	566

Table 1 (continued)

Experiment, Reporter: Suga						c.g.s. unit	
Run	h_1	U_1	v	$\epsilon \cdot 10^2$	$Re \cdot 10^{-3}$	F_d	$f_1 \cdot 10^3$
1	12.75	5.23	/	0.60	6.67	0.605	7.40
2	13.30	5.01	/	0.60	6.67	0.568	6.92
3	13.75	4.85	/	0.60	6.67	0.541	5.94
4	14.10	4.73	/	0.60	6.67	0.521	4.68
5	14.40	4.63	/	0.60	6.67	0.505	4.82
6	14.75	4.52	/	0.60	6.67	0.487	6.62
7	15.15	4.40	/	0.60	6.67	0.468	7.60
8	15.70	4.25	/	0.60	6.67	0.443	11.2
9	16.40	4.07	/	0.60	6.67	0.415	12.5
10	17.25	3.87	/	0.60	6.67	0.385	14.3
11	14.59	9.14	/	0.60	13.3	0.989	0.760
12	16.54	8.06	/	0.60	13.3	0.820	4.88
13	17.49	7.62	/	0.60	13.3	0.754	3.80
14	18.54	7.19	/	0.60	13.3	0.691	7.48
15	21.35	6.25	/	0.60	13.3	0.559	7.50
16	21.85	6.10	/	0.60	13.3	0.540	6.58
17	22.35	5.97	/	0.60	13.3	0.522	6.48
18	22.80	5.85	/	0.60	13.3	0.507	5.90
19	23.20	5.75	/	0.60	13.3	0.494	5.98
20	23.65	5.64	/	0.60	13.3	0.480	6.72
21	24.15	5.52	/	0.60	13.3	0.465	7.08
22	24.65	5.41	/	0.60	13.3	0.451	7.36
23	25.20	5.29	/	0.60	13.3	0.436	7.84
24	25.80	5.17	/	0.60	13.3	0.421	7.82
25	26.40	5.05	/	0.60	13.3	0.406	7.90
26	27.10	4.92	/	0.60	13.3	0.391	8.56
27	28.00	4.76	/	0.60	13.3	0.373	10.9
28	23.20	8.62	/	0.60	20.0	0.740	6.36
29	23.75	8.42	/	0.60	20.0	0.715	4.16
30	24.20	8.26	/	0.60	20.0	0.694	3.28
31	24.60	8.13	/	0.60	20.0	0.678	2.88
32	25.00	8.00	/	0.60	20.0	0.662	3.18
33	25.55	7.83	/	0.60	20.0	0.640	3.56
34	26.20	7.63	/	0.60	20.0	0.617	4.20
35	27.20	7.35	/	0.60	20.0	0.583	4.66
36	11.34	5.88	/	1.0	6.67	0.560	6.6
37	12.09	5.51	/	1.0	6.67	0.509	6.8
38	12.74	5.23	/	1.0	6.67	0.470	6.4
39	13.34	5.00	/	1.0	6.67	0.439	6.2
40	13.79	4.83	/	1.0	6.67	0.418	4.6
41	14.24	4.68	/	1.0	6.67	0.399	6.0
42	14.79	4.51	/	1.0	6.67	0.377	7.0
43	15.39	4.33	/	1.0	6.67	0.355	7.2
44	16.14	4.13	/	1.0	6.67	0.330	7.8
45	14.37	9.28	/	1.0	13.3	0.785	4.12
46	14.97	8.91	/	1.0	13.3	0.739	4.92
47	15.57	8.56	/	1.0	13.3	0.696	4.60
48	16.07	8.30	/	1.0	13.3	0.664	5.82
49	16.67	8.00	/	1.0	13.3	0.629	5.90

Table 1 (continued)

Run	h_1	U_1	ν	$\varepsilon \cdot 10^2$	$Re \cdot 10^{-3}$	F_d	$f_1 \cdot 10^3$
50	17.27	7.72	/	1.0	13.3	0.597	9.47
51	13.10	7.63	/	1.0	10.0	0.694	6.44
52	13.80	7.25	/	1.0	10.0	0.626	6.40
53	14.45	6.92	/	1.0	10.0	0.585	6.02
54	14.95	6.69	/	1.0	10.0	0.555	5.84
55	15.40	6.49	/	1.0	10.0	0.531	5.44
56	15.90	6.29	/	1.0	10.0	0.505	6.18
57	16.40	6.10	/	1.0	10.0	0.484	6.16
58	16.95	5.90	/	1.0	10.0	0.460	7.18
59	17.55	5.70	/	1.0	10.0	0.437	6.66
60	19.54	8.53	/	1.0	16.7	0.620	2.94
61	20.19	8.26	/	1.0	16.7	0.590	4.16
62	20.94	7.96	/	1.0	16.7	0.559	5.14
63	21.74	7.68	/	1.0	16.7	0.528	5.46
64	22.54	7.39	/	1.0	16.7	0.500	5.68
65	23.34	7.14	/	1.0	16.7	0.474	6.14
66	24.24	6.88	/	1.0	16.7	0.448	6.78
67	25.24	6.60	/	1.0	16.7	0.422	7.06
68	26.34	6.33	/	1.0	16.7	0.396	6.98
69	22.00	9.09	/	1.0	20.0	0.622	4.10
70	22.50	8.89	/	1.0	20.0	0.602	4.70
71	23.10	8.66	/	1.0	20.0	0.578	5.32
72	23.70	8.44	/	1.0	20.0	0.557	5.40
73	24.30	8.23	/	1.0	20.0	0.536	5.42
74	24.95	8.02	/	1.0	20.0	0.515	5.76
75	25.65	7.80	/	1.0	20.0	0.494	5.92
76	26.35	7.59	/	1.0	20.0	0.474	5.14
77	27.20	7.35	/	1.0	20.0	0.453	5.56
78	11.59	11.50	/	3.0	13.3	0.632	4.44
79	12.24	10.89	/	3.0	13.3	0.583	4.20
80	12.84	10.38	/	3.0	13.3	0.542	4.74
81	13.44	9.92	/	3.0	13.3	0.507	5.16
82	14.09	9.46	/	3.0	13.3	0.466	6.66
83	14.74	9.05	/	3.0	13.3	0.437	6.74
84	15.49	8.61	/	3.0	13.3	0.405	6.96
85	16.19	8.24	/	3.0	13.3	0.379	6.42
86	16.94	7.87	/	3.0	13.3	0.358	6.26
87	14.20	14.09	/	3.0	20.0	0.699	3.23
88	14.70	13.61	/	3.0	20.0	0.664	3.60
89	15.20	13.16	/	3.0	20.0	0.632	3.92
90	15.70	12.74	/	3.0	20.0	0.602	4.16
91	16.15	12.38	/	3.0	20.0	0.577	3.44
92	16.55	12.09	/	3.0	20.0	0.556	3.48
93	17.00	11.71	/	3.0	20.0	0.534	4.76
94	17.60	11.36	/	3.0	20.0	0.507	5.40
95	13.05	5.10	/	1.0	6.67	0.449	23.0
96	13.45	4.95	/	1.0	6.67	0.434	20.8
97	13.80	4.83	/	1.0	6.67	0.417	18.7
98	14.10	4.76	/	1.0	6.67	0.407	17.3
99	14.10	4.63	/	1.0	6.67	0.391	18.1
100	14.70	4.54	/	1.0	6.67	0.379	16.8

Table 1 (continued)

Run	h_1	U_1	ν	$\epsilon \cdot 10^2$	$R_e \cdot 10^{-3}$	F_d	$f_1 \cdot 10^3$
101	14.95	4.45	/	1.0	6.67	0.370	15.4
102	15.20	4.39	/	1.0	6.67	0.361	15.5
103	15.45	4.31	/	1.0	6.67	0.352	17.1
104	15.75	4.23	/	1.0	6.67	0.342	20.0
105	16.10	4.14	/	1.0	6.67	0.332	21.2
106	16.45	4.05	/	1.0	6.67	0.321	21.6
107	16.85	3.95	/	1.0	6.67	0.310	23.8
108	20.70	6.44	/	1.0	13.3	0.455	8.12
109	21.00	6.35	/	1.0	13.3	0.445	5.94
110	21.20	6.29	/	1.0	13.3	0.438	4.82
111	21.40	6.23	/	1.0	13.3	0.432	4.86
112	21.60	6.17	/	1.0	13.3	0.427	5.52
113	21.85	6.10	/	1.0	13.3	0.420	6.18
114	22.10	6.03	/	1.0	13.3	0.412	6.86
115	22.40	5.95	/	1.0	13.3	0.404	7.58
116	22.70	5.87	/	1.0	13.3	0.396	7.60
117	23.00	5.80	/	1.0	13.3	0.389	7.60
118	23.30	5.72	/	1.0	13.3	0.381	7.62
119	23.60	5.65	/	1.0	13.3	0.373	8.26
120	23.95	5.57	/	1.0	13.3	0.365	8.84
121	24.30	5.49	/	1.0	13.3	0.358	9.30
122	24.70	5.40	/	1.0	13.3	0.349	10.3
123	25.15	5.30	/	1.0	13.3	0.339	11.8
124	13.60	6.62	/	1.0	3.38	0.576	11.5
125	14.00	6.43	/	1.0	3.38	0.551	10.2
126	14.35	6.27	/	1.0	3.38	0.532	9.18
127	14.65	6.14	/	1.0	3.38	0.515	8.06
128	14.90	6.04	/	1.0	3.38	0.502	7.46
129	15.15	5.94	/	1.0	3.38	0.490	7.56
130	15.40	5.84	/	1.0	3.38	0.479	7.62
131	15.65	5.75	/	1.0	3.38	0.467	7.66
132	15.90	5.66	/	1.0	3.38	0.456	8.42
133	16.20	5.56	/	1.0	3.38	0.443	10.7
134	16.60	5.42	/	1.0	3.38	0.428	11.9
135	17.00	5.29	/	1.0	3.38	0.412	11.4
136	17.40	5.17	/	1.0	3.38	0.397	12.0
137	17.57	3.79	/	0.6	6.67	0.374	23.4
138	17.97	3.71	/	0.6	6.67	0.362	19.2
139	18.37	3.63	/	0.6	6.67	0.351	20.1
140	18.77	3.55	/	0.6	6.67	0.339	20.8
141	19.17	3.48	/	0.6	6.67	0.329	21.4
142	19.57	3.41	/	0.6	6.67	0.318	22.1
143	19.97	3.34	/	0.6	6.67	0.308	22.6
144	20.37	3.27	/	0.6	6.67	0.300	20.0
145	20.67	3.23	/	0.6	6.67	0.293	17.3
146	20.97	3.18	/	0.6	6.67	0.286	17.5
147	21.27	3.13	/	0.6	6.67	0.281	17.8
148	21.57	3.09	/	0.6	6.67	0.276	17.8
149	21.87	3.05	/	0.6	6.67	0.270	19.4
150	22.17	3.02	/	0.6	6.67	0.265	19.4
151	22.47	2.99	/	0.6	6.67	0.261	17.2

CHAPTER 183

TIDAL RESPONSE OF TWO-LAYER FLOW AT A RIVER MOUTH

by

Shizuo Yoshida*

and

Masakazu Kashiwamura**

ABSTRACT

This paper describes various features of tidal effects on the behavior of a salt wedge and on the mechanism of mixing between the salt water and the fresh water in the vicinity of a river mouth. The studies have been performed through experiments, field observations and theoretical considerations. The condition upon which the fresh water begins to show an intermittent flow-pattern owing to an increase of the tidal action, and the criterion of a transition of the mixing type from negligible into intense, were obtained, with two dimensionless parameters λ and θ . The former parameter λ is given by $\lambda = A_0/U_0 T_0$, in which T_0 is the tidal period, A_0 is the tidal amplitude of the sea level, and U_0 is the temporal mean velocity of the fresh water at the river mouth. The latter parameter θ is the so-called Keulegan number. Besides, it came evident that a tidal motion of the salt wedge couldn't be understood without a consideration of the internal wave inside the mouth, which were induced by the tide, in addition to a direct effect of the tide.

1. Introduction

Since early times, in Japan, river mouths have been utilized in many ways, for example, as fishery ports, navigation harbors, suppliers of water for irrigation and industries, etc. The river mouth, in this meaning, is considered to be an important base for all industries. Recently, with a growth of utilization of the river mouths, a serious problem has attracted public attention. It is water pollution. Saline pollution owing to the salt wedge has widely been known from old times, as a main difficulty to agriculture, chemical industries and to citizens' lives. Nowadays, in addition, sewage poured from citizens' lives, and waste from industries have come a new matter of the utmost concern, since they give a damage to coastal fisheries, and its results rebound to human life again, as a danger against human health.

* Research Assistant, Department of Engineering Science, Hokkaido University, Sapporo, Japan.

** Professor of Engineering Science, Hokkaido University, Sapporo, Japan.

To solve those problems, studies on the two-layer flow at a river mouth have an important role. Prediction of a length or a form of the salt wedge, control technique of its length¹⁾, an estimate of the area of river water expanding over the sea, outflow patterns varying with a degree of river discharge^{2),3),4),5)} etc. are those of already revealed to a certain degree, which have greatly served to increase a correct comprehension on mechanics of the problems. Most of them, however, have been investigated under a tideless condition, and many studies concerning the tidal effect are, at present, left unsolved yet. Needless to say, there have been many studies related to a tidal estuary, but most of them are directed to established types of mixing, namely, intense mixing or moderate mixing, where tidal variations of flow, level and saline concentration, from time to time, are usually ignored, and instead, temporal mean values are important.

The present authors intend, hereby, to describe a fine mechanism of the two-layer flow which varies in response to the tide. They deal, first, with an equipment for experiments and a method of measurements, which were adopted in the study, in Section 2, next, with a relationship between outflow patterns of the fresh water and the tide in Section 3, third, with a periodical motion of the salt wedge due to the tide in Section 4, and finally, with a problem of tidal mixing between the fresh water and the salt water, and also with a contribution of the tide to a transition from the negligible mixing type into the intense mixing type in Section 5.

2. Experimental Equipment

In order to observe the whole behavior of the two-layer flow which extends widely from the upstream of a river to the open sea, an equipment was designed as shown in Fig. 1, so as to consist of a large water vessel and a long straight channel which connects to the vessel at right angles. The vessel and the channel correspond to the sea and a river, respectively. Since they are made of transparent acrylic acid resin, for the purpose of marking dye in water being observable from outside. A tide generator is specially devised so that the water level may follow any curve of hydrographs. Its block diagram is shown in Fig. 2. Salt water in the vessel is separated by a wide vinyl sheet on the bottom, from water which is pumped in and out from below to change the water level. Thus, the salt water is moved bodily up and down, and is kept undisturbed.

As a movie camera is insufficient to observe the whole behavior of the salt wedge, another optical method is additionally adopted. The diagram of the optical system is shown in Fig. 1. Light pulses emitted from a xenon lamp intermittently at constant intervals, are made parallel by a concave mirror, and reflected perpendicularly at many plane mirrors which are lined up along the channel. Many light beams thus divided penetrate the channel transversely, pass through narrow slits of 0.3 mm in width, which are attached on the other side of the channel, and arrive at a long sheet of photosensitive paper, which moves along the channel by 0.3 mm, synchronously with every arrival of pulses. Since light is reflected or refracted at the water surface and the interface, both levels are exposed on the sheet, from time to time. Thus, a tidal change of the surface and the interface can be obtained at 10 cm intervals along the channel. The behavior of the two-layer flow outside the mouth are caught with a 8 mm movie camera, by the aid of fluorescein sodium liquid as a tracer.

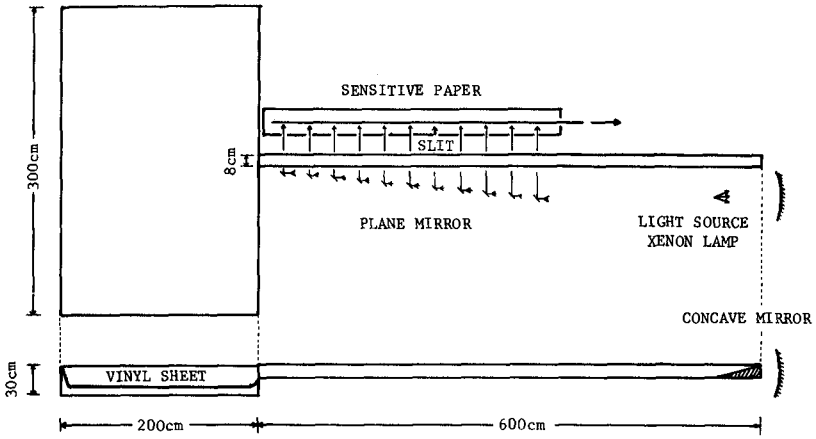


Figure 1.

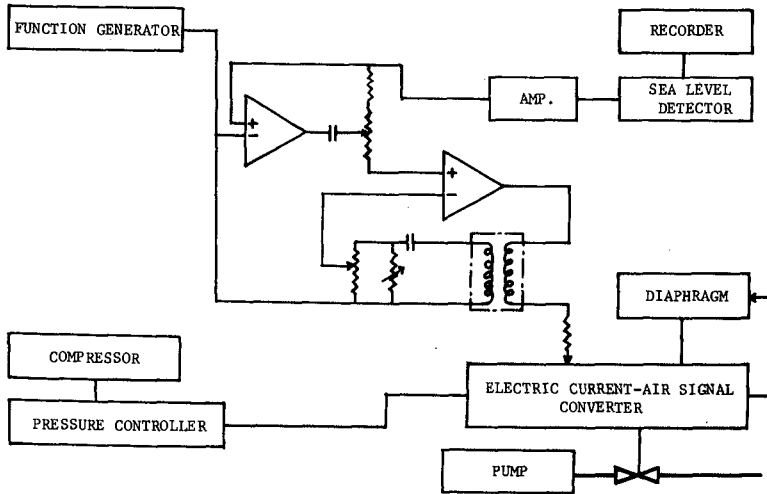


Figure 2

3. Tidal Change of Flow Pattern

An appearance of outflow pattern varies depending on only the amount of a river discharge, if it is assumed tideless. When the discharge grows, the outflow pattern approaches an extreme type called the E pattern, which resembles a turbulent jet of homogeneous fluid. On the other hand, if the discharge falls off, it reaches the other extreme type called the A pattern, whose stream lines extend slowly in all directions over the sea without turbulence. According to experiments, three transitional types lie between those extreme two, and they are called the B, C and D patterns. All patterns are shown in Fig. 3 (1), and they can be classified with two parameters, which are the Keulegan number θ and the Reynolds number R respectively, where $\theta = (\nu \epsilon g)^{1/3} / U_0$ and $R = U_0 b / \nu$. The symbol b is a cross-sectional mean velocity of the fresh water at the mouth, ν is a kinematic viscosity, and $\epsilon = (\rho_2 - \rho_1) / \rho_2$, where ρ_1 and ρ_2 are densities of the fresh water and the salt water respectively. The classification is shown in Fig. 3 (2).

When the tide exists, every pattern varies from time to time. At a flood tide, it has a trend to approach the A pattern, and at the ebb tide, it changes toward the E pattern. A degree of the tidal range dominates a change of the pattern. According to experiments, if an amplitude of the tide level is small, or a tidal period is long enough, the change is small, and the fresh water always flows out from the mouth over the whole tidal period. However, when the amplitude grows up excessively, or the tidal period decreases below a certain value, the fresh water sometimes stops or flows upstream at the flood. If it develops extremely, the fresh water, which has flown out at the ebb, cannot return into the river even at the flood, and it produces a special pattern, an "intermittent flow", every tidal cycle. In such a case, mixing of the fresh water and the salt water develops, and an adoption of the two-layer theory becomes impossible.

Two examples are shown in Figs. 4 and 5, which are those transferred from movie films. The former one is photographed on condition that the discharge is $6.70 \text{ cm}^3/\text{s}$, the tide amplitude is 1.70 cm , the tide period is 1380 sec and $\epsilon = 0.018$. If tideless, the upper values are those of the B, or C pattern, whose condition is $\theta R^{0.137} = 0.673$. However, the tide lets the fresh water change its flow pattern from time to time. Under the above condition, the upstream flow doesn't occur even at the flood. According to tidal hours, the flow pattern varies in such a manner that it shows the pattern C at the high and low waters, B at the flood, and E at the ebb. Fig. 5 is another example under condition that the discharge is $2.89 \text{ cm}^3/\text{s}$, the amplitude is 2.29 cm , the tidal period is 360 sec and $\epsilon = 0.020$. If tideless, the flow pattern belongs to B somewhat close to A with a relationship, $\theta R^{0.137} = 0.849$. Compared with the former case, in this case, the discharge and the period are so small that the tidal effect is strong. At every hour of the tide, the pattern shows A or B at the high and low waters, D at the ebb and an upstream flowing pattern at the flood, when the surface at the mouth is occupied by the salt water, namely, this type is an intermittent flow.

Other experimental results are all situated between those two cases, where sometimes the fresh water stops at the ebb, or sometimes the fresh water flows upstream in a type different from the intermittent flow.

Next, a criterion, upon which above various types occur, will be

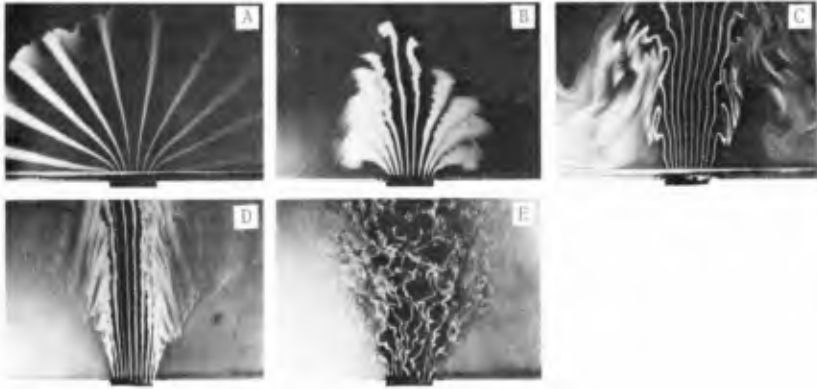


Figure 3(1).

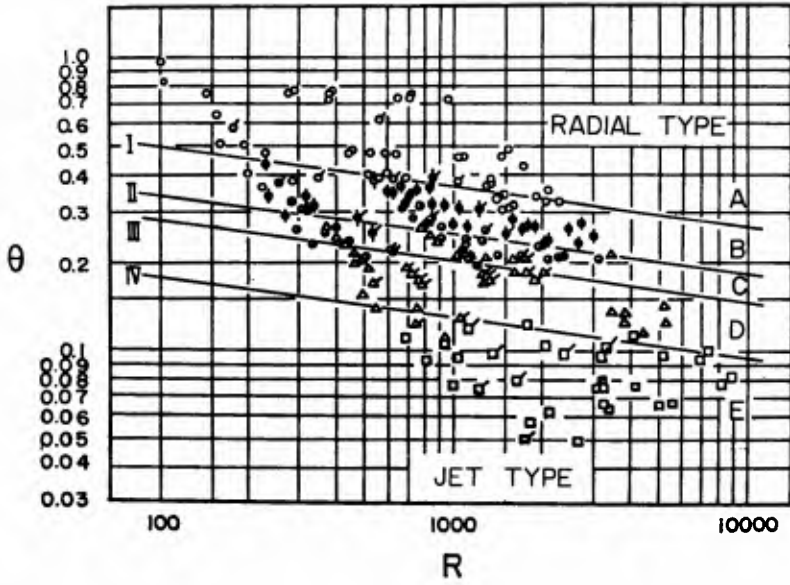
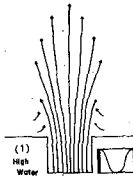


Figure 3(2).

Q	flow rate of the fresh water	6.7 ml/sec
A _w	amplitude	1.70 cm
T	period	1380 sec
C	$\frac{\rho_s - \rho_f}{\rho_s}$ = $\frac{\rho_s - \rho_f}{\rho_s} \cdot \frac{g \cdot b^3}{12 \cdot \nu^2}$	0.018
θ	Karleson number	0.245
R	Reynolds number, $\frac{U \cdot b}{\nu}$	1377



Q	flow rate of the fresh water	2.9 ml/sec
A _w	amplitude	2.20 cm
T	period	560 sec
E	$(\rho_s - \rho_f) / \rho_s$	0.020
θ	Karleson number	0.321
R	Reynolds number	1213

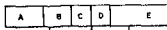
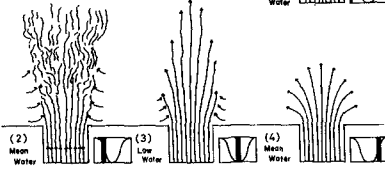
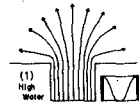


Figure 4.

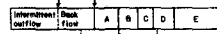
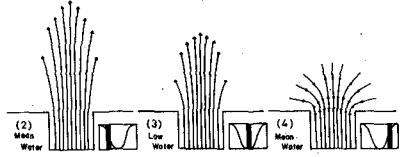


Figure 5.

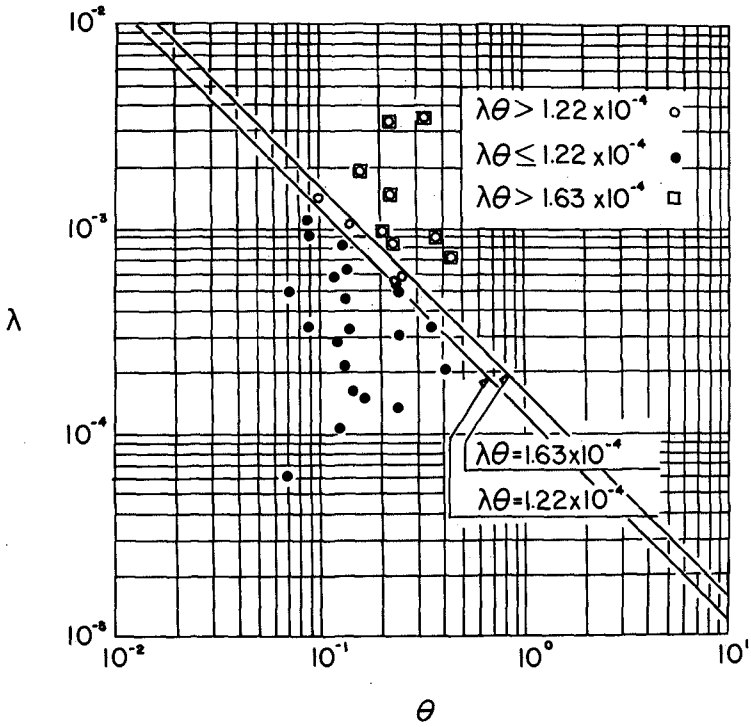


Figure 6.

discussed. Since a condition on which the fresh water flows upstream seems to arise, when the tidal current exceeds a temporal mean velocity of the fresh water, the ratio of both velocities will be a dimensionless parameter which dominates this problem. An intensity of the tidal current can be regarded as a function of A_0/T_0 , where A_0 is the amplitude of the tidal level and T_0 is the period. Therefore, the ratio λ , which is represented by $\lambda = A_0/U_0T_0$, should be a parameter required. In addition, the velocity U_0 of the fresh water is so deeply related to the two-layer flow system itself, that this problem seems to have a relation also to the Keulegan number θ .

Thus, by using those two parameters λ and θ , various patterns are classified as follows.

- $\lambda\theta < 1.22 \times 10^{-4}$: The fresh water always flows out, over the whole tidal period.
- $\lambda\theta = 1.22 \times 10^{-4}$: The fresh water stops at the flood.
- $1.22 \times 10^{-4} < \lambda\theta < 1.63 \times 10^{-4}$: The fresh water flows backward into the river, at the flood, but it is no intermittent flow.
- $\lambda\theta = 1.63 \times 10^{-4}$: The salt water covers the surface temporarily in the vicinity of the mouth, at the flood.
- $\lambda\theta > 1.63 \times 10^{-4}$: The intermittent flow occurs.

Those conditions are shown in Fig. 6. The value of U_0 is evaluated from the equation $U_0 = (egQ/b)^{1/3}$, which is derived from two equations, $Q = bh_1U_0$ and $U_0^2/egh = 1$, where Q and h_1 are temporal mean values of the discharge and a depth of the fresh water at the mouth, respectively. There arises a question whether the conditions thus obtained from experiments are valid for natural rivers or not. This will be discussed again in Section 5, with some theoretical consideration.

4. Tidal Change of Two-Layer Flow and Its Propagation

Problems of a stationary two-layer flow inside the river mouth are more or less related to those of the salt wedge. A prediction of a form of the salt wedge plays an important part for solving problems of this kind, and it is possible from the theory after Schijf-Schönfeld, by using a coefficient of interfacial resistance. Physical properties of the interfacial resistance have not fully been revealed yet, but studies on those are growing through experiments and field observations, along a definite line to relate the resistance with a certain parameter ψ , which is composed of the Reynolds number R and the interfacial Froude number F_1 , as $\psi = RF_1^2$.

Studies on the dynamical behavior of the two-layer flow which is under the tidal effect have been also developed in some degree mainly through field observations. For example, a front of the salt wedge is formed steep at the high water and is flattened at the low water; The surface level moves with not always the same phase with that of the interface; the salt wedge advances at the flood and retreats at the ebb, while the fresh water continuously flows down over the whole period, etc. Those are nowadays well-known facts, though fairly empirical.

The authors conducted a series of experiments with high accuracy on those problems, and also made field observations to test experimental

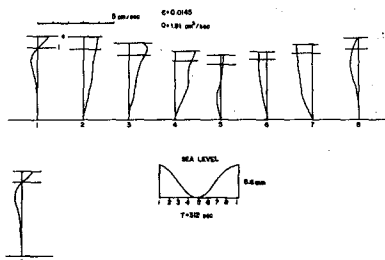


Figure 7(1).

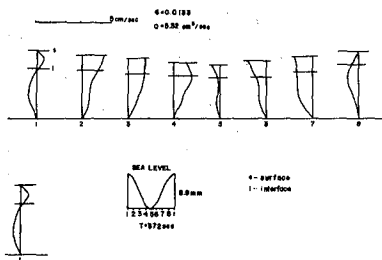


Figure 7(2).

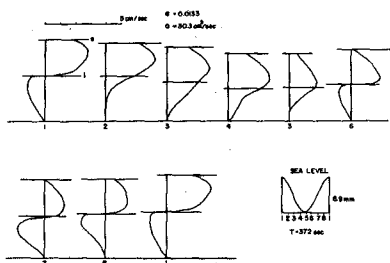


Figure 7(3).

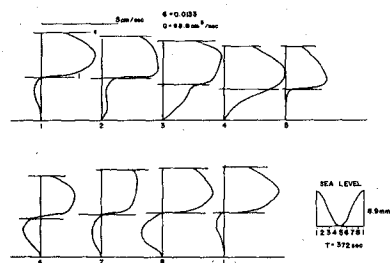


Figure 7(4).

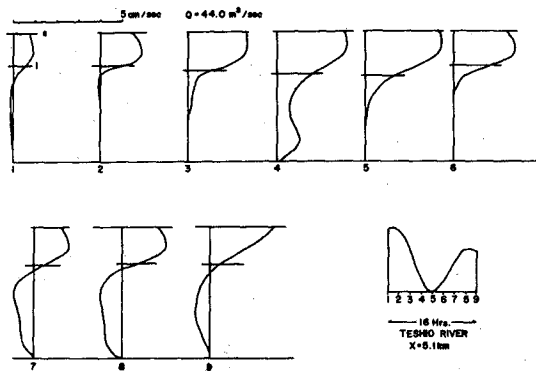


Figure 7(5).

results.

(a) Results of Model Experiments and Analyses

First, a change of the vertical distribution of velocity due to the tide is examined. Figs. 7 (1), (2), (3) and (4) show some examples. Observational points are 2.75 m upstream from the mouth, in cases of (1) and (2), and 1.3 m in (3) and (4). The discharge of the fresh water increases, in order, from (1) to (4). Fig. 8 shows a tidal change of salt concentration in the surface water (in electrical conductivity, $\mu\text{g}/\text{cm}$) at the mouth, at various values of discharge. Fig. 9 shows the same at different places inside the mouth. Throughout experiments, the tidal change of the level is given to move sinusoidally. If the discharge is small, for example, $Q = 1.91 \text{ cm}^3/\text{s}$ in Fig. 8, the salt water occupies the surface for some distance from the mouth at the flood, and it suggests an intermittent flow. This case belongs to a condition of the intermittent flow, $\lambda\theta > 1.63 \times 10^{-4}$, and the shape of the fresh water is sketched as shown in Fig. 10. When the discharge increases, the intermittent or upstream types disappear and the fresh water flows down every tidal hour, but on the other hand, the salt water beneath the fresh water, moves upstream and downstream according to the tidal hours. Such a case has frequently been experienced in field observations as shown in Fig. 7(5). However, the change of the interfacial level is more remarkable in field than in experiment.

As described above, the level, interface, velocity and salinity, change periodically with the tide at every point along the channel, and it suggests that those variations may propagate along the channel. Observations at two points, one of which is 50 cm upstream from the mouth and the other 350 cm, provide some properties of those propagations. Two examples are shown in Figs. 11 and 12. Experiments were performed with dye as a tracer and a movie camera. Fig. 11 is an example of no discharge, when the tidal periods are 33.3 sec and 100 sec. Both curves are different in phase with each other, where an exactly opposite trend can be found. This is because of that the case of 33.3 sec is resonant with the proper period of the channel which is 31.9 sec. According to a detailed observation at the upstream point, a change of velocity and level is observed always to have a phase difference $\pi/2$, the former being ahead of the latter. This fact is understood from a consideration that there occurs a cooscillating tide in the channel caused by the tide outside. Fig. 12 shows an example with the discharge $12.0 \text{ cm}^3/\text{s}$. The approximate behavior is almost the same with that of no discharge, since the amount of the discharge is relatively small. In those two examples, the effect of the external wave which is caused by the tide is dominant on the motion of water inside the channel, where the interface between the fresh water and the salt water moves at the same phase with the water surface.

The tidal current induced in the channel is next examined theoretically, in order to compare the observed results with it. If the channel has a constant depth and its length is small compared to the wave length of the external wave, equations of motion and continuity are given at the first approximation for an inviscid two-layer flow, as follows.

$$h_1 \frac{\partial u_1}{\partial x} + \frac{\partial}{\partial t} (\eta_1 - \eta_2) = 0 \quad (1)$$

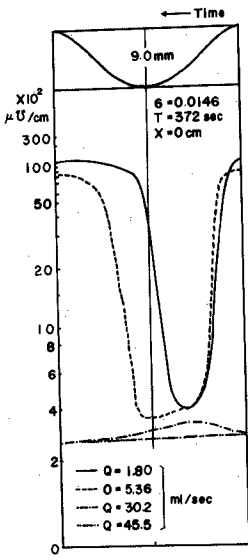


Figure 8.

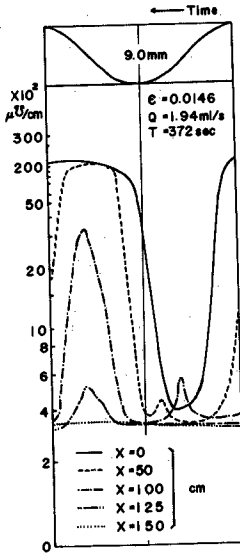


Figure 9.

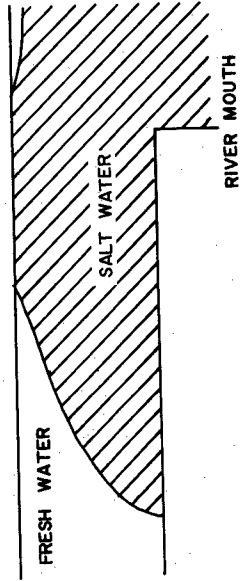


Figure 10.

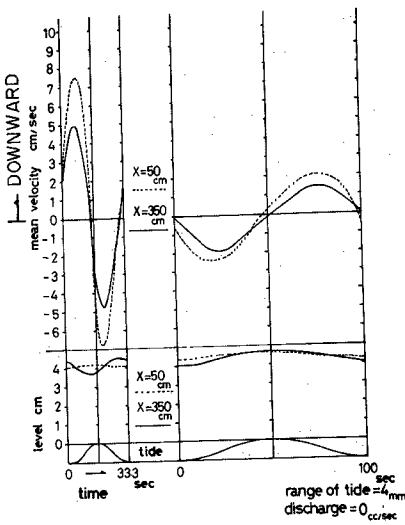


Figure 11.

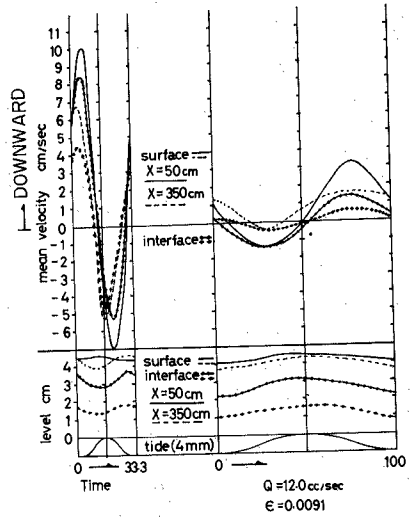


Figure 12.

$$h_2 \frac{\partial u_2}{\partial x} + \frac{\partial \eta_2}{\partial t} = 0 \quad (2)$$

$$\frac{\partial u_1}{\partial t} = -g \frac{\partial \eta_1}{\partial x} \quad (3)$$

$$\frac{\partial u_2}{\partial t} = -g \frac{\rho_1}{\rho_2} \frac{\partial \eta_1}{\partial x} - \epsilon g \frac{\partial \eta_2}{\partial x} \quad (4)$$

where t is time, x is a coordinate along the channel from the mouth, η_1 and η_2 are vertical deviations of the surface and the interface from their temporal mean values, h and u are depth and velocity at each layer, and subscripts 1 and 2 represent the upper and the lower layers. By combining four equations, the next form of u is derived.

$$\frac{\partial^4 u_1}{\partial t^4} - g (h_1 + h_2) \frac{\partial^4 u_1}{\partial t^2 \partial x^2} + \epsilon g^2 h_1 h_2 \frac{\partial^4 u_1}{\partial x^4} = 0 \quad (5)$$

By introducing new symbols C_s as a velocity of the external wave, and C_i as the internal wave, such as $C_s^2 = g (h_1 + h_2)$, and $C_i^2 = \epsilon g h_1 h_2 / (h_1 + h_2)$, a general solution, $u_1 = f(mx + \sigma t) + F(mx - \sigma t)$ is obtained from Eq. (5) under the condition $\epsilon \ll 1$, where $\sigma/m = C_{s,i}$ which represents both C_s and C_i together. Similarly u_2 , η_1 and η_2 are given in the same form with u_1 .

$$\eta_1 = \eta_{10} \cos (mx - \sigma t) \quad (6-1)$$

$$\eta_2 = \left(1 - \frac{gh_1}{C_{s,i}^2}\right) \eta_{10} \cos (mx - \sigma t) \quad (6-2)$$

$$u_1 = \frac{g}{C_{s,i}} \eta_{10} \cos (mx - \sigma t) \quad (6-3)$$

$$u_2 = \frac{C_{s,i}}{h_2} \left(1 - \frac{gh_1}{C_{s,i}^2}\right) \eta_{10} \cos (mx - \sigma t) \quad (6-4)$$

Since the upper end of the channel exists, it can be assumed that the velocity $u = 0$ at $x = \ell$ which is the distance from the mouth. Furthermore, putting the tide level $\eta_1 = \eta_{10} \cos (\sigma t + \epsilon)$ outside the mouth, solutions are given as follows.

$$\eta_1 = \eta_{10} \frac{\cos \{m(x - \ell)\}}{\cos m\ell} \cos (\sigma t + \epsilon) \quad (7-1)$$

$$\eta_2 = \left(1 - \frac{gh_1}{C_{s,i}^2}\right) \eta_{10} \frac{\cos \{m(x - \ell)\}}{\cos m} \cos (\sigma t + \epsilon) \quad (7-2)$$

$$u_1 = \frac{g}{C_{s,i}} \eta_{10} \frac{\sin \{m(x - \ell)\}}{\cos m\ell} \sin (\sigma t + \epsilon) \quad (7-3)$$

$$u_2 = \frac{C_{s,i}}{h_2} \left(1 - \frac{gh_1}{C_{s,i}^2}\right) \eta_{10} \frac{\sin \{m(x - \ell)\}}{\cos m\ell} \sin (\sigma t + \epsilon) \quad (7-4)$$

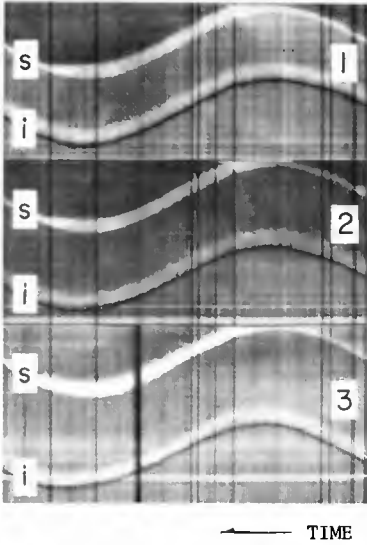


Figure 13.

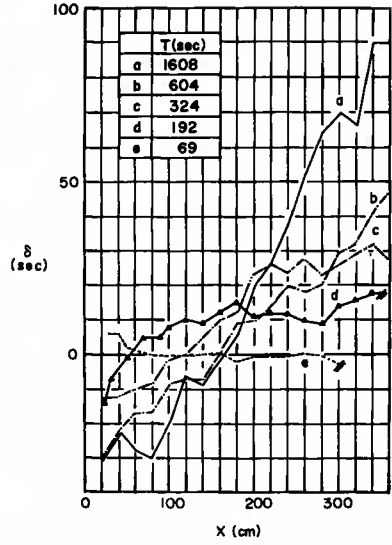


Figure 14.

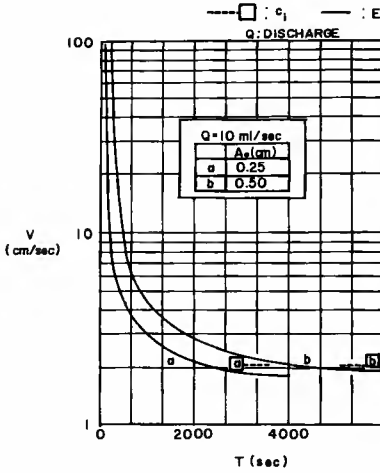


Figure 15(1).

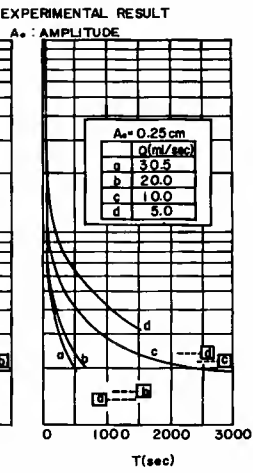


Figure 15(2).

Substituting experimental values which are shown in Fig. 12, as $\eta_{10} = 0.2$ cm, $T = 100$ sec and $l = 450$ cm, into Eq. (7-3), the value, $u_{10} \neq u_{20} = 1.36$ cm/s is found. This value is consistent well with the cross-sectional mean velocity, 1.2 cm/s, which is calculated from the lateral velocity distribution. Besides, the phase difference of the velocity and the level which has already been described as $\pi/2$, is also explained by those equations.

As pointed out like those, changes of the level and the velocity owing to the tide with the period 100 sec, coincide with those estimated from Eq. (7-3), where the propagation is based on the external wave. This fact, however, is not always true, because the interface grows remarkable with a distance from the mouth, and also with an increase of the tidal period. Such an example is shown in Fig. 13. These pictures are obtained through the technique by using the light-beam system which has already been described in Section 2. Since a propagation of the surface level is very fast, owing to its dependence on the external wave, the time difference cannot be detected at any station, but on the other hand, the interface is recognized to delay with a distance from the mouth. This means that the interface is affected more strongly by the internal wave. The experiments were made under condition that $Q = 9.67$ cm³/s, $\epsilon = 0.0067$, $\eta_{10} = 1.0$ cm, $T = 1623$ cm and a time interval of every exposure is 8.92 sec.

In order to investigate how the phase difference of the surface and the interface is related to the tidal period, experiments were repeated in a direction toward a decision of the time delay δ of the interface behind the surface, at various points along the channel. The results are shown in Fig. 14, in which $Q = 10$ cm³/s and $\eta_{10} = 0.27$ cm. From this figure, it can be understood that an increase of δ is approximately linear against x . Its gradient δ_i has a trend to grow steep with an increase of the tidal period. This means that a change of the interface propagates upstream with a certain velocity which depends on the tidal period. The velocity V is estimated undoubtedly as the reciprocal of δ_i . The dependency of V on the tidal period is seen also in Figs. 15 (1) and (2), in which the discharge or the tide amplitude is taken as a parameter, where the amplitude is very small compared with the whole depth.

From those results, it is found that V is exceedingly large at the period of 100 sec and the phase difference between the surface and the interface is negligible, but it decreases with a growth of the tidal period, and finally it converges to a certain small value. Those final values become to be independent of the tide amplitude, but they depend on only the discharge. Convergent values are very close to those calculated from the following equation which gives the velocity of an internal wave.

$$C_i = - \frac{U_2 h_1 + U_1 h_2}{h_1 + h_2} + \sqrt{g \frac{h_1 h_2}{h_1 + h_2} - \frac{(U_1 - U_2)^2 h_1 h_2}{(h_1 + h_2)^2}} \quad (8)$$

This coincidence proves that a change of the interface brought by the tide has a property of the internal gravity wave.

In conclusion, a short period of the tide produces only the external wave at both the surface and the interface, but a sufficiently long period of the tide causes the external wave at the surface and the internal wave

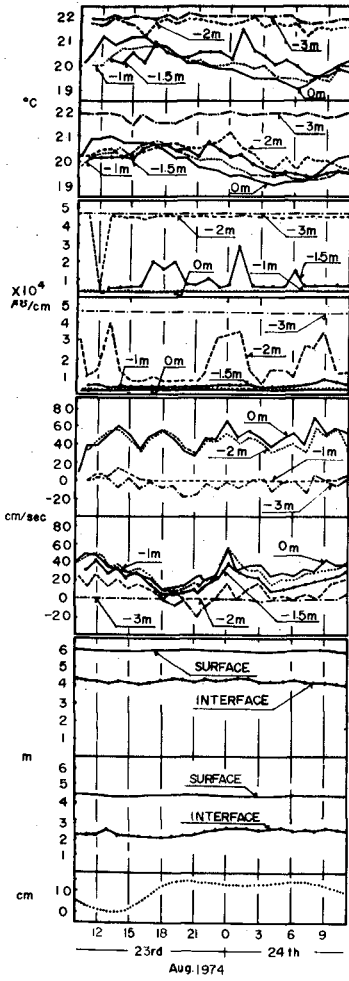


Figure 16.

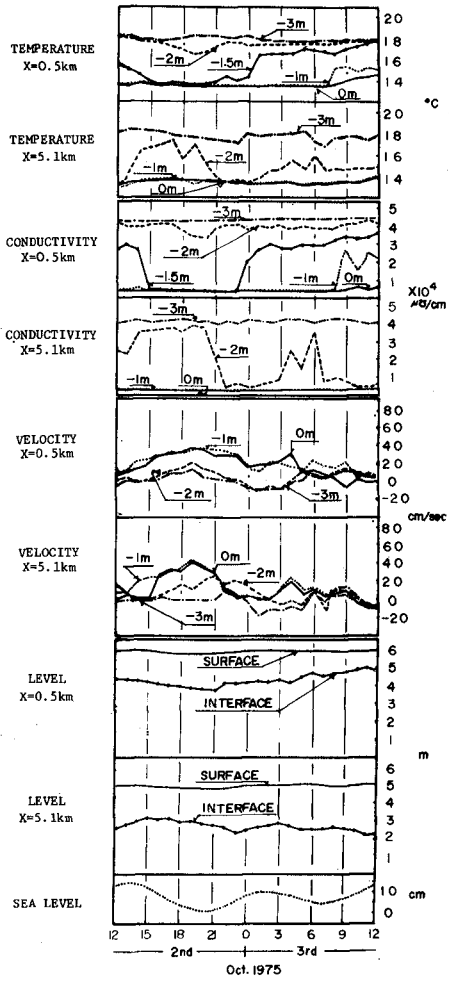


Figure 17.

at the interface. There is no theory sufficient to explain all those phenomena in detail yet, but it is not only interesting but also important for a study on the salt wedge. Under the condition of a long period, it must be noticed that a velocity of the flow in the salt layer also propagates with the velocity of the internal wave, although a velocity of the fresh water shows that of the external wave. Then, the surface level rises and falls almost simultaneously everywhere along the channel, nevertheless, the interface delays in time behind the surface, with an increase of the distance, because a propagation of the velocity of the salt water is very slow. In an extreme case, when the surface rises, the interface at a certain point may sometimes fall. It is possible that the origin of the internal wave is situated at some place inside the river mouth, from paying attention to Fig. 14. Needless to say, the occurrence of the internal wave is due to the tide, but the mechanism in what manner the tide passes through the mouth is still unknown and it belongs to the future study. If the tidal period is short enough, the effect of the internal wave disappears inside the mouth, and the interface rises and falls simultaneously at any point, as shown in Fig. 14.

(b) Field Observation of the Two-Layer Flow and Analyses

Figs. 16 and 17 show examples of field observation, at two stations along the Teshio River in Hokkaido. One is 0.5 km upstream from the mouth, and the other is 5.1 km. Observations at both stations were made at every one hour over the whole period of 25 hours. Since the Japan Sea to which the Teshio River opens, has a small tidal range of about 30 cm at its maximum, the length of the salt wedge is little affected by the tide. The relationship between the length and the river discharge is shown in Fig. 18. In the case of Fig. 16, as the discharge is about $90 \text{ m}^3/\text{s}$, the length of the salt wedge is estimated about 15 km. In Fig. 17, the length is expected 22 km, since the discharge is $44 \text{ m}^3/\text{s}$. According to the hydrograph obtained at the station of 18.3 km from the mouth, the change of the water level coincides with the tide, except flood days. This means that the external wave caused by the tide can travel for a great distance along the river without decay.

The surface level, interface velocity, water temperature and electrical conductivity were observed. It is noticeable that the change of the velocity contains irregular components whose periods are smaller than the tide, at the lower station. It seems to have been caused by the stormy weather which produces a seiche with a long period. After eliminating those components, the careful comparison of tidal components of the level, interface and velocity with each other, will lead to understanding that they are waves rather progressive towards upstream, than standing waves which have been discussed in the preceding section. This is evident from the fact that there is no reflection from the upstream of the river and the tide is caught without decay even at a very far station upstream from the river mouth.

In such a case, Proudman's solutions seems to be adoptable. The velocity is calculated from Eq. (6) as $u_{10} = 10.7 \text{ cm/s}$. This is very close to the cross-sectionally averaged value 13 cm/s , while the value at the center of the flow is 20 cm/s , as shown in Fig. 13. As described like those, since all the changes are thought progressive, there can be a phase difference at two stations upper and lower. However, the external wave is estimated as 7 m/s in velocity and its travel time is only 11 minutes over the distance of 4.6 km between both stations.

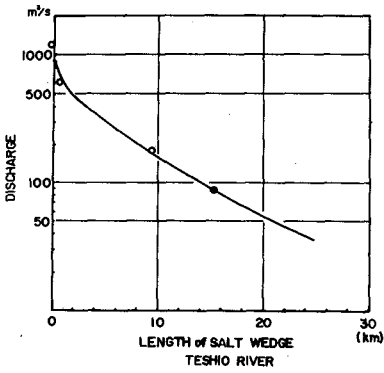


Figure 18.

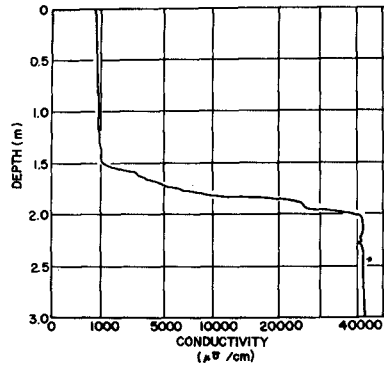


Figure 20.

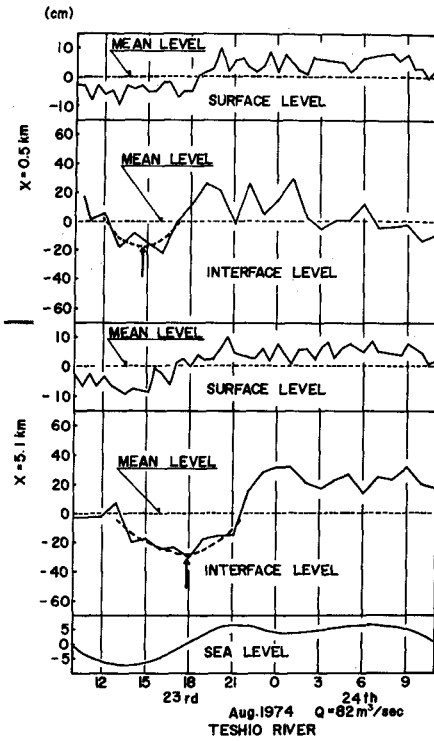


Figure 19(1).

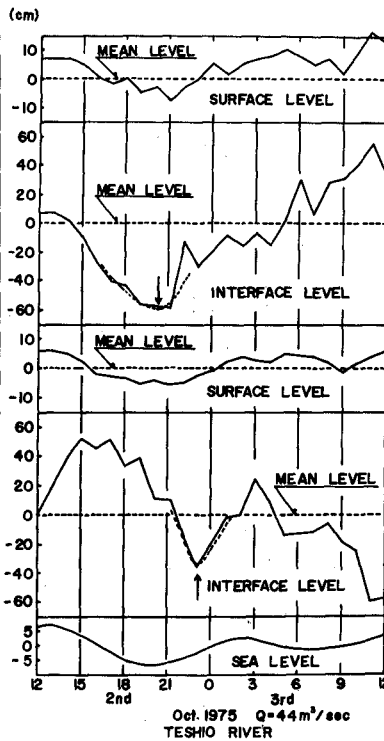


Figure 19(2).

Therefore, the time difference of the surface level is not detected between the two stations. For the purpose of finding of the detailed relationship between the surface and interface levels, enlarged figures are shown in Figs. 19 (1) and (2), in which the interface is defined as a level of 30,000 $\mu\text{S}/\text{cm}$ in electrical conductivity. A representative type of the vertical distribution of electrical conductivity which corresponds to density, is shown in Fig. 20. The time difference of the surface level and the interface is negligible at the lower station, but not at the upper station as easily expected. There are 3-4 hours in Fig. 19 (1) and 2.5-3 hours in Fig. 19 (2). They are approximately the same with values of the internal wave which passes through two stations, where the former is calculated 3.1 hours and the latter 2.7 hours by using Eq. (8).

From all those experienced in field observation, the tidal effect at the Teshio River can be regarded as the same with that experienced in the experiment of a long tidal period which has already been described. It must be stressed again that the velocity change in the salt layer propagates with a velocity of the internal wave also in field observations. However, the velocity of the fresh water doesn't seem, for the present, to have a property of propagation of the internal wave.

There are many other important problems unsolved. For example, the case in which the tidal range becomes comparable with the water depth; a problem of the degree of a change of the interface level, which is much larger in field than in experiment, etc. are belonging to future studies.

5. Tidal Mixing of Two Layers

In a case of a negligible tide, mixing of the two-layer flow is thought to occur by interfacial instability and turbulence, caused by an increase of the relative velocity of the two layers. In such a case, the salt wedge has another phenomenon. The increase of the relative velocity brings a retreat of the salt wedge and finally pushes it out from the river mouth into the sea. From those two facts, it is understandable that if the salt wedge exists inside the river, mixing of two layers is always weak or negligible. Therefore, the existence of various types of mixing has been, hitherto, considered to depend on the tidal effect. The intense mixing type of a density current inside a river mouth or an estuary is, for instance, possible only in a case of the great range of tide.

In order to test this point of view, the authors repeated experiments with various degrees of the tidal range. However, contrary to expectation, there occurred no intense mixing, nor moderate mixing but always a type of distinctly separated two-layer flow, at any large value of the tidal range. As has already been described, the channel used in the experiments has a smooth bed and smooth sides, since it is made of acrylic resin. According to another experiment in which roughness is given to the bed, flow patterns change completely and mixing occurs even with a relatively small tidal range.

Examples are shown in Figs. 21 (a), (b), (c) and (d), whose conditions are, $T = 200$ sec, $Q = 10$ cm^3/s , $\epsilon = 0.0067$ and the total depth is 4 cm. The roughness is given with rectangular wooden pieces having a square cross-section of 6 mm \times 6 mm and every spacing is 10 cm in distance. Figs. from (a) to (d) are photographed at the flood, where the amplitudes of the tidal range are $\eta_{10} = 4.9$ mm, 8.4 mm, 17.3 mm and 20.7 mm,

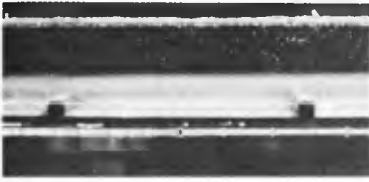


Figure 21(a).

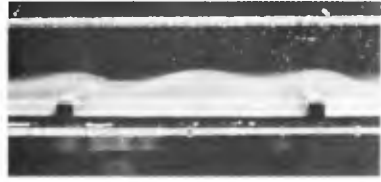


Figure 21(b).

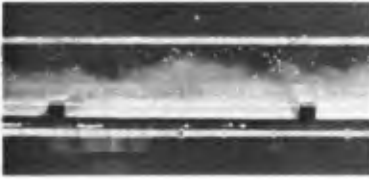


Figure 21(c).

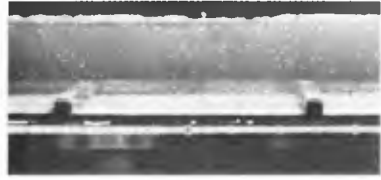


Figure 21(d).

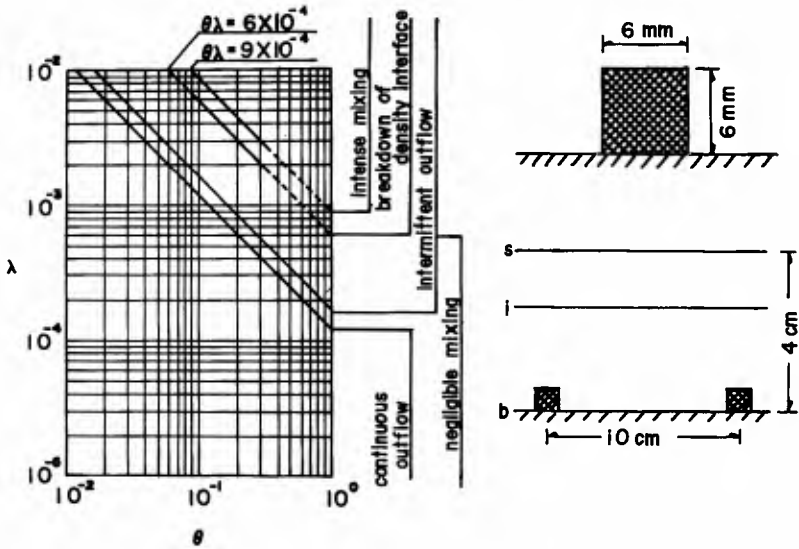


Figure 22.

respectively. The interface is distinct and straight horizontally in Fig. (a). Lee waves occur in Fig. (b), and the interface begins to break down in Fig. (c), in which many vortices produced behind wooden pieces move with the current, gradually growing and disturbing the interface, and finally break the interface in such a manner that vortices drag down the interface into themselves, and cause mixing of the two layers. A type of fully developed mixing is found in Fig. (d), which is that of the so-called intense mixing. In the case of Fig. (d), however, the interface has a trend to restore its original two-layer type at the ebb time. Therefore, in order to keep the intense type over the whole period, a larger amplitude is necessary.

As thus described, mixing is deeply dependent on the roughness of the channel and a strength of the tidal current. The degree of mixing is classified with two parameters λ and θ , which have already been used in the classifications of outflow pattern, as shown in Fig. 22. Although experiments are not so plentiful enough to derive the conclusion yet, within the limited range of values of θ , breaking of the interface occurs, when $\lambda\theta \geq 6 \times 10^{-4}$, and a transition to the intense mixing type is found, when $\lambda\theta \geq 9 \times 10^{-4}$. But the observational results in field are not so coincident with those values, that another new parameter should be introduced, instead of λ . According to field measurements, since the tidal current depends rather on a velocity of the external wave, than on the tidal period, another parameter such as $\lambda_U = KgA_0/C_S U_0$ was tried to take into account, but at present it is not successful. Unification of the results, both in field and experiment, by discovering a reasonable parameter, is an important problem for further study.

REFERENCES

- 1) Schijf, J. B and Schönfeld, J. C. : Proc. Minnesota, Intern. Hydr. Conv., IAHR, 1953.
- 2) Kashiwamura, M. and Yoshida, S. : Coast. Eng. Japan, Vol. 10, 1967.
- 3) Kashiwamura, M. and Yoshida, S. : 13th Kyoto Congr., IAHR, 1969.
- 4) Kashiwamura, M. and Yoshida, S. : Coast. Eng. Japan, Vol. 14, 1971.
- 5) Kashiwamura, M. and Yoshida, S. : Novosibirsk Symp. on Stratified Flow, IAHR, & Sci. Acad. USSR, 1972.
- 6) Simmons, H. B. : 2nd Conf. Coast. Eng., 1951.
- 7) Proudman, J. : "Dynamical Oceanography", Wiley, New York, 1953.

CHAPTER 184

EVALUATION OF AIR-SEA INTERFACE HEAT FLUX

ROBERT L. STREET¹, M.ASCE
A. WOODRUFF MILLER, JR.²

ABSTRACT

A theoretical analysis, laboratory experiments, and the routine availability of infrared remote sensors for boat, airplane or satellite use are combined to provide a simple method for evaluating the total heat flux through the air-water interface under nighttime field conditions in which the water surface is rough; all indications are that the technique can be extended to other conditions as well. To evaluate this flux all that is required is the local windspeed, the water surface temperature, a subsurface temperature, and the character of the sea surface. Conversely, the theory can also be applied to predict temperature differences across the interface if the heat transfer can be otherwise established.

INTRODUCTION

Rejection to the atmosphere is the ultimate fate of the heat released by thermal power plants. The probable development of off-shore nuclear plants and the existing coastal power plants make necessary an understanding of and a means of evaluating the effects of ocean waves and the wind on the total heat transfer and/or temperature gradients across the air-sea interface. This transfer is important to local ocean thermal conditions and as an input to the development of local climatology.

The key to estimating interface transfer is knowledge of the temperature structure in the aqueous boundary layer just beneath the air-

¹Professor, Department of Civil Engineering, Stanford University, Stanford, California 94305, U.S.A.

²Assistant Professor, Department of Civil Engineering, Brigham Young University, Provo, Utah 84602, U.S.A.

water interface. Saunders (1967) said, "For some decades it has been known that the surface is generally cooler than the subsurface water with the major temperature variation concentrated in the uppermost millimeters." He also noted, "When used from a near surface position, radiometers afford a unique tool for determining the magnitude of this surface anomaly, and ... it seems likely that they will become indispensable in field experiments where the transfer of heat, moisture and momentum are measured." Following this Hasse (1971) considered the heat flow through the surface. Disregarding initially the short wave radiation due to the sun, he developed a theoretical analysis, based on the diffusivity relationship of Reichardt, for the vertical transfer of heat in the aqueous boundary layer that is required to balance the heat loss (or gain) at the surface through evaporation, sensible heat transfer and effective back radiation. He then provided a theoretical relationship including the influence of the sun.

Using the insight provided by Saunders and Hasse, we have extended the latter's theoretical analysis, used our own laboratory experiments, and presumed the routine availability of infrared remote sensors for boat, airplane or satellite use to provide a simple method for evaluating the total heat flux through the air-water interface under *nighttime* field conditions in which the water surface is rough; all indications are that the technique can be extended to other conditions as well. To evaluate this flux all that is required is the local windspeed, the water surface temperature, a subsurface temperature, and the character of the sea surface. Conversely, the theory can also be applied to predict temperature differences across the interface if the heat transfer can be otherwise established.

The work of Scarpace and Green (1973) at Wisconsin gives a good illustration of the applicability of such a theory. Airborne thermal imagery (infrared radiometry) was used on thermal plumes. The imagery was supported by simultaneous data taken from boats. They reported:

The scanner is virtually impossible to calibrate from the air. It also gives no information on subsurface temperatures. Thus an intensive ground truth effort is essential to providing both accurate data and supporting information.

While the plane was overhead (sometimes shortly before and after), two or three surface craft measured underwater temperatures with Whitney resistance thermometers, while [a 40 ft R/V boat] made several passes over a predetermined course marked by 20 buoys. The PRT-5 [radiometer] was mounted on the bow.

Application of the method discussed below would either yield the heat transfer from the Scarpace and Green data or, combined with meteorological and wave data, obviate the need for either the subsurface or the PRT-5 data as ground truth.

BASIC THEORY

As mentioned above both Saunders and Hasse developed theories for the heat transfer and temperature difference relationship in the aqueous boundary layer. Saunders' theory was applicable across the so-called thermal sublayer where molecular effects are dominant, while Hasse's theory applies across a specific depth of the layer (as does ours). Interestingly the attempts to verify Saunders' theory have been made through experiments more relevant to Hasse's and our theories, leading to a diversity of results for Saunders' transfer coefficient λ .

Hasse (1971) suggests treating the flux Q_T in the aqueous surface layer in differential form as (Fig. 1)

$$Q_T = -\rho_w c_{p_w} K \frac{\partial T}{\partial z} \quad (1)$$

where $K = K(z)$ is the *effective* thermal diffusivity, T is the water temperature, ρ_w is the density of water, c_{p_w} is the heat capacity of water, and z is measured positive downward from the surface. If $\partial T/\partial x$ is essentially zero, and we speak of a steady mean flow so $\partial T/\partial t \equiv 0$, then

$$Q_T = -\rho_w c_{p_w} K \frac{dT}{dz} \quad (2)$$

In the surface layer Q_T is constant below the level of back radiation and in the absence of solar (incoming) radiation. We ignore the temperature effects on ρ_w and c_{p_w} across the thermal layers. Then,

$$\frac{dT}{dz} = -\left(\frac{Q_T}{\rho_w c_{p_w}}\right) \frac{1}{K(z)} \quad (3)$$

The key parameters of the problem are summarized as follows (see Fig. 1):

- h = mean surface roughness (wave) height
- k' = Kármán constant = 0.40
- Pr = molecular Prandtl number = ν_w/κ_w
- $U_{*w} = (\tau_o/\rho_w)^{\frac{1}{2}}$ = friction velocity in water
- z_b = depth of "bulk" water temperature measurement
- z_s = radiometer optical depth ($z_s \approx 140 \mu\text{m}$ for our experiments, while $z_s \approx 20 \mu\text{m}$ for a PRT-5)

- δ_t = thermal sublayer thickness
 δ_T = thermal layer matching thickness (i.e., the point at which the temperature profile becomes logarithmic)
 δ_v = viscous sublayer thickness
 κ_w = thermal diffusivity of water
 ν_w = kinematic viscosity of water
 τ_o = surface shear stress

We also define a set of nondimensional (Reynolds) numbers:

$$\begin{aligned}
 h^+ &= U_{*w} h / \nu_w; & z_b^+ &= U_{*w} z_b / \nu_w; & z_s^+ &= U_{*w} z_s / \nu_w; \\
 \delta_T^+ &= U_{*w} \delta_T / \nu_w; & \delta_t^+ &= U_{*w} \delta_t / \nu_w; & \delta_v^+ &= U_{*w} \delta_v / \nu_w
 \end{aligned}
 \tag{4}$$

Yaglom and Kader (1974) discussed the flow over and heat transfer from rough surfaces. They defined the functional form of the eddy viscosities and eddy diffusivities in the surface layers; we employ their formulations here. We also let $\Delta T_t = T_s - T_b$ where T_s and T_b are the "surface" and bulk water temperatures and the heat transfer coefficient becomes

$$\frac{1}{C_H} = \frac{\rho_w c_p U_{*w} \Delta T_t}{Q_T}
 \tag{5}$$

The immediate objective of our work was to obtain an explicit relationship between $1/C_H$ and the parameters of the flow. Our goals then were *first* to use our results from a laboratory experiment employing an infrared radiometer to relate δ_v^+ to h^+ for rough flows and *second* to employ this relation to predict $1/C_H$ for any rough flow. The experiments were run in the Stanford Wind, Water-Wave Research facility (Fig. 2).

The key to the analysis is prescription of $K(z)$. We have developed expressions based on Yaglom and Kader's analysis for fully rough wall flows, i.e., for $h^+ > 100$. Thus,

$$\epsilon_H = a_H' \nu_w (h^+)^{-3/2} (z^+)^3
 \tag{6}$$

$$\epsilon_M = a_M' \nu_w (h^+)^{-3/2} (z^+)^3
 \tag{7}$$

near the rough wall, where ϵ_H and ϵ_M are the eddy diffusivities for heat and momentum, respectively, and a_H' and a_M' are supposed constant for any given boundary geometry.

For the layers shown in Fig. 1 we must have

$$\text{a. at } z^+ = \delta_t^+ : \epsilon_H = a_H^+ \nu_w (h^+)^{-3/2} \quad (\delta_t^+)^3 = \kappa \quad (8)$$

$$\text{b. at } z^+ = \delta_v^+ : \epsilon_M = a_M^+ \nu_w (h^+)^{-3/2} \quad (\delta_v^+)^3 = \nu \quad (9)$$

$$\text{c. at } z^+ = \delta_T^+ : \epsilon_H = a_H^+ \nu_w (h^+)^{-3/2} \quad (\delta_T^+)^3 = k^+ \nu \delta_T^+ \quad (10)$$

Thus we require $\epsilon_H = \kappa$ at the edge of the thermal sublayer, $\epsilon_M = \nu$ at the edge of the viscous sublayer, and $\epsilon_H = k^+ U_{*w} z$ as a matching condition so the eddy diffusivity given by the cubic estimate matches that of the logarithmic layer (cf., Sec. 3.2, Kader and Yaglom, 1972). Using Eqs. (8-10) and other arguments (see, Street and Miller, 1976), we were able to conclude, first, that the classic relation

$$\delta_t^+ / \delta_v^+ = Pr^{-1/3} \quad (11)$$

is still valid, and, second, that

$$\delta_v^+ = k^{-1/3} \delta_T^{+2/3} \quad (12)$$

or

$$\delta_T^+ = 0.63 (\delta_v^+)^{1.5} \quad (12)$$

It follows that, if $K(z) = \kappa + \epsilon_H$, then

$$\text{a. in } z_s \leq z \leq \delta_T^+ : K(z) = \kappa [1 + (z^+ / \delta_T^+)^3] \quad (13a)$$

$$\text{b. in } \delta_T^+ \leq z \leq z_b : K(z) = \kappa (1 + 0.4 Pr z^+) \quad (13b)$$

Therefore, our basic equation (Eq. 3) can be integrated to give

$$\int_{T_s}^{T_b} dT = \left(\frac{-Q_T}{\rho_w c_p} \right) \int_{z_s}^{z_b} \frac{dz}{K(z)} \quad (14)$$

which leads to

$$\frac{1}{C_H} = \frac{\text{Pr}\delta_t^+}{3} \left[\frac{1}{2} \ln \left\{ \frac{(\delta_t^{+2} - \delta_t^+ z_s^+ + z_s^{+2})(\delta_t^+ + \delta_T^+)^2}{(\delta_t^{+2} - \delta_t^+ \delta_T^+ + \delta_T^{+2})(\delta_t^+ + z_s^+)^2} \right\} + (3)^{\frac{1}{2}} \left\{ \tan^{-1} \left(\frac{2\delta_T^+ - \delta_t^+}{(3)^{\frac{1}{2}}\delta_t^+} \right) - \tan^{-1} \left(\frac{2z_s^+ - \delta_t^+}{(3)^{\frac{1}{2}}\delta_t^+} \right) \right\} \right] \quad (15)$$

$$+ 2.5 \ln \left\{ \frac{1 + 0.4 \text{Pr}z_b^+}{1 + 0.4 \text{Pr}\delta_T^+} \right\}$$

EVALUATION OF RELATION BETWEEN δ_v^+ AND h^+

The data of Miller, et al. (1975) were used, together with Eq. (15), by Street and Miller (1976) to obtain an estimate of the relation between δ_v^+ and h^+ . Indeed Yaglom and Kader (1974) hypothesize (in effect) that

$$\delta_v^+ = a^+ (h^+)^{\frac{1}{2}} \quad (16)$$

Thus, we sought the constant a^+ for rough flows ($h^+ > 100$).

To establish a^+ we used 23 cases of wind-generated waves in the Stanford laboratory facility (Fig. 2) with water to air temperature differences of about 2.5, 5.0 and 7.5°C at fetches of 9.5 and 14.5 m (Miller, et al., 1975). The water surface temperatures were measured to $\pm 0.01^\circ\text{C}$ with an infrared radiometer employing an indium antimonide detector with a wave length range of 1.5 to 5.5 μm and an optical depth z_s of about 140 μm . (Extracting the surface temperature involved special calibration and computational techniques and consideration of the wave-length dependent, water and air, optical properties within the detector band width; details can be found in Miller, et al., 1975.) The thermal layer temperature difference ΔT_t was defined as the bulk water temperature T_b measured 100 mm below the mean interface minus the average temperature at $z = z_s = 140 \mu\text{m}$. The parameters used in calculating surface temperature and wave height were monitored continuously. Other parameters, such as mean free-stream air velocity, temperature and humidity, were obtained also. They formed the basis for calculating the total heat transfer and surface roughness Reynolds numbers h^+ through use of data collected by previous investigators in the Stanford channel.

From our experiments we derived the key result that $a^+ = 0.37$ so

$$\delta_v^+ = 0.37(h^+)^{\frac{1}{2}} \quad (17)$$

Thus, Yaglom and Kader's conjecture for rough solid surfaces applies as well to mobile surfaces and

$$\delta_v^+ = 0[(h^+)^{\frac{1}{2}}] \quad (18)$$

We also have from Eq. (11)

$$\delta_t^+ = 0.37(\text{Pr}^{-1/3})(h^+)^{1/2} \quad (19)$$

FIELD USE

The statistical distribution of wave heights in both laboratory and field is known to be a Rayleigh distribution. In addition, the similarity theory of Yaglom and Kader (1974) which underlies Eqs. (17) and (19) should not be scale dependent, a^+ being supposed to vary only with surface shape. Accordingly, we believe that Eqs. (17) and (19) should be valid in the field as well as in the laboratory, except perhaps in the presence of long-wave swell which should be subtracted before computing h^+ for the remaining sea (defined here as freshly generated waves).

Given that δ_v^+ and δ_t^+ are known via Eqs. (17) and (19) as functions of h^+ and Pr , we may use Eq. 15 with a minimum of measurements to obtain C_H . When C_H is known we can predict Q_T by measuring U_{*w} , the sea surface physical characteristics, the surface temperature (with an infrared radiometer to obtain T_s and, hence, ρ_w and c_{pw}) and the bulk water temperature T_b (in any convenient manner).

One possible approach to obtain U_{*w} and the necessary sea surface characteristics is as follows. Hsu (1974) shows that the dynamic roughness z_o of a water surface can be expressed as

$$z_o = \frac{1}{2} \frac{H}{(C/U_{*a})^2} \quad (20)$$

where H is the dominant wave height, C is its phase velocity and U_{*a} is the friction velocity in the atmospheric constant-flux layer. Using the results of Kondo, et al. (1973), Kondo (1975) determines that the mean surface roughness height h is given by

$$h = 30 z_o \quad (21)$$

for completely rough flow above the sea (established to occur when $U_{10} \geq 8 \text{ m}\cdot\text{s}^{-1}$ where U_{10} is the windspeed at 10 metres elevation). Of course, h can be measured directly also. Kondo (1975) also shows that the drag coefficient

$$C_D = (U_{*a}/U_{10})^2 = 10^{-3}(1.2 + 0.025 U_{10}) \quad (22)$$

for $U_{10} \geq 8 \text{ m}\cdot\text{s}^{-1}$. Applying the assumption of stress continuity across the interface yields

$$U_{*w} = (\rho_a/\rho_w)^{\frac{1}{2}} U_{*a} \quad (23)$$

where ρ_a is the air density. Given U_{10} and the temperatures in air and water, U_{*w} is found by the combination of Eqs. (23) and (22).

Hasse (1971), Saunders (1967), and others have followed the concept of stress continuity across the interface, according to Eq. (23). Wu₂ (1975) points out clearly that the fraction of the momentum flux $\rho_a U_{*a}^2$ from the air which goes to drift currents ranges from about 0.6 to 0.8 in the rough flow regime, the remaining flux going to wave generation. In a rough boundary case where eddying is driven by the drift current boundary layer flow and the random water wave motion together it is not entirely clear whether one should use U_{*w} or some fraction thereof as the reference velocity (the fraction ranging apparently from $\sqrt{0.6} \approx 0.8$ to $\sqrt{0.8} \approx 0.9$). We feel that, pending further evidence, the use of U_{*w} is best.

Thus, Eqs. (15), (17), (19), (21-23), and (12) are the needed set for prediction of the heat flux and temperature difference relationships for a given wind and sea state. Given basic physical data one can either predict ΔT_t from known Q_T or predict Q_T from known ΔT_t .

AN APPLICATION

An example illustrates the variation of parameters. Assume that T_b is 20°C so ν_w , ρ_w , c_{pw} and $Pr = 7.1$ are known. Take $T_{air} = 15^\circ\text{C}$ so ρ_a is known and assume $U_{*a} = 0.381$ (equivalent to $U_{10} = 10 \text{ m/s}$, for example). We employ a PRT-5 radiometer so $z_s = 20 \mu\text{m}$ and measure the bulk temperature at one of 3 depths, viz., $z_b = \delta_T$, $z_b = 1 \text{ cm}$ and $z_b = 10 \text{ cm}$.

Under these conditions $h^+ = (1.3 \times 10^4)h$ so $h^+ > 100$ when $h > 3/4 \text{ cm}$. One finds, for example,

$$z_s^+ = 0.27 (\delta_v^+ \geq 3.7, \delta_t^+ \geq 1.9 \text{ and}$$

$$\delta_T^+ \geq 4.5 \text{ for } h^+ \geq 100)$$

$$z_b^+ = \delta_T^+, 133 \text{ or } 1330$$

In Fig. 3 we show δ_v^+ and δ_t^+ as functions of h . As expected $\delta_t^+ \approx \frac{1}{2} \delta_v^+$ and both are proportional to \sqrt{h} . Figure 4 shows the inverse transfer coefficient C_H^{-1} as a function of h and z_b . As δ_T represents the point of transition to the fully turbulent, logarithmic temperature profile, $z_b = \delta_T$ corresponds to neglecting any temperature variation between δ_T and the actual measurement point for bulk temperature. As Saunders' theory neglects even the variation between $z = \delta_t$ and $z = \delta_T$, it is clear that comparison of laboratory or field measurements to Saunders' theory is moot because we cannot measure at $z = \delta_t$ which lies between the surface roughness. From this figure we see that neglecting the temperature variation in the logarithmic zone leads to an error of between 10 and 50 percent for $z_b = 10$ cm.

The final figure (Fig. 5) shows ΔT_t , i.e., the surface temperature depression for a typical field heat transfer value with all the previous assumptions in effect. Clearly a 1 to 2°C depression over 10 cm is worth considering.

The next step in our efforts will be to carry out the straightforward extension of our theory to daytime (significant solar radiation) conditions and to transition rough and smooth flow conditions.

Acknowledgment: This work was supported by the Meteorology Program, Atmospheric Sciences Division, National Science Foundation, through Grant DES73-06538.

REFERENCES

- Hasse, L. (1971). "The Sea Surface Temperature Deviation and the Heat Flow at the Sea-Air Interface," Bound.-Layer Met., 1, 368-379.
- Hsu, S. A. (1974). "A Dynamic Roughness Equation and Its Application to Wind Stress Determination at the Air-Sea Interface," J. Phys. Ocean., 4, 1, 116-120.
- Kader, B. A., and A. M. Yaglom (1972). "Heat and Mass Transfer Laws for Fully Turbulent Wall Flows," Int. J. Heat and Mass Transfer, 15, 2329-2351.

- Kondo, J., Y. Fujinawa, and G. Naito (1973). "High-Frequency Components of Ocean Waves and Their Relation to the Aerodynamic Roughness," J. Phys. Ocean., 3, 197-202.
- Kondo, J. (1975). "Air-Sea Bulk Transfer Coefficients in Diabatic Conditions," Bound.-Layer Met., 9, 91-112.
- Miller, A. W., Jr., R. L. Street, and E. Y. Hsu (1975). "The Structure of the Aqueous Thermal-Sublayer at an Air-Water Interface," Dept. of C.E. Tech. Rept. No. 195, Stanford University, Stanford, Calif. 94305.
- Saunders, P. M. (1967). "The Temperature at the Ocean-Air Interface," J. Atm. Sci., 24, 269-273.
- Scarpace, F. L., and T. Green, III (1973). "Dynamic Surface Temperature Structure of Thermal Plumes," Wat. Res. Res., 9, 1, 138-153.
- Street, R. L., and A. W. Miller, Jr. (1976). "Determination of the Aqueous Sublayer Thicknesses at an Air-Water Interface," Manuscript submitted for publication.
- Wu, Jin (1975). "Wind-Induced Drift Currents," J. Fluid Mech., 68, 1, 49-70.
- Yaglom, A. M., and B. A. Kader (1974). "Heat and Mass Transfer Between a Rough Wall and Turbulent Fluid Flow at High Reynolds and Péclet Numbers," J. Fluid Mech., 62, 3, 601-623.

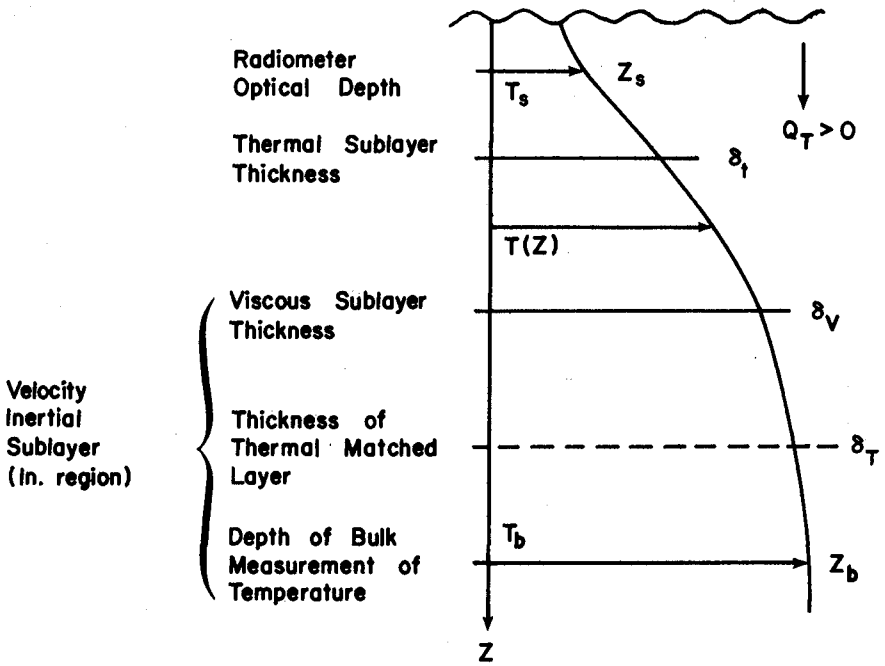


FIG. 1. SCHEMATIC OF AQUEOUS SURFACE LAYER.

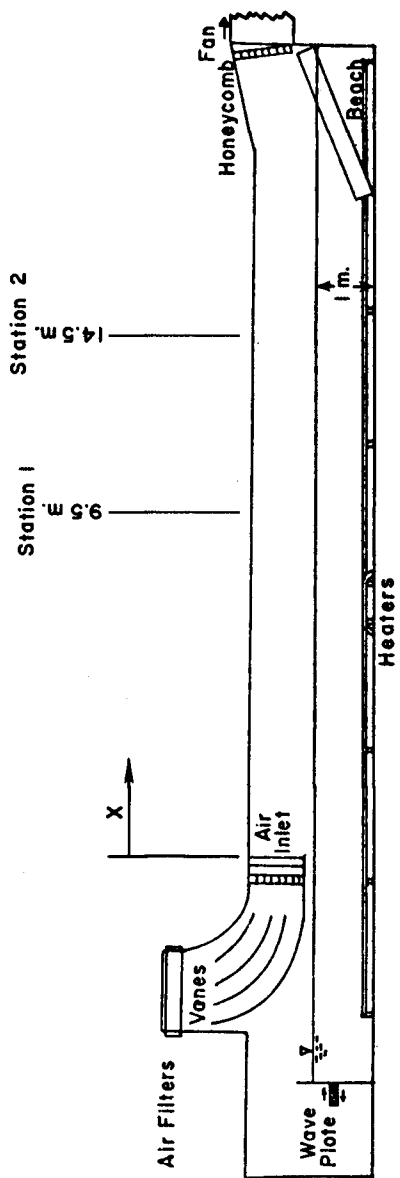


FIG. 2. SCHEMATIC OF STANFORD WIND, WATER-WAVE RESEARCH FACILITY.

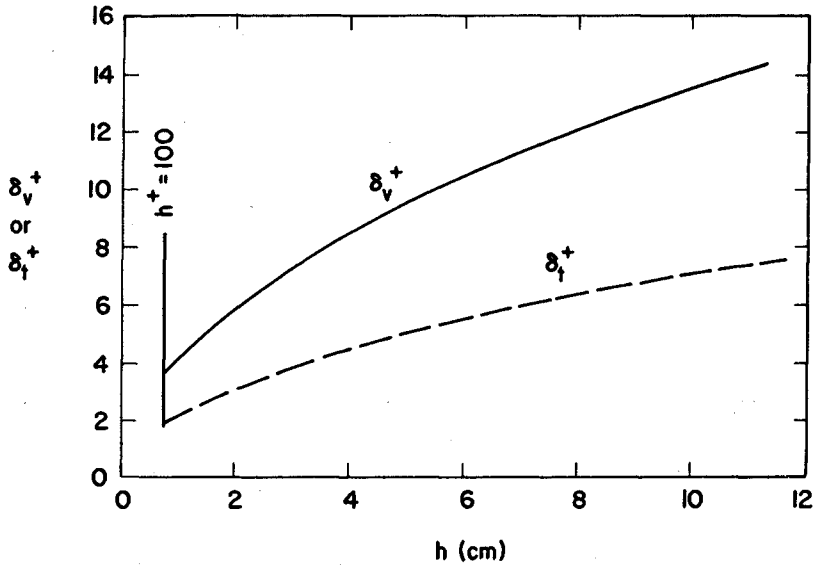


FIG. 3. VARIATION OF DIMENSIONLESS THERMAL AND VISCOUS SUBLAYER THICKNESS WITH MEAN WAVE HEIGHT FOR FULLY ROUGH BOUNDARY.

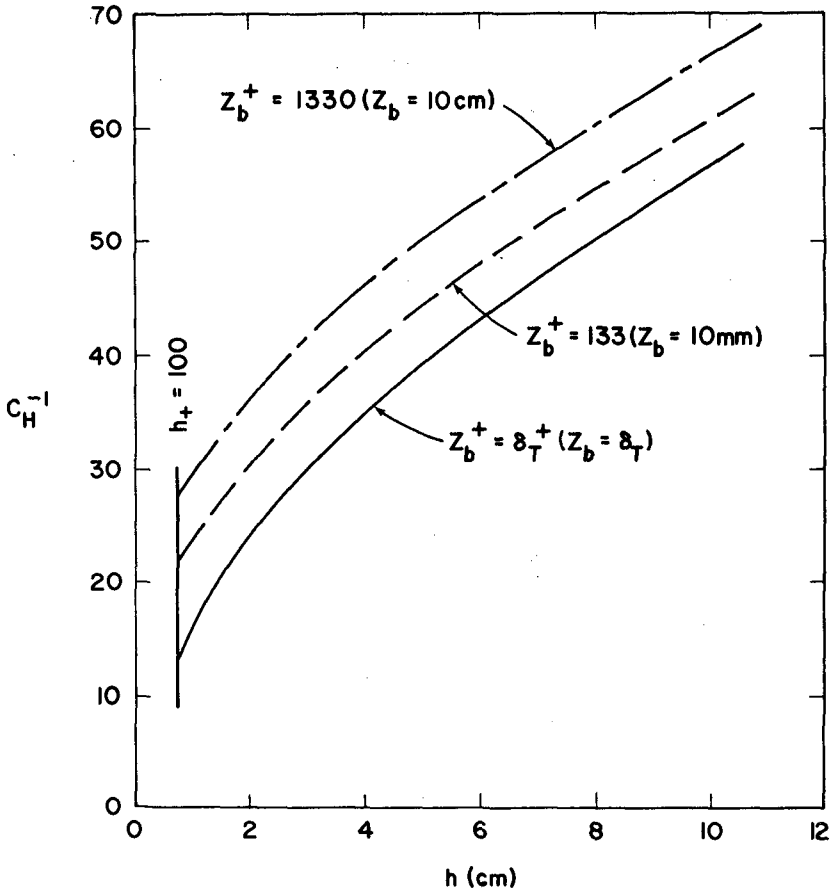


FIG. 4. VARIATION OF THE INVERSE OF THE TOTAL HEAT TRANSFER COEFFICIENT WITH MEAN WAVE HEIGHT FOR FULLY ROUGH BOUNDARY.

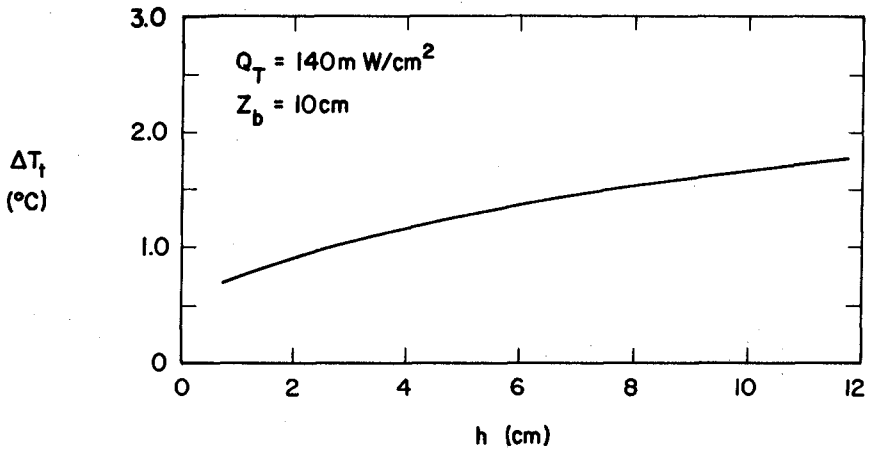


FIG. 5. VARIATION OF BULK-WATER TO SURFACE-WATER TEMPERATURE DIFFERENCE WITH MEAN WAVE HEIGHT FOR SPECIFIED Q_T AND Z_B AND A FULLY ROUGH SURFACE.

CHAPTER 185

STATE ESTIMATION OF ESTUARINE CIRCULATION AND WATER QUALITY BY NUMERICAL SIMULATION AND OBSERVATION

J. J. Leendertse; S. K. Liu

The Rand Corporation, Santa Monica, CA, U.S.A.

SUMMARY

This paper describes a hindcast of post-rainstorm coliform bacteria distributions in Jamaica Bay made by use of a water-quality simulation model of that bay and models of the surrounding drainage basins on the basis of tide, wind, and rainfall data. That hindcast is then compared with coliform estimates obtained by field sampling.

Although the investigators did not have access to the results of the field sampling until the hindcast was completed, the estimates obtained by simulation agree well with the estimates from field data. It is concluded that the models used here are capable of making predictions for engineering assessments.

INTRODUCTION

The City of New York is presently working to terminate the discharge of untreated combined sewer overflows after rainstorms by constructing Auxiliary Water Pollution Control Facilities (AWPCFs) around the periphery of Jamaica Bay (Fig. 1). The completion of this plan, together with ongoing upgrading of existing Water Pollution Control Facilities (WPCFs), would open the possibility of extensive use of the area for recreational purposes. Being within the City limits, it is ideally suited for that purpose.

Control of water pollution is generally a difficult task; extensive engineering analysis is required prior to committing large amounts of capital for the construction of facilities. The problems of analysis are compounded in this case, where water pollution control must be applied to the large intermittent discharges of relatively short duration caused by rainstorms.

For the optimal design of a control system as a whole and the auxiliary plants which are part of that system, the quality and quantity of the overflows, as well as the impact of each of the overflows upon the water quality in the bay, must be determined for rainstorms of different intensity and duration.

To optimize the design of AWPCFs with respect to required storage and treatment characteristics, it is particularly important to know the drainage basins' responses to rainstorms in quantity and quality of overflow, since overdesign would make the installations much more expensive to build and underdesign would impair the system's effectiveness. The tools for such assessments have been developed in a previous study [1]. Models of the different drainage basins around the bay are now available, and water-quality distributions can be computed by means of a two-dimensional model of the bay [2-7].

Figure 2 presents an overview of the Jamaica Bay urban estuarine water-quality simulation system. This figure shows the boundaries of several major drainage systems, together with the results of the water-quality simulation model for the bay itself.

The area around the bay is generally residential, with a large population. In certain areas there are more than 100 housing units per acre. However, along the northwestern shore of the bay much open undeveloped space still exists. These areas can be noted easily in the aerial photograph of the bay (Fig. 1), which is on the same scale as Fig. 2. It will also be noted that the islands in the bay are not developed except the Broad Channel community along the north-south connection through the bay.

Two airports are situated near the bay. A runway of John F. Kennedy International Airport extends onto a marshy island in the bay. The boundaries of the drainage basins near Kennedy Airport are not known exactly, but their storm-water discharges into the bay are accounted for and the discharge points are shown. Similarly, we accounted for a major storm-water discharge from a large, densely populated area west of the bay, namely, the Mill Basin separate system.

The effectiveness of the drainage basin models and the water-quality simulation model was evaluated by the observation, simulation, and state estimation of coliform distributions in Jamaica Bay resulting from a rainstorm during the period from May



Fig. 1--Aerial photograph of Jamaica Bay, Kennedy International Airport and vicinity, New York City, U.S.A. (Courtesy of U.S. Army Corps of Engineers)

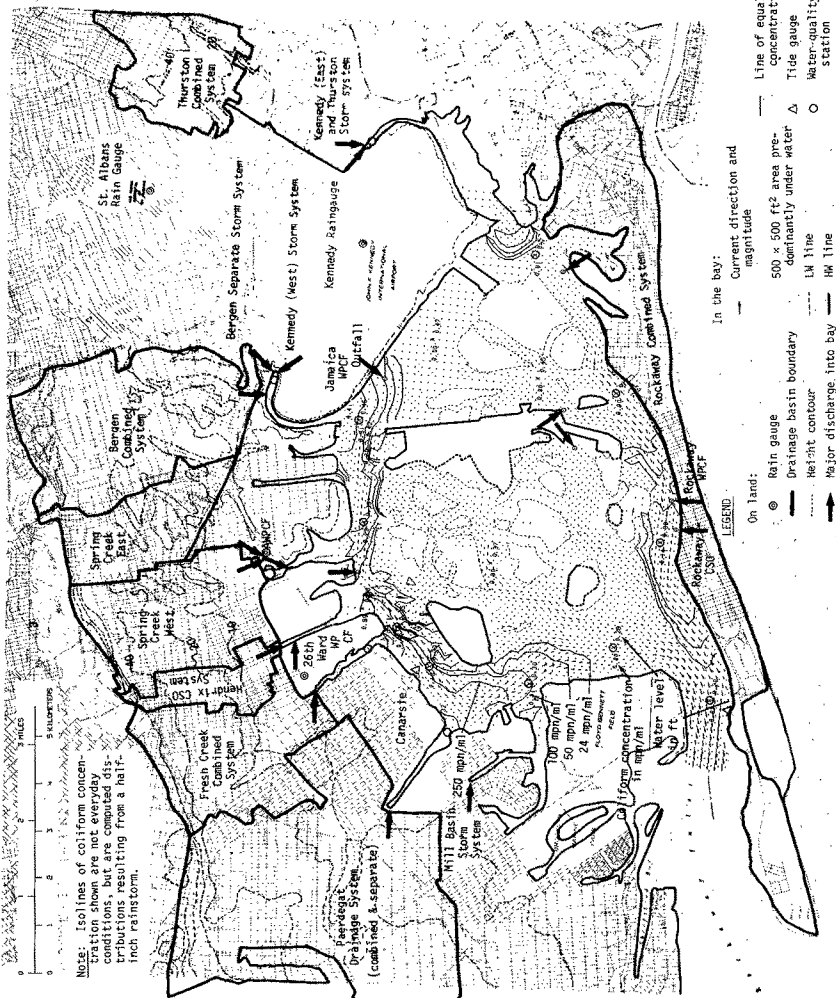


Fig. 2--Jamaica Bay urban-estuarine water-quality simulation system

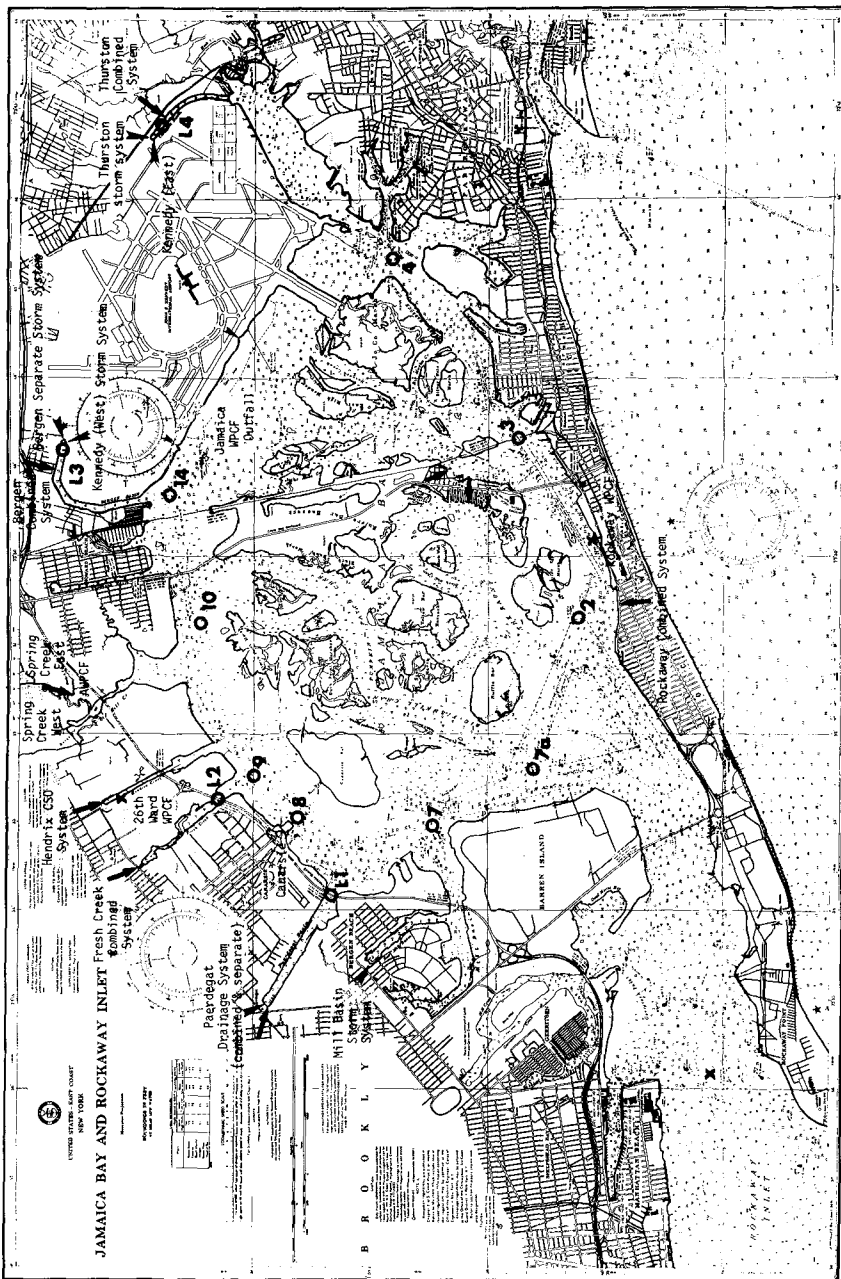


Fig. 3--Location of field sampling stations and the major discharges into Jamaica Bay

31 to June 3, 1972. This evaluation is presented in Ref. 7. In that experiment the results obtained by estimation agree well with those obtained by field measurement.

Because these predictive tools are important to the optimal design of the control system and its components, another evaluation was made based upon very extensive field measurements made by City personnel in the period of June 13 to June 17, 1973. To obtain from these models predictions completely unbiased by knowledge of observed water-quality data in the bay, the data from the observations were retained by the City until the predictions were completed. The present paper describes the results of this second evaluation experiment, in which state estimates obtained from field measurements were compared with estimates obtained from simulations.

DRAINAGE BASIN SIMULATIONS

The peripheral drainage areas of Jamaica Bay are served by nine major sanitary storm combined systems with a total drainage area of approximately 17,700 acres. An additional 19,000 acres of peripheral drainage areas have storm water systems which are separate from the sanitary system. These drainage systems, together with their points of discharge, are shown in Figs. 2 and 3. To simulate the water quality of the bay, the quantity and quality of discharge from these drainage areas during and after the storm must be determined.

These data were obtained by models for each of the drainage basins. Models were used because it is not physically possible to measure the quantity and quality of the time-varying overflows from each of the drainage systems simultaneously. Also, the City intends to use these drainage basin models for the real-time control of AWPCF operation after rainfall, as described in Ref. 1.

Consequently, the applicability of these models was proved in the experiment described here by predicting the time histories of the discharges and coliform concentrations from rainfall data. Thus, if the predictions made with the drainage basin model provided adequate input for the water-quality simulation and if the state estimates of coliform in the bay obtained by simulation agreed well with those obtained by observation, both types of models would be verified* and the models would be then considered suitable for use in prediction and control.

The drainage basin models use response functions which relate the overflow to the rainfall after taking into account depression storage of the rain and infiltration into the ground. For five of these basin models, the response functions were derived from extensive data sets of rainfall and the resulting overflow. These data, measured in 1970 and 1971 during a field study of water quality in the bay and inputs into the bay, were made available to us by the City. In determining the response functions from these data sets, we made extensive use of cross-spectral analysis, as described in Ref. 1. For those basins where these data were not available, response functions of a basin with similar hydrological and waste loading characteristics were used with modifications for the size of the basin.

* In a strict sense, compensating features do exist for these two types of models; they originate mainly from the time variability in the runoff quality estimates and the estimation of diffusive transport in the bay model. These characteristic compensating components would have equal probability of realization in future prediction when both models are used together. The expected variability of prediction should be similar to that determined from the present experiment.

To prepare the drainage system inputs of the water-quality simulation, the digitized rainfall data were first converted into effective net rainfall by estimating the system's imperviousness parameter and the depression storage. Then, for the free-flow system (i.e., no tidal influence downstream), the computed overflow hydrographs were obtained by means of numerical convolution of effective net rainfall and response functions.

For the downstream-controlled system, the time-varying overflow discharges were determined from the effective rainfall by a procedure which takes into account the water levels on each side of the tide gates in the overflow structure and the storage and flow characteristics of the sewer system. Determining these downstream-controlled discharges is much more complicated than for the free-flow discharges, since the former may have a delay of several hours for part or all of the discharged quantity when the tide gates close during high water.

The time histories of the bacterial concentration in each of the CSOs were computed from a formula that incorporates the basic mechanisms of surface washing, conduit dilution, and bottom scouring from within the system[1]. For the separate storm water systems, the quality of the discharge was based upon field data monitoring during a summer season, and a mean value of 70,000 MPN/ml was estimated.

A typical result of a drainage basin simulation is presented in Fig. 4. The hyetograph and the overflow, the response kernel, the overflow hydrograph, and the pollutograph are shown for the Thurston combined system.

The hyetograph is expressed in terms of inches per hour per unit area. The resulting system overflow is presented in the same graph in the same units for easy comparison. It will be noted that the total rainfall quantity is much larger than the overflow, since there is considerable loss from infiltration into the ground, especially within a large cemetery situated in the middle of this drainage area. Furthermore, part of this precipitation was handled by the WPCF as intercepted flow.

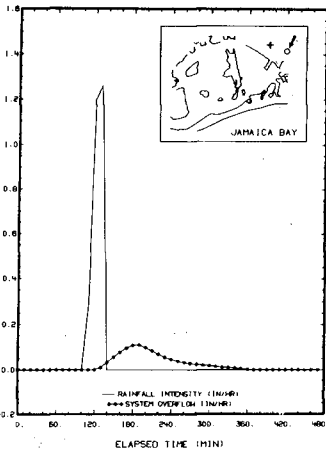
The location (+) of the rain gauge and the overflow (0) are indicated in the insert map on the hyetograph. The location of overflow as indicated refers to the location of the discharge in the two-dimensional model, not necessarily the actual geographical location due to the schematization. The zero reference for the elapsed time in this figure is at noon, June 13, 1973.

The rainfall intensity for this drainage basin was obtained from the rain gauge at John F. Kennedy International Airport.

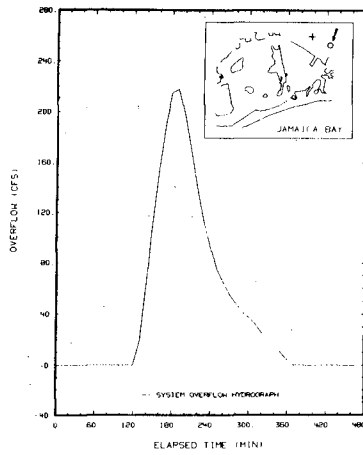
The coordinates of the response kernel are expressed in terms of cubic feet per second per inch. This unit was selected so that digitized rainfall data sensed from the tilting-bucket rain gauge (volume increments per 10 min) network installed in the drainage systems can be used directly to produce overflow discharges in cubic feet per second (cfs) through a simple machine computation.

The peak of the response kernel occurs at a time of one hour. As the rainfall intensity is strongly peaked, the overflow hydrograph also shows a peak, but at an elapsed time which is one hour later than the occurrence of the peak of the rainfall intensity.

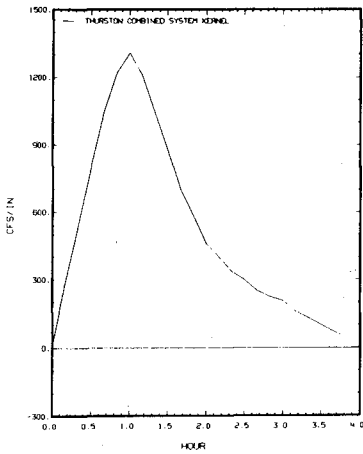
The overflow hydrograph is also presented in cfs. The pollutograph shows the time history of coliform concentration on the overflow in MPN/ml.



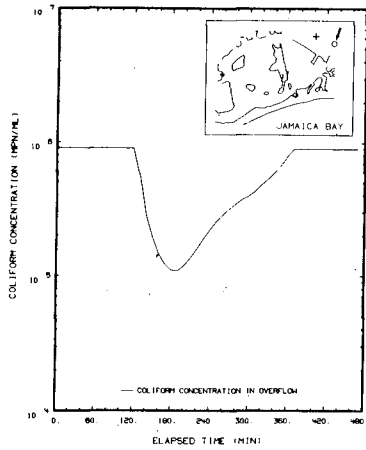
RAINFALL INTENSITY AND OVERFLOW (IN/HR)
THURSTON COMBINED SYSTEM



SYSTEM OVERFLOW HYDROGRAPH
THURSTON COMBINED SYSTEM



THURSTON COMBINED SYSTEM KERNEL



COLIFORM CONCENTRATION IN OVERFLOW
THURSTON COMBINED SYSTEM

Fig. 4--The rainfall intensity and overflow, the system overflow hydrograph, the system kernel, and the coliform concentration graphs of the Thurston Combined System

THE SIMULATIONS

The water-quality simulation was carried out for four calendar days from 0000 hr of June 13, 1973 through 2400 hr of June 16, 1973, with $T = 0$ at 0000 hr of June 13, which is approximately 14 hr before the beginning of the rainstorm. The time step of the simulation was 1 min ($\Delta t = 60$ sec). A coliform disappearance rate of 2.65×10^{-5} /sec, which corresponds to a 90-percent decay in concentration per day, was used throughout the simulation; this is the same as previously used. All the other parameters required for the simulation were kept the same as for the simulations of the previous rainstorm which was used for verification, as reported in Ref. 7.

The first simulation run which was made without the geostrophic boundary correction as described earlier caused some perturbations in the velocity field near the entrance. However, these local perturbations did not appear to influence the interior of the model.

In preparing the graphical outputs of the spatial distributions of coliform after the briefing, we noted that part of the records were lost because of a bad computer graphics tape. Also, from reviewing the drainage basin inflow time histories, we noted that several small values of inflow from the Rockaway CSO were inserted by mistake at the first hour of the second simulation day when the values should have been zero. For these reasons and because of our intention to try the geostrophic boundary correction, we made another simulation run without using any additional field information.

As mentioned earlier, this correction was made in anticipation of using this boundary information not only for this experiment, but also for a future investigation of the influence of a planned hurricane barrier in Rockaway Inlet. The major portion of the graphical results presented herein is from the second simulation. Charts with spatial distributions of velocities, mass transports, and coliform were obtained at time intervals of 124 min (2 lunar hr); a typical example of the velocity distribution is shown in Fig. 5. The following basic information is given in this chart, which represents the situation at 2235 min from the beginning of the simulation:

1. Clock time and date.
2. Wind speed (kn) and direction.
3. Locations and names of eighteen peripheral inputs, indicated by (O).
4. Tidal and wind-induced current velocity vector (2 ft/sec corresponding to a grid) on every point of the computation in each direction.
5. Current velocity and tide stage at eighteen stations throughout the bay. The value to the left of these current stations marked by (x) is the local velocity, the value to the right is the local water level.
6. Contours of equal velocity, with the values of the isolines indicated in the lower right corner of the chart. The lowest contour is at 0.2 ft/sec.

To relate the flow field to the tide stage, we also show in the figure a graph of the computed tide at Rockaway near the boundary of the model. The tide stage is indicated by a small arrow on the tide curve.

The velocities in Grassy Bay in the northeastern part of Jamaica Bay are very low: only in part do the vertically-averaged velocities exceed 0.2 ft/sec. If the veloc-

ies are a little smaller than 0.2 ft/sec, the vectors are not plotted, since their direction cannot be determined from the graphical output. The velocities in the inlet are the highest, exceeding 2 ft/sec.

Figure 6 shows, for the same time, the transports in cfs per ft width. The basic information on the chart is very similar to that of the velocities in Fig. 5. In this graph the isocontours of the transports are shown, as well as the transport vectors. Since the transports also reflect the depth, the figure shows more clearly the flow in the bay during the incoming flood tide. As water flows out of the channels onto the tidal flats, the transport intensities decrease towards the northeast. It will be noted that at this time the wildlife refuge in the center of the bay is filled to a large extent by flow in a northeasterly direction, through the so-called Pumpkin Patch Channel.

Grassy Bay is filled by the flood flow from the south as well as from the west. In order to study the flow pattern in this bay in more detail, the transport vectors in the bay were enlarged five times in comparison with the vector intensities in the remainder of the figure. The flow, through the deep channel which enters from the south, generates eddies in Grassy Bay, apparently by a kind of jet effect.

Figure 7 shows another typical result of the simulation. This graph shows the isocontours of the coliform concentrations as well as the velocity vectors and the area flooded at that time. This is shown by a dot (·) at the water-level point which participates in the computation at the time of plotting.

The condition represented by this figure shows that the marshes in the bay are only partially flooded. In contrast to figures shown in previous publications, the velocity vectors in all the graphs are now located at the point where the water depth is inserted. The vector is suppressed, however, if the velocity is smaller than 0.2 ft/sec. This method presents the submerged areas more clearly.

In this figure, the state estimates of coliform and water level are shown at the locations at which bay samples were obtained. The location at which this numerical data is presented is indicated by (x). The numerical value on the left of the mark in this case is the coliform concentration in 1000 MPN/ml, whereas the values on the right are water levels. The coliform estimate shown can assist in finding the values of the coliform contours.

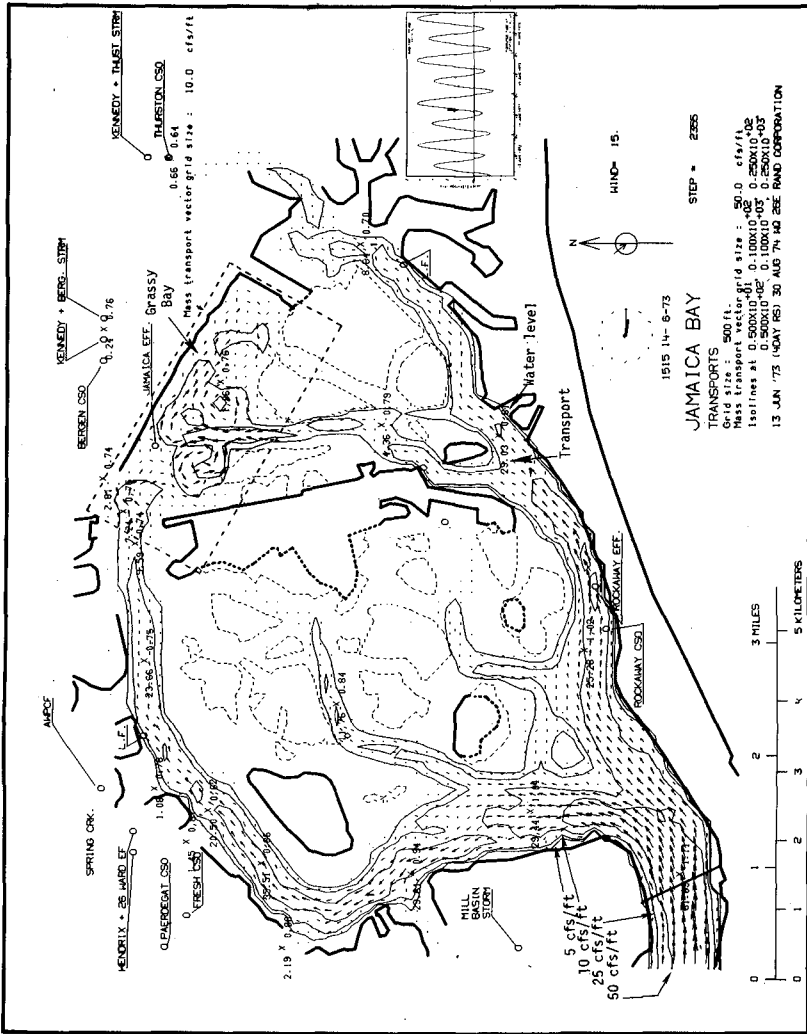


Fig. 6--Hindcasted transport distributions in Jamaica Bay on June 14, 1973 at 15 hr 15 min

STATE ESTIMATES OF COLIFORM FROM SIMULATION AND OBSERVATION

At thirteen stations in the bay, samples were taken which can be compared with the state estimates from the simulation. These comparisons are shown in Figs. 8 through 10

In these figures the 90-percent confidence interval is shown for the observations as well as for the computed estimates. The upper limit shown is the upper 95-percent confidence limit, and the lower is the lower 95-percent confidence limit. Thus, in a statistical sense, we have 90-percent confidence that the computed and observed estimates are within the interval of the limits shown. The interval of the observed coliform concentrations is determined by the nature of biological tests made. The interval of the computed estimates is the same as the number of tests used to determine the characteristics of the drainage basin model, and the confidence interval can be carried over from the drainage basin model results into the water-quality simulation.

Since animal life is present nearly everywhere in the bay, small randomly distributed coliform loads are being applied to the system continuously. Because the results of extensive coliform surveys made a few years ago indicated that these sources give a background level of about 10 MPN/ml, this value was added to the results of the simulation presented herein.

In Fig. 8 the observed coliform estimates agree well with the estimate by simulation; only two observed estimates are outside the confidence band of the simulation. These values are somewhat suspect, since these high values occur at about the same time at each station and thus have likely been processed in the same manner.

In Fig. 9 also only a very few observations are outside the confidence band. Generally we underestimated some high values in the second day of the simulation. An underestimate is quite well possible near discharges, since we are computing with averages in a 500×500 ft² area, which averages can be lower than observed if steep gradients are present.

In Fig. 10 as well only a few observations are outside the confidence limit.

A time-independent plot of the observed and the computed coliform concentration is presented in Fig. 11. In this diagram the ordinate represents the observed values, whereas the abscissa represents the computed values. The solid line across the diagram represents the location of all values in the hypothetical case that we were able to exactly predict computed values for and make error-free field observations. The six values denoted by cross hatches (+) indicate the discrepancies in the Paerdegat Basin as described earlier.

The model and the field sampling are far from being free of error, but we are able to indicate confidence bands. The confidence band representing the testing variability of the observed samples is delineated by dashed lines. Thus, according to the nature of the laboratory test, there is approximately a 10-percent probability that the actual number of bacteria in a given sample lies outside of these limits. Approximately the same confidence band also exists for the computed estimates, which are represented by a horizontal range of limits. This probabilistic behavior of the computed values is inherited from the water-quality inputs derived from the

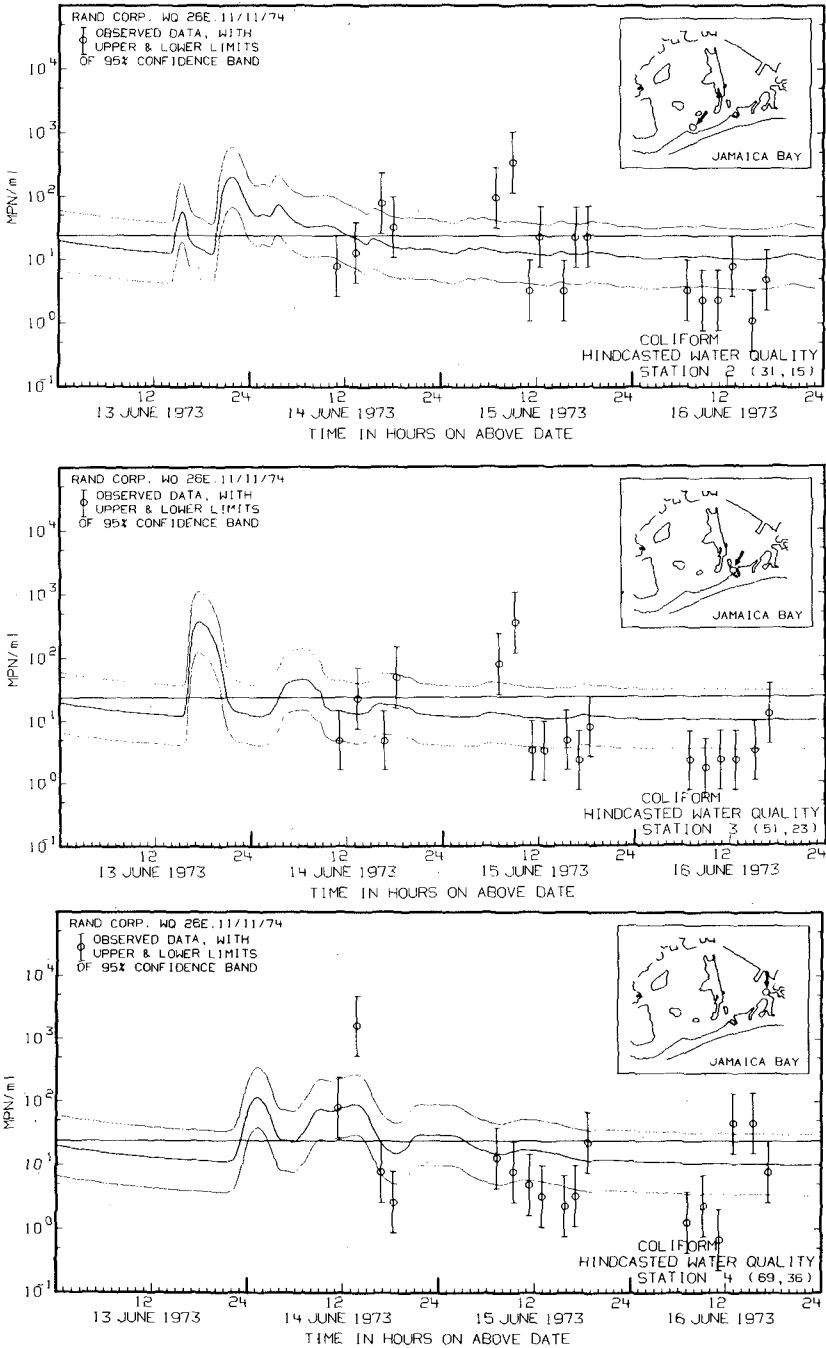


Fig. 8--Hindcasted coliform concentration histories and observed values at three stations in the southern part of Jamaica Bay

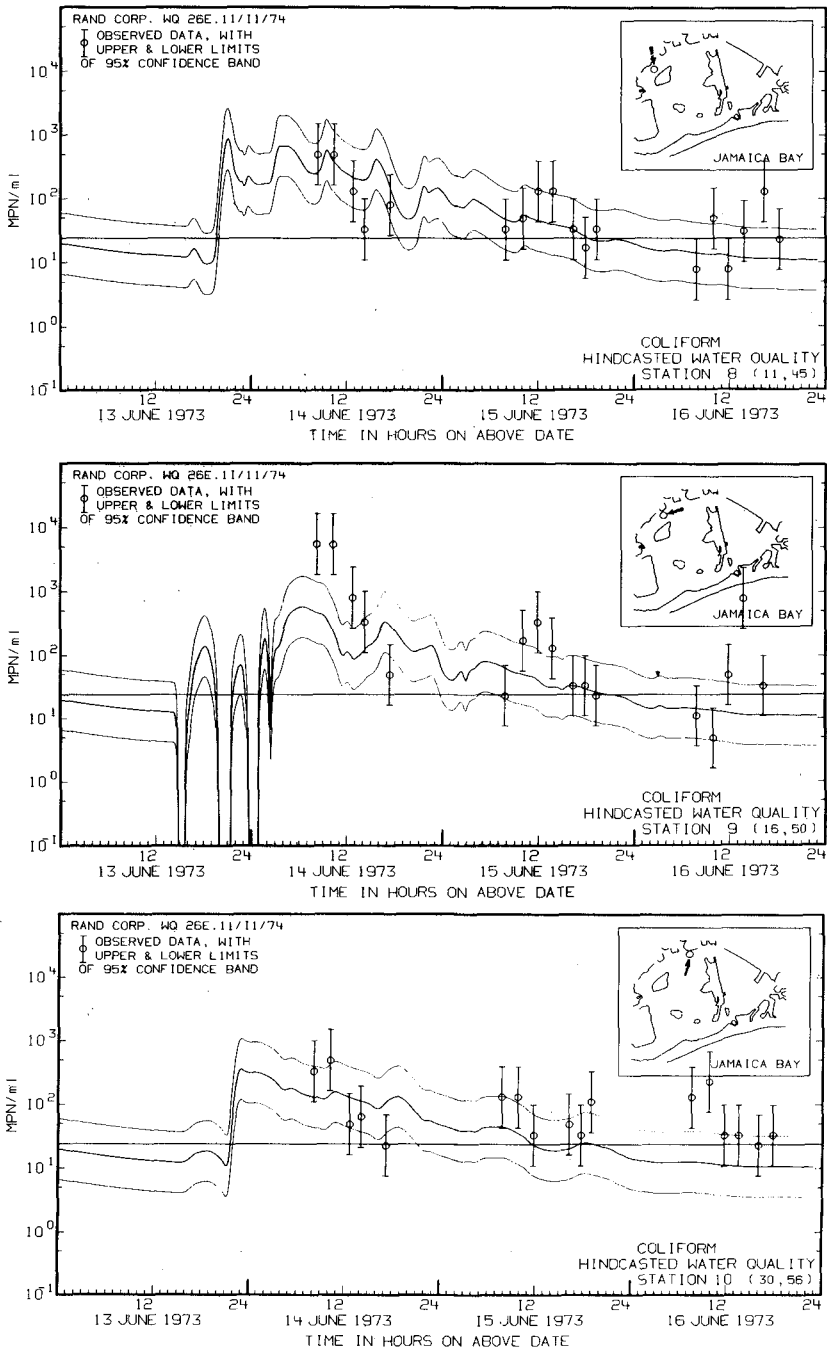


Fig. 9--Hindcasted coliform concentration histories and observed values at three stations in the northern part of Jamaica Bay, New York

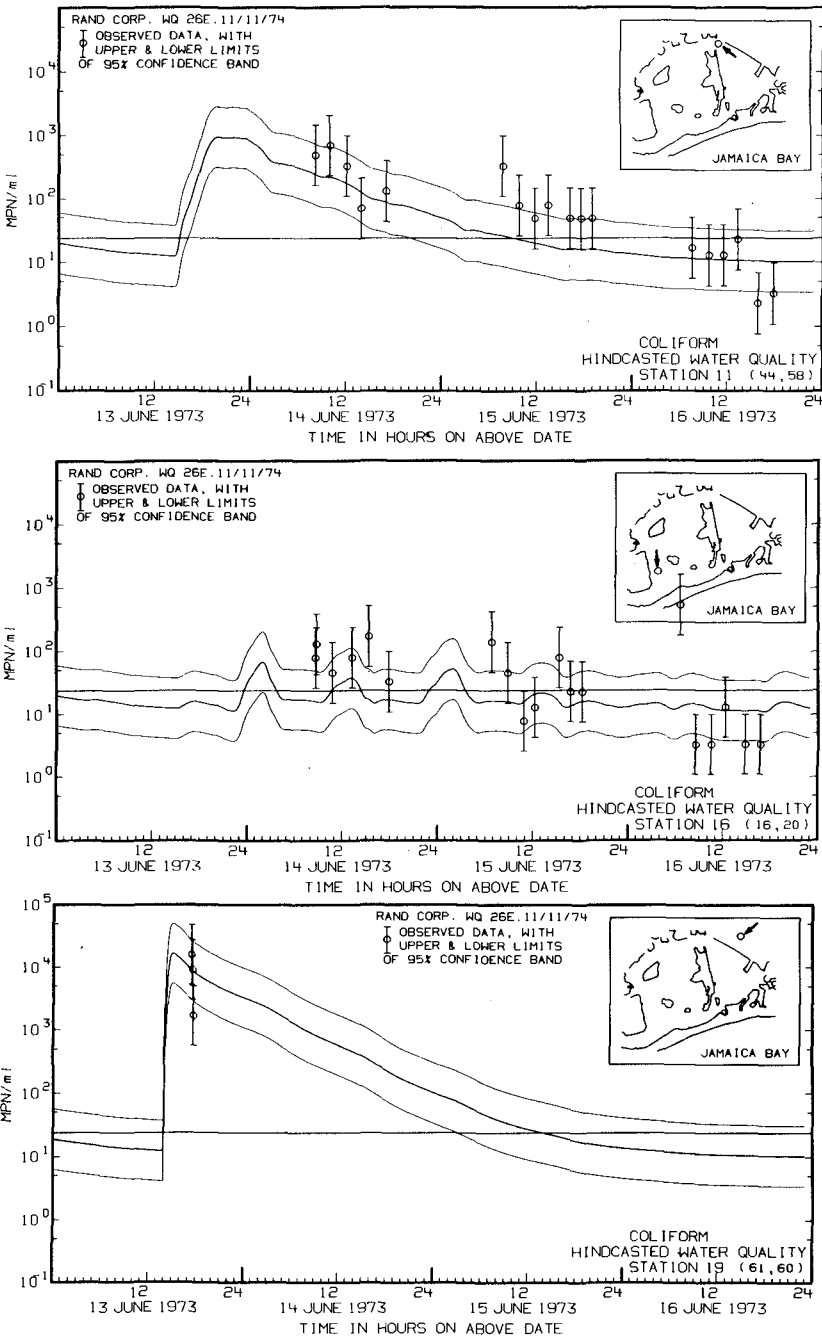


Fig. 10--Hindcasted coliform concentration histories and observed values at three stations in the western and northeastern part of Jamaica Bay, New York

peripheral drainage models and applied to this two-dimensional hydrodynamic computation of the bay water quality. Because the former derived its coliform prediction functions using observed coliform estimates, it is subject to a testing variability similar to that mentioned for the observed samples in the bay. The other error sources which contribute to the total deviation between the computed and the observed values are as follows:

- The resolvability of the rain gauge network.
- The prediction of overflow quantity.
- The time of discharge of the estimated overflow within the drainage system.
- The intercepted flow to the WPCF for the particular day and time.
- The computation of the flow in the water-quality model.
- The estimated parameters governing the diffusion and advection in the water-quality model.
- The sampling location in the field, especially in the vicinity of a discharge point where a sharp gradient exists.
- The resolvability of the grid system for representing computed estimates in the model.

In Fig. 11, no computed values lower than 10 MPN/ml are shown because of the assumption that a uniformly distributed background level of 10 MPN/ml exists in the bay. This value appears to overestimate the stations in the southernmost channel along the Rockaway peninsula, as indicated by the number of coliform observations lower than 10 MPN/ml.

It is apparent from the comparisons presented here and in the previous report that the models are able to make predictions quite well within the confidence bands. In the time-independent comparison (Fig. 11) it appears that only a small percentage (approximately 10 percent) is outside the expectation range. Thus, if other simulations are made, one would expect the results to be similar.

CONCLUSIONS

From the comparison of coliform estimates from observations in Jamaica Bay and the estimates obtained by simulation, it can be concluded that coliform density distributions in the bay, as well as discharges in the bay, can be predicted with confidence. Consequently, the models used in this investigation are capable of making predictions for engineering assessments.

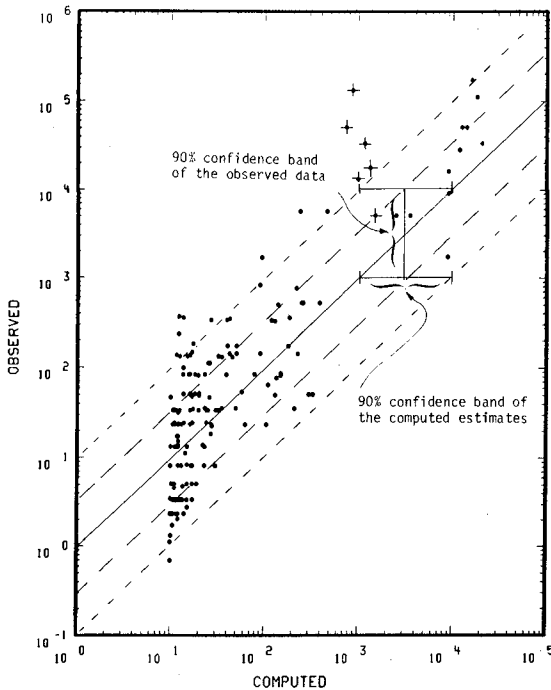


Fig. 11--Observed versus computed coliform state estimates with their confidence bands

ACKNOWLEDGMENTS

We appreciate greatly the action taken by Mr. Martin Lang, First Deputy Administrator of the Environmental Protection Administration of New York City, which resulted in the stringent test of the predictive capability of water quality in Jamaica Bay described in this report.

We also want to acknowledge the cooperation of Mr. Norman Nash, First Deputy Commissioner, and Mr. William Pressman of the Department of Water Pollution Control. The field studies used in this investigation were made by Messrs. S. Arella, M. Singer, and H. Innerfeld of the Department. During the study period Mr. Charles Samowitz was Commissioner of Water Resources.

The many graphs in this report were prepared by Ms. M. Lakatos and Ms. G. Burkholz. Our colleague Mr. A. Nelson made the simulations.

The development of the programs used in the data analysis is sponsored by the U.S. Geological Survey of the Department of the Interior and by the Data Processing Division of the Netherlands Rijkswaterstaat.

REFERENCES

1. Liu, Shiao-Kung, *Stochastic Analysis and Control of Urban Estuarine Water-Quality Systems: Vol. I, Estimation and Prediction*, The Rand Corporation, R-1622-NYC, December 1974.
2. Leendertse, J. J., *A Water-Quality Simulation Model for Well-Mixed Estuaries and Coastal Seas: Volume I, Principles of Computation*, The Rand Corporation, RM-6230-RC, February 1970.
3. Leendertse, J. J., and E. C. Gritton, *A Water-Quality Simulation Model for Well Mixed Estuaries and Coastal Seas: Vol. II, Computation Procedures*, The Rand Corporation, R-708-NYC, July 1971.
4. Leendertse, J. J., and E. C. Gritton, *A Water-Quality Simulation Model for Well Mixed Estuaries and Coastal Seas: Vol. III, Jamaica Bay Simulation*, The Rand Corporation, R-709-NYC, July 1971.
5. Leendertse, J. J., *A Water-Quality Simulation Model for Well Mixed Estuaries and Coastal Seas: Vol. IV, Jamaica Bay Tidal Flows*, The Rand Corporation, R-1009-NYC, July 1972.
6. Gritton, E. C., *A Water-Quality Simulation Model for Well Mixed Estuaries and Coastal Seas: Vol. V, Jamaica Bay Rainstorms*, The Rand Corporation, R-1010-NYC, July 1972.
7. Leendertse, Jan J., and Shiao-Kung Liu, *A Water-Quality Simulation Model for Well Mixed Estuaries and Coastal Seas: Vol. VI, Simulation, Observation, and State Estimation*, The Rand Corporation, R-1586-NYC, September 1974.
8. *Standard Methods for the Examination of Water and Waste Water*, 12th ed., American Public Health Association, October 1967.
9. *Influence of a Landfill on Water Pollution*, Phase 1 report, New York City Department of Health, 1965.
10. *Waste Discharge Characterization*, a task report submitted to the Department of Water Resources, Environmental Protection Administration, City of New York, by Engineering Science, Inc., May 1971.

CHAPTER 186

NUMERICAL MODELLING - AN AID TO ASSESSING FIELD DATA

H.P. Riedel¹ and F.L. Wilkinson²

ABSTRACT

After the completion of 5 years of field measurements, complemented by extensive numerical modelling in 1974, the hydraulics of Cockburn Sound, Western Australia, are now understood in enough detail to allow the rate of exchange of water between the Sound and the ocean to be determined. Flow patterns in Cockburn Sound tend to be complicated by the superimposition of many driving influences, the most important being wind, but by using the output of a numerical model most of these patterns are predictable.

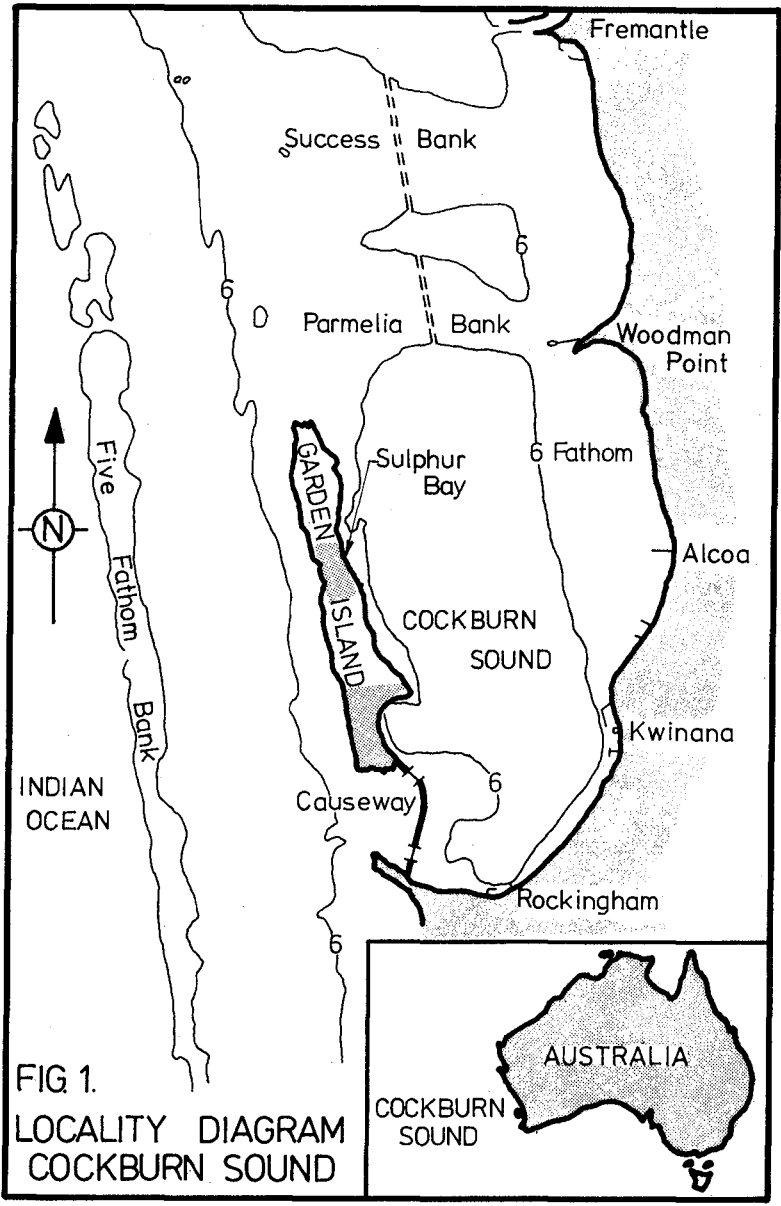
Current magnitudes within Cockburn Sound have not reduced so that the rate of dispersion of effluents released by the industrial complex on the eastern side of the Sound has not changed. However, flow rates through the southern entrance to Cockburn Sound have been reduced to between 30 to 45% of the rates which occurred prior to the causeway construction. This means that the mean discharge rate is now 570 m³/sec through the causeway bridges compared to a rate of about 1500 m³/sec before the causeway construction.

1. INTRODUCTION

The hydraulic and environmental conditions in Cockburn Sound, Western Australia (see locality map, Fig. 1), an area with a very small tidal range, have been the subject of intensive investigation since 1969 in order to assess the effect on Cockburn Sound currents of constructing a causeway, with two bridge openings, between Garden Island and the mainland. The causeway was constructed in the period 1971-1973 so that field data has been collected before, during and after completion of the project. However, because of the complexity of the driving forces which control currents in Cockburn Sound, much of the data collected before the start of 1974 appeared contradictory and there was still a large degree of uncertainty in the interpretation of the field data.

In 1972 some exploratory numerical modelling was conducted using 'System 21 - Jupiter', a general purpose system for studying two dimensional nearly horizontal flows which has been adequately described in the literature by Abbott et al (1). From these early numerical modelling runs, it appeared that the incomplete picture provided by the field data could be improved by detailed numerical modelling. Consequently, extensive numerical modelling of currents due to ocean currents, wind and tide were carried out both for currents caused by individual driving forces and for selected combinations of driving forces during July-August 1974.

1, 2 Maritime Works Branch,
Australian Government Department of Construction.



In all, 26 modelling runs were executed in order to compare water movements in Cockburn Sound before and after the causeway construction, in particular in areas where field measurements had given rise to ambiguities.

2. FACTORS CAUSING CURRENTS IN COCKBURN SOUND

Currents in Cockburn Sound are caused by the combination of several driving forces which may be sub-divided into primary and secondary groups. The available information shows that water exchange between Cockburn Sound and the ocean is predominantly governed by wind induced currents within Cockburn Sound and by oceanic currents moving north or south along the West Australian coast. Secondary influences are tides, surges during storms, long waves and short period waves. The current patterns and magnitudes are also largely influenced by bottom topography.

The magnitude of wind induced currents in an open body of water are typically up to 3% of the wind velocity. When considering wind effects on an enclosed or semi-enclosed body of water with a complex bottom topography, the cause and effect relationship between the wind and the water becomes quite complex. Consequently, the water current cannot be inferred directly from the wind velocity and must either be directly measured or theoretically determined by the use of modelling.

The oceanic current is derived from the West Australian current which is a large scale current present in deep water off the West Australian coast. See Neumann (2) for a more complete description. It is partially driven by other currents circulating in the Indian Ocean and is part of a larger oceanic system which is the result of a balance between geostrophic, inertial and prevailing wind driven currents. The oceanic current is then modified locally by :

- (i) the effect of wind systems along the West Australian coast;
- (ii) the intensity and rate of movement of atmospheric pressure systems;
- (iii) nearshore bottom topography

to yield currents at the boundaries of Cockburn Sound.

Either of the primary currents may dominate the flow field and mask the effect of any other current. Generally, ocean currents tend to be persistent, their time scale being of the order of days and many explanations of observed water movements must make reference to this parameter for a satisfactory interpretation of the data. Wind induced currents are relatively easy to detect and can easily be correlated with wind data. Many of the observed flow rates and patterns can easily be explained in terms of wind induced currents, especially when the velocity field is predicted from a numerical model. However, for short duration strong winds there have been instances where current directions are observed opposite to the wind direction due to the predominance of the ocean current, or the presence of a seiche of 2-3 hours period. The natural frequency of seiching for Cockburn Sound in the north-south direction is $2\frac{1}{2}$ hours.

Tidal currents are of small magnitude because of the small diurnal tidal range, however, the exchange of water between Cockburn Sound and the ocean caused by the tide is basically steady from day to day resulting in about 3% of the volume of Cockburn Sound being exchanged daily.

Currents induced by long and short period waves affect small scale water circulation rather than gross exchange. These currents are most noticeable in the shallow Southern Flats area, particularly at the bridge openings while in the bulk of the Sound they are often not detected.

With the construction of the causeway, current patterns and magnitudes have changed, significant changes being confined mainly to areas within 1500 metres of the causeway.

3. FIELD MEASUREMENTS

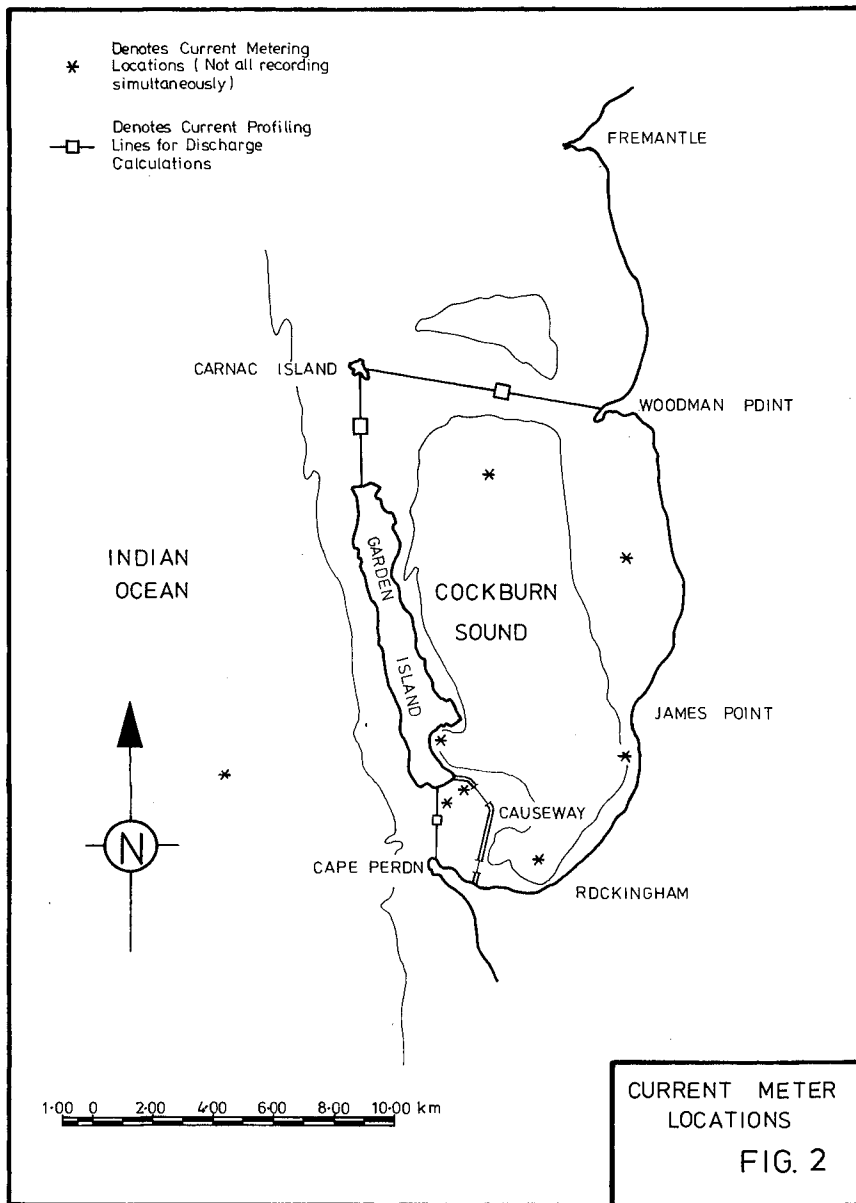
These measurements consist of

(a) Current Metering, which has been in progress for the full duration of the field measurements with current meters placed at the locations shown in Fig. 2 at various stages of the study. Unfortunately, conventional off the shelf meters, as used in this study, generally have two restrictions on their use. They have a threshold velocity of about 4 cm/sec so that they usually do not respond to the low velocities present in the deep waters of the Sound, and they tend to oscillate and give unreliable results if waves are present with periods greater than about 5 seconds. Consequently, most of the useable data has been confined to current measurements made across the Garden Island to Cape Peron gap.

These measurements were made in 1969-70 before the causeway and in 1974-75 after the causeway construction and form the basis for the quantitative assessment of discharges through the southern entrance to Cockburn Sound.

(b) Salinity-Temperature Metering, which was used at one metre depth intervals for about 30 points throughout Cockburn Sound. Measurements were conducted twice daily for periods up to 10 days in an attempt to track the motion of discrete bodies of water labelled by their salinity/temperature characteristics. Flushing rates estimated using this method were sometimes 5 times the rate estimated by other methods and indicated practically unchanged flushing rates before and after the causeway construction. The unchanged apparent flushing rates between 1971 and 1973 may be explained by current magnitudes after the causeway construction remaining constant through the intensification of a large scale circulation in the centre of Cockburn Sound. This occurred even though the nett discharge through the entrances to Cockburn Sound had changed significantly. Data using salinity metering has been ignored for any quantitative analysis, and no further data was collected after 1973.

(c) Float Drogue Tracking, which was used extensively up until 1974 with most of the tracking concentrated along the causeway route and within 1500 metres of the causeway. The main problem with the float drogues was wind drag on that portion of the float above the water surface. Also there is a partial integrating effect because of drag on the float as well as on the drogue vanes. Considering these factors the float drogues can only be expected to yield qualitative data in Cockburn Sound which is an extremely windy area.



(d) Dye Tracking, which consisted of instantaneously releasing a quantity (about 10 kg) of Fluoroscetin or Rhodamine B and then tracking the dye patch from aerial photos and/or by a fluorometer mounted in a runabout. It was attempted to obtain quantitative data but the information was only used for descriptive purposes because of problems with instrument operation.

(e) Tidal data. Tide records are available continuously for the port of Fremantle and, as would be expected, short term tide recordings taken within Cockburn Sound correlate well with the Fremantle data. The predominating feature of the West Australian coast in the vicinity of Fremantle is the very small, diurnal tidal range. The tidal range rarely exceeds 0.6 metres and tidal velocities tend to be negligible in water depths greater than 5 metres. The average tidal range is 0.4 metres which results in about 3% of the volume of water in Cockburn Sound being exchanged daily by this mode.

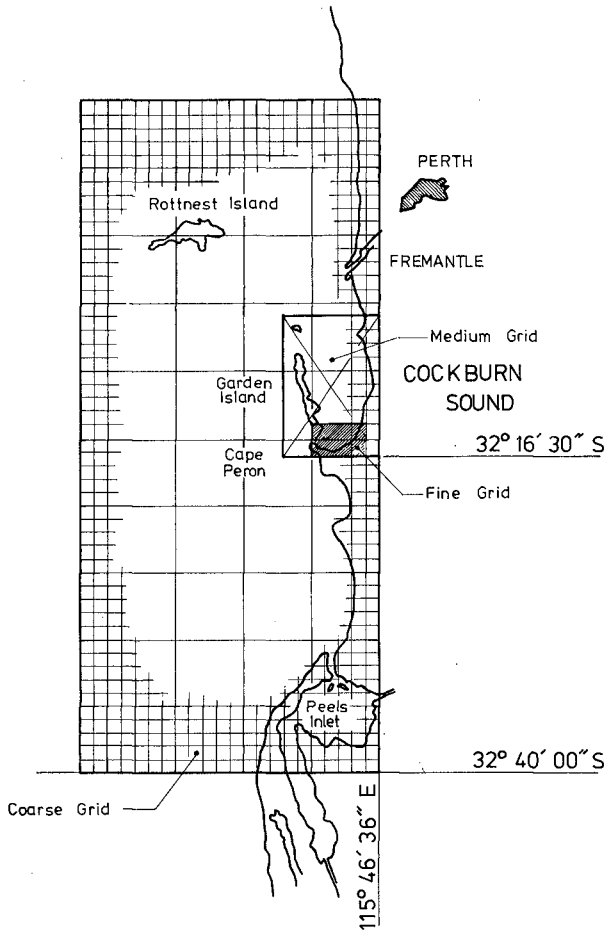
(f) Meteorological data. Wind and barometric pressure records were available from the Fremantle Port Authority and again the difference between observations of these parameters at Fremantle and within Cockburn Sound was negligible, except for a time lag in the wind, in particular in the arrival of the sea breeze. The wind data was necessary in estimating the component of water currents caused by wind shear and the barometric data usually explained any discrepancy between the predicted and observed tidal heights. It is also thought that the passage of intense pressure systems will induce seiching and water currents because of the 'inverted barometer' effect but it is difficult to isolate this phenomena when there are so many other driving influences present.

The overall picture presented by the collection of the above field data up to December 1973 was one of uncertainty and clarification was required, and it was thought that numerical modelling would be the method most likely to succeed.

4. THE NUMERICAL MODEL

Numerical modelling studies were made using System 21 'Jupiter', a computational system consisting of a set of computer routines with back up documentation which is used to construct a numerical model of any region of two dimensional nearly horizontal flow when presented with the hydrography of the region and operates the model from given initial and boundary conditions, wind velocities, atmospheric pressure differences, tidal-tractive forces, latitude and other external conditions as required. It provides output in the form of velocity and water surface level plots for selected regions on the complete computation field. A detailed description of the model may be found in Ref. (1)

In all, 26 computer runs were made using 3 different grid sizes with boundary conditions chosen to represent the most commonly occurring current generators. A very coarse grid (C) of 1 nautical mile spacing was used (Fig. 3) to include a sufficient ocean area so that the penetration of the oceanic current into Cockburn Sound could be reliably reproduced. Runs 1-4 were run on the coarse grid and were used as boundary conditions for medium grid runs involving the oceanic current. For these runs an oceanic current of 20 cm/sec was modelled for a real time duration of 13 hrs which was the time required to reach a steady condition.



MODEL GRIDS

Coarse Grid Spacing = 1 Nautical Mile

FIG. 3

A grid with a spacing of $1/3$ nautical mile, termed a medium grid (M), was used for most of the study to predict flow patterns and water throughput for Cockburn Sound. Run numbers 5-22 were based on the medium grid and covered all the commonly occurring wind, oceanic and tidal conditions affecting Cockburn Sound. The wind applied in runs 5-14 was increased linearly from 0 to 20 knots over a period of 3 hours and then held constant for the next 3 hours by which time a steady state had been reached.

In order to obtain a clear pattern of velocity vectors for tidal flows, runs Nos. 15 and 16, an extreme tide range of 0.8 m was modelled rather than the mean range of 0.4 m. A full diurnal tidal cycle was modelled and the only affect of the causeway was to push the null point of the tide within Cockburn Sound further south. As expected the tidal range did not change.

Runs 17 to 20 used a hot start from runs 1 to 4 respectively, ie. the boundary conditions at the edge of the medium grid were obtained from the steady condition of the coarse grid and held constant for 3 hours in order to let the medium grid runs reach a steady state. Then a SW or NW wind is applied in the same way as for runs 5 to 8.

Runs 21 and 22 on the medium grid were used to simulate a sea breeze pattern which is a common occurrence at Cockburn Sound during summer. The sea breeze cycle consists of an overnight land breeze from the NE followed by a change of the wind to the SW during the day.

Runs 25 and 26 were made on a fine grid (F) with a spacing of $1/9$ nautical mile and only covered the area in the vicinity of the causeway. This grid was not used to predict discharges but was used to look closely at seiching and other oscillations which may have been induced by varying boundary conditions arising from the influence of the sea-breeze.

Table 1 lists the modelling runs. By combinations or superposition of the results from the 26 runs it is possible to estimate the currents for any physically occurring situation. The only significant limitation in using the model is that it is depth integrated and so only gives velocities averaged over the depth at any point. This means that where wind shear is the driving force which moves the surface water roughly in the direction of the wind to a depth of, say, 10 metres, there may be a return current below this depth in order to satisfy continuity, but the numerical model effectively gives the average of these two components which may not resemble either of them. It is in this type of situation where discrepancies between field observed currents and numerically computed currents is most likely to occur. However, in shallow water areas the model will give a representative indication of the currents. The model is however, directly useful for estimating gross rates of water exchange as the depth averaged velocities relate directly to water transport or "flux".

TABLE 1 - MODEL RUNS

Run No.	Grid	Boundary Condition	Time step (sec)	Real time duration (Hrs)
1	C	N-S current w/o causeway	300	13
1A	C	N-S current w/o causeway (modified)	"	13
2	C	N-S current with causeway	"	13
3	C	S-N current w/o causeway	"	13
4	C	S-N current with causeway	"	13
5	M	SW wind w/o causeway	"	6
6	M	SW wind with causeway	"	6
6B	M	SW wind with causeway (modified)	"	6
7	M	NW wind w/o causeway	"	6
8	M	NW wind with causeway	"	6
9	M	E wind w/o causeway	"	6
10	M	E wind with causeway	"	6
11	M	S wind w/o causeway	"	6
12	M	S wind with causeway	"	6
13	M	N wind w/o causeway	"	6
14	M	N wind with causeway	"	6
15	M	Tide w/o causeway	"	25
16	M	Tide with causeway	"	25
17	M	N-S current, SW wind w/o causeway	"	14
18	M	N-S current, SW wind with causeway	"	14
19	M	S-N current, NW wind w/o causeway	"	14
20	M	S-N current, NW wind with causeway	"	14
21	M	Sea breeze w/o causeway	"	15
22	M	Sea breeze with causeway	"	15
25	F	Sea breeze w/o causeway	"	15
26	F	Sea breeze with causeway	"	15
25A	F	Sea breeze w/o causeway	15	2
26A	F	Sea breeze with causeway	15	2

5. COMPARISON OF FIELD DATA WITH NUMERICAL MODELLING SOLUTIONS

Comparison of field data with the numerical modelling solutions was divided into two categories - comparison of flow patterns on a qualitative basis as is possible with float drogue data, and comparison of measured discharges through the southern opening to Cockburn Sound. Both types of comparison can only be attempted in situation where wind controls the flow and wind fields are similar in the model and in the field. Direct comparison of oceanic current model runs with field information is not possible because this current was not measured successfully in the field. All the field data gathered at times for which there are model solutions with comparable wind fields are presented in the comparisons and any poor correlations can usually be explained by seiching, the oceanic current or tidal currents.

5.1 Flow Patterns

Float drogue measurements were made over a period of four years during which float tracks were obtained for all wind directions. However, in order to compare these current measurements with the model output it was considered that the wind should average at least 5 m/sec and not change in direction by more than 45° for a 6 hour duration. Six hours was chosen because in this time a wind induced current would approach a steady state condition.

The general type of results obtained are shown for the case of a SW wind, the most common weather condition, in Figs 4 and 5, which show flow patterns before and after the causeway construction respectively. Comparisons for other wind conditions give similar agreement but because of space limitations the results for only two other weather conditions will be shown.

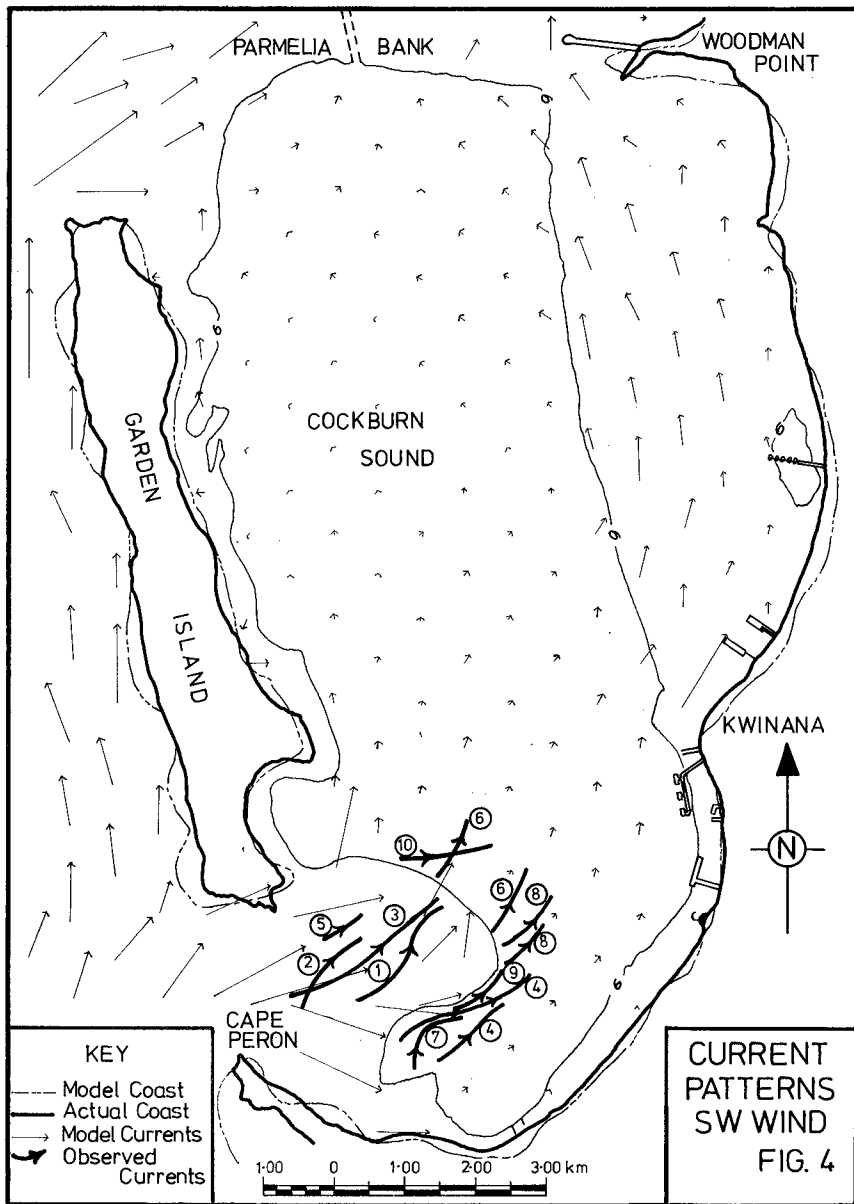
It is emphasised that the current pattern comparison is qualitative only and the current depicted by the float drogue paths show direction only and are not scaled. A quantitative comparison is not valid because the float drogue usually measures a surface current whereas the model calculates a current averaged over the whole depth and additionally there is a wind drag on the float which usually results in the velocity of the float drogue being higher than that of the water current. From a combination of these two effects the current magnitudes of the float drogues are on an average approximately 50% greater than the currents estimated by the comparable numerical model. However, the current directions taken by the float drogues were reproduced remarkably well by the models.

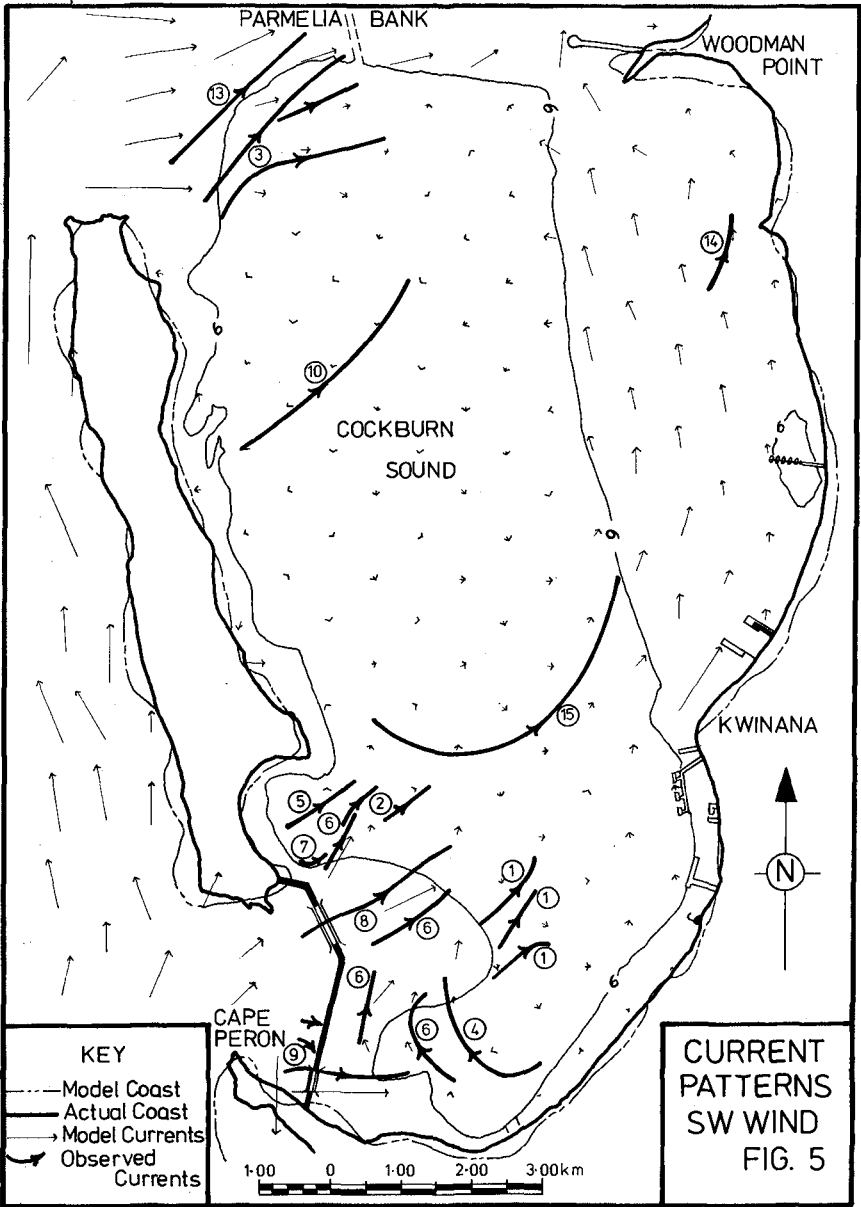
Fig. 4 shows the comparison between observed float drogue tracks and model predictions prior to the causeway construction. Each arrow shows the average path of 10 to 20 float drogues released at one time over a length of about 200 metres at the start of the arrow and excellent agreement occurs between the measurements and predictions except for days 2, 7 and 10.

The appearance of a possible eddy in track No. 7 is probably caused by the causeway construction having proceeded to the trestle bridge and flows in the Rockingham area could follow the post-causeway predictions which do show eddies in this area. The movement of float drogues on days 2 and 10 are not in agreement with the model prediction, possibly because on day 2 the wind was SSW to SW and on day 10 it was WSW to SW.

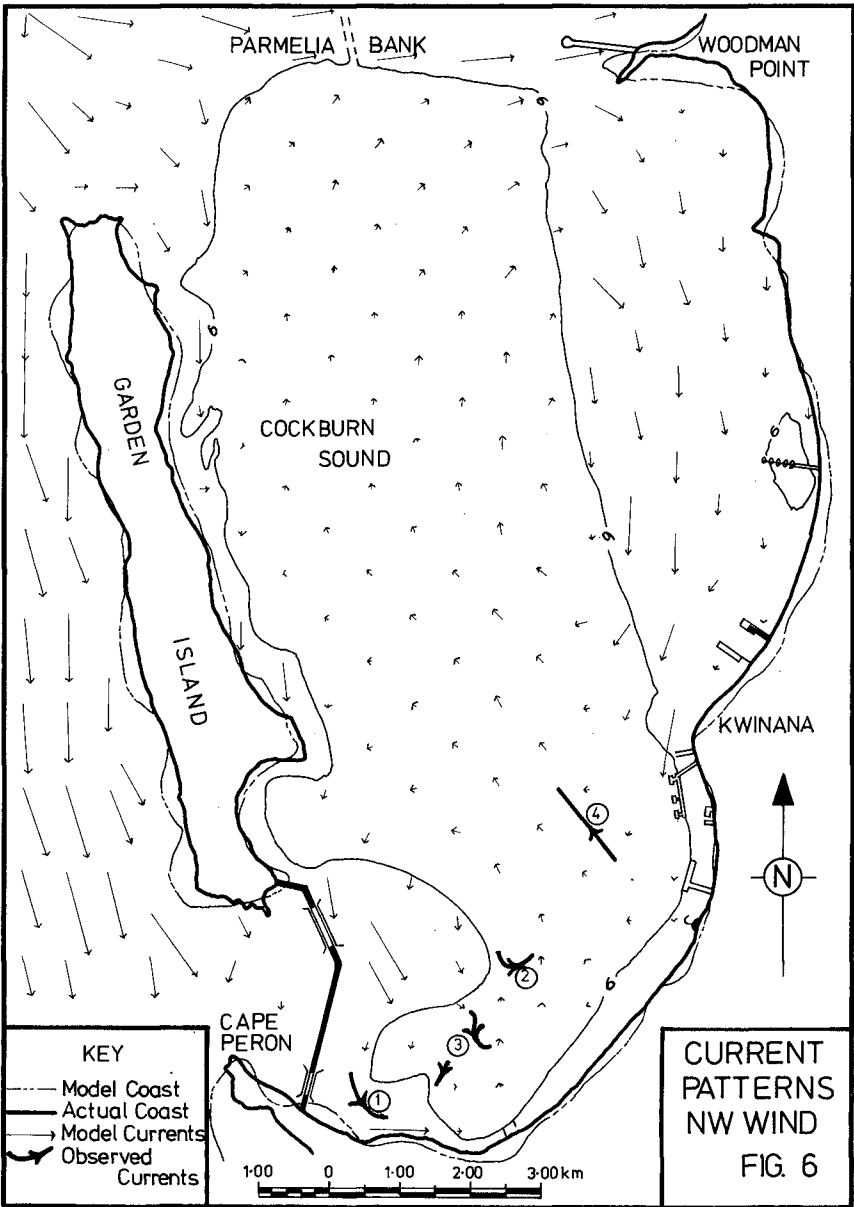
Since the causeway construction there were 15 occasions on which winds exceeded 5 m/sec from the SW during which float drogue measurements were made and these observations are shown in Fig. 5. Of these tracks only those of days 1 and 10 do not agree with the model predictions. Both these tracks exhibit obvious wind drag effects on the float and could illustrate a surface flow in the direction of the wind whereas the net flow as depicted by the model is slightly against the wind.

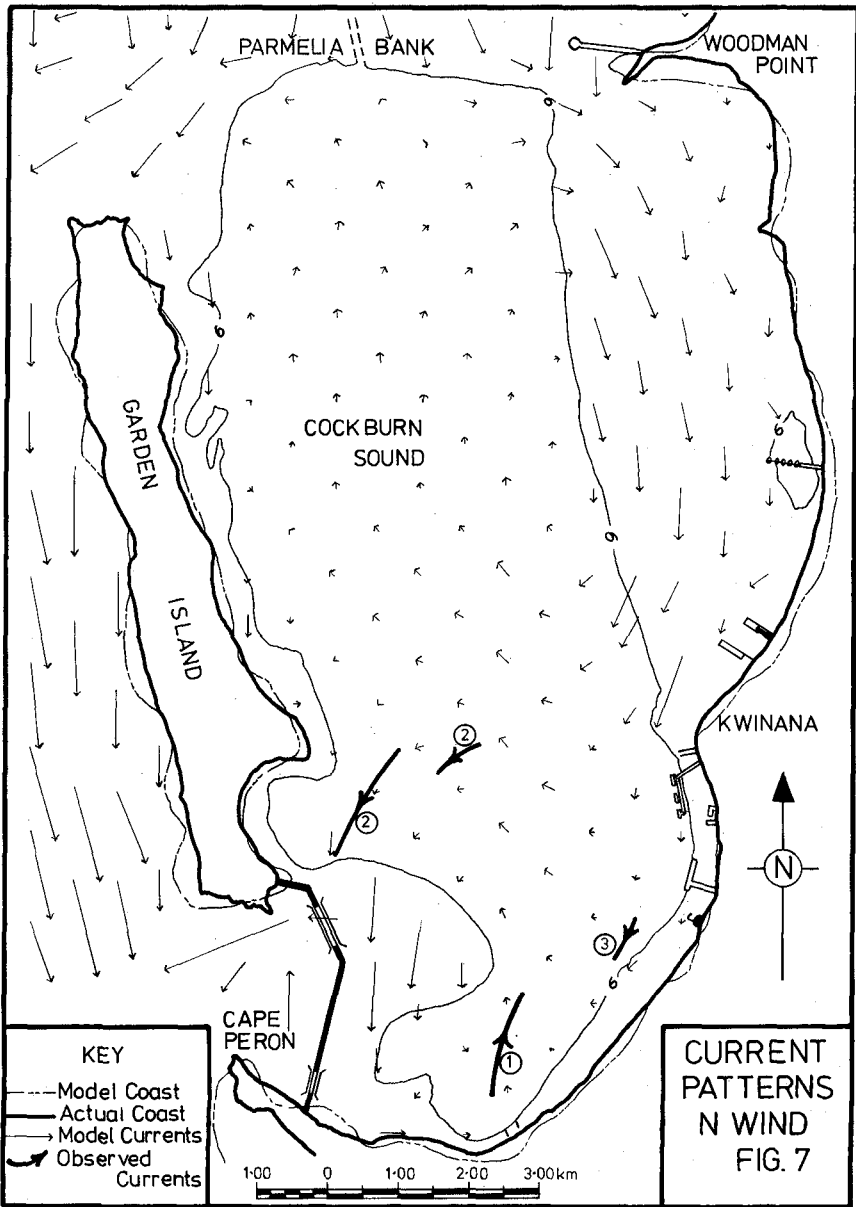
Fig. 6 shows the comparison between observed float drogue tracks and model predictions after the causeway construction for a NW wind and Fig. 7 shows a similar comparison for a N wind. Both these examples are presented because they show float drogue tracks which were difficult to understand without the model output. Figs. 6 & 7 show how each float drogue group follows the vector plot as depicted by the model. Yet using the float drogues alone it would not be possible to deduce the current patterns.





CURRENT PATTERNS SW WIND FIG. 5





5.2 Discharge Rates

Current magnitudes within Cockburn Sound and net discharges through Cockburn Sound are the most important factors controlling the ability of the Sound to adequately dissipate pollutants. A knowledge of these factors would also allow the determination of the most suitable discharge points for effluents into Cockburn Sound.

Discharges through Cockburn Sound have been measured both before and since the causeway construction. This information has been augmented by discharge calculations under similar conditions using numerical modelling. In general terms the following sections will show that current magnitudes in the bulk of the Sound are not reduced significantly but the net discharge of water through Cockburn Sound has been reduced on the average to 30-45% of the discharge which occurred before construction of the causeway.

5.2.1 Measured discharge rates before and after the causeway construction

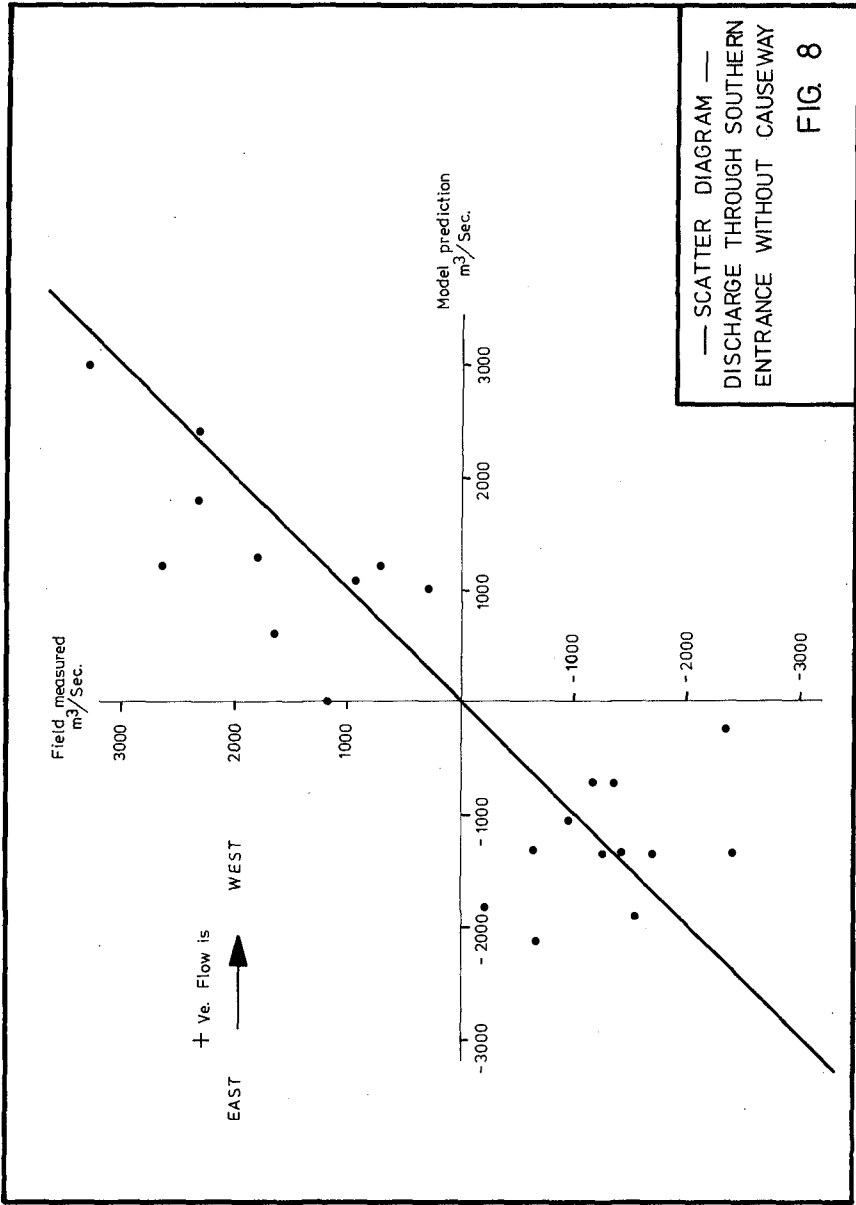
Field measurements in the form of twice daily current profiles were made at approximately two week intervals across the gap between Cape Peron and Collie Head for a period of 14 months during 1969-70. Measured discharge rates averaged over the two profiles taken on each day varied from 3300 m³/sec out of the Sound to 2400 m³/sec into the Sound via the southern entrance. The average magnitude of the flow rate over the 28 sets of readings taken during the 14 months was 1500 m³/sec.

Since July 1974 there have been regular current profile measurements under both of the causeway bridges and the range of discharge rates, averaged over a day's observations, up to January 1976 was 2700 m³/sec out of the Sound to 780 m³/sec into the Sound. It needs to be noted that the observation of 2700 m³/sec is double the rate of the next highest observation which in turn is 50% greater than the 3rd highest flow rate observed. In comparison, there were 6 observations of flow rates above 2,300 m³/sec prior to the causeway construction. Consequently a true comparison of flow rates can only be obtained by comparing means rather than extremes. The average magnitude of the flow rate over 33 sets of readings was 570 m³/sec, which is 38% of that occurring before the causeway was constructed.

The range of field measurements is shown in Figs. 8 and 9.

5.2.2 Discharge rates computed by the model before and after the causeway construction

The basic numerical model output which was used in the assessment of currents and discharges was the steady state solution reached after the application of a 20 knot wind from the direction of interest. A steady state condition was reached approximately 6 hours (prototype time) after the start of the wind. For the model runs where the forcing function was not steady such as for tidal runs, runs where a wind is superimposed on an oceanic current or sea breeze runs, the output was analysed at about one hourly intervals because a steady state condition did not exist. Table 2 compares the discharge through the southern opening with the causeway and without the causeway for each of the model runs.



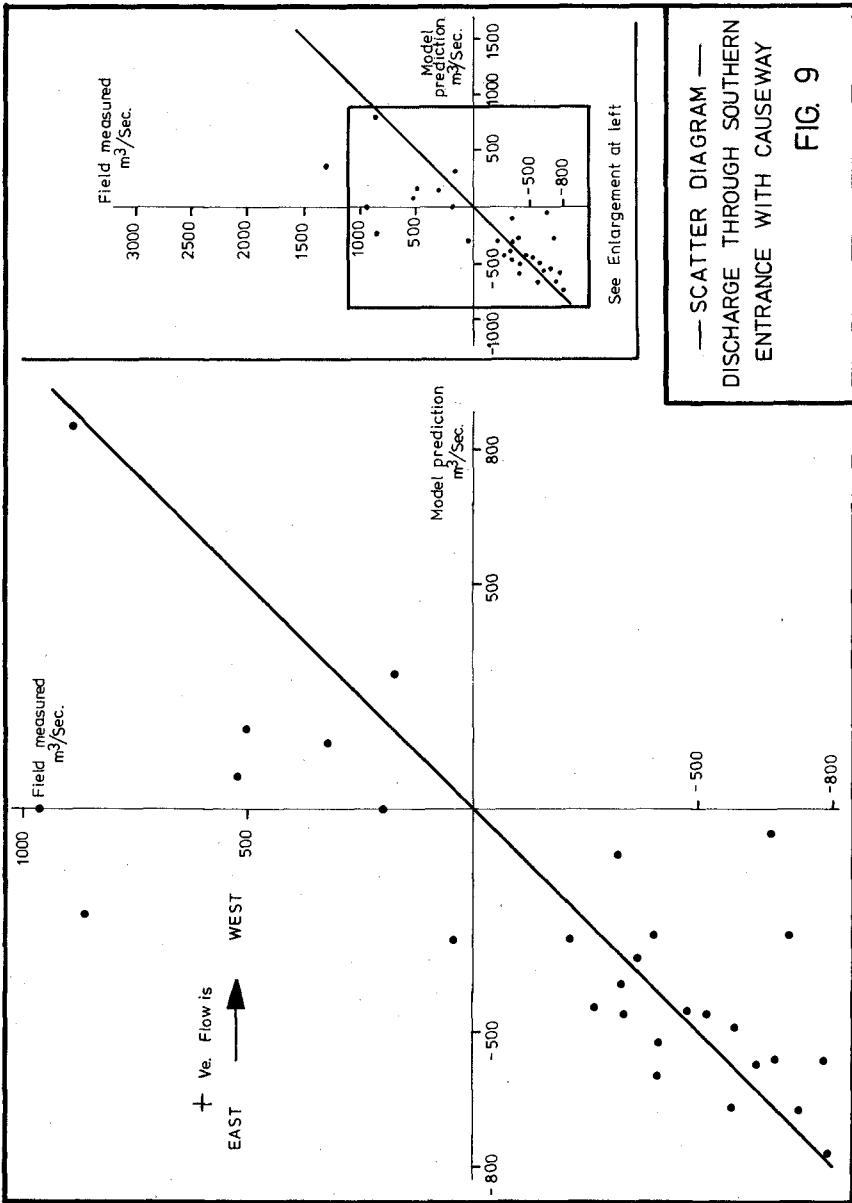


TABLE 2

Boundary Condition	Discharge (m ³ /sec)		Discharge with causeway Discharge w/o causeway %
	w/o causeway	with causeway	
20 knot N wind	+ 2410	+ 946	39
20 knot E wind	+ 1835	+ 780	42
20 knot S wind	- 2590	- 1020	39
20 knot SW wind	- 2780	- 1125	40
20 knot NW wind	+ 754	+ 240	32
NE wind	+ 2657	+ 725	26
N to S oceanic current	+ 3070	+ 1057	34
N to S oceanic current & sea breeze	+ 1062	+ 389	37
S to N oceanic current	- 2583	- 896	35
S to N oceanic current & NW wind	- 2126	- 779	37
Sinusoidal tide	varying		Range 29% - 40%

Table 2 shows that the numerical model predicts that on an average, weighted for frequency of occurrence of conditions, the discharge through the southern opening to Cockburn Sound has been reduced to 38% of the flow occurring before the causeway construction. This ties in closely with the discharge measurements reported in 5.2.1.

5.2.3 Comparison of measured and computed discharges.

In the comparison of measured and computed discharges as shown in the scatter diagrams of Figs. 8 and 9 it has been assumed that the relationship between wind speed and current is linear and that each of the measured currents is purely attributable to the wind blowing during the previous 6 hours. Consequently, there is quite a wide scatter on both diagrams, with the scatter reflecting the effects of the oceanic current, seiching and tidal flows. The redeeming feature in the scatter is that current magnitudes predicted by the model and those measured in the field correspond both before and after the causeway construction. It may be concluded that the model gives a good representation of net discharge through the southern entrance to Cockburn Sound and that if the magnitudes of the currents resulting from seiching and from the oceanic influence could be measured, and corrected for, the data points would exhibit less scatter.

5.2.4 Currents in the Bulk of Cockburn Sound

Inspection of the vector plots from the numerical model results shows that current magnitudes have not changed noticeably within Cockburn Sound for all runs except those involving the oceanic current. In some cases the extra constriction at the southern entrance has resulted in an intensified eddy in the centre of the Sound resulting in current magnitudes greater than those occurring prior to the causeway construction. See Cases 1, 3 and 5 of Table 3. An exception is the oceanic current which does not cause eddy formations because it is controlled by a simple head difference between the two ends of the Sound. In this case currents are reduced to 1/3 of the magnitude occurring prior to the cause, (cases 6 and 8). Usually the oceanic current does not occur on its own but is accompanied by a wind induced current so that generally currents have not changed in magnitude appreciably after the causeway construction, cases 7 and 9.

TABLE 3

Case	Boundary Condition	Gross Discharge across Section Between Sulphur Bay and Alcoa (m ³ /sec)	
		w/o causeway	with causeway
1	20 knot N wind	2840	3960
2	20 knot E wind	1890	1010
3	20 knot S wind	2730	3850
4	20 knot SW wind	2740	2310
5	20 knot NW wind	3230	3600
6	N to S oceanic current	3070	1060
7	N to S oceanic current and SW sea breeze	4550	4030
8	S to N oceanic current	2400	930
9	S to N oceanic current and NW wind	5770	4790

The only field data verification for currents in the bulk of Cockburn Sound comes from the salinity/temperature measurements which indicated that the rate of movement of bodies of water described by their salinity had not changed as a result of the causeway construction.

6. CONCLUSIONS

(i) For large bodies of water where wind generated currents greatly influence the flow, only sufficient field data should be obtained to determine the driving forces and then numerical modelling can be used as an effective tool in explaining and determining details of the flow field. More field data may then be desirable to confirm features of the flow highlighted by the model.

(ii) The exchange of water between Cockburn Sound and the Indian Ocean has been reduced to 30-45% of the exchange which occurred prior to the causeway construction. This figure is validated both by field data and numerical modelling.

(iii) Current magnitudes in the bulk of Cockburn Sound have remained nearly constant compared to those occurring before the causeway construction. Thus the rate of mixing or dispersion of effluents within the Sound has not changed significantly.

ACKNOWLEDGEMENTS

It is desired to express appreciation to Mr. Warwick-Smith, Secretary of the Australian Government Department of Construction, for permission to publish this paper. Nevertheless, the opinions expressed herein are those of the authors.

REFERENCES

1. Abbott M.B. et al 'System 21 - Jupiter - '
(A design system for two Dimensional Nearly-Horizontal Flows).
Jnl. of Hyd. Res. Vol. II (1973) No. 1.
2. Neumann, G. 'Ocean Currents'
Elsevier Publishing Co. 1968.

CHAPTER 187

WIND-DRIVEN CIRCULATION OF SAGINAW BAY

James H. Saylor¹ and Larry J. Danek²

ABSTRACT

A combination of Lagrangian measurements and fixed current meter moorings were used during the summer of 1974 and the winter of 1974-75 to determine the circulation patterns of Saginaw Bay. Because the bay is shallow, the water responds rapidly to wind changes. Distinct circulation patterns were determined for southwest and northeast winds. These directions parallel the major axis of the bay and were the prevailing wind directions during the study. A typical exchange rate between the inner and outer bay during moderate winds aligned with the bay axis is $3700 \text{ m}^3 \text{ s}^{-1}$. If sustained, this flushing rate would completely exchange the water of the inner bay in about 26.5 days. However, winds perpendicular to the axis of the bay cause little water to be exchanged and the residence time of water in the bay is much longer. Comparison of measured currents with the results of an independently-developed numerical model for the bay indicates there is good agreement between the observations and the simulation of the circulation in the shallow inner bay. Agreement is poor in the deeper outer bay, where specification of proper boundary conditions at the open mouth of the bay is important for meaningful model simulations. Ice cover during winter shields the water surface from wind stress. Currents are sluggish and driven almost entirely from interactions with the lake-scale circulation of Lake Huron.

INTRODUCTION

Saginaw Bay is a large and important embayment on the southwestern coast of Lake Huron, centered close to $44^{\circ}00'N$ latitude and $83^{\circ}20'W$ longitude (Figure 1). The mouth of Saginaw Bay (from Point Aux Barques to Au Sable Point) is 42 km wide with an average depth of 27 m. The bay's narrowest constriction is between Sand Point and Point Lookout, with a width of 20 km and a mean depth of only 4 m. A line between these two points forms an approximate boundary between the outer bay (mean depth 16 m) and the much shallower inner bay (mean depth 4.5 m). The bay is 83 km long with its major axis aligned 40° east of north. An important feature of the bay is the relatively deep channel that runs through the inner bay. It is aligned nearly parallel with the major axis of the bay and has a maximum depth of about 14 m.

¹National Oceanic and Atmospheric Administration, Great Lakes Environmental Research Laboratory, Ann Arbor, Michigan.

²NALCO Environmental Sciences, Northbrook, Illinois.

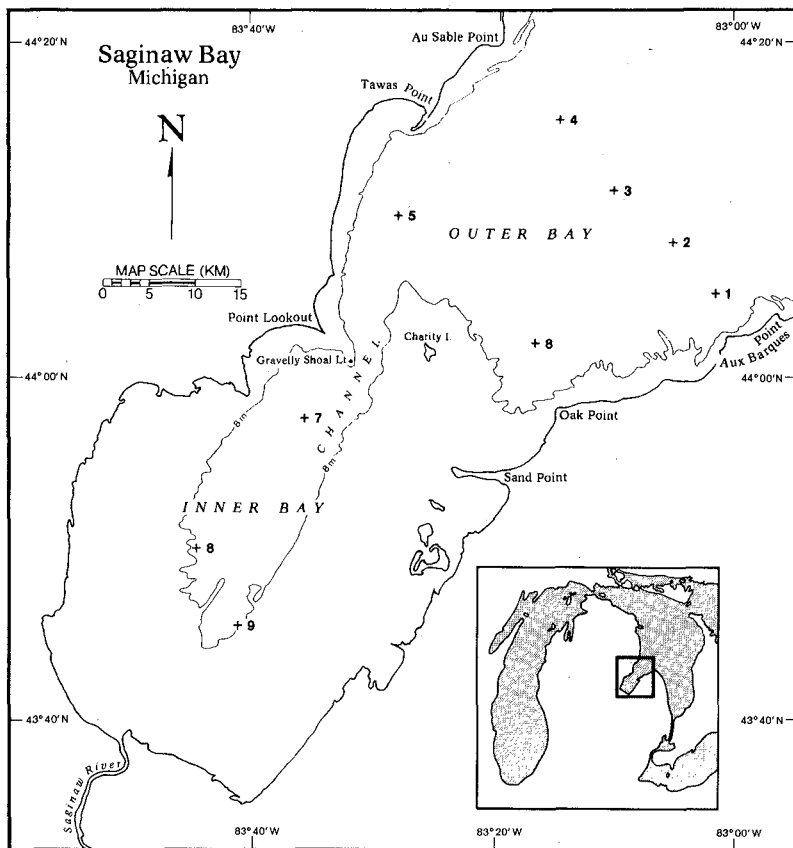


Figure 1. Location map of Saginaw Bay. Current meter moorings were placed at stations numbered 1 - 9, and wind speed and direction was recorded at the Gravelly Shoal Light.

The currents of Saginaw Bay and the character of Saginaw Bay-Lake Huron interactions are important because of the heavy load of pollutants entering Lake Huron through the bay. The Saginaw River drains an area of over 16,000 km² and discharges the wastes of the industrialized cities of Midland, Bay City, and Saginaw, Michigan. It is the largest tributary source of undesirable materials discharged to Lake Huron. A long residence time and the pattern of water mass movement within Saginaw Bay have adversely impacted parts of the bay. Several other rivers flow into the bay, but their combined discharge is small compared to that of the Saginaw River.

Because the inner reaches of Saginaw Bay are shallow and tidal amplitudes are negligible, currents in the inner bay are closely related to the wind. The outer bay, although also influenced by the local winds, interacts strongly with the large-scale circulation of Lake Huron. Several qualitative studies have been conducted on the circulation of Lake Huron and Saginaw Bay. Harrington (1895) and Johnson (1958) performed drift bottle studies on the lake and bay, and Ayers et al. (1956) used a dynamic height method developed for fresh water to determine the circulation in Lake Huron. Beeton et al. (1967) used chemical distributions to trace the water movements in the bay. These studies were in agreement in that all indicated currents in the bay were strongly dependent on local winds and were highly variable. A more recent study by Allender (1975) used a numerical model to simulate the circulation. This paper presents the results of a study using both Lagrangian and Eulerian current measuring techniques to determine the circulation patterns of the bay. Also presented are representative current speeds and volume transports for various wind conditions and a comparison of these results with the results of Allender's numerical model.

METHOD

Eighteen Geodyne model A-100 film recording current meters were installed in Saginaw Bay during May, 1974, and operated through October, 1974. As many as three of these Savonius rotor current meters were attached to an anchored line and suspended in the water column by a subsurface float. A small surface float attached to the end of a ground line 30 to 40 m in length was used to mark the location of the moorings and to aid in the recovery of the meters. Several of the meters failed because of mechanical and electrical problems leaving some holes in the planned sampling grid. Locations and depths of the meters are given in Figure 1 and Table 1. Each current meter sampled the velocity for a 50 s interval every 30 min and accumulated over 7200 data points for the duration of the study.

Drogues were tracked for three 2-week sessions, one session each in June, August, and October of 1974. The drogues consisted of a surface bouy plus a subsurface panel. The bouy was made from a pneumatic float and a radar reflector that extended 1.5 m above the water surface. The panel, a sheet metal current cross with a cross-sectional area of 1.86 m^2 , could be set to any desired depth in the water column. During this study the panels were set only at depths of 2 or 5 m and used almost exclusively in the shallow water of the inner bay where the use of moored current meters was impractical. The drogues were followed with a small tending vessel and sequentially positioned by radar with reference to anchored radar reflectors deployed at the site of each released drogue.

Wind speed and direction were measured at the Gravelly Shoal Light near Point Lookout. Data were continuously recorded on a strip chart by the use of a Bendix wind recording system and later digitized as hourly averages. The sensor location was approximately 23 m above the water surface. As the distance to the nearest point of land was 4.5 km, local interferences were minimal.

During the winter of 1974-75 an extensive study of currents and water

Table 1. Current meter locations and dates of operation during the May to October deployments.

Meter No.	Site No.	Latitude (N)	Longitude (W)	Depth (m)	Duration
2A	2	44°05.2'	83°02.4'	10	17 May-15 Oct.
2B	2	44°05.2'	83°02.4'	20	28 May-15 Oct.
2C	2	44°05.2'	83°02.4'	30	17 May-15 Oct.
3B	3	44°11.5'	83°10.9'	20	18 May-15 Oct.
3C	3	44°11.5'	83°10.9'	30	18 May-15 Oct.
4A	4	44°15.3'	83°15.0'	10	18 May-15 Oct.
4B	4	44°15.3'	83°15.0'	20	18 May-15 Oct.
5A	5	44°10.1'	83°28.9'	7	18 May-16 Aug.
5B	5	44°10.1'	83°28.9'	15	18 May- 3 Oct.
6A	6	44°02.3'	83°17.3'	7	17 May- 8 June
6B	6	44°02.3'	83°17.3'	10	17 May-16 Oct.
9A	9	43°45.6'	83°41.4'	7	20 May-18 Oct.

temperatures was performed in Lake Huron to determine the large-scale circulation of the lake. In this study many current meter moorings were placed along the west shore of Lake Huron and in the mouth of the bay. The moorings were in place from November, 1974 to May, 1975 and consisted of AMF Vector Averaging Current Meters, again of Savonius rotor design. Thus, the mouth of Saginaw Bay was instrumented for a period of almost one year, although a short gap in the records at the end of October and early November, 1974 exists. The entire bay is usually nearly isothermal so that the water mass is essentially homogeneous. Only during early summer in the deeper water at the mouth of the bay was any density stratification of significance observed.

RESULTS

Drogues

Since most of the inner bay was too shallow for current meter moorings, the drogue studies were concentrated in that area. During 25 days on the bay, 117 drogues were tracked for an average interval of 5 hr each. The

average speed for the drogues was 6.7 cm s^{-1} , while the highest speed measured was over 30 cm s^{-1} ; however the speeds in several areas of the bay varied considerably from the average. Near Point Lookout, where the channel has its narrowest constriction, the average speed was 10 cm s^{-1} . Water flow balancing the wind-driven transport in the shallow water southeast of the channel is funneled through this constriction causing the higher average speed. On the other hand, water in the southeast corner of the bay was nearly stagnant, with speeds of less than 4 cm s^{-1} . This is the same area where the highest ion concentrations were reported by Beeton et al. (1967). In the central part of the inner bay the speeds were typically slower in the channel (average speed 6.2 cm s^{-1}) than in the shallow water areas on either side (average speed 8.8 cm s^{-1}). There was no appreciable difference between the average speeds measured at 2 and 5 m depths.

As it was not possible to do a synoptic survey of the entire bay, the drogue data were compiled to present on one chart observations made during similar wind conditions in various parts of the bay thus providing a reasonably accurate picture of the circulation of the inner bay for certain wind directions. Transects for 7 days during which the wind was out of the southwest are shown in Figure 2. The drogue tracks show that the water in the

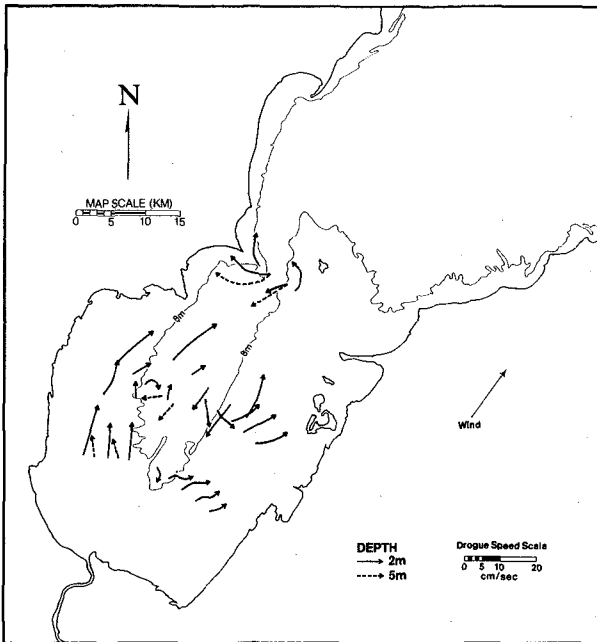


Figure 2. Compilation of drogue tracks observed during southwest wind.

inner bay generally moves to the northeast with the wind, except in the channel, where there is a counterflow to the southwest. The current in the southwest section of the bay, combined with the return flow in the channel, forms a crude clockwise gyre in that region, whereas the current in the shallow southeast area follows the shoreline and flows into the outer bay between Charity Island and Oak Point. Part of the water from the southeastern region of the inner bay also flows northeastward west of Charity Island, a part of this water may be recycled to the inner bay by the return flow southwestward in the channel. The flow distribution near Point Lookout shows that the return flow is confined to a rather narrow stream, with northeastward flow in the shallow water to each side. The drogue trajectories show that the return flow is still well defined further into the bay, although the apparent path of the flow does meander somewhat because of slightly different wind conditions during the separate days of observations.

On the day that drogues were deployed across the channel near Point Lookout, the wind was out of the southwest with an average speed of 5.8 m s^{-1} . Drogue panels set at 2 and 5 m made it possible to estimate the vertical profile of horizontal velocity and to compute the volume water entering the inner bay through the channel. The estimated transport was $3700 \text{ m}^3 \text{ s}^{-1}$ or 37 times the average flow of the Saginaw River. Since the volume of the inner bay was about $8.5 \times 10^9 \text{ m}^3$ during the time of the study, it would take only 26.5 days for this flow to replace the inner bay water.

On several days the wind changed rather abruptly during the drogue experiments presenting an opportunity to examine the response of the bay to sudden wind changes and to determine the time required for the return flow in the channel to develop. The response for a wind changing to one out of the southwest is that in all areas of the inner bay the water initially flows with the wind; after approximately 8 hr a return flow develops in the central channel. Of course residual currents and the intensity of the wind affect the circulation and the lag time before a return flow develops and a new equilibrium state is established, but this response time is typical for a moderate southwest wind. This result also agrees well with previous work on the bay (Johnson, 1958, and Allender, 1975). The current speed averaged about 3% of the wind speed in shallow water where the currents flow with the wind.

During the Lagrangian current studies the wind was usually out of the southwest, but there were a few occasions of northeast winds. The transects from these days indicate that water enters the inner bay between Charity Island and Oak Point and flows to the southwest in the shallow areas of the bay. The results also show a countercurrent in the channel flowing to the northeast, but there was insufficient data to estimate a volume exchange rate. With flow to the southwest on either side of the channel and a counterflow to the northeast in the channel, the circulation pattern is just reversed from that observed for a southwest wind.

Current meters

Since the largest part of the inner bay was too shallow for current meter moorings, most of the meters were deployed in the outer bay. Histograms of current direction were used to display the summer data. The

histograms were constructed by sorting the current direction into 40° sectors. The percentage of data points that fell into each sector was computed and the average speed for each sector was calculated (percentages of less than 5% are not shown). The average speeds were divided into three categories, low (less than 8 cm s^{-1}), medium (8 to 15 cm s^{-1}), and high (greater than 15 cm s^{-1}), and the results are displayed on the histograms. A similar histogram of wind data was computed, giving the direction toward which the wind was blowing (that is, to be consistent the oceanographic convention was also used for the wind direction so that a wind out of the north was plotted in the south sector).

Since the currents are so highly dependent on the local winds, the nature of the bay circulation during several well-defined meteorological events was examined. Histograms of current direction were computed for periods when the wind was relatively constant for at least two days. Since the two predominant wind directions during the summer of 1974 were out of the southwest and out of the northeast, the response of the bay to winds from these directions was analyzed.

The wind was constant out of the northeast on 22-27 June. Histograms computed for that period are shown in Figure 3. The results of this episode, which are typical of several episodes of northeast wind examined, show that the flow is characterized by a counterclockwise gyre in the outer bay; water enters the bay at the northern edge of the bay mouth, flushes through the outer bay in one large counterclockwise loop, and flows back into Lake Huron along the southern part of the bay mouth. Meter 9A suggests that a return flow has developed in the channel even that far into the bay, although the return current isn't as well defined as that for a southwest wind. An illustration of this flow pattern, combined with the circulation derived from the drogue results for a northeast wind in the inner bay, is shown in Figure 4. The vectors on the Figure represent a qualitative vertically averaged circulation pattern, with the length of the arrows proportional to flow intensity.

The wind was constant out of the southwest on 3-5 October (Figure 5). The histograms from this episode, which are similar to others computed for a southwest wind, are markedly different than those calculated for a northeast wind. The flow from Lake Huron enters the bay through the southern parts of the bay mouth, circulates through the outer bay in a clockwise direction, and flows out along the edge. Meter 9A shows the prominent return flow in the channel noted in the drogue studies. This circulation pattern, together with the flow pattern determined from the drogue studies for a southwest wind, is illustrated in Figure 6. The flow past station 5 is usually toward the southwest under both wind conditions, influenced more by the gross circulation and geometry of the bay than by the direct influence of the local winds. This site is in the zone of the return flow in the channel during southwest wind and in the inflow to Saginaw Bay from Lake Huron during northeast wind. Histograms computed for the entire length of the summer current meter records revealed a high variability of flow, with the current direction for some of the meters almost equally distributed around the compass. The meter at site 9, though, showed a dominant flow to the southwest because the prevailing winds during the summer were from the southwest. Wind from directions not nearly parallel to the bay axis drives a local circulation in the inner bay, but does not appear to cause much exchange of water with the outer bay.

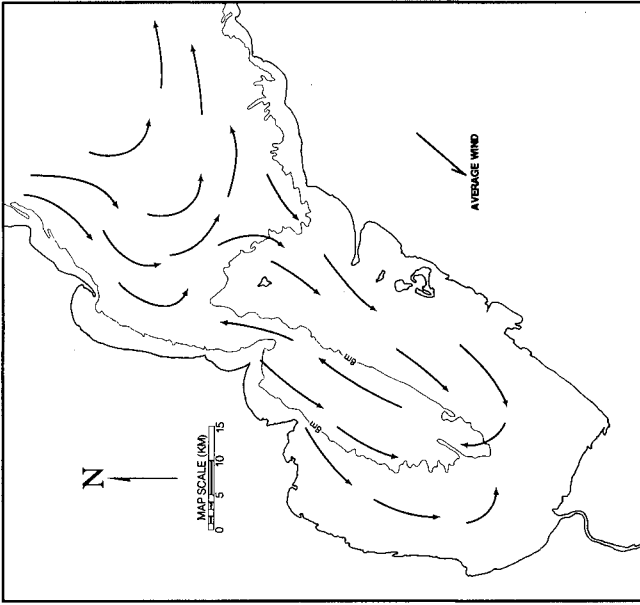


Figure 4. The circulation of Saginaw Bay driven by northeast wind.

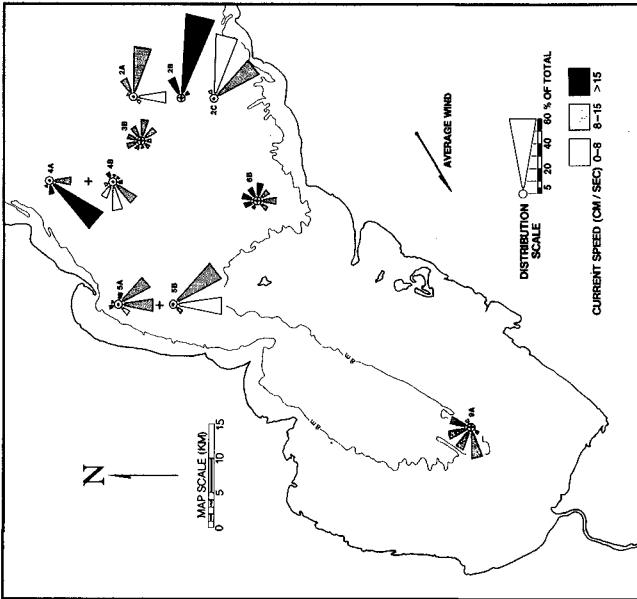


Figure 3. Current direction histograms during northeast wind, 22-27 June, 1974.

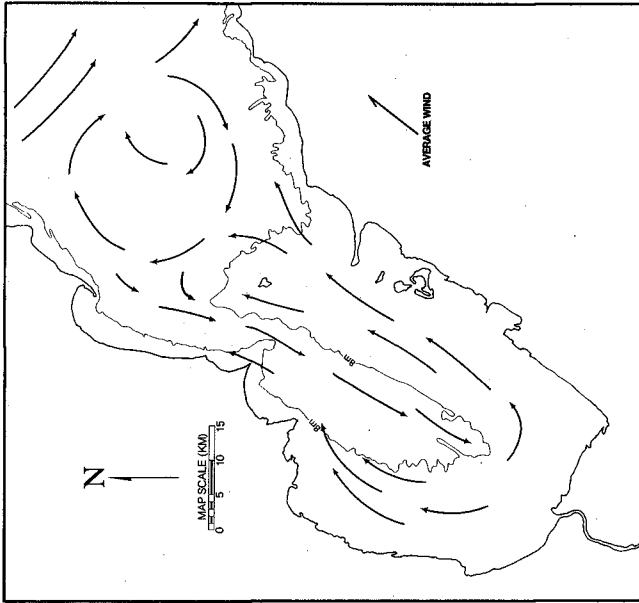


Figure 6. The circulation of Saginaw Bay driven by southwest wind.

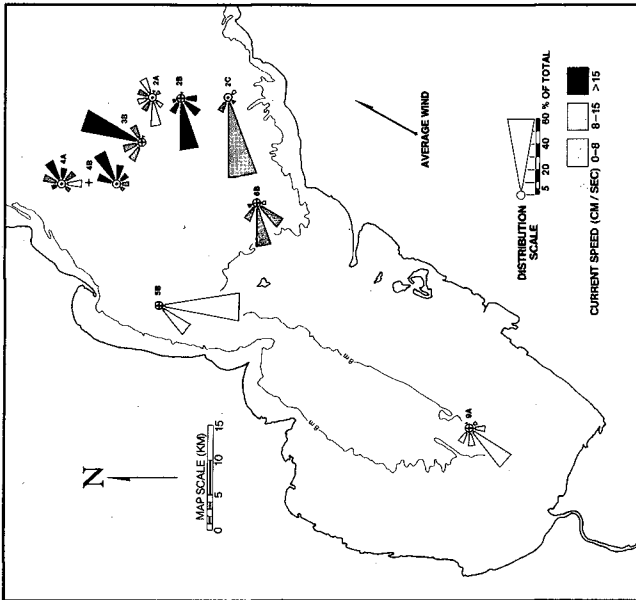


Figure 5. Current direction histograms during southwest wind, 3-5 October, 1974.

Winter current meters confirmed the same nature of outer bay circulation. Winter studies of Lake Huron have shown that southward flow along the west coast of the lake is the dominant feature of lake circulation. The rest of the lake responds to this flow in the form of one large cyclonic cell, returning water northward along the eastern coast. This persistent southward flow across the mouth of Saginaw Bay interacts strongly with the outer bay and plays a major role in determining its flow characteristics. Figure 7 shows an episode of lake scale current flow during moderate northerly winds in November of 1974. Current roses of water transport past each current meter are shown at the 15 m level. Wind run roses for this episode as recorded at five stations around the perimeter of the lake are shown in usual meteorological fashion here, being wind from the north and northeast at 5 to 6 m s^{-1} . This episode shows, as noted earlier for the summer studies, that north to northeasterly wind drives a counterclockwise loop of Lake Huron water through the outer bay. The average current speeds in the outer bay were 15 to 20 cm s^{-1} during this episode.

Ice cover during its peak development in winter covers the entire surface of Saginaw Bay, extending lakeward past all four current meter moorings placed in the mouth of the bay. Figure 8 shows another episode of wind similar to that of the November case, but during extensive lake ice cover. With ice extending from 10 to 15 km lakeward from the outer bay current meters, the currents in the bay are entirely different in character. Lake Huron retains its cyclonic flow pattern, but under the ice the bay mouth circulation loses its distinctive character. Flow is weak with average current speeds of a few cm s^{-1} . Thus, even the driving force of lake current interactions is lost during extensive winter ice cover, and the bay circulation must be very disorganized and sluggish.

MODEL COMPARISON

Allender (1975) simulated the bay using a finite difference method to solve the linear barotropic equations for two-dimensional motion. Because the development of such a model requires the specification of boundary conditions at the mouth of the bay, he examined water level records from within Saginaw Bay and from Lake Huron near the bay mouth and determined the dominant periods of oscillation of the surface stage. He then specified as boundary conditions periodic functions of the velocity field at the open boundary between Saginaw Bay and Lake Huron at periods of the observed dominant surface oscillations. The intensity of the flow field was adjusted to yield water surface oscillations with amplitudes near those observed on the bay. Figure 9 shows the circulation he calculated for a southwest wind, and Figure 10 shows the flow pattern driven by a northeast wind. A comparison of these results with the results of the field studies shows that there is very good agreement between the flow patterns in the inner bay. Both results show a distinct current in the channel flowing into the wind and flow in shallow water with the wind. The agreement in the outer bay for similar wind conditions is not close, however. The differences between the model and field study circulations are due to the strong influence of Lake Huron currents on the flow in the outer bay, effects which were not included in model development.

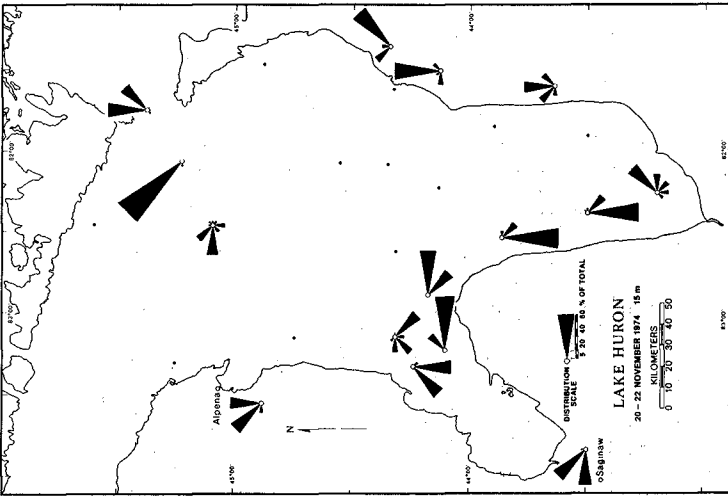


Figure 7. Current roses of water transport at the 15 m level during an episode of northerly wind in November, 1974.

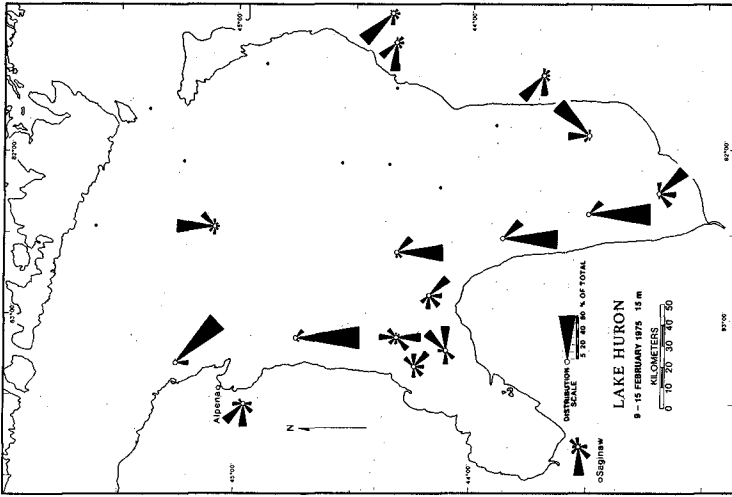


Figure 8. Current roses of water transport at the 15 m level during an episode of northerly wind with extensive ice cover on Saginaw Bay in February, 1975.

SAGINAW BAY NE WIND (12 knots): 2nd and 3rd mode forcing
 T = 10.0 hours
 → = .40 m²/sec

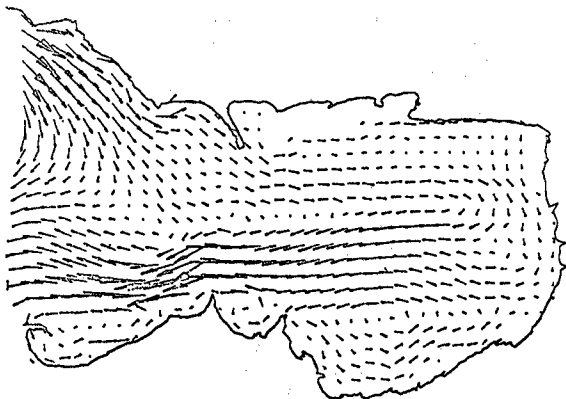


Figure 10. Currents in Saginaw Bay driven by a northeast wind with weak boundary forcing at periods of 3.3 and 2.0 hr (from Allender, 1975).

SAGINAW BAY SW WIND (12 knots): 2nd and 3rd mode forcing
 T = 10.0 hours
 → = .40 m²/sec

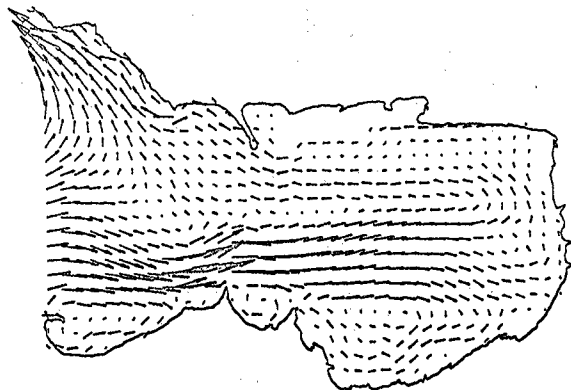


Figure 9. Currents in Saginaw Bay driven by a southwest wind with weak boundary forcing at periods of 3.3 and 2.0 hr (from Allender, 1975).

Spectral analyses of the current meter recordings reveal no significant periodic components in the flow field near the periods specified in model development, although during the density stratified season strong inertial period current flows are prominent near the bay-lake boundary. The dominant interaction between the bay and Lake Huron is controlled by the southward flowing coastal current structure in the lake, so that more realistic model development would necessarily include the dynamical effects of this interaction. Of course, the interaction of the lake and bay cannot be described without detailed field investigation, and the results of these surveys were not available for Allender's work.

SUMMARY

Currents in Saginaw Bay are quite variable and dependent on the local winds. The inner bay is especially susceptible to wind changes, but the circulation patterns developed are predictable for winds from the southwest or northeast, as a stable pattern develops within about 8 hr after a wind shift. Since wind from directions just slightly different than these cause only small perturbations to the flow field, as revealed during several of the drogue tracking intervals, it is felt that the two circulation charts are representative of wind from the southwest and northeast quadrants.

Winds blowing transverse to the longitudinal axis of the bay also cause the circulation pattern to change quickly. The flow pattern is more complex than when the wind is nearly parallel to the axis of the bay, but not enough data were collected under these wind conditions to determine a detailed circulation pattern. The outer bay responds less rapidly to wind changes and the current patterns are strongly influenced by currents in Lake Huron. The dominant southward flowing current along the west shore of Lake Huron frequently flushes through the outer bay. A northeast wind causes part of this current to flow through the outer bay in a counterclockwise loop, whereas the current flows past the mouth of the bay during southwest wind and drives a large clockwise eddy in the outer bay. The existence of such an eddy was suggested by Ayers et al. (1956). Ice cover during winter shields the water surface from wind stress and the bay circulation is very sluggish. Even the outer reaches of Saginaw Bay are decoupled from strong interaction with the currents flowing in Lake Huron as the ice fields grow lakeward of the bay mouth.

The comparison of results of this field study with those of a numerical model developed for the same area demonstrates the usefulness and validity of such modeling techniques. The agreement of the model with the actual data is excellent in the shallow water of the inner bay. However, the comparison also illustrates the importance and difficulty of prescribing proper boundary conditions at the open mouth of the bay. The model agrees well with the data far from the bay mouth, but breaks down near the open boundary. The choice of realistic boundary conditions is essential for the prediction of meaningful flow patterns, especially in this region where currents in Lake Huron are so important in influencing the circulation.

REFERENCES

- Allender, J.H.
1975. Numerical simulation of circulation and advection-diffusion processes in Saginaw Bay, Michigan. Ph. D. Thesis, University of Michigan, Ann Arbor.
- Ayers, J.C., D.V. Anderson, D.C. Chandler, and G.H. Lauff
1956. Currents and water masses of Lake Huron. Ontario Dept. of Lands and Forests, Res. Rept. No. 35, and Great Lakes Res. Institute, University of Michigan, Ann Arbor, Tech. Paper No. 1, 101 pp.
- Beeton, A.M., S.H. Smith, and F.F. Hooper
1967. Physical limnology of Saginaw Bay, Lake Huron. Great Lakes Fisheries Commission, Ann Arbor, Michigan, Tech. Rept. No. 12, 56 pp.
- Harrington, M.W.
1895. Surface currents of the Great Lakes, as deduced from the movements of bottle papers during the seasons of 1892, 1893, and 1894. U.S. Dept. of Agriculture, Wash., D.C, Weather Bur. Bulletin B, 14 pp.
- Johnson, J.H.
1958. Surface current studies of Saginaw Bay and Lake Huron. U.S. Fish and Wildlife Service, Special Scientific Rept. - Fisheries No. 267, 84 pp.

CHAPTER 188

PREDICTION OF POLLUTANT DISTRIBUTION IN ESTUARIES*

A. Y. Kuo and J. P. Jacobson
Department of Physical Oceanography and Hydraulics
Virginia Institute of Marine Science
Gloucester Point, Virginia 23062

ABSTRACT

A method was developed for predicting the distribution of sewage constituents which would result from a proposed sewage outfall in estuaries or coastal seas. The method is based on the mathematical relationship between the solutions of the mass-balance equations with and without a decay term and on the assumption that both the dispersion and decaying processes are linear, acting independently. The application of the method requires dye dispersion experiments and a numerical model employing the results of the experiments. This approach makes it possible to predict the concentration field of sewage constituents with differing decay rates by using tracer release experiment employing a conservative tracer.

The method has been applied to assess the environmental impact of a proposed sewage outfall in Hampton Roads, Virginia. Two dye dispersion experiments were performed, one a continuous release over a flood tide cycle and the other over an ebb tide cycle. Horizontal distributions of dye were measured at subsequent slack waters before flood and ebb. The results were used to predict the concentration fields of total nitrogen, total phosphorus, coliform bacteria, biochemical oxygen demand, dissolved oxygen deficit and chlorine residuals, which would result from the proposed sewage outfall.

INTRODUCTION

The dilution and mixing of sewage with receiving water may be considered a two-stage process. The first stage is the initial jet mixing. This initial mixing of the sewage jet with receiving water produces a broad field of diluted sewage. The second stage of mixing is the dispersion of sewage due to natural flow field as the diluted sewage field drifts with the ambient currents.

Models for the first stage, jet mixing, have been studied extensively (Fan, 1967; Fan and Brooks, 1969). These models are capable of delineating the concentration distribution of sewage constituents within the mixing zone.

* Virginia Institute of Marine Science Contribution No. 788.

The layout of diffuser ports, jet momentum, ambient currents and density difference are important parameters affecting the details of the mixing zone.

The second stage of mixing is dominated by the currents and turbulent characteristics of the receiving water. The far field distribution of sewage constituents outside the mixing zone is relatively insensitive to initial mixing. The ideal models for this stage of mixing are based on the equations of motion, continuity and mass balance of sewage constituents (Tracor, 1970). These models calculate the hydrodynamic characteristics, such as currents, density variations, turbulence of receiving water body and use them as inputs to the mass balance equation to calculate the concentration distribution. Due to the amount of field data required for the formulation and verification of this kind of model, it is not always feasible to resort to them for problem solving. Simple models based on the solutions of point or line source in a steady uniform flow field have been developed (Brooks, 1959; Csanady, 1973). The extension of these simple models to an estuarine environment where the flow field is non-uniform and oscillatory, is not straightforward. A purely analytical approach has yet to be developed.

The experimental approach of tracer release has been employed to delineate the far field distribution of pollutant discharge into a water body. Pritchard and Carter (1965) developed a method to estimate the concentration distribution of a nonconservative substance from that of a conservative substance which may be obtained with a field experiment. Their method is based on an empirical relationship that the concentration field of a continuous point source approaches its steady state with an exponential function of time. This paper describes a new approach using the concentration field of a conservative tracer to predict those of sewage constituents discharged from a proposed sewage outfall. This method makes it possible to describe the concentration fields of nonconservative substances without a large field effort to measure or calculate parameters, such as velocity field and dispersion coefficient, which are necessary for solving the mass-balance equation.

THEORETICAL BACKGROUND AND APPROACH

The concentration distribution of a sewage constituent in a receiving water body may be described by the mass balance equation

$$\frac{\partial c}{\partial t} + u \frac{\partial c}{\partial x} + v \frac{\partial c}{\partial y} + w \frac{\partial c}{\partial z} = \frac{\partial}{\partial x} (e_x \frac{\partial c}{\partial x}) + \frac{\partial}{\partial y} (e_y \frac{\partial c}{\partial y}) + \frac{\partial}{\partial z} (e_z \frac{\partial c}{\partial z}) - kc + S(x, y, z, t) \quad (1)$$

where

c is the concentration of sewage constituent,
 t is time,
 x, y, z are three orthogonal coordinates,
 u, v, w are velocity components,
 e_x, e_y, e_z are turbulent diffusion coefficients,
 k is decay rate,
 $S(x, y, z, t)$ is source or sink.

As it was stated previously, an ideal model would be the one based on the solution of equation (1) with the velocity components, turbulent diffusion coefficients, decay rate, and source as input parameters. The velocity field and diffusion coefficients have to be solved with a hydrodynamic model or measured in the field. Because of the efforts involved, developing such a model is often unfeasible.

An alternative way of obtaining the concentration distribution of a sewage constituent is to introduce a tracer at the proposed outfall location and measure the resulting concentration distribution. The release of the tracer should last long enough such that an equilibrium condition is achieved. Furthermore, different tracers have to be used to simulate sewage constituents of different decay rates. This direct experimental method is unfeasible in practice because

- 1) for each group of sewage constituents with a different decay rate, a tracer-release experiment has to be done,
- 2) tracers of a given decay rate cannot always be found.

The approach described here is to construct a simple model based on the relationship of concentration distributions between decaying and non-decaying substances. The experimental results of a non-decaying tracer provide the input data of the model and the concentration distributions of decaying substances are calculated.

The Model for a Steady Flow Field

If $N_0(x, y, z, t, t')$ and $N(x, y, z, t, t')$ are the concentration distributions, at time t , resulting from an instantaneous release at time $t = t'$ of non-decaying and decaying substances respectively, then

$$N(x, y, z, t, t') = N_0(x, y, z, t, t') \exp\{-k(t-t')\} \quad (2)$$

where k is the first order decay rate. In a steady flow field, the functions N and N_0 depend on $t - t'$, while they are independent of the time of release t' , therefore

$$N_0(x, y, z, t, t') = N_0(x, y, z, t-t') \quad (3)$$

and

$$N(x, y, z, t, t') = N(x, y, z, t-t') \quad (4)$$

If a tracer is introduced continuously at a constant rate (unit mass per unit time) for an infinitely long time, an equilibrium concentration field will be reached with

$$C_\infty(x, y, z) = \int_{-\infty}^t N(x, y, z, t-t') dt' \quad (5)$$

Let $\tau = t-t'$, equation (5) may be transformed into

$$C_\infty(x, y, z) = \int_0^\infty N(x, y, z, \tau) d\tau \quad (6)$$

and, substituting equations (2) and (3), it may also be obtained that

$$C_\infty(x, y, z) = \int_0^\infty N_0(x, y, z, \tau) \exp(-k\tau) d\tau \quad (7)$$

Mathematically, equation (7) states that the equilibrium concentration field of decaying substances may be calculated from the results of the tracer release experiment with a non-decaying tracer.

However, it is technically impossible to monitor continuously the history of a time-varying concentration field, $N_0(x, y, z, \tau)$. The continuous release of a tracer may be regarded as a succession of piece-wise continuous release of duration T . Equation (5) may be written as

$$C_\infty(x, y, z) = \sum_{n=1}^{\infty} \int_{t-nT}^{t-(n-1)T} N(x, y, z, t-t') dt' \quad (8)$$

Similarly, equations (6) and (7) become

$$C_{\infty}(x,y,z) = \sum_{n=1}^{\infty} \int_{(n-1)T}^{nT} N(x,y,z,\tau) d\tau \quad (9)$$

and

$$C_{\infty}(x,y,z) = \sum_{n=1}^{\infty} \int_{(n-1)T}^{nT} N_0(x,y,z,\tau) \exp(-k\tau) d\tau \quad (10)$$

If the time interval T is small compared with the time scale of decay, i.e. $1/k$, the decaying factor, $\exp(-k\tau)$, may be approximated by a constant $\exp(-\frac{2n-1}{2} kT)$ with an error less than $(kT)^3$, and equation (10) becomes

$$\begin{aligned} C_{\infty}(x,y,z) &= \sum_{n=1}^{\infty} \int_{(n-1)T}^{nT} N_0(x,y,z,\tau) d\tau \cdot \exp(-\frac{2n-1}{2} kT) \\ &= \sum_{n=1}^{\infty} C_{On}(x,y,z) \exp(-\frac{2n-1}{2} kT) \end{aligned} \quad (11)$$

where

$$C_{On}(x,y,z) = \int_{(n-1)T}^{nT} N_0(x,y,z,\tau) d\tau,$$

has a physical meaning as the concentration field resulting from a continuous release of a non-decaying substance over a time interval from nT to $(n-1)T$ in the past. Thus, the series C_{On} may be obtained from a field experiment in which a tracer is continuously released over a time period T and the concentration fields are measured at subsequent time instants $T, 2T, 3T, \dots, nT$ after the beginning of release. Equation (11) may then be used to calculate the equilibrium concentration field of any sewage constituent with decay rate k .

Extension of the Model to Tidal Estuaries

In the case of a non-steady flow field, the functions $N_0(x,y,z,t,t')$ and $N(x,y,z,t,t')$ not only depend on $t-t'$, but also on t' , the time when the tracers are introduced. The analysis in the previous section cannot be applied. However, the model may be easily extended to a tidal estuary if the flow field in the estuary is assumed periodic.

In estuaries where the tidal propagation dominates the flow field, the advective velocities u, v, w and diffusion

coefficients e_x , e_y , e_z are periodic functions of time. The period of fluctuation, one tidal cycle, may be used as the time unit and functions $N_0(x,y,z,n,n')$ and $N(x,y,z,n,n')$ may be defined as the concentration fields at a particular phase of the n^{th} tidal cycle resulting from instantaneous release at any phase of the n^{th} cycle. Because of periodicity, N_0 and N depend only on $n-n'$, while being independent of n' , thus

$$N_0(x,y,z,n,n') = N_0(x,y,z,n-n') \quad (12)$$

$$N(x,y,z,n,n') = N(x,y,z,n-n') \quad (13)$$

Therefore, the analysis of the previous section is still applicable if the time duration of a piece-wise continuous tracer release T equals a tidal cycle.

Equation (11) gives the equilibrium concentration at a particular phase of tide when the concentration fields are measured at that phase of successive tidal cycles. Of the concentration fields varying with phase of tide, the most significant ones are those at slack water before ebb (SBE) or high water slack and at slack water before flood (SBF) or low water slack because they are the extremes of the tidal excursion.

Let a non-decaying tracer be released continuously over a tidal cycle starting at slack water before ebb and let

$CH_n(x,y,z)$ be the measured concentration field at the n^{th} SBE after release begins,

$CL_n(x,y,z)$ be the measured concentration field at the n^{th} SBF after release begins,

then, according to equation (11), the equilibrium concentration field at SBE may be expressed as

$$CH(x,y,z) = \sum_{n=1}^{\infty} CH_n(x,y,z) \exp\left(-\frac{2n-1}{2} kT\right) \quad (14)$$

Since the concentration fields CL_n are not measured at the same tidal phase when the tracer-release begins or ends, the decaying factor of equation (11) has to be modified. The first concentration field CL_1 is measured at a time when the tracer has been released for only half of the tidal cycle. The average decaying factor is $\exp\left(-\frac{1}{4} kT\right)$. For $n \geq 2$, the

concentration fields CL_n are measured at $(n-1)$ tidal cycles after the mid-time of tracer release. The decaying factor is $\exp\{-(n-1)kT\}$. Therefore, equation (11) is modified to

$$CL(x,y,z) = CL_1(x,y,z)\exp(-\frac{1}{4}kT) + \sum_{n=2}^{\infty} CL_n(x,y,z)\exp\{-(n-1)kT\} \quad (15)$$

In deriving equation (11), the decaying factor $\exp(-k\tau)$ is approximated by a constant $\exp(-\frac{2n-1}{2}kT)$ over the time interval $t = (n-1)T$ to $t = nT$. The error introduced by this approximation may be reduced by shortening the duration of continuous tracer release T . For a tidal estuary, this may be easily achieved by separating the tracer-release into two parts: one continuous release over ebb tide and another continuous release over flood tide. Successive concentration fields at SBE and SBF are measured for both releases and constant decay factors applied to each of the measured concentration fields.

Let

$CHF_n(x,y,z)$ be the concentration field of flood tide release, measured at the n^{th} SBE,

$CHE_n(x,y,z)$ be the concentration field of ebb tide release, measured at the n^{th} SBE,

$CLF_n(x,y,z)$ be the concentration field of flood tide release, measured at the n^{th} SBF,

$CLE_n(x,y,z)$ be the concentration field of ebb tide release, measured at the n^{th} SBF.

then, for a non-decaying substance, the CH_n and CL_n in equations (14) and (15) may be expressed as

$$CH_n = CHF_n + CHE_n \quad (16)$$

$$CL_n = \begin{cases} CLF_{n-1} + CLE_n & n \geq 2 \\ CLE_n & n = 1 \end{cases} \quad (17)$$

The asymmetry of indices in equation (17) arises from the fact that CL_n is the concentration field at slack water before flood while the continuous tracer release is assumed to be from SBE to SBE.

For a decaying substance, different decaying factors are applied to the two parts of CH_n and CL_n , and equations (14) and (15) become

$$CH(x, y, z) = \sum_{n=1}^{\infty} CHF_n(x, y, z) \exp \left\{ - \left(\frac{2n-1}{2} - \frac{1}{4} \right) kT \right\} \\ + \sum_{n=1}^{\infty} CHE_n(x, y, z) \exp \left\{ - \left(\frac{2n-1}{2} + \frac{1}{4} \right) kT \right\} \quad (18)$$

$$CL(x, y, z) = \sum_{n=1}^{\infty} CLF_n(x, y, z) \exp \left\{ - \left(\frac{2n-1}{2} + \frac{1}{4} \right) kT \right\} \\ + \sum_{n=1}^{\infty} CLE_n(x, y, z) \exp \left\{ - \left(\frac{2n-1}{2} - \frac{1}{4} \right) kT \right\} \quad (19)$$

The adjustment of $\frac{1}{4} kT$ and $-\frac{1}{4} kT$ for the decaying factors of concentration fields of half-tidal cycle tracer releases improves the accuracy over a continuous full tidal cycle release.

FIELD EXPERIMENT

The model was used to study the proposed Nansemond Sewage Treatment Plant to be located on the south shore of the James River near the mouth of the Nansemond River. The outfall for this plant would be in Hampton Roads at a point roughly 12,000 feet (3,658 meters) from shore and a depth of 20 to 25 feet (6.1 to 7.6 meters), as shown in figure 1. The depth in Hampton Roads is much smaller than the horizontal dimensions of the water body. Vertical mixing by tidal currents is strong so that, at a location outside of the zone of initial mixing, the vertical variation of water constituent concentrations is negligible when compared with horizontal variations. The vertical homogeneity is especially true in late summer when the density stratification is weak and when the water quality problem is severe. Therefore, the horizontal distribution of concentration fields were measured in the tracer release experiments and vertical homogeneity was assumed. Vertical distribution of dye was measured at several locations during the field experiment and they confirmed the vertical homogeneity.

During the summer of 1974, two dye studies were conducted in Hampton Roads to simulate the release of pollutants during the flood and ebb cycles separately. The dispersion and transport of the dye, Rhodamine WT, were

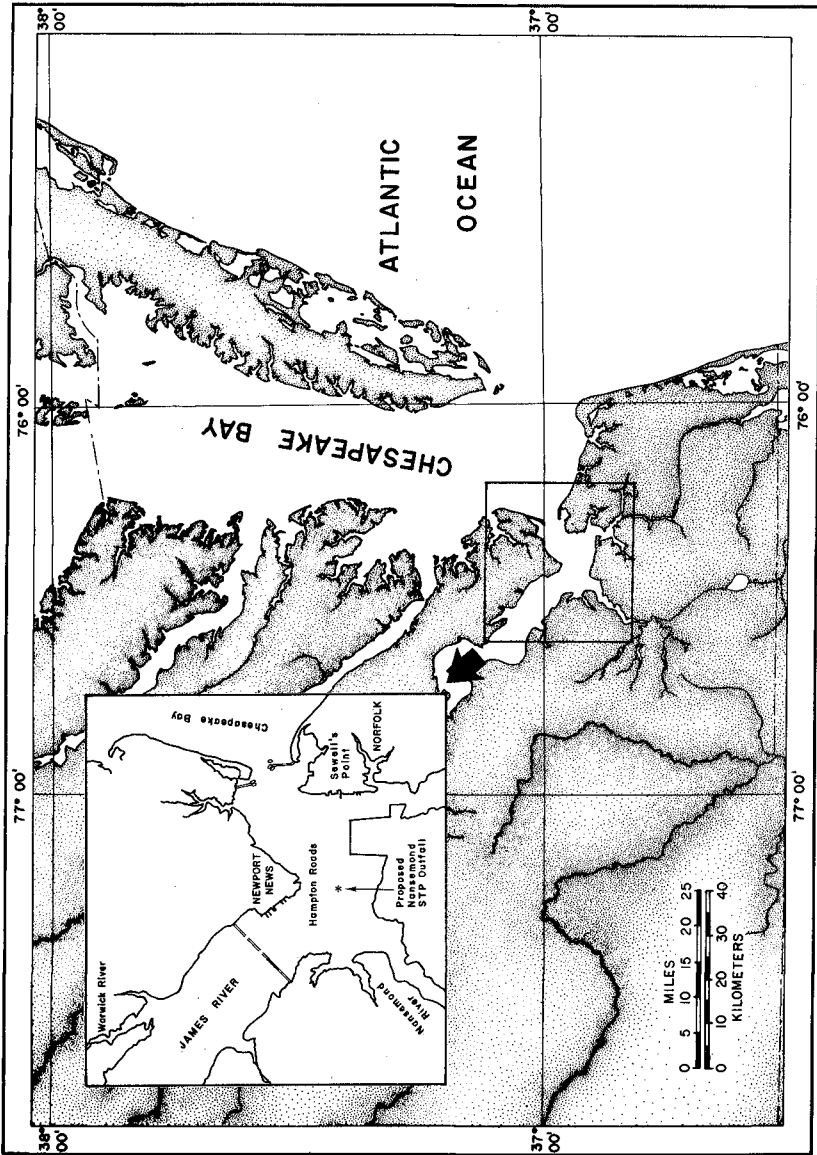
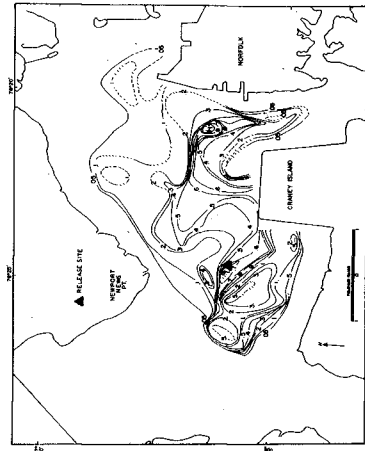


Figure 1. The location map of Hampton Roads and proposed Nansemond STP Outfall.

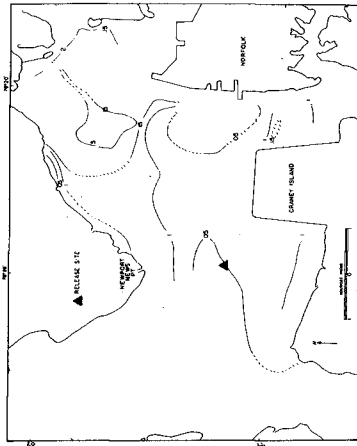
followed for a period of about four days in each experiment. Two moving boats equipped with flow-through fluorometers and Hastings-Raydist navigation units traversed the study area at slack waters before ebb and flood (SBE and SBF). Each boat moved from shore to shore in a zigzag fashion following the period of slack water as it progressed upriver. The near surface (1 ft. or 30.5 cm below surface) dye concentration was monitored continuously and location coordinates were recorded every ten seconds. The data from these cruises were transferred to a chart of the area and contours of equal dye concentration were drawn by hand.

The dispersion and transport of the dye can be seen in figure 2 which shows some samples of dye clouds following the ebb cycle release. No data are presented within the area labeled Initial Mixing Zone, since within that area, there was a significant vertical variation in dye concentration. Outside that area, the concentration was nearly uniform with depth. The initial plume at the first SBF is about six miles long but less than one mile wide (figure 2a). At the following SBE, one complete tidal cycle after the dye release began, the dye cloud reaches from shore to shore, as shown in figure 2b. The dye has been dispersed over a broad area, and the complex pattern of currents in Hampton Roads has broken the dye cloud into several patches. At the second SBF, figure 2c, the dye cloud has been further dispersed and moved downriver. By the fourth SBF, figure 2d, the dye has been dispersed over a large area so that the concentrations are quite low. Much of the dye has left the James and gone into Chesapeake Bay. Similar patterns were found for the dye clouds of the flood cycle release, samples of which are shown in figure 3.

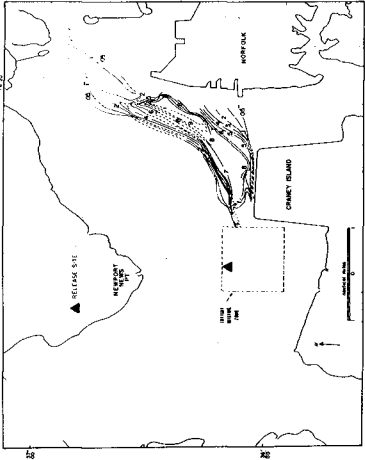
Data from the contours for the various slack waters for both flood and ebb releases were digitized for input to the computer. An 8.5 mile (13.7 kilometer) by 7 mile (11.3 kilometer) grid with 0.1 mile (0.161 kilometer) grid spacing was constructed and dye concentrations at each grid point were tabulated and read into the computer. Due to limited manpower and difficulties surveying at night in an area with a large volume of shipping, it was not possible to sample on every slack tide. Therefore an interpolation procedure was needed to provide the missing data. Values for the dye concentration one tidal cycle prior to and one tidal cycle after the slack with missing data were used to calculate the interim value (Kuo and Jacobson, 1975). Once this procedure had been accomplished, the summation process in equations (18) and (19) was completed and the equilibrium values were printed out on the grid points. This printout was then contoured and the equilibrium distributions were obtained.



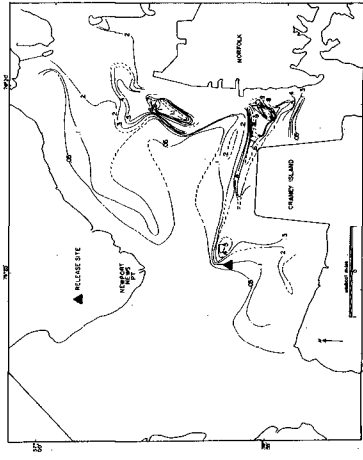
2a 0815, dye concentration in ppb.



2b 0915, dye concentration in ppb.

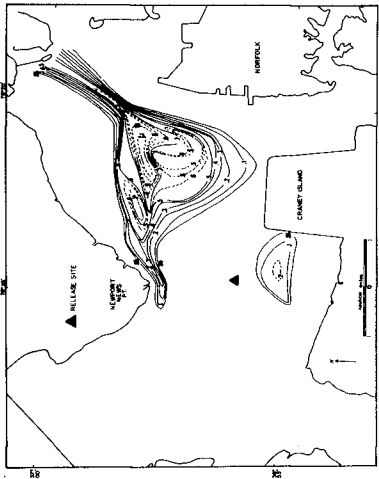


2c 1015, dye concentration in ppb.

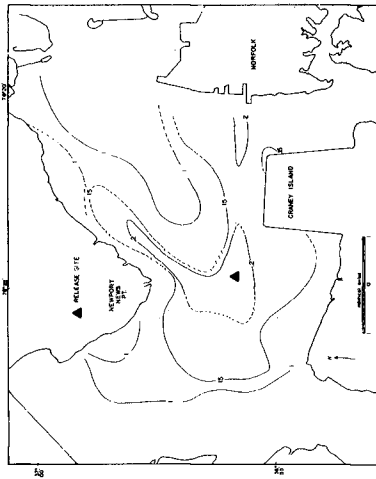


2d 1115, dye concentration in ppb.

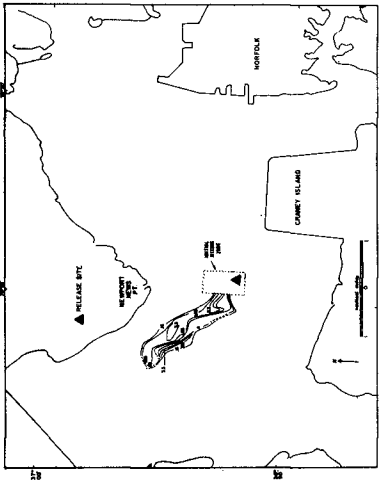
Figure 2. Samples of dye distributions from ebb tide release.



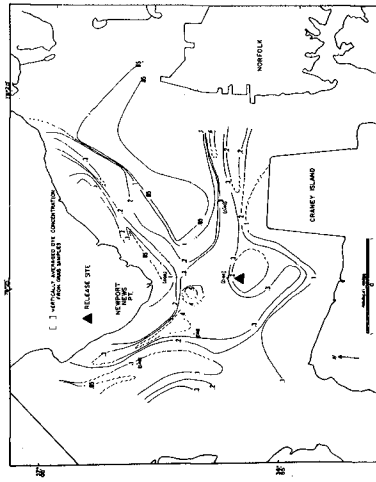
3b cm^2 , dye concentration in ppb.



3d cm^2 , dye concentration in ppb.



3a cm^2 , dye concentration in ppb.



3c cm^2 , dye concentration in ppb.

Figure 3. Samples of dye distributions from flood tide release.

Figure 4 shows the equilibrium concentration fields resulting from a continuous point source of 800 lb/day (363 kg/day). Equations (18) and (19) allow the simulation of the dispersion of nonconservative substances as well as conservative substances. In the figure one can compare the equilibrium concentration distributions for a conservative substance and one with a decay rate of 0.30 per day.

RESULTS

Using the designed effluent loadings of the proposed sewage treatment plant and the dye distribution data from the field experiment, the model was used to predict the distribution of total nitrogen, total phosphorus, biochemical oxygen demand, dissolved oxygen deficit, residual chlorine and coliform bacteria in Hampton Roads. The following are the designed average effluent loadings:

flow	:	16 MGD (0.702 m ³ /sec)
BOD ₅	:	4000 lb/day (1814 kg/day)
total nitrogen	:	25 mg/l (as N)
total phosphorus	:	10 mg/l (as P)
residual chlorine	:	2 ppm
fecal coliform	:	70/100 ml

In the simulation, total nitrogen and total phosphorus were assumed to be conservative substances. The predicted maximum concentrations of total nitrogen and total phosphorus are 40 µg/l and 25 µg/l respectively. Throughout Hampton Roads, concentrations are generally less than 10 µg/l for total nitrogen and 5 µg/l for total phosphorus. The dissolved oxygen deficit was estimated from the equilibrium relationship between reaeration and biochemical oxygen demand (both carbonaceous and nitrogenous). It was concluded that the DO deficit would be of the order of 0.1 mg/l in general, with a maximum of 0.4 mg/l near the initial mixing zone.

The toxicity of residual chlorine resulting from disinfection of treated wastewaters to estuarine organisms has recently been shown to vary widely with the species and the life history stage. For some organisms, e.g. oyster and clam larvae, 48 hours LC50 (50% lethal concentrations) as low as 0.001 ppm have been found (Roberts et al. 1975). In light of these findings and the fact that the James River estuary is the largest producer of seed oysters in Virginia the model was also used to estimate the potential impact of chlorine disinfection on sensitive species in the estuary. This was accomplished by applying the decay rate for chlorine and monochloramine to the field data of dye concentrations. The decay constant utilized was that determined by Bender, et al. (1975) who showed the decay of both chlorine and monochloramine to be approximately first order with $k = 0.05 \text{ hr}^{-1}$. Figures 5a and 5b show the predicted residual chlorine

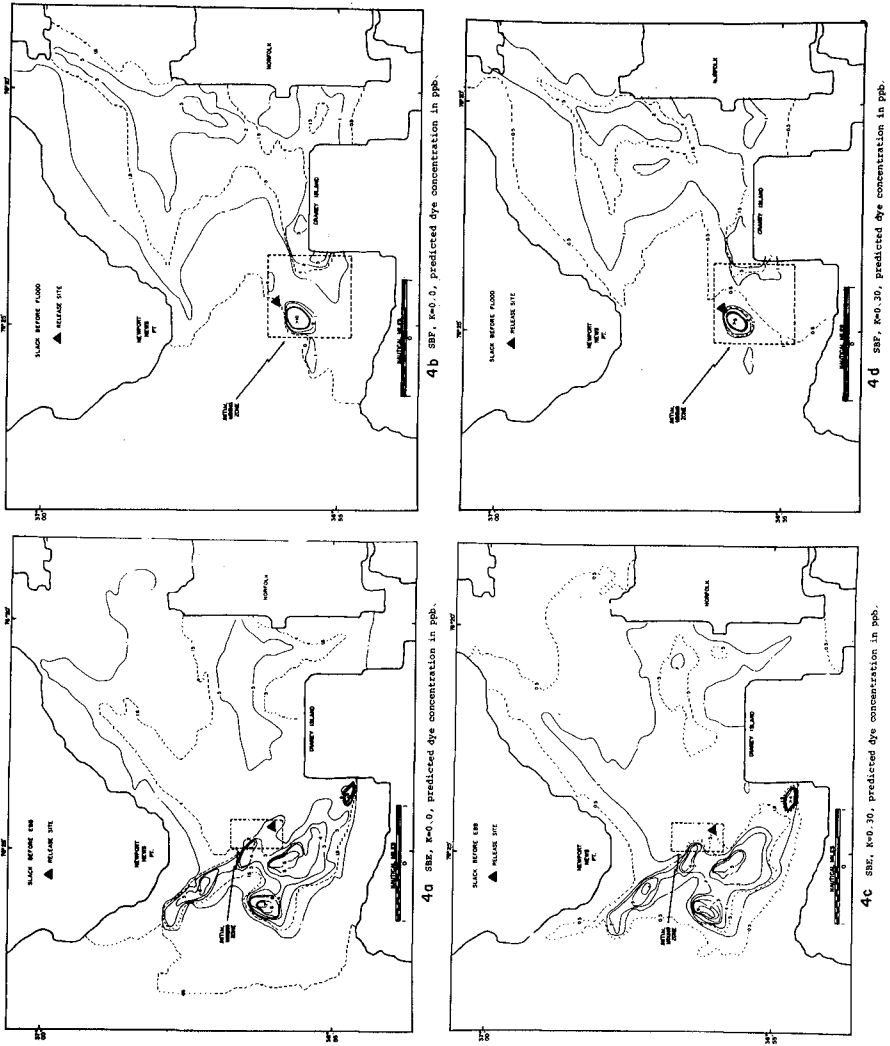
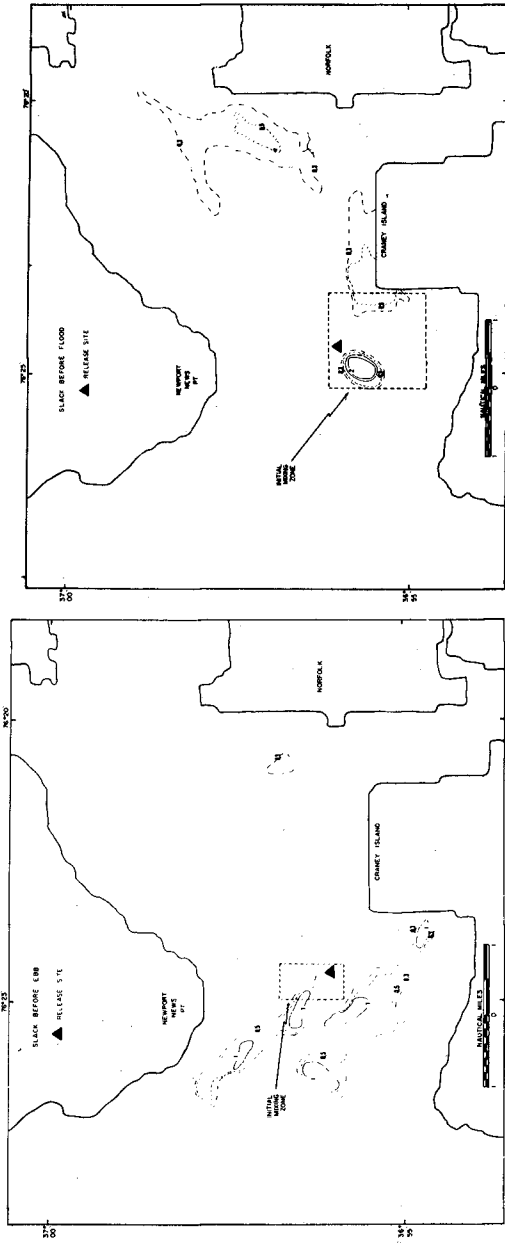


Figure 4. Equilibrium dye distributions from a continuous point source.



5a SBE, predicted chlorine distribution (ppb) for 1995 average loading.

5b SBF, predicted chlorine distribution (ppb) for 1995 average loading.

Figure 5. Concentration fields of residual chlorine.

distributions in the estuary at SBE and SBF respectively. As can be readily seen from inspection of figure 5a, considerable risk to oyster and clam larvae entrained in or passing through this segment seems likely.

Although not directly detrimental to marine organisms, the presence of coliform organisms above given levels in estuarine water is used by public health officials as an indicator of fecal contamination. If coliforms or fecal coliforms exceed accepted limits in a given segment of water the area is restricted for shellfish harvesting, thereby incurring an economic loss of valuable resources without actual damage to the shellfish population.

The model was used to predict the increase in ambient coliform concentrations as the result of proposed effluent loadings. The maximum bacteria level allowable in the effluent was set at 70 fecal coliforms per 100 milliliter of water. The model predicted that the maximum increase in ambient coliform levels was less than 1 per 100 ml. It was concluded that coliform loadings at this rate would not have a detrimental effect from the standpoint of shellfish closures. However, to cover the contingency of a breakdown in normal chlorinating procedures at a sewage treatment plant, an area around a sewage outfall was always designated that no shellfish might be taken within it. The model was used to simulate the coliform distribution which would result from the discharge of unchlorinated secondary effluent (3×10^5 fecal coliform/100 ml) for some specified length of time to simulate the discharge of unchlorinated effluent for finite duration. The summation in equations (18) and (19) was carried out to the first few terms corresponding to the duration of the point source. Figures 6a and 6b show the concentration distributions resulting from chlorination breakdown of half a tidal cycle.

DISCUSSION

The method presented in this paper has three elements: determining the dispersion and transport of a conservative substance released in a water body, some measure of the rate of decay or transformation of the wastewater constituents, and a set of mathematical procedures to combine this information and predict the distribution of nonconservative substances. All three elements will introduce some error. The effluent distributions which have been predicted appear reasonable to the oceanographers who have studied the tidal circulation in this region.

It is possible to note several limitations of the method. First, the determination of the physical dispersion and transport is time and site specific. That is, the results do not apply to other outfall locations nor do they

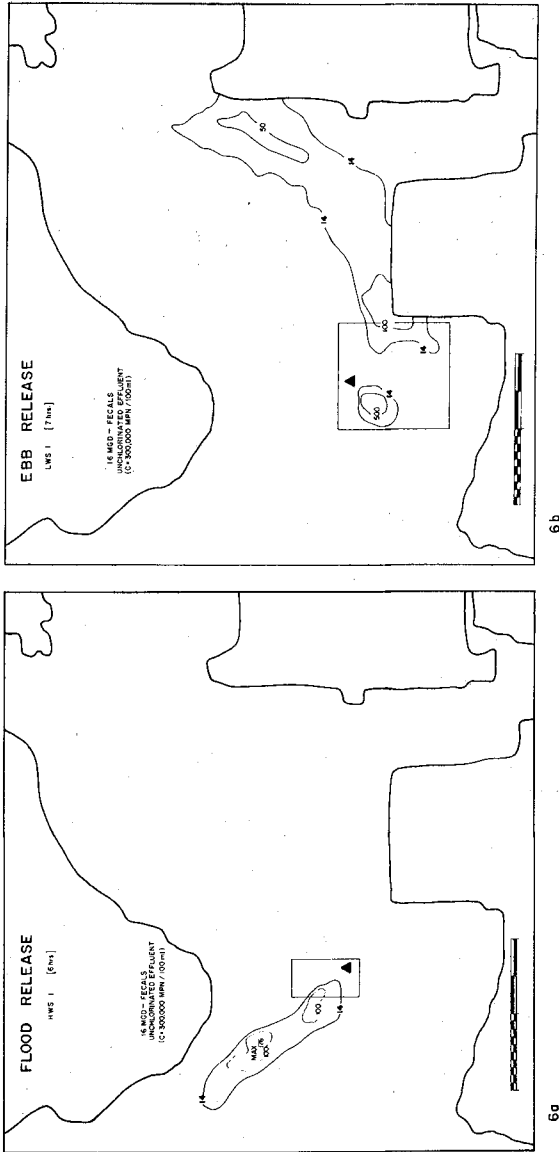


Figure 6. Fecal coliform distributions resulting from unchlorinated sewage.

necessarily apply to other times if the meteorological and hydrographic conditions have changed. An obvious example is that the results of the dye studies conducted in Hampton Roads during the summer of 1974 would not give good predictions for extreme events such as floods or hurricanes. It is not known to what extent the results will be modified when the estuary exhibits strong vertical salinity stratification, as occurs most winters and springs, but it is believed that the results will differ only slightly. If a hydraulic model is available for the water body under investigation, the tests could be repeated for different hydrographic conditions. The results then could be used to give the predictions for the corresponding conditions in the real world.

The rate of decay depends on many biological, geological and chemical processes and it is not always possible to determine a single rate of transformation which will be widely applicable. Therefore, values should be used which underestimate the rate of decay, and therefore provide conservative predictions since the residence time and concentrations will be over-estimated. The errors introduced by the mathematical manipulations are believed to be smaller than those introduced by the other two steps.

ACKNOWLEDGEMENTS

Many thanks are due to our colleagues, especially to Mr. E. P. Ruzecki for his capable supervision of the field study, and to Drs. C. S. Fang and B. J. Neilson for their suggestions and criticism.

This model was developed under the Cooperative State Agencies Program. The continuing support of the Virginia State Water Control Board is appreciated. The application of the model as described herein was supported by Hampton Roads Sanitation District Commission through McGaughy, Marshall & McMillan-Hazen and Sawyer: A Joint Venture. They are appreciated for the financial support and encouragement.

REFERENCES

- Bender, M. E., Roberts, M. H., Diaz, R. and R. J. Huggett, 1975. "Effects of Residual Chlorine on Estuarine Organisms," Proc. Biofouling Workshop, Johns Hopkins Univ., Baltimore, Maryland.
- Brooks, N. H., 1960. "Diffusion of Sewage Effluent in an Ocean Current," Proc. of First International Conf. on Waste Disposal in the Marine Environment, Univ. of California 1959, Pergamon Press, New York.

- Csanady, G. T., 1973. "Turbulent Diffusion in the Environment," D. Reidel Publishing Co., Boston, Mass.
- Fan, Loh-Nien, 1967. "Turbulent Buoyant Jets into Stratified or Flowing Ambient Fluids," W. M. Keck Lab. of Hydraulics and Water Resources Report No. KH-R-15, Calif. Inst. of Tech.
- Fan, Loh-Nien and N. H. Brook, 1969. "Numerical Solutions of Turbulent Buoyant Jet Problems," W. M. Keck Lab. of Hydraulics and Water Resources Report No. KH-R-18, Calif. Inst. of Tech.
- Kuo, A. Y. and J. P. Jacobson, 1975. "A Model for Predicting the Pollutant Distribution from an Outfall in a Tidal Estuary," Spec. Rep. No. 86 in Appl. Mar. Sci. and Ocean Eng., Vol. 5, VIMS.
- Pritchard, D. W. and H. H. Carter, 1965. "On the Prediction of the Distribution of Excess Temperature from a Heated Discharge in an Estuary," Tech. Rep. 33, Chesapeake Bay Inst., The Johns Hopkins Univ., Baltimore, Maryland.
- Roberts, M. H., Diaz, R., Bender, M. E. and R. J. Huggett, 1975. "Acute Toxicity of Chlorine to Selected Estuarine Species," J. of the Fisheries Res. Bd. of Canada, Vol. 32, No. 2.
- Tracor, Inc., 1971. "Estuarine Modeling: An Assessment," EPA, Water Pollution Control Research Series, 16070, DZV 02/71.

CHAPTER 189

NUMERICAL MODEL FOR DENSITY CURRENTS IN ESTUARIES

Karsten Fischer*

1. Introduction

In the estuarine mixing areas of salt water and fresh water the vertical stream velocity profile generally is strongly affected by the baroclinic forces, giving rise to upstream currents near the bottom. Such reverse currents occur not only in stratified estuaries, but also in estuaries of the well-mixed type [1], and they may cause problems like strong shoaling areas, salt intrusion, or difficulties when disposing wastes or dredged material [3]. The contributions of the salinity variations to the tidal motion are comparable to the contributions from the fresh water upland discharge [1]. For well-mixed estuaries with negligible fresh water discharge, the tidal velocities and water elevations may be obtained from numerical vertically averaged models or from physical homogeneous-flow models, but for all other conditions or desired results one has to use numerical vertically discretized models or physical inhomogeneous-flow models. As numerical and physical models have different properties and deficiencies, they may be used complementarily rather than concurrently [4], the farfield regime apparently becoming the domain of numerical models.

The increased public and scientific interest in water quality problems led to the development and application of baroclinic numerical tidal models [5, 6]. The present paper is concerned with the question, how well the action of baroclinic forces can be represented by numerical techniques. As a test example, the salt wedge problems is tackled. Studies on salt wedges by means of physical models have been very successful [1, 7], but mathematical approaches were confined to analytical solutions for the stationary salt wedge [8 - 10] and simple geometric boundaries only. The numerical approach is free from these restrictions, giving a solution of the complete equations of motion, continuity, and convection-diffusion simultaneously.

The main difficulty for the numerical model lies in the solution of the convection equation. The usual methods to solve the convection equation (like Forward Time / Centered Space, Upstream Differences, Lax-Wendroff, ADI, Leapfrog, or Galerkin-Finite Elements) break down when the convection of fairly sharp density jumps is to be calculated, as is the case for the salt wedge. Strong artificial diffusivity, mass losses, violations of the second law of thermodynamics or even unstable solutions are encountered. The numerical errors can be reduced considerably by using higher order difference approximations [11] at

*

Research Scientist, Sonderforschungsbereich 79, Technische Universität Hannover, F.R. Germany

the expense of higher numerical effort and more complicated boundary conditions, or by using a floating (Lagrangian) grid formulation; however, shearing and circulating flow forces the programmer to interpolate back to a fixed (Eulerian) grid from time to time, so that the advantage of the Lagrangian formulation in part gets lost, while the full numerical effort remains. In the baroclinic numerical model, errors in the convective solution may distort the whole model because of the faulty baroclinic forces (arising from a faulty density distribution) which act in the equations of motion. The question is, whether the numerical smoothing of sharp density jumps still allows for an adequate solution of the dynamics.

In the present paper, a new method for solving the convection equation is described, where the above mentioned numerical errors are reduced drastically. The numerical solution is compared to a semi-analytic one, ensuring the quality of the numerical method. A few exemplary calculations, showing the influence of bottom friction, barriers, and tidal motion on the shape of the salt wedge, demonstrate the versatility of the numerical model.

2. Numerical Method

Figure 1 shows the schematic salt wedge and the geometry used in the present investigation. We take a channel of constant depth a and length S , open at both ends. The lateral (y -) dependence is neglected. The freshwater discharge Q enters from the right. The salt wedge is formed by the sharp density jump between salt water (density ρ_1) and fresh water (density ρ_0) at $z = -t$, the thickness of the wedge over the bottom is r .

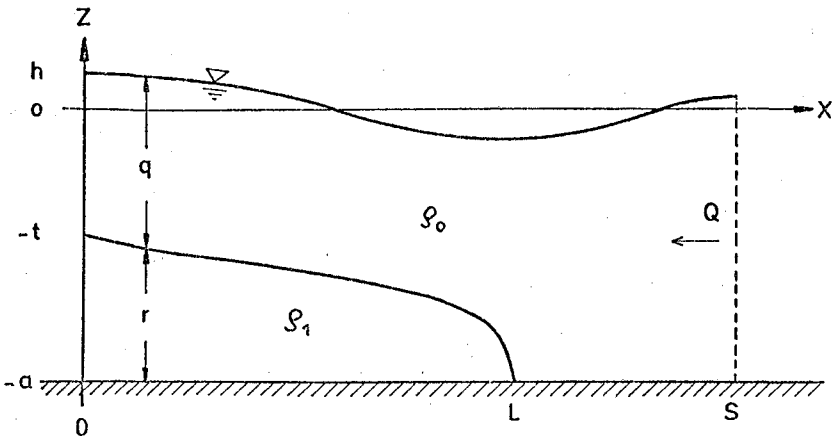


Figure 1. Salt wedge - schematic for definition of parameters.

The numerical solution is based on the following equations:
the equation of motion

$$\frac{\partial u}{\partial t} + \frac{1}{\rho} \frac{\partial p}{\partial x} - A \frac{\partial^2 u}{\partial z^2} = 0 \quad (1)$$

the hydrostatic pressure equation

$$\frac{\partial p}{\partial z} + \rho g = 0 \quad (2)$$

the continuity equation for incompressible flow

$$\frac{\partial u}{\partial x} + \frac{\partial w}{\partial z} = 0 \quad (3)$$

and the convection equation

$$\frac{\partial c}{\partial t} + u \frac{\partial c}{\partial x} + w \frac{\partial c}{\partial z} = 0 \quad (4)$$

where the concentration c is related to the density ρ by

$$c = \frac{\rho - \rho_0}{\rho} \quad (5)$$

u and w are the velocities in the x - and z -direction, respectively. p is the pressure, g the gravitational acceleration, ρ the density, and A the vertical eddy viscosity coefficient. In (1), the convective terms have been neglected in order to make an analytic solution possible which is needed for the comparison purpose. Eq. (1) still contains the terms responsible for tidal motion and salt wedge formation, and major effects from the convective terms should only be expected near the tip of the salt wedge where the velocity gradient is large. It will be shown that this is the region where the numerical errors are largest, but the comparison to experimental salt wedge profiles is good, so the neglect of the convective terms can be justified. In eq. (4) the diffusion terms were neglected for the same reason, i.e. the desired analytical solution works with two fluid layers of different density as depicted in fig. 1, while diffusion would create a continuous vertical density profile. For the numerical model, a certain amount of numerical diffusivity cannot be avoided, and an additional physical diffusion term would make the comparisons even more difficult.

For the numerical solution of the dynamic equations (1-3) the scheme of Suendermann [12] was used. The linearized equations are solved by an explicit leap - frog method, whereby the z -dependency of the velocity u is treated implicitly. The time-step of this procedure is limited by the step size along the x -axis through the Courant stability criterion.

For the numerical solution of the convection equation, a newly developed method was applied [13]. For simplicity, the method is explained for the one-dimensional case. The spatial density distribution is represented by Hermite interpolation functions; at the computational grid points, the density value ρ_j and its local gradient $(\frac{\partial \rho}{\partial x})_j$ are defined as time-dependent variables. For example, the density representation between grid points 0 and 1 is given by

$$\rho(x) = \rho_0 a(x) + \rho_1 b(x) + \left(\frac{\partial \rho}{\partial x}\right)_0 c(x) + \left(\frac{\partial \rho}{\partial x}\right)_1 d(x) \quad (6)$$

with the Hermite interpolation polynomials

$$\begin{aligned} a(x) &= 2x^3 - 3x^2 + 1 & b(x) &= -2x^3 + 3x^2 \\ c(x) &= x^3 - 2x^2 + x & d(x) &= x^3 - x^2 \end{aligned} \quad (7)$$

This representation has the following properties

$$\rho(0) = \rho_0, \rho(1) = \rho_1, \frac{\partial \rho}{\partial x}(0) = \left(\frac{\partial \rho}{\partial x}\right)_0, \frac{\partial \rho}{\partial x}(1) = \left(\frac{\partial \rho}{\partial x}\right)_1$$

The convection equation

$$\frac{\partial \rho}{\partial t} = -u \frac{\partial \rho}{\partial x} \quad (8)$$

is converted to the explicit difference equation

$$\rho_j^{n+1} = \rho_j^n - u_j \Delta t \left(\frac{\partial \rho}{\partial x}\right)_j^n \quad (9)$$

with j the spatial index and n the time-index, Δt is the time step.

For the gradient variables, another marching equation is needed. This equation is obtained from eq. (8) by spatial differentiation:

$$\frac{\partial}{\partial t} \left(\frac{\partial \rho}{\partial x}\right) = -u \frac{\partial^2 \rho}{\partial x^2} - \frac{\partial u}{\partial x} \frac{\partial \rho}{\partial x} \quad (10)$$

and transformed to the difference equation

$$\begin{aligned} \left(\frac{\partial \rho}{\partial x}\right)_j^{n+1} &= \left(\frac{\partial \rho}{\partial x}\right)_j^n - \frac{u_j \Delta t}{\Delta x} \left\{ \begin{aligned} &\frac{6}{\Delta x}(\rho_{j-1}^n - \rho_j^n) + 4 \left(\frac{\partial \rho}{\partial x}\right)_j^n + 2 \left(\frac{\partial \rho}{\partial x}\right)_{j-1}^n \\ &\frac{6}{\Delta x}(\rho_{j+1}^n - \rho_j^n) - 4 \left(\frac{\partial \rho}{\partial x}\right)_j^n - 2 \left(\frac{\partial \rho}{\partial x}\right)_{j+1}^n \end{aligned} \right\} \\ &\quad - \frac{u_{j+1} - u_{j-1}}{2 \Delta x} \left(\frac{\partial \rho}{\partial x}\right)_j^n \end{aligned} \quad (11)$$

where Δx is the spatial step size. The second term in the right-hand side of eq. (11) models the term $\frac{\partial^2 \rho}{\partial x^2}$ and is obtained from the evaluation of the second derivative of eq. (6), letting $x \rightarrow 0$; upstream differences are taken in eq. (11), where the upper line holds for $u_i > 0$, the lower line for $u_i < 0$. The third term on the r-h-s of eq. (11) is a spatial nonlinear term and was omitted in the calculations because of its destabilizing behaviour. It was found that eqs (9) and (11) together are linearly unstable, but stability could be achieved by a small correction to eq. (9). Instead of eq. (8), the form

$$\frac{\partial \rho}{\partial t} = -u \frac{\partial \rho}{\partial x} + \frac{u^2 \Delta t}{2} \frac{\partial^2 \rho}{\partial x^2} \tag{12}$$

was evaluated, where the corrective second term could immediately be taken from eq. (11).

The accuracy of the above described convective solution method is compared to several other methods in figure 2.

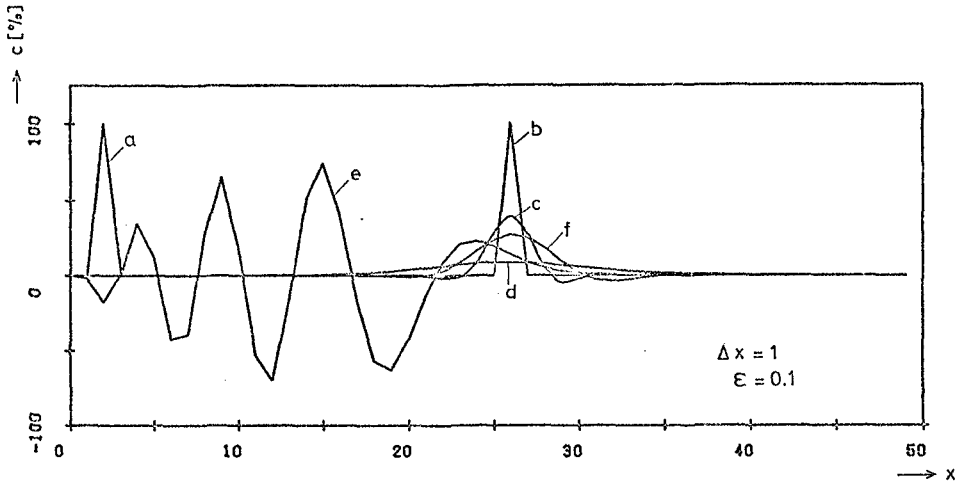


Figure 2. Numerical solution for convection of density spot.
 a) Initial, b) final density distribution (exact),
 c) present method, d) upstream differencing,
 e) forward time-centered space, f) Fromm's method.

As test example, the convection of a narrow density spot (initial width = $1 \cdot \Delta x$) over a distance $24 \cdot \Delta x$ was calculated by iterating over 240 time steps. The best approximation to the exact final density distribution is given by the present

method, which is even superior to the higher order method of Fromm [11]. The unstable character of the Forward Time-Centered Space method results in the strongly oscillating curve, while the Upstream Differencing scheme displays the strong numerical damping. Many other methods like Leapfrog, Lax-Windroff, Finite Elements or Flux-Corrected Transport can be shown to be inferior to the method of Fromm [13]; the present method gives comparatively very good results, uses simple boundary conditions and needs little numerical effort, only some more core space is needed for storing the gradient values.

In two dimensions, a second expression analogous to eq. (11) has to be evaluated numerically. The calculation can be done by fractional time steps, scanning through the coordinate directions successively, or by computing and adding the contributions from both coordinates simultaneously; the latter method was used here.

3. Semi - Analytic Solution to the Stationary Salt Wedge

Omitting the partial time derivative in eq. (1), a quadratic z -dependency of the velocity u can be obtained for each density layer (see fig. 1) separately, by integration. The non-slip condition is applied at the bottom:

$$u(-a) = 0 \quad (13)$$

The total flow across r is zero:

$$\int_{-a}^{-t} u(z) dz = 0 \quad (14)$$

Introducing the "baroclinic water level" k :

$$k(x) = h(x) - c q(x), \quad (15)$$

one gets for the velocity in the lower saline layer

$$u(z) = \frac{g}{6A} \frac{\partial k}{\partial x} \{ 3z^2 + 2(2a + t)z + a(a + 2t) \} \quad (16)$$

For the upper layer, the following two conditions are applied:

- 1.) the velocity $u(z)$ must be continuous at the interface $z = -t$.
- 2.) The total fresh water flow across q has the given constant value Q :

$$\int_{-t}^h u(z) dz = Q \quad (17)$$

For the velocity in the upper layer one gets

$$\begin{aligned}
 u(z) = & \frac{g}{2A} \frac{\partial h}{\partial x} z^2 + \frac{1}{3} \left\{ \frac{g}{A} \frac{\partial h}{\partial x} (2t - h) - \frac{g}{A} \frac{\partial k}{\partial x} \frac{r^2}{q} + \frac{6Q}{q^2} \right\} z \\
 & + \frac{1}{6} \left\{ \frac{g}{A} \frac{\partial h}{\partial x} t (t - 2h) + \frac{g}{A} \frac{\partial k}{\partial x} \frac{r^2}{q} (h - t) + \frac{12Q}{q^2} t \right\}
 \end{aligned} \quad (18)$$

For the calculation of the wedge shape $t(x)$ and the surface $h(x)$ two conditions are needed. They are obtained by considering the tangential forces:

1.) the stress at the surface is zero

$$\left. \frac{\partial u}{\partial z} \right|_{z=h} = 0 \quad (19)$$

2.) the stress at the interface is continuous

$$\left. \frac{\partial u}{\partial z} \right|_{z=-t-0} = \left. \frac{\partial u}{\partial z} \right|_{z=-t+0} \quad (20)$$

Inserting (16) in (20) and (18) in (19) and (20), one gets

$$\frac{\partial t}{\partial x} = \frac{1}{c} \frac{\partial h}{\partial x} \left(\frac{3}{2} \frac{h+t}{a-t} + 1 - c \right) \quad (21)$$

$$\frac{\partial h}{\partial x} = - \frac{12QA}{g(h+t)^2(4h+3a+t)} \quad (22)$$

This system of nonlinear, first - order differential equations was solved (to an arbitrary degree of accuracy) by numerical methods, and the solution is referred to as semi - analytic.

Dimensional analysis of (21) and (22) shows that x scales with a^4 while t and h scale with a , thereby establishing an affine relationship. Integrating (21) over the length L of the salt wedge gives the proportionality

$$L \sim \frac{gc}{QA} a^4 \quad (23)$$

where the remaining constant depends only on the relative depth of the salt wedge at the river mouth. Introducing the densimetric Froude- and Reynolds-numbers

$$Fr = \frac{Q}{\sqrt{cga^3}} \quad , \quad Re = \frac{\sqrt{cga^3}}{A}$$

one has

$$L \sim \frac{Re}{Fr} a \quad (24)$$

while the corresponding results of Keulegan [7] read

$$L \sim \frac{Re^{\frac{1}{4}}}{Fr^{\frac{5}{2}}} a \quad (25)$$

for natural rivers and

$$L \sim \frac{Re^{\frac{1}{2}}}{Fr^{\frac{5}{2}}} a \quad (26)$$

for hydraulic model flumes.

The difference in the results may arise from the simplifications in our theory, especially the constant eddy viscosity A and the non-slip condition (13).

4. Numerical Results

The computer code developed for the calculations permits the choice of variable step sizes in the vertical direction, variable bottom friction and bottom topography, and wind stresses at the surface. At the open boundaries upstream and downstream, the density distribution was kept fixed during the calculation. Care was taken that the salt wedge did not reach the upstream boundary. Since the buoyancy forces had been omitted in the initial differential equations, the hydrodynamically stable stratification had to be readjusted by averaging when a higher density value occurred above lower density values.

The fresh water discharge Q was taken as a dependent variable. As upstream and downstream boundary conditions the water levels were kept fixed. Stationary solutions were obtained after 10 000 time steps ($\hat{=}$ 4 weeks model time). The uniqueness of the solution was checked by starting from various density distributions; up to some minor differences in the velocity distribution, the same results were obtained in every case. More details of the calculations can be found in [14].

The following parameters were used throughout the calculations:

- Channel length $s = 36$ km, height $a = 13.7$ m
- Salt wedge thickness at the downstream end = 6.8 m, concentration = 3‰
- Eddy viscosity coefficient $A = 10^{-3} \text{ m}^2/\text{s}$
- Water levels upstream 4.7 cm, downstream 0.0 cm.

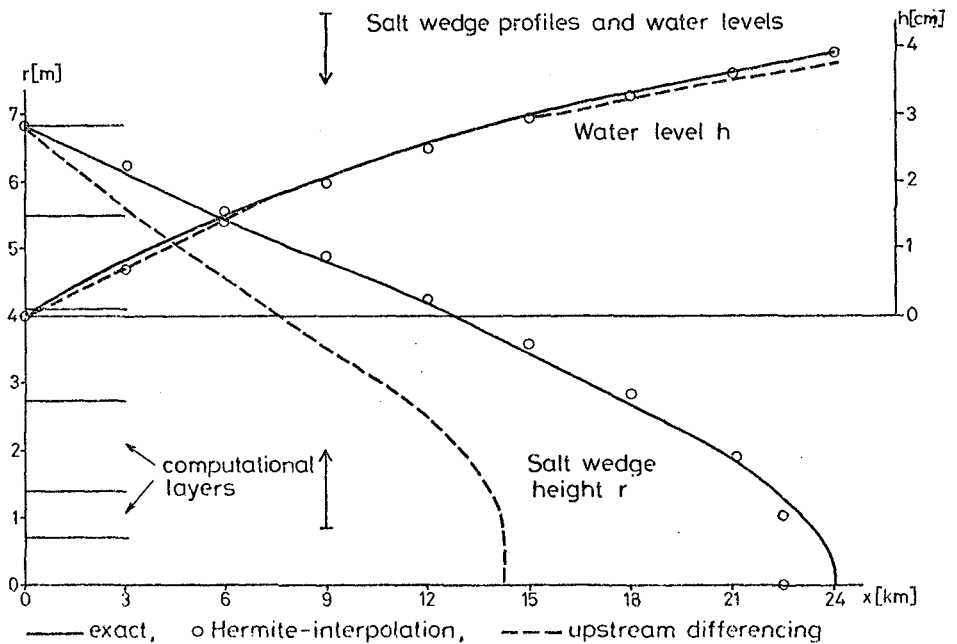


Figure 3. Stationary salt wedge profiles and water levels

Figure 3 shows the stationary salt wedges, computed by the various methods. For the present numerical method called "Hermite-interpolation", the 1.5% - isohaline was plotted as salt wedge boundary. The comparison to the semi-analytic curve called "exact" is good, major differences occur only at the tip of the wedge (where the neglect of the convective terms may play a significant role). It should be noted, however, that the wedge thickness in this region is comparable to the vertical grid spacing, as indicated in the figure. For comparison, another numerical solution is shown where the convection equation was solved by "upstream differencing". From this one can conclude that only the numerical high-precision solution of the convection equation leads to reasonable results in the field of highly stratified estuaries. The differences in the water level are less important, as shown in the upper part of the figure.

At $x = 9$ km, the vertical density profiles of the three different solutions are shown in figure 4.

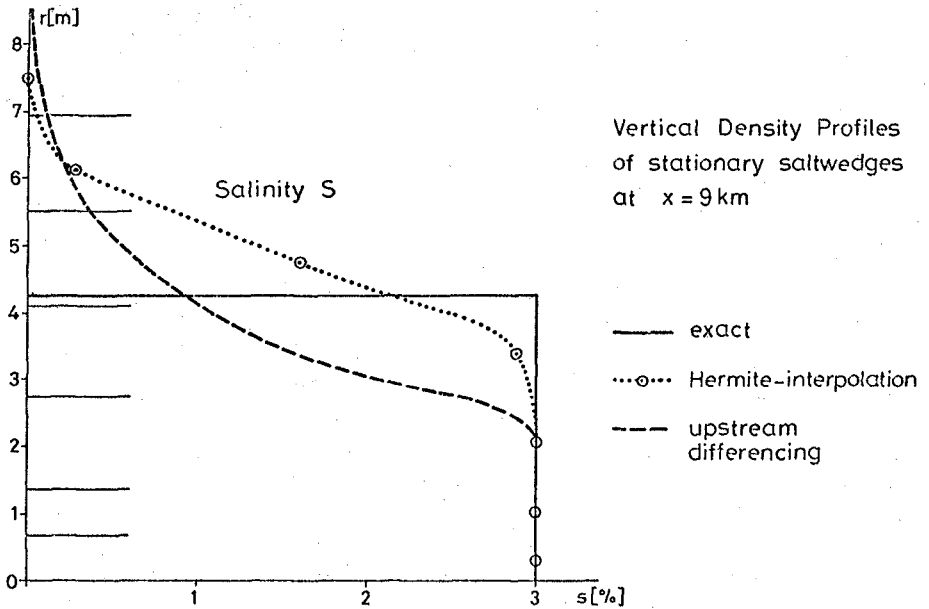


Figure 4. Vertical density profiles of stationary salt wedges from fig. 3. at $x = 9$ km

The sharp density jump of the exact representation is reproduced fairly well by the "Hermite-interpolation" method, while the "upstream differencing" - result shows a very long tail extending towards the channel surface.

All of the following numerical results are obtained with the method of "Hermite-interpolation". Figure 5 shows the changes in the shape of the salt wedge, when the density profile at the river mouth is altered.

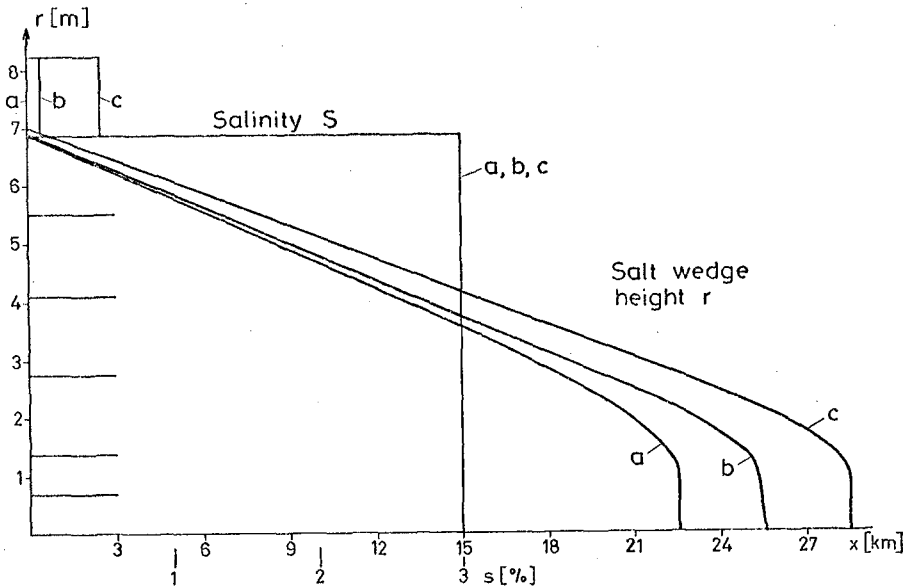


Figure 5. Vertical salinity profiles at river mouth $x = 0$ and corresponding salt wedges

From this figure one can see that little changes in the river mouth density cause substantial changes in the wedge length. This high sensibility of the baroclinic model will make the calibration of parameters in a realistic calculation easier, and it might be interesting to observe such an effect in natura.

Figure 6 shows the influence of bottom friction on the salt wedge shape; the dimensionless friction coefficient R is defined by the Taylor formula for the bottom stress

$$\tau = R u_b |u_b| \quad (27)$$

where u_b is the bottom velocity. With decreasing bottom friction the length of the salt wedge increases. One could have thought of an increased fresh water discharge (because of the decreased bottom friction) and a corresponding shortening of the salt wedge length (see eq. 23), but the opposite is true.

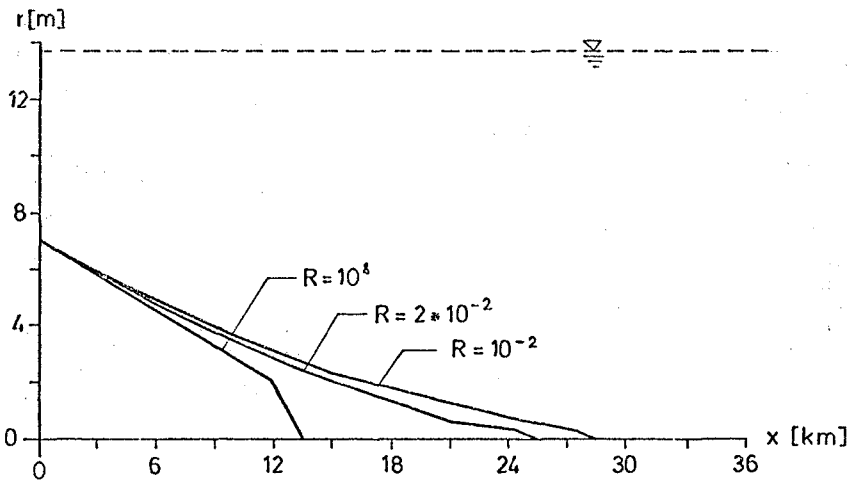


Figure 6. Influence of bottom friction R on salt wedge profile

The influence of a bottom barrier on the salt wedge form is demonstrated in fig. 7

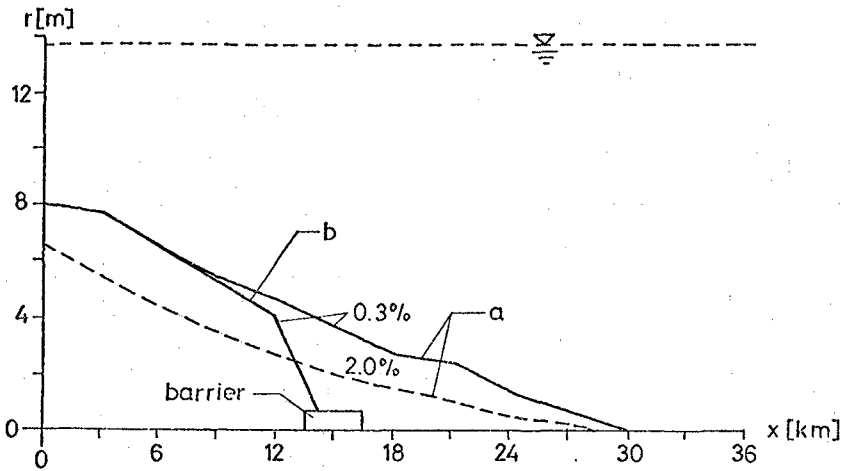


Figure 7. Influence of bottom barrier on salt wedge profile
a) without barrier, b) with barrier

As can be seen in the figure, a barrier height d which is about $1/3$ of the undisturbed salt wedge height, is fully sufficient to prevent the salt wedge from spreading out upstream. This result is contrary to Keulegan's [7] statement that the barrier must be as high as the salt wedge. The problem can be elucidated by considering the velocity distribution eq. 16. For the lower two thirds of the wedge height r , the fluid moves upstream. No salt water can be transported upstream across a barrier of height $d = 2r/3$, because the transport velocity above this level is downstream. In addition, the velocity profile near the bottom is changed by a barrier, so that a barrier height of only $r/3$ prohibits salt intrusion.

As a first instationary calculation, a tidal wave was superimposed on the fresh-water discharge. The data for the calculation are:

	upstream	downstream
- average water levels:	5.3 cm	0 cm
- tidal amplitude:	102.8 cm	102.8 cm
- tidal phase shift:	25.0 deg.	0 deg.
- salt wedge thickness:		7.0 m

The calculation was carried out until periodic conditions were obtained. Figure 8 shows the salt wedges at high and low water. The difference in length is not large, but the

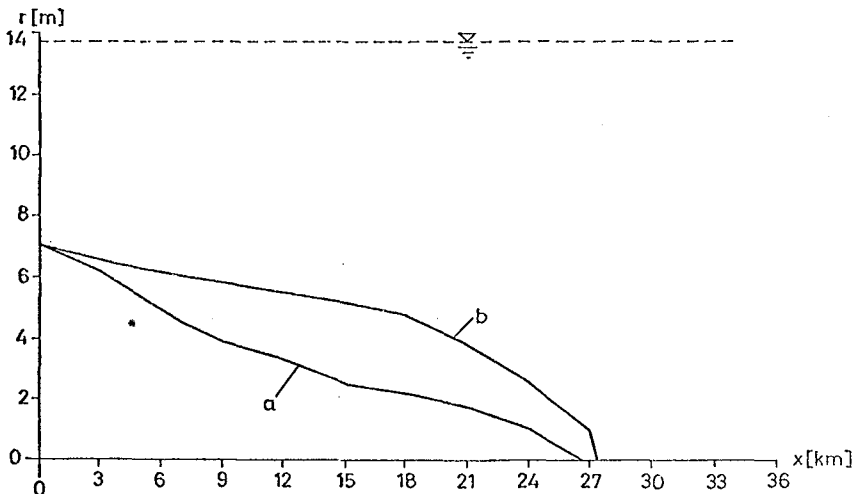


Figure 8. Salt wedge under tidal excitation. a) minimal, b) maximal salt water intrusion into the estuary

difference in salt wedge volume is. The constant height of the salt wedge at the downstream end is an unrealistic boundary condition and should be replaced by a tidally varying one. An indication of a computational instability was found near the tip of the wedge where the concentration at a single grid point was slowly but steadily increasing during the tidal periods. This effect can certainly be removed by more realistic boundary conditions and shall be further observed.

Finally, in order to show the relation of the present calculations to experimental data, the semi-analytic salt wedge curve is compared to Keulegan's [7] affine curve in figure 9.

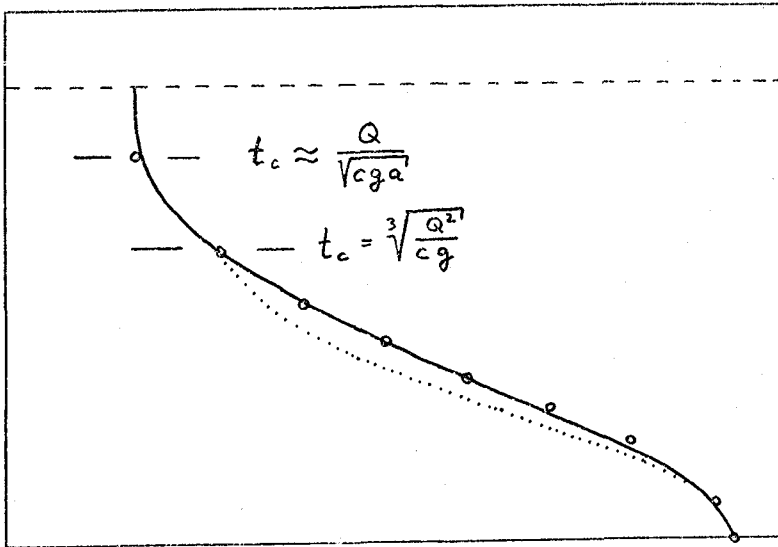


Figure 9. Comparison of semi-analytic salt wedge (full line) to experimental data. Dotted line: Keulegan's salt wedge [7], fitted to critical flow conditions at river mouth
Circles: Keulegan's salt wedge, fitted to present results
Dashed line: Water surface

Taking the point of critical flow in the fresh water layer as "river mouth",

$$t_c = \sqrt[3]{\frac{Q^2}{cg}} \quad (28)$$

the dotted curve, taken from Keulegan's table [7], should be compared to that piece of the semi-analytic solution curve covering the same x - interval. The comparison is rather bad, however, the relation (28) is based on homogeneous flow in both fluid layers and not very well justified experimentally [7]. Relaxing this condition and fitting Keulegan's curve (circles in fig. 9) to the present one, a very good comparison is obtained; the empirical critical depth for this case is

$$t_c \approx \frac{Q}{\sqrt{cga}} \quad (29)$$

In conclusion, the present numerical model appears to be well suited to calculate the hydrodynamics of highly stratified estuaries. Of course, the numerical problems in calculating partially mixed estuaries are comparatively small. The results of such a calculation are given in figure 10.

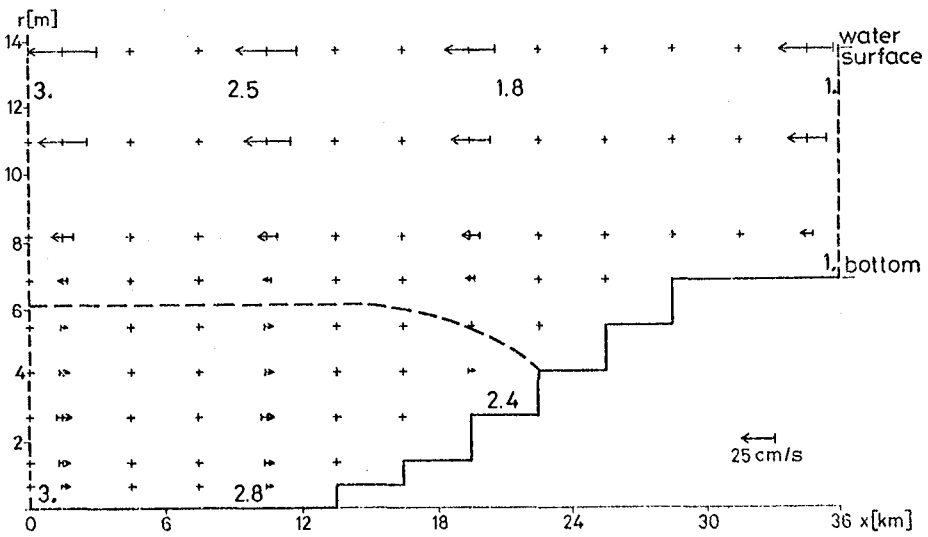


Figure 10. Horizontal velocities (arrows) and salinities (numbers) in a well - mixed estuary (stationary). Dashed line separates regions of upstream and downstream currents.

For this calculation, a horizontal and a vertical diffusion term were added to the density transport equation (4). The diffusion coefficients were taken as large as allowed by stability conditions for an explicit difference scheme. At the boundaries fully mixed conditions were prescribed (numbers indicate density values). The partial stratification in the interior had developed dynamically. The combined effects of longitudinal stratification and sloping bottom lead to a zone of upstream current velocity, indicated in the lower

left part of the figure. This upstream current apparently exists independently from the degree of vertical stratification in the estuary, but only caused by the longitudinal stratification. The tip of the upstream current zone or equally the tip of the salt wedge are known to be the areas of maximum shoaling [3]. In consequence, for longitudinally stratified estuaries no information about the sediment transport can be obtained from measurements of surface velocities or calculations with vertically averaged numerical models, and this seems to hold for vertically stratified and mixed estuaries as well.

5. Summary and Conclusions

A numerical model for density currents in estuaries was presented, combining a classical solution scheme for the dynamical equations with a new solution scheme for the transport equation. The effects of baroclinic forces caused by density differences were studied in a two-dimensional x-z-model, and the results for a stationary salt wedge were shown to be in good agreement with a semi-analytic solution and experimental data. The uniqueness of the numerical solution was checked by varying the initial and boundary conditions. The influence of bottom friction, a bottom barrier, and tidal motions were studied; and the stationary solution for a well - mixed estuary was obtained.

It was found that the accuracy of the results for stratified estuaries depends mainly on the quality of the convective solution scheme, and that the present method of "Hermite-interpolation" gives satisfactory results in every case. As a practical aspect, it was found that bottom barriers for preventing salt intrusion into estuaries need not be as high as the undisturbed salt wedge. For realistic calculations, the time - dependency of water levels and vertical density profiles at the open ends of the estuary must be known from measurements.

6. Acknowledgements

The present work was done by funds of the Deutsche Forschungsgemeinschaft, Sonderforschungsbereich 79 (Wasserforschung im Küstenbereich). The major part of the numerical programming and production was done by W. P. Wittorf, student at Technische Universität Hannover. The support with computer programs and helpful discussions by J. Suendermann is gratefully mentioned.

References

- 1.) A.T. Ippen, "Salinity Intrusion in Estuaries", in [2], chapter 13
- 2.) A.T. Ippen (ed.), "Estuary and Coastline Hydrodynamics", McGraw-Hill, New York 1966
- 3.) See [2], chapters 14, 15
- 4.) J.J. Dronkers, "Tidal Computations in Rivers and Coastal Waters", North-Holland Publ. Co., Amsterdam 1964, p. 18
- 5.) M.B. Abbott, J.A. Bertelsen, J.R. Warren, "Mathematical Modelling of Storm Surges in Stratified Flow", Abstracts 15th Int. Conf. on Coastal Eng., Honolulu 1976, p. 1
- 6.) J.J. Leendertse, R.C. Alexander, S.K. Liu, "A Three-Dimensional Model of Estuaries and Coastal Seas. Vol. 1, Principles of Computation", Report R - 1417 - OWRR, Rand Corporation, 1973
- 7.) G.H. Keulegan, "The Mechanism of an Arrested Saline Wedge", in [2], chapter 11
- 8.) F.A. Lee, Proc. ASCE Hydraul. Div. 100, 17 (1974)
- 9.) M. Rattray, E. Mitsuda, Estuarine and Coastal Marine Sci. 2, 375 (1974)
- 10.) B.P. Rigter, Proc. ASCE Hydraul. Div. 101, 765 (1975)
- 11.) J.E. Fromm, J. Comp. Phys. 3, 176 (1968)
- 12.) J. Suendermann, Mitt. Inst. Meereskunde Univ. Hamburg 19 (1971)
- 13.) K. Fischer, to be published
- 14.) W.P. Wittorf, Diplomarbeit, Techn. Univ. Hannover (1975), unpublished

CHAPTER 190

ENERGY DISSIPATION IN TIDAL ESTUARIES

by

Hans-Werner Partenscky ¹⁾

and

Günther Barg ²⁾

INTRODUCTION

In this study, the method for damped co-oscillating tides is used to evaluate damping and energy dissipation characteristics for various estuaries of different geometry and depth.

Of special interest are the damping and energy dissipation characteristics of the German tidal rivers such as Elbe, Weser and Ems in comparison with North-American tidal estuaries, since the former are characterized by deep navigation channels and relatively flat wadden areas at their lateral boundaries.

Harleman and Ippen have applied a mathematical model for co-oscillating tides to the Bay of Fundy and the Delaware estuary. This model gives information about the damping behaviour and energy distribution in the tidal estuaries.

Both of the above mentioned estuaries represent special cases since the geometric form of the Bay of Fundy allows it to be approximately represented as a rectangular chanal of constant width and depth, whereas for the Delaware Estuary one can assume a constant depth of water. Partenscky has applied an extended form of this model to the St. Lawrence Estuary.

The method of co-oscillating tides has now also been used in a mathematical model for the German tidal rivers such as Elbe, Weser and Ems. This method takes into account the influence of geometry and depth on the tidal motion and also the damping of the tidal wave due to friction and partial reflection. Data from gauges situated along the estuaries are needed as initial input for the calculation of the damping coefficient and the phase change. The wave amplitude and the time of highwater must be known from these stations.

1) Professor and Director, Franzius-Institute, Technical University of Hannover, Germany

2) Dipl.-Ing., Research Assistant, Franzius-Institute, Technical University of Hannover, Germany

DESCRIPTION OF THE GERMAN TIDAL RIVERS ELBE, WESER AND EMS

Fig. 1 shows a plan view of the German tidal rivers Elbe and Weser. Both rivers flow into the German Bay. The third mentioned river, the Ems, is a much smaller tidal river and not a so important navigation channel as Weser or Elbe. It flows more westwards near the boundary to the Netherlands into the Dollart. All three German tidal rivers have relatively flat wadden areas at their lateral boundaries.

The Elbe River is the largest German tidal river, it stretches from the mouth at Cuxhaven to the weir at Geesthacht. The width at the mouth is about 3300 m and the mean water depth is nearly 11 m.

The tidal estuary of the Weser River extends from Bremerhaven to the weir at Hemelingen. That is a distance of about 70 km. The harbour of Bremen is located nearly 5 km seaward from the weir of Hemelingen. 65 km downstream of Bremen at the bend near Bremerhaven the tidal river has a width of 1100 m and a mean water depth of 8 m.

In all three German tidal rivers the semidiurnal component is dominant, hence the tidal period is constant to 12.42 hours.

The cross-sections of the German tidal rivers are bounded upstream by weirs, so that one can assume total reflection of the tidal wave at these points.

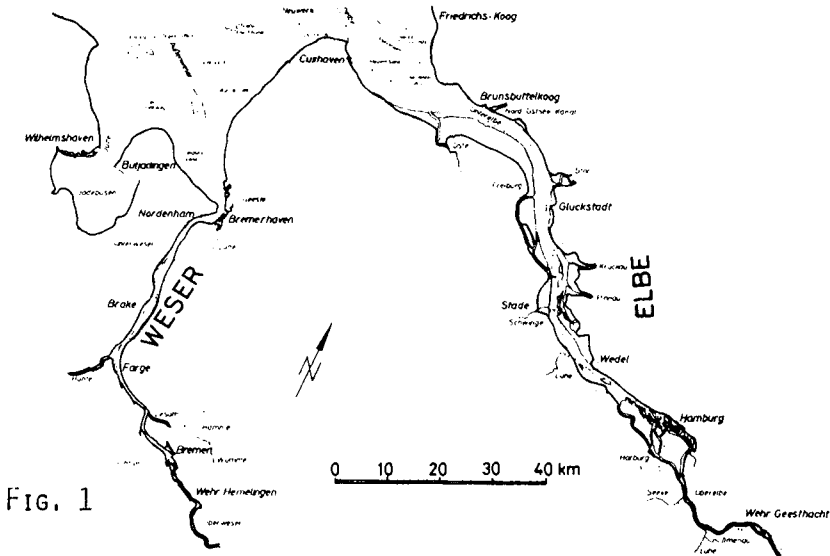


Fig. 1

ENERGY DISSIPATION AND DAMPING PARAMETERS.

Extensive prototype measurements at the Weser river are carried out by the Franzius-Institut to determine the influence of heat rejection of nuclear power plants on water quality parameters such as temperature and oxygen level. In this case, measurements in different cross sections of the river upstream and downstream of the cooling water intake over a stretch of about 40 km are carried out.

In order to examine the mixing process of seawater and freshwater in this area, it is useful to determine the longitudinal salinity distribution by conductivity measurements or chemical analysis. For given boundary conditions such as tidal motion and geometry of the estuary the longitudinal salinity distribution is a function of the freshwater discharge.

The stratification parameter $\beta = G/J$ is a useful parameter for this calculation, where G is the energy transported by the tidal wave with respect to the water mass of the examined area. J is the potential energy that the freshwater gains by increasing salinity.

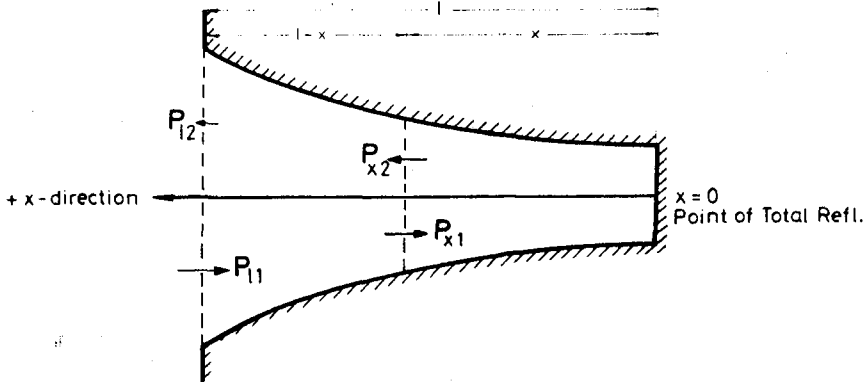


Fig. 2 Energy flux

The energy flux of a tidal wave is given by $P = E_{\text{tot}} \cdot c$ with

$$c = L/T = \frac{\sigma}{k}$$

To determine the resulting energy flux for a cross section at a point x , one must split the observed tidal wave into an incoming and a reflected component (Fig. 2).

For a cross section at $x > 0$ the resulting energy flux is

$$P_{Rx} = P_{x1} - P_{x2}$$

At the point of total reflection $P_{x1} = P_{x2}$ and there is of course no longitudinal energy transport.

The loss in potential and kinetic energy of the tidal wave between the river mouth and a point between the river mouth and the weir is $\Delta P_x = P_{RL} - P_{Rx}$.

Let ΔP_x be the wave energy transformed into heat by friction and turbulence, then we get the relative loss of energy G_x as the transformed energy related to the water mass in the segment $l - x$.

For the cross section with total reflection we get the energy dissipation $G_o = P_{RL}/M$.

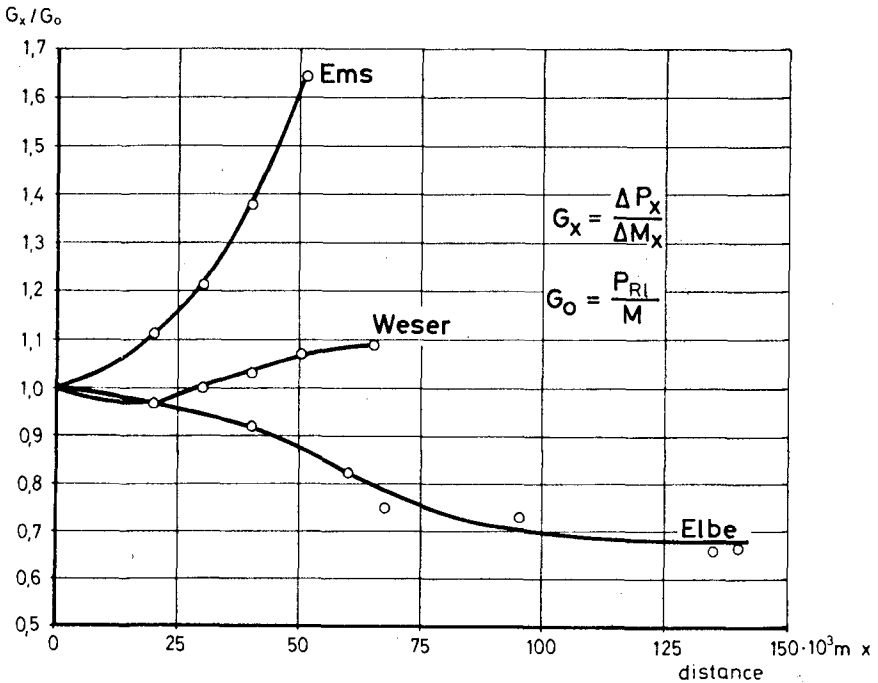


Fig. 3 Energy dissipation

An analysis of the energy dissipation with respect to G_o for all three examined German tidal rivers shows pronounced differences in the plotted curves. At the smallest tidal river, the Ems, the energy ratio G_x/G_o increases towards the mouth to 1,65. For the Weser, which is completely transformed into a navigation channel from the mouth up to the weir, the value is about 1,0. Contrarily

to the Ems, the Elbe River shows a decrease in the ratio towards the river mouth to 0,65.

To demonstrate these relationships, the resulting energy flux and the corresponding water mass in which the energy flux takes place are shown for the three tidal rivers as functions of distance in the diagram of Fig. 4. At $x=1$, i.e. at the seaward end of the examined tidal river the values of the energy flux and the water mass are assumed to be 100 %.

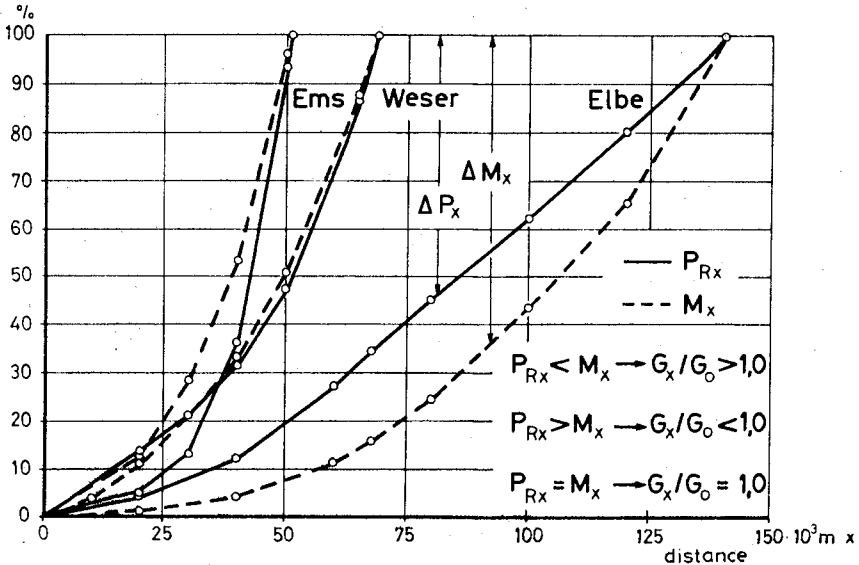


Fig. 4 Energy flux and water mass

With these assumptions, it can be clearly seen from the plots, that

$$\begin{array}{ll} \text{for } P_{Rx} < M_x & \text{it follows that } G_x/G_0 > 1 \\ P_{Rx} > M_x & G_x/G_0 < 1 \\ P_{Rx} = M_x & G_x/G_0 = 1 \end{array}$$

For the Weser River, the curve of water mass is almost identical to the curve for the energy flux. Accordingly, the energy ratio G_x/G_0 is about 1,0.

The variation is roughly only 10 % in the lower Weser and the energy dissipation can be assumed to be constant in the brackwater zone of the Weser.

The value G_x was used for tests to describe the longitudinal salinity distribution in the brackish area of the lower Weser.

The damping of the tidal wave is characterized by the damping coefficient μ which is important for the energy dissipation.

Referring to HARLEMAN and IPPEN, the equation for the damping coefficient was found by solving the equation for the local time of high water and the equation for the local amplitude of high water.

With application of Green's Law the local amplitude of high water is given by:

$$\eta_{xH} = a_o \left(\frac{b_o}{b_x}\right)^{1/2} \left(\frac{h_o}{h_x}\right)^{1/4} \left[e^{\mu x} \cos(\sigma t_H + kx) + e^{-\mu x} \cos(\sigma t_H - kx) \right]$$

and the corresponding time of high water is then:

$$\sigma t_H = \tan^{-1} (-\tan kx \cdot \tan \mu x)$$

For the damping coefficient follows then:

$$\cosh^2 \mu x = \frac{1}{2} \left[(N+1) + \sqrt{(N+1)^2 - 4 N \cos^2 \sigma t_H} \right]$$

$$\text{where } N = \frac{\eta_{xH}^2}{\eta_{oH}^2} \cdot \left(\frac{b_o}{b_x}\right)^{-1} \cdot \left(\frac{h_o}{h_x}\right)^{-1/2}$$

The reflected component of the resulting wave can be estimated from the value of μx . The component of the reflected wave is negligible as μx becomes very large. One arrives at an approximation of a progressive tidal wave without reflection.

In the case of no friction and total reflection at the closed end of the estuary, we get $\mu x = 0$ and the phase lag of the entrance of highwater $\sigma t_H = 0$.

In the study of real estuaries one finds values between these limits (Fig. 5).

Since the validity of Green's law is not satisfied in the German tidal rivers, the damping coefficient includes effects of friction, geometry and partial reflection of wave energy from the side walls of the estuary.

In comparison to the Elbe and Ems, the Weser River has the

smallest damping coefficient but the local change of this value is greater than for example in the lower part of the Elbe River as shown in Fig. 5.

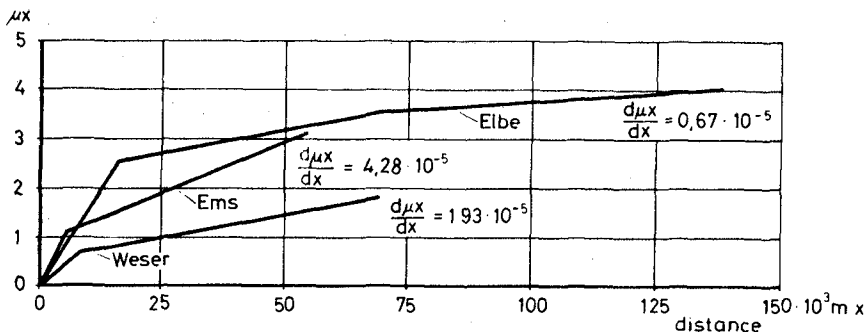


Fig. 5 Damping Parameter

The increase in the energy flux also shows this tendency.

Let the energy flux be 100 % at the river mouth and 0 % at the weir of these three rivers, then the decrease in energy flux from the river mouth to the point of reflection is greatest with the Ems and smallest in the Elbe. The energy flux at the half distance from the mouth to the weir is 10 % for the Ems ($x = 26 \text{ km}$), 27 % for the Weser ($x = 34 \text{ km}$) and 36 % for the Elbe ($x = 70 \text{ km}$) of the initial value at the river mouth.

In general, it can be stated that the greater the change in the damping coefficient, the greater the relative decrease of the energy flux will be.

In comparison with the North American tidal estuaries (such as Bay of Fundy, Delaware Estuary and St. Lawrence) the German tidal rivers Elbe, Weser and Ems are much smaller in size.

The examined estuaries can be classified in three general types:

- Estuaries of nearly rectangular geometry in plan view having an approximately constant water depth (Example: Bay of Fundy).
- Estuaries whose widths vary exponentially, whereas the mean water depth remains approximately constant (Examples: Delaware Estuary and Weser Estuary).
- Estuaries featuring an exponentially varying width and a continuous decrease in water depth towards the head of the estuary (Examples: St. Lawrence Estuary and Elbe Estuary).

Comparison of the damping behaviour and energy dissipation has been made in Figure 6 between the three North American and the three German estuaries.

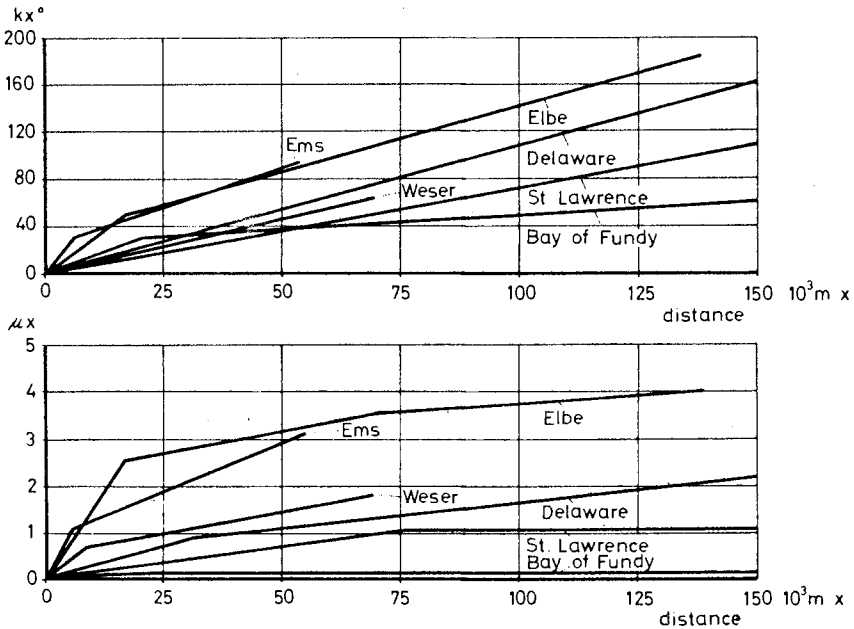


Fig. 6 Phase change and damping parameter

From the diagramm it is evident that the three North American tidal estuaries show smaller damping parameters at points equidistant from the reflection point than German tidal estuaries. This can be readily explained by the fact, that in the North American tidal estuaries due to their size the friction and geometry affect is of smaller importance than in the shallower and narrower German tidal rivers.

Only the mean water depth of the Delaware Estuary is nearly the same as the water depth of the German tidal rivers.

This relationship also can be seen from the plotted damping parameter versus distance x . The comparison is made for a distance of only 150 km seaward the point of total reflection, because all German tidal rivers are shorter.

The Bay of Fundy shows nearly no change of it very small

damping parameter with respect to the distance.
In the St. Lawrence Estuary there is a slope at the first 75 km and then the curve progress horizontal.

Only the Delaware Estuary shows nearly the same change of μx with respect to the distance x as the German tidal rivers Elbe and Weser.

BIBLIOGRAPHY

- | | |
|-------------------------------------|---|
| Partenscky, H.W. and Vincent, R.: | Tidal motion in the St. Lawrence Estuary
Extra.9.10.Conference on Coastal Engineering, Tokyo 1966 |
| Partenscky, H.W. and Louchard, L.: | The intrusion of salinity into the estuary of the St. Lawrence River.
Paper 101, 11.Conference on Coastal Engineering, London 1968 |
| Partenscky, H.W. and Warmoes, J.C.: | Damped co-oscillating tides with negative reflection at the end of the estuary
IAHR, Kyoto 1969 |
| Partenscky, H.W. and Marche, I.C.: | Deformation of Tidal Waves in Shallow Estuaries
Conference on Coastal Engineering, Vancouver July 1972. |

CHAPTER 191

ALGORITHM FOR VERTICAL DIFFUSION

Søren Peter Kjeldsen**)

ABSTRACT

A mathematical method and a computer algorithm is developed for the case of one-dimensional vertical mixing for an estuary with rather small advection. In the case under consideration varies the diffusion coefficients both with time and depth, and the case is therefore closer to actual estuaries than earlier computing methods that applies constant coefficients. Model experiments with a small grid oscillation with high frequencies in two fluids with different densities were performed to test the algorithm. Reynolds number for turbulence was near $1.6 \cdot 10^4$.

The results showed that the ratio between the stabilizing Brunt-Väisälä frequency and the agitating cyclic frequency was a governing parameter for the system, and dimensionless diffusion coefficients could be expressed as a function of this parameter.

INTRODUCTION

Pollution problems in the sea and in the adjacent estuaries play an important role in coastal engineering and demands more and more sophisticated computational technique to be solved in a satisfactory way.

This paper deals with the case where two fluids with different densities are found in an estuary, with very small advection. After initial mixing in outlets and jets has occurred a more calm phase will be found where a light fluid is overlying a more dense fluid, and vertical mixing is due only to local turbulence.

This situation is common in many cases where the coastal engineer is involved such as:

**) Senior research engineer, River and Harbour Laboratory at the Norwegian Institute of Technology, Trondheim, Norway.

- 1) Thermal power plants with density differences between heated water and cooler recipient water.
- 2) Water power plants with density differences between fresh water in the mountains and salt water in the recipient.
- 3) Outlets that belong to the municipal sewage system.
- 4) Outlets and rivers containing different kinds of sediments in suspension.

Figure 1 shows a typical Norwegian fjord. The advection that occurs here is mainly wind driven. (See H. Rye, 1973 [1]). The algorithm presented here can also be extended to include advection and treat a case like this, as outlined below.



Figure 1. Site for collection of field data. Romsdalsfjord, Norway.

MATHEMATICAL ANALYSIS

Let us now consider the one-dimensional case without advection. The problem under consideration is shown in Figure 2. A salinity profile varying with depth is slowly mixed due to local turbulence. In the case under consideration no current is acting and all diffusion is vertical.

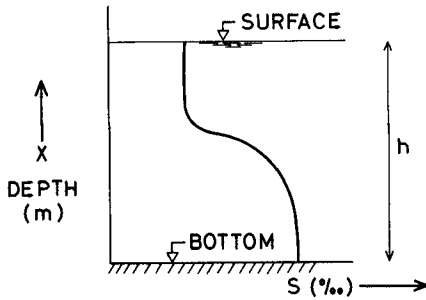


Figure 2. Definition of the problem.

The general equation for this situation is:

$$\frac{\partial s}{\partial t} = \frac{\partial}{\partial x} (D \cdot \frac{\partial s}{\partial x}) \quad (1)$$

D is the diffusion coefficient varying both with time and depth, x is the vertical co-ordinate, t is the time co-ordinate and s is the concentration of substance; here salinity (in other cases this could be heat or concentration of particles in suspension).

The boundary conditions for this situation are that the salt flux through the surface is zero, and that the time derivative of salinity integrated over the whole volume is zero as no material is transferred to the system from outside the control volume. (Eq. (2) and (3).)

$$FLUX_{x=h} = D \cdot \frac{\partial s}{\partial x} = 0 \quad (2)$$

$$\int_0^h \frac{\partial s}{\partial t} \cdot dx = 0 \quad (3)$$

Integration of the general equation with respect to x for a certain time kept constant gives

$$\int_0^x \frac{\partial s}{\partial t} \cdot dx = D \cdot \frac{\partial s}{\partial x} + CONSTANT \quad (4)$$

An integration constant appears here on the right side. This constant can be determined as shown in eq. (5) where the integration is taken over the whole volume.

$$CONSTANT = \int_0^h \frac{\partial s}{\partial t} \cdot dx - [D \cdot \frac{\partial s}{\partial x}]_{x=h} = 0 \quad (5)$$

The last term is the flux through the surface which is known to be zero, and the first term is also zero due to continuity. Thus the integration constant in eq. (4) is determined to be zero. The diffusion coefficient can then be found as the integral on the left hand side divided with the salinity gradient. Eq. (6) thus shows the determination of the diffusion coefficient for a certain time t_1 and a certain depth x_1 .

$$[D]_{x=x_1, t=t_1} = \frac{[\int_0^{x_1} \frac{\partial s}{\partial t} \cdot dx]_{t=t_1}}{[\frac{\partial s}{\partial x}]_{x=x_1, t=t_1}} \quad (6)$$

This result is now transferred to an algorithm for computer work.

Figure 3 shows the flow sheet of the computer version of the algorithm. The input is recorded density profiles. They are written out for each series or test.

AN ALGORITHM FOR VERTICAL DIFFUSION

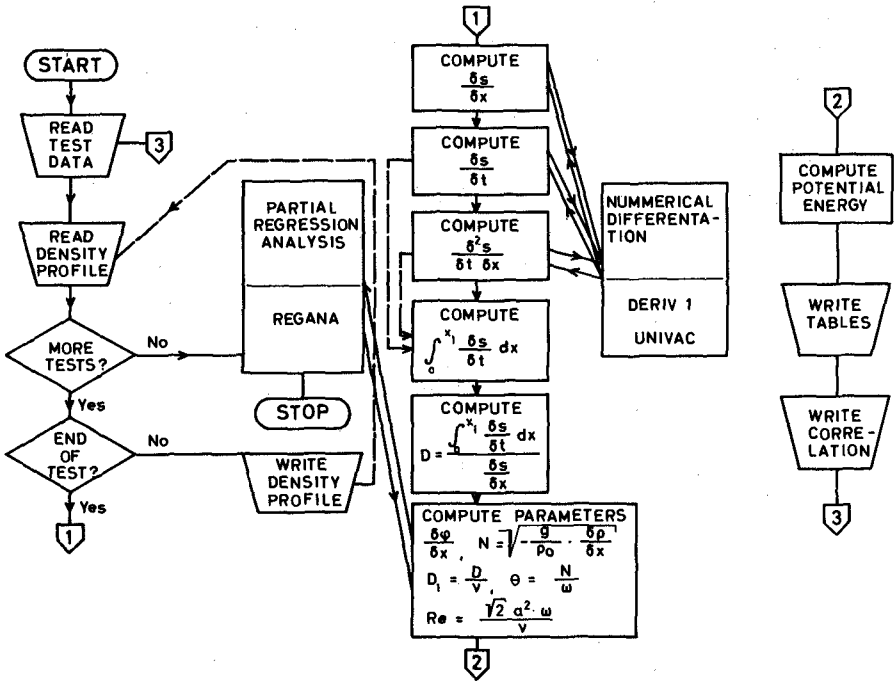


Figure 3. Flow diagram for algorithm.

A vital part of the programme is shown in two boxes, viz. a routine for numerical differentiation and a routine for a partial regression analysis. When a series of recordings is ended the computational part of the programme is called. This computes all the derivatives shown. Further, the programme uses a routine for numerical integration in which the input is both the salinity gradient with respect to time and the second derivative of salinity with respect to time and depth. From this the integral is found, and division with the local salinity gradient then gives the diffusion coefficients. Further, a special part of the programme computes all parameters that are considered necessary for the analysis of diffusion, such as density gradient, Brunt-Väisälä frequency, dimensionless diffusion coefficient, and Reynolds number for turbulence. The programme then goes on and computes potential energy and writes all parameters in tables.

Finally the regression analysis is called and it is then possible to investigate if there is any correlation between diffusion coefficients and selected density or turbulence parameters. This programme gives the final correlations directly. It takes density profiles as input and it gives the final correlation between diffusion coefficients and selected parameters immediately as output. It should, therefore, be an effective tool for research work in this field.

MODEL EXPERIMENTS

Experimental laboratory data for vertical mixing were used to test the algorithm. These were obtained in a small test tank that contained a layer of fresh water overlying a layer of salt water. A fine mesh grid was installed in the test tank and this could oscillate with different frequencies and amplitudes and thus generate the necessary turbulence. Two types of fine mesh grid were used, one with horizontal nets and one with vertical nets. Water samples could be extracted from the test tank through small tubes and the salinity was then determined with a conductivity meter. The temperature was kept constant during the tests. The test arrangement is shown in Figure 4.

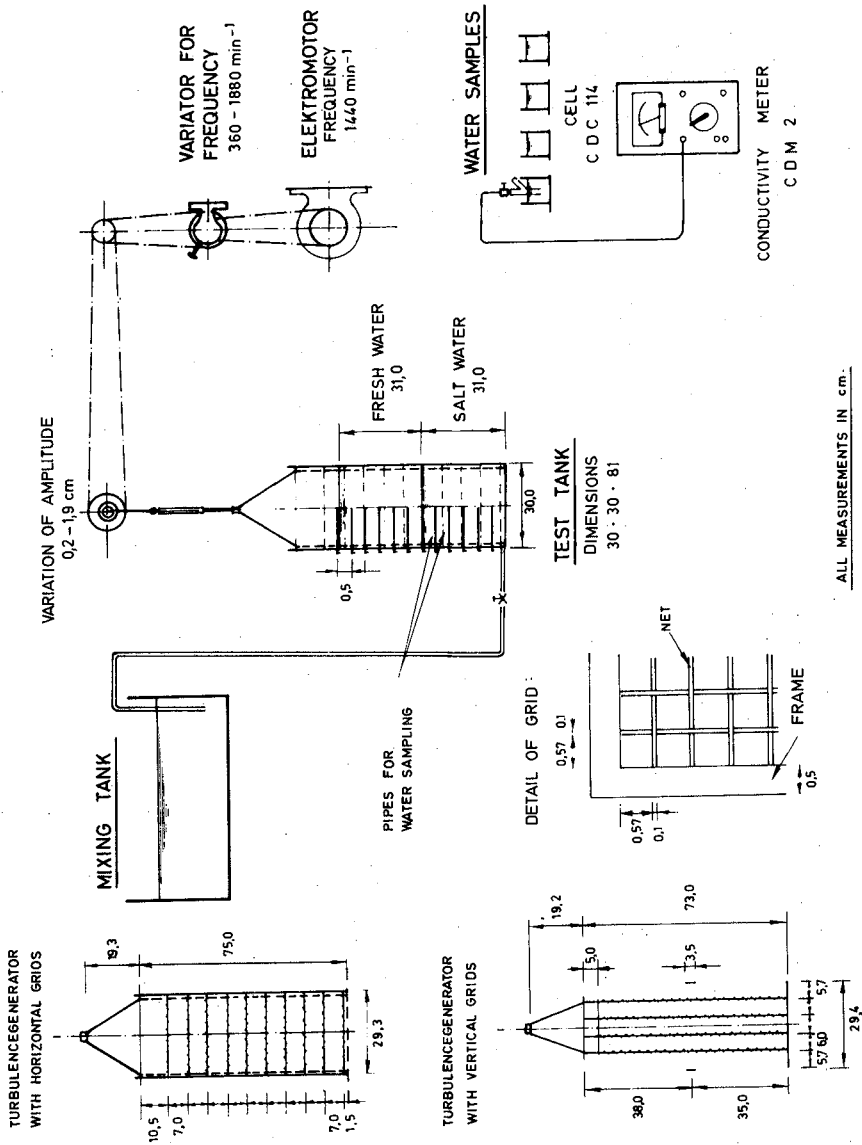


FIG. 4. MODEL ARRANGEMENT

RESULTS

Figure 5 shows a typical test result, after 2 minutes testing. The density profile is mixed to some extent. The Brunt-Väisälä frequency is the reference parameter for the density profile that is considered most important. It is defined by the equation:

$$N = \sqrt{-\frac{g}{\rho_0} \cdot \frac{\partial \rho}{\partial x}} \quad (7)$$

where g is the acceleration of gravity, ρ_0 is the local density and $\partial \rho / \partial x$ the density gradient. It can be derived from the density profile. It shows a clear maximum in a certain level. 2π divided by this frequency is the lowest period with which internal waves can exist, and the distribution of the Brunt-Väisälä frequency is thus one of the most important dynamical characteristics of an estuary. Corresponding with this we can here see the computed vertical diffusion coefficient from the algorithm. It has a local minimum where the Brunt-Väisälä frequency has its maximum, and it has two local tops. This illustrates the inverse proportionality between these two parameters.

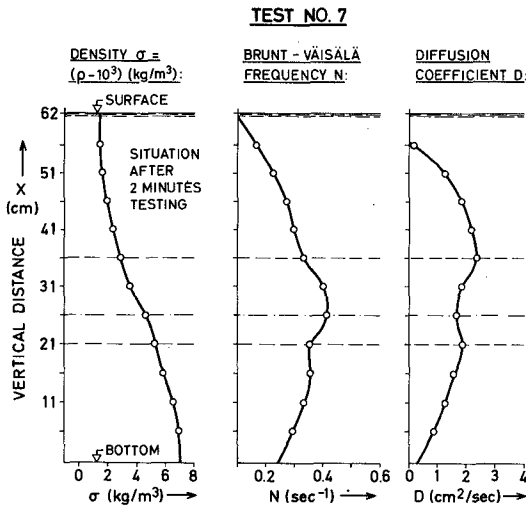


Figure 5. Test result after 2 minutes mixing.

Figure 6 shows a correlation between the diffusion coefficient and the squared Brunt-Väisälä frequency in one of the tests. The figure contains 154 points taken at different times during the 6 minutes test period. There is a considerable scatter. Still the partial regression analysis showed an inverse proportionality between the two parameters with a multiple correlation coefficient 0.94.

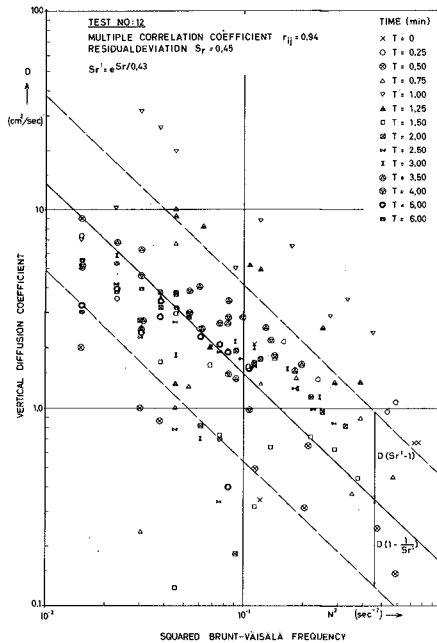


Fig. 6. Diffusion coefficient as a function of Brunt-Väisälä frequency.

Table 1 gives the equations for similar obtained correlations for all five performed tests.

TABLE 1
REGRESSION ANALYSIS NO 2

Level of significance to enter variable : 4.0
 Level of significance to delete variable : 4.0
 Minimum (residual variance/observed variance): 10^{-4}

Run	Correlation between D and N ²	Number of observations	Multiple corr. coefficient	Residual error	Anti-log residual error
No	Equation	m	r _{ij}	S _r	S _r ' = e ^{S_r'/0.4343}
7	$D = \frac{8.989 \cdot 10^{-2}}{(N^2)^{0.9928}}$	66	0.9535	0.5147	3.271
8	$D = \frac{4.957 \cdot 10^{-1}}{(N^2)^{0.9852}}$	33	0.9924	0.2886	1.944
9	$D = \frac{1.247 \cdot 10^{-1}}{(N^2)^{0.9551}}$	66	0.9630	0.4035	2.532
11	$D = \frac{2.572 \cdot 10^{-1}}{(N^2)^{0.9008}}$	66	0.9423	0.5620	3.648
12	$D = \frac{1.597 \cdot 10^{-1}}{(N^2)^{0.9604}}$	154	0.9414	0.4525	2.834

D = cm²/sec
 N = sec⁻¹

The power in the equation for the squared Brunt-Väisälä frequency is in the first test 0.99 obtained for 66 points. In the second test the power was 0.99 obtained for 33 points. In the following tests the power was 0.96 for 66 points and 0.90 for 66 points respectively, and in the last test the power was 0.96 for 154 points. Altogether 385 points were recorded and correlation coefficients varied between 0.94 and 0.99 as shown in the table.

The power for the squared Brunt-Väisälä frequency was thus in all cases found to be a little less than one.

Fig. 7 further illustrates that and shows the calculated best fit obtained from the regression analysis for all 5 tests performed, and the correlation coefficients. Further it is indicated that two types of grids, one horizontal and one vertical are used with different oscillating frequencies, and it is observed that the diffusion coefficient for both types of grids increases with increasing oscillation frequency.

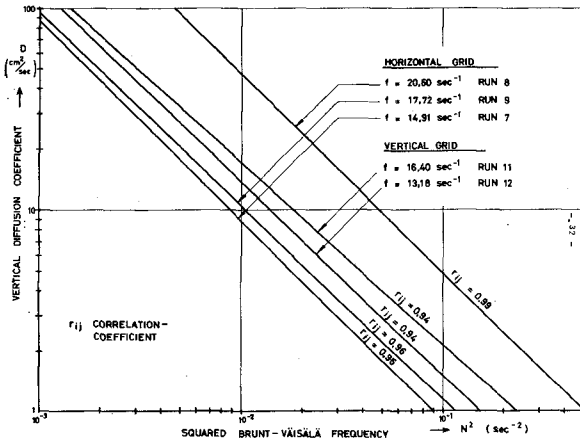


Fig. 7. Results of regression analysis. Diffusion coefficients as functions of Brunt-Väisälä frequencies.

The next step is then to relate the obtained results to the turbulence that acted in the test tank.

DESCRIPTION OF TURBULENCE

It is well known that if u denotes the velocity fluctuation in the turbulence then the scalar energy spectrum is given by equation (8) where κ is the wave number.

$$\overline{u^2} = 2 \int_0^{\infty} E(\kappa) d\kappa \quad (8)$$

We can then form a Reynolds number consisting of the root-mean-square of the velocity fluctuations multiplied by a characteristic length scale for the eddies l and divided by the kinematic viscosity (Eq. (8)).

$$Re = \frac{(\overline{u^2})^{1/2} \cdot l}{\nu} \quad (9)$$

Unfortunately it was not possible to make direct measurements of the turbulence when the tests were performed. A first estimate of the turbulence parameters is therefore extracted from the sinusoidal oscillation of the agitating grid. In

Fig. 8 one of the bars-in the grid is shown in the mean position and in positions with maximum amplitudes, where the velocity is zero. The streamlines according to potential flow theory are also shown for the case where the oscillating velocity is maximum.

OSCILLATING CYLINDER

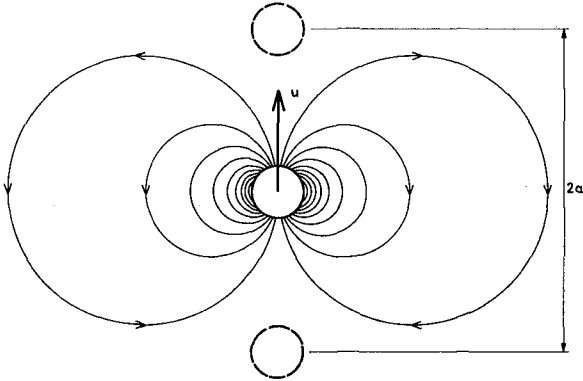


Fig. 8. Oscillating cylinder.

It is believed that it is the streamlines in this situation that dominate the flow pattern, as the velocity becomes smaller and the circles decrease near the amplitude maximum. Therefore as a first estimate the characteristic length of the eddies l is taken to twice the amplitude, a .

$$l = 2a \quad (10)$$

The validity of this approach to the macro-length scale is dependent on the Reynolds numbers for the oscillating cylinder. It will not be possible to obtain a better estimate without access to experimental data. Eddie shedding will occur from the back-side of the cylinder, but l is defined as the maximum length in which velocities can be correlated and it is therefore equation (10) and not the scale of the smaller eddies that is the best approximation for the scale of turbulence.

Further as a first approximation to the root mean square of the turbulent fluctuations the root mean square of grid velocity is taken as outlined in equation (11). ω is here the cyclic frequency in the oscillation. This is a reasonable first estimation as the added mass coefficient for an accelerated cylinder is near to one.

$$\overline{(u^2)}^{\frac{1}{2}} = \left[\frac{1}{T} \int_0^T a^2 \omega^2 \sin^2 (\omega t) dt \right]^{\frac{1}{2}} = \frac{\sqrt{2}}{2} a \omega \quad (11)$$

It is now possible to form the characteristic Reynolds numbers describing the turbulence. When the result for the root mean square of the velocity fluctuations and the characteristic length scale is set into equation (8) we obtain:

$$Re = \frac{\overline{(u^2)}^{\frac{1}{2}} \cdot l}{\nu} = \frac{\sqrt{2} a^2 \omega}{\nu} \quad (12)$$

In the experiments this Reynolds number was varied from $1 \cdot 10^4$ to $1.6 \cdot 10^4$, which indicates that a well developed turbulence was obtained.

It is possible to obtain a dimensionless parameter that describes the process, simply by forming the ratio between the stability frequency (the Brunt-Väisälä frequency N) and the agitating cyclic frequency ω .

$$\theta = \frac{N}{\omega} \quad (13)$$

All data for diffusion coefficients obtained in 3 different tests with the horizontal grid and with 3 different agitating frequencies were then correlated with this dimensionless number and presented in a dimensionless form, so that the ratio between diffusion coefficient and the kinematic viscosity is given. The result is shown in Fig. 9.

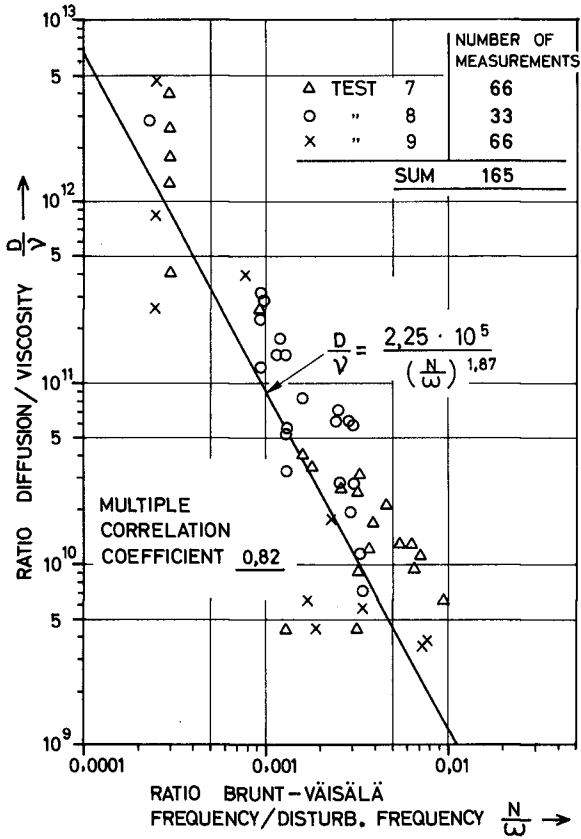


Fig. 9. Diffusion coefficients as a function of the ratio between stabilizing and agitating frequencies.

All data in the 3 different tests, 165 altogether, correlated with a multiple correlation frequency 0.82 and the equation obtained was:

$$\frac{D}{\nu} = \frac{2.25 \cdot 10^5}{\theta^{1.87}} = \frac{\text{CONSTANT}}{(N/\omega)^{1.87}} \quad (14)$$

The ratio between the diffusion coefficient and the kinematic viscosity can thus be expressed as a constant divided by the frequency ratio to the power 1.87.

A typical order of magnitude for the diffusion coefficients involved here is $10 \text{ cm}^2/\text{sec}$.

EXTENSION TO CASE INCLUDING ADVECTION

The general equation for three-dimensional diffusion with varying diffusion coefficients is:

$$\frac{\partial s}{\partial t} + U_x \frac{\partial s}{\partial x} + U_y \frac{\partial s}{\partial y} + U_z \frac{\partial s}{\partial z} = \frac{\partial}{\partial x} (D_x \cdot \frac{\partial s}{\partial x}) + \frac{\partial}{\partial y} (D_y \cdot \frac{\partial s}{\partial y}) + \frac{\partial}{\partial z} (D_z \cdot \frac{\partial s}{\partial z}) \quad (15)$$

Here x is the vertical coordinate while y and z are horizontal coordinates. If advection in one direction dominates, as in the case in many estuaries with wind driven circulation, we obtain:

$$\frac{\partial s}{\partial t} + U_y \frac{\partial s}{\partial y} = \frac{\partial}{\partial x} (D_x \frac{\partial s}{\partial x}) \quad (16)$$

Horizontal diffusion terms might be included here on the left side as a constant or as a function of space coordinates. For the vertical diffusion coefficient we can then obtain:

$$D_x = \frac{\int_0^x \frac{\partial s}{\partial t} dx + \int_0^x U_y \frac{\partial s}{\partial y} \cdot dx}{\frac{\partial s}{\partial x}} \quad (17)$$

If the current velocity is recorded the algorithm can then be extended and operated for a case with advection.

Field data in the form of density profiles, current profiles and wind, tide and wave recordings have already been collected from a typical Norwegian fjord which has been found suitable for further studies. This is the Romsdalsfjord earlier mentioned and shown in Fig. 1.

Use of the algorithm on the field data obtained here is in progress.

CONCLUSION

The purpose of this project was to develop a mathematical method that is able to treat the case of vertical diffusion with a diffusion coefficient varying with time and dept.

This was done and a computer programme was developed for the one-dimensional case without advection.

Model experiments were performed to test the algorithm. The results from these showed that the ratio between the stabilizing Brunt-Väisälä frequency and the agitating cyclic frequency was a governing parameter for the system and dimensionless diffusion coefficients could be expressed as a function of this parameter.

The algorithm can easily be extended to include advection, and is therefore usefull also for the treatment of field data in more complex situations.

This extension can be made step by step, and might include more and more terms in the general equation for diffusion in space and time with variable diffusion coefficients.

Further knowledge concerning development and decay of turbulence in the presence of a density profile is urgently needed.

ACKNOWLEDGEMENT

The author would like to epress his gratitude to Dr. T. Carstens, Head of Research at VHL, who suggested the experiments and gave advice on the paper. "Konsesjonsavgiftsfondet", The Fund of Licence Fees, The Norwegian Water Resources and Electricity Board sponsored the project.

REFERENCE

- [1] H. Rye 1973: " Wind currents in the Langfjord Norway". Division of Port and Ocean Engineering. The Norwegian Institute of Technology, Trondheim.

CHAPTER 192

DISPERSIVE TRANSPORT IN RIVER AND TIDAL FLOWS

by

R. B. Taylor¹

ABSTRACT

Analytical results are presented which describe the mechanisms of longitudinal dispersive mass transport in rectangular channels of finite and infinite widths for both unidirectional (river) and oscillatory (tidal) flow regimes. Emphasis is placed upon the discussion of results and the characteristics of longitudinal dispersive mass transport revealed by the analytical treatment. Expressions presented for the dispersion coefficient were obtained from solutions to four sets of boundary value problems for the velocity and concentration variation components u'' and c'' . Examination of these expressions reveals that in oscillatory flow the dispersive mass transport is described by a type of resonant interaction between the period of oscillation and the time scales of vertical and lateral mixing. The analysis also shows that for oscillatory flow regimes the effect of lateral shear becomes negligible for very wide channels and the three dimensional solution collapses to the two dimensional case in which vertical shear and mixing effects dominate. It is shown analytically that this is not the case in unidirectional flows. For this case the lateral shear and mixing effects dominate the corresponding vertical effects and dispersive mass transport increases without bound with increasing channel widths.

INTRODUCTION

Previous efforts (Bowden 1965; Holley et al. 1970; Fukuoka 1973) to describe the mechanism of dispersive mass transport in oscillatory flows have generally assumed that it is reasonable to describe this process through comparison by analogy to a similar process in a steady unidirectional flow. As will be seen from the results presented here, this assumption is misleading and can lead to erroneous results and conclusions. This is due to the fact that the dispersion process in oscillatory flow behaves quite differently from the corresponding process in unidirectional flow. Thus, unless the basic characteristics of dispersion are clearly understood for both types of flows, the interpretation of results can vary greatly depending upon the basis used for the comparison.

¹Florida Coastal Engineers, Inc., Jacksonville, Florida

The mechanisms of dispersion in unidirectional flow are better understood. The most useful analytical treatment of this problem and the one which appears to provide the best results was developed by Fischer (1967). However, to apply Fischer's results one must have a detailed knowledge of the variations in the velocity field within the flow cross section. Moreover, his analysis assumes that the vertical effects of viscosity and diffusivity are small when compared to the same effects acting laterally across the channel. While this seems reasonable and has provided good results, it does not provide an analytical basis for examining those conditions under which either the vertical or lateral effects would play a dominant role in the dispersion process. Results presented in this paper allow for this comparison and are generally supportive of Fischer's work.

STATEMENT OF THE PROBLEM

The approach used to obtain expressions for the longitudinal dispersion coefficient generally follows the methodology devised by Taylor (1953) and applied later by others which defines the dispersive flux as the correlation over space and/or time of the velocity and concentration cross-sectional variation components by means of the following relationships:

$$-E_L \frac{\partial \bar{c}}{\partial \xi} = \overline{u'' c''} \quad (\text{unidirectional flow}) \quad (1)$$

$$- \langle E_X \rangle_T \frac{\partial \bar{c}}{\partial \xi} = \langle \overline{u'' c''} \rangle_T \quad (\text{oscillatory flow}) \quad (2)$$

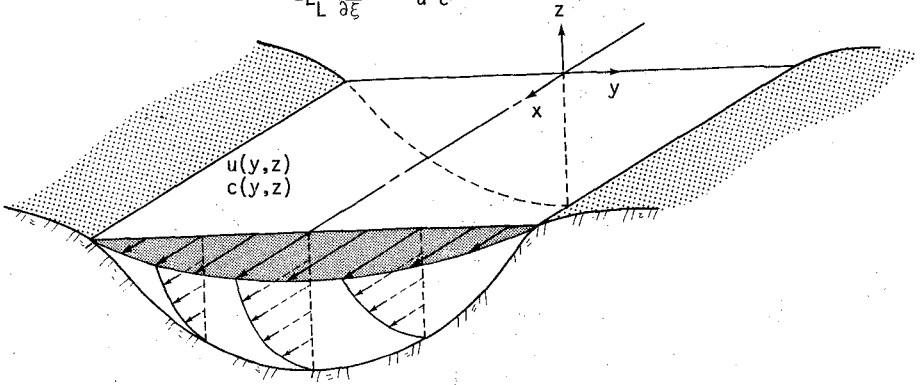
where the overbar denotes the spatial average of the variable over the flow cross section, and the notation $\langle \rangle_T$ denotes an average over the period of oscillation, T. The variables u'' and c'' are defined by:

$$u'' = u - \bar{u} \quad (3)$$

$$c'' = c - \bar{c} \quad (4)$$

where u and c are the velocity and concentration variables, and \bar{u} and \bar{c} are the corresponding cross-sectional mean values. In carrying out the analysis, strict adherence to the use of companion solutions to the equation of motion and the transport diffusion equation was followed to obtain solutions for u'' and c'' which most nearly reflected the kinematic structure of the flow field of the particular problem being investigated. This is particularly important for the case of oscillatory flow regimes where, as illustrated by Figure 1b, flow reversals occur in the lower momentum regions of the channel which significantly affect u'' during portions of the tidal cycle. These phenomena have been preserved here and represent a departure from the work of previous investigators in which temporal phase differences in the velocity field over the flow cross section have not been included (Holly and Harleman 1965; Okubo 1967; Holley, *et al.* 1970; Fukuoka 1973).

$$-E_L \frac{\partial \bar{c}}{\partial \bar{t}} = \overline{u''c''}$$

(a) RIVER

$$-\langle E_x \rangle_T \frac{\partial \bar{c}}{\partial \bar{t}} = \langle u''c'' \rangle_T$$

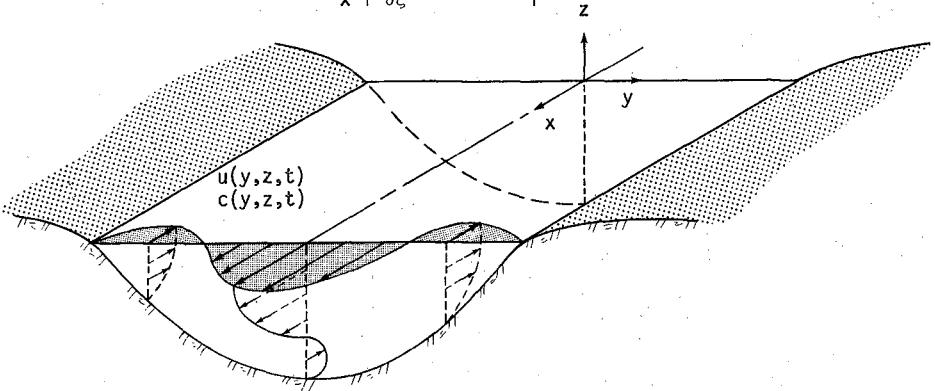
(b) TIDAL

FIGURE 1 - DESCRIPTIVE FLOW REGIMES AND ASSOCIATED DISPERSIVE MASS TRANSPORT RELATIONSHIPS

Expressions for the longitudinal dispersion coefficient were developed for the four combinations of flow and channel geometries previously mentioned. The analytical procedure was begun by solving the prescribed equation of motion for the velocity u for the particular flow regime and channel geometry under consideration. From this, an expression for u'' was obtained which in turn was used to force the companion form of the transport diffusion equation. Solutions to the transport diffusion equation then yielded expressions for the concentration variation component, c'' . Expressions for the longitudinal dispersion coefficient were obtained from Equations (1) and (2) by averaging the product $\text{Re}(u'') \cdot \text{Re}(c'')$ over the flow cross section, and for oscillatory flow by averaging again over the period of oscillation.

Boundary Value Problem Formulation

Several assumptions must be introduced to obtain forms of the governing equations that can be solved in a reasonable manner. These are described as follows:

- (a) The Boussinesq approximation is applied to the viscous terms in the equation of motion and the eddy viscosity coefficients, $\bar{\epsilon}_y$ and $\bar{\epsilon}_z$, are introduced. These coefficients are considered to be constant and equal to their spatial and temporal mean where appropriate.
- (b) Eddy diffusivity coefficients, \bar{K}_z and \bar{K}_y , are used to formulate the turbulent diffusion terms in the transport diffusion equation in a manner similar to that described for the viscous terms.
- (c) For purposes of the simplification of results and physical interpretation it is assumed that the eddy coefficients of viscosity and diffusivity are of equal magnitude. Thus, $\bar{K}_z = \bar{\epsilon}_z$, and $\bar{K}_y = \bar{\epsilon}_y$.
- (d) For steady unidirectional flow the pressure field is independent of time. If the flow is uniform then it can be assumed that

$$\frac{1}{\rho} \frac{\partial p}{\partial x} = K \quad (5)$$

where K is constant.

- (e) For oscillatory flow the pressure field is assumed to be temporally periodic, thus

$$\frac{1}{\rho} \frac{\partial p}{\partial x} = K e^{i\sigma t} \quad (6)$$

where σ is the angular frequency of oscillation and t is time.

(f) The velocity and concentration variables in oscillatory flow are assumed to be temporally periodic and of the form

$$u = u_s e^{i\sigma t} \quad (7)$$

$$c'' = c_s'' e^{i\sigma t} \quad (8)$$

where u_s and c_s'' are complex variables of the spatial coordinates defining position within the flow cross section. This formulation allows for temporal phase differences of u'' and c'' within the flow cross section.

The forms of the transport diffusion equations presented in all four boundary value problems are consistent with those used by previous investigators (Taylor 1953, 1954; Fischer 1967; Bowden 1965; Holley, et al., 1970) in which the concentration variable is viewed from a Lagrangian frame of reference traveling with the cross-sectional mean velocity. This transformation is accomplished by the introduction of the variable ξ defined as follows:

$$\xi = x - \bar{u}t \quad (\text{unidirectional flow}) \quad (9)$$

$$\xi = x - \int_0^t u(t') dt' \quad (\text{oscillatory flow}) \quad (10)$$

The first two sets of boundary value problems (BVP #1 and BVP #2) describe the dynamics of fluid motion and the transport diffusion of a substance in which only the vertical effects of shear and eddy diffusivity are considered. As shown by Figure 2, the x coordinate has been chosen to act along the principal flow axis while the z coordinate is defined positive upward from the channel bed. The two dimensional shear flow cases examined by these two boundary value problems incorporate essentially the same boundary conditions. For the equations of fluid motion the conditions of no-slip at the channel bed and zero shear at the free surface are applied; whereas for the transport diffusion equation the conditions of zero Fickian flux across the free surface and channel bed are used.

The boundary value problem formulations for three dimensional steady unidirectional and oscillatory flow regimes are presented by boundary value problems 3 and 4 (BVP #3 and BVP #4). Figure 3 illustrates the coordinate system used in these formulations. The origin has been located at the center of a rectangular region of height $2h$ and width w . The open rectangular channel is mathematically represented by the lower half of the full section shown in Figure 3. Selection of the coordinate system in this manner preserves the symmetry of the problem about the origin and, as will be shown later, correctly predicts the same dispersive mass transport for equal degrees of skewness in channel geometry in either the vertical or lateral directions. Equations (15) through (18) are of the same form as those presented for the two dimensional cases in BVP #1 and BVP #2 with additional terms included to account for the lateral effects of turbulent shear and diffusivity. Boundary conditions

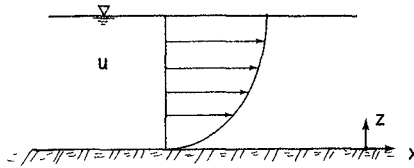


FIGURE 2 - DEFINITION SKETCH FOR TWO DIMENSIONAL SHEAR FLOW

BVP#1 : Two Dimensional Steady Unidirectional Flow

$$\text{EOM} : \frac{d^2 u}{dz^2} = \frac{K}{\bar{\epsilon}_z} \quad (11)$$

$$u = 0; z = 0$$

$$\frac{du}{dz} = 0; z = h$$

$$\text{TDE} : \bar{K}_z \frac{\partial^2 c''}{\partial z^2} = u'' \frac{\partial \bar{c}}{\partial \xi} \quad (12)$$

$$\frac{\partial c''}{\partial z} = 0; z = 0, h$$

BVP#2 : Two Dimensional Oscillatory Flow

$$\text{EOM} : \bar{\epsilon}_z \frac{\partial^2 u_s}{\partial z^2} - i\sigma u_s = K \quad (13)$$

$$u_s = 0; z = 0$$

$$\frac{\partial u_s}{\partial z} = 0; z = h$$

$$\text{TDE} : \bar{K}_z \frac{\partial^2 c_s''}{\partial z^2} - i\sigma c_s'' = u_s'' \frac{\partial \bar{c}}{\partial \xi} \quad (14)$$

$$\frac{\partial c_s''}{\partial z} = 0; z = 0, h$$

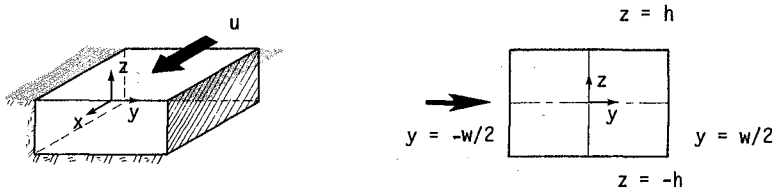


FIGURE 3 - DEFINITION SKETCH FOR THREE DIMENSIONAL SHEAR FLOW

BVP#3 : Three Dimensional Steady Unidirectional Flow

$$\underline{\text{EOM}} : \bar{\epsilon}_z \frac{\partial^2 u}{\partial z^2} + \bar{\epsilon}_y \frac{\partial^2 u}{\partial y^2} = K \quad (15)$$

$$u = 0; z = \pm h, y = \pm w/2$$

$$\underline{\text{TDE}} : \bar{K}_z \frac{\partial^2 c''}{\partial z^2} + \bar{K}_y \frac{\partial^2 c''}{\partial y^2} = u'' \frac{\partial \bar{c}}{\partial \xi} \quad (16)$$

$$\frac{\partial c''}{\partial z} = 0; z = \pm h$$

$$\frac{\partial c''}{\partial y} = 0; y = \pm w/2$$

BVP#4 : Three Dimensional Oscillatory Flow

$$\underline{\text{EOM}} : \bar{\epsilon}_z \frac{\partial^2 u_s}{\partial z^2} + \bar{\epsilon}_y \frac{\partial^2 u_s}{\partial y^2} - i\sigma u_s = K \quad (17)$$

$$u = 0; z = \pm h, y = \pm w/2$$

$$\underline{\text{TDE}} : \bar{K}_z \frac{\partial^2 c_s''}{\partial z^2} + \bar{K}_y \frac{\partial^2 c_s''}{\partial y^2} - i\sigma c_s'' = u_s'' \frac{\partial \bar{c}}{\partial \xi} \quad (18)$$

$$\frac{\partial c_s''}{\partial z} = 0; z = \pm h$$

$$\frac{\partial c_s''}{\partial y} = 0; y = \pm w/2$$

used include the conditions of no slip and zero Fickian flux at the sides of the full rectangular section.

Dispersion Coefficient Solutions

Solutions obtained for u'' and c'' from BVP #1 through BVP #4 were used as previously discussed to develop the corresponding expressions for the longitudinal dispersion coefficient. The reader is referred to Taylor (1974) for the detailed development of these expressions.

To simplify the expressions obtained, several mixing time scales were introduced. These are defined as follows:

- a. Vertical Mixing Time, $T_{cz} = h^2/\bar{K}_z$
- b. Lateral Mixing Time, $T_{cy} = w^2/4\bar{K}_y$
- c. Non-Dimensional Vertical Mixing Time, $T'_z = T_{cz}/T$
- d. Non-Dimensional Lateral Mixing Time, $T'_y = T_{cy}/T$
- e. Relative Mixing Time, $T'_c = T_{cz}/T_{cy}$

where T is defined as the period of flow oscillation.

The solution of Equations (11) and (12) for the case of two dimensional steady unidirectional flow is straightforward. The expression obtained for the longitudinal dispersion coefficient is given as

$$E_L = \frac{8u_{\max}^2 T_{cz}}{945} \quad (19)$$

where u_{\max} denotes the maximum cross-sectional velocity. Equation (19) has been expressed as a function of u_{\max} by maximizing the solution for u as a function of the pressure gradient modulus, K . This provides a relationship between u_{\max} and K that can be used to express the dispersion coefficient solutions in terms of the more useful parameter u_{\max} .

Except for the numerical constants, the expression given by Equation (19) is identical to that obtained by Taylor (1953) for steady flow in a circular tube. By itself it is of passing interest only. However, for comparative purposes later in this paper, it is noted from Equation (19) that in two dimensional unidirectional flow, the dispersive mass transport increases proportionally with increasing vertical mixing time.

For the case of oscillatory two dimensional shear flow, the solution of Equation (13) for the velocity has been known and documented for some time (Lamb 1945; Segall 1971). To obtain a solution for c''_s , the velocity variation

component was expanded in a Fourier cosine series, and a Fourier cosine series form of the solution for c_S'' in Equation (14) was correspondingly assumed. The assumed form for c_S'' and the expanded series form for u_S'' were then substituted into Equation (14) and the Fourier coefficients for c_S'' were solved for. Expressions obtained for u'' and c'' were then integrated over the flow cross section, and time-averaged over the period of oscillation to obtain the dispersive mass transport. This produced the following expression for the longitudinal dispersion coefficient as a function of u_{\max} , the temporal and spatial maximum of the velocity:

$$\langle E_X \rangle_T = \pi u_{\max}^2 T \frac{T^2}{Z} \frac{(\cosh 2 \sqrt{\pi T^1} \frac{Z}{Z} - \cos 2 \sqrt{\pi T^1} \frac{Z}{Z})}{(\cosh \sqrt{\pi T^1} \frac{Z}{Z} - \cos \sqrt{\pi T^1} \frac{Z}{Z})^2} \sum_{n=1}^{\infty} \frac{(n\pi)^2}{[(n\pi)^4 + (2\pi T^1 \frac{Z}{Z})^2]^2} \quad (20)$$

It should be noted that Equation (20) incorporates the effects of an oscillatory velocity shear profile which allows for temporal phase differences of the flow over the water column. It also demonstrates the dependence of the dispersion mechanism on both the vertical mixing time scale and the period of oscillation. Although this dual dependence has been pointed out by previous investigators (Okubo 1967; Holley *et al.*, 1970; Segall and Gidlund 1972; Fukuoka, 1973) the fundamental way in which these two time scales govern dispersive mass transport has not been identified. This will be discussed in the following section.

Equation (20) has also been expressed as a function of the pressure gradient modulus, K , and the excursion length of a surface particle during one-half of a period of oscillation. The reader is referred to Taylor (1974) for the development of these expressions. Results obtained from these, however, will be used later for discussion purposes.

Solutions for the longitudinal dispersion coefficient in three dimensional unidirectional and oscillatory flows were obtained by assuming double Fourier cosine series forms for u and c'' . Arguments of the cosine functions were selected to satisfy both the boundary conditions stated for BVP #3 and BVP #4 and the physical requirements of no-slip, zero shear stress and zero diffusive flux at the appropriate boundaries and points of the rectangular half-section corresponding to the open channel cross section. The remaining portions of the solution techniques used are similar to those described previously for the two dimensional shear flow cases. To obtain the dispersive mass transport, the product of the real parts of u'' and c'' were integrated over the full rectangular section shown in Figure 3 and the result divided by 2 to provide the actual dispersive mass transport in the rectangular open channel.

The expression thus obtained for the longitudinal dispersion coefficient as a function of u_{\max} for the three dimensional steady unidirectional flow case is stated in nondimensional form as

$$E_L' = \frac{E_L}{u_{\max}^2 T_{CZ}} \quad (21)$$

$$E_L' = \frac{64}{\pi^4 \phi'^2} \sum_{\ell=0}^{\infty} \sum_{k=0}^{\infty} \sum_{m=0}^{\infty} \sum_{n=0}^{\infty} \sum_{p=0}^{\infty} \sum_{q=0}^{\infty} \frac{\mu_{\ell k}}{\delta(\ell, k, m, n, p, q) R_{mn} R_{pq} R_{\ell k}} \quad (22)$$

where,

$$\delta(\ell, k, m, n, p, q) = [(2p+1)^2 - (2\ell)^2][(2q+1)^2 - (2k)^2][(2m+1)^2 - (2\ell)^2][(2n+1)^2 - (2k)^2]$$

$$R_{mn} = \left[\frac{(2m+1)\pi}{2} \right]^2 + T_C' \left[\frac{(2n+1)\pi}{2} \right]^2$$

$$R_{pq} = R_{mn} \text{ with } p \text{ replacing } m \text{ and } q \text{ replacing } n$$

$$R_{\ell k} = [(\ell\pi)^2 + T_C' (k\pi)^2]$$

$$\phi' = \sum_{m=0}^{\infty} \sum_{n=0}^{\infty} \frac{(-1)^{m+n}}{(2m+1)(2n+1)R_{mn}}$$

$$\mu_{\ell k} = \begin{cases} 1 & k \neq 0, \ell \neq 0 \\ \frac{1}{2} & k = 0, \text{ or } \ell = 0 \\ 0 & k = \ell = 0 \end{cases}$$

The non-dimensional form of the longitudinal dispersion coefficient obtained for the three dimensional oscillatory flow case (BVP #4) is presented on the following page as Equation (23). It is noted from an inspection of Equations (22) and (23) that:

(a) Dispersive mass transport in channels of finite width for both oscillatory and unidirectional flows is a function of both the vertical and lateral time scales of turbulent mixing through the variable T_C' .

Solution for Three Dimensional Oscillatory Flow (BVP #4)

$$E'_X = \frac{\langle E_X \rangle}{u_{max}^2 T} = \frac{32T_1^2}{\pi^4 \psi^2} \sum_{\ell=0}^{\infty} \sum_{k=0}^{\infty} \sum_{m=0}^{\infty} \sum_{n=0}^{\infty} \sum_{p=0}^{\infty} \sum_{q=0}^{\infty} \frac{\mu_{\ell,k} \{ [r_2(\ell,k) - (2\pi T_1^2)^2]^2 \cos \lambda + (2\pi T_1^2) \sin \lambda \}}{\delta'(\ell,k,m,n,p,q) r_1^2(m,n) r_1^2(p,q) r_2(\ell,k)} \quad (23)$$

where,

$$\delta'(\ell,k,m,n,p,q) = [(2p+1)^2 - (2\ell)^2][2q+1)^2 - (2k)^2][2m+1)^2 - (2n)^2] - (2k)^2$$

$$r_1(m,n) = \{ [\frac{(2m+1)\pi}{2}]^2 + T_1^2 [\frac{(2n+1)\pi}{2}]^2 \}^2 + (2\pi T_1^2)^2 \quad \alpha_1(m,n) = \tan^{-1} \frac{2\pi T_1^2}{[\frac{(2m+1)\pi}{2}]^2 + T_1^2 [\frac{(2n+1)\pi}{2}]^2}$$

$r_1(p,q) = r_1(m,n)$ with p replacing m and q replacing n

$$r_2(\ell,k) = \{ (\ell\pi)^2 + T_1^2 (k\pi)^2 \}^2 + (2\pi T_1^2)^2$$

$$\lambda = \alpha_1(m,n) - \alpha_1(p,q)$$

$$\mu_{\ell,k} = \begin{cases} 1, & k \neq 0, \quad \ell \neq 0 \\ \frac{1}{2}, & k = 0 \text{ or } \ell = 0 \\ 0, & k = \ell = 0 \end{cases}$$

$\alpha_1(p,q) = \alpha_1(m,n)$ with p replacing m and q replacing n

$$\psi^2 = \left\{ \sum_{m=0}^{\infty} \sum_{n=0}^{\infty} \frac{(-1)^{m+n} [r_1(m,n) - (2\pi T_1^2)^2]^2}{(2m+1)(2n+1)r_1(m,n)} \right\}^2$$

$$+ \left\{ 2\pi T_1^2 \sum_{m=0}^{\infty} \sum_{n=0}^{\infty} \frac{(-1)^{m+n}}{(2m+1)(2n+1)r_1(m,n)} \right\}^2$$

(b) The dispersive mass transport for the three dimensional oscillatory flow case is also a function of the period of oscillation through the variables T and T'_z .

DISCUSSION OF RESULTS

Two Dimensional Oscillatory Flow

Bowden (1965) was the first investigator to look at longitudinal dispersive mass transport in oscillatory flow. He found that for the case in which the period of oscillation is infinitely long the longitudinal dispersion coefficient is one-half the value of the same coefficient for a corresponding unidirectional flow having the same surface velocity, the same shear profile, and the same vertical eddy diffusivity. Okubo (1967) and Holley, *et al.* (1970) extended Bowden's work and demonstrated that the dispersion process in oscillatory flows was functionally dependent on both the time scale of vertical mixing and the period of oscillation. The manner in which Holley, *et al.* interpreted their results stimulated much of the interest in the work presented here, and will therefore be discussed for illustrative and comparative purposes.

Holley, *et al.* assumed a linear oscillatory profile for the spatial component of velocity of the form

$$u'' = \alpha z \sin \sigma t \quad (24)$$

where α is a constant, z is the vertical coordinate, and σ is the angular frequency of oscillation, $2\pi/T$. Proceeding in the same manner as described here, they then used this expression for u'' to obtain solutions for c'' and the longitudinal dispersion coefficient corresponding to the general case of two dimensional oscillatory flow, and the special case in which the period of oscillation is infinitely long. The dispersion coefficient for the infinitely long period of oscillation, E_∞ , was then used as the basis for comparison of the dispersion processes in oscillatory and unidirectional flows. This was accomplished by plotting the ratio of the dispersion coefficient for oscillatory flow divided by E_∞ versus the non-dimensional time T' defined as $1/T'_z$ as used here. This produced the results as shown by curve ① in Figure 4. The ordinate variable used in Figure 4 is normalized by the corresponding dispersion coefficient for unidirectional flow, E_L , which is exactly double the value of E_∞ . The results of Holley, *et al.* were adjusted accordingly.

For comparison purposes Figure 4 includes results obtained from the present work as shown by curves ② and ③. Curve ③ plots the ratio of Equation (20) divided by Equation (19) while curve ② plots the ratio of the corresponding forms of Equations (20) and (19) expressed as functions of the pressure gradient modulus, K .

The results depicted in Figure 4 demonstrate the fact that the relative magnitudes of the dispersion coefficients for oscillatory and unidirectional

flow vary considerably depending upon how one chooses to make the comparison. All three curves shown approach the limiting value of one-half for large periods of oscillation which agrees with the findings of Okubo (1967) and Bowden (1965). However, as T' decreases the curves begin to diverge considerably. The agreement between the results of Holley, *et al.* (1970) and the u_{\max} normalization of the results presented here is good for large values of T' . However, it becomes increasingly worse as T' decreases. The close agreement for large values of T' is not surprising since both curves ① and ③ were developed by requiring the surface amplitude of the velocity in the oscillatory flow field to be equal to the velocity at the surface in the unidirectional flow field. The divergence of the two curves with decreasing values of T' results from the use of a truly oscillatory velocity profile in the present work as compared to the one assumed by Holley, *et al.* in which the velocity remains temporally in phase over the water column. Thus, as the period of oscillation decreases the effect of inertial forces increases thereby increasing the effects of flow reversals over the water column on the dispersive mass transport.

Curve ② in Figure 4 serves to illustrate the dramatic difference in behavior of the dispersion process when one chooses to compare the oscillatory and unidirectional cases by requiring both flow regimes to have the same pressure gradient modulus, K . For unidirectional flow the pressure gradient and viscous forces are in equilibrium so as to produce a constant unidirectional shear flow for the dispersive transport of substance. In oscillatory flow, however, the pressure gradient is in constant balance with the time varying inertial and friction forces. As the period of oscillation decreases, the inertial effects become very large such that in the limiting case little or no flow would be induced. This results in little or no dispersive transport.

The dramatic difference in the behavior of the velocity and pressure gradient normalized solutions raises the question of whether or not a plot such as Figure 4 is the most meaningful method of illustrating the characteristics of dispersive mass transport in oscillatory flow. It also suggests that the non-dimensionalization of the oscillatory dispersion coefficient by the corresponding unidirectional flow coefficient may in fact mask the fundamental behavior characteristics of the dispersion process in oscillatory flow. This is shown to be true by plotting separately the expressions obtained for E_L and $\langle E_X \rangle_T$ versus T_{CZ} , the vertical mixing time. Figure 5 presents such a plot. In this figure, the longitudinal dispersion coefficient, $\langle E_X \rangle_T$, as given by Equation (20) is plotted versus the vertical mixing time, T_{CZ} , for four periods of oscillation ranging from 22,526 to 223,560 seconds and a u_{\max} of 1 ft./sec. Also plotted is the solution for the unidirectional flow coefficient, E_L , as given by Equation (19). This figure clearly shows the significantly different behavior of E_L and $\langle E_X \rangle_T$. The unidirectional flow coefficient varies directly with the vertical mixing time which for little or no turbulent mixing over the water column allows the shear flow to transport higher concentrations of substance far downstream. The behavior of the oscillatory flow coefficient, however, is governed by a type of resonant interaction between the period of oscillation and the vertical mixing time. As the period

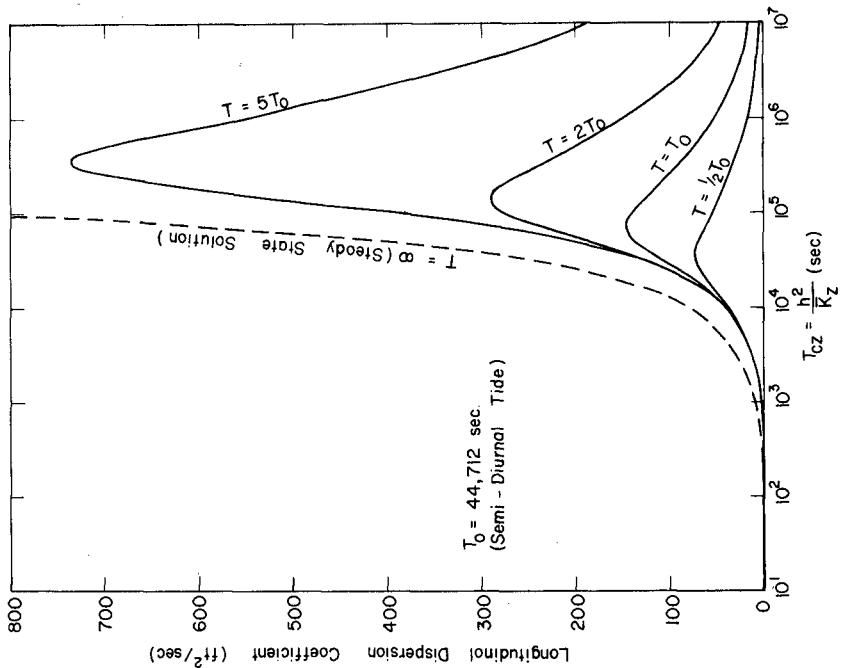


FIGURE 5 - COMPARISON OF DISPERSION PROCESSES AS A FUNCTION OF T_{cz}

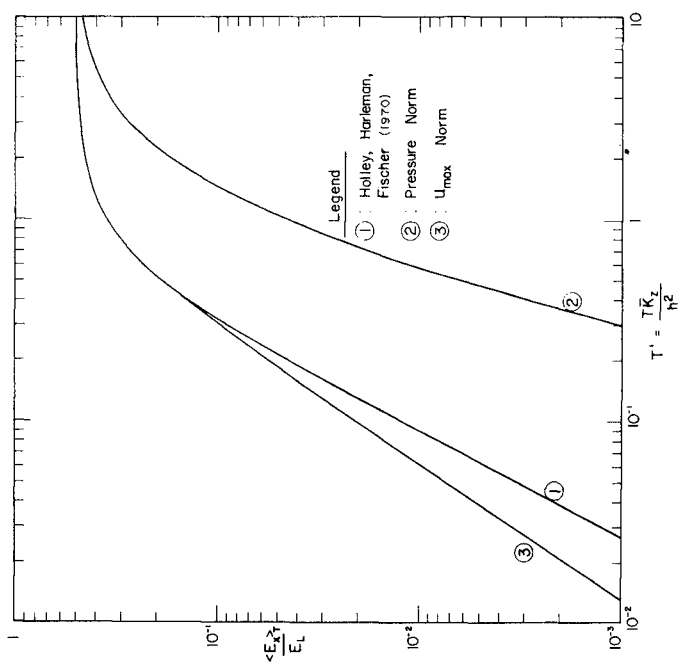


FIGURE 4 - NON-DIMENSIONAL DISPERSION COEFFICIENT $\langle E_x \rangle_T / E_L$, AS A FUNCTION OF T'

of oscillation is increased, the resonant peak shifts to the right and likewise increases until the limiting case is reached where the peak is infinitely large and the values predicted for $\langle E_x \rangle_T$ are exactly one-half those predicted for the unidirectional flow coefficient, E_L . The resonant characteristic of $\langle E_x \rangle_T$ also explains the abrupt decrease in the ratio of $\langle E_x \rangle_T / E_L$ as exhibited by the curves in Figure 4.

The physical reasoning behind the resonant behavior of $\langle E_x \rangle_T$ is surprisingly simple. Consider first the case where the period of oscillation is much greater than the vertical mixing time. In this situation, the rate of vertical mixing is so rapid that there is no time for the velocity shear profile to transport the substance longitudinally before it loses its identity through vertical mixing. Thus, the oscillatory and unidirectional flow dispersive processes behave in a similar manner and both are small. This corresponds to conditions found in the extreme left regions in Figure 5. If T is held constant and T_{cz} is allowed to increase, the oscillatory shear profile is then able to transport the substance farther downstream before excessive mixing occurs; thereby increasing the dispersive transport. Thus, the oscillatory case continues to behave in the same manner as the unidirectional case. This continues to be true until the optimum ratio between the period of oscillation and the vertical mixing time is reached. At this point, the dispersive mass transport in the oscillatory flow regime has reached its maximum. If, however, the vertical mixing time is increased beyond this point, the oscillatory nature of the flow begins to become a factor and the longitudinal dispersion is decreased. This trend continues as T_{cz} is increased further until the limiting case is reached in which there is little or no vertical mixing taking place during one or more periods of oscillation. For this situation an elemental volume initially residing in the water column at elevation z , and containing an initial concentration c , would remain at this elevation thus being transported over the closed pathline of flow, and returned to its initial position with no longitudinal dispersion having occurred. By comparison, in a unidirectional flow with little or no vertical mixing, the longitudinal dispersion would be very large.

Thus, it is seen that for an oscillatory flow regime, the longitudinal dispersive mass transport becomes small for both $T \ll T_{cz}$ and $T \gg T_{cz}$; whereas for a unidirectional flow the longitudinal dispersive mass transport varies directly with T_{cz} .

The family of curves implied by Figure 5 was collapsed into one summarizing curve by expressing $\langle E_x \rangle_T$ as given by Equation (20) in the following non-dimensional form:

$$E'_x = \frac{\langle E_x \rangle_T}{u_{\max}^2 T} \quad (25)$$

It is noted that the form of E'_x follows naturally from Equation (20). A

plot of E'_x versus the non-dimensional vertical mixing time T'_z is shown by Figure 6. As indicated, the maximum value of the longitudinal dispersion coefficient occurs when the vertical mixing time, T_{cz} , is 1.58 times the period of oscillation, T .

Three Dimensional Oscillatory Flow

The non dimensional form of the solution for the longitudinal dispersion coefficient in three dimensional oscillatory flow, as given by Equation (23), is plotted versus T'_z in Figure 7 for several values of the relative mixing time, T'_c . As stated earlier, the relative mixing time is defined as the ratio of the vertical mixing time scale to the lateral mixing time scale. Thus, small values of T'_c are indicative of a very wide shallow channel, whereas $T'_c = 1$ would represent a channel whose width is twice its depth provided $\bar{K}_z = \bar{K}_y$. T'_c can therefore be considered as a measure of the relative effects of vertical and lateral shear for a given width-to-depth ratio, and vertical and lateral eddy diffusivities. Values of T'_c ranging from 1×10^{-6} to 1 were used to develop the curves shown in Figure 7.

It is seen from Figure 7 that when both the vertical and lateral effects of shear and turbulent mixing are considered, the dispersion process in oscillatory flow is described by an infinite number of resonant curves as compared to the single curve presented in Figure 6 when only vertical effects are considered. The effect of varying T'_c causes changes in the shape of the curve, the maximum value of E'_x achieved, and the value of T'_z at which this maximum occurs.

The innermost curve shown in Figure 7 is identified by $T'_{c \leq} \times 10^{-6}$ on the left hand side of the peak and by $T'_c \leq 0.001$ on the right. A comparison of this curve and the one shown in Figure 6 shows that the general shapes of the two curves are nearly identical with both peaks occurring at $T'_z = 1.58$. The peak value of E'_x in Figure 6 is 3.27×10^{-3} whereas for the limiting curve in Figure 7 it is 3.07×10^{-3} or 6 percent below the value shown for the two dimensional case. Differences in these two curves are attributed to the number of terms used to generate Figure 7. Because the solution for E'_x as given by Equation (23) contains six infinite summations nested in series, some limitations were necessary in carrying out the required computations. By varying the upper bound on each of the sums, it was demonstrated that the solution converges upward to its limiting value. The convergence occurs reasonably rapidly; however, above an upper limit of 10 terms for each sum the rate of convergence is slowed considerably. The results presented here were computed using an upper bound of 10 on each sum; therefore, each value of E'_x includes approximately 1.2×10^6 terms. Notwithstanding this obvious

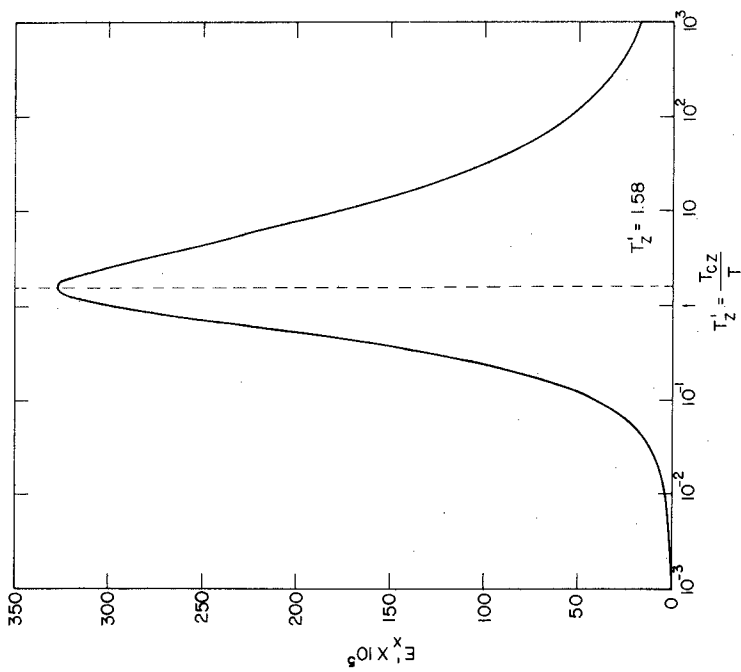


FIGURE 6 - E'_x AS A FUNCTION OF T'_z FOR TWO DIMENSIONAL OSCILLATORY SHEAR FLOW

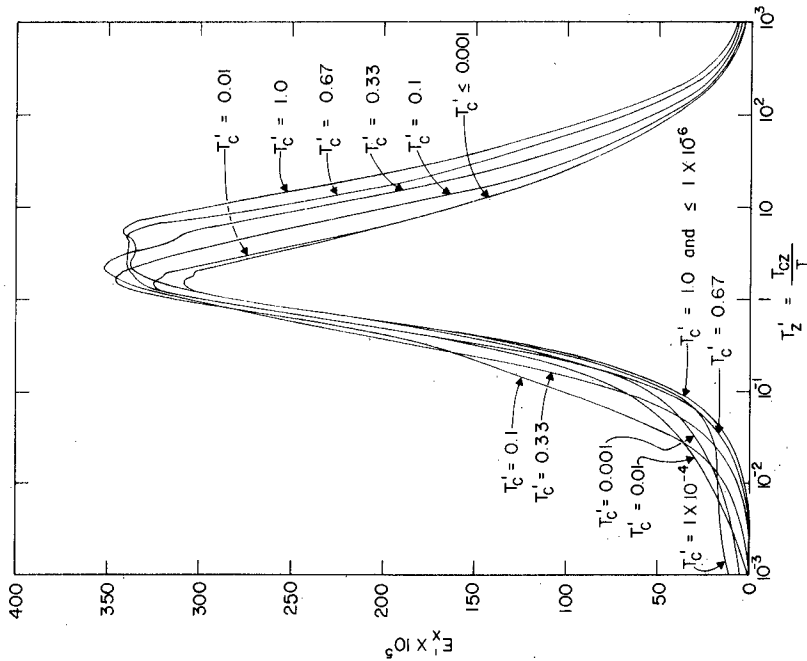


FIGURE 7 - E'_x AS A FUNCTION OF T'_z AND T'_c FOR THREE DIMENSIONAL OSCILLATORY SHEAR FLOW

limitation, it appears that the three dimensional solution for E'_x approaches the two dimensional solution for E'_x in the limit as $T'_c \rightarrow 0$.

Before passing, it is worthy to note the mathematical and physical symmetry of the dispersion process described by Equation (23). If T'_c had been inversely defined as T_{cy}/T_{cz} , Equation (23) would be of the same form with T'_y replacing T'_z everywhere, and the newly defined T'_c multiplying all complementary terms in r_1 , r_2 , and α_1 . This form of the solution would predict the same value of E'_x as the original formulation provided that u_{max} and T were the same, and that the new T'_y equaled the old T'_z and the new T'_c equaled the old T'_c . Stated another way, for the same u_{max} and T , a channel whose half-width was twice its depth would produce the same dispersive mass transport as a channel whose depth was twice its half-width provided that the ratio K_y/K_z for the first case equaled K_z/K_y in the second case. One way to show the symmetry of the solution about $T'_c = 1$ is by means of a plot such as Figure 8 in which isolines of E'_x are shown for channel geometries skewed in both width and depth. The lower half of this figure corresponds to geometries in which $w/2h > 1$ whereas the upper half corresponds to geometries in which $w/2h < 1$, provided that $K_z = K_y$.

Three Dimensional Steady Unidirectional Flow

Values for E'_L obtained from Equation (22) are plotted versus T'_c in Figure 9. In performing the computations, a summation limit of 12 was used on each of the six infinite summations included in the solution. By adjusting this value in a manner similar to that discussed for the oscillatory case, it was concluded that the solution as presented in Figure 9 is near that given by the infinite summations.

It is seen from Figure 9 that the longitudinal dispersion coefficient becomes very large with increasing channel widths. By comparison, if the definition of E'_L given by Equation (21) is applied to the two dimensional solution for E_L given by Equation (19) the result is

$$E_L = \frac{8}{945} = \text{constant} \quad (26)$$

This is shown in Figure 9 by the dotted line. The difference between the behavior of the two solutions is dramatic and for unidirectional flows supports Fischer's theory regarding the dominant effect of lateral shear on longitudinal dispersion in wide channels. It is apparent that the longitudinal dispersion for the three dimensional case increases without bound as the width of the

- Maximum Value of $E'_x = 354 \times 10^{-5}$ occurring at $T'_c = 0.25$ and $T'_z = 1.95$

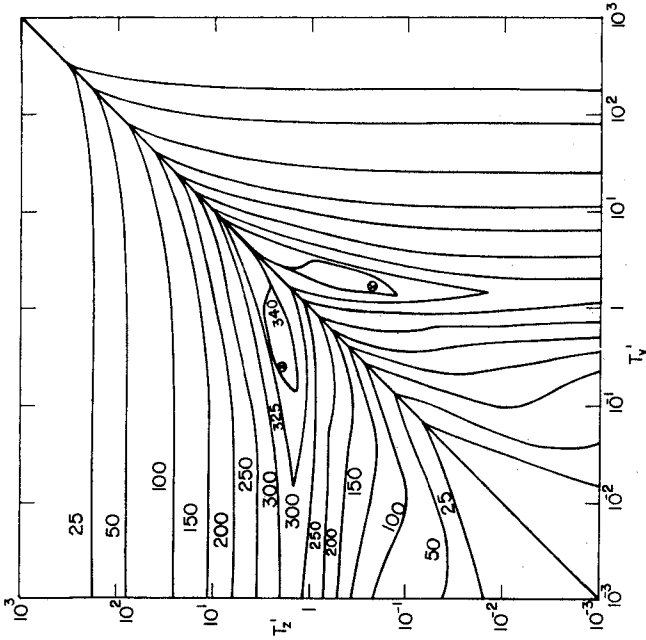


FIGURE 8 - SYMMETRIC DISPLAY OF ISOLINES OF $E'_x \times 10^5$ IN THREE DIMENSIONAL OSCILLATORY SHEAR FLOW

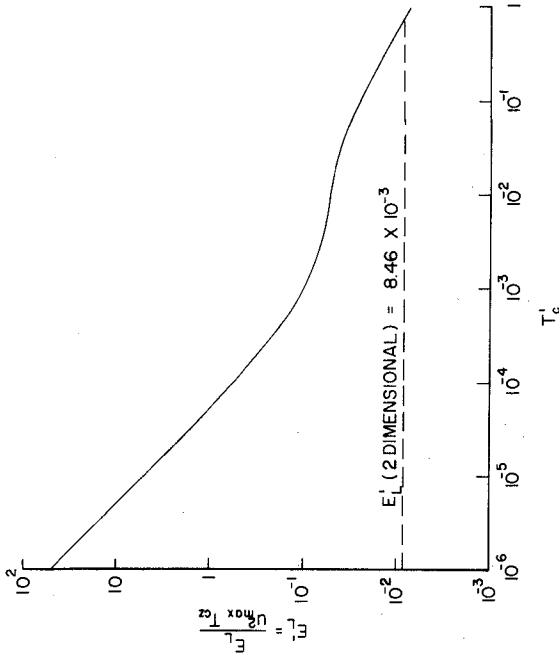


FIGURE 9 - E'_L AS A FUNCTION OF T'_c FOR TWO AND THREE DIMENSIONAL UNIDIRECTIONAL SHEAR FLOW

channel is increased correspondingly, whereas the longitudinal dispersion predicted for the two dimensional case remains independent of changes in the channel width.

The fact that the three dimensional solution does not approach the two dimensional solution in the limit as $T_c' \rightarrow 0$ is not surprising if one considers the physical characteristics of the unidirectional flow regime and the mathematical formulations of the two cases examined. The three dimensional problem has by definition a lateral shear effect which, no matter how wide the channel, is forever present. Conversely, the two dimensional problem by definition has no such effect. Thus, the presence of this shear coupled with a unidirectional flow and a long time scale of lateral mixing must produce a significantly higher longitudinal dispersive mass transport than would be produced in the case where the lateral effect is non-existent. This phenomena does not apply to the oscillatory flow case because of the completely different nature of the flow regime. In that situation, the oscillatory characteristics of the flow negate the effects of a large lateral mixing time by periodically transporting the water mass across a fixed point of reference rather than transporting it far downstream as in unidirectional flow.

It is noted that the solution given by Equation (22) is symmetrical about $T_c = 1$ in exactly the same manner as discussed for the three dimensional oscillatory flow case. Thus, the discussion presented applies equally to those channels whose geometries are skewed in depth rather than width provided the conditions previously discussed are satisfied. This, of course, would not include the period of oscillation, T .

SUMMARY AND CONCLUSIONS

Analytical expressions for the longitudinal dispersion coefficient have been presented for four cases of shear flows, namely:

- a. Unidirectional flow in an infinitely wide rectangular channel
- b. Oscillatory flow in an infinitely wide rectangular channel
- c. Unidirectional flow in a rectangular channel of finite width
- d. Oscillatory flow in a rectangular channel of finite width

Examination of these results shows that in oscillatory flow regimes the dispersion process is governed by a type of resonant interaction between the period of oscillation and the time scales of transverse mixing over the flow cross section. For two dimensional oscillatory flows in which lateral effects are not considered, this interaction is confined to the period of oscillation and the time scale of vertical mixing. The dispersion coefficient was found to reach its maximum value for this case when the vertical mixing time is 1.58 times the period of oscillation. For the case of three dimensional oscillatory flows in which both the vertical and lateral effects of shear and

turbulent mixing are considered, it was found that the inclusion of the lateral effects affected the shape of the resonant curve, the maximum value of the dispersion coefficient achieved, and the value of T_z^2 at which the maximum occurred. It was also shown that the three dimensional solution for the dispersion coefficient in oscillatory flow approaches the two dimensional solution in the limit for wide channels.

The solution presented for the dispersion coefficient in three dimensional unidirectional flow was shown to predict increasing dispersive mass transport as the channel width was increased correspondingly. Thus, the three dimensional solution does not collapse in the limit to the two dimensional case as was found for oscillatory flow. This behavior supports Fischer's (1967) theory regarding the dominant effect of lateral shear on longitudinal dispersion in wide channels.

ACKNOWLEDGEMENTS

The author would like to thank Robert G. Dean who, as his doctoral studies advisor, provided many hours of encouragement and scientific insight for the work presented.

REFERENCES

- Bowden, K.F., "Horizontal Mixing in the Sea Due to a Shearing Current," J. Fluid Mech., Vol. 21, 1965, pp. 83-95.
- Fischer, H.B., "The Mechanics of Dispersion in Natural Streams," J. Hyd. Div., ASCE, Vol. 93, No. HY6, 1967, pp.187-216.
- Fukouka, S. "Longitudinal Dispersion of Matter in Alternating Shear Flows," Res. Bull. No. C9, Dept. of Eng., James Cook University of North Queensland, 1973.
- Holley, E. R. and D. R. F. Harleman, "Dispersion of Pollutants in Estuary Type Flows," M.I.T. Hydro Lab Tech. Rpt. No. 74, 1965.
- Holley, E. R., Harleman, D. R. F. and H. B. Fischer, "Dispersion in Homogeneous Estuary Flow," J. Hyd. Div., ASCE, No. HY8, 1970, pp. 1691-1709.
- Lamb, H., Hydrodynamics, 6th ed., New York: Dover Publications, 1945.
- Okubo, A. "The Effect of Shear in an Oscillatory Current on Horizontal Diffusion from an Instantaneous Source," Int. J. of Oceanology and Limnology, Vol. 1, No. 3, 1967, pp. 194-204.
- Segall, B. A. Velocity Gradients and Their Influence on Dispersion in Oscillating Shear Flow, Ph.D. dissertation, New York University, at New York, June, 1971.
- Segall, B.A. and E. R. Gidlund, "Velocity Profiles and Dispersion in Estuarine Flow," J. San. Eng. Div., ASCE, Vol. 98, No. SA4, 1972.

- Taylor, G. I., "Dispersion of Soluble Matter in Solvent Flowing Slowly Through a Tube," Proc. Roy. Soc., A, Vol. 219, 1953, pp. 186-203.
- Taylor, G. I., "The Dispersion of Matter in Turbulent Flow Through a Pipe," Proc. Roy. Soc., A, Vol 223, 1954, pp. 446-468.
- Taylor, R. B., "Dispersive Mass Transport in Oscillatory and Unidirectional Flows," Coastal and Oceanographic Laboratory Tech. Rpt. No. 24, University of Florida, August, 1974.

CHAPTER 193

TIDAL STREAM FLOW SOLVED BY GALERKIN TECHNIQUE

By L. H. Smith & R. T. Cheng

Water Resources Division
U.S. Geological Survey

I. The Problem

The total discharges in a tidally influenced stream reach are known to be related to the stages (water levels) at the ends of the reach. The discharge-stage relationships can be derived from the conservation principles of mass and momentum under a few simplifying assumptions. Solutions of the governing equations with appropriate boundary and initial conditions give spatial and temporal variations of the flow in the reach. Practically, the most needed information are the instantaneous discharges, which, in many instances, provide guidance for water resources management decision making. Unfortunately, measuring the instantaneous discharge in a tidal reach is often difficult, tedious and costly. However, measuring the stages of a tidal reach is relatively simple, inexpensive and is done routinely. To determine discharges from measured water levels has been the subject of the present study.

The governing conservation equations of momentum and mass when written for unidirectional, constant density, transient flow are, respectively,

$$L_1(u, Z) = \frac{\partial u}{\partial t} + u \frac{\partial u}{\partial x} + g \frac{\partial Z}{\partial x} + G |u| u + (q/A)u = 0, \quad (1)$$

$$L_2(u, Z) = \frac{\partial Z}{\partial t} + u \frac{\partial Z}{\partial x} + (A/B) \frac{\partial u}{\partial x} + (S_0 + \frac{\partial A}{\partial x}/B)u - (q/B) = 0, \quad (2)$$

where

A = channel cross-sectional area

B = width of channel cross-section at water surface

g = gravitational acceleration,

G = $gn^2 / (1.49^2 R^{4/3})$, n being Manning's coefficient,

q = lateral inflow per unit length of channel,

R = hydraulic radius of a cross-section,

S_0 = slope of the channel bottom,

t = time,

u = average water velocity for cross-sectional area A,

x = direction of flow,

Z = elevation of water surface,

as indicated in Figure 1.

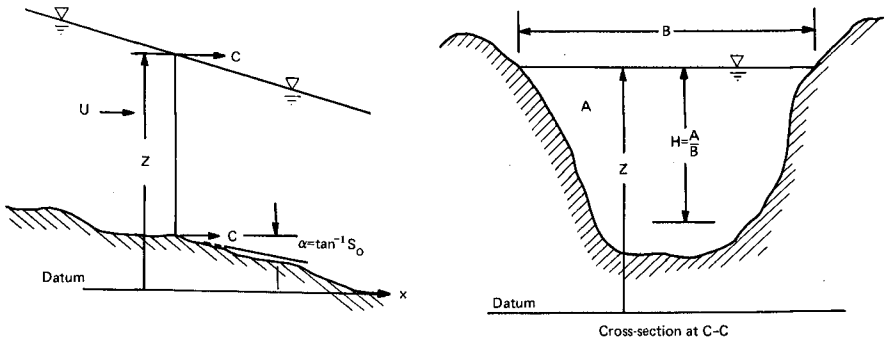


Figure 1. Schematic Diagram of a Tidal Reach

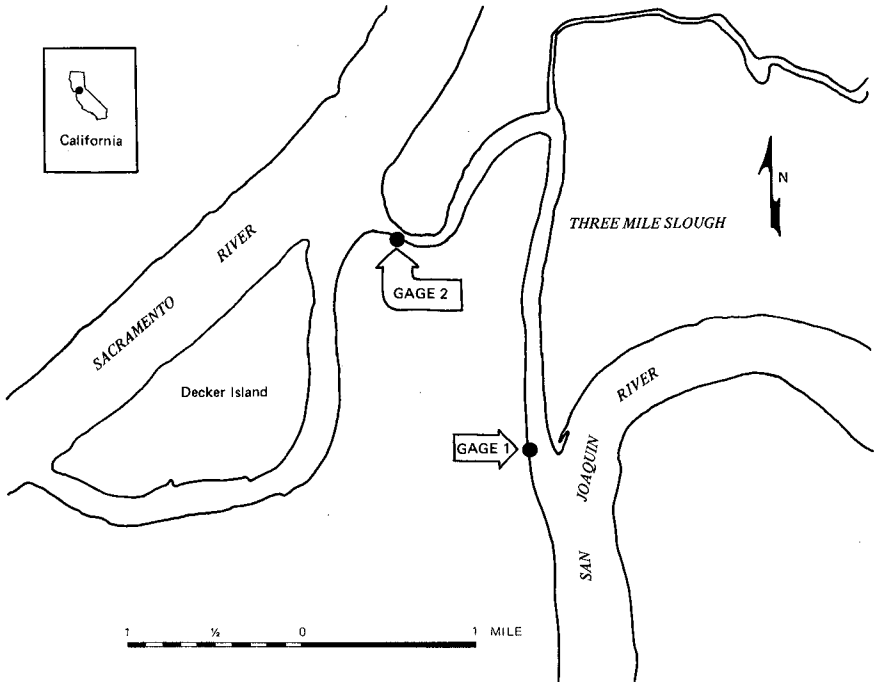


Figure 2. Plane View of Three-mile Slough, California

These equations assume that the flow is relatively uniform in any cross-section of the reach so that an average velocity u can be used to characterize the total discharge by Au . Though the cross-sectional area is treated as a variable, we further assume that A can be schematized by stacked trapezoids and that a linear representation of variation of A along the stream is sufficient. Stoker (1957), Chow (1959), Dronkers (1964) and Baltzer and Lai (1968) provide derivations and further discussion of these equations. The governing equations are coupled, nonlinear partial differential equations of hyperbolic type, which with specified water stages as the boundary conditions at ends of a channel segment, and initial conditions specified within the channel segment, form an initial-boundary value problem without known analytical solution.

Resorting to numerical techniques, Baltzer and Lai (1968) have considered the power series method, the implicit finite-difference method, and the method of characteristics to construct solutions of the discharges. Of these methods, the method of characteristics appears to produce the most accurate solutions. Recently, many classical variational techniques have attracted attention of researchers in relation to finite element methods, and use of the finite element methods in solid mechanics has been very fruitful.

Applications of the finite element techniques to hyperbolic equations are not yet numerous. Wang, et al. (1972) considered the one-dimensional primitive shallow water equation using cubic Hermite basis functions. Smith (1975) demonstrated that a Galerkin-finite element solution using linear basis functions compared favorably with those obtained by Baltzer and Lai (1968). Following a similar approach, a finite element solution of the Saint-Venant equation using linear basis functions was presented by Cooley and Moin (1976). They found that a stage boundary condition at each end of a channel segment must be implemented with the aid of the characteristic equations.

In this study we illustrate the use of cubic Hermite polynomials as basis functions in formulating a Galerkin-finite element solution to Eqs. (1) and (2). We explore the use of explicit and implicit time-differencing schemes. For a field case we compare measured discharges with discharges computed by the solution algorithm using measured stages as boundary values.

II. Galerkin-Finite Element Method

A. Galerkin Procedure

A general way to construct a finite element solution to a set of partial differential equations (such as (1) and (2)) is to employ the method of weighted residuals (Finlayson, 1972). For an M -th order approximate solution \bar{u} and \bar{Z} for the dependent variables u and Z , we write

$$\bar{u}(x,t) = \sum_{i=1}^M a_i(t) \psi_i(x), \text{ and} \quad (3)$$

$$\bar{Z}(x,t) = \sum_{i=1}^M b_i(t) \psi_i(x), \quad (4)$$

where ψ_i , $i=1,2,\dots, M$ are a carefully selected family of linearly independent functions called basis functions. If residual functions R_1 and R_2 are defined as

$$R_1(x,t) = L_1(\bar{u}, \bar{Z}), \text{ and}$$

$$R_2(x,t) = L_2(\bar{u}, \bar{Z}),$$

the method of weighted residuals obtains \bar{u} and \bar{Z} by making integrals of the residuals R_1 and R_2 vanish over the entire domain of interest with respect to certain weighting functions W_i , $i=1,2,\dots, M$. In other words,

$$\int_0^L R_1(x,t) W_i(x) dx = 0, \text{ and} \quad (5)$$

$$\int_0^L R_2(x,t) W_i(x) dx = 0, \quad (6)$$

for $i=1,2,\dots, M$, where L is the length of the entire channel segment of interest. When the weighting functions are defined and the integrals are evaluated, Eqs. (5) and (6) become a system of $2M$ simultaneous, ordinary differential equations of a_i 's and b_i 's, $i=1,2,\dots, M$. The Galerkin procedure assumes that $W_i = \psi_i$, and the classical Galerkin procedure is equivalent to the scheme of eigenfunction expansion for solution of boundary value problems. In finite element applications the basis functions ψ_i are neither complete nor orthogonal, so that the Galerkin procedure only implies that the weighted-averaged residuals are zero over the domain with respect to the basis functions.

Following the Galerkin procedure, and using Eqs. (1) - (4), Eqs. (5) and (6) can be written in matrix form as

$$[T] \frac{d\{a\}}{dt} + [P(a)]\{a\} + g [S]\{b\} + [Q(G|u| + q/A)]\{a\} = 0, \quad (7)$$

$$[T] \frac{d\{b\}}{dt} + [P(a)]\{b\} + [P(A/B)]\{a\} + [Q(S_0 + \frac{\partial A}{\partial x}/B)]\{a\} - [T]\{A/B\} = 0, \quad (8)$$

where

{ } = a column vector of dimension M ,

$$[T] = \int_0^L \psi_i \psi_j dx, \quad (9)$$

$$[S] = \int_0^L \psi_i \frac{\partial \psi_j}{\partial x} dx, \text{ and} \quad (10)$$

$$[P(f)] = \sum_{k=1}^M f_k U_{ijk}, \quad (11)$$

$$[Q(f)] = \sum_{k=1}^M f_k V_{ijk} \quad (12)$$

in which

$$U_{ijk} = \int_0^L \psi_i \frac{\partial \psi_j}{\partial x} \psi_k dx, \quad (13)$$

$$V_{ijk} = \int_0^L \psi_i \psi_j \psi_k dx, \text{ and} \quad (14)$$

for a given function $f(x)$ we write

$$f(x) = \sum_{k=1}^m f_k \psi_k(x). \quad (15)$$

Calculations for f_k are straightforward and clear when defined in terms of $\psi_k(x)$. Appendix I gives expressions for the above integrals in which $\psi_k(x)$ are cubic Hermite polynomials. In terms of local coordinates, the integrals defining the coefficient matrices have been evaluated explicitly. Appendix II contains specific entries for these matrices.

Application of the Galerkin-finite element procedure to the conservation equations produces the 2M - coupled, nonlinear, ordinary differential equations, Eqs. (7) and (8). In this study both the explicit and implicit finite-difference schemes have been used in the temporal space.

B. Explicit Time-differencing

Of the explicit time-differencing schemes, predictor-corrector schemes are well-suited for solving Eqs. (7) and (8). A fourth order Haming's modified predictor-corrector formula (Ralston and Wilf, 1960) has been employed in this study for which stages and discharges and their time-derivatives at three consecutive, equally-spaced times are used to predict their values at a fourth time. The time derivatives of the stages and discharges at the fourth time can thus be evaluated by Eqs. (7) and (8), and the processes repeated. A Runge-Kutta formula must be used up to the fourth time step to start the fourth order predictor-corrector. This integration scheme is explicit and requires relatively small time steps to maintain numerical stability. Because of its explicit nature, specification of stages at end boundaries must be implemented with the aid of characteristic equations (Cooley and Moin, 1976).

C. Implicit Time-differencing

Alternatively, in many applications an implicit Crank-Nicholson time differencing scheme which is numerically stable is preferred. Before applying a Crank-Nicholson scheme, we employ the quasi-linearization procedure to the governing equations, Eqs. (1) and (2).

1. Method of Quasi-linearization

As shown above the Galerkin procedure is general. When applied to nonlinear partial differential equations it only results in a system of nonlinear ordinary differential equations. The question of nonlinearity is dealt with by first linearizing the governing equations and introducing an iteration upon them. The Galerkin procedure is then applied to the linearized system to construct numerical solutions for each step of the iteration. This is plausible, and the following nonlinear terms are approximated by

$$u \frac{\partial u}{\partial x} \cong u^{(n)} \frac{\partial u^{(n+1)}}{\partial x} + u^{(n+1)} \frac{\partial u^{(n)}}{\partial x} - u^{(n)} \frac{\partial u^{(n)}}{\partial x} \tag{16}$$

$$u \frac{\partial Z}{\partial x} \cong u^{(n)} \frac{\partial Z^{(n+1)}}{\partial x} + u^{(n+1)} \frac{\partial Z^{(n)}}{\partial x} - u^{(n)} \frac{\partial Z^{(n)}}{\partial x} \tag{17}$$

where the superscript indicates the order of the iteration. When the $(n + 1)$ -th order solutions are sought, the n -th order solutions are known functions. Thus, Eqs. (16) and (17) are linear with respect to the $(n + 1)$ -th order solutions. Normally, the previous time solutions of u and Z are taken as the zeroth order solutions. It can be demonstrated that the quasi-linearization is but the extension of Newton's method to functional space. If convergence can be reached, the iteration converges at a quadratic rate (Bellman and Kalaba, 1965). Some nonlinearities in Eqs. (1) and (2) are weak and may be treated by a time delayed approximation. Thus Eqs. (1) and (2) become

$$\tilde{L}_1(u, Z) = \frac{\partial u}{\partial t} + u^{(n)} \frac{\partial u}{\partial x} + u \frac{\partial u^{(n)}}{\partial x} + g \frac{\partial Z}{\partial x} + G |u^{(o)}| u \tag{18}$$

$$- u^{(n)} \frac{\partial u^{(n)}}{\partial x} + (q/A) u = 0, \tag{19}$$

$$\tilde{L}_2(u, Z) = \frac{\partial Z}{\partial t} + u^{(n)} \frac{\partial Z}{\partial x} + u \frac{\partial Z^{(n)}}{\partial x} + \left[\frac{A}{B} \right]^{(o)} \frac{\partial u}{\partial x}$$

$$+ \left[S_o + \frac{\partial A}{\partial x} / B \right]^{(o)} u - \left[q/B \right] = 0,$$

where \tilde{L}_1 and \tilde{L}_2 are linear operators in which the superscript $(n + 1)$ is dropped for clarity, and terms with superscript (o) are treated with the time-delayed approximation.

By applying the Galerkin procedure, Eqs. (18) and (19) become, in matrix form,

$$[T] \frac{d\{a\}}{dt} + [P(\underline{a}^{(n)})] \{a\} + [P(\underline{a})] \{a\}^{(n)} + g [S] \{b\} \tag{20}$$

$$+ [Q [G | u| + q/A]^{(o)}] \{a\} - [P [\underline{a}^{(n)}]] \{a^{(n)}\} = 0,$$

$$[T] \frac{d\{b\}}{dt} + [P [\underline{a}^{(n)}]] \{b\} + [P (\underline{a})] \{b^{(n)}\} + [P [A^{(o)}/B]] \{a\} \tag{21}$$

$$+ [Q [S_o + \frac{\partial A}{\partial x} / B]^{(o)}] \{a\} - [T] \{q/B\} = 0,$$

in which the matrices $[T]$, $[S]$, $[P]$, and $[Q]$ are defined previously in Eqs. (9)-(12). Eqs. (20) and (21) are coupled, linear ordinary differential equations. At a particular time iterative solutions are obtained until $|\{a\} - \{a\}^{(n)}|$ and $|\{b\} - \{b\}^{(n)}|$ are less than a specified tolerance before further increment of time. Experience suggests that this criterion can usually be met within one or two quasi-linear iterations.

2. Crank-Nicholson Time-differencing Scheme

The Crank-Nicholson scheme is now applied to integrate Eqs. (20) and (21).

$$\text{Since } [P(a)]\{b\} = [P^*(b)]\{a\} \quad (22)$$

$$\text{where } [P^*(b)] = \sum_{j=1}^m U_{ijk} b_j$$

Eqs. (20) and (21) can be assembled such that they appear as

$$[C] \frac{d\{\xi\}}{dt} + [D]\{\xi\} = \{F\} \quad (23)$$

where the vector $\{\xi\}$ has dimension $2M$ and $\xi_{2i-1} = a_i$ and $\xi_{2i} = b_i$.

Using a finite-difference expression for $\frac{d}{dt}\{\xi\}$, we write Eq. (23) in the form

$$\left([C] + [D] / 2 \right) \left(\{\xi\}^+ - \{\xi\}^- \right) = \{F\} - [D]\{\xi\}^- / 2 \quad (24)$$

where $\{\xi\} = \{\xi(t_0)\}$ and $\{\xi\}^+ = \{\xi(t_0 + \Delta t)\}$.

The difference of the present and past $\{\xi\}$, i.e. $\{\xi\}^+ - \{\xi\}^-$, is actually solved to minimize possible round-off errors that could have been incurred in the computations. Because of the properties of the functions $\psi_i(x)$, the coefficient matrix $([C] + [D] / 2)$ is banded and diagonally dominant. An extended Cholesky algorithm (Tewarson, 1973) satisfactorily solves Eq. (24).

In summary, using an implicit time-difference scheme, we have (1) quasi-linearized the nonlinear partial differential equations, (2) applied the Galerkin procedure in the space domain, (3) integrated the resultant ordinary differential equations with respect to time by the Crank-Nicholson finite difference scheme.

III. A Case Study

Three-mile Slough, which is located about 40 miles northeast of San Francisco in the delta region of California's central valley, provides an interesting example of tide-induced, unsteady, open-channel flow. The slough is actually a channel approximately three miles in length connecting the Sacramento and San Joaquin Rivers, Fig. 2.

The long-period tidal waves propagate inland through Golden Gate, San Francisco Bay, San Pablo Bay, Carquinez Strait, Suisan Bay, and on. At the confluence of the San Joaquin River with the Sacramento River near the city of Pittsburgh, the waves divide and continue to propagate upstream in the separate river channels. Because of lesser distance above the confluence and because of greater channel depth, a translatory wave crest passes the Sacramento River end of Three-mile Slough from 30 to 45 minutes before the corresponding wave crest reaches the slough's San Joaquin River end. As a result, Three-mile Slough exhibits continuously and rapidly varying flow through each tidal cycle. Moreover, the direction of flow alternates with the passage of each successive wave. Because of the high degree of unsteadiness and alternating direction of the flow, this tidal reach was deemed desirable for trial evaluation of the discharge computation process.

In 1959, Water Resources Division of the U.S.G.S. conducted an extensive field investigation in this tidal reach. Two tidal gages were installed at the San Joaquin and at the Sacramento River ends to record water levels at 15-minute intervals. A field survey was also conducted to help establish its cross-sectional properties. During the months of July and August, 1959, gates blocked all the diversionary channels, and several sets of discharge measurements were made using current meters. These data were used to evaluate the computational schemes suggested in the present study.

Using the measured stage records at the ends of the Three-mile Slough (See Fig. 2) as inputs, the computations have been carried out by both the predictor-corrector and Crank-Nicholson schemes for several values of Manning coefficient. Figure 3 is a plot of measured and computed discharges obtained by the predictor-corrector scheme for three different Manning values. A Manning value of 0.038 gives a best over-all fit for this scheme. Since the discharge ranges between +35,000 cfs (ft^3/sec) to -35,000 cfs, it is quite likely that the Manning n value should have been treated as a function of the discharge. We have not included this feature in the present study, although implementation of a variable n in the model is plausible. For a Manning coefficient of 0.038, Figure 4 compares the computed discharges for the predictor-corrector and quasi-linearization schemes to those computed by the predictor-corrector scheme with linear basis functions. The predictor-corrector schemes both were run with a 1-minute time-step, and the Crank-Nicholson (quasi-linearization) scheme with a 5-minute time-step. The deviation of the quasi-linearization scheme is attributable to the different manner in which it handles the friction term. For a reach with channel geometry as regular and length as short as Three-mile Slough, there is little difference in the discharges computed using the Hermite and linear basis functions. All of the schemes compute discharges within 5 percent of the measured values.

IV. Discussion

In this study numerical solutions to the governing equation of a tidal reach have been constructed using a Galerkin-finite element approximation in space and finite-difference approximation in time. The computer algorithms have been successfully tested in a case study at Three-mile Slough, California, where a complete reversal of flow takes place in every semi-diurnal tidal cycle. The predictor-corrector

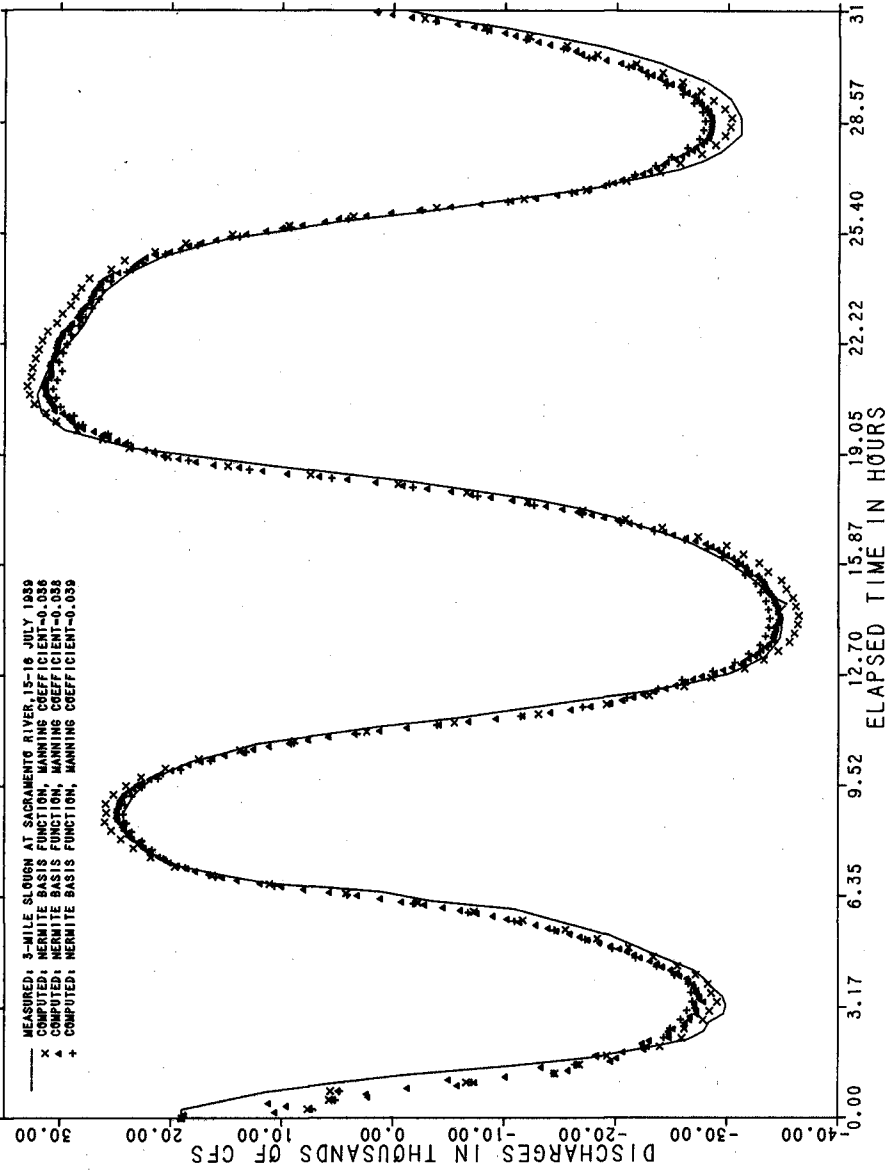


Figure 3. Comparison of the Computed and Measured Discharges at Sacramento River for Various Values of Manning Coefficient

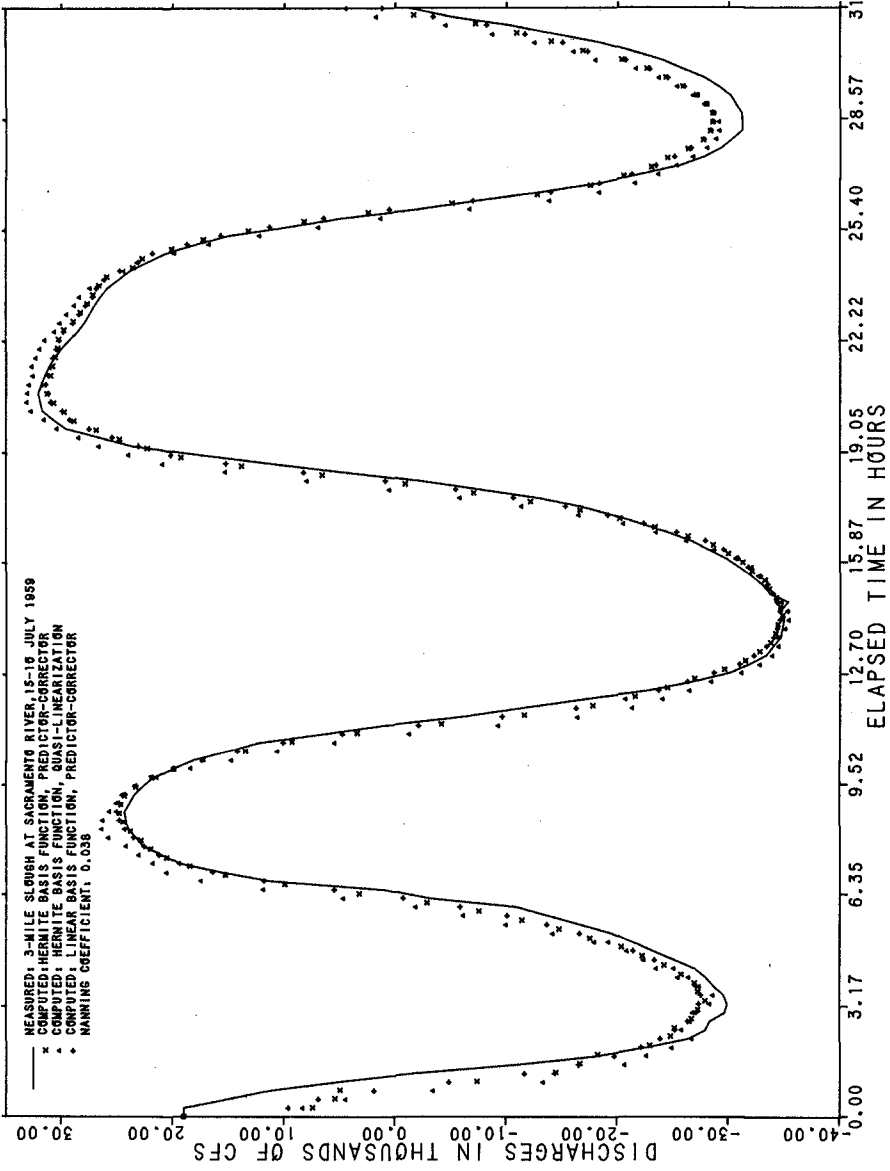


Figure 4. Discharges at Sacramento River Computed by Various Numerical Schemes

solution computes accurate discharges but requires use of the characteristic equations to implement the boundary conditions, and small time-steps to maintain numerical stability. The implicit Crank-Nicholson and quasi-linearization scheme has neither of these requirements. Although it requires longer computer time per time step, it permits the use of larger time steps. The total computer time requirements for the implicit and explicit methods are comparable. Good agreement between the measured and computed discharges suggests further applications of the present model to realistic field problems.

V. References

1. Baltzer, R. A. and Lai, V. C., 1968, Computer simulation of unsteady flow in waterways, Journal of Hydraulic Division, ASCE, Vol. 94, No. HY.4, p. 1083-1117.
2. Bellman, R. E. and Kalaba, R. E., 1965, Quasi-linearization and Nonlinear Boundary-Value Problems, Elsevier, New York
3. Chow, V. T., 1959, Open Channel Hydraulics, McGraw-Hill, New York, 680 p.
4. Cooley, R. L. and Moin, S. A., 1976, Finite Element Solution of Saint-Venant Equations, Journal of Hydraulic Division, ASCE, Vol. 102, No. HY.6, p. 759-775.
5. Dronkers, J. J., 1964, Tidal Computations in Rivers and Coastal Waters, North-Holland Publishing Co., Interscience, Amsterdam, p. 518.
6. Eisenberg, M. A., and Malvern, L. E., 1973, On Finite Element Integration in Natural Coordinates, Int. J. for Num. Meth. in Eng., Vol. 7, No. 4., p. 574-575.
7. Finlayson, B. A., 1972, The method of weighted residuals and variational principles, Academic Press, New York, 412 p.
8. Ralston, A. and Wilf, H. S., 1960, Mathematical Methods for Digital Computers, Wiley, New York, p. 95-109.
9. Smith, L. H., 1975, Finite element solution for one-dimensional unsteady flow in an open channel, (ABS.), Hydr. Eng. for Optional Use of Water Resources, Specialty Conference, ASCE, Seattle, Wash.
10. Stoker, J. J., 1957, Water Waves, Interscience, New York, 567 p.
11. Strang, G. and Fix, G. J., 1973, An Analysis of the Finite Element Method, Prentice-Hall, Englewood Cliffs, N.J.
12. Tewarson, R. P., 1973, Sparse Matrices, Academic Press, New York, 160 p.
13. Wang, H. H., Halpern, P., Douglas, Jr., J., and Dupont, T., 1972, Numerical Solutions of the One-Dimensional Primitive Equations Using Galerkin Approximations with Localized Basis Functions, Mon. Weath. Rev., Vol. 100, No. 10, p. 738-746.

Appendix I. Spatial Integration with Hermite Basis Functions

To facilitate easy application of the Galerkin procedure, we first partition the domain $[0, L]$ into N elements, i.e.,

$$0 = x_0 < x_1 < x_2 < \dots < x_n = L,$$

where the i -th element spans $[x_{i-1}, x_i]$. The local coordinates L_1 and L_2 are introduced such that any point x on the line element $[x_1, x_2]$ can be expressed as

$$x = L_1(x) x_1 + L_2(x) x_2 \quad (\text{I-1})$$

where

$$L_1(x) = \frac{x_2 - x}{x_2 - x_1}, \quad L_2(x) = \frac{x - x_1}{x_2 - x_1}$$

The functions L_1 and L_2 , known as the natural or local coordinates, are simply ratios of length when measured from x_2 and x_1 respectively, and satisfy

$$L_1 + L_2 = 1. \quad (\text{I-2})$$

Utilization of the properties of local coordinates significantly simplifies evaluation of integrals over the elements. General quadratures in terms of the local coordinates can be derived easily (Eisenberg and Malvern, 1973). For one-dimensional problems, we redefine, for the i -th element,

$$L_{i,1}(x) = \frac{x_i - x}{x_i - x_{i-1}}, \quad L_{i,2}(x) = \frac{x - x_{i-1}}{x_i - x_{i-1}}, \quad (\text{I-3})$$

then

$$\int_{x_{i-1}}^{x_i} L_{i,1}^\alpha L_{i,2}^\beta dx = \frac{\alpha! \beta! L_i}{(\alpha + \beta + 1)!}, \quad \text{where } L_i = x_i - x_{i-1}.$$

The cubic Hermit polynomials can be defined in natural coordinates as

$$\psi_{2i-1}(x) = \begin{cases} -2 L_{i,2}^3 + 3 L_{i,2}^2 & \text{if } x_{i-1} \leq x \leq x_i \\ 2 L_{i+1,2}^3 - 3 L_{i+1,2}^2 + 1 & \text{if } x_i \leq x \leq x_{i+1} \\ 0 & \text{otherwise,} \end{cases} \quad (I-4)$$

$$\psi_{2i}(x) = \begin{cases} L_{i,2}^2 L_{i,1} L_i & \text{if } x_{i-1} \leq x \leq x_i \\ L_{i+1,1}^2 L_{i,2} L_{i+1} & \text{if } x_i \leq x \leq x_{i+1} \\ 0 & \text{otherwise.} \end{cases} \quad (I-5)$$

The functions $\psi_{2i-1}(x)$ and $\psi_{2i}(x)$ are sketched in Fig. 5 for the sub-regions $[x_{i-1}, x_i]$ and $[x_i, x_{i+1}]$, or the i -th and $(i+1)$ -th elements.

Note that $\psi_{2i-1}(x_i) = 1$, $\psi_{2i}(x_i) = 0$, $\frac{d\psi_{2i-1}}{dx}(x_i) = 0$, and $\frac{d\psi_{2i}}{dx}(x_i) = 1$. (I-6)

These imply in Eqs. (3) and (4) of section II A that

$$\begin{aligned} a_{2i-1}(t) &= u(x_i, t), & a_{2i}(t) &= \left. \frac{\partial u}{\partial x} \right|_{x=x_i}, \\ b_{2i-1}(t) &= Z(x_i, t), & b_{2i}(t) &= \left. \frac{\partial Z}{\partial x} \right|_{x=x_i}. \end{aligned} \quad (I-7)$$

Thus \bar{u} and \bar{Z} are interpolation expressions for the functions u and Z in terms of their values and spatial gradients at the x_i . The $C^{(1)}$ -interpolating functions ψ_i constitute a basis for the set of $C^{(1)}$ -elements in one-dimensional problems (Strang and Fix, 1973). The numerical solutions are the discrete solutions of velocity and stage at each node, u_i and Z_i and their spatial gradients, $\frac{du_i}{dx}$ and $\frac{dZ_i}{dx}$.

Therefore, $C^{(1)}$ elements provide continuous approximate u , z , $\frac{du}{dx}$ and $\frac{dZ}{dx}$ but piecewise continuous second order derivatives.

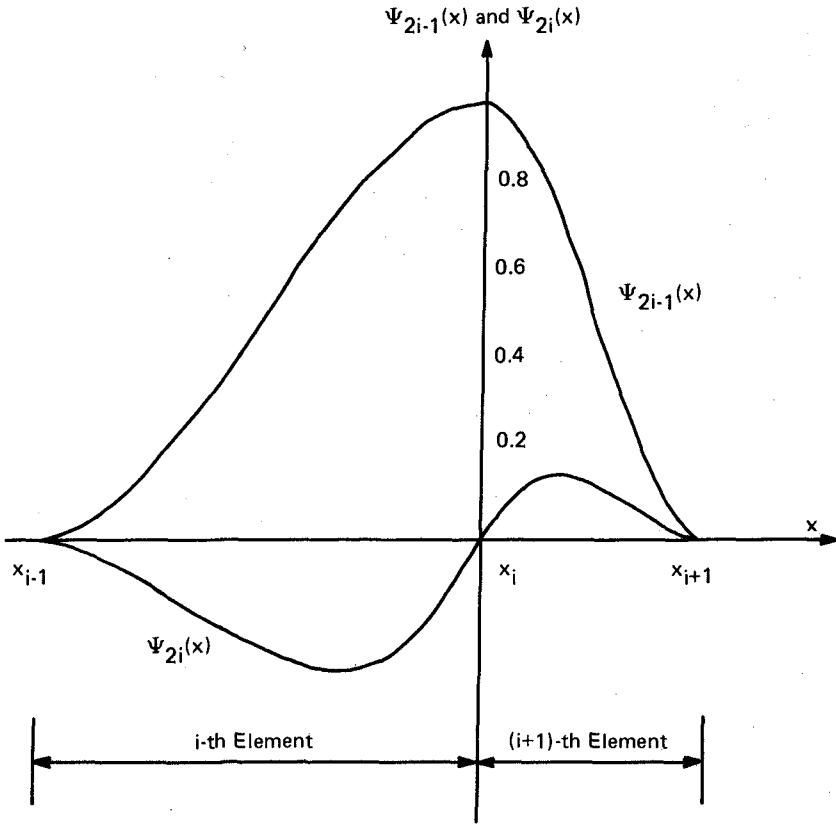


Figure 5. The Cubic Hermite Polynomial Shape Functions for i -th and $(i+1)$ -th Elements

Integrals defining the coefficient matrices, Eqs. (9)-(14), can now be examined. For example,

$$[T] = \sum_0^L \psi_i \psi_j dx = \sum_{k=1}^n \int_{x_{k-1}}^{x_k} \psi_i \psi_j dx. \quad (I-8)$$

Note that unless $i, j = 2k - 1, 2k, 2k + 1,$ or $2k + 2,$

$$\int_{x_{k-1}}^{x_k} \psi_i \psi_j dx = 0.$$

Therefore the elemental contribution to $[T]$ from $[x_{k-1}, x_k]$ can be given as

$$[T]^{(k)} = \frac{L_k}{420} \begin{bmatrix} \frac{156}{L_k} & 22 & \frac{54}{L_k} & -13 \\ 22 & 4 L_k & 13 & -3 L_k \\ \frac{54}{L_k} & 13 & \frac{156}{L_k} & -22 \\ -13 & -3 L_k & -22 & 4 L_k \end{bmatrix} \quad (I-9)$$

where the first through the fourth column and row represent rows and columns from $(2k-1)$ to $(2k+2)$ in the global (over-all) matrix. This recurrence formula constitutes the basic algorithm of the finite element method. The global matrix $[T]$ is formed by adding the elemental contributions to the proper rows and columns. Likewise, elemental

contributions of $[S]^{(k)}, [u_{ij}^{(k)}]_1, [v_{ij}^{(k)}]_1$ have been calculated and their values are given in Appendix II.

Appendix II. Elemental Contributions of Coefficient Matrices.

$$[S]^{(k)} = \int_{x_{k-1}}^{x_k} \psi_i \frac{d\psi_i}{dx} dx = \frac{1}{60} \begin{bmatrix} -30 & -6 L_k & -30 & 6 L_k \\ 6 L_k & 0 & -6 L_k & L_k^2 \\ 30 & 6 L_k & 30 & -6 L_k \\ -6 L_k & -L_k & 6 L_k & 0 \end{bmatrix}$$

$$[U_{ij}^{(k)}]_{\ell} = \int_{x_{k-1}}^{x_k} \psi_i \frac{d\psi_j}{dx} \psi_{\ell} dx, \text{ then}$$

when $\ell = 2k - 1$:

$$[U_{ij}^{(k)}]_{\ell} = \frac{1}{840} \begin{bmatrix} -280 & 100 L_k & 280 & -68 L_k \\ -50 L_k & 5 L_k^2 & 50 L_k & -11 L_k^2 \\ -140 & -16 L_k & 140 & -16 L_k \\ 34 L_k & 3 L_k^2 & -34 L_k & 5 L_k^2 \end{bmatrix},$$

when $\ell = 2K$:

$$[U_{ij}^{(k)}]_{\ell} = \frac{1}{840} \begin{bmatrix} -50 L_k & 5 L_k^2 & 50 L_k & -11 L_k^2 \\ -10 L_k^2 & 0 & 10 L_k^2 & -2 L_k^3 \\ -34 L_k & -5 L_k^2 & 34 L_k & -3 L_k^2 \\ 8 L_k^2 & L_k^3 & -8 L_k^2 & 3 L_k \end{bmatrix},$$

when $\ell = 2K + 1$

$$[U_{ij}^{(k)}]_{\ell} = \frac{1}{840} \begin{bmatrix} -140 & -16 L_k & 140 & -16 L_k \\ -34 L_k & -5 L_k^2 & 34 L_k & -3 L_k^2 \\ -280 & -68 L_k^2 & 280 & 100 L_k \\ 50 L_k & 11 L_k^2 & -50 L_k & -5 L_k^2 \end{bmatrix},$$

$$\ell = 2k + 2$$

$$\left[\begin{array}{c} v_{ij} \\ (k) \end{array} \right]_{\ell} = \begin{bmatrix} 34 L_k & 3 L_k^2 & -34 L_k & 5 L_k^2 \\ 8 L_k^2 & L_k^3 & -8 L_k^2 & L_k^3 \\ 50 L_k & 11 L_k^2 & -50 L_k & -5 L_k^2 \\ -10 L_k^2 & -2 L_k^2 & 10 L_k^2 & 0 \end{bmatrix}$$

$$\left[\begin{array}{c} v_{ij} \\ (k) \end{array} \right]_{\ell} = \int_{x_{k-1}}^{x_k} \psi_i \psi_j \psi_{\ell} dx,$$

$$\text{when } \ell = 2k - 1 :$$

$$\left[\begin{array}{c} v_{ij} \\ (k) \end{array} \right]_{\ell} = \frac{L_k}{2520} \begin{bmatrix} 774 & 97 L_k & 162 & -43 L_k \\ 97 L_k & 16 L_k^2 & 35 L_k & -9 L_k^2 \\ 162 & 35 L_k & 162 & -35 L_k \\ -43 L_k & -9 L_k^2 & -35 L_k & 8 L_k^2 \end{bmatrix},$$

$$\text{when } \ell = 2k :$$

$$\left[\begin{array}{c} v_{ij} \\ (k) \end{array} \right]_{\ell} = \frac{L_k}{2520} \begin{bmatrix} 97 L_k & 16 L_k^2 & 35 L_k & -9 L_k^2 \\ 16 L_k^2 & 3 L_k^3 & 8 L_k^2 & -2 L_k^3 \\ 35 L_k & 8 L_k^2 & 43 L_k & -9 L_k^2 \\ -9 L_k^2 & -2 L_k^3 & -9 L_k^2 & 2 L_k^3 \end{bmatrix},$$

when $\ell = 2k + 1$:

$$\left[v_{ij}^{(k)} \right]_{\ell} = \frac{L_k}{2520}$$

$$\begin{bmatrix} 162 & 35 L_k & 162 & -35 L_k \\ 35 L_k & 8 L_k^2 & 43 L_k & -9 L_k^2 \\ 162 & 43 L_k & 774 & -97 L_k \\ -35 L_k & -9 L_k^2 & -97 L_k & 16 L_k^2 \end{bmatrix}$$

when $\ell = 2k + 2$:

$$\left[v_{ij}^{(k)} \right]_{\ell} = \frac{L_k}{2520}$$

$$\begin{bmatrix} -43 L_k & -9 L_k^2 & -35 L_k & 8 L_k^2 \\ -9 & -2 L_k^3 & -9 L_k^2 & 2 L_k^3 \\ -35 L_k & -9 L_k^2 & -97 L_k & 16 L_k^2 \\ 8 L_k^2 & 2 L_k^3 & 16 L_k^2 & -3 L_k^3 \end{bmatrix}$$

CHAPTER 194

MODEL VERIFICATION FOR TIDAL CONSTITUENTS

By

R. W. Whalin,¹ F. C. Perry,² and D. L. Durham³

ABSTRACT

Installation and operation of an automated model data acquisition and control system have made it possible to make a quantum advance in the accuracy and time required for verification of tidal inlet (or estuary) hydraulic models. The flexible sampling rate (usually about 200 samples per model tidal cycle for each gage) and digital recording of these data make them ideal for harmonic analysis and comparison with prototype data defining the coefficients and phase for each tidal constituent at various key locations within the tidal lagoon and at an open-ocean station removed from the immediate influence of the tidal inlet. The concept used is to force the model with the M_2 tidal constituent with the amplitude being correct at the ocean tide gage. A harmonic analysis is performed at all other gage locations corresponding to the prototype measurements, and the amplitude and phase (relative to the ocean tide gage) are calculated and compared with the prototype data. Investigation of the relative phases between various gages quickly shows those areas where either more or less model roughness is required. It is reasonable to expect to be able to have all phases for the M_2 constituent verified within 1 degree. Tidal elevations can almost always be expected to be verified to within a maximum deviation of ± 0.1 ft in both tidal height and mean tide level. Upon verification of the M_2 constituent, which practically insures that the proper channel roughness is obtained, a progressive tide can be constructed; and it should be attempted to perform a verification for a 14.765-day (synoptic period for M_2 and S_2 components) progressive tide at east coast locations using the prototype measurements of tidal velocities for the final verification data. Should additional roughness be necessary, it will almost always be on the mud flats or marsh areas. Computations are made to illustrate the energy transfer from the M_2 constituent to higher order harmonics as the wave propagates from the ocean to the back of the estuary, and it is shown that this energy transfer is, at worst, the same order of magnitude in both the model and prototype.

The concept ventured in this paper has been applied to verification of the Murrells Inlet, South Carolina, hydraulic model. Model scales were 1:60 vertical and 1:200 horizontal (a distortion ratio of 3-1/3:1).

Major conclusions are that verification based on the M_2 constituent is feasible and was quite successful in the Murrells Inlet, South Carolina, model, and it is postulated that a method similar to that contained in this paper should be used for the verification of numerical models.

¹Chief, Wave Dynamics Division, Hydraulics Laboratory, USAE Waterways

²Experiment Station, Vicksburg, Miss.

³Captain, U. S. Army, Project Engineer and Research Coordinator, Wave Dynamics

Division, Hydraulics Laboratory, USAE Waterways Experiment Station, Vicksburg, Miss.

³Research Oceanographer, Wave Dynamics Division, Hydraulics Laboratory, USAE Waterways Experiment Station, Vicksburg, Miss.

INTRODUCTION

Design, construction, and operation of hydraulic models of tidal inlets in order to evaluate the effects of planned improvements to inlet-estuary systems are common problems undertaken in the Wave Dynamics Division. Usually the improvement consists of either proposed jetty construction to stabilize and maintain some project depth in an entrance channel or lengthening of existing jetties with an associated deepening of the entrance channel to accommodate larger and deeper-draft vessels. This type of problem has been common during the past 20 years and is anticipated to continue for the foreseeable future since there are about 340 navigable tidal inlets and river entrances along the east, Gulf, and west coasts of the continental United States.

Tidal inlet models are practically always distorted out of necessity for various reasons which will be mentioned but not discussed. Many times tidal inlets are large and the bathymetry includes flood and ebb tidal deltas which are quite shallow leading to large model energy attenuation and viscous friction scale effects on waves. These effects can be minimized through distortion and at the same time decrease model costs. It is extremely desirable to reproduce the entire tidal estuary for reasons which follow. Inclusion of the tidal estuary in the model results in the flexibility to study the effects of proposed improvements on the tidal prism, tidal circulation, tidal flushing, and salinity of the estuary. In addition, inclusion of the estuary should result in the correct nonlinear energy transfer from various tidal constituents to higher order harmonics. Deletion of a major portion of the estuary leaves reproduction of this phenomenon considerably more uncertain, although its importance is not well established but should perhaps be investigated on a case-by-case basis.

This paper focuses attention on the problem of model verification and reports on an attempt to verify a model by using the elevation and phase of the M_2 tidal constituent for the principal verification tool. A progressive tide was subsequently used in the final phase of verification. The model being used was of Murrells Inlet, South Carolina; and since this was a project study (not a research study), there are several experimental tests which should be conducted to supplement the knowledge gained in this investigation. These areas are pointed out and will, hopefully, be the subject of future research.

HYDRAULIC MODEL OF MURRELLS INLET, SOUTH CAROLINA, USA

This section gives a brief discussion of model design, instrumentation, and the automated data acquisition system used in the model study. Verification by tidal constituent is practically impossible without an automated data acquisition system which was an integral part of this model study.

Model Design

Murrells Inlet, South Carolina, is an unimproved inlet, Figure 1, with an existing main channel of only about -4.0 ft mlw which meanders and is not stable. The estuary is actually a well-mixed tidal lagoon of ocean salinity with no source of fresh water inflow except for surface runoff from rainfall. Figure 2 illustrates the model layout showing the head bay, wave generator locations, and locations of prototype and model tide gages and velocity ranges. Vertical scale of the model is 1:60 and horizontal scale is 1:200 resulting in a distortion of 3-1/3.

An interesting point to designers of hydraulic models is that a portion of the model bathymetry (seaward of the -22 ft mlw contour) is artificial in order to compensate for refraction due to bathymetric variations seaward of this contour which could not feasibly be installed in the model because of the extremely large distance seaward. This is a typical problem along the east and Gulf Coast of the United States. This represents the first use (at the Waterways Experiment Station) of an artificial bathymetry to correct for refraction seaward of the model limits and will be the subject of a future paper. A thorough discussion of this appears in the final report (Perry, 1976) to be published near the end of this calendar year. The artificial bathymetry was chosen to yield the approximate prototype energy distribution and wave direction at the -22 ft mlw contour from all wave directions of interest in the model study.

Instrumentation

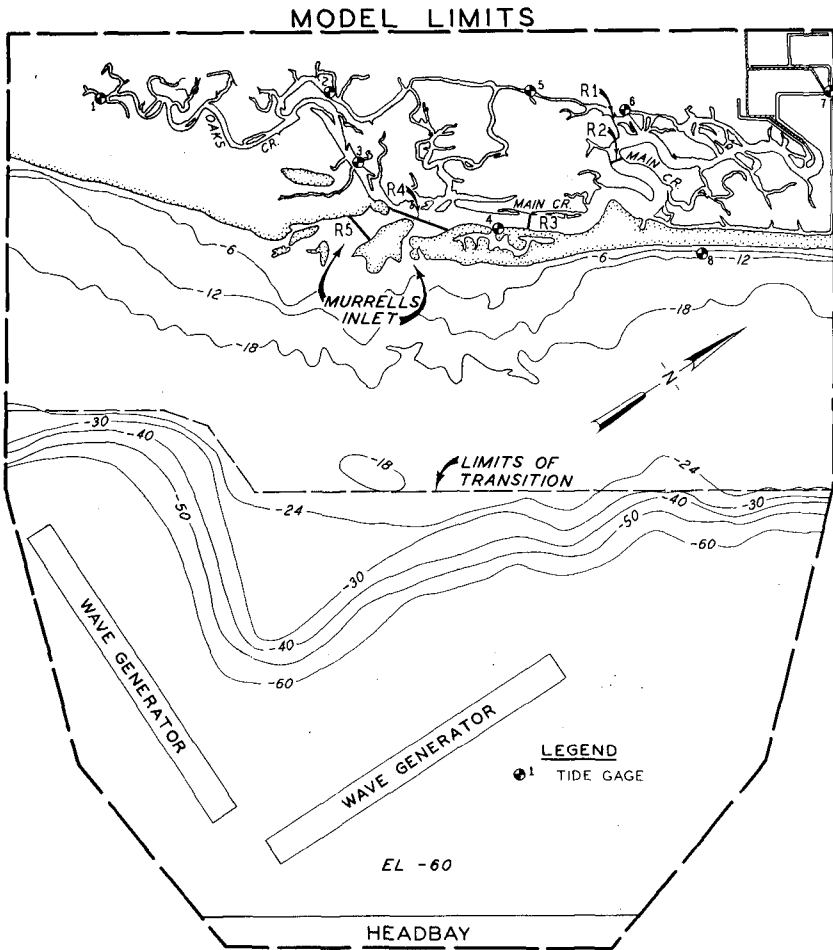
The principal information required in the verification process is tidal elevation data. Various types of tidal height sensors are in use; however, the Murrells Inlet model used a "bubbler system" or gage which measures small hydrostatic pressure changes associated with changes in model tidal elevations. The "bubbler system" consists of a high precision pressure transducer, a scanivalve device for sequencing input ports, and 48 pressure inputs. Durham *et al.* (1976) gives a thorough discussion of the model sensors. Wave gages also were installed in the model but are not discussed here since those data were not essential to the verification process. Velocities of tidal currents were measured with miniature Price-type current meters and with two electromagnetic velocity meters. Most data were acquired with the miniature Price meters, but the electromagnetic current meters seem to be quite promising for future model use.

Data Acquisition

An automated data acquisition and control system (acronym ADACS) has been designed, procured, installed, and is operational on wave and tidal inlet models at WES. Durham, *et al.* (1976) describes the system. The principal functions of ADACS are to provide automated acquisition of wave and tide data in a format compatible for digital reduction and analyses and automated control of model sensor calibration and of wave and tide generators.



Figure 1. Murrells Inlet, South Carolina.



MURRELLS INLET
MODEL LAYOUT

SCALES IN FEET

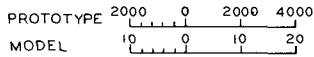


Figure 2. Model Layout.

Tidal elevation data for a programmed tide condition are collected from a specified number of tide sensors, digitized and recorded on magnetic tape or disc for future analysis. A flexible sampling scheme is used and is only limited in sampling rate by the scanivalve multiplexing rate. The sampling scheme used for this study consisted of the following (a) increment the scanivalve to the first data channel, (b) delay a specified time interval (usually 0.5 sec) to allow input pressure stabilization, (c) collect a specified number of samples (10 in this case), (d) average the voltage samples, (e) store the discrete sample in memory, (f) increment to the next channel, (g) repeat the above procedure, and (h) continue sequentially through the remaining channels. Using input parameters, the minicomputer calculates (1) the required timing interval between scanivalve multiplexing scans to provide the correct sampling rate, (2) the delay interval at each channel, and (3) the number of voltage samples to be digitized and averaged and initializes counters for determining completion of tidal tests. In addition, it provides an analog command signal through the digital to analog converter to the tide generator and lags the beginning of data acquisition by a specified number of tide cycles after starting the generator.

Due to thermal effects (zero drift) on the transducer output over a tidal test of 2-3 hours duration, the pressure transducer is calibrated prior to and at selected time intervals during each tidal test to provide accurate, update calibration data for scaling voltage (pressure) to tidal elevations. Durham et al. (1976) give a complete discussion of the calibration procedure.

A limited number of channels of tidal velocity can be measured by miniature, electromagnetic current meters which are monitored by ADACS. The collection of tidal velocities using ADACS has not been fully implemented at this time and is pending the completion of transducer evaluation which should be within the next year. Until such time, the majority of tidal velocity measurements are obtained manually by using a modified version of the miniature Price meters.

In addition to tide data, most tidal inlet studies require wave information. Generation and acquisition of wave data at specific tidal phases (normally high, low, and mean tide levels) are provided by ADACS. While controlling the tide generator and collecting tidal data, ADACS uses in-core timers to determine the occurrence of specified tidal phases at which times (1) the wave generators are turned on, (2) wave data at a specified sampling rate for a predetermined number of wave periods are collected at various locations in the model, (3) the completion of wave test for that tidal phase is detected, (4) the wave generators are turned off, and (5) in-core timers initialized to determine the next specified tidal phase for wave tests. These wave tests are performed normally during the middle cycle of a three-cycle tidal test. The instrumentation and procedure for collecting wave data are the same as described in Durham and Greer (1975).

At completion of the acquisition mode, the calibration, wave, and tide data have been recorded in binary form on magnetic tape or disc. Schematically, the automated procedures for analyzing tidal data are as follow:

1. Program Initialization

- (1) Input test parameters and option flags.
- (2) Read and decode data tape or disc file.
- (3) Demultiplex data files and scale data.

II. Tidal Data Analyses

- (1) Harmonic analysis using Least Squares techniques.
 - (a) Amplitude and phases of tidal constituents.
 - (b) Relative phases between gages.
- (2) Analyses of residual variances.
 - (a) Original versus Least Square estimate.
 - (b) Prototype tide versus model tide.
 - (c) Model base test versus model plans.
- (3) Graphic output of above results.

In addition to the above automated procedures, manual and photographic techniques are employed in tidal models to study general patterns of tidal circulation and to qualitatively define littoral transport and deposition patterns. Analyses of wave data are discussed by Durham and Greer (1975) and are basically auto-spectral and cross-spectral analyses, statistical analyses for wave heights and periods of wave signals at selected locations throughout the model, and computation of response functions or amplification factors from wave energy within the harbor or tidal inlet relative to incoming wave energy.

PROTOTYPE DATA

Model verification can be no better than the prototype data available for verification. Recent improvements and advances in acquisition of hydraulic model data (ADACS) have resulted in the situation where model data are almost invariably more accurate than the prototype data. The method of verification discussed in this paper was selected subsequent to collection of the prototype data (of course after evaluation of these data to ascertain their adequacy for such an approach). As a result the tidal elevation data are completely satisfactory, but the velocity data are not adequate to extract components of the various tidal constituents. Nonetheless, they are satisfactory for velocity verification during a portion of the progressive tide. The verification method described makes primary use of tidal elevation data.

Tidal Elevations

Prototype data on tidal elevations were obtained at seven locations in the tidal lagoon and one location on the open coast north of the

inlet. The gages were installed, operated, and analyzed by personnel of National Ocean Survey (NOS) of the National Oceanographic and Atmospheric Administration for a period of approximately 6 months. Gage locations are shown in Figure 2, and results of the NOS analysis of these data for the tidal constituents at the open-coast gage are shown in Table 1. As indicated in Table 1, the Murrells Inlet tidal regime is dominated by the principal lunar semidiurnal constituent M_2 . The M_2 variance represents approximately 90 percent of the tidal variance in Murrells Inlet.

Table 1: PROTOTYPE TIDAL CONSTITUENTS

Component	H(ft)	κ (deg)	Component	H(ft)	κ (deg)
J_1	.0175	106.75	L_2	.0673	214.91
K_1	.2623	112.04	N_2	.5628	187.69
M_1	.0157	117.33	S_2	.3635	214.63
O_1	.2209	122.62	S_4	.0342	49.64
P_1	.0868	112.04	S_6	.0083	356.56
Q_1	.0429	127.91	P_2	.0029	214.63
ρ_1	.0084	127.17	T_2	.0214	214.63
M_2	2.4020	201.30	ν_2	.1092	189.51
M_4	.0106	23.13	2N	.0749	174.08
M_6	.0065	152.89	2Q	.0057	133.20
M_8	.0109	311.58	00	.0095	101.46
K_2	.0989	214.63	λ	.0168	207.49

Tidal Velocities

Prototype tidal velocities were measured for a 14-hr period on 1 May 1974 at the ranges illustrated in Figure 2. Depending on the channel width and depth, currents were measured every 30 minutes for 1 to 3 stations (marked by buoys) on each range at 1 to 3 water depths per station (surface, mid-depth, and bottom). Bottom and surface measurements were 3 ft above the bottom and 3 ft below the surface, respectively. Price current meters were used with a direct readout on boat for both speed and direction. A hand-operated winch was installed on the boat for raising and lowering the current meters. These velocity data are summarized in their entirety in Perry (1976).

Bathymetry

Bathymetric data required for model construction were obtained by the U. S. Army Engineer District, Charleston, and consisted of a survey of the offshore area at 500-ft intervals normal to the shore established baseline out to the 30-ft contour where the topography was taken directly

from existing C&GS survey charts. The channels also were surveyed. Aerial photography (color infrared and black and white) was obtained at low water (while the gages were installed) from which the preceding high water line could be clearly distinguished. Spot elevations in the tidal lagoon also were obtained after inspection of the aerial photography in order to insure a good tie in between the prototype survey with the aerial photography.

MODEL VERIFICATION

Upon completion of construction of the Murrells Inlet hydraulic model the ADACS described previously had just been installed and became operational for Wave Dynamics Division models of harbors and tidal inlets. Availability of this new capability for acquisition and analysis of large quantities of model data led to the plan to attempt verification of Murrells Inlet model by using the M_2 tidal constituent and proceeding to use a progressive tide.

Procedure

In the past, verification of tidal inlet and estuary models has consisted of first matching model and prototype tide curves (recorded on a strip chart) at key locations within the estuary and on the open coast. This matching process was either performed by visual means or by a least squares analysis of a discrete (but relatively small) number of points during a tidal cycle. Adjustments in model roughness are made primarily on the basis of the tidal amplitude comparison but also considering the phase if there is an obvious disparity between model and prototype curves. It is difficult to visually detect relatively small phase differences if the relative phase of the tidal constituents is not known for either the model or prototype curves. Subsequent to verification of the tidal elevations, a tidal velocity verification is conducted where additional model friction adjustments are made. In the past, prototype data usually consist of a tide curve for several days (almost never an analysis of the amplitude and phase of the tidal constituents and their harmonics) and 13 or 25 hrs of velocity data at several stations along pertinent ranges in the inlet and estuary.

Upon considering the capabilities of the newly operational ADACS and the availability of prototype data on the amplitude and phase of the tidal constituents, it became apparent that we had the opportunity to possibly improve our model verification procedure with no increase in model testing cost (and potentially a decrease in future model testing costs). Considering the previous verification procedure, it was hypothesized that the time usually spent in velocity verification was probably really performing model roughness adjustments in order to make the tidal phases (model to prototype) agree. The basis for this hypothesis was that it is difficult to detect up to a 30-minute variation in phase when model and prototype data only consist of strip chart information which must be digitized and compared. Furthermore, the usual prototype velocity data consist of discrete velocity measurements every 20 to 30 minutes. A 5 to 20 minute variation in phase can, in some instances, make a large difference in velocity fields, especially at some critical

locations near channel intersections and large flooding marshes. Therefore, it was concluded that any new verification procedure should focus on adjustments in model roughness to verify both tidal amplitudes and phases throughout the estuary as closely as possible.

The desired verification procedure can be summarized as follows:

- a. Adjust the tide generator to reproduce M_2 , M_4 , M_6 , and M_8 at the open-coast gage.
- b. Calculate the amplitude and phase of M_2 at each gage in the inlet and estuary and tabulate the phases relative to the open-coast gage and relative to adjacent gages in the estuary and compare these calculations with one another. Also calculate the mean tide level at all gages and compare with that for the prototype.
- c. Readjust model roughness (preferably between two gages only), conduct another test, and again calculate the amplitude and relative phases at all gages for the M_2 constituent.
- d. Repeat Step c until a satisfactory verification has been achieved.
- e. Construct a progressive tide and perform a velocity verification for that portion of the progressive tide for which prototype data are available. This should be near the middle of the model progressive tide.

It should be noted that the desired procedure described above was not precisely followed due to various reasons such as problems with the tide controller and time constraints on the project schedule. Actually the tide generator was adjusted to reproduce the M_2 component at the open-ocean gage; however, the energy in M_4 , M_6 , and M_8 was not reproduced for this gage. Consequently, the energy in the overtides is not precisely what it should be; however, it is the correct order of magnitude. This will be discussed later in the paper in connection with energy transfer to higher order harmonics. The remainder of the procedure described above was followed. For emphasis, the parameter used to estimate the distribution (horizontal) of roughness elements is the relative phase of the M_2 tidal constituent and the mean tide level at different locations along a tidal channel relative to some reference location in the channel.

Elevation of the prototype tide at a specific location can be represented by

$$h(t) = H_0 + \sum_{i=1}^N f_i H_i \cos [\alpha_i t + (V_0 + \mu)_i - \kappa_i]$$

The harmonic analysis performed by NOS provided H_0 , and H_i , and κ_i for each tide gage. Other coefficients f_i , α_i , $(V_0 + \mu)_i$ can be obtained from tables (Schureman, 1940). The above equation can be rewritten in the form

$$h(t) = H_0 + \sum_{i=1}^N A_i \cos(\omega_i t + \phi_i)$$

which is used for model control and analyses of the hydraulic model data. A harmonic function composed of M_2 , M_4 , M_6 , and M_8 was used as the initial command signal to the model tide generator, and tidal heights were recorded simultaneously at all model tide gages. The model tidal elevation can be represented as

$$h_M(t) = \hat{h}_M(t) + \varepsilon(t) \equiv a_0 + \sum_{i=1}^N [a_i \cos(\omega_i t) + b_i \sin(\omega_i t)] + \varepsilon(t)$$

where $\hat{h}_M(t)$ is the calculated tidal elevation represented by a harmonic series of known frequencies and $\varepsilon(t)$ is noise. Since the noise level is unknown, the method of least squares is used to solve for the unknown coefficients (amplitudes and phases) for the M_2 , M_4 , M_6 , and M_8 tidal constituents by minimizing the variance of the sum of the squared difference between the measured model tidal elevation and the assumed form for the model tidal elevation.

Therefore, the harmonic coefficients for the model tidal height at each tide gage can be used to calculate the phases of the tidal constituents at each gage relative to tidal Gage 8 on the open ocean and the differences in the model and prototype relative phases can be determined.

The above procedure should, in principle, lead to an excellent verification including that for tidal velocities. It was decided to attempt to verify the tidal amplitudes within ± 0.1 ft and the phase of M_2 within ± 1.0 degree.

It appeared that the primary problem which might not be solved by the M_2 verification procedure enumerated above would be the situation where a spring tide caused a considerable amount of flow to occur over relatively flat marsh areas which might have little or no flow over them for the M_2 constituent of smaller amplitude. If such were the case, there would have been a lack of adjustment of model roughness in these areas. A minor problem somewhat analogous also could occur for a neap tide if there were too much roughness in relatively shallow channels. However, for tidal regimes dominated by M_2 variance, this procedure with emphasis placed on mean tide level verification as well as the M_2 constituent throughout the inlet should minimize this problem.

Consequently, the velocity data, practically always taken during a spring tide (if only one set is acquired), should be used for this final verification using a progressive tide in the model and making velocity measurements at the stage corresponding to that for which prototype data are available. Since the progressive tide should run for 15 or 30 days, depending on the location, this test will be quite long in the model and should be performed after all other verification tests.

Verification for the M_2 Constituent

Since this was the first time such a verification procedure was

attempted, it required more tests than originally contemplated to verify the M₂ constituent. However, the total time for verification was normal or less than that for similar models using the usual procedure. A total of 73 test runs were made leading up to the verified condition. This number included all runs, some of which were made to determine optimum sump water level and to repair the model tide generator which malfunctioned twice during the process. When testing was ongoing, two tests were conducted per day. Total elapsed time from initiation to completion of verification was about 4 months. With hindsight, it appears that 6-8 weeks might be sufficient on a similar future model study.

Tables 2, 3, 4, and 5 show some results of the M₂ constituent verification procedure after Runs 1, 36, and 73. Run No. 1 represents the first test, No. 36 an intermediate test, and No. 73 the verified condition.

For Run No. 1, Table 2 shows all model tidal amplitudes are too high (most by 0.3 ft) and Table 3 indicates the tide reaches all estuary gages too fast (relative to Gage 8 the phase differences range from about 6 degrees to 18 degrees). Table 4 shows there is about the correct amount of roughness between Gage 4 and 7, there is too much roughness or something is restricting the flow too much between Gages 6 and 7, there is too little roughness elsewhere, and the most roughness should be added between Gages 1 and 2 (a little but not much is needed between Gages 2 and 3). Actually there was an error in molding the channel between Gages 6 and 7, which did not allow enough flow through the channel. Table 5 illustrates that the mean tide level is too high everywhere except at Gage 3. It is readily apparent that an enormous amount of information has been gained by merely looking at Tables 2 through 5 for Run No. 1.

Table 2: M₂ CONSTITUENT TIDAL AMPLITUDES (FT)

Station	Prototype	Run No. 1		Run No. 36		Run No. 73	
		Model	Difference	Model	Difference	Model	Difference
1	1.788	2.150	+0.362	1.804	+0.016	1.716	-0.072
2	1.834	2.140	+0.306	1.922	+0.088	1.789	-0.045
3	1.866	2.070	+0.204	1.916	+0.050	1.797	-0.069
4	1.919	2.260	+0.341	1.974	+0.055	1.878	-0.041
5	1.885	2.220	+0.335	1.957	+0.072	1.838	-0.047
6	1.936	2.270	+0.334	1.986	+0.050	1.872	-0.064
7	1.865	1.950	+0.085	1.885	+0.020	1.819	-0.066
8	2.402	2.430	+0.028	2.412	+0.010	2.396	-0.006

Table 3: M₂ CONSTITUENT PHASE DIFFERENCES (DEG*)

Station to Station	Prototype	Run No. 1		Run No. 36		Run No. 73	
		Model	Difference	Model	Difference	Model	Difference
8-1	48.23	30.50	-17.73	45.14	-3.09	49.24	+1.01
8-2	33.40	26.50	- 6.90	32.20	-1.20	34.20	+0.80
8-3	19.52	13.80	- 5.72	19.20	-0.32	20.20	+0.68
8-4	20.69	13.80	- 6.89	21.40	+0.71	20.30	-0.39
8-5	32.66	23.90	- 8.76	32.30	-0.36	33.10	+0.44
8-6	33.23	21.20	-12.03	32.00	-1.23	32.50	-0.73
8-7	47.09	41.00	- 6.09	44.46	-2.63	46.80	-0.29

* 1 Degree = 2.07 minutes of prototype time.

Table 4: M₂ CONSTITUENT PHASE DIFFERENCES (DEG*)

Station to Station	Prototype	Run No. 1		Run No. 36		Run No. 73	
		Model	Difference	Model	Difference	Model	Difference
2-1	14.83	4.60	-10.23	12.94	-1.89	15.04	+0.21
3-1	28.71	17.30	-11.41	25.94	-2.77	29.04	+0.33
3-2	13.88	12.70	- 1.18	13.00	-0.88	14.00	+0.12
4-5	11.98	10.10	- 1.88	10.90	-1.08	12.80	+0.82
4-6	12.54	7.40	- 5.14	10.60	-1.94	12.20	-0.34
4-7	26.38	27.20	+ 0.82	23.06	-3.32	26.50	+0.12
5-6	0.57	-2.70	- 3.27	-0.30	-0.87	-0.60	-1.17
6-7	13.84	19.70	+ 5.86	12.46	-1.38	14.30	+0.46

* 1 Degree = 2.07 minutes of prototype time

Table 5: M₂ CONSTITUENT MEAN TIDE LEVELS (FT ABOVE MLW)

Station	Prototype	Run No. 1		Run No. 36		Run No. 73	
		Model	Difference	Model	Difference	Model	Difference
1	2.668	2.833	+0.165	2.499	-0.169	2.734	+0.046
2	2.674	2.831	+0.157	2.427	-0.247	2.695	+0.020
3	2.696	2.632	-0.062	2.249	-0.447	2.546	-0.150
4	2.715	2.733	+0.018	2.380	-0.335	2.663	-0.052
5	2.696	2.794	+0.098	2.432	-0.273	2.682	-0.014
6	2.680	2.755	+0.075	2.387	-0.293	2.655	-0.025
7	2.676	3.012	+0.336	2.523	-0.153	2.762	+0.086
8	2.344	2.557	+0.213	2.128	-0.216	2.365	+0.021

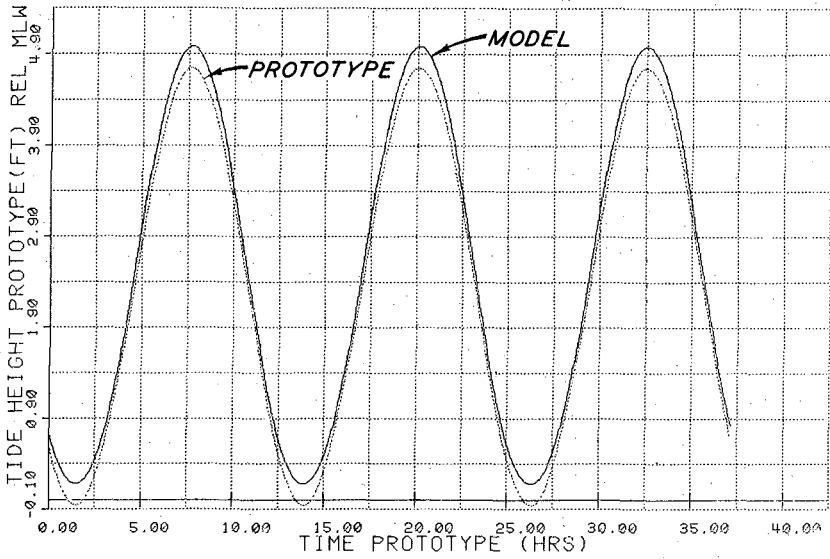
For Run No. 36, Table 2 shows that all tidal amplitudes are still too high but within 0.1 ft of the prototype, and Table 3 indicates the tide still reaches all gages except No. 4 too fast (relative to Gage 8), however, the largest phase difference has been reduced to 3 degrees. Table 5 shows more roughness is needed between all gages, but the most is needed between Gages 1 and 2 and 4 and 6. Table 5 illustrates that the mean tide level is too low at all model gages and by nearly 0.5 ft at Gage 4.

For Run No. 73, the verified condition, Table 2 shows that all model tidal amplitudes are less than the prototype but by only a few hundredths of a foot (the largest difference is 0.07 ft). Table 3 also indicates that about half of the phase differences are positive and half negative (relative to Gage 8) with the largest being 1 degree. Table 4 shows that the largest phase difference is 1.17 degrees and that is between Gages 7 and 8. Table 5 illustrates that the mean model tide level is larger than the prototype at about half the gages and smaller at the other half. The largest difference in the mean tide level is 0.086 ft. Figures 3 and 4 illustrate model and prototype tide curves for M₂ at Run No. 1 and Run No. 73 for Gage 8 and Gage 2, respectively.

To summarize the M₂ constituent verification, we have been successful in verifying the M₂ tidal amplitude to within +0.1 ft, the mean tide level

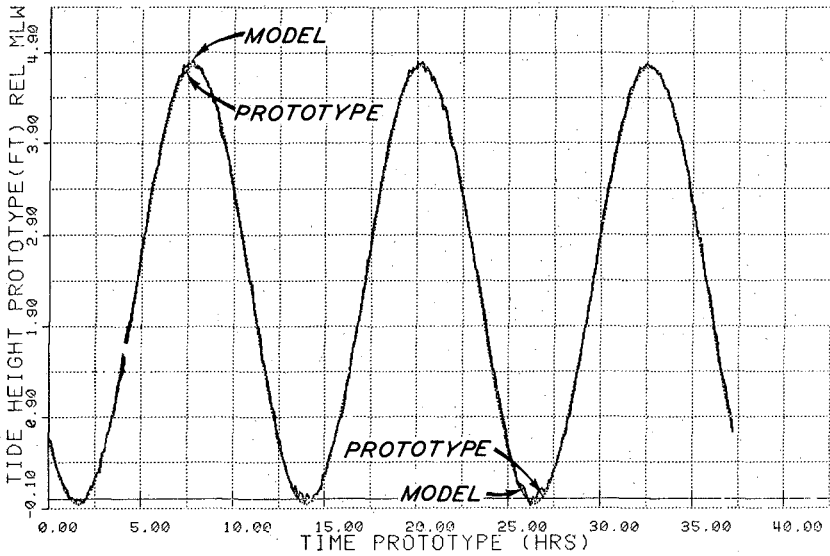
BEFORE VERIFICATION

MURRELLS INLET RUN NUMBER 1 GAGE NUMBER M-08



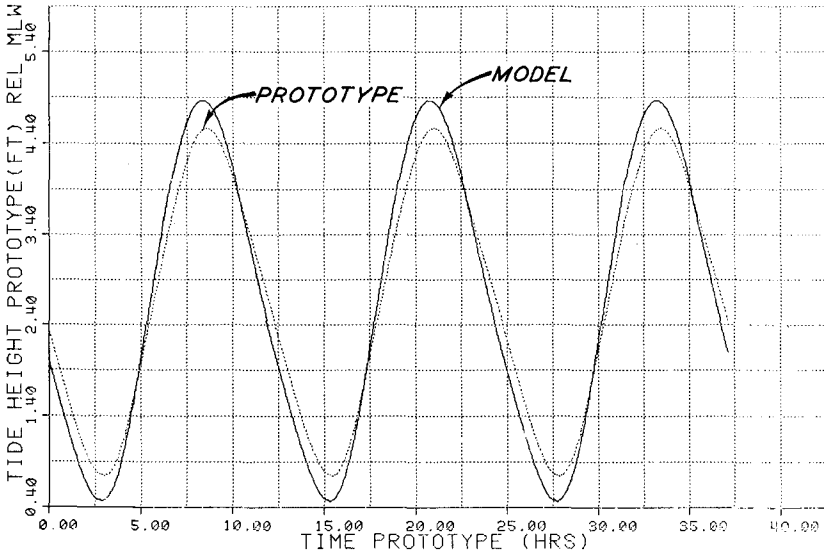
AFTER VERIFICATION

MURRELLS INLET RUN NUMBER 73 GAGE NUMBER M-08

Figure 3. M_2 Tidal Elevation Near Mouth of Murrells Inlet.

BEFORE VERIFICATION

MURRELLS INLET RUN NUMBER 1 GAGE NUMBER M-02



AFTER VERIFICATION

MURRELLS INLET RUN NUMBER 73 GAGE NUMBER M-02

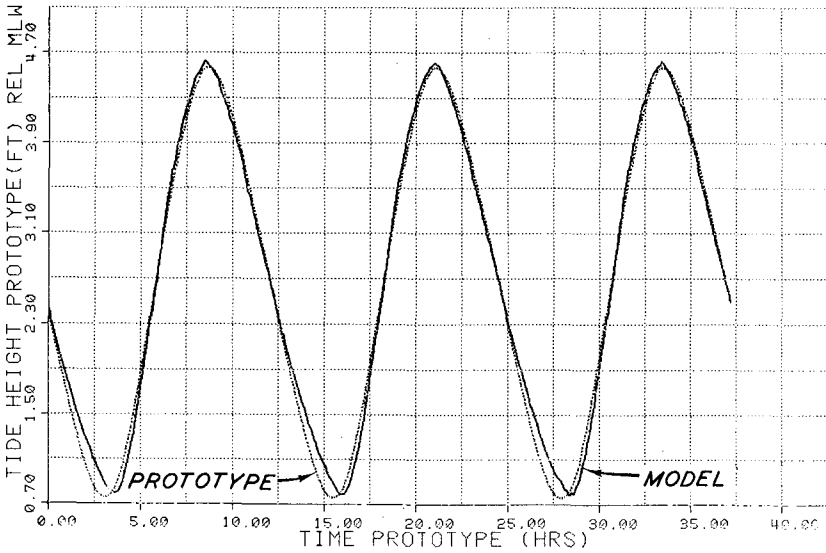


Figure 4. M_2 Tidal Elevation in Back Reach of Estuary.

to within ± 0.1 ft, and the phase of the M_2 constituent to within 1 degree relative to the phase at the open-ocean gage. This is considered to be an excellent M_2 constituent verification.

Verification for Progressive Tide

Due to the lack of prototype constituent velocity data, this portion of the verification was limited. A 15-day progressive tide consisting of the M_2 , S_2 , and their overtide constituents was generated in the model and velocities were measured at the 4 ranges for which prototype data were available. The velocity verification was considered adequate, and no adjustments in model roughness were made or additional verification tests conducted. Figure 5 illustrates a sample of the velocity verification.

DISCUSSION OF OTHER PERTINENT DATA

A brief discussion follows on the significance of other data acquired during the verification processes of the model study. Although these data have not been analyzed to glean their full potential some interesting and quite important information has been obtained.

Energy Transfer to Higher Order Harmonics

Table 6 shows a comparison of the model and prototype amplitudes for M_2 , and its overtides M_4 , M_6 , and M_8 . Gage 8 is the open-ocean gage and the model and prototype M_2 amplitudes are identical for all practical purposes. Unfortunately, sufficient time was not available to adjust the amplitudes of the overtides (M_4 , M_6 , and M_8) to coincide with the prototype data at Gage 8. However, the information contained in Table 6 is interesting and can be quite informative. The difference between amplitudes of the overtides in the estuary (Gages 1 to 7) and the open coast (Gage 8) represents a nonlinear transfer of energy from the principal lunar component M_2 to its harmonics M_4 , M_6 , and M_8 . Obviously this is occurring at a non-negligible rate in the prototype. It has often been questioned whether or not such nonlinear energy transfers occur in hydraulic models and to what degree. Unfortunately, this question cannot be answered completely from the data contained in Table 6 since the energy in M_4 , M_6 , and M_8 was not precisely adjusted at Gage 8. However, it is obvious that nonlinear energy transfer is occurring in the model and in more or less the correct proportion. Thus, the information in Table 6 is interpreted as preliminary confirmation that such nonlinear effects are occurring in approximate similitude (at least within the correct order of magnitude) in the hydraulic model. Several additional model tests should be conducted to confirm this indication and to unequivocally determine the relative degree of similitude of these nonlinear energy transfers.

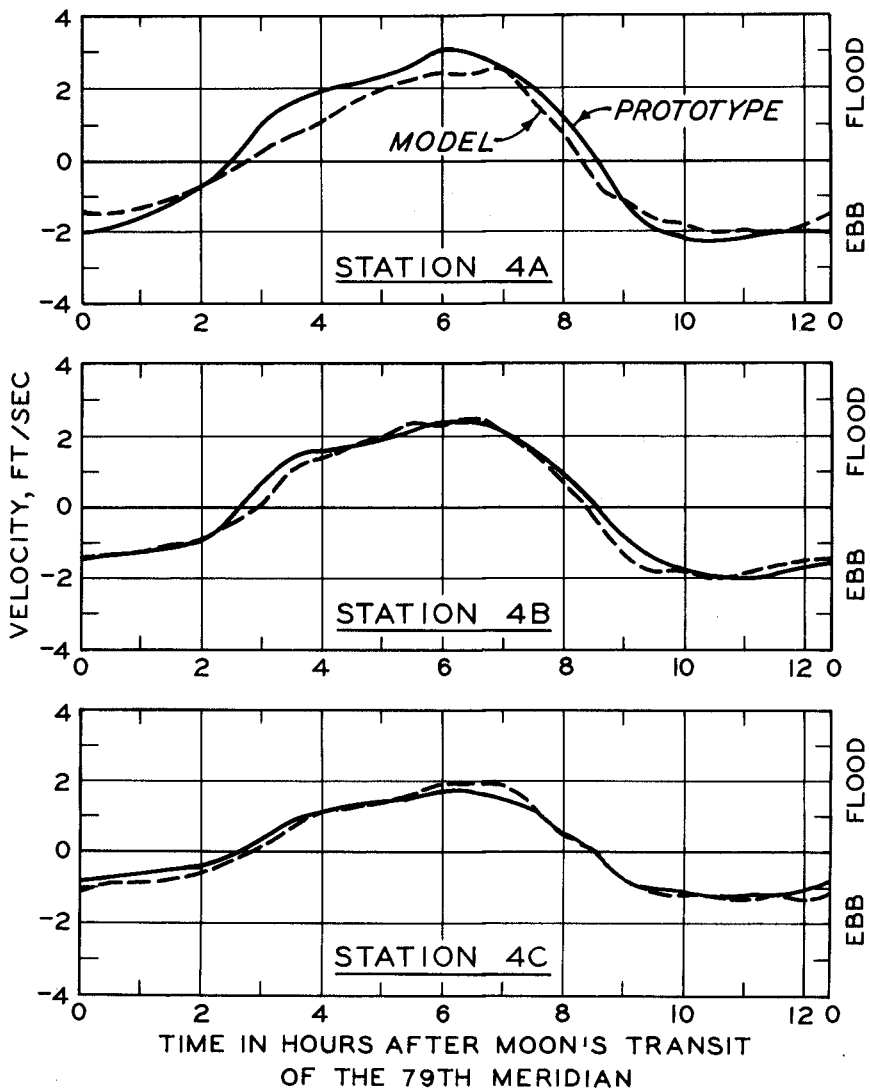


FIGURE 5. VERIFICATION OF MODEL VELOCITIES - MID-DEPTH

Table 6: ENERGY IN HIGHER ORDER HARMONICS (RUN NO. 73)

Gage	M_2 ft		M_4 ft (10^{-2})		M_6 ft (10^{-2})		M_8 ft (10^{-3})	
	Prototype	Model	Prototype	Model	Prototype	Model	Prototype	Model
1	1.7875	1.72	16.36	21.60	8.36	5.32	18.9	62.61
2	1.8344	1.79	15.43	20.77	4.74	4.00	15.9	33.96
3	1.8655	1.80	11.95	24.99	6.33	9.16	13.8	44.51
4	1.9192	1.88	16.75	33.23	4.10	6.91	12.2	26.61
5	1.8849	1.84	15.38	26.75	6.20	5.58	22.6	43.99
6	1.9363	1.87	10.49	23.63	8.74	5.00	31.7	33.15
7	1.8649	1.82	17.60	17.49	8.61	4.55	28.3	52.35
8	2.4020	2.40	1.06	3.54	0.65	1.02	10.9	5.93

Energy in Other Harmonics

A plot of the residual energy as a function of frequency was performed for each gage after each test in order to insure that a large residual energy was not present or that energy was not showing up in some characteristic frequency band which might be indicative of a malfunctioning tide control, sump, or pump, or perhaps an undesirable model resonance. No such problems were detected and the residual energy was always low.

NUMERICAL MODEL IMPLICATIONS

It is believed that results of this study have wide-ranging implications, in particular for numerical models. Recent advances (Butler and Raney, 1976) in numerical modeling of inlet-estuarine systems have finally made numerical modeling of well-mixed systems a viable engineering tool for the early stages of an inlet or estuarine improvement plan. While still having resolution disadvantages relative to a physical model, a numerical model may be a viable alternative in the planning stage to evaluate the relative adequacy of numerous plans while a physical model may and probably should be used as the principal tool for final design.

Since numerical models must be verified in much the same manner as physical models, it is hypothesized that the M_2 constituent verification is a superior method of numerical model verification. This brings many interesting numerical experiments immediately to mind. For instance, will the numerical model predict the nonlinear energy transfer to higher order harmonics as well as the physical model? Will the velocity verification, which is critical to numerical models, be essentially disposed of upon verification of both the amplitude and phase of the M_2 constituent?

It will be practically impossible to verify the numerical model (even the much faster implicit model of Butler and Raney, 1976) for a progressive tide due to computer time and cost limitations. However, the next generation of computers should solve this limitation. While advances in numerical modeling are taking place quite fast, more serious applications work is needed for them to realize their full potential and to complement physical hydraulic model studies to the fullest possible extent.

RECOMMENDATIONS FOR ADDITIONAL RESEARCH

Information emanating from the study reported herein has perhaps led to more questions than answers; however, it is believed a new set of questions have been raised and that our knowledge of model verification has advanced accordingly. As a result of the work performed, the following recommendations for additional research are made:

- a. Additional prototype velocity data should be collected at Murrells Inlet to define the velocity constituents. These data would form the basis for further physical model and numerical model verification experiments.
- b. Investigate the velocity constituent verification in the physical model of Murrells Inlet using both the M_2 tide and a progressive tide.
- c. Attempt to verify a numerical model for Murrells Inlet (Butler and Raney, 1976, appears to be the most applicable model) by use of the M_2 tidal constituent.
- d. Perform more physical model experiments specifically designed to investigate nonlinear phenomena occurring. In particular, adjust the model to open-coast gage and analyze the nonlinear energy transfer in model and prototype.
- e. Perform detailed numerical model experiments of the nonlinear phenomena present comparing these findings with both the physical model data and the prototype data.
- f. It may be possible to experimentally relate and quantify the number of roughness elements needed to relative phase lags.

CONCLUSIONS

The following conclusions are formulated as a result of this study:

- a. It is feasible to verify a physical hydraulic model by using tidal constituents.
- b. Verification by the M_2 constituent can be expected to be achieved within ± 0.1 ft in amplitude, within ± 0.1 ft in mean tide level, and ± 1 degree in phase.
- c. Verification by the M_2 constituent should be followed by verification for a spring tide to insure correct marsh and overbank roughness and a check for a neap tide condition would be wise. It is preferable to perform this verification with a progressive tide of at least 15 days duration which contains 1 spring and 1 neap tide.
- d. Prototype verification data collection should be designed to define the principal tidal constituents and their overtides for both the tidal elevation stations and the tidal velocity stations (i.e. a month of record is required as a minimum).

CHAPTER 195

Finite Element Model for Estuaries with Inter-Tidal Flats

Bruno Herrling*

Abstract

This paper deals with finite element formulations for the numerical computation of two-dimensional incompressible long-period shallow water waves. The described mathematical model is used to reproduce the dynamic situation occurring at the tidal propagation in estuaries. Areas which fall dry and wet again within a tidal cycle - so called inter-tidal flats - are taken into account.

Introduction

Since more than ten years the finite element method has been applied with considerable success in structural mechanics. In the last years the method was also used in fluid mechanics. Investigators like Grotkop [1], Connor, Wang [2], Davis, Taylor [3] and other made use of it to compute shallow water waves. But up to now inter-tidal flats - that are areas which fall dry and wet again within a tidal cycle - were not considered in these models. Only some investigators like for example Ramming [4] and Apelt, Gout, Szewczyk [5] took these areas into account using the finite difference method.

In the south eastern part of the North Sea in Europe many inter-tidal flats extend in front of the coast line. Without considering a natural phenomenon like that the hydrodynamic situation near these areas could be predicted only incompletely by a mathematical model. Therefore calculation algorithms for inter-tidal flat elements and for normal ones were developed, which are coupled in one mathematical model. The coupling is useful for saving computing time because only for elements of the first type much effort has to be made to include the permanent changing geometry of the area.

Basic Differential Equations

For the present problem two vertically averaged, horizontal velocities v_i ($i=0,1$) defined in a Cartesian coordinate system and the height of water level h (see Fig.1) are introduced as unknown parameters. The differential equations for this two-

* Dipl.-Ing., Scientific Assistant, Chair of Fluid Mechanics
Technical University Hannover, W.Germany

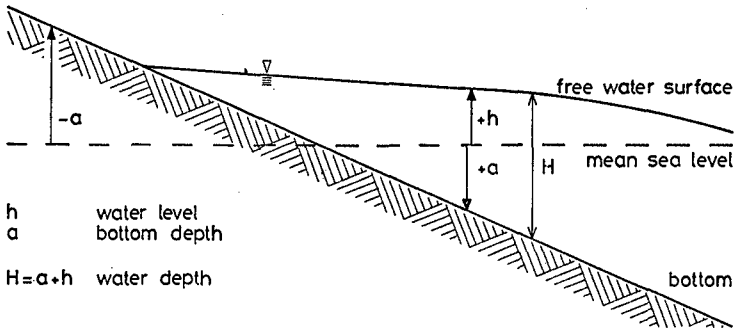


Fig.1 Definition Sketch Described in a Vertical Section

dimensional problem are obtained from the three-dimensional form of the continuity equation and the equations of motion by integrating over the depth (see e.g. Dronkers [6]). The vertically integrated equations received in this way are the continuity equation

$$h_{,t} + q_{i,i} - q^* = 0 \quad (1)$$

and the equations of motion (2)

$$v_{i,t} + v_j v_{i,j} + gh_{,i} + \frac{\lambda \sqrt{v_j v_j}}{a+h} v_i - \Omega \epsilon_{ij} v_j + \frac{1}{\rho} p_{0,i} - \frac{\mu_w \sqrt{W_j W_j}}{a+h} W_i = 0$$

with $i, j = 0, 1$ to be summed. In the continuity equation the flux per length q_i will be replaced by the relation

$$q_i = (a+h) v_i \quad (3)$$

later. q^* is the inflow in the area of computation and will be specified afterwards.

In the equations of motion there are special terms for bottom friction, Coriolis force, atmospheric pressure and wind force as usual - g signifies the acceleration due to the gravity, λ a dimensionless friction parameter, Ω the Coriolis parameter, which is a function of the latitude, ϵ_{ij} an alternating tensor, ρ the density of the water, p_0 the atmospheric pressure, μ_w a dimensionless wind friction parameter and W_i are components of the wind velocity.

In the equations (), $_{,i}$ and (), $_{,t}$ mean partial differentiations with respect to the coordinates x_i and to the time t .

Besides the friction term there are two further non-linear terms in the basic equations. For these the following linea-

rizations are realized:

$$q_i = (a + \bar{h}) v_i + (h - \bar{h}) \bar{v}_i \quad (4)$$

$$v_j v_{i,j} = \bar{v}_j v_{i,j} + v_j \bar{v}_{i,j} - \bar{v}_j \bar{v}_{i,j} \quad (5)$$

\bar{h} and \bar{v}_i are e.g. in time extrapolated values or values from the last step of iteration, when an iteration within each time step is used, or initial values of the time step when no better values are available.

Boundary conditions are the hydrographs of the water level or of the flux across the boundaries (see Fig.2):

$$h - \hat{h} = 0 \quad \text{on } S_h \quad (6)$$

$$q_i n_i + \hat{q} = 0 \quad \text{on } S_q \quad (7)$$

\hat{h} signifies a prescribed water level and \hat{q} a flux normal to the boundaries; \hat{q} is positive when the water flows in the area of computation. On closed boundaries \hat{q} is equal to zero.

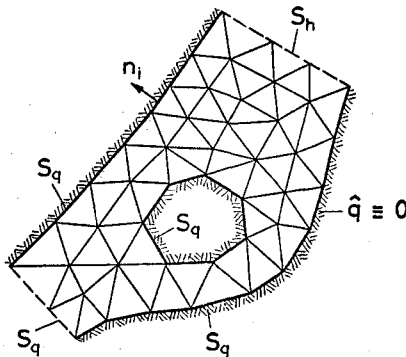


Fig.2 Designation of Boundaries

Finite Element Analysis

Because there exists no functional approach for the problem the method of weighted residuals is used and is the basic for

the application of the finite element method (see e.g. Zienkiewicz [7]). The domain of computation is subdivided into finite elements. For the integration of the weighted differential equations elements in space and time are chosen with linear shape functions θ_E and τ_T as described in Fig.3. In time the differential

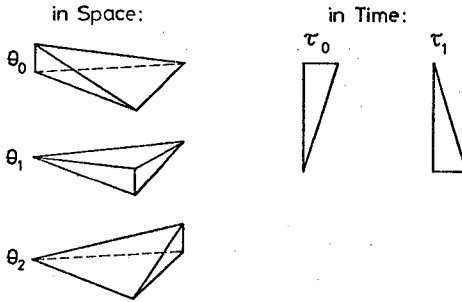
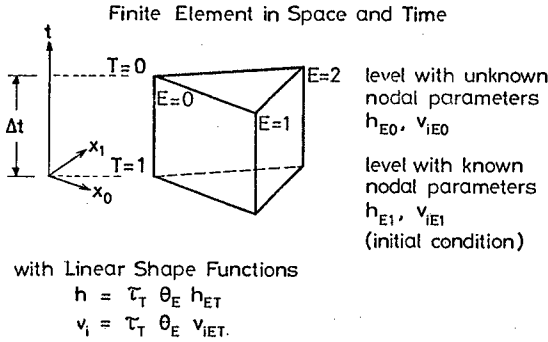


Fig.3 Discretization and Shape Functions

equations are solved in a stepwise manner as usual. The weighting functions

$$\delta h = \bar{\tau}_0 \theta_E \delta h_{E0}$$

and

$$\delta v_i = \bar{\tau}_0 \theta_E \delta v_{iE0}$$

are functions of space and time; δh_{E0} and δv_{iE0} are arbitrary values. In the present model the functions in space θ_E are identical with the shape functions (Galerkin method) though

in conformity with a new publication from Gärtner [8] better ones could be used. In time special weighting functions $\bar{\tau}_0$ (see Fig.4) are chosen to reduce the numerical damping. With

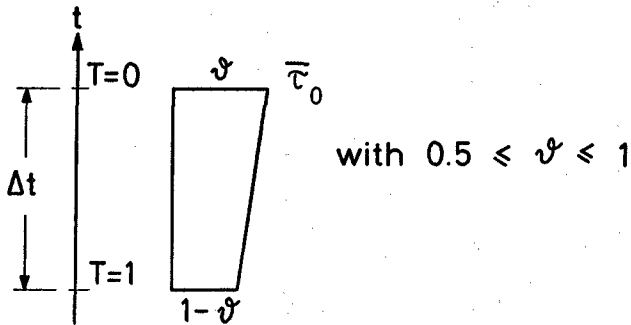


Fig.4 Weighting Function in Time

$\psi = 0.5$ the Crank-Nicolson time integrating factors are received and with $\psi = 1$ the method of Galerkin is again employed. The best value is near 0.5.

The continuity equation (1) is weighted with respect to δh

$$\iint_{At} \delta h (h_t + q_{i,i}) dt dA - \iint_{At} \delta h q dt dA - \int_t \delta h_K Q_K dt = 0 \quad (8)$$

Instead of q^* an areal distributed mass inflow q and a point source of mass inflow Q_K at node K of the system are introduced. After integrating by parts and insertion of the boundary conditions (7) on S_q equation (8) gets the form (9)

$$\iint_{At} \delta h h_t dt dA - \iint_{At} \delta h_{,i} q_i dt dA = \iint_{S_q t} \delta h \hat{q} dt ds + \iint_{At} \delta h q dt dA + \int_t \delta h_K Q_K dt$$

and finally after substitution of q_i and linearization according to (4)

$$\begin{aligned} \iint_{At} [\delta h h_t - \delta h_{,i} ([a+\bar{h}]v_i + [h-\bar{h}]\bar{v}_i)] dt dA = & \iint_{S_q t} \delta h \hat{q} dt ds + \iint_{At} \delta h q dt dA \\ & + \int_t \delta h_K Q_K dt \end{aligned} \quad (10)$$

The equations of motion (2) are weighted with respect to δv_i

$$\int_{\Delta t} \int_A \delta v_i [v_{i,t} + v_j v_{i,j} + gh_{,i} + \frac{\lambda \sqrt{v_j v_j}}{a+h} v_i - \Omega \epsilon_{ij} v_j + \frac{1}{\rho} p_{o,i} - \frac{\mu_w \sqrt{W_j W_j}}{a+h} W_i] dt dA = 0. \quad (11)$$

After the linearization (5) these equations receive the shape

$$\int_{\Delta t} \int_A \delta v_i [v_{i,t} + \bar{v}_j v_{i,j} + v_j \bar{v}_{i,j} - \bar{v}_j \bar{v}_{i,j} + gh_{,i} + \frac{\lambda \sqrt{\bar{v}_j \bar{v}_j}}{a+h} v_i - \Omega \epsilon_{ij} v_j + \frac{1}{\rho} p_{o,i} - \frac{\mu_w \sqrt{W_j W_j}}{a+h} W_i] dt dA = 0. \quad (12)$$

The integration of the weighted equations (10) and (12) is carried out in time t over a time interval Δt because of the stepwise solution algorithm and in space strictly speaking over the whole area A of the computation. As the finite element technique is used the integration in space can be reduced to an element area A_e . This leads to matrix equations of an element existing of nine equations with nine unknown parameters. As the integration have to be performed over the whole area A the matrix equations of all elements are added. So the big set of equations is received which have to be calculated in each time step.

The boundary condition (6) is inserted in the whole set of equations by erasing of lines and columns as usual in the finite element technique.

Area of Inter-Tidal Flats

Two basic problems appear when computing areas of inter-tidal flats in a mathematical model: First the difficulty to describe the physical situation near the changing water-land boundary (water boundary) and second the organizing problem when the boundaries of the mathematical model start to wander because some areas fall dry.

The author proposes the following procedure in principle for the solution of these problems:

- The discretization in space remains constant.
- Elements with at least one dry node in the end of a time step are approximately removed from the area of computation.
- In the partly flooded elements only the remaining volume of water is considered and is fixed as a function of the water level in the flooded nodes.

By these simplifications the dynamic is not exactly represented in the direct reach of the water boundary but the continuity is guaranteed. As this area is very small in comparison with the remaining model and the water depth mostly low the defect will be unimportant. On the other hand thus the whole organization of the program seems to be mastered in a

reasonable time.

To perform the proposed solution some postulated conditions have to be fulfilled:

- The boundaries of the flooded area are described by boundary integrals.
- In special nodes of the system an exactly defined mass inflow or outflow of water can be realized.
- An iteration is practicable within each time step to correct the actual boundary of computation and to improve the assumed volume of water in the partly flooded elements.
- A relaxation can be used to accelerate the iteration.
- For a better starting-point of the iteration the height of water level is extrapolated in the time direction with application of the least squares method.

In the following the procedure will be explained in detail. For the computation of a new time step there exist defined initial conditions of all parameters from the last time step. By an extrapolation in time with consideration of several known time levels the water level can be roughly predicted in all nodes.

Thus elements can be found which have three dry nodes at the end of a time step; these are dry elements (Fig.5). Further

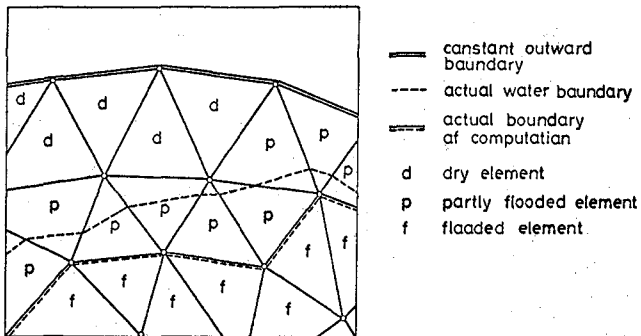


Fig.5 Various Boundaries in the Area of Inter-Tidal Flats

there are elements with one or two dry nodes, the so called partly flooded elements. All the other ones are flooded elements and these constitute the remaining mathematical model. The boundary between the flooded and the partly flooded elements - the actual boundary of computation - is described by boundary integrals. The actual water boundary is found by a horizontal extrapolation of the water level in adjacent flooded elements and is used to compute the remaining water volume (Fig.6). The difference of the water volume between

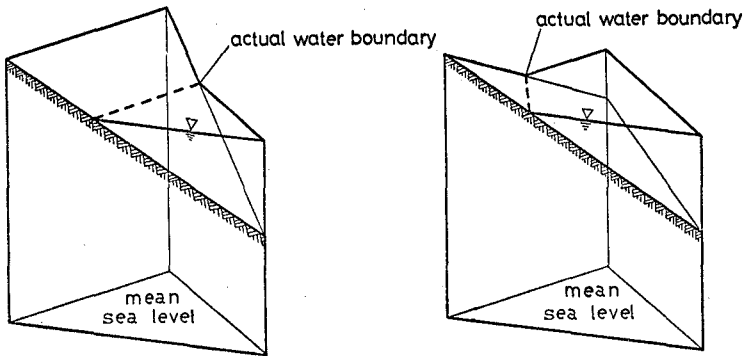


Fig.6 Partly Flooded Elements

the initial and the new state in the partly flooded and dry elements is given as a point source of mass inflow or outflow in or out of the remaining dynamic model in the same time step. By this the partly flooded elements effect the dynamic behaviour and correct the continuity in the flooded area. After computing the element matrices of the flooded elements and solving the set of equations the new water levels and velocities are received. These differ from the extrapolated values in general. By an iteration within the same time step the water levels are improved and by this the actual boundary of computation and the assumed volume of water in the partly flooded elements. The iteration is accelerated by a relaxation.

Numerical Computation

The program system MECCA (Modular Element Concept for Continuum Analysis) is used for the numerical computation. The modular constructed system (Fig.7) performs the always recurrent operations as being found in the finite element technique for boundary value problems or like in this case for initial and boundary value problems. MECCA manages organization problems such as input and output, data storage on disk packs, assembling and solving the set of equations and a graphic representation of the results. The input and partly the control over the sequence of program modules is managed by a problem oriented language (Fig.8). A special data organization (Fig.9) is prepared for the storage of the big and complex data sets.

The differential equations describing a physical process and the characteristics of an element are specified in a separate element program (Fig.7,8) which is linked to special modules

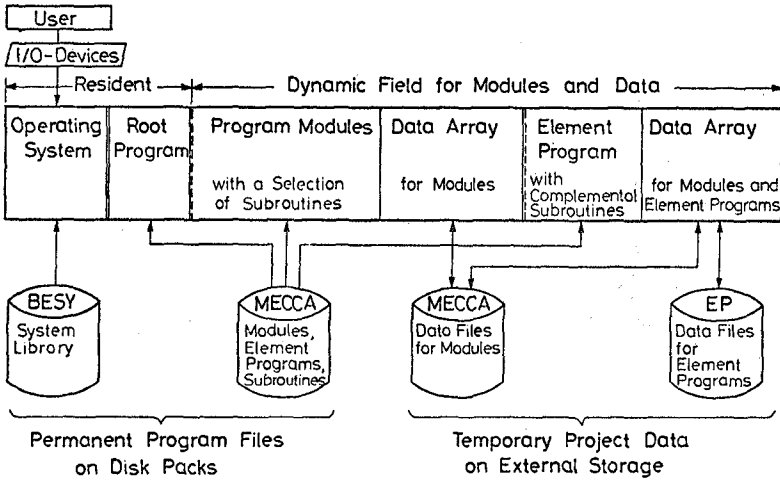


Fig.7 Allocation of the Computer by the Program System MECCA

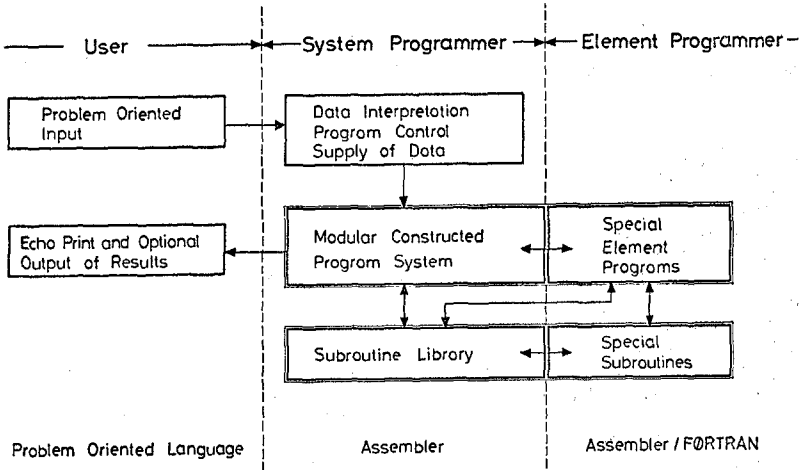


Fig.8 Schematic Organization of the Program System MECCA

of MECCA. Thus the possibility exists to couple different types of elements - in this case inter-tidal flat elements and normal ones - using common parameters in the connection nodes.

A first publication of MECCA happened by Beyer [9] and Herrling, Pfeiffer [10].

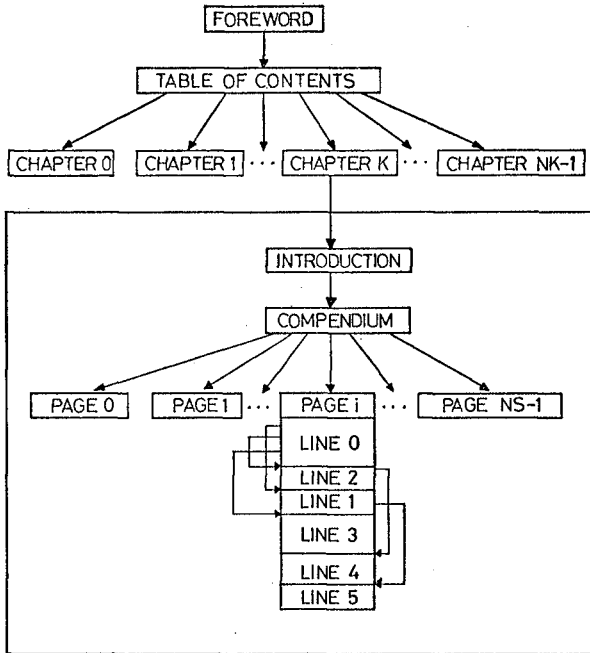


Fig.9 Set-up of a Data File

Numerical Results

The usefulness of the presented method is demonstrated by two examples: First a test of continuity is carried out in a basin falling dry partly, and in a second test the program is employed to the tide situation in the exterior Jade.

For the test of continuity a sloping basin has been chosen with a finite element network and a distribution of depth as shown in Fig.10. Three boundaries of the basin are closed and the other one is open. On this boundary the time dependent flux \hat{q} is described (see Fig.11). The discharge is so propor-

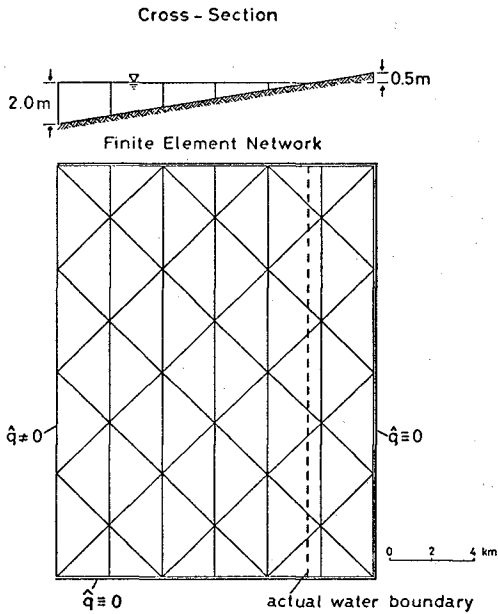


Fig.10 FE Network and Distribution of Depth

tioned that the water volume goes down for 1m in the whole basin.

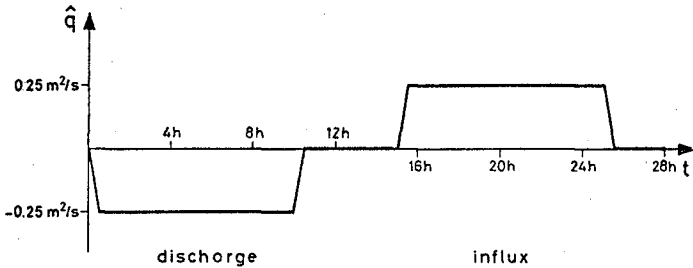


Fig.11 Prescribed Flux across the Boundary

In Fig.12 to 15 the numerical results are shown at different times. The time step Δt amounts to 30 minutes and 0.003 is the value of the friction coefficient.

ESTUARY MODEL

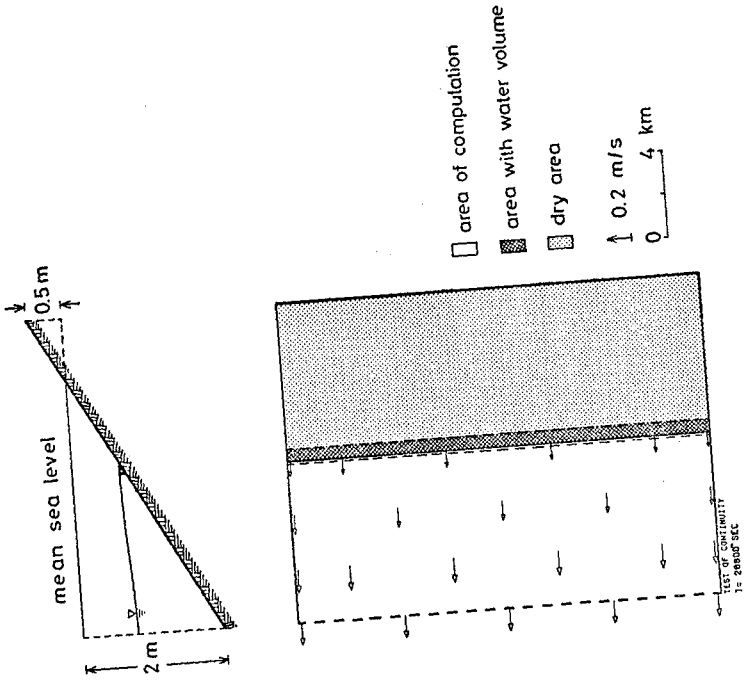


Fig. 12 State at 4 Hours

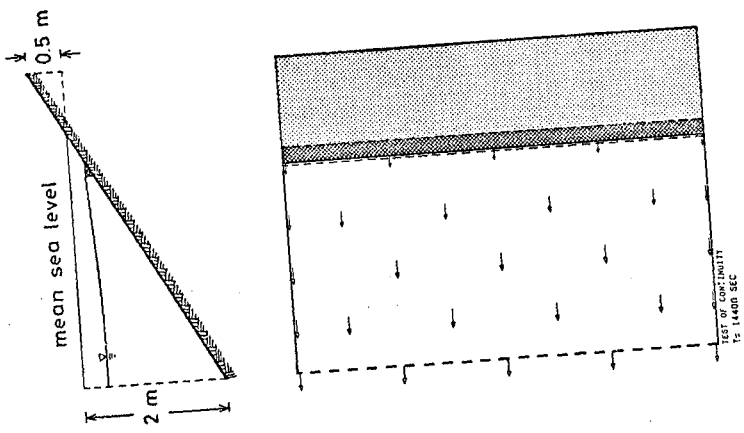


Fig. 13 State at 8 Hours

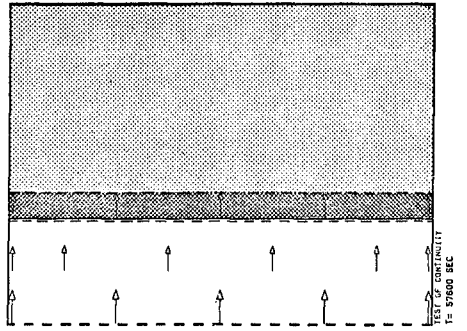
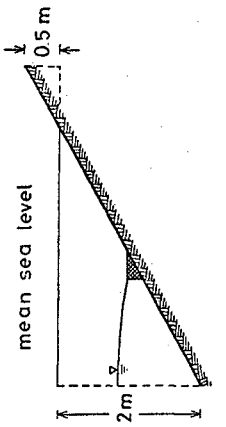
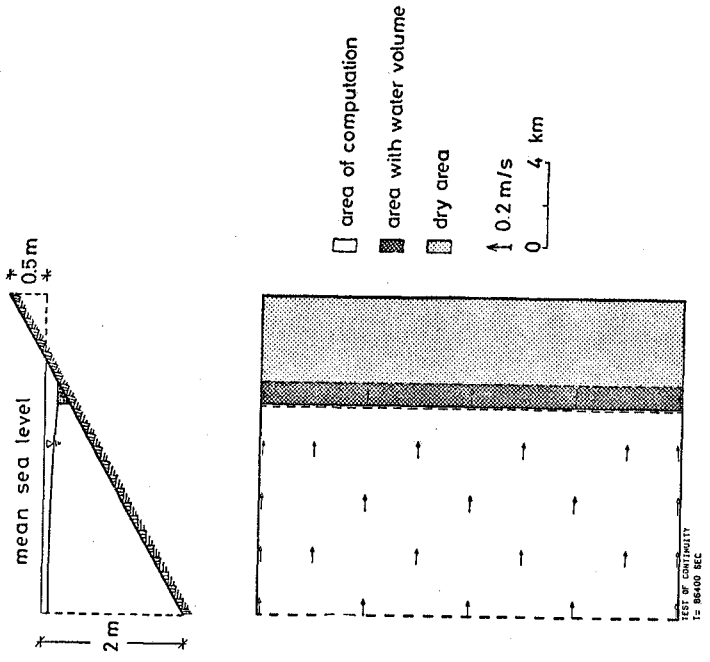


Fig.14 State at 16 Hours



area of computation
area with water volume
dry area
↑ 0.2 m/s
0 4 km

Fig.15 State at 24 Hours

As a second example the time dependent distribution of water levels and velocities in the exterior Jade (Fig.16) has been computed. The Jade is a German estuary in the south eastern part of the North Sea.

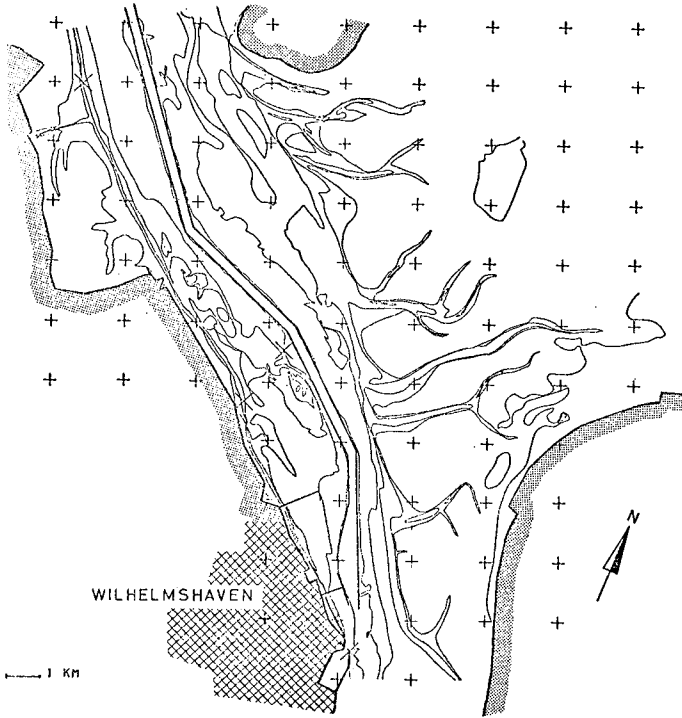


Fig.16 Topology of the Exterior Jade

Fig.17 shows the very coarse network of elements and Fig.18 the distribution of depth in the model. In this mathematical model two different types of elements are used (Fig.19). Boundary conditions are prescribed water levels at the open ends of the model (Fig.20). The friction coefficient has the value 0.003 and the time step amounts to 10 minutes. Fig.21 and 22 demonstrate the distribution of velocities and the areas of dry and partly flooded elements.

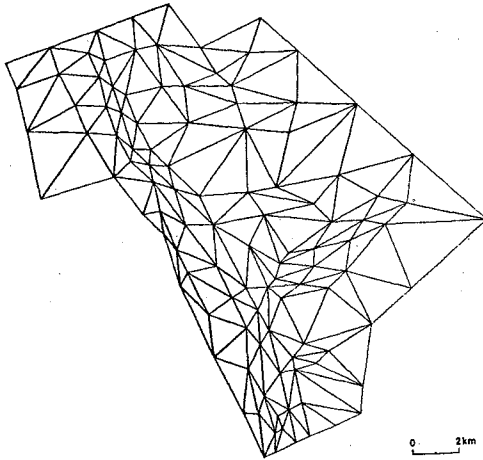


Fig.17 Network of Elements

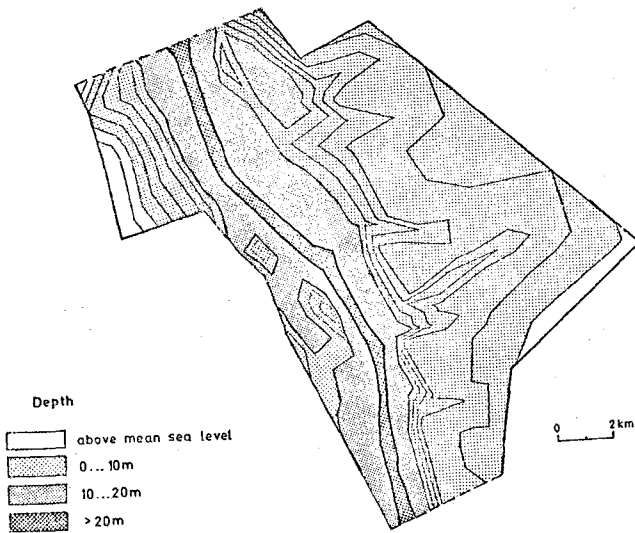


Fig.18 Distribution of Depth in the Model

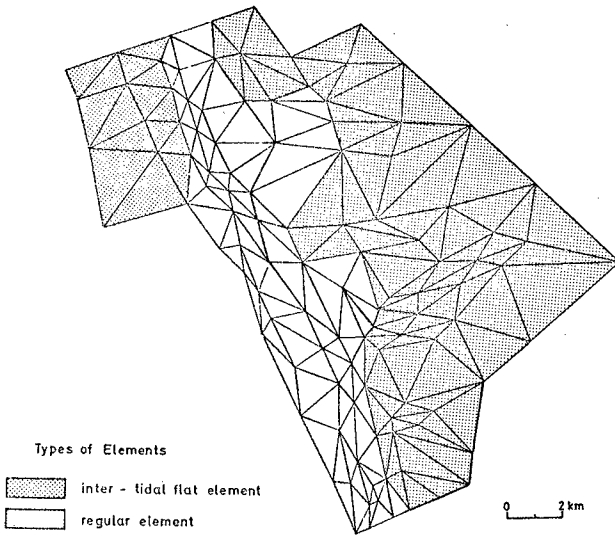


Fig.19 Used Types of Elements

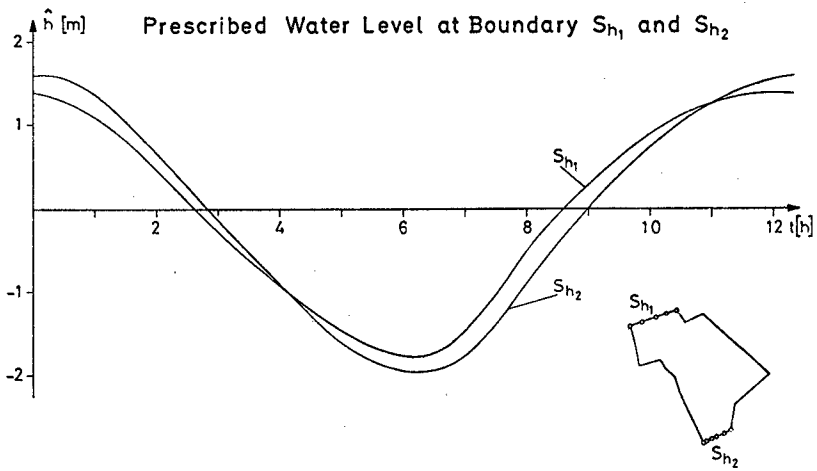


Fig.20 Boundary Conditions

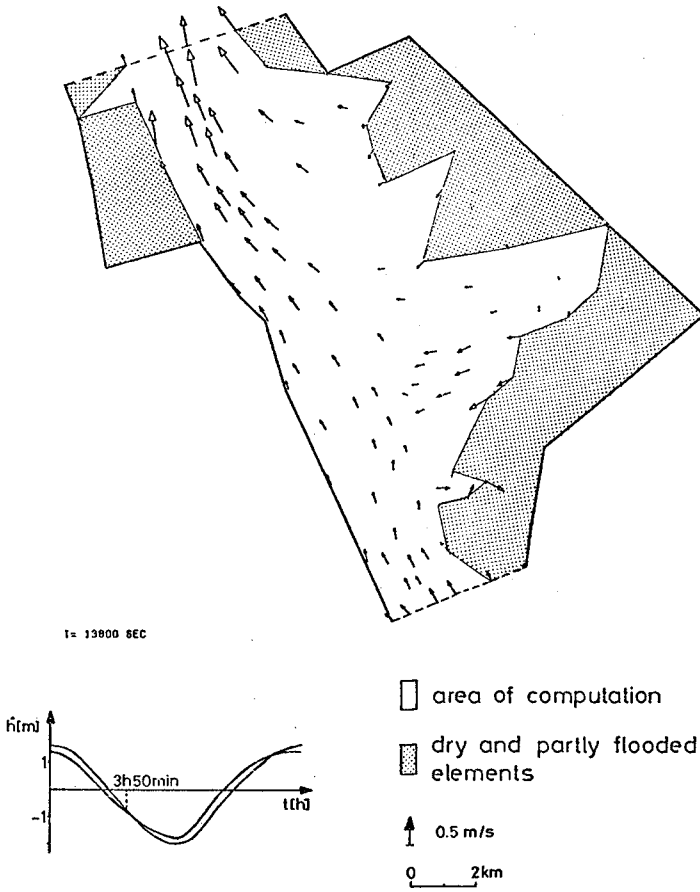


Fig.21 State at 3 h 50 min

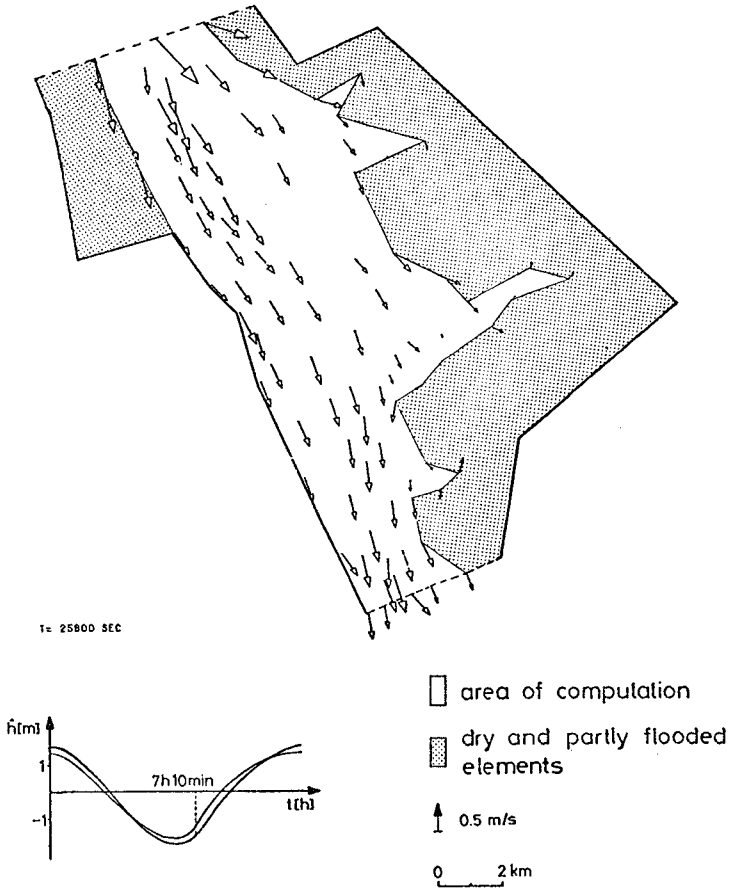


Fig.22 State at 7 h 10 min

Conclusion

The numerical results have shown that the new method is qualified to analyze the dynamic of estuaries with inter-tidal flats. In the mathematical model the dynamic behaviour is correct and the continuity of the water masses is guaranteed. The author hopes that he has provided a further contribution for a wide future application of the in hydrodynamics more and more advanced method of finite elements by the new opportunity to consider areas of inter-tidal flats in a mathematical model.

Acknowledgement

This investigation was supported by the Sonderforschungsbereich 79 (SFB 79) 'Wasserforschung im Küstenbereich' in Hannover, W.Germany. Moreover the author wants to thank Mr. J. Claussen for his support to realize the program [11] and to compute the numerical results and Dipl.-Ing. H. Hennlich for preparing the element network of the exterior Jade.

References

- [1] Grotkop, G., "Finite Element Analysis of Long-Period Water Waves", Computer Methods in Applied Mechanics and Engineering, Vol.2, No.2, May, 1973
- [2] Connor, J.J., Wang, J., "Finite Element Modelling of Hydrodynamic Circulation", Numerical Methods in Fluid Dynamics, ed.by Brebbia, C.A., Connor, J.J., Pentech Press, London, 1974
- [3] Taylor, C., Davis, J., " A Finite Element Model of Tides in Estuaries", Finite Element Methods in Flow Problems, ed.by Oden, J.T., Zienkiewicz, O.C., Gallagher, R.H., Taylor, C., UAH Press, Huntsville, Alabama, 1974
- [4] Ramming, H.-G., "Reproduction of Physical Processes in Coastal Areas", proceedings of the 13th Coastal Engineering Conference, Vancouver, Canada, 1972
- [5] Apelt, C.J., Gout, J.J., Szewczyk, A.A., "Numerical Modelling of Pollutant Transport and Dispersion in Bays and Estuaries", Numerical Methods in Fluid Dynamics, ed.by Brebbia, C.A., Connor, J.J., Pentech Press, London, 1974
- [6] Dronkers, J.J., "Tidal Computations in Rivers and Coastal Waters". North-Holland Publishing Company, Amsterdam, 1964

- [7] Zienkiewicz, O.C., "The Finite Element Method in Engineering Science", McGraw-Hill, London, 1971
- [8] Gärtner, S., "Trägermethode (engl. support method) - Ein Defektabgleich zur Berechnung von Transportprozessen und Flachwasserwellen mit der Methode der Finiten Elemente", Doctor Thesis, T.U. Hannover, 1976
- [9] Beyer, A., "Die mathematische Formulierung eines Programmsystems für die FEM", paper on the "VII. International Congress on the Application of Mathematics in Engineering (IKM)" in Weimar, DDR, 1975
- [10] Herrling, B., Pfeiffer, E., "Das Programmsystem MECCA, ein modulares Elementkonzept für die Kontinuumsanalyse", paper on the "VII. International Congress on the Application of Mathematics in Engineering (IKM)" in Weimar, DDR, 1975
- [11] Claussen, J., "Zur Berechnung von zweidimensionalen Flachwasserwellen unter Berücksichtigung von Wattflächen", Diplomarbeit, T.U. Hannover, 1976

CHAPTER 196

Calibration of Branched Estuary Models

by

James P. Bennett¹

INTRODUCTION

Unsteady flow models of one-dimensional channels or of channel networks are commonly calibrated using a combination of stage (water surface elevation) and discharge observations. In tidally influenced areas these observations may extend in time over several tidal cycles. Where there is an important mean flow discharge such as in a river harbor, observations must be repeated for a number of representative mean flow conditions.

Stage observations are commonly collected using recorders coupled to water surface floats mounted at various points on the channel banks. The initial costs of purchasing the recorders, installing them, and in the leveling necessary to determine datum are the primary expenses involved in collecting stage observations. For these observations the cost per observation decreases as the number increases.

In tidally influenced channels, accurate one-dimensional instantaneous discharge measurements are difficult if not impossible to obtain because of the rapidly changing flow velocity. In many locations, discharge measurements cannot be made throughout a tidal cycle because of safety restrictions. Finally, with respect to stage information, the cost of collecting discharge information can be extremely high. In addition, the cost per observation does not decrease with the number of observations.

With respect to the boundary conditions used to drive them, there are two main classes of unsteady flow models, the stage-stage models and the discharge-stage models. The former are driven by inputs of stage at all important external boundary points. The primary purpose of the stage-stage model is to determine the time history, or an average value of downstream discharge. Discharge-stage models are driven upstream by steady or time-variable observed or hypothetical discharges and downstream by observed or hypothetical stages. This type of model is used primarily in conjunction with solute transport models in predicting the location and concentration of dissolved substances, as in dissolved oxygen modeling.

¹U.S. Geological Survey, Reston, Va.

In light of the difficulty, danger, and relative expense of collecting discharge measurements, as compared to stage observations the question arises how best to locate in space and time the minimum number of discharge measurements required to calibrate an unsteady flow model. In fact, it should be asked if situations arise wherein unsteady flow models can be adequately calibrated without any discharge measurements. This paper is presented to discuss these questions. Illustrations are presented using field data collected to calibrate both stage-stage and discharge-stage flow models.

THEORY

Unsteady Flow Computation

The conservation of mass equation for a segment of one-dimensional open channel with no distributed inflow is

$$\frac{\partial A}{\partial t} + U \frac{\partial A}{\partial x} + A \frac{\partial U}{\partial x} = 0 \quad (1)$$

Wherein the independent variables are x downstream distance and t , time. The dependent variables are cross-sectional area, A , and downstream velocity U . The conservation of momentum equation is

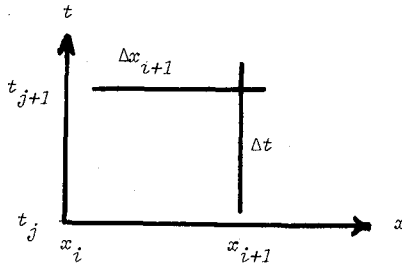
$$\frac{\partial U}{\partial t} + U \frac{\partial U}{\partial x} + g \left(\frac{\partial H}{\partial x} + S_f \right) = 0 \quad (2)$$

Wherein g is the gravitational constant, S_f is the friction slope and H is the stage. Cross-sectional area is expressed as a function of H and x . In (2) friction slope is expressed using Chezy's formulation

$$S_f = \frac{U^2}{C^2 D} \quad (3)$$

Wherein C is Chezy's discharge coefficient, the hydraulic depth, D , is A/T and T is the channel top width corresponding to a particular water surface elevation.

One of the most efficient schemes for solving the nonlinear hyperbolic partial differential equations 1 and 2 is Strelkoff's (1970) linear implicit technique presented here as modified by Bennett (1975). In this formulation, the following space-time convention is used,



and (1) becomes

$$\begin{aligned} & \frac{1}{2\Delta t} \left[T_{i+1}^j (H_{i+1}^{j+1} - H_{i+1}^j) + T_i^j (H_i^{j+1} - H_i^j) \right] \\ & + \frac{(U_{i+1}^j + U_i^j)}{2\Delta x_{i+1}} \left[(A_{i+1}^j - A_i^j) + T_{i+1}^j (H_i^{j+1} - H_i^{j+1}) - T_i^j (H_i^{j+1} - H_i^j) \right] \\ & + \frac{(A_{i+1}^j + A_i^j)}{2\Delta x_{i+1}} \left[U_{i+1}^{j+1} - U_i^{j+1} \right] = 0 \end{aligned} \quad (4)$$

while (2) becomes

$$\begin{aligned} & \frac{1}{2\Delta t} (U_{i+1}^{j+1} - U_{i+1}^j + U_i^{j+1} - U_i^j) + \frac{(U_{i+1}^j + U_i^j)}{2\Delta x_{i+1}} (U_{i+1}^{j+1} - U_i^{j+1}) + \\ & g \left[\frac{(H_{i+1}^{j+1} - H_i^{j+1})}{x_{i+1}} + \frac{1}{2} \left((S_f^j)_{i+1}^j + (S_f^j)_i^j + \left(\frac{\partial S_f}{\partial U} \right)_{i+1}^j (U_{i+1}^{j+1} - U_{i+1}^j) \right. \right. \\ & \left. \left. + \left(\frac{\partial S_f}{\partial U} \right)_i^j (U_i^{j+1} - U_i^j) + \left(\frac{\partial S_f}{\partial y} \right)_{i+1}^j (y_{i+1}^{j+1} - y_{i+1}^j) + \left(\frac{\partial S_f}{\partial y} \right)_i^j (y_i^{j+1} - y_i^j) \right) \right] = 0 \end{aligned} \quad (5)$$

Bennett (1975) lists the advantages and disadvantages of the linear implicit formulation in solving the single reach unsteady flow problem. He also describes a general model which allows the efficient extension of the linear implicit technique to the computation of unsteady flows in networks of open channels. This model uses a coding system referenced to the end cross-sections of channel segments intersecting at interior junctions to inform the solution algorithm to apply interior boundary conditions and thus carry the implicit formulation from one channel segment to another. Specific techniques are introduced to reduce the core storage required and to expedite the inversion of the resulting sparse, wide-banded coefficient matrix. The calculations described in the remainder of this paper were made using the general model.

Calibration

Calibration of a mathematical model is the process of adjusting model parameters to obtain best-fit of model predictions to a set or sets of observations. The best-fit criterion is the objective function, a single unique function of differences between observations and the corresponding predictions. "Best-fit" is achieved when the objective function is minimized. The parameter values producing this minimum comprise the optimum parameter set.

A number of automatic optimization routines have been used to derive optimum parameters for unsteady flow models. Becker and Yeh (1972) and (1973) use the influence coefficient algorithm. A modification of their scheme was used by Bennett (1975) and is incorporated into the general model discussed above. Yih and Davidson (1975) found the Marquardt algorithm to be the most efficient in obtaining longitudinal dispersion coefficients. The main disadvantage in the use of these routines is the large number of complete simulation runs that must be made before the optimum is reached. In unsteady flow simulation this can become quite expensive.

The most commonly used objective function is the mean square error, the average of the squares of difference between observations and predictions. The square root of the mean square error, the RMS (Root Mean Square Error) is used in this paper. It has the advantage of being expressed in the same units as the original predictions and observations, and is, therefore, more easily comparable to the values of the individual variables themselves. When the observation consists of two or more noncommensurable quantities such as a stage and discharge it becomes difficult to define the objective function to give the correct weight to each type of observation. In this case some normalizing function should be used to commensurate the contributions of the two types of observations to the objective function. The definitions of the normalizing functions of course, influence the final result of the calibration; they, therefore, must be defined with great care. Becker and Yeh (1972) use velocity and depth errors directly in their objective function. For the shallow flows that they worked with this places about equal weight on both types of observations, however, for deeper flows it would emphasize the depth. Bennett (1975) used the average value of depth to normalize errors in stage and the average absolute value of discharge to normalize errors in discharge. This scheme probably places too much weight on discharge.

In this paper we want to investigate the possibility of calibrating the two basic types of unsteady flow models using stage data alone. We will therefore work primarily with the RMS of stage errors. However, we will continuously monitor the RMS of discharge deviations to determine the effectiveness of our techniques.

THE STAGE-STAGE PROBLEM

Three Mile Slough

The data chosen to illustrate the stage-stage problem was collected jointly by the U.S. Geological Survey and the California Department of Water Resources in July and August, 1959. As shown in Figure 1 Three Mile Slough is the first connecting channel upstream of the confluence of the Sacramento and the San Joaquin Rivers. It is a natural channel which has been stabilized and diked.

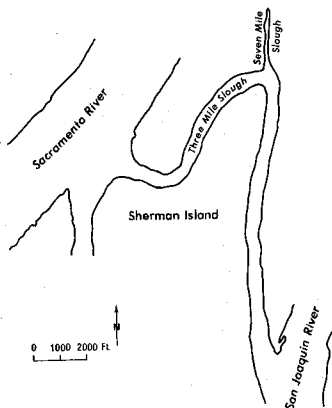


Figure 1. Three Mile Slough, a stage-stage problem.

At the two ends of the Slough the water surfaces in the rivers oscillate independently because of different travel times for tidal transients moving up the rivers from San Francisco Bay. Because of the independence of the water surface elevations at the two ends of the channel and because it is a relatively small channel connecting the two larger bodies of water, Three Mile Slough provides a classical example of the stage-stage problem.

There are seventeen sets of cross section descriptions available over the 3.2 mile length of the Slough, nine were used in the mathematical model. The side channel is a 2,300 foot segment of Seven Mile Slough presently closed off at the end away from Three Mile Slough. The only cross sectional properties available for Seven Mile Slough are average width and depth. These were used in the mathematical model. Little attention was paid to Seven Mile Slough during data collection because it was observed that this channel had little influence on the discharge picture in Three Mile Slough. Simulation results confirm this observation.

The tidal oscillations in the Sacramento and San Joaquin Rivers at the ends of Three Mile Slough were recorded digitally from direct reading floats at 15-minute intervals. The discharge observations used were obtained by summing the instantaneous contributions of individual discharge hydrographs for each of about twenty subsections at each end of the Slough. The individual hydrographs were prepared from standard discharge measurements made from boats. Each subsection was gaged about every 45 minutes.

Numerical Experiments

The investigation of the stage-stage problem, essentially a sensitivity analysis, was conducted as follows: (1) Fourier series were fit to the driving stages at the Sacramento (arbitrarily chosen as the upstream end of the Slough) and at the San Joaquin for a tidal day of twenty five hours. This was done, first, because it expedited interpolation between the observed stages, as stability conditions required a computation time interval on the order of six minutes rather than the fifteen minutes used in recording the data. Second, the analytical expressions for the driving stages allowed them to be shifted in time by any arbitrary increment, permitting the investigation of the influence of phase errors. The Fourier series stages were seldom as much as two-hundredths of a foot different than the original observations.

The mathematical model driven by the Fourier series stages was calibrated against upstream and downstream observed discharge by adjusting Chezy's C. The absence of intermediate discharge observations precluded the use of different C values for the three channel segments comprising the mathematical model. The optimum parameter value is $C = 75 \text{ ft}^{3/2}/\text{sec}$. and the corresponding value of the normalized RMS discharge error is .123 (12 percent).

For use as observations in the sensitivity analysis the calibrated model was used to compute stages at river miles .66, 1.26 (the intersections of Three Mile and Seven Mile Sloughs) and 2.44 measured upstream to downstream. This error-free numerically generated set of stage observations was used to perform the sensitivity analysis of a typical stage-stage unsteady flow model subjected to perturbations of its parameters and boundary conditions. Note that because of rounding the hypothetical observations to the nearest 0.01 ft, the normalized stage RMS errors for the error free data set is .00015 (0.015 percent). Again, because actual observations of discharge, were used, this corresponds to a normalized error of 0.123 in this variable.

The Discharge Coefficient

The effect of varying the Chezy discharge coefficient C on normalized RMS stage error and normalized RMS discharge error is shown in figure 2. For the stage error, the largest quantity given on figure 2 represents an RMS error of only 0.01 ft (to the nearest hundredth) at each of the three observation stations. The stage errors are systematic, that is the water surface elevation for C values not equal to $75 \text{ ft}^{3/2}/\text{sec}$. are always slightly lower than for this value. Figure 3 shows for the extreme cases of $C = 60 \text{ ft}^{3/2}/\text{sec}$. and $C = 90 \text{ ft}^{3/2}/\text{sec}$, the influence of the variations on the discharge at the Sacramento River end of the slough. When C is greater than $75 \text{ ft}^{3/2}/\text{sec}$. the amplitude of the discharge fluctuation is noticeably larger than for this value, while for a lesser, the amplitude is less. A similar pattern is observed at the San Joaquin end.

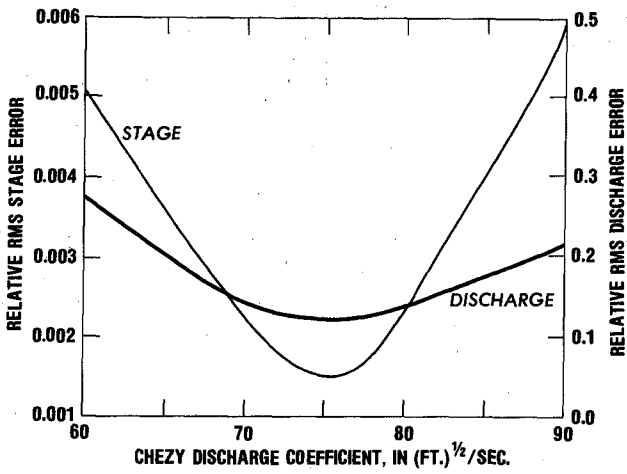


Figure 2. Effect of variation of Chezy C on normalized stage and discharge errors.

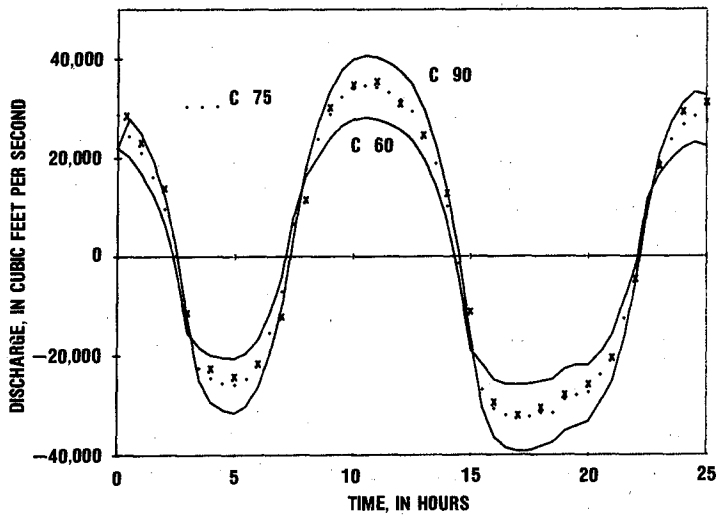


Figure 3. Observed and predicted discharge hydrographs for extreme values of Chezy C.

Using the error free stage observation set in performing the present sensitivity analysis has provided the answer to one of the questions posed earlier; namely, is it possible to calibrate a stage-stage model using stage observations alone. The answer is no, because while for the nonoptimum C values the deviation of stage from that observed for $C = 75 \text{ ft}^2/\text{sec}$ is systematic, it is too small to be observed in a real stage record collected in the field.

Figure 3 makes it possible to answer another of the questions posed in the introduction namely, where best in space and time to place discharge measurements to make the best use of them. In calibrating a stage-stage model the best positions in time are at the two extremes of positive and negative discharge to define the amplitude of the discharge fluctuation. At least two positive and two negative peaks should be observed for each mean flow condition of interest. At least in a reach as short as Three Mile Slough, the spacial location of the discharge measurements is unimportant and measurements at one cross section should be sufficient.

At this point the main questions posed concerning the calibration of a stage-stage model using a bias-free data set have been answered. The remaining topics in this section concern the influences of errors in the calibration data on the final product and describe how to detect these errors using auxiliary stage observations.

Cross-Sectional Area

The effect of variation of cross-sectional area on normalized RMS discharge error is shown on figure 4. The area ratio of this figure is a multiplicative factor applied in simulation to the true values of area and top-width of a cross section at any stage. At least for the magnitudes shown in figure 4, cross-sectional area has no discernable effect on the RMS stage error. Therefore, errors in cross-sectional area cannot be detected from stage records in the stage-stage problem.

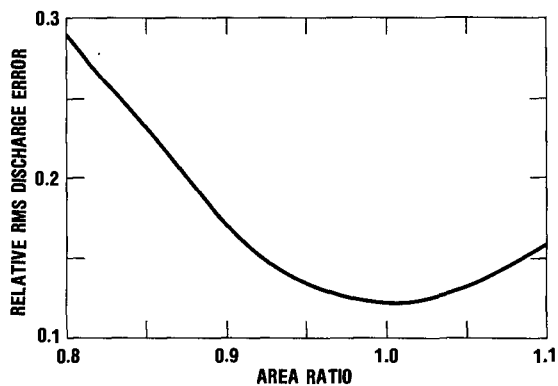


Figure 4. Effect of errors in cross-sectional area on discharge.

Decreasing the cross sectional area has the same quantitative effect on predicted discharge as decreasing the discharge coefficient, it increases the frictional resistance. Therefore, the amplitude of discharge fluctuation decreases as cross sectional area decreases. As can be seen from figure 4 for the same amount of area variation, the effect is more severe as the area decreases than as it increases. For relatively small errors in cross sectional area, say up to 20 percent a stage-stage model can probably be calibrated successfully. The C values will simply be erroneous and compensate for the errors in the cross sectional area. The section on discharge-stage models contains a discussion of the advantageous use of such compensating "errors" in calibrating a discharge-stage model.

Gage Datum

Assuming the intermediate gages are to correct datum, an error in the datum in one of the driving gages is distributed essentially linearly along the segment of channel between the driving gages. The error is easy to see because it appears as a vertical displacement between the observed and predicted water surface elevations at the intermediate gages. An approximate value for the error can easily be recovered by a simple linear extrapolation. Under normal operating conditions three to five hundredths of a foot should be detectable.

The effect of a positive datum shift at the upstream gage on the calculated tidal-cycle average downstream discharges for the simulation period are shown in table 1.

Table 1. Effects of datum shifts on downstream discharge.

Description	Average downstream discharge (cfs)	Steady uniform discharge (cfs)
Datum Shift		
" " = .05 ft	1572	6888
" " = .1 ft	3052	9741
" " = .2 ft	6116	13775

Also given in the table is a predicted approximate value for the steady-uniform flow in Three Mile Slough for $C = 75 \text{ ft}^{3/2}/\text{sec}$ where the amount of fall is equal to the datum shift. The unsteady nature of the flow causes the predicted average value to be less than that for steady uniform flow. The predicted average downstream discharge increases linearly with datum shift, rather than with the square root of it as does the steady-uniform flow discharge. This is probably an isolated occurrence because, of course, as shift increases average fall increases and tends to become dominant in determining the average value of discharge. As this happens the square root relationship has to come fully into effect.

The average value of 810 cfs for an observed downstream discharge seems large in comparison to the predicted value of 94 at zero shift. However, it should be kept in mind that 810 is somewhat less than two and one-half percent of the average of the absolute values of the observed discharges. This is well within measurement error for a single discharge measurement and surprisingly small when one considers the combined hydrograph technique that had to be used to convert the time-distributed measurements into the instantaneous values shown.

Driving Stage Timing

Errors in timing of driving stage gages can be caused by different speeds of the clocks driving the recorders, a missed punch, or erroneous starting or finishing times. They can be damaging because small errors are difficult to detect and, although it is apparently not so in the case illustrated here, small timing errors in driving stage can sometimes result in large errors in predicted discharge.

Figure 5 shows the effects of various time shifts of the stage record of the San Joaquin-gage on the normalized RMS stage error and normalized RMS discharge error. Figure 6 shows the effect of twelve minute shift on the records produced at the three intermediate stations.

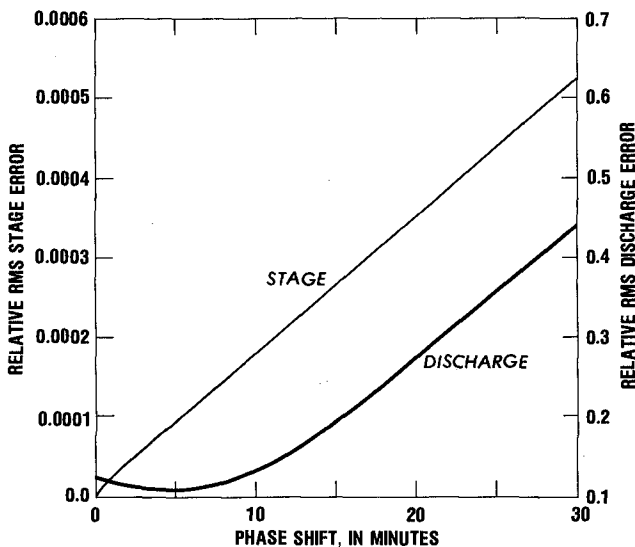


Figure 5. Effect of time phase shift of downstream gage on predicted stage and discharge.

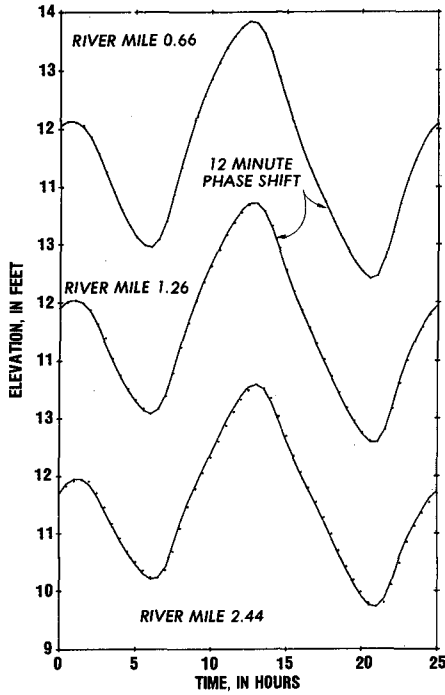


Figure 6. Effect of 12 minute time phase shift on predicted water surface elevations at the intermediate observation stations.

As can be seen from figure 6 the time shift is approximately linearly distributed amongst the auxiliary stations. If we can make the big assumption that the clocks on the intermediate recorders are accurate, the approximate value of the shift should be recoverable by linear extrapolation. For a real field situation where we can't be certain about the intermediate clocks either, but with conditions similar to the ones illustrated here it should at least be possible to discern a shift as small as six minutes.

Figure 5 shows a minimum in the normalized RMS discharge error at a value of time shift somewhere around five minutes. This indicates, first, that there was probably an undetected timing error of about this magnitude in the original stage records. It indicates, second, that this technique; that is, the construction of hypothetical shift versus normalized discharge error graphs, is a viable alternative to inspection of the intermediate stage records for finding possible timing errors.

In this example the increase in the normalized RMS discharge error is not significant until the time shift becomes something between 12 and 18 minutes that is between two and three times the time computation step and around fifteen times the Courant time step. That this magnitude of shift is permissible should not, however, be taken as a general conclusion because a number of factors such as the rapidity with which the driving stages change, the phase difference between them, and the length of the reach being modeled determine the allowable value before serious errors result.

THE DISCHARGE - STAGE PROBLEM Portland Harbor

The data selected to illustrate the discharge-stage problem comes from Portland Harbor, Oregon. As shown in figure 7, Portland Harbor consists of the lower 26 miles of the Willamette River from Willamette Falls to the Columbia River, the 21 miles of Multnomah Channel, and 56 miles of the Columbia River from Bonneville Dam to Columbia City Oregon. Forty-nine cross sections in seven different channel reaches provided an adequate representation of harbor geometry for use in the simulation model. Input boundary conditions for running the model consist of the mean flow discharges for the Columbia River at Bonneville and for the Willamette River at Willamette Falls and the Columbia River stage at Columbia City.

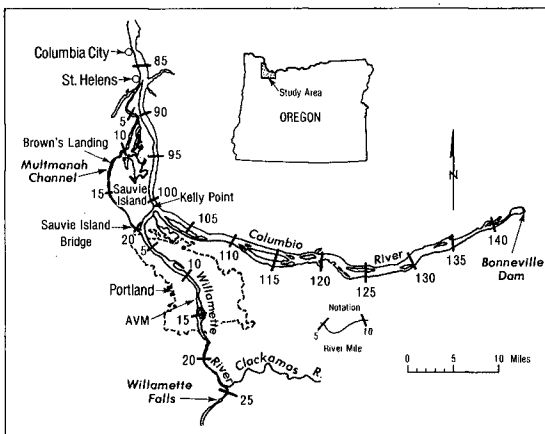


Figure 7. Portland Harbor, Oregon.

Cross section properties were obtained from recent soundings corrected to Columbia River datum and transcribed on a photomosaic of the Harbor by the Portland District of the U.S. Army Corps of Engineers. Calibration data were collected during four short term intensive data collection periods characterizing a range of mean flow conditions on the two rivers. Referring to figure 7, measured discharges were available at the Acoustic Velocity Meter (AVM), Willamette River mile (RM) 1, and Sauvie Island Bridge. Observed water surface elevations were available at the AVM, Kelly Point, St. Helens, and the Vancouver Interstate bridge (Vancouver). The discharge at the AVM was obtained at hourly intervals from the calibrated acoustic flow meter, at RM 1 by boat measurement, and at Sauvie Island Bridge by bridge measurement, all by standard U.S. Geological Survey techniques. The water surface elevations were obtained from floats and recorded digitally at 15 minute intervals. Bennett (1975) describes this data set in greater detail.

Calibration Procedure

Bennett (1975) gives calibration curves for Chezy C versus characteristic discharge drawn for the seven segments of the Portland Harbor model. The calibration curves were derived from the data set described here and another set which covered a wider range of discharges but consisted only of observations of stage and discharge at the AVM. In his study Bennett (1975) used the influence coefficient algorithm, an automatic optimization routine, to minimize an objective function which consisted of discharge prediction error normalized by local absolute mean discharge and water surface elevation prediction error normalized by local mean depth. In contrast the object of the present study is to calibrate the model manually as though only stage information were available. The results of using the two calibration procedures will be compared in some detail, however, first it is necessary to describe the manual calibration procedure used.

The first step in the manual calibration procedure is the adjustment of the mean value of stage and the RMS stage error at Kelly Point by varying the Chezy coefficient C in the two channel segments of the Columbia River between Columbia City and Kelly Point. This can be done essentially independent of Multnomah Channel because the stage at Kelly Point is primarily dependent on the much larger discharge of the Columbia River. For a predominantly unidirectional flow, aid in determining the amount of adjustment of the discharge coefficient required can be obtained by multiplying S_f by the length of reach and expanding the friction loss term as the first four terms in a power series in Chezy discharge coefficient. The resulting cubic equation in ΔC the required increment in the discharge coefficient, can be easily solved by synthetic division or Newton iteration.

For constant discharge, decreasing C has the effect of increasing the average predicted stage. A similar effect can be achieved by decreasing the cross-sectional area. Controlling the predicted stage by varying cross-sectional area has the advantage that C is left free, to a certain extent, to control the amplitude of the water surface elevation fluctuations. For the simulations reported here, the cross sectional-area of the Columbia River from Kelly Point to Columbia City was reduced by ten percent to allow

C to be large enough to force the amplitude of the stage fluctuations to that observed. This may be considered a questionable procedure because cross-sectional area is obtained from physical measurements made in the field. However, it should be realized that the cross sections used are at best random samples of those in the channel segments and as such may not be truly representative of the average conditions. Additionally, the field measurements may be inaccurate or incomplete, therefore, it is reasonable to permit small changes in cross-sectional properties to expedite calibration.

The second step in the manual calibration procedure is the adjustment of the predicted stage at the AVM and Vancouver by varying the C's in the Willamette and in the Columbia above Kelly Point. Calibration for these two stages can proceed simultaneously yet independently because the water surface elevations at these two locations are functions of the independent discharge in the two rivers and of the stage at Kelly Point which has been established in the previous calibration step. Because of the large natural cross sectional areas in the Willamette below Willamette Falls, the stage at the AVM is insensitive to discharge coefficient for the lower discharges. For these discharges it is determined almost entirely by the water surface elevation at Kelly Point.

The final step in the manual calibration procedure was an attempt to minimize the RMS stage error at St. Helens by varying the discharge coefficient in Multnomah Channel. The results of this, however, were not necessarily good in terms of discharge prediction because calibration of Multnomah Channel is essentially a stage-stage problem. The water surface elevation at St. Helens is determined by those at Columbia City and Kelly Point independent of the discharge coefficient value in the Channel. The entire calibration process described here was completed for each data set in less than fifteen simulation runs, a considerable savings compared to the fifty to seventy-five required for the automatic optimization procedure described by Bennett (1975).

Results

For the four data sets, table 2 gives the component prediction RMS errors and the corresponding normalized RMS errors for simulations using the optimum parameters resulting from the calibration procedure described above. In the table, these errors are compared to the corresponding ones resulting from simulations using the optimum parameters derived in the study by Bennett (1975). As might be expected the normalized stage RMS errors for all four data sets are smaller for the parameters derived using the above procedure while the normalized RMS discharge errors are all larger.

Whether or not the increase in accuracy of discharge prediction evidenced by the earlier technique as compared to the one described here is sufficient to merit the additional cost of collection of the necessary discharge data is a question that has to be answered based on the purposes for which the model will be used. To add perspective, typical model behavior for the

Table 2. RMS component errors and normalized RMS errors for stage-only and combined objective function calibration procedures.

Date	Type	Prediction error in feet				Normalized Stage Error	Prediction error in cfs			Normalized Discharge Errors
		AVM	Kelley Point	St. Helens	Vancouver		AVM	River Mile 1.0	Sauvie Island Bridge	
5/13/76	Stage-only	.15	.11	.08	.14	.00511	4197	9823	1102	.448
	joint	.12	.18	.09	.20	.00683	3473	7877	2533	.344
8/1/73	Stage-only	.21	.18	.08	.15	.00605	5360	7636	1176	.444
	Joint	.20	.40	.08	.34	.01184	3460	5746	2509	.285
12/5/73	Stage-only	.21	.20	.05	.23	.00708	3602	1993	2161	.054
	Joint	.22	.22	.29	.26	.00911	3626	3065	510	.039
6/12/24	Stage-only	.06	.03	.16	.09	.00280	1523	3660	900	.088
	Joint	.22	.58	.08	.14	.00723	1502	1446	2779	.060

parameters derived from the two calibration procedures is shown by the stage hydrographs of figure 8 and the discharge hydrographs of figure 9. The hydrographs were computed using boundary conditions and optimum parameters for the data set of 5-31-73. Casual inspection detects little difference between the agreement of either set of predictions with the observed data.

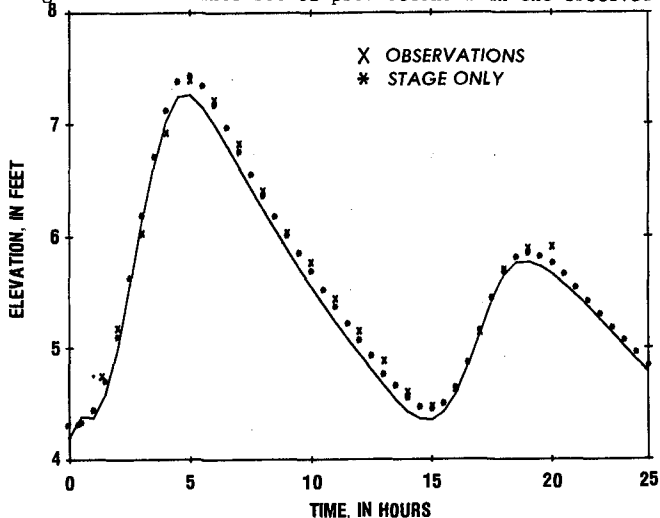


Figure 8. Predicted and observed stage hydrographs at Kelly Point for 5/31/73. Solid line curve reproduced from Bennett (1975).

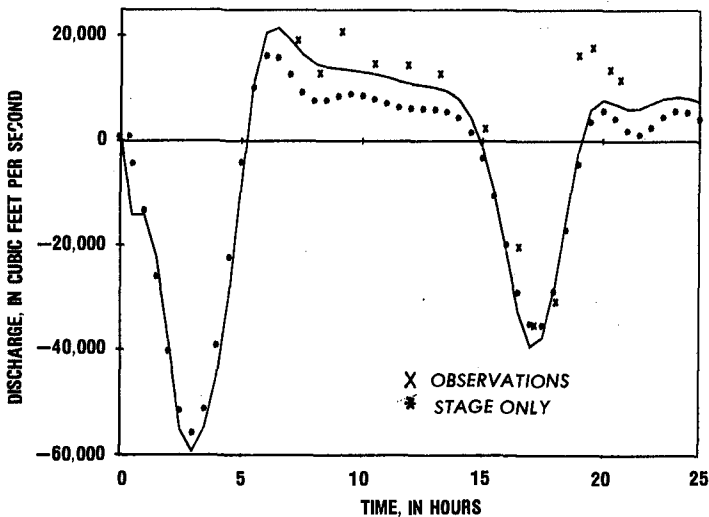


Figure 9. Predicted and observed discharge hydrographs at River Mile 1 for 5/31/73. Solid line curve reproduced from Bennett (1975).

Besides the accuracy of stage and discharge estimation another point which must be considered is the consistency of the parameter estimates obtained from the various data sets. Table 3 shows the C values for each of the seven channel segments of the harbor model. For the first three

Table 3. Channel segment discharge coefficients in $\text{ft}^{1/2}/\text{sec}$.

Channel segments Description	Date			
	5/31/75	8/1/73	12/5/73	6/12/74
Willamette: Falls to Multnomah Channel	90	90	90	90
Willamette: Multnomah Channel to Columbia	90	90	90	90
Multnomah Channel	85	85	85	85
Columbia: Bonneville Dam to Vancouver	60	60	60	60
Columbia: Vancouver to Willamette	195	200	96	120
Columbia: Willamette to Multnomah Channel	102	102	102	95
Columbia: Multnomah Channel to Columbia City	102	102	102	95

segments the values are the same for all data sets. The C value for the fourth segment was not adjusted in calibration because of lack of stage data above Vancouver. The optimum C value for the fifth segment behaves erratically in a fashion which can not be explained. Finally, the C values for the 6th and 7th segments are essentially constant. This is much more consistent behavior than demonstrated by the optimum C values obtained by Bennett (1975).

The reasons for the consistent behavior bear some discussion. First the AVM stages are not sensitive to C at the lower discharges, therefore, the C values for the first two segments are essentially set by the 12/5/76 data set. Second, Multnomah Channel is really a stage-stage problem, and should be fine-tuned using discharge information. This is beyond the scope of the technique being investigated. Third, the C values in the lower Columbia apparently decrease slightly, but only slightly with increasing discharge. Finally, as mentioned above, no explanation has been found for the behavior of C values in the short segment of the Columbia from Vancouver to the Willamette.

As explained earlier the model's intended use dictates acceptable prediction accuracy. However, Table 2 and figures 8 and 9 indicate that, with the possible exception of Multnomah Channel, the Portland Harbor model could have been calibrated acceptably for most purposes in the complete absence of discharge measurements. Whether or not detailed information concerning Multnomah Channel behavior is important in the final study will dictate how much attention should be paid to its calibration. If its behavior must be predicted accurately Multnomah Channel should be calibrated as in the stage-stage problem; that is, with discharge information collected at the extremes of ebb and flood flow.

Conclusions

Calibration of a stage-stage model requires the use of observed discharge. The best time for making the required discharge measurements is near the peaks of maximum and minimum downstream flow. Like variations in the Chezy discharge coefficient, errors in cross-sectional area can not be detected using auxiliary stage observation stations. On the other hand, gage datum discrepancies on the order of 0.05 ft and timing errors in one of the driving stage records on the order of 6 to 12 min. can be detected by comparing the predicted and observed stage records from such stations.

In most water quality modeling situations, discharge-stage models can be satisfactorily calibrated using only stage observations. The data used should cover as nearly as possible the range of mean flow discharges to be encountered in prediction.

References

- Becker, L. and W. W-G Yeh, 1972, 'Identification of parameters in unsteady open channel flows', Water Resources Research, 8 (4), p 956-965.
- Becker, L. and W. W-G. Yeh, 1973, 'Identification of multiple-reach channel parameters', Water Resources Research, 9 (2), p 326-335.
- Bennett, J. P., 1975 'General model to simulate flow in branched estuaries, ' Symposium on Modeling Techniques, 1, ASCE, p 643-662.
- Strelkoff, T., 1970, 'Numerical solution of Saint - Venant equations, ' Journal of the Hydraulics Division ASCE, 96 (HY1), p 223-254.
- Yih, S.-M., and B. Davidson, 'Identification in nonlinear distributed parameter water quality models ' Water Resources Research, 11 (5) p 693-704.

CHAPTER 197

MOVABLE BED TIDAL INLET MODELS

by

Subhash C. Jain¹

and

John F. Kennedy²

INTRODUCTION

Stabilization of tidal inlets is a major engineering problem that is frequently encountered in the development of harbors. The planning, design, and modification of these inlets under the dynamic conditions that generally characterize their surroundings is, at best, a complex and uncertain undertaking. Prediction of the sedimentary response of an existing inlet to artificial improvements and to changing environmental conditions, or of a new inlet to the expected ambient conditions, and the optimization of the layout in order to minimize undesirable accretion or erosion are major elements in the design of tidal inlets. Because of the complexity of the problem, movable bed hydraulic models often are employed, despite the questions that surround their validity, to investigate these responses and to guide designs. The success of a movable bed hydraulic model depends upon the proper choice of similitude conditions and modeling criteria. Unfortunately, the conditions of similitude still are not well defined, as many of the phenomena constituent to the processes involved are yet to be elucidated adequately and formulated. Moreover, it is not possible to satisfy simultaneously all of the similitude conditions that arise. The required grain size and density of the model bed material, the current exaggeration that may be required, the effects of geometric distortion, etc. cannot be determined by straightforward computations. These must be chosen to obtain the most favorable balance between all relevant phenomena. The criteria of similitude generally are specified by experimenters who have previous experience with this type of model. The execution of a model studies of this type is, therefore, largely an "art" and entails major elements of subjectivity.

The Iowa Institute of Hydraulic Research, under contract to Coastal Engineering Research Center, U.S. Army Corps of Engineers, is presently (1976) conducting a study to evaluate the reliability and effectiveness of movable bed, tidal inlet, hydraulic models as predictors of prototype behavior. The main emphasis of this study is on comparison of model predictions with observations made in the prototypes, and evaluation of model performance in the light of: (i) the criteria of similitude adopted; (ii) the sedimentary material and instrumentation utilized in the models; (iii) the experimental procedure followed; (iv) the quality of the prototype data utilized in verification of the models; and (v) the degree and accuracy of model verification. The scope of this study is limited to those models in which the area of interest is composed entirely of movable material and not of just a thin erodible layer placed over a fixed bathymetry. In the United States these model studies

¹ Research Engr., Inst. of Hyd. Res., Univ. of Iowa, Iowa City, Iowa, USA

² Director, Inst. of Hyd. Res., Univ. of Iowa, Iowa City, Iowa USA

have been conducted only by Waterways Experiment Station (WES), U.S. Army Corps of Engineers, Vicksburg, Mississippi.

SIMILITUDE CONDITIONS - WHY?

Is it always necessary to satisfy certain dynamic similitude conditions in a coastal mobile bed model? It is generally possible to find by a trial and error procedure a combination of waves and currents in the model which will produce the known bed configuration and transport sediment at the desired rate to a certain scale. Why not then use the empirical approach; i.e., the trial and error procedure? To answer this question let us examine what L.F. Vernon-Harcourt (1892) reported long ago on movable bed technology. According to him, a model can be used successfully to predict the possible effects of proposed modification: (a) if the originally existing conditions can be reproduced in the model; and (b) if, moreover, by placing regulating works in the model, the changes that were brought about by the training works actually built can be reproduced. The first of these conditions, i.e., the satisfactory reproduction of the originally existing conditions, may be obtained using a suitable combination of waves and currents, determined by trial and error, in the model. There is, however, no guarantee that satisfactory reproduction would be obtained using the same combination of waves and currents when the constructed works are placed in the model; i.e. that condition (b) will be satisfied. This dilemma was encountered in a model study reported by Reinalda (1960). In his study, the model results were compared with the prototype data for the period before and after the construction of groynes along the coast in the vicinity of the Thyboron channel on the east coast of Denmark. The horizontal and vertical scales of the model were 1:250 and 1:40, respectively. Ground Bakelite with mean diameter of 1.8 mm and a density of 1350 kg/m³ was used as sediment. The waves and currents were reproduced according to the Froude law. The sedimentological time scale was determined by comparing the rates of recession of the coastlines in the model and the prototype. Groynes were built in the model at locations and times at which prototype groynes were installed. The relationship between the sedimentological time scale in the model and the prototype time scale for both pre- and post-construction periods is shown in figure 1. For the period from 1874 to 1890 (before the construction of groynes) one year in the prototype corresponds to about 0.5 hours in the model, while after 1920 (following construction of groynes) one year in the prototype corresponds to roughly 2 hours in the model. The model, therefore, over-predicted the effectiveness of the groynes on the rate of recession of the shore-line by a factor of 4. Although the groynes in the model reduced the rate of recession of the shoreline as observed in the prototype, the rate of sediment transport in the model was not accurately reproduced in the model. It might have been possible, after numerous attempts, to find another combination of waves and currents which would have yielded the same time scale for both pre- and post-construction periods (although the probability of doing so is very small). But such a trial and error procedure is very time consuming and expensive. It can be applied only in those cases in which extensive prototype detailed data are available for comparison and model calibration.

The empirical approach, therefore, can be applied only in very few cases and with limited expectation of success. It follows that the realization of a satisfactory model can be achieved only by satisfying certain similitude conditions at the outset. As mentioned in the introduction, these conditions of similitude are still not well defined. A certain amount of experimentation to determine proper combinations of waves and currents and to calibrate each model will continue to be required to reproduce the prototype conditions satisfactorily, even if one has satisfied similitude requirements to the extent possible. But the refined procedure will certainly reduce the time required for model calibration. Moreover, the results from such models can be used with more confidence.

SIMILITUDE RELATIONS

Over the past several years many papers (Bijker, 1967; Fan and Le Méhauté, 1969; Yalin, 1971; Migniot, 1972; Kamphuis, 1975) have been written on similitude requirements for mobile bed coastal models. Dimensional analysis generally has been used to derive the nondimensional quantities which must assume equal values in model and prototype for similitude to attain. Any dependent property, A, of the flow may be expressed in terms of the independent variables by the following relationship:

$$A = f[H, L(\text{or } T_w), \sigma_w, \theta, T_t, d, U, \rho, \nu, \rho_s, D, \sigma_g, X, g] \quad (1)$$

in which

H = wave height	}	Wave parameters
L = wave length		
T_w = wave period		
σ_w = parameter to describe the distribution of wave heights and periods		
θ = wave direction		
T_t = tide period	}	Tide and current parameters
d = flow depth		
U = current velocity		
ρ = density of water	}	fluid parameters
ν = kinematic viscosity of water		
ρ_s = density of sediment particles	}	sediment parameters
D = diameter of sediment particles		
σ_g = parameter to describe the size distribution of sediment particles		
X = some characteristic horizontal dimension		
g = acceleration due to gravity		

Equation 1 may be expressed in dimensionless form as

$$\pi_A = \phi_A \left\{ \frac{H}{d}, \frac{L}{d}, \sigma_w, \sigma, \frac{T U}{X}, \frac{Ud}{v}, \frac{\rho_s}{\rho}, \frac{d}{D}, \sigma_g, \frac{d}{X}, \frac{U^2}{gd} \right\} \quad (2)$$

which is so general as to be of practically of little practical use without simplification. It can be said at the outset, however, that it is neither possible nor essential to have the values of all the dimensionless quantities appearing in (2) equal in model and prototype. There is general accord (Fan and Le Méhauté, 1969; Yalin, 1971; Migniot, 1972; Kamphius, 1975) that the waves should be scaled according to the Froude law, with the scales for wave length and wave height equal to the vertical geometric scale. This condition insures proper wave breaking and refraction in the model (provided the model bottom topography is correct by modelled), but the wave reflection and diffraction are not reproduced correctly (because the wavelength is not scaled according to the horizontal length scale). Normally the currents also should be simulated according to Froude law. But the correct simulation of shear velocity, as discussed below, requires a certain exaggeration of the current velocity. The parameters σ_w and θ can be satisfactorily simulated in the model if the wave machine is able automatically to produce a continuous succession of irregular waves of different heights, periods, and directions. Though it is possible to simulate σ_w (by a crushing and sieving process), it is normally disregarded. It remains to simulate the other four nondimensional parameters: Reynolds number, $Re = \frac{Ud}{v}$; density ratio, ρ_s/ρ ; ratio of flow depth to sediment size, d/D ; and model distortion, d/X .

Froude similitude permits dynamically scaled representation of the mean hydraulic flow in the model but does not take into consideration the motion of the sediment. In order to define a suitable model bed material (sediment size and density) and a model distortion which will reproduce sediment motion in the model which is similar to that in the prototype, let us examine how the various sediment transport mechanisms are related to the dimensionless variables. It should be mentioned that the nondimensional parameters given in (2) are not unique. It is possible, at least in principle, to express these nondimensional variables in an infinite number of alternate forms. The form of the dimensionless parameters which should have the same values both in prototype and model to achieve similitude is not obtained by dimensional analysis alone, but requires also consideration of the physical processes involved.

For the satisfactory simulation of sediment motion in a tidal inlet movable bed model, it is desirable that the following conditions be satisfied in the model:

1. The general shape of the beach be conserved.
2. The condition of incipient entrainment of the sediment be correctly simulated
3. The rate of sediment transport be correctly reproduced.

It should be stressed that it may be neither possible nor necessary in some cases to satisfy all these conditions. It is hoped that the results of the study involving comparison between model and prototype which currently (1976) is underway at Iowa will determine which of these conditions must be fulfilled for acceptable similitude to be achieved. Unfortunately, the relationships among the various nondimensional variables which arise in the aforementioned

conditions are not well formulated. Past investigators have used different relations and thus proposed different similitude conditions; these are summarized in a recent report by Kamphuis (1975). The following discussion is based upon the present state of knowledge of the roles of three conditions stated above.

Equilibrium Beach Profiles. A generally reliable relationship which will define the equilibrium beach profile in terms of independent variables has not been developed to date. Noda (1972) recently proposed some scale relations for equilibrium beach profiles, but Collins and Chesnutt (1975) concluded on the basis of their laboratory experiments that Noda's model laws predict only the shape of the foreshore region, and its general use was not recommended by them. Until a better relationship for the equilibrium beach profile is obtained, it is recommended that preliminary experiments in a two-dimensional wave tank be conducted to determine beach profiles using the selected model bed material and vertical and horizontal scales, for some characteristic model wave conditions. If the actual scale distortion of the resulting equilibrium beach does not agree that imposed in the wave tank experiments, it is necessary to adjust the imposed value of distortion until the values do agree.

Incipient Entrainment of Sediment. Presently only very limited experimental data are available on initiation of sediment motion by the combined action of waves and currents. The experimental information on initiation of sediment by currents or waves alone suggests that the initiation of sediment motion due to both waves and currents may be expressed by a relation similar to that of Shields (Vanoni, 1975) for steady unidirectional flows. The criterion for the incipient entrainment of sediment under the action of waves and currents can be expressed as

$$F_{*C} = f(R_{*C}) \quad (3)$$

where

$$R_{*C} = \frac{U_{*C} D}{\nu}$$

and

$$F_{*C} = \frac{U_{*C}}{\sqrt{g\gamma' D}}$$

in which U_{*C} is the critical shear velocity, $\gamma' = \frac{\gamma_s - \gamma}{\gamma}$ is the apparent specific weight of the submerged sediment, and γ and γ_s are specific weights of the fluid and sediment, respectively. Both F_{*C} and R_{*C} are based on shear velocity, U_{*C} , which is a dependent variable. Equation 3 is not a suitable basis for a similitude condition unless U_{*C} is known for the model and the prototype. Valembois (1960) expressed Shields' relation in the modified form

$$G = f(R_{*C}) \quad (4)$$

where $G = \frac{\gamma' g D^3}{\nu^2}$, the so-called grain parameter, is obtained by dividing F_{*C} by $(R_{*C})^2$. It is proposed here, for want of a better alternative, that for the simulation of incipient entrainment of sediment, the value of grain parameter, G , should be equal in model and prototype. This gives the following similitude condition:

$$\lambda_Y, \lambda_D^3 = \lambda_V^2 \quad (5)$$

in which λ represents the scaling factor (value in model/value in prototype) for the quantity symbolized by its suffix. It is assumed that λ_g is unity.

Sediment Transport. Experimental data on sediment transport under the combined action of waves and current are also very limited. Recently Lin (1972) conducted some tests in a model basin to study sediment transport due to inlet currents and waves approaching the shoreline at an angle of 10° . He used dimensional analysis and his experimental results to express the sediment transport rate as a function of Froude number, bottom shear stress, friction factor, and wave steepness. Another experimental study on sediment transport by currents and waves was conducted by Bijker (1967). He expressed the rate of sediment transport by the following relation:

$$\frac{q_s}{U_*^3 D} = 1.95 e^{-0.33 \frac{\gamma' g D}{\mu U_*^2}} \quad (6)$$

in which q_s is the volumetric sediment transport rate per unit width, U_* = shear velocity based on total shear stress due to both waves and currents, and μ is a "ripple factor". For correct simulation of the sediment transport in the model, the value of $\frac{\gamma' g D}{\mu U_*^2}$ should be the same both in the model and the prototype, i.e.,

$$\lambda_Y, \lambda_D = \lambda_\mu \lambda_{U_*}^2 \quad (7)$$

The scale of shear velocity can be written

$$\lambda_U = \lambda_{U_*} \lambda_C \quad (8)$$

where C is bed resistance coefficient. Assuming $\lambda_\mu \approx 1$, as found by Bijker (1967) in his experiments, the similitude condition^u for sediment transport becomes

$$\lambda_U = (\lambda_Y, \lambda_D)^{1/2} \lambda_C \quad (9)$$

Using (5), (8), and (9) it can be shown that

$$\lambda_{R_*} = 1 \quad (10)$$

where $R_* = \frac{U_* D}{\nu}$; that is if (5) and (9) are satisfied, then (10) is also satisfied. Equation 7 for $\lambda_\mu \approx 1$ reduces to the similitude condition that the particle Froude number based on the total shear velocity must be the same both in the model and the prototype.

STUDIES CONDUCTED AT WES

Through 1975 WES had conducted seven movable bed model studies of tidal inlets. Each study was conducted on an *ad hoc* basis, in that no general similitude requirements or modeling criteria were followed. The waves and currents required to produce satisfactory bed configurations were obtained by a trial and error procedure. Wave heights were exaggerated as much as possible without causing wave breaking to occur at entirely wrong locations. Two prototype hydrographic surveys conducted some time apart were used for model verification and calibration. A model distortion of five was adopted in all model studies. Sands with mean diameters ranging from 0.2 mm to 0.25 mm was used as a model bed materials in all models except the Galveston Harbor Entrance Model, in which coal with specific gravity of 1.4 and a median diameter of 1.4 mm was utilized. The WES studies have utilized plunger-type wave generators, which are adjusted manually to generate regular waves of desired height and period. In all model studies, waves were generated from one or more fixed directions. The bed configurations in the model were recorded manually using sounding rods graduated to 1 ft (prototype). Tides were produced using automatic tide generators.

For the verification of the movable bed models, fill and scour maps, both for prototype and model, were prepared and compared. In some studies the dredging volumes also were used in the model verification. If the general pattern of fill and scour in the model was similar to that in the prototype, the model was considered to have been satisfactorily verified. This "eye-ball" comparison of the scour and fill patterns involves, of course, a strong element of subjectivity.

A PROPOSAL FOR QUANTIFICATION OF MODEL VERIFICATION

It would be very useful to have a quantitative measure of the performance of movable bed tidal models. Some of the quantitative indicators being considered in the Iowa study are the following.

Let S_j be the total amount of scour and F_j be the total amount of fill over the j th profile during a given time Δt (see figure 2). Let Q_j be equal to $(S_j - F_j)$; thus Q_j is a measure of the net sediment transport across the j th profile in the given time. It is also a measure of the average depth change over the j th profile.

The degree to which the change in bed elevation along at a given profile or at a given point in the model is related to that in the prototype can be expressed by the correlation coefficients

$$R_S = \frac{1}{N-1} \sum_{j=1}^N \frac{(S_{jm} - \bar{S}_{jm})(S_{jp} - \bar{S}_{jp})}{\sigma_{Sm} \sigma_{Sp}} \quad (11)$$

$$R_F = \frac{1}{N-1} \sum_{j=1}^N \frac{(F_{jm} - \bar{F}_{jm})(F_{jp} - \bar{F}_{jp})}{\sigma_{Fm} \sigma_{Fp}} \quad (12)$$

$$R_Q = \frac{1}{N-1} \sum_{j=1}^N \frac{(Q_{jm} - \bar{Q}_{jm})(Q_{jp} - \bar{Q}_{jp})}{\sigma_{Qm} \sigma_{Qp}} \quad (13)$$

and

$$R_D = \frac{1}{\sum_{j=1}^N M_j - 1} \sum_{j=1}^N \sum_{i=1}^{M_j} \frac{(D_{ij} - \bar{D}_{ij})_m (D_{ij} - \bar{D}_{ij})_p}{\sigma_{Dm} \sigma_{Dp}} \quad (14)$$

in which D_{ij} is the change in the bottom elevation at a point (i,j) within the given time interval (figure 2), σ is the standard deviation of the quantity symbolized by the subscript, the overbar denotes the average value, and the suffixes m and p denote model and prototype, respectively,

If the model results were in perfect agreement with the prototype data, the correlation coefficients in (11) thru (14) would be unity. This would be too much to expect from a model with a high value of R_D , but the values of the other correlation coefficients in (11), (12), and (13) must be high (approaching unity) before a reasonable verification of the model can be said to have been achieved.

A CONCLUDING REMARK

In conclusion the writers take this opportunity to invite identification of other model prototype studies and other methods of analysis that could be used in the Iowa investigation of tidal inlet models.

ACKNOWLEDGEMENT

This work is a result of research sponsored by the U.S. Army Coastal Engineering Research Center under Contract DACW72-76-C-0003.

REFERENCES

- Bijker, E.W., "Some Considerations about Scales for Coastal Models with Movable Bed", Delft Hydraulic Laboratory, Publication No. 50, 1967.
- Collins, J.I. and Chesnutt, C.B., "Tests of the Equilibrium Profiles of Model Beaches and the Effects of Grain Shape and Size Distribution", Proc. of the Symposium on Modeling Technique, San Francisco, Calif., Sept. 1975.
- Fan, L.N., and Le Méhauté, B., "Coastal Movable Bed Model Technology", Tetra Tec., Report No. TC-131, 1969.
- Kamphuis, J.W., "The Coastal Mobile Bed Model", C.E. Research Report No. 75, Queen's University, Kingston, Ontario, Aug 1975.
- Migniot, C., "Représentation Des Transports et Des Depots de Sediments Dans Des Modeles Reduits Maritimes", Journee Technique sur la Simulation en Hydraulique Maritime, Moth Division Hydraulique, Paris, Mar 1972.
- Migniot C., Orgeron, C., and Biesel, F., "LCHF Coastal Sediment Modeling Techniques", Proc. of the Symposium on Modeling Techniques, San Francisco, Calif., Sept. 1975.
- Noda, E.K., "Equilibrium Beach Profile Scale-Model Relationship", Journal of the Waterways, Harbors and Coastal Engineering Division, ASCE, Vol. 98, No. WW4, Nov. 1972.
- Reinalda, R., "Scale Effects in Models with Littoral Sand-Drift", Delft Hydraulic Lab., Publication No. 22, Sept. 1960.
- Valembois, J., "Etude Sur Modele du Transport Littoral Conditions de Similitude", Proc. Seventh Congr. on Coastal Engineering, Vol. 1, Hague, Netherlands, Aug. 1960.
- Vanoni, V.A., *Sedimentation Engineering*, ASCE - Manual and Reports on Engineering Practice, No. 54, 1975.
- Vernon-Harcourt, L.F., "Improvement of the Maritime Portion of Rivers Including Their Outlets", Proc. 5th International Congress of (Inland) Navigation, 4th Section, 10th Question, Paper 51, 1892.
- Yalin, M.S., *Theory of Hydraulic Models*, MacMilan, London, 1971.

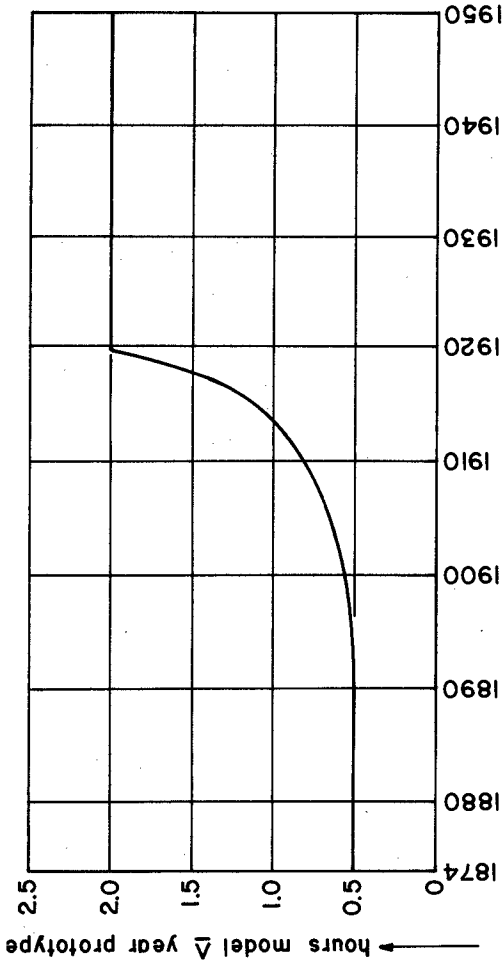


Figure 1 - Curve for the time scale

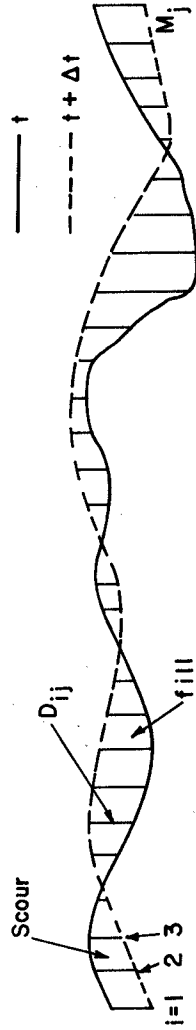


Figure 2 - j th cross-section profile

CHAPTER 198

CHURCHILL RIVER SALT-WATER TIDAL MODEL

by

Bruce D. Pratte*

1. BACKGROUND

The Port of Churchill is located just inside the mouth of the Churchill River, on the western shore of Hudson Bay (Fig. 1, Photo 1). Each shipping season, about 25×10^6 bushels of grain are shipped to Europe and Britain. The Port opens just after mid-July when Hudson Strait and Bay become relatively clear of ice. However, it is forced to close 3 months later by ice forming upstream in the rapids, sweeping down as slush ice at ebb tide, jamming between the ships and the dock and breaking mooring lines. Since the route to Europe is shorter and therefore the laid-in cost of the grain slightly less than from other Canadian ports, there is a demand to extend the operating season at Churchill. A feasibility study and field survey in 1965 by Dick (Refs. 1, 2) showed that the Port could remain open about 2 weeks longer than the present October 23 closing if the slush ice could be kept out of the harbour. To this end, the National Harbours Board in 1974 commissioned the Hydraulics Laboratory of the National Research Council of Canada to do an hydraulic model study of the harbour and estuary.



Photo 1. The Port of Churchill, Manitoba

* Associate Research Officer, Hydraulics Laboratory, National Research Council of Canada, Ottawa, Ontario, Canada.

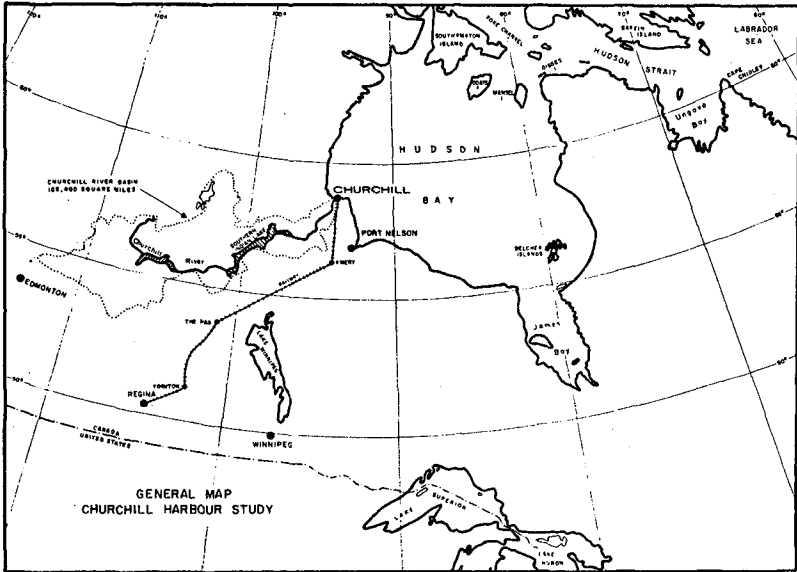


Fig. 1. Location Map of Churchill

2. OBJECT OF STUDY

The sponsor of the study required that various structures be examined for protecting the ships in the harbour from the current of slush ice, principally at ebb tide. Since the structure will be permanent, it must also not have detrimental effects during the rest of the year with regard to flow patterns and velocities and sedimentation. Although maintenance dredging is not a major problem in the harbour at present, averaging about 8,300 yd³ per year, the season is so short that it would be undesirable if excessive dredging were caused by implementation of one of the schemes. Ideally, the structure should produce a quiet harbour so that loading and turning of the ships can go on without the present concern for the high outflow ebb velocities at the dock.

Fig. 2 shows the extent of the area modelled, and how the dock is situated on the outside of a bend in the flow. The most obvious structure would be a deflector just upstream of the dock, and various deflectors formed a large part of the model investigation. Another, but considerably more expensive scheme is a dam from the dock over to Cackle's Point, incorporating a section with a weir with crest elevation above the extreme tidal highwater. In addition to excluding the slush ice from the harbour, it could serve as a causeway to the west shore of the river, opening it up for development and access to historic Fort Prince of Wales.

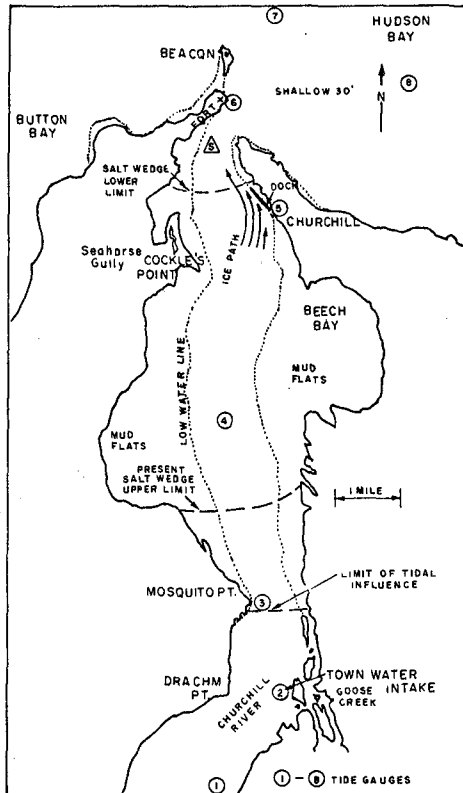


Fig. 2. Extent of Model

Since the river several hundred miles upstream is soon being partially diverted into the Nelson River system for power development, the freshwater discharge will be reduced in the harbour area from a present mean around 50,000 cfs down to about 20,000 cfs. However, there is the possibility of it going as low as say 2,000 cfs in the fall, so that the 1% salt-water limit of intrusion will move up the river past Mosquito Point. This will require relocating the town's fresh water intake pipe, presently at Goose Creek, Fig. 2, further upstream. The model was also expected to show how far upstream the salt will penetrate at extreme high tides and very low river discharges.

3. THE MODEL

To study all the required objectives, the model in Fig. 2 and Photo 2 was constructed of concrete over sand. It is 185 ft long, 55 ft wide, and extends the equivalent of 3

miles into Hudson Bay as the seaward salt water tidal boundary. The upstream end of the model is above the tidal limit and supplies a constant freshwater inflow by means of a head tank and vee-notch weir.



Photo 2. Churchill Tidal Model with Supply Manifold in Foreground, and a Dam Past the Dock.

3.1 Model Scales

Prototype/model length scales are $L_p/L_m = 400/1$ horizontal, $d_p/d_m = 50/1$ vertical, giving a vertical exaggeration or distortion of 8. This is necessary to achieve sufficient depth and turbulent flow in the shallow reaches of the river.

From the Froude (Fr) law for scaling of free surface flow phenomena, one derives the following relations:

$$\text{since } Fr_m = Fr_p, \quad V_m/\sqrt{gd_m} = V_p/\sqrt{gd_p},$$

$$\text{the velocity scale is } T_p/T_m = \frac{L_p}{L_m} \times \sqrt{\frac{gd_m}{gd_p}} = 56.5685;$$

(Thus a 12.4 hour tide cycle requires 13.1 minutes on the model.)

$$\text{The discharge scale is } Q_p/Q_m = \frac{V_p L_p d_p}{V_m L_m d_m} = 141,421.$$

Finally, the salt concentration, salinity or density is modelled in a 1/1 ratio, so that it is the same in model

and prototype, namely 28% out in Hudson Bay near the tidal boundary. Because the harbour is in an area of density stratification where a fresher surface layer at times flows in quite different directions to the bottom seawater layer, it was necessary that the model be a salt-water one, with freshwater river discharge. This of course gives rise to considerably more complex model control, and measurement and calibration of velocity and density.

3.2 Model Control

A large sump is kept up to seawater salinity by a Robertshaw pneumatic controller which causes a small amount of saturated brine, obtained from a pit of dissolving rock salt, to be injected into the intake of the 6 cfs seawater pump. A Schlumberger Solartron density meter monitors the density of a continuously sampled portion of the flow leaving the pump. This instrument works on the principle of the change in frequency of an oscillating pair of tubes through which the fluid travels, and senses extremely small changes in fluid density. Any deviation from the controller's set-point density causes the appropriate amount of brine to be injected. The brine is needed to make up for the dilution of the seawater caused by the steady freshwater river inflow.

The main seawater flow then enters a large head tank before flowing by gravity into the Hudson Bay end through a 32 feet long, 1 foot diameter manifold pipe. The 5 cfs inflow is constant. Tidal control is effected by a drain valve located in the corner of the model such that the flow drains toward it in the same direction as in the prototype. The valve is controlled by an on-line EAI-640 computer which compares the historical tide curve desired, to the level sensed by a floating water level sensor in Hudson Bay. Any error results in a signal to the valve to open (lower) or close (raise the water level). In addition to control of the tide, the computer also records for off-line plots and printouts, the water levels and velocities from gauges on the model to allow comparisons of different test conditions.

A 10 feet long weir near the valve follows the tidal water level. The overflow from this weir is set to twice the freshwater inflow rate, and passes through a 3-way 4 inch valve. When the tide is rising, this valve drains into the seawater sump. However, on falling tide when Hudson Bay gets a skin of fresher water from the river flow, this valve opens so as to bypass the "fresher" weir overflow down the sewer. Thus, the sump level is not filled up or degraded in salinity quite so much by the fresher water during a test.

3.3 Instrumentation

There are eight tide gauges located along the model. A glass ball float is attached to a stem which is free to move up and down inside a DCDT (direct-current differential transformer). Outputs of up to ± 3 volts D.C. are sensed by the computer and converted to water levels by a calibration equation. Five velocity meters are located in the estuary, and each incorporates a DCDT mounted horizontally, and has a 2 x 4 cm drag plate in the water suspended from thin frictionless straps (Photo 3). Movement of the plate by fluid drag causes the stem or core to move freely inside the DCDT. This meter is sensitive enough to measure velocities, both upstream and downstream, down to about 1 cm/sec, and up to 30 cm/sec. One disadvantage of the meter is that it must be carefully levelled, and therefore is not suited for traversing through the flow depth.

A newly developed velocity meter was also used. It comprises a very sensitive strain-gauged Kistler transducer, connected by a rod to a flat circular cylinder drag body. Velocities coming from any direction in the horizontal plane can be sensed by this instrument, and the resultant vector obtained from computer analysis of the output of the x and y axis strain gauges. This instrument was located where the flow direction swings appreciably as the tide changes, in the center of the estuary between the dock and Cockle's Point.



Photo 3. Drag-Plate Velocity Meter



Photo 4. Traversing "Salinity" Probe

Vertical velocity profiles were very difficult to obtain since the velocities were often low and the sensitive levelled drag-body velocity meters could not be traversed. Even miniature Kent and Ott laboratory-type propellor meters were not adequate. Therefore, a dye injection system was devised, which involved timing a puff of dye (injected normal to the flow direction) past a ruler located at the same depth. This system worked very well, and allowed vertical traverses. However, by the time velocities were measured at say 10 depths, the tide cycle was quite different than when starting the traverse. Therefore, several tide cycles had to be repeated in order to get enough measurements at different levels at the same point in the tide cycle.

Vertical salinity profiles in the model test locations were made by traversing a specially developed conductivity probe which continuously sucks a tiny sample of the water through a fixed volume past platinized electrodes, Photo 4. This instrument is similar to that constructed by the Delft Hydraulic Laboratory. A motorized traversing rig moves the probe through the full range of the depth at about 1 cm/sec. Response is very good although electrical calibration in standard solutions of "known conductivity" must be made frequently. Temperature is also monitored to allow conversion of conductivity to salinity by standard equations. Again, several tide cycles of testing were needed before enough points were available to plot a near instantaneous vertical salinity profile. This of course assumes the tides and salinity distributions repeat very well from cycle to cycle in the model.

To measure the 1‰ salinity penetration upstream towards Mosquito Point, a small Beckman conductivity probe was used.

4. MODEL CALIBRATION

In August 1974, temporary tide gauges were installed on the Churchill River at 4 and 2, Fig. 1, in addition to the long-time permanent gauge at the dock. A survey of elevations at 3 and 1 allowed their levels also to be tied in to these tide gauges. In 1965, Dick (2) made a field survey of prototype vertical velocity and salinity profiles at various locations near the harbour and estuary entrance. Also, penetration of the 1‰ salt-water limit was found to be about as shown on Fig. 1 at high tide. Mosquito Point, near 3 is a region of very rapidly flowing water, with large 5 to 8 feet diameter boulders on the bottom in less than 8 feet of water. At low tide and average river flow of about 50,000 cfs, the salt limit is pushed down just past the dock. There is a very strong density gradient seaward of this point with a fresher layer on the surface moving rapidly (5 fps) out to sea, and a nearly stagnant sea

water layer underneath trying to move up the estuary as a wedge. Surface movement of ice and of drogue bodies was observed or tracked by theodolite, giving vector paths as sketched in Fig. 1 approaching at about 30° to the dock.

Model calibration involved placing 2 cm wide stainless steel strips vertically into holes in the concrete bed of the model in the area from the entrance up to Cackle's Point, and coarse gravel in the shallow areas further up-stream. By trial, a distribution of this bed roughness was found which forced the model to reproduce the correct tide curves at each station. Due to the vertical distortion, $d_p/d_m = 8/1$, the deeper areas are exaggerated and tend to attract more flow in the model than would occur in the real river. Therefore, roughness was concentrated more in these deeper areas to create velocities in the various locations where measurements were available. The roughness of course has no effect at high water slack, but is very effective on falling or rising tide when velocities and head losses become significant.

Fig. 3 shows a comparison of model and prototype vertical velocity (from dye timing) and salinity profiles at 2.2 hours after low tide at location s, Fig. 1. The tide is rising and the seawater is flooding in beneath the fresher layer on top which even at this time is still ebbing seaward. By about 3 hours after low water, the surface layer itself will turn and start to be backed up into the estuary. The salinity profiles show the very marked stratified gradient at this station, in the estuary entrance, of 25‰ in the lower 35 feet and nearly fresh above. The thick lower layer

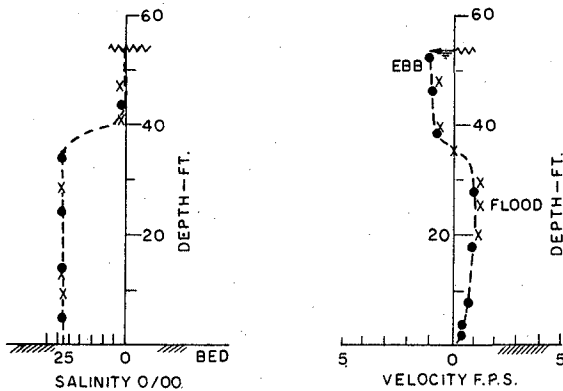


Fig. 3. Comparison of Model (x) and Prototype (o) 2.2 Hours after Low Tide

forces the freshwater layer to flow seaward at high velocity throughout the 2.5 hour period just after low water. This phenomena is of importance to the surface clearing of ice, as is the time, speed and duration of movement of the lower layer with respect to suspended sediment transport. Only with a salt-and-fresh water model can these effects be properly simulated.

Photographs of the movement of surface floats (styrofoam, paper punchings, or wood pieces) were also used in calibration of the model, and in testing various flow diverting structures. A Haselblad 500 EL camera mounted above the harbour area was computer-controlled to take a 5 second exposure at times of interest in the tide cycle, such as at maximum flood and ebb tide, and high and low water. Just after the shutter opened, an external blade was triggered to briefly cover the lens, producing a break in the streaks which the particles create on the film. This break is near the end of the streak where the particle came from. There are white strings 30 inches apart, or 1,000 feet prototype, stretched across the model just above the water surface, which allows one to scale off the length of each 5 second streak in the photograph, and determine the particle's velocity, direction and sense.

Velocity of the lower layer was measured by the current meters, but frequently dye was used to show flow direction and to colour the lower salt-water layer to observe its penetration up the dredged navigation channel, into the harbour, and further upstream. In fact, at low tide, the seawater layer was dyed just downstream of the dock, and the dye front observed to penetrate up to the same limit towards Mosquito Point as shown in Fig. 1 from the prototype observations of Dick. This dye limit corresponded well with that measured using the Beckman conductivity cell at the same spot but without dye.

Since an indication of any large changes which various structures might create in the bottom sediment movement was also required, gilsonite, bakelite, and fine crushed walnut shells (shelblast) were tried as tracers. The walnut shells were found most useful for a qualitative idea of likely bed erosion and deposition areas. Although no tracer studies were made in the prototype, it is known from a few bed samples Dick obtained, that the harbour area deposits are mostly medium to coarse sand of 0.4 to 0.9 mm median grain diameter, felt to come from up river, plus some fine, silty grey mud of 0.075 mm size. This mud may come from the photographically evident littoral drift zone around Button Bay, and be carried on flood tide up the estuary to settle out on the mud flats, and eventually in the harbour itself. Ignoring the cohesive effects of the silts, the sand may be expected to move as bed load for bed velocities greater than 0.5 to 0.8 fps.

5. TEST RESULTS

Since many tests were made, and since the results are proprietary information of the sponsor, only a few illustrative results of the investigation will be given here by permission. These results should not be considered as representing the sponsor's opinions or recommendations.

5.1 Deflector Upstream of Dock

Various configurations were tried, varying the length, angle to the flow, and tip curvature to lessen scour. Photos 5 and 6 show the ebb flow from left to right past the dock without and with a deflector. The deflector shown is a 1,200 feet long rubble mound structure. It provides adequate protection in the entire harbour area at ebb tide with the slush ice kept out, and with only a very weak clockwise re-circulating eddy present.

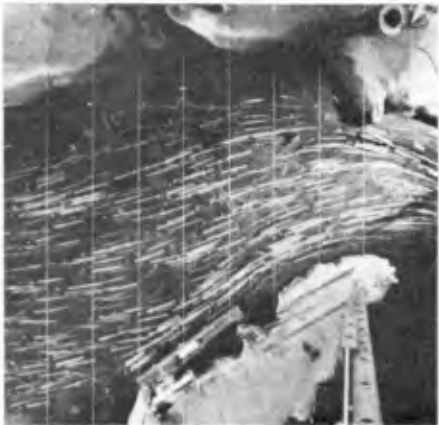


Photo 5. Surface Ebb Flow
Past Dock



Photo 6. Harbour Protection
with Deflector

At flood tide most of the returning ice flows up the shallow west side of the estuary across from the harbour, since that side then is on the outside of the bend for flood flow. Any ice trapped in the harbour on ebb tide was not packed in between deflector and dock on flood tide. Rather, the bottom seawater layer moves into the deep harbour area, locally raising the nearly stagnant freshwater layer on top and causing a superelevation so that the surface "ice" moves out around the deflector. This phenomena was unexpected, but indeed welcome since in the model, even a northwest wind failed to overcome the strong clearing effect. In the prototype, however, freezing cohesion of the real ice could alter this behaviour somewhat, and some small tugboat action might be needed to break up any persistent ice cover which forms.

Sediment placed in the harbour tended to stay there. However, walnut shells placed at A upstream of the deflector at ebb tide was vigorously moved northwest on the bed, at about 30° to the direction of the surface currents, Fig. 4. As the tide approached low water, the deflected flow slowed down, and was attracted more towards the deeper harbour, and a small number of walnut shells moved along the outer edge of the harbour at B, a few depositing in the downstream corner of the harbour at C and in the approach channel at D. Approximately 90% of the particles placed across the river section at A, simulating the sand bed-load coming down the river, were strongly moved out the narrow deep entrance mouth into Hudson Bay, not to return on flood tides. The few particles at D were carried up into the harbour on the next flood tide, and settled out in there in the areas hatched. Particles placed at E were cleared out by the strong bottom seawater currents at flood tide. Obviously

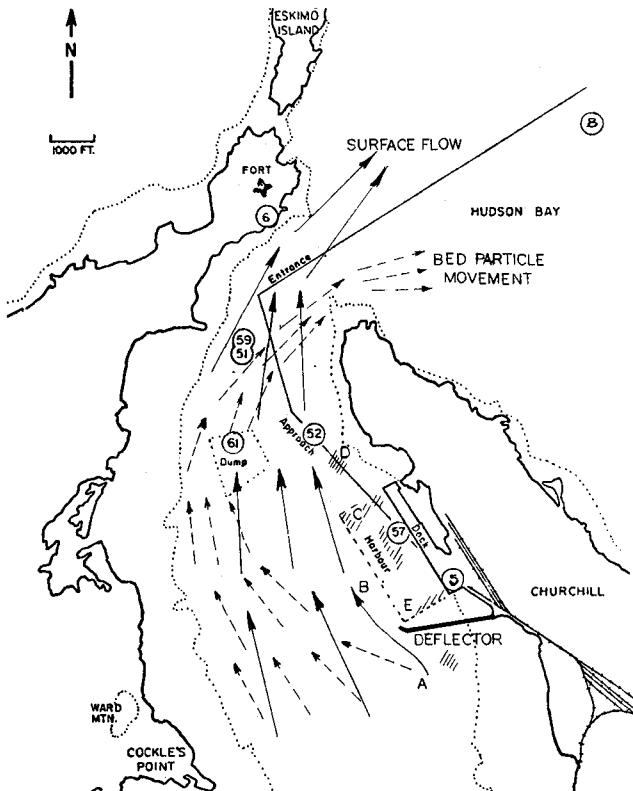


Fig. 4. Effect of Deflector on Ebb Bed Particle Movement Compared to Surface Flow Velocity Meter Locations Also Shown

sedimentation will be more of a problem in the harbour if this deflector were build, if indeed there is significant sediment coming down the river, a factor not yet well determined.

It is also expected that deposition of some sand, but mostly mud, will occur on the upstream side of the deflector, as shown by dye simulating any suspended silts brought in from Hudson Bay in the salt water layer.

5.2 Dam With Weir and Causeway

The second idea investigated was a dam extending the deflector over to Cockle's Point. Placement of a weir was tested for best results in the harbour. Photo 7 shows one scheme with a 2,600 feet long weir near the middle of the section. The crest elevation of +10 feet above mean water level was 0.4 foot above the highest recorded tide in the harbour of September 7, 1967, which had a 9.6 feet high water and a -6.9 feet low water. The weir length was chosen to pass the maximum expected flood flow of 100,000 cfs with a 5 feet head, giving a dammed level upstream of +15 feet, the highest suggested before significant flooding would occur.



Photo 7. Dam and Weir Upstream of Dock

The advantages of the dam were found to be as follows. First, the slush ice formed in the rapids becomes a static ice cover in the deep wide nearly-stagnant lake created by the dam. Therefore, no ice problem occurred in the harbour area, which in any case was protected from the direct weir overflow. Next, the harbour velocities were lowered, with mostly seawater of very low velocity moving slowly back and forth to fill the much reduced tidal prism between dam and Hudson Bay. Third, river-borne sediment was trapped in the lake, and did not get past the dam. The lake created by the dam was non-tidal and fresh, forming a

steady recreational area all year round, plus giving ready access to fresh water for the Port and town of Churchill. Finally, a roadway may be constructed on top of the dam and weir to provide safe access for development of the west shore and for tourism.

The disadvantages of the dam were found to be: firstly, extremely high cost due to material and equipment availability and overall size (almost 8,000 feet long); definite possibility of suspended material settling out due to the low velocities in the harbour area even though the surface freshwater layer from the weir is always moving seaward even at flood tide (except when river discharges are very low). The tests showed that at flows of 10,000 and 24,000 cfs, the tidal inflow near the bed predominates in duration over its outflow, allowing more time for littoral drift sediments to be brought in and deposit in the harbour. Thus, increased dredging is forecast, although conditions for dredging would be easier. The river is blocked to navigation, although small boats would likely be kept above the dam in any case. Some flooding of the area between the dam and Goose Creek will occur at flood flows nearing 100,000 cfs, requiring dykes and building relocations. Certain yearly maintenance costs would be incurred, and finally the harbour would not clear of ice until a few days later than normal.

5.3 Reduction of River Flow by Diversion

The Churchill River will soon have much of its flow diverted into the Nelson River several hundred miles upstream for power development. The effect of severely reduced flows on conditions in the harbour was investigated. Fig. 5 shows the drag-plate current meter velocities over two semi-diurnal tide cycles, for two test conditions, one with present average river flow of 50,000 cfs, and the other for an admittedly very small discharge of only 2,500 cfs. These two tests demonstrate the effect of a reduction in river flow. First, although not shown here, the high water levels at the dock are influenced mainly by Hudson Bay, and so were found to be almost the same. The low water, however, is about 0.6 foot lower with the small flow since only a small slope is then required to get this amount of freshwater out to Hudson Bay. Water levels further upriver are lowered dramatically, by over 4 feet at gauge 1, Fig. 2, so that the river becomes much narrower and shallower. The velocity meters located as in Fig. 4, showed interesting behaviour. Meter 51 was in the entrance in the surface layer and meter 59 was directly below it near the bed. With the 50,000 cfs flow, there was a 2.5 hour lag between the time the bottom seawater (59) began to move as inflow and the time when the surface layer (51) finally reversed also. However, with the 2,500 cfs river flow, the surface layer is so thin that virtually the whole flow from top to bottom

reverses direction at the same time. The tidal prism of the estuary which at high flows is filled by river and tide, will then be mainly filled by inflow from Hudson Bay. Thus inflow times will be longer and the velocities higher, and outflows will be shorter. The end result will be more time for littoral drift sediments to be carried into the estuary, and less time to be cleared out. On the favourable side of the question of reduced river discharges is the fact that less river flow will bring down less sand and sediments. In addition, less ice should be produced in the rapids by the smaller river cross-section. These two factors may well more than compensate for the increased siltation expected from Hudson Bay. The best recommendation now is to wait and see if the results of the diversion bear out the predictions from the model tests.

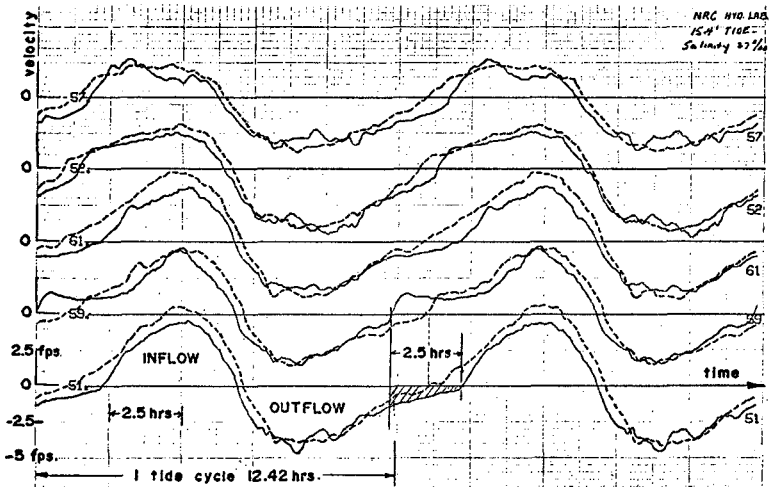


Fig. 5. Two Semi-Diurnal Tide Cycles Giving Velocities for 50,000 cfs (—) and 2,500 cfs (---) River Discharges

6. DISCUSSION

The purpose in presenting this model study is to encourage the use of salinity models in the study of flow phenomena where density effects are involved. Although not inexpensive to operate because of salt use, the model control and data acquisition by on-line computer was most effective in keeping testing to a minimum. Use of plastic pipe and concrete is recommended where possible to avoid corrosion problems. Even rusting, however, requires years before

significant damage occurs, and by then the equipment has certainly paid for itself in allowing better knowledge to be gained than from all-fresh water tests. Instruments made of type 316 stainless steel were found to resist corrosion very well.

The results of a few of the schemes tested on the model to improve conditions in Churchill harbour, particularly under ice-run conditions were described along with their advantages and drawbacks. Obviously no scheme was perfect, but at least the results should allow a better appraisal of the merits of each when the time comes to implement one at Churchill.

7. REFERENCES

1. Dick, T.M., "Limits to Navigation by Ice in Port of Churchill", Proceeding of ASCE, Journal of Waterways and Harbours Division, WW4, November 1967.
2. Limited distribution of National Research Council documents by T.M. Dick; 1 report on Feasibility of Extending Navigation Season at Churchill Harbour, and 3 laboratory memoranda on field measurements of velocity, temperature and salinity, and assessment of littoral drift and sedimentation.

8. ACKNOWLEDGEMENTS

To the National Harbours Board of Canada, the initiator and sponsor of this study.

CHAPTER 199

Analysis of Time Conditions for Hybrid Tidal Models

Klaus-Peter Holz*

Summary

Hybrid models for the investigation of tidal waves in rivers and estuaries are a combination of mathematical and hydraulic models, which are coupled under real-time conditions. The coupling procedure cannot be performed without some time delay which mainly depends on the time needed for the computation of the mathematical model and for the control operations on the instrumentation. An analysis of their influence on the accuracy of a hybrid model is given and experimental results from a feasibility study are presented.

Introduction

During recent years great advances have been made in the field of numerical models. Simple models which start from the assumption of vertically averaged velocities have quite often been applied for the simulation of far-field processes in tidal waters. They are of good economics and high physical reliability and have thus become standard tools for coastal engineers. However, when detailed three-dimensional investigations have to be performed, often mathematical models are less reliable than physical models are. This is due to the fact that only few numerical models of this type [1,2,3] are in use and still only few experience on the choice of physical coefficients is available. Furthermore the computational expense grows considerably. So it is reasonable to stick to physical models for three-dimensional investigations, which should be performed at the largest scale possible. However, a small section of an estuary can be modeled then only. For this the boundary conditions have to be known which often makes a separate investigation necessary. This can be per-

*Dr.-Ing., Universitätsdozent, Technische Universität Hannover

formed by setting up a physical model of the whole estuary at a much smaller scale. This technique would be rather expensive. A second approach can be made by using a far-field numerical model. However, now the near-field section has to be included into the computation which starts from the assumption of vertically averaged velocities. A considerable error may result from this simplification, which should not be allowed for. It can be avoided by a new investigation technique, in which the near-field section of the model is realized hydraulically and the outer area of the model, for which the far-field assumptions are valid, is set up numerically. Both models are coupled under real-time conditions and thus integrated into one new formulation, which we call a hybrid model. The three-dimensional physical model interacts dynamically with the two-dimensional numerically simulated part and vice versa. So no special boundary conditions have to be controlled on the physical model part. The only prescribed conditions are those for the outer mathematically simulated part.

The coupling technique between the hydraulic and numerical model follows the strategy of correcting the water-levels and the discharges on the boundary between both models within small fixed time-intervals, thus guaranteeing continuous condition between both models. The practical applicability of hybrid models depends on the computing time needed for the numerical model and on the time needed for performing the control operations on the instrumentation. These time-elements have to be analysed carefully. This will be done by some theoretical considerations and experimentally in a feasibility study which was run for an one-dimensional open channel system.

Hybrid Model

The hybrid model technique will be tested in principle for a rectangular straight channel of about 25m length. The tank is closed at one end and a sinus-shaped variation of the water-level is controlled at the other end (Fig.1).

The channel may be regarded as a hydraulic model of a system. For our investigations the model has to be reformulated in a hybrid way. It is cut into two parts (Fig.1) now, one of which still is a hydraulic model, whereas the other part is simulated numerically on a computer. As with respect to geometry and boundary conditions no changes have been made, the time history of the water-levels must remain the same for any station in the hydraulic model as well as for the hybrid formulation. A comparison between measured values in both model tests gives some idea on the accuracy and reliability of the hybrid approach.

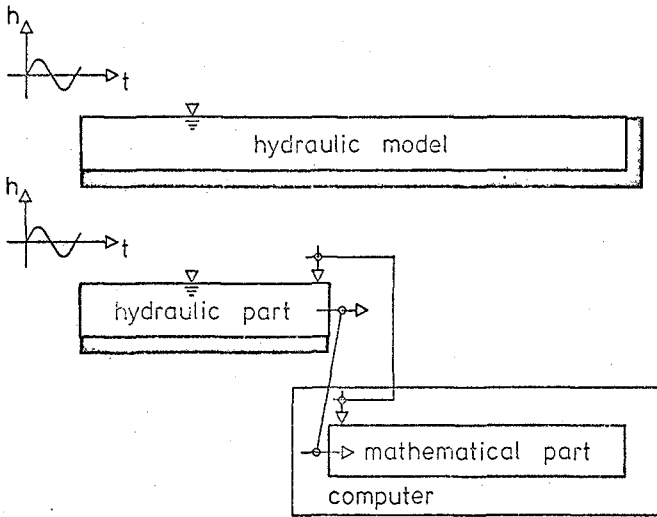


Fig. 1 Feasibility Study

The coupling procedure between the numerical and the physical model part is run on the same computer as the numerical model is (Fig.1). Within fixed time-intervals which we call the coupling intervals Δt , the water-level is measured at the coupling point in the hydraulic model and given as boundary condition to the mathematical model. Now the computation is performed for one time-step, which is equal to the coupling interval. The numerical model is thus updated from the time level of the last measurement to that for which the boundary condition is valid. The computed discharge is then given for control to a pump-system on the hydraulic part (Fig.1). If this procedure works within very small intervals, continuous water-levels and discharge on either side of the coupling point can be expected. Practically, however, the coupling interval cannot be made arbitrary small as within each interval some time must be spent on the computation of the numerical model and some further time for setting the pump-system to the computed discharge values. These time-elements determine not only the frequency of the coupling procedure but they also represent a time-delay between measuring and having the pump set to the computed new position. So they strongly influence the behaviour of the hybrid model which is seen from Fig. 2, in which a comparison is made between water-levels h and discharges q measured in the complete hydraulic model and the corresponding values h^* and q^* in a hybrid for-

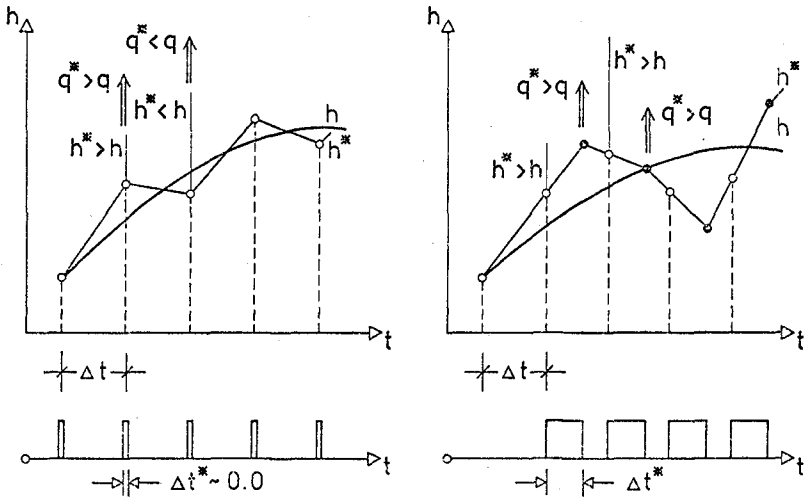


Fig. 2 Coupling Procedure

mulation.

The left side of Fig.2 shows a situation when the delay is assumed to be nearly zero. The coupling procedure starts by measuring a water-level h^* and gives this as boundary condition to the numerical model. This now computes a discharge q^* which will be bigger than the corresponding q in the hydraulic model if h^* was measured higher than h . When now q^* is controlled on the pump it causes the water-level to sink for the time Δt of the coupling interval and so the next measured value h^* will be lower than h . A lower water-level h^* now leads to a computed discharge q^* which is smaller than q and thus the water-level starts rising again. This oscillation around the correct value can no longer be guaranteed when the time-delay is taken into consideration. This is shown on the right side of Fig.2. The water-level keeps rising during all the time needed for the computation of the value q^* for the discharge which, when available, does no longer corresponds to the actual water-level. The computed discharge is too small now and the next water-level will remain too high. But then a rather strong variation of the discharge may follow which will surely induce a considerable error and may even make the system to run out of control. An analytical analysis of such conditions can hardly be given due to the nonlinearity of the describing differential equations. So

experiments have to be run in order to find out, up to which delay the hybrid model will give satisfactory answers.

Time Elements

Time delays inherent in the coupling procedure are basically caused by three elements (Fig.3).

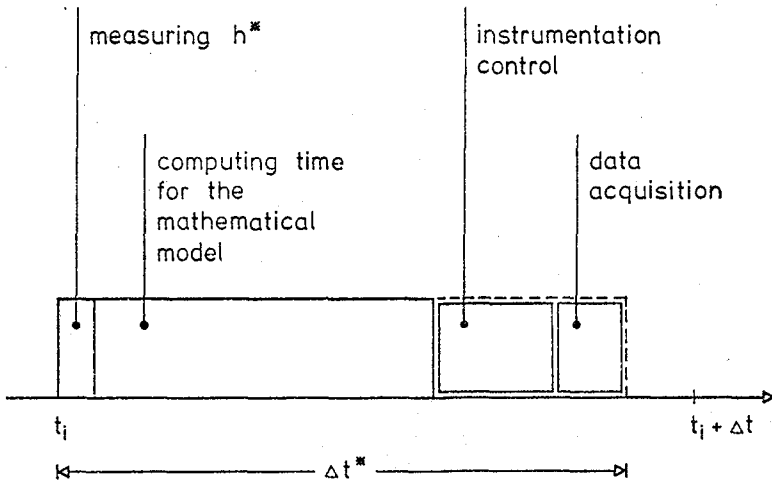


Fig. 3 Time Elements

Within one coupling interval the water-level has to be measured which takes a very short time only. An interrupt is generated by the computer, the sampling performed via the multiplexer and the analog signal from the instrumentation converted into a digital form. A brief subroutine subsequently transforms the measured value into the wanted water-level quantity taking the calibration curve of the instrumentation into account. Performing all these operations takes mostly less than 0.01 sec. So this time element is very small and can be neglected for further considerations. The second step within the coupling routine is the computation of the mathematical model. This may take a considerable amount of time depending on the size of the system and the chosen numerical algorithm for solving the differential equations. These are given by the equation of motion

$$v, _t + v v, _x + g h, _x + R v = J \quad (1)$$

and the equation of mass conservation

$$h, _t + h v, _x + v h, _x = 0 . \quad (2)$$

v is the velocity, h the water-level, J the bottom slope and R stands for a parametric term including turbulence and friction. Numerical solutions mostly start from the linearized version of the equations

$$v, _t + \bar{v} v, _x + g h, _x + R v = J \quad (3)$$

$$h, _t + \bar{h} v, _x + \bar{v} h, _x = 0 \quad (4)$$

The bar-marked quantities are assumed to be known and are chosen identical to the initial conditions for the actual computational time-step.

The numerical solution schemes can be formulated in quite different ways using either a finite difference or a finite element approach. In any case a set of explicit equations is obtained if the problem is formulated explicitly or an equation system will result if an implicit strategy is chosen. With respect to the real-time application in a hybrid model, the computational expense of both formulations has to be analyzed. The solution of the equation system can be performed rather economically by the double-sweep algorithm [4,5], but explicit schemes are still more economical if a comparison is made on a per step basis. However, these schemes are not unconditionally stable and so often several computational steps are necessary to arrive at a time-level the solution for which is obtained by implicit schemes within only one step. So implicit schemes may become again faster on the coupling interval basis. Furthermore the time-step may be varied arbitrarily without altering space discretizations due to the stability properties of such schemes. These considerations lead to the use of a double-sweep implicit model for this study.

The third time-element is represented by the control operations on the pump when this is set to the computed new discharge value. This can be performed either under direct computer control or by using additional technical equipment. In any case the computed discharge must first of all be converted into an electrical or mechanical quantity. This is achieved by a simple subroutine referring to the calibration curve of the pump. Then this digital value is given via an output relay to the instrumentation. If this is set to the

new position in only one step this would surely be the most time saving way in a real-time application, however, a sudden change in discharge will cause big disturbances near the coupling point and thus falsify the next measurement of the water-level h^* . So it is preferable to vary the flow conditions slowly bringing the instrumentation up to the new position by an independent unit being supplied with a clock and a counter or in a more flexible and cheaper way by the computer itself using the interrupt facilities. The gradient, by which the new position is approached, can then be determined by a software solution but then the computer is kept busy and cannot yet start the next coupling interval. So this time must be considered to be the third time-element. However, as the computer calculations are performed much faster than output signals can be given to the instrumentation, this time-element may include additional functions. During intermediate intervals data acquisition routines for the hydraulic model can be run and thus a task be taken into account, for which in many laboratories computers originally have been made available. From this then follows that for hybrid models mostly no additional installations are needed.

Besides this way of performing the control operations, which can be programmed very easily, there is still a more complex alternative. In this again the interrupt facilities of the computer are used, now interrupting the computing process of the numerical model for control and data acquisition. This leads to a more complicated software solution, but allows for neglecting the third time-element in all considerations. So the only element, causing any delay, is the computing time of the numerical model.

Experimental Tests

The test series on the time conditions are run for the system shown by Fig.4.

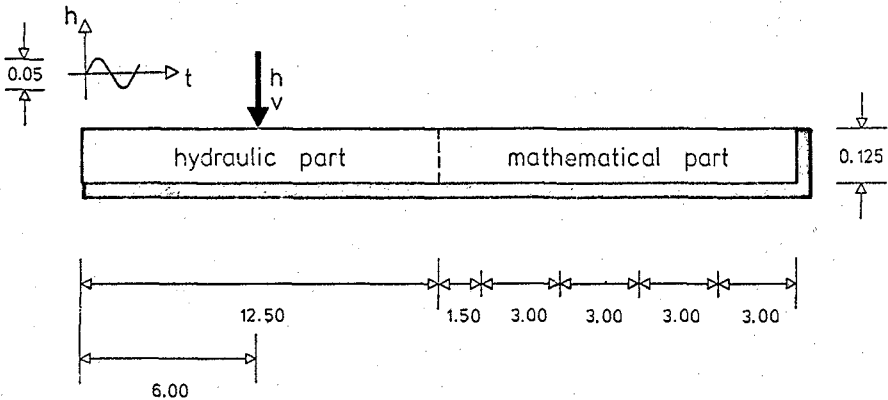


Fig. 4 Hybrid Model

At the left hand side a sinus-shaped variation of the water-level with an amplitude of 2.5 cm and a period of 300 sec is generated. The mean water depth is 12.5 cm. These values correspond to conditions which are often found in estuary studies of shallow water areas. The numerical part of the model is discretized by 5 elements thus giving a computation time of about 0.1 sec per time-step. For comparisons between the original hydraulic and the later hybrid model the time-history of water-levels and velocities is gauged at always the same station (Fig.4) in the hydraulic model part. Any discrepancy in the results can than be interpreted as an error induced by the hybrid realization and by increased or decreased time-elements.

The first test concerns a minimum of delay. The computed new discharge q^* is then available after 0.1 sec already, but the control operations on the instrumentation need much more time. So a coupling interval of $\Delta t = 1$ sec is chosen within which the numerical model takes 0.1 sec, the control operations take 0.7 sec and 0.2 sec are left for data acquisition. The results from this test for the hydraulic and hybrid formulation are given by Fig.5. In the upper part a comparison for the water-levels over 5 tidal cycles is made. It shows very good agreement. The same can be stated for the velocities as shown in the lower part of Fig.5. The rather nervous behaviour of these curves must be explained from the instrumentation. A thermo-element based instrument had been used, giving the resultant velocity component at one fixed point only. As no artificial damping on the analog output was made and no averaging performed, turbulent variations are still inherent in the data. The decreasing magnitude of the velocities for the first three periods has to be explained by the fact that the system starts from rest. Quasi stationary conditions are not obtained up to the fourth period.

The object of the experiments is to find out up to which size the computing time of the numerical model can be extended. So a further test is run with a delay of 2.1 sec. As the coupling interval is made $\Delta t = 2.0$ sec, all control operations have to interrupt the computation of the numerical model. Due to programming simplification no interrupt is allowed within the first 0.1 sec of a coupling interval, in which all measuring procedures are run. So finally a delay of 2.1 sec results. Figure 6 shows the comparison for the water-levels. In the lower part of the figure a detailed analysis for two periods is made. Referring to the water-levels measured in the original hydraulic model the error for the hybrid formulation can be calculated on a per centage basis. The errors found do not exceed the range of 1%. So the difference between measured water-levels in the hydraulic and hybrid model is of about 1.5 mm at maximum, or when referring to the tidal range of 50 mm, of about 3%. An error of this magnitude, however, seems still to be acceptable as this is within the same range of accuracy in which in many cases also field-data are.

A further extension of the time-delay up to 3.1 sec leads to

only slightly increased errors. More interesting to note, however, is the fact, that small local disturbances on the

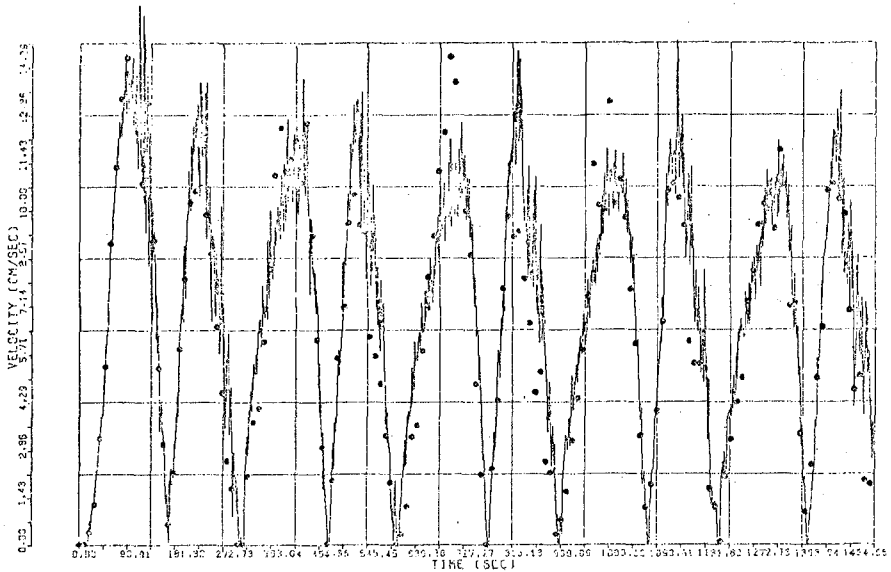
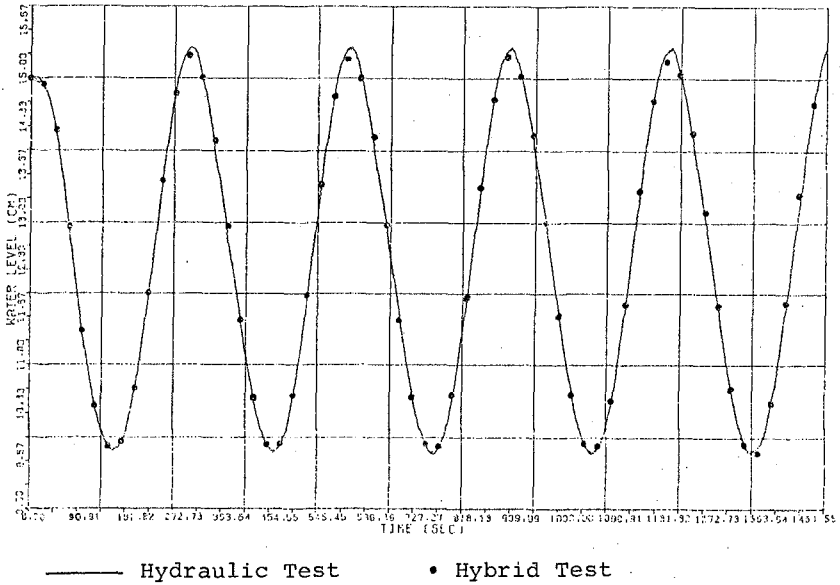


Fig. 5 Comparison of Hybrid and Hydraulic Test, Delay 0.1 sec

measured water-levels at the coupling point, as for instance caused by air bubbles in the water, induce very heavy oscillations of the water-level. Though these mostly disappear after slack water, in general test run at this and further extended time-delays gave no satisfactory agreement with hydraulic model tests.

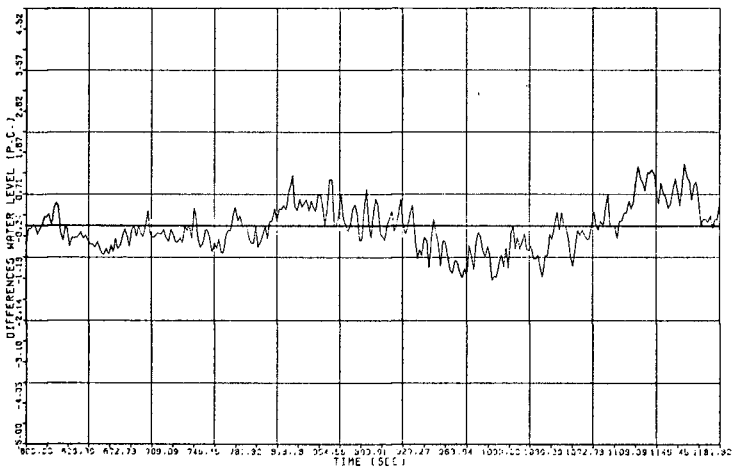
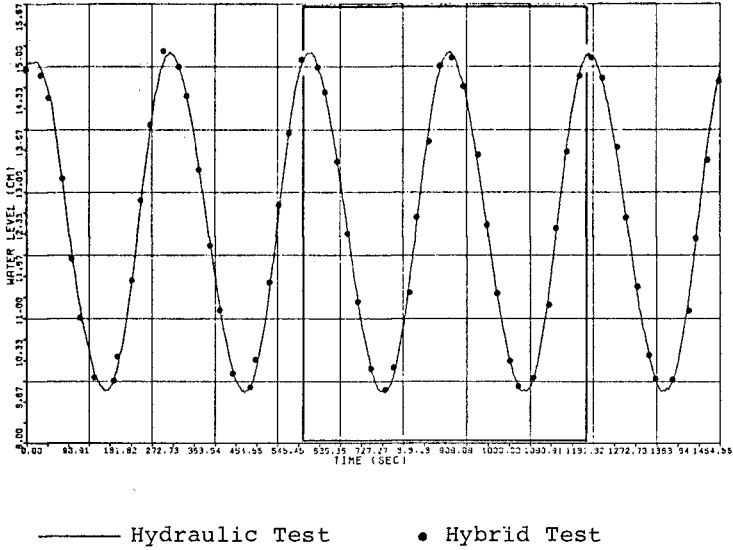


Fig. 6 Comparison of Water-Level, Delay 2.1 sec

Conclusions

A feasibility study was run on the realization of a hybrid model technique for open channel flow situations. An analysis on the time-delay, caused by the computation of the numerical model part, showed that for the system under investigation a delay of about 2 sec lead to an error of about 1.0% for the water-levels. This magnitude seems to be acceptable in practical applications, as it is of the same order, of which in many cases field data are. On the other hand a time of 2 sec allows for the computation of about 100 elements in the used numerical model. In many investigations this number is fully sufficient for a good representation of the far-field area of a system. So these results lead to the conclusion, that the hybrid model technique can readily be applied in practical investigations.

Acknowledgement

The study was carried out in the Sonderforschungsbereich 79 at the Technische Universität Hannover under sponsorship of the Deutsche Forschungsgemeinschaft.

The author wants to thank the team working on this project for good cooperation and many interesting discussions.

References

- [1] LEENDERTSE, J.J., ALEXANDER, R.C., LIU, S.-K., A Three-Dimensional Model for Estuaries and Coastal Seas, Vol.1, Principles of Computation, Report R-1417-OWRR, Rand Corporation, 1973
- [2] SÜNDERMANN, J., Die hydro-dynamisch numerische Berechnung der Vertikalstruktur von Bewegungsvorgängen in Kanälen und Becken, Mitt.Inst.Meereskunde, H.19, Univ.Hamburg, 1971
- [3] EBELING, H., Berechnung der Vertikalstruktur bei Flachwasserwellen mit der Methode der Finiten Elemente, Diss. Techn.Univ.Hannover, 1976
- [4] DRONKERS, J.J., Tidal Computations for Rivers, Coastal Areas and Seas, J.Hydr.Div., 95, 1965, pp 29-64
- [5] SCHULZE, K.-W., Eine problemorientierte Sprache zur Dynamik offener Gerinne, Mitt. Sonderforschungsbereich 79, Techn.Univ.Hannover, H.1, 1973

CHAPTER 200

PLANFORM INFLUENCE ON FLUSHING AND CIRCULATION IN SMALL HARBORS

by

Ronald E. Nece¹, Roger A. Falconer², and Toshiro Tsutsumi³

ABSTRACT

Laboratory data showing the influence of planform geometry on the tidal flushing characteristics of small harbors of simple surface shape. The tide ranges, water depths, and planform areas are typical of those encountered in small-boat marinas in Puget Sound, Washington. Each harbor investigated had a single, asymmetric entrance.

Flushing and circulation patterns within such harbors depend strongly upon the characteristics of the angular momentum established within the basin and upon the effective penetration distance into the basin of the stream of ambient water entering the harbor on the flood tide.

Experimental results confirm that best gross tidal flushing occurs when rectangular harbors have an aspect ratio L/B near unity, and that rounded interior corners of the basin has little effect on the gross tidal flushing but does improve local exchange. Aspect ratios L/B less than 3 lead to the creation of more than one circulation cell (gyre) within the basin.

INTRODUCTION

This paper reports on a laboratory study of tide-induced circulation in small, constructed harbors. Effects of wind and waves upon water motions within the harbors are not considered.

The study was keyed to the continuing demand for more small-boat marinas in Puget Sound, Washington. A common construction approach is to dredge the marina basin from a tideflat area, with the dredged material providing fill for parking lots, dry land work and storage areas, etc. A breakwater is provided on the seaward side, usually with a single asymmetric entrance located to provide best wave protection. Surface areas typically range from 10 to 30 acres, with provisions for from 200 to 800 boat moorages. Such marinas can truly be classified as "small" harbors.

Questions related to water quality are of considerable importance in

-
1. Professor of Civil Engineering, University of Washington, Seattle, Washington, U.S.A.
 2. Graduate Student, Department of Civil Engineering, Imperial College, London, Great Britain.
 3. Technical Official, Civil Engineering Research Institute of Hokkaido Development Bureau, Sapporo, Japan.

the planning and design of such harbors. Of particular concern in the Puget Sound area is the potential impact of water quality in marinas on fish, particularly migrating juvenile salmon. Poor tidal flushing can lead to detrimental algal growths and low dissolved oxygen contents, dangerous to the migrating fish. It becomes imperative in the design of new marinas, and in the design evaluation leading to the legal permission to proceed with construction, that both the gross tidal flushing and the local circulation patterns within the proposed basins be considered. The particular concern of the present study is the question of how much the basin planform geometry affects the overall exchange and the internal circulation patterns.

The approach followed has been to utilize physical models. Numerical modeling procedures have been employed to study flow fields in existing small harbors (e.g., Grubert (1)), but in order to predict actual water exchanges a convective-diffusion solution would have to be superimposed on the hydrodynamic solution. Efficacy of the numerical techniques depends upon a valid determination of the separation streamline of the flood currents around the edges of the harbor entrance and on the time-and-space unsteady circulation cell which is initially engendered by this separation phenomenon, as well as upon the correct representation of diffusion coefficients. For designed but not built basins, the physical model approach has been considered the more economical and graphical approach to a combination of design tool and screen (2).

The laboratory tests described here utilized single-fluid vertically distorted models with a 10:1 distortion ratio. Such models do not properly scale diffusion-dispersion processes (3); therefore, the assumption must be made the convective transport is the dominant mode of water exchange and that diffusion per se is of less significance, allowing the use of tracer dyes in the model. This assumption has been used in a number of specific model studies of tidal exchange in small harbors subject to fairly large tides, where tidal currents are the dominant circulation feature (2). Field verification studies of water exchange are still needed; the models do reproduce depth-averaged velocities in the small harbors (4).

Because the tidal currents are indeed quite strong in the basins modeled it is safe to ignore Coriolis as well as wind and wave effects, and because the basins are relatively short and deep the absence of a friction calibration is not viewed as a major concern. Results are restricted to non-stratified harbors having no fresh water inflow; this is indeed the situation for the well-mixed water bodies which have been investigated so far in the Puget Sound marina studies. These limitations are listed here because they do restrict the generality of the results.

RANGE OF TESTS

The laboratory studies were treated as model studies of idealized basin shapes. The scale ratios were 1:500 horizontal, 1:50 vertical. Tides were restricted to repetitive, sinusoidal tides of constant period of 10.52 minutes in the model corresponding, via Froude law scaling relations, to a 12.4-hour semi-diurnal tide.

Gross water exchange (flushing) was determined by measuring changes in the concentration of fluorescent dye Rhodamine-WT in the basin over a number of cycles. Ink dye was used for visual observation of internal circulation patterns. Laboratory techniques and details of the tidal model basin used have been described previously (2,4).

Flushing data are presented in terms of E, the average per-cycle exchange coefficient, defined as that fraction of the water in the basin at high water slack which is removed from the basin and replaced by ambient water during the cycle ending at the next high water slack. The choice of selecting the period from high-water to high-water is arbitrary, but leads to a simple comparison with the tidal prism ratio, defined conventionally as

$$\text{Tidal Prism Ratio (TPR)} = \frac{(\text{Basin Vol. at High Tide}) - (\text{Basin Vol. at Low Tide})}{\text{Basin Volume at High Tide}}$$

where the numerator is known as the "tidal prism." A "flushing efficiency" is defined as

$$\eta = \frac{E}{\text{TRR}} \times 100, \text{ percent}$$

and compares measured water exchanges with those predicted by the simple tidal prism theory.

Three planforms--rectangular, rectangular with rounded corners, and circular--were investigated. For simplicity, vertical walls and horizontal basin bottoms were used in all cases. The basin planforms and notation used are shown in Figure 1. Semi-circular "jetties" were used at the entrance in each case.

The basin area was maintained at 1.25×10^6 square feet (28.7 acres). The equivalent $L/B = 1.00$ basin (which was not tested) has a side length of 1180 feet, or approximately 0.2 mi. The mean depth d within the harbor was 16 feet, taken at mean water level. The three tide ranges used in the tests were: neap, 4 feet; mean, 8 feet; spring, 12 feet. These values are representative of small boat basins in Puget Sound. The range of L/B in the rectangular basin tests varied from 0.20 to 5.00, more than spanning the usual range of aspect ratios found in such small harbors with single entrances aligned with one side wall. Entrance widths w were 125, 250, and 500 feet; the first is the most representative of field dimensions, and is emphasized most in following results. Data are presented in terms of equivalent prototype dimensions.

TIDAL FLUSHING

Essentials of the flushing (water exchange) test results are summarized in Figure 2 on which are shown data for three entrance widths w , three tides H , for rectangular basins over the aspect ratio L/B range 0.2 to 5.0. No data points are shown on Figure 2; a representative set is shown on Figure 3, illustrating the degree of experimental scatter which can be obtained in the rather sensitive exchange tests.

A few conclusions are apparent. Over the range of L/B from $2/3$ to 3.2 there is relatively little variation in exchange coefficient E for a given tide range H . The overall flushing falls off markedly for L/B less than $1/3$ and greater than 3 . This trend holds for the narrow entrance widths w . The dip in the E -curve near $L/B = 1.0$ is confirmed by the test points in Figure 3. At the larger tides H , the narrower entrance generally produces better overall flushing. As H decreases, the flushing efficiency η increases; this behavior has been noted on model studies of specific marinas having the very short entrance channel lengths used in the present tests.

Effects of L/B and w noted above are linked to the angular momentum of the complex flow within the harbor. The preservation of this angular momentum, associated with the deflection of flood tide flows through the entrance, is especially important to the internal circulation and, hence, harbor flushing. Circulation cells, or gyres, are created on the flood tide flow by moments of effective stresses associated with flow separation past the breakwater. These cells grow in both circulation strength and in size until they occupy a significant part of the basin, and may persist well into the ebb phase of the tidal cycle. As a consequence of the angular momentum established within the basin, even in the absence of longshore currents ebb flows are often skewed instead of leaving the basin in a direction parallel to the entrance axis. Higher velocities occur near the basin perimeter, and lower velocities near its center. These conditions in some respects are comparable to those occurring when tangential entrance jets of small size are used to produce a slow-moving large-scale circulation in water supply reservoirs (5). This angular momentum allows the inflowing ambient water to sweep past a major portion of the interior boundaries of the basin without losing its identity through diffusion. Thus, factors which contribute to increased angular momentum would be expected to improve overall flushing.

A preliminary simple angular momentum control volume analysis was made which considered shear forces on the walls and bottom of the basin and pressure forces on the walls; these would enter calculations of angular momentum about a vertical axis at the basin center. While details of these forces were not considered because interior velocities were not known, it was demonstrated that the optimum rectangular planform for maximizing the interior velocities at any instant of time is a square, $L/B = 1.0$ (6). For a constant surface area A the square planform has the minimum boundary perimeter, so that for a given H , w combination there is the greatest possibility in such small harbors that the ambient water entering as a two-dimensional jet will be able to circumnavigate the basin. Water which so completes the circuit around the boundary has a velocity component along the breakwater side of the basin as it approaches the entrance from within (clockwise, in Figure 1); if this not fully mixed ambient stream reaches the entrance at about high water slack some of it will be deflected back into the basin but some will exit the basin and not accomplish any effective exchange. The dips on the E -curves near $L/B = 1.0$ on Figures 2 and 3 reflect this phenomenon.

The 125-foot entrance width w is narrow enough to lend itself to the above reasoning over the full L/B range tested, and the 250-foot width nearly so. For the 500-foot width, tested for the 8-foot tide only, at small L/B the entrance width approached L and for large L/B for the constant surface area the width w approached B , and in neither case do the foregoing angular momentum considerations apply. Actual entrance widths are seldom much less than

the smallest (125 feet) valve tested, due to navigation considerations.

The reason for the fall-off in E for L/B less than 1/3 and greater than 3 will be discussed in the next section.

Figure 4 shows there is little difference in gross flushing performance between the rectangular and rounded-corner basins of equal aspect ratio. The benefit of the rounded interior corners is that local separation zones, hence areas of relatively stagnant water, are eliminated; this is a point of concern to fisheries resource managers.

Figure 5 reflects the data of Figure 2, and indicates more clearly that the flushing efficiency for these short-entrance basins increases as the tide range H decreases. This is contrary to what can happen if entrance channels are longer or if exterior constraints such as a detached breakwater located athwart the channel axis impede the free exchange of basin and ambient waters, so that at the smaller tide ranges some of water exhausted from the basin on the ebb is returned to the basin on the flood.

Figures 6 and 7 indicate very little difference in the flushing performance of rectangular and rounded-corner basins with L/B = 1.0 and of a circular basin of the same surface area. At the "mean" tide of 8.0 feet flushing coefficients are nearly identical, and all exchange coefficients are above 80 percent. Extrapolation of these results to tide ranges of less than 4 feet may not be safe. It also is pointed out again that the combination of A, H, and d tested apply to limited geographical areas.

CIRCULATION PATTERNS IN HARBOR

Insight into the mechanisms of the tidal flushing process can be gained by considering the path and distance penetrated into the harbor on the flood tide by the inflow stream of ambient water and by relating this distance to the planform geometry of the basin. This section deals with a simple correlation of these quantities.

Experimental results are shown in Figure 8 for two tidal ranges for each of four harbor geometries. Small tubular drogues, weighted to provide adequate vertical penetration so that the drogues move with the local depth-averaged velocity, were released at the center of the entrance at the time of mean water level crossing and were tracked through the basin for the subsequent one-quarter cycle to high water slack. The locations of the drogues at one-eighth and one-fourth of the tidal period T after release are indicated, as well as the paths followed. The effect of doubling the range H from 4 feet to 8 feet is apparent.

For the elongated basins of L/B = 3.20 and L/B = 0.31, the drogue paths indicate how two circulation cells are developed in the harbors. For the inlet orientation shown the cell near the harbor entrance is clockwise in each case, while that in the rear portion of the harbor is counterclockwise. The drogue pathlines for these two configurations do not show that part of the ambient water stream does not follow the plotted pathline into the rear section of the harbor but rather moves into the gyre in the front section of the harbor. Figure 8 indicates pathlines for water entering at the time of mean

water level crossing. Ambient water entering the basin prior to this time on the flood tide has followed much the same path after initial development of the cell inside the harbor entrance; as a consequence, at the time of high water slack there are currents moving along the walls of the harbor and toward the mouth.

For purposes of comparison, a penetration distance p has been defined as the distance traveled along its pathline by a particle of water which enters the basin at the time of the mean sea level crossing, which for practical purposes in an entrance of the type used in the present study is the time of maximum velocity of the flood tide current. The flood current has maximum or near-maximum momentum at this arbitrarily selected but convenient time, and from consideration of conservation of momentum of the inflow "jet" it possesses the capability of penetrating a maximum distance into the basin in a finite time. The following simple analysis considers the penetration distance p at high water slack, a time $T/4$ after water entrance into the basin. Notation is shown in the definition sketch, Figure 9. The rounded jetties used in the tests minimized contraction of the inflow as it passed through the inlet, so that a one-dimensional condition of uniform velocity V_0 over the entrance area $w d$ could be a reasonable assumption.

The inflow stream initially flows parallel to one wall in the harbor planforms studied, but in all cases ultimately deflects from its initial direction. The choice remains, in a simple momentum correlation, whether to employ a wall-jet analysis or a slot-jet analysis. In either case, neither of which matches the physics of the tidal currents in the small harbors, the expression for the velocity v along the streamline of maximum velocity is

$$\frac{v}{V_0} = C \left(\frac{x}{w} \right)^{-1/2}$$

Values of the constant C are 3.45 for the wall-jet (7) and 2.28 for the slot-jet (8), respectively. Assuming that the steady flow relations can be applied to a water particle moving along this streamline, integration of the expression $v = dx/dt$ along the initial direction of motion, x , gives

$$x = \left(\frac{3}{2} C \right)^{2/3} V_0^{2/3} w^{1/3} t^{2/3}$$

It remains to relate V_0 to the tidal range and to the basin geometry. Applying the simple one-dimensional continuity equation for a sinusoidal tide of range H and period T to the basin of planform area A and inlet cross-sectional area $w d$ at the mean water level, V_0 at this time is given by

$$V_0 = \frac{\pi H}{T} \frac{A}{w d}$$

Interchanging the penetration distance p for the distance along the x -direction gives

$$p = \left(\frac{3}{2} \pi C \right)^{2/3} \frac{H^{2/3}}{w^{1/3}} \left(\frac{A}{d} \right)^{2/3} \left(\frac{\pi T}{T} \right)^{2/3}$$

where n = the fractional part of the tidal cycle after $t = 0$ at which p is evaluated.

The results of Figure 8 have been replotted in Figure 10, in which the maximum value $n = 1/4$ represents conditions at high water slack. The slot-jet value of $C = 2.28$ was used because it correlates more closely with the experimental observations; the wall-jet empirical constant C over-predicts the penetration. Numerical agreement with the jet models considered could not be expected, but the test results do show agreement in the form of the penetration distance vs. time relationships. Therefore, the form of the last equation given above can be used to predict changes in the ambient-water penetration into a harbor with variations in tidal range H or in harbor geometry parameters A , d , and w .

CONCLUSIONS

The effect of planform geometry upon the tidal flushing characteristics of small harbors with single asymmetric entrances has been studied for simple, rectangular basins in which wind and stratification effects are negligible and tidal action is the dominant flow-producing mechanism. When harbor aspect ratios exceed 3 or are less than $1/3$, multiple circulation cells exist within the harbor and the basin-average tidal flushing is reduced. So long as the aspect ratio is kept within these limits there is relatively little variation in the tidal exchange coefficient, E , with L/B for a given tidal range H , although best flushing occurs when the aspect ratio is close but not necessarily equal to unity, the value predicted by simple considerations of angular momentum of the internal tidal currents.

The experimental data indicate that rounding interior corners of the harbor does not improve the gross flushing. The elimination of sharp interior corners does, however, eliminate local stagnation zones and thus improves local water exchange and local water quality. This latter consideration is important to the safety of fish which pass through or temporarily reside in small-boat basins of the size range tested. In the Puget Sound area of Washington, this point is of particular concern in the safe migration of juvenile salmon. Figure 11 illustrates changes in typical marina planform shapes for small-boat basins in the Puget Sound region which have in some part been brought about by considerations of tidal flushing and internal circulation patterns, particularly the latter.

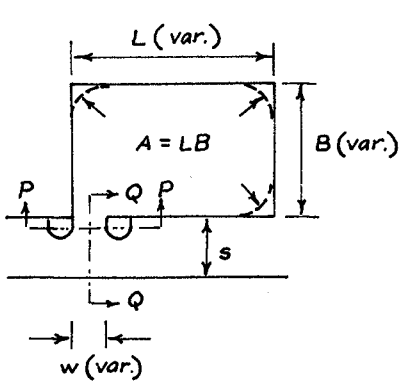
Results of this study may be used to answer some of the hydraulic questions considered in the design of such harbors and may reduce the need for individual model studies on a case-by-case basis.

ACKNOWLEDGMENT

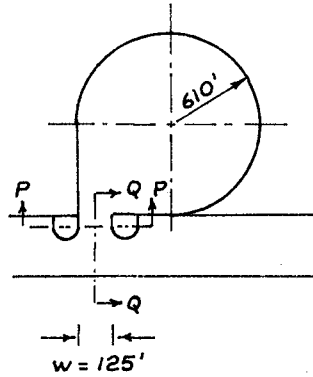
The experiments reported were conducted in the C. W. Harris Hydraulics Laboratory, University of Washington, Seattle, U.S.A.

REFERENCES

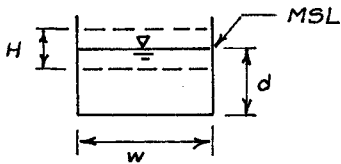
1. Grubert, J. P., "Numerical Computation of Two-Dimensional Flows," Journ. of the Waterways, Harbors, and Coastal Eng. Division, ASCE, 102, No. WW1, February 1976, pp. 1-12.
2. Nece, R. E. and E. P. Richey, "Application of Physical Tidal Models in Harbor and Marina Design," Proceedings of the Symposium on Modeling Techniques, ASCE, San Francisco, California, September 1975, pp. 783-801.
3. Harleman, D. R. F., "Pollution in Estuaries," Chapter 14 in Estuary and Coastline Hydrodynamics (A. T. Ippen, Ed.), McGraw-Hill, 1966.
4. Nece, R. E. and E. P. Richey, "Flushing Characteristics of Small-Boat Marinas," Proceedings of the Thirteenth Coastal Engineering Conference, Vancouver, Canada, July 1972, pp. 2499-2512.
5. Sobey, R. J. and S. B. Savage, "Jet-Forced Circulation in Water-Supply Reservoirs," Journal of the Hydraulics Division, ASCE, 100, No. HY12, December 1974, pp. 1809-1828.
6. Falconer, R. A., "Tidal Circulation Effects in Rectangular Harbors," MSCE Thesis, University of Washington, Seattle, Washington, 1974, 97 pp. (unpublished).
7. Rajaratnam, N., "The Hydraulic Jump as a Wall Jet," Journal of the Hydraulics Division, ASCE, 91, No. HY5, September 1965, pp. 107-132.
8. Albertson, M. L., Y. B. Dai, R. A. Jensen and H. Rouse, "Diffusion of Submerged Jets," Transactions ASCE, 115, 1950, pp. 639-664.



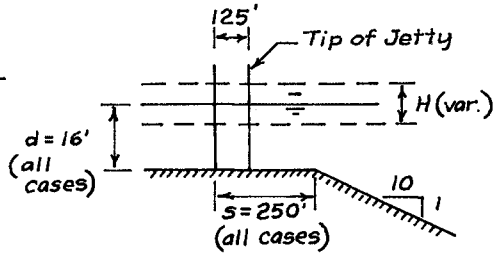
Plan - Rectangular Basin
 (Note: $r = 250'$, all cases,
 Rounded Corner Basin)



Plan - Circular Basin
 (Note: Surface Area = LB)



Sect. P-P



Sect. Q-Q

Vertical Wall, Level Bottom Basin:

$$TPR = \frac{H}{d + \frac{H}{2}}$$

$$\eta = \frac{E}{TPR} \times 100$$

FIGURE 1. Definition and notation diagram.

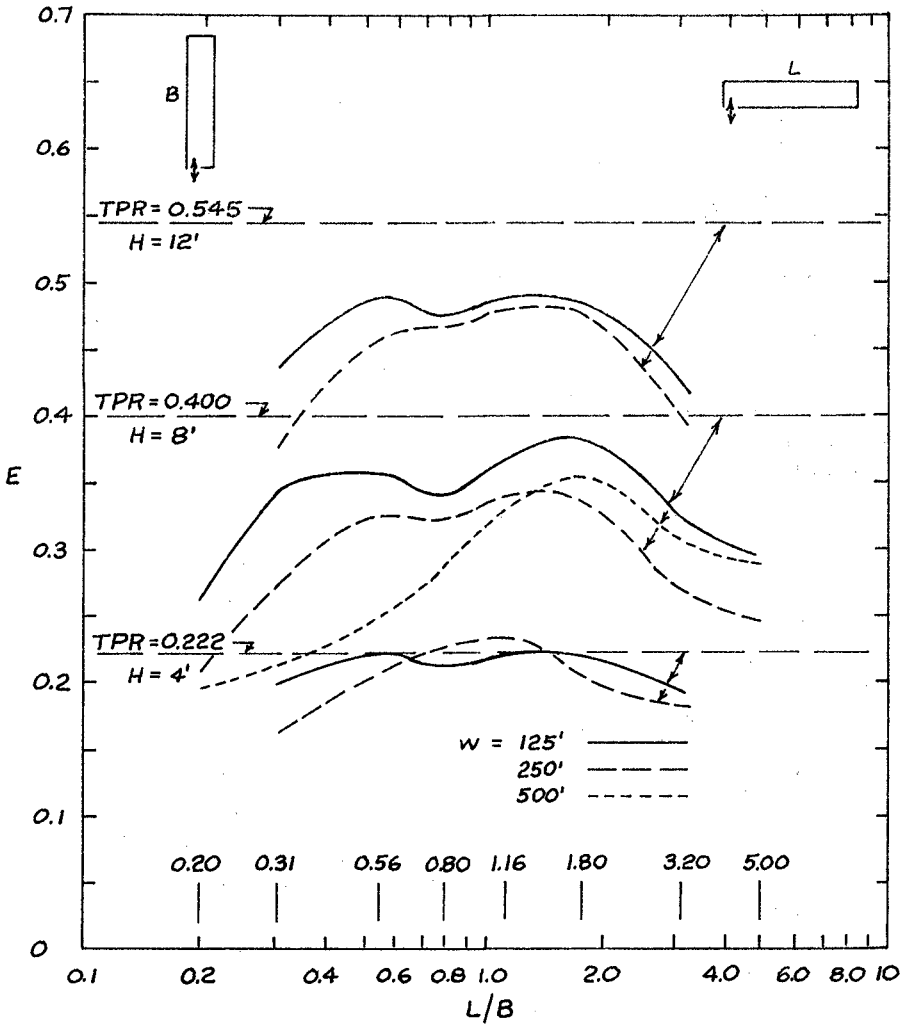


FIGURE 2. Flushing data summary, rectangular harbor.

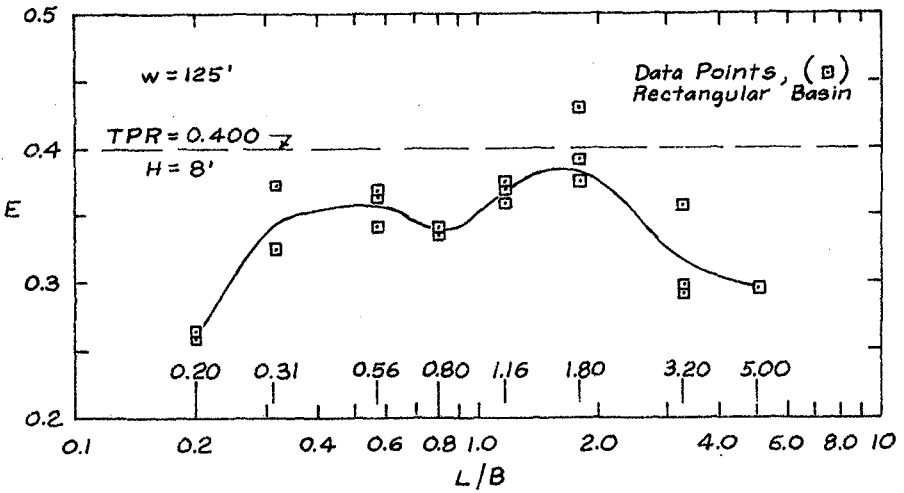


FIGURE 3. Representative data set, rectangular harbor, $H = 8$ feet, $w = 125$ feet.

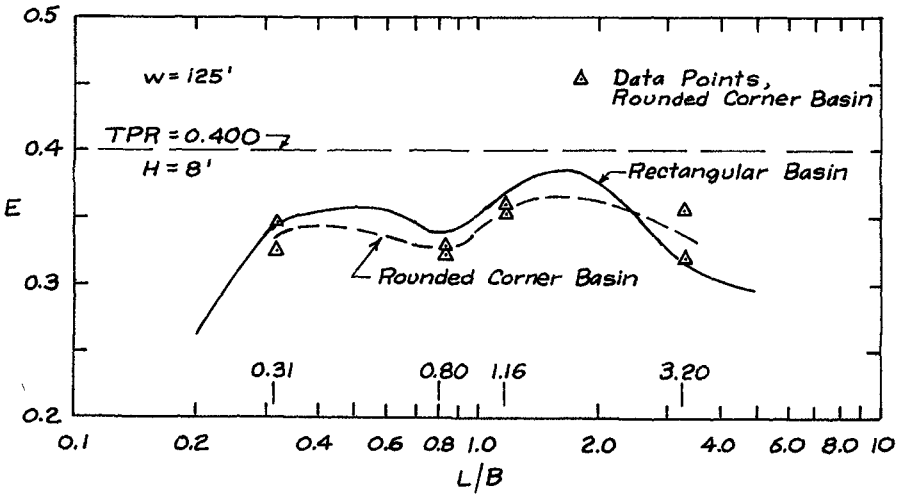


FIGURE 4. Comparison of flushing performance, rectangular basin and rounded corner basin, $H = B'$, $w = 125'$.

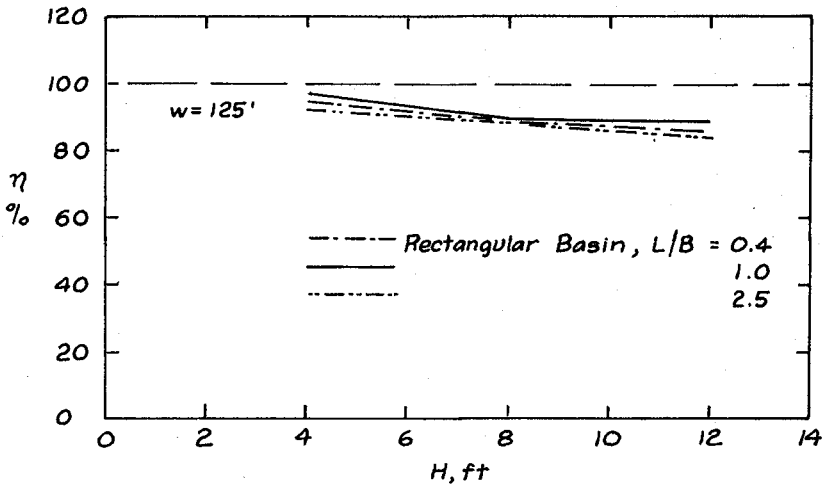


FIGURE 5. Variation of flushing efficiency with tide range, regular basin, $w = 125$ feet.

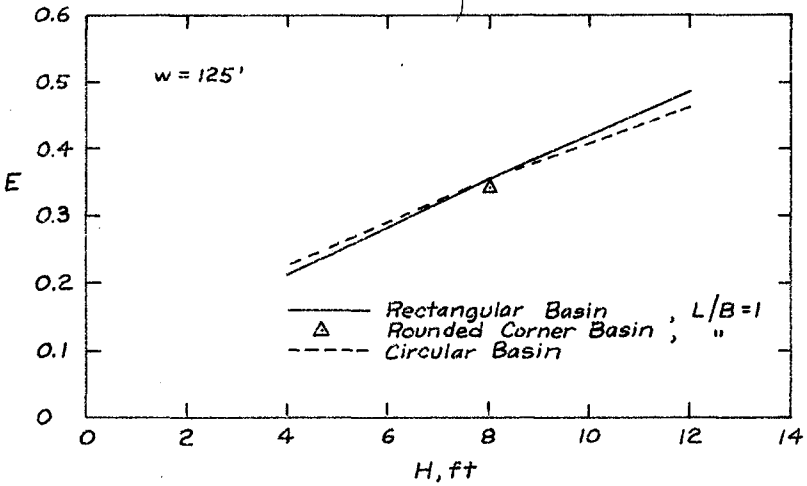


FIGURE 6. Comparison of flushing performance, circular and "square" basins.

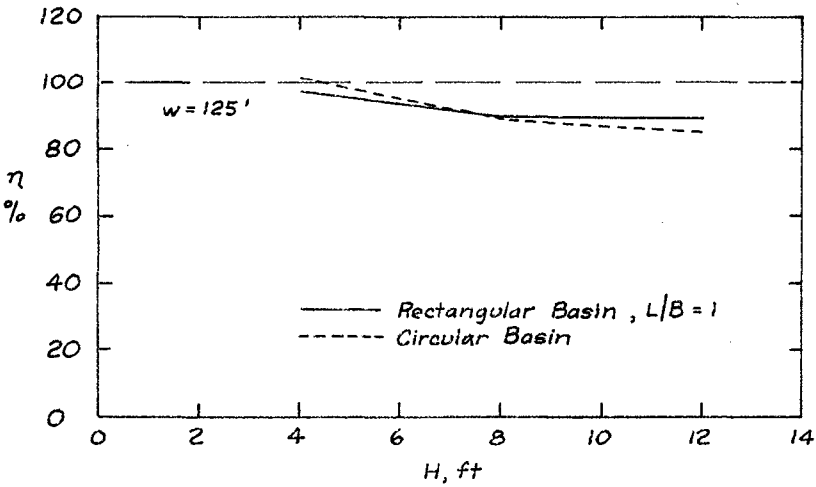
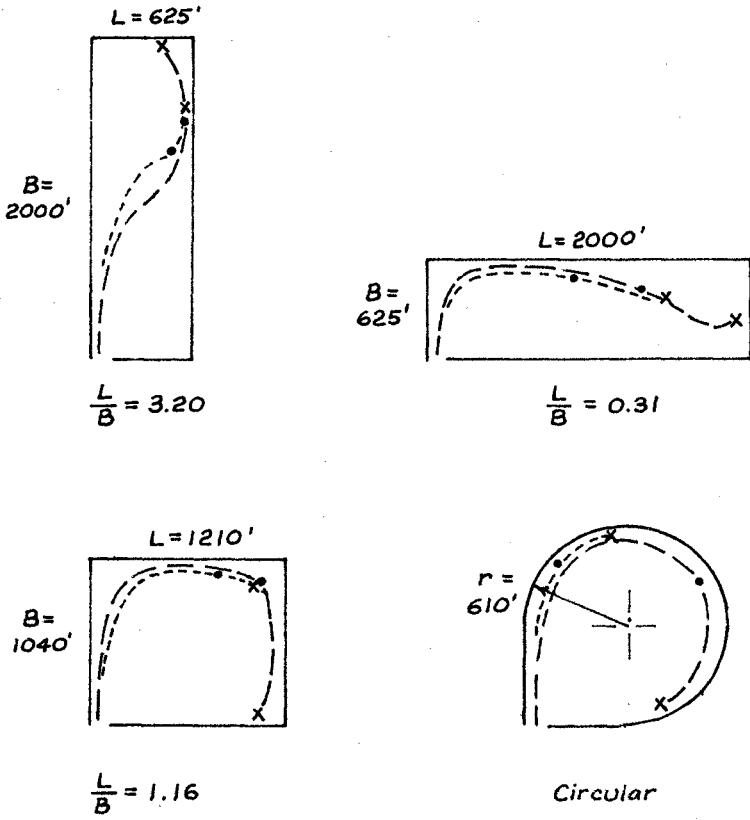


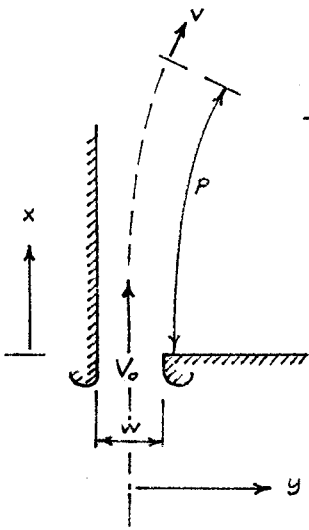
FIGURE 7. Flushing efficiency, circular and "square" basins.



$w = 125'$, $d = 16'$

Time from MSL		Tide Range
$\frac{T}{8}$	•	$H = 4'$ ----
$\frac{T}{4}$	x	$H = 8'$ ---

FIGURE 8. Inlet jet paths and penetration distances for four harbor planforms.



$$\frac{v}{V_0} = 2.28 \left(\frac{P}{w} \right)^{-1/2} ; C = 2.28$$

$$P = \left(\frac{3}{2} \pi C \right)^{2/3} \frac{H^{2/3}}{w^{1/3}} \left(\frac{A}{d} \right)^{2/3} \left(\frac{nT}{T} \right)^{2/3}$$

$n = 0 @ MWL$

FIGURE 9. Definition diagram, jet penetration analysis.

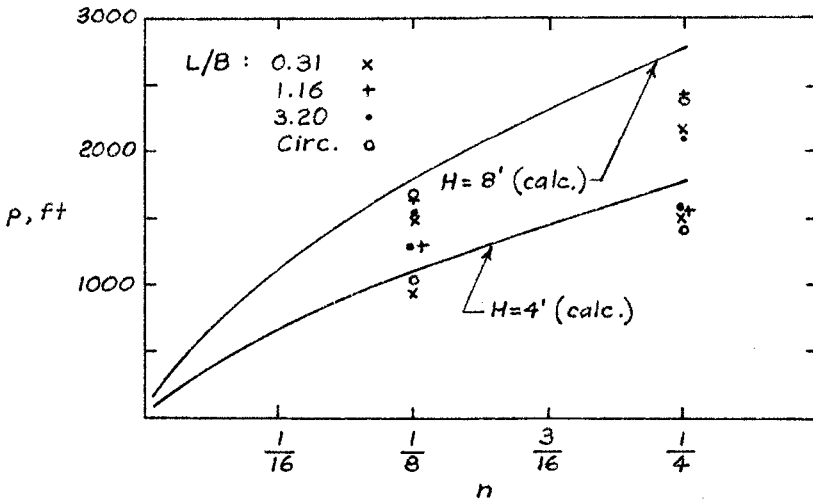


FIGURE 10. Jet penetration measurement data.

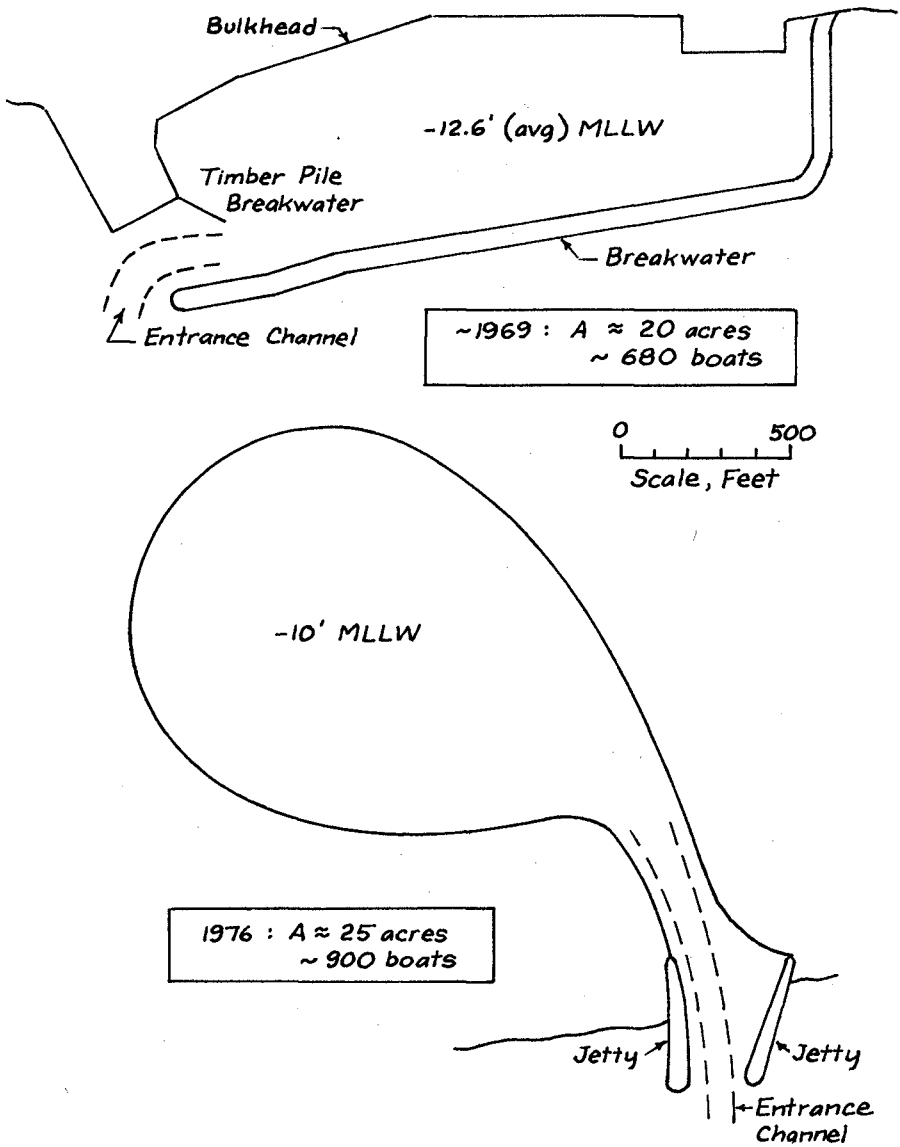


FIGURE 11. Changes in marina planform design to achieve improved internal circulation.

CHAPTER 201

COASTAL PROBLEMS IN SRI LANKA

Frans Gerritsen¹ and Summa R. Amarasinghe²

ABSTRACT

As an island state with about 900 miles of coastline, Sri Lanka is endowed with a large natural resource: its 720 miles of sandy beaches. The coastal zone is under stress by a burgeoning population, living in the coastal belt, and a variety of other demands with conflicting interests. Due to natural causes and interference of men, erosion is a serious problem in the densely populated southwest part of the island.

This paper describes the principal characteristics of the coastal environment and discusses the nature of some of the basic problems. In the recommendations, emphasis is placed on the setting up of an organizational structure to study the problems, both in the field and in the laboratory, with respect to the management aspects in the coastal zone.

INTRODUCTION

The island of Sri Lanka, 25,000 square miles in area with a coastal perimeter of about 900 miles (at least 80% of which are sandy beaches) is located at the southern tip of India; it lies between 6° and 10° north latitudes and between 79° and 82° east longitude. It has a population of 13 million and of this as many as two million are concentrated in the southwestern coastal belt up to a distance of 100 miles south of the capital city of Colombo (see map, Fig. 1).

A coastal retreat, due to erosion by the sea (at one point up to 1,000 ft in the last 50 years), has resulted in the loss of several square miles of the coast especially in the densely populated southwestern region. Of the several protective structures, viz. boulder revetments, sea walls and later on groins, erected in the last few decades only some were successful in combatting the erosion problem. In more recent times the problem has been aggravated by both the direct and indirect consequences of sand and coral mining and other engineering and industrial activity in the coastal zone by numerous individuals and organizations. The rapid development of the country's tourist industry in the last decade has had its impact on the coastal zone. The preservation, restoration, and environmental control of the beaches and above all the effective management of the coastal zone has high priority in the country's development plans.

It was obviously futile to permit illegal and uncontrolled operations to continue on the coast and then spend large sums of money to protect the coast. In addition, existing legislation for seashore protection was weak, while a solution was also necessary for the socio-economic problem of those engaged in the illegal mining of sand and coral for a livelihood. In this connection,

¹Professor, Dept. of Ocean Engineering, University of Hawaii.

²Head, Coast Conservation Division, Colombo Port Commission, Colombo, Sri Lanka (formerly Ceylon).

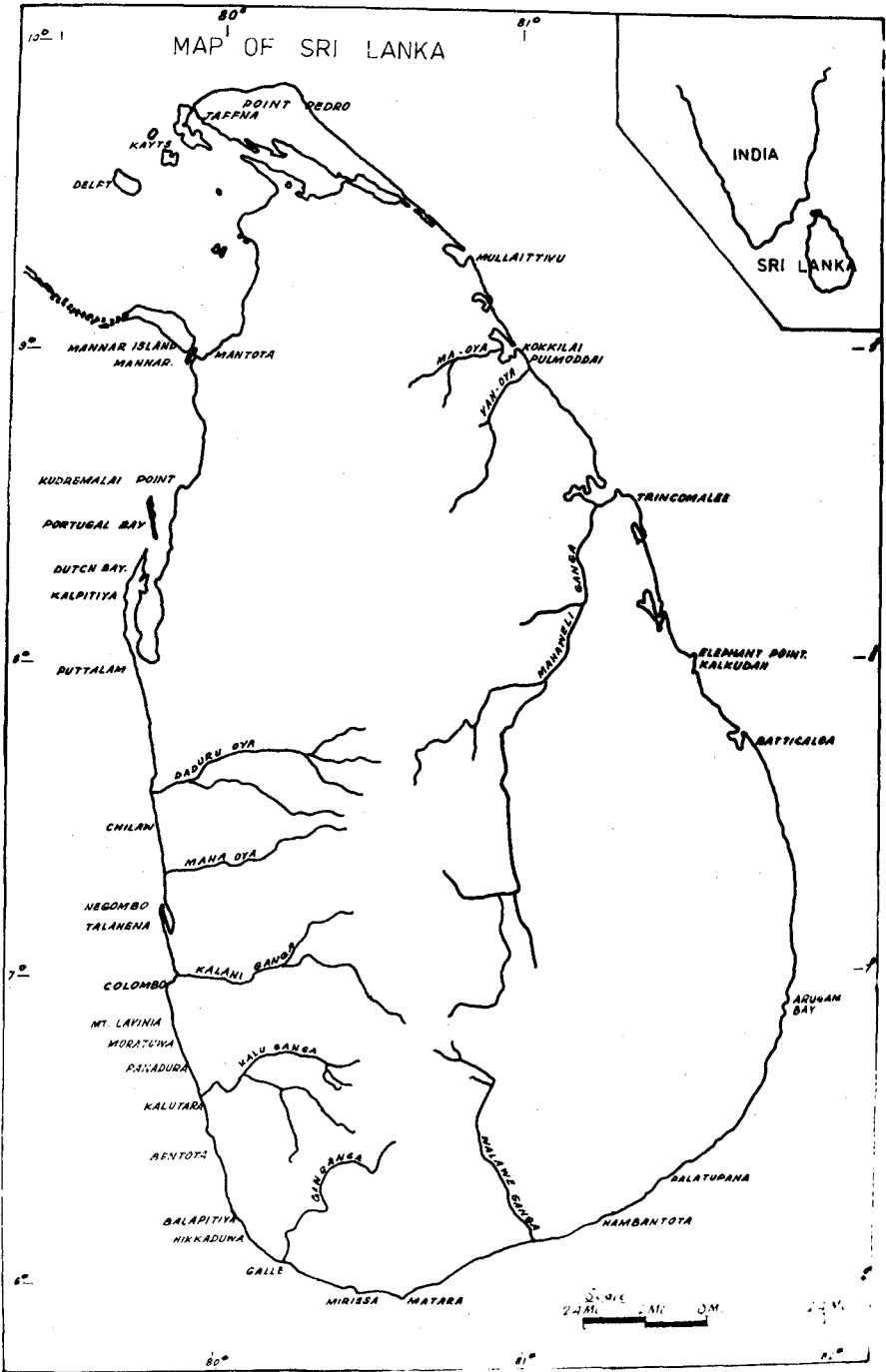


FIG. 1 MAP OF SRI LANKA

proposals made by the Ministry of Shipping and Tourism three years ago and accepted by the government consisted broadly of: (a) the creation of a single authority to control, regulate and coordinate all activity within the coastal zone which may have adverse effects on coast conservation in Sri Lanka; and (b) the framing of separate legislation for the conservation of the country's coast.

Action as proposed above was pursued by seeking assistance from the United Nations for the services of an expert in coastal engineering. In this capacity the senior author spent three months in Sri Lanka (July - September, 1974) to study the coastal problems, to recommend solutions and to make appropriate recommendations for a Coastal Zone Management Program in Sri Lanka. Furthermore, the Colombo Port Commission and the Ministry of Shipping and Tourism, in collaboration with the country's Legal Draughtsman's Department drafted new legislation for coast conservation in Sri Lanka. This draft legislation is now awaiting debate in the country's National State Assembly.

DISCUSSION OF ENVIRONMENTAL FACTORS

Prior to discussing the particular coastal problems in the State, this section provides information on the environment and the general characteristics of the littoral drift.

Geology

The major portion of the island (about nine-tenth) consists of crystalline rocks of Archaean age, with narrow belts of sediments in the coastal zone [1]. Extensive development of sedimentary rock is found along the northwest coast of the island, where limestones of Miocene age are found. Beaches are found all around the island. Along considerable portions of the west coast a shallow coastal reef of sedimentary sandstone of recent age is found. This reef has been a stabilizing factor against beach erosion. The reef runs parallel to the shoreline between Colombo and Mt. Lavinia; at other locations (Negombo, North of Colombo) it makes a small angle with the present shoreline.

Along the greater part of the southwestern and eastern shoreline, beaches are situated between rocky headlands of gneis or granite. In many locations, beaches are backed by lagoons, estuarine deltas and marshes indicative of progradation and coastal rectification that followed a phase of submergence [1]. Cliff coasts occur in the south of the island between Dondera and Tangalle and in the Trincomalee area on the northeast coast.

As to the possibility of tilting of the island around an east-west axis (between Colombo and Pottuvil) with the southern portion of the island going down, this theory has been dismissed by Swan [1]. Instead there seems more evidence for a steady rise in sea level in post Würm times, with minor oscillations superimposed thereon.

The present phase of increased erosion seems due to a slight rise in sea level since the mid-19th century.

Coral reefs are found along parts of the west and east coast. Most coral beds are dead but live coral is still found near Hikkaduwa on the southwest coast and near Trincomalee on the east coast.

Winds and Waves

There are two distinct climatological periods--the southwest monsoon from May to September and the northeast monsoon from November to January. Waves from the southwest are predominant during the southwest monsoon, although waves from the northwest occur occasionally. Winds from the southwest are considerably stronger than from the northeast and the wave conditions on the west coast during the southwest monsoon are more severe than on the east coast during the northeast monsoon. In both cases, the height and period of the significant waves are somewhat reduced during periods of high wind speed due to a limited fetch length, so that the condition of a fully-developed sea will not be reached (Fig. 2).

Waves from the southwest have a median significant height of about 5 ft with a significant period of 5 1/2-6 sec; whereas, waves from the northeast have a median significant wave height of about 3 ft with a significant period of approximately 4 1/2 sec.

In addition to the waves generated by the wind there is the southern swell (from directions between south and southeast), originated by winds and storms on the southern hemisphere. It has a significant effect on the direction and magnitude of the littoral drift.

Tides and Currents

Tides are predominantly semi-diurnal; the tidal range varies approximately between 1.5 and 2.0 ft during spring tides and between 0.3 and 0.8 ft during neap tides [2]. In addition, there is a small seasonal variation.

General ocean circulation around Sri Lanka depends on the monsoon season, as shown in Fig. 3. In a study on oceanographic conditions [3] currents along the west coast were found to run in northerly direction during the southwest monsoon and in southerly direction during the northeast monsoon. The strength of these currents was usually less than 0.5 ft/sec in the Colombo area, but got as high as 1.7 ft/sec in the Galle area. Occasionally considerably higher values (up to 2.9 ft/sec) were observed for no obvious reasons.

Tidal currents become important in the vicinity of tidal inlets and at the mouths of bays and lagoons. Near the breaker zone, wave induced currents become significant and are a primary cause for the movement of sand along the shoreline.

Rainfall and Hydrology

Rainfall is heavy in the mountain areas of the central part of the country, about 100 inches per year, and very heavy on the southwestern slopes of the central hills (up to 200 inches per year). In the coastal belt it averages 50 inches per year. The extreme southeast and northeast coastal zones are dry; the annual rainfall there is below 50 inches.

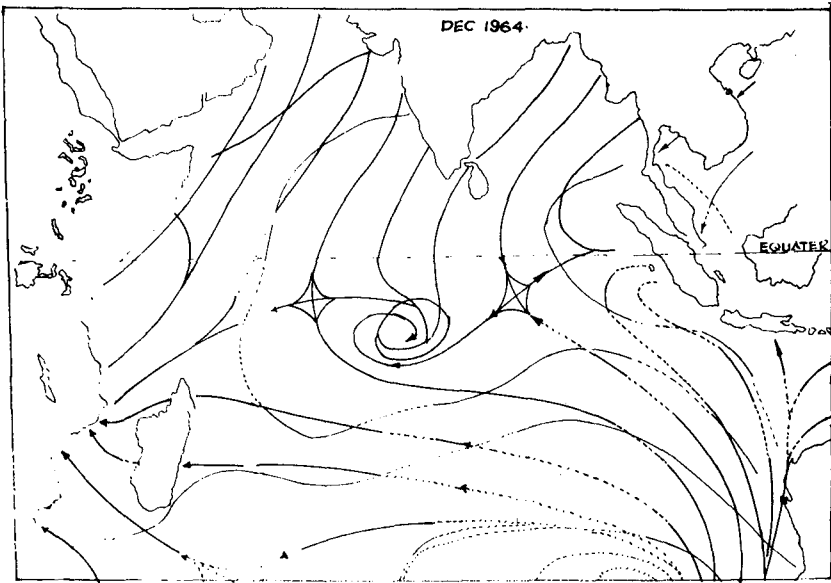
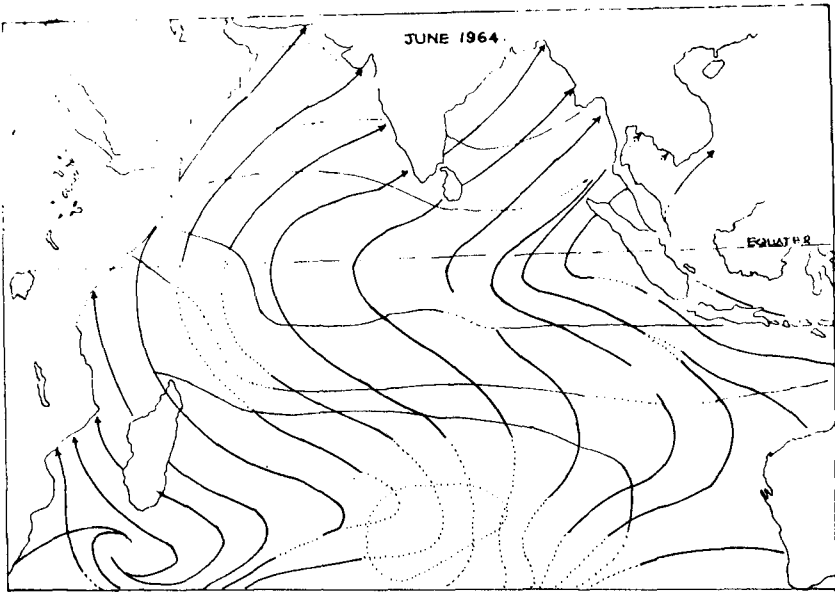


FIG. 2 WIND CIRCULATION PATTERNS IN INDIAN OCEAN

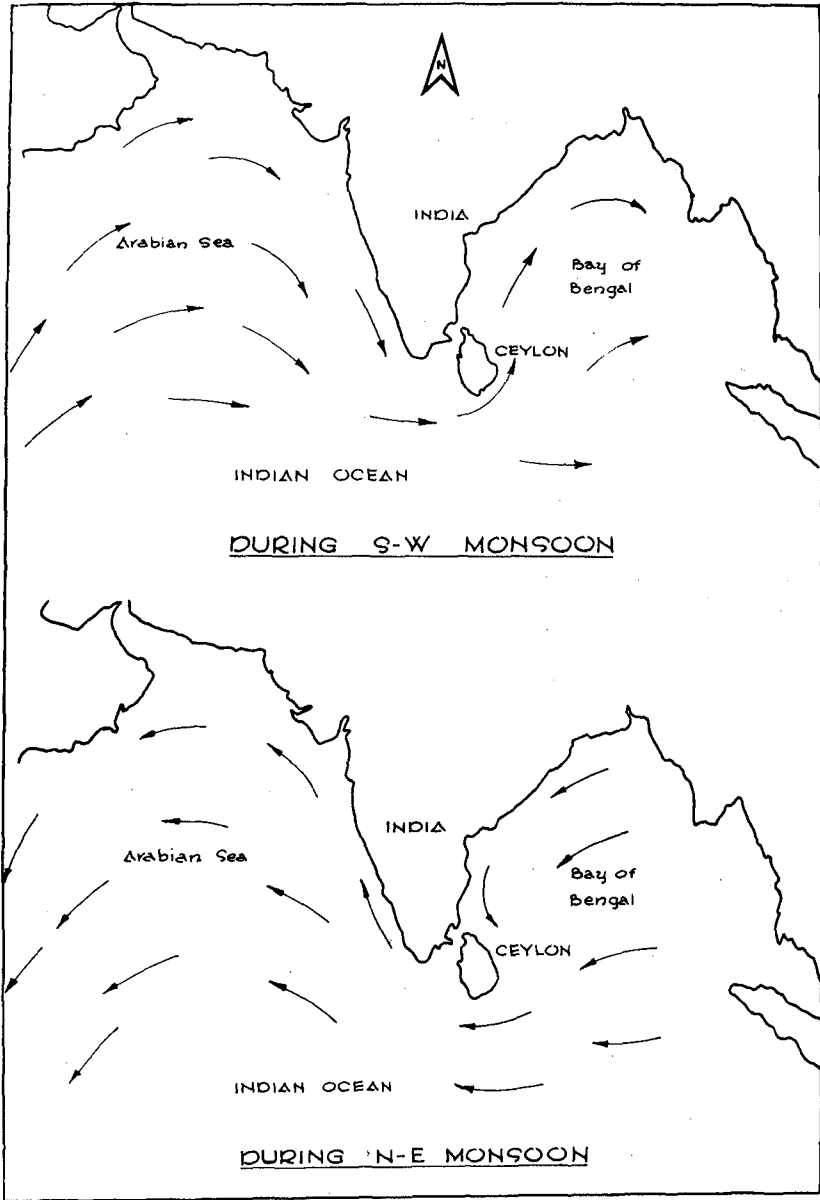


FIG. 3 OCEAN CURRENTS OFF SRI LANKA

The greater part of the precipitation in Sri Lanka returns to the atmosphere through evapotranspiration [2]. The remaining part is discharged to the ocean by a number of rivers of different sizes, which originate in the central highlands and flow toward the coastline. The largest rivers are the Dadura Oye*, north of Chilaw; the Kalani Ganga*, north of Colombo; and the Kalatura Ganga, all on the west coast and the Mahawela Ganga, flowing into Trincomalee Bay on the east coast. These rivers carry large amounts of sediment (sand) to the various coastal sections.

In a number of locations the rivers discharge their sediments into a coastal lagoon where part of the sediment load is temporarily deposited. The steeper the river, the greater the current velocities and the larger the size of the sediment particles that can be transported.

Littoral Drift

The wave climate responsible for the littoral drift along Sri Lanka's shoreline is strongly related to the monsoon periods. Along the west coast the southwesterly waves induce a littoral transport in a northerly direction. Occasionally the drift is reversed during periods of northwesterly storms. The northerly drift is reinforced by the effect of the southern swell for most of the west and southwest coasts. Locally the littoral drift is reversed due to wave refraction and/or diffraction.

During the southwest monsoon, the southwest coast of the island has a nodal point of the littoral drift in the vicinity of Hikkaduwa (see Fig. 1). North of this point the waves are moving sediments in northwesterly direction, south of there in southeasterly direction. In the vicinity of a nodal point the sediments transported by the waves must be supplied from upland or from local sources and often this supply is not adequate to meet the demand. The rate of erosion in this area is the largest in the State (see Fig. 4); in addition, natural erosion here is reinforced by offshore mining of coral. Along the east coast the drift is predominantly to the north during the southwest monsoon under the effect of the southern swell. During the northeast monsoon the transport is basically southward under the predominant effect of the wind-generated waves from the northeast. The southeast coastal area of the state is an area of deposition, as is the northeast coast of the Jaffna Peninsula.

PROBLEMS IN THE COASTAL ZONE

Erosion

The causes of erosion in Sri Lanka can be broadly classified as due to: (a) natural erosion, (b) erosion and sedimentation due to man-made activity, and (c) erosion due to biological activity.

Natural erosion has manifested itself in the formation of a series of bays on the southwest coast suspended by rocky headlands most of which form reasonable stable shorelines. The eroding tendencies of convex shorelines have also resulted in the long term in the creation of several exposed reefs especially on the southwest coast where beach material has been removed by currents over the years. These shorelines have had to be protected by the construction of revetments and in some places by groins.

* Local words for "river".

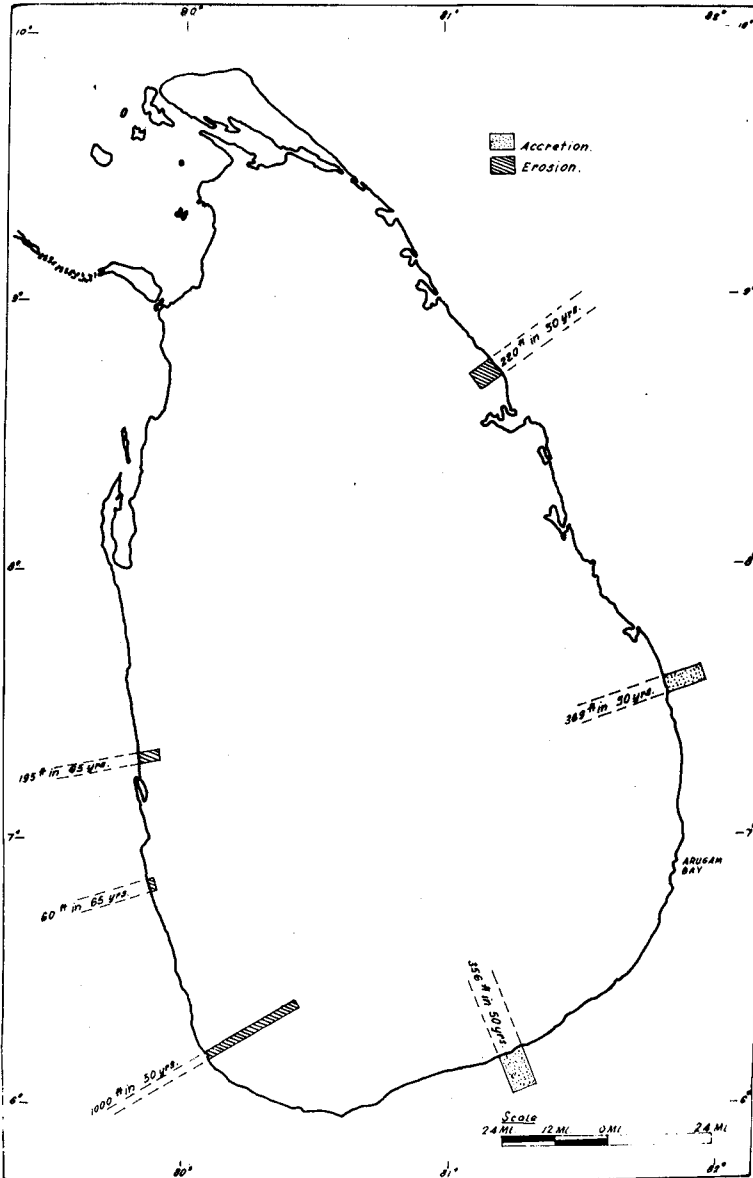


FIG. 4 TYPICAL SHORELINE CHANGES (rates of erosion or accretion) SINCE 1910

Another aspect of natural erosion is the cyclic changes of shorelines adjacent to tidal inlets. An example of the latter is the erosion pattern at the Kalutara inlet where the Kalu Ganga, which discharges the largest volume of water in Sri Lanka, has a fluctuating river mouth. Coast erosion of the adjacent shoreline occurs either on the north or south shores depending on the position of the inlets and the mechanism of the littoral drift in its vicinity. The inlet or river mouth is also called outfall because it allows the discharge of flood water into the ocean. Reference is made to the following section for further discussion.

The existence of a deep canyon or a deep harbor entrance traversing the coastline may act as a barrier to the littoral drift resulting in erosion of the downdrift shoreline. Such a barrier most likely exists in the entrance to Trincomalee Harbor on the east coast, where the predominantly northerly drift caused by the southern swell is interrupted by the over 100-fathom deep entrance to Trincomalee Harbor. Erosion of the shoreline to the north of Trincomalee as seen in Fig. 4 seems to be the result of this condition.

By far the largest contribution to problems of erosion and sedimentation of the island's shoreline has been made by the interference by man with the natural processes that occur in the coastal zone. Such activity in Sri Lanka has consisted of: (a) the legal and illegal mining of sand and coral from the coastal zone, the latter usually by the destruction of reefs; (b) construction of training works at outlets of rivers and streams for drainage purposes without adequate consideration of the consequences to the adjacent shoreline; (c) construction of fishery harbors to meet demands of national priorities without adequate investigation and study; and, (d) the construction of emergency protective works against sea erosion, such as groins and seawalls, to satisfy pressures resulting from the density of human habitation in the coastal zone and which in the long term have adverse consequences on adjacent coastal areas. The problem has been aggravated in recent years especially with the development of the tourist industry and the consequent demand for beach-oriented recreation areas. These and the siting of several activities conflicting with one another in coastal areas, with little concern for coast conservation, have led to the urgent need for coastal area planning. Examples of some of these problems are described later in this section.

The biological reason for erosion mentioned earlier is the destruction of some of the reefs in the Trincomalee area of the east coast by the coral eating starfish (*Acanthaster Planci*). The starfish found abundantly in this region are since 1974 being collected and destroyed under a program executed by the Fisheries Department. In 1974 a team of six divers collected and buried about 24,000 starfish in a period of about three months. It has been suggested that a likely cause for the outburst of starfish attack since about 1972 is a direct consequence of the collection of tropical fish for export (an expanding activity in recent years), some of which are the natural predators of the starfish larvae. Investigations made by the Fisheries Department over the last two years have revealed that the presence of starfish is fortunately confined only to the Trincomalee region of the island's coastal waters giving rise to the hope that the present program of eliminating this menace would have successful results.

Coastal Inlet ProblemsKalutara Inlet

An excellent example of unplanned activity in a coastal area resulting in multiple-use conflicts is found at the outfall of the Kalu Ganga, one of the island's major rivers. Figure 5 shows five significant positions of the outfall between 1921 and 1976. In 1921 the outfall was at the northern extremity of the barrier beach and the lagoon had been enclosed by the sandbar to form a lake. Changes between 1921 and 1931 resulted in the re-opening of the lagoon and the migration of the outfall to the south combined with a seaward shift of the southern sandbar. The migration to the south continued until 1940 when the outfall was close to the southern extremity, at which stage the outfall was diverted back to the north by artificially opening up a channel close to the northern end. The migration to the south increased rapidly thereafter and the outfall shifted back to the southern end by 1943 where it remained until after 1954, when once more a northerly shift was affected by artificial means. From 1926 to 1940 the position of the outfall oscillated between north of mid-way to the northern end. It was during this period that severe erosion was experienced on the shoreline to the north of this area, necessitating the construction of a field of groins which was successful to arrest the local erosion. After 1940 the southerly migration commenced once more up to the present position of the outfall at a point south of the mid-way mark. This time, however, the effects were going to be disastrous as an entrepreneur had obtained a lease of the land on the southern sandbar from the Government Agent of Kalutara (the Chief Executive of the Government's district administration) in 1973, and with foreign collaboration had commenced the building of a 72-room hotel (to service the growing tourist industry), at an estimated cost of one million US dollars. He then found to his alarm that the outfall was migrating towards his hotel site and his land area was dwindling daily until in 1976 the distance of the outfall from the hotel had reduced to 410 feet. Based on a plan prepared by the Coast Conservation Division of the Colombo Port Commission, the entrepreneur undertook the construction of a combination of boulder groins and rubble revetments to hold the head of the southern spit from further recession and to train the outfall of the river at this point. The first phase of the project has been successfully completed and the immediate danger seems to have receded. These protective works are estimated to cost 50,000 US dollars, which is 5% of the main investment on the hotel. An interesting aspect of this problem was that in view of the heavy river discharge and the periodic flooding of low-lying land in the coastal zone upstream, the need to train the outfall was always under consideration by the Department of Irrigation (vested with the responsibility for inland waterways). The need for costly and time-consuming hydraulic studies and the absence of habitation and activity on the migrating sandbars presumably lent low priority to the study of this project. The lack of coastal area planning becomes apparent when considering the fact that neither the Department of Irrigation nor the Coast Conservation Division were consulted prior to the commencement of the hotel project either by the entrepreneur or the local approving the project. To complicate matters further, a fishery harbor consisting of a channel from the sea to the lagoon, its entrance protected by two breakwaters projecting to the sea complemented by an offshore breakwater parallel to the shoreline was proposed for construction at a point south of the hotel, with a view to using the lagoon for the mooring of craft. The obvious consequence of this proposal would have been downdrift beach erosion north of the breakwaters to additionally affect the

hotel from the seaside. Even if the hotel project was not undertaken, it was clear that the fishery harbor proposal had to be studied together with the project of training the outfall and an investigation of the effect on the adjacent shoreline, in order to obtain a meaningful solution. Fortunately, action on the harbor proposal has been deferred pending further study. The total problem of the Kalutara inlet demonstrates so very well the need for and importance of integrated field and laboratory studies, as well as coastal zone management.

Panadura Inlet

The Panadura outfall (Fig. 6) drains the waters of a large inland lake bordered by several acres of cultivated paddy land. The runoff being low during the non-monsoonal period on the west coast (i.e. from October to April), the outfall tended to close up with the formation of a sandbar as the tidal prism is insufficient to keep it open by means of tidal flushing. The consequence of this situation was the destruction of vast tracts of paddy land by flooding, usually at the commencement of the monsoonal rains. It was usual to open the sandbar by mechanical means to drain the flood waters, but this was too late to prevent the damage. The Department of Irrigation therefore constructed a groin or jetty on the south bank of the outfall to train the waters to keep the outlet always open by means of tidal flushing. This project was completed a few years ago and has successfully achieved the objective of a permanently open outfall. In addition, this has facilitated the navigation of fishing boats to mooring areas within the river throughout the year; a boon to dwellers of this area engaged in the fishing industry. An adverse consequence of this project, however, has been the severe erosion of the shoreline to the north caused by a partial interruption of the littoral drift (despite the beneficial effect on a "clair voie", an opening in the updrift jetty, that promotes sand bypassing to the downdrift coast) and a change in the littoral drift gradient along the downdrift coast. The Coast Conservation Division has since been engaged in the construction of protective works in the affected area utilizing its own funds. Artificial nourishment would provide an attractive solution in this case, dredging sand deposits from the inlet and from the lagoon and pumping these to the downdrift shore. A small dredge suitable for this work is presently available in Sri Lanka. The outfall scheme had obviously not taken into account the problem of this consequence when studies for the outfall design were carried out--another example of poor coastal area planning. The economic evaluation of the original project needs then to be reviewed to accommodate the additional cost of the coast protective works. Several problems of a similar nature exist, while the construction of several outfall works schemes around the island are envisaged. It is hoped that this short fall in planning would be recognized and corrected in the design of future works.

Fishery Harbors

As an example of a coastal fishery harbor, the harbor at Tangalle will be discussed (Photo. 4). Tangalle is a seaside town, 22 miles east of the southern tip of the island; it has an expanding fishing industry, therefore, the site was chosen for the construction of a fishery harbor in 1964, as one of the first of a network of such harbors planned for the development of the island's fishing industry. Local pressures compelled the government to direct

the immediate construction of this harbor precluding the apparent luxury of time-consuming pre-design studies. Based on a hydrographic survey chart, the layout was planned to consist of a main breakwater parallel to the shoreline partially enclosing the bay and a second minor breakwater at right angles to the shoreline and within the shadow of the main breakwater. Adequate depths existed in the bay to accommodate the class of craft catered for and the need for dredging was minimal. The usually closed outfall of an apparently small stream (but with an appreciable sediment carrying capacity during heavy rainfall), was presumably ignored as inconsequential during the short time available for planning and design, and the design seemed to lay stress on protection of the harbor from wave attack only. There was, in addition, a littoral drift from east to west during the northeast monsoon to be reckoned with. The result of the construction (the main breakwater first) was the rapid silting-up of the harbor even while construction was progressing. A quick solution was necessary and it was decided to block the littoral drift and divert the river discharge by the construction of another breakwater normal to the shoreline on the west bank of the outfall. Providentially, success was immediate, when in addition to overcoming the sediment problem, a beach built itself up between the breakwaters normal to the shoreline, and this proved to be an excellent spending beach for the dissipation of wave energy. Dredging of the harbor has since been undertaken in a reduced water area as shore structures have been built in areas reclaimed by the unexpected siltation. The almost ideal layout of the harbor as it now stands, achieved by accident, has entailed considerable additional expenditure. The importance of pre-design study has now been realized by those concerned as an essential ingredient in the economy of coastal engineering structures.

Coral and Sand Mining in the Coastal Zone

This activity although illegal for most areas has been carried out in particular areas for several decades and the consequences of which are now proving to be serious especially in areas with strong tendencies for natural erosion, e.g. the southwest coast of Sri Lanka.

Coral mining (providing lime for the building industry) has been concentrated within a coastal area about 22 miles north of Galle on the west coast. Coral is obtained by breaking the reef with sharp instruments and by digging in the nearshore and low-lying coastal areas. The excavated material is then burnt in neighborhood kilns and the extracted lime (calcium oxide) is supplied by the producer to the building industry usually through middlemen. It has been estimated that the quantity of coral removed from this area exceeds 75,000 tons per year. This in turn represents a retreat inland of the affected 6-mile stretch of shoreline of about 6 ft per year, only taking into account the sand required to fill in the gaps, while the effect of weakening the protective function of the coral reef and the removal of coral from the littoral drift will be additional in the occurrence of erosion. It has been further estimated that about 20,000 people in this area are dependent on this illegal activity for their livelihood. While existing legislation is weak and new legislation has been prepared, solution of the socio-economic problem is primary in eliminating this destructive activity. As a large percentage of lime for the building industry is supplied from this area, alternative sources of this material have been proposed to meet the demand when coral mining activity in the coastal zone is terminated.

Sand mining, mostly illegal, is also carried out extensively in the coastal zone, especially at the Kelani river outfall, the Kalutara inlet, and south of the Panadura outfall on the west coast. The total quantity mined from these areas would exceed 325,000 cubic yards per year, while legal mining at Pulmoddai on the northeast coast by the State Mineral Sands Corporation for extraction of ilmenite, rutile and zircon, accounts for about 200,000 cubic yards per year in a three mile stretch of foreshore and backshore areas. The consequences of the latter operation will need to be considered in the economic evaluation of the mineral extraction project. The new legislation provides for the control of sand mining in the coastal zone and as before alternative sources have been proposed to meet the commercial demand for sand.

POTENTIAL OF SRI LANKA BEACHES FOR RECREATION

Sri Lanka possesses a number of beautiful beaches and an attractive climate for vacationing. The temperature of the water of the ocean varies between narrow boundaries and is therefore attractive for swimming. Calm sea conditions and gently sloping beaches are present on the west coast during the northeast monsoon and similarly on the east coast during the southwest monsoon. Beach-oriented resort development has taken place in Bentota and Negombo on the west coast, and Kalkudah and just north of Trincomalee on the east coast. The better beaches are found on the east coast where many of them are yet unspoiled by man in the sparsely populated areas where access is hindered by low-key communication development. Arugam Bay on the east coast and the region between Galle and Matara on the southwest coast are other beach recreational areas gaining in popularity in recent years.

Resort developers have sought the assistance of the Coast Conservation Division for the provision of safe bathing areas during the monsoonal period of such areas and for neighborhood beach development. In many such cases, studies are to be undertaken for optimum solutions to be determined, while the topography of some areas have lent themselves to evolving solutions both economical and unusual. An example of the latter is the building of a "sea-pool", where only a narrow beach exists at present on a sandstone reef which drops sharply into the sea making any attempt at swimming a hazardous exercise. A bathing enclosure was therefore excavated by blasting an area 150 x 50 ft out of the sandstone ledge (leaving adequate seaside cover for coast protection) and removing a 6-8 ft layer of sandstone down to the sand base below, which provides bathing depths up to about 8 ft. Sea water enters the pool through a natural inlet at one end and wave attack (when present), is controlled by artificially placed boulder protection on the seaside edge of the sandstone ledge.

PLANNING GUIDELINES PROPOSED

Interest shown by those concerned in the conservation of the country's coast led to the development of a United Nations project in 1974 for the solution of Sri Lanka's coastal problems. The expert's recommendations include the establishment of a Coastal Engineering Research Center to be

located within a separate administrative organization for Coast Conservation, along with training of local personnel and curricula development in Coastal Engineering at the University of Ceylong, as the main features of the Program. Complementarily, new legislation titled "Coast Conservation" was prepared and is now awaiting debate in the country's legislature.

The main provisions of this law are:

1. The appointment of a Director of Coast Conservation to be statutorily responsible for the control and management of the coastal zone and the permitting of all schemes of work therein.
2. The creation of a Coastal Advisory Council to advise the Minister in charge of the subject on matters concerning coast conservation.
3. The control of excavation of material within the coastal zone.

Major uses in the Coastal Zone of Sri Lanka that would need to be considered to define shore objectives are: recreation and aesthetic aspects; resource extraction; waste disposal; transportation; residential, commercial, and industrial development; and ecological aspects. After examining techniques for achieving the objectives, a coastal area management plan would be formulated for the purpose of implementation. Some of the studies considered immediately necessary for this Plan are:

1. Physical information of the coast to include an inventory of all maritime structures in Sri Lanka.
2. An estimate of annual mining of coral and sand and the corresponding demand of the building industry.
3. Alternative sources of sand and lime for the building industry.
4. A census of those engaged in illegal mining of coral and sand and the provision of alternative sources of employment.
5. A benefit/cost evaluation of maritime structures built for coast protection in Sri Lanka.

CONCLUSIONS AND RECOMMENDATIONS

1. The coastal zone is of increasing importance for Sri Lanka as a natural resource and deserves careful management and protection.
2. Coastal erosion is a serious threat to the beaches of the State, and particularly to the southwest coast, which is the area of highest population density. Three causes of erosion may be distinguished: natural erosion; man-made erosion; and erosion due to biological activity.
3. Among the adverse effects of the actions by men, most significant are the construction of ill-designed harbors and coastal protection works (seawalls and groins) and the mining of sand and coral from various coastal areas.
4. Solution of the various problems can only be found after a thorough understanding of the coastal processes is obtained. Such understanding may vary between the realization of possible adverse effects of a groin or groin system on the adjacent beaches and the complexities of the sediment transport mechanism in natural inlets or constructed outfalls.

5. The construction of seawalls too close to the waterline as a measure of coastal protection is usually ineffective; it possibly induces increased erosion. Measures to cope with bluff erosion should be tied in with a scheme to stabilize the beach.

6. The mining of sand or coral from eroding areas should be prohibited.

7. Schemes of new fishery harbors on the southwest coast should be based on the results of careful analysis of the sediment transport of the coastal regime. This will usually require both field and model studies prior to the design and construction.

8. For the study and planning of coastal measures the organization of a Coastal Engineering Research Center is recommended. Such a center will be charged with the field and model studies and will give guidance to the branches engaged in engineering design.

9. To solve the problems associated with the conflicting demands on the coastal zone the establishment of a Department of Coast Conservation is recommended under the Ministry of Shipping and Tourism with the power to define priorities and prepare new legislation.

10. For the staffing on the new research center it will be necessary to establish educational programs in coastal engineering at the various campuses of the University of Sri Lanka. The educational aspects will also include training of coastal engineers abroad.



PHOTO 1 SEVERE EROSION ON SOUTHWEST COAST DUE TO COMBINED EFFECTS OF NATURAL CAUSES AND CORAL MINING. NOTE THE REMOVAL OF EXPOSED CORAL.

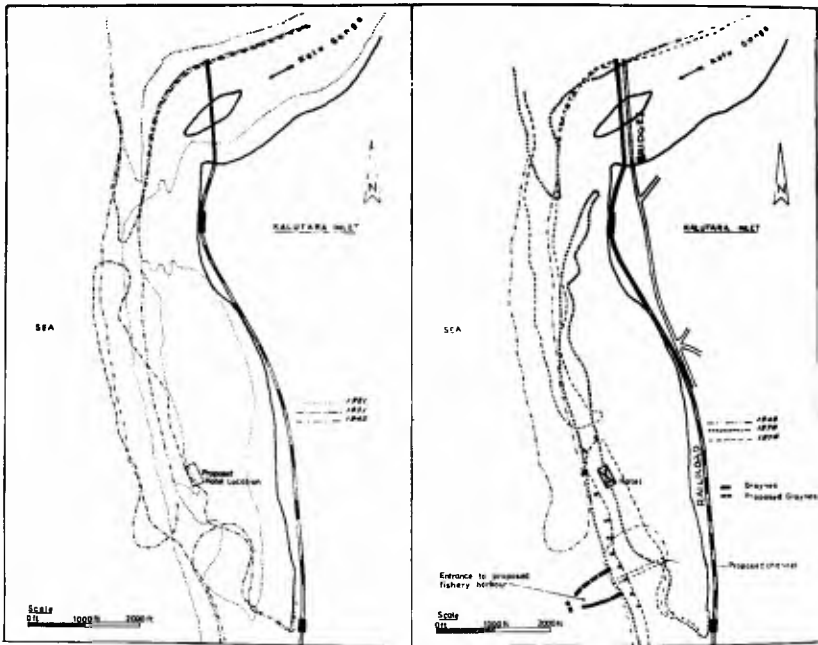


FIG. 5 MIGRATION OF UNIMPROVED INLET AT KALUTARA



PHOTO 2 KALUTARA INLET



PHOTO 3 PANADURA INLET



PHOTO 4 TANGALLE FISHERY HARBOR

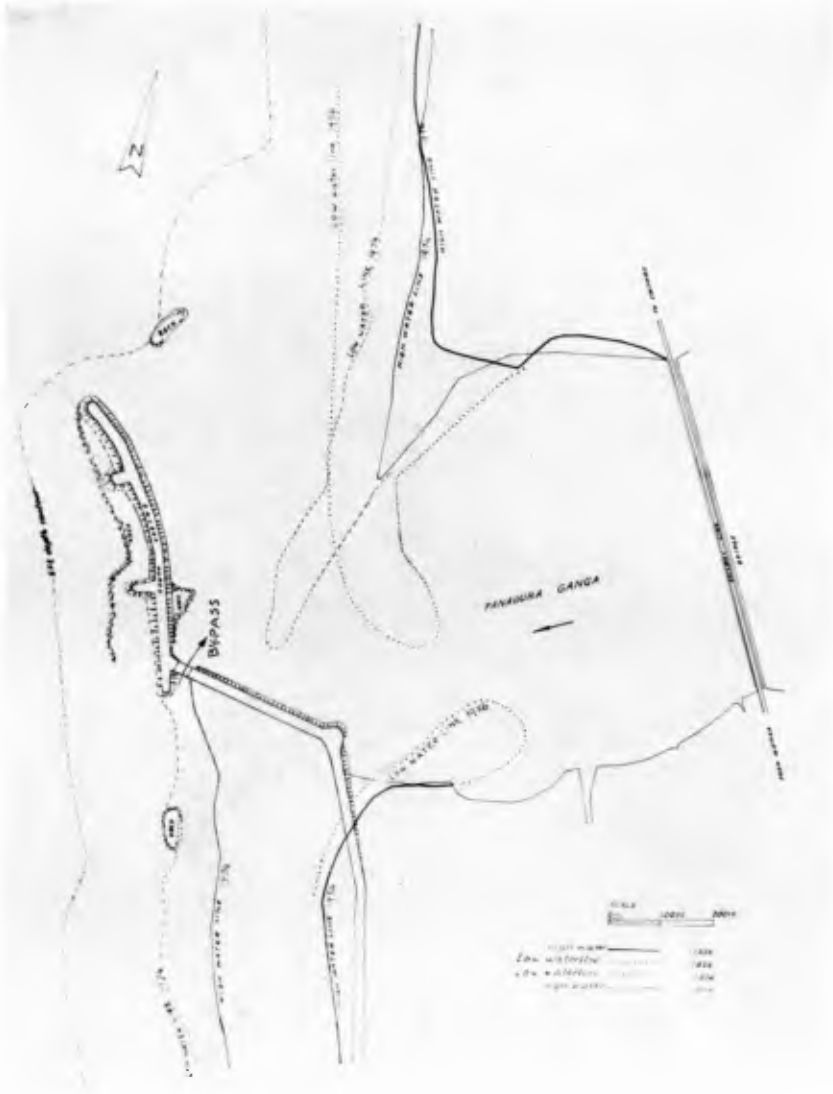


FIG. 6 PANADURA INLET SHORELINE CHANGES CONSEQUENT TO INLET TRAINING WORKS TO AVOID CLOSURE OF RIVER MOUTH FOR UPSTREAM FLOOD PROTECTION PURPOSES.

SELECTED REFERENCES

1. Swan, Bernard, "Coastal Erosion Principles and a Classification of South-West Ceylon's Beaches on the Basis of their Erosional Stability", The Ceylon Geographer, Vol. 19, Nos. 1-4, January-December 1965.
2. Zeper, J., "Sea Erosion Studies and Recommendations on Coastal Protection in Ceylon", Netherlands Bureau for International Technical Assistance, The Hague, Netherlands, August 1960.
3. Humphreys, Howard and Sons, Consulting Engineers, Reading, England, "Report on Oceanographic Studies, March 1971, prepared under United Nations Development Program and World Health Organization.
4. Eaton, Richard O., "Coast Protection and Coastal Resource Development in Ceylon", Report in compliance with United States International Cooperation Administration Project Implementation, 1961.
5. Gerritsen, F., "Coastal Engineering in Sri Lanka", Report on UN mission, June 2B - October 3, 1974.

ACKNOWLEDGEMENTS

The authors wish to thank the UNOP for supporting the Sri Lanka Coastal Engineering Project and the Government of Sri Lanka for initiating action on this study. Special thanks are due to Mr. P.B. Karandawala, Secretary of the Ministry of Shipping and Tourism, whose active interest since 1970 and the assignment of high priority to the country's coastal problems contributed greatly to the positive action in the field of coastal area planning.

The authors record their deep appreciation of all the assistance given and contribution made by Mr. H.V. Dayananda, Engineer Coastal Research and Investigations of the Colombo Port Commission, and his team of Port Commission Hydrographers, in the collection of data, and the preparation of maps, photographs and diagrams. Thanks are also due to the Colombo Port Commission without whose facilities this work would not have been possible.

The authors thank Mildred Frank of the Department of Ocean Engineering for the typing of the manuscript.

CHAPTER 202

ENVIRONMENTAL IMPACTS ON AN ISLAND COMMUNITY

Gordon A. Chapman¹

INTRODUCTION

The environmental impacts of coastal engineering projects generally affect island communities to a greater degree than they would affect continental land mass communities. This occurs because of the smaller land area; close interdependence and interaction of land and sea communities, both natural and human; and relatively small projects having relatively large overall impacts on island ecosystems.

The natural flora and fauna of Pacific Islands have developed rather precariously unbalanced communities that are extremely fragile and susceptible to change, both natural and man induced. This susceptibility dictates that, where possible, man induced or proposed changes, such as coastal engineering projects, should be designed such that as little change as possible occurs to the natural environment. Additionally, the natural resources of island communities are generally limited and this too dictates that conservation practices be employed that assure the highest and best use of those limited resources.

The purpose of this paper is to indicate the environmental effects of a major coastal engineering project on an island community. This will be accomplished by describing the environmental quality control monitoring program that has been performed as an integral part of the Honolulu International Airport (HIA) Reef Runway construction project on Oahu, Hawaii, and presenting the initial findings of that environmental monitoring program.

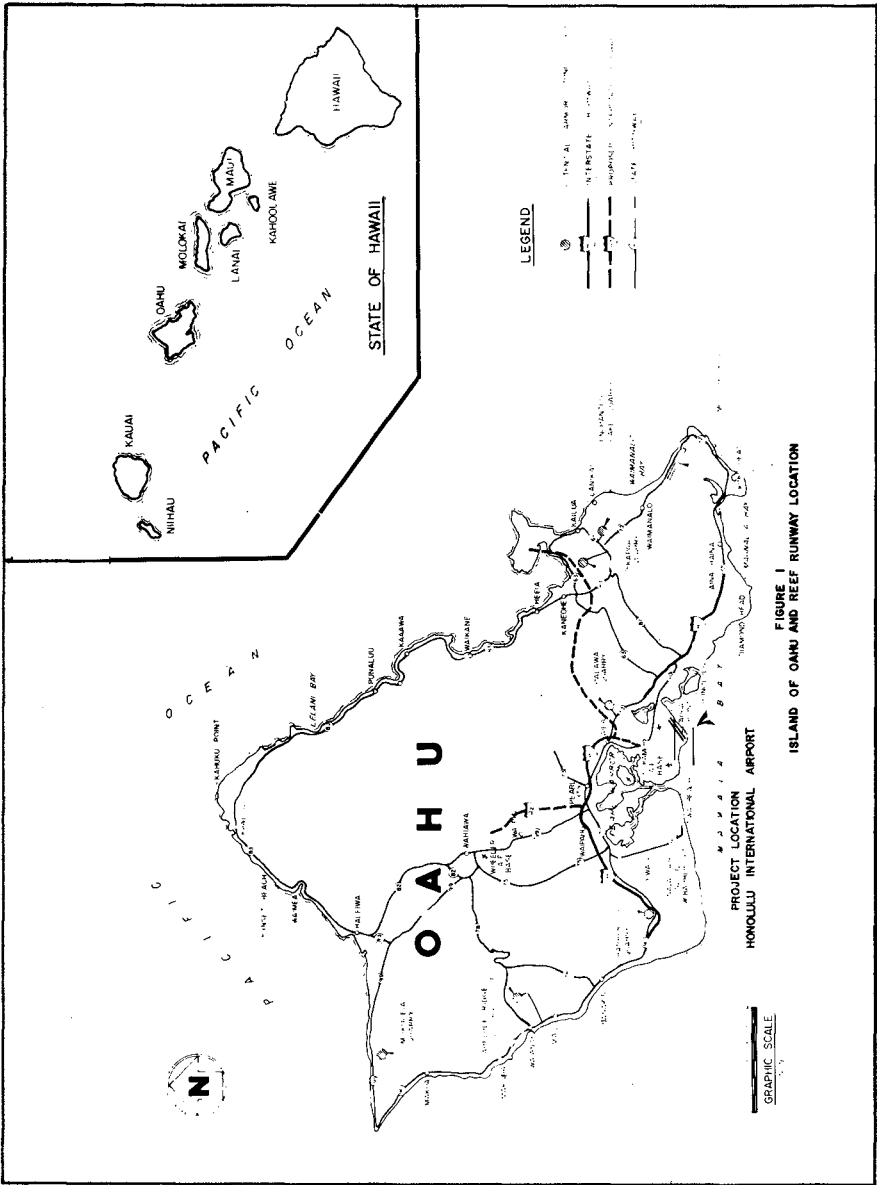
The Honolulu International Airport reef runway planning and design began in earnest in 1968 and 1969 with hydrographic and topographic surveys, foundation investigations, two- and three-dimensional hydraulic model studies, and environmental studies that were conducted (J. K. K. Look, 1970; Berger, 1971; Sunn, et al, 1969). These studies, and others, were utilized to determine the technical feasibility, and to gather the engineering and environmental data for final design and construction.

The Reef Runway, located south of the HIA runway system on the fringing coral reef, seaward of Keehi Lagoon, in Mamala Bay, is 12,000 feet long and 200 feet wide. The runway and taxiway complex is protected from the sea by a 16,000-foot long protective structure constructed of rock and dollose (Figure 1).

MATERIALS AND METHODS

The Reef Runway environmental monitoring program began during the 1970-1972 period when various oceanographic, marine biology and ecology, water quality, and avifauna baseline studies were conducted (J. K. K. Look, 1971; Berger, 1971; Harvey, et al, 1971; Sunn, et al, 1972a; Bathen, 1970). During the initial planning and design

¹Senior Environmental Analyst, The Ralph M. Parsons Company, Honolulu, Hawaii.



phases of the Reef Runway project, and during the preparation of the Environmental Impact Statement (Federal Aviation Administration, 1972), it was determined that extensive baseline studies as well as a construction period monitoring program were required. The baseline studies were needed to adequately describe existing conditions and to predict probable environmental impacts of the project, and the monitoring program to ensure compliance with all applicable State and Federal environmental protection regulations during construction activities.

The "during construction" water quality monitoring program was initiated in June, 1973, approximately one month prior to the start of construction and continued until August 30, 1976, approximately one month following major offshore and onshore construction activities. The program consisted of bimonthly water quality sampling, initially at 19 preselected stations, and finally at 13 of the original stations and one added station (Figure 2). Dissolved oxygen (D.O.) was measured using a Yellow Springs D.O. probe and turbidity measured with a standard 30 c.m. diameter Secchi disk. In-situ measurements of temperature and salinity were made utilizing a Beckman in-situ thermister probe and induction salinometer. Laboratory measurements of pH, total phosphorus, and total Kjeldahl nitrogen were made. Station depths varied from 6 feet to 45 feet, with most being 15 to 20 feet. All in-situ measurements and water samples were taken at mid-depths. Sampling was accomplished at different times of the day and at varying tidal, wind, and weather conditions.

Water quality sampling was conducted on 88 separate days during the 38-month period the reef runway environmental monitoring program existed. Over 1,300 samples were collected and 9,000 separate data entries have been recorded.

RESULTS

In order to assess the effects of the reef runway construction on Keehi Lagoon water quality, six water quality parameters have been analyzed in general and four in detail for five lagoon and two open ocean monitoring stations. Of the six parameters (temperature, salinity, turbidity, dissolved oxygen, total Kjeldahl nitrogen, and total phosphorus), the latter four have been analyzed in detail. Arithmetic means, standard deviations and geometric means of field and laboratory measurements have been calculated for annual, bi-annual, quarterly and seasonal periods. Quarterly arithmetic mean, standard deviation and geometric mean data for the stations analyzed are presented in Table 1.

Prior to regular monitoring activities, baseline data for most of the sampling stations shown on Figure 2 was assembled from various preconstruction studies. This baseline data and applicable State of Hawaii Water Quality Standards (State of Hawaii, 1974) formed the standards against which water quality readings during construction were measured. Keehi Lagoon, with the exception of the small boat marina areas along the eastern shoreline (Figure 2), is classified by the State Water Quality Standards as Class A waters. The small boat marina areas are Class B waters. Baseline data available for Stations 2, 2b, 3, 4, 6, 22 and 24 is presented in Table 2.

TEMPERATURE AND SALINITY

Temperature and salinity are two of the most potent physical factors in the life of marine organisms. They largely characterize the physicochemical properties of a given body of water (Kinne, 1963). There exists a complex correlation between the biological effects of temperature and salinity. Temperature can modify the effects

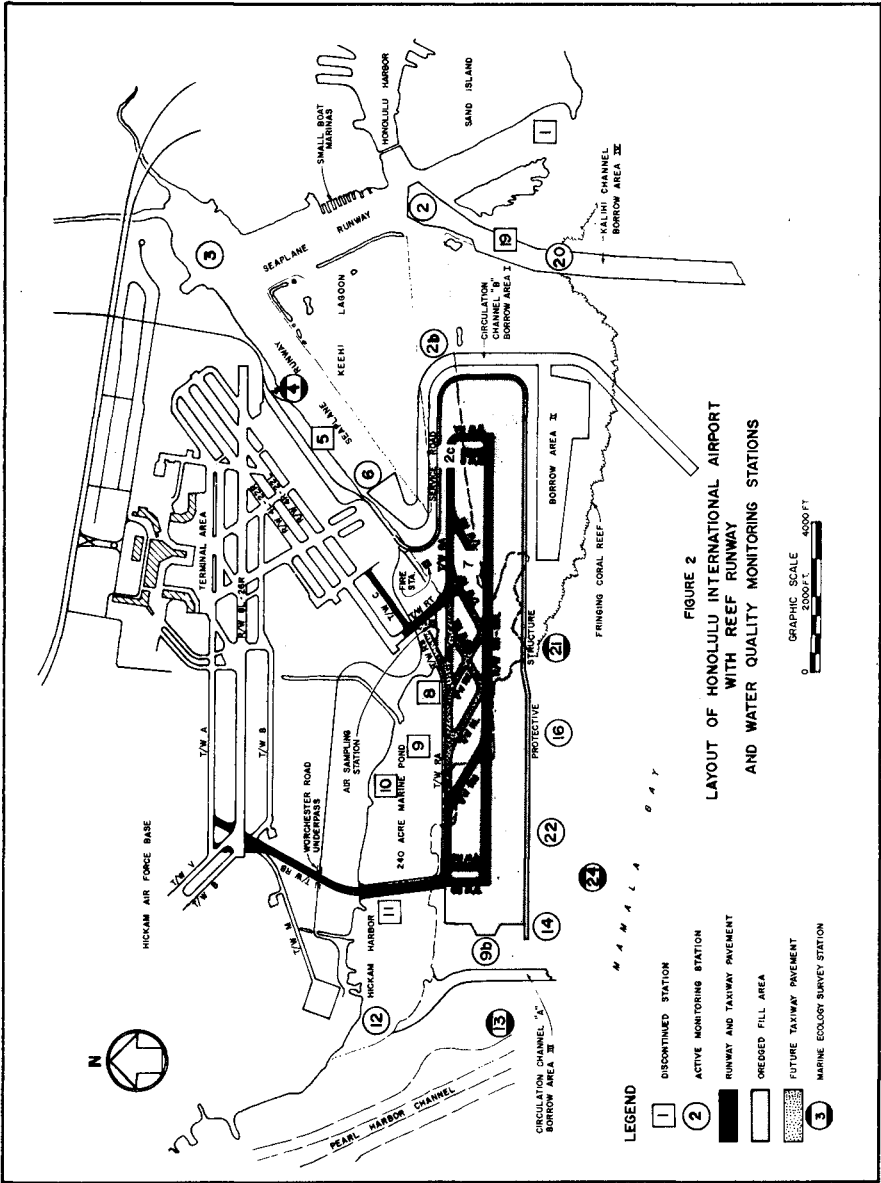


TABLE 1
REEF RUNWAY WATER QUALITY ANALYSIS
QUARTERLY ARITHMETIC MEAN, STANDARD DEVIATION AND GEOMETRIC MEAN
FOR STATIONS 2, 2b, 3, 4, 6, 22 and 24

STA.	QTR.	SECCHI DISK (ft.)			O.O. (mg/l)			TOTAL N (mg/l)			TOTAL P (mg/l)		
		ARITH. MEAN	STO. DEV.	GEOM. MEAN	ARITH. MEAN	STO. DEV.	GEOM. MEAN	ARITH. MEAN	STO. DEV.	GEOM. MEAN	ARITH. MEAN	STO. DEV.	GEOM. MEAN
2	1	7.04	1.30	6.93	5.94	0.50	5.92	0.226	0.11	0.198	0.022	0.01	0.01
	2	7.33	2.70	7.00	5.47	0.41	5.45	0.108	0.08	0.069	0.022	0.01	0.019
	3	7.11	1.52	6.97	6.16	0.32	6.15	0.143	0.12	0.068	0.022	0.01	0.019
	4	6.33	0.61	6.31	5.88	0.33	5.87	0.281	0.08	0.266	0.018	0.02	0.013
	5	6.67	1.75	6.50	6.17	0.42	6.15	0.253	0.19	0.190	0.021	0.02	0.007
	6	5.36	0.69	5.32	6.17	0.29	6.16	0.258	0.14	0.201	0.051	0.02	0.045
	7	5.67	1.72	5.42	6.55	0.39	6.54	0.257	0.08	0.246	0.029	0.02	0.024
	8	4.71	1.25	4.58	6.50	0.54	6.48	0.346	0.21	0.281	0.028	0.01	0.026
	9	6.38	1.49	6.24	6.48	0.23	6.47	0.386	0.19	0.336	0.041	0.02	0.038
	10	6.25	1.89	6.02	6.27	0.58	6.24	0.259	0.19	0.202	0.040	0.02	0.035
	11	8.67	1.60	8.51	6.94	0.28	6.93	0.481	0.25	0.418	0.033	0.01	0.032
	12	7.00	2.22	6.47	6.85	0.62	6.82	0.330	0.14	0.297	0.051	0.03	0.045
	13	11.00	2.92	10.59	6.27	0.34	6.26	0.344	0.19	0.288	0.071	0.02	0.068
2b	1	5.79	1.18	5.66	6.12	0.62	6.09	0.215	0.10	0.174	0.017	0.01	0.015
	2	5.00	1.53	4.78	5.52	0.18	5.52	0.117	0.11	0.061	0.024	0.01	0.023
	3	6.00	1.93	5.63	6.01	0.53	5.99	0.155	0.11	0.115	0.026	0.01	0.026
	4	6.08	2.26	5.69	5.67	0.24	5.66	0.327	0.25	0.249	0.024	0.01	0.021
	5	5.25	0.85	5.18	6.47	0.60	6.44	0.252	0.22	0.176	0.030	0.03	0.010
	6	5.93	0.86	5.87	5.90	0.42	5.88	0.244	0.13	0.202	0.047	0.03	0.040
	7	5.42	1.79	5.07	6.65	0.62	6.62	0.482	0.22	0.418	0.039	0.02	0.036
	8	4.79	1.22	4.64	6.53	0.35	6.52	0.304	0.06	0.297	0.028	0.01	0.025
	9	6.88	0.21	6.87	6.55	0.39	6.54	0.328	0.11	0.313	0.053	0.02	0.049
	10	5.25	1.11	5.14	6.22	0.33	6.21	0.233	0.15	0.163	0.050	0.01	0.048
	11	7.17	0.90	7.11	7.08	0.59	7.06	0.214	0.12	0.174	0.050	0.02	0.047
	12	6.50	1.26	6.39	7.00	0.48	6.98	0.349	0.24	0.276	0.059	0.02	0.052
	13	5.25	1.30	5.05	6.57	0.29	6.56	0.544	0.22	0.500	0.042	0.01	0.042
3	1	4.44	0.76	4.37	6.33	0.49	6.31	0.223	0.14	0.173	0.034	0.03	0.027
	2	4.83	1.75	4.53	6.38	0.51	6.36	0.169	0.09	0.145	0.026	0.01	0.025
	3	5.33	1.60	5.02	6.57	0.38	6.56	0.160	0.10	0.133	0.032	0.01	0.030
	4	4.17	0.47	4.14	6.85	0.68	6.82	0.352	0.13	0.313	0.028	0.04	0.014
	5	4.58	1.02	4.48	6.80	0.74	6.76	0.368	0.17	0.037	0.035	0.02	0.019
	6	4.50	0.89	4.41	5.91	0.35	5.90	0.348	0.24	0.238	0.052	0.03	0.046
	7	3.42	0.67	3.35	6.72	0.64	6.68	0.413	0.16	0.380	0.047	0.03	0.038
	8	3.64	0.52	3.61	6.53	0.37	6.52	0.343	0.33	0.255	0.032	0.01	0.032
	9	4.50	0.35	4.49	6.48	0.33	6.47	0.161	0.09	0.139	0.042	0.02	0.034
	10	3.92	0.67	3.85	6.63	0.24	6.63	0.388	0.22	0.317	0.045	0.01	0.043
	11	5.50	0.96	5.41	6.80	0.24	6.80	0.314	0.51	0.309	0.044	0.01	0.043
	12	5.08	0.61	5.05	6.88	0.55	6.86	0.390	0.16	0.352	0.062	0.02	0.054
	13	4.00	0.00	4.00	6.63	0.47	6.62	0.380	0.25	0.317	0.029	0.02	0.025
4	1	4.31	0.64	4.26	6.47	0.42	6.45	0.159	0.10	0.122	0.019	0.01	0.018
	2	4.78	1.47	4.60	6.56	0.41	6.54	0.155	0.12	0.121	0.026	0.01	0.024
	3	5.56	1.76	5.24	6.63	0.57	6.61	0.452	0.26	0.357	0.027	0.02	0.022
	4	4.67	0.80	4.60	6.70	0.71	6.66	0.574	0.13	0.558	0.037	0.02	0.032
	5	5.92	0.73	5.87	6.62	0.82	6.56	0.351	0.28	0.256	0.024	0.02	0.013
	6	5.29	1.16	5.16	6.41	0.70	6.38	0.230	0.14	0.196	0.034	0.01	0.030
	7	4.08	0.73	4.02	7.08	0.52	7.06	0.326	0.11	0.304	0.040	0.01	0.039
	8	3.93	0.62	3.88	6.77	0.27	6.77	0.387	0.18	0.354	0.026	0.01	0.022
	9	4.75	0.43	4.73	6.78	0.23	6.77	0.231	0.06	0.223	0.043	0.02	0.038
	10	4.25	0.38	4.23	6.63	0.24	6.63	0.407	0.33	0.302	0.023	0.01	0.021
	11	5.00	0.65	4.96	6.98	0.31	6.97	0.462	0.24	0.376	0.044	0.02	0.040
	12	5.08	0.61	5.05	7.15	0.77	7.11	0.417	0.16	0.385	0.062	0.03	0.057
	13	4.75	0.83	4.68	6.63	0.39	6.62	0.509	0.10	0.498	0.067	0.03	0.060

TABLE 1 (Continued)

STA.	QTR.	SECCHI DISK (ft.)			D.O. (mg/l)			TOTAL N (mg/l)			TOTAL P (mg/l)		
		ARITH. MEAN	STD. DEV.	GEOM. MEAN	ARITH. MEAN	STD. DEV.	GEOM. MEAN	ARITH. MEAN	STD. DEV.	GEOM. MEAN	ARITH. MEAN	STD. DEV.	GEOM. MEAN
6	1	4.21	0.83	4.13	6.59	0.44	6.58	0.175	0.11	0.129	0.017	0.01	0.016
	2	4.06	0.98	3.91	6.14	0.35	6.13	0.257	0.26	0.110	0.025	0.01	0.025
	3	5.44	1.54	5.25	6.42	0.41	6.41	0.450	0.28	0.356	0.031	0.01	0.026
	4	4.50	0.91	4.40	6.63	0.81	6.59	0.587	0.36	0.496	0.040	0.01	0.038
	5	5.25	0.99	5.15	6.50	0.66	6.47	0.523	0.32	0.433	0.018	0.02	0.012
	6	5.07	1.37	4.85	5.73	0.61	5.74	0.298	0.16	0.243	0.018	0.01	0.019
	7	3.83	0.75	3.76	6.65	0.64	6.62	0.285	0.08	0.272	0.039	0.01	0.036
	8	3.71	0.52	3.68	6.74	0.46	6.73	0.284	0.12	0.253	0.034	0.01	0.031
	9	4.25	0.43	4.23	6.48	0.13	6.47	0.253	0.10	0.223	0.132	0.17	0.059
	10	4.33	1.07	4.19	6.50	0.25	6.50	0.319	0.18	0.260	0.039	0.02	0.030
	11	5.50	0.91	5.42	6.82	0.47	6.80	0.348	0.22	0.261	0.034	0.02	0.031
	12	4.17	1.77	3.80	7.23	0.73	7.20	0.305	0.24	0.227	0.031	0.01	0.030
	13	6.25	2.28	5.89	6.57	0.25	6.56	0.390	0.19	0.324	0.047	0.01	0.045
22	1	15.92	3.36	15.50	5.48	0.48	5.46	0.216	0.11	0.163	0.023	0.02	0.021
	2	16.67	2.91	16.36	5.78	0.42	5.76	0.174	0.17	0.089	0.011	0.01	0.009
	3	17.44	1.95	17.32	6.39	0.35	6.38	0.185	0.21	0.081	0.024	0.02	0.017
	4	19.00	0.58	18.99	6.20	0.16	6.20	0.537	0.18	0.503	0.034	0.03	0.034
	5	18.50	3.40	18.10	5.93	0.36	5.92	0.257	0.14	0.168	0.019	0.01	0.014
	6	17.86	2.23	17.71	6.10	0.46	6.08	0.337	0.25	0.276	0.038	0.03	0.028
	7	15.67	4.50	14.88	6.62	0.27	6.61	0.447	0.48	0.259	0.040	0.04	0.036
	8	16.43	5.04	15.14	6.34	0.21	6.34	0.215	0.07	0.197	0.033	0.03	0.031
	9	12.50	5.72	13.54	6.65	0.22	6.65	0.284	0.06	0.278	0.019	0.02	0.017
	10	17.33	4.11	16.76	6.44	0.29	6.36	0.165	0.10	0.127	0.042	0.03	0.033
	11	18.00	1.73	17.91	7.04	0.42	7.03	0.493	0.23	0.448	0.045	0.04	0.042
	12	15.33	5.50	14.44	6.75	0.78	6.70	0.330	0.15	0.283	0.041	0.04	0.040
	13	16.67	4.71	15.87	6.15	0.05	6.15	0.354	0.20	0.308	0.053	0.05	0.051
24*	1	---	---	---	---	---	---	---	---	---	---	---	---
	2	40.00	0.00	40.00	5.86	0.28	5.85	0.087	0.06	0.074	0.018	0.01	0.017
	3	31.00	9.18	29.38	6.38	0.40	6.36	0.127	0.19	0.063	0.027	0.02	0.022
	4	31.83	7.90	30.76	6.20	0.25	6.19	0.283	0.18	0.189	0.036	0.04	0.020
	5	31.50	5.99	30.91	5.98	0.51	5.96	0.211	0.07	0.200	0.010	0.01	0.007
	6	35.00	7.07	34.11	6.11	0.38	6.10	0.243	0.14	0.155	0.029	0.01	0.026
	7	32.50	9.01	31.05	6.48	0.44	6.47	0.429	0.16	0.399	0.034	0.01	0.031
	8	35.14	10.01	32.63	6.25	0.34	6.16	0.259	0.08	0.245	0.034	0.02	0.030
	9	37.50	4.33	37.22	6.55	0.43	6.53	0.292	0.17	0.234	0.041	0.01	0.040
	10	35.83	6.07	35.25	6.48	0.19	6.48	0.235	0.17	0.128	0.024	0.01	0.020
	11	31.67	10.27	28.94	6.94	0.29	6.93	0.408	0.14	0.375	0.037	0.02	0.032
	12	34.50	8.14	33.17	7.07	0.58	7.04	0.304	0.11	0.284	0.051	0.02	0.046
	13	28.33	13.12	24.10	6.40	0.10	6.40	0.331	0.11	0.314	0.039	0.01	0.039

State of Hawaii Water Quality Standards for:

D.O. = > 5.0 mg/l
 Total N = < 0.150 mg/l
 Total P = < 0.025 mg/l
 Secchi Disk ± 10 percent from natural conditions

Qtrly. Periods: 1 = Jun 1973 to Sep 1973
 2 = Oct 1973 to Dec 1973
 3 = Jan 1974 to Mar 1974
 4 = Apr 1974 to Jun 1974
 5 = Jul 1974 to Sep 1974
 6 = Oct 1974 to Dec 1974
 7 = Jan 1975 to Mar 1975
 8 = Apr 1975 to Jun 1975
 9 = Jul 1975 to Sep 1975
 10 = Oct 1975 to Dec 1975
 11 = Jan 1976 to Mar 1976
 12 = Apr 1976 to Jun 1976
 13 = Jul 1976 to Aug 1976

*Station 24 monitoring started in Oct 1973.

of salinity and change, either enlarge, narrow, or shift the salinity range of an organism; and salinity can modify the effects of temperature accordingly (Kinne, 1963; McLeese, 1956; Dehmel, 1960).

TABLE 2
BASELINE DATA
STATIONS 2, 2b, 3, 4, 6, 22 AND 24

Station	Water Quality Parameter					
	Temperature (°C)	Salinity (0/00)	Turbidity * (Lower Limit-Ft.)	D.O. (mg/l)	Total N (mg/l)	Total P (mg/l)
2	26.5	34.57	3.5	NA	NA	NA
2b	27.3	34.84	3.0	3.73	0.16	0.025
3	27.3	34.64	2.5	5.39	0.20	0.024
4	25.9	34.24	3.0	NA	NA	NA
6	25.6	34.69	2.5	5.35	NA	NA
22	27.2	NA	NA	5.62	0.09	0.030
24	NA	NA	NA	NA	NA	NA

NA - Not Available

*Turbidity lower limits were established by subtracting twice the standard deviation from mean Secchi disk readings taken during pre-construction studies (Sunn, et al, 1972).

Mid-depth temperature readings taken at Stations 2, 2b, 3, 4, 6, 22 and 24 demonstrate characteristics similar to those for open ocean conditions in the tropics. That is, fairly narrow variations ($+5^{\circ}\text{C}$) between high and low readings, and normal variations between summer and winter months. Table 3 indicates high and low quarterly arithmetic means, standard deviation, and geometric means for temperature data collected.

TABLE 3
TEMPERATURE DATA
STATIONS 2, 2b, 3, 4, 6, 22 AND 24

Station	High (°C)				Low (°C)			
	Arith. Mean	Std. Dev.	Geom. Mean	Qtr.	Arith. Mean	Std. Dev.	Geom. Mean	Qtr.
2	27.33	0.68	27.33	5	23.10	0.51	23.09	11
2b	27.20	0.44	27.20	5	23.30	0.77	23.29	11
3	27.98	0.91	27.97	5	23.38	1.03	23.36	7
4	27.83	0.82	27.82	5	23.20	0.92	23.18	11
6	27.90	0.68	27.89	5	22.95	1.31	22.91	7
22	26.75	0.38	26.95	5	23.32	0.43	23.31	11
24	26.85	0.35	26.85	5	23.30	0.46	23.30	11

All high temperature readings were taken during the fifth quarter (July-September, 1974) and low readings were taken during the seventh quarter (January-March, 1975) and the eleventh quarter (January-March, 1976). The lowest average temperature was recorded at Station 6 and the highest average at Station 3. The temperature ranges and patterns indicated in Table 3 are comparable to those described in the literature for similar estuarine water bodies (Ekman, 1953, Sverdrup, et al, 1942).

Salinity, like water temperature, is influenced by outside forces, primarily water temperature and wind. Salinity ranges for individual and/or all stations collectively varies only slightly, less than two parts per thousand (0/00 - Table 4). As with temperature, the highest salinity values are found in the spring and summer months (April-August, 1976) and generally, the lowest in the winter months (January-March, 1974).

TABLE 4
SALINITY DATA
STATIONS 2, 2b, 3, 4, 6, 22 AND 24

Station	High (0/00)				Low (0/00)			
	Arith. Mean	Std. Dev.	Geom. Mean	Qtr.	Arith. Mean	Std. Dev.	Geom. Mean	Qtr.
2	36.00	0.12	36.00	13	34.50	0.24	34.50	3
2b	35.93	0.08	35.92	13	34.46	0.25	34.25	3
3	36.17	0.36	36.16	12	34.00	0.45	33.99	3
4	35.88	0.11	35.87	13	33.83	0.44	33.83	3
6	36.03	0.13	36.02	13	33.76	0.40	33.76	3
22	36.00	0.16	36.00	13	34.73	0.52	34.73	1
24	36.10	0.28	36.10	13	34.82	0.04	34.82	3

The one exception occurred at Station 22 where the lowest average was recorded during the June-September, 1973 period. Higher ambient air temperatures and generally stronger tradewind conditions cause greater evaporation rates to occur in the summer months, resulting in higher salinity values. Conversely, lower ambient air temperatures, less tradewind activity, and greater inflows of fresh water, tend to cause lower salinities in the winter months.

TURBIDITY

The possibility of significantly decreasing water clarity as a result of dredging activities was believed to be potentially one of the most detrimental construction effects on the marine environment of Keehi Lagoon. High turbidity and associated suspended solids would reduce the amount of light available for photosynthesis, would smother bottom dwelling organisms, and if ingested, affect the vital life processes of marine organisms (Johannes, 1972). Although occasional violations of Secchi disk lower limits occurred, generally water clarity at all stations was not significantly different from baseline conditions.

High and low quarterly arithmetic mean, standard deviation, and geometric mean Secchi disk data are shown in Table 5. All low Secchi disk readings occurred during the April-September period and high readings occurred throughout the three-year program. Low readings can be expected during the summer months since the south coast of Oahu is subjected to fairly heavy southerly swell and wave action during those months.

DISSOLVED OXYGEN

Dissolved oxygen (D.O.) is an important environmental parameter since low levels, i.e., less than 5.0 milligrams per liter (mg/l) may significantly affect marine life. A complex set of factors, including organic decay, photosynthesis, and respiration affect D.O. values to range from less than 5.0 mg/l to over 8.5 mg/l or supersaturation on any given day. Oxygen saturation is dependent upon temperature and salinity, but roughly ranges from 6.8 to 7.1 mg/l for the temperature ranges generally recorded in the Keehi Lagoon area.

TABLE 5
SECCHI DISK DATA
STATIONS 2, 2b, 3, 4, 6, 22 AND 24

Station	High (Ft.)				Low (Ft.)			
	Arith. Mean	Std. Dev.	Geom. Mean	Qtr.	Arith. Mean	Std. Dev.	Geom. Mean	Qtr.
2	11.00	2.92	10.59	13	4.71	1.25	4.58	8
2b	7.17	0.90	7.11	11	4.79	1.22	4.64	8
3	5.50	0.96	5.41	11	4.17	0.47	4.14	4
4	5.92	0.73	5.87	5	3.93	0.62	3.88	8
6	6.25	2.28	5.89	13	3.71	0.52	3.68	8
22	19.00	0.58	18.99	4	12.50	5.72	13.54	9
24	40.00	0.00	40.00	2	28.33	13.12	24.10	13

State of Hawaii Class A Water Quality Standard for D.O. is values greater than 5.0 mg/l except from natural causes, e.g., heavy phytoplankton bloom and ensuing temporary depletion of dissolved oxygen. Table 6 indicates that all quarterly means for all stations fall within the generally accepted range of values, i.e., between 5.0 and 7.0 mg/l.

TABLE 6
DISSOLVED OXYGEN DATA
STATIONS 2, 2b, 3, 4, 6, 22 AND 24

Station	High (mg/l)				Low (mg/l)			
	Arith. Mean	Std. Dev.	Geom. Mean	Qtr.	Arith. Mean	Std. Dev.	Geom. Mean	Qtr.
2	6.94	0.28	6.93	11	5.47	0.41	5.45	2
2b	7.08	0.59	7.06	11	5.52	0.18	5.52	2
3	6.88	0.55	6.86	12	5.91	0.35	5.90	6
4	7.15	0.77	7.11	12	6.41	0.70	6.38	6
6	7.23	0.73	7.20	12	5.73	0.61	5.74	6
22	7.04	0.42	7.03	11	5.48	0.48	5.46	1
24	7.07	0.58	7.04	12	5.86	0.28	5.85	2

Table 6 also indicates that all high D.O. readings were recorded during the January-June, 1976 period and that all low readings, with the exception of Station 22, occurred during the October-December period. The low readings for Station 22 occurred during June-September, 1973 period.

All D.O. values are at acceptable levels, indicating adequate O₂ levels for marine biological processes. However, unrecorded bottom level readings, particularly at Stations 3 and 4, have, on occasion, indicated greatly depleted O₂ levels (less than 2.0 mg/l), indicating a lack of water mixing, overpopulation by planktonic organisms, or extreme putrefaction or eutrophication conditions.

NUTRIENTS

The significance of total Kjeldahl nitrogen and total phosphorus levels is difficult to assess due to the wide variation in natural conditions. For example, State of

Hawaii Standards for Class A waters are often exceeded in pristine open ocean waters surrounding Hawaii (Tetra Tech, 1976). The measured levels of nitrogen and phosphorus in Keehi Lagoon vary widely. In some cases, it has been possible to determine exact or definite probable causes of high nutrient readings. In other cases, the causes of extremely high or low readings was not apparent even after investigating several probable causes.

As an example of the wide range of nutrient levels recorded, nitrogen levels at Station 4 have varied from less than 0.010 mg/l (August 20, 1973) to 1.080 mg/l (December 4, 1975) and phosphorus readings have varied from less than 0.001 mg/l (August 30, 1974) to 0.075 mg/l (September 11, 1975). Similar extreme high and low readings have been recorded for all stations, inside and outside Keehi Lagoon. Tables 7 and 8 indicate nutrient data collected.

TABLE 7
TOTAL KJELOHL NITROGEN DATA
STATIONS 2, 2b, 3, 4, 6, 22 AND 24

Station	High (mg/l)				Low (mg/l)			
	Arith. Mean	Std. Dev.	Geom. Mean	Qtr.	Arith. Mean	Std. Dev.	Geom. Mean	Qtr.
2	0.481	0.247	0.418	11	0.108	0.075	0.069	2
2b	0.544	0.216	0.500	13	0.117	0.110	0.061	2
3	0.413	0.156	0.380	7	0.160	0.101	0.133	3
4	0.509	0.103	0.498	12	0.155	0.119	0.121	2
6	0.587	0.359	0.496	4	0.175	0.105	0.129	1
22	0.493	0.227	0.448	11	0.165	0.098	0.127	10
24	0.429	0.162	0.399	7	0.087	0.056	0.074	2

TABLE 8
TOTAL PHOSPHORUS
STATIONS 2, 2b, 3, 4, 6, 22 AND 24

Station	High (mg/l)				Low (mg/l)			
	Arith. Mean	Std. Dev.	Geom. Mean	Qtr.	Arith. Mean	Std. Dev.	Geom. Mean	Qtr.
2	0.071	0.021	0.068	13	0.018	0.016	0.013	4
2b	0.059	0.023	0.052	12	0.017	0.010	0.015	1
3	0.062	0.017	0.059	12	0.026	0.008	0.025	2
4	0.067	0.029	0.060	13	0.019	0.006	0.018	1
6	0.047	0.011	0.045	13	0.017	0.007	0.016	1
22	0.053	0.013	0.051	13	0.011	0.008	0.009	2
24	0.051	0.024	0.046	12	0.010	0.009	0.007	5

Low nitrogen readings occur generally during the fall (October-December) and winter (January-March) months while high readings occur during the winter, spring (April-June) and summer (July-September) months. All stations exceed Class A Standards (0.15 mg/l). Generally, it can be expected that nitrogen readings will be highest after the period of most rapid utilization of nitrate by plants in the spring and summer, and then generally decrease. Also, it has been found that higher quantities of nitrite are generally found in surface waters during the summer and autumn and

therefore definitely associated with the distribution of density and of water temperature (Sverdrup, 1942). These findings indicate that the low fall and winter month readings and high spring and summer month readings are fairly typical of naturally occurring situations. However, high winter readings for total nitrogen are atypical and may, in Keehi Lagoon, be caused by storm water runoff inflows.

Low phosphorus readings were found during the spring and summer months, except for Stations 3 and 22, and exceed Class A water standards. Generally, the values recorded are fairly atypical of natural conditions. Highest phosphorus values generally occur during the winter, and lowest values during the summer, when phytoplankton growth has been great.

It is known that in shallow water communities, e.g., Keehi Lagoon, bottom sediments may be a large reservoir of phosphorus. Even the release of a small part of this phosphorus could significantly increase the concentration in the water. When O_2 levels in bottom waters are reduced (e.g., from organic pollution) phosphate is released from the sediments. Dredging, with the consequent suspension of oxygen-consuming sediment particles, may increase total phosphorus concentrations (Ferguson Wood and Johannes, 1975).

As noted previously, bottom D.O. readings have indicated extremely low levels (less than 2.0 mg/l). This fact, acting in concert with the large amount of suspended sediment particles and disturbance of bottom conditions, may be the cause of high summer total phosphorus values recorded. However, also to be considered are the outside influences of drainage canals, streams, and sewer outfalls.

MARINE ECOLOGY SURVEYS

During the conduct of the water quality monitoring program, quarterly marine ecology surveys were being performed at four of the water quality stations (4, 13, 21 and 24 - Figure 2). Three of the stations (13, 21 and 24) are located seaward of the construction project on reef tops (15 to 40 feet below the surface). These reef tops have been exposed to little, if any, environmental stress (Bowers, 1976). Station 4 is located within Keehi Lagoon in an area that has been exposed to stress, including siltation, industrial pollution, and domestic sewage pollution (Bowers, 1976).

Live coral coverage of the substratum, numbers of sea urchins and fish, and zooplankton samples were recorded and collected. Coral coverage varied considerably from one quarterly monitoring period to the next. However, it appears that this variation represents an estimate of the natural variation inherent in the distribution of coral colonies throughout the station area.

The variations in numbers of sea urchins and fish that were observed were due, in part, to natural movements in and out of the station areas, requirements for irregular habitats, and mobility of the organisms.

Table 9 indicates yearly variations of coral coverage, numbers of urchins and fish, and total zooplankton types found at the four stations.

TABLE 9
YEARLY VARIATIONS OF MARINE ORGANISMS

Year	Percent Coral Coverage			Number Of Urchins Observed			Number Of Fish Observed			Number Of Zooplankton Types Observed		
	1	2	3	1	2	3	1	2	3	1	2	3
Station												
4	No Coral Observed			No Urchins Observed			Two Fish Observed During Three Years			15.5	15.7	17.0
13	34.3	45.0	47.3	11.2	46.0	47.0	475	620	476	20.2	17.0	19.0
21	21.5	20.5	20.3	2.0	2.2	2.7	592	710	442	17.7	16.5	16.5
24	26.3	25.5	25.8	7.2	7.5	14.0	557	418	416	18.0	14.7	16.7

CIRCULATION

Hawaii is located in an eastern central Pacific anti-cyclonic gyre. It is thought that water approaches the island of Oahu from the northeast in the winter and from the south to southeast in the spring and summer, depending on the position of the gyre (Sverdrup, 1942; R. M. Towill Corp., 1975). The winds, waves, tides, configuration of the coastline, and the bathymetry strongly influence the flow of water around the island at any given location. Flows in and out of major estuaries, e.g., Keehi Lagoon or Pearl Harbor, with each tide result in important local effects. The circulation in the entire Mamala Bay area (Figure 1) is strongly influenced by winds and tides, and therefore, varies seasonally (R. M. Towill Corp., 1975).

Circulation studies conducted prior to the construction of the reef runway (Bathen, 1970; Summ, et al, 1969) indicated that there were weak but definite flows of water inward over the barrier reef and westward around Ahua Point to the Hickam Harbor area and on out to the open ocean (Figures 3 and 4). Since the reef runway has blocked this flow, water entering Keehi Lagoon via Honolulu Harbor, Kalihi and Moanalua Streams, Kalihi Channel, and over the reef, must now pass over the reef, back through Kalihi Channel or out Circulation Channel "B" (Figure 2).

Prior to the dredging of Circulation Channel "B", a circulation study was performed (R. M. Towill Corp., 1976a) that indicated most outward flow as occurring in Kalihi Channel (Figure 5).

Recent post-construction aerial observations of Keehi Lagoon and the reef runway project area indicate that there is now a definite outflow of water in Circulation Channel "B". A portion of this outward flow can be seen on Figure 6. Circulation Channel "B" is approximately 500 feet wide at the surface, with a bottom width of 300 feet. The channel is dredged to minus 45-50 feet.

DISCUSSION

The obvious environmental impact of the reef runway project has been the covering of over 850 acres of coral reef flat with over 19 million cubic yards of dredged coral materials. This has resulted in some changes to the water quality and circulation patterns of Keehi Lagoon.

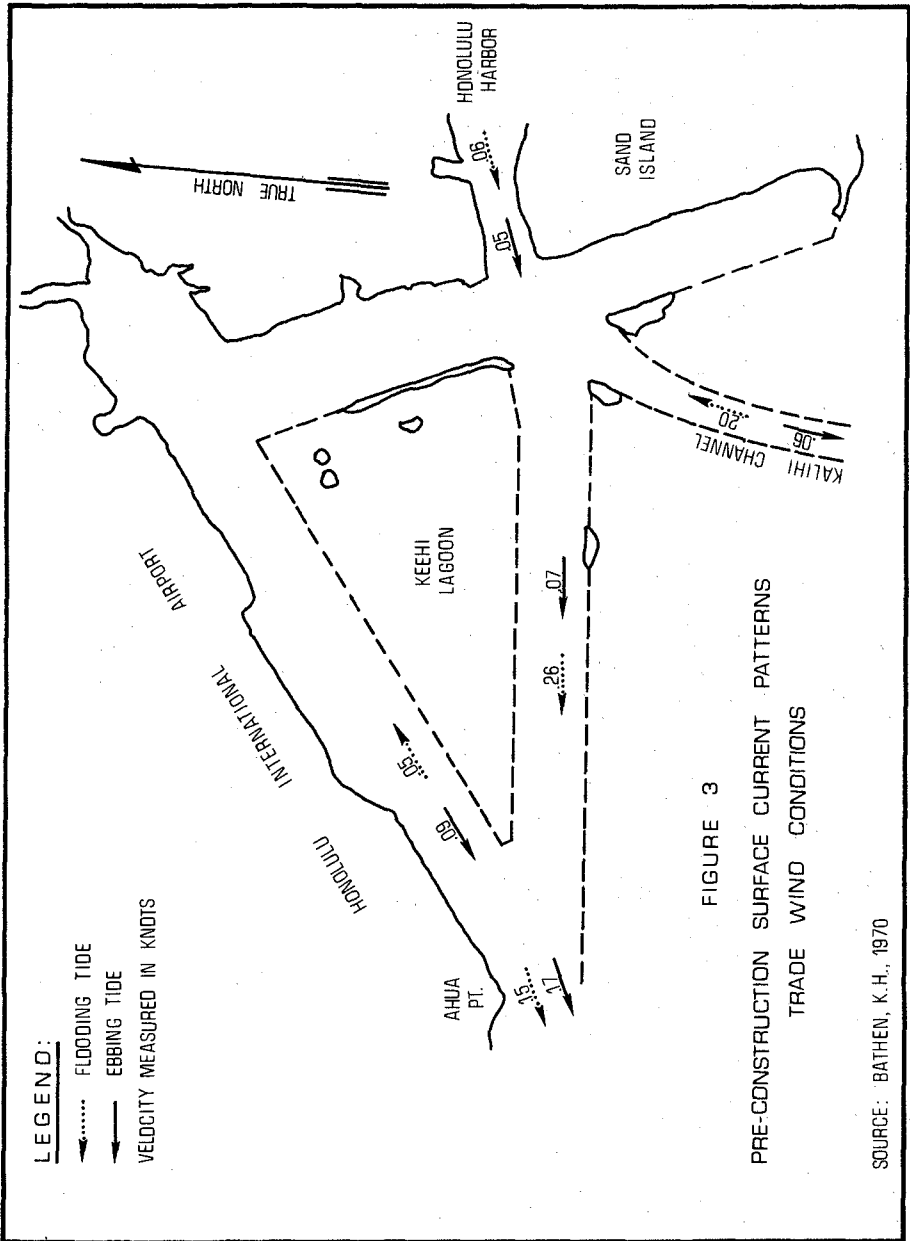


FIGURE 3
PRE-CONSTRUCTION SURFACE CURRENT PATTERNS
TRADE WIND CONDITIONS

SOURCE: BATHEN, K.H., 1970

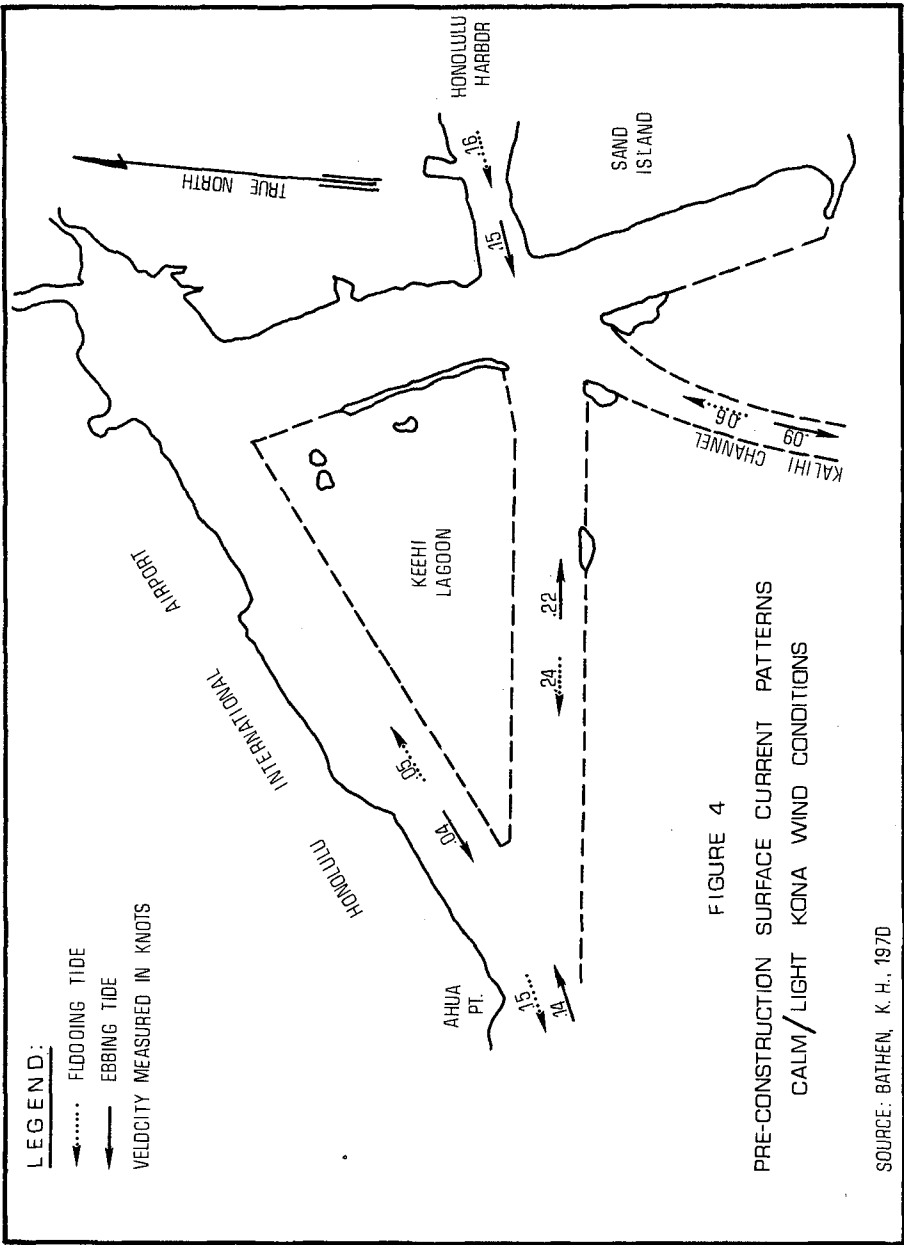


FIGURE 4
PRE-CONSTRUCTION SURFACE CURRENT PATTERNS
CALM/LIGHT KONA WIND CONDITIONS

SOURCE: BATHEN, K. H., 1970

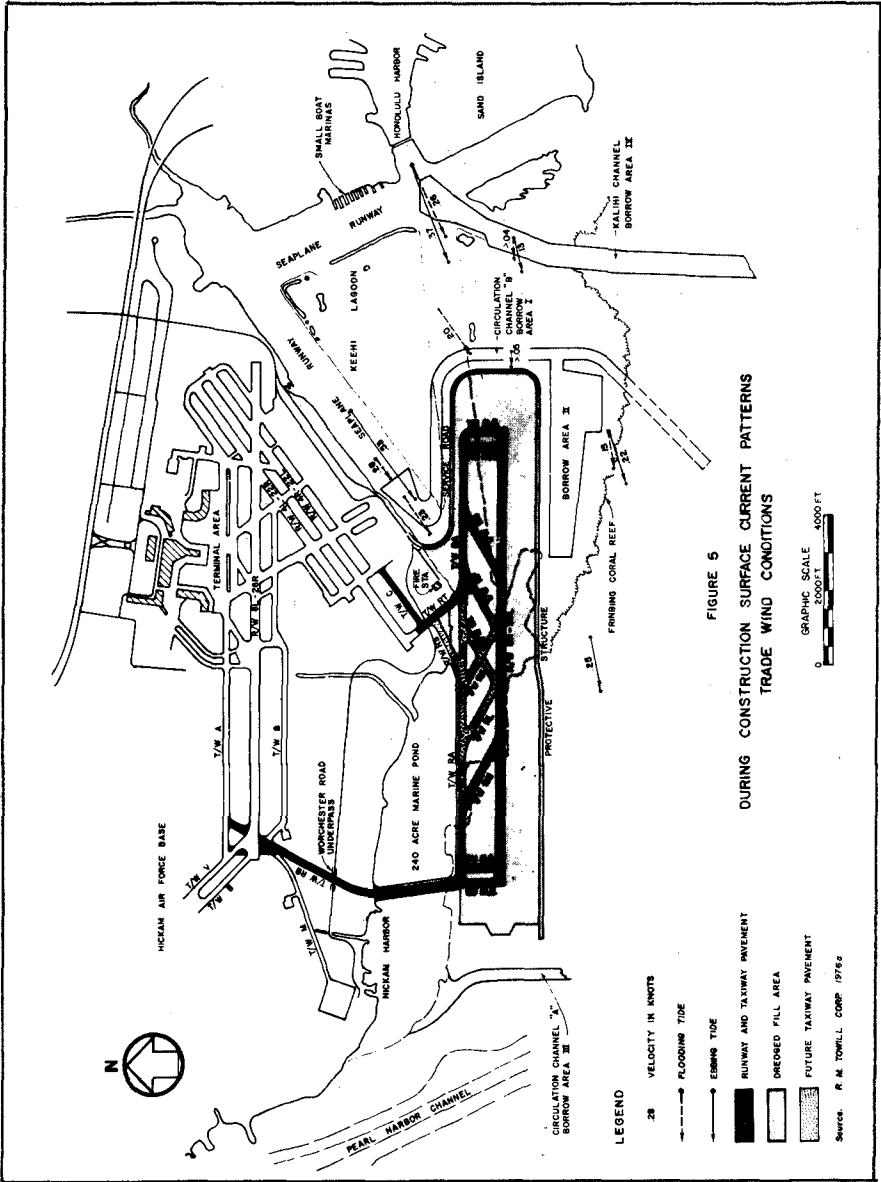




Figure 6 Aerial View of Reef Runway, September, 1976.

Temperature and salinity levels at the seven stations analyzed (2, 2b, 3, 4, 6, 22 and 24) do not appear to indicate variations other than normal seasonal differences. That is, highest temperatures were found during the summer months and lowest during winter months. Highest salinity values were recorded during the spring and summer months and lowest values were recorded during the winter months, except at Station 22 where the lowest average was recorded during the summer. The reason for this anomaly is unclear, but it appears to be a local condition and not indicative of a long term situation.

Water clarity at all stations except two (3 and 24) is greater now than before the reef runway construction. It was apparent during the construction and dredging activities, that as dredging and filling approached any particular station, that water clarity decreased. However, as these activities proceeded by a given station and the area allowed to restabalize, water clarity increased. The exceptions to this are Stations 3 and 24. Station 3 is influenced by fresh water inflow from Kalihi and Moanalua streams. This inflow is generally silt laden and causes minor daily variations in water clarity. The effects of construction appear to have affected the water quality at Station 3 only to the degree that circulation patterns have been altered. Possibly resulting in decreased flow rates out of the area. However, until a detailed circulation study has been performed, definitive conclusions cannot be reached.

Station 24 is influenced by swell, wave, and offshore current action. It appears that dredging in Borrow Area II and Circulation Channel "B", plus the present outflow of water through Channel "B" may be causing some silt build-up along the 40- to 60-foot bottom contours. During the ecological surveys, a fine layer of silt was occasionally observed on corals at Station 24. However, it appears that this silt is naturally carried away by subsurface currents and is dispersed over a wide area. During spring and summer southerly swell conditions, this silt is placed into suspension and decreases water clarity. This condition is expected to continue for several years until the borrow areas and circulation channel have been cleansed of fine silts.

Dissolved oxygen levels at all stations indicate that construction activities have had little, if any, effect. As indicated previously, all sampling was performed at mid-depths and as such stratification of the various water quality parameters was not measured. However, unrecorded bottom D.O. measurements did indicate O_2 depleted conditions. These readings were made prior to completion of Circulation Channel "B" and it is, therefore, not possible at this time to indicate whether flushing or mixing within the lagoonal water column is occurring.

The general increases in nutrient levels (total Kjeldahl nitrogen and total phosphorus) that appear to be occurring are difficult to assess due to numerous other influences. As noted above, Kalihi and Moanalua Streams and Honolulu Harbor enter Keehi Lagoon. The Sand Island Sewer Outfall, which presently disposes of over 55 million gallons of raw sewage daily, is less than two miles upwind the reef runway project area. Predominant currents flow towards the reef runway area. It is known (Ferguson Wood and Johannes, 1975) that dredging operations cause the release of nutrients stored in bottom sediments. It is also possible that if subsurface current flows through Keehi Lagoon have increased as a result of Circulation Channel "B", nutrients could be released from bottom sediments through increased scouring and the resultant suspension of silt particles in the water column.

An indication of the effects of changes in water quality that have occurred is provided by the marine ecology surveys. As noted previously, percent coral coverage variations that have occurred tend to indicate natural variation rather than one produced by construction activities or abrupt changes in water quality. Sea urchin and fish counts also tend to indicate variations due to natural causes rather than construction induced changes. Bowers (1976) reports that variations in numbers of sea urchins similar to those found at the reef runway have also been observed at other areas on Oahu, and that these variations may be natural cyclic occurrences.

The variations in the numbers of fish and fish species observed during the 3-year monitoring period can be generally explained by changes in the underwater visibility and natural fish movements.

The variations in the numbers and types of zooplankton observed does not indicate any general trend. The relatively small changes that have occurred, tend to imply that natural variation as opposed to environmental stress conditions, such as construction, are responsible for the variations in total plankton types noted.

CONCLUSIONS

As noted previously, a major purpose of the reef runway environmental monitoring program was the detection of non-compliance with State of Hawaii and construction project specification water quality standards.

Of major importance was the early detection of turbidity violations. Turbidity was controlled through the use of sea curtains and the requirement that all dredged spoil material be pumped into confined areas. Only in a few instances did turbidity levels go below allowable standards, and these situations were quickly and easily corrected. Violations of other water quality standards, e.g. nutrient levels, have also occurred. However, it appears that these violations have not been entirely due to construction efforts, but more likely, due to outside influences. As noted, when water quality, circulation, and marine biological factors are considered, it appears, at this time, that the reef runway construction project has not had any negative impacts. Definitive conclusions regarding the long-term effects of the reef runway project will not be possible until future water quality, circulation, and marine ecology studies have been conducted.

The analysis of water quality data collected during the reef runway project, and examinations of water quality data collected during other coastal engineering projects in Hawaii, suggests that present State Water Quality Standards require review and adjustment to reflect naturally occurring conditions. As noted previously, studies (Tetra Tech, 1976) have shown that pristine open ocean water, on the windward and leeward sides of Oahu and other islands, does not meet State Water Quality Standards. Studies performed at other construction sites on other Hawaiian islands also tend to indicate these findings (Sunn, et al, 1972b and 1975; Oceanic Foundation, 1975; J. K. K. Look, 1972; U.S. Army Engineers, 1976).

The long-term environmental effects of the reef runway construction can only be determined following additional data reduction analyses, and future water quality, circulation, and marine ecological studies. These studies, which should be conducted over at least a one-year period following major offshore construction efforts, will provide the data base upon which fairly definitive conclusions can be reached.

ACKNOWLEDGEMENTS

The preparation of this paper would not have been possible without the valuable assistance and guidance of Mr. Owen Miyamoto, Chief, Airports Division, Mr. Robert S. Chun, Airports Engineer, and Mr. Frank Okimoto, Engineer, Airports Division, State of Hawaii Department of Transportation. The field work, compilation and reporting of data collected was performed by Messrs. Frank Doyle, F. L. Vuillemont, and Roy Tsutsui of the R. M. Towill Corporation. Their assistance, perseverance, and patience are gratefully acknowledged. I would especially like to extend my sincere thanks to Messrs. Lowell Anderson and Francois Iragui, Reef Runway Project Managers, The Ralph M. Parsons Company, for their financial and moral assistance and their perseverance and dedication to complete a program that, at times, contributed additional problems to an already complex construction sequence and methods situation. Finally, I would like to thank Ms. Francee Matlock for her patience and help in preparing the tables and typing the manuscript.

Without all of this help, the monitoring program would not have been possible. One of the pleasures inherent in the completion of a research project is the opportunity to express gratitude to all those who made it possible.

REFERENCES

- Bathen, K. H., 1970. The Circulation In Keehi Lagoon, Oahu, Hawaii, during July and August, 1968. University of Hawaii, Hawaii Inst. Mar. Biol. Tech. Rept. No. 17.

- Berger, A., 1971. Keehi Lagoon Bird Survey. Final report submitted to The Ralph M. Parsons Company. Xerox M.S.
- Bowers, R. M., 1976. Reef runway monitoring program marine ecology survey final report. In: Environmental Quality Control Monitoring Program For The Reef Runway, Final Report, R. M. Towill Corporation.
- Dehnel, P. A., 1960. Effect of temperature and salinity on the oxygen consumption of two intertidal crabs. Biol. Bull. Woods Hole, 118(2): 215-249.
- Ekman, S., 1953. Zoogeography of the Sea. Sidgwick and Jackson, Ltd., London, 417 pp.
- Federal Aviation Administration, 1972. Final Environmental Impact Statement, Reef Runway Project, Honolulu International Airport, Honolulu, Hawaii, 86 pp.
- Ferguson Wood, E. J. and R. E. Johannes, 1975. Tropical Marine Pollution. Elsevier Scientific Publishing Company, New York, 192 pp.
- Harvey, G. W., R. Q. Palmer, J. R. Walker, and T. D. Krishna Kartha, 1971. Plan to enhance water quality in Keehi Lagoon and ponds makai of proposed reef runway 8R26L. Final report prepared for The Ralph M. Parsons Company.
- James K. K. Look Laboratory of Ocean Engineering, 1970. Hydraulic Model study, proposed reef runway, Honolulu International Airport. Report prepared for State of Hawaii Department of Transportation. Department of Ocean Engineering, University of Hawaii.
- James K. K. Look Laboratory of Ocean Engineering, 1972. Dredging Operation monitoring and environmental study, Kawaihae Harbor, Hawaii. Technical Report No. 25, University of Hawaii-Look Lab-72-25.
- Johannes, R. E., 1972. Coral reefs and pollution. In: M. Ruvio (Ed.), Marine Pollution and Sea Life. Fishing News (Books), London, pp. 364-371.
- Kinne, O., 1963. The effects of temperature and salinity on marine and brackish water animals. In: H. Barnes (Ed.), Oceanography and Marine Biology. Allen-Unwin, London, pp. 301-340.
- McLeese, D. W., 1956. Effects of temperature, salinity, and oxygen on the survival of the American lobster. J. Fish. Res. Bd. Canada, 13(2): 247-272.
- Oceanic Foundation, 1975. A three-year environmental study of Honokohau Harbor, Hawaii. Report prepared for U.S. Army Corps of Engineers, 101 pp.
- Office of Environmental Quality Control and Keehi Lagoon Task Force, 1971. Report on Keehi Lagoon and Waikiki Beach water quality. Report prepared for the Governor, State of Hawaii.

- R. M. Towill Corporation, 1975. Final environmental impact statement for Honouliuli wastewater treatment plant and Barbers Point outfall system, Supplement. Report prepared for Div. of Sewers, Dept. of Public Works, City and County of Honolulu.
- R. M. Towill Corporation, 1976a. Reef runway water circulation study (construction phase). Report prepared for The Ralph M. Parsons Company, 36 pp.
- R. M. Towill Corporation, 1976b. Environmental quality control monitoring program for the reef runway - final report. Report prepared for The Ralph M. Parsons Company, 210 pp.
- State of Hawaii, Department of Health, 1974. Public Health Regulations, Chapter 37-A, Water Quality Standards, 11 pp.
- Sunn, Low, Tom and Hara, Inc., 1969. Current study in connection with proposed reef runway, Honolulu International Airport. Report prepared for Univ. of Hawaii Center for Engineering Research, 50 pp.
- Sunn, Low, Tom and Hara, Inc., 1972a. Environmental quality control for the construction of the reef runway, Honolulu International Airport. Report prepared for The Ralph M. Parsons Company, 100 pp.
- Sunn, Low, Tom and Hara, Inc., 1972b. Estimates of environmental impact of construction in Nawiliwili Bay water quality and ecosystems. Report prepared for Corps of Engineers, Honolulu, Hawaii, 60 pp.
- Sunn, Low, Tom and Hara, Inc., 1975. Final report of Nawiliwili small boat harbor post-construction survey. Report prepared for Corps of Engineers, Honolulu, Hawaii, 55 pp.
- Sverdrup, H. U., M. W. Johnson, and R. H. Fleming, 1942. The Oceans: Their Physics, Chemistry, and General Biology, Prentice-Hall, Inc., Englewood Cliffs, N. J., 1060 pp.
- Tetra Tech, Inc., 1976. Final Report: Study areas II and VI-C water quality analysis and environmental assessments, Oahu, Hawaii. Report prepared for National Commission on Water Quality, 300 pp.
- U.S. Army Engineer District Honolulu, Hawaii, 1976. Draft environmental impact statement for Barbers Point Harbor, 200 pp.

CHAPTER 203

STUDY OF AN ARTIFICIAL ISLAND

by

J.P. LEPETIT and S. MOREAU *

1 - INTRODUCTION

The location of large surface industrial zones along sea shores often competes with other coastal activities, such as recreational pursuits, fishing, nature reserves, etc. The construction of an artificial island in the sea, near the shore, is a solution to which it will perhaps be necessary to have recourse in the fairly near future. The design of such a project poses many problems particularly in respect of its impact on the environment. We present here the results of a study which examines this aspect.

The problems are as follows :

- influence of the island on the local wave climate, or swell, and consequent shoreline changes,
- influence of the island on tidal currents and resulting evolution of the sandy sea bed,
- dispersion of industrial effluents.

The effect of the island on swell and on shore stability and the calculation of pollutant dispersion are approached by the use of mathematical models ; the effect of the island on tidal currents is analysed on a reduced scale physical model.

* Division Hydraulique Maritime - Laboratoire National d'Hydraulique Electricite de France - Chatou - France.

2 - IMPACT ON THE SHORE

The impact on the shore is determined by computer calculations [1] of the wave pattern and of its resulting effect on littoral drift (fig. 1). The computation of the wave pattern takes account of refraction, due to variations in water depth, and diffraction, due to the presence of the island : both mechanisms are computed independently and then combined by multiplying the coefficients of wave height variation so obtained.

The variations in wave height and incidence along the shore are determined for each wave period and direction considered ; then, using a classical littoral drift formula, the variation in the discharge of sand is estimated. By summing the volumes of sand transported by waves in each category considered, weighted according to their frequency of occurrence, the net sand transport along the shore can be obtained. The stage-by-stage evolution of the shoreline is derived by calculation of the continuity.

During the computation the discharge of sand is modified daily according to changes in the orientation of the shoreline, and the computation of the wave pattern is repeated every three years. This computation is carried out for the existing situation in the absence of the island, and then repeated with the island present.

Without the island, waves (6s period, 4 m annual significant height) originating from directions between west and north-east produce a net littoral drift eastwards of 10 to 20 m³/day on a straight east-west shore consisting of fine sand (0,25 mm).

The location of an island, 3500 m offshore, induces the formation of a tombolo with erosion of the beach on either side. Due to the predominant direction of littoral drift, the north-south axis of the tombolo is slightly west of the intersection of the north-south axis of the island with the shore (fig. 2). However, the drift being low, the shoreline changes are rather slow. The average shoreline advance is 0,30 m/year with a 2200 m long island & 0,45 m/year with a 3500 m long island. The average rates of shoreline recession are 0,10 m/year and 0,25 m/year respectively.

Shoreline changes may be prevented by periodical dredging. The construction of groynes on the shore on either side of the island would also reduce the volume of sand trapped in the sheltered zone between island and shore.

[1] LEPETIT J.P. Transport littoral : essais et calculs. Proc. 13th Conf. Coastal Engineering. Vancouver 1972.

3 - IMPACT ON CURRENTS AND BATHYMETRY

This is analysed on a reduced scale model with a fixed bed (horizontal scale 1/1000, vertical scale 1/100) equipped with tide and current generators. The surface current paths are measured by taking time exposures of floats before and after the construction of the island on the model. The effect of the island can be assessed from charts indicating zones of increase and decrease in current velocity (fig.3).

A 700 m wide island oriented in the direction of maximum long shore currents has little significant effect on discharge. However, appreciable changes occur near the island. Decreases in velocity are noted around the island, both upstream and downstream. On both sides of the island, particularly between the island and the shore, increase occur. In both cases the maximum change in velocity is 25 %.

The result is very sensitive to several parameters which are :

- the length of the island
- the width of the island
- the distance from the shore
- and the shape of the island itself.

More tests are necessary to understand the effect of each parameter but as regards the increase of velocity between the shore and the island it seems that this variation is more important when the island is wider, is nearer from the shore and is shorter.

A particular shape of the upstream extremity of the island with deflects the current seawards reduces the increase of velocity between the island and the shore (fig. 4).

When the sea bed is sandy, these results may be used to give an indication of the likely zones of deposition and erosion. Thus, it is possible to extrapolate the formation of a sand bank behind the island, and an area of scour between the island and the shore ; furthermore, such an eroded area may limit the accretion of the shore due to wave refraction.

4 - EFFLUENT DISPERSION

The dispersion of industrial effluents is assessed by a stage-by-stage computer calculation, 2 dimensional in plan, which takes into account convection and dispersion due to tidal currents. The dispersion coefficient used is about $5 \text{ m}^2/\text{s}$ in each horizontal direction. Concentrations are assumed to be uniform throughout the depth - an assumption which is satisfied during strong tidal currents. The current values used in the computation are those measured with the island represented on the physical model.

With a slightly rotating, reversing tidal current parallel to the shore, having a maximum velocity of 1 m/s and an effluent discharge of 200 m³/s seawards from the centre of the island, the surface areas affected by concentrations of 10 % and 20 % of the discharged concentration are approximately and respectively 2 km² and 0,5 km² (fig. 5).

Computations carried out for a nearby coastal site with reversing but non-rotating currents give 10 % concentrations over areas 2 to 3 times greater. For a site inside of an estuary the areas concerned are even more higher (fig. 6).

The comparison therefore favours discharging effluents into the open sea, but the difference is due to several factors whose effects are difficult to assess - distance from the shore, stronger residual current, rotating currents and also greater depth.

A more succinct assessment is carried out by simulating the effluent discharge by coloured water on a reduced scale model. The results obtained are in relatively good agreement with the computed results, perhaps because the convection by tidal currents is the major effect and precisely the currents introduced in the calculation are those recorded on the model where dye tests are made.

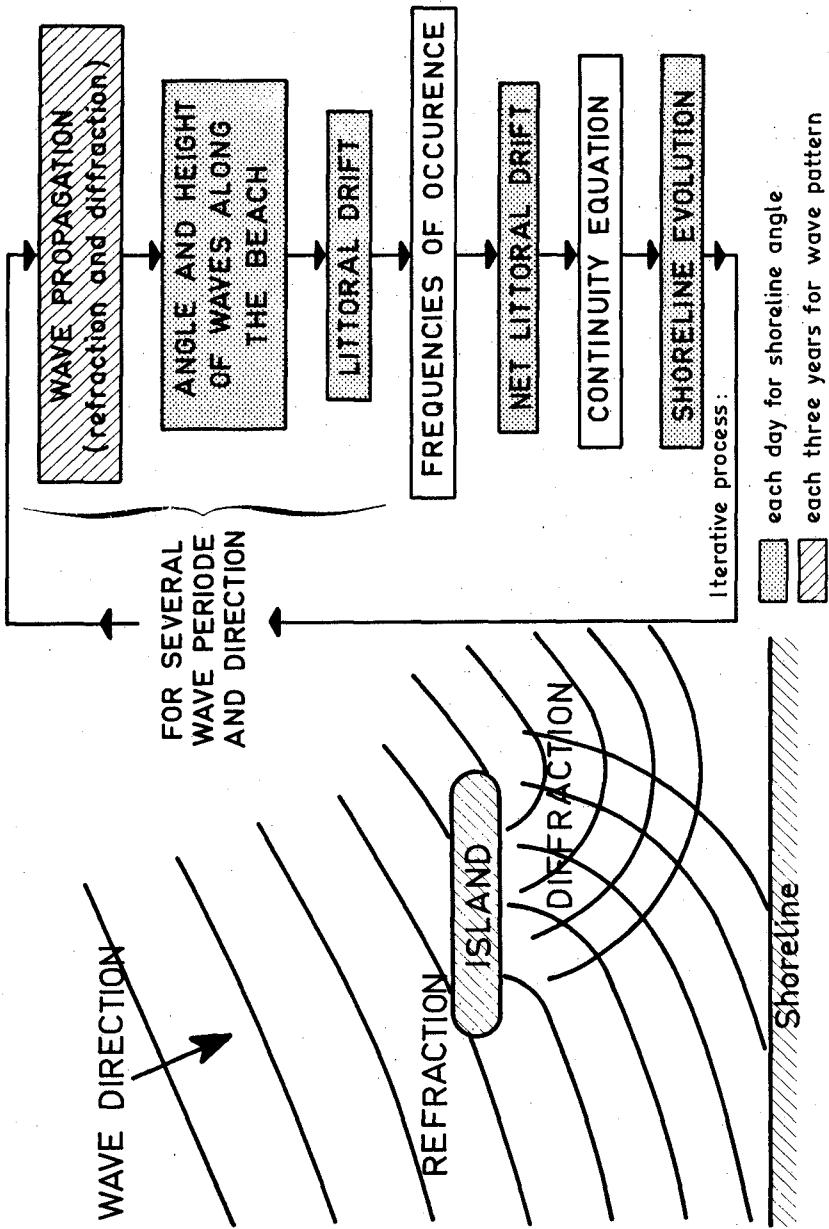


Fig.1- COMPUTATION OF SHORE CHANGES

Beach material
- Sand
- $D_{50} = 0.25\text{mm}$

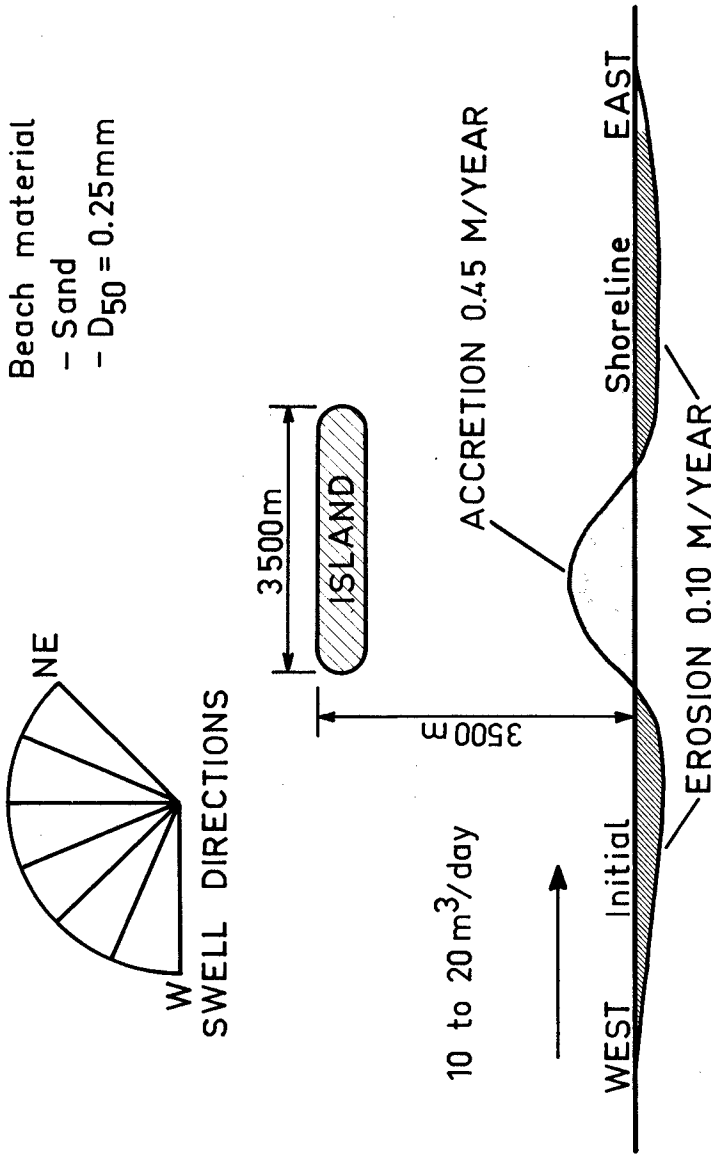


Fig.2 - TYPICAL SHORE EVOLUTION

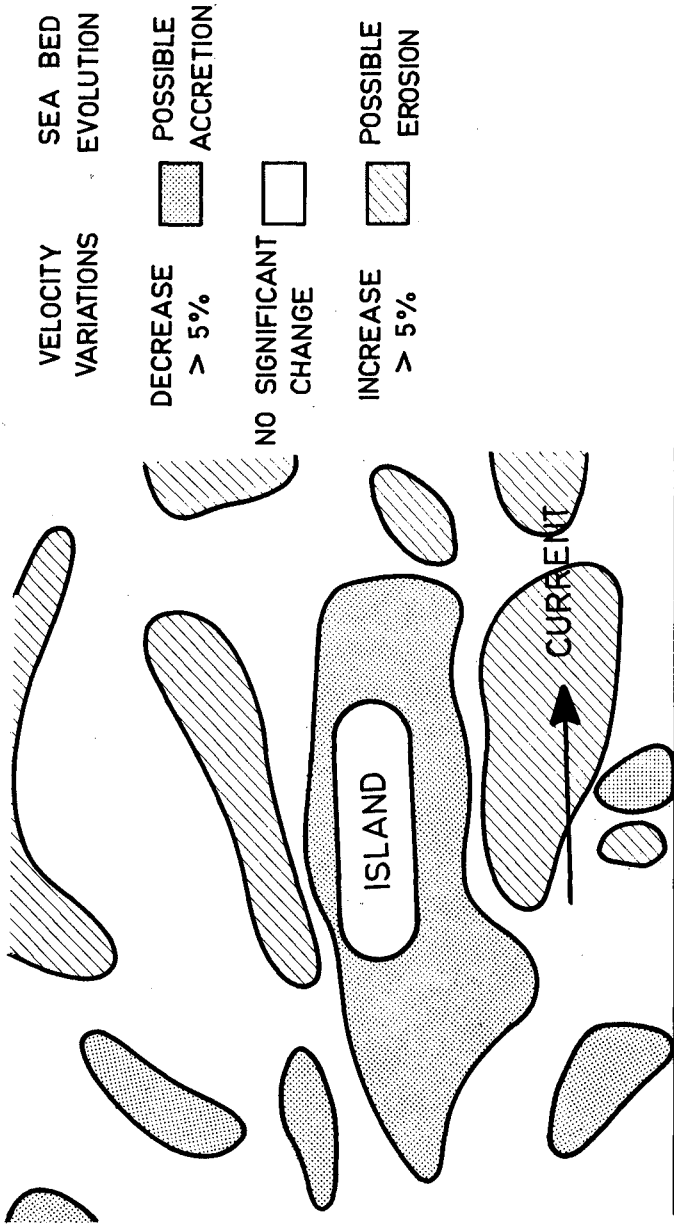


Fig.3 - EFFECT OF ISLAND ON TIDAL CURRENTS

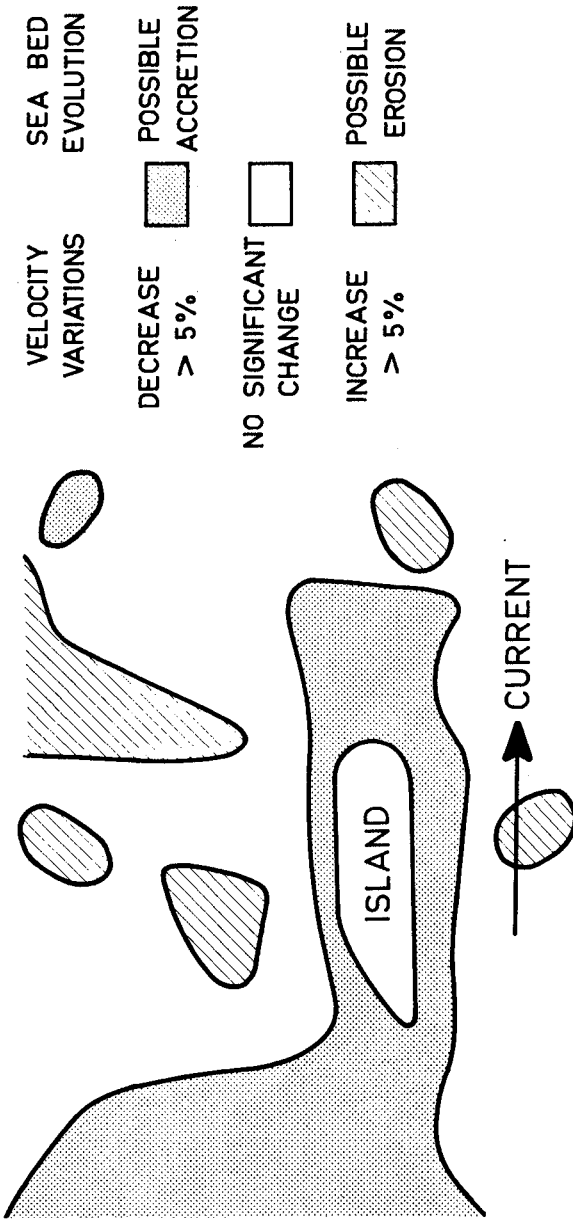


Fig.4 - REDUCTION OF THE EFFECT ON TIDAL CURRENTS

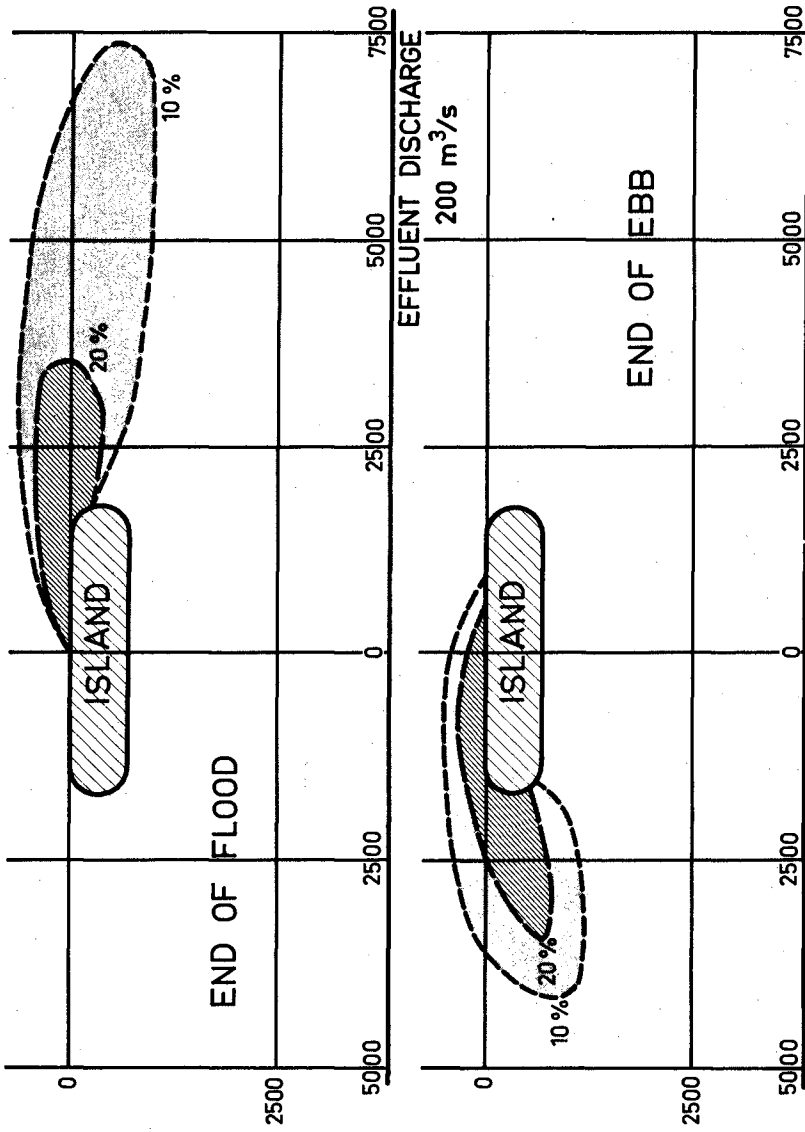


Fig.5- DISPERSION OF AN EFFLUENT

	SITE	TIDAL EXCURSION (km)	DRIFT (km/tide)
---	in estuary	22	1
- - -	on the coast	15	1
—	offshore	12	5

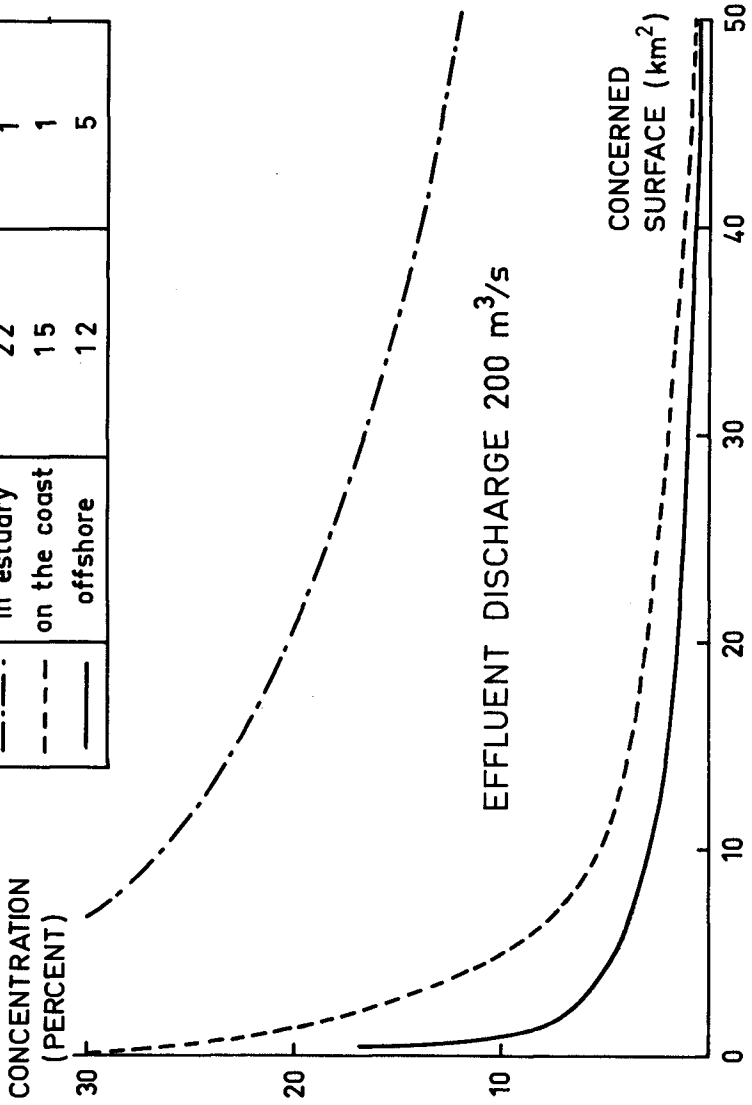


Fig.6 - COMPARISON WITH DISPERSION IN OTHER SITES

CHAPTER 204

WAVE INDUCED OSCILLATIONS OF HARBORS WITH VARIABLE DEPTH

by

F. Raichlen¹ and E. Naheer²

ABSTRACT

A numerical method is presented to treat the wave-induced oscillations of a harbor with a variable depth and width. A two-dimensional finite difference approach is used inside the harbor matched at the entrance to a solution for the open-sea based on the Helmholtz Equation which includes incident, reflected, and radiated wave energy. Examples of the response and the modal shapes of the water surface are presented for harbors with simple and complex shapes.

INTRODUCTION

In recent years significant progress has been made in developing analytical models to determine the response of harbors to incident waves. The ultimate objective in such research is to be able to treat a harbor with variable depth, planform, and coastline configuration, and with a variable interior reflectivity. Such a model would be extremely useful in preliminary design work and guiding laboratory studies of the phenomenon.

Early theoretical investigations of harbor resonance concentrated on harbors with constant depth and simple geometric shapes. Examples of these studies are: Miles and Munk (1961) and Ippen and Goda (1962). One of the major results of these investigations was the realization that the open-sea was important in allowing for the loss of energy radiated from a harbor. For the steady-state excitation of a harbor the radiated energy from the harbor to the open-sea is an important aspect of the response problem, and provides a form of "dissipation" in an otherwise inviscid theoretical approach. Methods were presented which demonstrated, quite well, (particularly the study of Ippen and Goda (1962)) the effect on the harbor response of geometric characteristics of the harbor, such as the ratios of: width to length and entrance width to harbor width.

Lee (1969), Hwang and Tuck (1970), and Lee and Raichlen (1971) investigated the problem of the wave-induced oscillations of constant depth harbors of arbitrary shape. Numerical methods were developed to treat the problem of a complex harbor with perfectly reflecting interior boundaries. In the study of Hwang and Tuck (1970) the open-sea and the harbor were treated as one region; Lee (1969) and Lee and Raichlen (1971) treated the harbor and the open-sea separately, then matched the solutions at the harbor entrance. (This difference leads to the study reported herein.)

Several approaches have been proposed to determine the response of harbors with variable shape and depth to incident waves, e.g., Raichlen (1965), Wilson et al. (1965), Olsen and Hwang (1971), and Chen and Mei (1974). Comments are made by Miles (1974) relative to the applicability of certain of these methods, and the interested reader is directed to that publication.

A two-dimensional approach was presented by Raichlen (1965) to treat the oscillations of long waves in closed basins of arbitrary planform and variable depth. This was extended, in an approximate fashion, to the case of a harbor

¹Professor of Civil Engineering, W. M. Keck Lab. of Hydr. and Water Res., Calif. Inst. of Tech., Pasadena, CA, USA.

²Graduate Research Assistant, W. M. Keck Lab. of Hydr. and Water Res., Calif. Inst. of Tech., Pasadena, CA, USA.

connected to the open-sea. The major assumption in the case of the harbor was that a node existed at the harbor entrance. It was realized at the time that this was a serious limitation to the analysis, especially in view of the work of Ippen and Goda (1962) where it was shown, for rectangular harbors, that only for small ratios of width to length and large ratios of entrance width to harbor width is this assumption reasonable. Suggestions were made for improving this, but these were not attempted at the time.

The objective of the study reported herein is to eliminate this imposed entrance condition and develop a simple method which allows the wave amplitude at the entrance to adjust naturally to the external and internal waves similar to the analyses presented by Ippen and Goda (1962) and Lee (1969) for simple and complex shapes, respectively. The harbor and the ocean are considered as two separate regions with the wave amplitude and the water surface slope obtained in each region matched at the harbor entrance. In this manner, it is possible to use analytical approaches which are different in each of the two regions.

ANALYTICAL CONSIDERATIONS

In this section the analytical method used will be discussed considering in order: the solution inside the harbor, the solution in the open-sea, and the solution for the combined region. There are certain limitations which are placed on the solution which may or may not restrict its application. These are:

- (1) Only shallow water waves are considered.
- (2) The problem is reduced to a two-dimensional problem; no surface variations are allowed in the harbor in a direction perpendicular to the *talweg* of the harbor.
- (3) The open-sea has a constant depth equal to the average depth at the entrance.
- (4) The coastline is assumed to be straight.

Harbor Region

The solution for the interior of the harbor follows the method proposed by Raichlen (1965), and it will be summarized here. A body of water is considered with a length l measured along the natural coordinate direction s , see Fig. 1. The natural coordinate is directed along the *talweg* which is the line which smoothly connects the deepest parts of the body of water. The variation of surface width and cross-section area perpendicular to the s -direction are denoted as $b(s)$ and $A(s)$, respectively.

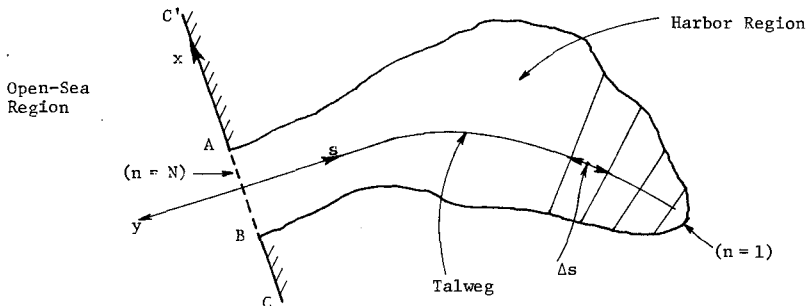


Fig. 1. Definition Sketch of Harbor and Open-Sea Regions.

For long waves with small amplitude the equation of continuity for the fluid body may be written as:

$$\frac{\partial}{\partial s} (Au) + b \frac{\partial \eta}{\partial t} = 0 \quad (1)$$

where u is the water partical velocity in the s -direction averaged over the cross-section and η is the amplitude of the water surface relative to the mean water level.

Neglecting friction, the equation of motion in the s -direction for two-dimensional flow (without body forces) is:

$$\frac{\partial u}{\partial t} + u \frac{\partial u}{\partial s} = - \frac{1}{\rho} \frac{\partial p}{\partial s} \quad (2)$$

where ρ is the density of the fluid and p is the local pressure. For small amplitude shallow water waves, the pressure can be assumed hydrostatic:

$$p = \gamma(\eta - z) \quad (3)$$

where γ is the specific weight of the fluid and the coordinate direction z is positive upwards. Neglecting the convective acceleration in Eq. 2 (which is reasonable for this small amplitude approach), Eqs. 2 and 3 can be combined to give:

$$\frac{\partial \eta}{\partial s} = - \frac{\partial u / \partial t}{g} \quad (4)$$

Eq. 4 states that the local water surface slope in the s -direction is given by the ratio of the local acceleration to the acceleration of gravity. It is assumed that the amplitude variation of the free surface can be expressed as a separable function of space and time as:

$$\eta = \eta(s) \cos \sigma t \quad (5)$$

where σ is the circular wave frequency, 2π /wave period. Differentiating the continuity equation (Eq. 1) with respect to time, substituting for the local acceleration from Eq. 4 and using Eq. 5 in the resulting expression, the following is obtained:

$$\frac{\partial}{\partial s} \left[A \frac{\partial \eta}{\partial s} \right] + \frac{b\sigma^2}{g} \eta = 0 \quad (6)$$

Eq. 6 can be expanded into an equation of the Sturm-Lionville form:

$$A \frac{d^2 \eta}{ds^2} + \frac{dA}{ds} \frac{d\eta}{ds} + \lambda_m b \eta = 0 \quad (7)$$

where $\lambda_m = \frac{\sigma^2}{g}$ $m = 1, 2, \dots, M$

and λ_m is a characteristic or an eigenvalue of the problem, and A and b are functions of s alone. Wilson et al. (1965) describe two boundary conditions that may exist at the end of the basin opposite to the entrance:

- (1) The cross-section area tends to zero or,
- (2) there is perfect reflection from the end.

From Eq. 7, these conditions can be expressed respectively as:

$$(1) \quad A = 0 \quad \frac{dA}{ds} \frac{d\eta}{ds} + \lambda_m b \eta = 0 \quad (8a)$$

$$(2) \quad \frac{d\eta}{ds} = 0 \quad \Lambda \frac{d^2\eta}{ds^2} + \lambda_m b \eta = 0 \quad (8b)$$

If both conditions exist simultaneously, the trivial case of $\eta = 0$ is obtained from Eq. 7. In addition, inherent in the assumption of $\Lambda = 0$ at the end is the fact that $b \neq 0$ at that point; if not, Eq. 7 reduces to $\frac{dA}{ds} \frac{d\eta}{ds} = 0$. Thus, the two boundary conditions at the closed end of the harbor are somewhat restrictive, although they do cover most of the interesting problems.

To obtain a numerical solution to Eq. 7, the basin is divided into N cross-sections spaced a distance Δs apart, where $\Delta s = \ell / (N-1)$; the cross-sections are perpendicular to the *talweg*. The section $n=1$ is the closed end of the basin and $n=N$ is at the entrance which communicates with the open-sea. The first and second derivatives are expressed in finite difference form using central differences, and Eq. 7 becomes:

$$a_{n,n-1} \eta_{n-1} + a_{n,n} \eta_n + a_{n,n+1} \eta_{n+1} = \Lambda_m \eta_n \quad (9)$$

where:

$$a_{n,n-1} = -\frac{1}{b_n} \left[A_n - \frac{1}{4}(A_{n+1} - A_{n-1}) \right] \quad a_{n,n} = 2A_n/b_n$$

$$a_{n,n+1} = -\frac{1}{b_n} \left[A_n + \frac{1}{4}(A_{n+1} - A_{n-1}) \right] \quad \Lambda_m = \lambda_m \Delta s^2$$

For the boundary condition where the area at the end section ($n=1$) goes to zero, Eq. 8a, forward differences are used to define the derivatives and Eq. 8a becomes:

$$a_{1,1} \eta_1 + a_{1,2} \eta_2 = \Lambda_m \eta_1 \quad (10a)$$

where:

$$a_{1,1} = (A_2/b_2) = -a_{1,2}$$

Therefore, the wave amplitude at the next section ($n=2$) can be expressed in terms of the amplitude at section $n=1$ from Eq. 10a as:

$$\eta_2 = \left(1 - \frac{b_2 \sigma^2 \Delta s^2}{g \Lambda_2} \right) \eta_1 = E_2 \eta_1 \quad (10b)$$

In the case of perfect reflection from the end boundary ($n=1$) when the depth does not go to zero, the water surface slope becomes zero in accordance with Eq. 8b. This equation could be written in difference form similar to that shown in Eqs. 10a and 10b. However, to obtain a solution a zero water surface slope can be forced to occur at the end by using the "mirror-image" method proposed by Raichlen (1965). In that method the basin is extended one cross-section beyond the end wall to construct a mirror image; for example, for reflections at $n=1$ a cross-section at $n=0$ is defined with $A_0 = A_2$, $b_0 = b_2$ and $\eta_0 = \eta_2$. In this manner, by symmetry about $n=1$, a zero water surface slope is forced at $n=1$. The difference equations written for this are:

$$a_{1,2} \eta_2 + a_{1,1} \eta_1 = \Lambda_m \eta_1 \quad (11a)$$

where

$$a_{1,1} = (2A_1/b_1) = -a_{1,2}$$

Hence, the wave amplitude at $n=2$ can be expressed in terms of the amplitude at the end of the basin as:

$$\eta_2 = \left(1 - \frac{b_1 \sigma^2 \Delta s^2}{2gA_1} \right) \eta_1 = E_2' \eta_1 \quad (11b)$$

It should be recalled, the analytical method used is to obtain a solution inside the harbor that can be matched at the entrance to a solution obtained by a different method for the outside region (the open-sea). To accomplish this, an inside solution must be evaluated at the entrance, $n=N$. Eq. 9 and the appropriate boundary condition (Eq. 10b or 11b) is used for this. In this regard, it is instructive to look first at the wave amplitude at the cross-section $n=3$.

$$\eta_3 = \frac{1}{A_2 + \frac{1}{4}(A_3 - A_1)} \left\{ \left[\frac{1}{4}(A_3 - A_1) - A_2 \right] + \left[2A_2 - \frac{b_2 \sigma^2 \Delta s^2}{g} \right] \left[E_2 \text{ or } E_2' \right] \right\} \eta_1 = E_3 \eta_1 \quad (12)$$

Therefore, knowing the wave amplitude at the end of the basin, $n=1$, and the cross-section geometry and wave period, the wave amplitude at $n=3$ can be evaluated. Proceeding iteratively, the amplitudes at arbitrary cross-sections are expressed as:

$$\eta_{n-1} = E_{n-1} \eta_1 \quad (13a)$$

and

$$\eta_n = E_n \eta_1 \quad (13b)$$

where E_n is a coefficient which can be evaluated easily.

Using backward differences, the water surface slope at the entrance ($n=N$) is approximated as:

$$\frac{d\eta_N}{ds} = \frac{\eta_N - \eta_{N-1}}{\Delta s} = F_N \eta_1 \quad (14)$$

where

$$F_N = \frac{E_N - E_{N-1}}{\Delta s} .$$

For any cross-section, E_n (and ultimately F_N) is determined by arbitrarily setting $\eta_1 = 1$ and the calculating $\eta_2, \eta_3, \dots, \eta_N$ iteratively. Dividing η_N and η_{N-1} by η_1 , the desired values of E_N and E_{N-1} are obtained, and the slope of the water surface (or the velocity) at the entrance is defined.

The wave amplitude η is a complex quantity which, at the entrance ($n=N$), can be written as:

$$\eta_N = \eta_N^{(R)} + i \eta_N^{(I)} \quad (15)$$

where $\eta_N^{(R)}$ and $\eta_N^{(I)}$ are the real and imaginary parts of the entrance wave amplitude, respectively, and thus provide both amplitude and phase information.

Open-Sea Region

The solution for the open-sea region is taken from Lee (1969) and will be summarized here; the interested reader is directed to the publication cited for

a more comprehensive description. As mentioned previously, for this development the open-sea is assumed to be a constant depth equal to the average depth at the harbor entrance. If a separable solution of the velocity potential ϕ is sought, within the limitations of small amplitude wave theory, the following expression can be used for the velocity potential:

$$\phi(x, y, z; t) = -\frac{1}{i\sigma} \frac{a_1 g \cosh k(h+z)}{\cosh kh} f(x, y) e^{-i\sigma t} \quad (16a)$$

and hence:

$$\eta(x, y; t) = a_1 f(x, y) e^{-i\sigma t} \quad (16b)$$

wherein a_1 is the wave amplitude, k is the wave number, and h is the depth. From Laplace's Equation ($\nabla^2 \phi = 0$) it is found that the spacial wave function, f , must satisfy the Helmholtz Equation:

$$\frac{\partial^2 f}{\partial x^2} + \frac{\partial^2 f}{\partial y^2} + k^2 f = 0 \quad (17)$$

In the outside region the wave function is defined as:

$$f_{out} = f_{inc} + f_{ref} + f_{rad} \quad (18a)$$

where f_{inc} is the incident wave function, f_{ref} is the wave function for the reflected wave, and f_{rad} is the wave function for the wave which is radiated outward from the harbor entrance. From Eq. 16b the wave amplitude can be expressed as:

$$\eta = a_1 (f_{inc} + f_{ref} + f_{rad}) e^{-i\sigma t} \quad (18b)$$

Referring to Fig. 1, the following boundary conditions are imposed on f_{out} .

$$(1) \quad \frac{\partial f_{out}}{\partial n} = 0 \text{ on } \overline{AC'} \text{ and } \overline{BC} \text{ at } y=0 \quad (19a)$$

$$(2) \quad \frac{\partial f_{out}}{\partial n} = -c \text{ on } \overline{AB} \text{ at } y=0 \quad (19b)$$

$$(3) \quad f_{out} \rightarrow (f_{inc} + f_{ref}) \text{ as } (x^2 + y^2) \rightarrow \infty \quad (19c)$$

The first boundary condition implies a zero velocity along the impermeable coastline where n is the normal to the boundary. The second boundary condition expresses the average velocity across the entrance in terms of the solution of the velocity obtained from inside the harbor. (This does not pertain to the immediate solution sought, but it is presented here for its usefulness later.) The third boundary condition ensures the radiated wave system, f_{rad} , disappears with increasing distance from the harbor entrance and the wave becomes simply a standing wave at infinity.

Lee (1969) obtains the radiated wave function using Weber's solution for the Helmholtz Equation (Eq. 17) letting the standing wave amplitude at infinity be a_1 , i.e., $(f_{inc} + f_{ref}) = 1$. Thus the wave function along the entrance is written as:

$$f_{out}(x, 0) = 1 - \frac{i}{2} \int_{\overline{AB}} C(x, 0) H_0^{(1)}(kr) dx \quad (20)$$

where $H_0^{(1)}(kr)$ is the Hankel function of the first kind and zero order chosen as a fundamental solution of the Helmholtz Equation. If variations in amplitude and velocity across the entrance in the x direction are considered small, f_{out} and $C(x,0)$ in Eq. 20 can be replaced by their values averaged over the width of the entrance: \bar{f}_{out} and \bar{C} . Hence, from Eq. 20 one obtains

$$\bar{f}_{out} = 1 - \frac{i}{2} \left[J_c + i \frac{2}{\pi} Y_c \right] b_N \bar{C} \quad (21)$$

where:

$$J_c = 1 - \frac{1}{6} \left(\frac{kb_N}{2} \right)^2 + \frac{1}{60} \left(\frac{kb_N}{2} \right)^4 - \frac{1}{1008} \left(\frac{kb_N}{2} \right)^6 + \frac{1}{25920} \left(\frac{kb_N}{2} \right)^8 + \dots$$

$$Y_c = \left[\ln \left(\frac{kb_N}{2} \right) + \gamma - \frac{3}{2} \right] - \frac{1}{6} \left(\frac{kb_N}{2} \right)^2 \left[\ln \left(\frac{kb_N}{2} \right) + \gamma - \frac{19}{12} \right] + \frac{1}{60} \left(\frac{kb_N}{2} \right)^4 \left[\ln \left(\frac{kb_N}{2} \right) + \gamma - \frac{55}{30} \right] - \frac{1}{1008} \left(\frac{kb_N}{2} \right)^6 \left[\ln \left(\frac{kb_N}{2} \right) + \gamma - \frac{353}{168} \right] + \frac{1}{25920} \left(\frac{kb_N}{2} \right)^8 \left[\ln \left(\frac{kb_N}{2} \right) + \gamma - \frac{826}{360} \right] + \dots$$

and: $\gamma = 0.5772157$ (Euler's constant). (To handle relatively large ratios of entrance width to wave length, the numerical computations for J_c and Y_c are carried to terms of order $(kb_N/2)^8$.)

Solution for the Combined Regions

Eq. 21 provides a first approximation to the outside wave function, f_{out} , and hence the wave amplitude in terms of an unknown average water surface slope, \bar{C} , at the harbor entrance. Since the \bar{C} can be complex, it is described by the derivative of Eq. 15 with respect to the s-direction, i.e., $\bar{C} = (1/a_1)(d\eta_N/ds)$. This substituted into Eq. 21 provides a general expression for the wave function at the entrance averaged over the entrance width. Separating the resulting expression into the real and imaginary parts the following are obtained:

$$\eta_N^{(R)} = a_1 + \frac{1}{2} \left[J_c \frac{d\eta_N^{(I)}}{ds} + \frac{2}{\pi} Y_c \frac{d\eta_N^{(R)}}{ds} \right] b_N \quad (22a)$$

$$\eta_N^{(I)} = -\frac{1}{2} \left[J_c \frac{d\eta_N^{(R)}}{ds} - \frac{2}{\pi} Y_c \frac{d\eta_N^{(I)}}{ds} \right] b_N \quad (22b)$$

Substituting Eqs. 13 and 14 obtained from the interior solution into Eqs. 22, the latter can be rewritten as:

$$\eta_1^{(R)} = \frac{a_1}{E_N} + \frac{1}{2} \left[J_c F_N \eta_1^{(I)} + \frac{2}{\pi} Y_c F_N \eta_1^{(R)} \right] \frac{b_N}{E_N} \quad (23a)$$

$$\eta_1^{(I)} = -\frac{1}{2} \left[J_c F_N \eta_1^{(R)} - \frac{2}{\pi} Y_c F_N \eta_1^{(I)} \right] \frac{b_N}{E_N} \quad (23b)$$

Eqs. 23a and 23b can be solved simultaneously for the real and the imaginary parts of η_1 , the amplitude at the end of the harbor ($n=1$):

$$\eta_1^{(R)} = a_i (E_N - \frac{1}{\pi} Y_c F_N b_N) / \alpha_N \quad (24a)$$

$$\eta_1^{(I)} = a_i (-\frac{1}{2} J_c F_N b_N) / \alpha_N \quad (24b)$$

where:

$$\alpha_N = \left(E_N - \frac{1}{\pi} Y_c F_N b_N \right)^2 + \left(\frac{1}{2} J_c F_N b_N \right)^2.$$

If the response function for the harbor is defined as the ratio of the wave amplitude at a position in the harbor (e.g., at the backwall, $n=1$) divided by the amplitude at the entrance if the entrance were closed, then from Eqs. 24 this becomes (for the backwall):

$$R_1 = \frac{1}{a_i} \left[\left(\eta_1^{(R)} \right)^2 + \left(\eta_1^{(I)} \right)^2 \right]^{1/2} \quad (25)$$

The amplification factor, R_1 , can be evaluated by setting the standing wave amplitude to unity ($a_i=1$) and substituting Eqs. 24a and b into Eq. 25. With reference to Eq. 13, the response at any other location becomes:

$$R_n = E_n R_1 \quad (26)$$

where E_n is defined, as before, from an expression similar to Eq. 12. Therefore, from Eqs. 24, 25, and 26 the response of a variable depth harbor to incident waves can be investigated keeping in mind the restrictions imposed on the solution by the assumptions stated previously.

DISCUSSION OF RESULTS

In evaluating this method of analysis, a harbor of simple geometry was considered first. This was a rectangular harbor with a width w , a linearly varying depth, and a fully open entrance connected directly to the open-sea. The depth of the open-sea region was set equal to the depth at the harbor entrance. The ratio of the depth at the backwall of the harbor to that at the entrance varied from zero to unity. The ratio of the harbor width to the length for the case considered was: $w/l = 0.194$; the same ratio as the constant depth case considered by Ippen and Goda (1962) and Lee (1969).

The response curves obtained are presented in Fig. 2 for four ratios of depths at the backwall to the entrance: $h_1/h_2 = 0, 0.67, 0.33, 1.0$. The ordinate is the response function as defined by Eq. 25 and the abscissa is the product of the harbor length and the wave number based on the wave period and the depth of water at the harbor entrance. The response for $h_1/h_2 = 1$ is the same as obtained by Ippen and Goda (1962) and Lee (1969). As the slope of the bottom increases the amplification at resonance increases significantly and the maximum response shifts to smaller values of $k_2 l$. Note that as $k_2 l$ tends to zero (the wave length tends to infinity) the response tends to unity, i.e., the wave length is so large that the wave essentially does not "see" the harbor and the amplitude is the same as the standing wave with the harbor entrance

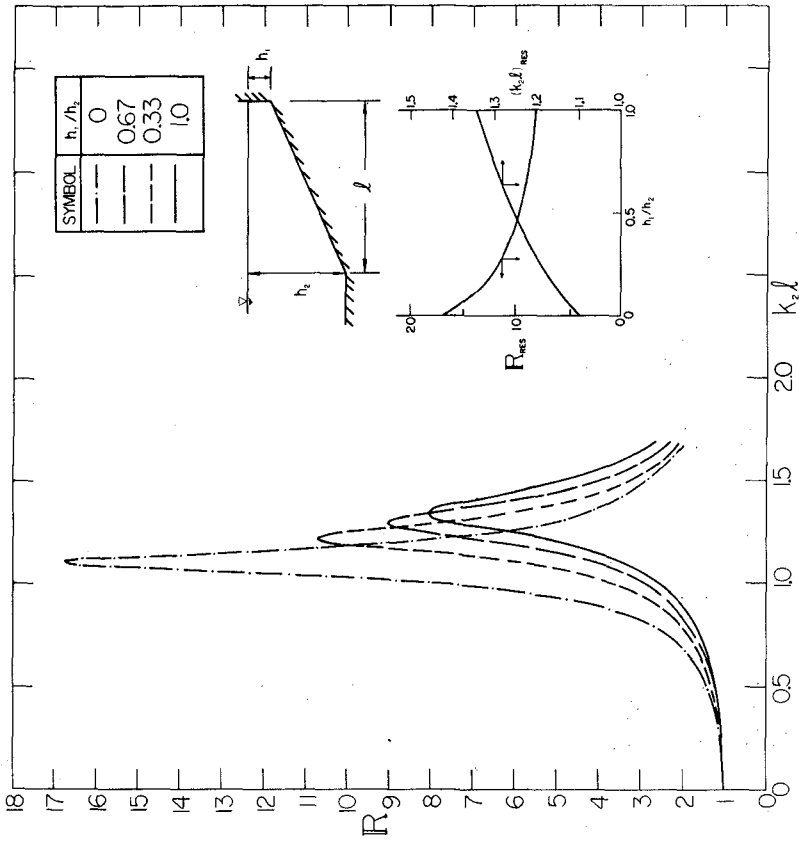


Fig. 2. Response at the Backwall of a Rectangular Harbor with a Linearly Varying Depth; the Fundamental Mode (length = 31.15 cm, width = 6.03 cm, $h_2 = 7.62$ cm).

closed. The variation of the amplification and the product $k_2 l$ at resonance with the depth ratio are presented in the inset to Fig. 2; it is apparent that the effect of the change in depth on the amplification at resonance is much more significant than the effect on the resonant wave number, k_2 . The former can be considered an effect of shoaling; the latter also is an effect of shoaling and represents a change in the resonant wave length caused by the change in mean depth.

In Fig. 3 the response of a fully open rectangular harbor with a linearly varying depth is presented for two cases: a width to length of 0.1 and 1.0; the fundamental mode is shown for each case. (It should be noted, the response function is presented logarithmically along the ordinate.) The amplification at resonance is reduced by nearly an order of magnitude by increasing the ratio of width to length in the same amount. In addition, the resonant wavelength increases as the width of the harbor increases (the resonant wave number decreases). In fact, it appears that if the width were great enough compared to the length, the response at the backwall would be equal to unity independent of wave number. This is the case where the harbor is so wide compared to the length that it simply becomes like the coastline.

In Fig. 4 the variation of the relative amplitude with relative length is shown for the fundamental mode of three harbors with a varying ratio of width to length. For the three cases the ratio of the depth at the backwall to the depth at the entrance is zero. The results of the numerical analysis are shown along with the exact solution of Lamb (1945) for a long wave in a canal with a linearly varying depth, and the agreement is good. At $x/l=1$ the entrance effect can be seen, and as the ratio of width to length, w/l , decreases, the relative amplitude at the entrance also decreases. In fact, it appears that if $w/l \gg 1$ the amplitude in the harbor would be approximately uniform in the x -direction; this is the same trend observed in Fig. 3 as w/l increases.

An example of the response of a harbor with a more general shape is the case of Apra Harbor, Guam, M. I. This harbor was chosen because of the availability of the results of hydraulic model tests which were conducted in the late 1940's to evaluate certain inner harbor modifications and the design of a proposed breakwater (see Knapp and Vanoni (1949)).

A schematic drawing of the harbor is presented in Fig. 5. In the analysis, the outer harbor was limited near the East end by a series of shoals; in the hydraulic model one proposed method to protect the inner harbors was to build a series of breakwaters connecting certain of the shoals. In the analytical model the shoal-breakwater location and the LST berth were considered to be closed ends and the results were compared to the experimental results with the breakwaters in place. The general direction of the *talweg* is shown in Fig. 5 and the areas and surface widths of sections perpendicular to the *talweg* are shown in Fig. 6. The depth averaged over the cross-section varies from approximately 60 ft at the entrance to a maximum of 113 ft about one-third of the harbor length from the entrance and 18 ft near the LST berth.

A response curve obtained for this harbor is presented in Fig. 7; the ordinate is the ratio of wave amplitude at the LST berth (see Fig. 5) to that at the harbor entrance with the entrance closed. The abscissa is the product of the wave number and the harbor length along the *talweg*; the length used is 16,000 ft with the harbor divided into 33 sections. The theoretical response curve exhibits six modes of oscillation for the range of kl shown. This response curve must be somewhat in error, since the oscillations corresponding to the response shown in Fig. 7 are two-dimensional and three-dimensionality would probably become important in such a harbor for the higher modes of oscillation. Nevertheless, this does show certain aspects of the response in a variable depth, arbitrary shaped harbor.

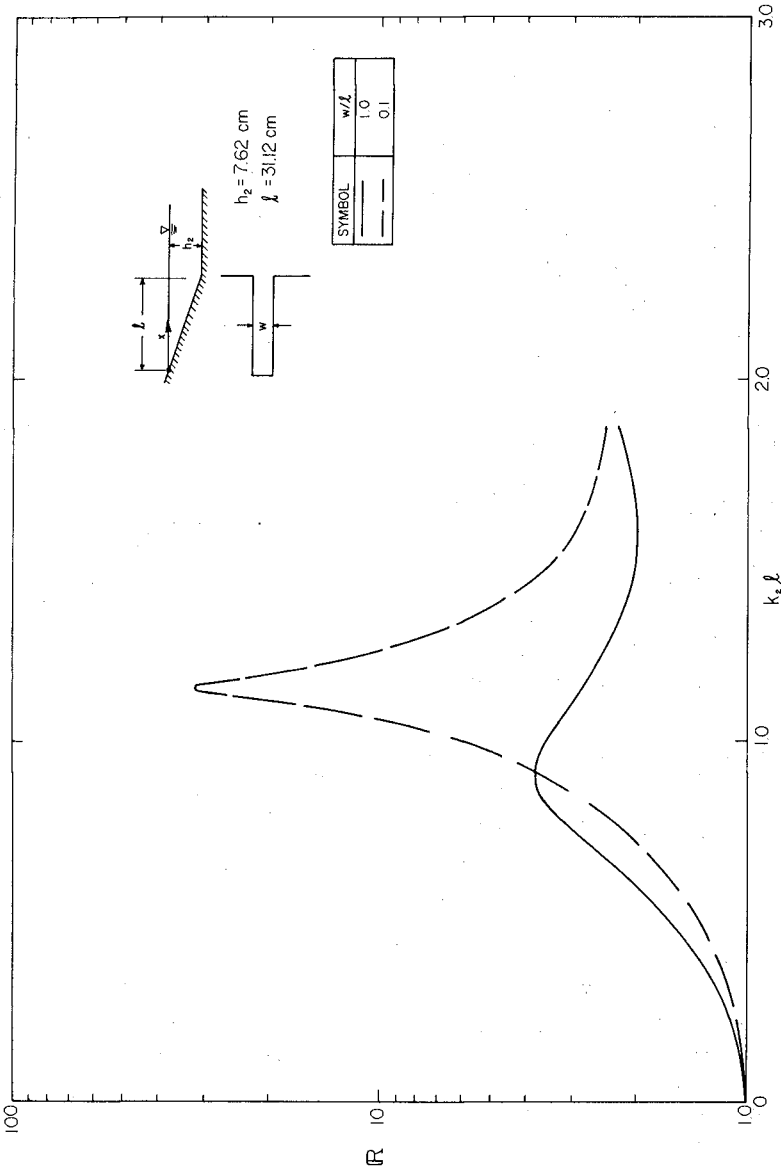


Fig. 3. Response at the Backwall of a Rectangular Harbor with a Linearly Varying Depth ($h_1/h_2 = 0$); the Fundamental Mode.

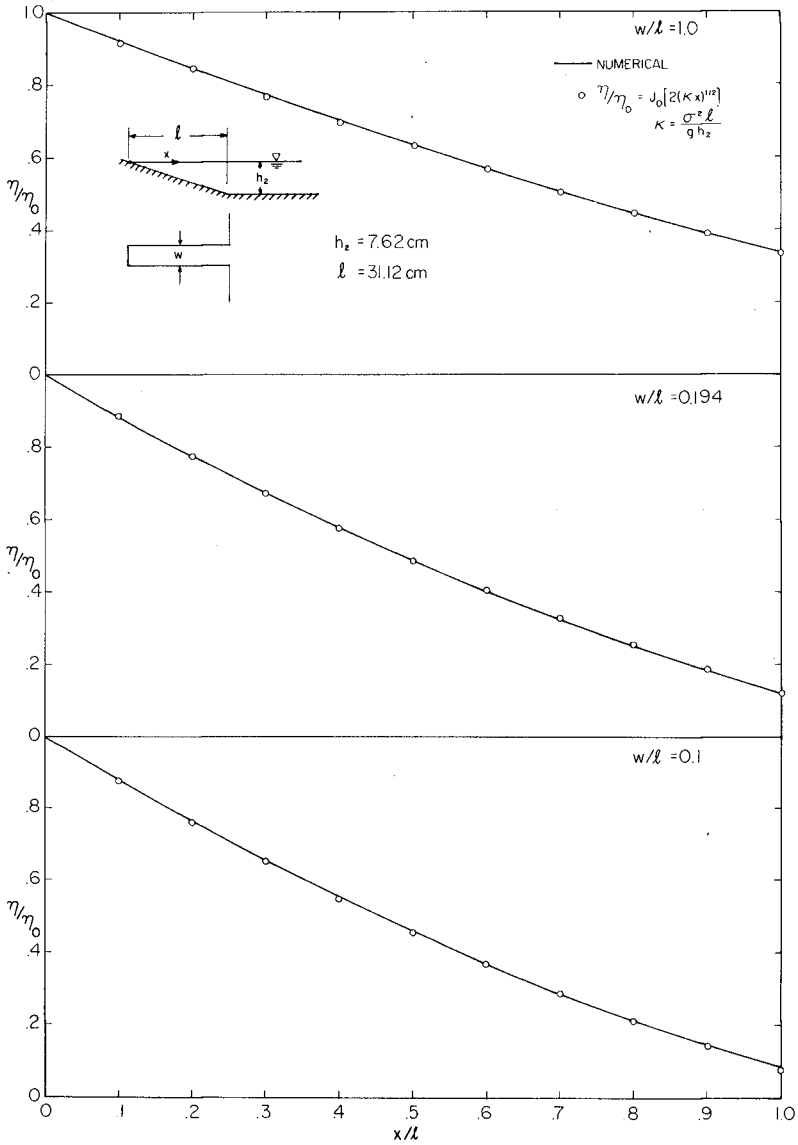


Fig. 4. Relative Wave Amplitude vs. Relative Length for the Fundamental Mode.

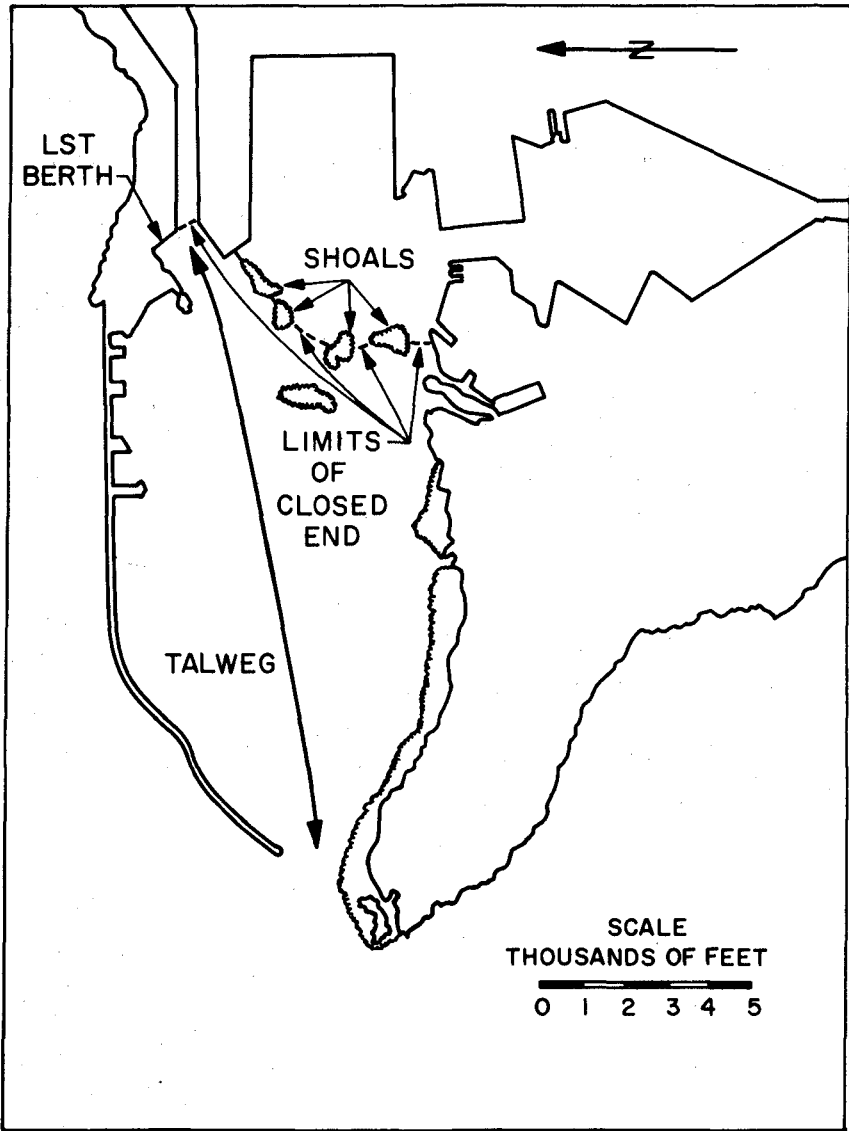


Fig. 5. Schematic Drawing of Apra Harbor, Guam, M.I.

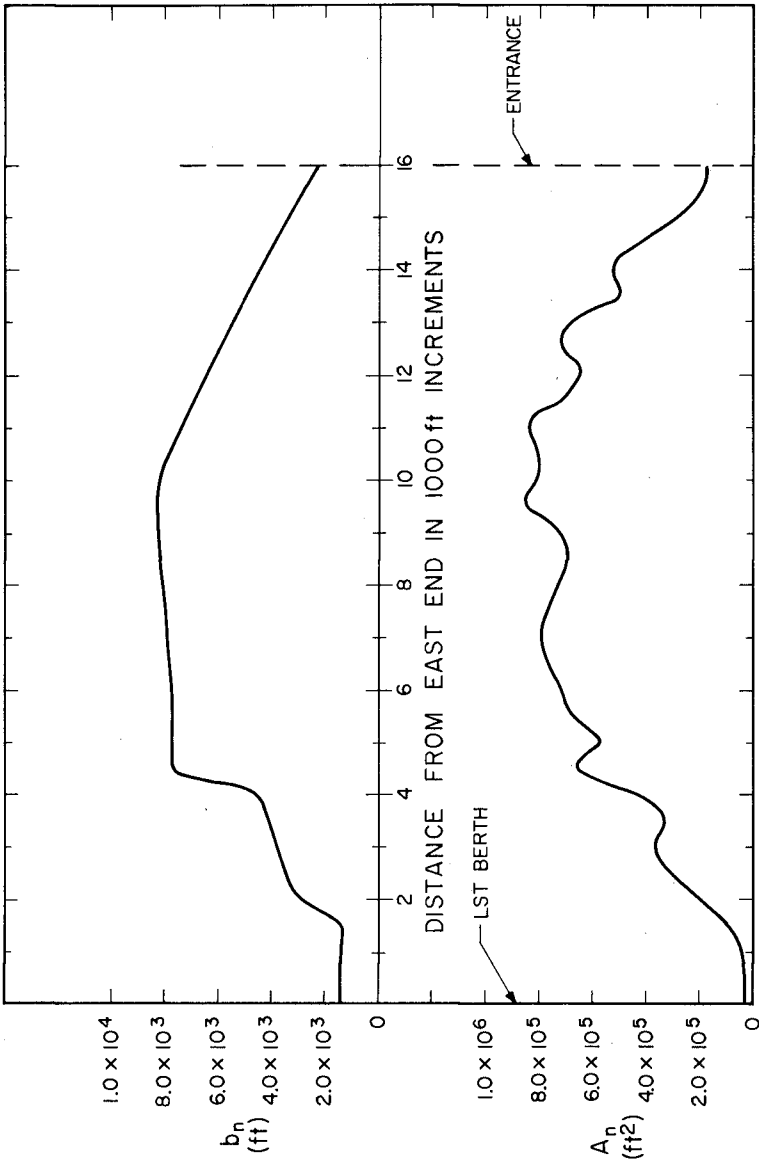


Fig. 6. Variation of Surface Width and Cross-Section Area, Apra Harbor, Guam, M.I.

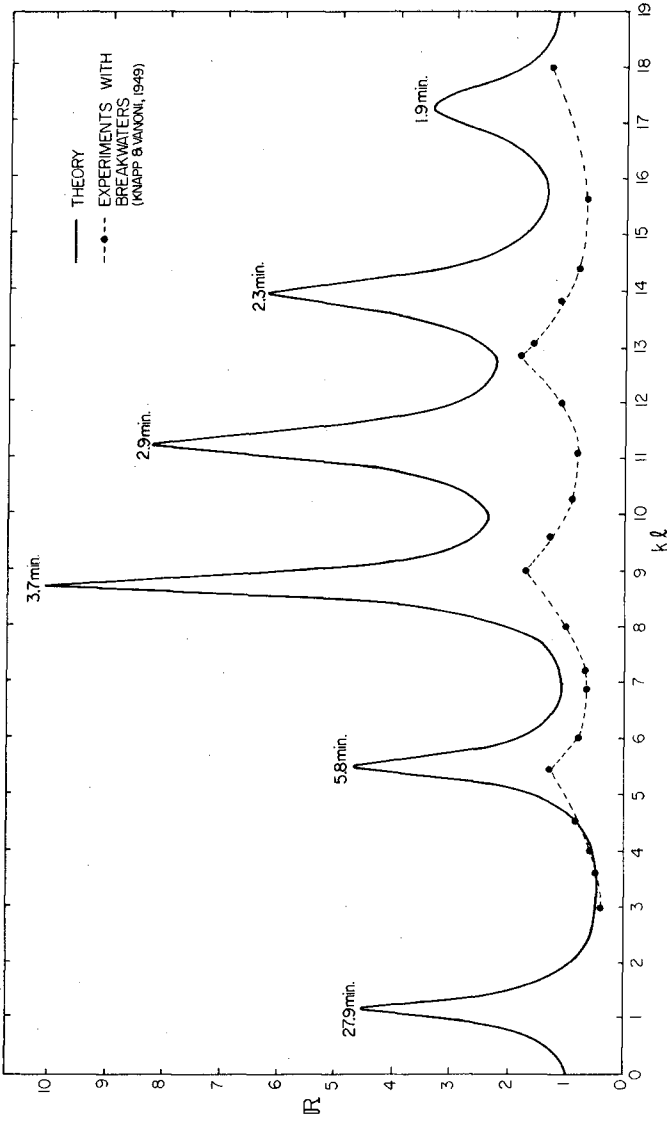


Fig. 7. Response Curve at the LST Berth, Apra Harbor, Guam, M.I.

The experimental data presented in Fig. 7 were obtained by Knapp and Vanoni (1949); the definition of the response function used in that study was not precisely the same as that used in the theory. In their experiments the amplification factor was defined as the ratio of the maximum amplitude at the location of interest to the maximum amplitude outside the harbor with the entrance open. Since there must be an effect on the outside wave due to the harbor, in comparing the experiments to the theory one would expect differences. In Fig. 7 the agreement in the shape of the response curve perhaps is reasonable for the second and third modes but considerably poorer thereafter. This may be due to the failure of a two-dimensional theory in describing the higher modes of oscillation where three-dimensionality must be important as well as the differences mentioned between the theory and the experiments.

The periods of the various modes are shown in Fig. 7 next to the peaks. It is noted that the lowest mode, the fundamental, has a period of 27.9 min; the maximum amplification for $0 < k\ell < 19$ is exhibited by the third mode with a period of 3.7 min. (These periods are based on an average depth of 84.7 ft inside the harbor.) The shape of the water surface for the first three modes are shown in Fig. 8 where the local amplification factor (R_n in Eq. 26) is plotted as a function of distance from the LST berth along the *talweg*. By plotting in this manner, the relative importance of mode shape at a given location can be observed. An interesting feature of Fig. 8 is the water surface amplitude at the entrance ($n=N$). For these three modes the classical condition of a node at the entrance certainly is not met. Thus, the approach proposed by Raichlen (1965) and Wilson et al. (1965) would be in error in predicting both the resonant periods and the mode shapes.

For a rectangular harbor with a similar geometry ($2b/\ell \cong 0.33$ and $d/b = 0.5$) the value of $k\ell$ at resonance for the first mode would be 1.15. (It should be noted, the width of both the harbor and the entrance used for this computation are approximate.) Referring to Fig. 7, the value of $k\ell$ at resonance for the first mode, the pumping mode, is about the same as that predicted for the corresponding mode for the rectangular harbor. Hence, the fact that a node does not exist at the entrance is partly due to the aspect ratio of the harbor and partly due to the partially closed condition.

The second basin investigated was Monterey Bay, California. This bay has experienced problems due to long period oscillations in the past, and in connection with an approximate numerical model presented by Raichlen (1965) and Wilson et al. (1965) it is of some interest. This is a large bay with a length along the *talweg* of approximately 56,000 ft from the shore to the entrance, a maximum width near the entrance of 138,000 ft and an average depth which decreases from 581 ft at the entrance to nearly zero at the shore. The longitudinal variation of the surface width and cross-section area are presented in Fig. 9. For the numerical calculations the harbor was divided into 20 sections.

The response curve for a location at the shoreline ($n=1$) is presented in Fig. 10. It is interesting that due to the shape of the basin, the modes of oscillation are not defined as distinctly as those for Apra Harbor shown in Fig. 7. Nevertheless, the first three modes of oscillation are evident in Fig. 10 and are defined therein. For this harbor the ratio of width to length is nearly 2.5, thus three-dimensional effects would be expected for higher modes of oscillation. The results of the two-dimensional analysis of Raichlen (1965) and Wilson et al. (1965) for this case are indicated along the abscissa; in those analyses a node was assumed at the entrance. That this is not so is evident from Fig. 10 and is emphasized even more in Fig. 11 where the shape of the water surface is shown for the first three modes of oscillation. It is seen that nodal conditions

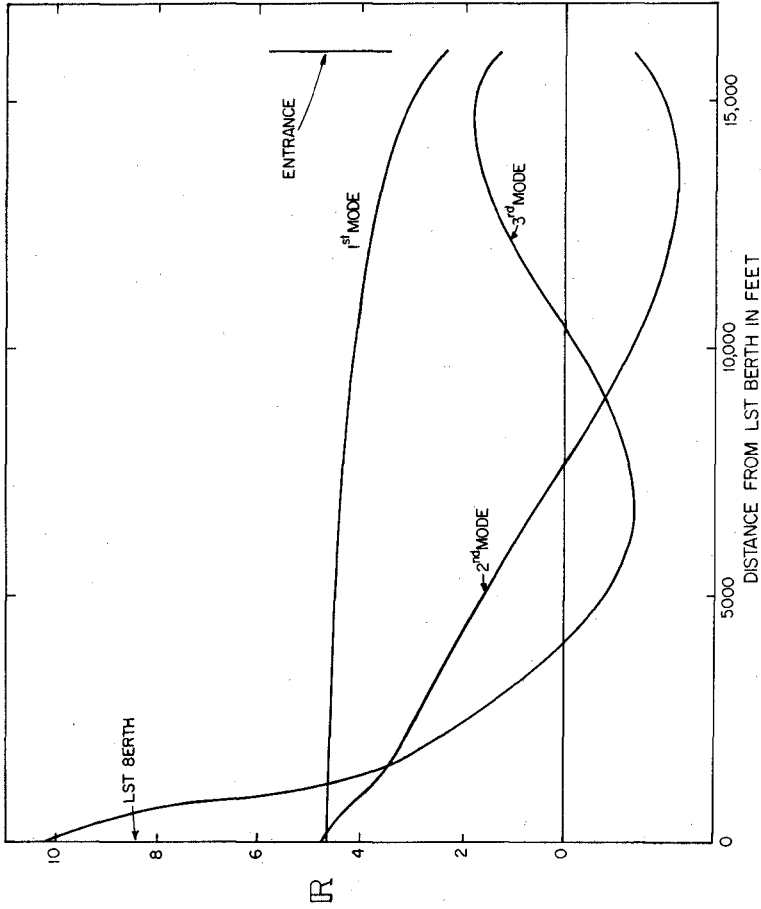


Fig. 8. The Shape of Three Modes of Oscillation for Apra Harbor, Guam, M.I.

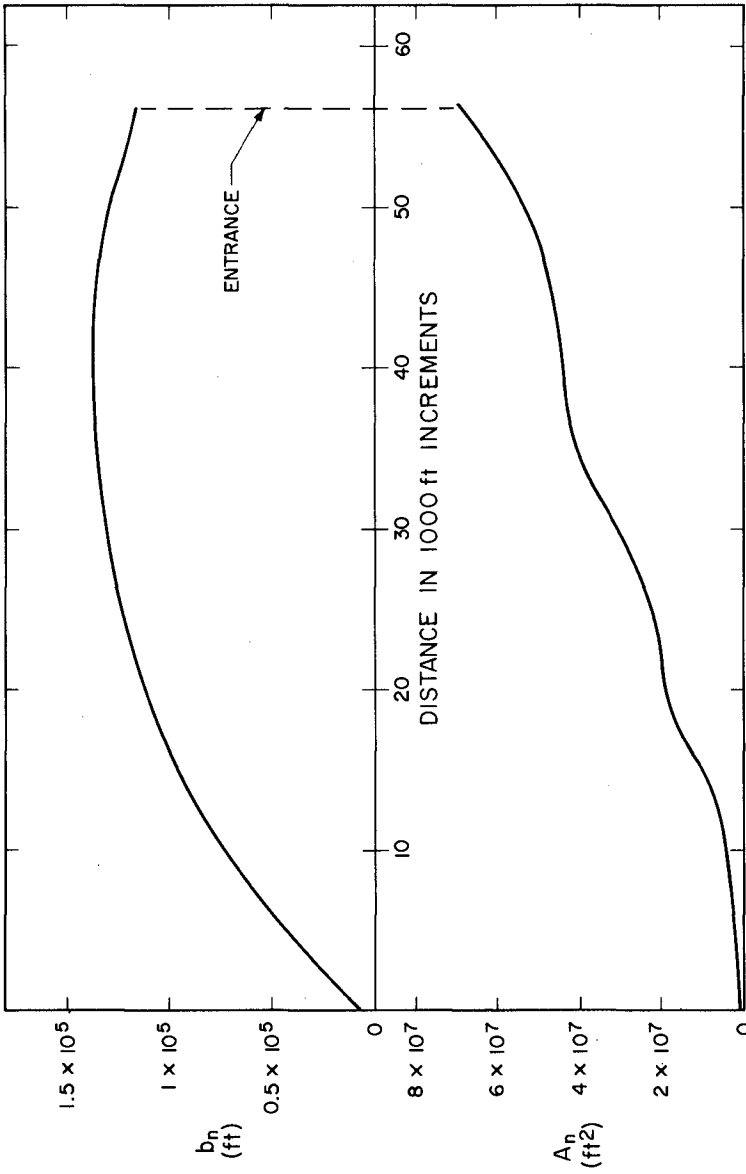


Fig. 9. Variation of Surface Width and Cross-Section Area, Monterey Bay, California.

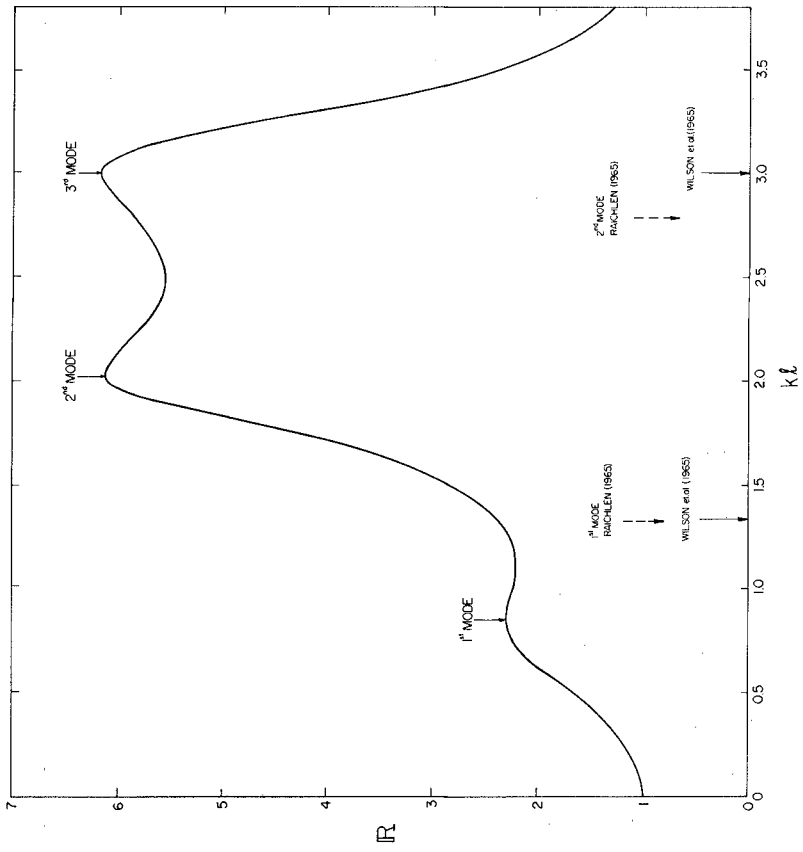


Fig. 10. Response Curve at the Backwall of Monterey Bay, California.

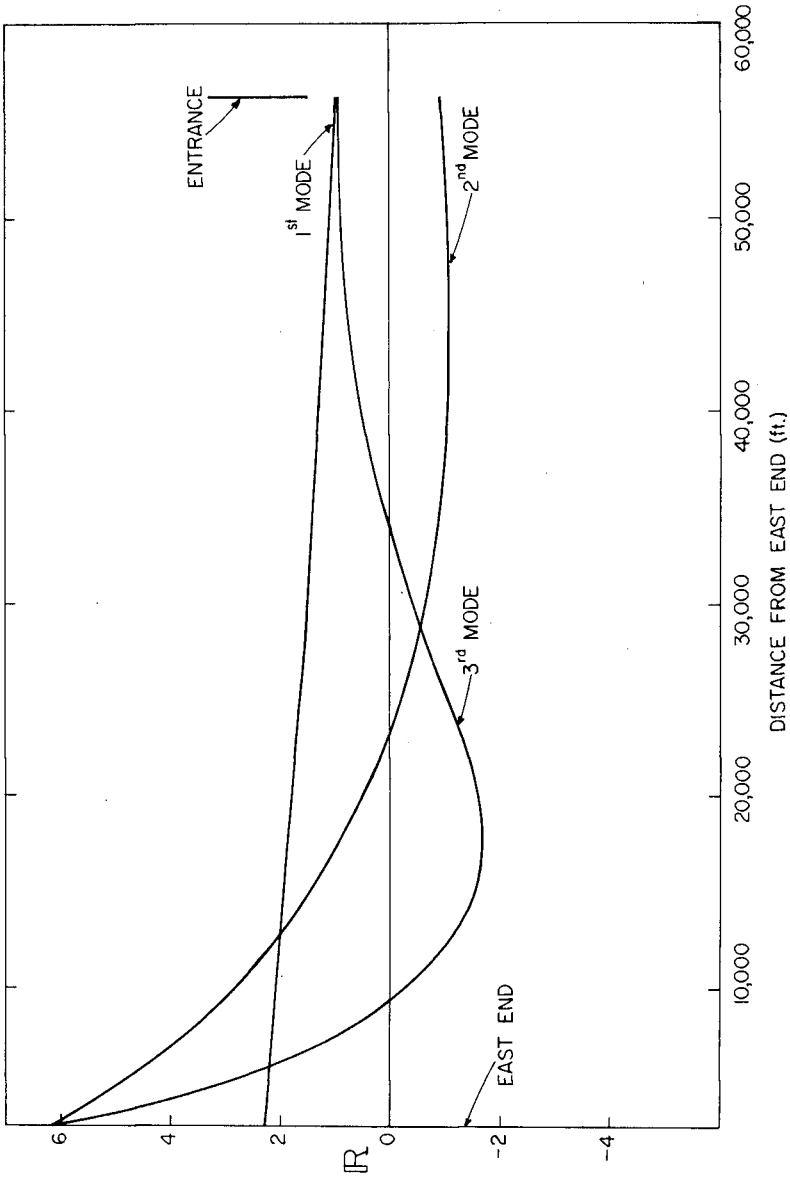


Fig. 11. The Shape of Three Modes of Oscillation for Monterey Bay, California.

are not met for any of these modes of oscillation. This emphasizes the importance of not imposing entrance boundary conditions for a harbor. The conditions at the entrance must respond naturally, depending upon the shape of the basin and the period of the incident waves.

CONCLUSIONS

The following major conclusions may be drawn from this study:

1. Using matching conditions at the entrance to a harbor it is possible to use two completely different methods of analyses in the two domains: the harbor region and the open-sea region.
2. Reasonably good agreement is found for the period of the lower modes of oscillation measured experimentally compared to the results of the numerical analysis for a harbor with a relatively complex shape.
3. The boundary condition at the entrance of a harbor must be allowed to develop naturally and a particular amplitude such as a node cannot be forced to occur. In the event this is done, the response of a harbor determined numerically may be considerably in error.

ACKNOWLEDGMENTS

This research was supported in part by the National Science Foundation Grant AEN72-03587A2 in a continuing study of the generation, propagating and coastal effects of tsunamis.

REFERENCES

- Chen, H. S., and Mei, C. C., "Oscillations and Wave Forces in an Offshore Harbor," Report 190, R. M. Parsons Lab. for Water Resources and Hydrodynamics, MIT, Cambridge, Mass., 1974.
- Hwang, L.-S., and Tuck, E. O., "On the Oscillation of Harbors of Arbitrary Shape," J. Fluid Mech., 42(3), 1970.
- Ippen, A. T., and Goda, Y., "Wave Induced Oscillations in Harbors: The Solution of a Rectangular Harbor Connected to the Open Sea," Report No. 59, Hydrodynamics Lab., MIT, Cambridge, Mass., 1962.
- Knapp, R. T., and Vanoni, V. A., "Model Studies of Apra Harbor, Guam, M.I.," Calif. Inst. of Tech., Hydrodynamics Lab., Report N-63, June 1949.
- Lamb, H., "Hydrodynamics," 6th Edition, Dover Publications, 1945.
- Lee, J. J., "Wave-Induced Oscillations in Harbors of Arbitrary Shape," Report KH-R-20, W. M. Keck Lab. of Hyd. and Water Res., Calif. Inst. of Tech., 1969 (see also J. Fluid Mech., Vol. 45, Part 2, 1971).
- Lee, J. J., and Raichlen, F., "Wave-Induced Oscillations in Harbors with Connected Basins," Report KH-R-26, W. M. Keck Lab. of Hyd. and Water Res., Calif. Inst. of Tech., 1971 (see also JWWH, ASCE, Aug. 1972).
- Miles, J. W., "Harbor Seiching," Annual Review of Fluid Mechanics, Vol. 6, 1974.
- Miles, J. W., and Munk, W. H., "Harbor Paradox," JWWH, ASCE, 87, WW3, 1961.
- Olsen, K., and Hwang, L.-S., "Oscillations in a Bay of Arbitrary Shape and Variable Depth," J. Geophys. Res., 76(21), July 1971.
- Raichlen, F., "Long Period Oscillation in Basins of Arbitrary Shape," Proc. Santa Barbara Coastal Engineering Conference, 1965.
- Wilson, B. W., Hendrickson, J. A., and Kilmer, R. E., "Feasibility Study for a Surge-Action Model of Monterey Harbor, California," Science Engineering Associates Report, Oct. 1965.

CHAPTER 205

PROBABLE UTILIZATION LEVEL FOR A BARGE HARBOR

Martin T. Czerniak¹
Choule J. Sonu²

INTRODUCTION

The main consideration in harbor master planning is to maximize the amount of time that the harbor can be used. The potential level of harbor utilization can be evaluated by analyzing vessel performance during harbor operations in terms of the range of imposed environmental conditions. The harbor utilization level is expressed statistically as the probable amount of time that the harbor can be used as planned.

In this paper, a siting study for a towboat-barge harbor will be described. This example will demonstrate the use of harbor utilization statistics for a simplified case of a single-purpose harbor and a single design vessel. This scheme can be applied to more complex cases of multi-purpose harbors used by a variety of vessels. The purpose of this paper is twofold. First, it outlines the basic concept of harbor utilization statistics and their value to harbor master planning. While it seems that studies of this type would have been undertaken in the past, at present no examples have been found by the authors among published literature. Secondly, considering the lack of published information, it is beneficial to record some practical experience regarding towboat and barge systems as design vessels.

APPLICATION

Many harbor operations can be analyzed using harbor utilization statistics. For example, an evaluation of entrance/exit conditions will lead to utilization statistics that define the percentage of time that vessels can safely negotiate the harbor entrance. The loading/unloading/berthing utilization can also be considered. This calculation would involve the wave height in the berth area of the harbor and may influence harbor configuration by revealing the need for additional breakwater sections (LeMehaute, 1976). A "harbor-of-refuge" can be better planned to provide safe entrance and safe mooring during storms if utilization statistics are compiled for the types of small craft generally found in nearby waters.

Harbor utilization statistics can be interpreted in terms of the economic and functional feasibility of a specific harbor configuration, location, and operational plan. The computations will reveal how harbor utilization can be improved by plan modifications. Economic analyses are improved because the benefits attributable to the harbor's presence can be more accurately established.

¹Senior Engineer and ²Principal Engineer,
Tetra Tech, Inc., Pasadena, California, U.S.A.

PROCEDURE

Once the design vessels and the intended purpose of the harbor have been decided, three steps are necessary to determine the utilization level of a particular harbor operation:

- (1) Identify the environmental parameters which influence vessel behavior during the harbor operation of interest;
- (2) Determine the "critical level" of each parameter beyond which safe operations are jeopardized;
- (3) Determine the probable amount of time that the harbor will be closed due to the exceedance or joint exceedance of the "critical levels."

Often the occurrence statistics for the important parameters that are identified in step 1 will not be directly available from environmental data summaries. In such cases, appropriate engineering analyses must be employed to develop the needed data from the available statistics. For example, if it has been determined (step 2) that the maximum allowable wave height in the berth area of a proposed harbor is 40 cm, then refraction and diffraction techniques must be used to establish all the incident wave conditions that will result in this wave height there. Once these conditions are known, data summaries of incident wave height, period and direction can be used to establish the probability of exceeding the allowable wave agitation in the berth area (step 3).

EXAMPLE: TOWBOAT - BARGE HARBOR

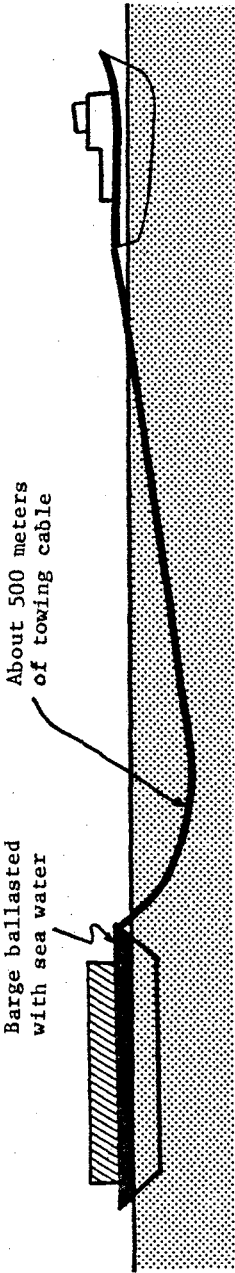
Harbor utilization statistics were used to select the best site during the master planning of a proposed harbor for the central California coast. The proposed harbor must provide year round safe entrance and unloading conditions for barges in order to maintain the delivery schedule of construction materials for the development of the Vandenburg Air Force Base. Due to the nature of the coastline, a "shoreline harbor" is required. That is, primary harbor protection is provided by breakwaters, and the harbor basin is located seaward of the existing shoreline. The vessels that will be used for the delivery operation are ocean-going towboats, which commonly draw about 4.5 meters, connected by a towing cable to a medium-sized commercial barge. These barges are about 115 meters long, 25 meters wide, and have a loaded draft of about 4 meters when not ballasted with sea water.

Step 1: Identify Parameters: Three parameters are judged most important in defining the amount of time that the towboat-barge system can safely enter the harbor: (1) the wave height one to four kilometers offshore of the harbor entrance, (2) the wind speed, and (3) the visibility level.

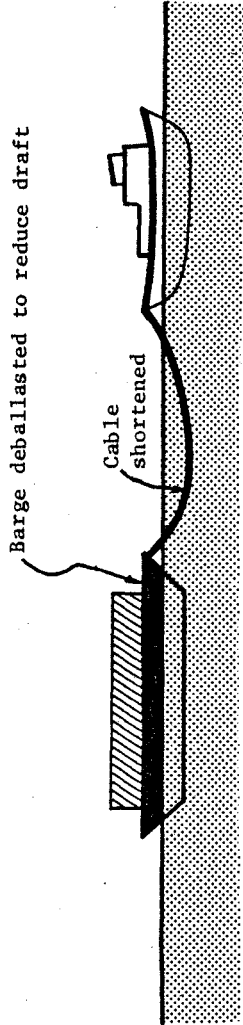
The procedure used by the vessel in approaching and entering the harbor must be known in order to judge which oceanographic and meteorological factors are most important to safety. While underway on the open ocean, about 500 meters of towing cable connect the towboat and the barge (Brady, 1967). As shown in Figure 1a, the tow cable takes a catenary shape and functions as a "spring" to absorb the ship motions of both vessels. Generally, the barge will be ballasted during ocean towing, which helps to reduce its amplitude of response to the waves. Prior to entering the harbor, perhaps one to four kilometers offshore of the harbor entrance, the cable must be shortened for better towing control and the barge must be deballasted of sea water to reduce its draft. In this condition (Figure 1b), the spring action provided by the cable is considerably reduced and the cable could be in danger of parting if the towboat and barge do not ride the wave synchronously. Now deballasted, the barge will respond more to the wave action than it will under ocean-going conditions thus increasing tension in the cable.

The likelihood of a navigational mishap is highest during this period of approach to the harbor. High wave heights during the time when the tow cable is shortened and the barge deballasted may cause the cable to part or the barge to capsize. High winds may make the barge difficult to control while towing, especially if the cargo is bulky and presents a large "sail" area. For the proposed harbor, the vessels must come broadside to the predominant wind direction in order to enter the harbor. Thus, with the slower vessel speed necessary near the harbor, high wind speeds may cause the barge to drift from the course set by the towboat and strike the breakwater or other vessels. Poor visibility is especially hazardous in this case because dense fog is common along the central California coast. No electronic vessel traffic guidance system will be available at the harbor, a condition which when coupled with the rugged wave climate and brisk winds, makes the safe transit of a towed barge into an open-coast harbor quite dependent upon good visibility.

Breaker conditions are not included among the factors influencing the harbor entrance utilization level. By proper planning it is possible to locate the harbor entrance at a depth such that the occurrence of breaker conditions alone would not close the harbor. Two cases must be considered in this planning. First, when the sea state is too high to permit the vessels to safely execute their harbor approach procedures, they must lay off the coast until conditions are more favorable. In this case, the occurrence of high offshore waves effectively closes the harbor to the towboat and barge traffic and it does not matter if the waves are breaking across the harbor entrance. In the second case, the sea state is low enough to permit a normal approach to the harbor and the location of the breaker zone with respect to the harbor entrance is important. For maximum utilization, the harbor entrance should be negotiable by vessels under any wave conditions that the harbor can be safely approached. In this study the minimum depth for the outer breakwaters defining the harbor entrance was taken to be the breaker depth for the highest 2% of the waves in the Rayleigh distribution for the maximum sea state defining the limit of safe vessel approach procedures.



(a) Ocean towing



(b) Entering Harbor

Figure 1: Towing Conditions a) under open ocean towing, and b) while entering the harbor

Step 2: Critical Levels: The critical values of offshore wave height, wind speed, and visibility beyond which safe navigation is jeopardized depends upon the vessel size and type, the operational procedures, and the acceptable risk. Due to the lack of published data on critical levels vis-a-vis design vessels, the harbor engineer must analytically determine them or rely on experienced advice and judgment in selecting them.

An analytical determination of the actual critical wave height for safe operation of the towboat-barge system would require knowledge of the cable-breaking conditions and the risk probability of collision and grounding as a function of wave agitation and vessel response. Such an analysis is costly and time-consuming, and for this reason towboat operators familiar with the central California coast were consulted. While commercial barges commonly operate successfully during offshore wave heights of about three meters (John Turner, personal communication), harbor entrance procedures involving barge deballasting and the shortening of the tow wire require a calmer sea state. Thus, the critical values defining safe navigation were judged to be:

- Critical wave height, $H_c = 2$ meters
- Critical wind speed, $U_c = 20$ knots
- Critical visibility level, $V_c = 1/4$ mile

Although some level of operational risk is implicit in selecting "critical levels," the actual risk will, in fact, vary on a case-by-case basis for each vessel transit into the harbor. This is caused by variables which cannot be realistically considered such as the experience and judgment of the towboat captain and the condition of the equipment.

Step 3: Exceedance Statistics: The harbor cannot be entered safely by the towboat and barge when one or more of the three governing environmental parameters exceed the critical level. The equation which expresses the expected amount of time that the harbor will be closed, $P(\text{closure})$, is:

$$P(\text{closure}) = P(H_c) + P(U_c) + P(V_c) - P(H_c, U_c) - P(H_c, V_c) - P(U_c, V_c) + P(H_c, U_c, V_c)$$

(1) (2) (3) (4) (5) (6) (7)

In this equation, all the terms on the right side express the probability of occurrence or joint occurrence of environmental conditions more severe than those which are safe for navigation. As such, $P(H_c)$ indicates the probability that the wave height exceeds the critical wave height, $P(V_c)$ indicates the probability that the visibility is worse than the critical visibility, and $P(H_c, U_c)$ indicates the probability that both the critical wave height and critical wind speed are exceeded.

The first three terms of the P(closure) equation are determined from cumulative probability distribution plots of the data. Since the probability of the joint occurrence of high waves and high winds is significant, term (4) of the P(closure) equation must be evaluated. This value can be evaluated using a joint exceedance probability plot, as shown in Figure 2 for the January statistics in the study area. Using this figure, the probability that winds greater than 20 knots and offshore waves higher than 2 meters occur simultaneously is 5.5%.

In the study area, most events of poor visibility are caused by fog or haze. Intuitively then, it would seem that poor visibility would be largely a calm weather phenomenon, not occurring when wind speed and wave heights are high. An evaluation of the available data showed this to be true more than 99.9% of the time. In practical usage, therefore, events of high wind or high waves are mutually exclusive of events of poor visibility in this area, causing terms (5), (6), and (7) to drop out of the P(closure) equation.

Results: With P(closure) determined by an evaluation of terms (1), (2), (3) and (4), the harbor utilization is solved by $1-P(\text{closure})$. For the example problem, harbor utilization statistics were compiled for two potential harbor sites using data supplied by the U. S. Air Force and by the Summary of Synoptic Meteorological Observations (SSMO). The results are given in Table 1 and plotted by month in Figure 3. Note that site A would provide a higher overall harbor utilization level, but that the two sites differ markedly in the probability of supercritical conditions for each of the three important parameters. These differences are consistent with the varying site conditions, including coastal exposure, air flow patterns and local shoreline topography. This example illustrates how harbor utilization statistics help provide a rational comparison among potential harbor sites which possess counterbalancing siting characteristics. Harbor utilization can be improved over the level shown in Figure 3 by the selection of larger design vessels which can safely operate under more severe environmental conditions.

ECONOMIC IMPLICATIONS

When monetary values are assigned to harbor operational time and harbor down time, the harbor utilization concept provides a basis for a rational comparison of harbor costs and benefits. As an evaluation of berthing and unloading conditions may indicate that one potential harbor site requires more breakwater sections than another in order to achieve the same utilization level, the relative construction costs are also indicated.

The economic feasibility of harbor protection by breakwaters can also be addressed. For example, consider Figure 4 which shows the annual cumulative probability distribution of wave heights at a potential harbor site. Table 2 summarizes the various navigation conditions which ships using the harbor would encounter and the probability of occurrence of each condition based on the wave statistics given in Figure 4. The

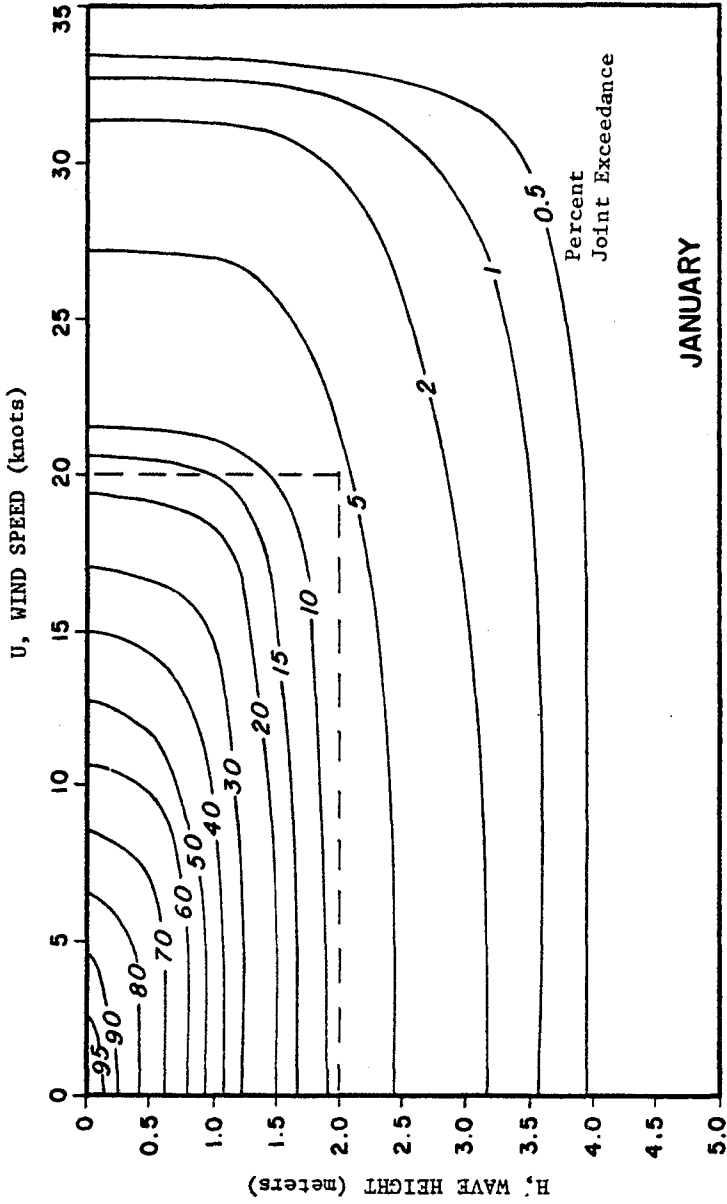


Figure 2: Joint Exceedance Probability (in percent) for Wave Heights and Wind Speeds. (Intersection of dashed lines indicates that the percent joint exceedance of wind speeds >20 knots and wave heights >2.0 meters is 5.5%).

Table 1
HARBOR ENTRANCE UTILIZATION STATISTICS
FOR TWO POTENTIAL HARBOR SITES

Month	Percent of Time Harbor Is Closed by Factor					Harbor Utilization Level
	Visibility P(V<1/4 mi)	Offshore Wave Height P(H>2 m)	Wind Speed P(U≥20 kts)	Correction for Joint Occurrence P(H>2,U>20)	Total Percent Nonoperational Time P(closure)	(Percent Operational Time)
Site A						
JAN.	2.0	9.6	0.3	5.5	6.4	93.6
FEB.	2.8	14.5	0.9	6.1	12.1	87.9
MAR.	3.3	18.0	1.5	8.8	14.0	86.0
APR.	2.7	20.3	1.7	12.5	12.2	87.8
MAY	4.9	22.2	0.7	15.0	12.8	87.2
JUNE	7.4	18.6	0.9	13.0	13.9	86.1
JULY	12.5	13.0	0.1	8.4	17.2	82.8
ADG.	12.8	13.6	0.1	5.7	20.8	79.2
SEPT.	9.7	6.5	0.3	4.7	11.8	88.2
OCT.	7.5	10.8	0.8	5.9	13.2	86.8
NOV.	3.7	12.4	0.4	4.8	11.7	88.3
DEC.	2.9	16.3	1.0	6.6	13.6	86.4
Site B						
JAN.	1.1	14.6	11.0	5.5	21.2	78.8
FEB.	2.0	5.0	15.1	6.1	16.0	84.0
MAR.	0.9	10.0	20.5	8.8	22.6	77.4
APR.	1.1	10.0	19.6	12.5	18.2	81.8
MAY	2.1	6.2	22.3	15.0	15.6	84.4
JUNE	1.4	9.3	32.9	13.0	30.6	69.4
JULY	1.7	1.7	24.0	8.4	19.0	81.0
AUG.	2.3	6.6	29.7	5.7	32.9	67.1
SEPT.	2.2	4.3	27.2	4.7	29.0	71.0
OCT.	2.8	4.2	16.7	5.9	17.8	82.2
NOV.	2.2	11.7	10.9	4.8	20.0	80.0
DEC.	1.5	9.7	14.0	6.6	18.6	81.4

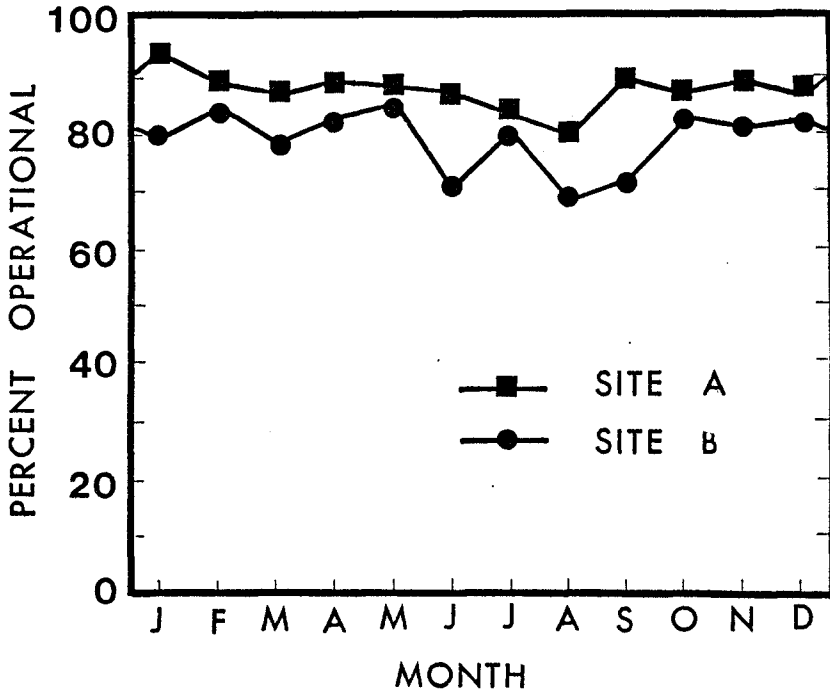


Figure 3: Harbor Entrance Utilization Level by Towboat-Barge Systems for Two Alternate Harbor Sites (for wave height >2 meters, wind speeds >20 knots, and visibility <1/4 mile).

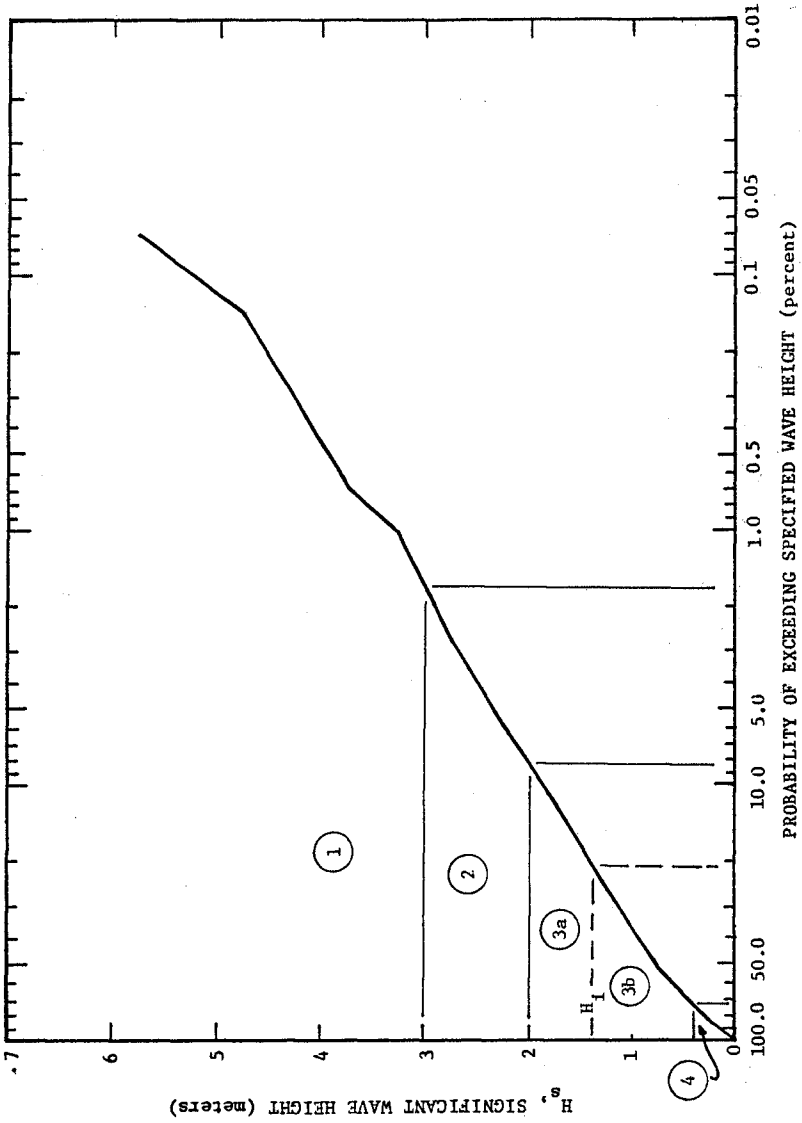


Figure 4: Annual Probability Distribution of Waves at a Potential Harbor Site Showing Range of Navigational Conditions Experienced by Approaching Ships

Table 2

DESCRIPTION AND PROBABILITY OF OCCURRENCE OF
NAVIGATIONAL CONDITIONS

Condition	Description	Incident Wave Height Outside Harbor (meters)	Annual Probability of Occurrence (percent)
1	Sea traffic not possible	$H > 3$	1.6
2	Sea traffic possible, but cannot safely enter harbor	$3 > H > 2$	6.4
3a	Ships can enter harbor but cannot safely unload cargo	$2 > H > H_i$	67.0
3b	Ships can unload cargo in sheltered harbor area, but could not unload without protection of breakwater	$H_i > H > 0.4$	
4	Ships can unload cargo even without shelter of breakwater	$0.4 > H > 0$	25.0

allowable wave height for unloading depends upon the particular cargo, the method of unloading, the type of ship being unloaded, and the location of stowage aboard ship. If the allowable wave height in the berth area is 40 cm for a particular set of unloading conditions, then there exists an incident wave height outside the harbor, H_i , which after transformation will result in the 40 cm wave in the harbor. For incident wave heights between 0.4 and H_i meters, breakwater protection is required to unload the cargo (condition 3b in Table 2). For incident wave heights between H_i and 2 meters, the ships can safely enter the harbor, but cannot unload because wave heights at the berth will be greater than 40 cm (condition 3a). For maximum harbor utilization, therefore, it is clear that the harbor should be designed so that ships can unload any time that they can safely enter the harbor.

During condition 4, the breakwater is not needed at all, and the ships can unload while moored at a pier or quay. Under conditions 1 and 2, the harbor cannot be utilized, no matter how well designed and situated. Only during condition 3 is the cost of the breakwater being converted usefully into increased harbor operating time.

SUMMARY

A method of determining the probable amount of time that a harbor will be operational has been outlined. This method requires the harbor engineer to evaluate vessel performance capabilities in terms of environmental parameters. These "harbor utilization statistics" are a valuable tool for harbor master planning because they provide a rational means of comparing alternate harbor sites in terms of their functional and economic feasibility.

The use of harbor utilization statistics has been illustrated herein by a study to site a barge harbor along the central California coast. Although this example provides a simplified case of a single-purpose harbor and a single design vessel, the scheme should provide valuable results for a number of other harbor studies:

- Safety analysis of harbors for the shipment or receiving of hazardous cargoes.
- Improved planning and design of small "harbors-of-refuge" in terms of safe entrance, anchorage, and berthing during storms of various intensities and for the various types of small craft generally found in nearby waters.
- Rational harbor site selection among alternative locations having counterbalancing beneficial and detrimental characteristics.
- More realistic economic analyses of costs and benefits of harbor construction.

ACKNOWLEDGMENTS

The study reported on in this paper was performed for the U. S. Department of the Air Force, Space and Missile Systems Organization, Los Angeles. The authors appreciate their cooperation and the meteorological data provided by them. The authors also appreciate the valuable suggestions made by Bernard LeMehaute and Raymond Rodrigue of Tetra Tech during the course of this study and the editorial suggestions of Allene S. Czerniak.

REFERENCES

1. Brady, Edward M. (1967), Tugs, Towboats, and Towing, Cornell Maritime Press, Inc., Cambridge, Maryland, 256 p.
2. LeMehaute, Bernard (1976), "Wave Agitation Criteria for Harbors," Proceedings, 15th International Coastal Engineering Conference.
3. Turner, John J., President of Pacific Towboat and Salvage Company, Long Beach, California.

CHAPTER 206

APPLICATION OF CERC SPECIAL REPORT NO. 2

by James W. Dunham, F. ASCE

Coastal Engineer, Moffatt & Nichol, Engineers, Long Beach, Calif.

PURPOSE AND SCOPE

The purpose of this paper is to discuss the new manual titled Small Craft Harbors: Design, Construction and Operation, published by the U. S. Army Corps of Engineers Coastal Engineering Research Center (CERC) as Special Report No. 2 dated December 1974. The objective of the manual is to enable anyone with a basic engineering background to plan and design small craft harbors or do so with the help of one or more specialists. The manual outlines methods of investigating the problems involved and the various engineering, economic and environmental criteria to be applied. It covers much of the planning and design considerations discussed by the A.S.C.E. Committee on Small Craft Harbors in manuals and reports on engineering practice, #50, "Report on Small Craft Harbors 1969". However, it also incorporates a considerable amount of additional information in the form of special design and construction techniques, certain rules of thumb commonly accepted in marina design practice, and observations as to elements of good practice in this field. It provides a compendium of planning data gleaned through a nationwide canvassing of marina operators, marina design engineers, and trades people who provide commonly used marina construction products. Also included in the manual are some of the design and construction requirements of various Federal, state and local government agencies having jurisdiction over, or assisting with the development of small craft harbors.

CONTENT

SR-2 takes the reader step by step through the process of planning and designing a marina, beginning with site analysis and ending with the functional design of structures. It covers the special problems of harbor sites on rivers, in interior lakes and bays, in roadsteads and along open continental shorelines. Environmental considerations such as snow, wind, ice, fog, waves, surge, tides, littoral drift, river deposits, material sources, soils and seismic activity are discussed. Ecological and sociological factors are evaluated as they relate to harbor construction and operation. The special problems of entrance design under various conditions are discussed at length, including methods of construction and the capabilities and limitations of presently available construction equipment. The proper layout of the various components of a marina for functional efficiency is demonstrated, and rules of thumb are given for allocating space. Detail design criteria are then presented for such items as basin geometry, perimeter stabilization, fixed and floating docks, geometric requirements for various types and sizes of craft, launching equipment, etc., along with charts and graphs for layout and design. Numerous line drawings and photographs are presented to illustrate both good and inferior design.

Following the planning and design chapters of SR-2 is a description of the roles played by various Federal, state, and local governments in marina financing, construction, and operation. Because a successful marina requires a sound economic foundation, one chapter deals with feasibility studies, pre-design planning, and methods of financing. Construction contracting and timing are discussed, operating principles are outlined, and some of the more important features of marina maintenance are described. Statistical data on U.S. marina practice derived from replies to questionnaires are tabulated, and 12 case studies are presented to illustrate different planning, management, and design techniques.

It is the intention of CERC to eventually incorporate a manual such as this as an appendix to its Coastal Engineering Manual which will extend the present Shore Protection Manual coverage to all facets of the coastal engineering discipline. This initial effort by CERC in the small craft harbors field was pursued through a contract with Moffatt & Nichol, Engineers, of Long Beach, California, to prepare such a manual under a set of general guidelines as to content. Although this placed the responsibility for the publication primarily with that firm, every effort was made to reflect the soundest thinking in marina design construction and operation that evolved through the many contacts made with personnel living daily with marina design and operation problems. Because it was impossible to contact personnel in many areas, some features may have been overlooked or additional criteria should have been included to cover special cases or conditions of environment.

COMMENTS INVITED

In the preface of SR-2 is the statement "Comments on this Publication are invited". Because the intent of CERC is to upgrade SR-2 to the status of a manual of proven worth and highest possible quality for inclusion as an appendix to the Coastal Engineering Manual, it is imperative that all personnel actively engaged in the small craft harbors field review the publications and submit comments to CERC. Thus, the purpose of presenting this paper at a coastal engineering conference is to call the attention of the coastal engineering profession to the existence of this publication and to solicit comments on it. Most desirable would be comments concerning ideas that were not included or that were covered insufficiently and could be improved upon by inclusion of additional information. Comments of a general nature, such as which parts of the manual are considered too detailed and which too general would also be welcome. Comments should be addressed to the Director, Coastal Engineering Research Center, Kingman Building, Fort Belvoir, Virginia 22060.

SR-2 is available from the Superintendent of Documents, U.S. Government Printing Office, Washington, D.C. 20402, under Stock No. 0822-00091. Checks should be made payable to the Superintendent of Documents. The price, postpaid, is \$4.50 in the United States, Canada, and some Latin American countries. The price to other foreign countries is \$5.63, postpaid.

Subject Index

- Accidents; Collisions; Harbor structures; Mooring; Moorings; Offshore drilling; Ships; Wave tanks**
Protection of Maritime Structures Against Ship Collisions, Kazuki Oda and Shositiro Nagai, 2810
- Aeolian soils; Barriers; Beach erosion; Erosion; Islands (landforms); Sediment deposits; Surges**
Barrier Island Dynamics: Overwash Processes and Eolian Transport, Stephen P. Leatherman, 1958
- Aerial photography; Bathymetry; Beach erosion; Beaches; Field investigations; Littoral current; Sediment deposits; Sediment transport; Suspended sediments**
Field Investigation of Sediment Transport Pattern in a Closed System, Tsuguo Sunamura and Kiyoshi Horikawa, 1240
- Air bubbles; Air flow rates; Manifold air injection systems; Model tests; Orifices; Pipes; Porous materials**
Guidelines for the Design of Air Bubble Systems, Nabil Ismail, 2994
- Air entrainment; Damage; Dikes; Impact; Revetments; Wave action; Wave energy**
Response of Seadykes due to Wave Impacts, Alfred Fuhrboter, Hans H. Dette and J. Grune, 2604
- Air flow rates; Manifold air injection systems; Model tests; Orifices; Pipes; Porous materials; Air bubbles**
Guidelines for the Design of Air Bubble Systems, Nabil Ismail, 2994
- Airports; Breakwaters; Hawaii; Reefs; Slope protection; Slope stability**
Design and Construction of Protective Structure for New Reef Runway at Honolulu International Airport, Wilfred D. Darling, 2589
- Air-water interfaces; Heat flux; Heat transfer; Infrared scanners; Infrared scanning; Remote sensing; Water temperature**
Evaluation of Air-Sea Interface Heat Flux, Robert L. Street and A. Woodruff Miller, Jr., 3208
- Alabama; Bays (topographic features); Sedimentation; Sediment deposits; Sediment distribution; Sediment transport; Tidal effects**
Sediment Transportation and Deposition Models for Mobile Bay, Alabama, Gary G. April, Samuel Ng and C. Everett Brett, 2092
- Alaska; Beach erosion; Geomorphology; Glacial erosion; Glaciers; Glaciology**
Geomorphology of the Southern Coast of Alaska, Miles O. Hayes, Christopher H. Ruby, Michael F. Stephen and Stephen J. Wilson, 1992
- Algorithms; California; Discharge (water); Numerical analysis; Tidal currents; Tidal effects**
Tidal Stream Flow Solved by Galerkin Technique, L. H. Smith and Ralph T-S Cheng, 3358
- Algorithms; Diffusion; Estuaries; Frequency analysis; Hydraulic models; Mathematical models; Mixing**
Algorithm for Vertical Diffusion, Soren Peter Kjeldsen, 3321
- Armoring (streambed); Breakwaters; Experimentation; Stresses; Testing**
Experimental Studies of Stresses Within the Breakwater Armor Piece "Dolos", Omar J. Lillevang and Wayne E. Nickola, 2519
- Armoring (streambed); Breakwaters; Failure; Slope protection; Slope stability; Wave action; Wave energy; Wave period**
Armour Blocks as Slope Protection, A. F. Whillock and W. A. Price, 2564
- Armoring (streambed); Breakwaters; Model tests; Scale effect; Stability; Wave height; Wave period; Wave runoff**
Large Scale Model Tests of Placed Stone Breakwaters, Charles K. Sollitt and Donald H. DeBok, 2572
- Australia; Estuaries; Flooding; Hydrographic surveys; Jetties; River flow; Sandbars; Training walls**
Results of River Mouth Training on the Clarence Bar, New South Wales, Australia, Cyril D. Floyd and Bruce M. Druery, 1738
- Automation; Forecasting; Hurricanes; Storm surges; Weather forecasting**
Automated Forecasting of Extratropical Storm Surges, N. Arthur Pore, 906
- Barges; Economic analysis; Environmental effects; Harbors; Performance; Safety; Site selection; Utilization**
Probable Utilization Level for a Barge Harbor, Martin T. Czerniak and Choule J. Sonu, 3557
- Barriers; Beach erosion; Erosion; Islands (landforms); Sediment deposits; Surges; Aeolian soils**
Barrier Island Dynamics: Overwash Processes and Eolian Transport, Stephen P. Leatherman, 1958
- Barriers; Beaches; Canada; Littoral current; Littoral drift; Morphology; Sandbars; Sediment deposits; Wave energy**
Process and Morphology Characteristics of Two Barrier Beaches in the Magdalen Islands, Gulf of St. Lawrence, Canada, E. H. Owens, 1975
- Barriers; Breakwaters; California; Jetties; Littoral current; Littoral drift; Sediment transport; Surf; Wave energy**
Longshore Transport at a Total Littoral Barrier, Richard O. Bruno and Christopher G. Gable, 1203
- Barriers; Finite differences; Shallow water; Simulation; Walls; Water waves; Wave action; Waves**
Action of Non-Linear Waves at a Solid Wall, Mohamed S. Nasser and John A. McCorquodale, 815
- Bathymetry; Beach erosion; Beaches; Field investigations; Littoral current; Sediment deposits; Sediment transport; Suspended sediments; Aerial photography**
Field Investigation of Sediment Transport Pattern in a Closed System, Tsuguo Sunamura and Kiyoshi Horikawa, 1240

- Bathymetry; Groins (structures); Littoral drift; Sandbars; Sediment transport; Verification inspection; Wave height; Wave spectrum**
Experimental Verification of Groyne Theory, C. H. Hulsbergen, W. T. Bakker and G. van Bochove, 1439
- Bays (topographic features); Beach erosion; Breakwaters; Shore protection; Wave action; Wave energy**
Headland Defense of Coasts, Richard Silvester, 1394
- Bays (topographic features); Beach erosion; Erosion; Jetties; Oregon; Sedimentation; Sediment deposits; Shoaling**
Changes due to Jetties at Tillamook Bay, Oregon, Paul D. Komar and Thomas A. Terich, 1791
- Bays (topographic features); Sedimentation; Sediment deposits; Sediment distribution; Sediment transport; Tidal effects; Alabama**
Sediment Transportation and Deposition Models for Mobile Bay, Alabama, Gary G. April, Samuel Ng and C. Everett Brett, 2092
- Beach erosion; Beaches; Breakwaters; Construction; Harbor structures; Japan; Ocean bottom; Shoaling; Topographical factors**
Topographic Change Resulting from the Construction of a Harbor on a Sandy Beach, Kashima Port, Norio Tanaka and Shoji Sato, 1824
- Beach erosion; Beaches; California; Equilibrium; Tidal effects; Wave energy; Wave spectrum**
Beach Profiles at Torrey Pines, California, David G. Aubrey, Douglas L. Inman and Charles E. Nordstrom, 1297
- Beach erosion; Beaches; Computer models; Slopes; Wave spectrum**
Study of Equilibrium Beach Profiles, Robert A. Dalrymple and William W. Thompson, 1277
- Beach erosion; Beaches; Equilibrium; Gravel; Laboratory tests; Littoral current; Sediment transport; Shore protection; Wave energy**
Equilibrium Profiles and Longshore Transport of Coarse Material Under Oblique Wave Attack, E. van Hijum, 1258
- Beach erosion; Beaches; Field investigations; Littoral current; Sediment deposits; Sediment transport; Suspended sediments; Aerial photography; Bathymetry**
Field Investigation of Sediment Transport Pattern in a Closed System, Tsuguo Sunamura and Kiyoshi Horikawa, 1240
- Beach erosion; Beach nourishment; Bypasses; Erosion; Great Lakes; Michigan; Sand; Shore protection; Water levels**
Sand-Bypass and Shore Erosion, Bridgman, Michigan, C. N. Johnson and L. W. Hiipakka, 1361
- Beach erosion; Beach nourishment; Dynamics; Equilibrium; Erosion; Reflection; Sandbars; Sand traps; Three-dimensional; Wave action**
Three Dimensional Tests on Dynamic Equilibrium and Artificial Nourishment, J. William Kamphuis and R. M. Myers, 1532
- Beach erosion; Beach nourishment; Equilibrium; Forecasting; France; Marinas; Ports**
Impact of Yachting Marinas on Beaches, J. P. Lepetit, 1844
- Beach erosion; Beach nourishment; Erosion; Littoral current; Recreational facilities; Storms; Storm surges; Wave action; Wave energy**
Cape Hatteras Beach Nourishment, John S. Fisher and Wilson N. Felder, 1512
- Beach erosion; Breakwaters; Japan; Ocean bottom; Shore protection; Subsidence**
Changes of Sea Bed Due to Detached Breakwaters, Osamu Toyoshima, 1572
- Beach erosion; Breakwaters; Shore protection; Wave action; Wave energy; Bays (topographic features)**
Headland Defense of Coasts, Richard Silvester, 1394
- Beach erosion; Climatic data; Estuaries; Estuarine environment; Sediment deposits; Sediment distribution; Sediments; Tidal effects; Wave action**
Factors Influencing Estuary Sediment Distribution, Mary P. Kendrick and B. V. Derbyshire, 2072
- Beach erosion; Eigenvalues; Impulses; Responses; Stability; Statistical analysis; Storms; Variability**
Stability and Impulse Response of Empirical Eigenfunctions, Clinton D. Winant and David G. Aubrey, 1312
- Beach erosion; Erosion; Field tests; Groins (structures); Laboratory tests; Littoral drift; Shore protection; Storms; Water temperature; Wave height**
Laboratory Investigation of Shore Erosion Processes, Ernest F. Brater and David Ponce-Campos, 1493
- Beach erosion; Erosion; Groins (structures); Rip currents; Waves; Wave tanks**
Groin Length and the Generation of Edge Waves, Michael K. Gaughan and Paul D. Komar, 1459
- Beach erosion; Erosion; Islands (landforms); Sediment deposits; Surges; Aeolian soils; Barriers**
Barrier Island Dynamics: Overwash Processes and Eolian Transport, Stephen P. Leatherman, 1958
- Beach erosion; Erosion; Jetties; Oregon; Sedimentation; Sediment deposits; Shoaling; Bays (topographic features)**
Changes due to Jetties at Tillamook Bay, Oregon, Paul D. Komar and Thomas A. Terich, 1791
- Beach erosion; Geomorphology; Glacial erosion; Glaciers; Glaciology; Alaska**
Geomorphology of the Southern Coast of Alaska, Miles O. Hayes, Christopher H. Ruby, Michael F. Stephen and Stephen J. Wilson, 1992
- Beach erosion; Investigations; Japan; Littoral current; Littoral drift; Slopes**
Concept for Inferring the Littoral Drift Trend, Masataro Hattori and Takasuke Suzuki, 1223
- Beach erosion; New Jersey; Sandbars; Sea level; Sedimentation; Sediment deposits; Sediment transport; Tidal currents**
Offshore Sedimentary Processes and Responses Near Beach Haven — Little Egg Inlets, New Jersey, Thomas McKinney, Joseph T. DeAlteris, Yung Y. Chao, Lloyd Stahl and James Roney, 1899

- Beaches; Beach nourishment; Breakwaters; Hawaii; Recreational facilities; Shore protection; Swimming**
Proposed "Improvement" of Kaimu Beach, Hawaii, Doak C. Cox, Franciscus Gerritsen and Theodore T. Lee, 1552
- Beaches; Beach nourishment; Groins (structures); Hydrographic surveys; Monitoring; Shore protection**
Comprehensive Monitoring of a Beach Restoration Project, Omar H. Shemdin, H. K. Brooks, Z. Ceylanli and S. L. Harrell, 1477
- Beaches; Breaking; Resonance; Surges; Turbulence; Wave height; Wave runup; Waves**
Resonant Interactions for Waves Breaking on a Beach, Robert T. Guza and Anthony J. Bowen, 560
- Beaches; Breakwaters; Construction; Harbor structures; Japan; Ocean bottom; Shoaling; Topographical factors; Beach erosion**
Topographic Change Resulting from the Construction of a Harbor on a Sandy Beach, Kashima Port, Norio Tanaka and Shoji Sato, 1824
- Beaches; Breakwaters; Enclosures; Groins (structures); Israel; Recreational facilities; Social needs**
Enclosing Scheme for Bathing-Beach Development, Joseph Tauman, 1425
- Beaches; California; Equilibrium; Tidal effects; Wave energy; Wave spectrum; Beach erosion**
Beach Profiles at Torrey Pines, California, David G. Aubrey, Douglas L. Inman and Charles E. Nordstrom, 1297
- Beaches; Canada; Littoral current; Littoral drift; Morphology; Sandbars; Sediment deposits; Wave energy; Barriers**
Process and Morphology Characteristics of Two Barrier Beaches in the Magdalen Islands, Gulf of St. Lawrence, Canada, E. H. Owens, 1975
- Beaches; Computer models; Slopes; Wave spectrum; Beach erosion**
Study of Equilibrium Beach Profiles, Robert A. Dalrymple and William W. Thompson, 1277
- Beaches; Deformation; Periodic functions; Phase velocity; Water depth; Wave energy; Wave height; Waves**
Deformation up to Breaking of Periodic Waves on a Beach, Ib A. Svendsen and J. Buhr Hansen, 477
- Beaches; Equilibrium; Gravel; Laboratory tests; Littoral current; Sediment transport; Shore protection; Wave energy; Beach erosion**
Equilibrium Profiles and Longshore Transport of Coarse Material Under Oblique Wave Attack, E. van Hijum, 1258
- Beaches; Field investigations; Littoral current; Sediment deposits; Sediment transport; Suspended sediments; Aerial photography; Bathymetry; Beach erosion**
Field Investigation of Sediment Transport Pattern in a Closed System, Tsuguo Sunamura and Kiyoshi Horikawa, 1240
- Beaches; Flowmeters; Friction coefficient (hydraulic); Rip currents; Surf; Turbulence**
Lateral and Bottom Forces on Longshore Currents, David A. Huntley, 645
- Beaches; Inlets (waterways); Littoral current; Littoral drift; Surf; Tidal currents; Wave recorders (water waves)**
Changes in Inlet Offset due to Stabilization, Dennis K. Hubbard, 1812
- Beaches; Inlets (waterways); Sandbars; Sand traps; Shoaling; Tidal effects**
Capacity of Inlet Outer Bars to Store Sand, Todd L. Walton, Jr. and William D. Adams, 1919
- Beaches; Japan; Littoral drift; Ocean currents; Rip currents; Wave recorders (water waves)**
Nearshore Current on a Gently Sloping Beach, Tamio Sasaki, Kiyoshi Horikawa and Shintaro Hotta, 626
- Beaches; Ocean waves; Resonance; Simulation; Water levels; Wave height; Wave runup**
Wave Run-Up on a Simulated Beach, A. J. Sutherland, J. N. Sharma and Omar H. Shemdin, 752
- Beach nourishment; Beach sands; Littoral current; Predictions; Sediment deposits; Sediment transport**
Predictive Equations Regarding Coastal Transport, D. H. Swart, 1113
- Beach nourishment; Breakwaters; Hawaii; Recreational facilities; Shore protection; Swimming; Beaches**
Proposed "Improvement" of Kaimu Beach, Hawaii, Doak C. Cox, Franciscus Gerritsen and Theodore T. Lee, 1552
- Beach nourishment; Bypasses; Erosion; Great Lakes; Michigan; Sand; Shore protection; Water levels; Beach erosion**
Sand-Bypass and Shore Erosion, Bridgman, Michigan, C. N. Johnson and L. W. Hiipakka, 1361
- Beach nourishment; Coastal engineering; Recreational facilities; Shore protection; Sri Lanka**
Coastal Problems in Sri Lanka, Franciscus Gerritsen and Summa R. Amarasinghe, 3487
- Beach nourishment; Dynamics; Equilibrium; Erosion; Reflection; Sandbars; Sand traps; Three-dimensional; Wave action; Beach erosion**
Three Dimensional Tests on Dynamic Equilibrium and Artificial Nourishment, J. William Kamphuis and R. M. Myers, 1532
- Beach nourishment; Equilibrium; Forecasting; France; Marinas; Ports; Beach erosion**
Impact of Yachting Marinas on Beaches, J. P. Lepetit, 1844
- Beach nourishment; Erosion; Littoral current; Recreational facilities; Storms; Storm surges; Wave action; Wave energy; Beach erosion**
Cape Hatteras Beach Nourishment, John S. Fisher and Wilson N. Felder, 1512
- Beach nourishment; Groins (structures); Hydrographic surveys; Monitoring; Shore protection; Beaches**
Comprehensive Monitoring of a Beach Restoration Project, Omar H. Shemdin, H. K. Brooks, Z. Ceylanli and S. L. Harrell, 1477
- Beach sands; Littoral current; Predictions; Sediment deposits; Sediment transport; Beach nourishment**
Predictive Equations Regarding Coastal Transport, D. H. Swart, 1113

- Bedding materials; Bed ripples; Ripple marks; Sand; Sonar detection; Wave action; Wave generation**
Wave-Formed Ripples in Nearshore Sands, John R. Dingle and Douglas L. Inman, 2109
- Bed forms; Circulation; Inlets (waterways); Littoral current; Littoral drift; Sand; Scouring; Sediment transport; South Carolina; Tidal currents**
Sand Circulation Pattern at Price Inlet, South Carolina, Duncan M. FitzGerald, Dag Nummedal and Timothy W. Kana, 1868
- Bed forms; Inlets (waterways); Ocean bottom; Scale effect; Sediment transport; Simulation models; Tidal effects; Wave energy**
Tidal Inlet Flow Dynamics and Sediment Movement, Jerry L. Machemehl, N. E. Bird and A. N. Chambers, 1681
- Bed load; Current meters; Friction coefficient (hydraulic); Inlets (waterways); Tidal effects**
Measurement of Bed Friction in Tidal Inlets, Ashish J. Mehta, R. J. Byrne and Joseph T. DeAlteris, 1701
- Bed ripples; Ripple marks; Sand; Sonar detection; Wave action; Wave generation; Bedding materials**
Wave-Formed Ripples in Nearshore Sands, John R. Dingle and Douglas L. Inman, 2109
- Berths; Dolphins (structures); Head losses; Mass; Shallow water; Tanker ships; Water depth**
Added Masses of Large Tankers Berthing to Dolphins, Taizo Hayashi and Masujiro Shirai, 2830
- Bottom water; Continental shelf; Cyclic loads; Foundations; Ocean bottom; Offshore structures; Predictions; Stability; Wave action; Wave energy**
Prediction of Wave-Induced Seafloor Movements, Leland Milo Kraft, Jr. and David James Watkins, 1605
- Boundary value problems; Breakwaters; Permeability; Sea walls; Two-dimensional; Water depth; Water waves; Wave height**
Method of Analyses for Two-Dimensional Water Wave Problems, Takeshi Iijima, Chung Ren Chou and Akinori Yoshida, 2717
- Boundary value problems; Coastal engineering; Computation; Periodic variations; Refraction; Wave energy; Wave propagation; Waves**
Physics and Mathematics of Waves in Coastal Zones, H. Lundgren, 880
- Breaking; Breakwaters; Friction coefficient (hydraulic); Littoral drift; Ocean currents; Three-dimensional; Wave dispersion; Wave height; Waves**
Non-Uniform Alongshore Currents, Michael R. Gourlay, 701
- Breaking; Coastal engineering; Field tests; Littoral drift; Ocean currents; Photogrammetry; Stereophotography; Water levels; Waves**
Terrestrial Photogrammetric Measurements of Breaking Waves and Longshore Currents in the Nearshore Zone, Joseph W. Maresca, Jr. and Erwin Seibel, 681
- Breaking; Dimensional analysis; Experimentation; Surf; Wave height; Wave period; Waves; Wave spectrum**
Wave Spectrum of Breaking Wave, Toru Sawaragi and Koichiro Iwata, 580
- Breaking; Gravity waves; Solitary waves; Time dependence; Wave height; Waves; Wave velocity**
Recent Developments in the Study of Breaking Waves, Michael S. Longuet-Higgins, 441
- Breaking; Periodic variations; Shoaling; Slopes; Wave period; Wave runup; Waves**
Set-Up and Run-Up in Shoaling Breakers, William G. Van Dorn, 738
- Breaking; Refraction; Shoaling; Wave action; Wave dispersion; Wave height; Waves; Wave velocity**
Refraction of Finite-Height and Breaking Waves, James R. Walker, 507
- Breaking; Resonance; Surges; Turbulence; Wave height; Wave runup; Waves; Beaches**
Resonant Interactions for Waves Breaking on a Beach, Robert T. Guza and Anthony J. Bowen, 560
- Breaking; Surf; Three-dimensional; Two-dimensional; Wave equations; Wave height**
Three-Dimensional Conditions of Surf, William L. Wood, 525
- Breaking energy; Secondary waves; Wave height; Wave period; Wave recorders (water waves); Wave spectrum; Wave velocity**
Kinematics of Breaking Waves, Edward B. Thornton, James J. Galvin, Frank L. Bub and David P. Richardson, 461
- Breakwaters; Buoys; Energy dissipation; Field tests; Floating bodies; Scale effect; Tethered tests; Wave action; Wave energy; Wave spectrum; Wave tanks**
Design, Analysis and Field Test of a Dynamic Floating Breakwater, D. J. Agerton, G. H. Savage and K. C. Stotz, 2792
- Breakwaters; Caissons; Concrete (reinforced); Cylindrical bodies; Model tests; Pressure cells; Shock tests; Strain; Strain gages**
Cylindrical Caisson Breakwater: Strain Model Tests, Helge Gravesen, Finn P. Brodersen, Jorn S. Larsen and H. Lundgren, 2357
- Breakwaters; California; Jetties; Littoral current; Littoral drift; Sediment transport; Surf; Wave energy; Barriers**
Longshore Transport at a Total Littoral Barrier, Richard O. Bruno and Christopher G. Gable, 1203
- Breakwaters; Coastal engineering; Costs; Erosion; Groins (structures); Revetments; Sea walls; Shore protection**
Low-Cost Shoreline Protection, Billy L. Edge, John G. Housley and George M. Watts, 2888
- Breakwaters; Coastal structures; Experimentation; Field tests; Scour; Scouring; Water levels; Wave action; Wave height**
Local Scour and Current Around a Porous Breakwater, Shintaro Hotta and Nobuo Marui, 1590
- Breakwaters; Coastal structures; Israel; Littoral drift; Sedimentation; Sediment deposits; Sediment transport; Shore protection**
Protection by Means of Offshore Breakwaters, I. Fried, 1407

- Breakwaters; Construction; Harbor structures; Japan; Ocean bottom; Shoaling; Topographical factors; Beach erosion; Beaches**
Topographic Change Resulting from the Construction of a Harbor on a Sandy Beach, Kashima Port, Norio Tanaka and Shoji Sato, 1824
- Breakwaters; Costs; Erosion; Great Lakes; Groins (structures); Shore protection; Storms**
Low-Cost Shore Protection on the Great Lakes: A Demonstration/Research Program, John M. Armstrong, 2858
- Breakwaters; Damage; Hydraulic models; Rubble; Rubble mounds; Stability; Wave action; Wave energy**
Effect of Broken Dolosse on Breakwater Stability, D. Donald Davidson and Dennis G. Markle, 2544
- Breakwaters; Deltas; Hydraulic models; Nigeria; Sedimentation; Sediment concentration; Sediment distribution; Sediment transport**
Sedimentation Studies on the Niger River Delta, Ramiro Mayor-Mora, Preben Mortensen and Jorgen Fredsoe, 2151
- Breakwaters; Dredges; Dredging; Sedimentation; Sediment deposits; Sediment transport**
Sedimentation Problems at Offshore Dredged Channels, A. A. Kadib, 1756
- Breakwaters; Enclosures; Groins (structures); Israel; Recreational facilities; Social needs; Beaches**
Enclosing Scheme for Bathing-Beach Development, Joseph Tauman, 1425
- Breakwaters; Experimentation; Stresses; Testing; Armoring (streambed)**
Experimental Studies of Stresses Within the Breakwater Armor Piece "Dolos", Omar J. Lillevang and Wayne E. Nickola, 2519
- Breakwaters; Failure; Harbors; Harbor structures; Hydraulic models; Model tests; Portugal**
Design of Main Breakwater at Sines Harbour, John Dorrington Mettam, 2499
- Breakwaters; Failure; Slope protection; Slope stability; Wave action; Wave energy; Wave period; Armoring (streambed)**
Armour Blocks as Slope Protection, A. F. Whillock and W. A. Price, 2564
- Breakwaters; Floating bodies; Forecasting; Harbors; Marinas; Model studies; Mooring; Moorings**
Floating Breakwater Performance, Bruce H. Adec, 2777
- Breakwaters; Friction coefficient (hydraulic); Littoral drift; Ocean currents; Three-dimensional; Wave dispersion; Wave height; Waves; Breaking**
Non-Uniform Alongshore Currents, Michael R. Gourlay, 701
- Breakwaters; Hawaii; Recreational facilities; Shore protection; Swimming; Beaches; Beach nourishment**
Proposed "Improvement" of Kaimu Beach, Hawaii, Doak C. Cox, Franciscus Gerritsen and Theodore T. Lee, 1552
- Breakwaters; Hawaii; Reefs; Slope protection; Slope stability; Airports**
Design and Construction of Protective Structure for New Reef Runway at Honolulu International Airport, Wilfred D. Darling, 2589
- Breakwaters; Japan; Ocean bottom; Shore protection; Subsidence; Beach erosion**
Changes of Sea Bed Due to Detached Breakwaters, Osamu Toyoshima, 1572
- Breakwaters; Laboratory tests; Permeability; Reflection; Wave height**
Laboratory Study of Pervious Core Breakwaters, Hideo Kondo, Satoshi Toma and Kenji Yano, 2643
- Breakwaters; Laboratory tests; Rubble mounds; Wave action; Wave dispersion; Wave energy; Waves**
Wave Transmission Through Trapezoidal Breakwaters, Ole Secher Madsen and Stanley M. White, 2662
- Breakwaters; Model tests; Scale effect; Stability; Wave height; Wave period; Wave runup; Armoring (streambed)**
Large Scale Model Tests of Placed Stone Breakwaters, Charles K. Sollitt and Donald H. DeBok, 2572
- Breakwaters; Oscillation; Sediment transport; Unsteady flow; Wave equations; Waves**
Quantitative Description of Sediment Transport, Ole Secher Madsen and William D. Grant, 1093
- Breakwaters; Overtopping; Rubble mounds; Wave action; Wave energy; Waves; Wave spectrum**
Overtopping of Rubble-Mound Breakwaters by Irregular Waves, Yvon Ouellet and Pierre Eubanks, 2756
- Breakwaters; Permeability; Sea walls; Two-dimensional; Water depth; Water waves; Wave height; Boundary value problems**
Method of Analyses for Two-Dimensional Water Wave Problems, Takeshi Ijima, Chung Ren Chou and Akinori Yoshida, 2717
- Breakwaters; Reflection; Slitting; Wave action; Wave damping; Wave energy**
Slit-Type Breakwater: Box-Type Wave Absorber, Shoshtiro Nagai and Shohachi Kakuno, 2697
- Breakwaters; Resonance; Rubble; Rubble mounds; Slope stability; Stability; Surf; Wave period; Wave runup**
New Design Principles for Rubble Mound Structures, Per Moller Bruun and Ali Riza Gunbak, 2429
- Breakwaters; Shore protection; Wave action; Wave energy; Bays (topographic features); Beach erosion**
Headland Defense of Coasts, Richard Silvester, 1394
- Buoyancy; Diffusers; Dilution; Discharge (water); Eddies; Experimentation; Jets; Slots**
Negatively Buoyant Slot Jets, D. M. Shahrabani and J. D. Ditmars, 2976
- Buoyancy; Fluid mechanics; Gravitation; Ocean currents; Spreading; Time dependence; Wastewater**
Buoyancy-Driven Gravitational Spreading, Robert C.Y. Koh, 2956
- Buoys; Energy dissipation; Field tests; Floating bodies; Scale effect; Tethered tests; Wave action; Wave energy; Wave spectrum; Wave tanks; Breakwaters**
Design, Analysis and Field Test of a Dynamic Floating Breakwater, D. J. Agerton, G. H. Savage and K. C. Stotz, 2792

- Bypasses; Erosion; Great Lakes; Michigan; Sand; Shore protection; Water levels; Beach erosion; Beach nourishment**
Sand-Bypass and Shore Erosion, Bridgman, Michigan, C. N. Johnson and L. W. Hiipakka, 1361
- Bypasses; Jet pumps; Littoral current; Sand; Shore protection; Surf**
A Sand Bypassing System Using a Jet Pump, E. C. McNair, Jr., 1342
- Caissons; Concrete (reinforced); Cylindrical bodies; Tidal tests; Pressure cells; Shock tests; Strain; Strain gages; Breakwaters**
Cylindrical Caisson Breakwater: Strain Model Tests, Helge Gravsen, Finn P. Brodersen, Jorn S. Larsen and H. Lundgren, 2357
- Caissons; Model tests; Overturning tests; Wave action; Wave energy; Wave height; Wave period**
Wave Forces on Aquare Caissons, G. R. Mogridge and W. W. Jamieson, 2271
- Calibration; Discharge (water); Estuaries; Open channel flow; Water meters; Water quality**
Calibration of Branched Estuary Models, James P. Bennett, 3416
- California; Coastal engineering; Coastal structures; Numerical analysis; Wave energy; Wave recorders (water waves)**
Regional Network for Coastal Engineering Data, Richard J. Seymour and Meredith H. Sessions, 60
- California; Discharge (water); Numerical analysis; Tidal currents; Tidal effects; Algorithms**
Tidal Stream Flow Solved by Galerkin Technique, L. H. Smith and Ralph T-S Cheng, 3358
- California; Equilibrium; Tidal effects; Wave energy; Wave spectrum; Beach erosion; Beaches**
Beach Profiles at Torrey Pines, California, David G. Aubrey, Douglas L. Inman and Charles E. Nordstrom, 1297
- California; Jetties; Littoral current; Littoral drift; Sediment transport; Surf; Wave energy; Barriers; Breakwaters**
Longshore Transport at a Total Littoral Barrier, Richard O. Bruno and Christopher G. Gable, 1203
- Canada; Density currents; Hydraulic models; Saline water-freshwater interfaces; Salinity; Salt water intrusion; Tidal effects**
Churchill River Salt-Water Tidal Model, Bruce D. Pratte, 3445
- Canada; Littoral current; Littoral drift; Morphology; Sandbars; Sediment deposits; Wave energy; Barriers; Beaches**
Process and Morphology Characteristics of Two Barrier Beaches in the Magdalen Islands, Gulf of St. Lawrence, Canada, E. H. Owens, 1975
- Cavities; Deep water; Explosions; Predictions; Wave generation; Wave height; Wave propagation; Waves**
Calculations of Waves Formed From Surface Cavities, Charles L. Mader, 1079
- Channels (waterways); Dunes; Dune sands; Sand waves; Sediment transport; Tidal effects; West Germany**
Transport Mechanism in Tidal Dunes, Horst Nasner, 2136
- Channels (waterways); River regulation; Sandbars; Sediment transport; Stability; Tidal effects; Tidal hydraulics; Tidal waters**
Stability of Tidal Channels Dependent on River Improvement, Volker Barthel, 1775
- Circulation; Inlets (waterways); Littoral current; Littoral drift; Sand; Scouring; Sediment transport; South Carolina; Tidal currents; Bed forms**
Sand Circulation Pattern at Price Inlet, South Carolina, Duncan M. FitzGerald, Dag Nummedal and Timothy W. Kana, 1868
- Climatic data; Estuaries; Estuarine environment; Sediment deposits; Sediment distribution; Sediments; Tidal effects; Wave action; Beach erosion**
Factors Influencing Estuary Sediment Distribution, Mary P. Kendrick and B. V. Derbyshire, 2072
- Climatic data; Ocean waves; Wave energy; Wave height; Wavemeters; Wave recorders (water waves); Waves**
Wave Climate Analysis for Engineering Purpose, Hans H. Dette and Alfred Fuhrboter, 10
- Climatology; Coastal engineering; Ocean waves; Spectral analysis; Statistical analysis; Wave forecasting; Wave period; Waves; Wave spectrum**
Ocean Wave Statistics from FNWC Spectral Analysis, Warren C. Thompson and F. Michael Reynolds, 238
- Coastal engineering; Coastal plains; Japan; Power spectra; Refraction; Shoaling; Tsunamis; Warning systems**
Transformation of Tsunamis in a Coastal Zone, Shigehisa Nakamura, Haruo Higuchi and Yoshito Tsuchiya, 988
- Coastal engineering; Coastal structures; Data collection; Data collection systems; Hydrographic surveys; Waves; Wind (meteorology)**
Data Collection and Analysis for Coastal Projects, E. Loewy, K. G. Witthaus, L. Summers and R. J. Maddrell, 43
- Coastal engineering; Coastal structures; Directional measurement; Sediment transport; Wave energy; Wavemeters**
Wave Direction Computations with Three Gage Arrays, D. Esteve, 349
- Coastal engineering; Coastal structures; Numerical analysis; Wave energy; Wave recorders (water waves); California**
Regional Network for Coastal Engineering Data, Richard J. Seymour and Meredith H. Sessions, 60
- Coastal engineering; Coastal structures; Stability; Wave energy; Wave height; Wave period; Waves**
Consecutive High Waves in Coastal Waters, Winfried Siefert, 171
- Coastal engineering; Computation; Periodic variations; Refraction; Wave energy; Wave propagation; Waves; Boundary value problems**
Physics and Mathematics of Waves in Coastal Zones, H. Lundgren, 880
- Coastal engineering; Costs; Erosion; Groins (structures); Revetments; Sea walls; Shore protection; Breakwaters**
Low-Cost Shoreline Protection, Billy L. Edge, John G. Housley and George M. Watts, 2888

- Coastal engineering; Currents; Littoral drift; Ocean currents; Sediment transport; Storm surges; Tidal marshes**
Currents in Tidal Flats During Storm Surges, Harald Gohren, 959
- Coastal engineering; Environmental factors; Monitoring; Nuclear power plants; Social impact**
Coastal Environment and a Nuclear Power Plant, Ralph A. de la Parra, 3014
- Coastal engineering; Field tests; Littoral drift; Ocean currents; Photogrammetry; Stereophotography; Water levels; Waves; Breaking**
Terrestrial Photogrammetric Measurements of Breaking Waves and Longshore Currents in the Nearshore Zone, Joseph W. Maresca, Jr. and Erwin Seibel, 681
- Coastal engineering; India; Statistical analysis; Wave height; Wavemeters; Wave recorders (water waves); Wave spectrum**
Ocean Wave Record Analysis by Tucker's Method — An Evaluation, Jade Dattatri and Irvathur Vasudeva Nayak, 289
- Coastal engineering; Ocean waves; Spectral analysis; Statistical analysis; Wave forecasting; Wave period; Waves; Wave spectrum; Climatology**
Ocean Wave Statistics from FNWC Spectral Analysis, Warren C. Thompson and F. Michael Reynolds, 238
- Coastal engineering; Ocean waves; Taiwan; Wave height; Wave period; Waves; Wind speed**
Waves Off Taichung Coast of Taiwan, Charles C.C. Chang, M. H. Wang and J. T. Juang, 129
- Coastal engineering; Recreational facilities; Shore protection; Sri Lanka; Beach nourishment**
Coastal Problems in Sri Lanka, Francisus Gerritsen and Summa R. Amarasinghe, 3487
- Coastal plains; Japan; Power spectra; Refraction; Shoaling; Tsunamis; Warning systems; Coastal engineering**
Transformation of Tsunamis in a Coastal Zone, Shigehisa Nakamura, Haruo Higuchi and Yoshito Tsuchiya, 988
- Coastal structures; Cooling water; Intake systems; Mathematical models; Nuclear power plants; Numerical analysis; Refraction; Sediment transport; Wave dispersion; Waves**
Application of a Sediment Transport Model, C. A. Fleming and J. N. Hunt, 1184
- Coastal structures; Damping; Numerical analysis; Wave action; Wave energy; Wave runoff; Wave velocity**
Numerical Calculation of Wave Forces on Structures, B. D. Nichols and C. W. Hirt, 2254
- Coastal structures; Data collection; Data collection systems; Hydrographic surveys; Waves; Wind (meteorology); Coastal engineering**
Data Collection and Analysis for Coastal Projects, E. Loewy, K. G. Withaus, L. Summers and R. J. Maddrell, 43
- Coastal structures; Directional measurement; Sediment transport; Wave energy; Wavemeters; Coastal engineering**
Wave Direction Computations with Three Gage Arrays, D. Esteva, 349
- Coastal structures; Experimentation; Field tests; Scour; Scouring; Water levels; Wave action; Wave height; Breakwaters**
Local Scour and Current Around a Porous Breakwater, Shintaro Hotta and Nobuo Marui, 1590
- Coastal structures; Hazards; Tsunamis; Wave action; Wave energy; Wave generation; Wave height**
Tsunami Hazard and Design of Coastal Structures, George Pararas-Carayannis, 2248
- Coastal structures; Israel; Littoral drift; Sedimentation; Sediment deposits; Sediment transport; Shore protection; Breakwaters**
Protection by Means of Offshore Breakwaters, I. Fried, 1407
- Coastal structures; Lateral forces; Pile foundations; Steel piles; Structural design**
Concepts in Design of Coastal Structures, Casimir J. Kray, 2209
- Coastal structures; Numerical analysis; Wave energy; Wave recorders (water waves); California; Coastal engineering**
Regional Network for Coastal Engineering Data, Richard J. Seymour and Meredith H. Sessions, 60
- Coastal structures; Random processes; Reflection; Water waves; Wave dispersion; Wave energy; Wave spectrum**
Decomposition of Co-Existing Random Wave Energy, Dennis B. Morden, Eugene P. Richey and Derald R. Christensen, 846
- Coastal structures; Stability; Wave energy; Wave height; Wave period; Waves; Coastal engineering**
Consecutive High Waves in Coastal Waters, Winfried Siefert, 171
- Coastal topographic features; Eigenvalues; Responses; Rip currents; Velocity distribution; Water waves; Wave equations**
Rip-Current and Coastal Topography, Mikio Hino, 1326
- Coliform bacteria; Drainage; Estuaries; Runoff; Sampling; Simulation; Water circulation; Water quality**
State Estimation of Estuarine Circulation and Water Quality by Numerical Simulation and Observation, Jan J. Leendertse and S. K. Liu, 3223
- Collisions; Harbor structures; Mooring; Moorings; Offshore drilling; Ships; Wave tanks; Accidents**
Protection of Maritime Structures Against Ship Collisions, Kazuki Oda and Shositiro Nagai, 2810
- Computation; Periodic variations; Refraction; Wave energy; Wave propagation; Waves; Boundary value problems; Coastal engineering**
Physics and Mathematics of Waves in Coastal Zones, H. Lundgren, 880
- Computerized simulation; Concrete (blocks); Harbor structures; Quays; Reflection; Revetments; Shore protection; Wave dispersion**
Quay Wall with Wave Absorber "Igloo", Naofumi Shiraishi, Robert Q. Palmer and Hiroshi Okamoto, 2677

- Computer models; Forecasting; Hurricanes; Numerical analysis; Storm surges; Tropical cyclones**
SPLASH — A Model for Forecasting Tropical Storm Surges, Celso S. Barrientos and Chester P. Jelecnianski, 941
- Computer models; Slopes; Wave spectrum; Beach erosion; Beaches**
 Study of Equilibrium Beach Profiles, Robert A. Dalrymple and William W. Thompson, 1277
- Concrete (blocks); Harbor structures; Quays; Reflection; Revetments; Shore protection; Wave dispersion; Computerized simulation**
 Quay Wall with Wave Absorber "Igloo", Naofumi Shiraishi, Robert Q. Palmer and Hiroshi Okamoto, 2677
- Concrete (blocks); Permeability; Reservoirs; Sea walls; Wave energy; Wave period**
 Permeable Seawall with Reservoir and the Use of "Warock", Takeshi Iijima, Enzoh Tanaka and Hideaki Okuzono, 2623
- Concrete (reinforced); Cylindrical bodies; Model tests; Pressure cells; Shock tests; Strain; Strain gages; Breakwaters; Caissons**
 Cylindrical Caisson Breakwater: Strain Model Tests, Helge Gravesen, Finn P. Brodersen, Jorn S. Larsen and H. Lundgren, 2357
- Construction; Harbor structures; Japan; Ocean bottom; Shoaling; Topographical factors; Beach erosion; Beaches; Breakwaters**
 Topographic Change Resulting from the Construction of a Harbor on a Sandy Beach, Kashima Port, Norio Tanaka and Shoji Sato, 1824
- Continental shelf; Cyclic loads; Foundations; Ocean bottom; Offshore structures; Predictions; Stability; Wave action; Wave energy; Bottom water**
 Prediction of Wave-Induced Seafloor Movements, Leland Milo Kraft, Jr. and David James Watkins, 1605
- Continental shelf; Storms; Storm surges; Storm water; Wave energy; Wave height; Wave period; Wave recorders (water waves); Waves; Wave spectrum**
 Extreme Wave Parameters Based on Continental Shelf Storm Wave Records, R. E. Haring, A. R. Osborne and L. P. Spencer, 151
- Convection; Diffusion; Dispersion; Finite element method; Numerical analysis; Stratification; Two phase flow**
 Numerical Modeling of Dispersion in Stratified Waters, George C. Christodoulou and Jerome J. Connor, 3138
- Cooling water; Cylindrical bodies; Field tests; Intake structures; Nuclear power plants; Wave dispersion; Wave energy**
 Wave Pressures on Large Circular Cylindrical Structure, Hiroshi Nakamura, 2290
- Cooling water; Intake systems; Mathematical models; Nuclear power plants; Numerical analysis; Refraction; Sediment transport; Wave dispersion; Waves; Coastal structures**
 Application of a Sediment Transport Model, C. A. Fleming and J. N. Hunt, 1184
- Costs; Erosion; Great Lakes; Groins (structures); Shore protection; Storms; Breakwaters**
 Low-Cost Shore Protection on the Great Lakes: A Demonstration/Research Program, John M. Armstrong, 2858
- Costs; Erosion; Groins (structures); Revetments; Sea walls; Shore protection; Breakwaters; Coastal engineering**
 Low-Cost Shoreline Protection, Billy L. Edge, John G. Housley and George M. Watts, 2888
- Current meters; Friction coefficient (hydraulic); Inlets (waterways); Tidal effects; Bed load**
 Measurement of Bed Friction in Tidal Inlets, Ashish J. Mehta, R. J. Byrne and Joseph T. DeAlteris, 1701
- Current meters; Water circulation; Wave recorders (water waves); Wind pressure; Wind tides**
 Wind-Driven Circulation of Saginaw Bay, James H. Saylor and Larry J. Danek, 3262
- Currents; Dredging; Estuaries; Harbors; Littoral drift; Sand traps; Storms; Wave action**
 Design and Behaviour of Sandtraps in Regions of High Littoral Drift, P. C. Saxena, Pashhayannur P. Vaidyaraman and R. Srinivasan, 1377
- Currents; Finite elements; Gravity waves; Predictions; Refraction; Surf; Water depth; Waves**
 Current Depth Defraction Using Finite Elements, Ove Skovgaard and Ivar G. Jonsson, 721
- Currents; Great Lakes; Harbors; Seiches; Tidal effects; Water levels; Wave generation**
 Hydraulics of Great Lakes Inlet — Harbors Systems, Robert M. Sorensen and William N. Seelig, 1646
- Currents; Littoral drift; Ocean currents; Sediment transport; Storm surges; Tidal marshes; Coastal engineering**
 Currents in Tidal Flats During Storm Surges, Harald Gohren, 959
- Currents (water); Interactions; Turbulence; Wave action; Wave damping; Wave dispersion; Wave energy; Wave velocity**
 Interaction of Waves and a Turbulent Current, J. D.A. van Hoften and Susumu Karaki, 404
- Cyclic loads; Foundations; Ocean bottom; Offshore structures; Predictions; Stability; Wave action; Wave energy; Bottom water; Continental shelf**
 Prediction of Wave-Induced Seafloor Movements, Leland Milo Kraft, Jr. and David James Watkins, 1605
- Cylinders; Drag; Hydraulic models; Lift; Oscillations; Reynolds number; Stream flow; Water flow; Wave action; Wave energy**
 High Reynolds Number Oscillating Flow by Cylinders, Tokuo Yamamoto and John H. Nath, 2321
- Cylindrical bodies; Drag; Force; Oscillation; Roughness (hydraulic); Vortices; Water flow**
 Forces on Rough-Walled Circular Cylinders in Harmonic Flow, Turgut Sarpkaya, 2301
- Cylindrical bodies; Field tests; Intake structures; Nuclear power plants; Wave dispersion; Wave energy; Cooling water**
 Wave Pressures on Large Circular Cylindrical Structure, Hiroshi Nakamura, 2290

- Cylindrical bodies; Flow separation; Oscillations; Pressure distribution; Vortices; Wakes; Water waves**
Flow Separation, Wake Vortices and Pressure Distribution Around a Circular Cylinder under Oscillatory Waves, Yuichi Iwagaki and Hajime Ishida, 2341
- Cylindrical bodies; Model tests; Pressure cells; Shock tests; Strain; Strain gages; Breakwaters; Caissons; Concrete (reinforced)**
Cylindrical Caisson Breakwater: Strain Model Tests, Helge Gravesen, Finn P. Brodersen, Jorn S. Larsen and H. Lundgren, 2357
- Damage; Dikes; Impact; Revetments; Wave action; Wave energy; Air entrainment**
Response of Seadykes due to Wave Impacts, Alfred Fuhrboter, Hans H. Dette and J. Grune, 2604
- Damage; Hydraulic models; Rubble; Rubble mounds; Stability; Wave action; Wave energy; Breakwaters**
Effect of Broken Dolosse on Breakwater Stability, D. Donald Davidson and Dennis G. Markle, 2544
- Damping; Energy dissipation; Estuaries; Stratification; Tidal effects; Wave energy; West Germany**
Energy Dissipation in Tidal Estuaries, Hans-Werner Partensky and Gunther Barg, 3312
- Damping; Numerical analysis; Wave action; Wave energy; Wave runoff; Wave velocity; Coastal structures**
Numerical Calculation of Wave Forces on Structures, B. D. Nichols and C. W. Hirt, 2254
- Data collection; Data collection systems; Hydrographic surveys; Waves; Wind (meteorology); Coastal engineering; Coastal structures**
Data Collection and Analysis for Coastal Projects, E. Loewy, K. G. Witthaus, L. Summers and R. J. Maddrell, 43
- Data collection systems; Hydrographic surveys; Waves; Wind (meteorology); Coastal engineering; Coastal structures; Data collection**
Data Collection and Analysis for Coastal Projects, E. Loewy, K. G. Witthaus, L. Summers and R. J. Maddrell, 43
- Deep water; Explosions; Predictions; Wave generation; Wave height; Wave propagation; Waves; Cavities**
Calculations of Waves Formed From Surface Cavities, Charles L. Mader, 1079
- Deformation; Periodic functions; Phase velocity; Water depth; Wave energy; Wave height; Waves; Beaches**
Deformation up to Breaking of Periodic Waves on a Beach, Ib A. Svendsen and J. Buhr Hansen, 477
- Delaware; New Jersey; Probability; Simulation; Simulation models; Storm surges**
Simulation Model for Storm Surge Probabilities, Mohammad H. Fallah, J. N. Sharma and Cheng Y. Yang, 934
- Deltas; Hydraulic models; Nigeria; Sedimentation; Sediment concentration; Sediment distribution; Sediment transport; Breakwaters**
Sedimentation Studies on the Niger River Delta, Ramiro Mayor-Mora, Preben Mortensen and Jorgen Fredsoe, 2151
- Density currents; Estuaries; Friction coefficient (hydraulic); Mathematical models; Numerical analysis; Saline water intrusion; Stratification; Transport phenomena**
Numerical Model for Density Currents in Estuaries, Karsten Fischer, 3295
- Density currents; Flow patterns; Mathematical models; Scour; Scouring; Stratified flow; Troughs**
Generation of Troughs by Density Currents, Hans Speekenbrink, 2170
- Density currents; Hydraulic models; Saline water-freshwater interfaces; Salinity; Salt water intrusion; Tidal effects; Canada**
Churchill River Salt-Water Tidal Model, Bruce D. Pratte, 3445
- Diffraction; Mach number; Reflection; Walls; Water waves; Wave height**
Mach-Reflection as a Diffraction Problem, Udo Berger and Soren Kohlhasse, 796
- Diffusers; Dilution; Discharge (water); Eddies; Experimentation; Jets; Slots; Buoyancy**
Negatively Buoyant Slot Jets, D. M. Shahrabani and J. D. Ditmars, 2976
- Diffusers; Dilution; Mixing; Outfall sewers; Site selection; Water quality**
Design Procedures for Ocean Outfalls, Jeffrey A. Layton, 2919
- Diffusers; Discharge (water); Hydraulic models; Nuclear power plants; Plume detection; Plumes; Thermal pollution; Two phase flow**
Field Studies of Submerged-Diffuser Thermal Plumes with Comparisons to Predictive Model Results, A. A. Frigo, Richard A. Paddock and J. D. Ditmars, 3028
- Diffusers; Environmental effects; Hydrodynamics; Ocean engineering; Outfall sewers; Underwater pipelines**
Design Considerations for the Sand Island and Barbers Point Outfalls, Robert C.Y. Koh, Norman H. Brooks and Floyd Louis Vuillemot, 2941
- Diffusion; Dispersion; Finite element method; Numerical analysis; Stratification; Two phase flow; Convection**
Numerical Modeling of Dispersion in Stratified Waters, George C. Christodoulou and Jerome J. Connor, 3138
- Diffusion; Eddies; Estuaries; Interfaces; Saline water-freshwater interfaces; Salinity; Salt water intrusion; Stratification**
Determination of the Interfacial Eddy Diffusion Coefficient of a Highly Stratified Estuary, Yu-Hwa Wang, 3158
- Diffusion; Eddies; Hydraulic models; Scale effect; Statistical analysis; Tidal effects; Turbulence**
Horizontal Diffusion in Tidal Models and Scaling Criteria for Thermal-Hydraulic Model Tests, Gerd Flugge, 3097

- Diffusion; Estuaries; Frequency analysis; Hydraulic models; Mathematical models; Mixing; Algorithms**
Algorithm for Vertical Diffusion, Soren Peter Kjeldsen, 3321
- Dikes; Discharge (water); Overtopping; Periodic variations; Wave height; Wave runup; Waves**
Characteristics of Flow in Run-Up of Periodic Waves, Ary Roos and Jurjen A. Battjes, 781
- Dikes; Echo sounding; Field investigations; Instrumentation; Ocean waves; Scale effect; Storm surges; Wave equations; Wave height; Wave period; Wave runup**
Wave Run-Up in Field Measurements with Newly Developed Instrument, Heie F. Erchinger, 767
- Dikes; Impact; Revetments; Wave action; Wave energy; Air entrainment; Damage**
Response of Seadykes due to Wave Impacts, Alfred Fuhrboter, Hans H. Dette and J. Grune, 2604
- Dilution; Discharge (water); Eddies; Experimentation; Jets; Slots; Buoyancy; Diffusers**
Negatively Buoyant Slot Jets, D. M. Shahrabani and J. D. Ditmars, 2976
- Dilution; Mixing; Outfall sewers; Site selection; Water quality; Diffusers**
Design Procedures for Ocean Outfalls, Jeffrey A. Layton, 2919
- Dimensional analysis; Experimentation; Surf; Wave height; Wave period; Waves; Wave spectrum; Breaking**
Wave Spectrum of Breaking Wave, Toru Sawaragi and Koichiro Iwata, 580
- Directional measurement; Sediment transport; Wave energy; Wavemeters; Coastal engineering; Coastal structures**
Wave Direction Computations with Three Gage Arrays, D. Esteve, 349
- Discharge (water); Eddies; Experimentation; Jets; Slots; Buoyancy; Diffusers; Dilution**
Negatively Buoyant Slot Jets, D. M. Shahrabani and J. D. Ditmars, 2976
- Discharge (water); Effluents; Field tests; Mathematical models; Numerical analysis; Water flow; Wave energy; Wind pressure**
Numerical Modelling -- An Aid to Assessing Field Data, H. P. Riedel and F. L. Wilkinson, 3243
- Discharge (water); Estuaries; Open channel flow; Water meters; Water quality; Calibration**
Calibration of Branched Estuary Models, James P. Bennett, 3416
- Discharge (water); Hydraulic models; Nuclear power plants; Plume detection; Plumes; Thermal pollution; Two phase flow; Diffusers**
Field Studies of Submerged-Diffuser Thermal Plumes with Comparisons to Predictive Model Results, A. A. Frigo, Richard A. Paddock and J. D. Ditmars, 3028
- Discharge (water); Hydraulic models; Nuclear power plants; Prototype tests; Temperature distribution; Thermal diffusion; Thermal pollution; Water temperature**
Thermal Discharges: Prototype vs. Hydraulic Model, Gary C. Parker, Ching S. Fang and Albert Y. Kuo, 3049
- Discharge (water); Interfacial tension; Stability; Stratified flow; Thermal pollution; Turbulence**
Interfacial Instability in Stratified Flow, Richard H. French, 3124
- Discharge (water); Numerical analysis; Tidal currents; Tidal effects; Algorithms; California**
Tidal Stream Flow Solved by Galerkin Technique, L. H. Smith and Ralph T-S Cheng, 3358
- Discharge (water); Overtopping; Periodic variations; Wave height; Wave runup; Waves; Dikes**
Characteristics of Flow in Run-Up of Periodic Waves, Ary Roos and Jurjen A. Battjes, 781
- Dispersion; Distribution; Dyes; Estuaries; Predictions; Sewage disposal; Sewage effluents; Tracers; Water pollution**
Prediction of Pollutant Distribution in Estuaries, Albert Y. Kuo and John P. Jacobson, 3276
- Dispersion; Effluent reuse; Effluents; Islands (landforms); Scale effect; Shore protection; Tidal currents**
Study of an Artificial Island, J. P. Lepetit and S. Moreau, 3526
- Dispersion; Finite element method; Numerical analysis; Stratification; Two phase flow; Convection; Diffusion**
Numerical Modeling of Dispersion in Stratified Waters, George C. Christodoulou and Jerome J. Connor, 3138
- Dispersion; Mass transfer; Open channel flow; River flow; Sediment transport; Tidal currents**
Dispersive Transport in River and Tidal Flows, R. B. Taylor, 3336
- Distribution; Dyes; Estuaries; Predictions; Sewage disposal; Sewage effluents; Tracers; Water pollution; Dispersion**
Prediction of Pollutant Distribution in Estuaries, Albert Y. Kuo and John P. Jacobson, 3276
- Distribution functions; Distribution patterns; Frequency; Ocean waves; Surface waves; Wave energy; Wave spectrum**
Directional Spectral of Ocean Surface Waves, Hisashi Mitsuyasu and S. Mizuno, 329
- Distribution patterns; Frequency; Ocean waves; Surface waves; Wave energy; Wave spectrum; Distribution functions**
Directional Spectral of Ocean Surface Waves, Hisashi Mitsuyasu and S. Mizuno, 329
- Distribution patterns; Wave height; Wavelengths; Waves; Wave spectrum; Wave tanks; Wind (meteorology)**
Wave Height Distribution of Wind Waves Over Long Waves, Shan-Hwei Ou and Frederick L.W. Tang, 388
- Dolphins (structures); Head losses; Mass; Shell water; Tanker ships; Water depth; Berths**
Added Masses of Large Tankers Berthing to Dolphins, Taizo Hayashi and Masujiro Shirai, 2830
- Drag; Force; Oscillation; Roughness (hydraulic); Vortices; Water flow; Cylindrical bodies**
Forces on Rough-Walled Circular Cylinders in Harmonic Flow, Turgut Sarpkaya, 2301

- Drag; Force; Separation; Spheres; Water circulation; Wave action; Wave energy**
Forces on a Sphere Under Linear Progressive Waves, Scott A. Jenkins and Douglas L. Inman, 2413
- Drag; Hydraulic models; Lift; Oscillations; Reynolds number; Stream flow; Water flow; Wave action; Wave energy; Cylinders**
High Reynolds Number Oscillating Flow by Cylinders, Tokuo Yamamoto and John H. Nath, 2321
- Drag; Inertial forces; Submerged flow; Underwater structures; Wave action; Wave energy**
Wave Forces on Submerged Objects, Suphat Vongvisessomjai and Richard Silvester, 2387
- Drainage; Estuaries; Runoff; Sampling; Simulation; Water circulation; Water quality; Coliform bacteria**
State Estimation of Estuarine Circulation and Water Quality by Numerical Simulation and Observation, Jan J. Leendertse and S. K. Liu, 3223
- Dredges; Dredging; Sedimentation; Sediment deposits; Sediment transport; Breakwaters**
Sedimentation Problems at Offshore Dredged Channels, A. A. Kadib, 1756
- Dredging; Estuaries; Estuarine environment; San Francisco; Sediments; Spoil; Tracers (radioactive)**
Tracing Estuarine Sediments by Neutron Activation, Richard M. Ecker, John F. Sustar and William T. Harvey, 2009
- Dredging; Estuaries; Harbors; Littoral drift; Sand traps; Storms; Wave action; Currents**
Design and Behaviour of Sandtraps in Regions of High Littoral Drift, P. C. Saxena, Pazhayanur P. Vaidyaraman and R. Srinivasan, 1377
- Dredging; Sedimentation; Sediment deposits; Sediment transport; Breakwaters; Dredges**
Sedimentation Problems at Offshore Dredged Channels, A. A. Kadib, 1756
- Dunes; Dune sands; Movable bed models; Sediment transport; Tidal currents; Tidal effects**
Origin of Submarine Dunes, Mehmet S. Yalin, 2127
- Dunes; Dune sands; Sand waves; Sediment transport; Tidal effects; West Germany; Channels (waterways)**
Transport Mechanism in Tidal Dunes, Horst Nasner, 2136
- Dune sands; Movable bed models; Sediment transport; Tidal currents; Tidal effects; Dunes**
Origin of Submarine Dunes, Mehmet S. Yalin, 2127
- Dune sands; Sand waves; Sediment transport; Tidal effects; West Germany; Channels (waterways); Dunes**
Transport Mechanism in Tidal Dunes, Horst Nasner, 2136
- Dyes; Estuaries; Predictions; Sewage disposal; Sewage effluents; Tracers; Water pollution; Dispersion; Distribution**
Prediction of Pollutant Distribution in Estuaries, Albert Y. Kuo and John P. Jacobson, 3276
- Dynamics; Equilibrium; Erosion; Reflection; Sandbars; Sand traps; Three-dimensional; Wave action; Beach erosion; Beach nourishment**
Three Dimensional Tests on Dynamic Equilibrium and Artificial Nourishment, J. William Kamphuis and R. M. Myers, 1532
- Echo sounding; Field investigations; Instrumentation; Ocean waves; Scale effect; Storm surges; Wave equations; Wave height; Wave period; Wave runup; Dikes**
Wave Run-Up in Field Measurements with Newly Developed Instrument, Heie F. Erchingler, 767
- Ecology; Environmental effects; Littoral drift; Marinas; Seismic studies; Site selection**
Application of CERC Special Report No.2, James W. Dunham, 3570
- Economic analysis; Environmental effects; Harbors; Performance; Safety; Site selection; Utilization; Barges**
Probable Utilization Level for a Barge Harbor, Martin T. Czerniak and Choule J. Sonu, 3557
- Eddies; Estuaries; Interfaces; Saline water-freshwater interfaces; Salinity; Salt water intrusion; Stratification; Diffusion**
Determination of the Interfacial Eddy Diffusion Coefficient of a Highly Stratified Estuary, Yu-Hwa Wang, 3158
- Eddies; Experimentation; Jets; Slots; Buoyancy; Diffusers; Dilution; Discharge (water)**
Negatively Buoyant Slot Jets, D. M. Shahrabani and J. D. Ditmars, 2976
- Eddies; Hydraulic models; Scale effect; Statistical analysis; Tidal effects; Turbulence; Diffusion**
Horizontal Diffusion in Tidal Models and Scaling Criteria for Thermal-Hydraulic Model Tests, Gerd Flugge, 3097
- Effluent reuse; Effluents; Islands (landforms); Scale effect; Shore protection; Tidal currents; Dispersion**
Study of an Artificial Island, J. P. Lepetit and S. Moreau, 3526
- Effluents; Field tests; Mathematical models; Numerical analysis; Water flow; Wave energy; Wind pressure; Discharge (water)**
Numerical Modelling — An Aid to Assessing Field Data, H. P. Riedel and F. L. Wilkinson, 3243
- Effluents; Islands (landforms); Scale effect; Shore protection; Tidal currents; Dispersion; Effluent reuse**
Study of an Artificial Island, J. P. Lepetit and S. Moreau, 3526
- Eigenvalues; Impulses; Responses; Stability; Statistical analysis; Storms; Variability; Beach erosion**
Stability and Impulse Response of Empirical Eigenfunctions, Clinton D. Winant and David G. Aubrey, 1312
- Eigenvalues; Responses; Rip currents; Velocity distribution; Water waves; Wave equations; Coastal topographic features**
Rip-Current and Coastal Topography, Mikio Hino, 1326
- Enclosures; Groins (structures); Israel; Recreational facilities; Social needs; Beaches; Breakwaters**
Enclosing Scheme for Bathing-Beach Development, Joseph Tauman, 1425

- Energy conversion; Surface waves; Thermal energy; Thermal gradient; Two phase flow; Water flow**
Flow Field Near an Ocean Thermal Energy Conversion Plant, D. M. Sheppard, G. M. Powell and I. B. Chou, 3068
- Energy dissipation; Estuaries; Stratification; Tidal effects; Wave energy; West Germany; Damping**
Energy Dissipation in Tidal Estuaries, Hans-Werner Partenscky and Gunther Barg, 3312
- Energy dissipation; Field tests; Floating bodies; Scale effect; Tethered tests; Wave action; Wave energy; Wave spectrum; Wave tanks; Breakwaters; Buoys**
Design, Analysis and Field Test of a Dynamic Floating Breakwater, D. J. Agerton, G. H. Savage and K. C. Stotz, 2792
- Energy equation; Littoral current; Littoral drift; Rip currents; Sediment transport; Shore protection**
Longshore Transport Prediction — SPM 1973 Equation, Cyril J. Galvin and Philip Vitale, 1133
- Environmental effects; Harbors; Performance; Safety; Site selection; Utilization; Barges; Economic analysis**
Probable Utilization Level for a Barge Harbor, Martin T. Czerniak and Choule J. Sonu, 3557
- Environmental effects; Hawaii; Islands (landforms); Monitoring; Reefs; Runways; Water quality**
Environmental Impacts on an Island Community, Gordon A. Chapman, 3506
- Environmental effects; Hydrodynamics; Ocean engineering; Outfall sewers; Underwater pipelines; Diffusers**
Design Considerations for the Sand Island and Barbers Point Outfalls, Robert C.Y. Koh, Norman H. Brooks and Floyd Louis Vuillemot, 2941
- Environmental effects; Inlets (waterways); Littoral drift; New Jersey; Scouring; Sea level; Tidal effects; Tidal waters**
Beach Haven and Little Egg Inlets, A Case Study, Joseph T. DeAlteris, Thomas McKinney and James Roney, 1881
- Environmental effects; Littoral drift; Marinas; Seismic studies; Site selection; Ecology**
Application of CERC Special Report No.2, James W. Dunham, 3570
- Environmental factors; Monitoring; Nuclear power plants; Social impact; Coastal engineering**
Coastal Environment and a Nuclear Power Plant, Ralph A. de la Parra, 3014
- Equilibrium; Erosion; Reflection; Sandbars; Sand traps; Three-dimensional; Wave action; Beach erosion; Beach nourishment; Dynamics**
Three Dimensional Tests on Dynamic Equilibrium and Artificial Nourishment, J. William Kamphuis and R. M. Myers, 1532
- Equilibrium; Forecasting; France; Marinas; Ports; Beach erosion; Beach nourishment**
Impact of Yachting Marinas on Beaches, J. P. Lepetit, 1844
- Equilibrium; Gravel; Laboratory tests; Littoral current; Sediment transport; Shore protection; Wave energy; Beach erosion; Beaches**
Equilibrium Profiles and Longshore Transport of Coarse Material Under Oblique Wave Attack, E. van Hijum, 1258
- Equilibrium; Tidal effects; Wave energy; Wave spectrum; Beach erosion; Beaches; California**
Beach Profiles at Torrey Pines, California, David G. Aubrey, Douglas L. Inman and Charles E. Nordstrom, 1297
- Erosion; Erosion control; Gullies; Netherlands; Shore protection; Weed control; Weeds**
Recent Applications of Artificial Seaweed in the Netherlands, Henk G.H. ten Hoopen, 2905
- Erosion; Field tests; Groins (structures); Laboratory tests; Littoral drift; Shore protection; Storms; Water temperature; Wave height; Beach erosion**
Laboratory Investigation of Shore Erosion Processes, Ernest F. Brater and David Ponce-Campos, 1493
- Erosion; Great Lakes; Groins (structures); Shore protection; Storms; Breakwaters; Costs**
Low-Cost Shore Protection on the Great Lakes: A Demonstration/Research Program, John M. Armstrong, 2858
- Erosion; Great Lakes; Michigan; Sand; Shore protection; Water levels; Beach erosion; Beach nourishment; Bypasses**
Sand-Bypass and Shore Erosion, Bridgman, Michigan, C. N. Johnson and L. W. Hiipakka, 1361
- Erosion; Groins (structures); Revetments; Sea walls; Shore protection; Breakwaters; Coastal engineering; Costs**
Low-Cost Shoreline Protection, Billy L. Edge, John G. Housley and George M. Watts, 2888
- Erosion; Groins (structures); Rip currents; Waves; Wave tanks; Beach erosion**
Groin Length and the Generation of Edge Waves, Michael K. Gaughan and Paul D. Komar, 1459
- Erosion; Islands (landforms); Sediment deposits; Surges; Aeolian soils; Barriers; Beach erosion**
Barrier Island Dynamics: Overwash Processes and Eolian Transport, Stephen P. Leatherman, 1958
- Erosion; Jetties; Oregon; Sedimentation; Sediment deposits; Shoaling; Bays (topographic features); Beach erosion**
Changes due to Jetties at Tillamook Bay, Oregon, Paul D. Komar and Thomas A. Terich, 1791
- Erosion; Littoral current; Recreational facilities; Storms; Storm surges; Wave action; Wave energy; Beach erosion; Beach nourishment**
Cape Hatteras Beach Nourishment, John S. Fisher and Wilson N. Felder, 1512
- Erosion; Movable bed models; Prototype tests; Scale effect; Scour; Scouring; Tidal waters; Tides**
Movable Bed Tidal Inlet Models, Subhash C. Jain and John F. Kennedy, 3435
- Erosion; Reflection; Sandbars; Sand traps; Three-dimensional; Wave action; Beach erosion; Beach nourishment; Dynamics; Equilibrium**
Three Dimensional Tests on Dynamic Equilibrium and Artificial Nourishment, J. William Kamphuis and R. M. Myers, 1532

- Erosion control; Gullies; Netherlands; Shore protection; Weed control; Weeds; Erosion**
Recent Applications of Artificial Seaweed in the Netherlands, Henk G.H. ten Hoopen, 2905
- Estuaries; Estuarine environment; San Francisco; Sediments; Spoil; Tracers (radioactive); Dredging**
Tracing Estuarine Sediments by Neutron Activation, Richard M. Ecker, John F. Sustar and William T. Harvey, 2009
- Estuaries; Estuarine environment; Sediment deposits; Sediment distribution; Sediments; Tidal effects; Wave action; Beach erosion; Climatic data**
Factors Influencing Estuary Sediment Distribution, Mary P. Kendrick and B. V. Derbyshire, 2072
- Estuaries; Feasibility; Hydraulic models; Mathematical models; Rivers; Tidal effects; Time**
Analysis of Time Conditions for Hybrid Tidal Models, Klaus-Peter Holz, 3460
- Estuaries; Finite element method; Numerical analysis; Shallow water; Tidal effects; Tidal marshes; Water waves**
Finite Element Model for Estuaries with Inter-Tidal Flats, Bruno Herrling, 3396
- Estuaries; Flooding; Hydrographic surveys; Jetties; River flow; Sandbars; Training walls; Australia**
Results of River Mouth Training on the Clarence Bar, New South Wales, Australia, Cyril D. Floyd and Bruce M. Druey, 1738
- Estuaries; Flooding; Inlets (waterways); Tidal currents; Tidal effects; Tidal energy; Tidal hydraulics; Vortices**
Harbour Inlets on Tidal Estuaries, Hans Vollmers, 1854
- Estuaries; Flooding; River flow; Sandbars; Sedimentation; Sediment deposits; Wave action; Wave energy**
Morphodynamics of a Wave-Dominated River Mouth, L. D. Wright, 1721
- Estuaries; Frequency analysis; Hydraulic models; Mathematical models; Mixing; Algorithms; Diffusion**
Algorithm for Vertical Diffusion, Soren Peter Kjeldsen, 3321
- Estuaries; Friction coefficient (hydraulic); Mathematical models; Numerical analysis; Saline water intrusion; Stratification; Transport phenomena; Density currents**
Numerical Model for Density Currents in Estuaries, Karsten Fischer, 3295
- Estuaries; Harbors; Littoral drift; Sand traps; Storms; Wave action; Currents; Dredging**
Design and Behaviour of Sandtraps in Regions of High Littoral Drift, P. C. Saxena, Pazhayanur P. Vaidyaraman and R. Srinivasan, 1377
- Estuaries; Interfaces; Saline water-freshwater interfaces; Salinity; Salt water intrusion; Stratification; Diffusion; Eddies**
Determination of the Interfacial Eddy Diffusion Coefficient of a Highly Stratified Estuary, Yu-Hwa Wang, 3158
- Estuaries; Landforms; Nonuniform flow; Open channel flow; Specific energy**
Concept of Minimum Specific Energy and Its Relation to Natural Forms, Gordon R. McKay and Ahad K. Kazempour, 2186
- Estuaries; Open channel flow; Water meters; Water quality; Calibration; Discharge (water)**
Calibration of Branched Estuary Models, James P. Bennett, 3416
- Estuaries; Predictions; Sewage disposal; Sewage effluents; Tracers; Water pollution; Dispersion; Distribution; Dyes**
Prediction of Pollutant Distribution in Estuaries, Albert Y. Kuo and John P. Jacobson, 3276
- Estuaries; Reservoirs; Tidal currents; Tidal effects; Tidal hydraulics; Tidal marshes; Wave height; Waves**
Waves Used for Inter-Tidal Design and Construction, D. C. Keiller and T. D. Ruxton, 23
- Estuaries; Runoff; Sampling; Simulation; Water circulation; Water quality; Coliform bacteria; Drainage**
State Estimation of Estuarine Circulation and Water Quality by Numerical Simulation and Observation, Jan J. Leendertse and S. K. Liu, 3223
- Estuaries; Saline water-freshwater interfaces; Saline water intrusion; Salinity; Stratified flow; Tracers**
Dynamics of a Longitudinally Stratified Estuary, Jorg Imberger, 3108
- Estuaries; Saline water-freshwater interfaces; Salinity; Salt water intrusion; Tidal currents; Tidal effects; Two phase flow**
Tidal Response of Two-Layer Flow at a River Mouth, Shizuo Yoshida and Masakazu Kashiwamura, 3189
- Estuaries; Stratification; Tidal effects; Wave energy; West Germany; Damping; Energy dissipation**
Energy Dissipation in Tidal Estuaries, Hans-Werner Partenscky and Gunther Barg, 3312
- Estuarine environment; San Francisco; Sediments; Spoil; Tracers (radioactive); Dredging; Estuaries**
Tracing Estuarine Sediments by Neutron Activation, Richard M. Ecker, John F. Sustar and William T. Harvey, 2009
- Estuarine environment; Sediment deposits; Sediment distribution; Sediments; Tidal effects; Wave action; Beach erosion; Climatic data; Estuaries**
Factors Influencing Estuary Sediment Distribution, Mary P. Kendrick and B. V. Derbyshire, 2072
- Experimentation; Field tests; Scour; Scouring; Water levels; Wave action; Wave height; Breakwaters; Coastal structures**
Local Scour and Current Around a Porous Breakwater, Shintaro Hotta and Nobuo Marui, 1590
- Experimentation; Jets; Slots; Buoyancy; Diffusers; Dilution; Discharge (water); Eddies**
Negatively Buoyant Slot Jets, D. M. Shahrabani and J. D. Ditmars, 2976
- Experimentation; Random processes; Wave energy; Wave period; Wave recorders (water waves); Waves; Wave spectrum**
Estimation of Incident and Reflected Waves in Random Wave Experiments, Yoshimi Goda and Yasumasa Suzuki, 828

- Experimentation; Stresses; Testing; Armoring (streambed); Breakwaters**
Experimental Studies of Stresses Within the Breakwater Armor Piece "Dolos", Omar J. Lillevang and Wayne E. Nickola, 2519
- Experimentation; Surf; Wave height; Wave period; Waves; Wave spectrum; Breaking; Dimensional analysis**
Wave Spectrum of Breaking Wave, Toru Sawaragi and Koichiro Iwata, 580
- Explosions; Predictions; Wave generation; Wave height; Wave propagation; Waves; Cavities; Deep water**
Calculations of Waves Formed From Surface Cavities, Charles L. Mader, 1079
- Failure; Harbors; Harbor structures; Hydraulic models; Model tests; Portugal; Breakwaters**
Design of Main Breakwater at Sines Harbour, John Dorrington Mettam, 2499
- Failure; Slope protection; Slope stability; Wave action; Wave energy; Wave period; Armoring (streambed); Breakwaters**
Armour Blocks as Slope Protection, A. F. Whillock and W. A. Price, 2564
- Failures; Laboratory tests; Sandbars; Scale effect; Scour; Scouring; Underwater pipelines; Wave action**
Scour Around Model Pipelines Due to Wave Action, John B. Herbich, 1624
- Feasibility; Hydraulic models; Mathematical models; Rivers; Tidal effects; Time; Estuaries**
Analysis of Time Conditions for Hybrid Tidal Models, Klaus-Peter Holz, 3460
- Fenders; Force; Harmonic functions; Mooring; Moorings; Oscillations; Wave action; Wave energy; Wave period**
Subharmonic Components in Hawser and Fender Forces, J. H. van Oorschot, 2840
- Fetch; Great Lakes; Wave energy; Wave equations; Wave height; Wave period; Waves; Wave spectrum**
Applications of Empirical Fetch-Limited Spectral Formulas to Great Lakes Waves, Paul C. Liu, 113
- Fetch; Ocean waves; Wave energy; Wave forecasting; Waves; Wave spectrum; Wind forces; Wind speed**
Application of Fetch Area Method in Monsoon Wave Hindcasting, Nai-Kuang Liang, Shih-Tsan Tang and Ben-Juen Lee, 258
- Field investigations; Instrumentation; Ocean waves; Scale effect; Storm surges; Wave equations; Wave height; Wave period; Wave runup; Dikes; Echo sounding**
Wave Run-Up in Field Measurements with Newly Developed Instrument, Heie F. Erchinger, 767
- Field investigations; Littoral current; Sediment deposits; Sediment transport; Suspended sediments; Aerial photography; Bathymetry; Beach erosion; Beaches**
Field Investigation of Sediment Transport Pattern in a Closed System, Tsuguo Sunamura and Kiyoshi Horikawa, 1240
- Field tests; Floating bodies; Scale effect; Tethered tests; Wave action; Wave energy; Wave spectrum; Wave tanks; Breakwaters; Buoys; Energy dissipation**
Design, Analysis and Field Test of a Dynamic Floating Breakwater, D. J. Agerton, G. H. Savage and K. C. Stotz, 2792
- Field tests; Groins (structures); Laboratory tests; Littoral drift; Shore protection; Storms; Water temperature; Wave height; Beach erosion; Erosion**
Laboratory Investigation of Shore Erosion Processes, Ernest F. Brater and David Ponce-Campos, 1493
- Field tests; Intake structures; Nuclear power plants; Wave dispersion; Wave energy; Cooling water; Cylindrical bodies**
Wave Pressures on Large Circular Cylindrical Structure, Hiroshi Nakamura, 2290
- Field tests; Littoral drift; Ocean currents; Photogrammetry; Stereophotography; Water levels; Waves; Breaking; Coastal engineering**
Terrestrial Photogrammetric Measurements of Breaking Waves and Longshore Currents in the Nearshore Zone, Joseph W. Maresca, Jr. and Erwin Seibel, 681
- Field tests; Mathematical models; Numerical analysis; Water flow; Wave energy; Wind pressure; Discharge (water); Effluents**
Numerical Modelling — An Aid to Assessing Field Data, H. P. Riedel and F. L. Wilkinson, 3243
- Field tests; Ocean bottom; Ocean waves; Wave action; Wave dispersion; Wave energy; Wave velocity**
Near-Bottom Water Motion Under Ocean Waves, Robert A. Grace, 2371
- Field tests; Scour; Scouring; Water levels; Wave action; Wave height; Breakwaters; Coastal structures; Experimentation**
Local Scour and Current Around a Porous Breakwater, Shintaro Hotta and Nobuo Marui, 1590
- Finite differences; Shallow water; Simulation; Walls; Water waves; Wave action; Waves; Barriers**
Action of Non-Linear Waves at a Solid Wall, Mohamed S. Nasser and John A. McCorquodale, 815
- Finite element method; Numerical analysis; Shallow water; Tidal effects; Tidal marshes; Water waves; Estuaries**
Finite Element Model for Estuaries with Inter-Tidal Flats, Bruno Herrling, 3396
- Finite element method; Numerical analysis; Stratification; Two phase flow; Convection; Diffusion; Dispersion**
Numerical Modeling of Dispersion in Stratified Waters, George C. Christodoulou and Jerome J. Connor, 3138
- Finite elements; Gravity waves; Predictions; Refraction; Surf; Water depth; Waves; Currents**
Current Depth Defraction Using Finite Elements, Ove Skovgaard and Ivar G. Jonsson, 721
- Floating bodies; Forecasting; Harbors; Marinas; Model studies; Mooring; Moorings; Breakwaters**
Floating Breakwater Performance, Bruce H. Adee, 2777

- Floating bodies; Scale effect; Tethered tests; Wave action; Wave energy; Wave spectrum; Wave tanks; Breakwaters; Buoys; Energy dissipation; Field tests**
Design, Analysis and Field Test of a Dynamic Floating Breakwater, D. J. Agerton, G. H. Savage and K. C. Stotz, 2792
- Flooding; Hydrographic surveys; Jetties; River flow; Sandbars; Training walls; Australia; Estuaries**
Results of River Mouth Training on the Clarence Bar, New South Wales, Australia, Cyril D. Floyd and Bruce M. Druery, 1738
- Flooding; Inlets (waterways); Tidal currents; Tidal effects; Tidal energy; Tidal hydraulics; Vortices; Estuaries**
Harbour Inlets on Tidal Estuaries, Hans Vollmers, 1854
- Flooding; Predictions; Storm surges; Tsunamis; Wave runup**
Tsunami Inundation Prediction, Charles L. Bretschneider and Pieter G. Wybro, 1006
- Flooding; River flow; Sandbars; Sedimentation; Sediment deposits; Wave action; Wave energy; Estuaries**
Morphodynamics of a Wave-Dominated River Mouth, L. D. Wright, 1721
- Flood plain insurance; Hurricanes; Storms; Tidal effects; Tidal energy; Warning systems**
Hurricane Tide Frequencies on the Atlantic Coast, Francis P. Ho, 886
- Flowmeters; Friction coefficient (hydraulic); Rip currents; Surf; Turbulence; Beaches**
Lateral and Bottom Forces on Longshore Currents, David A. Huntley, 645
- Flowmeters; Ocean currents; Rip currents; Time dependence; Wave height; Wave period; Wave spectrum; Wave velocity**
Time Dependent Fluctuations in Longshore Currents, Guy A. Meadows, 660
- Flow patterns; Mathematical models; Scour; Scouring; Stratified flow; Troughs; Density currents**
Generation of Troughs by Density Currents, Hans Speckenbrink, 2170
- Flow separation; Oscillations; Pressure distribution; Vortices; Wakes; Water waves; Cylindrical bodies**
Flow Separation, Wake Vortices and Pressure Distribution Around a Circular Cylinder under Oscillatory Waves, Yuichi Iwagaki and Hajime Ishida, 2341
- Fluid mechanics; Gravitation; Ocean currents; Spreading; Time dependence; Wastewater; Buoyancy**
Buoyancy-Driven Gravitational Spreading, Robert C.Y. Koh, 2956
- Flushing; Harbors; Tidal currents; Tidal hydraulics; Tides; Washington; Water circulation; Water depth**
Planform Influence on Flushing and Circulation in Small Harbors, Ronald C. Nece, Roger A. Falconer and Toshiro Tsutsumi, 3471
- Force; Harmonic functions; Mooring; Moorings; Oscillations; Wave action; Wave energy; Wave period; Fenders**
Subharmonic Components in Hawser and Fender Forces, J. H. van Oorschot, 2840
- Force; Oscillation; Roughness (hydraulic); Vortices; Water flow; Cylindrical bodies; Drag**
Forces on Rough-Walled Circular Cylinders in Harmonic Flow, Turgut Sarpkaya, 2301
- Force; Separation; Spheres; Water circulation; Wave action; Wave energy; Drag**
Forces on a Sphere Under Linear Progressive Waves, Scott A. Jenkins and Douglas L. Inman, 2413
- Forecasting; France; Marinas; Ports; Beach erosion; Beach nourishment; Equilibrium**
Impact of Yachting Marinas on Beaches, J. P. Lepetit, 1844
- Forecasting; Harbors; Marinas; Model studies; Mooring; Moorings; Breakwaters; Floating bodies**
Floating Breakwater Performance, Bruce H. Adee, 2777
- Forecasting; Hurricanes; Numerical analysis; Storm surges; Tropical cyclones; Computer models**
SPLASH — A Model for Forecasting Tropical Storm Surges, Celso S. Barrientos and Chester P. Jelesnianski, 941
- Forecasting; Hurricanes; Storm surges; Weather forecasting; Automation**
Automated Forecasting of Extratropical Storm Surges, N. Arthur Pore, 906
- Forecasting; Hurricanes; Wave action; Wave forecasting; Wind forces; Wind speed**
Hurricane Wind and Wave Forecasting Techniques, Charles L. Bretschneider and Elaine E. Tamaye, 202
- Foundations; Ocean bottom; Offshore structures; Predictions; Stability; Wave action; Wave energy; Bottom water; Continental shelf; Cyclic loads**
Prediction of Wave-Induced Seafloor Movements, Leland Milo Kraft, Jr. and David James Watkins, 1605
- France; Marinas; Ports; Beach erosion; Beach nourishment; Equilibrium; Forecasting**
Impact of Yachting Marinas on Beaches, J. P. Lepetit, 1844
- Frequency; Ocean waves; Surface waves; Wave energy; Wave spectrum; Distribution functions; Distribution patterns**
Directional Spectral of Ocean Surface Waves, Hisashi Mitsuyasu and S. Mizuno, 329
- Frequency analysis; Hydraulic models; Mathematical models; Mixing; Algorithms; Diffusion; Estuaries**
Algorithm for Vertical Diffusion, Soren Peter Kjeldsen, 3321
- Friction coefficient (hydraulic); Inlets (waterways); Tidal effects; Bed load; Current meters**
Measurement of Bed Friction in Tidal Inlets, Ashish J. Mehta, R. J. Byrne and Joseph T. DeAlteris, 1701
- Friction coefficient (hydraulic); Interfaces; Two phase flow; Wave equations; Wave height; Wave velocity**
Friction at the Interface of Two-Layered Flows, Nobuyuki Tamai, 3169
- Friction coefficient (hydraulic); Littoral drift; Ocean currents; Three-dimensional; Wave dispersion; Wave height; Waves; Breaking; Breakwaters**
Non-Uniform Alongshore Currents, Michael R. Gourlay, 701

- Friction coefficient (hydraulic); Mathematical models; Numerical analysis; Saline water intrusion; Stratification; Transport phenomena; Density currents; Estuaries**
Numerical Model for Density Currents in Estuaries, Karsten Fischer, 3295
- Friction coefficient (hydraulic); Numerical analysis; Propagation; Shallow water; Tsunamis; Wave height**
Tsunami Propagation in the Pacific Ocean, Manfred Engel and Wilfried Zahel, 971
- Friction coefficient (hydraulic); Ocean bottom; Ripple marks; Shallow water; Turbulent diffusion**
Consideration on Friction Coefficient for Sea Bottom, Toru Sawaragi, Koichiro Iwata and Masayoshi Kubo, 595
- Friction coefficient (hydraulic); Rip currents; Surf; Turbulence; Beaches; Flowmeters**
Lateral and Bottom Forces on Longshore Currents, David A. Huntley, 645
- Friction coefficient (hydraulic); Wave dispersion; Wave height; Wavelengths; Wave propagation; Waves**
Transformation of Nonlinear Long Waves, Nobuo Shuto, 423
- Geomorphology; Glacial erosion; Glaciers; Glaciology; Alaska; Beach erosion**
Geomorphology of the Southern Coast of Alaska, Miles O. Hayes, Christopher H. Ruby, Michael F. Stephen and Stephen J. Wilson, 1992
- Glacial erosion; Glaciers; Glaciology; Alaska; Beach erosion; Geomorphology**
Geomorphology of the Southern Coast of Alaska, Miles O. Hayes, Christopher H. Ruby, Michael F. Stephen and Stephen J. Wilson, 1992
- Glaciers; Glaciology; Alaska; Beach erosion; Geomorphology; Glacial erosion**
Geomorphology of the Southern Coast of Alaska, Miles O. Hayes, Christopher H. Ruby, Michael F. Stephen and Stephen J. Wilson, 1992
- Glaciology; Alaska; Beach erosion; Geomorphology; Glacial erosion; Glaciers**
Geomorphology of the Southern Coast of Alaska, Miles O. Hayes, Christopher H. Ruby, Michael F. Stephen and Stephen J. Wilson, 1992
- Gravel; Laboratory tests; Littoral current; Sediment transport; Shore protection; Wave energy; Beach erosion; Beaches; Equilibrium**
Equilibrium Profiles and Longshore Transport of Coarse Material Under Oblique Wave Attack, E. van Hījum, 1258
- Gravitation; Ocean currents; Spreading; Time dependence; Wastewater; Buoyancy; Fluid mechanics**
Buoyancy-Driven Gravitational Spreading, Robert C.Y. Koh, 2956
- Gravity waves; Predictions; Refraction; Surf; Wave depth; Waves; Currents; Finite elements**
Current Depth Defraction Using Finite Elements, Ove Skovgaard and Ivar G. Jonsson, 721
- Gravity waves; Solitary waves; Time dependence; Wave height; Waves; Wave velocity; Breaking**
Recent Developments in the Study of Breaking Waves, Michael S. Longuet-Higgins, 441
- Great Lakes; Groins (structures); Shore protection; Storms; Breakwaters; Costs; Erosion**
Low-Cost Shore Protection on the Great Lakes: A Demonstration/Research Program, John M. Armstrong, 2858
- Great Lakes; Harbors; Seiches; Tidal effects; Water levels; Wave generation; Currents**
Hydraulics of Great Lakes Inlet — Harbors Systems, Robert M. Sorensen and William N. Seelig, 1646
- Great Lakes; Michigan; Sand; Shore protection; Water levels; Beach erosion; Beach nourishment; Bypasses; Erosion**
Sand-Bypass and Shore Erosion, Bridgman, Michigan, C. N. Johnson and L. W. Hiipakka, 1361
- Great Lakes; Wave action; Wave height; Wave period; Waves; Wave spectrum; Wind speed**
Great Lakes Wave Information, D. T. Resio and L. W. Hiipakka, 92
- Great Lakes; Wave energy; Wave equations; Wave height; Wave period; Waves; Wave spectrum; Fetch**
Applications of Empirical Fetch-Limited Spectral Formulas to Great Lakes Waves, Paul C. Liu, 113
- Groins (structures); Hydrographic surveys; Monitoring; Shore protection; Beaches; Beach nourishment**
Comprehensive Monitoring of a Beach Restoration Project, Omar H. Shemdin, H. K. Brooks, Z. Ceylanli and S. L. Harrell, 1477
- Groins (structures); Inlets (waterways); Islands (landforms); Sandbars; Shore protection; Tidal currents**
Inlet Changes of the East Frisian Islands, Gunter Luck, 1938
- Groins (structures); Israel; Recreational facilities; Social needs; Beaches; Breakwaters; Enclosures**
Enclosing Scheme for Bathing-Beach Development, Joseph Tauman, 1425
- Groins (structures); Laboratory tests; Littoral drift; Shore protection; Storms; Water temperature; Wave height; Beach erosion; Erosion; Field tests**
Laboratory Investigation of Shore Erosion Processes, Ernest F. Brater and David Ponce-Campos, 1493
- Groins (structures); Littoral drift; Sandbars; Sediment transport; Verification inspection; Wave height; Wave spectrum; Bathymetry**
Experimental Verification of Groyne Theory, C. H. Hulsbergen, W. T. Bakker and G. van Bochove, 1439
- Groins (structures); Revetments; Sea walls; Shore protection; Breakwaters; Coastal engineering; Costs; Erosion**
Low-Cost Shoreline Protection, Billy L. Edge, John G. Housley and George M. Watts, 2888
- Groins (structures); Rip currents; Waves; Wave tanks; Beach erosion; Erosion**
Groin Length and the Generation of Edge Waves, Michael K. Gaughan and Paul D. Komar, 1459
- Groins (structures); Shore protection; Storms; Breakwaters; Costs; Erosion; Great Lakes**
Low-Cost Shore Protection on the Great Lakes: A Demonstration/Research Program, John M. Armstrong, 2858

- Gullies; Netherlands; Shore protection; Weed control; Weeds; Erosion; Erosion control**
Recent Applications of Artificial Seaweed in the Netherlands, Henk G.H. ten Hoopen, 2905
- Harbors; Harbor structures; History; Jetties; Rubble mounds; Wave action; Wave energy**
Design and Construction of Humboldt Jetties, 1880 to 1975, Orville T. Magoon, Robert L. Sloan and Nobuyuki Shimizu, 2474
- Harbors; Harbor structures; Hydraulic models; Model tests; Portugal; Breakwaters; Failure**
Design of Main Breakwater at Sines Harbour, John Dorrington Mettam, 2499
- Harbors; Littoral drift; Sand traps; Storms; Wave action; Currents; Dredging; Estuaries**
Design and Behaviour of Sandtraps in Regions of High Littoral Drift, P. C. Saxena, Pazhayanur P. Vaidyaraman and R. Srinivasan, 1377
- Harbors; Marinas; Model studies; Mooring; Moorings; Breakwaters; Floating bodies; Forecasting**
Floating Breakwater Performance, Bruce H. Adee, 2777
- Harbors; Performance; Safety; Site selection; Utilization; Barges; Economic analysis; Environmental effects**
Probable Utilization Level for a Barge Harbor, Martin T. Czerniak and Choule J. Sonu, 3557
- Harbors; Seiches; Tidal effects; Water levels; Wave generation; Currents; Great Lakes**
Hydraulics of Great Lakes Inlet — Harbors Systems, Robert M. Sorensen and William N. Seelig, 1646
- Harbors; Tidal currents; Tidal hydraulics; Tides; Washington; Water circulation; Water depth; Flushing**
Planform Influence on Flushing and Circulation in Small Harbors, Ronald C. Nece, Roger A. Falconer and Toshiro Tsutsumi, 3471
- Harbor structures; History; Jetties; Rubble mounds; Wave action; Wave energy; Harbors**
Design and Construction of Humboldt Jetties, 1880 to 1975, Orville T. Magoon, Robert L. Sloan and Nobuyuki Shimizu, 2474
- Harbor structures; Hydraulic models; Model tests; Portugal; Breakwaters; Failure; Harbors**
Design of Main Breakwater at Sines Harbour, John Dorrington Mettam, 2499
- Harbor structures; Japan; Ocean bottom; Shoaling; Topographical factors; Beach erosion; Beaches; Breakwaters; Construction**
Topographic Change Resulting from the Construction of a Harbor on a Sandy Beach, Kashima Port, Norio Tanaka and Shoji Sato, 1824
- Harbor structures; Mooring; Moorings; Offshore drilling; Ships; Wave tanks; Accidents; Collisions**
Protection of Maritime Structures Against Ship Collisions, Kazuki Oda and Shositiro Nagai, 2810
- Harbor structures; Quays; Reflection; Revetments; Shore protection; Wave dispersion; Computerized simulation; Concrete (blocks)**
Quay Wall with Wave Absorber "Igloo", Naofumi Shiraishi, Robert Q. Palmer and Hiroshi Okamoto, 2677
- Harmonic functions; Mooring; Moorings; Oscillations; Wave action; Wave energy; Wave period; Fenders; Force**
Subharmonic Components in Hawser and Fender Forces, J. H. van Oorschot, 2840
- Hawaii; Islands (landforms); Monitoring; Reefs; Runways; Water quality; Environmental effects**
Environmental Impacts on an Island Community, Gordon A. Chapman, 3506
- Hawaii; Recreational facilities; Shore protection; Swimming; Beaches; Beach nourishment; Breakwaters**
Proposed "Improvement" of Kaimu Beach, Hawaii, Doak C. Cox, Franciscus Gerritsen and Theodore T. Lee, 1552
- Hawaii; Reefs; Slope protection; Slope stability; Airports; Breakwaters**
Design and Construction of Protective Structure for New Reef Runway at Honolulu International Airport, Wilfred D. Darling, 2589
- Hazards; Tsunamis; Wave action; Wave energy; Wave generation; Wave height; Coastal structures**
Tsunami Hazard and Design of Coastal Structures, George Pararas-Carayannis, 2248
- Head losses; Mass; Shallow water; Tanker ships; Water depth; Berths; Dolphins (structures)**
Added Masses of Large Tankers Berthing to Dolphins, Taizo Hayashi and Masujiro Shirai, 2830
- Heat flux; Heat transfer; Infrared scanners; Infrared scanning; Remote sensing; Water temperature; Air-water interfaces**
Evaluation of Air-Sea Interface Heat Flux, Robert L. Street and A. Woodruff Miller, Jr., 3208
- Heat transfer; Infrared scanners; Infrared scanning; Remote sensing; Water temperature; Air-water interfaces; Heat flux**
Evaluation of Air-Sea Interface Heat Flux, Robert L. Street and A. Woodruff Miller, Jr., 3208
- History; Jetties; Rubble mounds; Wave action; Wave energy; Harbors; Harbor structures**
Design and Construction of Humboldt Jetties, 1880 to 1975, Orville T. Magoon, Robert L. Sloan and Nobuyuki Shimizu, 2474
- Hurricanes; Numerical analysis; Storm surges; Tropical cyclones; Computer models; Forecasting**
SPLASH — A Model for Forecasting Tropical Storm Surges, Celso S. Barrientos and Chester P. Jelesnianski, 941
- Hurricanes; Storms; Tidal effects; Tidal energy; Warning systems; Flood plain insurance**
Hurricane Tide Frequencies on the Atlantic Coast, Francis P. Ho, 886
- Hurricanes; Storm surges; Weather forecasting; Automation; Forecasting**
Automated Forecasting of Extratropical Storm Surges, N. Arthur Pore, 906
- Hurricanes; Wave action; Wave forecasting; Wind forces; Wind speed; Forecasting**
Hurricane Wind and Wave Forecasting Techniques, Charles L. Bretschneider and Elaine E. Tamaye, 202

- Hydraulic models; Lift; Oscillations; Reynolds number; Stream flow; Water flow; Wave action; Wave energy; Cylinders; Drag**
High Reynolds Number Oscillating Flow by Cylinders, Tokuo Yamamoto and John H. Nath, 2321
- Hydraulic models; Mathematical models; Mixing; Algorithms; Diffusion; Estuaries; Frequency analysis**
Algorithm for Vertical Diffusion, Soren Peter Kjeldsen, 3321
- Hydraulic models; Mathematical models; Rivers; Tidal effects; Time; Estuaries; Feasibility**
Analysis of Time Conditions for Hybrid Tidal Models, Klaus-Peter Holz, 3460
- Hydraulic models; Model tests; Portugal; Breakwaters; Failure; Harbors; Harbor structures**
Design of Main Breakwater at Sines Harbour, John Dorrington Mettam, 2499
- Hydraulic models; Movable bed models; Scale effect; Sediment transport; Tracers (radioactive); West Germany**
Sand Movement Investigations by Means of Radioactive Tracers in a Hydraulic Model and in the Field, Hans Rohde, 2027
- Hydraulic models; Nigeria; Sedimentation; Sediment concentration; Sediment distribution; Sediment transport; Breakwaters; Deltas**
Sedimentation Studies on the Niger River Delta, Ramiro Mayor-Mora, Preben Mortensen and Jorgen Fredsoe, 2151
- Hydraulic models; Nuclear power plants; Plume detection; Plumes; Thermal pollution; Two phase flow; Diffusers; Discharge (water)**
Field Studies of Submerged-Diffuser Thermal Plumes with Comparisons to Predictive Model Results, A. A. Frigo, Richard A. Paddock and J. D. Ditmars, 3028
- Hydraulic models; Nuclear power plants; Prototype tests; Temperature distribution; Thermal diffusion; Thermal pollution; Water temperature; Discharge (water)**
Thermal Discharges: Prototype vs. Hydraulic Model, Gary C. Parker, Ching S. Fang and Albert Y. Kuo, 3049
- Hydraulic models; Predictions; Prototype tests; Scale effect; Surface tension; Thermal diffusion; Viscosity; Water temperature**
Adaptability of Prediction Method of Hydraulic Model Experiment for Thermal Diffusion, Masanobu Kato and Akira Wada, 3082
- Hydraulic models; Prototype tests; Roughness (hydraulic); Tidal currents; Tidal effects; Tidal energy**
Model Verification for Tidal Constituents, R. W. Whalin, F. C. Perry and D. L. Durham, 3377
- Hydraulic models; Rubble; Rubble mounds; Stability; Wave action; Wave energy; Breakwaters; Damage**
Effect of Broken Dolosse on Breakwater Stability, D. Donald Davidson and Dennis G. Markle, 2544
- Hydraulic models; Saline water-freshwater interfaces; Salinity; Salt water intrusion; Tidal effects; Canada; Density currents**
Churchill River Salt-Water Tidal Model, Bruce D. Pratte, 3445
- Hydraulic models; Scale effect; Statistical analysis; Tidal effects; Turbulence; Diffusion; Eddies**
Horizontal Diffusion in Tidal Models and Scaling Criteria for Thermal-Hydraulic Model Tests, Gerd Flugge, 3097
- Hydraulic models; Three-dimensional; Water waves; Wave generation; Waves**
3-D Hydraulic Model of Wave Generated by Displacements, Shin-Lin Liu and Robert L. Wiegel, 1060
- Hydrodynamics; Ocean engineering; Outfall sewers; Underwater pipelines; Diffusers; Environmental effects**
Design Considerations for the Sand Island and Barbers Point Outfalls, Robert C.Y. Koh, Norman H. Brooks and Floyd Louis Vuillemot, 2941
- Hydrographic surveys; Jetties; River flow; Sandbars; Training walls; Australia; Estuaries; Flooding**
Results of River Mouth Training on the Clarence Bar, New South Wales, Australia, Cyril D. Floyd and Bruce M. Druery, 1738
- Hydrographic surveys; Monitoring; Shore protection; Beaches; Beach nourishment; Groins (structures)**
Comprehensive Monitoring of a Beach Restoration Project, Omar H. Shemdin, H. K. Brooks, Z. Ceylanli and S. L. Harrell, 1477
- Hydrographic surveys; Waves; Wind (meteorology); Coastal engineering; Coastal structures; Data collection; Data collection systems**
Data Collection and Analysis for Coastal Projects, E. Loewy, K. G. Witthaus, L. Summers and R. J. Maddrell, 43
- Hydromechanics; Numerical analysis; Simulation; Storm surges**
Generalized Model for Storm Surges, Gour-Tsyh Yeh and Fei-Fan Yeh, 921
- Impact; Revetments; Wave action; Wave energy; Air entrainment; Damage; Dikes**
Response of Seadykes due to Wave Impacts, Alfred Fuhrboter, Hans H. Dette and J. Grune, 2604
- Impulses; Responses; Stability; Statistical analysis; Storms; Variability; Beach erosion; Eigenvalues**
Stability and Impulse Response of Empirical Eigenfunctions, Clinton D. Winant and David G. Aubrey, 1312
- India; Statistical analysis; Wave height; Wavemeters; Wave recorders (water waves); Wave spectrum; Coastal engineering**
Ocean Wave Record Analysis by Tucker's Method — An Evaluation, Jade Dattatri and Irvathur Vasudeva Nayak, 289
- Inertial forces; Submerged flow; Underwater structures; Wave action; Wave energy; Drag**
Wave Forces on Submerged Objects, Suphat Vongvisessomjai and Richard Silvester, 2387
- Infrared scanners; Infrared scanning; Remote sensing; Water temperature; Air-water interfaces; Heat flux; Heat transfer**
Evaluation of Air-Sea Interface Heat Flux, Robert L. Street and A. Woodruff Miller, Jr., 3208

- Infrared scanning; Remote sensing; Water temperature; Air-water interfaces; Heat flux; Heat transfer; Infrared scanners**
 Evaluation of Air-Sea Interface Heat Flux, Robert L. Street and A. Woodruff Miller, Jr., 3208
- Inlets (waterways); Islands (landforms); Sandbars; Shore protection; Tidal currents; Groins (structures)**
 Inlet Changes of the East Frisian Islands, Gunter Luck, 1938
- Inlets (waterways); Japan; Tidal effects; Tidal energy; Tidal hydraulics; Tidal waters; Wave energy**
 Characteristics of Tidal Inlets on the Pacific Coast of Japan, Toshiyuki Shigemura, 1666
- Inlets (waterways); Littoral current; Littoral drift; Sand; Scouring; Sediment transport; South Carolina; Tidal currents; Bed forms; Circulation**
 Sand Circulation Pattern at Price Inlet, South Carolina, Duncan M. FitzGerald, Dag Nummedal and Timothy W. Kana, 1868
- Inlets (waterways); Littoral current; Littoral drift; Surf; Tidal currents; Wave recorders (water waves); Beaches**
 Changes in Inlet Offset due to Stabilization, Dennis K. Hubbard, 1812
- Inlets (waterways); Littoral drift; New Jersey; Scouring; Sea level; Tidal effects; Tidal waters; Environmental effects**
 Beach Haven and Little Egg Inlets, A Case Study, Joseph T. DeAlteris, Thomas McKinney and James Roney, 1881
- Inlets (waterways); Ocean bottom; Scale effect; Sediment transport; Simulation models; Tidal effects; Wave energy; Bed forms**
 Tidal Inlet Flow Dynamics and Sediment Movement, Jerry L. Machemehl, N. E. Bird and A. N. Chambers, 1681
- Inlets (waterways); Sandbars; Sand traps; Shoaling; Tidal effects; Beaches**
 Capacity of Inlet Outer Bars to Store Sand, Todd L. Walton, Jr. and William D. Adams, 1919
- Inlets (waterways); Tidal currents; Tidal effects; Tidal energy; Tidal hydraulics; Vortices; Estuaries; Flooding**
 Harbour Inlets on Tidal Estuaries, Hans Vollmers, 1854
- Inlets (waterways); Tidal effects; Bed load; Current meters; Friction coefficient (hydraulic)**
 Measurement of Bed Friction in Tidal Inlets, Ashish J. Mehta, R. J. Byrne and Joseph T. DeAlteris, 1701
- Instrumentation; Ocean waves; Scale effect; Storm surges; Wave equations; Wave height; Wave period; Wave runup; Dikes; Echo sounding; Field investigations**
 Wave Run-Up in Field Measurements with Newly Developed Instrument, Heie F. Erchinger, 767
- Intake structures; Nuclear power plants; Wave dispersion; Wave energy; Cooling water; Cylindrical bodies; Field tests**
 Wave Pressures on Large Circular Cylindrical Structure, Hiroshi Nakamura, 2290
- Intake systems; Mathematical models; Nuclear power plants; Numerical analysis; Refraction; Sediment transport; Wave dispersion; Waves; Coastal structures; Cooling water**
 Application of a Sediment Transport Model, C. A. Fleming and J. N. Hunt, 1184
- Interactions; Turbulence; Wave action; Wave damping; Wave dispersion; Wave energy; Wave velocity; Currents (water)**
 Interaction of Waves and a Turbulent Current, J. D.A. van Hoften and Susumu Karaki, 404
- Interfaces; Saline water-freshwater interfaces; Salinity; Salt water intrusion; Stratification; Diffusion; Eddies; Estuaries**
 Determination of the Interfacial Eddy Diffusion Coefficient of a Highly Stratified Estuary, Yu-Hwa Wang, 3158
- Interfaces; Two phase flow; Wave equations; Wave height; Wave velocity; Friction coefficient (hydraulic)**
 Friction at the Interface of Two-Layered Flows, Nobuyuki Tamai, 3169
- Interfacial tension; Stability; Stratified flow; Thermal pollution; Turbulence; Discharge (water)**
 Interfacial Instability in Stratified Flow, Richard H. French, 3124
- Investigations; Japan; Littoral current; Littoral drift; Slopes; Beach erosion**
 Concept for Inferring the Littoral Drift Trend, Masataro Hattori and Takasuke Suzuki, 1223
- Islands (landforms); Monitoring; Reefs; Runways; Water quality; Environmental effects; Hawaii**
 Environmental Impacts on an Island Community, Gordon A. Chapman, 3506
- Islands (landforms); Ocean bottom; Oceanography; Refraction; Resonance**
 Resonant Refraction by Round Islands, Richard E. Meyer, 866
- Islands (landforms); Sandbars; Shore protection; Tidal currents; Groins (structures); Inlets (waterways)**
 Inlet Changes of the East Frisian Islands, Gunter Luck, 1938
- Islands (landforms); Scale effect; Shore protection; Tidal currents; Dispersion; Effluent reuse; Effluents**
 Study of an Artificial Island, J. P. Lepetit and S. Moreau, 3526
- Islands (landforms); Sediment deposits; Surges; Aeolian soils; Barriers; Beach erosion; Erosion**
 Barrier Island Dynamics: Overwash Processes and Eolian Transport, Stephen P. Leatherman, 1958
- Israel; Littoral drift; Sedimentation; Sediment deposits; Sediment transport; Shore protection; Breakwaters; Coastal structures**
 Protection by Means of Offshore Breakwaters, I. Fried, 1407
- Israel; Recreational facilities; Social needs; Beaches; Breakwaters; Enclosures; Groins (structures)**
 Enclosing Scheme for Bathing-Beach Development, Joseph Tauman, 1425
- Japan; Littoral current; Littoral drift; Slopes; Beach erosion; Investigations**
 Concept for Inferring the Littoral Drift Trend, Masataro Hattori and Takasuke Suzuki, 1223

- Japan; Littoral drift; Ocean currents; Rip currents; Wave recorders (water waves); Beaches**
Nearshore Current on a Gently Sloping Beach, Tamio Sasaki, Kiyoshi Horikawa and Shintaro Hotta, 626
- Japan; Models; Numerical analysis; Statistical models; Tsunamis; Wave dispersion; Wave height**
Numerical Models of Huge Tsunamis Off the Sanriku Coast, Toshio Iwasaki, 1044
- Japan; Ocean bottom; Shoaling; Topographical factors; Beach erosion; Beaches; Breakwaters; Construction; Harbor structures**
Topographic Change Resulting from the Construction of a Harbor on a Sandy Beach, Kashima Port, Norio Tanaka and Shoji Sato, 1824
- Japan; Ocean bottom; Shore protection; Subsidence; Beach erosion; Breakwaters**
Changes of Sea Bed Due to Detached Breakwaters, Osamu Toyoshima, 1572
- Japan; Power spectra; Refraction; Shoaling; Tsunamis; Warning systems; Coastal engineering; Coastal plains**
Transformation of Tsunamis in a Coastal Zone, Shigehisa Nakamura, Haruo Higuchi and Yoshito Tsuchiya, 988
- Japan; Tidal effects; Tidal energy; Tidal hydraulics; Tidal waters; Wave energy; Inlets (waterways)**
Characteristics of Tidal Inlets on the Pacific Coast of Japan, Toshiyuki Shigemura, 1666
- Jet pumps; Littoral current; Sand; Shore protection; Surf; Bypasses**
A Sand Bypassing System Using a Jet Pump, E. C. McNair, Jr., 1342
- Jets; Slots; Buoyancy; Diffusers; Dilution; Discharge (water); Eddies; Experimentation**
Negatively Buoyant Slot Jets, D. M. Shahrabani and J. D. Ditmars, 2976
- Jetties; Littoral current; Littoral drift; Sediment transport; Surf; Wave energy; Barriers; Breakwaters; California**
Longshore Transport at a Total Littoral Barrier, Richard O. Bruno and Christopher G. Gable, 1203
- Jetties; Oregon; Sedimentation; Sediment deposits; Shoaling; Bays (topographic features); Beach erosion; Erosion**
Changes due to Jetties at Tillamook Bay, Oregon, Paul D. Komar and Thomas A. Terich, 1791
- Jetties; River flow; Sandbars; Training walls; Australia; Estuaries; Flooding; Hydrographic surveys**
Results of River Mouth Training on the Clarence Bar, New South Wales, Australia, Cyril D. Floyd and Bruce M. Druey, 1738
- Jetties; Rubble mounds; Wave action; Wave energy; Harbors; Harbor structures; History**
Design and Construction of Humboldt Jetties, 1880 to 1975, Orville T. Magoon, Robert L. Sloan and Nobuyuki Shimizu, 2474
- Laboratory tests; Littoral current; Sediment transport; Shore protection; Wave energy; Beach erosion; Beaches; Equilibrium; Gravel**
Equilibrium Profiles and Longshore Transport of Coarse Material Under Oblique Wave Attack, E. van Hijum, 1258
- Laboratory tests; Littoral drift; Shore protection; Storms; Water temperature; Wave height; Beach erosion; Erosion; Field tests; Groins (structures)**
Laboratory Investigation of Shore Erosion Processes, Ernest F. Brater and David Ponce-Campos, 1493
- Laboratory tests; Ocean waves; Random variables; Simulation; Waves; Wave tanks**
Random Wave Simulation in a Laboratory Wave Tank, Akira Kimura and Yuichi Iwagaki, 368
- Laboratory tests; Permeability; Reflection; Wave height; Breakwaters**
Laboratory Study of Pervious Core Breakwaters, Hideo Kondo, Satoshi Toma and Kenji Yano, 2643
- Laboratory tests; Rubble mounds; Wave action; Wave dispersion; Wave energy; Waves; Breakwaters**
Wave Transmission Through Trapezoidal Breakwaters, Ole Secher Madsen and Stanley M. White, 2662
- Laboratory tests; Sandbars; Scale effect; Scour; Scouring; Underwater pipelines; Wave action; Failures**
Scour Around Model Pipelines Due to Wave Action, John B. Herbich, 1624
- Laboratory tests; Sediment concentration; Sediments; Sediment samplers; Water flow**
Iowa Sediment Concentration Measuring System, Tatsuaki Nakato, Frederick A. Locher, John R. Glover and John F. Kennedy, 2060
- Landforms; Nonuniform flow; Open channel flow; Specific energy; Estuaries**
Concept of Minimum Specific Energy and Its Relation to Natural Forms, Gordon R. McKay and Ahad K. Kazempour, 2186
- Lateral forces; Pile foundations; Steel piles; Structural design; Coastal structures**
Concepts in Design of Coastal Structures, Casimir J. Kray, 2209
- Lift; Oscillations; Reynolds number; Stream flow; Water flow; Wave action; Wave energy; Cylinders; Drag; Hydraulic models**
High Reynolds Number Oscillating Flow by Cylinders, Tokuo Yamamoto and John H. Nath, 2321
- Littoral current; Littoral drift; Morphology; Sandbars; Sediment deposits; Wave energy; Barriers; Beaches; Canada**
Process and Morphology Characteristics of Two Barrier Beaches in the Magdalen Islands, Gulf of St. Lawrence, Canada, E. H. Owens, 1975
- Littoral current; Littoral drift; Rip currents; Sediment transport; Shore protection; Energy equation**
Longshore Transport Prediction — SPM 1973 Equation, Cyril J. Galvin and Philip Vitale, 1133
- Littoral current; Littoral drift; Sand; Scouring; Sediment transport; South Carolina; Tidal currents; Bed forms; Circulation; Inlets (waterways)**
Sand Circulation Pattern at Price Inlet, South Carolina, Duncan M. FitzGerald, Dag Nummedal and Timothy W. Kana, 1868

- Littoral current; Littoral drift; Sediment transport; Surf; Wave energy; Barriers; Breakwaters; California; Jetties**
 Longshore Transport at a Total Littoral Barrier, Richard O. Bruno and Christopher G. Gable, 1203
- Littoral current; Littoral drift; Slopes; Beach erosion; Investigations; Japan**
 Concept for Inferring the Littoral Drift Trend, Masataro Hattori and Takasuke Suzuki, 1223
- Littoral current; Littoral drift; Surf; Tidal currents; Wave recorders (water waves); Beaches; Inlets (waterways)**
 Changes in Inlet Offset due to Stabilization, Dennis K. Hubbard, 1812
- Littoral current; Predictions; Sediment deposits; Sediment transport; Beach nourishment; Beach sands**
 Predictive Equations Regarding Coastal Transport, D. H. Swart, 1113
- Littoral current; Recreational facilities; Storms; Storm surges; Wave action; Wave energy; Beach erosion; Beach nourishment; Erosion**
 Cape Hatteras Beach Nourishment, John S. Fisher and Wilson N. Felder, 1512
- Littoral current; Sand; Shore protection; Surf; Bypasses; Jet pumps**
 A Sand Bypassing System Using a Jet Pump, E. C. McNair, Jr., 1342
- Littoral current; Sediment deposits; Sediment transport; Suspended sediments; Aerial photography; Bathymetry; Beach erosion; Beaches; Field investigations**
 Field Investigation of Sediment Transport Pattern in a Closed System, Tsuguo Sunamura and Kiyoshi Horikawa, 1240
- Littoral current; Sediment transport; Shore protection; Wave energy; Beach erosion; Beaches; Equilibrium; Gravel; Laboratory tests**
 Equilibrium Profiles and Longshore Transport of Coarse Material Under Oblique Wave Attack, E. van Hijum, 1258
- Littoral drift; Marinas; Seismic studies; Site selection; Ecology; Environmental effects**
 Application of CERC Special Report No.2, James W. Dunham, 3570
- Littoral drift; Morphology; Sandbars; Sediment deposits; Wave energy; Barriers; Beaches; Canada; Littoral current**
 Process and Morphology Characteristics of Two Barrier Beaches in the Magdalen Islands, Gulf of St. Lawrence, Canada, E. H. Owens, 1975
- Littoral drift; New Jersey; Scouring; Sea level; Tidal effects; Tidal waters; Environmental effects; Inlets (waterways)**
 Beach Haven and Little Egg Inlets, A Case Study, Joseph T. DeAlteris, Thomas McKinney and James Roncy, 1881
- Littoral drift; Ocean currents; Photogrammetry; Stereophotography; Water levels; Waves; Breaking; Coastal engineering; Field tests**
 Terrestrial Photogrammetric Measurements of Breaking Waves and Longshore Currents in the Nearshore Zone, Joseph W. Maresca, Jr. and Erwin Seibel, 681
- Littoral drift; Ocean currents; Rip currents; Sediment transport; Wave height; Wave phases**
 Physical Aspects of Wave-Induced Nearshore Current System, Masaru Mizuguchi and Kiyoshi Horikawa, 607
- Littoral drift; Ocean currents; Rip currents; Wave recorders (water waves); Beaches; Japan**
 Nearshore Current on a Gently Sloping Beach, Tamio Sasaki, Kiyoshi Horikawa and Shintaro Hotta, 626
- Littoral drift; Ocean currents; Sediment transport; Storm surges; Tidal marshes; Coastal engineering; Currents**
 Currents in Tidal Flats During Storm Surges, Harald Gohren, 959
- Littoral drift; Ocean currents; Three-dimensional; Wave dispersion; Wave height; Waves; Breaking; Breakwaters; Friction coefficient (hydraulic)**
 Non-Uniform Alongshore Currents, Michael R. Gourlay, 701
- Littoral drift; Rip currents; Sediment transport; Shore protection; Energy equation; Littoral current**
 Longshore Transport Prediction — SPM 1973 Equation, Cyril J. Galvin and Philip Vitale, 1133
- Littoral drift; Sand; Scouring; Sediment transport; South Carolina; Tidal currents; Bed forms; Circulation; Inlets (waterways); Littoral current**
 Sand Circulation Pattern at Price Inlet, South Carolina, Duncan M. FitzGerald, Dag Nummedal and Timothy W. Kana, 1868
- Littoral drift; Sandbars; Sands; Secondary waves; Sediment transport; Wave propagation; Waves**
 Sand Transport by Waves, E. W. Bijker, E. van Hijum and P. Vellinga, 1149
- Littoral drift; Sandbars; Sediment transport; Verification inspection; Wave height; Wave spectrum; Bathymetry; Groins (structures)**
 Experimental Verification of Groynes Theory, C. H. Hulsbergen, W. T. Bakker and G. van Bochove, 1439
- Littoral drift; Sand traps; Storms; Wave action; Currents; Dredging; Estuaries; Harbors**
 Design and Behaviour of Sandtraps in Regions of High Littoral Drift, P. C. Saxena, Pazhhayannur P. Vaidyaraman and R. Srinivasan, 1377
- Littoral drift; Sedimentation; Sediment deposits; Sediment transport; Shore protection; Breakwaters; Coastal structures; Israel**
 Protection by Means of Offshore Breakwaters, I Fried, 1407
- Littoral drift; Sediment transport; Surf; Wave energy; Barriers; Breakwaters; California; Jetties; Littoral current**
 Longshore Transport at a Total Littoral Barrier, Richard O. Bruno and Christopher G. Gable, 1203
- Littoral drift; Shore protection; Storms; Water temperature; Wave height; Beach erosion; Erosion; Field tests; Groins (structures); Laboratory tests**
 Laboratory Investigation of Shore Erosion Processes, Ernest F. Brater and David Ponce-Campos, 1493

- Littoral drift; Slopes; Beach erosion; Investigations; Japan; Littoral current**
Concept for Inferring the Littoral Drift Trend, Masataro Hattori and Takasuke Suzuki, 1223
- Littoral drift; Surf; Tidal currents; Wave recorders (water waves); Beaches; Inlets (waterways); Littoral current**
Changes in Inlet Offset due to Stabilization, Dennis K. Hubbard, 1812
- Mach number; Reflection; Walls; Water waves; Wave height; Diffraction**
Mach-Reflection as a Diffraction Problem, Udo Berger and Soren Kohlhase, 796
- Manifold air injection systems; Model tests; Orifices; Pipes; Porous materials; Air bubbles; Air flow rates**
Guidelines for the Design of Air Bubble Systems, Nabil Ismail, 2994
- Marinas; Model studies; Mooring; Moorings; Breakwaters; Floating bodies; Forecasting; Harbors**
Floating Breakwater Performance, Bruce H. Adee, 2777
- Marinas; Ports; Beach erosion; Beach nourishment; Equilibrium; Forecasting; France**
Impact of Yachting Marinas on Beaches, J. P. Lepetit, 1844
- Marinas; Seismic studies; Site selection; Ecology; Environmental effects; Littoral drift**
Application of CERC Special Report No.2, James W. Dunham, 3570
- Mass; Shallow water; Tanker ships; Water depth; Berths; Dolphins (structures); Head losses**
Added Masses of Large Tankers Berthing to Dolphins, Taizo Hayashi and Masujiro Shirai, 2830
- Mass transfer; Open channel flow; River flow; Sediment transport; Tidal currents; Dispersion**
Dispersive Transport in River and Tidal Flows, R. B. Taylor, 3336
- Mathematical models; Mixing; Algorithms; Diffusion; Estuaries; Frequency analysis; Hydraulic models**
Algorithm for Vertical Diffusion, Soren Peter Kjeldsen, 3321
- Mathematical models; Nuclear power plants; Numerical analysis; Refraction; Sediment transport; Wave dispersion; Waves; Coastal structures; Cooling water; Intake systems**
Application of a Sediment Transport Model, C. A. Fleming and J. N. Hunt, 1184
- Mathematical models; Numerical analysis; Saline water intrusion; Stratification; Transport phenomena; Density currents; Estuaries; Friction coefficient (hydraulic)**
Numerical Model for Density Currents in Estuaries, Karsten Fischer, 3295
- Mathematical models; Numerical analysis; Water flow; Wave energy; Wind pressure; Discharge (water); Effluents; Field tests**
Numerical Modelling — An Aid to Assessing Field Data, H. P. Riedel and F. L. Wilkinson, 3243
- Mathematical models; Rivers; Tidal effects; Time; Estuaries; Feasibility; Hydraulic models**
Analysis of Time Conditions for Hybrid Tidal Models, Klaus-Peter Holz, 3460
- Mathematical models; Scour; Scouring; Stratified flow; Troughs; Density currents; Flow patterns**
Generation of Troughs by Density Currents, Hans Speekenbrink, 2170
- Michigan; Sand; Shore protection; Water levels; Beach erosion; Beach nourishment; Bypasses; Erosion; Great Lakes**
Sand-Bypass and Shore Erosion, Bridgman, Michigan, C. N. Johnson and L. W. Hiipakka, 1361
- Mixing; Algorithms; Diffusion; Estuaries; Frequency analysis; Hydraulic models; Mathematical models**
Algorithm for Vertical Diffusion, Soren Peter Kjeldsen, 3321
- Mixing; Outfall sewers; Site selection; Water quality; Diffusers; Dilution**
Design Procedures for Ocean Outfalls, Jeffrey A. Layton, 2919
- Models; Numerical analysis; Statistical models; Tsunamis; Wave dispersion; Wave height; Japan**
Numerical Models of Huge Tsunamis Off the Sanriku Coast, Toshio Iwasaki, 1044
- Model studies; Mooring; Moorings; Breakwaters; Floating bodies; Forecasting; Harbors; Marinas**
Floating Breakwater Performance, Bruce H. Adee, 2777
- Model tests; Orifices; Pipes; Porous materials; Air bubbles; Air flow rates; Manifold air injection systems**
Guidelines for the Design of Air Bubble Systems, Nabil Ismail, 2994
- Model tests; Overturning tests; Wave action; Wave energy; Wave height; Wave period; Caissons**
Wave Forces on Aquare Caissons, G. R. Mogridge and W. W. Jamieson, 2271
- Model tests; Portugal; Breakwaters; Failure; Harbors; Harbor structures; Hydraulic models**
Design of Main Breakwater at Sines Harbour, John Dorrington Mettam, 2499
- Model tests; Pressure cells; Shock tests; Strain; Strain gages; Breakwaters; Caissons; Concrete (reinforced); Cylindrical bodies**
Cylindrical Caisson Breakwater: Strain Model Tests, Helge Gravesen, Finn P. Brodersen, Jorn S. Larsen and H. Lundgren, 2357
- Model tests; Scale effect; Stability; Wave height; Wave period; Wave runoff; Armoring (streambed); Breakwaters**
Large Scale Model Tests of Placed Stone Breakwaters, Charles K. Sollitt and Donald H. DeBok, 2572
- Monitoring; Nuclear power plants; Social impact; Coastal engineering; Environmental factors**
Coastal Environment and a Nuclear Power Plant, Ralph A. de la Parra, 3014
- Monitoring; Reefs; Runways; Water quality; Environmental effects; Hawaii; Islands (landforms)**
Environmental Impacts on an Island Community, Gordon A. Chapman, 3506

- Monitoring; Shore protection; Beaches; Beach nourishment; Groins (structures); Hydrographic surveys**
Comprehensive Monitoring of a Beach Restoration Project, Omar H. Shemdin, H. K. Brooks, Z. Ceylanli and S. L. Harrell, 1477
- Mooring; Moorings; Breakwaters; Floating bodies; Forecasting; Harbors; Marinas; Model studies**
Floating Breakwater Performance, Bruce H. Adee, 2777
- Mooring; Moorings; Offshore drilling; Ships; Wave tanks; Accidents; Collisions; Harbor structures**
Protection of Maritime Structures Against Ship Collisions, Kazuki Oda and Shositiro Nagai, 2810
- Mooring; Moorings; Oscillations; Wave action; Wave energy; Wave period; Fenders; Force; Harmonic functions**
Subharmonic Components in Hawser and Fender Forces, J. H. van Oorschot, 2840
- Moorings; Breakwaters; Floating bodies; Forecasting; Harbors; Marinas; Model studies; Mooring**
Floating Breakwater Performance, Bruce H. Adee, 2777
- Moorings; Offshore drilling; Ships; Wave tanks; Accidents; Collisions; Harbor structures; Mooring**
Protection of Maritime Structures Against Ship Collisions, Kazuki Oda and Shositiro Nagai, 2810
- Moorings; Oscillations; Wave action; Wave energy; Wave period; Fenders; Force; Harmonic functions; Mooring**
Subharmonic Components in Hawser and Fender Forces, J. H. van Oorschot, 2840
- Morphology; Sandbars; Sediment deposits; Wave energy; Barriers; Beaches; Canada; Littoral current; Littoral drift**
Process and Morphology Characteristics of Two Barrier Beaches in the Magdalen Islands, Gulf of St. Lawrence, Canada, E. H. Owens, 1975
- Movable bed models; Prototype tests; Scale effect; Scour; Scouring; Tidal waters; Tides; Erosion**
Movable Bed Tidal Inlet Models, Subhash C. Jain and John F. Kennedy, 3435
- Movable bed models; Scale effect; Sediment transport; Tracers (radioactive); West Germany; Hydraulic models**
Sand Movement Investigations by Means of Radioactive Tracers in a Hydraulic Model and in the Field, Hans Rohde, 2027
- Movable bed models; Sediment transport; Tidal currents; Tidal effects; Dunes; Dune sands**
Origin of Submarine Dunes, Mehmet S. Yalin, 2127
- Mud flats; Viscosity; Wave action; Wave dispersion; Wave energy; Wave functions; Wave height**
Wave Action and Bottom Movements in Fine Sediments, Michael W. Tubman and Joseph N. Suhayda, 1168
- Netherlands; Shore protection; Weed control; Weeds; Erosion; Erosion control; Gullies**
Recent Applications of Artificial Seaweed in the Netherlands, Henk G.H. ten Hoopen, 2905
- New Jersey; Probability; Simulation; Simulation models; Storm surges; Delaware**
Simulation Model for Storm Surge Probabilities, Mohammad H. Fallah, J. N. Sharma and Cheng Y. Yang, 934
- New Jersey; Sandbars; Sea level; Sedimentation; Sediment deposits; Sediment transport; Tidal currents; Beach erosion**
Offshore Sedimentary Processes and Responses Near Beach Haven — Little Egg Inlets, New Jersey, Thomas McKinney, Joseph T. DeAlteris, Yung Y. Chao, Lloyd Stahl and James Roney, 1899
- New Jersey; Scouring; Sea level; Tidal effects; Tidal waters; Environmental effects; Inlets (waterways); Littoral drift**
Beach Haven and Little Egg Inlets, A Case Study, Joseph T. DeAlteris, Thomas McKinney and James Roney, 1881
- Nigeria; Sedimentation; Sediment concentration; Sediment distribution; Sediment transport; Breakwaters; Deltas; Hydraulic models**
Sedimentation Studies on the Niger River Delta, Ramiro Mayor-Mora, Preben Mortensen and Jorgen Fredsoe, 2151
- Nonuniform flow; Open channel flow; Specific energy; Estuaries; Landforms**
Concept of Minimum Specific Energy and Its Relation to Natural Forms, Gordon R. McKay and Ahad K. Kazempour, 2186
- Nuclear power plants; Numerical analysis; Refraction; Sediment transport; Wave dispersion; Waves; Coastal structures; Cooling water; Intake systems; Mathematical models**
Application of a Sediment Transport Model, C. A. Fleming and J. N. Hunt, 1184
- Nuclear power plants; Plume detection; Plumes; Thermal pollution; Two phase flow; Diffusers; Discharge (water); Hydraulic models**
Field Studies of Submerged-Diffuser Thermal Plumes with Comparisons to Predictive Model Results, A. A. Frigo, Richard A. Paddock and J. D. Ditmars, 3028
- Nuclear power plants; Prototype tests; Temperature distribution; Thermal diffusion; Thermal pollution; Water temperature; Discharge (water); Hydraulic models**
Thermal Discharges: Prototype vs. Hydraulic Model, Gary C. Parker, Ching S. Fang and Albert Y. Kuo, 3049
- Nuclear power plants; Social impact; Coastal engineering; Environmental factors; Monitoring**
Coastal Environment and a Nuclear Power Plant, Ralph A. de la Parra, 3014
- Nuclear power plants; Wave dispersion; Wave energy; Cooling water; Cylindrical bodies; Field tests; Intake structures**
Wave Pressures on Large Circular Cylindrical Structure, Hiroshi Nakamura, 2290
- Numerical analysis; Oscillations; Responses; Water depth; Water surface profiles; Wave action; Wave energy**
Wave Induced Oscillations of Harbors with Variable Depth, Fredric Raichlen and Ehud Naheer, 3536

- Numerical analysis; Propagation; Shallow water; Tsunamis; Wave height; Friction coefficient (hydraulic)**
Tsunami Propagation in the Pacific Ocean, Manfred Engel and Wilfried Zahel, 971
- Numerical analysis; Propagation; Shore protection; Simulation; Tsunamis**
Numerical Simulation of Tsunamis Originating in the Peru-Chile Trench, A. W. Garcia and H. L. Butler, 1025
- Numerical analysis; Refraction; Sediment transport; Wave dispersion; Waves; Coastal structures; Cooling water; Intake systems; Mathematical models; Nuclear power plants**
Application of a Sediment Transport Model, C. A. Fleming and J. N. Hunt, 1184
- Numerical analysis; Saline water intrusion; Stratification; Transport phenomena; Density currents; Estuaries; Friction coefficient (hydraulic); Mathematical models**
Numerical Model for Density Currents in Estuaries, Karsten Fischer, 3295
- Numerical analysis; Shallow water; Tidal effects; Tidal marshes; Water waves; Estuaries; Finite element method**
Finite Element Model for Estuaries with Inter-Tidal Flats, Bruno Herrling, 3396
- Numerical analysis; Simulation; Storm surges; Hydromechanics**
Generalized Model for Storm Surges, Gour-Tsyh Yeh and Fei-Fan Yeh, 921
- Numerical analysis; Statistical models; Tsunamis; Wave dispersion; Wave height; Japan; Models**
Numerical Models of Huge Tsunamis Off the Sanriku Coast, Toshio Iwasaki, 1044
- Numerical analysis; Storm surges; Tropical cyclones; Computer models; Forecasting; Hurricanes**
SPLASH — A Model for Forecasting Tropical Storm Surges, Celso S. Barrientos and Chester P. Jelesnianski, 941
- Numerical analysis; Stratification; Two phase flow; Convection; Diffusion; Dispersion; Finite element method**
Numerical Modeling of Dispersion in Stratified Waters, George C. Christodoulou and Jerome J. Connor, 3138
- Numerical analysis; Tidal currents; Tidal effects; Algorithms; California; Discharge (water)**
Tidal Stream Flow Solved by Galerkin Technique, L. H. Smith and Ralph T-S Cheng, 3358
- Numerical analysis; Water flow; Wave energy; Wind pressure; Discharge (water); Effluents; Field tests; Mathematical models**
Numerical Modelling — An Aid to Assessing Field Data, H. P. Riedel and F. L. Wilkinson, 3243
- Numerical analysis; Wave action; Wave energy; Wave runoff; Wave velocity; Coastal structures; Damping**
Numerical Calculation of Wave Forces on Structures, B. D. Nichols and C. W. Hirt, 2254
- Numerical analysis; Wave energy; Wave recorders (water waves); California; Coastal engineering; Coastal structures**
Regional Network for Coastal Engineering Data, Richard J. Seymour and Meredith H. Sessions, 60
- Ocean bottom; Oceanography; Refraction; Resonance; Islands (landforms)**
Resonant Refraction by Round Islands, Richard E. Meyer, 866
- Ocean bottom; Ocean waves; Wave action; Wave dispersion; Wave energy; Wave velocity; Field tests**
Near-Bottom Water Motion Under Ocean Waves, Robert A. Grace, 2371
- Ocean bottom; Offshore structures; Predictions; Stability; Wave action; Wave energy; Bottom water; Continental shelf; Cyclic loads; Foundations**
Prediction of Wave-Induced Seafloor Movements, Leland Milo Kraft, Jr. and David James Watkins, 1605
- Ocean bottom; Ripple marks; Shallow water; Turbulent diffusion; Friction coefficient (hydraulic)**
Consideration on Friction Coefficient for Sea Bottom, Toru Sawaragi, Koichiro Iwata and Masayoshi Kubo, 595
- Ocean bottom; Scale effect; Sediment transport; Simulation models; Tidal effects; Wave energy; Bed forms; Inlets (waterways)**
Tidal Inlet Flow Dynamics and Sediment Movement, Jerry L. Machemehl, N. E. Bird and A. N. Chambers, 1681
- Ocean bottom; Shoaling; Topographical factors; Beach erosion; Beaches; Breakwaters; Construction; Harbor structures; Japan**
Topographic Change Resulting from the Construction of a Harbor on a Sandy Beach, Kashima Port, Norio Tanaka and Shoji Sato, 1824
- Ocean bottom; Shore protection; Subsidence; Beach erosion; Breakwaters; Japan**
Changes of Sea Bed Due to Detached Breakwaters, Osamu Toyoshima, 1572
- Ocean currents; Photogrammetry; Stereophotography; Water levels; Waves; Breaking; Coastal engineering; Field tests; Littoral drift**
Terrestrial Photogrammetric Measurements of Breaking Waves and Longshore Currents in the Nearshore Zone, Joseph W. Maresca, Jr. and Erwin Seibel, 681
- Ocean currents; Rip currents; Sediment transport; Wave height; Wave phases; Littoral drift**
Physical Aspects of Wave-Induced Nearshore Current System, Masaru Mizuguchi and Kiyoshi Horikawa, 607
- Ocean currents; Rip currents; Time dependence; Wave height; Wave period; Wave spectrum; Wave velocity; Flowmeters**
Time Dependent Fluctuations in Longshore Currents, Guy A. Meadows, 660
- Ocean currents; Rip currents; Wave recorders (water waves); Beaches; Japan; Littoral drift**
Nearshore Current on a Gently Sloping Beach, Tamio Sasaki, Kiyoshi Horikawa and Shintaro Hotta, 626

- Ocean currents; Sediment transport; Storm surges; Tidal marshes; Coastal engineering; Currents; Littoral drift**
Currents in Tidal Flats During Storm Surges, Harald Gohren, 959
- Ocean currents; Spreading; Time dependence; Wastewater; Buoyancy; Fluid mechanics; Gravitation**
Buoyancy-Driven Gravitational Spreading, Robert C.Y. Koh, 2956
- Ocean currents; Three-dimensional; Wave dispersion; Wave height; Waves; Breaking; Breakwaters; Friction coefficient (hydraulic); Littoral drift**
Non-Uniform Alongshore Currents, Michael R. Gourlay, 701
- Ocean engineering; Outfall sewers; Underwater pipelines; Diffusers; Environmental effects; Hydrodynamics**
Design Considerations for the Sand Island and Barbers Point Outfalls, Robert C.Y. Koh, Norman H. Brooks and Floyd Louis Vuillemot, 2941
- Oceanography; Refraction; Resonance; Islands (landforms); Ocean bottom**
Resonant Refraction by Round Islands, Richard E. Meyer, 866
- Ocean waves; Radar equipment; Wave height; Wavemeters; Wave recorders (water waves); Wave spectrum**
Wave Measurements in Open Ocean, Davidson T. Chen, Benjamin S. Yaplee, Donald L. Hammond and Paul Bey, 72
- Ocean waves; Random variables; Simulation; Waves; Wave tanks; Laboratory tests**
Random Wave Simulation in a Laboratory Wave Tank, Akira Kimura and Yuichi Iwagaki, 368
- Ocean waves; Resonance; Simulation; Water levels; Wave height; Wave runoff; Beaches**
Wave Run-Up on a Simulated Beach, A. J. Sutherland, J. N. Sharma and Omar H. Shemdin, 752
- Ocean waves; Scale effect; Storm surges; Wave equations; Wave height; Wave period; Wave runoff; Dikes; Echo sounding; Field investigations; Instrumentation**
Wave Run-Up in Field Measurements with Newly Developed Instrument, Heie F. Erchinger, 767
- Ocean waves; Spectral analysis; Statistical analysis; Storms; Wave height; Wave spectrum**
Six-Parameter Wave Spectra, Michel K. Ochi and E. Nadine Hubble, 301
- Ocean waves; Spectral analysis; Statistical analysis; Wave forecasting; Wave period; Waves; Wave spectrum; Climatology; Coastal engineering**
Ocean Wave Statistics from FNWC Spectral Analysis, Warren C. Thompson and F. Michael Reynolds, 238
- Ocean waves; Surface waves; Wave energy; Wave spectrum; Distribution functions; Distribution patterns; Frequency**
Directional Spectral of Ocean Surface Waves, Hisashi Mitsuyasu and S. Mizuno, 329
- Ocean waves; Taiwan; Wave height; Wave period; Waves; Wind speed; Coastal engineering**
Waves Off Taichung Coast of Taiwan, Charles C.C. Chang, M. H. Wang and J. T. Juang, 129
- Ocean waves; Wave action; Wave dispersion; Wave energy; Wave velocity; Field tests; Ocean bottom**
Near-Bottom Water Motion Under Ocean Waves, Robert A. Grace, 2371
- Ocean waves; Wave action; Wave height; Wave propagation; Wave spectrum**
Revisions in Wave Data Presentation, Laurence Draper, 3
- Ocean waves; Wave energy; Wave forecasting; Waves; Wave spectrum; Wind forces; Wind speed; Fetch**
Application of Fetch Area Method in Monsoon Wave Hindcasting, Nai-Kuang Liang, Shih-Tsan Tang and Ben-Juen Lee, 258
- Ocean waves; Wave energy; Wave height; Wavemeters; Wave recorders (water waves); Waves; Climatic data**
Wave Climate Analysis for Engineering Purpose, Hans H. Dette and Alfred Fuhrboter, 10
- Offshore drilling; Ships; Wave tanks; Accidents; Collisions; Harbor structures; Mooring; Moorings**
Protection of Maritime Structures Against Ship Collisions, Kazuki Oda and Shositiro Nagai, 2810
- Offshore structures; Predictions; Stability; Wave action; Wave energy; Bottom water; Continental shelf; Cyclic loads; Foundations; Ocean bottom**
Prediction of Wave-Induced Seafloor Movements, Leland Milo Kraft, Jr. and David James Watkins, 1605
- Offshore structures; Prototype tests; Scour; Scouring; Wave action; Wave energy; Wharves**
Wave Action on Large Off-Shore Structures, C. J. Apelt and A. Macknight, 2228
- Open channel flow; River flow; Sediment transport; Tidal currents; Dispersion; Mass transfer**
Dispersive Transport in River and Tidal Flows, R. B. Taylor, 3336
- Open channel flow; Specific energy; Estuaries; Landforms; Nonuniform flow**
Concept of Minimum Specific Energy and Its Relation to Natural Forms, Gordon R. McKay and Ahad K. Kazemipour, 2186
- Open channel flow; Water meters; Water quality; Calibration; Discharge (water); Estuaries**
Calibration of Branched Estuary Models, James P. Bennett, 3416
- Oregon; Sedimentation; Sediment deposits; Shoaling; Bays (topographic features); Beach erosion; Erosion; Jetties**
Changes due to Jetties at Tillamook Bay, Oregon, Paul D. Komar and Thomas A. Terich, 1791
- Orifices; Pipes; Porous materials; Air bubbles; Air flow rates; Manifold air injection systems; Model tests**
Guidelines for the Design of Air Bubble Systems, Nabil Ismail, 2994
- Oscillation; Roughness (hydraulic); Vortices; Water flow; Cylindrical bodies; Drag; Force**
Forces on Rough-Walled Circular Cylinders in Harmonic Flow, Turgut Sarpkaya, 2301
- Oscillation; Sediment transport; Unsteady flow; Wave equations; Waves; Breakwaters**
Quantitative Description of Sediment Transport, Ole Secher Madsen and William D. Grant, 1093

- Oscillations; Pressure distribution; Vortices; Wakes; Water waves; Cylindrical bodies; Flow separation**
Flow Separation, Wake Vortices and Pressure Distribution Around a Circular Cylinder under Oscillatory Waves, Yuichi Iwagaki and Hajime Ishida, 2341
- Oscillations; Responses; Water depth; Water surface profiles; Wave action; Wave energy; Numerical analysis**
Wave Induced Oscillations of Harbors with Variable Depth, Fredric Raichlen and Ehud Naheer, 2536
- Oscillations; Reynolds number; Stream flow; Water flow; Wave action; Wave energy; Cylinders; Drag; Hydraulic models; Lift**
High Reynolds Number Oscillating Flow by Cylinders, Tokuo Yamamoto and John H. Nath, 2321
- Oscillations; Wave action; Wave energy; Wave period; Fenders; Force; Harmonic functions; Mooring; Moorings**
Subharmonic Components in Hawser and Fender Forces, J. H. van Oorschot, 2840
- Outfall sewers; Site selection; Water quality; Diffusers; Dilution; Mixing**
Design Procedures for Ocean Outfalls, Jeffrey A. Layton, 2919
- Outfall sewers; Underwater pipelines; Diffusers; Environmental effects; Hydrodynamics; Ocean engineering**
Design Considerations for the Sand Island and Barbers Point Outfalls, Robert C.Y. Koh, Norman H. Brooks and Floyd Louis Vuillemot, 2941
- Overtopping; Periodic variations; Wave height; Wave runup; Waves; Dikes; Discharge (water)**
Characteristics of Flow in Run-Up of Periodic Waves, Ary Roos and Jurjen A. Batjjes, 781
- Overtopping; Rubble mounds; Wave action; Wave energy; Waves; Wave spectrum; Breakwaters**
Overtopping of Rubble-Mound Breakwaters by Irregular Waves, Yvon Ouellet and Pierre Eubanks, 2756
- Overtopping; Scale effect; Shore protection; Slopes; Wave equations; Wave runup**
Wave Overtopping Equation, J. Richard Weggel, 2737
- Overturning tests; Wave action; Wave energy; Wave height; Wave period; Caissons; Model tests**
Wave Forces on Aquare Caissons, G. R. Mogridge and W. W. Jamieson, 2271
- Performance; Safety; Site selection; Utilization; Barges; Economic analysis; Environmental effects; Harbors**
Probable Utilization Level for a Barge Harbor, Martin T. Czerniak and Choule J. Sonu, 3557
- Periodic functions; Phase velocity; Water depth; Wave energy; Wave height; Waves; Beaches; Deformation**
Deformation up to Breaking of Periodic Waves on a Beach, Ib A. Svendsen and J. Buhr Hansen, 477
- Periodic variations; Refraction; Wave energy; Wave propagation; Waves; Boundary value problems; Coastal engineering; Computation**
Physics and Mathematics of Waves in Coastal Zones, H. Lundgren, 880
- Periodic variations; Shoaling; Slopes; Wave period; Wave runup; Waves; Breaking**
Set-Up and Run-Up in Shoaling Breakers, William G. Van Dorn, 738
- Periodic variations; Wave height; Wave runup; Waves; Dikes; Discharge (water); Overtopping**
Characteristics of Flow in Run-Up of Periodic Waves, Ary Roos and Jurjen A. Batjjes, 781
- Permeability; Reflection; Wave height; Breakwaters; Laboratory tests**
Laboratory Study of Pervious Core Breakwaters, Hideo Kondo, Satoshi Toma and Kenji Yano, 2643
- Permeability; Reservoirs; Sea walls; Wave energy; Wave period; Concrete (blocks)**
Permeable Seawall with Reservoir and the Use of "Warock", Takeshi Ijima, Enzoh Tanaka and Hideaki Okuzono, 2623
- Permeability; Sea walls; Two-dimensional; Water depth; Water waves; Wave height; Boundary value problems; Breakwaters**
Method of Analyses for Two-Dimensional Water Wave Problems, Takeshi Ijima, Chung Ren Chou and Akinori Yoshida, 2717
- Phase velocity; Water depth; Wave energy; Wave height; Waves; Beaches; Deformation; Periodic functions**
Deformation up to Breaking of Periodic Waves on a Beach, Ib A. Svendsen and J. Buhr Hansen, 477
- Photogrammetry; Stereophotography; Water levels; Waves; Breaking; Coastal engineering; Field tests; Littoral drift; Ocean currents**
Terrestrial Photogrammetric Measurements of Breaking Waves and Longshore Currents in the Nearshore Zone, Joseph W. Maresca, Jr. and Erwin Seibel, 681
- Pile foundations; Steel piles; Structural design; Coastal structures; Lateral forces**
Concepts in Design of Coastal Structures, Casimir J. Kray, 2209
- Pipes; Porous materials; Air bubbles; Air flow rates; Manifold air injection systems; Model tests; Orifices**
Guidelines for the Design of Air Bubble Systems, Nabil Ismail, 2994
- Plume detection; Plumes; Thermal pollution; Two phase flow; Diffusers; Discharge (water); Hydraulic models; Nuclear power plants**
Field Studies of Submerged-Diffuser Thermal Plumes with Comparisons to Predictive Model Results, A. A. Frigo, Richard A. Paddock and J. D. Ditmars, 3028
- Plumes; Thermal pollution; Two phase flow; Diffusers; Discharge (water); Hydraulic models; Nuclear power plants; Plume detection**
Field Studies of Submerged-Diffuser Thermal Plumes with Comparisons to Predictive Model Results, A. A. Frigo, Richard A. Paddock and J. D. Ditmars, 3028

- Porous materials; Air bubbles; Air flow rates; Manifold air injection systems; Model tests; Orifices; Pipes**
Guidelines for the Design of Air Bubble Systems, Nabil Ismail, 2994
- Ports; Beach erosion; Beach nourishment; Equilibrium; Forecasting; France; Marinas**
Impact of Yachting Marinas on Beaches, J. P. Lepetit, 1844
- Portugal; Breakwaters; Failure; Harbors; Harbor structures; Hydraulic models; Model tests**
Design of Main Breakwater at Sines Harbour, John Dorrington Mettam, 2499
- Power spectra; Refraction; Shoaling; Tsunamis; Warning systems; Coastal engineering; Coastal plains; Japan**
Transformation of Tsunamis in a Coastal Zone, Shigehisa Nakamura, Haruo Higuchi and Yoshito Tsuchiya, 988
- Predictions; Prototype tests; Scale effect; Surface tension; Thermal diffusion; Viscosity; Water temperature; Hydraulic models**
Adaptability of Prediction Method of Hydraulic Model Experiment for Thermal Diffusion, Masanobu Kato and Akira Wada, 3082
- Predictions; Refraction; Surf; Water depth; Waves; Currents; Finite elements; Gravity waves**
Current Depth Defraction Using Finite Elements, Ove Skovgaard and Ivar G. Jonsson, 721
- Predictions; Sediment deposits; Sediment transport; Beach nourishment; Beach sands; Littoral current**
Predictive Equations Regarding Coastal Transport, D. H. Swart, 1113
- Predictions; Sewage disposal; Sewage effluents; Tracers; Water pollution; Dispersion; Distribution; Dyes; Estuaries**
Prediction of Pollutant Distribution in Estuaries, Albert Y. Kuo and John P. Jacobson, 3276
- Predictions; Stability; Wave action; Wave energy; Bottom water; Continental shelf; Cyclic loads; Foundations; Ocean bottom; Offshore structures**
Prediction of Wave-Induced Seafloor Movements, Leland Milo Kraft, Jr. and David James Watkins, 1605
- Predictions; Storm surges; Tsunamis; Wave runoff; Flooding**
Tsunami Inundation Prediction, Charles L. Bretschneider and Pieter G. Wybro, 1006
- Predictions; Wave generation; Wave height; Wave propagation; Waves; Cavities; Deep water; Explosions**
Calculations of Waves Formed From Surface Cavities, Charles L. Mader, 1079
- Pressure cells; Shock tests; Strain; Strain gages; Breakwaters; Caissons; Concrete (reinforced); Cylindrical bodies; Model tests**
Cylindrical Caisson Breakwater: Strain Model Tests, Helge Gravesen, Finn P. Brodersen, Jorn S. Larsen and H. Lundgren, 2357
- Pressure distribution; Vortices; Wakes; Water waves; Cylindrical bodies; Flow separation; Oscillations**
Flow Separation, Wake Vortices and Pressure Distribution Around a Circular Cylinder under Oscillatory Waves, Yuichi Iwagaki and Hajime Ishida, 2341
- Probability; Simulation; Simulation models; Storm surges; Delaware; New Jersey**
Simulation Model for Storm Surge Probabilities, Mohammad H. Fallah, J. N. Sharma and Cheng Y. Yang, 934
- Propagation; Shallow water; Tsunamis; Wave height; Friction coefficient (hydraulic); Numerical analysis**
Tsunami Propagation in the Pacific Ocean, Manfred Engel and Wilfried Zahel, 971
- Propagation; Shore protection; Simulation; Tsunamis; Numerical analysis**
Numerical Simulation of Tsunamis Originating in the Peru-Chile Trench, A. W. Garcia and H. L. Butler, 1025
- Prototype tests; Roughness (hydraulic); Tidal currents; Tidal effects; Tidal energy; Hydraulic models**
Model Verification for Tidal Constituents, R. W. Whalin, F. C. Perry and D. L. Durham, 3377
- Prototype tests; Scale effect; Scour; Scouring; Tidal waters; Tides; Erosion; Movable bed models**
Movable Bed Tidal Inlet Models, Subhash C. Jain and John F. Kennedy, 3435
- Prototype tests; Scale effect; Surface tension; Thermal diffusion; Viscosity; Water temperature; Hydraulic models; Predictions**
Adaptability of Prediction Method of Hydraulic Model Experiment for Thermal Diffusion, Masanobu Kato and Akira Wada, 3082
- Prototype tests; Scour; Scouring; Wave action; Wave energy; Wharves; Offshore structures**
Wave Action on Large Off-Shore Structures, C. J. Apelt and A. Macknight, 2228
- Prototype tests; Temperature distribution; Thermal diffusion; Thermal pollution; Water temperature; Discharge (water); Hydraulic models; Nuclear power plants**
Thermal Discharges: Prototype vs. Hydraulic Model, Gary C. Parker, Ching S. Fang and Albert Y. Kuo, 3049
- Quays; Reflection; Revetments; Shore protection; Wave dispersion; Computerized simulation; Concrete (blocks); Harbor structures**
Quay Wall with Wave Absorber "Igloo", Naofumi Shiraishi, Robert Q. Palmer and Hiroshi Okamoto, 2677
- Radar equipment; Wave height; Wavemeters; Wave recorders (water waves); Wave spectrum; Ocean waves**
Wave Measurements in Open Ocean, Davidson T. Chen, Benjamin S. Yaplee, Donald L. Hammond and Paul Bey, 72
- Random processes; Reflection; Water waves; Wave dispersion; Wave energy; Wave spectrum; Coastal structures**
Decomposition of Co-Existing Random Wave Energy, Dennis B. Morden, Eugene P. Richey and Derald R. Christensen, 846
- Random processes; Wave energy; Wave period; Wave recorders (water waves); Waves; Wave spectrum; Experimentation**
Estimation of Incident and Reflected Waves in Random Wave Experiments, Yoshimi Goda and Yasumasa Suzuki, 828

- Random variables; Simulation; Waves; Wave tanks; Laboratory tests; Ocean waves**
Random Wave Simulation in a Laboratory Wave Tank, Akira Kimura and Yuichi Iwagaki, 368
- Recreational facilities; Shore protection; Sri Lanka; Beach nourishment; Coastal engineering**
Coastal Problems in Sri Lanka, Franciscus Gerritsen and Summa R. Amarasinghe, 3487
- Recreational facilities; Shore protection; Swimming; Beaches; Beach nourishment; Breakwaters; Hawaii**
Proposed "Improvement" of Kaimu Beach, Hawaii, Doak C. Cox, Franciscus Gerritsen and Theodore T. Lee, 1552
- Recreational facilities; Social needs; Beaches; Breakwaters; Enclosures; Groins (structures); Israel**
Enclosing Scheme for Bathing-Beach Development, Joseph Tauman, 1425
- Recreational facilities; Storms; Storm surges; Wave action; Wave energy; Beach erosion; Beach nourishment; Erosion; Littoral current**
Cape Hatteras Beach Nourishment, John S. Fisher and Wilson N. Felder, 1512
- Reefs; Runways; Water quality; Environmental effects; Hawaii; Islands (landforms); Monitoring**
Environmental Impacts on an Island Community, Gordon A. Chapman, 3506
- Reefs; Slope protection; Slope stability; Airports; Breakwaters; Hawaii**
Design and Construction of Protective Structure for New Reef Runway at Honolulu International Airport, Wilfred D. Darling, 2589
- Reflection; Revetments; Shore protection; Wave dispersion; Computerized simulation; Concrete (blocks); Harbor structures; Quays**
Quay Wall with Wave Absorber "Igloo", Naofumi Shiraiishi, Robert Q. Palmer and Hiroshi Okamoto, 2677
- Reflection; Sandbars; Sand traps; Three-dimensional; Wave action; Beach erosion; Beach nourishment; Dynamics; Equilibrium; Erosion**
Three Dimensional Tests on Dynamic Equilibrium and Artificial Nourishment, J. William Kamphuis and R. M. Myers, 1532
- Reflection; Slitting; Wave action; Wave damping; Wave energy; Breakwaters**
Slit-Type Breakwater: Box-Type Wave Absorber, Shositiro Nagai and Shohachi Kakuno, 2697
- Reflection; Walls; Water waves; Wave height; Diffraction; Mach number**
Mach-Reflection as a Diffraction Problem, Udo Berger and Soren Kohlhasse, 796
- Reflection; Water waves; Wave dispersion; Wave energy; Wave spectrum; Coastal structures; Random processes**
Decomposition of Co-Existing Random Wave Energy, Dennis B. Morden, Eugene P. Richey and Derald R. Christensen, 846
- Reflection; Wave height; Breakwaters; Laboratory tests; Permeability**
Laboratory Study of Pervious Core Breakwaters, Hideo Kondo, Satoshi Toma and Kenji Yano, 2643
- Refraction; Resonance; Islands (landforms); Ocean bottom; Oceanography**
Resonant Refraction by Round Islands, Richard E. Meyer, 866
- Refraction; Sediment transport; Wave dispersion; Waves; Coastal structures; Cooling water; Intake systems; Mathematical models; Nuclear power plants; Numerical analysis**
Application of a Sediment Transport Model, C. A. Fleming and J. N. Hunt, 1184
- Refraction; Shoaling; Tsunamis; Warning systems; Coastal engineering; Coastal plains; Japan; Power spectra**
Transformation of Tsunamis in a Coastal Zone, Shigehisa Nakamura, Haruo Higuchi and Yoshito Tsuchiya, 988
- Refraction; Shoaling; Wave action; Wave dispersion; Wave height; Waves; Wave velocity; Breaking**
Refraction of Finite-Height and Breaking Waves, James R. Walker, 507
- Refraction; Surf; Water depth; Waves; Currents; Finite elements; Gravity waves; Predictions**
Current Depth Defraction Using Finite Elements, Ove Skovgaard and Ivar G. Jonsson, 721
- Refraction; Wave energy; Wave propagation; Waves; Boundary value problems; Coastal engineering; Computation; Periodic variations**
Physics and Mathematics of Waves in Coastal Zones, H. Lundgren, 880
- Remote sensing; Water temperature; Air-water interfaces; Heat flux; Heat transfer; Infrared scanners; Infrared scanning**
Evaluation of Air-Sea Interface Heat Flux, Robert L. Street and A. Woodruff Miller, Jr., 3208
- Reservoirs; Sea walls; Wave energy; Wave period; Concrete (blocks); Permeability**
Permeable Seawall with Reservoir and the Use of "Warock", Takeshi Ijima, Enzoh Tanaka and Hideaki Okuzono, 2623
- Reservoirs; Tidal currents; Tidal effects; Tidal hydraulics; Tidal marshes; Wave height; Waves; Estuaries**
Waves Used for Inter-Tidal Design and Construction, D. C. Keiller and T. D. Ruxton, 23
- Resonance; Islands (landforms); Ocean bottom; Oceanography; Refraction**
Resonant Refraction by Round Islands, Richard E. Meyer, 866
- Resonance; Rubble; Rubble mounds; Slope stability; Stability; Surf; Wave period; Wave runup; Breakwaters**
New Design Principles for Rubble Mound Structures, Per Moller Bruun and Ali Riza Gunbak, 2429
- Resonance; Simulation; Water levels; Wave height; Wave runup; Beaches; Ocean waves**
Wave Run-Up on a Simulated Beach, A. J. Sutherland, J. N. Sharma and Omar H. Shemdin, 752
- Resonance; Surges; Turbulence; Wave height; Wave runup; Waves; Beaches; Breaking**
Resonant Interactions for Waves Breaking on a Beach, Robert T. Guza and Anthony J. Bowen, 560

- Responses; Rip currents; Velocity distribution; Water waves; Wave equations; Coastal topographic features; Eigenvalues**
Rip-Current and Coastal Topography, Mikio Hino, 1326
- Responses; Stability; Statistical analysis; Storms; Variability; Beach erosion; Eigenvalues; Impulses**
Stability and Impulse Response of Empirical Eigenfunctions, Clinton D. Winant and David G. Aubrey, 1312
- Responses; Water depth; Water surface profiles; Wave action; Wave energy; Numerical analysis; Oscillations**
Wave Induced Oscillations of Harbors with Variable Depth, Fredric Raichlen and Ehud Naheer, 3536
- Revetments; Sea walls; Shore protection; Breakwaters; Coastal engineering; Costs; Erosion; Groins (structures)**
Low-Cost Shoreline Protection, Billy L. Edge, John G. Housley and George M. Watts, 2888
- Revetments; Shore protection; Wave dispersion; Computerized simulation; Concrete (blocks); Harbor structures; Quays; Reflection**
Quay Wall with Wave Absorber "Igloo", Naofumi Shiraishi, Robert Q. Palmer and Hiroshi Okamoto, 2677
- Revetments; Wave action; Wave energy; Air entrainment; Damage; Dikes; Impact**
Response of Seadykes due to Wave Impacts, Alfred Fuhrboter, Hans H. Dette and J. Grune, 2604
- Reynolds number; Stream flow; Water flow; Wave action; Wave energy; Cylinders; Drag; Hydraulic models; Lift; Oscillations**
High Reynolds Number Oscillating Flow by Cylinders, Tokuo Yamamoto and John H. Nath, 2321
- Rip currents; Sediment transport; Shore protection; Energy equation; Littoral current; Littoral drift**
Longshore Transport Prediction — SPM 1973 Equation, Cyril J. Galvin and Philip Vitale, 1133
- Rip currents; Sediment transport; Wave height; Wave phases; Littoral drift; Ocean currents**
Physical Aspects of Wave-Induced Nearshore Current System, Masaru Mizuguchi and Kiyoshi Horikawa, 607
- Rip currents; Surf; Turbulence; Beaches; Flowmeters; Friction coefficient (hydraulic)**
Lateral and Bottom Forces on Longshore Currents, David A. Huntley, 645
- Rip currents; Time dependence; Wave height; Wave period; Wave spectrum; Wave velocity; Flowmeters; Ocean currents**
Time Dependent Fluctuations in Longshore Currents, Guy A. Meadows, 660
- Rip currents; Velocity distribution; Water waves; Wave equations; Coastal topographic features; Eigenvalues; Responses**
Rip-Current and Coastal Topography, Mikio Hino, 1326
- Rip currents; Wave recorders (water waves); Beaches; Japan; Littoral drift; Ocean currents**
Nearshore Current on a Gently Sloping Beach, Tamio Sasaki, Kiyoshi Horikawa and Shintaro Hotta, 626
- Rip currents; Waves; Wave tanks; Beach erosion; Erosion; Groins (structures)**
Groin Length and the Generation of Edge Waves, Michael K. Gaughan and Paul D. Komar, 1459
- Ripple marks; Sand; Sonar detection; Wave action; Wave generation; Bedding materials; Bed ripples**
Wave-Formed Ripples in Nearshore Sands, John R. Dinger and Douglas L. Inman, 2109
- Ripple marks; Shallow water; Turbulent diffusion; Friction coefficient (hydraulic); Ocean bottom**
Consideration on Friction Coefficient for Sea Bottom, Toru Sawaragi, Koichiro Iwata and Masayoshi Kubo, 595
- River flow; Sandbars; Sedimentation; Sediment deposits; Wave action; Wave energy; Estuaries; Flooding**
Morphodynamics of a Wave-Dominated River Mouth, L. D. Wright, 1721
- River flow; Sandbars; Training walls; Australia; Estuaries; Flooding; Hydrographic surveys; Jetties**
Results of River Mouth Training on the Clarence Bar, New South Wales, Australia, Cyril D. Floyd and Bruce M. Druery, 1738
- River flow; Sediment transport; Tidal currents; Dispersion; Mass transfer; Open channel flow**
Dispersive Transport in River and Tidal Flows, R. B. Taylor, 3336
- River regulation; Sandbars; Sediment transport; Stability; Tidal effects; Tidal hydraulics; Tidal waters; Channels (waterways)**
Stability of Tidal Channels Dependent on River Improvement, Volker Barthel, 1775
- Rivers; Tidal effects; Time; Estuaries; Feasibility; Hydraulic models; Mathematical models**
Analysis of Time Conditions for Hybrid Tidal Models, Klaus-Peter Holz, 3460
- Roughness (hydraulic); Tidal currents; Tidal effects; Tidal energy; Hydraulic models; Prototype tests**
Model Verification for Tidal Constituents, R. W. Whalin, F. C. Perry and D. L. Durham, 3377
- Roughness (hydraulic); Vortices; Water flow; Cylindrical bodies; Drag; Force; Oscillation**
Forces on Rough-Walled Circular Cylinders in Harmonic Flow, Turgut Sarpkaya, 2301
- Rubble; Rubble mounds; Slope stability; Stability; Surf; Wave period; Wave runoff; Breakwaters; Resonance**
New Design Principles for Rubble Mound Structures, Per Moller Bruun and Ali Riza Gunbak, 2429
- Rubble; Rubble mounds; Stability; Wave action; Wave energy; Breakwaters; Damage; Hydraulic models**
Effect of Broken Dolosse on Breakwater Stability, D. Donald Davidson and Dennis G. Markle, 2544

- Rubble mounds; Slope stability; Stability; Surf; Wave period; Wave runoff; Breakwaters; Resonance; Rubble**
New Design Principles for Rubble Mound Structures, Per Moller Bruun and Ali Riza Gunbak, 2429
- Rubble mounds; Stability; Wave action; Wave energy; Breakwaters; Damage; Hydraulic models; Rubble**
Effect of Broken Dolosse on Breakwater Stability, D. Donald Davidson and Dennis G. Markle, 2544
- Rubble mounds; Wave action; Wave dispersion; Wave energy; Waves; Breakwaters; Laboratory tests**
Wave Transmission Through Trapezoidal Breakwaters, Ole Secher Madsen and Stanley M. White, 2662
- Rubble mounds; Wave action; Wave energy; Harbors; Harbor structures; History; Jetties**
Design and Construction of Humboldt Jetties, 1880 to 1975, Orville T. Magoon, Robert L. Sloan and Nobuyuki Shimizu, 2474
- Rubble mounds; Wave action; Wave energy; Waves; Wave spectrum; Breakwaters; Overtopping**
Overtopping of Rubble-Mound Breakwaters by Irregular Waves, Yvon Ouellet and Pierre Eubanks, 2756
- Runoff; Sampling; Simulation; Water circulation; Water quality; Coliform bacteria; Drainage; Estuaries**
State Estimation of Estuarine Circulation and Water Quality by Numerical Simulation and Observation, Jan J. Leendertse and S. K. Liu, 3223
- Runways; Water quality; Environmental effects; Hawaii; Islands (landforms); Monitoring; Reefs**
Environmental Impacts on an Island Community, Gordon A. Chapman, 3506
- Safety; Site selection; Utilization; Barges; Economic analysis; Environmental effects; Harbors; Performance**
Probable Utilization Level for a Barge Harbor, Martin T. Czerniak and Choule J. Sonu, 3557
- Saline water-freshwater interfaces; Saline water intrusion; Salinity; Stratified flow; Tracers; Estuaries**
Dynamics of a Longitudinally Stratified Estuary, Jorg Imberger, 3108
- Saline water-freshwater interfaces; Salinity; Salt water intrusion; Stratification; Diffusion; Eddies; Estuaries; Interfaces**
Determination of the Interfacial Eddy Diffusion Coefficient of a Highly Stratified Estuary, Yu-Hwa Wang, 3158
- Saline water-freshwater interfaces; Salinity; Salt water intrusion; Tidal currents; Tidal effects; Two phase flow; Estuaries**
Tidal Response of Two-Layer Flow at a River Mouth, Shizuo Yoshida and Masakazu Kashiwamura, 3189
- Saline water-freshwater interfaces; Salinity; Salt water intrusion; Tidal effects; Canada; Density currents; Hydraulic models**
Churchill River Salt-Water Tidal Model, Bruce D. Pratte, 3445
- Samplers; Sampling; Sediment concentration; Sediment samplers; Sediment sampling; Surf; Suspended sediments; Wave action**
Measurement of Suspended Sediment in the Surf Zone, F. A. Kilner, 2045
- Sampling; Sediment concentration; Sediment samplers; Sediment sampling; Surf; Suspended sediments; Wave action; Samplers**
Measurement of Suspended Sediment in the Surf Zone, F. A. Kilner, 2045
- Sampling; Simulation; Water circulation; Water quality; Coliform bacteria; Drainage; Estuaries; Runoff**
State Estimation of Estuarine Circulation and Water Quality by Numerical Simulation and Observation, Jan J. Leendertse and S. K. Liu, 3223
- Saline water intrusion; Salinity; Stratified flow; Tracers; Estuaries; Saline water-freshwater interfaces**
Dynamics of a Longitudinally Stratified Estuary, Jorg Imberger, 3108
- Saline water intrusion; Stratification; Transport phenomena; Density currents; Estuaries; Friction coefficient (hydraulic); Mathematical models; Numerical analysis**
Numerical Model for Density Currents in Estuaries, Karsten Fischer, 3295
- Salinity; Salt water intrusion; Stratification; Diffusion; Eddies; Estuaries; Interfaces; Saline water-freshwater interfaces**
Determination of the Interfacial Eddy Diffusion Coefficient of a Highly Stratified Estuary, Yu-Hwa Wang, 3158
- Salinity; Salt water intrusion; Tidal currents; Tidal effects; Two phase flow; Estuaries; Saline water-freshwater interfaces**
Tidal Response of Two-Layer Flow at a River Mouth, Shizuo Yoshida and Masakazu Kashiwamura, 3189
- Salinity; Salt water intrusion; Tidal effects; Canada; Density currents; Hydraulic models; Saline water-freshwater interfaces**
Churchill River Salt-Water Tidal Model, Bruce D. Pratte, 3445
- Salinity; Stratified flow; Tracers; Estuaries; Saline water-freshwater interfaces; Saline water intrusion**
Dynamics of a Longitudinally Stratified Estuary, Jorg Imberger, 3108
- Salt water intrusion; Stratification; Diffusion; Eddies; Estuaries; Interfaces; Saline water-freshwater interfaces; Salinity**
Determination of the Interfacial Eddy Diffusion Coefficient of a Highly Stratified Estuary, Yu-Hwa Wang, 3158
- Salt water intrusion; Tidal currents; Tidal effects; Two phase flow; Estuaries; Saline water-freshwater interfaces; Salinity**
Tidal Response of Two-Layer Flow at a River Mouth, Shizuo Yoshida and Masakazu Kashiwamura, 3189
- Salt water intrusion; Tidal effects; Canada; Density currents; Hydraulic models; Saline water-freshwater interfaces; Salinity**
Churchill River Salt-Water Tidal Model, Bruce D. Pratte, 3445

- Sand; Scouring; Sediment transport; South Carolina; Tidal currents; Bed forms; Circulation; Inlets (waterways); Littoral current; Littoral drift**
Sand Circulation Pattern at Price Inlet, South Carolina, Duncan M. FitzGerald, Dag Nummedal and Timothy W. Kana, 1868
- Sand; Shore protection; Surf; Bypasses; Jet pumps; Littoral current**
A Sand Bypassing System Using a Jet Pump, E. C. McNair, Jr., 1342
- Sand; Shore protection; Water levels; Beach erosion; Beach nourishment; Bypasses; Erosion; Great Lakes; Michigan**
Sand-Bypass and Shore Erosion, Bridgman, Michigan, C. N. Johnson and L. W. Hiipakka, 1361
- Sand; Sonar detection; Wave action; Wave generation; Bedding materials; Bed ripples; Ripple marks**
Wave-Formed Ripples in Nearshore Sands, John R. Dingler and Douglas L. Inman, 2109
- Sandbars; Sands; Secondary waves; Sediment transport; Wave propagation; Waves; Littoral drift**
Sand Transport by Waves, E. W. Bijker, E. van Hijum and P. Vellinga, 1149
- Sandbars; Sand traps; Shoaling; Tidal effects; Beaches; Inlets (waterways)**
Capacity of Inlet Outer Bars to Store Sand, Todd L. Walton, Jr. and William D. Adams, 1919
- Sandbars; Sand traps; Three-dimensional; Wave action; Beach erosion; Beach nourishment; Dynamics; Equilibrium; Erosion; Reflection**
Three Dimensional Tests on Dynamic Equilibrium and Artificial Nourishment, J. William Kamphuis and R. M. Myers, 1532
- Sandbars; Scale effect; Scour; Scouring; Underwater pipelines; Wave action; Failures; Laboratory tests**
Scour Around Model Pipelines Due to Wave Action, John B. Herbich, 1624
- Sandbars; Sea level; Sedimentation; Sediment deposits; Sediment transport; Tidal currents; Beach erosion; New Jersey**
Offshore Sedimentary Processes and Responses Near Beach Haven — Little Egg Inlets, New Jersey, Thomas McKinney, Joseph T. DeAlteris, Yung Y. Chao, Lloyd Stahl and James Roney, 1899
- Sandbars; Sedimentation; Sediment deposits; Wave action; Wave energy; Estuaries; Flooding; River flow**
Morphodynamics of a Wave-Dominated River Mouth, L. D. Wright, 1721
- Sandbars; Sediment deposits; Wave energy; Barriers; Beaches; Canada; Littoral current; Littoral drift; Morphology**
Process and Morphology Characteristics of Two Barrier Beaches in the Magdalen Islands, Gulf of St. Lawrence, Canada, E. H. Owens, 1975
- Sandbars; Sediment transport; Stability; Tidal effects; Tidal hydraulics; Tidal waters; Channels (waterways); River regulation**
Stability of Tidal Channels Dependent on River Improvement, Volker Barthel, 1775
- Sandbars; Sediment transport; Verification inspection; Wave height; Wave spectrum; Bathymetry; Groins (structures); Littoral drift**
Experimental Verification of Groyne Theory, C. H. Hulsbergen, W. T. Bakker and G. van Bochove, 1439
- Sandbars; Shore protection; Tidal currents; Groins (structures); Inlets (waterways); Islands (landforms)**
Inlet Changes of the East Frisian Islands, Gunter Luck, 1938
- Sandbars; Training walls; Australia; Estuaries; Flooding; Hydrographic surveys; Jetties; River flow**
Results of River Mouth Training on the Clarence Bar, New South Wales, Australia, Cyril D. Floyd and Bruce M. Drucry, 1738
- Sands; Secondary waves; Sediment transport; Wave propagation; Waves; Littoral drift; Sandbars**
Sand Transport by Waves, E. W. Bijker, E. van Hijum and P. Vellinga, 1149
- Sand traps; Shoaling; Tidal effects; Beaches; Inlets (waterways); Sandbars**
Capacity of Inlet Outer Bars to Store Sand, Todd L. Walton, Jr. and William D. Adams, 1919
- Sand traps; Storms; Wave action; Currents; Dredging; Estuaries; Harbors; Littoral drift**
Design and Behaviour of Sandtraps in Regions of High Littoral Drift, P. C. Saxena, Pashhayannur P. Vaidyaraman and R. Srinivasan, 1377
- Sand traps; Three-dimensional; Wave action; Beach erosion; Beach nourishment; Dynamics; Equilibrium; Erosion; Reflection; Sandbars**
Three Dimensional Tests on Dynamic Equilibrium and Artificial Nourishment, J. William Kamphuis and R. M. Myers, 1532
- Sand waves; Sediment transport; Tidal effects; West Germany; Channels (waterways); Dunes; Dune sands**
Transport Mechanism in Tidal Dunes, Horst Nasner, 2136
- San Francisco; Sediments; Spoil; Tracers (radioactive); Dredging; Estuaries; Estuarine environment**
Tracing Estuarine Sediments by Neutron Activation, Richard M. Ecker, John F. Sustar and William T. Harvey, 2009
- Scale effect; Scour; Scouring; Tidal waters; Tides; Erosion; Movable bed models; Prototype tests**
Movable Bed Tidal Inlet Models, Subhash C. Jain and John F. Kennedy, 3435
- Scale effect; Scour; Scouring; Underwater pipelines; Wave action; Failures; Laboratory tests; Sandbars**
Scour Around Model Pipelines Due to Wave Action, John B. Herbich, 1624
- Scale effect; Sediment transport; Simulation models; Tidal effects; Wave energy; Bed forms; Inlets (waterways); Ocean bottom**
Tidal Inlet Flow Dynamics and Sediment Movement, Jerry L. Machemehl, N. E. Bird and A. N. Chambers, 1681

- Scale effect; Sediment transport; Tracers (radioactive); West Germany; Hydraulic models; Movable bed models**
Sand Movement Investigations by Means of Radioactive Tracers in a Hydraulic Model and in the Field, Hans Rohde, 2027
- Scale effect; Shore protection; Slopes; Wave equations; Wave runup; Overtopping**
Wave Overtopping Equation, J. Richard Weggel, 2737
- Scale effect; Shore protection; Tidal currents; Dispersion; Effluent reuse; Effluents; Islands (landforms)**
Study of an Artificial Island, J. P. Lepetit and S. Moreau, 3526
- Scale effect; Stability; Wave height; Wave period; Wave runup; Armoring (streambed); Breakwaters; Model tests**
Large Scale Model Tests of Placed Stone Breakwaters, Charles K. Sollitt and Donald H. DeBok, 2572
- Scale effect; Statistical analysis; Tidal effects; Turbulence; Diffusion; Eddies; Hydraulic models**
Horizontal Diffusion in Tidal Models and Scaling Criteria for Thermal-Hydraulic Model Tests, Gerd Flugge, 3097
- Scale effect; Storm surges; Wave equations; Wave height; Wave period; Wave runup; Dikes; Echo sounding; Field investigations; Instrumentation; Ocean waves**
Wave Run-Up in Field Measurements with Newly Developed Instrument, Heie F. Erchinger, 767
- Scale effect; Surface tension; Thermal diffusion; Viscosity; Water temperature; Hydraulic models; Predictions; Prototype tests**
Adaptability of Prediction Method of Hydraulic Model Experiment for Thermal Diffusion, Masanobu Kato and Akira Wada, 3082
- Scale effect; Tethered tests; Wave action; Wave energy; Wave spectrum; Wave tanks; Breakwaters; Buoys; Energy dissipation; Field tests; Floating bodies**
Design, Analysis and Field Test of a Dynamic Floating Breakwater, D. J. Agerton, G. H. Savage and K. C. Stotz, 2792
- Scour; Scouring; Stratified flow; Troughs; Density currents; Flow patterns; Mathematical models**
Generation of Troughs by Density Currents, Hans Speekenbrink, 2170
- Scour; Scouring; Tidal waters; Tides; Erosion; Movable bed models; Prototype tests; Scale effect**
Movable Bed Tidal Inlet Models, Subhash C. Jain and John F. Kennedy, 3435
- Scour; Scouring; Underwater pipelines; Wave action; Failures; Laboratory tests; Sandbars; Scale effect**
Scour Around Model Pipelines Due to Wave Action, John B. Herbich, 1624
- Scour; Scouring; Water levels; Wave action; Wave height; Breakwaters; Coastal structures; Experimentation; Field tests**
Local Scour and Current Around a Porous Breakwater, Shintaro Hotta and Nobuo Marui, 1590
- Scour; Scouring; Wave action; Wave energy; Wharves; Offshore structures; Prototype tests**
Wave Action on Large Off-Shore Structures, C. J. Apelt and A. Macknight, 2228
- Scouring; Sea level; Tidal effects; Tidal waters; Environmental effects; Inlets (waterways); Littoral drift; New Jersey**
Beach Haven and Little Egg Inlets, A Case Study, Joseph T. DeAlteris, Thomas McKinney and James Roney, 1881
- Scouring; Sediment transport; South Carolina; Tidal currents; Bed forms; Circulation; Inlets (waterways); Littoral current; Littoral drift; Sand**
Sand Circulation Pattern at Price Inlet, South Carolina, Duncan M. FitzGerald, Dag Nummedal and Timothy W. Kana, 1868
- Scouring; Stratified flow; Troughs; Density currents; Flow patterns; Mathematical models; Scour**
Generation of Troughs by Density Currents, Hans Speekenbrink, 2170
- Scouring; Tidal waters; Tides; Erosion; Movable bed models; Prototype tests; Scale effect; Scour**
Movable Bed Tidal Inlet Models, Subhash C. Jain and John F. Kennedy, 3435
- Scouring; Underwater pipelines; Wave action; Failures; Laboratory tests; Sandbars; Scale effect; Scour**
Scour Around Model Pipelines Due to Wave Action, John B. Herbich, 1624
- Scouring; Water levels; Wave action; Wave height; Breakwaters; Coastal structures; Experimentation; Field tests; Scour**
Local Scour and Current Around a Porous Breakwater, Shintaro Hotta and Nobuo Marui, 1590
- Scouring; Wave action; Wave energy; Wharves; Offshore structures; Prototype tests; Scour**
Wave Action on Large Off-Shore Structures, C. J. Apelt and A. Macknight, 2228
- Sea level; Sedimentation; Sediment deposits; Sediment transport; Tidal currents; Beach erosion; New Jersey; Sandbars**
Offshore Sedimentary Processes and Responses Near Beach Haven — Little Egg Inlets, New Jersey, Thomas McKinney, Joseph T. DeAlteris, Yung Y. Chao, Lloyd Stahl and James Roney, 1899
- Sea level; Tidal effects; Tidal waters; Environmental effects; Inlets (waterways); Littoral drift; New Jersey; Scouring**
Beach Haven and Little Egg Inlets, A Case Study, Joseph T. DeAlteris, Thomas McKinney and James Roney, 1881
- Sea walls; Shore protection; Breakwaters; Coastal engineering; Costs; Erosion; Groins (structures); Revetments**
Low-Cost Shoreline Protection, Billy L. Edge, John G. Housley and George M. Watts, 2888
- Sea walls; Two-dimensional; Water depth; Water waves; Wave height; Boundary value problems; Breakwaters; Permeability**
Method of Analyses for Two-Dimensional Water Wave Problems, Takeshi Ijima, Chung Ren Chou and Akinori Yoshida, 2717

- Sea walls; Wave energy; Wave period; Concrete (blocks); Permeability; Reservoirs**
Permeable Seawall with Reservoir and the Use of "Warock", Takeshi Iijima, Enzoh Tanaka and Hideaki Okuzono, 2623
- Secondary waves; Sediment transport; Wave propagation; Waves; Littoral drift; Sandbars; Sands**
Sand Transport by Waves, E. W. Bijker, E. van Hijum and P. Vellinga, 1149
- Secondary waves; Wave height; Wave period; Wave recorders (water waves); Wave spectrum; Wave velocity; Breaking energy**
Kinematics of Breaking Waves, Edward B. Thornton, James J. Galvin, Frank L. Bub and David P. Richardson, 461
- Sedimentation; Sediment concentration; Sediment distribution; Sediment transport; Breakwaters; Deltas; Hydraulic models; Nigeria**
Sedimentation Studies on the Niger River Delta, Ramiro Mayor-Mora, Preben Mortensen and Jorgen Fredsoe, 2151
- Sedimentation; Sediment deposits; Sediment distribution; Sediment transport; Tidal effects; Alabama; Bays (topographic features)**
Sediment Transportation and Deposition Models for Mobile Bay, Alabama, Gary G. April, Samuel Ng and C. Everett Brett, 2092
- Sedimentation; Sediment deposits; Sediment transport; Breakwaters; Dredges; Dredging**
Sedimentation Problems at Offshore Dredged Channels, A. A. Kadib, 1756
- Sedimentation; Sediment deposits; Sediment transport; Shore protection; Breakwaters; Coastal structures; Israel; Littoral drift**
Protection by Means of Offshore Breakwaters, I. Fried, 1407
- Sedimentation; Sediment deposits; Sediment transport; Tidal currents; Beach erosion; New Jersey; Sandbars; Sea level**
Offshore Sedimentary Processes and Responses Near Beach Haven — Little Egg Inlets, New Jersey, Thomas McKinney, Joseph T. DeAlteris, Yung Y. Chao, Lloyd Stahl and James Roney, 1899
- Sedimentation; Sediment deposits; Shoaling; Bays (topographic features); Beach erosion; Erosion; Jetties; Oregon**
Changes due to Jetties at Tillamook Bay, Oregon, Paul D. Komar and Thomas A. Terich, 1791
- Sedimentation; Sediment deposits; Wave action; Wave energy; Estuaries; Flooding; River flow; Sandbars**
Morphodynamics of a Wave-Dominated River Mouth, L. D. Wright, 1721
- Sediment concentration; Sediment distribution; Sediment transport; Breakwaters; Deltas; Hydraulic models; Nigeria; Sedimentation**
Sedimentation Studies on the Niger River Delta, Ramiro Mayor-Mora, Preben Mortensen and Jorgen Fredsoe, 2151
- Sediment concentration; Sediments; Sediment samplers; Water flow; Laboratory tests**
Iowa Sediment Concentration Measuring System, Tatsuki Nakato, Frederick A. Locher, John R. Glover and John F. Kennedy, 2060
- Sediment concentration; Sediment samplers; Sediment sampling; Surf; Suspended sediments; Wave action; Samplers; Sampling**
Measurement of Suspended Sediment in the Surf Zone, F. A. Kilner, 2045
- Sediment deposits; Sediment distribution; Sediments; Tidal effects; Wave action; Beach erosion; Climatic data; Estuaries; Estuarine environment**
Factors Influencing Estuary Sediment Distribution, Mary P. Kendrick and B. V. Derbyshire, 2072
- Sediment deposits; Sediment distribution; Sediment transport; Tidal effects; Alabama; Bays (topographic features); Sedimentation**
Sediment Transportation and Deposition Models for Mobile Bay, Alabama, Gary G. April, Samuel Ng and C. Everett Brett, 2092
- Sediment deposits; Sediment transport; Beach nourishment; Beach sands; Littoral current; Predictions**
Predictive Equations Regarding Coastal Transport, D. H. Swart, 1113
- Sediment deposits; Sediment transport; Breakwaters; Dredges; Dredging; Sedimentation**
Sedimentation Problems at Offshore Dredged Channels, A. A. Kadib, 1756
- Sediment deposits; Sediment transport; Shore protection; Breakwaters; Coastal structures; Israel; Littoral drift; Sedimentation**
Protection by Means of Offshore Breakwaters, I. Fried, 1407
- Sediment deposits; Sediment transport; Suspended sediments; Aerial photography; Bathymetry; Beach erosion; Beaches; Field investigations; Littoral current**
Field Investigation of Sediment Transport Pattern in a Closed System, Tsuguo Sunamura and Kiyoshi Horikawa, 1240
- Sediment deposits; Sediment transport; Tidal currents; Beach erosion; New Jersey; Sandbars; Sea level; Sedimentation**
Offshore Sedimentary Processes and Responses Near Beach Haven — Little Egg Inlets, New Jersey, Thomas McKinney, Joseph T. DeAlteris, Yung Y. Chao, Lloyd Stahl and James Roney, 1899
- Sediment deposits; Shoaling; Bays (topographic features); Beach erosion; Erosion; Jetties; Oregon; Sedimentation**
Changes due to Jetties at Tillamook Bay, Oregon, Paul D. Komar and Thomas A. Terich, 1791
- Sediment deposits; Surges; Aeolian soils; Barriers; Beach erosion; Erosion; Islands (landforms)**
Barrier Island Dynamics: Overwash Processes and Eolian Transport, Stephen P. Leatherman, 1958
- Sediment deposits; Wave action; Wave energy; Estuaries; Flooding; River flow; Sandbars; Sedimentation**
Morphodynamics of a Wave-Dominated River Mouth, L. D. Wright, 1721
- Sediment deposits; Wave energy; Barriers; Beaches; Canada; Littoral current; Littoral drift; Morphology; Sandbars**
Process and Morphology Characteristics of Two Barrier Beaches in the Magdalen Islands, Gulf of St. Lawrence, Canada, E. H. Owens, 1975

- Sediment distribution; Sediments; Tidal effects; Wave action; Beach erosion; Climatic data; Estuaries; Estuarine environment; Sediment deposits**
Factors Influencing Estuary Sediment Distribution, Mary P. Kendrick and B. V. Derbyshire, 2072
- Sediment distribution; Sediment transport; Breakwaters; Deltas; Hydraulic models; Nigeria; Sedimentation; Sediment concentration**
Sedimentation Studies on the Niger River Delta, Ramiro Mayor-Mora, Preben Mortensen and Jorgen Fredsoe, 2151
- Sediment distribution; Sediment transport; Tidal effects; Alabama; Bays (topographic features); Sedimentation; Sediment deposits**
Sediment Transportation and Deposition Models for Mobile Bay, Alabama, Gary G. April, Samuel Ng and C. Everett Brett, 2092
- Sediments; Sediment samplers; Water flow; Laboratory tests; Sediment concentration**
Iowa Sediment Concentration Measuring System, Tatsuaki Nakato, Frederick A. Locher, John R. Glover and John F. Kennedy, 2060
- Sediments; Spoil; Tracers (radioactive); Dredging; Estuaries; Estuarine environment; San Francisco**
Tracing Estuarine Sediments by Neutron Activation, Richard M. Ecker, John F. Sustar and William T. Harvey, 2009
- Sediments; Tidal effects; Wave action; Beach erosion; Climatic data; Estuaries; Estuarine environment; Sediment deposits; Sediment distribution**
Factors Influencing Estuary Sediment Distribution, Mary P. Kendrick and B. V. Derbyshire, 2072
- Sediment samplers; Sediment sampling; Surf; Suspended sediments; Wave action; Samplers; Sampling; Sediment concentration**
Measurement of Suspended Sediment in the Surf Zone, F. A. Kilner, 2045
- Sediment samplers; Water flow; Laboratory tests; Sediment concentration; Sediments**
Iowa Sediment Concentration Measuring System, Tatsuaki Nakato, Frederick A. Locher, John R. Glover and John F. Kennedy, 2060
- Sediment sampling; Surf; Suspended sediments; Wave action; Samplers; Sampling; Sediment concentration; Sediment samplers**
Measurement of Suspended Sediment in the Surf Zone, F. A. Kilner, 2045
- Sediment transport; Beach nourishment; Beach sands; Littoral current; Predictions; Sediment deposits**
Predictive Equations Regarding Coastal Transport, D. H. Swart, 1113
- Sediment transport; Breakwaters; Deltas; Hydraulic models; Nigeria; Sedimentation; Sediment concentration; Sediment distribution**
Sedimentation Studies on the Niger River Delta, Ramiro Mayor-Mora, Preben Mortensen and Jorgen Fredsoe, 2151
- Sediment transport; Breakwaters; Dredges; Dredging; Sedimentation; Sediment deposits**
Sedimentation Problems at Offshore Dredged Channels, A. A. Kadib, 1756
- Sediment transport; Shore protection; Breakwaters; Coastal structures; Israel; Littoral drift; Sedimentation; Sediment deposits**
Protection by Means of Offshore Breakwaters, I. Fried, 1407
- Sediment transport; Shore protection; Energy equation; Littoral current; Littoral drift; Rip currents**
Longshore Transport Prediction — SPM 1973 Equation, Cyril J. Galvin and Philip Vitale, 1133
- Sediment transport; Shore protection; Wave energy; Beach erosion; Beaches; Equilibrium; Gravel; Laboratory tests; Littoral current**
Equilibrium Profiles and Longshore Transport of Coarse Material Under Oblique Wave Attack, E. van Hijum, 1258
- Sediment transport; Simulation models; Tidal effects; Wave energy; Bed forms; Inlets (waterways); Ocean bottom; Scale effect**
Tidal Inlet Flow Dynamics and Sediment Movement, Jerry L. Machemehl, N. E. Bird and A. N. Chambers, 1681
- Sediment transport; South Carolina; Tidal currents; Bed forms; Circulation; Inlets (waterways); Littoral current; Littoral drift; Sand; Scouring**
Sand Circulation Pattern at Price Inlet, South Carolina, Duncan M. FitzGerald, Dag Nummedal and Timothy W. Kana, 1868
- Sediment transport; Stability; Tidal effects; Tidal hydraulics; Tidal waters; Channels (waterways); River regulation; Sandbars**
Stability of Tidal Channels Dependent on River Improvement, Volker Barthel, 1775
- Sediment transport; Storm surges; Tidal marshes; Coastal engineering; Currents; Littoral drift; Ocean currents**
Currents in Tidal Flats During Storm Surges, Harald Gohren, 959
- Sediment transport; Surf; Wave energy; Barriers; Breakwaters; California; Jetties; Littoral current; Littoral drift**
Longshore Transport at a Total Littoral Barrier, Richard O. Bruno and Christopher G. Gable, 1203
- Sediment transport; Suspended sediments; Aerial photography; Bathymetry; Beach erosion; Beaches; Field investigations; Littoral current; Sediment deposits**
Field Investigation of Sediment Transport Pattern in a Closed System, Tsuguo Sunamura and Kiyoshi Horikawa, 1240
- Sediment transport; Tidal currents; Beach erosion; New Jersey; Sandbars; Sea level; Sedimentation; Sediment deposits**
Offshore Sedimentary Processes and Responses Near Beach Haven — Little Egg Inlets, New Jersey, Thomas McKinney, Joseph T. DeAlteris, Yung Y. Chao, Lloyd Stahl and James Roney, 1899
- Sediment transport; Tidal currents; Dispersion; Mass transfer; Open channel flow; River flow**
Dispersive Transport in River and Tidal Flows, R. B. Taylor, 3336

- Sediment transport; Tidal currents; Tidal effects; Dunes; Dune sands; Movable bed models**
Origin of Submarine Dunes, Mehmet S. Yalin, 2127
- Sediment transport; Tidal effects; Alabama; Bays (topographic features); Sedimentation; Sediment deposits; Sediment distribution**
Sediment Transportation and Deposition Models for Mobile Bay, Alabama, Gary G. April, Samuel Ng and C. Everett Brett, 2092
- Sediment transport; Tidal effects; West Germany; Channels (waterways); Dunes; Dune sands; Sand waves**
Transport Mechanism in Tidal Dunes, Horst Nasner, 2136
- Sediment transport; Tracers (radioactive); West Germany; Hydraulic models; Movable bed models; Scale effect**
Sand Movement Investigations by Means of Radioactive Tracers in a Hydraulic Model and in the Field, Hans Rohde, 2027
- Sediment transport; Unsteady flow; Wave equations; Waves; Breakwaters; Oscillation**
Quantitative Description of Sediment Transport, Ole Secher Madsen and William D. Grant, 1093
- Sediment transport; Verification inspection; Wave height; Wave spectrum; Bathymetry; Groins (structures); Littoral drift; Sandbars**
Experimental Verification of Groyne Theory, C. H. Hulsbergen, W. T. Bakker and G. van Bochove, 1439
- Sediment transport; Wave dispersion; Waves; Coastal structures; Cooling water; Intake systems; Mathematical models; Nuclear power plants; Numerical analysis; Refraction**
Application of a Sediment Transport Model, C. A. Fleming and J. N. Hunt, 1184
- Sediment transport; Wave energy; Wavemeters; Coastal engineering; Coastal structures; Directional measurement**
Wave Direction Computations with Three Gage Arrays, D. Esteva, 349
- Sediment transport; Wave height; Wave phases; Littoral drift; Ocean currents; Rip currents**
Physical Aspects of Wave-Induced Nearshore Current System, Masaru Mizuguchi and Kiyoshi Horikawa, 607
- Sediment transport; Wave propagation; Waves; Littoral drift; Sandbars; Sands; Secondary waves**
Sand Transport by Waves, E. W. Bijker, E. van Hijum and P. Vellinga, 1149
- Seiches; Tidal effects; Water levels; Wave generation; Currents; Great Lakes; Harbors**
Hydraulics of Great Lakes Inlet — Harbors Systems, Robert M. Sorensen and William N. Seelig, 1646
- Seismic studies; Site selection; Ecology; Environmental effects; Littoral drift; Marinas**
Application of CERC Special Report No.2, James W. Dunham, 3570
- Separation; Spheres; Water circulation; Wave action; Wave energy; Drag; Force**
Forces on a Sphere Under Linear Progressive Waves, Scott A. Jenkins and Douglas L. Inman, 2413
- Sewage disposal; Sewage effluents; Tracers; Water pollution; Dispersion; Distribution; Dyes; Estuaries; Predictions**
Prediction of Pollutant Distribution in Estuaries, Albert Y. Kuo and John P. Jacobson, 3276
- Sewage effluents; Tracers; Water pollution; Dispersion; Distribution; Dyes; Estuaries; Predictions; Sewage disposal**
Prediction of Pollutant Distribution in Estuaries, Albert Y. Kuo and John P. Jacobson, 3276
- Shallow water; Simulation; Walls; Water waves; Wave action; Waves; Barriers; Finite differences**
Action of Non-Linear Waves at a Solid Wall, Mohamed S. Nasser and John A. McCorquodale, 815
- Shallow water; Tanker ships; Water depth; Berths; Dolphins (structures); Head losses; Mass**
Added Masses of Large Tankers Berthing to Dolphins, Taizo Hayashi and Masujiro Shirai, 2830
- Shallow water; Tidal effects; Tidal marshes; Water waves; Estuaries; Finite element method; Numerical analysis**
Finite Element Model for Estuaries with Inter-Tidal Flats, Bruno Herrling, 3396
- Shallow water; Tsunamis; Wave height; Friction coefficient (hydraulic); Numerical analysis; Propagation**
Tsunami Propagation in the Pacific Ocean, Manfred Engel and Wilfried Zahel, 971
- Shallow water; Turbulent diffusion; Friction coefficient (hydraulic); Ocean bottom; Ripple marks**
Consideration on Friction Coefficient for Sea Bottom, Toru Sawaragi, Koichiro Iwata and Masayoshi Kubo, 595
- Ships; Wave tanks; Accidents; Collisions; Harbor structures; Mooring; Moorings; Offshore drilling**
Protection of Maritime Structures Against Ship Collisions, Kazuki Oda and Shositiro Nagai, 2810
- Shoaling; Bays (topographic features); Beach erosion; Erosion; Jetties; Oregon; Sedimentation; Sediment deposits**
Changes due to Jetties at Tillamook Bay, Oregon, Paul D. Komar and Thomas A. Terich, 1791
- Shoaling; Slopes; Wave period; Wave runup; Waves; Breaking; Periodic variations**
Set-Up and Run-Up in Shoaling Breakers, William G. Van Dorn, 738
- Shoaling; Tidal effects; Beaches; Inlets (waterways); Sandbars; Sand traps**
Capacity of Inlet Outer Bars to Store Sand, Todd L. Walton, Jr. and William D. Adams, 1919
- Shoaling; Topographical factors; Beach erosion; Beaches; Breakwaters; Construction; Harbor structures; Japan; Ocean bottom**
Topographic Change Resulting from the Construction of a Harbor on a Sandy Beach, Kashima Port, Norio Tanaka and Shoji Sato, 1824

- Shoaling; Tsunamis; Warning systems; Coastal engineering; Coastal plains; Japan; Power spectra; Refraction**
Transformation of Tsunamis in a Coastal Zone, Shigehisa Nakamura, Haruo Higuchi and Yoshito Tsuchiya, 988
- Shoaling; Wave action; Wave dispersion; Wave height; Waves; Wave velocity; Breaking; Refraction**
Refraction of Finite-Height and Breaking Waves, James R. Walker, 507
- Shoaling; Wave equations; Wave functions; Waves; Wave velocity**
Wave Shoaling of Finite Amplitude Waves, Masataka Yamaguchi and Yoshito Tsuchiya, 497
- Shock tests; Strain; Strain gages; Breakwaters; Caissons; Concrete (reinforced); Cylindrical bodies; Model tests; Pressure cells**
Cylindrical Caisson Breakwater: Strain Model Tests, Helge Gravesen, Finn P. Brodersen, Jørn S. Larsen and H. Lundgren, 2357
- Shore protection; Beaches; Beach nourishment; Groins (structures); Hydrographic surveys; Monitoring**
Comprehensive Monitoring of a Beach Restoration Project, Omar H. Shemdin, H. K. Brooks, Z. Ceylanli and S. L. Harrell, 1477
- Shore protection; Breakwaters; Coastal engineering; Costs; Erosion; Groins (structures); Revetments; Sea walls**
Low-Cost Shoreline Protection, Billy L. Edge, John G. Housley and George M. Watts, 2888
- Shore protection; Breakwaters; Coastal structures; Israel; Littoral drift; Sedimentation; Sediment deposits; Sediment transport**
Protection by Means of Offshore Breakwaters, I. Fried, 1407
- Shore protection; Energy equation; Littoral current; Littoral drift; Rip currents; Sediment transport**
Longshore Transport Prediction — SPM 1973 Equation, Cyril J. Galvin and Philip Vitale, 1133
- Shore protection; Simulation; Tsunamis; Numerical analysis; Propagation**
Numerical Simulation of Tsunamis Originating in the Peru-Chile Trench, A. W. Garcia and H. L. Butler, 1025
- Shore protection; Slopes; Wave equations; Wave runoff; Overtopping; Scale effect**
Wave Overtopping Equation, J. Richard Weggel, 2737
- Shore protection; Sri Lanka; Beach nourishment; Coastal engineering; Recreational facilities**
Coastal Problems in Sri Lanka, Franciscus Gerritsen and Summa R. Amarasinghe, 3487
- Shore protection; Storms; Breakwaters; Costs; Erosion; Great Lakes; Groins (structures)**
Low-Cost Shore Protection on the Great Lakes: A Demonstration/Research Program, John M. Armstrong, 2858
- Shore protection; Storms; Water temperature; Wave height; Beach erosion; Erosion; Field tests; Groins (structures); Laboratory tests; Littoral drift**
Laboratory Investigation of Shore Erosion Processes, Ernest F. Brater and David Ponce-Campos, 1493
- Shore protection; Subsidence; Beach erosion; Breakwaters; Japan; Ocean bottom**
Changes of Sea Bed Due to Detached Breakwaters, Osamu Toyoshima, 1572
- Shore protection; Surf; Bypasses; Jet pumps; Littoral current; Sand**
A Sand Bypassing System Using a Jet Pump, E. C. McNair, Jr., 1342
- Shore protection; Swimming; Beaches; Beach nourishment; Breakwaters; Hawaii; Recreational facilities**
Proposed "Improvement" of Kaimu Beach, Hawaii, Doak C. Cox, Franciscus Gerritsen and Theodore T. Lee, 1552
- Shore protection; Tidal currents; Dispersion; Effluent reuse; Effluents; Islands (landforms); Scale effect**
Study of an Artificial Island, J. P. Lepetit and S. Moreau, 3526
- Shore protection; Tidal currents; Groins (structures); Inlets (waterways); Islands (landforms); Sandbars**
Inlet Changes of the East Frisian Islands, Gunter Luck, 1938
- Shore protection; Water levels; Beach erosion; Beach nourishment; Bypasses; Erosion; Great Lakes; Michigan; Sand**
Sand-Bypass and Shore Erosion, Bridgman, Michigan, C. N. Johnson and L. W. Hiipakka, 1361
- Shore protection; Wave action; Wave energy; Bays (topographic features); Beach erosion; Breakwaters**
Headland Defense of Coasts, Richard Silvester, 1394
- Shore protection; Wave dispersion; Computerized simulation; Concrete (blocks); Harbor structures; Quays; Reflection; Revetments**
Quay Wall with Wave Absorber "Iglou", Naofumi Shiraiishi, Robert Q. Palmer and Hiroshi Okamoto, 2677
- Shore protection; Wave energy; Beach erosion; Beaches; Equilibrium; Gravel; Laboratory tests; Littoral current; Sediment transport**
Equilibrium Profiles and Longshore Transport of Coarse Material Under Oblique Wave Attack, E. van Hijum, 1258
- Shore protection; Weed control; Weeds; Erosion; Erosion control; Gullies; Netherlands**
Recent Applications of Artificial Seaweed in the Netherlands, Henk G.H. ten Hoopen, 2905
- Simulation; Simulation models; Storm surges; Delaware; New Jersey; Probability**
Simulation Model for Storm Surge Probabilities, Mohammad H. Fallah, J. N. Sharma and Cheng Y. Yang, 934
- Simulation; Storm surges; Hydromechanics; Numerical analysis**
Generalized Model for Storm Surges, Gour-Tsyh Yeh and Fei-Fan Yeh, 921
- Simulation; Tsunamis; Numerical analysis; Propagation; Shore protection**
Numerical Simulation of Tsunamis Originating in the Peru-Chile Trench, A. W. Garcia and H. L. Butler, 1025

- Simulation; Walls; Water waves; Wave action; Waves; Barriers; Finite differences; Shallow water**
Action of Non-Linear Waves at a Solid Wall, Mohamed S. Nasser and John A. McCorquodale, 815
- Simulation; Water circulation; Water quality; Coliform bacteria; Drainage; Estuaries; Runoff; Sampling**
State Estimation of Estuarine Circulation and Water Quality by Numerical Simulation and Observation, Jan J. Leendertse and S. K. Liu, 3223
- Simulation; Water levels; Wave height; Wave runoff; Beaches; Ocean waves; Resonance**
Wave Run-Up on a Simulated Beach, A. J. Sutherland, J. N. Sharma and Omar H. Shemdin, 752
- Simulation; Waves; Wave tanks; Laboratory tests; Ocean waves; Random variables**
Random Wave Simulation in a Laboratory Wave Tank, Akira Kimura and Yuichi Iwagaki, 368
- Simulation models; Storm surges; Delaware; New Jersey; Probability; Simulation**
Simulation Model for Storm Surge Probabilities, Mohammad H. Fallah, J. N. Sharma and Cheng Y. Yang, 934
- Simulation models; Tidal effects; Wave energy; Bed forms; Inlets (waterways); Ocean bottom; Scale effect; Sediment transport**
Tidal Inlet Flow Dynamics and Sediment Movement, Jerry L. Machemehl, N. E. Bird and A. N. Chambers, 1681
- Site selection; Ecology; Environmental effects; Littoral drift; Marinas; Seismic studies**
Application of CERC Special Report No.2, James W. Dunham, 3570
- Site selection; Utilization; Barges; Economic analysis; Environmental effects; Harbors; Performance; Safety**
Probable Utilization Level for a Barge Harbor, Martin T. Czerniak and Choule J. Sonu, 3557
- Site selection; Water quality; Diffusers; Dilution; Mixing; Outfall sewers**
Design Procedures for Ocean Outfalls, Jeffrey A. Layton, 2919
- Sitting; Wave action; Wave damping; Wave energy; Breakwaters; Reflection**
Slit-Type Breakwater: Box-Type Wave Absorber, Shositiro Nagai and Shohachi Kakuno, 2697
- Slope protection; Slope stability; Airports; Breakwaters; Hawaii; Reefs**
Design and Construction of Protective Structure for New Reef Runway at Honolulu International Airport, Wilfred D. Darling, 2589
- Slope protection; Slope stability; Wave action; Wave energy; Wave period; Armoring (streambed); Breakwaters; Failure**
Armour Blocks as Slope Protection, A. F. Whillock and W. A. Price, 2564
- Slopes; Beach erosion; Investigations; Japan; Littoral current; Littoral drift**
Concept for Inferring the Littoral Drift Trend, Masataro Hattori and Takasuke Suzuki, 1223
- Slopes; Wave equations; Wave runoff; Overtopping; Scale effect; Shore protection**
Wave Overtopping Equation, J. Richard Weggel, 2737
- Slopes; Wave period; Wave runoff; Waves; Breaking; Periodic variations; Shoaling**
Set-Up and Run-Up in Shoaling Breakers, William G. Van Dorn, 738
- Slopes; Wave spectrum; Beach erosion; Beaches; Computer models**
Study of Equilibrium Beach Profiles, Robert A. Dalrymple and William W. Thompson, 1277
- Slope stability; Airports; Breakwaters; Hawaii; Reefs; Slope protection**
Design and Construction of Protective Structure for New Reef Runway at Honolulu International Airport, Wilfred D. Darling, 2589
- Slope stability; Stability; Surf; Wave period; Wave runoff; Breakwaters; Resonance; Rubble; Rubble mounds**
New Design Principles for Rubble Mound Structures, Per Moller Bruun and Ali Riza Gunbak, 2429
- Slope stability; Wave action; Wave energy; Wave period; Armoring (streambed); Breakwaters; Failure; Slope protection**
Armour Blocks as Slope Protection, A. F. Whillock and W. A. Price, 2564
- Slots; Buoyancy; Diffusers; Dilution; Discharge (water); Eddies; Experimentation; Jets**
Negatively Buoyant Slot Jets, D. M. Shahrabani and J. D. Ditmars, 2976
- Social impact; Coastal engineering; Environmental factors; Monitoring; Nuclear power plants**
Coastal Environment and a Nuclear Power Plant, Ralph A. de la Parra, 3014
- Social needs; Beaches; Breakwaters; Enclosures; Groins (structures); Israel; Recreational facilities**
Enclosing Scheme for Bathing-Beach Development, Joseph Tauman, 1425
- Solitary waves; Time dependence; Wave height; Waves; Wave velocity; Breaking; Gravity waves**
Recent Developments in the Study of Breaking Waves, Michael S. Longuet-Higgins, 441
- Sonar detection; Wave action; Wave generation; Bedding materials; Bed ripples; Ripple marks; Sand**
Wave-Formed Ripples in Nearshore Sands, John R. Dingler and Douglas L. Inman, 2109
- South Carolina; Tidal currents; Bed forms; Circulation; Inlets (waterways); Littoral current; Littoral drift; Sand; Scouring; Sediment transport**
Sand Circulation Pattern at Price Inlet, South Carolina, Duncan M. FitzGerald, Dag Nummedal and Timothy W. Kana, 1868
- Specific energy; Estuaries; Landforms; Nonuniform flow; Open channel flow**
Concept of Minimum Specific Energy and Its Relation to Natural Forms, Gordon R. McKay and Ahad K. Kazempour, 2186
- Spectral analysis; Statistical analysis; Storms; Wave height; Wave spectrum; Ocean waves**
Six-Parameter Wave Spectra, Michel K. Ochi and E. Nadine Hubble, 301

- Spectral analysis; Statistical analysis; Wave forecasting; Wave period; Waves; Wave spectrum; Climatology; Coastal engineering; Ocean waves**
Ocean Wave Statistics from FNWC Spectral Analysis, Warren C. Thompson and F. Michael Reynolds, 238
- Spheres; Water circulation; Wave action; Wave energy; Drag; Force; Separation**
Forces on a Sphere Under Linear Progressive Waves, Scott A. Jenkins and Douglas L. Inman, 2413
- Spoil; Tracers (radioactive); Dredging; Estuaries; Estuarine environment; San Francisco; Sediments**
Tracing Estuarine Sediments by Neutron Activation, Richard M. Ecker, John F. Sustar and William T. Harvey, 2009
- Spreading; Time dependence; Wastewater; Buoyancy; Fluid mechanics; Gravitation; Ocean currents**
Buoyancy-Driven Gravitational Spreading, Robert C.Y. Koh, 2956
- Sri Lanka; Beach nourishment; Coastal engineering; Recreational facilities; Shore protection**
Coastal Problems in Sri Lanka, Francisus Gerritsen and Summa R. Amarasinghe, 3487
- Stability; Statistical analysis; Storms; Variability; Beach erosion; Eigenvalues; Impulses; Responses**
Stability and Impulse Response of Empirical Eigenfunctions, Clinton D. Winant and David G. Aubrey, 1312
- Stability; Stratified flow; Thermal pollution; Turbulence; Discharge (water); Interfacial tension**
Interfacial Instability in Stratified Flow, Richard H. French, 3124
- Stability; Surf; Wave period; Wave runup; Breakwaters; Resonance; Rubble; Rubble mounds; Slope stability**
New Design Principles for Rubble Mound Structures, Per Moller Bruun and Ali Riza Gunbak, 2429
- Stability; Tidal effects; Tidal hydraulics; Tidal waters; Channels (waterways); River regulation; Sandbars; Sediment transport**
Stability of Tidal Channels Dependent on River Improvement, Volker Barthel, 1775
- Stability; Wave action; Wave energy; Bottom water; Continental shelf; Cyclic loads; Foundations; Ocean bottom; Offshore structures; Predictions**
Prediction of Wave-Induced Seafloor Movements, Leland Milo Kraft, Jr. and David James Watkins, 1605
- Stability; Wave action; Wave energy; Breakwaters; Damage; Hydraulic models; Rubble; Rubble mounds**
Effect of Broken Dolosse on Breakwater Stability, D. Donald Davidson and Dennis G. Markle, 2544
- Stability; Wave energy; Wave height; Wave period; Waves; Coastal engineering; Coastal structures**
Consecutive High Waves in Coastal Waters, Winfried Siefert, 171
- Stability; Wave height; Wave period; Wave runup; Armoring (streambed); Breakwaters; Model tests; Scale effect**
Large Scale Model Tests of Placed Stone Breakwaters, Charles K. Sollitt and Donald H. DeBok, 2572
- Statistical analysis; Statistical distributions; Wave energy; Wave height; Wave period**
Characteristic Wave Period, Madhav Manohar, Ismail E. Mobarek and N. A. El Sharky, 273
- Statistical analysis; Storms; Variability; Beach erosion; Eigenvalues; Impulses; Responses; Stability**
Stability and Impulse Response of Empirical Eigenfunctions, Clinton D. Winant and David G. Aubrey, 1312
- Statistical analysis; Storms; Wave height; Wave spectrum; Ocean waves; Spectral analysis**
Six-Parameter Wave Spectra, Michel K. Ochi and E. Nadine Hubble, 301
- Statistical analysis; Tidal effects; Turbulence; Diffusion; Eddies; Hydraulic models; Scale effect**
Horizontal Diffusion in Tidal Models and Scaling Criteria for Thermal-Hydraulic Model Tests, Gerd Flugge, 3097
- Statistical analysis; Wave forecasting; Wave period; Waves; Wave spectrum; Climatology; Coastal engineering; Ocean waves; Spectral analysis**
Ocean Wave Statistics from FNWC Spectral Analysis, Warren C. Thompson and F. Michael Reynolds, 238
- Statistical analysis; Wave height; Wavemeters; Wave recorders (water waves); Wave spectrum; Coastal engineering; India**
Ocean Wave Record Analysis by Tucker's Method -- An Evaluation, Jade Dattatri and Irvathur Vasudeva Nayak, 289
- Statistical distributions; Wave energy; Wave height; Wave period; Statistical analysis**
Characteristic Wave Period, Madhav Manohar, Ismail E. Mobarek and N. A. El Sharky, 273
- Statistical models; Tsunamis; Wave dispersion; Wave height; Japan; Models; Numerical analysis**
Numerical Models of Huge Tsunamis Off the Sanriku Coast, Toshio Iwasaki, 1044
- Steel piles; Structural design; Coastal structures; Lateral forces; Pile foundations**
Concepts in Design of Coastal Structures, Casimir J. Kray, 2209
- Stereophotography; Water levels; Waves; Breaking; Coastal engineering; Field tests; Littoral drift; Ocean currents; Photogrammetry**
Terrestrial Photogrammetric Measurements of Breaking Waves and Longshore Currents in the Nearshore Zone, Joseph W. Maresca, Jr. and Erwin Seibel, 681
- Storms; Breakwaters; Costs; Erosion; Great Lakes; Groins (structures); Shore protection**
Low-Cost Shore Protection on the Great Lakes: A Demonstration/Research Program, John M. Armstrong, 2858

- Storms; Storm surges; Storm water; Wave energy; Wave height; Wave period; Wave recorders (water waves); Waves; Wave spectrum; Continental shelf**
Extreme Wave Parameters Based on Continental Shelf Storm Wave Records, R. E. Haring, A. R. Osborne and L. P. Spencer, 151
- Storms; Storm surges; Wave action; Wave energy; Beach erosion; Beach nourishment; Erosion; Littoral current; Recreational facilities**
Cape Hatteras Beach Nourishment, John S. Fisher and Wilson N. Felder, 1512
- Storms; Tidal effects; Tidal energy; Warning systems; Flood plain insurance; Hurricanes**
Hurricane Tide Frequencies on the Atlantic Coast, Francis P. Ho, 886
- Storms; Variability; Beach erosion; Eigenvalues; Impulses; Responses; Stability; Statistical analysis**
Stability and Impulse Response of Empirical Eigenfunctions, Clinton D. Winant and David G. Aubrey, 1312
- Storms; Water temperature; Wave height; Beach erosion; Erosion; Field tests; Groins (structures); Laboratory tests; Littoral drift; Shore protection**
Laboratory Investigation of Shore Erosion Processes, Ernest F. Brater and David Ponce-Campos, 1493
- Storms; Wave action; Currents; Dredging; Estuaries; Harbors; Littoral drift; Sand traps**
Design and Behaviour of Sandtraps in Regions of High Littoral Drift, P. C. Saxena, Pazhhayannur P. Vaidyaraman and R. Srinivasan, 1377
- Storms; Wave height; Wave spectrum; Ocean waves; Spectral analysis; Statistical analysis**
Six-Parameter Wave Spectra, Michel K. Ochi and E. Nadine Hubble, 301
- Storm surges; Delaware; New Jersey; Probability; Simulation; Simulation models**
Simulation Model for Storm Surge Probabilities, Mohammad H. Fallah, J. N. Sharma and Cheng Y. Yang, 934
- Storm surges; Hydromechanics; Numerical analysis; Simulation**
Generalized Model for Storm Surges, Gour-Tsyh Yeh and Fei-Fan Yeh, 921
- Storm surges; Storm water; Wave energy; Wave height; Wave period; Wave recorders (water waves); Waves; Wave spectrum; Continental shelf; Storms**
Extreme Wave Parameters Based on Continental Shelf Storm Wave Records, R. E. Haring, A. R. Osborne and L. P. Spencer, 151
- Storm surges; Surf; Water level fluctuations; Water levels; Wave action; Wave energy; Waves; Wave spectrum**
Energy Spectra of Irregular Surf Waves, Fritz Busching, 539
- Storm surges; Tidal marshes; Coastal engineering; Currents; Littoral drift; Ocean currents; Sediment transport**
Currents in Tidal Flats During Storm Surges, Harald Gohren, 959
- Storm surges; Tropical cyclones; Computer models; Forecasting; Hurricanes; Numerical analysis**
SPLASH — A Model for Forecasting Tropical Storm Surges, Celso S. Barrientos and Chester P. Jelesnianski, 941
- Storm surges; Tsunamis; Wave runup; Flooding; Predictions**
Tsunami Inundation Prediction, Charles L. Bretschneider and Pieter G. Wybro, 1006
- Storm surges; Wave action; Wave energy; Beach erosion; Beach nourishment; Erosion; Littoral current; Recreational facilities; Storms**
Cape Hatteras Beach Nourishment, John S. Fisher and Wilson N. Felder, 1512
- Storm surges; Wave equations; Wave height; Wave period; Wave runup; Dikes; Echo sounding; Field investigations; Instrumentation; Ocean waves; Scale effect**
Wave Run-Up in Field Measurements with Newly Developed Instrument, Heic F. Erchinger, 767
- Storm surges; Weather forecasting; Automation; Forecasting; Hurricanes**
Automated Forecasting of Extratropical Storm Surges, N. Arthur Pore, 906
- Storm water; Wave energy; Wave height; Wave period; Wave recorders (water waves); Waves; Wave spectrum; Continental shelf; Storms; Storm surges**
Extreme Wave Parameters Based on Continental Shelf Storm Wave Records, R. E. Haring, A. R. Osborne and L. P. Spencer, 151
- Strain; Strain gages; Breakwaters; Caissons; Concrete (reinforced); Cylindrical bodies; Model tests; Pressure cells; Shock tests**
Cylindrical Caisson Breakwater: Strain Model Tests, Helge Gravesen, Finn P. Brodersen, Jørn S. Larsen and H. Lundgren, 2357
- Strain gages; Breakwaters; Caissons; Concrete (reinforced); Cylindrical bodies; Model tests; Pressure cells; Shock tests; Strain**
Cylindrical Caisson Breakwater: Strain Model Tests, Helge Gravesen, Finn P. Brodersen, Jørn S. Larsen and H. Lundgren, 2357
- Stratification; Diffusion; Eddies; Estuaries; Interfaces; Saline water-freshwater interfaces; Salinity; Salt water intrusion**
Determination of the Interfacial Eddy Diffusion Coefficient of a Highly Stratified Estuary, Yu-Hwa Wang, 3158
- Stratification; Tidal effects; Wave energy; West Germany; Damping; Energy dissipation; Estuaries**
Energy Dissipation in Tidal Estuaries, Hans-Werner Partenscky and Gunther Barg, 3312
- Stratification; Transport phenomena; Density currents; Estuaries; Friction coefficient (hydraulic); Mathematical models; Numerical analysis; Saline water intrusion**
Numerical Model for Density Currents in Estuaries, Karsten Fischer, 3295
- Stratification; Two phase flow; Convection; Diffusion; Dispersion; Finite element method; Numerical analysis**
Numerical Modeling of Dispersion in Stratified Waters, George C. Christodoulou and Jerome J. Connor, 3138
- Stratified flow; Thermal pollution; Turbulence; Discharge (water); Interfacial tension; Stability**
Interfacial Instability in Stratified Flow, Richard H. French, 3124

- Stratified flow; Tracers; Estuaries; Saline water-freshwater interfaces; Saline water intrusion; Salinity**
Dynamics of a Longitudinally Stratified Estuary, Jorg Imberger, 3108
- Stratified flow; Troughs; Density currents; Flow patterns; Mathematical models; Scour; Scouring**
Generation of Troughs by Density Currents, Hans Speekenbrink, 2170
- Stream flow; Water flow; Wave action; Wave energy; Cylinders; Drag; Hydraulic models; Lift; Oscillations; Reynolds number**
High Reynolds Number Oscillating Flow by Cylinders, Tokuo Yamamoto and John H. Nath, 2321
- Stresses; Testing; Armoring (streambed); Breakwaters; Experimentation**
Experimental Studies of Stresses Within the Breakwater Armor Piece "Dolos", Omar J. Lillevang and Wayne E. Nickola, 2519
- Structural design; Coastal structures; Lateral forces; Pile foundations; Steel piles**
Concepts in Design of Coastal Structures, Casimir J. Kray, 2209
- Submerged flow; Underwater structures; Wave action; Wave energy; Drag; Inertial forces**
Wave Forces on Submerged Objects, Suphat Vongvisessomjai and Richard Silvester, 2387
- Subsidence; Beach erosion; Breakwaters; Japan; Ocean bottom; Shore protection**
Changes of Sea Bed Due to Detached Breakwaters, Osamu Toyoshima, 1572
- Surf; Bypasses; Jet pumps; Littoral current; Sand; Shore protection**
A Sand Bypassing System Using a Jet Pump, E. C. McNair, Jr., 1342
- Surf; Suspended sediments; Wave action; Samplers; Sampling; Sediment concentration; Sediment samplers; Sediment sampling**
Measurement of Suspended Sediment in the Surf Zone, F. A. Kilner, 2045
- Surf; Three-dimensional; Two-dimensional; Wave equations; Wave height; Breaking**
Three-Dimensional Conditions of Surf, William L. Wood, 525
- Surf; Tidal currents; Wave recorders (water waves); Beaches; Inlets (waterways); Littoral current; Littoral drift**
Changes in Inlet Offset due to Stabilization, Dennis K. Hubbard, 1812
- Surf; Turbulence; Beaches; Flowmeters; Friction coefficient (hydraulic); Rip currents**
Lateral and Bottom Forces on Longshore Currents, David A. Huntley, 645
- Surf; Water depth; Waves; Currents; Finite elements; Gravity waves; Predictions; Refraction**
Current Depth Defraction Using Finite Elements, Ove Skovgaard and Ivar G. Jonsson, 721
- Surf; Water level fluctuations; Water levels; Wave action; Wave energy; Waves; Wave spectrum; Storm surges**
Energy Spectra of Irregular Surf Waves, Fritz Busching, 539
- Surf; Wave energy; Barriers; Breakwaters; California; Jetties; Littoral current; Littoral drift; Sediment transport**
Longshore Transport at a Total Littoral Barrier, Richard O. Bruno and Christopher G. Gable, 1203
- Surf; Wave height; Wave period; Waves; Wave spectrum; Breaking; Dimensional analysis; Experimentation**
Wave Spectrum of Breaking Wave, Toru Sawaragi and Koichiro Iwata, 580
- Surf; Wave period; Wave runup; Breakwaters; Resonance; Rubble; Rubble mounds; Slope stability; Stability**
New Design Principles for Rubble Mound Structures, Per Moller Bruun and Ali Riza Gunbak, 2429
- Surface tension; Thermal diffusion; Viscosity; Water temperature; Hydraulic models; Predictions; Prototype tests; Scale effect**
Adaptability of Prediction Method of Hydraulic Model Experiment for Thermal Diffusion, Masanobu Kato and Akira Wada, 3082
- Surface waves; Thermal energy; Thermal gradient; Two phase flow; Water flow; Energy conversion**
Flow Field Near an Ocean Thermal Energy Conversion Plant, D. M. Sheppard, G. M. Powell and I. B. Chou, 3068
- Surface waves; Wave energy; Wave spectrum; Distribution functions; Distribution patterns; Frequency; Ocean waves**
Directional Spectral of Ocean Surface Waves, Hisashi Mitsuyasu and S. Mizuno, 329
- Surges; Aeolian soils; Barriers; Beach erosion; Erosion; Islands (landforms); Sediment deposits**
Barrier Island Dynamics: Overwash Processes and Eolian Transport, Stephen P. Leatherman, 1958
- Surges; Turbulence; Wave height; Wave runup; Waves; Beaches; Breaking; Resonance**
Resonant Interactions for Waves Breaking on a Beach, Robert T. Guza and Anthony J. Bowen, 560
- Suspended sediments; Aerial photography; Bathymetry; Beach erosion; Beaches; Field investigations; Littoral current; Sediment deposits; Sediment transport**
Field Investigation of Sediment Transport Pattern in a Closed System, Tsuguo Sunamura and Kiyoshi Horikawa, 1240
- Suspended sediments; Wave action; Samplers; Sampling; Sediment concentration; Sediment samplers; Sediment sampling; Surf**
Measurement of Suspended Sediment in the Surf Zone, F. A. Kilner, 2045
- Swimming; Beaches; Beach nourishment; Breakwaters; Hawaii; Recreational facilities; Shore protection**
Proposed "Improvement" of Kaimu Beach, Hawaii, Doak C. Cox, Franciscus Gerritsen and Theodore T. Lee, 1552
- Taiwan; Wave height; Wave period; Waves; Wind speed; Coastal engineering; Ocean waves**
Waves Off Taichung Coast of Taiwan, Charles C.C. Chang, M. H. Wang and J. T. Juang, 129

- Tanker ships; Water depth; Berths; Dolphins (structures); Head losses; Mass; Shallow water**
 Added Masses of Large Tankers Berthing to Dolphins, Taizo Hayashi and Masujiro Shirai, 2830
- Temperature distribution; Thermal diffusion; Thermal pollution; Water temperature; Discharge (water); Hydraulic models; Nuclear power plants; Prototype tests**
 Thermal Discharges: Prototype vs. Hydraulic Model, Gary C. Parker, Ching S. Fang and Albert Y. Kuo, 3049
- Testing; Armoring (streambed); Breakwaters; Experimentation; Stresses**
 Experimental Studies of Stresses Within the Breakwater Armor Piece "Dolos", Omar J. Lillevang and Wayne E. Nickola, 2519
- Tethered tests; Wave action; Wave energy; Wave spectrum; Wave tanks; Breakwaters; Buoys; Energy dissipation; Field tests; Floating bodies; Scale effect**
 Design, Analysis and Field Test of a Dynamic Floating Breakwater, D. J. Agerton, G. H. Savage and K. C. Stotz, 2792
- Thermal diffusion; Thermal pollution; Water temperature; Discharge (water); Hydraulic models; Nuclear power plants; Prototype tests; Temperature distribution**
 Thermal Discharges: Prototype vs. Hydraulic Model, Gary C. Parker, Ching S. Fang and Albert Y. Kuo, 3049
- Thermal diffusion; Viscosity; Water temperature; Hydraulic models; Predictions; Prototype tests; Scale effect; Surface tension**
 Adaptability of Prediction Method of Hydraulic Model Experiment for Thermal Diffusion, Masanobu Kato and Akira Wada, 3082
- Thermal energy; Thermal gradient; Two phase flow; Water flow; Energy conversion; Surface waves**
 Flow Field Near an Ocean Thermal Energy Conversion Plant, D. M. Sheppard, G. M. Powell and I. B. Chou, 3068
- Thermal gradient; Two phase flow; Water flow; Energy conversion; Surface waves; Thermal energy**
 Flow Field Near an Ocean Thermal Energy Conversion Plant, D. M. Sheppard, G. M. Powell and I. B. Chou, 3068
- Thermal pollution; Turbulence; Discharge (water); Interfacial tension; Stability; Stratified flow**
 Interfacial Instability in Stratified Flow, Richard H. French, 3124
- Thermal pollution; Two phase flow; Diffusers; Discharge (water); Hydraulic models; Nuclear power plants; Plume detection; Plumes**
 Field Studies of Submerged-Diffuser Thermal Plumes with Comparisons to Predictive Model Results, A. A. Frigo, Richard A. Paddock and J. D. Ditmars, 3028
- Thermal pollution; Water temperature; Discharge (water); Hydraulic models; Nuclear power plants; Prototype tests; Temperature distribution; Thermal diffusion**
 Thermal Discharges: Prototype vs. Hydraulic Model, Gary C. Parker, Ching S. Fang and Albert Y. Kuo, 3049
- Three-dimensional; Two-dimensional; Wave equations; Wave height; Breaking; Surf**
 Three-Dimensional Conditions of Surf, William L. Wood, 525
- Three-dimensional; Water waves; Wave generation; Waves; Hydraulic models**
 3-D Hydraulic Model of Wave Generated by Displacements, Shin-Lin Liu and Robert L. Wiegel, 1060
- Three-dimensional; Wave action; Beach erosion; Beach nourishment; Dynamics; Equilibrium; Erosion; Reflection; Sandbars; Sand traps**
 Three Dimensional Tests on Dynamic Equilibrium and Artificial Nourishment, J. William Kamphuis and R. M. Myers, 1532
- Three-dimensional; Wave dispersion; Wave height; Waves; Breaking; Breakwaters; Friction coefficient (hydraulic); Littoral drift; Ocean currents**
 Non-Uniform Alongshore Currents, Michael R. Gourlay, 701
- Tidal currents; Beach erosion; New Jersey; Sandbars; Sea level; Sedimentation; Sediment deposits; Sediment transport**
 Offshore Sedimentary Processes and Responses Near Beach Haven — Little Egg Inlets, New Jersey, Thomas McKinney, Joseph T. DeAlteris, Yung Y. Chao, Lloyd Stahl and James Roney, 1899
- Tidal currents; Bed forms; Circulation; Inlets (waterways); Littoral current; Littoral drift; Sand; Scouring; Sediment transport; South Carolina**
 Sand Circulation Pattern at Price Inlet, South Carolina, Duncan M. FitzGerald, Dag Nummedal and Timothy W. Kana, 1868
- Tidal currents; Dispersion; Effluent reuse; Effluents; Islands (landforms); Scale effect; Shore protection**
 Study of an Artificial Island, J. P. Lepetit and S. Moreau, 3526
- Tidal currents; Dispersion; Mass transfer; Open channel flow; River flow; Sediment transport**
 Dispersive Transport in River and Tidal Flows, R. B. Taylor, 3336
- Tidal currents; Groins (structures); Inlets (waterways); Islands (landforms); Sandbars; Shore protection**
 Inlet Changes of the East Frisian Islands, Gunter Luck, 1938
- Tidal currents; Tidal effects; Algorithms; California; Discharge (water); Numerical analysis**
 Tidal Stream Flow Solved by Galerkin Technique, L. H. Smith and Ralph T-S Cheng, 3358
- Tidal currents; Tidal effects; Dunes; Dune sands; Movable bed models; Sediment transport**
 Origin of Submarine Dunes, Mehmet S. Yalin, 2127
- Tidal currents; Tidal effects; Tidal energy; Hydraulic models; Prototype tests; Roughness (hydraulic)**
 Model Verification for Tidal Constituents, R. W. Whalin, F. C. Perry and D. L. Durham, 3377
- Tidal currents; Tidal effects; Tidal energy; Tidal hydraulics; Vortices; Estuaries; Flooding; Inlets (waterways)**
 Harbour Inlets on Tidal Estuaries, Hans Vollmers, 1854

- Tidal currents; Tidal effects; Tidal hydraulics; Tidal marshes; Wave height; Waves; Estuaries; Reservoirs**
Waves Used for Inter-Tidal Design and Construction, D. C. Keiller and T. D. Ruxton, 23
- Tidal currents; Tidal effects; Two phase flow; Estuaries; Saline water-freshwater interfaces; Salinity; Salt water intrusion**
Tidal Response of Two-Layer Flow at a River Mouth, Shizuo Yoshida and Masakazu Kashiwamura, 3189
- Tidal currents; Tidal hydraulics; Tides; Washington; Water circulation; Water depth; Flushing; Harbors**
Planform Influence on Flushing and Circulation in Small Harbors, Ronald C. Nece, Roger A. Falconer and Toshiro Tsutsumi, 3471
- Tidal currents; Wave recorders (water waves); Beaches; Inlets (waterways); Littoral current; Littoral drift; Surf**
Changes in Inlet Offset due to Stabilization, Dennis K. Hubbard, 1812
- Tidal effects; Alabama; Bays (topographic features); Sedimentation; Sediment deposits; Sediment distribution; Sediment transport**
Sediment Transportation and Deposition Models for Mobile Bay, Alabama, Gary G. April, Samuel Ng and C. Everett Brett, 2092
- Tidal effects; Algorithms; California; Discharge (water); Numerical analysis; Tidal currents**
Tidal Stream Flow Solved by Galerkin Technique, L. H. Smith and Ralph T-S Cheng, 3358
- Tidal effects; Beaches; Inlets (waterways); Sandbars; Sand traps; Shoaling**
Capacity of Inlet Outer Bars to Store Sand, Todd L. Walton, Jr. and William D. Adams, 1919
- Tidal effects; Bed load; Current meters; Friction coefficient (hydraulic); Inlets (waterways)**
Measurement of Bed Friction in Tidal Inlets, Ashish J. Mehta, R. J. Byrne and Joseph T. DeAlteris, 1701
- Tidal effects; Canada; Density currents; Hydraulic models; Saline water-freshwater interfaces; Salinity; Salt water intrusion**
Churchill River Salt-Water Tidal Model, Bruce D. Pratte, 3445
- Tidal effects; Dunes; Dune sands; Movable bed models; Sediment transport; Tidal currents**
Origin of Submarine Dunes, Mehmet S. Yalin, 2127
- Tidal effects; Tidal energy; Hydraulic models; Prototype tests; Roughness (hydraulic); Tidal currents**
Model Verification for Tidal Constituents, R. W. Whalin, F. C. Perry and D. L. Durham, 3377
- Tidal effects; Tidal energy; Tidal hydraulics; Tidal waters; Wave energy; Inlets (waterways); Japan**
Characteristics of Tidal Inlets on the Pacific Coast of Japan, Toshiyuki Shigemura, 1666
- Tidal effects; Tidal energy; Tidal hydraulics; Vortices; Estuaries; Flooding; Inlets (waterways); Tidal currents**
Harbour Inlets on Tidal Estuaries, Hans Vollmers, 1854
- Tidal effects; Tidal energy; Warning systems; Flood plain insurance; Hurricanes; Storms**
Hurricane Tide Frequencies on the Atlantic Coast, Francis P. Ho, 886
- Tidal effects; Tidal hydraulics; Tidal marshes; Wave height; Waves; Estuaries; Reservoirs; Tidal currents**
Waves Used for Inter-Tidal Design and Construction, D. C. Keiller and T. D. Ruxton, 23
- Tidal effects; Tidal hydraulics; Tidal waters; Channels (waterways); River regulation; Sandbars; Sediment transport; Stability**
Stability of Tidal Channels Dependent on River Improvement, Volker Barthel, 1775
- Tidal effects; Tidal marshes; Water waves; Estuaries; Finite element method; Numerical analysis; Shallow water**
Finite Element Model for Estuaries with Inter-Tidal Flows, Bruno Herrling, 3396
- Tidal effects; Tidal waters; Environmental effects; Inlets (waterways); Littoral drift; New Jersey; Scouring; Sea level**
Beach Haven and Little Egg Inlets, A Case Study, Joseph T. DeAlteris, Thomas McKinney and James Roney, 1881
- Tidal effects; Time; Estuaries; Feasibility; Hydraulic models; Mathematical models; Rivers**
Analysis of Time Conditions for Hybrid Tidal Models, Klaus-Peter Holz, 3460
- Tidal effects; Turbulence; Diffusion; Eddies; Hydraulic models; Scale effect; Statistical analysis**
Horizontal Diffusion in Tidal Models and Scaling Criteria for Thermal-Hydraulic Model Tests, Gerd Flugge, 3097
- Tidal effects; Two phase flow; Estuaries; Saline water-freshwater interfaces; Salinity; Salt water intrusion; Tidal currents**
Tidal Response of Two-Layer Flow at a River Mouth, Shizuo Yoshida and Masakazu Kashiwamura, 3189
- Tidal effects; Water levels; Wave generation; Currents; Great Lakes; Harbors; Seiches**
Hydraulics of Great Lakes Inlet — Harbors Systems, Robert M. Sorensen and William N. Seelig, 1646
- Tidal effects; Wave action; Beach erosion; Climatic data; Estuaries; Estuarine environment; Sediment deposits; Sediment distribution; Sediments**
Factors Influencing Estuary Sediment Distribution, Mary P. Kendrick and B. V. Derbyshire, 2072
- Tidal effects; Wave energy; Bed forms; Inlets (waterways); Ocean bottom; Scale effect; Sediment transport; Simulation models**
Tidal Inlet Flow Dynamics and Sediment Movement, Jerry L. Machemehl, N. E. Bird and A. N. Chambers, 1681
- Tidal effects; Wave energy; Wave spectrum; Beach erosion; Beaches; California; Equilibrium**
Beach Profiles at Torrey Pines, California, David G. Aubrey, Douglas L. Inman and Charles E. Nordstrom, 1297

- Tidal effects; Wave energy; West Germany; Damping; Energy dissipation; Estuaries; Stratification**
Energy Dissipation in Tidal Estuaries, Hans-Werner Partenscky and Gunther Barg, 3312
- Tidal effects; West Germany; Channels (waterways); Dunes; Dune sands; Sand waves; Sediment transport**
Transport Mechanism in Tidal Dunes, Horst Nasner, 2136
- Tidal energy; Hydraulic models; Prototype tests; Roughness (hydraulic); Tidal currents; Tidal effects**
Model Verification for Tidal Constituents, R. W. Whalin, F. C. Perry and D. L. Durham, 3377
- Tidal energy; Tidal hydraulics; Tidal waters; Wave energy; Inlets (waterways); Japan; Tidal effects**
Characteristics of Tidal Inlets on the Pacific Coast of Japan, Toshiyuki Shigemura, 1666
- Tidal energy; Tidal hydraulics; Vortices; Estuaries; Flooding; Inlets (waterways); Tidal currents; Tidal effects**
Harbour Inlets on Tidal Estuaries, Hans Vollmers, 1854
- Tidal energy; Warning systems; Flood plain insurance; Hurricanes; Storms; Tidal effects**
Hurricane Tide Frequencies on the Atlantic Coast, Francis P. Ho, 886
- Tidal hydraulics; Tidal marshes; Wave height; Waves; Estuaries; Reservoirs; Tidal currents; Tidal effects**
Waves Used for Inter-Tidal Design and Construction, D. C. Keiller and T. D. Ruxton, 23
- Tidal hydraulics; Tidal waters; Channels (waterways); River regulation; Sandbars; Sediment transport; Stability; Tidal effects**
Stability of Tidal Channels Dependent on River Improvement, Volker Barthel, 1775
- Tidal hydraulics; Tidal waters; Wave energy; Inlets (waterways); Japan; Tidal effects**
Characteristics of Tidal Inlets on the Pacific Coast of Japan, Toshiyuki Shigemura, 1666
- Tidal hydraulics; Tides; Washington; Water circulation; Water depth; Flushing; Harbors; Tidal currents; Tidal effects**
Planform Influence on Flushing and Circulation in Small Harbors, Ronald C. Nece, Roger A. Falconer and Toshiro Tsutsumi, 3471
- Tidal hydraulics; Vortices; Estuaries; Flooding; Inlets (waterways); Tidal currents; Tidal effects; Tidal energy**
Harbour Inlets on Tidal Estuaries, Hans Vollmers, 1854
- Tidal marshes; Coastal engineering; Currents; Littoral drift; Ocean currents; Sediment transport; Storm surges**
Currents in Tidal Flats During Storm Surges, Harald Gohren, 959
- Tidal marshes; Water waves; Estuaries; Finite element method; Numerical analysis; Shallow water; Tidal effects**
Finite Element Model for Estuaries with Inter-Tidal Flats, Bruno Herrling, 3396
- Tidal marshes; Wave height; Waves; Estuaries; Reservoirs; Tidal currents; Tidal effects; Tidal hydraulics**
Waves Used for Inter-Tidal Design and Construction, D. C. Keiller and T. D. Ruxton, 23
- Tidal waters; Channels (waterways); River regulation; Sandbars; Sediment transport; Stability; Tidal effects; Tidal hydraulics**
Stability of Tidal Channels Dependent on River Improvement, Volker Barthel, 1775
- Tidal waters; Environmental effects; Inlets (waterways); Littoral drift; New Jersey; Scouring; Sea level; Tidal effects**
Beach Haven and Little Egg Inlets, A Case Study, Joseph T. DeAlteris, Thomas McKinney and James Roney, 1881
- Tidal waters; Tides; Erosion; Movable bed models; Prototype tests; Scale effect; Scour; Scouring**
Movable Bed Tidal Inlet Models, Subhash C. Jain and John F. Kennedy, 3435
- Tidal waters; Wave energy; Inlets (waterways); Japan; Tidal effects; Tidal hydraulics**
Characteristics of Tidal Inlets on the Pacific Coast of Japan, Toshiyuki Shigemura, 1666
- Tides; Erosion; Movable bed models; Prototype tests; Scale effect; Scour; Scouring**
Movable Bed Tidal Inlet Models, Subhash C. Jain and John F. Kennedy, 3435
- Tides; Washington; Water circulation; Water depth; Flushing; Harbors; Tidal currents; Tidal hydraulics**
Planform Influence on Flushing and Circulation in Small Harbors, Ronald C. Nece, Roger A. Falconer and Toshiro Tsutsumi, 3471
- Time; Estuaries; Feasibility; Hydraulic models; Mathematical models; Rivers; Tidal effects**
Analysis of Time Conditions for Hybrid Tidal Models, Klaus-Peter Holz, 3460
- Time dependence; Wastewater; Buoyancy; Fluid mechanics; Gravitation; Ocean currents; Spreading**
Buoyancy-Driven Gravitational Spreading, Robert C.Y. Koh, 2956
- Time dependence; Wave height; Wave period; Wave spectrum; Wave velocity; Flowmeters; Ocean currents; Rip currents**
Time Dependent Fluctuations in Longshore Currents, Guy A. Meadows, 660
- Time dependence; Wave height; Waves; Wave velocity; Breaking; Gravity waves; Solitary waves**
Recent Developments in the Study of Breaking Waves, Michael S. Longuet-Higgins, 441
- Topographical factors; Beach erosion; Beaches; Breakwaters; Construction; Harbor structures; Japan; Ocean bottom; Shoaling**
Topographic Change Resulting from the Construction of a Harbor on a Sandy Beach, Kashima Port, Norio Tanaka and Shoji Sato, 1824
- Tracers; Estuaries; Saline water-freshwater interfaces; Saline water intrusion; Salinity; Stratified flow**
Dynamics of a Longitudinally Stratified Estuary, Jorg Imberger, 3108

- Tracers; Water pollution; Dispersion; Distribution; Dyes; Estuaries; Predictions; Sewage disposal; Sewage effluents**
Prediction of Pollutant Distribution in Estuaries, Albert Y. Kuo and John P. Jacobson, 3276
- Tracers (radioactive); Dredging; Estuaries; Estuarine environment; San Francisco; Sediments; Spoil**
Tracing Estuarine Sediments by Neutron Activation, Richard M. Ecker, John F. Sustar and William T. Harvey, 2009
- Tracers (radioactive); West Germany; Hydraulic models; Movable bed models; Scale effect; Sediment transport**
Sand Movement Investigations by Means of Radioactive Tracers in a Hydraulic Model and in the Field, Hans Rohde, 2027
- Training walls; Australia; Estuaries; Flooding; Hydrographic surveys; Jetties; River flow; Sandbars**
Results of River Mouth Training on the Clarence Bar, New South Wales, Australia, Cyril D. Floyd and Bruce M. Druery, 1738
- Transport phenomena; Density currents; Estuaries; Friction coefficient (hydraulic); Mathematical models; Numerical analysis; Saline water intrusion; Stratification**
Numerical Model for Density Currents in Estuaries, Karsten Fischer, 3295.
- Tropical cyclones; Computer models; Forecasting; Hurricanes; Numerical analysis; Storm surges**
SPLASH — A Model for Forecasting Tropical Storm Surges, Celso S. Barrientos and Chester P. Jelesnianski, 941
- Troughs; Density currents; Flow patterns; Mathematical models; Scour; Scouring; Stratified flow**
Generation of Troughs by Density Currents, Hans Speekenbrink, 2170
- Tsunamis; Numerical analysis; Propagation; Shore protection; Simulation**
Numerical Simulation of Tsunamis Originating in the Peru-Chile Trench, A. W. Garcia and H. L. Butler, 1025
- Tsunamis; Warning systems; Coastal engineering; Coastal plains; Japan; Power spectra; Refraction; Shoaling**
Transformation of Tsunamis in a Coastal Zone, Shigehisa Nakamura, Haruo Higuchi and Yoshito Tsuchiya, 988
- Tsunamis; Wave action; Wave energy; Wave generation; Wave height; Coastal structures; Hazards**
Tsunami Hazard and Design of Coastal Structures, George Pararas-Carayannis, 2248
- Tsunamis; Wave dispersion; Wave height; Japan; Models; Numerical analysis; Statistical models**
Numerical Models of Huge Tsunamis Off the Sanriku Coast, Toshio Iwasaki, 1044
- Tsunamis; Wave height; Friction coefficient (hydraulic); Numerical analysis; Propagation; Shallow water**
Tsunami Propagation in the Pacific Ocean, Manfred Engel and Wilfried Zahel, 971
- Tsunamis; Wave runup; Flooding; Predictions; Storm surges**
Tsunami Inundation Prediction, Charles L. Bretschneider and Pieter G. Wybro, 1006
- Turbulence; Beaches; Flowmeters; Friction coefficient (hydraulic); Rip currents; Surf**
Lateral and Bottom Forces on Longshore Currents, David A. Huntley, 645
- Turbulence; Diffusion; Eddies; Hydraulic models; Scale effect; Statistical analysis; Tidal effects**
Horizontal Diffusion in Tidal Models and Scaling Criteria for Thermal-Hydraulic Model Tests, Gerd Flugge, 3097
- Turbulence; Discharge (water); Interfacial tension; Stability; Stratified flow; Thermal pollution**
Interfacial Instability in Stratified Flow, Richard H. French, 3124
- Turbulence; Wave action; Wave damping; Wave dispersion; Wave energy; Wave velocity; Currents (water); Interactions**
Interaction of Waves and a Turbulent Current, J. D.A. van Hoften and Susumu Karaki, 404
- Turbulence; Wave height; Wave runup; Waves; Beaches; Breaking; Resonance; Surges**
Resonant Interactions for Waves Breaking on a Beach, Robert T. Guza and Anthony J. Bowen, 560
- Turbulent diffusion; Friction coefficient (hydraulic); Ocean bottom; Ripple marks; Shallow water**
Consideration on Friction Coefficient for Sea Bottom, Toru Sawaragi, Koichiro Iwata and Masayoshi Kubo, 595
- Two-dimensional; Water depth; Water waves; Wave height; Boundary value problems; Breakwaters; Permeability; Sea walls**
Method of Analyses for Two-Dimensional Water Wave Problems, Takeshi Ijima, Chung Ren Chou and Akinori Yoshida, 2717
- Two-dimensional; Wave equations; Wave height; Breaking; Surf; Three-dimensional**
Three-Dimensional Conditions of Surf, William L. Wood, 525
- Two phase flow; Convection; Diffusion; Dispersion; Finite element method; Numerical analysis; Stratification**
Numerical Modeling of Dispersion in Stratified Waters, George C. Christodoulou and Jerome J. Connor, 3138
- Two phase flow; Diffusers; Discharge (water); Hydraulic models; Nuclear power plants; Plume detection; Plumes; Thermal pollution**
Field Studies of Submerged-Diffuser Thermal Plumes with Comparisons to Predictive Model Results, A. A. Frigo, Richard A. Paddock and J. D. Dittmars, 3028
- Two phase flow; Estuaries; Saline water-freshwater interfaces; Salinity; Salt water intrusion; Tidal currents; Tidal effects**
Tidal Response of Two-Layer Flow at a River Mouth, Shizuo Yoshida and Masakazu Kashiwamura, 3189
- Two phase flow; Water flow; Energy conversion; Surface waves; Thermal energy; Thermal gradient**
Flow Field Near an Ocean Thermal Energy Conversion Plant, D. M. Sheppard, G. M. Powell and I. B. Chou, 3068

- Two phase flow; Wave equations; Wave height; Wave velocity; Friction coefficient (hydraulic); Interfaces**
Friction at the Interface of Two-Layered Flows, Nobuyuki Tamai, 3169
- Underwater pipelines; Diffusers; Environmental effects; Hydrodynamics; Ocean engineering; Outfall sewers**
Design Considerations for the Sand Island and Barbers Point Outfalls, Robert C.Y. Koh, Norman H. Brooks and Floyd Louis Vuillemot, 2941
- Underwater pipelines; Wave action; Failures; Laboratory tests; Sandbars; Scale effect; Scour; Scouring**
Scour Around Model Pipelines Due to Wave Action, John B. Herbich, 1624
- Underwater structures; Wave action; Wave energy; Drag; Inertial forces; Submerged flow**
Wave Forces on Submerged Objects, Suphat Vongvisessomjai and Richard Silvester, 2387
- Unsteady flow; Wave equations; Waves; Breakwaters; Oscillation; Sediment transport**
Quantitative Description of Sediment Transport, Ole Secher Madsen and William D. Grant, 1093
- Utilization; Barges; Economic analysis; Environmental effects; Harbors; Performance; Safety; Site selection**
Probable Utilization Level for a Barge Harbor, Martin T. Czerniak and Choule J. Sonu, 3557
- Variability; Beach erosion; Eigenvalues; Impulses; Responses; Stability; Statistical analysis; Storms**
Stability and Impulse Response of Empirical Eigenfunctions, Clinton D. Winant and David G. Aubrey, 1312
- Velocity distribution; Water waves; Wave equations; Coastal topographic features; Eigenvalues; Responses; Rip currents**
Rip-Current and Coastal Topography, Mikio Hino, 1326
- Verification inspection; Wave height; Wave spectrum; Bathymetry; Groins (structures); Littoral drift; Sandbars; Sediment transport**
Experimental Verification of Groyne Theory, C. H. Hulsbergen, W. T. Bakker and G. van Bochove, 1439
- Viscosity; Water temperature; Hydraulic models; Predictions; Prototype tests; Scale effect; Surface tension; Thermal diffusion**
Adaptability of Prediction Method of Hydraulic Model Experiment for Thermal Diffusion, Masanobu Kato and Akira Wada, 3082
- Viscosity; Wave action; Wave dispersion; Wave energy; Wave functions; Wave height; Mud flats**
Wave Action and Bottom Movements in Fine Sediments, Michael W. Tubman and Joseph N. Suhayda, 1168
- Vortices; Estuaries; Flooding; Inlets (waterways); Tidal currents; Tidal effects; Tidal energy; Tidal hydraulics**
Harbour Inlets on Tidal Estuaries, Hans Vollmers, 1854
- Vortices; Wakes; Water waves; Cylindrical bodies; Flow separation; Oscillations; Pressure distribution**
Flow Separation, Wake Vortices and Pressure Distribution Around a Circular Cylinder under Oscillatory Waves, Yuichi Iwagaki and Hajime Ishida, 2341
- Vortices; Water flow; Cylindrical bodies; Drag; Force; Oscillation; Roughness (hydraulic)**
Forces on Rough-Walled Circular Cylinders in Harmonic Flow, Turgut Sarpkaya, 2301
- Wakes; Water waves; Cylindrical bodies; Flow separation; Oscillations; Pressure distribution; Vortices**
Flow Separation, Wake Vortices and Pressure Distribution Around a Circular Cylinder under Oscillatory Waves, Yuichi Iwagaki and Hajime Ishida, 2341
- Walls; Water waves; Wave action; Waves; Barriers; Finite differences; Shallow water; Simulation**
Action of Non-Linear Waves at a Solid Wall, Mohamed S. Nasser and John A. McCorquodale, 815
- Walls; Water waves; Wave height; Diffraction; Mach number; Reflection**
Mach-Reflection as a Diffraction Problem, Udo Berger and Soren Kohlhasse, 796
- Warning systems; Coastal engineering; Coastal plains; Japan; Power spectra; Refraction; Shoaling; Tsunamis**
Transformation of Tsunamis in a Coastal Zone, Shigehisa Nakamura, Haruo Higuchi and Yoshito Tsuchiya, 988
- Warning systems; Flood plain insurance; Hurricanes; Storms; Tidal effects; Tidal energy**
Hurricane Tide Frequencies on the Atlantic Coast, Francis P. Ho, 886
- Washington; Water circulation; Water depth; Flushing; Harbors; Tidal currents; Tidal hydraulics; Tides**
Planform Influence on Flushing and Circulation in Small Harbors, Ronald C. Nece, Roger A. Falconer and Toshiro Tsutsumi, 3471
- Wastewater; Buoyancy; Fluid mechanics; Gravitation; Ocean currents; Spreading; Time dependence**
Buoyancy-Driven Gravitational Spreading, Robert C.Y. Koh, 2956
- Water circulation; Water depth; Flushing; Harbors; Tidal currents; Tidal hydraulics; Tides; Washington**
Planform Influence on Flushing and Circulation in Small Harbors, Ronald C. Nece, Roger A. Falconer and Toshiro Tsutsumi, 3471
- Water circulation; Water quality; Coliform bacteria; Drainage; Estuaries; Runoff; Sampling; Simulation**
State Estimation of Estuarine Circulation and Water Quality by Numerical Simulation and Observation, Jan J. Leendertse and S. K. Liu, 3223
- Water circulation; Wave action; Wave-energy; Drag; Force; Separation; Spheres**
Forces on a Sphere Under Linear Progressive Waves, Scott A. Jenkins and Douglas L. Inman, 2413

- Water circulation; Wave recorders (water waves); Wind pressure; Wind tides; Current meters**
Wind-Driven Circulation of Saginaw Bay, James H. Saylor and Larry J. Danek, 3262
- Water depth; Berths; Dolphins (structures); Head losses; Mass; Shallow water; Tanker ships**
Added Masses of Large Tankers Berthing to Dolphins, Taizo Hayashi and Masujiro Shirai, 2830
- Water depth; Flushing; Harbors; Tidal currents; Tidal hydraulics; Tides; Washington; Water circulation**
Planform Influence on Flushing and Circulation in Small Harbors, Ronald C. Nece, Roger A. Falconer and Toshiro Tsutsumi, 3471
- Water depth; Water surface profiles; Wave action; Wave energy; Numerical analysis; Oscillations; Responses**
Wave Induced Oscillations of Harbors with Variable Depth, Fredric Raichlen and Ehud Naheer, 3536
- Water depth; Water waves; Wave height; Boundary value problems; Breakwaters; Permeability; Sea walls; Two-dimensional**
Method of Analyses for Two-Dimensional Water Wave Problems, Takeshi Iijima, Chung Ren Chou and Akinori Yoshida, 2717
- Water depth; Wave energy; Wave height; Waves; Beaches; Deformation; Periodic functions; Phase velocity**
Deformation up to Breaking of Periodic Waves on a Beach, Ib A. Svendsen and J. Buhr Hansen, 477
- Water depth; Waves; Currents; Finite elements; Gravity waves; Predictions; Refraction; Surf**
Current Depth Defraction Using Finite Elements, Ove Skovgaard and Ivar G. Jonsson, 721
- Water flow; Cylindrical bodies; Drag; Force; Oscillation; Roughness (hydraulic); Vortices**
Forces on Rough-Walled Circular Cylinders in Harmonic Flow, Turgut Sarpkaya, 2301
- Water flow; Energy conversion; Surface waves; Thermal energy; Thermal gradient; Two phase flow**
Flow Field Near an Ocean Thermal Energy Conversion Plant, D. M. Sheppard, G. M. Powell and I. B. Chou, 3068
- Water flow; Laboratory tests; Sediment concentration; Sediments; Sediment samplers**
Iowa Sediment Concentration Measuring System, Tatsuaki Nakato, Frederick A. Locher, John R. Glover and John F. Kennedy, 2060
- Water flow; Wave action; Wave energy; Cylinders; Drag; Hydraulic models; Lift; Oscillations; Reynolds number; Stream flow**
High Reynolds Number Oscillating Flow by Cylinders, Tokuo Yamamoto and John H. Nath, 2321
- Water flow; Wave energy; Wind pressure; Discharge (water); Effluents; Field tests; Mathematical models; Numerical analysis**
Numerical Modelling — An Aid to Assessing Field Data, H. P. Riedel and F. L. Wilkinson, 3243
- Water level fluctuations; Water levels; Wave action; Wave energy; Waves; Wave spectrum; Storm surges; Surf**
Energy Spectra of Irregular Surf Waves, Fritz Busching, 539
- Water levels; Beach erosion; Beach nourishment; Bypasses; Erosion; Great Lakes; Michigan; Sand; Shore protection**
Sand-Bypass and Shore Erosion, Bridgman, Michigan, C. N. Johnson and L. W. Hiipakka, 1361
- Water levels; Wave action; Wave energy; Waves; Wave spectrum; Storm surges; Surf; Water level fluctuations**
Energy Spectra of Irregular Surf Waves, Fritz Busching, 539
- Water levels; Wave action; Wave height; Breakwaters; Coastal structures; Experimentation; Field tests; Scour; Scouring**
Local Scour and Current Around a Porous Breakwater, Shintaro Hotta and Nobuo Marui, 1590
- Water levels; Wave generation; Currents; Great Lakes; Harbors; Seiches; Tidal effects**
Hydraulics of Great Lakes Inlet — Harbors Systems, Robert M. Sorensen and William N. Seelig, 1646
- Water levels; Wave height; Wave runup; Beaches; Ocean waves; Resonance; Simulation**
Wave Run-Up on a Simulated Beach, A. J. Sutherland, J. N. Sharma and Omar H. Shemdin, 752
- Water levels; Waves; Breaking; Coastal engineering; Field tests; Littoral drift; Ocean currents; Photogrammetry; Stereophotography**
Terrestrial Photogrammetric Measurements of Breaking Waves and Longshore Currents in the Nearshore Zone, Joseph W. Maresca, Jr. and Erwin Seibel, 681
- Water meters; Water quality; Calibration; Discharge (water); Estuaries; Open channel flow**
Calibration of Branched Estuary Models, James P. Bennett, 3416
- Water pollution; Dispersion; Distribution; Dyes; Estuaries; Predictions; Sewage disposal; Sewage effluents; Tracers**
Prediction of Pollutant Distribution in Estuaries, Albert Y. Kuo and John P. Jacobson, 3276
- Water quality; Calibration; Discharge (water); Estuaries; Open channel flow; Water meters**
Calibration of Branched Estuary Models, James P. Bennett, 3416
- Water quality; Coliform bacteria; Drainage; Estuaries; Runoff; Sampling; Simulation; Water circulation**
State Estimation of Estuarine Circulation and Water Quality by Numerical Simulation and Observation, Jan J. Leendertse and S. K. Liu, 3223
- Water quality; Diffusers; Dilution; Mixing; Outfall sewers; Site selection**
Design Procedures for Ocean Outfalls, Jeffrey A. Layton, 2919

- Water quality; Environmental effects; Hawaii;**
Islands (landforms); Monitoring; Reefs; Runways
 Environmental Impacts on an Island Community,
 Gordon A. Chapman, 3506
- Water surface profiles; Wave action; Wave energy;**
Numerical analysis; Oscillations; Responses; Water depth
 Wave Induced Oscillations of Harbors with
 Variable Depth, Fredric Raichlen and Ehud
 Naheer, 3536
- Water temperature; Air-water interfaces; Heat flux;**
Heat transfer; Infrared scanners; Infrared scanning; Remote sensing
 Evaluation of Air-Sea Interface Heat Flux, Robert
 L. Street and A. Woodruff Miller, Jr., 3208
- Water temperature; Discharge (water); Hydraulic models; Nuclear power plants; Prototype tests; Temperature distribution; Thermal diffusion; Thermal pollution**
 Thermal Discharges: Prototype vs. Hydraulic Model, Gary C. Parker, Ching S. Fang and Albert Y. Kuo, 3049
- Water temperature; Hydraulic models; Predictions; Prototype tests; Scale effect; Surface tension; Thermal diffusion; Viscosity**
 Adaptability of Prediction Method of Hydraulic Model Experiment for Thermal Diffusion, Masanobu Kato and Akira Wada, 3082
- Water temperature; Wave height; Beach erosion; Erosion; Field tests; Groins (structures); Laboratory tests; Littoral drift; Shore protection; Storms**
 Laboratory Investigation of Shore Erosion Processes, Ernest F. Brater and David Ponce-Campos, 1493
- Water waves; Cylindrical bodies; Flow separation; Oscillations; Pressure distribution; Vortices; Wakes**
 Flow Separation, Wake Vortices and Pressure Distribution Around a Circular Cylinder under Oscillatory Waves, Yuichi Iwagaki and Hajime Ishida, 2341
- Water waves; Estuaries; Finite element method; Numerical analysis; Shallow water; Tidal effects; Tidal marshes**
 Finite Element Model for Estuaries with Inter-Tidal Flats, Bruno Herrling, 3396
- Water waves; Wave action; Waves; Barriers; Finite differences; Shallow water; Simulation; Walls**
 Action of Non-Linear Waves at a Solid Wall, Mohamed S. Nasser and John A. McCorquodale, 815
- Water waves; Wave dispersion; Wave energy; Wave spectrum; Coastal structures; Random processes; Reflection**
 Decomposition of Co-Existing Random Wave Energy, Dennis B. Morden, Eugene P. Richey and Derald R. Christensen, 846
- Water waves; Wave equations; Coastal topographic features; Eigenvalues; Responses; Rip currents; Velocity distribution**
 Rip-Current and Coastal Topography, Mikio Hino, 1326
- Water waves; Wave generation; Waves; Hydraulic models; Three-dimensional**
 3-D Hydraulic Model of Wave Generated by Displacements, Shin-Lin Liu and Robert L. Wiegell, 1060
- Water waves; Wave height; Boundary value problems; Breakwaters; Permeability; Sea walls; Two-dimensional; Water depth**
 Method of Analyses for Two-Dimensional Water Wave Problems, Takeshi Ijima, Chung Ren Chou and Akinori Yoshida, 2717
- Water waves; Wave height; Diffraction; Mach number; Reflection; Walls**
 Mach-Reflection as a Diffraction Problem, Udo Berger and Soren Kohlbase, 796
- Wave action; Beach erosion; Beach nourishment; Dynamics; Equilibrium; Erosion; Reflection; Sandbars; Sand traps; Three-dimensional**
 Three Dimensional Tests on Dynamic Equilibrium and Artificial Nourishment, J. William Kamphuis and R. M. Myers, 1532
- Wave action; Beach erosion; Climatic data; Estuaries; Estuarine environment; Sediment deposits; Sediment distribution; Sediments; Tidal effects**
 Factors Influencing Estuary Sediment Distribution, Mary P. Kendrick and B. V. Derbyshire, 2072
- Wave action; Currents; Dredging; Estuaries; Harbors; Littoral drift; Sand traps; Storms**
 Design and Behaviour of Sandtraps in Regions of High Littoral Drift, P. C. Saxena, Pazhayannur P. Vaidyaraman and R. Srinivasan, 1377
- Wave action; Failures; Laboratory tests; Sandbars; Scale effect; Scour; Scouring; Underwater pipelines**
 Scour Around Model Pipelines Due to Wave Action, John B. Herbich, 1624
- Wave action; Samplers; Sampling; Sediment concentration; Sediment samplers; Sediment sampling; Surf; Suspended sediments**
 Measurement of Suspended Sediment in the Surf Zone, F. A. Kilner, 2045
- Wave action; Wave damping; Wave dispersion; Wave energy; Wave velocity; Currents (water); Interactions; Turbulence**
 Interaction of Waves and a Turbulent Current, J. D.A. van Hoften and Susumu Karaki, 404
- Wave action; Wave damping; Wave energy; Breakwaters; Reflection; Slitting**
 Slit-Type Breakwater: Box-Type Wave Absorber, Shositiro Nagai and Shohachi Kakuno, 2697
- Wave action; Wave dispersion; Wave energy; Wave functions; Wave height; Mud flats; Viscosity**
 Wave Action and Bottom Movements in Fine Sediments, Michael W. Tubman and Joseph N. Suhayda, 1168
- Wave action; Wave dispersion; Wave energy; Waves; Breakwaters; Laboratory tests; Rubble mounds**
 Wave Transmission Through Trapezoidal Breakwaters, Ole Secher Madsen and Stanley M. White, 2662
- Wave action; Wave dispersion; Wave energy; Wave velocity; Field tests; Ocean bottom; Ocean waves**
 Near-Bottom Water Motion Under Ocean Waves, Robert A. Grace, 2371

- Wave action; Wave dispersion; Wave height; Waves; Wave velocity; Breaking; Refraction; Shoaling**
Refraction of Finite-Height and Breaking Waves, James R. Walker, 507
- Wave action; Wave energy; Air entrainment; Damage; Dikes; Impact; Revetments**
Response of Seadykes due to Wave Impacts, Alfred Fuhrboter, Hans H. Dette and J. Grune, 2604
- Wave action; Wave energy; Bays (topographic features); Beach erosion; Breakwaters; Shore protection**
Headland Defense of Coasts, Richard Silvester, 1394
- Wave action; Wave energy; Beach erosion; Beach nourishment; Erosion; Littoral current; Recreational facilities; Storms; Storm surges**
Cape Hatteras Beach Nourishment, John S. Fisher and Wilson N. Felder, 1512
- Wave action; Wave energy; Bottom water; Continental shelf; Cyclic loads; Foundations; Ocean bottom; Offshore structures; Predictions; Stability**
Prediction of Wave-Induced Seafloor Movements, Leland Milo Kraft, Jr. and David James Watkins, 1605
- Wave action; Wave energy; Breakwaters; Damage; Hydraulic models; Rubble; Rubble mounds; Stability**
Effect of Broken Dolosse on Breakwater Stability, D. Donald Davidson and Dennis G. Markle, 2544
- Wave action; Wave energy; Cylinders; Drag; Hydraulic models; Lift; Oscillations; Reynolds number; Stream flow; Water flow**
High Reynolds Number Oscillating Flow by Cylinders, Tokuo Yamamoto and John H. Nath, 2321
- Wave action; Wave energy; Drag; Force; Separation; Spheres; Water circulation**
Forces on a Sphere Under Linear Progressive Waves, Scott A. Jenkins and Douglas L. Inman, 2413
- Wave action; Wave energy; Drag; Inertial forces; Submerged flow; Underwater structures**
Wave Forces on Submerged Objects, Suphat Vongvisessomjai and Richard Silvester, 2387
- Wave action; Wave energy; Estuaries; Flooding; River flow; Sandbars; Sedimentation; Sediment deposits**
Morphodynamics of a Wave-Dominated River Mouth, L. D. Wright, 1721
- Wave action; Wave energy; Harbors; Harbor structures; History; Jetties; Rubble mounds**
Design and Construction of Humboldt Jetties, 1880 to 1975, Orville T. Magoon, Robert L. Sloan and Nobuyuki Shimizu, 2474
- Wave action; Wave energy; Numerical analysis; Oscillations; Responses; Water depth; Water surface profiles**
Wave Induced Oscillations of Harbors with Variable Depth, Fredric Raichlen and Ehud Naheer, 3536
- Wave action; Wave energy; Wave generation; Wave height; Coastal structures; Hazards; Tsunamis**
Tsunami Hazard and Design of Coastal Structures, George Pararas-Carayannis, 2248
- Wave action; Wave energy; Wave height; Wave period; Caissons; Model tests; Overturning tests**
Wave Forces on Aquare Caissons, G. R. Mogridge and W. W. Jamieson, 2271
- Wave action; Wave energy; Wave period; Armoring (streambed); Breakwaters; Failure; Slope protection; Slope stability**
Armour Blocks as Slope Protection, A. F. Whillock and W. A. Price, 2564
- Wave action; Wave energy; Wave period; Fenders; Force; Harmonic functions; Mooring; Moorings; Oscillations**
Subharmonic Components in Hawser and Fender Forces, J. H. van Oorschot, 2840
- Wave action; Wave energy; Wave runup; Wave velocity; Coastal structures; Damping; Numerical analysis**
Numerical Calculation of Wave Forces on Structures, B. D. Nichols and C. W. Hirt, 2254
- Wave action; Wave energy; Waves; Wave spectrum; Breakwaters; Overtopping; Rubble mounds**
Overtopping of Rubble-Mound Breakwaters by Irregular Waves, Yvon Ouellet and Pierre Eubanks, 2756
- Wave action; Wave energy; Waves; Wave spectrum; Storm surges; Surf; Water level fluctuations; Water levels**
Energy Spectra of Irregular Surf Waves, Fritz Busching, 539
- Wave action; Wave energy; Wave spectrum; Wave tanks; Breakwaters; Buoys; Energy dissipation; Field tests; Floating bodies; Scale effect; Tethered tests**
Design, Analysis and Field Test of a Dynamic Floating Breakwater, D. J. Agerton, G. H. Savage and K. C. Stotz, 2792
- Wave action; Wave energy; Wharves; Offshore structures; Prototype tests; Scour; Scouring**
Wave Action on Large Off-Shore Structures, C. J. Apelt and A. Macknight, 2228
- Wave action; Wave forecasting; Wind forces; Wind speed; Forecasting; Hurricanes**
Hurricane Wind and Wave Forecasting Techniques, Charles L. Bretschneider and Elaine E. Tamaye, 202
- Wave action; Wave generation; Bedding materials; Bed ripples; Ripple marks; Sand; Sonar detection**
Wave-Formed Ripples in Nearshore Sands, John R. Dingler and Douglas L. Inman, 2109
- Wave action; Wave height; Breakwaters; Coastal structures; Experimentation; Field tests; Scour; Scouring; Water levels**
Local Scour and Current Around a Porous Breakwater, Shintaro Hotta and Nobuo Marui, 1590
- Wave action; Wave height; Wave period; Waves; Wave spectrum; Wind speed; Great Lakes**
Great Lakes Wave Information, D. T. Resio and L. W. Hiipakka, 92

- Wave action; Wave height; Wave propagation; Wave spectrum; Ocean waves**
Revisions in Wave Data Presentation, Laurence Draper, 3
- Wave action; Waves; Barriers; Finite differences; Shallow water; Simulation; Walls; Water waves**
Action of Non-Linear Waves at a Solid Wall, Mohamed S. Nasser and John A. McCorquodale, 815
- Wave damping; Wave dispersion; Wave energy; Wave velocity; Currents (water); Interactions; Turbulence; Wave action**
Interaction of Waves and a Turbulent Current, J. D.A. van Hoften and Susumu Karaki, 404
- Wave damping; Wave energy; Breakwaters; Reflection; Slitting; Wave action**
Slit-Type Breakwater: Box-Type Wave Absorber, Shositiro Nagai and Shohachi Kakuno, 2697
- Wave dispersion; Computerized simulation; Concrete (blocks); Harbor structures; Quays; Reflection; Revetments; Shore protection**
Quay Wall with Wave Absorber "Iglou", Naofumi Shiraishi, Robert Q. Palmer and Hiroshi Okamoto, 2677
- Wave dispersion; Wave energy; Cooling water; Cylindrical bodies; Field tests; Intake structures; Nuclear power plants**
Wave Pressures on Large Circular Cylindrical Structure, Hiroshi Nakamura, 2290
- Wave dispersion; Wave energy; Wave functions; Wave height; Mud flats; Viscosity; Wave action**
Wave Action and Bottom Movements in Fine Sediments, Michael W. Tubman and Joseph N. Suhayda, 1168
- Wave dispersion; Wave energy; Waves; Breakwaters; Laboratory tests; Rubble mounds; Wave action**
Wave Transmission Through Trapezoidal Breakwaters, Ole Secher Madsen and Stanley M. White, 2662
- Wave dispersion; Wave energy; Wave spectrum; Coastal structures; Random processes; Reflection; Water waves**
Decomposition of Co-Existing Random Wave Energy, Dennis B. Morden, Eugene P. Richey and Derald R. Christensen, 846
- Wave dispersion; Wave energy; Wave velocity; Currents (water); Interactions; Turbulence; Wave action; Wave damping**
Interaction of Waves and a Turbulent Current, J. D.A. van Hoften and Susumu Karaki, 404
- Wave dispersion; Wave energy; Wave velocity; Field tests; Ocean bottom; Ocean waves; Wave action**
Near-Bottom Water Motion Under Ocean Waves, Robert A. Grace, 2371
- Wave dispersion; Wave height; Japan; Models; Numerical analysis; Statistical models; Tsunamis**
Numerical Models of Huge Tsunamis Off the Sanriku Coast, Toshio Iwasaki, 1044
- Wave dispersion; Wave height; Wavelengths; Wave propagation; Waves; Friction coefficient (hydraulic)**
Transformation of Nonlinear Long Waves, Nobuo Shuto, 423
- Wave dispersion; Wave height; Waves; Breaking; Breakwaters; Friction coefficient (hydraulic); Littoral drift; Ocean currents; Three-dimensional Non-Uniform Alongshore Currents, Michael R. Gourlay, 701**
- Wave dispersion; Wave height; Waves; Wave velocity; Breaking; Refraction; Shoaling; Wave action**
Refraction of Finite-Height and Breaking Waves, James R. Walker, 507
- Wave dispersion; Waves; Coastal structures; Cooling water; Intake systems; Mathematical models; Nuclear power plants; Numerical analysis; Refraction; Sediment transport**
Application of a Sediment Transport Model, C. A. Fleming and J. N. Hunt, 1184
- Wave energy; Air entrainment; Damage; Dikes; Impact; Revetments; Wave action**
Response of Seadykes due to Wave Impacts, Alfred Fuhrboter, Hans H. Dette and J. Grune, 2604
- Wave energy; Barriers; Beaches; Canada; Littoral current; Littoral drift; Morphology; Sandbars; Sediment deposits**
Process and Morphology Characteristics of Two Barrier Beaches in the Magdalen Islands, Gulf of St. Lawrence, Canada, E. H. Owens, 1975
- Wave energy; Barriers; Breakwaters; California; Jetties; Littoral current; Littoral drift; Sediment transport; Surf**
Longshore Transport at a Total Littoral Barrier, Richard O. Bruno and Christopher G. Gable, 1203
- Wave energy; Bays (topographic features); Beach erosion; Breakwaters; Shore protection; Wave action**
Headland Defense of Coasts, Richard Silvester, 1394
- Wave energy; Beach erosion; Beaches; Equilibrium; Gravel; Laboratory tests; Littoral current; Sediment transport; Shore protection**
Equilibrium Profiles and Longshore Transport of Coarse Material Under Oblique Wave Attack, E. van Hījum, 1258
- Wave energy; Beach erosion; Beach nourishment; Erosion; Littoral current; Recreational facilities; Storms; Storm surges; Wave action**
Cape Hatteras Beach Nourishment, John S. Fisher and Wilson N. Felder, 1512
- Wave energy; Bed forms; Inlets (waterways); Ocean bottom; Scale effect; Sediment transport; Simulation models; Tidal effects**
Tidal Inlet Flow Dynamics and Sediment Movement, Jerry L. Machemehl, N. E. Bird and A. N. Chambers, 1681
- Wave energy; Bottom water; Continental shelf; Cyclic loads; Foundations; Ocean bottom; Offshore structures; Predictions; Stability; Wave action**
Prediction of Wave-Induced Seafloor Movements, Leland Milo Kraft, Jr. and David James Watkins, 1605
- Wave energy; Breakwaters; Damage; Hydraulic models; Rubble; Rubble mounds; Stability; Wave action**
Effect of Broken Dolosse on Breakwater Stability, D. Donald Davidson and Dennis G. Markle, 2544

- Wave energy; Breakwaters; Reflection; Slitting; Wave action; Wave damping**
Slit-Type Breakwater: Box-Type Wave Absorber, Shositiro Nagai and Shohachi Kakuno, 2697
- Wave energy; Cooling water; Cylindrical bodies; Field tests; Intake structures; Nuclear power plants; Wave dispersion**
Wave Pressures on Large Circular Cylindrical Structure, Hiroshi Nakamura, 2290
- Wave energy; Cylinders; Drag; Hydraulic models; Lift; Oscillations; Reynolds number; Stream flow; Wave flow; Wave action**
High Reynolds Number Oscillating Flow by Cylinders, Tokuo Yamamoto and John H. Nath, 2321
- Wave energy; Drag; Force; Separation; Spheres; Wave circulation; Wave action**
Forces on a Sphere Under Linear Progressive Waves, Scott A. Jenkins and Douglas L. Inman, 2413
- Wave energy; Drag; Inertial forces; Submerged flow; Underwater structures; Wave action**
Wave Forces on Submerged Objects, Suphat Vongvissomsomjai and Richard Silvester, 2387
- Wave energy; Estuaries; Flooding; River flow; Sandbars; Sedimentation; Sediment deposits; Wave action**
Morphodynamics of a Wave-Dominated River Mouth, L. D. Wright, 1721
- Wave energy; Harbors; Harbor structures; History; Jetties; Rubble mounds; Wave action**
Design and Construction of Humboldt Jetties, 1880 to 1975, Orville T. Magoon, Robert L. Sloan and Nobuyuki Shimizu, 2474
- Wave energy; Inlets (waterways); Japan; Tidal effects; Tidal energy; Tidal hydraulics; Tidal waters**
Characteristics of Tidal Inlets on the Pacific Coast of Japan, Toshiyuki Shigemura, 1666
- Wave energy; Numerical analysis; Oscillations; Responses; Water depth; Water surface profiles; Wave action**
Wave Induced Oscillations of Harbors with Variable Depth, Fredric Raichlen and Ehud Nahcer, 3536
- Wave energy; Wave equations; Wave height; Wave period; Waves; Wave spectrum; Fetch; Great Lakes**
Applications of Empirical Fetch-Limited Spectral Formulas to Great Lakes Waves, Paul C. Liu, 113
- Wave energy; Wave forecasting; Waves; Wave spectrum; Wind forces; Wind speed; Fetch; Ocean waves**
Application of Fetch Area Method in Monsoon Wave Hindcasting, Nai-Kuang Liang, Shih-Tsan Tang and Ben-Juen Lee, 258
- Wave energy; Wave functions; Wave height; Mud flats; Viscosity; Wave action; Wave dispersion**
Wave Action and Bottom Movements in Fine Sediments, Michael W. Tubman and Joseph N. Suhayda, 1168
- Wave energy; Wave generation; Wave height; Coastal structures; Hazards; Tsunamis; Wave action**
Tsunami Hazard and Design of Coastal Structures, George Pararas-Carayannis, 2248
- Wave energy; Wave height; Wavemeters; Wave recorders (water waves); Waves; Climatic data; Ocean waves**
Wave Climate Analysis for Engineering Purpose, Hans H. Dette and Alfred Fuhrboter, 10
- Wave energy; Wave height; Wave period; Caissons; Model tests; Overturning tests; Wave action**
Wave Forces on Aquare Caissons, G. R. Mogridge and W. W. Jamieson, 2271
- Wave energy; Wave height; Wave period; Statistical analysis; Statistical distributions**
Characteristic Wave Period, Madhav Manohar, Ismail E. Mobarak and N. A. El Sharaky, 273
- Wave energy; Wave height; Wave period; Wave recorders (water waves); Waves; Wave spectrum; Continental shelf; Storms; Storm surges; Storm water**
Extreme Wave Parameters Based on Continental Shelf Storm Wave Records, R. E. Haring, A. R. Osborne and L. P. Spencer, 151
- Wave energy; Wave height; Wave period; Waves; Coastal engineering; Coastal structures; Stability**
Consecutive High Waves in Coastal Waters, Winfried Siefert, 171
- Wave energy; Wave height; Waves; Beaches; Deformation; Periodic functions; Phase velocity; Water depth**
Deformation up to Breaking of Periodic Waves on a Beach, Ib A. Svendsen and J. Buhr Hansen, 477
- Wave energy; Wavemeters; Coastal engineering; Coastal structures; Directional measurement; Sediment transport**
Wave Direction-Computations with Three Gage Arrays, D. Esteve, 349
- Wave energy; Wave period; Armoring (streambed); Breakwaters; Failure; Slope protection; Slope stability; Wave action**
Armour Blocks as Slope Protection, A. F. Whillock and W. A. Price, 2564
- Wave energy; Wave period; Concrete (blocks); Permeability; Reservoirs; Sea walls**
Permeable Seawall with Reservoir and the Use of "Warock", Takeshi Ijima, Enzoh Tanaka and Hideaki Okuzono, 2623
- Wave energy; Wave period; Fenders; Force; Harmonic functions; Mooring; Moorings; Oscillations; Wave action**
Subharmonic Components in Hawser and Fender Forces, J. H. van Oorschot, 2840
- Wave energy; Wave period; Wave recorders (water waves); Waves; Wave spectrum; Experimentation; Random processes**
Estimation of Incident and Reflected Waves in Random Wave Experiments, Yoshimi Goda and Yasumasa Suzuki, 828
- Wave energy; Wave propagation; Waves; Boundary value problems; Coastal engineering; Computation; Periodic variations; Refraction**
Physics and Mathematics of Waves in Coastal Zones, H. Lundgren, 880

- Wave energy; Wave recorders (water waves); California; Coastal engineering; Coastal structures; Numerical analysis**
Regional Network for Coastal Engineering Data, Richard J. Seymour and Meredith H. Sessions, 60
- Wave energy; Wave runup; Wave velocity; Coastal structures; Damping; Numerical analysis; Wave action**
Numerical Calculation of Wave Forces on Structures, B. D. Nichols and C. W. Hirt, 2254
- Wave energy; Waves; Breakwaters; Laboratory tests; Rubble mounds; Wave action; Wave dispersion**
Wave Transmission Through Trapezoidal Breakwaters, Ole Secher Madsen and Stanley M. White, 2662
- Wave energy; Waves; Wave spectrum; Breakwaters; Overtopping; Rubble mounds; Wave action**
Overtopping of Rubble-Mound Breakwaters by Irregular Waves, Yvon Ouellet and Pierre Eubanks, 2756
- Wave energy; Waves; Wave spectrum; Storm surges; Surf; Water level fluctuations; Water levels; Wave action**
Energy Spectra of Irregular Surf Waves, Fritz Busching, 539
- Wave energy; Wave spectrum; Beach erosion; Beaches; California; Equilibrium; Tidal effects**
Beach Profiles at Torrey Pines, California, David G. Aubrey, Douglas L. Inman and Charles E. Nordstrom, 1297
- Wave energy; Wave spectrum; Coastal structures; Random processes; Reflection; Water waves; Wave dispersion**
Decomposition of Co-Existing Random Wave Energy, Dennis B. Morden, Eugene P. Richey and Derald R. Christensen, 846
- Wave energy; Wave spectrum; Distribution functions; Distribution patterns; Frequency; Ocean waves; Surface waves**
Directional Spectral of Ocean Surface Waves, Hisashi Mitsuyasu and S. Mizuno, 329
- Wave energy; Wave spectrum; Wave tanks; Breakwaters; Buoys; Energy dissipation; Field tests; Floating bodies; Scale effect; Tethered tests; Wave action**
Design, Analysis and Field Test of a Dynamic Floating Breakwater, D. J. Agerton, G. H. Savage and K. C. Stotz, 2792
- Wave energy; Wave velocity; Currents (water); Interactions; Turbulence; Wave action; Wave damping; Wave dispersion**
Interaction of Waves and a Turbulent Current, J. D.A. van Hoften and Susumu Karaki, 404
- Wave energy; Wave velocity; Field tests; Ocean bottom; Ocean waves; Wave action; Wave dispersion**
Near-Bottom Water Motion Under Ocean Waves, Robert A. Grace, 2371
- Wave energy; West Germany; Damping; Energy dissipation; Estuaries; Stratification; Tidal effects**
Energy Dissipation in Tidal Estuaries, Hans-Werner Partenscky and Gunther Barg, 3312
- Wave energy; Wharves; Offshore structures; Prototype tests; Scour; Scouring; Wave action**
Wave Action on Large Off-Shore Structures, C. J. Apelt and A. Macknight, 2228
- Wave energy; Wind pressure; Discharge (water); Effluents; Field tests; Mathematical models; Numerical analysis; Water flow**
Numerical Modelling — An Aid to Assessing Field Data, H. P. Riedel and F. L. Wilkinson, 3243
- Wave equations; Coastal topographic features; Eigenvalues; Responses; Rip currents; Velocity distribution; Water waves**
Rip-Current and Coastal Topography, Mikio Hino, 1326
- Wave equations; Wave functions; Waves; Wave velocity; Shoaling**
Wave Shoaling of Finite Amplitude Waves, Masataka Yamaguchi and Yoshito Tsuchiya, 497
- Wave equations; Wave height; Breaking; Surf; Three-dimensional; Two-dimensional**
Three-Dimensional Conditions of Surf, William L. Wood, 525
- Wave equations; Wave height; Wave period; Wave runup; Dikes; Echo sounding; Field investigations; Instrumentation; Ocean waves; Scale effect; Storm surges**
Wave Run-Up in Field Measurements with Newly Developed Instrument, Heie F. Erchinger, 767
- Wave equations; Wave height; Wave period; Waves; Wave spectrum; Fetch; Great Lakes; Wave energy**
Applications of Empirical Fetch-Limited Spectral Formulas to Great Lakes Waves, Paul C. Liu, 113
- Wave equations; Wave height; Wave velocity; Friction coefficient (hydraulic); Interfaces; Two phase flow**
Friction at the Interface of Two-Layered Flows, Nobuyuki Tamai, 3169
- Wave equations; Wave runup; Overtopping; Scale effect; Shore protection; Slopes**
Wave Overtopping Equation, J. Richard Weggel, 2737
- Wave equations; Waves; Breakwaters; Oscillation; Sediment transport; Unsteady flow**
Quantitative Description of Sediment Transport, Ole Secher Madsen and William D. Grant, 1093
- Wave forecasting; Wave period; Waves; Wave spectrum; Climatology; Coastal engineering; Ocean waves; Spectral analysis; Statistical analysis**
Ocean Wave Statistics from FNWC Spectral Analysis, Warren C. Thompson and F. Michael Reynolds, 238
- Wave forecasting; Waves; Wave spectrum; Wind forces; Wind speed; Fetch; Ocean waves; Wave energy**
Application of Fetch Area Method in Monsoon Wave Hindcasting, Nai-Kuang Liang, Shih-Tsan Tang and Ben-Juen Lee, 258
- Wave forecasting; Wind forces; Wind speed; Forecasting; Hurricanes; Wave action**
Hurricane Wind and Wave Forecasting Techniques, Charles L. Bretschneider and Elaine E. Tamaye, 202

- Wave functions; Wave height; Mud flats; Viscosity; Wave action; Wave dispersion; Wave energy**
Wave Action and Bottom Movements in Fine Sediments, Michael W. Tubman and Joseph N. Suhayda, 1168
- Wave functions; Waves; Wave velocity; Shoaling; Wave equations**
Wave Shoaling of Finite Amplitude Waves, Masataka Yamaguchi and Yoshito Tsuchiya, 497
- Wave generation; Bedding materials; Bed ripples; Ripple marks; Sand; Sonar detection; Wave action**
Wave-Formed Ripples in Nearshore Sands, John R. Dingler and Douglas L. Inman, 2109
- Wave generation; Currents; Great Lakes; Harbors; Seiches; Tidal effects; Water levels**
Hydraulics of Great Lakes Inlet — Harbors Systems, Robert M. Sorensen and William N. Seelig, 1646
- Wave generation; Wave height; Coastal structures; Hazards; Tsunamis; Wave action; Wave energy**
Tsunami Hazard and Design of Coastal Structures, George Pararas-Carayannis, 2248
- Wave generation; Wave height; Wave propagation; Waves; Cavities; Deep water; Explosions; Predictions**
Calculations of Waves Formed From Surface Cavities, Charles L. Mader, 1079
- Wave generation; Waves; Hydraulic models; Three-dimensional; Water waves**
3-D Hydraulic Model of Wave Generated by Displacements, Shin-Lin Liu and Robert L. Wiegel, 1060
- Wave height; Beach erosion; Erosion; Field tests; Groins (structures); Laboratory tests; Littoral drift; Shore protection; Storms; Water temperature**
Laboratory Investigation of Shore Erosion Processes, Ernest F. Brater and David Ponce-Campos, 1493
- Wave height; Boundary value problems; Breakwaters; Permeability; Sea walls; Two-dimensional; Water depth; Water waves**
Method of Analyses for Two-Dimensional Water Wave Problems, Takeshi Ijima, Chung Ren Chou and Akinori Yoshida, 2717
- Wave height; Breaking; Surf; Three-dimensional; Two-dimensional; Wave equations**
Three-Dimensional Conditions of Surf, William L. Wood, 525
- Wave height; Breakwaters; Coastal structures; Experimentation; Field tests; Scour; Scouring; Water levels; Wave action**
Local Scour and Current Around a Porous Breakwater, Shintaro Hotta and Nobuo Marui, 1590
- Wave height; Breakwaters; Laboratory tests; Permeability; Reflection**
Laboratory Study of Pervious Core Breakwaters, Hideo Kondo, Satoshi Toma and Kenji Yano, 2643
- Wave height; Coastal structures; Hazards; Tsunamis; Wave action; Wave energy; Wave generation**
Tsunami Hazard and Design of Coastal Structures, George Pararas-Carayannis, 2248
- Wave height; Diffraction; Mach number; Reflection; Walls; Water waves**
Mach-Reflection as a Diffraction Problem, Udo Berger and Soren Kohlhasse, 796
- Wave height; Friction coefficient (hydraulic); Numerical analysis; Propagation; Shallow water; Tsunamis**
Tsunami Propagation in the Pacific Ocean, Manfred Engel and Wilfried Zahel, 971
- Wave height; Japan; Models; Numerical analysis; Statistical models; Tsunamis; Wave dispersion**
Numerical Models of Huge Tsunamis Off the Sanriku Coast, Toshio Iwasaki, 1044
- Wave height; Mud flats; Viscosity; Wave action; Wave dispersion; Wave energy; Wave functions**
Wave Action and Bottom Movements in Fine Sediments, Michael W. Tubman and Joseph N. Suhayda, 1168
- Wave height; Wavelengths; Wave propagation; Waves; Friction coefficient (hydraulic); Wave dispersion**
Transformation of Nonlinear Long Waves, Nobuo Shuto, 423
- Wave height; Wavelengths; Waves; Wave spectrum; Wave tanks; Wind (meteorology); Distribution patterns**
Wave Height Distribution of Wind Waves Over Long Waves, Shan-Hwei Ou and Frederick L.W. Tang, 388
- Wave height; Wavemeters; Wave recorders (water waves); Waves; Climatic data; Ocean waves; Wave energy**
Wave Climate Analysis for Engineering Purpose, Hans H. Dette and Alfred Fuhrboter, 10
- Wave height; Wavemeters; Wave recorders (water waves); Wave spectrum; Coastal engineering; India; Statistical analysis**
Ocean Wave Record Analysis by Tucker's Method — An Evaluation, Jade Dattatri and Irvathur Vasudeva Nayak, 289
- Wave height; Wavemeters; Wave recorders (water waves); Wave spectrum; Ocean waves; Radar equipment**
Wave Measurements in Open Ocean, Davidson T. Chen, Benjamin S. Yaple, Donald L. Hammond and Paul Bey, 72
- Wave height; Wave period; Caissons; Model tests; Overturning tests; Wave action; Wave energy**
Wave Forces on Aquare Caissons, G. R. Mogridge and W. W. Jamieson, 2271
- Wave height; Wave period; Statistical analysis; Statistical distributions; Wave energy**
Characteristic Wave Period, Madhav Manohar, Ismail E. Mobarek and N. A. El Sharaky, 273
- Wave height; Wave period; Wave recorders (water waves); Waves; Wave spectrum; Continental shelf; Storms; Storm surges; Storm water; Wave energy**
Extreme Wave Parameters Based on Continental Shelf Storm Wave Records, R. E. Haring, A. R. Osborne and L. P. Spencer, 151
- Wave height; Wave period; Wave recorders (water waves); Wave spectrum; Wave velocity; Breaking energy; Secondary waves**
Kinematics of Breaking Waves, Edward B. Thornton, James J. Galvin, Frank L. Bub and David P. Richardson, 461

- Wave height; Wave period; Wave runup; Armoring (streambed); Breakwaters; Model tests; Scale effect; Stability**
 Large Scale Model Tests of Placed Stone Breakwaters, Charles K. Sollitt and Donald H. DeBok, 2572
- Wave height; Wave period; Wave runup; Dikes; Echo sounding; Field investigations; Instrumentation; Ocean waves; Scale effect; Storm surges; Wave equations**
 Wave Run-Up in Field Measurements with Newly Developed Instrument, Heic F. Erchinger, 767
- Wave height; Wave period; Waves; Coastal engineering; Coastal structures; Stability; Wave energy**
 Consecutive High Waves in Coastal Waters, Winfried Siefert, 171
- Wave height; Wave period; Waves; Wave spectrum; Breaking; Dimensional analysis; Experimentation; Surf**
 Wave Spectrum of Breaking Wave, Toru Sawaragi and Koichiro Iwata, 580
- Wave height; Wave period; Waves; Wave spectrum; Fetch; Great Lakes; Wave energy; Wave equations**
 Applications of Empirical Fetch-Limited Spectral Formulas to Great Lakes Waves, Paul C. Liu, 113
- Wave height; Wave period; Waves; Wave spectrum; Wind speed; Great Lakes; Wave action**
 Great Lakes Wave Information, D. T. Resio and L. W. Hiiipakka, 92
- Wave height; Wave period; Waves; Wind speed; Coastal engineering; Ocean waves; Taiwan**
 Waves Off Taichung Coast of Taiwan, Charles C.C. Chang, M. H. Wang and J. T. Juang, 129
- Wave height; Wave period; Wave spectrum; Wave velocity; Flowmeters; Ocean currents; Rip currents; Time dependence**
 Time Dependent Fluctuations in Longshore Currents, Guy A. Meadows, 660
- Wave height; Wave phases; Littoral drift; Ocean currents; Rip currents; Sediment transport**
 Physical Aspects of Wave-Induced Nearshore Current System, Masaru Mizuguchi and Kiyoshi Horikawa, 607
- Wave height; Wave propagation; Waves; Cavities; Deep water; Explosions; Predictions; Wave generation**
 Calculations of Waves Formed From Surface Cavities, Charles L. Mader, 1079
- Wave height; Wave propagation; Wave spectrum; Ocean waves; Wave action**
 Revisions in Wave Data Presentation, Laurence Draper, 3
- Wave height; Wave runup; Beaches; Ocean waves; Resonance; Simulation; Water levels**
 Wave Run-Up on a Simulated Beach, A. J. Sutherland, J. N. Sharma and Omar H. Shemdin, 752
- Wave height; Wave runup; Waves; Beaches; Breaking; Resonance; Surges; Turbulence**
 Resonant Interactions for Waves Breaking on a Beach, Robert T. Guza and Anthony J. Bowen, 560
- Wave height; Wave runup; Waves; Dikes; Discharge (water); Overtopping; Periodic variations**
 Characteristics of Flow in Run-Up of Periodic Waves, Ary Roos and Jurjen A. Battjes, 781
- Wave height; Waves; Beaches; Deformation; Periodic functions; Phase velocity; Water depth; Wave energy**
 Deformation up to Breaking of Periodic Waves on a Beach, Ib A. Svendsen and J. Buhr Hansen, 477
- Wave height; Waves; Breaking; Breakwaters; Friction coefficient (hydraulic); Littoral drift; Ocean currents; Three-dimensional; Wave dispersion**
 Non-Uniform Alongshore Currents, Michael R. Gourlay, 701
- Wave height; Waves; Estuaries; Reservoirs; Tidal currents; Tidal effects; Tidal hydraulics; Tidal marshes**
 Waves Used for Inter-Tidal Design and Construction, D. C. Keiller and T. D. Ruxton, 23
- Wave height; Waves; Wave spectrum; Wind forces; Wind speed**
 Parametric Representation of a Wind-Wave Field, Henrik Rye and Roald Svec, 183
- Wave height; Waves; Wave velocity; Breaking; Gravity waves; Solitary waves; Time dependence**
 Recent Developments in the Study of Breaking Waves, Michael S. Longuet-Higgins, 441
- Wave height; Waves; Wave velocity; Breaking; Refraction; Shoaling; Wave action; Wave dispersion**
 Refraction of Finite-Height and Breaking Waves, James R. Walker, 507
- Wave height; Wave spectrum; Bathymetry; Groins (structures); Littoral drift; Sandbars; Sediment transport; Verification inspection**
 Experimental Verification of Groyne Theory, C. H. Hulsbergen, W. T. Bakker and G. van Bochove, 1439
- Wave height; Wave spectrum; Ocean waves; Spectral analysis; Statistical analysis; Storms**
 Six-Parameter Wave Spectra, Michel K. Ochi and E. Nadine Hubble, 301
- Wave height; Wave velocity; Friction coefficient (hydraulic); Interfaces; Two phase flow; Wave equations**
 Friction at the Interface of Two-Layered Flows, Nobuyuki Tamai, 3169
- Wavelengths; Wave propagation; Waves; Friction coefficient (hydraulic); Wave dispersion; Wave height**
 Transformation of Nonlinear Long Waves, Nobuo Shuto, 423
- Wavelengths; Waves; Wave spectrum; Wave tanks; Wind (meteorology); Distribution patterns; Wave height**
 Wave Height Distribution of Wind Waves Over Long Waves, Shan-Hwei Ou and Frederick L.W. Tang, 388
- Wavemeters; Coastal engineering; Coastal structures; Directional measurement; Sediment transport; Wave energy**
 Wave Direction Computations with Three Gage Arrays, D. Esteva, 349

- Wavemeters; Wave recorders (water waves); Waves; Climatic data; Ocean waves; Wave energy; Wave height**
Wave Climate Analysis for Engineering Purpose, Hans H. Dette and Alfred Fuhrboter, 10
- Wavemeters; Wave recorders (water waves); Wave spectrum; Coastal engineering; India; Statistical analysis; Wave height**
Ocean Wave Record Analysis by Tucker's Method -- An Evaluation, Jade Dattatri and Irvathur Vasudeva Nayak, 289
- Wavemeters; Wave recorders (water waves); Wave spectrum; Ocean waves; Radar equipment; Wave height**
Wave Measurements in Open Ocean, Davidson T. Chen, Benjamin S. Yaplee, Donald L. Hammond and Paul Bey, 72
- Wave period; Armoring (streambed); Breakwaters; Failure; Slope protection; Slope stability; Wave action; Wave energy**
Armour Blocks as Slope Protection, A. F. Whillock and W. A. Price, 2564
- Wave period; Caissons; Model tests; Overturning tests; Wave action; Wave energy; Wave height**
Wave Forces on Aquare Caissons, G. R. Mogridge and W. W. Jamieson, 2271
- Wave period; Concrete (blocks); Permeability; Reservoirs; Sea walls; Wave energy**
Permeable Seawall with Reservoir and the Use of "Warock", Takeshi Iijima, Enzoh Tanaka and Hideaki Okuzono, 2623
- Wave period; Fenders; Force; Harmonic functions; Mooring; Moorings; Oscillations; Wave action; Wave energy**
Subharmonic Components in Hawser and Fender Forces, J. H. van Oorschot, 2840
- Wave period; Statistical analysis; Statistical distributions; Wave energy; Wave height**
Characteristic Wave Period, Madhav Manohar, Ismail E. Mobarek and N. A. El Sharaky, 273
- Wave period; Wave recorders (water waves); Waves; Wave spectrum; Continental shelf; Storms; Storm surges; Storm water; Wave energy; Wave height**
Extreme Wave Parameters Based on Continental Shelf Storm Wave Records, R. E. Haring, A. R. Osborne and L. P. Spencer, 151
- Wave period; Wave recorders (water waves); Waves; Wave spectrum; Experimentation; Random processes; Wave energy**
Estimation of Incident and Reflected Waves in Random Wave Experiments, Yoshimi Goda and Yasumasa Suzuki, 828
- Wave period; Wave recorders (water waves); Wave spectrum; Wave velocity; Breaking energy; Secondary waves; Wave height**
Kinematics of Breaking Waves, Edward B. Thornton, James J. Galvin, Frank L. Bub and David P. Richardson, 461
- Wave period; Wave runup; Armoring (streambed); Breakwaters; Model tests; Scale effect; Stability; Wave height**
Large Scale Model Tests of Placed Stone Breakwaters, Charles K. Sollitt and Donald H. DeBok, 2572
- Wave period; Wave runup; Breakwaters; Resonance; Rubble; Rubble mounds; Slope stability; Stability; Surf**
New Design Principles for Rubble Mound Structures, Per Moller Bruun and Ali Riza Gunbak, 2429
- Wave period; Wave runup; Dikes; Echo sounding; Field investigations; Instrumentation; Ocean waves; Scale effect; Storm surges; Wave equations; Wave height**
Wave Run-Up in Field Measurements with Newly Developed Instrument, Heic F. Erchinger, 767
- Wave period; Wave runup; Waves; Breaking; Periodic variations; Shoaling; Slopes**
Set-Up and Run-Up in Shoaling Breakers, William G. Van Dorn, 738
- Wave period; Waves; Coastal engineering; Coastal structures; Stability; Wave energy; Wave height**
Consecutive High Waves in Coastal Waters, Winfried Siefert, 171
- Wave period; Waves; Wave spectrum; Breaking; Dimensional analysis; Experimentation; Surf; Wave height**
Wave Spectrum of Breaking Wave, Toru Sawaragi and Koichiro Iwata, 580
- Wave period; Waves; Wave spectrum; Climatology; Coastal engineering; Ocean waves; Spectral analysis; Statistical analysis; Wave forecasting**
Ocean Wave Statistics from FNWC Spectral Analysis, Warren C. Thompson and F. Michael Reynolds, 238
- Wave period; Waves; Wave spectrum; Fetch; Great Lakes; Wave energy; Wave equations; Wave height**
Applications of Empirical Fetch-Limited Spectral Formulas to Great Lakes Waves, Paul C. Liu, 113
- Wave period; Waves; Wave spectrum; Wind speed; Great Lakes; Wave action; Wave height**
Great Lakes Wave Information, D. T. Resio and L. W. Hiipakka, 92
- Wave period; Waves; Wind speed; Coastal engineering; Ocean waves; Taiwan; Wave height**
Waves Off Taichung Coast of Taiwan, Charles C.C. Chang, M. H. Wang and J. T. Juang, 129
- Wave period; Wave spectrum; Wave velocity; Flowmeters; Ocean currents; Rip currents; Time dependence; Wave height**
Time Dependent Fluctuations in Longshore Currents, Guy A. Meadows, 660
- Wave phases; Littoral drift; Ocean currents; Rip currents; Sediment transport; Wave height**
Physical Aspects of Wave-Induced Nearshore Current System, Masaru Mizuguchi and Kiyoshi Horikawa, 607
- Wave propagation; Waves; Boundary value problems; Coastal engineering; Computation; Periodic variations; Refraction; Wave energy**
Physics and Mathematics of Waves in Coastal Zones, H. Lundgren, 880
- Wave propagation; Waves; Cavities; Deep water; Explosions; Predictions; Wave generation; Wave height**
Calculations of Waves Formed From Surface Cavities, Charles L. Mader, 1079

- Wave propagation; Waves; Friction coefficient (hydraulic); Wave dispersion; Wave height; Wavelengths**
Transformation of Nonlinear Long Waves, Nobuo Shuto, 423
- Wave propagation; Waves; Littoral drift; Sandbars; Sands; Secondary waves; Sediment transport**
Sand Transport by Waves, E. W. Bijker, E. van Hijum and P. Vellinga, 1149
- Wave propagation; Wave spectrum; Ocean waves; Wave action; Wave height**
Revisions in Wave Data Presentation, Laurence Draper, 3
- Wave recorders (water waves); Beaches; Inlets (waterways); Littoral current; Littoral drift; Surf; Tidal currents**
Changes in Inlet Offset due to Stabilization, Dennis K. Hubbard, 1812
- Wave recorders (water waves); Beaches; Japan; Littoral drift; Ocean currents; Rip currents**
Nearshore Current on a Gently Sloping Beach, Tamio Sasaki, Kiyoshi Horikawa and Shintaro Hotta, 626
- Wave recorders (water waves); California; Coastal engineering; Coastal structures; Numerical analysis; Wave energy**
Regional Network for Coastal Engineering Data, Richard J. Seymour and Meredith H. Sessions, 60
- Wave recorders (water waves); Waves; Climatic data; Ocean waves; Wave energy; Wave height; Wavemeters**
Wave Climate Analysis for Engineering Purpose, Hans H. Dette and Alfred Fuhrboter, 10
- Wave recorders (water waves); Waves; Wave spectrum; Continental shelf; Storms; Storm surges; Storm water; Wave energy; Wave height; Wave period**
Extreme Wave Parameters Based on Continental Shelf Storm Wave Records, R. E. Haring, A. R. Osborne and L. P. Spencer, 151
- Wave recorders (water waves); Waves; Wave spectrum; Experimentation; Random processes; Wave energy; Wave period**
Estimation of Incident and Reflected Waves in Random Wave Experiments, Yoshimi Goda and Yasumasa Suzuki, 828
- Wave recorders (water waves); Wave spectrum; Coastal engineering; India; Statistical analysis; Wave height; Wavemeters**
Ocean Wave Record Analysis by Tucker's Method — An Evaluation, Jade Dattatri and Irvathur Vasudeva Nayak, 289
- Wave recorders (water waves); Wave spectrum; Ocean waves; Radar equipment; Wave height; Wavemeters**
Wave Measurements in Open Ocean, Davidson T. Chen, Benjamin S. Yaplee, Donald L. Hammond and Paul Bey, 72
- Wave recorders (water waves); Wave spectrum; Wave velocity; Breaking energy; Secondary waves; Wave height; Wave period**
Kinematics of Breaking Waves, Edward B. Thornton, James J. Galvin, Frank L. Bub and David P. Richardson, 461
- Wave recorders (water waves); Wind pressure; Wind tides; Current meters; Water circulation**
Wind-Driven Circulation of Saginaw Bay, James H. Saylor and Larry J. Danck, 3262
- Wave runup; Armoring (streambed); Breakwaters; Model tests; Scale effect; Stability; Wave height; Wave period**
Large Scale Model Tests of Placed Stone Breakwaters, Charles K. Sollitt and Donald H. DeBok, 2572
- Wave runup; Beaches; Ocean waves; Resonance; Simulation; Water levels; Wave height**
Wave Run-Up on a Simulated Beach, A. J. Sutherland, J. N. Sharma and Omar H. Shemdin, 752
- Wave runup; Breakwaters; Resonance; Rubble; Rubble mounds; Slope stability; Stability; Surf; Wave period**
New Design Principles for Rubble Mound Structures, Per Moller Bruun and Ali Riza Gunbak, 2429
- Wave runup; Dikes; Echo sounding; Field investigations; Instrumentation; Ocean waves; Scale effect; Storm surges; Wave equations; Wave height; Wave period**
Wave Run-Up in Field Measurements with Newly Developed Instrument, Heie F. Erchinger, 767
- Wave runup; Flooding; Predictions; Storm surges; Tsunamis**
Tsunami Inundation Prediction, Charles L. Bretschneider and Pieter G. Wybro, 1006
- Wave runup; Overtopping; Scale effect; Shore protection; Slopes; Wave equations**
Wave Overtopping Equation, J. Richard Weggel, 2737
- Wave runup; Waves; Beaches; Breaking; Resonance; Surges; Turbulence; Wave height**
Resonant Interactions for Waves Breaking on a Beach, Robert T. Guza and Anthony J. Bowen, 560
- Wave runup; Waves; Breaking; Periodic variations; Shoaling; Slopes; Wave period**
Set-Up and Run-Up in Shoaling Breakers, William G. Van Dorn, 738
- Wave runup; Waves; Dikes; Discharge (water); Overtopping; Periodic variations; Wave height**
Characteristics of Flow in Run-Up of Periodic Waves, Ary Roos and Jurjen A. Battjes, 781
- Wave runup; Wave velocity; Coastal structures; Damping; Numerical analysis; Wave action; Wave energy**
Numerical Calculation of Wave Forces on Structures, B. D. Nichols and C. W. Hirt, 2254
- Waves; Barriers; Finite differences; Shallow water; Simulation; Walls; Water waves; Wave action**
Action of Non-Linear Waves at a Solid Wall, Mohamed S. Nasser and John A. McCorquodale, 815
- Waves; Beaches; Breaking; Resonance; Surges; Turbulence; Wave height; Wave runup**
Resonant Interactions for Waves Breaking on a Beach, Robert T. Guza and Anthony J. Bowen, 560

- Waves; Beaches; Deformation; Periodic functions; Phase velocity; Water depth; Wave energy; Wave height**
Deformation up to Breaking of Periodic Waves on a Beach, Ib A. Svendsen and J. Buhr Hansen, 477
- Waves; Boundary value problems; Coastal engineering; Computation; Periodic variations; Refraction; Wave energy; Wave propagation**
Physics and Mathematics of Waves in Coastal Zones, H. Lundgren, 880
- Waves; Breaking; Breakwaters; Friction coefficient (hydraulic); Littoral drift; Ocean currents; Three-dimensional; Wave dispersion; Wave height**
Non-Uniform Alongshore Currents, Michael R. Gourlay, 701
- Waves; Breaking; Coastal engineering; Field tests; Littoral drift; Ocean currents; Photogrammetry; Stereophotography; Water levels**
Terrestrial Photogrammetric Measurements of Breaking Waves and Longshore Currents in the Nearshore Zone, Joseph W. Maresca, Jr. and Erwin Seibel, 681
- Waves; Breaking; Periodic variations; Shoaling; Slopes; Wave period; Wave runup**
Set-Up and Run-Up in Shoaling Breakers, William G. Van Dorn, 738
- Waves; Breakwaters; Laboratory tests; Rubble mounds; Wave action; Wave dispersion; Wave energy**
Wave Transmission Through Trapezoidal Breakwaters, Ole Secher Madsen and Stanley M. White, 2662
- Waves; Breakwaters; Oscillation; Sediment transport; Unsteady flow; Wave equations**
Quantitative Description of Sediment Transport, Ole Secher Madsen and William D. Grant, 1093
- Waves; Cavities; Deep water; Explosions; Predictions; Wave generation; Wave height; Wave propagation**
Calculations of Waves Formed From Surface Cavities, Charles L. Mader, 1079
- Waves; Climatic data; Ocean waves; Wave energy; Wave height; Wavemeters; Wave recorders (water waves)**
Wave Climate Analysis for Engineering Purpose, Hans H. Dette and Alfred Fuhrboter, 10
- Waves; Coastal engineering; Coastal structures; Stability; Wave energy; Wave height; Wave period**
Consecutive High Waves in Coastal Waters, Winfried Siefert, 171
- Waves; Coastal structures; Cooling water; Intake systems; Mathematical models; Nuclear power plants; Numerical analysis; Refraction; Sediment transport; Wave dispersion**
Application of a Sediment Transport Model, C. A. Fleming and J. N. Hunt, 1184
- Waves; Currents; Finite elements; Gravity waves; Predictions; Refraction; Surf; Water depth**
Current Depth Defraction Using Finite Elements, Ove Skovgaard and Ivar G. Jonsson, 721
- Waves; Dikes; Discharge (water); Overtopping; Periodic variations; Wave height; Wave runup**
Characteristics of Flow in Run-Up of Periodic Waves, Ary Roos and Jurjen A. Battjes, 781
- Waves; Estuaries; Reservoirs; Tidal currents; Tidal effects; Tidal hydraulics; Tidal marshes; Wave height**
Waves Used for Inter-Tidal Design and Construction, D. C. Keiller and T. D. Ruxton, 23
- Waves; Friction coefficient (hydraulic); Wave dispersion; Wave height; Wavelengths; Wave propagation**
Transformation of Nonlinear Long Waves, Nobuo Shuto, 423
- Waves; Hydraulic models; Three-dimensional; Water waves; Wave generation**
3-D Hydraulic Model of Wave Generated by Displacements, Shin-Lin Liu and Robert L. Wiegel, 1060
- Waves; Littoral drift; Sandbars; Sands; Secondary waves; Sediment transport; Wave propagation**
Sand Transport by Waves, E. W. Bijker, E. van Hijum and P. Vellinga, 1149
- Waves; Wave spectrum; Breaking; Dimensional analysis; Experimentation; Surf; Wave height; Wave period**
Wave Spectrum of Breaking Wave, Toru Sawaragi and Koichiro Iwata, 580
- Waves; Wave spectrum; Breakwaters; Overtopping; Rubble mounds; Wave action; Wave energy**
Overtopping of Rubble-Mound Breakwaters by Irregular Waves, Yvon Ouellet and Pierre Eubanks, 2756
- Waves; Wave spectrum; Climatology; Coastal engineering; Ocean waves; Spectral analysis; Statistical analysis; Wave forecasting; Wave period**
Ocean Wave Statistics from FNWC Spectral Analysis, Warren C. Thompson and F. Michael Reynolds, 238
- Waves; Wave spectrum; Continental shelf; Storms; Storm surges; Storm water; Wave energy; Wave height; Wave period; Wave recorders (water waves)**
Extreme Wave Parameters Based on Continental Shelf Storm Wave Records, R. E. Haring, A. R. Osborne and L. P. Spencer, 151
- Waves; Wave spectrum; Experimentation; Random processes; Wave energy; Wave period; Wave recorders (water waves)**
Estimation of Incident and Reflected Waves in Random Wave Experiments, Yoshimi Goda and Yasumasa Suzuki, 828
- Waves; Wave spectrum; Fetch; Great Lakes; Wave energy; Wave equations; Wave height; Wave period**
Applications of Empirical Fetch-Limited Spectral Formulas to Great Lakes Waves, Paul C. Liu, 113
- Waves; Wave spectrum; Storm surges; Surf; Water level fluctuations; Water levels; Wave action; Wave energy**
Energy Spectra of Irregular Surf Waves, Fritz Busching, 539
- Waves; Wave spectrum; Wave tanks; Wind (meteorology); Distribution patterns; Wave height; Wavelengths**
Wave Height Distribution of Wind Waves Over Long Waves, Shan-Hwei Ou and Frederick L.W. Tang, 388

- Waves; Wave spectrum; Wind forces; Wind speed; Fetch; Ocean waves; Wave energy; Wave forecasting**
Application of Fetch Area Method in Monsoon Wave Hindcasting, Nai-Kuang Liang, Shih-Tsan Tang and Ben-Juen Lee, 258
- Waves; Wave spectrum; Wind forces; Wind speed; Wave height**
Parametric Representation of a Wind-Wave Field, Henrik Rye and Roald Svee, 183
- Waves; Wave spectrum; Wind speed; Great Lakes; Wave action; Wave height; Wave period**
Great Lakes Wave Information, D. T. Resio and L. W. Hiipakka, 92
- Waves; Wave tanks; Beach erosion; Erosion; Groins (structures); Rip currents**
Groin Length and the Generation of Edge Waves, Michael K. Gaughan and Paul D. Komar, 1459
- Waves; Wave tanks; Laboratory tests; Ocean waves; Random variables; Simulation**
Random Wave Simulation in a Laboratory Wave Tank, Akira Kimura and Yuichi Iwagaki, 368
- Waves; Wave velocity; Breaking; Gravity waves; Solitary waves; Time dependence; Wave height**
Recent Developments in the Study of Breaking Waves, Michael S. Longuet-Higgins, 441
- Waves; Wave velocity; Breaking; Refraction; Shoaling; Wave action; Wave dispersion; Wave height**
Refraction of Finite-Height and Breaking Waves, James R. Walker, 507
- Waves; Wave velocity; Shoaling; Wave equations; Wave functions**
Wave Shoaling of Finite Amplitude Waves, Masataka Yamaguchi and Yoshito Tsuchiya, 497
- Waves; Wind (meteorology); Coastal engineering; Coastal structures; Data collection; Data collection systems; Hydrographic surveys**
Data Collection and Analysis for Coastal Projects, E. Loewy, K. G. Withaus, L. Summers and R. J. Maddrell, 43
- Waves; Wind speed; Coastal engineering; Ocean waves; Taiwan; Wave height; Wave period**
Waves Off Taichung Coast of Taiwan, Charles C.C. Chang, M. H. Wang and J. T. Juang, 129
- Wave spectrum; Bathymetry; Groins (structures); Littoral drift; Sandbars; Sediment transport; Verification inspection; Wave height**
Experimental Verification of Groyne Theory, C. H. Hulsbergen, W. T. Bakker and G. van Bochove, 1439
- Wave spectrum; Beach erosion; Beaches; California; Equilibrium; Tidal effects; Wave energy**
Beach Profiles at Torrey Pines, California, David G. Aubrey, Douglas L. Inman and Charles E. Nordstrom, 1297
- Wave spectrum; Beach erosion; Beaches; Computer models; Slopes**
Study of Equilibrium Beach Profiles, Robert A. Dalrymple and William W. Thompson, 1277
- Wave spectrum; Breaking; Dimensional analysis; Experimentation; Surf; Wave height; Wave period; Waves**
Wave Spectrum of Breaking Wave, Toru Sawaragi and Koichiro Iwata, 580
- Wave spectrum; Breakwaters; Overtopping; Rubble mounds; Wave action; Wave energy; Waves**
Overtopping of Rubble-Mound Breakwaters by Irregular Waves, Yvon Ouellet and Pierre Eubanks, 2756
- Wave spectrum; Climatology; Coastal engineering; Ocean waves; Spectral analysis; Statistical analysis; Wave forecasting; Wave period; Waves**
Ocean Wave Statistics from FNWC Spectral Analysis, Warren C. Thompson and F. Michael Reynolds, 238
- Wave spectrum; Coastal engineering; India; Statistical analysis; Wave height; Wavemeters; Wave recorders (water waves)**
Ocean Wave Record Analysis by Tucker's Method — An Evaluation, Jade Dattatri and Irvathur Vasudeva Nayak, 289
- Wave spectrum; Coastal structures; Random processes; Reflection; Water waves; Wave dispersion; Wave energy**
Decomposition of Co-Existing Random Wave Energy, Dennis B. Morden, Eugene P. Richey and Derald R. Christensen, 846
- Wave spectrum; Continental shelf; Storms; Storm surges; Storm water; Wave energy; Wave height; Wave period; Wave recorders (water waves); Waves**
Extreme Wave Parameters Based on Continental Shelf Storm Wave Records, R. E. Haring, A. R. Osborne and L. P. Spencer, 151
- Wave spectrum; Distribution functions; Distribution patterns; Frequency; Ocean waves; Surface waves; Wave energy**
Directional Spectral of Ocean Surface Waves, Hisashi Mitsuyasu and S. Mizuno, 329
- Wave spectrum; Experimentation; Random processes; Wave energy; Wave period; Wave recorders (water waves); Waves**
Estimation of Incident and Reflected Waves in Random Wave Experiments, Yoshimi Goda and Yasumasa Suzuki, 828
- Wave spectrum; Fetch; Great Lakes; Wave energy; Wave equations; Wave height; Wave period; Waves**
Applications of Empirical Fetch-Limited Spectral Formulas to Great Lakes Waves, Paul C. Liu, 113
- Wave spectrum; Ocean waves; Radar equipment; Wave height; Wavemeters; Wave recorders (water waves)**
Wave Measurements in Open Ocean, Davidson T. Chen, Benjamin S. Yaple, Donald L. Hammond and Paul Bey, 72
- Wave spectrum; Ocean waves; Spectral analysis; Statistical analysis; Storms; Wave height**
Six-Parameter Wave Spectra, Michel K. Ochi and E. Nadine Hubble, 301
- Wave spectrum; Ocean waves; Wave action; Wave height; Wave propagation**
Revisions in Wave Data Presentation, Laurence Draper, 3

- Wave spectrum; Storm surges; Surf; Water level fluctuations; Water levels; Wave action; Wave energy; Waves**
Energy Spectra of Irregular Surf Waves, Fritz Busching, 539
- Wave spectrum; Wave tanks; Breakwaters; Buoys; Energy dissipation; Field tests; Floating bodies; Scale effect; Tethered tests; Wave action; Wave energy**
Design, Analysis and Field Test of a Dynamic Floating Breakwater, D. J. Agerton, G. H. Savage and K. C. Stotz, 2792
- Wave spectrum; Wave tanks; Wind (meteorology); Distribution patterns; Wave height; Wavelengths; Waves**
Wave Height Distribution of Wind Waves Over Long Waves, Shan-Hwei Ou and Frederick L.W. Tang, 388
- Wave spectrum; Wave velocity; Breaking energy; Secondary waves; Wave height; Wave period; Wave recorders (water waves)**
Kinematics of Breaking Waves, Edward B. Thornton, James J. Galvin, Frank L. Bub and David P. Richardson, 461
- Wave spectrum; Wave velocity; Flowmeters; Ocean currents; Rip currents; Time dependence; Wave height; Wave period**
Time Dependent Fluctuations in Longshore Currents, Guy A. Meadows, 660
- Wave spectrum; Wind forces; Wind speed; Fetch; Ocean waves; Wave energy; Wave forecasting; Waves**
Application of Fetch Area Method in Monsoon Wave Hindcasting, Nai-Kuang Liang, Shih-Tsan Tang and Ben-Juen Lee, 258
- Wave spectrum; Wind forces; Wind speed; Wave height; Waves**
Parametric Representation of a Wind-Wave Field, Henrik Rye and Roald Svee, 183
- Wave spectrum; Wind speed; Great Lakes; Wave action; Wave height; Wave period; Waves**
Great Lakes Wave Information, D. T. Resio and L. W. Hiipakka, 92
- Wave tanks; Accidents; Collisions; Harbor structures; Mooring; Moorings; Offshore drilling; Ships**
Protection of Maritime Structures Against Ship Collisions, Kazuki Oda and Shositiro Nagai, 2810
- Wave tanks; Beach erosion; Erosion; Groins (structures); Rip currents; Waves**
Groin Length and the Generation of Edge Waves, Michael K. Gaughan and Paul D. Komar, 1459
- Wave tanks; Breakwaters; Buoys; Energy dissipation; Field tests; Floating bodies; Scale effect; Tethered tests; Wave action; Wave energy; Wave spectrum**
Design, Analysis and Field Test of a Dynamic Floating Breakwater, D. J. Agerton, G. H. Savage and K. C. Stotz, 2792
- Wave tanks; Laboratory tests; Ocean waves; Random variables; Simulation; Waves**
Random Wave Simulation in a Laboratory Wave Tank, Akira Kimura and Yuichi Iwagaki, 368
- Wave tanks; Wind (meteorology); Distribution patterns; Wave height; Wavelengths; Waves; Wave spectrum**
Wave Height Distribution of Wind Waves Over Long Waves, Shan-Hwei Ou and Frederick L.W. Tang, 388
- Wave velocity; Breaking; Gravity waves; Solitary waves; Time dependence; Wave height; Waves**
Recent Developments in the Study of Breaking Waves, Michael S. Longuet-Higgins, 441
- Wave velocity; Breaking; Refraction; Shoaling; Wave action; Wave dispersion; Wave height; Waves**
Refraction of Finite-Height and Breaking Waves, James R. Walker, 507
- Wave velocity; Breaking energy; Secondary waves; Wave height; Wave period; Wave recorders (water waves); Wave spectrum**
Kinematics of Breaking Waves, Edward B. Thornton, James J. Galvin, Frank L. Bub and David P. Richardson, 461
- Wave velocity; Coastal structures; Damping; Numerical analysis; Wave action; Wave energy; Wave runoff**
Numerical Calculation of Wave Forces on Structures, B. D. Nichols and C. W. Hirt, 2254
- Wave velocity; Currents (water); Interactions; Turbulence; Wave action; Wave damping; Wave dispersion; Wave energy**
Interaction of Waves and a Turbulent Current, J. D.A. van Hoften and Susumu Karaki, 404
- Wave velocity; Field tests; Ocean bottom; Ocean waves; Wave action; Wave dispersion; Wave energy**
Near-Bottom Water Motion Under Ocean Waves, Robert A. Grace, 2371
- Wave velocity; Flowmeters; Ocean currents; Rip currents; Time dependence; Wave height; Wave period; Wave spectrum**
Time Dependent Fluctuations in Longshore Currents, Guy A. Meadows, 660
- Wave velocity; Friction coefficient (hydraulic); Interfaces; Two phase flow; Wave equations; Wave height**
Friction at the Interface of Two-Layered Flows, Nobuyuki Tamai, 3169
- Wave velocity; Shoaling; Wave equations; Wave functions; Waves**
Wave Shoaling of Finite Amplitude Waves, Masataka Yamaguchi and Yoshito Tsuchiya, 497
- Weather forecasting; Automation; Forecasting; Hurricanes; Storm surges**
Automated Forecasting of Extratropical Storm Surges, N. Arthur Pore, 906
- Weed control; Weeds; Erosion; Erosion control; Gullies; Netherlands; Shore protection**
Recent Applications of Artificial Seaweed in the Netherlands, Henk G.H. ten Hoopen, 2905
- Weeds; Erosion; Erosion control; Gullies; Netherlands; Shore protection; Weed control**
Recent Applications of Artificial Seaweed in the Netherlands, Henk G.H. ten Hoopen, 2905

- West Germany; Channels (waterways); Dunes; Dune sands; Sand waves; Sediment transport; Tidal effects**
Transport Mechanism in Tidal Dunes, Horst Nasner, 2136
- West Germany; Damping; Energy dissipation; Estuaries; Stratification; Tidal effects; Wave energy**
Energy Dissipation in Tidal Estuaries, Hans-Werner Partenscky and Gunther Barg, 3312
- West Germany; Hydraulic models; Movable bed models; Scale effect; Sediment transport; Tracers (radioactive)**
Sand Movement Investigations by Means of Radioactive Tracers in a Hydraulic Model and in the Field, Hans Rohde, 2027
- Wharves; Offshore structures; Prototype tests; Scour; Scouring; Wave action; Wave energy**
Wave Action on Large Off-Shore Structures, C. J. Apelt and A. Macknight, 2228
- Wind forces; Wind speed; Fetch; Ocean waves; Wave energy; Wave forecasting; Waves; Wave spectrum**
Application of Fetch Area Method in Monsoon Wave Hindcasting, Nai-Kuang Liang, Shih-Tsan Tang and Ben-Juen Lee, 258
- Wind forces; Wind speed; Forecasting; Hurricanes; Wave action; Wave forecasting**
Hurricane Wind and Wave Forecasting Techniques, Charles L. Bretschneider and Elaine E. Tamayc, 202
- Wind forces; Wind speed; Wave height; Waves; Wave spectrum**
Parametric Representation of a Wind-Wave Field, Henrik Rye and Roald Svee, 183
- Wind (meteorology); Coastal engineering; Coastal structures; Data collection; Data collection systems; Hydrographic surveys; Waves**
Data Collection and Analysis for Coastal Projects, E. Loewy, K. G. Witthaus, L. Summers and R. J. Maddrell, 43
- Wind (meteorology); Distribution patterns; Wave height; Wavelengths; Waves; Wave spectrum; Wave tanks**
Wave Height Distribution of Wind Waves Over Long Waves, Shan-Hwei Ou and Frederick L.W. Tang, 388
- Wind pressure; Discharge (water); Effluents; Field tests; Mathematical models; Numerical analysis; Water flow; Wave energy**
Numerical Modelling — An Aid to Assessing Field Data, H. P. Riedel and F. L. Wilkinson, 3243
- Wind pressure; Wind tides; Current meters; Water circulation; Wave recorders (water waves)**
Wind-Driven Circulation of Saginaw Bay, James H. Saylor and Larry J. Danek, 3262
- Wind speed; Coastal engineering; Ocean waves; Taiwan; Wave height; Wave period; Waves**
Waves Off Taichung Coast of Taiwan, Charles C.C. Chang, M. H. Wang and J. T. Juang, 129
- Wind speed; Fetch; Ocean waves; Wave energy; Wave forecasting; Waves; Wave spectrum; Wind forces**
Application of Fetch Area Method in Monsoon Wave Hindcasting, Nai-Kuang Liang, Shih-Tsan Tang and Ben-Juen Lee, 258
- Wind speed; Forecasting; Hurricanes; Wave action; Wave forecasting; Wind forces**
Hurricane Wind and Wave Forecasting Techniques, Charles L. Bretschneider and Elaine E. Tamayc, 202
- Wind speed; Great Lakes; Wave action; Wave height; Wave period; Waves; Wave spectrum**
Great Lakes Wave Information, D. T. Resio and L. W. Hiipakka, 92
- Wind speed; Wave height; Waves; Wave spectrum; Wind forces**
Parametric Representation of a Wind-Wave Field, Henrik Rye and Roald Svee, 183
- Wind tides; Current meters; Water circulation; Wave recorders (water waves); Wind pressure**
Wind-Driven Circulation of Saginaw Bay, James H. Saylor and Larry J. Danek, 3262

Author Index

- Adams, William D.**
See Todd L. Walton, Jr., 1919
- Adee, Bruce H.**
Floating Breakwater Performance, 2777
- Agerton, D. J.**
Design, Analysis and Field Test of a Dynamic
Floating Breakwater, with G. H. Savage and K. C.
Stotz, 2792
- Amarasinghe, Summa R.**
See Franciscus Gerritsen, 3487
- Apelt, C. J.**
Wave Action on Large Off-Shore Structures, with A.
Macknight, 2228
- April, Gary G.**
Sediment Transportation and Deposition Models for
Mobile Bay, Alabama, with Samuel Ng and C.
Everett Brett, 2092
- Armstrong, John M.**
Low-Cost Shore Protection on the Great Lakes: A
Demonstration/Research Program, 2858
- Aubrey, David G.**
Beach Profiles at Torrey Pines, California, with
Douglas L. Inman and Charles E. Nordstrom, 1297
See Clinton D. Winant, 1312
- Bakker, W. T.**
See C. H. Hulsbergen, 1439
- Barg, Gunther**
See Hans-Werner Partensky, 3312
- Barrientos, Celso S.**
SPLASH — A Model for Forecasting Tropical Storm
Surges, with Chester P. Jelesnianski, 941
- Barthel, Volker**
Stability of Tidal Channels Dependent on River
Improvement, 1775
- Battjes, Jurjen A.**
See Ary Roos, 781
- Bennett, James P.**
Calibration of Branched Estuary Models, 3416
- Berger, Udo**
Mach-Reflection as a Diffraction Problem, with
Soren Kohlhase, 796
- Bey, Paul**
See Davidson T. Chen, 72
- Bijker, E. W.**
Sand Transport by Waves, with E. van Hijum and P.
Vellinga, 1149
- Bird, N. E.**
See Jerry L. Machemehl, 1681
- Bowen, Anthony J.**
See Robert T. Guza, 560
- Brater, Ernest F.**
Laboratory Investigation of Shore Erosion Processes,
with David Ponce-Campos, 1493
- Bretschneider, Charles L.**
Hurricane Wind and Wave Forecasting Techniques,
with Elaine E. Tamaye, 202
Tsunami Inundation Prediction, with Pieter G.
Wybro, 1006
- Brett, C. Everett**
See Gary G. April, 2092
- Brodersen, Finn P.**
See Helge Gravesen, 2357
- Brooks, H. K.**
See Omar H. Shemdin, 1477
- Brooks, Norman H.**
See Robert C.Y. Koh, 2941
- Bruno, Richard O.**
Longshore Transport at a Total Littoral Barrier, with
Christopher G. Gable, 1203
- Braun, Per Moller**
New Design Principles for Rubble Mound Structures,
with Ali Riza Gunbak, 2429
- Bub, Frank L.**
See Edward B. Thornton, 461
- Busching, Fritz**
Energy Spectra of Irregular Surf Waves, 539
- Butler, H. L.**
See A. W. Garcia, 1025
- Byrne, R. J.**
See Ashish J. Mehta, 1701
- Ceylanli, Z.**
See Omar H. Shemdin, 1477
- Chambers, A. N.**
See Jerry L. Machemehl, 1681
- Chang, Charles C.C.**
Waves Off Taichung Coast of Taiwan, with M. H.
Wang and J. T. Juang, 129
- Chao, Yung Y.**
See Thomas McKinney, 1899
- Chapman, Gordon A.**
Environmental Impacts on an Island Community,
3506
- Chen, Davidson T.**
Wave Measurements in Open Ocean, with Benjamin
S. Yaplee, Donald L. Hammond and Paul Bey, 72
- Cheng, Ralph T-S**
See L. H. Smith, 3358
- Chou, Chung Ren**
See Takeshi Ijima, 2717
- Chou, I. B.**
See D. M. Sheppard, 3068
- Christensen, Derald R.**
See Dennis B. Morden, 846

- Christodoulou, George C.**
Numerical Modeling of Dispersion in Stratified Waters, with Jerome J. Connor, 3138
- Connor, Jerome J.**
See George C. Christodoulou, 3138
- Cox, Doak C.**
Proposed "Improvement" of Kaimu Beach, Hawaii, with Francis G. Gerritsen and Theodore T. Lee, 1552
- Czerniak, Martin T.**
Probable Utilization Level for a Barge Harbor, with Choulei J. Sonu, 3557
- Dalrymple, Robert A.**
Study of Equilibrium Beach Profiles, with William W. Thompson, 1277
- Danek, Larry J.**
See James H. Saylor, 3262
- Darling, Wilfred D.**
Design and Construction of Protective Structure for New Reef Runway at Honolulu International Airport, 2589
- Dattatri, Jade**
Ocean Wave Record Analysis by Tucker's Method — An Evaluation, with Irvathur Vasudeva Nayak, 289
- Davidson, D. Donald**
Effect of Broken Dolosse on Breakwater Stability, with Dennis G. Markle, 2544
- DeAlteris, Joseph T.**
Beach Haven and Little Egg Inlets, A Case Study, with Thomas McKinney and James Roney, 1881
See Ashish J. Mehta, 1701
See Thomas McKinney, 1899
- DeBok, Donald H.**
See Charles K. Sollitt, 2572
- de la Parra, Ralph A.**
Coastal Environment and a Nuclear Power Plant, 3014
- Derbyshire, B. V.**
See Mary P. Kendrick, 2072
- Dette, Hans H.**
Wave Climate Analysis for Engineering Purpose, with Alfred Fuhrboter, 10
See Alfred Fuhrboter, 2604
- Dingler, John R.**
Wave-Formed Ripples in Nearshore Sands, with Douglas L. Inman, 2109
- Ditmars, J. D.**
See D. M. Shahrabani, 2976
See A. A. Frigo, 3028
- Draper, Laurence**
Revisions in Wave Data Presentation, 3
- Druery, Bruce M.**
See Cyril D. Floyd, 1738
- Dunham, James W.**
Application of CERC Special Report No.2, 3570
- Durham, D. L.**
See R. W. Whalin, 3377
- Ecker, Richard M.**
Tracing Estuarine Sediments by Neutron Activation, with John F. Sustar and William T. Harvey, 2009
- Edge, Billy L.**
Low-Cost Shoreline Protection, with John G. Housley and George M. Watts, 2888
- El Sharaky, N. A.**
See Madhav Manohar, 273
- Engel, Manfred**
Tsunami Propagation in the Pacific Ocean, with Wilfried Zahel, 971
- Erchinger, Heie F.**
Wave Run-Up in Field Measurements with Newly Developed Instrument, 767
- Esteva, D.**
Wave Direction Computations with Three Gage Arrays, 349
- Eubanks, Pierre**
See Yvon Ouellet, 2756
- Falconer, Roger A.**
See Ronald C. Nece, 3471
- Fallah, Mohammad H.**
Simulation Model for Storm Surge Probabilities, with J. N. Sharma and Cheng Y. Yang, 934
- Fang, Ching S.**
See Gary C. Parker, 3049
- Felder, Wilson N.**
See John S. Fisher, 1512
- Fischer, Karsten**
Numerical Model for Density Currents in Estuaries, 3295
- Fisher, John S.**
Cape Hatteras Beach Nourishment, with Wilson N. Felder, 1512
- FitzGerald, Duncan M.**
Sand Circulation Pattern at Price Inlet, South Carolina, with Dag Nummedal and Timothy W. Kana, 1868
- Fleming, C. A.**
Application of a Sediment Transport Model, with J. N. Hunt, 1184
- Floyd, Cyril D.**
Results of River Mouth Training on the Clarence Bar, New South Wales, Australia, with Bruce M. Druery, 1738
- Flugge, Gerd**
Horizontal Diffusion in Tidal Models and Scaling Criteria for Thermal-Hydraulic Model Tests, 3097
- Fredsoe, Jorgen**
See Ramiro Mayor-Mora, 2151
- French, Richard H.**
Interfacial Instability in Stratified Flow, 3124
- Fried, I.**
Protection by Means of Offshore Breakwaters, 1407

- Frigo, A. A.**
Field Studies of Submerged-Diffuser Thermal Plumes with Comparisons to Predictive Model Results, with Richard A. Paddock and J. D. Ditmars, 3028
- Fuhrboter, Alfred**
Response of Seadykes due to Wave Impacts, with Hans H. Dette and J. Grune, 2604
See Hans H. Dette, 10
- Gable, Christopher G.**
See Richard O. Bruno, 1203
- Galvin, Cyril J.**
Longshore Transport Prediction — SPM 1973 Equation, with Philip Vitale, 1133
- Galvin, James J.**
See Edward B. Thornton, 461
- Garcia, A. W.**
Numerical Simulation of Tsunamis Originating in the Peru-Chile Trench, with H. L. Butler, 1025
- Gaughan, Michael K.**
Groin Length and the Generation of Edge Waves, with Paul D. Komar, 1459
- Gerritsen, Franciscus**
Coastal Problems in Sri Lanka, with Summa R. Amarasinghe, 3487
See Doak C. Cox, 1552
- Glover, John R.**
See Tatsuaki Nakato, 2060
- Goda, Yoshimi**
Estimation of Incident and Reflected Waves in Random Wave Experiments, with Yasumasa Suzuki, 828
- Gohren, Harald**
Currents in Tidal Flats During Storm Surges, 959
- Gourlay, Michael R.**
Non-Uniform Alongshore Currents, 701
- Grace, Robert A.**
Near-Bottom Water Motion Under Ocean Waves, 2371
- Grant, William D.**
See Ole Secher Madsen, 1093
- Gravesen, Helge**
Cylindrical Caisson Breakwater: Strain Model Tests, with Finn P. Brodersen, Jorn S. Larsen and H. Lundgren, 2357
- Grune, J.**
See Alfred Fuhrboter, 2604
- Gunbak, Ali Riza**
See Per Moller Bruun, 2429
- Guza, Robert T.**
Resonant Interactions for Waves Breaking on a Beach, with Anthony J. Bowen, 560
- Hammond, Donald L.**
See Davidson T. Chen, 72
- Hansen, J. Buhr**
See Ib A. Svendsen, 477
- Haring, R. E.**
Extreme Wave Parameters Based on Continental Shelf Storm Wave Records, with A. R. Osborne and L. P. Spencer, 151
- Harrell, S. L.**
See Omar H. Shemdin, 1477
- Harvey, William T.**
See Richard M. Ecker, 2009
- Hattori, Masataro**
Concept for Inferring the Littoral Drift Trend, with Takasuke Suzuki, 1223
- Hayashi, Taizo**
Added Masses of Large Tankers Berthing to Dolphins, with Masujiro Shirai, 2830
- Hayes, Miles O.**
Geomorphology of the Southern Coast of Alaska, with Christopher H. Ruby, Michael F. Stephen and Stephen J. Wilson, 1992
- Herbich, John B.**
Scour Around Model Pipelines Due to Wave Action, 1624
- Herrling, Bruno**
Finite Element Model for Estuaries with Inter-Tidal Flats, 3396
- Higuchi, Haruo**
See Shigehisa Nakamura, 988
- Hiiipakka, L. W.**
See D. T. Resio, 92
See C. N. Johnson, 1361
- Hino, Mikio**
Rip-Current and Coastal Topography, 1326
- Hirt, C. W.**
See B. D. Nichols, 2254
- Ho, Francis P.**
Hurricane Tide Frequencies on the Atlantic Coast, 886
- Holz, Klaus-Peter**
Analysis of Time Conditions for Hybrid Tidal Models, 3460
- Horikawa, Kiyoshi**
See Masaru Mizuguchi, 607
See Tamio Sasaki, 626
See Tsuguo Sunamura, 1240
- Hotta, Shintaro**
Local Scour and Current Around a Porous Breakwater, with Nobuo Marui, 1590
See Tamio Sasaki, 626
- Housley, John G.**
See Billy L. Edge, 2888
- Hubbard, Dennis K.**
Changes in Inlet Offset due to Stabilization, 1812
- Hubble, E. Nadine**
See Michel K. Ochi, 301
- Hulsbergen, C. H.**
Experimental Verification of Groyne Theory, with W. T. Bakker and G. van Bochove, 1439

Hunt, J. N.

See C. A. Fleming, 1184

Huntley, David A.

Lateral and Bottom Forces on Longshore Currents, 645

Ijima, Takeshi

Method of Analyses for Two-Dimensional Water Wave Problems, with Chung Ren Chou and Akinori Yoshida, 2717

Permeable Seawall with Reservoir and the Use of "Warock", with Enzoh Tanaka and Hideaki Okuzono, 2623

Imberger, Jorg

Dynamics of a Longitudinally Stratified Estuary, 3108

Inman, Douglas L.

See David G. Aubrey, 1297

See John R. Dingle, 2109

See Scott A. Jenkins, 2413

Ishida, Hajime

See Yuichi Iwagaki, 2341

Ismail, Nabil

Guidelines for the Design of Air Bubble Systems, 2994

Iwagaki, Yuichi

Flow Separation, Wake Vortices and Pressure Distribution Around a Circular Cylinder under Oscillatory Waves, with Hajime Ishida, 2341

See Akira Kimura, 368

Iwasaki, Toshio

Numerical Models of Huge Tsunamis Off the Sanriku Coast, 1044

Iwata, Koichiro

See Toru Sawaragi, 580

See Toru Sawaragi, 595

Jacobson, John P.

See Albert Y. Kuo, 3276

Jain, Subhash C.

Movable Bed Tidal Inlet Models, with John F. Kennedy, 3435

Jamieson, W. W.

See G. R. Mogridge, 2271

Jelesnianski, Chester P.

See Celso S. Barrientos, 941

Jenkins, Scott A.

Forces on a Sphere Under Linear Progressive Waves, with Douglas L. Inman, 2413

Johnson, C. N.

Sand-Bypass and Shore Erosion, Bridgman, Michigan, with L. W. Hiipakka, 1361

Jonsson, Ivar G.

See Ove Skovgaard, 721

Juang, J. T.

See Charles C.C. Chang, 129

Kadib, A. A.

Sedimentation Problems at Offshore Dredged Channels, 1756

Kakuno, Shohachi

See Shositiro Nagai, 2697

Kamphuis, J. William

Three Dimensional Tests on Dynamic Equilibrium and Artificial Nourishment, with R. M. Myers, 1532

Kana, Timothy W.

See Duncan M. FitzGerald, 1868

Karaki, Susumu

See J. D.A. van Hofen, 404

Kashiwamura, Masakazu

See Shizuo Yoshida, 3189

Kato, Masanobu

Adaptability of Prediction Method of Hydraulic Model Experiment for Thermal Diffusion, with Akira Wada, 3082

Kazemipour, Ahad K.

See Gordon R. McKay, 2186

Keiller, D. C.

Waves Used for Inter-Tidal Design and Construction, with T. D. Ruxton, 23

Kendrick, Mary P.

Factors Influencing Estuary Sediment Distribution, with B. V. Derbyshire, 2072

Kennedy, John F.

See Tatsuki Nakato, 2060

See Subhash C. Jain, 3435

Kilner, F. A.

Measurement of Suspended Sediment in the Surf Zone, 2045

Kimura, Akira

Random Wave Simulation in a Laboratory Wave Tank, with Yuichi Iwagaki, 368

Kjeldsen, Soren Peter

Algorithm for Vertical Diffusion, 3321

Koh, Robert C.Y.

Buoyancy-Driven Gravitational Spreading, 2956

Design Considerations for the Sand Island and Barbers Point Outfalls, with Norman H. Brooks and Floyd Louis Vuillemot, 2941

Kohlhase, Soren

See Udo Berger, 796

Komar, Paul D.

Changes due to Jetties at Tillamook Bay, Oregon, with Thomas A. Terich, 1791

See Michael K. Gaughan, 1459

Kondo, Hideo

Laboratory Study of Pervious Core Breakwaters, with Satoshi Toma and Kenji Yano, 2643

Kraft, Leland Milo, Jr.

Prediction of Wave-Induced Seafloor Movements, with David James Watkins, 1605

Kray, Casimir J.

Concepts in Design of Coastal Structures, 2209

Kubo, Masayoshi

See Toru Sawaragi, 595

- Kuo, Albert Y.**
Prediction of Pollutant Distribution in Estuaries, with John P. Jacobson, 3276
See Gary C. Parker, 3049
- Larsen, Jorn S.**
See Helge Gravesen, 2357
- Layton, Jeffrey A.**
Design Procedures for Ocean Outfalls, 2919
- Leatherman, Stephen P.**
Barrier Island Dynamics: Overwash Processes and Eolian Transport, 1958
- Lee, Ben-Juen**
See Nai-Kuang Liang, 258
- Lee, Theodore T.**
See Doak C. Cox, 1552
- Leendertse, Jan J.**
State Estimation of Estuarine Circulation and Water Quality by Numerical Simulation and Observation, with S. K. Liu, 3223
- Lepetit, J. P.**
Impact of Yachting Marinas on Beaches, 1844
Study of an Artificial Island, with S. Moreau, 3526
- Liang, Nai-Kuang**
Application of Fetch Area Method in Monsoon Wave Hindcasting, with Shih-Tsan Tang and Ben-Juen Lee, 258
- Lillevang, Omar J.**
Experimental Studies of Stresses Within the Breakwater Armor Piece "Dolos", with Wayne E. Nickola, 2519
- Liu, Paul C.**
Applications of Empirical Fetch-Limited Spectral Formulas to Great Lakes Waves, 113
- Liu, S. K.**
See Jan J. Leendertse, 3223
- Liu, Shin-Lin**
3-D Hydraulic Model of Wave Generated by Displacements, with Robert L. Wiegel, 1060
- Locher, Frederick A.**
See Tatsuaki Nakato, 2060
- Loewy, E.**
Data Collection and Analysis for Coastal Projects, with K. G. Witthaus, L. Summers and R. J. Maddrell, 43
- Longuet-Higgins, Michael S.**
Recent Developments in the Study of Breaking Waves, 441
- Luck, Gunter**
Inlet Changes of the East Frisian Islands, 1938
- Lundgren, H.**
Physics and Mathematics of Waves in Coastal Zones, 880
See Helge Gravesen, 2357
- Machemehl, Jerry L.**
Tidal Inlet Flow Dynamics and Sediment Movement, with N. E. Bird and A. N. Chambers, 1681
- Macknight, A.**
See C. J. Apelt, 2228
- Maddrell, R. J.**
See E. Loewy, 43
- Mader, Charles L.**
Calculations of Waves Formed From Surface Cavities, 1079
- Madsen, Ole Secher**
Quantitative Description of Sediment Transport, with William D. Grant, 1093
Wave Transmission Through Trapezoidal Breakwaters, with Stanley M. White, 2662
- Magoon, Orville T.**
Design and Construction of Humboldt Jetties, 1880 to 1975, with Robert L. Sloan and Nobuyuki Shimizu, 2474
- Manohar, Madhav**
Characteristic Wave Period, with Ismail E. Mobarek and N. A. El Sharaky, 273
- Maresca, Joseph W., Jr.**
Terrestrial Photogrammetric Measurements of Breaking Waves and Longshore Currents in the Nearshore Zone, with Erwin Seibel, 681
- Markle, Dennis G.**
See D. Donald Davidson, 2544
- Marui, Nobuo**
See Shintaro Hotta, 1590
- Mayor-Mora, Ramiro**
Sedimentation Studies on the Niger River Delta, with Preben Mortensen and Jorgen Fredsoe, 2151
- McCorquodale, John A.**
See Mohamed S. Nasser, 815
- McKay, Gordon R.**
Concept of Minimum Specific Energy and Its Relation to Natural Forms, with Ahad K. Kazempour, 2186
- McKinney, Thomas**
Offshore Sedimentary Processes and Responses Near Beach Haven — Little Egg Inlets, New Jersey, with Joseph T. DeAlteris, Yung Y. Chao, Lloyd Stahl and James Roney, 1899
See Joseph T. DeAlteris, 1881
- McNair, E. C., Jr.**
A Sand Bypassing System Using a Jet Pump, 1342
- Meadows, Guy A.**
Time Dependent Fluctuations in Longshore Currents, 660
- Mehta, Ashish J.**
Measurement of Bed Friction in Tidal Inlets, with R. J. Byrne and Joseph T. DeAlteris, 1701
- Mettam, John Dorrington**
Design of Main Breakwater at Sines Harbour, 2499
- Meyer, Richard E.**
Resonant Refraction by Round Islands, 866
- Miller, A. Woodruff, Jr.**
See Robert L. Street, 3208
- Mitsuyasu, Hisashi**
Directional Spectral of Ocean Surface Waves, with S. Mizuno, 329

- Mizuguchi, Masaru**
Physical Aspects of Wave-Induced Nearshore Current System, with Kiyoshi Horikawa, 607
- Mizuno, S.**
See Hisashi Mitsuyasu, 329
- Mobarek, Ismail E.**
See Madhav Manohar, 273
- Mogridge, G. R.**
Wave Forces on Aquare Caissons, with W. W. Jamieson, 2271
- Morden, Dennis B.**
Decomposition of Co-Existing Random Wave Energy, with Eugene P. Richey and Derald R. Christensen, 846
- Moreau, S.**
See J. P. Lepetit, 3526
- Mortensen, Preben**
See Ramiro Mayor-Mora, 2151
- Myers, R. M.**
See J. William Kamphuis, 1532
- Nagai, Shositiro**
Slit-Type Breakwater: Box-Type Wave Absorber, with Shohachi Kakuno, 2697
See Kazuki Oda, 2810
- Naheer, Ehud**
See Fredric Raichlen, 3536
- Nakamura, Hiroshi**
Wave Pressures on Large Circular Cylindrical Structure, 2290
- Nakamura, Shigehisa**
Transformation of Tsunamis in a Coastal Zone, with Haruo Higuchi and Yoshito Tsuchiya, 988
- Nakato, Tatsuaki**
Iowa Sediment Concentration Measuring System, with Frederick A. Locher, John R. Glover and John F. Kennedy, 2060
- Nasner, Horst**
Transport Mechanism in Tidal Dunes, 2136
- Nasser, Mohamed S.**
Action of Non-Linear Waves at a Solid Wall, with John A. McCorquodale, 815
- Nath, John H.**
See Tokuo Yamamoto, 2321
- Nayak, Irvathur Vasudeva**
See Jade Dattatri, 289
- Nece, Ronald C.**
Planform Influence on Flushing and Circulation in Small Harbors, with Roger A. Falconer and Toshiro Tsutsumi, 3471
- Ng, Samuel**
See Gary G. April, 2092
- Nichols, B. D.**
Numerical Calculation of Wave Forces on Structures, with C. W. Hirt, 2254
- Nickola, Wayne E.**
See Omar J. Lillevang, 2519
- Nordstrom, Charles E.**
See David G. Aubrey, 1297
- Nummedal, Dag**
See Duncan M. FitzGerald, 1868
- Ochi, Michel K.**
Six-Parameter Wave Spectra, with E. Nadine Hubble, 301
- Oda, Kazuki**
Protection of Maritime Structures Against Ship Collisions, with Shositiro Nagai, 2810
- Okamoto, Hiroshi**
See Naofumi Shiraishi, 2677
- Okuzono, Hideaki**
See Takeshi Ijima, 2623
- Osborne, A. R.**
See R. E. Haring, 151
- Ou, Shan-Hwei**
Wave Height Distribution of Wind Waves Over Long Waves, with Frederick L.W. Tang, 388
- Ouellet, Yvon**
Overtopping of Rubble-Mound Breakwaters by Irregular Waves, with Pierre Eubanks, 2756
- Owens, E. H.**
Process and Morphology Characteristics of Two Barrier Beaches in the Magdalen Islands, Gulf of St. Lawrence, Canada, 1975
- Paddock, Richard A.**
See A. A. Frigo, 3028
- Palmer, Robert Q.**
See Naofumi Shiraishi, 2677
- Pararas-Carayannis, George**
Tsunami Hazard and Design of Coastal Structures, 2248
- Parker, Gary C.**
Thermal Discharges: Prototype vs. Hydraulic Model, with Ching S. Fang and Albert Y. Kuo, 3049
- Partenscky, Hans-Werner**
Energy Dissipation in Tidal Estuaries, with Gunther Barg, 3312
- Perry, F. C.**
See R. W. Whalin, 3377
- Ponce-Campos, David**
See Ernest F. Brater, 1493
- Pore, N. Arthur**
Automated Forecasting of Extratropical Storm Surges, 906
- Powell, G. M.**
See D. M. Sheppard, 3068
- Pratte, Bruce D.**
Churchill River Salt-Water Tidal Model, 3445
- Price, W. A.**
See A. F. Whillock, 2564
- Raichlen, Fredric**
Wave Induced Oscillations of Harbors with Variable Depth, with Ehud Naheer, 3536

- Resio, D. T.**
Great Lakes Wave Information, with L. W. Hiipakka, 92
- Reynolds, F. Michael**
See Warren C. Thompson, 238
- Richardson, David P.**
See Edward B. Thornton, 461
- Richey, Eugene P.**
See Dennis B. Morden, 846
- Riedel, H. P.**
Numerical Modelling — An Aid to Assessing Field Data, with F. L. Wilkinson, 3243
- Rohde, Hans**
Sand Movement Investigations by Means of Radioactive Tracers in a Hydraulic Model and in the Field, 2027
- Roney, James**
See Joseph T. DeAlteris, 1881
See Thomas McKinney, 1899
- Roos, Ary**
Characteristics of Flow in Run-Up of Periodic Waves, with Jurjen A. Battjes, 781
- Ruby, Christopher H.**
See Miles O. Hayes, 1992
- Ruxton, T. D.**
See D. C. Keiller, 23
- Rye, Henrik**
Parametric Representation of a Wind-Wave Field, with Roald Svee, 183
- Sarpkaya, Turgut**
Forces on Rough-Walled Circular Cylinders in Harmonic Flow, 2301
- Sasaki, Tamio**
Nearshore Current on a Gently Sloping Beach, with Kiyoshi Horikawa and Shintaro Hotta, 626
- Sato, Shoji**
See Norio Tanaka, 1824
- Savage, G. H.**
See D. J. Agerton, 2792
- Sawaragi, Toru**
Consideration on Friction Coefficient for Sea Bottom, with Koichiro Iwata and Masayoshi Kubo, 595
Wave Spectrum of Breaking Wave, with Koichiro Iwata, 580
- Saxena, P. C.**
Design and Behaviour of Sandtraps in Regions of High Littoral Drift, with Pazhhayannur P. Vaidyaraman and R. Srinivasan, 1377
- Saylor, James H.**
Wind-Driven Circulation of Saginaw Bay, with Larry J. Danek, 3262
- Seelig, William N.**
See Robert M. Sorensen, 1646
- Seibel, Erwin**
See Joseph W. Maresca, Jr., 681
- Sessions, Meredith H.**
See Richard J. Seymour, 60
- Seymour, Richard J.**
Regional Network for Coastal Engineering Data, with Meredith H. Sessions, 60
- Shahrabani, D. M.**
Negatively Buoyant Slot Jets, with J. D. Ditmars, 2976
- Sharma, J. N.**
See A. J. Sutherland, 752
See Mohammad H. Fallah, 934
- Shemdin, Omar H.**
Comprehensive Monitoring of a Beach Restoration Project, with H. K. Brooks, Z. Ceylanli and S. L. Harrell, 1477
See A. J. Sutherland, 752
- Sheppard, D. M.**
Flow Field Near an Ocean Thermal Energy Conversion Plant, with G. M. Powell and I. B. Chou, 3068
- Shigemura, Toshiyuki**
Characteristics of Tidal Inlets on the Pacific Coast of Japan, 1666
- Shimizu, Nobuyuki**
See Orville T. Magoon, 2474
- Shirai, Masujiro**
See Taizo Hayashi, 2830
- Shiraishi, Naofumi**
Quay Wall with Wave Absorber "Iglou", with Robert Q. Palmer and Hiroshi Okamoto, 2677
- Shuto, Nobuo**
Transformation of Nonlinear Long Waves, 423
- Siefert, Winfried**
Consecutive High Waves in Coastal Waters, 171
- Silvester, Richard**
Headland Defense of Coasts, 1394
See Suphat Vongvisessornjai, 2387
- Skovgaard, Ove**
Current Depth Defraction Using Finite Elements, with Ivar G. Jonsson, 721
- Sloan, Robert L.**
See Orville T. Magoon, 2474
- Smith, L. H.**
Tidal Stream Flow Solved by Galerkin Technique, with Ralph T-S Cheng, 3358
- Sollitt, Charles K.**
Large Scale Model Tests of Placed Stone Breakwaters, with Donald H. DeBok, 2572
- Sonu, Choule J.**
See Martin T. Czerniak, 3557
- Sorensen, Robert M.**
Hydraulics of Great Lakes Inlet — Harbors Systems, with William N. Seelig, 1646
- Speekenbrink, Hans**
Generation of Troughs by Density Currents, 2170
- Spencer, L. P.**
See R. E. Haring, 151
- Srinivasan, R.**
See P. C. Saxena, 1377

- Stahl, Lloyd**
See Thomas McKinney, 1899
- Stephen, Michael F.**
See Miles O. Hayes, 1992
- Stotz, K. C.**
See D. J. Agerton, 2792
- Street, Robert L.**
Evaluation of Air-Sea Interface Heat Flux, with A. Woodruff Miller, Jr., 3208
- Suhayda, Joseph N.**
See Michael W. Tubman, 1168
- Summers, L.**
See E. Loewy, 43
- Sunamura, Tsuguo**
Field Investigation of Sediment Transport Pattern in a Closed System, with Kiyoshi Horikawa, 1240
- Sustar, John F.**
See Richard M. Ecker, 2009
- Sutherland, A. J.**
Wave Run-Up on a Simulated Beach, with J. N. Sharma and Omar H. Shemdin, 752
- Suzuki, Takasuke**
See Masataro Hattori, 1223
- Suzuki, Yasumasa**
See Yoshimi Goda, 828
- Svee, Roald**
See Henrik Rye, 183
- Svendsen, Ib A.**
Deformation up to Breaking of Periodic Waves on a Beach, with J. Buhr Hansen, 477
- Swart, D. H.**
Predictive Equations Regarding Coastal Transport, 1113
- Tamai, Nobuyuki**
Friction at the Interface of Two-Layered Flows, 3169
- Tamaye, Elaine E.**
See Charles L. Bretschneider, 202
- Tanaka, Enzoh**
See Takeshi Ijima, 2623
- Tanaka, Norio**
Topographic Change Resulting from the Construction of a Harbor on a Sandy Beach, Kashima Port, with Shoji Sato, 1824
- Tang, Frederick L.W.**
See Shan-Hwei Ou, 388
- Tang, Shih-Tsan**
See Nai-Kuang Liang, 258
- Tauman, Joseph**
Enclosing Scheme for Bathing-Beach Development, 1425
- Taylor, R. B.**
Dispersive Transport in River and Tidal Flows, 3336
- ten Hoopen, Henk G.H.**
Recent Applications of Artificial Seaweed in the Netherlands, 2905
- Terich, Thomas A.**
See Paul D. Komar, 1791
- Thompson, Warren C.**
Ocean Wave Statistics from FNWC Spectral Analysis, with F. Michael Reynolds, 238
- Thompson, William W.**
See Robert A. Dalrymple, 1277
- Thornton, Edward B.**
Kinematics of Breaking Waves, with James J. Galvin, Frank L. Bub and David P. Richardson, 461
- Toma, Satoshi**
See Hideo Kondo, 2643
- Toyoshima, Osamu**
Changes of Sea Bed Due to Detached Breakwaters, 1572
- Tsuchiya, Yoshito**
See Masataka Yamaguchi, 497
See Shigehisa Nakamura, 988
- Tsutsumi, Toshiro**
See Ronald C. Nece, 3471
- Tubman, Michael W.**
Wave Action and Bottom Movements in Fine Sediments, with Joseph N. Suhayda, 1168
- Vaidyaraman, Pazhhayannur P.**
See P. C. Saxena, 1377
- van Bochove, G.**
See C. H. Hulsbergen, 1439
- Van Dorn, William G.**
Set-Up and Run-Up in Shoaling Breakers, 738
- van Hijum, E.**
Equilibrium Profiles and Longshore Transport of Coarse Material Under Oblique Wave Attack, 1258
See E. W. Bijker, 1149
- van Hoften, J. D.A.**
Interaction of Waves and a Turbulent Current, with Susumu Karaki, 404
- van Oorschot, J. H.**
Subharmonic Components in Hawser and Fender Forces, 2840
- Vellinga, P.**
See E. W. Bijker, 1149
- Vitale, Philip**
See Cyril J. Galvin, 1133
- Vollmers, Hans**
Harbour Inlets on Tidal Estuaries, 1854
- Vongvisessomjai, Suphat**
Wave Forces on Submerged Objects, with Richard Silvester, 2387
- Vuillemot, Floyd Louis**
See Robert C.Y. Koh, 2941
- Wada, Akira**
See Masanobu Kato, 3082
- Walker, James R.**
Refraction of Finite-Height and Breaking Waves, 507

- Walton, Todd L., Jr.**
Capacity of Inlet Outer Bars to Store Sand, with
William D. Adams, 1919
- Wang, M. H.**
See Charles C.C. Chang, 129
- Wang, Yu-Hwa**
Determination of the Interfacial Eddy Diffusion
Coefficient of a Highly Stratified Estuary, 3158
- Watkins, David James**
See Leland Milo Kraft, Jr., 1605
- Watts, George M.**
See Billy L. Edge, 2888
- Weggel, J. Richard**
Wave Overtopping Equation, 2737
- Whalin, R. W.**
Model Verification for Tidal Constituents, with F. C.
Perry and D. L. Durham, 3377
- Whillock, A. F.**
Armour Blocks as Slope Protection, with W. A.
Price, 2564
- White, Stanley M.**
See Ole Secher Madsen, 2662
- Wiegel, Robert L.**
See Shin-Lin Liu, 1060
- Wilkinson, F. L.**
See H. P. Riedel, 3243
- Wilson, Stephen J.**
See Miles O. Hayes, 1992
- Winant, Clinton D.**
Stability and Impulse Response of Empirical
Eigenfunctions, with David G. Aubrey, 1312
- Witthaus, K. G.**
See E. Loewy, 43
- Wood, William L.**
Three-Dimensional Conditions of Surf, 525
- Wright, L. D.**
Morphodynamics of a Wave-Dominated River
Mouth, 1721
- Wybro, Pieter G.**
See Charles L. Bretschneider, 1006
- Yalin, Mehmet S.**
Origin of Submarine Dunes, 2127
- Yamaguchi, Masataka**
Wave Shoaling of Finite Amplitude Waves, with
Yoshito Tsuchiya, 497
- Yamamoto, Tokuo**
High Reynolds Number Oscillating Flow by
Cylinders, with John H. Nath, 2321
- Yang, Cheng Y.**
See Mohammad H. Fallah, 934
- Yano, Kenji**
See Hideo Kondo, 2643
- Yaplee, Benjamin S.**
See Davidson T. Chen, 72
- Yeh, Fei-Fan**
See Gour-Tsyh Yeh, 921
- Yeh, Gour-Tsyh**
Generalized Model for Storm Surges, with Fei-Fan
Yeh, 921
- Yoshida, Akinori**
See Takeshi Ijima, 2717
- Yoshida, Shizuo**
Tidal Response of Two-Layer Flow at a River
Mouth, with Masakazu Kashiwamura, 3189
- Zahel, Wilfried**
See Manfred Engel, 971

